Polyhedron 28 (2009) 2001–2009

Contents lists available at ScienceDirect

Polyhedron

journal homepage: www.elsevier.com/locate/poly

Structures and magnetic properties of imidazolate-bridged tetranuclear and polymeric copper(II) complexes

Nobumasa Koyama, Ryo Watanabe, Takayuki Ishida *, Takashi Nogami, Tamizo Kogane *

Department of Applied Physics and Chemistry, The University of Electro-Communications, Chofugaoka 1-5-1, Chofu, Tokyo 182-8585, Japan

ARTICLE INFO

Article history:
Available online 12 January 2009

Keywords:
Imidazole
Copper(II) ion
Supramolecular chemistry
Magnetic property
Molecular grid

ABSTRACT

Eight kinds of imidazolate-bridged copper(II) complexes were found to be classified into two categories from the magnetic properties. The crystal structures of $[Cu(L)(\mu\text{-im})]_n$ (Him = imidazole; L = nonane-4,6-dionate, 2,6-dimethylheptane-3,5-dionate) and $[Cu(L)(\mu\text{-im})]_4$ (L = nonane-4,6-dionate, 1-phenylbutane-1,3-dionate) were determined, to reveal that they consist of polymeric chains and tetranuclear cycles, respectively. Note that the nonane-4,6-dionate derivative gave the two phases. The Bonner–Fisher model (a one-dimensional antiferromagnetic chain model) was plausibly applied to $[Cu(L)(\mu\text{-im})]_n$ for the best fit, while a square model was to $[Cu(L)(\mu\text{-im})]_4$. The complexes with unknown crystal structures were also subjected to magnetic measurements, and the tetra- and polymeric structures could be clearly distinguished from each other by fitting the magnetic data to appropriate models. The exchange parameters were comparable for both series ($2J/k_B = -78$ to -97 K) because the structurally common bridges Cu–N(eq)–N(eq)–Cu afford comparable magnitudes of couplings.

© 2008 Elsevier Ltd. All rights reserved.

1. Introduction

Oligonuclear and polymeric copper(II) coordination compounds attract much attention in materials chemistry; for example, Kahn's magnetic material building-blocks [1], Yaghi and co-workers' metal-organic frameworks [2], and Lehn's supramolecular chemistry approach [3]. Some peculiar enzyme functions are based on oligonuclear copper clusters in laccase and ascorbate oxidase [4], where imidazolates and histidinates play a role of bridging ligands. Copper(II) imidazolate systems afford a variety of structures of self-assembled supramolecular coordination complexes, e.g., trinuclear cycles [5], tetranuclear cycles or [2 × 2] grids [6–10], discrete linear systems [11–16], polymeric chains [17,18], layers [19–21], and 3-D networks [19,22].

One of the authors (T.K.) reported imidazolate-bridged copper(II) complexes $[Cu(\beta\text{-diketonato})(\mu\text{-im})]_x$ (Him stands for imidazole) [23], but their crystal structures have not yet been reported. Generally, there are difficulties in preparing single crystals of polymeric coordination compounds, and also in characterizing compounds as infinite polymers or cyclic oligomers solely from the spectroscopic and elemental analyses. We will report here the crystal structures of $[Cu(dnbm)(\mu\text{-im})]_x$ as two phases, infinite polymer and cyclic tetramer (for structural formula, see below). Preliminary results have been reported in the previous letter [24], and the present report will further discuss the following issue. When the crystal structure analysis is unsuccessful owing to the poor crystallinity, their magnetic measurements would help prediction of crystal structures. The magnetic properties of the complexes whose crystal structures were unknown were analyzed according to the model of a polymer- or tetramer-based spin system.

2. Results

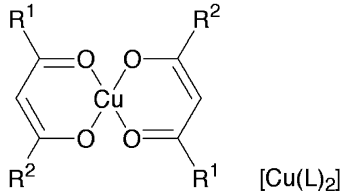
2.1. Preparation

The β-diketones (HL) employed are pentane-2,4-dione (Hacac), heptane-3,5-dione (Hdprm), nonane-4,6-dione (Hdnbm), 2,6-dimethylheptane-3,5-dione (Hdibm), 2,2,6,6-tetramethylheptane-3,5-dione (Hdpm), (1-phenylbutane-1,3-dione (Hbzac) and 1-(2-thienyl)butane-1,3-dione (Htac), and their copper(II) complexes are represented as $[Cu(L)_2]$ (Scheme 1).

Imidazolate-bridged copper(II) complexes $[Cu(L)(\mu\text{-im})]_n$ have been prepared in ethanol [23], and they were efficiently obtained in methanol as well. The reactions of $[Cu(L)_2]$ with two molar equiv. of imidazole gave polymeric complexes $[Cu(L)(\mu\text{-im})]_n$ ($[Cu(acac)(\mu\text{-im})]_n$ (**1p**), $[Cu(dprm)(\mu\text{-im})]_n$ (**2p**), $[Cu(dibm)(\mu\text{-im})]_n$ (**4p**) and $[Cu(dpm)(\mu\text{-im})]_n$ (**5p**)), and tetranuclear $[Cu(bzac)(\mu\text{-im})]_4$ (**6t**). However, $[Cu(dnbm)_2]$ gave tetranuclear $[Cu(dnbm)(\mu\text{-im})]_4$ (**3t**) instead of polymeric $[Cu(dnbm)(\mu\text{-im})]_n$ (**3p**) under these conditions. Complex $[Cu(dnbm)(\mu\text{-im})]_n$ (**3p**) was obtained by the reaction of $[Cu(dnbm)_2]$ with two molar equiv. of imidazole in ethanol. Complex $[Cu(tac)(\mu\text{-im})]_4$ (**7t**) prepared

* Corresponding authors. Tel.: +81 42 443 5490; fax: +81 42 443 5501 (T. Ishida).
E-mail addresses: ishi@pc.uec.ac.jp (T. Ishida), kogane@crc.uec.ac.jp (T. Kogane).

0277-5387/$ - see front matter © 2008 Elsevier Ltd. All rights reserved.
doi:10.1016/j.poly.2008.12.004



$[Cu(acac)_2]$	$R^1 = R^2 = CH_3$
$[Cu(dprm)_2]$	$R^1 = R^2 = C_2H_5$
$[Cu(dnbm)_2]$	$R^1 = R^2 = n\text{-}C_3H_7$
$[Cu(dibm)_2]$	$R^1 = R^2 = i\text{-}C_3H_7$
$[Cu(dpm)_2]$	$R^1 = R^2 = t\text{-}C_4H_9$
$[Cu(bzac)_2]$	$R^1 = CH_3$, $R^2 = C_6H_5$
$[Cu(tac)_2]$	$R^1 = CH_3$, $R^2 = C_4H_3S$ (2-thienyl)

Scheme 1. Abbreviations and formulas of copper(II) β-diketonates.

according to the previous report [23] was used for the magnetic measurements. Here, the notation **p** and **t** denote polymeric and tetranuclear, respectively.

2.2. Molecular structures

Fig. 1 shows the molecular structure of **3p**. The complex consists of a helix, which has a dinuclear crystallographically independent unit [{Cu(dnbm)(μ-im)}$_2$] as a repeating motif. The intramolecular nearest-neighboring Cu1···Cu2 and Cu2···Cu1* distances are 5.9016(10) and 5.8973(11) Å, respectively. The Cu ions have a CuN_2O_2 coordination environment with two nitrogen atoms from two imidazolates and two oxygen atoms from a dnbm ligand. Selected geometrical parameters are summarized in Table 1. Although the geometry about the copper ions Cu1 and Cu2 is approximately square-planar, the O1–Cu1–N1, O2–Cu1–N4$^{\#}$, O3–Cu2–N3, and O4–Cu2–N2 bond angles are considerably smaller than ideal square-planar angle of 180°, being bent toward opposite directions to form a saddle structure. Namely, the coordination around the copper ions is considerably distorted from square-planar toward tetrahedral (d-SP). The Cu1 ion is located slightly above the mean basal O1–O2–N1–N4$^{\#}$ plane by 0.018(3) Å, and the Cu2 ion above the mean basal O3–O4–N2–N3 plane by 0.053(3) Å.

There are eight copper ions in a pitch along a crystallographic 4_2 screw axis in **3p**, contrary to the expectation from the cis configuration of the N–Cu–N coordination, which seems suitable for a fourfold axis involving four copper ions. It may be related to the d-SP structures at Cu1 and Cu2. The Cu1···Cu2···Cu1* angle (134.66(2)°) is considerably larger than, while the Cu2···Cu1*···Cu2* angle (89.64(2)°) is close to, the ideal right angle. The alternating irregular angles are responsible for the formation of a Cu_8-based chain and not a Cu_4-based helix or a tetrameric macrocycle.

Fig. 2 shows the molecular structure of **4p**. A dinuclear unit is crystallographically independent. A zig-zag chain structure is formed in a space group *C*2/*c*, which contains four copper units in a pitch. As the N–Cu–O angles of 150.37(15)–173.13(15)° indicate, Cu1 has an almost square planer structure (n-SP), while Cu2 has a d-SP one. The dislocations from the mean N_2O_2 planes are small (0.053(12) and 0.031(2) Å, respectively), owing to the saddle structures.

The Cu···Cu distances (5.8865(7) and 5.9239(7) Å) of **4p** are comparable with those of **3p**. The nearest-neighboring Cu···Cu···Cu angles are 102.925(10)° and 132.817(11)°, being suitable for such a zig-zag chain and quite different from that of **3p**. The steric bulkiness of peripheral substituents (*n*-propyl *versus* isopropyl) may affect the molecular packing in the crystal. Basically, the Cu–N and Cu–O distances as well as the N–Cu–N and O–Cu–O angles of **4p** are in typical ranges and just comparable to those of **3p**. Since the Cu–N bonds can rotate in solution, the geometry seems to be fixed in a suitable packing motif on crystallization. Thus, in comparison between **3p** and **4p**, the mutual geometry between neighboring units is different, which is caused by torsion around the Cu–N bonds.

We found that [Cu(dnbm)(μ-im)] has two phases, **3p** and **3t**. As Fig. 3 shows the molecular structure of **3t**, four Cu ions construct a rectangle arrangement affording a [2 × 2]-molecular grid. A half of the molecule of **3t** is crystallographically independent owing to centrosymmetry in a space group $P\bar{1}$. The intramolecular Cu1···Cu2 and Cu1···Cu2† distances are 5.8694(7) and 5.8933(10) Å, respectively. The Cu2†···Cu1···Cu2 and Cu1···Cu2···Cu1† angles are 89.951(12)° and 90.049(12)°, respectively.

As for the CuN_2O_2 coordination environments in **3t**, the O3–Cu2–N3† and O4–Cu2–N2 are much smaller than the angle of 180°, and, giving saddle-type distortion. Such an out-of-plane deformation has also been reported in the imidazolate-bridged Cu_4 macrocyle [8]. The coordination around the Cu1 ion is n-SP, while Cu2 is d-SP. This finding seems to be similar to that of the bisimidazolato copper(II) compound possessing a d-SP/n-SP–mixed tetranuclear framework. [26]. The dislocations of Cu1 and Cu2 ions are small (0.049(3) and 0.082(3) Å, respectively) from the mean basal N_2O_2 planes, owing to the saddle structures. As the side view (Fig. 3b) shows, the two basal planes are slightly canted with each other by 7.7(1)°.

Fig. 4 shows the molecular structure of **6t**. The refinement was unsatisfactory because **6t** gave only tiny crystals. Large standard deviations remained and thermal displacement factors were somewhat unrealistic for several carbon atoms. However, the *R* factors were decreased to be relatively small (ca. 0.06), and we can safely conclude that **6t** has a tetranuclear macrocyclic structure, or a molecular [2 × 2] grid, in a space group $P\bar{1}$. A dinuclear unit is crystallographically independent. The nearest-neighboring Cu···Cu···Cu angles are nearly 92° and 88°. The molecular structure of **6t** is almost identical to that of **3t** except for the peripheral substituents, and furthermore the molecular packings are also similar to each other in the comparable crystal lattices.

2.3. Magnetic properties

We measured magnetic susceptibilities (χ_{mol}) of polycrystalline specimens of the present compounds on a SQUID magnetometer. The X-ray diffraction study revealed the crystal structures of **3p**, **4p**, **3t**, and **6t**, and we will check the consistency between the structure and magnetic properties. Fig. 5a and 5b show the χ_{mol} versus *T* plots for polymeric **3p** and **4p**, respectively, on the basis of a copper(II) ion.

The χ_{mol} value of **3p** was increased on cooling from 300 K, reached a broad maximum around 60 K, and gradually decreased. This behavior clearly indicates the presence of dominant antiferromagnetic coupling. An extrapolation of the χ_{mol} curvature to 0 K seems to give a non-zero χ_m intercept. Usually such behavior is related with the infinite Heisenberg $S = 1/2$ antiferromagnetic chain, as originally predicted by Bonner and Fisher [27], and so far confirmed by many experiments [28]. Cyclic $S = 1/2$ antiferromagnetic clusters having even number of the spin sources would show null χ_{mol} at $T \rightarrow 0$ K. Thus, the non-zero χ_{mol} at $T \rightarrow 0$ K is regarded as a fingerprint of infinite chain structures. On further cooling, the χ_{mol} value of **3p** was further decreased with a turning point around 10 K. The origin of this anomaly is not clear at present, but might be explained in terms of a spin-Peierls transition [29]. Namely, a strong singlet–dimer formation takes place to reduce drastically the magnetic susceptibility. To estimate the exchange coupling within a chain, we used the data above 15 K. Assuming the

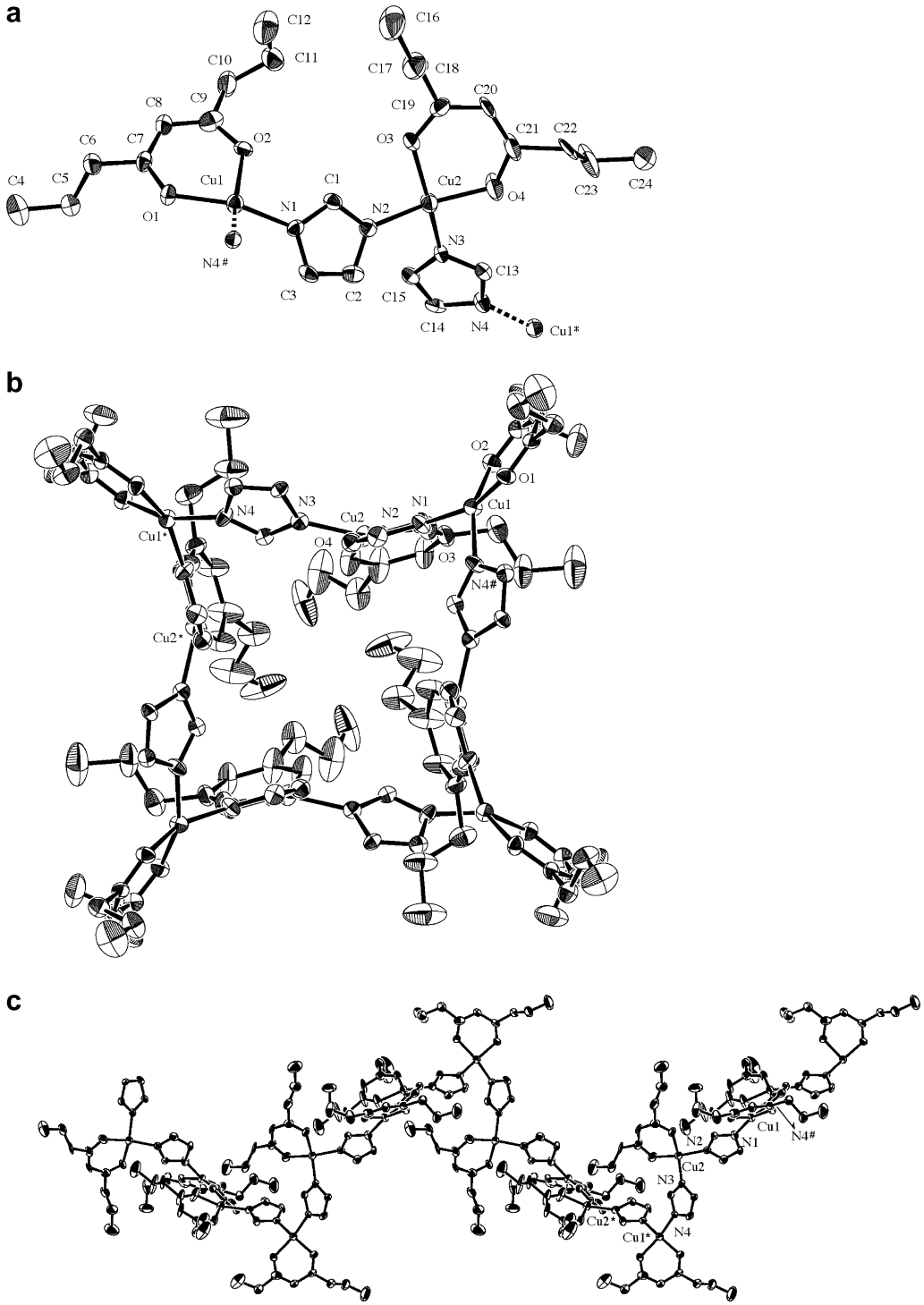


Fig. 1. X-ray crystal structure of $[Cu(dnbm)(\mu\text{-im})]_n$ (**3p**). (a) Crystallographically independent unit. Only a major conformation is shown for the C23–C24 portion. Thermal ellipsoids are drawn at the 50% probability level. Hydrogen atoms are omitted. (b) Top and (c) side views of a chain. Eight repeating units are drawn. Symmetry operation codes of $*$ and # are $-y$, $-1/2+x$, $-1/2+z$ and $1/2+y$, $-x$, $1/2+z$, respectively.

equally-spaced $S = 1/2$ magnetic chain and the Heisenberg spin Hamiltonian as $H = -\Sigma 2JS_i \cdot S_{i+1}$, we applied the following expression [27] with $x = |J|/k_BT$:

$$\chi_{mol} = \frac{N_A\mu_B^2 g^2}{k_B T}\,\frac{0.25 + 0.14995x + 0.30094x^2}{1.0 + 1.9862x + 0.68854x^2 + 6.0626x^3}. \quad (1)$$

The best fit gave $-89.8(7)$ K with $g = 2.04(2)$ for **3p**. According to the Bonner–Fisher analysis, T_{max} at which χ_{mol} shows a rounded maximum is simply related with J as expressed by Eq. (2) [27]. The χ_m peak position around 60 K for **3p** agrees well with the calculated J value:

$$k_B T_{max}/|J| = \text{ca. } 1.28. \quad (2)$$

Similarly, **4p** exhibited a Bonner–Fisher-type behavior (Fig. 5b). However, in sharp contrast to the case of **3p**, the χ_{mol} value of **4p** turned to increase again below 10 K, suggesting a slight contamination with Curie impurity. We analyzed the experimental data using the Bonner–Fisher model plus a Curie contribution (Eq. (3)).

Table 1
Selected bond lengths (Å) and angles (°).

Compounds	3p	4p	3t
Cu1–O1	1.918(3)	1.938(3)	1.913(3)
Cu1–O2	1.932(4)	1.935(3)	1.929(4)
Cu1–N1	1.954(5)	1.958(3)	1.935(4)
Cu1–N4	1.954(5)[a]	1.977(3)[b]	1.932(5)[c]
Cu2–O3	1.923(4)	1.950(3)	1.919(4)
Cu2–O4	1.920(4)	1.926(3)	1.918(3)
Cu2–N2	1.981(5)	1.941(3)	1.957(3)
Cu2–N3	1.944(5)	1.954(3)	1.967(4)
O1–Cu1–N1	158.46(19)	173.13(15)	154.9(2)
O2–Cu1–N4	156.73(18)[a]	167.59(16)[b]	152.2(2)[c]
O3–Cu2–N3	159.08(19)	150.37(15)	162.6(2)
O4–Cu2–N2	161.3(2)	152.82(15)	171.5(2)

[a] N4 is a symmetry-related equivalence with $-y, -1/2+x, -1/2+z$.
[b] N4 is a symmetry-related equivalence with $1/2-x, -1/2+y, 3/2-z$.
[c] N4 is a symmetry-related equivalence with $1-x, 2-y, -z$.

$$\chi_{mol} = \frac{N_A \mu_B^2 g^2}{k_B T} \frac{0.25 + 0.14995x + 0.30094x^2}{1.0 + 1.9862x + 0.68854x^2 + 6.062x^3} + \frac{C_{imp}}{T}. \quad (3)$$

The best fit gave $2J/k_B = -93.1(6)$ K with $g = 2.129(5)$ and $C_{imp} = 0.00695(4)$ cm^3 mol^{-1} for **4p**. The obtained J is very close to that of **3p**, despite of the different helix motives.

Although the crystal structures of **1p**, **2p**, and **5p** are unknown, we measured their magnetic susceptibility to predict the crystal structures. Fig. 6 shows the results of them. They showed a broad maximum and non-zero χ_{mol} at $T \to 0$ K. This behavior strongly suggests that they are antiferromagnetically correlated infinite chains, just like **3p** and **4p**. There also were Curie tails. The Bonner–Fisher model (i.e., Eq. (3)) was applied, giving $2J/k_B = -96(2)$ K, $g = 2.01(4)$, and $C_{imp} = 0.00725(9)$ cm^3 K mol^{-1} for **1p**, $2J/k_B = -96.9(3)$ K, $g = 2.09(2)$, and $C_{imp} = 0.0086(2)$ cm^3 K mol^{-1} for **2p**, and $2J/k_B = -85(1)$ K, $g = 2.13(2)$, and $C_{imp} = 0.00232(8)$ cm^3 K mol^{-1} for **5p**. The calculated curves well reproduced the experimental data (solid lines in Fig. 6). Thus, we assume that they would be chains.

The content of the Curie impurity varied from 0.6% to 2% depending on the specimens investigated here, but the coupling parameters are close to each other (from −85 to −97 K for **1p**–**5p**). This finding supports the assumption that the structurally common bridges Cu–N(eq)–N(eq)–Cu afford comparable magnitudes of couplings. They largely depend on the coordination sites, equatorial and axial, where the nitrogen atoms are coordinated [30].

The χ_{mol} versus T pots of tetrameric **3t** and **6t** (Fig. 7) exhibited a distinctly different feature from those of **3p** and **4p**. Namely, zero χ_{mol} values are suggested at $T \to 0$ K. As for **3t**, the χ_{mol} value increased on lowering temperature and reached a maximum around 55 K. After that the χ_{mol} value turned to decrease somewhat steeply toward $\chi_{mol} = 0$ cm^3 mol^{-1}. A Curie impurity was included, as indicated with a sharp upturn at the lowest temperature region.

A square model involving four $S = 1/2$ spins leads to the Heisenberg spin Hamiltonian as $H = -2J(S_1 \cdot S_2 + S_2 \cdot S_3 + S_3 \cdot S_4 + S_4 \cdot S_1)$. The molar magnetic susceptibility can be written as Eq. (4) [6,7,10] by applying Kambe's vector coupling method [31] and the van Vleck equation:

$$\chi_{mol} = \frac{N_A \mu_B^2 g^2}{k_B T} \frac{2 + 5\exp(2J/k_B) + \exp(-2J/k_B)}{7 + 5\exp(2J/k_B) + 3\exp(-2J/k_B) + \exp(-4J/k_B)} + \frac{C_{imp}}{T}. \quad (4)$$

A Curie impurity term was added. The experimental data of **3t** were fitted to Eq. (4) to give $2J/k_B = -81.0(2)$ K, $g = 2.061(2)$, and

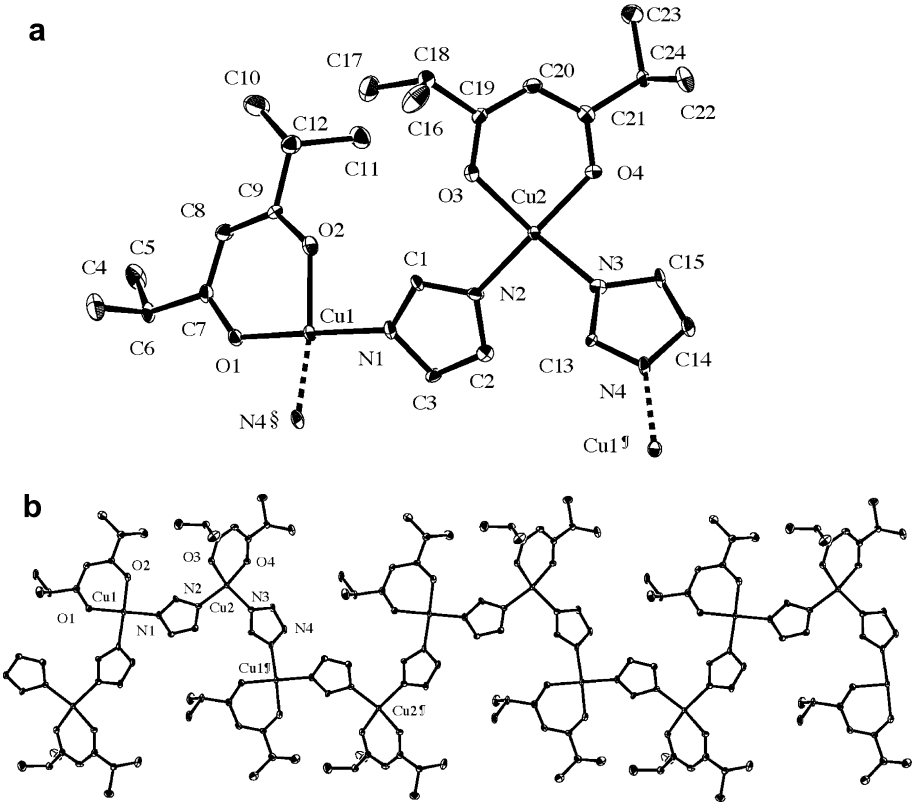


Fig. 2. X-ray crystal structure of [Cu(dibm)(μ-im)]$_n$ (**4p**). (a) Crystallographically independent unit. Thermal ellipsoids are drawn at the 50% probability level. Hydrogen atoms are omitted. (b) Side views of a chain. Six repeating units are drawn. Symmetry operation codes of § and ¶ are $1/2-x, -1/2+y, 3/2-z$, and $1/2-x, 1/2+y, 3/2-z$, respectively.

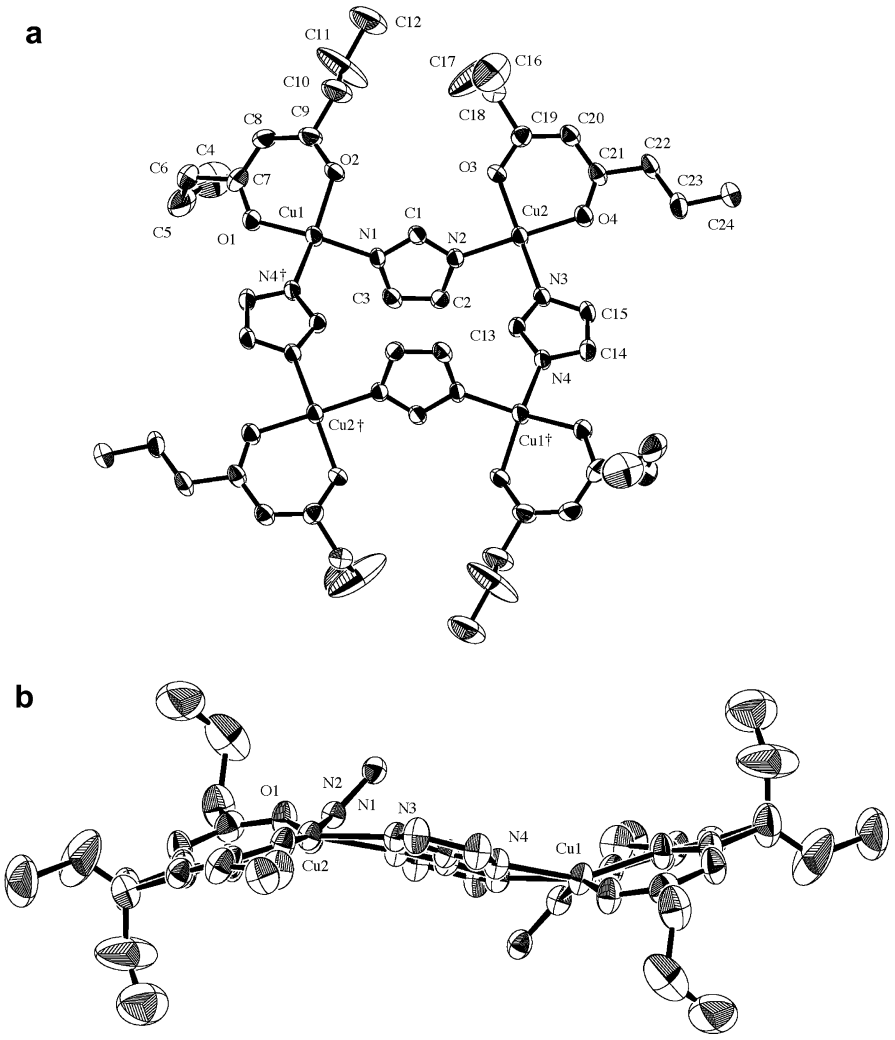


Fig. 3. X-ray crystal structure of [Cu(dnbm)(μ-im)]$_4$ (**3t**). (a) Top and (b) side views. Thermal ellipsoids are drawn at the 30% probability level. Hydrogen atoms are omitted. Symmetry operation code of † is $1-x, 2-y, -z$.

C_{imp} = 0.0203(2) cm^3 K mol^{-1}. The dotted line in Fig. 7a implies the first term in Eq. (3) after the subtraction of the Curie term. This line approaches to 0 cm^3 mol^{-1} at $T \rightarrow 0$ K.

The data of **6t** were similarly analyzed (Fig. 7b). The data on **6t** were fitted to Eq. (4) and the parameters were optimized as: $2J/k_B = -78(1)$ K, $g = 2.13(2)$, and $C_{imp} = 0.00662(8)$ cm^3 K mol^{-1}. The J value is very close to that of **3t**.

The crystal structure of **7t** is unknown, but we measured its magnetic susceptibility (Fig. 7b). The data on **7t** were also well fitted to Eq. (4) rather than Eq. (3). The molecular structure was suggested to be a square tetramer. The parameters were optimized as: $2J/k_B = -85.0(8)$ K, $g = 2.27(1)$, and $C_{imp} = 0.00230(6)$ cm^3 K mol^{-1}. The calculated curves well reproduced the experimental data. Thus, we predict that **7t** would consist of a cyclic tetramer.

3. Discussion

3.1. Synthesis

Complexation reactions of [Cu(L)$_2$] with imidazole are very sensitive to the nature of the β-diketonato ligand as well as to the reaction conditions, sometimes giving different products depending upon the solvent used. For convenience, [Cu(L)$_2$] can be classified into [Cu(L^1)$_2$], [Cu(L^2)$_2$], and [Cu(L^3)$_2$] (HL^1, HL^2, and HL^3 stand for aliphatic β-diketones, aroyl- or hetaroylacetones and fluorinated β-diketones, respectively).

The reactions of [Cu(L^1)$_2$] and [Cu(L^2)$_2$] with two molar equiv. of imidazole in methanol or ethanol gave polymeric and tetranuclear complexes ([Cu(L^1)(μ-im)]$_n$ and [Cu(L^2)(μ-im)]$_4$), respectively. The [Cu(dnbm)$_2$] case is exceptional. A mixture of [Cu(dnbm)$_2$] with two molar equiv. of imidazole gave **3t** under the same conditions. On the other hand, when a mixture solution was concentrated gradually on heating, yielding **3p** (see Section 5).

Complexation reactions of [Cu(L)$_2$] with pyrazole gave different products. The complexes [Cu(L^1)$_2$] afforded di- or tetranuclear complexes, while [Cu(L^2)$_2$] afforded pyrazolate-bridged complexes, 1:1 and/or 1:2 adducts [32]. Furthermore, [Cu(L^1)$_2$] afforded different products depending upon the solvents used. By successive addition of imidazole, [Cu(acac)$_2$] gave no isolable imidazolate complex in chloroform [25], while gave **1p** instead of the imidazolate complex in ethanol or methanol [23]. It has been reported that [Cu(L^3)$_2$] such as [Cu(hfac)$_2$] (Hhfac stands for 1,1,1,5,5,5-hexafluoropentane-2,4-dione) afforded 1:1 and/or 1:2 adducts in chloroform because of their stronger coordination ability [25].

3.2. Crystal structures

Chaudhuri et al. prepared cyclic tri- and tetranuclear copper(II) complexes [5,6], where non-substituted imidazolate was utilized

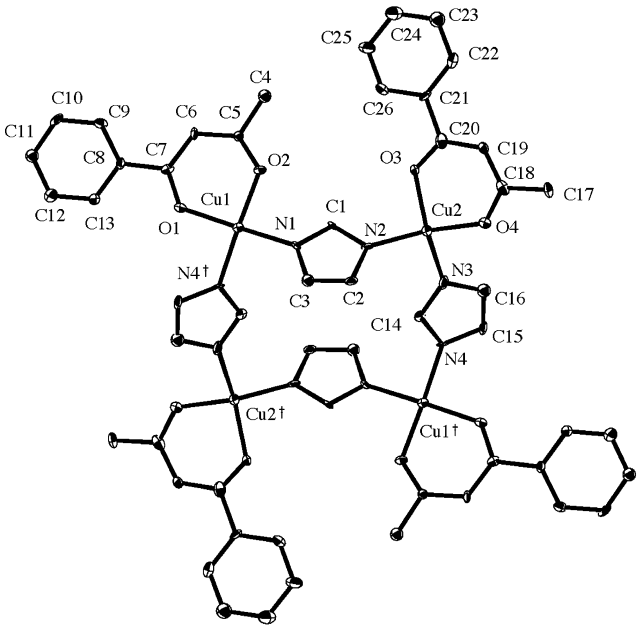


Fig. 4. X-ray crystal structure of [Cu(bzac)(μ-im)]$_4$ (**6t**). Thermal ellipsoids are drawn at the 50% probability level. Hydrogen atoms are omitted. Symmetry operation code of † is $2-x$, $1-y$, $-z$.

as a bridge; namely, $[Cu_3(tacn)_3(\mu\text{-im})_3](ClO_4)_3$ and $[Cu_4(tacn)_4(\mu\text{-im})_4](ClO_4)_4 \cdot 2H_2O$ (tacn = 1,4,7-triazacyclononane). The capping ligands are tridentate and neutral. Consequently, the copper ions were square-pyramidal. Counter ions (ClO_4^-) did not work as ligands. On the other hand, the present compounds have monoanionic β-diketonate chelates as a cap. All of the copper ions are tetra-coordinated (actually n-SP and d-SP). There is no counter anion in the crystal lattice. However, the tetranuclear skelton $[Cu_4(\mu\text{-im})_4]$ of **3t** is similar to that of $[Cu_4(tacn)_4(\mu\text{-im})_4](ClO_4)_4 \cdot 2H_2O$ [6] as well as other known tetramers [7–10].

In the present study, the capping ligands are simple β-diketonates, which occupy two equatorial sites in a cis manner. Accordingly, the imidazolate N atoms are coordinate at the rest position in a cis manner. The N(im)–Cu–N(im) angles close to 90° favors tetranuclear macrocycles. Though several imidazolate-based preorganized ligands have been utilized for development of [2 × 2] grids [6–10], the combination of commercially available copper(II) diketonates and the unsubstituted imidazolate ion is also versatile for this purpose.

3.3. Magnetic properties

The magnetic data of **1p**–**5p** were analyzed by the Bonner–Fisher model as an equally-spaced model. We have to think possible fittings to alternating-chain and rectangle models, because the crystallographic analysis indicates that there are two kinds of exchange couplings. The present analysis brought about averaged values from two independent parameters, J and αJ, where α is alternation parameter. In more precise treatment using the Heisenberg spin Hamiltonian as $H = -\Sigma(2JS2_{2i-1} \cdot S_{2i} + 2\alpha JS_{2i} \cdot S_{2i+1})$, we could adopt an alternating antiferromagnetic chain model [33]. One may imagine the singlet–triplet model [34] in case of the $\alpha = 0$ limit, and accordingly the χ_{mol} value approaches to null at $T \rightarrow 0$ K when α is close to zero. On the other hand, the χ_{mol} versus T profile appears just like the Bonner–Fisher curve when α is close to unity. The present results on **1p**–**5p** exhibited the non-zero χ_{mol} at the $T \rightarrow 0$ K limit, which guarantees that an approximation as an equally-spaced chain model is valid. Moreover, the possibility of

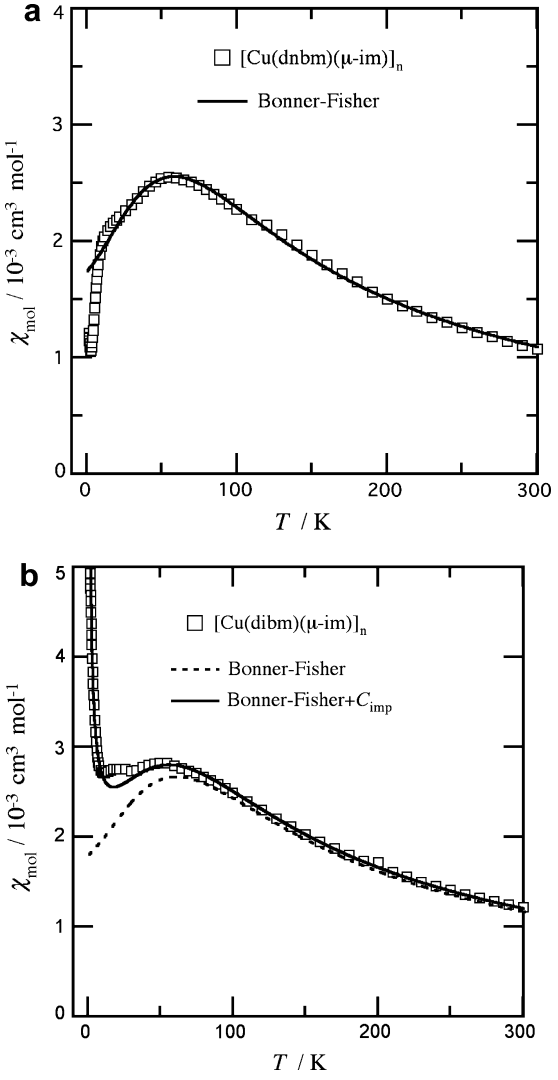


Fig. 5. Temperature dependence of molar magnetic susceptibility (χ_{mol}) for (a) [Cu(dnbm)(μ-im)]$_n$ (**3p**) and (b) [Cu(dibm)(μ-im)]$_n$ (**4p**). The solid and dotted lines represent the best fit curves. See the text for the equations and parameters.

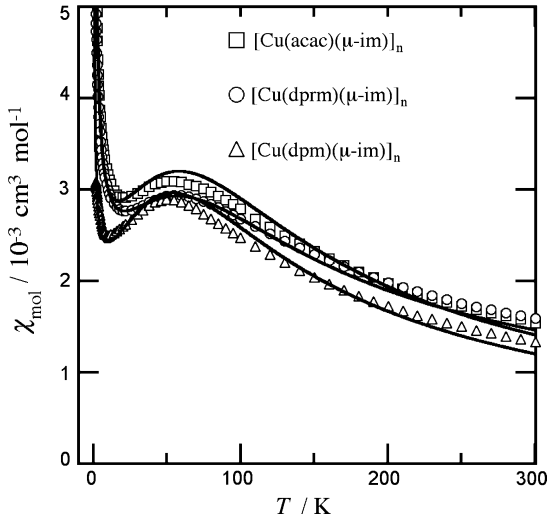


Fig. 6. Temperature dependence of molar magnetic susceptibility (χ_{mol}) for [Cu(acac)(μ-im)]$_n$ (**1p**), [Cu(dprm)(μ-im)]$_n$ (**2p**), and [Cu(dpm)(μ-im)]$_n$ (**5p**). The solid lines represent the best fit curves. See the text for the equations and parameters.

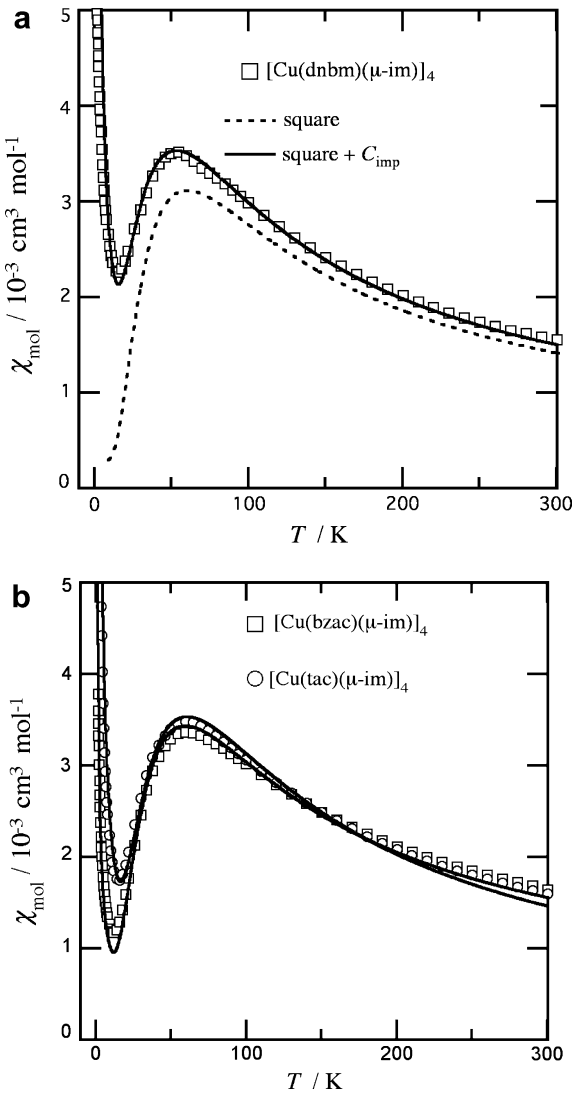


Fig. 7. Temperature dependence of χ_{mol} for (a) [Cu(dnbm)(μ-im)]$_4$ (**3t**) and (b) [Cu(bzac)(μ-im)]$_4$ (**6t**) and [Cu(tac)(μ-im)]$_4$ (**7t**). The solid and dotted lines represent the best fit curves. See the text for the equations and parameters.

the cyclic structures such as a tetramer is completely discarded. Compounds **1p**, **2p**, and **5p** consist of chains as well as **3p** and **4p**. The reports on imidazolate-bridged copper(II) chains are rare [17,18], in which the copper ions were weekly bonded with ligands in an axial manner. To our knowledge, the present work is the first characterization of one-dimensional imidazolate-bridged copper(II) chains showing appreciable antiferromagnetic couplings.

The magnetic data of **3t**, **6t**, and **7t** were analyzed by the square model as an equally-spaced model. Similarly, possibility of rectangle models deserves discussion, because the crystallographic analysis indicates that there are two crystallographic independent copper ions in a tetramer. We actually tried to fit the data of **7t** as well as **3t** and **6t** to the alternating antiferromagnetic chain model [32] and the rectangle model [7]. We eventually found that the latter analysis more likely from the better fit. Furthermore, we also found that the analysis based on the equal spacing satisfactorily reproduced the experimental results.

The structurally common bridges Cu–N$_{im}$(eq)–N$_{im}$(eq)–Cu afford comparable magnitudes of couplings. The 2J values were observed between −78 and −97 K for both the chains and cycles investigated here, and accordingly the α value should be 0.80 at the most. Hence, though an alternating parameter α should be introduced, α was found to be close to unity.

The exchange parameters for the present compounds fell in a typical range of superexchange couplings between copper(II) ions across imidazolates [5–10]. The mechanism of the superexchange coupling was previously discussed by Kolks et al. [7] and Chaudhuri et al. [6]. The σ-pathway across the nitrogen lone-pairs has been pointed out, like other diazaaromatic-bridged systems [35]. The present exchange couplings are much larger than that of imidazolate-bridged copper(II) chains having the *N*-equatorial–*N*-axial bridging motif (for example, $2J/k_B = -5.2$ K [18]).

4. Concluding remarks

The magnetic properties of **1p**–**5p**, **3t**, **6t**, and **7t** were found to be devided into two categories: the Bonner–Fisher model was plausibly applied to polymeric [Cu(L)(μ-im)]$_n$ for the best fit, while a square model to tetrameric [Cu(L)(μ-im)]$_4$. We could not determine the crystal structures of **1p**, **2p**, **5p**, and **7t** at present. It is difficult to characterize compounds as infinite polymers or cyclic oligomers solely from the spectroscopic and elemental analyses. The polymeric and tetranuclear structures could be clearly distinguished from each other by fitting the magnetic data to theoretical curves.

We utilized a simple imidazolate anion for linking several copper(II) diketonates without preorganization of the ligands. It should be noted that the combination of simple copper(II) diketonates and imidazolate ion is versatile for supramolecular chemistry.

5. Experimental

5.1. Materials

Bis(β-diketonato)copper(II) complexes employed were [Cu(acac)$_2$], [Cu(dprm)$_2$], [Cu(dnbm)$_2$], [Cu(dibm)$_2$], [Cu(dpm)$_2$] and [Cu(bzac)$_2$]. They were prepared by the reported method [23]. Imidazole (Tokyo Chemical Industry Co.) was recrystallized from light petroleum (b.p. range 30–70 °C).

The imidazolate-bridged complexes **1p**–**5p** and **6t** are previously characterized except for melting points. However, these complexes and **3t** were prepared for X-ray diffraction study and magnetic measurements according to the following method. Complex **7t** prepared by the previous report [23] was applied for magnetic measurements.

[Cu(acac)(μ-im)]$_n$ (**1p**). The complex [Cu(acac)$_2$] (103.2 mg, 0.39 mmol) was dissolved in methanol (20 ml) with two molar equiv. of imidazole (53.3 mg, 0.78 mmol). The solution was refluxed for 2 h. After standing for a few days, a violet precipitate was formed. The product was filtered, washed with a small amount of methanol, and dried *in vacuo*. The yield was 33.5 mg (37%). Mp. 182–185 °C.

[Cu(dprm)(μ-im)]$_n$ (**2p**). This complex was prepared according to a similar method to that described for **1p**. The yield was 39%. Mp. 183–186 °C.

[Cu(dnbm)(μ-im)]$_n$ (**3p**). The complex [Cu(dnbm)$_2$] (74.8 mg, 0.20 mmol) was dissolved in ethanol (15 ml) with two molar equiv. of imidazole (27.3 mg, 0.40 mmol). The solution was refluxed for 2 h and the solvent was concentrated gradually on heating. Black fine needles were formed during the concentration. They were filtered, washed with a small amount of ethanol, and dried *in vacuo*, giving 17.3 mg of **3p** (30%). Mp. 153–156 °C.

[Cu(dnbm)(μ-im)]$_4$ (**3t**). The complex [Cu(dnbm)$_2$] (74.8 mg, 0.20 mmol) was dissolved in ethanol (15 ml) with two molar equiv. of imidazole (27.3 mg, 0.40 mmol). The solution was stirred at

Table 2
Selected crystallographic data for **3p**, **4p**, **3t**, and **6t**.

Compounds	3p	4p	3t	6t
Formula	$C_{12}H_{18}CuN_2O_2$	$C_{12}H_{18}CuN_2O_2$	$C_{48}H_{72}Cu_4N_8O_8$	$C_{52}H_{48}Cu_4N_8O_8$
Formula weight	285.83	285.83	1143.32	1167.18
Habit	black block	blue platelet	blue prism	blue prism
Dimension (mm^3)	$0.36 \times 0.18 \times 0.09$	$0.2 \times 0.2 \times 0.2$	$0.51 \times 0.4 \times 0.24$	$0.08 \times 0.05 \times 0.01$
T (K)	97	90	296	90
Crystal system	tetragonal	monoclinic	triclinic	triclinic
Space group	$P4_2/n$	$C2/c$	$P\bar{1}$	$P\bar{1}$
a (Å)	21.047(15)	28.03(4)	8.396(6)	8.168(18)
b (Å)	21.047(15)	16.91(2)	12.616(6)	11.39(3)
c (Å)	12.334(11)	11.125(18)	13.738(8)	13.16(3)
α (°)	90	90	93.78(4)	95.23(7)
β (°)	90	95.03(6)	99.89(5)	91.78(6)
γ (°)	90	90	106.49(5)	103.72(7)
V (Å^3)	5764(7)	5254(13)	1364.3(14)	1183(5)
Z	16	16	1	1
D_{calc} (g cm^{-3})	1.390	1.445	1.391	1.639
Unique data	5764	6012	5987	5353
μ (Mo Kα) (mm^{-1})	1.591	1.655	1.593	1.840
R (F)[a] ($I > 2\sigma(I)$)	0.0566	0.0546	0.0580	0.0569
$R_w(F^2)$[b] (all data)	0.0588	0.0978	0.0737	0.0806

[a] $R = \Sigma||F_o| - |F_c||/\Sigma|F_o|$.
[b] $R_w = [\sum w(F_o^2 - F_o^2)^2 / \sum w(F_o^2)]^{1/2}$.

room temperature for 2 h, and allowed to stand at room temperature for 10 days. The resultant bluish black blocks were filtered, washed with a small amount of ethanol, and dried *in vacuo*. The yield was 10.3 mg (18%). Mp. 113–114 °C.

[Cu(dibm)(μ-im)]$_n$ (**4p**). The complex [Cu(dibm)$_2$] (50.8 mg, 0.14 mmol) was dissolved in methanol (10 ml) with two molar equiv. of imidazole (18.4 mg, 0.27 mmol). The solution was refluxed for 2 h. After standing for a few days, dark blue needles were formed. They were filtered, washed with a small amount of methanol, and dried *in vacuo*. The yield was 16.2 mg (40%). Mp. 183–185 °C.

[Cu(dpm)(μ-im)]$_n$ (**5p**). This complex was prepared by a similar method to that described for complex **1p**. The yield was 85%. Mp. >195 °C.

[Cu(bzac)(μ-im)]$_4$ (**6t**). The complex [Cu(bzac)$_2$] (100.2 mg, 0.26 mmol) was dissolved in methanol (25 ml) with two molar equiv. of imidazole (35.3 mg, 0.52 mmol). The solution was refluxed for 2 h. After standing for a few days, dark green crystals were formed. They were filtered, washed with a small amount of methanol and dried *in vacuo*. The yield was 35.1 mg (46%). Mp. 185–187 °C.

5.2. X-ray crystallographic analysis

X-Ray diffraction data of **3p, 4p, 3t**, and **6t** were collected on a Rigaku R-axis RAPID diffractometer or a Rigaku Saturn-70 CCD diffractometer with graphite monochromated MoKα radiation (λ = 0.71069 Å). The structures were directly solved by a heavy-atom method and expanded using Fourier techniques in the CRYSTALSTRUCTURE 3.8.2 program package [36]. Numerical absorption correction was used. All of the hydrogen atoms were located at calculated positions and the parameters were refined as "riding". The thermal displacement parameters of non-hydrogen atoms were refined anisotropically. Full-matrix least-squares methods were applied using all of the unique reflection data. Selected crystallographic data are listed in Table 2. Preliminary crystallographic analysis on **6t** was also performed.

5.3. Magnetic measurements

Magnetic properties of polycrystalline specimens of **1p**–**5p, 3t, 6t,** and **7t** were measured at 5000 Oe in a temperature range down to 1.8 K on a Quantum Design MPMS SQUID magnetometer. The magnetic responses were corrected with diamagnetic blank data of the sample holder measured separately. The diamagnetic contribution of the sample itself was estimated from Pascal's constants.

Acknowledgements

This work was supported by Grants-in-Aid for Scientific Research (Nos. 15073101, 16550121, and 19550135) from the Ministry of Education, Culture, Sports, Science and Technology, Japan.

Appendix A. Supplementary data

CCDC 702612, 702613, 702869, and 702870 contain the supplementary crystallographic data for **3p**, **3t**, **4p**, and **6t**, respectively. These data can be obtained free of charge via http://www.ccdc.cam.ac.uk/conts/retrieving.html, or from the Cambridge Crystallographic Data Centre, 12 Union Road, Cambridge CB2 1EZ, UK; fax: (+44) 1223-336-033; or e-mail: deposit@ccdc.cam.ac.uk. Supplementary data associated with this article can be found, in the online version, at doi:10.1016/j.poly.2008.12.004.

References

[1] O. Kahn, Molecular Magnetism, VCH, New York, 1993.
[2] M. Eddaoudi, D.B. Moler, H. Li, B. Chen, T.M. Reineke, M. O'Keefe, O.M. Yaghi, Acc. Chem. Res. 34 (2001) 319.
[3] J.-M. Lehn, Supramolecular Chemistry: Concepts and Perspective, VCH, Weinheim, 1995.
[4] A. Messerschmidt, R. Huber, Eur. J. Biochem. 187 (1990) 341.
[5] P. Chaudhuri, I. Karpenstein, M. Winter, C. Butzlaff, E. Bill, A.X. Trautwein, U. Florke, H.J. Haupt, J. Chem. Soc., Chem. Commun. (1992) 321.
[6] P. Chaudhuri, I. Karpenstein, M. Winter, M. Lengen, C. Butzlaff, E. Bill, A.X. Trautwein, U. Flörke, H.-J. Haupt, Inorg. Chem. 32 (1993) 888.
[7] G. Kolks, S.J. Lippard, J.V. Waszezak, H.R. Lilienthal, J. Am. Chem. Soc. 104 (1982) 717.
[8] S. Mukherjee, T. Weyhermüller, E. Bill, P. Chaudhuri, Eur. J. Inorg. Chem. (2001) 4209.
[9] W.A. Alves, G. Cerchiaro, A. Paduan-Filho, D.M. Tomazela, M.N. Eberlin, A.M.D.C. Ferreira, Inorg. Chim. Acta 358 (2005) 3581.
[10] T. Higa, M. Moriya, Y. Shimazaki, T. Yajima, F. Tani, S. Karasawa, M. Nakano, Y. Naruta, O. Yamauchi, Inorg. Chim. Acta 360 (2007) 3304.
[11] C.A. Koch, C.A. Reed, G.A. Brewer, N.P. Rath, W.R. Scheidt, G. Gupta, G. Lang, J. Am. Chem. Soc. 111 (1989) 7645.
[12] (a) E. Colacio, M. Ghazi, R. Klevekas, M. Klinga, F. Lloret, J.M. Moreno, Inorg. Chem. 39 (2000) 2770;

(b) E. Colacio, J.M. Dominguez-Vera, M. Ghazi, R. Liveskas, M. Klinga, J.M. Moreno, Inorg. Chem. 37 (1998) 3040.
[13] N. Matsumoto, K. Inoue, M. Ohba, H. Okawa, S. Kida, Bull. Chem. Soc. Jpn. 65 (1992) 2283.
[14] J.M. Dominguez-Vera, N. Galvez, E. Colacio, R. Cuesta, J.-P. Costes, J.-P. Laurent, J. Chem. Soc., Dalton Trans. (1996) 861.
[15] R. Boca, M. Hvastijova, J. Kozisek, M. Valko, H. Ehrenberg, H. Fuess, W. Haase, I. Svoboda, R. Werner, Inorg. Chem. Commun. 8 (2005) 548.
[16] Y.F. Song, C. Massera, M. Quesada, I.A. Koval, Patrick Gamez, A.M.M. Lanfredi, J. Reedijk, Eur. J. Inorg. Chem. (2004) 4566.
[17] S.H. Rahaman, H. Chowdhury, D. Bose, G. Mostafa, H.-K. Fun, B.K. Ghosh, Inorg. Chem. Commun. 8 (2005) 1041.
[18] N. Matsumoto, T. Nozaki, H. Ushio, K. Motoda, M. Ohba, G. Mago, H. Okawa, J. Chem. Soc., Dalton Trans. (1993) 2157.
[19] N. Masciocchi, S. Bruni, E. Cariati, F. Cariati, S. Galli, A. Sironi, Inorg. Chem. 40 (2001) 5897.
[20] N. Masciocchi, G.A. Ardizzoia, G. LaMonica, A. Maspero, S. Galli, A. Sironi, Inorg. Chem. 40 (2001) 6983.
[21] (a) S.J. Retting, A. Storr, D.A. Suumers, R.C. Thompson, J. Trotter, J. Am. Chem. Soc. 119 (1997) 8675;
(b) S.J. Retting, V. Sanchez, A. Storr, R.C. Thompson, J. Trotter, J. Chem. Soc., Dalton Trans. (2000) 3931.
[22] (a) Y.-Q. Tian, C.-X. Cai, X.-M. Ren, C.-Y. Duan, Y. Xu, S. Gao, X.-Z. You, Chem. Eur. J. 9 (2003) 5673;
(b) J.-P. Zhang, X.-M. Chen, Chem. Commun. (2006) 1689.
[23] T. Kogane, R. Hirota, Bull. Chem. Soc. Jpn. 53 (1980) 91.
[24] R. Watanabe, N. Koyama, T. Nogami, T. Ishida, T. Kogane, Chem. Lett. 38 (2009) 30.
[25] J.T. Chen, S.M. Wang, J. Chin. Chem. Soc. 18 (1971) 213.
[26] (a) J. Peisach, P. Aisen, W.E. Blumberg, The Biochemistry of Copper, Academic Press, 1966;
(b) J.A.J. Jarvis, A.F. Wells, Acta Crystallogr. 13 (1960) 1027.
[27] J.C. Bonner, M.E. Fisher, Phys. Rev. A 135 (1964) 640.
[28] (a) R. Feyerherm, S. Abens, D. Günther, T. Ishida, M. Meissner, M. Meschke, T. Nogami, M. Steiner, J. Phys.: Condens. Matter 12 (2000) 8495;
(b) R. Feyerherm, T. Ishida, T. Nogami, M. Seiner, Mol. Cryst. Liq. Cryst. 335 (1999) 947.
[29] (a) J.S. Miller, Extended Linear Chain Compounds, Plenum Press, New York, 1983;
(b) K. Mukai, N. Wada, J.B. Jamali, N. Achiwa, Y. Narumi, K. Kindo, T. Kobayashi, K. Amaya, Chem. Phys. Lett. 257 (1996) 538.
[30] (a) N. Koyama, T. Ishida, T. Nogami, T. Kogane, Polyhedron 27 (2008) 2341;
(b) M. Yasui, Y. Ishikawa, N. Akiyama, T. Ishida, T. Nogami, F. Iwasaki, Acta Crystallogr., Sect. B 57 (2001) 288.
[31] K. Kambe, J. Phys. Soc. Jpn 5 (1950) 48.
[32] T. Kogane, T. Yamamoto, M. Hayashi, R. Hirota, C.A. Horiuchi, Polyhedron 14 (1995) 2475.
[33] (a) W.E. Estes, D.P. Gavel, W.E. Hatfield, D. Hodgson, Inorg. Chem. 17 (1978) 1415;
(b) W.E. Hatfield, J. Appl. Phys. 52 (1981) 1985.
[34] B. Bleaney, K.D. Bowers, Proc. R. Soc. London, Ser. A 214 (1952) 451.
[35] T. Ishida, T. Kawakami, S.-i. Mitsubori, T. Nogami, K. Yamaguchi, H. Iwamura, J. Chem. Soc., Dalton Trans. (2002) 3177.
[36] CRYSTALSTRUCTURE, version 3.8.2, Rigaku/MSC, The Woodlands, TX 77381, 2003–2007, USA.

Polyhedron 28 (2009) 2010–2016

Contents lists available at ScienceDirect

Polyhedron

journal homepage: www.elsevier.com/locate/poly

Chemical assembly of an antiferromagnetic macrocyclic molecule containing two inner Co^{II} centers from polymeric cobalt pivalate

Konstantin Tokarev [a], Mikhail Kiskin [a,*], Aleksei Sidorov [a], Grygory Aleksandrov [a], Artem Bogomyakov [b,1], Vladimir Novotortsev [a], Igor Eremenko [a]

[a] N.S. Kurnakov Institute of General and Inorganic Chemistry, Russian Academy of Sciences, Leninsky Prosp. 31, 119991 Moscow, GSP-1, Russian Federation
[b] International Tomography Centre, Siberian Branch, Russian Academy of Sciences, Institutskaya Str. 3a, 630090 Novosibirsk, Russian Federation

ARTICLE INFO

Article history:
Available online 3 January 2009

Keywords:
Coordination polymer
Binuclear complexes
Transition metals
Carboxylate ligands
Amine ligand
Schiff-base macrocycle
X-ray study
Magnetic measurements

ABSTRACT

The reaction of the polymer $\{Co(Piv)_2\}_n$ (Piv is the pivalic acid anion) with triethylenetetramine (L^1) ($M:L^1 = 2:1$) in MeCN affords the polymeric compound $[Co_2L^1(\eta^2\text{-}Piv)_2(\mu\text{-}Piv)_2]_n$ (**1**) containing asymmetric dicobalt units coordinated by one chelate ligand L^1. The reaction of **1** with an additional amount of L^1 ($M:L^1 = 1:1$) in MeCN gives rise to the binuclear molecule $Co_2L^1{}_2(Piv)_4$ (**2**), where L^1 acts as a chelate-bridging ligand. Compounds analogous to **2** with M = Fe (**3**) were prepared by the reaction of the polymer $\{Fe(Piv)_2\}_n$ with L^1 in MeCN using the reagent ratio $M:L^1 = 1:1$. The reaction of the compound $CoL^1{}_2(Piv)_4$ (**2**) with isophthalaldehyde (L^2) produces the binuclear complex $Co_2L^3(Piv)_4$ (**4**) containing the new [2 + 2] macrocyclic ligand L^3 as a result of condensation of L^1 with L^2. All newly synthesized compounds were characterized by X-ray diffraction and magnetic measurements.

© 2008 Elsevier Ltd. All rights reserved.

1. Introduction

The molecular assembly of macrocyclic molecules on metal centers is typical of lanthanide species [1,2]; nevertheless, the use of d metals in these processes was also documented [3–6]. The main problem in the latter case is low solubility of the final complexes or the formation of large amounts of by-products. In our investigations, we used pivalate derivatives of different metals, which made it possible to manipulate metal complexes having good solubility in organic solvents.

To assemble a macrocycle, we chose triethylenetetramine as the starting building block and isophthalaldehyde as the cross-linking agent. Transition metal ions are known to generally form mononuclear complexes with triethylenetetramine, which is coordinated as a tetradentate chelate (Scheme 1a) [7–20]. However, triethylenetetramine can also act as a chelate-bridging ligand (Scheme 1b) [21–23].

For this reason, we made attempts to use these properties to assemble a new heterocyclic molecule from the tetraamine ligand and isophthalaldehyde, which are bound to the metal centers as mediators in this process.

2. Experimental

2.1. Synthesis

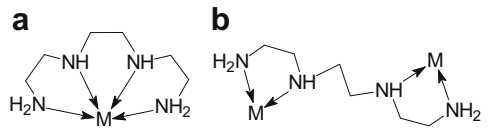
New complexes were synthesized in freshly distilled acetonitrile using the standard Schlenk techniques. The starting materials were purchased from commercial sources and were used without purification. The initial compounds $[Co(Piv)_2]_n$ and $[Fe(Piv)_2]_n$ were synthesized according to the known procedure [24,25].

$[Co_2L^1(\eta^2\text{-}Piv)_2(\mu\text{-}Piv)_2]_n$ (1). *Method A.* A mixture of $[Co(Piv)_2]_n$ (0.4 g, 1.54 mmol) and triethylenetetramine (0.11 g, 0.77 mmol) in MeCN (30 ml) was refluxed at 80 °C for 0.5 h. The resulting purple solution was kept at room temperature for 24 h. Purple needle-like crystals suitable for X-ray diffraction thus formed were collected, washed with cold MeCN, and dried under a stream of argon. The yield of **1** was 0.41 g (80%). Found: C, 46.8; H, 8.0; N, 8.5% $C_{26}H_{54}Co_2N_4O_8$ (%): C, 46.71; H, 8.14; N, 8.38. IR (KBr) ν/cm^{-1}: 3376 m, 3276 m, 2964 s, 2872 m, 1564 s, 1548 s, 1536 s, 1408 s, 1456 m, 1416 s, 1360 s, 1224 m, 1072 w, 1000 w, 964 w, 900 w, 892 w, 792 w, 604 w.

Method B. A solution of **2** (0.3 g, 0.37 mmol) in MeCN was added to $[Co(Piv)_2]_n$ (0.19 g, 0.74 mmol), and the reaction mixture was refluxed at 80 °C for 0.5 h. The resulting purple solution was filtered and kept at room temperature for 24 h. Purple needle-like crystals suitable for X-ray diffraction were collected, washed with cold MeCN, and dried under a stream of argon. The yield of **1** was

* Corresponding author. Tel.: +7 495 955 4835; fax: +7 495 952 1279.
E-mail address: mkiskin@igic.ras.ru (M. Kiskin).
[1] Fax: +7 383 333 1399.

0277-5387/$ - see front matter © 2008 Elsevier Ltd. All rights reserved.
doi:10.1016/j.poly.2008.12.002



Scheme 1. Coordination modes of triethylenetetramine to the metal centers: chelate (a) and chelate-bridging (b).

0.42 g (85%). Found: C, 46.7; H, 8.0; N, 8.4% $C_{26}H_{54}Co_2N_4O_8$ (%): C, 46.71; H, 8.14; N, 8.38. IR (KBr) ν/cm^{-1}: 3376 m, 3276 m, 2964 s, 2872 m, 1564 s, 1548 s, 1536 s, 1408 s, 1456 m, 1416 s, 1360 s, 1224 m, 1072 w, 1000 w, 964 w, 900 w, 892 w, 792 w, 604 w.

$Co_2L^1{}_2(Piv)_4$ (2). *Method A*. A solution of triethylenetetramine (0.09 g, 0.62 mmol) in MeCN (5 ml) was added to a solution of **1** (0.41 g, 0.61 mmol) in MeCN (20 ml). The reaction mixture was refluxed at 80 °C for 0.5 h. The resulting dark-red solution was concentrated to 5 ml, cooled to room temperature, and allowed to stand for several hours, after which red crystals suitable for X-ray diffraction precipitated. The crystals were washed with cold MeCN and dried under a stream of argon. The yield of **2** was 0.44 g (89%). Found: C, 47.1; H, 9.0; N, 13.7% $C_{32}H_{72}Co_2N_8O_8$ (%): C, 47.17; H, 8.91; N, 13.75. IR (KBr) ν/cm^{-1}: 3752 w, 3380 w, 3276 m, 2964 s, 2948 s, 2868 m, 1668 w, 1564 s, 1480 s, 1456 m, 1404 s, 1356 s, 1224 m, 1048 w, 976 w, 884 m, 792 m, 596 w, 396 w.

Method B. A solution of triethylenetetramine (0.15 g, 1.00 mmol) in MeCN (15 ml) was added to $[Co(Piv)_2]_n$ (0.26 g, 1.00 mmol). The reaction mixture was refluxed at 80 °C for 0.5 h. The resulting dark-red solution was concentrated to 5 ml, cooled to room temperature, and allowed to stand for several hours, after which red crystals suitable for X-ray diffraction precipitated. The crystals were washed with cold MeCN and dried under a stream of argon. Found: C, 47.2; H, 8.9; N, 13.6% $C_{32}H_{72}Co_2N_8O_8$ (%): C, 47.17; H, 8.91; N, 13.75. The yield of **2** was 0.37 g (90%). IR (ν, cm^{-1}): 3752 w, 3380 w, 3276 m, 2964 s, 2948 s, 2868 m, 1668 w, 1564 s, 1480 s, 1456 m, 1404 s, 1356 s, 1224 m, 1048 w, 976 w, 884 m, 792 m, 596 w, 396 w.

$Fe_2L^1{}_2(Piv)_4$ (3). A solution of triethylenetetramine (0.04 g, 0.39 mmol) in MeCN (15 ml) was added to $[Fe(Piv)_2]_n$ (0.10 g, 0.39 mmol). The resulting colorless solution was refluxed at 80 °C for 0.5 h, concentrated to 10 ml, and kept at room temperature for 72 h. The colorless crystals that precipitated were washed with cold MeCN and dried under a stream of argon. The yield of **3** was 0.12 g (78%).

$Co_2L^3(Piv)_4$ (4). A solution of **2** (0.32 g, 0.39 mmol) and isophthalaldehyde (0.11 g, 0.80 mmol) in MeCN (20 ml) was refluxed at 80 °C for 1 h. The resulting red solution was kept at room temperature for 48 h. Pink crystals that precipitated were washed with cold MeCN and dried under a stream of argon. The yield of **4** was 20–25%. Found: C, 57.1; H, 7.7; N, 12.0%. $C_{50}H_{79}Co_2N_9O_8$ (%): C, 57.08; H, 7.57; N, 11.9. IR (KBr) ν/cm^{-1}: 3419 w, 3260 w, 3156w, 3075 w, 2958 m, 2922 m, 2864 m, 1700 w, 1643 s, 1586 s, 1570 s, 1533 s, 1482 m, 1431 m, 1401 m, 1353 m, 1304 w, 1224 m, 1176 w, 1125 w, 1018 m, 974 m, 897 m, 879 w, 807 w, 792 m, 690 w, 605 w.

2.2. Methods

Microanalyses were carried out on a Carlo Erba CHN elemental analyzer. IR spectra were recorded on a Specord M80 spectrometer in KBr pellets (4000–400 cm^{-1}). Magnetic measurements were carried out on an MPMS-5S SQUID magnetometer (Quantum Design) in the temperature range 2–300 K in a magnetic field of up to 5 kOe. The molar magnetic susceptibility χ was calculated including diamagnetic corrections. The effective magnetic moment was calculated by the formula $\mu_{eff} = (8\chi T)^{1/2}$.

2.3. X-ray data collection

The X-ray data sets for complexes **1**–**4** were collected on a Bruker AXS SMART APEX II diffractometer equipped with a CCD detector (graphite monochromator, ω scanning technique, scan step 0.3°, exposure time per frame 10 s) using a standard procedure [26]. Semi-empirical absorption corrections for all complexes were applied (min/max transmission was 0.8186/0.6628 for **1**, 0.8841/0.8497 for **2**, 0.8515/0.7373 for **3**, and 0.9690/0.9570 for **4**) [27]. The structures were solved by direct methods and using Fourier techniques and were refined by the full-matrix least squares against F^2 with anisotropic thermal parameters for all non-hydrogen atoms. The hydrogen atoms in compounds **1**–**4** were positioned geometrically and refined using the riding model. All

Table 1
Crystallographic parameters and details of the structure refinement for complexes **1**–**4**.

Complex/parameter	**1**	**2**	**3**	**4**
Formula	$C_{26}H_{54}Co_2N_4O_8$	$C_{32}H_{72}Co_2N_8O_8$	$C_{32}H_{72}Fe_2N_8O_8$	$C_{50}H_{79}Co_2N_9O_8$
Formula weight	668.59	814.84	808.68	1052.08
T (K)	120(2)	100(2)	120(2)	293(2)
Crystal system	triclinic	monoclinic	monoclinic	triclinic
Space group	$P\bar{1}$	$P2_1/n$	$P2_1/c$	$P\bar{1}$
a (Å)	9.151(2)	9.504(3)	19.181(3)	9.671(2)
b (Å)	11.339(3)	10.386(3)	10.464(2)	12.860(3)
c (Å)	16.828(5)	21.643(6)	21.704(4)	13.022(3)
α (°)	89.696(5)	90	90	70.319(4)
β (°)	99.567(4)	100.301(6)	108.201(4)	83.339(4)
γ (°)	104.231(4)	90	90	70.227(4)
V (Å^3)	1667.8(7)	2102.0(10)	4138.1(13)	1435.0(6)
Z	2	2	4	1
D_{calc} (g cm^{-3})	1.331	1.281	1.298	1.217
μ (mm^{-1})	1.042	0.842	0.755	0.633
Total number of reflections/unique	7071/5697	10604/4228	28202/9803	12497/5651
R_{int}	0.1248	0.1541	0.0889	0.0943
θ_{max} (°)	25.35	26.44	28.03	26.37
S	0.993	0.972	1.001	0.953
R_1 ($I > 2\sigma(I)$)	0.0808	0.0682	0.0662	0.0700
wR_2 ($I > 2\sigma(I)$)	0.1460	0.1115	0.1400	0.1150
R_1 (all data)	0.2212	0.1740	0.1482	0.1701
wR_2 (all data)	0.1790	0.1371	0.1599	0.1447

calculations were carried out with the use of the SHELX97 program package [28]. The crystallographic parameters and the refinement statistics are given in Table 1.

3. Results and discussion

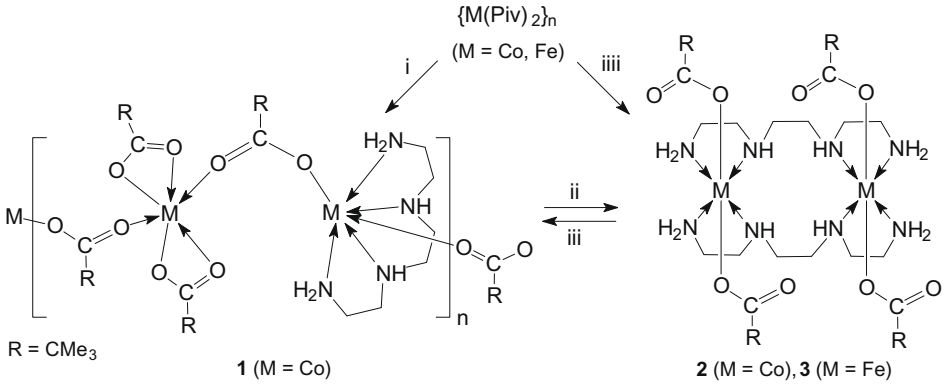
3.1. Synthesis and X-ray diffraction study

In the first step, the polymer $[Co(Piv_2)]_n$ was found to react with triethylenetetramine (reagent ratio M: L^1 = 2: 1) in MeCN (80 °C) to form the new polymer $[Co_2L^1(\eta^2\text{-Piv})_2(\mu\text{-Piv})_2]_n$ (**1**) (Scheme 2).

The X-ray diffraction study showed that the polymeric chain consists of non-symmetric dicobalt units, in which the metal atoms are held together by the bridging pivalate group (Fig. 1, Table 2). The binuclear unit contains only one chelate triethylenetetramine molecule, which is bound to one cobalt atom (type a, Scheme 1), whereas the second metal center is coordinated by two chelate pivalate groups. The adjacent binuclear fragments in the polymer are also linked together by the bridging pivalate groups. Hence, each cobalt atom has a distorted octahedral environment (CoO_6 or CoN_4O_2). The hydrogen atoms of the amine groups form hydrogen bonds with the carboxylate oxygen atoms (Table 3, Fig. 1).

In the next step, the addition of L^1 to polymer **1** (reagent ratio M: L^1 = 2: 1) resulted in the formation of the binuclear molecule $Co_2L^1{}_2(Piv)_4$ (**2**) (Scheme 2). However, the addition of the initial polymer $[Co(Piv_2)]_n$ to a MeCN solution of **2** (reagent ratio **2**: $[Co(Piv_2)]_n$ = 1: 1) again initiated the formation of polymeric compound **1**. Compound **2** can also be prepared by the reaction of $[Co(Piv_2)]_n$ with L^1 in MeCN (80 °C) (reagent ratio M: L^1 = 1: 1) (Scheme 2). The iron-containing binuclear analogue $M_2L^1{}_2(Piv)_4$ (M = Fe (**3**)) was synthesized starting from $[Fe(Piv_2)]_n$ by the reaction with L^1 in MeCN (80 °C) (reagent ratio M: L^1 = 1: 1) (Scheme 2).

According to the X-ray diffraction data for **2** and **3** (Table 1), the binuclear units in both compounds have similar structures (Fig. 2). The metal(II) atoms (in two independent molecules for complex **3**)



Scheme 2. Formation of complexes **1**, **2**, and **3** [(i), L^1 (M: L^1 = 2: 1), MeCN, Ar, 80 °C; (ii), L^1 (M: L^1 = 2: 1), MeCN, Ar, 80 °C; (iii), $[Co(Piv_2)]_n$ (M: $[Co(Piv_2)]_n$ = 1: 1), MeCN, Ar, 80 °C; (iiii), L^1 (M: L^1 = 1: 1, MeCN, Ar, 80 °C].

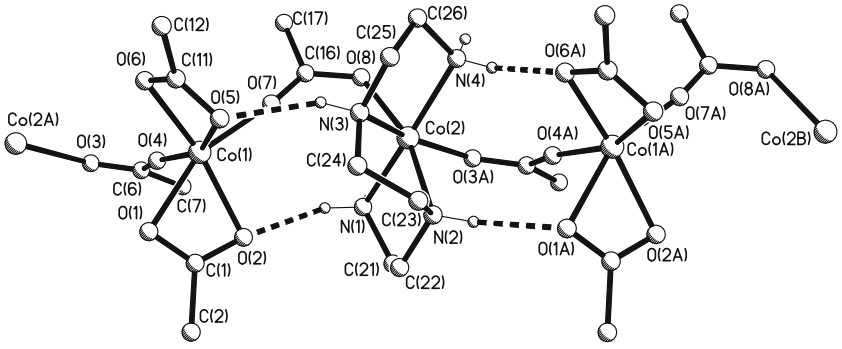


Fig. 1. Fragment of the polymeric chain of compound **1** (methyl groups are omitted for clarity).

Table 2
Selected bond lengths [Å] and bond angles [°] for complexes **1**–**4**.

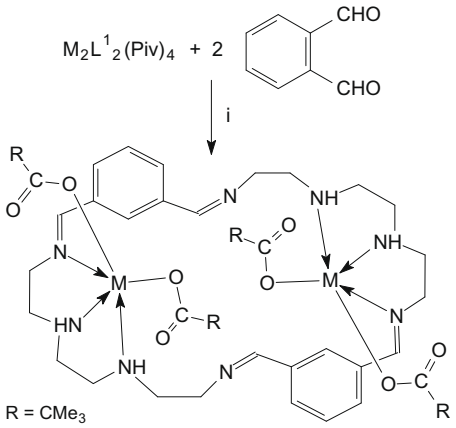
Complex/parameter	1	2	3[a]	4
M···M	4.657(2), 4.669(2)	5.713(2), 7.680(2)[b]	5.505(1), 5.736(1), 7.485(1)[b], 7.588(1)[b]	9.242(2), 7.456(2)[b], 8.663(2)[b]
M–O (μ-Piv)	2.018(8)–2.125(6)			
M–O (η^1-Piv)		2.034(4), 2.104(3)	2.037(3) – 2.083(3)	1.984(3), 2.048(3)
M–O (η^2-Piv)	2.126(6)–2.185(6)			
M–N	2.122(7)–2.193(7)	2.141(4)–2.245(5)	2.200(4)–2.313(3)	2.072(3), 2.228(4), 2.234(4)
C–O	1.226(10)–1.284(10)	1.157(8)–1.346(9)	1.251(5)–1.343(7)	1.225(5)–1.263(5)
Angle O–C–O	119.5(9)–123.9(9)	123.1(6), 123.7(5)	118.4(6)–125.0(4)	125.8(4), 122.9(4)

[a] For two independent molecules.
[b] Intermolecular.

Table 3
Hydrogen bonds [Å] and bond angles [°] for complexes **1**–**4**.

1		3[a]	
H(N1)···O2	2.05	H(N3)···O2	2.14
Angle N1–H1A–O2	160.5	Angle N3–H3E–O2	140.3
H(N3)···O5	2.18	H(N4)···O4	2.13
Angle N3–H3–O5	144.4	Angle N4–H4D–O4	147.3
H(N2)···O1A	2.19	H(N1)···O2[b]	2.04
Angle N2–H2–O1A	146.1	Angle N1–H1B–O2[b]	160.2
H(N4)···O6A	2.10	H(N1)···O4[b]	2.12
Angle N4–H4–O6A	160.7	Angle N1–H1A–O4[b]	154.5
2		**4**	
H(N1)···O4	2.14	H(N2)···O2	2.29
Angle N1–H1A–O4	139.2	Angle N2–H2A–O2	132.7
N3···O2	2.934	H(N3)···N4[b]	2.58
H(N4)···O4[b]	2.14	N3···N4[b]	3.379
Angle N4–H4D–O4[b]	148.3	Angle N3–H3D–N4[b]	147.6
		N2···O2[b]	3.290
		H(N2)···O2[b]	2.87
		Angle N2–H2A–O2[b]	109.6

[a] For two independent molecules.
[b] Intermolecular.



Scheme 3. Formation of the binuclear complex $[M_2L^3(Piv)_4]$ (M = Co (**4**)) [(i), MeCN, Ar, 80 °C].

are in a distorted octahedral environment formed by four nitrogen atoms of two equatorial ligands L^1 and two oxygen atoms of two axial terminal pivalate groups. In molecules **2** and **3**, the tetraamine ligands L^1 act as chelate-bridging ligands and are coordinated to the adjacent metal centers (type b, Scheme 1) *via* two M–N bonds (Table 2). In the complex molecules, hydrogen bonding is present between the carboxylate oxygen atoms and the amine protons and between the binuclear units (Table 3).

In the next step of the assembly of the macrocycle, we used isophthalaldehyde (L^2) as the cross-linking agent. Formally, the tetraamine ligands L^1 in binuclear molecule **2** are ready for condensation with L^2. The reaction of complexes **2** with L^2 in MeCN (reagent ratio M: L^2 = 1: 1) afforded the binuclear structure $M_2L^3(Piv)_4$ (M = Co (**4**)) containing the new [2 + 2] macrocyclic ligand L^3 as a condensation product of L^1 and L^2 (Scheme 3).

According to the X-ray diffraction data, the 30-membered macrocycle containing eight nitrogen atoms is the main structural unit of centrosymmetric binuclear molecule **4** (Fig. 3, Table 2). However, only six N atoms are bound to two inner Co(II) centers. The metal atoms Co(1)···Co(2) are at a nonbonded distance (Co···Co 9.242(2) Å). In addition, the Co(II) atom is coordinated by two oxygen atoms of the terminal carboxylate anions. Therefore, each cobalt atom is in a disordered tetragonal pyramidal ligand environment (Fig. 3). Hydrogen bonding is present between the

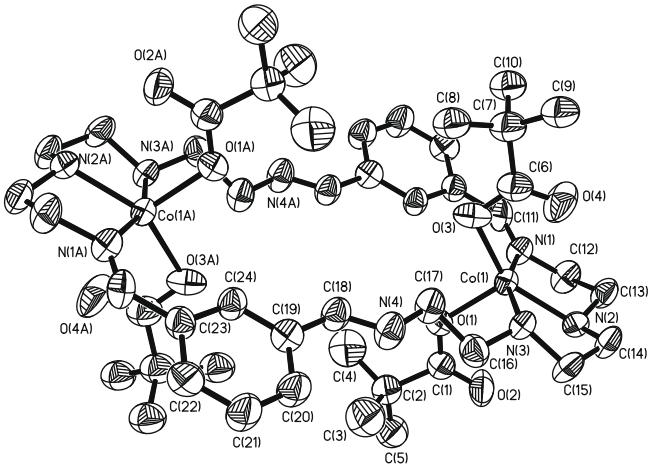


Fig. 3. Structure of the complex $Co_2L^3(Piv)_4$ (**4**).

oxygen atoms of the terminal carboxylate groups and the hydrogen atoms of the coordinated amine groups (Table 3, Fig. 4).

In the crystal structure, adjacent molecules **4** self-assemble *via* weak intermolecular hydrogen bonds between the nitrogen atoms (N(4) of the ligand L^3 and the protons of the amine groups (N(3)), which are not coordinated to the metal centers (Co···Co

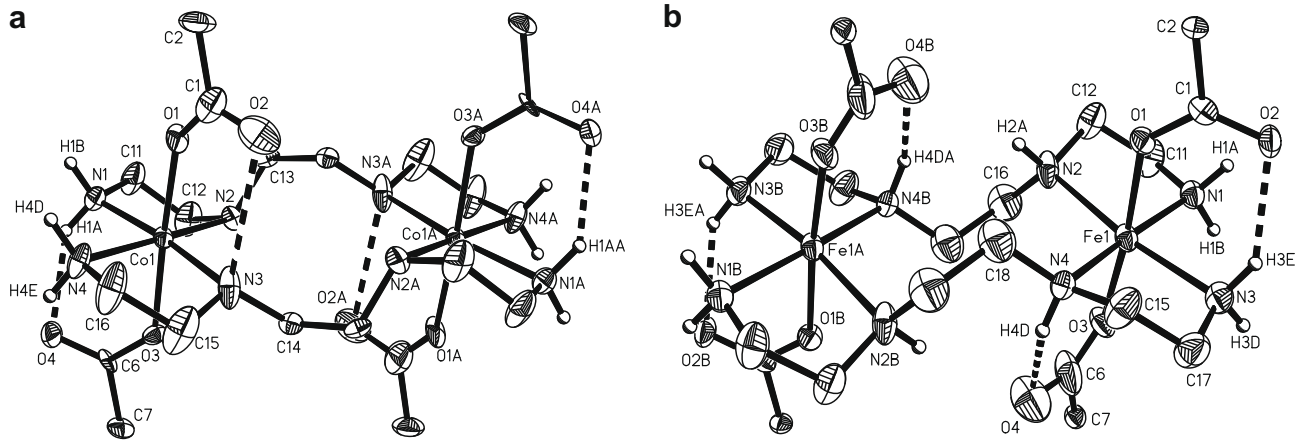


Fig. 2. Structure of the binuclear complexes $M_2L^1{}_2(Piv)_4$ (M = Co (*a*), Fe (*b*)) (methyl groups are omitted for clarity).

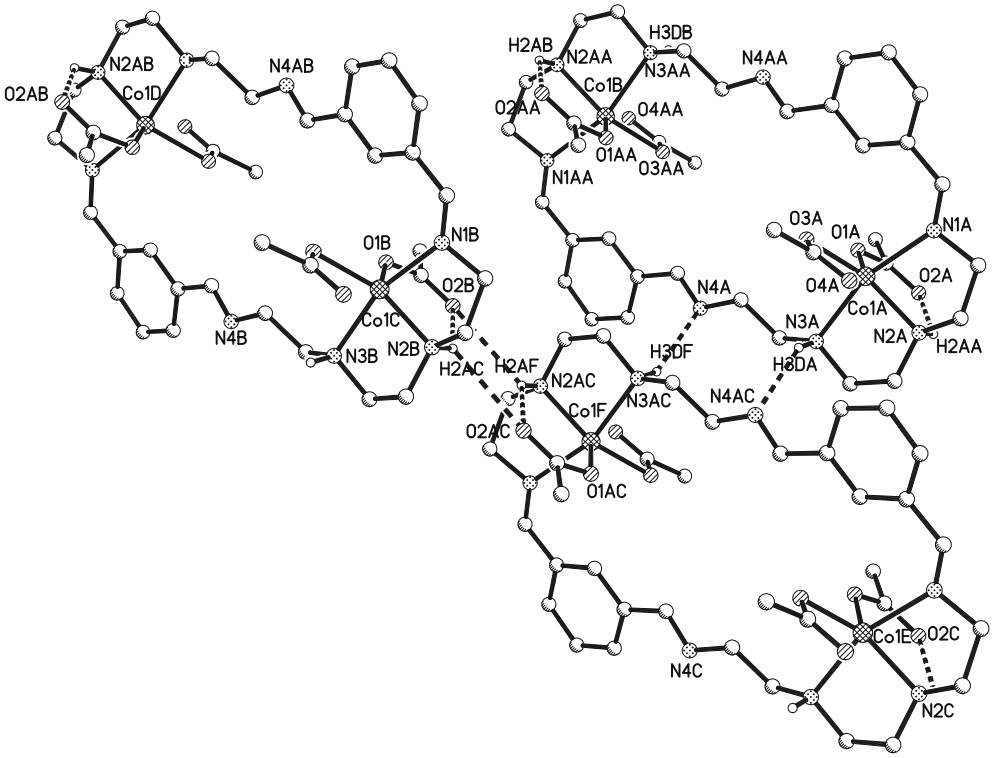


Fig. 4. Fragment of the supramolecular layer in crystal structure of complex **4** (methyl groups are omitted for clarity). Selected distances (Å): Co1A···Co1B 9.242(2), Co1A···Co1F 8.663(2), Co1A···Co1E 9.671(2), Co1F···Co1C 7.456(2).

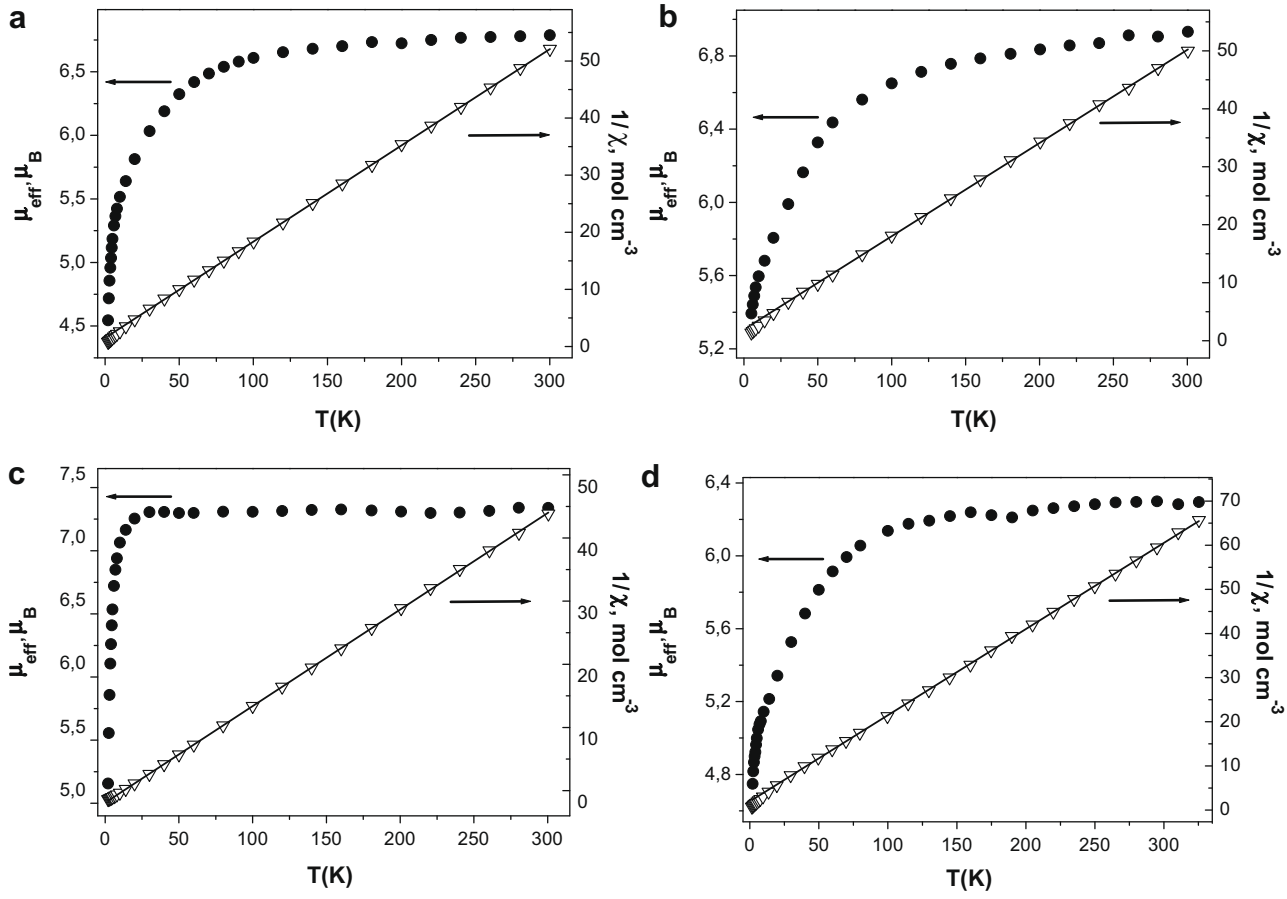


Fig. 5. Magnetic properties of complexes **1** (*a*), **2** (*b*), **3** (*c*), and **4** (*d*): temperature dependence of magnetic moment (●), plot $1/\chi$ vs. T (▽) and calculated data as solid line.

8.663(2) Å) and the oxygen atoms (O2) of the terminal carboxylate groups and the hydrogen atoms (N2) of the coordinated amine groups (Co···Co 7.456(2) Å) (Table 3), to form a supramolecular layer (Fig. 4).

3.2. Magnetic properties

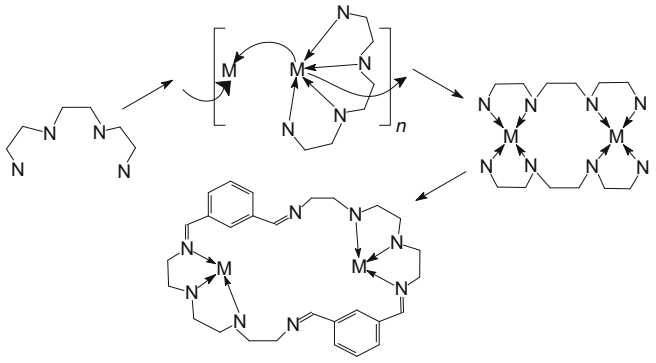
Magnetic measurements of the newly synthesized cobalt(II)-containing complexes **1**, **2**, and **4** revealed the strong temperature dependence of the magnetic moment (Fig. 5). All complexes have a similar temperature dependence of the magnetic moments. The magnetic moments μ_{eff} are 6.79 and 6.91 μ_B at 300 K and 6.30 μ_B at 325 K for complexes **1**, **2**, and **4**, respectively. The experimental effective magnetic moments are substantially larger than the theoretical pure spin value μ_{calc} = 5.48 μ_B (for two spins, $S = 3/2$, $g = 2$), which is attributed to the orbital contribution to the magnetic susceptibility typical of Co^{II} ions and the g factor >2. The magnetic moments first smoothly and then more sharply decrease with decreasing temperature and reach 4.55, 5.39, and 4.75 μ_B at 2 K for complexes **1**, **2**, and **4**, respectively. The exchange interaction parameters were estimated from the Curie–Weiss law because it is difficult to precisely calculate these parameters because of the large orbital contribution to the magnetic susceptibility typical of Co^{II} ions in an octahedral environment. Complex **1** exists as a polymeric chain, in which Co^{II} ions are coupled by exchange interactions through the bridging carboxylate anions. In the temperature range of 50–300 K, the plot $\chi^{-1}(T)$ for complex **1** follows the Curie–Weiss law ($\chi = C/(T-\theta)$) with C = 5.91 (2.955 per cobalt atom) and $\theta/k = -8.8$ K (Fig. 5, Table 4). The negative value of θ/k is indicative of the presence of antiferromagnetic exchange interactions, which are responsible for a decrease in the magnetic moment at low temperatures. For complex **2**, the Curie constant C = 6.22 and $\theta/k = -12$ K (Fig. 5, Table 4). Intramolecular interactions between the Co^{II} ions through the Co(1)–N(2)–C(13)–C(14A)–N(3A)–Co(1A) aliphatic ligand are possible. In addition, intermolecular interactions through the Co(1)–O(3)–C(6)=O(4)···H–N(4A)–Co(1A) channel can also exist. Therefore, in the solid phase, the Co^{II} ions form exchange-bound chains because of which it is impossible to analyze the magnetic properties based on the expression for the susceptibility of exchange-bound dimers. In the structure of complex **4**, there are also interactions between the Co^{II} ions of the adjacent molecules through the hydrogen bonds between the coordinated carboxylate group and the amine nitrogen atom of the ligand and between the amine nitrogen atom of the ligand and the imine nitrogen atom of the ligand belonging to the adjacent molecules. The plot χ^{-1}(T) for complex **4** follows the Curie–Weiss law (Fig. 5, Table 4).

For iron compound **3**, the temperature dependence is more complicated. In the temperature range 300–30 K, the effective magnetic moment (μ_{eff}) decreases only slightly from 7.24 to 7.20 μ_B (Fig. 5). However, at helium temperatures μ_{eff} decreases sharply to 5.06 μ_B (2 K). The magnetic moment μ_{eff} at room temperature is similar to the calculated magnetic moment for two iron(II) ($S = 2$, $g = 2$) ions (μ_{calc} = 6.93 μ_B). In the structure of **3**, as in complex **2**, there are exchange-bound chains of Fe^{II} ions, in which antiferromagnetic exchange interactions prevail (Fig. 5, Table 4).

Table 4
Calculated Curie–Weiss parameters for compound **1**–**4**.

Complex	C, cm^3 K mol^{-1}	θ/k, K
1	5.912 ± 0.007 (2.96/calc. 2.8–3.4/)[a]	−8.8 ± 0.2
2	6.22 ± 0.02 (3.11/calc. 2.8–3.4/)[a]	−12.0 ± 0.7
3	6.54 ± 0.01 (3.27/calc. 3/)[a]	−0.6 ± 0.3
4	5.11 ± 0.01 (2.56/calc. 2.8–3.4/)[a]	−9.6 ± 0.4

[a] Per one metal atom.



Scheme 4. Schematic representation of the phase assembly of macrocyclic complex **4**.

To conclude, we found that binuclear complex **2** with chelate-bridging tetraamine ligands can be used as a building block to assemble macrocyclic species. The present investigation showed that the formation of the macrocyclic molecule at cobalt centers as mediators of chemical assembly proceeds in a stepwise fashion (Scheme 4).

Acknowledgments

This study was supported by the Russian Foundation for Basic Research (Project Nos. 06-03-32742, 07-03-00707, 07-03-12131, 07-03-12210, 08-03-00091, and 08-03-00343), the Council on Grants of the President of the Russian Federation (Grants NSh-1324.2008.3, NSh-1518.2008.3), the Federal Agency for Science and Innovations (Lot 1.3), the Russian Science Support Foundation, the Russian Academy of Science, the Siberian Branch of the Russian Academy of Sciences and the Department of Chemistry and Materials Science.

Appendix A. Supplementary data

Supplementary data associated with this article can be found, in the online version, at doi:10.1016/j.poly.2008.12.002.

References

[1] V. Alexander, Chem. Rev. 95 (1995) 273. and refs. therein.
[2] D.E. Fenton, P.A. Vigato, Chem. Soc. Rev. 17 (1988) 69.
[3] N.V. Gerbeleu, V.B. Arion, J. Burgess, Template Synthesis of Macrocyclic Compounds, Wiley-VCH, 1994. and refs. therein.
[4] D. Meyerstein, Coordination Chemistry Reviews 185–186 (1999) 141.
[5] K. Gloe (Ed.), Macrocyclic Chemistry: Current Trends and Future Perspectives, vol. 105–119, Springer, Netherlands, 2005.
[6] R.M. Izatt, J.J. Christensen, Progress in Macrocyclic Chemistry, vol. 1, John Wiley & Sons, 1979.
[7] M.K. Saha, U. Mukhopadhyay, I. Bernal, Dalton Trans. (2004) 1466.
[8] F. Brezina, Z. Travnicek, Z. Sindelar, R. Pastorek, J. Marek, Transition Met. Chem. 24 (1999) 459.
[9] R. Boca, M. Boca, M. Gembicky, L. Jager, C. Wagner, H. Fuess, Polyhedron 23 (2004) 2337.
[10] M.R. Burke, M.F. Richardson, P.J. McCarthy, J. Crystallogr. Spectrosc. Res. 14 (1984) 143.
[11] R.K. Wismer, R.A. Jacobson, Inorg. Chim. Acta 7 (1973) 477.
[12] M. Dwyer, I.E. Maxwell, Inorg. Chem. 9 (1970) 1459.
[13] I. Bernal, Inorg. Chim. Acta 96 (1985) 99.
[14] I. Bernal, J. Cetrullo, Inorg. Chim. Acta 120 (1986) 109.
[15] H. Chun, B.J. Salinas, I. Bernal, Eur. J. Inorg. Chem. (1999) 723.
[16] Y. Kitamura, J.G. Leipoldt, A. Roodt, Inorg. Chim. Acta 149 (1988) 125.
[17] J. Cai, X. Hu, X. Feng, L. Ji, I. Bernal, Acta Crystallogr., Sect. B 57 (2001) 45.
[18] I. Bernal, J. Cai, J. Certrullo, S.S. Massoud, Struct. Chem. 5 (1994) 265.
[19] M. Gembicky, R. Boca, L. Jager, C. Wagner, Inorg. Chem. Commun. 3 (2000) 566.

[20] Z.-W. Mao, M.-Q. Chen, X.-S. Tan, J. Liu, W.-X. Tang, Inorg. Chem. 34 (1995) 2889.
[21] R.D. Willett, Acta Crystallogr., Sect. C 43 (1987) 1494.
[22] J. Cai, X.-P. Hu, J.-H. Yao, L.-N. Ji, Inorg. Chem. Commun. 4 (2001) 478.
[23] G.-M. Wang, Y.-Q. Sun, G.-Y. Yang, J. Solid State Chem. 179 (2006) 1545.
[24] I.L. Eremenko, M.A. Kiskin, I.G. Fomina, A.A. Sidorov, G.G. Aleksandrov, V.N. Ikorskii, Yu.G. Shvedenkov, Yu.V. Rakitin, V.M. Novotortsev, J. Cluster Sci. 16 (2005) 331.
[25] I.G. Fomina, G.G. Aleksandrov, Zh.V. Dobrokhotova, O.Yu. Proshenkina, M.A. Kiskin, Yu.A. Velikodnyi, V.N. Ikorskii, V.M. Novotortsev, I.L. Eremenko, Russ. Chem. Bull. 55 (2006) 1909.
[26] SMART (Control) and SAINT (Integration) Software, Version 5.0, Bruker AXS Inc., Madison, WI, 1997.
[27] G.M. Sheldrick, SADABS, Program for Scanning and Correction of Area Detector Data, Göttingen University, Göttingen, Germany, 1997.
[28] G.M. Sheldrick, SHELX-97: Program for the Solution of Crystal Structures, Göttingen, Germany, 1997.

Polyhedron 28 (2009) 2017–2025

Contents lists available at ScienceDirect

Polyhedron

journal homepage: www.elsevier.com/locate/poly

Linear Mn^{II}_3 and cubane Mn^{II}_4 carboxylate clusters derived from di-2-pyridyl ketone: Synthesis, characterization and magnetic properties

Constantinos C. Stoumpos [a], Nikolia Lalioti [a], Ian A. Gass [b], Konstantinos Gkotsis [a], Alexandros A. Kitos [a], Harikleia Sartzi [a], Constantinos J. Milios [a,b], Catherine P. Raptopoulou [c], Aris Terzis [c], Euan K. Brechin [b,*], Spyros P. Perlepes [a,*]

[a] Department of Chemistry, University of Patras, 265 04 Patras, Greece
[b] School of Chemistry, The University of Edinburgh, West Mains Road, EH9 3JJ Edinburgh, UK
[c] Institute of Materials Science, NCSR "Demokritos", 153 10 Aghia Paraskevi, Attikis, Greece

ARTICLE INFO

Article history:
Available online 12 January 2009

Keywords:
Di-2-pyridyl ketone metal complexes
Linkage isomers
Magnetic susceptibility data
Manganese(II) clusters
Manganese(II) cubanes

ABSTRACT

The employment of di-2-pyridyl ketone, $(py)_2CO$, in manganese(II) benzoate chemistry is reported. The syntheses, crystal structures and spectroscopic (IR, EPR) characterization are described for $[Mn^{II}_3(O_2CPh)_6\{(py)_2CO\}_2]$ (**1**), $[Mn^{II}_3(O_2CPh)_6\{(py)_2CO\}_2]\cdot 2MeCN$ (**2** · 2MeCN) and $[Mn^{II}_4(O_2CPh)_4\{(py)_2C(OH)O\}_4]$ (**3**), where $(py)_2C(OH)O^-$ is the monoanion of the *gem*-diol form of $(py)_2CO$. Variable-temperature, magnetic susceptibility studies on **3** have also been performed. Complexes **1** and **2** · 2MeCN are linkage isomers. The trinuclear molecules of both complexes have a linear structure, with one $\eta^1{:}\eta^2{:}\mu_2$ and two *syn, syn*- $\eta^1{:}\eta^1{:}\mu_2$ $PhCO_2^-$ groups spanning each pair of Mn^{II} atoms. The terminal Mn^{II} atoms are each capped by one κ^2N,N' $(py)_2CO$ ligand in orange **1** and one κ^2N,O $(py)_2CO$ molecule in the yellow isomer **2** · 2MeCN. The molecule of **3** has a cubane topology with the Mn^{II} centers and the deprotonated oxygen atoms from the $\eta^1{:}\eta^3{:}\eta^1{:}\mu_3$ ligands occupying alternate vertices of the cube. A terminal monodentate $PhCO_2^-$ group completes a distorted octahedral coordination at each Mn^{II} atom. The IR data are discussed in terms of the coordination modes of the ligands that are present in the complexes. The X-band EPR spectra of powdered **1** and **2** at 4 K indicate that the populated spin states exhibit a zero-field splitting, while the spectrum of **3** at 18 K is consistent with the presence of magnetically interacting Mn^{II} atoms in the solid state. The magnetic properties of **3** in the 300–5 K range have been modelled with two *J* values, which reveal weak antiferromagnetic interactions within the molecule. Some suggestions have been made concerning the great stability of complex **3**.

© 2009 Elsevier Ltd. All rights reserved.

1. Introduction

Molecular Mn carboxylate cluster chemistry continues to attract intense attention from many research groups around the world. The reasons for this are many, but the two most important ones are the relevance of the chemistry of Mn to bioinorganic chemistry [1] and to the ongoing efforts to develop new routes to high-spin molecules [2] and single-molecule magnets (SMMs) [3]. SMMs are molecules that retain their magnetization below a blocking temperature (T_B) in the absence of an applied field, thus representing a molecular, "bottom up" approach to nanoscale magnets.

In this study, we have sought to extend our previous work where we had employed di-2-pyridyl ketone ($(py)_2CO$, Scheme 1) in Mn acetate reactions, and had obtained structurally interesting new complexes [4]. Due to its highly activated carbonyl group, $(py)_2CO$ is a unique ligand [5]. Water, among other nucleophiles [5,6], has been shown to add to the carbonyl group *upon coordination of the 2-pyridyl rings and/or the carbonyl oxygen* forming the ligand $\{(py)_2C(OH)_2\}$ [the *gem*-diol form of $(py)_2CO$]. Upon deprotonation, the latter can function either as mono- or dianionic ligand depending on the reaction conditions. Herein, we report the synthetic investigation of the $Mn^{II}/PhCO_2^-/(py)_2CO$ reaction system that resulted in the isolation of three manganese(II) benzoate clusters. Portions of this work have been communicated [7].

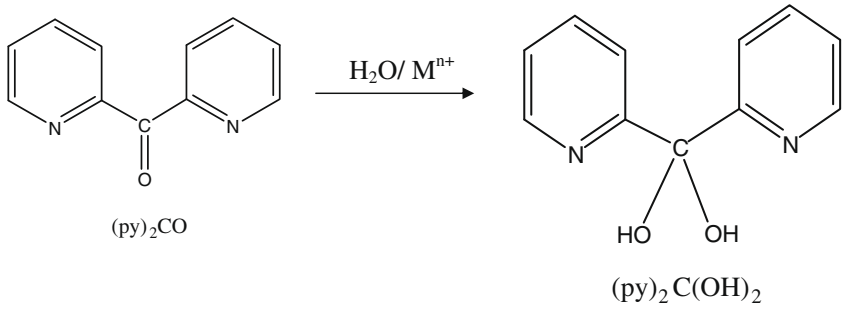
2. Experimental

2.1. General information and techniques

All manipulations were performed under aerobic conditions using materials (reagent grade) and solvents as received.

* Corresponding authors. Tel.: +44 131 650 7545 (E.K. Brechin), tel.: +30 2610 997146; fax: +30 2610 997118 (S.P. Perlepes).
E-mail addresses: ebrechin@staffmail.ed.ac.uk (E.K. Brechin), perlepes@patreas.upatras.gr (S.P. Perlepes).

0277-5387/$ - see front matter © 2009 Elsevier Ltd. All rights reserved.
doi:10.1016/j.poly.2008.12.001



Scheme 1. Ligands discussed in the text. Note that $(py)_2C(OH)_2$ and its anions do not exist as free species but exist only in their respective metal complexes. M^{n+} = metal ion; n = 2, 3.

$Mn(O_2CPh)_2 \cdot 2H_2O$ was prepared as described elsewhere [8]. Microanalyses (C, H, N) were performed by the University of Ioannina (Greece) Microanalytical Laboratory using an EA Carlo Erba analyzer.

IR spectra (4000–400 cm^{-1}) were recorded on a Perkin–Elmer 16 PC FT-IR spectrometer with samples prepared as KBr pellets. FT-Raman spectra were recorded on a Bruker IFS 66v interferometer with a FT-Raman FRA 106 module. The compounds were excited by the 1064 nm line of a Nd:YAG laser operating at 200 mW. For each spectrum, 1000 scans were recorded and averaged. Solid state EPR spectra in the 4.2–300 K range were recorded on a Bruker ER 200D-SRC X-band spectrometer equipped with an Oxford ESR 9 cryostat. Dc magnetic measurements were carried out on a polycrystalline sample of the cubane complex (vide infra) using a Quantum Design MPMS SQUID magnetometer operating at a constant magnetic field of 0.1 T between 5.0 and 300 K. The experimental molar susceptibility was corrected for the diamagnetic contribution from the sample holder and the diamagnetic response from the sample, which was evaluated from Pascal's constants.

2.2. Compound preparation

2.2.1. $[Mn_3(O_2CPh)_6\{(py)_2CO\text{-}\kappa^2N,N'\}_2]$ (**1**), $[Mn_3(O_2CPh)_6\{(py)_2CO\text{-}\kappa^2N,O\}_2]\cdot 2MeCN$ (**2**·2MeCN) and $[Mn_4(O_2CPh)_4\{(py)_2C(OH)O\}_4]$ (**3**) in a mixture

A colourless solution of $Mn(O_2CPh)_2\cdot 2H_2O$ (300 mg, 0.9 mmol) in freshly distilled MeCN (20 ml) was treated with solid $(py)_2CO$ (110 mg, 0.6 mmol) under mild stirring. The solid soon dissolved and the colour of the solution turned to bright yellow. Stirring was maintained for 20 min, and the solution flask was sealed and left undisturbed overnight. After several hours the solution began to afford a mixture of orange crystals of **1** and yellow crystals of **2**·2MeCN, while the colour of the solution faded to orange. One crystal from each compound was removed from the mixture and its identity was crystallographically established. The orange crystals proved to be complex **1,** while the unstable yellow crystals corresponded to complex **2**·2MeCN. After 3 days, the precipitation was judged to be complete producing more orange crystals and no yellow ones. The ratio of orange to yellow crystals was estimated to be approximately 4:1; the combined yield of the precipitated materials was about 55%. After 1 week a quantity of colourless polyhedral crystals, crystallographically identified as $[Mn_4(O_2CPh)_4\{(py)_2C(OH)O\}_4]$ (**3**), was precipitated in 30% yield, while the supernatant mother solution was colourless. The reaction mixture was then left to slowly evaporate in the air and upon atmospheric oxidation the $(py)_2CO$-free known compound $[Mn_6O_2(O_2CPh)_{10}(MeCN)_4]$ formed as brown rectangular plates in ~10% yield (all yields are based on the total Mn content of the reaction mixture).

2.2.2. $[Mn_3(O_2CPh)_6\{(py)_2CO\text{-}\kappa^2N,N'\}_2]$ (**1**)

A colourless solution of $Mn(O_2CPh)_2\cdot 2H_2O$ (300 mg, 0.9 mmol) in freshly distilled MeCN (20 ml) was treated with solid $(py)_2CO$ (110 mg, 0.6 mmol) under mild stirring. The solid ligand soon dissolved and the colour of the solution instantly turned to bright yellow. Then a reflux condenser was attached to the reaction flask and the solution maintained under reflux for 24 hours under vigorous stirring. The colour of the solution gradually turned to orange. The reaction flask was cooled to room temperature and left undisturbed to produce orange crystals of pure **1** over a period of 3 days. The crystals were filtered, washed with Et_2O (2 × 3 ml) and dried in the air. 60% yield.

IR (KBr pellet, cm^{-1}): ν = 3062m, 2828w, 1710s, 1602s, 1560s, 1474m, 1446sh, 1432m, 1386sb, 1296m, 1258w, 1222m, 1016m, 950m, 802m, 776m, 750w, 724s, 678s, 636m. *Anal.* Calc. for $C_{64}H_{46}O_{14}N_4Mn_3$ (1259.9): C, 61.01; H, 3.69; N, 4.45. Found: C, 60.67; H, 3.55; N, 4.52%.

2.2.3. $[Mn_3(O_2CPh)_6\{(py)_2CO\text{-}\kappa^2N,O\}_2]\cdot 2MeCN$ (**2** · 2MeCN)

A colourless solution of $Mn(O_2CPh)_2\cdot 2H_2O$ (600 mg, 1.8 mmol) in freshly distilled MeCN (20 ml) was treated with solid $(py)_2CO$ (220 mg, 1.2 mmol) in small portions under gentle stirring. The solid ligand soon dissolved and the bright yellow solution obtained was left undisturbed to produce a yellow microcrystalline powder. The powder was collected after 6 h, since after that time orange crystals of **1** began to form. The yellow material was collected by filtration, washed with Et_2O (2 × 3 ml) and dried in the air. The yield was 30%. (KBr pellet, cm^{-1}): ν = 3064m, 2830w, 1640s, 1596s, 1546br, 1470m, 1430sh, 1408s, 1384sh, 1296w, 1268w, 1028m, 1016m, 978w, 772m, 724s, 678m, 640w, 615sh. The solid analyzed as solvent-free. *Anal.* Calc. for $C_{64}H_{46}O_{14}N_4Mn_3$ (1259.9): C, 61.01; H, 3.69; N, 4.45. Found: C, 60.87; H, 3.73; N, 4.40%.

2.2.4. $[Mn_4(O_2CPh)_4\{(py)_2C(OH)O\}_4]$ (**3**)

To a colourless solution of $Mn(O_2CPh)_2\cdot 2H_2O$ (167 mg, 0.5 mmol) in "wet" CH_2Cl_2 (25 ml) was added solid $(py)_2CO$ (92 mg, 0.5 mmol). The solid soon dissolved to yield a pale yellow solution. The solution became colourless after 30 min of stirring. The solution was layered with *n*-hexane (50 ml). Slow mixing gave large, polyhedral crystals of the product after 3 days in 90% yield. The crystals were collected by filtration, washed with Et_2O (2 × 3 ml) and dried in the air. IR (KBr pellet, cm^{-1}): ν = 3416br, 1596s, 1558s, 1434m, 1390s, 1292w, 1258w, 1222m, 1016m, 950m, 774m, 726s, 680m, 662w, 636m. *Anal.* Calc. for $C_{72}H_{56}O_{16}N_8Mn_4$ (1509.0): C, 57.30; H, 3.75; N, 7.43. Found: C, 57.42; H, 3.96; N, 7.33%.

2.3. Single-crystal X-ray crystallography

A crystal of **1** was mounted in air, while crystals of **2**·2MeCN and **3** were mounted in capillary. Diffraction measurements were made

on a Crystal Logic Dual Goniometer diffractometer using graphite-monochromated Mo radiation. Complete crystal data and parameters for data collection and processing are listed in Table 1. Unit cell dimensions were determined and refined by using the angular settings of 25 automatically centered reflections in the range $11^\circ < 2\theta < 23^\circ$. Intensity data were recorded using the θ-2θ scan method. Three standard reflections monitored every 97 reflections showed less than 3% variation and no decay. Lorentz, polarization corrections were applied using the Crystal Logic software package.

The structures were solved by direct methods using SHELXS-86 [9] and refined by full-matrix least-squares techniques on F^2 with SHELXL-97 [10]. For the structure of **1**, all hydrogen atoms were located by difference maps and refined isotropically. In the case of **2** · 2MeCN, all hydrogen atoms were located by difference maps and refined isotropically, except those of the MeCN solvate which were introduced at calculated positions as riding on their respective bonded atom. For the structure of **3**, all hydrogen atoms were introduced at calculated positions as riding on bonded atoms. For all three structures, all non-hydrogen atoms were refined using anisotropic thermal parameters.

3. Results and discussion

3.1. Synthetic comments

The $Mn(O_2CPh)_2{\cdot}2H_2O/(py)_2CO$ reaction system in freshly distilled MeCN is complicated. The 1.5:1 reaction gave a bright yellow solution, which upon storage in a *closed* flask gradually turned to orange within ~10 h giving a mixture of yellow and orange crystals in a visual ratio ~1:1. The orange crystals are stable in the atmosphere, whereas the yellow ones collapse rapidly giving a yellow powder. To our surprise, both dried samples gave almost identical analytical results corresponding to the empirical formula $Mn(O_2CPh)_2\{(py)_2CO\}_{0.7}$. Our curiosity increased when we looked at the IR spectra of the two samples. The spectra of the orange and yellow materials exhibit a strong band at 1710 and 1640 cm^{-1}, respectively, attributable to ν(C=O) and suggesting [11] that the ligand is present in its rare [5] ketone $(py)_2CO$ form (Scheme 1) in both compounds. Thus, we decided to collect full single-crystal, X-ray data sets for the two samples. Crystallography revealed that the orange and yellow crystals correspond to the compounds $[Mn^{II}_3(O_2CPh)_6\{(py)_2CO\text{-}\kappa^2N, N'\}_2]$ (**1**) and $[Mn^{II}_3(O_2CPh)_6\{(py)_2CO\text{-}\kappa^2N, O\}_2]{\cdot}2MeCN$ (**2**·2MeCN), respectively. Though the molecular coordination formula of the two complexes is identical, there is a major difference associated with the coordination (ligation) mode of $(py)_2CO$. In complex **1** the ligand is coordinated through the two pyridyl N atoms forming a 6-membered chelating ring, whereas in **2**·2MeCN the donor atoms of $(py)_2CO$ are the carbonyl O atom and the pyridyl N atom thus forming a 5-membered chelating ring (vide infra). With hindsight, the different coordination sphere of the external Mn^{II} atoms in the trinuclear molecules justifies the different colours of the compounds. Also the instability of the yellow crystals in the normal laboratory atmosphere is explained by the easy loss of the solvate MeCN molecules from the crystal lattice.

If the storage time of the initial reaction solution increases from several hours to ~3 days, the percentage of the orange crystals increases leading to a final visual ratio of ~4:1. At this point the yield was ~55%, based on the total available Mn. Prolonged storage (>1 week) of the initial reaction solution in a closed flask led to the slow precipitation of a third product in the form of colourless, polyhedral crystals, together with a sporadic precipitation of few orange crystals of **1,** in 30% yield (again based on the total available Mn). The colourless crystals were crystallographically shown to be $[Mn_4(O_2CPh)_4\{(py)_2C(OH)O\}_4]$ (**3**). The Mn^{II}-mediated nucleophilic attack of H_2O [from the solvent and $Mn(O_2CPh)_2{\cdot}2H_2O$] on the carbonyl group is responsible for the formation of the *gem*-diolate(-1) ligand $(py)_2C(OH)O^-$ [5]. The electrophilic character of the carbonyl carbon atom of $(py)_2CO$ is increased by coordination of the carbonyl oxygen to Mn^{II} (direct polarization) and/or coordination of the more remote pyridyl nitrogens (induced polarization) in solution [5].

Complexes **1**, **2** · 2MeCN and **3** are not the only products from the $Mn(O_2CPh)_2{\cdot}2H_2O/(py)_2CO$ reaction system in MeCN! If the initial reaction solution- that already had led to the three manganese(II) complexes- was left to slowly evaporate in the air, its colour turned to brown and few reddish-brown rectangular plates of the known $(py)_2CO$-free, mixed valence cluster $[Mn^{II}_4Mn^{III}_2O_2(O_2CPh)_{10}(MeCN)_4]$ (**4**) [12] appeared as a by-product [12]; the yield was ~10% (based on the total available Mn). The identity of **4** was confirmed by elemental analyses, IR spectrum, and a unit cell determination and comparison with the authentic material [12]. Complex **4** contains a $\{Mn_6O_2\}^{10+}$ core that can be conveniently described as two edge-sharing Mn_4 tetrahedra at the center of each of which is a μ_4-O^{2-} group [12,13].

With the identities of **1**–**3** established, convenient syntheses of pure materials were sought under alternative reaction conditions. First, we decided to take full advantage of the fact that the colour of the solution reflects the identity of the dominant species present, i.e. the solution is yellow when the first yellow crystals of **2**·2MeCN appear and orange when the main quantity of the orange crystals of **1** form. Second, we wondered why two trinuclear products form. The answer to this question was provided by Toyama et al. who carried out excellent synthetic and NMR studies on Ru^{II}/Cl^-/DMSO/$(py)_2CO$ chemistry [14]. These researchers concluded that the κ^2N,O coordination mode of the $(py)_2CO$ ligand is *kinetically* favourable, while the κ^2N,N' mode is the *thermodynamically* stable ligation mode. Thus, when the reaction mixture in MeCN was maintained under reflux for 24 h its colour changed progressively from yellow to orange, bypassing the precipitation

Table 1
Crystallographic data for complexes **1**, **2**·2MeCN and **3.**

Parameter	**1**	**2**·2MeCN	**3**
Formula[a]	$C_{64}H_{46}Mn_3N_4O_{14}$	$C_{68}H_{52}Mn_3N_6O_{14}$	$C_{72}H_{56}Mn_4N_8O_{16}$
M	1259.86	1341.98	1509.03
Crystal size (mm)	0.15 × 0.25 × 0.50	0.10 × 0.25 × 0.50	0.10 × 0.20 × 0.50
Crystal system	triclinic	triclinic	tetragonal
Space group	$P\bar{1}$	$P\bar{1}$	I-42d
a(Å)	12.086(4)	14.328(10)	14.564(10)
b(Å)	11.481(4)	10.957(9)	14.564(10)
c(Å)	11.771(4)	11.197(9)	38.27(3)
α(°)	80.92(1)	99.58(3)	90.00(0)
β(°)	68.34(1)	109.05(2)	90.00(0)
γ(°)	69.73(1)	99.47(3)	90.00(0)
V(Å^3)	1423.2(8)	1593(2)	8117(11)
Z	2	2	4
T/K	293(2)	293(2)	298(2)
$2\theta_{max}$(°)	50.00	48.02	50.00
λ/Å[b]	0.71073	0.71073	0.71073
$\rho_{calc.}$/(g cm^{-3})	1.470	1.399	1.235
μ (mm^{-1})	0.728	0.656	0.671
Measd./ independent reflns. (R_{int})	5267/ 4992(0.0100)	5309/ 5008(0.0355)	3881/ 3579(0.0189)
Obsd. reflns. [$I > 2\sigma(I)$]	3998	3620	2819
R_1[c]	0.0473	0.0448	0.0560
wR_2[d]	0.1223	0.1099	0.1861
GOF on F^2	1.108	1.095	1.124
$(\Delta\rho)_{max,min}$/(e Å^{-3})	0.862,−0.475	0.369,−0.275	0.950,−0.376

[a] Including solvate molecules.
[b] Mo-Kα radiation, graphite monochromator.
[c] $R_1 = \sum(|F_o| - |F_c|)/\sum(|F_o|)$ for observed reflections.
[d] $wR_2 = \{\sum[w(F_o^2 - F_c^2)^2]/\sum[w(F_o^2)^2]\}^{1/2}$ for all data.

of the kinetic product **2** and leading to the clean isolation of **1** in good yield (~60%), according to the chemical Eq. (1). For the isolation of **2** we employed a

$$3Mn^{II}(O_2CPh)_2\cdot 2H_2O + 2\ (py)_2CO \xrightarrow[T,24\ h]{MeCN} \underset{\text{orange } \mathbf{1}}{[Mn^{II}_3(O_2CPh)_6\{(py)_2CO\}_2]} + 6H_2O \quad (1)$$

different route. Since compound **2** is the first product that forms (evident from the bright yellow colour of the initial solution), we used nearly saturated solutions of $Mn(O_2CPh)_2\cdot 2H_2O$ and $(py)_2CO$ (1.5:1) in MeCN at room temperature, carefully mixed in order to avoid precipitation of the starting materials. After ~1 h, yellow microcrystals of **2**·2MeCN began to precipitate. The precipitation was interrupted after ~6 h, by filtering the mixture and collecting the polycrystalline material. The formation of **2** is summarized in Eq. (2). The route produced **2** in 30% yield. We could not optimize

$$3Mn^{II}(O_2CPh)_2\cdot 2H_2O + 2\ (py)_2CO \xrightarrow[RT,6\ h]{MeCN} \underset{\text{yellow } \mathbf{2}}{[Mn^{II}_3(O_2CPh)_6\{(py)_2CO\}_2]} + 6H_2O \quad (2)$$

the procedure, because after ~6 h the first crystals of **1** appeared. Once formed and isolated, the orange complex **1** does not transform into **2** in MeCN even though the reaction mixture is stirred or refluxed overnight.

The pure complex **3** was easily prepared by the 1:1 (this ratio was adopted after the crystal structure solution of this cluster) reaction between $Mn(O_2CPh)_2\cdot 2H_2O$ and $(py)_2CO$ in CH_2Cl_2 containing few drops of H_2O (<0.5 ml). The obtained colourless solution was layered with *n*-hexane to afford the product in almost quantitative yields (~90%). The formation of the tetranuclear cluster is summarized in Eq. (3). The

$$4\ Mn^{II}(O_2CPh)_2\cdot 2H_2O + 4\ (py)_2CO \xrightarrow{\text{"wet" } CH_2Cl_2} \underset{\text{colourless } \mathbf{3}}{[Mn^{II}_4(O_2CPh)_4\{(py)_2C(OH)O\}_4]} + 4\ PhCO_2H + 4H_2O \quad (3)$$

excess benzoates act as a base facilitating the single deprotonation of the *gem*-diol form of the ligand. This reaction represents a general synthetic method for the isolation of $Mn^{II}/\{(py)_2C(OH)O^-/RCO_2^-$ cubanes irrespective of the nature of R [15]. Complex **3** is the only product that can be isolated from the $Mn(O_2CPh)_2\cdot 2H_2O/(py)_2CO$ reaction mixtures in "wet" CH_2Cl_2 even if basic and/or oxidizing conditions are applied (albeit in lower yields) stressing its great thermodynamic stability. The latter can be attributed to the formation of four intramolecular H bonds, typical for all $(py)_2C(OH)O^-/RCO_2^-$-based 3d metal cubanes; in addition, all the 12 phenyl and pyridyl rings present in the molecule of **3** interact in pairs forming intramolecular π–π stacking interaction, which also provide stability. In spite of this stability, recent results from our group indicate that complex **3** can be oxidized and hydrolyzed under very strong conditions forming mixed-valence Mn_8 and Mn_{20} clusters, fragments of which are structurally related to **3** [16].

Complexes **1** and **2** react spontaneously with H_2O and undergo partial oxidation by the atmospheric oxygen in MeCN giving a mixture of **3** and **4**, as expected. *Assuming* a 3:1 molar ratio of the products, such a reaction can be represented by the balanced Eq. (4):

$$6[\underset{\mathbf{1}\text{ or }\mathbf{2}}{Mn_3(O_2CPh)_6\{(py)_2CO\}_2}] + 13H_2O + 4MeCN + \frac{1}{2}O_2 \xrightarrow{MeCN} 3[\underset{\mathbf{3}}{Mn_4(O_2CPh)_4\{(py)_2C(OH)O\}_4}] + [\underset{\mathbf{4}}{Mn_6O_2(O_2CPh)_{10}(MeCN)_4}] + 14PhCO_2H \quad (4)$$

3.2. Vibrational spectra

The IR spectrum of **1** shows a strong band at 1710 cm^{-1}, suggesting that the organic ligand is present in its ketone form [11,17]. This mode is situated at higher wavenumber than that in the spectrum of free $(py)_2CO$ (1684 cm^{-1}), confirming the non-participation of the ketone group in coordination in complex **1**. The low wavenumber (1640 cm^{-1}) for the ν(C=O) vibration in the IR spectrum of the yellow isomer **2** is due to the carbonyl oxygen coordination. The ν(C=O) mode appears as a medium-intensity peak at 1679 and 1638 cm^{-1} in the Raman spectra of **1** and **2**, respectively. The IR spectrum of **3** does not exhibit a band in the region for the carbonyl stretching vibration as expected, with the nearest band at 1596 cm^{-1} which can be assigned as a pyridyl stretching mode [this band has also a $\nu_{as}(CO_2)$ character] raised from 1582 cm^{-1}, as observed earlier [18] upon complex formation involving hydration of $(py)_2CO$.

In the IR spectrum of **3**, the strong band at 1390 cm^{-1} is assigned to the $\nu_s(CO_2)$ mode (the corresponding Raman peak appears at 1397 cm^{-1}). The difference Δ, where $\Delta = \nu_{as}(CO_2) - \nu_s(CO_2)$, is 1596–1390 = 206 cm^{-1}; the value of this parameter is larger than that for NaO_2CPh (184 cm^{-1}), as expected [19] for the monodentate mode of carboxylate ligation. In the IR spectrum of **1** the bands at 1602 and 1560 cm^{-1} are assigned to $\nu_{as}(CO_2)$, both features undoubtedly representing two overlapping bands; the $\nu_s(CO_2)$ modes appear at 1432 and 1386 cm^{-1}. The appearance of two distinct bands for each mode reflects the presence of two different types of $PhCO_2^-$ groups in the complex (vide infra). The 1602, 1386 cm^{-1} (Δ = 216 cm^{-1}) pair are assigned [19,20] to the $\eta^1{:}\eta^2{:}\mu_2$ benzoate, while the 1560, 1432 cm^{-1} pair (Δ = 128 cm^{-1}) to the bidentate bridging ($\eta^1{:}\eta^1{:}\mu_2$) benzoates (vide infra). An analogous spectral situation is seen in **2**, with the 1596, 1384 cm^{-1} (Δ = 212 cm^{-1}) pair representing the monoatomically-bridged $\eta^1{:}\eta^2{:}\mu_2$ $PhCO_2^-$ group, and the 1546, 1408 cm^{-1} (Δ = 138 cm^{-1}) the bidentate bridging $PhCO_2^-$ ligands.

3.3. Description of structures

The molecular structures of complexes **1–3**, are depicted in Figs. 1–3. Selected interatomic distances and angles are listed in Tables 2–4.

Complex **1** crystallizes in the triclinic space group $P\bar{1}$. Its crystal structure consists of trinuclear $[Mn_3(O_2CPh)_6\{(py)_2CO\}_2]$ molecules. The central metal center [Mn(2)] is located on a crystallographic inversion center and thus the trinuclear molecule adopts a linear structure. Mn(2) is coordinated by six oxygen atoms belonging to six $PhCO_2^-$ groups. One $\eta^1{:}\eta^2{:}\mu_2$ and two *syn*, *syn*- $\eta^1{:}\eta^1{:}\mu_2$ carboxylate groups span each pair of neighbouring Mn^{II} atoms. The terminal metal ions [Mn(1), Mn(1′)] are each capped by one bidentate chelating - *N*,*N*′ (κ^2*N*,*N*′) $(py)_2CO$ ligand (Scheme 2).

The $Mn(2)O_6$ octahedron is almost perfect with the Mn(2)—O bond lengths and the *cis* O—Mn(2) —O bond angles being in the ranges 2.133(2)–2.214(2) Å and 86.8–93.2(1)°, respectively. The $Mn(1)N_2O_4$ octahedron is distorted; the main distortion arises from the acute O(6)—Mn(1)—O(7) angle [56.8(1)°]. TheMn—N and Mn—O bond lengths agree well with values expected for octahedral high-spin Mn^{II} complexes [4,17,21]. The C(6)–O(1) bond distance [1.210(6) Å] is typical for a carbon–oxygen double bond [14]. The coordination of the bridging benzoate oxygen [O(6), O(6')] is slightly pyramidal [$\sum$°O(6) = 346.2°]. The Mn(1)–O(6)–Mn(2) angle is 105.9(1)°.

The six-membered chelating ring Mn(1)NCCCN adopts a slightly boat conformation with the Mn(1) and C(6) atoms 0.032 and 0.099 Å, respectively, below the plane defined by the remaining

four atoms. The dihedral angle between the two pyridyl rings of the $(py)_2CO$ ligand is 10.0°.

Complex **2**·2MeCN crystallizes also in the triclinic space group $P\bar{1}$. Its crystal structure consists of centrosymmetric trinuclear $[Mn_3(O_2CPh)_6\{(py)_2CO\}_2]$ molecules and solvate MeCN molecules; the latter will not be further discussed. The structure of the trinuclear molecule that is present in **2**·2MeCN is similar to that present in **1**. The main differences are: (i) The termini of the $\{Mn(O_2CPh)_3Mn(O_2CPh)_3Mn\}$ unit in the former are each capped by the bidentate chelating - *N,O* (κ^2*N,O*) $(py)_2CO$ ligand (Scheme 2); (ii) the Mn(1)NO_5 octahedron in **2**·2MeCN is more distorted than the corresponding Mn(1)N_2O_4 polyhedron in **1**. For example, the average value of the three *trans* coordination angles around Mn(1) is 154.1(1)° in **2**·2MeCN compared to 161.3(1)° in **1**. The more severe distortions in the former arise from the acute O(6)–Mn(1)–O(7) angle of 57.5(1)° (such an acute angle is also present in the structure of **1**) and the five-membered chelating ring Mn(1)NCCO with a narrow N(1)–Mn(1)–O(1) angle [70.4(1)°]; and (iii) the intraligand pyridyl ring angle is considerably larger in **2**·2MeCN (49.6°) than in **1** (10.0°); this is a consequence of the different coordination modes of the ligand.

An exciting structural feature of **2**·2MeCN is the κ^2*N,O* ligation mode of $(py)_2CO$, see Scheme 2. Complex **2**·2MeCN is only the third structurally characterized example of a metal complex that contains $(py)_2CO$ in its κ^2*N,O* coordination mode; the previous two examples are complex *trans* (Cl), *cis* (S)-$[Ru^{II}Cl_2\{(py)_2CO\text{-}\kappa^2N,O\}(DMSO\text{-}S)_2]$ [14] and the organometallic compound $[(\eta^5\text{-}C_5H_5)Rh\{(py)_2CO\text{-}\kappa^2N,O\}]$ [22]. The κ^2*N,N'* mode is the familiar coordination mode of $(py)_2CO$ in complexes containing this ligand in its ketone form [5,11,14,23].

Complexes **1** and **2**·2MeCN are linkage isomers. This is the first case of true linkage isomerism in the coordination chemistry of $(py)_2CO$. Toyama et al. have recently studied the complexes *cis* (Cl), *cis* (S)-$[Ru^{II}Cl_2\{(py)_2CO\text{-}\kappa^2N,N'\}(DMSO\text{-}S)_2]$ and (the above mentioned) *trans* (Cl), *cis* (S)-$[Ru^{II}Cl_2\{(py)_2CO\text{-}\kappa^2N,O\}(DMSO\text{-}S)_2]$ [14], which can be considered as linkage isomers; however, these complexes also exhibit geometrical isomerism.

Complexes **1** and **2**·2MeCN join a small family of structurally characterized, trinuclear complexes containing the $[Mn^{II}_3(\eta^1{:}\eta^1{:}\mu_2\text{-}O_2CR)_4(\eta^1{:}\eta^2{:}\mu_2\text{-}O_2CR)_2]^0$ core [21,24]. The benzoate members of this family are listed in Table 5. Such complexes have been important in the establishment of the "carboxylate shift" concept [25]. Of the various types of metal-carboxylate binding modes,

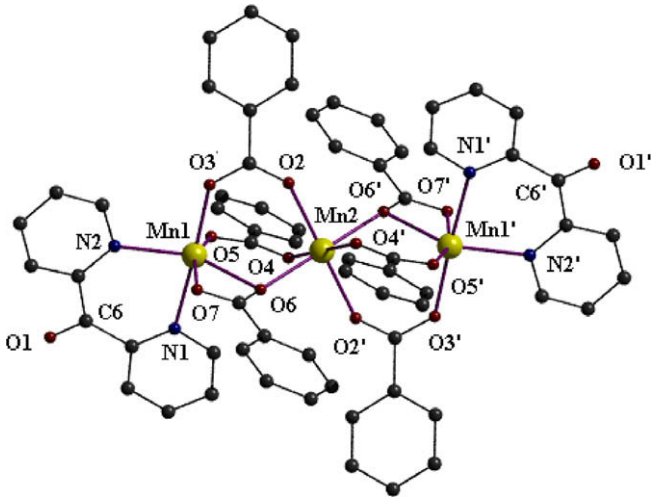


Fig. 1. Partially labeled plot of the molecular structure of complex **1**. Primes are used for symmetry related (−*x*, −*y*, −*z* +1) atoms.

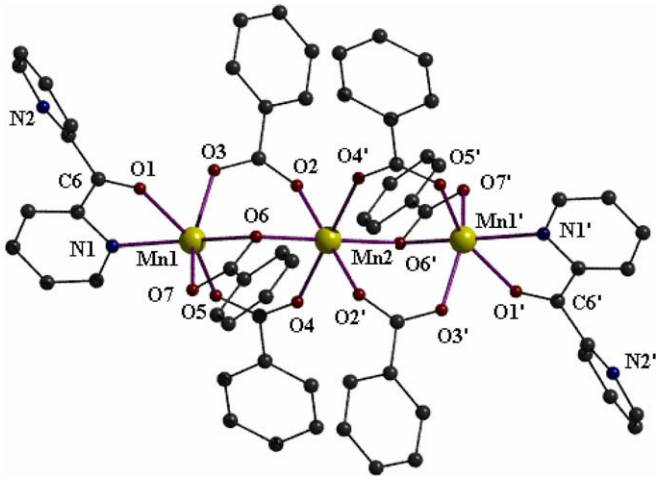


Fig. 2. Partially labeled plot of the linear trinuclear molecule present in complex **2**·2MeCN. Primes are used for symmetry related (−*x*, −*y*, −*z*) atoms.

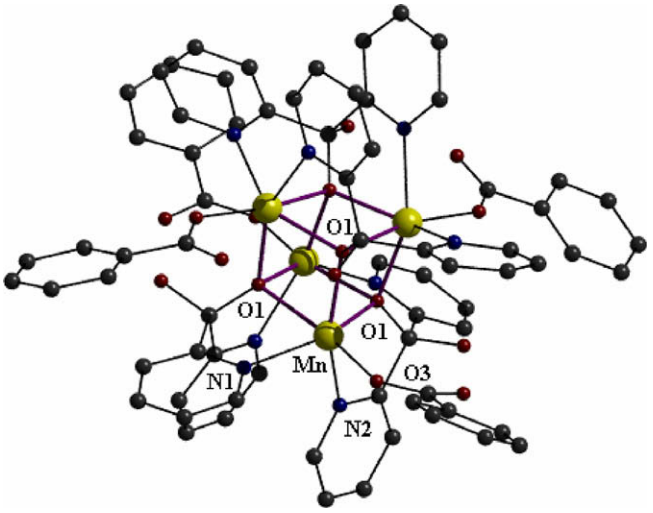


Fig. 3. Partially labeled plot of the cubane molecule present in complex **3**. Only the donor atoms of one Mn^{II} center are labeled. O(1) is the donor atom of the $(py)_2C(OH)O^-$ ligand, while O(3) is the coordinated oxygen atom of the $PhCO_2^-$ group.

Table 2
Selected interatomic distances (Å) and angles (°) for complex **1**.

Interatomic distances			
Mn(1)...Mn(2)	3.552(2)	Mn(1)–O(6)	2.238(2)
Mn(1)–N(1)	2.304(3)	Mn(1)–O(7)	2.346(3)
Mn(1)–N(2)	2.240(3)	Mn(2)–O(2)	2.133(2)
Mn(1)–O(3)	2.116(2)	Mn(2)–O(4)	2.137(3)
Mn(1)–O(5)	2.093(3)	Mn(2)–O(6)	2.214(2)
Bond angles			
N(1)–Mn(1)–N(2)	83.7(1)	O(3)–Mn(1)–O(5)	91.5(1)
N(1)–Mn(1)–O(3)	174.4(1)	O(3)–Mn(1)–O(6)	96.4(1)
N(1)–Mn(1)–O(5)	84.1(1)	O(3)–Mn(1)–O(7)	94.7(1)
N(1)–Mn(1)–O(6)	88.3(1)	O(5)–Mn(1)–O(6)	106.4(1)
N(1)–Mn(1)–O(7)	90.5(1)	O(5)–Mn(1)–O(7)	162.6(1)
N(2)–Mn(1)–O(3)	94.1(1)	O(6)–Mn(1)–O(7)	56.8(1)
N(2)–Mn(1)–O(5)	104.6(1)	O(2)–Mn(2)–O(4)	86.8(1)
N(2)–Mn(1)–O(6)	147.0(1)	O(2)–Mn(2)–O(6)	91.1(1)
N(2)–Mn(1)–O(7)	91.2(1)	O(4)–Mn(2)–O(6)	91.5(1)

Table 3
Selected interatomic distances (Å) and angles (°) for complex **2** · 2MeCN.

Interatomic distances			
Mn(1)...Mn(2)	3.573(2)	Mn(1)–O(6)	2.322(3)
Mn(1)–N(1)	2.260(3)	Mn(1)–O(7)	2.208(3)
Mn(1)–O(1)	2.311(3)	Mn(2)–O(2)	2.136(3)
Mn(1)–O(3)	2.089(3)	Mn(2)–O(4)	2.142(3)
Mn(1)–O(5)	2.070(3)	Mn(2)–O(6)	2.272(3)
Bond angles			
N(1)–Mn(1)–O(1)	70.4(1)	O(3)–Mn(1)–O(6)	92.0(1)
N(1)–Mn(1)–O(3)	100.2(1)	O(3)–Mn(1)–O(7)	145.8(1)
N(1)–Mn(1)–O(5)	90.1(1)	O(5)–Mn(1)–O(6)	105.7(1)
N(1)–Mn(1)–O(6)	156.4(1)	O(5)–Mn(1)–O(7)	97.0(1)
N(1)–Mn(1)–O(7)	104.1(1)	O(6)–Mn(1)–O(7)	57.5(1)
O(1)–Mn(1)–O(3)	81.2(1)	O(2)–Mn(2)–O(4)	88.6(1)
O(1)–Mn(1)–O(5)	160.2(1)	O(2)–Mn(2)–O(6)	89.5(1)
O(1)–Mn(1)–O(6)	91.9(1)	O(4)–Mn(2)–O(6)	90.6(1)
O(1)–Mn(1)–O(7)	84.7(1)	Mn(1)–O(6)–Mn(2)	102.2(1)
O(3)–Mn(1)–O(5)	106.7(1)		

Table 4
Selected interatomic distances (Å) and angles (°) for complex **3**.

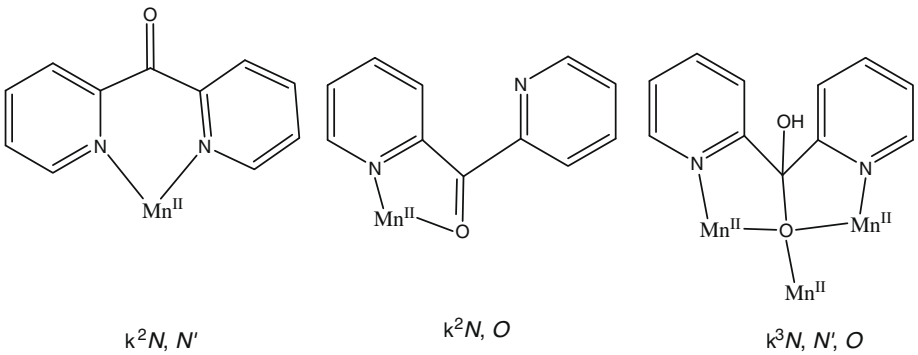
Interatomic distances		Bond angles	
Mn...Mn	3.353(2), 3.445(2)	N(1)–Mn–N(2)	93.8(2)
Mn–N(1)	2.250(6)	N(1)–Mn–O(1)	71.6(2), 109.0(2), 146.0(2)
Mn–N(2)	2.273(5)	N(1)–Mn–O(3)	96.2(2)
Mn–O(1)	2.170(4), 2.178(4), 2.327(4)	N(2)–Mn–O(1)	72.3(2), 98.2(2), 154.3(2)
Mn–O(3)	2.086(5)	N(2)–Mn–O(3)	90.4(2)
		O(1)–Mn–O(3)	98.4(2), 114.3(2), 165.4(2)
		O(1)–Mn–O(1)	78.8(1), 79.8(1), 82.1(1)
		Mn–O(1)–Mn	96.4(1), 99.7(1), 100.9(2)

monodentate (monoatomic) bridging between metal centers offers great flexibility. Analysis [25] of the structural features of discrete complexes containing monodentate/monoatomic bridging carboxylates shows that they can be grouped into three classes, depending upon the strength of the interaction of the non-bridging, or dangling (O_d), oxygen atom [O(7) in complexes **1** and **2**·2MeCN] with one of the bridged metal ions [Mn(1) in **1** and **2**·2MeCN]. The application of this analysis to trinuclear Mn^{II} benzoate complexes is demonstrated in Scheme 3 and Table 5. The monoatomic bridging mode is postulated to be an important intermediate between the other, more common carboxylate attachment modes, based on observed variation of the geometry for monoatomic bridges in structurally characterized metal complexes. The movement from monoatomic bridging to the other binding modes has been termed the "carboxylate shift" [25]; such a shift is considered to be kinetically important in carboxylate-containing metalloproteins. Complex **2**·2MeCN is characterized by a small *D* value, $B > D$, a rather long Mn...Mn distance, a small difference between $C–O_d$ and $C–O_b$ (indicating significant delocalization of the double bond), a large tilt ($\alpha-\beta$) of the $\eta^1:\eta^2:\mu_2$ carboxylate group toward Mn(1) and the significant distortion of the coordination geometry of Mn(1). Thus, compound **2**·2MeCN has a strong interaction between Mn(1) and O_d, i.e. O(7), and can be placed in class III in Lippard's classification scheme [25]. Based on analogous arguments, complex **1** is placed in class II in the "carboxylate shift" classification scheme.

Complex **3** crystallizes in the tetragonal space group *I*-42*d*. Its structure consists of tetranuclear $[Mn_4(O_2CPh)_4\{(py)_2C(OH)O\}_4]$ molecules. The molecule of **4** lies on an inverse four-fold axis (S_4 symmetry) and the asymmetric unit contains a quarter of the cluster molecule. The tetranuclear molecule has a cubane $[Mn^{II}_4(\mu_3\text{-}OR')_4]^{4+}$ core with Mn^{II} atoms and μ_3-O atoms occupying alternate vertices. Thus, the molecule consists of two interpenetrating tetrahedra: one of four μ_3-O atoms originating from the $(py)_2C(OH)O^-$ ions and one of four Mn^{II} atoms. In addition to three μ_3-O atoms, each Mn^{II} center is coordinated to two N atoms that belong to two different $(py)_2C(OH)O^-$ ligands and to one O atom that belongs to a monodentate $PhCO_2^-$ group. Thus, the chromophore is $Mn^{II}N_2O_4$. One octahedral face of each Mn^{II} atom is occupied by the three alkoxide-type O atoms and the other consists of the remaining donor atoms.

One O atom of each $(py)_2(OH)O^-$ ligand remains protonated and unbound to the metals. The resultant monoanion functions as a κ^3N,N',O (or $\eta^1:\eta^1:\eta^3:\mu_3$) ligand forming two five-membered MnNCCO chelating rings with two different Mn^{II} atoms (these rings share a common C—O edge) and an alkoxide-type bond to a third metal ion (Scheme 2). This ligation mode is common in the coordination chemistry of hydrated di-2-pyridyl ketone [5].

The Mn_4 tetrahedron is distorted by compression along an S_4 axis and this gives four shorter Mn^{II}...Mn^{II} distances (3.353 Å) and two longer (3.445 Å). There are two types of Mn—O(alkoxide-type) bonds for each Mn^{II} atom: one bond is long (2.327 Å), whereas the two other bonds are shorter (average 2.174 Å). The cube deviates from the ideal geometry. The internal cube angles at the metal vertices (R'O–Mn–OR') average 80.2°, whereas the corresponding angles at the alkoxide corners (Mn–OR'-Mn) are considerably larger averaging 99.0°. An ideal cubane has twelve equal bond lengths and twenty four bond angles at 90°. Such an ideal situation is not encountered in practice, notably because three bonds at 90° are rarely observed at the bridging O atom. An sp^3 hybridized O atom would have three angles at 109.5°, and this may be achieved by compressing the four oxygens along the body diagonals of the cube

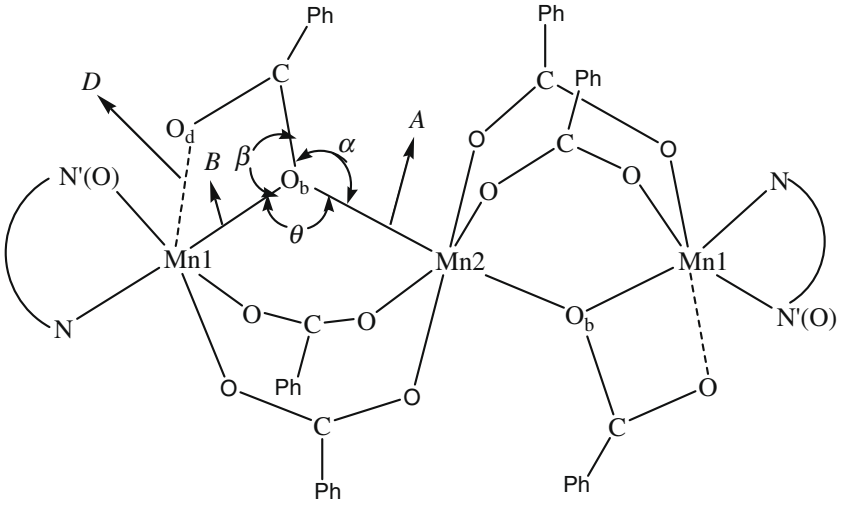


Scheme 2. The crystallographically established coordination modes of the ligands $(py)_2CO$ and $(py)_2C(OH)O^-$ in complexes **1–3**.

Table 5
Pertinent structural properties[a] for trinulear Mn^{II} complexes containing the $[Mn^{II}_3(\eta^1{:}\eta^1{:}\mu_2\text{-}O_2CPh)_4(\eta^1{:}\eta^2{:}\mu_2\text{-}O_2CPh)_2]^0$ core.

Complex	*B*(Å)	*D*(Å)	*A*(Å)	Mn–Mn (Å)	C–O_b(Å)	C–O_d(Å)	θ(°)	β(°)	α(°)
$[Mn_3(O_2CPh)_6(bpy)_2]$[b]	2.285	2.274	2.239	3.588	1.284	1.257	104.9	90.5	135.0
$[Mn_3(O_2CPh)_6\{(py)(ph)CO\}_2]$[c]	2.261	2.249	2.240	3.603	1.275	1.247	106.3	90.3	140.2
$[Mn_3(O_2CPh)_6\{(py)CO\}_2]$(**1**)[d]	2.238	2.346	2.214	3.552	1.278	1.246	105.9	93.6	146.7
$[Mn_3(O_2CPh)_6\{(py)CO\}_2]\cdot 2MeCN$ (**2**·2MeCN)[d]	2.322	2.208	2.272	3.573	1.259	1.246	102.2	87.6	135.3

Abbreviations: bpy = 2,2'-bipyridine; (py)(ph)CO=phenyl 2-pyridyl ketone.
[a] See Scheme 3 for the definition of the structural parameters given in this table.
[b] Ref. [24f].
[c] Ref. [21].
[d] This work.



Scheme 3. The schematic structures of complexes **1** and **2** · 2MeCN showing the dangling (O_d) and bridging (O_b) oxygen atoms of the $\eta^1{:}\eta^2{:}\mu_2$ carboxylate groups of the benzoate ligands, and defining the geometry of monoatomic carboxylate-bridged polymetallic centers in relation to the "carboxylate shift" mechanism proposed by Lippard [25]; the values of the relevant structural parameters for **1** and **2** · 2MeCN and other trinuclear complexes containing the $[Mn^{II}_3(\eta^1{:}\eta^1{:}\mu_2\text{-}O_2CPh)_4(\eta^1{:}\eta^2{:}\mu_2\text{-}O_2CPh)_2]^0$ core are listed in Table 5.

(tetrahedral distortion), increasing the angles at oxygen, but concurrently decreasing the angles at the metal below 90°. The magnitude of this effect may be measured by calculating the sum of the angles at an oxygen vertex, the value for an ideal cubane being 270° and that for an sp^3 oxygen 328.5° [26]. In the case of **3**, this sum is 297.0°. The ratio of the mean O...O distance to the mean Mn...Mn distance may be also taken as a measure of the tetrahedral distortion; a value of one is expected for a perfect cube [26]. This ratio is 0.85 for **3.**

There are several secondary interactions within the cubane molecule that justify its extreme stability towards further reactivity. These are conveniently summarized in Table 6 and shown in Fig. 4. Four, symmetry related H bonds form, with the protonated O atom of the $(py)_2C(OH)O^-$ ligand as the donor and the uncoordinated O atom of the monodentate $PhCO_2^-$ group as the acceptor. In addition, the aromatic rings of the molecule stack in six pairs through π–π interactions [27]. These interactions are of two types: four interactions are between one pyridyl ring of a $(py)_2C(OH)O^-$ ligand and the aromatic ring of the $PhCO_2^-$ group and two between pyridyl rings of adjacent $(py)_2C(OH)O^-$ ligands, with the former being weaker than the latter. By contrast with its $MeCO_2^-$ analogue $[Mn_4^{II}(O_2CMe)_4\{(py)_2C(OH)O\}_4]$ [4], which lacks the four Ph...py interactions, complex **3** is thermodynamically stable being the only product from the $Mn^{II}/PhCO_2^-$ /$(py)_2CO$ system in H_2O-containing organic solvents, whereas the acetate cluster is readily oxidized and hydrolyzed to afford cluster $[Mn_{10}^{II}Mn_4^{III}O_4(O_2CMe)_{20}\{(py)_2C(OH)O\}_4]$; the structure of the latter is based on cubane subunits [4].

A few Mn^{II} cubanes containing the $[Mn_4^{II}(\mu_3\text{-}OR')_4]^{4+}$ core have been reported previously [4,17,28,29]. Complexes **1–3** join a handful of structurally characterized Mn complexes containing various forms of $(py)_2CO$ as ligands [4,28f,30].

3.4. EPR and magnetic studies

At 300 K, the X-band EPR spectra of **1** and **2**·2MeCN are very broad (more than 4000 G). At 10 K, fine structure is resolved, while at 4 K the two spectra are similar and quite complicated with resonances at $g = \sim 6.3$, ~3.4, ~2.0 and ~1.7. This indicates that the populated spin state at 4 K exhibits zero-field splitting [24b,24c]. If the ZFS effects were negligible, i.e., $|J| > |A|$ (A is the hyperfine splitting parameter), a narrow signal would be expected with g around 2. However, if the ZFS is considerable, this signal should be split into several features, and thus signals at low fields may be observed, as found here.

Variable-temperature dc magnetic susceptibility data were collected on a powdered microcrystalline sample of **3** (Fig. 5) in the temperature range 300-5 K under an applied field of 0.1 T. The room temperature $\chi_M T$ value is 16.5 $cm^3\,mol^{-1}\,K$, slightly lower than the expected value of 17.5 $cm^3\,mol^{-1}\,K$ for four $S = 5/2$ uncoupled spin carriers with $g = 2$. The $\chi_M T$ product remains practically constant down to 50 K and then decreases sharply upon further cooling, reaching a value of 5.57 $cm^3\,mol^{-1}\,K$ at 5 K. This behaviour is indicative of weak antiferromagnetic exchange interactions between the Mn^{II} centers [4,17,28d,28h]. Since the spin carriers are all d^5 Mn^{II} atoms, and therefore orbital

Table 6
Intracubane hydrogen bonding and π–π staking details for complex **3.**

D-H...A *H-bonds*[a]	D...A [Å]	H...A [Å]	DHA [°]
O[(py)$_2$C(OH)O$^-$]-H...O(PhCO$_2^-$)	2.693	1.884	168.3

Interaction	Centroid...Centroid [Å]	Plane...Plane [Å]	Displacement angle [°][b]	Plane...Plane angle [°]
π–π interactions				
Ph...Py	4.368	3.376	18.4	16.8
Py...Py	3.632	3.093	22.1	16.7

[a] A = acceptor; D = donor.
[b] The angle between the ring normal and the vector that connects the ring centroids.

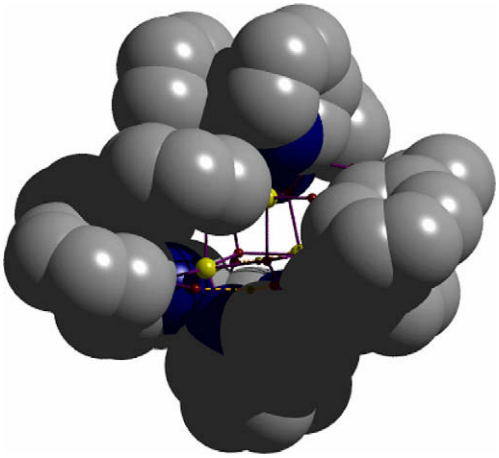


Fig. 4. The secondary intramolecular interactions of **3**. The π–π interacting pairs are shown as space-filling models, while some H bonds are depicted as dotted lines.

singlet (S) ions, only the isotropic part of the exchange interaction was considered.

When a symmetrical spin Hamiltonian with all coupling constants assumed to be equal was applied, the high temperature data could not be reproduced. The actual S_4 symmetry of the complex was taken into account in order to find a more accurate Hamiltonian. This suggested the use of the spin Hamiltonian given in Eq. (5). The J_1

$$H = -2J_1(S_1S_2 + S_1S_4 + S_2S_3 + S_3S_4) - 2J_2(S_1S_3 + S_2S_4) \quad (5)$$

parameter was attributed to the four shorter Mn^{II}...Mn^{II} distances of 3.353 Å with corresponding Mn–O(1)–Mn angles of 96.4 and 100.9°. The J_2 parameter was attributed to the two longer Mn^{II}...Mn^{II} distances of 3.445 Å with corresponding Mn–O(1)–Mn angles of 99.7°. The exchange interaction model used is illustrated in Scheme 4. The simulation was performed using the program MAGPACK [31]. The best fit parameters are J_1 = -0.25 cm^{-1}, J_2 = -0.10 cm^{-1} and g = 1.97. The ground state of the complex was found to be S = 0, with S = 1 and S = 2 excited states 0.6 and 1.8 cm^{-1} above the ground state, respectively. Any ZFS together with the close spacing of the S levels and their Zeeman M_S components when in an applied magnetic field, make the calculation of the magnetization, M, very difficult to achieve by use of the DS_Z^2-type spin Hamiltonians [28h]. Previous detailed studies [28c] have shown that small D values ($-0.5 \leqslant D \leqslant 0.5$ cm^{-1}) have essentially no effect on the $\chi_M T$ vs. T plots for such Mn$_4^{II}$ systems.

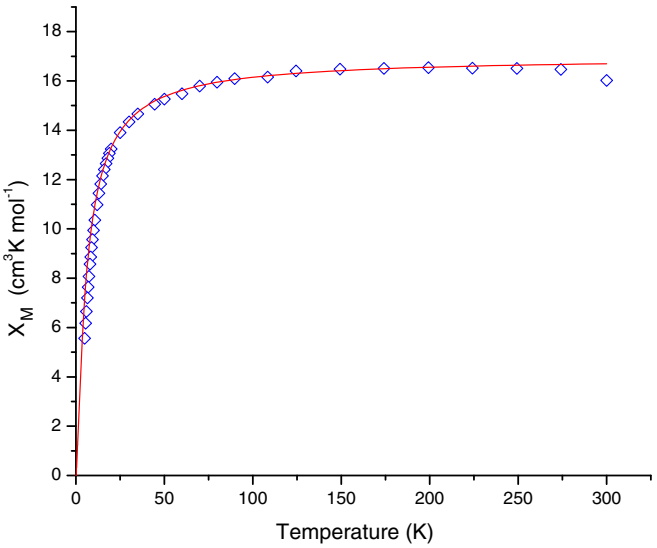
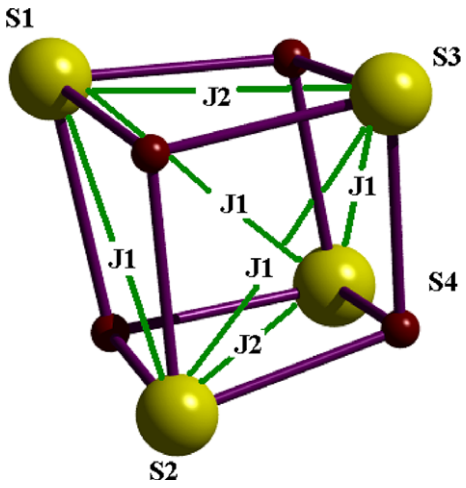


Fig. 5. Plot of $\chi_M T$ vs. T for a powdered sample of complex **3**. The solid line represents the simulation of the experimental data.



Scheme 4. Exchange interaction model used for **3**.

The weak antiferromagnetic J values for **3** are within the narrow range (from −0.10 to −4.11 cm^{-1}) reported for other cubane complexes containing the [Mn$_4^{II}$ (μ_3-OR')$_4$]$^{4+}$ core [4,17,28b,28d,28f–h,29b]. In particular, the J values are close to those (−0.10 and −0.19 cm^{-1}) of the structurally similar complex [Mn$_4^{II}$ (O_2CMe)$_4$ {(py)$_2$C(OH)O}$_4$] [4].

The X-band powder EPR spectrum of **3** at 1.8 K exhibits an almost featureless broad resonance with a $g \sim 2$-value. The broadness of the isotropic absorption is consistent with the presence of magnetically interacting Mn^{II} centers in the solid state [32].

4. Concluding comments

The present work extends the body of results that emphasize the ability of (py)$_2$CO-based ligands to form new structural types in 3d-metal chemistry. The employment of (py)$_2$CO in reactions with Mn(O_2CPh)$_2$·2H_2O has provided access to three neutral Mn^{II} complexes, two novel Mn$_3^{II}$ linkage isomers and one Mn$_4^{II}$ cubane. The trinuclear complexes are reactive and transform into the cubane cluster and a known mixed-valent, (py)$_2$CO-free Mn$_4^{II}$Mn$_2^{III}$ cluster. The intramolecular H-bonding and π–π stacking interactions that are present in the cubane are considered responsible for its great stability towards reactivity. This work demonstrates the flexibility, versatility and synthetic potential of combining (py)$_2$CO with carboxylate ligands. We currently explore synthetic methods

for isolating Mn^{II} benzoate clusters that involve the dianionic ligand $(py)_2CO_2^{2-}$ and for preparing Mn^{III} (or $Mn^{II/III}$) benzoate clusters that contain various forms of $(py)_2CO$.

Supplementary data

Crystallographic data in CIF format have been deposited at the Cambridge Crystallographic Data Center with CCDC Nos. 660964; 660965 and 660966 for **1**, **2**·2MeCN and **3**, respectively. Copies of this information may be obtained free of charge from The Director, CCDC, 12 Union Road, Cambridge, CB2 1EZ, UK (Fax: +44 1223 336033; e-mail: deposit@ccdc.cam.ac.uk or http://www.ccdc.cam.ac.uk). Supplementary data associated with this article can be found, in the online version, at doi:xxx.

Acknowledgements

This work was supported by the EPSRC and Leverhulme Trust (to E.K.B.), and by the Operation and Vocational II (EPEAEK II) and particularly the program PYTHAGORAS (Grant b. 365.037 to S.P.P).

References

[1] (a) For recent reviews see J. Barber, J.W. Murray, Coord. Chem. Rev. 252 (2008) AA233;
(b) C.S. Mullins, V.L. Pecoraro, Coord. Chem. Rev. 252 (2008) 416.
[2] (a) For example, see A.M. Ako, I.J. Hewitt, V. Mereacre, R. Clérac, W. Wernsdorfer, C.E. Anson, A.K. Powell, Angew. Chem., Int. Ed. 45 (2006) 4926;
(b) Th.C. Stamatatos, K.A. Abboud, W. Wernsdorfer, G. Christou, Angew. Chem., Int. Ed. 46 (2007) 884.
[3] (a) For reviews, see G. Aromi, E.K. Brechin, Struct. Bonding 122 (2006) 1;
(b) D. Gatteschi, R. Sessoli, Angew. Chem., Int. Ed. 42 (2003) 268.
[4] C.C. Stoumpos, I.A. Gass, C.J. Milios, N. Lalioti, A. Terzis, G. Aromi, S.J. Teat, E.K. Brechin, S.P. Perlepes, Dalton Trans. (2009) 307.
[5] For a review, see: G.S. Papaefstathiou, S.P. Perlepes, Comments Inorg. Chem. 23 (2002) 249.
[6] (a) For example, see Y. Li, S. Xiang, T. Sheng, J. Zhang, S. Hu, R. Fu, X. Huang, X. Wu, Inorg. Chem. 45 (2006) 6577;
(b) B.F. Abrahams, T.A. Hudson, R. Robson, Chem. Eur. J. 12 (2006) 7095.
[7] C.C. Stoumpos, I.A. Gass, C.J. Milios, E. Kefalloniti, C.P. Raptopoulou, A. Terzis, N. Lalioti, E.K. Brechin, S.P. Perlepes, Inorg. Chem. Commun. 11 (2008) 196.
[8] M.W. Wemple, H.-L. Tsai, S. Wang, J.P. Claude, W.E. Streib, J.C. Huffman, D.N. Hendrickson, G. Christou, Inorg. Chem. 35 (1996) 6437.
[9] G.M. Sheldrick, SHELXS-86, Structure Solving Problem, University of Göttingen, Germany, 1986.
[10] G.M. Sheldrick, SHELXL-97, program for the Refinement of Crystal Structures from Diffraction Data, University of Göttingen, Germany, 1997.
[11] E. Katsoulakou, N. Lalioti, C.P. Raptopoulou, A. Terzis, E. Manesi-Zoupa, S.P. Perlepes, Inorg. Chem. Commun. 5 (2002) 719.
[12] M.A. Halcrow, W.E. Streib, K. Folting, G. Christou, Acta Crystallogr. C51 (1995) 1263.
[13] Th.C. Stamatatos, D. Foguet-Albiol, S.P. Perlepes, C.P. Raptopoulou, A. Terzis, C.S. Patrickios, G. Christou, A.J. Tasiopoulos, Polyhedron 25 (2006) 1737.
[14] M. Toyama, M. Nakahara, N. Nagao, Bull. Chem. Soc. Jpn. 80 (2007) 937.
[15] C.C. Stoumpos, E.K. Brechin, S.P. Perlepes, unpublished results.
[16] C.C. Stoumpos, C. Lampropoulos, S.P. Perlepes, G. Christou, manuscript in preparation.
[17] G.S. Papaefstathiou, A. Escuer, F.A. Mautner, C. Raptopoulou, A. Terzis, S.P. Perlepes, R. Vicente, Eur. J. Inorg. Chem. (2005) 879.
[18] P.K. Byers, A.J. Canty, L.M. Engelhardt, J.M. Patrick, A.H. White, J. Chem. Soc., Dalton Trans. (1985) 981.
[19] G.B. Deacon, R.J. Phillips, Coord. Chem. Rev. 33 (1980) 227.
[20] (a) S.P. Perlepes, A. Libby, W.E. Streib, K. Folting, G. Christou, Polyhedron 11 (1992) 923;
(b) G. Christou, S.P. Perlepes, E. Libby, K. Folting, J.C. Huffman, R.J. Webb, D.N. Hendrickson, Inorg. Chem. 29 (1990) 3657;
(c) J.-P. Costes, F. Dahan, J.-P. Laurent, Inorg. Chem. 24 (1985) 1018.
[21] C.J. Milios, Th.C. Stamatatos, P. Kyritsis, A. Terzis, C.P. Raptopoulou, R. Vicente, A. Escuer, S.P. Perlepes, Eur. J. Inorg. Chem. (2004) 2885.
[22] C. Godart, S.B. Duckett, S. Parsons, R.N. Perutz, Chem. Commun. (2003) 2332.
[23] (a) For example, see F. Zhang, E.M. Prokopchuk, M.E. Broczkowski, M.C. Jennings, R.J. Puddephatt, Organometallics 25 (2006) 1583;
(b) C. Kanaras, B.L. Westcott, G. Crundwell, J.B. Updegraff III, M. Zeller, A.D. Hunter, S.O. Sommerer, Z. Kristallogr. 219 (2004) 1;
(c) K.N. Crowder, S.J. Garcia, R.L. Burr, J.M. North, M.H. Wilson, B.L. Conley, P.E. Fanwick, P.S. White, K.D. Sienerth, R.M. Granger III, Inorg. Chem. 43 (2004) 72;
(d) S. Zhu, W.W. Brennessel, R.G. Harrison, L. Que Jr., Inorg. Chim. Acta 337 (2002) 32;
(e) G.B. Deacon, C.M. Kepert, N. Sahely, B.W. Skelton, L. Spiccia, N.C. Thomas, A.H. White, J. Chem. Soc., Dalton Trans. (1999) 275;
(f) A.D.Q. Ferreira, A. Bino, D. Gibson, Inorg. Chim. Acta 265 (1997) 155.
[24] (a) D.P. Kessissoglou, Coord. Chem. Rev. 185–186 (1999) 837;
(b) B. Albela, M. Corbella, J. Ribas, I. Castro, J. Sletten, H. Stoeckli-Evans, Inorg. Chem. 37 (1998) 788;
(c) S. Ménage, S.E. Vitols, P. Bergerat, E. Codjovi, O. Kahn, J.-J. Girerd, M. Guillot, X. Solans, T. Calvet, Inorg. Chem. 30 (1991) 2666;
(d) V. Tangoulis, D.A. Malamatari, K. Soulti, V. Stergiou, C.P. Raptopoulou, A. Terzis, Th.A. Kabanos, D.P. Kessissoglou, Inorg. Chem. 35 (1996) 4974;
(e) R.L. Rardin, P. Poganiuch, A. Bino, D.P. Goldberg, W.B. Tolman, S. Li, S.J. Lippard, J. Am. Chem. Soc. 114 (1992) 5240;
(f) J.B. Vincent, G. Christou, Adv. Inorg. Chem. Radiochem. 33 (1989) 197;
(g) R.A. Reynolds III, W.R. Dunham, D. Coucouvanis, Inorg. Chem. 37 (1988) 1232;
(h) K. Tsuneyoshi, H. Kobavashi, H. Miyamae, Acta Crystallogr. 49C (1993) 233.
[25] R.L. Rardin, W.B. Tolman, S.J. Lippard, New J. Chem. 15 (1991) 417.
[26] K. Isele, F. Gigon, A.F. Williams, G. Bernardinelli, P. Franz, S. Decurtins, Dalton Trans. (2007) 332.
[27] C. Janiak, J. Chem. Soc., Dalton Trans. (2000) 3885.
[28] (a) For example, see S. Brooker, V. McKee, W.B. Shepard, L.K. Pannell, J. Chem. Soc., Dalton Trans. (1987) 2555;
(b) J. Aussoleil, P. Cassoux, P. de Loth, J.-P. Tuchagues, Inorg. Chem. 28 (1989) 3051;
(c) K.L. Taft, A. Caneschi, L.E. Pence, C.D. Delfs, G.C. Papaefthymiou, S.J. Lippard, J. Am. Chem. Soc. 115 (1993) 11753;
(d) L.E. Pence, A. Caneschi, S.J. Lippard, Inorg. Chem. 35 (1996) 3069;
(e) S. Brooker, V. McKee, T. Metcalfe, Inorg. Chim. Acta 246 (1996) 171;
(f) M.-L. Tong, S.-L. Zheng, J.-X. Shi, Y.-X. Tong, H.K. Lee, X.-M. Chen, J. Chem. Soc., Dalton Trans. (2002) 1727;
(g) M. Nihei, N. Hoshino, T. Ito, H. Oshio, Chem. Lett. (2002) 1016;
(h) T.A. Hudson, K.J. Berry, B. Moubaraki, K.S. Murray, R. Robson, Inorg. Chem. 45 (2006) 3549.
[29] (a) A.F. Williams, Dalton Trans. (2008) 818;
(b) T. Shiga, H. Oshio, Sci. Techn. Adv. Mater. 6 (2005) 565.
[30] (a) C.M. Zaleski, E.C. Depperman, C. Dendrinou-Samara, M. Alexiou, J.W. Kampf, D.P. Kessissoglou, M.L. Kirk, V.L. Pecoraro, J. Am. Chem. Soc. 127 (2005) 12862;
(b) Th.C. Stamatatos, K.A. Abboud, W. Wernsdorfer, G. Christou, Angew. Chem., Int. Ed. 47 (2008) 6694;
(c) Th.C. Stamatatos, V. Nastopoulos, A.J. Tasiopoulos, E.E. Moushi, W. Wernsdorfer, G. Christou, S.P. Perlepes, Inorg. Chem. 47 (2008) 10081.
[31] (a) J.J. Borrás-Almenar, J.-M. Clemente, E. Coronado, B.S. Tsukerblat, Inorg. Chem. 38 (1999) 6081;
(b) J.-M. Clemente, E. Coronado, B.S. Tsukerblat, J. Comput. Chem. 22 (2001) 985.
[32] (a) A. Gelasco, A. Askenas, V.L. Pecoraro, Inorg. Chem. 35 (1996) 1419;
(b) S. Theil, R. Yerande, R. Chikate, F. Dahan, A. Bousseksou, S. Padhye, J.-P. Tuchagues, Inorg. Chem. 36 (1997) 6279.

Polyhedron 28 (2009) 2026–2028

Contents lists available at ScienceDirect

Polyhedron

journal homepage: www.elsevier.com/locate/poly

Dimethyl sulfoxide oxidation mediated by a copper(II) diamine complex: A possible source of problem in the synthesis of molecular magnetic compounds

Rafael A. Allão [a], Jackeline S. Martins [a], Antonio S. Florencio [a], Guilherme P. Guedes [a], José Walkimar de M. Carneiro [a], Mauricio Lanznaster [a], Sauli Santos Jr [b,c], Maria G.F. Vaz [a,*]

[a] Universidade Federal Fluminense, Departamento de Química Inorgânica, Instituto de Química, Outeiro de São João Batista, 24020-141 Niterói, RJ, Brazil
[b] Universidade Federal do Tocantins, Laboratório de Física, Campus de Palmas, 77020-120 Palmas, TO, Brazil
[c] Universidade Federal de Goiás, Curso de Física, Campus de Jataí, 75804-120 Jataí, GO, Brazil

ARTICLE INFO

Article history:
Available online 23 January 2009

Keywords:
Molecular magnetism
Dimethyl sulfoxide
1D-antiferromagnetic chains
DFT calculations

ABSTRACT

In the present work we report a reaction in which dimethyl sulfoxide, initially used as solvent, undergoes oxidation to form sulfate, which then participates to the formation of a linear one-dimensional copper chain. Indeed, using $[Cu(bipy)Cl_2]$, a building block largely applied in synthesis of molecular magnetic compounds, the coordination compound $[Cu(bipy)(H_2O)_2(SO_4)]_n$, where bipy = 2,2′-bipyridine was obtained. Magnetic characterization of complex shows a weak antiferromagnetic interaction between the copper(II) ions with $J = -0.53\ cm^{-1}$. DFT calculations demonstrate that the pathway for the weak antiferromagnetic interaction is through the sulfate bridge.

© 2008 Elsevier Ltd. All rights reserved.

Dimethyl sulfoxide (DMSO) is a well-known molecule due to its important applications in chemistry and molecular biology. It is largely used as aprotic polar solvent which dissolves a large number of substances, turning it particularly useful in chemical reactions, crystallization processes, chemical analyses, biological studies and in coordination chemistry [1]. Several examples in the literature report the preparation of molecular magnetic compounds using DMSO as the reaction solvent and, in many cases, Cu(II) is the metallic ion involved. As examples, one-dimensional chain [2], two-dimensional [3], interlocked systems [4] and compounds with optical properties [5] have been described. Furthermore, DMSO can also influence the magnetic properties of crystalline compounds [6]. Synthetic chemists usually assume that DMSO is a quite inert solvent for the preparation of coordination compounds. However, when a series of building blocks for molecular magnets were prepared in our laboratories, using copper(II) chloride, diamine ligands and DMSO as the solvent, sulfate containing complexes were obtained. In spite of the large number of papers describing the ability of O_2 activation by copper complexes in solution [7] and the catalytic properties of such complexes in oxidative processes [8], no reference was found about the possibility of generating unexpected products due to DMSO oxidation.

The reaction between $[Cu(bipy)Cl_2]$ [9] and the 4,4′-sulfonyl-bis(phenylamino)bis(ethyl-2-oxoacetato) (**L01**) ligand [10] in DMSO provided needle shaped green crystals, identified as $[Cu(bipy)(H_2O)_2(SO_4)]_n$. When the reaction was carried out in the same experimental conditions, except for the absence of the **L01** ligand, the product was also obtained [11]. Under identical conditions, reactions of the similar precursors yielded one-dimensional compounds of formula $[Cu(en)(H_2O)_2(SO_4)]_n$ and $[Cu(H_2O)_2(phen)(SO_4)]_n$, where en = 1,2-ethylenediamine and phen = 1,10-phenantroline. In order to understand the origin of the sulfate ions, a spot test in the mother liquor was performed with barium chloride aqueous solution. As result, no detectable amount of sulfate ion was found, suggesting a slow formation of SO_4^{2-} due to oxidation of DMSO.

Magnetic measurements for $[Cu(bipy)(H_2O)_2(SO_4)]_n$ were performed on a Cryogenic SX-600 SQUID magnetometer in a range of 2–300 K with an applied field of 0.1 T. Diamagnetic correction was evaluated from Pascal's constants. The field dependence of the magnetization was measured in the field range 0–6 T at 1.8 K. χ_M and $1/\chi_M$ plots as a function of temperature are displayed in Fig. 1. $1/\chi_M$ can be nicely fitted to the Curie–Weiss law ($\chi_M = C/(T - \theta)$). The values obtained for Curie and Weiss constants are 0.37 emu. mol^{-1} and −0.13 K, respectively. These values are expected for an antiferromagnetic chain with a $S = 1/2$ that presents weak interactions through the SO_4^{2-} bridge [12]. Based on the structure of $[Cu(bipy)(H_2O)_2(SO_4)]_n$, we attempted to reproduce the experimental magnetic data considering a Heisenberg 1-D Hamiltonian for antiferromagnetic chains [13]

$$H = -J\sum_{i=1}^{n-1} S_{A_i} S_{A_{i+1}}$$

* Corresponding author. Tel.: +55 21 26292354; fax: +55 21 26292129.
E-mail address: mariavaz@vm.uff.br (M.G.F. Vaz).

0277-5387/$ - see front matter © 2008 Elsevier Ltd. All rights reserved.
doi:10.1016/j.poly.2008.12.021

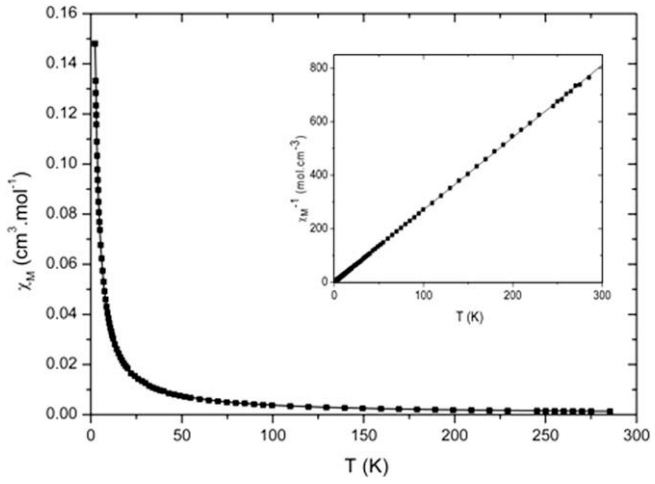


Fig. 1. Temperature dependence of χ_M of $[Cu(bipy)(H_2O)_2(SO_4)]_n$ (squares). Line corresponds to the best fit. Inset: $1/\chi_M$ data as a function of the temperature (squares) fitted to the Curie–Weiss law (line).

and

$$\chi = \frac{Ng^2\beta^2[0.25 + 0.074975x + 0.075235x^2]}{kT[1 + 0.9931x + 0.172135x^2 + 0.757825x^3]},$$

where $x = |J|/kT$.

The best fit parameters were $J = -0.53$ cm^{-1} and $g = 2.01$. Magnetic measurements as a function of the applied magnetic showed a field of 6 T is not enough to override the antiferromagnetic interactions and reach saturation, preventing the magnetization to follow a paramagnetic behavior at 1.8 K.

The crystal structure of $[Cu(bipy)(H_2O)_2(SO_4)]_n$ has been previously described [14]. In the complex the copper atom is in a distorted octahedral environment. Two nitrogen atoms of the diamine groups and two water molecules are in the equatorial plane, whereas the apical positions are occupied by two oxygen atoms of the sulfate ions. Each sulfate ion is bound to two copper ions forming a 1D chain. Each chain is connected to another one through hydrogen bonds between oxygen atoms of sulfate and hydrogen atoms of water molecules. Inspection of the crystal structure shows two pathways through which the antiferromagnetic coupling may occur (Fig. 2). The first one is through the sulfate bridge (model **a**), binding the copper atoms and the second one is through the intermolecular hydrogen bounds (model **b**). Furthermore, there is not a consensus in literature about the main pathway in which the magnetic interaction occurs [12,15]. In order to examine how magnetic orbitals could be involved in the exchange interactions, DFT calculations were performed for $[Cu(bipy)(H_2O)_2(SO_4)]_n$ in GAUSSIAN 03W program package (G03W) [16] employing the Becke's three-parameters hybrid functional (B3) [17] and the Lee-Yang-Parr's gradient-corrected correlation functional (LYP) [18] – B3LYP method. The TZVP basis set was applied for all other atoms [19]. Geometries were fully optimized under these conditions (B3LYP/TZVP). The values of the coupling constants J were obtained using the broken symmetry approach [20]. The optimized geometry is in good agreement with structural experimental parameters. For the model **a**, the magnetic orbital has a small contribution from the d_z2 orbital centered on the copper atoms and a large contribution from the π^* orbital of the sulfate bridge. The d_z2 orbital is directed to the sulfate ion in the apical positions. In this case the value obtained for the coupling constant was $J = -0.20$ cm^{-1}. In the same way as found for **a**, the magnetic orbital of **b** model presents large contributions of a π^* orbital of the sulfate bridge. However, the active orbital centered on the copper atom is a $d_x2 - {}_y2$ instead of a d_z2 one. The coupling constant calculated for model **b** is $J = -0.04$ cm^{-1}. Both models underestimate the value of the experimental coupling constant, but there is a clear difference between the magnitudes of the two calculated values. The magnetic interactions described by model **a** are closer to the experimental values than those obtained with model **b**, showing that the magnetic interaction occurs through the sulfate bridge.

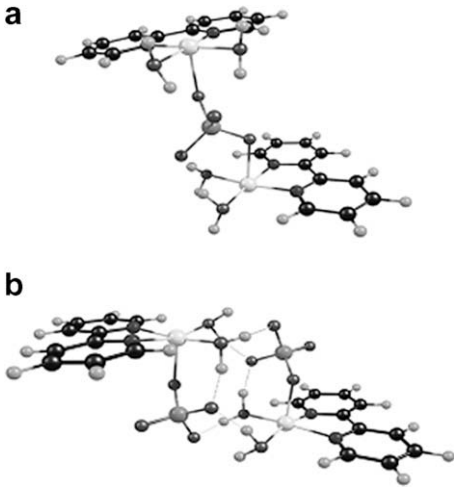


Fig. 2. Models a and b used in DFT calculations for $[Cu(bipy)(H_2O)_2(SO_4)]_n$.

As copper(II) salts and diamine ligands are ordinary reactants applied in the syntheses of molecular magnets, these results showed the possibility of obtaining undesired sub-products formation in reactions where DMSO is used as solvent. Formation of the sulfate copper chains does not depend on the nature of the organic ligands involved in the reactions. Moreover, the obtained chains are insoluble in all investigated solvents, therefore the precipitation of traces of the insoluble paramagnetic compounds can be considered as a possible contamination source which can lead to misleading interpretation of the magnetic behavior, as was recently described [21].

Acknowledgements

The authors would like to acknowledge the financial support from FAPERJ, CNPq, CAPES and LDRX-UFF, Dr. Stéphane Soriano, Dr. Claudio Sangregorio, Dr. Javier Ellena for the discussions and Dr. Miguel A. Novak for the help with the magnetic measurements.

References

[1] M. Calligaris, Coord. Chem. Rev. 248 (2004) 351.
[2] V. Tangoulis, D. Panagoulis, C.P. Raptopoulou, C. Dendrinou-Samara, Dalton Trans. (2008) 1752.
[3] M.L. Kahn, C. Mathonière, O. Kahn, Inorg. Chem. 38 (1999) 3692.
[4] O. Cador, M.G.F. Vaz, H.O. Stumpf, C. Mathoniere, O. Kahn, Synth. Met. 122 (2001) 559.
[5] C.L.M. Pereira, A.C. Doriguetto, C. Konzen, L.C. Meira-Belo, U.A. Leitao, N.G. Fernandes, Y.P. Mascarenhas, J. Ellena, A.L. Brandl, M. Knobel, H.O. Stumpf, Eur. J. Inorg. Chem. 24 (2005) 5018.
[6] M.G.F. Vaz, E.F. Pedroso, N.L. Speziali, M.A. Novak, A.F.C. Alcantara, H.O. Stumpf, Inorg. Chim. Acta 326 (2001) 65.
[7] (a) X. Liu, A. Qiu, D.T. Sawyer, J. Am. Chem. Soc. 115 (1993) 3239;
(b) G. Izzet, J. Zeitouny, H. Akdas-Killig, Y. Frapart, S. Ménage, B. Douziech, I. Jabin, Y. Mest, O. Reinaud, J. Am. Chem. Soc. 130 (2008) 914.
[8] (a) H. Sigel, C. Flierl, R. Griesser, J. Am. Chem. Soc. 91 (1969) 1061;
(b) C. Jallabert, C. Lapinte, H. Riviere, J. Mol. Cat. 14 (1982) 75;
(c) I.E. Markó, P.R. Giles, M. Tsukazaki, S.M. Brown, C.J. Urch, Science 274 (1996) 2044;
(d) R. Csonka, J. Kaizer, M. Giorgi, M. Réglier, L. Hajba, J. Mink, G. Speier, Inorg. Chem. 47 (2008) 6121;
(e) S. Chattopadhyay, T.C.W. Mak, Inorg. Chem Commun. 3 (2000) 111.

[9] M. Hernández-Molina, J. González-Platas, C. Ruiz-Pérez, F. Lloret, M. Julve, Inorg. Chim. Acta 284 (1999) 258.
[10] C.L. Muenchenstein, H.R.B. Gelterkinden, M.D. Frenkendorf, French Patent no. 1567434 (1969).
[11] In a round-bottom flask, [Cu(bipy)Cl_2] (58.0 mg, 0.20 mmol) and 5.0 mL of DMSO were refluxed during 7 h. The reaction solution was stocked at room temperature. After four weeks, the color of the solution changed from green to blue and some days after, needle blue crystals were obtained. These crystals were isolated by filtration and washed with hot water. Yield: 12.0 mg (19%). Selected IR data (cm^{-1}): 3107 and 3033 (ν C–H bipyridine), 1601 (ν C–H aromatic) and 1301 (ν S=O). *Anal*. Calc. for $C_{10}H_{12}N_2O_6SCu$: C, 34.53; H, 3.51; N, 8.22%. Found: C, 34.52; H, 3.52; N, 8.06%.
[12] C. Nicolini, W.M. Reiff, J. Solid State Chem. 44 (1982) 141.
[13] O. Kahn, Molecular Magnetism, VCH, Weinheim, 1993.
[14] T.C. Tedenac, N.D. Phong, C. Aviens, M. Maurin, J. Inorg. Nucl. Chem. 38 (1976) 85.
[15] O. Kravchyna, A. Kaplienko, M. Kajnakova, Low Temp. Phys. 30 (2004) 820.
[16] M.J. Frisch, G.W. Trucks, H.B. Schlegel, G.E. Scuseria, M.A. Robb, J.R. Cheeseman, J.A. Montgomery Jr., T. Vreven, K.N. Kudin, J.C. Burant, J.M. Millam, S.S. Iyengar, J. Tomasi, V. Barone, B. Mennucci, M. Cossi, G. Scalmani, N. Rega, G.A. Petersson, H. Nakatsuji, M. Hada, M. Ehara, K. Toyota, R. Fukuda, J. Hasegawa, M. Ishida, T. Nakajima, Y. Honda, O. Kitao, H. Nakai, M. Klene, X. Li, J.E. Knox, H.P. Hratchian, J.B. Cross, V. Bakken, C. Adamo, J. Jaramillo, R. Gomperts, R.E. Stratmann, O. Yazyev, A.J. Austin, R. Cammi, C. Pomelli, J.W. Ochterski, P.Y. Ayala, K. Morokuma, G.A. Voth, P. Salvador, J.J. Dannenberg, V.G. Zakrzewski, S. Dapprich, A.D. Daniels, M.C. Strain, O. Farkas, D.K. Malick, A.D. Rabuck, K. Raghavachari, J.B. Foresman, J.V. Ortiz, Q. Cui, A.G. Baboul, S. Clifford, J. Cioslowski, B.B. Stefanov, G. Liu, A. Liashenko, P. Piskorz, I. Komaromi, R.L. Martin, D.J. Fox, T. Keith, M.A. Al-Laham, C.Y. Peng, A. Nanayakkara, M. Challacombe, P.M.W. Gill, B. Johnson, W. Chen, M.W. Wong, C. Gonzalez, J.A. Pople, GAUSSIAN 03, Gaussian, Inc., Wallingford, CT, 2004.
[17] A.D. Becke, J. Chem. Phys. 98 (1993) 5648.
[18] C. Lee, W. Yang, R.G. Parr, Phys. Rev. B 37 (1988) 785.
[19] (a) A. Schaefer, H. Horn, R. Ahlrichs, J. Chem. Phys. 97 (1992) 2571;
(b) A. Schaefer, C. Huber, R. Ahlrichs, J. Chem. Phys. 100 (1994) 5829.
[20] A. Bencini, F. Totti, C.A. Daul, K. Doclo, P. Fantucci, V. Barone, Inorg. Chem. 36 (1997) 5022.
[21] O. Cador, A. Caneshi, D. Rovai, C. Sangregorio, R. Sessoli, L. Sorace, Inorg. Chim. Acta 361 (2008) 3882.

Polyhedron 28 (2009) 2029–2035

Contents lists available at ScienceDirect

Polyhedron

journal homepage: www.elsevier.com/locate/poly

A novel class of tetrairon(III) single-molecule magnets with graphene-binding groups

Chiara Danieli [a,*], Andrea Cornia [a], Claudia Cecchelli [a], Roberta Sessoli [b], Anne-Laure Barra [c], Glauco Ponterini [a], Barbara Zanfrognini [a]

[a] Department of Chemistry and INSTM Research Unit, University of Modena and Reggio Emilia, Via G. Campi 183, 41100 Modena, Italy
[b] Department of Chemistry and INSTM Research Unit, University of Florence, Via della Lastruccia 3, 50019 Sesto Fiorentino (FI), Italy
[c] Grenoble High Magnetic Field Laboratory – CNRS, BP 166, 25 Avenue des Martyrs, 38042 Grenoble Cedex 9, France

ARTICLE INFO

Article history:
Available online 21 January 2009

Keywords:
Single-molecule magnets
Spectroscopic characterizations
HF-EPR spectroscopy
Tetrairon(III) complexes

ABSTRACT

Tripods of general formula R'–O–$CH_2C(CH_2OH)_3$ are excellent site-specific ligands for the preparation of functionalized Fe_4 single-molecule magnets. Herein, we describe the synthesis and characterization of two novel complexes designed to bind graphene surfaces, in which the R group consists of an alkyl spacer $–(CH_2)_n–$ (n = 6 and 10) and a terminal pyrenyl moiety. The site-specific ligand substitution on $[Fe_4(OMe)_6(dpm)_6]$ (Hdpm = dipivaloylmethane) with the new tripods has been studied with ^{2}H NMR on isotopically-enriched samples, revealing that, once formed, these clusters are stable in solution over long timescales. It was not possible to isolate the new compounds as crystalline solids, nevertheless they were chemically characterized by elemental analysis and ^{1}H NMR. The presence of the pyrenyl ending groups prompted us to investigate the effect of metal complexation on fluorescence, and a full pyrene-to-iron cluster excitation energy transfer was observed. The analysis of the magnetic behaviour revealed an S = 5 ground spin state with a negative zero-field splitting parameter D = –0.42 cm^{-1}.

© 2009 Elsevier Ltd. All rights reserved.

1. Introduction

Tetrairon(III) complexes with a propeller-like structure (also known as "ferric stars") are among the most appealing single-molecule magnets (SMM) for application in molecular spintronics and quantum computing [1]. Since the discovery of the archetypal tetrairon(III) SMM, the compound $[Fe_4(OMe)_6(dpm)_6]$ [2] (**1**, Hdpm = dipivaloylmethane), several derivatives have been obtained by selective replacement of the six methoxide bridges with tripods H_3L = R–$C(CH_2OH)_3$. The products of the reaction are usually obtained as pure, crystalline materials and display enhanced magnetic properties as compared with the parent compound **1**. Moreover, the R group can be chosen so as to bring additional functionalities, such as surface-binding capability [3–7]. We have recently shown that tetrairon(III) SMM can be successfully anchored to native gold surfaces by using R groups containing thioacetyl moieties, with full retention of magnetic properties [8]. In a different approach, tripods bearing a terminal double bond were reacted with H-terminated silicon substrates to give arrays of molecular receptors designed for SMM binding [7]. The first CNT-SMM hybrids (CNT = carbon nanotube) were also successfully realized by exploiting the noncovalent π-stacking interaction between pristine CNT and a Fe_4 derivative functionalized with pyrenyl units [9]. The tripodal ligand used (**H_3C4**, Scheme 1) is a derivative of pentaerythritol and comprises a short C4 alkyl spacer. In the present work we wish to describe the synthesis of two additional pyrene-functionalized SMM, **2** and **3**, bearing longer spacers (**H_3C6** and **H_3C10** in Scheme 1). The new compounds were characterized with NMR and fluorescence spectroscopy, and the magnetic properties were measured with DC magnetometry and HF-EPR spectroscopy.

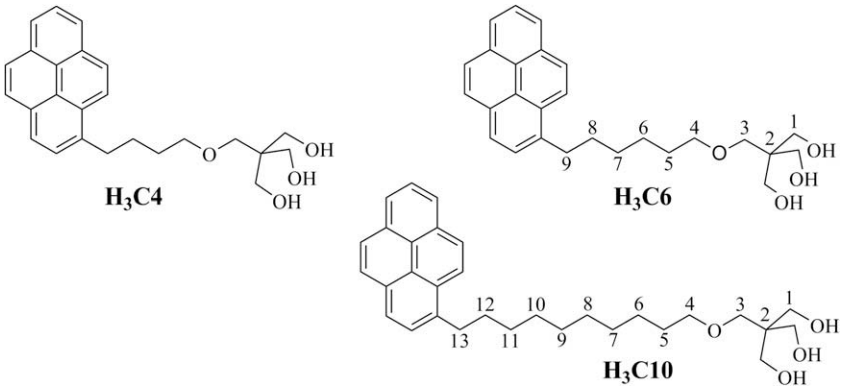
2. Experimental

2.1. Materials and methods

All the chemicals were of reagent-grade quality and used as received, unless otherwise stated. Anhydrous THF and diethyl ether, predried over $CaCl_2$, were distilled from Na/benzophenone shortly before use. MeOH was carefully dried by treatment with Mg/I_2 and distilled prior to use. Anhydrous toluene, *n*-hexane, dichloromethane (DCM) and 1,2-dichloroethane (DCE) were obtained by distillation over CaH_2. Toluene and *n*-hexane were stored over Na wires, while DCM and DCE were stored over 4-Å molecular sieves in the dark.

* Corresponding author. Tel.: +39 59 2055030; fax: +39 59 373543.
E-mail addresses: cdanieli@unimore.it (C. Danieli), acornia@unimore.it (A. Cornia), roberta.sessoli@unifi.it (R. Sessoli), anne-laure.barra@grenoble.cnrs.fr (A.-L. Barra).

0277-5387/$ - see front matter © 2009 Elsevier Ltd. All rights reserved.
doi:10.1016/j.poly.2008.12.024



Scheme 1. Tripodal ligands functionalized with pyrenyl moieties.

(1-Methyl-2,6,7-trioxabicyclo[2.2.2]octan-4-yl)methanol [10], 6-bromohexanoyl chloride [11], 10-bromodecanoyl chloride [12], $[Fe_4(OMe)_6(dpm)_6]$ (**1**) [3], and $[Fe_4(OMe)_6(dpm\text{-}d_{18})_6]$ (**1-*d***) [3] were synthesized according to literature procedures.

All the solutions used for NMR and fluorescence experiments were prepared with anhydrous solvents and were stored excluding any possible contamination. The NMR spectra were recorded at 302 K with a Bruker FT-DPX200 NMR spectrometer. Proton chemical shifts are reported relative to TMS, while deuteron chemical shifts are referenced to acetone-d_6, as external standard (δ = 2.16 ppm). The protons of the pyrenyl ring are abbreviated as C*H*Py. ESI Mass spectra were obtained with an ESI Waters ZQ-4000 instrument; C, H analysis was performed using a Carlo Erba EA1110 CHNS-O automatic analyser.

2.2. Synthesis of the compounds

2.2.1. 6-Bromo-1-(pyren-1-yl)hexan-1-one (*4*)

Pyrene (2.478 g, 12.25 mmol) and 6-bromohexanoyl chloride (2.180 g, 10.21 mmol) were dissolved in 29 mL of anhydrous DCE under N_2, the mixture was cooled to −10 °C and $AlCl_3$ (1.633 g, 12.25 mmol) was added portionwise in 20 min. The reaction mixture turned to a dark color and was allowed to reach room temperature slowly and stirred overnight. Excess $AlCl_3$ was quenched with crushed ice, the resulting aqueous phase was saturated with solid NaCl, 50 mL of fresh DCE were added and the layers separated. The organic phase was washed with saturated NaCl, dried over $MgSO_4$, filtered and concentrated in vacuo. The crude product was purified with column chromatography on silica gel (petroleum ether–DCM: 7:3) to yield **4** as a yellowish solid (3.014 g, 78%). ^{1}H NMR ($CDCl_3$): δ (ppm) 8.88 (d, J = 9.4 Hz, 1H, C*H*Py); 8.30–8.00 (m, 8H, C*H*Py); 3.44 (t, J = 6.7 Hz, 2H, CH_2Br); 3.21 (t, J = 7.2 Hz, 2H, CH_2CO); 2.02–1.82 (m, 4H, CH_2CH$_2$Br, CH_2CH$_2$CO); 1.68–1.52 (m, 2H, CH_2). ^{13}C NMR ($CDCl_3$): δ (ppm) 206.60 (*C*O); 129.53 (*C*HPy); 129.43 (*C*HPy); 127.05 (*C*HPy); 126.38 (*C*HPy); 126.22 (*C*HPy); 125.97 (*C*HPy); 124.75 (*C*HPy); 123.99 (*C*HPy); 42.25 (*C*H$_2$); 33.55 (*C*H$_2$); 32.65 (*C*H$_2$); 27.93 (*C*H$_2$); 23.99 (*C*H$_2$).

2.2.2. 1-(6-Bromohexyl)pyrene (*5*)

To a stirred suspension of $AlCl_3$ (0.880 g, 6.60 mmol) in 9 mL of anhydrous Et_2O under N_2, $LiAlH_4$ (6.6 mL, 1-M solution in Et_2O) was added dropwise. To the resulting milky reaction mixture, a solution of **4** (1.00 g, 2.64 mmol) in 12.5 mL of anhydrous DCM was slowly added dropwise. The reaction turned orange with a white precipitate and was stirred at room temperature for 1 h. Excess $LiAlH_4$ was quenched by careful addition of crushed ice, then 2.5-M HCl was added until acidic pH. The reaction was extracted with Et_2O (2 × 50 mL), the combined organic phases were washed with saturated NaCl, dried over $MgSO_4$, filtered and concentrated in vacuo to yield **5** as a yellow solid (0.864 g, 92%), which was used without further purification (98% + from ^{1}H NMR). ^{1}H NMR ($CDCl_3$): δ (ppm) 8.29 (d, J = 9.2 Hz, 1H, C*H*Py); 8.20–7.96 (m, 7H, C*H*Py); 7.87 (d, J = 7.8 Hz, 1H, C*H*Py); 3.42 (t, J = 6.7 Hz, 2H, CH_2Br); 3.36 (t, J = 7.7 Hz, 2H, CH_2Py); 1.97–1.81, (m, 4H, CH_2CH$_2$Br, CH_2CH$_2$Py); 1.59–1.50 (m, 4H, CH_2). ^{13}C NMR ($CDCl_3$): δ (ppm) 136.34 (*C*^{IV}Py); 130.93 (*C*^{IV}Py), 129.76 (*C*^{IV}Py); 127.51 (*C*HPy); 127.20 (*C*HPy); 127.16 (*C*HPy); 126.54 (*C*HPy); 125.77 (*C*HPy); 124.82 (*C*HPy); 124.77 (*C*HPy); 124.65 (*C*HPy); 123.39 (*C*HPy); 33.84 (*C*H$_2$); 33.40 (*C*H$_2$); 32.76 (*C*H$_2$); 31.63 (*C*H$_2$); 28.84 (*C*H$_2$); 28.09 (*C*H$_2$).

2.2.3. 2-(Hydroxymethyl)-2-((6-(pyren-1-yl)hexyloxy)methyl)-propane-1,3-diol (***H$_3$C6***)

To a stirred suspension of NaH (0.289 g, 60% w/w dispersion in mineral oil, 12.0 mmol) in 17 mL of anhydrous THF under N_2, (1-methyl-2,6,7-trioxabicyclo[2.2.2]octan-4-yl)methanol (0.193 g, 1.20 mmol) was added as a solid in one portion. The mixture was stirred at room temperature for 1 h, then a solution of **5** (0.484 g, 1.32 mmol) in 7 mL of THF was added dropwise, followed by tetrabutylammonium bromide (TBABr) (0.020 g, 0.053 mmol). The reaction was stirred at room temperature for 3 days under N_2, excess NaH was quenched with careful addition of MeOH, the solution was acidified with 2.5-M HCl until pH 1. The solvent was removed in vacuo and the crude material was purified with column chromatography on silica gel (DCM, gradient elution to DCM–MeOH: 10:1) to yield the intermediate monoacetylated product **AcH$_2$C6** (0.200 g, 0.432 mmol) and a small amount of the desired compound **H$_3$C6** (0.030 g, 6%). The monoacetylated product (0.200 g, 0.432 mmol) was dissolved in 4 mL of anhydrous MeOH, NaOMe (0.015 mL, 2.94-M solution in methanol, 0.044 mmol) was added and the mixture was stirred under N_2 for 1 day at room temperature. Finally, a drop of 2.5-M HCl was added and the solvent removed in vacuo to yield **H$_3$C6** as a light yellow solid (0.178 g, 98%).

^{1}H NMR for **AcH$_2$C6** ($CDCl_3$): δ (ppm) 8.29 (d, J = 9.4 Hz, 1H, C*H*Py); 8.20–7.95 (m, 7H, C*H*Py); 7.87 (d, J = 7.8 Hz, 1H, C*H*Py); 4.19 (s, 2H, CH_2OCO); 3.69–3.55 (m, 4H, CH_2OH); 3.43 (s, 2H, OCH_2-C^{IV}); 3.42 (t, J = 6.2 Hz, 2H, CH$_2$CH_2O); 3.36 (t, J = 7.6 Hz, 2H, CH_2Py); 2.08 (s, 3H, CH_3CO); 1.96–1.81 (m, 2H, CH_2); 1.66–1.38 (m, 6H, CH_2).

^{1}H NMR for **H$_3$C6** (DMSO-d_6): δ (ppm) 8.35–8.00 (m, 8H, C*H*Py); 7.92 (d, J = 7.9 Hz, 1H, C*H*Py); 4.15 (t, J = 5.3 Hz, 3H, O*H*); 3.39 (d, J = 5.3 Hz, 6H, CH_2OH); 3.35–3.26 (m, 6H, CH_2OCH_2, CH_2Py); 1.83–1.69 (m, 2H, CH_2); 1.55–1.25 (m, 6H, CH_2). ^{13}C NMR (DMSO-d_6): δ (ppm) 137.00 (*C*^{IV}Py); 130.85 (*C*^{IV}Py); 130.37 (*C*^{IV}Py);

129.10 (C^{IV}Py); 127.96 (C^{IV}Py); 127.39 (*C*HPy); 127.34 (*C*HPy); 127.09 (*C*HPy); 126.33 (*C*HPy); 126.01 (*C*HPy); 124.83 (*C*HPy); 124.65 (*C*HPy); 124.20 (C^{IV}Py); 123.37 (*C*HPy); 70.71 (CH_2O); 69.62 (CH_2O); 61.00 (CH_2OH); 45.43 (C^{IV}); 32.51 (CH_2); 31.46 (CH_2); 29.06 (CH_2); 28.82 (CH_2); 25.52 (CH_2).

Anal. Calc. for **H_3C6**, $C_{27}H_{32}O_4$: C, 77.11; H, 7.67. Found: C, 76.77; H, 8.01%.

2.2.4. [Fe_4(C6)$_2$(dpm)$_6$] (**2**)

To a stirred solution of **1** (0.075 g, 0.050 mmol) in 20 mL of dry toluene, **H_3C6** (0.052 g, 0.12 mmol) was added and the resulting mixture was stirred for 40 h. The solvent was carefully removed in vacuo without warming, the resulting dark orange solid was stirred with 10 mL of anhydrous *n*-hexane for 30 min, and the suspension obtained was filtered on a G4 sintered glass frit. Removal of the solvent in vacuo without warming afforded **2** as a dark orange solid (0.081 g, 75%).

Anal. Calc. for **2**·C_6H_{14}, $Fe_4O_{20}C_{126}H_{186}$: C, 67.41; H, 8.37. Found: C, 67.35; H, 8.37%.

2.2.5. 10-Bromo-1-(pyren-1-yl)decan-1-one (**6**)

Pyrene (2.430 g, 12.00 mmol) and 10-bromodecanoyl chloride (2.700 g, 10.00 mmol) were dissolved in 28 mL of anhydrous DCE under N_2, the mixture was cooled to 0 °C and $AlCl_3$ (1.600 g, 12.00 mmol) was added portionwise in 20 min. The reaction turned to a dark color and was allowed to reach room temperature slowly and stirred overnight. Excess $AlCl_3$ was quenched with crushed ice, the resulting aqueous phase was saturated with solid NaCl, 50 mL of fresh DCE were added and the layers separated. The organic layer was washed with saturated NaCl, dried over $MgSO_4$, filtered and concentrated in vacuo. The crude product was purified with column chromatography on silica gel (petroleum ether–DCM: 7:3) to yield **6** as a yellow solid (3.450 g, 83%). ^{1}H NMR ($CDCl_3$): δ (ppm) 8.88 (d, J = 9.4 Hz, 1H, *CH*Py); 8.30–7.98 (m, 8H, *CH*Py); 3.39 (t, J = 6.8 Hz, 2H, CH_2Br); 3.19 (t, J = 7.3 Hz; 2H, CH_2CO); 1.94–1.76 (m, 4H, CH_2CH_2Br, CH_2CH_2CO); 1.53–1.31 (m, 10H, CH_2). ^{13}C NMR ($CDCl_3$): δ (ppm) 205.25 (*C*O); 133.53 (C^{IV}Py); 132.91 (C^{IV}Py); 131.08 (C^{IV}Py); 130.56 (C^{IV}Py); 129.42 (*C*HPy); 129.32 (*C*HPy); 129.23 (C^{IV}Py); 127.04 (*C*HPy); 126.33 (*C*HPy); 126.15 (*C*HPy); 125.95 (*C*HPy); 125.91 (*C*HPy); 124.82 (*C*HPy); 124.35 (C^{IV}Py); 123.98 (*C*HPy); 42.63 (CH_2CO); 33.96 (CH_2Br); 32.81 (CH_2); 29.35 (CH_2); 29.25 (CH_2); 28.68 (CH_2); 28.13 (CH_2); 24.97 (CH_2).

2.2.6. 1-(10-Bromodecyl)pyrene (**7**)

To a stirred suspension of $AlCl_3$ (0.919 g, 6.90 mmol) in 9 mL of anhydrous Et_2O under N_2, $LiAlH_4$ (6.90 mL, 1-M solution in Et_2O) was added dropwise. To the resulting milky reaction mixture, a solution of **6** (1.20 g, 2.76 mmol) in 8 mL of anhydrous DCM was slowly added dropwise. The reaction turned orange with a white precipitate and was stirred at room temperature for 2 h. Excess $LiAlH_4$ was quenched by careful addition of crushed ice, then 2.5-M HCl was added until acidic pH. The reaction was extracted with Et_2O (2 × 50 mL), the combined organic phases were washed with saturated NaCl, dried over $MgSO_4$, filtered and concentrated in vacuo to yield **7** as a yellow solid (1.142 g, 98%), which was used without further purification (98% + from ^{1}H NMR). ^{1}H NMR ($CDCl_3$): δ (ppm) 8.31 (d, J = 9.4 Hz, 1H, *CH*Py); 8.21–7.97 (m, 7H, *CH*Py); 7.88 (d, J = 7.8 Hz, 1H, *CH*Py); 3.41 (t, J = 6.4 Hz, 2H, CH_2Br); 3.36 (t, J = 7.8 Hz, 2H, CH_2Py); 1,96–1.78 (m, 4H, CH_2CH_2Br, CH_2CH_2Py); 1.59–1.24 (m, 12H, CH_2). ^{13}C NMR ($CDCl_3$): δ (ppm) 137.30 (C^{IV}Py); 131.52 (C^{IV}Py); 131.00 (C^{IV}Py); 129.75 (C^{IV}Py); 129.46 (C^{IV}Py); 128.66 (C^{IV}Py); 127.57 (*C*HPy); 127.23 (*C*HPy); 127.11 (*C*HPy); 126.51 (*C*HPy); 125.76 (*C*HPy); 124.80 (*C*HPy); 124.64 (*C*HPy); 123.53 (*C*HPy); 34.00 (CH_2Br); 33.61 (CH_2); 32.88 (CH_2); 31.93 (CH_2); 29.80 (CH_2); 29.56 (CH_2); 29.52 (CH_2); 29.44 (CH_2); 28.78 (CH_2); 28.20(CH_2).

2.2.7. 2-(Hydroxymethyl)-2-((10-(pyren-1-yl)decyloxy)methyl)-propane-1,3-diol (**H_3C10**)

To a stirred suspension of NaH (0.716 g, 60% w/w dispersion in mineral oil, 17.9 mmol) in 25 mL of anhydrous THF under N_2, (1-methyl-2,6,7-trioxabicyclo[2.2.2]octan-4-yl)methanol (0.287 g, 1.79 mmol) was added as a solid portionwise. The mixture was stirred at room temperature for 1 h, then a solution of **7** (0.834 g, 1.98 mmol) in 3 mL of THF was added dropwise, followed by TBABr (0.030 g, 0.079 mmol). The reaction was stirred at room temperature for 5 days under N_2, excess NaH was quenched with careful addition of MeOH, the solution was acidified with 2.5-M HCl until pH 1. The solvent was removed in vacuo and the crude material was purified with column chromatography on silica gel (DCM, gradient elution to DCM–MeOH: 1:1) to yield the intermediate monoacetylated product **AcH_2C10** (0.486 g, 0.937 mmol) and **H_3C10** (0.243 g, 28%). Compound **AcH_2C10** (0.486 g, 0.937 mmol) was dissolved in 9 mL of anhydrous MeOH, NaOMe (0.032 mL, 2.94-M solution in methanol, 0.094 mmol) was added and the mixture was stirred under N_2 for one day at room temperature, a drop of 2.5 M HCl was added and the solvent removed in vacuo to yield **H_3C10** as a dark yellow solid (0.437 g, 99%).

^{1}H NMR for **AcH_2C10** ($CDCl_3$): δ (ppm) 8.28 (d, J = 9.4 Hz, 1H, *CH*Py); 8.18–7.94 (m, 7H, *CH*Py); 7.86 (d, J = 7.8 Hz, 1H, *CH*Py); 4.20 (s, 2H, CH_2OCO); 3.71–3.57 (m, 4H, CH_2OH); 3.43–3.29 (m, 6H, OCH_2C^{IV}, CH_2CH_2O, CH_2Py); 3.04 (br s, 2H, O*H*); 2.09 (s, 3H, CH_3CO); 1.85–1.79 (m, 2H, CH_2CH_2Py); 1.60–1.29 (m, 14H, CH_2). ^{13}C NMR ($CDCl_3$) δ (ppm) 171.65 (*C*O); 137.32 (C^{IV}Py); 131.47 (C^{IV}Py); 130.96 (C^{IV}Py); 129.68 (C^{IV}Py); 128.61 (C^{IV}Py); 127.52 (*C*HPy); 127.21 (*C*HPy); 127.07 (*C*HPy); 126.45 (*C*HPy); 125.74 (*C*HPy); 125.08 (C^{IV}Py); 124.76 (*C*HPy); 124.59 (*C*HPy); 123.51 (*C*HPy); 72.26 (CH_2); 72.06 (CH_2); 63.67 (CH_2); 63.35 (CH_2); 53.41 (C^{IV}); 44.67 (CH_2); 33.57 (CH_2); 31.91 (CH_2); 29.80 (CH_2); 29.55 (CH_2); 29.46 (CH_2); 29.39 (CH_2); 26.06 (CH_2); 20.80 (CH_3).

^{1}H NMR for **H_3C10** (DMSO-d_6) δ (ppm) 8.28 (d, J = 9.3 Hz, 1H, *CH*Py); 8.17–7.93 (m, 7H, *CH*Py); 7.85 (d, J = 7.9 Hz, 1H, *CH*Py); 3.70 (s, 6H, CH_2OH); 3.42 (s, 2H, OCH_2C^{IV}); 3.38 (t, J = 6.6 Hz, 2H, CH_2CH_2O); 3.33 (t, J = 7.8 Hz, 2H, CH_2Py); 3.12 (br s, 3H, O*H*) 1.93–1.78 (m, 2H, CH_2); 1.60–1.28 (m, 14H, CH_2). ^{13}C NMR ($CDCl_3$) δ (ppm) 137.40 (C^{IV}Py); 131.56 (C^{IV}Py); 131.04 (C^{IV}Py); 129.78 (C^{IV}Py); 128.70 (C^{IV}Py); 127.62 (*C*HPy); 127.30 (*C*HPy); 127.15 (*C*HPy); 126.54 (*C*HPy); 125.82 (*C*HPy); 125.19 (C^{IV}Py); 124.85 (*C*HPy); 124.68 (*C*HPy); 123.60 (*C*HPy); 73.55 (CH_2O); 72.23 (CH_2O); 64.45 (CH_2OH); 44.98 (C^{IV}); 33.66 (CH_2); 32.00 (CH_2); 29.89 (CH_2); 29.63 (CH_2); 29.55 (CH_2); 29.48 (CH_2); 26.15 (CH_2).

Anal. Calc. for **H_3C10,** $C_{31}H_{40}O_4$: C, 78.11; H, 8.46. Found: C, 77.89; H, 8.76%.

2.2.8. [Fe_4(C10)$_2$(dpm)$_6$] (**3**)

To a stirred solution of **1** (0.080 g, 0.053 mmol) in 20 mL of dry toluene, **H_3C10** (0.063 g, 0.13 mmol) was added and the resulting mixture was stirred for 40 h. The solvent was carefully removed in vacuo without warming, the resulting dark orange solid was stirred with 12 mL of anhydrous *n*-hexane for 30 min, and the suspension obtained was filtered on a G4 sintered glass frit. Removal of the solvent in vacuo without warming afforded **3** as a dark orange solid (0.098 g, 81%).

Anal. Calc. for **3**·0.5C_6H_{14}, $Fe_4O_{20}C_{131}H_{195}$: C, 68.01; H, 8.50. Found: C, 67.54; H, 8.51%.

2.3. Fluorescence spectra

Fluorescence emission spectra were recorded with a Spex Jobin Yvon FluoroMax 2 spectrofluorometer, using a triangular cell and front-face irradiation. Spectral bandwidth was around 2 nm.

2.4. Magnetic measurements

DC magnetic data were recorded using a Cryogenic S600 SQUID magnetometer. The temperature dependence of the M/H ratio (assumed to correspond to the static susceptibility) was measured on 15.77- and 13.51-mg samples of **2** and **3**, respectively, in applied fields of 10 kOe from 300 to 30 K and of 1 kOe from 30 to 1.9 K to suppress saturation effects. The isothermal magnetization of the same samples was also measured at 1.9, 2.5 and 4.5 K in fields up to 50 kOe.

Data reduction was carried out using the following molecular weights and diamagnetic contributions (estimated from Pascal's constants): for **2**, 2244.24 and -1408×10^{-6} emu mol^{-1} (corresponding to **2**·C_6H_{14}); for **3**, 2313.37 and -1464×10^{-6} emu mol^{-1} (corresponding to **3**·0.5C_6H_{14}).

2.5. EPR spectra

High-Frequency EPR (HF-EPR) spectra were recorded at the Grenoble High Magnetic Field Laboratory on a homebuilt spectrometer working in single-pass mode, at temperatures of 5, 10 and 20 K. Gunn diodes operating at 95 or 115 GHz, equipped with a frequency doubler were used as source excitation. The amorphous samples of **2** and **3** used for the experiments were crushed using a mortar and pestle and pressed in a pellet. Spin-Hamiltonian calculations and simulation of HF-EPR spectra were carried out as described elsewhere [5]. The uncertainty in the spin-Hamiltonian parameters obtained by simulation of HF-EPR spectra is of the order of ±1 on the last significant digit.

3. Results and discussion

3.1. Synthesis

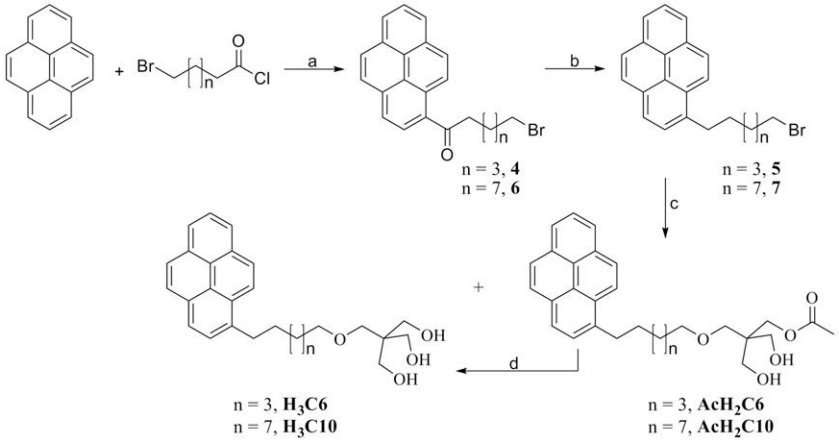
The two novel pyrenyl ligands were synthesised as shown in Scheme 2. Pyrene was acylated with the appropriate ω-bromoalkanoyl chloride through a classical Friedel-Crafts reaction [12,13]. The subsequent reduction of the carbonyl moiety was carried out in mild conditions [14] to give the corresponding 1-(ω-bromoalkyl)pyrene (**5**, **7**) in good yields without need of purification. The next step, i.e. the coupling reaction of 1-(ω-bromoalkyl)pyrene with (1-methyl-2,6,7-trioxabicyclo[2.2.2]octan-4-yl)methanol, proved not to be trivial. Literature procedures employing KOH in DMSO [15,16] lead almost exclusively to the formation of elimination by-products. Strictly anhydrous conditions with NaH as base and catalytic TBABr proved to be the most successful strategy to the desired products. Interestingly, the work-up conditions allowed to isolate both the totally deprotected tripods and the monoacetylated derivatives, which were quantitatively hydrolyzed to give the target compounds **H_3C6** and **H_3C10**.

The coordinating ability of the two new ligands was tested using ^{2}H NMR. When samples are isotopically enriched on the *t*Bu groups of dpm$^-$ ligands, the paramagnetically-shifted ^{2}H NMR signals allow to easily monitor structural changes in the tetrairon(III) core [3,5]. Toluene solutions of the deuterated complex [$Fe_4(OMe)_6$(dpm-d_{18})$_6$] (**1-*d***) showed time dependent ^{2}H NMR spectra, as previously reported for Et_2O solutions [3]. If spectra are recorded immediately after the dissolution two distinct signals appear at δ = 10.3 and at 12.7 ppm in a 91:9 ratio, which are assigned respectively to the intact tetrairon(III) species and to a magnetically uncoupled Fe(dpm) complex. After 24 h, the latter signal is largely dominant and after 6 days dpm$^-$ is present exclusively as monomeric Fe(dpm) complexes and as free ligand (δ = 0.9 ppm) (Fig. 1a).

The above-described trend is drastically affected if an excess of tripodal ligand (2.7 eq.) is added to a 1.6 mM solution of **1-*d*** in toluene (see Fig. 1b and c). The ratio between the signals at 10.3 ppm and at 12.7 ppm is 4:1 short after preparation and raises to 7:1 after 24 h. After 6 days the spectra are dominated by the resonance from intact tetrairon(III) complexes, with only very weak signals at 12.7 ppm and at 0.9 ppm. Thus, the two tripods **H_3C6** and **H_3C10** show the same coordinating ability and stabilize tetrairon(III) complexes over long timescales. Indeed, very similar spectra were obtained using the shorter-chain ligand **H_3C4**, whose tetrairon(III) complex could be isolated in crystalline form [9].

To gain further evidence, the same solutions were analysed with ESI-MS, a unique tool for the determination of the molecular mass of large and labile molecules. The ESI (+) spectra revealed signals centred at m/z = 2289 and 2401, attributable to [**2-*d*** + Na^+] and [**3-*d*** + Na^+], respectively. A remarkable agreement between the theoretical masses and the reconstructed ESI isotope patterns was found, thus confirming the ^{2}H NMR data.

Unfortunately, all attempts to isolate product clusters in crystalline form failed. The complexes were thus assembled in dry toluene solution using excess ligand, the solvent was removed in vacuo and the solid was extracted with dry *n*-hexane, since the solubility of **H_3C6** and **H_3C10** in this solvent is as low as 10^{-5} M (data obtained by UV–Vis analysis of saturated solutions). Solvent removal from the filtered extracts led to **2** and **3** as dark orange amorphous solids in good yield.



Scheme 2. Synthesis of the ligands **H_3C6** and **H_3C10**. Experimental conditions: (a) $AlCl_3$, DCE, −10 °C to room temperature, 18 h; (b) $AlCl_3$, $LiAlH_4$, Et_2O/DCM, 1–2 h room temperature; (c) (1-methyl-2,6,7-trioxabicyclo[2.2.2]octan-4-yl)methanol, NaH, THF, TBABr, 3–5 days, room temperature and (d) NaOMe, MeOH, room temperature, 1 day.

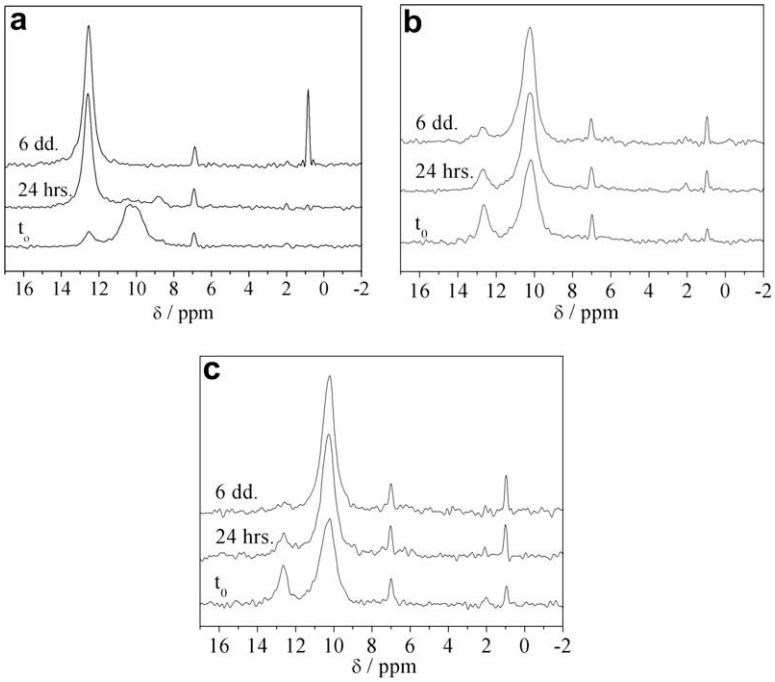


Fig. 1. Time-dependent ^{2}H NMR spectra of tetrairon(III) complexes in toluene solution at 302 K (t_0 labels freshly prepared solutions). (a) 1.57 mM solution of **1-*d***. (b) 1.55 mM solution of **1-*d*** with addition of excess tripodal ligand **H_3C6**. (c) 1.64 mM solution of **1-*d*** with addition of excess tripodal ligand **H_3C10**.

3.2. Solution characterization

Tetrairon(III) clusters with general formula $[Fe_4(L)_2(dpm)_6]$, although strongly paramagnetic, exhibit a quite distinctive ^{1}H NMR resonance arising from *t*Bu protons, whose very broad signal is observed at ca. 10.4 ppm at room temperature. The tripodal ligands L^{3-}, when coordinated, do not show any observable NMR signal from ^{1}H nuclei lying closer to the metal centers, such as C1 hydrogens and the first few CH_2 groups of alkyl substituents (refer to Scheme 1 for the atom numbering) [5]. The ^{1}H NMR spectrum of **2** in toluene-d_8 is presented in Fig. 2a. In addition to the above-mentioned *t*Bu signal, the spectrum comprises a group of broad resonances at 7.93–7.70 ppm arising from the 18 aromatic protons of the pyrenyl rings, which display unresolved hyperfine splittings. In the spectral region spanned by C1, C3, C4 and C9 hydrogens of the free ligand (δ = 3.6–3.1 ppm), a broad signal is observed at 3.3 ppm, whose integrated intensity corresponds to four protons only. This resonance is assigned to C9 protons, which lie farthest from the metal centers (see Supporting Information for the ^{1}H NMR spectrum of **H_3C10** in toluene-d_8). Integration of the broad signal at 1.72–1.33 ppm also indicates that, beside C4, additional protons of the aliphatic spacer escape NMR detection, thus lending further support to metal complexation. The longer alkyl spacer in **3** coherently affords sharper NMR resonances from pyrenyl and C13 hydrogens, as shown in Fig. 2b. Finally, traces of *n*-hexane are clearly detectable in both spectra (ca. 1.0 and 0.5 molecules per cluster for **2** and **3**, respectively).

Pyrenyl derivatives are widely used as fluorescent probe molecules for crucial applications, as chemosensors for metal ions [17], optical switches [18] and hybridization fluorescence sensors for polynucleotides [19], just to cite few. The fluorescence changes of pyrene hydroxamate derivatives due to metal ion complexation were studied in detail by Fages and coworkers. Complexation of iron(III) by a trichromophoric tripodal hydroxamate ligand was found to induce almost quantitative quenching of the fluorescence emission of the ligand [20].

The fluorescence spectra of dilute solutions of **H_3C6** and **H_3C10** (Fig. 3) in toluene show the monomer emission, patterned in five principal vibronic bands, while the broad excimer emission around 485 nm is almost not detectable, as expected for dilute solutions of pyrene derivatives. The relative intensity of peak III to peak I (see Fig. 3), known to be solvent sensitive, was found to be around

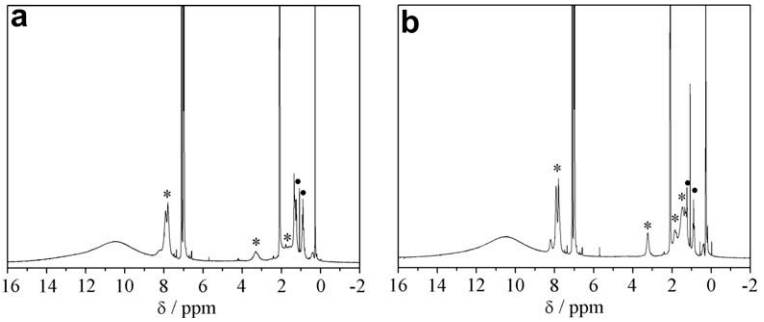


Fig. 2. ^{1}H NMR spectra of **2** (a) and **3** (b) in toluene-d_8. The signals labelled with $*$ are ascribed to tripodal ligands, while the signals marked with ● are due to traces of *n*-hexane.

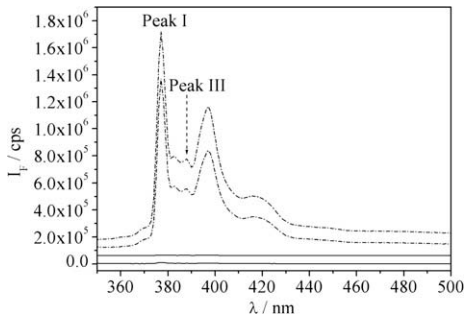


Fig. 3. Fluorescence spectra of 10^{-4} M solutions of **2** (grey, upper solid line) and **3** (black, lower solid line) in toluene. The fluorescence spectra of the free ligands **H_3C6** (grey, upper dash-dot line) and **H_3C10** (black, lower dash-dot line) are also reported for comparison at similar concentration (ligand and cluster samples were totally absorbing at λ_{exc} = 300 nm).

0.43, smaller than for toluene solutions of unsubstituted pyrene [21], but similar to the ratio found with other 1-substituted pyrene derivatives [22]. The spectra of **2** and **3** revealed a virtually complete excitation energy transfer (EET) from the S_1 state of pyrene to the chromophoric iron cluster ($\Phi_{EET} \geqslant 0.99$ for **2**, $\Phi_{EET} \sim 1$ for **3**, respectively, see Fig. 3). The residual very weak fluorescence might be attributed to traces of free ligand.

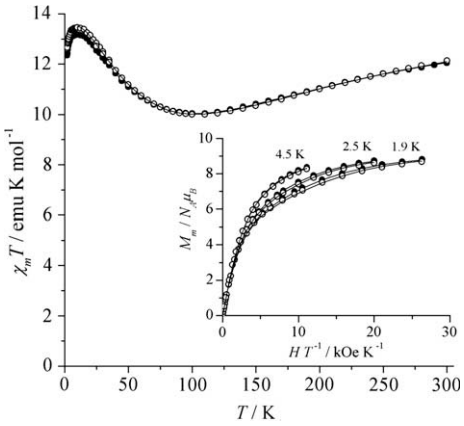


Fig. 4. DC magnetic properties of **2** (solid symbols) and **3** (void symbols). The solid lines provide the best fit to the experimental data with the following spin-Hamiltonian parameters: (for **2**) J_1 = 13.79(2) cm^{-1}, J_2 = −0.903(14) cm^{-1}, g = 1.8782(5); (for **3**) J_1 = 14.48(4) cm^{-1}, J_2 = −0.46(2) cm^{-1}, g = 1.8996(8). The inset shows isothermal magnetization data, along with the best-fit simulations obtained with (for **2**) D = −0.349(4) cm^{-1}, g = 1.852(3) and (for **3**) D = −0.386(6) cm^{-1}, g = 1.858(4). The spin-Hamiltonians used are defined in Ref. [5].

A full EET is consistent with the observation that the efficiency of quenching was independent of the length of the spacer alkyl chain.

3.3. Magnetic properties and HF-EPR spectra

The magnetic properties of **2** and **3** have been investigated using magnetic measurements and HF-EPR spectroscopy on powder samples. The $\chi_m T$ product of **2** and **3**, where χ_m is molar magnetic susceptibility and T is absolute temperature, is reported in Fig. 4 as a function of T. The overall trend is typical for tetrairon(III) propellers, the low-T increase of the magnetic moment being due to the selective population of the ground S = 5 state [3]. However, the maximum $\chi_m T$ value observed around 10 K in the two compounds is 13.2 emu K mol^{-1} (**2**) and 13.4 emu K mol^{-1} (**3**), hence ca. 10% lower than the Curie constant for an S = 5 spin state (15.0 emu K mol^{-1} with g = 2.00, as appropriate for high-spin iron(III)). The discrepancy, which exceeds the experimental accuracy of magnetic measurements, is confirmed by the unphysically low g values obtained by the quantitative analysis of $\chi_m T$ versus T and M_m versus H data (see caption to Fig. 4) using a well-established spin-Hamiltonian formalism [5]. The fit is otherwise excellent and affords spin-Hamiltonian parameters close to those observed in many other tetrairon(III) propellers [3,5]. It is likely that diamagnetic or weakly magnetic impurities arising from chemical manipulations contribute to decrease the magnetic response of the investigated samples, which are noncrystalline and difficult to purify.

Deeper insight was provided by the fine structure of the ground spin state as revealed by variable-temperature HF-EPR at 190 and 230 GHz. The spectra recorded at the higher frequency are gathered in Fig. 5, while 190-GHz spectra can be found in the Supporting Information. They are typical for high-spin species with an easy axis anisotropy [23] and can be accurately reproduced with the following spin-Hamiltonian parameters, as defined in Ref. [5]: for **2**, D = −0.421 cm^{-1}, E = 0.009 cm^{-1}, $B_4^0 = 1.8 \times 10^{-5}$ cm^{-1}; for **3**, D = −0.422 cm^{-1}, E = 0.008 cm^{-1}, $B_4^0 = 2.3 \times 10^{-5}$ cm^{-1} (S = 5 and g = 2.000 ± 0.005 throughout). Thus, the two complexes have identical magnetic anisotropy within experimental error. Furthermore, their spin-Hamiltonian parameters are typical for tetrairon(III) propellers $[Fe_4(L)_2(dpm)_6]$, in which the tripodal ligands adopt a η^2, η^2, η^2, μ_4 coordination mode [3–7].

4. Conclusion

Two novel tetrairon(III) SMM designed to bind graphene surfaces through pyrenyl groups were synthesised using new tripodal ligands with spacers of different length. Although the new compounds could not be isolated as crystalline solids suitable for X-ray diffraction studies, their molecular structure was inferred from

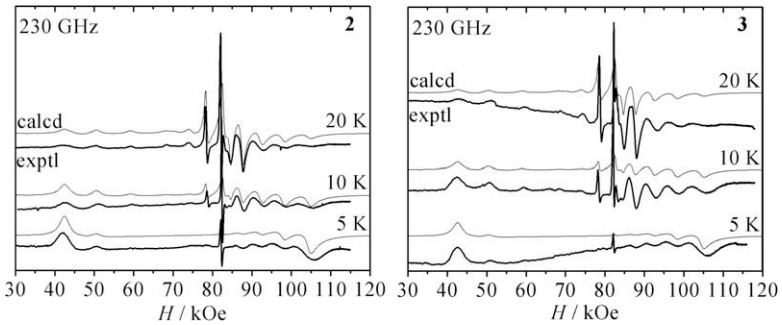


Fig. 5. HF-EPR spectra of **2** and **3** recorded at 230 GHz and at three different temperatures. The free electron resonance is found at H_0 = 82.1 kOe. The thin lines are best-fit simulations obtained with the parameters reported in the text.

^{1}H NMR and fluorescence spectra, magnetic measurements and HF-EPR. In particular, the typical ground spin state of $[Fe_4(L)_2(dpm)_6]$ complexes ($S = 5$ with a negative D parameter) was clearly revealed by HF-EPR.

Acknowledgments

We gratefully acknowledge Mr. Luca Zuppiroli (Department of Organic Chemistry, Faculty of Industrial Chemistry, University of Bologna, Italy) for ESI-MS experiments and the staff of CIGS (Centro Interdipartimentale Grandi Strumenti, University of Modena and Reggio Emilia) for assistance during ^{2}H NMR experiments.

This work was supported by the European Union through ERANET project "NanoSci-ERA: NanoScience in the European Research Area" (SMMTRANS) and NE "MAGMANET" (FP6-NMP3-CT-2005-515767).

Appendix A. Supplementary data

Supplementary data associated with this article can be found, in the online version, at doi:10.1016/j.poly.2008.12.024.

References

[1] (a) L. Bogani, W. Wernsdorfer, Nat. Mater. 7 (2008) 179. and references cited therein;
(b) E.K. Brechin, Chem. Commun. (2005) 5141;
(c) M. Mannini, F. Pineider, Ph. Sainctavit, L. Joly, A. Fraile-Rodriguez, M.-A. Arrio, W. Wernsdorfer, A. Cornia, D. Gatteschi, R. Sessoli, Adv. Mater. 21 (2009) 167;
(d) C. Schlegel, J. van Slageren, M. Manoli, E.K. Brechin, M. Dressel, Phys. Rev. Lett. 101 (2008) 147203;
(e) R.W. Saalfrank, A. Scheurer, I. Bernt, F.W. Heinemann, A.V. Postnikov, V. Schünemann, A.X. Trautwein, M.S. Alam, H. Rupp, P. Müller, Dalton Trans. (2006) 2865.
[2] A.-L. Barra, A. Caneschi, A. Cornia, F. Fabrizi de Biani, D. Gatteschi, C. Sangregorio, R. Sessoli, L. Sorace, J. Am. Chem. Soc. 121 (1999) 5302.
[3] S. Accorsi, A.-L. Barra, A. Caneschi, G. Chastanet, A. Cornia, A.C. Fabretti, D. Gatteschi, C. Mortalò, E. Olivieri, F. Parenti, P. Rosa, R. Sessoli, L. Sorace, W. Wernsdorfer, L. Zobbi, J. Am. Chem. Soc. 128 (2006) 4742.
[4] A. Cornia, A.C. Fabretti, P. Garrisi, C. Mortalò, D. Bonacchi, D. Gatteschi, R. Sessoli, L. Sorace, W. Wernsdorfer, A.-L. Barra, Angew. Chem. Int. Ed. 43 (2004) 1136.
[5] A.-L. Barra, F. Bianchi, A. Caneschi, A. Cornia, D. Gatteschi, L. Gorini, L. Gregoli, M. Maffini, F. Parenti, R. Sessoli, L. Sorace, A.M. Talarico, Eur. J. Inorg. Chem. 26 (2007) 4145.
[6] A. Cornia, L. Gregoli, C. Danieli, A. Caneschi, R. Sessoli, L. Sorace, A.-L. Barra, W. Wernsdorfer, Inorg. Chim. Acta 361 (2008) 3481.
[7] G.G. Condorelli, A. Motta, G. Pellegrino, A. Cornia, L. Gorini, I.L. Fragalà, C. Sangregorio, L. Sorace, Chem. Mater. 20 (2008) 2405.
[8] M. Mannini, F. Pineider, Ph. Sainctavit, C. Danieli, E. Otero, C. Sciancalepore, A.M. Talarico, M.-A. Arrio, A. Cornia, D. Gatteschi, R. Sessoli, Nat. Mater., in press.
[9] L. Bogani, C. Danieli, E. Biavardi, N. Bendiab, A.-L. Barra, E. Dalcanale, W. Wernsdorfer, A. Cornia, Angew. Chem. Int. Ed. 48 (2009) 746.
[10] T.J. Dunn, W.L. Neumann, M.M. Rogic, S.R. Woulfe, J. Org. Chem. 55 (1990) 6368.
[11] R. Srinivasan, M. Uttamchandani, S.Q. Yao, Org. Lett. 8 (2006) 713.
[12] P. Babu, N.M. Sangeetha, P. Vijaykumar, U. Maitra, K. Rissanen, A.R. Raju, Chem. Eur. J. 9 (2003) 1922.
[13] S.S. Atik, C.L. Kwan, L.A. Singer, J. Am. Chem. Soc. 101 (1979) 5696.
[14] A.K. Boal, V.M. Rotello, J. Am. Chem. Soc. 124 (2002) 5019.
[15] R.A. Findeis, L.H. Gade, Dalton Trans. (2003) 249.
[16] J.A. Camerano, M.A. Casado, M.A. Ciriano, F.J. Lahoz, L.A. Oro, Organometallics 24 (2005) 5147.
[17] A.P. de Silva, H.Q.N. Gunaratne, T. Gunnlaugsson, A.J.M. Huxley, C.P. McCoy, J.T. Rademacher, T.E. Rice, Chem. Rev. 97 (1997) 1515.
[18] P. Wessig, S. Czapla, U. Schedler, Helv. Chim. Acta 91 (2008) 1166.
[19] A.A. Martí, S. Jockusch, N. Stevens, J. Ju, N. Turro, Acc. Chem. Res. 40 (2007) 402.
[20] F. Fages, S. Leroy, T. Soujanya, J.-E. Sohna Sohna, Pure Appl. Chem. 73 (2001) 411.
[21] K. Kalyanasundaram, J.K. Thomas, J. Am. Chem. Soc. 99 (1977) 2039.
[22] B. Bodenant, F. Fages, M.-H. Delville, J. Am. Chem. Soc. 120 (1998) 7511.
[23] A.-L. Barra, L.-C. Brunel, D. Gatteschi, L. Pardi, R. Sessoli, Acc. Chem. Res. 31 (1998) 460.

Polyhedron 28 (2009) 2036–2038

Contents lists available at ScienceDirect

Polyhedron

journal homepage: www.elsevier.com/locate/poly

Spin transition in heptanuclear star-shaped iron(III)–antimony(V) NCS- and CN-bridged compounds

F. Renz [a,b,*], C. Zaba [a], L. Roßberg [a], St. Jung [a,b], M. Klein [a,b], G. Klingelhöfer [a], A. Wünsche [a], S. Reinhardt [a], M. Menzel [c]

[a] Institute for Inorganic Chemistry and Analytical Chemistry, Johannes Gutenberg-University, Duesbergweg 10-14, D-55099 Mainz, Germany
[b] Institute for Inorganic Chemistry, Leibniz University Hannover, Callin Str. 9, D-30167 Hannover, Germany
[c] Federal Institute for Materials Research and Testing (BAM), Richard-Willstätter Str. 11, D-12489 Berlin, Germany

ARTICLE INFO

Article history:
Available online 13 May 2009

Keywords:
Heptanuclear
High-spin molecule
Sb^V
Multistability
Multiple spin transition

ABSTRACT

The precursor $[Fe^{III}(L)Cl]$ (LH_2 = *N*,*N*′-bis(2′-hydroxy-benzyliden)-1,6-diamino-3-azahexane) has been prepared and Mössbauer spectroscopy assigned a high-spin ($S = 5/2$) state at room temperature. The precursor is combined with the bridging units $[Sb^V(X)_6]^-$ ($X = CN^-$, NCS^-) to yield star-shaped heptanuclear clusters $[(LFe^{III}–X)_6Sb^V]Cl_5$. The star-shaped compounds are in general high-spin systems at room temperature. On cooling to 20 K some of the iron(III) centers switch to the low-spin state as indicated by Mössbauer spectroscopy, i.e. multiple electronic transitions. While the cyano-bridged complex performs a multiple spin transition the thiocyanate-compound shows no significant population at both temperatures.

© 2009 Published by Elsevier Ltd.

1. Introduction

The phenomenon of switching molecules is an important researchers field in various scientific disciplines. An approach is to generate multistable molecules, i.e. physically and chemically induced transition between electronic states [1]. For multinuclear compounds the spin transition is rare [1].

Our systematic approach [2–13] enabled us to apply chemical tuning on pentadentate ligand Fe(III) complexes as building units $[LFe^{III}–X]$ (L = bis(3-salicylidene aminopropyl) amine) and show multistability, e.g. multiple thermally induced transitions between low-spin (LS) $^2T(O_h)$ and high-spin (HS) $^6A(O_h)$ in various star-shaped compounds: tetranuclear [4], heptanuclear [3,5–9], nonanuclear [2,3,6–9] and dodecanuclear [10].

In the present work, we extend this approach and introduce a novel heptanuclear system. With antimony we introduce a main-group element as star-shaped center and modify the bridging units between cyanide and thiocyanate. Such pentanuclear Fe_6Sb compounds may be capable of performing six spin transitions in one cluster, e.g. between 6 and 30 unpaired electrons. Such star-shaped heptanuclear Fe_6Sb systems are potential spin crossover systems. Their high-spin to low-spin switching was investigated by Mössbauer spectroscopy.

2. Experimental

The ligand LH_2 = *N*,*N*′-bis(2′-hydroxy-benzyliden)-1,6-diamino-3-azahexane has been prepared [8]. Complexation with Fe(III) gives the used iron precursor $[Fe^{III}(L)Cl]$ (=[2,3/H/Sal-H/Fe/Cl]) (Fig. 1). The precursor is combined with the bridging central units $[Sb^V(X)_6]^-$ ($X = CN^-$, NCS^-) to yield star-shaped heptanuclear clusters $[(LFe^{III}–X)_6Sb^V]Cl_5$ (=[2,3/H/Sal-H/Fe/$Sb(X)_6$]) (see Fig. 2).

2.1. Precursor

The precursor was prepared as described in literature [8]. The dark brown powder was characterized by IR and ESI.

2.2. $[Sb^V(X)_6]^-$ ($X = CN^-$, NCS^-)

The antimony pseudohalogenides cyanides and thiocyanates were prepared with their analogous compound of antimony chloride and potassium cyanide and potassium thiocyanate in acetone under nitrogen atmosphere. The mixtures stirred for 6 days under reflux.

2.3. Heptanuclear clusters $[(LFe^{III}–X)_6Sb^V]Cl_5$ (=[2,3/H/Sal-H/Fe/$Sb(X)_6$]) ($X = CN^-$, NCS^-)

The complexes were prepared in analogy to the literature [2,8]. The reaction solution stirred for 30 min and cooled for 5 days. The products were characterized by ESI-MS, IR- and Mössbauer spectroscopy.

* Corresponding author. Address: Leibniz Universität Hannover Institut für Anorganische Chemie, Callin Str. 9, D-30167 Hannover, Germany. Tel.: +49 511 762 4541.
E-mail address: franz.renz@acd.uni-hannover.de (F. Renz).

0277-5387/$ - see front matter © 2009 Published by Elsevier Ltd.
doi:10.1016/j.poly.2008.12.027

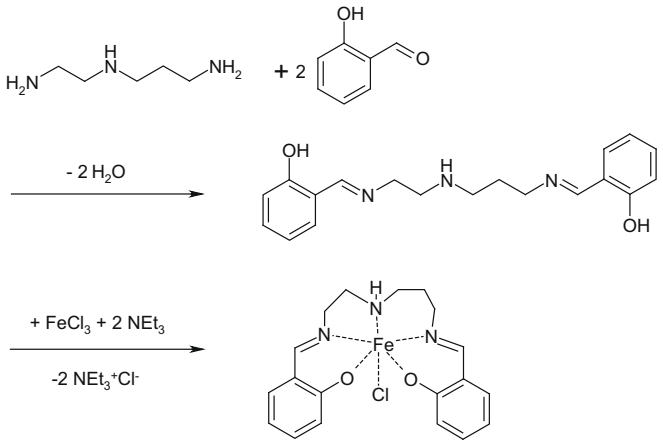


Fig. 1. Synthesis of the $[Fe^{III}(L)Cl]$ precursor.

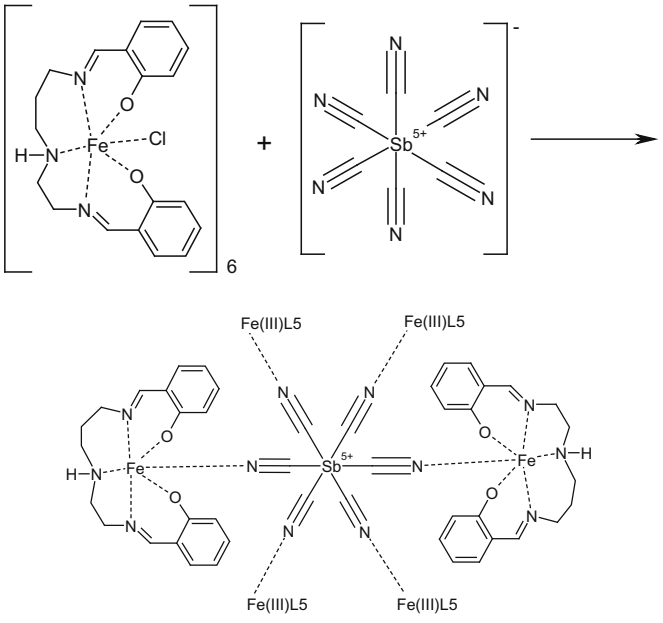


Fig. 2. Synthesis of the $[(LFe^{III}–X)_6Sb^V]Cl_5$ clusters, i.e. [2,3/H/Sal-H/Fe/Sb(X)6], (X = CN^-, NCS^-).

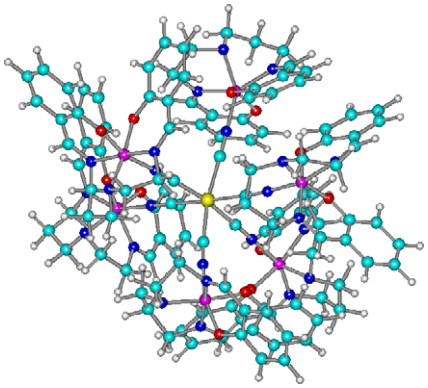


Fig. 3. MM+ structure of the $[(LFe^{III}–NC)_6Sb^V]^{5+}$.

2.3.1. IR-spectroscopy

A conventional MIR-IR spectrometer is used at ambient temperatures.

2.3.2. Mössbauer spectroscopy

The Mössbauer spectra were recorded using constant acceleration Mössbauer spectrometers. As a source ^{57}Co in rhodium is used.

3. Results and discussion

The schematic structure of the [2,3/H/Sal-H/Fe/Sb(X)$_6$] (X = CN^-, NCS^-) complexes are heptanuclear in star-shaped geometry. The complexes are characterized by IR-spectroscopy. They show, that a stretching vibration for a typical CN-bond shifts on bridging from 2080 to above 2100 cm^{-1}. For a typical NCS-bond this effect is less pronounced on bridging from 2050 to above 2060 cm^{-1}.

As central star-element antimony was used in the oxidation-state +5. This antimony(V) is coordinated to six precursors bridged via cyanide or rhodanide. The MM+ force field structure of the $[(LFe^{III}–NC)_6Sb^V]^{5+}$ complex is shown in Fig. 3.

Fig. 4 and Table 1 show the Mössbauer spectra and data of $[(LFe^{III}–NC)_6Sb^V]Cl_5$. At room temperature a doublet is seen which is characteristic for iron(III) in the high-spin state with 66% of the area fraction. A second doublet is characteristic for iron(III) in the low-spin state. On cooling to 20 K the same two doublets are observed being characteristic for iron(III) in the low-spin and high-spin state. Some of the molecules have been converted from high-spin to the low-spin state. This is indicative for a thermally-induced spin-crossover.

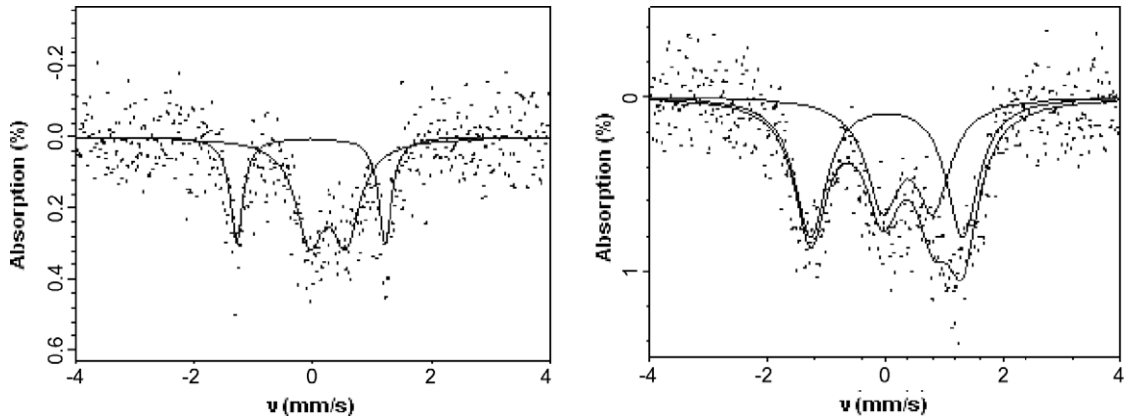


Fig. 4. Mößbauer spectra of $[(LFe^{III}–NC)_6Sb^V]Cl_5$ measured at 300 K (left) and 20 K (right).

Table 1
Mössbauer parameter of $[(LFe^{III}–NC)_6Sb^V]Cl_5$ for Fe at room temperature and 20 K.

	Fe/295 K	Fe/20 K	Comparison
	2 doublets symmetric	2 doublets symmetric	
δ (mm/s)	**1. D** 0.252	**1. D** 0.388	Rel. Fe/Rh
Δ (mm/s)	0.608	0.855	
Fraction /%	66.2	44.1	−22.1
δ (mm/s)	**2. D** −0.032	**2. D** 0.026	Rel. Fe/Rh
Δ (mm/s)	2.496	2.580	
Fraction (%)	33.8	55.9	+22.1

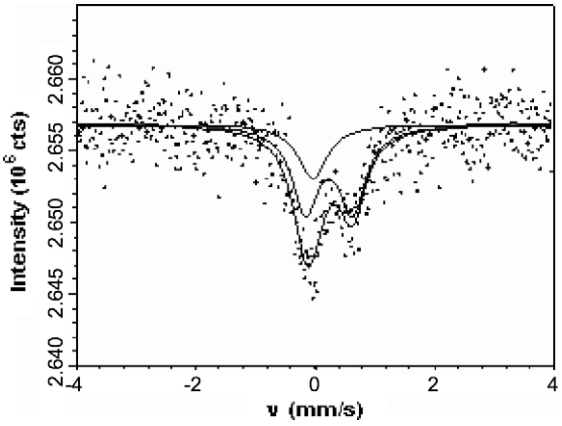


Fig. 5. Mößbauer spectra of $[(LFe^{III}–NCS)_6Sb^V]Cl_5$ measured at 300 K.

Fig. 5 shows the Mössbauer spectra of $[(LFe^{III}–NCS)_6Sb^V]Cl_5$ at room temperature. The spectra shows an asymmetric signal which is indicative for iron(III) in the high-spin state. There is no sign of iron(III) in the low-spin state. The modification of the cyano-bridge by a thiocyanate-bridge eliminates the iron(III) in the low-spin state at room temperature.

4. Conclusion

The ^{57}Fe-Mössbauer data indicate that the $[(LFe^{III}–NC)_6Sb^V]Cl_5$ show multiple spin transitions between iron(III) in the high-spin and low-spin state. Changing the bridging unit from CN^- to NCS^- all iron-centers in $[(LFe^{III}–NCS)_6Sb^V]Cl_5$ are converted to Fe(III) in the high-spin state at 300 K.

The results show that the CN-bridged compound performs molecular switching. Modification of the bridging unit from cyanide to thiocyanate keeps all units in the high-spin state at 300 K. This proves the usage of main group elements such as antimony as central atoms in switching molecules.

Acknowledgements

This work was partly funded by the University of Mainz (“Forschungsfond”; MWFZ), the Leibniz University of Hannover, and the “Deutsche Forschungsgemeinschaft” (DFG: Re-1627/1-3).

References

[1] P. Gütlich, P. van Koningsbruggen, F. Renz, In Optical Spectra and Chemical Bonding in Transition Metal Complexes, Structure and Bonding, Springer-Verlag 107 (2004) 27.
[2] F. Renz, P. Kerep, Hyperfine Interact. 156–157 (2004) 371.
[3] F. Renz, P. Kerep, Polyhedron 24 (2005) 2849.
[4] R. Herchel, R. Boča, M. Gembickŷ, J. Kožiŝek, F. Renz, Inorg. Chem. 43 (2004) 4103.
[5] M. Gembicky, R. Boca, F. Renz, Inorg. Chem. Commun. 3 (2000) 662.
[6] F. Renz, J. Hefner, D. Hill, M. Klein, Polyhedron 26 (2007) 2330.
[7] F. Renz, D. Hill, P. Kerep, M. Klein, R. Müller-Seipel, F. Werner, Hyperfine Interact. 168 (2006) 1051.
[8] F. Renz, P. Kerep, D. Hill, M. Klein, Hyperfine Interact. 168 (2006) 981–987.
[9] M. Klein, F. Renz, Hyperfine Interact. 168 (2006) 1001.
[10] F. Renz, D. Hill, M. Klein, J. Hefner, Polyhedron 26 (2007) 2325.
[11] R. Boca, Y. Fukuda, M. Gembicky, R. Herchel, R. Jarosciak, W. Linert, F. Renz, J. Yuzurihara, Chem. Phys. Lett. 325 (2000) 411.
[12] M. Glockle, W. Kaim, A. Klein, E. Roduner, G. Hubner, S. Zalis, J. van Slageren, F. Renz, P. Gütlich, Inorg. Chem. 40 (2001) 2256.
[13] M. Boca, P. Baran, R. Boca, H. Fuess, G. Kickelbick, W. Linert, F. Renz, I. Svoboda, Inorg. Chem. 39 (2000) 3205.

Polyhedron 28 (2009) 2039–2043

Contents lists available at ScienceDirect

Polyhedron

journal homepage: www.elsevier.com/locate/poly

The DFT rationalization of exchange and anisotropy in one-dimensional *d-p* magnets: The [Mn^{III}(porphyrin)][TCNE] case study

Fanica Cimpoesu [a,*], Marilena Ferbinteanu [b], Bogdan Frecuş [c], Mihai A. Gîrţu [c,*]

[a] Institute of Physical-Chemistry, Splaiul Independenţei 202, Bucharest 060021, Romania
[b] University of Bucharest, Inorganic Chemistry Department, Dumbrava Roşie 23, Bucharest 020462, Romania
[c] Ovidius University od Constanţa, Department of Physics, Bd. Mamaia 124, Constanţa 900527, Romania

ARTICLE INFO

Article history:
Available online 24 February 2009

Keywords:
Manganese porphyrin
Density functional theory
Exchange interactions
Ligand Field modeling
Magnetic anisotropy

ABSTRACT

We report here numerical experiments, modeling and interpretations dealing with the magnetic interactions necessary for building nano-scale magnets in quasi-one-dimensional systems based on the assembling of [Mn(porphyrin)]$^+$ magnetically anisotropic *d* units and TCNE-*p*-type spin carriers. The magnetic ordering and its coupling parameter are studied by Broken Symmetry DFT calculations for various model structures, allowing for the rationalization of geometry dependence of the effective exchange. The roles of the phenyl substituent, as well as of the basis set and the DFT functional used in the computation are discussed. The intrinsic anisotropy of these systems is studied in an original manner, extracting Ligand Field and Spin Orbit parameters by combined fits to non-relativistic and relativistic DFT calculations, allowing the explicit estimation of the Zero Field Splitting parameters.

© 2009 Elsevier Ltd. All rights reserved.

1. Introduction

The [Mn^{III}(porphyrin)]$^+$[cyanocarbon]$^-$ compounds form one of the most extensively studied families of molecular magnets [1]. The first member of the family was [MnTPP][TCNE] · *x*S [2], where (TPP = *meso*-tetraphenylporphyrinato, TCNE = tetracyanoethylene, and S = toluene). Since then a large variety of related compounds has been synthesized and characterized [3]. The manganese–porphyrin magnetic compounds are quasi-one-dimensional electron transfer salts consisting of chains of alternating metalloporphyrin electron donors and cyanocarbon electron acceptors. The adjacent spins along these chain alternate, $S_1 = 2$ on the donor and $S_2 = 1/2$ on the acceptor. This family of magnets provides the opportunity for the study of magnetic ordering because it offers a wide range of controlling factors [4]. For example the cyanocarbon bridge connecting the adjacent porphyrins can be varied to influence the intrachain interactions; different organic constituents can be added at the periphery of the porphyrin to affect the interchain interactions and, thereby, build up or reduce three-dimensional magnetic order; various solvents that may induce glassy behavior can be incorporated into the structure [4].

The mechanism for magnetic ordering proposed for the manganese–porphyrin compounds [MnTPP][TCNE] · *x*S, (S = toluene, *ortho*-xylene, and *ortho*-dichlorobenzene, etc.) is based on strong intrachain exchange, weak interchain dipole–dipole interactions and modest single-ion anisotropy all leading to canted magnetic ordering at low temperatures. The antiferromagnetic coupling (by strong kinetic superexchange of the order of 70 cm^{-1}) along the chain of unequal alternating spins leads to a 1D ferrimagnetic spin configuration [5]. Then, in the absence of superexchange pathways between the chains, the classical dipole–dipole interaction (coupling of about 10^{-3}–10^{-2} cm^{-1}) together with the onsite SIA (estimated to about 1–3 K) were proposed to produce canted magnets with critical temperatures around 10–15 K [5].

The motivation of the mechanism put forth was based on the results of fits of the dc susceptibility data to a model of alternating classical and quantum spins [6], which provided *J* of about −50 to −100 cm^{-1}, for certain [MnTPP][TCNE] · *x*S systems [5]. The fit was good in the range 50–350 K but at low temperatures deviations occurred, attributed to interchain interactions. However, an independent confirmation of the strength of the intrachain interaction and of the size of the single-ion anisotropy has been lacking.

A first theoretical approach attempted to correlate the critical temperatures with the overlap between the π^* SOMO of [TCNE]$^-$ and the d_z^2 SOMO of [Mn^{III}P]$^+$ [7]. Later on, CASSCF, CASPT2 and DFT/B3LYP calculations qualitatively reproduced the antiferromagnetic intrachain coupling and ferrimagnetic spin configuration along the chains [8]. However, it was found that the DFT techniques tend to overestimate the exchange coupling constant, while the ab initio approaches underestimate the experimental *J*s [8]. Moreover, based on the results obtained it was impossible to assign the mechanism of magnetic ordering in this family of compounds [8].

* Corresponding authors. Tel.: +40241606418; fax: +40241618372.
E-mail addresses: cfanica@yahoo.com (F. Cimpoesu), girtu@univ-ovidius.ro, mihai.girtu@gmail.com (M.A. Gîrţu).

0277-5387/$ - see front matter © 2009 Elsevier Ltd. All rights reserved.
doi:10.1016/j.poly.2009.01.014

More recently, Broken Symmetry DFT studies of the manganese–porphyrin–cyanocarbon dimer provided antiferromagnetic exchange constants of different strengths, depending on the functional used [9]. In this case, all DFT results underestimated the experimental value, obtained based on the Seiden fit, best results being obtained with UDFT/B3LYP, followed by UDFT/B2LYP and UHF. A subsequent study allowed the calculation of the zero-field-splitting that showed that the TCNE coordination hardly affects the magnetic anisotropy of $[Mn^{III}P]^+$, influencing significantly only the ferrimagnetic spin alignment [10]. The method used was based on UDFT calculations with BLYP, B2LYP and B3LYP functionals, the values obtained for D being all negative (about -0.8 to $-3.3\ cm^{-1}$) suggesting Ising-like anisotropy. The transverse component, E, was found to be at least two orders of magnitude smaller than D. Again, the three functionals provided different values, best results being obtained with UDFT/B3LYP.

Given the interest in this family of quasi-1D magnetic compounds, we report here DFT numerical experiments on the exchange coupling and magnetic anisotropy in manganese–porphyrin–cyanocarbon dimers.

2. Calculations

DFT calculations were carried out with the Gaussian03 [11] and ADF [12] packages using triple zeta polarized basis sets (6-311G* and TZP, respectively). The programs and functionals were used in the estimation of exchange coupling constant via Broken Symmetry calculations [13].

The reference system consisted in an experimental structure of the manganese–tetraphenyl–porphyrin system $[Mn^{III}TPP]^+[TCNE]^-$ [14]. In constructing the model dimer we added a Li^+ ion to the terminal CN group of the $[TCNE]^-$ radical, to mimic the polarization effects of the next metal ion. Furthermore, a HCN group *trans* coordinated to Mn^{III} is a substitute for the TCNE on the other side of the continued polymer. The resulting dimer proposed as a model for $[Mn^{III}TPP]^+[TCNE]^-$ systems is $\{(HCN)[MnTPP]^+[TCNE]^-Li^+\}$, with a $S_1 = 2$ on Mn^{III} and $S_2 = 1/2$ on $[TCNE]^-$.

Further idealization was done replacing the phenyl groups with H atoms and symmetrizing the slight deviation from the tetragonal symmetry, reducing the model to simple porphyrin within D_{4h} point group. The cartesian coordinates of the $[MnP]^+$ and $[MnTPP]^+$ units are presented in the Supplementary Data.

3. Results and discussion

3.1. Broken Symmetry calculations of exchange constants

The Yamaguchi–Onishi approach [15] was used to handle the BS DFT output and calculate the exchange constant. The illustration of the Broken Symmetry calculation is shown in Fig. 1, which gives an overall positive spin in the case of the unrestricted high spin (HS) system and the segregation of α and β bulk spin densities on MnTPP and TCNE units at the proper Broken Symmetry (BS) state computed at low spin projection. In both HS and BS spin density maps we observe areas with slight spin polarization.

Table 1
Broken Symmetry calculations of the J coupling constant in $[MnP]^+[TCNE]^-$ and $[MnTPP]^+[TCNE]^-$ dimers, reflecting the role of the phenyl substituent, the basis set and the DFT functional.

System	Code	Basis	Functional	$J\ (cm^{-1})$
[MnTPP][TCNE]	G03	6-311G*	B3LYP	−72.32
[MnTPP][TCNE]	G03	6-31G*	B3LYP	−73.97
[MnTPP][TCNE]	G03	6-311G*	BP86	−153.83
[MnTPP][TCNE]	G03	6-31G*	BP86	−153.15
[MnP][TCNE]	G03	6-311G*	B3LYP	−79.55
[MnP][TCNE]	G03	6-311G*	BP86	−182.70
[MnP][TCNE]	ADF	TZP	BP86	−171.74

Since the numerical calculations are usually performed on simplified models with porphyrin instead of the substituted ligands, we studied the impact of the substituent on the computed exchange constant. We also checked the influence of the basis set and the functional used. Moreover, the Gaussian and ADF calculations allowed the comparison between the Gaussian and the Slater-type atomic basis sets. The data are summarized in Table 1.

We note that the relative small differences between the computed J parameters of the $[MnP]^+$ and the substituted $[MnTPP]^+$, suggests that the use of H atoms instead of phenyl groups is a reasonable computational simplification. The conclusion that the organic constituents added at the periphery of the porphyrin have little effect on the intrachain exchange coupling is consistent with experimental suggestions that they affect mainly the interchain interactions by keeping the chains further apart and/or providing superexchange pathways [4].

From the data in Table 1 it can be seen that, once polarization effects are included, the differences between the basis sets do not lead to significant variations of the exchange constants. The functional, however, exerts a sensible role. It can be seen that the Becke-Perdew (BP86) functional gives higher absolute values of negative J, compared with the hybrid Becke and Lee-Yang-Parr (B3LYP) method. Corroborating this with the UHF versus UB3LYP comparison showing weaker antiferromagnetic coupling in the non-correlated HF case [9] we can infer that the functional part tends to give larger antiferromagnetic part, possibly overestimating its absolute values in certain circumstances. This issue deserves further exploration and a direct comparison to experiment, in order to determine the subtle balance between the better account of dynamical correlation and problems in long range functional dependence [16].

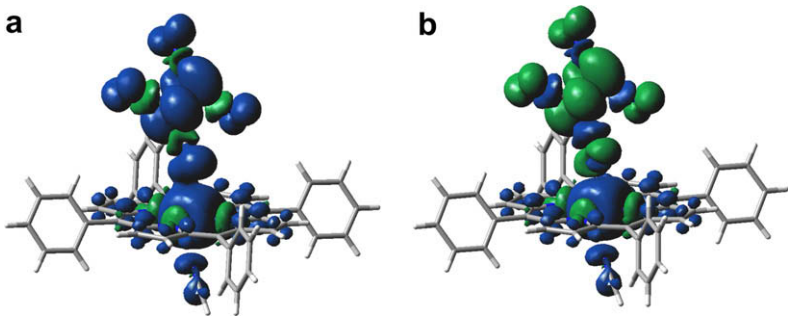


Fig. 1. The spin density isosurfaces for the [MnTPP][TCNE] system in unrestricted DFT (UB3LYP) calculations. (a) The high spin case (HS, $S_z = 5/2$) AND (b) the Broken Symmetry "low spin" configuration (BS, $S_z = 3/2$).

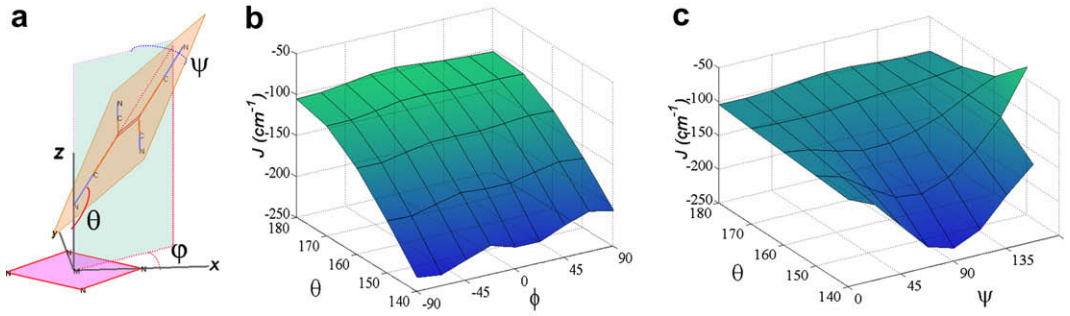


Fig. 2. (a) The geometry parameters defining the mutual orientation of the MnP and TCNE planes; (b) and (c) the dependence of computed J coupling constant ($J(\theta,\varphi)$ at $\Psi = 0$ and $J(\theta,\Psi)$ at $\varphi = 0$, respectively). The results are from Broken Symmetry (BS) BP86/6-311G* calculations with G03 code on the [MnP][TCNE] system.

Further, we studied the influence of the mutual orientation between the metal ion and the organic ligand on the strength of the exchange interaction. The important geometry parameters are shown in Fig. 2a. The orientation of the coordinating N≡C– group with respect to the metal ion is described by the angle θ, θ = Mn–N–C. The angle φ can be described either as the angle between the x axis of the porphyrin plane and the projection of the N≡C– group on that plane, or as the dihedral of a selected N(P)–Mn–N–C sequence. The angle Ψ, describes the rotation of the TCNE plane around the coordinating N≡C– group. The angle Ψ is the dihedral between the Mn–NC and TCNE planes. The Mn–NC is represented in Fig. 2a as a vertical plane, perpendicular to the porphyrin frame. At $\Psi = 0$ the TCNE plane is also perpendicular to the porphyrin.

Fig. 2b displays the dependence of the exchange coupling on θ and φ. It can be seen that the angle θ controls the σ and π overlapping, whereas the φ rotation does not change this balance, having a smaller effect. Fig. 2c presents the dependence of J on θ and Ψ. The Ψ parameter also defines the orientation of the p spin carrier with respect of the d-orbitals. At $\theta = 0$, when the NC group is aligned along the z axis, the Ψ angle does not change the balance of σ and π interaction channels. It affects only the distribution of the π effects among the yz and xz d-orbitals and since these are degenerate in the tetragonal symmetry, the Ψ dependence is not active, as is seen in the plateau of Fig. 2c. At lower values of θ, when the Ψ is about 90° the overlap between the p and the z^2 spin carriers is maximized, increasing the antiferromagnetism. At $\Psi = 0°$ or 180° the routes to z^2 are only orthogonal and, therefore, ferromagnetic. The other channels of π-type overlap, p-d_{xz} and p-d_{yz} remain antiferromagnetic, yielding in the sum the negative total J but with reduced magnitude. This explains the strong Ψ dependence in the lower θ side of Fig. 2c. A more detailed, analytical, description of these effects, realized by model fit to the computed J parametric surfaces is under construction.

3.2. Relativistic calculations and analytical modeling of magnetic anisotropy

The magnetic anisotropy is challenging to calculate, particularly in usual DFT codes, where there is no direct routine for it. An interesting and reliable approach was proposed by Yamaguchi and coworkers [17]. Their original program, GSO-ZFS, uses a wave function provided for instance by a preliminary Gaussian calculation, to compute the spin-orbit integrals and estimate the Zero Field Spitting (ZFS) by means of a perturbation scheme. The ZFS parameters obtained by the same group for $[Mn^{III}P]^+$ complexes [10] were in agreement with previous phenomenological estimations [5] and experimental values [18].

Here we approach the calculation of ZFS in the DFT frame by a different route, using results from ADF non-relativistic and relativistic calculations, followed by an appropriate handling with a Ligand Field (LF) and Spin Orbit (SO) model based on the following Hamiltonian:

$$\hat{H} = \hat{H}_{LF} + \hat{H}_{SO}. \tag{1}$$

The Ligand Field part is conveniently expressed in terms of standard tetragonal parameters Dq, Ds and Dt [19]:

$$\hat{H}_{LF} = 14Dq\sqrt{\pi}\left[Y_4^0 + \sqrt{\frac{5}{14}}(Y_4^4 + Y_4^{-4})\right] - 14Dt\sqrt{\pi}Y_4^0 - 14Ds\sqrt{\frac{\pi}{5}}Y_2^0, \tag{2}$$

where Y_l^m are the spherical harmonics, considered as operators. The energies of the d-orbitals are more transparently expressed by converting the set of Ds and Dt parameters into δ_e and δ_t

$$\delta_e = 2Ds - 6Dt, \tag{3a}$$
$$\delta_t = -Ds + 4Dt, \tag{3b}$$

which measure directly the gaps between the orbitals originating from the e_g and t_{2g} octahedral reference.

The Spin Orbit Hamiltonian in the one-electron form is:

$$\hat{H}_{SO} = \xi\hat{l}\cdot\hat{s}. \tag{4}$$

Our approach consists of the following steps:

(i.1). Non-relativistic DFT calculations provide orbital energies (Table 2) related to the LF parameters, $10Dq$, δ_e and δ_t (Table 3) by the formulas given in the second column of Table 2 and illustrated schematically on the left side of Fig. 3a.

(i.2). Relativistic DFT calculations determine molecular orbital energies (Table 4) used to evaluate the SO coupling parameter, ξ, by fitting the calculated energies with those provided by the 10 × 10 LF + SO Hamiltonian matrix (matrix A1, in the Supplementary Data) of the d spin-orbitals; the LF parame-

Table 2
Non-relativistic DFT calculations (with BP86/TZP setting in ADF code) providing the LF levels in the square-planar $[Mn^{III}(P)]^+$ and elongated octahedron $[Mn^{III}(P)(NCH)_2]^+$ complexes. The data are Kohn-Sham orbital energies, conventionally shifted to the barycenter.

Ligand Field formalism		Non-relativistic DFT	
D_{4h} point group symmetry	Ligand Field energies	$[Mn^{III}(P)]^+$ $\Delta\varepsilon$ (cm^{-1})	$[Mn^{III}(P)(NCH)_2]^+$ $\Delta\varepsilon$ (cm^{-1})
b_{2g} (xy)	$-4Dq - 2\delta_t$	−8572	−11151.7
e_g (xz,yz)	$-4Dq + \delta_t$	−2829.4	−5142.7
a_{1g} (z^2)	$6Dq - \delta_e$	−4087.6	5850.9
b_{1g} ($x^2 - y^2$)	$6Dq + \delta_e$	18,318.4	15,586.2

Table 3
Ligand Field parameters fitting the non-relativistic energies from Table 2.

Fitted Ligand Field parameters	$[Mn^{III}(P)]^+$ (cm^{-1})	$[Mn^{III}(P)(NCH)_2]^+$ (cm^{-1})
$10Dq$	11,859	17,864
δ_e	11,203	4867
δ_t	1914	2003

ters used in the LF + SO Hamiltonian matrix are those obtained in the previous step; the relationships between the orbital energies are illustrated on the right side of Fig. 3a.

(i.3). The LF and SO parameters obtained from the one-electron scheme of orbital energies are further used into the full many-electron LF + SO Hamiltonian applied to the ^5D term that corresponds to the d^4 configuration of the Mn^{III} ion (Fig. 3b). The SO coupling (expressed by the 25 × 25 Hamiltonian matrix discussed in formulas A3 of the Supplementary Data) splits the ^5D term into $(2L + 1)(2S + 1) = 25$ states, which can be further grouped based on their symmetry with respect to the LF interaction (Fig. 3b).

(i.4). The lowest energy levels with the same symmetry provided by the numerical diagonalization of the 25 × 25 Hamiltonian matrix in the previous step (the five levels with $^5B_{1g}$ symmetry in Fig. 3b) are the Zero-Field-Splitted levels from where the D parameter is obtained.

The advantage of the outlined procedure resides in the direct numerical calculation of the D parameter, with no need for the perturbation expressions usually invoked to express the ZFS terms as function of LF and SO parameters. By using a direct fit of the model Hamiltonians to DFT computed molecular orbitals and having the advent of D_{4h} symmetry that simplifies the model, it is not necessary to perform the projection techniques outlined by Atanasov et al. for extracting LF [20] and SO [21] parameters from DFT calculations.

The numerical experiments were applied comparatively to the idealized square-planar $[Mn^{III}(P)]^+$ and elongated octahedron $[Mn^{III}P(NCH)_2]^+$ complexes. The $[Mn^{III}(P)]^+$ unit, without axial ligands, was taken to discriminate the contribution due to the porfirine ligand itself. The $[Mn^{III}P(NCH)_2]^+$ case is taken to mimic the magnetic anisotropy of the manganese ion embedded in the chains of $[Mn^{III}TPP]^+[TCNE]^-$. In order to keep the convenient D_{4h} symmetry, the unit was idealized taking axially placed NCH groups as surrogate for the coordinating effect of the TCNE ligands along the chain. The fit following the steps *i*.1–*i*.4 described above gives rise to LF parameters placed in the usual range of strong field ligands and significant axial magnetic anisotropy.

The relation of orbital and spectral terms and the role played by the LF and SO effects is illustrated schematically in Fig. 3a and b. In

Table 4
Relativistic molecular orbital energies (DFT calculations with BP86/TZP using ADF).

D_{4h} double group symmetry	$[Mn^{III}(P)]^+$ $\Delta\varepsilon$ (cm^{-1})	$[Mn^{III}(P)(NCH)_2]^+$ $\Delta\varepsilon$ (cm^{-1})
Relativistic DFT		
$e_g^{3/2}$	−8509.1	−11,135.2
$e_g^{1/2}$	−4468.3	5818.5
$e_g^{1/2}$	−2839.1	−5400.6
$e_g^{3/2}$	−2629.4	−4957.0
$e_g^{3/2}$	18,445.8	15,674.5
Fitted Spin Orbit coupling		
ξ (cm^{-1})	480.8	374.6

the ^5D term the LF part can be simply taken as reverse of the orbital (d^1) scheme, since the d^4 configuration can be interpreted as an one-hole configuration. In this way, there is no need for explicit two-electron (Racah-type) parameters, the orbital data being sufficient for the recovery of the spectral terms and magnetic anisotropy of the d^4 ion. Passing from d^1 (orbital) to the d^4 (spectral term) description the $\xi\hat{l}\cdot\hat{s}$ one-electron Spin Orbit coupling is converted into the $\lambda\hat{L}\cdot\hat{S}$ Hamiltonian when taking $\lambda = \xi/6$.

The $10Dq$ parameter (Table 3) is higher in the modeled $[Mn^{III}P(NCH)_2]^+$complex than in the $[Mn^{III}(P)]^+$ unit because of axial ligand supplementary contribution into the former. In turn, the axial LF anisotropy expressed by the δ_e parameter is higher in the $[Mn^{III}(P)]^+$ because of the absence of axial ligands. The higher LF anisotropy can be qualitatively related to the larger absolute value of the ZFS parameter modeled in the $[Mn^{III}(P)]^+$ unit, $D = -0.65\ cm^{-1}$, as compared with $D = -0.40\ cm^{-1}$ in the $[Mn^{III}P(NCH)_2]^+$. The negative sign is determined by the stabilization of the $^5B_{1g}$ as LF groundstate. Although, the absolute parameters of the ZFS might be slightly underestimated, overall, the values of the D constant are consistent with those reported previously [5,10,17].

Our approach also provides the other LF–SO driven states corresponding to the ^5D set, or in other words, the Zero Field Splitting of all the Ligand Field spectral terms. Thus, it is interesting to note that the ZFS levels of the excited $^5A_{1g}$ states are fitted with a positive parameter, $D(^5A_{1g}) = +1.77\ cm^{-1}$ for $[Mn^{III}P(NCH)_2]^+$, and $D(^5A_{1g}) = +1.07\ cm^{-1}$ for $[Mn^{III}P(NCH)_2]^+$. This result is in line with the fact that in a compressed octahedron this state becomes lowest, imposing reversed magnetic anisotropy.

4. Conclusions

We reported calculations providing the magnetic exchange and anisotropy for $[Mn^{III}(porphyrin)]^+[TCNE]^-$ systems. By means of Broken Symmetry DFT calculations we studied the role of the Mn-TCNE bonding geometry on the intrachain exchange. We demonstrated that the phenyl substituent has a small influence on the

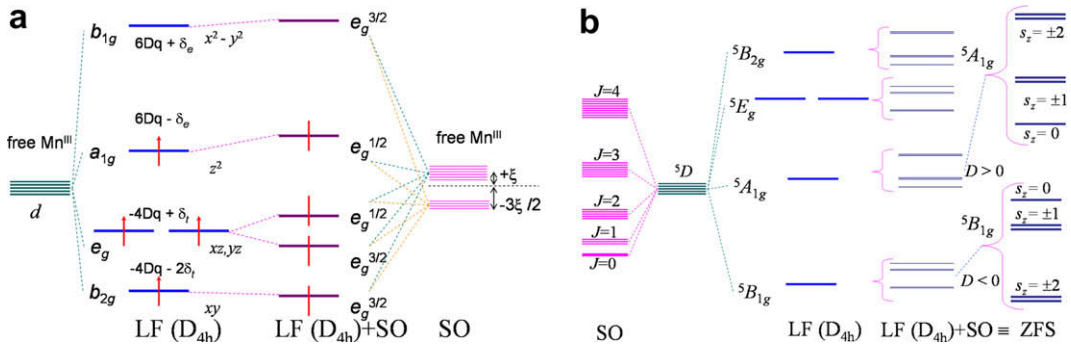


Fig. 3. The scheme of the Ligand Field (LF) + Spin Orbit effects (SO) in D_{4h} symmetry for: (a) one-electron states (*d*-orbitals) and (b) poly-electronic spectral terms of the d^4 configuration. The right extreme of the (b) panel shows the magnification of the ZFS pattern in the $^5B_{1g}$ ($D < 0$) and $^5A_{1g}$ ($D > 0$) terms.

intrachain coupling and confirmed that the values of J depend strongly on the DFT functional used. The ZFS parameters obtained by means of a combined relativistic and non-relativistic calculation are consistent with previous results, while the method proposed has the advantage of being very explicit in combining modern calculations and basic phenomenological concepts. Further exploration of the computation and modeling aspects, as well as the explicit correlation with available experimental data, make the object of future studies. The effect of the lower symmetry of the pseudo-tetragonal unit makes the object of future studies.

Acknowledgements

The authors acknowledge financial support from the Romanian Ministry of Education and Research through CNCSIS research grants PN2-PCE 174/2007 and PN2-PCCE 239/2009. Mihai A. Gîrţu is indebted to Professor Ken-ichi Sugiura, from Tokyo Metropolitan University, Japan, for providing structural data.

Appendix A. Supplementary data

Supplementary crystallographic data can be obtained free of charge via http://www.ccdc.cam.ac.uk/conts/retrieving.html, or from the Cambridge Crystallographic Data Centre, 12 Union Road, Cambridge CB2 1EZ, UK; fax: (+44) 1223-336-033, or e-mail: deposit@ccdc.ac.uk.

Supplementary data associated with this article can be found, in the online version, at doi:10.1016/j.poly.2009.01.014.

References

[1] M.A. Gîrţu, in: H.S. Nalwa (Ed.), Magnetic Nanostructures, American Scientific Publishers, Stevenson Ranch, CA, 2002, p. 360.
[2] J.S. Miller, J.C. Calabrese, R.S. McLean, A.J. Epstein, Adv. Mater. 4 (1992) 498.
[3] W. Hibbs, D.K. Rittenberg, K.-i. Sugiura, B.M. Burkhart, B.G. Morin, A.M. Arif, L. Liable-Sands, A.L. Rheingold, M. Sundaralingam, A.J. Epstein, J.S. Miller, Inorg. Chem. 40 (2001) 1915.
[4] A.J. Epstein, C.M. Wynn, M.A. Gîrţu, W.B. Brinckerhoff, K-i. Sugiura, J.S. Miller, Mol. Cryst. Liq. Cryst. 305 (1997) 321.
[5] C.M. Wynn, M.A. Gîrţu, W.B. Brinckerhoff, K-i. Sugiura, J.S. Miller, A.J. Epstein, Chem. Mater. 9 (1997) 2156;
C.M. Wynn, M.A. Gîrţu, K-i. Sugiura, E.J. Brandon, J.L. Manson, J.S. Miller, A.J. Epstein, Synth. Met. 85 (1997) 1695.
[6] J. Seiden, J. Phys. (Paris) Lett. 44 (1983) L-947.
[7] E.J. Brandon, C. Kollmar, J.S. Miller, J. Am. Chem. Soc. 120 (1998) 1822.
[8] J. Ribas-Arino, J.J. Novoa, J.S. Miller, J. Mater. Chem. 16 (2006) 2600.
[9] K. Koizumi, M. Shoji, Y. Kitagawa, T. Taniguchi, T. Kawakami, M. Okumura, K. Yamaguchi, Polyhedron 24 (2005) 2720.
[10] R. Takeda, K. Koizumi, M. Shoji, H. Nitta, S. Yamanaka, M. Okumura, K. Yamaguchi, Polyhedron 26 (2007) 2309.
[11] M.J. Frisch, G.W. Trucks, H.B. Schlegel, G.E. Scuseria, M.A. Robb, J.R. Cheeseman, J.A. Montgomery Jr., T. Vreven, K.N. Kudin, J.C. Burant, J.M. Millam, S.S. Iyengar, J. Tomasi, V. Barone, B. Mennucci, M. Cossi, G. Scalmani, N. Rega, G.A. Petersson, H. Nakatsuji, M. Hada, M. Ehara, K. Toyota, R. Fukuda, J. Hasegawa, M. Ishida, T. Nakajima, Y. Honda, O. Kitao, H. Nakai, M. Klene, X. Li, J.E. Knox, H.P. Hratchian, J.B. Cross, V. Bakken, C. Adamo, J. Jaramillo, R. Gomperts, R.E. Stratmann, O. Yazyev, A.J. Austin, R. Cammi, C. Pomelli, J.W. Ochterski, P.Y. Ayala, K. Morokuma, G.A. Voth, P. Salvador, J.J. Dannenberg, V.G. Zakrzewski, S. Dapprich, A.D. Daniels, M.C. Strain, O. Farkas, D.K. Malick, A.D. Rabuck, K. Raghavachari, J.B. Foresman, J.V. Ortiz, Q. Cui, A.G. Baboul, S. Clifford, J. Cioslowski, B.B. Stefanov, G. Liu, A. Liashenko, P. Piskorz, I. Komaromi, R.L. Martin, D.J. Fox, T. Keith, M.A. Al-Laham, C.Y. Peng, A. Nanayakkara, M. Challacombe, P.M.W. Gill, B. Johnson, W. Chen, M.W. Wong, C. Gonzalez, J.A. Pople, Gaussian 03, Revision C.02, Gaussian Inc., Wallingford, CT, 2004.
[12] ADF2006.01, SCM, Theoretical Chemistry, Vrije Universiteit, Amsterdam, The Netherlands, <http://www.scm.com>;
G. te Velde, F.M. Bickelhaupt, S.J.A. van Gisbergen, C. Fonseca Guerra, E.J. Baerends, J.G. Snijders, T. Ziegler, J. Comput. Chem. 22 (2001) 931;
C. Fonseca Guerra, J.G. Snijders, G. te Velde, E.J. Baerends, Theor. Chem. Acc. 99 (1998) 391.
[13] L. Noodleman, J. Chem. Phys. 74 (1981) 5737;
A. Bencini, F. Totti, Int. J. Quant. Chem. 101 (2005) 819.
[14] K-i. Sugiura, A. Arif, D.K. Rittenberg, J. Schweizer, L. Öhrstrom, A.J. Epstein, J.S. Miller, Chem. Eur. J. 3 (1997) 138;
Ken-ichi Sugiura, Tokyo Metropolitan University, Japan, private communication.
[15] M. Mitani, H. Mori, Y. Takano, D. Yamaki, Y. Yoshioka, K. Yamaguchi, Chem. Phys. 113 (2000) 4035;
T. Onishi, Y. Takano, Y. Kitagawa, T. Kawakami, Y. Yoshioka, K. Yamaguchi, Polyhedron 20 (2001) 1177.
[16] T. Leininger, H. Stoll, H.-J. Werner, A. Savin, Chem. Phys. Lett. 275 (1997) 151;
T. Sato, T. Tsuneda, K. Hirao, Mol. Phys. 103 (2005) 1151.
[17] M. Shoji, K. Koizumi, T. Hamamoto, T. Taniguchi, R. Takeda, Y. Kitagawa, T. Kawakami, M. Okumura, S. Yamanaka, K. Yamaguchi, Polyhedron 24 (2005) 2708.
[18] D.P. Goldberg, J. Telser, J. Krzystek, A.G. Montalban, L.-C. Brunel, A.G.M. Barrett, B.M. Hoffman, J. Am. Chem. Soc. 119 (1997) 8722;
J. Krzystek, J. Telser, L.A. Pardi, D.P. Goldberg, B.M. Hoffman, L.-C. Brunel, Inorg. Chem. 38 (1999) 6121.
[19] A.B.P. Lever, E.I. Solomon, in: E.I. Solomon, A.B.P. Lever (Eds.), Inorganic Electronic Structure and Spectroscopy, vol. I, John Willey and Sons, New York, 1999, p. 10 (and references therein).
[20] M.A. Atanasov, C.A. Daul, C. Rauzy, Chem. Phys. Lett. 367 (2003) 737.
[21] M.A. Atanasov, C. Rauzy, P. Baettig, C.A. Daul, J. Quantum Chem. 102 (2005) 119.

Polyhedron 28 (2009) 2044–2052

Contents lists available at ScienceDirect

Polyhedron

journal homepage: www.elsevier.com/locate/poly

Theory of chemical bonds in metalloenzymes XII: Electronic and spin structures of metallo–oxo and isoelectronic species and spin crossover phenomena in oxygenation reactions

Kizashi Yamaguchi [a,*], Mitsuo Shoji [b], Hiroshi Isobe [a], Syusuke Yamanaka [a], Jiro Shimada [c], Yasutaka Kitagawa [b], Mitsutaka Okumura [b]

[a] Center for Quantum Science and Technology Under Extreme Conditions (KYOKUGEN), Osaka University, Machikaneyama 1-1, Toyonaka, Osaka 560-8531, Japan
[b] Department of Chemistry, Graduate School of Science, Osaka University, Toyonaka, Osaka 560-0043, Japan
[c] NEC Corporation, Tsukuba, Ibaraki 305-8501, Japan

ARTICLE INFO

Article history:
Available online 6 February 2009

Keywords:
Fe(IV)=O core
O
O_2
Spin crossover
Broken-symmetry
Multideterminants
Isoelectronic analogy
Model Hamiltonian

ABSTRACT

The broken-symmetry (BS) and multideterminant approaches to atomic oxygen (O), molecular oxygen (O_2) and iron–oxo (Fe(IV)=O) core in P450 have elucidated electronic structures of the ground triplet and excited singlet states, which indicate isoelectronic characteristics of the species. The dissociation processes of the O–O and Fe–O double bonds are also examined to clarify the radical character, namely O-atom property responsible for radical mechanism of hydroxylations of alkanes and epoxidation of alkenes. This isolobal analogy has indeed enabled us to propose possible reaction mechanisms of oxygenation reactions by the Fe(IV)=O species on the basis of available theoretical and experimental results for O and O_2. Similarly an isolobal analogy of the σ^* bond among Fe(IV)=O, dioxirane, peracids, etc. indicates the common electrophilic property for the oxygenation reactions. The small energy gaps between the high- and low-spin states of the transition structures and intermediates generated in the oxygenation reactions are found to be origins for spin crossover phenomena along the reaction pathways of these reactions.

© 2009 Published by Elsevier Ltd.

1. Introduction

Active oxygen, oxyradicals and their metal-trapped species such as M=O, MOOH, etc. play important roles in various oxygenation reactions [1]. Past decades, electronic structures of metalloenzymes that catalyze oxygenation reactions have been extensively investigated by optical, magnetic, and many other experimental techniques [2–15]. Accumulated experimental results have elucidated a unified picture that the compound I consisted of the high-valent iron–oxo core [Fe(IV)=O] and ligand radical (•L), [(Fe(IV)=O) (•L)], is a common active species in catalase, peroxidase, P450, etc. Theoretical calculations [1] have also been performed for elucidation of electronic structure and reactivity of the compound I.

Transition-metal oxygen systems are generally characterized as strongly correlated electron systems with charge, spin, and orbital freedom [19,20]. For example, iron ions in heme enzymes exhibit valence fluctuations from divalent Fe(II) to pentavalent Fe(V) state, depending on ligand and other environment effects. The spin states of these species are variable from a low-spin singlet (diamagnetic, $S = 0$) to a high-spin (for example, sextet $S = 5/2$) state by changes in the ligand fields and other factors. Several d-orbital configurations are also feasible even in the same spin state, which results in different spatial symmetry states with near degeneracy. This is a difficult theoretical situation which often causes several computational troubles and misunderstanding in some cases.

As shown previously [1,19,20], the ground triplet and excited singlet states are not so separated in energy in the case of atomic oxygen (O), molecular oxygen (O_2) and high-valent iron–oxo [Fe(IV)=O] species as well as copper (gold)–oxo species [Cu(III)=O and Au(III)=O], as shown in Fig. 1. Isoelectronic character for these species leads to possible analogies for the reactivities among them. For example, spin crossover from $^3O_2$ to $^1O_2$ occurs in chemiluminescene reactions [through reductive activation of $^3O_2$ by complete electron transfer (efficient case) or direct bonding interaction between $^3O_2$ and a substrate (inefficient case)] [21]. The spin inversion may be equally expected for hydroxylation reactions of alkanes and epoxidation of alkenes by the Fe(IV)=O core in P450 and related synthetic model compounds [1–20].

In this paper (part XII of this series), both broken-symmetry (BS) and multideterminant (MR) methods are examined to calculate the energy levels of the ground and excited states of the isoelectronic species in Fig. 1. The relative stabilities among the

* Corresponding author. Tel.: +81 6 68505404; fax: +81 6 68505550.
E-mail address: yama@chem.sci.osaka-u.ac.jp (K. Yamaguchi).

0277-5387/$ - see front matter © 2009 Published by Elsevier Ltd.
doi:10.1016/j.poly.2009.01.024

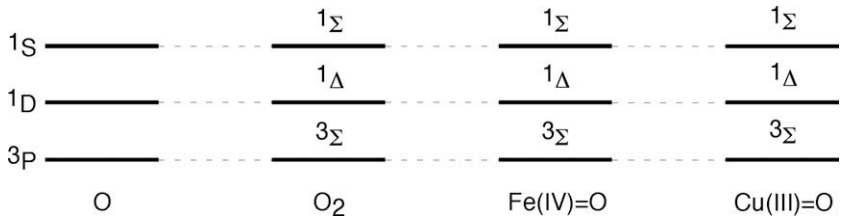


Fig. 1. The ground triplet and excited singlet states of the isoelectronic species, O, O_2, Fe(IV)=O, and Cu(III)=O.

different electronic and spin states of the Fe(IV)=O cores are analyzed from the view point of the configuration mixing of the zwitterionic (ZW) and/or charge-transfer (CT) configurations. To this end, theoretical backgrounds for the isolobal analogy are given in Section 2, and model Hamiltonians are solved analytically. The isolobal analogy provides possible reaction modes for epoxidation and hydroxylation reactions as discussed in Section 3. Finally, present computational results are discussed in relation to spin crossover phenomena in oxygenation reactions.

2. Theoretical background for the isolobal analogy

2.1. Restricted HF (RHF) and RDFT molecular orbitals of O_2 (O) and Fe(IV)=O

Here, the theoretical background for the isolobal analogy is briefly discussed. The restricted Hartree–Fock (RHF) and restricted Kohn–Sham (KS) density functional theory (RDFT) solutions are introduced in relation to the MO-theoretical description of the iron–oxo species [1]. The atomic orbitals of the fragments (O and Fe) are given by Fig. 2A. The molecular orbitals (MO) of O=O are expressed by the linear combinations of 2p-AOs (LCAO) as follows:

$$\phi(\pi_{x(y)}) = N^{-1}\{2px_1(2py_1) + 2px_2(2py_2)\} \quad (1a)$$

$$\phi(\pi^*_{x(y)}) = N^{-1}\{2px_1(2py_1) - 2px_2(2py_2)\} \quad (1b)$$

where the O–O σ-orbitals $\phi(\sigma)$ are neglected. The MOs of O=O are depicted in Fig. 2B. The orbital configurations of O_2 (O), O_2^- ($O^{\cdot-}$), and O_2^{2-} (O^{2-}) are depicted in Fig. 3B (A).

The molecular orbitals of the Fe(IV)=O are given by the LCAO approximations of the fragment AOs.

$$\phi(\pi_{x(y)}) = N^{-1}\{c_1 3dx_1(3dy_1) + c_2 2px_2(2py_2)\} \quad (2a)$$

$$\phi(\pi^*_{x(y)}) = N^{-1}\{c'_1 3dx_1(3dy_1) - c'_2 2px_2(2py_2)\} \quad (2b)$$

where c_i (i = 1, 2) denotes the LCAO coefficient. The dπ–pπ MOs of Fe(IV)=O are depicted in Fig. 2C. The orbital configurations of Fe(IV)=O, Fe(V)=O, and Fe(VI)=O are depicted in Fig. 3C and D. The energy levels of π_w and π_w^* (w = x and y) orbitals of O, O_2, and Fe(IV)=O are degenerate in energy. In this sense, these species are isolobal (or isoelectronic) [1].

The bond order (b) of O_2^m (m = 2 + ~2−) is defined by the occupation numbers of the MOs: $(\sigma)^a(\pi_x)^b(\pi_y)^c(\pi_y^*)^d(\pi_x^*)^e(\sigma^*)^f$. It is formally 3 for O_2^{2+} (m = 2+), since a = b = c = 2 and d = e = f = 0. The bond orders are, respectively, 2.5, 2.0, 1.5, and 1.0 for O_2^{1+}, O_2, O_2^-, and O_2^{2-}. Similarly, the bond order (b) for the high-valent Fe(VI)=O is 3.0 like O_2^{2+}. The b-values for Fe(V)=O, Fe(IV)=O, Fe(III)=O, and Fe(II)=O are, respectively, 2.5, 2.0, 1.5, and 1.0. The O_2 and Fe(IV)=O are isoelectronic from the view point of the bond order b = 2 as shown in Fig. 1. However, these RHF and RDFT pictures often break down because of strong electron and spin correlations described below.

2.2. Configuration interaction methods for O_2 (O) and Fe(IV)=O

As an example of the MR methods, configuration interaction methods are introduced here. As illustrated in Fig. 3, the O^{2-}, O_2^{2-}, and Fe(II)=O are regarded as the closed-shell singlet species, which are described by the single Slater determinant $|\pi_x^*\overline{\pi_x^*}\pi_y^*\overline{\pi_y^*}|$. On the other hand, the $O^{\cdot-}$, O_2^-, and Fe(V)=O species have the open-shell doublet state, for which the two configurations with the same energy are available (^{2}D state). The O, O_2, and Fe(IV)=O have the open-shell triplet ground state (Fig. 3). Since these species

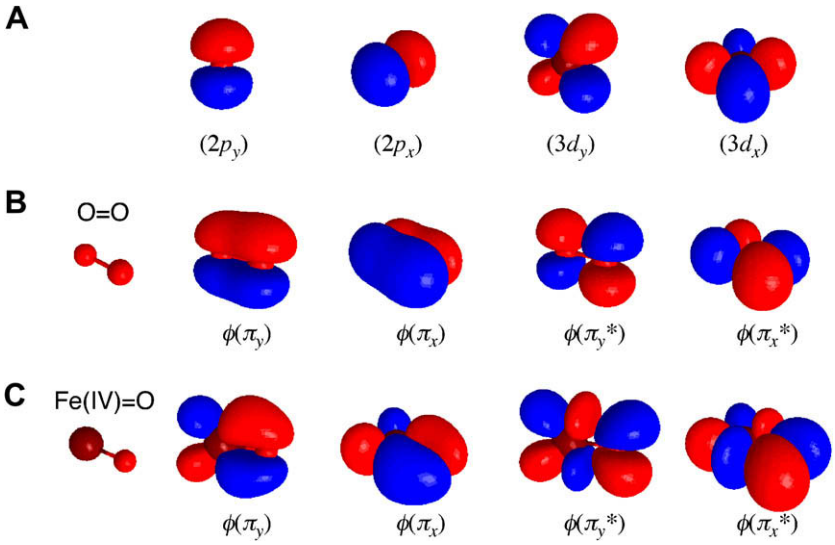


Fig. 2. (A) Atomic orbitals (AO) of the fragment atoms, O and metal (M), (B) the bonding and antibonding molecular π orbitals (π-MO) of O_2 and (C) the bonding and antibonding dπ–pπ MOs of Fe(IV)=O.

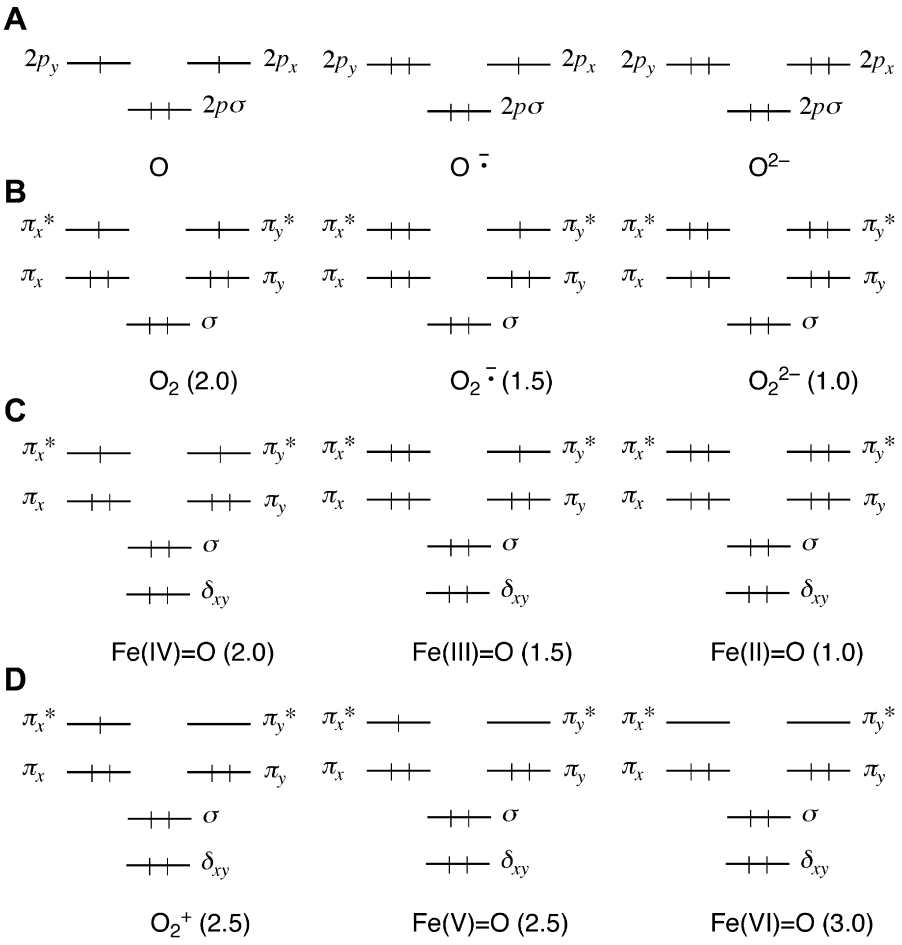


Fig. 3. Electronic configurations of the neutral, monoanion, and dianion states of (A) atomic oxygen (O) and (B) molecular oxygen. (C) electronic configurations of the tetra-, tri-, and divalent iron–oxo species Fe(X)=O and (D) those of O_2 cation, Fe(V)=O and Fe(VI)=O. The values in parentheses are the bond orders.

have the degenerate π_x^* (p_x) and π_y^* (p_y) orbitals, two closed-shell $|\pi_x^*\overline{\pi_x^*}|$ (= Δ_{xx}) and $|\pi_y^*\overline{\pi_y^*}|$ (= Δ_{yy}) and two diradical configurations $|\pi_x^*\overline{\pi_y^*}|$ (= Δ_{xy}) and $|\overline{\pi_x^*}\pi_y^*|$ (= Δ_{yx}) can be constructed, as illustrated in Fig. 4A. The configuration interaction (CI) between the degenerated configurations provides the $^{1,3}\Sigma$ and $^1\Delta$ states, as shown in Fig. 4B. The closed-shell (zwitterionic, Δ_{xx} = ZWI and Δ_{yy} = ZWII) and diradical (Δ_{xy} = DRI and Δ_{yx} = DRII) states are spontaneously degenerate in energy at the $^1\Delta$ state of O_2 and Fe(IV)=O. On the other hand, the $^{1,3}\Sigma$ states are given by the resonant ZW and DR configurations, respectively (Fig. 4B). Thus, the isolectronic state correlation diagrams for O, O_2, and Fe(IV)=O are available, as shown in Fig. 1 [1].

2.3. BS MO approaches to dissociation process of the covalent bonds of O_2, O_2^-, and O_2^{2-}

The broken-symmetry (BS) MO method is briefly introduced here. The dianion of molecular oxygen (O_2^{2-}) has the O–O σ-bond at the equilibrium geometry (bond order = 1), since all the bonding and antibonding π orbitals are doubly occupied (π-bond order = 0). As an example, let us consider the O–O dissociation process of O_2^{2-} on the basis of the BS MO approximation. The bonding and antibonding σ MOs are given by the RHF [restricted Kohn–Sham (RKS)] method.

$$\phi(\sigma) = N^{-1}(2pz_1 - 2pz_2) \tag{3a}$$

$$\phi(\sigma^*) = N^{-1}(2pz_1 + 2pz_2) \tag{3b}$$

where N is the normalizing factor. The bonding orbital is doubly occupied near the equilibrium geometry, being responsible for the stable closed-shell covalent bond (see Fig. 3). However, the RHF (RKS) orbitals are reorganized into the different orbitals for different spins (DODS) MOs if the O–O bond length exceeds a certain limit.

$$\psi^{\pm}(\sigma) = \cos\theta\phi(\sigma) \pm \sin\theta\phi(\sigma^*) \tag{4a}$$

$$\psi^{\pm}(\sigma^*) = \mp\sin\theta\phi(\sigma) \pm \cos\theta\phi(\sigma^*) \tag{4b}$$

where θ is the orbital mixing parameter. The MO bifurcation process and BS MOs are schematically depicted in Fig. 5A. The BS MOs become the atomic orbitals at the dissociation limit ($R = \infty$).

$$\psi^+(\sigma) = \psi^-(\sigma^*) = 2pz_1 \tag{5a}$$

$$\psi^-(\sigma) = \psi^+(\sigma^*) = -2pz_2 \tag{5b}$$

Therefore, the diradical BS configuration, $|\psi^+(\sigma)(\uparrow)\overline{\psi^-(\sigma)(\downarrow)}|$ (or $|\overline{\psi^+(\sigma)(\downarrow)}\psi^-(\sigma)(\uparrow)|$), reduces to the simple valence-bond (VB) configuration, $|2pz_1\overline{2pz_2}|$ (or $|\overline{2pz_1}2pz_2|$) in the Heitler–London theory. The O–O dissociation process of O_2^{2-} is explained by the following MO-VB scheme.

$$^1[\mathrm{O\text{–}O}]^{2-} \rightarrow {}^1[\ominus\ \overset{\uparrow\ \downarrow}{\mathrm{O}\overset{\delta\bullet}{\text{----}}\bullet\delta}\ \mathrm{O}\ominus\ ] \rightarrow {}^1[{}^2(\ominus\ \mathrm{O}\bullet\uparrow) + {}^2(\downarrow\bullet\mathrm{O}\ominus)] \tag{6a}$$

where ⊖ (or –) denotes the closed-shell lone pair. The O^- radical anion is correctly generated from O_2^{2-} in the unified MO-VB scheme.

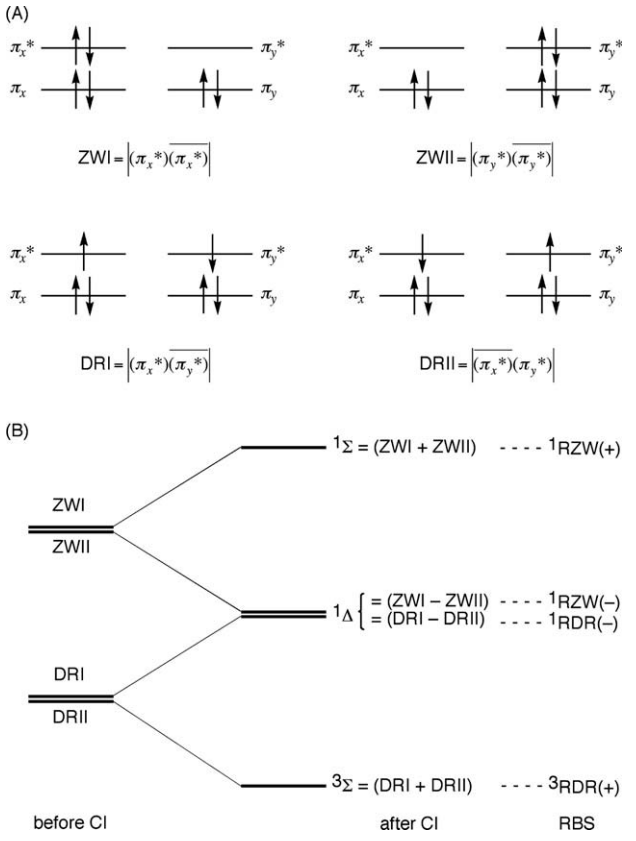


Fig. 4. (A) The orbital configurations of the diradical (DR) and zwitterionic (ZW) configurations and (B) energy levels of the DR and ZW states before and after configuration interaction (CI).

One of the π^*-orbital becomes half-occupied in the case of $O_2^{-\cdot}$ (Figs. 3 and 5). The delocalized π^*-orbital is deformed into the localized BS π^*-orbital at the O–O elongated O^-. The dissociation process of $O_2^{-\cdot}$ can be expressed by the unified MO-VB scheme as

$$^2[O{=}{=}O]^{-\cdot} \rightarrow {}^2[\uparrow \overset{\bullet}{O}\overset{\uparrow}{\delta\bullet}\cdots\overset{\downarrow}{\bullet\delta}O\ominus] \rightarrow {}^2[{}^3(\uparrow \overset{\bullet}{O}\bullet\uparrow) + {}^2(\downarrow\bullet O\ominus)] \qquad (6b)$$

The triplet O atom and doublet O anion radical are formed smoothly within the different orbitals for different spins (DODS) BS scheme. On the other hand, two π^*-orbitals are half-occupied in the case of triplet molecular oxygen ($^3O_2$). The O–O dissociation process of $^3O_2$ is given by the unified MO-VB scheme as

$$^3[O{=}{=}O] \rightarrow {}^3[\uparrow \overset{\bullet}{O}\overset{\uparrow}{\delta\bullet}\cdots\overset{\downarrow}{\bullet\delta}\overset{\bullet}{O}\uparrow] \rightarrow {}^3[{}^3(\uparrow \overset{\bullet}{O}\bullet\uparrow) + {}^1(\downarrow\bullet\overset{\bullet}{O}\uparrow)] \qquad (6c)$$

Thus, the triplet and singlet O atoms are generated at the dissociation limit under the DODS-type BS approximation, as can be easily recognized by the axial spin vector expression. However, two triplet O atoms should be generated at the ground state in this process.

To obtain correctly two ^3O atoms at the dissociation limit, the more general spin orbitals (GSO) [22] than the DODS MOs are necessary, as shown in Fig. 6. The GSO is given by the mixture of the up- and down-spins (namely, two-component spinor).

$$\varphi(\mathrm{GSO}) = \psi^+\alpha + \psi^-\beta = \begin{pmatrix}\psi^+\\ \psi^-\end{pmatrix} \qquad (7)$$

GSO permits the local spin rotation to obtain two ^3O atoms at the dissociation limit.

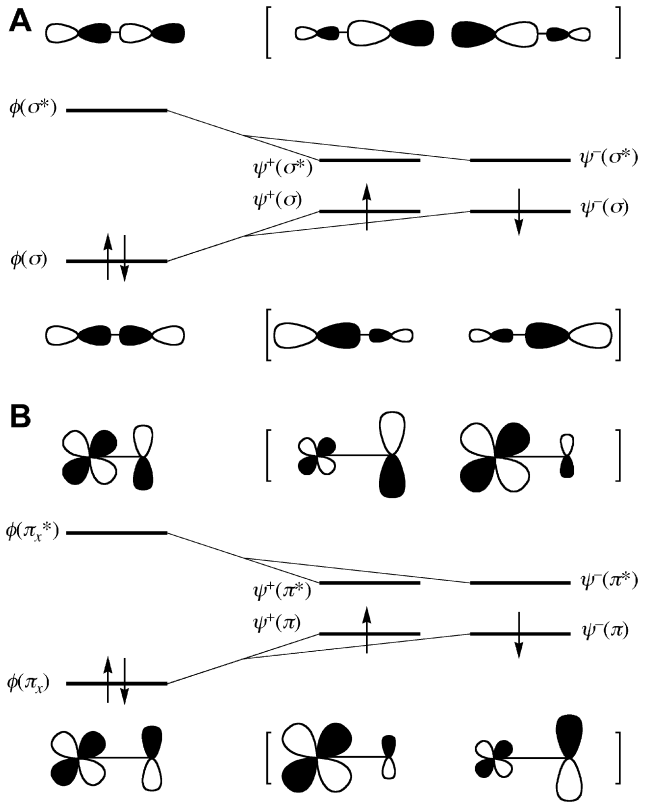


Fig. 5. Orbital correlation diagram for the dissociation process of (A) O–O σ-bond and (B) dπ–pπ bond.

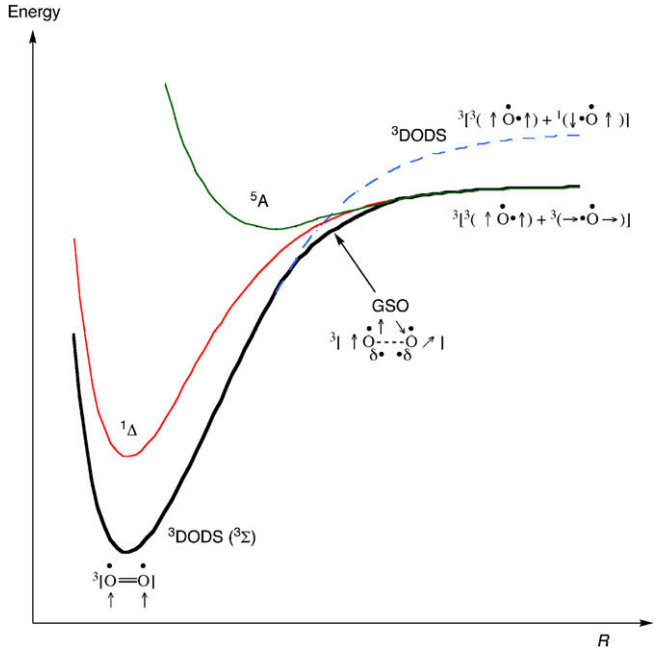


Fig. 6. The potential energy curves of the O–O dissociation process of molecular oxygen. The local spin rotation described by general spin orbital (GSO) is necessary at the intermediary stage, although the different orbitals for different spin (DODS) description is feasible at the equilibrium geometry.

$$^3[\uparrow \overset{\bullet}{O}\overset{\uparrow}{\delta\bullet}\cdots\overset{\downarrow}{\bullet\delta}\overset{\bullet}{O}\uparrow] \rightarrow {}^3[\uparrow \overset{\bullet}{O}\overset{\uparrow}{\delta\bullet}\cdots\overset{\searrow}{\bullet\delta}\overset{\bullet}{O}\nearrow] \rightarrow {}^3[{}^3(\uparrow \overset{\bullet}{O}\bullet\uparrow) + {}^3(\rightarrow\bullet\overset{\bullet}{O}\rightarrow)] \qquad (6d)$$

The detailed mathematical expression of this process by GSO has been given in our previous paper [22]. The dissociation of a covalent bond is thus described by the unified MO-VB scheme as

$$^{S}[\mathrm{MO}] \rightarrow {}^{S}[\mathrm{MO}+\mathrm{VB}] \rightarrow {}^{S}[\mathrm{VB}](S = \text{spin state}) \tag{6e}$$

The MO and VB (atomic orbital AO) pictures are useful for near equilibrium and near dissociation limit, respectively. However, the exact description of the intermediate region, [MO + VB] region, is not at all easy because of the dual character. It is noteworthy that the transition state regions of oxygenation reactions are often classified into this regime. The BS MO description is one of the simple but practical approaches even to this region, although it exhibits the so-called spin symmetry breaking. The recovery of spin symmetry from BS MO has been accompanied by the approximate spin projection (AP) scheme in this series of papers.

2.4. Resonating BS MO methods and approximate spin projection

Here, the recovery of the broken spin symmetry by the resonating BS (RBS) and approximate spin projection (AP) procedures is briefly described. The single Slater determinant is utilized in the case of the broken-symmetry (BS) MO description of the open-shell states of O_2 and Fe(IV)=O. The ground triplet state of O_2 (O) and Fe(IV)=O (namely the core of cpd II) is given by the single determinant as $|\pi_x^*(\uparrow)\pi_y^*(\uparrow)|$ ($S = 1$) or $|\pi_x^*(\downarrow)\pi_y^*(\downarrow)|$ ($S = -1$), where the weak spin polarizations (SP) of other doubly occupied MOs are neglected. The lowest-spin (LS) BS MO solutions are expressed by the DR configurations as $|\overline{\pi_x^*(\uparrow)}\pi_y^*(\downarrow)|$ ($\equiv |\psi^+(\pi_x^*)\overline{\psi^-(\pi_x^*)}|$) [$DR_a$ ($\uparrow\downarrow$), $S_z = 0$] or $|\pi_x^*(\downarrow)\overline{\pi_y^*(\uparrow)}|$ ($\equiv |\overline{\psi^+(\pi_x^*)}\psi^-(\pi_x^*)|$) [$DR_b$ ($\downarrow\uparrow$), $S_z = 0$], where the SP effects are also neglected. However, these BS DR configurations are degenerate in energy, leading to the resonating BS (RBS) states consisted of in and out of phase combinations of them, as illustrated in Fig. 7A. The RBS states are responsible for the $^1\Delta_{xy}$ and $^3\Sigma$ states, respectively. This in turn means that each BS MO configuration is nothing but a counter part of the exact $^1\Delta_{xy}$ and $^3\Sigma$ states, and therefore, its energy is given by the half sum of their energies: $E(^{LS}\mathrm{BS}) \cong [^1E(\Delta_{xy}) + {}^3E(^3\Sigma)]/2$, as illustrated in Fig. 7A. The elimination of the $^3\Sigma$ component from the ^{LS}BS configuration by the approximate spin projection procedure (AP BS) provides the projected energy for the $^1\Delta_{xy}$ state, which is close to that of the $^1\Delta_{xy}$ state by the CI (see Fig. 7A). Similarly, the elimination of the quartet component from the LS doublet BS solutions of cpd I provides the projected doublet energies (^{2}AP BS), as shown in the previous papers [1,19,20].

2.5. BS MO descriptions of metal–oxo species

Here, the broken-symmetry (BS) descriptions of the metal–oxo species are briefly examined before the detailed discussions of the iron–oxo bonds. The bonding and antibonding $\pi_{x(y)}$ MOs by the RHF(RKS) are given by the linear combination of dπ and pπ [= 2px(y)] AOs.

$$\phi(\pi_x) = c_1 3d\pi_x + c_2 2p\pi_x \tag{8a}$$
$$\phi(\pi_x^*) = c_1' 3d\pi_x - c_2' 2p\pi_x \tag{8b}$$

where the c_i (c_i') denote the LCAO coefficients. The bonding BS MOs are given by the HOMO (π_x) and LUMO (π_x^*) mixing as follows (see Fig. 5B):

$$\psi^+(\pi_x) = \cos\theta_1\phi(\pi_x) + \sin\theta_1\phi(\pi_x^*) \tag{9a}$$
$$= \cos\omega(3d\pi_x) + \sin\omega(2p\pi_x) \tag{9b}$$
$$\psi^-(\pi_x) = \cos\theta_2\phi(\pi_x) - \sin\theta_2\phi(\pi_x^*) \tag{9c}$$
$$= \cos\eta(2p\pi_x) + \sin\eta(3d\pi_x) \tag{9d}$$

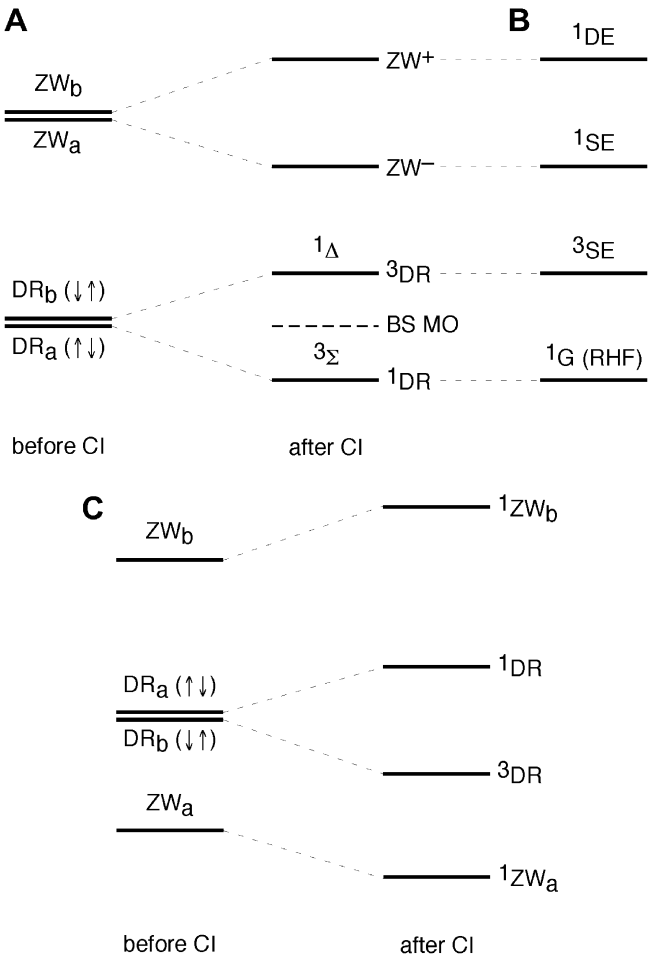


Fig. 7. (A) Energy diagrams of the DR and ZW states for the ground DR state before and after CI, (B) energy diagrams of the ground (G), single (SE) and double (D) excitation states for the closed-shell (^{1}RHF) species, and (C) energy diagrams of the DR and ZW states for the ground ZW state before and after CI.

where θ_1 (θ_2) and ω (η) are the mixing coefficients of MOs and AOs, respectively. Two parameters are necessary for the metal–oxo (M=O) bonds, since the electronegativities of the metal (M) and oxygen (O) sites are different, leading to definition of the ionicity parameter

$$y = \frac{\alpha_M - \alpha_O}{U} (\neq 0) \tag{10a}$$

where α_M and α_O denote the Coulomb integrals of M and O, respectively, and U is the effective on-site Coulomb repulsion integral ($U = U_M - U_O$) under the Hückel–Hubbard (HH) model examined previously [1,19–21]. On the other hand, the covalent bonding parameter is defined by

$$x = -\frac{\beta}{U} \tag{10b}$$

where β denotes the resonance integral for HH model. As shown previously [1], the BS HF (KS) equations can be analytically solved in the case of the HH model and LCAO coefficients of BS MOs are expressed by functions of the ionicity (y) and covalent (x) parameters.

As an example, let us consider the dissociation limit of the M–O bond for simple explanation. The two parameter theory (ω, η) in Eq. (9) can describe both diradical (DR) and zwitterionic (ZW) configurations [23]:

$$\left.\begin{aligned}\psi^{+}(\pi_x) &= 3d\pi_x(\omega=0)\\ \psi^{-}(\pi_x) &= 2p\pi_x(\eta=0)\end{aligned}\right\}(\uparrow)\,\dot{\mathrm{M}}-\dot{\mathrm{O}}\;(\downarrow)\equiv \mathrm{DR_a}\;(\uparrow\downarrow) \tag{11a}$$

$$\left.\begin{aligned}\psi^{+}(\pi_x) &= 2p\pi_x(\omega=\pi/2)\\ \psi^{-}(\pi_x) &= 2p\pi_x(\eta=0)\end{aligned}\right\}^{\oplus}\mathrm{M}-\mathrm{O}^{\ominus}\equiv \mathrm{ZW_a} \tag{11b}$$

$$\left.\begin{aligned}\psi^{+}(\pi_x) &= 3d\pi_x(\omega=0)\\ \psi^{-}(\pi_x) &= 3d\pi_x(\eta=\pi/2)\end{aligned}\right\}^{\ominus}\mathrm{M}-\mathrm{O}^{\oplus}\equiv \mathrm{ZW_b} \tag{11c}$$

This means that the M=O bond in the intermediate dissociation region is generally expressed by the mixing of DR_a (↑↓), ZW_a and ZW_b configurations in the VB (AO) CI scheme. The BS MO description (followed by AP) in (9) is, therefore, one of the practical approximations to the exact VB-CI approach to this regime.

The antibonding BS MOs are also given by the two parameters as follows (see Fig. 5).

$$\psi^{+}(\pi_x^*) = -\sin\theta_1\phi(\pi_x)+\cos\theta_1\phi(\pi_x^*) \tag{12a}$$

$$= -\sin\omega(3d\pi_x)+\cos\omega(2p\pi_x) \tag{12b}$$

$$\psi^{-}(\pi_x^*) = -\sin\theta_2\phi(\pi_x)+\cos\theta_2\phi(\pi_x^*) \tag{12c}$$

$$= -\sin\eta(2p\pi_x)+\cos\eta(3d\pi_x) \tag{12d}$$

where ± signs are determined by the orthogonality condition of BS MOs. The antibonding BS MOs are reduced to the AOs at the dissociation limit ($R=\infty$) [23].

$$\left.\begin{aligned}\psi^{+}(\pi_x^*) &= 2p\pi_x(\omega=0)\\ \psi^{-}(\pi_x^*) &= 3d\pi_x(\eta=0)\end{aligned}\right\}(\downarrow)\,\dot{\mathrm{M}}-\dot{\mathrm{O}}\;(\uparrow)\equiv \mathrm{DR_b}\;(\downarrow\uparrow) \tag{13a}$$

$$\left.\begin{aligned}\psi^{+}(\pi_x^*) &= -3d\pi_x(\omega=\pi)/2\\ \psi^{-}(\pi_x^*) &= 3d\pi_x(\eta=0)\end{aligned}\right\}^{\ominus}\mathrm{M}-\mathrm{O}^{\oplus}\equiv \mathrm{ZW_b} \tag{13b}$$

$$\left.\begin{aligned}\psi^{+}(\pi_x^*) &= 2p\pi_x(\omega=0)\\ \psi^{-}(\pi_x^*) &= -2p\pi_x(\eta=\pi/2)\end{aligned}\right\}^{\oplus}\mathrm{M}-\mathrm{O}^{\ominus}\equiv \mathrm{ZW_a} \tag{13c}$$

Thus, the doubly excited configuration $|\pi_x^*\overline{\pi_x^*}|$ (or $|\overline{\pi_x}\pi_x|$) corresponds to the DR_b (↓↑), ZW_b or ZW_a state at the dissociation limit, depending on the magnitude of the ionicity (y) and covalency (x) parameters. This means that the BS MO doubly excited (DE) states are generally expressed by the mixing of these three VB (AO) configurations.

The singly excited states are also explained by the VB (AO) CI terms at the dissociation limit:

Ⓐ $$\left|\psi^{+}(\pi_x)\overline{\psi^{-}(\pi_x^*)}\right| = \left|3d\pi_x\,\overline{3d\pi_x}\right| \quad \left(^{\ominus}\mathrm{M{-}O}^{\oplus}\equiv \mathrm{ZW_b}\right) \tag{14a}$$

$$\left|\psi^{+}(\pi_x^*)\overline{\psi^{-}(\pi_x)}\right| = \left|2p\pi_x\,\overline{2p\pi_x}\right| \quad \left(^{\oplus}\mathrm{M{-}O}^{\ominus}\equiv \mathrm{ZW_a}\right) \tag{14b}$$

Ⓑ $$\left|\psi^{+}(\pi_x)\overline{\psi^{-}(\pi_x^*)}\right| = -\left|2p\pi_x\,\overline{3d\pi_x}\right| \quad \left((\downarrow)\,\dot{\mathrm{M}}{-}\dot{\mathrm{O}}\;(\uparrow),\ \mathrm{DR_b}\;(\downarrow\uparrow)\right) \tag{15a}$$

$$\left|\psi^{+}(\pi_x^*)\overline{\psi^{-}(\pi_x)}\right| = -\left|3d\pi_x\,\overline{2p\pi_x}\right| \quad \left((\uparrow)\,\dot{\mathrm{M}}{-}\dot{\mathrm{O}}\;(\downarrow),\ \mathrm{DR_a}\;(\uparrow\downarrow)\right) \tag{15b}$$

Ⓒ $$\left|\psi^{+}(\pi_x)\overline{\psi^{-}(\pi_x^*)}\right| = -\left|3d\pi_x\,\overline{2p\pi_x}\right| \quad \left((\uparrow)\,\dot{\mathrm{M}}{-}\dot{\mathrm{O}}\;(\downarrow),\ \mathrm{DR_a}\;(\uparrow\downarrow)\right) \tag{16a}$$

$$\left|\psi^{+}(\pi_x^*)\overline{\psi^{-}(\pi_x)}\right| = -\left|2p\pi_x\,\overline{3d\pi_x}\right| \quad \left((\downarrow)\,\dot{\mathrm{M}}{-}\dot{\mathrm{O}}\;(\uparrow),\ \mathrm{DR_b}\;(\downarrow\uparrow)\right), \tag{16b}$$

where A, B, and C correspond to the parameter sets ($\omega=\eta=0$), ($\omega=\pi/2$, $\eta=0$), and ($\omega=0$, $\eta=\pi/2$), respectively. The singly excited states of diradical (DR) correspond to the zwitterionic (ZW) configurations (see Fig. 7A), whereas the singly excited states of ZW are given by the DR configurations (see Fig. 7C). Therefore, the configuration mixing (CI) of BS MO configurations provide the symmetry-adapted (SA) ground and excited states, as shown in Fig. 7. The DR state reduces to the closed-shell RHF state for nonradical species. The RHF CI scheme for the species is depicted in Fig. 7B, where the ground state (^{1}G) is well-described by ^{1}RHF and excited states are given by singly (SE) and doubly (DE) excited configurations, respectively. Further detailed descriptions of BS MO CI and related VB (AO) CI are given in our previous papers [23]. We have examined the BS MO descriptions of metal–oxo bonds (for example, Cr=O, Mn=O and Fe=O) on the basis of the unrestricted Hartree–Fock (UHF) calculations [1]. It was found that the analytical solutions of the BS UHF equations with two parameters (ω, η) are useful for qualitative understanding of the nature of labile metal–oxo bonds which are determined by subtle balances of the ionicity (y) and covalent (x) parameters. The computational results by ab initio BS UHF are also well-explained on the basis of the theoretical formula (9–16).

2.6. BS MO descriptions of iron–oxo species

The molecular orbital configuration of hyper high-valent Fe(VI)=O is expressed by the bonding orbitals in Fig. 3D. The σ, π_x, π_y orbitals of Fe(VI)=O at the equilibrium geometry ($R_{Fe-O}\leqslant 1.65$) are stable closed-shell pairs, indicating that the bond order is 3.0. This means that the Fe(VI)=O bond is regarded as singlet oxene structure with triple bond as in the case of Mn(V)=O [1]. Since the d-orbital level is deep for the high-valent Fe(X) state (X = VI–IV), the ionicity parameter (y) in Eq. (10) is not so large, leading to the formation of strong covalent bonds instead of the ionic bond. However, such a stable oxene triplet bond should not exhibit the high oxygenation reactivity. This in turn suggests that elongation of the Fe–O triple bond and/or decrease of the bond order by reduction of the Fe(VI) center are necessary for high reactivity of the Fe=O bonds.

The dissociation of Fe(VI)=O is mainly expressed by the decrease of the covalency parameter (x) [namely the resonance integral (β)]. The change of the bonding property is, therefore, expressed by the MO-VB scheme.

$$^1[\mathrm{Fe(VI)}{\equiv}\mathrm{O}] \rightarrow {}^1\left[\mathrm{Fe(IV)}\begin{matrix}\delta\bullet\uparrow\\ \delta\bullet\uparrow\end{matrix}\!\!\cdots\!\!\begin{matrix}\downarrow\bullet\delta\\ \downarrow\bullet\delta\end{matrix}\mathrm{O}\right] \rightarrow {}^1\left[{}^3\mathrm{Fe(IV)}\begin{matrix}\bullet\uparrow\\ \bullet\uparrow\end{matrix} + {}^3\left(\downarrow\dot{\mathrm{O}}\downarrow\right)\right] \tag{17}$$

The stable dπ-pπ orbitals (π_x and π_y) are reorganized into broken-symmetry (BS) orbitals in Fig. 5 in the intermediate region, where the triplet ^{3}O radical character is not negligible, as illustrated by the spin vector model. The ^{3}Fe(IV) ($S=1$) and ^{3}O ($S=-1$) fragments are generated at the dissociation limit, although the total spin state is singlet.

The antibonding π_x^* orbital is half-occupied in the case of ^{2}[Fe(V)≡≡O], where the bond order is formally 2.5. The bonding and antibonding π_x^* orbitals are deformed into the BS orbitals in Fig. 5 in the dissociation region. Therefore, the Fe–O dissociation process is expressed by the MO-VB scheme as

$$^2[\mathrm{Fe(V)}{\equiv}{\equiv}\mathrm{O}] \rightarrow {}^2\left[\mathrm{Fe(III)}\begin{matrix}\delta\bullet\uparrow\\ \downarrow\bullet\end{matrix}\!\!\cdots\!\!\begin{matrix}\downarrow\bullet\delta\\ \mathrm{O}\end{matrix}\right] \rightarrow {}^2\left[{}^2\mathrm{Fe(III)}\begin{matrix}\bullet\uparrow\\ \bullet\end{matrix} + {}^3\left(\downarrow\dot{\mathrm{O}}\downarrow\right)\right], \tag{18}$$

where triplet ^{3}O atom is generated at the dissociation limit.

The other antibonding π_y^* orbital is also half-occupied in the ^{3}[Fe(IV)=O] species with the formal bond order 2 (double bond), namely the metal–oxo bond as shown in Fig. 3C. The Fe–O dissociation process is given by the following MO-VB scheme

$$^3[\mathrm{Fe(IV)}{=}\mathrm{O}] \rightarrow {}^3\left[\mathrm{Fe(II)}\begin{matrix}\delta\bullet\uparrow\\ \delta\bullet\uparrow\end{matrix}\!\!:\!:\!:\!:\!\!\begin{matrix}\downarrow\bullet\delta\\ \downarrow\bullet\delta\end{matrix}\mathrm{O}\right] \rightarrow {}^3\left[{}^3\mathrm{Fe(II)}\begin{matrix}\bullet\uparrow\\ \bullet\uparrow\end{matrix} + {}^3\left(\downarrow\bullet\mathrm{O}\bullet\downarrow\right)\right], \tag{19}$$

where the triplet state of ^{3}Fe(II) is expressed with the atomic configuration: $^3[(\delta_{xy})^2(3d\pi x)^2(3d\pi y)^1(\sigma^*)^1]$. The spin crossover from the triplet to the quintet configuration $^5[(\delta_{xy})^1(\delta_{xy}{}^*)^1((3d\pi x)^2(3d\pi y)^1(\sigma^*)^1)$ is feasible if the exchange interaction on the Fe(II) site

is predominant. On the other hand, the local spin crossover occurs from the triplet excited state of ^{3}Fe(II) to the singlet ground state: ^{1}Fe(II) = $^1[(\delta_{xy})^2(3d\pi x)^2(3d\pi y)^2]$, under the condition that the ligand field for Fe(II) is strong enough to stabilize this closed-shell configuration. The electron transfer from Fe(II) to atomic oxygen (^{3}O) takes place if the ligand field of Fe(II) is electron donating as

$$^3[^1\mathrm{Fe(II)}\ ^3\dot{\dot{\mathrm{O}}}] \rightarrow {}^3[^2\mathrm{Fe(III)}\text{–}^2\mathrm{O}\bar{\bullet}] \rightarrow {}^3[^3\mathrm{Fe(IV)}\text{–}^1\mathrm{O}^{2-}] \quad (20)$$

where the triplet state of ^{3}Fe(IV) is expressed with $^3[(\delta_{xy})^2(3d\pi x)^1(3d\pi y)^1]$. The last oxygen dianion structure is formally proposed for the metal–oxo species, although the oxygen atom site in the structure should exhibit the nucleophilic property. Variations of the nature of iron–oxo bonds are qualitatively expressed by changes of the ionicity (y) and covalency (x) parameters in the BS MO scheme, as shown in Section 2.5. These parameters are of course subtle functions of types of ligands and substituents introduced, together with environmental effects such as solvent and protein fields in biological systems. As shown in Eqs. (17)–(20), the high-valent Fe(X)=O bonds exhibit more or less the triplet O diradical character. This is the reason why we have proposed the ^{3}O-atom model for electrophilic hydroxylation reactions by the species.

The excited singlet state $^1\Delta$ of Fe(IV)=O exhibits the dual characteristics, as illustrated in Fig. 4: one is the diradical (DR) configuration [$^1\Delta_{xy(yx)}$ state in the present paper] and the other is expressed with the zwitterionic (ZW) configuration [$^1\Delta_{xx(yy)}$]. These configurations correlate, respectively, with the diradical $^1[(2px)^1(2py)^1]$ and ionic $^1[(2px)^2(2py)^0$ or $(2px)^0(2py)^2]$ components of the excited $^1\Delta$ state of O atom. The isoelectronic analogy leads to our proposal of the ^{1}O model for hydroxylation reactions with $^1\Delta$ state of Fe(IV)=O. The $^1\Delta_{xy}$ and $^1\Delta_{xx}$ configurations of O-atom should prefer, respectively, the abstraction and insertion reactions. It is noteworthy that the mechanisms of hydroxylation reactions by ^{1,3}O atom are well understood on both experimental and theoretical grounds, as illustrated in Fig. 3 [1].

3. Discussions and concluding remark

3.1. BS calculations of metal–oxo species

The broken-symmetry (BS) calculations have been performed for transition-metal oxo species to confirm qualitative pictures presented in preceding sections [1,23]. The binding energies for the naked system, M=O (**1**), were calculated by using the BS Hartree–Fock (UHF) and hybrid density functional theory (UDFT), UB3LYP, and post UHF, namely, coupled–cluster (CC) method, UCCSD(T). The calculated binding energies for the $^2\Pi$-state of CuO are 2.69 and 2.37 eV by the UB3LYP and UCCSD(T) methods [24–29], in compatible with the experimental value (2.75 eV). The corresponding values for the $^5\Pi$-state of CrO are 4.34 and 3.71 eV, as compared with the experiment (4.41 eV). These results are not at all trivial, since the experimental binding energies can be reproduced by the less expensive BS DFT (UB3LYP) instead of time-consuming CCSD(T). The spin contamination errors in the BS approach are not so serious at least for energetics.

The BS UHF calculations [1] of the simplest model, O=M(NH_2)$_2$ (**2**) for transition-metal oxo porphyrine systems were also performed to confirm variations of the nature of the M–O bonds with changes of oxidation number (m) of transition metal ions [M = Cr(m), Mn(m), and Fe(m), m = 2–5]. It was found that the oxygen site of **2** is indeed variable from nucleophilic to electrophilic, depending on the m-value of these ions, for example [1],

$$\mathrm{Fe}(m{+}2)\mathrm{O}^{2-} \leftrightarrow \mathrm{Fe}(m{+}1)\mathrm{O}^{1-} \leftrightarrow \mathrm{Fe}(m)\mathrm{O}^{0} \leftrightarrow \mathrm{Fe}(m{-}1)\mathrm{O}^{+} \quad (21)$$

These variations are consistent with the qualitative pictures in Section 2.6. The high-valent iron–oxo species (Fe(IV)=O) often undergoes electrophilic reactions such as epoxidation of olefins. Thus, the isoelectronic analogy between O, O_2, Fe(IV)=O and Cu(III)=O in Fig. 1 is useful for qualitative understanding of electrophilic oxygenation reactions.

The BS calculations are useful for elucidation of covalent (x) and ionicity (y) parameters (in (10)) in model complexes and metalloenzymes as shown in this series of papers. In fact, the essence of the BS computational results can be extracted by using the effective Hückel–Hubbard (HH) model

$$H = \sum \alpha_i a_i^+ a_i + \sum \beta_{ij} a_i^+ b_j + \sum U_{ii} a_i^+ a_i a_i^+ a_i + \sum V_{ij} a_i^+ a_i b_j^+ b_j \quad (22)$$

where V_{ij} denotes the nearest neighbor Coulomb interaction. Several model Hamiltonians such as t(b)-J Hamiltonian [19,20] can be derived from this model. However, the BS methods are hardly applicable to several excited states, leading to the multireference (MR) approach for quantitative purpose. Several computational results based on the CAS-type approaches such as CASDFT will be shown elsewhere. These results are also expressed by the full CI scheme based on the model Hamiltonian in Eq. (22) as described in Section 2.

3.2. Isoelectronic analogy among O_2 (O) and Fe(IV)=O species

The isoelectronic analogy between O_2 and Fe(IV)=O in Fig. 1 lend support to propose common reaction intermediates in addition (epoxidation) reactions of the species to C=C double bonds, as shown in Fig. 8. A lot of our and other groups computational results on O_2 reactions [1,30,31] would be indeed transferable to understand reaction mechanisms of the Fe(IV)=O core. For example, four different intermediate [or transition structure (TS)] are conceivable, depending on the types of alkenes. The 1,4-diradical (DR) and metal DR (MDR) intermediate (or TS) are feasible for alkenes with less electron donating groups. For example, our BS calculations on the singlet oxygen ($^1O_2$) plus ethylene system indicated that 1,4-diradical (DR) mechanism was more favorable than the perepoxide (PE) mechanism [1,30]. Recent CASSCF and CASPT2 calculations on the same system [31] have concluded that perepoxide turns out to be attainable only by passing through the diradical, due to the nature of the critical points involved. Similarly our early BS calculation showed that metal 1,4-diradical (MDR) mechanism was more favorable than the metal perepoxide (MPE) mechanism [1]. Recent DFT calculations by Visser et al. also concluded the same result [32]. On the other hand, the 1,4-zwitterion (ZW) and metal ZW (MZW) species may be more stable than the DR and MDR in the case of alkenes with electron donating group. For example, the MZW for the Fe(IV)=O core may undergo the 1,2-cation shift at C=C double bond, leading to the so-called NIH shift [33]. The conversion from DR(MDR) to ZW(MZW) can be grasped with variations of the ionicity (y) and covalent (x) parameters on the theoretical grounds as shown in Section 2 [1]. The electron transfer (ET) and metal ET (MET) diradical intermediates may be generated in the case of strongly electron-rich alkenes such as dimethoxy ethylene. The MET is indeed formed in the one-electron oxidation step of phenol and amines by peroxydases with the Fe(IV)=O core, the so-called compound (cpd) I (or II) [34].

Possible mechanisms of hydroxylation reactions of alkanes are also available on the basis of the isoelectronic analogy between O and Fe(IV)=O as illustrated in Fig. 9. Both diradical (DR) and zwitterionic (ZW) mechanisms may be conceivable theoretically, depending on the strength of electron donating property of substituents introduced, though recent DFT calculations [2–21] usually favor the DR mechanism to the ZW mechanism. On the other hand, the electrophilic property of the peroxo species such as dioxirane,

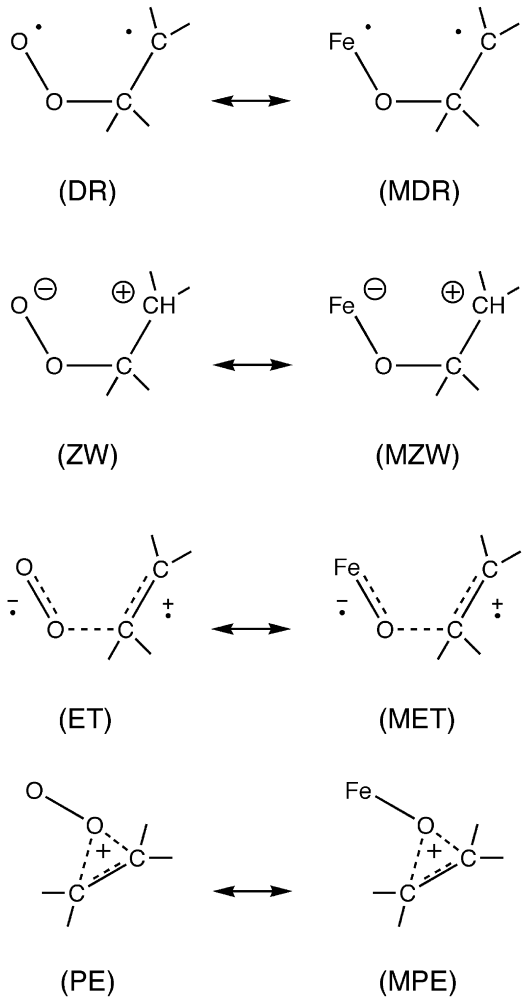


Fig. 8. Possible mechanisms of oxygen transfer reactions to alkenes on the basis of isoelectronic analogy between molecular oxygen and Fe(IV) core in P450.

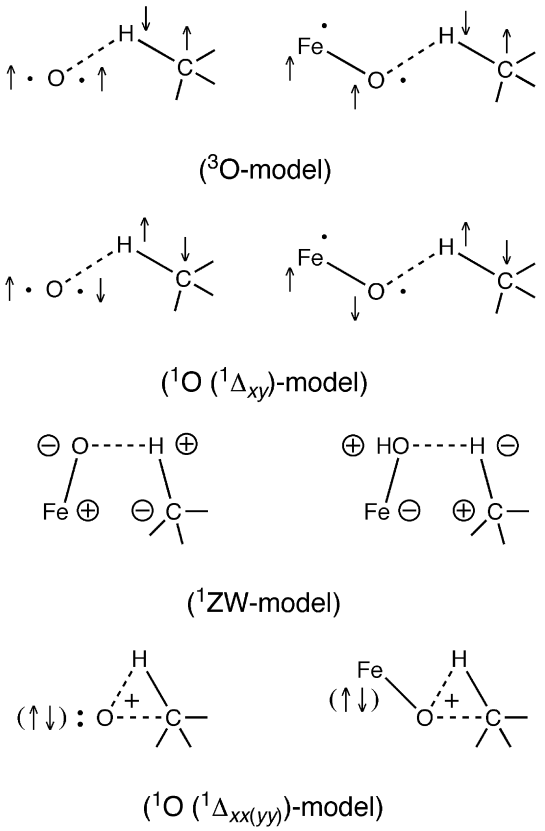


Fig. 9. Possible mechanisms of oxygen transfer reactions to alkanes on the basis of isoelectronic analogy between atomic and molecular oxygens and Fe(IV) core in P450.

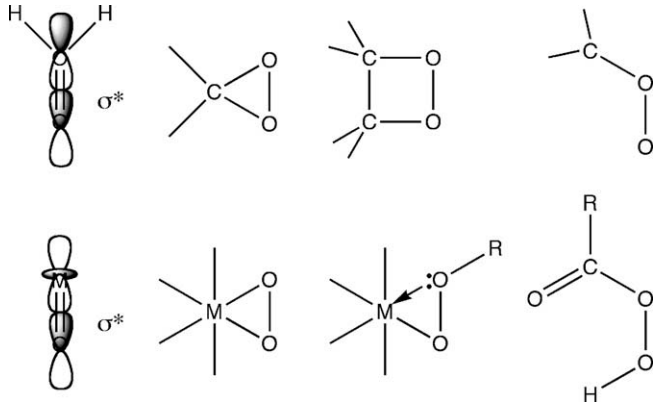


Fig. 10. Electrophilic properties of the σ* orbital of the O–O bond in several peroxides and metal oxo and metal peroxo species.

dioxetane, carbonyloxide, peracids, etc. may be understood by the existence of the lower-lying σ* orbital (LUMO) of these species as illustrated in Fig. 10. The electrophilic nature of the σ* orbital of the transition-metal oxo (M=O) species, transition-metal hydro(-alkyl)-peroxides, etc. plays an important role in several oxygenation reactions [1–20]. Thus, our BS MO analysis of metal–oxo bonds during 1985–1992 [1] has elucidated theoretical frameworks and possibilities in mechanisms of their oxygenation reaction of alkanes and alkenes, as illustrated in Figs. 8–10. The theoretical efforts in past decades have already been summarized in the review articles [1]. Recently, ab initio BS MO calculations [18–21] for realistic models including environmental effects have been extensively carried out to conclude which mechanism is more favorable than others. Such efforts are expected to elucidate reasonable mechanisms of oxygenation reactions on the theoretical grounds.

3.3. Concluding remarks

The electronic structures of the isoelectronic species, O, O_2, and Fe(IV)=O have been investigated on the basis of both broken-symmetry (BS) and multireference (MR) methods. In Section 2, the BS and MR descriptions of the ground (G) and low-lying excited states of these species were presented to elucidate the diradical (DR) and zwitterionic (ZW) characters of these states. The energy gap between the high-spin (HS) and low-spin (LS) DR states is rather small, often showing the spin crossover in the reaction pathways of oxygenation reactions [1,22]. Thus the oxygenation reactions are regarded as an interesting field for the molecular magnetism at least from the theoretical viewpoint. The reaction schemes of hydroxylation of alkanes and epoxidation of alkenes by the Fe(IV)=O core have been explained by the isolobal analogy, namely the triplet (^3O, $^3O_2$) and singlet (^1O, $^1O_2$) models, together with the electrophilic model based on the σ* orbital, for oxygenation reactions in Fig. s1 and Figs. 8–10. These models are found to be useful for qualitative understanding of ab initio DFT computational results on the Fe(IV)=O cores in model complexes and enzymes. The model Hamiltonians are also solved analytically to extract essential features of the DFT computational results.

Acknowledgement

This study is funded by the New Energy and Industrial Technology Development Organization (NEDO) through Development of Basic Technologies for Advanced Production Methods Using Microorganism Functions.

References

[1] (a) K. Yamaguchi, Y. Takahara, T. Fueno, in: V.H. Smith Jr., H.F. Scheafer III, K. Morokuma (Eds.), Applied Quantum Chemistry, D. Reidel, Boston, 1986. p. 155;
(b) K. Yamaguchi, in: A.A. Frimer (Ed.), Singlet Oxygen, vol. III, CRC Press, Boca Raton, FL, 1985. p. 237;
(c) K. Yamaguchi, Y. Takahara, T. Fueno, in: W. Ando, Y. Moro-oka (Eds.), The Role of Oxygen in Chemistry and Biology, Elsevier, Amsterdam, 1988. p. 263;
(d) K. Yamaguchi, Y. Takahara, T. Fueno, I. Saito, T. Matsuura, in: O. Hayaishi, E. Niki, M. Kondo, T. Yoshikawa (Eds.), Medical, Biological and Chemical Aspects of Free Radicals, Elsevier, Amsterdam, 1989. p. 993;
(e) K. Yamaguchi, K. Takada, Y. Otsuji, K. Mizuno, in: W. Ando (Ed.), Peroxide, John and Wiley, 1992. p. 2.

[2] (a) T. Omura, Y. Ishimura, Y. Fujii-Kriyama (Eds.), Cytochrome P-450, Kodansha, Tokyo, 1993;
(b) M. Sono, M.P. Roach, E.D. Coulter, J.H. Dawson, Chem. Rev. 96 (1996) 2841;
(c) H. Li, in: A. Messerschmidt, R. Huber, T. Poulos, K. Wieghardt (Eds.), Handbook of Metalloproteins, Wiley, Oxford, 2001. p. 267;
(d) B. Meunier, S.P. de Visser, S. Shaik, Chem. Rev. 104 (2004) 3947;
(e) I.G. Denisov, T.M. Makris, S.G. Sligar, I. Schlichting, Chem. Rev. 105 (2005) 2253.

[3] (a) J.T. Groves, R.C. Haushalter, M. Nakamura, T.E. Nemo, B.J. Evans, J. Am. Chem. Soc. 103 (1981) 2884;
(b) J.T. Groves, J. Chem. Educ. 62 (1985) 928.

[4] T. Egawa, H. Shimada, Y. Ishimura, Biochem. Biophys. Res. Commun. 201 (1994) 1464.

[5] C.E. MacBeth, A.P. Colombek, V.G. Young Jr., C. Yang, K. Kuczera, M.P. Hendrich, A.S. Borovik, Science 289 (2000) 939.

[6] C.A. Grapperhaus, B. Mienert, E. Bill, T. Weyhermüller, K. Wieghardt, Inorg. Chem. 39 (2000) 5306.

[7] J.-U. Rohde, J.-H. In, M.H. Lim, W.W. Brennessel, M.R. Bukowski, A. Stubra, E. Münck, W. Nam, L. Que Jr., Science 299 (2003) 1037.

[8] C.E. MacBeth, R. Gupta, K.R. Mitchell-Koch, V.G. Young Jr., G.H. Lushington, W.H. Thompson, M.P. Hendrich, A.S. Borovik, J. Am. Chem. Soc. 126 (2004) 2556.

[9] J. Kaizer, E.T. Klinker, N.Y. Oh, J.-U. Rohde, W.J. Song, A. Stubna, J. Kim, E. Münck, W. Nam, L. Que Jr., J. Am. Chem. Soc. 126 (2004) 472.

[10] J.-U. Rohde, S. Torelli, X. Shan, M.H. Lim, E.J. Klinker, J. Kaizer, K. Chen, W. Nam, L. Que Jr., J. Am. Chem. Soc. 126 (2004) 16750.

[11] O. Pestovsky, S. Stoian, E.L. Bominaar, X. Shan, E. Münck, L. Que Jr., A. Bakac, Angew. Chem., Int. Ed. Engl. 44 (2005) 6871.

[12] J.F. Berry, E. Bill, E. Bothe, T. Weyhermüller, K. Wieghardt, J. Am. Chem. Soc. 127 (2005) 11550.

[13] M.R. Bukowki, K.D. Koehntop, A. Stubna, E.L. Bominaar, J.A. Halfen, E. Münck, W. Nam, L. Que Jr., Science 310 (2005) 1000.

[14] J.-U. Rohde, L. Que Jr., Angew. Chem., Ind. Ed. Engl. 44 (2005) 2255.

[15] N.Y. Oh, Y. Suh, M.J. Park, M.S. Seo, J. Kim, W. Nam, Angew. Chem., Int. Ed. Engl. 44 (2005) 4235.

[16] (a) F. Ogliaro, N. Harris, S. Cohen, M. Filatov, S.P. de Visser, S. Shaik, J. Am. Chem. Soc. 122 (2000) 8977;
(b) F. Ogliaro, S. Cohen, S.P. de Visser, S. Shaik, J. Am. Chem. Soc. 122 (2000) 12892;
(c) F. Ogliaro, S.P. de Visser, S. Cohen, P.K. Sharma, S. Shaik, J. Am. Chem. Soc. 124 (2002) 2806;
(d) J.C. Schöneboom, S. Cohen, H. Lin, S. Shaik, W. Thiel, J. Am. Chem. Soc. 126 (2004) 4017;
(e) S. Shaik, D. Kumar, S.P. de Visser, A. Altun, W. Thiel, Chem. Rev. 105 (2005) 2279;
(f) D. Kumar, H. Hirao, L. Que Jr., S. Shaik, J. Am. Chem. Soc. 127 (2005) 8026;
(g) H. Hirao, D. Kumar, L. Que Jr., S. Shaik, J. Am. Chem. Soc. 128 (2006) 8590.

[17] (a) K. Yoshizawa, Y. Shiota, Y. Kagawa, Bull. Chem. Soc. Jpn. 73 (2000) 2669;
(b) K. Yoshizawa, J. Organomet. Chem. 635 (2001) 100;
(c) T. Kamachi, K. Yoshizawa, J. Am. Chem. Soc. 125 (2003) 4652.

[18] (a) V. Gaullar, R.A. Friesner, J. Am. Chem. Soc. 126 (2004) 8501;
(b) T. Jovanovic, R. Farid, R.A. Friesner, A.E. McDermott, J. Chem. Soc. 127 (2005) 13548;
(c) K.P. Ravindranatharn, E. Gallicchio, R.A. Friesner, A.E. McDermott, R.M. Levy, J. Am. Chem. Soc. 128 (2006) 5786.

[19] (a) M. Shoji, H. Isobe, T. Saito, H. Yabushita, K. Koizumi, Y. Kitagawa, S. Yamanaka, T. Kawakami, M. Okumura, M. Hagiwara, K. Yamaguchi, Int. J. Quant. Chem. 108 (2008) 631;
(b) M. Shoji et al., Int. J. Quant. Chem. 107 (2008) 3250.

[20] H. Isobe, S. Nishihara, M. Shoji, S. Yamanaka, J. Shimada, M. Hagiwara, K. Yamaguchi, Int. J. Quant. Chem. 108 (2008) 2991.

[21] H. Isobe, S. Yamanaka, S. Kuramitsu, K. Yamaguchi, J. Am. Chem. Soc. 130 (2008) 132.

[22] S. Yamanaka, K. Yamaguchi, Bull. Chem. Soc. Jpn. 77 (2004) 1269.

[23] K. Yamaguchi, T. Fueno, Chem. Phys. 19 (1978) 199.

[24] H. Isobe, T. Soda, Y. Kitagawa, Y. Takano, T. Kawakami, Y. Yoshioka, K. Yamaguchi, Int. J. Quant. Chem. 85 (2001) 34.

[25] M.J. Frisch, G.W. Trucks, H.B. Schlegel, G.E. Scuseria, M.A. Robb, J.R. Cheeseman, J.A. Montgomery Jr., T. Vreven, K.N. Kudin, J.C. Burant, J.M. Millam, S.S. Iyengar, J. Tomasi, V. Barone, B. Mennucci, M. Cossi, G. Scalmani, N. Rega, G.A. Petersson, H. Nakatsuji, M. Hada, M. Ehara, K. Toyota, R. Fukuda, J. Hasegawa, M. Ishida, T. Nakajima, Y. Honda, O. Kitao, H. Nakai, M. Klene, X. Li, J.E. Knox, H.P. Hratchian, J.B. Cross, C. Adamo, J. Jaramillo, R. Gomperts, R.E. Stratmann, O. Yazyev, A.J. Austin, R. Cammi, C. Pomelli, J.W. Ochterski, P.Y. Ayala, K. Morokuma, G.A. Voth, P. Salvador, J.J. Dannenberg, V.G. Zakrzewski, S. Dapprich, A.D. Daniels, M.C. Strain, O. Farkas, D.K. Malick, A.D. Rabuck, K. Raghavachari, J.B. Foresman, J.V. Ortiz, Q. Cui, A.G. Baboul, S. Clifford, J. Cioslowski, B.B. Stefanov, G. Liu, A. Liashenko, P. Piskorz, I. Komaromi, R.L. Martin, D.J. Fox, T. Keith, M.A. Al-Laham, C.Y. Peng, A. Nanayakkara, M. Challacombe, P.M.W. Gill, B. Johnson, W. Chen, M.W. Wong, C. Gonzalez, J.A. Pople, GAUSSIAN 03, Revision C.02, Gaussian Inc., Wallingford CT, 2004.

[26] M.W. Schmidt, K.K. Baldridge, J.A. Boatz, S.T. Elbert, M.S. Gordon, J.J. Jensen, S. Koseki, N. Matsunaga, K.A. Nguyen, S. Su, T.L. Windus, M. Dupuis, J.A. Montgomery, J. Comput. Chem. 14 (1993) 1347.

[27] (a) A.J.H. Wachters, J. Chem. Phys. 52 (1970) 1033;
(b) C.W. Bauschlicher Jr., S.R. Langhoff, L.A. Barnes, J. Chem. Phys. 91 (1989) 2399.

[28] (a) P.C. Hariharan, J.A. Pople, Theor. Chim. Acta. 28 (1973) 213;
(b) T. Clark, J. Chandrasekhar, G.W. Spitznagel, P.v.R. Schleyer, J. Comp. Chem. 4 (1983) 294;
(c) M.J. Frisch, J.A. Pople, J.S. Binkley, J. Chem. Phys. 80 (1984) 3265.

[29] (a) D. Mukherjee, S. Pal, Adv. Quant. Chem. 20 (1989) 291;
(b) R.J. Bartlett, Int. J. Mol. Sci. 3 (2002) 579;
(c) F.A. Evangelista, W.D. Allen, H.F. Schaefer III, J. Chem. Phys. 125 (2006) 154113.

[30] (a) K. Yamaguchi, T. Fueno, I. Saito, T. Matsuura, Tetrahedron Lett. 36 (1979) 3433;
(b) K. Yamaguchi, S. Yabushita, T. Fueno, Chem. Phys. Lett. 70 (1980) 27;
(c) idem. Ibid. 78 (1981) 572.

[31] (a) M. Hotokka, B. Roos, P. Siegbahn, J. Am. Chem. Soc. 105 (1983) 5263;
(b) G. Tonachini, H.B. Schlegel, F. Bernardi, M.A. Robb, J. Am. Chem. Soc. 112 (1990) 483;
(c) A. Maranzana, G. Ghigo, G. Tonachini, J. Am. Chem. Soc. 122 (2000) 1414.

[32] (a) S.P. de Vissser, F. Ogliaro, S. Shaik, Chem. Commun. (2001) 2322;
(b) S.P. de Visser, F. Ogliaro, N. Harris, S. Shaik, J. Am. Chem. Soc. 123 (2001) 3037.

[33] (a) G. Guroff, J.W. Daly, D.M. Jerina, J. Renson, B. Witkop, S. Udenfriend, Science 157 (1967) 1524;
(b) D.M. Jerina, J.W. Daly, Science 185 (1974) 573.

[34] (a) F.P. Guengerich, Chem. Res. Toxicol. 14 (2001) 611;
(b) P.R. Ortiz de Montellano, J.J. De Voss, Nat. Prod. Rep. 19 (2002) 477.

Polyhedron 28 (2009) 2053–2057

Contents lists available at ScienceDirect

Polyhedron

journal homepage: www.elsevier.com/locate/poly

Mesophase and magnetic behavior in cobalt(II) and iron(II) compounds

Shinya Hayami [a,*], Yoshihiro Kojima [a], Daisuke Urakami [a], Kazuchika Ohta [b], Katsuya Inoue [a,c]

[a] Department of Chemistry, Graduate School of Science, Hiroshima University, 1-3-1 Kagamiyama, Higashi-Hiroshima 739-8526, Japan
[b] Smart Materials Science and Technology, Shinshu University, 3-15-1 Tokida, Ueda 386-8567, Japan
[c] Institute for Advanced Material Research, Hiroshima University, 1-3-1 Kagamiyama, Higashi-Hiroshima 739-8526, Japan

ARTICLE INFO

Article history:
Available online 6 February 2009

Keywords:
Metallomesogen
Spin-crossover
Liquid crystal

ABSTRACT

The metal complexes with long alkyl chains $[Co(C16\text{-}terpy)_3](BF_4)_2$ (**1**) and $[Fe(C16\text{-}terpy)_2](BF_4)_2$ (**2**) were synthesized and the physical properties of the complex were characterized by magnetic susceptibility, Mössbauer spectroscopy, polarizing optical microscopy, differential scanning calorimetry, and X-ray scattering, where C16-terpy is 4′-hexadecyloxy-2,2′:6′,2″-terpyridine. Variable-temperature magnetic susceptibility measurements and/or Mössbauer studies revealed that the complex **1** exhibited unique spin transition ($T_{1/2}\downarrow$ = 217 K and $T_{1/2}\uparrow$ = 260 K) induced by structural phase transition, and the complex **2** was in the low-spin state in the temperature region of 5–400 K before the first mesophase transition. The cobalt(II) and iron(II) complexes exhibited liquid-crystal properties in the temperature range of 371–528 K and 466–556 K, respectively. After mesophase transition, the complex **1** exhibited only slight spin transition ($T_{1/2}\downarrow$ = 266 K and $T_{1/2}\uparrow$ = 279 K), and the complex **2** was in the low-spin state. The compounds with multifunction, i.e., magnetic property and liquid-crystal properties, are important in the development of molecular materials.

© 2009 Elsevier Ltd. All rights reserved.

1. Introduction

Liquid crystals are fascinating functional materials, and are important in the field of advance materials such as electrooptic devices. Generally, liquid crystals used in the display is organic liquid crystals, organic liquid crystals are diamagnetic and can be easily oriented by an electric field. The construction of metal-containing liquid crystals (metallomesogens) has recently attracted a great deal of attention [1–7]. Metallomesogens have unpaired electron, spin, and the control of liquid crystal property used spin characters is very interesting. The investigation for magnetic liquid crystals containing rare-earth ions has been reported, because these ions often have a large magnetic anisotropy [1]. Furthermore, side chain nickel(II) polymeric compounds have been synthesized and the compounds have exhibited cooperative magnetic properties toward constructing of ferromagnets with liquid-crystal properties [3]. Therefore, liquid crystals that can be controlled by a several of external fields have been developed.

Recently, Fujigaya et al. have reported the spin-crossover (SCO) iron(II) compounds triggered by a phase transition [8], and the similar materials reported by Kimizuka et al. [9,10]. The compounds exhibit phase transition (crystal ⇆ melt)-triggered SCO behavior. Gaspar et al. have also investigated the synchronicity both transition, spin transition and solid–liquid crystal transition in iron(II) complexes [11]. Chang et al. have reported a synchronic bistability of valence tautomerism and crystal–melt phase transition [12]. Recently, we have also investigation the possibility to synchronize between the motion of the long alkyl chains and spin states [7,13–16]. Putting a metal complex cores with SCO in the liquid crystals is expected to show novel physical properties base of a synergy between magnetic and liquid crystal properties toward external stimuli.

We aim at constructing metal complexes with SCO and liquid crystal properties. Here we focused on the cobalt(II) and iron(II) compounds $[Co(C16\text{-}terpy)_3](BF_4)_2$ (**1**) and $[Fe(C16\text{-}terpy)_2](BF_4)_2$ (**2**) (C16-terpy is 4′-hexadecyloxy-2,2′:6′,2″-terpyridine) in order to develop novel metallomesogens.

2. Experimental

2.1. Synthesis

The ligand 4′-hexadecyloxy-2,2′:6′,2″-terpyridine (C16-terpy) was synthesized as follows: 2,6-bis(2-pyridyl)-4(1*H*)-pyridone (0.5 g, 2.00 mmol), K_2CO_3 (0.332 g, 3.00 mmol), and 1-bromohexadecane (0.73 g, 3.00 mmol) were mixed in DMF (50 ml). The mixture was stirred vigorously at 80 °C for one day. After cooling at r.t., the mixture was poured into ice/water. The pale purple precipitates was filtrated and washed with hot acetone and hexane. The product was dissolved in $CHCl_3$, and the solution was washed with 10% K_2CO_3 in water. The separated organic solution was dried

* Corresponding author. Tel./fax: +81 82 424 7418.
E-mail address: hayami@hiroshima-u.ac.jp (S. Hayami).

0277-5387/$ - see front matter © 2009 Elsevier Ltd. All rights reserved.
doi:10.1016/j.poly.2009.01.029

using anhydrous Na_2SO_4 and concentrated to give white powders; yield: (0.94 g, 97%). ^1H NMR ($CDCl_3$): δ = 8.70 (d, J = 4.0, 2H), 8.62 (d, J = 8.0, 2H), 8.01 (s, 2H), 7.85 (td, J = 8.0, 1.5, 2H), 7.32 (ddd, J = 7.5, 4.5, 1.0, 2H), 4.22 (t, J = 6.5, 2H) 1.86–1.26 (m, 28H), 0.88 (t, J = 7.0, 3H). Selected FT-IR data [ν/cm^{-1}] using KBr disk: 2919, 2848, 1582, 1469, 1446, 1407, 1359, 1202, 1030, 796.

The compound [Co(C_{16}-terpy)$_2$](BF_4)$_2$ · MeOH (**1** · **MeOH**) was synthesized as follows: the ligand C16-terpy (170 mg, 0.36 mmol) was dissolved in $CHCl_3$/MeOH (20 ml) and was added to solution of Co(BF_4)$_2$ · $6H_2O$ (60 mg, 0.18 mmol) in MeOH (10 ml). The brown orange solution was concentrated to about 10 ml, the micro crystals were filtered and recrystallized slowly from MeOH; yield: 94 mg (43%); brown orange crystals. *Anal.* Calc. for $C_{63}H_{90}O_3N_6B_2F_8Co_1$: C, 62.43; H, 7.48; N, 6.93; Co, 4.86. Found: C, 62.48; H, 7.53; N, 6.98; Co, 4.93%. The elemental analyses for **1** after removing MeOH molecules are as follows: Calc. for $C_{62}H_{86}O_2N_6B_2F_8Co_1$, C, 63.11; H, 7.35; N, 7.12; Co, 4.99. Found: C, 63.21; H, 7.42; N, 7.20; Co, 4.83%.

The iron(II) compound [Fe(C_{16}-terpy)$_2$](BF_4)$_2$ · acetone (**2** · **acetone**) was synthesized as follows: under nitrogen atmosphere, C16-terpy (300 mg, 0.633 mmol) was dissolved in $CHCl_3$/MeOH (20 ml) and was added to mixture solution of $FeCl_2$ · $4H_2O$ (63 mg, 0.317 mmol) and $NaBF_4$ (69 mg, 0.317 mmol) in $CHCl_3$/MeOH (ca. 10 cm^3). The purple solution was concentrated to about 20 ml, the micro crystals were filtered and recrystallized from Aceton/EtOH; yield: 215 mg (85%); purple needle crystals. *Anal.* Calc. for $C_{65}H_{92}Cl_2Fe_1N_6O_{11}$: C, 61.95; H, 7.36; N, 6.67; Fe, 4.43. Found: C, 62.10; H, 7.22; N, 7.10; Fe, 4.21%. The elemental analyses for **2** after removing acetone molecules are as follows: *Calc.* for $C_{62}H_{86}O_2N_6B_2F_8Fe_1$, C, 63.28; H, 7.37; N, 7.14; Fe, 4.75. Found: C, 63.19; H, 7.22; N, 7.09; Fe, 4.53%.

2.2. Physical experiments

All elemental analyses date were obtained at the Service Center of the Elemental Analysis of Organic compounds, Department of Chemistry, Kyushu University. Metal analyses were done on a Shimadzu AA-625-11 Atomic Absorption/Flame Emission Spectrometer. Infrared spectra were recorded using KBr disk with a JASCO FT-IR-410. All NMR measurements were performed on a Bruker AVANCE SERIES DPX 400 instrument operating at 400 MHz. Differential Scanning Calorimetry (DSC) thermal analysis was carried out on a SHIMADZU DSC50 differential scanning calorimeter. Optical polarized microscopy was carried out on a Nippon Chemical Industrial corporation polarization microscope OPTICAL POL with a Yanagimoto factory MODEL MP-J3 micro melting point meter. Powder X-ray diffraction (XRD) studies were performed on a Rigaku X-ray diffractometer RAD-2A with 2.0 kW Cu Kα X-ray. The magnetic susceptibilities $\chi(T)$ were measured between 5 and 400 K with a superconducting quantum interference device magnetometer (Quantum Design MPMS-5S) in an external field of 0.5 T. The Mössbauer spectrometer with a ^{57}Co/Rh source was driven in the transmission mode. The measurements at low temperature were performed with a closed-cycle helium refrigerator (Iwatani Co., Ltd.).

3. Results and discussion

Single crystals **1** · **MeOH** were isolated as MeOH adducts by slow recrystallization from MeOH solvent. Fig. 1a shows the molecular structure for **1** · **MeOH**. Each of the cobalt(II) ions are octahedrally coordinated by six nitrogen atoms in two C16-terpy ligands, i.e., an N_6 donor set. The values of the bond lengths are typical LS and HS cobalt(II) compounds. The long alkyl chains $C_{16}H_{33}O$ which forms a rod like structure are stuck out of 4′-position in the terpyridine moiety. On the other hand, the single crystal X-ray analysis was done for **2** · **acetone**. Fig. 1b shows the structure when complex **2** · **acetone** is in the low-spin state. The structure of **2** · **acetone** is similar to that of **1** · **MeOH**. The values of the bond lengths are consistent with those for typical LS iron(II) compounds.

The temperature dependence of the magnetic susceptibility for the compound **1** was measured in the form of the χ_mT versus T curve, where χ_m is the molar magnetic susceptibility and T the temperature (Fig. 2). The χ_mT value for **1** gradually decreases from 1.58 cm^3 K mol^{-1} at 400 K to 0.41 cm^3 K mol^{-1} at 226 K, and the gradually decrease of the χ_mT value shows normal thermal SCO behavior. Further cooling, the χ_mT value increases abruptly at around $T_{1/2}\downarrow$ = 217 K to 2.01 cm^3 K mol^{-1} at 206 K. The magnetic behavior shows that compound **1** exhibits spin transition from LS state to HS state on cooling. On heating, the χ_mT products undulation between 1.70 and 2.15 cm^3 K mol^{-1} in the temperature range from 5 to 251 K. On further heating, the χ_mT values abruptly dropped at around $T_{1/2}\uparrow$ = 260 K, showing the transition from HS to LS state. Then the χ_mT value gradually increases in the temperature range from 267 to 400 K. In the additional cycle, the wide thermal hysteresis loop (ΔT = 43 K) remained unchanged in the successive thermal cycle. On the other hand, Mössbauer spectrum was measured at room temperature K for the complex **2** (Fig. 3a). A doublet with *Q.S.* (quadrupole splitting) = 1.18 mm s^{-1} and *I.S.* (isomer shift) = 0.22 mm s^{-1} was observed for **2**, at 300 K, which corresponded to the LS state of iron(II) compounds. Magnetic property for the complex **2** was also followed by measurements of the molar magnetic susceptibility χ_m as a function of temperature in the temperature range of 300–570 K by using SQUID for high temperatures. The χ_mT value for the complex **2** is equal to 0.32 cm^3 K mol^{-1} over room temperature, which shows that the iron(II) ions remain in the LS state although there is some influence by impurities of a quartz pipe and quartz wool.

Liquid-crystalline properties were confirmed by differential scanning calorimetry (DSC), polarizing optical microscopy (POM),

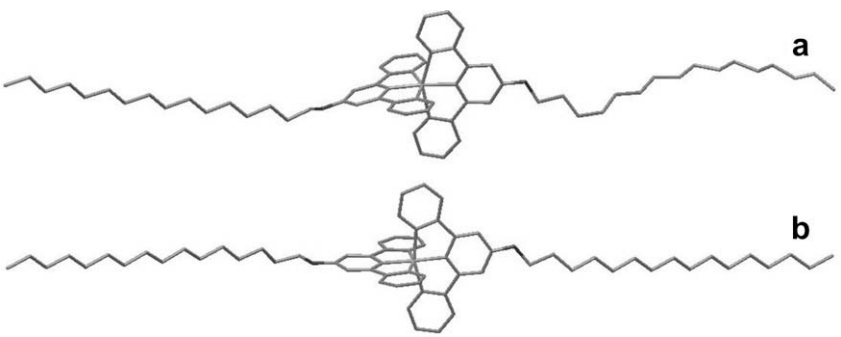


Fig. 1. Molecular structure of the cobalt(II) compound **1** · **MeOH** (a) and the iron(II) compound **2** · **acetone** (b).

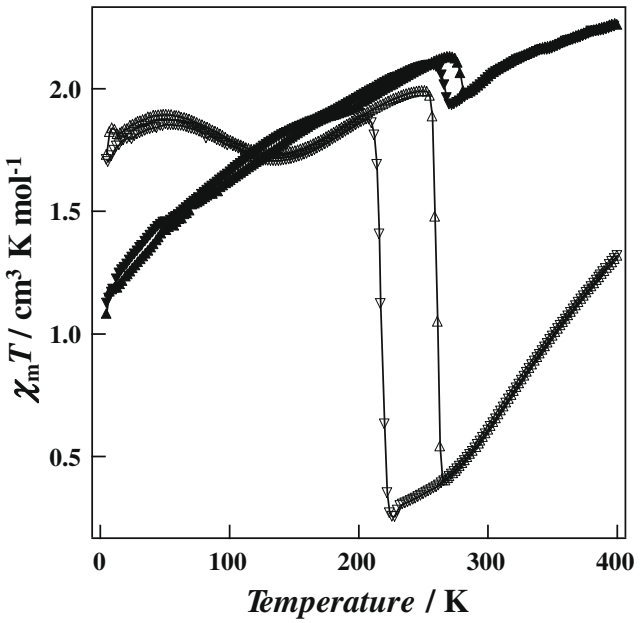


Fig. 2. $\chi_m T$ versus T plots for the complex **1**. The magnetic susceptibilities were measured on heating (△) and cooling (▽) before mesophase transition, and on heating (▲) and cooling (▼) after mesophase transition between 5 and 400 K.

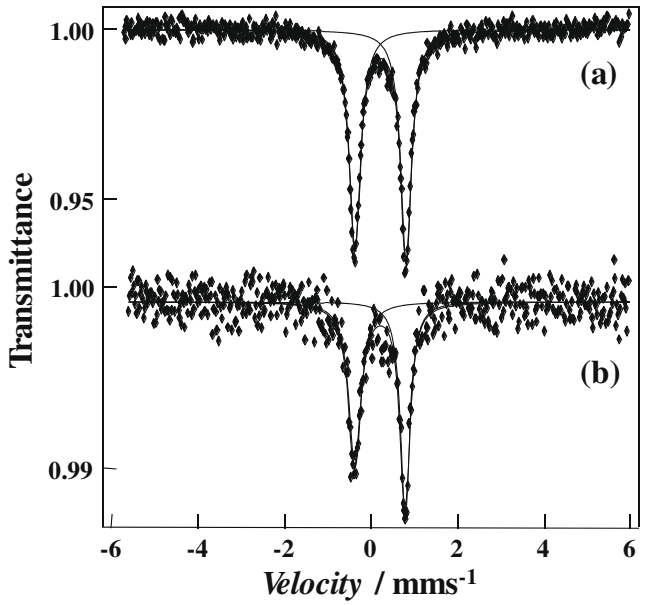


Fig. 3. Mössbauer spectra for **2** at room temperature. (a) Spectrum before mesophase transition. (b) Spectrum after mesophase transition.

and X-ray scattering (PXRD). Phase transition enthalpies were measured by carrying out DSC thermal analysis. The results are summarized in Table 1. Four peaks were observed at 371, 430, 511 and 528 K for **1**. The DSC peak (ΔH = 36.8 kJ mol^{-1}) at 371 K to a crystal-mesophase (SmE) transition, and that (ΔH = 13.7 kJ mol^{-1}) at 430 K is assigned to a SmE-SmC phase transition. Further heating, the peak at 511 K is assigned to a SmC-SmA phase transition, and that at 528 K is melting point. On the other hand, four peaks were observed at 448, 461, 466 and 556 K for **2**. Two peaks at 448 and 461 K is assigned to crystal (K_1) to crystal (K_2) and K_2 to K_3 transitions, respectively. Further heating, the peak at 466 K is assigned to K_3 to mesophase (D_{L2}) transition, and that at 556 K is melting point.

The mesophase was studied by hot-stage polarized optical microscopy, and identified as the mesophases based on the textures observed by optical microscopy for **1** and **2** (Fig. 4). Fig. 4a at 390 K, (b) at 490 K and (c) at 520 K show the texture of SmE, SmC and SmA phases, respectively. Fig. 4d at 520 K shows the texture of D_{L2} phase.

Temperature-dependent X-ray diffraction measurements were carried out to confirm this mesophase. Figs. 5 and 6 show the powder X-ray diffraction patterns of the crystal and mesophase states for the compounds **1** and **2**. A sharp reflection in the small-angle (2θ = 5.3°) with d-spacing of 16.7 Å was detected for **1** at 300 K (crystal phase). At 390 K, the peak of 2θ = 5.3° disappeared and a new peak appeared at 2θ = 4.6° (d = 19.2 Å) (SmE phase). At 490 K, the peak of 2θ = 4.6° disappeared and a new peak appeared at 2θ = 2.7° (d = 32.7 Å) (SmC phase). The peak of 2θ = 2.7° shifted to that of 2θ = 2.66° (d = 33.2 Å). The peak of 2θ = 21.5° (d = 4.1 Å) becomes broad at the same time. A sharp reflection in the small-angle (2θ = 4.7°) with d-spacing of 18.8 Å was detected for **2** at 300 K (K_1 phase). At 450 K, a new peak appeared at 2θ = 4.5° (d = 19.6 Å) (K_2 phase). At 463 K, the peak of 2θ = 4.5° shifted to that of 2θ = 4.4° (d = 20.1 Å). At 490 K, the peak of 2θ = 4.4° and 4.7° disappeared and a new peak appeared at 2θ = 2.6° (d = 34.0 Å) (D_{L2} phase).

The temperature dependence of the magnetic susceptibility for the compound **1** was measured after mesophase transition (Fig. 2).

Table 1
Phase transition temperatures and enthalpy changes for **1** and **2**.

Compound	Phase → Phase (T (K); ΔH / kJ mol^{-1})
1	K $\xrightarrow{371}$ SmE $\xrightarrow{430}$ SmC $\xrightarrow{511}$ SmA $\xrightarrow{528}$ I.L.(decomp.) [36.8] [13.7] [−] [−]
2	$K_1 \xrightarrow{448} K_2 \xrightarrow{461} K_3 \xrightarrow{466} D_{L2} \xrightarrow{556}$ I.L.(decomp.) [28.8] [4.55]

Phase nomenclature: K = crystal, SmA = smectic A mesophase, SmC = smectic C mesophase, SmE = smectic E mesophase, I.L. = isotropic liquid.

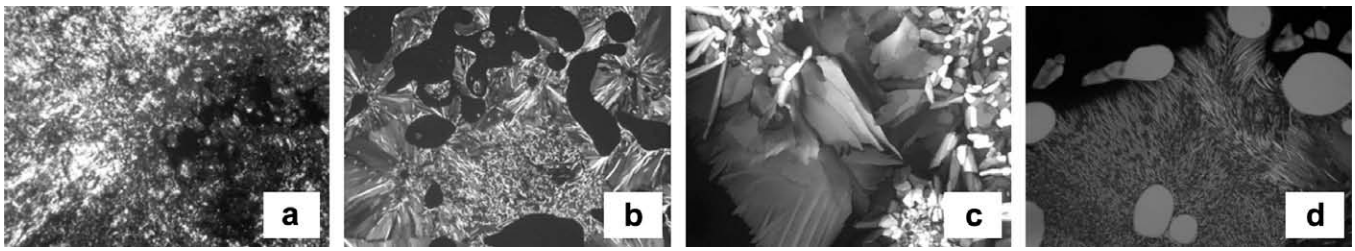


Fig. 4. Texture of the complex **1** and **2** under crossed polarizers at various temperatures. The texture (a) at 390 K is assigned to SmE phase, (b) at 490 K is assigned to SmC phase and (c) at 520 K is assigned to SmA phase for **1**. The texture (d) at 520 K is assigned to D_{L2} phase.

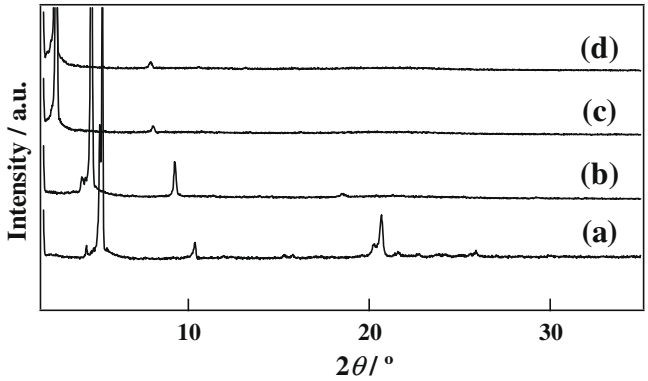


Fig. 5. Temperature dependence of powder XRD patterns for **1** (a) at 300 K, (b) at 390 K, (c) at 490 K and (d) at 520 K.

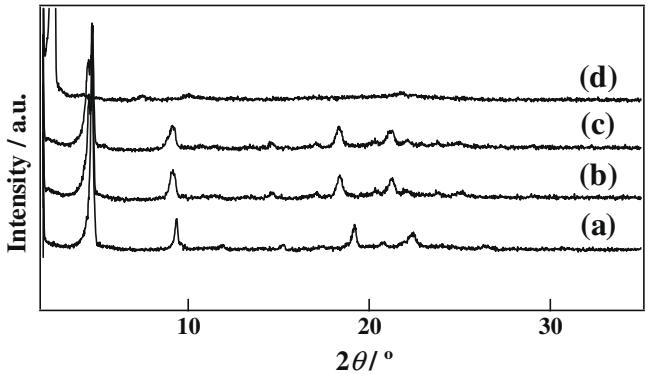


Fig. 6. Temperature dependence of powder XRD patterns for **2** (a) at 300 K, (b) at 450 K, (c) at 463 K and (d) at 500 K.

The $\chi_m T$ value for **1** gradually decreases from 2.26 cm^3 K mol^{-1} at 400 K to 1.93 cm^3 K mol^{-1} at 272 K. Further cooling, the $\chi_m T$ value slightly jump at around $T_{1/2}\downarrow$ = 266 K to 2.10 cm^3 K mol^{-1} at 256 K. The magnetic behavior shows that compound **1** exhibits slight spin transition induced by structural phase transition. On heating, the $\chi_m T$ gradually increases between 1.12 and 2.13 cm^3 K mol^{-1} in the temperature range from 5 to 271 K. On further heating, the $\chi_m T$ values slightly dropped at around $T_{1/2}\uparrow$ = 279 K. Then the $\chi_m T$ value gradually increases in the temperature range from 282 to 400 K. In the additional cycle, the wide thermal hysteresis loop (ΔT = 13 K) remained unchanged in the successive thermal cycle. The jump may be explained by increasing orientation of micro-crysytalline particles with anisotropic paramagnetic susceptibility. The magnetic results show that molecular arrangement for the complex **1** keeps condition as it is if the molecular arrangement is gathered once. On the other hand, Mössbauer spectrum was measured at room temperature K after mesophase transition for the complex **2** (Fig. 3b). A doublet with *Q.S.* (quadrupole splitting) = 1.17 mm s^{-1} and *I.S.* (isomer shift) = 0.21 mm s^{-1} was observed for **2**, at 300 K, which corresponded to the LS state of iron(II) compounds. The magnetic property for **2** is in the LS state, and both of the Mössbauer spectra give same parameters before and after mesophase transition.

4. Conclusions

The metal complexes with long alkyl chains $[Co(C16\text{-}terpy)_3](BF_4)_2$ (**1**) and $[Fe(C16\text{-}terpy)_2](BF_4)_2$ (**2**) were synthesized and the physical properties of the complex were characterized. The complex **1** exhibited unique spin transition ($T_{1/2}\downarrow$ = 217 K and $T_{1/2}\uparrow$ = 260 K) induced by structural phase transition, and the complex **2** was in the low-spin state in the temperature region of 5–400 K before the first mesophase transition. The compound **1** exhibited mesophase transitions, K to SmE at 371 K, SmE to SmC at 430 K, SmC to SmA at 511 K, and the compound **2** also exhibited mesophase transitions, K_3 to D_{L2} at 466 K. We believe that our approach, i.e., the co-occurrence of magnetic and liquid-crystal properties, can be widely applied, not only in the design of liquid-crystal materials with magnetism but also in the design of a variety of switchable molecular compounds.

Acknowledgements

This work was supported by "Development of Molecular Devices in Ferroelectric Metallomesogens" in 2006 from the New Energy and Industrial Technology Development Organization (NEDO) of Japan, and Grant-in-Aids for Science Research (No. 20350028) from the Ministry of Education, Culture, Sports, Science and Technology of the Japanese Government.

References

[1] K. Binnemans, Y.G. Galyametdinov, R.V. Deun, D.W. Bruce, S.R. Collinson, A.P. Polishchuk, I. Bikchantaev, W. Haase, A.V. Prosvirin, L. Tinchurina, I. Litvinov, A. Gubajdullin, A. Rakhmatullin, K. Uytterhoeven, L.V. Meervelt, J. Am. Chem. Soc. 122 (2000) 4335.
[2] K. Ohta, N. Yamaguchi, I. Yamamoto, J. Mater. Chem. 8 (1998) 2637.
[3] R. Werner, K. Falk, S. Ostrovsky, W. Haase, Macromol. Chem. Phys. 202 (2001) 2813.
[4] C. Piechocki, J. Simon, A. Skoulios, D. Guillon, P. Weber, J. Am. Chem. Soc. 104 (1982) 5245.
[5] A.M. Giround-Godquin, J.C. Marchon, J. Phys. Lett. 45 (1984) L681.
[6] Y. Galyametdinov, V. Ksenofontov, A. Prosvirin, I. Ovchinnikov, G. Ivanova, P. Gütlich, W. Haase, Angew. Chem., Int. Ed. 40 (2001) 4269.
[7] S. Hayami, K. Danjobara, K. Inoue, Y. Ogawa, N. Matsumoto, Y. Maeda, Adv. Mater. 16 (2004) 869.
[8] T. Fujigaya, D.-L. Jiang, T. Aida, J. Am. Chem. Soc. 125 (2003) 14690.
[9] N. Kimizuka, S.-H. Lee, T. Kunitake, Angew. Chem., Int. Ed. 39 (2000) 389.

[10] K. Kuroiwa, T. Shibata, A. Takada, N. Nemoto, N. Kimizuka, J. Am. Chem. Soc. 126 (2004) 2016.
[11] M. Seredyuk, A.B. Gaspar, V. Ksenofontov, Y. Galyametdinov, J. Kusz, P. Gütlich, J. Am. Chem. Soc. 130 (2008) 1431.
[12] D. Kiriya, H.C. Chang, S. Kitagawa, J. Am. Chem. Soc. 130 (2008) 5515.
[13] S. Hayami, Y. Shigeyoshi, M. Akita, K. Inoue, K. Kato, K. Osaka, M. Takata, R. Kawajiri, T. Mitani, Y. Maeda, Angew. Chem., Int. Ed. 44 (2005) 4899.
[14] S. Hayami, R. Moriyama, Y. Shigeyoshi, R. Kawajiri, T. Mitani, M. Akita, K. Inoue, Y. Maeda, Inorg. Chem. 44 (2005) 7295.
[15] S. Hayami, N. Motokawa, A. Shuto, N. Masuhara, T. Someya, Y. Ogawa, K. Inoue, Y. Maeda, Inorg. Chem. 46 (2007) 1789.
[16] S. Hayami, R. Moriyama, A. Shuto, Y. Maeda, K. Ohta, K. Inoue, Inorg. Chem. 46 (2007) 7692.

Polyhedron 28 (2009) 2058–2062

Contents lists available at ScienceDirect

Polyhedron

journal homepage: www.elsevier.com/locate/poly

Determination of spin susceptibility and intrachain exchange interaction of $S = 1/2$ one-dimensional antiferromagnetic Heisenberg chain $[Cu(OH)(NO_3)(pydz)]H_2O$ by solid-state high-resolution NMR

Tetsuya Yamada, Goro Maruta *, Sadamu Takeda *

Division of Chemistry, Faculty of Science and Graduate School of Science, Hokkaido University, Sapporo, Hokkaido 060-0810, Japan

ARTICLE INFO

Article history:
Available online 10 February 2009

Keywords:
Highly one-dimensional antiferromagnetic chain
Strong antiferromagetic interaction
Spin susceptibility
Solid-state high-resolution ^{13}C NMR
DFT calculation

ABSTRACT

Spin susceptibility of $S = 1/2$ one-dimensional antiferromagnetic Heisenberg chain $[Cu(OH)(NO_3)(pydz)]H_2O$ (pydz = pyridazine), which was difficult to be estimated from magnetic susceptibility measurements, was determined by measuring the temperature dependence of solid-state high-resolution ^{13}C MAS (magic angle spinning) NMR and by performing theoretical calculation. From fitting to theoretical formula for $S = 1/2$ one-dimensional chain model, one-dimensional intrachain exchange interaction J/k_B was estimated at 590–695 K (Hamiltonian = $J\sum S_i \cdot S_j$). We also evaluated that the ratio $\frac{k_B T_N}{J}$, which expresses a degree of one-dimensionality, is less than 3.4×10^{-3}. This result indicates that $[Cu(pydz)(OH)(NO_3)]H_2O$ has high one-dimensionality.

© 2009 Elsevier Ltd. All rights reserved.

Low-dimensional magnetic coordination polymers have attracted much attention in recent years because of many specific properties due to enhanced quantum fluctuation. In particular, one-dimensional electron spin system is one of the most popular quantum spin systems exhibiting interesting properties such as, Haldane gap for integer spin systems or gapless spin excitation levels for half integer spin systems [1–3]. Although they have been studied for a long time and some specific properties were found, new quantum properties have been still discovered such as single chain magnet [4,5] or field-induced gap [6–8], suggesting that one-dimensional system is still developing field.

Strong magnetic interaction within one-dimensional chain system enables us to apply an ideal model of no long-range ordering to the experimental results; specific properties of one-dimensionality may be observed in higher temperature region. Coordination polymer $[Cu(OH)(NO_3)(pydz)]H_2O$ is expected to be one of the strongest $S = 1/2$ one-dimensional antiferromagnetic Heisenberg chain [9–13] by considering from its crystal structure and very small magnetic moment at room temperature [14]. There are three bridging ligands in $[Cu(OH)(NO_3)(pydz)]H_2O$, which are hydroxyl ion, nitrate ion and pyridazine between adjacent copper(II) ions as shown in Fig. 1.

It is known that hydroxyl as a ligand plays an important role to enhance magnetic interaction [15] and magnetic moment of this compound measured at room temperature, which is $1.08\mu_B$, is much smaller than about $1.9\mu_B$ of typical copper coordination polymers. These properties suggest that $[Cu(OH)(NO_3)(pydz)]H_2O$ has strong antiferromagnetic interaction.

It is difficult to determine the spin susceptibility for strong antiferromagnetic coordination polymers, because magnetic susceptibility measurement observes not only spin susceptibility χ_{spin} but also other contributions. Observed value can be written as shown in Eq (1) [16,17]:

$$\chi_{obs} = \chi_{spin} + \chi_{dia} + \chi_{TIP} + \cdots, \quad (1)$$

which includes diamagnetic component χ_{dia} and temperature independent paramagnetism χ_{TIP}, for example. When spin susceptibility is as small as other contributions due to strong antiferromagnetic interaction, spin susceptibility cannot be evaluated correctly from magnetic susceptibility measurement. In fact, spin susceptibility χ_{spin} has never been reported for $[Cu(OH)(NO_3)(pydz)]H_2O$. So we need to determine spin susceptibility from other methods. In this report, we elucidated the spin susceptibility by solid-state high-resolution NMR and theoretical calculations.

One-dimensionality is suggested by the ratio of $\frac{k_B T_N}{J}$, where J/k_B is one-dimensional intrachain exchange interaction and T_N is Neel temperature. We estimated J/k_B and upper limit of T_N from spin susceptibility determined by solid-state high-resolution NMR and magnetic susceptibility measurement, respectively. We found that $[Cu(OH)(NO_3)(pydz)]H_2O$ has very high one-dimensionality compared with other structurally one-dimensional coordination polymer [10,18].

$[Cu(OH)(NO_3)(pydz)]H_2O$ was prepared by the literature method [14]. After $Cu(NO_3)_2 3H_2O$ (0.58 g, 2.4 mmol) was dissolved

* Corresponding authors. Tel.:+81 11 706 3505; fax: +81 11 706 4841 (S. Takeda).
E-mail addresses: maruta@sci.hokudai.ac.jp (G. Maruta), stakeda@sci.hokudai.ac.jp (S. Takeda).

0277-5387/$ - see front matter © 2009 Elsevier Ltd. All rights reserved.
doi:10.1016/j.poly.2009.01.038

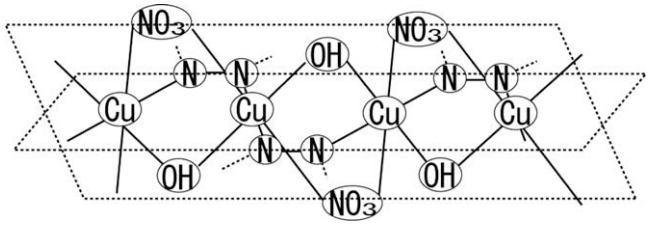


Fig. 1. Linear chains structure of $[Cu(OH)(NO_3)(pydz)]H_2O$. Nitrogen atoms coordinating to copper are from pyridazine molecule. Two planes shown by broken lines mean the planes made up with Cu–NO_3–Cu and Cu–pyridazine–Cu, respectively.

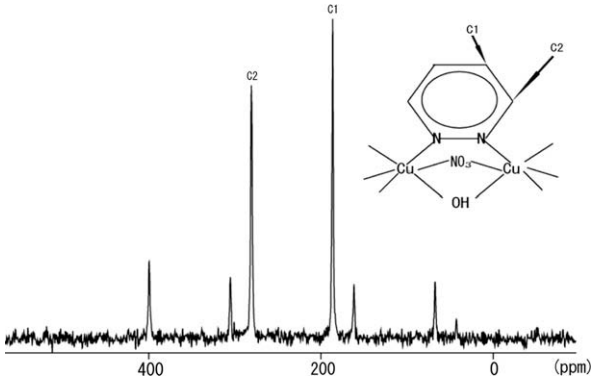


Fig. 2. ^{13}C MAS NMR spectrum of $[Cu(OD)(NO_3)(pydz\text{–}d^4)]D_2O$ at 9 kHz and room temperature. C1 and C2 are assignments of inequivalent pyridazine carbon atoms which are marked in inserted molecular diagram of $[Cu(OD)(NO_3)(pydz\text{–}d^4)]D_2O$.

in water (10 ml), pyridazine (0.174 ml, 2.4 mmol) was added with stirring the solution. The blue color of $Cu(NO_3)_2 3H_2O$ turned into dark-blue. This solution was concentrated to 2 ml by heating and ethanol (8 ml) was added. After sample was left at room temperature for 4–5 days, blue crystals formed. Elemental analysis for C, H and N showed good agreement with calculation. Anal. *Calc.* for $[Cu(OH)(NO_3)(pydz)]H_2O$: C, 19.95; H, 2.95; N, 17.45. Found: C, 20.01; H, 2.86; N, 17.66%. The powder X-ray diffraction of this complex agreed very well with previous report [14].

Solid-state high-resolution ^{13}C MAS (magic angle spinning) NMR was measured for deuterated sample $[Cu(OD)(NO_3)(pydz\text{–}d^4)]D_2O$ by spin echo pulse sequence synchronized with sample rotation and with Bruker DSX300 spectrometer at 7.03 T of external field, where resonant frequency for ^{13}C was 75.4 MHz. The spinning rate of the samples was 9 kHz. The ^{13}C NMR shift was measured from the external reference of hexamethylbenzene (carbon of methyl group: 17.17 ppm from TMS). Temperature dependence of ^{13}C NMR was measured between 190 and 420 K. Difference in temperature between thermometer of MAS probe and sample was calibrated by temperature dependence of ^{207}Pb NMR for $Pb(NO_3)_2$ [19].

Using the GAUSSIAN-98 software package, we performed UB3LYP calculation on a dimer for coordination polymer chain of $[Cu(OH)\text{-}(NO_3)(pydz)]H_2O$. As a reference, we also made calculation on a dimmer model for one-dimensional compound $[CuCl_2\text{-}(pydz)]$. Used basis set was LanL2DZ. The geometric structure of the dimer model was extracted from the crystal structure reported in a Ref. [14].

Temperature dependence of DC susceptibility was measured between 2 and 300 K in an applied magnetic field of 1 T with SQUID magnetometer (Quantum Design MPMS). Samples were put into a gelatin capsule for the measurement. Susceptibility of the gelatin capsule was also measured and was subtracted from the raw data of the sample.

Spin susceptibility can be determined indirectly by temperature dependence of NMR shift, because NMR shift depends on spin susceptibility as described as follows:

$$\delta_{para} = \frac{A}{N_A \hbar \gamma g \mu_B} \chi_{spin}, \tag{2}$$

$$\delta = \delta_{para} + \delta_{dia}, \tag{3}$$

where δ_{para} is paramagnetic shift which is caused by the Fermi contact term and dipole interaction term, A is hyperfine coupling constant (hfcc), δ_{dia} is diamagnetic chemical shift, γ is nuclear magnetogyric ratio, g is g-value and μ_B is Bohr magneton of electron spin. Although NMR is indirect method to determine spin susceptibility, it has great advantage to observe not the χ_{obs} in magnetic susceptibility measurement but the χ_{spin}. So we could determine χ_{spin} for $[Cu(OH)(NO_3)(pydz)]H_2O$ to discuss the intrachain magnetic interaction. Observed NMR shift δ is proportional to χ_{spin} and hfcc and includes temperature independent δ_{dia}. As a result, for determining spin susceptibility through NMR measurement, we need three parameters, i.e. δ, A and δ_{dia}. Fig. 2 shows ^{13}C MAS NMR spectrum at 9 kHz and room temperature for deuterated sample $[Cu(OD)(NO_3)(pydz\text{–}d^4)]D_2O$.

C1 and C2 is isotropic shift assigned to two inequivalent carbon atoms of pyridazine ligands. Assignment was confirmed by a measurement of partially deuterated pyridazine sample $[Cu(OH)\text{-}(NO_3)(pydz\text{–}d^2)]H_2O$. D-atom is bonded to C1 and H-atom is bonded to C2. When H–C1 of pyridazine is deuterated, dipolar interaction between carbon and hydrogen becomes very weak due to much smaller nuclear magnetogyric ratio of deuterium. As a result, line width of ^{13}C NMR peak becomes narrow for carbon atom bonded to deuterium atom and the C(–D) peak is concretely assigned. Narrow NMR spectrum shown in Fig. 2 is a result for fully deuterated pyridazine ligand in the complex. Peaks except for C1 and C2 are spinning side bands. Large shift from TMS was attributed to paramagnetic shift due to delocalization of lone pair electrons from copper to pyridazine ligand. Observed shifts of C1 and C2 correspond to δ in Eq. (3). Temperature dependence of δ of C1 and C2 are shown in Fig. 3.

Since the sample decomposed above 405 K and large change of NMR spectrum occurred, measurements at higher temperatures was impossible. Temperature dependence of shifts was due to a change of spin susceptibility as shown in Eq. (2). Because it was found from magnetic susceptibility measurement that magnetization decreased as temperature decreased in the range of NMR measurement, NMR shift to the lower frequency of each peak with decreasing temperature was considered to come from weakened paramagnetism. And diamagnetic chemical shift of pyridazine carbon atom locates near 150 ppm. From these behaviors of NMR shifts, it was expected that both hyperfine coupling constants and electron spin densities of carbon atoms in pyridazine ligand are positive. Additionally, in variation of shift with temperature, there are differences between C1 and C2. While shift of C1 changes only 4–5 ppm, that of C2 changes 10 ppm in the same temperature region. Because C2 is nearer to copper ion than C1, electron spin density at C2 is larger than C1 as explained later from theoretical calculation. As a result, NMR shift of C2 is influenced strongly by electron spins of copper ions more than that of C1.

From NMR measurement, we could obtain δ at each temperature. To evaluate the value of χ_{spin} of $[Cu(OH)(NO_3)(pydz)]H_2O$, we need the values of hfcc A and δ_{dia}, which could not be determined from the present NMR measurement due to the limited temperature region of the measurement without decomposition of the sample. So we attempted to use the calculated value of hfcc A and experimental value of δ_{dia} of similar one-dimensional $S = 1/2$ antiferromagnetic Heisenberg chain $[CuCl_2(pydz)]$. This compound has analogous crystal structure to the $[Cu(OH)(NO_3)(pydz)]H_2O$

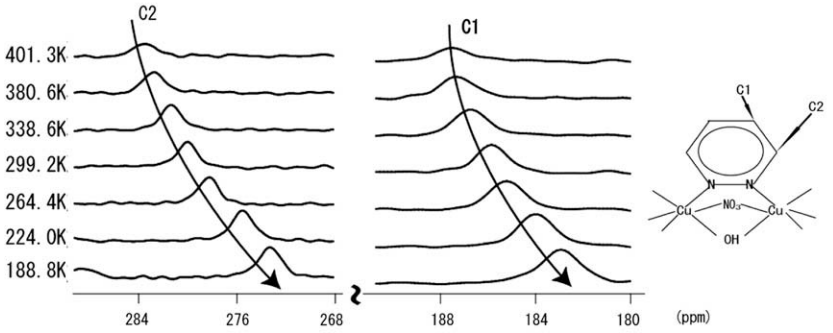


Fig. 3. Temperature dependence of ^{13}C MAS NMR spectra of [Cu(OD)(NO_3)(pydz–d^4)]D_2O between 188.8 and 401.3 K. Arrows follow temperature dependence of each peak.

[20]. Since [$CuCl_2$(pydz)] has smaller antiferromagnetic interaction than that of [Cu(OH)(NO_3)(pydz)]H_2O probably due to absence of hydroxyl bridging ligands, all the values of χ_{spin}, hfcc A and δ_{dia} can be determined by NMR and magnetic susceptibility measurements. Spin susceptibility χ_{spin} dominates the magnetic susceptibility of [$CuCl_2$(pydz)]. From the theoretical calculation based on DFT, we evaluated hfcc A of C1 and C2 both for [$CuCl_2$(pydz)] and [Cu(OH)(NO_3)(pydz)]H_2O. Table 1 shows theoretical and experimental value of hfcc A for [Cu(OH)(NO_3)(pydz)]H_2O and [$CuCl_2$-(pydz)]. Experimental value for [$CuCl_2$(pydz)] was obtained by using Eq. (2) with experimental results of ^{13}C NMR and magnetic susceptibility measurements as shown in Figs. 4–6 which were determined at first time in this work.

Table 1
Theoretical and experimental values of hfcc for [Cu(OH)(NO_3)(pydz)]H_2O and [$CuCl_2$(pydz)]. C1 and C2 mean the carbon atoms shown in Figs. 2 and 3.

	Hyperfine coupling constant (MHz)	
	C1	C2
Theoretical		
[Cu(OH)(NO_3)(pydz)]H_2O	1.3	4.4
[$CuCl_2$(pydz)]	1.7	3.1
Experimental		
[$CuCl_2$(pydz)]	2.4	3.3

For [$CuCl_2$(pydz)], theoretical hfcc values almost coincide with experimental hfcc both for C1 and C2, indicating that DFT calculation is valid. Theoretical values of hfcc of [Cu(OH)(NO_3)(pydz)]H_2O and [$CuCl_2$(pydz)] are similar to each other. This result indicates that there are similar circumstances about carbon atoms of pyridazine between the two coordination polymers, and that calculated hfcc A for [Cu(OH)(NO_3)(pydz)]H_2O and experimentally determined δ_{dia} of [$CuCl_2$(pydz)] can be used for the discussion of mag-

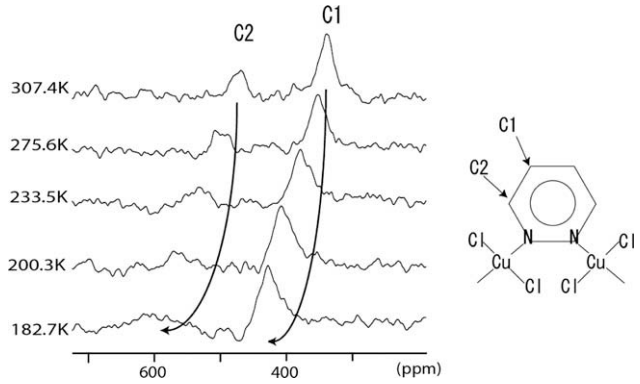


Fig. 5. Temperature dependence of ^{13}C MAS NMR spectra of [$CuCl_2$(pydz)] between 182.7 and 307.4 K. Arrows follow temperature dependence of each peak.

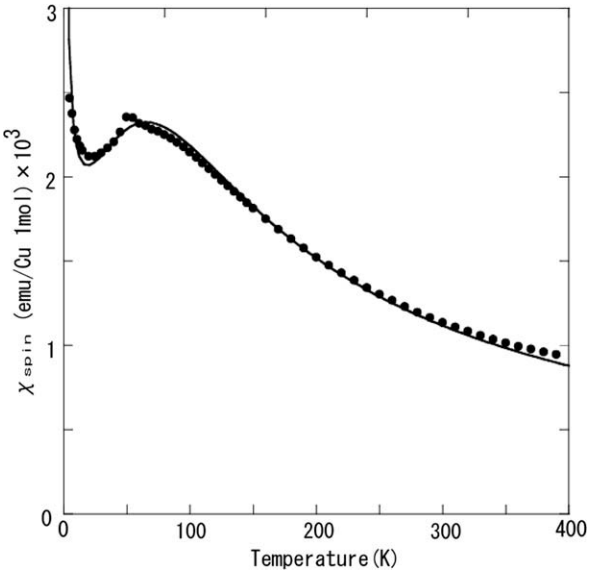


Fig. 4. Spin susceptibility of [$CuCl_2$(pydz)] from magnetic measurement. Solid curve is theoretical fit. J/k_B was estimated to 105 K.

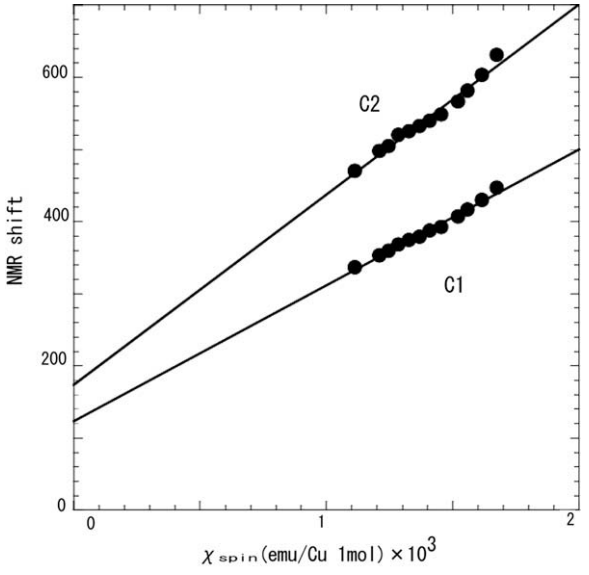


Fig. 6. Dependency of NMR shift of carbon atoms in [$CuCl_2$(pydz)] for spin susceptibility.

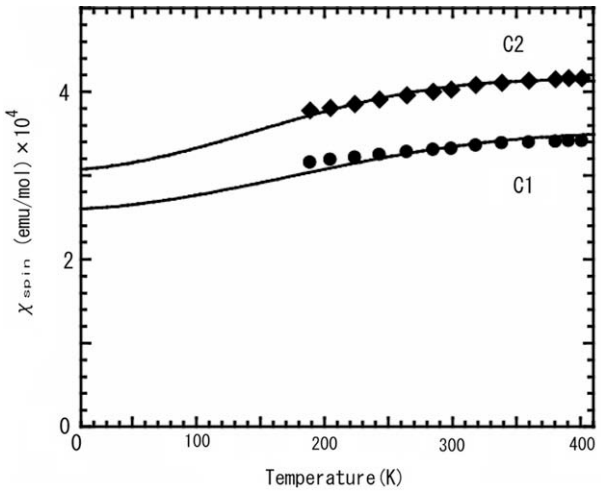


Fig. 7. Spin susceptibility of $[Cu(OH)(NO_3)(pydz)]H_2O$ obtained from NMR measurement. Closed circles and squares indicate spin susceptibility determined from each peak of C1 and C2. Solid curves represent the fit to Eq. (4).

netic interaction in a one-dimensional chain of $[Cu(OH)(NO_3)(pydz)]H_2O$. Now we have the values of hfcc A and δ_{dia} for $[Cu(OH)(NO_3)(pydz)]H_2O$ and we are able to discuss the spin susceptibility of $[Cu(OH)(NO_3)(pydz)]H_2O$.

Spin susceptibility was determined by Eq. (2). Fig. 7 shows spin susceptibility of $[Cu(OH)(NO_3)(pydz)]H_2O$ derived, as explained above.

Temperature range of plots is 188.1–401.3 K, where NMR measurement was performed. Upper plot in Fig. 7 is spin susceptibility determined from ^{13}C NMR shift of C1 and lower plot is from C2. Extrapolated solid lines were calculated based on theoretical formula called E.A.T. model [21,22], which can be written as follows:

$$\chi_{E.A.T.} = g^2\left(\frac{N\mu_B^2}{4k_B}\right)F(x)\frac{1}{T}, \tag{4}$$

$$F(x) = \frac{1 + 0.08516x + 0.23351x^2}{1 + 0.73382x + 0.13696x^2 + 0.53568x^3}, \tag{5}$$

where $x = J/k_BT$. E.A.T. model is a model that is a revision of well-known one-dimensional Bonner–Fischer model, and is superior to original model in the lower temperature region. Spin susceptibility of $[Cu(OH)(NO_3)(pydz)]H_2O$ could be fitted well by E.A.T. model. Here, g-value was fixed to 2.1 which value is often found for copper coordination polymers. As a result one-dimensional intrachain exchange interaction J/k_B was estimated to be 695 and 590 K for C1 and C2, respectively, which indicates J/k_B is 590–695 K. This result indicates that $[Cu(OH)(NO_3)(pydz)]H_2O$ has very strong antiferromagnetic intrachain interaction.

Although there are a few reports about stronger one-dimensional antiferromagnetic chain such as Sr_2CuO_3 ($J/k_B \sim 2600$ K) [9,10] and $[NiBr(chxn)_2]Br_2$ ($J/k_B = 2500$ K) [11] so far, this coordination polymer must be one of the most important antiferromagnetic chain with the strongest intrachain interaction among the copper coordination one-dimensional polymers.

Finally, we evaluated one-dimensionality of $[Cu(OH)(NO_3)(pydz)]H_2O$. One-dimensionality can be estimated from the ratio of Neel temperature T_N and J/k_B as shown in Eq. (6):

$$R = \frac{k_BT_N}{J}. \tag{6}$$

One-dimensional system, which has the smaller value of R, exhibits magnetic ordering at the lower temperature and finally approaches to the ideal one-dimensional chain that never undergoes the phase transition.

Table 2
List of J/k_B, T_N and the ratio $R = \frac{k_BT_N}{J}$ of some coordination polymers which have good one-dimensionality [9,10,13,18,23–25].

	J/k_B (K)	T_N (K)	k_BT_N/J
Sr_2CuO_3	2600	5.4	2.1×10^{-3}
$Sr_2Cu(PO_4)_2$	143	0.085	5.9×10^{-4}
$Cu(C_6H_5COO)_2 \cdot 3H_2O$	17.2	0.0008	4.7×10^{-5}
$[Cu(OH)(NO_3)(pydz)]H_2O$	590–695	<2	$<3.4 \times 10^{-3}$

In this study, we also performed magnetic susceptibility measurements down to 2 K for $[Cu(OH)(NO_3)(pydz)]H_2O$. Since no anomaly was found in the temperature range of the experiment, T_N is expected to be lower than 2 K. Tentatively, we estimated upper limit of the ratio of one-dimensionality from our experimental values, which is $R < \frac{2}{590} = 3.4 \times 10^{-3}$. Table 2 shows one-dimensional antiferromagnetic compounds found so far, together with the present compound $[Cu(OH)(NO_3)(pydz)]H_2O$.

Although Sr_2CuO_3 has the strongest intrachain interaction, one-dimensionality is inferior to other coordination polymers, which have weaker intrachain interaction than Sr_2CuO_3. In fact, $Cu(C_6H_5COO)_2 \cdot 3H_2O$ is the most ideal one-dimensional system at very low temperature, to our knowledge, though this coordination polymer exhibits only small J/k_B. The ratio $\frac{k_BT_N}{J}$ of present compound $[Cu(OH)(NO_3)(pydz)]H_2O$ is as large as Sr_2CuO_3 at least. This result indicates that $[Cu(OH)(NO_3)(pydz)]H_2O$ is a coordination polymer, that has large J/k_B and possibly better one-dimensionality with chemically tunable organic bridging ligands.

We determined NMR shift, hyperfine coupling constant, diamagnetic NMR chemical shift of pyridazine ligand of $S = 1/2$ one-dimensional antiferromagnetic Heisenberg chain $[Cu(OH)(NO_3)(pydz)]H_2O$ by using ^{13}C MAS NMR in the temperature region from about 190 to 400 K and by theoretical study based on DFT. From derived physical values, small spin susceptibility of antiferromagnetic Heisenberg chain $[Cu(OH)(NO_3)(pydz)]H_2O$ was elucidated and one-dimensional intrachain exchange interaction J/k_B was estimated to 590–695 K, which is very large among one-dimensional coordination polymers with organic ligands. We also evaluated one-dimensionality for $[Cu(OH)(NO_3)(pydz)]H_2O$ by considering the ratio $\frac{k_BT_N}{J}$ in this compound. It was estimated that the ratio $\frac{k_BT_N}{J}$ is much less than 3.4×10^{-3}. This ratio indicates that $[Cu(pydz)(OH)(NO_3)]H_2O$ has very good one-dimensionality.

Acknowledgments

This research was supported by Grant-in-Aid for Scientific Research on Priority Areas "Application of Molecular Spins" Area No. 769, Proposal No. 15087201 and for Scientific Research (B) 18350002 from the Ministry of Education, Culture, Sports, Science and Technology of Japan.

References

[1] F.D.M. Haldane, Phys. Rev. Lett. 50 (1983) 1153.
[2] J. Des Cloizeaux, J. Pearson, J. Phys. Rev. 128 (1962) 2131.
[3] L.D. Faddeev, L. Takahtajan, Phys. Lett. A 85 (1981) 375.
[4] A. Caneschi, D. Gatteschi, N. Lalioti, C. Sangregorio, R. Sessoli, G. Venture, A. Vindigni, A. Rettori, M.G. Pini, M.A. Novak, Angew. Chem., Int. Ed. 40 (2001) 1760.
[5] R. Clerac, H. Miyasaka, M. Yamashita, C. Coulon, J. Am. Chem. Soc. 124 (2002) 12837.
[6] D.C. Dender, P.R. Hammar, D.H. Reich, C. Broholm, G. Aeppli, Phys. Rev. Lett. 79 (1997) 1750.
[7] T. Asano, H. Nojiri, Y. Inagaki, J.P. Boucher, T. Sakon, Y. Ajiro, M. Motokawa, Phys. Rev. Lett. 84 (2000) 5880.
[8] M. Oshikawa, I. Affleck, Phys. Rev. Lett. 79 (1997) 2883.
[9] N. Motoyama, H. Eisaki, S. Uchida, Phys. Rev. Lett. 76 (1996) 3212.
[10] K.M. Kojima, Y. Fudamoto, M. Larkin, G.M. Luke, J. Merrin, B. Nachumi, Y.J. Uemura, N. Motoyama, H. Eisaki, S. Uchida, K. Yamada, Y. Endoh, S. Hosoya, B.J. Sternlieb, G. Shirane, Phys. Rev. Lett. 78 (1997) 1787.

[11] S. Takaishi, M. Kano, H. Kitagawa, Y. Furukawa, K. Kumagai, R. Ikeda, Chem. Lett. (2002) 856.
[12] S.K. Satija, J.D. Axe, G. Shirane, H. Yoshizawa, K. Hirakawa, Phys. Rev. B 21 (1980) 2001.
[13] A.A. Belik et al., J. Solid State Chem. 178 (2005) 3461.
[14] L. Carlussi, G. Ciani, M. Moret, A. Sironi, J. Chem. Soc., Dalton. Trans. (1994) 2397.
[15] V.H. Crawford, H.W. Richardson, J.R. Wasson, D.J. Hodgson, W.E. Hatfield, Inorg. Chem. 15 (1976) 2107.
[16] R. Kurland, B.R. Mcgervey, J. Magn. Reson. 2 (1970) 286.
[17] J.P. Jesson, G.N. La Mar, W. De, W. Horrocks Jr, R.H. Holm, NMR of Paramagnetic Molecules, Academic Press, 1973.
[18] T. Lancaster, S.J. Blundell, M.L. Brooks, P.J. Baker, F.L. Pratt, J.L. Manson, C.P. Landee, C. Baines, Phys. Rev. B 73 (2006) 020410(R).
[19] A. Bielecki, D.P. Burum, J. Magn. Reson. A 116 (1995) 215.
[20] Th. Fetzer, A. Lentz, T. Debaerdemaeker, O. Abou-Ei-Wafa, Z. Naturforsch. 45b (1990) 199.
[21] S. Eggert, I. Affleck, M. Takahashi, Phys. Rev. Lett. 73 (1994) 332.
[22] R. Feyerherm, S. Abens, D. Günther, T. Ishida, M. Meißner, M. Meschke, T. Nogami, M. Steiner, J. Phys.: Condens. Matter 12 (2000) 8495.
[23] Y. Karaki, R. Masutomi, M. Kubota, H. Ishimoto, T. Asano, Y. Ajiro, Physica B 329–333 (2003) 1002.
[24] M. Date et al., Progr. Theor. Phys. 46 (1970) 194.
[25] K. Takeda, J. Phys. Soc. Japan 49 (1980) 162.

Polyhedron 28 (2009) 2063–2069

Contents lists available at ScienceDirect

Polyhedron

journal homepage: www.elsevier.com/locate/poly

Electron spin density distribution of a series of nitroxide radicals with five-member ring as studied by solid-state ^{1}H, ^{2}H and ^{13}C NMR

Yasuhiro Kawahashi, Goro Maruta *, Sadamu Takeda *

Department of Chemistry, Faculty of Science and Graduate School of Science, Hokkaido University, Sapporo 060-0810, Japan

ARTICLE INFO

Article history:
Available online 27 March 2009

Keywords:
Organic radicals
Five-member ring
Hyperfine coupling constants
Solid-state high-resolution ^{1}H, ^{2}H, and ^{13}C NMR
Electron spin density distribution

ABSTRACT

Stable nitroxide radicals are useful to construct molecular magnetic systems. Particularly, radicals substituted by –COOH and $–CONH_2$ can be coordinated to magnetic metal ions and may be used as cladding reagents of gold nano-particles for modifying magnetism. Nitroxide molecules with unsaturated five-member ring have almost planner structure and electron spin delocalization may be expected. We determined the hyperfine coupling constants (hfcc) of ^{1}H, ^{2}H and ^{13}C of a series of nitroxide radicals with five-member ring. Experimental values of hfcc were compared with those deduced from calculations based on density functional theory. The electron spin density distribution at β position of ring was sensitive to the ring structure, although the electron spin density at β position is small compared with N–O site. Magnetic susceptibility and UV–Vis absorption spectra were also measured and discussed.

© 2009 Elsevier Ltd. All rights reserved.

Stable organic radicals substituted by –COOH and $–CONH_2$ can be coordinated to magnetic metal ions and may be used as cladding reagents of gold nano-particles for bringing about specific magnetism. For this purpose, electron spin density distribution in the radical molecules is important. As a candidate of such organic radicals, we investigated the electron spin density distribution by paramagnetic shift of solid-state high-resolution ^{1}H, ^{2}H and ^{13}C NMR spectrum for powder crystalline samples and by calculation based on density functional theory for four radicals shown in Scheme 1, *i.e.* (**1**) 3-carboxy-2,2,5,5-tetramethyl-1-pyrrolidinyloxy, (**2**) 3-carboxy-2,5-dihydro-2,2,5,5-tetramethyl-1H-pyrrol-1-yloxy, (**3**) 3-(aminocarbonyl)-2,5-dihydro-2,2,5,5-tetramethyl-1H-pyrrol-1-yloxy, and (**4**) carboxy-2,5-dihydro-2,2,5,5-tetramethyl-1H-imidazol-1-yloxy 3-oxide.

Although it is known that major electron spin density locates on N–O site and methyl groups for stable nitroxide radicals, electron spin density distribution of other part of the molecule is important for use of these organic radicals as a building block of molecular magnetic systems. Since linkage between the organic radicals and metal ions or metal nano particles is mostly formed through this other part (–COOH, –CONH2, etc. in the present case), one of the aim of present study is to investigate the electron spin density distribution of five-member ring and functional groups, which locate opposite the N–O site. Ring structure of five-member ring radicals is chair shape (compound **1** in this paper) or almost planner (other compounds **2**–**4** in this paper), while nitroxide radicals with six member ring mostly exhibit chair shape. Then it is also the aim of this study to clarify how the planarity affects the electron spin density distribution in the five-member ring radicals by experiments and DFT calculation.

Specimens **1**, **2** and **3** were purchased from Acrōs Organics, where **4** from Aldrich and were used as obtained for experiments except ^{2}H NMR of partially deuterated (–COOD) specimen of **1**. This deuteration was performed by several times of recrystallization from CD_3OD. Guaranteed purity was 98%, 99%, 99%, and 98% for **1**, **2**, **3**, and **4**, respectively. Since it was found that compound **4** degraded and electron spin disappeared by 10–15% as described later, we only present only the result of UV–Vis absorption spectrum and DFT calculation for **4**.

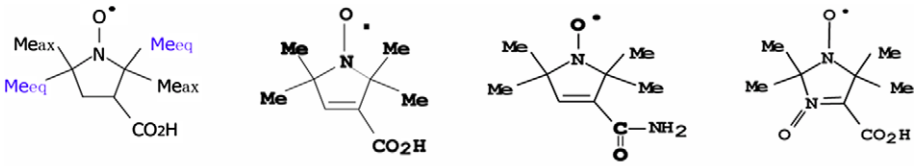
Magic angle spinning (MAS) ^{1}H and ^{13}C NMR spectra were measured at 294 K with Bruker DSX300 spectrometer. Spinning rate was 25 kHz for ^{1}H and 9 kHz for ^{13}C NMR by using 2.5 and 4 mm Zirconia rotor, respectively. Temperature raise by sample spinning was corrected by chemical shift of ^{207}Pb NMR spectrum of $PbNO_3$. Hyperfine coupling constant (hfcc) at each atom of the radical molecule can be determined from isotropic shift δ_{iso} of each NMR signal, which is measured by MAS technique. The observed isotropic shift on a ppm scale consists of Fermi contact term, pseudo contact (dipolar) term, and temperature independent diamagnetic term, as follows [1–3]:

$$\delta_{iso} = \delta_{Fermi} + \delta_{pseudo} + \delta_{dia} \quad (1)$$

$$\delta_{Fermi} = \frac{\mu_B}{3k_BT} \cdot \frac{A_{Ferm}}{\gamma_{nuc}/2\pi} \left(\frac{g_{xx} + g_{yy} + g_{zz}}{3} \right) S(S+1) \quad (2)$$

* Corresponding authors. Tel.: +81 11 706 3505; fax: +81 11 706 4841.
E-mail addresses: maruta@sci.hokudai.ac.jp (G. Maruta), stakeda@sci.hokudai.ac.jp (S. Takeda).

0277-5387/$ - see front matter © 2009 Elsevier Ltd. All rights reserved.
doi:10.1016/j.poly.2009.02.045



1 2 3 4

Scheme 1.

$$\delta_{\text{pseudo}} = \frac{\mu_B^2}{18k_B\text{Tr}^3}[\{2g_{zz}^2 - (g_{xx}^2 + g_{yy}^2)\}(3\cos^2\theta - 1) - 3(g_{xx}^2 - g_{yy}^2)\sin^2\theta\cos 2\Omega]S(S+1) \quad (3)$$

where A_{Fermi} is the Fermi coupling constant of the relevant nucleus in the unit of herz, T is the absolute temperature, γ_{nuc} is the nuclear gyromagnetic ratio, r is the distance between electron spin and nucleus, and others have usual meanings. Eq. (3) displays a contribution from anisotropy of g value of unpaired electron spin to the observed NMR isotropic shift. The anisotropy of the g value is very small for typical nitroxide radical crystals; *e.g.* 2.00620 ± 0.0040 [4]. Thus in our case, the contribution of the pseudo contact term is estimated to be less than 0.01 MHz for r = 0.18 nm, and the pseudo contact term in Eq. (3) can be neglected in comparison with the Fermi contact term to determine the hfcc A_{nuc} (=A_{Fermi}). By using molar magnetic susceptibility χ_M, Eqs. (1) and (2) can be written by [5]:

$$\delta_{\text{iso}} = \frac{A_{\text{nuc}}}{\gamma_{\text{nuc}}/2\pi}\cdot\frac{\chi_M}{N_A g\mu_B} + \delta_{\text{dia}} \quad (4)$$

Experimentally determined hfcc A_{nuc} (=A_{Fermi}) is proportional to the electron spin density $\rho(R_{\text{nuc}})$ at the relevant nuclear position R_{nuc} as follows:

$$A_{\text{nuc}}(=A_{\text{Fermi}}) = \frac{8\pi}{3}g\mu_B\cdot\frac{\gamma_{\text{nuc}}}{2\pi}\rho(R_{\text{nuc}}) \quad (5)$$

Hyperfine coupling constant A_{nue} can be determined experimentally from Eq. (4). However, since the signal accumulation for ^{13}C NMR at natural abundance required over night acquisition or more, it was difficult to measure temperature dependence of the NMR shift δ_{iso}. Therefore, we derived hfcc A_{nue} from the data measured at 294 K. Temperature dependence of magnetic susceptibility of the powder crystalline samples were also measured and are shown in Fig. 1. Curie–Weiss fitting gave Weiss temperature θ = −8.42 K (R = 1.00), −2.31 K (R = 1.00), for **1** and **3**, respectively. Although compound **4** degraded before the measurements as mentioned above and observed $\chi_M T$ value was 0.32 at 300 K, which was considerably smaller than the expected value of 0.375, preliminary value of Weiss temperature was estimated to be very small $\theta \sim -0.1$ K.

Since antiferromagnetic interactions are small, radical spin almost behaves as Curie spin and hfcc A_{nue} can be estimated from Eq. (4) with the observed isotropic shift at 294 K by using chemical shift δ_{dia} of diamagnetic compound with similar structure.

Theoretical calculation of hyperfine coupling constants A_{nue} were performed for single molecule with UB3LYP/6–31+G(d,p) based on DFT of GAUSSIAN98 program package [6]. Molecular structure of **4**, of which the crystal structure has never been reported, was optimized by calculation with UB3LYP/6–31+G(d,p). Reported crystal structures and optimized structures were used for the calculation for **1**, **2** and **3** [7,8]. Calculated results are listed in Tables 1–4.

^{1}H and ^{13}C NMR spectra of **1** are shown in Fig. 2 together with numbering scheme of carbon atoms. Three irradiation frequencies were chosen to cover all of the signals of ^{13}C NMR spectrum. Peaks indicated by stars were assigned to spinning side bands by changing the spinning rate. Assignment of ^{1}H and ^{13}C NMR spectral lines

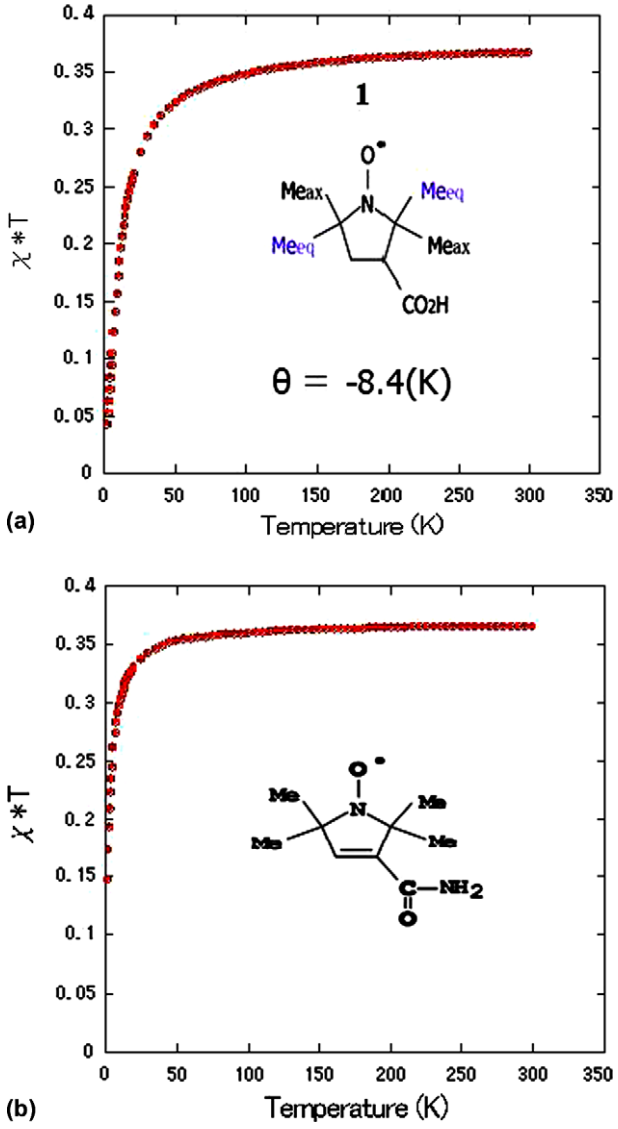


Fig. 1. Magnetic susceptibility multiplied by absolute temperature χT plotted as a function of temperature and Weiss temperature: (a) compound **1** and (b) compound **3**.

were based on the theoretical calculations. Assignment of hydrogen atom of –COOH was based on temperature dependent MAS ^{2}H NMR spectra of partially deuterated compound (–COOD). Powder crystalline sample of **1** is racemic and hfcc A_{nue} was calculated for the structure in a crystal of pure L-form. Comparison between the experimental values and those of calculations is indicated in Table 1. Agreement between the experimental values and calculation is fairly good except for C4, C5 and related hydrogen atoms. Calculation for hydrogen atom of –COOH also deviates from exper-

Table 1
Hyperfine coupling constants (hfcc) of each atom of **1** determined by solid-state high-resolution NMR and calculation with UB3LYP/6–31+G(d,p) based on DFT of GAUSSIAN98 program package.

	Calculated: crystal structure	Calculated: optimized structure	Observed value
Hfcc of ^{13}C/MHz			
C1	11	14	16
C2	24	24	33
C3	−16	−16	−16
C4	−0.36	−0.31	0.2
C5	−0.27	−0.18	1.3
C6	−14	−15	−16
C7	22	23	33
C8	9.9	13	16
C9	0.35	0.07	0.24
Hfcc of ^{1}H/MHz			
Me eq1	−1.26	−0.95	−1.10
Me ax2	−0.26	0.07	0.33
Me ax7	0.21	0.27	0.33
Me eq8	−0.84	−1.01	−1.07
CO2H	−0.03	−0.03	0.36
H1	−0.03	−0.31	−0.66
H2	−0.41	−0.55	−0.81
H3	−0.01	−0.02	−0.61

Table 2
Hyperfine coupling constants of each atom of **2** determined by solid-state high-resolution NMR and calculation with UB3LYP/6–31+G(d,p) based on DFT of GAUSSIAN98 program package.

	Calculated: crystal structure	Calculated: optimized structure	Observed value
Hfcc of ^{13}C/MHz			
C1	−1.13	−1.09	−0.36
C2	−0.61	−0.75	−0.18
C3	−0.42	−0.53	−0.48

Table 3
Hyperfine coupling constants (hfcc) of each atom of **3** determined by solid-state high-resolution NMR and calculation with UB3LYP/6–31+G(d,p) based on DFT of GAUSSIAN98 program package.

	Calculated: crystal structure	Calculated: optimized structure	Observed value
Hfcc of ^{13}C/MHz			
C1	−15	−14	
C2	−0.76	−0.68	−0.76
C3	−0.47	−0.63	+1.56
C4	−16	−15	
C5	−0.84	−0.87	−0.37
C6	18	16	
C7	19	16	
C8	18	18	
C9	18	19	
Hfcc of ^{1}H/MHz			
H	−1.39	−1.43	0.73
Average of Me	−0.56	−0.65	−0.53
Me6	−0.37	−0.51	
Me7	−0.43	−0.75	
Me8	−0.73	−0.61	
Me9	−0.69	−0.73	
NH2	0.26	−0.04	0.11

imental value. This is probably due to racemic crystal used for the measurement and hydrogen bonding between –COOH and >N–O· radical site in the crystal. Actually, temperature variation of MAS ^{2}H NMR spectrum of –COOD split into two peaks in the temperature range between 200 and 300 K, which correspond to D- and L-form in the racemic powder crystalline sample [9]. While X-ray diffraction experiment for a racemic single crystal gave an averaged structure for random mixing of D- and L-form [10], MAS ^{2}H NMR spectrum of –COOD detected slightly different local environments of –COOD···O–N (nitroxide) hydrogen bonding. Temperature variation of the two shift gave hfcc of deuterium A_D = +0.04 and +0.08 MHz, respectively. These values correspond to hfcc of respective protons A_H = +0.56 and +0.28 MHz. An average of these two values almost coincides with +0.36 MHz derived from unresolved MAS ^{1}H NMR shown in Fig. 2. In general, resolution of MAS ^{2}H NMR spectrum is much better than that of MAS ^{1}H NMR spectrum, since MAS is not efficient for dipolar coupled protons due to rapid spin diffusion during sample rotation and spin diffusion is very slow for deuteron.

We are interested in the variation of electron spin density distribution on the five-member ring by introducing double bond and hetero atom into the ring. ^{13}C NMR spectrum of **2**, which has

Table 4
Hyperfine coupling constants (hfcc) of each atom of **4** calculated with UB3LYP/6–31+G(d,p) based on DFT of GAUSSIAN98 program package.

	Calculated: optimized structure
Hfcc of ^{13}C and ^{15}N/MHz	
C1	−18
C3	0.63
C4	−15
C6	16
C7	16
C10	−1.06
C12	19
C13	19
N2	0.67
Hfcc of ^{1}H/MHz	
H	−0.10
Average of Me	−0.61
Me6	−0.56
Me7	−0.56
Me12	−0.65
Me13	−0.65

C=C double bond in the ring, is shown in Fig. 3. Peaks indicated by stars are spinning side bands. Calculated and experimentally determined hfcc are listed in Table 2.

Compound **3** has also C=C double bond in the ring and –$CONH_2$ group is introduced instead of –COOH of compound **2**. ^{1}H, ^{13}C NMR spectra are shown in Fig. 4. For ^{13}C NMR spectrum, peaks indicated by stars are spinning side bands. Calculated and experimentally determined hfcc are compared in Table 3.

From the NMR measurements of the three radical compounds with five-member ring **1**–**3**, we found that there is significant difference in hfcc A_{nue} of β position of the ring, *i.e.* +1.3, −0.48, and +1.56 for C5 of **1**, C3 of **2**, and C3 of **3**, respectively. Most of single occupied molecular orbital (SOMO) is composed of p(π^*) orbital of nitroxide group. Five-member ring of **1** is not planar but has chair conformation and SOMO is distributed to >CH_2 moiety via hyper-conjugation between hydrogen atoms of >CH_2 moiety and p(π^*) orbital of nitroxide group. This hyper-conjugation induces positive hfcc (+1.3 MHz) of β position. On the other hand, there exists a node of SOMO at β position of the ring of **2**. This is one of the significant differences between the two compounds. Fig. 5 illustrates differences of delocalization of SOMO among the four compounds.

To estimate experimentally the change of electronic state of these radicals, we also measured UV–Vis absorption spectra at room temperature for solutions of **1**, **3**, and **4** together with TEMPOL with six member ring of chair conformation. The experimental results are summarized in Fig. 6a. Fig. 6b indicates a good correlation between the experimental values of maximum absorption wave length and those of DFT calculation (UB3LYP/6–31+G(d,p). The π–π^* transitions appear between 200 and 300 nm. Typical n–π^* transition of nitroxide radicals can be seen between 400 and

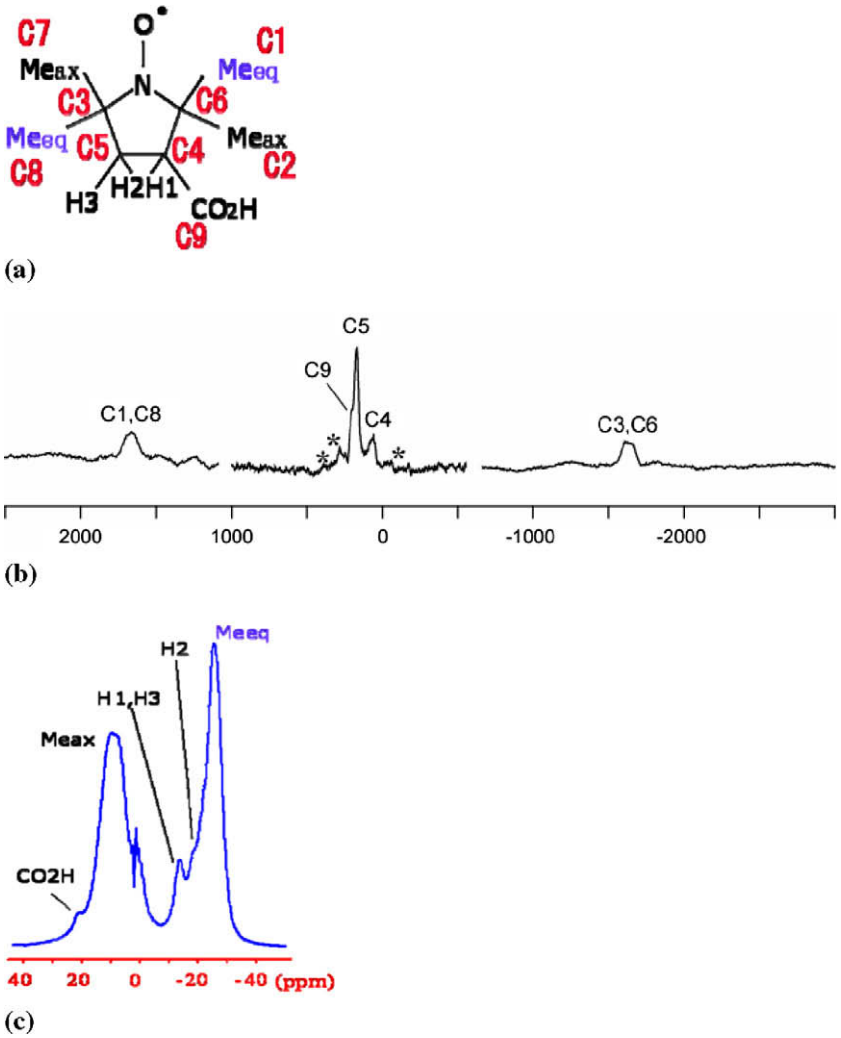


Fig. 2. Magic angle spinning ^{1}H and ^{13}C NMR of **1** measured at 294 K.

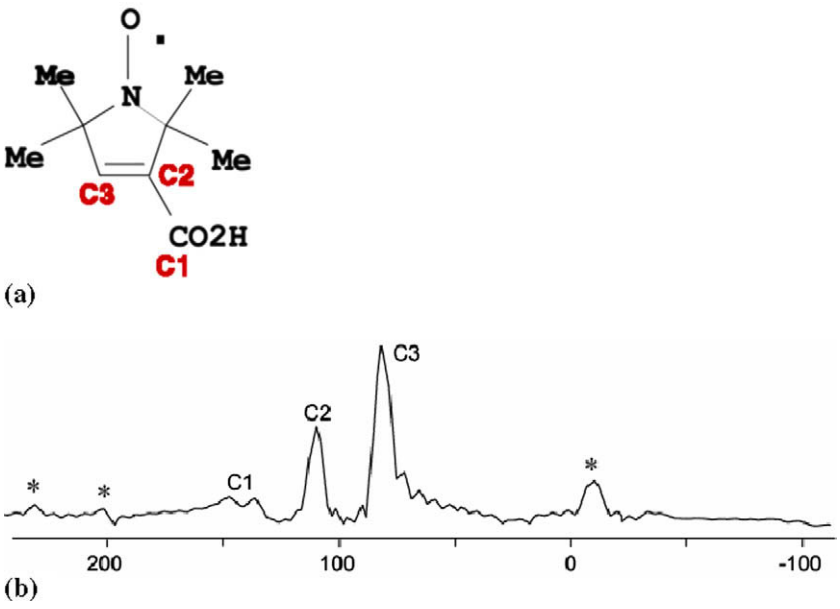


Fig. 3. Magic angle spinning ^{13}C NMR of **2** measured at 294 K.

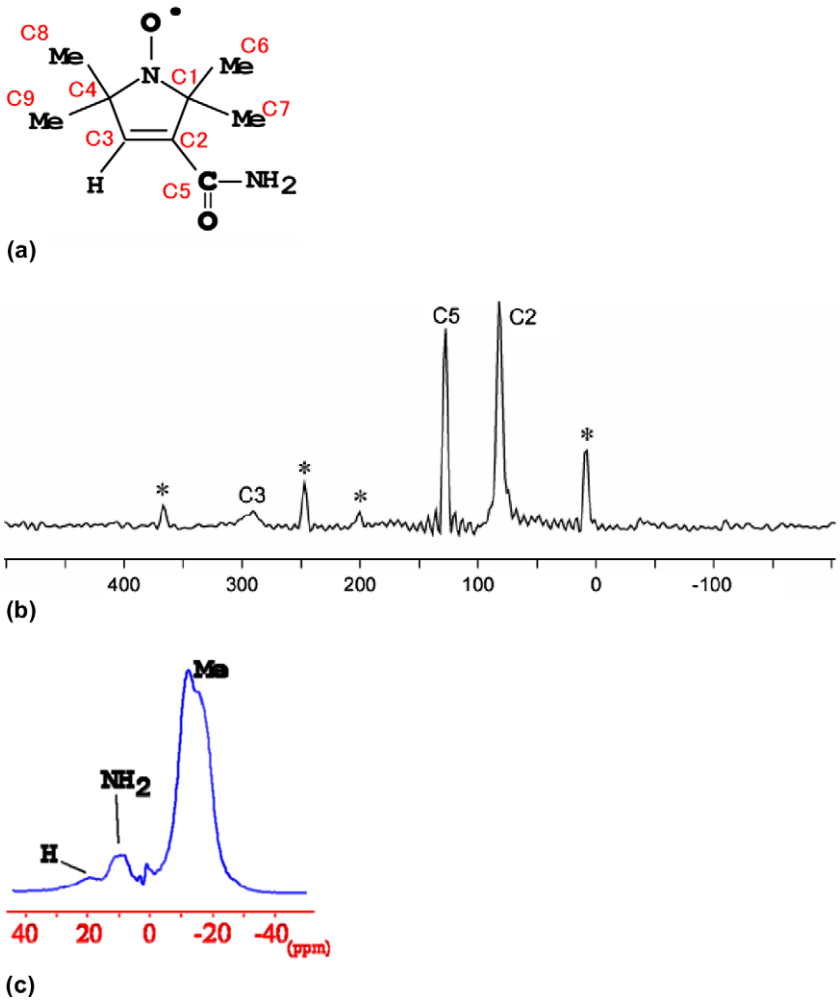


Fig. 4. Magic angle spinning ^{1}H and ^{13}C NMR of **3** measured at 294 K.

500 nm. We also performed unrestricted ZINDO calculation with GAUSSIAN03 program, and found that the results were not good: the calculated wavelengths of the n–π^* transitions were 700–800 nm, while the observed values located 400–500 nm.

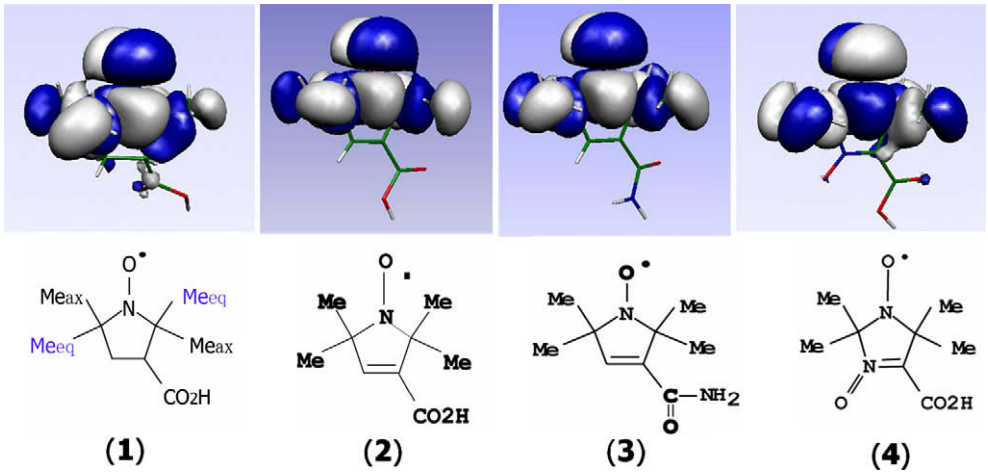


Fig. 5. Different distribution of single occupied molecular orbitals (SOMO) among **1**, **2**, **3** and **4**.

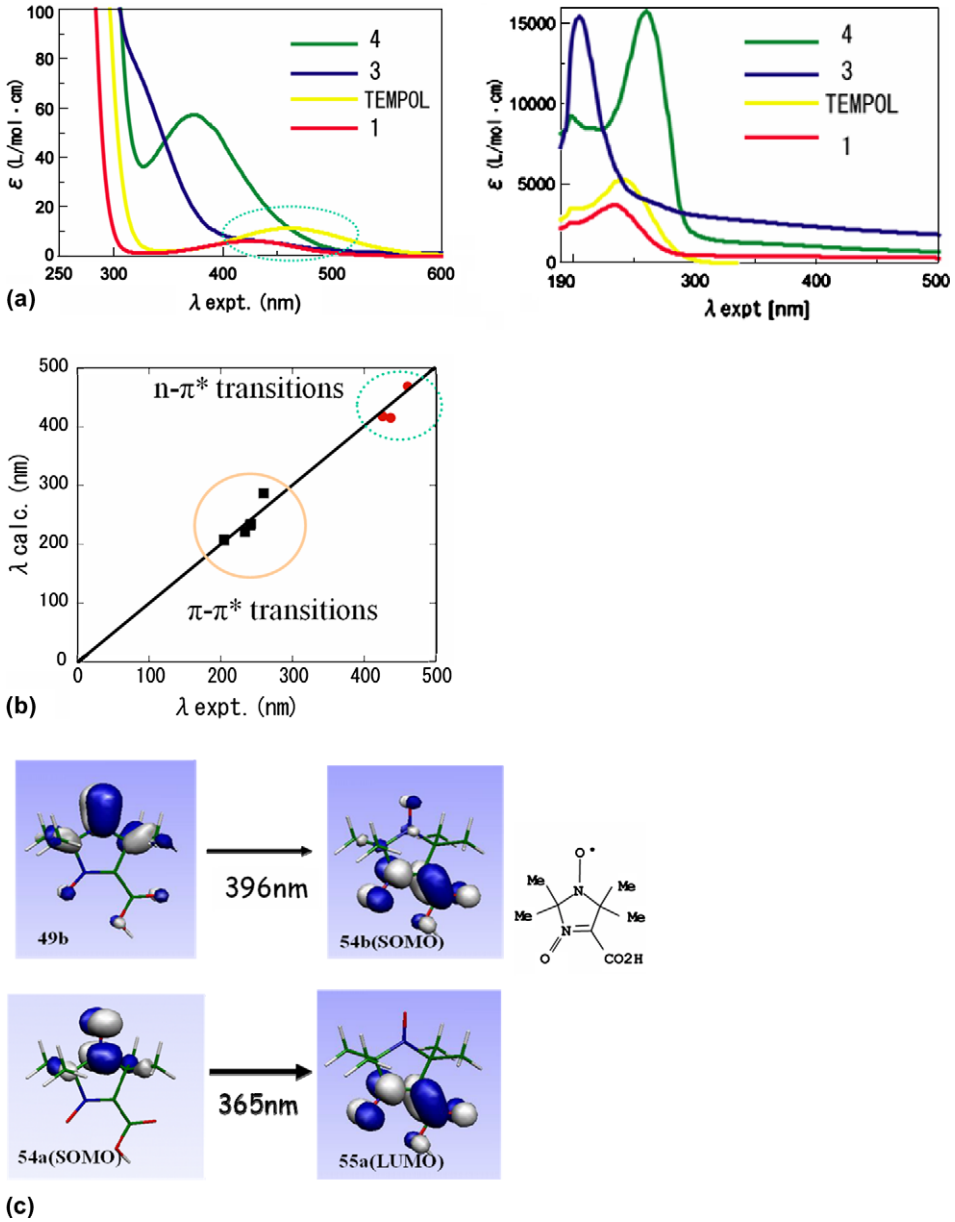


Fig. 6. (a) UV–Vis absorption spectra of solutions of radicals. Ordinate is magnified in left hand side spectra. (b) Correlation between calculated peak positions and observed one. (c) Contribution of excitations to the absorption peak around 400 nm of **4**.

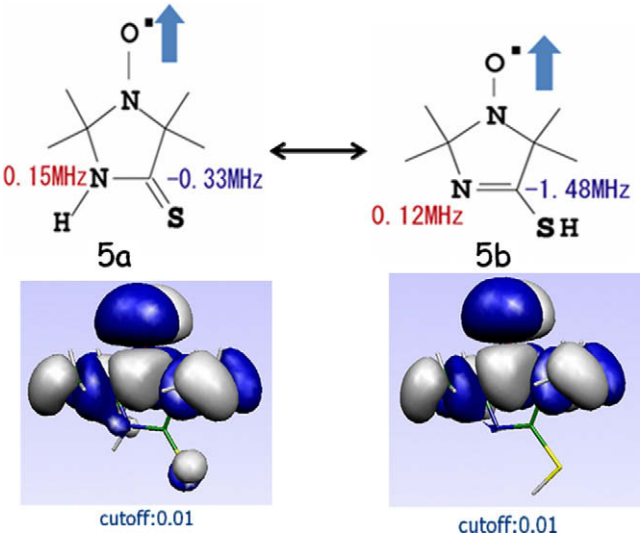


Fig. 7. Change of delocalization of SOMO between (a) thion and (b) thiol form of **5**.

In addition to these π–π^* and n–π^* transitions, relatively strong absorption was observed between 300 and 400 nm for **3** and **4**. These molecules have planar unsaturated ring structures. Since the calculation is fairly reliable as shown in Fig. 6b, an origin of this absorption band can be estimated from the calculation. One of the transitions, which contributes to this band of **4**, is 49b → 54b(SOMO) (396 nm). This transition corresponds to a dramatic change of orbital distribution as depicted in Fig. 6c. Transition of 54a(SOMO) → 55a(LUMO) locates at 365 nm, which is close to the previous transition. Optical control of transient spin density distribution with near visible light may be possible for **4**.

Synthesis of a similar radical with unsaturated five-member ring and with sulfur atom, 2,2,5,5-tetramethyl-4-thion-3-imidazoline-1-oxyl (**5a**), was reported [11–13]. This radical molecule may be changed to thiol form (**5b**) as depicted in Fig. 7 and is interesting as one of the cladding reagents for gold nano-particles for a specific magnetism. Therefore, we also tried to calculate delocalization of SOMO for the two isomers and an energy difference between them by DFT method mentioned above. Molecular structures of **5a** and **5b** were optimized by the same method as for **1**–**4**. Radical **5a** is energetically stable by 45 kJ/mol compared with **5b**. Difference of SOMO delocalization between **5a** and **5b** is depicted in Fig. 7, where numerical values shown are calculated hfcc of nitrogen and carbon atoms.

Magnetic metal complexes with these organic radicals as magnetic ligands are now under study.

Acknowledgments

This research was supported by Grant-in-Aid for Scientific Research on Priority Areas "Application of Molecular Spins" Area No. 769, Proposal No. 15087201 and by Grant-in-Aid for Scientific Research (B) 18350002 from the Ministry of Education, Culture, Sports, Science and Technology of Japan.

References

[1] H.M. McConnell, D.B. Chesnut, J. Chem. Phys. 28 (1959) 107.
[2] R.J. Kurland, B.R. McGarvey, J. Magn. Reson. 2 (1970) 286.
[3] G. Maruta, S. Takeda, R. Imachi, T. Ishida, T. Nogami, K. Yamaguchi, J. Am. Chem. Soc. 121 (1999) 424.
[4] D. Bordeaux, J. Lajzerowicz-Bonneteau, R. Briere, H. Lemaire, A. Rassat, Org. Magn. Reson. 5 (1973) 47.
[5] G. Maruta, S. Takeda, A. Yamaguchi, T. Okuno, K. Awaga, Polyhedron 22 (2003) 1989.
[6] M.J. Frisch, G.W. Trucks, H.B. Schlegel, G.E. Scuseria, M.A. Robb, J.R. Cheeseman, V.G. Zakrzewski, J.A. Montgomery Jr., R.E. Stramann, J.C. Burant, S. Dapprich, J.M. Millan, A.D. Daniels, K.N. Kudin, M.C. Strain, O. Farkas, J. Tomasi, V. Barone, M. Cossi, R. Cammi, B. Mennucci, C. Pomelli, C. Adamo, S. Clifford, J. Ochteski, G.A. Petersson, P.Y. Ayala, Q. Cui, K. Morokuma, P. Salvador, J.J. Dannenberg, D.K. Malick, A.D. Rabuck, K. Raghavachari, J.B. Foresman, J. Cioslowski, J.V. Ortiz, A.G. Baboul, B.B. Stefanov, G. liu, A. Liashenko, P. Piskorz, I. Komaromi, R. Gomperts, R.L. Martin, D.J. Fox, T. Keith, M.A. Al-Laham, C.Y. Peng, A. Nanayakkara, M. Challacombe, P.M.W. Gill, B. Johnson, W. Chen, M.W. Wong, J.L. Andres, C. Gonzalez, M. Hea-Gordon, E.S. Replogle, J.A. Pople, GAUSSIAN-98, Revision A.11.1, Gaussian Inc., Pittsburgh, PA, 2001.
[7] K.M. Ibne-Rasa, R.H.P.J. Ciabattoni, J.O. Edwards, J. Am. Chem. Soc. 95 (1973) 7896.
[8] J.W. Turlery, F.P. Boer, Acta Crystallogr., Sect. B 28 (1972) 1641.
[9] S. Takeda, Y. Nagayama, G. Maruta, unpublished results.
[10] (a) B. Chion, J. Lajzerowicz, D. Bordeaux, A. Collet, J. Jacques, J. Phys. Chem. 82 (1978) 2682;
(b) P.J. Cox, S. Blaney, S.W. Love, N. Shankland, D.B. Sheen, J. Chem. Crystallogr. 25 (1995) 845.
[11] N.G. Vanifatoba, M.V. Evstiferov, V.V. Martin, Zh. Anal. Kim. 43 (1988) 435 (Sov. J. Anal. Chem. 43 (1988) 341).
[12] M.V. Evstiferov, N.G. Vanifatova, O.M. Petrukhin, Izv. Akad. Nauk SSSR, Ser. Kim. (1989) 019 (Bull. Acad. Sci. USSR, Div. Chem. Sci. 38 (1989) 921).
[13] A.I. Korin, M.V. Evstiferov, I.A. Grigor'ev, V.A. Reznikov, G. Grampp, Izv. Akad. Nauk, Ser. Kim. (1999) 2005 (Russ. Chem. Bull. 48 (1999) 1982).

Polyhedron 28 (2009) 2070–2074

Contents lists available at ScienceDirect

Polyhedron

journal homepage: www.elsevier.com/locate/poly

Tungstoarsenate(III) polyoxoanions as inorganic ligands for polynuclear copper complexes

Firasat Hussain [a], Chris Ritchie [a], Robert W. Gable [a], Boujemaa Moubaraki [b], Keith S. Murray [b], Colette Boskovic [a,*]

[a] School of Chemistry, University of Melbourne, Victoria 3010, Australia
[b] School of Chemistry, Monash University, Clayton, Victoria 3800, Australia

ARTICLE INFO

Article history:
Available online 20 February 2009

Keywords:
Polynuclear complexes
Copper
Polyoxometalates
Tungstoarsenates
Bipyridine ligands
Hydrothermal synthesis
Magnetic properties

ABSTRACT

A trinuclear copper(II) complex and a tetranuclear copper(II) complex that each incorporate a 9-tungstoarsenate(III) polyoxoanion ligand and several 2,2′-bipyridine (2,2′-bpy) ligands co-crystallize as the acid form: $H_4[\{Cu(2,2'\text{-bpy})\}_3(\alpha\text{-}AsW_9O_{33})] \cdot [\{Cu(2,2'\text{-bpy})_2\}\{Cu(2,2'\text{-bpy})\}_3(\alpha\text{-}AsW_9O_{33})] \cdot 38H_2O$ (**1**). Compound **1** was obtained from a hydrothermal reaction employing the trivacant lacunary polyoxometalate $[\alpha\text{-}AsW_9O_{33}]^{9-}$ as a precursor. The α-isomeric form of the parent ion is retained in both product anions. Four different coordination modes are observed for the seven copper centers, with unusual structural distortions imposed by the steric bulk of the polyanion. Intra- and intermolecular π-stacking of the 2,2′-bpy ligands are both evident. Variable temperature magnetic susceptibility, magnetization and EPR data are consistent with very weak antiferromagnetic interactions between the copper centers that are likely mediated by the π-stacking of the 2,2′-bpy ligands.

Crown Copyright © 2009 Published by Elsevier Ltd. All rights reserved.

1. Introduction

Polyoxometalates (POMs) are an important class of inorganic compounds that exhibit a diverse compositional range and significant structural versatility [1]. One of the best known families of POMs are the heteropoly Keggin ions $[XM_{12}O_{40}]^{n-}$ (X = heteroatom, M = Mo and W). While a variety of main group or transition elements can act as heteroatoms in these species, the lone pair of electrons on elements such as arsenic(III) are stereoactive, preventing the formation of the closed plenary Keggin ions and instead giving rise to polyanions with more open structures, such as the trivacant lacunary Keggin ion $[\alpha\text{-}AsW_9O_{33}]^{9-}$ [2]. The exploration of these species as inorganic ligands for polynuclear complexes of other metals has afforded a number of new species. The reaction of other transition metals with $[\alpha\text{-}XW_9O_{33}]^{9-}$ (X = As(III), Sb(III) and Bi(III)) leads to polynuclear complexes with "sandwich" type structures, whereby two, three of four heterometals are "sandwiched" between two $[XW_9O_{33}]^{n-}$ POM ligands [3]. The POM $[\alpha\text{-}AsW_9O_{33}]^{9-}$ has also proved an excellent starting material for the synthesis of larger and more structurally elaborate polynuclear complexes of 3d or 4f metals including: $[K\subset\{Eu(H_2O)_2(AsW_9O_{33})\}_6]^{35-}$, $[Cs\subset\{Eu\text{-}(H_2O)_2(AsW_9O_{33})\}_4]^{23-}$, $[(CuCl)_6(AsW_9O_{33})_2]^{12-}$, $[Ce_4As_4W_{38}(H_2O)_{12}O_{136}]^{16-}$, $[Gd_6As_6W_{65}O_{229}(OH)_4(H_2O)_{12}(OAc)_2]^{38-}$ and $[Yb_{10}As_{10}W_{88}O_{308}(OH)_8(H_2O)_{28}(OAc)_4]^{40-}$ [4–7].

The functionalization of POMs with other transition metals or discrete coordination complexes is increasingly being pursued to enhance or modulate the physical properties of the POMs [8]. These species can alternatively be considered as metal complexes of inorganic POM ligands. In any case, the resulting hybrid species have considerable potential for applications as functional materials. To this end, several molecular copper complexes that feature different polyoxotungstates as inorganic ligands, in combination with the organic ligand 2,2′-bpy, have been reported: $[\{Cu(2,2'\text{-bpy})(H_2O)\}_2\{Cu(2,2'\text{-bpy})\}_2(\alpha\text{-}SbW_9O_{33})]^-$, $\{Cu(2,2'\text{-bpy})(H_2O)\}\{Cu(2,2'\text{-bpy})\}_3\{Cu(2,2'\text{-bpy})_2\}(\beta\text{-}GeW_8O_{31})]$, $[\{\{Cu(2,2'\text{-bpy})(H_2O)\}\{Cu(2,2'\text{-bpy})\}_4(\beta\text{-}GeW_9O_{34})\}_2]$ and $[\{Cu(2,2'\text{-bpy})\}_8(\beta\text{-}PW_8O_{31})2]^{2-}$ [9–11]. Similarly, the related ligand 1,10-phenathroline (phen) features in the molecular copper–tungstoarsenate(V) complex $[\{Cu\ (phen)\}_8(\beta\text{-}AsW_8O_{31})_2]^{2-}$, which has the same structure as $[\{Cu\text{-}(2,2'\text{-bpy})\}_8(\beta\text{-}PW_8O_{31})_2]^{2-}$ [12]. However, to the best of our knowledge there has been no report to date of any 3d metal complex incorporating both 2,2′-bpy and tungstoarsenate(III or V) ligands.

Herein we describe the synthesis, crystal structure and magnetic and EPR investigations of a compound comprised of the two new polynuclear complexes $[\{Cu(2,2'\text{-bpy})\}_3(\alpha\text{-}AsW_9O_{33})]^{3-}$ (**1a**) and $[\{Cu(2,2'\text{-bpy})_2\}\{Cu(2,2'\text{-bpy})\}_3(\alpha\text{-}AsW_9O_{33})]^-$ (**1b**) (Fig. 1) that co-crystallize as the acid form.

* Corresponding author. Tel.: +61 3 8344 4971; fax: +61 3 9347 5180.
E-mail address: c.boskovic@unimelb.edu.au (C. Boskovic).

0277-5387/$ - see front matter Crown Copyright © 2009 Published by Elsevier Ltd. All rights reserved.
doi:10.1016/j.poly.2009.02.009

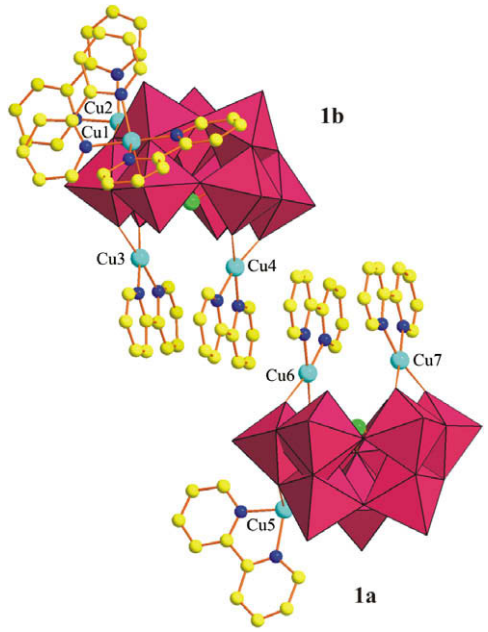


Fig. 1. Combined polyhedral/ball and stick representation of complexes **1a** and **1b** in the asymmetric unit of compound **1**. The red octahedra represent WO_6 units and the color code of the balls is: Cu (cyan), N (blue), C (yellow) and As (green). H atoms are omitted for clarity. (For interpretation of the references to color in this figure legend, the reader is referred to the web version of this article.)

Table 1
Crystallographic data for $H_4[\{Cu(2,2'\text{-bpy})\}_3(\alpha\text{-}AsW_9O_{33})] \cdot [\{Cu(2,2'\text{-bpy})_2\}\{Cu(2,2'\text{-bpy})\}_3(\alpha\text{-}AsW_9O_{33})] \cdot 38H_2O$ (**1** · $38H_2O$).

Parameter	**1** · $38H_2O$
Formula	$As_2C_{80}H_{144}N_{16}Cu_7O_{104}W_{18}$
Formula weight (g mol^{-1})	6898.03
Crystal class	monoclinic
Space group	$P2_1/c$
Unit cell dimensions	
a (Å)	13.912(4)
b (Å)	40.787(11)
c (Å)	29.010(8)
α (°)	90
β (°)	93.097(7)
γ (°)	90
V (Å^3)	16437(8)
Z	4
T (K)	130(2)
ρ_{calc} (g cm^{-3})	2.787
μ (mm)	13.925
Reflections measured	58303
Unique reflections	17113
R_{int}	0.1237
Observed data [$I > 2\sigma(I)$]	11647
R_1w[a]	0.0866
wR_2[b]	0.2048

[a] $I > 2\sigma(I)$.
[b] F^2, all data.

2. Experimental

2.1. Compound preparation

All manipulations were performed under aerobic conditions, using materials as received.

2.2.1. $H_4[\{Cu(2,2'\text{-}2,2'\text{-bpy})\}_3(AsW_9O_{33})] \cdot [\{Cu(2,2'\text{-bpy})_2\}\{Cu(2,2'\text{-bpy})\}_3(AsW_9O_{33})]$ (**1**)

Equimolar amounts of $Na_9[AsW_9O_{33}]$, $CuCl_2 \cdot 2H_2O$, and 2,2′-bpy (0.15 mmol of each) were added to a teflon-lined autoclave with 15 ml of 0.5 M NaOAc/AcOH buffer (pH 4.7). The mixture was heated at 438 K for 24 h and then cooled at a rate of 2 K h^{-1}. This afforded blue crystals that were suitable for single crystal X-ray diffraction and a sample for crystallography was maintained in contact with the mother liquor. The crystals were isolated by filtration, washed with cold distilled water and air dried to give a yield of *ca.* 40%. Some of the water molecules of crystallization are lost upon drying, with thermogravimetric analysis consistent with three H_2O molecules. *Anal.* Calc. for $H_4[\{Cu(2,2'\text{-bpy})\}_3(AsW_9O_{33})] \cdot [\{Cu(2,2'\text{-}2,2'\text{-bpy})_2\}\{Cu(2,2'\text{-}2,2'\text{-bpy})\}_3(AsW_9O_{33})] \cdot 3H_2O$ ($As_2C_{80}H_{74}N_{16}Cu_7O_{69}W_{18}$): W, 52.80; N, 3.58; H, 1.19; C, 16.33; Na, 0. Found: W, 49.30; N, 3.41; H, 1.53; C, 16.37; Na, 0.11%. IR. (KBr pellets, cm^{-1}): 1473(m), 1446(s), 1315(w), 1252(w), 1160(w), 1060(w), 1034(w) 1018(w), 942(vs), 885(vs), 774(vs), 729(m), 706(s), 484(w).

2.2. General and physical measurements

Infrared spectra (KBr disk) were recorded on a BioRad 175 FTIR spectrometer. Elemental analyses were performed at Chemical and Microanalytical Services, Belmont, Australia. Thermogravimetric analyses were performed on a Mettler Toledo thermal analyser. Variable temperature magnetic susceptibility and magnetization measurements were performed with a Quantum Design MPMS SQUID magnetometer equipped with a 5 T magnet. Three sets of DC magnetic susceptibility data were collected with magnetic fields of 0.01, 0.10 and 1.0 T. Pascal's constants were used to estimate the diamagnetic correction for the compound. EPR spectra were recorded on microcrystalline samples with a Bruker FT ECS-106 spectrometer.

2.3. X-ray crystallography

The intensity data of all compounds were collected on a Bruker CCD diffractometer using graphite monochromated Mo Kα radiation (λ = 0.71073 Å). Crystals were transferred directly from the mother liquor to a protective oil, which was used to prevent solvent loss. The structures were solved using direct methods and refined using a full-matrix least squares procedure based on F^2 using all data [13]. The crystallographic data are provided in Table 1.

3. Results and discussion

3.1. Syntheses

Compound **1** was obtained from the hydrothermal reaction of equimolar amounts of $Na_9[\alpha\text{-}AsW_9O_{33}]$ [2], $CuCl_2$ and 2,2′-bpy in sodium acetate buffer at 165 °C. Compound **1** could be obtained reproducibly in approximately 40% yield, based on 2,2′-bpy as the limiting reagent. Efforts to improve the yield by varying the reaction stoichiometry to better reflect the final composition of the compound were unsuccessful.

The use of the pre-formed lacunary POM $[\alpha\text{-}AsW_9O_{33}]^{9-}$ as a precursor for compound **1** is in stark contrast to the syntheses of related Cu-2,2′-bpy complexes of $[SbW_9O_{33}]^{9-}$, $[GeW_9O_{34}]^{10-}$, $[GeW_8O_{31}]^{10-}$ and $[PW_8O_{31}]^{9-}$ and the Cu-phen complex of $[AsW_8O_{31}]^{9-}$, all of which involve the hydrothermal reactions of Na_2WO_4, $CuCl_2$ and 2,2′-bpy or phen with Sb_2O_3, GeO_2, H_3PO_4 or Na_3AsO_4 [9–12]. Despite the hydrothermal conditions there is no evidence for any fragmentation or isomerization of the $[\alpha\text{-}AsW_9O_{33}]^{9-}$ starting material during the formation of compound **1**. Both fragmentation and isomerization to the β isomeric form have been observed previously during the formation of other large

complexes from reactions involving $[\alpha\text{-}AsW_9O_{33}]^{9-}$ performed at ambient temperature and pressure [6,7].

3.2. Description of structures

Single-crystal X-ray diffraction reveals that the asymmetric unit of compound **1** contains two different anionic complexes: **1a** (a trinuclear Cu complex) and **1b** (a tetranuclear Cu complex), together with water molecules. Molecules **1a** and **1b** are both derivatized $[\alpha\text{-}AsW_9O_{33}]^{9-}$ fragments. The POM fragments in each species are bound to three {Cu(2,2′-bpy)} units, with complex **1b** also incorporating a {Cu(2,2′-bpy)$_2$} unit. Selected interatomic distances associated with the coordination of the Cu centers are provided in Table 2. Two of the {Cu(2,2′-bpy)} units occupy lacunary sites of each of the POMs, with the Cu atoms bound through terminal O atoms that are terminal in the parent POM. These are Cu6 and Cu7 for **1a** and Cu3 and Cu4 for **1b**. The atoms Cu4 and Cu7 are bound to O atoms from the same edge-shared $\{W_3O_{13}\}$ triad in the POMs (Fig. 2a), while Cu3 and Cu6 are bound to O atoms from different edge-shared triads (Fig. 2b). It seems that the steric requirements of the 2,2′-bpy ligands prevent the binding of a third Cu center to the lacunary site of the trivacant POM, as the remaining {Cu(2,2′-bpy)} units coordinate to non-lacunary sites on the exterior of the POM, with Cu2 and Cu5 each binding to four bridging O atoms in **1a** and **1b**, respectively (Fig. 2c). These Cu centers bind at the interface between two edge-shared triads and are therefore each coordinated to two edge-sharing and two corner-sharing doubly bridging O atoms of the parent POM. A similar binding mode has been observed previously for two {Cu(2,2′-bpy)} units bound to $[\alpha\text{-}SbW_9O_{33}]^{9-}$ in the complex [{Cu(2,2′-bpy)(H$_2$O)}$_2${Cu(2,2′-bpy)}$_2$(α-SbW_9O_{33})] [9]. The [Cu(2,2′-bpy)$_2$]$^{2+}$ fragment in **1b** also binds to a non-lacunary site of the POM, coordinating to a terminal O atom in addition to a weak bond (2.68(2) Å) to an edge-sharing bridging O atom in the same triad (Fig. 2d). This arrangement of the Cu-2,2′-bpy fragments affords C_1 point symmetry for **1b**, while small structural distortions give rise to a deviation from ideal C_s point symmetry for **1a**.

Of the seven copper centers in compound **1**, four are four-coordinate with square planar geometries (Cu3, Cu4, Cu6 and Cu7), two are six-coordinate with distorted octahedral geometries (Cu2 and Cu5) and one is strictly five-coordinate with a long sixth Cu–O bond giving rise to an octahedrally distorted trigonal bipyramidal geometry (Cu1). Selected interatomic distances for the Cu centers are provided in Table 1. Bond valence sum calculations performed on the Cu atoms are consistent with seven divalent Cu ions [16]. The four four-coordinate Cu centers display coordination typical for square planar Cu^{II}, with Cu–O and Cu–N bond distances in the range 1.87–1.92 and 1.95–1.99 Å, respectively. The two distorted octahedral Cu centers each have N_2O_4 coordination spheres with Cu–N bond distances of 1.95–2.00 Å. Each of these centers has two Cu–O bonds of length 1.95–2.01 Å, *trans* to the Cu–N bonds. The remaining Cu–O bonds are longer, with bond distances of 2.27–2.41 Å. In addition, the *trans* O–Cu–O angles associated with these bonds are 127.1(8)° and 129.3(9)° for Cu5 and Cu2, respectively, whereas the *trans* O–Cu–N angles are in the range 172–175°. Thus this coordination geometry is best described as *cis*-distorted octahedral, with the distortion evidently due to the steric requirements of the bulky POM unit. The remaining copper center, Cu1, is strictly five-coordinate with an N_4O coordination sphere and distorted trigonal bipyramidal geometry. The atoms N2 and N4 occupy the axial sites of the trigonal bipyramid with Cu–N bond distances of 1.96(3) and 1.95(3) Å, while the atoms N1, N3 and O28 occupy the equatorial sites with Cu–N, Cu–N and Cu–O bond distances of 2.04(3), 2.14(3) and 2.07(3) Å, respectively. The O–Cu–N bond angles within the equatorial plane are 92(1)° and 147(1)°, while the N–Cu–N angle is 121(1). The atom O21 lies approximately on the equatorial plane and participates in a weak bond with Cu1 with a Cu···O separation of 2.68(2) Å. The Cu···O21 vector approximately bisects the Cu–N3 and Cu–O28 vectors, giving rise to the observed octahedral distortion to the trigonal bipyramidal coordination geometry of Cu1.

The 2,2′-bpy ligands of the copper ions that occupy the lacunary sites of the POM fragments participate in extensive intra- and intermolecular π-stacking interactions that extend along the crystallographic *a* direction (Fig. 3). These π–π interactions contract the intramolecular separation between these copper atoms to 4.36(1) and 4.45(1) Å for **1a** and **1b**, respectively. In addition intermolecular π–π interactions are also observed between pairs of 2,2′-bpy ligands coordinated to Cu1 and Cu2 centers from neighbouring molecules.

The absence of sodium cations in the X-ray structure and the very small percentage of sodium evident in the elemental analysis

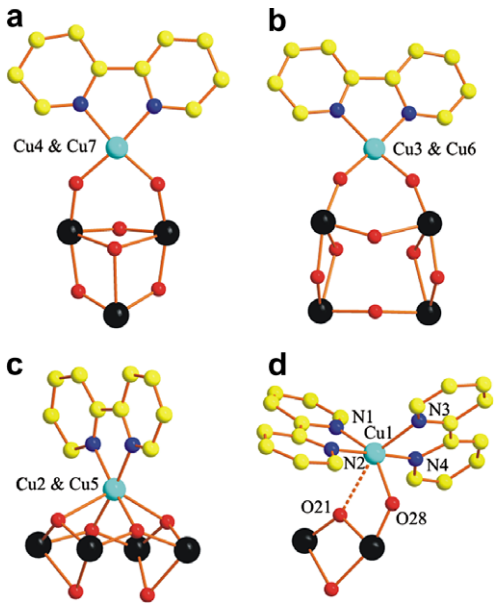


Fig. 2. Ball and stick representations of the four Cu coordination modes in compound **1**.

Table 2
Selected interatomic distances (Å) for **1** · 38H$_2$O.

Parameter	**1a**		**1b**	
Cu–O	Cu5–O37	2.01(3)	Cu1–O21	2.68(2)
	Cu5–O38	2.32(3)	Cu1–O28	2.07(3)
	Cu5–O57	2.41(2)	Cu2–O4	2.02(2)
	Cu5–O60	1.97(2)	Cu2–O5	2.36(3)
	Cu6–O35	1.86(3)	Cu2–O10	2.27(2)
	Cu6–O56	1.89(2)	Cu2–O18	1.95(2)
	Cu7–O45	1.90(2)	Cu3–O2	1.88(3)
	Cu7–O62	1.91(2)	Cu3–O8	1.88(3)
			Cu4–O23	1.93(2)
			Cu4–O31	1.89(2)
Cu–N	Cu5–N11	1.95(2)	Cu1–N1	2.04(3)
	Cu5–N12	1.99(3)	Cu1–N2	1.96(3)
	Cu6–N13	1.95(3)	Cu1–N3	2.14(3)
	Cu6–N14	1.99(3)	Cu1–N4	1.95(3)
	Cu7–N15	1.94(3)	Cu2–N5	1.96(3)
	Cu7–N16	1.98(3)	Cu2–N6	1.99(3)
			Cu3–N7	1.96(3)
			Cu3–N8	1.98(3)
			Cu4–N9	2.01(3)
			Cu4–N10	1.98(3)
Cu···Cu	Cu6···Cu7	4.36(1)	Cu3···Cu4	4.45(1)

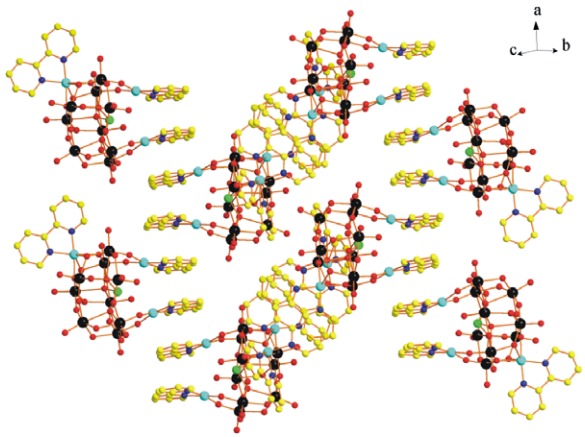


Fig. 3. Crystal packing of compound **1**. The color code of the balls is: W (black), Cu (cyan), N (blue), C (yellow), As (green) and O (red). Water molecules and H atoms are omitted for clarity. (For interpretation of the references to color in this figure legend, the reader is referred to the web version of this article.)

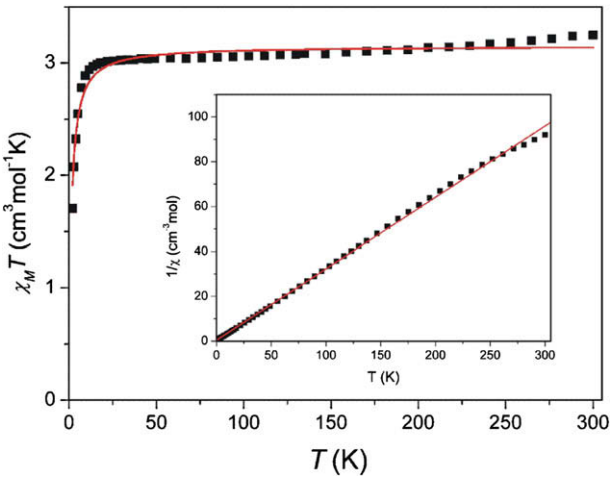


Fig. 4. Plot $\chi_M T$ vs. T for compound **1** obtained with a magnetic field of 1 T. The inset is a plot of $1/\chi_M$ vs. T and the solid line is the fit to the Curie–Weiss law as described in the text.

data imply the presence of four additional protons in compound **1a** to balance the charge of the anionic complexes. Bond valence sum calculations performed on the O atoms are consistent with all oxo rather than hydroxo ligands [14]. However, there is insufficient evidence to determine whether these acid protons are protonating the hydrate water molecules or the POM surface, with both of these protonation modes having been observed previously in POM chemistry [15].

3.3. Infrared spectroscopy

The infrared spectrum of compound **1** was recorded between 400 and 4000 cm^{-1} as a pressed KBr disk. Two regions are distinctive and useful for the identification of the compound. Four peaks that are characteristic of the 2,2′-bpy ligand are clearly evident at 1446(s), 1315(w), 1252(w) and 1160(w). These peaks have previously been employed to differentiate between the spectra of phosphotungstate POMS incorporating 2,2′-bpy and 4,4′-bpy complexes of Cu(II) [11]. In the region between 500 and 1000 cm^{-1} the peak at 942(vs) cm^{-1} can be assigned to the W=O stretching vibration and the peaks at 885(vs), 774(vs), 729(m) and 706(s) can be assigned to the different W–O–W and Cu–O–W and As–O–W stretching vibrations [17].

3.4. Magnetochemistry

Variable temperature magnetic susceptibility data were measured for compound **1** with magnetic fields of 0.01, 0.1 and 1 T and essentially superimposable data were obtained with the different fields (Fig. 4). The value of $\chi_M T$ decreases gradually from 3.25 to 3.01 cm^3 mol^{-1} K as the temperature is decreased from 300 to 20 K, before decreasing sharply to reach a value of 1.70 cm^3 mol^{-1} K at 2 K. The data between 2 and 300 K were fit to the Curie–Weiss law (inset of Fig. 4) to yield Curie and Weiss constants of 3.14 cm^3 mol^{-1} K and −1.3 K, respectively. This Curie constant is consistent with the value of 3.15 cm^3 mol^{-1} K calculated for seven non-interacting Cu^{II} ($S = 1/2$) ions with $g = 2.19$, which is within the range of $g = 2.1$–2.3 that is typical for Cu^{II} complexes [18]. This essentially Curie behavior indicates that the magnetic interactions between the Cu centers are minimal, with the small negative Weiss constant and the low temperature decrease in $\chi_M T$ consistent with very weak antiferromagnetic coupling. This is most likely intramolecular (Cu3···Cu4, Cu6···Cu7) and mediated by the π–π interactions between the 2,2′-bpy ligands in each complex [19].

The structurally related compound [{Cu(2,2′-bpy)$_2$-(H$_2$O)}$_2${Cu(2,2′-bpy)}$_2$(α-SbW$_9$O$_{33}$)]$^-$ also displays Curie–Weiss behavior in the temperature range 110–300 K [9]. Although a ferromagnetic Weiss constant is observed in this case, the origin of the apparent ferromagnetic coupling is not clear. In contrast, in the related compound [{{Cu(2,2′-bpy)(H$_2$O)}{Cu(2,2′-bpy)}$_4$(α-GeW$_9$O$_{34}$)}$_2$], a considerably stronger antiferromagnetic coupling is observed ($2J = -34.2$ cm^{-1}), which is due to the presence of μ$_3$–O bridge between two CuO$_3$N$_2$ moieties and a tungsten center [10].

Low temperature magnetization data were collected between 2 and 10 K for compound **1**. Although these data do not appear to show saturation behavior at fields up to 5 T, the magnetization at 2.0 K and 5.0 T is 6.5 BM, which is consistent with seven Cu(II) centers in compound **1**.

3.5. EPR spectroscopy

X-band EPR spectra were measured on a microcrystalline sample of compound **1** at 110 and 298 K. The room temperature spectrum features a single broad isotropic signal with an effective g value of 2.13. This g value is consistent with the value obtained from fitting the variable temperature magnetic susceptibility data. At 110 K the EPR spectrum appears to display some axial character suggestive of $g_{||} > g_{\perp}$, although a clearly defined peak associated with $g_{||}$ is not observed. This may reflect the origin of the spectrum as an average of the signals due to the seven different Cu centers in compound **1**, which includes four centers with square planar coordination geometry, two centers with *cis*-distorted octahedral geometry and one center with octahedrally distorted trigonal bipyramidal coordination (Fig. 2). Thus only limited information can be extracted from these data. These X-band EPR spectra do not provide any information about any magnetic exchange interactions between the Cu(II) centers and Q-band EPR spectroscopy would be required to probe this aspect in order to detect $\Delta M_s = 1$ and $\Delta M_s = 2$ lines arising from neighbouring Cu(II) centers [20].

4. Conclusions

In summary, an initial exploration of the potential of [α-AsW$_9$O$_{33}$]$^{9-}$ as a precursor for the hydrothermal synthesis of new POM-ligated copper complexes has afforded the first two copper complexes of tungstoarsenate and 2,2′-bpy ligands. Four different

Cu coordination geometries are observed including unusual *cis*-distorted octahedral and octahedrally distorted trigonal bipyramidal geometries, where the distortions are imposed by the steric requirements of the POM. Intra- and intermolecular π-stacking interactions between the 2,2′-bpy ligands of the Cu centers that occupy the lacunary POM sites extend along the crystallographic *a* direction. Magnetic studies indicate very weak antiferromagnetic interactions between the Cu centers that are likely mediated by these π−π interactions.

Acknowledgements

We thank Craig Gourlay and Victor Ng for collecting the EPR spectra. This work was supported by the Australian Research Council.

References

[1] (a) M.T. Pope, Heteropoly and Isopoly Oxometalates, Springer-Verlag, Berlin, 1983;
(b) C.L. Hill, Chem. Rev. 98 (1998) 1;
(c) J.J. Borraás-Almenar, E. Coronado, A. Müller, M.T. Pope (Eds.), Polyoxometalate Molecular Science, Kluwer, Dordrecht, The Netherlands, 2003.
[2] C. Tourné, A. Revel, G. Tourné, M. Vendrell, C.R. Acad. Sci. Paris, Ser. C 277 (1973) 643.
[3] (a) M.T. Pope, Comp. Coord. Chem. II 4 (2003) 635. and references therein;
(b) L.H. Bi, M. Reicke, U. Kortz, B. Keita, L. Nadjo, R.J. Clark, Inorg. Chem. 43 (2004) 3915. and references therein.
[4] K. Fukaya, T. Yamase, Angew. Chem., Int. Ed. 42 (2003) 654.
[5] T. Yamase, K. Fukaya, H. Nojiri, Y. Ohshima, Inorg. Chem. 45 (2006) 7698.
[6] W. Chen, Y. Li, Y. Wang, E. Wang, Z. Su, Dalton Trans. (2007) 4293.
[7] F. Hussain, R.W. Gable, M. Speldrich, P. Kögerler, C. Boskovic, Chem. Commun. (2009) 328.
[8] (a) M.T. Pope, A. Müller (Eds.), Polyoxometalate Chemistry: From Topology via Self-Assembly to Applications, Kluwer, Dordrecht, 2001;
(b) C.L. Hill, Comp. Coord. Chem. II 4 (2003) 679;
(c) L. De Long, E. Burkholder, L. Cronin, Chem. Soc. Rev. 36 (2007) 105.
[9] J. Wang, P. Ma, J. Li, J. Niu, Chem. Lett. 35 (2006) 994.
[10] C.M. Wang, S.T. Zheng, G.Y. Yang, Inorg. Chem. 46 (2007) 616.
[11] L. Lisnard, A. Dolbecq, P. Mialane, J. Marrot, E. Codjovi, F. Sécheresse, Dalton Trans. (2005) 3913.
[12] J. Wang, W. Wang, J. Niu, Inorg. Chem. Commun. 10 (2007) 1054.
[13] G.M. Sheldrick, SHELX97, Programs for Crystal Structure Analysis, Institut für Anorganische Chemie der Universität Göttingen, Tammanstrasse 4, D-3400 Göttingen, Germany, 1998.
[14] I.D. Brown, D. Altermatt, Acta Crystallogr. B41 (1985) 244.
[15] (a) G.M. Brown, M.R. Noe-Spirlet, W.R. Busing, H.A. Levy, Acta Crystallogr. B33 (1977) 1038;
(b) V.W. Day, W.G. Klemperer, D.J. Maltbie, J. Am. Chem. Soc. 109 (1987) 2991;
(c) C. Boskovic, M. Sadek, R.T.C. Brownlee, A.M. Bond, A.G. Wedd, J. Chem. Soc., Dalton Trans. (2001) 187.
[16] N.E. Brese, M. O'Keefe, Acta Crystallogr. B47 (1991) 192.
[17] (a) L.G. Detusheva, L.I. Kuznetsova, L.S. Dovlitova, V.A. Likholobov, Russ. Chem. Bull. Int. Ed. 52 (2003) 370;
(b) C. Craciun, D. Rusu, L. Pop-Fanea, M. Hossu, M. Rusu, L. David, J. Radioanal. Nucl. Chem. 264 (2005) 589.
[18] R.L. Carlin, Magnetochemistry, Springer-Verlag, Berlin, 1986.
[19] M. Vazquez, A. Taglietti, D. Gatteschi, L. Sorace, C. Sangregorio, A.M. Gonzalez, M. Maneiro, R.M. Pedrido, M.R. Bermejo, Chem. Commun. (2003) 1840.
[20] (a) A. Bencini, D. Gatteschi, EPR of Exchange Coupled Systems, Springer-Verlag, Berlin, 1990;
(b) J.R. Pilbrow, Transition Ion Electron Paramagnetic Resonance, Oxford University Press, Oxford, 1991.

Polyhedron 28 (2009) 2075–2079

Contents lists available at ScienceDirect

Polyhedron

journal homepage: www.elsevier.com/locate/poly

Doping effect of nonmagnetic impurity on the spin-Peierls-like transition in the quasi-one-dimensional (quasi-1D) spin system of 1-(4′-nitrobenzyl)pyridinium bis(maleonitriledithiolato)nickelate

Xiao-Ming Ren [a,b,*], Guang-Xiang Liu [a], Heng Xu [a], Tomoyuki Akutagawa [c], Takayoshi Nakamura [c]

[a] Provincial Key Lab of Anhui for Coordination Compounds, Anqing Normal College, Anqing 246011, PR China
[b] College of Science, Nanjing University of Technology, Nanjing 210009, PR China
[c] Research Institute for Electronic Science, Hokkaido University, Sapporo 060-0812, Japan

ARTICLE INFO

Article history:
Available online 20 February 2009

Keywords:
Bis(maleonitriledithiolato)nickelate
Spin-Peierls-like transition
Nonmagnetic doping
Magnetic property
Crystal structure

ABSTRACT

A nonmagnetic compound, $[NO_2BzPy][Cu(mnt)_2]$ (mnt^{2-} = maleonitriledithiolate; NO_2BzPy^+ = 1-(4′-nitrobenzyl)pyridinium), is isostructural with $[NO_2BzPy][Ni(mnt)_2]$, which is a quasi-1D spin system and exhibits a spin-Peierls-like transition with J = 192 K in the gapless state and spin energy gap = 738 K in the dimerization state, respectively. Further, five nonmagnetic impurity doped compounds $[NO_2BzPy][Cu_xNi_{1-x}(mnt)_2]$ (x = 0.04–0.74) were prepared, and their crystal structures as well as magnetic properties were investigated. The nonmagnetic doping causes the suppression of the spin transition with an average rate of 139(13) K/percentage of dopant concentration, and the transition collapse is estimated at around $x > 0.5$.

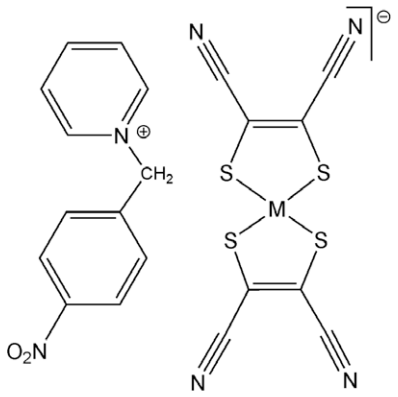
© 2009 Elsevier Ltd. All rights reserved.

1. Introduction

Impurity doping of a low-dimensional magnetic system often results in non-intuitive ground states and transition behavior differing from that of the parent material [1–7]. Lots of investigations for doping magnetic impurity with different spins have been done theoretically and experimentally for the low-dimensional inorganic magnetic systems since the first inorganic spin-Peierls compound $CuGeO_3$ was discovered [1–8]. In contrast, the examples of an impurity doping on the low-dimensional molecular magnetic system are very rare [9–12] even if the molecular spin-Peierls transition compounds have been known much earlier than the inorganic one [13–15]. One of crucial reasons to cause the above-mentioned situation is that the molecular structure is usually so complicated that it is not easy to find a suitable dopant that match with the parent material in both molecular structure and valence. In our previous study, we observed a peculiar spin-Peierls-like transition in 1-(4′-nitrobenzyl)pyridinium bis(maleonitriledithiolato)nickelate (Scheme 1 and abbreviated as $[NO_2BzPy][Ni(mnt)_2]$) [12]. This compound possesses columnar stacks along c-axis with cations and anions segregated, and the regular anionic stack can be considered as a uniform magnetic chain with $S = 1/2$ since the $[Ni(mnt)_2]^-$ monoanion bears a half spin. The magnetic exchange nature is antiferromagnetic (AFM) above transition temperature, while below that a spin gap is opened with the spin chain dimerization [16]. Instead of $[Ni(mnt)_2]^-$ monoanion with nonmagnetic $[Au(mnt)_2]^-$ monoanion, the compound of $[NO_2BzPy][Au(mnt)_2]$, which is isostructural with $[NO_2BzPy][Ni(mnt)_2]$, was obtained, and the effect of nonmagnetic $[NO_2BzPy][Au(mnt)_2]$ doping in the lattice of $[NO_2BzPy][Ni(mnt)_2]$ on the spin-Peierls-type transition was further investigated [17]. The doped systems $[NO_2BzPy][Au_xNi_{1-x}(mnt)_2]$ exhibit that: (1) within an anionic stack, $[Au(mnt)_2]^-$ substituting $[Ni(mnt)_2]^-$ does not change the crystal structure of $[Ni(mnt)_2]^-$ compound, moreover, the $[Ni(mnt)_2]^-$ and $[Au(mnt)_2]^-$ anions could not be distinguished from the single-crystal structure temperatures above 10 K; (2) even though an anionic stack exhibits a disordered structural feature, the magnetic behavior does not show a random spin system characteristic in the heavier doped system ($x \geqslant 0.49$), additionally, the fits for temperature dependence of magnetic susceptibility indicated the presence of stronger AFM coupling interaction between the $[Ni(mnt)_2]^-$ anions which are separated by the nonmagnetic $[Au(mnt)_2]^-$ species; (3) the transition is suppressed by nonmagnetic doping and collapsed at around $x > 0.27$, and in a heavier doped system with $x = 0.49$, the spin gap vanishes and a gapless phase is achieved again, and this magnetic behavior resembles to the phenomena observed in inorganic spin-Peierls transition systems such as $CuGO_3$ [1–3] and $TlCuCl_3$ [4], however, the transition collapses when x value is much higher than those found in the inorganic spin-Peierls transition systems and (4) single-crystal EPR measurements and theoretical analysis for the

* Corresponding author. Address: Provincial Key Lab of Anhui for Coordination Compounds, Anqing Normal College, Anqing 246011, PR China. Tel./fax: +86 556 5500090.
E-mail address: xmren@njut.edu.cn (X.-M. Ren).

0277-5387/$ - see front matter © 2009 Elsevier Ltd. All rights reserved.
doi:10.1016/j.poly.2009.02.008



(Abbr. as $[NO_2BzPy][M(mnt)_2]$ and M = Ni or Cu)

Scheme 1.

sample of $[NO_2BzPy][Au_{0.57}Ni_{0.43}(mnt)_2]$ disclosed the existence of intermolecular charge transfer between the adjacent $[Ni(mnt)_2]^-$ and $[Au(mnt)_2]^-$ species in an anionic stack [18].

It is well known that the structural feature of a nonmagnetic dopant strongly influence the magnetic transition behavior in a spin-Peierls system, this very important theme forms the background of the present work. The nonmagnetic compound $[NO_2BzPy][Cu(mnt)_2]$ is isostructural with the nonmagnetic compound $[NO_2BzPy][Au(mnt)_2]$ as well as the spin-Peierls-like transition compound $[NO_2BzPy][Ni(mnt)_2]$, compared with $[NO_2BzPy][Au(mnt)_2]$, the molecular geometric parameters in $[Cu(mnt)_2]^-$ species are much closer to those in $[Ni(mnt)_2]^-$ anion than $[Au(mnt)_2]^-$ species (the averaged M–S distances: d_{Au-S} = 2.3085, d_{Cu-S} = 2.1886 and d_{Ni-S} = 2.1466 Å; and the averaged ∠S—M—S bite angles: ∠S—Au—S = 90.50°, ∠S—Cu—S = 92.37° and ∠S—Ni—S = 92.44° in above-mentioned three compounds). In this contribution, we further investigate the crystal structures and magnetic properties of a series of compounds with a formula $[NO_2BzPy][Cu_xNi_{1-x}(mnt)_2]$ (x = 0–1 and it represents the molar fraction of Cu in a doped system).

Table 1
Elemental analyses (C, H and N), molar ratio of $[Cu(mnt)_2]^-$ to $[Ni(mnt)_2]^-$ in the starting materials and the occupation factor of Cu(Ni) in the final crystal structural refinement for $[NO_2BzPy][Cu_xNi_{1-x}(mnt)_2]$ (x = 0.04–0.74).

	Calculated			Found			Cu:Ni[a]	Cu:Ni[b]
	C	H	N	C	H	N		
x = 0.04	43.3	2.00	15.2	43.1	2.05	15.0	0.05:0.95	0.04:0.96
x = 0.12	43.3	2.00	15.1	43.0	2.03	14.9	0.10:0.90	0.12:0.88
x = 0.32	43.2	1.99	15.1	43.4	2.06	14.8	0.33:0.67	0.32:0.68
x = 0.50	43.1	1.99	15.1	43.1	2.02	15.2	0.49:0.51	0.50:0.50
x = 0.74	43.1	1.99	15.1	42.8	2.00	15.3	0.75:0.25	0.74:0.26

[a] The molar ratio in the starting materials.
[b] The results from ICP measurements.

2. Experimental

2.1. Preparation of compounds

$[NO_2BzPy][Ni(mnt)_2]$ and $[NO_2BzPy]_2[Cu(mnt)_2]$ were prepared according to the published procedures [16,19].

$[NO_2BzPy][Cu(mnt)_2]$: The compound $[NO_2BzPy]_2[Cu(mnt)_2]$ was oxidized by 0.75 equivalent of I_2 to afford $[NO_2BzPy][Cu(mnt)_2]$ (yield: ~72%). Single crystals suitable for X-ray structural analysis were obtained by diffusing diethyl ether into an acetonitrile solution of $[NO_2BzPy][Cu(mnt)_2]$. Elemental *Anal.* Calc. for $C_{20}H_{11}N_6O_2S_4Cu$: C, 43.0; H, 1.98; N, 15.0%. Found: C, 42.8; H, 2.04; N, 14.9%.

$[NO_2BzPy][Cu_xNi_{1-x}(mnt)_2]$: Each doped compound was prepared according to the procedure employed in the literature [17], and the product is needle- or block-shaped crystals which are suitable for X-ray structural analysis. The molar ratio of $[NO_2BzPy][Ni(mnt)_2]$ to $[NO_2BzPy][Cu(mnt)_2]$ in the starting materials and the results of elemental analyses for C, H and N for $[NO_2BzPy][Cu_xNi_{1-x}(mnt)_2]$ (x = 0.04–0.74) are presented in Table 1.

2.2. Physical measurements

Elemental analyses were performed with a Perkin–Elmer 240 analytical instrument. IR spectra were recorded on Bruker Vector 22 spectrophotometer (KBr disc). The molar ratio of Ni-to-Cu for each alloy compound was determined by inductively coupled plasma-atomic emission spectrometer (ICP-AES, Atomscan Advantage, USA). Magnetic susceptibility measurement over the range of 2–350 K for each polycrystalline sample was carried out using a Quantum Design MPMS-XL superconducting quantum interference device (SQUID) magnetometer under 1.0 T.

2.3. X-ray structural analyses

Crystallographic data were collected using a Rigaku Raxis-Rapid diffractometer with Mo Kα (λ = 0.71073 Å) radiation from a graphite monochromator. Structures were solved by direct method using the SHELXL-97 software package [20]. The non-hydrogen atoms were refined anisotropically using the full-matrix least-squares method on F^2. It is similar to the $[NO_2BzPy]$-$[Au_xNi$

Table 2
Crystallographic data for $[NO_2BzPy][Cu_xNi_{1-x}(mnt)_2]$ with molecular formula of $C_{20}H_{11}Cu_xNi_{1-x}N_6O_2S_4$ at 293 K.

	x = 0.04	x = 0.12	x = 0.32	x = 0.50	x = 0.74	x = 1
CCDC no.	705213	705214	705215	705216	705217	705212
Molecular mass	554.49	554.88	555.84	556.71	557.87	559.13
Space group	$P2(1)/c$	$P2(1)/c$	$P2(1)/c$	$P2(1)/c$	$P2(1)/c$	$P2(1)/c$
a (Å)	12.192(2)	12.194(2)	12.198(2)	12.152(2)	12.180(2)	12.217(2)
b (Å)	26.543(5)	26.546(5)	26.516(5)	26.448(5)	26.479(5)	26.559(5)
c (Å)	7.2383(14)	7.2556(15)	7.2511(15)	7.2930(15)	7.3027(15)	7.3433(15)
β (°)	102.82(3)	102.94(3)	102.97(3)	103.15(3)	103.19(3)	103.42(3)
V (Å^3), Z	2284.0(8), 4	2289.0(8), 4	2285.4(8), 4	2282.6(8), 4	2293.1(8), 4	2317.6(8), 4
μ (mm^{-1})	1.251	1.257	1.280	1.301	1.320	1.334
λ (Å)	0.71073	0.71073	0.71073	0.71073	0.71073	0.71073
ρ (g cm^{-3})	1.613	1.610	1.615	1.620	1.616	1.602
R_1	0.0331	0.0288	0.0572	0.1138	0.0439	0.0419
wR_2	0.0817	0.0647	0.1100	0.3746	0.1271	0.0699

$R_1 = \sum(||F_o| - |F_c||)/\sum|F_o|$, $wR_2 = \sum w(|F_o|^2 - |F_c|^2)^2/\sum w(|F_o|^2)^2]^{1/2}$.

$_{1-x}$(mnt)$_2$] compounds that the [Cu(mnt)$_2$]$^-$ anions distribute randomly in the [Ni(mnt)$_2$]$^-$ stack for all doped crystals of [NO$_2$BzPy][Cu$_x$Ni$_{1-x}$(mnt)$_2$] at 293 K, and the occupancy factors of Cu and Ni atoms for each doped sample were defined by ICP measurement. All hydrogen atoms were placed at calculated positions (C–H = 0.930 Å for benzene or pyridine rings and 0.970 Å for methylene) and refined riding on the parent atoms with U(H) = 1.2 × U_{eq} (bonded C atom). Details of the lattice parameters, data collections, and refinements for [NO$_2$BzPy][Cu$_x$Ni$_{1-x}$(mnt)$_2$] (x = 0.04–1) at 293 K are summarized in Table 2.

3. Results and discussion

3.1. Description of crystal structures

Crystal structure of [NO$_2$BzPy][Cu(mnt)$_2$] at 293 K: This compound crystallizes in monoclinic space group *P2(1)/c*, and it is isostructural with the compounds [NO$_2$BzPy][Ni(mnt)$_2$] and [NO$_2$BzPy][Au(mnt)$_2$]. The asymmetric unit in a cell is comprised of a coupled of [Cu(mnt)$_2$]$^-$ and NO$_2$BzPy$^+$. The [Cu(mnt)$_2$]$^-$ anion possesses roughly a planar geometry (Fig. 1a), and the Cu–S lengths range from 2.1844(8) to 2.1982(8) Å, these values are close to the Ni–S lengths [2.1409(7)–2.1565(6) Å] in [NO$_2$BzPy][Ni(mnt)$_2$], and shorter than the Au–S lengths [2.303(2)–2.3153(19) Å] in [NO$_2$BzPy][Au(mnt)$_2$]. The S–Cu–S bite angles of 92.08(3)° and 92.66(3)° are also close to the S–Ni–S values

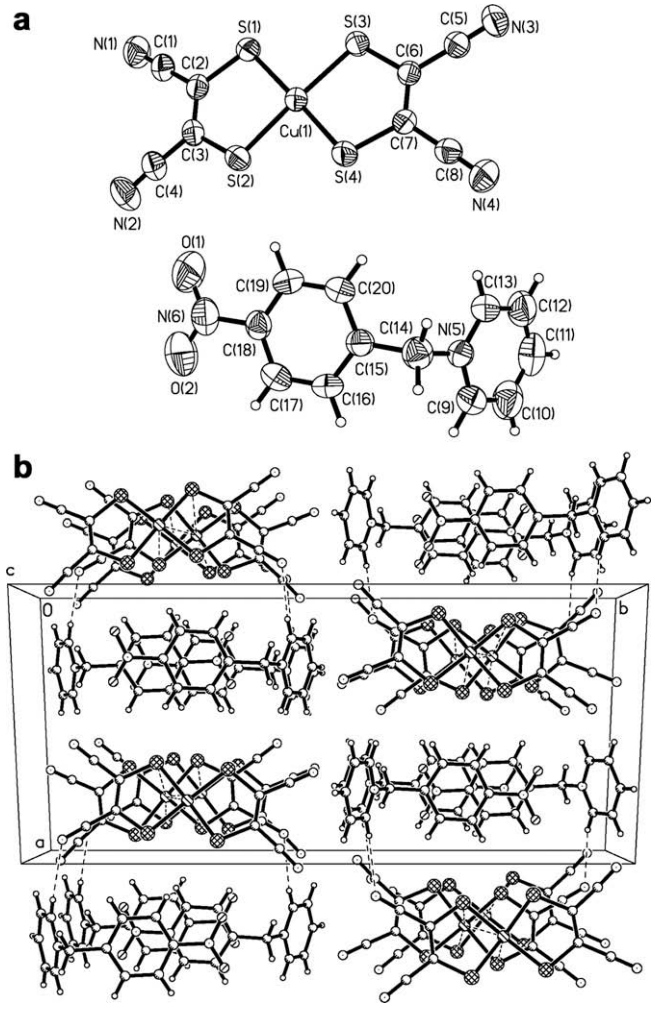


Fig. 1. (a) ORTEP view with displacement ellipsoids at 50% possibility level and (b) packing diagram of [NO$_2$BzPy][Cu(mnt)$_2$] projected along *c*-axis.

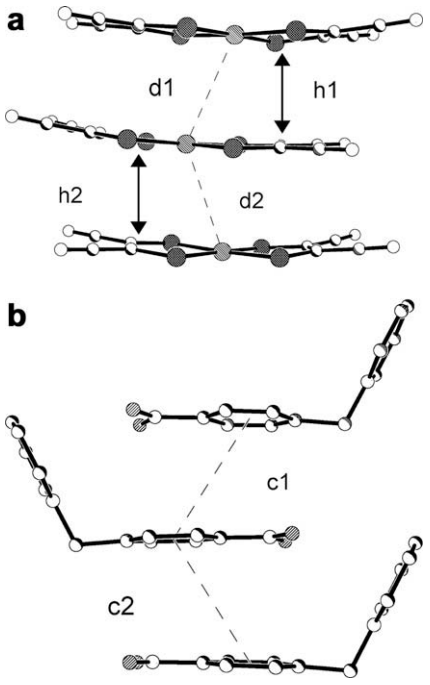


Fig. 2. (a) Distances of M···M (d_1 and d_2) and interplane between neighboring anions (h_1 and h_2) and (b) central-to-central distance between adjacent benzene rings (c_1 and c_2).

[92.32(3)° and 92.56(3)°] in [NO$_2$BzPy][Ni(mnt)$_2$]. The molecular conformation of [NO$_2$BzPy]$^+$ cation in [Cu(mnt)$_2$]$^-$ compound resembles to that in [Ni(mnt)$_2$]$^-$ compound. For example, the dihedral angles of pyridine ring and benzene ring with the reference plane C$_{Ar}$–CH$_2$–N$_{Py}$ are 88.3° and 64.8° in [Cu(mnt)$_2$]$^-$ compound versus 86.9° and 65.2° in [Ni(mnt)$_2$]$^-$ compound, respectively. The pyridine and benzene rings makes a dihedral angle of 90.2° in [NO$_2$BzPy][Cu(mnt)$_2$] and 95.0° in [NO$_2$BzPy][Ni(mnt)$_2$].

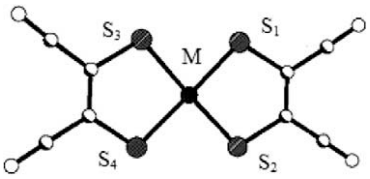
Both anions and cations form, respectively, the segregated stacks that run parallel to *c*-axis (Fig. 1b). Within anionic stacks, the face-to-face anions slid along *b*-axis and eclipse each other. The interplane distances between the adjacent [Cu(mnt)$_2$]$^-$ anions, which is defined by four coordinated S atoms, are h_1 = 3.507 and h_2 = 3.493 Å (Fig. 2a), while the adjacent Cu···Cu distances are exactly identical with d_1 = d_2 = 3.895 Å. The cationic stack is also regular with a uniform central-to-central distance of 4.280 Å between neighboring benzene rings (cf. Fig. 2b).

Crystal structures of [NO$_2$BzPy][Cu$_x$Ni$_{1-x}$(mnt)$_2$] (x = 0.04–0.74) at 293 K: As shown in Table 2, each compound with formula [NO$_2$BzPy][Cu$_x$Ni$_{1-x}$(mnt)$_2$] (x = 0.04–0.74) is isostructural to the parent compounds with very similar lattice parameters. The M–S lengths and S–M–S bite angles along with their estimated standard deviations are presented in Table 3. With the doping concentration x increases, the distances of M···M, M···S, S···S and interplanar distances between the nearest neighbors (h_1, h_2 refer to Fig. 2a) within an anionic stack change gradually and monotonically (cf. Fig. 3), and this characteristic of structural variation is distinct from the [NO$_2$BzPy][Au$_x$Ni$_{1-x}$(mnt)$_2$] systems.

3.2. Magnetic susceptibilities

The magnetic behavior of each [NO$_2$BzPy][Cu$_x$Ni$_{1-x}$(mnt)$_2$] (x = 0–1) was determined on its polycrystalline sample from 2 to 350 K. These compounds are isostructural with each other. Therefore, it is reasonable to suppose that the diamagnetism for each compound of [NO$_2$BzPy][Cu$_x$Ni$_{1-x}$(mnt)$_2$] is equal roughly to the magnetic susceptibility of [NO$_2$BzPy][Cu(mnt)$_2$]. The corrected

Table 3
The coordinated bond lengths (Å) and angles (°) in an anionic moiety for $[NO_2BzPy][Cu_xNi_{1-x}(mnt)_2]$ (x = 0–1).



	x = 0	x = 0.04	x = 0.12	x = 0.32	x = 0.50	x = 0.74	x = 1
M–S_1	2.1409(7)	2.1418(9)	2.1452(7)	2.1426(12)	2.158(4)	2.1647(9)	2.1844(8)
M–S_2	2.1442(6)	2.1443(9)	2.1488(6)	2.1451(12)	2.160(4)	2.1649(8)	2.1844(9)
M–S_3	2.1446(7)	2.1450(9)	2.1511(7)	2.1481(12)	2.162(4)	2.1668(9)	2.1872(9)
M–S_4	2.1565(6)	2.1555(8)	2.1611(6)	2.1562(12)	2.180(4)	2.1757(8)	2.1982(8)
S_1–M–S_2	92.32(3)	92.22(4)	92.16(3)	92.26(5)	92.15(15)	92.16(4)	92.08(3)
S_3–M–S_4	92.56(3)	92.48(4)	92.43(3)	92.51(5)	92.56(15)	92.62(3)	92.66(3)

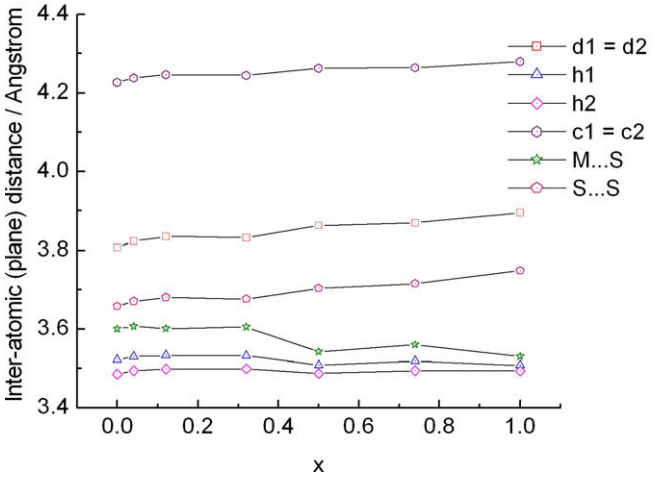


Fig. 3. Variations of interatomic and interplane distances between neighboring anions in a stack (h_1 and h_2; see Fig. 2) as x for $[NO_2BzPy][Cu_xNi_{1-x}(mnt)_2]$ (x = 0–0.74) at 293 K and $[NO_2BzPy][Ni(mnt)_2]$ at 273 K [16].

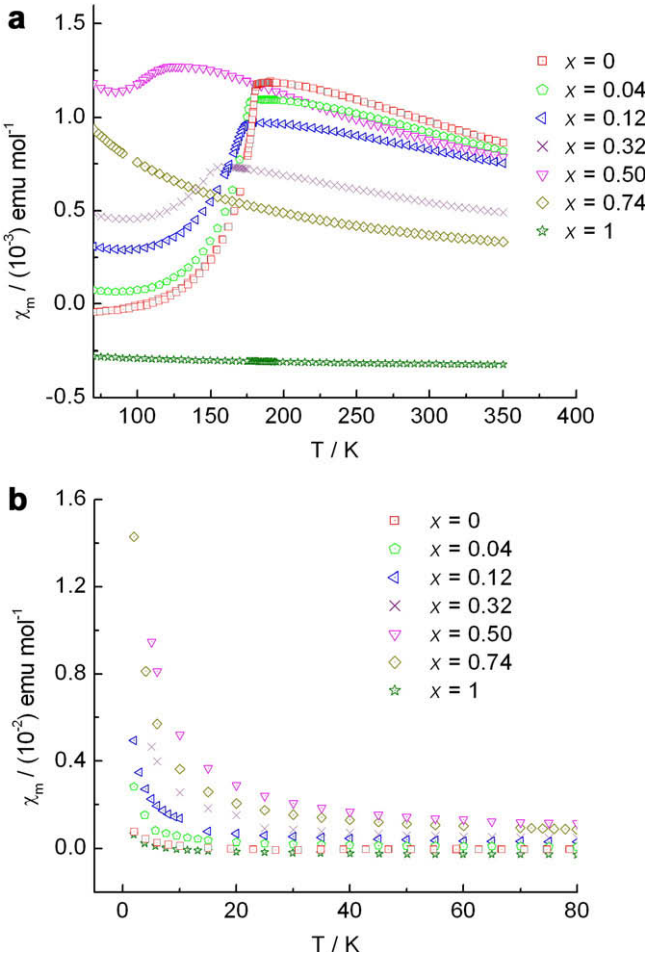


Fig. 4. Plots of $\chi_m(T)$ versus T for $[NO_2BzPy][Cu_xNi_{1-x}(mnt)_2]$ (x = 0–1) in the temperature range of (a) 70–350 K and (b) 2–80 K.

molar paramagnetic susceptibilities of $[NO_2BzPy][Cu_xNi_{1-x}(mnt)_2]$ (x = 0–0.74) as well as the nonmagnetic compound of $[NO_2BzPy][Cu(mnt)_2]$ are given in Fig. 4 as $\chi_m = f(T)$, from which it can be found that the nonmagnetic compound of $[NO_2BzPy][Cu(mnt)_2]$ clearly shows diamagnetism behavior (with negative magnetic susceptibilities).

For the parent compound of $[NO_2BzPy][Ni(mnt)_2]$ (x = 0), as reported in our previous work [16], a magnetic transition occurs around 181 K, and the phenomenology of the magnetic transition closely resembles that of a spin-Peierls transition. The spin gap with the value of 738 K in dimerized state was estimated from the fits of the magnetic susceptibility data in low temperature phase, and the magnetic exchange interaction with J/k_B = 192(3) K [17] in high temperature phase was evaluated from the analysis for magnetic susceptibility data utilizing a regular antiferromagnetic Heisenberg model for a S = ½ linear chain system [21].

As displayed in Fig. 4a and b, the nonmagnetic doping causes (1) the molar magnetic susceptibility decreasing with x value increase when x < 0.5; (2) an onset of a strong paramagnetic background in the low temperature region and (3) a damping of the spin transition. These behaviors are similar to the doped systems of $[NO_2BzPy][Au_xNi_{1-x}(mnt)_2]$ [17]. It is understandable that the nonmagnetic doping induces the strong paramagnetic background in the low temperature region for the doped sample since the antiferromagnetic spin chains of $[Ni(mnt)_2]^-$ are broken at the position of nonmagnetic dopants $[Cu(mnt)_2]^-$, moreover, the spin number in a chain should be randomly even and odd in equal probability. Therefore, the spin at the end of any odd numbered spin chain becomes uncoupled, giving a contribution to the paramagnetic susceptibility, and this contribution is dominant especially for heavily doped systems. In the doped system at x = 0.5, the broad maximum of magnetic susceptibility appears in the χ_m–T plot which is a typical characteristic of a lowered dimensionality of spin system due to the existence of short-range ordering. It is

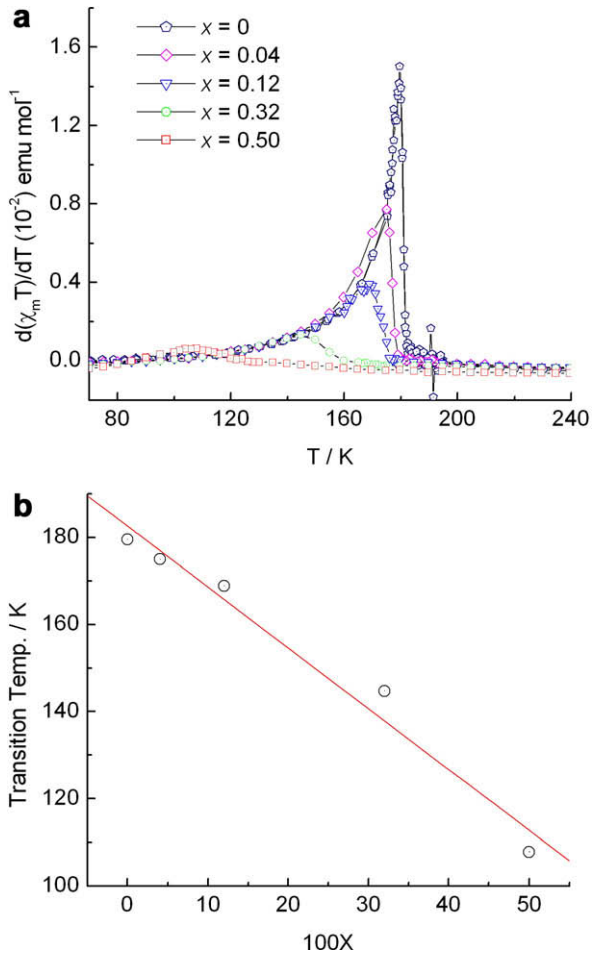


Fig. 5. (a) Plots of $d(\chi_m T)/dT$ versus T for $[NO_2BzPy][Cu_xNi_{1-x}(mnt)_2]$ (x = 0–0.5) and (b) the x dependences of T_C.

noteworthy that the transition is still observed with the χ_m value clear dropping in the χ_m–T plot even if the change is small. In the heavily doped system of x = 0.74, the shape of $\chi_m(T)$–T plot is totally different from other doped systems, in which the typical characteristic of a lowered dimensionality of spin system (with a broad maximum of magnetic susceptibility) and the magnetic transition disappear, and the temperature dependences of magnetic susceptibility exhibits a simple Curie–Weiss behavior. Fig. 5a depicts the derivative curves of $\chi_m T$ versus T for $[NO_2BzPy][Cu_xNi_{1-x}(mnt)_2]$ (x = 0–0.5) and Fig. 5b plots the corresponding x dependences of T_C, which is defined as the peak temperature in the $d(\chi_m T)/dT$–T plot. The values of $T_C(x)$ reduce linearly up to $x \leqslant 0.5$, and it is expressed as $T_C = 182(3)–139(13)x$ (K). Compared with the $[NO_2BzPy][Au_xNi_{1-x}(mnt)_2]$ system, where $T_C = 180(2)–221(12)x$ (K), the $[NO_2BzPy][Cu_xNi_{1-x}(mnt)_2]$ system exhibits higher x value of the transition collapsing and smaller x dependence of T_C shift.

4. Conclusion

Summarily, we synthesized and characterized structurally five nonmagnetic doped compounds with a formula $[NO_2BzPy][Cu_xNi_{1-x}(mnt)_2]$ (x = 0.04–0.74), and investigated the nonmagnetic impurities effects on the spin-Peierls-like transition in a quasi-1D spin system of $[NO_2BzPy][Ni(mnt)_2]$. The nonmagnetic impurities suppress the spin-Peierls-like transition, and the transition temperature T_C reduces at an average rate of 139(13) K/percentage of nonmagnetic dopant. The transition collapse is estimated around $x > 0.5$. Compared with the $[NO_2BzPy][Au_xNi_{1-x}(mnt)_2]$ system, the $[NO_2BzPy][Cu_xNi_{1-x}(mnt)_2]$ system shows higher x values of the transition collapsing and smaller x dependence of T_C shift, and these differences may be originate from the molecular structure distinction between $[Cu(mnt)_2]^-$ and $[Au(mnt)_2]^-$ anions, for example, the average Au–S length is around 0.15 Å longer than the average Ni–S length whereas the average Cu–S length is similar to the Ni–S distance.

Supplementary data

CCDC 705212–705217 contain the supplementary crystallographic data for each compound of $[NO_2BzPy][Cu_xNi_{1-x}(mnt)_2]$ (x = 0.04–1). These data can be obtained free of charge via http://www.ccdc.cam.ac.uk/conts/retrieving.html, or from the Cambridge Crystallographic Data Centre, 12 Union Road, Cambridge CB2 1EZ, UK; fax: (+44) 1223-336-033; or e-mail: deposit@ccdc.cam.ac.uk.

Acknowledgments

X.M. Ren thanks the Natural Science Foundation for Outstanding Scholars of Anhui Province, PR China (Grant Nos. 044-J-04011 and 2005hbz20).

References

[1] M. Hase, I. Terasaki, Y. Sasago, K. Uchinokura, Phys. Rev. Lett. 71 (1993) 4059.
[2] S.B. Oseroff, S.W. Cheong, B. Aktas, M.F. Hundley, Z. Fisk, L.W. Rupp Jr., Phys. Rev. Lett. 74 (1995) 1450.
[3] T. Masuda, A. Fujioka, Y. Uchiyama, I. Tsukada, K. Uchinokura, Phys. Rev. Lett. 80 (1998) 4566.
[4] A. Osawa, T. Ono, H. Tanaka, Phys. Rev. B 66 (2002) 020405.
[5] M. Isobe, Y. Ueda, J. Mag. Mag. Mater. 177–181 (1998) 671.
[6] M. Lohmann, H.-A. Krug von Nidda, A. Loidl, E. Morré, M. Dischner, C. Geibel, Phys. Rev. B 61 (2000) 9523.
[7] T. Otsuka, M. Yoshimaru, K. Awaga, H. Imai, T. Inabe, N. Wada, M. Ogata, J. Phys. Soc. Jpn. 70 (2001) 2711.
[8] V.N. Glazkov, A.I. Smirnov, H.-A. Krug von Nidda, A. Loidl, K. Uchinokura, T. Masuda, Phys. Rev. Lett. 94 (2005) 057205.
[9] M. Mito, S. Tanaka, T. Kawae, K. Takeda, M. Yanagimoto, K. Mukai, Physica B 329–333 (2003) 1150.
[10] K. Mukai, K. Suzuki, K. Ohara, J.B. Jamali, N. Achiwa, J. Phys. Soc. Jpn. 68 (1999) 3078.
[11] K. Mukai, Y. Shimobe, J.B. Jamali, N. Achiwa, J. Phys. Chem. B 103 (1999) 10876.
[12] X. Ribas, A. Sironi, N. Masciocchi, E.B. Lopes, M. Almeida, J. Veciana, C. Rovira, Inorg. Chem. 44 (2005) 2358.
[13] J.W. Bray Jr., H.R. Hart, L.V. Interrante, I.S. Jacobs, J.S. Kasper, G.D. Watkins, S.H. Wee, J.C. Bonner, Phys. Rev. Lett. 35 (1975) 744.
[14] I.S. Jacobs, J.W. Bray Jr., H.R. Hart, L.V. Interrante, J.S. Kasper, G.D. Watkins, D.E. Prober, J.C. Bonner, Phys. Rev. B 14 (1976) 3036.
[15] S. Huizinga, J. Kommandeur, G.A. Sawatzky, B.T. Thole, K. Kopinga, W.J.M. de Jonge, J. Roos, Phys. Rev. B 19 (1979) 4723.
[16] X.M. Ren, Q.J. Meng, Y. Song, C.J. Hu, C.S. Lu, X.Y. Chen, Inorg. Chem. 41 (2002) 5686.
[17] X.M. Ren, T. Akutagawa, S. Noro, S. Nishihara, T. Nakamura, Y. Yoshida, K. Inoue, J. Phys. Chem. B 110 (2006) 7671.
[18] X.M. Ren, Y.X. Sui, G.X. Liu, J.L. Xie, J. Phys. Chem. A112 (2008) 8009.
[19] X.M. Ren, J. Ma, C.S. Lu, S.Z. Yang, Q.J. Meng, P.H. Wu, Dalton Trans. (2003) 1345.
[20] G.M. Sheldrick, SHELXL-97, Program for the Refinement of Crystal Structure, University of Göttingen, Germany, 1997.
[21] D.C. Johnston, R.K. Kremer, M. Troyer, X. Wang, A. Klümper, S.L. Bud'ko, A.F. Panchula, P.C. Canfield, Phys. Rev. B 61 (2000) 9558.

Polyhedron 28 (2009) 2080–2086

Contents lists available at ScienceDirect

Polyhedron

journal homepage: www.elsevier.com/locate/poly

Electronic structures of newly designed two-dimensional high-spin organic polymers

Akihiro Ito *, Haruhiro Ino, Kazuyoshi Tanaka

Department of Molecular Engineering, Graduate School of Engineering, Kyoto University, Nishikyo-ku, Kyoto 615-8510, Japan

ARTICLE INFO

Article history:
Available online 28 February 2009

Keywords:
High-spin organic polymer
Arylamine
Poly(radical cation)
Crystal orbital

ABSTRACT

Practical two-dimensional high-spin organic polymers are newly designed and the electronic structures are examined on the basis of the ab initio two-dimensional unrestricted Hartree–Fock crystal orbital (UHF-CO) method. The present polymers can be oxidized up to six electrons per unit cell, and it is predicted that the three-electron and six-electron oxidations per unit cell lead to the high-spin organic polymers having superdegenerate band structures originating from the characteristic non-bonding crystal orbital patterns.

© 2009 Elsevier Ltd. All rights reserved.

1. Introduction

Polymer-based organic ferromagnets have been attracting much attention since Mataga's proposal [1]. This is firstly because the design of such polymers is conceptually straightforward and secondly because magnetic interaction through covalent intramolecular pathway can be expected to be strong compared with that through intermolecular pathway in the known crystalline ferromagnets composed of stable radical molecules [2].

In the polymer-based approach, the entire polymer can be constructed from two units: (i) a spin-containing (SC) unit and (ii) a ferromagnetic coupling (FC) unit [3]. The concept of FC unit is equivalent to appropriate choice of spacer connecting between SC units. To date, 1,3-benzenediyl and/or 1,3,5-benzenetriyl are well-known FC units. When two SC units are connected by 1,3-benzenediyl, the resulting diradical has inevitably two nearly degenerate non-bonding molecular orbitals (NBMOs) (for example, *m*-benzoquinodimethane). These NBMOs distribute over common atoms and therefore strong exchange interactions are expected to occur between two radical spins, leading to a high-spin preference [4]. This mechanism is closely related to the Hund's rule in atomic physics. Employing several kinds of SC units, a lot of polymers and their oligomer model molecules have been investigated along this line [5,6]. However, authentic preparation of organic polymer-based ferromagnets still remains questionable [7].

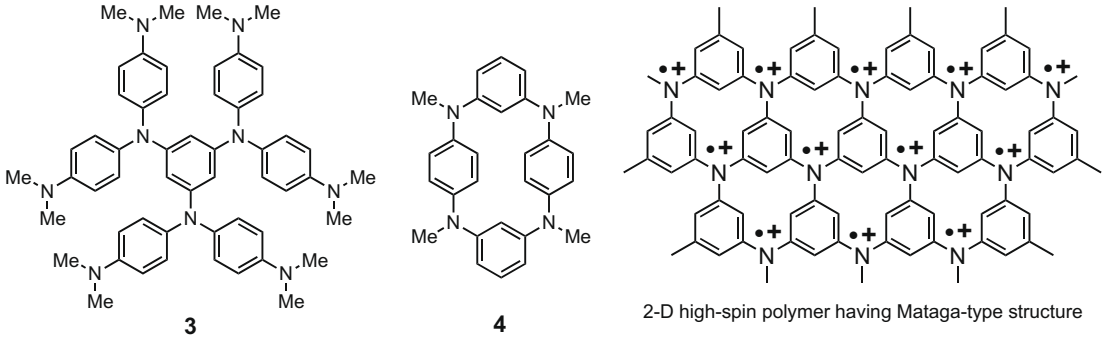
On the other hand, over the past 40 years, a considerable number of theoretical studies have been made on several organic high-spin model polymers. On the analogy of the NBMOs in high-spin molecules, the concept of "superdegeneracy" has been introduced into the half-filled bands for possible ferromagnetic polymers [8,9]. Furthermore the elaborate density functional studies have been performed to give more reliable information on the electronic structures of ferromagnetic one-dimensional (1-D) polymers and dendrimers [10].

As is well-known as Mermin and Wagner's theorem, in 1-D spin systems [11], the magnetic long range order cannot be accomplished at finite temperature. Moreover, for practical application of the 1-D magnetic polymer, generation of the spinless sites due to incomplete oxidation or decomposition leads to disappearance of high-spin correlation. Hence, 2-D or 3-D spin network is indispensable to the realization of defect-tolerant high-spin polymers [2].

Recently, we have investigated the polycationic states of a series of oligoarylamines in order to prepare two-dimensional (2-D) high-spin polymers [12–17]. These stable polycationic species are found to be in their high-spin ground states, probably due to the combination of the strong FC unit (1,3,5-benzenetriyl and 1,3-benzenediyl) and the robust SC unit (semiquinone radical cation of *para*-phenylenediamine). For example, the trication of the dendritic oligoarylamine **3** has quartet ground state [13], and the dication of the macrocyclic oligoarylamine **4** has triplet ground state [14]. When we design the arylamine-based 2-D high-spin polymers, the Mataga-type polymer is inappropriate for the candidate (Scheme 1). This is because such a molecular structure does not allow the planar 2-D structure due to the sterically overcrowded molecular structure. On the other hand, polymers **1** and **2** having *meta*- and *para*-phenylene linkage make it possible to maintain planar 2-D structure (Fig. 1). Polymers **1** and **2** contain six and nine nitrogen atoms per unit cell, respectively. Hence, three-electron oxidation per unit cell of **1** leads to complete generation of semiquinone radical cation (hereafter we denote this cationic state as

* Corresponding author. Tel.: +81 75 383 2550; fax: +81 75 383 2556.
E-mail address: aito@scl.kyoto-u.ac.jp (A. Ito).

0277-5387/$ - see front matter © 2009 Elsevier Ltd. All rights reserved.
doi:10.1016/j.poly.2009.02.016



Scheme 1.

1[3+]). Likely, six-electron oxidation per unit cell of **2** leads to complete generation of semiquinone radical cation (**2**[6+]). These charged polymers are of great importance for realization of the planar 2-D high-spin organic polymers. In particular, the realization of the high-spin organic polymers with the layered structures such as **1** and **2** opens the possibility of the control of their spin states by facilitating the reversible and partial inclusion and/or exclusion of the counter ions like the graphite intercalation compounds.

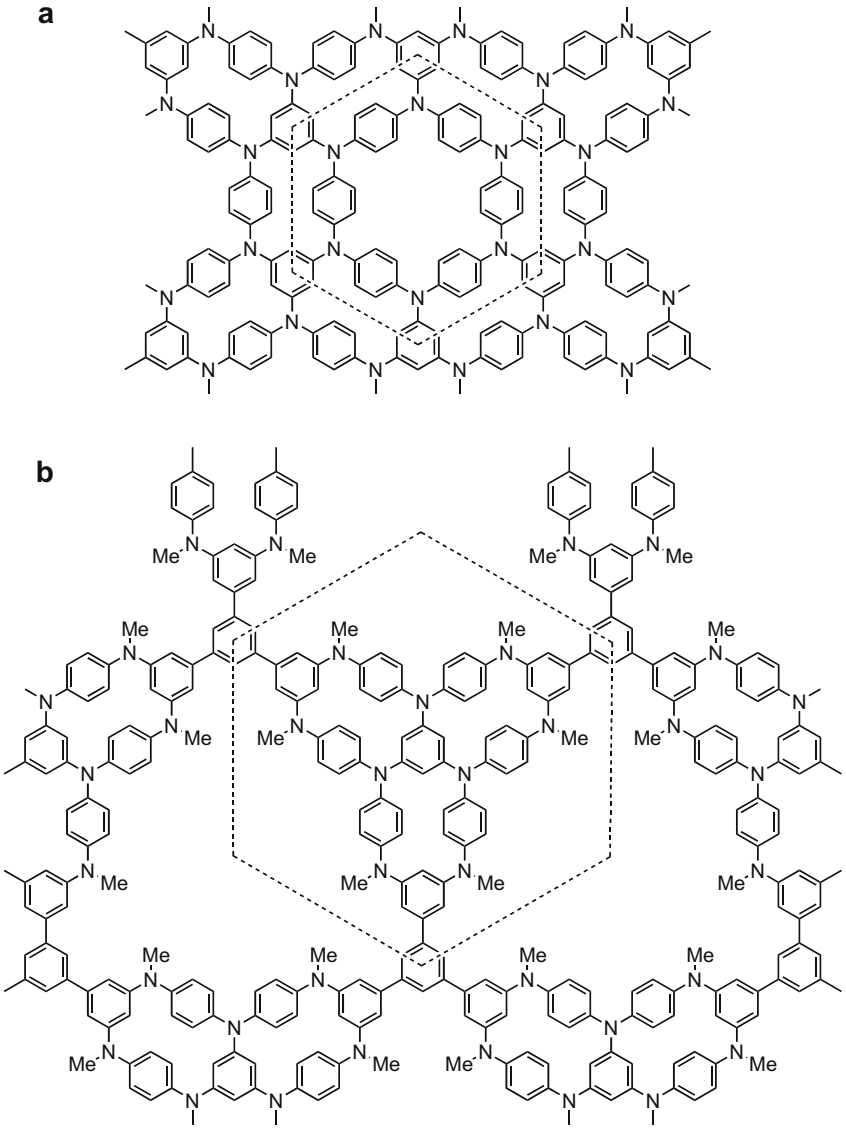


Fig. 1. Arylamine-based 2-D polymers: (a) **1** and (b) **2**. The unit cells are enclosed by broken lines.

Hence, it is worth while examining the spin electronic structures of these oxidized polymers prior to the future synthetic chemical studies.

In this paper, the newly designed 2-D magnetic polymer composed of 1,3,5-benzenetriamines as FC units and of *para*-phenylenediamines as SC units are examined on the basis of the ab initio 2-D unrestricted Hartree–Fock crystal orbital (UHF-CO) method. The aim of this study is to predict the spin electronic structures of the oxidized 2-D polymers **1**[3+], **1**[6+], **2**[3+] and **2**[6+].

2. Method of calculation

All the calculations of the novel 2-D polymers were carried out on the basis of ab initio UHF-CO method implemented in CRYSTAL98 package [18]. The 6-21G basis sets were utilized in this study [19]. To check the basis set dependency, we have performed UHF-CO calculations employing 3-21G, 4-31G and 6-31G* basis sets [19]. As a result, tendency of energy band structures remains unchanged except for the total energies.

The 2-D polymers, **1** and **2**, are classified by the layer groups belonging to a subset of the 230 space groups: $P\bar{3}1m$ for **1** and $P312$ for **2**. The unit cells for **1** and **2** correspond to the enclosed areas in Fig. 1a and b. Prior to the UHF-CO calculations, we determined the unit cell geometry by the geometry optimizations of the model clusters (Fig. 2) on the basis of the semi-empirical molecular orbital method (AM1 [20]). Several X-ray crystal structures of the arylamine molecules relating to the present molecular structure in the unit cell have been already reported [14,21–23]. The essential features from these X-ray studies are as follows: (i) all the nitrogen atoms lie in a plane and (ii) the 1,3,5-benzenetriyl rings are in the plane defined by the nitrogen atoms, while the *para*-phenylene rings are significantly canted out of the plane. The cant angle depends on the molecules studied and ranges from 40° to 80°. However, the cant angles from the reported tetraazacyclophane molecules are within 40–60°, [14,22] which are in good accordance with the values (59.0° for **1** and 47.2° for **2**) of the AM1-geometries. In the geometry optimization process, no restriction on the cant angle of *para*-phenylene rings was imposed. However, 1,3,5-benzenetriyl rings were assumed to retain coplanarity with the plane defined by the nitrogen atoms. As a result, the global planarity of the present polymers can be guaranteed by the fact that all the nitrogen atoms lie in a plane, whereas the local planarity is not guaranteed owing to canting of *para*-phenylene rings. Furthermore, the other geometrical parameters were in reasonable agreement with those of the reported X-ray structures.

Finally we performed the ab initio UHF-CO calculations for the neutral and charged states of the polymers **1** and **2** employing the above-mentioned optimized unit cells. The charged unit cell for the charged polymers must be compensated by the counter ions. In the present calculations, a uniform background charge was imposed to neutralize the charge in the unit cell [18]. Note that the same unit cell geometries were used for both the neutral and cationic states. This is because the 2-D networked structures are too rigid to be easily deformed. Actually, the DFT calculations on the tetraazacyclophane molecule demonstrated that the backbone structure in the neutral state remains unchanged even in the higher charged state [14]. Therefore, the present calculations can give qualitatively reliable results for the spin electronic structures of the polymers **1** and **2**.

3. Results and discussion

The geometries for the unit cells studied here are shown in Fig. 2. The bond lengths and angles take reasonable values in comparison with the reported X-ray structures of the related arylamine molecules [14,21–23]. The cant angles of the *para*-phenylene units in **1** and **2** are calculated to be 59.0° and 47.2°, respectively, and therefore, the π-conjugation between the 1,3,5-benzenetriyl and *para*-phenylene rings is expected to become weak compared to the hypothetical planar structures of **1** and **2** (Fig. 1).

The calculated total energies per unit cell are listed in Table 1. Apparently, the high-spin states are energetically more stable than the low-spin states for the cationic forms of **1** and **2** generated by three-electron and six-electron oxidations per unit cell. Herein it should be noted that, in the **2**[6+], all the nitrogen atoms are oxidized. In this case, it is natural that the quinoid deformation takes place and leads to diamagnetic polymers. However, this kind of deformation in the 2-D polymers is anticipated to need considerable energy compared to that in the oligomers. Therefore when the polymer **2** can be fully oxidized, **2**[6+] is highly expected to become a high-spin polymer.

The high-spin preference for the cationic states of **1** and **2** can be explained by the band structures (Fig. 3). In **1**[3+], the α-spin highest occupied crystal orbital (HOCO) bands (178–180) are less than 0.25 eV in width (Fig. 3a). These flat bands give the physical origin for the high-spin preference. On the other hand, the corre-

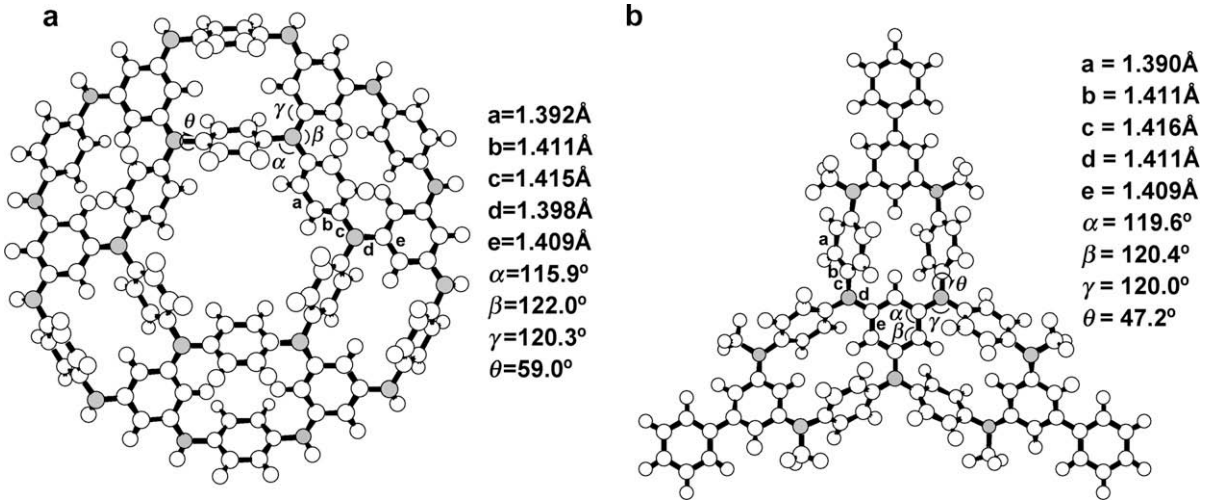


Fig. 2. AM1-optimized geometries of the unit cells for the ab initio SCF-UHF-CO calculations of the 2-D polymers: (a) **1** and (b) **2**.

Table 1
Total energies (in Hartree) per unit cell of the high-spin and low-spin states in the cationic forms of 2-D polymers **1** and **2**.

	Charge per unit cell	High-spin state	Low-spin state	ΔE_{L-H}[a]
1	neutral	−2135.280	–	–
	+3	−2135.132	−2135.020	3.1
	+6	−2135.370	−2134.936	11.8
2	neutral	−3209.923	–	–
	+3	−3209.940	−3209.803	3.7
	+6	−3209.823	−3209.104	19.6

[a] Energy differences (in eV) between the high-spin and low-spin states. The positive value means the high-spin preference.

sponding frontier β-spin bands are broader than the α-spin bands. The broadness of the β-spin bands stems from two reasons. First, the all-*para*-phenylene linkage exists in the polymer backbone, as is apparent from the unit cell structure in Fig. 1a. Second, **1**[3+] is of partially oxidized form. Turning now to the fully oxidized **1**[6+], the α-spin HOCO bands (175–180) are less than 0.06 eV in width, and moreover, the corresponding β-spin bands are also flat, originating from the fully oxidized form (Fig. 3c). The bands become so flat that the magnetic spins will be localized considerably. Again, these narrow bands give the physical origin for the high-spin preference for **1**[6+]. More noteworthy is that the partially oxidized **2**[3+] has completely flat band structures, as shown in Fig. 3b. This contrast between **1**[3+] and **2**[3+] is explainable by inspection of the CO patterns. As shown in Fig. 4a, the α-spin HOCOs (178–180) for **1**[3+] at the Γ point are delocalized over the entire polymer backbone, whereas the α-spin HOCOs (274–276) for **2**[3+] at the Γ point are mainly localized on the triphenylbenzene rings (Fig. 4b). Consequently, the highly localized HOCOs result in the flat bands even in **2**[3+]. In addition, the orbital patterns of the HOCOs at the Γ point for **1**[3+] are formed by those of the non-bonding molecular orbitals (NBMOs) of 1,3-benzenediamine and 1,3,5-benzenetriamine (Fig. 4c and d). Consequently, the non-bonding HOCOs result in the flat bands in **2**[3+].

The α-spin HOCOs for **1**[6+] (175–180) and **2**[6+] (271–276) at the Γ point are shown in Fig. 5. In **1**[6+], the six spin-containing α-spin HOCOs are separated into non-, doubly-, and triply-degenerate COs, and these COs are quasi-degenerate (Fig. 5a). Moreover, all the HOCOs in **1**[6+] are localized more than those in **1**[3+]. On the one hand, the upper three non- and doubly-degenerate COs (274–276) in **2**[6+] lie about 2 eV above the lower three non- and doubly-degenerate COs (271–273) (Fig. 5b). Similar to the HOCOs in **2**[3+], those in **2**[6+] have also highly localized character. However, the AO coefficients are mainly distributed to the hexaphenylbenzenetriamine moieties. As a whole, it was clarified that the nature of the HO α-bands of the cationic forms of **1** and **2** are clearly constructed from the NBMOs of 1,3-benzenediamine and 1,3,5-benzenetriamine.

Let us now look at the spin density distributions for **1**[3+], **1**[6+], **2**[3+], and **2**[6+], as shown in Fig. 6. In **1**[3+] and **1**[6+], most of the spin densities concentrate on 1,3,5-benzenetriamine moieties due to the large cant angle of the *para*-phenylene rings. The spin den-

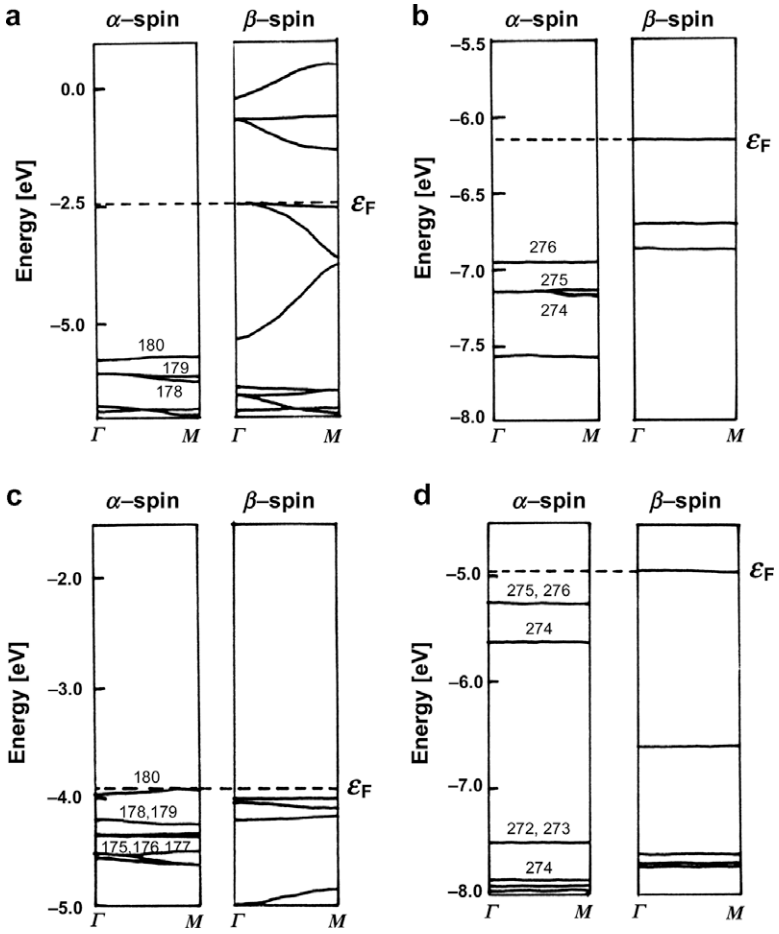


Fig. 3. Calculated band structures along the Γ–M direction of the Brillouin zone for the high-spin states of (a) **1**[3+], (b) **2**[3+], (c) **1**[6+], and (d) **2**[6+]. The broken lines designate the Fermi level.

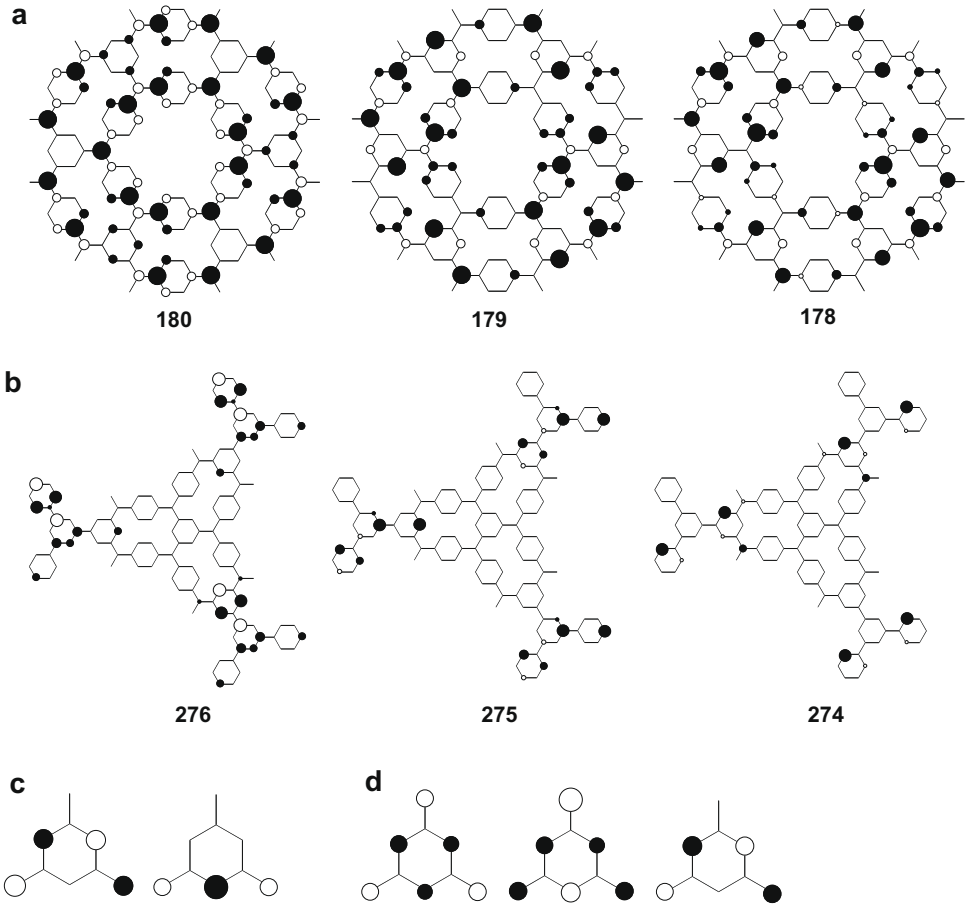


Fig. 4. α-spin HOCO patterns at the Γ point for the high-spin states of (a) **1**[3+] and (b) **2**[3+], and the schematic NBMOs of (c) 1,3-benzenediamine and (d) 1,3,5-benzenetriamine. The CO patterns are depicted after the expansion of the actual molecular structures onto the plane of the page. The radii of the black and white circles correspond to the coefficients of *p*-type atomic orbitals (AOs) and the only AOs with their coefficients larger than 0.02 are shown in this figure. The HOCOs can be regarded as psuedo-π-bands.

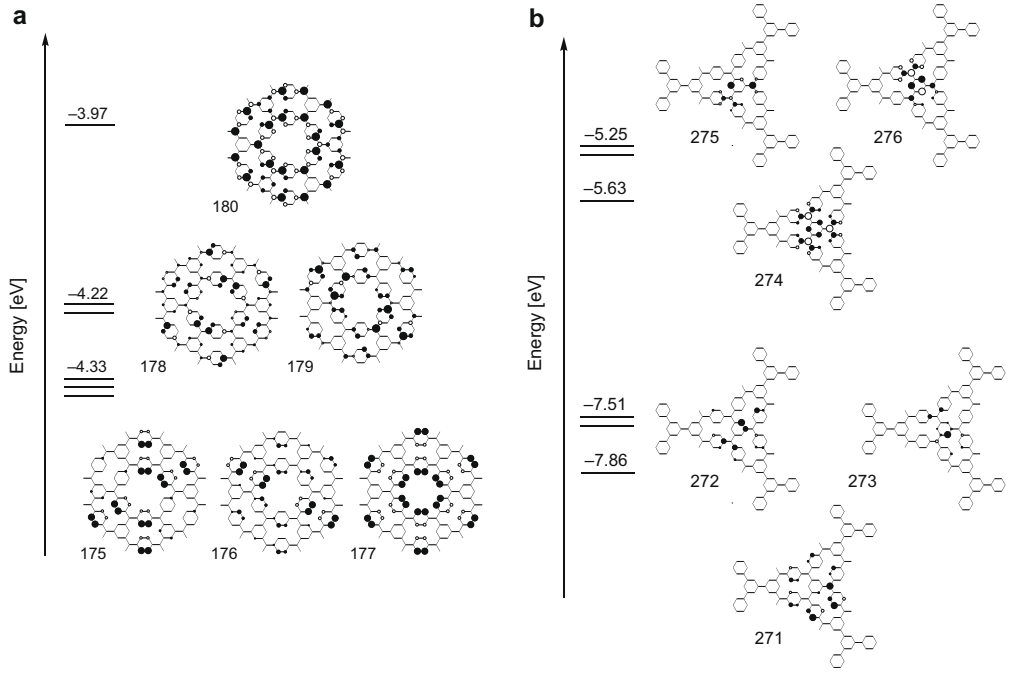


Fig. 5. α-spin HOCO patterns at the Γ point for the high-spin states of (a) **1**[6+] and (b) **2**[6+]. The CO patterns are depicted after the expansion of the actual molecular structures onto the plane of the page. The radii of the black and white circles correspond to the coefficients of *p*-type atomic orbitals (AOs) and the only AOs with their coefficients larger than 0.02 are shown in this figure. The HOCOs can be regarded as psuedo-π-bands.

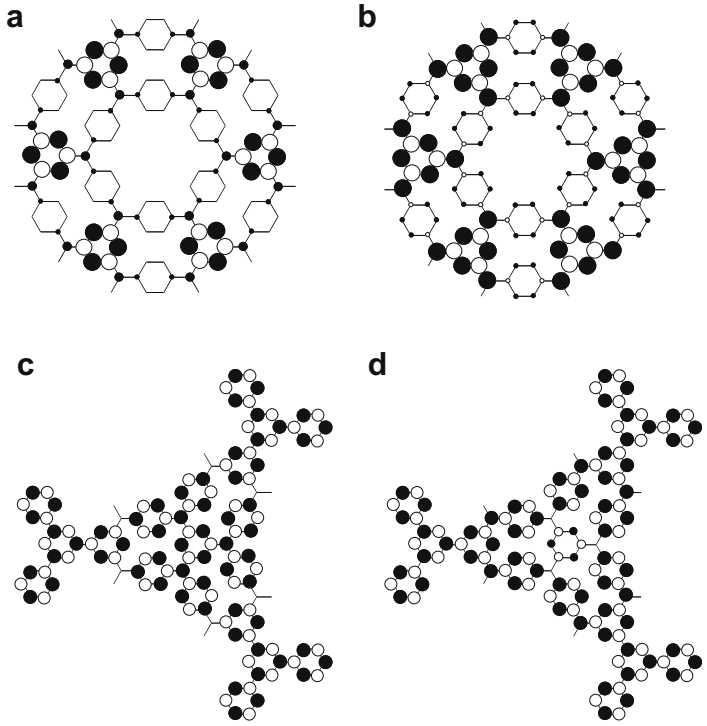


Fig. 6. Schematic representation of the Mulliken spin density distributions of (a) **1**[3+], (b) **1**[6+], (c) **2**[3+], and (d) **2**[6+]. They are depicted after the expansion of the actual molecular structures onto the plane of the page. The solid and white circles show the positive and negative spin densities, respectively, and their radii are in proportion to the magnitudes of the spin density. Only the spin density larger than 0.05 is shown in this figure.

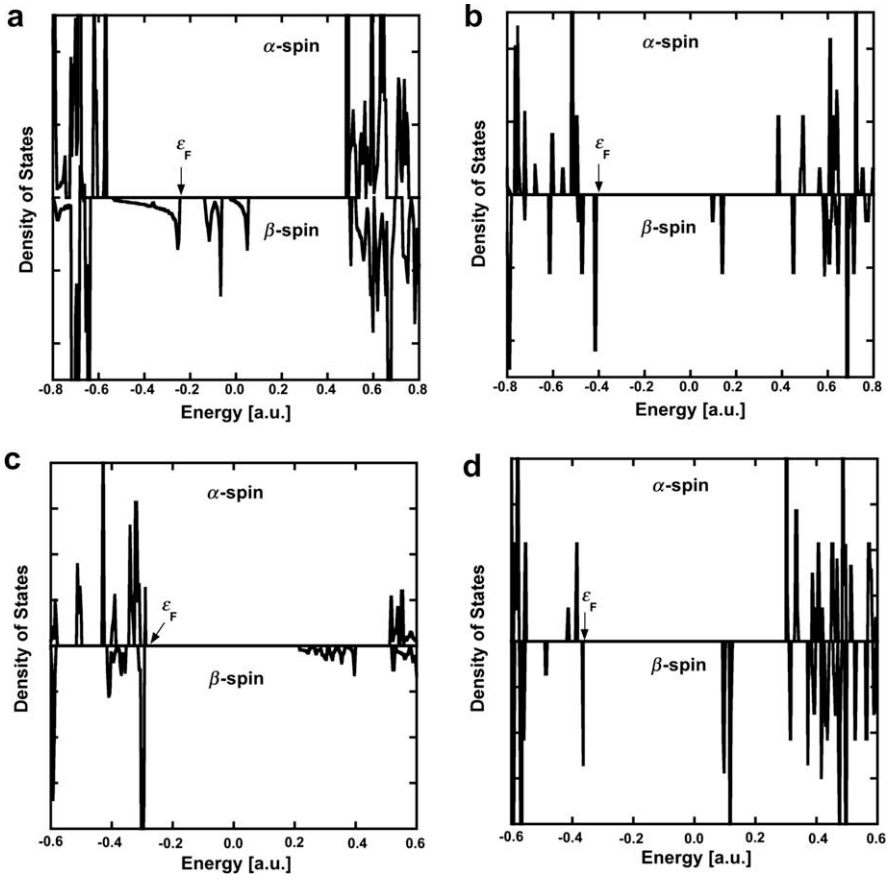


Fig. 7. The density of states for the high-spin states of (a) **1**[3+], (b) **2**[3+], (c) **1**[6+], and (d) **2**[6+]. The arrows designate the Fermi level.

sity on the nitrogen atoms increases with going from **1**[3+] to **1**[6+]. On the other hand, in **2**[6+], a considerable amount of spin flows into the *para*-phenylene rings through spin polarization effect [24], by which the positive and negative spin densities appear alternately in the two polymers. However, the spin densities on the nitrogen atoms of 1,3-benzenediamine or 1,3,5-benzenetriamine moieties are so small that we can conclude that **2**[3+] and **2**[6+] are spin localized systems.

The density of states (DOS) for **1**[3+], **1**[6+], **2**[3+], and **2**[6+] are shown in Fig. 7. From the calculated results, these high-spin polymers are expected to be insulating, because of a considerably large band gaps between the HOCO bands and the lowest unoccupied crystal orbital (LUCO) bands.

4. Conclusion

We have investigated the electronic structures of newly designed 2-D high-spin polymers **1** and **2** composed of the strong FC unit (1,3,5-benzenetriyl and 1,3-benzenediyl) and the stable SC unit (semiquinone radical cation of *para*-phenylenediamine). According to the ab initio UHF-CO calculations of cationic states of **1** and **2**, it was found that the high-spin preference is maintained in **1**[3+], **1**[6+], **2**[3+], and **2**[6+]. This indicates that the oligomer model study of **1** and **2** will be fruitful.

Acknowledgements

This work was supported by a Grant-in-Aid for Scientific Research (B) (20350065) from Japan Society for the Promotion of Science (JSPS). Numerical calculations were partly carried out at the Supercomputer Laboratory of the Institute for Chemical Research of Kyoto University.

References

[1] N. Mataga, Theor. Chim. Acta 10 (1968) 372.
[2] A. Rajca, Chem. Rev. 94 (1994) 871.
[3] D.A. Dougherty, Acc. Chem. Res. 24 (1991) 88.
[4] W.T. Borden, E.R. Davidson, J. Am. Chem. Soc. 99 (1977) 4587.
[5] J.A. Crayton, J.N. Devine, J.C. Walton, Tetrahedron 56 (2000) 7829.
[6] A. Rajca, Chem. Eur. J. 8 (2002) 4834.
[7] Organic π-conjugated polymers having very large magnetic moment and magnetic order at low temperature have been reported: A. Rajca, J. Wongsriratanakul, S. Rajca, Science 294 (2001) 1503.
[8] T. Hughbanks, J. Am. Chem. Soc. 107 (1985) 6851.
[9] T. Hughbanks, M. Kertesz, Mol. Cryst. Liq. Cryst. 176 (1989) 115.
[10] M. Mitani, D. Yamaki, Y. Takano, Y. Kitagawa, Y. Yoshioka, K. Yamaguchi, J. Chem. Phys. 113 (2000) 10486.
[11] N.D. Mermin, H. Wagner, Phys. Rev. Lett. 17 (1966) 1133.
[12] A. Ito, A. Taniguchi, T. Yamabe, K. Tanaka, Org. Lett. 1 (1999) 741.
[13] A. Ito, H. Ino, Y. Matsui, K. Tanaka, K. Kanemoto, T. Kato, J. Phys. Chem. A 108 (2004) 5715.
[14] A. Ito, Y. Ono, K. Tanaka, Angew. Chem., Int. Ed. 39 (2000) 1072.
[15] Y. Hirao, H. Ino, A. Ito, K. Tanaka, T. Kato, J. Phys. Chem. A 110 (2006) 4866.
[16] Y. Hirao, H. Ishizaki, A. Ito, T. Kato, K. Tanaka, Eur. J. Org. Chem. (2007) 186.
[17] A. Ito, S. Inoue, Y. Hirao, K. Furukawa, T. Kato, K. Tanaka, Chem. Commun. (2008) 3242.
[18] V.R. Saunders, R. Dovesi, C. Roetti, M. Causà, N.M. Harrison, R. Orlando, C.M. Zicovich-Wilson, CRYSTAL98 User's Manual, University of Turin and Daresbury Laboratory, 1999.
[19] W.J. Hehre, P. Radom, P.v.R. Schleyer, J.A. Pople, Ab Initio Molecular Orbital Theory, Wiley, New York, 1986.
[20] M.J.S. Dewar, E.G. Zoebisch, E.F. Healy, J.J.P. Stewart, J. Am. Chem. Soc. 107 (1985) 3902.
[21] K. Yoshizawa, A. Chano, A. Ito, K. Tanaka, T. Yamabe, H. Fujita, J. Yamauchi, M. Shiro, J. Am. Chem. Soc. 114 (1992) 5998.
[22] S.I. Hauck, K.V. Lakshmi, J.F. Hartwig, Org. Lett. 1 (1999) 2057.
[23] X.Z. Yan, J. Pawles, T. Goodson III, J.F. Hartwig, J. Am. Chem. Soc. 127 (2005) 9105.
[24] K. Yamaguchi, Y. Toyoda, T. Fueno, Synth. Met. 19 (1987) 81.

Polyhedron 28 (2009) 2087–2091

Contents lists available at ScienceDirect

Polyhedron

journal homepage: www.elsevier.com/locate/poly

Magnetostructural examination of Mn(III) complexes $[Mn(cyclam)X_2]^+$ with strong axial ligands

Haruyuki Baba, Motohiro Nakano *

Division of Applied Chemistry, Graduate School of Engineering, Osaka University, 2-1 Yamadaoka, Suita, Osaka 565-0871, Japan

ARTICLE INFO

Article history:
Available online 25 February 2009

Keywords:
Magnetic anisotropy
Ligand field
Angular-overlap model (AOM)
Manganese(III)

ABSTRACT

Three novel Mn(III) cyclam complexes, $[Mn(cyclam)(NCBH_3)_2](CF_3SO_3)$, $[Mn(cyclam)(NCBPh_3)_2](CF_3SO_3)$, and $[Mn(cyclam)(NCSe)_2](CF_3SO_3)\cdot H_2O$, have been synthesized. These complexes are in the high-spin state between 4 and 350 K, and show large zero-field splittings. The crystal structure of $[Mn(cyclam)(NCBH_3)_2](CF_3SO_3)$ was determined where the axial elongation of Mn–N bonds is found to be the largest among the homologue complexes. Ligand field in the $[Mn(cyclam)X_2]^+$ complex series was examined by angular-overlap model calculation.

© 2009 Elsevier Ltd. All rights reserved.

1. Introduction

The magnetism of Mn(III) complexes receives much attention recently because their large magnetic anisotropy serves useful pinning potentials for magnetization reversal in various nanomagnets [1] and their complicated d^4 electron configurations provide a potential for multiple bistabilities including spin-crossover and the Jahn–Teller effects [2–5].

A series of Mn(III) complexes, *trans*-$[Mn(cyclam)X_2]^+$ (cyclam = 1,4,8,11-tetraazacyclotetradecane, X^- = axial anionic ligand), has been extensively studied, focusing on the electronic structure and magnetic properties, which may take high-spin $(e_g)^1(t_{2g})^3$ or low-spin $(t_{2g})^4$ electron configurations [6–11]. Within the series, only one low-spin species is known with $X^- = CN^-$ [11], and no spin-crossover complexes are reported yet. We are interested in the stronger side of a range of axial ligand field, and obtained three novel complexes with $X^- = NCBH_3^-$ (**1**), $NCBPh_3^-$ (**2**), and $NCSe^-$ (**3**), exploring the spin-crossover boundary on the interaction parameter space. The crystal structure of *trans*-$[Mn(cyclam)(NCBH_3)_2](CF_3SO_3)$ (**1**) was solved and reported in detail. Several known complexes [8,9,11] were also prepared along with novel ones and their magnetic susceptibilities were measured aiming to determine the magnetic anisotropy parameter (uniaxial zero-field splitting parameter D) as a guide scale of axial ligand field. By applying angular-overlap model and extended Hückel molecular orbital calculations, the relation between magnetic anisotropy and electronic structure was discussed for a series of $[Mn(cyclam)X_2]^+$ complexes.

2. Experimental

Commercially available solvents and chemicals were used without further purification. The reaction procedures of **1** and **2** were carried out in ambient atmosphere. The reaction procedure of **3** was performed under an argon atmosphere using standard Schrenk technique. The complex $[Mn(cyclam)(OH_2)_2](CF_3SO_3)\cdot H_2O$ was prepared according to the literature method [8]. Elemental analyses were carried out at the Laboratory for Instrumental Analysis, Graduate School of Engineering, Osaka University. IR spectra were recorded on a JASCO FT/IR-300E.

2.1. Synthesis

2.1.1. $[Mn(cyclam)(NCBH_3)_2](CF_3SO_3)$ (**1**)

To an aqueous solution (3 mL) of $[Mn(cyclam)(OH_2)_2](CF_3SO_3)_3\cdot H_2O$ (378 mg, 0.5 mmol) was added an aqueous solution (2 mL) of $NaNCBH_3$ (62.9 mg, 1.0 mmol) at room temperature and the mixture was stirred. Sky-blue solid precipitated immediately was filtered off and dried in air (yield 135 mg, 56%). Infrared spectrum (KBr disk, cm^{-1}): 2184 (ν{C≡N}), 2350 (ν{B–H}). *Anal.* Calc. for $C_{13}H_{30}B_2F_3MnN_6O_3S$: C, 32.26; H, 6.25; N, 17.36. Found: C, 31.77; H, 6.18; N, 17.35%. For X-ray crystallographic analysis, an aqueous solution (1.5 mL) of $NaNCBH_3$ (13.1 mg, 0.21 mmol) was carefully layered on an aqueous solution (1 mL) of $[Mn(cyclam)(OH_2)_2](CF_3SO_3)_3\cdot H_2O$ (76.1 mg, 0.10 mmol) to yield sky-blue single crystals in 2 h.

2.1.2. $[Mn(cyclam)(NCBPh_3)_2](CF_3SO_3)$ (**2**)

A mixture of KCN (130 mg, 2.0 mmol) and BPh_3 (484 mg. 2.0 mmol) in ethanol (2.5 mL) at room temperature was stirred for 1 h to give a clear solution. To an aqueous solution (2 mL) of

* Corresponding author. Tel./fax: +81 6 6879 4588.
E-mail address: moto@ch.wani.osaka-u.ac.jp (M. Nakano).

0277-5387/$ - see front matter © 2009 Elsevier Ltd. All rights reserved.
doi:10.1016/j.poly.2009.02.013

$[Mn(cyclam)(OH_2)_2](CF_3SO_3)_3 \cdot H_2O$ (756 mg, 1.0 mmol) was added the ethanolic solution and the mixture was stirred. Immediately yellowish green solid was precipitated and filtered off. The solid was washed by ethanol, and dried in air (yield 357 mg, 38%). Infrared spectrum (KBr disk, cm^{-1}): 2171 (ν\{C≡N\}). *Anal.* Calc. for $C_{49}H_{54}B_2F_3MnN_6O_3S$: C, 62.57; H, 5.79; N, 8.93. Found: C, 62.30; H, 5.82; N, 8.98%.

2.1.3. $[Mn(cyclam)(NCSe)_2](CF_3SO_3) \cdot H_2O$ (**3**)

To a solution of KSeCN (143 mg, 0.99 mmol) in acetonitrile (10 mL) was added a solution of $[Mn(cyclam)(OH_2)_2](CF_3SO_3)_3 \cdot H_2O$ (378 mg, 0.50 mmol) in the same solvent (5 mL) at room temperature. The deep purple solution changed to a clear orange solution immediately after stirring. After 20 min, the solution was completely evaporated in vacuo. In half volume of solvent evaporated a dark-orange solid started to precipitate. The solid was washed by ethanol and dried in vacuo (yield 86.7 mg, 28%). Infrared spectrum (KBr disk, cm^{-1}): 2055 (ν\{C≡N\}). *Anal.* Calc. for $C_{13}H_{26}F_3MnN_6O_4SSe_2$: C, 24.69; H, 4.14; N, 13.29. Found: C, 24.68; H, 3.78; N, 13.23%.

2.2. X-ray structure determination

Single crystal structure determination was performed on the compound **1** at 123 K using a Rigaku RAXIS RAPID imaging-plate area detector with graphite monochromated Mo Kα radiation (λ = 0.071073 nm). The structure was solved by direct methods [12] and expanded using Fourier techniques [13]. The positions of all non-hydrogen atoms were refined anisotropically. Hydrogen atoms were included and their positions were refined using a riding model. All calculations were performed using the CRYSTALSTRUCTURE crystallographic software package [14,15]. Detail on the data collections and refinements are summarized in Table 1.

2.3. Magnetic susceptibilities

Magnetic measurements of **1** and **2** were carried out on a Quantum Design MPMS-XL5 SQUID magnetometer equipped with reciprocating sample option (RSO) at magnetic fields of 1.0 and 5.0 T. Magnetic measurement of **3** was carried out on a Quantum Design MPMS-2 SQUID magnetometer at a field of 1.0 T. Polycrystalline samples were mounted in calibrated gelatin capsules held at the center of a polypropylene straw fixed to the end of the sample rod.

Table 1
Crystal data and structure refinement for **1**.

trans-$[Mn(cyclam)(NCBH_3)_2](CF_3SO_3)$	
Formula	$C_{13}H_{30}B_2F_3MnN_6O_3S$
Formula weight	484.03
Crystal system	orthorhombic
Space group	$P2_12_12_1$
a (Å)	8.6989(5)
b (Å)	13.3506(8)
c (Å)	19.3131(10)
α (°)	90.0
β (°)	90.0
γ (°)	90.0
V (Å^3)	2242.9(2)
Z	4
D_{calc} (g cm^{-3})	1.433
Crystal color, habit	blue, prism
Crystal dimensions (mm)	0.15 × 0.10 × 0.10
F(000)	1008.00
μ (Mo Kα)	7.315 cm^{-1}
R_1 [$I > 1.50\sigma(I)$]	0.0717
wR_2 [$I > 1.50\sigma(I)$]	0.0823
Goodness of fit	1.070
Flack parameter [16]	0.49

3. Results and discussion

3.1. Molecular structure of $[Mn(cyclam)(NCBH_3)_2](CF_3SO_3)$ (**1**)

Crystal structure was determined for the complex **1** which crystallizes in the non-centrosymmetric space group $P2_12_12_1$. The molecular structure is depicted in Fig. 1. The counter anion $CF_3SO_3^-$ links neighboring complex cations via weak hydrogen bonds O···H–N forming a chain structure along *c*-axis (Fig. 2).

The coordination environment around Mn(III) is elongated-octahedron type. The equatorial Mn–N distances fall in a range of 0.2004–0.2034 nm. The axial Mn–N distances are significantly longer than them, being 0.2209 and 0.2215 nm. These values are the longest among axial Mn–N distances in the hitherto-reported $[Mn(cyclam)X_2]^+$ complexes [6–11]. The Mn–N and N≡C bonds in Mn···$NCBH_3$ axial coordination are non-collinear with the Mn–N–C angle of 169.4–173.7°, which gives rise to a small deviation from tetragonal symmetry, while the axial Mn–N bond is almost normal to the equatorial N_4 plane with the tilt angle of 1.06° (Table 2).

3.2. Magnetic properties

Isofield magnetizations of **1** and **2** were measured from 2 to 350 K, and the ones of **3** were from 4 to 350 K. All the compounds showed effective magnetic moments μ_{eff} of 4.9–5.2μ_B at room temperature, which agree well with the spin-only value of 4.9μ_B (S = 2) expected for a high-spin d^4 electron configuration of Mn(III) (Fig. 3). The μ_{eff} drops observed at low temperature should be attributable to the zero-field splitting accompanying with tetragonal coordination environment, rather than to antiferromagnetic intermolecular interactions. The uniaxial zero-field splitting

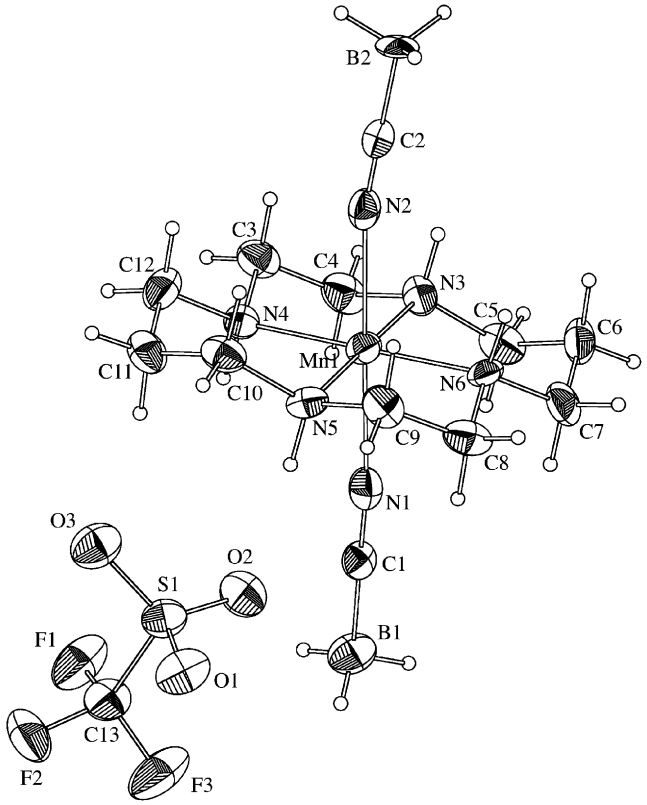


Fig. 1. Molecular structure of *trans*-$[Mn(cyclam)(NCBH_3)_2](CF_3SO_3)$ (**1**). All H atoms are shown as open circles, and thermal ellipsoids for heavier atoms are drawn at the 50% probability level.

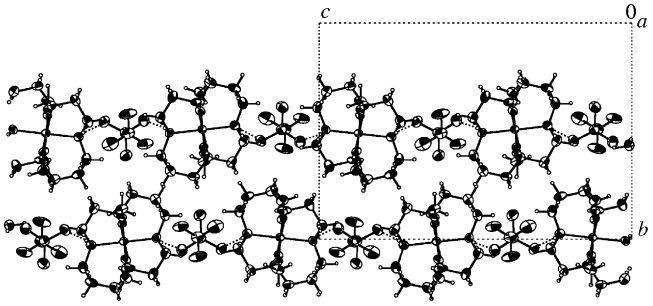


Fig. 2. Chain structure of *trans*-[Mn(cyclam)($NCBH_3$)$_2$](CF_3SO_3) with weak hydrogen bonds along *c*-axis.

parameter *D* of **1**, **2** and **3** were estimated by assuming random orientation of crystallites (Table 3).

3.3. Magnetic anisotropy analysis on the basis of AOM

Extended Hückel molecular orbital calculations [18] were made to figure out one-electron orbital energies for the complexes with X^- = Cl^-, Br^-, I^-, $NCBH_3^-$, NCO^-, NCS^-, N_3^-, CN^-, ClO_4^-, NO_3^-, and NO_2^- using their crystallographic coordinates [6–11]. The orbital energies of five d-character molecular orbitals are depicted in Fig. 4. It is obvious that the d_{z^2} orbitals are strongly affected by σ-donor character of axial ligands, while the orbital energy of the $d_{x^2-y^2}$ orbitals are dominated by the equatorial ligand cyclam and kept almost unchanged at around −8.2 eV throughout the series. Non-bonding t_{2g} orbitals found below −12 eV are slightly lifted by π-donor/acceptor character of the axial ligands, providing a single and a doubly degenerate levels. In spite that the splitting in the t_{2g} orbitals are much smaller than that in e_g orbitals, this small splitting plays an essential role in the low-spin electronic configuration under a very strong ligand field.

One-electron orbital energies obtained from extended Hückel molecular orbital calculations are useful to estimate ligand-field parameters. The angular-overlap model (AOM), instead of a conventional cubic harmonics expansion, was adopted to describe the ligand fields in [Mn(cyclam)X_2]$^+$ complexes, since it is more convenient to attribute the effect of individual ligand to the AOM parameters representing localized σ and π donors (e_σ and e_π, respectively). For an octahedral complex *trans*-[ML_4X_2] of D_{4h} symmetry, the orbital-energy relations:

$$E(x^2-y^2) = 3e_\sigma(\mathrm{L}), \quad (1)$$

$$E(z^2) = e_\sigma(\mathrm{L}) + 2e_\sigma(\mathrm{X}), \quad (2)$$

$$E(yz) = E(zx) = 2e_\pi(\mathrm{L}) + 2e_\pi(\mathrm{X}), \quad (3)$$

$$E(xy) = 4e_\pi(\mathrm{L}) \cong 0, \quad (4)$$

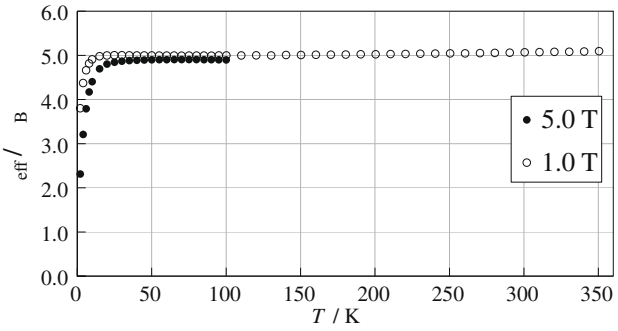


Fig. 3. The temperature dependence of effective magnetic moment of a polycrystalline sample of *trans*-[Mn(cyclam)($NCBH_3$)$_2$](CF_3SO_3) from 2 to 350 K. At temperatures lower than 50 K, the effective magnetic moment shows a drop caused by the zero-field splitting.

Table 3
Uniaxial zero-field splitting parameter *D* of *trans*-[Mn(cyclam)X_2]$^+$ complexes.

Axial ligand X	Spin state	D/hc (cm^{-1})	References
I	HS	0.82*	this work
Br	HS	−1.67	[17]
$NCBH_3$	HS	−4.65*	this work
$NCBPh_3$	HS	−5.76*	this work
NCSe	HS	−9.05*	this work
NCO	HS	−10.26*	this work
CN	LS	51.02*	this work

* Apparent value estimated by fitting of magnetic susceptibility data.

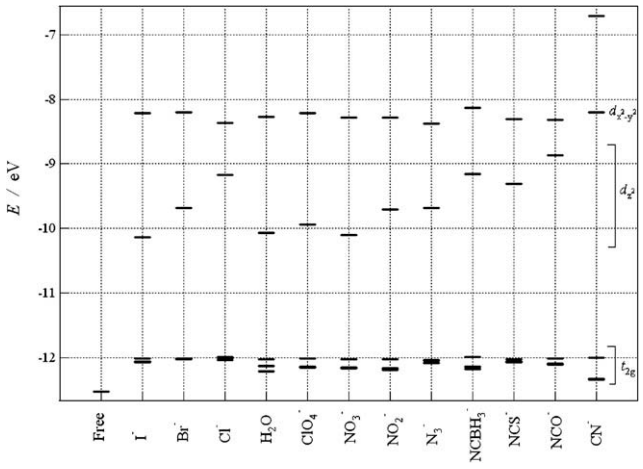


Fig. 4. 3d-levels for *trans*-[Mn(cyclam)X_2]$^{+/3+}$ estimated by extended Hückel calculations. Anions noted on the abscissa stand for the axial ligand X in the complex.

Table 2
Comparison of structural data for *trans*-[Mn(cyclam)X_2]$^{+/3+}$ complexes.

Axial ligand X	Spin state	Coordination sphere	Average Mn–X distance (Å)	Average Mn–N_{cyclam} distance (Å)	τ (°)[a]	References
I	HS	4N, 2I	2.9416(2)	2.028(2)	3.71	[8]
Br	HS	4N, 2Br	2.689(1)	2.029(6)	3.28	[6]
Cl	HS	4N, 2Cl	2.527(1)	2.035(3)	2.50	[6,7]
OH_2	HS	4N, 2O	2.187(8)	2.037(6)	7.80	[8]
ClO_4	HS	4N, 2O	2.1909(9)	2.0280(7)	8.71	[8]
NO_3	HS	4N, 2O	2.221(4)	2.036(7)	−4.49	[6]
NO_2	HS	4N, 2O	2.188(12)	2.034(3)	−5.90	[8]
N_3	HS	6N	2.175(3)	2.041(3)	3.76	[10]
NCS	HS	6N	2.166(17)	2.038(4)	1.48	[6]
$NCBH_3$	HS	6N	2.212(7)	2.020(9)	1.06	this work
NCO	HS	6N	2.148(4)	2.043(4)	1.40	[9]
CN	LS	4N, 2C	2.007(4)	2.029(4)	1.30	[11]

[a] Tilt angle τ is defined as the angle between the normal to the equatorial MnN_4 plane and the Mn–X bond [8].

Table 4
AOM parameters of *trans*-$[Mn(cyclam)X_2]^{+/3+}$ extracted from extended Hückel energy levels.

Axial ligand X	$e_\sigma(X)/hc$ (cm^{-1})	$e_\pi(X)/hc$ (cm^{-1})	$e_\sigma(L)/hc$ (cm^{-1})
I	3860	800	11 600
Br	5660	970	11 650
Cl	7930	960	11 200
OH_2	4220	420	11 440
ClO_4	4640	490	11 600
NO_3	4070	490	11 410
NO_2	5700	410	11 410
N_3	5900	860	11 160
$NCBH_3$	7830	410	11 820
NCS	7290	840	11 340
NCO	9100	710	11 330
CN	17 660	−260	11 640

are known for σ-donor equatorial ligand L and σ,π-donor axial ligand X, where $E(d)$ stands for the one-electron orbital energy of d-character orbital [19]. These relations were used to extract AOM parameter values compiled in Table 4. If $e_\pi(X)$ is negative, *i.e.* $E(yz)$, $E(zx) < E(xy)$, the axial ligand behaves as a π-acceptor rather than a π-donor. In this case, the possible low-spin electronic configuration is orbitally-degenerate $\{(d_{yz})(d_{zx})\}^3(d_{xy})^1$, not $(d_{xy})^2(d_{yz})^1(d_{zx})^1$, which is subject to the Jahn–Teller instability. It may be responsible for the tilting of axial ligands observed in $X^- = CN^-$ [11].

Although there is a report that the magnetic anisotropy in the high-spin $[Mn(cyclam)I_2]^+$ complex may be dominated by MLCT excited states mixing into the high-spin $^5B_1$ ground state [20], the contribution of such low-energy MLCT excited states is very rare and reliably ignored in most of the $[Mn(cyclam)X_2]^+$ complexes. Thus, the magnetic anisotropies of them were simulated taking only d-orbitals into account. Fig. 5 shows the zero-field splitting parameter (D) of $[Mn(cyclam)X_2]^+$ series mapped on an interaction parameter plane $e_\sigma(X)$–$e_\pi(X)$, which was calculated from the longitudinal Zeeman splitting simulations based on the AOM in conjunction with typical values for Mn(III) electronic parameters: Racah's parameters $B/hc = 1140\ cm^{-1}$ and $C/B = 4.3$ [21]; spin-orbit coupling $\zeta/hc = 355\ cm^{-1}$ [19]; Stevens' orbital reduction factor $k = 0.8$ [22]; and the AOM parameter of equatorial cyclam ligands $e_\sigma(L)/hc = 10000\ cm^{-1}$. The red broken curve on the map is a spin-crossover boundary separating high-spin ($S = 2$) and low-spin ($S = 1$) region. On this map, $e_\sigma(X)$ and $e_\pi(X)$ values of several complexes summarized in Table 4 are also plotted. This map suggested that the high-spin complex **1** does not have strong enough ligand field to break Hund's rule, and the cyanohydroborate anion behaves as not a π-acceptor expected but a weak π-donor for Mn^{3+}. Given the comparison of D-value in Table 4, complexes **2** and **3** appear to be located between **1** and $[Mn(cyclam)(NCO)_2]^+$. Although the D map was obtained on the basis of rather naïve AOM model, the agreement with experimental values is satisfactory in semiquantitative level. Comparing these plots with the spin-crossover boundary curve, it is revealed that the attainment of spin-crossover Mn(III) cyclam complexes requires stronger σ-donor and π-acceptor ligands than the complexes **1**–**3** have.

4. Conclusion

The manganese(III) complexes **1**–**3** were newly prepared and found to be in the high-spin state. The magnetic measurements of them revealed very large uniaxial zero-field splittings D in **1**–**3**. The crystal structures of **1** and analogous complexes were utilized in extended Hückel and AOM calculations, providing useful information of the spin-crossover boundary of $[Mn(cyclam)X_2]^+$ series.

Supplementary data

CCDC 705754 contains the supplementary crystallographic data for complex **1**. These data can be obtained free of charge via http://www.ccdc.cam.ac.uk/conts/retrieving.html, or from the Cambridge Crystallographic Data Centre, 12 Union Road, Cambridge CB2 1EZ, UK; fax: (+44) 1223-336-033; or e-mail: deposit@ccdc.cam.ac.uk.

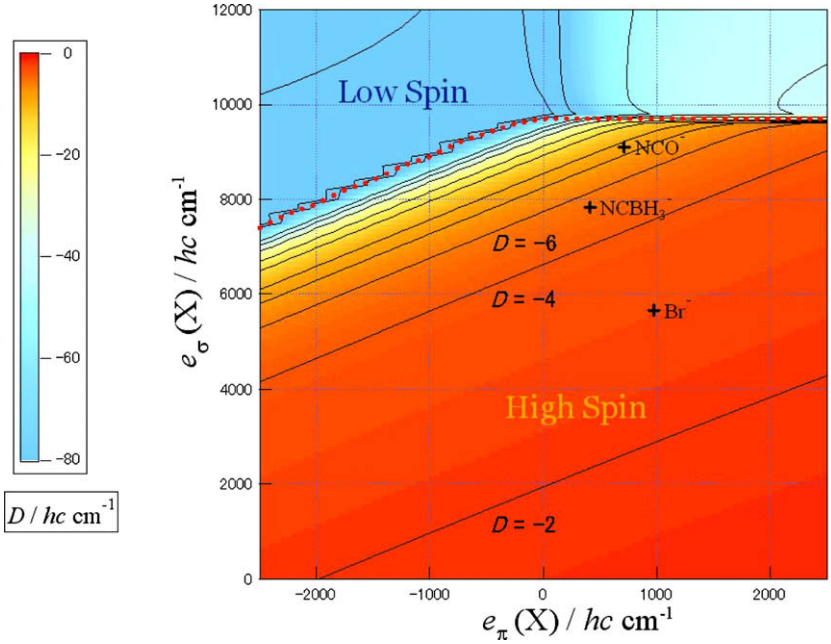


Fig. 5. Zero-field splitting parameter D of $[Mn(cyclam)X_2]^+$ complexes as a function of axial ligand AOM parameters $e_\sigma(X)$ and $e_\pi(X)$. Several points from Table 4 are also plotted on the map. The spin-crossover boundary is shown as a red dotted curve.

Acknowledgments

The authors would like to thank Prof. Takayoshi Kuroda-Sowa in Kinki University and Dr. Tetsuya Takeuchi at Low Temperature Center in Osaka University for magnetic measurements. We also appreciate Dr. Nobuko Kanehisa for X-ray crystal structure determinations.

References

[1] (a) R. Sessoli, D. Gatteschi, A. Caneschi, M.A. Novak, Nature 365 (1993) 141;
(b) R. Sessoli, H.-L. Tsai, A.R. Schake, S. Wang, J.B. Vincent, K. Folting, D. Gatteschi, G. Christou, D.N. Hendrickson, J. Am. Chem. Soc. 115 (1993) 1804;
(c) D. Gatteschi, A. Caneschi, L. Pardi, R. Sessoli, Science 265 (1994) 1054;
(d) H.J. Eppley, H.-L. Tsai, N. de Vries, K. Folting, G. Christou, D.N. Hendrickson, J. Am. Chem. Soc. 117 (1995) 301;
(e) L. Thomas, F. Lionti, R. Ballou, D. Gatteschi, R. Sessoli, B. Barbara, Nature 383 (1996) 145;
(f) J. Villain, F. Hartman-Boutron, R. Sessoli, A. Rettori, Europhys. Lett. 27 (1997) 159;
(g) S.L. Castro, Z. Sun, C.M. Grant, J.C. Bollinger, D.N. Hendrickson, G. Christou, J. Am. Chem. Soc. 120 (1998) 2365;
(h) D. Ruiz, Z. Sun, B. Albela, K. Folting, J. Ribas, G. Christou, D.N. Hendrickson, Angew. Chem., Int. Ed. 37 (1998) 300;
(i) Z. Sun, D. Ruiz, E. Rumberger, C.D. Incarvito, K. Folting, A.L. Rheingold, G. Christou, D.N. Hendrickson, Inorg. Chem. 37 (1998) 4758;
(j) W. Wernsdorfer, N. Aliaga-Alcalde, D.N. Hendrickson, G. Christou, Nature 416 (2002) 406;
(k) W. Wernsdorfer, S. Bhaduri, C. Boskovic, G. Christou, D.N. Hendrickson, Phys. Rev. B 65 (2002) 180403;
(l) S. Hill, E.S. Edwards, N. Aliaga-Alcalde, G. Christou, Science 302 (2003) 1015;
(m) D. Gatteschi, R. Sessoli, Angew. Chem., Int. Ed. 42 (2003) 268;
(n) M. Soler, W. Wernsdorfer, K. Folting, M. Pink, G. Christou, J. Am. Chem. Soc. 126 (2004) 2156;
(o) M. Murugesu, M. Habrych, W. Wernsdorfer, K.A. Abboud, G. Christou, J. Am. Chem. Soc. 126 (2004) 4766;
(p) H. Oshio, N. Hoshino, T. Ito, M. Nakano, J. Am. Chem. Soc. 126 (2004) 8805;
(q) A.J. Tasiopoulos, A. Vinslava, W. Wernsdorfer, K.A. Abboud, G. Christou, Angew. Chem., Int. Ed. 43 (2004) 2117;
(r) A.K. Boudalis, B. Donnadieu, V. Nastopoulos, J.M. Clemente-Juan, A. Mari, Y. Sanakis, J.-P. Tuchagues, S.P. Perlepes, Angew. Chem., Int. Ed. 43 (2004) 2266;
(s) H. Miyasaka, R. Clerac, W. Wernsdorfer, L. Lecren, C. Bonhomme, K. Sugiura, M. Yamashita, Angew. Chem., Int. Ed. 43 (2004) 2801.
[2] Y. Garcia, P. Gütlich, Top. Curr. Chem. 234 (2004) 49.
[3] P.G. Sim, E. Sinn, J. Am. Chem. Soc. 103 (1981) 241.
[4] M. Nakano, G. Matsubayashi, T. Matsuo, Phys. Rev. B 65 (2002) 212412.
[5] G.G. Morgan, K.D. Murnaghan, H. Müller-Bunz, V. McKee, C.J. Harding, Angew. Chem., Int. Ed. 45 (2006) 7192.
[6] P.A. Daugherty, J. Glerup, P.A. Goodson, D.J. Hodgson, K. Michelsen, Acta Chem. Scand. 45 (1991) 244.
[7] P.-K. Chan, C.-K. Poon, J. Chem. Soc., Dalton Trans. (1976) 858.
[8] S. Mossin, H.O. Sørensen, H. Weihe, J. Glerup, I. Søtofte, Inorg. Chim. Acta 358 (2005) 1096.
[9] A.D. Rae, S. Mossin, H.O. Sørensen, Acta Crystallogr., Sect. B 61 (2004) 407.
[10] K. Meyer, J. Bendix, N. Meltzler-Norte, T. Weyhermüller, K. Wieghardt, J. Am. Chem. Soc. 120 (1998) 7260.
[11] S. Mossin, H.O. Sørensen, H. Weihe, Acta Crystallogr., Sect. C 58 (2002) m204.
[12] A. Altomare, G. Cascarano, C. Giacovazzo, A. Guagliardi, M. Burla, G. Polidori, M. Camalli, J. Appl. Crystallogr. 27 (1994) 435.
[13] P.T. Beurskens, G. Admiraal, G. Beurskens, W.P. Bosman, R. de Gelder, R. Israel, J.M.M. Smits, The DIRDIF-99 Program System, Technical Report of the Crystallography Laboratory, University of Nijmegen, The Netherlands, 1999.
[14] CRYSTALSTRUCTURE 3.8, Crystal Structure Analysis Package, Rigaku and Rigaku Americas, 9009 New Trails Dr. The Woodlands, TX 77381, USA, 2000–2007.
[15] J.R. Carruthers, J.S. Rollett, P.W. Betteridge, D. Kinna, L. Pearce, A. Larsen, E. Gabe, CRYSTALS Issue 11, Chemical Crystallography Laboratory, Oxford, UK, 1999.
[16] H.D. Flack, Acta Crystallogr., Sect. A 39 (1983) 876.
[17] S. Mossin, M. Stefan, P.T. Heerdt, A. Bouwen, E. Goovaerts, H. Weihe, Appl. Magn. Reson. 21 (2001) 587.
[18] (a) M. Wolfsberg, L.J. Helmholtz, J. Chem. Phys. 20 (1952) 837;
(b) R. Hoffmann, J. Chem. Phys. 39 (1963) 1397;
(c) R. Hoffmann, W.N. Lipscomb, J. Chem. Phys. 36 (1962) 2179;
(d) J.H. Ammeter, H.-B. Burgi, J.C. Thibeault, R. Hoffmann, J. Am. Chem. Soc. 100 (1978) 3686;
(e) C. Mealli, D.M. Proserpio, J. Chem. Educ. 67 (1990) 399.
[19] B.N. Figgis, M.A. Hitchman, Ligand Field Theory and Its Applications, Wiley-VCH, 2000.
[20] S. Mossin, H. Weihe, A.-L. Barra, J. Am. Chem. Soc. 124 (2002) 8764.
[21] A. Bencini, I. Ciofini, M.G. Uytterhoeven, Inorg. Chim. Acta 274 (1998) 90.
[22] (a) J.J. Salzmann, H.H. Schmidtke, Inorg. Chim. Acta 3 (1969) 207;
(b) S.A. Cotton, Inorg. Nucl. Chem. Lett. 8 (1972) 371;
(c) N. Juranić, Spectrochim. Acta 36A (1980) 249.

Polyhedron 28 (2009) 2092–2096

Contents lists available at ScienceDirect

Polyhedron

journal homepage: www.elsevier.com/locate/poly

Quantum dynamic simulations for single molecular magnets using anisotropic spin models

T. Kawakami [a,*], H. Nitta [a], M. Takahata [a], M. Shoji [a], Y. Kitagawa [a], M. Nakano [b], M. Okumura [a], K. Yamaguchi [b]

[a] Department of Chemistry, Graduate School of Science, Osaka University, Osaka 560-0043, Japan
[b] Department of Materials Engineering Science, Graduate School of Engineering Science, Osaka University, Osaka 560-8531, Japan

ARTICLE INFO

Article history:
Available online 6 March 2009

Keywords:
Quantum dynamic simulation
Single molecular magnets

ABSTRACT

We performed quantum spin dynamics in anisotropic electron-spin systems to clarify the mechanism in single molecular magnets (SMM) theoretically. Usually, SMMs have large negative anisotropic D value and the large total spin angular moment (S_{total}). The splitting ground spin states in one SMM molecule are usually caused by the anisotropic terms (D and E), which become more important as well as isotropic term (J). In order to examine the effects of such anisotropic magnetic terms, model systems with large spin multiplicity of the ground state (S_{total} = 5 and 2) were treated. First, energy diagram in external magnetic field is shown, since negative D terms are responsible to the zero-field magnetic moment. Next, the quantum Liouvile approach is used for our spin dynamics simulation involving the relaxation processes of the system. Our simulations in S_{total} = 5 system successfully reproduced magnetic quantum tunneling (MQT) behavior in DC-external magnetic field. Moreover, in S_{total} = 2 system under AC-external magnetic field, frequency dependence of real (χ') and imaginary (χ'') parts of χ can be shown with Fourier transformation. Our theoretically drawn half circles in Cole-Cole plot (χ' versus χ'') will give information to many experimental studies.

© 2009 Elsevier Ltd. All rights reserved.

1. Introduction

Recently, low-dimensional magnetic materials have been actively investigated in relation to the so-called nano-science. For example, single molecular magnets (SMM) have been interesting targets both experimentally and theoretically [1–8]. In such the novel molecules classified in zero-dimension (0D), there are many sophisticated features, which are attracting most of scientists. For example, it is reported that magnetic hysteresis in SMMs ($S_{total} \approx 10$) is appeared by using dual stable spin states, though that is caused by moving domain-wall in bulk magnetic materials ($S_{total} \approx 10^5$). Many SMMs are the molecules that have large magnetic anisotropy (D) as well as the large total spin angular moment (S_{total} (or S)). For example, famous SMM molecules: Fe8 ($Fe_8O_2(OH)_{12}(tacn)_6$, tacn = 1,4,7-triazacyclononane) [3,4], Mn12-act ($Mn_{12}(CH_3COO)_{16}(H_2O)_4]_{12}]2CH_3COOH4H_2O$) [5–7] and Mn4 ($Mn_4O_3Cl_4(O_2CEt)_3Py_3$) [8] have been reported. Both molecules possess the large spin moment (S_{total} = 10) as ground spin state and their spin structure is anisotropic. Two spin states (M = +10 and −10) for such Mn12-ac and Fe8 molecules are the most stable and energy barrier (blocking temperature: 25 K for Fe8 and 67 K for Mn12-act) between both states exist for spin-flipping. Many scientists have been synthesized many related molecules and measured chemical or physical properties. Generally speaking, SMM molecules possess remarkable properties: (1) Large spin multiplicity of the ground state, (2) anisotropic magnetization (easy axis type), (3) activation energy ΔE for the magnetization reversal (magnetic hysteresis) and (4) magnetic quantum tunneling (MQT) between sub-levels (step structure in hysteresis loop). In particular, these SMMs are expected to candidates for elemental qubit devices in quantum computers as next generation calculation machine. They have a clear advantage concerning anisotropy of the magnetic moment and long relaxation time.

In the series of our previous studies, we have studied the excitation energy transfer in aggregated systems such as dendrimer molecules, where exciton migration with exciton–phonon interaction is very important [9–13]. Our simulation achieved theoretical prediction of dynamic features in aggregated systems. The results gave much information to experimental scientists. Now we have smoothly extended the theory to spin dynamics involving spin-phonon interaction that play important roles in several types of molecular magnetism [14,15].

The relaxation processes in the spin dynamics are focused in this study. We perform spin dynamics in strongly correlated electron-spin systems in order to clarify the phase relaxation in spin

* Corresponding author.
E-mail address: kawakami@chem.sci.osaka-u.ac.jp (T. Kawakami).

0277-5387/$ - see front matter © 2009 Elsevier Ltd. All rights reserved.
doi:10.1016/j.poly.2009.02.032

clusters. In our study, we consider the phenomenoligical relaxation parameters for the relaxation terms of the quantum Liouville equation.

Quantum spin Hamiltonian is considered in order to investigate behavior of quantum spin under external magnetic field (DC or AC). Especially, for simplified model systems for SMM molecules, anisotropic terms in Hamiltonian become important. Quantum Liouville approach with this Hamiltonian is used for the dynamics involving the relaxation processes of the system. Simple model systems (S_{total} = 5 and 2) are considered as the simplest example of SMMs.

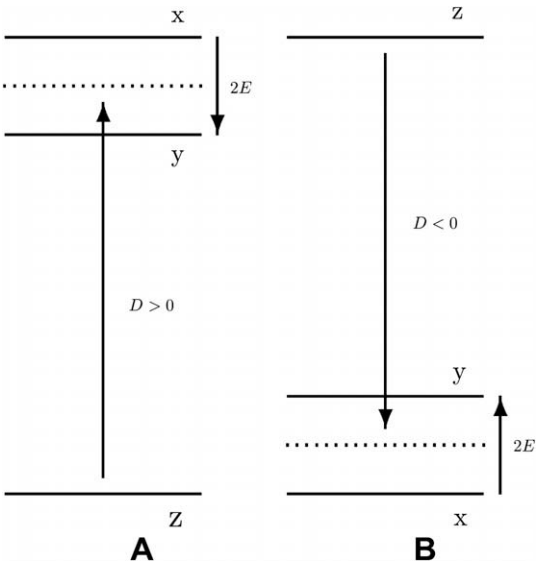


Fig. 1. The energy diagrams for anisotropic spins are shown, when the spin is on $\mathbf{u}_x$, $\mathbf{u}_y$ or $\mathbf{u}_z$ axis. Magnetic parameters D and E are called axial and transverse parameter, respectively. Two cases of positive and negative D are shown in (A) and (B), respectively, though the sign of E is not essential. Usually, single molecular magnets (SMM) have large negative D as well as the large total spin moment (S_{total} (or S)).

2. Theoretical background

2.1. Anisotropic quantum spin Hamiltonian

General spin Hamiltonian with spin-orbit coupling and external magnetic field $\mathbf{H}_0$ is defined as

$$\hat{H} = \lambda(\hat{\mathbf{L}} \cdot \hat{\mathbf{S}}) + (\hat{\mathbf{L}} + g_e\hat{\mathbf{S}})\mu_B\mathbf{H}_0 \tag{1}$$

Here, if we apply perturbation procedure and ignore higher terms, we can obtain effective Hamiltonian:

$$\hat{H}_{\text{eff}} = \langle 0|\hat{H}|0\rangle + \sum_{n\neq 0} \frac{\langle 0|\hat{H}|n\rangle\langle n|\hat{H}|0\rangle}{E_0 - E_n} \tag{2}$$

and finally,

$$\hat{H}_{\text{eff}} = \mu_B\hat{\mathbf{S}}g_e(1 - \lambda\Lambda)\mathbf{H}_0 + D\{\hat{S}_z^2 - S(S+1)/3\} + E(\hat{S}_x^2 - \hat{S}_y^2) \tag{3}$$

The tensor Λ in first term shows spatial symmetry of system and second and third terms are related to magnetic anisotropy.

Here, let us describe the zero-field splitting (ZFS) Hamiltonian of the magnetic anisotropy as

$$\hat{H}_{\text{ZFS}} = D\hat{S}_z^2 + E(\hat{S}_x^2 - \hat{S}_y^2) \tag{4}$$

under the suitable coordinates. Here, the parameter D and E are called axial and transverse parameters, and S is the total spin vector. If the ZFS tensor D can be calculated and diagonalized ($\mathbf{u}_x$, $\mathbf{u}_y$, $\mathbf{u}_z$), the diagonal elements are ordered and values D and E are defined. [16] The sign of E is not essential, since $\mathbf{u}_x$ and $\mathbf{u}_y$ can be swapped. Therefore, we ignore the sign of E in the present study. The energy diagrams for anisotropic spins are shown in Fig. 1. Magnetic properties between positive and negative D systems are different. Usually, SMMs have large negative D and large S. In Fig. 2A double well potential ($D < 0$) are depicted and each spin state ($M_S = S, S-1, \ldots, -S+1, -S$), which are illustrated in Fig. 2B as direction of magnetic field, has discrete levels. There are two ground states ($M_S = \pm S$), and the energy barrier between the two states is not zero. If the two valley states can be taken as 0 and 1, we can use as data storage units. Of course, spin transitions between each

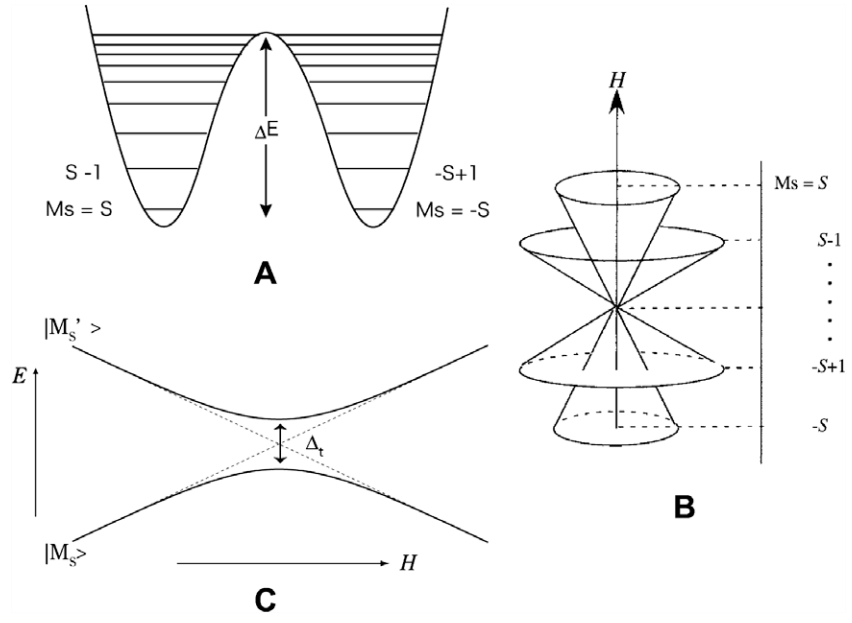


Fig. 2. (A) Double well potential ($D < 0$) are depicted. There are two ground states ($M_S = \pm S$), and the energy barrier between the two states is not zero. (B) All spin states ($M_S = S, S-1, \ldots, -S+1, -S$) are illustrated as direction of magnetic field. (C) In the non-zero E value case, tunnel splitting by the level mixing between $\mathbf{u}_x$ and $\mathbf{u}_y$ axis will occur and avoided crossing have appeared.

spin state are also very important. In the non-zero E value case, tunnel splitting by the level mixing between $\mathbf{u}_x$ and $\mathbf{u}_y$ axis will occur and avoided crossing are appeared in Fig. 2C.

Here, we append external magnetic field term into Eq. (4):

$$\hat{H}_{\mathrm{ZFC+ext}} = D\hat{S}_z^2 + E(\hat{S}_x^2 - \hat{S}_y^2) + \hat{H}_{\mathrm{ext}} \tag{5}$$

Here, direction of magnetic field $\mathbf{H}_0$ is set to apply in xz-plane and defined as

$$\hat{H}_{\mathrm{ext}} = -g_e\mu_B\mathbf{H}_0\cdot\hat{\mathbf{S}} = -g_e\mu_B H_0[\cos\theta\hat{S}_z + \sin\theta\hat{S}_x] \tag{6}$$

The parameter $\mathbf{H}_0$ is magnitude of magnetic field and θ is angle between z-axis and magnetic field.

2.2. Spin dynamics simulation with QME procedure

As a continuation of previous work, we have further examined the relaxation processes of electron spin via spin-phonon interaction. [14,15,17–19] Here, at the first step of this spin dynamics, these interactions are treated phenomenologically. Quantum master equation (QME) procedure is important in order to describe spin dynamics theoretically. In generally the time evolution of spin population ($\rho(t)$) is described by the master equation:

$$i\hbar\frac{\partial}{\partial t}\rho = [\hat{H}(t), \rho(t)] - i\Gamma\rho(t) \tag{7}$$

where the second term on the right side represents a relaxation term in the Markov approximation.

The total Hamiltonian ($\hat{H}_{\mathrm{tot}}(t)$) is expressed by the sum of the Hamiltonian ($\hat{H}_s$) for the spin parts and some interaction parts ($\hat{H}_{\mathrm{int}}$). In this study, since simulations are performed in spin systems, operator O_i is setting to spin operator S_x:

$$\hat{H}_{\mathrm{tot}} = \hat{H}_s + \sum_{i,q_i}\Omega_{q_i}c_{q_i}^{\dagger}c_{q_i} + \sum_i \hat{O}_i(\kappa_i^* c_i^{\dagger} + \kappa_i c_i) + g_e\mu_B\mathbf{H}(t)\cdot\hat{\mathbf{S}} \tag{8}$$

where the second, third and forth terms are indicate phonon parts, spin-phonon interaction and external magnetic field, respectively. For the first term ($\hat{H}_s$) we employ the anisotropic spin Hamiltonian ($\hat{H}_{\mathrm{ZFC}}$) of Eq. (4) and suitable values for both parameters D and E are set manually in our simulation.

Now we consider the ground multiplet electron-spin systems. Detailed formulation for Eq. (7) can be re-written by

$$\dot{\rho}_{\alpha\beta} = -i[\hat{H}_S + \hat{H}_{\mathrm{int}}, \rho]_{\alpha\beta} - \sum_{mn}\Gamma_{\alpha\beta;mn}\rho_{mn} \tag{9-1}$$

$$\dot{\rho}_{\alpha\alpha} = -\sum_{mn}\Gamma_{\alpha\alpha;mm}\rho_{mm} \tag{9-2}$$

In addition, the relaxation term in Eq. (7) can be considered as two types of mechanisms, i.e., population and coherent damping mechanisms. The detailed damping (Γ_{mn}) parameters in Eqs. (9-1) and (9-2) can be represented by

$$\Gamma_{\alpha\beta;mn} = \sum_k\sum_i[\delta_{n\beta}(\hat{O}_i)_{\alpha k}(\hat{O}_i)_{km}\gamma_i(\omega_{mk}) + \delta_{m\alpha}(\hat{O}_i)_{nk}(\hat{O}_i)_{k\beta}\gamma_i(\omega_{nk})] - \sum_i[(\hat{O}_i)_{\alpha m}(\hat{O}_i)_{n\beta}\gamma_i(\omega_{n\beta}) + (\hat{O}_i)_{\alpha m}(\hat{O}_i)_{n\beta}\gamma_i(\omega_{m\alpha})] \tag{10-1}$$

$$\Gamma_{\alpha\alpha;mm} = \sum_k\sum_i[\delta_{m\alpha}\{(\hat{O}_i)_{\alpha k}(\hat{O}_i)_{km} + (\hat{O}_i)_{mk}(\hat{O}_i)_{k\alpha}\}\gamma_i(\omega_{mk})] - 2\sum_i[(\hat{O}_i)_{\alpha m}(\hat{O}_i)_{m\alpha}\gamma_i(\omega_{m\alpha})] \tag{10-2}$$

Here, feeding (γ_{mn}) parameters also defined by

$$\gamma_i(\omega) = \frac{2\gamma_i^0}{1+e^{-\beta\omega}} \tag{10-3}$$

These feeding parameters are determined in a manner that the spin states relax from higher-lying to lower-lying states with the velocities, which depend on energy levels difference.

3. Results and discussion

3.1. Magnetic hysterisis and tunneling of magnetization

First, we employ spin model ($S_{\mathrm{total}} = 5$) as a simple spin cluster for SMM molecule, where for example 10-centered electro-spins with all ferromagnetic couplings are one of candidate cases. This model has 11 spin states ($2S + 1 = 11$) and each state is indicated by ($S = 5$: $M = 5,4,3,2,1,0,-1,-2,-3,-4,-5$). Fig. 3A shows the schematic energy levels of this spin systems on external magnetic field H (0–0.4 T). The spin Hamiltonian of Eq. (5) are employed and the anisotropic parameters are fixed at $D = -0.5\ \mathrm{cm}^{-1}$ and $E = 0\ \mathrm{cm}^{-1}$. In this system, the spin states $|S = 5 : M = \pm 5\rangle$ have ground energy at zero external magnetic field and split into two states under non-zero field. Each spin state is strongly influenced by magnetic field and show Zeeman splitting. In this figure, we can find several crossing points between two different spin states. If anisotropic parameter E is set to non-zero, each crossing points turn to avoided-level crossing points as shown in Fig. 2C. In such case, the tunneling of magnetization, i.e. MQT, which has been reported by experimental studies in many SMM crystals, is expected.

Thus, we set anisotoropic transverse parameter E to $0.01\ \mathrm{cm}^{-1}$ and run QME spin simulation. The simulation was performed numerically using (4,4) Runge-Kutta method by using Eqs. (9-1) and (9-2). The relaxation parameter (γ^0) for spin-phonon coupling is set to be $0.05\ \mathrm{cm}^{-1}$ and sweep rate (dH/dt) for external magnetic field is 0.01. The results of our simulation are depicted in Fig. 3B, where curvature of magnetization $-\langle S_z\rangle$ values (opposite direction to external magnetic field) is drawn to magnetic field. Static

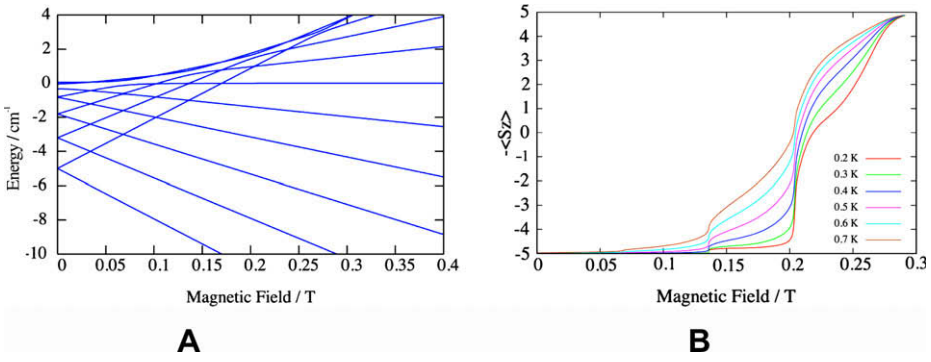


Fig. 3. We employ spin model ($S_{\mathrm{total}} = 5$) as a simple spin cluster for SMM molecule. (A) The schematic energy levels of this spin systems under external magnetic field. The spin Hamiltonian of Eq. (5) is employed and the anisotropic parameters are fixed at $D = -0.5\ \mathrm{cm}^{-1}$ and $E = 0\ \mathrm{cm}^{-1}$. (B) Anisotoropic transverse parameter E was set to be $0.01\ \mathrm{cm}^{-1}$ and run QME spin simulation. The results of our simulation are depicted in static magnetic field (DC).

magnetic fields (DC) are swept from 0 to 0.3 T and we can find out magnetization jumps at the avoided-level crossing point. The relaxation speed of magnetization increases, when magnitude of external magnetic field matches up to avoid level crossing points. Thus, step-like curvature is reproduced. External temperature is fixed to be $T = 0.2, 0.3, \ldots, 0.7$ K and we confirmed the magnetic hysteresis that magnetization at near 0 K remains even in the field being 0 T. The transition ratio between ground and excited levels in lower temperature regions becomes small, because thermal excitation ratio decreases.

3.2. AC-magnetic susceptibility and Cole-Cole plot

In previous section static (DC) external magnetic field was introduced into the system. In order to study SMM molecules concerning many interesting experimental studies, spin dynamic simulation for AC-magnetic susceptibility is also very important. Such magnetic response under the periodically driven fields depends on the frequency of the external magnetic field. Thus, frequency dependence of real (χ') and imaginary (χ'') parts of χ could be shown with Fourier transformation.

$$\chi(\omega) = \int dt e^{i\omega t}\chi(t) = \chi'(\omega) + i\chi''(\omega) \tag{11}$$

We assume that χ values can be described with linear relaxation (Debye type). Fig. 4 shows our obtained results in the case of $S_{\text{total}} = 2$, where for example four-centered electro-spins with all ferromagnetic couplings are one of candidate cases. Here, calculations for smaller S_{total} system were progressed, because the results for larger S_{total} system will be more complicated and hard to understand. Same procedure of numerical calculations depended on our QME simulation were carried out, except for alternative magnetic field in Eq. (6). The spin Hamiltonian of Eq. (5) are employed and the anisotropic parameters are fixed at $D = -0.5\ \text{cm}^{-1}$ and $E = 0\ \text{cm}^{-1}$. The relaxation parameter (γ^0) for spin-phonon coupling is $0.1\ \text{cm}^{-1}$ and amplitude of external magnetic field is 0.1 T. External temperature is fixed to be $T = 0.4, 0.5, \ldots, 2.0$ K and we can find out drastic changing of curvature of both χ' and χ'' terms. In this figure, temperature dependency is found, which implies response speeds against alternative external field will be sensitive to simulation temperature.

Moreover, let us re-plot the data in Fig. 4 into Fig. 5. Our theoretically drawn half circles in Cole-Cole plot (χ' versus χ'') will give information to experimental studies. In this figure, we can find that regular circles are realized in higher temperature case. On the other hand, in lower temperature system each circle becomes to be distorted. It is implied that divergence from linear-like decrement of spin relaxation time especially in lower temperature regions.

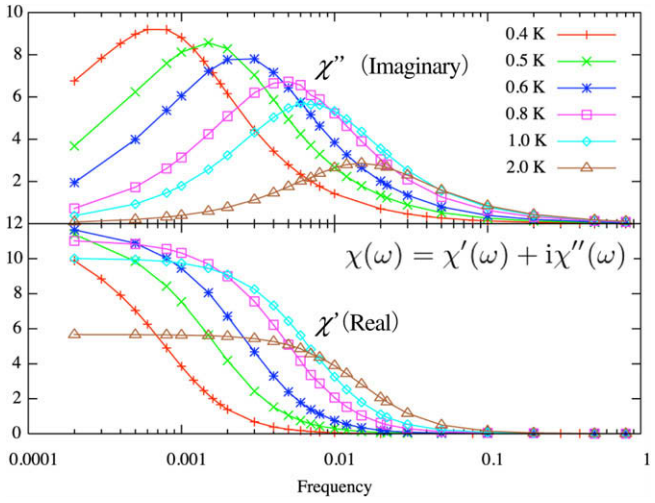


Fig. 4. Our QME simulation was carried out under AC magnetic field in Eq. (6). The anisotropic parameters are fixed at $D = -0.5\ \text{cm}^{-1}$ and $E = 0\ \text{cm}^{-1}$. AC-magnetic susceptibility in $S_{\text{total}} = 2$ system is shown, where frequency dependence of real (χ') and imaginary (χ'') parts of χ can be shown with Fourier transformation.

4. Conclusion

We have performed spin dynamics in electron-spin system using the quantum Liouville equation with the relaxation process

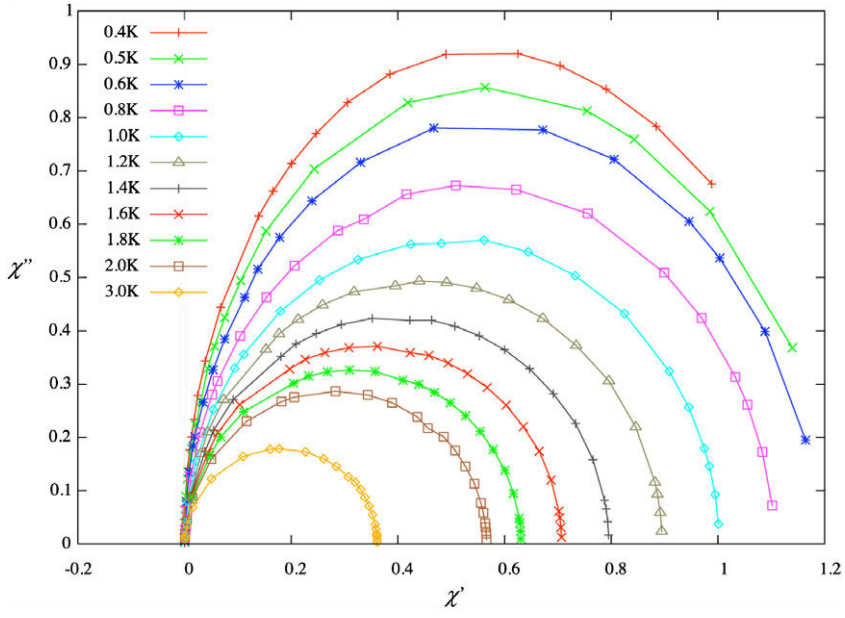


Fig. 5. The Cole-Cole (χ' versus χ'') plot, which was obtained by re-plotting the data in Fig. 4.

between spin states. These spin dynamics of the SMM-like spin system are simulated using QME approach. For the $S_{total} = 5$ spin systems, we consider the Zeeman splitting by external static magnetic field (DC). We examine the spin dynamics in variable magnitude of the external field and obtain tunneling of magnetization. Magnetic hysteresis and magnetization jump are seen in our simulation. It is worth considering our theoretical results for understanding magnetic nature of SMM molecules. For the $S_{total} = 2$ spin systems, we extend our spin dynamic simulation to that under alternative external magnetic field (AC). Our results in several temperatures are analyzed by Fourier transformation and plotted into χ', χ'' versus frequency and Cole-Cole plots. Our calculation of AC-magnetic susceptibility will give us much information of magnetic nature of SMM molecules. The relaxation processes are expected to be obedient except for lower temperature regions. Though real SMM molecules possess larger spin multiplicity of the ground state than our employing systems, our simulation will help us design newer SMMs as well as analyze the reported SMMs.

In addition to our spin dynamic simulation in this paper, we also can evaluate physical parameters by all *ab initio* MO procedures. Both *D* and *E* values in our simulation can be calculated for both model and real systems. These parameters are related to one of two terms: spin–spin dipole coupling (e.g. in organic ferromagnets) [18,20] or spin-orbit coupling (e.g. in metal complex) [16,21]. For the other parameters, i.e. *J* (Heisenberg Hamiltonian) [22], *t*, *U* (Hubbard, *t*–*J* Hamiltonian) [22] and ***d*** (Dzyaloshinskii–Moriya interaction) [16,21] have been treated theoretically in our studies. Thus, our all theoretical approach for A to Z is feasible and very unique.

In a previous report [14,15], we have discussed the superposed and entangled states of quantum systems. In this word, SMM molecules are one of good candidate of calculation and memory devices (qubit) in quantum computer. In fact, the quantum computing was realized by using seven nuclear spins by NMR technique. [23] One of the required conditions for quantum computing by the use of these systems (the magnetic moment in electron-spin or nuclear-spin, Rabi oscillation, etc.) is that the coherence time should be longer than the gating time. Efficiency of the small spin cluster in order to explore novel magnetic materials can be confirmed. This study is the first theoretical step for the rational design of quantum spin structures in SMM molecules.

Acknowledgment

This work was supported by Grant-in-Aid for Scientific Research (Nos. 19750005, 19350070 and 20038036) from Japan Society for the promotion of Science (JSPS).

References

[1] D. Gatteschi, R. Sessoli, Angew. Chem., Int. Ed. 42 (2003) 268.
[2] W. Wernsdorfer, Adv. Chem. Phys. 118 (2001) 99.
[3] Y. Pontillon, A. Caneschi, D. Gatteschi, R. Sessoli, E. Ressouche, J. Schweizer, E. Lelievre-Berna, J. Am. Chem. Soc. 121 (1999) 5342.
[4] L. Sorace, W. Wernsdorfer, C. Thirion, A.-L. Barra, M. Pacchioni, D. Mailly, B. Barbara, Phys. Rev. B 68 (2003) 220407.
[5] A. Caneschi, D. Gatteschi, R. Sessoli, J. Schweizer, Physica B 241–243 (1998) 600.
[6] R. Sessoli, D. Gatteschi, A. Caneschi, M.A. Novak, Nature 365 (1993) 141.
[7] L. Thomas, F. Lionti, R. Ballou, D. Gatteschi, R. Sessoli, B. Barbara, Nature 383 (1996) 145.
[8] W. Wernsdorfer, N. Aliaga-Alcalde, D.N. Hendrickson, G. Christou, Nature 416 (2002) 406.
[9] M. Takahata, M. Nakano, K. Yamaguchi, Synth. Met. 137 (2003) 875.
[10] H. Fujita, M. Nakano, M. Takahata, K. Yamaguchi, Synth. Met. 137 (2003) 1391.
[11] M. Takahata, M. Nakano, K. Yamaguchi, J. Theor. Comp. Chem. 2 (2003) 459.
[12] M. Takahata, M. Nakano, S. Yamada, K. Yamaguchi, Int. J. Quant. Chem. 95 (2003) 472.
[13] H. Nitta, M. Shoji, M. Takahata, M. Nakano, D. Yamaki, K. Yamaguchi, J. Photochem. Photobiol. A: Chem. 178 (2006) 264.
[14] M. Takahata, M. Shoji, S. Yamanaka, M. Nakano, K. Yamaguchi, Polyhedron 24 (2005) 2653.
[15] M. Takahata, M. Shoji, H. Nitta, R. Takeda, S. Yamanaka, M. Okumura, M. Nakano, K. Yamaguchi, Int. J. Quant. Chem. 105 (2005) 615.
[16] R. Takeda, Doctor Thesis, 2007.
[17] M. Takahata, Doctor Thesis, 2005.
[18] M. Shoji, Doctor Thesis, 2007.
[19] H. Nitta, Master Thesis, 2007.
[20] M. Shoji, K. Koizumi, T. Hamamoto, T. Taniguchi, R. Takeda, Y. Kitagawa, T. Kawakami, M. Okumura, S. Yamanaka, K. Yamaguchi, Polyhedron 24 (2005) 2708.
[21] R. Takeda, S. Mitsuo, S. Yamanaka, K. Yamaguchi, Polyhedron 24 (2005) 2238.
[22] T. Kawakami, T. Taniguchi, Y. Kitagawa, Y. Takano, H. Nagao, K. Yamaguchi, Mol. Phys. 100 (2002) 2641.
[23] Lieven M.K. Vandersypen, Matthias Steffen, Gregory Breyta, Costantino S. Yannoni, Mark H. Sherwood, Isaac L. Chuang, Nature 414 (2001) 883.

Polyhedron 28 (2009) 2097–2102

Contents lists available at ScienceDirect

Polyhedron

journal homepage: www.elsevier.com/locate/poly

Cadmium thiosemicarbazide complexes as precursors for the synthesis of nanodimensional crystals of CdS

S.N. Mlondo [a], N. Revaprasadu [a], P. Christian [b], M. Helliwell [b], P. O'Brien [b,*]

[a] Department of Chemistry, University of Zululand, Private Bag X1001, KwaDlangezwa 3886, South Africa
[b] The School of Chemistry and Manchester Materials Science Centre, University of Manchester, Oxford Road, Manchester, M13 9PL, UK

ARTICLE INFO

Article history:
Received 23 September 2008
Accepted 12 February 2009
Available online 17 April 2009

Keywords:
CdS
Thiosemicarbazide
Rods

ABSTRACT

The single X-ray structures of the thiosemicarbazide complexes $[Cd(NH_2CSNHNH_2)Cl_2]_n \cdot H_2O$ (**A**) and $[Cd(NH_2CSNHNH_2)_2Cl_2]_n$ (**B**) are reported. Both compounds have been found to be effective as single source precursors for the preparation of CdS nanomaterials. Thermal decomposition of the precursors in hexadecylamine (HDA) results in the formation of nanorods of different dimensions. The powder X-ray diffraction patterns of the nanodimensional materials reveal differences in the phases of the CdS synthesized from the two complexes. The particles synthesized from both precursors show quantum confinement effects in their absorption spectra, with the evidence of a broad defect emission in their photoluminescence spectra.

© 2009 Elsevier Ltd. All rights reserved.

1. Introduction

Rods of semiconductor nanoparticles were prepared by Alivisatos et al. [1] by adding hexylphosphonic acid (HPA) in an attempt to modify crystal growth. Numerous reports on the synthesis of metal chalcogenide nanorods, including those of CdSe [2], CdTe [3] and CdS [4–7], followed. Peng et al. have studied various factors that influence the formation of particles with non-spherical morphologies for CdSe [8]. Their work suggests that the nature of the precursor, the rate of nucleation and the nature of the capping agent are all potential factors affecting particle morphology. We have recently shown that the ratio of surface area to volume [7] and feed ratios are significant parameters in the formation of these small particles [9]. In Peng's work, cadmium chalcogenide (CdE; E = S, Se) nanoparticles were synthesized using CdO and $Cd(O_2CCH_3)_2$ together with an alkylphosphonic acid. The study showed that the rod shaped particles formed in reactions with high monomer concentrations. At intermediate monomer concentrations the nanoparticles grow to give a mixture of spheres and rods. At low monomer concentrations the particles are exclusively close to spherical. There have been relatively few reports of the preparation of nanorods of CdS by colloidal routes [10–17], and such work remains of current interest.

Group IIB metal complexes of thiosemicarbazides and thiosemicarbazones have been themselves identified as compounds which have potential for applications as non-linear optic materials [18,19]. Cadmium complexes of these ligands are thermally stable with large second harmonic generation (SHG) efficiencies [20,21].

Here we report the synthesis and structure of two cadmium complexes containing the thiosemicabazide ligand, and the preparation of CdS rods via their thermal decomposition in hexadecylamine (HDA). Thiosemicarbazide has been shown to be a good ligand for a range of metals, including zinc, mercury, cadmium and nickel [22,23]. Furthermore the related bis-bromo complex is also known for cadmium [24]. This earlier work suggests that these complexes offer an excellent opportunity for the study of the effects of the ligand system on the formation of nanomaterials.

2. Experimental

2.1. Materials

Ethanol, methanol, toluene, chloroform, thiosemicarbazide (analytical grade), hexadecylamine (HDA), tri-n-octylphosphine and cadmium chloride (analytical grade) were purchased from Aldrich. All the reagents were used as purchased without further purification.

2.2. Physical measurements

Absorption spectra were measured on a Helios B UV-spectrophotometer in chloroform in a 1 cm path length cell. Photoluminescence measurements were carried out on a Horiba Fluorolog-3 (FL3-22) in chloroform with a 1 cm path length. The p-XRD data were collected on a Bruker D8 diffractometer with a Cu Kα source. TEM were recorded on a Philips CM200 microscope with a 200 kV

* Corresponding author. Tel.: +44 161 2754652; fax: +44 161 2754616.
E-mail address: paul.obrien@man.ac.uk (P. O'Brien).

0277-5387/$ - see front matter © 2009 Elsevier Ltd. All rights reserved.
doi:10.1016/j.poly.2009.02.046

accelerating voltage. Samples were prepared by dispersing the particles in toluene and evaporating a droplet onto a carbon coated copper grid. X-ray diffraction single crystal data were collected with a Bruker Smart APEX CCD area detector equipped with an Oxford Cryosystem low-temperature device [25], using Mo Kα radiation and ω scans. Data were corrected for Lorentz and polarisation factors. The crystal data collection parameters are given in Table 1. Absorption corrections were applied to all data. All the structures were solved by direct methods using SHELXS-97. All the structures were completed by iterative cycles of ΔF-syntheses and full-matrix least squares refinement. All non-H atoms were refined anisotropically. In all the structures difference Fourier syntheses were employed in positioning idealised methyl-hydrogen atoms, which were assigned isotropic thermal parameters [U(H) = 1.5 Ueq(C)] and allowed to ride on their parent C-atoms [C–H 0.93 Å]. All refinements were against F^2 and used SHELXL-97 [26]. The thermal ellipsoids of the crystal structures are contoured at 50% probability.

2.3. Synthesis of the precursors

2.3.1. Synthesis of $[Cd(NH_2CSNHNH_2)Cl_2]_n{\cdot}H_2O$ (A)

$CdCl_2$ (2.5 g, 13 mmol) and thiosemicarbazide (2.5 g, 26 mmol) were each dissolved in ethanol (70 mL), and reacted. A creamy white precipitate immediately formed upon mixing, which was re-dissolved in hot methanol (100 mL) and left to cool slowly at room temperature. The flakes obtained were re-crystallised in hot water (100 mL). After 3 days, brown crystals of a flat square shape were obtained. The product contained some creamy white prismatic crystals (showed to be complex **B**, which were removed from the product by hand). The brown crystals of a flat square shape, $[Cd(NH_2CSNHNH_2)Cl_2]_n{\cdot}H_2O$ (**A**) (3.1 g) were analysed. The structure of complex **A** is shown in Fig. 1. Micro analysis: expected, C 6.3, H 2.2, N 21.9; found, C 6.2, H 2.2, N 21.0. Yield: 85%. Significant IR bands (cm^{-1}): ν(N–H) 2347, 3165, 3441; ν(C–N) 1589; ν(N–N) 1371; ν(C=S) 1049; ν(Cd–Cl) 250; ν(Cd–S) 198.

2.3.2. Synthesis of $[Cd(NH_2CSNHNH_2)_2Cl_2]_n$(**B**)

Cadmium chloride (1.1 g, 6 mmol) and thiosemicarbazide (1.1 g, 12 mmol) were each dissolved in hot ethanol (50 mL) in a 1:2 molar ratio, and reacted. A white precipitate was collected by filtration, dried under vacuum, and re-dissolved in hot methanol (100 mL). The solution was quickly filtered with suction whilst hot, which enhances the cooling rate. The supernatant formed a white precipitate, which was filtered, re-crystallised in 100 mL of water and left for approximately 2 days to crystallise, giving white prismatic crystals of $[Cd(NH_2CSNHNH_2)_2Cl_2]_n{\cdot}$(**B**) (1.5 g). The structure of complex **B** is shown in Fig. 2 and the packing diagram in Fig. 3. Micro analysis: expected, C 4.1, H 1.7, N 14.4; found, C 4.3, H 2.4, N 14.4. The materials were used as prepared [27]. Yield: 85%. Significant IR bands (cm^{-1}): ν(N–H) 2355, 3167, 3448; ν(C–N) 1592; ν(N–N) 1380; ν(C=S) 1039; ν(Cd–Cl) 257; ν(Cd–S) 201.

2.3.3. Decomposition of precursor (**A**) to nanodispersed CdS

Hexadecylamine (HDA) (4 g) was degassed at 120 °C for 30 min. The HDA was then heated to 180 °C under nitrogen. Complex **A** (0.25 g, 0.855 mmol) was suspended in tri-n-octylphosphine (4 mL) and injected into the hot HDA. The reaction was allowed to proceed for 30 min and the resultant yellow suspension was then cooled to 70 °C and the product isolated by washing with methanol (2 × 50 mL) and centrifuging. A similar procedure was used to decompose complex **B** (0.25 g, 0.684 mmol).

3. Results and discussion

3.1. Precursor structure

3.1.1. Structure of complex (**A**) $[Cd(NH_2CSNHNH_2)Cl_2]_n{\cdot}H_2O$

The structure of complex **A** (Fig. 1) is very similar to that reported by Woode et al. [28], showing only a small variation in the unit cell with a similar bonding arrangement. The compound crystallises into the monoclinic Cc space group. Complex **B** (Fig. 2), on the other hand, crystallises in the monoclinic C2/c space group. The lattice of complex **B** consists of infinite chains of $CdCl_4$ units linked into CdL_2 units via a Cd–S–Cd bridge (L is a thiosemicarbazide). The chloride ions lie almost symmetrically around the cadmium centre in the $CdCl_4$ moiety in a square planar geometry. The sulfur bridge is generated though a thiosemicarbazide ligand which lies fractionally closer to the $CdCl_4$ moiety than CdL_2 (cf 2.735(1) Å vs 2.862(1) Å). This is probably the result of the thiosemicarbazide molecules tilted orientation toward the $CdCl_4$ moiety (N(1)–S(1)–Cd(1) 86° cf 98° for Cd(2)). The CdL_2 units have the two thiosemicarbazide ligands lying in a square planer arrangement bound through both the sulfur and the nitrogen atoms. This results in a considerably shorter Cd–S bond for the chelating ligand than for the bridging ligand (Cd(2)–S(1) 2.862(1) Å cf Cd(2)–S(1) 2.589(1) Å). There are significant inter-chain and intra-chain bonding through NH–S and NH–Cl interactions (eg Cl(1)–N′(2) 3.400(3) Å; Cl(2)–N′(1) 3.234(3) Å; S(2)–N′(3) 3.582(3) Å;

Table 1
Crystal data collection parameters.

	Complex B	Complex A
Empirical formula	$CH_7CdCl_2N_3OS$	$C_2H_{10}CdCl_2N_6S_2$
Formula weight	292.46	365.58
Temperature (K)	100(2)	100(2)
Wavelength (Å)	0.71073	0.71073
Crystal system, SG	monoclinic, *Cc*	monoclinic, *C2/c*
A (Å)	*a* = 10.136(2)	*a* = 16.103(6)
B (Å)	*b* = 13.893(3)	*b* = 8.074(3)
C (Å)	*c* = 6.8116(1)	*c* = 16.483(6)
β (°)	β = 124.655(3)	β = 95.011(6)
Volume (Å^3)	789.1(3)	2134.9(14)
Z	4	8
Absorption coefficient (mm^{-1})	6.637	2.903
F(0 0 0)	560	1424
Reflections collected/unique	2229/1118	2187/2187
Completeness to theta	99.1%	
Refinement method	Full-matrix least-squares on F^2	Full-matrix least-squares on F^2
Final R[a] indices [$I > 2\delta(I)$]	R^1 = 0.0417, wR^2 = 0.1163	R^1 = 0.0213, wR^2 = 0.0544
R indices (all data)[b]	R^1 = 0.0420, wR^2 = 0.1167	R^1 = 0.0206, wR^2 = 0.0538

[a] All observed data.
[b] All unique data.

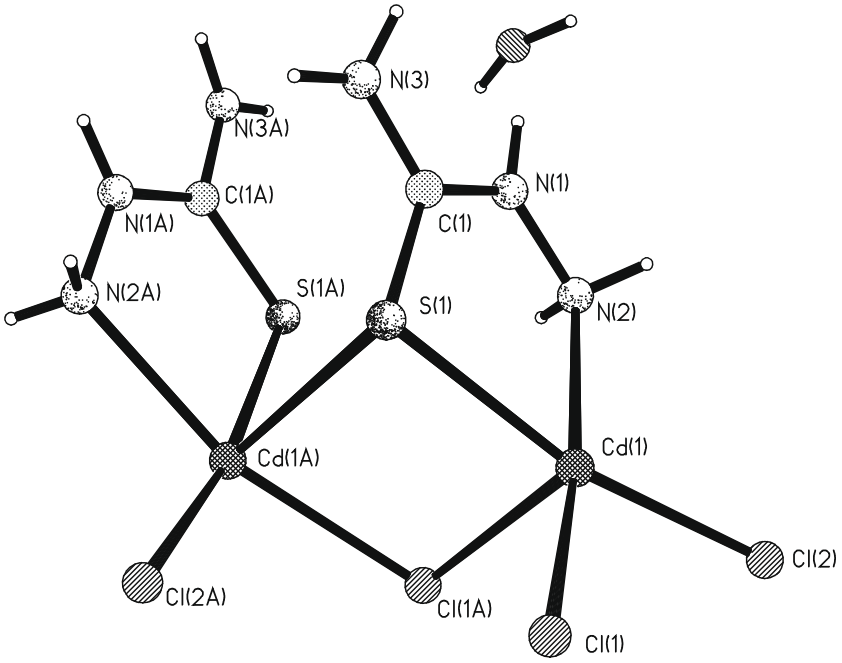


Fig. 1. Structure of complex **A**.

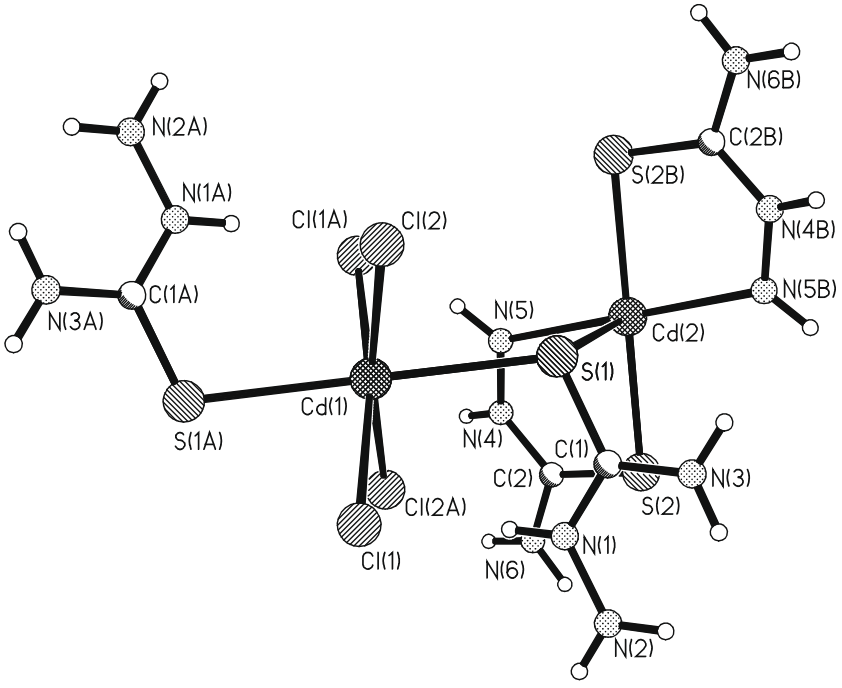


Fig. 2. Structure of complex **B**.

S(2)–N′(2) 3.395 Å). It is interesting to note the effect of the chelation of the thiosemicarbazide ligand on the length of the Cd–S bond. In both structures chelation results in a Cd–S bond length of 2.585(3) Å, whereas the non-chelate has a bond length of 2.860(3) Å. Selected bond lengths and bond angles for both complexes are shown in Tables 2 and 3, respectively.

3.1.2. Thermal analysis of the precursors

The thermogravimetric (TGA) decomposition data for both the precursors is shown in Fig. 4. The major difference in the decomposition profiles of the two compounds is difference of *ca.* 50 °C in the major decomposition step. Complex **A** showed major decomposition at 200 °C, which is attributed to the loss of the thiosemicarbazide ligand. Complex **B** showed an initial mass loss of approximately 4.5%, which is associated with the loss of water (4.9% calculated). Thereafter, **B** showed major decomposition starting at approximately 250 °C. The decomposition of both precursors continued gradually up to about 500 °C. The difference shown by the complexes upon decomposition is most likely an effect of the structural changes, which could explain why different nanomaterials of different phases were formed. The decomposition patterns, however, seem consistent with two compounds which have very

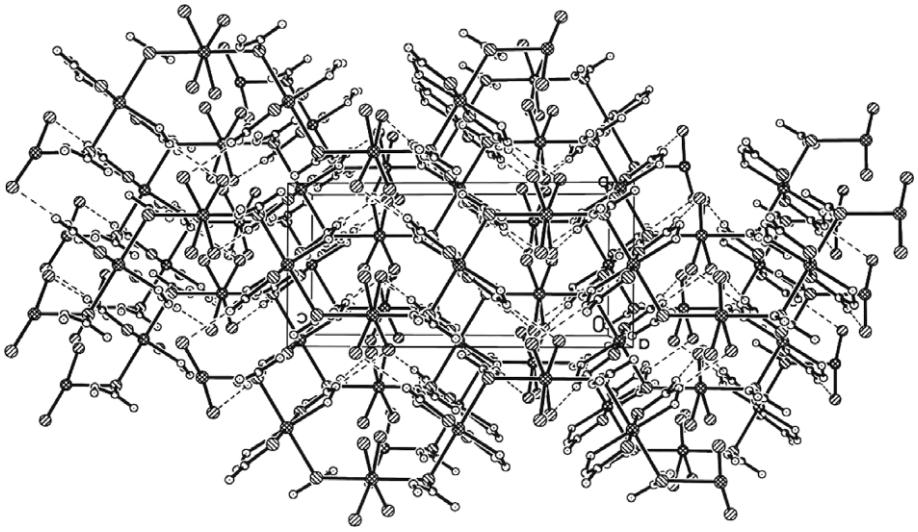


Fig. 3. Packing diagram of complex **B**.

Table 2
Selected bond lengths for complexes **A** and **B**.

Complex A	Length (Å)	Complex B	Length (Å)
Cd(1)–N(2)	2.407(8)	Cd(1)–Cl(2)	2.6252(9)
Cd(1)–Cl(2)	2.511(2)	Cd(1)–Cl(2)	2.6252(9)
Cd(1)–S(1)	2.585(3)	Cd(1)–Cl(1)	2.6318(9)
Cd(1)–Cl(1)	2.629(3)	Cd(1)–Cl(1)	2.6318(9)
Cd(1)–Cl(1)	2.648(3)	Cd(1)–S(1)	2.7351(1)
Cd(1)–S(1)	2.860(3)	Cd(1)–S(1)	2.7351(1)
Cd(1)–N(2)	2.407(8)	Cd(2)–N(5)	2.343(2)
Cd(1)–Cl(2)	2.511(2)	Cd(2)–N(5)	2.343(2)
Cd(1)–S(1)	2.585(3)	Cd(2)–S(2)	2.5886(1)
		Cd(2)–S(2)	2.5886(1)
		Cd(2)–S(1)	2.8621(1)
		Cd(2)–S(1)	2.8621(1)

Table 3
Selected Bond Angles for compounds **A** and **B**.

Complex B	Angle (°)	Complex A	Angle (°)
N(2)–Cd(1)–Cl(2)	92.71(2)	Cl(2)–Cd(1)–Cl(2)	87.59(4)
N(2)–Cd(1)–S(1)	76.03(2)	Cl(2)–Cd(1)–Cl(1)	171.058(2)
Cl(2)–Cd(1)–S(1)	167.73(7)	Cl(2)–Cd(1)–Cl(1)	89.60(3)
N(2)–Cd(1)–Cl(1)	163.94(2)	Cl(2)–Cd(1)–Cl(1)	89.60(4)
Cl(2)–Cd(1)–Cl(1)	100.27(8)	Cl(2)–Cd(1)–Cl(1)	171.060(2)
S(1)–Cd(1)–Cl(1)	90.11(7)	Cl(1)–Cd(1)–Cl(1)	94.40(4)
N(2)–Cd(1)–Cl(1)	92.2(2)	Cl(2)–Cd(1)–S(1)	89.99(2)
Cl(2)–Cd(1)–Cl(1)	94.08(8)	Cl(2)–Cd(1)–S(1)	90.13(2)
S(1)–Cd(1)–Cl(1)	91.25(1)	Cl(1)–Cd(1)–S(1)	81.53(2)
Cl(1)–Cd(1)–Cl(1)	96.21(1)	Cl(1)–Cd(1)–S(1)	98.36(2)
N(2)–Cd(1)–S(1)	86.3(2)	Cl(2)–Cd(1)–S(1)	90.13(2)
Cl(2)–Cd(1)–S(1)	83.68(8)	Cl(2)–Cd(1)–S(1)	89.99(2)
S(1)–Cd(1)–S(1)	90.64(1)	Cl(1)–Cd(1)–S(1)	98.36(2)
Cl(1)–Cd(1)–S(1)	85.82(9)	Cl(1)–Cd(1)–S(1)	81.53(2)
Cl(1)–Cd(1)–S(1)	177.22(5)	S(1)–Cd(1)–S(1)	179.84(3)
		N(5)–Cd(2)–N(5)	180.00(1)
		N(5)–Cd(2)–S(2)	78.24(6)
		N(5)–Cd(2)–S(2)	101.76(6)
		N(5)–Cd(2)–S(2)	101.76(6)
		N(5)–Cd(2)–S(2)	78.24(6)
		S(2)–Cd(2)–S(2)	180/00(1)
		N(5)–Cd(2)–S(1)	86.62(7)
		N(5)–Cd(2)–S(1)	93.37(7)
		S(2)–Cd(2)–S(1)	85.86(2)
		S(2)–Cd(2)–S(1)	94.14(2)
		N(5)–Cd(2)–S(1)	93.38(7)
		N(5)–Cd(2)–S(1)	86.63(7)
		S(2)–Cd(2)–S(1)	94.14(2)
		S(2)–Cd(2)–S(1)	85.86(2)
		S(1)–Cd(2)–S(1)	180.00(2)

similar structures and nominal formulae. The mechanism in which the CdS nanomaterials are formed is perhaps by the decomposition process. An overall ~50% mass loss is consistent with the formation of CdS, and it would appear that at 500 °C neither precursors approach this degree of decomposition. It does however seem likely that some $CdCl_2$ would also be formed and that the decomposition of this would require the higher temperatures. In the nanoparticle synthesis experiments the formation of $CdCl_2$ would not be a problem as it seems likely that it would be dissolved in the reaction media.

3.2. Preparation of CdS nanomaterials

The complexes were both decomposed in hexadecylamine at 180 °C for 30 min. In each case a pale yellow product was isolated. The UV absorption spectra (Fig. 5) were recorded and showed a significant blue shift in the band edge compared to that for bulk CdS (515 nm) (for materials synthesized using complex **A** the band edge was at 418 nm, and using complex **B** at 430 nm). The photoluminescence spectra (Fig. 5) both showed a large broad peak at 500 nm, which is consistent with the traps/defects in cadmium sulfide. Powder XRD of the materials showed a significant difference between the two products (Fig. 6). The product from complex **A** gave the typical hexagonal diffraction pattern (JCPDS 41–1049). However, the diffraction pattern for **B** was more difficult to interpret. On an initial examination, the pattern seems close to cubic, typified by the absence of the {1 0 2} and {1 0 3} lines. The sharp diffraction line at $2\theta = 25°$ cannot be ignored, as it is consistent with the {1 0 0} plane for the hexagonal form of CdS. The p-XRD results can be best understood in light of the morphology of the material (Figs. 7 and 8). In both cases there is a predominance of anisotropic material. Whilst the aspect ratios of the materials are approximately the same, there is a significant difference in the widths of the rods. Compound **A** gave rods with widths approaching the Bohr radius of 6.0 nm (±1.5 nm), however compound **B** results in rods with significantly smaller widths of 3.0 nm (±0.5 nm). These rod widths are consistent with the observed UV absorption spectra. Furthermore measurement of the lattice spacing of the rods leads to the conclusion that the long axis is the *c*-axis of the unit cell. If the p-XRD patterns are considered in light of this data, it may be seen that diffraction from the {1 0 0} planes will

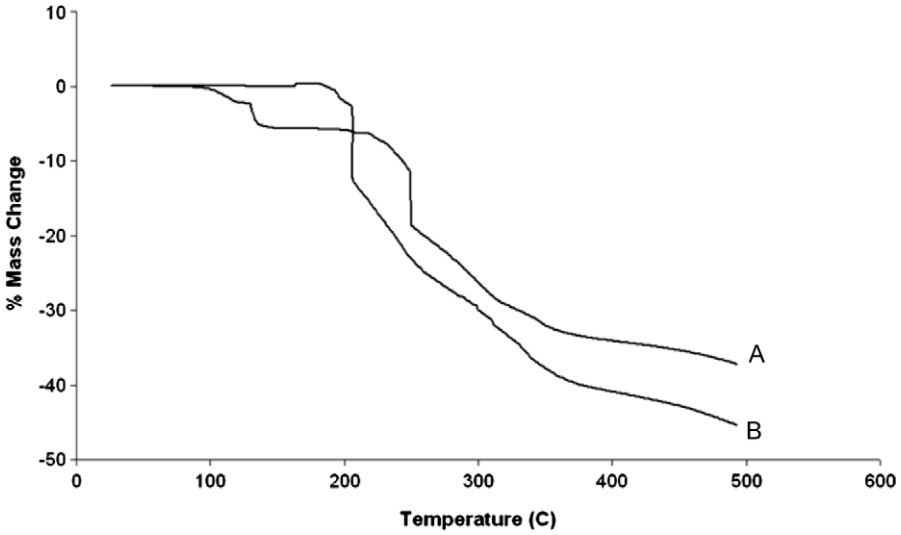


Fig. 4. TGA plots for the decomposition of **A** and **B** under nitrogen.

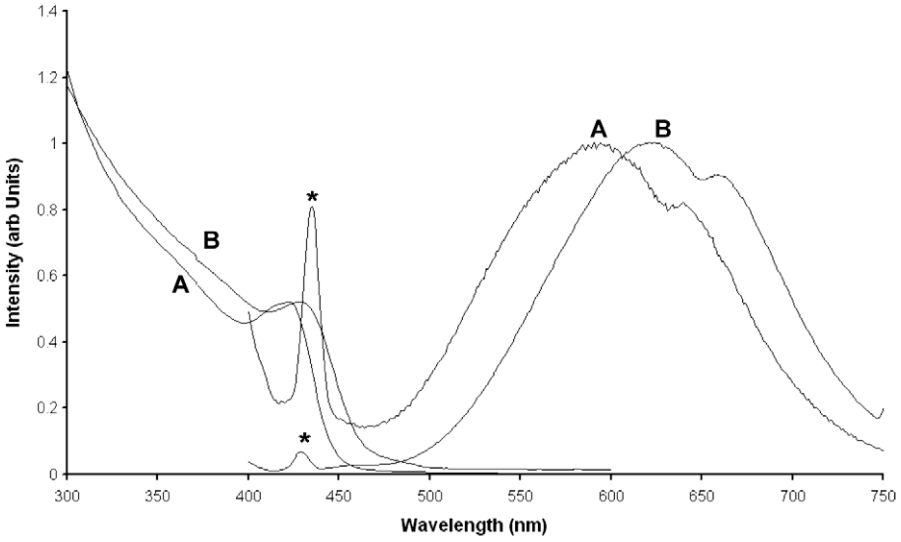


Fig. 5. UV and PL spectra of nanorods in chloroform. Absorption at approximately 425 nm, emission at approximately 600 nm. *Toluene Raman band.

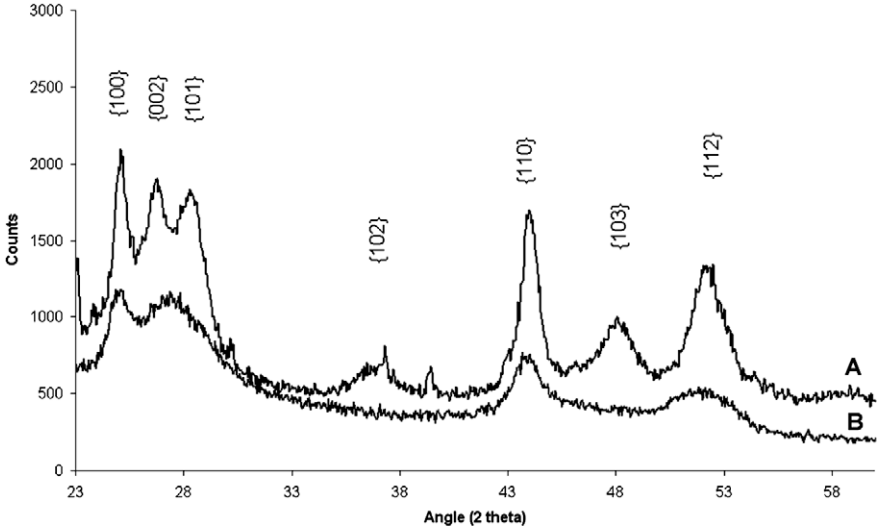


Fig. 6. XRD of CdS rods prepared from complexes **A** and **B** with hexagonal lattice planes marked.

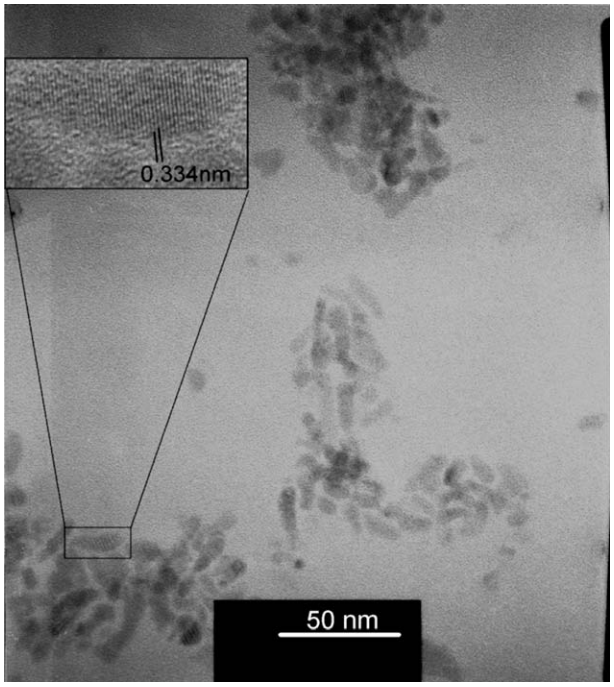


Fig. 7. TEM of nanorods prepared from complex **A** at 180 °C in HDA.

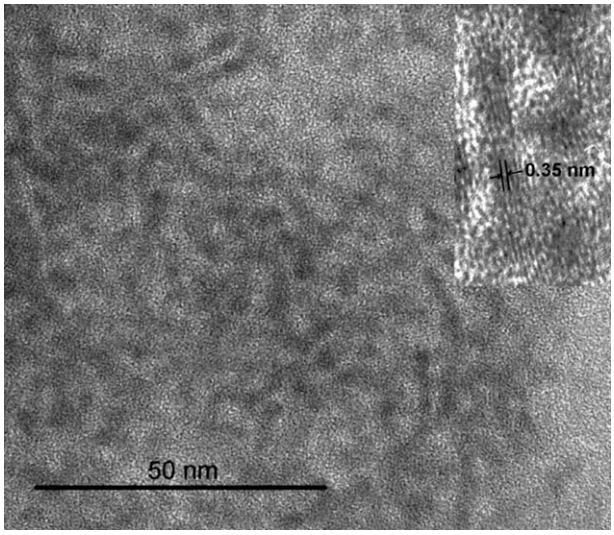


Fig. 8. TEM of nanorods prepared from complex **B** at 180 °C in HDA.

approximate to an infinite lattice much more closely than planes with contributions from an orthogonal axis. Taking this into account one would expect to see a broadening of the {0 0 2} and {1 0 1} lines as well as the {1 1 0} and {1 1 2} lines. Furthermore the broadening of the {1 1 2} line should be greater than that for the {1 1 0} line, as is observed here in sample **A**.

4. Conclusions

Cadmium thiosemicarbazide complexes are useful precursors for the preparation of anisotropic cadmium sulfide nanomaterials. Furthermore the nature of the precursor and the ease of thermal decomposition can significantly affect the morphology of the final products.

5. Supplementary data

CCDC 602904 and 602905 contain the supplementary crystallographic data for this paper. These data can be obtained free of charge via http://www.ccdc.cam.ac.uk/conts/retrieving.html, or from the Cambridge Crystallographic Data Centre, 12 Union Road, Cambridge CB2 1EZ, UK; fax: (+44) 1223-336-033; or e-mail: deposit@ccdc.cam.ac.uk.

Acknowledgements

We would like to thank the EPSRC, RCUK and the NRF South Africa for funding, that made this work possible.

References

[1] X.G. Peng, L. Manna, W.D. Yang, J. Wickham, J. Scher, A. Kadavanich, A.P. Alivisatos, Nature 404 (2000) 59.
[2] C.-C. Chen, C.-Y. Chao, Z.-H. Lang, Chem. Mater. 12 (2000) 1516.
[3] S.D. Bunge, K.M. Krueger, T.J. Boyle, M.A. Rodriguez, T.J. Headley, V.L. Colvin, J. Mater. Chem. 13 (2003) 1705.
[4] H. Zhang, X. Ma, J. Xu, D. Yang, J. Cryst. Growth 263 (2004) 372.
[5] X. Wu, Y. Tao, J. Cryst. Growth 242 (2002) 309.
[6] O. Conde, A.G. Rolo, M.J.M. Gomes, C.R. Ricolleau, D.J. Barber, J. Cryst. Growth 247 (2003) 371.
[7] P. Christian, P. O'Brien, Chem. Commun. (2005) 2817.
[8] Z. Peng, X. Peng, J. Am. Chem. Soc. 124 (2002) 3343.
[9] P.J. Thomas, P. O'Brien, J. Am. Chem. Soc. 128 (17) (2006) 5615.
[10] P. Christian, P. O'Brien, J. Chem. Commun. (2005) 2817.
[11] Y. Li, X. Li, C. Yang, Y. Li, J. Mater. Chem. 13 (2003) 2641.
[12] P.S. Nair, T. Radhakrishnan, N. Revaprasadu, G.A. Kolawole, P. O'Brien, Chem. Commun. (2002) 564.
[13] J.A. Ascencio, P. Santiago, L. Rendon, U. Pal, Appl. Phys. A 78 (2004) 5.
[14] J. Joo, H.B. Na, T. Yu, J.H. Yu, Y.W. Kim, F. Wu, J.Z. Zhang, T. Hyeon, J. Am. Chem. Soc. 125 (2003) 11100.
[15] Y. Li, X. Li, C. Yang, Y. Li, J. Mater. Chem. 13 (2003) 2631.
[16] X. Ge, Y. Ni, Z. Zang, Rad. Phys. Chem. 64 (2002) 223.
[17] B.A. Simmons, S. Li, V.T. John, G.L. McPerson, A. Bose, W. Zhou, J. He, Nanoletters 2 (2002) 263.
[18] Y. Tian, C. Duan, C. Zhao, X. You, T.C.W. Mak, Z. Zhang, Inorg. Chem. 36 (1997) 1247.
[19] S.X. Dou, M.H. Jiang, Z.S. Zhao, X.T. Tao, Appl. Phys. Lett. 54 (12) (1999) 1989.
[20] D. Xu, X.T. Tao, M.H. Jiang, Z.S. Shao, Rengonjingti (Chinese) 16 (1987) 1.
[21] X.T. Tao, N. Zhang, D. Yuan, D. Xu, W. Yu, M. Jiang, Non-linear Opt. Prop. Org. Mater. III (1990) 835.
[22] D.S. Mahadevappaan, A.S. Anandamurthy, Aust. J. Chem. 25 (1972) 1565.
[23] R.E. Ballard, D.B. Powell, U.A. Jayasooriya, Acta Crystallogr., Sect. B 30 (1974) 1111.
[24] F. Nicolo, H. El Ghaziri, G. Capuis, Acta Crystallogr., Sect. C 44 (1988) 975.
[25] J. Cosier, A.M. Glazer, J. Appl. Crystallogr. 19 (1986) 105.
[26] SHELXL-PC Package, Bruker Analytical X-ray Systems, Madison, WI, 1998.
[27] P.S. Nair, T. Radhakrishnan, N. Revaprasadu, G.A. Kolawole, P. O'Brien, Chem. Commun. (2002) 564.
[28] M.K. Woode, R.F. Bryan, D.A. Bekoe, Acta Crystallogr., Sect. C 43 (1987) 2324.

Polyhedron 28 (2009) 2103–2112

Contents lists available at ScienceDirect

Polyhedron

journal homepage: www.elsevier.com/locate/poly

Synthesis and structures of nickel(II) and copper(II) compounds of 5,5,7,13-tetramethyl-13-nitro-1,4,8,11-tetraazacyclotetradecane and the 13-ethyl-5,5,7-trimethyl-homologue

Neil F. Curtis [a,*], Kelly Flood [b], Ward T. Robinson [b,c], Joyce M. Waters [d]

[a] School of Chemical and Physical Sciences, Victoria University of Wellington, Box 600, Wellington 6140, New Zealand
[b] Chemistry Department, University of Canterbury, Christchurch, New Zealand
[c] Chemistry Department, University of Malaya, Kuala Lumpur, Malaysia
[d] Institute of Fundamental Sciences – Chemistry, Albany Campus, Massey University, Auckland, New Zealand

ARTICLE INFO

Article history:
Received 4 December 2008
Accepted 13 February 2009
Available online 3 March 2009

Keywords:
Nicke(II) compound
Copper(II) compound
Cyclic tetraamine
Tetraaza macrocycle
Oxalato chain-polymer
Tetrachlorozincate(II)
Aquotrichlorozincate(II)
Crystal structure

ABSTRACT

Reduction by $NaBH_4$ of the imine functions of (5,7,7,13-tetramethyl-13-nitro-1,4,8,11-tetraazacyclotetradec-4-ene)-nickel(II) and -copper(II), and of their 13-ethyl-5,7,7-trimethyl-homologues, yield the nitro-substituted cyclic tetraamine cations (5,5,7,13-tetramethyl-13-nitro-1,4,8,11-tetraazacyclotetradecane)-nickel(II) and -copper(II), $[M(neh)]^{2+}$, and (13-ethyl-5,5,7-trimethyl-homologues, $[M(nph)]^{2+}$, respectively. The nickel(II) cations form square–planar, singlet ground, state salts with poorly coordinating anions and octahedral, triplet ground state, compounds with additional ligands, *trans*-β-$[Ni(neh)A_2]$, $A^- = Cl^-$, NCS^- and *trans*-β-$[Ni(neh)A_2](ClO_4)_2$, X = NH_3, MeCN, all with nitrogen configuration III, 1*R*,4*R*,8*S*,11*S* = β. With oxalate the chain-polymeric compound *catena-trans*-β-$[Ni(neh)(\mu\text{-}C_2O_4)]_n \cdot 3n(H_2O)$ is formed. Folded macrocycle compounds *cis*-α-$[Ni(neh)(C_5H_7O_2)]ClO_4$ and *cis*-α-$[\{Ni(neh)\}_2(C_2O_4)](ClO_4)_2$ are formed with the chelates acetylacetonate and oxalate, with configuration 1*R*,4*R*,8*R*,11R = α. These react with $HClO_4$ to form metastable α-$[Ni(neh)](ClO_4)_2$ with retention of configuration. The copper(II) cations form crimson salts with poorly coordinating anions and compounds of the type β-[Cu(neh)A]ClO_4 of varying shades of blue with coordinating anions. Structures of singlet ground state square–planar nickel(II) compounds β-$[Ni(neh)](ClO_4)_2 \cdot H_2O$, β-$[Ni(neh)](ClO_4)_2$, β-$[Ni(neh)]_2[ZnCl_3(OH_2)]_2[ZnCl_4] \cdot H_2O$ and α-$[Ni(neh)](ClO_4)_2$, the triplet ground state chain-polymeric compound *catena-trans*-β-$[Ni(neh)(\mu\text{-}C_2O_4)]_n \cdot 3n(H_2O)$ and of square–pyramidal β-$[Cu(nph)Cl]ClO_4$ are reported.

© 2009 Elsevier Ltd. All rights reserved.

1. Introduction

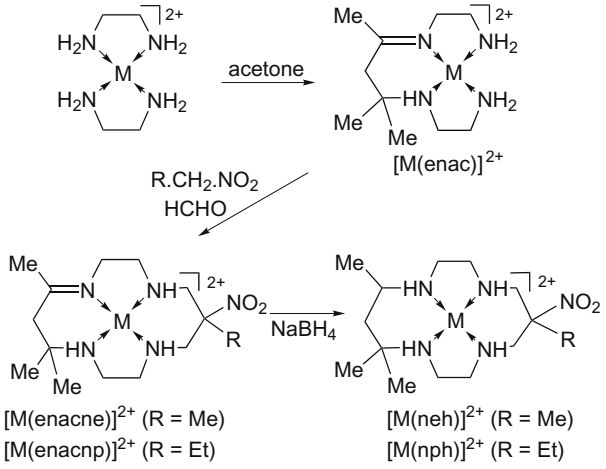
Numerous metal-ion azamacrocycle compounds have been prepared by ring-closing Mannich-like reactions of the terminal primary amine groups of linear amine complexes with methanal plus a diprotic carbon acid [1–3]. Reactions with methanal plus nitroalkanes, R–CH_2–NO_2, link terminal NH_2 groups of polyamines by forming a 1,5-diaza chelate ring with 3*R*,3-nitro substituents. Complexes of linear tetraamines react to give cyclic tetraamine products with single (nitro plus alkyl) substituents and structures have been reported for the copper(II) compounds with 13–16-membered macrocyclic rings [4–8].

Metal-ion amine–imine compounds, including azamacrocycle compounds, have been prepared by condensation reactions of metal amine complexes with acetone [9]. Reactions of bis(ethane-1,2-diamine)-nickel(II) or -copper(II) with acetone yield (4,6,6-trimethyl-3,7-diazanon-3-ene-1,9-diamine)-nickel(II) or -copper(II), $[M(enac)]^{2+}$ [10,11], which react with methanal and nitroethane (or nitropropane) to yield the nitro-substituted imine–triamine azamacrocyclic cations (5,7,7,13-tetramethyl-13-nitro-1,4,8,11-tetraazacyclotetradec-4-ene)-nickel(II) or -copper(II), $[M(enacne)]^{2+}$ {or from nitropropane (13-ethyl-5,7,7-trimethyl-13-nitro-1,4,8,11-tetraazacyclotetradec-4-ene)-nickel(II) or -copper(II), $[M(enacnp)]^{2+}$} [12–14], see Scheme 1.

Structures have been determined for $[Ni(enacne)][ZnCl_4]$ [12], $[Cu(enacnp)(OH_2)](ClO_4)_2$ [13], $[Cu(enacnp)][Ni(CN)_4] \cdot H_2O$ [14] and $[Cu(enacne)(NCS)]ClO_4 \cdot H_2O$ [15]. The structures of $[Ni(enacne)][ZnCl_4]$, $[Cu(enacnp)(OH_2)](ClO_4)_2$ and $[Cu(enacne)(NCS)]ClO_4 \cdot H_2O$ have disorder manifest as superimposed 5,7,7-trimethyl-4-ene and 5,5,7-trimethyl-7-ene structures, with disorder of the N4 or N8 location of the imine function and of the C5 or C7 location of the *gem*-dimethyl function. This was attributed to co-crystallisation of enantiomers arising from the C13 chiral centre [12].

* Corresponding author. Tel.: +64 4463 6514; fax: +64 4 463 5237.
E-mail address: neil.curtis@vuw.ac.nz (N.F. Curtis).

0277-5387/$ - see front matter © 2009 Elsevier Ltd. All rights reserved.
doi:10.1016/j.poly.2009.02.019



Scheme 1. Preparations of $[M(enac)]^{2+}$, $[M(neh)]^{2+}$ and $[M(nph)]^{2+}$, M = Ni(II), Cu(II).

In this communication, the preparations and properties of compounds of nitro-substituted cyclic tetraamines formed by the reduction of the imine functions of $[M(enacne/np)]^{2+}$ cations by $NaBH_4$ are described, and the structures of compounds of the resulting nitro-substituted cyclic tetraamines neh and nph are reported.

2. Results

Reduction by $NaBH_4$ of $[Ni(enacne)]^{2+}$, $[Ni(enacnp)]^{2+}$, $[Cu(enacne)]^{2+}$ and $[Cu(enacnp)]^{2+}$ as perchlorate salts, was studied in a variety of solvents. The imine functions were reduced leaving the nitro functions unaffected, forming the cyclic tetraamine cations $[Ni(neh)]^{2+}$, $[Ni(nph)]^{2+}$, $[Cu(neh)]^{2+}$ and $[Cu(nph)]^{2+}$ respectively, see Scheme 1.

The properties of the these cations are generally similar to those of their amine–imine analogues, $[M(enacne)]^{2+}$ and $[M(enacnp)]^{2+}$ [12–15].

The nickel(II) cations form orange coloured singlet ground state salts with poorly coordinating anions (such as perchlorate or chlorozincates) with nitrogen configurations III [16], 1*RS*,4*RS*,8*SR*,11*SR*, labeled as β. The cations coordinate additional ligands to form triplet ground state octahedrally coordinated compounds. With unidentate coordinating anions the cations form *trans*-compounds, also with configuration III, (e.g. *trans*-β-$[Ni(neh)(NCS)_2]$ and *trans*-β-$[Ni(neh)Cl_2]$). Crimson β-$[Ni(neh)(NH_3)_2](ClO_4)_2$, which separates from concentrated ammonia solution, loses the ammonia on exposure to the atmosphere. A grey–green bis(acetonitrile) adduct which crystallises from acetonitrile slowly loses the acetonitrile on exposure to the atmosphere. A grey–green-coloured chain-polymeric μ-oxalato compound, *catena*-β-$[Ni(neh)(\mu\text{-}C_2O_4)]_n \cdot 3n(H_2O)$ crystallises when oxalate is added to a neutral aqueous solution of $[Ni(neh)](ClO_4)_2$.

With the chelates oxalate and pentane-2,4-dionate the water-insoluble blue-coloured compounds *cis*-α-$[Ni(neh)(acac)]ClO_4$ and *cis*-α-$[\{Ni(neh)\}_2(C_2O_4)](ClO_4)_2$ are formed. These have the macrocycle folded with nitrogen configuration V, 1*RS*,4*RS*,8*RS*,11*RS*, labeled as α. Reaction of α-$[Ni(neh)(acac)]ClO_4$ with acid yields a solution containing metastable α-$[Ni(neh)]^{2+}$. The very slow interconversion between the nitrogen configurations in acid solution enabled preparation of metastable square–planar α-$[Ni(neh)](ClO_4)_2$. Similar reactions have been observed for other nickel(II) tetraaza macrocycle compounds [17–20].

The copper(II) cations form dark red salts with poorly coordinating anions, and with coordinating anions form compounds of various shades of blue, such as $[Cu(neh)X]ClO_4$, $X = Cl^-$, NCS^- or NO_2^-.

3. Structural studies

See Section 5.2 for crystallographic details.

Slow crystallisation of the perchlorate salt of $[Ni(neh)]^{2+}$ from water gave dark-orange coloured crystals of the monohydrate **3.1**. More rapid crystallization from water, or crystallization from organic solvents, gave light orange coloured crystals of the unhydrated salt, which has a poorly ordered structure **3.2**, which is described in the Supplementary data.

Attempts to prepare the tetrachlorozincate salt gave a product with an unusual stoichiometry, shown for structure **3.3** to have both tetrachlorozincate(II) and aqua-trichlorozincate(II) anions. The structure **3.5** is of a chain-polymeric compound with $Ni(neh)^{2+}$ cations linked by oxalate ions. The metastable square–planar compound α-$[Ni(neh)](ClO_4)_2$ is reported as structure **3.4**. The poorly ordered structure **3.6** of square–pyramidal β-$[Cu(nph)Cl]ClO_4$ is described in the Supplementary data.

3.1. The structure of 1RS,4RS,7RS,8SR,11SR,13RS-(5,5,7,13-tetramethyl-13-nitro-1,4,8,11-tetraazacyclotetradecane)nickel(II) perchlorate hydrate, β-$[Ni(neh)](ClO_4)_2 \cdot H_2O$

The asymmetric unit of this compound consists of two singlet ground state nickel(II) cations, four perchlorate anions and two water molecules. See Fig. 1 for a view of the asymmetric unit. The nickel(II) ions are in square–planar coordination by the four secondary amine nitrogen atoms of the cyclic tetraamine 5,5,7,13-tetramethyl-13-nitro-1,4,8,11-tetraazacyclotetradecane. Cation 1 has Ni1 and ring atoms N1–C14, with water molecule including O1 weakly interacting in one axial site and cation 2 has Ni2, ring atoms N21–N34 and water O2. See Fig. 2 for a view of the cation 1 and associated water molecule and Table 1 for dimensions of the cations.

The cations show small tetrahedral distortions of the N_4 donor group (r.m.s. displacements of N-atoms from the N_4 planes are ±0.043(1) Å for cation 1, with Ni1 0.0242(6) Å from the plane and ±0.047(1) Å for cation 2, with Ni2 0.0469(6) Å from the plane). The dimensions about the nickel(II) ions are normal for square–planar singlet ground state nickel(II), with all Ni–N distances similar, with mean Ni–N = 1.95(2) Å. The five-membered chelate rings

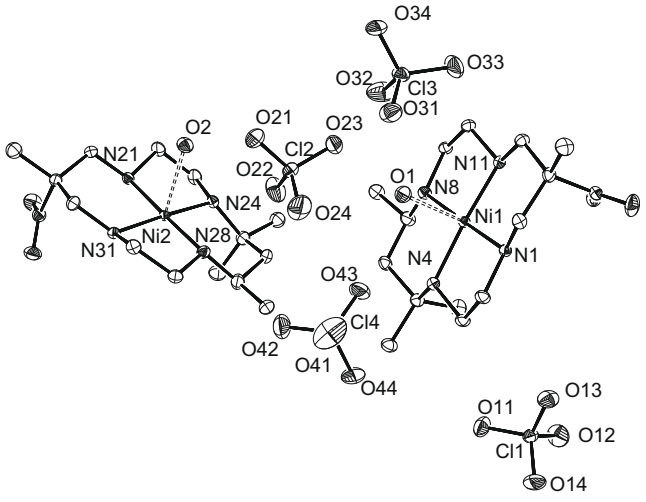


Fig. 1. The asymmetric unit for β-$[Ni(neh)](ClO_4)_2 \cdot H_2O$, drawn [30] with probability ellipsoids at the 50% confidence level, with hydrogen atoms omitted.

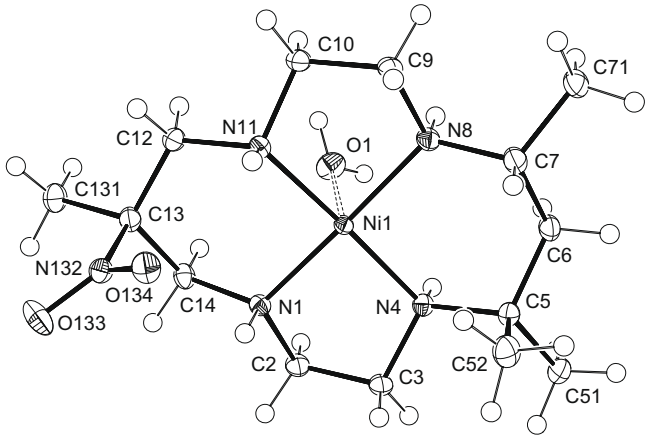


Fig. 2. The cation 1 and associated water molecule for β-[Ni(neh)]$(ClO_4)_2 \cdot H_2O$, drawn [30] as for Fig. 1, with hydrogen atoms shown as circles of arbitrary radius.

Table 1
Selected dimensions (Å, °) for β-[Ni(neh)]$(ClO_4)_2 \cdot H_2O$.

Atoms	Dimension	Atoms	Dimension
Ni1–N1	1.929(6)	Ni2–N21	1.943(5)
Ni1–N4	1.953(6)	Ni2–N24	1.949(5)
Ni1–N8	1.931(7)	Ni2–N28	1.957(6)
Ni1–N11	1.952(6)	Ni2–N31	1.954(5)
N1–Ni1–N4	87.0(3)	N21–Ni2–N24	86.4(2)
Ni1–O1	2.566(7)	Ni2–O2	2.592(7)
N1–Ni1–N8	178.2(3)	N21–Ni2–N28	179.1(2)
N1–Ni1–N11	92.0(2)	N21–Ni2–N31	94.7(2)
N4–Ni1–N8	93.6(3)	N24–Ni2–N28	92.8(2)
N4–Ni1–N11	178.0(3)	N24–Ni2–N31	178.7(2)
N8–Ni1–N11	87.5(3)	N28–Ni2–N31	86.2(2)

have asymmetric gauche conformations and the six-membered chelate rings both have chair conformations. The axially oriented C13-nitro substituent and the axial component of the C5-dimethyl group are oriented to the same side of the N_4 plane. Atomic displacements from NiN_2 chelate planes are listed in Table S1 in the Supplementary data.

The cations both have the 1*S*,4*S*,8*R*,11*R* nitrogen configuration III, usual for cyclam-like tetraamines in planar coordination, with approximate mirror symmetry (for cation 1 through C13, Ni1 and C6) apart from the axially oriented methyl substituent (C52)H_3 and nitro group (N132, O133, O134), and analogously for cation 2. The atoms C7 and C13 (and C27 and C33) are also chiral centres, C13 because of the different substitutions present at C5 and C7, with overall configuration 1*S*,4*S*,7*R*,8*R*,11*R*,13*R* for both cations.

The main difference between the two cations is in the orientation of the nitro groups, which is apparently determined by local hydrogen bonding. For cation 1 the nitro group is aligned approximately with the direction N11···C13, while for cation 2 the nitro group is aligned approximately normal to Ni2···C23 (with O131···C14 = 2.68 Å and O132···C14 = 2.75 Å).

The cations each occur as inversion related pairs in the unit cell, linked by a hydrogen bond (N1–H1···O132 ($-x$, $-y$, $-z$) or N21–H21···O232 ($-x$, $-y$, $-z$). The closest axial approach to each nickel ion is by a water molecule (including O1 for Ni1 and O2 for Ni2), on the side of the NiN_4 'plane' remote from the axial methyl and nitro groups (angles O–Ni–N range from 88.49(5) to 92.95(5)° for Ni1 and from 89.54(5) to 92.76(5)° for Ni2). The cations, anions and water molecules are linked by hydrogen bonding, listed in Table S2 of the Supplementary data. The structure shows no indication of the disorder in the location of the axial methyl substituents observed for structures **3.2, 3.3, 3.5** and **3.6.**

3.2. The structure of 1RS,4RS,7RS,8SR,11SR,13RS-(5,5,7,13-tetramethyl-13-nitro-1,4,8,11-tetraazacyclotetradecane)nickel(II) perchlorate, β-[Ni(neh)]$(ClO_4)_2$

Disorder of the perchlorate ions precluded a satisfactory structural solution for this compound, which is described more fully in the Supplementary data, with selected dimensions listed in Table S3 and hydrogen bonds in Table S4. The cations are similar to those of the previous compound, as shown in Fig. 1, but probably with disorder in location of the axial methyl group, arising from co-crystallisation of enantiomers. The compound unusually has three cations in the asymmetric unit, arranged in sequence in columns, as shown in Fig. 3. Poorly ordered perchlorate ions interleave with the cations, with weak axial interactions by the nickel(II) ions with perchlorate ion oxygen atoms.

3.3. The structure of bis-1RS,4RS,7RS,8SR,11SR,13RS-(5,5,7,13-tetramethyl-13-nitro-1,4,8,11-tetraazacyclotetradecane)nickel(II) bis(aquatrichlorozincate) tetrachlorozincate hydrate, β-[Ni(neh)]$_2$[$ZnCl_3(H_2O)$]$_2$[$ZnCl_4$] · H_2O

The asymmetric unit of this orange coloured, singlet ground state, compound contains two square–planar (tetraazamacrocycle)nickel(II) cations, labeled as for **3.1**, three anions and an independent water molecule including O1. One anion is a tetrachlorozincate(II) ion (including zinc atom Zn1 and chloride ions Cl11–Cl14) while the other two anions are aqua-trichlorozincate(II) ions (one including Zn2, water oxygen O2 and chloride ions Cl21–Cl23 and the other including Zn3, water oxygen atom O3 and partial occupancy chloride ions Cl31–Cl36). See Table 2 for dimensions and Fig. 4 for a view of the asymmetric unit.

The two cations have generally similar structures; similar to the cation shown in Fig. 1, though their environments differ. The dimensions about the nickel(II) ions are normal for square–planar singlet ground state nickel(II), with all Ni–N distances similar, with

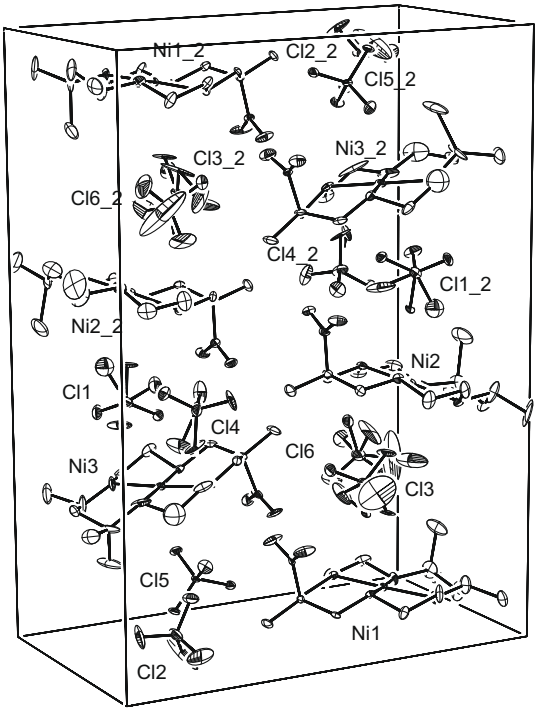


Fig. 3. View of β-[Ni(neh)]$(ClO_4)_2$ down the *b* axis of the unit cell, drawn [30] with ellipsoids at 30% probability, with hydrogen atoms omitted. The symmetry operation 2 = $-x$, $y + 1/2$, $-z$.

Table 2
Selected dimensions (Å, °) for β-[Ni(neh)]$_2$[ZnCl$_3$(H$_2$O)]$_2$[ZnCl$_4$] · H$_2$O.

Atoms	Dimension	Atoms	Dimension
Ni1–N1	1.929(6)	Ni2–N21	1.943(5)
Ni1–N4	1.953(6)	Ni2–N24	1.949(5)
Ni1–N8	1.931(7)	Ni2–N28	1.957(6)
Ni1–N11	1.952(6)	Ni2–N31	1.954(5)
N1–Ni1–N4	87.0(3)	N21–Ni2–N24	86.4(2)
N1–Ni1–N8	178.2(3)	N21–Ni2–N28	179.1(2)
N1–Ni1–N11	92.0(2)	N21–Ni2–N31	94.7(2)
N8–Ni1–N4	93.6(3)	N24–Ni2–N28	92.8(2)
N4–Ni1–N11	178.0(3)	N24–Ni2–N31	178.7(2)
N8–Ni1–N11	87.5(3)	N28–Ni2–N31	86.2(2)

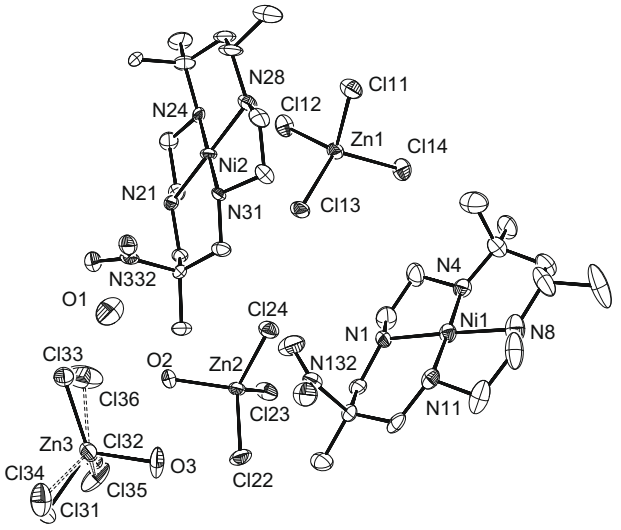


Fig. 4. The asymmetric unit for β-[Ni(neh)]$_2$[ZnCl$_3$(H$_2$O)]$_2$[ZnCl$_4$] · H$_2$O, drawn [30] as for Fig. 1.

mean Ni–N = 1.95(2) Å. The N$_4$ donor sets are near co-planar [r.m.s. displacements of N-atoms from N$_4$ planes are ±0.028(3) Å for the cation 1 and ±0.007(3) Å for the cation 2, with the Ni-atoms in-plane]. The angle between the two N$_4$ planes is 38.2(2)°. The cations have the configuration III of the coordinated nitrogen centres and a macrocycle conformation similar to that of the perchlorate salts, above, see Table S5 in the Supplementary data for displacements of atoms from the NiN$_2$ chelate planes.

When the structure was refined with an initially assumed 5,5,7-trimethyl structure of the cations then significant residual electron density was present in the axial substitution sites of both C7 and C27, while the freely refined site occupation factor (sof) of the axial methyl groups (C52)H$_3$ and (C252)H$_3$ were ca. 0.7. These residual peaks were assigned as partial occupancy axial methyl groups (C72)H$_3$ and (C272)H$_3$, as described elsewhere [12,21]. Refinement with complementary sof for (C52)H$_3$ and (C72)H$_3$, {and also C252)H$_3$ and (C272)H$_3$}, i.e. with superimposed 5,5,7-trimethyl and 5,7,7-trimethyl arrangements, led to the sof for (C52)H$_3$ of 0.70(2) and for (C72)H$_3$ of 0.30(2) for the cation 1, and with corresponding values of 0.72(2) and 0.28(2) for the cation 2.

The configuration of the major disorder component for both cations is 1*S*,4*S*,7*S*,8*R*,11*R*,13*R* and that of the minor component is 1*R*,4*R*,7*R*,8*S*,11*S*,13*S* (after renumbering as 5,5,7-trimethyl- to comply with IUPAC nomenclature) so the disorder components are enantiomers arising from the chiral centres C13 and C33, respectively.

Apart from the axial methyl group, the cations have approximate mirror symmetry through C13, C131, N15, Ni and C6 (or through C23, C231, N25, Ni2 and C26) respectively. The five-membered chelate rings have asymmetrical gauche conformations. The 13-methyl-13-nitro-substituted chelate rings have chair conformations, with the nitro substituent axially oriented. The trimethyl-substituted chelate rings also have chair conformations with the axially oriented methyl substituent oriented to the same side of the N$_4$ plane as the nitro substituent. The nitro-substituents are aligned approximately normal to the direction Ni···C13. The conformations of the macrocycles for the two cations are generally similar, but differ in detail, indicating the flexibility of these rings, with details of conformation determined by the environment.

The cations including Ni2 occur in the unit cell as inversion related pairs, with Ni2···Ni2 (−*x* + *1*, −*y* + *1*, −*z* + *1*) = 6.792(2) Å, linked by N–H···O–N inter-pair hydrogen bonds (as also observed for [Ni(enacne)][ZnCl$_4$] [12]). Close approaches of partial occupancy axial methyl substituents, C52···C72 (−*x*, −*y* + *1*, −*z* + *1*) = 2.37(2) Å, implies correlation of the site occupancies. The cations including Ni1 also occur as inversion related pairs, but the macrocycle cations are "back to back", with Ni1···Ni1 (−*x* + *1*, −*y* + *1*, −*z* + *1*) = 8.582(2) Å. There is no close interaction between the axial methyl substituents for the pairs for these cations.

The nickel(II) ions have only distant axial interactions: Ni1···Cl23 (*x*, *y* + *3/2*, −*z* + *1/2*) = 3.269(2); Ni1···Cl14 (*x*, *y* + *1/2*, −*z* + *1/2*) = 3.529(2); Ni2···Cl13 = 3.182(2) and Ni2···O333 (−*x* + *1*, −*y* + *1*, −*z* + *1*) = 3.622(5) Å.

The anions [(Zn1)Cl$_4$]$^{2-}$ and [(Zn2)Cl$_3$(OH$_2$)]$^-$ have approximately tetrahedral geometries. The anion [(Zn3)Cl$_3$(OH$_2$)]$^-$ shows disorder, which was modeled with two sets of three chloride ions, refined with complementary sof, arranged about the (Zn3)···(O3) axis, Cl31, Cl32 and Cl33 with sof = 0.75(2) and Cl34, Cl35 and Cl36 with sof = 0.25(2), with the sets rotated relatively by about 10°. There was no indication of similar disorder for the Zn2 anion. Bond lengths for the anions are in the ranges: Zn1–Cl, 2.240(2)–2.290(2); Zn2–O2, 2.022(5); Zn2–Cl, 2.230(2)–2.260(2); Zn3–O3, 2.024(6); Zn3–Cl (major components) 2.20(1)–2.284(4) Å.

The cations, anions and independent water molecule are linked by hydrogen bonds, listed in Table S6 of the Supplementary data.

3.4. The structure of 1RS,4RS,7SR,8RS,11RS,13RS-(5,5,7,13-tetramethyl-13-nitro-1,4,8,11-tetraazacyclotetradecane)nickel(II) perchlorate, α-[Ni(neh)](ClO$_4$)$_2$

The asymmetric unit of this orange compound consists of two (tetraazamacrocycle)nickel(II) cations, labeled as for structure **3.1**, and four perchlorate ions. The two cations have similar structures, with the nickel(II) ions in square–planar coordination by the four secondary amine nitrogen atoms of the macrocycle, the cation including Ni1 is shown in Fig. 5. The dimensions of the NiN$_4$O groups are normal for singlet ground state [Ni(tetraazamacrocycle)]$^{2+}$ cations, see Table 3. The Ni–N distances are similar, with mean value 1.932(8) Å, slightly shorter than the values for the configuration III cations of **3.1** and **3.3**. The N$_4$ donor groups show slight tetrahedral twisting, with r.m.s. displacements of ±0.066(3) Å for the N atoms and 0.014(2) Å for Ni1, with values ±0.018(3) and 0.018(2) Å for cation 2. A perchlorate ion oxygen atom interacts weakly in one axial coordination site for each cation (Ni1···O11 = 2.790(5), Ni2···O21 = 2.572(5) Å).

The cations are enantiomers, both with nitrogen configuration V of the secondary amine centres. Cation 1 has the 1*S*,4*S*,8*S*,11*S* configuration and cation 2 the 21*R*,24*R*,28*R*,31*R* configuration. This configuration is least strained for the azamacrocycle in folded coordination but is metastable in planar coordination, as it forces the macrocycle to adopt a non-optimum conformation, with the two six-membered chelate rings in twist conformations [17–20]. Displacements of atoms from the NiN$_2$ chelate planes are shown in Table 4, which should be compared with the values for the usual configuration III atomic displacements in Tables S1, S3 and S5.

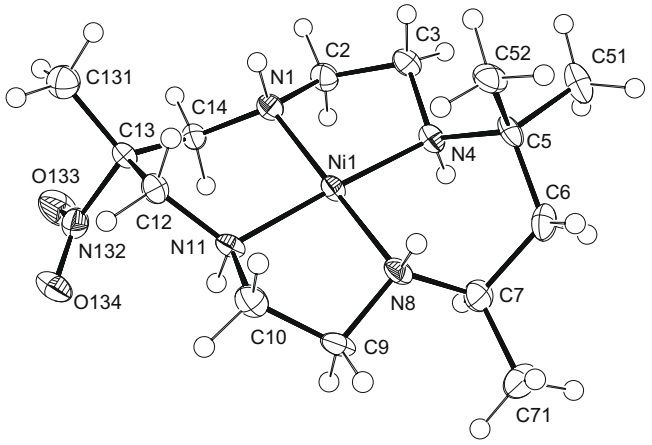


Fig. 5. The cation 1 for α-[Ni(neh)](ClO$_4$)$_2$, drawn as for Fig. 2.

Table 3
Selected dimensions for α-[Ni(neh)](ClO$_4$)$_2$.

Atoms	Distance (Å)	Atoms	Angle (°)
Ni1–N1	1.928(4)	N1–Ni1–N4	87.6(2)
Ni1–N4	1.938(4)	N1–Ni1–N8	176.8(2)
Ni1–N8	1.926(4)	N1–Ni1–N11	92.2(2)
Ni1–N11	1.932(4)	N4–Ni1–N8	93.5(2)
Ni1–O11	2.791(5)	N4–Ni1–N11	175.2(2)
Ni2–N21	1.932(4)	N8–Ni1–N11	87.0(2)
Ni2–N24	1.928(4)	N21–Ni2–N24	87.7(2)
Ni2–N28	1.926(4)	N21–Ni2–N28	176.4(2)
Ni2–N31	1.921(4)	N21–Ni2–N31	91.9(2)
Ni2–O21	2.569(5)	N24–Ni2–N28	93.3(2)
		N24–Ni2–N31	174.3(2)
		N28–Ni2–N31	87.4(2)

The conformation adopted orients the C51 and C71 methyl substituents equatorially and the C52 methyl substituent axially (and similarly for the C251, C271, C252 and C332 methyl groups), with the axially interacting perchlorate ion on the less crowded side, opposite to C52 (or C252). The C131 (C231) methyl and N132 (N332) nitro nitrogen atoms are approximately equally displaced from the NiN$_4$ plane, with the nitro groups oriented approximately normal to the Ni1···C13 (or Ni2···C133) directions. There is no indication of disorder in the location of the axial methyl substituents as observed for other [Ni(neh)]$^{2+}$ compounds.

Hydrogen bonds, which link the anions and cations, are listed in Table S7 of the Supplementary data.

3.5. The structure of catena-(bis(μ^2-oxalato-O,O')-1RS,4RS,7RS,8SR,11SR,13RS-(5,5,7,13-tetramethyl-13-nitro-1,4,8,11-tetraazacyclotetradecane)nickel(II)·trihydrate, catena-trans-[β-Ni(neh)(μ-C$_2$O$_4$)]$_n$ · 3n(H$_2$O)

This pale grey–green-coloured triplet ground state compound has a chain-polymeric structure, with square–planar β-[Ni(neh)]$^{2+}$ cations linked axially by bridging bis-unidentate oxalato groups. The asymmetric unit includes one azamacrocyclic nickel(II) cation, one bridging oxalate ion and three independent water molecules, see Figs. 6 and 7. The dimensions about the nickel(II) ion, shown in Table 5, are normal for triplet ground state octahedral Ni(II). The Ni1-O1 distance is slightly shorter than the Ni1-O2^A (symmetry operation A = x + 1/2, −y + 1/2, z + 1/2) distance although O1 is on the more crowded side of the macrocycle, towards which the axially oriented methyl and nitro-substituents are oriented. The N$_4$ group is near co-planar, with r.m.s tetrahedral twisting of ±0.001(1) Å, with Ni1 displaced by 0.039(1) Å from the plane towards O1. The five-membered chelate rings have gauche conformations and the six-membered chelate rings chair

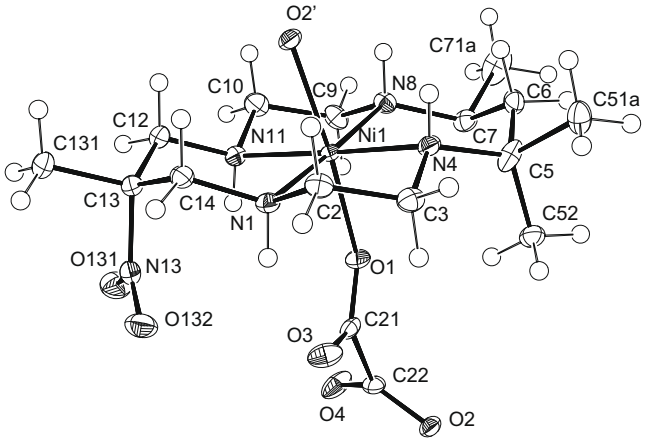


Fig. 6. The repeating unit for *catena*-β-[Ni(neh)(μ-C$_2$O$_4$)]$_n$ · 3n(H$_2$O), drawn [30] as for Fig. 1. Symmetry operation 4 = x + 1/2 − y + 1/2, z + 1/2.

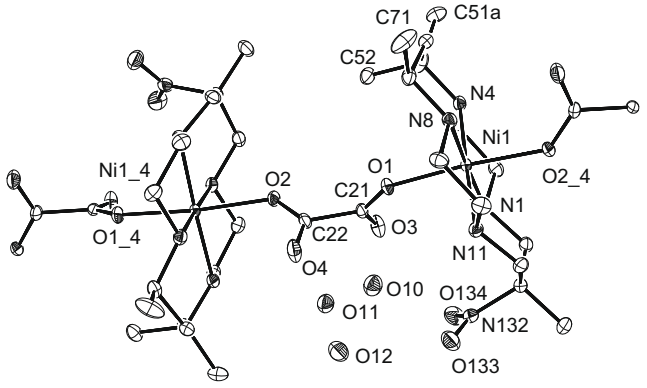


Fig. 7. The cation of *catena-trans*-β-[Ni(neh)(μ-C$_2$O$_4$)]$_n$ · 3n(H$_2$O), drawn [30] as for Fig. 2. Sites C52, C72, and C51 have partial occupancy, see text. Note the different orientation of the nitro group as compared with that in Fig. 2.

Table 4
Displacement (Å) of selected atoms from mean planes for α-[Ni(neh)](ClO$_4$)$_2$.

Plane	Atoms, displacement
Ni1, N1, N4	C2, 0.460(8); C3, −0.228(8)
Ni1, N8, N11	C9, 0.321(8); C10, −0.436(8)
Ni1, N4, N8	C5, −0.79(8); C6, −0.109(9); C7, 0.741(8); C51, −0.84(1); C52 −2.245(7); C71, 1.11(1)
Ni1, N1, N11	C12, −1.620(5); C13, −0.891(7); C14, 0.270(7); C131, −1.897(9);N132, −0.192(6); O133, 0.568(8); O134, −0.433(5)
Ni2, N21, N24	C22, −0.518(8);C23, 0.192(8)
Ni2, N28, N31	C29, −0.401(8); C30, 0.347(8)
Ni2, N24, N28	C25, 0.839(8); C26, 0.17(9); C27, −0.678(8); C251, 0.85(1); C252, 2.27(7); C271, −0.98(1)
Ni2, N21, N31	C32, 0.743(8); C33, 0.024(9); C34, −0.679(8); C331, 0.96(1); N332, −1.11(1); O333, 1.96(1); O334, −1.12(1)

Table 5
Selected dimensions (Å, °) for *catena-trans*-[β-Ni(neh)(μ-C_2O_4)]$_n$·3*n*(H_2O).

Atoms	Dimension	Atoms	Dimension
Ni1–N1	2.084(2)	N1–Ni1–N4	85.70(7)
Ni1–N4	2.084(2)	N1–Ni1–N8	177.71(7)
Ni1–N8	2.065(2)	N1–Ni1–N11	93.56(7)
Ni1–N11	2.083(2)	N4–Ni1–N8	94.55(7)
Ni1–O1	2.093(2)	N4–Ni1–N11	177.78(6)
Ni1–O2^A	2.142(2)	O1–Ni1–O2^A	174.61(6)
O1–C21	1.258(3)	N1–Ni1–O2^A	85.78(6)
O3–C21	1.246(3)	N4–Ni1–O2^A	88.90(6)
O2–C22	1.259(2)	N8–Ni1–O2^A	91.98(6)
O4–C22	1.254(3)	N11–Ni1–O2^A	88.97(6)
C21–C22	1.540(3)	O1–C21–O3	126.9(2)
N1–Ni1–O1	94.10(6)	O2–C22–O4	126.6(2)
N4–Ni1–O1	96.47(6)	O1–C21–C22	115.1(2)
N8–Ni1–O1	88.11(6)	O2–C22–C21	115.6(2)
N11–Ni1–O1	85.65(6)	O3–C21–C22	118.0(2)
Ni1^A–O2–C22	131.6(1)	O4–C22–C21	117.8(2)
		O133–N132–O134	123.7(2)

Symmetry operation A = $x + ½ - y + 1/2$, $z + ½$.

conformations, the overall conformation being similar to those of **3.1** and **3.3**, although the Ni–N distances are appreciably longer. The nitro group is aligned approximately normal to the C13···Ni1 direction. Displacements of atoms from NiN_2 chelate planes are listed in Table S8 of the Supplementary data.

As for the chlorozincate salt, **3.3**, the axial component of the *gem*-dimethyl group is disordered over sites axial with respect to ring atoms C5 and C7. The structure was refined with complementary sof for the two sites (sof of (C52)H_3 = 0.654(5)), with the disorder attributed to the presence of the enantiomers in ca. 2:1 proportions. The disorder components have the NH–C(Me)$_2$–CH_2CH(Me)–NH chelate ring reversed, which would be expected to lead to some disorder of all the atoms of the chelate ring. Site (C51)H_3 was resolved into sites (C51A)H_3 and (C51B)H_3, which were refined with the same complementary sof.

The linked macrocycle cations have Ni1···Ni1^A = 7.378 Å, with N_4 planes inclined at 5.3(1)° and twisted relatively (torsion angles N1–N8···N8^A–N4^A = 50.6(1)° and N4–N11···N11^A–N4^A = 56.1(1)°). The torsion angle O1–C21–C22–O2 = 114.8(1)°. The NH groups, oxalate ion and water molecules are linked by hydrogen bonding, listed in Table S9 of the Supplementary data.

3.6. The structure of chloro-1RS,4RS,7RS,8SR,11SR,13RS-(13-ethyl-5,5,7-trimethyl-13-nitro-1,4,8,11-tetraazacyclotetradecane)copper(II) perchlorate, β-[Cu(nph)Cl]ClO_4

This blue compound has a square–pyramidal cation with a near co-planar cyclic tetraamine N_4 group and an axially coordinated chloride ion (r.m.s. displacements from the N_4 plane are: N atoms: ±0.003(3), Cu1, 0.155(6); Cl1, 2.788(6) Å). Mean Cu–N = 2.02(1) and Cu–Cl = 2.637(3) Å, see Fig. 8. Disorder in the location of the

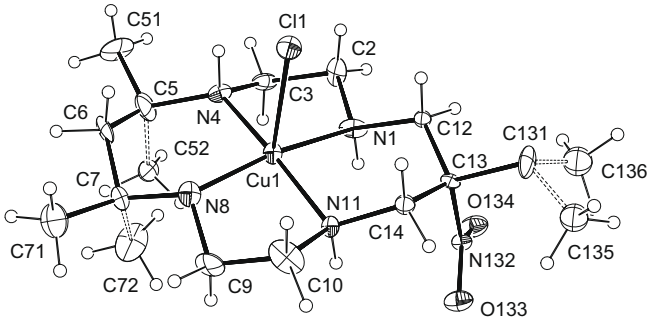


Fig. 8. The cation of β-[Cu(nph)Cl]ClO_4, drawn [30] as for Fig. 2. Sites C52, C72, C135 and C136 have partial occupancy, see text.

axial methyl substituents, methyl group of the ethyl substituent and of the perchlorate ion precluded a fully satisfactory solution of the structure, which is described more fully in the Supplementary data, with dimensions listed in Table S10.

4. Discussion

The azamacrocycle cations [M(enacne/np)]$^{2+}$, M = Ni(II) or Cu(II), are formed by a combination of two template condensations; an aldol-like reaction of bis(ethane-1,2-diamine) complexes with acetone to form the trimethyl-1-amine-3-imine linked [M(enac)]$^{2+}$ cation [9–11], and a Mannich-like reaction of [M(enac)]$^{2+}$ with methanal and the diprotic acid nitroethane to form the 2-methyl-2-nitro-1,3-diamine link [1–8]. The resulting "hybrid" macrocycle cation, [M(enacne)]$^{2+}$, combines features of the (5,5,7,12,12,14-hexamethyl-1,4,8,11-tetraazacyclotetrdeca-4,11-diene)metal(II) cation, [M (*trans*[14]diene)]$^{2+}$ [9] and 6,13-dimethyl-6,13-dinitro-1,4,8,11-tetraazacyclotetrdecane)metal(II), [M(dino)]$^{2+}$ macrocyclic ligand cations [1,22]. Both [Ni(*trans*[14]-diene)]$^{2+}$ and [Ni(dino)]$^{2+}$ predominantly form singlet ground state compounds, the axially oriented methyl and nitro-substituents hindering access to the axial coordination sites of the metal ions. In contrast, the [Ni(enacne)]$^{2+}$ cation forms triplet ground state compounds, both *trans* with axially coordinated ammonia and a variety of anions and *cis* with the macrocycle folded to accommodate a chelate additional ligand [12].

The imine functions of the [Ni(*trans*-[14]diene)]$^{2+}$ and [Ni(enacne)]$^{2+}$ cations are reduced by $NaBH_4$ to form the (5,5,7,12,12,14-hexamethyl-1,4,8,11-tetraazacyclotetradecane) and (5,7,7,13-tetramethyl-13-nitro-1,4,8,11-tetraazacyclotetradecane) cyclic tetraamine cations, respectively. The first occurs as C-*meso* and C-*rac* stereoisomers, which are readily separated for the nickel(II) cations because the C-*rac* isomer, tet*b*, has a much greater propensity to form compounds with chelate additional ligands with the macrocycle folded in the 1*RS*,4*RS*,8*RS*,11*RS* nitrogen configuration V than the C-*meso* isomer tet*a* [9]. The [M(enacne)]$^{2+}$ cations have a chiral centre at C13 so could, in principle, give rise to stereoisomeric reduction products, though for both nickel(II) and copper(II) one product was isolated, in ca. 75% yield. Appreciable amounts of tarry degraded material formed, so the potential yield of other products is small.

For all the structures of compounds of enacne/enacnp and neh/nph, as yet reported, the macrocycle is in square–planar coordination with the 1*SR*,4*SR*,8*RS*,11*RS* nitrogen configuration, III [16], which is least strained for planar coordination of cyclam-like azamacrocycles. For all these structures the nitro-substituent is axially oriented on a chair conformation chelate ring, to the same side of the "plane" as the axial component of the *gem*-dimethyl group. For [Ni(neh)]$(ClO_4)_2 \cdot H_2O$, structure **3.1**, the asymmetric unit contains two independent cations, both with the 1*S*,4*S*,7*R*,8*R*,11*R*,13*R* configuration; inversion centres ensuring chiral balance for the unit cell. It would appear that the $NaBH_4$ reduction of [Ni(enacne)]$^{2+}$ yields exclusively, or at least predominantly, the 7*RS*,13*RS* stereo-isomers.

Assessment of the stereochemistry for both the enacne and neh cations for several of the structures determined is complicated by the occurrence of disorder arising from co-crystallisation of cations with the N5-N8 trimethyl-amine-imine (enacne) or N5–N8 trimethyl-diamine (neh) chelate rings reversed. These disorder components for the enacne compounds are the 13*R* and 13*S* enantiomers, or for the neh cations the 7*R*,13*R* and 7*S*,13*S* enantiomers, typically present in ca. 0.7:0.3 proportions.

This disorder is not present for the singlet ground state perchlorate salt hydrate, structure **3.1**, but is present for the tetrachlorozincate salt, structure **3.3** (and probably also for the unhydrated

perchlorate salt, structure **3.2**) and is also present for the triplet ground state *catena*-μ-oxalato compound, structure **3.5**, which has appreciably longer Ni–N bond lengths. It is not present for the α-configuration perchlorate salt, **3.4**, which has a quite different conformation.

The same disorder phenomenon was observed for [Cu(enacne/np)]$^{2+}$ compounds [12–15] and is present for the [Cu(nph)(Cl)]ClO_4 structure **3.6**.

For the cyclic amine–imine compounds [Ni(enacne)][$ZnCl_4$], [Cu(enacnp)(OH_2)]$(ClO_4)_2$ and [Cu(enacne)(NCS)]$ClO_4{\cdot}H_2O$ this disorder leads to superposition of amine–imine chelate rings with inherently asymmetric conformations, with resulting intermediate C=N/C–N distances and apparent long C–CH_3 distances to the minor component axial methyl substituents. For the tetraamine compounds, now reported, these distances are more "normal", since reversal of the N4–N8 diamine chelate ring leads to smaller distortions in the chelate ring conformation.

As anticipated, the properties of the nickel(II) and copper(II) coordination compounds of the triamine–imine (enacne/enacnp) and tetraamine (neh/nph) azamacrocycles are generally similar. The [Ni(neh/nph)]$^{2+}$ cations exist as singlet ground state β-configuration cations in solutions in polar solvents such as water and as salts with poorly coordinating anions. The tendency of these cations to form triplet ground state *trans*-di-ligand compounds depends largely on the extent to which the axially oriented substituents "block" access to the axial coordination sites. The 'hybrid' [Ni(enacne)]$^{2+}$ cation forms such octahedrally coordinated compounds more readily than either of the 'parent' [Ni(*trans*[14]-diene)]$^{2+}$ or [Ni(dino)]$^{2+}$ cations. As examples, both [Ni(neh)]$^{2+}$and [Ni(enacne)]$^{2+}$ crystallize from water as triplet ground state compounds with chloride and thiocyanate ions, while the 'parent' cations do not. The formation of a triplet ground state bis(acetonitrile) adduct by [Ni(neh)]$(ClO_4)_2$, but not by [Ni(enacne)]$(ClO_4)_2$, may indicate that the more flexible neh ligand enables adoption of a conformation with less repulsion between the axial substituents and axially coordinated ligands. The tendency of the cations to form folded macrocycle compounds with chelates is also largely determined by interactions involving axial substituents, as exemplified by the facile formation of such species by the C-*rac* cation [Ni(tet*b*]$^{2+}$ and the resistance to such folding by the C-*meso* cation [Ni(teta)]$^{2+}$. The formation of triplet ground state α-[Ni(enacne)(O_2N)]ClO_4 but singlet ground state β-[Ni(neh)]$NO_2{\cdot}ClO_4 \cdot H_2O$ may indicate easier folding by the enacne macrocycle. Both [Ni(enacne)]$^{2+}$ and [Ni(neh)]$^{2+}$ form water-insoluble folded macrocycle compounds α-[Ni(L)(acac)]$(ClO_4)_2$ and α-[{Ni(L)}$_2(C_2O_4)$]-$(ClO_4)_2$, but it is not clear to what extent the insolubility is driving their formation. The *trans*-coordinated chain-polymer *catena-trans*-β-[Ni(neh)(μ-C_2O_4)]$_n \cdot 3n(H_2O)$ (structure **3.5**) crystallizes when oxalate is added to an aqueous solution containing [Ni(neh)]$^{2+}$. The compound is stable in aqueous solution but in the presence of perchlorate ions slowly converts to the insoluble di-nuclear bis-bidentate μ^4-oxalato compound α-[{Ni(neh)}$_2$-(C_2O_4)]$(ClO_4)_2$.

There is one other example in the Cambridge Structural Database [23] of a nickel(II) compound with an oxalato-bridged chain-polymeric structure similar to structure **3.5**; *catena*-(3,14-dimethyl-2,6,13,17-tetraazatricyclo(14.4.01.18.07.12)docosane)(μ-C_2O_4)nickel(II) dihydrate) [24], and one other with a chain-polymeric structure with the "non-bridging" oxygen atoms of the oxalate ion in bidentate coordination to another nickel(II) ion; [Ni_2(1,4,8,11-tetraazacyclotetradecane)$_2$(μ^3-C_2O_4)]$_n(ClO_4)_{2n} \cdot n(H_2O)$ [25].

Reaction with acid of the folded macrocycle α-configuration oxalato or propane-2,4-dionato compounds removes the chelate by protonation and produces a solution containing the square–planar α-configuration cation. This is metastable in acid solution but slowly in neutral and rapidly in basic solution converts to the stable β-configuration cation. These properties are similar to those observed with other nickel(II) cyclic tetraamine compounds [17–20].

The cations [Cu(neh/nph)]$^{2+}$ form dark red salts with poorly coordinating anions and compounds of varying shades of blue with coordinating anions such as Cl^-, NCS^-, NO_2^-, etc. [Cu(nph)]$(ClO_4)_2$ crystallises as the red anhydrous compound from non-aqueous solvents, but as a blue hydrate from water. Both cations form very sparingly soluble blue compounds with tetracyanonickelate(II), analogous to [Cu(nph){Ni$(CN)_4$}] $\cdot H_2O$ [14], which has trinuclear [(neh)Cu–NC–Ni$(CN)_2$–CN–Cu(neh)]$^{2+}$ cations.

The square–pyramidal structure **3.6** of β-[Cu(nph)Cl]ClO_4 has a structure similar to that of β-[Cu(neh)(NCS)]$ClO_4 \cdot H_2O$ [14], which also has disorder in the location of the axial methyl group. The displacement of the copper(II) ion from the N_4 best plane for these compounds varies with the strength of the interaction with the axial ligand, being 0.246(2) Å for [Cu(enacnp)$_2${Ni$(CN)_4$}]$^{2+}$ with strongly bound tetracyanonickelate(II), 0.205(2) Å for [Cu(enacne)(NCS)]$ClO_4{\cdot}H_2O$, 0.155(6) Å for [Cu(nph)Cl]ClO_4 and 0.143(1) Å for [Cu(enacnp)(OH_2)]$(ClO_4)_2$ [13–15].

The orientation of the nitro group appears to be determined largely by local hydrogen bonding interactions. For β-[Ni(neh)]$(ClO_4)_2 \cdot H_2O$ (cation 1), β-[Ni(neh)]$_2$[$ZnCl_3(H_2O)$]$_2$[$ZnCl_4$] $\cdot$ $0.5H_2O$, α-[Ni(neh)]$(ClO_4)_2$, β-[Ni(neh)](μ-C_2O_4)]$_n \cdot 3n(H_2O)$ and β-[Cu(nph)Cl]ClO_4, and for [Ni(enacne)][$ZnCl_4$] [12] the nitro group is aligned approximately parallel with the M···C13 direction whereas for β-[Ni(neh)]$(ClO_4)_2 \cdot H_2O$ (cation 2), the three cations of β-[Ni(neh)]$(ClO_4)_2$ and the [Cu(enacne/np)]$^{2+}$ compounds the group is aligned approximately parallel with the direction Cu···C13 [12,16].

The 13- and 14-membered nitro-substituted cyclic tetraamine copper(II) compounds (formed from linear tetraamines, methanal and nitroethane [4–8]) have the nitro group axially oriented on chair conformation chelate rings and oriented normal to the Cu···C(NO_2) direction, while the 15- and 16-membered ring compounds have the relevant chelate ring in a boat conformation with the nitro group 'parallel', with one oxygen atom weakly interacting in an axial coordination site.

5. Experimental

5.1. Preparation of compounds

The cyclic tetraamine(metal) cations, [M(neh/nph)]$^{2+}$, were prepared by $NaBH_4$ reduction of the imine functions of the triamine–imine cations, [M(enacne/np)]$^{2+}$, which were prepared as previously reported [12,13]. The tetraamine compounds are distinguishable from the triamine–imine precursor compounds by the absence of a ν(C=N) band at ca. 1655 cm^{-1} in the IR. The IR spectra of neh and nph analogues are generally indistinguishable. Bands in the "fingerprint" region arising from other species generally could not be assigned because of the complexity of the neh/nph spectrum. The nitro-substituted cyclic tetraamine cations are resistant to acid (other than nitric acid which rapidly oxidizes them) but are very slowly degraded in base.

Compounds containing perchlorate are potentially explosive and should be treated with caution.

5.1.1. *β-(5,5,7,13-Tetramethyl-13-nitro-1,4,8,11-tetraazacyclotetradecane)nickel(II) perchlorate, β-[Ni(neh)](ClO$_4$)$_2$, structures **3.1** and **3.2***

Ni(enacne)]$(ClO_4)_2$ (2 g) was dissolved in water (50 cm^3) and $NaBH_4$ (0.15 g, 1:1 mol equivalents; excess $NaBH_4$ reduces the yield of product) added, when gentle effervescence occurred and a blue–violet borohydrido complex [Ni(enacne)(BH_4)]ClO_4 formed and sometimes precipitated. The solution was left at ambient tem-

perature for 2d, while gentle effervescence occurred and any initial precipitate redissolved. The solution was filtered, acidified with perchloric acid and allowed to evaporate to small volume, while the orange product crystallised. This was filtered off, washed with ethanol and recrystallised from hot acetonitrile. A pale grey–green acetonitrile *adduct* slowly crystallised on standing (IR: ν(NH) 3286, 3208, ν(C≡N) 2307, 2277, 2253; $\nu_{asym}(NO_2)$ 1553 cm^{-1}). This adduct was filtered off and washed with cold ethanol. It slowly lost the acetonitrile on exposure to the atmosphere, though large crystals were quite persistent. The solid was boiled with ethanol, when the orange perchlorate salt crystallised. This *product* was filtered from the cold solution and recrystallised from hot water, methanol or acetone (containing a few drops of water)/propan-2-ol in ca. 75% yield. The crystallisation of the acetonitrile adduct purifies the material from any traces of unreduced [Ni(enacne)]$(ClO_4)_2$ which is much more soluble in this solvent. If the IR spectrum showed any ν(C=N) absorption at 1665 cm^{-1} then the recrystallisation from acetonitrile was repeated. *Anal.* Calc. for $C_{14}H_{31}Cl_2N_5NiO_{10}$: C, 30.1; H, 5.6; N, 12.5. Found for a sample of the anhydrous salt recrystallised from acetone/propan-2-ol: C, 30.3; H, 5.7; N, 12.6%. Spectra; IR (KBr) ν_{max} (cm^{-1}): ν(NH), 3221sh, 3194; $\nu_{as}(NO_2)$, 1552. Visible (water) λ_{max}: 462 (nm); ε: 46 mol^{-1} cm^{-1} dm^3.

Large well-formed, dark-orange crystals of the *monohydrate* (structure **3.1**) crystallised on slow evaporation from water, with water bands in the IR spectrum (KBr) ν_{max} (cm^{-1}): ν(OH), 3592, 3523; ν(NH), 3202; δ(HOH), 1637; $\nu_{as}(NO_2)$ 1556. This hydrate slowly effloresced in the atmosphere.

5.1.2. bis-β-(5,5,7,13-Tetramethyl-13-nitro-1,4,8,11-tetraazacyclotetradecane)nickel(II) tetrachlorozincate(II) bis(aquatrichlorozincate(II)) hydrate, β-[Ni(neh)]$_2$ [$ZnCl_4$][$ZnCl_3(OH_2)$] · H_2O, structure **3.3**

Zinc(II) chloride in small excess was added to a solution of [Ni(neh)]$(ClO_4)_2$ in hot 10:1 acetone: water. The orange crystalline *solid* was filtered off and recrystallised from hot water. *Anal.* Calc. for $C_{28}H_{68}Cl_{10}N_{10}Ni_2O_7Zn_3$: C, 25.4; H, 5.2; N, 10.6 Found: C, 25.1; H, 5.2; N, 10.3%. IR (KBr) ν_{max} (cm^{-1}): ν(OH), (3367, 3313)vs, br; ν(NH), 3219, 3109; δ(HOH), 1646sh, 1620; $\nu_{as}(NO_2)$, (1558,1546)s, sp.

5.1.3. α-(5,5,7,13-Tetramethyl-13-nitro-1,4,8,11-tetraazacyclotetradecane)nickel(II) perchlorate, α-[Ni(neh)]$(ClO_4)_2$, structure **3.4**

α-[Ni(neh)(acac)]ClO_4 (5.1.8, 1 g) was dissolved in acetone (10 cm^3) and aqueous perchloric acid (5 cm^3, 10%) added, when the colour changed from blue to orange. The orange *product* which crystallised as the solution evaporated was recrystallised by evaporation from acetone/propan-2-ol. The compound slowly isomerizes in solution to form the β-cation. IR (KBr) ν_{max} (cm^{-1}): ν(NH), 3203; $\nu_{as}(NO_2)$, 1558.

5.1.4. trans-β-(5,5,7,13-Tetramethyl-13-nitro-1,4,8,11-tetraazacyclotetradecane)(dithiocyanato-N)nickel(II), trans-β-[Ni(neh)$(NCS)_2$]

Sodium thiocyanate was added to a hot aqueous solution of [Ni(neh)]$(ClO_4)_2$. Salmon coloured crystals of the *product* were filtered from the cold solution and recrystallised from hot water. The compound is sparingly soluble in cold water, forming an orange coloured (dissociated) solution. It is soluble in a variety of polar organic solvents e.g. acetonitrile, acetone, dichloromethane, etc, forming blue–violet (associated) solutions. *Anal.* Calc. for $C_{16}H_{31}N_7NiS_2O_2$: C, 40.3; H, 6.6; N, 20.6. Found: C, 40.4; H, 6.7; N, 20.6%. IR (KBr): ν_{max} (cm^{-1}) ν(NH), ν(NH), 3300, 3233, all w; ν(NCS^-), 2061vs, sp; $\nu_{as}(NO_2)$, 1546sp.

5.1.5. trans-Dichloro-β-(5,5,7,13-tetramethyl-13-nitro-1,4,8,11-tetraazacyclotetradecane)nickel(II), trans-β-[Ni(neh)Cl_2]

A few drops of concentrated hydrochloric acid was added to a hot concentrated aqueous solution of the perchlorate salt. The pale lavender coloured *product* was filtered from the cold solution and recrystallised from hot water. *Anal.* Calc. for $C_{14}H_{31}N_5Cl_2NiO_2$: C, 39.0; H, 7.2; N, 12.2. Found: C, 39.4; H, 7.3; N, 12.3%. IR (KBr): ν_{max} (cm^{-1}) ν(NH), 3279, 3223w, 3025; $\nu_{as}(NO_2)$, 1554s.

5.1.6. Catena-trans-bis(μ-oxalato-O,O′)-β-[(5,5,7,13-tetramethyl-13-nitro-1,4,8,11-tetraazacyclotetradecane- k^4)nickel(II)·trihydrate, catena-trans-β-[Ni(neh)(μ-C_2O_4)]$_n$·3n(H_2O), structure **3.5**

Diethylammonium oxalate (0.5 g in 5 cm^3 water) was added to a solution of [Ni(neh)Cl_2] (0.5 g in 5 cm^3 water). The pale lavender coloured *product* which slowly crystallised was filtered off and washed with a little cold water, then recrystallised from water. *Anal.* Calc. for $C_{16}H_{37}N_5NiO_7$: C, 38.3; H, 7.4; N, 13.9. Found: C, 38.5; H, 7.1; N, 13.8%. IR (KBr) ν_{max} (cm^{-1}): ν(OH), 3587, 3486; ν(NH), 3263, 3177; δ(HOH), ν_{as}(OCO), $\nu_{as}(NO_2)$ 1647, 1583vs, 1543, 1564.

Note: The compound is stable in solution in water but in the presence of perchlorate ions converts to insoluble *cis*-α-[{Ni(neh)}$_2(C_2O_4)$]$(ClO_4)_2$.

5.1.7. cis-α-(5,5,7,13-Tetramethyl-13-nitro-1,4,8,11-tetraazacyclotetradecane)nickel(II)] nitrite·perchlorate hydrate, β-[Ni(neh]NO_2 · ClO_4 · H_2O

This orange coloured *compound* was prepared as for the thiocyanato compound, 5.14, by substituting sodium nitrite and recrystallised from water. *Anal.* Calc. for $C_{14}H_{33}ClN_6NiO_9$: C, 32.1; H, 6.4; N, 16.1. Found: C, 32.5; H, 6.2; N, 16.2%. IR (KBr) ν_{max} (cm^{-1}): ν(OH), 3437br; ν(NH), 3295w, 3258, 3204, 3087; δ(HOH), 1655; $\nu_{as}(NO_2)$, 1547sp.

5.1.8. cis-α-(5,5,7,13-Tetramethyl-13-nitro-1,4,8,11-tetraazacyclotetradecane)(pentane-2,4-dionato)nickel(II) perchlorate, cis-α-[Ni(neh)(acac)]ClO_4

Pentane-2,4-dione (acetylacetone), in small excess was added to a hot aqueous solution of [Ni(neh)]$(ClO_4)_2$, followed by dilute aqueous ammonia. The blue *precipitate* that formed was filtered from the cold solution, washed with water, and recrystallised from acetone/propan-2-ol. *Anal.* Calc. for $C_{19}H_{38}ClN_5NiO_8$: C, 40.8; H, 6.9; N, 12.5. Found: C, 41.2; H, 6.2; N, 12.7%. IR (KBr) ν_{max} (cm^{-1}): ν(NH), 3307w, 3275, 3261; $\nu_{as}(NO_2)$, 1547, ν($acac^-$), 1597, 1518, 1400, all sp.

5.1.9. bis-cis-(5,5,7,13-Tetramethyl-13-nitro-1,4,8,11-tetraazacyclotetradecane)(-oxalato)nickel(II) perchlorate, cis-α-[{Ni(neh)}$_2$(μ-C_2O_4)]$(ClO_4)_2$

(a) Oxalic acid in small excess was added to a solution of [Ni(neh)(acac)]ClO_4 in ethanol, when the sparingly soluble blue product crystallised.
(b) Sodium oxalate and dilute aqueous ammonia were added to an aqueous solution of [Ni(neh)]$(ClO_4)_2$ and the solution heated, when the product slowly crystallised.

The *product* was filtered off and washed with water, then ethanol. *Anal.* Calc. for $C_{15}H_{31}ClN_5NiO_8$: C, 35.8; H, 6.2; N, 13.9. Found: C, 35.8; H, 6.3; N, 13.5%. IR (KBr) ν_{max} (cm^{-1}): ν(NH), 3274; ν_{as}(CO), 1651vs,sp, 1598w; $\nu_{as}(NO_2)$, 1546; $\nu(CO)_{sym}$, 1307 $\nu_3(ClO_4^-)$, 1102, 1066 $\nu_4(ClO_4^-)$, 624.

5.1.10. β-(13-Ethyl-5,5,7-trimethyl-13-nitro-1,4,8,11-tetraazacyclotetradecane)-nickel(II) perchlorate, β-Ni(nph)](ClO$_4$)$_2$

This orange *compound* was prepared by reduction of [Ni(enacnp)](ClO$_4$)$_2$ and purified by crystallization of the acetonitrile adduct, as for the neh homologue 5.11. *Anal.* Calc. for $C_{15}H_{33}Cl_2N_5NiO_{10}$: C, 31.4; H, 5.8; N, 12.2. Found: C, 31.7; H, 5.9; N, 12.4%.

5.1.11. (13-Ethyl-5,5,7-trimethyl-13-nitro-1,4,8,11-tetraazacyclotetradecane)nickel(II) tetrachlorozincate(II) hemihydrate, [Ni(nph)][ZnCl$_4$] · 0.5H$_2$O

This orange *compound* was prepared as for the [Ni(neh)]$^{2+}$, chlorozincate salt. *Anal.* Calc. for $C_{15}H_{34}Cl_4N_5NiO_{2.5}Zn$ requires: C 30.5; H, 5.8; N, 11.8. Found: C, 30.4; H, 5.6; N, 11.8%.

5.1.12. β-(5,5,7,13-Tetramethyl-13-nitro-1,4,8,11-tetraazacyclotetradecane)-copper(II) perchlorate, β-[Cu(neh)](ClO$_4$)$_2$

[Cu(enacne)](ClO$_4$)$_2$ (2 g) was dissolved in acetonitrile/methanol (20 cm^3 of a 1:1 mixture). NaBH$_4$ (0.15 g. 1: 1 mol proportions, in 10 cm^3 of the same solvent mixture) was added. The solution effervesced and a dark chocolate coloured solid slowly precipitated. This slowly redissolved to leave a purple solution with a small amount of black precipitate. After ca. 24 h. the solution was filtered, acidified with dilute perchloric acid and allowed to evaporate to small volume. The crimson *product* was filtered from the cold solution, washed with ethanol and recrystallised from hot water or acetonitrile/propan-2-ol. Yield ca. 80%. Recrystallisation is ineffective in removing any traces of unreduced [Cu(enacne)](ClO$_4$)$_2$, indicated by the presence of a ν(C=N) band at ca. 1665 cm^{-1} in the IR. Precipitation and recrystallisation of [Cu(neh)Cl]ClO$_4$, 5.115, removes this contaminant and the perchlorate salt can be reformed by evaporation of an aqueous solution containing 1.1 mol proportions of perchloric acid, with a final recrystallisation from hot water. *Anal.* Calc. for $C_{14}H_{31}Cl_2CuN_5O_{10}$: C, 29.8; H, 5.5; N, 12.4. Found: C, 30.0; H, 5.3; N, 12.4%. Spectra, IR (KBr) ν_{max} (cm^{-1}): ν(NH), 3267w, 3209; ν_{as}(NO$_2$), 1551, 1540. Visible (water) λ_{max}: 514 (nm), ε 94 cm^{-1} mol^{-1} dm^3.

5.1.13. β-(5,5,7,13-Tetramethyl-13-nitro-1,4,8,11-tetraazacyclotetradecane)-copper(II) tetrachlorozincate(II), β-[Cu(neh)][ZnCl$_4$]

This red *compound* was prepared as for the nickel compound, 5.12. *Anal.* Calc. for $C_{14}H_{31}Cl_4CuN_5O_2Zn$: C, 29; H, 5.5; N, 12.2. Found: C, 29.7; H, 5.3; N, 12.2%. IR (KBr) ν_{max} (cm^{-1}): ν(NH) 3247, 3220w, 3197, 3164; ν_{as}(NO$_2$) 1548.

Table 6
Crystallographic details.

Compound	β-[Ni(neh)](ClO$_4$)$_2$ · H$_2$O[a]	β-[Ni(neh)](ClO$_4$)$_2$	β-[Ni(neh)]$_2$[ZnCl$_4$][ZnCl$_3$(OH)]$_2$H$_2$O	α-[Ni(neh)](ClO$_4$)$_2$	*catena*-β-[Ni(neh)-(μ-C$_2$O$_4$)]$_n$· 3*n*(H$_2$O)	β-[Cu(nph)Cl]ClO$_4$
Formula	$C_{14}H_{33}Cl_2N_5NiO_{11}$	$C_{14}H_{31}Cl_2N_5NiO_{10}$[b]	$C_{28}H_{63}Cl_{10}N_{10}Ni_2O_7Zn_3$[c]	$C_{14}H_{31}C2N_5NiO_{10}$[d]	$C_{16}H_{37}N_5NiO_9$[e]	$C_{15}H_{31}Cl_2CuN_5O_6$[f]
Formula weight	559.03	577.06	1319.91	559.03	502.22	511.89
Crystal system	monoclinic	monoclinic	monoclinic	triclinic	monoclinic	orthorhombic
Space group	*P*2(1)/c	*P*2(1)	*P*2(1)/c	$P\bar{1}$	*P*2(1)/n	*P* na 2(1)
Space group hall	−*P* 2*ybc*	*P*2 *yb*	−*P* 2*ybc*	−*P*$\bar{1}$	−*P* 2*yn*	*P* 2*c*–2*n*
a (Å)	18.103(4)	16.160(1)	20.853(2)	11.693(2)	8.2657(1)	36.01(2)
b (Å)	16.392(3)	9.2803(5)	15.352(1)	13.878(2)	20.0635(3)	10.394(7)
c (Å)	15.567(3)	22.315(2)	17.524(1)	14.835(2)	13.9824(2)	6.005(4)
α (°)	90	90	90	90.325(2)	90	90
β (°)	98.53(3)	90.293(2)	114.830(3)	91.149(2)	101.521(1)	90
γ (°)	90	90	90	106.325(2)	90	90
V (Å^3)	4568.4(2)	3346.6(4)	5091.3(6)	2309.8(5)	2272.10(5)	2247(3)
Z	4	4	4	2	4	4
Cell detection: reflection	9906	4926	3215	5113	7041	1369
Range θ_{min}, θ_{max} (°)	2.6 → 30.5	2.5 → 29.5	2.5 → 28.6	2.3 → 30.4		2.3 → 26.0
T (K)	153(2)	293(2)	100(2)	100(2)	90(2)	133(2)
Crystal, size (mm)	0.10 × 0.20 × 0.35	0.07 × 0.20 × 0.70	0.16 × 0.17 × 0.26	0.08 × 0.20 × 0.25	0.10 × 0.11 × 0.34	0.65 × 0.28 × 0.03
ρ_{calc} (g/cm^3)	1.678	1.664	1.722	1.608	1.465	1.513
F(000)	2416	1752	2692	1168	1072	1068
μ (mm^{-1})	1.149	1.171	2.694	1.131	0.910	1.250
T_{max}, T_{min}	0.689, 0.894	0.921, 0.755	0.650, 0.538	0.699, 0.913	0.915, 0.747	0.96, 0.80
Reflections number (avge. *R* eqiv.)	313301 (0.0183)	16516 (0.0664)	8421 (0.0548)	13947 (0.0213)	28277 (0.0390)	9517 (0.0622)
Index range *h*	−25 → 25	−21 → 21	−20 → 20	−16 → 16	−9 → 9	−38 → 44
Index range *k*	−18 → 23	−6 → 12	−16 → 13	−18 → 18	−23 → 23	−12 → 11
Index range *l*	−22 → 21	−29 → 16	−18 → 17	−20 → 21	−15 → 17	−7 → 7
θ range (°)	1.1 → 30.5	1.8 → 28.5	1.7 → 21.9	1.3 → 30.4	1.80 → 25	2.04 → 26.54
Reflections total	11559	12286	5122	11067	3994	4224
Reflections [$I > 2\sigma$ (I)]	9311	8528	3658	9278	3303	3486
Parameters (restraints)	619(4)	926(7)	596(4)	575(0)	321(4)	260(16)
Goodness-of-fit (GOF) on F^2 [all data]	1.04	1.02	0.96	1.12	1.02	1.18
Final *R* indexes [$I > 2\sigma$(I)]	R_1, 0.028; R_w, 0.077	R_1, 0.054; R_w, 0.132	R_1, 0.042; R_w, 0.100	R_1, 0.068; R_w, 0.177	R_1, 0.030; R_w, 0.074	R_1, 0.099; R_w, 0.221
Final *R* indexes [all data]	R_1, 0.040; R_w, 0.0826	R_1, 0.082; R_w, 0.145	R_1, 0.073; R_w, 0.116	R_1, 0.077; R_w, 0.182	R_1, 0.041; R_w, 0.080	R_1, 0.125; R_w, 0.234

[a] β-(5,5,7,13-Tetramethyl-13-nitro-1,4,8,11-tetraazacyclotetradecane-κ^4)nickel(II) perchlorate monohydrate.
[b] β-(5,5,7,13-Tetramethyl-13-nitro-1,4,8,11-tetraazacyclotetradecane-κ^4)nickel(II) perchlorate. Flack coefficient 0.43(2) [29].
[c] bis-β-{(5,5,7,13-Tetramethyl-13-nitro-1,4,8,11-tetraazacyclotetradecane-κ^4)nickel(II)} bis{aquatrichlorozincate(II)} tetrachlorozincate(II) hydrate.
[d] α-(5,5,7,13-Tetramethyl-13-nitro-1,4,8,11-tetraazacyclotetradecane-κ^4)nickel(II) perchlorate monohydrate.
[e] *catena*-μ-oxalato-*trans*-β-(5,5,7,13-Tetramethyl-13-nitro-1,4,8,11-tetraazacyclotetradecane-κ^4)-(μ-oxalato-κ^2)nickel(II) trihydrate.
[f] β-Chloro(13-ethyl-5,5,7-trimethyl-1,4,8,11-tetraazacyclotetradecane-κ^4)(thiocyanato-*N*)copper(II) perchlorate. Flack coefficient reported by SHELX as 0.00 [29].

5.1.14. β-(5,5,7,13-Tetramethyl-13-nitro-1,4,8,11-tetraazacyclotetradecane)-copper(II) tetracyanonickelate(II) dihydrate, β-[Cu(neh){Ni(CN)$_4$}] · 2H$_2$O

An aqueous solution of $Na_2[Ni(CN)_4] \cdot 3H_2O$ (0.8 g) was added slowly to a warm aqueous solution of $[Cu(neh)](ClO_4)_2$ (1 g, equimolar proportions). The sparingly soluble blue precipitate was filtered off and washed with water. *Anal.* Calc. for C, 38.3; H, 6.3; N, 22.4. Found: C, 38.4; H, 6.3; N, 22.6%. IR (KBr) ν_{max} (cm^{-1}): ν(OH), 3568, 3444; ν(NH), 3300, 3272w, 3227; ν(CN), 2146, 2124; δ(HOH), 1614; $\nu_{as}(NO_2)$, 1547.

5.1.15. Chloro-β-(13-ethyl-5,5,7,13-tetramethyl-13-nitro-1,4,8,11-tetraazacyclotetradecane)copper(II) perchlorate, β-[Cu(neh)Cl]ClO$_4$

A few drops of concentrated hydrochloric acid were added to a methanol solution of $[Cu(neh)](ClO_4)_2$, followed by propan-2-ol. The blue product was filtered off and recrystallised from hot methanol/propan-2-ol. *Anal.* Calc. for $C_{14}H_{31}Cl_2CuN_5O_4$: C, 33.6; H, 6.3; N, 14.0. Found: C, 33.9; H, 6.3; N, 13.9%. IR (KBr) ν_{max} (cm^{-1}): ν(NH) 3241, $\nu_{as}(NO_2)$ 1553.

5.1.16. β-(5,5,7,13-Tetramethyl-13-nitro-1,4,8,11-tetraazacyclotetradecane) (thiocyanato)copper(II) perchlorate, β-[Cu(neh)(NCS)]ClO$_4$

Blue crystals of the *product* which separated when NaCNS was added to a hot aqueous solution of $[Cu(neh)](ClO_4)_2$ were recrystallised from hot methanol. *Anal.* Calc. for $C_{15}H_{31}ClCuN_6O_6S$: C, 34.5; H, 6.0; N, 16.1. Found: C, 34.7; H, 5.9; N, 16.2%. IR (KBr) ν_{max} (cm^{-1}): ν(NH), 3229; ν(CNS$^-$), 2048; $\nu_{as}(NO_2)$ 1548.

5.1.17. Nitrito-β-(5,5,7,13-tetramethyl-13-nitro-1,4,8,11-tetraazacyclotetra-decane)copper(II) perchlorate, β-[Cu(neh)(ONO)]ClO$_4$

Blue *crystals* which separated when $NaNO_2$ was added to a hot aqueous solution of $[Cu(neh)](ClO_4)_2$ were recrystallised from hot water. *Anal.* Calc. for $C_{14}H_{31}ClCuN_6O_8$: C, 32.9; H, 6.1; N, 16.5. Found: C, 33.1; H, 6.1; N, 16.5%. IR (KBr) ν_{max} (cm^{-1}): ν(NH) 3224, 3119, $\nu_{as}(NO_2)$ 1550; $\nu_{as}(NO_2^-)$, 1266.

5.1.18. β-(13-Ethyl-5,5,7-trimethyl-13-nitro-1,4,8,11-tetraazacyclotetradecane)-copper(II) perchlorate, β-[Cu(nph)](ClO$_4$)$_2$

This magenta coloured *compound* was prepared by reduction of $[Cu(enacnp)](ClO_4)_2$, as for the neh homologue, 5.1.12. *Anal.* Calc. for $C_{15}H_{33}Cl_2CuO_{10}$: C, 31.2; H, 5.8; N, 12.1. Found: C, 31.5; H, 5.5; N, 12.2%. IR (KBr) ν_{max} (cm^{-1}): ν(NH) 3232w, 3186; $\nu_{as}(NO_2)$ 1553. The compound formed a blue hydrate when crystallised slowly from water.

*5.1.19. Chloro-β-(13-ethyl-5,5,7-trimethyl-13-nitro-1,4,8,11-tetraazacyclotetra-decane)copper(II) perchlorate, β-[Cu(nph)Cl](ClO$_4$, structure **3.6***

This blue *compound* was prepared as for the $[Cu(neh)]^{2+}$ homologue, 5.1.15. *Anal.* Calc. for $C_{15}H_{33}Cl_2CuN_5O_6$: C, 35.1; H, 6.5; N, 13.6. Found: C, 35.1; H, 6.4; N, 13.6%.

5.1.20. β-(13-Ethyl-5,5,7-trimethyl-13-nitro-1,4,8,11-tetraazacyclotetradecane)-copper(II) tetrachlorozincate hemihydrate, β-[Cu(nph)][ZnCl$_4$] · 0.5H$_2$O

This red *compound* was prepared as for the neh homologue, 5.113. *Anal.* Calc. for $C_{15}H_{34}Cl_4N_5NiO_{2.5}$: C, 30.5; H, 5.8; N, 11.9 Found: C, 30.4; H, 5.6; N, 11.8%.

5.2. Crystallography

Diffraction data was collected by using Bruker C.C.D. diffractometers [26] with graphite monochromaticized Mo Kα radiation (λ, 0.71073 Å), with phi and omega scans, and corrected for absorption [26,27]. See Table 6 for details.

The structures were solved by direct methods (SHELXS) [28] and refined on F^2 (SHELXL) [28], with anisotropic thermal parameters, except where specified. Hydrogen atoms bonded to C and N are in calculated positions, with their positions refined using a riding model with SHELXL defaults. Hydrogen atoms of water molecules were located from difference synthesis and their positions refined with DFIX (0.82 Å) constraints.

The structures with C5/C7 disorder in the location of the axial methyl groups were refined with complementary sof for these groups. For the oxalato compound 3.5 this disorder model was extended to atom C51.

Appendix A. Supplementary data

CCDC 711742, 711743, 711744, 711745, 711746, and 711747 contain the supplementary crystallographic data for β-[Ni(neh)](ClO$_4$)$_2$ · H$_2$O; β-[Ni(neh)]$_2$[ZnCl$_3$(H$_2$O)]$_2$[ZnCl$_4$] · 0.5H$_2$O; α-[Ni(neh)](ClO$_4$)$_2$; *catena-trans*-β-Ni(neh)(μ-C$_2$O$_4$)]$_n$·3n(H$_2$O)and β-[Cu(nph)Cl]ClO$_4$. These data can be obtained free of charge via http://www.ccdc.cam.ac.uk/conts/retrieving.html, or from the Cambridge Crystallographic Data Centre, 12 Union Road, Cambridge CB2 1EZ, UK; fax: (+44) 1223-336-033; or e-mail: deposit@ccdc.cam.ac.uk. Supplementary data associated with this article can be found, in the online version, at doi:10.1016/j.poly.2009.02.019.

References

[1] P. Comba, N.F. Curtis, G.A. Lawrance, A.M. Sargeson, B.W. Skelton, A.H. White, Inorg. Chem. 25 (1986) 4260.
[2] P.V. Bernhardt, G.A. Lawrance, Coord. Chem. Rev. 104 (1990) 297.
[3] G.A. Lawrance, M. Maeder, E.N. Wilkes, Rev. Inorg. Chem. 13 (1993) 199.
[4] G.A. Lawrance, M. Rossignoli, B.W. Skelton, A.H. White, Aust. J. Chem. 40 (1987) 1441.
[5] P. Comba, N.F. Curtis, G.A. Lawrance, M.A. O'Leary, B.W. Skelton, A.H. White, J. Chem. Soc., Dalton Trans. (1988) 2145.
[6] P. Comba, N.F. Curtis, G.A. Lawrance, M.A. O'Leary, B.W. Skelton, A.H. White, J. Chem. Soc., Dalton Trans. (1988) 497.
[7] G.A. Lawrance, M.A. O'Leary, Polyhedron 6 (1987) 1291.
[8] G.A. Lawrance, M. Maeder, M.A. O'Leary, F.H. Woon, Polyhedron 9 (1990) 2227.
[9] N.F. Curtis, Coord. Chem. Rev. 3 (1966) 3.
[10] N.F. Curtis, J. Chem. Soc., Dalton Trans. (1972) 1357.
[11] N.F. Curtis, H.K.J. Powell, H. Puschmann, C.E.F. Rickard, J.M. Waters, Inorg. Chim. Acta 355 (2003) 25.
[12] N.F. Curtis, K. Flood, W.T. Robinson, Polyhedron 25 (2006) 1313.
[13] N.F. Curtis, H. Puschmann, Polyhedron 25 (2006) 1204.
[14] N.F. Curtis, H. Puschmann, Acta Cryst. Sect. C 60 (2004) m410.
[15] N.F. Curtis, K. Flood, W.T. Robinson, unpublished observations.
[16] B. Bosnich, C.K. Poon, M.L. Tobe, Inorg. Chem. 4 (1965) 1102.
[17] N.F. Curtis, D.A. Swann, T.N. Waters, J. Chem. Soc., Dalton Trans. (1973) 1963.
[18] D.F. Cook, N.F. Curtis, C.E.F. Rickard, J.M. Waters, D.C. Weatherburn, Inorg. Chim. Acta 355 (2003) 1.
[19] D.F. Cook, N.F. Curtis, O.P. Gladkikh, D.C. Weatherburn, Inorg. Chim. Acta 355 (2003) 15.
[20] D.F. Cook, N.F. Curtis, C.E.F. Rickard, J.M. Waters, Polyhedron 24 (2005) 3022.
[21] N.F. Curtis, K. Flood, C.E.F. Rickard, W.T. Robinson, J.M. Waters, Polyhedron 28 (2009) 739.
[22] N.F. Curtis, G.J. Gainsford, A. Siriwardena, D.C. Weatherburn, Aust. J. Chem. 46 (1993) 755.
[23] Cambridge Structural Database, Cambridge Crystallographic Data Centre, (2008).
[24] J.C. Kim, J.H. Cho, A.J. Lough, Inorg. Chim. Acta 317 (2001) 252.
[25] H. Liu, W. Gu, G. Xu, Y. Feng, Y. Kou, L. Feng, S. Yan, D. Liao, P. Cheng, Inorg. Chem. Comm.10 (2007) 1099.
[26] Bruker SMART (Version 5.054), SADABS (Version 2.03) and Saint (Version 6.02A), Bruker AXS Inc., Madison, Wisconsin, USA, 1997.
[27] R.H. Blessing, Acta Cryst., Sect. A 51 (1995) 33.
[28] G.M. Sheldrick, SHELXTL (Version 5.10), Programs for the solution and refinement of crystal structures, 1997.
[29] H.D. Flack, Acta Cryst., A 39 (1983) 876.
[30] L.J. Farrugia, ORTEP-32, J. Appl. Cryst. 30 (1997) 565.

Polyhedron 28 (2009) 2113–2118

Contents lists available at ScienceDirect

Polyhedron

journal homepage: www.elsevier.com/locate/poly

Synthesis, structural characterisation and thermal decomposition of a new organic–inorganic hybrid material $(C_5H_{14}N_2)[Cu(SO_4)_2(H_2O)_4]\cdot H_2O$

Fadhel Hajlaoui [a], Samia Yahyaoui [a], Houcine Naïli [a,*], Tahar Mhiri [a], Thierry Bataille [b]

[a] Laboratoire de l'Etat Solide, Département de Chimie, Faculté des Sciences de Sfax, BP 1171, 3000 Sfax, Tunisia
[b] Sciences Chimiques de Rennes (UMR CNRS 6226), Groupe Matériaux Inorganiques, Chimie Douce et Réactivité, Université de Rennes I, Avenue du Général Leclerc, 35042 Rennes cedex, France

ARTICLE INFO

Article history:
Received 3 February 2009
Accepted 23 March 2009
Available online 31 March 2009

Keywords:
Chemical synthesis
Crystal structure
2-Methylpiperazine
Thermal decomposition
Hydrogen bonds
Transition metal sulfate

ABSTRACT

The crystal structure of copper sulfate templated by 2-methylpiperazine, $(C_5H_{14}N_2)[Cu(SO_4)_2(H_2O)_4]\cdot H_2O$, was investigated using single crystal X-ray diffraction data. At room temperature, it crystallises in the monoclinic $P2_1/n$ space group with the following unit-cell parameters: $a = 6.9153(1)$, $b = 23.1295(3)$, $c = 10.4472(1)$ Å, $\beta = 104.227(1)^\circ$, $V = 1619.75(4)$ Å^3 and $Z = 4$. The Cu^{II} cation adopts a slightly distorted octahedral geometry, arising from four water molecules and two sulfate tetrahedra leading to the formation of $[Cu(SO_4)_2(H_2O)_4]$ units. The structure consists of isolated $[Cu(SO_4)_2(H_2O)_4]^{2-}$ anions, 2-methylpiperazinediium cations $(C_5H_{14}N_2)^{2+}$ and water molecules connected by a three-dimensional hydrogen-bond network. The thermal decomposition of the precursor, studied by thermogravimetry and temperature-dependent X-ray powder diffraction, proceeds through four stages giving rise to the copper oxide.

© 2009 Elsevier Ltd. All rights reserved.

1. Introduction

In the past decades, a variety of organically templated metal sulfates with fascinating architectures and desirable physical properties have also attracted considerable attention [1]. A great interest has been shown in some double sulfates of trivalent metal with monovalent aliphatic ammonium cations because of their ferroelastic and ferroelectric properties [2–6]. So far, there are few data on the double sulfates of divalent transition metal cations with mono or divalent organic amines cations [7–19]. By analogy with trivalent metal sulfates showing a para-ferroelectric transition upon cooling [3–6], it was expected that such divalent metal sulfates would exhibit this feature. The use of non-centrosymmetric amine groups, instead of alkylamines, may help crystallize disordered phases at room temperature. Cation ordering at low temperature would thus provide acentric structures that are the basic condition to have ferroelectricity. In order to expand upon the emergent chemistry of templated metal sulfate, a new compound using 2-methylpiperazine as a template and copper as a transition metal has been synthesized. In this paper, we report the chemical preparation, the structural study and the thermal behavior of title compound.

2. Experimental

2.1. Synthesis

Single crystals of the compound $(C_5H_{14}N_2)[Cu(SO_4)_2(H_2O)_4]\cdot H_2O$ were grown as follows: 1 mmol of the copper sulfate pentahydrate $CuSO_4\cdot 5H_2O$ (99%, Merck); 1 mmol of 2-methylpiperazine (98%, ACROS Organics) and 1 mmol of sulfuric acid H_2SO_4 (96%, Carlo Erba) were mixed together in a minimum amount of distilled water. The clear solutions were stirred for 15 min and allowed to stand at room temperature. After a few days, blue prismatic crystals were formed. The product was filtered off and washed with a small amount of distilled water.

2.2. Structure determination and refinement

Although in some cases beautiful crystals of macroscopic dimensions were obtained (e.g., $0.336 * 0.153 * 0.334$ mm^3), the preparation proved to be difficult. Finally smashing the crystals gave fragments suitable for analysis.

Single-crystal X-ray data of $(C_5H_{14}N_2)[Cu(SO_4)_2(H_2O)_4]\cdot H_2O$ were collected at room temperature on a Nonius Kappa CCD diffractometer using Mo Kα radiation ($\lambda = 0.71073$ Å) through the programm COLLECT [20]. Correction for Lorentz-polarisation effect, peak integration and background determination were carried out with the program DENZO [21]. Frame scaling and unit-cell parameters refinement were performed with the program SCALEPACK [21].

* Corresponding author. Tel.: +216 98 66 00 26; fax: +216 74 274 437.
E-mail address: houcine_naili@yahoo.com (H. Naïli).

0277-5387/$ - see front matter © 2009 Elsevier Ltd. All rights reserved.
doi:10.1016/j.poly.2009.03.024

Analytical absorption corrections were performed by modeling the crystal faces using NUMABS [22]. The crystal structure has been solved in the monoclinic symmetry, space group $P2_1/n$ according to the automated search for space group available in WINGX [23]. Transition metal and sulfur atoms were located using direct methods with the program SHELXS-97 [24]. The oxygen atoms and the organic moiety were found from successive Fourier calculations using SHELXL-97 [25]. The aqua H atoms and those bonded to N atoms were located in a difference Fourier map and their positions and isotropic displacement parameters were refined. Within the water molecules, the O–H and H–H distances were restrained to 0.85(2) and 1.39(2) Å, respectively, so that the H–O–H angle approach the theoretical values, 105.4°. H atoms bonded to C atoms were positioned geometrically (the C–H bonds were fixed at 0.97 Å) and allowed to ride on their parent atoms. Crystallographic data and the results of the least-squares structure refinement are given in Table 1. Bond distances and angles calculated from the final atomic coordinates, as well as probable hydrogen bonds, are listed in Tables 2 and 3.

Table 1
Crystallographic data for $(C_5H_{14}N_2)[Cu(SO_4)_2(H_2O)_4]\cdot H_2O$.

Empirical formula	$C_5H_{24}CuN_2O_{13}S_2$
Formula weight (g/mol)	447.92
T (K)	293(2)
Crystal system	monoclinic
Space group	$P2_1/n$
a (Å)	6.9153(1)
b (Å)	23.1295(3)
c (A)	10.4472(l)
β (°)	104.227(1)
V (Å^3)	1619.75(4)
Z	4
ρ_{cal}	1.837
Crystal size (mm^3)	0.336 * 0.153 * 0.334
Habit–colour	prism–blue
λ (Mo Kα) (Å)	0.71073
Extinction coefficient	0.0140(16)
μ (mm^{-1})	1.674
Θ range (°)	3.16–39.37
Index ranges	$-12 \leqslant h \leqslant 9$
	$-41 \leqslant k \leqslant 41$
	$-18 \leqslant l \leqslant 18$
Unique data	9607
Observed data [$I > 2\sigma(I)$]	7084
F(000)	932
Refinement method	full matrix least-squares on $\lvert F^2\rvert$
R_1	0.05
WR_2	0.136
Goodness-of-fit (GOF)	1.037
No. parameters	249
Transmission factors	0.5810 and 0.8102
Largest difference map peak and hole (e Å^{-3})	−1.591 and 0.960

2.3. Thermal analyses

Thermogravimetric analysis for $(C_5H_{14}N_2)[Cu(SO_4)_2(H_2O)_4]\cdot H_2O$ was carried out with a Rigaku Thermoflex instrument. The 80.82 mg powdered sample was spread evenly in a large sample holder to avoid mass effects. The TG run was performed in flowing air with a heating rate of 15° Ch^{-1} from room temperature to 900 °C. The temperature-dependent X-ray (TDXD) was performed with a D5005 powder diffractometer (Bruker AXS) using Cu Kα radiation [λ(Kα_1) = 1.5406 Å, λ(Kα_2) = 1.5444 Å] selected with a diffracted-beam graphite monochromator, and equipped with an Anton Paar HTK1200 high-temperature oven camera. The thermal decomposition of the compound was carried out in air, with a heating rate of 14.4° Ch^{-1} from ambient to 870 °C.

2.4. IR spectroscopy

All IR measurements were obtained using a Perkin Elmer 1600 FT spectrometer. Samples were diluted with spectroscopic KBr and pressed into a pellet. Scans were run over the range 400–4000 cm^{-1}.

3. Results and discussion

3.1. Description of the crystal structure of $(C_5H_{14}N_2)[Cu(SO_4)_2(H_2O)_4]\cdot H_2O$

All of the transition metal sulfates templated by amines described in the literature show similar structures. However, the arrangement of the polyhedra and the organic molecules within these structures is slightly different. Consequently, we were able to distinguish different arrangement types and space groups [26–34]. The crystal structure of the new 2-methylpiperazinediium

Table 2
Selected bond distances (Å) and angles (°).

Octahedron around Cu		Tetrahedron around S1		Within the organic moiety	
Cu–OW1	1.9505(12)	S1–O1	1.4578(14)	N1–C4	1.492(2)
Cu–OW2	1.9727(12)	S1–O2	1.4797(15)	N1–C1	1.499(2)
Cu–OW3	1.9802(12)	S1–O3	1.4834(11)	N2–C3	1.488(2)
Cu–OW4	1.9828(12)	S1–O4	1.4837(12)	N2–C2	1.490(2)
Cu–O3	2.3418(11)	O1–S1–O2	110.30(9)	C1–C5	1.511(3)
Cu–O7	2.3672(11)	O1–S1–O3	110.60(8)	C1–C2	1.519(2)
OW1–Cu–OW2	90.15(5)	O1–S1–O4	110.34(9)	C3–C4	1.514(2)
OW1–Cu–OW3	175.00(6)	O2–S1–O3	107.92(8)	C4–N1–C1	112.48(12)
OW1–Cu–OW4	90.17(5)	O2–S1–O4	109.68(10)	C3–N2–C2	111.21(13)
OW1–Cu–O3	93.25(5)	O3–S1–O4	107.93(7)	N1–C1–C5	109.49(14)
OW1–Cu–O7	91.22(5)	tetrahedron around S2		N1–C1–C2	108.95(13)
OW2–Cu–OW3	88.26(5)	S2–O5	1.4691(14)	C5–C1–C2	111.35(16)
OW2–Cu–OW4	179.27(5)	S2–O6	1.4690(13)	N2–C2–C1	111.46(14)
OW2–Cu–O3	91.10(5)	S2–O7	1.4735(11)	N2–C3–C4	110.03(15)
OW2–Cu–O7	92.57(5)	S2–O8	1.4964(12)	N1–C4–C3	109.93(14)
OW3–Cu–OW4	91.37(5)	O5–S2–O6	110.17(9)		
OW3–Cu–O3	91.52(5)	O5–S2–O7	110.45(8)		
OW3–Cu–O7	84.11(5)	O5–S2–O8	109.09(8)		
OW4–Cu–O3	89.54(5)	O6–S2–O7	108.94(8)		
OW4–Cu–O7	86.77(5)	O6–S2–O8	109.37(8)		
O3–Cu–O7	174.21(4)	O7–S2–O8	108.80(7)		

Table 3
Hydrogen-bonding geometry (Å, °)

D–H···A	d(D–H) (Å)	d(H···A) (Å)	d(D···A) (Å)	∠D–H···A (°)
OW1–H11···O4^{i}	0.853(15)	1.827(15)	2.679(2)	176(2)
OW1–H12···OW5	0.840(14)	1.785(15)	2.622(2)	174(2)
OW2–H21···O2^{ii}	0.902(16)	1.815(16)	2.694(2)	164(2)
OW2–H22···O4	0.908(16)	1.815(16)	2.680(2)	159(3)
OW3–H31···O8^{iii}	0.867(16)	1.916(17)	2.761(2)	164(3)
OW3–H32···O8^{iv}	0.879(16)	1.899(17)	2.769(2)	171(2)
OW4–H41···O8	0.890(16)	1.902(17)	2.769(2)	164(3)
OW4–H42···O5^{iv}	0.903(16)	1.752(18)	2.641(2)	168(3)
OW5–H52···O6^{v}	0.942(16)	1.897(17)	2.805(2)	161(2)
OW5–H51···O2	0.941(17)	1.95(2)	2.808(2)	151(3)
N1–H1A···O7^{vi}	0.90	1.88	2.761(2)	166.0
N1–H1B···O6^{vii}	0.90	1.85	2.731(2)	165.1
N2–H2A···O3	0.90	1.83	2.720(2)	168.9
N2–H2B···O1^{i}	0.90	1.88	2.740(2)	160.1

Symmetry codes: $^{i}x-1, y, z$; $^{ii}x-1/2, -y+1/2, z-1/2$; $^{iii}x+1, y, z$; $^{iv}-x, -y, -z$; $^{v}x+1/2, -y+1/2, z+1/2$; $^{vi}x, y, z+1$; $^{vii}x+1, y, z+1$.

copper disulfate obtained her, crystallizes in the centrosymmetric space group $P2_1/n$. It consists of isolated $[Cu(SO_4)_2(H_2O)_4]^{2-}$, $(C_5H_{14}N_2)^{2+}$ and H_2O units connected by a complex hydrogen-bond network only. Fig. 1 shows a view of the structure of $(C_5H_{14}N_2)[Cu(SO_4)_2(H_2O)_4] \cdot H_2O$ down the crystallographic *a*-axis.

In the molecular material, the coordination polyhedra around the copper cations are slightly distorted octahedra located in a general position and coordinated by two oxygen atoms of sulfate groups at a distances $Cu–O_3 = 2.3418(11)$ and $Cu–O_7 = 2.3672(11)$ Å and four corners of water molecules (Cu–OW distances vary from 1.9509(12) to 1.9828(12) Å). The values of O–Cu–O angles are between 84.11(5) and 179.27(5)° (Table 2). The copper octahedra are separated from one to each other with a shortest metal–metal distance of Cu–Cu = 6.706 Å. Since, this intermetallic distance is shorter than those found in other compounds previously reported, e.g. $Cu–Cu_{min} = 6.953$ Å and $Co–Co_{min} = 6.803$ Å in dabco and ethylenediamine related sulfates, respectively, it can be the origin of some interesting magnetic interactions at low temperature. This result demonstrates that the structural arrangement and the distances between the metallic centers depend on the size and the shape of the amino group involved in these structures. Within a formula unit, two types of sulfate oxygen atoms are distinguished: six oxygen atoms are hydrogen bonded to water molecules or to the organic cations and two oxygen atoms bonded to Cu atom. It should be noted that the shortest S–O bond lengths are observed for oxygen atoms H-bonded to water molecules or to 2-methylpiperazinediium cations, S–O distances range from 1.4578(14) to 1.4964(12) Å. The distances and angles in the sulfate groups as quoted in Table 2 and they indicate that their shapes are slightly distorted. These geometric characteristics do not present any particularity and they are comparable to those observed in some sulfate compounds templated by others amines groups. Each Cu octahedron shares two oxygen atoms with two sulfate groups to form $[Cu(SO_4)_2(H_2O)_4]$ units. These latest are stabilized and connected together through OW–H···O hydrogen bonds giving rise to a three-dimensional inorganic framework. Fig. 2 represents one $[Cu(SO_4)_2(H_2O)_4]$ group, indicating that two oxygen atoms belonging to the sulfate groups participate in the coordination sphere of the copper atom. Indeed, each metallic octahedron is connected not only to two sulfate groups by corners sharing but also to four other sulfate tetrahedra via H-bonds: one in a bidentate manner and three others in a monodentate fashion (Fig. 3). These octahedra are linked also, via OW–H···O hydrogen bonds, to one free water molecule in a monodentate manner. This neighboring environment is different from that found in the ethylenediamine related sulfate [33], where the cobalt octahedron is surrounded only by six sulfate tetrahedra via H-bonds: two in a bidentate manner and four others in a monodentate fashion. Within the OW–H···O intermolecular H-bonds, the OW···O distances range from 2.622(2) to 2.808(2) Å and the OW–H–O angles are comprised between 151(3) and 176(2)° (Table 3). The negative charge of the inorganic part is compensated by the 2-methylpiperazinediium cations which are located on general position in the inorganic framework cavities (Fig. 1). The characteristic bond distances and angles within the protonated diamine molecule, listed in Table 2, are in agreement with those observed in other compounds containing similar amine groups [18,30,35]. Fig. 4 shows that each organic cation engages its hydrogen atoms bonded to N atoms in N–H···O hydrogen bonds. Thus, it is connected to four neighboring $[Cu(SO_4)_2(H_2O)_4]$ groups and participates in the structure cohesion. The N···O distances vary from 2.720(2) to 2.7616(2) Å and the N–H–O angles range between 160.1 and 168.9° (Table 3).

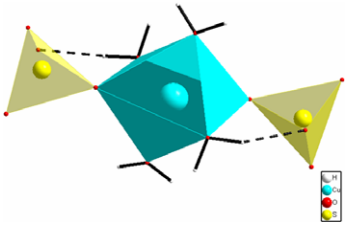


Fig. 2. The $[Cu(SO_4)_2(H_2O)_4]$ units in the structure.

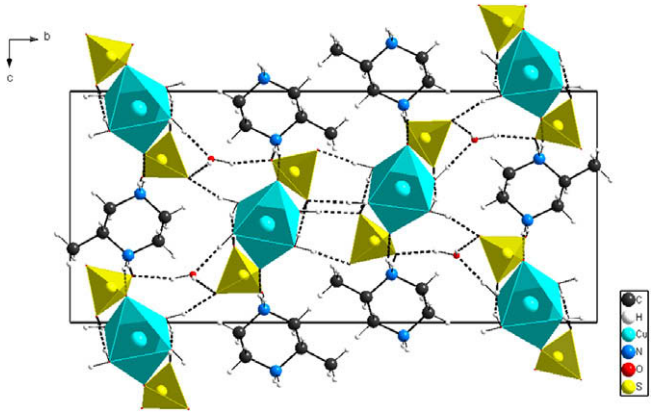


Fig. 1. View of the structure of $(C_5H_{14}N_2)[Cu(SO_4)_2(H_2O)_4] \cdot H_2O$ down the crystallographic *a*-axis. Hydrogen bonds are represented by dashed lines.

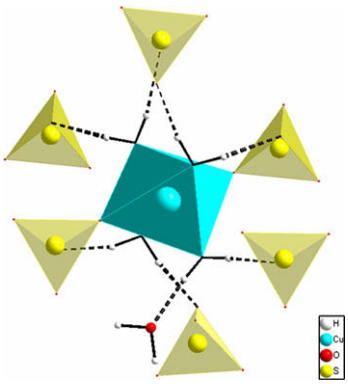


Fig. 3. Octahedron environment around the Cu atom, in the structure of $(C_5H_{14}N_2)[Cu(SO_4)_2(H_2O)_4] \cdot H_2O$.

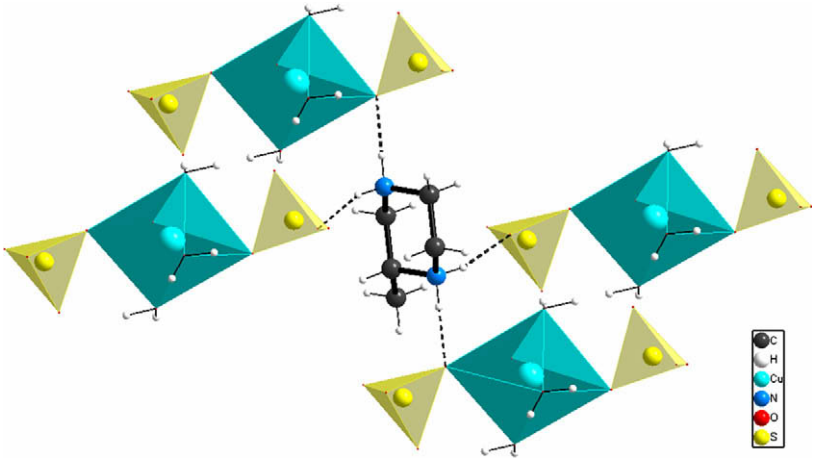


Fig. 4. H-bonds established between $(C_5H_{14}N_2)^{2+}$ and sulfate tetrahedra in the structure of $(C_5H_{14}N_2)[Cu(SO_4)_2(H_2O)_4] \cdot H_2O$.

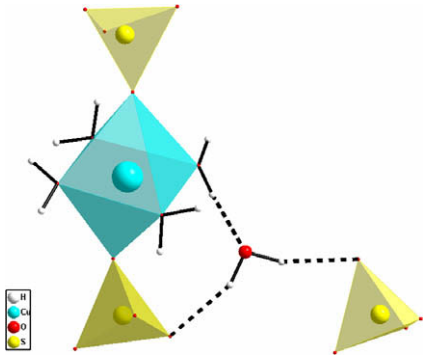


Fig. 5. H-bonds established between the free H_2O molecule, sulfate tetrahedra and copper octahedron in the structure of $(C_5H_{14}N_2)[Cu(SO_4)_2(H_2O)_4] \cdot H_2O$.

In the hybrid materials, the presence of free water molecules plays an important role in the cohesion of the structure [30,32] because they participate in more hydrogen bonds than the other water molecules (three hydrogen bonds for OW5, shown in Table 3). In these hydrogen-bonded interactions, the OW5···O (where OW5 plays the role of a donor) distance range from 2.805(2) to 2.808(2) Å and the OW···OW5 (where OW5 plays the role of an acceptor) distance is 2.622(2) Å. Hence, OW5 is more weakly linked than those found in other water molecules observed in the present structure. The OW5–H···O angles vary from 151(3)° to 161(2)° and OW–H···OW5 angle has the value 174(2)°. The free water molecule OW5 is surrounded by two sulfate tetrahedra and one copper octahedron; connect to each other via, OW–H···O, hydrogen bonds. It is not participating in the environment of copper. It accepts only one hydrogen bond, by one of its free electronic doublets, from the Cu octahedron, and it is donating two hydrogen bonds to two oxygen atoms of sulfate tetrahedra. The environment of the free water molecule is shown in Fig. 5.

The presence of the template in this structure is confirmed using IR spectroscopy, with C–H and N–H bonds measured at 1456 and 1610 cm^{-1}, respectively. C–H and N–H stretches are observed at 2990 and 2782 cm^{-1}, respectively. S–O and S=O stretches are centered on 1120 cm^{-1}. These data are in agreement also of the double protonation of the organic moiety.

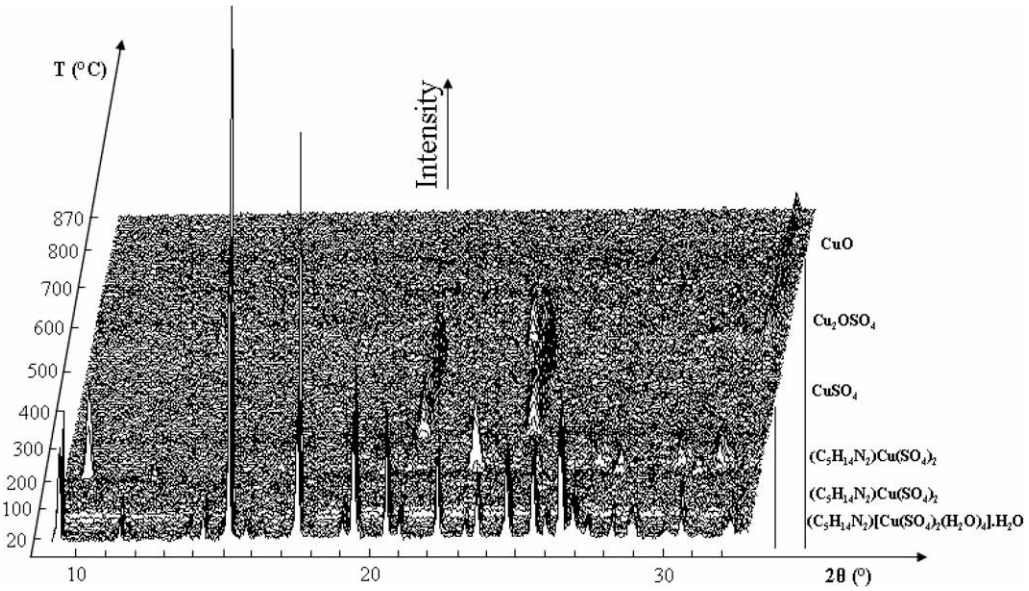


Fig. 6. TDXD plot for the decomposition of $(C_5H_{14}N_2)[Cu(SO_4)_2(H_2O)_4] \cdot H_2O$ in air (14.4° Ch^{-1} from 20 to 870 °C).

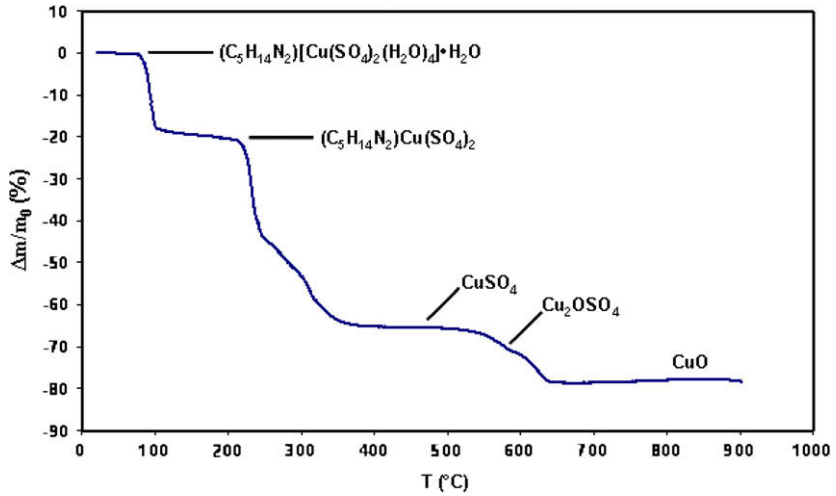


Fig. 7. TG curve for the decomposition of $(C_5H_{14}N_2)[Cu(SO_4)_2(H_2O)_4] \cdot H_2O$ in flowing air.

3.2. Thermal behavior of the precursors

Fig. 6 shows the successive powder patterns obtained during the thermal decomposition of $(C_5H_{14}N_2)[Cu(SO_4)_2(H_2O)_4] \cdot H_2O$, in air in the temperature range 20–870 °C. The TG curve, carried out with a heating rate of 15° Ch^{-1} between 25 and 900 °C, appears in Fig. 7. The first transformation occurs in the temperature range 71–202 °C. The weight loss of 20.7% is in agreement with the departure of five water molecules (cal. weight loss of 20.1%), thus leading to the anhydrous phase, $(C_5H_{14}N_2)Cu(SO_4)$, amorphous to X-rays (Fig. 6). At 220 °C, some diffraction lines emerge from the background. At this temperature no weight loss is observed in the TG curve. From these observations, it was concluded that the anhydrous phase crystallises. It can be noted that a similar thermal behavior has already been observed for $(C_4H_{14}N_2)[M^{II}(H_2O)_6](SO_4)_2 \cdot 4H_2O$ with M^{II} = Co and Ni templated by 1,4-butanediamine [32]. Unfortunately, high background contribution and instability of diffracted intensities did not allow further structural investigations of the compound. $(C_5H_{14}N_2)Cu(SO_4)$ is not stable and decomposes into $CuSO_4$ (weight loss 65.38%). As shown in Fig. 6, some diffraction lines appear to coexist with $CuSO_4$ in the temperature range 550–600 °C. They are attributed to Cu_2OSO_4, as also evidenced by the weight loss of 71.21% (cal. 73.29%) observed in the TG curve at the inflection point (T = 590 °C). The final transformation corresponds to the formation of copper oxide, CuO, which crystallises immediately after Cu_2OSO_4 starts to decompose.

4. Concluding remarks

The title compound templated by 2-methylpiperazine was prepared by the slow evaporation method and characterised by single crystal X-ray diffraction, powder thermodiffractometry and thermogravimetric analyses. It crystallises in the monoclinic system, space group $P2_1/n$. The structure consists of $[Cu(SO_4)_2(H_2O)_4]$ units, built from copper (II) octahedron and two sulfate tetrahedra linked by corner sharing, water molecules, and diprotonated 2-methylpiperazine cations connected together by hydrogen bonds only. The thermal decomposition of the precursors leads to amorphous and crystalline anhydrous phases, respectively. We believe that the centric crystal structure of the title compound was expected from the racemic character of the amine used in the synthesis. The use of the chiral form of this amine (S or R) would allow us to obtain possible acentric organic–inorganic salts. More extensive studies using this synthetic approach should giving rise to a new class of ferroelectrics at room temperature, stable within a wider temperature range. Additional work with XRD, dielectric and thermocurrent measurements are under way and will give more insight into the structural and the physical characteristics of these materials [36].

Appendix A. Supplementary data

CCDC 718821 contains the supplementary crystallographic data for **1**. These data can be obtained free of charge via http://www.ccdc.cam.ac.uk/conts/retrieving.html, or from the Cambridge Crystallographic Data Centre, 12 Union Road, Cambridge CB2 1EZ, UK; fax: (+44) 1223-336-033; or e-mail: deposit@ccdc.cam.ac.uk.

References

[1] C.N.R. Rao, J.N. Behera, M. Dan, Chem. Soc. Rev. 35 (2006) 375.
[2] L.F. Kirpichnikova, L.A. Shuvalov, N.R. Ivanov, B.N. Prasolov, E.F. Andreyev, Ferroelectrics 96 (1989) 313.
[3] A. Pietraszko, K. Lukaszewicz, L.F. Kirpichnikova, Polish J. Chem. 67 (1993) 1877.
[4] L.F. Kirpichnikova, E.F. Andreev, N.R. Ivanov, L.A. Shuvalov, V.M. Varikash, Kristallografiya 33 (1988) 1437.
[5] A.N. Holden, B.T. Matthias, W.J. Merz, J.P. Remeika, Phys. Rev. 98 (1955) 546.
[6] N. Galesic, V.B. Jordanovska, Acta Crystallogr., Sect. C 48 (1992) 256.
[7] M. Fleck, L. Bohaty, E. Tillmanns, Solid State Sci. 6 (2004) 469.
[8] J.-X. Pan, G.-Y. Yang, Y.-Q. Sun, Acta Crystallogr., Sect. E 59 (2003) m286.
[9] A. Rujiwatra, J. Limtrakul, Acta Crystallogr., Sect. E 61 (2005) m1403.
[10] S. Chaabouni, S. Kamoun, A. Daoud, T. Mhiri, Acta Crystallogr., Sect. C 52 (1996) 505.
[11] Y.-L. Fu, Z.-W. Xu, J.-L. Ren, S.W. Ng, Acta Crystallogr., Sect. E 61 (2005) m1639.
[12] C.N. Morimoto, E.C. Lingafelter, Acta Crystallogr., Sect. B 26 (1970) 335.
[13] V. Jordanovska, S. Aleksovska, J. Siftar, J. Thermal Anal. 38 (1992) 1563.
[14] Y.-J. Zhao, X.-H. Li, S. Wang, Acta Crystallogr., Sect. E 61 (2005) m671.
[15] I. Turel, I. Leban, M. Zupancic, P. Bukovec, K. Gruber, Acta Crystallogr., Sect. C 52 (1996) 2443.
[16] M. Rademeyer, Acta Crystallogr., Sect. E 60 (2004) m993.
[17] W. Rekik, H. Naïli, T. Mhiri, T. Bataille, Acta Crystallogr., Sect. E 61 (2005) m629.
[18] W. Rekik, H. Naïli, T. Bataille, T. Roisnel, T. Mhiri, Inorg. Chim. Acta 359 (2006) 3954.
[19] H. Naïli, W. Rekik, T. Bataille, T. Mhiri, Polyhedron 25 (2006) 3543.
[20] Nonius, Kappa CCD Program Software, Nonius BV, Delft, The Netherlands, 1998.
[21] Z. Otwinowski, W. Minor, C.W. Carter, R.M. Sweet (Eds.), Methods in Enzymology, vol. 276, Academic Press, New York, 1997, p. 307.
[22] J. de Meulenaer, H. Tompa, Acta Cryst. 19 (1965) 1014.
[23] L. Farrugia, J. Appl. Crystallogr. 32 (1999) 837.
[24] G.M. Sheldrick, SHELXS-97, Programs for Crystal Solution, University of Göttingen, Germany, 1997.
[25] G.M. Sheldrick, SHELXL-97, Programs for Crystal Structure Refinement, University of Göttingen, Germany, 1997.
[26] M. Doran, A.J. Norquist, D. O'Hare, Chem. Commun. (2002) 2946.
[27] T. Bataille, D. Louër, J. Mater. Chem. 12 (2002) 3487.
[28] C. Ruiz-Valero, C. Cascales, B. Gomez-Lor, E. Gutierrez-Puebla, M. Iglesias, M.A. Monge, N. Snejko, J. Mater. Chem. 12 (2002) 3073.

[29] E.A. Muller, R.J. Cannon, A.N. Sarjeant, K.M. Ok, P.S. Halasyamani, A.J. Norquist, Cryst. Growth Des. 5 (2005) 1913.
[30] S. Yahyaoui, W. Rekik, H. Naïli, T. Mhiri, T. Bataille, Solid State Chem. 180 (2007) 3560.
[31] W. Rekik, H. Naïli, T. Mhiri, T. Bataille, J. Chem. Crystallogr. 37 (2006) 147.
[32] W. Rekik, H. Naïli, T. Mhiri, T. Bataille, Solid State Sci. 11 (2009) 614.
[33] W. Rekik, H. Naïli, T. Mhiri, T. Bataille, Mater. Res. Bull. 43 (2007) 2709.
[34] W. Rekik, H. Naïli, T. Bataille, T. Mhiri, J. Organomet. Chem. 691 (2006) 4725.
[35] A.M. Chippindale, A.D. Bond, A.D. Law, A.R. Cowley, J. Solid State Chem. 136 (1998) 227.
[36] F. Hajlaoui, S. Yahyaoui, H. Naïli, T. Bataille, in preparation.

Polyhedron 28 (2009) 2119–2122

Contents lists available at ScienceDirect

Polyhedron

journal homepage: www.elsevier.com/locate/poly

Ovalbumin mediated synthesis of Mn_3O_4

Zehra Durmus [a], Abdulhadi Baykal [a,*], Hüseyin Kavas [b], Mikail Direkçi [c], Muhammet S. Toprak [d]

[a] Department of Chemistry, Fatih University, B.Çekmece, 34500 Istanbul, Turkey
[b] Department of Physics, Fatih University, B.Çekmece, 34500 Istanbul, Turkey
[c] Department of Physics, Bozok University, 66200 Yozgat, Turkey
[d] Functional Materials Division, Royal Institute of Technology, SE16440 Stockholm, Sweden

ARTICLE INFO

Article history:
Received 18 February 2009
Accepted 24 March 2009
Available online 31 March 2009

Keywords:
Sol–gel processes
Nanocomposites
Spinels
Functional applications
Ovalbumin

ABSTRACT

By using Mn^{2+} and Mn^{3+} salts, and freshly extracted ovalbumin, Mn_3O_4 nanocrystals have been synthesized successfully. The X-ray diffraction results indicated that the synthesized nanoparticles have only the spinel structure without the presence of any other phase impurities. As the ovalbumin–water mixture was highly basic, the process did not require any use of base to increase the pH where hydrolysis took place. A gel formed where water soluble ovalbumin proteins served as a perfect matrix for entrapment of metal ions (Mn^{2+} and Mn^{3+}). Upon heat treatment, the dried gel precursor decomposed into nanocrystalline Mn_3O_4. The discrepancy between the crystallite size from XRD and particle size SEM analysis reveals polycrystalline nature of the synthesized particles with this route. EPR analysis of Mn_3O_4 shows a narrow and symmetric line indicating the absence of hyperfine splitting.

© 2009 Elsevier Ltd. All rights reserved.

1. Introduction

Manganese oxides have attracted considerable interest due to their wide range of applications in catalysis, ion-exchange materials, electrochemical materials, high-density magnetic storage media, solar energy transformation and molecular adsorption [1–6]. Hausmannite, Mn_3O_4 with the spinel structure, is an important oxide which can be used as an active catalyst for the oxidation of methane and carbon monoxide [7] and the selective reduction of nitrobenzene [8] as well as electrode materials for batteries; moreover, it is an effective material to prevent air pollution and limit the emission of NO_x and volatile organic compounds from waste gases of different origins [9].

Various methods have been reported for the synthesis of Mn_3O_4 nanoparticles. Among these methods, high-temperature and hydrothermal methods are generally adopted in conventional processes for the synthesis of Mn_3O_4. Almost all oxides, hydroxides, carbonates, nitrates and sulfates of manganese can serve as precursors to produce Mn_3O_4 at about 1000 °C in air [10]. However, these processes are economically unviable. Recently, chemical bath deposition [11], sol–gel technique [12], oxidation–precipitation method [13], reflux [14] and the co precipitation method [15] have been employed to prepare Mn_3O_4. It is becoming very important to find simple and cost effective routes to synthesize Mn_3O_4 nanoparticles by application of cheap, non-toxic and environmentally friendly precursors.

Egg white proteins (ovalbumin) have various types of functional properties such as gelling, foaming, emulsification, heat setting and binding adhesion [16]. Besides the advantage of its solubility in water and its tendency to associate with metal ions in solution, egg white proteins have also been used as a binder cum gel to shape material, especially bulk and porous ceramics [17]. The use of egg white not only simplifies the process but also would provide another preference process to synthesize of nanocrystalline ceramic particles in an environmentally friendly and cheap way. Up to now, Dhara [17], Kumari et al. [18] and Maensiri et al. [19] used egg white as a water soluble polymeric matrix to produce nanocrystalline alumina, $LiMn_2O_4$ and $NiFe_2O_4$, respectively.

Hereby, we report an innovative approach for the synthesis of Mn_3O_4 based on calcination of a dried gel precursor obtained by freshly extracted ovalbumin mediated synthesis. To the best of our knowledge, this study is the first report on the synthesis of Mn_3O_4 nanocrystals using egg white.

2. Experimental

2.1. Synthesis of Mn_3O_4 nanoparticles in the presence of egg white

Mn (II) acetate dihydrate, $(Mn(ac)_2) \cdot 2H_2O$ and Mn (III) acetylacetonate, $Mn(acac)_3$, of reagent grade, were obtained from Merck. All chemicals were used without further purification. Firstly, water–egg white mixture was prepared (3:2 volume ratio). 60 ml of egg white was stirred with 40 ml deionized water with vigorously at room temperature until a homogeneous solution was obtained. Subsequently, stoichiometric amount of $Mn(ac)_2$ and

* Corresponding author. Tel.: +90 212 866 33 00x2061; fax: +90 212 866 34 02.
E-mail address: hbaykal@fatih.edu.tr (A. Baykal).

0277-5387/$ - see front matter © 2009 Elsevier Ltd. All rights reserved.
doi:10.1016/j.poly.2009.03.026

$Mn(acac)_3$ (with the molar ratio of 1:2) were added slowly into egg white–water solution. During addition of Mn salts the solution was stirred magnetically at room temperature for 2 h to obtain a clear solution. Throughout the whole process, no pH adjustment was necessary as the pH of the solution was measured as ~9. Then the yellow–orange mixed solution was evaporated by heating at 80 °C for several hours until a dried gel precursor was obtained. The dried mass was crushed into powder using a mortar and pestle and then calcined in a box-furnace at 800 °C 3 h in air.

2.2. Characterization

X-ray powder diffraction (XRD) analysis was conducted on a Huber JSODEBYEFLEX 1001 diffractometer operated at 40 kV and 35 mA using Cu Kα radiation.

Fourier transform infrared (FT-IR) spectra of the samples were recorded in transmission mode with a Perkin Elmer BX FT-IR infrared spectrometer using KBr diluted pellets in the range of 4000–400 cm^{-1}.

The thermal stability was determined by thermogravimetric analysis (TGA, Perkin Elmer Instruments model, STA 6000). The TGA thermogram was recorded for 5 mg of powder sample at a heating rate of 10 °C min in the temperature range of 30–800 °C under nitrogen atmosphere.

Scanning electron microscopy (SEM) analysis was performed, in order to investigate the microstructure of the sample, using FEI XL40 Sirion FEG Digital Scanning Microscope. Samples were coated with gold at 10 mA for 2 min prior to SEM analysis.

Transmission electron microscopy (TEM) analysis was performed using a FEI Tecnai G2 Sphera microscope. A drop of diluted sample in alcohol was dripped on the TEM grid.

A conventional X-band (f = 9.8 GHz) Bruker EMX model EPR spectrometer employing an ac magnetic field (modulation frequency: 100 kHz) modulation technique was used for magnetic characterization. Operating conditions were 20.07 mW microwave power, 15 G modulation amplitude, center field 8000 G, time constant 40.96 ms and sweep time 41.94 s with multiple accumulations to enhance the signal-to-noise ratio.

3. Results and discussion

3.1. XRD analysis

A typical XRD pattern of the as-synthesized powder is shown in Fig. 1. All diffraction peaks were indexed to the tetragonal Mn_3O_4 (which are consistent bulk value ICDD Card no. 24-0734). The lattice parameters were calculated as a = 5.76(3) and b = 9.47(1) Å using the d-spacing values and the respective (hkl) parameters. The average size of the crystallites, D_{XRD}, was estimated as 22 ± 10 nm from the diffraction pattern using the line profile fitting of Mn_3O_4 diffraction peaks as described in Wejrzanowski et al. [20] and Pielaszek [21]. The line profile, shown in Fig. 1, is fitted for 14 peaks with the following Miller indices: (101), (112), (200), (013), (211), (004), (220), (213), (204), (015), (312), (303), (321) and (224).

3.2. FT-IR analysis

FT-IR analysis was performed for the sample prepared by the calcination of the dried gel precursor and the spectrum is presented in Fig. 2. In the range of 1000–400 cm^{-1}, two main metal–oxygen bands at ~606 and 478 cm^{-1} were observed in the FT-IR spectrum which are associated with the coupling between Mn–O stretching modes of tetrahedral A- and octahedral B-sites [22,23].

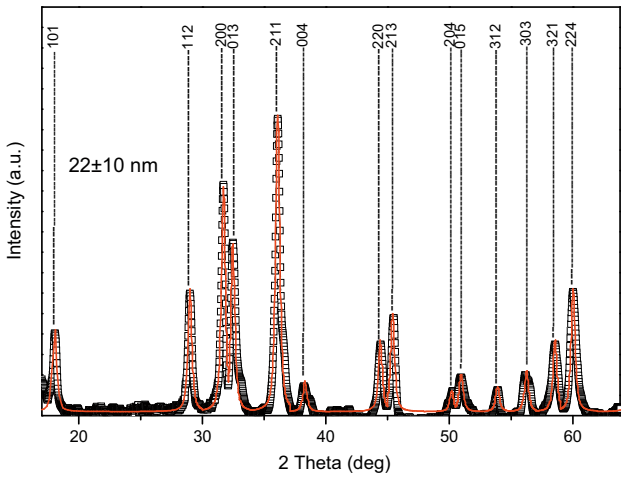


Fig. 1. XRD pattern of Mn_3O_4 particles (obtained upon calcination of dried gel precursor 800 °C) and line profile fitting.

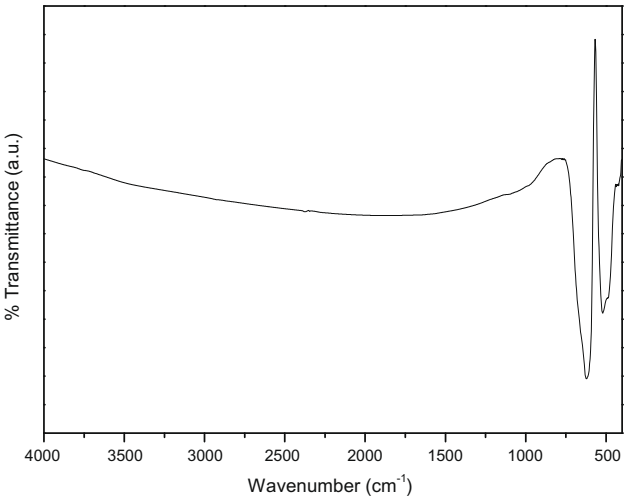


Fig. 2. FT-IR spectrum of as-synthesized Mn_3O_4 upon calcination of the dried gel precursor at 800 °C.

3.3. Thermal analysis

Thermal stability of the precursor powder and final powder has been analyzed using TGA. Thermograms for both samples are presented in Fig. 3. Calcined powder shows no weight loss, as all organic residues have been removed, that reveals the stability of obtained Mn_3O_4 nanoparticles. Precursor powder shows an overall weight loss of ~75%. According to the differential thermogram, DTG, presented in the inset of Fig. 3 there is four-step weight loss (indicated with arrows) for the precursor powder, of mainly ovalbumin, matrix the first one at <200 °C, a shoulder at ~240 °C, the most intense one at ~300 °C and a secondary shoulder one at ~450 °C. The observed thermogram perfectly matches that of pure ovalbumin reported by Kumari et al. [18] above 200 °C. Weight loss up to 200 °C is due to the adsorbed water and boiling of organic residues released from Mn salts. Weight loss around ~240 °C suggests that water molecules in albumin are strongly bonded to the protein molecules and that it takes higher energies to remove them. The considerable weight loss at ~300 °C and the shoulder at ~450 °C is due to the decomposition of proteins in ovalbumin.

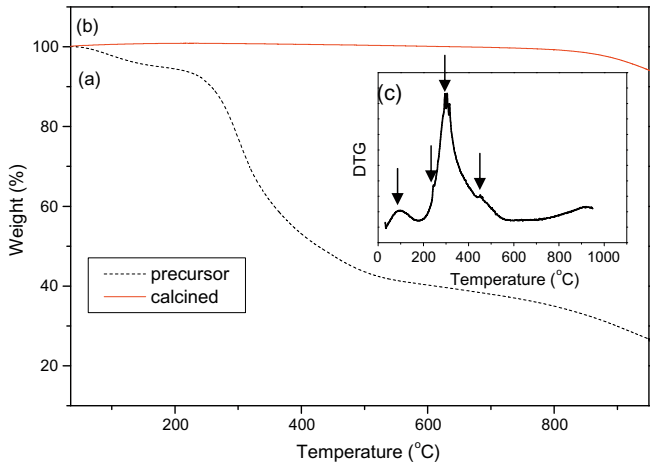


Fig. 3. TGA thermograms of (a) as-made dried gel precursor; (b) final powder after calcination of dried gel precursor; and (c) differential thermogram, DTG, of the precursor in (a).

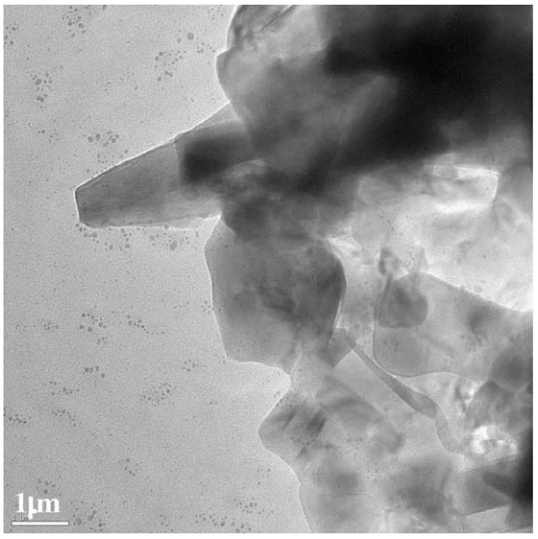


Fig. 5. TEM micrograph of Mn_3O_4 particles obtained upon calcination of the dried gel precursor at 800 °C.

3.4. SEM analysis

SEM analysis was performed to investigate the morphology of synthesized Mn_3O_4 powder and micrographs taken at different magnifications are presented in Fig. 4. Particles were observed to have various morphologies and a wide range of sizes making it difficult to assess the average size from the micrographs. Non-spherical morphology of particles with smooth surfaces suggests the shape is controlled by the entrapment in the dried gel, mainly due to the ovalbumin proteins that confines and stabilizes the metal ions in the gel. Particles with well-defined smooth surfaces are in majority with sizes ranging from ~150 nm up to ~2 μm. The particle size is much larger than the crystallite size obtained from XRD indicating the polycrystalline nature of the observed particle morphologies.

3.5. TEM analysis

Morphology of Mn_3O_4 particles were also investigated by TEM and a micrograph is presented in Fig. 5 which shows a strong agglomeration. Even though particles have lateral dimensions on the order of 1–2 μm levels, their high transparency under TEM reveals a sheet like morphology.

3.6. EPR analysis

The magnetic properties of the as-synthesized Mn_3O_4 were measured using EPR technique in X band and the resultant spectrum is presented in Fig. 6. The EPR spectrum can be used to detect Mn^{2+} and Mn^{4+}, whereas Mn^{3+} is usually not detected due to the complete splitting of the energy levels (no ground state degeneracy) [24].

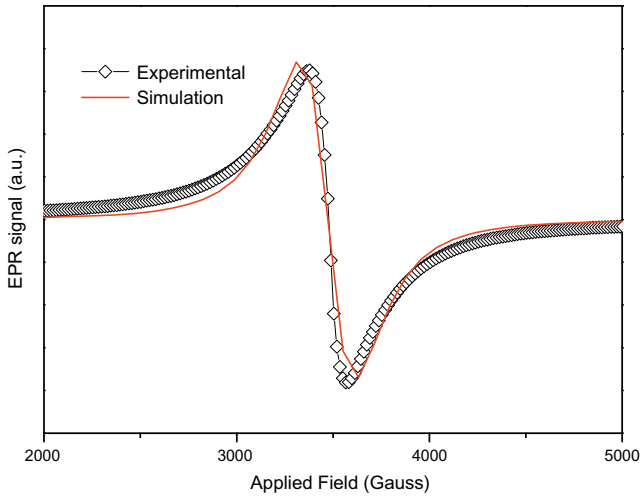


Fig. 6. First derivative of EPR signal (◇) and simulation (–) for Mn_3O_4 particles obtained upon calcination of the dried gel precursor at 800 °C.

Fig. 6 shows room temperature EPR spectrum of Mn_3O_4 including a narrow and symmetric line with its Gaussian simulation signal. The hyperfine splitting is not observed. EPR lines have a peak to peak line-width of 195 G, resonance field of 3475 G and g value

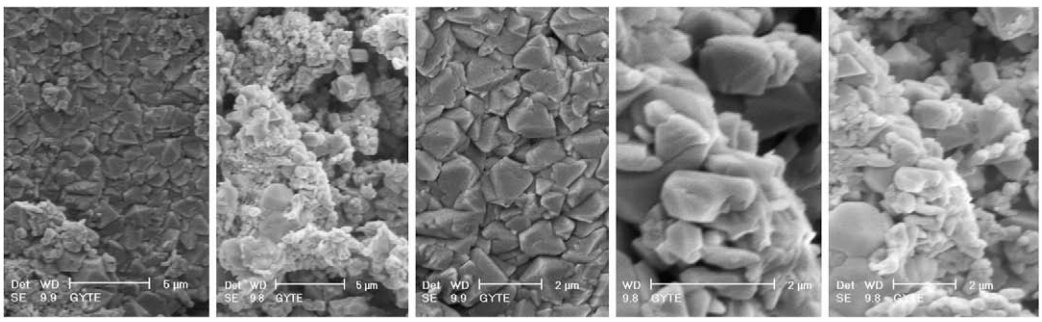


Fig. 4. SEM micrographs of Mn_3O_4 particles, obtained upon the calcination of the dried gel precursor at 800 °C, at different magnifications.

of 2.01. Srinivasan et al. [25] have reported on the temperature dependence of ΔH, Hr and g parameters of Mn_3O_4 in detail. Our results are in accordance with their room temperature observations, where ΔH, Hr and g have been reported as 405 Oe, 3170 Oe and 2.01 at 9 GHz. Huber et al. [26] suggested effective g value of the unlike spin in the exchanged–coupled system as follows:

$$g_{eff} = \frac{g_A S_A(S_A+1)N_A + g_B S_B(S_B+1)N_B}{S_A(S_A+1)N_A + S_B(S_B+1)N_B}$$

where g_A and g_B are the g values, S_A and S_B are spin moments, N_A and N_B are the relative concentrations of A and B sites, respectively. At $Mn^{+2}[Mn^{+3}]_2\ O_4$, by assuming that Mn^{+2} has $g_A = 2$ and using $S_A = 5/2$ and $S_B = 2$ are spin moments, $N_A = 1$ and $N_B = 2$ and experimental g value as $g_{eff} = 2.01$, the Mn^{+3} in B site has g value 2.02 that means unquenched orbital moment resulting unsplitted EPR line [25]. EPR spectrum and exchange coupled equation reveal the absence of hyperfine splitting in the final powder.

4. Conclusion

A novel, environment friendly route utilizing freshly extracted ovalbumin, and Mn^{2+} and Mn^{3+} salts, has been successfully used for the synthesis of Mn_3O_4 nanocrystals. High pH value of ovalbumin–water mixture self-regulated the pH for hydrolysis of metal ions. Water soluble ovalbumin proteins formed a gel and served as a matrix for entrapment of Mn^{2+} and Mn^{3+} ions. The dried gel precursors decomposed into nanocrystalline Mn_3O_4 upon calcination. Crystallite size was estimated as 22 ± 10 nm by XRD line profile fitting and particle size observed from SEM is in the range of 150 nm–2 μm. This discrepancy indicated polycrystalline nature of synthesized nanoparticles. EPR analysis showed a narrow and symmetric line indicating the absence of hyperfine splitting. Presented synthetic route is simple, cost effective, cheap and environmentally friendly that can be applied for the synthesis of other oxide systems.

Acknowledgements

The authors are thankful to the Fatih University, Research Project Foundation (Contract No.: P50020803-2) and Turkish Ministry of Industry and Trade (Contract No.: 00185.STZ.2007-2) for financial support of this study. The fellowship from Knut and Alice Wallenberg's Foundation for Dr. M.S. Toprak is thankfully acknowledged (No.: UAW2004.0224).

References

[1] A.R. Armstrong, P.G. Bruce, Nature 381 (1996) 499.
[2] Y.F. Shen, R.P. Zerger, R.N. Deguzman, S.L. Suib, L. Mccurdy, D.I. Potter, C.L. Oyoung, Science 260 (1993) 511.
[3] M.C. Bernard, H.L. Goff, B.V. Thi, J. Electrochem. Soc. 140 (1993) 3065.
[4] A.H. De Vries, L. Hozoi, R. Broer, Phys. Rev. B 66 (2002) 035108.
[5] Y. Yamashita, K. Mukai, J. Yoshinobu, M. Lippmaa, T. Kinoshita, M. Kawasaki, Surf. Sci. 514 (2002) 54.
[6] Y.C. Zhang, T. Qiao, X.Y. Hu, J. Solid State Chem. 177 (2004) 4093.
[7] E.R. Stobbe, B.A.D. de Boer, J.W. Geus, Catal. Today 47 (1999) 161.
[8] E.J. Grootendorst, Y. Verbeek, V. Ponce, J. Catal. 157 (1995) 706.
[9] M.F.M. Zwinkels, S.G. Jaras, P.G. Menon, T.A. Griffik, Catal. Rev. Sci. Eng. 35 (1993) 319.
[10] A. Vazquez-Olmos, G. Redon, R. Rodriguez-Gattorno, M.E. Mata-Zamora, F. Morales-Leal, A.L. Fernandez-Osorio, J.M. Saniger, J. Colloid Interface Sci. 291 (2005) 175.
[11] W.S. Kijlstra, J.C.M.L. Daamen, J.M. Vandegraaf, B. Vanderlinden, E.K. Poels, A. Bliek, Appl. Catal. B 7 (1996) 337.
[12] E. Mendelovici, A. Sagarzazu, Thermochim. Acta 133 (1988) 93.
[13] T. Ozkaya, A. Baykal, H. Kavas, Y. Köseoğlu, M.S. Toprak, Physica B 403 (2008) 3760.
[14] A. Baykal, Y. Köseoğlu, M. Senel, Central Eur. J. Chem. 5 (1) (2007) 169.
[15] E. Finocchio, G. Busca, Catal. Today 70 (2001) 213.
[16] Y. Mine, Trends Food Sci. Technol. 6 (1995) 225.
[17] S. Dhara, J. Am. Ceram. Soc. 88 (2005) 2003.
[18] T. Sri Devi Kumari, R. Kannan, T. Prem Kumar, Ceramic Int., doi:10.1016/j.ceramint.2008.08.020.
[19] S. Maensiri, C. Masingboon, B. Boonchom, S. Seraphin, Scripta Mater. 56 (2007) 797.
[20] T. Wejrzanowski, R. Pielaszek, A. Opalinska, H. Matysiak, W. Łojkowski, K.J. Kurzydłowski, Appl. Surf. Sci. 253 (2006) 204.
[21] R. Pielaszek, Analytical expression for diffraction line profile for polydispersive powders, Appl. Crystallography, in: Proceedings of the XIX Conference, Krakow, Poland, 2003, p. 43.
[22] W. Wang, C. Xu, G. Wang, Y. Liu, C. Zheng, Adv. Mater. 14 (2002) 837.
[23] N. Gupta, A. Verna, S.C. Kashyap, D.C. Dube, J. Magn. Magn. Mater. 308 (2007) 137.
[24] W.S. Kijlstra, E.K. Poels, A. Bliek, B.M. Weckhuysen, R.A. Schoonheydt, J. Phys. Chem. B 101 (1997) 309.
[25] G. Srinivasan, M.S. Seehra, Phys. Rev. B 28 (1983) 1.
[26] D.L. Huber, Phys. Rev. B 12 (1975) 31.

Polyhedron 28 (2009) 2123–2130

Contents lists available at ScienceDirect

Polyhedron

journal homepage: www.elsevier.com/locate/poly

Functionalised β-diketonate polynuclear lanthanoid hydroxo clusters: Synthesis, characterisation, and magnetic properties

Philip C. Andrews [a], Tobias Beck [a,b], Benjamin H. Fraser [a], Peter C. Junk [a,*], Massimiliano Massi [a,c], Boujemaa Moubaraki [a], Keith S. Murray [a], Morry Silberstein [d]

[a] School of Chemistry, Monash University, Melbourne, Victoria 3800, Australia
[b] On Exchange from Faculty of Chemistry, University of Göttingen, 37077 Göttingen, Germany
[c] Department of Applied Chemistry, Curtin University of Technology, Perth, Western Australia 6845, Australia
[d] School of Medicine Nursing and Health Sciences, Monash University, Melbourne, Victoria 3800, Australia

ARTICLE INFO

Article history:
Received 16 February 2009
Accepted 24 March 2009
Available online 12 April 2009

Keywords:
Lanthanoids
β-Diketones
Crystal structures
Magnetic susceptibility
Metal-hydroxo clusters

ABSTRACT

The controlled hydrolysis of lanthanoid trichloride hexahydrate (Ln = Nd, Eu, Ho) in methanol with the β-diketone ligands dibenzoylmethane and 1,3-bis(4-ethoxyphenyl)propane-1,3-dione yielded tetranuclear and pentanuclear hydroxo clusters for Eu and Ho. In contrast, performing the reaction in the presence of 1,3-bis(4-methoxyphenyl)propane-1,3-dione yielded a mononuclear complex for Nd. The compounds were structurally characterised by means of single crystal X-ray diffraction, showing that the increased bulkiness of the ligand due to the ethoxy functionalities does not affect the capability of the diketonate to stabilize the cluster core. Variable temperature dc susceptibility magnetic measurements were made on the clusters and were indicative of very weak to zero antiferromagnetic, intra-cluster coupling. Variable frequency ac data recorded at low temperatures did not show any evidence for single molecule magnet (SMM) behaviour, unlike the recent reported case of the analogue $[Dy_5(OH)_5(\mathbf{Ph_2acac})_{10}]$, where $\mathbf{Ph_2acac}^-$ is the dibenzoylmethanide ligand.

© 2009 Elsevier Ltd. All rights reserved.

1. Introduction

Over the past decade, the hydrolysis of lanthanoid salts (LnX_3 X = Cl, I, OTf, ClO_4) performed under "controlled conditions" and in the presence of "protecting ligands", to avoid extensive formation of insoluble hydroxide species, has allowed the isolation and characterisation of a wide variety of polynuclear oxo/hydroxo clusters [1]. Although these polynuclear cages have been envisaged for some time as precursors for the preparation of novel functional materials, due to the properties associated with the f electrons of the rare earths such as luminescence [2], magnetism [3], and Lewis acidity [1f,4], very few results in this context have so far been reported. The only relevant examples reported for their application describe their catalytic activity in polymerisation and oxidation reactions [4]. By contrast, the incorporation of polynuclear lanthanoid cages into hybrid organic/inorganic polymeric networks or molecular frameworks has been successfully attempted [5]. Despite these early results, there is still little known about the chemistry and reactivity of the rare earth clusters. In all the synthetic procedures, formation of the polynuclear cage is the ultimate step and no further reactions aimed at modifying either the metal core or the encapsulating ligands have been described. As a result, questions about the stability of the clusters under specific reaction conditions or the possibility of introducing different functional groups on the outer shell in a preformed cage remain unanswered. As part of our ongoing research into obtaining functionalisable clusters, we have pursued cluster formation using β-diketonates obtained from dibenzoylmethane ($\mathbf{Ph_2acac}$H) with short chain ether groups in the *para* position of both phenyl rings. The preparation of tetranuclear and pentanuclear lanthanoid hydroxo clusters, via hydrolysis of lanthanoid chlorides with β-diketonates as ligands, is now well established [4,6]. It is also well known that less bulky ligands promote the formation of larger clusters and vice versa [6,7]. In exploring the chemistry and reactivity of rare earth oxo/hydroxo clusters, we have also probed the relationship between the overall steric bulk of the ligand and the size of the cage (in terms of number of Ln^{3+} ions) which results from this synthetic procedure. This can provide valuable information on whether small modifications to the outer shell can cause a collapse of the cage as a result of changes in the steric demand of the ligands. To achieve this goal we used an "inverse approach", i.e. firstly modifying the ligand with subsequent cluster formation. As such, methoxy and ethoxy functionalities were added in the *para* positions of both the phenyl rings of $\mathbf{Ph_2acac}$H and analogous reactions to the ones which give the unmodified $\mathbf{Ph_2acac}^-$ ligated clusters were carried out. Moreover, a detailed investigation of the magnetic properties of these polynuclear cages has been conducted, in view of their possible use as single molecule magnets (SMMs) [8]. While the

* Corresponding author. Tel.: +61 3 9905 4570; fax: +61 3 9905 4597.
E-mail address: peter.junk@sci.monash.edu.au (P.C. Junk).

0277-5387/$ - see front matter © 2009 Elsevier Ltd. All rights reserved.
doi:10.1016/j.poly.2009.03.031

present work was in progress, a paper describing the SMM features of $[Dy_5(OH)_5(\mathbf{Ph_2acac})_{10}]$, isostructural to the Ho and Eu clusters reported in this work, has just appeared [3c]. Variable frequency ac susceptibility studies have shown that the present Ho_5 and Eu_5 clusters are essentially flat in the out-of-phase ac χ''_M versus T (2–10 K) region, with the merest hint of an increase indicating they are either not SMMs or that the blocking temperature is below 2 K. In contrast, the Dy_5 analogue showed characteristic maxima in χ''_M at ~3 K, pointing to slow relaxation of the magnetisation [3c]. The static dc magnetic susceptibilities of the present compounds show Curie–Weiss behaviour, some with plateaus in susceptibilities at low temperatures, that is indicative of weak to zero antiferromagnetic intra-cluster coupling.

2. Experimental

2.1. General procedures

Chemicals were obtained from Sigma–Aldrich and used as received. ^{1}H and ^{13}C NMR spectra were recorded on a Bruker AM 200 and AM 300 spectrometers. Chemical shifts were recorded on the δ scale and referenced to the solvent. Infrared spectra were recorded on a Perkin–Elmer 1600 Series FTIR using solid state pellets (KBr). Melting points were measured on a Stuart Scientific Melting Point Apparatus SMP3 in an open capillary and were not corrected. Elemental Analyses were performed by the Campbell Microanalytical Laboratory, Department of Chemistry, University of Otago, Dunedin, New Zealand. Crystallographic data were obtained on a Bruker X8 APEX CCD at the temperature of 123 K. The data for $[Nd(\mathbf{5})_3(DMF)_2]$ were collected on an Enraf-Nonius KAPPA CCD at the temperature of 123 K. All compounds were measured with Mo Kα radiation generated by a fine-focus sealed tube using a graphite monochromator. Scans were performed in φ and ω and 0.5° frames were recorded. All the molecular structures were solved using the program SHELXS-97 [9]. Refinement was carried out with the program SHELXL-97 against F^2 using least-square methods [9]. For the X-ray data refer to Table 3. Magnetic measurements were performed using a Quantum Design MPMS 5 Squid for dc studies and a Quantum Design PPMS instrument for ac susceptibilities, as described previously [10]. Samples of mass ~20 mg were checked for crystallite torquing anomalies, due to magnetic anisotropy, by making mulls in Vaseline and comparing to the neat powder samples. The ac frequencies employed on the PPMS machine were 10, 50, 100, 250, 500, 750, 1000, 1250, 1500 Hz with the accompanying dc (static) field of about 3 Oe.

2.2. Synthesis of methyl 4-methoxybenzoate (*1*)

Methyl 4-hydroxybenzoate (6.0 g, 40 mmol) was dissolved in dry DMF (80 ml). K_2CO_3 (16.6 g, 120 mmol) was added and the suspension was stirred for 10 min. Methyliodide (3.8 ml, 60 mmol) was then added dropwise. After stirring for 14 h, water (100 ml) and ethyl acetate (500 ml) were added. The aqueous phase was separated from the organic layer, which was washed with water (8 × 250 ml), dried over $MgSO_4$ and evaporated to dryness to yield **1** as a yellow solid. Yield: 6.42 g (97%). M.p. 51–52 °C. ^{1}H NMR (200 MHz, $CDCl_3$): δ = 3.84 (s, 3H, CH_3O), 3.86 (s, 3H, $COOCH_3$), 6.86–6.93 (m, 2H, 2-H, 6-H), 7.93–8.01 (m, 2H, 3-H, 5-H). ^{13}C NMR (50 MHz, $CDCl_3$): δ = 51.9 ($COOCH_3$), 55.5 (CH_3O), 113.7 (C3, C5), 122.7 (C1), 131.7 (C2, C6), 163.4 (C4), 167.0 ($COOCH_3$). MS (ESI): m/z = 166.8 $[MH]^+$.

2.3. Synthesis of methyl 4-ethoxybenzoate (*2*)

Methyl 4-hydroxybenzoate (6.0 g, 40 mmol) was dissolved in dry DMF (80 ml). K_2CO_3 (19.3 g, 140 mmol) was added and the suspension was stirred for 10 min. Ethyliodide (4.8 ml, 60 mmol) was added dropwise. After stirring for 14 h, water (100 ml) and ethyl acetate (500 ml) were added. The aqueous phase was separated from the organic layer, which was washed with water (8 × 250 ml), dried over $MgSO_4$ and evaporated to dryness to yield **2** as a white solid. Yield: 6.98 g (97%). M.p. 37–38 °C. ^{1}H NMR (300 MHz, $CDCl_3$): δ = 1.43 (t, J = 7.0 Hz, 3H, CH_3CH_2O), 3.88 (s, 3H, CH_3O), 4.08 (q, J = 7.0 Hz, 2H, CH_3CH_2O), 6.88–6.92 (m, 2H, 2-H, 6-H), 7.96–8.00 (m, 2H, 3-H, 5-H). ^{13}C NMR (50 MHz, $CDCl_3$): δ = 14.8 (CH_3CH_2O), 51.9 (CH_3O), 63.8 (CH_3CH_2O), 114.2 (C3, C5), 122.6 (C1), 131.7 (C2, C6), 162.9 (C4), 167.0 ($COOCH_3$). MS (ESI): m/z = 202.9 $[MNa]^+$, 181.2 $[MH]^+$.

2.4. Synthesis of 4-methoxycetophenone (*3*)

4-Hydroxyacetophenone (5.5 g, 40 mmol) was dissolved in dry DMF (80 ml). K_2CO_3 (18 g, 130 mmol) was added and the suspension was stirred for 10 min. Methyliodide (3.8 ml, 60 mmol) was added dropwise. After stirring for 16 h, water (100 ml) and ethyl acetate (500 ml) were added. The aqueous phase was separated from the organic layer, which was washed with water (12 × 250 ml), dried over $MgSO_4$ and evaporated to dryness to yield **3** as a pale yellow solid. Yield: 5.86 g (98%). M.p. 40–41 °C. ^{1}H NMR (200 MHz, $CDCl_3$): δ = 2.54 (s, 3H, CH_3), 3.87 (s, 1H, CH_3O), 6.90–6.97 (m, 2H, 3-H, 5-H), 7.90–7.97 (m, 2H, 2-H, 6-H). ^{13}C NMR (50 MHz, $CDCl_3$): δ = 26.5 (CH_3), 55.6 (CH_3O), 113.8 (C3, C5), 130.5 (C1), 130.8 (C2, C6), 163.6 (C4), 196.9 ($COCH_3$). MS (ESI): m/z = 150.8 $[MH]^+$.

2.5. Synthesis of 4-ethoxy acetophenone (*4*)

4-Hydroxyacetophenone (5.5 g, 40 mmol) was dissolved in dry DMF (80 ml). K_2CO_3 (18 g, 130 mmol) was added and the suspension was stirred for 10 min. Ethyliodide (4.8 ml, 60 mmol) was added dropwise. After stirring for 16 h, water (100 ml) and ethyl acetate (500 ml) were added. The aqueous phase was separated from the organic layer, which was washed with water (12 × 250 ml), dried over $MgSO_4$ and evaporated to dryness to yield **4** as a beige solid. Yield: 5.86 g (99%). M.p. 38–39 °C. ^{1}H NMR (200 MHz, $CDCl_3$): δ = 1.44 (t, J = 7.0 Hz, 3H, CH_3CH_2O), 2.54 (s, 3H, CH_3), 4.12 (q, J = 7.0 Hz, 2H, CH_3CH_2O), 6.87–6.95 (m, 2H, 3-H, 5-H), 7.88–7.96 (m, 2H, 2-H, 6-H). ^{13}C NMR (50 MHz, $CDCl_3$): δ = 14.8 (CH_3CH_2O), 26.4 (CH_3), 63.8 (CH_3CH_2O), 114.3 (C3, C5), 130.3 (C1), 130.7 (C2, C6), 163.0 (C4), 196.9 ($COCH_3$). MS (ESI): m/z = 186.9 $[MNa]^+$, 164.9 $[MH]^+$.

2.6. Synthesis of 1,3-bis(4-methoxyphenyl)propane-1,3-dione (*5H*)

NaH (2.0 g of 60% dispersion in mineral oil, 50 mmol) was added to a mixture of dry DMSO and anhydrous THF (1:2, 150 ml). Compounds **1** (3.3 g, 20 mmol) and **3** (2.2 g, 15 mmol) were dissolved in dry THF (20 ml) and added dropwise to the NaH-suspension while cooling with an ice bath. The brown mixture was allowed to warm up to room temperature after stirring for 1 h, and it was heated to 40 °C and stirred for 16 more h. The THF was evaporated under reduced pressure, water was added (100 ml), and the residue was neutralised with hydrochloric acid (10%) to pH 7. The mixture was then extracted with ethyl acetate (2 × 300 ml), and the combined organic layers were washed with water (10 × 250 ml), dried over $MgSO_4$, and evaporated to dryness. The crude product was recrystallised from ethanol. Compound **5**H was obtained as light brown needles. Yield: 2.22 g (52%). M.p. 119–120 °C. ^{1}H NMR (as mixture of keto and enol forms) (200 MHz, $CDCl_3$): δ = 3.87 (s, 6H, CH_3O), 4.53 (s, CH_2), 6.73 (s, 1H, CH), 6.91–7.01 (m, 4H, 3-H, 3-H, 5-H, 5-H), 7.93–8.03 (m, 4H, 2-H, 2-H, 6-H, 6-H). ^{13}C NMR (50 MHz, $CDCl_3$): δ = 55.6 (CH_3O), 91.6

(COCH$_2$CO), 114.1 (C3, C3, C5, C5), 128.4 (C1, C1), 129.2 (C2, C2, C6, C6), 163.2 (C4, C4), 184.8 (CO). IR (KBr pellet): ν = 2925 (m), 2849 (m), 1604 (s), 1498 (s), 1204 (m), 120 (s), 1229 (s), 1186 (s), 1171 (s), 1116 (m), 1022 (m), 842 (m), 781 (s), 722 (m), 634 (w) cm^{-1}. MS (ESI): m/z = 307.0 [MNa]$^+$, 285.0 [MH]$^+$.

2.7. Synthesis of 1,3-bis(4-ethoxyphenyl)propane-1,3-dione (**6**H)

NaH (2.0 g of 60% dispersion in mineral oil, 50 mmol) was added to a mixture of dry DMSO and anhydrous THF (1:2, 150 ml). Compounds **2** (4.3 g, 24 mmol) and **4** (2.2 g, 20 mmol) were dissolved in dry THF (20 ml) and added dropwise to the NaH-suspension while cooling with an ice bath. The brown mixture was allowed to warm up to room temperature after stirring for 1 h and it was heated to 40 °C and stirred for 16 more h. The THF was evaporated under reduced pressure, water was added (100 ml), and the residue was neutralised with hydrochloric acid (10%) to pH 7. The mixture was extracted with ethyl acetate (2 × 300 ml) and the combined organic layers were washed with water (8 × 100 ml), dried over $MgSO_4$ and evaporated to dryness. The crude product was recrystallized from ethanol. **6**H was obtained as thin yellow plates. Yield: 4.62 g (74%). M.p. 137–138 °C. ^{1}H NMR (300 MHz, $CDCl_3$): δ = 1.45 (t, J = 7.0 Hz, 6H, CH_3CH$_2$O), 4.11 (q, J = 7.0 Hz, 4H, CH$_3$CH_2O), 4.52 (s, CH$_2$), 6.72 (s, 1H, CH), 6.90–6.98 (m, 4H, 3-H, 3-H, 5-H, 5-H), 7.93–8.03 (m, 4H, 2-H, 2-H, 6-H, 6-H). ^{13}C NMR (50 MHz, $CDCl_3$): δ = 14.8 (*C*H$_3$CH$_2$O), 63.9 (CH$_3$*C*H$_2$O), 91.6 (CO*C*H$_2$CO), 114.5 (C3, C3, C5, C5), 128.2 (C1, C1), 129.2 (C2, C2, C6, C6), 162.6 (C4, C4), 196.9 (CO). IR (KBr pellet): ν = 2981 (m), 2936 (m), 2891 (m), 1604 (s), 1506 (m), 1389 (m), 1302 (m), 1254 (s), 1229 (s), 1190 (m), 1173 (s), 1120 (s), 1042 (s), 919 (m), 851 (m), 835 (w), 815 (w), 785 (s), 729 (w), 702 (w), 670 (w), 652 (w), 605 (m) cm^{-1}. MS (ESI): m/z = 335.0 [MNa]$^+$, 313.1 [MH]$^+$.

2.8. Synthesis of [Nd(**5**)$_3$(DMF)$_2$]

$NdCl_3 \cdot 6H_2O$ (0.36 g, 1.0 mmol) and **5**H (0.57 g, 2.0 mmol) were added to 50 ml methanol. Once both reagents were completely dissolved, NEt_3 (0.84 ml, 6.0 mmol) was then added dropwise. After stirring the reaction mixture for 13 h, the solvent was evaporated under reduced pressure. The solid was washed with toluene (3 × 10 ml) and then dissolved in DMF (5 ml). Green block shaped crystals were obtained by slow evaporation after 6 months. Yield (not optimised): 0.17 g (15%). *Anal.* Calc. for $C_{57}H_{59}N_2NdO_{14}$: C, 60.04; H, 5.22; N, 2.46. Found: C, 59.78; H, 5.32; N, 2.43%. IR (KBr pellet) ν: 2933 (w), 2835 (w), 1663 (w), 1641 (m), 1658 (s), 1525 (s), 148,5 (s), 1459 (s), 1430 (s), 1376 (s), 1302 (m), 1249 (s), 1217 (m), 1168 (m), 1103 (s), 1061 (w), 1022 (m), 936 (m), 842 (w), 780 (m) cm^{-1}.

2.9. Synthesis of [Eu$_4$(OH)$_2$(**Ph$_2$acac**)$_{10}$]

$EuCl_3 \cdot 6H_2O$ (0.37 g, 1.0 mmol) and **Ph$_2$acac**H (0.45 g, 2.0 mmol) were added to 50 ml methanol. Once both reagents were completely dissolved, NEt_3 (0.84 ml, 6.0 mmol) was then added dropwise. After stirring the reaction mixture for 13 h, the solvent was evaporated under reduced pressure. The residue was stirred in toluene (15 ml) and filtered. The resulting yellow solid was washed with ethanol (3 × 30 ml) and then dissolved in chloroform (5 ml). Bright yellow crystals were obtained by slow diffusion of hexane into this solution. Yield (not optimised) 0.21 g (15%). *Anal.* Calc. for $C_{150}H_{132}Eu_4O_{22}$: C, 62.24; H 4.60. Found: C, 62.32; H, 4.05%. IR (KBr pellet): ν 3058 (m), 1597 (s), 1556 (s), 1520 (s), 1480 (s), 1455 (s), 1401 (s), 1312 (s), 1223 (m), 1179 (m), 1126 (w), 1069 (m), 1024 (m), 1000 (w), 940 (m), 842 (w), 812 (w), 784 (m), 752 (m), 720 (s), 686 (s), 618 (m), 604 (m) cm^{-1}.

2.10. Synthesis of [Eu$_5$(OH)$_5$(**6**)$_{10}$]

Compound **6**H (0.62 g, 2.0 mmol) was dissolved in a mixture of methanol/THF (1:1, 50 ml), and $EuCl_3 \cdot 6H_2O$ (0.37 g, 1.0 mmol) was added. Once both reagents were completely dissolved, NEt_3 (0.84 ml, 6.0 mmol) was then added dropwise. After stirring for 16 h the solvents were evaporated and toluene (30 ml) was added to the residue. The mixture was stirred for 2 h and filtered. The toluene solution was left undisturbed to evaporate to yield yellow crystals after 1 week. Yield (not optimised): 0.24 g (28%). *Anal.* Calc. for $C_{204}H_{211}Eu_5O_{45}$: C, 59.15; H, 5.13. Found: C, 58.81; H, 5.22%. IR (KBr pellet): ν 3435 (m), 2978 (m), 2928 (m), 1603 (s), 1546 (s), 1527 (s), 1490 (s), 1430 (m), 1387 (m), 1303 (m), 1255 (s), 1220 (s), 1179 (s), 1130 (m), 1115 (m), 1044 (s), 1008 (w), 922 (m), 844 (m), 782 (s), 704 (w), 632 (w) cm^{-1}.

2.11. Synthesis of [Ho$_5$(OH)$_5$(**Ph$_2$acac**)$_{10}$]

$HoCl_3 \cdot 6H_2O$ (0.38 g, 1.0 mmol) and **Ph$_2$acac**H (0.56 g, 2.5 mmol) were added to 50 ml methanol. Once both reagents were completely dissolved, NEt_3 (0.84 ml, 6.0 mmol) was added dropwise. The solution was stirred for 16 h and then evaporated to dryness under reduced pressure. The residue was stirred in toluene (15 ml) and the remaining white solid was filtered off. The filtrate was allowed to stand undisturbed at room temperature to yield yellow crystals after 5 days. Yield (not optimised): 0.10 g (16%). *Anal.* Calc. for $C_{150}H_{115}Ho_5O_{25}$: C, 57.34; H, 3.69. Found: C, 57.67; H, 3.83%. IR (KBr pellet): ν 3455 (sb), 1605 (s), 1553 (s), 1522 (s), 1480 (s), 1458 (s), 1397 (s), 1314 (m), 1281 (m), 1223 (m), 1181 (w), 1068 (w), 1051 (w), 1022 (w), 941 (w), 784 (w), 750 (m), 716 (m), 686 (m), 610 (m) cm^{-1}.

2.12. Synthesis of [Ho$_5$(OH)$_5$(**6**)$_{10}$]

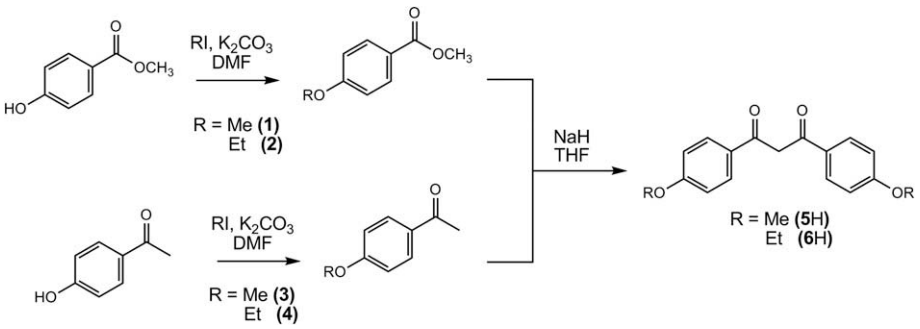
Compound **6**H (0.62 g, 2.0 mmol) was dissolved in a mixture of methanol/THF (1:1, 50 ml), and $HoCl_3 \cdot 6H_2O$ (0.38 g, 1.0 mmol) was added. Once both reagents were completely dissolved, NEt_3 (0.84 ml, 6.0 mmol) was then added dropwise. After stirring for 16 h the solvents were evaporated and toluene (30 ml) was added to the residue. The mixture was stirred for 2 h and filtered. The filtrate was allowed to stand undisturbed at room temperature to yield yellow crystals after 5 days. Yield (not optimised): 0.16 g (18%). *Anal.* Calc. for $C_{197}H_{203}Ho_5O_{45}$: C, 57.49; H, 4.97. Found: C, 57.73; H, 5.08%. IR (KBr pellet): ν 3456 (sb), 2977 (m), 1604 (s), 1560 (m), 1546 (m), 1528 (m), 1491 (s), 1388 (m), 1303 (s), 1254 (m), 1220 (m), 1173 (s), 1115 (w), 1044 (m), 922 (w), 844 (w), 782 (s), 632 (w) cm^{-1}.

3. Results and discussion

3.1. Synthesis of the functionalised ligands and preparation of the polynuclear clusters

The functionalised ligands 1,3-bis(4-methoxyphenyl)propane-1,3-dione (**5**H) and 1,3-bis(4-ethoxyphenyl)propane-1,3-dione (**6**H) were prepared in two steps, as shown in Scheme 1. First, the corresponding 4-hydroxyacetophenone and methyl 4-hydroxybenzoate precursors were treated with MeI or EtI in DMF to produce either the methoxy compounds **1** and **3** or the ethoxy functionalised compounds **2** and **4**. Subsequently, via Claisen condensation, **5**H and **6**H were obtained through coupling of **1** with **3** or **2** with **4** respectively using NaH in dry THF. Only the symmetrical versions of the β-diketones were prepared and investigated in this work.

The cluster compounds were prepared according to the literature procedure [4] by treating 1 equiv. of the corresponding hy-

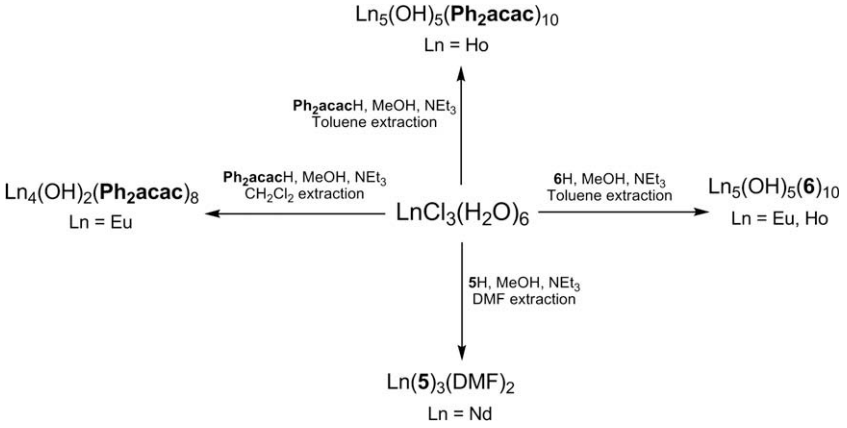


Scheme 1. Synthesis of the functionalised β-diketonate ligands 5 and 6.

drated lanthanoid chloride ($LnCl_3(H_2O)_6$, Ln = Nd, Eu, Ho) with 2 equiv. of ligand (**Ph$_2$acac**H, **5**H, or **6**H) in the presence of an excess of triethylamine in methanol. When the ligands **Ph$_2$acac**H or **6**H were used, the cluster compounds were extracted with toluene or dichloromethane after complete removal of the methanol. The organic phase was then washed with water to remove any unreacted triethylamine along with residual triethylammonium chloride or lanthanoid salt. This procedure yielded the tetranuclear cluster $[Eu_4(OH)_2(\mathbf{Ph_2acac})_8]$ as well as the pentanuclear clusters $[Eu_5(OH)_5(\mathbf{6})_{10}]$ and $[Ho_5(OH)_5(\mathbf{6})_{10}]$. The reaction of the lanthanoid chlorides with **5**H yielded products with poor solubility in toluene, chlorinated solvents or alcohols. Therefore, they were dissolved in DMF and allowed to stand undisturbed. After several months, single crystals suitable for X-ray diffraction were obtained starting from $NdCl_3$ and **5**H. The structure was identified as a mononuclear complex of formula $[Nd(\mathbf{5})_3(DMF)_2]$. At present, due to the insolubility of the product, it is still unclear whether this mononuclear complex was the only species formed in the initial reaction mixture or resulted from deaggregation of a polynuclear cluster in DMF. However, previous studies on polynuclear oxo/hydroxo lanthanoid clusters have shown these cages are unstable in water but relatively stable in highly polar organic solvents such as DMF or DMSO [3d]. By comparison with these results it seems likely that the poor solubility of the complex prevents its further growth into an hydroxo cluster. A summary of the reactions attempted and the corresponding products is given in Scheme 2.

3.2. Crystallography

The tetranuclear $[Eu_4(OH)_2(\mathbf{Ph_2acac})_8]$ and the pentanuclear $[Ho_5(OH)_5(\mathbf{Ph_2acac})_{10}]$ are isostructural with previously reported clusters and will not be described in any detail within this work. Small differences in bond lengths, primarily due to the lanthanoid contraction [11], are provided in Table 1. Interestingly though, in



Scheme 2. Summary of the attempted reactions and corresponding obtained products.

Table 1
Selected bond lengths for $[Eu_4(OH)_2(\mathbf{Ph_2acac})_{10}]$ and $[Ho_5(OH)_5(\mathbf{Ph_2acac})_{10}]$.

Ligand	$[Eu_4(OH)_2(\mathbf{Ph_2acac})_{10}]$	Bond (Å)	$[Ho_5(OH)_5(\mathbf{Ph_2acac})_{10}]$	Bond (Å)
OH	Eu(1)–O(1)	2.410(4)	Ho(1)–O(1) (μ_3-OH)	2.312(4)
OH	Eu(2)–O(1)	2.343(4)	Ho(1)–O(2) (μ_4-OH)	2.560(2)
η^2-Diketonate	Eu(1)–O(4)	2.325(4)	Ho(1)–O(5)	2.277(4)
η^2-Diketonate	Eu(1)–O(5)	2.337(4)	Ho(1)–O(6)	2.273(4)
(μ-O)-η^2-Diketonate	Eu(2)–O(8)	2.343(4)	Ho(1)–O(4)	2.343(4)
(μ-O)-η^2-Diketonate	Eu(2)–O(9)	2.443(4)	Ho(1)–O(3)	2.342(4)
(μ-O)-η^2-Diketonate	Eu(1)–O(9)	2.469(4)	Ho(1)–O(3)#	2.427(4)
(μ-O)$_2$-η^2-Diketonate	Eu(1)–O(2)	2.556(4)		
(μ-O)$_2$-η^2-Diketonate	Eu(1)–O(3)	2.555(4)		
(μ-O)$_2$-η^2-Diketonate	Eu(2)–O(2)#	2.483(4)		
(μ-O)$_2$-η^2-Diketonate	Eu(2)–O(3)#	2.489(4)		
	#: $-x$, $-y+1$, $-z+1$		#: y, $-x+3/2$, z	

the case of Eu both tetranuclear and pentanuclear clusters are formed. It is known that bigger lanthanoids prefer tetranuclear cages where each metal cation is nonacoordinated, whereas smaller ones tend to form pentanuclear cages with octacoordinated metal ions [6]. In this respect, Eu represents the borderline of this trend.

The Nd complex [Nd(**5**)$_3$(DMF)$_2$] (Fig. 1) crystallises in the triclinic space group $P\bar{1}$. The metal is overall octacoordinated by three diketonate ligands, which all adopt a chelating configuration, and two molecules of DMF. Two of the ligands lie on a plane with the third almost perpendicular, whereas the other face of the complex is occupied by the two coordinated solvent molecules. A third molecule of DMF resides in the crystal lattice. The structure does not show any appreciable intermolecular hydrogen bonding, however, the phenyl rings of the diketonate ligands form a π-stacking network exhibiting offset face-to-face bonding with an average distance of 3.6 Å and a vertex-to-face bonding (C–H═C_6H_4 centroid 3.1 Å).

[Eu$_5$(OH)$_5$(**6**)$_{10}$], and [Ho$_5$(OH)$_5$(**6**)$_{10}$] (Fig. 2, where only the Ho cage is reported) are isostructural, showing only small differences in bond lengths between the oxygen atoms of the diketonate and hydroxo ligands due to the lanthanoid contraction passing from Eu to Ho [11] (see Table 2). The structure and geometry of the pentanuclear cage is isostructural with previously published pentanuclear clusters with dibenzoylmethanide ligands. In this case however, the presence of the ethoxy groups in the ligands lowers the symmetry and the compounds crystallise in a monoclinic space group ($C2/c$). Four toluene molecules are present in the lattice. There is no appreciable evidence of either intermolecular hydrogen bonding or π-stacking.

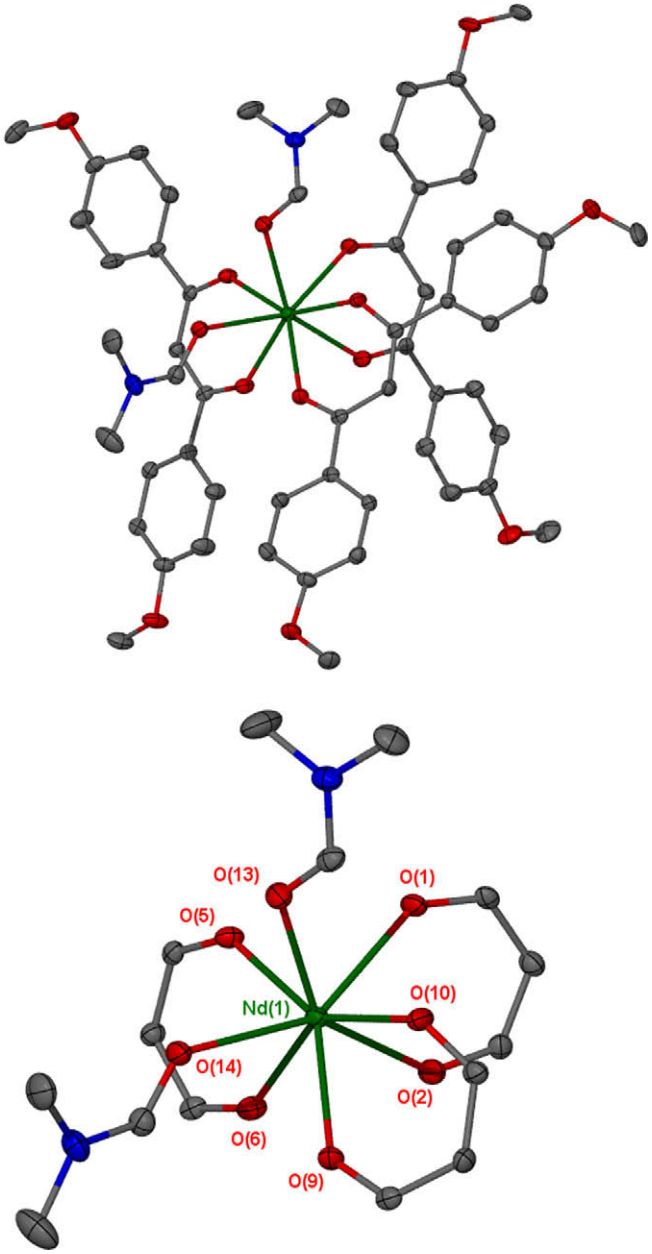


Fig. 1. X-ray crystal structure of [Nd(**5**)$_3$(DMF)$_2$] (top) and coordination environment around the Nd cation (bottom) with ellipsoids at 50% probability. Hydrogen atoms are omitted for clarity.

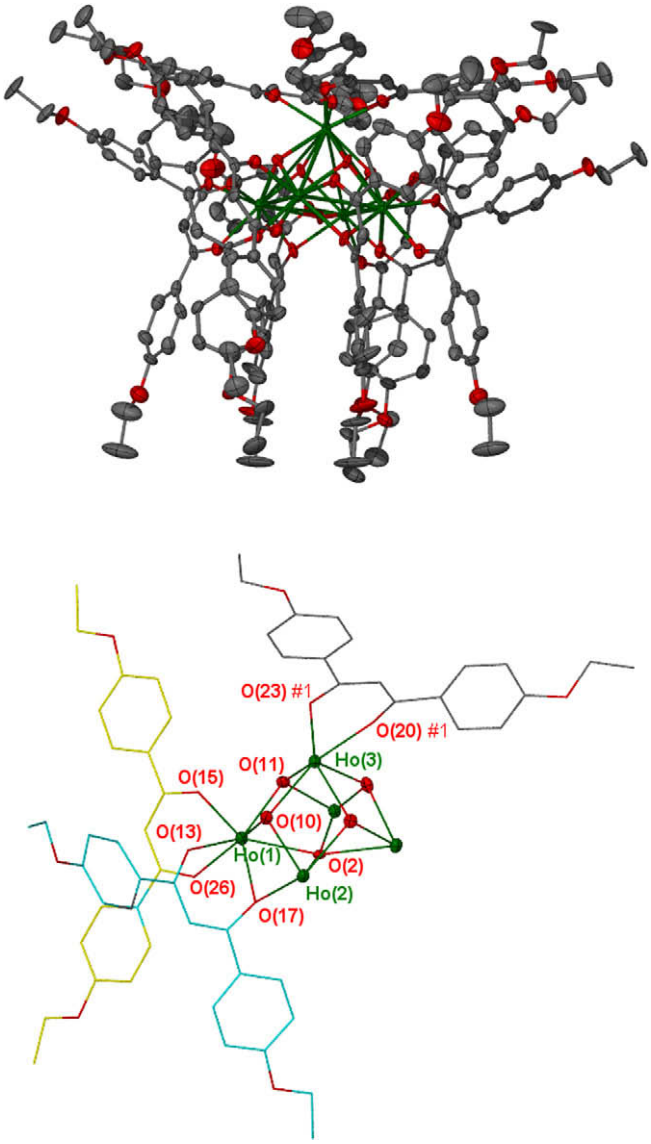


Fig. 2. X-ray crystal structure of [Ho$_5$(OH)$_5$(**6**)$_{10}$] (top) and cluster core (bottom) showing with one ligand chelating (yellow), one ligand chelating/bridging (blue) and one ligand chelating the apical holmium atom (grey). Ellipsoids at 50% probability for core atoms. Hydrogen atoms omitted for clarity, labelling only for atoms that are part of the asymmetric unit and #1 $-x, y, 1/2 - z$. (For interpretation of the references to colour in this figure legend, the reader is referred to the web version of this article.)

3.3. Magnetic measurements on the cluster compounds

The plots of the dc μ_{eff} and χ_M values, per Eu_4 in $[Eu_4(OH)_2(\mathbf{Ph_2acac})_8] \cdot 2\ CHCl_3 \cdot$ hexane, are given in Fig. 3. It can be seen that the μ_{eff} values decrease gradually from 6.5 μ_B (3.25 μ_B per Eu) at 300 K to 0.75 μ_B at 2 K (0.37 μ_B per Eu). The corresponding χ_M values show a broad maximum/plateau between ~70 and 30 K, possibly due to medium strength antiferromagnetic (antiparallel) coupling of the f^6 spins. This plateau region is followed by a rapid, Curie-like increase in χ_M that commonly (in d-block clusters) originates from traces of monomeric (more strongly) paramagnetic impurities. Single ion Eu(III) compounds display μ_{eff} values at 300 K of ~3.4 μ_B, compared to a calculated value of ~3.61 μ_B obtained after consideration of ligand field and spin–orbit splitting of the ^7F free-ion ground state (to give J levels 0 ($^7F_0$ ground level), 1, 2, 3, 4, 5, 6) and thermal population of the first excited $^7F_1$ level following its splitting by first order Zeeman magnetic field effects (H), together with second order Zeeman contributions (H^2) [12,13]. Because of large spin–orbit coupling constants in f-block ions, the separation of the $^7F_0$ and $^7F_1$ levels is of the order of the Boltzmann energy kT (210 K at 300 K) and thus monomeric Eu(III) compounds will show a significant temperature dependence in μ_{eff}, with a zero value calculated at 0 K. Thus, in clusters of the present kind, sorting the spin–spin coupling from the single-ion ligand field/spin–orbit effects is not trivial. The plateau in χ_M at low temperatures might originate from a combination of second order Zeeman (TIP, temperature independent susceptibilities) single-ion effects and weak intra-cluster antiferromagnetic coupling. Very similar plots of μ_{eff} (expressed as $\chi_M T$) and χ_M, versus temperature to those given in Fig. 3 have recently been reported for tetranuclear (chain) species $[Eu_2(L^1)_2(1,10\text{-phen})_2(H_2O)_5] \cdot 3H_2O$, where L^1 is *m*-sulphophenylphosphonate, (μ_{eff} at 300 K = 3.39 μ_B, per Eu) for which antiferromagnetic coupling was suggested [2b], and in the framework structures $[Eu(benzenetricarboxylate)(H_2O)]_n$ and $\{[Eu_2(2\text{-amino-1,4-benzene-dicarboxylate})_3 \cdot (dmf)_4] \cdot 2dmf\}_n$ for which the thermal population of $^7F_1$ levels was invoked, with spin–spin coupling across the carboxylate bridges being assumed to be negligible to weak [14].

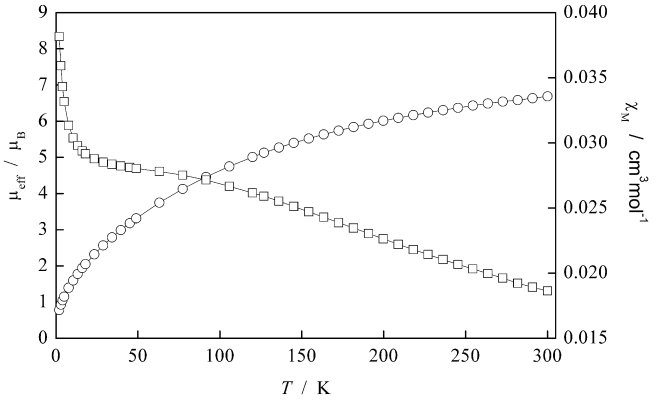


Fig. 3. Plots of molar magnetic susceptility, χ_M, per Eu_4 (squares) and effective magnetic moment, μ_{eff}, per Eu_4 (circles) for $[Eu_4(OH)_2(Ph_2acac)_8] \cdot$ hexane $\cdot$ 2chloroform. The solid lines are just guides to the eye.

The plots of μ_{eff} and χ_M, per Eu_5, versus temperature for $[Eu_5(OH)_5(\mathbf{6})_{10}] \cdot 4$ toluene are given in Fig. 4 and generally have a similar shape to those in Fig. 3, but with a higher plateau value in χ_M between 60 and 10 K, because of the extra Eu(III) centre in this

Table 2
Selected bond lengths for $[Eu_5(OH)_5(\mathbf{6})_{10}]$ and $[Ho_5(OH)_5(\mathbf{6})_{10}]$.

Ligand	$[Eu_5(OH)_5(\mathbf{6})_{10}]$	Bond (Å)	$[Ho_5(OH)_5(\mathbf{6})_{10}]$	Bond (Å)
μ_3-OH	Eu(1)–O(1)	2.360(7)	Ho(1)–O(2)	2.334(6)
μ_4-OH	Eu(1)–O(3)	2.544(2)	Ho(1)–O(1)	2.587(2)
η^2-Diketonate	Eu(1)–O(16)	2.329(6)	Ho(1)-O(12)	2.262(6)
η^2-Diketonate	Eu(1)–O(17)	2.312(6)	Ho(1)–O(13)	2.285(6)
(μ-O)-η^2-Diketonate	Eu(2)–O(12)	2.377(6)	Ho(1)–O(8)	2.347(6)
(μ-O)-η^2-Diketonate	Eu(2)–O(13)	2.393(6)	Ho(1)–O(9)	2.329(6)
(μ-O)-η^2-Diketonate	Eu(1)–O(13)	2.494(7)	Ho(2)–O(9)	2.420(6)

Table 3
Crystal data and structure refinement for $[Nd(\mathbf{5})_3(DMF)_2]$, $[Eu_4(OH)_2(\mathbf{Ph_2acac})_{10}]$, $[Eu_5(OH)_5(\mathbf{6})_{10}]$, $[Ho_5(OH)_5(\mathbf{Ph_2acac})_{10}]$, and $[Ho_5(OH)_5(\mathbf{6})_{10}]$.

	$[Nd(\mathbf{5})_3(DMF)_2]$	$[Eu_4(OH)_2(\mathbf{Ph_2acac})_{10}]$	$[Eu_5(OH)_5(\mathbf{6})_{10}]$	$[Ho_5(OH)_5(\mathbf{Ph_2acac})_{10}]$	$[Ho_5(OH)_5(\mathbf{6})_{10}]$
Formula	$C_{60}H_{66}N_3NdO_{15}$	$C_{158}H_{128}C_{16}Eu_4O_{22}$	$C_{218}H_{227}Eu_5O_{45}$	$C_{178}H_{147}Ho_5O_{25}$	$C_{218}H_{227}Ho_5O_{45}$
Formula weight	1213.40	3199.14	4326.80	3510.61	4391.65
Crystal system	triclinic	triclinic	monoclinic	tetragonal	monoclinic
Space group	$P\bar{1}$	$P\bar{1}$	$C2/c$	$P4/n$	$C2/c$
a (Å)	14.297(2)	15.275(3)	35.217(5)	19.640(3)	34.758(7)
b (Å)	14.338(2)	16.111(3)	17.000(3)	19.640(3)	17.061(3)
c (Å)	16.268(3)	16.580(4)	33.440(5)	19.076(2)	33.283(4)
α (°)	107.24(3)	117.22(3)	90	90	90
β (°)	113.85(4)	109.38(3)	95.33(3)	90	94.39(3)
γ (°)	94.18(3)	91.85(2)	90	90	90
Volume (Å^3)	2841.2(8)	3339.4(12)	19934(5)	7358.2(18)	19679(6)
ρ_{calcd} (mg m^{-3})	1.418	1.590	1.442	1.584	1.482
Z	2	1	4	2	4
μ (mm^{-1})	0.984	2.045	1.628	2.730	2.065
Reflections collected	49 423	33 983	121 698	163 904	49 582
Unique reflections	15 687	19 397	16 964	10 876	14 132
R_{int}	0.1067	0.0356	0.0880	0.0723	0.0691
R_1 [$I > 2\sigma(I)$]	0.0459	0.0674	0.0966	0.0626	0.0670
wR_2 [all data]	0.1115	0.1361	0.1774	0.1123	0.1231
Goodness-of-fit	1.038	1.220	1.316	1.263	1.253

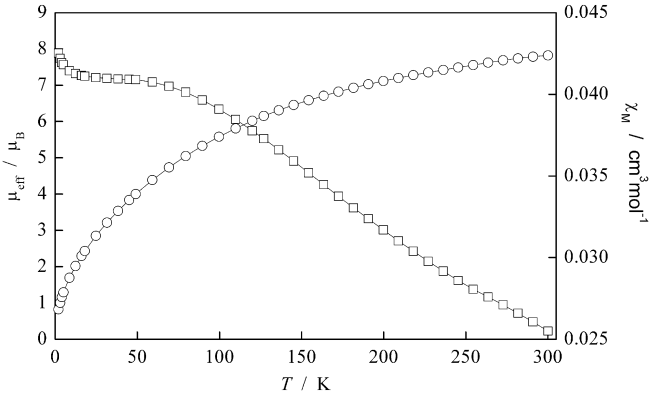


Fig. 4. Plots of molar magnetic susceptility, χ_M, per Eu_5 (squares) and effective magnetic moment, μ_{eff}, per Eu_5 (circles) for $[Eu_5(OH)_5(6)_{10}] \cdot 4$ toluene.

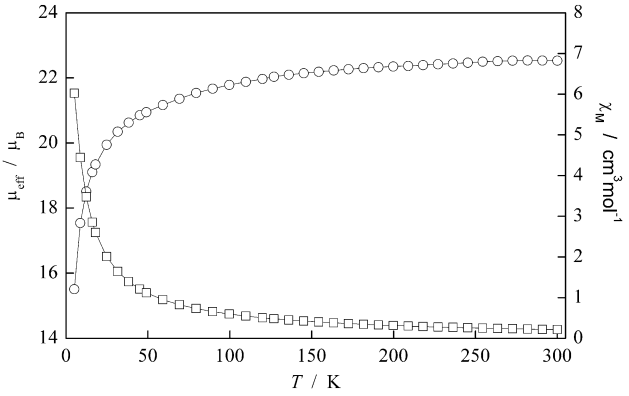


Fig. 5. Plots of molar magnetic susceptility, χ_M, per Ho_5 (squares) and effective magnetic moment, μ_{eff}, per Ho_5 (circles) for $[Ho_5(OH)_5(\mathbf{6})_{10}] \cdot 4$ toluene.

cluster. The room temperature value of μ_{eff}, per Eu, of 3.54 μ_B (7.89 μ_B, per Eu_5), is again typical of Eu(III) compounds and the temperature variation poses the same questions that were discussed for the tetranuclear compound, above, in that the ligand field/spin–orbit effects can not easily be untangled from any antiferromagnetic coupling, although the latter appears to be very weak. The Eu...Eu distances in the crystal structure, of 3.6–3.9 Å, connected by hydroxide are probably longer than the *cis*-carboxylate bridging in the benzenecarboxylate network systems [14] and similar to one of the phosphonate bridging distances (3.81 Å) in $[Eu_2(L^1)_2(1,10\text{-phen})_2(H_2O)_5] \cdot 3H_2O$ [2b]. Thus, from a chemical/structural perspective, it is difficult to predict whether spin coupling between Eu(III) centres is significant, or whether the magnetism is largely single-ion in origin. The examples cited, and the present Eu_4 and Eu_5 clusters, all show rather similar magnetic moment plots irrespective of the bridging ligands employed.

The plot of μ_{eff} and χ_M, per Ho_5, versus temperature for $[Ho_5(OH)_5(\mathbf{6})_{10}] \cdot 4$ toluene is given in Fig. 5. The μ_{eff} values gradually decrease from 22.4 μ_B at 300 K (10.01 μ_B per Ho(III)) to 15.5 μ_B at 4.2 K (6.93 μ_B per Ho(III)). The corresponding χ_M/T plot shows Curie–Weiss behaviour. The Ho(III) f^{10} configuration, with a $^5I_8$ free-ion ground state, typically leads to observed values of ~10.4 μ_B in monomeric systems, and this compares well to the calculated $g(J(J+1))^{0.5}$ value of 10.6 μ_B. Since spin–orbit coupling, second order Zeeman and ligand field effects do not influence the magnetism, as was the case in Eu(III), the decrease in μ_{eff} values with decreasing temperature strongly suggests that antiferromagnetic coupling is occurring in this cluster, via the hydroxo bridges. It is not strong enough, however, to give a maximum in χ_M, a characteristic feature of antiferromagnetic coupling, at least in d-block

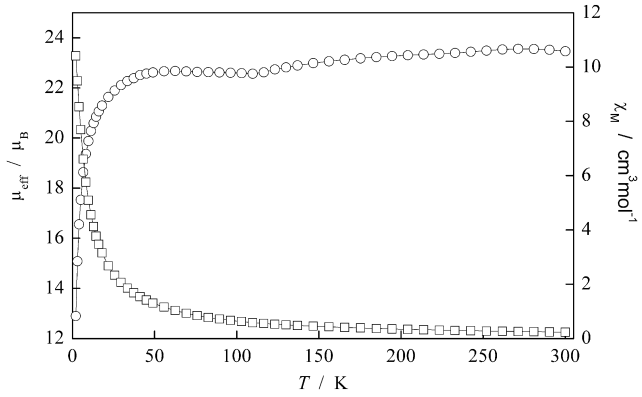


Fig. 6. Plots of molar magnetic susceptility, χ_M, per Ho_5 (squares) and effective magnetic moment, μ_{eff}, per Ho_5 (circles) for $[Ho_5(OH)_5(\mathbf{Ph_2acac})_{10}] \cdot 4$ toluene.

cluster systems. There appear to be few, if any Ho(III) clusters to make comparisons of the present data to. Some metallocrown 15-MC-5 complexes containing both Ho(III) and Cu(II), in dimeric or helical structures, show values of μ_{eff} of 10.4 μ_B at 300 K, decreasing to 7.85 μ_B at 2 K, due to the constituent f^{10} and d^1 spin centres. Exchange coupling parameters could not be obtained for such a complicated situation [15].

The magnetism plots for $[Ho_5(OH)_5(\mathbf{Ph_2acac})_{10}]$ are given in Fig. 6, and, while showing a μ_{eff} value at 300 K similar in size to that of $[Ho_5(OH)_5(\mathbf{6})_{10}] \cdot 4$ toluene, viz. 10.42 μ_B, there is an unusual but reproducible shallow dip at ~100 K, followed, below 50 K, by a rapid decrease with μ_{eff} reaching 5.72 μ_B at 2 K. Assuming that trace impurities are not present, and that there is no phase change at ~100 K, it would appear that changing the β-diketonate ligand from $\mathbf{6}^-$ to $\mathbf{Ph_2acac}^-$ leads to small differences in the magnetism and in the electronic structure of these Ho_5 clusters.

To probe for SMM behaviour in the present clusters, and in view of the very recent report of this important feature occurring, below ~3 K, in an isostructural Dy(III) cluster, $[Dy_5(OH)_5(\mathbf{Ph_2acac})_{10}]$ [3c], the latter showing dc μ_{eff} versus T plots rather like those in Fig. 6, measurements of the dynamic ac in-phase, χ'_M, and out-of-phase, χ''_M, values were made on the clusters between 10 and 2 K, in frequencies of 50–1500 Hz under a close to zero dc applied field. The temperature dependence of χ'_M was Curie–Weiss-like, as in the dc χ_M plots, while the χ''_M values remained close to zero between 10 and 2 K, with only the merest hint of frequency dependent increases at close to 2 K. This contrasts with the clear maxima, at ~3 K, observed in the χ''_M versus T plots for $[Dy_5(OH)_5(\mathbf{Ph_2acac})_{10}]$. Thus we would require facilities to measure χ''_M below 2 K, with a dc field applied to move any frequency dependent maxima above 2 K.

4. Conclusions

The reaction of functionalised β-diketones, as analogues of dibenzoylmethane bearing *para* ethoxy group, with Eu and Ho trichlorides yielded tetranuclear and pentanuclear hydroxo clusters. These structures demonstrate that the increased bulkiness of the ligand has no effect on the formation of the cluster core. On the other side, the methoxy functionalised β-diketone yielded a Nd mononuclear complex. It is still unclear whether this complex does not grow into a cluster due to its limited solubility in the reaction medium or as a cause of deaggregation in polar solvents like DMF. The magnetic studies on the present clusters of Eu(III) and Ho(III) show typical temperature dependent magnetic moment data for these ions. Any antiferromagnetic coupling, within the clusters, is very weak and the decrease in magnetic moments with decreasing temperature is largely due to thermal depopulation of Zeeman lev-

els that originate from the Eu(III) single ion energy levels formed after the free ion states have been split by ligand field and spin–orbit coupling effects. Low temperature plateaus in the molar susceptibilities of the Eu(III) clusters are probably due to second order Zeeman effects rather than to antiferromagnetic coupling. It is likely that antiferromagnetic coupling across the hydroxo bridges is occurring in the Ho(III) clusters since spin–orbit splittings and Zeeman population effects are much less applicable than in the Eu(III) analogues. While there are some hints of SMM behaviour in the Eu and Ho clusters, below 2 K, we do not see the typical maxima in the out-of-phase ac susceptibilities, at different frequencies, recently observed in a closely related pentanuclear Dy(III) cluster [3c]. In other work on large Ln(III) clusters containing different bridging groups than those employed here, some of us have realised, as in Ref. [3c], that to observe SMM features in homometallic Ln(III) species, Dy(III) ($S = 5/2$; $^6H_{15/2}$ ground state) is the lanthanide ion of choice [16]. Much more work on different lanthanoids is needed, however, to test this idea.

5. Supplementary data

CCDC 701176–701180 contain the supplementary crystallographic data for this paper. These data can be obtained free of charge via <http://www.ccdc.cam.ac.uk/conts/retrieving.html>, or from the Cambridge Crystallographic Data Centre, 12 Union Road, Cambridge CB2 1EZ, UK; fax: (+44) 1223-336-033; or e-mail: deposit@ccdc.cam.ac.uk.

Acknowledgments

The authors want to thank Dr. Craig Forsyth (Monash University) and Dr. Regine Herbst-Irmer (Universität Göttingen) for the help provided regarding the crystal structures. Prof. George M. Sheldrick (Fakultät für Chemie, Universität Göttingen) is also gratefully acknowledged for Tobias Beck's student exchange program at Monash University. This work was supported by the Australian Research Council, Monash University and Bayer Schering Pharma.

References

[1] (a) Z. Zheng, Chem. Commun. (2001) 2521;
(b) R. Wang, Z. Zheng, T. Jin, R.T. Staples, Angew. Chem., Int. Ed. 38 (1999) 1813;
(c) R. Anwander, Angew. Chem., Int. Ed. 37 (1998) 599;
(d) Z. Zák, P. Unfried, G. Gieser, J. Alloys Compd. 257 (1997) 175;
(e) M.T. Gamer, P.W. Roesky, Inorg. Chem. 44 (2005) 5963;
(f) D.M. Lyubov, C. Doring, G.K. Fukin, A.V. Cherkasov, A.S. Shavyrin, R. Kempe, A.A. Trifonov, Organometallics 27 (2008) 2905;
(g) D.-S. Zhang, B.-Q. Ma, T.-Z. Jin, S. Gao, C.-H. Yan, T.C.W. Mak, New J. Chem. 24 (2000) 61;
(h) A. Babai, A.-V. Mudring, Z. Anorg. Allg. Chem. 632 (2006) 1956;
(i) R. Wang, M.D. Carducci, Z. Zheng, Inorg. Chem. 39 (2000) 1836.
[2] (a) J.-W. Cheng, J. Zhang, S.-T. Zheng, G.-Y. Yang, Chem. Eur. J. 14 (2008) 88;
(b) Z.-Y. Du, H.-B. Xu, J.-G. Mao, Inorg. Chem. 45 (2006) 9780;
(c) T. Kajiwara, K. Katagiri, M. Hasegawa, A. Ishii, M. Ferbinteanu, S. Takaishi, T. Ito, M. Yamashita, N. Iki, Inorg. Chem. 45 (2006) 4880.
[3] (a) C. Michaelis, W. Bauhofer, H. Buchkremer-Hermanns, R.K. Kremer, A. Simon, G.J. Miller, Z. Anorg. Allg. Chem. 618 (1992) 98;
(b) J.-J. Zhang, S.-M. Hu, S.-C. Xiang, T. Sheng, X.-T. Wu, Y.-M. Li, Inorg. Chem. 45 (2006) 7173;
(c) T.M. Gamer, Y. Lan, P.W. Roesky, A.K. Powell, R. Clerac, Inorg. Chem. 47 (2008) 6581;
(d) N. Mahé, O. Guillou, C. Daiguebonne, Y. Gérault, A. Caneschi, C. Sangregorio, J.Y. Chane-Ching, P.E. Car, T. Roisnel, Inorg. Chem. 44 (2005) 7743.
[4] P.W. Roesky, G. Canesco-Melchor, A. Zulys, Chem. Commun. (2004) 738.
[5] (a) S. Yang, S.I. Troyanov, A.A. Popov, M. Krause, L. Dunsch, J. Am. Chem. Soc. 128 (2006) 16733;
(b) X. Gu, D. Xue, Inorg. Chem. 46 (2007) 3212;
(c) X.-J. Zheng, L.-P. Jin, S. Gao, Inorg. Chem. 43 (2004) 1600.
[6] (a) V. Baskar, P.W. Roesky, Z. Anorg. Allg. Chem. 631 (2005) 2782;
(b) V. Baskar, P.W. Roesky, Dalton Trans. (2006) 676;
(c) S. Datta, V. Baskar, H. Li, P.W. Roesky, Eur. J. Inorg. Chem. (2007) 4216.
[7] (a) G. Xu, Z.-M. Wang, Z. He, Z. Lu, C.-S. Liao, C.-H. Yan, Inorg. Chem. 41 (2002) 6802;
(b) R. Wang, D. Song, S. Wang, Chem. Commun. (2002) 368.
[8] (a) M. Cavallini, M. Facchini, C. Albonetti, F. Biscarini, Phys. Chem. Chem. Phys. 10 (2008) 784;
(b) J. Tang, I.J. Hewitt, N.T. Madhu, G. Chastanet, W. Wernsdorfer, C.E. Hanson, C. Benelli, R. Sessoli, A.K. Powell, Angew. Chem., Int. Ed. 45 (2006) 1729;
(c) J. Luzon, K. Bernot, I.J. Hewitt, C.E. Hanson, A.K. Powell, R. Sessoli, Phys. Rev. Lett. 100 (2008) 247205;
(d) L.F. Chibotaru, L. Ungur, A. Soncini, Angew. Chem., Int. Ed. 47 (2008) 4126;
(e) J.-P. Costes, J.-P. Dahan, W. Wernsdorfer, Inorg. Chem. 45 (2006) 45.
[9] G.M. Sheldrick, Acta Cryst. A 64 (2008) 112.
[10] L.M. Wittick, K.S. Murray, B. Moubaraki, S.R. Batten, L. Spiccia, K.J. Berry, Dalton Trans. 1 (2004) 1003.
[11] S. Cotton, Lanthanide and Actinide Chemistry, John Wiley, England, 2006.
[12] (a) B.N. Figgis, Introduction to Ligand Fields, John Wiley, England, 1966 (Chapter 13);
(b) R.L. Carlin, Magnetochemistry, Springer-Verlag, New York, 1986 (Chapter 9).
[13] M. Gerloch, E.C. Constable, Transition Metal Chemistry, Wiley-VCH, 1994 (Chapter 10).
[14] (a) J. Yang, Q. Yue, G. -D. Li, J.-J. Cao, G.-H. Li, Jie-Sheng, Inorg. Chem. 45 (2006) 2857;
(b) C.A. Black, J.S. Costa, W.T. Fu, C. Massera, O. Roubeau, S.J. Teat, G. Aromi, P. Gamez, J. Reedijk, Inorg. Chem. 48 (2009) 1062.
[15] C.M. Zaleski, E.C. Depperman, J.W. Kampf, M.L. Kirk, V.L. Pecoraro, Inorg. Chem. 45 (2006) 10022.
[16] A.S.R. Chesman, D.R. Turner, B. Moubaraki, K.S. Murray, G.B. Deacon, S.R. Batten, Chem. Eur. J. 15 (2009), doi:10.1002/chem.200900400.

Polyhedron 28 (2009) 2131–2136

Contents lists available at ScienceDirect

Polyhedron

journal homepage: www.elsevier.com/locate/poly

3D zinc(II) coordination polymers built up by triazole and benzene-polycarboxylate anions: Synthesis, crystal structure, thermal and photoluminescence characterization

Durga Sankar Chowdhuri [a], Abhinandan Rana [a], Madhusudan Bera [a], Ennio Zangrando [b], Sudipta Dalai [a,*]

[a] Department of Chemistry and Chemical Technology, Vidyasagar University, Midnapore, 721 102 WB, India
[b] Dipartimento di Scienze Chimiche, University of Trieste, 34127 Trieste, Italy

ARTICLE INFO

Article history:
Received 12 January 2009
Accepted 2 April 2009
Available online 18 April 2009

Keywords:
Coordination polymer of zinc(II)
1,2,4-Triazole
Trimesic acid
Benzene-1,2,4,5-tetracarboxylic acid
Photoluminescence

ABSTRACT

Two coordination polymers of the formula $[Zn_5(tmaH)_4(trz)_2(H_2O)_4]$ (**1**) and $[Zn_3(bta)(trz)_2(H_2O)_4]\cdot 2H_2O$ (**2**) [$tmaH_3$ = benzene-1,3,5-tricarboxylic acid/trimesic acid, trzH = 1,2,4-triazole, $btaH_4$ = benzene-1,2,4,5-tetracarboxylic acid] have been synthesized and structurally characterized by X-ray single crystal diffraction analysis. Both complexes are 3D coordination polymers containing $[Zn_4(trz)_2]$ units connected by benzene-carboxylate anions. In particular, an undulated layer containing 6- and 18-membered rings is outlined in the network of **1**. Hydrogen bonds, involving the coordinated and lattice water molecules with carboxylate oxygen atoms, contribute to the stabilization of the networks. Their thermal stability was investigated by thermogravimetric analysis. The fluorescence spectrum of **1** features two peaks at 419 and 323 nm, originating from a π–π^* intraligand transition and LMCT, respectively. For **2** a broad band at 410 nm is assigned solely as a π–π^* intraligand transition.

© 2009 Elsevier Ltd. All rights reserved.

1. Introduction

Metal organic frameworks (MOFs) [1–3] have been an area of increasing interest due to their topology and potential application in the field of ion exchange [4–6], catalysis [7–9], luminescence [10–12] and gas storage [13–16]. Among the variety of organic molecules used as linkers in the design of supramolecular networks, aromatic polycarboxylates (O-donor) and heterocyclic N rings are the most widely used ligands due to their rigidity in structure and flexibility in coordination modes [17–24].

Several metal organic supramolecular structures based on $tmaH_3$ [$tmaH_3$ = benzene-1,3,5-tricarboxylic acid/trimesic acid] and $btaH_4$ [benzene-1,2,4,5-tetracarboxylic], in the form of differently deprotonated anions, have been reported. The examples show an extensive application of these ligands towards transition metal ions with the aim to build architectures of high dimensionality [25–30]. Polyaza heterocycle trzH [1,2,4-triazole] and its derivatives are very interesting ligands with N-donor centers, which can produce interesting networks with novel topologies [31–37]. TrzH can function as a neutral bridging ligand to two metal sites or as a bridge between three metal centers in the azolate form (trz^-). By exploiting the ligating behavior of these two types (O- and N-donors) of ligands, interesting novel networks can be synthesized.

In this work we report the hydrothermal synthesis, structural characterization, thermal and photoluminescence properties of two new coordination complexes showing a 3D network, namely $[Zn_5(tmaH)_4(trz)_2(H_2O)_4]$ (**1**) and $[Zn_3(bta)(trz)_2(H_2O)_4]\cdot 2H_2O$ (**2**).

2. Result and discussions

2.1. Preparation of the complexes

Zinc(II) complexes **1** and **2** were obtained by reacting zinc(II)acetate and 1,2,4-triazole with benzene-1,3,5-tricarboxylic acid and benzene-1,2,4,5-tetracarboxylic acid, respectively. The pH of both of reaction mixtures were adjusted to five by adding NaOH solution. Both the isolated compounds are air-stable, less soluble in water and alcohols, but soluble in solvents with pronounced donor properties.

2.2. Structure description of *1*

An ORTEP view of the three crystallographically independent Zn(II) coordination spheres is depicted in Fig. 1 and selected bond lengths and angles are reported in Table 1. The three independent metals present different coordination environments, Zn(1) and Zn(3) having distorted tetrahedral NO_3 and N_2O_2 donor sets, respectively, neglecting a long Zn–O(carboxylate) distance of 2.271(3) Å for the latter. The Zn(1)- and Zn(3)-N(triazole) coordination bond lengths are between 2.000(3) and 2.024(3) Å, those

* Corresponding author. Fax: +91 3222 275 329.
E-mail address: icsd2@yahoo.com (S. Dalai).

0277-5387/$ - see front matter © 2009 Elsevier Ltd. All rights reserved.
doi:10.1016/j.poly.2009.04.008

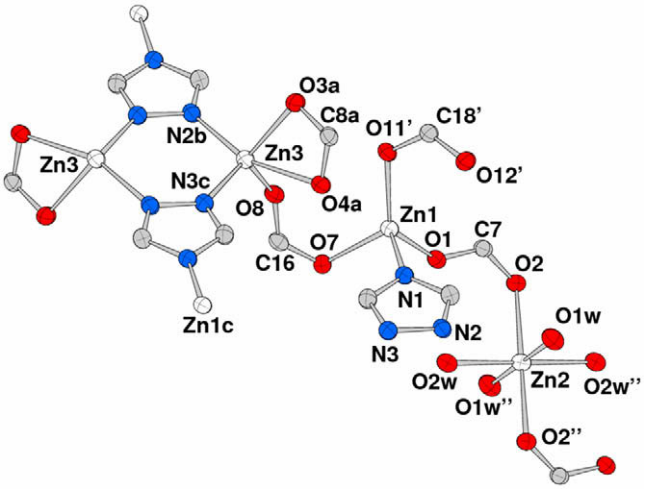


Fig. 1. ORTEP drawing (35% probability ellipsoids) showing the metal coordination spheres of **1**. Symmetry codes: (′) $x, -y+1/2, z+1/2$; (″) $-x+1, -y, -z+1$; (a) $-x+2, y+1/2, -z+3/2$; (b) $x+1, y, z$; (c) $-x+2, -y+1, -z+1$.

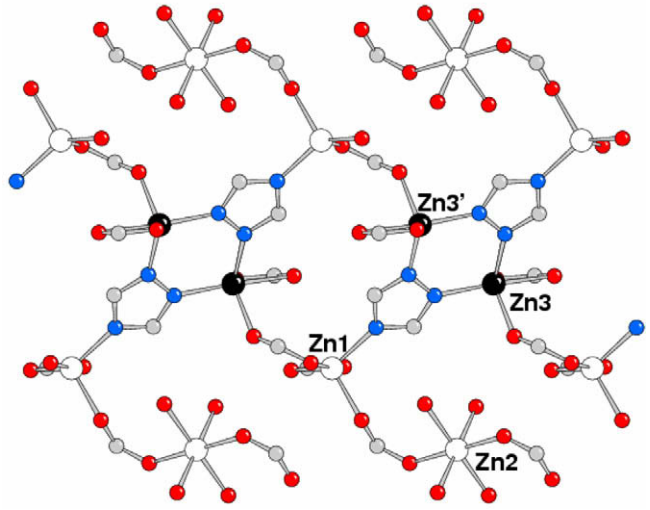


Fig. 2. Crystal packing of **1**: the layer parallel to the ab plane contains the $[Zn_4(trz)_2]$ units.

Table 1
Selected bond lengths (Å) and angles (°) for complex **1**.

Zn(1)–N(1)	2.000(3)	Zn(2)–O(2w)	2.063(3)
Zn(1)–O(1)	2.005(3)	Zn(3)–N(3c)	2.010(3)
Zn(1)–O(7)	2.001(2)	Zn(3)–N(2b)	2.024(3)
Zn(1)–O(11′)	1.941(2)	Zn(3)–O(3a)	2.072(2)
Zn(2)–O(2)	2.060(2)	Zn(3)–O(8)	2.000(3)
Zn(2)–O(1w)	2.159(3)	Zn(3)–O(4a)	2.271(3)
N(1)–Zn(1)–O(1)	102.69(11)	O(2)–Zn(2)–O(2w″)	87.85(10)
N(1)–Zn(1)–O(7)	96.81(11)	O(2w″)–Zn(2)–O(1w)	92.00(12)
O(11′)–Zn(1)–N(1)	126.35(11)	O(2w)–Zn(2)–O(1w)	88.00(12)
O(11′)–Zn(1)–O(1)	113.88(10)	N(3c)–Zn(3)–N(2b)	105.89(11)
O(7)–Zn(1)–O(1)	97.35(10)	N(2b)–Zn(3)–O(3a)	100.37(11)
O(11′)–Zn(1)–O(7)	114.91(10)	O(8)–Zn(3)–N(2b)	96.93(11)
O(2)–Zn(2)–O(1w)	87.00(11)	N(3c)–Zn(3)–O(3a)	117.02(12)
O(2)–Zn(2)–O(1w″)	93.00(11)	O(8)–Zn(3)–N(3c)	118.86(11)
O(2)–Zn(2)–O(2w)	92.15(10)	O(8)–Zn(3)–O(3a)	113.15(10)

Symmetry codes: (′) $x, -y+1/2, z+1/2$; (″) $-x+1, -y, -z+1$; (a) $-x+2, y+1/2, -z+3/2$; (b) $x+1, y, z$; (c) $-x+2, -y+1, -z+1$.

with O-carboxylate fall in a larger range from 1.941(2) to 2.072(2) Å. On the other hand, the Zn(2) ion, located on an inversion center, presents an octahedral O_6 chromophore, with Zn–OH_2 bond lengths of 2.159(3) and 2.063(3) Å, and Zn–O(carboxylate) distances of 2.060(2) Å. All these values are within the range usually observed for Zn(II) compounds containing five-membered azaheterocycles and benzene-carboxylate anions [38–44]. Fig. 2 shows the centrosymmetric $[Zn_4(trz)_2]$ unit and the bridging behavior of the triazolato ligand coordinating two Zn(3) ions spaced at 3.807 Å, while the Zn(1)–Zn(3) and Zn(1)–Zn(3′) distances are 6.070 and 5.956 Å, respectively. In addition, the metals are linked by carboxylate groups having sin-anti bridging behavior (intermetallic Zn(1)–Zn(2) and Zn(1)–Zn(3) distances of 5.048 and 4.353 Å). The described connections give rise to an undulated layer comprising 6- and 18-membered rings (Fig. 2). These undulated metal layers are further connected by bridging benzene-1-carboxylic-3,5-carboxylato dianions to form a 3D network (Fig. 3), which is reinforced by H-bonds involving the aquo and carboxylate oxygen atoms. Strong interactions (O–H···O distance of *ca.* 2.6 Å; Table 1S in SI) are measured for the H-bonds occurring between the carboxylic groups. Here the 1,3,5-tricarboxylate dianions show different behavior, one acts as μ_3-bridging/monocoordinating, the other as μ_3-bridging/chelating species (Fig. 1S in SI). It is interesting to note that the carboxylate groups involved in metal bridging are tilted with respect to the benzene ring by 39.6(2)° (C7/O1/O2) and 23.2(2)° (C16/O7/O8), while the other $-CO_2$ groups are almost coplanar with the ring atoms.

2.3. Structure description of **2**

The two crystallographic independent ions, Zn(1) and Zn(2), exhibit a N_2O_4 octahedral and a distorted N_2O_2 tetrahedral coordination environment, respectively. Fig. 4 depicts the crystal structure, while a selection of bond lengths and angles is collected in Table 2. The coordination bond distances of Zn(2) are almost comparable, being in the range 1.922(4) to 1.993(4) Å, the Zn(1)–O(1w), Zn(1)–N(1) and Zn(1)–O(2w) distances vary from 2.070(5) to 2.100(4) and 2.146(4) Å, respectively. The deprotonated triazole ligand bridges three metal ions forming an isosceles triangle, the base being defined by two Zn(2) ions spaced at 3.611 Å, while the two Zn(1)–Zn(2) distances are 5.993 and 6.170 Å. These values are comparable to those measured in the structure of **1**. The crystal structure can be described as being built up of – $Zn(1)(H_2O)_4$ – $[Zn(2)_2(trz)_2]$ – arrays running in the ac plane, which are linked by μ_4-tetrabenzene-carboxylate anions (Fig. 5) to form a 3D architecture. Each carboxylate group is tilted by about 54.9(4)° with respect to the phenyl ring, having one oxygen atom coordinating a metal ion and the other acting as a H-bond acceptor for an aquo ligand. The conformation assumed by the carboxylate groups is likely attained for steric reasons in order to accomplish metal coordination and H-bond interactions. The described H-bonding scheme together with interactions realized by lattice water molecules and carboxyl groups contribute to the stabilization of the overall crystal structure (O–H···O distances in the range 2.640–2.836 Å) (Table 1S in SI).

2.4. PXRD study

The simulated and measured XRD patterns of compounds **1** (Fig. 6a) and **2** (Fig. 6b) match well, indicating that the solid structures are unchanged during the crystallization process.

2.5. Thermal study

The thermal decomposition profiles for **1** and **2** are shown in Figs. 7 and 8, respectively. Compound **1** is thermally stable up to 40 °C. On further heating, the compound is dehydrated in two steps

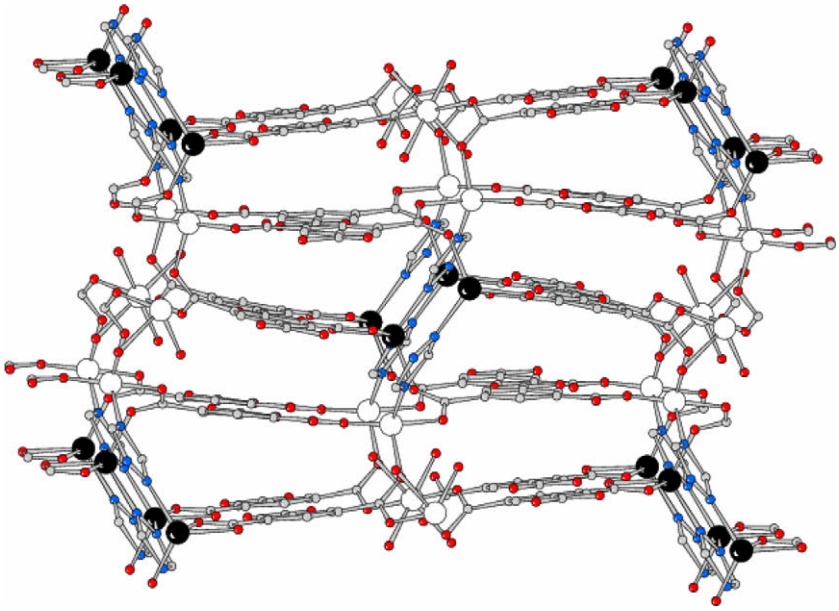


Fig. 3. 3D structure of **1** showing the bridging benzene-carboxylato anions connecting the undulated layers [Zn(3) evidenced as black spheres].

(four coordinated water molecules, mass loss *ca.* 5%, Calc. 5.2%) in the temperature range 40–250 °C. The deaquation temperature range is significant, with the presence of two types of strong hydrogen bonding of the coordinated water molecules (O–H: 2.6 and 2.8 Å). The deaquated species collapsed further upon heating as the Zn centers fail to attain a stable geometry after the removal of the coordinated water molecules. A rapid weight loss (*ca.* 9.8%, Calc. 9.9%) between 260 and 340 °C corresponds to the loss of the trz^- ligand, and sharp weight loss (*ca.* 59%, Calc. 60.8%) between 350 and 630 °C is attributed to the loss of the $tmaH^{2-}$ ligand. Compound **2** undergoes a preliminary dehydration process between 80 and 130 °C, corresponding to the loss of a total of six water molecules in two steps (mass loss *ca.* 15%, Calc. 15.6%), indicating the presence of coordinated and non-coordinated water molecules. The subsequent step between 350 and 460 °C is associated with the loss of the bta^{4-} ligand with a mass loss of *ca.* 36% (Calc. 36.2%). Finally the trz^- ligand is lost (mass loss *ca.* 19%, Calc. 19.7%) between 725 and 770 °C.

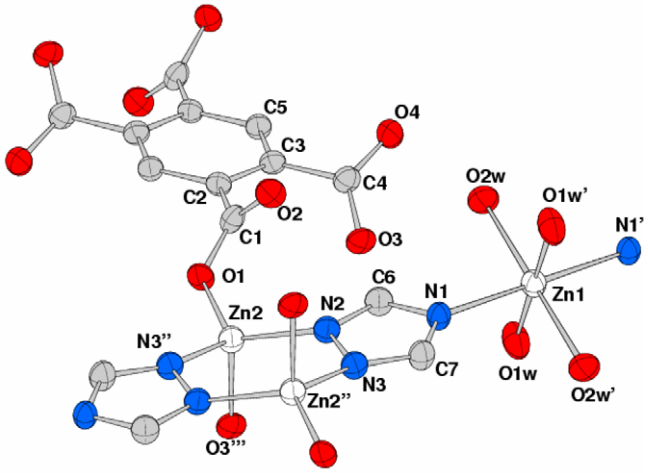


Fig. 4. ORTEP drawing (35% probability ellipsoids) showing the metal coordination spheres of **2**. Symmetry codes: (′) $-x+1, -y, -z+2$; (″) $-x, -y, -z+1$; (‴) $-x+1, -y, -z+1$.

Table 2
Coordination bond distances (Å) and angles (°) for complex **2**.

Zn(1)–N(1)	2.100(4)	Zn(2)–N(3″)	1.983(5)
Zn(1)–O(1w)	2.070(5)	Zn(2)–O(1)	1.922(4)
Zn(1)–O(2w)	2.146(4)	Zn(2)–O(3‴)	1.993(4)
Zn(2)–N(2)	1.995(5)		
O(1w′)–Zn(1)–N(1)	90.38(18)	O(1)–Zn(2)–N(3″)	120.68(18)
O(1w)–Zn(1)–N(1)	89.62(18)	O(1)–Zn(2)–O(3‴)	98.42(17)
N(1)–Zn(1)–O(2w′)	90.27(18)	N(3″)–Zn(2)–O(3‴)	101.06(18)
N(1)–Zn(1)–O(2w)	89.73(18)	O(1)–Zn(2)–N(2)	118.46(17)
O(1w)–Zn(1)–O(2w′)	93.0(2)	N(3″)–Zn(2)–N(2)	108.94(18)
O(1w)–Zn(1)–O(2w)	87.0(2)	O(3‴)–Zn(2)–N(2)	105.74(18)

Symmetry codes: (′) $-x+1, -y, -z+2$; (″) $-x, -y, -z+1$; (‴) $-x+1, -y, -z+1$.

2.6. Photoluminescence study

The luminescence study of the ligands and complexes has been performed in the solid state at room temperature. The two polycarboxylates *i.e.* $tmaH_3$ and $btaH_4$, give no fluorescence response, whereas the azole trzH shows an emission band around 370 nm with $\lambda_{ex} = 300$ nm (Fig. 2S in SI). Compound **1** shows two peaks: a major peak at 323 nm and a weak emission at 419 nm when excited at 278 nm (Fig. 9). For compound **2** a bright fluorescence at 410 nm with a broad emission band has been found when the complex is excited at 320 nm (Fig. 10). During a comparison of the emission properties of the complexes with the trzH ligand, the red shifted band by 49 nm (for **1**) and 40 nm (for **2**) can be assigned as a π–π^* intraligand charge transfer of the triazole ring. On the contrary, for **1**, the 323 nm band, blue shifted by ~47 nm, can be assigned as a ligand-to-metal charge transfer (LMCT) transition. The probable reason for this is that the triazole ring is a deprotonated π-excessive system which is coordinated to the Zn(II) center by displacing one hydrogen atom. The coordination of Zn(II) with the trz^- ring decreases the electron density of the trz^- ring, which is responsible for the weakening of the strength of emission.

3. Conclusion

The reaction of the 1,2,4-triazole ligand and zinc(II) metal with aromatic polycarboxylates affords interesting polymeric architec-

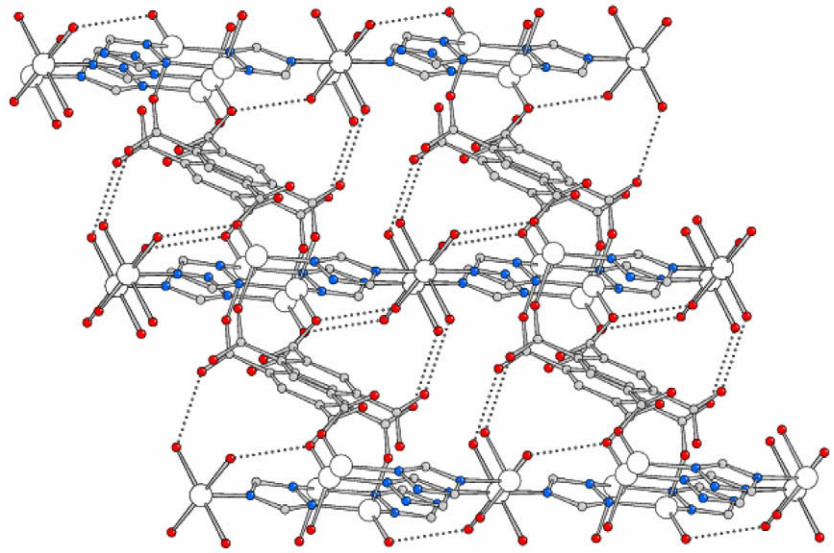


Fig. 5. 3D crystal packing of **2** viewed down the *a*-axis with H-bonds indicated (dotted lines). Guest water molecules are not shown.

tures. In this work, the combination of the 1,2,4-triazolate anion (trz^-) with the benzene-1,3,5-tricarboxylate dianion ($tmaH^{2-}$) or the fully deprotonated benzene-1,2,4,5-tetracarboxylate (bta^{4-}) with Zn(II) ions leads to two 3D coordination networks. The X-ray structural analysis of the compounds revealed that both the polymeric structures comprise centrosymmetric $[Zn_4(trz)_2]$ fragments where each triazolato ligand bridges three metal ions. In particular, an undulated layer containing 6- and 18-membered rings is outlined in the crystal structure of **1**. A photoluminescence study revealed that the red shifted band for both compounds is due to a π–π^* intraligand charge transfer of the triazole ring, while the blue shifted band in **1** is due to LMCT. The synthesis of these compounds demonstrates that the proper combination of polycarboxylates and 1,2,4-triazole derivatives is an excellent way to synthesize interesting high dimensional networks/MOFs.

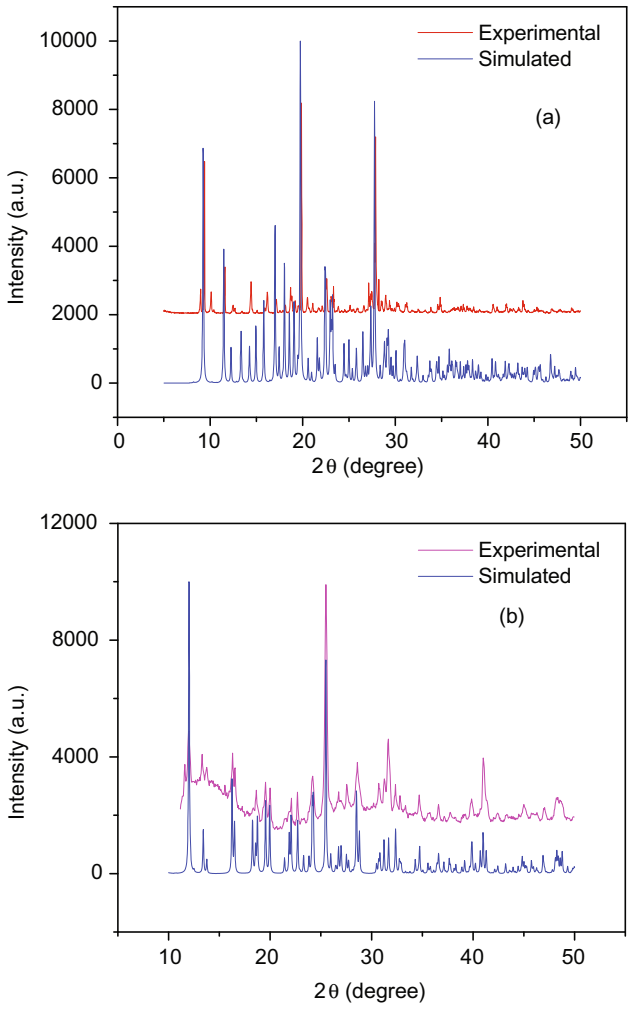


Fig. 6. PXRD patterns (experimental and simulated) for (a) **1** and (b) **2**.

4. Experimental

4.1. Materials and physical measurements

All the chemicals for the synthesis were used as received. Zinc acetate dihydrate was obtained from MERCK. Benzene-1,3,5-tricar-

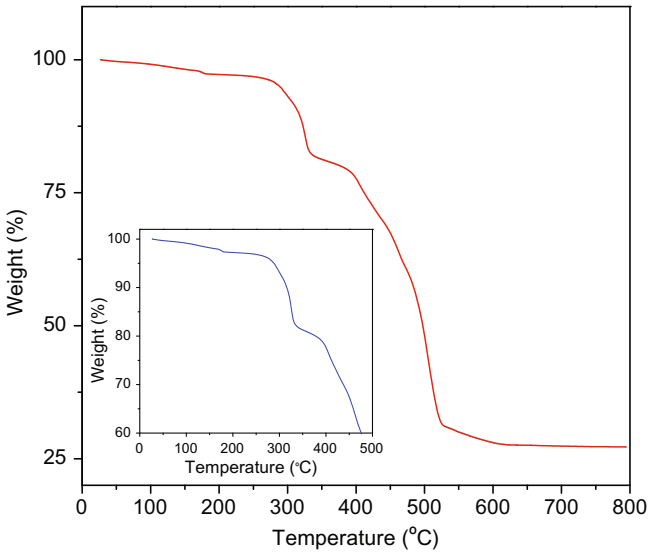


Fig. 7. TG analysis of **1** in the temperature range 25–800 °C with a heating rate of 10 °C/min under N_2 atmosphere.

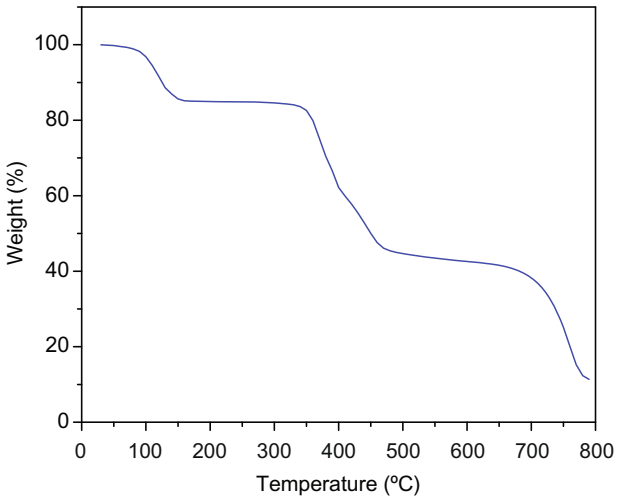


Fig. 8. TG analysis of **2** in the temperature range 25–800 °C with a heating rate of 10 °C/min under N_2 atmosphere.

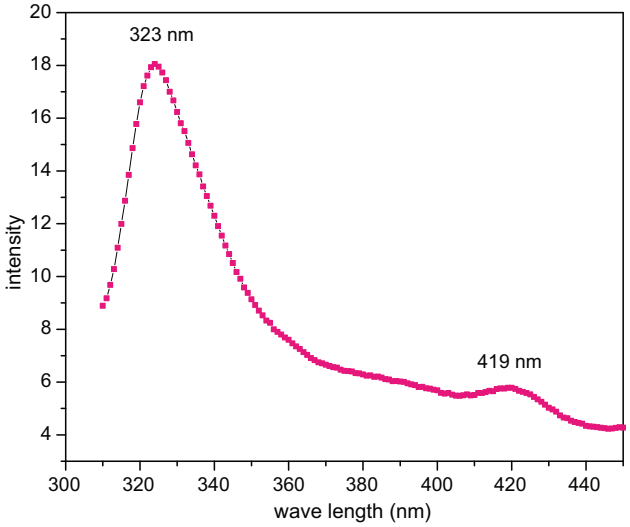


Fig. 9. Solid state emission spectra of **1** at room temperature (λ_{ex} = 278 nm).

boxylic acid, benzene-1,2,4,5-tetracarboxylic acid and 1,2,4-triazole were purchased from SIGMA–ALDRICH Inc. IR specta for **1** and **2** were recorded in a JASCO FT/IR-6200 using the ATR technique in the range 4000–400 cm^{-1}. Elemental analyses (C, H, N) were performed using a Perkin–Elmer 240C elemental analyzer. Thermogravimetric analysis (TGA) were done under nitrogen (flow rate of 20 mL min^{-1}) with a Metler Toledo (SDTA 851e) analyzer in the temperature range 25–800 °C, with a heating rate of 10 °C/min. X ray powder diffraction data were recorded on a BRUKER AXS D8 advance instrument using Cu Kα radiation. The fluorescence spectra of the ligands and compounds were measured in the solid state at room temperature using a HITACHI F-7000 spectrofluorimeter.

4.2. Synthesis of $\{[Zn_5(tmaH)_4(trz)_2(H_2O)_4]\}_n$ (**1**)

A mixture of $Zn(CH_3COOH)_2{\cdot}2H_2O$ (0.5 mmol, 0.109 g), $tmaH_3$ (0.5 mmol, 0.105 g) and trzH (0.5 mmol, 0.034 g) in a molar ratio of 1:1:1 was taken in deionized water (8 mL). The pH of the solution was adjusted to ~5 with 1(M) NaOH solution. The solution was transferred into 23 mL Teflon-lined stainless steel vessel and heated at 160 °C for 72 h. The mixture was allowed to cool to room

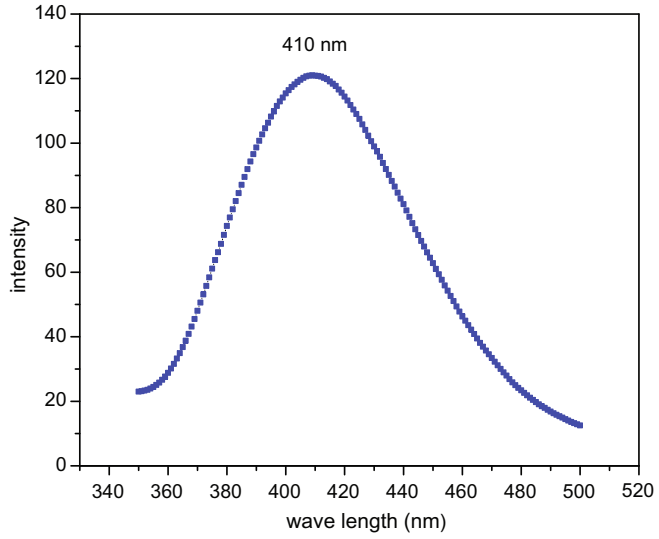


Fig. 10. Solid state emission spectra of **2** recorded at room temperature (λ_{ex} = 320 nm).

temperature and the resulting colorless needle-shaped crystals were isolated by decanting the supernatant liquid, and were washed with deionized water, ethanol and dried in air. Yield: 75%. *Anal.* Calc. for $C_{40}H_{28}N_6O_{28}Zn_5$ (1367.53): C, 35.12; H, 2.06; N, 6.14. Found: C, 35.09; H, 2.12; N, 6.20%.

4.3. Synthesis of $\{[Zn_3(bta)(trz)_2(H_2O)_4{\cdot}2H_2O]\}_n$ (**2**)

Compound **2** was prepared by a similar procedure to that described for the synthesis of **1**. The ligand $btaH_4$ (0.5 mmol, 0.127 g) was used instead of $tmaH_3$. After cooling the solution to room temperature, colorless needle-shaped crystals were isolated by filtering the supernatant liquid, and were washed with deionized water, ethanol and dried in air. Yield: 60%. *Anal.* Calc. for

Table 3
Crystallographic data and details of refinements for compounds **1** and **2**.

	1	**2**
Empirical formula	$C_{40}H_8N_6O_{28}Zn_5$	$C_{14}H_{18}N_6O_{14}Zn_3$
Formula mass (g mol^{-1})	1367.53	690.45
Crystal system	monoclinic	triclinic
Space group	$P\,2_1/c$	$P\bar{1}$
a (Å)	8.685(3)	7.574(3)
b (Å)	13.029(3)	8.433(3)
c (Å)	19.154(3)	10.189(4)
α (°)		104.07(2)
β (°)	93.94(2)	99.78(2)
γ (°)		112.03(2)
V ($Å^3$)	2162.3(10)	560.0(4)
Z	2	1
$\rho_{calc.}$ (g cm^{-3})	2.100	2.048
μ (Mo Kα) (mm^{-1})	2.849	3.273
F(0 0 0)	1368	346
θ Range (°)	1.89–29.64	2.88–27.09
No. collected data	24724	6613
Unique data	5821	2135
R_{int}	0.0501	0.0418
Data $I > 2\sigma(I)$	3652	1302
Refined parameters	372	187
$R1$[a] $[I > 2\sigma(I)]$	0.0422	0.0454
$wR2$[a] $[I > 2\sigma(I)]$	0.1000	0.1063
Goodness of fit (GOF)[b]	0.876	0.857
Residuals (e $Å^{-3}$)	0.421, −0.679	0.584, −0.499

[a] $R1 = \Sigma||Fo| - |Fc||/\Sigma|Fo|$, $wR2 = [\Sigma w(Fo^2 - Fc^2)^2/\Sigma w(Fo^2)^2]^{1/2}$.
[b] $GOF = \{\Sigma[w(Fo^2 - Fc^2)^2]/(n-p)\}^{1/2}$.

$C_{14}H_{18}N_6O_{14}Zn_3$ (690.45): C, 24.35; H, 2.62; N, 12.17. Found: C, 24.29; H, 2.80; N, 12.25%.

4.4. IR study

The IR spectral analysis of compounds **1** and **2** shows a broad band in the region 3200–3500 cm^{-1} [ν(O–H)], suggesting the presence of H_2O molecules [45]. ν_{as}(OCO), ν_s(OCO) bands appear at ~1620, ~1424 cm^{-1} for compound **1** and ~1635, ~1455 cm^{-1} for compound **2**, respectively, indicating the carboxylate is involved in the coordination.

4.5. Crystallographic data collection and refinement

Diffraction data collections were carried out at room temperature on a Nonius DIP-1030H system, using Mo Kα radiation, λ = 0.71073 Å. Cell refinement, indexing and scaling of all the data sets were performed using the programs DENZO and SCALEPACK [46]. The structures were solved by direct methods and subsequent Fourier analyses, and refined by the full-matrix least-squares method using SHELXl97 [47] based on F^2 with all reflections. Hydrogen atoms bonded to carbon were included at calculated positions, while those of water molecules were located in a difference Fourier map and refined with distance constraints. All the calculations were performed using the WINGX System, Ver 1.70.01 [48]. Crystallographic data are given in Table 3.

Acknowledgement

Financial support from DST, New Delhi (Fast Track Proposal:SR/FTP/CS-26/2007) is gratefully acknowledged to carry out this work.

Appendix A. Supplementary data

CCDC 706471 and 714415 contains the supplementary crystallographic data for **1** and **2**. These data can be obtained free of charge via http://www.ccdc.cam.ac.uk/conts/retrieving.html, or from the Cambridge Crystallographic Data Centre, 12 Union Road, Cambridge CB2 1EZ, UK; fax: (+44) 1223-336-033; or e-mail: deposit@ccdc.cam.ac.uk. Supplementary data associated with this article can be found, in the online version, at doi:10.1016/j.poly.2009.04.008.

References

[1] C. Janiak, J. Chem. Soc., Dalton Trans. (2003) 2781.
[2] C.N.R. Rao, S. Natarajan, R. Vaidhyanathan, Angew. Chem., Int. Ed. 43 (2004) 1466.
[3] S. Kitagawa, R. Kitaura, S. Noro, Angew. Chem., Int. Ed. 43 (2004) 2334.
[4] A.N. Khlobystov, N.R. Champness, C.J. Roberts, S.B. Tendler, C. Thompson, M. Schroder, CrystEngComm (2002) 426.
[5] J. Fan, L. Gan, H. Kawaguchi, Y. Sun, K.B. Yu, X. Tang, Chem.-Eur. J. 9 (2003) 3965.
[6] R. Custelcean, T.J. Haverlock, B.A. Moyer, Inorg. Chem. 45 (2006) 6446.
[7] (a) M. Fujita, Y.J. Kwon, S. Washizu, K. Ogura, J. Am. Chem. Soc. 116 (1994) 1151;
(b) F.X.L. Xamena, A. Abad, A. Corma, H. Garcia, J. Catal. 250 (2007) 294;
(c) F.X.L. Xamena, O. Casanova, R.G. Tailleur, H. Garcia, A. Corma, J. Catal. 255 (2008) 220.
[8] J.S. Seo, D. Whang, H. Lee, S.I. Jun, J. Oh, Y.J. Jeon, K. Kim, Nature 404 (2000) 982.
[9] C.D. Wu, A. Hu, L. Zhang, W.B. Lin, J. Am. Chem. Soc. 127 (2005) 8940.
[10] X.J. Zheng, C.Y. Sun, S.Z. Lu, F.H. Liao, S. Gao, L. Jin, J. Eur, J. Inorg. Chem. (2004) 3262.
[11] J.H. He, J.H. Yu, Y.T. Zhang, Q.H. Pan, R.R. Xu, Inorg. Chem. 44 (2005) 9279.
[12] J. Yang, Q. Yuo, J.J. Cao, G.H. Li, J.S. Chen, Inorg. Chem. 45 (2006) 2857.
[13] (a) N. L Rosi, J. Eckert, M. Eddaoudi, D.T. Vodak, O. Kim, M. Keeffe, O.M. Yaghi, Science 300 (2003) 1127;
(b) J.-R. Li, Y. Tao, Q. Yu, X.-H. Bu, H. Sakamoto, S. Kitagawa, Chem. -Eur. J. 14 (2008) 2771.
[14] (a) B.L. Chen, N.W. Ockwig, A.R. Millward, D.S. Contreras, O.M. Yaghi, Angew. Chem., Int. Ed. 44 (2005) 4745;
(b) M. Latroche, S. Surble, C. Serre, C. Mellot-Draznieks, P.L. Llewellyn, J.S. Chang, S.H. Jhung, G. Férey, Adv. Mater. 19 (2007) 2246.
[15] (a) J.L.C. Rowsell, O.M. Yaghi, J. Am. Chem. Soc. 128 (2006) 1304;
(b) H.J. Choi, M. Dincă, J.R. Long, J. Am. Chem. Soc. 130 (2008) 7848.
[16] (a) H. Chun, D.N. Dybtsev, H. Kim, K. Kim, Chem.-Eur. J. 11 (2005) 3521;
(b) M. Dincă, J.R. Long, Angew. Chem., Int. Ed. 47 (2008) 6766.
[17] O.M. Yaghi, M. O'Keeffe, M.N.W. Ockwig, H.K. Chae, M. Eddaoudi, J. Kim, Nature 423 (2003) 705.
[18] B. Moulton, M. Zaworotko, Chem. Rev. 101 (2001) 1629.
[19] X.L. Wang, C. Qin, E.B. Wang, L. Xu, Z.M. Su, C.W. Hu, Angew. Chem., Int. Ed. 43 (2004) 5036.
[20] Y.J. Lu, Coord. Chem. Rev. 241 (2003) 327.
[21] P.S. Mukherjee, S. Dalai, G. Mostafa, E.T. Zangrando, H.T. Lu, G. Rogez, T. Mallah, N. Ray Chaudhuri, Chem. Commun. (2001) 1346.
[22] S. Dalai, P.S. Mukherjee, E. Zangrando, F. Lloret, N. Ray Chaudhuri, J. Chem. Soc., Dalton Trans. (2002) 822.
[23] S. Dalai, P.S. Mukherjee, G. Rogez, T. Mallah, M.G.B. Drew, N. Ray Chaudhuri, Eur. J. Inorg. Chem. (2002) 3292.
[24] S. Kitagawa, S. Noro, Coordination polymers: infinite systems, in: J.A. McCleverty, T.J. Meyer (Eds.), Comprehensive Coordination Chemistry II, vol. 7, Elsevier, New York, 2004, pp. 231–261.
[25] M. Du, X.-J. Jiang, X.-J. Zhao, Inorg. Chem. 45 (2006) 3998 (and references therein).
[26] B.B. Ding, Y.-Q. Weng, Z.W. Mao, C.-K. Lam, X.-M. Chen, B.-H. Ye, Inorg. Chem. 44 (2005) 8836.
[27] C. Daiguebonne, A. Deluzet, M. Camara, K. Boubekeur, N. Audebrand, Y. Gerault, C. Baux, O. Guillou, Cryst. Growth Des. 3 (2003) 1015 (and references therein).
[28] S.K. Ghosh, P.K. Bharadwaj, Inorg. Chem. 43 (2004) 5180.
[29] Q.-G. Zhai, C.-Z. Lu, X.-Y. Wu, S.R. Batten, Cryst. Growth Des. 11 (2007) 2332.
[30] X. Shi, G. Zhu, X. Wang, G. Li, Q. Fang, G. Wu, G. Tian, M. Xue, X. Zhao, R. Wang, S. Qiu, Cryst. Growth Des. 5 (2005) 207.
[31] H. Park, J.F. Britten, U. Mueller, J.Y. Lee, J. Li, J.B. Parise, Chem. Mater. 19 (2007) 1302.
[32] H. Park, D.M. Moureau, J.B. Parise, Chem. Mater. 18 (2006) 525.
[33] Q.G. Zhai, C.Z. Lu, X.-Y. Wu, S.R. Batten, Cryst. Growth Des. 7 (2007) 2332.
[34] H. Park, G. Krigsfeld, J.B. Parise, Cryst. Growth Des. 7 (2007) 736.
[35] Q.-Y. Li, F.-K. Zheng, W.-Q. Zou, M.-F. Wua, G.-C. Guo, A.-Q. Wua, J.-S. Huang, Inorg. Chem. Commun. 11 (2008) 969.
[36] B. Liu, X.-C. Zhang, Inorg. Chem. Commun. 11 (2008) 1162.
[37] X. He, C.-D. Wub, M.-X. Li, S.R. Batten, Inorg. Chem. Commun. 11 (2008) 1378.
[38] D. Krishnamurthy, R. Murugavel, Ind. J. Chem., Sect. A: Inorg., Bio-inorg., Phys., Theor. Anal. Chem. 42 (2003) 2267.
[39] Y.-Y. Liu, J.-F. Ma, J. Yang, Z.-M. Su, Inorg. Chem. 46 (2007) 3027.
[40] Q. Wang, M.-J. Wu, X.-G. Wang, Zhao, Acta Crystallogr., Sect. E: Struct. Rep. Online 62 (2006) m2496.
[41] M.J. Plater, M.R.St. Foreman, R.A. Howie, J.M.S. Skakle, E. Coronado, C.J. Gomez-Garcia, T. Gelbrich, M.B. Hursthouse, Inorg. Chim. Acta 319 (2001) 159.
[42] Z. An, H. Sun, R.-S. Wang, Acta Crystallogr., Sect. E: Struct. Rep. Online 61 (2005) m2157.
[43] C.D. Wu, C.-Z. Lu, D.-M. Wu, H.-H. Zhuang, J.-S. Huang, Inorg.Chem. Commun. 4 (2001) 561.
[44] Z. An, R.-S. Wang, Acta Crystallogr., Sect. E: Struct. Rep. Online 62 (2006) m2493.
[45] K. Nakamoto, Infrared and Raman Spectra of Inorganic and Coordination Compounds, 5th ed., John Wiley and Sons, New York, 1997.
[46] Z. Otwinowski, W. Minor, Processing of X-ray diffraction data collected in oscillation Mode, in: C.W. Carter Jr., R.M. Sweet (Eds.), Methods in Enzymology, vol. 276, Academic Press, New York, 1997, p. 307.
[47] G.M. Sheldrick, University of Göttingen, Germany, SHELX97 Programs for Crystal Structure Analysis (Release 97-2), 1998.
[48] L.J.J. Farrugia, Appl. Crystallogr. 32 (1999) 837.

Polyhedron 28 (2009) 2137–2148

Contents lists available at ScienceDirect

Polyhedron

journal homepage: www.elsevier.com/locate/poly

Synthesis, characterization, molecular and supramolecular structures of nickel(II) complexes derived from α-diketone and α-ketoaldehyde bisaroylhydrazones

Nahed M.H. Salem [a], Amal R. Rashad [a], Laila El Sayed [a], W. Haase [b], Magdi F. Iskander [a,*]

[a] Chemistry Department, Faculty of Science, Alexandria University, P.O. Box 426, Ibrahimia, Alexandria 21321, Egypt
[b] Institut fur Physikalische Chemie, AG Kondensierte Materie, Fachbereich Chemie, Technische Universitat Darmstadt, Petersenstrasse 20, D-64287 Darmstadt, Germany

ARTICLE INFO

Article history:
Received 26 February 2009
Accepted 7 April 2009
Available online 16 April 2009

Keywords:
Bisaroylhydrazones
Nickel(II)complexes
Ammonia and imidazole complexes
X-ray molecular structures

ABSTRACT

A new series of nickel(II) complexes derived from symmetrical diacetyl bisaroylhydrazones [Ni(L^1-R)] and unsymmetric phenylglyoxal bisaroylhydrazones [Ni(L^2-R)] have been prepared and characterized. X-ray crystal and molecular structures of [Ni(L^1-H)], [Ni(L^1-pCH_3O)] and [Ni(L^1-pNO_2)] have been determined. In these complexes, the Ni(II) is in a distorted square planar environment and the aroylhydrazone acts as dinegative tetradentate ligand forming a 5,5,5-tricyclic chelate ring. Reaction of [Ni(L^1-R)] with aqueous ammonia afforded the paramagnetic five coordinate [Ni(L^1-R)(NH_3)] while [Ni(L^2-R)] gave the diamagnetic square planar [Ni(L^2-R)(NH_3)] complexes. Reaction of [Ni(L^1-R)] complexes with imidazole gave the corresponding paramagnetic octahedral bis(imidazole) adducts. X-ray structures of both [Ni(L^1-H)(HIm)$_2$] and [Ni(L^1-pNO_2)(HIm)$_2$] suggest a distorted octahedral structure where the bisaroylhydrazone occupies the basal plane while the two imidazoles occupy the axial sites. The molecular units are associated together forming triple stranded helical chains. With imidazole the [Ni(L^2-R)] series gave the corresponding diamagnetic mono(imidazole) [Ni(L^2-R)(HIm)] complexes, The X-ray structure of {Ni(L^2-pCH_3)(HIm)] suggest square planar arrangement around the Ni(II) where the bisaroylhydrazone acts as dinegative NNO tridentate ligand forming with the Ni(II) a 5,6-bicyclic chelate ring the fourth coordination site is occupied by imidazole nitrogen.

© 2009 Elsevier Ltd. All rights reserved.

1. Introduction

The coordination chemistry of tridentate aroylhydrazones derived from ortho hydroxyaldehydes and ketones [1–11], 2-N-heterocyclic aldehydes and ketones [12–17], β-diketones [18–23] and α-ketomonooximes [24–28] have been extensively studied. Besides their interesting coordination chemistry, tridentate aroylhydrazones and their transition metal complexes show a wide spectrum of biological and pharmacological activities [29–34]. Less attention, however, was paid for a systematic study on the coordination chemistry of tetradentate bisaroylhydrazones derived from α-ketoaldehydes and α-diketones. Some of the diacetyl bis-aroylhydrazone nickel(II) complexes have been prepared and characterized [35–38]. In these complexes the bis aroylhydrazone ligand was found to act as a dinegative NNOO tetradentate anion where the central Ni(II) is coordinated to two imine nitrogens and the two deprotonated enolimide oxygens forming the 5,5,5-membered tricyclic chelate ring system. This mode of chelation was confirmed by X-ray structural analysis of the Ni(II) complexes with diacetyl bis(benzoylhydrazone) and bis(*p*-methoxybenzoylhydrazone) [35,37]. Moreover, square planar Ni(II) complex with diacetyl bisbenzoylhydrazone was found to act as Lewis acid and its interaction with different types of Lewis bases has been studied spectrophotometrically [39–42]. Only octahedral bis(pyridine) adduct was isolated and partially characterized [39]. Reactions with bidentate heterocyclic bases, however, proceeded with the rupture of one of the two coordinated oxygens and eventually gave the monobase adduct. The bis(aroylhydrazone) ligand acted as dinegative NNO tridentat anion, forming with the central Ni(II) a 5,5-membered bicyclic chelate ring [43]. In the present paper, we describe the synthesis and characterization of a new series of nickel(II) complexes derived from both symmetric diacetyl bis-aroylhydrazones (H_2L^1-R) (**1**, $R_1 = R_2 = CH_3$, $R_3 = C_6H_5$, *p*-$CH_3{\cdot}C_6H_4$, *p*-$CH_3O{\cdot}C_6H_4$, *p*-$Cl{\cdot}C_6H_4$ or *p*-$NO_2{\cdot}C_6H_4$) and unsymmetric phenylglyoxal bisaroyl – hydrazones (H_2L^2-R) (**1**, $R_1 = H$, $R_2 = C_6H_5$, $R_3 = C_6H_5$, *p*-$CH_3{\cdot}C_6H_4$, *p*-$OCH_3{\cdot}C_3H_4$, *p*-$Cl{\cdot}C_6H_4$, *p*-$NO_2{\cdot}C_6H_4$). The X-ray crystal and molecular structure of [Ni(L^1-pNO_2)] has been determined and compared with the previously reported X-ray

* Corresponding author. Tel.: +20 3 3911794; fax: +20 3 5932488.
E-mail address: m.iskander@link.net (M.F. Iskander).

0277-5387/$ - see front matter © 2009 Elsevier Ltd. All rights reserved.
doi:10.1016/j.poly.2009.04.007

structures of [Ni(L^1-H)] and [Ni(L^1-pCH_3O)] [35,37]. The reactions of both [Ni(L^1-R)] and [Ni(L^2-R)] series with ammonia and imidazole have been also studied aiming to investigate the effect of the nature of substituents on the C–C backbone of the ligands on the reactivity of this type of nickel(II) complexes. The X-ray structures of representative bis- and monoimidazole complexes obtained, respectively, from the reaction of imidazole with [Ni(L^1-R)] and [Ni(L^2-R)] have been determined.

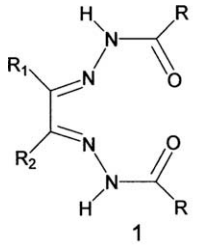
2. Experimental

2.1. Materials

Diacetyl and phenylglyoxal were obtained from Aldrich and used without further purification. Hydrazine hydrate (99%) (BDH), imidazole and nickel acetate tetrahydrate (BDH) were also used without further purification. Aroylhydrazines were prepared, as previously described [27], by the hydrazinolysis of aromatic carboxylic methyl esters in methanol.

2.2. Preparation of bisaroylhydrazones (*1*)

Bisaroylhydrazones were prepared as previously described by the condensation of diacetyl or phenylglyoxal with two equimolar amounts of aroylhydrazine in acidified ethanol [36]. The infrared, ultraviolet-visible and ^{1}H NMR spectral data of the prepared bisaroylhydrazones are deposited as Supplementary data.



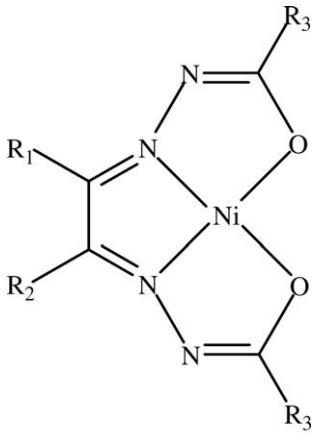
1

R_1	R_2	R	Abbreviation
CH_3	CH_3	C_6H_5	H_2L^1-H
CH_3	CH_3	p-$CH_3C_6H_4$	H_2L^1-pCH_3
CH_3	CH_3	p-$CH_3OC_6H_4$	H_2L^1-pCH_3O
CH_3	CH_3	p-ClC_6H_4	H_2L^1-pCl
CH_3	CH_3	p-$NO_2C_6H_4$	H_2L^1-pNO_2
H	C_6H_5	C_6H_5	H_2L^2-H
H	C_6H_5	p-$CH_3C_6H_4$	H_2L^2-pCH_3
H	C_6H_5	p-$CH_3OC_6H_4$	H_2L^2-pCH_3O
H	C_6H_5	p-ClC_6H_4	H_2L^2-pCl
H	C_6H_5	p-$NO_2C_6H_5$	H_2L^2-pNO_2

2.3. Preparation of nickel(II) complexes

*2.3.1. Preparation of [NiL^1-R] (**2**, $R_1 = R_2 = CH_3$, $R_3 = C_6H_5$, p-CH_3·C_6H_4, p-CH_3O·C_6H_4, p-Cl·C_6H_4 and p-NO_2·C_6H_4) and [NiL^2-R]·nH_2O (**2**, $R_1 = H$, $R_2 = C_6H_5$, R_3 = p-CH_3·C_6H_4, p-CH_3O·C_6H_4, p-Cl·C_6H_4 and p-NO_2·C_6H_4) complexes*

A hot solution of potassium hydroxide (0.02 mol) in ethanol (15 ml) was added to a suspension of the appropriate bisaroylhydrazone (**1**, $R_1 = R_2 = CH_3$, $R_3 = C_6H_5$, p-CH_3·C_6H_4, p-CH_3O·C_6H_4, p-Cl·C_6H_4 and p-NO_2·C_6H_4; R_1 = H, $R_2 = C_6H_5$, R_3 = p-CH_3·C_6H_4, p-CH_3O·C_6H_4, p-Cl·C_6H_4 and p-NO_2·C_6H_4) (0.01 mol) in ethanol (50 ml). To the resulting yellow solution, a hot solution of nickel(II) acetate tetrahydrate (0.01 mol) in ethanol (25 ml) was added. The mixture was then refluxed, with constant stirring, for 2 h. The isolated complex was then filtered off, recrystallized from benzene and then dried under vacuum. Single crystals of [Ni(L^1-H)] and [Ni(L^1-pCH_3O)], suitable for X-ray diffraction studies were selected from the recrystallised batches, while crystals of benzene solvate [Ni(L^1-pNO_2)]·1/2C_6H_6 were isolated from the mother liquor after kept for 1 month.



2

*[Ni(L^1-H)] (**2**, $R_1 = R_2 = CH_3$, $R_3 = C_6H_5$).* Yield: 70%. *Anal.* Calc. for $C_{18}H_{16}N_4O_2Ni$: C, 57.04; H, 4.25; N, 14.78. Found: C, 57.20; H, 4.27; N, 14.74%. IR (KBr) (cm^{-1}): 1587 m, ν(C=N–N=C); 1552 m ν(N=C–C=N); 1372s, 1297s, amide III [ν(C–N) + ν(C–O)]. UV–Vis(CH_2Cl_2, λ_{max}/nm (log ε)): 275(4.22); 324(4.19); 390(4.23) (L–L*); 628sh, 684(3.13); 752 (2.98) (MLCT). Magnetic moment (μ_{eff}, μ_β): diamagnetic.

*[Ni(L^1-pCH_3)] (**2**, $R_1 = R_2 = CH_3$, R_3 = p-CH_3·C_6H_4).* Yield: 72%. *Anal.* Calc. for $C_{20}H_{20}N_4O_2Ni$: C, 59.01; H, 4.95; N, 13.76. Found: C, 58.82; H, 4.99; N, 13.56%. IR (KBr) (cm^{-1}): 1608s, 1587s ν(C=N–N=C); 1552 m, ν(N=C–C=N); 1386s, 1293s, amide III [ν(C–N) + ν(C–O)]. UV–Vis (CH_2Cl_2, λ_{max}/nm (log ε)): 239(4.38); 282(4.20); 330(4.24), 397(4.32) (L–L*); 471(3.33) (LMCT); 623sh; 681(3.19); 748(2.98) (MLCT). Magnetic moment (μ_{eff}, μ_β): diamagnetic.

*[Ni(L^1-pCH_3O)] (**2**, $R_1 = R_2 = CH_3$, R_3 = p-CH_3O·C_6H_4).* Yield: 66%. *Anal.* Calc. for $C_{20}H_{20}N_4O_4Ni$: C, 54.71; H, 4.59; N, 12.76. Found: C, 54.74; H, 4.58; N, 12.62%. IR (KBr) (cm^{-1}): 1603s ν(C=N–N=C); 1552 m, ν(N=C–C=N); 1372s, 1250s, amide III [ν(C–N) + ν(C–O)]. UV–Vis (CH_2Cl_2, λ_{max}/nm (log ε): 252(4.45); 341(4.17); 410(4.39) (L–L*); 470sh (LMCT); 629sh, 677(3.29); 742(3.07) (MLCT). Magnetic moment (μ_{eff}, μ_β): diamagnetic.

*[(Ni(L^1-pCl)] (**2**, $R_1 = R_2 = CH_3$, R_3 = p-Cl·C_6H_4).* Yield: 68%. *Anal.* Calc. for $C_{18}H_{14}N_4O_2Cl_2Ni$: C, 48.27; H, 3.15; N, 12.51. Found: C, 48.30; H, 3.30; N, 12.30%. IR (KBr) (cm^{-1}): 1582 m ν(C=N–N=C); 1550 m, ν(N=C–C=N); 1382s, 1291s, amide III [ν(C–N) + ν (C–O)]. UV–Vis (CH_2Cl_2 (saturated solution), λ_{max}/nm (log ε)): 242; 282; 328; 390 (L–L*); 468sh (LMCT); 635sh, 681; 752 (MLCT). Magnetic moment (μ_{eff}, μ_β): diamagnetic.

*[Ni(L^1-pNO_2)] (**2**, $R_1 = R_2 = CH_3$, R_3 = p-NO_2·C_6H_4).* Yield: 73%. *Anal.* Calc. for $C_{18}H_{14}N_6O_6Ni$: C, 46.09; H, 3.01; N, 17.92. Found: C, 46.21; H, 3.14; N, 17.32%. IR (KBr) (cm^{-1}): 1603s, 1587s, ν(C=N–N=C); 1555sh ν(N=C–C=N); 1343s, 1270s, amide III [ν(C–N) + ν (C–O)]. UV–Vis (CH_2Cl_2, λ_{max}/nm (log ε)): 320(4.19); 334sh; 395(4.27) (L–L*), 470(3.19) (LMCT); 658(2.96); 703(2.97); 771sh (MLCT). Magnetic moment (μ_{eff}, μ_β): diamagnetic.

*[Ni(L^2-H)] (**2**, $R_1 = H$, $R_2 = C_6H_5$, $R_3 = C_6H_5$).* Yield: 46%. *Anal.* Calc. for $C_{22}H_{16}N_4O_2Ni$: C, 61.87; H, 3.78; N, 13.12. Found: C, 61.80; H, 3.86; N, 13.08%. IR (KBr) (cm^{-1}): 1610 m, 1580 m, ν(C=N–N=C); 1552 m, 1530 m ν(N=C–C=N); 1390s, 1297s, amide III [ν(C–N) + ν (C–O)]. UV–Vis (CH_2Cl_2 (saturated solution), λ_{max}/nm (log ε)): 240(4.58), 303(4.45), 385sh (L–L*); 425(3.43) (LMCT); 635 (MLCT). Magnetic moment (μ_{eff}, μ_β): diamagnetic.

*[Ni(L^2-pCH_3)]·H_2O (**2**, $R_1 = H$, $R_2 = C_6H_5$, R_3 = p-CH_3·C_6H_4).* Yield: 58%. *Anal.* Calc. for $C_{24}H_{22}N_4O_3Ni$: C, 60.92; H, 4.69; N, 11.84. Found: C, 60.47; H, 4.40; N, 12.31%. IR (KBr) (cm^{-1}): 1609s, 1579s, ν(C=N–N=C); 1553 m, 1535, ν(N=C–C=N); 1395s, 1369s, amide III [ν(C–N) + ν (C–O)]. UV–Vis (CH_2Cl_2 (saturated solution),

λ_{max}/nm (log ε)): 240(4.58); 303sh (L–L*); 425(3.43) (LMCT); 638 (MLCT). Magnetic moment (μ_{eff}, μ_β): diamagnetic.

*Ni(L^2-pCH$_3$O)]·H$_2$O (**2**, R_1 = H, R_2 = C_6H_5, R_3 = p-CH$_3$O·C_6H_4).* Yield: 60%. *Anal.* Calc. for $C_{24}H_{22}N_4O_5Ni$%: C, 57.06; H, 4.39; N, 11.09. Found: C, 57.52; H, 4.40; N, 11.65%. IR (KBr) (cm^{-1}): 1605s, 1585s, ν(C=N–N=C); 1535, ν(N=C–C=N); 1373s, 1250s, amide III [ν(C–N) + ν(C–O)]. UV–Vis (CH_2Cl_2, λ_{max}/nm (log ε)): 363sh (L–L*); 430 (LMCT); 560(3.30); 641(3.08) (MLCT). Magnetic moment (μ_{eff}, μ_β): diamagnetic.

*[Ni(L^2-pCl)]·2H$_2$O (**2**, R_1 = H, R_2 = C_6H_5, R_3 = p-Cl·C_6H_4).* Yield: 56%. *Anal.* Calc. for $C_{22}H_{18}N_4O_4Cl_2Ni$: C, 49.67; H, 3.41; N, 10.53. Found: C, 49.14; H, 2.96; N, 10.39%. IR (KBr) (cm^{-1}): 1620s, 1597s, ν(C=N–N=C); 1570s, 1550s, ν(N=C–C=N) 1383s, 1253s, amide III [ν(C–N) + ν(C–O)]. UV–Vis (CH_2Cl_2 (saturated solution), λ_{max}/nm (log ε)): 240sh, 309sh; 409 (L–L*); 425sh (LMCT); 644 (MLCT). Magnetic moment (μ_{eff}, μ_β): diamagnetic.

2.3.2. Preparation of [Ni(L^1-R)(NH_3)] complexes

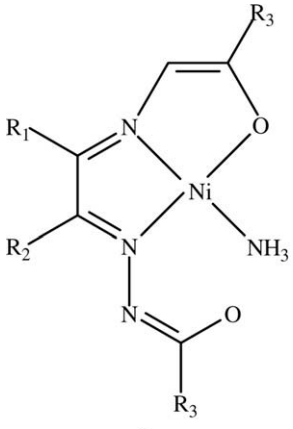
To a hot suspension of diacetyl bis(aroylhydrazone)(**1**, R_1 = R_2 = CH_3, R_3 = p-Cl·C_6H_4 and p-NO_2·C_6H_4) (0.01 mol) in ethanol (20 ml), a hot solution of nickel(II) acetate tetrahydrate (0.01 mol) in ethanol (20 ml) was added. The resulting green mixture turned red upon treating with aqueous ammonia (3 ml of 30% ammonia solution). The red solution was then stirred for 1/2 h, during which a reddish brown precipitate separated out, was filtered off and dried in air. In the case of R_3 = C_6H_5, p-CH_3·C_6H_4 and p-CH_3O·C_6H_4 only the [Ni(L^1-R)] complexes were isolated.

[(Ni(L^1-pCl(NH_3)]. Yield: 38%. *Anal.* Calc. For $C_{18}H_{17}N_5O_2Cl_2Ni$: C, 46.50; H, 3.69; N, 15.06. Found: C, 46.88; H, 3.65; N, 14.60%. IR (KBr) (cm^{-1}): 3320m, 3246m, 3190m, ν(N–H) (NH_3); 1640s δ(N–H); 1584s, ν(C=N–N=C); 1550sh, ν(N=C–C=N). Magnetic moment (μ_{eff}, μ_β): 2.70.

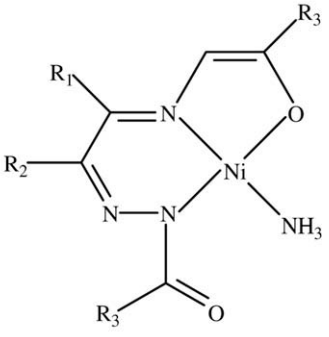
[Ni(L^1-pNO$_2$(NH_3)]·H$_2$O. Yield: 35%. *Anal.* Calc. For $C_{18}H_{19}N_7O_7Ni$: C, 42.89; H, 3.80; N, 19.45. Found: C, 42.74; H, 3.70; N, 18.85%. IR (KBr) (cm^{-1}): 3375m, 3283m, 3264m, 3237m, ν(N–H) (NH_3); 1642s, δ(N–H), 1602, ν(C=N–N=C), 1568, ν(N=C–C=N). Magnetic moment (μ_{eff}, μ_β): 2.64.

2.3.3. Preparation of [Ni(L^2-R)(NH_3)] (**4**, R_1 = H, R_2 = C_6H_5, R_3 = p-CH$_3$·C_6H_4, p-CH$_3O$·C_6H_4, p-Cl·C_6H_4 and p-NO_2·C_6H_4) complexes

The [Ni(L^2-R)(NH_3)] (**4**, R_1 = H, R_2 = C_6H_5, R_3 = C_6H_5, p-CH_3·C_6H_4, p-CH_3O·C_6H_4, p-Cl·C_6H_4 and p-NO_2·C_6H_4) complexes were prepared using the same procedure described for *[Ni(L^1-R)(NH_3)]* complexes.



3



4

*[Ni(L^2-H)(NH_3)] (**4**, R_1 = H, R_2 = C_6H_5, R_3 = C_6H_5).* Yield: 41%. *Anal.* Calc. for $C_{22}H_{19}N_5O_2Ni$: C, 59.50; H, 4.31; N, 15.77. Found: C, 59.52, H, 4.31; N, 15.73%. IR (KBr) (cm^{-1}): 3360m, 3324m, 3255m, ν(N–H) (NH_3); 1655, amide I [ν(C=O)];1635s δ(N–H); 1600s, 1575s, ν(C=N–N=C); 1555m, 1535m, ν(N=C–C=N). UV–Vis (CH_2Cl_2, λ_{max}/nm (log ε)): 233(4.35), 259sh, 288(4.53), 357(3.94) (L–L*); 442(3.84) (LMCT); 468 (3.83), 655(sh) (MLCT). Magnetic moment (μ_{eff}, μ_β): diamagnetic.

*[Ni(L^2-pCH$_3$)(NH_3)]·1/2H$_2$O (**4**, R_1 = H, R_2 = C_6H_5, R_3 = p-CH$_3$·C_6H_4).* Yield: 48%. *Anal.* Calc. for $C_{24}H_{24}N_5O_{2.5}Ni$%: C, 59.91; H, 5.03; N, 14.55. Found: C, 59.47; H, 4.86; N, 14.64%. IR (KBr) (cm^{-1}): 3365, 3325, 3255, 3115, ν(N–H) (NH_3); 1655sh, amide I [ν(C=O)]; 1640s, δ(N–H), 1603s, ν(C=N–N=C), 1555s, 1533s, ν(N=C–C=N). UV–Vis (CH_2Cl_2, λ_{max}/nm (log ε)): 285(4.57), 360(3.97) (L–L*); 435(3.84) (LMCT); 475(3.85), 655sh (MLCT). Magnetic moment (μ_{eff}, μ_β): diamagnetic.

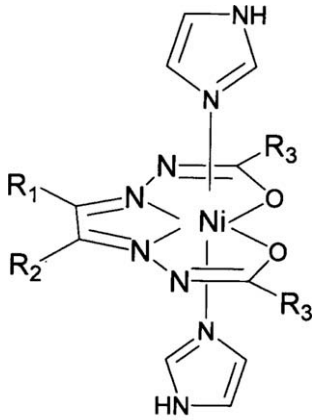
*[Ni(L^2-pCH$_3$O)(NH_3)]·2H$_2$O (**4**, R_1 = H, R_2 = C_6H_5, R_3 = p-CH$_3$O·C_6H_4).* Yield: 56%. *Anal.* Calc. for $C_{24}H_{27}N_5O_6Ni$: C, 53.36; H, 5.04; N, 12.97. Found: C, 53.85; H, 4.89, N, 12.97%. IR (KBr) (cm^{-1}): 3377m, 3356m, 3321m, 3247m, 3187m, ν(N–H) (NH_3); 1657m amide I [ν(C=O)]; 1640s, δ(N–H); 1600s, 1570s, ν(C=N–N=C); 1552m, 1535m, ν(N=C–C=N). UV–Vis (CH_2Cl_2, λ_{max} / nm (log ε)): 262sh, 288 (4.56), 367 (4.07) (L – L*); 435 (3.92) (LMCT); 475 (3.92), 652 (2.08) (MLCT). Magnetic moment (μ_{eff}, μ_β): diamagnetic.

*[Ni(L^2-pCl)(NH_3)] (**4**, R_1 = H, R_2 = C_6H_5, R_3 = p-Cl·C_6H_4).* Yield: 60%. *Anal.* Calc. for $C_{22}H_{17}N_5O_2Cl_2Ni$: C, 51.51; H, 3.34; N, 13.65. Found: C, 51.46, H, 3.35, N, 13.54%. IR (KBr) (cm^{-1}): 3370m, 3311m, 3155m, 3155m, ν(N–H) (NH_3); 1660sh, amide I [ν(C=O)]; 1637s, δ(N–H); 1585s, ν(C=N–N=C); 1534m, ν(N=C–C=N). UV–Vis (CH_2Cl_2 saturated solution, λ_{max}/nm (log ε)): 225, 288, 365 (L–L*), 435 (LMCT), 470 (MLCT). Magnetic moment (μ_{eff}, μ_β): diamagnetic.

*[Ni(L^2-pNO$_2$)(NH_3)] (**4**, R_1 = H, R_2 = C_6H_5, R_3 = p-NO$_2$·C_6H_4).* Yield: 60%. *Anal.* Calc. for $C_{22}H_{17}N_7O_6Ni$: C, 49.47; H, 3.21; N, 18.36. Found: C, 49.45; H, 3.26; N, 18.38%. IR (KBr) (cm^{-1}): 3318, 3252, 3186, 3108, ν(N–H) (NH_3); 1658sh, amide I [ν(C=O)]; 1643s, δ(N–H); 1595s, 1570s, ν(C=N–N=C); 1535sh, ν(N=C–C=N). UV–Vis (CH_2Cl_2 saturated solution, λ_{max}/nm (log ε)): 275 (L–L*), 435 (LMCT); 500sh (MLCT). Magnetic moment (μ_{eff}, μ_β): diamagnetic.

2.3.4. Preparation of [Ni(L^1-R)(HIm)$_2$] (**5**, R_1 = R_2 = CH_3, R_3 = C_6H_5, p-CH$_3$ · C_6H_4, p-CH$_3O$ · C_6H_4, p-Cl · C_6H_4 and p-NO_2 · C_6H_4)

Bis(imidazole) nickel(II) complexes were prepared by adding a hot suspension of diacetyl bisaroylhydrazone (0.01 mol) in acetonitrile (20 ml) to a hot solution of nickel(II) acetate tetrahydrate (0.01 mol) in ethanol (20 ml). The resulting green complex was then treated with a large excess of solid imidazole (0.08 mol) to give a dark red solution. The resulted solution was filtered and then evaporated to half its original volume. On cooling, the formed crystals were filtered off and dried in air.



5

*[Ni(L^1-H)(HIm)$_2$] · H_2O (**5**, $R_1 = R_2 = CH_3$, $R_3 = C_6H_5$).* Yield: 58%. *Anal.* Calc. for $C_{24}H_{26}N_8O_3Ni$: C, 54.06; H, 4.91; N, 21.01. Found: C, 54.21; H, 4.79; N, 21.25%. IR (KBr) (cm^{-1}): 3135m, ν(N–H); 3049m, 2930m, 2848m [(ν(N–H) + ν(C–H)]; 1585m, ν(C=N–N=C); 1548m, 1533, ν(N=C–C=N); 1343s, 1287s, amide III [ν(C–N) + ν(C–O)]. Magnetic moment (μ_{eff}, μ_β): 3.22.

*[Ni(L^1-pCH_3)(HIm)$_2$] (**5**, $R_1 = R_2 = CH_3$, R_3 = p-CH_3·C_6H_4).* Yield: 55%. *Anal.* Calc. for $C_{26}H_{28}N_8O_2Ni$: C, 57.48; H, 5.20; N, 20.63. Found: C, 57.24; H, 5.19; N, 20.32%. IR (KBr) (cm^{-1}): 3127m, ν(N–H); 3057m, 2951m, 2850m [(ν(N–H) + ν(C–H)]; 1601m, ν(C=N–N=C); 1570, ν(N=C–C=N); 1336s, 1288s, amide III [ν(C–N) + ν(C–O)]. Magnetic moment (μ_{eff}, μ_β): 3.30.

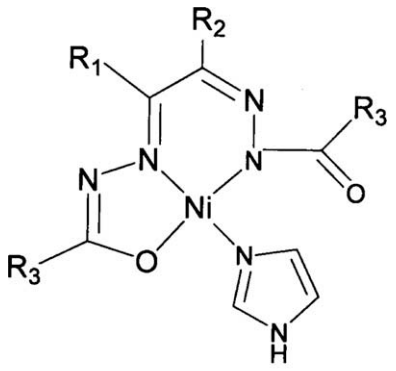
*[Ni(L^1-pCH_3O)(HIm)$_2$]·1/2H_2O (**5**, $R_1 = R_2 = CH_3$, R_3 = p-CH_3O·C_6H_4).* Yield: 55%. *Anal.* Calc. for $C_{26}H_{29}N_8O_{4.5}Ni$: C, 53.36; H, 4.99; N, 19.14. Found: C, 53.28; H, 4.90; N, 19.08%. IR (KBr) (cm^{-1}): 3112m, ν(N–H); 3050, 2929, 2838 [(ν(N–H) + ν(C–H)]; 1601s, 1582, ν(C=N–N=C); 1540s, ν(N=C–C=N); 1349s, 1249s, amide III [ν(C–N) + ν (C–O)]. Magnetic moment (μ_{eff}, μ_β): 3.60.

*[Ni(L^1-pCl)(HIm)$_2$]·1/2H_2O (**5**, $R_1 = R_2 = CH_3$, R_3 = p-Cl.C_6H_4).* Yield: 53%. *Anal.* Calc. for $C_{24}H_{23}N_8O_{2.5}Cl_2Ni$: C, 48.60; H, 3.91; N, 18.89. Found: C, 48.51; H, 3.77; N, 18.98%. IR (KBr) (cm^{-1}): 3138m, ν(N–H); 3074m, 2961m, 2925, 2860 [(ν(N–H) + ν(C–H)]; 1580m, ν(C=N–N=C); 1540, ν(N=C–C=N); 1363s, 1292s, amide III, ν(C–N). Magnetic moment (μ_{eff}, μ_β): 3.15.

*[Ni(L^1-pNO_2)(HIm)$_2$] (**5**, $R_1 = R_2 = CH_3$, R_3 = p-NO_2·C_6H_4).* Yield: 54%. *Anal.* Calc. for $C_{24}H_{22}N_{10}O_6Ni$: C, 47.63; H, 3.66; N, 23.14. Found: C, 47.59; H, 3.64; N, 22.74%. IR (KBr) (cm^{-1}): 3132m, ν(N–H); 3060m, 2950m, 2864m [(ν(N–H) + ν(C–H)]; 1600m, ν(C=N–N=C); 1535m, ν(N=C–C=N)1340s, 1286s, amide III, ν(C–N). Magnetic moment (μ_{eff}, μ_β): 3.17.

2.3.5. Preparation of [Ni(L^2-R)(HIm)] (**6**, R_1 = H, $R_2 = C_6H_5$, R_3 = p-CH_3·C_6H_4, p-CH_3O·C_6H_4, p-Cl·C_6H_4 and p-NO_2·C_6H_5)

To a hot suspension of phenylglyoxal bisaroylhydrazone (0.01 mol) in acetonitrile (20 ml), a hot solution of nickel(II) acetate tetrahydrate (0.01 mol) in ethanol (20 ml) was added. The resulting green complex was then treated with a large excess of solid imidazole (0.05 mol) to give a dark red solution. The resulted solution was filtered, then evaporated to half its original volume. After cooling, the formed red crystals were filtered off.



6

*[Ni(L^2-H)(Him)] (**6**, R_1 = H, $R_2 = C_6H_5$, $R_3 = C_6H_5$).* Yield: 60%. *Anal.* Calc. for $C_{25}H_{20}N_6O_2Ni$: C, 60.64; H, 4.07; N, 16.97. Found: C, 60.52; H, 4.05; N, 16.93%. IR (KBr) (cm^{-1}): 3131s, ν(N–H); 3050, 2969, 2932 [ν(N–H) + ν(C–H)]; 1660sh, 1643, amide I, ν(C=O); 1616s, 1598s, ν(C=N–N=C); 1570s, 1552m, ν(N=C–C=N); 1366s, 1291s, amide III [ν(C–N) + ν (C–O)]. UV–Vis (DMF), λ_{max}/nm (log ε): 308(4.50), 367(sh) (L–L*); 475(3.80), 490(3.62) (LMCT); 570(3.44), 625(3.58) (MLCT). Magnetic moment (μ_{eff}, μ_β): diamagnetic.

*[Ni(L^2-pCH_3)(HIm)] (**6**, R_1 = H, $R_2 = C_6H_5$, R_3 = p-CH_3 · C_6H_4).* Yield: 58%. *Anal.* Calc. for $C_{27}H_{24}N_6O_2Ni$: C, 61.98; H, 4.62; N, 16.06. Found: C, 61.47; H, 4.65; N, 15.55%. IR (KBr) (cm^{-1}): 3171s, ν(N–H); 3061, 2967, 2919, 2859 [ν(N–H) + ν(C–H)]; 1660s, 1628s, amide I, ν(C=O); 1608s, 1587, ν(C=N–N=C); 1570, 1552, ν(N=C–C=N); 1396s, 1291s, amide III [ν(C–N) + ν (C–O)]. UV–Vis (DMF), λ_{max}/nm (log ε): 305(4.48), 367(sh) (L–L*); 477(3.75), 487(3.60) (LMCT); 570(3.37), 620(3.50) (MLCT). Magnetic moment (μ_{eff}, μ_β): diamagnetic.

*[Ni(L^2-pCH_3O)(HIm)] (**6**, R_1 = H, $R_2 = C_6H_5$, R_3 = p-CH_3O · C_6H_4).* Yield: 64%. *Anal.* Calc. for $C_{27}H_{24}N_6O_4Ni$: C, 58.41; H, 4.36; N, 15.14. Found: C, 58.49; H, 4.34; N, 15.06%. IR (KBr) (cm^{-1}): 3171s, ν(N–H); 3061, 2967, 2919, 2859 [ν(N–H) + ν(C–H)]; 1660s, 1628s, amide I, ν(C=O); 1608s, 1587, ν(C=N–N=C); 1570, 1552, ν(N=C–C=N); 1396s, 1291s, amide III [ν(C–N) + ν (C–O)]. UV–Vis (DMF), λ_{max}/nm (log ε): 305(4.48), 367(sh) (L–L*); 477(3.75), 487(3.60) (LMCT); 570(3.37), 620(3.50) (MLCT). Magnetic moment (μ_{eff}, μ_β): diamagnetic.

*[Ni(L^2-pCl)(HIm)] (**6**, R_1 = H, $R_2 = C_6H_5$, R_3 = p-Cl·C_6H_4).* Yield: 62%. *Anal.* Calc. for $C_{25}H_{18}N_6O_2Cl_2Ni$: C, 53.24; H, 3.22; N, 14.90. Found: C, 52.79; H, 3.26; N, 15.40%. IR (KBr) (cm^{-1}): 3133s, ν(N–H); 3077, 2968, 2860 [ν(N–H) + ν(C–H)]; 1660m, 1634m, amide I, ν(C=O); 1613s, 1594s, ν(C=N–N=C); 1560, 1535, ν(N=C–C=N) 1392s, 1297s, amide III [ν(C–N) + ν(C–O)]. UV–Vis (DMF), λ_{max}/nm (log ε): 305(4.46), 367(sh) (L–L*); 477(3.70), 481(3.69) (LMCT); 560(3.36), 610(3.47), 652(sh) (MLCT). Magnetic moment (μ_{eff}, μ_β): diamagnetic.

*[Ni(L^2-pNO_2)(HIm)] (**6**, R_1 = H, $R_2 = C_6H_5$, R_3 = p-NO_2·C_6H_4):* Yield: 62%. *Anal.* Calc. for $C_{25}H_{18}N_8O_6Ni$: C, 51.29; H, 3.10; N, 19.16. Found: C, 51.35; H, 3.13; N, 19.02%. IR (KBr) (cm^{-1}): 3218s, 3152m, ν(N–H); 3080, 3050, 2972, 2934 [ν(N–H) + ν(C–H)]; 1650s, amide I, ν(C=O); 1599m, ν(C=N–N=C); 1550, 1526, ν(N=C–C=N); 1345s, 1287s, amide III, [ν(C–N) + ν(C–O)]. UV–Vis (DMF), λ_{max}/nm (log ε): 377sh (L–L*); 480(3.95) LMCT, 495(3.82), 648(3.18) (MLCT). Magnetic moment (μ_{eff}, μ_β): diamagnetic.

2.4. Physical measurements

The infrared spectra were recorded on a Perkin–Elmer 1430 Data system and/or a Perkin–Elmer (FT-IR) Paragon 1000 PC spectrophotometer. Solid samples were examined as KBr discs. The ultraviolet and visible absorption spectra were recorded on V-530 UV–Vis. recording spectrophotometer, Jasco, using 10 mm quartz cells and/or a double beam ratio recording Lambada 4B Perkin–Elmer spectrophotometers. ^{1}H NMR spectra were recorded on Brucker WM 300 using tetramethylsilane (TMS) as an internal standard. Magnetic susceptibilities of powdered dried samples were recorded on a Faraday-type magnetometer using a sensitive computer controlled D-200 Cahn RG microbalance. The magnetic field applied was ~1.5 T [44]. Experimental susceptibility data were corrected for the underlying diamagnetism using Pascal's constants.

X-ray diffraction data were collected on CrysAlis CCD, Oxford Diffraction limited, version 1.70.14 (2002), using graphite monochromated Mo Kα radiation (λ = 0.71013 Å). The structures were solved by direct method with SHELXS-97 [45]; refinement was done by full-matrix least squares on F^2 using the SHEXL-97 [45]. Drawings of the molecules were produced with ORTEP 3 [46] or PLATON [47].

3. Results and discussion

3.1. Synthesis and characterization

In ethanol, the reaction of both symmetrical diacetyl bisaroylhydrazones, (H_2L^1-R), and unsymmetrical phenylglyoxal bisaroylhydrazone (H_2L^2-R) with nickel(II) acetate tetrahydrate in the presence of KOH, respectively afforded the corresponding neutral nickel(II) chelates [Ni(L^1-R)] (**2**, $R_1 = R_2 = CH_3$ and $R_3 = C_6H_5$, *p*-$CH_3{\cdot}C_6H_4$, *p*-$CH_3O{\cdot}C_6H_4$, *p*-$Cl{\cdot}C_6H_4$, and *p*-$NO_2{\cdot}C_6H_4$) and [Ni(L^2-R)]·nH_2O (**2**, $R_1 = H$, $R_2 = C_6H_5$, $R_3 = p$-$CH_3{\cdot}C_6H_4$, *p*-$CH_3O{\cdot}C_6H_4$ or *p*-$Cl{\cdot}C_6H_4$). The IR spectra of these nickel(II) complexes lack absorption bands which could be attributed to ν(N–H), amide(I) ν(C=O) and amide (II) bands, but exhibit instead a very intense band at *ca.* 1625–1580 cm^{-1} due to ν(C=N–N=C). The ν(N=C–C=N) of the diimine residue which appears at *ca* 1610–1570 cm^{-1} in the spectra of metal free ligands are shifted to lower frequencies, 1550–1535 cm^{-1}, in the corresponding Ni(II) complexes. These spectral data suggest the deprotonation of the two amide residues of the bisaroylhydrazone ligand and the bisaroylhydrazones in these nickel(II) complexes act as dinegative N_2O_2 tetradentate ligands [35–37]. At room temperature (298 K), the prepared monoligand nickel(II) complexes [Ni(L^1-R)] and [Ni(L^2-R)]·nH_2O were found to be diamagnetic, indicating square planar arrangement with $^1A_{1g}$ ground state. The solution electronic absorption spectra (UV–Vis) of these complexes in dichloromethane are in agreement with this assignment [48]. The absorption bands at *ca* 239–282 and 321–397 nm can be related to the different L–L* transitions of the highly conjugated dinegative ligand anion. Similar to other square planar nickel(II) complexes [48], the band located around 410– 71 nm is most probably due to a LMCT transition(s), while the three absorption bands in the regions 623–658, 681–703 and 742–771 nm can be fairly attributed to the different $d(M) \rightarrow \pi^*(L)$ transitions (MLCT) [36]. The recorded spectra lack weak absorptions due to the different d–d transitions which are most probably hidden under the very intense LMCT band. The position of MLCT absorption bands in the spectra of the square planar nickel(II) complexes [Ni(L^1-R)] and [Ni(L^2-R)]·nH_2O were found to be affected by the nature of p-substituents in the aroylhydrazone residue. The energy of the MLCT bands, measured in wavenumber (cm^{-1}), can be correlated with Hammett's σ_p constant and plot of wavenumber against σ_p gave a straight line with a negative slope confirming the MLCT origin of these absorption bands.

On using aqueous ammonia, the reaction of H_2L^1-R (**1**, $R_1 = R_2 = CH_3$, $R_3 = C_6H_5$, *p*-$CH_3{\cdot}C_6H_4$, *p*-$CH_3O{\cdot}C_6H_4$) with Ni$(CH_3COO)_2{\cdot}4H_2O$ using (1:1) molar ratio in ethanol resulted in the formation of the diamagnetic square planar neutral complexes [Ni(L^1-R] (**2**) which are identical to those isolated in the absence of aqueous ammonia.. In these reactions, aqueous ammonia acts as proton acceptor which facilitates the deprotonation of the bishydrazone ligands. However, with bishydrazones having electron withdrawing substituents (**1**, $R_1 = R_2 = CH_3$, $R_3 = p$-$Cl{\cdot}C_6H_4$ or *p*-$NO_2{\cdot}C_6H_4$), the reaction proceeded with the formation of the monoammine complexes [Ni(L^1-R)·NH_3]. The IR spectra of both [Ni(L^1-pCl)·NH_3] and [Ni(L^1-pNO_2)·NH_3] lack absorptions due to hydrazone ν(N–H), amide I ν(C=O) and amide II, implying the deprotonation of both aroylhydrazone arms. The spectra, also, show a series of bands at 3365, 3320, 3245 cm^{-1} due to the different vibration modes of coordinated NH_3, besides bands at *ca.* 1640, 1580 and 1550 cm^{-1} due to δ(N–H) of NH_3, ν(C=N–N=C) and ν(N=C–C=N) respectively. The solid complexes are paramagnetic with magnetic moments being within the range 2.60–2.70 μ_β (298 K). From the stoichiometry, infrared spectral data and magnetic measurements, a distorted square pyramidal structure can be tentatively assigned for these solid complexes, where the four donor atoms of the dinegative bishydrazone ligand are coordinated to the Ni(II) forming the equatorial plane while ammonia occupies the fifth coordination site. It seems that these complexes are stable only in the solid state. However in solution, complete deammination occurs and the solution electronic spectra of both [Ni(L^1-pCl)·NH_3] and [Ni(L^1-pNO_2)·NH_3] in dichloromethane are quite similar to those recorded for the parent square planar complexes.

The reaction of unsymmetric bisaroylhydrazones H_2L^2-R with Ni$(CH_3COO)_2{\cdot}4H_2O$ in the presence of aqueous ammonia gave the corresponding monoammine complexes of the general formula [Ni(L^2-R)·NH_3]·nH_2O. Different from [Ni(L^1-pCl)·NH_3] and [Ni(L^1-pNO_2)·NH_3] which are paramagnetic, the prepared nickel(II) complexes [Ni(L^2-R)·NH_3]·nH_2O are diamagnetic, suggesting square planar arrangement around the Ni(II) ion. The electronic absorption spectra of these complexes in dichloromethane display three absorptions due to L–L* transitions at *ca* 220, 270 and 360 nm, besides a strong LMCT absorption band at *ca* 445 nm. The spectra also display three MLCT absorption bands within the range 470–660 nm, confirming a square planar structure. In these square planar nickel(II) complexes, the bisaroylhydrazone must act as a dinegative tridentate anion while the NH_3 occupies the fourth coordination site. Thus two coordination modes **3** or **4** can be proposed for these complexes. The presence of a very intense amide I [ν(C=O)] band at 1650–1666 cm^{-1} in the IR spectra of these complexes suggest the deprotonation of the hydrazone N–H proton and structure **4** can be tentatively assigned for these complexes where the bisaroylhydrazone acts as dinegative NNO tridentate anion and is coordinated to the Ni(II) via deprotonated enolimine oxygen, imine nitrogen and deprotonated hydrazone nitrogen forming a 5,6-membered bicyclic chelate system.

In ethanol–acetonitrile mixture, the reaction of complexes [Ni(L^1-R)] complexes with excess solid imidazole (HIm) (8 equiv.) afforded the corresponding bis(imidazole) nickel(II) complexes [Ni(L^1-R)$(HIm)_2$] (**5**, $R_1 = R_2 = CH_3$, $R = C_6H_5$, *p*-$CH_3{\cdot}C_6H_4$, *p*-$CH_3O{\cdot}C_6H_4$, *p*-$Cl{\cdot}C_6H_4$ or *p*-$NO_2{\cdot}C_6H_4$). The IR spectra of these bis(imidazole) complexes display absorption bands at 3135–3115 cm^{-1} region due to ν(N–H) of the coordinated imidazole besides a series of bands at 3075–3050, 2972–2930 and 2920–2835 cm^{-1} which can be attributed to [ν(C–H) + ν(N–H)] coupled vibrations. Similar to the IR spectra of the parent square planar complexes [Ni(L^1-R)], the spectra of bis(imidazole) complexes [Ni(L^1-R)$(HIm)_2$] do not show any absorptions due to hydrazone υ(N–H) and amide I band (νC=O), but display intense bands at 1600–1575 cm^{-1} and 1555–1530 cm^{-1} due to ν(C=N–N=C) and ν(N=C–C=N), respectively, confirming the deprotonation of both hydrazone arms and the bis(aroylhydrazone) acts as a dinegative NNOO tetradentate ligand. The [Ni(L^1-R)$(HIm)_2$] complexes were found to be paramagnetic with magnetic moments (μ_{eff} = 3.15–3.50 μ_β) suggesting octahedral structure (**5**, $R_1 = R_2 = CH_3$, $R_3 = C_6H_5$, *p*-$CH_3{\cdot}C_6H_4$, *p*-$CH_3O{\cdot}C_6H_4$, *p*-$Cl{\cdot}C_6H_4$ or *p*-$NO_2{\cdot}C_6H_4$). The octahedral structure of both [Ni(L^1-H)$(HIm)_2$] and [Ni(L^1-pNO_2)$(HIm)_2$] has been confirmed by X-ray structural analysis.

Different from the reaction of [Ni(L^1-R)] (**2**) with imidazole which gave the bis(imidazole) complexes, [Ni(L^1-R)$(HIm)_2$] (**5**), the Ni(II) complexes derived from unsymmetric phenylglyoxal bishydrazones [Ni(L^2-R)]·nH_2O afforded the corresponding mono(imidazole) complexes [Ni(L^2-R)(HIm)] (**6**, $R_1 = H$, $R_2 = C_6H_5$, $R_3 = p$-$CH_3{\cdot}C_6H_4$, *p*-$CH_3O{\cdot}C_6H_4$, *p*-$Cl{\cdot}C_6H_4$ and *p*-$NO_2{\cdot}C_6H_4$). The IR spectral patterns of the mono(imidazole) complexes are more less similar to those recorded for the analogous mono(ammine) complexes and show a series of absorption bands at 3218–3131, 1660–1645, 1610–1580 cm^{-1}, respectively, due to ν(N–H) of the coordinated imidazole, amide I [ν(C=O)] of the uncoordinated

Table 1
Crystal data and structure refinement for [Ni(L^1-H)], [Ni(L^1-pCH_3O)] and [Ni(L^1-pNO_2)] complexes.

	[Ni(L^1-H)]	[Ni(L^1-pCH_3O)]	[Ni(L^1-pNO_2)]
Empirical formula	$C_{18}H_{16}N_4NiO_2$	$C_{20}H_{20}N_4NiO_4$	$C_{21}H_{17}N_6NiO_6$
Formula weight	379.06	439.11	508.12
Temperature (K)	299(2)	299(2)	299(2)
Wavelength (A)	0 .7 1073	0.71073	0.71073
Crystal system	orthorhombic	monoclinic	monoclinic
Space group	*Pbca*	*C2/c*	P21/n
Unit cell dimensions			
a (Å)	6.6415(8)	12.057(1)	8.6378(9)
b (Å)	28.430(3)	19.338(2)	11.6264(9)
c (Å)	18.162(2)	8.765(1)	21.484(1)
α (°)	90	90	90
β (°)	90	112.24(1)	93.375(8)
γ (°)	90	90	90
V (Å^3)	3429.3(7)	1891.6(3)	2153.9(3)
Z	8	4	4
D_{calc} (Mg m^{-3})	1.468	1.542	1.567
Absorption coefficient (mm^{-1})	1.150	1.062	0.954
F (0 0 0)	1568	912	1044
Crystal size (mm)	0.56 × 0.06 × 0.04	0.52 × 0.40 × 0.08	0.50 × 0.10 × 0.10
θ range for data collection (°)	4.30–26.37	4.14–26.37	4.19–26.37
Limiting indices	$-8 \leqslant h \leqslant 4$, $-35 \leqslant k \leqslant 34$, $-22 \leqslant l \leqslant 22$	$-15 \leqslant h \leqslant 15$, $-23 \leqslant k \leqslant 23$, $-10 \leqslant l \leqslant 5$	$-10 \leqslant h \leqslant 7$, $-14 \leqslant k \leqslant 14$, $-26 \leqslant l \leqslant 26$
Reflections collected	22 610	5764	14 858
Independent reflections (R_{int})	3482 (0.1692)	1899 (0.0293)	4340 (0.0423)
Completeness to θ	26.37 99.3%	26.37 97.8%	26.37 98.5%
Absorption correction	analytical	analytical	analytical
Maximum and minimum transmission	0.9538 and 0.5531	0.9199 and 0.6082	0.9107 and 0.6471
Refinement method	Full-matrix least-squares on F^2	full-matrix least-squares on F^2	full-matrix least-squares on F^2
Data/restraints/parameters	3482/0/226	1899/0/134	4340/0/307
Goodness-of-fit on F^2	1.044	1.077	0.950
Final *R* indices ($I > 2\sigma(I)$)	$R_1 = 0.0774$, $wR_2 = 0.1351$	$R_1 = 0.0370$, $wR_2 = 0.1000$	$R_1 = 0.0430$, $wR_2 = 0.1018$
R indices (all data)	$R_1 = 0.2679$, $wR_2 = 0.2053$	$R_1 = 0.0435$, $wR_2 = 0.1035$	$R_1 = 0.0838$, $wR_2 = 0.1171$
Largest difference in peak and hole (e A^{-3})	0.633 and −0.482	0.526 and −0.293	0.337 and −0.268

R_3-C=O residue, and ν(C=N–N=) of the deprotonated aroylhydrazone arm. The prepared mono(imidazole) complexes are diamagnetic indicating square planar arrangement around the central Ni(II) ion. The recorded electronic absorption spectra, in dichloromethane, are in agreement with this assignment.

3.2. X-ray molecular and supramolecular structures

3.2.1. Square planar nickel(II) complexes [Ni(L^1-R)] (**2**, $R_1 = R_2 = CH_3$ and $R_3 = C_6H_5$, p-CH_3O·C_6H_4, and p-NO_2·C_6H_4)

The crystal data and structural refinement parameters for [Ni(L^1-H)], [Ni(L^1-pCH_3O)] and [Ni(L^1-pNO_2)]·1/2C_6H_6 are listed in Table 1, while selected bond distances (Å) and bond angles (°) are collected in Table 2. The X-ray structures of [Ni(L^1-H)], [Ni(L^1-pCH_3O)] have been previously reported [35,37]. The X-ray structure of the newly prepared [Ni(L^1-pNO_2)] · 1/2C_6H_6 together with the atomic numbering scheme are, respectively, shown in Fig. 1. In these complexes the Ni(II) ion is in a distorted square planar environment where the bisaroylhydrazone ligand in these complexes acts as a dinegative N_2O_2 tetradentate ligand, forming the expected 5,5,5-membered tricyclic chelate ring system [35–37]. The bond distances of Ni–O1 and Ni–O2 in both [Ni(L^1-H)] and [Ni(L^1-pNO_2)], and Ni–O1 and Ni–O1# (#, $1 - x, y, -z + 1/2$) in [Ni(L^1-pCH_3O)], Table 2, are within the range 1.874–1.896 Å which are significantly higher than the range (1.83–1.86 Å) reported for square planar Ni(II) complexes with tridentate and tetradentate aroylhydrazones having, respectively, 5,6-membered bicyclic and 5,5,6-membered tricyclic chelate rings [3,5,22,21], but are comparable with the range (1.87–1.91 Å) reported for nickel(II) aroylhydrazone oxime complexes with 5,5-membered bicyclic chelate system [26]. This can be related to the steric constraints imposed by the 5,5,5- membered tricyclic chelate system. The Ni–N1 and Ni–N3 bond distance range (1.79–1.80 Å), Table 2, is relatively shorter than the range (1.82–1.84 Å) reported for square planar Ni(II) complexes derived from both mononegative tridentate and dinegative tetradentate aroylhydrazones. The observed decrease

Table 2
Selected bond distances (Å) and bond angles (°) for [Ni(L^1-H)], [Ni(L^1-pNO_2)] and [Ni(L^1-pCH_3O).

	[Ni(L^1-H)]	[Ni(L^1-pNO_2)]	[Ni(L^1-pCH_3O)]	
Ni–O1	1.874(5)	1.8958(18)	Ni–O1	1.8814(15)
Ni–N1	1.793(6)	1.805(2)	Ni–N1	1.7935(17)
Ni–N3	1.804(6)	1.791(2)	Ni–N1#1	1.7935(17)
Ni–O2	1.884(5)	1.882(2)	Ni–N1#1	1.8814(15)
C1–O1	1.316(9)	1.303(3)	C1–O1	1.305(3)
C1–C2	1.448(10)	1.471(4)	C1–C2	1.472(3)
C1–N2	1.334(10)	1.331(4)	C1–N2	1.329(3)
N1–N2	1.361(8)	1.373(3)	N1–N2	1.370(2)
C8–N1	1.310(9)	1.297(3)	C8–N1	1.304(3)
C8–C9	1.489(11)	1.477(4)	C8–C9	1.484(3)
C9–N3	1.316(9)	1.290(4)	N1–Ni1–N1#1	84.29(11)
N3–N4	1.371(8)	1.384(4)	N1–Ni–O1	83.47(7)
C10–N4	1.349(9)	1.323(4)	N1#1–Ni–O1#	83.47(7)
C10–C11	1.455(10)	1.471(4)	N1#1–Ni–O1	167.70(7)
C10–O2	1.305(9)	1.299(3)	N1–Ni–O1#1	167.70(7)
N1–Ni–O1	83.5(3)	83.69(9)	O–Ni–O1#1	108.80(10)
N1–Ni–N3	84.9(3)	82.94(11)	O1–C1–N2	124.01(19)
N3–Ni–O2	83.1(3)	83.97(10)	C1–N2–N1	105.98(17)
O1–Ni–O2	109.6(2)	109.35(8)	C8–N1–N2	124.65(18)
N1–Ni–O2	167.9(3)	166.83(9)	N1–C8–C9	124.29(19)
N3–Ni–O1	168.3(3)	166.54(11)	N1–C8–C8#1	110.82
O1–C1–N2	122.7(7)	124.5(3)		
N2–C1–C2	118.6(8)	116.6(3)		
C1–N2–N1	106.6(6)	106.5(2)		
C8–N1–N2	124.3(7)	124.8(3)		
N1–C8–C9	110.4(8)	110.6(3)		
N3–C9–C8	111.5(7)	110.3(3)		
C9–N3–N4	125.1(7)	124.1(2)		
C10–N4–N3	105.5(7)	106.3(2)		
O2–C10–N4	123.5(8)	124.4(3)		
O2–C10–C11	118.5(8)	118.0(3)		

#1 Symmetry transformations used to generate equivalent atoms: -x, y, -z + 1/2.

in both Ni–N1 and Ni–N3 bond distances may be due to appreciable (Ni–N) π-interactions usually observed in coordinated diimine systems. The bond distance ranges for C–N (imide) [C1–N2, C10–N4] (1.32–1.33 Å) and C–O [C1–O1, C10–O2] (1.29–1.32 Å) are consistent with the deprotonation of the enolimine tautomer [11,17,20,21,49]. The ligand C–N (imine) [C8–N1, C9–N3], hydrazine [N1–N2, N3–N4], C–N(imide) [C1–N2, C10–N4] and C–O [C1–O1, C10–O2] are intermediate between formal single and double bonds indicating delocalization over the 5,5,5-membered tricyclic chelate system.

The structures of these square planar Ni(II) complexes show interesting supramolecular architectures depending on the nature of substituents in the hydrazone phenyl rings. No classic hydrogen bonds are found in the crystal lattice of these complexes. However, in the unsubstituted complex [Ni(L^1-H)], two molecules are interconnected by two reciprocal C6H···O2 (C6···O2 = 3.487 Å) hydrogen bonds, forming a hydrogen bonded dimer. While in [Ni(L^1-pCH_3O)], each molecular unit is linked to four different neighboring molecular units via two pairs of reciprocal C9H···O2 (C9···O2 = 3.523 Å) hydrogen bonds giving rise to a two dimensional stepped sheet extending parallel to the ac-plane. Each molecular unit, in the stepped sheet, is stacked from both sides to two adjacent molecular units of inverted symmetry via two reciprocal edge to face CH···π interactions between the C9H*A* methyl proton and (C2–C7) phenyl π system [(CH9*A*···Cg1) = 2.816 Å, where Cg1 refers to the phenyl ring centroid] forming a one dimensional array of stacked molecular units as shown in Fig. 2. The dimensions of this CH···π interaction are consistent with those reported for other systems [50]. The Ni(II) coordination planes in this stacked array are parallel to each other and the distance between two successive planes is 3.36 Å. Both CH···O and CH···π non-covalent interactions combine to form a three dimensional network of molecular units.

In the crystal lattice of [Ni(L^1pNO$_2$)]·1/2C_6H_6, one of the nitro group oxygens (O4) is engaged in hydrogen bonding with the methyl

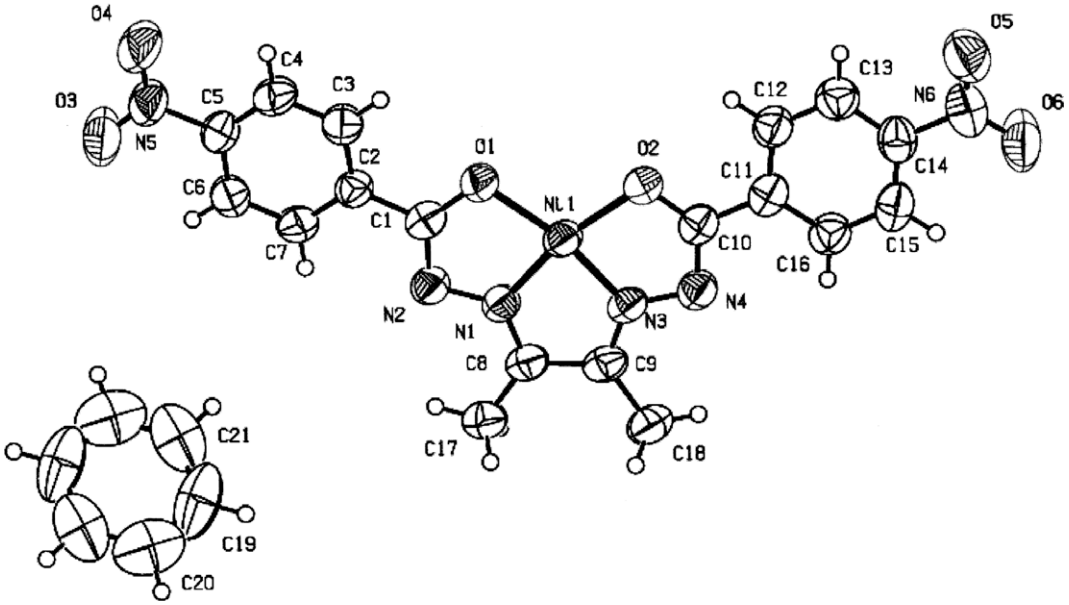


Fig. 1. ORTEP representation of [Ni(L^1-pNO$_2$)] with labeling atoms.

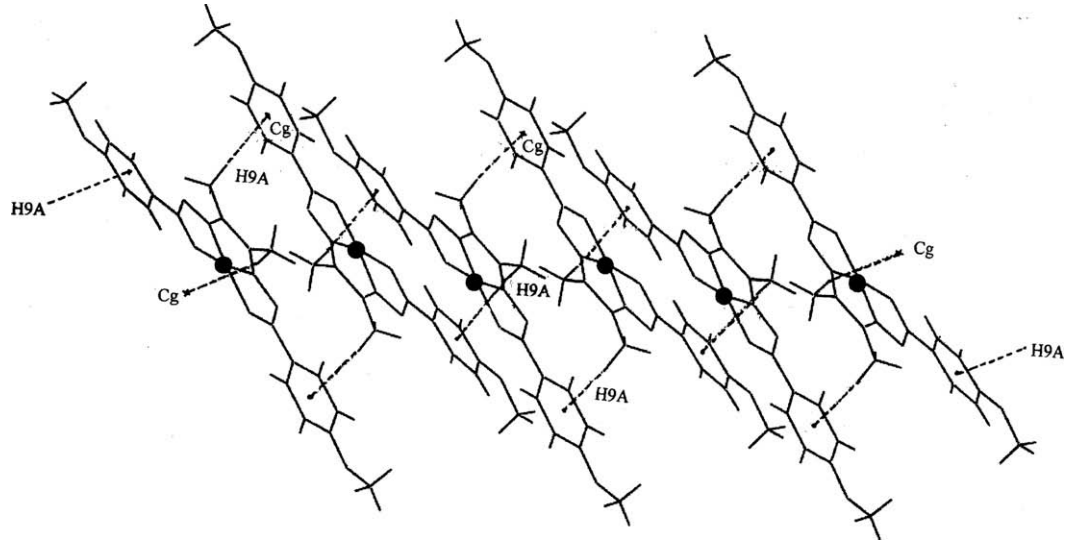


Fig. 2. CH···π non-covalent bond interactions in [Ni(L^1-pCH_3O)] complex.

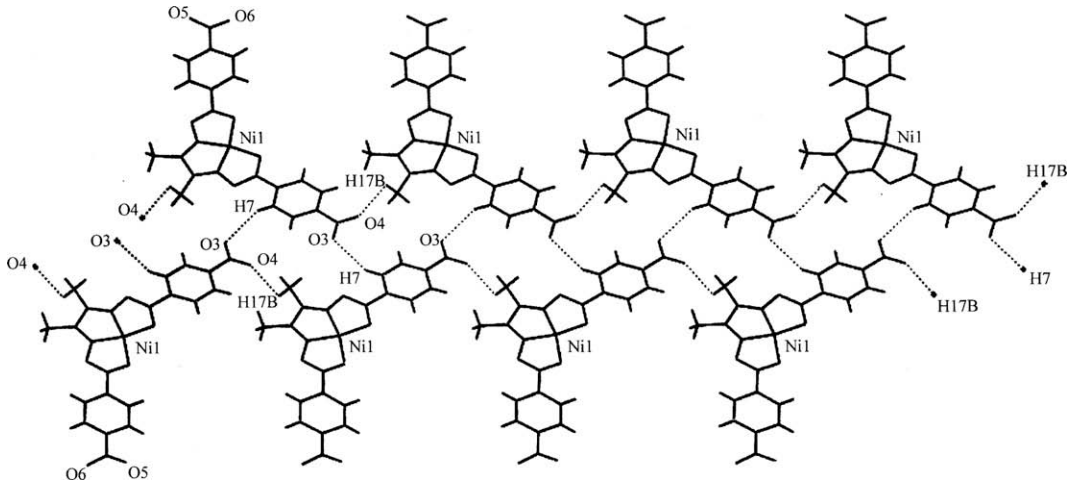


Fig. 3. Intra- and Interchain CH···O non-covalent bond interactions in [Ni(L^1-pNO_2)] double chains.

proton (H17B) of the neighboring molecule (CH17B···O4, C17···O4 = 3.19 Å) giving rise to an infinite chain propagating along b axis. This chain is connected to another adjacent chain of inverted symmetry by pairs of reciprocal hydrogen bonds between the other nitro group oxygens (O3) of chain 1 and the phenyl ring H7 protons of chain 2 (C7H···O3 = 3.281 Å) forming an infinite strand of double chains as shown in Fig. 3. The parameters of (CH17B···O4) [C–H17B = 0.96 Å, H17B···O4 = 2.672 Å, C17···O4 = 3.19 Å and C17–H17B–O4 angle = 114.79°] are in the typical range reported for such interaction [51,52]. The benzene molecules in the unit cell do not show any non-covalent intermolecular interactions.

3.2.2. Bis(imidazole) and mono(imidazole) nickel(II) complexes

The crystal data and structural refinement parameters for the bis(imidazole) nickel(II) complexes, [Ni(L^1-H)$(HIm)_2$] · 1/3H_2O, [Ni(L^1-NO_2)$(HIm)_2$] and the mono(imidazole) Ni(II) complex [Ni(L^2-pCH_3)(HIm)] are, respectively, listed in Table 3. The structures of [Ni(L^1-H)$(HIm)_2$] and [Ni(L^1-NO_2)$(HIm)_2$] together with their atomic numbering scheme are, respectively, shown in Figs. 4 and 5. Selected bond distances (Å) and bond angles (°) for [Ni(L^1-H)$(HIm)_2$] · 1/3H_2O and [Ni(L^1-NO_2)$(HIm)_2$] are listed in Table 4. The crystal structure of [Ni(L^1-H)$(HIm)_2$] · 1/3H_2O consists of three crystallographically independent molecular units, namely Ni1, Ni2

Table 3
Crystal data and structure refinement for [Ni(L^1-H)$(HIm)_2$], [Ni(L^1-pNO_2)$(HIm)_2$] and [Ni(L^2-pCH_3)(HIm)] complexes.

	[Ni(L^1-H)$(HIm)_2$]	[Ni(L^1-pNO_2)$(HIm)_2$]	[Ni(L^2-pCH_3)(HIm)]
Empirical formula	$C_{72}H_{74}N_{24}Ni_3O_7$	$C_{24}H_{22}N_{10}NiO_6$	$C_{27}H_{24}N_6NiO_2$
Formula weight	1563.68	605.23	523.23
T (K)	299(2)	299(2)	296(2)
λ (Å)	0.71073	0.71073	1.54180
Crystal system	monoclinic	monoclinic	monoclinic
Space group	$C2/c$	$P21/c$	$P21/c$
Unit cell dimensions			
a (Å)	70.257(13)	25.681(1)	12.552(2)
b (Å)	8.493(2)	13.0453(8)	11.616(2)
c (Å)	26.737(9)	8.0847(5)	17.949(3)
α (°)	90	90	90
β (°)	105.64(3)	92.911(5)	106.26(1)
γ (°)	90	90	90
V (Å^3)	15 363(7)	2705.0(3)	2512.4(7)
Z	8	4	4
D_{Calc} (Mg m^{-3})	1.352	1.486	1.383
Absorption coefficient (mm^{-1})	0.796	0.776	1.409
F (0 0 0)	6512	1248	1088
Crystal size (mm)	0.44 × 0.20 × 0.18	0.60 × 0.60 × 0.30	0.475 × 0.40 × 0.125
θ Range for data collection	4.08–27.24	4.12–26.37	3.84–66.96
Limiting indices	$-79 \leqslant h \leqslant 88$, $-10 \leqslant k \leqslant 10$, $-33 \leqslant l \leqslant 34$	$-32 \leqslant h \leqslant 31$, $-15 \leqslant k \leqslant 16$, $-6 \leqslant l \leqslant 10$	$-14 \leqslant h \leqslant 1$, $0 \leqslant k \leqslant 13$, $-20 \leqslant l \leqslant 21$
Reflections collected	64 901	18 657	4691
Independent reflections (R_{int})	16 399 (0.1074)	5441 (0.0383)	4474 (0.0376)
Completeness to θ	27.24 95.5%	26.37 98.7%	66.96 99.9 %
Absorption correction	semi-empirical from equivalents	analytical	empirical
Maximum and minimum transmission	0.9761 and 0.8909	0.8255 and 0.7030	0.7364 and 0.5268
Refinement method	full-matrix least-squares on F^2	full-matrix least-squares on F^2	full-matrix least-squares on F^2
Data/restraints/parameters	16 399/2/961	5441/0/379	4474/1/380
Goodness-of-fit on F^2	1.002	1.049	1.062
Final R indices $I > 2\sigma(I)$	R_1 = 0.0969, wR_2 = 0.2592	R_1 = 0.0400, wR_2 = 0.1041	R_1 = 0.0306, wR_2 = 0.1011
R indices (all data)	R_1 = 0.2095, wR_2 = 0.3350	R_1 = 0.0501, wR_2 = 0.1093	R_1 = 0.0428, wR_2 = 0.1052
Largest difference in peak and hole (e Å^{-3})	1.172 and −0.573	0.433 and −0.342	0.294 and −0.224

and Ni3 molecular units, in addition to one water molecule while that of $[Ni(L^1\text{-}NO_2)(HIm)_2]$ consists of one type of discrete molecular units. The central Ni(II) in each of the three molecular units of $[Ni(L^1\text{-}H)(HIm)_2]\cdot 1/3H_2O$ as well as in $[Ni(L^1\text{-}NO_2)(HIm)_2]$ is six coordinate in a distorted octahedral geometry, where the dinegative bisaroylhydrazone ligand occupies the equatorial plane while the two imidazole rings are situated in the two apical positions. The bite angles in the three molecular units of $[Ni(L^1\text{-}H)(HIm)_2]\cdot 1/3H_2O$ and $[Ni(L^1\text{-}NO_2)(HIm)_2]$, Table 4, are less than 90° while the trans angles in the equatorial planes are much less than 180°. The axial angles formed between the central Ni and the coordinated imidazole nitrogens, N5–Ni–N7, N13–Ni–N15, and N21–Ni–N23, in Ni1, Ni2, and Ni3 molecular units of $[Ni(L^1\text{-}H)(HIm)_2]\cdot 1/3H_2O$ are 156.2(3)°, 154.8(3)° and 161.1(3)°, respectively, while the

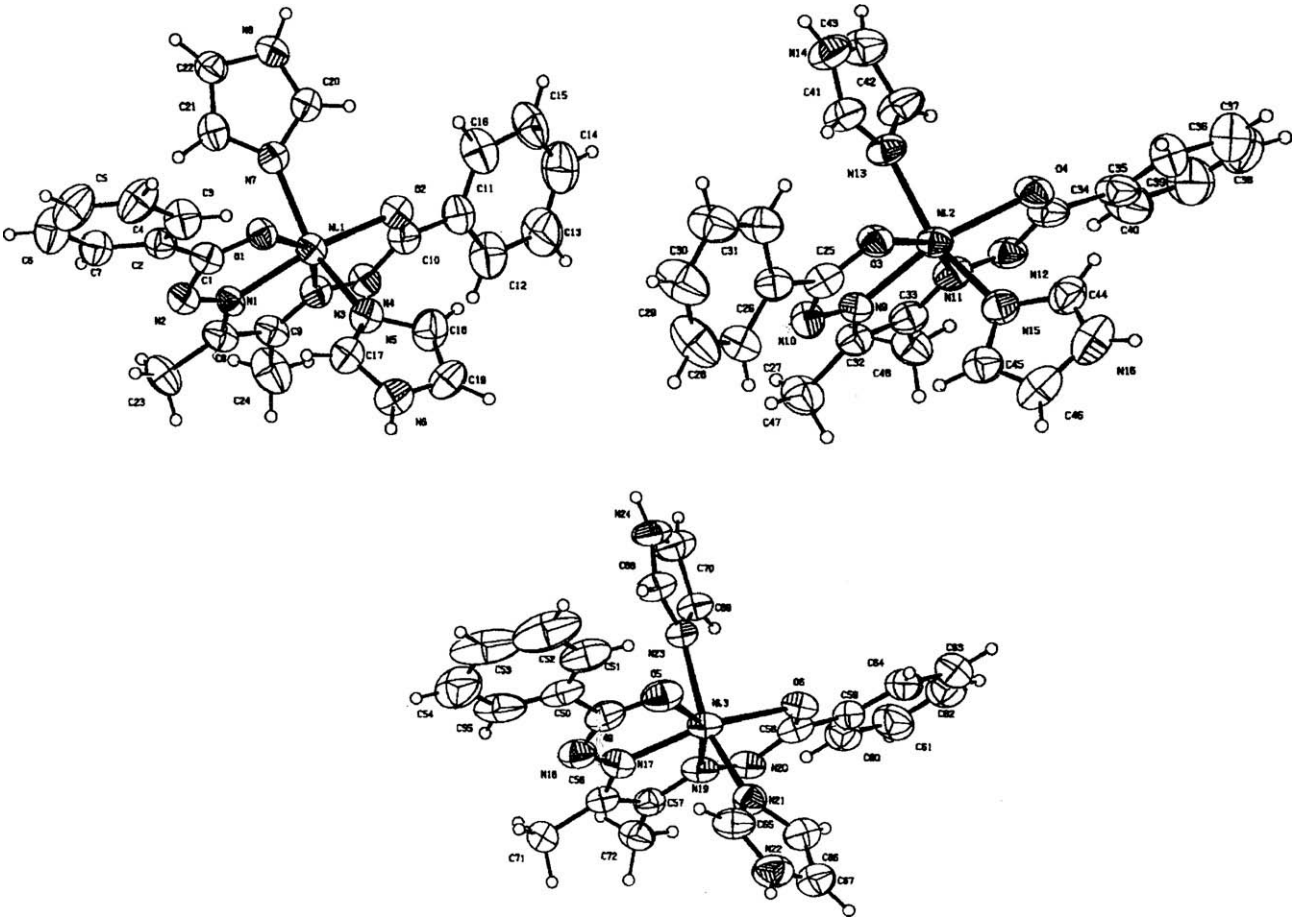


Fig. 4. ORTEP representation of the three crystallographic independent molecular units of $[Ni(L^1\text{-}H)(HIm)_2]$ with labeling atoms.

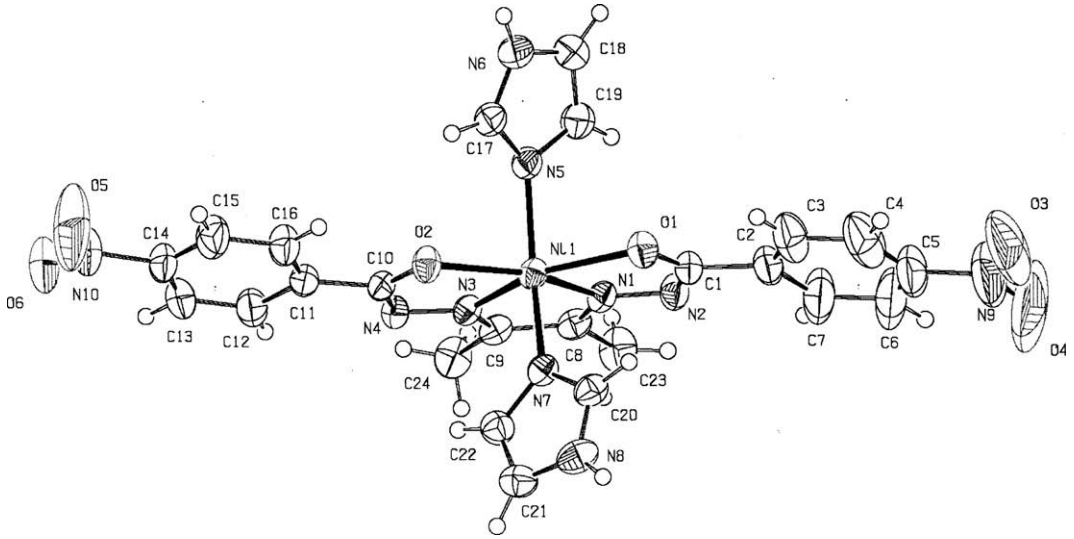


Fig. 5. ORTEP representation of $[Ni(L^1\text{-}pNO_2)(HIm)_2]$ with labeling atoms.

corresponding angle (N5–Ni–N7) in $[Ni(L^1\text{-}NO_2)(HIm)_2]$ is 159.09°. Hereafter, the imidazole ring in these complexes are designated by the tertiary nitrogen directly coordinated to the Ni(II).

The N–H protons of the two coordinated imidazole rings in both $[Ni(L^1\text{-}H)\cdot(HIm)_2]\cdot 1/3\ H_2O$ and $[Ni(L^1\text{-}NO_2)(HIm)_2]$ play a crucial role in their crystal packing. In $[Ni(L^1\text{-}H)\cdot(HIm)_2]\cdot 1/3\ H_2O$, the Ni1, Ni2 and Ni3 molecular units are involved in different supramolecular assemblies. The N6H proton of the N5 imidazole ring in Ni1 molecular unit is involved in intermolecular hydrogen bond formation, N6H···O1 (N6···O1 = 2.720 Å), *i*th the enolimine oxygen O1 of one adjacent Ni1 molecular unit while the other N8H proton of the N7 imidazole ring forms N8H···N2 (N8···N2 = 2.864 Å) hydrogen bond with the hydrazone N2 nitrogen of another adjacent Ni1 molecular units, giving rise to a supramolecular triple stranded helical chain (Ni1 chain) propagating along *b*-axis as shown in Fig. 6a. The Ni2 molecular units are also linked together via N16H···N10 (N16···N10 = 3.080 Å) hydrogen bonds, forming a linear chain extended along *b*-axis. In this chain, two successive Ni2 molecular units are further linked to one Ni3 molecular unit via N14H···O6 (N14···O6 = 2.934 Å) and N24H···O4 (N24···O4 = 2.75.53 Å) hydrogen bonds, respectively, thus the interconnected Ni2- and Ni3-molecular units form mono stranded helical chain (Ni2–Ni3 chain) extended parallel to the *b*-axis as shown in Fig. 6b. The Ni2–Ni3 helical chain is stabilized by CH···π interactions between the N13 imidazole C43H proton and the (C49–C54) phenyl π system, and between the phenyl (C59–C64) phenyl C63H proton and N23 imidazole π system. Similarly, the Ni3 molecular units are also linked to the adjacent Ni2 molecular units, forming another Ni2–Ni3 chain but of inverted symmetry. The Ni2–Ni3 chains are connected together by water bridges where the water H7*2* protons are involved in hydrogen bond formation with the enolimine O2 oxygens of the Ni2 molecular units while the water O7 oxygens form hydrogen bonds with the imidazole N22–H protons of Ni3 molecular units (N22H···O7, N22···O7 = 2.839 Å) of the neighboring Ni2–Ni3 chain giving rise to a two-dimensional sheet of helical chains extending parallel to *bc*-plane. In the crystal lattice of $[Ni(L^1\text{-}H)\cdot(HIm)_2]\cdot 1/3H_2O$, the Ni1 molecular units of Ni1 chains are connected from both sides to Ni2 and Ni3 molecular units by C23···N12 and C52H···C12, respectively. Thus the Ni1 chains are embedded between the two extended sheets originated from Ni2 and Ni3 molecular units.

In $[Ni(L^1\text{-}NO_2)(HIm)_2]$ the molecular units are linked together by N6H···O1 (N6···O1 = 2.763 Å) and a trifurcated hydrogen bond between N8H imidazole proton and N3 imine nitrogen (N8H···N3, N8···N3 = 2.622 Å), N4 hydrazine nitrogen (N8H···N4, N8···N4 = 2.642 Å) and N5 imidazole nitrogen (N8H···N5, N8···N5 = 2.559 Å), giving rise to a supramolecular triple stranded helical chain propagating along the *c*-axis more or less similar to Ni1 chain in $[Ni(L^1\text{-}H)(HIm)_2]\cdot 1/3H_2O$. The helical chain is further stabilized by intrachain C–H···π interactions between aromatic C16H and N7 imidazole π system [50]. In the crystal lattice of $[Ni(L^1\text{-}NO_2)(HIm)_2]$ the helical chains are linked together by CH····N non-covalent bond interactions between H23A methyl protons of one chain and N2 hydrazine nitrogen of the adjacent chain, forming a sheet of infinite

Table 4
Selected bond distances (Å) and bond angles (°) for $[Ni(L^1\text{-}H)(HIm)_2]$ and $[Ni(L^1\text{-}H)(HIm)_2]$ complexes.

$[Ni(L^1\text{-}H)(HIm)_2]$							$[Ni(L^1\text{-}pNO_2)(HIm)_2]$
Ni1 Molecular unit		Ni2 Molecular unit		Ni3 Molecular unit			
N1–Ni1	2.029(5)	N9–Ni2	2.002(6)	N17–Ni3	2.015(7)	N1–Ni1	2.0077(18)
O1–Ni1	2.275(5)	O3–Ni2	2.178(5)	O5–Ni3	2.243(7)	O1–Ni1	2.2397(16)
O2– Ni1	2.151(5)	O4–Ni2	2.69(6)	O6– Ni3	2.280(5)	O2– Ni1	2.1726(15)
N3– Ni1	1.995(6)	N11–Ni2	1.997(6)	N19–Ni3	1.999(6)	N3– Ni1	1.9881(18)
N5–Ni1	2.034(6)	N15–Ni2	2.048(7)	N21–Ni3	2.051(7)	N5–Ni1	2.0725(19)
N7– Ni1	2.070(6)	N13–Ni2	2.057(6)	N23– Ni3	2.053(7)	N7– Ni1	2.0481(18)
C1–O1	1.271(9)	C25–O3	1.266(10)	C49–O5	1.290(12)	C1–O1	1.274(3)
C1–C2	1.462(11)	C25–C26	1.495(12)	C49–C50	1.497(14)	C1–C2	1.500(3)
C1–N2	1.378(10)	C25–N10	1.338(10)	C49–N18	1.296(12)	C1–N2	1.328(3)
N1–N2	1.405(8)	N9–N10	1.388(9)	N17–N18	1.368(9)	N1–N2	1.370(3)
C8–N1	1.307(9)	C32– N9	1.297(9)	C56–N17	1.278(10)	C8–N1	1.299(3)
C8–C9	1.480(12)	C32–C33	1.465(11)	C56–C57	1.486(11)	C8–C9	1.475(3)
C9–N3	1.281(9)	C33–N11	1.310(10)	C57–N19	1.298(9)	C9–N3	1.299(3)
N3–N4	1.359(8)	N11–N12	1.354(9)	N19 –N20	1.382(9)	N3–N4	1.369(2)
C10–N4	1.351(10)	C34–N12	1.330(10)	C58–N20	1.332(10)	C10–N4	1.343(3)
C10–O2	1.277(9)	C34–O4	1.275(10)	C58–O6	1.251(10)	C10–O2	1.266(3)
C10–C11	1.478(12)	C34–C35	1.516(13)	C58–C59	1.529(12)	C10–C11	1.494(3)
N1–Ni1–O1	72.1(2)	N9–Ni2–O3	74.5(2)	N17–Ni3–O5	73.0(3)	N1–Ni1–O1	73.51(7)
N3–Ni1–N1	78.3(3)	N11–N2–N9	78.6(3)	N19–Ni3–N17	77.8(3)	N3–Ni1–N1	78.27(7)
N7–Ni1–O1	8 2.3(2)	N13–Ni2–O3	85.8(2)	N23–Ni3–O5	86.5(3)	N7–Ni1–O1	85.77(7)
N7–Ni1–O2	8 5.0(2)	N13–Ni2–O4	86.2(2)	N23–Ni3–O6	83.3(2)	N7–Ni1–O2	87.39(7)
N5–Ni1–O2	88.3(2)	N15–Ni2–O4	84.3(3)	N21–Ni3–O6	84.3(3)	N5–Ni1–O2	86.01(7)
N3–Ni1–N5	96.2(3)	N11–Ni2–N15	100.0(3)	N17–Ni3–N21	96.2(3)	N3–Ni1–N5	101.63(7)
O2–Ni1–O1	134.47(19)	O3–Ni2–O4	134.7(2)	O5–Ni3–O6	135.9(3)	O2–Ni1–O1	133.18(6)
N5–Ni1–O1	8 6.3(2)	O3–Ni2–N15	84.3(3)	N21–Ni3–O5	87.6(3)	N5–Ni1–O1	84.36(7)
N5–Ni1–N7	156.2(3)	N15–Ni2–N13	154.8(3)	N21–Ni3–N23	161.1(3)	N5–Ni1–N7	159.09(7)
N1–Ni1–O2	153.4(2)	N9–Ni2–O4	150.6(2)	N17–Ni3–O6	151.0(2)	N1–Ni1–O2	153.29(7)
O1–C1–C2	120.2(7)	O3–C25–C26	118.8(7)	O5–C49–C50	116.8(10)	O1–C1–C2	118.9(2)
N2–C1–C2	113.9(7)	N10–C25–C26	114.9(7)	N18–C49–C50	114.7(11)	N2–C1–C2	114.3(2)
O1–C1–N2	125.9(7)	O3–C25–N10	126.2(8)	O5–C49–N18	128.6(9)	O1–C1–N2	126.8(2)
C1–N2–N1	106.1(6)	C25–N10–N9	108.0(6)	C49–N18–N17	107.8(8)	C1–N2–N1	108.87(18)
N2–N1–C8	118.8(6)	C32–N9–N10	122.2(6)	C56–N17–N18	120.0(7)	N2–N1–C8	120.67(18)
N1–C8–C9	112.5(7)	N9–C32–C33	114.1(7)	N17–C56–C57	114.3(7)	N1–C8–C9	113.83(19)
N3–C9–C8	115.8(7)	N11–C33–C32	114. 2(7)	N19–C57–C56	112. 9(7)	N3–C9–C8	113.65 (19)
C9–N3–N4	121.8(6)	C33–N11–N12	119.5(7)	C57–N19–N20	119.4(6)	C9–N3–N4	121.25(18)
C10–N4–N3	1 0 7.9(6)	C34–N12–N11	1 0 9.6(7)	C58–N20–N19	108.4(7)	C10–N4–N3	108.08(16)
O2–C10–N4	126.1(7)	O4–C34–N12	124.7(8)	O6–C58–N20	127.9(8)	O2–C10–N4	126.62(19)
O2–C10–C11	118.3(8)	O4–C34–C35	115.9(8)	O6–C58–C59	118.5(8)	O2–C10–C11	118.72(19)

chains extended parallel to the *bc*-plane. The chains in one sheet are further interconnected to symmetry inverted chains of the adjacent sheet by C24HC···O6, C24H*A*···O5 and C21H···O5 interactions, giving rise to two dimensional arrays of helical chains.

The structure of the monoimidazole complex, [Ni(L^2-pCH_3)(HIm)], together with the atomic numbering scheme is shown in Fig. 7. Selected bond distances (Å) and bond angles (°) for [Ni(L^2-pCH_3)(HIm)] are listed in Table 5. The central nickel (II) in [Ni(L^2-pCH_3)(HIm)] is in a distorted square planar geometry, being coordinated to the imine N1 nitrogen [Ni–N1 = 1.8154(17) Å] and the deprotonated enolimide O1 oxygen [Ni–O1 = 1.8721(14) Å] of the aldehydic arm, besides the deprotonated hydrazide N3 nitrogen of the phenyl arm, forming a 5,6-membered bicyclic chelate ring. The ketoamide O2 oxygen of the phenyl arm remains uncoordinated. It is thus apparent that the bis(aroylhydrazone) molecule acts as a dinegative NNO tridentate ligand rather than the expected dinegative NNOO tetradentate ligand. The fourth coordination site is occupied by the N5 imidazole nitrogen [Ni–N5 = 1.899(17) Å]. This unexpected coordination mode can be related to the unsymmetric nature of the coordinated bis(aroylhydrazone) ligand. The imidazole N6–H proton is involved in hydrogen bond formation with the uncoordinated ketoamide O2 oxygen forming, hydrogen bonded dimer. In this dimer, the two imidazole rings are involved in π–π stacking interaction [Cg5···Cg5 = 4.102 Å]. The hydrogen

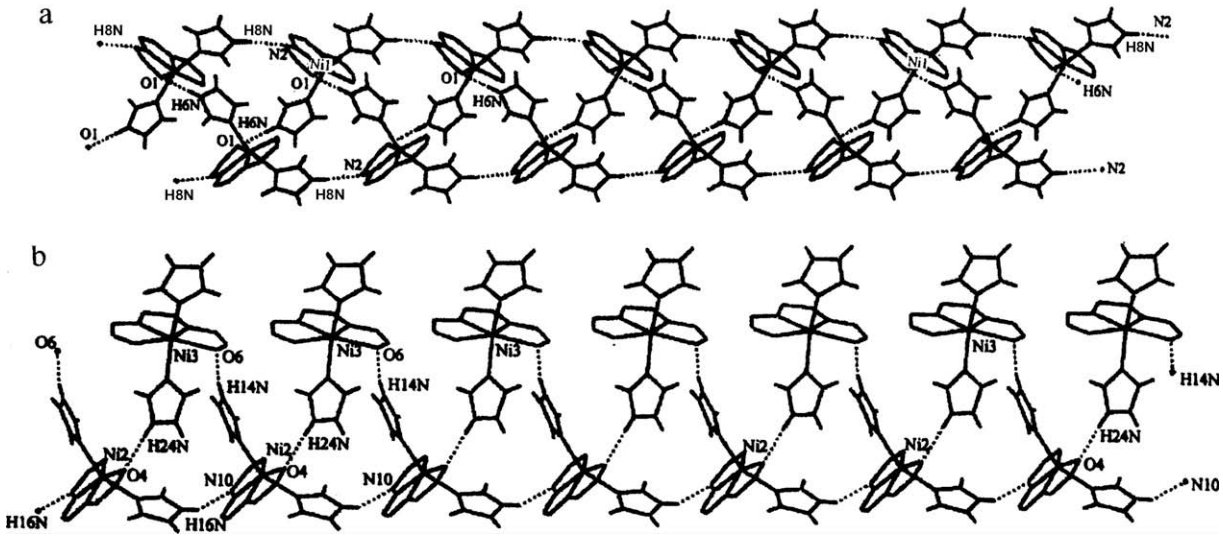


Fig. 6. Ni1- and Ni2–Ni3-chains in [Ni(L^1-H)$(HIm)_2$] complex: (a) triple stranded helical Ni1-chain and (b) Ni2–Ni3 helical chain.

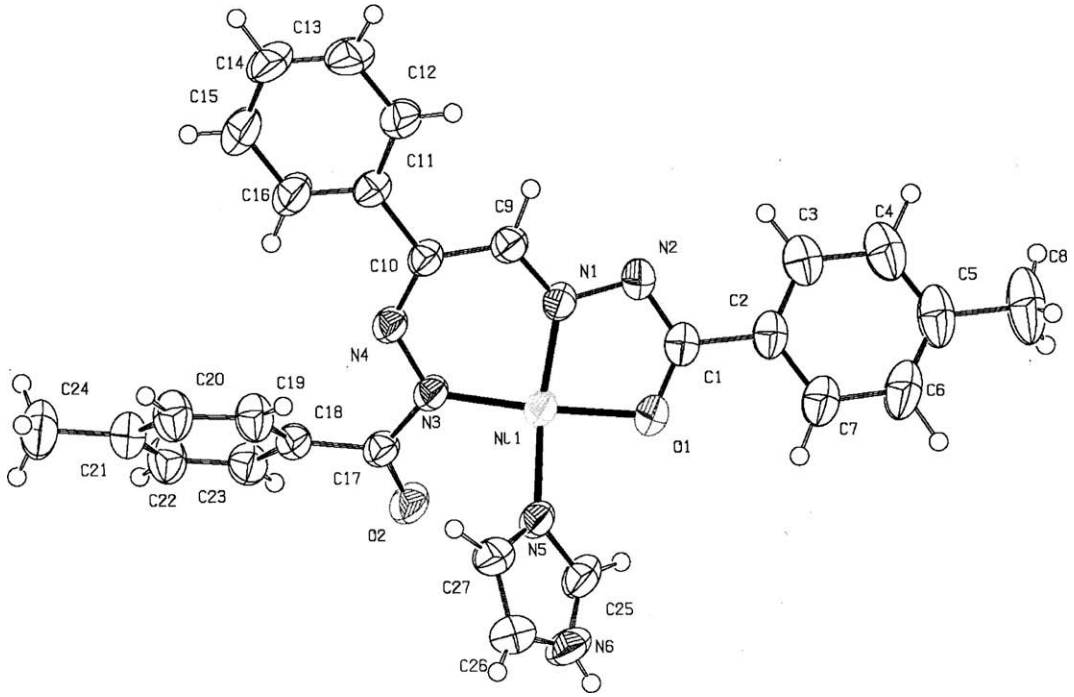


Fig. 7. ORTEP representation of [Ni(L^2-pCH_3)(HIm)] with labeling atoms.

Table 5
Selected bond distances (Å) and bond angles (°) for [Ni(L^2-pCH_3)(HIm)] complex.

Bond distances (Å)		Bond angles (°)	
Ni–N1	1.8154(17)	N1–Ni–O1	83.16(6)
Ni–N3	1.8695(16)	N1–Ni–N3	92.16(7)
Ni–N5	1.8990(17)	N3–Ni–N5	96.63(7)
Ni–O1	1.8721(14)	O1–Ni–N5	89.49(7)
C1–C1	1.481(3)	N1–Ni–N5	165.76(7)
C1–O1	1.294(2)	N3–Ni–O1	171.09(7)
C1–N2	1.312(3)	O1–C1–C2	119.80(18)
N1–N2	1.392(2)	N2–C1–C2	117.53(19)
C9–N1	1.298(2)	N2–C1–O1	122.67(17)
C9–C10	1.432(3)	C1–N2–N1	107.80(16)
C10–C11	1.494(2)	C9–N1–N2	115.94(17)
C10–N4	1.298(2)	N1–C9–C10	122.41(19)
N3–N4	1.352(2)	C9–C10–C11	119.00(17)
C17– N3	1.398(2)	N4–C10– C11	115.36(16)
C17–C18	1.493(3)	C10–N4–N3	121.79(15)
C17–O2	1.224(2)	N4–N3–C17	109.95(14)
		N3–C17–C18	120.57(16)
		O2–C17–N3	120.02(17)
		O2–C17–C18	119.39(17)

bonded dimers are linked together by two pairs of reciprocal CH···π interactions between the C12H proton of the phenylglyoxal phenyl (C11–C16) ring and the N5 imidazole π-system [C12H···Cg5 = 2.790 Å] giving rise to a linear chain propagating along b-axis. The chain of dimers is further stabilized by C9H···C7 interactions [C9···C7 = 3.569 Å]. In the crystal lattice, the hydrogen bonded dimers chain are interconnected by reciprocal C23H····C9 interactions.

Acknowledgments

Thanks are due to BMBF/Forschungszentrm, Jüelich, ÖA-IB/Wo WTZ for supporting this bilateral project.

Appendix A. Supplementary data

CCDC 721269, 721270, 72171, 721272, 721273 and 721274 contain the supplementary crystallographic data for [Ni(L^1-H)], [Ni(L^1-pCH_3O)], [Ni(L^1-pNO_2)] · 1/2C_6H_6, [Ni(L^1-H)(HIm)$_2$] · 1/3H_2O, [Ni(L^1-NO_2)(HIm)$_2$] and [Ni(L^2-pCH_3)(HIm)], respectively. These data can be obtained free of charge via http://www.ccdc.cam.ac.uk/conts/retrieving.html, or from the Cambridge Crystallographic Data Centre, 12 Union Road, Cambridge CB2 1EZ, UK; fax: (+44) 1223-336-033; or e-mail: deposit@ccdc.cam.ac.uk. Supplementary data associated with this article can be found, in the online version, at doi:10.1016/j.poly.2009.04.007.

References

[1] H. Liu, Z. Lu, D. Niu, J. Coord. Chem. 61 (2008) 4040.
[2] H. Liu, H. Wang, F. Gao, D. Niu, Z. Lu, J. Coord. Chem. 60 (2007) 2671.
[3] A. Roth, A. Buchholz, M. Gartner, A. Malassa, H. Gorls, G. Vaughan, W. Plass, Z. Anorg, Allg. Chem. 633 (2007) 2009.
[4] R. Reveendran, S. Pal, Inorg. Chim. Acta 359 (2006) 3212.
[5] R.B.N. Bessy, K.M.R. Prathapachandra, E. Suresh, Struct. Chem. 17 (2006) 201.
[6] S. Das, S. Pal, J. Mol. Struct. 753 (2005) 68.
[7] F. Borbone, V. Caruso, R. Centore, A. De Maria, A. Fort, M. Fusco, B. Panuzi, A. Reviello, A. Tuzi, Eur. J. Inorg. Chem. (2004) 2467.
[8] F. Cariati, V. Caruso, R. Centore, W. Marcolli, A. De Maria, B. Panunz, A. Reviello, A. Tuzi, Inorg. Chem. 41 (2002) 6597.
[9] S. Pal, Proc. Indian Acad. Sci. (Chem. Sci.) 114 (2002) 417.
[10] R. Dinda, P. Sengupta, S. Ghosh, H. Mayer Figge, W.S. Sheldrick, J. Chem. Soc., Dalton. Trans. (2002) 4434.
[11] M.F. Iskander, T.E. Khalil, W. Haase, R. Werner, I. Svoboda, H. Fuess, Polyhedron 20 (2001) 2787.
[12] M.F. Iskander, T.E. Khalil, R. Werner, W. Haase, I. Svoboda, H. Fuess, Polyhedron 19 (2000) 949.
[13] S. Banerjee, S. Sen, S. Basak, S. Mitra, D.L. Hughes, C. Desplanches, Inorg. Chim. Acta 361 (2008) 2707.
[14] R. Raveendram, S. Pal, Polyhedron 24 (2005) 57.
[15] J. Grewe, A. Hagenbach, B. Shomburg, R. Alberto, Anorg. Allg. Chem. 629 (2003) 303.
[16] S. Pal, S. Pal, J. Chem. Soc., Dalton Trans. (2000) 2102.
[17] N.R. Sangeetha, S. Pal, Polyhedron 19 (2000) 1593.
[18] A. Chaudhury, B. Geetha, N.R. Sangeetha, V. Kavita, V. Susila, S. Pal, J. Coord. Chem. 48 (1999) 87.
[19] A. Sarkar, S. Pal, Polyhedron 25 (2006) 1689.
[20] S. Das, S. Pal, J. Mol. Struct. 741 (2005) 183.
[21] A. Mukhopadhyay, S. Pal, Polyhedron 23 (2004) 1997.
[22] A. Mukhopadhyay, G. Padmaja, S. Pal, S. Pal, Inorg. Chem. Commun. 6 (2003) 381.
[23] S. Das, G.P. Muthukumaragopal, S. Pal, S. Pal, New J. Chem. 27 (2003) 1102.
[24] N.R. Sangeetha, C.K. Pal, P. Ghosh, S. Pal, J. Chem. Soc., Dalton Trans. (1996) 3293.
[25] N.M.H. Salem, L. El-Sayed, M.F. Iskander, Polyhedron 27 (2008) 3215.
[26] N.M.H. Salem, L. El-Sayed, S. Foro, W. Haase, M.F. Iskander, Polyhedron 26 (2007) 4161.
[27] N.M.H. Salem, L. El-Sayed, W. Haase, M.F. Iskander, J. Coord. Chem. 58 (2005) 1327.
[28] M.F. Iskander, L. El-Sayed, N.M.H. Salem, R. Werner, W. Haase, J. Coord. Chem. 56 (2003) 1075.
[29] D.S. Kalinowski, D.R. Richardson, Pharmacol. Rev. 57 (2005) 547.
[30] B. Mladanova, D.S. Ivanov, M.H. Umbreit, J. Klos, S. Konstantinov, M. Karaivanova, Pharmacia 50 (2003) 3.
[31] J. Patole, U. Sandbhor, S. Padhye, D.N. Deobagkar, C.E. Anson, A. Powell, Bioorg. Med. Chem. Lett. 13 (2003) 51.
[32] E.W. Ainscough, A.M. Brodie, W.A. Denny, G.J. Finlay, S.A. Gothe, J.D. Ranford, J. Inorg. Biochem. 77 (1999) 125.
[33] E.W. Ainscough, A.M. Brodie, A.J. Dobbs, J.D. Ranford, J.M. Waters, Inorg. Chim. Acta 267 (1998) 27.
[34] L.L. Koh, O.L. Kon, K.W. Loh, Y.C. Long, J.D. Ranford, A.L.C. Tan, Y.Y. Tjan, J. Inorg. Biochem. 72 (1998) 155.
[35] A. Bacchi, Mauro Carcelli, O. Francescangeli, F. Neve, P. Pelagatti, C. Pelizzi, Inorg. Chem. Commun. 2 (1999) 255.
[36] L. El-Sayed, M.F. Iskander, N.M. Hawash, S.S. Massoud, Polyhedron 17 (1998) 199.
[37] V.G. Yusupov, M.T. Toshev, G.G. Aleksandrov, N.A. Parpiev, M.M. Karimov, Kh.B. Dustov, O.V. Sharopov, Koord. Khim. 14 (1988) 985.
[38] L. Sacconi, Z. Anorg. Allg. Chem. 275 (1954) 249.
[39] L. Sacconi, G. Lombardo, P. Paoletti, J. Chem. Soc. (1958) 848.
[40] L. Sacconi, G. Lombardo, R. Ciofalo, J. Am. Chem. Soc. 82 (1960) 4181.
[41] L. Sacconi, G. Lombardo, P. Paoletti, J. Am. Chem. Soc. 82 (1960) 4185.
[42] L. Sacconi, G. Lombardo, J. Am. Chem. Soc. 82 (1960) 6266.
[43] D. Dakternieks, A. Orlandini, L. Sacconi, Inorg. Chim. Acta 29 (1978) L205.
[44] S. Gehring, P. Paulus, W. Haase, Inorg. Chem. 32 (1993) 54.
[45] G.M. Sheldrick, SHELXS-97, SHELXL-97: Programs for Crystal Structure Analysis, University of Göttingen, Göttingen, Germany, 1998.
[46] C.K. Johnson, M.N. Burnett, ORTEPIII. Report ORNL-6895, Oak Ridge National Laboratory, TN, USA, 1996.
[47] A.L. Spek, PLATON, A Multipurpose Crystallographic Tool, Utrecht University, Utrecht, The Netherlands, 2002.
[48] A.B.P. Lever, Inorganic Electronic Spectroscopy, 2nd ed., Elsevier, Amestrdam, 1984.
[49] S.C. Chan, L.L. Koh, P.-H. Leung, J.D. Ranford, K.Y. Sim, Inorg. Chem. Acta 236 (1995) 101.
[50] M. Nishio, M. Hirota, Y. Umezawa, CH/π interaction. Evidence, Nature and Consequences, John Wiley and Sons Inc., New York, 1998.
[51] G.R. Desiraju, Acc. Chem. Res. 29 (1996) 441.
[52] G.R. Desiraju, Acc. Chem. Res. 24 (1991) 290.

Polyhedron 28 (2009) 2149–2156

Contents lists available at ScienceDirect

Polyhedron

journal homepage: www.elsevier.com/locate/poly

X-ray structure and spectroscopic characterization of doubly-bridged binuclear copper(II) complexes in symmetric and asymmetric coordination environments

Gnana S. Siluvai *, Narasimha N. Murthy

Department of Chemistry, Indian Institute of Technology, Madras 600 036, India

ARTICLE INFO

Article history:
Received 15 October 2008
Accepted 7 April 2009
Available online 16 April 2009

Keywords:
Symmetrical and unsymmetrical dicopper(II) complexes
X-ray crystal structures
Solution magnetic moment
Paramagnetic ^{1}H NMR

ABSTRACT

μ-1,3-Acetamide or acetate bridged, symmetric and asymmetric dicopper(II) complexes *viz* $[Cu_2(P1\text{-}O^-)(NHAc^-)](ClO_4)_2$ (**1**), $[Cu_2(P2\text{-}O^-)(OAc^-)](ClO_4)_2$ (**2**) and $[Cu_2(P2'\text{-}O^-)(OAc^-)(H_2O)](ClO_4)_2$ (**3**) were synthesized by employing classic dinucleating ligands; P1-OH, P2-OH (symmetric), and P2′-OH (asymmetric) having trivial differences in their ligand frame work. Solid state structures of these complexes were determined by X-ray crystallography. In solution, they were also characterized by various spectroscopic techniques, which includes ESI-MS, FT-IR, optical, solution magnetic moment, paramagnetic ^{1}H NMR and EPR. The solution magnetic moment of these complexes at room temperature suggests a weak magnetic interaction between the two Cu(II) centers.

Published by Elsevier Ltd.

1. Introduction

Nature has specially designed many dinuclear metalloprotein active sites with carboxylate and histidine rich ligand donors located in chemically different environments around the two metal centers, an asymmetry that may also involve the coordination numbers and the geometry of the metal centers [1–4]. These two metal centers are often found in close proximity (3–4 Å) and are bridged *via* oxo, hydroxo, carboxylate or imidazolate groups, such as to allow electronic interaction, which in turn is manifested in the physical properties of the metalloenzymes and so in model complexes, such as redox potentials, optical and magnetic characteristics. One, two or three bridging groups are usually encountered, for example: one imidazolate bridge in the defense enzyme Cu–Zn superoxide dismutase, one oxygen and one carboxylate in the diiron enzyme ribonucleotide reductase B_2, one hydroxy and two carboxylates in the diiron enzyme deoxyhemerythrin. Such binuclear structures have been well recognized to play key roles in various stereo-selective and specific biological functions such as dioxygen (O_2) activation, hydroxylation of –C–H bonds, hydrolytic cleavage of peptide and phosphoesters bonds of DNA and RNA, and several others [5–8].

Consequently, the design and synthesis of such binuclear metal complexes are challenging for the stimulation of new types of co-operative binuclear activation chemistry and their implications in the magnetic and electronic interactions in such systems for the better understanding of the various physicochemical properties of the natural enzymes [9–11]. This has led to the synthesis of a number of dicopper(II) complexes with different bridging patterns including hydroxo, alkoxo, phenoxo, imidazolate or carboxylate alone or with their combinations [12–37]. These dicopper complexes are found to have weak to strong spin–coupling between the two copper centers with intriguing modulation in their proton NMR features [12,38–42]. Among them the interesting ones are the weakly coupled systems with a shorter net electronic relaxation time (τ_s) of $\sim 10^{-11}$ s.

Here, we report the synthesis and characterization of three new dicopper(II) complexes namely $[Cu_2(P1\text{-}O^-)(NHAc^-)](ClO_4)_2$ (**1**), $[Cu_2(P2\text{-}O^-)(OAc^-)](ClO_4)_2$ (**2**) and $[Cu_2(P2'\text{-}O^-)(OAc^-)(H_2O)](ClO_4)_2$ (**3**) with a combination of chemically similar (**2**) and dissimilar (**1** and **3**) coordination environments around the two copper(II) centers (Chart 1), in order to understand more about the unique features of coordination asymmetry in binuclear systems.

2. Experimental

2.1. General

All reagents were purchased from commercial sources and used without further purification. Solvents were dried and purified under nitrogen using standard methods and distilled immediately

* Corresponding author. Address: Department of Science and Engineering, School of Medicine, Oregon Health and Science University, 20000 NW Walker Road, Beaverton, OR 97006, USA. Tel.: +1 503 7481086/2906157; fax: +1 503 7481464.
E-mail address: siluvaig@ebs.ogi.edu (G.S. Siluvai).

0277-5387/$ - see front matter Published by Elsevier Ltd.
doi:10.1016/j.poly.2009.04.006

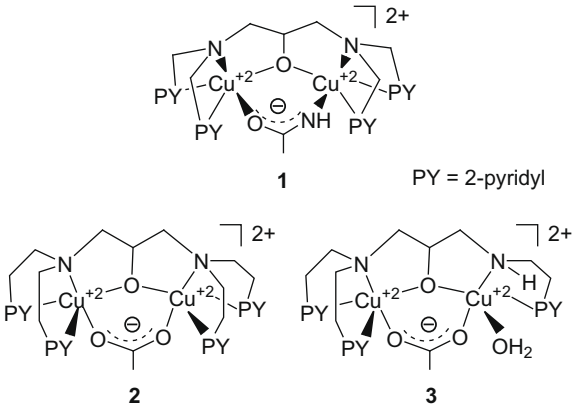


Chart 1. A representation of the binuclear copper(II) complexes **1**, **2** and **3**.

before use. Electronic spectra were measured on a Varian Cary 5E model UV–Vis–NIR spectrometer. Infrared spectra were obtained on a Shimadzu IR470 spectrometer using KBr disk/nujol mull. CHN data were obtained from Perkin–Elmer Model 2004 Series-2 CHN–S–O analyzer. Electro spray mass spectra were recorded on a Q-Tof micro hybrid quadrupole time of flight mass spectrometer. Samples are prepared in acetonitrile and were introduced into the ESI source through a syringe pump at the rate of 5 μL per min. The ESI capillary was set at 3.5 kV; the cone voltage range was 20–40 V and an average of 6–8 scans were used to observe the final spectra.

JEOL 400 or Bruker 400 spectrometers were used to record 1D spectra. Spectral width used to measure the spectra is −100–300 ppm. The carrier frequency is set at the middle of the spectral window. 1D spectra were obtained using a 90° pulse of 8–9 μs duration with 32 K data points and are the average of 1000–2000 scans. The relaxation delay used for the measurement was 0.1 s, as the rate of relaxation of the protons is of the order of ms. The shift values reported are those positive to TMS are downfield and those negative are upfield shifted. Signal assignment is partial. EPR spectra were obtained for frozen solutions of 1–2 mM concentration in DMF on a Varian E-112 spectrometer operating at X-band equipped with a liquid N_2 Dewar insert using 4 mm-OD quartz tubes at 77 K, and calibration was effected using a powder sample of 2,2-diphenyl-1-picrylhydrazyl (DPPH; $g = 2.0037$). The ligands *N,N′,N″,N‴*-tetrakis(2-pyridylmethyl)1,3-diamino-2-propanol (P1-OH), *N,N′,N″,N‴*-tetrakis(2-pyridylethyl)1,3-diamino-2-propanol (P2-OH), and *N,N′,N″*-tris(2-pyridylethyl)1,3-diamino-2-propanol (P2′-OH) were synthesized according to published procedures [43,44]. P2′-OH was obtained as a second fraction during the purification of P2-OH ligand.

Caution: Perchlorate salts of metal complexes with organic ligands are potentially explosive. Although no problems were encountered in this work, only small amounts of material should be prepared and handled with caution.

2.2. Solution magnetic moment

Room temperature magnetic moments were determined by Evans' method [45]. In a coaxial NMR tube (one tube placed in another, 5 mm OD) with the outer tube containing a known concentration of the metal complex (10–20 mM), in a deuterated solvent (acetonitrile-d_3/nitromethane-d_3) and the inner tube or capillary with only the solvent is taken. The ^{1}H NMR spectrum (0–10 ppm) of the solvent in the inner tube placed in an empty standard NMR tube was recorded and its position was fixed at its original position (e.g. CH_3CN at 1.97 ppm). Then the empty tube was replaced by the one, which contain the metal-complex solution. The spectrum of this solution and that of solvent in the inner tube were recorded simultaneously. The position of acetonitrile (solvent) for both the samples was noted. Solvent in the capillary remained at it's original position, while that in the complex shifted from its original position due to bulk susceptibility of the metal complex. The difference in the shift ($\Delta\nu$) called paramagnetic chemical shift was noted. This is related to the molar susceptibility (χ_M) (Eq. (1)) from which the magnetic moment (μ) (Eq. (2)) is calculated.

$$\chi_M = \frac{3}{4\pi}\frac{\Delta\nu}{\nu_0}\frac{1000}{c} + \chi_0 - \chi_D \quad (1)$$

where, $\Delta\nu$ = paramagnetic shift of the solvent = $\nu^{sol}_{internal} - \nu^{sol}_{external}$, ν = frequency of the NMR spectrometer, c = concentration of the metal complex used, L/mol, χ_0 = solvent susceptibility, χ_D = diamagnetic correction of the metal complex (-452.72×10^{-6} (**1**), -465.62×10^{-6} (**2**), and -416.12×10^{-6} (**3**) cgs units).

$$\mu = 2.84\sqrt{\frac{\chi_M \times T}{n}} \quad (2)$$

where χ_M = total molar susceptibility, T = temperature of measurement and n = nuclearity of the complex.

2.3. $[Cu_2(P1\text{-}O^-)(NHAc^-)](ClO_4)_2$ (**1**)

To $Cu(ClO_4)_2 \cdot 6H_2O$ (0.15 g, 0.4 mmol) in MeOH (1 mL), a mixture of P1-OH (0.1 g, 0.2 mmol) and Et_3N (25 μL, 0.2 mmol) in MeOH (3 mL) was added under N_2. Acetamide (0.013 g, 0.2 mmol) and Et_3N (25 μL, 0.2 mmol) mixture was introduced to the above solution, to obtain bluish-green precipitate. The reaction mixture was stirred for 2 h, then filtered and washed with methanol, and dried to obtain light blue precipitate as **1** (0.13 g; yield, 70%). UV–Vis (CH_3CN) [λ_{max}, nm (ε, M^{-1} cm^{-1})]: 290 (2335), 670 (135), 885 (331). IR (ν, cm^{-1}; KBr disk): 1559, 2847 (s, νCH_3CONH^-), 1098 (s, νClO_4^-). *Anal.* Calc. for $[Cu_2(P1\text{-}O^-)(NHAc^-)](ClO_4)_2$, $C_{29}H_{33}Cl_2Cu_2N_7O_{10}$: C, 41.58; H, 3.97; N, 11.71. Found: C, 41.95; H, 3.62; N, 11.14%. Magnetic moment (Evans, CD_3CN): 1.92 μ_B/Cu^{2+}. ^{1}H NMR (CD_3CN, RT, 400 MHz): δ = 256.5, 210.4, 206.3, 70.4, 68.2, 64.0, 58.9, 50.4, 43.9, 32.8, 30.0, 27.5, 27.3, 26.7, 26.2, 24.7, 24.4, 21.8, 20.9, 13.4, 10.7, 10.5, 10.3, 10.2. X-band EPR (DMF, 90 K): $g_{\|} = 2.20$, $g_{\perp} = 2.12$, $A_{\|} = 110$ G. ESI-MS: *m/z*, 738 (20%), $[Cu_2(P1\text{-}O^-)(NHAC^-)(ClO_4^-)]^+$ and *m/2z*, 318 (100%) $[Cu_2(P1\text{-}O^-)(NHAc^-)]^{2+}$.

2.4. $[Cu_2(P2\text{-}O^-)(OAc^-)](ClO_4)_2$ (**2**)

A sample of $Cu(ClO_4)_2 \cdot 6H_2O$ (0.32 g, 0.9 mmol) in MeOH (2 ml) was slowly added to a mixture of predissolved ligand P2-OH (0.2 g, 0.45 mmol), AcOH (26 mg, 0.45 mmol) and NEt_3 (89 mg, 0.9 mmol) in MeOH (5 ml). A bluish green precipitate that formed immediately was washed with MeOH to obtain a microcrystalline product of **2** (0.32 g; yield, 89%). UV–Vis (CH_3CN) [λ_{max}, nm (ε, M^{-1} cm^{-1})]: 360 (796), 685 (281), 980 (58). IR (KBr disk, cm^{-1}): 1565, 1467 (s, OAc^-), 1092 (s, ClO_4^-). *Anal.* Calc. for $[Cu_2(P2\text{-}O^-)(OAc^-)](ClO_4)_2$, $C_{33}H_{40}Cl_2Cu_2N_6O_{11}$: C, 44.30; H, 4.51; N, 9.39. Found: C, 44.54; H, 4.62; N, 8.94%. ^{1}H NMR (CD_3NO_2, RT, 400 MHz): δ = 251.0, 219.2, 177.8, 92.8, 33.4, 28.8, 21.1, 18.0, 16.7, 14.9, 14.0, 13.8, 10.4, 9.3, 8.5, −5.5, −6.6, −6.8, −11.9, −17.7. EPR (DMF, 90 K): $g = 2.32$, $g_{\perp} = 2.03$ and $|\Delta M_s| = 2$ at $g = 3.90$, $A_{\|} = 150$ G. Magnetic moment (Evans, CD_3NO_2): 1.93 μ_B/Cu^{2+}. ESI-MS: *m/z*, 795 (45%) $[Cu(P2\text{-}O^-)(OAc^-)(ClO_4^-)]^+$ and *m/2z*, 347.5 (100%) $[Cu(P2\text{-}O^-)(OAc^-)]^+$.

2.5. $[Cu_2(P2'\text{-}O^-)(OAc^-)(H_2O)](ClO_4)_2$ (**3**)

To an ethanolic solution of $Cu(ClO_4)_2 \cdot 6H_2O$ (0.182 g, 0.4938 mmol), P2′-OH (0.1 g, 0.2469 mmol) in ethanol (2 mL) was

added followed by a mixture of acetic acid (0.015 g, 0.2469 mmol) and Et_3N (62.5 μL, 0.5 mmol) in ethanol (2 mL). Immediately after the addition, light blue colored precipitate crashed out. This was filtered, washed with additional ethanol (10 mL) and vacuum dried. This was further purified by recrystallization from CH_2Cl_2 to afford 0.142 g (yield, 80%) of $[Cu_2(P2'\text{-}O^-)(OAc^-)(H_2O)](ClO_4)_2$, **3** as blue crystals. UV–Vis (CH_3CN) [λ_{max}, nm (ε, $M^{-1}\,cm^{-1}$)]: 355 (513), 670 (728). IR data (KBr disk, ν/cm^{-1}): 1558, 1455 (s, CH_3COO^-), 1088 (s, ClO_4^-) and 3504 (b, H_2O). *Anal.* Calc. for $[Cu_2(P2'\text{-}O^-)(OAc^-)(H_2O)](ClO_4)_2$, $C_{26}H_{35}Cl_2Cu_2N_5O_{12}$: C, 38.67; H, 4.37; N, 8.67. Found: C, 38.96; H, 4.26; N, 8.23%. ^1H NMR (CD_3CN, RT, 400 MHz): δ = 266.4, 247.6, 233.5, 225.8, 220.0, 215.8, 181.6, 174.5, 155.1, 145.6, 141.0, 105.4, 97.9, 95.8, 90.6, 88.3, 47.4, 36.8, 35.9, 35.4, 32.8, 32.3, 31.9, 31.4, 30.5, 29.3, 28.2, 27.6, 21.0, 20.1, 18.9, 18.5, 17.7, 16.8, 16.4, 15.9, 14.7, 14.1, 13.2, 10.5, 10.4, 10.2, 9.2, 9.0, 8.8, 8.6, 8.5, 8.2, −5.5, −5.9, −6.7, −6.9, −8.3, −12.2, −14.8, −17.3, −17.6, −17.9, −18.7, −19.8 and −20.6. EPR (DMF, 90 K): $g_{\|}$ = 2.48, 2.45, $g_{\perp}$ = 2.14 and $A_{\|}$ = 125 and 140 G. Magnetic moment (Evans, CD_3CN): 1.88 μ_B/Cu^{2+}. ESI-MS: *m*/*z*, 690 (30%) $[Cu(P2'\text{-}O^-)(OAc^-)(ClO_4^-)]^+$ and *m*/2*z*, 295 (100%) $[Cu(P2'\text{-}O^-)(OAc^-)]^+$.

2.6. X-ray crystallography

Crystals of **1**, **2** and **3** were obtained by solvent evaporation from CH_3CN or CH_2Cl_2. Crystals of approximate size $0.3 \times 0.2 \times 0.2\ mm^3$ were mounted and covered with epoxy resin before data collection and data were collected at 293(2) K. Diffraction data were recorded with the $\omega/2\theta$ scan mode on a Mo Kα radiation (λ kα = 0.71073 Å). The data were corrected for absorption using *Psi*-scan. The unit cell parameters were obtained by a least squares fit of 25 reflections ($2.02° < 2\theta < 24.97°$). Complexes **1** and **2** belong to orthorhombic system, and **3** belongs to monoclinic crystal system. The unit cell parameters and information related to intensity data collection are summarized in Table 2. The structures were solved by direct methods and refined by full-matrix least squares techniques using SHELXL-97 [46] program, which provided most non-hydrogen atoms. All non-hydrogen atoms were refined with anisotropic displacement parameters. Solvent hydrogens were located through difference Fourier Map. All other hydrogens were geometrically fixed and riding model refinement was performed. During the refinement, wR_2 was optimized according to $wR2 = [\sum[w(F_o^2 - F_c^2)2]/\sum[w(F_o^2)^2]]^{1/2}$ with $w = 1/[\sigma^2(F_o^2) + (aP)^2 + bP]$ for $P = (F_o^2 + 2F_c^2)/3$ where, *a* and *b* as free variables, [*a* = 0.1233, 0.0467, 0.0859 and *b* = 18.93, 18.99, 6.4619 for **1**·CH_3CN, **2**·CH_3OH and **3**, respectively]. Molecular graphics were of ORTEP3 (WINGX) program [47].

3. Results and discussion

3.1. Synthesis and characterization

The dicopper complexes **1**, **2** and **3** were synthesized by straightforward methods *via* the reaction of copper(II) perchlorate with a mixture of primary and auxiliary ligands; P1-OH/P2-OH/P2′-OH, acetamide/acetic acid and 2 equivalents of Et_3N in ethanol to afford > 70% yield. They were characterized by solid state FT-IR, solution state magnetic moment (Evans measurement), optical, elemental (CHN) analysis, paramagnetic ^1H NMR, and mass spectrometry including X-ray crystal structure determination.

IR spectra of **1**, **2** and **3** display the bands expected for the counterion (ClO_4^-), and acetamide/acetate coligands (Table 1). Complex **1** shows acetamide –C=O stretch at 1559 cm^{-1} and –NH stretch at 2847 cm^{-1}. Complexes **2** and **3** show two characteristic carboxylate stretching vibrations around 1460 and 1560 cm^{-1}. A difference in ($\nu_{as} - \nu_s$) value of ~110 cm^{-1}, in agreement with the presence of a carboxylate group bridging the two copper(II) ions in μ-1,3-coordination mode [48]. All the three complexes exhibit a strong stretch around 1090 cm^{-1} corresponding to free perchlorate.

Table 1
Selected spectral data for **1**, **2** and **3**.

Complex	UV–Vis[a] λ, nm (ε, $M^{-1}\,cm^{-1}$)	IR (cm^{-1})[b]	μ[h] (μ_B/Cu^{II})	^1H NMR (ppm)	EPR[k]
1	890 (330),	2847[c]	1.92	0 to 250[j]	$g_{\|}$ = 2.20
	670 (135),	1559[d]			$g_{\perp}$ = 2.12
	290 (2335)	1098[g]			$A_{\|}$ = 110 G
2	685 (281),	1467[e]	1.93	−20 to 250[i]	$g_{\|}$ = 2.32
	980 (45),	1565[f]			$g_{\perp}$ = 2.03
	360 (796)	1092[g]			$A_{\|}$ = 151 G
3	670 (728),	1455[e]	1.88	−25 to 270[j]	$g_{\|}$ = 2.48, 2.45
	980 (58),	1558[f]			$g_{\perp}$ = 2.14
	355 (513)	1088[g]			$A_{\|}$ = 125, 140 G

[a] Two millimolar in CH_3CN solution.
[b] KBr mull.
[c] ν_{N-H} of NHAc.
[d] $\nu_{C=O}$ of NHAc.
[e] ν_s of OAc.
[f] ν_a of OAc.
[g] $\nu_{(ClO_4)}^{-}$.
[h] Solution state, room temperature.
[i] CD_3NO_2.
[j] CD_3CN.
[k] Frozen glass in DMF at 90 K.

Complexes **1** and **3** exhibit very clean ESI-MS spectra in acetonitrile solvent, containing two major peaks corresponding to the monocationic and dicationic molecular species. Complex **1** shows a peak at *m*/*z* 738 (20%) corresponding to the monocationic species $[Cu_2(P1\text{-}O^-)(NHAc^-)(ClO_4^-)]^+$ and at *m*/2*z* 318.4 (100%) corresponding to the dicationic species $[Cu_2(P1\text{-}O^-)(NHAc^-)]^{2+}$ (Fig. S1). Complex **3** showed a peak at *m*/*z* 690 (30%) with the characteristic isotopic distribution attributable to $[Cu_2(P2'\text{-}O^-)(OAc^-)(ClO_4^-)]^+$ ion; besides, a major peak at *m*/2*z* 295 (100%) corresponding to $[Cu_2(P2'\text{-}O^-)(OAc^-)]^{2+}$ is also consistent with **3** (Fig. S3). FAB MS of the complex **2** showed a peak at *m*/*z* 795 (45%) corresponding to the monocation $[Cu_2(P2\text{-}O^-)(OAc^-)(ClO_4^-)]^+$ (Fig. S2). Interestingly, it also showed a peak at *m*/*z* 690 corresponding to the monocation of complex **3** $[Cu_2(P2'\text{-}O^-)(OAc^-)(ClO_4^-)]^+$ with 75% isotopic abundance indicating that the conversion of P2-OH to P2′-OH is facile.

Solution magnetic moments of **1**, **2** and **3** were measured in deuterated acetonitrile/nitromethane solvent by Evan's method [45]. The room temperature effective magnetic moment (μ_{eff}) values for **1**, **2** and **3** are 1.92, 1.93 and 1.88 μ_B/Cu^{2+}, respectively. These magnetic moment values correspond to the presence of a spin of $s = 1/2$ as like mononuclear copper(II) complexes, which in turn indicate their weak spin–spin coupling.

3.2. Electronic absorption spectroscopy

The electronic absorption spectra of **1**, **2** and **3** are shown in Fig. 1. The peak positions of the spectral components are summarized with their molar extinction coefficients in Table 1. Complex **1** has an intense low energy band maximum at 890 nm (330 $M^{-1}\,cm^{-1}$) and a well defined high energy shoulder at 670 nm (135 $M^{-1}\,cm^{-1}$), which are assigned to d_{xy},$d_{x2-y2} \rightarrow d_{z2}$ and $d_{xz,yz} \rightarrow d_{z2}$ transitions of a trigonal bipyramidal Cu(II) center with unpaired electron on the d_{z2} orbital [49]. The dicopper(II) complexes **2** and **3** display similar absorption pattern in the electronic spectra (Fig. 1). Both show a charge transfer transition, L (alkoxo) → Cu^{2+} at 355 nm (ε = ~750 $M^{-1}\,cm^{-1}$) and two d–d transitions, one at 685 nm (ε = ~300 $M^{-1}\,cm^{-1}$) region, and an-

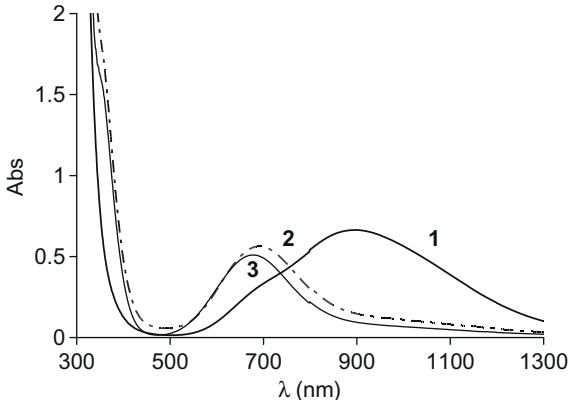


Fig. 1. The overlay of the optical spectra of **1**, **2** and **3** (2 mM in CH_3CN).

other weak low energy broad shoulder centered at 1000 nm ($\varepsilon = \sim 50\ M^{-1}\ cm^{-1}$) region. The d–d transitions of **3** are slightly shifted towards higher energy region than that of **2**. They are assigned to $d_{xz,yz,xy} \rightarrow d_{x2-y2}$ and $d_{z2} \rightarrow d_{x2-y2}$ transitions, respectively, which in turn represent the presence of square pyramidal Cu(II) centers with d_{x2-y2} orbital, holding the unpaired electron [49–51].

3.3. X-ray structures of the dicopper(II) complexes *1*, *2* and *3*

Complexes **1**, **2** and **3** were recrystallized from CH_3CN/CH_2Cl_2 solutions by solvent evaporation, and analyzed as $[Cu_2(P1\text{-}O^-)(NHAc^-)](ClO_4)_2$ (**1**), $[Cu_2(P2\text{-}O^-)(OAc^-)](ClO_4)_2$ (**2**) and $[Cu_2(P2'\text{-}O^-)(OAc^-)(H_2O)](ClO_4)_2$ (**3**), respectively from X-ray structure. Crystallographic data and selected geometric information for **1**, **2** and **3** are given in Tables 2 and 3. The structural diagrams are presented in Figs. 2–4 with the counter anions omitted for clarity. Complexes **1** and **2** crystallize in the orthorhombic space group, *Pbca* ($Z = 8$), whereas complex **3** crystallizes in the monoclinic space group, $P2_1/c$ ($Z = 4$). All are found binuclear. The copper(II) centers are doubly bridged by the alkoxo oxygen atom (O1) from the dinucleating ligand back bone and the acetamide/acetate bidentate supporting ligand from the bottom.

Table 2
Summary of crystal and refinement data for $[Cu_2(P1\text{-}O^-)(NHAc^-)](ClO_4)_2 \cdot CH_3CN$ (**1**); $[Cu_2(P2\text{-}O^-)(OAc^-)](ClO_4)_2 \cdot CH_2Cl_2$ (**2**); and $[Cu_2(P2'\text{-}O^-)(OAc^-)(H_2O)](ClO_4)_2$ (**3**).

Parameter	[a]**1**	[b]**2**	[c]**3**
Formula	$C_{31}H_{33}N_8O_{10}Cu_2Cl_2$	$C_{34}H_{42}N_6O_{11}Cu_2Cl_4$	$C_{26}H_{35}N_5O_{12}Cu_2Cl_2$
Mw	875.63	979.62	807.57
Wavelength	0.71073 (Mo Kα)	1.5418 (Cu Kα)	0.71073 (Mo Kα)
T	293(2)	293(2)	293(2)
Crystal system	orthorhombic	orthorhombic	monoclinic
a (Å)	11.610(2)	16.504(5)	13.238(5)
b (Å)	18.378(15)	23.457(8)	12.778(6)
c (Å)	34.822(7)	21.487(3)	20.616(14)
α (°)	90	90	90
β (°)	90	90	108.34(6)
γ (°)	90	90	90
V (Å^3)	7430(6)	8318(4)	3310(3)
D_{calcd} (g/cm^3)	1.566	1.564	1.611
Z	8	8	4
Space group	*Pbca*	*Pbca*	$P2_1/c$
Reflections collcd	6509	7533	6068
Reflections used	2690	4831	5800
Absolute coefficient (mm^{-1})	1.354	1.513	
Range of *h*, *k*, *l*	0 → 13, 0 → 21, 0 → 41	−19 → 0, 0 → 28, 0 → 25	0 → 15, 0 → 15, −24 → 23
Goodness-of-fit (GOF) on F^2	1.041	1.089	1.023
Data	6509	7533	5800
Restraints	1	2	1
Parameters	482	547	428
R ($I > 2\sigma(I)$)	0.0668	0.0572	0.0553
wR_2	0.1866	0.1032	0.1471

$wR_2 = [\sum[w(F_o^2 - F_c^2)]2]/\sum[w(F_o^2)^2]]^{1/2}$ with $w = 1/[\sigma^2(F_o^2) + (aP)^2 + bP]$ for $P = (F_o^2 + 2F_c^2)/3$ where *a* and *b* as free variables [*a* = 0.1233, 0.0467, and 0.0859 for **1**, **2** and **3**; *b* = 18.93, 18.99, and 6.4619 for **1**, **2** and **3**, respectively].

[a] Two thousand six hundred and ninety reflections $I > 2\sigma(I)$.

[b] Four thousand eight hundred and thirty one reflections $I > 2\sigma(I)$.

[c] Five thousand and eight hundred reflections $I > 2\sigma(I)$.

Table 3
Selected bond distances (Å) and angles (°) for **1**, **2** and **3**.

Parameters	**1**	**2**	**3**
Distances (Å)			
Cu1···Cu2	3.409(6)	3.540(1)	3.498(3)
Cu1–O1	1.887(6)	1.925(3)	1.919(4)
Cu1–O2	1.928(6)	1.963(3)	1.972(4)
Cu1–N1	2.065(8)	2.071(4)	2.098(4)
Cu1–N2	2.035(8)	2.021(4)	2.037(4)
Cu1–N3	2.215(8)	2.320(4)	2.240(5)
Cu2–O1	1.906(6)	1.926(3)	1.929(3)
Cu2–N7/O3	1.916(8)	1.950(3)	1.933(4)
Cu2–N6/O4	2.155(9)	2.252(4)	2.617(4)
Cu2–N4	2.058(7)	2.088(4)	1.991(5)
Cu2–N5	2.047(7)	2.017(4)	2.051(4)
C4–O2	1.266(10)	1.242(6)	1.231(6)
C4–N7/O3	1.269(11)	1.251(6)	1.254(6)
Angles (°)			
Cu1–O1–Cu2	128.0(3)	133.25(16)	130.70(17)
O1–Cu1–N2	139.9(3)	157.79(17)	156.79(17)
O2–Cu1–N1	177.3(3)	175.88(16)	171.90(17)
O–Cu1–N(rest)	84.9–100.9	85.87–109.02	85.10–100.15
O1–Cu1–O2	97.8(3)	91.97(13)	93.22(15)
N–Cu1–N(range)	80.6–114.1	92.70–93.82	93.24–103.06
O1–Cu2–N5	141.7(3)	166.26(16)	168.25(18)
O3/N7–Cu2–N4	178.2(3)	171.20(16)	168.60(2)
O–Cu2–N(rest)	83.8–108.1	85.70–98.16	83.51–89.50
O1–Cu2–O3/N7	97.6(3)	94.65(13)	94.60(16)
N–Cu2–N(range)	82.3(3)	91.55–95.48	94.6(2)
O2–C4–O3/N7	124.9(8)	127.4(5)	126.2(5)

The binuclear copper(II) centers of **1** are in distorted trigonal bipyramidal ligand environment, where a μ_2-bridging alkoxide (O1) and two pyridyl nitrogens (N2, N3 or N5, N6) from the binucleating ligand occupy the three basal coordination site and an asymmetrically *syn*, *syn*-coordinated acetamide group (O2/N7) and a tertiary amine nitrogen (N1/N4) from the ligand occupies the apical sites thereby establishing CuN_3O_2 and CuN_4O chromophores around Cu1 and Cu2, respectively (Fig. 2). The intervening bridges, alkoxide donor (O1) and acetamide donors (O2 and N7) respectively, lie on the equatorial and axial sites, anticipated to

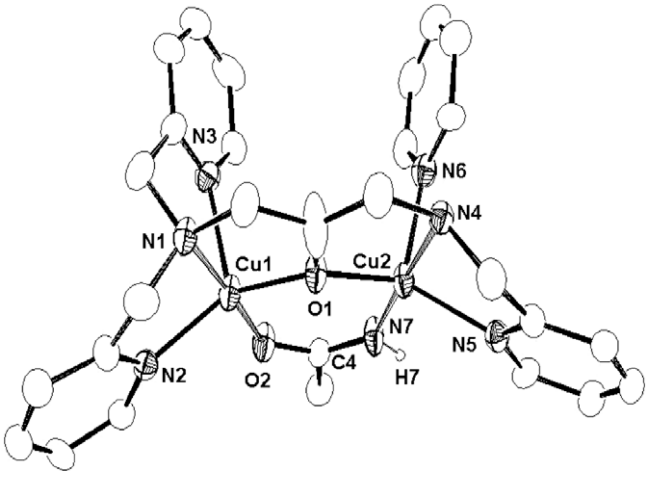


Fig. 2. X-ray structure (25% ellipsoids) of **1**.

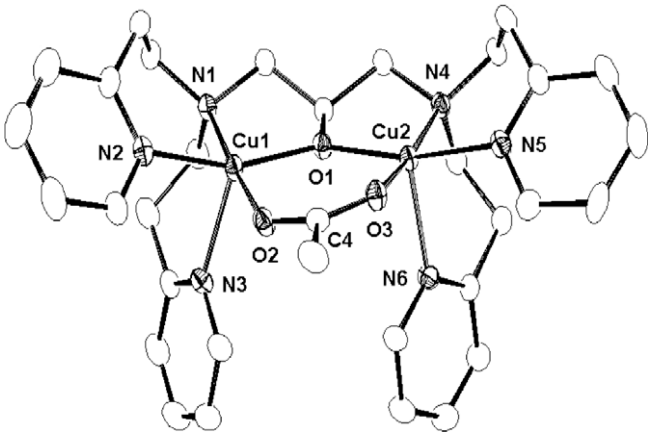


Fig. 3. X-ray structure (25% ellipsoids) of **2**.

induce weak magnetic interaction between the two copper(II) centers.

Unlike **1**, the copper(II) centers in **2** and **3** are each in a distorted square pyramidal ligand environment, where an amine nitrogen (N1/N4), a μ_2-bridging alkoxide/phenoxide (O1) and one pyridyl nitrogen (N2/N5) from the binucleating ligand and a symmetrically *syn*, *syn*-coordinated carboxylate group (O2/O3) take up the four basal coordination sites of the square plane. The apical sites are occupied by two *cis*-oriented pyridyl nitrogens (N3 and N6) from the binucleating ligand in the symmetric complex **2**. In the asymmetric complex **3**, one of the apical sites is occupied by an exogenous water oxygen atom (O4) at a distance of 2.617 Å due to the lack of another pyridyl nitrogen atom, which in turn makes the molecule asymmetric. Complex **2** has two CuN_3O_2 chromophores, and complex **3** has CuN_2O_3 and CuN_3O_2 chromophores around the copper(II) centers. Unlike complex **1**, in **2** and **3**, both the intervening bridge donors, alkoxide (O1) and acetate donors (O2 and O3) lie on the square plane.

The geometrical parameters (τ_1 and τ_2) of ~0.61 (**1**), 0.3 and 0.08 (**2**), and 0.25 and 0.005 (**3**), again indicate distorted trigonal bipyramidal and square pyramidal geometries around the copper centers, respectively [52]. The copper atoms are out of their mean planes by ~0.12 Å (**1**), ~0.18 Å (**2**), and ~0.16 Å (**3**). Dihedral angle between the trigonal and square planes containing Cu1 and Cu2 in **1**, **2** and **3** are 23.42, 21.9, and 26.47°, respectively. The two copper centers of **1**, **2** and **3** are separated by 3.41, 3.54, and 3.498 Å and make a ∠Cu1–O1–Cu2 angle of 128.0, 133.3 and 130.7°, respectively indicating an increase of ∠Cu1–O1–Cu2 angle with Cu···Cu distance. Unpredictably, complex **2** having a flexible two methylenes linker ligand P2-OH has larger Cu···Cu separation and Cu–O–Cu angle, compared to complex **1** holding a one methylene linker ligand P1-OH.

The apical Cu–N bonds in **2** and **3** are longer than the average basal Cu–N bonds by (0.25–0.30 Å) as is always observed in square pyramidal copper(II) complexes containing binucleating ligands and also the bond distances involving them are not equal pinpointing distortion of the square–pyramids. There is an asymmetry in the coordination distances around Cu1 and Cu2 in **1** due to acetamide ($NHAc^-$) bridge; also the latter seems to bridge strongly compared to acetate, which is apparent from the Cu–O and Cu–N distances (Table 3). There is no significant difference in the C–O/C–N bond distances of acetamide/acetate auxiliary bridges suggesting complete delocalization of the bridge.

Table 4 gives selected bond parameters and magnetic data of carboxylate bridged dicopper(II) complexes containing dinucleating ligand analogous to P1-OH. In such complexes, the important bond parameters (Cu···Cu separation and the Cu–O–Cu angle) that

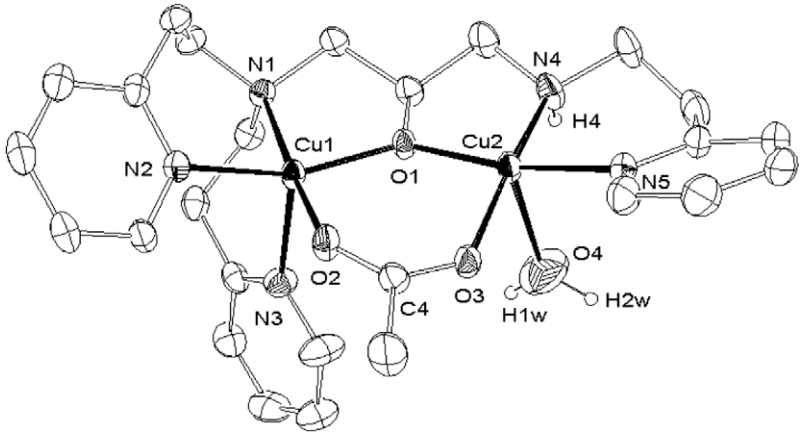


Fig. 4. X-ray structure (25% ellipsoids) of **3**.

Table 4
Comparison of bond parameters of carboxylate bridged dicopper(II) complexes

Complexes	M···M (Å)	M–O–M (°)	O–C–O	Geomet.	μ (BM/Co); J (cm^{-1})	Ref.
$[Cu_2(P1\text{-}O^-)(NHAc^-)]^{2+}$, **1**	3.409(6)	128.0(3)	124.9(8)	tbp	1.92; –[a]	this work
$[Cu_2(P2\text{-}O^-)(OAc^-)]^{2+}$, **2**	3.540(1)	133.3(2)	127.4(5)	sp	1.93; –[a]	this work
$[Cu_2(P2'\text{-}O^-)(OAc^-)(H_2O)]^{2+}$, **3**	3.498(3)	130.7(17)	126.2(5)	sp	1.88; –[a]	this work
$[Cu_2(P1\text{-}O^-)(OAc^-)]^{2+}$, **4**	3.418(2)	128.8(3)	127.2(9)	tbp	1.91; 44.2	[12]
$[Cu_2(L1\text{-}O^-)(OAc^-)]^{2+}$, **5**	3.541(1)	132.0(2)	126.8(4)	tbp	–[a]; –[a]	[36]
$[Cu_2(L2\text{-}O^-)(OAc^-)]^{2+}$, **6**	3.359(1)	115.4(2)	125.6(6)	tbp	2.58; +16.4	[16]
$[Cu_2(L3\text{-}O^-)(OAc^-)]^{2+}$, **7**	3.459(2)	130.6(5)	129(1)	tbp	1.89; 12	[37]

Where, L1-O^- – 1,3-bis[bis(2-(6-methylpyridyl)methyl)amino]-2-propanolate; L2-O^- – *N,N,N′,N′*-tetrakis[(2-(1-methylimidazolyl))methyl]-1,3-diaminopropan-2-ol; L3-O^- – *N,N,N′,N′*-tetrakis[(2-(1-ethylbenzimidazolyl))methyl]-1,3-diaminopropan-2-ol.

[a] Unknown/not measured.

dictate predominantly the magnetic property depend primarily on the dinucleating ligand present and coordination geometry. Cu···Cu separation of **1**, **2** and **3** lie between 3 and 4 Å, and the same is observed for analogous carboxylate bridged dicopper(II) complexes [12,16,36,37]. The O–C–O carboxylate bond angle is quite deviated from the trigonal angle and is constantly observed above 120°.

3.4. Paramagnetic ^{1}H NMR spectroscopy of the dicopper(II) complexes *1*, *2* and *3*

Complex **1** is an unsymmetrical complex, where the auxiliary ligand acetamide induces coordination asymmetry with N_3O_2 and N_4O coordination around the two copper(II) centers. Because of this, it shows twice the number of resonances (Fig. 5) as compared to the acetate analogue $[Cu_2(P1\text{-}O^-)(OAc^-)]^{2+}$ [12]. As the molecule is asymmetric, all the protons impart individual resonances. There are totally 25 resonances, all downfield shifted. The acetamide bridged complex **1** adopts the same trigonal bipyramidal geometry, like that of the acetate bridged analogue $[Cu_2(P1\text{-}O^-)(OAc^-)]^{2+}$ and hence, the chemical shifts of various protons are comparable, except that all the signals are now doubled in number. All the methylene hydrogens are not clearly resolved to show separate signals. For convenience, the methylene pair hydrogens together are labeled as α/β. The pyridyl signals are assigned based on the acetate analogue, since their chemical shifts are not expected to be affected much because of acetamide coordination. The signals at 27.5 and 32.8 ppm are assigned to the $-CH_3$ and –NH resonances of the acetamide bridge, respectively on the basis of their integration ratio. This assignment is tentative.

The *C*2-symmetric complex $[Cu_2(P2\text{-}O^-)(OAc^-)]^{2+}$, **2** exhibits a ^{1}H NMR spectrum with signals spanning from δ 250 to −20 and most line widths are less than 100 Hz. There are 20 sharp signals. Among them, 15 signals are down-fielded and 5 are up-fielded (Fig. 6). Signal assignment for **2** is achieved using a combination of measurements: Signal integration, the proximity of the hydrogens from the metal center measured from X-ray structure and line-widths that correlates with the through bond electron delocalization (Table 5). All the methylene hydrogens are inequivalent due to their diastereotopic nature. For similar dinuclear copper complexes, the solution state Cu–H distances from T_1 measurement concord well with the solid state Cu–H distances from X-ray structure data [12,38–41]. And hence, the signals for the protons H6, Ha, H6′ and Ha′ that are very close to copper are the far downfield shifted in the NMR spectrum and are assigned in accordance with their solid state Cu–H distances. As anticipated these proton signals have broader line widths and thus short T_2 values. The methylene hydrogen (CH) and the second methylene hydrogens (CH_2) are found to have negative spin density through spin polarization, and as anticipated, they are seen in the negative region.

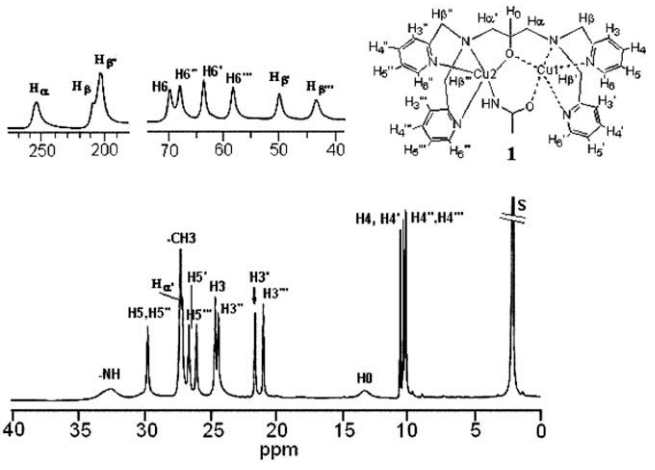


Fig. 5. A 400 MHz ^{1}H NMR of **1** in $CH_3CN\text{-}d_3$ at RT.

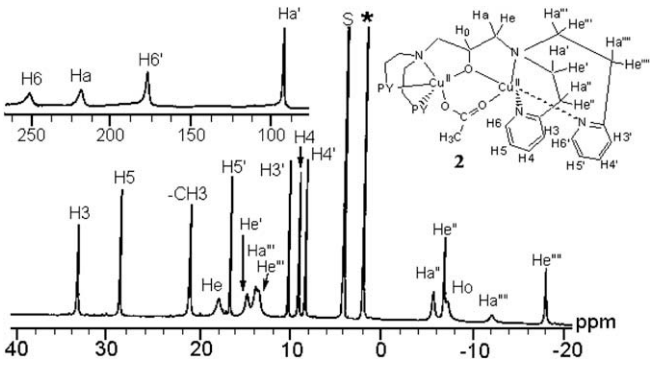


Fig. 6. A 400 MHz ^{1}H NMR spectrum of **2** in CD_3NO_2 at RT. ∗ represents peaks due to solvent impurities.

Table 5
Comparison of structural and ^{1}H NMR data of **2**.

H's	Signal (δ, ppm)	$\nu_{1/2}$ (Hz)	R_{Cu-H} (Å) X-ray	^{1}H Int. ratio
H6	251	272	2.93	2
Ha	219.2	234	2.99	2
H6′	177.8	60	3.11	2
Ha′	92.8	52	3.15	2
H3	33.4	42	4.93	2
H5	28.8	32	4.96	2
0	21.1	53	4.98	3
He	18	60	3.67	2
H5′	16.7	21	5.18	2
He′	14.9	59	3.5	2
Ha‴	14		3.52	2
He‴	13.8		3.83	2
H3′	10.4	32	5.19	2
H4	9.3	32	5.68	2
H4′	8.5	21	6.01	2
Ha″	−5.5	74	2.9	2
He″	−6.6		3.2	2
H_0	−6.8		3.18	1
Ha⁗	−11.9	263	4.05	2
He⁗	−17.7	63	4.22	2

Although the axial (H_a) and equatorial (H_e) hydrogens are the geminal methylene hydrogens, H_a is close to copper, whereas H_e is away from copper. This is due to the conformational change that causes Cu–N–C–$H_{a/e}$ dihedral angle variation, thereby M–$H_{a/e}$ distances change significantly between the axial and equatorial hydrogens. The measured dihedral angles for the different methylenes from X-ray crystal structure are *viz* H_a and H_e, 172.9 and 70°; $H_{a'}$ and $H_{e'}$, 165.7 and 75.9°; and $H_{a''}$ and $H_{e''}$, 142.7 and 99.4°. Hence, H_a's are expected to be far downfield shifted than H_e's and the same is observed as well. The spectral assignment is purely partial. Variable temperature measurements were carried out between the temperature range −251 to +348 K in CD_3NO_2 solvent. Most of the resonances except those in the diamagnetic region are temperature dependent. As the temperature increases, the signals move towards the diamagnetic region (Fig. S4). The intercepts of the various signals in the plot of chemical shifts *versus* $1/T$ (Curie plot) lie within ±20 ppm indicating that the chemical shifts are predominantly contact in origin [42].

The unsymmetrical analogue of **2** $[Cu_2(P2'\text{-}O^-)(OAc^-)(H_2O)]^{2+}$ (**3**) having the asymmetric polypodal ligand P2′-OH with one ethyl pyridyl arm on one side and two ethyl pyridyl arms on the other side gives a complicated ^{1}H NMR spectrum (Fig. 7) and notably, with the same spectral span range like **2** at 25 °C. With the

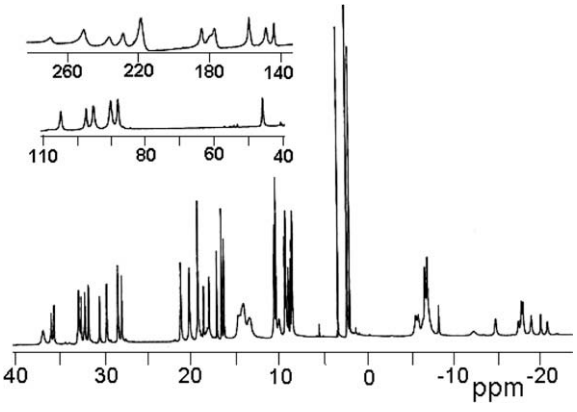


Fig. 7. A 400 MHz ^{1}H NMR spectrum of **3** in CD_3CN at RT.

unsymmetrical structure, all the hydrogens present in the molecule now become magnetically inequivalent, and hence resonances correspond to all the protons sprout up in the ^{1}H NMR spectrum. The diastereotopic methylenes are not resolved out and they show signals correspond to two inequivalent sets. All the remaining hydrogens are well resolved. Variable temperature measurements were carried out between the temperature range 258–298 K in CD_3CN (Fig. S5). Like complex **2**, here also most of the resonances except those in the diamagnetic region are temperature dependent and the spectral width narrows with increasing temperature.

3.5. EPR spectroscopy

The dicopper(II) complexes show characteristic EPR spectra (Figs. S6–S8). The X-band EPR spectra of **1**, **2** and **3** have been measured in the parallel mode and in frozen DMF glass state at LN_2 temperature and the '*g*' parameters are tabulated below (Table 1). All displayed $g_{\|} > g_{\perp}$ and $g_{\|} > 2.15$, representative of five-coordinated Cu(II) complexes with strained geometry. Complex **1** shows two overlapping four-line pattern in the $g_{\|}$ region and a pattern characteristic of tbp geometry with an average spacing of 110 G (Fig. S6). The $g_{\|}$ and $g_{\perp}$ values of **1**, 2.20 and 2.12, respectively, are well near to each other indicating their geometry is a mixture of tbp and sp. Whereas, the binuclear copper(II) complexes **2** and **3** provide a nearly axial spectra with $g_{\|} > g_{\perp}$, consistent with $d_{x^2-y^2}$ being the highest energy half-occupied molecular orbital. In addition to that, complex **2** shows a "half-field" signal (~1250 G) correspond to the forbidden $|\Delta M_s = 2|$ transition at $g = 3.90$ (Fig. S7), and is characteristic of dinuclear Cu^{2+} species with a weak magnetic coupling [53].

Acknowledgements

Gnana S. Siluvai is thankful to Indian Institute of Technology Madras for financial support in the form of a fellowship. The authors gratefully acknowledge Dr. Babu Varghese for X-ray structure solution.

Appendix A. Supplementary data

CCDC 671961, 250729 and 250730 contains the supplementary crystallographic data for this paper. These data can be obtained free of charge via http://www.ccdc.cam.ac.uk/conts/retrieving.html, or from the Cambridge Crystallographic Data Centre, 12 Union Road, Cambridge CB2 1EZ, UK; fax: (+44) 1223-336-033; or e-mail: deposit@ccdc.cam.ac.uk. Supplementary data associated with this article can be found, in the online version, at doi:10.1016/j.poly.2009.04.006.

References

[1] C. Belle, J.-L. Pierre, Eur. J. Inorg. Chem. (2003) 4137.
[2] S.J. Lippard, J.M. Berg, Principles of Bioinorganic Chemistry, University Science Books, Mill Valley, CA, 1994.
[3] J.M. Berg, J.L. Tymoczko, L. Stryer, Biochemistry, fifth ed., W.H. Freeman, New York, 2002.
[4] R.H. Holm, P. Kennepohl, E.I. Solomon, Chem. Rev. 96 (1996) 2239.
[5] K.D. Karlin, Z. Tyeklar, Bioinorganic Chemistry of Copper, Chapman and Hall, New York, 1993.
[6] N. Strater, W.N. Lipscomb, T. Klabunde, B. Krebs, Angew. Chem. Int. Ed. 35 (1996) 2024.
[7] W.N. Lipscomb, N. Strater, Chem. Rev. 96 (1996) 2375.
[8] C. Liu, M. Wang, T. Zhang, H. Sun, Coord. Chem. Rev. 248 (2004) 147.
[9] K.D. Karlin, Science 261 (1993) 701.
[10] E.A. Lewis, W.B. Tolman, Chem. Rev. 104 (2004) 1047. and references therein.
[11] E.Y. Tshuva, S.J. Lippard, Chem. Rev. 104 (2004) 987.
[12] N.N. Murthy, K.D. Karlin, I. Bertini, C. Luchinat, J. Am. Chem. Soc. 119 (1997) 2156.
[13] N.N. Murthy, M.M. Tahir, K.D. Karlin, J. Am. Chem. Soc. 115 (1993) 10404.
[14] A. Neves, L.M. Rossi, I. Vencato, V. Drago, W. Haase, R. Werner, Inorg. Chim. Acta 281 (1998) 111.
[15] A. Neves, L.M. Rossi, A. Horn Jr., I. Vencato, A.J. Bortoluzzi, C. Zucco, A.S. Mangrich, Inorg. Chem. Commun. 2 (1999) 334.
[16] H. Nie, S.M.J. Aubin, M.S. Mashuta, R.A. Porter, A.F. Richardson, D.N. Hendrickson, R.N. Buchanan, Inorg. Chem. 35 (1996) 3325.
[17] G.D. Fallon, K.S. Murray, Inorg. Chim. Acta 96 (1985) L53.
[18] T. Kawata, M. Yamanaka, S. Ohba, Y. Nishida, M. Nagamatsu, T. Tokii, M. Kato, W.S. Omar, Bull. Chem. Soc. Jpn. 65 (1992) 2739.
[19] W. Mazurek, B.J. Kennedy, K.S. Murray, M.J. O'Conner, J.R. Rodgers, M.R. Snow, A.G. Wedd, P.R. Zwak, Inorg. Chem. 24 (1985) 3258.
[20] C. Fernandes, A. Neves, A.J. Bortoluzzi, A.S. Mangrich, R. Eva, S. Bruno, S. Erineu, Inorg. Chim. Acta 320 (2001) 12.
[21] A. Neves, L.M. Rossi, A.J. Bortoluzzi, A.S. Mangrich, W. Hasse, R. Werner, J. Braz. Chem. Soc. 12 (2001) 747.
[22] G. Pavel, M. Luken, N. Moller, A. Rompel, B. Krebs, Inorg. Chem. Commun. 4 (2001) 753.
[23] K. Bertoncello, G.D. Fallon, J.H. Hodgkin, K.S. Murray, Inorg. Chem. 27 (1988) 4750.
[24] J.H. Satcher Jr, W.W. Droege, T.J.R. Weakley, R.T. Taylor, Inorg. Chem. 34 (1995) 3317.
[25] M. Suzuki, H. Kanatomi, Y. Demura, I. Murase, Bull. Chem. Soc. Jpn. 57 (1984) 1003.
[26] S. Mandal, R. Mukherjee, Inorg. Chim. Acta 359 (2006) 4019.
[27] S. Gupta, A. Mukherjee, M. Nethaji, A.R. Chakravarty, Polyhedron 24 (2005) 1922.
[28] P. Chaudhuri, R. Wagner, T. Weyhermuller, Inorg. Chem. 46 (2007) 5134.
[29] M. Kato, T. Tanase, M. Mikuriya, Inorg. Chem. 45 (2006) 2925.
[30] I.A. Koval, K. van der Schilden, A.M. Schuitema, P. Gamez, C. Belle, J.-L. Pierre, M. Lu1ken, B. Krebs, O. Roubeau, J. Reedijk, Inorg. Chem. 44 (2005) 4372.
[31] C. Belle, C. Beguin, I. Gautier-Luneau, S. Hamman, C. Philouze, J.L. Pierre, F. Thomas, S. Torelli, Inorg. Chem. 41 (2002) 479.
[32] L.M. Rossi, A. Neves, A.J. Bortoluzzi, R. Horner, B. Szpoganicz, H. Terenzi, A.S. Mangrich, E. Pereira-Maia, E.E. Castellano, W. Haase, Inorg. Chim. Acta 358 (2005) 1807.
[33] R. Gupta, S. Mukherjee, R. Mukherjee, J. Chem. Soc., Dalton Trans. (1999) 4025.
[34] S.-F. Huang, Y.-C. Chou, P. Misra, C.-J. Lee, S. Mohanta, H.-H. Wei, Inorg. Chim. Acta 357 (2004) 1627.
[35] A.M. Thomas, G.C. Mandal, S.K. Tiwary, R.K. Rath, A.R. Chakravarty, J. Chem. Soc., Dalton Trans. (2000) 1395.
[36] K. Yamaguchi, F. Akagi, S. Fujinami, M. Suzuki, M. Shionoya, S. Suzuki, J. Chem. Soc. Chem. Commun. (2001) 375.
[37] V. Mckee, M. Zuaguli, J.V. Dagadigian, M.A. Patch, C.A. Reed, J. Am. Chem. Soc. 106 (1984) 4765.
[38] J.M. Brink, R.A. Rose, R.C. Holz, Inorg. Chem. 35 (1996) 2878.
[39] V. Clementi, C. Luchinat, Acc. Chem. Res. 31 (1998) 351.
[40] R.C. Holz, J.M. Brink, Inorg. Chem. 33 (1994) 4609.
[41] J.H. Satcher Jr., A.L. Balch, Inorg. Chem. 34 (1995) 3371.
[42] I. Bertini, P. Turano, NMR of paramagnetic molecules, in: L.J. Berliner, J. Reuben (Eds.), Biological Magnetic Resonance, vol. 12, Plenum press, NY, 1993.
[43] K.C. Michael, W.H. Armstrong, J. Am. Chem. Soc. 111 (1989) 9121.
[44] K.D. Karlin, Z. Tyeklar, A. Farooq, M.S. Haka, P. Ghosh, R.W. Cruse, Y. Gultneh, J.C. Hayes, P.J. Toscano, J. Zubieta, Inorg. Chem. 31 (1992) 1436.
[45] D.F. Evans, J. Chem. Soc. (1959) 2003.
[46] G.M. Sheldrick, SHELXL97, Program for Crystal Structure Refinement, Gottingen, Germany, 1997.
[47] L.J. Farrugia, J. Appl. Cryst. 32 (1999) 837.
[48] B. Deacon, R.J. Phillips, Coord. Chem. Rev. 33 (1980) 227.
[49] B.J. Hathaway, Comprehensive Coordination Chemistry, vol. 5, Pergamon, New York, 1987. p. 533.

[50] A.B.P. Lever, Inorganic Electronic Spectroscopy, Elsevier Science Publishers B.V., Amsterdam, 1984. p. 553.
[51] U. Rajendran, R. Viswanathan, M. Palaniandavar, N. Laskiminaraya, J. Chem. Soc., Dalton Trans. (1994) 1219.
[52] A.W. Addison, T.N. Rao, J. Chem. Soc., Dalton Trans. (1984) 1349.
[53] S. Marciela, A. Neves, R. Horner, A.J. Bortoluzzi, B. Szpoganics, C. Zucco, R.A.N. Silva, V. Drago, A.S. Mangrich, W.A. Ortiz, W.A.C. Passos, M.C.B. De Oliveira, T. Hernan, Inorg. Chem. 42 (2003) 8353.

Polyhedron 28 (2009) 2157–2164

Contents lists available at ScienceDirect

Polyhedron

journal homepage: www.elsevier.com/locate/poly

Synthesis, crystal structures and spectral studies of square planar nickel(II) complexes containing an ONS donor Schiff base and triphenylphosphine

M. Muthu Tamizh [a], Kurt Mereiter [b], Karl Kirchner [c], B. Ramachandra Bhat [d], R. Karvembu [a,*]

[a] Department of Chemistry, National Institute of Technology, Tanjore Road, Tiruchirappalli 620 015, Tamil Nadu, India
[b] Institute of Chemical Technologies and Analytics, Vienna University of Technology, A-1060 Vienna, Austria
[c] Institute of Applied Synthetic Chemistry, Vienna University of Technology, A-1060 Vienna, Austria
[d] Department of Chemistry, National Institute of Technology, Surathkal 575 025, India

ARTICLE INFO

Article history:
Received 13 May 2008
Accepted 10 April 2009
Available online 24 April 2009

Keywords:
Schiff base ligand
Triphenylphosphine
Ni(II) complexes
Spectral studies
Crystal structures

ABSTRACT

Five mononuclear nickel(II) complexes, *viz.* [Ni(L1)(PPh_3)] (**1**), [Ni(L2)(PPh_3)] (**2**), [Ni(L3)(PPh_3)] (**3**), [Ni(L4)(PPh_3)] (**4**) and [Ni(L5)(PPh_3)] (**5**) (where L1, L2, L3, L4 and L5 are dianions of *N*-(2-mercaptophenyl) salicylideneimine, 5-methyl-*N*-(2-mercaptophenyl)salicylideneimine, 5-chloro-*N*-(2-mercaptophenyl) salicylideneimine, 5-bromo-*N*-(2-mercaptophenyl)salicylideneimine and *N*-(2-mercaptophenyl)naphthylideneimine, respectively), have been synthesized and characterized by means of elemental analysis, electronic, IR, ^1H, ^{13}C and ^{31}P NMR spectroscopy. Single crystal X-ray analysis of two of the complexes (**1** and **5**) has revealed the presence of a square planar coordination geometry (ONSP) about nickel. The crystal structures of the complexes are stabilized by intermolecular π–π stacking between the ligands (L) and by various C–H···π interactions.

© 2009 Elsevier Ltd. All rights reserved.

1. Introduction

The synthesis of geometrically distorted nickel(II) complexes with mixed N and S donor sets is the research interest of many groups [1]. Nickel is present in the active sites of several important classes of metalloproteins, such as 2-mercaptoethanol-inhibited urease and Ni/Fe hydrogenases [2]. The nickel coordination sphere in both of these metalloenzyme systems contains N and S donor sets. These features led to increased interest in the synthesis of nickel(II) complexes with mixed N,S donating chelates as structural and spectroscopic models of the active sites. There are many reports available for nickel(II) complexes with N,S donor ligands [3], but nickel(II) complexes containing N,S donor ligands as well as triphenylphosphine are very rare [4]. Complexes of this kind are interesting in terms of both models of the active sites and homogeneous catalysis.

In addition, *N*-(2-mercaptophenyl)salicylideneimine exhibits different kinds of coordination modes with different metal ions. It behaves as a bifunctional tridentate ligand with Tc(V), Re(V), Ru(II) and Ru(III) [5–7]. The same ligand shows monofunctional tridentate coordination with Co(II), Cu(II) and Zn(II) [8] and monofunctional bidentate coordination with Ru(I) [9]. Hence, we intend to investigate the coordination behaviour of *N*-(2-mercaptophenyl)salicylideneimine, its derivatives and *N*-(2-mercaptophenyl)naphthylideneimine with Ni(II). Here, we report square planar nickel(II) complexes of O,N,S donor ligands and triphenylphosphine. These complexes were characterized by IR, electronic and NMR spectral data. The structures of two complexes have been determined by single crystal X-ray crystallography. The general structures of the ONS Schiff base ligands used in this study are depicted in Fig. 1.

2. Experimental

2.1. Materials

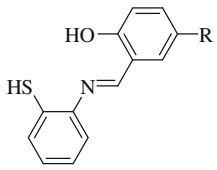
All the chemicals used were of analytical grade. Solvents were purified and dried according to standard procedures [10]. $NiCl_2{\cdot}6H_2O$ was purchased from Qualigens Fine Chemicals and was used without further purification. The starting complex [$NiCl_2(PPh_3)_2$] was prepared by the reaction between $NiCl_2{\cdot}6H_2O$ and triphenylphosphine in glacial acetic acid [11]. The Schiff base ligands were prepared by the condensation between salicylaldehyde, its derivatives or 2-hydroxy-1-naphthaldehyde and *o*-aminothiophenol in ethanol [5,12].

2.2. Physical measurements

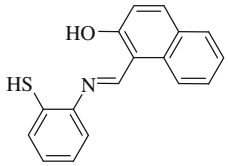
Electronic spectra were measured on a Perkin Elmer EZ 301 UV–Vis double beam spectrophotometer for CH_3CN solutions of the complexes in the 200–800 nm range. FT-IR spectra were recorded

* Corresponding author. Tel.: +91 422 2501801; fax: +91 431 2503632.
E-mail address: kar@nitt.edu (R. Karvembu).

0277-5387/$ - see front matter © 2009 Elsevier Ltd. All rights reserved.
doi:10.1016/j.poly.2009.04.021



R	Ligand
H	H_2L1
CH_3	H_2L2
Cl	H_2L3
Br	H_2L4



Ligand
H_2L5

Fig. 1. General structures of the ligands.

on a Perkin Elmer Spectrum One FT-IR spectrometer as KBr pellets in the frequency range 400–4000 cm^{-1}. The C, H, N and S contents were determined by a Thermoflash EA1112 series elemental analyzer. ^1H, ^{13}C, HSQC and HMBC NMR spectra were recorded in a Bruker AMX 400 instrument using TMS as the internal standard. ^{31}P NMR spectra were recorded in a Bruker AMX 400 instrument in $CDCl_3$ with H_3PO_4 as a reference. Melting points were determined with a Khora digital melting point apparatus.

2.3. X-ray crystallography

Single crystals of **1** and **5** for X-ray diffraction studies were grown at room temperature from a dichloromethane solution by the diffusion of diethyl ether vapour. Diffraction data were collected on a Bruker SMART APEX CCD diffractometer using graphite monochromated Mo Kα radiation (λ = 0.71073 Å). The structures were solved by direct methods (SHELXS-97) [13] and refined by full-matrix least squares fitting based on F^2 using the program SHELXL-97 [14]. All non-hydrogen atoms were refined with anisotropic displacement parameters. All H atoms were located by difference Fourier syntheses and were then included in the refinement with idealized geometry riding on the atoms to which they were bonded.

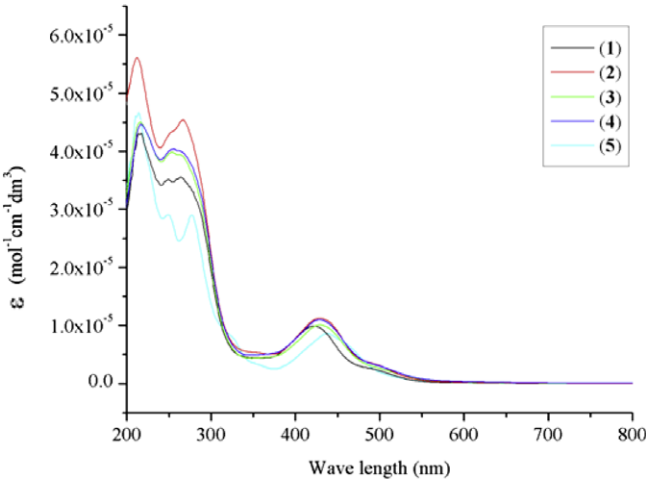


Fig. 2. Electronic spectra of the nickel(II) complexes.

2.4. Synthesis of Ni(II) complexes

All the complexes were prepared by stirring an ethanolic solution of $[NiCl_2(PPh_3)_2]$ with dichloromethane solutions of the ligands in a 1:1 molar ratio for 2 h at 25–27 °C. The resulting dark brown solutions were concentrated to approximately 3 cm^3 and cooled. Hexane (20 cm^3) was then added, whereupon the product complex separated. The brown coloured complex was filtered, washed with ethanol and then with hexane, and dried in *vacuo*. The formation of complex was checked by TLC.

$[Ni(L1)(PPh_3)]$ (**1**) is prepared from $[NiCl_2(PPh_3)_2]$ (0.5 g; 0.764 mmol) and H_2L1 (0.175 g; 0.764 mmol). Yield: 59%. *Anal*Calc.

Table 1
Infrared spectral data (cm^{-1}) for the ligands and their Ni(II) complexes.

Compound	ν(C=N)	ν(C–O)	ν(C–S)	ν(Ni–O)	ν(Ni–N)	Bands due to PPh_3
H_2L1	1614	1316	754			
H_2L2	1622	1323	756			
H_2L3	1621	1321	753			
H_2L4	1612	1317	757			
H_2L5	1610	1304	757			
(**1**)	1607	1334	746	528	457	1433, 1095, 691
(**2**)	1615	1341	744	532	455	1435, 1096, 693
(**3**)	1619	1325	743	527	455	1434, 1093, 695
(**4**)	1603	1326	752	529	459	1437, 1098, 694
(**5**)	1598	1321	750	529	456	1435, 1097, 695

Table 2
^1H, ^{13}C and ^{31}P NMR spectral data of the Ni(II) complexes.

Complex	^1H (ppm)	^{13}C (ppm)	^{31}P (ppm)
(**1**)	6.4–8.0 (m, 23H, aromatic), 8.9 (d, *J* = 10.36 Hz, 1H, –CH=N–)	163.98, 154.51, 149.82, 143.98, 143.85, 134.84, 134.72, 133.98, 133.00, 130.59, 130.57, 129.43, 129.00, 128.62, 128.60, 128.21, 128.11, 126.70, 121.88, 121.63, 119.30, 115.44, 114.84	22.3
(**2**)	2.3 (s, 3H, $–CH_3$), 6.3–8.0 (m, 22H, aromatic), 8.8 (d, *J* = 9.36 Hz, 1H, –CH=N–)	162.44, 154.25, 149.99, 144.46, 144.32, 135.95, 134.86, 134.72, 132.73, 130.55, 130.42, 129.69, 129.08, 128.63, 128.20, 128.07, 128.02, 126.52, 124.23, 121.83, 121.35, 118.84, 114.76, 20.23	22.3
(**3**)	6.3–8.0 (m, 22H, aromatic), 8.8 (d, *J* = 9.03 Hz, 1H, –CH=N–)	162.53, 153.46, 149.43, 144.48, 144.33, 134.79, 134.66, 133.94, 131.84, 130.70, 130,67, 129.36, 128.74, 128.66, 128.28, 128.14, 127.06, 123.07, 122.03, 119.90, 119.54, 114.95	22.4
(**4**)	6.3–8.0 (m, 22H, aromatic), 8.8 (d, *J* = 9.34 Hz, 1H, –CH=N–)	162.83, 153.39, 149.91, 144.42, 144.24, 136.46, 135.06, 134.79, 134.66, 130.72, 130.67, 129.35, 128.73, 128.66, 128.29, 128.16, 127.09, 123.50, 122.05, 120.83, 114.97, 106.28	22.5
(**5**)	6.3–8.1 (m, 25H, aromatic), 8.8 (d, *J* = 10.27 Hz,1H, –CH=N–)	164.93, 151.12, 148.32, 143.23, 142.96, 134.84, 134.63, 134.19, 130.64, 130.60, 129.70, 129.08, 128.80, 128.32, 128.10, 127.58, 127.06, 126.03, 124.24, 122.77, 121.98, 118.94, 114.85, 110.29	25.2

for $C_{31}H_{24}NNiOPS$: C, 67.90; H, 4.41; N, 2.55; S, 5.85. Found: C, 67.02; H, 3.96; N, 2.41; S, 6.11%. $\lambda_{max}(\varepsilon)$ CH_3CN: 213(42900), 249(35135), 264(35496), 422(9885) nm(dm^3 mol^{-1} cm^{-1}). Decomposition temperature 230 °C.

[Ni(L2)(PPh_3)] (**2**) is prepared from [$NiCl_2(PPh_3)_2$] (0.25 g; 0.382 mmol) and H_2L2 (0.093 g; 0.382 mmol). Yield: 67%. *Anal*Calc. for $C_{32}H_{26}NNiOPS$: C, 68.35; H, 4.66; N, 2.49; S, 5.70. Found: C, 67.99; H, 4.23; N, 2.80; S, 6.00%. $\lambda_{max}(\varepsilon)$ CH_3CN: 216(56603), 253(43880), 267(45735), 431(11252) nm(dm^3 mol^{-1} cm^{-1}). Decomposition temperature 234 °C.

[Ni(L3)(PPh_3)] (**3**) is prepared from [$NiCl_2(PPh_3)_2$] (0.5 g; 0.764 mmol) and H_2L3 (0.202 g; 0.764 mmol). Yield: 58%. *Anal*Calc. for $C_{31}H_{23}ClNNiOPS$: C, 63.90; H, 3.98; N, 2.40; S, 5.32. Found: C, 63.34; H, 3.52; N, 2.56; S, 5.85%. $\lambda_{max}(\varepsilon)$ CH_3CN: 216(45411), 253(40015), 267(39532), 429(10094) nm(dm^3 mol^{-1} cm^{-1}). Decomposition temperature 246 °C.

[Ni(L4)(PPh_3)] (**4**) is prepared from [$NiCl_2(PPh_3)_2$] (0.5 g; 0.764 mmol) and H_2L4 (0.25 g; 0.764 mmol). Yield: 40%. *Anal.* Calc. for $C_{31}H_{23}BrNNiOPS$: C, 59.37; H, 2.23; N, 2.55; S, 5.11. Found: C, 59.18; H, 2.45; N, 2.27; S, 5.71%. $\lambda_{max}(\varepsilon)$ CH_3CN: 212(45269), 253(40509), 267(40334), 428(11001) nm(dm^3 mol^{-1} cm^{-1}). Decomposition temperature 239 °C.

[Ni(L5)(PPh_3)] (**5**) is prepared from [$NiCl_2(PPh_3)_2$] (0.5 g; 0.764 mmol) and H_2L5 (0.214 g; 0.764 mmol). Yield: 57%. *Anal.* Calc. for $C_{35}H_{26}NNiOPS$: C, 70.26; H, 4.38; N, 2.34; S, 5.36. Found: C, 69.66; H, 3.85; N, 2.18; S, 6.53%. $\lambda_{max}(\varepsilon)$ CH_3CN: 199(46749), 249(29007), 276(28964), 328(7516), 438(8550), 468(5901) nm (dm^3 mol^{-1} cm^{-1}). Decomposition temperature 245 °C.

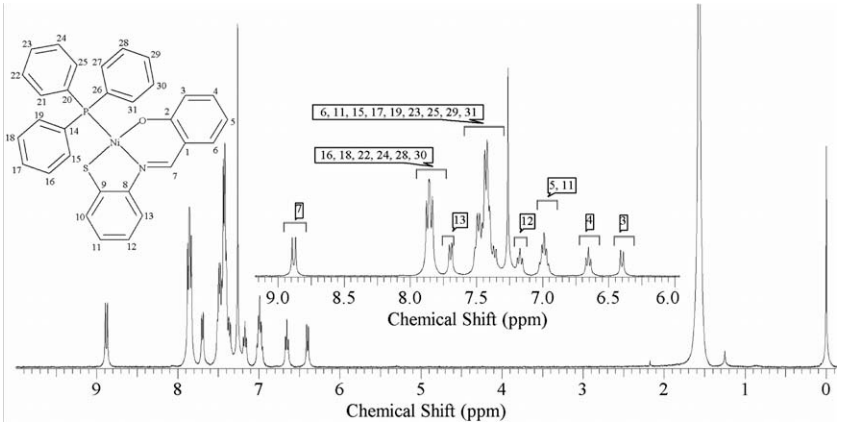


Fig. 3. ^1H NMR spectrum of [Ni(L1)(PPh_3)].

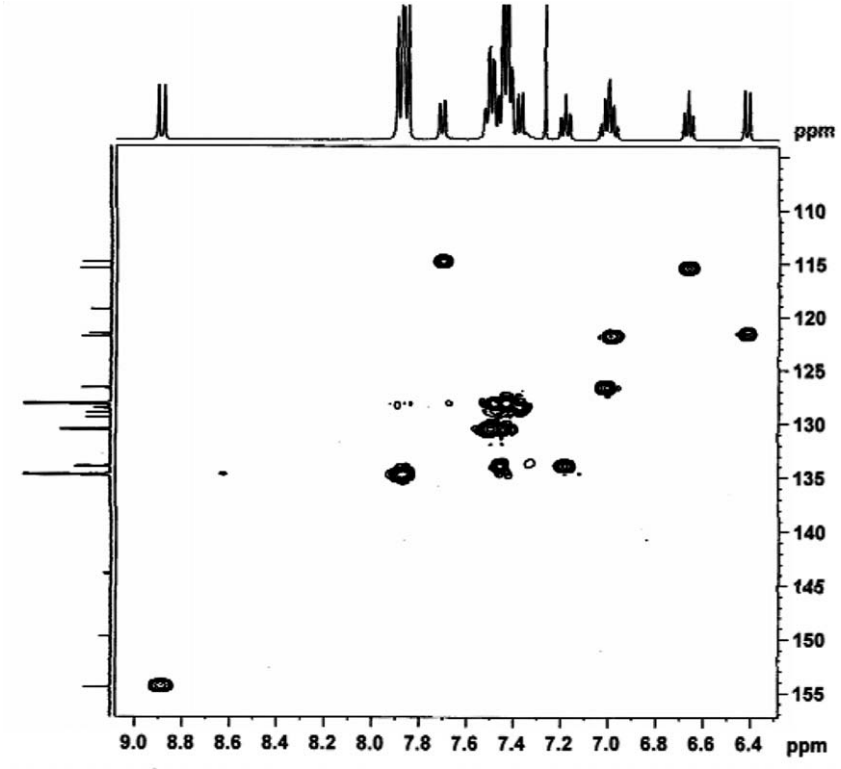


Fig. 4. HSQC spectrum of [Ni(L1)(PPh_3)].

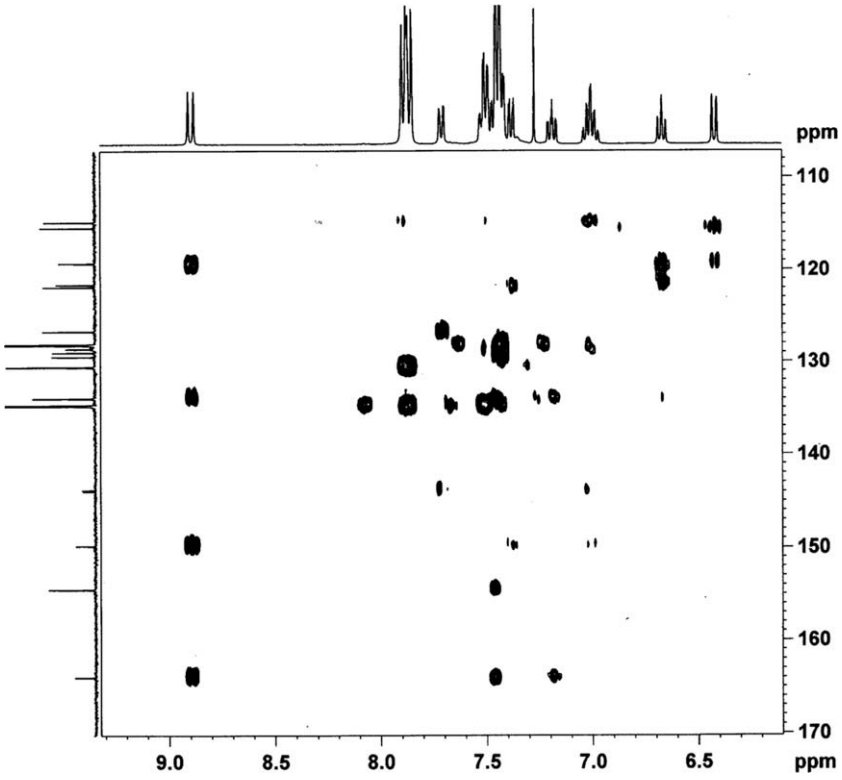


Fig. 5. HMBC spectrum of [Ni(L1)(PPh_3)].

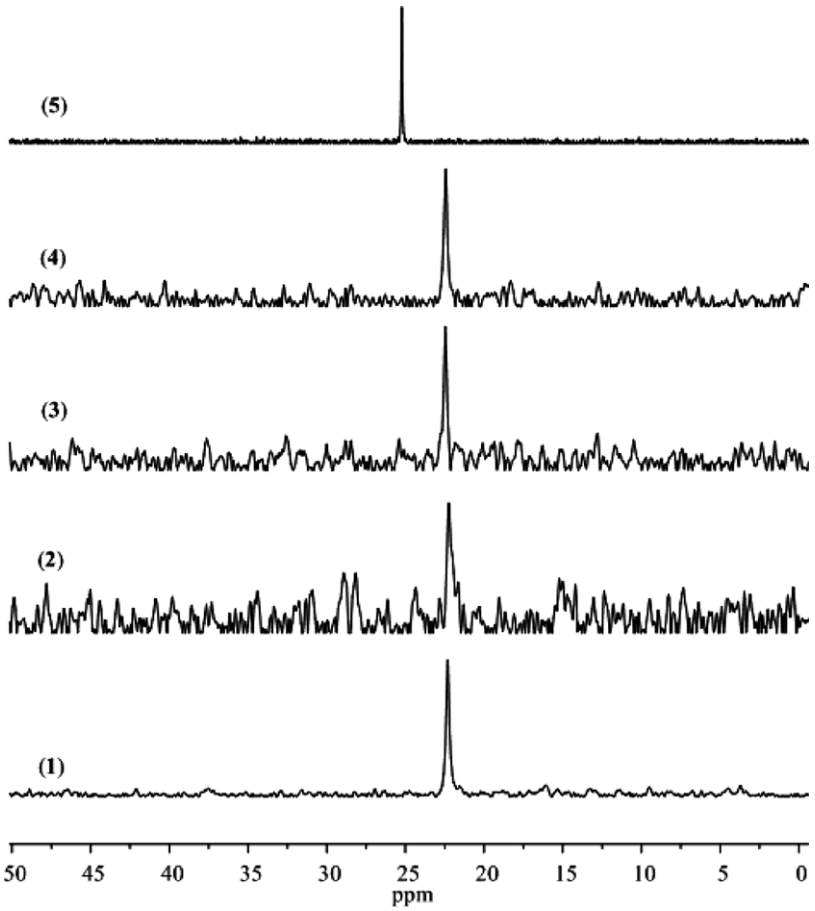


Fig. 6. ^{31}P NMR spectra of the nickel(II) complexes.

Table 3
Crystal data, data collection and structure refinement parameters for (**1**) and (**5**).

Parameters	(**1**)	(**5**)
Empirical formula	$C_{31}H_{24}NNiOPS$	$C_{35}H_{26}NNiOPS$
Formula weight	548.25	598.31
Colour	dark brown	dark brown
Habit	block	block
Crystal dimensions (mm)	0.52 × 0.42 × 0.35	0.59 × 0.55 × 0.48
Crystal system	triclinic	monoclinic
Space group	$P\bar{1}$	$P2_1/c$
a (Å)	8.9703(4)	13.1734(4)
b (Å)	9.9644(4)	17.2572(6)
c (Å)	14.3335(6)	12.6594(4)
α (°)	99.836(1)	90
β (°)	94.904(1)	130.720(1)
γ (°)	97.785(1)	90
Volume (Å^3)	1242.95(9)	2795.82(16)
Z	2	4
T (K)	100(2)	100(2)
D_C (Mg/m^3)	1.465	1.421
Absorption coefficient (mm^{-1})	0.955	0.856
F(0 0 0)	568	1240
λ (Å)	Mo Kα (0.71073)	Mo Kα (0.71073)
θ Range (°)	2.58–29.96	2.33–29.99
Scan type	ω, φ	ω, φ
Index ranges	$-12 \leqslant h \leqslant 12$, $-13 \leqslant k \leqslant 13$, $-20 \leqslant l \leqslant 20$	$-18 \leqslant h \leqslant 17$, $-20 \leqslant k \leqslant 24$, $-17 \leqslant l \leqslant 17$
Reflections collected/ unique	18 052/7114	29 095/8103
R_{int}	0.0161	0.0185
Refinement method	full-matrix least-squares on F^2	full-matrix least-squares on F^2
Diffractometer	Bruker SMART APEX CCD	Bruker SMART APEX CCD
Absorption correction	multi-scan SADABS	multi-scan SADABS
Final R indices R_1/wR_2 [$I > 2\sigma(I)$]	0.0285/0.0750	0.0244/0.0651
R_1/wR_2 (all data)	0.0302/0.0762	0.0269/0.0665
Goodness-of-fit (GOF) on F^2	1.051	1.038
$\Delta\rho_{max.}$ (e Å^{-3})	0.70 and −0.26	0.42 and −0.33
Data/restraints/ parameters	7114/0/325	8103/117/361

3. Results and discussion

The reaction of equimolar ratios of the ligands (H_2L) and [$NiCl_2(PPh_3)_2$] yielded the new complexes of the general formula [Ni(L)(PPh_3)] (L = dianionic Schiff base ligand) in moderate to good yield. All the present complexes were brown in colour. They were found to be soluble in CH_2Cl_2, CH_3CN, C_6H_6, DMSO, DMF and C_2H_5OH. The analytical data for these complexes are in good agreement with the above molecular formula. In all the reactions, it has been observed that the Schiff base behaves as a bifunctional tridentate ligand by substituting one of the triphenylphosphine ligands and both the chloride ions from the starting complex.

3.1. Electronic spectra

The electronic spectra of the complexes (Fig. 2) **1**, **2**, **3** and **4** in CH_3CN showed four bands in the region 198–431 nm. The bands appearing in the region 198–267 nm have been assigned to intraligand transitions. A less intense band in range 423–431 nm corresponds to a forbidden $d \rightarrow d$ transition. Complex **5** displayed six bands in the 199–469 nm range. The extra bands are due to the additional phenyl ring present in the ligand. Four bands in the region 199–323 nm are due to intraligand transitions and two bands at 438 and 469 nm are due to forbidden $d \rightarrow d$ transitions. The same behaviour has been observed in the electronic spectra of other similar square planar nickel(II) complexes [4,15].

3.2. IR spectra

Selected IR bands of the ligands and complexes are listed in Table 1. The spectra of the ligands exhibit a strong band around 1610–1622 cm^{-1}, which is assigned to a ν(C=N) vibration. As a result of coordination, this band shifts to a lower wavenumber by *ca.* 10 cm^{-1} in the complexes [4,16]. The band in the region

Table 4
Selected bond lengths (Å) and angles (°).

(**1**)		(**5**)	
Ni(1)–O(1)	1.8496(9)	Ni(1)–O(1)	1.8448(8)
Ni(1)–N(1)	1.9096(10)	Ni(1)–N(1)	1.8956(8)
Ni(1)–S(1)	2.1359(3)	Ni(1)–S(1)	2.1369(3)
Ni(1)–P(1)	2.2164(3)	Ni(1)–P(1)	2.1894(3)
S(1)–C(9)	1.7512(12)	S(1)–C(12)	1.7499(10)
P(1)–C(20)	1.8196(12)	P(1)–C(24)	1.8202(10)
P(1)–C(26)	1.8211(11)	P(1)–C(30)	1.8206(10)
P(1)–C(14)	1.8214(11)	P(1)–C(18)	1.8228(10)
O(1)–C(2)	1.2995(14)	O(1)–C(2)	1.2968(12)
N(1)–C(7)	1.3054(15)	N(1)–C(11)	1.3137(12)
N(1)–C(8)	1.4268(14)	N(1)–C(13)	1.4247(13)
C(1)–C(2)	1.4088(16)	C(1)–C(2)	1.4134(14)
C(8)–C(9)	1.3960(16)	C(12)–C(13)	1.4012(13)
C(1)–C(7)	1.4216(17)	C(1)–C(11)	1.4169(14)
O(1)–Ni(1)–N(1)	95.37(4)	O(1)–Ni(1)–N(1)	94.34(3)
O(1)–Ni(1)–S(1)	173.98(3)	O(1)–Ni(1)–S(1)	175.08(2)
N(1)–Ni(1)–S(1)	89.32(3)	N(1)–Ni(1)–S(1)	90.15(3)
O(1)–Ni(1)–P(1)	82.58(3)	O(1)–Ni(1)–P(1)	85.10(2)
N(1)–Ni(1)–P(1)	174.75(3)	N(1)–Ni(1)–P(1)	177.24(3)
S(1)–Ni(1)–P(1)	93.056(12)	S(1)–Ni(1)–P(1)	90.311(11)
C(9)–S(1)–Ni(1)	98.64(4)	C(12)–S(1)–Ni(1)	97.76(3)
C(20)–P(1)–C(26)	104.11(5)	C(24)–P(1)–C(30)	106.73(5)
C(20)–P(1)–C(14)	104.63(5)	C(24)–P(1)–C(18)	104.79(4)
C(26)–P(1)–C(14)	105.55(5)	C(30)–P(1)–C(18)	102.19(4)
C(20)–P(1)–Ni(1)	113.56(4)	C(24)–P(1)–Ni(1)	105.04(3)
C(26)–P(1)–Ni(1)	107.01(4)	C(30)–P(1)–Ni(1)	117.88(3)
C(14)–P(1)–Ni(1)	120.57(4)	C(18)–P(1)–Ni(1)	119.02(3)
C(2)–O(1)–Ni(1)	128.25(8)	C(11)–N(1)–C(13)	118.87(9)
C(7)–N(1)–C(8)	118.68(10)	C(11)–N(1)–Ni(1)	123.28(7)
C(7)–N(1)–Ni(1)	122.90(8)	C(13)–N(1)–Ni(1)	117.73(6)
C(8)–N(1)–Ni(1)	118.37(8)	C(2)–O(1)–Ni(1)	127.63(7)
N(1)–C(7)–C(1)	127.12(11)	N(1)–C(11)–C(1)	127.45(9)
C(2)–C(1)–C(7)	122.53(11)	C(2)–C(1)–C(11)	120.51(9)
C(8)–C(9)–S(1)	118.42(8)	C(13)–C(12)–S(1)	118.67(8)

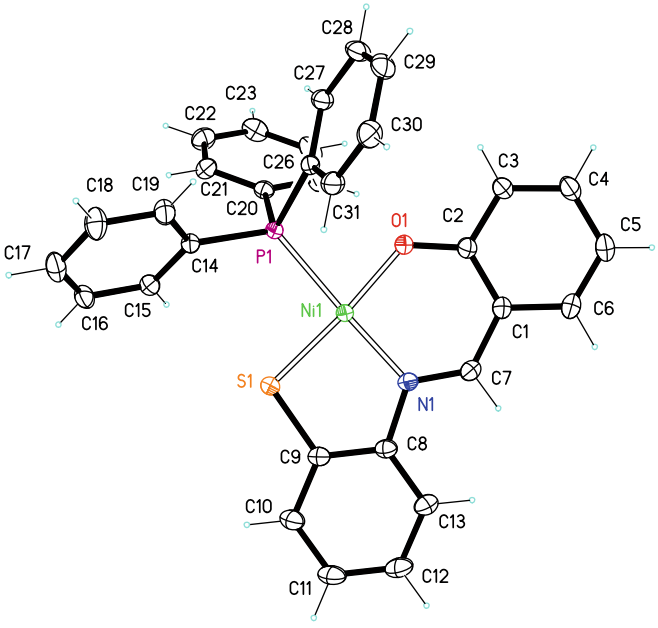


Fig. 7. Molecular structure of complex **1** showing 50% displacement ellipsoids.

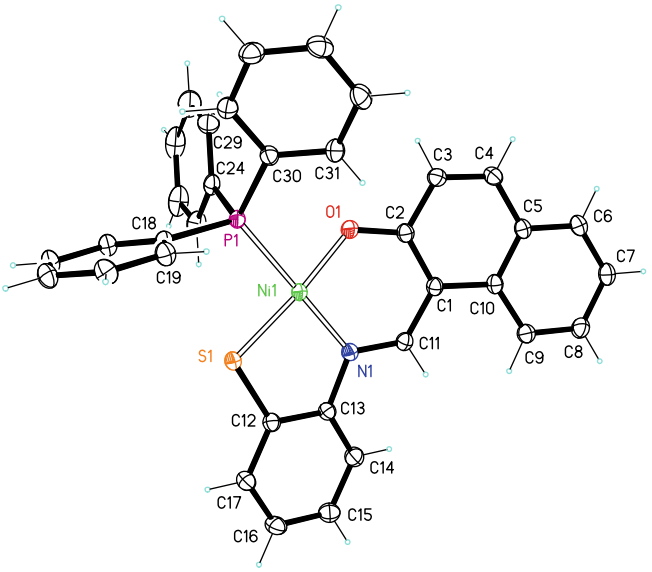


Fig. 8. Molecular structure of complex **5** showing 50% displacement ellipsoids.

1304–1323 cm^{-1}, which is assigned to phenolic ν(C–O) in the free ligand, is shifted to a higher wavenumber in the complexes, suggesting the coordination of the phenolic oxygen atom to the nickel ion [4,16]. A weak band observed in the region 753–757 cm^{-1}, corresponding to ν(C–S) in the ligands, shifts to a lower wavenumber (743–752 cm^{-1}) which supports sulfur coordination with the nickel centre [17]. The bands around 530 and 460 cm^{-1} in all the complexes are assigned to ν(Ni–O) and ν(Ni–N), respectively [18]. Bands due to triphenylphosphine also appear in the expected region [19].

3.3. NMR spectra

^{1}H, ^{13}C and ^{31}P NMR spectral data of the complexes are given in Table 2. All the nickel(II) complexes exhibit a multiplet around 6.3–8.1 ppm, which has been assigned to the protons of the phenyl groups present in triphenylphosphine and the Schiff base ligand. A doublet observed at 8.8 ppm in the complexes has been assigned to the azomethine proton (–C=N–) [20]. Complex **3** exhibits a singlet at 2.3 ppm, corresponding to methyl protons. The absence of a resonance due to phenolic and thiolato hydrogen atoms indicates the deprotonation of these groups and the Schiff bases behave as dianionic ligands. The ^{1}H NMR spectrum of **1** is depicted in Fig. 3. In the ^{13}C NMR spectra of all the complexes, azomethine carbon resonances are observed in the 151.12–154.49 ppm range. The resonances for C–S, C–N, C–O and C–P are observed in the regions 129.00–129.69, 149.32–149.99, 162.44–164.93 and 142.96–144.48 ppm, respectively [21,22]. The ^{13}C NMR and DEPT 135 spectra of **1** revealed the presence of seven different carbons (119.30, 129.00, 129.46, 143.85, 143.98, 149.82 and 163.98 ppm). This indicates that the three quaternary carbons arising from triphenylphosphine aromatic units are in different magnetic environments. The HSQC correlation spectrum of **1** (Fig. 4) establishes the connection between the imine proton (δ_H = 8.89, d, J = 10.36 Hz, 1H) and C-7 (δ_C = 154.51). The interaction of the imine proton (δ_H = 8.89, d, J = 10.36 Hz, 1H) with three quaternary carbons *viz.* C-1 (δ_C = 119.30), C-2 (δ_C = 163.98) and C-8 (δ_C = 149.82) and the methine carbon C-6 (δ_C = 134.00) has been understood from the HMBC correlation spectrum (Fig. 5). The ^{31}P NMR spectra of all the complexes exhibit a singlet around 22.3–25.2 ppm, suggesting the presence of one coordinated triphenylphosphine ligand in these nickel(II) complexes [23]. The ^{31}P NMR spectra of all the complexes are given in Fig. 6.

3.4. X-ray crystallography

The compounds **1** and **5** were structurally determined by X-ray crystallography. The crystallographic and measurement data are shown in Table 3 and representative bond lengths and bond angles are listed in Table 4. Figs. 7 and 8 present thermal ellipsoid representations of complexes **1** and **5**, respectively. In both the complexes, the nickel(II) atom is four coordinated in a square planar geometry by the Schiff base and triphenylphosphine ligands. The Schiff base acts as a tridentate ligand through the thiolato sulfur atom, the imine N and the phenolic O atom. Two units of [Ni(L1)(PPh_3)] and four units of [Ni(L5)(PPh_3)] are present in their respective unit cells. As expected for four coordinate d^8 metal complexes, the structure of **1** adopts a nearly ideal square planar geometry with O–Ni–S and N–Ni–P bond angles of 173.98(3) and 174.75(3)°, respectively [24]. The other angles around the nickel(II)

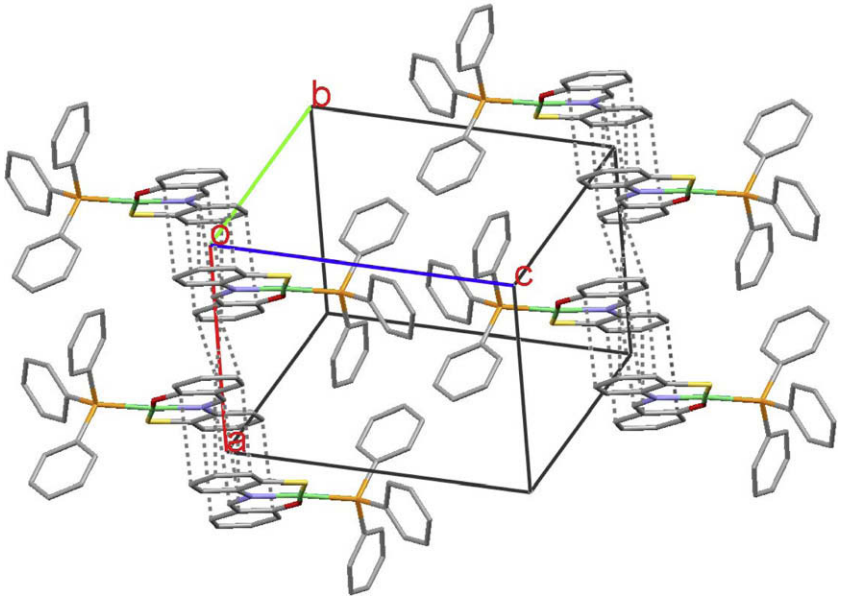


Fig. 9. Schematic drawing of the crystal packing of **1** showing the π–π stacking parallel to the *a*-axis. Hydrogen atoms are omitted.

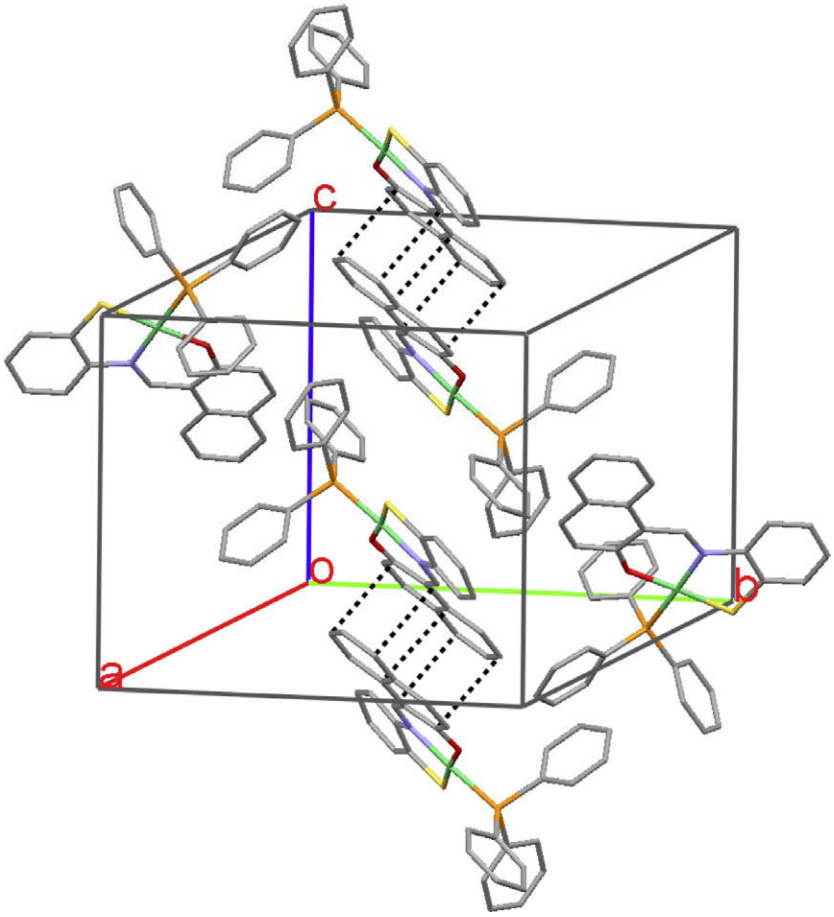


Fig. 10. Schematic drawing of the crystal packing of **5** showing the π–π stacking between pairs of complexes *via* their naphthyl moieties. Hydrogen atoms are omitted.

atom deviate slightly from the ideal value (90°), ranging from 82.58(3) to 95.37(4)°. In structure **5**, the O–Ni–S and N–Ni–P bond angles are 175.08(2) and 177.24(3)°, respectively and other angles around nickel(II) are in the range 85.10(2) to 94.34(3)°. The Ni–P, Ni–O, Ni–N and Ni–S bond distances are in the usual range in both complexes [4]. Disregarding triphenylphosphine, complex **1** is essentially planar, showing a r.m.s. deviation of 0.030 Å of the non-hydrogen atoms from a common least-squares plane, from which the P atom deviates by 0.324(1) Å. Complex **5** is distinctly more aplanar showing for the Ni(L5) moiety a r.m.s. deviation of 0.154 Å from planarity and a significant twist between the phenyl and the naphthyl residues of L5 (interplanar angle 14.15(5)°). These differences between [Ni(L1)(PPh_3)] and [Ni(L5)(PPh_3)] are attributable to differences in crystal packing and intermolecular interactions. The intermolecular interactions in [Ni(L1)(PPh_3)] are characterized by comparatively weak π–π stacks of L1, forming continuous chains along the *a*-axis (Fig. 9). In [Ni(L5)(PPh_3)], there are pairs of complexes π–π stacked via their naphthyl moieties (Fig. 10). The PPh_3 moieties in both [Ni(L1)(PPh_3)] and [Ni(L5)(PPh_3)] do not show π–π stacking but contribute by various C–H···π interactions to the coherence of the structures.

4. Conclusion

Mononuclear Ni(II) complexes of the type [Ni(L)(PPh_3)] (L = ONS donor Schiff base ligand) were prepared and characterized by NMR, IR and electronic spectroscopy. Structures of two complexes were determined by X-crystallography, which are stabilized by intermolecular π–π stacking between the ligands (L) and by various C–H···π interactions.

Supplementary data

CCDC 663130 and 653443 contain the supplementary crystallographic data for **1** and **5**. These data can be obtained free of charge via http://www.ccdc.cam.ac.uk/conts/retrieving.html, or from the Cambridge Crystallographic Data Centre, 12 Union Road, Cambridge CB2 1EZ, UK; fax: (+44) 1223-336-033; or e-mail: deposit@ccdc.cam.ac.uk.

Acknowledgements

R.K. and B.R.B. are thankful to the Technical Education Quality Improvement Program (TEQIP) for financial support under the institution networking scheme. K.K. also thanks TEQIP, NITT, for the award of a Visiting Professorship. R.K. and M.M. gratefully acknowledge CSIR [01(2137)/07/EMR-II] for financial support. We thank Dr. K. Shanmugasundaram and Mr. S. Ganesamoorthy, Syngene International Pvt. Ltd., Bangalore for useful discussion regarding 2D NMR.

References

[1] (a) R.K. Henderson, E. Bouwman, A.L. Spek, J. Reedijk, Inorg. Chem. 36 (1997) 4616;
(b) B. Adhikari, O.P. Anderson, R. Hazell, S.M. Miller, C.E. Olsen, H. Toftlund, J. Chem. Soc., Dalton Trans. (1997) 4539;

(c) H. Frydendahl, H. Toftlund, J. Becher, J.C. Dutton, K.S. Murray, L.F. Taylor, O.P. Anderson, E.R.T. Tiekink, Inorg. Chem. 34 (1995) 4467.
[2] (a) A. Volbeda, M.-H. Charon, E.C. Piras, M. Frey, J.C. Fontecilla-Camps, Nature 373 (1995) 580;
(b) S. Wang, M.H. Lee, R.P. Hausinger, P.A. Clark, D.E. Wilcox, R.A. Scott, Inorg. Chem. 33 (1994) 1589.
[3] (a) N. Goswami, D.M. Eichhorn, Inorg. Chem. 38 (1999) 4329;
(b) E.M. Jouad, A. Riou, M. Allain, M.A. Khan, G.M. Bouet, Polyhedron 20 (2001) 67.
[4] R. Prabhakaran, R. Karvembu, T. Hashimoto, K. Shimizu, K. Natarajan, Inorg. Chim. Acta 358 (2005) 2093.
[5] F. Tisato, F. Refosco, U. Mazzi, G. Bandoli, M. Nicolini, J. Chem. Soc., Dalton Trans. (1987) 1693.
[6] C. Jayabalakrishnan, K. Natarajan, Transition Met. Chem. 27 (2002) 75.
[7] S. Priyarega, R. Prabhakaran, K.R. Aranganayagam, R. Karvembu, K. Natarajan, Appl. Organomet. Chem. 21 (2007) 788.
[8] A.A. Soliman, W. Linert, Thermochim. Acta 338 (1999) 65.
[9] M.M.H. Khalil, M.M. Aboaly, R.M. Ramadan, Spectrochim. Acta, Part A 61 (2005) 157.
[10] A.I. Vogel, Textbook of Practical Organic Chemistry, fifth ed., Longman, London, 1989.
[11] J. Venanzi, J. Chem. Soc. (1958) 719.
[12] L.D. Albin, M. Jacobson, D.B. Olson, US Patent 5426,085, 1995.
[13] G.M. Sheldrick, Acta Crystallogr., Sect. A 46 (1990) 467.
[14] G.M. Sheldrick, SHELX-97, Programs for Crystal Structure Analysis (Release 97-2), University of Göttingen, Germany, 1997.
[15] M. Akbar Ali, S.M.G. Hossain, S.M.M.H. Majumder, M. Nazimuddin, M.T.H. Tarafder, Polyhedron 6 (1987) 1653.
[16] J.E. Kovacic, Spectrochim. Acta, Part A 23 (1967) 183.
[17] V. Philip, V. Suni, M.R.P. Kurup, M. Nethaji, Polyhedron 23 (2004) 1233.
[18] A.A. Soliman, G.G. Mohamed, Thermochim. Acta 421 (2004) 151.
[19] R. Karvembu, K. Natarajan, Polyhedron 21 (2002) 219.
[20] R. Karvembu, S. Hemalatha, R. Prabhakaran, K. Natarajan, Inorg. Chem. Comm. 6 (2003) 486.
[21] J. Gradinaru, A. Forni, V. Druta, S. Quici, A. Britchi, C. Deleanu, N. Gerbeleu, Inorg. Chim. Acta 338 (2002) 169.
[22] S.K. Gupta, P.B. Hitchcock, Y.S. Kushwah, G.S. Argal, Inorg. Chim. Acta 360 (2007) 2415.
[23] C. Jayabalakrishnan, R. Karvembu, K. Natarajan, Transition Met. Chem. 27 (2002) 790.
[24] D.J. Darensbourg, C.G. Ortiz, J. Yarbrough, Inorg. Chem. 42 (2003) 6915.

Polyhedron 28 (2009) 2165–2170

Contents lists available at ScienceDirect

Polyhedron

journal homepage: www.elsevier.com/locate/poly

Preparation and characterisation of mononuclear Pd(II) complexes with 1,8-bis(3,5-dimethyl-1-pyrazolyl)-3,6-dithiaoctane (bddo) ligand: Spectroscopy studies and crystal structure of *trans*-[Pd(SCN)$_2$(bddo)]

Antonio de León [a], Josefina Pons [a,*], Jordi García-Antón [a], Xavier Solans [b,1], Mercè Font-Bardía [b], Josep Ros [a,*]

[a] Departament de Química, Facultat de Ciències, Unitat de Química Inorgànica, Universitat Autònoma de Barcelona, 08193-Bellaterra-Cerdanyola, Barcelona, Spain
[b] Cristal.lografia, Mineralogia i Dipòsits Minerals, Universitat de Barcelona, Martí i Franquès s/n, 08028-Barcelona, Spain

ARTICLE INFO

Article history:
Received 19 March 2009
Accepted 10 April 2009
Available online 23 April 2009

Keywords:
N,S ligand
Palladium
Crystal structure

ABSTRACT

Mononuclear palladium(II) complexes containing a pyrazole-thioether ligand, with general formula *trans*-[Pd(X)$_2$(bddo)] (X = CN$^-$ (**1**), SCN$^-$ (**2**) or N$_3^-$ (**3**); bddo = 1,8-bis(3,5-dimethyl-1-pyrazolyl)-3,6-dithiaoctane), have been prepared. Similar reactivity carried out with pyridine or triphenylphosphine has been assayed. When pyridine is used, a mixture of [Pd(bddo)(py)$_2$](BF$_4$)$_2$ ([**4**](BF$_4$)$_2$) and [Pd(bddo)](BF$_4$)$_2$ is obtained. When triphenylphosphine is used, only [Pd(bddo)](BF$_4$)$_2$ is obtained. The complexes have been characterised by elemental analyses, conductivity measurements, IR and NMR spectroscopies. X-ray crystal structure of *trans*-[Pd(SCN)$_2$(bddo)] (**2**) is presented. In this complex the metal atom is coordinated by the two azine nitrogen atoms of the pyrazole rings and two SCN$^-$ anions in *trans* disposition.

© 2009 Elsevier Ltd. All rights reserved.

1. Introduction

The role of ligands in coordination and organometallic chemistry does not need emphatic presentation since their fundamental importance in determining the morphology and the chemical–physical properties of the molecules. For example, a rich variety of coordination modes is observed for pyrazole hybrid ligands [1] and their complexes have been successfully employed in catalysis [2], chemotherapy [3], electrochemical reduction [4], magnetic coupling [5] and metallo-supramolecular chemistry [6].

For this reason, in our group, we have studied and reported the synthesis and characterisation of ligands combining a pyrazolyl group with some other donor groups, in particular, with S (thiol or thioether) [7] with the objective of introducing ligands with different nature in the coordination sphere of the metal.

We have investigated the reactivity of the complex [PdCl(μ-med)]$_2$ (Hmed = *N*-(2-mercaptoethyl)-3,5-dimethylpyrazole), with monodentate (pyridine, triphenylphosphine, cyanide, thiocyanate and azide) or bidentate ligands (bipyridine and bis(diphenylphosphine)ethane) [8].

Recently, we have studied the reactivity of [PdCl(bdtp)](BF$_4$) (bdtp = 1,5-bis(3,5-dimethyl-1-pyrazolyl)-3-thiapentane) with pyridine, triphenylphosphine, cyanide, thiocyanate or azide ligands, yielding the complexes [Pd(bdtp)(X)](BF$_4$)$_2$ (X = py, PPh$_3$) and [Pd(X)(bdtp)](BF$_4$) (X = CN$^-$, SCN$^-$ and N$_3^-$) [9].

In a previous paper, the synthesis and characterisation of [PdCl$_2$(bddo)] and [Pd(bddo)](BF$_4$)$_2$ (bddo = 1,8-bis(3,5-dimethyl-1-pyrazolyl)-3,6-dithiaoctane) have been presented [7a]. Here, we extend the study of the coordinative properties of bddo ligand towards Pd(II). Reaction of [PdCl$_2$(bddo)] with cyanide, thiocyanate or azide in the presence of AgBF$_4$ or NaBF$_4$ produces the complexes [Pd(X)$_2$(bddo)] (X = CN$^-$ (**1**), SCN$^-$ (**2**) and N$_3^-$ (**3**)). Reaction of [PdCl$_2$(bddo)] with pyridine yields a mixture of [Pd(bddo)(py)$_2$](BF$_4$)$_2$ ([**4**](BF$_4$)$_2$) and [Pd(bddo)](BF$_4$)$_2$. When the reaction is carried out with triphenylphosphine, [Pd(bddo)](BF$_4$)$_2$ is the only complex that is obtained (Scheme 1).

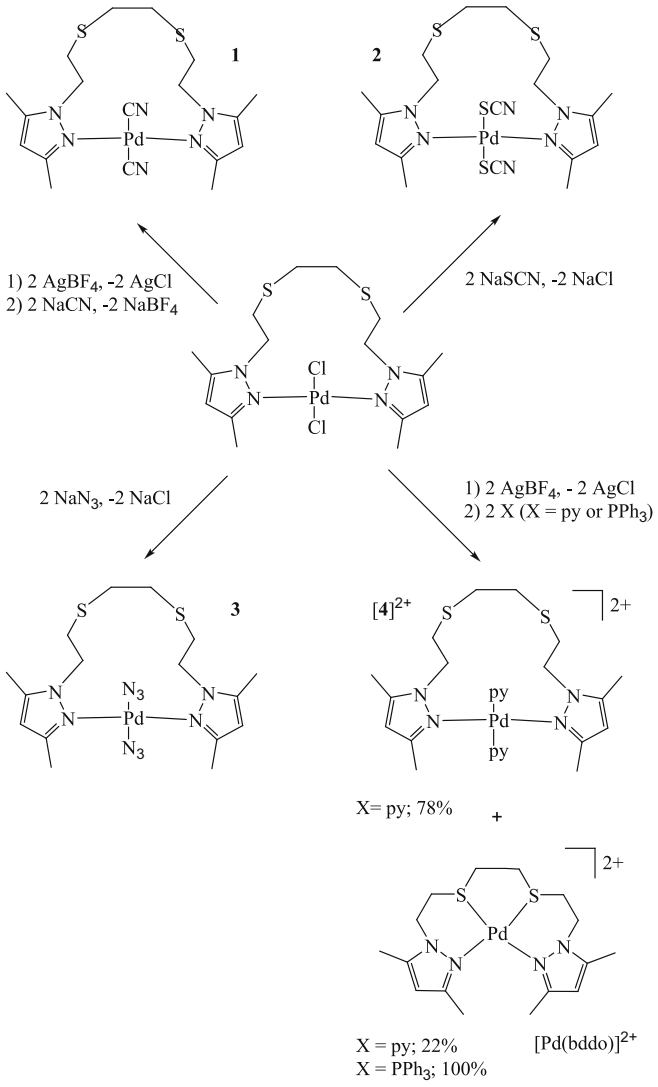
2. Results and discussion

2.1. Synthesis and spectroscopic properties of the complexes

Reaction of [PdCl$_2$(bddo)] [7a] with two equivalents of NaBF$_4$ in the presence of two equivalents of NaSCN or NaN$_3$, and in a mixture of CH$_2$Cl$_2$/MeOH (1:1), yields the complexes [Pd(X)$_2$(bddo)] (X = SCN$^-$ (**2**) or N$_3^-$ (**3**)). When identical conditions are used in an attempt to prepare the corresponding [Pd(CN)$_2$(bddo)] (**1**) complex, displacement of the bddo ligand occurs, yielding Na$_2$[Pd(CN)$_4$] [10]. A new synthetic route has been tried. Complex [Pd(bddo)(CH$_3$CN)$_2$](BF$_4$)$_2$ is formed by the reaction of [PdCl$_2$(bddo)] with two equivalents of AgBF$_4$ in a mixture of CH$_2$Cl$_2$/CH$_3$CN (2:1) at room temperature. Two equivalents of NaCN are then added to the solution of [Pd(bddo)(CH$_3$CN)$_2$](BF$_4$)$_2$, yielding [Pd(CN)$_2$(bddo)] (**1**) (Scheme 1).

* Corresponding authors. Fax: +34 93 581 31 01 (J. Pons).
E-mail address: Josefina.Pons@uab.es (J. Pons).
[1] Deceased on September 3, 2007.

0277-5387/$ - see front matter © 2009 Elsevier Ltd. All rights reserved.
doi:10.1016/j.poly.2009.04.013



Scheme 1.

When $[PdCl_2(bddo)]$ reacts with two equivalents of $AgBF_4$ in CH_2Cl_2:CH_3CN:CH_3OH (2:1:1) and then two equivalents of pyridine (py) are added, a mixture of two complexes, $[Pd(bddo)(py)_2](BF_4)_2$ (78%) ([**4**]$(BF_4)_2$) and $[Pd(bddo)](BF_4)_2$ (22%), is obtained. $[Pd(bddo)](BF_4)_2$ had already been described in a previous paper by some of the authors of this work, and its presence in the mixture has been confirmed by comparison of the ^{1}H NMR spectra. ^{1}H NMR spectrum of the mixture has also been used to determine the ratio of [**4**]$(BF_4)_2$ (δ(C–H_{pz}) = 6.18 ppm) and $[Pd(bddo)](BF_4)_2$ (δ(C–H_{pz}) = 6.26 ppm) complexes (integration of C–H_{pz} signals, see Section 4). Unfortunately, isolation of the two complexes by silica gel chromatography was unsuccessful. Recrystallisations of the mixture with different solvents have been carried out but pure products could not be obtained.

When a similar reaction is used to prepare the complex $[Pd(bddo)(PPh_3)_2](BF_4)_2$, we obtain $[Pd(bddo)](BF_4)_2$ as a pure product [7a].

Complexes **1–3** and the mixture of [**4**]$(BF_4)_2$ and $[Pd(bddo)(PPh_3)_2](BF_4)_2$ have been characterised by elemental analyses, conductivity measurements and spectroscopic methods.

The elemental analyses confirm the stoichiometries proposed for the compounds. The positive ionisation spectra (ESI(+)) of **1–3** gave peaks with m/z values at 519, 583 and 551, respectively, corresponding to {100%, ($[Pd(X)_2(bddo)] + Na)^+$)}, (X = CN^-, SCN^- and N_3^-).

The conductivity data in acetonitrile are in agreement with non-electrolytes for compounds **1–3** [11].

IR spectra of complexes **1–3** and the mixture of [**4**]$(BF_4)_2$ and $[Pd(bddo)](BF_4)_2$ are similar to that of $[PdCl_2(bddo)]$, the most characteristic bands being those attributable to the pyrazolyl group: $\nu(C{=}C)_{pz}$ and $\nu(C{=}N)_{pz}$ between 1557 and 1546 cm^{-1}. The IR spectrum of the mixture of [**4**]$(BF_4)_2$ and $[Pd(bddo)](BF_4)_2$ presents bands, attributable to [**4**]$(BF_4)_2$, that are assigned to $(\nu(C{=}C)_{ar})_{py}$ and $(\nu(C{=}N)_{ar})_{py}$ at 1601 cm^{-1}, $(\delta(C{-}H)_{oop})_{py}$ at 701 cm^{-1} and ν(B–F) at 1066 cm^{-1}. [12] The terminal CN^- groups in **1** give rise to a band at 2140 cm^{-1}, typical of monodentate cyanides [13]. Complex **2** exhibits a strong band at 2111 cm^{-1} indicative of S-bond thiocyanates [13a–c,14]. Finally, the IR spectrum of **3** displays a strong band at 2024 cm^{-1} attributable to azide groups [13a,15]. The IR spectra of the complexes in the 650–250 cm^{-1} region have also been studied. In all cases, they show bands attributable to ν(Pd–N) between 463 and 419 cm^{-1}. Moreover, bands attributable to $\nu(Pd{-}C_{cyanide})$ at 412 cm^{-1} (**1**), $\nu(Pd{-}S_{thiocyanate})$ at 342 cm^{-1} (**2**) and $\nu(Pd{-}N_{azide})$ at 473 cm^{-1} (**3**) were also assigned [13a,15].

The ^{1}H, ^{13}C{^{1}H}NMR, COSY and HSQC spectra for complexes **1–3** were recorded in $(CD_3)_2CO$ and show the signals of coordinated ligands. HSQC spectra were used to assign the protons and carbons of the $SCH_2CH_2N_{pz}$ and the SCH_2CH_2S fragments. NMR data are reported in the Section 4.

NMR spectra of compound **2** and **3** were studied in more detail. Study of the $SCH_2CH_2N_{pz}$ fragment as an AA'XX' system gave a set of coupling constants for each complex. These constants are consistent with the simulated spectra obtained with the aid of the *g* NMR program [16]. Fig. 1 shows the experimentally determined and simulated spectra of the $SCH_2CH_2N_{pz}$ and the SCH_2CH_2S fragments for **2**. In the ^{1}H NMR spectrum of complexes **2** and **3,** we observe two multiplets corresponding to one CH_2 of the $SCH_2CH_2N_{pz}$ fragment each. The two protons of each CH_2 group are isocrones but each of them presents one ^2J coupling constant with the geminal proton and two ^3J coupling constants with the vicinal protons, due to the rigidity of the bddo ligand once it is complexed (NMR data can be found in the Section 4).

The coupling constants obtained for the $SCH_2CH_2N_{pz}$ fragment of complexes **2** and **3** are comparable to those obtained for $[PdCl_2(bddo)]$ [7a]. This indicates that the bddo ligand presents the same coordination behaviour in $[PdCl_2(bddo)]$ and complexes **2** and **3**: the ligand coordinates the Pd(II) centre through the azine nitrogens of the two pyrazolyl rings and the thioether groups remain uncoordinated. This type of coordination is corroborated by the X-ray crystal structure of $[PdCl_2(bddo)]$ [7a] and complex **2** (Fig. 2).

The ^{1}H NMR spectrum of complex **1** could not be further studied due to the broadness of the signals corresponding to the $SCH_2CH_2N_{pz}$ fragment. However, the number of signals and their positions is similar to those found for $[PdCl_2(bddo)]$, and complexes **2** and **3**. This would indicate that the bddo ligand also coordinates the Pd(II) centre in **1** through the azine nitrogens of the two pyrazolyl rings.

*2.2. Description of the crystal and molecular structure of trans-$[Pd(SCN)_2(bddo)]$ (**2**)*

The structure of **2** consist of discrete *trans*-$[Pd(SCN)_2(bddo)]$ units packed according to van der Waals forces (Fig. 2). Some selected bond lengths and bond angles for this complex are listed in Table 1.

The palladium atom is coordinated by two pyrazolic nitrogens and two sulfur atoms from the thiocyanate ligands in a distorted square-planar geometry. The tetrahedral distortion can be observed in the mean separation [0.077 Å] of the atoms linked to

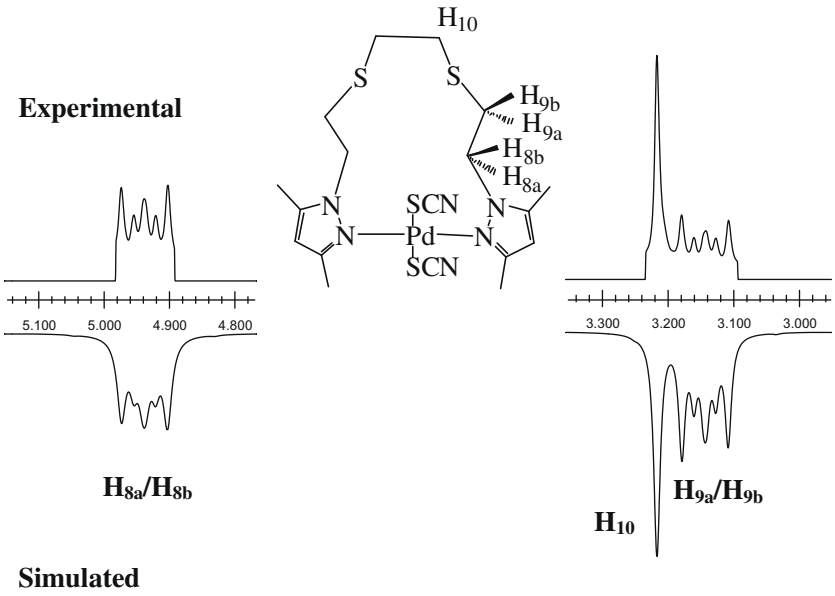


Fig. 1. The 250-MHz ^{1}H NMR and the simulated *g* NMR spectra for H_8, H_9 and H_{10} protons of the $N_{pz}CH_2CH_2S$ and SCH_2CH_2S fragments of $[Pd(SCN)_2(bddo)]$ (**2**), including the numbering of the H_8, H_9 and H_{10} protons.

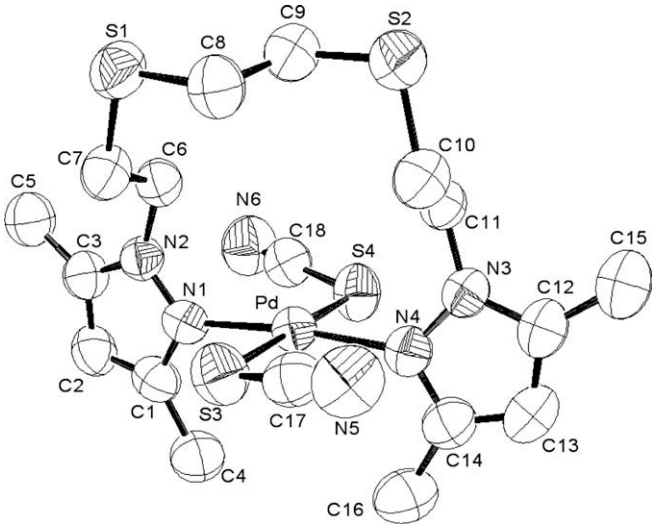


Fig. 2. ORTEP drawing of $[Pd(SCN)_2(bddo)]$ (**2**), showing all non-hydrogen atoms and the atom numbering scheme; 50% probability amplitude displacement ellipsoids are shown.

Table 1
Selected bond lengths (Å) and bond angles (°) for **2**.

Pd–N(1)	2.047(3)	Pd–S(3)	2.352(2)
Pd–N(4)	2.025(3)	Pd–S(4)	2.320(2)
N(4)–Pd–N(1)	172.67(12)	N(1)–Pd–S(4)	93.73(9)
N(4)–Pd–S(4)	85.45(10)	N(1)–Pd–S(3)	85.33(9)
N(4)–Pd–S(3)	95.34(11)	S(4)–Pd–S(3)	178.49(5)

the Pd atom in relation to the mean plane. Tetrahedral distortion of the square-planar geometry can also be observed in the angles S3–Pd–S4 and N1–Pd–N4, of 178.49(5)° and 172.67(12)°, respectively. The dihedral angle between the planes N1–Pd–S3 and N4–Pd–S4 is 7.33°. The pyrazolyl groups are *trans* to each other. The bddo ligand acts as a bidentate chelate, and form one thirteen membered ring.

The PdN_2S_2 *core* (N pyrazole and S thiocyanate) is found in three complexes in the literature [14a,17]. The Pd–N_{pz} (2.025(3) Å, 2.047(3) Å) and Pd–S_{SCN} (2.320(2) Å, 2.352(2) Å) distances are of the same order as those found in the literature for this kind of complexes. For the Pd–N_{pz} bonds, the literature describes distances between 1.979 and 2.141 Å [9], and for Pd–S_{SCN}, the described bond distances lay between 2.278 and 2.448 Å [18].

The values of the Pd–S–C angles are 104.20(18)° and 105.62(16)° for Pd–S3–C17 and Pd–S4–C18, respectively. These angles agree with the values observed for other complexes found in the literature (104.8(1)° for $[Pd(SCN)_2(HPz)_2]$ (HPz = pyrazol) [14a], 106.2(2)° for $[Pd(SCN)_2(phmPz)_2]$ (phmPz = 1-phenyl-3-methylpyrazole) [14a], 102.0(1)° for $[Pd(SCN)_2(HdmPz)_2]_n$ (HdmPz = 3,5-dimethylpyrazole) [17], 107.3° for $[Pd\{Ph_2P(CH_2)_3NMe_2\}(SCN)(NCS)]$ [19]) and 102.71(10)° for $[Pd(SCN)_2(PTA)_2](SCN)_2$ (PTA = 1,3,5-triaza-7-phosphaadamantane) [20].

The values of S–C–N angles in the thiocyanate groups are 176.5(5)° (S3–C17–N5) and 173.9(5)° (S4–C18–N6). These angles are of the same order as those found in the aforementioned complexes [17–20] and show that the thiocyanate groups are nearly linear. In addition, the bond length values of S–C (1.612(6) Å, 1.712(5) Å) and C–N (1.187(6) Å, 1.121(6) Å), indicate the dominance of the mesomeric S–C≡N form [17].

3. Conclusion

The present paper reports the reaction of the complex $[PdCl_2(bddo)]$ with cyanide, thiocianate, azide, pyridine and triphenylphosphine, in the presence of $AgBF_4$ or $NaBF_4$. In these complexes, the chlorine ligands are replaced by anionic ligands (cyanide, thiocianate, or azide) to yield the complexes *trans*-$[Pd(X)_2(bddo)]$ (X = CN^-, SCN^- and N_3^-). In these complexes, the bddo ligand shows bidentate coordination (*NN*).

When neutral ligand piridine reacts with the complex $[PdCl_2(bddo)]$, a mixture of $[Pd(bddo)(py)_2](BF_4)_2$ and $[Pd(bddo)](BF_4)_2$ complexes has been obtained. Only one complex, $[Pd(bddo)](BF_4)_2$, has been obtained when the neutral ligand is triphenylphosphine.

In summary, in these complexes, the presence of monodentate anionic ligands (CN^-, SCN^- or N_3^-) produces complexes in which the bddo ligand coordinates de Pd(II) centre in a *NN* mode. When monodentate neutral ligands (py or PPh_3) are used, the *NSSN* coor-

dination of the bddo ligand is favoured. ^{1}H NMR experiments have proven to be highly useful to determine the coordination mode of the bddo ligand in these complexes.

4. Experimental

4.1. General details

The reactions were carried out under nitrogen atmosphere using vacuum line and Schlenk techniques. All reagents were commercial grade materials and were used without further purification. Solvents were dried and distilled according to standard procedures and stored under nitrogen. Samples of $[PdCl_2(bddo)]$ were prepared as described in the literature [7a]. Elemental analyses (C, H, N, S) were carried out by the staff of Chemical Analyses Service of the Universitat Autònoma de Barcelona on a Carlo Erba CHNS EA-1108 instrument. Conductivity measurements were performed at room temperature (r.t.) in 10^{-3} M acetonitrile solution, employing a CyberScan CON 500 (Euthech instrument) conductimeter. Infrared spectra were run on a Perkin Elmer FT spectrophotometer, series 2000 cm^{-1} as KBr pellets or polyethylene films in the range 4000–250 cm^{-1}. ^{1}H, ^{13}C{^{1}H} NMR COSY and HSQC spectra were recorded on a NMR-FT Bruker AC-250 MHz spectrometer, $(CD_3)_2CO$ solution at 298 K. ^{1}H NMR and ^{13}C{^{1}H} NMR chemical shifts (δ) were determined relative to internal TMS and are given in ppm. Mass spectra were obtained with an Esquire 3000 ion-trap mass spectrometer from Bruker Daltonics.

4.2. Synthesis of the complexes

4.2.1. Synthesis of the complex $[Pd(CN)_2(bddo)]$ (**1**)

A solution of 0.21 mmol (0.040 g) of $AgBF_4$ in methanol (5 ml) was added dropwise, under vigorous stirring, to a solution of 0.10 mmol (0.050 g) of $[PdCl_2(bddo)]$ in 10 ml of CH_2Cl_2/CH_3CN (2:1). Afterwards, stirring was stopped, and AgCl was filtered off through a Celite pad. Then, a solution of 0.20 mmol (0.010 g) of NaCN dissolved in 5 ml of CH_3OH was added. The mixture was stirred for 12 h. Then, when the volume of the resultant solution was reduced to roughly 5 ml, the product precipitated as a yellow solid. This solid was filtered, washed with diethyl ether and dried under vacuum.

Compound ***1****:* Yield: 0.032 g (66%). ($C_{18}H_{26}N_6PdS_2$): Anal. Calc.: C, 43.50; H, 5.27; N, 16.91; S, 12.90. Found: C, 43.70; H, 5.30; N, 16.87; S, 13.10%. MS(ESI(+)): *m*/*z* (%) = 519 (100) ($[Pd(CN)_2$-(bddo)] + Na)$^+$. Conductivity (Ω^{-1} cm^2 mol^{-1}, 1.01 10^{-3} M in acetonitrile): 114. IR (KBr, cm^{-1}): 3022 ν(C–H)$_{ar}$, 2959, 2915 ν(C–H)$_{al}$, 2140 ν(CN), 1557 (ν(C=C), ν(C=N))$_{ar}$, 1465, 1424 (δ(C=C), δ(C=N))$_{ar}$, 798 δ(C–H)$_{oop}$. (Polyethylene, cm^{-1}): 440 ν(Pd–N), 412 ν(Pd–C). ^{1}H NMR ($(CD_3)_2CO$ solution, 250 Hz, 298 K) δ: 6.15 [2H, s, C*H*(pz)], 4.83 [4H, br, $N_{pz}CH_2$CH2S], 3.49 [4H, s, SCH_2CH_2S], 3.36 [4H, br, NpzCH_2CH_2S], 2.32 [6H, s, CH_3(pz)], 2.27 [6H, s, CH_3(pz)] ppm. ^{13}C{^{1}H} NMR ($(CD_3)_2CO$ solution, 63 MHz, 298 K) δ: 154.4 (pz-*C*), 143.8 (pz-*C*), 116.6 (*C*N), 105.0 (*C*H(pz)), 48.7 ($N_{pz}CH_2CH_2S$), 32.1 ($N_{pz}CH_2CH_2S$, SCH_2CH_2S), 13.6 (*C*H_3(pz)), 11.0 (*C*H_3(pz)) ppm.

4.2.2. Synthesis of the complex $[Pd(X)_2(bddo)]$ ($X = SCN^-$ (**2**), and N_3^- (**3**))

A solution of 0.40 mmol (0.032 g) of NaSCN or 0.40 mmol (0.026 g) of NaN_3 dissolved in 5 ml of CH_3OH was added to another solution of 0.19 mmol (0.100 g) of $[PdCl_2(bddo)]$ in 10 ml of CH_2Cl_2. In both cases, the colour changed from orange to red. Immediately after, 0.40 mmol (0.044 g) of $NaBF_4$ in methanol (5 ml) were added. The solutions were stirred for 12 h, and then, they were filtered through a pad of Celite. When the volumes of the resultant solutions were reduced to roughly 5 ml, the products precipitated as orange solids. These solids were filtered and dried under vacuum.

Compound ***2****:* Yield: 0.085 g (78%). ($C_{18}H_{26}N_6PdS_4$): Anal. Calc.: C, 38.53; H, 4.67; N, 14.98; S, 22.86. Found: C, 38.30; H, 4.50; N, 14.90; S, 23.05%. MS(ESI(+)): *m*/*z* (%) = 583 (100) ($[Pd(SCN)_2(bddo)]$ + Na)$^+$. Conductivity (Ω^{-1} cm^2 mol^{-1}, 1.00 10^{-3} M in acetonitrile): 82. IR (KBr, cm^{-1}): 3136 ν(C–H)$_{ar}$, 2974, 2922 ν(C–H)$_{al}$, 2111 ν(CN), 1554 (ν(C=C), ν(C=N))$_{ar}$, 1465, 1422 (δ(C=C), δ(C=N))$_{ar}$, 813 δ(C–H)$_{oop}$. (Polyethylene, cm^{-1}): 463 ν(Pd–N), 342, 321 ν(Pd–S). ^{1}H NMR ($(CD_3)_2CO$ solution, 250 Hz, 298 K) δ: 6.24 [2H, s, C*H*(pz)], 4.94 [4H, m, ^2J = 13.12 Hz, ^3J = 12.18 Hz, ^3J = 4.00 Hz, $N_{pz}CHHCH_2S$], 3.22 [4H, s, SCH_2CH_2S], 3.14 [4H, m, ^2J = 13.12 Hz, ^3J = 12.18 Hz, ^3J = 4.00 Hz, $N_{pz}CH_2CHHS$], 2.84 [6H, s, CH_3(pz)], 2.44 [6H, s, CH_3(pz)] ppm. ^{13}C{^{1}H} NMR ($(CD_3)_2CO$ solution, 63 MHz, 298 K) δ: 150.7 (pz-*C*), 146.7 (pz-*C*), 116.5 (S*C*N), 110.6 (*C*H(pz)), 51.2 ($N_{pz}CH_2CH_2S$), 34.3 (SCH_2CH_2S), 30.3 ($N_{pz}CH_2CH_2S$), 14.8 (*C*H_3(pz)), 11.2 (*C*H_3(pz)) ppm.

Compound ***3****:* Yield: 0.078 g (76%). ($C_{16}H_{26}N_{10}PdS_2$): Anal. Calc.: C, 36.33; H, 4.95; N, 26.48; S, 12.12. Found: C, 36.10; H, 4.85; N, 26.23; S, 12.05%. MS(ESI(+)): *m*/*z* (%) = 551 (100) ($[Pd(N_3)_2(bddo)]$ + Na)$^+$. Conductivity (Ω^{-1} cm^2 mol^{-1}, 1.01 10^{-3} M in acetonitrile): 106. IR (KBr, cm^{-1}): 3122 ν(C–H)$_{ar}$, 2995, 2937 ν(C–H)$_{al}$, 2024 ν(N$_3$), 1551 (ν(C=C), ν(C=N))$_{ar}$, 1475, 1426 (δ(C=C), δ(C=N))$_{ar}$, 797 δ(C–H)$_{oop}$. (Polyethylene, cm^{-1}): 473, 445 ν(Pd–N). ^{1}H NMR ($(CD_3)_2CO$ solution, 250 Hz, 298 K) δ: 6.17 [2H, s, C*H*(pz)], 4.96 [4H, m, ^2J = 12.70 Hz, ^3J = 11.80 Hz, ^3J = 4.90 Hz, $N_{pz}CHHCH_2S$], 3.23 [4H, s, SCH_2CH_2S], 3.09 [4H, m, ^2J = 12.70 Hz, ^3J = 11.80 Hz, ^3J = 4.90 Hz, $N_{pz}CH_2CHHS$], 2.96 [6H, s, CH_3(pz)], 2.44 [6H, s, CH_3(pz)] ppm. ^{13}C{^{1}H} NMR ($(CD_3)_2CO$ solution, 63 MHz, 298 K) δ: 150.4 (pz-*C*), 144.5 (pz-*C*), 108.9 (*C*H(pz)), 50.7 ($N_{pz}CH_2CH_2S$), 33.6 (SCH_2CH_2S), 30.1 ($N_{pz}CH_2CH_2S$), 14.1 (*C*H_3(pz)), 11.1 (*C*H_3(pz)) ppm.

Coupling constants for complexes **2** and **3** were obtained with the aid of the *g* NMR program [16].

4.2.3. Reaction of $[PdCl_2(bddo)]$ with pyridine

A solution of 0.21 mmol (0.040 g) of $AgBF_4$ in methanol (5 ml) was added dropwise and with vigorous stirring to another solution of 0.10 mmol (0.053 g) of $[PdCl_2(bddo)]$ in a mixture of CH_2Cl_2/CH_3CN (2:1, 10 ml). After 5 minutes, stirring was stopped, and AgCl was filtered off through a Celite pad. Then, a solution of 0.23 mmol (0.018 g) of pyridine in dichloromethane (3 ml) was added. The solution was stirred for 12 h. When the volume of the resultant solution was reduced to roughly 5 ml, an orange solid precipitated. This solid was filtered and washed with diethyl ether, yielding a mixture of $[Pd(bddo)(py)_2](BF_4)_2$ [**4**]$(BF_4)_2$ and $[Pd(bddo)](BF_4)_2$. Isolation of the two complexes by silica gel chromatography (60 Å) or recrystallisation with different solvents was unsuccessful.

$[4](BF_4)_2$ + $[Pd(bddo)](BF_4)_2$: Yield: 0.052 g (68%) (78% [**4**]$(BF_4)_2$ + 22% [Pd(bddo)]$(BF_4)_2$). IR (KBr, cm^{-1}): 3077 ν(C–H)$_{ar}$, 2979, 2922 ν(C–H)$_{al}$, 1601 ((ν(C=C), ν(C=N))$_{py}$, 1546 (ν(C=C), ν(C=N))$_{pz}$, 1454, 1414 (δ(C=C), δ(C=N))$_{ar}$, 1066 ν(B–F), 765 (δ(C–H)$_{oop}$)$_{pz}$, 701 (δ(C–H)$_{oop}$)$_{py}$. (Polyethylene, cm^{-1}): 443, 419 ν(Pd–N). ^{1}H NMR ($(CD_3)_2CO$ solution, 250 Hz, 298 K) δ: **$[4](BF_4)_2$**, (78%): 8.87, 8.28, 7.83 [7.8H, m, Py], 6.18 [1.6H, s, C*H*(pz)], 4.55 [3.1H, m, $N_{pz}CH_2CH_2S$], 3.23 [3.1H, m, $N_{pz}CH_2CH_2S$], 3.11 [3.1H, s, S–CH_2–CH_2–S], 2.37 [4.7H, s, CH_3(pz)], 2.35 [4.7H, s, CH_3(pz)] ppm. **$[Pd(bddo)](BF_4)_2$**, (22%): 6.28 [0.4H, s, C*H*(pz)], 5.50, 5.19 [0.4H/0.4H, m, $N_{pz}CHHCH_2S$], 3.78, 3.72 [0.4H/0.4H, m, $N_{pz}CH_2CHHS$], 3.11 [0.9H, m, S–CH_2–CH_2–S], 2.52 [0.7H, s, CH_3(pz)], 1.99 [0.7H, s, CH_3(pz)] ppm. ^{13}C{^{1}H} NMR ($(CD_3)_2CO$ solution, 63 MHz, 298 K) δ: **$[4](BF_4)_2$**: 150.6 (pz-*C*), 141.4 (pz-*C*), 126.8 (Py), 107.0 (*C*H(pz)), 51.2 ($N_{pz}CH_2CH_2S$), 37.2 (SCH_2CH_2S), 33.8 ($N_{pz}CH_2CH_2S$), 14.5 (*C*H_3(pz)), 10.8 (*C*H_3(pz)) ppm. **$[Pd(bddo)](BF_4)_2$**: 152.1 (pz-*C*), 147.0 (pz-*C*), 108.9 (*C*H(pz)), 63.5 ($N_{pz}CH_2CH_2S$), 48.3 (SCH_2CH_2S), 31.4 ($N_{pz}CH_2CH_2S$), 13.2 (*C*H_3(pz)), 11.8 (*C*H_3(pz)) ppm.

Table 2
Crystallographic data for **2**.

Empirical formula	$C_{18}H_{26}N_6PdS_4$
Formula weight	561.09
Temperature (K)	293(2)
Crystal System	orthorhombic
Space group	$P2_12_12_1$
Unit cell dimensions	
a (Å)	12.213(6)
b (Å)	13.655(6)
c (Å)	14.823(4)
U (Å^3)	3563.1(19)
Z	4
D_{calc} (g.cm^{-3})	1.508
μ (mm^{-1})	1.105
F(0 0 0)	1144
Crystal size (mm^{-1})	0.2 × 0.1 × 0.1
θ range (°)	2.63–30.00
Index range	$-18 \leqslant h \leqslant 18$, $-19 \leqslant k \leqslant 19$, $-22 \leqslant l \leqslant 22$
Reflexions collected/unique	30 651/7125 [R_{int} = 0.0498]
Completeness to θ (%)	98.8
Absorption correction	none
Data/restraints/parameters	7125/6/266
Goodness-of-fit (GOF)	1.121
Final R_1, ωR_2	0.0418, 0.0967
R_1 (all data), ωR_2	0.0556, 0.1012
Residual electron density (e Å^{-3})	0.306 and −0.640

*4.2.4. X-ray crystal structure for compound **2***

Suitable crystals for X-ray diffraction of compound **2** were obtained through crystallisation from acetonitrile-diethylether solution (1:1).

A prismatic crystal was selected and mounted on a MAR345 diffractometer with an image plate detector. Unit-cell parameters were determined from 2038 reflections (3° < θ < 31°) and refined by least-squares method. Intensities were collected with graphite monochromatized Mo Kα radiation. 30 651 reflections were measured in the range 2.63° ⩽ θ ⩽ 30.00°. About 7125 of which were non-equivalent by symmetry (R_{int} (on I) = 0.079). About 5885 reflections were assumed as observed applying the condition $I > 2\sigma(I)$. Lorentz-polarization but no absorption corrections were made.

The structure was solved by Direct methods, using SHELXS97 computer program [21], and refined by full-matrix least-squares method with SHELXL97 computer program [22] using 30 651 reflections, (very negative intensities were not assumed). The function minimised was $\sum\omega||F_O|^2 - |F_C|^2|^2$, where $\omega = [\sigma^2(I) + (0.0414P)^2 + 0.0658P]^{-1}$ and $P = (|F_O|^2 + 2|F_C|^2)/3$. All H atoms were computed and refined, using a riding model, with an isotropic temperature factor equal to 1.2 times the equivalent temperature factor of the atom which are linked. The final $R(F)$ factor and $R_w(F^2)$ values as well as the number of parameters and other details concerning the refinement of the crystal structure are gathered in Table 2.

Supplementary data

CCDC 723189 contains the supplementary crystallographic data for complex **2**. These data can be obtained free of charge via http://www.ccdc.cam.ac.uk/conts/retrieving.html, or from the Cambridge Crystallographic Data Centre, 12 Union Road, Cambridge CB2 1EZ, UK; fax: (+44) 1223-336-033; or e-mail: deposit@ccdc.cam.ac.uk.

Acknowledgments

In memory of Prof. Xavier Solans Huguet.

Support by the Spanish Ministerio de Educacion y Cultura (projecte CTQ2007-63913 BQU) is gratefully acknowledged.

References

[1] (a) S. Kealey, N.J. Long, P.W. Miller, A.J.P. White, P.B. Hitchcock, A. Gee, Dalton Trans. (2007) 2823;
(b) R. Mukherjee, Coord. Chem. Rev. 203 (2000) 151;
(c) G. La Monica, G.A. Ardizzoia, Prog. Inorg. Chem. 46 (1997) 151;
(d) S. Trofimenko, Scorpionates: The Coordination Chemistry of Polypyrazolylborate Ligands, Imperial College Press., London, UK, 1999;
(e) S. Trofimenko, Chem. Rev. 93 (1993) 943;
(f) S. Trofimenko, Prog. Inorg. Chem. 34 (1986) 115;
(g) S. Trofimenko, Chem. Rev. 72 (1972) 497;
(h) P.K. Byers, A.J. Canty, R.T. Honeyman, Adv. Organomet. Chem. 34 (1992) 1.
[2] (a) V. Montoya, J. Pons, V. Branchadell, J. García-Antón, X. Solans, M. Font-Bardía, J. Ros, Organometallics 27 (2008) 1084;
(b) A. Orejón, C. Claver, L.A. Oro, A. Elduque, M.T. Pinillos, J. Mol. Catal. A: Chem. 136 (1998) 279;
(c) H. Shumann, H. Hemling, V. Ravindar, Y. Badrieh, J. Blum, J. Organomet. Chem. 469 (1994) 213;
(d) D. Carmona, A. Mendoza, J. Ferre, F.J. Lahoz, L.A. Oro, J. Organomet. Chem. 431 (1992) 87;
(e) L.A. Oro, D. Carmona, P.L. Pérez, A. Tiripicchio, M. Tiripicchio-Camellini, J. Chem. Soc., Dalton Trans. (1989) 1427;
(f) C. Claver, P. Kalck, M. Ridmy, A. Thorez, L.A. Oro, M.T. Pinillos, M.C. Apreda, F.H. Cano, C. Foces-Foces, J. Chem. Soc., Dalton Trans. (1988) 1523;
(g) L.A. Oro, M. Campo, D. Carmona, J. Mol. Catal. 39 (1987) 341;
(h) J. Jezierska, A. Jezierski, B. Jezooska, I. Trzebiatawska, A. Ozarowshi, Inorg. Chim. Acta 68 (1983) 7.
[3] (a) K. Sakai, Y. Tomita, T. Ue, K. Goshima, M. Ohminato, T. Tsubomura, K. Matsumoto, K. Ohmura, K. Kawakami, Inorg. Chim. Acta 297 (2000) 64;
(b) N. Saha, A. Saha, A. Misra, Polyhedron 13 (1994) 2025.
[4] A.G.M.M. Hossain, T. Nagaoka, K. Ogura, Eletrochim. Acta 41 (1996) 2773.
[5] (a) B. Ma, J. Li, P.I. Djurovich, M. Yousufuddin, R. Bau, M.E. Thompson, J. Am. Chem. Soc. 127 (2005) 28;
(b) W. Lu, M.C.W. Chan, N. Zhu, C.M. Che, C. Li, Z. Hui, J. Am. Chem. Soc. 126 (2004) 7639;
(c) S.W. Lai, M.C.W. Chan, T.C. Cheung, S.M. Peng, C.M. Che, Inorg. Chem. 38 (1999) 4046;
(d) J. Pons, F.J. Sánchez, A. Labarta, J. Casabó, F. Teixidor, A. Caubet, Inorg. Chim. Acta 208 (1993) 167;
(e) D.J. Hodgson, B.J. Schwartz, T.N. Sorrell, Inorg. Chem. 28 (1989) 2226;
(f) J. Pons, X. López, J. Casabó, F. Teixidor, A. Caubet, J. Rius, C. Miravitlles, Inorg. Chim. Acta 195 (1992) 61;
(g) J. Casabó, J. Pons, K.S. Siddiqi, F. Teixidor, E. Molins, C. Miravitlles, J. Chem. Soc., Dalton Trans. (1989) 1401.
[6] (a) M. Guerrero, J. Pons, V. Branchadell, T. Parella, X. Solans, M. Font-Bardía, J. Ros, Inorg. Chem. 47 (2008) 11084;
(b) Q.F. Sun, K.M.C. Wong, L.X. Liu, H.P. Huang, S.Y. Yu, V.W.W. Yam, Y.Z. Li, Y.J. Pan, K.C. Yu, Inorg. Chem. 47 (2008) 2142;
(c) S.Y. Yu, H.P. Huang, S.H. Li, Q. Jiao, Y.Z. Li, B. Wu, Y. Sei, K. Yamaguchi, Y.J. Pan, H.W. Ma, Inorg. Chem. 44 (2005) 9471;
(d) Z.X. Zhang, H. Huang, S.Y. Yu, J. Chin. Inorg. Chem. 20 (2004) 849. and references therein.
[7] (a) J. García-Antón, J. Pons, X. Solans, M. Font-Bardía, J. Ros, Eur. J. Inorg. Chem. (2002) 3319;
(b) J. García-Antón, J. Pons, X. Solans, M. Font-Bardía, J. Ros, Eur. J. Inorg. Chem. (2003) 2992;
(c) J. García-Antón, J. Pons, X. Solans, M. Font-Bardía, J. Ros, Eur. J. Inorg. Chem. (2003) 3952;
(d) J. García-Antón, J. Pons, X. Solans, M. Font-Bardía, J. Ros, Inorg. Chim. Acta 355 (2003) 87;
(e) J. García-Antón, R. Mathieu, N. Lugan, J. Pons, J. Ros, J. Organomet. Chem. 689 (2004) 1599;
(f) J. García-Antón, J. Pons, J. Ros, X. Solans, M. Font-Bardía, Acta Crystallogr., Sect. E 60 (2004) m1087;
(g) A. Rimola, M. Sodupe, J. Ros, J. Pons, Eur. J. Inorg. Chem. (2006) 447;
(h) A. de León, J. Pons, J. García-Antón, X. Solans, M. Font-Bardía, J. Ros, Polyhedron 26 (2007) 2921;
(i) A. de León, J. Pons, J. García-Antón, X. Solans, M. Font-Bardía, J. Ros, Inorg. Chim. Acta 360 (2007) 2071;
(j) A. de León, J. Pons, J. García-Antón, X. Solans, M. Font-Bardía, J. Ros, J. Chem. Crystallogr. 37 (2007) 801;
(k) A. de León, J. Pons, J. García-Antón, X. Solans, M. Font-Bardía, J. Ros, Polyhedron 26 (2007) 2498.
[8] (a) J. García-Antón, J. Pons, X. Solans, M. Font-Bardía, J. Ros, Inorg. Chim. Acta 357 (2004) 571;
(b) A. de León, J. Pons, J. García-Antón, X. Solans, M. Font-Bardía, J. Ros, Inorg. Chim. Acta 362 (2009) 1528.
[9] A. de León, J. Pons, J. García-Antón, X. Solans, M. Font-Bardía, J. Ros, Inorg. Chim. Acta, accepted for publication, doi:10.1016/j.ica.2009.04.045.
[10] J.M. Harrington, S. Bart Jones, R.D. Hancock, Inorg. Chim. Acta 358 (2005) 4473.
[11] W.J. Geary, Coord. Chem. Rev. 7 (1971) 81.
[12] D.H. Williams, I. Fleming, Spectroscopic Methods in Organic Chemistry, McGraw-Hill, London, UK, 1995.
[13] (a) K. Nakamoto, Infrared and Raman, Spectra of Inorganic and Coordination Compounds, fifth ed., John Wiley and Sons, New York, USA, 1997;

(b) G. Siedle, P.G. Lassahn, V. Lozan, C. Janiak, B. Kersting, Dalton Trans. (2007) 52;
(c) G. Siedle, B. Kersting, Dalton Trans. (2006) 2114;
(d) J.A. Davies, F.R. Hartley, S.G. Murray, Inorg. Chim. Acta 41 (1980) 249;
(e) J.A. Davies, F.R. Hartley, S.G. Murray, M.A. Pierce-Butler, J. Chem. Soc., Dalton Trans. (1983) 1305.
[14] (a) A.V.G. Netto, R.C.G. Frem, A.E. Mauro, R.H.A. Santos, J.R. Zoia, Transition Met. Chem. 27 (2002) 279;
(b) R.A. Bailey, S.L. Nozak, T.W. Michelsen, W.N. Mills, Coord. Chem. Rev. 4 (1971) 407.
[15] T.M. Klapötke, R. Polborn, T. Schütt, Z. Anorg. Allg. Chem. 626 (2000) 1444.
[16] P.H.M. Butzlelaar, *g* NMR ver. 4.0 IvorySoft, Cherwell Scientific, Oxford, UK, 1997.
[17] A.V.G. Netto, R.C.G. Frem, A.E. Mauro, E.T. de Almeida, A.M. Santana, J. de Souza Jr., R.H.A. Santos, Inorg. Chim. Acta 350 (2003) 252.
[18] F.A. Allen, Acta Crystallog. B 58 (2002) 380.
[19] G.R. Clark, G.J. Palenik, Inorg. Chem. 9 (1970) 12.
[20] A.M.M. Meij, S. Otto, A. Roodt, Acta Crystallogr., Sect. C: Cryst. Struct. Commun. C59 (2003) m352.
[21] G.M. Sheldrick, SHELXS-97, Program for Crystal Structure Determination, University of Göttingen, Germany, 1997.
[22] G.M. Sheldrick, SHELXL-97, Program for Crystal Structure Refinement, University of Göttingen, Germany, 1997.

Polyhedron 28 (2009) 2171–2178

Contents lists available at ScienceDirect

Polyhedron

journal homepage: www.elsevier.com/locate/poly

Synthesis, electrochemical, *in situ* spectroelectrochemical and *in situ* electrocolorimetric characterization of new phthalocyanines peripherally fused to four flexible crown ether moieties

Zekeriya Bıyıklıoğlu [a], Atıf Koca [b], Halit Kantekin [a,*]

[a] Department of Chemistry, Faculty of Arts and Sciences, Karadeniz Technical University, 61080 Trabzon, Turkey
[b] Department of Chemical Engineering, Faculty of Engineering, Marmara University, Göztepe 34722, İstanbul, Turkey

ARTICLE INFO

Article history:
Received 12 March 2009
Accepted 12 April 2009
Available online 6 May 2009

Keywords:
Crown ether
Metallophthalocyanine
Synthesis
Cyclic voltammetry
Spectroelectrochemistry
Chromaticity diagram

ABSTRACT

Novel Ni(II), Zn(II), Co(II) and Cu(II) phthalocyanines with four peripheral 4-[methyleneoxy(18-crown-6)] groups have been synthesized via the cyclic tetramerization of 4-[{(18-crown-6)-yl}methyleneoxy]phthalonitrile and the corresponding metal salts ($NiCl_2$, $Zn(CH_3COO)_2$, $CoCl_2$ and $CuCl_2$). The thermal stabilities of the metal-free and metallophthalocyanine compounds were determined by thermogravimetric analysis. The structures of the target compounds were confirmed using elemental analysis, IR, ^{1}H-NMR, ^{13}C-NMR, UV–Vis and MS spectral data. Voltammetric and *in situ* spectroelectrochemical measurements show that while the cobalt phthalocyanine complex gives both metal-based and ring-based redox processes, the metal-free, nickel, zinc and copper phthalocyanines show only ring-based reduction and oxidation processes. An *in situ* electrocolorimetric method has been applied to investigate the color of the electro-generated anionic and cationic forms of the complexes.

© 2009 Elsevier Ltd. All rights reserved.

1. Introduction

The synthesis of metal-free and metallophthalocyanines has been an area of intense research activity for over 50 years [1–3]. In recent years, much effort has been dedicated to the synthesis and characterization of novel phthalocyanine derivatives having interesting electrical, optical, gas sensing and catalytic properties by making slight differences in peripheral substitution [4–7]. Remarkable progress has been made in the past decade in the use of phthalocyanine derivatives as sensitizers for photodynamic therapy of cancer [8–11]. The range of solubility of the phthalocyanines becomes very important for these applications, since many phthalocyanines are poorly soluble in organic solvents. The solubility of Pcs can be enhanced by adding different kinds of substituents, such as long chain alkyl, alkylthio or alkoxy groups at the periphery positions of the phthalocyanine ring [12–15].

Attachment of crown ether groups to the phthalocyanine ring significantly increases the solubility of phthalocyanines in many organic solvents, leading to significant advances in research such as biological modelling, homogeneous catalysis, alkaline or earth alkaline and lanthanide metal extractions [16,17].

Microwaves have been used previously for the synthesis of phthalocyanines and there is a wide range of references on the topic [18–23]. In this paper, we describe the synthesis and characterization of metal-free **4** and metallophthalocyanines **5**, **6**, **7** and **8**, containing four flexible 18-crown-6(1,4,7,10,13,16-hexaoxacyclooctadecane) moieties on the periphery through methyleneoxy bridges, by microwave irradiation. Also, we have investigated the voltammetric, *in situ* spectroelectrochemical and *in situ* electrocolorimetric responses of the metallophthalocyanines in solution to open a way to their possible electrochromic application, depending on the spectroelectrochemical and chromaticity data. It is well known that many phthalocyanine complexes show excellent electrochromic properties [24–26] both in solution and as films. Therefore, we report here the *in situ* electrocolorimetric analysis of the phthalocyanines to determine the possible electrochromic application of the complexes, because the electrocolorimetry technique provides a more precise way to define colour of the electro-generated species [27].

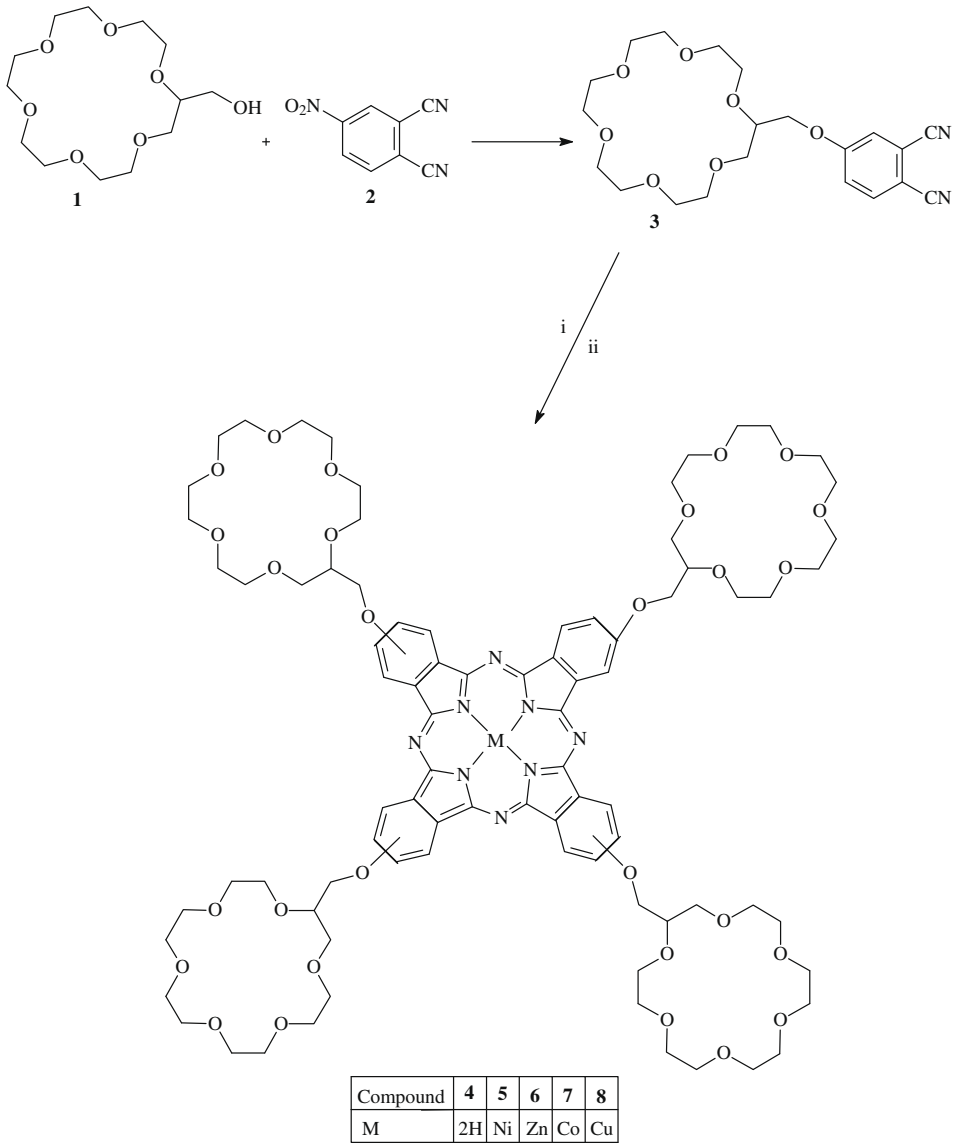
2. Results and discussion

2.1. Synthesis and characterizations

The synthesis of the new metal-free and metallophthalocyanines is shown in Scheme 1. The first step in the synthetic procedure was to obtain 4-[{(18-crown-6)yl}methyleneoxy] phthalonitrile (**3**). This reaction involves the nucleophilic aromatic nitro displacement of 4-nitrophthalonitrile with 2-hydroxymethyl(18-crown-6) (**1**) in the presence of K_2CO_3 as the base in dry dimethylformamide (DMF) at 50 °C [28]. Conversion of

* Corresponding author. Tel.: +90 462 377 2589; fax: +90 462 325 3196.
E-mail address: halit@ktu.edu.tr (H. Kantekin).

0277-5387/$ - see front matter © 2009 Elsevier Ltd. All rights reserved.
doi:10.1016/j.poly.2009.04.036



Compound	4	5	6	7	8
M	2H	Ni	Zn	Co	Cu

Scheme 1. The synthesis of the metal-free phthalocyanine and metallophthalocyanines. (i) *n*-Pentanol, DBU. (ii) MW, 175 °C, 350 W and metal salts.

4-[{(18-crown-6)yl}methyleneoxy]phthalonitrile (**3**) into the metal-free phthalocyanine (**4**) was accomplished in *n*-pentanol in the presence of a few drops of 1,8-diazabicyclo[5.4.0]undec-7-ene (DBU) as a strong base at reflux temperature under argon atmosphere. Cyclotetramerization of the dinitrile compound **3** in the presence of anhydrous metal salts [$NiCl_2$, $Zn(CH_3COO)_2$, $CoCl_2$ and $CuCl_2$] gave the desired metallophthalocyanines, **5**–**8** in 2-(dimethylamino)ethanol by microwave irradiation. Characterization of the products involved a combination of methods including FT-IR, ^{1}H NMR, elemental analysis, UV–Vis spectroscopy and mass spectroscopy.

In the IR spectra, the formation of compound **3** was clearly confirmed by the disappearance of the OH and NO_2 bands at 3338 and 1538–1355 cm^{-1} and the appearance of the C≡N band at 2229 cm^{-1}. In the ^{1}H NMR spectrum of **3**, the OH group of compound **1** disappeared, as expected. The ^{1}H NMR spectrum of **3** showed new signals at δ = 7.65 (d, 1H, Ar–H), 7.31 (s, 1H, Ar–H), 7.18 (d, 1H, Ar–H), belonging to aromatic protons. The ^{13}C NMR spectrum of **3** indicated the presence of nitrile carbon atoms in **3** at δ = 115.76 and 115.33 ppm. The mass spectrum of compound **3**, which shows a peak at m/z = 459 [M+K], supports the proposed formula for this compound.

After conversion of the dinitrile **3** to phthalocyanines **4**–**8**, the sharp C≡N vibration around 2229 cm^{-1} disappeared in the FT-IR spectra. The NH stretching absorption of the inner core of the metal-free phthalocyanine **4** was observed at 3285 cm^{-1}. The ^{1}H NMR spectrum of compound **4** indicates aromatic protons at δ 7.64, 7.27 and 7.17 ppm, and the aliphatic ether protons at δ 4.07–3.59 ppm. The NH protons of **4** could not be observed owing to the probable strong aggregation of the molecules [29]. The mass spectrum of **4** displayed the $[M]^+$ parent ion peak at m/z = 1683, which confirms the same structure. The IR spectra of metallophthalocyanines **5**–**8** are very similar. The ^{1}H-NMR spectra of complexes **5**–**6** showed almost identical chemical shifts. ^{1}H-NMR measurement of the cobalt(II) and copper(II) phthalocyanine **7**, **8** were precluded owing to their paramagnetic nature. In the mass spectra of the Ni, Zn, Co and Cu phthalocyanines, the presence of molecular ion peaks at m/z = 1741 $[M+H]^+$, 1786 $[M+K]^+$, 1740 $[M]^+$ and 1745 $[M]^+$, respectively, confirmed the proposed structures.

The thermal behaviour of the metal-free and metallophthalocyanines were investigated by thermogravimetric analysis/differential thermal analysis (TG/DTA). Although the thermal stabilities of phthalocyanines is well known, the phthalocyanine compounds are not stable above 340 °C. The initial decomposition temperature

Table 1
Thermal properties of the phthalocyanines.

Compound	M	Initial decom. temp. (°C)	Main decom. temp. (°C)
4	2H	379	409
5	Ni	376	399
6	Zn	388	419
7	Co	340	364
8	Cu	359	373

decreased in the order: **6** > **4** > **5** > **8** > **7** (Table 1). The DTA curves exhibited exothermic changes for all the phthalocyanines (**4**–**8**) in the region investigated [30].

The metal-free and metallophthalocyanines display typical electronic spectra with two strong absorption regions, one of them in the UV region at about 300–350 nm (B-band) and the other one in the visible region at 600–700 nm (Q-band) [31]. The electronic absorption spectra of the metal-free phthalocyanine (**4**), nickel(II) phthalocyanine (**5**), zinc(II) phthalocyanine (**6**) in chloroform at room temperature are shown in Fig. 1. In the UV–Vis spectrum of the metal-free derivative **4** (in $CHCl_3$) split Q-bands appeared at 707, 674 and 647 nm, while the B-bands remained at 365 and 300 nm. The UV–Vis spectra of the metallophthalocyanines **5**–**8** (in $CHCl_3$) exhibited an intense single Q-band absorption for $\pi \rightarrow \pi^*$ transitions around 677–692 nm and B-bands in the UV region around 293–383 nm [32,33].

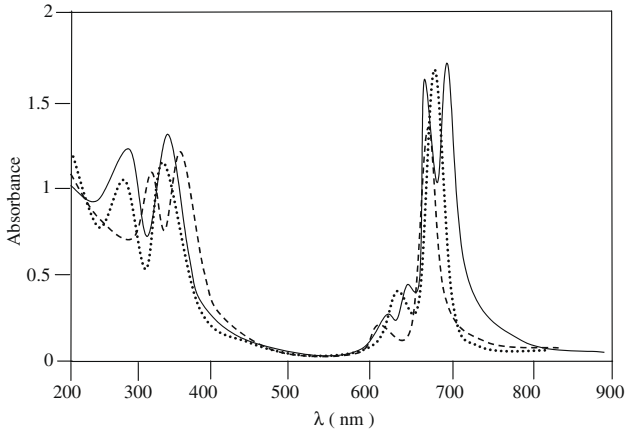


Fig. 1. UV–Vis spectra of compounds **4** (**––**), **5** (—) and **6** (···) in chloroform.

2.2. Electrochemical measurements

The solution redox properties of the complexes (**4**–**8**) were studied using cyclic voltammetry (CV) and square wave voltammetry (SWV) measurements in dichloromethane (DCM), containing 0.10 mol dm^{-3} tetrabutylammonium perchlorate (TBAP) on a Pt electrode. Table 2 lists the assignments of the redox couples, half-wave peak potentials ($E_{1/2}$) and the difference between the first oxidation and reduction processes ($\Delta E_{1/2}$). $\Delta E_{1/2}$ reflects the HOMO–LUMO gap for metal free Pcs and it is related to the HOMO–LUMO gap in MPc species. The $E_{1/2}$ values are shifted to more negative potentials when compared with the reported data for redox processes in other metallophthalocyanine complexes [31,34–42].

H_2Pc (**4**), NiPc (**5**), ZnPc (**6**) and CuPc (**8**) give very similar voltammetric responses with small potential shifts due to the different metal centers. Based on the well-known electrochemical behavior of phthalocyanine complexes, all the couples of these complexes are assigned to the phthalocyanine ring. The nature of the redox couples was also confirmed below using spectroelectrochemistry measurements. Figs. 2 and 3 illustrate the CVs of **5** and **6** as representative for MPcs having redox inactive metal centers. Both complexes give three reduction and two oxidation couples within the potential window of the DCM/TBAP electrolyte system. All complexes show an aggregation tendency in solution, so the redox couples are split into two waves due to electron transfer of aggregated and monomeric species. Diluting solutions of the complexes causes peak current of the waves assigned to the aggregated species to decrease more than that of the monomeric species, supporting existence of the aggregation-disaggregation equilibrium.

Table 2
Voltammetric data of the complexes with the related metallophthalocyanines for comparison.

Complex		Ring oxidations		M^{III}/M^{II}	M^{II}/M^{I}	Ring reductions			[b]$\Delta E_{1/2}$	Ref.
4 (H_2Pc)	[a]$E_{1/2}$ vs. SCE		0.86			−0.72	−1.09	−1.42	1.58	tw
5 (NiPc)	[a]$E_{1/2}$ vs. SCE	[c]1.51	0.89(0.64)			−0.86	−1.25	−1.65[c]	1.50	tw
6 (ZnPc)	[a]$E_{1/2}$ vs. SCE	1.36	0.65			−1.14(−0.98)	−1.42(−1.31)	−1.63	1.63	tw
7 (CoPc)	[a]$E_{1/2}$ vs. SCE		0.83(0.61)		−0.28	−1.46			0.89	tw
8 (CuPc)	[a]$E_{1/2}$ vs. SCE		0.77			−0.98(−0.83)	−1.67(−1.40)		1.60	tw
[e]CuPc	$E_{1/2}$ (in DCM)		0.82			−0.86	−1.25		1.68	[50]
[f]ZnPc	$E_{1/2}$ (in DCM)		0.78			−0.83	−1.24	−1.55	1.61	[51]
[g]CoPc	$E_{1/2}$ (in DMSO)			0.45	−0.37	−0.28			0.82	[42]
[h]CoPc	$E_{1/2}$ (in DMSO)		0.99	0.49	−0.36	−1.27		−1.83	0.85	[52]
[i]ZnPc	$E_{1/2}$ (in DCM)					−0.78		−1.01		[48]
[j]ZnPc	$E_{1/2}$ (in DCM)		0.85			−0.75		−1.16	1.60	[40]
[j]CoPc	[d]$E_{1/2}$ (in DCM)			0.45	−0.42	−1.30			0.87	[40]
[k]CuPc	$E_{1/2}$ (in DCM)					−0.86	−1.26			[49]

tw: This work.
[a] $E_{1/2} = (E_{pa} + E_{pc})/2$ at 0.100 V s^{-1} for reversible processes and E_{pa} or E_{pc} for irreversible processes ($E_{1/2}$ values of the aggregated species are given in parentheses).
[b] $\Delta E_{1/2} = \Delta E_{1/2}$ (first oxidation) − $\Delta E_{1/2}$ (first reduction) = HOMO–LUMO gap for metallophthalocyanines having an electro-inactive metal center (metal-to-ligand (MLCT) or ligand to metal (LMCT) charge transfer transition gap for MPc having a redox active metal center).
[c] The process is recorded with SWV.
[d] Potential vs. Fc/Fc^+.
[e] Substituted with 2-nitro-9,16,23-tri{[(benzo-15-crown-5)-4′-yl]oxy} moieties.
[f] Substituted with tetra {[(benzo-15-crown-5)-4′-yl]oxy} moieties.
[g] Substituted with tetrakis-[4-nitro-2-(octyloxy)phenoxy] moieties.
[h] Substituted with tetrakis-6-(-thiophene-2-carboxylate)-hexylthio moieties.
[i] Substituted with tetrakis-octafluoro pentoxy moieties.
[j] Substituted with tetrapentafluorobenzyloxy moieties.
[k] Substituted with tetrabutyl moieties.

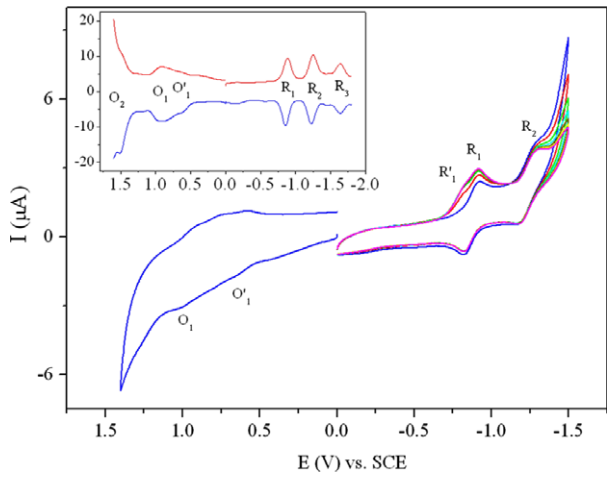


Fig. 2. Repetetive CVs of **5** recorded at 0.100 mV s^{-1} scan rate on Pt in DCM/TBAP (inset: SWVs of **5**. SWV parameters: pulse size = 100 mV; frequency:25 Hz).

Redox couples and splitting of them are illustrated by SWV scans. Switching potentials do not affect the peak character of the complex considerably. However, repetitive CV cycles affect the aggregation–disaggregation equilibriums of the complexes. In case of **6**, second split wave of the first reduction process (R′1) increases in current with repetitive CV cycles, indicating monomerization of the aggregated species under potential cycling. However, aggregation of **5** increases with repetitive CV cycles, since R′1 increases with continuous CV cycles. Aggregations of the complexes are also observed with the UV–Vis spectra during *in situ* spectroelectrochemical measurements, even at much diluted solutions, as given below.

Fig. 4 shows the CV and SWV of CoPc (**7**). Within the electrochemical window of TBAP/DCM in the CV measurements, **7** undergoes one oxidation and three reduction processes. CV and SWV analysis show that **7** also has an aggregation-disaggregation equilibria in solution, thus the redox couples split into two waves due to electron transfer of the aggregated and monomeric species. Assignments of the redox couple are confirmed by spectroelectrochemical measurements, which are given below.

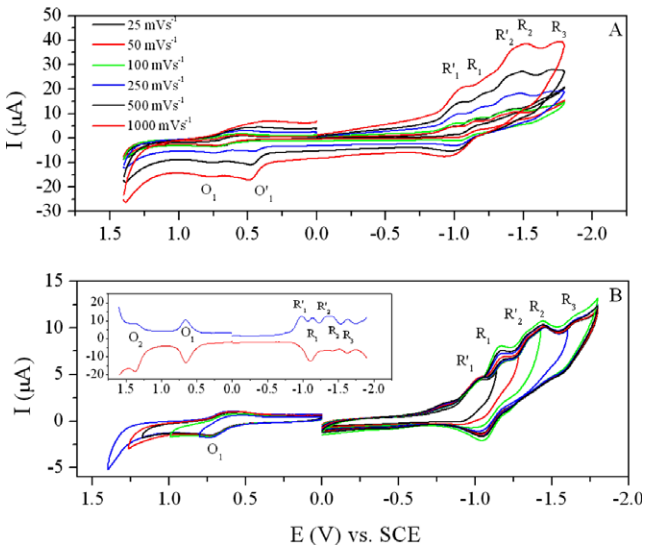


Fig. 3. (A) CVs of **6** recorded at different scan rates on Pt in DCM/TBAP. (B) CVs of **6** recorded with different switching potentials at 0.100 mV s^{-1} scan rate (inset: SWVs of **6**. SWV parameters: pulse size = 100 mV; frequency:25 Hz).

2.3. Spectroelectrochemical studies

Spectroelectrochemical studies were employed to confirm the assignments in the CVs of the complexes. The complexes **4**–**6** and **8** all have redox inactive metal centers, therefore, the *in situ* UV–Vis spectral changes indicated ligand-based characters of all the redox couples of **4**–**6** and **8**. The UV–Vis spectral chances of NiPc (**5**) are given in Fig. 5 as a representative of a MPc having a redox inactive metal center. During controlled potential reductions of **5** at −1.00 V potential application, intensity of the Q-band at 672 nm decreases without shift, while two new bands at 580 and 936 nm (charge transfer region) are recorded. At the same time, the B2-band at 374 nm increases in intensity. Observation of a band at 630 nm before and after this process indicates the presence of the aggregated species. This process gives clear isosbestic points at 335, 387, 610 and 728 nm in the spectra. These spectroscopic changes are characteristic of Pc ring reduction and confirm the CV assignment of the couple to the $[Ni^{II}Pc^{-2}]/[Ni^{II}Pc^{-3}]^{-1}$ process (Fig. 5A) [43–45]. Spectroscopic changes during controlled potential application at −1.50 V support further reduction of the monoanionic species, $[Ni^{II}Pc^{-3}]^{-1}$, to $[Ni^{II}Pc^{-4}]^{-2}$ (Fig. 5B). Decrease of the Q-band intensity without shift and observation of new bands in the charge transfer region at 490, 793 and 877 nm are characteristic of a ring reduction process. During oxidation of **5** (Fig. 5C), absorption of the Q-band decreases in intensity without shift, while new bands between 450 and 550 nm and at 748 nm appear with an increase in intensity. Clear isosbestic points were recorded at 375, 588 and 708 nm in the spectra. These changes are typical of ring-based oxidation and are assigned to the $[Ni^{II}Pc^{-2}]/[Ni^{II}Pc^{-1}]^{+1}$ processes [43–45].

The color change of the complexes during the redox processes were recorded using *in situ* colorimetric measurements. Fig. 5D gives the chromaticity diagrams of the complex **5** recorded simultaneously during the spectroelectrochemical measurements. Without any potential application, the solution of **5** is greenish blue ($x = 0.277$ and $y = 0.336$). As the potential is stepped from 0 to −1.00 V, color of the neutral **5**, $[Ni^{II}Pc^{-2}]$, starts to change and light blue color ($x = 0.268$ and $y = 0.298$) of the monoanionic form of **5**, $[Ni^{II}Pc^{-3}]^{-1}$, was obtained at the end of the first reduction. Similarly color of the dianionic species, $[Ni^{II}Pc^{-4}]^{-2}$, was recorded as light purple ($x = 0.318$ and $y = 0.316$). The monocationic species $[Ni^{II}Pc^{-1}]^{+1}$ has a reddish blue color ($x = 0.343$ and $y = 0.350$). Measurement of the *xyz* coordinates allows quantification of each color of the redox species, which is very important to decide their possible electrochromic application.

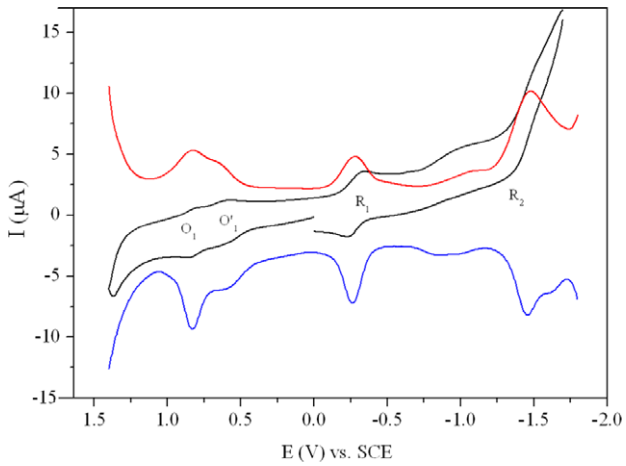


Fig. 4. CVs of **7** recorded at 0.100 mV s^{-1} scan rate on Pt in DCM/TBAP (inset: SWVs of **7**. SWV parameters: pulse size = 100 mV; frequency:25 Hz).

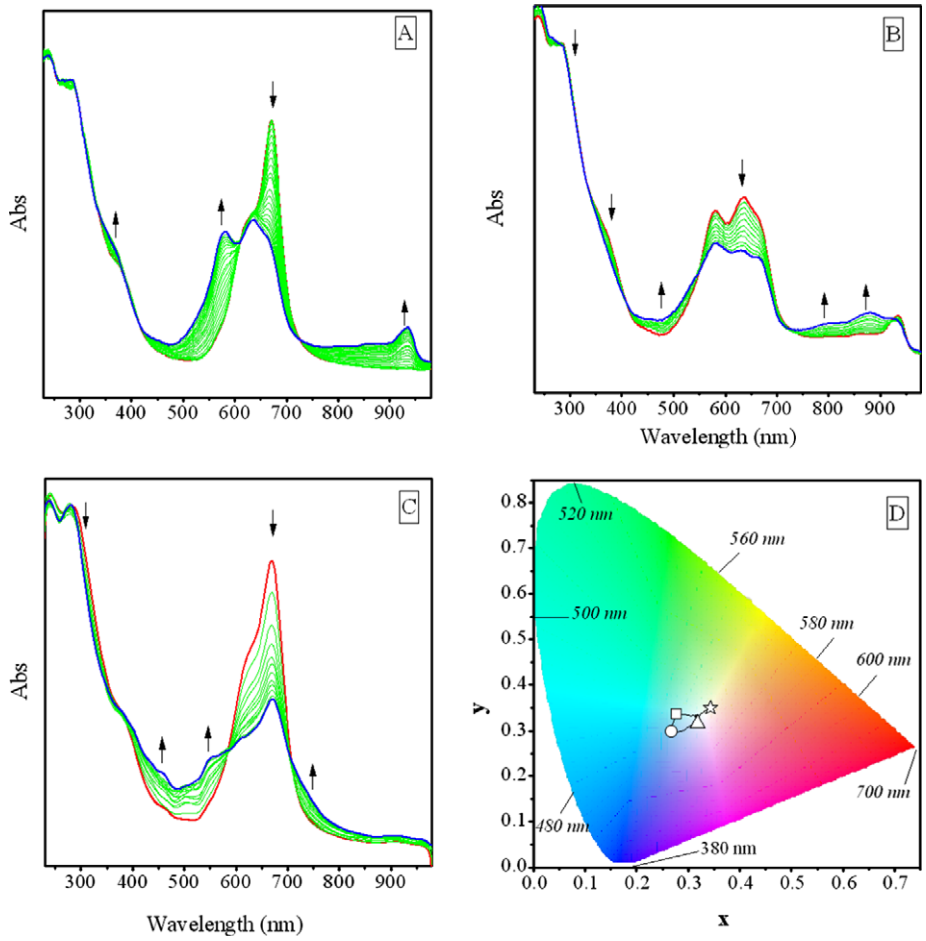


Fig. 5. *In situ* UV–Vis spectral changes of **5**. (A) E_{app} = −0.70 V. (B) E_{app} = −1.50 V. (C) E_{app} = 1.10 V. (D) Chromaticity diagram of **5** (each symbol represents the color of electrogenerated species; □ : neutral **5**, $Ni^{II}Pc^{-2}$, ○ : $Ni^{II}Pc^{-3}$, △: $Ni^{II}Pc^{-4}$, ☆ : $Ni^{II}Pc^{-}$).

Fig. 6 represents the *in situ* UV–Vis spectral changes and *in situ* recorded chromaticity diagram of CoPc (**7**) in DCM/TBAP during potential application at potentials of the redox processes. Shifting of the Q-band from 675 to 706 nm and observation of a new band at 450 nm indicate metal center reduction of **7** at −0.55 V potential application (Fig. 6A). At the same time, the B-band shifts from 297 to 307 nm with an increase in intensity. This process resulted in clear isosbestic points at 325, 388, 564 and 690 nm in the spectra. A color change from greenish blue (x = 0.254 and y = 0.340) to yellow (x = 0.382 and y = 0.433) was recorded, as shown in the chromaticity diagram (Fig. 6D). These spectroscopic data confirm our earlier assignment of the first reduction couple to $[Co^{II}Pc^{-2}]/[Co^{I}Pc^{-2}]^{1-}$. Further reduction of $[Co^{I}Pc^{-2}]^{1-}$ at −1.20 V indicates a ligand-based redox process, because the Q-band at 706 nm decreases without shift while a new broad band is recorded at 540 nm. At the same time, the B-band decreases in intensity while the band at 450 nm decreases slightly in intensity with red shifting (Fig. 6B). Clear isosbestic points were observed at 345, 400, 613 and 764 nm in the spectra. A color change from yellow to orange (x = 0.397 and y = 0.373) was recorded (Fig. 6D). These changes confirm our earlier assignment of a second reduction couple to $[Co^{I}Pc^{-2}]^{1-}/[Co^{I}Pc^{-3}]^{2-}$. Fig. 5C represents the spectral changes during the oxidation process of the complex. During 0.95 V potential application, a decrease of the Q-band at 675 nm without shift and observation of new bands at 528 and 760 nm indicate a ligand-based process and it is assigned to $[Co^{II}Pc^{-2}]/[Co^{II}Pc^{-1}]^{1+}$ [46–50]. A greenish blue color changes to light red (x = 0 .355 and y = 0.343) occurs during the oxidation process.

3. Experimental

2-Hydroxymethyl(18-crown-6) (**1**) and 4-nitrophthalonitrile (**2**) were prepared according to the reported procedures [51,52]. All reagents and solvents were of reagent grade quality and were obtained from commercial suppliers. All solvents were dried and purified as described by Perrin et al. [53]. The IR spectra were recorded on a Perkin–Elmer 1600 FT-IR Spectrophotometer, using KBr pellets or NaCl discs. ^{1}H and ^{13}C NMR spectra were recorded on a Varian Mercury 200 MHz spectrometer in $CDCl_3$, chemical shifts were reported (δ) relative to Me_4Si as an internal standard. Mass spectra were measured on a Micromass Quatro LC/ULTIMA LC-MS/MS spectrometer. The elemental analyses were performed on a Costech ECS 4010 instrument. A Seiko II Exstar 6000 thermal analyzer was used to record the DTA curves under a nitrogen atmosphere with a heating rate of 20 °C min^{-1} in the temperature range 30–900 °C using platinum crucibles. Melting points were measured on an electrothermal apparatus and are uncorrected. Optical spectra in the UV–Vis region were recorded with a Unicam UV2-100 spectrophotometer, using 1 cm pathlength cuvettes at room temperature.

3.1. Synthesis of 4-[{(18-crown-6)-yl)methyleneoxy]phthalonitrile (3)

2-Hydroxymethyl-18-crown-6 (**1**) (2.5 g, 8.49 mmol) was dissolved in anhydrous DMF (25 ml) under N_2 atmosphere, and 4-nitrophthalonitrile (**2**) (1.46 g, 8.49 mmol) was added to the solution. After stirring for 10 min, finely ground anhydrous K_2CO_3

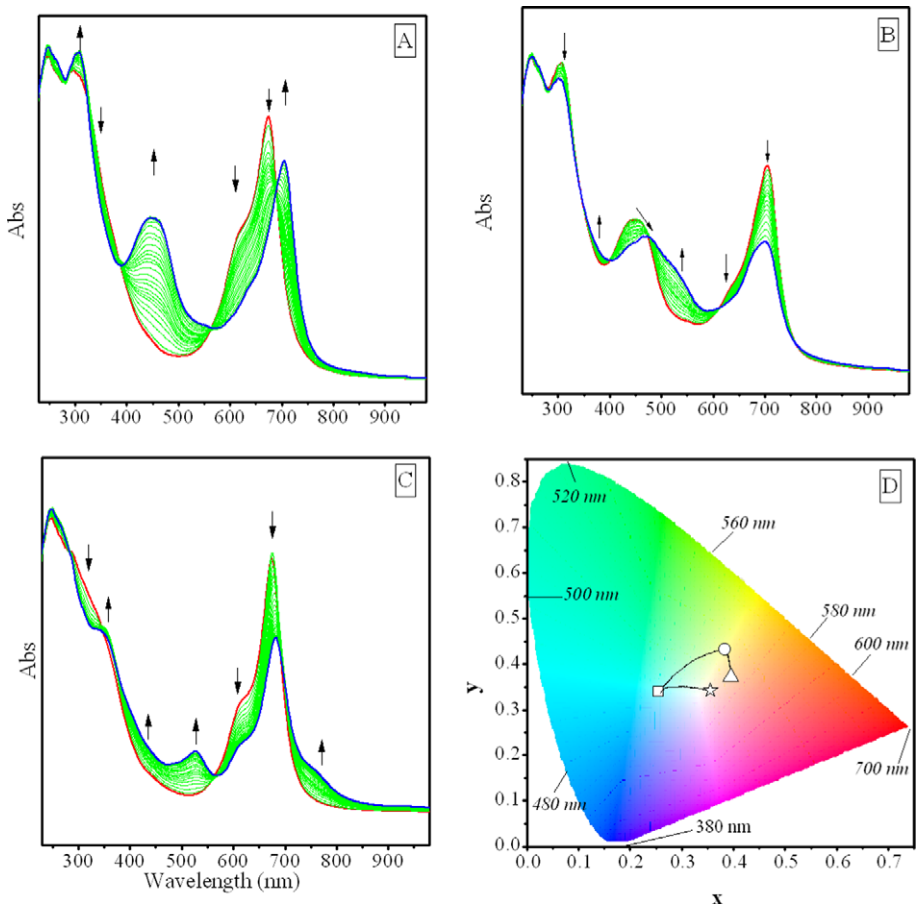


Fig. 6. *In situ* UV–Vis spectral changes of **7**. (A) E_{app} = −0.70 V. (B) E_{app} = −1.25 V. (C) E_{app} = 1.10 V. (D) Chromaticity diagram of **7** (each symbol represents the color of electrogenerated species; □ : neutral **7**, $Co^{II}Pc^{-2}$, ○ : $Co^{I}Pc^{-2}$, △ $Co^{I}Pc^{-3}$, ☆ : $Co^{II}Pc^{-}$).

(3.51 g, 25.47 mmol) was added portion-wise over 2 h, with efficient stirring. The reaction mixture was stirred under N_2 at 50 °C for 3 days. Then the solution was poured into ice-water (100 ml) and the aqueous phase was extracted with chloroform (3× 40 ml). The combined extracts were dried over anhydrous sodium sulfate. Purification of the product was accomplished by column chromatography with silica gel (eluent chloroform). 1.50 g (42%). *Anal.* Calc. for $C_{21}H_{28}N_2O_7$: C, 59.99; H, 6.71; N, 6.66. Found: C, 59.93; H, 6.74; N, 6.62%. IR (KBr tablet), ν_{max}/cm^{-1}: 3071 (Ar–H), 2923–2851 (Aliph. C–H), 2229 (C≡N), 1597, 1562, 1491, 1464, 1350, 1320, 1254, 1115, 1028, 951, 840, 525. ^{1}H NMR. ($CDCl_3$), (δ: ppm): 7.65 (d, 1H, Ar–H), 7.31 (s, 1H, Ar–H), 7.18 (d, 1H, Ar–H), 4.21 (d, 2H, CH–CH_2–O), 3.94–3.56 (m, 23H, CH_2–O). ^{13}C NMR. ($CDCl_3$), (δ: ppm): 162.11, 135.10, 119.86, 119.75, 117.21, 115.76, 115.33, 107.09, 76.41, 71.20, 70.86, 70.67, 70.49, 70.08, 69.79, 69.23. MS (ES^+), (m/z): 459 $[M+K]^+$.

3.2. Metal-free phthalocyanine (**4**)

A mixture of 4-[{(18-crown-6)-yl}methyleneoxy]phthalonitrile (**3**) (0.25 g, 0.59 mmol) and 0.59 mmol of 1.8-diazabicyclo[5.4.0]undec-7-ene (DBU) (0.4 ml) in 2.5 ml of dry n-pentanol was heated and stirred at 160 °C for 24 h under N_2. After the reaction mixture was cooled and decanted, the remaining dark green solid was dissolved in ethanol (20 ml) and precipitated by adding diethyl ether. The precipitated green solid product was filtered off, and then dried. The obtained green solid product was purified by aluminium oxide column chromatography, using only chloroform as the solvent system. Yield: 97 mg (39%). *Anal.* Calc. for $C_{84}H_{114}N_8O_{28}$: C, 59.93; H, 6.82; N, 6.65. Found: C, 59.98; H, 6.84; N, 6.69%. IR (KBr tablet) ν_{max}/cm^{-1}: 3285 (N–H), 3065 (Ar–H), 2924–2862 (Aliph. C–H), 1643, 1602, 1520, 1487, 1352, 1287, 1242, 1110, 835, 749. ^{1}H NMR. ($CDCl_3$), (δ: ppm): 7.64 (d, 4H, Ar–H), 7.27 (s, 4H, Ar–H), 7.17 (m, 4H, Ar–H), 4.07-3.59 (m, 100H, CH_2–O). UV–Vis (chloroform): λ_{max}/nm: [(10^{-5} ε dm^3 mol^{-1} cm^{-1})]: 300 (5.08), 365 (5.12), 614 (4.51), 647 (4.65), 674 (5.20), 707 (5.23). MS (ES^+), (m/z): 1683 $[M]^+$.

3.3. Nickel(II) phthalocyanine (**5**)

A mixture of 4-[{(18-crown-6)-yl}methyleneoxy]phthalonitrile (**3**) (0.25 g, 0.59 mmol), anhydrous $NiCl_2$ (19 mg, 0.15 mmol) and 2-(dimethylamino)ethanol (2.5 ml) was irradiated in a microwave oven at 175 °C, 350 W for 8 min. After cooling to room temperature the reaction mixture refluxed with ethanol to precipitate the product, which was filtered off. The green solid product was washed with hot ethanol, water, diethyl ether and dried *in vacuo*. The obtained green solid product was purified by aluminium oxide column chromatography, using only chloroform:methanol (100:2) as the solvent system. Yield: 123 mg (48%). *Anal.* Calc. for $C_{84}H_{112}N_8O_{28}Ni$: C, 57.97; H, 6.49; N, 6.44. Found: C, 57.61; H, 6.89; N, 7.01%. IR (KBr tablet) ν_{max}/cm^{-1}: 3060 (Ar–H), 2901-2875 (Aliph. C–H), 1610, 1468, 1351, 1284, 1246, 1103, 954, 834, 745. ^{1}H NMR. ($CDCl_3$), (δ:ppm): 7.70 (m, 4H, Ar–H), 7.28 (s, 4H, Ar–H), 7.21 (m, 4H, Ar–H), 4.15–3.66 (m, 100H, CH_2–O). UV–Vis (chloroform): λ_{max}/nm: [(10^{-5} ε dm^3 mol^{-1} cm^{-1})]: 332 (5.42), 383 (5.07), 608 (4.47), 677 (5.12). MS (ES^+), (m/z): 1741 $[M+H]^+$.

3.4. Zinc(II) phthalocyanine (**6**)

The same procedure as above was adopted by using compound **3** (0.25 g, 0.59 mmol), anhydrous $Zn(CH_3COO)_2$ (27 mg, 0.15 mmol) and 2-(dimethylamino)ethanol (2.5 ml). The obtained green solid product was purified by aluminium oxide column chromatography, using only chloroform:methanol (100:2) as the solvent system. Yield: 139 mg (54%). *Anal.* Calc. for $C_{84}H_{112}N_8O_{28}Zn$: C, 57.74; H, 6.46; N, 6.41. Found: C, 57.60; H, 6.71; N, 6.50%. IR (KBr tablet) ν_{max}/cm^{-1}: 3065 (Ar–H), 2910–2880 (Aliph. C–H), 1605, 1488, 1394, 1351, 1287, 1247, 1104, 956, 834, 748. ^1H NMR. ($CDCl_3$), (δ: ppm): ^1H NMR. ($CDCl_3$), (δ: ppm): 7.54 (d, 4H, Ar–H), 7.14 (s, 4H, Ar–H), 6.98 (m, 4H, Ar–H), 4.01–3.45 (m, 100H, CH_2–O). UV–Vis (chloroform): λ_{max}/nm: [(10^{-5} ε dm^3 mol^{-1} cm^{-1})]: 293 (5.06), 356 (5.07), 620 (4.62), 686 (5.21). MS (ES^+), (m/z): 1786 $[M+K]^+$.

3.5. Cobalt(II) phthalocyanine (**7**)

The same procedure as above was adopted by using compound **3** (0.25 g, 0.59 mmol), anhydrous $CoCl_2$ (19 mg, 0.15 mmol) and 2-(dimethylamino)ethanol (2.5 ml). The obtained green solid product was purified by aluminium oxide column chromatography, using only chloroform:methanol (100:2) as the solvent system. Yield: 159 mg (61%). *Anal.* Calc. for $C_{84}H_{112}N_8O_{28}Co$: C, 57.96; H, 6.49; N, 6.44. Found: C, 57.74; H, 6.79; N, 6.56%. IR (KBr tablet) ν_{max}/cm^{-1}: 3021 (Ar–H), 2905–2868 (Aliph. C–H), 1608, 1470, 1351, 1286, 1246, 1102, 956, 833, 752. UV–Vis (chloroform): λ_{max}/nm: [(10^{-5} ε dm^3 mol^{-1} cm^{-1})]: 347 (5.11), 368 (5.13), 617 (4.71), 692 (5.19). MS (ES^+), (m/z): 1740 $[M]^+$.

3.6. Copper(II) phthalocyanine (**8**)

The same procedure as above was adopted by using compound **3** (0.25 g, 0.59 mmol), anhydrous $CuCl_2$ (15 mg, 0.15 mmol) and 2-(dimethylamino)ethanol (2.5 ml). The obtained green solid product was purified by aluminium oxide column chromatography, using only chloroform:methanol (100:2) as the solvent system. Yield: 143 mg (55%). *Anal.* Calc. for $C_{84}H_{112}N_8O_{28}Cu$: C, 57.80; H, 6.47; N, 6.42. Found: C, 57.98; H, 6.83; N, 6.60%. IR (KBr tablet) ν_{max}/cm^{-1}: 3010 (Ar–H), 2900–2873 (Aliph. C–H), 1598, 1486, 1454, 1351, 1288, 1189, 1104, 955, 833. UV–Vis (chloroform): λ_{max}/nm: [(10^{-5} ε dm^3 mol^{-1} cm^{-1})]: 322 (5.03), 360 (5.05), 620 (4.62), 689 (5.08). MS (ES^+), (m/z): 1745 $[M]^+$.

3.7. Electrochemical, in situ spectroelectrochemical and in situ electrocolorimetric measurements

The electrochemical and spectroelectrochemical measurements were carried out with a Gamry Reference 600 potentiostat/galvanostat controlled by an external PC and utilizing a three-electrode configuration at 25 °C. For CV and SWV measurements, the working electrode was a Pt disc with a surface area of 0.071 cm^2. The surface of the working electrode was polished with a diamond suspension before each run. A Pt wire served as the counter electrode. A saturated calomel electrode (SCE) was employed as the reference electrode and separated from the bulk of the solution by a double bridge. Ferrocene was used as an internal reference. TBAP in DCM was employed as the supporting electrolyte at a concentration of 0.10 mol dm^{-3}. High purity N_2 was used to remove dissolved O_2 for at least 15 min prior to each run and to maintain a nitrogen blanket during the measurements. IR compensation was applied to the CV and SWV scans to minimize the potential control error.

UV–Vis absorption spectra and chromaticity diagrams were measured by an OceanOptics QE65000 diode array spectrophotometer. *In situ* spectroelectrochemical measurements were carried out by utilizing a three-electrode configuration of a thin-layer quartz spectroelectrochemical cell at 25 °C. The working electrode was Pt tulle. A Pt wire counter electrode separated by a glass bridge and a SCE reference electrode separated from the bulk of the solution by a double bridge were used.

In situ electrocolorimetric measurements, under potentiostatic control, were obtained using an OceanOptics QE65000 diode array spectrophotometer with a color measurement mode by utilizing a three-electrode configuration of a thin-layer quartz spectroelectrochemical cell. The standard illuminant A with 2° observer at constant temperature in a light booth designed to exclude external light was used. Prior to each set of measurements, background color coordinates (x, y and z values) were taken at open-circuit, using the electrolyte solution without MPc under study. During the measurements, readings were taken as a function of time under kinetic control, however only the color coordinates at the beginning and end of each redox processes were reported.

4. Conclusion

In this work, we describe the synthetic procedure and characterization of new soluble metal-free and metallophthalocyanines substituted with four flexible 18-crown-6 ether groups through methyleneoxy bridges. Also, the thermal properties of the phthalocyanines were examined by thermogravimetric analysis. Through the introduction of crown ether groups into peripheral positions of phthalocyanines, the solubility in organic solvents increased. A good solubility of phthalocyanine in organic solvents is becoming more important for technological materials. Voltammetric and spectroelectrochemical studies show that while metal free, zinc, copper and nickel phthalocyanine complexes give ligand-based, redox processes, the cobalt phthalocyanine complex gives both metal and ligand-based redox processes. Definite determination of the colors of the electro-generated anionic and cationic form of the complexes is important to decide any possible electrochromic application of the complexes. Electrochromic applications of the complexes are under investigation.

Acknowledgement

This study was supported by The Scientific & Technological Research Council of Turkey (TÜBİTAK, Project No.: 107T429).

References

[1] F. Moser, A.L. Thomas, The Phthalocyanines, CRC Press, Boca Raton, 1983.
[2] C.C. Leznoff, A.B.P. Lever, Phthalocyanines: Properties and Applications, vols. 1–2, VCH, New York, 1989–1993.
[3] Ö. Bekaroğlu, Appl. Organomet. Chem. 10 (1996) 605.
[4] E. Hamuryudan, Z.A. Bayır, Ö. Bekaroğlu, Dye Pigment 43 (1999) 77.
[5] P. Matlaba, T. Nyokong, Polyhedron 21 (2002) 2463.
[6] N.B. McKeown, Phthalocyanine Materials; Synthesis, Structure and Function; Cambridge University Press: Cambridge, 1998.
[7] S.Y. Yu, O.H. Luo, M.C. Shen, X.Y. Huang, W.H. Yang, Z. Zhang, Inorg. Chim. Acta 223 (1994) 181.
[8] R. Bonnett, Chem. Soc. Rev. 24 (1995) 19.
[9] E.A. Lukyanets, J. Porphy. Phthalocyan. 3 (1999) 424.
[10] M. Sanchez, E. Fache, D. Bonnet, B. Meunier, J. Porphy. Phthalocyan. 5 (2001) 867.
[11] A. Bilgin, B. Ertem, Y. Gök, Supramol. Chem. 17 (2005) 277.
[12] E. Hamuryudan, Ö. Bekaroğlu, J. Chem. Res. (S) 11 (1993) 460.
[13] Z.A. Bayır, E. Hamuryudan, Ö. Bekaroğlu, J. Chem. Res. (S) 12 (1999) 702.
[14] H.Y. Yenilmez, İ. Özçeşmeci, A.İ. Okur, A. Gül, Polyhedron 23 (2004) 787.
[15] M. Selçukoğlu, E. Hamuryudan, Dyes Pigment 74 (2007) 17.
[16] H.Y. An, J.S. Bradshaw, R.M. Izatt, Z.M. Yan, Chem. Rev. 94 (1994) 939.
[17] Y. Gök, S.Z. Yıldız, Polyhedron 16 (1997) 113.
[18] Z. Bıyıklıoğlu, H. Kantekin, M. Özil, J. Organomet. Chem. 692 (2007) 2436.
[19] H. Kantekin, Z. Bıyıklıoğlu, Dyes Pigment 77 (2008) 98.
[20] H. Kantekin, Z. Bıyıklıoğlu, Dyes Pigment 77 (2008) 432.
[21] Z. Bıyıklıoğlu, H. Kantekin, J. Organomet. Chem. 693 (2008) 505.
[22] Z. Bıyıklıoğlu, H. Kantekin, Polyhedron 27 (2008) 1650.
[23] Z. Bıyıklıoğlu, E.T. Güner, S. Topçu, H. Kantekin, Polyhedron 27 (2008) 1707.

[24] R.J. Mortimer, Electrochim. Acta 44 (1999) 2971.
[25] A. Koca, T. Ceyhan, M.K. Erbil, A.R. Özkaya, Ö. Bekaroğlu, Chem. Phys. 340 (2007) 283.
[26] C.C. Leznoff, A.B.P. Lever (Eds.), Phthalocyanines: Properties and Applications, vol. 1–4, VCH, Weinheim, 1996.
[27] Y.A. Udum, A. Durmus, G.E. Gunbas, L. Toppare, Org. Electron. 9 (2008) 501.
[28] İ. Gürol, V. Ahsen, J. Porphy. Phthalocyan. 4 (2000) 621.
[29] H. Kantekin, M. Rakap, Y. Gök, H.Z. Şahinbaş, Dyes Pigment 74 (2007) 21.
[30] A. Bilgin, A. Mendi, U. Yıldız, Polymer 47 (2006) 8462.
[31] M.K. Şener, A. Koca, A. Gül, M.B. Koçak, Polyhedron 26 (2007) 1070.
[32] İ. Gürol, V. Ahsen, Ö. Bekaroğlu, J. Chem. Soc., Dalton Trans. 4 (1994) 497.
[33] G. Gümüş, A. Gül, V. Ahsen, New J. Chem. 21 (1997) 589.
[34] A. Koca, M.K. Şener, M.B. Koçak, A. Gül, Int. J. Hydrogen Energy 31 (2006) 2211.
[35] C.A. Donders, S. Liu, C. Loosli, L. Sanguinet, A. Neels, S. Decurtins, Tetrahedron 62 (2006) 3543.
[36] Ş. Bayar, H.A. Dinçer, E. Gonca, Dyes Pigment 80 (2009) 156.
[37] R. Decréau, M. Chanon, M. Julliard, Inorg. Chim. Acta 293 (1999) 80.
[38] A. Koca, A.R. Özkaya, M. Selçukoğlu, E. Hamuryudan, Electrochim. Acta 52 (2007) 2683.
[39] A.B.P. Lever, E.R. Milaeva, G. Speier, in: C.C. Leznoff, A.B.P. Lever (Eds.), The Redox Chemistry of Metallophthalocyanines in Solution in Phthalocyanines: Properties and Applications, vol. 3, VCH, New York, 1993, pp. 5–27.
[40] D. Kulaç, M. Bulut, A. Altındal, A.R. Özkaya, B. Salih, Ö. Bekaroğlu, Polyhedron 26 (2007) 5432.
[41] A.R. Özkaya, A. Gürek, A. Gül, Ö. Bekaroğlu, Polyhedron 16 (1997) 1877.
[42] A.B.P. Lever, S.R. Pickens, P.C. Minor, S. Licoccia, B.S. Ramaswany, K. Magnell, J. Am. Chem. Soc. 103 (1981) 6800.
[43] M.J. Stilman, in: C.C. Leznoff, A.B.P. Lever (Eds.), Phthalocyanines: Properties and Applications, vol. 3, VCH Publishers, New York, 1993.
[44] J. Obirai, T. Nyokong, Electrochim. Acta 50 (2005) 3296.
[45] K. Hesse, D. Schlettwein, J. Electroanal. Chem. 476 (1999) 148.
[46] A. Koca, M.K. Şener, M.B. Koçak, A. Gül, Transition Met. Chem. 30 (2005) 399.
[47] R.H. Campbell, G.A. Health, G.T. Hefter, R.C.S. McQueen, J. Chem. Soc., Chem. Commun. (1983) 1123.
[48] Y. Arslanoğlu, A. Koca, E. Hamuryudan, Polyhedron 26 (2007) 891.
[49] E. Hamuryudan, Dyes Pigment 68 (2006) 151.
[50] T. Sugimori, S. Horike, M. Handa, K. Kasuga, Inorg. Chim. Acta 278 (1998) 253.
[51] S.J. Jungk, J.A. Moore, R.D. Gandour, J. Org. Chem. 48 (1983) 1116.
[52] G.J. Young, W. Onyebuagu, J. Org. Chem. 55 (1990) 2155.
[53] D.D. Perin, W.L.F. Armarego, D.R. Perin, Purification of Laboratory Chemicals, 2nd ed. Pergamon Press, New York, 1985.

Polyhedron 28 (2009) 2179–2182

Contents lists available at ScienceDirect

Polyhedron

journal homepage: www.elsevier.com/locate/poly

Supramolecular structure of the polymeric Eu(III) complex with pyridine-2,6-dicarboxylic acid

Josef Hamacek [a,*], Soumaila Zebret [a], Gérald Bernardinelli [b,*]

[a] Department of Inorganic, Analytical and Applied Chemistry, University of Geneva, 30 quai E.-Ansermet, CH-1211 Geneva 4, Switzerland
[b] Laboratory of X-ray Crystallography, University of Geneva, 24 Quai E.-Ansermet, 1211 Geneva 4, Switzerland

ARTICLE INFO

Article history:
Received 1 December 2008
Accepted 12 April 2009
Available online 21 April 2009

Keywords:
Europium complex
Dipicolinate
Supramolecular
Polymeric
Crystal structure

ABSTRACT

The europium complex with pyridine-2,6-dicarboxylic acid forms three-dimensional polymers in the solid state. The crystal structure of this assembly shows that europium cation is nine-coordinated and the first coordination sphere contains four water molecules. Mono(dipicolinate) structural units are interconnected by bridging carboxylate oxygens to provide a compact supramolecular structure with a high density.

© 2009 Elsevier Ltd. All rights reserved.

1. Introduction

The Ln(III) complexes with organic ligands containing carboxylic groups are of durable interest for their usually high thermodynamic stability and peculiar magnetic and luminescent properties. Pyridine-2,6-dicarboxylic acid (dipicolinic acid, H_2DPA) is one of suitable polydentate ligands and three dipicolinate are necessary for an efficient Ln(III) coordination (coordination number 9). These $[Ln(DPA)_3]^{3-}$ complexes have been extensively studied by X-ray crystallography at the beginning of the eighties [1]. The crystal structures of tris(dipicolinato)lanthanide complexes reveal the formation of triclinic phases for Ce–Dy and hexagonal, monoclinic, and orthorhombic phases for Ho–Lu [1,2], where discrete mononuclear anionic complexes $[Ln(DPA)_3]^{3-}$ are arranged in columns and interconnected by H-bonds. The solid state structure of tris(dipicolinato)lanthanide complexes was also studied with the intention of preparing mixed lanthanide/transition metal oxides by thermal decomposition [3–5]. These complexes with saturated coordination sphere exhibit interesting luminescent properties [6,7], which can be further tuned by introducing suitable substituents on the pyridine ring [8]. In solution, the stability constants of $[Ln(DPA)_3]^{3-}$ complexes determined by potentiometry reach relatively high values ($\log \beta_{13}$ = 19–22, Ln = La–Lu) [9]. Due to a high symmetry (D_3), tris(dipicolinato)lanthanide complexes were extensively used for development of paramagnetic NMR tools for structural analysis (lanthanide shift reagents) [10–13].

In addition to $[Ln(DPA)_3]^{3-}$ complexes described above, several reports deal with unsaturated Ln(III) complexes containing two dipicolinate anions bound to the same lanthanide cation. Bis(dipicolinato)lanthanide complexes $[Ln(HDPA)(DPA)(H_2O)_2]$ were prepared systematically (Ln = La–Yb) [4,14–16], or as side products (Eu) [5]. These neutral complexes crystallise in monoclinic phases and adopt a polymeric structure, where one $Hdipic^-$ ligand is coordinated only to one metal, while the second DPA^{2-} also participates on the coordination of neighbouring metal ions through bridging carboxylate oxygens.

$Ln_2(DPA)_3$ complexes represent an intermediate structure between bis and mono(dipicolinate) complexes. While the first Ln(III) cation is coordinated by two DPA molecules forming an anionic complex, the second Ln(III) cation is coordinated by only one DPA (cationic complex). Both complexes are interconnected by carboxylate bridges to form 3D microporous coordination polymers [17].

Mono(dipicolinate) complexes $[Ln(DPA)]^+$ were characterised in solution by their stability constants [9] and by NMR [13]. However, to the best of our knowledge, no crystal structure of mono(dipicolinate) lanthanide complexes was reported. Only recently, lanthanide selenite–DPA compounds forming two-dimensional clusters were characterised by crystallography [18]. In this contribution we report on the crystal structure of europium mono(dipicolinate) complex. This unprecedented polymeric structure completes the series of Ln(III) complexes with dipicolinic acid summarised above and illustrates a high versatility of Ln(III)–DPA complexes.

* Corresponding authors. Tel.: +41 22 379 6413; fax: +41 22 379 6830 (J. Hamacek), tel.: +41 22 379 6413; fax: +41 22 379 6108 (G. Bernardinelli).
E-mail addresses: Josef.Hamacek@unige.ch (J. Hamacek), Gerald.Bernardinelli@cryst.unige.ch (G. Bernardinelli).

0277-5387/$ - see front matter © 2009 Elsevier Ltd. All rights reserved.
doi:10.1016/j.poly.2009.04.011

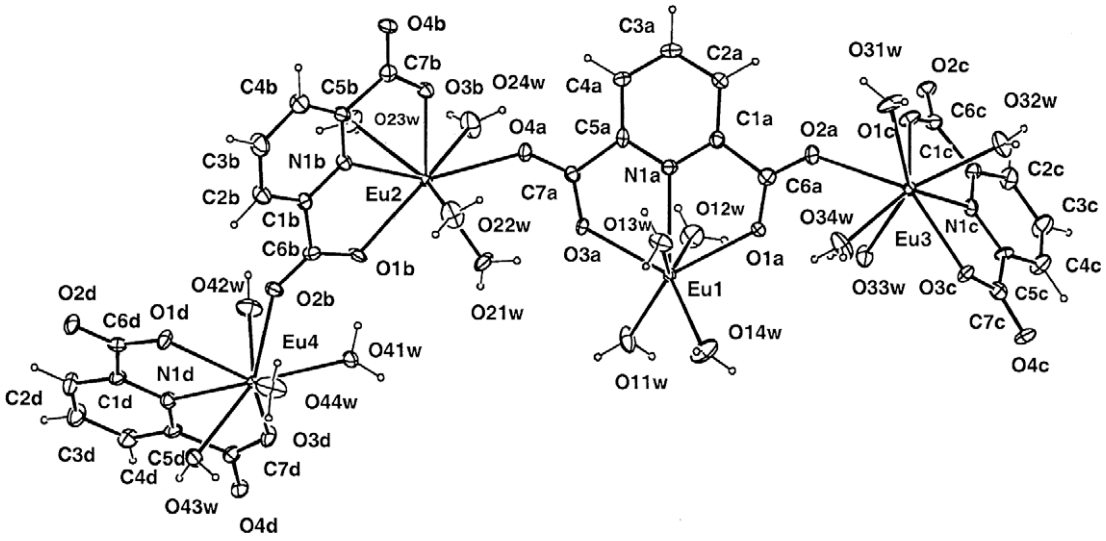


Fig. 1. The asymmetric unit of the $\{[Eu(C_7H_3NO_4)(H_2O)_4]_4(ClO_4)_4\}_\infty$ (**1**) polymer with the atom numbering.

2. Experimental

2,6-Dipicolinic acid (p.a.) was purchased from Acros Organics. The europium and lanthanum perchlorate salts were prepared from the corresponding oxides (Rhodia, 99.99%) according to literature procedures [19]. Ln(III) content of solid salts was determined by complexometric titrations with Titriplex III (Merck) in the presence of urotropine and xylene orange.

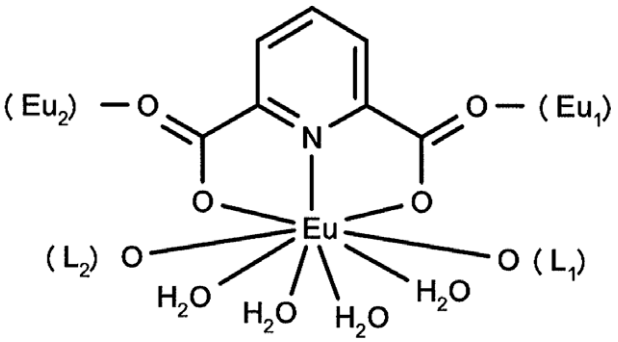
2.1. X-ray crystal data of $\{[Eu(C_7H_3NO_4)(H_2O)_4]_4(ClO_4)_4\}_\infty$ (*1*)

Dipicolinic acid ($\sim 10^{-2}$ M) was dissolved in water and 1 eq of $Eu(ClO_4)_3$ was added. The X-ray quality transparent crystals were obtained by slow evaporation at room temperature. The raw data were collected at 200 K on a Stoe IPDS diffractometer with graphite monochromated Mo [Kα] radiation ($\lambda = 0.7107$ Å). The structure was solved by direct methods (SIR97) [20]. All other calculations were performed with XTAL [21] programme package. The crystallographic data and the details of structural refinements are the following: $M = 1954.4$, crystal system trigonal, space group $R\bar{3}$, $a = 28.7051(11)$ (Å), $c = 35.1997(17)$ (Å), $V = 25\,118(2)$ (Å^3), $D_c = 2.325$ g cm^{-1}, $\mu = 4.75$ mm^{-1}, $Z = 18$, $T = 150$ K, 82 855 collected reflections, 10 933 independent reflections ($R_{int} = 0.045$) and 7702 observed reflections [$F_0 > 4\sigma(F_0)$], 840 refined parameters, $R = 0.024$, $\omega R = 0.025$. The hydrogen atoms of water molecules have been observed and refined with restraints on bond lengths and bond angles and blocked in the last cycles. Two ClO_4^- are located in general positions and do not show disorder. The two other perchlorates of the asymmetric unit are located on various special positions and show large disorders.

3. Results and discussion

Upon complexation of lanthanides with DPA^{2-}, the ^{1}H NMR signal related to the aromatic protons of the free ligand ($\delta = 8.33$) disappears and the ^{1}H NMR spectrum of the Eu(III) complex in D_2O ($[Eu]_{tot}/[DPA]_{tot} = 1$) shows two separate signals with the relative peak area in the ratio 1:2. The peak splitting is compatible with the pyridine protons in C_2-symmetrical environment ($\delta_H(D_2O)$ 4.5 (1H, t), 2.6 (2H, d)). The resulting paramagnetic shift for *para* and *meta* protons can be calculated according to $\Delta^{para}_{m,p} = \delta_{dia} - \delta_{exp}$, where δ_{exp} is the chemical shift of the paramagnetic Eu(III) complex. δ_{dia} corresponds to a diamagnetic shift measured for an analogous lanthanum complex. The calculated values for the monometallic complex $[Eu(DPA)]^+$ ($\Delta^{para}_p = 3.8$; $\Delta^{para}_m = 5.6$) are in agreement with the report of Alsaadi ($\Delta^{para}_p = 3.74$; $\Delta^{para}_m = 5.6$) [13]. No signal belonging to $[Eu(DPA)_2]^-$ and $[Eu(DPA)_3]^{3-}$ complexes was identified in the spectrum.

The X-ray crystal structure shows that the Eu(III) complex with DPA^{2-} crystallises in trigonal space group ($R\bar{3}$) with the asymmetric unit composed of four $[Eu(DPA)(H_2O)_4]^+$ building blocks (Fig. 1). Each europium cation in this crystal structure is nine-coordinated by one molecule of dipicolinic acid (three coordinating atoms), two oxygens coming from the carboxylate groups of neighbouring $Eu(DPA)^+$, and four water molecules (Scheme 1). The coordination sphere of Eu(III) is best described as a distorted mono-capped square antiprismatic site, where pyridine nitrogen caps the rectangular face formed by two carbonyl oxygens and two water molecules. In the polymer, both carboxylate groups of DPA^{2-} act as



Scheme 1. Coordination sphere around the europium cation.

Table 1
Average bond lengths in mono-, bis- and tris(dipicolinato)europium complexes.

	$[Eu(DPA)]^+$	$[Eu(HDPA)(DPA)]$[a]	$[Eu(DPA)_3]^{3-}$[b]
Eu–N	2.56(1)	2.57(1)	2.53(1)
Eu–O	2.43(1)	2.48(4)	2.45(1)
Eu–O(water)	2.45(2)	2.41(3)	
Eu–O(bridge)	2.48(1)	2.44(1)	

[a] Calculated with data in Ref. [5].
[b] Calculated with data in Ref. [3].

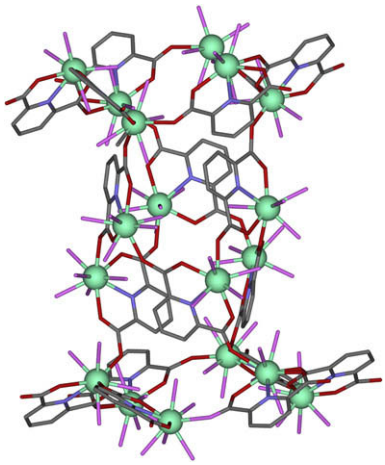


Fig. 2. Partial side view of the 3D cylinder running along the [0 0 1] direction in **1**. The hydrogens and perchlorates are omitted for clarity.

bidentate ligands with bridging functions. This binding mode advantageously increases the number of coordination bonds between Eu(III) and the DPA^{2-} ligands. The Eu–O and Eu–N distances in **1** are close to these found in Eu(III) complexes with two or three dipicolinates (Table 1). However, the average distances between Eu(III) and bridging oxygens are slightly longer than in the bis(dipicolinate)europium complex. The shortest Eu–N distances are found for tris(dipicolinates), which indicates a better encapsulation of Eu(III) in the coordination cavity. The calculated density of $\{[Eu(C_7H_3NO_4)(H_2O)_4]_4(ClO_4)_4\}_\infty$ amounts to 2.33 g cm^3. This value can be compared with 1.99 g cm^{-3} and 1.65 g cm^{-3} measured for $[Eu(HDPA)(DPA)(H_2O)_2]\cdot 4H_2O$ [5] and for $Cs_3[Eu(DPA)_3]\cdot 9H_2O$ [3], respectively. It shows that the density decreases about 0.34 g cm^{-3} per DPA^{2-} ligand bound to the Eu(III) cation.

Detailed scrutiny of the crystal structure **1** shows that the $[Eu(DPA)]^+$ complexes form the three-dimensional polymers with a cylindrical arrangement parallel to the *c* axis (Fig. 2). This supramolecular structure can be better described as an alternation of "cavities" and "tunnels" evidenced schematically in Fig. 3, (L = DPA^{2-}, the atom numbering is related to Fig. 1). The "cavities" are constituted by six monomeric units (three $Eu3L^c$ and three $Eu4L^d$) located around the $\bar{3}$ axis and represented on Fig. 4a. These "cavities" are interconnected by the "tunnels" composed of three units $Eu1L^aEu2L^b$ along a three-fold axis (Fig. 4b and c). The resulting cylindrical arrangements are further connected through $O4^c$ and $O4^d$ (oxygens located on L^c and L^d coordinated to Eu3 and Eu4, respectively), which form the bridges by coordinating the cations Eu2 and Eu1 of neighbouring cylinders (Fig. 3). The perchlorate anions are located in different general and special positions inside and outside of the cylinders formed by the complexes. Interestingly, these cylinders can be considered as monodimensional nanotunnels along the *c* axis with anions or solvent molecules sitting inside. A view of the crystal packing along the [0 0 1] direction evidencing the hexagonal "cavities" and "tunnels" is given in Fig. 5.

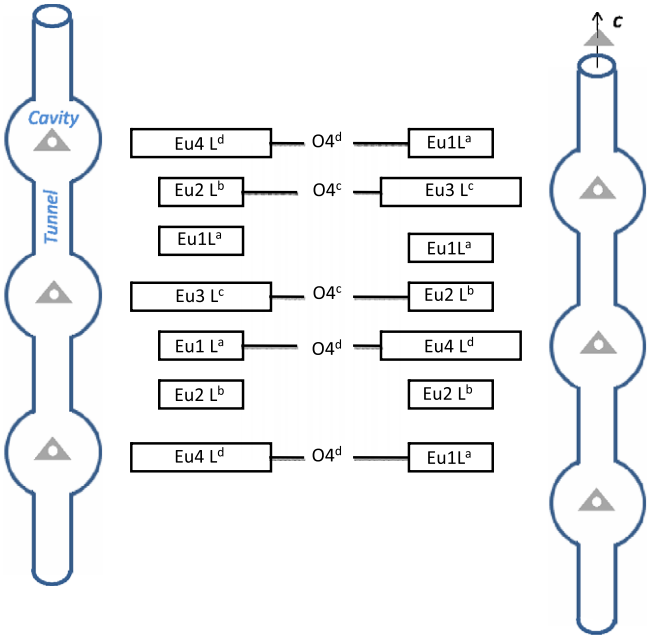


Fig. 3. Schematic representation of the supramolecular structure of **1**.

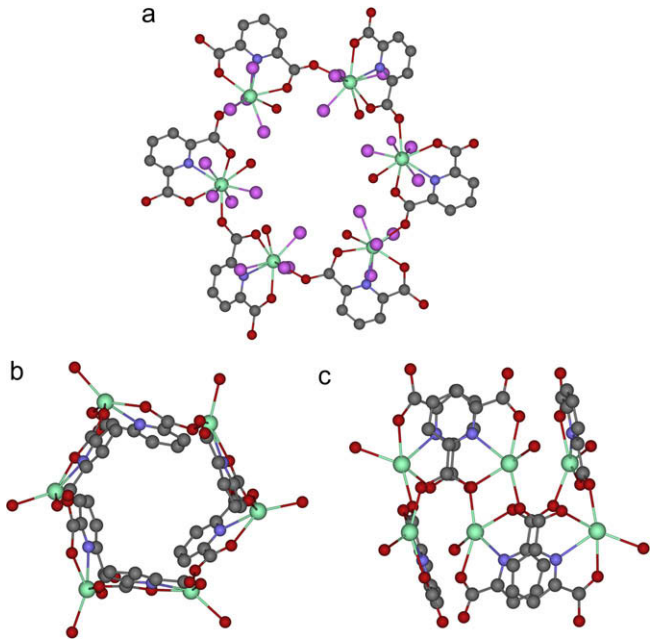


Fig. 4. (a) View of the "cavity" along the c axis. (b) View of the "tunnel" along the c axis. (c) View of the "tunnel" perpendicularly to the c axis. The hydrogens and perchlorates are omitted for clarity. Coordinated water molecules are omitted in (b) and (c).

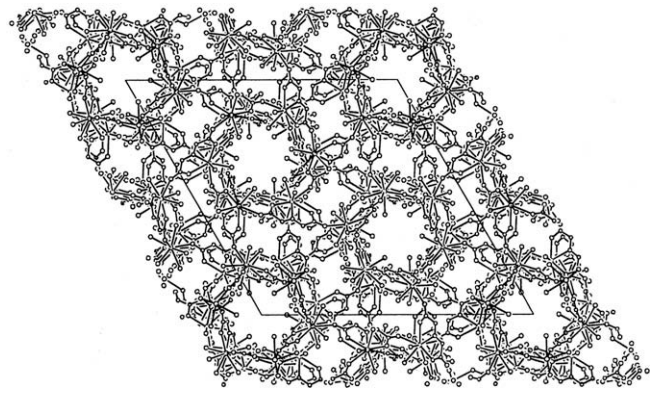


Fig. 5. View of the crystal packing of **1** along the [0 0 1] direction. The hydrogens and perchlorates are omitted for clarity.

4. Conclusion

The structure of mono(dipicolinato)europium complex in the solid state has been elucidated by X-ray crystallography. The self-assembly of $[Eu(DPA)(H_2O)_4]^+$ units leads to the formation of a peculiar polymeric network, where Eu(III) cations are nine-coordinated and all carboxylate groups of DPA^{2-} behave in a bidentate fashion. A tendency to form polymeric complexes increases along the series $[Eu(DPA)_3]^{3-}$, [Eu(HDPA)(DPA)], $Eu(DPA)]^+$ and reflects the decrease of occupancy of Eu(III) coordination sphere by chelating ligands. Although only the Eu(III) complex is presented, the formation of similar structures with remaining lanthanides is expected. However, the three-dimensional solid state arrangement is most probably not preserved in solution. This study demonstrates that unsaturated lanthanide complexes possessing carboxylic functions may be advantageously used for designing 3D metalloorganic frameworks.

Acknowledgements

This work was supported by the University of Geneva and the Swiss National Science Foundation.

Appendix A. Supplementary data

CCDC 706852 contains the supplementary crystallographic data for $\{[Eu(C_7H_3NO_4)(H_2O)_4]_4(ClO_4)_4\}_\infty$ (**1**). These data can be obtained free of charge via http://www.ccdc.cam.ac.uk/conts/retrieving.html, or from the Cambridge Crystallographic Data Centre, 12 Union Road, Cambridge CB2 1EZ, UK; fax: (+44) 1223-336-033; or e-mail: deposit@ccdc.cam.ac.uk.

References

[1] (a) J. Albertsson, Acta Chem. Scand. 24 (1970) 1213;
(b) J. Albertsson, Acta Chem. Scand. 26 (1972) 985;
(c) J. Albertsson, Acta Chem. Scand. 26 (1972) 1005;
(d) J. Albertsson, Acta Chem. Scand. 26 (1972) 1023.
[2] (a) P.A. Brayshaw, J.M. Harrowfield, A.N. Sobolev, Acta Crystallogr., Sect. C: Cryst. Struct. Commun. C 51 (1995) 1799;
(b) A. Mondry, P. Starynowicz, J. Alloys Compd. 225 (1995) 367.
[3] (a) P.A. Brayshaw, J.-C.G. Bünzli, P. Froidevaux, J.M. Harrowfield, Y. Kim, A.N. Sobolev, Inorg. Chem. 34 (1995) 2068;
(b) J.M. Harrowfield, Y. Kim, B.W. Skelton, A.H. White, Aust. J. Chem. 48 (1995) 807.
[4] K. Saravanan, S. Govindarajan, Synth. React. Inorg., Met.-Org., Nano-Met. 35 (2005) 143.
[5] P.A. Brayshaw, A.K. Hall, W.T.A. Harrison, J.M. Harrowfield, D. Pearce, T.M. Shand, B.W. Skelton, C.R. Whitaker, A.H. White, Eur. J. Inorg. Chem. 34 (2005) 1127.
[6] (a) C. Reinhard, H.U. Güdel, Inorg. Chem. 41 (2002) 1048;
(b) M.R. George, C.A. Golden, M.C. Grossel, R.J. Curry, Inorg. Chem. 45 (2006) 1739;
(c) E.B. Sveshnikova, P.A. Shakhverdov, T.A. Shakhverdov, V.E. Lanin, R.U. Safina, B.M. Bolotin, V.L. Ermolaev, Opt. Spectrosc. 95 (2003) 898;
(d) H.G. Brittain, Inorg. Chem. 17 (1978) 2762;
(e) M.H.V. Werts, N. Nerambourg, D. Pelegry, Y. Le Grand, M. Blanchard-Desce, Photochem. Photobiol. Sci. 4 (2005) 531.
[7] A.-S. Chauvin, F. Gumy, D. Imbert, J.-C.G. Bünzli, Spectrosc. Lett. 37 (2004) 517. Erratum: Spectrosc. Lett. 40 (2006) 193.
[8] (a) A.-L. Gassner, C. Duhot, J.-C.G. Bünzli, A.-S. Chauvin, Inorg. Chem. 47 (2008) 7802;
(b) A. Picot, A. D'Aleo, P.L. Baldeck, A. Grichine, A. Duperray, C. Andraud, O. Maury, J. Am. Chem. Soc. 130 (2008) 1532.
[9] (a) I. Grenthe, J. Am. Chem. Soc. 83 (1961) 360;
(b) I. Grenthe, Acta Chem. Scand. 17 (1963) 2487.
[10] (a) J.F. Desreux, C.N. Reilley, J. Am. Chem. Soc. 98 (1976) 2105;
(b) C.N. Reilley, B.W. Good, J.F. Desreux, Anal. Chem. 47 (1975) 2110.
[11] N. Ouali, B. Bocquet, S. Rigault, P.-Y. Morgantini, J. Weber, C. Piguet, Inorg. Chem. 41 (2002) 1436.
[12] H. Donato Jr., R.B. Martin, J. Am. Chem. Soc. 94 (1972) 4129.
[13] (a) B.M. Alsaadi, F.J.C. Rossotti, R.J.P. Williams, J. Chem. Soc., Dalton Trans. (1980) 597;
(b) B.M. Alsaadi, F.J.C. Rossotti, R.J.P. Williams, J. Chem. Soc., Chem. Commun. (1977) 527.
[14] A. Anagnostopoulos, J. Coord. Chem. 4 (1975) 231.
[15] A. Fernandes, J. Jaud, J. Dexpert-Ghys, C. Brouca-Cabarrecq, Polyhedron 20 (2001) 2385.
[16] (a) P. Guerriero, U. Casellato, S. Sitran, P.A. Vigato, R. Graziani, Inorg. Chim. Acta 133 (1987) 337;
(b) N. Okabe, H. Kyoyama, Acta Crystallogr., Sect. E 58 (2002) m226;
(c) K. Ghosh Sujit, K. Bharadwaj Parimal, Inorg. Chem. 42 (2003) 8250;
(d) Z. Li, S. Wang, Q. Zhang, X. Yu, Acta Crystallogr., Sect. E: Struct. Rep. Online E 63 (2007) m2438;
(d) F. Miao, J. Wang, T. Jin, J. Liu, H. Zhang, C. Huang, Chin. J. Inorg. Chem. (Wuji Huaxue Xuebao) 8 (1992) 180;
(e) C.-X. Cheng, H.-W. Liu, Z.-Q. Hu, F.-H. Luo, M.-N. Cao, Acta Crystallogr., Sect. E: Struct. Rep. E 63 (2007) m1.
[17] (a) H.-L. Gao, L. Yi, B. Zhao, X.-Q. Zhao, P. Cheng, D.-Z. Liao, S.-P. Yan, Inorg. Chem. 45 (2006) 5980;
(b) S.K. Ghosh, P.K. Bharadwaj, Eur. J. Inorg. Chem. (2005) 4886;
(c) W. Brzyska, W. Ozga, Thermochim. Acta 247 (1994) 329.
[18] X.-F. Guo, M.-L. Feng, Z.-L. Xie, J.-R. Li, X.-Y. Huang, Dalton Trans. (2008) 3101.
[19] J.-F. Desreux, in: J.-C.G. Bünzli, G.R. Choppin (Eds.), Lanthanide Probes in Life Chemical and Earth Sciences, Elsevier Publishing Co., Amsterdam, 1989, p. 43 (Chapter 2).
[20] A. Altomare, M.C. Burla, M. Camalli, G. Cascarano, C. Giacovazzo, A. Guagliardi, A.G.G. Moliterni, G. Polidori, R. Spagna, J. Appl. Cryst. 32 (1999) 115.
[21] S.R. Hall, H.D. Flack, J.M. Stewart (Eds.), XTAL 3.2 User's Manual, Universities of Western Australia, Geneva and Maryland, 1992.

Polyhedron 28 (2009) 2183–2186

Contents lists available at ScienceDirect

Polyhedron

journal homepage: www.elsevier.com/locate/poly

Aerobic oxidation of tetrahydrofuran by a series of iron (III) containing POSS compounds

Michael T. Hay [a,*], Steven J. Geib [b,1], Derek A. Pettner [a,2]

[a] Penn State Beaver, 100 University Drive, Monaca, PA 15061, USA
[b] University of Pittsburgh, 309 Chevron Building, Pittsburgh, PA 15260, USA

ARTICLE INFO

Article history:
Received 30 October 2008
Accepted 15 April 2009
Available online 23 April 2009

Keywords:
POSS
Iron complexes
Aerobic oxidation
X-ray crystal structures

ABSTRACT

A series of iron (III) containing POSS compounds, $[Bu_4N][(R)_7Si_7O_{12}FeCl]$ (R = isobutyl- (**1**), ethyl- (**2**), phenyl- (**3**), and cyclopentyl- (**4**)) were investigated as potential catalysts for aerobic oxidation of tetrahydrofuran (THF). The oxidation products for this reaction were characterized by IR, GC and GC–MS. The major oxidation product was γ-butyrolactone ($C_4H_6O_2$, GBL); while the two minor products were 2-hydroxy-THF and its tautomer, 4-hydroxybutanal. A third minor oxidative product is believed to be an isomer of dihydroxy-THF. THF free syntheses of **2**–**4** have been developed and all three compounds were characterized by elemental analysis, IR, and X-ray diffraction studies. The crystallographic data for **1**–**4** demonstrate a similar iron coordination sphere between the four compounds, but the different substitutents on the various POSS. The corresponding turnover numbers for the aerobic oxidation of THF suggest that smaller substitutents on the POSS ligands improve the stability of the catalytic species. When compared to other published catalytic iron systems, these turnover numbers appear to be the largest for the aerobic conversion of THF to GBL.

© 2009 Elsevier Ltd. All rights reserved.

1. Introduction

Metal containing polyhedral oligomeric silsesquioxanes (POSS) have been used to model a variety of industrial catalysts consisting of silica (SiO_2) supported metals [1,2]. As a result, our laboratory has been investigating the use of POSS ligands as potential models for the Fe-ZSM-5 catalyst [3]. During this process, we synthesized and fully characterized four different iron (III)-containing POSS compounds, $[Bu_4N][(R)_7Si_7O_{12}FeCl]$ (R = isobutyl- (**1**), ethyl- (**2**), phenyl- (**3**), and cyclopentyl- (**4**)) (Fig. 1).

In the crystal structure of the isobutyl derivative (**1**) an equivalent of γ-butyrolactone ($C_4H_6O_2$, GBL) had crystallized with the complex [4]. Since GBL had not been added to the reaction mixture, we hypothesized that it was formed from the aerobic oxidation of the solvent, tetrahydrofuran (C_4H_8O, THF), during the synthesis of **1** (Reaction 1).

The aerobic oxidation of ethers, such as THF, has been facilitated by a variety of transition metal complexes [5–12]. However, oxidation of ethers using an iron containing complex is especially significant because of iron's importance in biological reactions [13,14]. We offer here our results of the controlled aerobic oxidation of THF in the presence of four different iron (III) chloro-POSS compounds (**1**–**4**) and a control of iron (III) chloro complex that does not contain the POSS, $[Bu_4N][FeCl_4]$ (**5**). In addition, we present the synthesis and structural characterization of the ethyl- (**2**) and phenyl- (**3**) derivatives, and an improved synthesis and structural characterization for the cyclopentyl- derivative (**4**) [15].

2. Experimental

2.1. Materials and instrumentation

All procedures were performed under aerobic conditions. Hexane and toluene were dried over Na and stored over 4 Å molecular sieves. Acetonitrile was dried over CaH_2 and stored over 4 Å molecular sieves. IR spectra were recorded on a Nicolet Impact 410 FTIR Spectrometer using a KBr pellet or NaCl plates. Elemental analysis was performed by Galbraith Laboratories Inc. (Knoxville, TN) using a Perkin–Elmer 240 CHN Analyzer. Gas chromatography (GC) was recorded on a GOW-MAC Series 400 Thermal Conductivity GC using a carbowax column. Gas chromatography–mass spectrometry (GC–MS) analysis was performed on an Agilent 6890 gas chromatograph coupled to a Waters GCT time-of-flight mass spectrometer using a Varian VF5-MS column (20 m, 0.18 mm i.d., 0.15 μm) programmed from 40 (1 min hold) to 300 °C at 15 °C/min) operating in 20 to 1 split injection mode (Injector T = 250 °C). The compounds were ionized via electron ionization. The X-ray diffraction data were collected under a cooled N_2 stream

* Corresponding author. Tel.: +1 724 773 3876; fax: +1 724 773 3557.
E-mail addresses: mth7@psu.edu (M.T. Hay), geib@pitt.edu (S.J. Geib).
[1] Tel.: +1 412 624 1131; fax: +1 412 624 8611.
[2] Tel.: +1 724 773 3876; fax: +1 724 773 3557.

0277-5387/$ - see front matter © 2009 Elsevier Ltd. All rights reserved.
doi:10.1016/j.poly.2009.04.014

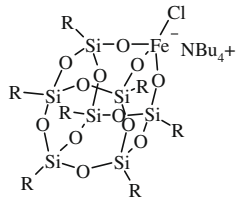
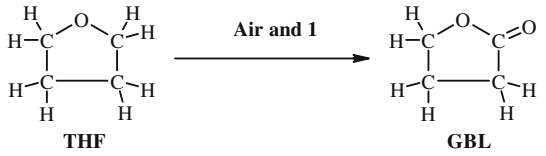


Fig. 1. Iron (III) chloro-POSS compounds, R = isobutyl- (**1**), ethyl- (**2**), phenyl- (**3**), and cyclopentyl- (**4**)



Reaction 1. Oxidation of tetrahydrofuran to γ-butyrolactone.

at 150 K on a Bruker Apex CCD diffractometer (sealed-tube Mo radiation) which is controlled via Bruker Smart software. Trisilanolethyl-POSS, $(CH_3CH_2)_7Si_7O_{12}H_3$, the trisilanolphenyl-POSS, $(C_6H_5)_7Si_7O_{12}H_3$, and the trisilanolcyclopentyl-POSS, (cyclo-$C_5H_9)_7$-$Si_7O_{12}H_3$ were all obtained from Hybrid Plastics or as a gift from Dr. Andre Lee from Michigan State University and used as received. Triethylamine, anhydrous tetrahydrofuran (THF), γ-butyrolactone (GBL), and dodecane were all obtained from Sigma–Aldrich chemical and used as received. Compound **1** was synthesized as described in the literature [16]. Compound **5** was prepared according to the literature procedure [17].

2.2. Synthesis of compound *2*

A colorless solution of the trisilanol-POSS, $(CH_3CH_2)_7Si_7O_{12}H_3$, (0.200 g, 0.336 mmol) in toluene (4.0 mL) was treated with 3 equiv. of triethylamine (141 μL, 1.01 mmol). The mixture was stirred for 5 min at room temperature before 1 equiv. of solid **5** (0.148 g, 0.336 mmol) was added. The yellow solid did not immediately dissolve. After stirring for 10 min, the solution had turned yellow and a precipitate had formed. A white precipitate was collected by filtration. The yellow filtrate was concentrated in vacuo giving a yellow oil, which was then extracted with acetonitrile. A majority of the yellow oil dissolved except for a small amount of insoluble white precipitate. These were removed by filtration, and the filtrate was concentrated in vacuo to give yellow crystalline material, which was then extracted with toluene and then concentrated in vacuo to afford a yellow powder after being dried under vacuum.

2.2.1. Compound *2*

Yield: 83.9%. *Anal.* Calc. for $C_{30}H_{71}FeClNO_{12}Si_7$ (925.81): C, 38.92; H, 7.73; N, 1.51. Found: C, 38.89; H, 7.63; N, 1.54%. IR (KBr, ν (cm^{-1})): 2967s, 2877s, 1481m, 1461m, 1415w, 1383w, 1252s, 1086vs, 940s, 881m, 753s, 696vs, 492s, 458s.

2.3. Synthesis of compounds *3* and *4*

Compounds **3** and **4** were prepared following a procedure analogous to the synthesis of **2**. Similar molar quantities of the appropriate trisilanol-POSS were used, but due to their lower solubility in toluene, twice the volume of solvent was used as well as longer reaction times were necessary.

2.3.1. Compound *3*

Yield: 82.2%. *Anal.* Calc. for $C_{58}H_{71}FeClNO_{12}Si_7$ (1262.09): C, 55.19; H, 5.67; N, 1.11. Found: C, 55.12; H, 5.49; N, 1.12%. IR (KBr, ν (cm^{-1})): 3137w, 3071s, 3049s, 2965s, 2931s, 2874s, 2719w, 1961m, 1891m, 1824m, 1776m, 1593s, 1480s, 1431s, 1381s, 1068vs, 879s, 744vs, 694vs, 645s, 594m, 551s.

2.3.2. Compound *4*

Yield: 73.8%. *Anal.* Calc. for $C_{51}H_{99}FeClNO_{12}Si_7$ (1206.24): C, 50.78; H, 8.27; N, 1.16. Found: C, 50.61; H, 8.72; N, 1.26%. IR (KBr, ν (cm^{-1})): 2948vs, 2864s, 1481m, 1471m, 1454m, 1383m, 1243s, 1099vs, 1040vs, 943s, 906w, 736m, 496vs.

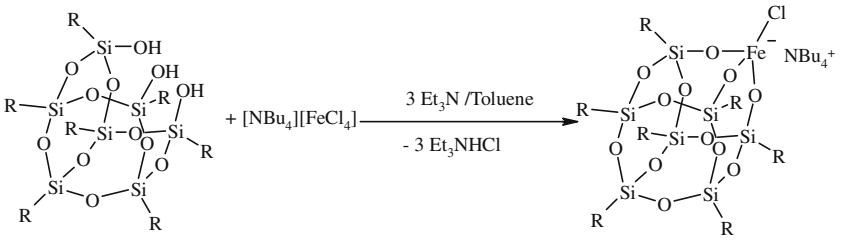
2.4. X-ray analysis of iron (III) chloro-POSS compounds

Crystallization of **2** from a minimum amount of toluene afforded yellow crystals of **2**. $C_{30}H_{71}ClFeNO_{12}Si_7$, M = 925.81, monoclinic space group, $P2_1/c$, a = 9.8962(5), b = 29.5660(15), c = 16.1237(8) Å, β = 90.7710(10)°, V = 4717.2(4) Å^3, Z = 4, D_{calc} = 1.302 Mg/m^3; F(0 0 0) = 1976, μ_{Mo} = 0.422 mm^{-1}; crystal dimensions: 0.32 × 0.28 × 0.25 mm. The structure was solved via direct methods. Least-squares refinement on F^2 using all reflections converged to R_{F^2} = 15.29%. One of the ethyl methylene carbons was disordered 50:50 over two sites.

Crystallization of **3** from a minimum amount of toluene afforded yellow crystals of **3**. $C_{58}H_{71}ClFeNO_{12}Si_7$–2($C_6H_5CH_3$), M = 1446.36, monoclinic space group, $P2_1/n$, a = 15.079(3), b = 20.224(4), c = 25.423(4) Å, β = 100.642(4)°, V = 7619(2) Å^3, Z = 4, D_{calc} = 1.261 Mg/m^3; F(0 0 0) = 3052, μ_{Mo} = 0.401 mm^{-1}; crystal dimensions: 0 0.22 × 0.34 × 0.35 mm. The structure was solved via direct methods. Least-squares refinement on F^2 using all reflections converged to R_{F^2} = 27.52%. There are two toluene solvate molecules per asymmetric unit which were constrained to fit approximately rigid hexagons. The crystal was very weakly diffracting which caused problems in the refinement including poorly shaped ADP's, unexpected variations in U_{eq} values, and some atypical bond lengths. These problems are noted in the checkcif report. Crystallization of **4** from a minimum amount of toluene afforded yellow crystals of **4**. $C_{51}H_{99}ClFeNO_{12}Si_7$, M = 1206.24, monoclinic space group, $P2_1/c$, a = 15.4303(16), b = 22.127(2), c = 40.539(4) Å, β = 93.408(2)°, V = 13817(2) Å^3, Z = 8, D_{calc} = 1.159 Mg/m^3; F(0 0 0) = 5192, μ_{Mo} = 0.428 mm^{-1}; crystal dimensions: 0.21 × 0.28 × 0.34 mm. The structure was solved via direct
methods. Least-squares refinement on F^2 using all reflections converged to R_{F^2} = 23.54%. Crystals diffracted very weakly which caused problems in the refinement including poorly shaped ADP's, unexpected variations in U_{eq} values, and some atypical bond lengths. These problems are noted in the checkcif report. One of the cyclopentyl groups was disordered over two 50% occupancy orientations.

2.5. Aerobic oxidation of the tetrahydrofuran

In a 10-mL micro-scale round bottom flask, 0.0500 mol% of the iron complex was dissolved in 2.00 mL of THF. The resulting solution was golden yellow. Three stacked micro-scale water condensers were added to the round bottom flask to prevent evaporation of the solvent. The mixture was stirred for 5 days at room temperature. Afterwards, the reaction mixture was analysed by infrared spectroscopy (IR) and gas chromatography (GC). Dodecane was used as an internal standard during the GC analysis, and the turnover number from four separate trials were averaged to give the reported values. On separate occasions, similar reaction mixtures were analysed by gas chromatography–



Reaction 2. THF free synthesis of **1**–**4**.

mass spectrometry (GC–MS) to determine the identities of the THF oxidation products.

3. Results and discussion

3.1. Synthesis of iron (III) chloro-POSS compounds

The conversion of THF to GBL was originally detected when **1** was synthesized and crystallized in a solution of THF under aerobic conditions [4]. A general THF free synthesis was therefore developed in order to prepare **1**–**4** (Reaction 2). The corresponding POSS trisilanol was treated with 3 equiv. of triethylamine in toluene. Although **5** was insoluble in toluene, the reaction between **5** and the POSS ligand still occurred albeit slower and with a considerable amount of stirring. After reaction times ranging from 5 to 60 min, depending on the POSS, triethyl ammonium chloride salt and a small amount of unreacted **5** were removed by filtration. The resulting yellow toluene solution was concentrated under reduced pressure to give a yellow oil, which was then extracted with acetonitrile. The trisilanol POSS ligands are insoluble in acetonitrile, while **1–4** are soluble, therefore unreacted trisilanol POSS ligand can be easily removed from the reaction mixture increasing the purity of the product. A final extraction with either hexane or toluene, depending on the product, resulted in the formation of **1–4** in relatively high yields.

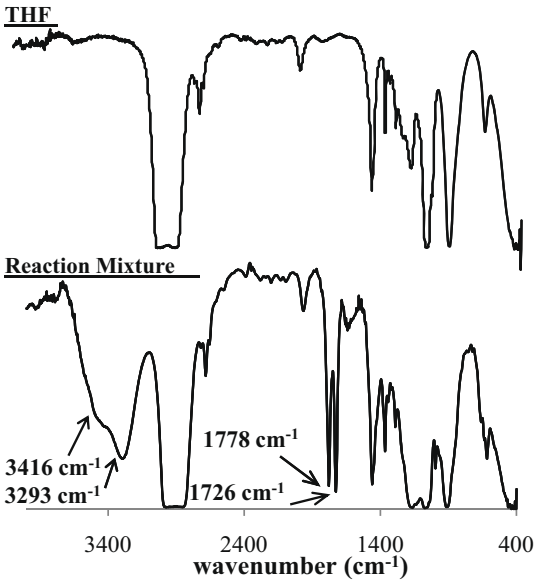


Fig. 2. Infrared spectral data of pure THF (top) and a typical reaction mixture (bottom).

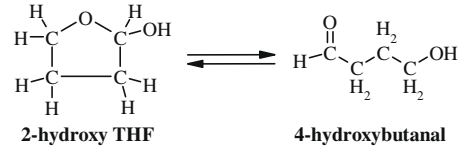
3.2. X-ray analysis of iron (III) chloro-POSS compounds

The iron (III) center in **2**–**4** all have the same coordination geometry previously observed in **1** [15,16], a distorted tetrahedral geometry composed of a single chlorine atom and three trisilanate oxygen atoms. The Fe–Cl bond distances in **1**–**4** are very similar [Fe–Cl: **1**, 2.2536(10) Å; **2**, 2.2534(5) Å, **3**, 2.227(2) Å, and **4**, 2.256(1) Å], while the average Fe–$O_{trisilanate}$ bond length of **1–4** are also very close [Fe–$O_{trisilanate}$: **1**, 1.842 (±0.008) Å; **2**, 1.84 (±0.01) Å, **3**, 1.835(±.009) Å, and **4**, 1.825(±.009) Å]. Clearly, the four complexes are structurally comparable within the coordination environment of the iron and differ only in the type and thus the size of the hydrocarbon substitutents on the POSS ligand.

3.3. Aerobic oxidation of the tetrahydrofuran

A yellow solution of 0.0500 mol% **1–5** in anhydrous THF was stirred open to the atmosphere for five days. The IR spectrum of the reaction mixtures of each sample was compared to the IR spectrum of pure THF (Fig. 2). New bands were detected that are indicative of oxidation products: a shoulder at 3416 cm^{-1}, a broad band at 3293 cm^{-1}, and two sharper bands at 1778 cm^{-1} and 1726 cm^{-1}. The peaks in the 3000 cm^{-1} range are characteristic of hydroxyl (–OH) functionality, while the peaks in the 1700 cm^{-1} range support the presence of carbonyl (C=O) groups [18]. The 1778 cm^{-1} peak is consistent with the IR of pure GBL obtained in our laboratory as well as the literature value [19].

According to the GC–MS results, GBL was confirmed as the major oxidation product for the aerobic oxidation of THF. In addition, two minor products were also detected. The more abundant of the two minor species was 2-hydroxy-THF. The shoulder at 3416 cm^{-1} in the IR also supports its presence [20]. It can undergo a ring-chain tautomerism to form 4-hydroxybutanal [21], however, the GC–MS did not detect the ring opened species (Reaction 3). In the liquid phase, however, the 1726 cm^{-1} peak in the IR is consistent with 4-hydroxybutanal [22]. Therefore, it is possible that either the gas phase equilibrium favoured the cyclic tautomer in the MS or the ring-opened form did not elute from the GC column. The third most abundant species detected by the GC–MS is believed to be a dihydroxy-THF molecule. An M^+ peak of 104 in the mass spec is consistent with a molecular formula of $C_4H_8O_3$, and the broad band at 3293 cm^{-1} in the IR would also support the presence of a second hydroxyl containing species. We were unable to definitively confirm which dihydroxy-THF isomer was present in the reaction mixture.



Reaction 3. Ring-chain tautomerism of 2-hydroxy-THF and 4-hydroxybutanal.

Table 1
Turnover numbers for THF oxidation products.

Iron (III) chloro complex	THF to GBL turnover number	Total oxidation turnover number
Isobutyl POSS (**1**)	74 (±7)	100 (±8)
Ethyl POSS (**2**)	114 (±9)	170 (±10)
Phenyl POSS (**3**)	89 (±7)	130 (±10)
Cyclopentyl POSS (**4**)	82 (±7)	120 (±9)
No POSS (**5**)	6 (±2)	14 (±3)

As of this study, it is not clear that the iron (III) chloro-POSS complexes (**1–4**) remain intact during the oxidation of THF, and are thus responsible for the catalytic conversion of THF to GBL. In our previous report [4], we showed that an equivalent of GBL co-crystallized with **1**, suggesting that **1** remains intact during the oxidation of THF. In this work, though, we were unable to isolate **1–4** from any of the THF reaction mixtures, possibly due to its low concentration. Also, the iron (III) center is paramagnetic [4], making simple spectroscopic methods for characterizing the catalytic iron species difficult. It is possible that the iron (III) chloro-POSS complexes could function as a pre-catalyst by potentially loosing the chloride ligand or reacting with water or oxygen to generate the catalytic species. As a result, we calculated turnover numbers for the THF oxidation reaction based on the initial number of moles of iron (III) in **1–5**.

Since the reaction mixture contained multiple oxidation products of THF, we calculated both the THF to GBL turnover numbers as well as the turnover numbers for the total oxidation of THF (Table 1). The iron (III) chloro-POSS complexes (**1–4**) generated between 74 and 114 equiv. of GBL per mole of iron (III), while the total number of oxidation equivalents per iron (III) ranged from 100 to 170. As a control, **5** was dissolved in THF under the same conditions and only 6 turnovers of GBL and 14 total oxidation turnovers were measured. Apparently, the POSS ligand enhances the stability of the catalytic species resulting in the higher turnover numbers. This may be a result of the POSS ligand's electron withdrawing ability, which would result in a more Lewis acidic iron center [23].

To place the iron (III) chloro-POSS system's turnover numbers in context, a review of the literature was conducted revealing only two previously published examples of the catalytic oxidation of THF to GBL by dioxygen in the presence of an iron complex. The first system used $FeCl_2{\cdot}$(1.5 THF) under a pressure of dioxygen and carbon dioxide [14]. The second system used a carboxylate-bridged diiron complex in the presence of a triarylphosphine in air-saturated THF [13]. Both systems produce multiple THF oxidation products, including GBL. Approximately 2.5 turnovers of GBL were obtained after a reaction time of about 8 days from the $FeCl_2{\cdot}$(1.5 THF) system, while the carboxylate-bridged diiron system did not report turnover numbers. Therefore, the iron (III) chloro-POSS system appears to provide the highest published THF to GBL turnovers for an iron system to date.

4. Conclusion

Clearly, the GBL observed in the crystal structure of **1** is formed by the aerobic oxidation of THF [4]. By first synthesizing the four iron (III)-containing POSS compounds (**1–4**) in toluene and then dissolving them in THF, we have demonstrated that all four complexes are capable of either catalysing this oxidation reaction or acting as pre-catalysts. The low turnover numbers observed with **5** supports that the presence of the POSS ligand significantly stabilizes the catalysts allowing for dramatically higher yields of GBL. A comparison of the turnover numbers for **1–4** also shows that by varying the substitutent on the POSS, the stability of the catalyst can be improved: the POSS with the smallest substitutent, **2,** provides the most stable catalyst.

Supplementary data

CCDC 706342, 706344 and 706343 contain the supplementary crystallographic data for **2**, **3** and **4**. These data can be obtained free of charge via http://www.ccdc.cam.ac.uk/conts/retrieving.html, or from the Cambridge Crystallographic Data Centre, 12 Union Road, Cambridge CB2 1EZ, UK; fax: (+44) 1223-336-033; or e-mail: deposit@ccdc.cam.ac.uk.

Acknowledgements

We thank the University College of the Pennsylvania State University for their financial support. Special thanks go to Dr. Andre Lee (Michigan State University) for providing several samples of the trisilanol POSS and Dr. Robert Minard (Pennsylvania State University) for his assistance in obtaining and interpreting the GC–MS data.

References

[1] F.J. Feher, T.A. Budzichowski, Polyhedron 14 (1995) 3239.
[2] H.C.L. Abbenhuis, Chemistry – A European Journal 6 (2000) 25.
[3] A. Zecchina, M. Rivallan, G. Berlier, C. Lamberti, G. Ricchiardi, Phys. Chem. Chem. Phys. 9 (2007) 3483.
[4] M.T. Hay, B.J. Hainaut, S.J. Geib, Inorg. Chem. Commun. 6 (2003) 431.
[5] A. Datta, M. Agarwal, S. Dasgupta, Catal. Surveys from Asia 8 (2004) 171.
[6] T. Straub, A.M.P. Koskinen, Inorg. Chem. Commun. 5 (2002) 1052.
[7] M. Shi, J. Chem. Res.-S 9 (1998) 592.
[8] S. Minakata, E. Imai, Y. Ohshima, K. Inaki, I. Ryu, M. Komatsu, Chem. Lett. (1996) 19.
[9] M.T. Reetz, K. Tollner, Tetrahedron Lett. 36 (1995) 9461.
[10] E. Hata, T. Takai, Chem. Lett. (1993) 1513.
[11] A. Sen, M.R. Lin, L.C. Kao, A.C. Hutson, J. Am. Chem. Soc. 114 (1992) 6385.
[12] A.K. Fazlurrahman, J.C. Tsai, K.M. Nicholas, J. Chem. Soc. – Chem. Commun. (1992) 1334.
[13] R.F. Moreira, E.Y. Tshuva, S.J. Lippard, Inorg. Chem. 43 (2004) 4427.
[14] M. Aresta, C. Fragale, E. Quaranta, I. Tommasi, J. Chem. Soc. – Chem. Commun. (1992) 315.
[15] P.A. Shapley, W.S. Bigham, M.T. Hay, Inorg. Chim. Acta 345 (2003) 255.
[16] M.T. Hay, S.J. Geib, Acta Crystallogr., Sect. E – Struct. Rep. Online 63 (2007) M445.
[17] M.T. Hay, S.J. Geib, Acta Crystallogr., Sect. E – Struct. Rep. Online 61 (2005) M190.
[18] H.K. Hall, R. Zbinden, J. Am. Chem. Soc. 80 (1958) 6428.
[19] R. Mecke, R. Mecke, A. Lüttringhaus, Chem. Ber. 90 (1957) 975.
[20] A.G.M. Barrett, H.B. Broughton, S.V. Attwood, A.A.L. Gunatilaka, J. Org. Chem. 51 (1986) 495.
[21] A. Lebedev, L. Leite, M. Fleisher, V. Stonkus, Chem. Heterocycl. Compd. (New York) (Translation of Khimiya Geterotsiklicheskikh Soedinenii) 36 (2000) 775–778.
[22] S. Oka, Bull. Chem. Soc. Jpn. 35 (1962) 986–989.
[23] R. Duchateau, U. Cremer, R.J. Harmsen, S.I. Mohamud, H.C.L. Abbenhuis, R.A. van Santen, A. Meetsma, S.K.H. Thiele, M.F.H. van Tol, M. Kranenburg, Organometallics 18 (1999) 5447.

Polyhedron 28 (2009) 2187–2195

Contents lists available at ScienceDirect

Polyhedron

journal homepage: www.elsevier.com/locate/poly

Antibacterial and antifungal activity of metal(II) complexes of acylhydrazones of 3-isatin and 3-(*N*-methyl)isatin

María C. Rodríguez-Argüelles [a,*], Roberto Cao [b], Ana M. García-Deibe [c], Corrado Pelizzi [d], Jesús Sanmartín-Matalobos [c,*], Franca Zani [e]

[a] Departamento de Química Inorgánica, Universidade de Vigo, 36310 Vigo, Spain
[b] Laboratorio de Bioinorgánica, Facultad de Química, Universidad de La Habana, La Habana, 10400 Cuba, Cuba
[c] Departamento de Química Inorgánica, Universidade de Santiago de Compostela, 15782 Santiago de Compostela, Spain
[d] Dipartimento di Chimica Generale ed Inorganica, Chimica Analitica, Chimica Fisica, Università di Parma, 43100 Parma, Italy
[e] Dipartimento Farmaceutico, Università di Parma, 43100 Parma, Italy

ARTICLE INFO

Article history:
Received 10 December 2008
Accepted 23 December 2008
Available online 20 May 2009

Keywords:
Isatin
Acylhydrazones
Metal complexes
Antibacterial activity
Antifungal activity

ABSTRACT

Cobalt(II), nickel(II), copper(II) and zinc(II) complexes of 2-thiophenecarbonyl hydrazone of 3-isatin (H_2L^1) and 2-furoic hydrazones of 3-isatin (H_2L^2) and 3-(*N*-methyl)isatin (HL^3), with general composition $[M(L)_2] \cdot nX$, where X is ethanol or/and water, were synthesised and characterised. The molecular structure of HL^3 showed that it crystallised in the keto form, which is also the more abundant tautomer for the three hydrazone ligands in solution. The three ligands behave as κ^2-*O,N* donors in the cobalt(II) and zinc(II) complexes. The X-ray crystal structure of pseudotetrahedral $[Zn(HL^1)_2] \cdot 1.75MeOH$ confirmed the *O,N* coordination mode of the two monodeprotonated ligands in their keto forms. Secondary interactions of zinc ions with the O atoms of each isatin keto residue provoke a substantial distortion towards a square pyramidal form. The interaction of the isatin keto residues is stronger in the three nickel(II) complexes where the three acylhydrazones can be considered as κ^3-*O,N,O* donors.

The free ligands and their complexes were evaluated *in vitro* as antimicrobial agents against a panel of Gram positive and Gram negative bacteria, as well as, yeasts and moulds. Among the tested microorganisms, *Haemophilus influenzae* was the most sensitive strain, especially to H_2L^1 and its complexes.

© 2009 Elsevier Ltd. All rights reserved.

1. Introduction

Acylhydrazones are known to present a wide spectrum of biological properties, such as analgesic, anti-inflammatory, antithrombotic, antinociceptive and antiplatelet [1]. In some cases, the biological activity has been related to the chelating property of the acylhydrazones [2].

Acylhydrazones can behave as κ^2-*O,N* or κ^3-*O,N,X* ligands to form stable coordination compounds with different transition metal ions [3]. We have recently reported the interesting biological properties of cobalt(II), nickel(II), copper(II) and zinc(II) complexes of 3-isatin- and *N*-methyl-isatin-3-picolinoylhydrazone [4] as well as of 2-thiophenecarbonyl and isonicotinoyl hydrazones of 3-(*N*-methyl)isatin [5].

Following this research line, here we describe the synthesis and structural characterisation of some Co(II), Ni(II), Cu(II) and Zn(II) complexes of 2-thiophenecarbonyl hydrazone of 3-isatin, H_2L^1, 2-furoic hydrazone of 3-isatin, H_2L^2, and 2-furoic hydrazone of 3-(*N*-methyl)isatin, HL^3 (Scheme 1). Moreover, we report the antibacterial and antifungal activities of all the synthesised compounds.

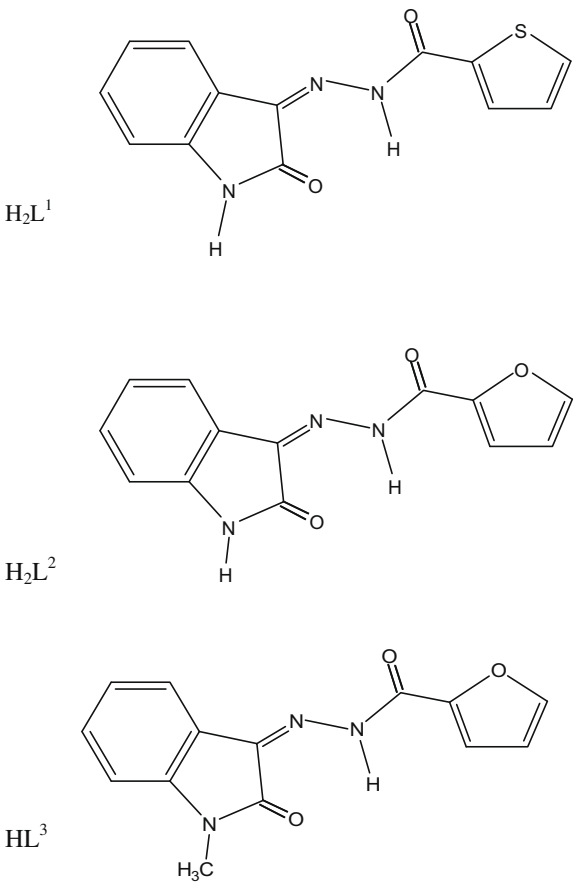
2. Experimental

2.1. Materials and measurements

All reagents and solvents were of reagent grade. Elemental analyses were performed with a Carlo-Erba 1108 analyser. The nuclear magnetic resonance (NMR) spectra were recorded on a Bruker ARX-400 using dimethyl sulfoxide-d_6 (DMSO-d_6) as solvent. Infrared (IR) spectra in the 4000–400 cm^{-1} range were recorded on a Bruker V-22 spectrophotometer with the samples prepared as KBr discs. Magnetic susceptibility measurements were performed on pulverised samples at room temperature (RT) with an Alfa MSB-MK1 balance. Diffuse reflectance spectra were recorded on a Shimadzu UV-3101 PC spectrophotometer.

* Corresponding authors. Tel.: +34 986 812410; fax: +34 986 812556 (M.C. Rodríguez-Argüelles), tel.: +34 981 591076; fax: +34 981 597525 (J. Sanmartín-Matalobos).
E-mail addresses: mcarmen@uvigo.es (M.C. Rodríguez-Argüelles), jesus.sanmartin@usc.es (J. Sanmartín-Matalobos).

0277-5387/$ - see front matter © 2009 Elsevier Ltd. All rights reserved.
doi:10.1016/j.poly.2008.12.038



Scheme 1. Representations of H_2L^1, H_2L^2 and HL^3.

2.2. Synthesis of compounds

2.2.1. Synthesis of ligands

The ligands, 2-thiophenecarbonyl hydrazone of 3-isatin, H_2L^1, 2-furoic hydrazone of 3-isatin, H_2L^2, and 2-furoic hydrazone of 3-(*N*-methyl)isatin, HL^3, were obtained by refluxing an ethanol solution of isatin- or *N*-methyl-isatin and the corresponding hydrazide (2-thiophenecarboxylic or 2-furoic hydrazide), following a general procedure previously reported [6]. Powdered solids obtained by cooling were filtrated, washed with ethanol and dried under vacuum. The slow evaporation at room temperature of an ethanol solution of HL^3 led to the isolation of some crystals adequate to their study by diffraction of X-ray.

2.2.1.1. H_2L^1. Anal. Calc. for $C_{13}H_9N_3O_2S$: C, 57.7; H, 3.3; N, 15.5; S, 11.8. Found for yellow solid: C, 57.5; H, 3.3; N, 15.3; S, 12.1%. M.p. 235 °C. Yield 83%. IR (KBr, cm^{-1}, s: strong, m: medium, w: weak, sh: shoulder, br: broad, v br: very broad): ν(NH) 3421w, br, 3168m, v br, 3113w, br; ν(CO) 1732s, 1653s; ν(CN) 1593s; ν(CN) + δ(NH) 1512m. NMR δ(^{1}H, DMSO-d_6, 400 MHz, ppm, s: singlet, d: doublet, t: triplet and m: multiplet) = 11.64 (1H, s, *H*N1), 10.84 (1H, s, *H*N3), 8.17 (1H, d, *H*C13), 8.07 (1H, d, *H*C7), 8.01 (1H, d, *H*C11), 7.39 (1H, t, *H*C5), 7.26 (1H, m, *H*C12), 7.06 (1H, t, *H*C6), 6.91 (1H, d, *H*C4), NMR δ(^{13}C, DMSO-d_6, 100 MHz, ppm) = 164.50 (C9), 162.00 (C1), 143.91 (C3), 138.91 (C2), 134.90 (C11), 134.49 (C10), 133.96 (C13), 132.68 (C5), 127.64 (C12), 126.41 (C7), 121.69 (C6), 115.29 (C8), 110.54 (C4); λ (nm) = 240, 278, 324, 432.

2.2.1.2. H_2L^2. Anal. Calc. for $C_{13}H_9N_3O_3$: C, 61.2; H, 3.5; N, 16.5. Found for yellow solid: C, 61.2; H, 3.4; N, 16.4%. M.p. 266 °C. Yield 83%. IR (cm^{-1}, KBr): ν(NH) 3261m, 3187m, br, 3111m; ν(CO) 1720s, 1666s; ν(CN) 1609s; ν(CN) + δ(NH) 1511m. δ(^{1}H, DMSO-d_6, 400 MHz, ppm) = 13.86 (1H, s, $HO1_{enol}$), 11.51 (1H, s, *H*N1), 11.34 (1H, s, $HN3_{enol}$), 10.85 (1H, s, *H*N3), 8.05 (1H, d, *H*C13), 7.96 (1H, d, *H*C7), 7.63 (1H, d, *H*C11), 7.60 (1H, d, $HC7_{enol}$), 7.41 (1H, t, *H*C5), 7.40 (1H, t, $HC5_{enol}$), 7.12 (1H, t, $HC6_{enol}$), 7.08 (1H, t, *H*C6), 6.96 (1H, d, $HC4_{enol}$), 6.92 (1H, d, *H*C4), 6.80 (1H, m, $HC12_{enol}$), 6.78 (1H, m, *H*C12), δ(^{13}C, DMSO-d_6, 100 MHz, ppm) = 164.54 (C9), 162.80 ($C9_{enol}$), 157.09 (C1), 146.98 (C13), 146.89 ($C13_{enol}$), 145.43 (C10), 143.90 (C3), 142.45 ($C3_{enol}$), 140.00 (C2), 132.76 (C5), 131.76 ($C5_{enol}$), 126.29 (C7), 122.62 ($C6_{enol}$), 121.74 (C6), 120.93 ($C7_{enol}$), 119.69 ($C8_{enol}$), 118.66 (C11), 115.40 (C8), 112.83 ($C12_{enol}$), 112.36 (C12), 111.11 ($C4_{enol}$), 110.65 (C4).

2.2.1.3. HL^3. Anal. Calc. for $C_{14}H_{11}N_3O_3$: C, 62.4; H, 4.1, N, 15.6. Found for yellow solid: C, 62.3; H, 4.1; N, 15.6%. M.p. 197 °C. Yield 62%. IR (cm^{-1}, KBr): ν(NH) 3453m, v br; ν(CO) 1713s, 1678s; ν(CN) 1606s; ν(CN) + δ(NH) 1516m. δ (^{1}H, DMSO-d_6, 400 MHz, ppm) = 13.78 (1H, s, $HO1_{enol}$), 11.55 (1H, s, *H*N1), 8.05 (1H, d, *H*C13), 7.99 (1H, d, *H*C7), 7.63 (1H, d, *H*C11), 7.49 (1H, t, *H*C5), 7.43 (1H, t, $HC5_{enol}$), 7.18 (1H, t, $HC6_{enol}$), 7.15 (1H, t, *H*C6), 7.10 (1H, d, *H*C4), 6.78 (1H, m, *H*C12), 3.23 (1H, m, H_3CN3_{enol}), 3.19 (1H, m, H_3CN3), δ(^{13}C, DMSO-d_6, 100 MHz, ppm) = 163.21 (C9), 160.93 ($C9_{enol}$), 157.10 (C1), 147.00 (C13), 146.90 ($C13_{enol}$), 145.42 (C10), 144.91 (C3), 143.65 ($C3_{enol}$), 139.80 (C2), 132.62 (C5), 131.63 ($C5_{enol}$), 125.95 (C7), 123.12 ($C6_{enol}$), 122.21 (C6), 120.54 ($C7_{enol}$), 118.94 ($C8_{enol}$), 118.73 (C11), 114.73 (C8), 112.85 ($C12_{enol}$), 112.35 (C12), 109.87 ($C4_{enol}$), 109.27 (C4), 25.92 (CN3), 25.58 ($CN3_{enol}$); λ (nm) = 238, 262, 388, 430.

2.2.2. Synthesis of complexes

Complexes were obtained by refluxing for 6–12 h an ethanol suspension of each metal acetate ($ZnAc_2$, $CuAc_2$, $NiAc_2$ and $CoAc_2$) and corresponding free ligands in a 1:2 molar ratio. The resulting suspension was stirred at room temperature for about 24–72 h. Powder solids obtained by cooling, were filtrated, washed with ethanol and dried under vacuum. After several attempts of recrystallisation of all these solids in ethanol–methanol solutions, only small single crystals of $[Zn(HL^1)_2] \cdot 1.75MeOH$ could be obtained by slow evaporation, at room temperature from a solution of $[Zn(HL^1)_2] \cdot EtOH$.

2.2.2.1. $[Zn(HL^1)_2] \cdot EtOH$. Anal. Calc. for $C_{28}H_{22}N_6O_5S_2Zn$: C, 51.6; H, 3.4; N, 12.9; S, 9.8. Found for orange solid: C, 51.3; H, 3.2; N, 12.7; S, 10.0%. M.p. >300 °C. Yield 50%. IR (KBr, cm^{-1}): ν(NH + OH) 3177w, br, 3143m, v br, 3064w; ν(CO) 1703s, 1690s; ν(CN) 1611s; ν(CN) + δ(NH) 1531m. δ(^{1}H, DMSO-d_6, 400 MHz, ppm) = 11.22 (1H, s, *H*N3), 8.24 (1H, d, *H*C7), 7.97 (1H, d, *H*C13), 7.91 (1H, d, *H*C11), 7.44 (1H, br, *H*C5), 7.24 (2H, m, *H*C6, *H*C12), 7.05 (1H, d, *H*C4), δ(^{13}C, DMSO-d_6, 100 MHz, ppm) = 173.12 (C1), 166.50 (C9), 143.11 (C3), 138.86 (C10), 135.23 (C2), 132.90 (C11), 132.34 (C5), 131.86 (C13), 128.28 (C12), 126.52 (C7), 123.07 (C6), 116.34 (C8), 111.64 (C4).

2.2.2.2. $[Cu(HL^1)_2] \cdot 2.5H_2O$. Anal. Calc. for $C_{26}H_{21}CuN_6O_{6.5}S_2$: C, 48.1; H, 3.3; N, 12.9; S, 9.9. Found for brown solid: C, 48.3; H, 3.3; N, 12.9; S, 9.8%. M.p. = 271 °C. Yield 89%. IR (KBr, cm^{-1}): ν(NH + OH) 3447m, v br; ν(CO) 1683m, br; ν(CN) 1612s; ν(CN) + δ(NH) 1527m. μ (R.T., BM) = 1.8.

2.2.2.3. $[Ni(HL^1)_2] \cdot 0.5H_2O$. Anal. Calc. for $C_{26}H_{17}N_6NiO_{4.5}S_2$: C, 51.3; H, 2.8; N, 13.8; S, 10.5. Found for brown solid: C, 51.2; H, 2.7; N, 13.7; S, 10.9%. M.p. >300 °C. Yield 47%. IR (KBr, cm^{-1}): ν(NH) 3390m, v br; ν(CO) 1660s; ν(CN) 1617s; ν(CN) + δ(NH) 1527m. μ

(R.T., BM) = 3.1; λ (nm) = 236, 282, 354 [intraligand absorptions], 482 [ML charge transfer], 625, 690 [$\nu_2\ ^3T_{1g}(F) \leftarrow\ ^3A_{2g}(F)$], 1040 [$\nu_1\ ^3T_{2g}(F) \leftarrow\ ^3A_{2g}(F)$].

2.2.2.4. $[Co(HL^1)_2] \cdot H_2O$. Anal. Calc. for $C_{26}H_{18}CoN_6O_5S_2$: C, 50.6; H, 2.9; N, 13.6; S, 10.4. Found for brown solid: C, 50.3; H, 2.9; N, 13.6; S, 10.6%. M.p. = 215°C. Yield 37%. IR (KBr, cm^{-1}): ν(NH + OH) 3421m, v br; ν(CO) 1677s, br; ν(CN) 1612s; ν(CN) + δ(NH) 1526m. μ(R.T., BM) = 4.7; λ (nm) = 240, 284, 342, 448 [intraligand absorptions], 512 [ML charge transfer], 665, 740 [$\nu_3\ ^4T_1(P) \leftarrow\ ^4A_2(F)$].

2.2.2.5. $[Zn(HL^2)_2] \cdot 2H_2O$. Anal. Calc. for $C_{27}H_{19}N_6O_{5,5}Zn$: C, 51.2; H, 3.3; N, 13.8. Found for orange solid: C, 51.4; H, 3.3; N, 13.6%. M.p. = 270 °C. Yield 76%. IR (KBr, cm^{-1}): ν(NH + OH) 3443m, v br, 3141m, br; ν(CO) 1699s, br; ν(CN) 1615s, br; ν(CN) + δ(NH) 1517m. δ(^{1}H, DMSO-d_6, 400 MHz, ppm) = 11.26 (1H, s, *H*N3$_{enol}$), 8.26 (1H, d, *H*C7), 8.00 (1H, d, *H*C13), 7.48 (1H, d, *H*C11), 7.43 (1H, t, *H*C5), 7.22 (1H, t, *H*C6), 7.05 (1H, d, *H*C4), 6.74 (1H, m, *H*C12), δ(^{13}C, DMSO-d_6, 100 MHz, ppm) = 169.79 (C1), 166.62 (C9), 149.10 (C10), 146.97 (C13), 143.01 (C3), 135.26 (C2), 132.30 (C5), 126.63 (C7), 123.11 (C6), 117.14 (C11), 116.25 (C8), 112.40 (C12), 111.65 (C4).

2.2.2.6. $[Cu(HL^2)_2] \cdot 2H_2O$. Anal. Calc. for $C_{26}H_{10}CuN_6O_8$: C, 51.4; H, 3.3; N, 13.8. Found for brown solid: C, 51.6; H, 3.3 N, 13.6%. M.p. = 260°C. Yield 44%. IR (KBr, cm^{-1}): ν(NH + OH) 3392m, v br; ν(CO) 1680s, br; ν(CN) 1613s; ν(CN) + δ(NH) 1578m. μ (R.T., BM) = 1.9.

2.2.2.7. $[Ni(HL^2)_2] \cdot H_2O$ EtOH. Anal. Calc. for $C_{28}H_{24}N_6NiO_8$: C, 53.3; H, 3.8; N, 13.3. Found for brown solid: C, 53.1; H, 3.9; N, 13.3%. M.p. >300 °C. Yield 71%. IR (KBr, cm^{-1}): ν(NH + OH) 3419m, v br; ν(CO) 1661s, br; ν(CN) 1613s; ν(CN) + δ(NH) 1577m. μ (R.T., BM) = 3.2.

2.2.2.8. $[Co(HL^2)_2] \cdot 1.5H_20$ EtOH. Anal. Calc. for $C_{29}H_{25}CoN_6O_{7.5}$: C, 52.5; H, 3.9; N, 13.1. Found for deep red solid: C, 52.2; H, 3.8; N, 12.9%. M.p. = 280°C. Yield 50%. IR (KBr, cm^{-1}): ν(NH + OH) 3417m, v br; ν(CO) 1672s, br; ν(CN) 1614s; ν(CN) + δ(NH) 1577m. μ (R.T., BM) = 4.6.

2.2.2.9. $[Zn(L^3)_2] \cdot 0.75H_2O$. Anal. Calc. for $C_{28}H_{21.5}N_6O_{6.75}Zn$: C, 54.6; H, 3.5; N, 13.6. Found for orange solid: C, 54.6; H, 3.5; N, 13.3%. M.p. >300 °C. Yield 62%. IR (KBr, cm^{-1}): ν(NH + OH) 3474m, v br; ν(CO) 1685s, br; ν(CN) 1608s; ν(CN) + δ(NH) 1525m. δ(^{1}H, DMSO-d_6, 400 MHz, ppm) = 8.31 (1H, d, *H*C7), 8.00 (1H, d, *H*C13), 7.51 (1H, t, *H*C5), 7.49 (1H, d, *H*C11), 7.29 (1H, t, *H*C6), 7.23 (1H, d, *H*C4), 6.75 (1H, m, *H*C12), 3.21 (1H, m, H_3CN3), δ(^{13}C, DMSO-d_6, 100 MHz, ppm) = 169.81 (C1), 165.25 (C9), 149.01 (C10), 147.06 (C13), 144.25 (C3), 134.90 (C2), 132.21 (C5), 126.43 (C7), 123.55 (C6), 117.32 (C11), 115.81 (C8), 112.43 (C12), 110.25 (C4), 26.61 (CN3).

2.2.2.10. $[Cu(L^3)_2] \cdot 0.5H_2O$. Anal. Calc. for $C_{28}H_{20}CuN_6O_6$: C, 55.2; H, 3.5; N, 13.8. Found for brown solid: C, 55.2; H, 3.4; N, 13.7%. M.p. >300 °C. Yield 65%. IR (KBr, cm^{-1}): ν(NH) 3455m, v br; ν(CO) 1672s; ν(CN) 1605s; ν(CN) + δ(NH) 1522m. μ (R.T., BM) = 2.1 λ (nm) = 242, 262, 336 [intraligand absorptions], 486 [ML charge transfer].

2.2.2.11. $[Ni(L^3)_2] \cdot 0.5H_2O$. Anal. Calc. for $C_{28}H_{21}N_6NiO_{6.5}$: C, 55.7; H, 3.5; N, 13.9. Found for brown solid: C, 55.4; H, 3.4; N, 13.8%. M.p. >300 °C. Yield 65%. IR (KBr, cm^{-1}): ν(NH) 3445m, v br; ν(CO) 1665s; ν(CN) 1604s; ν(CN) + δ(NH) 1524m. μ (R.T., BM) = 3.1; λ (nm) = 270, 334 [intraligand absorptions], 486 [ML charge transfer], 658 [$\nu_2\ ^3T_{1g}(F) \leftarrow\ ^3A_{2g}(F)$], 1090 [$\nu_1\ ^3T_{2g}(F) \leftarrow\ ^3A_{2g}(F)$].

2.2.2.12. $[Co(L^3)_2] \cdot 0.5H_2O$. Anal. Calc. for $C_{28}H_{20}CoN_6O_6$: C, 55.6; H, 3.4; N, 13.9. Found for brown solid: C, 55.6; H, 3.3; N, 13.7%. M.p. >300 °C. Yield 63%. IR (KBr, cm^{-1}): ν(NH) 3453m, v br; ν(CO) 1673s; ν(CN) 1604s; ν(CN) + δ(NH) 1504m. μ (R.T., BM) = 4.6; λ (nm) = 242, 274, 334 [intraligand absorptions], 500 [ML charge transfer], 646, 726 [$\nu_3\ ^4T_1(P) \leftarrow\ ^4A_2(F)$].

2.3. Single crystal X-ray diffraction measurements for HL^3 and $[Zn(HL^1)_2] \cdot 1.75MeOH$

The most significant crystal and refinement data for HL^3 and $[Zn(HL^1)_2] \cdot 1.75MeOH$ are summarised in Table 1. Orange prismatic single crystals of HL^3 and $[Zn(HL^1)_2] \cdot 1.75MeOH$ were mounted on a fibreglass, and their X-ray diffraction data were collected at room temperature on a Bruker CCD Smart 1000 diffractometer, employing graphite monochromated Mo Kα radiation (λ = 0.71073 Å). Data reduction was performed using the SAINT package [7], and involved corrections for Lorentz, polarisation and absorption (SADABS) effects [8]. The structures were solved by direct methods (SHELXS-97) [9], and refined by full-matrix least-squares techniques on all F^2 (SHELXL-97) [9]. In the case of HL^3, all the H atoms were introduced in calculated positions, excluding that bonded to N1, which was located in the Fourier maps. Molecular graphics were represented by ORTEP-3 for Windows [10].

Several crystals of $[Zn(HL^1)_2] \cdot 1.75MeOH$ were mounted, but data collected revealed not only severe non-merohedral twinning, but a poor diffraction ability as well. In fact, the best of these data sets only displays a θ_{max} of ca. 23°. Despite these inconveniences, the structure could be clearly solved using direct methods (SHELXS-97) [9], and even refined by standard Fourier techniques based on weighted full-matrix least-squares on F^2 (SHELXL-97) [9], with a final R_1 = 0.0974. This procedure allowed modelling with some restraints the disorder observed for some solvated methanol molecules, and for the thiophene rings of both ligand units. This latter can be described as a rotation of 180° around the pivot C atoms (C110 and C210), which leads to find two different occupation sites for the S atoms [S101 and S11′ (0.68:0.32); S201 and S21′ (0.79:0.21)], and their opposite C atoms [C111 and C11′ (0.68:0.32); C211 and C21′

Table 1
Crystal data and structure refinement for HL^3 and $[Zn(HL^1)_2] \cdot 1.75MeOH$.

Compound	HL^3	$[Zn(HL^1)_2] \cdot 1.75MeOH$
Empirical formula	$C_{14}H_{11}N_3O_3$	$C_{27.75}H_{23}N_6O_{5.75}S_2Zn$
Formula weight	269.26	662.01
Crystal system	monoclinic	monoclinic
Space group	$P2_1/c$	$P2_1/n$
Unit cell dimensions		
a (Å)	10.774(2)	14.350(3)
b (Å)	7.4526(16)	16.908(3)
c (Å)	16.149(4)	15.041(3
β (°)	101.850(5)	112.78(1)
V (Å^3)	1269.0(5)	3364.7(11)
Z	4	4
D_{calc} (Mg/m^3)	1.409	1.307
Absorption coefficient (mm^{-1})	0.102	0.899
F(0 0 0)	560	1358
Crystal size (mm^3)	0.22 × 0.22 × 0.15	0.12 × 0.10 × 0.08
θ Range for data collection (°)	1.93–28.00	1.67–23.27
Reflection collection/ independent reflection (R_{int})	7903/3022 (0.1186)	5870/3275 (0.0586)
Data/restraints/parameters	3022/0/186	3275/0/386
Goodness-of-fit on F^2	0.697	0.970
Final *R* indices ($I > 2\sigma(I)$)	R_1 = 0.0499, wR_2 = 0.0874	R_1 = 0.0974, wR_2 = 0.2599
R indices (all data)	R_1 = 0.2021, wR_2 = 0.1152	R_1 = 0.2273, wR_2 = 0.3443
Largest difference in peak and hole (e Å^{-3})	0.169 and −0.208	0.771 and −0.389

(0.79:0.21)]. Non-H atoms were anisotropically treated, except C and O atoms with low occupation sites. All the H atoms were added theoretically and treated as riding on concerned atoms. In view of the data quality, a detailed analysis of the dimensions seems inadvisable and consequently, bond distances and angles should be interpreted with some caution, but the molecular structure determined for the complex appears unambiguous.

2.4. Antimicrobial activity

All the ligands and their complexes were assayed for their *in vitro* growth inhibitory activity using the twofold broth dilution technique [11]. All determinations were performed in triplicate and confirmed by three separate experiments.

Since the compounds are virtually water insoluble, samples were dissolved in dmso. In order to test final concentrations ranging from 200 to 0.15 μg/mL, further dilutions were prepared in the test media (Haemophilus Test Medium for *Haemophilus influenzae*, Mueller Hinton Broth for the remaining bacteria and Sabouraud Liquid Medium for fungi). Solvent never exceeded 1% v/v and controls containing broth media supplemented with only dmso at the same dilutions used in the experiments were found inactive. The final inoculum size was 5×10^4 bacteria/mL and 1×10^3 fungi/mL. After incubation at 37 °C for 24 h (bacteria) or at 30 °C for 48 h (fungi), the minimal inhibitory concentrations (MICs, μg/mL) were determined as the lowest concentrations of drug in the medium where no microbial growth was visible.

To evaluate the minimal bactericidal concentrations (MBCs, μg/mL) and the minimal fungicidal concentrations (MFCs, μg/mL), 100 μL from each clear sample were removed and transferred in tubes containing 1 mL of fresh medium and then incubated at 37 °C for 24 h (bacteria) and 30 °C for 48 h (fungi).

The antimicrobial activity was investigated against some Gram positive and Gram negative bacteria, as well as yeasts and moulds that are related below:

- Gram positive bacteria: *Bacillus megaterium* BGSC 7A2, *Bacillus subtilis* ATCC 6633, *Bacillus thuringiensis* var. *kurstaki* BGSC 4D1, *Sarcina lutea* ATCC 9341, *Staphylococcus aureus* ATCC 25923, *Staphylococcus epidermidis* ATCC 12228 and clinical isolates of methicillin-resistant *S. aureus*, methicillin-resistant *S. epidermidis*, *Staphylococcus haemolyticus*, *Streptococcus agalactiae*, *Streptococcus faecalis* and *Streptococcus faecium*;
- Gram negative bacteria: *Enterobacter cloacae* ATCC 23355, *Escherichia coli* SPA 27, *Proteus vulgaris* ATCC 13315, *Pseudomonas aeruginosa* ATCC 9027, *Salmonella typhimurium* ATCC 14028, *Serratia marcescens* ATCC 8100 and clinical isolates of *H. influenzae*, *Klebsiella pneumoniae* and *Proteus mirabilis*.
- Yeasts: *Candida tropicalis* ATCC 1369, *Saccharomyces cerevisiae* ATCC 9763.
- Moulds: *Aspergillus niger* ATCC 6275.

Since $[Co(HL^1)_2] \cdot H_2O$ showed antifungal activity, we expanded the test in liquid medium to other yeasts such as *Candida albicans* ATCC 10231, clinical isolates of *Candida guilliermondii*, *Candida parapsilosis* and *Cryptococcus neoformans*. Moulds including *Pseudallescheria boydii*, *Sporothrix schenkii*, some dermatophytes (*Epidermophyton floccosum*, *Microsporum gypseum*, *Trichophyton mentagrophytes*) and phytopathogenic fungi (*Alternaria tenuis* ATCC 11680, *Botrytis cinerea*, *Fusarium* sp., *Fusicladium dendriticum, Sclerotinia minor*) were also tested by the twofold agar dilution method. The dmso solution of $[Co(HL^1)_2] \cdot H_2O$ was serially diluted in Sabouraud dextrose agar to give a range of concentrations from 200 to 1.5 μg/mL. The inocula were prepared from exponentially growing cultures and were performed by applying the strains on the agar surface. Growth controls were included. The minimal inhibitory concentration (MIC) was read as the lowest concentration of the compound in the agar where no visible growth of the moulds took place after 14 days of incubation at 25 °C.

3. Results and discussion

The empirical formula of the complexes of the general type $[M(L)_2] \cdot nX$, where M = Co(II), Ni(II), Cu(II) or Zn(II) and X = ethanol, water, was calculated on the basis of C, H and N microanalysis. Excluding $[Cu(L^3)_2] \cdot 0.5H_2O$, attempts to prepare a series of complexes by reaction of metal chlorides and free ligands were unsuccessful, despite some reaction conditions such as time, temperature, pH and even molar ratios (1:1 instead of 1:2) were altered. The reason for obtaining only complexes with 1:2 (metal:ligand) molar ratio could be attributed to the two bulky terminal moieties of the ligands. According to physicochemical characterisation data the three ligands coordinated with elimination of the hydrazine proton, which is the most labile of all. This is agreement with the structure observed for $[Zn(HL^1)_2] \cdot 1.75MeOH$, characterised by X-ray diffraction.

All the obtained metal complexes were soluble in dmso and dmf, but insoluble in water and most organic solvents. Although dmso and dmf are considered coordinating solvents they did not compete in the coordination sphere with any of the three ligands. In fact, all the complexes dissolved in dmso for their study by NMR spectroscopy are stable for long periods of time.

3.1. Crystal structure of HL^3

The molecular structure of HL^3 is depicted in Fig. 1. The planarity of the ligand is expressed in the low value for the dihedral angle between the isatin and hydrazide residues. The most significant bond distances and angles are listed in Table 2. The bond distances in the acylhydrazone chain are in good agreement with others reported elsewhere (Table 3) [4,5,12]. The O1–C1 distance (about 1.217 Å) is indicative of a keto tautomer for this compound in the solid state at room temperature. The mean distance in the isatin aromatic ring is 1.394 Å which is also similar to those found in isatin 3-picolinoyl hydrazone [4].

N1–C1, N1–N2 and N2–C2 bonds display different configurations, which can be described as *Z*, *E* and *Z*, respectively. This spatial array [5] seems clearly influenced by an intramolecular bifurcated hydrogen bond [N1–H···O2 (about 2.744 Å) and N1–H···O3 (about 2.665 Å)].

3.2. Crystal structure of $[Zn(HL^1)_2] \cdot 1.75MeOH$

The most significant bond distances and angles are summarised in Tables 4 and 5, respectively. An ORTEP representation of this zin-

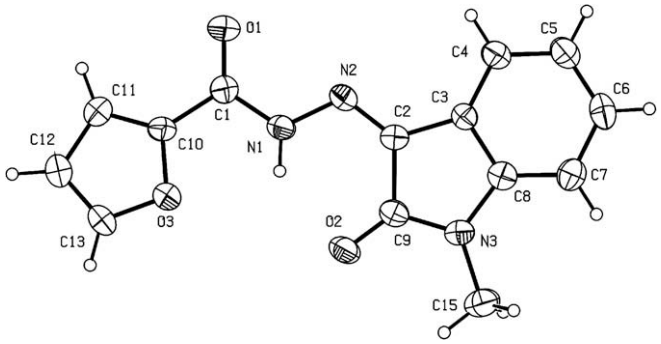


Fig. 1. Molecular structure of HL^3.

Table 2
Selected bond distances (Å) and angles (°) for HL^3.

Atoms	Distances (Å)	Atoms	Angle (°)
O1–C1	1.2173	N1–C1–C10	113.83
C1–C10	1.4694	O1–C1–C10	122.23
N1–C1	1.3644	O1–C1–N1	124.13
N1–N2	1.3733	C1–N1–N2	120.73
N2–C2	1.2873	C2–N2–N1	116.62
O2–C9	1.2263	N2–C2–C9	127.53
N3–C9	1.3583	N2–C2–C3	125.73
N3–C8	1.4163	C9–N3–C8	110.52
N3–C15	1.4603	C9–N3–C15	124.43
O3–C10	1.3633	C8–N3–C15	125.13
O3–C13	1.3753	C10–O3–C13	105.52

Table 3
Selected bond distances (Å) for 2-thiophenecarbonyl hydrazone of 3-(*N*-methyl)isatin (A), isonicotinoyl hydrazone of 3-(*N*-methyl)isatin (B), picolinoyl hydrazone of 3-isatin (C) and isonicotinoyl hydrazone of 3-isatin (D).

Bonds	A [5]	B [5]	C [4]	D [12]
O1–C1	1.230(9)	1.218(2)	1.229(7)	1.229(3)
C1–C10	1.474(10)	1.503(2)	1.492(8)	1.505(5)
N1–C1	1.356(9)	1.372(2)	1.351(7)	1.356(1)
N1–N2	1.347(7)	1.369(2)	1.387(2)	1.376(4)
N2–C2	1.288(8)	1.290(2)	1.280(7)	1.296(5)
N3–C8	1.409(8)	1.418(2)	1.395(9)	1.404(5)
N3–C9	1.363(8)	1.360(2)	1.373(7)	1.354(5)
N3–C15	1.457(8)	1.458(2)		

Table 4
Selected bond distances for $[Zn(HL^1)_2] \cdot 1.75MeOH$.

Atoms	Distance	Atoms	Distance
Zn1–N102	2.086(15)	Zn1–N202	2.002(14)
Zn1–O101	2.053(11)	Zn1–O201	2.062(11)
O101–C101	1.293(18)	O201–C201	1.283(18)
C101–C110	1.41(2)	C201–C210	1.42(2)
N102–C102	1.27(2)	N202–C202	1.273(19)
N101–N102	1.379(18)	N202–N201	1.358(16)
C101–N101	1.3291(9)	C201–N201	1.35(2)
C102–C109	1.48(2)	C202–C209	1.53(2)
C109–O102	1.26(2)	C209–O202	1.22(2)
Zn1···O102	2.558(13)	Zn1···O202	2.569(12)

Table 5
Selected angles for $[Zn(HL^1)_2] \cdot 1.75MeOH$.

Atoms	Angle	Atoms	Angle
N202–Zn1–O101	120.3(5)	N202–Zn1–O201	77.4(6)
O101–Zn1–O201	102.1(4)	O101–Zn1–N102	77.6(6)
N202–Zn1–N102	152.8(6)	O201–Zn1–N102	121.3(5)
C101–O101–Zn1	111.1(12)	C201–O201–Zn1	109.5(12)
O101–C101–N101	126.0(17)	O201–C201–N201	126.7(17)
O101–C101–C110	118.5(18)	O201–C201–C210	115(2)
C101–N101–N102	110.9(15)	C101–N101–N102	110.9(15)
C102–N102–N101	123.4(16)	C102–N102–N101	123.4(16)
C101–N101–N102	110.9(15)	C201–N201–N202	107.5(14)
N102–C102–C109	117.8(19)	N202–C202–C209	115.8(17)

c(II) complex is shown in Fig. 2, with its corresponding numbering scheme.

The asymmetric unit contains a discrete molecule of the neutral complex with solvated methanol molecules that show some disorder and partial occupation sites. The molecular structure shows the coordination of two monodeprotonated ligands behaving as chelating *N*,*O*-donors. The zinc ion assumes in $[Zn(HL^1)_2] \cdot 1.75MeOH$ a geometry that could be described as pseudo-tetrahedral, with Zn–O and Zn-N bond lengths ranging 2.0–2.1 Å, what is usual for this type of ligands [4]. The geometry of the complex presents a substantial distortion towards a square pyramidal form due to weak secondary interactions between the O atoms (O102 and O202) of each isatin residue and the metal centre. The obtained Zn···O distances (about 2.55 Å) are too long to be considered as true coordinated bonds.

The spatial array of the coordinated ligand is allowed by an extended planarity, with a configuration of the N101–C101, N101–N102 and N102–C102 bonds which can be described as *Z*, *E* and *E*, respectively. Geometric parameters around C101 and C201 seem to indicate the presence of keto forms for the coordinated ligand, as occurred in HL^3 and some other related free ligands [4,5,12].

The crystal packing scheme seems supported by substantial H-bonding between the amine atoms and one of the solvated methanol molecules. In addition, some intermediate and weak π–π stacking interactions, as well as σ–π contacts can be also worthy of mention.

3.3. NMR studies

The use of two-dimensional, COSY (correlation spectroscopy), HMQC (heteronuclear multiple quantum correlation) and HMBC (heteronuclear multiple bond correlation) experiments have allowed a full assignment for H- and C-signals of free ligands and their zinc(II) complexes.

Free ligands. H_2L^1, H_2L^2 and HL^3 are mainly in keto form in DMSO-d_6 solution. In fact, we did not detect neither H- nor C-signals for the enol form of H_2L^1. However, the presence of the corresponding enol forms of H_2L^2 and HL^3 in solution is unquestionable. Thus, the keto:enol molar ratios could be assessed for about 5:1 and 4:1 in H_2L^2 and HL^3, respectively. Fig. 3 (bottom) shows the ^{13}C spectrum of H_2L^2 that illustrates the keto–enol equilibrium affecting –N(1)H–C1(O)– bonds.

In the enol form C9, C7, C5 and C3 signals are upfield shifted respect to the keto form, while C12, C8, C6 and C4 signals experiment an inverse effect. Among the observed signals for both forms, C8 and C7 are the most influenced by the keto-enol equilibrium (shifted in about 5.5 ppm). Similarly, Fig. 4 shows that the most affected H-signals are attributed to *H*C7 and *H*N(3) (shifted in about 0.5 ppm).

Comparison of ^{13}C NMR spectra of H_2L^1 and H_2L^2 allows to observe the influence of the heteroatom on the C-atom signals of furan and thiophene rings. Thus, C10 and C13 result more deshielded when the heteroatom is O than when is S, whereas for C1, C11 and C12 occurs the inverse. Similarly, the deshielding effect on H11, H12 and H13 atoms is more marked when the heteroatom is S that when is O.

Zinc complexes. Comparison of ^1H NMR spectra of zinc complexes and the corresponding free ligands allows the following observations:

(i) The absence of the signal assigned to *H*N(1) proton in the three zinc(II) complexes is indicative of the monodeprotonation of their respective ligands.
(ii) A slight downfield shift (0.2–0.4 ppm) for *H*N(3), *H*C7, *H*C6 and *H*C4 proton signals respect to their corresponding free ligands is interpreted as due to the complexation of the zinc(II) ion through N(2). This is illustrated in Fig. 4 for the H_2L^2–$[Zn(HL^2)_2] \cdot 2H_2O$ pair.
(iii) A very slight upfield shift (0.1 ppm) undergone by *H*C11 and *H*C13 proton signals is coherent with the participation of O(1) in the metal coordination.
(iv) *H*C5 and *H*C12 proton signals remained virtually unaffected upon the metal coordination.

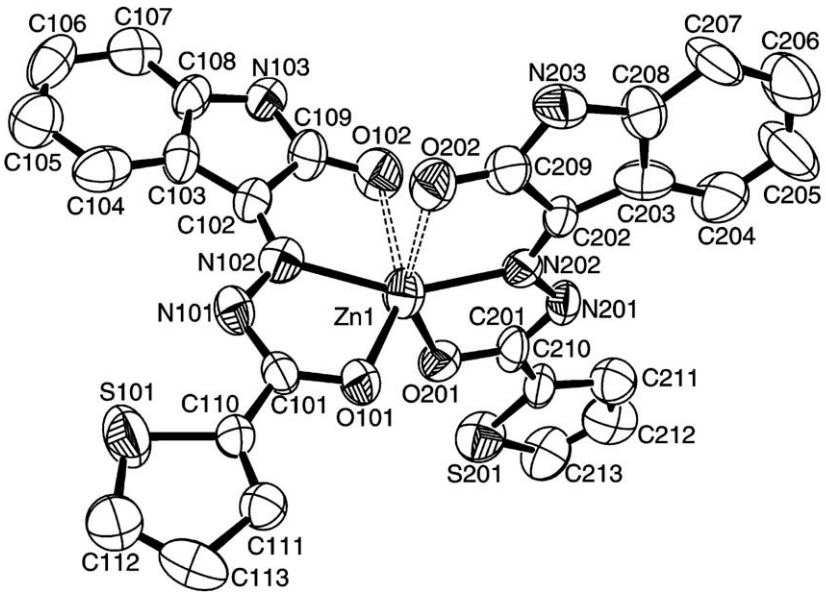


Fig. 2. ORTEP representation of [Zn(HL^1)] at 40% probability. Solvated methanol molecules, H atoms, and disordered S and C atoms of the thiophene residues with lower occupation sites have been omitted for clarity.

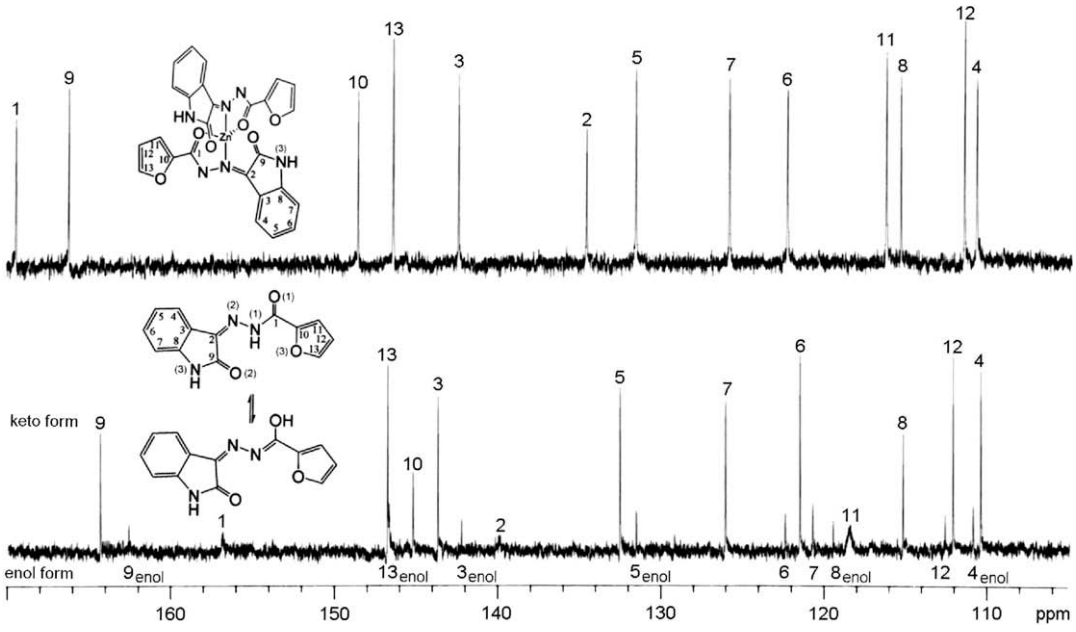


Fig. 3. ^{13}C NMR spectra of H_2L^2 (bottom) and $[Zn(HL^2)_2] \cdot 2H_2O$ (top) using DMSO-d_6 as solvent.

The comparative study of ^{13}C NMR spectra of zinc complexes and the corresponding free ligands allows us to conclude that the most affected C-signals by the complexation are those attributed to C1 (bonded to O1) and C2 (bonded to N2). In particular, C1 signal underwent a downfield shift (about 12.7 ppm) in $[Zn(HL^2)_2]\cdot 2H_2O$, while C2 signal underwent an upfield shift in the mentioned zinc complex of H_2L^2 (about 4.7 ppm). The remaining signals show shifts below 3.7 ppm, being about 2.1 ppm for C9 (bonded to O2). Based on this, the three ligands can be considered as O(1), N(2)-donors in their zinc(II) complexes, which is in agreement with that described for the molecular structure of $[Zn(HL^1)_2] \cdot 1.75$MeOH.

3.4. IR spectra

The IR spectra of the complexes showed very broad bands in the 4000–3000 cm^{-1} region, corresponding to the presence of solvent molecules (ethanol or/and water) associated through hydrogen bonds. For an accurate interpretation of the IR spectra of the Zn(II), Cu(II), Ni(II) and Co(II) complexes we used our previous reports on 3-(*N*-methyl)isatin-3-picolinoyl hydrazone [4] and 3-(*N*-methyl)isatin-2-thiophenecarbonyl hydrazone [5] complexes. Both ligands and their nickel(II) complexes were structurally characterised by X-ray diffraction. These Ni(II) complexes resulted to be octahedral (μ_{eff} = 3.1–3.2 BM) with the ligands behaving as κ^3-*O*,*N*,*O*.

In the IR spectra of all synthesised metal complexes the ν(CN) band of each ligand (1593–1609 cm^{-1}) was shifted up to 1604–1617 cm^{-1}. Additionally, a shift of the ν(CN) + δ(NH) band from 1511–1516 cm^{-1} (free ligands) up to 1517–1578 cm^{-1} was also observed. Both shifts, which include the effect provoked by the back-donation to the coordinated metal ions, express the participation of the hydrazone nitrogen atom in the coordination. The

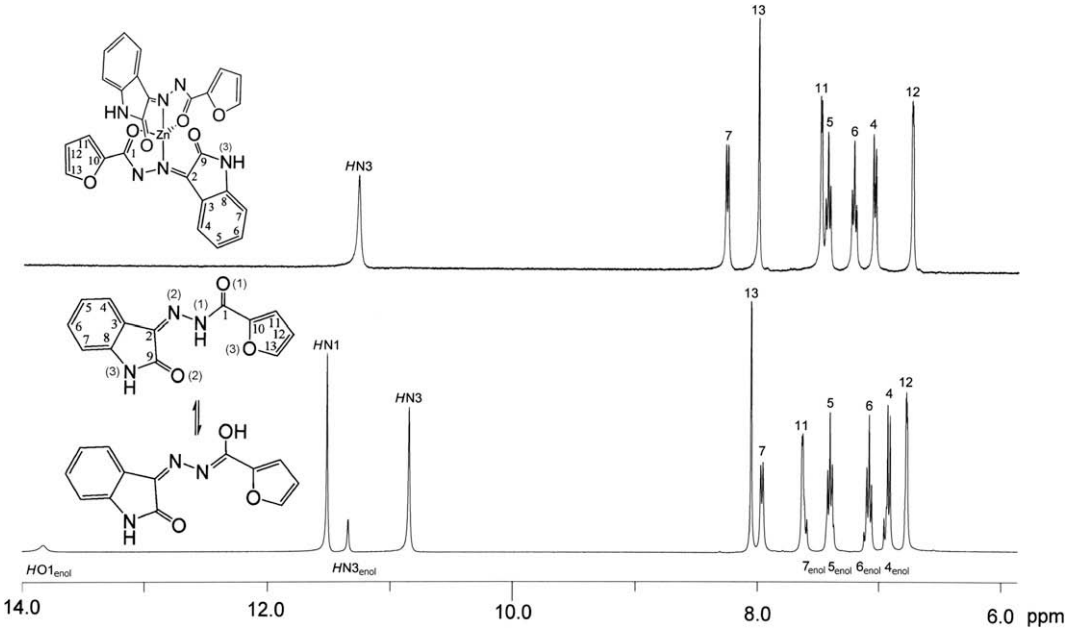


Fig. 4. ^{1}H NMR spectra of H_2L^2 (bottom) and $[Zn(HL^2)_2] \cdot 2H_2O$ (top) using DMSO-d_6 as solvent.

highest shifts were observed for the complexes of HL^3. Apparently, the methyl group substituted in the isatin ring of HL^3 provokes an electronic effect that acts contrary to the shift induced by coordination to the metal ion. Coincidently, the smallest shifts were also observed when comparing the ^{13}C NMR spectra of HL^3 and $[Zn(L^3)_2] \cdot 0.75H_2O$.

The ν(CO) band of the aliphatic carbonyl group was also analysed. The band shifted from 1732–1713 cm^{-1} (free ligands) down to 1703–1660 cm^{-1} in the complexes. Actually, two ν(CO) bands were recorded for the free ligands, with an extra one at 1678–1653 cm^{-1} since two carbonyl groups are present. The highest wavelength corresponds to aliphatic carbonyl and the lowest to the isatin carbonyl group. Upon coordination the band of this latter group overlaps with the shifted aliphatic carbonyl group band.

The three nickel(II) complexes presented the highest shift in the ν(CO) band, down to 1660–1665, a shift similar to that observed in the reported complexes with 3-(*N*-methyl)isatin-3-picolinoyl hydrazone [4] and 3-(*N*-methyl)isatin-2-thiophenecarbonyl hydrazone [5]. The nickel(II) complexes with these latter two ligands were reported to present an octahedral structure with the carbonyl isatin group also participating in the coordination, although less intensely than the aliphatic carbonyl group, according to X-ray structural analysis.

3.5. Magnetism and diffuse reflectance

The μ_{eff} values obtained for $[Ni(HL^1)_2] \cdot 0.5H_2O$, $[Ni(HL^2)_2] \cdot H_2O \cdot EtOH$ and $[Ni(L^3)_2] \cdot 0.5H_2O$ at room temperature, 3.1, 3.2 and 3.1 BM, respectively, correspond to octahedral geometries [5,13–15] with the ligands acting as κ^3-*O,N,O*, as already analysed from the IR spectra. Additionally, the diffuse reflectance spectra of $[Ni(HL^1)_2] \cdot 0.5H_2O$ (Fig. 5) and $[Ni(HL^2)_2] \cdot H_2O \cdot EtOH$ show two electronic transitions, ν_1 $[^3T_{2g}(F) \leftarrow {}^3A_{2g}(F)]$ and ν_2 $[^3T_{1g}(F) \leftarrow {}^3A_{2g}(F)]$, in the 1040–1090 and 625–690 nm ranges, respectively, characteristic for octahedral nickel(II) complexes. A similar spectrum was reported for the nickel(II) complex of 3-(*N*-methyl)isatin-2-thiophenecarbonyl hydrazone [5] with a doublet at 618 and 676 nm. This latter complex presented a octahedral distorted coordination environment with Ni–O distances at 2.059 and 2.236 Å [5]. In the $[Ni(HL^1)_2] \cdot 0.5H_2O$ spectrum (Fig. 5), the ν_2 absorption

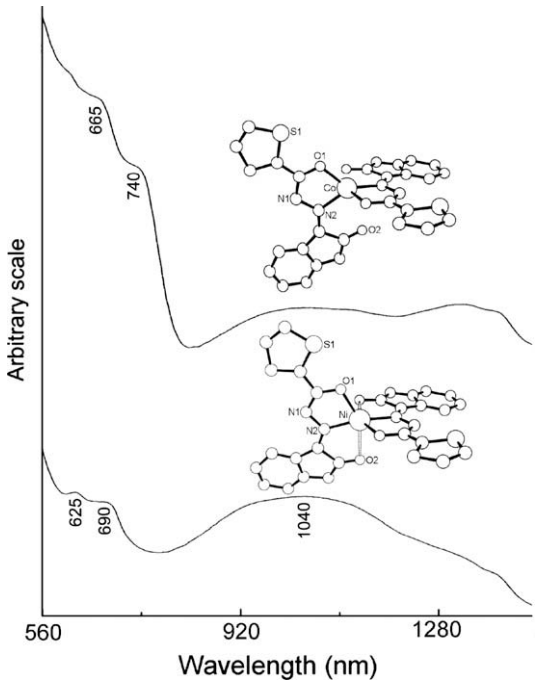


Fig. 5. Diffuse reflectance spectra (in the range 560–1460 nm) for two representative complexes $[Co(HL^1)_2] \cdot H_2O$ (top) and $[Ni(HL^1)_2] \cdot 0.5H_2O$ (bottom).

was also observed as a splitted band that can be attributed to the previously described distortion.

The μ_{eff} values of $[Co(HL^1)_2] \cdot H_2O$, $[Co(HL^2)_2] \cdot 1.5H_2O$ EtOH and $[Co(L^3)_2] \cdot 0.5H_2O$ (4.7, 4.6 and 4.6 BM, respectively) fall within the range characteristic for high spin tetrahedral cobalt(II) complexes. This is coherent with κ^3-*O,N* behaviour of the three ligands in their respective Co(II) complexes. The diffuse reflectance spectra of $[Co(HL^1)_2] \cdot H_2O$ (Fig. 5) and $[Co(L^3)_2] \cdot 0.5H_2O$ in the visible region presented the asymmetric ν_3 $^4T_1(P) \leftarrow {}^4A_2(F)$ band, characteristic of a Co(II) ion with tetrahedral geometry [5,13,16–18]. However, examination of the infrared region did not lead to an unequivocal

identification of the weak band associated with the ν_2 transition $^4T_1(F) \leftarrow {}^4A_2(F)$.

The absence of detectable bands in the 500–800 nm range for the diffuse reflectance spectrum of $[Cu(L^3)_2] \cdot 0.5H_2O$ (obscured by a strong charge-transfer band tailing) does not permit a structural proposition with certainty. However, the Jahn–Teller effect and the fact that the interaction between the metal centre and the O atom of the isatin residue is weak are arguments to dismiss a hexa-coordination. The magnetic moment values obtained for the copper(II) complexes with H_2L^1, H_2L^2 and HL^3 were 1.8, 1.9 and 2.1 BM, respectively. The relatively high value of $[Cu(L^3)_2] \cdot 0.5H_2O$ should be attributed to a distortion of the assumed square planar structure due to the steric effect induces by the methyl group substituted in the isatin ring.

3.6. Antimicrobial activity

The *in vitro* antimicrobial activity of H_2L^1, H_2L^2 and HL^3 and their metal complexes together with isatin and 2-furoic hydrazide (whose condensation gave H_2L^2), was assayed against representative Gram positive and Gram negative bacteria, yeasts and moulds (Table 6). It must be noted that the antimicrobial activity of the remaining starting compounds (*N*-methyl isatin and 2-thiophenecarboxilic acid hydrazide as well as the metal salts used in this work) has been previously reported [5] presenting low activity against the studied strains (except Zn(II) salts versus *H. influenzae*) [5]. Therefore, the values reported in Table 6 should be attributed mainly to the undissociated complexes. Moreover, dimethyl sulfoxide used as solvent did not influence the growth of the tested microorganisms.

3.6.1. Antibacterial activity

Several of the tested compounds inhibit the growth of the Gram positive bacteria listed in Table 6. Among these particular substances, $[Zn(HL^1)_2] \cdot EtOH$ and $[Zn(L^3)_2] \cdot 0.75\ H_2O$ inhibit the growth of *B. subtilis* at 25 μg/mL while $[Cu(HL^1)_2] \cdot 2.5H_2O$, $[Ni(HL^1)_2] \cdot 0.5H_2O$, $[Co(HL^1)_2] \cdot H_2O$, $[Ni(L^3)_2] \cdot 0.5H_2O$ and $[Co(L^3)_2] \cdot 0.5H_2O$ show a smaller effectiveness (MIC 50 μg/mL) against the cited microorganism. $[Zn(HL^1)_2] \cdot EtOH$ is also the most effective compound against *S. aureus* (MIC 50 μg/mL).

The compounds exhibiting MIC values $\leqslant$ 50 μg/mL against *B. subtilis* or *S. aureus* were tested against a wide variety of Gram positive bacteria including methicillin-resistant strains of *S. aureus* and *S. epidermidis*. MIC values reported in Table 7 show that complexes of H_2L^1 are effective towards almost all the tested microorganisms (MICs 12–100 μg/mL), while the effectiveness of complexes of HL^3 generally is limited to bacilli and can be qualified as modest.

Remarkably, all free ligands and their metal complexes proved to be effective in controlling the growth of Gram negative *H. influenzae* a very harmful bacterium to humans (Table 6) being the most potent agents H_2L^1 and its complexes (MICs 1.5–3 μg/mL). So, among all the tested microorganisms, *H. influenzae* appears to be the most sensitive strain. On the contrary, a poor inhibition of Gram negative *E. coli* was observed.

Ligands and complexes active against *H. influenzae* (MIC $\leqslant$ 50 μg/mL) were tested against other Gram negative bacteria as *E. cloacae*, *K. pneumoniae*, *P. mirabilis*, *P. vulgaris*, *P. aeruginosa*, *S. typhimurium* and *S. marcescens*. Only a moderate degree of inhibition against *P. vulgaris* for $[Zn(HL^1)_2] \cdot EtOH$ and $[Ni(HL^1)_2] \cdot 0.5H_2O$ at 50 μg/mL and for $[Cu(HL^1)_2] \cdot 2.5H_2O$ at 100 μg/mL was observed, whereas both ligands H_2L^1 and HL^3 and complexes $[Zn(HL^2)_2] \cdot 2H_2O$ and $[Co(L^3)_2] \cdot 0.5H_2O$ were active at 200 μg/mL.

All the active compounds exhibited bacteriostatic properties, as it is deduced from their MBC values higher than the corresponding MICs (Tables 6 and 7).

3.6.2. Antifungal activity

Of all the compounds assayed against *S. cerevisiae*, *C. tropicalis* and *A. niger* (Table 6) only $[Co(HL^1)_2] \cdot H_2O$ showed antifungal properties against the first one (MIC 100 μg/mL). MFC value higher than 200 μg/mL evidenced fungistatic activity.

To more extensively investigate the spectrum of its antifungal activity, we tested a higher number of yeasts and moulds including some dermatophytes and phytopathogenic fungi cited in epigraph 2.3. As a result, a moderate inhibitory activity was detected towards the assayed dermatophyte fungi *E. floccosum* (MIC 12 μg/mL), *T. mentagrophytes* (MIC 25 μg/mL) and *M. gypseum* (MIC 50 μg/mL), as well as towards the phytopathogenic fungi *A. tenuis* (MIC 50 μg/mL), *Botrytis cinerea* (MIC 100 μg/mL) and *S. minor* (MIC 200 μg/mL).

Table 6
Antimicrobial activity, expressed as MIC (μg/mL), as well as MBC or MFC (in brackets), both in μg/mL.

Compound	Bacteria[a]				Fungi[b]		
	BS	SA	EC	HI	SC	CT	AN
H_2L^1	100 (>200)	200 (>200)	>200	1.5 (3)	>200	>200	>200
$[Zn(HL^1)_2] \cdot EtOH$	25 (100)	50 (>200)	100 (>200)	3 (6)	>200	>200	>200
$[Cu(HL^1)_2] \cdot 2.5H_2O$	50 (100)	100 (>200)	>200	1.5 (3)	>200	>200	>200
$[Ni(HL^1)_2] \cdot 0.5H_2O$	50 (>200)	100 (>200)	>200	1.5 (3)	>200	>200	>200
$[Co(HL^1)_2] \cdot H_2O$	50 (>200)	200 (>200)	200 (>200)	1.5 (3)	100 (>200)	>200	>200
H_2L^2	>200	>200	>200	50 (200)	>200	>200	>200
$[Zn(HL^2)_2] \cdot 2H_2O$	100 (>200)	100 (>200)	200 (>200)	25 (100)	>200	>200	>200
$[Cu(HL^2)_2] \cdot 2H_2O$	>200	>200	>200	100 (>200)	>200	>200	>200
$[Ni(HL^2)_2] \cdot H_2O \cdot EtOH$	>200	>200	>200	100 (>200)	>200	>200	>200
$[Co(HL^2)_2] \cdot 1.5H_2O \cdot EtOH$	>200	>200	>200	50 (100)	>200	>200	>200
HL^3	>200	>200	>200	3 (25)	>200	>200	>200
$[Zn(L^3)_2] \cdot 0.75H_2O$	25 (>200)	>200	>200	12 (>200)	>200	>200	>200
$[Cu(L^3)_2] \cdot 0.5H_2O$	>200	>200	>200	25 (>200)	>200	>200	>200
$[Ni(L^3)_2] \cdot 0.5H_2O$	50 (>200)	>200	>200	12 (100)	>200	>200	>200
$[Co(L^3)_2] \cdot 0.5H_2O$	50 (>200)	>200	>200	25 (>200)	>200	>200	>200
Isatin	>200	>200	>200	25 (50)	>200	>200	>200
2-Furoic hydrazide	>200	>200	>200	>200	>200	>200	>200

[a] Gram positive bacteria: *Bacillus subtilis* ATCC 6633 (BS) and *Staphylococcus aureus* ATCC 25923 (SA). Gram negative bacteria: *Escherichia coli* SPA 27 (EC) and *Haemophilus influenzae* (HI).
[b] Yeasts: *Saccharomyces cerevisiae* ATCC 9763 (SC) and *Candida tropicalis* ATCC 1369 (CT). Mould: *Aspergillus niger* ATCC 6275 (AN).

Table 7
Antimicrobial activity of the most active compounds against some Gram positive bacteria expressed as MIC and MBC (in brackets), both in μg/mL.

Bacteria	$[Zn(HL^1)_2] \cdot EtOH$	$[Cu(HL^1)_2] \cdot 2.5H_2O$	$[Ni(HL^1)_2] \cdot 0.5H_2O$	$[Co(HL^1)_2] \cdot {\cdot}H_2O{\cdot}$	$[Zn(L^3)_2] \cdot 0.75H_2O$	$[Ni(L^3)_2] \cdot 0.5H_2O$	$[Co(L^3)_2] \cdot 0.5H_2O$
Bacillus megaterium	25 (>200)	50 (100)	50 (>200)	50 (100)	200 (>200)	100 (>200)	200 (>200)
Bacillus thuringiensis var. *kurstaki*	25 (>200)	100 (>200)	50 (>200)	100 (>200)	100 (>200)	>200	100 (>200)
Sarcina lutea	25 (>200)	50 (>200)	50 (>200)	50 (>200)	>200	>200	100 (>200)
Staphylococcus aureus methicillin-resistant	50 (>200)	100 (>200)	50 (>200)	100 (>200)	>200	>200	>200
Staphylococcus epidermidis	50 (>200)	100 (>200)	100 (>200)	100 (>200)	>200	>200	>200
Staphylococcus epidermidis methicillin-resistant	>200	100 (>200)	>200	>200	>200	>200	>200
Staphylococcus haemolyticus	50 (>200)	100 (>200)	100 (>200)	100 (>200)	>200	>200	200 (>200)
Streptococcus agalactiae	25 (>200)	100 (>200)	12 (>200)	50 (>200)	>200	>200	>200
Streptococcus faecalis	50 (>200)	100 (>200)	100 (>200)	100 (>200)	>200	>200	>200
Streptococcus faecium	25 (>200)	50 (>200)	50 (>200)	100 (>200)	>200	>200	>200

4. Conclusions

Three new acylhydrazone ligands and their metal complexes, $[M(L)_2] \cdot n$X, were synthesised and characterised. The X-ray molecular structure of HL^3 showed that this ligand crystallised in the keto form, which was also the more abundant tautomer for the three ligands in solution. Physicochemical studies allow to said that the three acylhydrazones coordinated as monoanionic *O*,*N*-donors to cobalt(II) and zinc(II) ions, which are tetracoordinated. In $[Zn(HL^1)_2] \cdot 1.75MeOH$ secondary interactions of the O atoms of each isatin residue with zinc(II) provokes a substantial distortion of the pseudo-tetrahedral geometry. For the nickel(II) complexes, carbonyl isatin groups of the three ligands coordinate strongly enough to consider them presenting a *O*,*N*,*O*-donor behaviour to give a distorted octahedral geometry.

The free ligands and their complexes were evaluated *in vitro* as antimicrobial agents against a panel of Gram positive and Gram negative bacteria, as well as yeasts and moulds. Among the tested microorganisms, *H. influenzae* appears to be the most sensitive strain. H_2L^1 and its metal complexes were active against Gram positive bacteria such as *B. subtilis* methicillin-susceptible and methicillin-resistant as well as *S. aureus*, being $[Zn(HL^1)_2] \cdot EtOH$, the most active compound. It must be emphasised that the studied metal complexes were more active than the free ligands and metal salts [5]. Moreover, $[Co(HL^1)_2] \cdot H_2O$ showed antifungal properties against dermatophytes and some phytopathogenic fungi.

Supplementary data

CCDC 662397 and 708535 contain the supplementary crystallographic data for this paper. These data can be obtained free of charge via http://www.ccdc.cam.ac.uk/conts/retrieving.html, or from the Cambridge Crystallographic Data Centre, 12 Union Road, Cambridge CB2 1EZ, UK; fax: (+44) 1223 336 033; or e-mail: deposit@ccdc.cam.ac.uk.

Acknowledgements

Authors thank Berta Covelo and Sonia Escudero (Universidade de Vigo, CACTI) for technical support. M.C.R.A. thanks Xunta de Galicia (Spain) for a grant.

References

[1] C.A.M. Fraga, E.J. Barreiro, Cur. Med. Chem. 13 (2006) 167.
[2] P.V. Bernhardt, J. Mattsson, D.R. Richardson, Inorg. Chem. 45 (2006) 752.
[3] M.F. Iskander, L. El-Sayed, N.M.H. Salem, W. Haase, H.J. Linder, S. Foro, Polyhedron 23 (2004) 23.
[4] M.C. Rodríguez Argüelles, M. Belicchi Ferrari, F. Bisceglie, C. Pelizzi, G. Pelosi, S. Pinelli, M. Sassi, J. Inorg. Biochem. 98 (2004) 313.
[5] M.C. Rodríguez Argüelles, S. Mosquera Vázquez, P. Tourón Touceda, J. Sanmartín, A. García Deibe, M. Belicchi Ferrari, G. Pelosi, C. Pelizzi, F. Zani, J. Inorg. Biochem. 101 (2007) 138.
[6] C. Lorenzini, C. Pelizzi, G. Pelizzi, G. Predieri, J. Chem. Soc., Dalton Trans. (1983) 2155.
[7] SMART (Control) and SAINT (Integration) Software, Bruker Analytical X-ray Systems, Madison, WI, 1994.
[8] SADABS: Area-Detector Absorption Correction, Siemens Industrial Automation, Inc., Madison, WI, 1996.
[9] G.M. Sheldrick, SHELX-97, A Program for the Refinement of Crystal Structures from X-ray Data, University of Göttingen, Germany, 1997.
[10] L.J. Farrugia, J. Appl. Cryst. 30 (1997) 565 (Based on ORTEP-III (v. 1.0.3), M.N. Burnett, C.K. Johnson, Report ORNL-6895. Oak Ridge National Laboratory, Oak Ridge, Tennessee, 1996).
[11] J.H. Jorgensen et al., Antimicrobial agents and susceptibility testing, Section VIII, in: P.R. Murray, E.J. Baron, M.A. Pfaller, F.C. Tenover, R.H. Yolken (Eds.), Manual of Clinical Microbiology, ASM Press, Washington, DC, 1999, p. 1467.
[12] Y. Sun, J. Lu, D. Zhang, H. Song, Anal. Sci. 22 (2006) 237.
[13] M.M. Mashaly, T.M. Ismail, S.B. El-Maraghy, H.A. Habib, J. Coord. Chem. 57 (2004) 1099.
[14] S.S. Konstantinovic, B.C. Radovanovic, Z. Cakic, V. Vasic, J. Serb. Chem. Soc. 68 (2003) 641.
[15] A. Cukurovali, I. Yilmaz, S. Kirbag, Transition Met. Chem. 31 (2006) 207.
[16] K. Sone, Y. Fukuda, Inorganic Thermochromism, Springer, Heidelberg, 1987.
[17] X. Lin, D.M.J. Doble, A.J. Blake, A. Harrison, C. Wilson, M. Schröder, J. Am. Chem. Soc. 125 (2003) 9476.
[18] S.M.E. Khalil, H.S. Selleem, B.A. El-Shetary, M. Shebl, J. Coord. Chem. 55 (2002) 883.

Polyhedron 28 (2009) 2196–2200

Contents lists available at ScienceDirect

Polyhedron

journal homepage: www.elsevier.com/locate/poly

One-dimensional coordination polymers of praseodymium(III)–vanadium(V) complexes with pyridine-2,6-dicarboxylic acid

Taoyun Zhu [a,d], Koichi Murokawa [a,d], Kazuyoshi Uematsu [b,d], Tadashi Ishigaki [c,d], Kenji Toda [a,d], Hirokazu Okawa [c,d], Mineo Sato [b,d,*]

[a] Graduate School of Science and Technology, Niigata University, 8050 Ikarashi 2-nocho, Niigata 950-2181, Japan
[b] Department of Chemistry and Chemical Engineering, Niigata University, 8050 Ikarashi 2-nocho, Niigata 950-2181, Japan
[c] Center for Transdisciplinary Research, Niigata University, Ikarashi 2-no-cho, Niigata 950-2181, Japan
[d] Department of Earth Science and Technology, Faculty of Engineering and Resource Science, Akita University, Tegata Gakuen-machi, Akita 010-8502, Japan

ARTICLE INFO

Article history:
Received 26 September 2008
Accepted 15 January 2009
Available online 6 June 2009

Keywords:
Rare earth complexes
Crystal structure
Pyridine-2,6-dicarboxylic acid
Coordination polymer

ABSTRACT

This paper represents the hydrothermal synthesis of new isomorphous lanthanide–vanadium complexes with one-dimensional coordination polymers: $[Pr_2(VO_2)_2(dipic)_4(H_2O)_9] \cdot nH_2O$ with dipic = pyridine-2,6-dicarboxylic acid and $n = 7.75$. The structure determination shows a unique one-dimensional structure in which three types of chains run along the *c*-axis: the chain of positively charged praseodymium complexes bridged by a dipic ligand ($[Pr(dipic)(H_2O)_5]^+$), the chain of negatively charged, stacked vanadium complexes ($[VO_2(dipic)]^-$), and the chain of neutral praseodymium complexes with a bridged dipic ligand and a coordinating dipic ligand ($[Pr(dipic)[VO_2(dipic)](H_2O)_4]$). Such one-dimensional chains provide open channels which can accommodate water molecules. Not only accommodated water molecules but also ones coordinated to praseodymium ions were easily removed and absorbed upon heating at 200 °C and exposure of humidity at room temperature, respectively.

© 2009 Elsevier Ltd. All rights reserved.

1. Introduction

The synthesis and assembly of metal–organic frameworks (MOFs) through coordination of metal ions with multifunctional organic ligands are one of the current interests as a new class of porous materials [1–4]. The interests in these materials span from purely academic aspects of chemistry and physics to applications such as separation, catalysis, and potential fuel gas storage [5–9].

A large number of the works have so far been done on the coordination polymers containing transition metals because of their well-defined coordination geometries which can make an artificial design of MOFs easy. On the other hand, the use of lanthanide elements for constructing MOFs is usually unsuitable and hard to control the coordination geometries of MOFs due to their high coordination numbers. Nevertheless, owing to important magnetic and luminescence properties of lanthanide elements, a growing development in the field of MOFs containing lanthanide ions have provided the wide applications of light conversion molecular devices based on a charge transfer type luminescence from antenna ligands to central lanthanide ions [10–40]. However, in most of them, only lanthanide ions are employed to construct efficient MOF structures. Incorporation of 3d transition elements into a MOF structure, thus creation of 3d–4f metal-based MOF structure, may provide us a great opportunity for constructing desirable architectures of the MOF assisted by the combination of flexible coordination manners of lanthanide ions and stereochemical preference coordination ones of transition metal ions. A few examples have been reported for 3d–4f metal-based MOFs with a 3D nanotubular coordination polymer and a 1D channel coordination polymer [14,22,26,35,38–40].

Since lanthanide ions have a high affinity for hard donor atoms and ligands such as oxygen or hybrid oxygen–nitrogen atoms, pyridine-2,6-dicarboxylic acid (dipic) which has been frequently employed in the architectures for lanthanide coordination polymers is adopted in this study as a multicarboxylate ligand. Among the 3d–4f metal-based MOFs reported so far, 3d-transition ions such as Cu^{2+}, Fe^{2+}, Mn^{2+}, and Ni^{2+} were widely used in order to build metal centers as nodes in the MOF frameworks. Vanadium(V) has a preference for tetrahedral and square-pyramidal coordination against oxygen atoms, implying a possibility to act as a multi-connected metal node in the 3D frameworks. In spite of the fact, vanadium ions have been little employed in the construction of MOFs. Here, we report a series of one-dimensional coordination polymers consisting of praseodymium(III) and vanadium(V) complexes with dipic. To our knowledge, these are the first example of 3d–4f metal-based coordination polymers containing vanadium as a 3d transition ion.

* Corresponding author. Tel./fax: +81 25 262 6768.
E-mail address: msato@eng.niigata-u.ac.jp (M. Sato).

0277-5387/$ - see front matter © 2009 Elsevier Ltd. All rights reserved.
doi:10.1016/j.poly.2009.01.010

2. Experimental

2.1. Characterization

Qualitative and quantitative chemical analyses for the single crystal were undertaken by an electron probe microanalysis (EPMA) using a Shimadzu EPMA-8705. Elemental analyses for C, H, and N were carried out using Flash EA1112 microanalyzer. Thermogravimetric analysis (TG) and differential thermal analysis (DTA) were carried out at a heating rate of 5 °C min^{-1} in air using a Seiko Denshi TG-DTA 6300. The IR spectra were recorded on a Shimadzu FT-IR 4200 spectrometer using KBr disk. Magnetic susceptibility data were collected on a powdered sample with use of a SQUID magnetometer on a Quantum Design MPMS-5S. Data were corrected for diamagnetism of the ligands estimated from Pascal's constants [41].

2.2. Synthesis

$[Pr_2(VO_2)_2(dipic)_4(H_2O)_9]\cdot nH_2O$ was hydrothermally synthesized at 150 °C for 72 h in a 40 mL Teflon-lined steel autoclave under autogenous pressure. The starting solution was prepared by mixing Pr_6O_{11} (0.5 mmol), pyridine-2,6-dicarboxylate (3 mmol), V_2O_5 (1.5 mmol), and deionized water with a molar ratio of 2:1:2:1:555 (total volume, 15 mL), and its pH value was adjusted to 3.05 by hydrochloric acid. After the hydrothermal reaction, the autoclave was slowly cooled to room temperature, and plate-like crystals were produced. The yield of the compound was about 70 mol% per Pr. *Anal.* Calc. for $C_{28}H_{45.5}N_4O_{36.75}Pr_2V_2$: C, 23.85; H, 3.25; N, 3.97%. Found: C, 23.55; H, 3.15; N, 3.3%. Heavy atoms ratio by EPMA: Pr:V = 1.0:0.99.

2.3. Structural determination

Crystallographic data of the compound were collected on a Rigaku RAXIS-RAPID single crystal diffractometer equipped with an imaging plate area detector with graphite monochromated Mo Kα radiation with $\lambda = 0.71073$ Å at a temperature of 93 K. The data processing was accomplished with the Crystal Structure processing program [24]. The structure was solved by direct methods using the program SIR97 [42] and refined by full-matrix least-squares techniques against F^2 using the SHELXTL-97 crystallographic software package [43]. All non-H atoms were easily found from the difference Fourier map and refined anisotropically. The hydrogen atoms on the dipic molecules were positioned geometrically and included in the refinement as riding, whereas the hydrogen atoms on the water molecules coordinated to praseodymium ions were first geometrically fixed so that the distance of O–H in water molecules was 0.85 Å, and then in the final refinement stages were refined isotropically without constraint. On the other hand, some of hydrogen atoms on solvent-like water molecules, several oxygen atoms of which were highly disordered, were unassigned.

3. Results and discussion

The formula, $[Pr_2(VO_2)_2(dipic)_4(H_2O)_9]\cdot 7.75H_2O$, is deduced from the structural determination of single crystal, the elemental analyses, and the TG measurement. Magnetic susceptibilities of the compound were also measured in the temperature range from 5 to 300 K. The $\chi_M T$ value is equal to 3.15 $cm^3\,K\,mol^{-1}$ at room temperature, which is fairly agreement with its expected value (3.20) per chemical formulae deduced from the assumption of Pr^{3+} ion with $^3H_4$ ground state and V^{5+} ion (d^0).

3.1. Description of the crystal structure of $[Pr_2(VO_2)_2(dipic)_4(H_2O)_9]\cdot nH_2O$

Crystal data, intensity measurements, and structure refinements are summarized in Table 1. Selected bond distances are listed in Table 2. The hydrogen bonds parameters which could be assigned are shown in Table 3.

The asymmetric unit for the compound is shown in Fig. 1. There are two types of praseodymium ions. Not as understood directly by insight from Fig. 1, both of Pr1 and Pr2 have a nine-folded coordination environment. Pr1 is coordinated by two carboxylic oxygen atoms and a nitrogen atom of a dipic molecule with tridentate coordination, one of carboxylic oxygen atoms of another dipic molecule with bridging coordination, four water molecules, and finally one of oxygen atoms of a dioxovanadyl group, thus forming the nine-folded coordination environment. The coordination environment around Pr2 is almost the same as that around Pr1 except for an additional coordination of a water molecule instead of one of oxygen atoms of a dioxovanadyl group. The Pr–O(carboxylic) bond distances ranging from 2.492 to 2.497 Å for Pr1 and from 2.500 to 2.514 Å for Pr2, the Pr–N(pyridinic) bond distances of 2.594 Å for Pr1 and 2.566 Å for Pr(2), and Pr–O(water) bond distances ranging from 2.497 to 2.573 Å for Pr1 and from 2.477 to 2.532 Å for Pr2 are all comparable to those reported previously. The polyhedron of both praseodymium coordination spheres for the compound may be best described as a distorted tricapped trigonal prism, but the distortion is so remarkable. There are also two kinds of vanadium atoms in the compound. The asymmetric unit also contains two crystallographically independent vanadium atoms. V1 is a five-folded coordination by two oxo ligands and the tridentate ligand of a dipic molecule. The oxo ligands (O31 and O32) of V1 have two distinct bond distances to V1: one is a longer distance of 1.638 Å for V1–O31 which takes part in the coordination to Pr1, the other a shorter distance of 1.614 Å for V1–O32 which seems to participate in hydrogen bonding to O14W (Table 3). The situation in the coordination around V2 is somewhat different from to that around V1 because of no coordination to praseodymium central ions. The longer distance (1.626 Å) found for the O42–V2 bond is indicative for participation of hydrogen bonding although the bond was not able to be identified in the crystal structure refinement, and the short one (1.608 Å) found for the O41–V2 bond indicates the existence of V=O bond. The bond lengths and angles found in the compound are primarily similar to those observed for $[VO_2(dipic)]$ motifs previously reported [44,45]. The structure refinement finally satisfied showed 7.75 mol of water molecule in the asymmetric unit in spite of the fact that the TG measurement suggested an existence of approximately eight water molecules, as discussed in later. These water molecules are classified into two groups; one is the molecules coordinating praseodymium ions (O11W, O12W, O13W, and O14W for Pr1, and O21W, O22W, O23W, O24W, and O15W for Pr2, respectively) and the other the molecules isolated as a water of crystallization, some oxygen atoms of which are highly disordered.

The structural architecture constructed in the compound is one-dimensional, consisting of three types of chains, all running along the *c-axis* (Fig. 2). In the first type of chains containing Pr2 (Fig. 2a), a dipic molecule plays two roles; one acts as a tridentate ligand for praseodymium, the other as a bridging one for adjacent praseodymium ions through one of oxygen atoms of a carboxylic group. The $[VO_2(dipic)]$ motif of V1 is connected, as a pendant arm, with Pr1 of this chain via one of its oxo group. Formally, the chain is neutral, expressed as $[Pr(dipic)[VO_2(dipic)](H_2O)_4]$. The fundamental structure of the second type of chains containing Pr, as shown in Fig. 3b, is substantially the same as that of the first type except for no existence of $[VO_2(dipic)]$ motif, which is replaced by a water molecule. The principal unit of the chain is pos-

Table 1
Crystal data and structure refinement for $[Pr_2(VO_2)_2(dipic)_4(H_2O)_9]\cdot nH_2O$.

Empirical formula	$C_{28}H_{34}N_4O_{36.75}Pr_2V_2$
Formula weight	1398.32
T (K)	93
Wavelength (Mo Kα) (Å)	0.71073
Crystal system	orthorhombic
Space group	*Pbca*
Unit cell dimensions	
a (Å)	44.706(1)
b (Å)	25.9243(6)
c (Å)	8.0798(2)
V (Å^3)	9364.2(4)
Z	8
D_{calc} (g cm^{-3})	2.032
Absorption coefficient (Mo Kα) (mm^{-1})	2.551
F(000)	5696
Crystal size (mm)	0.2 × 0.2 × 0.2
Index ranges	$-58 \leqslant h \leqslant 58$, $-33 \leqslant k \leqslant 33$, $-10 \leqslant l \leqslant 10$
Reflections collected/unique (R_{int})	57135/10674 (0.0474)
Absorption correction	None
Refinement method	full-matrix least-squares on F^2
Data/restraints/parameters	10674/22/798
Goodness-of-fit on F^2	1.148
Final R indices [I > 2σ(I)]	R_1 = 0.0457, wR_2 = 0.0972
R indices (all data)	R_1 = 0.0542, wR_2 = 0.1042
Largest difference in peak and hole (e Å^{-1})	2.152 and −0.967

Table 3
Hydrogen bonds (Å) and angles (°) for $[Pr_2(VO_2)_2(dipic)_4(H_2O)_9]\cdot nH_2O$.

D–H···A	d(D–H)	d(H···A)	d(D···A)	∠(DHA)
O(11W)–H(11A)···O(3C)	0.848	2.35	3.119(5)	151
O(11W)–H(11B)···O(2D)[a]	0.848	1.899	2.736(5)	169
O(12W)–H(12B)···O(4B)[a]	0.848	2.007	2.833(5)	164
O(13W)–H(13A)···O(5W)	0.851	1.888	2.728(6)	169
O(13W)–H(13B)···O(2D)	0.849	2.01	2.784(5)	152
O(14W)–H(14A)···O(32)[b]	0.851	1.92	2.737(5)	160
O(14W)–H(14B)···O(1C)[b]	0.851	1.85	2.666(5)	159
O(21W)–H(21A)···O(4D)[c]	0.849	2.02	2.809(5)	155
O(21W)–H(21B)···O(2A)[d]	0.845	1.88	2.698(5)	162
O(22W)–H(22A)···O(1B)[f]	0.847	1.94	2.758(5)	161
O(22W)–H(22B)···O(1W)[f]	0.848	1.904	2.750(7)	176
O(23W)–H(23A)···O(4D)[c]	0.849	2.15	2.866(5)	143
O(23W)–H(23B)···O(1W)	0.849	1.885	2.725(6)	169
O(25W)–H(25B)···O(1B)	0.848	1.914	2.757(5)	173
O(1W)–H(1WA)···O(4C)[e]	0.849	1.974	2.813(6)	169
O(5W)–H(5WB)···O(3D)[f]	0.848	2.036	2.879(6)	172

Symmetry codes:
[a] x, y, z + 1.
[b] −x + 3/2, −y + 1, z − 1/2.
[c] −x + 1, y + 1/2, −z + 1/2.
[d] x, −y + 3/2, z − 1/2.
[e] −x + 1, −y + 1, −z + 1.
[f] x, y, z − 1.

itively charged, expressed as $[Pr(dipic)(H_2O)_5]^+$. The third type only consisting of the $[VO_2(dipic)]^-$ units formally negatively charged is, strictly speaking, not a chain but a kind of stacking sequence of the units (Fig. 3c). The pyridine rings of dipic molecules are stacked with a decline angle of 34.7° against (001) plane. The driving force of occurrence of the stacking sequence seems to be resulted from hydrogen bonding between oxygen atoms of the oxo group and water molecules of crystallization [11,16,19,23,31,34] although the hydrogen bonding was not fully specified. Totally, the assembly of three kinds of chains running along the *c-axis* makes open cannels, where a large amount of water molecules are populated, as shown in Fig. 3.

3.2. Thermal stability

The thermal stability of the compound has been investigated using TG and powder X-ray diffraction measurements (Figs. 4 and 5). The TG, performed from room temperature to 800 °C, shows two types of major weight losses in this temperature range.

Table 2
Selected interatomic distances (Å) for $[Pr_2(VO_2)_2(dipic)_4(H_2O)_9]\cdot nH_2O$.

Around Pr1		Around Pr2	
Pr1–O31	2.484(3)	Pr2–O22W	2.477(4)
Pr1–O1D[a]	2.492(3)	Pr2–O2C	2.500(3)
Pr1–O1C	2.496(3)	Pr2–O2A	2.504(3)
Pr1–O1A	2.497(3)	Pr2–O21W	2.508(3)
Pr1–O14W	2.497(3)	Pr2–O2B[b]	2.514(3)
Pr1–O13W	2.505(3)	Pr2–O24W	2.520(4)
Pr1–O11W	2.540(3)	Pr2–O25W	2.526(3)
Pr1–O12W	2.573(3)	Pr2–O23W	2.532(4)
Pr1–N11	2.594(4)	Pr2–N21	2.566(4)
Around V1		Around V2	
V1–O32	1.614(3)	V2–O41	1.608(5)
V1–O31	1.638(3)	V2–O42	1.626(5)
V1–O3A	1.955(4)	V2–O4A	1.989(4)
V1–O3C	2.000(4)	V2–O4C	2.012(4)
V1–N31	2.080(4)	V2–N41	2.092(4)

Symmetry codes:
[a] −x + 3/2, −y + 1, z − 1/2.
[b] x, −y + 3/2, z − 1/2.

The first weight loss initiated at about 40 °C, accompanied with endothermic heats, implying the elimination of water molecules. With a careful insight, one can observed two step weight loss processes for this region. The first step accompanying a weight loss of 10.1 wt% corresponds to the loss of eight water molecules, and the second step (12.8 wt%) corresponds to the loss of nine water molecules. On the basis of the crystal structure of the compound, it could be concluded that the first step is responsible for the elimination of the guest water molecules populated in the channel while the second step is responsible for the elimination of water molecules coordinated to praseodymium ions. On the hand, the high temperature weight loss with an initiation temperature of about 350 °C involves a complicated multi-step process. Since these steps accompany exothermic heats, this weight loss may be attributed from the elimination due to the combustion of four dipic molecules. The observed weight loss is 50.3 wt%, fairly con-

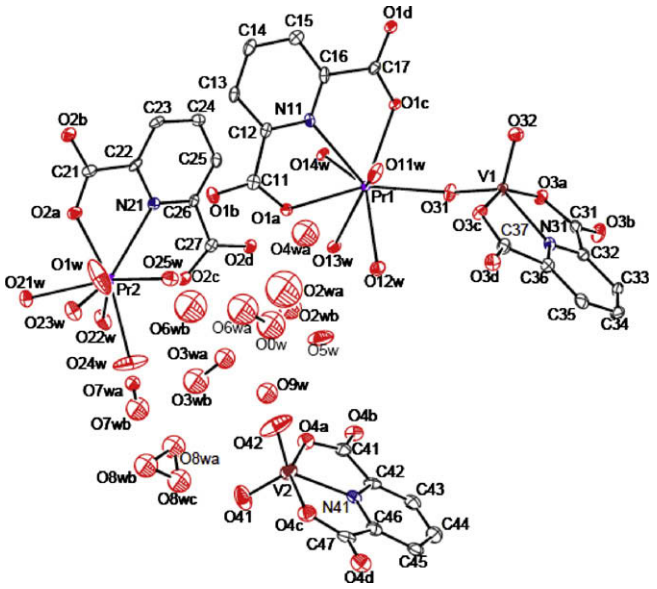


Fig. 1. ORTEP view of the asymmetric unit of $[Pr_2(VO_2)_2(dipic)_4(H_2O)_9]\cdot nH_2O$, showing 50% probability displacement ellipsoids. H atoms are omitted for clarity.

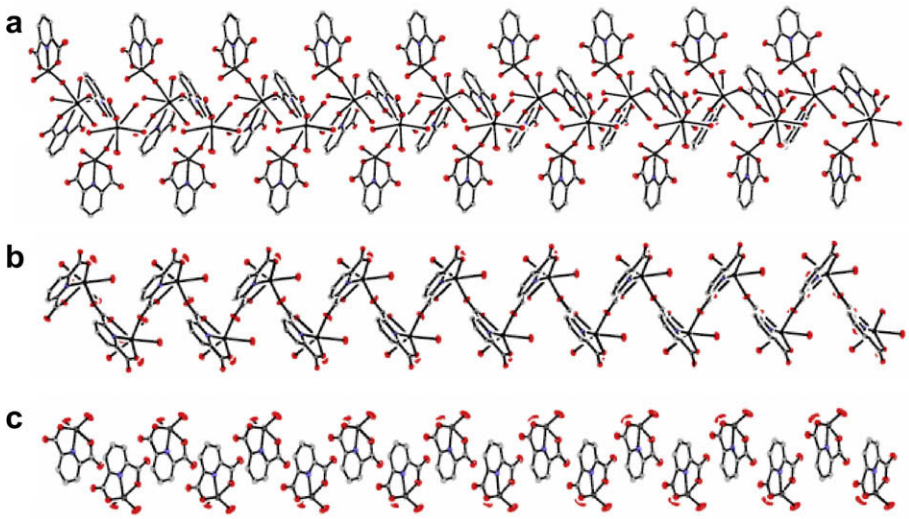


Fig. 2. Three types of continuous chains found in $[Pr_2(VO_2)_2(dipic)_4(H_2O)_9] \cdot nH_2O$, running along the *c*-axis; $[Pr(dipic)[VO_2(dipic)](H_2O)_4]]_n$ (a), $[[Pr(dipic)(H_2O)_5]^+]_n$ (b), and $[[VO_2(dipic)]^-]_n$ (c).

sistent with the calculated one (53.8 wt%). The powder XRD studies were performed for the as-synthesized sample, the sample heated at 200 °C for 3 h, and the samples obtained after the heated sample was kept upon exposure of 100% relative humidity for 24 h (Fig. 5). The crystalline compound becomes amorphous upon the release of water molecules by heating it at 200 °C. Such an amorphous material, however, recover its crystal structure upon the exposure of water vapor at room temperature, as shown in Fig. 5c. This result implies that the amorphous phase still has micro-porous frameworks for accommodation of water molecules. In fact, the sample which absorbs water molecules and recovers its crystal frame-

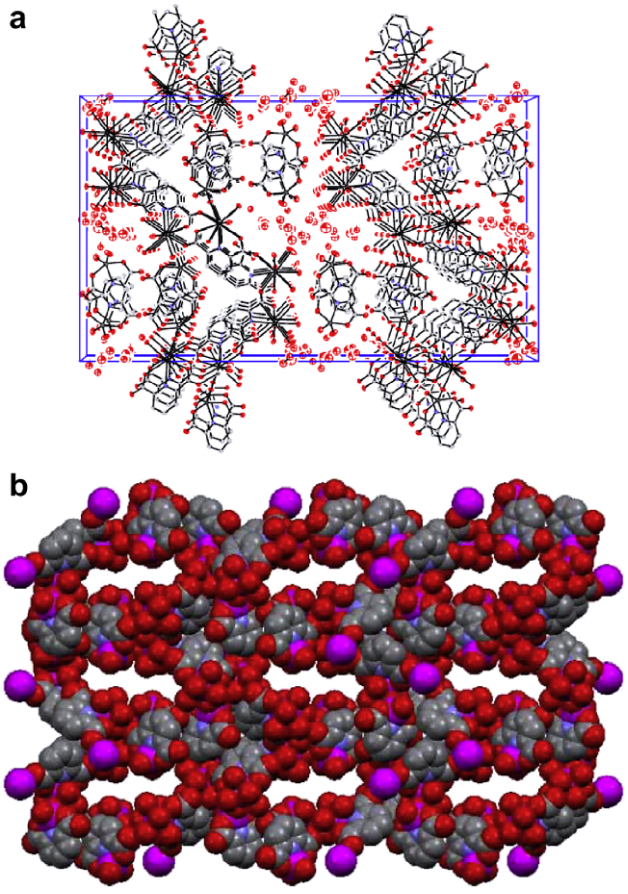


Fig. 3. Packing view (a) and CPK representation (b) for $[Pr_2(VO_2)_2(dipic)_4(H_2O)_9] \cdot nH_2O$ projected along to the *c*-axis for the total view.

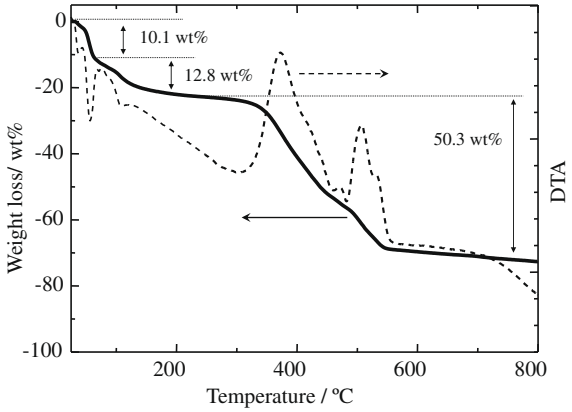


Fig. 4. TG-DTA curves for as-synthesized crystal of $[Pr_2(VO_2)_2(dipic)_4(H_2O)_9] \cdot nH_2O$.

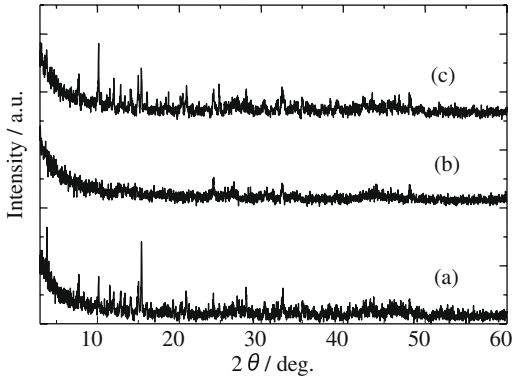


Fig. 5. Powder X-ray diffraction patterns for the as-synthesized sample (a), he sample heated at 200 °C for 3 h (b), and the sample obtained after the heated sample was kept upon exposure of 100% relative humidity for 24 h (c).

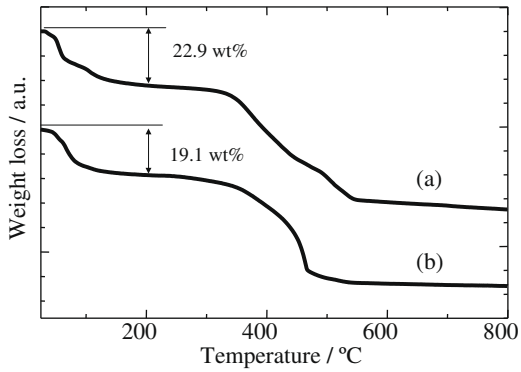


Fig. 6. TG-DTA curves for as-synthesized sample (a) and the sample obtained after the heated sample was kept upon exposure of humidity (b).

works exhibits almost the same thermal behavior in the TG measurement as that of the as-grown crystal (Fig. 6).

4. Conclusion

One-dimensional coordination polymers based on 3d–4f metal-based MOFs have been synthesized under a hydrothermal condition. XRD analysis reveals that it is crystallized in an orthorhombic crystal system. The compounds are constructed from three kinds of continuous chains, which provide open channels in the interstitials among them. Guest water molecules accommodated in the channels can be easily removed and absorbed upon heating and exposure of humidity, respectively.

Acknowledgments

This work was supported by a Grant-in-Aid for Scientific Research (no. 440, Panoscopic Assembling and High Ordered Functions for Rare Earth Materials, and no. 17042012) from the Japanese Ministry of Education, Culture, Sports, Science, and Technology. A part of this work was also supported by the Grant-in-Aid for Scientific Research from the Japanese Ministry of Education, Science, Sports and Culture (no. 18350104).

Appendix A. Supplementary data

CCDC 702698 contain the supplementary crystallographic data for the compound. These data can be obtained free of charge via http://www.ccdc.cam.ac.uk/conts/retrieving.html, or from the Cambridge Crystallographic Data Centre, 12 Union Road, Cambridge CB2 1EZ, UK; fax: (+44) 1223 336 033; or e-mail: deposit@ccdc.cam.ac.uk. Supplementary data associated with this article can be found, in the online version, at doi:10.1016/j.poly.2009.01.010.

References

[1] M. Eddaoudi, J. Kim, N. Rosi, D. Vodak, J. Wachter, M. O'Keeffe, O.M. Yaghi, Science 296 (2002) 469.
[2] X. Xu, M. Nieuwenhuyzen, S.L. James, Angew. Chem., Int. Ed. Engl. 41 (2002) 764.
[3] O.M.Yaghi, M. O'Keefe, N.W. Ockwig, H.K. Chae, M. Eddaoudi, J. Kim, Nature 423 (2003) 705.
[4] E.Y. Lee, M.P. Suh, Angew. Chem., Int. Ed. Engl. 43 (2004) 2798.
[5] R. Robson, S.R. Batten, Angew. Chem., Int. Ed. Engl. 37 (1998) 1460.
[6] M. Eddaoudi, D.B. Moler, H. Li, B. Chen, T.M. Reineke, M. O'Keefe, O.M. Yaghi, Acc. Chem. Res. 34 (2001) 319.
[7] S. Kitagawa, R. Kitaura, S. Noro, Angew. Chem., Int. Ed. Engl. 43 (2004) 2334.
[8] C.N.R. Rao, S. Natarajan, R. Vaidyanathan, Angew. Chem., Int. Ed. Engl. 43 (2004) 1466.
[9] D. Bradshaw, J.B. Claridge, E.J. Cussen, M.J. Rosseinsky, Acc. Chem. Res. 38 (2005) 273.
[10] P.A. Brayshaw, J.M. Harrowfield, A.N. Sobolev, Acta Crystallogr., Sect. C 51 (1995) 1799.
[11] G. Swarnabala, M.V. Rajasekharan, Inorg. Chem. 37 (1998) 1483.
[12] G.A. van Albada, S. Gorter, J. Reedijk, Polyhedron 18 (1999) 1821.
[13] A. Fernandes, J. Jaud, J. Dexpert-Ghys, C. Brouca-Cabarrecq, Polyhedron 20 (2001) 2385.
[14] R. Baggio, M.T. Garland, Y. Moreno, O. Peña, M. Perec, E. Spodine, J. Chem. Soc., Dalton Trans. (2000) 2061.
[15] N. Okabe, H. Kyoyama, Acta Crystallogr., Sect. E 58 (2002) m226.
[16] L. Chen, X.-H. Yin, M.-Y. Tan, C.-G. Xia, K.-B. Yu, Acta Crystallogr., Sect. E 58 (2002) m666.
[17] C. Brouca-Cabarrecq, A. Fernandes, J. Jaud, J.P. Costes, Inorg. Chim. Acta 332 (2002) 54.
[18] B. Zhao, P. Cheng, Y. Dai, C. Cheng, D.Z. Liao, S.P. Yan, Z.H. Jiang, G.L. Wang, Angew. Chem., Int. Ed. Engl. 42 (2003) 934.
[19] S.K. Ghosh, P.K. Bharadwaj, Inorg. Chem. 42 (2003) 8250.
[20] S.K. Ghosh, P.K. Bharadwaj, Inorg. Chem. 43 (2004) 2293.
[21] B. Zhao, X.-Y. Chen, P. Cheng, D.-Z. Liao, S.-P. Yan, Z.-H. Jian, J. Am. Chem. Soc. 126 (2004) 15394.
[22] B. Zhao, P. Cheng, X. Chen, C. Cheng, W. Shi, D. Liao, S. Yan, Z. Jiang, J. Am. Chem. Soc. 126 (2004) 3012.
[23] M. Rafizadeh, M. Ranjbar, V.M. Rafizadeh, M. Ranjbar, V. Amani, Acta Crystallogr., Sect. E 60 (2004) m479.
[24] L. Duan, Y. Li, F. Liu, E. Wang, X. Wang, C. Hu, L. Xu, J. Mol. Struct. 689 (2004) 269.
[25] S.K. Ghosh, P.K. Bharadwaj, Inorg. Chem. 44 (2005) 3156.
[26] Y.-P. Cai, C.-Y. Su, G.-B. Li, Z.-W. Mao, C. Zhang, A.-W. Xu, B.-S. Kang, Inorg. Chim. Acta 358 (2005) 1298.
[27] M. Rafizadeh, V. Amani, E. Iravani, B. Neumüller, Z. Anorg. Allg. Chem. 631 (2005) 952.
[28] B. Zhao, L. Yi, Y. Dai, X.-Y. Chen, P. Cheng, D.-Z. Liao, S.-P. Yan, Z.-H. Jiang, Inorg. Chem. 44 (2005) 911.
[29] H. Aghabozorg, B. Nakhjavan, M. Ghadermazi, F. Ramezanipour, Acta Crystallogr., Sect. E 62 (2006) m1527.
[30] B. Jia, X.-G. Meng, S.-M. Shi, Z.-Q. Hu, F.-H. Luo, Acta Crystallogr., Sect. E 62 (2006) m1799.
[31] Y. Liu, J.-M. Dou, D.-Q. Wang, X.-X. Zhang, L. Zhou, Acta Crystallogr., Sect. E 62 (2006) m2794.
[32] M. Rafizadeh, V. Amani, Acta Crystallogr., Sect. E 62 (2006) m90.
[33] M.R. George, C.A. Golden, M.C. Grossel, R.J. Curry, Inorg. Chem. 45 (2006) 1739.
[34] H.-L. Gao, L. Yi, B. Zhao, X.-Q. Zhao, P. Cheng, D.-Z.G. Liao, S.-P. Yan, Inorg. Chem. 45 (2006) 5980.
[35] F.-Q. Wang, X.-J. Zheng, Y.-H. Wan, C.-Y. Sun, Z.-M. Wang, K.-Z. Wang, L.-P. Jin, Inorg. Chem. 46 (2007) 2956.
[36] S. Tanase, P.M. Gallego, R. de Gelder, W.T. Fu, Inorg. Chim. Acta 360 (2007) 102.
[37] C. Brouca-Cabarrecq, J. Dexpert-Ghys, A. Fernandes, J. Jaud, J.C. Trombem, Inorg. Chim. Acta 361 (2008) 2909.
[38] J.-W. Cheng, S.-T. Zheng, G.-Y. Yang, Inorg. Chem. 47 (2008) 4930.
[39] H. Deng, Z. Liu, Y. Qiu, Y. Li, M. Zeller, Inorg. Chem. Commun. 11 (2008) 978.
[40] V. Mereacre, D. Prodius, A.M. Ako, N. Kaur, J. Lipkowski, C. Simmons, N. Dalal, I. Geru, C.E. Anson, A.K. Powell, C. Turta, Polyhedron 27 (2008) 2459.
[41] P. Pascal, Ann. Chim. Phys. 19 (1910) 5.
[42] A. Altomare, M. Burla, M. Camalli, G. Cascarano, C. Giacovazzo, A. Guagliardi, A. Moliterni, G. Polidori, R. Spagna, J. Appl. Cryst. 32 (1999) 115.
[43] G.M. Sheldrick, SHELX97, Program for the Refinement of Crystal Structures, University of Göttingen, Germany, 1997.
[44] B. Nuber, J. Weiss, K. Wieghardt, Z. Naturforsch. 33B (1978) 265.
[45] L. Yang, A.L. Cour, O.P. Anderson, D.V. Crans, Inorg. Chem. 41 (2002) 6322.

Polyhedron 28 (2009) 2201–2205

Contents lists available at ScienceDirect

Polyhedron

journal homepage: www.elsevier.com/locate/poly

NMR and *ab initio* studies of Mg^{2+}, Ca^{2+}, Zn^{2+}, Cu^{2+} alizarin complexes

Marek Doskocz [a,b,*], Karolina Kubas [c], Anna Frąckowiak [c], Roman Gancarz [c]

[a] Chair and Department of Toxicology, Silesian Piasts University of Medicine in Wrocław, ul. Traugutta 57/59, 50-417 Wrocław, Poland
[b] Department of Bioorganic Chemistry, Faculty of Chemistry, Wroclaw University of Technology, Wybrzeże Wyspiańskiego 27, 50-370 Wrocław, Poland
[c] Department of Medicinal Chemistry and Microbiology, Faculty of Chemistry, Wroclaw University of Technology, Wybrzeże Wyspiańskiego 27, 50-370 Wrocław, Poland

ARTICLE INFO

Article history:
Received 26 August 2008
Accepted 30 January 2009
Available online 28 March 2009

Keywords:
Metal
Alizarin
Complexation
NMR
DFT

ABSTRACT

Complexation of Mg^{2+}, Ca^{2+}, Zn^{2+} and Cu^{2+} with alizarin, characterized by NMR and theoretical studies (DFT, B3LYP/6-31G(*d,p*) PCM and NMR GIAO B3LYP/IGLOIII), indicated that the metal ion is attached to two hydroxyl groups in a bidentate mode. The alternative complexation in the bidentate mode, with only one hydroxyl group and a carbonyl oxygen, is less possible as it has a higher energy.

© 2009 Elsevier Ltd. All rights reserved.

1. Introduction

Anthraquinones are one of the most important natural compounds which are applied widely in medicine as drugs [1] and antineoplastic agents [2], in industry as dyes and dye-related compounds [3], in environmentally friendly synthesis of hydrogen peroxide [4], as analytical reagents, indicators and in many other areas [5–7]. One of the most well known anthraquinones is alizarin (1,2-dihydroxy-9,10-anthraquinone) which can be isolated from plants, for example from *Radix Rubiae tinctorum* L. Its crucial feature is a strong ability to chelate ions such as calcium, zinc, magnesium and copper. Alizarin is also believed to be responsible for the biological activity of *Rubia tinctorum* extracts in nephrolithiasis, since kidney stones are composed mostly of calcium and magnesium salts [8].

On the other hand the above mentioned ions are common in biological structures. They activate chemical bonds making them more suitable to undergo various chemical reactions [9]. Calcium is a major bone component and plays an important role in transferring signals in many biochemical routes, for example the sight process or muscular contraction. Zinc activates many essential enzymes, such as alcohol dehydrogenase or the digestive enzyme carboxypeptidase, by creating a complex with the active site. The zinc ion is also an important structural component in proteins involved in nucleic acid binding [10]. Magnesium stimulates the first factor of chlorophyll photosynthesis, it is also needed to prompt the ATP moiety or DNA polymerase. The copper ion plays a role in oxidation processes [11].

Nuclear Magnetic Resonance (NMR) is a useful technique for studying the structure of chemical and biological systems, from small molecules to complicated structures such as nucleic acids and proteins. Chemical shifts and spin–spin coupling serve to recognize the molecular conformation, composition and environment of the moiety. However, the investigation and understanding of the relationships between molecular structure and measured NMR parameters can sometimes be quite difficult, and need the support of theoretical calculations.

In this work we describe the studies of alizarin and its metal complexes using the NMR technique and theoretical DFT calculations.

2. Experimental and computations details

NMR experiments were performed on commercially available alizarin and metal salts (Fluka®). In the NMR studies, the alizarin was dissolved in DMSO-d_6 at a concentration of 30 mg/6.00 ml of solvent and concentration of metal 0.195, 0.168, 0.212, 0.223 mol/dm^3 ($Mg(NO_3)_2 \cdot 6H_2O$, $Zn(NO_3)_2 \cdot 6H_2O$, $Ca(NO_3)_2 \cdot 4H_2O$, $Cu(NO_3)_2 \cdot 2H_2O$). The solvent was supplied from Dr Glaser AG (Basel, Switzerland). The NMR spectra were recorded at room temperature on a Bruker Avance DRX300 instrument, operating at 300.13 MHz for 1H nuclei and 75.46 MHz for 13C nuclei. The NMR spectra at the temperatures 293, 313, 333 and 353 K for the solution of alizarin and the zinc salt were recorded on a Bruker Avance AMX600 instrument operating at 600.58 MHz for 1H nuclei. Proton decoupling was achieved by power gated decoupling using

* Corresponding author. Address: Chair and Department of Toxicology, Silesian Piasts University of Medicine in Wrocław, ul. Traugutta 57/59, 50-417 Wrocław, Poland. Tel.: +48 694615532.
E-mail address: marek.doskocz@tox.am.wroc.pl (M. Doskocz).

0277-5387/$ - see front matter © 2009 Elsevier Ltd. All rights reserved.
doi:10.1016/j.poly.2009.01.046

the Waltz 16 sequence. The spectra were referenced to the solvent line of DMSO (δH = 2.50 ppm quintuplet, δC = 39.43 ppm septuplet) as internal standards. NMR spectra were analyzed using the MestreC program [12].

In the theoretical study of the structure of the complex, Becke's three parameters functional approach with the Vosko et al. local correlation part and the Lee et al. non-local part, abbreviated as B3LYP, was applied [13]. The calculations of geometry were performed using the standard 6-31G(*d*,*p*) basis set [14]. The effect of the solvent of the calculated structures has been taken into account with Barone and Cossi's implementation [15]. The polarizable conductor model (CPCM) continuum solvatation method with Klamt's [16] and explicit from 4 to 6 water molecules and five DMSO molecules was applied. The NMR parameters were calculated using the coupled perturbed density functional theory (CP-DFT) method with the B3LYP functional by including the diamagnetic spin–orbit, paramagnetic spin–orbit, Fermi-contact and spin-dipolar terms [17]. This functional is believed to be in a good agreement with experimental data [18]. A IGLO III base [19] was applied to the calculations of the NMR properties for carbon, hydrogen and oxygen atoms and a standard base 6-31G(*d*) for the zinc atom. The same solvent models as employed for the geometry optimization were used in the calculation of the scalar coupling. The computations were carried out using the Gaussian 03 suite of codes [20], and the results were visualized by applying the ChemCraft package [21].

3. Results and discussions

Alizarin (1,2-dihydroxy-9,10-anthraquinone) is the one of the most popular hydroxyanthraquinones and is often selected as a model system Fig. 1.

The effect of complexation of alizarin has been studied by various techniques, such as IR, UV–Vis, NMR, MS and theoretical modelling [22–26]. Alizarin has favourable donor-centers, namely oxygen atoms from carbonyl (C=O) and hydroxyl (OH) groups [22]. They create good binding sites for divalent cations. In aqueous solution (physiological conditions), metal cations are always present in the hydrated form. The number of water molecules in the hydratation sphere of the cations amounts to 12 ± 2 water molecules for Ca^{2+} and 13 ± 2 for Mg^{2+} [27]. The most important water molecules create the first solvatation sphere and this corresponds to the coordinate number of the metal. The typical coordination number for Ca^{2+}, Mg^{2+}, Zn^{2+} and Cu^{2+} is six [9,28]. A good model for complexes of anthraquinone with metal cations must always include the hydration shell of the metal cation [29]. The hydrated metal cation may interact with the anthraquinone via its outer shell (Fig. 2a), inner shell and in bidentate fashions (Fig. 2b and c).

Our calculations have shown that the bidentate binding form is the preferred structure of alizarin complexes with metal ions (Fig. 2b and c). The one of the two structures, which is lower in energy, is seen on coordination to calcium metal (Fig. 2c). This result correlates with the conclusion about the structure of the complex proposed by Brewer [25]. The energy difference between structures b and c equals 0.85 kcal/mol (Fig. 2) for the alizarin complex with Mg^{2+}, 3.82 kcal/mol for the complex with Ca^{2+}, and 1.62 kcal/mol for the complex with Zn^{2+}. The stability of the structure shown in Fig. 2c is strengthened due to the formation of strong hydrogen bonding O–H···O=C, which is manifested by the shorter H···O distance (in the case of the calcium complex it equals 1.6 and 1.9 Å for the structures in Fig. 2c and b, respectively). In water solution at various pH values there are possibilities of other interactions to the ones analyzed above, for example the metal ion can interact with $MeOH^+$, $Me(OH)_2$ and the ligand as anthraquinone$^-$ or antraquinone-H^+. Such interactions, however, are not analyzed in this paper.

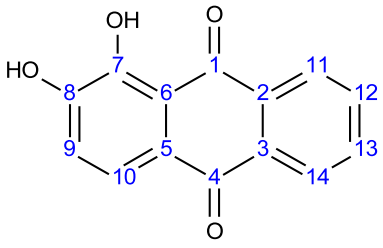


Fig. 1. The alizarin structure with the carbon atoms numbering.

The interaction between the anthraquinone and the metal may be manifested in some changes of geometry and the magnetic properties of anthraquinone. By our calculations we have found that the planarity of alizarin is not disturbed after complexation to the metal. The root mean square deviation (RMSD) from planarity for the carbon, oxygen and aromatic-hydrogen atoms is very small (in the range of 0.03 Å). However the interaction between the anthraquinone and the metal is expected to influence the chemical shifts of the nearby atoms. This change can be observed by ^{1}H NMR and ^{13}C{^{1}H} NMR techniques. (Figs. 3 and 4 and Table 1).

The ^{1}H NMR spectra for alizarin alone, and with $Mg(NO_3)_2$, $Ca(NO_3)_2$ and $Zn(NO_3)_2$ in DMSO-d_6, and the ^{1}H NMR spectra for alizarin with $Zn(NO_3)_2$ at various temperatures show small differences, lower than 0.13 ppm (Table 1), between the chemical shift for the pure and complexed alizarin. The changes of the chemical shift for the ^{13}C{^{1}H} NMR spectra are lower than 0.54 ppm. In all cases the addition of the metal salt to the solution results in upfield shifts. However there is a big change in the shape of the ^{1}H NMR signal (Figs. 3 and 4). The two hydroxyl hydrogen signals for alizarin dissolved in DMSO are wide, indicating their dynamics. The signal further to the left (12.56 ppm) was identified as the one attached to the hydroxyl group at C7. Our calculations have also shown that it should be shifted upfield with respect to the hydrogen atom of hydroxyl group at C8. When the complex is being formed, the hydrogen of the hydroxyl group at C7 becomes significantly narrowed whereas the hydrogen atom attached to the hydroxyl group at C8 becomes even wider than that in alizarin. This occures for the complexes with magnesium and zinc. In the case of the complex with calcium, the signal from the hydrogen atom of hydroxyl group at C8 is slightly narrowed but to a much smaller extent than the other one. The spectrum of the complex with copper shows very wide signals due to the paramagnetic nature of that metal. The aromatic region and proton H7 are visible in the ^{1}H NMR spectrum as broad signals and the signal from the H8 proton has disappeared, as in the case of the other complexes.

The interpretation of the above observation is as follows. Formation of the complex of alizarin with the metal in a fashion shown in Fig. 2c, i.e. by the oxygens from both hydroxyl groups, should result in weaker binding of the corresponding hydroxyl hydrogen atoms to the corresponding oxygen atoms. In fact the calculated O–H distance of the hydroxyl group is the shortest one (0.968) Å and it does not take part in the interaction with the metal ion attached to the C8 carbon atom, which is shown in structure Fig. 2a. In the structures presented in Fig. 2b and c, the distance becomes equal, 0.970 Å. Due to the above effect, the signals of the hydroxyl hydrogens atoms in the NMR spectra should be wider as they are dynamically less restricted. However the hydrogen attached to the hydroxyl group at C7 becomes trapped by the carbonyl oxygen. This effect is confirmed by the calculations which indicate the shortening of the H···O distance and lengthening of the O–H distance in the O–H···O fragment. In the presented magnesium complex (Fig. 2) the (C7)O–H distances equal 0.974, 0.997 and 1.017 Å and the (C7)OH···O distances equal 2.025,

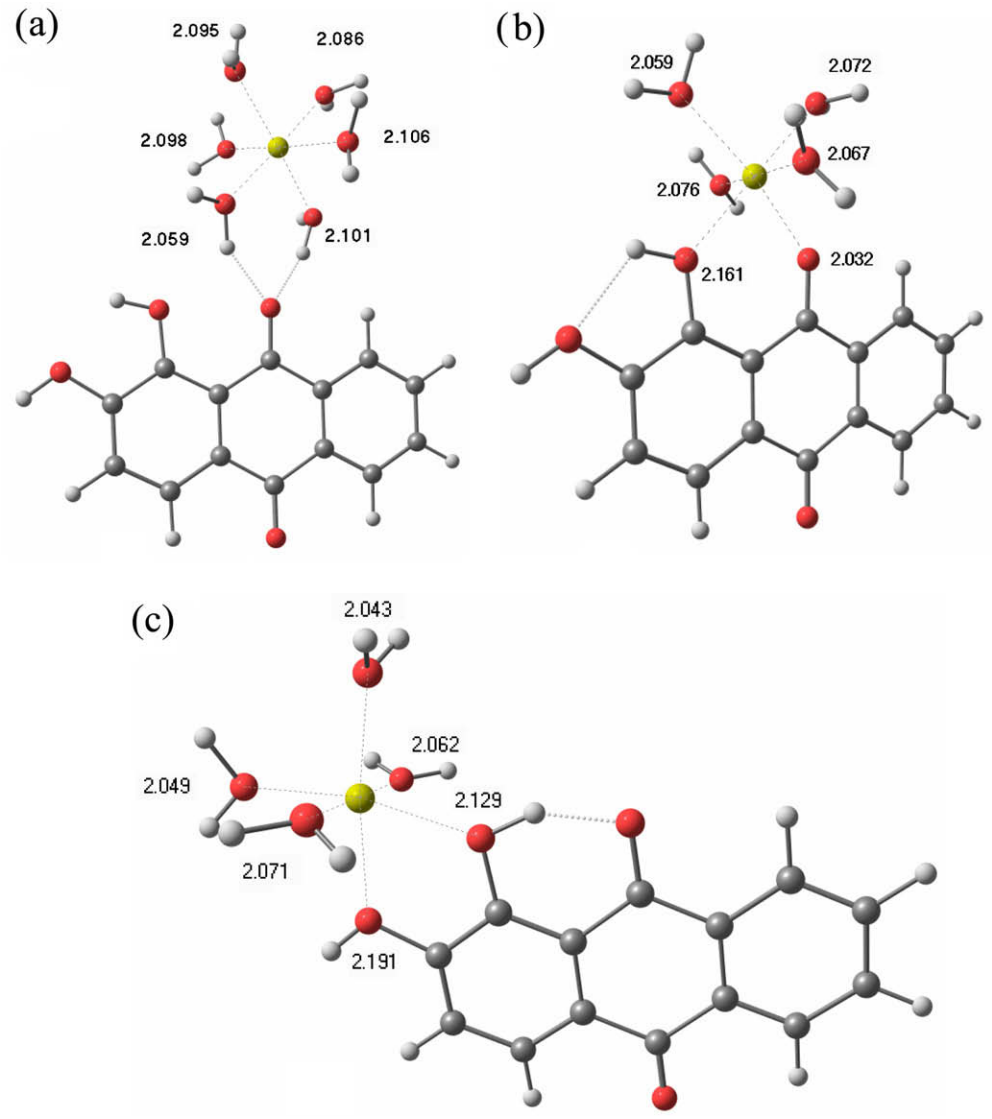


Fig. 2. Binding modes of Mg^{2+} cations to alizarine. The presented structures were optimized at the B3LYP/6-31G(*d*,*p*) level of theory with the PCM solvent model. (a) Outer-shell binding; (b) bidentate binding to oxygens from carbonyl and hydroxyl groups; (c) bidentate binding to oxygen from both hydroxyl groups.

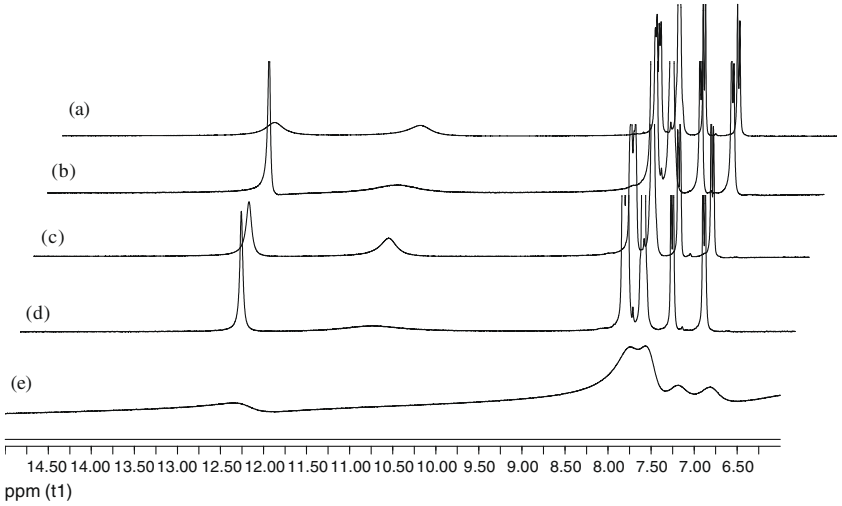


Fig. 3. The ^1H NMR spectra in DMSO-d_6 for (a) alizarin, (b) alizarin with $Mg(NO_3)_2$, (c) alizarin with $Ca(NO_3)_2$, (d) alizarin with $Zn(NO_3)_2$, (e) alizarin with $Cu(NO_3)_2$.

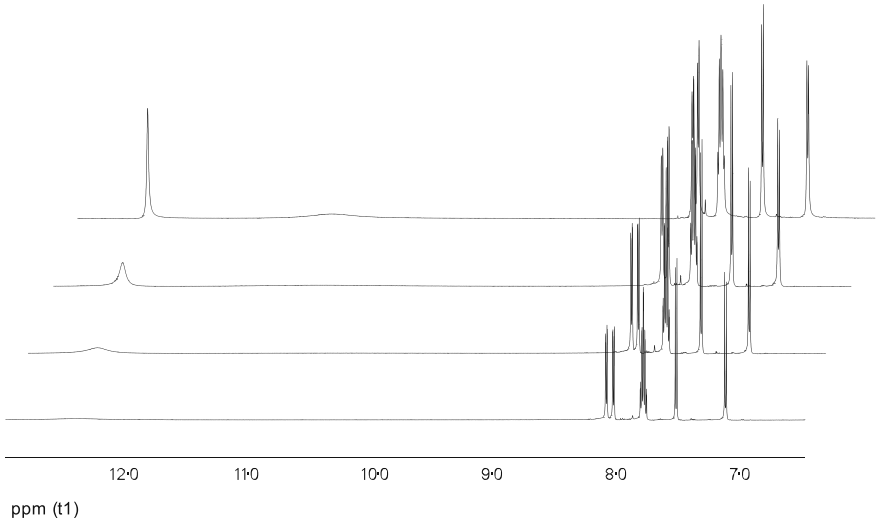


Fig. 4. The ^{1}H NMR spectra of alizarin and $Zn(NO_3)_2$ in DMSO-d_6 recorded at various temperatures (293, 313, 333 and 353 K).

Table 1
Experimental and theoretical chemical shifts [ppm] for alizarin and its complexes with metal ions.

Atom number of alizarin*	Experimental δ	$\Delta\delta = \delta_{(\text{alizarin with metal})} - \delta_{(\text{alizarin})}$**			Theoretical δ	Error %	$\Delta\delta^{\text{theor}} = \delta^{\text{theor}}_{(\text{alzarin and } Zn^{2+})} - \delta^{\text{theor}}_{(\text{alzarin})}$**	
		Mg^{2+}	Ca^{2+}	Zn^{2+}			c***	b***
H7	12.56	0.13	0.05	0.12	13.52	7.6	2.47	−5.66
H8	10.86	−0.10	−0.04	−0.04	7.07	34.9	0.29	0.20
H11	8.11	0.12	0.08	0.11	8.63	6.4	0.06	0.04
H14	8.06	0.11	0.04	0.11	8.56	6.2	0.09	0.06
H12 and 13 multiplet	7.84	0.08	0.02	0.07	8.22	5.0	0.13	0.15
					8.19	4.5	0.09	0.09
H10	7.55	0.12	0.04	0.12	8.12	7.5	0.17	0.23
H9	7.15	0.09	0.03	0.09	7.58	6.1	0.24	0.21
C1	188.56	0.36	0.14	0.36	199.19	7.0	1.22	−0.81
C4	180.28	0.47	0.18	0.48	191.01	6.0	0.23	−0.54
C8	152.61	0.41	0.20	0.42	161.65	5.9	−7.50	−3.50
C7	150.64	0.43	0.20	0.44	158.22	5.0	−4.85	−5.38
C13	134.91	0.54	0.22	0.53	143.61	6.5	1.91	2.57
C12	133.83	0.54	0.22	0.54	142.15	6.2	0.92	0.82
C3	133.35	0.29	0.12	0.30	140.92	5.7	−0.24	−0.56
C2	132.61	0.27	0.12	0.29	139.97	5.6	−1.13	0.11
C14	126.54	0.44	0.17	0.44	134.99	6.7	0.83	0.56
C11	126.28	0.45	0.18	0.46	134.55	6.6	0.94	2.36
C5	123.58	0.34	0.13	0.35	130.94	6.0	2.75	1.92
C10	120.98	0.51	0.20	0.50	129.52	7.1	1.31	3.56
C9	120.67	0.46	0.19	0.45	126.11	4.5	2.17	1.82
C6	116.02	0.28	0.12	0.28	121.99	5.1	0.89	1.46

Δ Indicates the difference in chemical shift between non-complexed and complexed alizarin.
Error Indicates the predicted relative percentage error theoretical versus experimental.
* The final assignment is based on the analysis of the data from theoretical calculations.
** The experimental chemical shift difference between NMR signals for alizarin and its complex and the calculated chemical shift difference between NMR signals for alizarin and its complex.
*** The structure C is analogous to the structure presented in Fig. 2c but with the zinc ion, B corresponds to Fig. 2b, also with zinc ion.

1.971 and 1.578 Å, respectively for the structures presented in Fig. 2a–c.

It finally results in restricting the freedom of the hydrogen atom at the C7 hydroxyl group and narrowing its signal in the ^{1}H NMR spectra. The phenomena described above confirms the mode of binding in the way shown in Fig. 2c, but it neglects other modes of binding.

Dimethyl sulfoxide is a strong aprotic donor solvent and it can efficiently intersolvate the d-element ions of Cu^{2+} and Zn^{2+}. The considered interaction between the metal and the DMSO molecule is: $M^{2+}\cdots O{=}S(CH_3)_2$. Models of this same interaction between the ion and solvent were researched by El-Nahas [30]. The calculation of the model with DMSO gives similar results to that where water molecules are used as the solvent. The structures for the DMSO model are presented in the Supplementary data.

Heating a mixture of alizarin with $Zn(NO_3)_2$ in DMSO (from 20 to 80 °C) results in widening of the signals corresponding to both hydrogen atoms attached to hydroxyl group, since at the elevated temperatures the dynamics of these hydrogen atoms increase. (Fig. 4) The above experiment additionally supports our previous conclusion.

Theoretically, the calculated chemical shifts strongly correlate with the calculated values. For most of the hydrogens the predicted error is within the 4–8% range and for carbon atoms it is lower than 11%. The highest value of predicted error for the proton signal of H8 (from the hydroxyl group) is 34%. The calculation of the

chemical shift for structures DB and DC (supplementary material) with the explicit influence of the –O–H8···O (solvent) hydrogen bond gives more appropriate results. The experimental chemical shift of H8 for alizarin is 10.86 ppm, and the theoretical value is 7.20 ppm, in structures DC and DB it is 11.85 and 12.47 ppm, respectively. The tendency of most experimental ($\Delta\delta$) and theoretical ($\Delta\delta^{theor}$) chemical shift differences between complexed and non-complexed alizarin is the same and it is of a positive value (Table 1). The structure of the complexes which correlates in the best way with the theoretical and experimental data is the structure in which the metal interacts in a bidentate mode to both oxygen atoms from hydroxyl groups (Fig. 1c).

4. Conclusions

Alizarin acts as a bidendate ligand on forming complexes with metal ions. From the possible structures, the one with the metal attached to two hydroxyl oxygen atoms is of lower energy. A theoretical calculation of the structure of the complex and NMR parameter analysis lead to the same conclusion.

In the ^{1}H NMR and ^{13}C{^{1}H} NMR spectra, the chemical shift difference between the free ligand and the ligand complexed to metal is too small and is not useful in studies of the mode of complexation. However the change of the shape of the signals from the hydroxyl group (O–H) is informative.

Acknowledgement

The authors thank Dr. Vladimir Synchrovsky from UCB Prague for a discussion about the solvatation model. We would also like to thank the Poznań and Wroclaw Supercomputing and Networking Centers and Academic Computer Centre in Gdansk for a generous allotment of computer time.

Appendix A. Supplementary data

The cartesian coordinates for the bidendate structures B and C (Table 1), the solvatation models for Ca^{2+}, Mg^{2+} and Zn^{2+} ions and the solvatation model with DMSO molecules in the complex of alizarin and Zn^{2+}, and their ^{13}C{^{1}H} NMR spectra are available in the supporting material.

Supplementary data associated with this article can be found, in the online version, at doi:10.1016/j.poly.2009.01.046.

References

[1] P. Bányai, N. Kuzovkina, L. Kursinszki, É. Szőke, Chromatogr. Suppl. 63 (2006) 111.
[2] Q. Huang, G. Lu, H.-M. Shen, M.C.M. Chung, C.N. Ong, Interscience (2006) 609.
[3] L.G. Angelini, L. Pistelli, P. Belloni, A. Bertoli, S. Panconesi, Indust. Crops Products 6 (1997) 303.
[4] J.M. Campos-Martin, G. Blanco-Brieva, J.L.G. Fierro, Angew. Chem. Int. Ed. 49 (2006) 6952.
[5] V. Ya Fain, M.A. Ryabov, B.E. Zaitsev, Rus. J. Org. Chem. 41 (5) (2005) 707.
[6] V. Ya Fain, M.A. Ryabov, B.E. Zaitsev, Rus. J. Gen. Chem. 74 (10) (2004) 1558.
[7] A. Vasconsuleo, R. Boland, Plant Sci. 172 (2007) 861.
[8] H. Puchtler, S.N. Meloan, M.S. Terry, J. Histochem. Cytochem. 17 (2) (1968) 110.
[9] F.C. Lightstone, E. Schwegler, R.Q. Hood, F. Gygi, G. Galli, Chem. Phys. Lett. 343 (2001) 549.
[10] J.M. Berg, J. Biol. Chem. 265 (1990) 6513.
[11] J.M. Berg, J. Tymoczko, L. Stryer, Biochemistry (2002).
[12] J.C. Cobas, Concept. Magn. Reson. 19A (2) (2003) 80.
[13] M. Cossi, N. Rega, G. Scalmani, J. Comp. Chem. 24 (6) (2003) 669.
[14] A.D. Becke, J. Chem. Phys. 98 (1993) 564.
[15] M.F. Michelle, J.P. Wiliam, J.H. Warren, J.S. Binkley, M.S. Gordon, D.J. DeFrees, J.A. Pople, J. Chem. Phys. 77 (1982) 3654.
[16] F. Eckert, A. Klamt, AIChE J. 48 (2002) 369.
[17] V. Sychrovsky, J. Sponer, L. Trantirek, B. Schneider, J. Am. Chem. Soc. 128 (2006) 6823.
[18] V. Sychrovsky, J. Grafenstein, J. Chem. Phys. 113 (9) (2000) 3530.
[19] W. Kutzelnigg, U. Fleischer, M. Schindler, The IGLO-Method: Ab-initio Calculation and Interpretation of NMR Chemical Shifts and Magnetic Susceptibilities, vol. 23, Springer-Verlag, Haidelberg, 1990.
[20] GAUSSIAN 03: M.J. Frisch, G.W. Trucks, H.B. Schlegel, G.E. Scuseria, M.A. Robb, J.R. Cheeseman, J.A. Montgomery Jr., T. Vreven, K.N. Kudin, J.C. Burant, J.M. Millam, S.S. Iyengar, J. Tomasi, V. Barone, B. Mennucci, M. Cossi, G. Scalmani, N. Rega, G.A. Petersson, H. Nakatsuji, M. Hada, M. Ehara, K. Toyota, R. Fukuda, J. Hasegawa, M. Ishida, T. Nakajima, Y. Honda, O. Kitao, H. Nakai, M. Klene, X. Li, J.E. Knox, H.P. Hratchian, J.B. Cross, V. Bakken, C. Adamo, J. Jaramillo, R. Gomperts, R.E. Stratmann, O. Yazyev, A.J. Austin, R. Cammi, C. Pomelli, J.W. Ochterski, P.Y. Ayala, K. Morokuma, G.A. Voth, P. Salvador, J.J. Dannenberg, V.G. Zakrzewski, S. Dapprich, A.D. Daniels, M.C. Strain, O. Farkas, D.K. Malick, A.D. Rabuck, K. Raghavachari, J.B. Foresman, J.V. Ortiz, Q. Cui, A.G. Baboul, S. Clifford, J. Cioslowski, B.B. Stefanov, G. Liu, A. Liashenko, P. Piskorz, I. Komaromi, R.L. Martin, D.J. Fox, T. Keith, M.A. Al-Laham, C.Y. Peng, A. Nanayakkara, M. Challacombe, P.M.W. Gill, B. Johnson, W. Chen, M.W. Wong, C. Gonzalez, J.A. Pople, Revision C.02; Gaussian Inc., Wallingford, CT, 2004.
[21] ChemCraft, G.A. Zhurko, <http://www.chemcraftprog.com>, 2006.
[22] V.Y. Fain, B. Zaitsev, M.A. Ryabov, Rus. J. Coord. Chem. 30 (5) (2004) 365.
[23] N. Komiha, O.K. Kabbaj, M. Chraibi, J. Mol. Struct. 594 (2002) 135.
[24] Y. Kubo, T. Ishida, A. Kobayashi, T.D. James, J. Mater. Chem. 15 (2005) 2889.
[25] D.G. Brewer, J.A. Pag, Canadian J. Chem. 41 (1963) 1695.
[26] P. Soubayrol, G. Dana, P.P. Man, Magnet. Reson. Chem. 34 (1996) 638.
[27] A.A. Zavitsas, J. Phys. Chem. B 105 (32) (2001) 7805.
[28] G.W. Marini, K.R. Liedl, B.M. Rode, J. Phys. Chem. A 103 (51) (1999) 11387.
[29] J.E. Šponer, J.V. Burda, J. Leszczynki, J. Šponer, in: Computational Studies of RNA and DNA, Springer, Netherlands, 2006.
[30] A.M. El-Nahas, Chem. Phys. Lett. 365 (2002) 251.

Polyhedron 28 (2009) 2206–2218

Contents lists available at ScienceDirect

Polyhedron

journal homepage: www.elsevier.com/locate/poly

Effect of substituent position and lithium, sodium and potassium on the electronic structure of *o*-, *m*- and *p*-methoxybenzoic acids

M. Kalinowska, G. Świderski, W. Lewandowski *

Department of Chemistry, Bialystok Technical University, Zamenhofa 29, 15-435 Białystok, Poland

ARTICLE INFO

Article history:
Received 2 August 2008
Accepted 19 March 2009
Available online 12 April 2009

Keywords:
Methoxybenzoic acids
Alkali metal methoxybenzoates
Spectroscopic studies
Quantum mechanical calculations

ABSTRACT

We have studied the effect of the substituent position in the ring, and lithium, sodium and potassium ions on the electronic structure of *o*-, *m*- and *p*-methoxybenzoic acids (anisic acids) by the use of FT-IR, FT-Raman, Ar matrix FT-IR and ^{1}H NMR methods, and *ab initio* calculations at the B3LYP/6-311++G** level of theory. Characteristic shifts of the bands in the spectra and changes in the band intensities along the metal and ligand series were observed. On the basis of the obtained results we may answer the questions: (1) do the substituents in the benzene ring influence the electronic charge distribution in the carboxylic group of anisic acids and alkali metal anisates, (2) do the metal ions affect the electronic charge distribution in the methoxy group, (3) in what way do the alkali metals affect the electronic system of *o*-, *m*- and *p*-anisic acids? The substitution of lithium, sodium and potassium ions in the carboxylic group of *o*-, *m*- and *p*-anisic acids causes changes in the values of bond lengths and angles, and in the electronic charge distribution in the carboxylic group, methoxy group and aromatic ring. The influence of alkali metals on the electronic structure of the ligands is weaker than the effect of methoxy substituents. The effect of Li, Na and K ions on the aromatic ring of the ligands is mostly noticeable in the case of the *ortho* isomer. The carboxylic and methoxy groups situated in *ortho* positions in the ring weaken the effect of the alkali metals on the electronic charge distribution in the carboxylic anion and methoxy group.

© 2009 Elsevier Ltd. All rights reserved.

1. Introduction

Methoxybenzoic acids (anisic acids) are naturally occurring compounds and their biological activity is widely described. They are known to be important inhibitors in the growth of bacteria [1] and they influence the catalytic activity of many enzymes [2]. For example *p*-anisic acid is an inhibitor of phospholipase A_2. The crystal structure of an anisic acid – bound triple mutant of phospholipase A_2 revealed that the small molecule of anisic acid is located in the active site of the enzyme. One of the carboxylate oxygen atoms is coordinated to the calcium ion, and the second carboxylate oxygen atom is hydrogen bonded to the phenolic hydroxyl group of tyrosine (Tyr69) [3]. The biological activity of molecules is determined by their molecular structure, i.e. the kind and position of substituent and the kind of metal coordinated through the carboxylic group. There is a direct relationship between chemical structure and the biological properties of chemical compounds. For example, Maffei et al. showed that methoxy-substituted benzoic acids decrease isocitrate lyase (ICL) activity, whereas hydroxyl-substituted benzoic acids generally increase ICL activity [4]. Our studies on 3,5-dihydroxy- and 2,6-dihydroxybenzoates as well as 3,5-dichloro- and 2,6-dichlorobenzoates showed that the highest antimicrobial activity towards *Bacillus subtilis* and *Staphylococus ureus* posses alkali metal 3,5-dichlorobenzoates [5]. Among the studied complexes of *m*-iodobenzoic and pyridine-carboxylic acids with alkali metals and transition metals, the highest antimicrobial activity towards the selected microorganisms was showed by Zn *m*-iodobenzoate and Ag picolinate [6]. To better understand the mechanisms of action of chemical compounds on biological systems it is essential to carry out physico-chemical studies of model compounds. The results of this study make it possible to predict some properties of a molecule, such as reactivity, durability of complex compounds as well as the nature of the interactions of these compounds with their biological targets (e.g. receptors in the cell or important cell components) and a kinship to enzymes. From this point of view it is very important to study the effect of substituents and metals on biologically important ligands such as anisic acids [7].

In this paper we have studied the effect of metals (lithium, sodium and potassium) and the position of a methoxy substituent in the ring on the electronic system of *o*-, *m*- and *p*-anisic acids by the use of infrared (FT-IR), Raman (FT-Raman), nuclear magnetic resonance spectroscopy (^{1}H NMR) and quantum mechanical calculations (optimized structure, theoretical IR and NMR spectra, atomic charge distribution using NPA, ChelpG and MK methods).

* Corresponding author. Tel.: +48 85 469790; fax: +48 85 7469782.
E-mail address: w-lewando@wp.pl (W. Lewandowski).

0277-5387/$ - see front matter © 2009 Elsevier Ltd. All rights reserved.
doi:10.1016/j.poly.2009.03.030

It is worth mentioning that to our knowledge no calculations have been reported so far for alkali metal anisates and the spectroscopic data are incomplete and have mainly been performed for anisic acids.

2. Experimental

The alkali metal anisates were prepared by dissolving the appropriate weighed amount of the anisic acids in an aqueous solution of the alkali metal hydroxides in a stoichiometric ratio of 1:1. The anhydrous compounds were obtained after the evaporation the solvent on a vapour bath, and drying at 160 °C in a dryer under reduced pressure. The metal:ligand ratio is 1:1, which was proven by elementary analysis of the synthesized compounds. The results for the *o*-anisates are as follows: lithium *o*-anisate: %C = 60.01, %H = 4.32, C:H element ratio = 1.17:1; sodium *o*-anisate: %C = 55.07, %H = 4.04 (C:H = 1.14:1); potassium *o*-anisate: %C = 49.94, %H = 3.67, (C:H = 1.13:1). The results of elementary analysis for *m*-anisates: lithium *m*-anisate: %C = 60.42, %H = 4.37, (C:H = 1.16:1); sodium *m*-anisate: %C = 53.81, %H = 4.11 (C:H = 1.10:1); potassium *m*-anisate: %C = 49.96, %H = 3.80, (C:H = 1.10:1). The results of elementary analysis for *p*-anisates: lithium *p*-anisate: %C = 60.71, %H = 4.37, (C:H = 1.17:1); sodium *p*-anisate: %C = 54.57, %H = 3.98 (C:H = 1.15:1); potassium *p*-anisate: %C = 50.55, %H = 3.77, (C:H = 1.13:1). The calculated percentage composition of carbon and hydrogen atoms in anisate molecules are as follows: for lithium anisate %C = 60.78, calc.%H = 4.46; for sodium anisate %C = 55.18; %H = 4.05; for potassium anisate: %C = 50.51; %H = 3.71, (C:H = 1.14:1).

The IR spectra were recorded with an Equinox 55 spectrometer within the range 400–4000 cm^{-1}. Samples in the solid state were measured in a KBr matrix – pellets were obtained with a hydraulic press under 739 MPa pressure. Raman spectra of solid samples in capillary tubes were recorded in the range 400–4000 cm^{-1} with a FT-Raman accessory of the Perkin–Elmer system 2000. The resolution of the spectrometer was 1 cm^{-1}. Argon matrices were produced by deposition of the sample into a stream of gas onto a KBr window held at 20 K in a Displex 202 cryostat. The compound, contained in a glass tube, was heated to 333 K. During irradiation and subsequent spectral measurements, the matrix temperature was kept at 20 K. As irradiation sources, the following were used: (1) an 899 ring laser (Coherent), pumped by a Coherent Innova 300 argon laser; (2) an ILA 120 argon laser; (3) a 300 W xenon lamp (ILC). The NMR spectra in DMSO solution were recorded with a Bruker Varian Tectron 500 MHz unit at room temperature. TMS was used as an internal reference. The optimized geometries, NPA (Natural Population Analysis), ChelpG (CHarges from ELectrostatic Potentials using a Grid based method), MK (Merz–Singh–Kollman) atomic charges and IR wavenumbers were calculated at the B3LYP/6-311++G** level of theory using the Gaussian 98W program [8]. Additionally the AIM theory of Bader [9] (the theory of atoms in molecules) was used to localize bond critical points and to calculate their properties: electron densities at bond critical points (ρBCP) and electron densities at ring critical points (ρRCP). All AIM calculations were performed using the AIM2000 program [10]. The aromaticity indices (HOMA – *the harmonic oscillator model of aromaticity index*, I_6 – *the Bird's aromaticity index*, BAC – *the bond alternation coefficient*, A_j – *the first aromaticity index formulated by Julg and François*) were calculated for optimal geometrical structures of anisic acid and the anisates [11,12]. Literature structural data were used in this discussion. The average estimated standard deviation (esd) of the carbon–carbon bond lengths was less than 0.01 Å.

3. Results and discussion

3.1. Geometries of methoxybenzoic acids

The geometries of the anisic acids were calculated using the B3LYP/6-311++G** level of theory. Different conformers were taken into consideration (Fig. 1). All structures were checked by vibrational analysis (no imaginary wavenumbers) and their be-

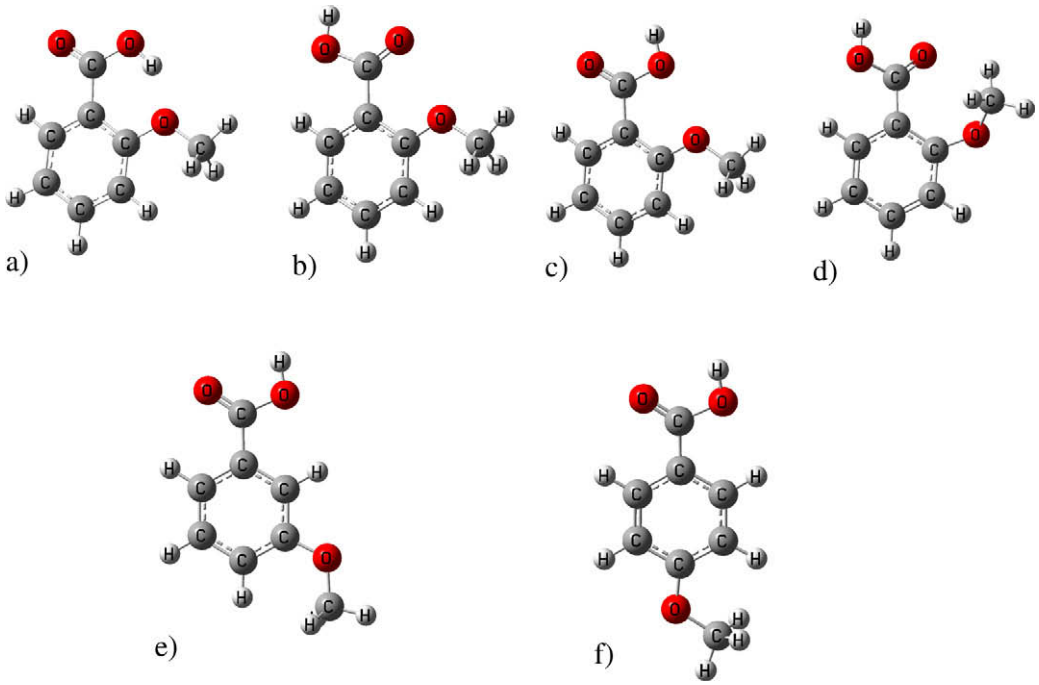


Fig. 1. Calculated structures of methoxybenzoic acid; *o*-methoxybenzoic acids: (a) $E = -535{,}500$ au, dipole moment = 7.06 D; (b) $E = -535.497$ au, dipole moment = 2.72 D; (c) $E = -535.497$ au, dipole moment = 3.75 D and (d) $E = -535.493$ au, dipole moment = 1.94 D; (e) *m*-methoxybenzoic acid, $E = -353.504$ au, dipole moment = 3.31 D; (f) *p*-methoxybenzoic acid, $E = -535.507$ au, dipole moment = 3.85 D.

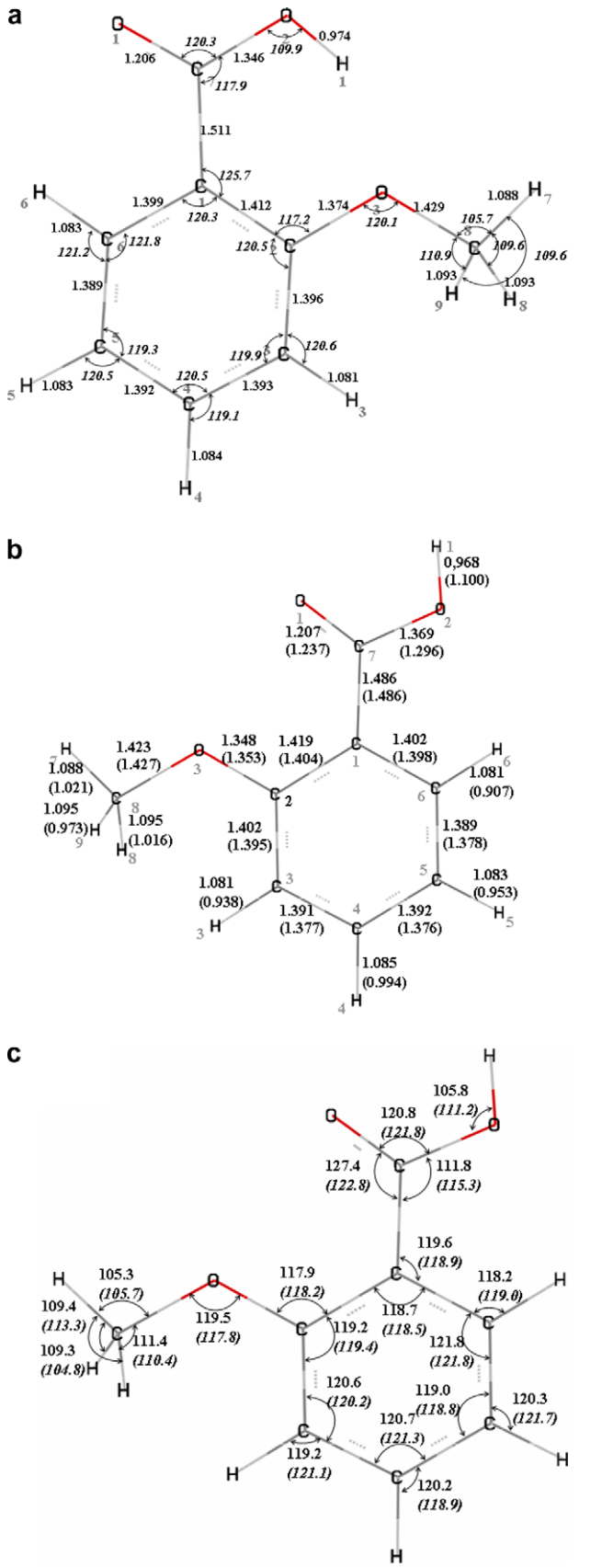


Fig. 2. (a) Calculated bond lengths [Å] and angles [°] (italics) for *o*-anisic acid (structure no. 1a in Fig. 1). (b) Calculated and experimental bond lengths [Å] (experimental values are given in parenthesis [16]) for *o*-anisic acid (structure no. 1b in Fig. 1). (c) Calculated and experimental angles [°] (experimental values are given in parenthesis [16] for *o*-anisic acid (structure no. 1b in Fig. 1).

haved as energy minima. The structure of *o*-anisic acid (Fig. 1a) is a conformer of minimum energy. The molecule is stabilized by intramolecular hydrogen bonds between the oxygen atom of the methoxy group and the hydrogen atom of the carboxylic group. The existence of hydrogen bonds was previously proven by calculations at the B3LYP/6-311++G** level in the gas phase [13] and in solutions [14,15]. The other geometries of *o*-anisic acid were also taken into account (Fig. 1b–d), but our discussion is constrained to the structure no. 1b in Fig. 1 because of the same location of the substituents as in the experimental crystal structure [16]. The conformers of *m*-anisic acid and *p*-anisic acid with the lowest energy are shown in Fig. 1e and Fig. 1f, respectively. In the case of *p*-anisic acid, the mutual position of the methoxy and carboxylic groups is similar as in the crystal structure [17]. An X-ray structure for *m*-anisic acid was not found.

Comparing the studied structures, we found quite good agreement between the calculated and experimental data (with the exception of the carboxylic and methoxy group distances and angles). The computations were done for an isolated compound, whereas in the solid state the molecules are held together by intermolecular forces, predominantly hydrogen bonds. The calculated conformers of *o*-anisic acid are shown in Fig. 2 (a – with hydrogen bonds, and b, c – without hydrogen bonds). The hydrogen bonds clearly influence the geometry of the *o*-methoxybenzoic acid molecule, especially bond lengths and angles in the carboxylic and methoxy groups. The other geometric parameters change insignificantly. The interaction between the carboxylic and methoxy groups affects the geometry of the ring. Both experimental and theoretical C1–C2, C2–C3 and C6–C1 bond lengths in *o*-anisic acid are longer than the other distances in the aromatic ring. The slight influence of the carboxylic group on the methoxy group hydrogen H7 is seen. The C8–H7 distance is shorter than the C8–H8 and C8–H9 lengths.

The optimized geometry of *m*-anisic acid at the B3LYP/6-311++G** level is displayed in Fig. 3. Almost all the bonds are of similar length, being longer than the conjugated C–C bond of the benzene ring (approximately 1.390 Å). The optimized geometrical parameters for *p*-anisic acid are given in Fig. 4a and b. Especially surprisingly is short length of the C5–C6 bond (1.370 Å).

Comparing the *ortho*, *meta* and *para* isomers of methoxybenzoic acid one may see a distinct effect of the substituents on the geometrical parameters of the molecules. The bond lengths and angles located in the neighbourhood of carboxylic and methoxy groups undergo remarkable alternations. Namely, in the 2a and 2b conformers the C6–C1, C1–C2 and C2–C3 distances are longer than the other bonds distances in the ring (both experimental and calculated data). In the *meta* isomer, the C6–C1, C2–C3, C3–C4 and C4–C5 bonds lengths are the longest in the ring. In the *para* isomer, the C6–C1, C1–C2, C3–C4 and C4–C5 distances are longer than the other C–C bonds in the aromatic ring. Moreover, the dependency between the alternation of bond lengths in the aromatic ring and the aromatic properties of molecule, which was discussed previously in our paper [18], is very interesting. The geometric criterion of aromaticity is based on the fact that the essential factor in aromaticity stabilization is the π-electron delocalization manifested in the following: planar geometry, equalization of the bond lengths and angles, and symmetry. Following this idea, geometry-based aromaticity indexes were formulated and successfully applied for the determination of the aromatic character of mono- and polycyclic compounds [19,20]. The geometrical indexes calculated on the basis of theoretical and experimental bond lengths are gathered in Table 1. The experimental [21,22] and calculated data (this paper) for the benzoic acid molecule are also included and discussed below. On the basis of the obtained indexes we could arrange the acids according to an increase in the aromatic properties of the molecules. Namely, the values of the aromaticity indexes increase

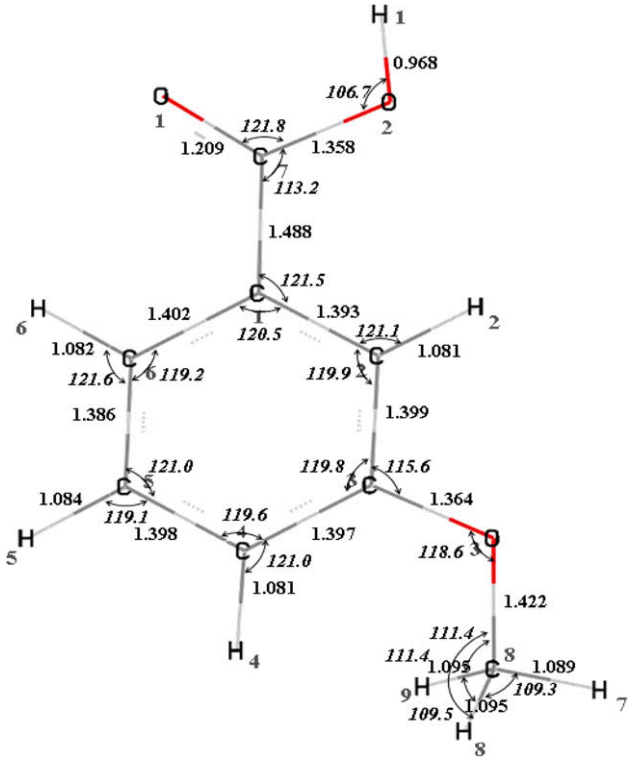


Fig. 3. Calculated bond lengths [Å] and angles [°] (italics) for *m*-anisic acid.

in the order: *o*- → *p*- → *m*- isomers, which suggests that the stabilization of the π-electron system increases in the series *o*- → *p*- → *m*- methoxybenzoic acids (the conformer of *o*-anisic acid with intramolecular hydrogen bonding was not taken into account). Moreover, the difference between the highest and the lowest values of angles between the carbon atoms in the aromatic ring, Δα(CCC), is higher for the *ortho* isomer, compared to the *meta* and *para* isomers, and the values of Δ(CC) decrease in the order as mentioned above (i.e. *o*- → *p*- → *m*-). One may see that calculation of the Δ(CC) and Δα(CCC) values are sufficient for a preliminary estimation of the aromatic properties of the studied systems. Comparing the geometrical indexes obtained for the 2a and 2b conformers of *o*-methoxybenzoic acid we may see that the presence of the intramolecular hydrogen bonds clearly stabilizes the π-electron system of the molecule. The aromaticity indexes are higher for the 2a structure (with hydrogen bonds) compared to 2b (without hydrogen bonds), and the I_6 index is even higher for the 2a structure than the *meta* isomer.

3.2. Geometries of alkali metal methoxybenzoates

The geometrical parameters for lithium, sodium and potassium *m*- and *p*-methoxybenzoates, calculated at the B3LYP/6-311++G** level, are gathered in Tables S1 and S2 (see Supplementary data). The structural data for *o*-methoxybenzoates were reported previously [7]. Comparing the effect of alkali metal ions and substituents on the structure of the ligand, one may say that the metal ions do not evoke such large changes in bond lengths and angles as the methoxy substituent in the aromatic ring. The bond lengths that change more than 0.003 Å in the series: Li → Na → K anisates are displayed in Fig. 5. The alkali metal ions mostly influence the bond lengths and angles in the carboxylic group (which is to be expected) and what is interesting is that they influence the methoxy group geometry. In the series of Li → Na → K *o*-, *m*- and *p*-methoxybenzoates, the C7–O1, C7–O2 and O3–C8 distances decrease, whereas the C1–C7 and C–O3 bond lengths extend. Moreover,

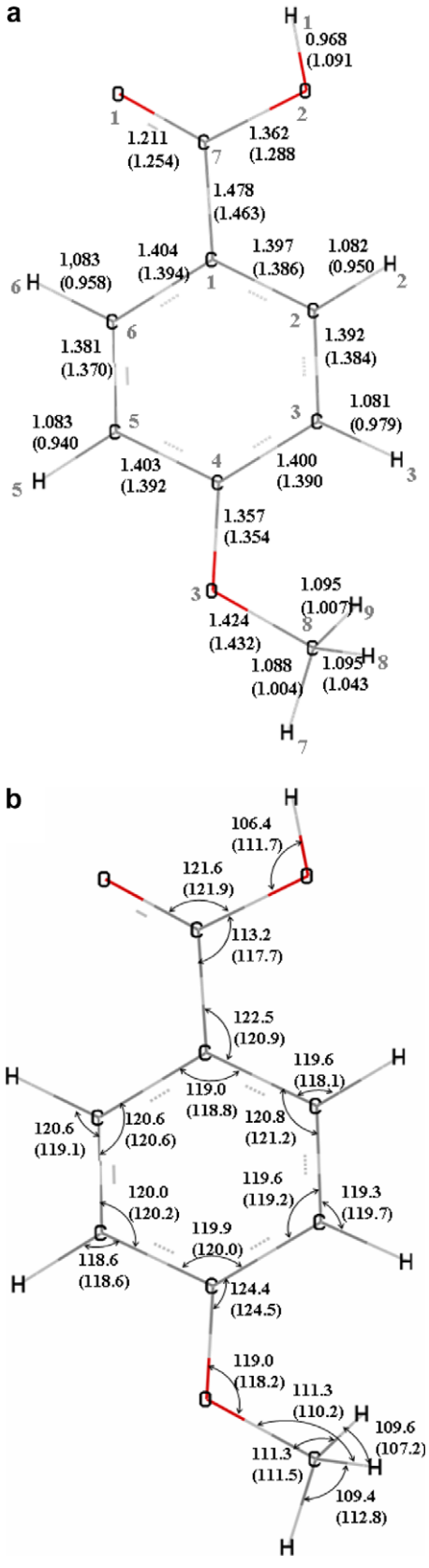


Fig. 4. (a) Calculated and experimental bond lengths [Å] (experimental values are given in parenthesis [17]) for *p*-anisic acid. (b) Calculated and experimental angles [°] (experimental values are given in parenthesis [17]) for *p*-anisic acid.

Table 1
The geometry-based indexes of aromaticity calculated on the basis of geometrical parameters calculated at B3LYP/6-311++G** level.

	Benzoic acid			*m*-Anisic acid	*p*-Anisic acid		*o*-Anisic acid		
	Exp. [21]	Exp. [22]	Calc.	Calc.	Exp. [17]	Calc.	Exp. [16]	Calc. 1b*	Calc. 1a
Δ(CC) [Å]	0.022	0.020	0.008	0.016	0.024	0.023	0.036	0.029	0.023
Δα(CCC) [°]				1.8		1.8		3.1	2.5
HOMA	0.988	0.969	0.982	0.977	0.983	0.966	0.956	0.947	0.966
BAC	0.924	0.918	0.950	0.920	0.881	0.879	0.873	0.902	0.919
Aj	0.995	0.995	0.998	0.997	0.993	0.993	0.981	0.989	0.994
I_6	87.76	80.84	96.89	90.52	93.34	88.88	89.47	85.86	93.69

* Structures 1a and 1b are presented in Fig. 1.

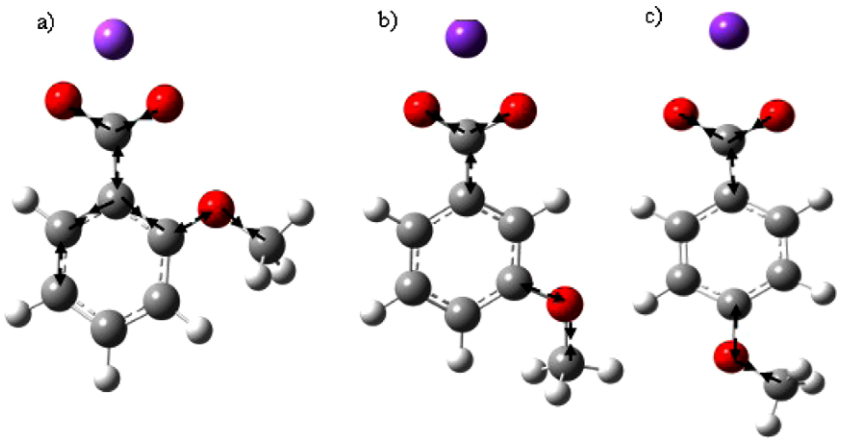


Fig. 5. The change of bond lengths more than 0.003 Å in the series: Li → Na → K (a) *o*-anisates; (b) *m*-anisates and (c) *p*-anisates. The symbols mean: ←→ an increase in bond lengths; →← a decrease in bond lengths; the colors mean: grey – carbon, white – hydrogen, red – oxygen, violet – alkali metal. (For interpretation of the references to color in this figure legend, the reader is referred to the web version of this article.)

the C6–C1–C2, C3–C4–C5, C–O3–C8, H–C–H (in the methoxy group) angles decrease, and the O1–C7–O2 angle increases along the series Li → Na → K anisates. The existence of some regular changes in the distance and angles of molecules suggests that other parameters such as atomic charges of molecules or position of wavenumbers in the IR or Raman spectra may also change regularly in the same fashion for methoxybenzoates. The biggest changes in the geometry of the ring is seen in the case of the *ortho* isomer (Fig. 5).

Similarly as was done in the case of the anisic acids, the aromaticity indexes for the anisates were calculated and gathered in Table S3. The substitution of a metal ion in the carboxylic group does not cause such evident alternations in the values of indexes, as in the case of the change of substituent in the aromatic ring. Generally, the values of indexes increase in the order: Li → Na → K methoxybenzoates, which suggests an increase in the aromatic properties of the molecules in the above series and therefore the stabilization of the π-electron system. In the case of *m*- and *p*-anisates, the values of the indexes stay almost unchanged, whereas for *o*-anisates the indexes change more clearly. This may mean that the alkali metal ions affect the electronic system of ligand to the highest degree when the substituent is in the *ortho* position in the ring and the effect is poorly observed for a *meta* position of the methoxy substituent in the ring.

3.3. Atomic charges

The calculated NPA, ChelpG and MK atomic charges for *o*-, *m*- and *p*-anisic acids and anisates are gathered in Tables S4–S6, respectively. In Table 2 the total atomic charges of the carboxylic and methoxy groups as well as the aromatic rings of studied molecules are given. The position of the substituent affects the electronic charge distribution in the ligand. Namely, the electronic charge density of the methoxy group increases in the series: *o*- → *p*- → *m*- anisic acids, in the case of the carboxylic group the charge generally increases in the order: *o*- → *m*- → *p*- (in the case of NPA charges: *o*- ∼ *m*- → *p*-), and the charge density of the ring changes along the series: *p*- → *m*- → *o*-. The lowest charge density of the methoxy and carboxylic groups, as well as the highest charge density of the ring, is observed in the case of *o*-anisic acid. This is probably caused by the so-called "ortho effect". The main part of the "ortho effect" consists of polar and steric effects which influence the acidity of the carboxylic acids [23]. A methoxy group in the *meta* position in the ring possesses electron withdrawing properties, whereas in the *para* position in the ring it is an electron donating group. When the substituent group has electron withdrawing character, the negative charge of the carboxylic group of the benzoate derivative decreases (stabilization of the carboxylic anion). On the other hand, a methoxy substituent in the *para* posi-

Table 2
The calculated at B3LYP-6-311++G** level total atomic charges [e] for the carboxylic and methoxy groups, as well as the aromatic ring.

	o-Anisic acid (1a)			*o*-Anisic acid (1b)		
	NPA	ChelpG	MK	NPA	ChelpG	MK
$-OCH_3$	−0.223	−0.141	−0.066	−0.179	−0.093	−0.066
−COOH	0.015	0.034	0.066	−0.015	−0.032	0.008
Carbons of ring	−0.668	−0.305	−0.573	−0.663	−0.300	−0.537
	m-Anisic acid			*p*-Anisic acid		
$-OCH_3$	−0.211	−0.180	−0.184	−0.201	−0.178	−0.173
−COOH	−0.013	−0.062	−0.029	−0.032	−0.072	−0.053
Carbons of ring	−0.665	−0.266	−0.485	−0.524	−0.224	−0.353

Table 3
Topological parameters for *o*-methoxybenzoic acid with intramolecular hydrogen bond [au] (bond critical points numbering in Fig. 6/bond lengths numbering in Fig. 2a).

BCP	Bond length	ρ	Hessian eigenvalues			$\nabla^2\rho$
1	C4–C5	0.310556	−0.65204	−0.54392	0.322053	−0.8739
2	C3–C4	0.307843	−0.64271	−0.53376	0.321641	−0.85484
3	C2–C3	0.308644	−0.65237	−0.52357	0.319829	−0.85611
4	C1–C2	0.300603	−0.63263	−0.51156	0.330533	−0.81365
5	C6–C1	0.306121	−0.63643	−0.53193	0.325459	−0.8429
6	C5–C6	0.311605	−0.65277	−0.54636	0.320538	−0.8786
7	C2–O3	0.274426	−0.52756	−0.5272	0.734497	−0.32026
8	**H1–O3**	**0.039926**	**−0.06514**	**−0.06042**	**0.269723**	**0.144167**
9	O2–H1	0.352303	−1.79659	−1.76816	1.069997	−2.49475
10	C7–O2	0.302829	−0.65636	−0.65253	0.789837	−0.51905
11	C1–C7	0.254306	−0.51427	−0.45974	0.373075	−0.60093
12	O3–C8	0.23885	−0.39308	−0.39206	0.507952	−0.27718
13	C7–O1	0.420244	−1.12495	−1.02459	1.939298	−0.21024
14	C6–H6	0.286063	−0.78342	−0.77463	0.554795	−1.00326
15	C5–H5	0.282162	−0.75446	−0.73869	0.521167	−0.97198
16	C4–H4	0.282586	−0.75561	−0.7456	0.523955	−0.97726
17	C3–H3	0.282143	−0.7505	−0.73149	0.516351	−0.96564
18	C8–H7	0.285318	−0.78788	−0.75565	0.547804	−0.99573
19	C8–H8	0.281441	−0.76686	−0.73519	0.539707	−0.96234
20	C8–H9	0.281444	−0.76687	−0.73523	0.539738	−0.96236
RCP						
21		0.021436	−0.01647	0.081794	0.091234	0.156559
22		0.015781	−0.01356	0.048848	0.059432	0.09472

ρ-Electron density, $\nabla^2\rho$-Laplacian of the electron density.

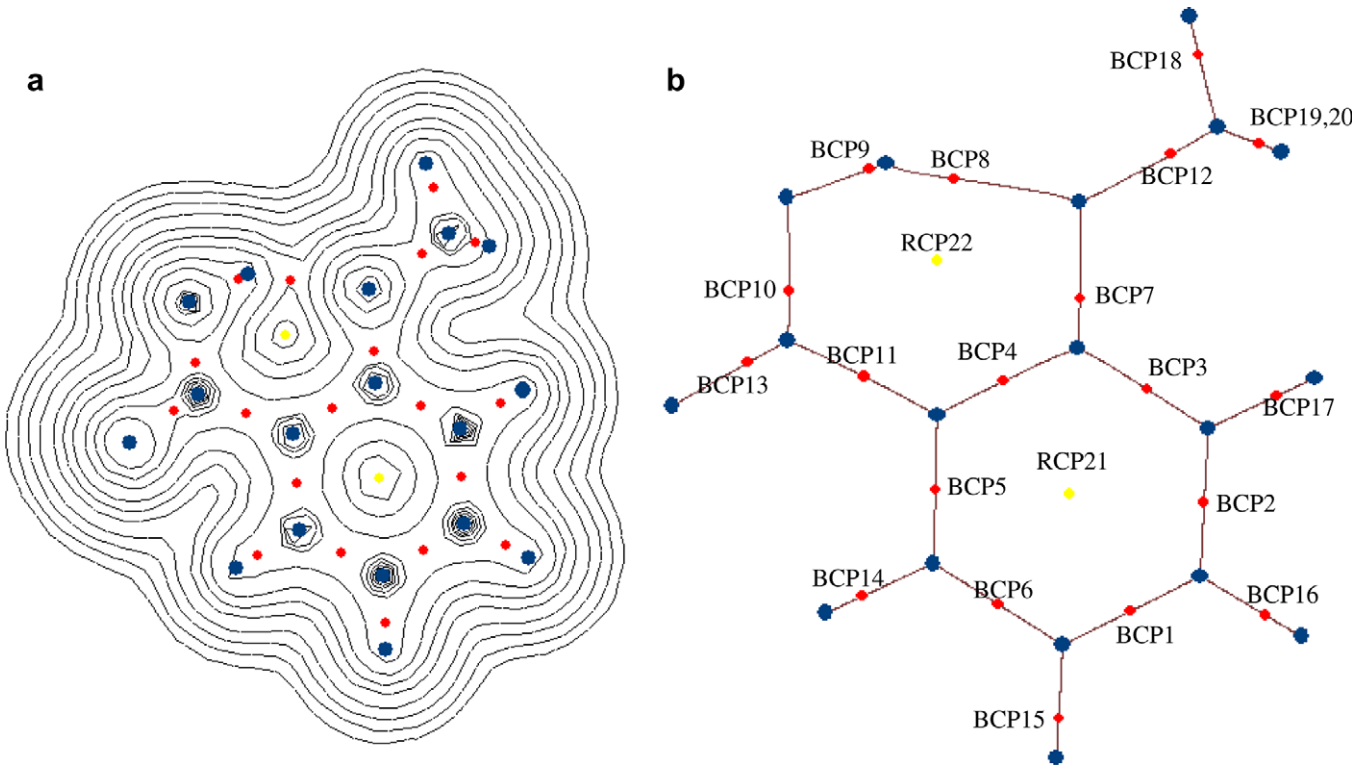


Fig. 6. (a) Contour maps of electron density for *o*-methoxybenzoic acid and (b) critical points assignment: (●) nuclear position; (●) ring critical point; (●) bond critical point.

tion is an electron donating group which causes an increase in the electronic charge distribution and destabilization of the carboxylic anion. It explains the highest electronic charge density of the methoxy and carboxylic groups in the case of *m*- and *p*-anisic acids, respectively.

Comparing the calculated atomic charges for two conformers of *o*-methoxybenzoic acid (1a – with intramolecular hydrogen bonds and 1b – without hydrogen bonds) we may notice that conformer 1a clearly possesses higher electronic charge density on the C1 (except for NPA charge) and O3 atoms, and lower electronic charge density on the H1 and O1 atoms. As a result of this, the total NPA, ChelpG and MK atomic charges of the methoxy group are lower in the case of the 1a conformer compared with the 1b conformer, and inversely – the total atomic charge of the carboxylic group is lower in the case of the 1b structure. Whereas the total atomic charge on the aromatic ring carbon atoms is slightly lower in the case of the 1a conformer. We can see that the existence of intramolecular hydrogen bonds clearly influences the electron

density in the carboxylic and methoxy groups, and therefore it influences the reactivity and properties of the molecules. To study the presence of intramolecular hydrogen bonds in *o*-methoxybenzoic acid, the Bader theory (AIM) was applied. The results of topological analysis are gathered in Table 3 and Fig. 6. The calculations prove the existence of hydrogen bonds between the oxygen atom of the methoxy group and the hydrogen atom of the carboxylic group. In general, the hydrogen bond critical points are associated with small densities and positive Laplacians [24,25]. The electron density at the H···O bond critical point is equal to 0.039926 au. According to the criterion applied in literature, the formed hydrogen bond has weak character [26]. Moreover, the intramolecular hydrogen bond strongly stabilizes the molecule by forming a six-membered quasi aromatic ring with RCP = 0.015781 au (RCP = 0.021436 au for the real aromatic ring of *o*-anisic acid).

It is worth mentioning that the NPA, ChelpG and MK atomic charges located on the C1, C2, C6, C7 and O1 atoms and on the aromatic ring carbons connected with the methoxy substituent change (i.e. increase or decrease) in the series: *o*- → *p*- → *m*- anisic acids. In the case of the C3, C8 and O3 atoms, only the NPA and MK atomic charges change in the same fashion. The calculated values of the atomic charges depend on the type of applied method. This is extremely visible in the case of the methoxy group hydrogens. Namely, the NPA atomic charges on H7, H8 and H9 atoms remain almost unchanged, but the values of the ChelpG atomic charges decrease in the series *o*- → *m*- → *p*- methoxybenzoic acids. In contrast, the values of the MK atomic charges decrease along the series *o*- → *p*- → *m*- anisic acids.

The substitution of metal ions in place of the carboxylic group hydrogen causes a decrease in the electronic charge density on the C1 atom and an increase on C2, C4, C6, O1, O2, H7, H8 and H9 atoms compared to the corresponding atomic charges calculated for the acid. The atomic charges on the other atoms change insignificantly or increase/decrease depending on the applied method. Namely, for *o*-anisates, the electronic charge density on H4 and H5 atoms increase compared to the values of the charges calculated for *o*-anisic acid; for *m*-anisates, the electronic charge density on the C7 atom decreases, whereas that on the O3 atom increases compared to the values of the charges calculated for *m*-anisic acid; for *p*-anisates, the charges on the C3, C5 and C8 atoms decrease, and on the O3 atom increases in comparison with *p*-anisic acid. The calculated total electronic charge density of the methoxy group increases in the series: acid → Li → Na → K anisates. The total electronic charge density of the carboxylic group is higher in anisate molecules than the corresponding acids and it decreases in the order: Li → Na → K anisates. The total electronic charge density of the ring increases in the series: Li → Na → K anisates (NPA method). The total electronic charge density of ring calculated for *o*- and *m*- anisates is higher than that calculated for the corresponding acids, but in the case of *p*-anisates it is lower than that for *p*-anisic acid. This tendency is displayed in Fig. 7.

3.4. Vibrational wavenumbers

Replacement of the carboxylic group hydrogen with a metal ion brings about characteristic changes in the IR and Raman spectra of the metal anisates in comparison with the spectra of the ligand. The disappearance of bands for the symmetric and asymmetric valence vibrations: stretching ν(C=O) [*o*-anisic acid: 1693 and 1669 cm^{-1} (IR), and 1639 cm^{-1} (Raman); *m*-anisic acid: 1693 cm^{-1} (IR) and 1627 cm^{-1} (Raman); *p*-anisic acid: 1686 cm^{-1} (IR)], in-plane bending β(C=O) [*m*-anisic acid: 808 cm^{-1} (IR) and 811 cm^{-1} (Raman); *p*-anisic acid: 735 cm^{-1} (IR)] as well as out-of-plane bending γ(C=O) of the carbonyl group [*o*-anisic acid: 653 (IR) and 650 (Raman) cm^{-1}; *m*-anisic acid: 580 cm^{-1} (IR) and 582 cm^{-1} (Raman); *p*-anisic acid: 548 cm^{-1} (IR)]; disappearance of stretching vibrations ν(O–H) in the range: *o*-anisic acid: 3056–2818 (IR) cm^{-1}; *m*-anisic acid: 2676–2533 cm^{-1} (IR); *p*-anisic acid: 2728–2520 cm^{-1} (IR)], deformation vibrations:β(O–H) [*o*-anisic acid: 1409 cm^{-1} (IR); *m*-anisic acid: 1417 cm^{-1} (IR); *p*-anisic acid: 1427 cm^{-1} (IR) and 1421 cm^{-1} (Raman)] and γ(O–H) [*m*-anisic acid: 935 cm^{-1} (IR); *p*-anisic acid: 928 cm^{-1} (IR)]; appearance of bands of the asymmetric and symmetric vibrations of the carboxylate anion $\nu_{as}(COO^-)$, $\nu_s(COO^-)$ as well as $\beta_{as}(COO^-)$, $\beta_s(COO^-)$, and disappearance or changes in positions and intensities of some aromatic bands are observed. The FT-IR spectra of the anisic acids are shown in Fig. 8.

Thanks to the FT-IR Argon matrix, it is possible to distinguish between hydrogen bonds present in the molecule of *o*-anisic acid. In the region of OH stretching vibrations, i.e. 3728–3358 cm^{-1} a few bands appear (see Fig. 9). The most intense band is assigned to the OH stretches of the monomer, whereas the weaker bands at 3364 and 3358 cm^{-1} correspond to associated molecules. Reva et al. have claimed that using different Ar matrix-to-sample ratios

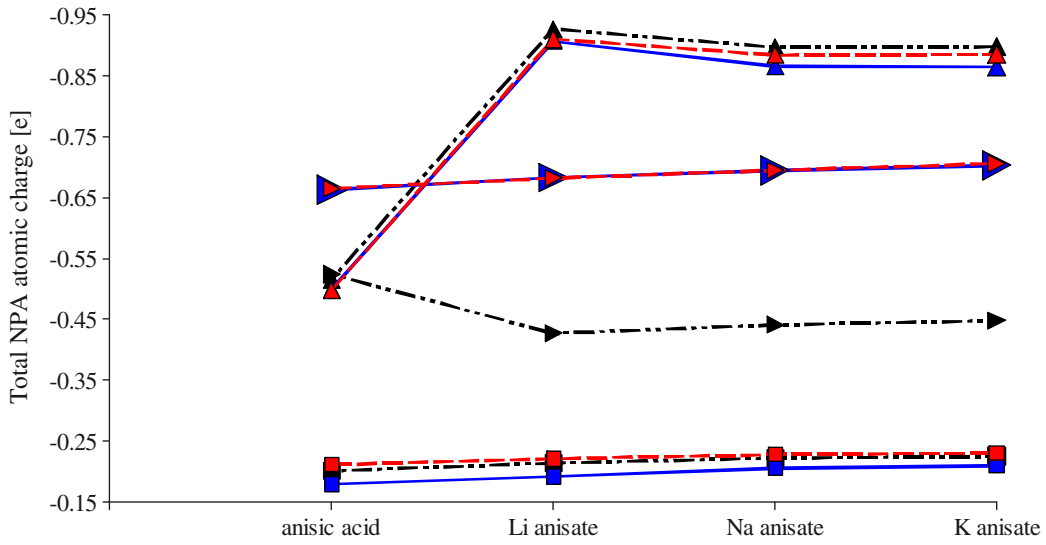


Fig. 7. The total NPA atomic charge calculated at the B3LYP/6-311++G** level for *o*-anisic acid and *o*-anisates (line: —), for *m*-anisic acid and *m*-anisates (line: - - -) as well as for *p*-anisic acid and *p*-anisates (line:). The following symbols stand for: ■ methoxy group, ► ring, ▲ carboxylic group.

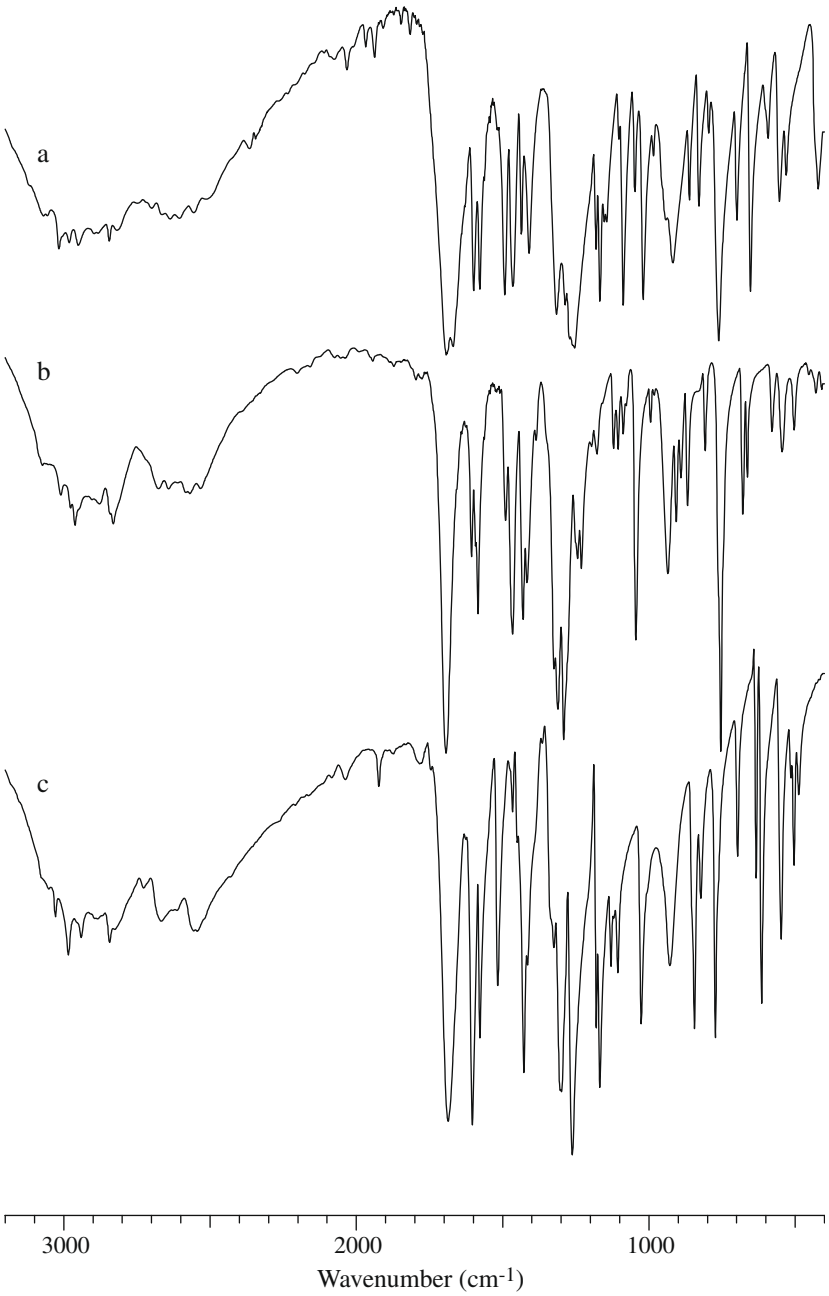


Fig. 8. The FT-IR spectra of: (a) *o*-anisic acid; (b) *m*-anisic acid; (c) *p*-anisic acid.

it is possible to study the existence of benzoic acid monomers as well as cyclic dimers with two H-bonds and linear dimers with single H-bonds [27,28]. Moreover the calculated wavenumbers showed that the formation of intramolecular hydrogen bonds in the *o*-anisic acid molecule lowers the band wavenumbers of the OH stretches. In the C═O stretching region several bands occurred in the Ar matrix IR spectra of *o*-anisic acid. The bands at 1768 and 1762 cm^{-1} are assigned to vibrations of monomers, whereas a very weak band at 1735 cm^{-1} corresponds to the vibration of a dimer. Moreover the βOH, *v*C-(OCH_3), *v*OCH_3 and γC═O vibrations are also affected by the presence of H-bonds.

The position of the substituent in the aromatic ring affects the vibrations of anisic acid molecules. In the Table 4 the selected wavenumbers of bands present in the IR and Raman spectra of anisic acids, sodium anisates as well as benzoic acid and sodium benzoate are gathered. Comparing the wavenumbers of the corresponding bands one can see that the methoxy substituent influences the electronic system of ligand to a larger extent than a metal substituted in the carboxylic group. Substitution of the methoxy group in the ring causes shifts of selected bands to over 100 cm^{-1}. Whereas substitution of metal ions in the place of the carboxylic group hydrogen of anisic acid causes displacement of the corresponding bands by a maximum of about 20 cm^{-1}. Moreover, it seems that the metal more strongly affects the electronic system of benzoic acid than anisic acid. Generally, we can see (Table 4) that more bands disappear in the IR and Raman spectra of sodium benzoate compared with the spectra of benzoic acid than occurs in the case of anisates and anisic acids. Namely, three main aromatic bands (i.e. 8a, 19a, 19b) disappear in the IR spectrum of sodium benzoate compared with the IR spectrum of the acid. Band no. 8b is absent in the Raman spectrum of the sodium salt, but it is present in the Raman spectrum of benzoic acid. The

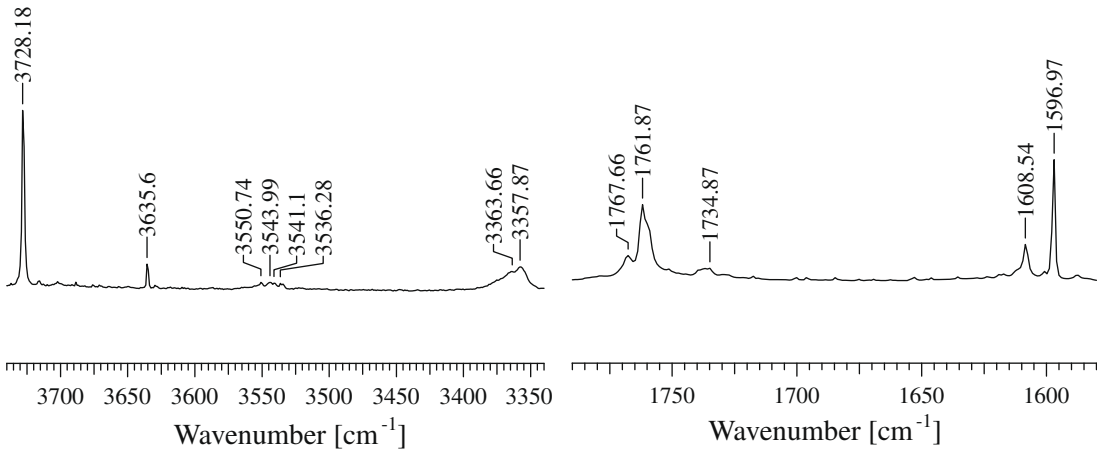


Fig. 9. The selected regions of the IR Argon matrix spectrum of *o*-anisic acid.

Table 4
The wavenumbers [cm^{-1}] of selected aromatic bands from the IR and Raman spectra of selected compounds.

Compound		8a	8b	19a	19b	14	18b	18a	10a	4	6b
Benzoic acid	IR	1604m*	1586m	1498w	1455s	1324vs	1073m	1027m	856vw	668s	617vw
	R	1603s	1586vw	–	1460vw	1326w	–	1027m	855vw	–	616s
Na benzoate	IR	–	1597vs	–	–	1306w	1068m	1029m	819m	684sh	–
	R	1605s	–	1493w	1436m	–	–	1033m	825w	–	617m
o-Anisic acid	IR	1578s	1599s	1436s	1492s		1019s	1088s	796m	–	–
	R	1581m	1600vs	1437w	1493w		1021vw	–	797vw	–	–
Na *o*-anisate	IR	1596vs	1612vs	1438m	1487m		1020m	1101w	781w	704w	660m
	R	1597s	1621vw	1441vw	1487vw		1022vw	1102vw	782s	–	663m
m-Anisic acid	IR	1584s	1606s	1430s	1490s	1324sh	1105m	1088m		679m	504m
	R	1587w	1605m	1430vw	–	1325vw	–	1078vw		680vw	–
Na *m*–anisate	IR	–	1600m	–	1486m	–	–	1075vw		678w	501w
	R	–	1601w	1419w	1486vw	–	–	1077vw		669vw	502vw
p-Anisic acid	IR	1604vs	1577s	1517s	1427s	1304s	1106s	–	823m	697m	633m
	R	1610s	1581w	–	1421vw	1304vw	–	1012vw	825m	699vw	635vw
Na *p*-anisate	IR	1612s	1597vs	1515m	–	1314w	1096m	–	–	694w	635w
	R	1616w	–	1518vw	1435w	1319vw	1098vw	–	816vw	696vw	636vw

* s – strong; m – medium; w – weak; v – very; sh – shoulder.

rest of the bands are shifted toward lower or higher wavenumbers. Moreover the maximum of the band displacement amounts to 37 cm^{-1} in the IR spectra and 30 cm^{-1} in the Raman spectra (band no. 10a). This may suggest that the methoxy substituent slightly weakens the effect of the metal on the aromatic system of the ligand.

The effect of metals on the electronic system of the ligand depends on the position of the methoxy substituent in the ring. Taking into account the four main aromatic bands present in the spectra of *o*-, *m*- and *p*-anisic acids, i.e. no. 8a, 8b, 19a and 19b (a simplified interpretation of the origin of spectral bands and notation by Varsanyi [29] is used), one may observe the influence of the alkali metals on the aromatic system of the ligand. In Table 4 the spectroscopic data for the sodium salt and anisic acids are gathered, and similar dependencies occur for the lithium and potassium salts as well. Bands no. 8a (IR and Raman spectra), 8b (IR spectra), 14 (IR and Raman spectra) and 18b (IR and Raman spectra) disappear in the spectrum of Na *m*-anisate. The rest of the bands mentioned in Table 4 undergo a displacement in the spectrum of the salt toward lower wavenumbers by a maximum of 13 cm^{-1}. On the other hand, in the spectra of sodium *o*-anisate most of the bands are shifted toward higher wavenumbers compared with the corresponding bands in the spectrum of the acid (except bands no. 19b and 10a – their wavenumbers slightly decrease in the IR and Raman spectra of the salts). Moreover bands no. 4 and 6b appear in the spectra of the salt, but they are absent in the spectra of the ligand. In the case of *p*-anisate, some of the bands are shifted toward higher wavenumber, i.e. 8a (IR, R), 8b (IR), 19b (R) and 14 (IR, R), the remaining bands are shifted toward lower wavenumbers or they disappear. Bands no. 8a, 8b, 18a and 10a from the IR and Raman spectra of sodium *o*-anisate and bands no. 8b, 19b and 14 from the IR and Raman spectra of sodium *p*-anisate undergo a significant displacement (>10 cm^{-1}) compared with the spectra of the acids. This effect is stronger in the case of the *ortho* isomer. Analysis of the spectroscopic data shows that the effect of the metals on the electronic system of the ligand is different in the case of *meta*, *ortho* and *para* isomers of anisic acid. This is probably caused by different electron donating-withdrawing properties of the substituent. The methoxy substituent in the *meta* position in the ring possesses electron withdrawing character and causes a decrease in the electronic charge distribution in the ring of the salt. This is revealed in a decrease in the numbers, wavenumbers and/or intensities of the bands for metal complexes in comparison to the appropriate bands in the spectra of the ligand. It is caused by a decrease in the force constants of the bonds and polarization of the C–C and C–H bonds in the ring [18]. In the case of the *ortho* isomer, the close proximity of the methoxy and carboxy substituents plays an important role in increasing the negative charge of the ring in *o*-anisate molecules, which induces the displacement of aromatic bands toward higher wavenumbers in comparison to the corresponding bands in the spectrum of *o*-anisic acid. A methoxy substituent in the *para* position in the ring shows

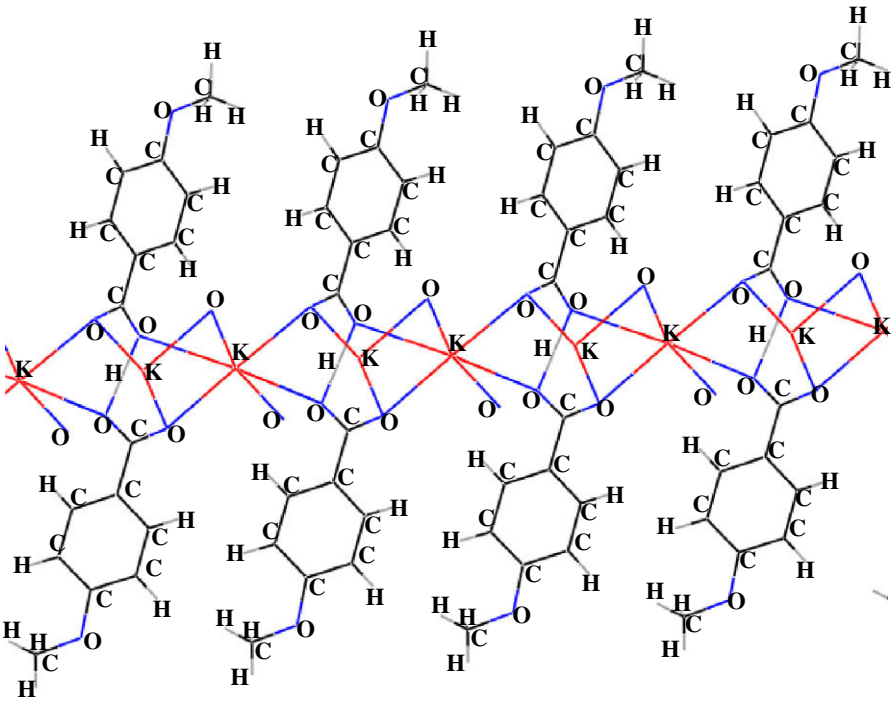


Fig. 10. Crystal structure of potassium *p*-anisate [30].

electron donating character, causing an increase in the negative charge density of the ring, and the carboxylic group as well (the negative charge density of the COO^- group is higher in the case of *p*-anisate compared to *o*-anisate and *m*-anisate, and this is described below). The effect of metals on the electronic structure of the ligand cannot be described by a simple model, the intermolecular interactions which stabilize the system should be taken into consideration as well. Comparing the theoretical and experimental data it should be kept in mind that calculations were performed for an isolated molecule, whereas in fact molecular interactions exist. In Fig. 10 the crystal structure of potassium *p*-anisate is presented. A comparison of that structure with simple calculated models (e.g. in Fig. 5) shows how big a simplification is assumed during the calculations [30].

In the IR and Raman spectra of the salts, some of the bands assigned to aromatic ring vibrations are shifted toward lower wavenumbers in the series: Li → Na → K anisates, i.e. bands no. 20a (~3070 cm^{-1}), 20b (~3025 cm^{-1}), 8b (~1605 cm^{-1}), 8a (~1590 cm^{-1}), 18a (~1100 cm^{-1}), 17b (~940 cm^{-1}), 10a (~780 cm^{-1}), 11 (~750 cm^{-1}) and 6b (~660 cm^{-1}) in the spectra of *o*-anisates; 19b (~1480 cm^{-1}), 3 (~1315 cm^{-1}), 7a (~1280 cm^{-1}), 13 (~1250 cm^{-1}), 18a (~1080 cm^{-1}), 17a (~900 cm^{-1}), 7b (~870 cm^{-1}) and 6b (~500 cm^{-1}) in the spectra of *m*-anisates; 20b (~3050 cm^{-1}), 8b (~1600 cm^{-1}), 19a (~1510 cm^{-1}), 14 (~1310 cm^{-1}), 9a (~1135 cm^{-1}), 18a (~1005 cm^{-1}) and 6a (615 cm^{-1}) in the spectra of *p*-anisates. The decrease in the wavenumbers of the aromatic bands along with the change of the complexed metal cation or ring substituent is interpreted by some authors as only an

Table 5
The wavenumbers [cm^{-1}] of selected bands from IR (experimental and theoretical) and Raman (R) (experimental) spectra of anisic acid and anisates.

Vibrations		*o*-Anisic acid	*o*-Anisates			*m*-Anisic acid	*m*- Anisates			*p*-Anisic acid	*p*-Anisates		
			Li	Na	K		Li	Na	K		Li	Na	K
$\nu_{as}(CH_3)$	IR	2981s*	2977w	2977w	–					2986m	2964w	2954w	2958w
	R	2982vw	2977vw	2978vw	–					2985vw	2962vw	2954vw	2958vw
	Calc.	3139	3131	3126	3123					3140	3134	3130	3128
$\nu_{as}(CH_3)$	IR	2951s	2944w	2944w	2958w	2961s	2942vw	2942vw	2944vw	2941m	2943w	2935w	2934w
	R	2953w	2946w	2943vw	2952w	2945vw	2942vw	2942vw	2944vw	2942vw	–	2939vw	2935vw
	Calc.	3071	3059	3052	3049	3137	3030	3130	3125	3091	3065	3061	3058
$\nu_s(CH_3)$	IR	2845s	2842w	2841w	2841w	2831s	2835w	2833w	2833w	2844m	2840w	2834w	2838w
	R	2846w	2844w	2843w	2843w	2832vw	2835vw	2835vw	2836vw	2840vw	2844vw	2838vw	2840vw
	Calc.	3010	3000	2996	2994	3005	3000	2997	2996	3012	3006	3003	3002
$\delta(CH_3)$	IR	1465s	1465s	1465m	1468m	1466s	–	–	1465m	1466m	–	–	1472w
	R	1464w	1460vw	–	–	1456w	–	–	–	–	–	–	–
	Calc.	1503	1499	1501	1502	1505	1505	1506	1506	1503	1504	1505	1506
$\rho(CH_3)$	IR	1167s	1164m	1164w	1160w	1121m	1128m	1115w	1111m	1130s	1128vw	–	–
	R	1167s	1165m	1161m	1162m	1123vw	–	1125vw	–	1135vw	–	–	–
	Calc.	1166	1163	1166	1166	1167	1166	1168	1167	1166	1167	1167	1167
νO-(CH_3)	IR	1048m	1049m	1047m	1047m	1045s	1039w	1040w	1038m	1027s	1034m	1035m	1031m
	R	1050s	1050vs	1049vs	1049vs	1045vw	1040vw	1044vw	1039vw	1023vw	1037vw	–	1030vw
	Calc.	1050	1053	1056	1056	1075	1072	1073	1072	1052	1058	1060	1061

* s – strong; m – medium; w – weak; v – very; sh – shoulder.

Table 6
The wavenumbers [cm^{-1}] of $\Delta\nu(COO^-)$ and $\Delta\beta(COO^-)$ from IR (experimental and calculated) and Raman (R) (experimental) spectra of lithium, sodium and potassium anisates.

		o-Anisates		
		Li	Na	K
$\Delta\nu(COO^-)$	IR	166	170	171
	R	171	181	173
	Calc.	130	159	174
$\Delta\beta(COO^-)$	IR	–	338	328
	R	–	–	329
	Calc.	407	463	463
		m-Anisates		
$\Delta\nu(COO^-)$	IR	151	154	161
	R	–	181	164
	Calc.	119	158	174
$\Delta\beta(COO^-)$	IR	232	236	241
	R	–	–	–
	Calc	269	231	221
		p-Anisates		
$\Delta\nu(COO^-)$	IR	127	124	137
	R	147	–	147
	Calc.	99	142	158
$\Delta\beta(COO^-)$	IR	303	319	327
	R	–	–	316
	Calc.	335	330	323

effect of the increase in the atomic mass of the cation or the substituent. Our previous studies showed that the most important factor causing the decrease in the wavenumbers of the aromatic bands is the ionic potential of the metal ions [31–33].

The substitution of alkali metals in the carboxylic group of anisic acid causes changes in the electronic charge distribution of the methoxy group as well. It is mostly visible in the case of bands assigned to the asymmetric stretching vibrations of the methoxy group $\nu_{as}(CH_3)$ (~2980 and ~2950 cm^{-1}) (Table 5). In the spectra of anisates these bands are shifted towards lower wavenumbers (or disappear) compared with the spectra of the acids, and they clearly decrease in wavenumbers along the series: Li → Na → K. The smallest differences between the position of the bands assigned to the methoxy group vibrations are visible in the spectra of *o*-acid and its salts, for example the band attributed to $\nu_{as}(CH_3)$ appears at 2981 cm^{-1} in the spectrum of *o*-anisic acid, and at 2977 cm^{-1} in the spectra of the Li and Na *o*-anisates (there is a lack of this band in the spectrum of K *o*-anisate). Whereas, in the spectra of *m*- and *p*-anisic acids, the discussed band is located at 2961 and 2986 cm^{-1}, respectively. In the spectra of Li, Na and K *m*- and *p*-anisates, $\nu_{as}(CH_3)$ is present at 2942, 2942 and 2944 cm^{-1}, and at 2964, 2954 and 2958 cm^{-1}, respectively. In Table 6 the differences between the wavenumbers of the asymmetric and symmetric stretching and deforming vibrations of the carboxylic group are gathered. In the IR and Raman spectra of *o*-anisates, the bands of $\nu_{as}(COO^-)$ are generally located at higher wavenumbers and $\nu_s(COO^-)$ are present at lower wavenumbers compared to the corresponding bands in the spectra of *m*- and *p*-anisates. The same situation is seen in the case of $\beta_{as}(COO^-)$ and $\gamma_s(COO^-)$. As a consequence, the values of $\Delta\nu(COO^-)$ and $\Delta\beta(COO^-)$ are higher in the case of Li, Na and K *o*-anisates than *m*-, *p*-anisates. Moreover the change of metal in the series Li→Na→K causes somewhat larger changes in the value of $\Delta\nu(COO^-)$ and $\Delta\beta(COO^-)$ of *m*-anisates and *p*-anisates than *o*-anisates. Probably the carboxylic and methoxy groups situated in the *ortho* position in the ring weaken the effect of the alkali metals on the electronic charge distribution in the carboxylic anion. Additionally, one can see that in the case of alkali metal salts, the IR and Raman wavenumbers of $\Delta\nu(COO^-)$ and $\Delta\beta(COO^-)$ decrease in the series *o*- → *m*- → *p*-anisates, which according to the calculated total atomic charge indicates an increase in the negative charge density of the carboxylic group in the same series. This was previously explained by electron withdrawing and electron donating properties of the methoxy substituent situated in the *meta* and *para* position in the ring, respectively. The stabilization effect of the *ortho* position of the methoxy group has not been completely described so far and it is explained by steric and polar effects [23].

3.5. ^1H NMR spectra of anisic acid and anisates

The chemical shifts of the protons from experimental and calculated ^1H NMR spectra of anisic acid and Li, Na and K anisates are displayed in Fig. 11. In the spectra of anisates, the proton signals are shifted downfield in comparison to the corresponding signals in the spectrum of the acid. Moreover the general tendency for the decrease of chemical shift of particular protons in the series: Li → Na → K is noticeable. It points at an increase in the screening of aromatic protons as a consequence of the circular current weakening. The highest differences between the values of chemical shifts present in the spectra of acid and salts are mostly visible in the case of *ortho* isomer.

4. Conclusions

1. The substitution of lithium, sodium and potassium ions in the carboxylic group of *o*-, *m*- and *p*-anisic acids causes changes in the values of bond lengths, angles and in the electronic charge distribution in the carboxylic group, methoxy group and aromatic ring. The values of the aromaticity indexes increase in the order: *o*- → *p*- → *m*- isomers which suggests that the aromaticity of the studied systems increases in the series *o*- → *p*- → *m*- methoxybenzoic acids. The presence of intramolecular hydrogen bonds causes an increase in the aromaticity of the *o*-anisic acid molecule. The electronic charge density of the methoxy group increases in the series: *o*- → *p*- → *m*- anisic acids. In the case of the carboxylic group, the charge generally increases in the order: *o*- → *m*- → *p*-, and the charge density of the ring changes along the series: *p*- → *m*- → *o*-. Such distribution of the negative charge may be explained by the electron donating and electron withdrawing properties of the methoxy group situated in the *o*-, *m*- and *p*- position in the ring.
2. On the basis of the spectroscopic data, the values of the aromaticity indexes and the atomic charges, it was shown that the influence of the alkali metals on the electronic structure of the ligands is weaker than the effect of the methoxy substituents. The calculated total electronic charge density of the methoxy group increases in the series: acid → Li → Na → K anisates. The total electronic charge density of the carboxylic group is higher in the case of anisates than the coresponding acids, and decreases in the order: Li → Na → K anisates. The total electronic charge density of the ring increases in the series: Li → Na → K anisates (NPA method). The effect of the metals on the electronic system of the ligand depends on the position of the methoxy substituent in the ring and the electron donating-withdrawing properties of substituent. In the case of the *ortho* isomer, steric and polar effects additionally play an important part in the increase in the negative charge of the ring in *o*-anisates. On the basis of IR, Raman and ^1H NMR data it is concluded that the effect of Li, Na and K on the aromatic ring of the ligand is mostly noticeable in the case of the *ortho* isomer. The bands in vibrational spectra, which are responsible for oscillation or deformation, change their wavenumbers depending on the structure of the ligand.

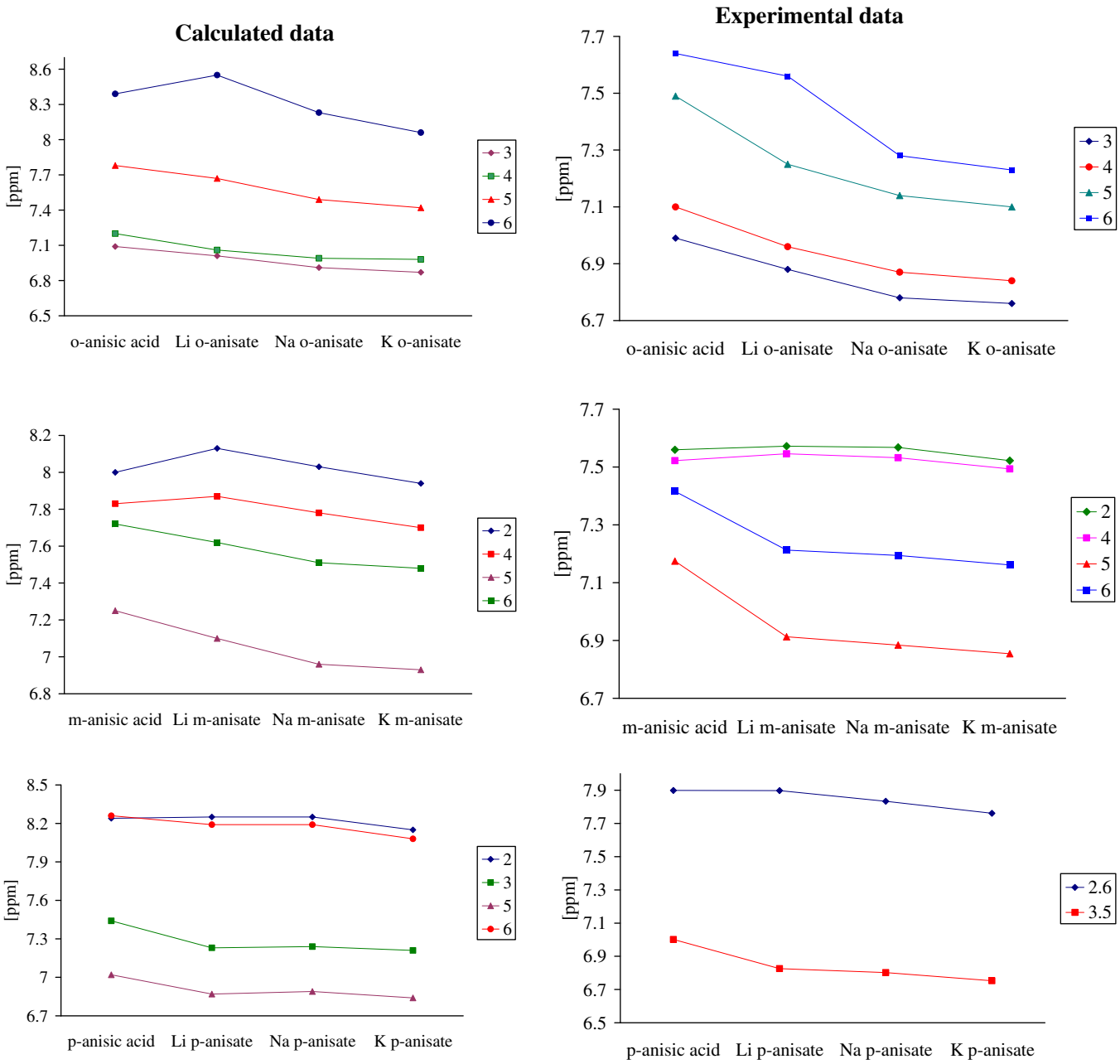


Fig. 11. The chemical shifts of protons from calculated (B3LYP/6-311++G** GIAO; TMS) and experimental ^{1}H NMR spectra of anisic acids and Li, Na and K anisates (proton numbering in Figs. 2–4).

3. It is assumed that the carboxylic and methoxy groups situated in the *ortho* position in the ring weaken the effect of alkali metals on the electronic charge distribution in the carboxylic anion and methoxy group. Additionally, one can see that the IR and Raman wavenumbers of $\Delta\nu(COO^-)$ and $\Delta\beta(COO^-)$ decrease in the series *o*– → *m*- → *p*-anisates, which according to the calculated total atomic charge indicates an increase in the negative charge density of the carboxylic group in the same series.

Acknowledgements

This work was supported by the Polish Scientific Committee (KBN's grant no. N N305 267534) and the Technical University in Bialystok (grant no. S/WBiIS/21/2007).

Appendix A. Supplementary data

Supplementary data associated with this article can be found, in the online version, at doi:10.1016/j.poly.2009.03.030.

References

[1] S. Kanchan, D.N.S. Jayachandra, Can. J. Bot. 59 (1981) 199.
[2] J.F. Lynas, B. Walker, Bioorg. Med. Chem. Lett. 7 (1997) 1133.
[3] K. Sekar, S. Vaijayanthi Mala, M. Yogavel, D. Velmurugan, Ming-Jye Poi, B.S. Vishwanath, T.V. Gowda, A. Arokia Jeyaprakash, M.-D. Tai, J. Mol. Biol. 333 (2003) 367.
[4] M. Maffei, C.M. Bertea, F. Garneri, S. Scannerini, Plant Sci. 141 (1999) 139.
[5] M. Kalinowska, R. Świsłocka, M. Borawska, J. Piekut, W. Lewandowski, Spectrochim. Acta Part A 70 (2008) 126.
[6] M. Kalinowska, R. Świsłocka, W. Lewandowski, J. Mol. Struct. 834–836 (2007) 419.

[7] M. Kalinowska, R. Świsłocka, W. Lewandowski, J. Mol. Struct. 792–793 (2006) 130.
[8] M.J. Frisch, G.W. Trucks, H.B. Schlegel, G.E. Scuseria, M.A. Robb, J.R. Cheeseman, V.G. Zakrzewski, J.A. Montgomery Jr., R.E. Stratmann, J.C. Burant, S. Dapprich, J.M. Millam, A.D. Daniels, K.N. Kudin, M.C. Strain, O. Farkas, J. Tomasi, V. Barone, M. Cossi, R. Cammi, B. Mennucci, C. Pomelli, C. Adamo, S. Clifford, J. Ochterski, G.A. Petersson, P.Y. Ayala, Q. Cui, K. Morokuma, N. Rega, P. Salvador, J.J. Dannenberg, D.K. Malick, A.D. Rabuck, K. Raghavachari, J.B. Foresman, J. Cioslowski, J.V. Ortiz, A.G. Baboul, B.B. Stefanov, G. Liu, A. Liashenko, P. Piskorz, I. Komaromi, R. Gomperts, R.L. Martin, D.J. Fox, T. Keith, M.A. Al-Laham, C.Y. Peng, A. Nanayakkara, M. Challacombe, P.M.W. Gill, B. Johnson, W. Chen, M.W. Wong, J.L. Andres, C. Gonzalez, M. Head-Gordon, E.S. Replogle, J.A. Pople, Gaussian 98, Revision A.11.2 Inc., Pittsburgh PA, 2001.
[9] R.F.W. Bader, Atoms in Molecules. A Quantum Theory, Oxford University Press, New York, 1990.
[10] AIM2000 designed by Friedrich Biegler-König, University of Applied Sciences, Bielefeld, Germany.
[11] A. Julg, P. François, Chem. Pap. 49 (1995) 128.
[12] T.M. Krygowski, A. Ciesielski, M.K. Cyrański, J. Mol. Struct. 374 (1996) 277.
[13] Y.Y. Kharitonov, I.I. Oleinik, Dokl. Akad. Nauk SSSR 294 (1987) 151.
[14] O. Exner, P. Fiedler, M. Buděšinský, J. Kulhánek, J. Org. Chem. 64 (1999) 3513.
[15] I.I. Schuster, J. Chem. Soc., Perkin Trans. 2 (2002) 1961.
[16] M. Parvez, Acta Crystallogr., Sect. C 43 (1987) 2243.
[17] R. Fausto, A. Matos-Beja, J.A. Paixao, J. Mol. Struct. 435 (1997) 207.
[18] M. Kalinowska, E. Siemieniuk, A. Kostro, W. Lewandowski, J. Mol, Struct.: Theochem. 761 (2006) 129.
[19] R.H. Mitchell, Chem. Rev. 101 (2001) 1301.
[20] T.M. Krygowski, M.K. Cyrański, Chem. Rev. 101 (2001) 1385.
[21] G. Bruno, L. Randaccio, Acta Crystallogr., Sect. B 36 (1980) 1711.
[22] R. Feld, M.S. Lehmann, K.W. Muir, J.C. Speakman, Z. Kristallogr., Kristallgeom., Kristallphys., Kristallchem. 157 (1981) 215.
[23] S. Böhm, P. Fiedler, O. Exner, New J. Chem. 28 (2004) 67.
[24] S. Wojtulewski, S.J. Grabowski, Chem. Phys. Lett. 378 (2003) 388.
[25] W. Lewandowski, G. Świderski, R. Świsłocka, S. Wojtulewski, P. Koczoń, J. Phys. Org. Chem. 18 (2005) 918.
[26] I. Rozas, I. Alkorta, J. Elguero, J. Am. Chem. Soc. 122 (2000) 11154.
[27] I.D. Reva, S.G. Stepanian, J. Mol. Struct. 349 (1995) 337.
[28] S.G. Stepanian, I.D. Reva, E.D. Radchenko, G.G. Sheina, Vibr. Spectr. 11 (1996) 123.
[29] G. Varsanyi, Assignments for Vibrational Spectra of 700 Benzene Derivatives, Akademiai Kiado, Budapest, 1973.
[30] R. Winpenny, A. Smith, S. Parsons, D. Messenger, Private Communication (2005).
[31] W. Lewandowski, M. Kalinowska, H. Lewandowska, J. Inorg. Biochem. 99 (2005) 1407.
[32] M. Samsonowicz, R. Świsłocka, E. Regulska, W. Lewandowski, Int. J. Quant. Chem. 107 (2007) 480.
[33] W. Lewandowski, M. Kalinowska, H. Lewandowska, Inorg. Chim. Acta 358 (2005) 2155.

Polyhedron 28 (2009) 2219–2227

Contents lists available at ScienceDirect

Polyhedron

journal homepage: www.elsevier.com/locate/poly

Copper(II) complexes of methylated glycine derivatives: Effect of methyl substituent on their DNA binding and nucleolytic property

Hoi Ling Seng [a], Kong Wai Tan [b], Mohd Jamil Maah [b], Wee Tee Tan [c], Hirokazu Hamada [d], Makoto Chikira [d], Chew Hee Ng [a,*]

[a] Faculty of Engineering and Science, Universiti Tunku Abdul Rahman, 53100 Kuala Lumpur, Malaysia
[b] Chemistry Department, Universiti Malaya, 50603 Kuala Lumpur, Malaysia
[c] Chemistry Department, Universiti Putra Malaysia, 43400 Serdang, Malaysia
[d] Department of Applied Chemistry, Chuo University, Tokyo 112-8551, Japan

ARTICLE INFO

Article history:
Received 23 January 2009
Accepted 20 March 2009
Available online 29 March 2009

Keywords:
Copper complexes
Amino acids
Methylated glycine
DNA binding
Oxidative cleavage
Nucleolytic efficiency

ABSTRACT

A set of copper(II) complexes of glycine and methylated glycine derivatives, $Cu(aa)_2$, consisting of C-dimethylglycine, L-alanine, *N*-dimethylglycine and sarcosine, was investigated for their DNA binding and nucleolytic properties by means of EPR and visible spectroscopy, and electrophoresis. They bind weakly to DNA with apparent binding constants in the range $1.8–2.9 \times 10^3\ M^{-1}$ with very similar orientation. No DNA cleavage is observed in the absence of exogenous agents. Copper(II) complexes of *N*-methylated derivatives bind to DNA more stereo-specifically and less strongly, and their oxidative DNA cleavage is less efficient than those of the corresponding C-methylated derivatives in the presence of hydrogen peroxide (H_2O_2) alone, or sodium ascorbate (NaHA) alone or tandem H_2O_2–NaHA. The oxidative DNA cleavage mechanism in the three systems involves a common copper(I) species. Neocuproine can inhibit DNA cleavage by these complexes.

© 2009 Elsevier Ltd. All rights reserved.

1. Introduction

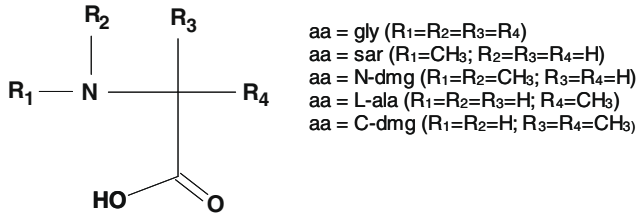
Although, copper is essential to animals, it can also induce toxicity. This toxicity is due to those reactions of the redox-active copper ions which generate reactive oxygen species (ROS) via a Fenton or Haber–Weiss mechanism [1]. Copper(II), Cu^{2+}, has been implicated in many diseases such as Wilson's disease, Menkes disease, Alzheimer's disease, Parkinson's disease, prion disease, other neurodegenerative diseases and cataract [2]. ROS can be produced by Cu^{2+} in the presence of hydrogen peroxide or ascorbate anion or both hydrogen peroxide and ascorbate [1–5]. The ROS thus produced can cause damage to protein, DNA or cellular membrane. Recently, it was reported that even the antioxidant metalloenzyme, copper–zinc superoxide dismutase (Cu–Zn-SOD) could cleave DNA in the presence of hydrogen peroxide or mercaptoethanol [6].

Copper complexes with amino acids are both important biologically and interesting. Many low-molecular-weight copper complexes with amino acids and amino acid derivatives act as anti-inflammatory, antiulcer, anticonvulsant, anticancer, and/or radiation protection agents [7]. They can assume a variety of coordination geometries, from irregular square planar, distorted planar, flattened tetrahedral, and distorted square–pyramidal to distorted octahedral, as observed in their experimental crystal structures [7].

However, copper(II) ion chelated with amino acid can harm DNA by either oxidative or hydrolytic cleavage, depending on the amino acid involved [8–10]. A recent study has investigated the effects of pH, concentration of both amino acid and hydrogen peroxide, and the type of amino acids (glycine, lysine, L-alanine) on the kinetics of ·OH radicals formation from the reaction of copper(II)-amino acid mixtures with hydrogen peroxide [11]. Similar reaction is also involved in the oxidative cleavage of DNA by copper(II) complexes of *N*,*N*′-dimethylglycine and other ligands [8]. A widely accepted view of the mechanism of DNA cleavage by copper(II) complexes details the binding of the complexes to the DNA and their subsequent reaction with hydrogen peroxide to generate the ·OH radicals on site to cleave the DNA. Of relevance are the studies of the binding of copper(II) complexes of some amino acids with DNA fibers using EPR spectroscopy and the results have shown that the nature and orientation of binding of the complexes were influenced by the amino acids used (glycine, serine, threonine, lysine and arginine) [12,13]. This paper reports the effect of the number and position of methyl substituent(s) on (i) the relative quantity of hydroxyl radicals produced by the reaction of the copper(II) chelated methyl-derivatives of glycine (general structure of ligands is depicted in Scheme 1), $Cu(aa)_2$, with hydrogen peroxide, and (ii) the oxidative cleavage of DNA by these complexes in the

* Corresponding author.
E-mail address: ngch@utar.edu.my (C.H. Ng).

0277-5387/$ - see front matter © 2009 Elsevier Ltd. All rights reserved.
doi:10.1016/j.poly.2009.03.022



Structure of amino acid, aa

Scheme 1.

presence of either hydrogen peroxide or sodium ascorbate or both these exogenous reagents. In addition, the interaction of these complexes with DNA was investigated by EPR and ethidium bromide (EB) quenching assay studies.

2. Experimental

2.1. Reagents and materials

Most of the reagents were of analytical grade and were used as supplied. The pBR 322, gene ruler 1 Kb DNA ladder, ethidium bromide, loading buffer, Tris and agarose were bought from BioSyn Tech (Fermentas). Salmon testes DNA was purchased from Sigma Chemical Co. (USA). All solutions for DNA experiments were prepared with ultra-pure water from a Elga PURELAB ULTRA Bioscience water purification system with UV light accessory. The borate buffer was prepared from 0.1 M boric acid aqueous solution in which the pH was adjusted with NaOH aqueous solution till pH 8.5. The borate buffer pH 8.5 contains borate at 0.1 M. All stock solutions of H_2O_2 in water and metal complexes in borate buffer were freshly prepared daily.

2.2. Physical measurements

The C, H and N microanalysis was carried out with a Perkin Elmer 2400 CHN analyser. Infrared spectra of all compounds were recorded as KBr pellets using Perkin–Elmer FT-IR spectrometer in the frequency range 4000–400 cm^{-1}. UV–Vis spectroscopic measurement was carried out on a Perkin Elmer Lambda 40. Fluorescence measurements were performed using a Perkin–Elmer LS55 photoluminescence spectrometer. The EPR data of the copper complexes were obtained with a JEOL RE-2X spectrometer.

2.3. Synthesis of $Cu(aa)_2$ complexes

The aqua*bis*(*N*,*N*-dimethylglycinato)copper(II), Cu(N-dmg)$_2$ and *cis*-aqua*bis*(glycinato)copper(II), *cis*-Cu(gly)$_2$, complexes were synthesized by previously reported procedures [8,14]. The FTIR of Cu(N-dmg)$_2$ and *cis*-Cu(gly)$_2$ were identical with those of aqua*bis*(*N*,*N*-dimethylglycinato)copper(II) [8] and *cis*-aqua-*bis*(glycinato)copper(II) [14], respectively. The *bis*(C-dimethylglycinato)copper(II), Cu(C-dmg)$_2$, *bis*(L-alaninato)copper(II), Cu(L-ala)$_2$, and *bis*(sarcosinato)copper(II), Cu(sar)$_2$ were prepared by reacting freshly prepared copper(II) hydroxide with the respective amino acid as in the previously reported procedure [8].

2.3.1. Elemental analysis for $Cu(aa)_2$ complexes

Cu(C-dmg)$_2$: *Anal.* Calc for Cu($C_8H_{16}N_2O_4$): C, 35.88; H, 6.02; N, 10.46. Found: C, 35.91; H, 5.84; N, 10.36%. For Cu(sar)$_2$: *Anal.* Calc. for Cu($C_6H_{12}N_2O_4$)(H_2O)$_2$: C, 26.13; H, 5.85; N, 10.16. Found: C, 26.32; H, 5.66; N, 10.15%. For Cu(L-ala)$_2$: *Anal.* Calc. for Cu($C_6H_{12}N_2O_4$): C, 30.06; H, 5.05; N, 11.69. Found: C, 30.11; H, 4.88; N, 11.61%. For Cu(N-dmg)$_2$: *Anal.* Calc. for Cu($C_8H_{16}N_2O_4$)(H_2O)] · 2H_2O: C, 29.86; H, 6.89; N, 8.70. Found: C, 29.95; H, 6.85; N, 8.53%.

2.4. PNDA assay of ·OH radicals from $Cu(aa)_2 + H_2O_2$

The reactions of Cu(aa)$_2$ and copper(II) salt in borate buffer pH 8.5 with H_2O_2 were carried out merely to investigate the relative amount of hydroxyl radicals produced. The reactions were monitored at 5-min intervals over duration of 15 min. A PNDA assay was used for this purpose and the procedure has been previously described [9]. The production of ·OH radicals from the reactions of the copper nitrate and the Cu(aa)$_2$ complexes (100 μM) in borate buffer pH 8.5 with 20 μM H_2O_2 was assayed by the use of *p*-nitrodimethylaniline (PNDA) indicator (56 μM) according to a previous procedure [9]. The % bleaching of the PNDA after time *t* (minutes) was calculated by using the formula $(A_o - A_t)/A_t \times 100$, where A_o and A_t are the absorbance of the PNDA in the reaction mixture at initial time and at time *t*. Initial absorbance reading was measured within 30 s.

2.5. Preparation of DNA pellets and fibers

The DNA from salmon testes was dissolved in 20 mM NaCl to make a solution of approximately 1 mM DNA base pair concentration. Subsequently, the complex solution was added drop wise to the DNA, and stirred for approximately 12 h at 4 °C. The resulting solutions were adjusted to a pH of 8.4 with sodium hydroxide and hydrochloric acid throughout the experiments. The DNA-pellet was obtained by ultracentrifugation of the mixed solution at 60 000 rpm for 7 h. The DNA fibers were prepared from the pellet as previously reported [9].

2.6. EPR spectra

X-band (9.2 GHz) EPR spectra at ambient temperature and −150 °C were measured on a JEOL RE-2X spectrometer with 100 kHz field modulation of 0.5 mT. The magnetic field was calibrated with an NMR field meter EFM-2000 (ECHO Electronics LTD). The microwave frequency was measured on Anritsu MF2412A frequency counter. The EPR spectra were measured at different angles of Φ between the fiber axis and the static magnetic field.

2.7. DNA cleavage experiments

The reaction mixtures were prepared as follows: 1 μl of 10 μM H_2O_2 or 1 μl of 2 μM ascorbic acid were added to the mixture of 0.5 μl of supercoiled plasmid DNA pBR322 (0.25 μg/μl) and 2 μl of 500 μM copper(II) complexes or salt followed by dilution with borate buffer pH 8.5 to a total volume of 20 μl. The reactions were performed after incubating the reaction mixture at 37 °C for 2 h in the presence or/and absence of complexes or copper salt. 3 μl of 6× loading buffer was added to 20 μl of the reaction mixtures and electrophoresis was performed at 80 V for 90 min in Tris-acetate-EDTA (TAE) buffer, pH 8.1, using 1.25% agarose gel. After electrophoresis, the agarose gel was stained with ethidium bromide solution (0.5 μg/ml).

Agarose gel electrophoresis experiments were carried out on supercoiled plasmid DNA pBR322 (4.4 Kb) using a horizontal gel system. For the cleavage studies, each 20 μL sample consisted of the complex dissolved in buffer, DNA, and the required volume of additional buffer. All samples were incubated in the dark in a water-bath at a temperature of 37 °C for 2 h. For the oxidative or reductive cleavage studies, incubation of the samples was similarly carried out. The DNA cleavage profile was analyzed using 1.25%

agarose gel in a horizontal gel tank set with a running time of 2 h, at a constant voltage of 80 V. Each reaction mixture consisted of 0.5 μg/μL DNA and borate buffer pH 8.5 unless otherwise mentioned. The resultant DNA bands after the electrophoresis step for each set of experiments were stained with ethidium bromide before being photographed under UV light using a Syngene Bio Imaging system and the digital image was viewed with Gene Flash software.

For the DNA cleavage by $Cu(aa)_2$ in the presence of hydrogen peroxide alone or sodium ascorbate (NaHA) alone, mechanistic experiments were similarly carried out to test the effect of radical scavengers sodium azide (NaN_3), thiourea, tiron, and DMSO on the DNA cleavage. Neocuproine (a Cu(I)-specific chelator) was also used to test any cleavage inhibition. To identify formation of Cu(I)-intermediate species, additional spectroscopic experiments were undertaken to obtain the visible spectra of (i) CuI + neocuproine; (ii) $Cu(aa)_2 + H_2O_2$ + neocuproine; (iii) $Cu(aa)_2$ + NaHA + neocuproine. CuI and neocuproine stock solutions were prepared in methanol–water (2:1 v/v) while the $Cu(aa)_2$ were dissolved in borate buffer pH 8.5. All final reaction mixtures were obtained by topping up with borate buffer pH 8.5.

2.8. Ethidium bromide quenching assay

Calf thymus DNA (CT-DNA) was obtained from Sigma Chemical Co. (USA), and used as received. Stock solution of DNA was prepared by dissolving nucleic acids in buffer solution, stored at 4 °C more than 24 h with gentle shaking occasionally to get homogeneity, and used within 2 days. The concentrations of CT-DNA per nucleotide phosphate [DNA] were calculated according to the absorbance at 260 nm by using extinction coefficient of DNA = 6400 M^{-1} cm^{-1}.

Ethidium bromide quenching assay were performed by measuring the emission of ethidium bromide bound to DNA which shows the enhanced emission intensity due to its intercalative binding to DNA. The competitive binding of the complexes to the DNA reduces the emission intensity of ethidium bromide (EB) with either the bound complex quenching the emission or a displacement of the bound ethidium bromide from the bound to the free state. Fluorescence measurements were performed using a Perkin–Elmer LS55 photoluminescence spectrometer. All the fluorescence measurements were taken at λ_{ex} of 545 nm and λ_{em} of 600 nm at room temperature.

In this experiment, 0.32 μM ethidium bromide was added to 10 μM CT-DNA solution. After that, the mixture was incubated overnight to reach saturation condition. Varied complex concentrations in borate buffer (pH 8.5) were added to the EB-DNA solution. After the mixtures were incubated for 2 h, their fluorescence intensity was measured after each addition. The fluorescence intensities were plotted against the complex concentration to yield a curve that showed the relative extent of quenching of DNA-bound EB. The values of the apparent binding constant, K_{app}, of the $Cu(aa)_2$ complexes were calculated from the equation $K_{app,Cu(aa)_2}$ [$Cu(aa)_2$] = $K_{app,EB}$[EB], where $K_{app,EB}$ is the apparent binding constant of EB assumed to be 10^7 M^{-1}, $K_{app,Cu(aa)_2}$ is the apparent binding constant of $Cu(aa)_2$, [EB] is the concentration of EB used and [$Cu(aa)_2$] is the concentration of the $Cu(aa)_2$ at 50% quenching [15].

3. Results and discussion

3.1. DNA interaction with $Cu(aa)_2$

It is well known that DNA cleavage by copper(II) complexes involves binding of the complexes to DNA. In fact, DNA binding studies with copper(II) complexes of some amino acids have been reported [12,13]. This study attempts to investigate whether the nature of the binding of the $Cu(aa)_2$ complexes affects their nucleolytic property, and thereby help to understand the effect of the position and number of methyl substituent on the nucleolytic property of a series of copper(II) methyl-substituted glycine derivatives. Two experiments were conducted, viz. EPR study to investigate the binding of the complexes with highly oriented DNA fibers where the fiber is rotated through an angle Φ (from 0–90°) with respect to the static magnetic field, B (Fig. 1) and EB-quenching assay to find the binding strength of the $Cu(aa)_2$.

The EPR spectra of all the $Cu(aa)_2$ complexes on B-form DNA at room temperature (r.t.) are similar (Fig. 2). The intensity of the typical Cu(II) spectral peaks are maximum at $\Phi = 0°$ and decreases to zero at $\Phi = 90°$. As such, all the $Cu(aa)_2$ complexes are oriented in a similar fashion with the $g_{//}$ axis parallel to the B-DNA fiber axis. This indicates that the presence of methyl groups does not greatly alter the binding orientation of the $Cu(aa)_2$ to the DNA. However, the binding structures are still unclear and need further investigation. Nevertheless, the angular Φ dependence of the EPR spectra of B-form DNA at room temperature is more prominent for Cu(N-dmg)$_2$ and $Cu(sar)_2$, suggesting that these copper(II) complexes with *N*-methylated glycine derivatives are orientated more stereo-specifically than the other $Cu(aa)_2$ complexes (Fig. 2d and e). Freezing of the B-DNA fiber randomized the orientation of all the complexes except that of Cu(N-dmg)$_2$ (data not shown). This result implies that the hydrogen bonding of amino protons of the complexes with solvated water was randomly modulated by micro iceberg formation in the DNA fibers; the *N*-methyl groups in N-dmg protected such randomization. Therefore, there is distinct differences in the interaction of the *N*-methylated $Cu(aa)_2$ and the C-methylated $Cu(aa)_2$ with the DNA.

To investigate further the binding interaction between the $Cu(aa)_2$ and DNA, an EB-quenching assay was carried out to compare the DNA binding strength. Subsequent calculation of the apparent binding constants of the $Cu(aa)_2$ complexes from the classical Stern–Volmer equation at 50% quenching of DNA-bound EB, the order of increasing binding strength of the $Cu(aa)_2$ complexes is found to be $Cu(sar)_2$ < *cis*-$Cu(gly)_2$ < Cu(N-dmg)$_2$ < $Cu(L\text{-ala})_2$ < Cu(C-dmg)$_2$ (Table 1). The C-methylated $Cu(aa)_2$, i.e. Cu(C-dmg)$_2$ and $Cu(L\text{-ala})_2$, binds more strongly to the DNA by ~1–1.5× more than the *N*-methylated $Cu(aa)_2$, i.e. Cu(N-dmg)$_2$ and $Cu(sar)_2$. Although, not intercalators themselves, these $Cu(aa)_2$ complexes (binding constant range $1.882–2.936 \times 10^3$ M^{-1}) bind to DNA much more weakly than classical intercalators (with binding constants of the order of 10^5 M^{-1}) [16]. Those copper(II) complexes,

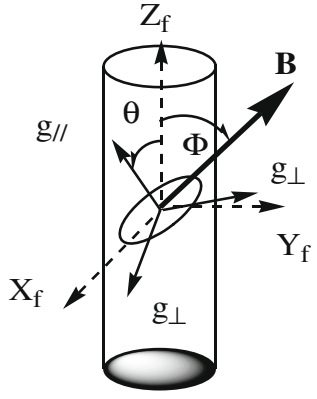


Fig. 1. The coordinate system used for the calculation of EPR line shapes. Static magnetic field **B**, DNA-fiber axes (X_f, Y_f, Z_f), and *g*-tensor axes ($g_{//}$, $g_\perp$). Φ and θ are the angles of the **B** and $g_{//}$ axes from Z_f, respectively.

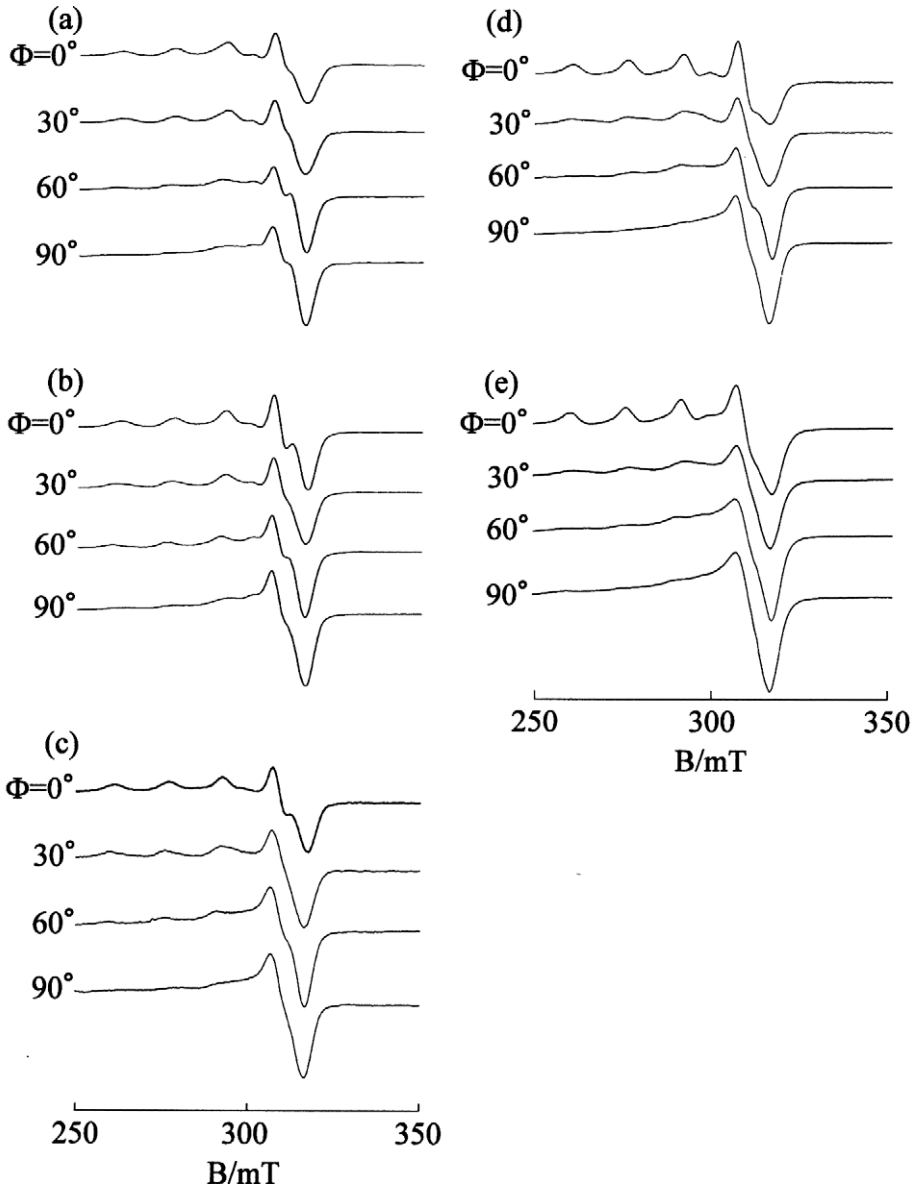


Fig. 2. EPR spectra of Cu(II) glycine derivatives on B-form DNA at r.t. (a) Cu(II)(gly):$g_{//} = 2.26$, $A_{//} = 0.0163\ cm^{-1}$; (b) Cu(II)(C-dmg)$_2$: $g_{//} = 2.25$, $A_{//} = 0.0163\ cm^{-1}$; (c) Cu(II)(L-ala)$_2$: $g_{//} = 2.26$, $A_{//} = 0.0164\ cm^{-1}$; (d) Cu(II)(N-dmg)$_2$: $g_{//} = 2.27$, $A_{//} = 0.0164\ cm^{-1}$; (e) Cu(II)(sar)$_2$: $g_{//} = 2.27$, $A_{//} = 0.0164\ cm^{-1}$.

which binds by partial intercalation, can have binding constant in the magnitude of $10^4\ M^{-1}$ [17]. Nevertheless, the binding constants of Cu(aa)$_2$ are comparable to [Cu(imda)(phen)(H$_2$O)] (K_b, $0.60 \times 10^3\ M^{-1}$; imda = iminodiacetic acid; phen = 1,10-phenanthroline) and [Cu(imda)(5,6-dmp)] (K_b, $3.9 \times 10^3\ M^{-1}$; 5,6-dmp = 5,6-dimethyl-1,10-phenanthroline) which bind to DNA by partial intercalation and groove binding, respectively [18]. The Cu(aa)$_2$ complexes are probably groove binders.

Table 1
Ethidium quenching assay results for the Cu(aa)$_2$.

Complex	Concentration at 50% quenching/μM	Binding constant/M^{-1}
Cu(C-dmg)$_2$	1090	2.936×10^3
Cu(L-ala)$_2$	1554	2.058×10^3
Cu(N-dmg)$_2$	1560	2.050×10^3
cis-Cu(gly)$_2$	1597	2.003×10^3
Cu(sar)$_2$	1770	1.882×10^3

3.2. DNA cleavage by Cu(aa)$_2$ in presence of exogenous agents

This section examines the effect of the position and number of methyl substituent of the copper(II) chelated methylated glycine derivatives, Cu(aa)$_2$, on the nucleolytic property of these complexes in the absence and presence of exogenous agents. The mono- and di-C-methylated (i.e. α-carbon) glycine complexes are Cu(L-ala)$_2$ and Cu(C-dmg)$_2$, respectively while those of the corresponding *N*-amino nitrogen methylated glycine complexes are Cu(sar)$_2$ and Cu(N-dmg)$_2$. The pH value of 8.5 for the nucleolytic experiments was selected to avoid partial dissociation of the Cu(aa)$_2$ complexes at lower pH values. No precipitation was observed in preparing stock solutions of Cu(aa)$_2$ in borate buffer at pH 8.5. To obtain distinct gel images for comparison and achieve the above objective, the concentration of the Cu(aa)$_2$ was optimised. As the Cu(aa)$_2$ complexes alone did not cleave the DNA under our experimental conditions, DNA cleavage experiments were conducted in the presence of (i) hydrogen peroxide alone, (ii) so-

dium ascorbate alone, and (iii) both hydrogen peroxide and sodium ascorbate together.

3.2.1. DNA cleavage by $Cu(aa)_2$ in presence of H_2O_2

Incubating the DNA alone or in the presence of 10 μM H_2O_2 in borate buffer at pH 8.5 for 2 h at 37 °C did not result in any degradation of DNA. About 500 μM of either $CuCl_2$ or $Cu(aa)_2$ also did not cleave DNA in the absence of 10 μM H_2O_2 under the above experimental conditions (Fig. 3). All the copper compounds can induce DNA cleavage in the presence of H_2O_2. The copper(II) complexes of the C-methylated glycine derivatives, i.e. $Cu(C\text{-}dmg)_2$ and $Cu(L\text{-}ala)_2$ (Fig. 3: lanes **11** and **14**, respectively) are better nucleolytic agents as they were able to convert all the supercoiled DNA to nicked and linear DNA. However, the copper(II) complexes of the *N*-methylated glycine derivatives, i.e. $Cu(N\text{-}dmg)_2$ and $Cu(sar)_2$, are the least efficient as some supercoiled DNA still remained uncleaved (Fig. 3: lanes **12** and **15**, respectively). The order of nucleolytic efficiency is $Cu(C\text{-}dmg)_2 > Cu(L\text{-}ala)_2 \simeq$ *cis*-$Cu(gly)_2 > Cu(N\text{-}dmg)_2 \simeq Cu(sar)_2$.

Interestingly, the $CuCl_2$(aq.) can only nick some supercoiled pBR322 (Fig. 3, lane **5**) while the $Cu(aa)_2$ complexes can induce a greater amount of DNA cleavage. This suggests chelation of each of the investigated amino acid to the copper(II) ion enhances its nucleolytic efficiency. This is unlike the tetradentate amino acid, *N*,*N*-ethylenediaminediacetic acid, which upon chelation to copper(II) ion diminished its nucleolytic efficiency [9]. This suggests bidentate amino acid chelated to copper(II) ion can cause more damage to DNA than copper(II) ion in the borate buffer solution. In conclusion, it can be said that $Cu(aa)_2$ with C-methyl substituent are better nucleolytic agents than those with *N*-methyl substituent in the presence of hydrogen peroxide.

The cause of DNA cleavage by copper(II) complexes in the presence of hydrogen peroxide has been attributed to the formation of hydroxyl radicals [19,20]. Nakajima et al. had previously proposed that the hydroxyl radical was produced by a two step reactions in a copper(II)-hydrogen peroxide system: (i) $Cu(II) + H_2O_2 \rightarrow Cu(I) + HOO^{\cdot} + H^+$; and (ii) $Cu(I) + H_2O_2 \rightarrow Cu(II) + OH^- + {}^{\cdot}OH$ [21]. The H_2O_2 has a dual function, i.e. acting initially as reducing agent and then as oxidizing agent. As expected, a hydroxyl radical scavenger, thiourea, inhibited the DNA cleavage by most of the $Cu(aa)_2$ complexes in the presence of hydrogen peroxide (Fig. 4, lanes **12–15**). The degree of inhibition apparently varies with each $Cu(aa)_2$. Unexpectedly, thiourea enhanced the DNA cleavage by $Cu(sar)_2$ (Fig. 4, lane **16**) and copper(II) ions (Fig. 4, lane **6**). As far as we know, this is the first instance of selective activation of a copper(II) complex and copper(II) ion by thiourea towards cleavage of DNA in the presence of hydrogen peroxide. We are currently investigating this further to elucidate this unusual phenomenon.

Consequently, we investigate the difference in nucleolytic efficiency of the $Cu(aa)_2$ by using a PNDA assay to compare the amount of hydroxyl radicals produced from the reaction of $Cu(aa)_2$ with hydrogen peroxide in borate buffer at pH 8.5. In the PNDA assay, the amount of bleaching of the yellow PNDA is directly proportional to the ·OH radicals produced as the reaction stoichiometric ratio of PNDA: ·OH is 1:1 [9]. As can be seen from Fig. 5, the inferred order of increasing ·OH radical production is $Cu(NO_3)_2 < Cu(sar)_2 < Cu(N\text{-}dmg)_2 <$ *cis*-$Cu(gly)_2 < Cu(L\text{-}ala)_2 < Cu(C\text{-}dmg)_2$. As the order of nucleolytic efficiency shows a similar trend, i.e. $Cu(N\text{-}dmg)_2 \simeq Cu(sar)_2 < Cu(L\text{-}ala)_2 \simeq$ *cis*-$Cu(gly)_2 < Cu(C\text{-}dmg)_2$, the nucleolytic efficiency may be attributed to the difference in the rate of ·OH radical production and the resultant amount of radicals produced. This difference in production of ·OH radicals by the $Cu(aa)_2$ complexes may be the result of a number of factors, such as steric hindrance to binding of H_2O_2 or ^-OOH due to methyl groups at the amino nitrogen, electronic effect of electron donating methyl substituent, and difference in redox property of the $Cu(aa)_2$. A previous study by Raja et al. found that the number of methyl groups and their position on the tridentate pyridylmethylethylenediamine ligands in a series of copper (II) complexes affect their DNA binding and nucleolytic efficiency [22]. Among the three complexes, two complexes were less efficient in cleaving the DNA than the third one and this was attributed to the presence of the more sterically hindered ligands in the former. Shao et al. similarly attributed the difference in the decreasing order of nucleolytic

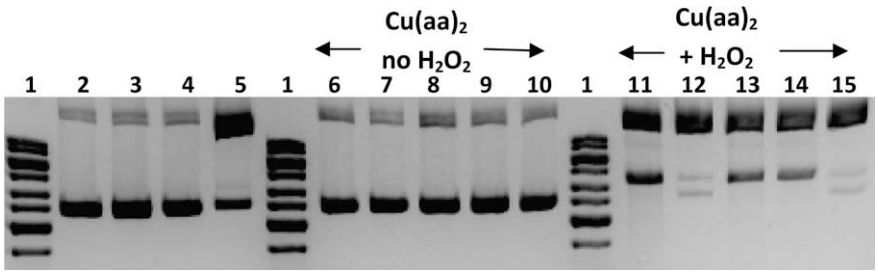


Fig. 3. Electrophoresis results of incubating pBR322 (0.5 μg/μL) with 500 μM of each $Cu(aa)_2$ complexes at 37 °C in borate buffer pH 8.5 in an oven incubator for 2 h in the absence and presence of 10 μM H_2O_2. Lanes **1** are gene ruler 1 Kb DNA ladder; lane **2**, DNA alone; lane **3**, DNA + 10 μM H_2O_2; lane **4**, DNA + 500 μM $CuCl_2$; lane **5**, DNA + 500 μM $CuCl_2$ + 10 μM H_2O_2. Lanes **6–10** DNA + $Cu(aa)_2$ alone: **6**, $Cu(C\text{-}dmg)_2$; **7**, $Cu(N\text{-}dmg)_2$; **8**, *cis*-$Cu(gly)_2$; **9**, $Cu(L\text{-}ala)_2$; **10**, $Cu(sar)_2$. Lanes **11–15** DNA + $Cu(aa)_2$ + 10 μM H_2O_2: **11**, $Cu(C\text{-}dmg)_2$; **12**, $Cu(N\text{-}dmg)_2$; **13**, *cis*-$Cu(gly)_2$; **14**, $Cu(L\text{-}ala)_2$; **15**, $Cu(sar)_2$.

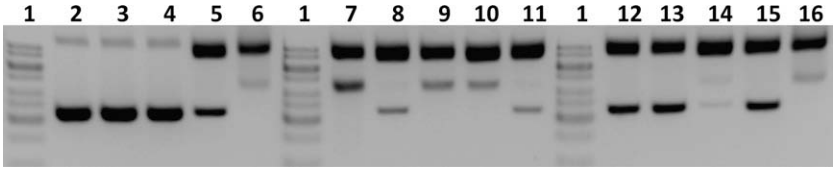


Fig. 4. Electrophoresis results of incubating pBR322 (0.5 μg/μL) with 500 μM of each $Cu(aa)_2$ complexes with 10 μM H_2O_2 at 37 °C in borate buffer pH 8.5 in an oven incubator for 2 h in the absence and presence of thiourea. Lanes **1** are gene ruler 1 Kb DNA ladder; lane **2**, DNA alone; lane **3**, DNA + 250 μM thiourea; lane **4**, DNA + 500 μM $CuCl_2$; lane **5**, DNA + 500 μM $CuCl_2$ + 10 μM H_2O_2; lane **6**: DNA + 500 μM $CuCl_2$ + 10 μM H_2O_2 + 250 μM thiourea. Lanes **7–11** DNA + $Cu(aa)_2$ + 10 μM H_2O_2: **7**, $Cu(C\text{-}dmg)_2$; **8**, $Cu(N\text{-}dmg)_2$; **9**, *cis*-$Cu(gly)_2$; **10**, $Cu(L\text{-}ala)_2$; **11**, $Cu(sar)_2$. Lanes **12–16** DNA + $Cu(aa)_2$ + 10 μM H_2O_2 + 250 μM thiourea; **12**, $Cu(C\text{-}dmg)_2$; **13**, $Cu(N\text{-}dmg)_2$; **14**, *cis*-$Cu(gly)_2$; **15**, $Cu(L\text{-}ala)_2$; **16**, $Cu(sar)_2$.

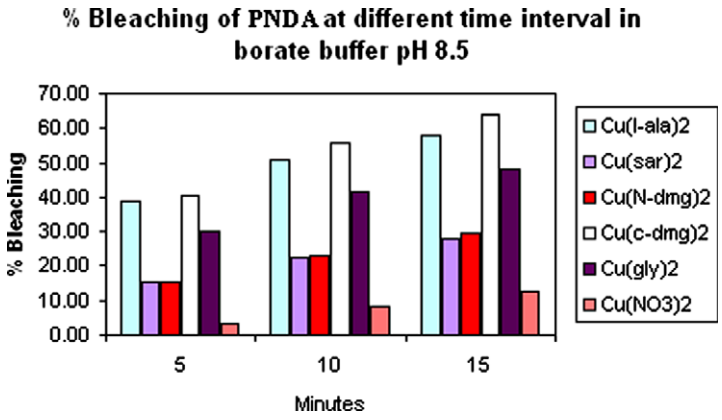


Fig. 5. PNDA assay to determine the amount of hydroxyl radicals from the reaction of $Cu(aa)_2$ with H_2O_2 at 5-min intervals for 15 min.

property of three copper(II) complexes of aminoquinoline derivatives to increasing steric hindrance of the amino-substituent of the ligands [23]. Others have also reported steric and electronic effects, enantiospecificity and reactive orientation as factors that determine the nature of the DNA binding and nucleolytic efficiency of 26 derivatives of $[Salen\text{-}Mn(III)]^+$ [24]. As for the redox factor, a recent study found that the rate of oxidation of DNA by a series of complexes based on $Ru(tpy)(bpy)O^{2+}$ (with electron-donating or -withdrawing substituent in the polypyridyl ligands) had correlation with the order of redox potentials of these complexes [25]. Thus, similar factors may affect the nucleolytic efficiency of the present $Cu(aa)_2$ complexes.

One of the mechanisms of DNA cleavage by copper(II) complexes in the presence of hydrogen peroxide involves binding of the metal complex species to the DNA and subsequent DNA cleavage by ·OH radicals produced at the binding sites [19–21,26,27]. The order of increasing binding strength of the $Cu(aa)_2$ complexes has been found to be $Cu(sar)_2$ < *cis*-$Cu(gly)_2$ < $Cu(N\text{-}dmg)_2$ < $Cu(L\text{-}ala)_2$ < $Cu(C\text{-}dmg)_2$ (Table 1, Section 3.1). The order of increasing ·OH radical production is $Cu(sar)_2$ < $Cu(N\text{-}dmg)_2$ < *cis*-$Cu(gly)_2$ < $Cu(L\text{-}ala)_2$ < $Cu(C\text{-}dmg)_2$ (Fig. 5). Thus, the greater nucleolytic efficiency of the copper(II) C-methylated glycine derivatives compared to those of *N*-methylated glycine derivatives can be attributed to both the greater binding strength of these complexes and higher ·OH radical production. Similar dependence of nucleolytic efficiency on the DNA binding strength has been observed for various series of copper(II) complexes [15,28,29].

3.3. DNA cleavage by $Cu(aa)_2$ in the presence of sodium ascorbate alone or of both sodium ascorbate and H_2O_2

The $CuCl_2$ and all the $Cu(aa)_2$ complexes do not cleave the DNA in the absence of sodium ascorbate (Fig. 6, lanes **4**, **6–10**). DNA in the presence of 2 μM of sodium ascorbate showed no DNA cleavage (Fig. 6, lane **3**). However, DNA incubated with 500 μM of $CuCl_2$ in the presence of 2 μM of sodium ascorbate could nick a small amount of supercoiled plasmid DNA (Fig. 6, lane **5**). Except for $Cu(sar)_2$, the other $Cu(aa)_2$ complexes induced more extensive nicking of the DNA. No double nicking of DNA to produce linear DNA was observed. This suggests that chelating the bidentate amino acid to the copper(II) ion normally enhanced its nucleolytic efficiency in the presence of ascorbate. By comparing the nucleolytic efficiency of the copper(II) C-methylated glycine derivatives with those of the *N*-methylated glycine derivatives, the same conclusion is again obtained as that for the DNA cleavage by $Cu(aa)_2$ in the presence of hydrogen peroxide. However, *cis*-$Cu(gly)_2$ (instead of $Cu(C\text{-}dmg)_2$) is the most efficient nucleolytic agent in the presence of sodium ascorbate as all the supercoiled DNA was converted to nicked DNA (Fig. 6, lane **13**).

The ROS scavenging experiment for the reaction of DNA with $Cu(aa)_2$ in the presence of sodium ascorbate was carried out to determine the active species responsible for DNA cleavage. No distinct DNA cleavage inhibition was detected for thiourea, sodium azide and tiron (results not shown). Thus, no detectable ·OH, singlet oxygen ($^1O_2$), and superoxide anion radical (O_2^-) is produced. The DNA cleavage by $Cu(aa)_2$ in the presence of sodium ascorbate (NaHA) may be due to the formation of ascorbyl (=ascorbate) radical as the active cleavage agent. Ascorbate is known to be a one electron donor and electron transfer results in formation of ascorbyl radical [30,31]. However, there is total inhibition of DNA cleavage by neocuprione, a Cu(I)-specific chelator (Fig. 7A). The present DNA cleavage by $Cu(aa)_2$ seems to be different from the that by $[Cu(phen)(L\text{-}threo)(H_2O)](ClO_4)$ in the presence of ascorbate where inhibition by DMSO indicated the role of ·OH radicals [32]. Additional experiment with DMSO shows no inhibition of DNA cleavage by all the $Cu(aa)_2$ (data not shown). Thus, ascorbyl radicals may be

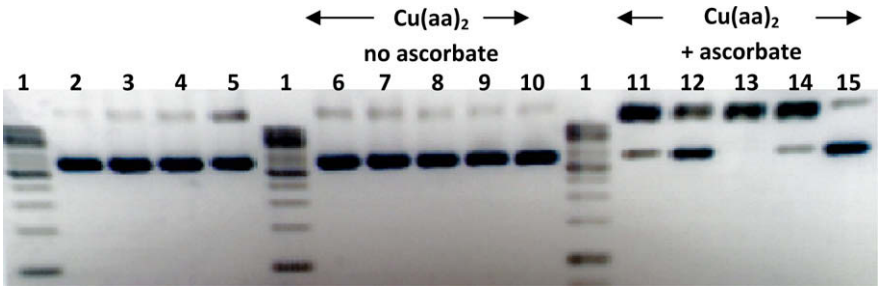


Fig. 6. Electrophoresis results of incubating pBR322 (0.5 μg/μL) with 500 μM of each $Cu(aa)_2$ complexes at 37 °C in Borate buffer pH 8.5 in an oven incubator for 2 h in the absence and presence of 2 μM sodium ascorbate. Lanes labeled **1** are gene ruler 1 Kb DNA ladder; lane **2**, DNA alone; lane **3**, DNA + 2 μM sodium ascorbate; lane **4**, DNA + 500 μM $CuCl_2$; lane **5**, DNA + 500 μM $CuCl_2$ + 2 μM sodium ascorbate. Lanes **6–10** DNA + $Cu(aa)_2$ alone: **6**, $Cu(C\text{-}dmg)_2$; **7**, $Cu(N\text{-}dmg)_2$; **8**, *cis*-$Cu(gly)_2$; **9**, $Cu(L\text{-}ala)_2$; **10**, $Cu(sar)_2$. Lanes **11–15** DNA + $Cu(aa)_2$ + 2 μM sodium ascorbate: **11**, $Cu(C\text{-}dmg)_2$; **12**, $Cu(N\text{-}dmg)_2$; **13**, *cis*-$Cu(gly)_2$; **14**, $Cu(L\text{-}ala)_2$; **15**, $Cu(sar)_2$.

the active cleaving species in the DNA cleavage by $Cu(aa)_2$ in the presence of ascorbate alone.

In the above discussion on the mechanism of DNA cleavage by (i) $Cu(aa)_2$ in the presence of H_2O_2 and (ii) $Cu(aa)_2$ in the presence of ascorbate, there seems a common and essential initial step in the process. In both cases, the Cu(II) species seems to have been reduced to the Cu(I) species. To verify this, spectroscopic experiments on the reactions of the 500 μM $Cu(aa)_2$ with (i) H_2O_2 (10 mM) in the presence of neocuproine (750 μM), and with (ii) ascorbate (200 μM) in the presence of neocuproine (250 μM), were carried out. For each $Cu(aa)_2$ tested in both series of experiments, there was appearance of a new intense band at 456 nm (Fig. 8 spectra A and B show only spectra for $Cu(L\text{-ala})_2$). The formation of the Cu(I)–neocuproine species was confirmed by comparison with the spectrum of a solution of copper(I) iodide with neocuproine which has a λ_{max} at 456 nm (Fig. 8 Spectrum C). In view of this, DNA cleavage mechanism by $Cu(aa)_2$ is likely to involve the following reactions:

$$Cu(II) + H_2O_2 \rightarrow Cu(I) + HOO^{\cdot} + H^+ \quad (1)$$

$$Cu(I) + H_2O_2 \rightarrow Cu(II) + HO^- + {}^{\cdot}OH \quad (2)$$

$$Cu(II) + AH^- \rightarrow Cu(I) + A^{\cdot -} + H^+ \quad (3)$$

where Cu(II) represents copper(II) species, Cu(I) represents copper(I) species, $HOO^{\cdot}$ represents the hydroperoxo (= hydroperoxyl) radical, AH^- is the ascorbate anion and $A^{\cdot -}$ is the ascorbyl radical. Reaction (1) is not likely to directly responsible for DNA cleavage as the hydroperoxo radicals are reported to have little or no ability to induce DNA cleavage [33]. A crucial step in the inhibition by neocuproine for the $Cu(aa)_2$–H_2O_2 system may involve the oxidatively stable Cu(I)–neocuproine species which were not oxidized by H_2O_2 [34]. Consequently, reaction (2) did not occur and no hydroxyl radicals were formed to cleave the DNA.

To investigate the inhibition of DNA cleavage by the $Cu(aa)_2$-ascorbate system by neocuproine, we monitor the various $Cu(aa)_2$–neocuproine mixtures spectroscopically and found that there was a distinct shift of the λ_{max} of the $Cu(aa)_2$ to longer wavelengths, indicating partial or total displacement of coordinated aa^- ligands by neocuproine to form a series of new species (Fig. 9 and Table 2) whose λ_{max} values are close to that of Cu(II)–neocuproine

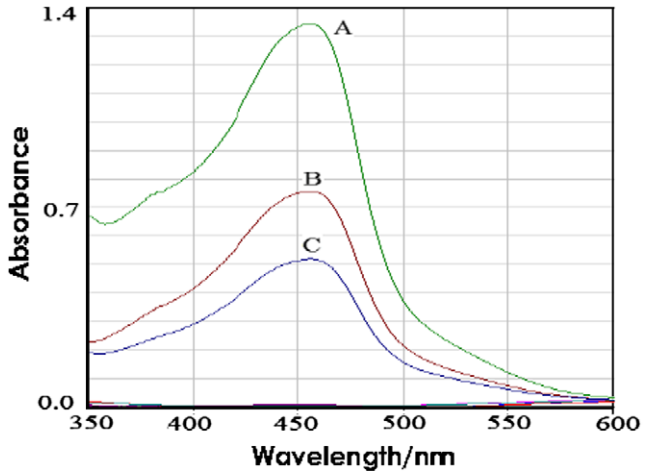


Fig. 8. Visible spectra of (A) 500 μM $Cu(L\text{-ala})_2$ in the presence of 10 mM H_2O_2 + 750 μM neocuproine; (B) 500 μM $Cu(L\text{-ala})_2$ in the presence of 200 μM NaHA + neocuproine; (C) CuI + neocuproine.

at 689 nm. Thus, the Cu(II)–neocuproine species can be formed in the DNA-$Cu(aa)_2$-NaHA mixtures in the presence of neocuproine. Inhibition of DNA cleavage cannot be directly due to formation of this Cu(II)–neocuproine species as the copper(II) oxidation state has not been reported to be stabilized. In fact, Cu(II)–neocuproine has been extensively used as an oxidizing agent for a variety of antioxidants in the CUPRAC method [35]. In fact, a blue methanolic solution of Cu(gg)(dmp) (gg = glycylglycinate; dmp = neocuproine) has been reported to eventually becomes yellow by a neocuproine-promoted reduction of Cu(II) to form the stable $Cu(I)(dmp)_2^+$ [36]. Hall et al. have reported that copper(II)–neocuproine complexes can easily be reduced to the copper(I) state and this reduction is more rapid if the solution is boiled [37]. No explanation was given for the reduction of the copper(II)–neocuproine in the absence of any reducing agent. Thus, the DNA-bound $Cu(aa)_2$ species can be converted to DNA-bound Cu(II)–neocuproine species and be still readily reduced to DNA-bound Cu(I)–neocuproine species by

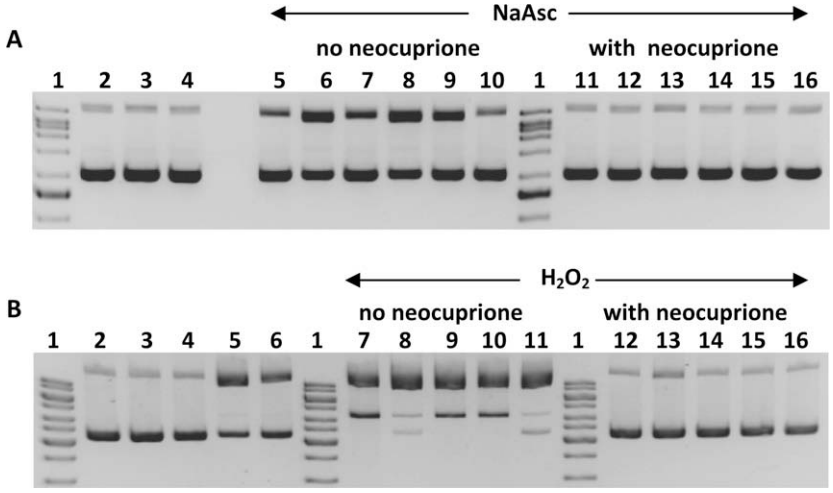


Fig. 7. Electrophoresis results of incubating pBR322 (0.5 μg/μL) with 500 μM of $CuCl_2$ or $Cu(aa)_2$ complexes with exogeneous reagent at 37 °C in borate buffer pH 8.5 in an oven incubator for 2 h in the absence and presence of 500 μM neocuproine (A) or 250 μM neocuproine (B). A: Lanes **1**–**16**: Reactions with 2 μM NaHA. Lanes **1** are gene ruler 1 Kb DNA ladder; lane **2**, DNA alone; lane **3**, DNA + 500 μM neocuproine; lane **4**, DNA + 2 μM NaHA. Lanes **5**–**10** no neocuprione: lane **5**, $CuCl_2$; lane **6**, $Cu(C\text{-dmg})_2$; **7**, $Cu(N\text{-dmg})_2$; **8**, *cis*-$Cu(gly)_2$; **9**, $Cu(L\text{-ala})_2$; **10**, $Cu(sar)_2$. Lanes 11–16 with neocuproine added. Lane **11**, $CuCl_2$; lane **12**, $Cu(C\text{-dmg})_2$; **13**, $Cu(N\text{-dmg})_2$; **14**, *cis*-$Cu(gly)_2$; **15**, $Cu(L\text{-ala})_2$; **16**, $Cu(sar)_2$. **B: Lanes 1–16:** Reactions with 10 μM H_2O_2. Lanes **1** are gene ruler 1 Kb DNA ladder; lane **2**, DNA alone; lane **3**, DNA + 250 μM neocuproine; lane **4**, DNA + 500 μM $CuCl_2$; lane **5**, DNA + 500 μM $CuCl_2$ + 10 μM H_2O_2; lane **6**: DNA + 500 μM $CuCl_2$ + 10 μM H_2O_2 + 250 μM neocuproine. Lanes **7**–**11:** DNA + $Cu(aa)_2$ + 10 μM H_2O_2: **7**, $Cu(C\text{-dmg})_2$; **8**, $Cu(N\text{-dmg})_2$; **9**, *cis*-$Cu(gly)_2$; **10**, $Cu(L\text{-ala})_2$; **11**, $Cu(sar)_2$. Lanes **12**–**16:** DNA + $Cu(aa)_2$ + 10 μM H_2O_2 + 250 μM neocuproine: **12**, $Cu(C\text{-dmg})_2$; **13**, $Cu(N\text{-dmg})_2$; **14**, *cis*-$Cu(gly)_2$; **15**, $Cu(L\text{-ala})_2$; **16**, $Cu(sar)_2$.

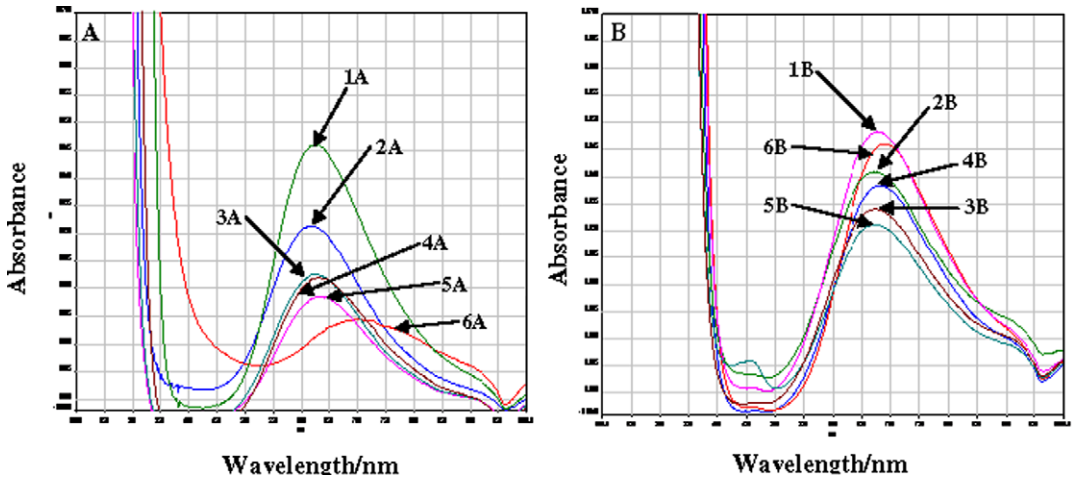


Fig. 9. (A) Spectra of 500 μM of $Cu(aa)_2$: $Cu(N\text{-}dmg)_2$, **1A**; $Cu(C\text{-}dmg)_2$, **2A**; $Cu(L\text{-}ala)_2$, **3A**; $Cu(sar)_2$, **4A**; *cis*-$Cu(gly)_2$, **5A**; $CuCl_2$, **6A**; (B) Spectra of 500 μM Cu(aa)2 + 500 μM neocuproine: $Cu(N\text{-}dmg)_2$, **1B**; $Cu(C\text{-}dmg)_2$, **2B**; $Cu(L\text{-}ala)_2$, **3B**; Cu(sar)2, **4B**; *cis*-$Cu(gly)_2$, **5B**; $CuCl_2$, **7B**. Absorbance and wavelength scales are the same for both (A) and (B).

Table 2
Visible spectral data (λ_{max} and absorbance(A)) of 500 μM $Cu(aa)_2$ alone and 500 μM $Cu(aa)_2$ + 500 μM neocuproine in borate buffer pH 8.5.

Amino acid, aa^-	λ_{max}/nm (A)	
	$Cu(aa)_2$	$Cu(aa)_2$ + neocuproine
Gly	645(0.019)	677(0.031)
C-dmg	622(0.032)	676 (0.041)
L-ala	625(0.022)	676(0.034)
N-dmg	628(0.046)	681(0.048)
Sar	633(0.022)	681(0.038)
	$CuCl_2$	$CuCl_2$ + neocuproine
	706(0.014)	689(0.046)

ascorbate to produce ascorbyl radical. However, the ascorbyl radicals may be formed further from the DNA and prevented from reaching the DNA by the Cu(I)–DNA–neocuproine complex as it was established that the initial $Cu(aa)_2$ binds very weakly to the DNA. Further investigation is needed to confirm this proposed inhibition of DNA cleavage by neocuproine in the $Cu(aa)_2$-ascorbate system.

As thus far, no comparison has been made for the use of H_2O_2 alone, sodium ascorbate (or ascorbic acid) alone, and the combination of H_2O_2 and sodium ascorbate to activate copper(II) complexes for DNA cleavage, we have done so for our series of $Cu(aa)_2$ complexes. In all cases (including the $CuCl_2$), the nucleolytic efficiency of $Cu(aa)_2$ increases in the following order in the presence of exogenous agent: sodium ascorbate < hydrogen peroxide < {hydrogen peroxide + sodium ascorbate} (Fig. 10). For the DNA cleavage by $Cu(aa)_2$ in the presence of both sodium ascorbate and H_2O_2, the order of nucleolytic efficiency is $Cu(sar)_2$ < $Cu(N\text{-}dmg)_2$ < $Cu(L\text{-}ala)_2$ < $Cu(C\text{-}dmg)_2$ < *cis*-$Cu(gly)_2$. Again the copper(II) complexes

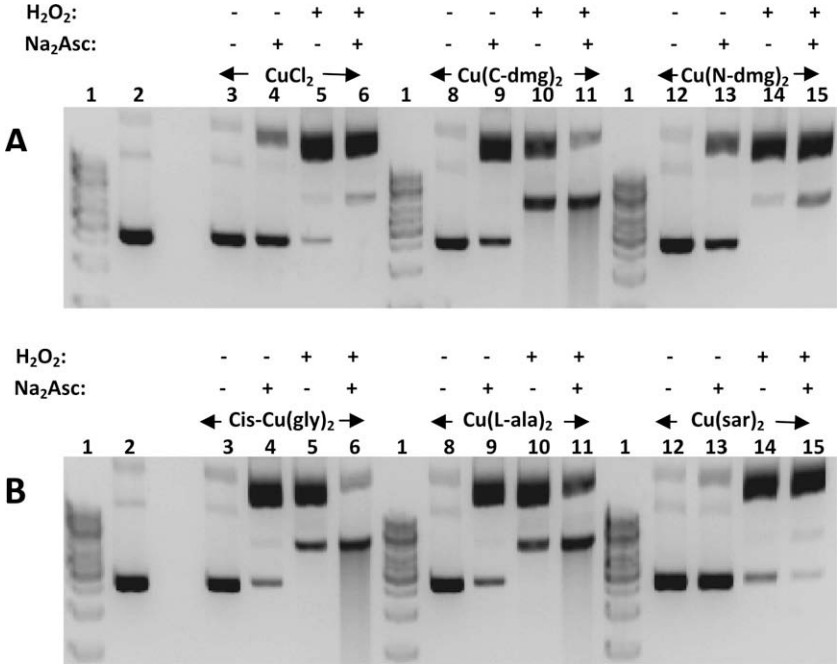


Fig. 10. Electrophoresis results of incubating pBR322 (0.5 μg/μL) with 500 μM of each $Cu(aa)_2$ complexes at 37 °C in Borate buffer pH 8.5 in an oven incubator for 2 h in the absence and presence of exogenous agents (10 μM H_2O_2; 2 μM sodium ascorbate; 10 μM H_2O_2 + 2 μM sodium ascorbate). A: $CuCl_2$, $Cu(C\text{-}dmg)_2$, $Cu(N\text{-}dmg)_2$; B: *cis*-$Cu(gly)_2$, $Cu(L\text{-}ala)_2$, $Cu(sar)_2$.

of C-methylated glycine derivatives cleave the DNA better than the copper(II) complexes of the *N*-methylated glycine derivatives. The higher DNA cleavage by $Cu(aa)_2$-NaHA-H_2O_2 system can be attributed to the more efficient production of ·OH by virtue of more Cu(I) species produced through reactions (1) and (3).

In conclusion, the $Cu(aa)_2$ complexes bind weakly to the DNA with a similar orientation. Nevertheless, the differences in binding between the copper(II) C-methylated glycine derivatives and the copper(II) *N*-methylated glycine derivatives are distinguishable. The electrophoresis results show that the nucleolytic property of the former complexes are better than that of the latter in the presence of hydrogen peroxide alone or sodium ascorbate alone or both combination of hydrogen peroxide and sodium ascorbate. For mechanism of the cleavage reaction, reduction of Cu(II) to Cu(I) species by hydrogen peroxide or ascorbate has been confirmed.

Acknowledgements

The authors acknowledged the contribution of their respective universities, and in particular, the research grant from the Malaysian Ministry of Science, Technology and Innovation (E-science Project No. 02-02-11-SF0033) and the grant from Research Institute of Science and Engineering, Chuo University.

References

[1] M.E. Letelier, A.M. Lepe, M. Faúndez, J. Salazar, R. Marín, P. Aracena, H. Speisky, Chem. Biol. Interact. 151 (2005) 71.
[2] M.F. Ahmad, D. Singh, A. Taiyab, T. Ramakrishna, B. Raman, Ch.M. Rao, J. Mol. Biol. 382 (2008) 812.
[3] L. Cai, J. Koropatnick, M.G. Cherian, Chem. Biol. Interact. 96 (1995) 143.
[4] E.S. Henle, J. Biol. Chem. 272 (1997) 19095.
[5] D.-H. Lee, T.R. O'Connor, G.P. Pfeifer, Nucleic Acids Res. 30 (16) (2002) 3566.
[6] Y.-C. Han, T. Shen, W. Jiang, Q.-F. Xia, C.-L. Liu, J. Inorg. Biochem. 101 (2007) 214.
[7] J.R.J. Sorenson, in: G. Berthon (Ed.), Handbook on Metal–Ligand Interactions in Biological Fluids: Bioinorganic Medicine, vol. 2, Marcel Dekker, New York, 1995, pp. 1128–1139.
[8] C.H. Ng, H.K. Alan Ong, C.W. Kong, K.K. Su, S.W. Ng, J. Coord. Chem. 59 (2006) 1089.
[9] C.H. Ng, H.K. Alan Ong, C.W. Kong, K.W. Tan, Raja Noor Zaliha, B.M. Yamin, S.W. Ng, Polyhedron 25 (2006) 3119.
[10] R. Ren, P. Yang, W.-J. Zheng, Z.-C. Hua, Inorg. Chem. 39 (2000) 5454.
[11] T.-Y. Lin, C.-H. Wu, J. Catal. 232 (2005) 117.
[12] M. Chikira, M. Inoue, R. Nagane, W. Harada, H. Shindo, J. Inorg. Biochem. 66 (1997) 131.
[13] W. Harada, T. Nojima, A. Shibayama, H. Ueda, H. Shindo, M. Chikira, J. Inorg. Biochem. 64 (1996) 273.
[14] H.C. Freeman, M.R. Snow, I. Nitta, K. Tomita, Acta Cryst. 17 (1964) 1463.
[15] A. Rajendran, B.U. Nair, Biochim. Biophys. Acta 1760 (2006) 1794.
[16] H. Li, X.-Y. Le, D.-W. Pang, H. Deng, Z.-H. Xu, Z.-H. Lin, J. Inorg. Biochem. 99 (2005) 2240.
[17] M. Chauhan, F. Arjmand, Chem. Biodiversity 3 (2006) 660.
[18] B. Selvakumar, V. Rajendiran, P.U. Maheswari, H. Stoeckli-Evans, M. Palaniandavar, J. Inorg. Biochem. 100 (2006) 316.
[19] V. Uma, M. Kanthimathi, T. Weyhermuller, B.U. Nair, J. Inorg. Biochem. 99 (2005) 2299.
[20] T. Kobayashi, T. Okuno, T. Suzuki, M. Kunita, S. Ohba, Y. Nishida, Polyhedron 17 (1998) 1553.
[21] A. Nakima, Y. Ueda, World J. Microbiol. Biotechnol. 24 (2008) 1253.
[22] A. Raja, V. Rajendiran, P.U. Maheswari, R. Balamurugan, C.A. Kilner, M.A. Halcrow, M. Palaniandavar, J. Inorg. Biochem. 99 (2005) 1717.
[23] Y. Shao, J.-Y. Zhang, C. Tu, C.-H. Dai, Q. Xu, Z.-J. Guo, J. Inorg. Biochem. 99 (2005) 1490.
[24] D.J. Gravert, J.H. Griffin, Inorg. Chem. 35 (1996) 4837.
[25] B.T. Farrer, H.H. Thorp, Inorg. Chem. 39 (2000) 44.
[26] M.S.S. Babu, K.H. Reddy, P.G. Krishna, Polyhedron 26 (2007) 572.
[27] Q. Jiang, N. Xiao, P.-F. Shi, Y.-G. Zhu, Z.-J. Guo, Coord. Chem. Rev. 251 (2007) 1951.
[28] R. Rao, A.K. Patra, P.R. Chetana, Polyhedron 27 (2008) 1343.
[29] V. Uma, M. Elango, B.U. Nair, Eur. J. Inorg. Chem. 22 (2007) 3484.
[30] T. Iyanagi, I. Yamazaki, K.F. Anan, Biochim. Biophys. Acta 806 (1985) 255.
[31] G.R. Buettner, B.A. Jurkiewicz, Free Rad. Biol. Med. 14 (1993) 49.
[32] S.-C. Zhang, Y.-G. Zhu, C. Tu, H.-Y. Wei, Z. Yang, L.-P. Lin, J. Ding, J.-F. Zhang, Z.-J. Guo, J. Inorg. Biochem. 98 (2004) 2099.
[33] T. Paul, M.J. Young, I.E. Hill, K.U. Ingold, Biochemistry 39 (2000) 4129.
[34] D.R. Graham, L.E. Marshall, K.A. Reich, D.S. Sigman, J. Am. Chem. Soc. 102 (1980) 5421.
[35] K. Sözgen, S.D. Cekic, E. Tütem, R. Apak, Talanta 68 (2006) 1601.
[36] C.J. Simmons, M. Lundeen, K. Seff, Inorg. Chem. 17 (1978) 1429.
[37] J.R. Hall, N.K. Marchant, R.A. Plowman, Aust. J. Chem. 15 (1962) 480.

Polyhedron 28 (2009) 2228–2232

Contents lists available at ScienceDirect

Polyhedron

journal homepage: www.elsevier.com/locate/poly

X-ray structural and electrochemical analysis of η^6-*p*-cymene ruthenium complexes with chelating S∩N ligands derived from 2-(methylthio)aniline and substituted benzaldehydes

Christopher G. Hamaker *, Dominic P. Halbach

Department of Chemistry, Illinois State University, Campus Box 4160, Normal, IL 61790, USA

ARTICLE INFO

Article history:
Received 12 February 2009
Accepted 24 March 2009
Available online 29 March 2009

Keywords:
Ruthenium
Schiff bases
Coordination chemistry
Crystal structure
Electrochemistry

ABSTRACT

A series of cationic, half-sandwich ruthenium complexes with the general formula $[(\eta^6\text{-}p\text{-cymene})RuCl(S\cap N)]^+$, (S∩N = MeS-$C_6H_4$-2-N=CHAr, **1a–f**) have been studied by cyclic voltammetry and X-ray crystallography. The complexes **1a–e** undergo irreversible oxidations and the results are compared to related complexes. The molecular structures of **1d**[PF_6] and **1f**[PF_6] were determined by X-ray crystallography.

© 2009 Elsevier Ltd. All rights reserved.

1. Introduction

Schiff bases are popular ligands in coordination chemistry due to their easy syntheses and their ability to be easily modified both sterically and electronically [1]. There are many examples of chelating Schiff base ligands that are potentially anionic, but neutral bidentate varieties are less common. Common examples are the 2-pyridylimines, $NC_5H_4CH{=}NR$, [2] and phosphinoimines derived from 2-(diphenylphosphino)benzaldehyde [3]. Recently, we have reported the synthesis and coordination chemistry of two classes of thioether-containing Schiff base ligands. One class is derived from the reaction of 2-(methylthio)aniline with aldehydes [4] and the other from the reaction of 2-(alkylthio)benzaldehydes with amines [5]. The first class of ligands, which form a five-membered chelate ring upon coordination to a metal center, has been shown to be susceptible to hydrolysis upon coordination to metal centers, while the second class with six-membered chelate rings is much more stable with respect to hydrolysis. In fact, our initial attempts to crystallize the compounds resulted in the isolation of the 2-methylthioaniline complex [4]. After several days under an ambient atmosphere, the Schiff base ligand bound to the ruthenium center completely hydrolyzes. Using X-ray crystallography, we can examine the changes in the ligand structure upon coordination to a metal center and how these changes may affect the hydrolytic stability of the Schiff bases upon coordination to the ruthenium center.

Arene ruthenium complexes are versatile compounds and have found use in catalysis [6] and medicine [7]. Investigation of the structural and electrochemical properties of η^6-arene ruthenium complexes can provide insight into their utility. There are very few reports of electrochemical studies on cationic arene ruthenium complexes [5,8]. Significant information can be obtained by investigating the effect of ligand structure on the properties of transition metal complexes.

The present work is an extension of our previous studies of $[(\eta^6\text{-}p\text{-cymene})RuCl(S\cap N)]^+$ complexes [4,5]. Herein we report the electrochemical properties and X-ray crystal structures of some η^6-*p*-cymene ruthenium complexes with our first generation of S∩N Schiff base ligands [4] and compare them to related complexes.

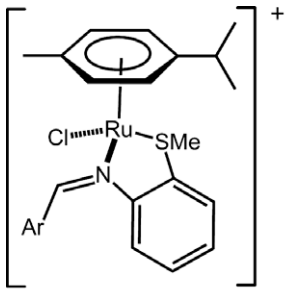
2. Results and discussion

2.1. Electrochemical behavior

The $[(\eta^6\text{-}p\text{-cymene})RuCl(MeSC_6H_4\text{-}2\text{-}N{=}CH\text{-}C_6H_4\text{-}p\text{-}X)]^+$ complexes **1a–e** (Scheme 1) were analyzed by cyclic voltammetry. All of the complexes show an irreversible Ru(II) to Ru(III) oxidation between 1196 and 1336 mV versus ferrocene/ferrocenium (Table 1). As expected, electron donating groups on the ligand reduce the oxidation potential while electron withdrawing groups increase the oxidation potential. To that end, complex **1d** (X = NO_2)

* Corresponding author. Tel.: +1 309 438 7659; fax: +1 309 438 5538.
E-mail address: chamake@ilstu.edu (C.G. Hamaker).

0277-5387/$ - see front matter © 2009 Elsevier Ltd. All rights reserved.
doi:10.1016/j.poly.2009.03.021



compound	Ar
a	4-$C_6H_4CH_3$
b	4-$C_6H_4OCH_3$
c	4-C_6H_4Cl
d	4-$C_6H_4NO_2$
e	C_6H_5
f	3,5-$C_6H_3(OCH_3)_2$

1a-f

Scheme 1.

is the most difficult to oxidize, while complex **1b** (X = OCH_3) is the easiest. A plot of E_{pa} versus Hammett constant, σ, reveals a linear relationship (Fig. 1) with a slope of about 134 mV/σ, which is very similar to the previously reported [(η^6-*p*-cymene)RuCl(RSC_6H_4-2-CH=NAr)]$^+$complexes [5]. In fact, the oxidation potentials for **1a–e** are very near those of our previously reported complexes. All of the complexes are easier to oxidize the than the reported phosphine complex [(η^6-*p*-cymene)RuCl(dppf)]$^+$ [8b] but more difficult to oxidize than the analogous phosphine imine complex [(η^6-*p*-cymene)RuCl($Ph_2PCH_2P(Ph_2)$=NC_5F_4N)]$^+$ [8c].

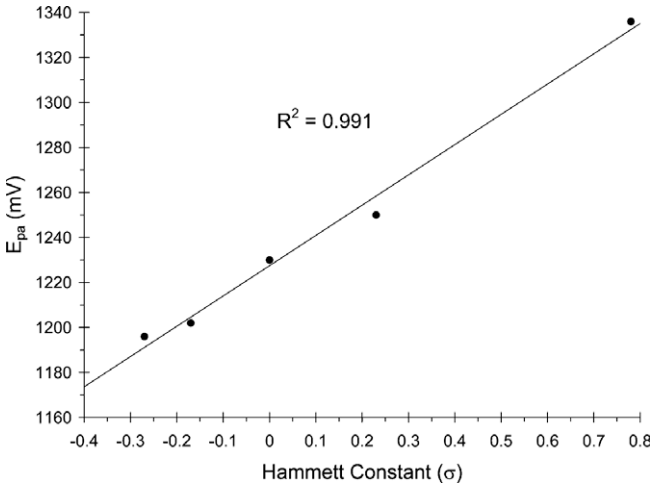


Fig. 1. A plot of E_{pa} vs. Hammett constant, σ, for the ruthenium complexes **1a–e**.

2.2. X-ray crystallographic analysis

Single crystal X-ray structure analyses were carried out for compounds **1d**[PF_6] (Fig. 2) and **1f**[PF_6] (Fig. 3). Crystallographic data are given in Table 2 and selected bond lengths (Table 3) and angles (Table 4) are also given along with relevant bond lengths and angles for the free ligand $MeSC_6H_4$-2-N=CH-3,5-$C_6H_3(OCH_3)_2$ [9]. In the ruthenium complexes, the S∩N ligands are coordinated in an η^2 fashion resulting in a five-membered ring. The complexes adopt the familiar piano stool geometry. The ruthenium atom is situated 1.688(15) and 1.6954(10) Å from the centroid of the *p*-cymene ring in **1d** and **1f**, respectively. These distances are shorter than those in the previously characterized [(η^6-*p*-cymene)RuCl(RSC_6H_4-2-CH=NAr)]$^+$complexes [5], but are in agreement with other structurally characterized cationic η^6-*p*-cymene ruthenium complexes [10]. The bond angles for the leg portion of the piano stool range from approximately 79–80° for the N(1)–Ru–S angle to approximately 91–92° for the S–Ru–Cl angle.

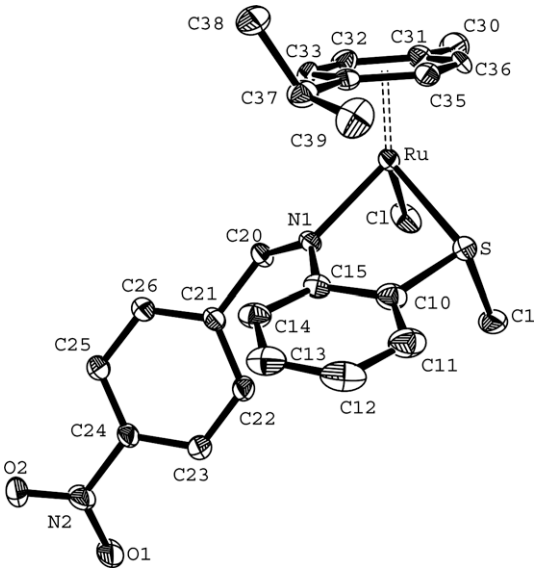


Fig. 2. Structural diagram of complex **1d** showing the atom-numbering scheme (50% probability ellipsoids). Hydrogen atoms are omitted for clarity.

Table 1
Selected electrochemical data for cationic arene ruthenium complexes with the general formula [(η^6-arene)RuCl(L∩L)]$^+$.

Complex	E_{pa} (mV)[a]	Ref.
[(η^6-*p*-Cymene)RuCl(MeS-C_6H_4-2-N=CH-C_6H_4-4-Me)]$^+$, **1a**	1202[b]	this work
[(η^6-*p*-Cymene)RuCl(MeS-C_6H_4-2-N=CH-C_6H_4-4-OMe)]$^+$, **1b**	1196[b]	this work
[(η^6-*p*-Cymene)RuCl(MeS-C_6H_4-2-N=CH-C_6H_4-4-Cl)]$^+$, **1c**	1250[b]	this work
[(η^6-*p*-Cymene)RuCl(MeS-C_6H_4-2-N=CH-C_6H_4-4-NO_2)]$^+$, **1d**	1336[b]	this work
[(η^6-*p*-Cymene)RuCl(MeS-C_6H_4-2-N=CH-C_6H_5)]$^+$, **1e**	1230[b]	this work
[(η^6-*p*-Cymene)RuCl($PhCH_2S$-C_6H_4-2-CH=N-C_6H_4-4-OMe)]$^+$	1193[b]	[5]
[(η^6-*p*-Cymene)RuCl(Me_2CHS-C_6H_4-2-CH=N-C_6H_4-4-OMe)]$^+$	1207[b]	[5]
[(η^6-*p*-Cymene)RuCl(CH_3CH_2S-C_6H_4-2-CH=N-C_6H_4-4-OMe)]$^+$	1180[b]	[5]
[(η^6-*p*-Cymene)RuCl($PhCH_2S$-C_6H_4-2-CH=N-C_6H_4-4-Br)]$^+$	1255[b]	[5]
[(η^6-*p*-Cymene)RuCl($PhCH_2S$-C_6H_4-2-CH=N-C_6H_4-4-Me)]$^+$	1205[b]	[5]
[(η^6-*p*-Cymene)RuCl($PhCH_2S$-C_6H_4-2-CH=N-C_6H_4-3-CF_3)]$^+$	1270[b]	[5]
[(η^6-*p*-Cymene)RuCl($PhCH_2S$-C_6H_4-2-CH=N-C_6H_2-2,4,6-Me_3)]$^+$	1331[b]	[5]
[(η^6-*p*-Cymene)RuCl(dppf)]$^+$	1420[c]	[8b]
[(η^6-*p*-Cymene)RuCl($Ph_2PCH_2P(Ph_2)$=NC_5F_4N)]$^+$	980[d]	[8c]

[a] Reported vs. ferrocene/ferrocenium couple.
[b] Recorded at a scan rate of 100 mV/s in acetonitrile with 0.1 M [Bu_4N][PF_6] as the supporting electrolyte.
[c] dppf = 1,1′-bis(diphenylphosphino)ferrocene. Recorded at a scan rate of 100 mV/s in dichloromethane with 0.03 M [Bu_4N][PF_6] as the supporting electrolyte [8b].
[d] Recorded at a scan rate of 100 mV/s in 1:1 acetonitrile:dichloromethane with 0.1 M [Bu_4N][ClO_4] as the supporting electrolyte [8c].

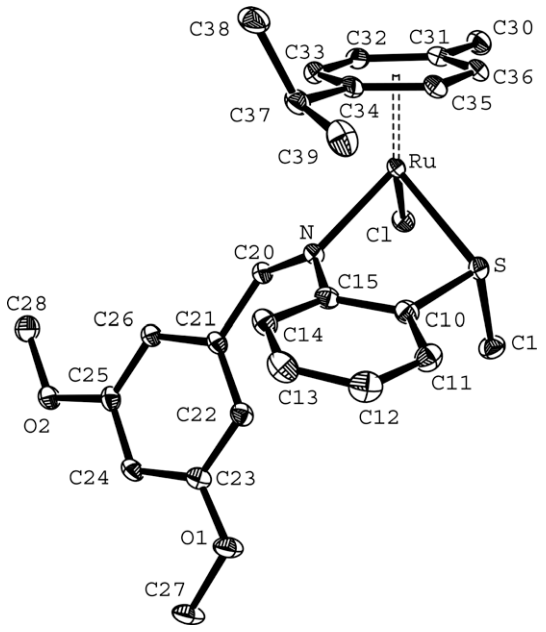


Fig. 3. Structural diagram of complex **1f** showing the atom-numbering scheme (50% probability ellipsoids). Hydrogen atoms are omitted for clarity.

Table 2
Crystallographic data for **1d**[PF_6] and **1f**[PF_6].

	1d[PF_6]	**1f**[PF_6]
Empirical formula	$C_{24}H_{26}ClF_6N_2O_2PRuS$	$C_{24}H_{31}ClF_6NO_2PRuS$
Formula weight	688.02	703.07
Temperature/K	100 (2)	100 (2)
Wavelength/Å	0.71073	0.71073
Crystal system	monoclinic	triclinic
Space group	*Cc*	$P\bar{1}$
a/Å	12.399 (4)	10.5636 (4)
b/Å	16.477 (5)	11.0491 (4)
c/Å	13.032 (4)	12.8779 (5)
α/°	90	83.0356 (7)
β/°	92.170 (6)	84.0994 (7)
γ/°	90	69.0045 (7)
Volume/Å^3	2660.5 (14)	1390.08 (9)
Z	4	2
D_{calc}/g cm^{-3}	1.718	1.680
μ (Mo Kα)/mm^{-1}	0.897	0.859
F(000)	1384	712
Crystal size/mm^3	0.35 × 0.15 × 0.14	0.40 × 0.27 × 0.27
θ range/°	2.06 – 28.28	1.98 – 28.28
Limiting indices	$-16 \leqslant h \geqslant 16$ $-21 \leqslant k \geqslant 21$ $-17 \leqslant l \geqslant 17$	$-14 \leqslant h \geqslant 14$ $-14 \leqslant k \geqslant 14$ $-17 \leqslant l \geqslant 17$
Reflections collected	13375	14529
Independent reflections (R_{int})	6435 (0.031)	6875 (0.015)
Max. and min. transmission	0.882 and 0.644	0.790 and 0.726
Data/restraints/parameters	6435/2/344	6875/0/353
Goodness-of-fit (GOF) on F^2	1.118	1.048
Final *R* indices [$I > 2\sigma(I)$]	R_1 = 0.0325 wR_2 = 0.0805	R_1 = 0.0225 wR_2 = 0.0574
Final *R* indices (all data)	R_1 = 0.0332 wR_2 = 0.0820	R_1 = 0.0234 wR_2 = 0.0580
Largest difference in peak and hole (e Å^{-3})	0.426 and −0.670	0.634 and −0.782

Looking at an overlay of the structures of **1d** and **1f** (Fig. 4) using the program Mercury [11], the two structures are very similar. The largest angle differences are the angles around the imine carbon C20 (Table 4). Another difference, which is evident in the overlay of the two structures, is the orientation of the C10–C15 benzene ring of the ligand. The angle between the mean plane of the η^6-*p*-cymene ligand and the mean plane of the C10–C15 benzene ring is 20.97(8)° in **1d** and 14.57(7)° in **1f**. The C10–C15 ring is **1f** is probably pushed further away from the arene substituent on the imine due to the increased steric bulk of the 3,5-methoxy groups. This also explains the larger S–Ru–Cl angle in **1d**, 92.09(4)°, compared to complex **1f**, 90.934(12)°.

Comparing the structure of complex **1f** with that of the free ligand $MeSC_6H_4$-2-N=CH-3,5-$C_6H_3(OCH_3)_2$ [9], the bond distances

Table 3
Selected bond lengths (Å) for **1d** and **1f** and the free ligand $MeSC_6H_4$-2-N=CH-3,5-$C_6H_3(OCH_3)_2$.

BOND	**1d**	**1f**	Free ligand[a]
Ru–N(1)	2.099 (3)	2.1022 (12)	
Ru–Cl	2.3906 (10)	2.3838 (3)	
Ru–S	2.3748 (11)	2.3931 (4)	
Ru–Cent[b]	1.688 (15)	1.6954 (10)	
C1–S	1.816 (4)	1.8177 (15)	1.7955(16)
C10–S	1.777 (4)	1.7789 (15)	1.7633(14)
C15–N(1)	1.436 (4)	1.4327 (7)	1.4154(16)
C20–N(1)	1.287 (4)	1.2915 (18)	1.2744(19)

[a] Ref. [10].
[b] Cent = *p*-cymene ring centroid.

Table 4
Selected bond angles (°) for **1d** and **1f** and the free ligand $MeSC_6H_4$-2-N=CH-3,5-$C_6H_3(OCH_3)_2$.

BOND	**1d**	**1f**	Free ligand[a]
N(1)–Ru–S	80.32 (8)	79.18 (3)	
S–Ru–Cl	92.05 (4)	90.934 (12)	
N(1)–Ru–Cl	85.48 (8)	86.14 (3)	
C10–S–Ru	97.17 (13)	95.62 (5)	
C10–S–C1	100.02 (18)	99.99 (7)	102.41(7)
Ru–S–C1	113.16 (17)	114.94 (5)	
N(1)–C20–C21	127.6 (3)	129.86 (13)	122.99(13)
C16–N–C20	122.4 (3)	122.63 (12)	118.09(12)

[a] Ref. [10].

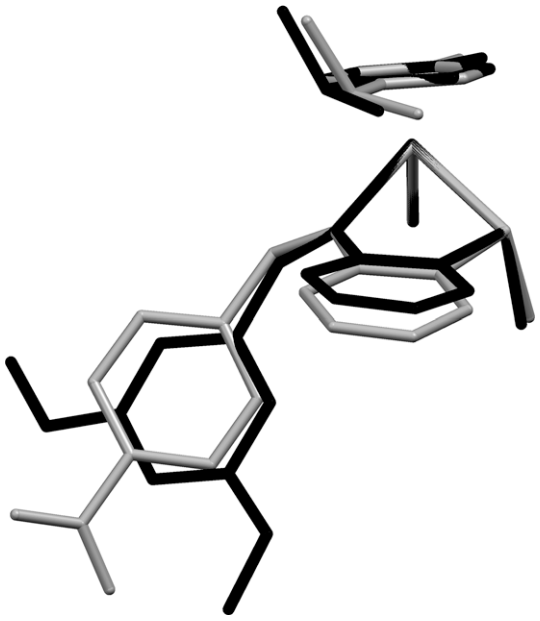


Fig. 4. Overlay of the crystal structures of complexes **1d** (grey) and **1f** (black) generated using the program Mercury.

are all very similar (Table 3). The only significant differences are in the angles of the imine and thioether portions of the compounds. The N–C20–C21 angle is about 6.9° smaller in the free ligand while the C16–N–C20 angle is about 4.5° smaller. Additionally, the imine is in the *cis* configuration when coordinated to the ruthenium center but in the *trans* configuration in the free ligand (Fig. 5). This change in imine geometry is not required for coordination (either the *cis*- or *trans*-imine could coordinate to the metal center). However, the *cis*-geometry minimizes steric interactions between the arene substituent on the imine and the metal center. The C10–S–C1 bond angle decreases by about 2.4° upon coordination of the ligand to the ruthenium center, again most likely due to increased steric repulsion from the ruthenium fragment. The decreased bond angles around C20, N, and S most likely are the reason for the slight lengthening of the bonds involving those three atoms as shown in Table 3.

Of primary interest is the bite angle of the S∩N ligands in these complexes; 80.32(8)° in **1d** and 79.18(3)° in **1f**. They are significantly smaller than the bite angles of our previously reported RSC_6H_4-2-CH=NAr, which form six-membered rings upon coordination with bite angles in the $[(\eta^6$-*p*-cymene)RuCl(RSC_6H_4-2-CH=NAr)$]^+$ complexes of 86.86(12)°–89.22(4)° (Table 5). This smaller bite angle in the MeS-C_6H_4-2-N=CHAr ligands, along with the changes in the imine bond angles and geometry, may explain the instability of complexes **1a–f** towards hydrolysis [4].

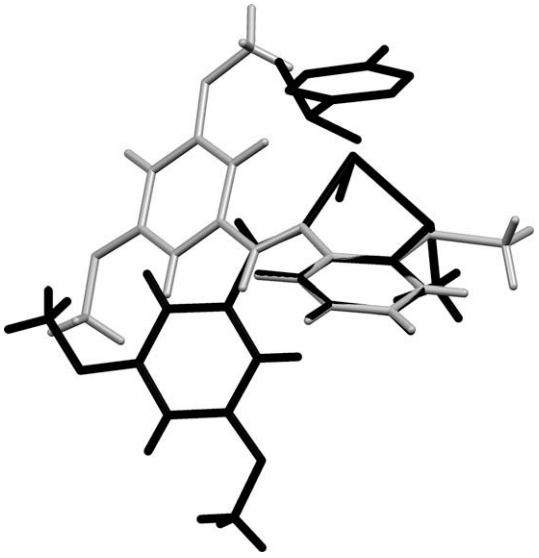


Fig. 5. Overlay of the crystal structures of complex **1f** (black) and the free ligand $MeSC_6H_4$-2-N=CH-3,5-$C_6H_3(OCH_3)_2$ (grey) generated using the program Mercury.

Table 5
Selected bite angles (°) for several cationic arene ruthenium complexes with the general formula $[(\eta^6$-*p*-cymene)RuCl(N∩S)$]^+$.

Complex	N–Ru–S	Ref.
$[(\eta^6$-*p*-Cymene)RuCl(MeS-C_6H_4-2-N=CH-C_6H_4-4-NO_2)$]^+$, **1d**	80.32 (8)	this work
$[(\eta^6$-*p*-Cymene)RuCl($MeSC_6H_4$-2-N=CH-C_6H_3-3,5-$(OCH_3)_2$)$]^+$, **1f**	79.18 (3)	this work
$[(\eta^6$-*p*-Cymene)RuCl($PhCH_2S$-C_6H_4-2-CH=N-C_6H_4-4-OMe)$]^+$	86.82 (12)	[5]
$[(\eta^6$-*p*-Cymene)RuCl($PhCH_2S$-C_6H_4-2-CH=N-C_6H_2-2,4,6-$(CH_3)_3$)$]^+$	87.20 (6)	[5]
$[(\eta^6$-*p*-Cymene)RuCl(Me_2CHS-C_6H_4-2-CH=N-C_6H_4-4-CH_3)$]^+$	89.22 (4)	[5]
$[(\eta^6$-*p*-Cymene)RuCl(MeS-C_6H_4-2-NH_2)$]^+$	81.63 (5)	[4]

3. Conclusions

While the arene ruthenium complexes of our S∩N Schiff base ligands derived from 2-methylthioaniline have similar electrochemical properties to those with S∩N ligands derived from 2-(alkylthio)benzaldehydes, the decrease in bite angle may lead to more reactive metal complexes with respect to hydrolysis.

4. Experimental

4.1. General considerations

All reagents were of commercial grade and used without further purification. The ruthenium complexes were synthesized using the literature procedure [4] and their analytical and spectroscopic data are reported there. The electrochemical studies were carried out in acetonitrile using a BAS CV-50W potentiostat. A conventional three-electrode cell consisting of a platinum disk working electrode, a platinum wire auxiliary electrode and a Ag/AgCl reference electrode was used. The cyclic voltammograms were run in 0.1 M $[Bu_4N][PF_6]$ at a scan rate of 100 mV/s. The scanning limits were +0.5 to +1.9 V versus Ag/AgCl, and the ferrocene/ferrocenium couple appeared at +445 mV versus the Ag/AgCl reference. All potentials are reported versus the ferrocene/ferrocenium couple.

4.2. X-ray crystallography

Orange X-ray quality crystals of complexes **1b**$[PF_6]$ and **1f**$[PF_6]$ were isolated by layering a solution of the complex in dry 1,2-dichloroethane with dry *n*-heptane under a nitrogen atmosphere. Data were collected at Youngstown State University on a Bruker AXS SMART APEX CCD-equipped diffractometer at −173 °C using MoKα radiation (λ = 0.71073 Å) from a graphite monochromater. Cell refinement and data reduction were accomplished using SAINT+ [12]. The data were corrected for absorption through use of the SADABS procedure. See Table 2 for a summary of crystal data and X-ray collection information.

Solution and data analysis were performed using the WinGX software package [13]. The structures were solved by direct methods using the program SIR2002 [14]. The refinements were completed using the program SHELX-97 [15]. Hydrogen atoms were assigned positions based on the geometries of their attached carbons. See Table 2 for final refinement parameters.

Acknowledgements

C.G.H. wishes to thank Illinois State University for financial support (URG-FRA award). D.P.H. wishes to thank the Illinois State University Chemistry Department for receipt of a Kurz Summer Graduate Fellowship. The authors also wish to thank Matthias Zeller and Allen D. Hunter of the Youngstown State University X-ray Crystallography Laboratory for collection of low-temperature, CCD X-ray data. The diffractometer was funded by NSF grant 0087210, by Ohio Board of Regents grant CAP-491, and by Youngstown State University.

Appendix A. Supplementary data

CCDC 667817 and 667818 contain the supplementary crystallographic data for **1d**$[PF_6]$ and **1f**$[PF_6]$. These data can be obtained free of charge via http://www.ccdc.cam.ac.uk/conts/retrieving.html, or from the Cambridge Crystallographic Data Centre, 12 Union Road, Cambridge CB2 1EZ, UK; fax: (+44) 1223-336-033; or e-mail: deposit@ccdc.cam.ac.uk.

References

[1] (a) P.G. Cozzi, Chem. Soc. Rev. 33 (2004) 410;;
(b) C.-M. Che, J.-S. Huang, Coord. Chem. Rev. 242 (2003) 97.
[2] (a) J. Song, Q. Shan, F. Xu, X. Lu, Tetrahedron 63 (2007) 5148;
(b) J. Cloete, S.F. Mapolie, J. Mol. Catal. A 243 (2006) 221.
[3] (a) J. Best, J.M. Wilson, H. Adams, L. Gonsalvi, M. Peruzzini, A. Haynes, Organometallics 26 (2007) 1960;
(b) P. Crochet, J. Gimeno, J. Borge, S. Garcia-Granda, New J. Chem. 27 (2003) 414.
[4] C.G. Hamaker, D.P. Halbach, Inorg. Chim. Acta 359 (2006) 846.
[5] D.P. Halbach, C.G. Hamaker, J. Organomet. Chem. 691 (2006) 3349.
[6] (a) L. Delaude, A. Demonceau, A.F. Noels, Curr. Org. Chem. 10 (2006) 203;
(b) K. Severin, Corr. Org. Chem. 10 (2006) 217.
[7] (a) C. Scolaro, A. Bergamo, L. Brescacin, R. Delfino, M. Cocchietto, G. Laurenczy, T.J. Geldbach, G. Sava, P.J. Dyson, J. Med. Chem. 48 (2005) 4161;
(b) A. Dorcier, P.J. Dyson, C. Gossens, U. Rothlisberger, R. Scopelliti, I. Tavernelli, Organometallics 24 (2005) 2114.
[8] (a) P. Štěpnička, J. Ludvík, J. Caniver, G. Süss-Fink, Inorg. Chim. Acta 359 (2006) 2369;
(b) J.-F. Mai, Y. Yamamoto, J. Organomet. Chem. 560 (1998) 223;
(c) V. Cadierno, P. Crochet, J. García-Alvarez, S.E. García-Garrido, J. Gimeno, J. Organomet. Chem. 663 (2002) 32.
[9] C.G. Hamaker, D.P. Halbach, Acta Cryst. E62 (2006) o2149.
[10] F.H. Allen, Acta Cryst. B58 (2002) 380.
[11] I.J. Bruno, J.C. Cole, P.R. Edgington, M.K. Kessler, C.F. Macrae, P. McCabe, J. Pearson, R. Taylor, Acta Cryst. B58 (2002) 389.
[12] Bruker, SAINT Integration Software for Single-Crystal Data Frames – *h*, *k*, *l*, Intensity; Bruker Advanced X-ray Solutions, Madison, Wisconsin, 1999.
[13] L.J. Farrugia, J. Appl. Cryst. 32 (1999) 837.
[14] M.C. Burla, M. Camalli, B. Carrozzini, G.L. Cascarano, C. Giacovazzo, G. Polidori, R. Spagna, J. Appl. Cryst. 36 (2003) 1103.
[15] G.M. Sheldrick, SHELX-97: Programs for Crystal Structure Analysis (Release 97-2), University of Göttingen, Germany, 1997.

Polyhedron 28 (2009) 2233–2239

Contents lists available at ScienceDirect

Polyhedron

journal homepage: www.elsevier.com/locate/poly

Templated growth of smart nanocomposite thin films: Hybrid aerosol assisted and atmospheric pressure chemical vapour deposition of vanadyl acetylacetonate, auric acid and tetraoctyl ammonium bromide

Manfredi Saeli [a], Russell Binions [b,*], Clara Piccirillo [b], Geoffrey Hyett [b], Ivan P. Parkin [b]

[a] Università degli Studi di Palermo, Dipartimento di Progetto e Costruzione Edilizia (DPCE), Viale delle Scienze 90128 Palermo, Italy
[b] Christopher Ingold Laboratories, Department of Chemistry, University College London, 20 Gordon Street, London WC1H 0AJ, United Kingdom

ARTICLE INFO

Article history:
Received 6 November 2008
Accepted 24 March 2009
Available online 31 March 2009

Keywords:
CVD
Nanocomposite
Thermochromism
Aerosol
Hybrid

ABSTRACT

Hybrid aerosol assisted and atmospheric pressure chemical vapour deposition methodology has been utilised to produce nanocomposite thin films of gold nanoparticles and vanadium dioxide from vanadyl acetylacetonate and auric acid. The addition of tetraoctyl ammonium bromide (TOAB) to the precursor solution gave control of the size and distribution of gold nanoparticles in the vanadium oxide matrix. These reactions led to vanadium dioxide films with reduced crystallite sizes and enhanced thermochromic properties. The films were analysed by X-ray diffraction, scanning electron microscopy and X-ray photoelectron spectroscopy. Their optical and thermochromic behaviour was also determined. This hybrid method shows great potential for the production of nanocomposite thin films with good physical properties.

Crown Copyright © 2009 Published by Elsevier Ltd. All rights reserved.

1. Introduction

The production and use of nanoparticles is a major research theme worldwide [1]. Many applications of these nanoparticles will rely on their incorporation into a host matrix. The production of a nanocomposite can change the physical properties of both the host matrix and the nanoparticles. Additionally the resulting nanocomposite serves both to immobilize the nanoparticles and to render them chemically inert. Much work has focused on the production of metallic nanoparticles incorporated into a semi-conductor matrix [1–8], this has led to improvements in photocatalysis [1,9,10], photoanodes [11], and various chromatic films [12,13].

Here we describe a one step hybrid chemical vapour deposition route for producing nanocomposite thin films. Gold nanoparticles are preformed in solution using tetraoctylammonium bromide as a surfactant in methanol and transported to the reaction chamber using an aerosol. A conventional atmospheric pressure chemical vapour deposition (APCVD) reaction is used to grow the semi-conductor matrix; in this case vanadium dioxide, at the same time ensuring that gold nanoparticles are encapsulated in the growing vanadium dioxide film.

Vanadium dioxide is a material that has shown potential for use as an intelligent glazing material [14,15]. The material has a metal to semiconductor transition (MST) where there is a structural change from a higher temperature rutile structure to a lower temperature monoclinic structure [16]. This structural transition results in a change in electrical conductivity and optical properties. The monoclinic phase is a semiconductor and generally transparent to solar radiation, whereas the rutile material is metallic and reflects a wide range of solar radiation. Work has been conducted in recent years to try and reduce the transition temperature of the vanadium dioxide MST by adding dopants [17,18], of which tungsten has been the most successful dopant reducing the MST by 20–25 °C per atom % [19].

In this work, we focus on using gold nanoparticles to improve the properties of vanadium dioxide films. Gold nanoparticles have a surface plasmon resonance that is strongly absorbing, the frequency of which is strongly dependent on the dielectric properties of the host matrix as well as the size and shape of the nanoparticles [20,21]. By using nanoparticles of the right size and shape, the properties of the resulting films can be tuned. The use of auric acid and colloidal gold suspensions used in aerosol assisted chemical vapour deposition (AACVD) to produce gold nanoparticle films have been reported [22,23]. However, the use of auric acid alone led to films with a wide nanoparticle size distribution [22]. It has been shown that the use of a coordinating surfactant controlled the size and shape of the deposited gold nanoparticles [23]. Indeed gold doped vanadium dioxide composites produced using reactive ion beam sputtering followed by annealing and laser ablation have received attention as fast optical switches [24,25]. Attempts to produce gold doped vanadium dioxide films from a single source

* Corresponding author. Tel.: +44 207 679 4658.
E-mail address: r.binions@ucl.ac.uk (R. Binions).

0277-5387/$ - see front matter Crown Copyright © 2009 Published by Elsevier Ltd. All rights reserved.
doi:10.1016/j.poly.2009.03.025

AACVD reaction have proved futile as there appears to be an adduct reaction on mixing solutions of vanadium and gold precursors [26]. There are no cheap and easily available gold precursors for use in APCVD, there is however potentially an abundance of precursors that can be used in AACVD as the precursor limitations of APCVD do not apply [27,28], indeed previous work has reported the use of auric acid [22,23].

This hybrid technique of combining aerosol assisted and atmospheric pressure gas streams [26] has advantages over other techniques for the deposition of nanocomposites; firstly it is highly flexible, a wide variety of semiconductor metal oxides are grown using APCVD, whilst AACVD has the potential to deliver any solution of preformed nanoparticles. Secondly CVD is industrially well known and has wide application in the microelectronics and glazing industry, it has a number of established advantages such as conformal coating and good substrate adherence.

Here we show that using the hybrid technique, high quality vanadium dioxide–gold nanocomposites can be made. The use of the surfactant tetraoctylammonium bromide (TOAB) in the film formation allowed for greater control of nanoparticles.

2. Experimental

A 98% nitrogen, 2% oxygen mixture was obtained from the British Oxygen Company (BOC) and used as supplied in the plain line. Nitrogen (99.99%) was obtained from BOC and used as supplied in the bubbler lines. Coatings were obtained on SiO_2 coated float glass. Combined AA/AP CVD experiments were conducted on 150 mm × 45 mm × 3 mm pieces of glass using a flat-bed cold-walled CVD reactor. The glass was cleaned prior to use by washing with petroleum ether (60–80 °C) and isopropanol and then dried in air. A graphite block containing a Whatman cartridge heater was used to heat the glass substrate. The temperature of the substrate was monitored by a Pt–Rh thermocouple. Independent thermocouple measurements indicated that temperature gradients of up to 50 °C cm^{-1} were observable at a substrate temperature of 600 °C across the surface of the glass. The rig was designed so that four independent gas lines could be used. All gas handling lines, regulators and flow valves were made of stainless steel and were 6.5 mm internal diameter except for the inlet to the mixing chamber and the exhaust line from the apparatus that were 13 mm in diameter. In these experiments three gas lines were used. Gases came directly from a cylinder and were preheated by passing along 2 m lengths of stainless steel tubing, which were curled and inserted inside a tube furnace. The temperatures of all the gas inlet lines were monitored by Pt–Rh thermocouples and Eurotherm heat controllers.

Vanadyl acetylacetonate (99.99%) was obtained from Aldrich and used without further purification and was placed into a stainless steel bubbler. The bubbler was heated to 175 °C by a heating jacket and vanadyl acetylacetonate introduced into the gas streams by passing hot nitrogen gas through the bubbler. Auric acid (40 mg, 0.117 mmol 99.9%, obtained from Aldrich and used without further purification) was dissolved in 25 ml methanol and placed into a glass flask. In experiments using TOAB, between 1.00 and 0.06 g was added to the reaction flask and stirred for 10 min prior to the deposition experiment. An aerosol was generated at room temperature by use of a PIFCO air humidifier. Nitrogen was passed through the aerosol mist, thus forcing the aerosol particles encapsulated with precursor into the heated reaction chamber.

The two components of the system were transported using stainless steel pipes 13 mm internal diameter respectively. The pipes were attached directly to the reaction chamber of the coater. Gas flows were adjusted using suitable regulators and flow controllers. The exhaust from the reactor was vented directly into the extraction system of a fume cupboard. This deposition setup has been described in more detail previously [26]. All of the apparatus was baked out with nitrogen at 150 °C for 30 min before use. Deposition experiments were conducted by heating the horizontal-bed reactor and the bubblers to the desired temperatures before diverting the nitrogen line through the bubbler and hence to the reactor. Deposition experiments were timed by use of a stopwatch and were conducted between 30 s and 30 min in order to vary the thickness of the samples. The maximum possible deposition temperature with this equipment was 600 °C. At the end of the deposition only nitrogen was allowed to flow over the glass substrate until the substrate was sufficiently cool to handle (~60 °C). Samples were handled and stored in air. Substrate temperature for deposition was kept constant at 525 °C as this has been found to be the optimal temperature to grow monoclinic vanadium dioxide thin films from vanadyl acetylacetonate. Due to the nature of the graphite heating block there are changes in thickness that correlate with the temperature gradient across the substrate however, a highly uniform area 2 cm × 5 cm in the middle of the substrate is always observed, it is this area that is referred to when discussing the uniformity of the films.

Electron microprobe analysis was obtained on a JEOL EMA and referenced against vanadium and oxygen standards. EDAX and WDAX were conducted using a Phillips XL30 ESEM instrument. SEM images were acquired on a Jeol 6301F field emission instrument. X-ray diffraction patterns were measured on a Bruker Gadds D8 diffractometer using monochromated (Cu $K\alpha_{1+2}$) radiation in the reflection mode using a glancing incident angle of 5°. Reflectance and transmission spectra were recorded between 300 and 2500 nm on a Perkin–Elmer Lambda 950 UV–Vis spectrometer. UV–Vis spectra were obtained using a Helios double beam instrument. Raman spectra were acquired on a Renishaw Raman system 1000 using a helium–neon laser of wavelength 632.8 nm. The Raman system was calibrated against the emission lines of neon. Transmittance-temperature studies were performed on a Perkin–Elmer 457 grating spectrometer set to 4000 cm^{-1}. An aluminium temperature cell controlled by RS resistive heaters, Eurotherm temperature controllers and k-type thermocouples were used to manipulate sample temperature. Sample temperature was measured using a k-type thermocouple taped directly onto the film surface. Film thickness was measured directly by scanning electron microscopy then correlated with EDAX and optical transmission data.

3. Results

Composite VO_2/Au nanoparticle films were grown by the use of hybrid aerosol assisted/atmospheric pressure CVD from [$HAuCl_4$] and tetraoctylammonium bromide (TOAB) in methanol (the aerosol component) and [$VO(acac)_2$] (the atmospheric pressure component). The films showed good surface coverage, uniformity and reproducibility. Film thickness could be easily varied by increasing or decreasing the time of deposition. In all cases at least the first 75% of the substrate is covered, similar to that observed previously with VO_2 films produced from the APCVD reaction of vanadyl acetylacetonate and with other APCVD systems such as those that produce metal oxide and metal phosphide materials [29–33]. Similarly there are changes in thickness that correlate with the temperature gradient across the substrate surface as seen previously [29–33] and a highly uniform area 2 cm × 5 cm in the middle of the substrate. The colour of the films (Table 1) could be altered substantially with a range of blues and greens being produced in contrast to the yellow/brown colour normally associated with monoclinic vanadium dioxide; this is attributed to the inclusion of gold nanoparticles in the VO_2 matrix. UV/Vis absorbance

Table 1
Summary of experimental conditions and chemical analysis. Flow conditions were constant for all experiments; Plain flow = 2 L min^{-1}, $VO(acac)_2$ Bubler flow = 4 L min^{-1} and Aerosol flow = 1 L min^{-1}.

Sample	Contents of AACVD flask	EDAX/WDAX/XRD phase	Au/V ratio	λ max in visible transmission/nm	λ max in visible reflection/nm
1	40 mg $HAuCl_4$ 1.00 g TOAB	VO_2 (m) + Au	0.52	493	495
2	40 mg $HAuCl_4$ 0.50 g TOAB	VO_2 (m) + Au	0.15	493	530
3	40 mg $HAuCl_4$ 0.25 g TOAB	VO_2 (m) + Au	0.96	566	559
4	40 mg $HAuCl_4$ 0.12 g TOAB	VO_2 (m) + Au	0.09	566	545
5	40 mg $HAuCl_4$ 0.06 g TOAB	VO_2 (m) + Au	0.29	561	596
6	40 mg $HAuCl_4$ No TOAB	VO_2 (m) + Au	0.35	570	591

spectroscopy of the gold doped films indicates that a plasmon resonance band is present; however this is very broad, ~100 nm, due to significant variation of gold nanoparticle size (Fig. 1). The strength of the band correlates strongly with the gold to vanadium ratio in the films. The addition of TOAB into the precursor flask causes a significant shift in the SPR centre (Fig. 1).

The films from the hybrid CVD reaction were also more adherent than films of vanadium dioxide or gold produced using AACVD [22,23]; they passed the Scotch tape test and could not be wiped off with a piece of towelling. The films could however, be marked with a brass or steel stylus similar to films of VO_2 produced previously [19,34,35]. The films were found to be electrically insulating

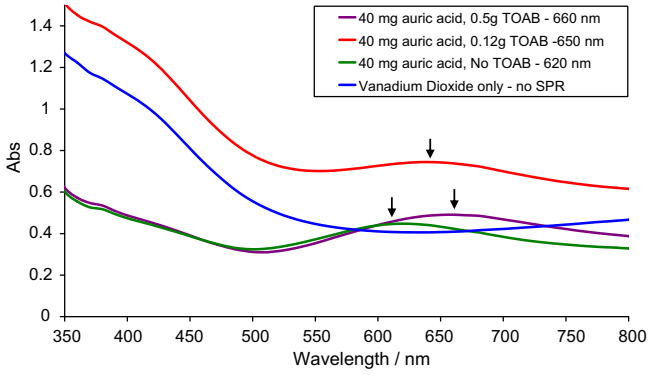


Fig. 1. UV/Vis spectroscopy and surface plasmon centres of typical samples of a VO_2/Au nanoparticle film produced using the hybrid AA/AP CVD methodology grown with TOAB and without TOAB. The arrows mark the position of the surface plasmon band resonance centre. The absorbance spectrum of a VO_2 film is included for comparison.

suggesting that the amount of gold in the films was not enough to exceed the percolation limit. Details of experimental conditions are given in Table 1.

Scanning electron microscopy (Fig. 2) of the samples indicates an island growth morphology. Typically for samples produced with TOAB (Samples 1–5) a smaller average island size of 75 nm (Fig. 2A) is seen compared with 150 nm (Fig. 2B) for those produced without.

Analysis with energy dispersive analysis of X-rays indicated that the films contained gold and vanadium (summarised in Table 1) and no contaminant, at least to the limit of detection of the methodology (around 1/2 atom % depending on the element).

Backscattered electron imaging (Fig. 3) and EDAX spot analysis indicated that gold is found amongst the crystallites on the surface, rather than segregating as independent gold crystallites as seen as a result of the sol gel process [36]. There were stark differences between the gold crystallites grown with TOAB (Fig. 3A) and those grown without (Fig. 3B). The gold crystallites in films grown with TOAB formed spherical agglomerates with a diameter in the region of 70 ± 10 nm. The gold crystallites in films grown without TOAB were very different; the crystallite agglomerates were smaller, around 40 nm diameter, and highly interconnected with no particular shape.

X-ray diffraction analysis (Fig. 4.) indicates that in all cases cubic gold and monoclinic vanadium dioxide are formed, though the films were not particularly crystalline. The films were quite thin and a large broad hump centred at 24 2θ is seen from the amorphous glass substrate. The gold crystallite size was evaluated using Scherrer equation, it was found that for samples produced with TOAB the crystallite size was 13 ± 3 nm in diameter, where as crystallites produced without the use of TOAB were smaller, measuring 8 ± 2 nm in diameter. Annealing in nitrogen at 500 °C for 2 h did

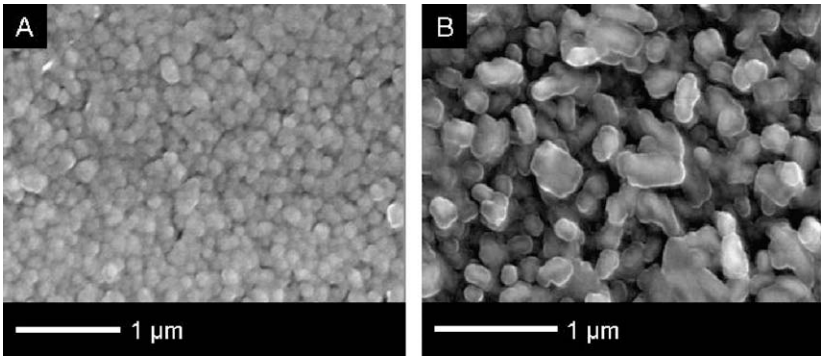


Fig. 2. Secondary electron scanning electron microscopy pictures of typical samples of a VO_2/Au nanoparticle film produced using the hybrid AA/AP CVD methodology grown (A) with TOAB and (B) without TOAB.

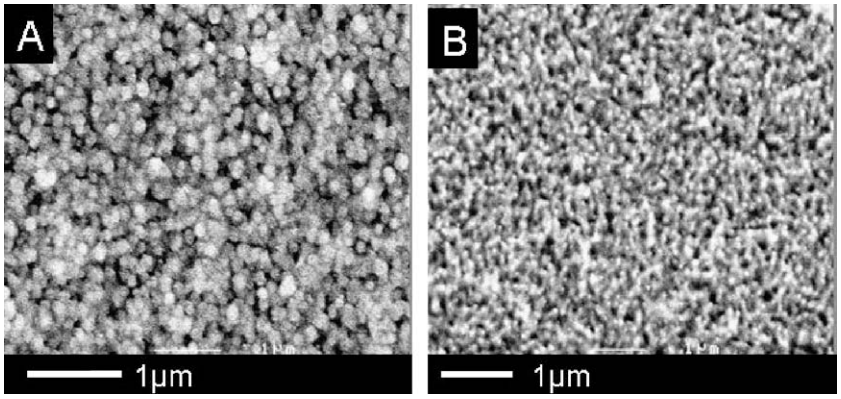


Fig. 3. Back scattered secondary electron scanning electron microscopy of typical samples of a VO_2/Au nanoparticle film produced using the hybrid AA/AP CVD methodology grown (A) with TOAB and (B) without TOAB.

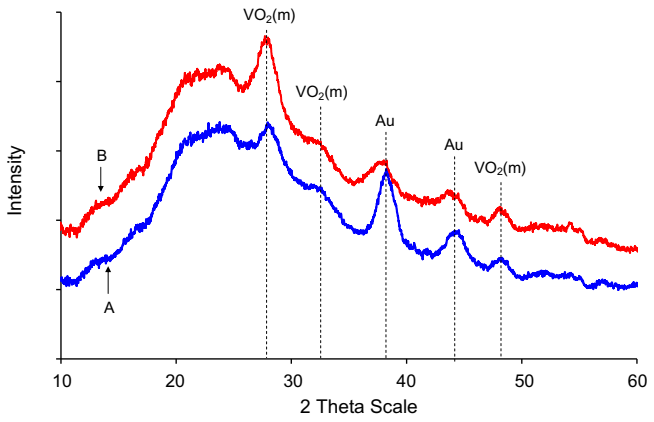


Fig. 4. X-ray Diffraction patterns of typical samples of a VO_2/Au nanoparticle film produced using the hybrid AA/AP CVD methodology grown (A) with TOAB and (B) without TOAB.

not improve the crystallinity of the VO_2 phase in the films, however peaks relating to V_2O_5 appeared in the X-ray diffraction pattern. Indeed in some cases there is some evidence of the formation of V_2O_5 in the as produced samples. This is not entirely unexpected as previous work on vanadium dioxide by APCVD has seen a similar phenomenon and has shown that surface V_2O_5 does not effect the thermochromic behaviour of the bulk film [19,34,35]. X-ray photoelectron analysis (XPS, Fig. 5A and C.) of the sample surface suggests a variety of vanadium environments due to the broadness and asymmetry of the peaks, we believe V_2O_5 to be present only at the surface; indeed, on etching only a single vanadium environment (V_{2p} at 516.8 and 523.4 eV) is observed consistent with vanadium dioxide. XPS shows that gold is found in a single metallic environment, Au_{4f} 83.6 and 87.2 eV (Fig. 5B and D), this indicates several things: there are no other detectable gold compounds present in the film, there is no un-reacted precursor on the film surface and indicates that the gold is present only as gold nanoparticles on the surface and in the bulk of the host film matrix. XPS and Raman spectroscopy were used to evaluate carbon contamination in the films; insignificant amounts of carbon, less than 1 atom%, could be detected in the bulk of the films using XPS. More carbon was detected on the surface of the films using XPS but is most likely from an external source. Raman spectroscopy produced no signal, specifically no signal from graphitic carbon (at 1000 cm^{-1}) was observed suggesting that the level of carbon is below the detection limit of this method and that the films are poor Raman scatterers possibly due to surface morphology effects.

As seen with un-doped and tungsten doped samples prepared by CVD [19,34,35] a large change in transmission is observable at 2500 nm (Fig. 6), typically 35–40% comparable with previous literature values [19,34,35]. The reflectance spectrum is different (Fig. 6) there is only a small change of around 10% on undergoing the transition. This is similar to previous examples of gold doped VO_2 films produced using this hybrid methodology [26].

All of the films show thermochromic behaviour with reduced transition temperatures compared to un-doped VO_2 single crystals (typically 66–68 °C) [16] and compared to un-doped VO_2 thin films (50–66 °C depending on the growth conditions) [35]. Typically the hysteresis width (Fig. 7) of gold doped vanadium dioxide thin films is in the range of 15–20 °C. The films produced with TOAB in (Samples 1–5) had lower transition temperatures, typically 42–45 °C, than the films without TOAB (Sample 6) where the transition temperature was in the region 50–54 °C.

4. Discussion

The hybrid aerosol assisted atmospheric pressure chemical vapour deposition reaction of vanadyl acetylacetonate and auric acid lead to the production of thin films of gold nanoparticle doped monoclinic vanadium dioxide thin films. Addition of TOAB to the precursor solution led to significant changes in the functional properties and colour of the deposited films.

The addition of gold nanoparticles into the film lead to the observation of a surface plasmon resonance band. The position of this band determines the overall colour and is dependent upon three factors: the inter-particle distance, particle size and the refractive index of the host matrix [20,21]. The refractive index of the host matrix is assumed constant between samples so the only factors that effect the surface plasmon resonance (SPR) are the size and distance between gold nanoparticles.

For films grown without TOAB the SPR centre is 620 nm, the use of 0.5 g or more TOAB in the reaction moves the SPR centre to 660 nm. Using less than 0.5 g TOAB in the reaction causes a smaller change in the SPR centre. The more TOAB used in the reaction the more profound the effect; the addition of smaller amounts of TOAB, 0.06–0.25 g, leads to a shift in the visible reflection peak from 591 to 559 nm but no significant change in the visible transmission peak. Samples produced with a larger amount of TOAB, 0.5 or 1.00 g, had profound changes in both the visible transmission and reflectance peaks and appeared blue as both the transmission and reflection peaks were shifted to ~495 nm. This is because as more gold nanoparticles agglomerates are templated (i.e. with increasing levels of TOAB) the agglomerates are more discreet and regular in size and shape (Fig. 3) and the effect of the SPR band

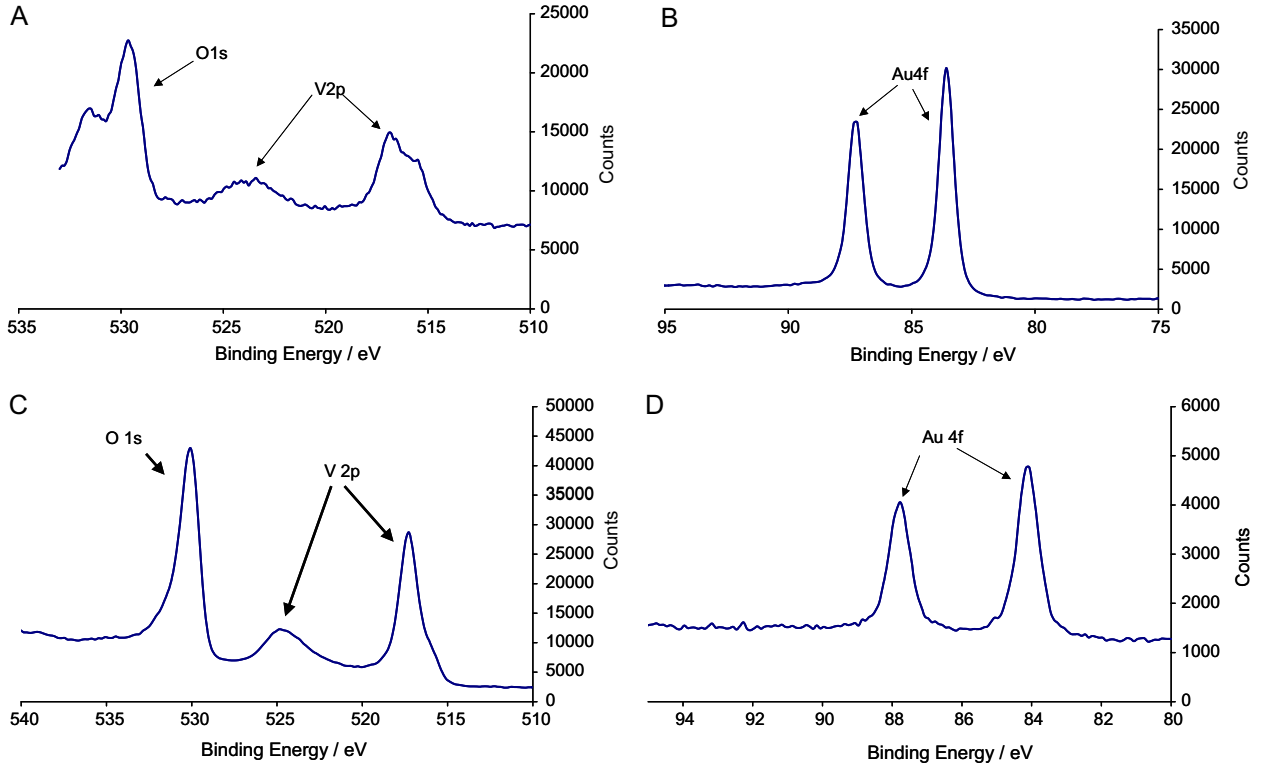


Fig. 5. X-Ray Photoelectron Spectroscopy of typical samples of a VO_2/Au nanoparticle film produced using the hybrid AA/AP CVD methodology grown (A) with TOAB vanadium and oxygen region, (B) with TOAB gold region, (C) without TOAB vanadium and oxygen region and (D) without TOAB gold region.

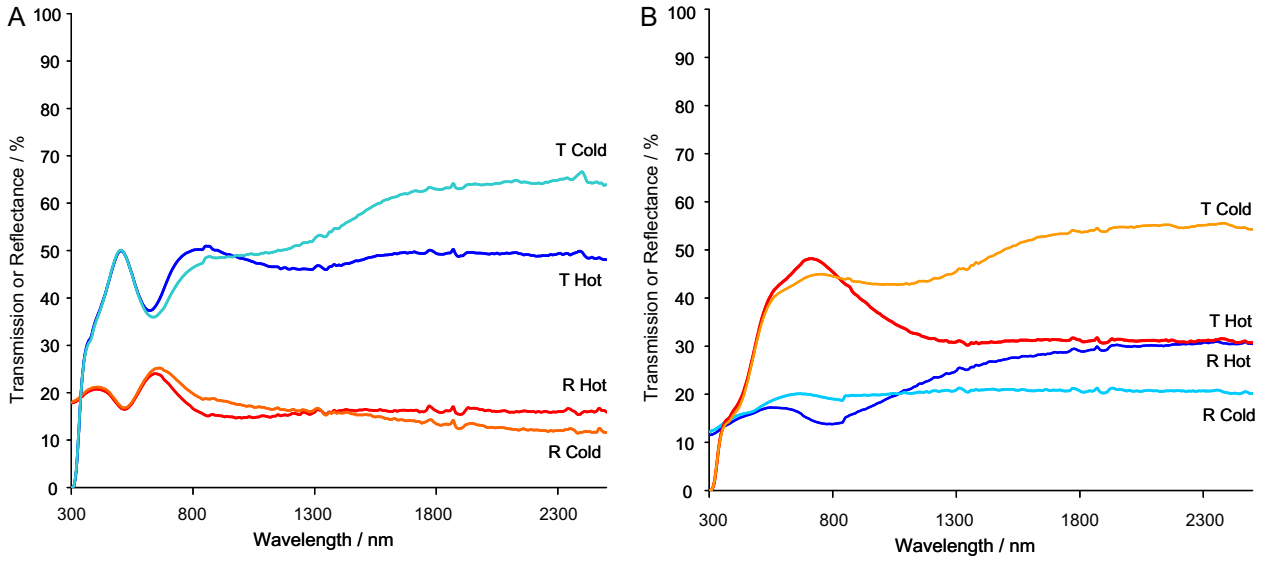


Fig. 6. Transmission and Reflection Data for typical samples of a VO_2/Au nanoparticle film produced using the hybrid AA/AP CVD methodology grown (A) with TOAB and (B) without TOAB.

is stronger. Where no TOAB or lower levels of TOAB (less than 0.25 g) were used, nanoparticle agglomerates had a wide variety of shapes and sizes and were more heavily interconnected; in these instances the effect of the SPR band is weak and there is no significant change in the colour of the films.

As mentioned in the results section the microstructure of the films is significantly altered due to the use of TOAB in the reaction; in depositions without TOAB the island size of vanadium dioxide particles is around 150 nm and there is significant interconnectivity between agglomerates (Fig. 2B), similar to that previously seen [35], whilst with the use of TOAB the agglomerate size is reduced to 75 nm and leads to a more discreet, rounded morphology. A similar effect is seen when observing the gold nanoparticles in the films using backscattered electron imaging (Fig. 3). The films produced without TOAB show a variety of gold nanoparticle shapes and sizes, significant but random agglomeration and interconnectivity. The films produced using TOAB are very different, the gold nanoparticle agglomerates are uniform in shape and size (~75 nm diameter spheres). This is due to a surfactant effect caused by the TOAB that has been seen previously [23]. It is less

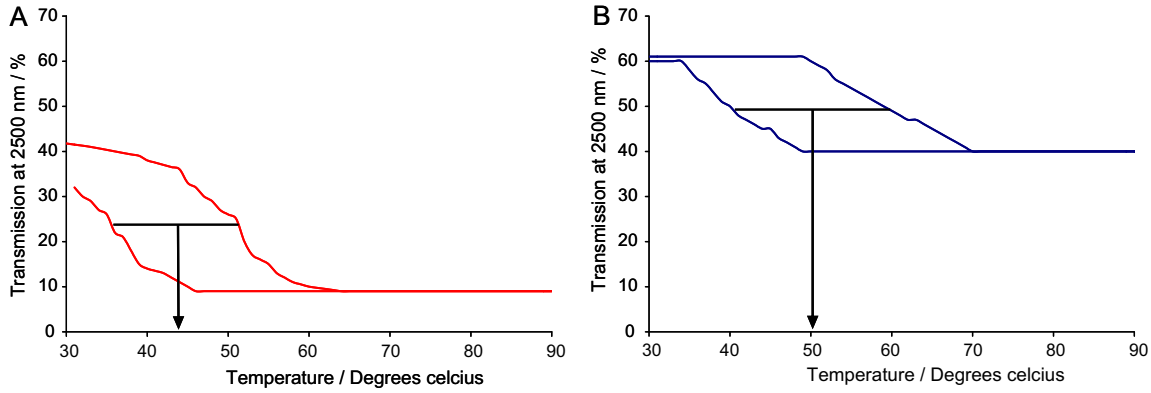


Fig. 7. Hysteresis behaviour of typical samples of a VO_2/Au nanoparticle film produced using the hybrid AA/AP CVD methodology grown of (A) with TOAB and (B) without TOAB.

expected that the use of TOAB would cause a change in the overall film morphology between films grown under otherwise identical conditions.

In all cases a large change in transmission is observable at 2500 nm (Fig. 6), typically 30–40% comparable with previous literature values [19,34,35]. The reflectance spectra show a smaller change of 10–15% (Fig. 6) on undergoing the transition. This is attributable to the metallic nature of the gold nanoparticles and the rough looking film surface (Fig. 2). Un-doped or tungsten doped films of monoclinic vanadium dioxide do not have as significant a metallic contribution to the reflectance and the change at 2500 nm on undergoing the MST is around 25% [19,20,29,34,35].

All of the films show thermochromic behaviour with reduced transition temperatures. Typically the hysteresis width (Fig. 7) of gold doped vanadium dioxide thin films is relatively wide in the range of 15–20 °C compared to 10 °C as seen with some tungsten doped samples produced by APCVD [19,34,35] and 10–15 °C seen for films produced by Sol–Gel methodology [36], though this is comparable to films of this type produced previously using the hybrid method [26]. The hysteresis width seemed to be independent of the amount of gold present in the film. Ideally the hysteresis width would be as narrow as possible in order to maximise the energy saving effect the coating would have. Hysteresis width has been attributed to several factors such as a variety of grain size [37] and or crystallographic orientation [35]. Indeed the transition temperature is reduced to ~50 °C for samples grown without the use of TOAB and to as low as 42 °C with films grown with TOAB, which is independent of the amount of gold in the films. It is likely that this reduction for the films grown without TOAB is caused by strain as a result of preferential orientation as observed previously [26,35], although this is difficult to quantify as the films are thin and poorly crystalline. The additional reduction of the transition temperature to 42 °C seen in films produced by TOAB is harder to explain. The average island size is smaller and agglomeration more, this may lead to higher strain in the films though this is difficult to evaluate in the absence of quality X-ray diffraction data. TOAB has been used previously to template gold nanoparticles in AACVD [23] causing a surfactant effect in solution before aerosol generation. The effect was to direct the size and shape of the nanoparticles. This is occurring in this instance as well and it may be that the uniform size of templated gold crystallites in the films produced with TOAB help lead to this additional reduction in transition temperature.

The use of TOAB in hybrid aerosol assisted atmospheric pressure chemical vapour deposition reactions leads to several interesting effects. There is a change in morphology of the overall film that is unexpected and can be potentially exploited to enhance the properties of the film. The gold nanoparticle agglomerates are effectively templated; we anticipate that the use of a different surfactant will lead to different size and shape nanoparticle agglomerates. It also seems that the vanadium dioxide islands are templated; to test this some depositions were performed with TOAB but no gold in the precursor flask. The resultant morphologies were very similar to those obtained here. The use of TOAB also leads to an additional reduction on the thermochromic transition temperature, this is attributed to the introduction of additional strain in the film caused by this template effect.

5. Conclusion

The use of hybrid aerosol assisted and atmospheric pressure chemical vapour deposition methodology has afforded nanocomposite thin films of a vanadium dioxide matrix hosting gold nanoparticles. This methodology is a one step process using a solution of preformed nanoparticles and shows great promise for producing other nanocomposites. The use of TOAB in these reactions adds a further level of control over the reaction product than has been previously seen using this hybrid methodology. Unexpectedly the TOAB was found to template not just the growth of gold nanoparticles incorporated in the film, but the growth of the film itself. This introduced additional strain into the film and caused a reduction in the thermochromic transition temperature.

Acknowledgments

This research was supported financially as part of the EU project TERMOGLAZE. Pilkington glass are thanked for the provision of glass substrates. IPP thanks the Wolfson trust for a merit award. RB thanks the Royal Society for a Dorothy Hodgkin fellowship. Mr. Kevin Reeves is thanked for invaluable assistance with electron microscopy. MS thanks the University of Palermo “Esperto di Nanotecnologie per i Beni Culturali” for funding.

References

[1] V. Subramanian, E.E. Wolf, P.V. Kamat, J. Am. Chem. Soc. 126 (2004) 4943.
[2] T. Ung, L.M. Liz-Marzan, P. Mulvaney, Colloids Surf. A: Physicochem. Eng. Aspects 202 (2002) 119.
[3] X. Xu, M. Stevens, M.B. Cortie, Chem. Mater. 16 (2004) 2259.
[4] Z. Liu, H. Wang, H. Li, X. Wang, Appl. Phys. Lett. 72 (1998) 1823.
[5] T. Mokari, H. Sertchook, A. Aharoni, Y. Ebenstein, D. Avnir, U. Banin, Chem. Mater. 17 (2005) 258.
[6] K. Naoi, Y. Ohko, T. Tatsuma, J. Am. Chem. Soc. 126 (2004) 3664.
[7] C. Yang, M. Kalwei, F. Schuth, K. Chao, Appl. Catal., A: Gen. 254 (2003) 289.
[8] M. Lee, L. Chae, K.C. Lee, Nanostruct. Mater. 11 (1999) 195.

[9] D. Lahiri, V. Subramanian, T. Shibata, E.E. Wolf, B.A. Bunker, P.V. Kamat, J. Appl. Phys. 93 (2003) 2575.
[10] S. Schimpf, M. Lucas, C. Mohr, U. Rodemerck, A. Bruckne, J. Radnik, H. Hofmeister, P. Claus, Catal. Today 72 (2002) 63.
[11] Y. Hida, H. Kozuka, Thin Solid Films 476 (2005) 264.
[12] T. He, Y. Ma, Y. Cao, W. Yang, J. Yao, Phys. Chem. Chem. Phys. 4 (2002) 1637.
[13] T. He, Y. Ma, Y. Cao, W. Yang, J. Yao, J. Electroanal. Chem. 514 (2001) 129.
[14] C.G. Granqvist, Thin Solid Films 193 (1990) 730.
[15] C.G. Granqvist, Adv. Mater. 15 (2003) 1789.
[16] K.D. Rogers, Powder Diffract. 8 (1993) 240.
[17] T.E. Phillips, R.A. Murray, T.D. Poelher, Mater. Res. Bull. 22 (1997) 113.
[18] F. Beteille, R. Morineau, J. Livage, M. Nagano, Mater. Res. Bull. 32 (1997) 1109.
[19] T.D. Manning, I.P. Parkin, M.E. Pemble, D.W. Sheel, D. Vernardou, Chem. Mater. 16 (2004) 744.
[20] T. Ung, L.M. Liz-Marzan, P. Mulvaney, Colloids Surf. A: Physicochem. Eng. Aspects 202 (2002) 119.
[21] S. Link, M. El-Sayed, in: V.I. Klimnov (Ed.), Semiconductor and Metal Nanocrystals, Marcel Dekker, New York, 2004, p. 45.
[22] R.G. Palgrave, I.P. Parkin, J. Am. Chem. Soc. 128 (2006) 1587.
[23] R.G. Palgrave, I.P. Parkin, Chem. Mater. 19 (2007) 4639.
[24] M. Maaza, O. Nemravoui, C. Sella, A.C. Beye, Gold Bull. 38 (2005) 100.
[25] S. Chen, H. Ma, X. Yi, H. Wang, X. Tao, M. Chem, X. Li, C. Ke, Infrared Phys. Technol. 45 (2004) 239.
[26] R. Binions, I.P. Parkin, C. Piccirillo, C.J. Carmalt, R.G. Palgrave, Chem. Vap. Deposition 1–2 (2008) 33.
[27] W.B. Cross, I.P. Parkin, Chem. Commun. 14 (2003) 1696.
[28] R. Binions, C.J. Carmalt, I.P. Parkin, Thin Solid Films 416 (2004) 9469.
[29] R. Binions, C.S. Blackman, C.J. Carmalt, I.P. Parkin, S.A. O'Neill, K.C. Molloy, L. Apostolico, Polyhedron 21 (2002) 1943.
[30] R. Binions, C.J. Carmalt, I.P. Parkin, Polyhedron 22 (2003) 1683.
[31] R. Binions, C.J. Carmalt, I.P. Parkin, Polyhedron 25 (2006) 3032.
[32] R. Binions, I.P. Parkin, Meas. Sci. Technol. 18 (2007) 190.
[33] R. Binions, C.J. Carmalt, I.P. Parkin, Chem. Mater. 16 (2004) 2489.
[34] T.D. Manning, I.P. Parkin, J. Mater. Chem. 14 (2004) 2554.
[35] R. Binions, C. Piccirillo, G. Hyett, I.P. Parkin, J. Mater. Chem. 17 (2007) 4652.
[36] E. Cavanna, J.P. Segaud, J. Livage, Mater. Res. Bull. 34 (1999) 167.
[37] F. Beleille, L. Mazerolles, J. Livage, Mater. Res. Bull. 34 (1999) 2177.

Polyhedron 28 (2009) 2240–2248

Contents lists available at ScienceDirect

Polyhedron

journal homepage: www.elsevier.com/locate/poly

Electrochemical synthesis and characterization of zinc(II) complexes with pyrimidine-2-thionato ligands and their adducts with N,N donors

Antonio Rodríguez [a,*], Antonio Sousa-Pedrares [b], José A. García-Vázquez [b], Jaime Romero [b], Antonio Sousa [b]

[a] Departamento de Química Fundamental, Universidade da Coruña, 15071-A Coruña, Spain
[b] Departamento de Química Inorgánica, Universidad de Santiago de Compostela, 15782-Santiago de Compostela, Spain

ARTICLE INFO

Article history:
Received 30 October 2008
Accepted 27 March 2009
Available online 5 April 2009

Keywords:
Zinc
Electrochemistry
S ligands
Heterocycles

ABSTRACT

Zinc complexes with pyrimidine-2-thionato ligands with the general formula $[Zn(RpymS)_2]$ can be easily obtained by electrochemical oxidation of a zinc anode in a cell containing an acetonitrile solution of the appropriate thione (RpymSH, R = 4,6-Me_2,5-Et; 4-CF_3 and 4,6-CF_3,Me). When 2,2′-bipyridine (bipy) or 1,10-phenanthroline (phen) were added to the cell, the corresponding adducts $[Zn(RpymS)_2L]$ were also obtained (L = bipy, phen). All of the compounds have been characterized by microanalysis, mass spectrometry, IR spectroscopy and, for compounds that were sufficiently soluble, by ^1H and ^{13}C NMR spectroscopy. The compounds $[Zn(4,6\text{-}Me_2,5\text{-}EtpymS)_2(MeOH)]$ (**4**), $[Zn(4\text{-}CF_3pymS)_2(phen)]$ (**7**) and $[Zn(4,6\text{-}CF_3,MepymS)_2(bipy)]$ (**9**) were also characterized by X-ray diffraction. The structures of all of these complexes consist of discrete molecules. In complex **4**, the pyrimidine-2-thionato acts as an S,N bidentate chelating ligand. The coordination number for Zn is five and the fifth position is occupied by an oxygen atom from a methanol molecule. In **7** and **9**, the coordination number for the metal centre is four. In these cases the thionato ligands show a monodentate behaviour, using the exocyclic sulfur to bind the zinc atom.

© 2009 Elsevier Ltd. All rights reserved.

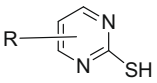
1. Introduction

Much of the interest in Zn–sulfur chemistry results from the potential relevance of these compounds in biological systems. Zinc complexes with N,S donors can be used as models for the study of metalloproteins and metalloenzymes [1]. In fact, the molecular structure of liver alcohol dehydrogenase (LADH) includes zinc atoms coordinated by two cysteine thiolates, a hystidine nitrogen and a water molecule [2]. In LADH, the catalytic cycle is initiated by displacement of one oxygen donor ligand molecule (water) by another (the alcohol substrate), which transiently binds to the zinc centre in LADH prior to displacement [3]. It is also well known that several alcohol dehydrogenases and thiolate alkylating enzymes contain the unusual NS_2ZnX coordination, where N represents a hystidine molecule, S a cysteinate group and X the catalytic site [4]. In the same way, many metabolic processes involve heterocyclic thiones, which have been known to play an important role in these reactions (e.g. 6-amino-2-thiouracil [5] exhibits antiviral and chemotherapeutic activity), and such activity is enhanced when they are administrated as metal complexes [6,7]. Moreover, thionato complexes derived from pyrimidine have been proposed as new chemotherapy agents [8–10] and the capability of the heterocyclic amines to act as carrier moieties [11,12] in order to react with plasma proteins led to increased interest in their metal complexes. This fact is consistent with the structural requirements for cytotoxic activity. In many cases, it seems probable that complex formation is implicated in the biological action of these pyrimidine derivatives [13]. The study of the interaction between metal ions and pyrimidine derivatives could provide a great deal of information related to the interactions of these metals with nucleic acids constituents [14]. In fact, it has been proposed that Zn(II) complexes could be directly involved in the addition of a mononucleotide to the free end of a DNA molecule [15].

Zinc complexes with ligands containing the thioamide group have also applications in many other fields and bis(N-oxopyridine-2-thionato)zinc(II), commonly known as zinc pyrithione, is an effective antifungal agent and is used as the active component of some antidandruff shampoo products [16]. Moreover, although the usual mode of binding for thioamides involves the formation of four-membered chelate rings through sulfur and nitrogen coordination [17], pyrimidine thiones and the corresponding thionatos have the potential to bind the metal ion by coordination with sulfur, nitrogen or a combination of the two [18–21]; these bindings could leave some potential donor atoms free and those positions would enhance the biological activity. When both sulfur and nitrogen atoms bind the metal centre (zinc), the N–Zn bond seems to be stronger than the S–Zn bond [22].

* Corresponding author. Tel.: +34 81 167000; fax: +34 81 167065.
E-mail address: amrodriguezc@udc.es (A. Rodríguez).

0277-5387/$ - see front matter © 2009 Elsevier Ltd. All rights reserved.
doi:10.1016/j.poly.2009.03.029



R = 4,6-Me_2,5-Et; 4-CF_3 ; 4,6-CF_3,Me

Scheme 1.

As part of our continued interest in the coordination chemistry of heterocyclic thione compounds, we report here the synthesis and characterization of zinc complexes with several pyrimidine-2-thionato ligands (Scheme 1). Ligands of this type are amongst the most versatile and unique in their coordination form [23], yielding complexes with unusual geometries, variable nuclearities and great structural diversity [21,24]. Moreover, the presence in these ligands of different substituents allows the possibility of investigating the influence of the nature and location of the substituents in the heterocyclic ring on the coordinative behaviour of these ligands and on the structure of the corresponding complexes. All of the compounds were obtained by using an electrochemical procedure that involves the anodic oxidation of a zinc foil in a solution of the corresponding ligand. For the synthesis of the heteroleptic complexes, 2,2′-bipyridine (bipy) or 1,10-phenanthroline (phen) were added to the cell solution.

2. Experimental

2.1. Materials and characterization

1,1,1-Trifluoro-2,4-pentanedione, thiourea, 3-ethyl-2,4-pentanedione, 1,1,1-trifluoroacetone, benzaldehyde, 4-trifluoromethylpyrimidine-2-thione; 1,10-phenanthroline and 2,2′-bipyridine are commercial products and were used as supplied. Zinc was used as a foil and washed with hydrochloric acid and brushed prior to use.

Elemental analyses were performed with a Carlo–Erba EA microanalyser. IR spectra were recorded as KBr mulls on a Bruker IFS-66 V Spectrophotometer. ^{1}H and ^{13}C NMR spectra were recorded on a Bruker AMX 300 MHz instrument with $CDCl_3$ or [D_6] DMSO as solvent. Chemical shifts are given in relative to TMS as the internal standard. The mass spectra (FAB) were recorded on a Micromass Autospec spectrometer, with 3-nitrobenzyl alcohol as the matrix material.

2.2. Synthesis of [4,6-Me_2,5-EtpymSH] (**1**)

This ligand was prepared by using a synthetic route previously reported for another pyrimidine-2-thiones [25]. 3-Ethyl-2,4-pentanedione (8.92 g, 0.069 mol, 9.35 mL) was dissolved in ethanol (70 mL) and concentrated hydrochloric acid (10 mL) was added at room temperature. The mixture was stirred under argon for 30 min and a solution of thiourea (8.47 g, 0.11 mol, 1.6 equiv.) in ethanol (150 mL) was added dropwise by cannula. This mixture was heated under reflux for 24 h.

The solvent was removed by vacuum distillation and the solid was treated with 2 M NaOH (150 mL). The mixture was filtered and the solution was acidified to pH 6 with 2 M H_2SO_4 at low temperature. A yellow solid was obtained and was filtered off. This product was recrystallized from $CHCl_3$ (Yield: 6.928 g; 59.21%). *Anal.* Calc. for $C_8H_{12}N_2S$ (168.26): C, 57.11; N, 16.65; H, 7.19; S, 19.06. Found: C, 57.113; N, 16.78; H, 7.36; S, 19.04%. IR (KBr/cm^{-1}): 3100–3200 (m, br); 1650 (s), 1610 (s), 1580 (w), 1559 (m), 1450 (m), 1430 (w), 1420 (w), 1380 (w), 1350 (w), 1320 (s), 1300 (w), 1280 (w), 1220 (m), 1200 (m), 1180 (w), 1160 (m), 1150 (m), 1090 (w), 1060 (w), 1020 (m), 990 (w), 970 (m), 940 (w), 930 (w), 920 (w), 850 (w), 840 (w), 820 (w), 770 (m), 680 (m), 660 (m), 640 (w), 620 (w), 590 (w), 580 (w), 560 (w), 490 (w), 460 (m), 380 (m). ^{1}H NMR (300 MHz, $CDCl_3$): δ = 13.00 (s, 1 H, NH); 1.07 (t. 3H, H_9); 2.44 (s, 3H, C_7/$C_{7'}$) 2. 52 (q, 2H, H_8) ppm. ^{13}C NMR (300 MHz, $CDCl_3$): δ = 171.7 (s, C_2); 165.7 (s, C_4); 165. 6 (s, C_6); 124 (s, C_5); 13.35 (s, C_7); 13.29 ($C_{7'}$); 20.6 (s, C_8); 1.43 (s, C_9) ppm. MS m/z = 169 (M^+); 335.2 (M_2^+).

2.3. Synthesis of [4,6-CF_3MepymSH] (**2**)

A slightly different method was used for the synthesis of this ligand; it was obtained by direct reaction between thiourea (2.428 g, 32 mmol) and 1,1,1-trifluoro-2,4-pentanedione (5 g, 32 mmol) in ethanol in the presence of concentrated hydrochloric acid (1 mL) as a catalyst. The mixture was heated under reflux for 2 h and the resulting dusty yellow solid was filtered off (Yield: 4.45 g; 71.8%). *Anal.* Calc. for $C_6H_5F_3N_2S$ (194.17): C, 37.11; H, 2.60; N, 14.43; S, 16.51. Found: C, 36.89; H, 2.60; N, 15.26; S, 16.08%. IR (KBr/cm^{-1}): 3100–3200 (m, br), 1615 (vs), 1590 (vs), 1440 (m), 1350 (vs), 1320 (w), 1200 (s, br), 1130 (m), 1100 (m), 1030 (w), 970 (s), 920 (m), 860 (w), 850 (m), 705 (w), 660 (w), 595 (w), 530 (m), 510 (w), 570 (m), 450 (m), 370 (w) cm^{-1}. ^{1}H NMR (300 MHz [D_6] DMSO): δ = 14.40 (s, 1 H, NH), 7.19 (s, 1 H, H_5), 2.39 (s, 3H, CH_3). ^{13}C NMR (300 MHz [D_6] DMSO) δ = 181.00 and 172.13 (s, C_2); 155.86 and 153.72 (q $^2J_{13C-19F}$ = 35 Hz, C_4); 104.89 (s, C_5); 163.61 (s, C_6); 119.27 and 119.67 (q, $^1J_{13C-19F}$ = 275 Hz, CF_3); 23.45 and 18.46 (s, CH_3) ppm. MS (FAB): m/z = 194 (M^+).

2.4. Electrochemical synthesis

The cells consisted of zinc foil (anode) and a platinum wire (cathode) in contact with the thione solution in acetonitrile. A small amount of tetraethylammonium perchlorate acted as an electrolyte. The cell can be summarized as $M_{(+)}/CH_3CN$ + RpymSH + L′/$Pt_{(-)}$. All of the syntheses were carried out at room temperature and the current intensity was kept at 10 mA. In all of the reactions hydrogen was evolved at the cathode and the yellow or orange colour of solutions faded. At the end of the reactions the solids were isolated by filtration.

Caution: Although no problem was encountered in this work, all perchlorate compounds are potentially explosive and should be handled in small quantities and with great care!

2.4.1. Synthesis of [Zn(4,6-Me_2,5-EtpymS)$_2$](H_2O) (**3**)

The electrolysis of a solution of 4,6-Me_2,5-EtpymSH (150 mg, 0.89 mmol) gave a pale yellow solution and no solid was obtained after filtration. A total of 29 mg (0.89 mmol) of zinc was dissolved from the anode. After the evaporation of the solvent at room temperature a dusty pale yellow solid was obtained (Yield: 109 mg; 44%), which was identified as [Zn(4,6-Me_2,5-EtpymS)$_2$](H_2O). *Anal.* Calc. for $C_{16}H_{24}N_4S_2ZnO$ (416.07): C, 45.99; N, 13.41; H, 5.79; S, 15.34. Found: C, 46.01; N, 13.77; H, 6.18; S, 15.03%. IR (KBr/cm^{-1}): 3500 (m, br); 2990 (m); 1550 (s), 1460 (w), 1430 (w), 1370 (m), 1350 (w), 1280 (s), 1160 (m), 1120 (w), 1070 (m), 1000 (w), 970 (w), 930 (w), 770 (w), 610 (w), 580 (m, br) cm^{-1}. ^{1}H NMR (300 MHz, $CDCl_3$): δ = 1.39 (t, 3H, CH_3); 2.37 (s, 6H, CH_3); 2.45 (q, 2H, –CH_2–) ppm. ^{13}C NMR (300 MHz, $CDCl_3$): δ = 21 (s, C_8); 127.85 (S, C_5); 165.4 (s, C_4/C_6); 175.0 (s, C_2) ppm. MS (FAB): m/z = 631 [Zn_2(4,6-Me_2EtpymS)$_3$]; 399 [Zn(4,6-Me_2EtpymS)$_2$]; 231 [Zn(4,6-Me_2EtpymS)]. Crystals of [Zn(4,6-Me_2,5-EtpymS)$_2$ (MeOH)](MeOH) (**4**) suitable for X-ray diffraction were obtained by recrystallization of the initial product from methanol.

2.4.2. Synthesis of [Zn(4-CF_3pymS)$_2$] (**5**)

A solution of 4-CF_3pymSH (150 mg, 0.83 mmol) in acetonitrile was electrolyzed and 17 mg (0.27 mmol) of zinc were dissolved from the anode. As the current was flowing a suspension was

obtained in the cell and the initial orange colour became pale yellow. The suspension was filtered to give a dusty pale yellow solid (Yield: 60 mg; 34%). *Anal.* Calc. for $C_{10}H_4N_4F_6S_2Zn$ (421.91): C, 28.35; N, 13.44; H, 0.95; S, 15.13. Found: C, 29.09; N, 13.22; H, 1.20; S, 14.69%. IR (KBr/cm^{-1}): 1580 (s), 1550 (vs), 1480 (m), 1460 (m), 1440 (s), 1420 (s), 1350 (vs), 1310 (s), 1290 (m), 1200 (vs), 1190 (s), 1160 (s), 1150 (s), 1130 (s), 110 (s), 1070 (w), 1050 (w), 1040 (w), 1020 (m), 1000 (w), 970 (m), 900 (w), 830 (s), 820 (s), 770 (s), 730 (s), 680 (w), 670 (s), 650 (m), 630 (m), 590 (w), 520 (w), 460 (m), 440 (w), 410 (m), 350 (m), 320 (m) cm^{-1}. ^{1}H NMR (300 MHz, $CDCl_3$): δ = 7.25 (d, 1H, H_5); 8.49 (d, 1H, H_6) ppm. ^{13}C NMR (300 MHz, $CDCl_3$): δ = 109.3 (s, C_5); 121.30 (q, C_7); 154.5 (q, $^2J_{13C-19F}$ = 111 Hz, C_4); 168.69 (s, C_6); 181.09 (s, C_2) ppm. The signals in the mass spectra were not identified.

2.4.3. Synthesis of [Zn(4-CF$_3$pymS)$_2$(bipy)] (**6**)

A total of 17 mg (0.27 mmol) of Zn were dissolved from the anode when the thione (150 mg, 0.83 mmol) was electrolyzed. Bipy (65 mg, 0.42 mmol) was also added to the cell solution. As the process was taking place, the initial orange solution became a dark yellow suspension. The mixture was filtered and a pale yellow dusty solid was obtained (Yield: 130 mg; 54%). *Anal.* Calc. for $C_{20}H_{12}N_6F_6S_2Zn$ (579.98): C, 41.43; N, 14.49; H, 2.09; S, 11.06. Found: C, 41.47; N, 14.66; H, 2.12; S, 11.53%. IR (KBr/cm^{-1}): 1590 (s), 1550 (vs), 1480 (m), 1460 (m), 1440 (s), 1420 (s), 1340 (vs, br), 1310 (s), 1240 (m), 1200 (vs, br), 1190 (s), 1160 (w), 1150 (w), 1140 (m), 1110 (m), 1070 (w), 1050 (w), 1040 (w), 1020 (m), 1000 (m), 970 (m), 900 (w), 830 (m), 820 (s), 770 (s), 730 (s), 680 (w), 670 (s), 650 (m), 630 (m), 590 (w), 520 (w), 460 (m), 430 (w), 410 (m), 350 (m), 320 (m) cm^{-1}. ^{1}H NMR (300 MHz [D_6] DMSO): δ = 7.31 (d, 1H, H_5); 8.76 (wide, 1H, H_6); bipy: 7.92 (d, 2H, $H_5/H_{5'}$); 8.11 (wide, 2H, $H_4/H_{4'}$); 8.55 (d, 2H, $H_3/H_{3'}$); 9.1 (d, 2H, $H_6/H_{6'}$) ppm. ^{13}C NMR (300 MHz [D_6] DMSO) δ = 114.95 (s, C_5); 162.10 (s, C_6); 148.90 (bipy $C_6/C_{6'}$) ppm. MS (FAB): m/z = 399 [Zn(4-CF$_3$pymS)(bipy)].

2.4.4. Synthesis of [Zn(4-CF$_3$pymS)$_2$(phen)] (**7**)

The result of the electrolytic process was a yellow dusty solid (Yield: 148 mg; 59%). Thione (150 mg, 0.83 mmol), phen (84 mg, 0.46 mmol) and Zn (0.22 mg) were used for this reaction. *Anal.* Calc. for $C_{22}H_{12}N_6F_6S_2Zn$ (601.98): C, 43.76; N, 13.92; H, 2.00; S, 10.62. Found: C, 44.16; N, 14.24; H, 2.02; S, 10.99%. IR (KBr/cm^{-1}): 1610 (m), 1600 (s, br), 1530 (m), 1500 (m), 1480 (w), 1430 (m), 1420 (s), 1330 (s, br), 1210 (s), 1190 (m), 1160 (w), 1140 (w), 1130 (w), 110 (m), 1090 (m), 1070 (w), 990 (w), 970 (m), 860 (w), 850 (m), 830 (m), 820 (m), 780 (w), 720 (s), 680 (w), 670 (s), 640 (m), 460 (m), 440 (w), 420 (m), 360 (m) cm^{-1}. ^{1}H NMR (300 MHz [D_6] DMSO): δ = 7.92 (d, 1H, H_5); 8.87 (d, 2H, H_6); phen: 8.09 (br, 2H, H_8/H_3); 8.29 (s, 2H, H_5/H_6); 9.01 (d, 2H, H_5/H_6); 9.11 (d, 2H, H_2/H_9) ppm. ^{13}C NMR (300 MHz [D_6] DMSO) δ = 95.3 (s, C_7); 114.9 (s, C_5); 154.45 (q, C_4); 168.08 (s, C_6); 168.67 (s, C_2); phen: 127.03 (s, C_3/C_8); 128.75 (s, C_5/C_7); 128.75 (s, C_{4a}/C_{6a}); 139.46 (s, C_4/C_6); 139.85 (s, C_{4b}/C_{6b}); 148.71 (s, C_2/C_9) ppm. MS (FAB): m/z = 425 [Zn(4-CF$_3$pymS)(phen)]. Crystals of **7** used for X-ray diffraction studies were obtained by recrystallization from ethanol.

2.4.5. Synthesis of [Zn(4,6-CF$_3$MepymS)$_2$] (**8**)

Electrolysis of an acetonitrile solution of 4,6-CF$_3$MepymSH (0.152 g, 0.78 mmol) using a zinc anode gave a pale yellow solution rather than a solid. A total of 29 mg (0.44 mmol) of Zn was dissolved from the anode. The solvent was evaporated and a dark yellow dusty solid was obtained (Yield: 62 mg; 35%). This product was identified as Zn(4,6-CF$_3$MepymS)$_2$. *Anal.* Calc. for $C_{12}H_8N_4F_6S_2Zn$ (449.94): C, 31.90; N, 12.27; H, 1.80; S, 14.21. Found: C, 32.92; N, 12.27; H, 2.40; S, 13.40%. IR (KBr/cm^{-1}): 1575 (vs), 1540 (vs), 1479 (m), 1430 (m), 1385 (vs), 1360 (m), 1270 (vs), 1220 (s), 1190 (s), 1170 (m), 1140 (s), 1110 (m), 1030 (w), 990 (w), 980 (w), 940 (w), 920 (m), 850 (s), 780 (w), 710 (s), 550 (m), 510 (w), 460 (m) cm^{-1}. ^{1}H NMR (300 MHz, $CDCl_3$): δ = 2.38 (s, 3H, CH_3); 6.94 (s, 1H, H_5) ppm. ^{13}C NMR (300 MHz, $CDCl_3$) ppm: δ = 23.78 (CH_3); 111 (C_5); 169.16 (C_6); 182 (C_2). MS (FAB): m/z = 710 [Zn_2(4,6-CF$_3$MepymS)$_3$]; 451 (M^+); 257 [Zn(4,6-CF$_3$MepymS)].

2.4.6. Synthesis of [Zn(4,6-CF$_3$MepymS)$_2$(bipy)] (**9**)

Thione (200 mg, 1.03 mmol) and bipyridine (80 mg, 0.51 mmol) were initially dissolved for this synthesis. The process caused the dissolution of 46 mg (0.72 mmol) of the zinc anode. Once more, a solid was not obtained at the end of the electrolytic process but a pale yellow solution, which was slowly concentrated at room temperature to give a colourless crystalline solid. These crystals were not suitable for X-ray diffraction studies (Yield: 90 mg; 29%). The analytical data confirmed that this solid was [Zn(4,6-CF$_3$MepymS)$_2$(bipy)]. *Anal.* Calc. for $C_{22}H_{16}F_6N_6S_2Zn$ (606.01): C, 43.07; N, 13.82; H, 2.65; S, 10.55. Found: C, 43.07; N, 13.62; H, 2.53; S, 10.13%. IR (KBr/cm^{-1}): 1590 (s), 1570 (vs), 1540 (vs), 1480 (m), 1460 (m), 1440 (s), 1380 (s, br), 1360 (s), 1310 (m), 1270 (s), 1260 (s), 1220 (s), 1180 (m), 1160 (m), 1140 (s), 1120 (w), 1100 (w), 1020 (w), 1000 (w), 970 (m), 910 (m, br), 880 (w), 840 (vs), 810 (w), 770 (vs), 730 (s), 710 (vs), 650 (m), 630 (w), 550 (m), 480 (w), 460 (w), 440 (w), 410 (m), 350 (m) cm^{-1}. ^{1}H NMR (300 MHz, $CDCl_3$): δ = 2.39 (s, 3H, CH_3), 6.83 (s, 1H, H_5); bipy: 7.59 (dd, 2H, $H_5/H_{5'}$); 8.10 (dd, 2H, $H_4/H_{4'}$), 8.26 (d, 2H, $H_3/H_{3'}$), 9.00 (d, 2H, $H_6/H_{6'}$) ppm. ^{13}C NMR (300 MHz, $CDCl_3$): δ = 24.58 (s, CH_3); 109.58 (s, C_5); 121.68 (q, CF_3), 149.6 (q, $^2J_{13C-19F}$ = 91 Hz, C_4) 168.9 (s, C_6); 182 (s, C_2); 126.79 (bipy, $C_3/C_{3'}$); 140.63 (bipy $C_5/C_{5'}$) ppm. MS (FAB): m/z = 413 ([Zn(4,6-CF$_3$MepymS)(bipy)]. Crystals of **9** suitable for X-ray diffraction studies were obtained by recrystallization of the initial product from ethanol/dichloromethane.

2.4.7. Synthesis of [Zn(4,6-CF$_3$MepymS)$_2$(phen)] (**10**)

A total of 62 mg (0.97 mmol) of zinc was dissolved through electrolysis of the corresponding ligand (200 mg, 1.03 mmol). In this case, phen (62 mg, 0.97 mmol) was added to the initial solution. As the current flowed the initial yellow solution became orange in colour. Solid did not appear during the reaction and partial evaporation of the solvent at room temperature gave a dusty brown solid (Yield: 80 mg; 20%), which was identified as [Zn(4,6-CF$_3$MepymS)$_2$(phen)]. *Anal.* Calc. for $C_{24}H_{16}F_6N_6S_2Zn$ (630.01): C, 45.62; N, 13.30; H, 2.55; S, 10.15. Found: C, 46.63; N, 12.30; H, 2.56; S, 9.93%. IR (KBr/cm^{-1}): 1610 (w), 1570 (s), 1540 (s), 1510 (w, br), 1480 (w), 1460 (w), 1420 (s), 1380 (s, br), 1360 (m), 1300 (w), 1260–70 (vs, br), 1220 (s), 1180 (w), 1160 (w), 1140 (m, br), 1100 (m), 970 (m), 910 (m), 860 (w), 840 (s), 770 (w), 730 (s), 710 (s), 550 (m), 470 (w), 450 (w), 420 (w), 350 (w) cm^{-1}. ^{1}H NMR (300 MHz, $CDCl_3$): δ = 2.33 (s, 3H, CH_3); 6.67 (s, 1H, H_5); phen: 7.89 (dd, 2H, H_3/H_8); 8.02 (s, 2H, H_5/H_6); 8.47 (d, 2H, H_4/H_7); 9.23 (wide s, 2H, H_2/H_9) ppm. ^{13}C NMR (300 MHz, $CDCl_3$): δ = 24.47 (s, CH_3), 109.58 (s, C_5), 122.51 (q, CF_3), 155.2 (q, C_4); 168, 9 (s, C_6); 182.0 (s, C_2); phen: 125, 63 (s, C_8/C_3), 127.43 (s, C_6/C_5), 129.55 (s, C_{4a}/C_{6a}); 139.49 (s, C_4/C_7); 141.65 (s, C_{4b}/C_{6b}); 149.55 (s, $C_2(C_9)$ ppm. MS (FAB): m/z = 629 (M^+), 437 [Zn, (4,6-CF$_3$MepymS)phen], 263 [Zn(4,6-CF$_3$MepymS)].

2.5. X-ray crystal structural determination

Intensity data sets for all compounds were collected with the use of a Smart-CCD-1000 Bruker diffractometer (Mo Kα radiation, λ = 0.71073 Å) equipped with a grafite monochromator. All crystals were measured at 293 K. The omega and phi scans technique was employed to measure intensities in all crystals. No decomposition

Table 1
Crystal data and structure refinement for **4**, **7** and **9**.

	4	**7**	**9**
Empirical formula	$C_{18}H_{30}N_4O_2S_2Zn$	$C_{22}H_{12}F_6N_6S_2Zn$	$C_{44}H_{32}F_{12}N_{12}S_4Zn_2$
Formula mass	463.95	603.87	1215.80
Crystal system	monoclinic	orthorhombic	monoclinic
Space group	*P*2(1)/*c*	*Pbcn*	*P*2(1)
a (Å)	7.840(8)	21.471(5)	8.632(2)
b (Å)	18.932(18)	9.501(5)	21.393(6)
c (Å)	15.369(14)	11.677(5)	13.669(4)
α (°)	90	90.000 (5)	90
β (°)	96.801	90.000(5)	93.723(4)
γ (°)	90	90.000(5)	90
Volume [Å^3]	2265(4)	2382.1(17)	2518.9(11)
Z	4	4	2
D_{calc} (Mg m^{-3})	1.360	1.684	1.603
μ (Mo Kα) (mm^{-1})	1.288	1.278	1.209
F(0 0 0)	976	1208	1224
Crystal size (mm)	0.24 × 0.20 × 0.09	0.28 × 0.20 × 0.03	0.97 × 0.30 × 0.12
T (K)	293(2)	293(2)	292(2)
Number of reflections collected	19 786	18 037	31 449
Number of independent reflections	4634	2037	12 003
Goodness of fit (GOF) on F^2	1.041	1.055	1.050
R[a]	0.0421	0.0401	0.0398
wR_2[b]	0.0809	0.0792	0.0866

[a] $R_1 = \Sigma[|F_o|-|F_c|]/\Sigma[|F_o|]$.
[b] $wR_2 = [\Sigma(F_o^2 - F_c^2)^2]/\Sigma(F_o^2)^2]^{1/2}$.

of the crystals happened during data collection. The intensities of all data sets were corrected for Lorentz and polarization effects. Absorption effects in all compounds were corrected using the program SADABS [26]. The crystal structures of all compounds were solved by direct methods. Crystallographic programs used for structure solution and refinement were those of SHELX 97 [27]. Scattering factors were those provided with the SHELX program system. Missing atoms were located in the difference Fourier map and included in subsequent refinement cycles. The structures were refined by full-matrix least-squares refinement on F^2, using anisotropic displacement parameters for all non-hydrogen atoms. Hydrogen atoms attached to carbons in the three compounds were placed geometrically and refined using a riding model, including free rotation about C–C bonds for methyl groups, with C–H distances of 0.93–0.97 Å. For all compounds, hydrogen atoms were refined with U_{iso} constrained at 1.2 (for non-methyl groups) and 1.5 (for methyl groups) times U_{eq} of the carrier C atom. Hydrogen atoms attached to oxygens (structure of complex **4**) were found and refined isotropically.

Table 1 summarizes pertinent details of the data collections and structure refinements, while Tables 2, 4 and 5 list important geometrical data for all compounds. Ortep3 [28] drawings with the numbering scheme used are shown in Figs. 1, 3 and 4.

Table 2
Selected bond lengths [Å] and angles [°] for [Zn(4,6-Me_2,5-EtpymS)$_2$(MeOH)] (**4**).

Zn(1)–O(1)	2.058(4)	Zn(1)–S(1)	2.377(2)
Zn(1)–N(1)	2.196(3)	S(1)–C(1)	1.741(4)
Zn(1)–N(3)	2.235(3)	S(2)–C(9)	1.738(4)
Zn(1)–S(2)	2.3318(19)		
O(1)–Zn(1)–N(1)	89.53(13)	N(3)–Zn(1)–S(2)	69.51(10)
O(1)–Zn(1)–N(3)	92.29(13)	O(1)–Zn(1)–S(1)	113.40(12)
N(1)–Zn(1)–N(3)	177.54(11)	N(1)–Zn(1)–S(1)	69.31(10)
O(1)–Zn(1)–S(2)	114.99(12)	N(3)–Zn(1)–S(1)	111.40(9)
N(1)–Zn(1)–S(2)	108.20(10)	S(2)–Zn(1)–S(1)	131.53(5)

a: #1: −*x*, −*y*, −*z* + 2.

Table 4
Selected bond lengths [Å] and angles [°] for [Zn(4-CF_3pymS)$_2$(phen)] (**7**).

Zn(1)–S(1)	2.2929(13)	Zn(1)–N(3)	2.119(4)
Zn(1)–S(1)#1	2.2929(13)	Zn(1)–N(3)#1	2.119(4)
S(1)–C(1)	1.724(4)		
N(3)–Zn(1)–N(3)#1	79.0(2)	N(3)–Zn(1)–S(1) #1	101.43(11)
N(3)–Zn(1)–S(1)	119.63(10)	N(3)#1–Zn(1)–S(1)#1	119.63(10)
N(3)#1–Zn(1)–S(1)	101.43(11)	S(1)–Zn(1)–S(1)#1	126.66(7)

a: #1: −*x* + 1, *y*, −*z* + 3/2.

Table 3
π–π interactions for **4**, **7** and **9**.

π–π	Cg–Cg[a] (Å)	α[b]	β[c]	γ[d]	Cg(*I*)_J[e]	Cg(*J*)_I[f]
(4)						
π[N1,N2,C1–C4]–π[N1,N2,C1–C4]#3	3.997	0.02	28.86	28.86	3.500	3.500
π[N3,N4,C9–C12]–π[N3,N4,C9–C12]#2	3.912	0.00	25.65	25.65	3.527	3.527
(7)						
π[N3,C6–C10]–π[N3,C6–C10]#3	3.779	0.03	19.64	19.64	3.559	3.559
(9)						
π[N6,C18–C22]–π[N12,C40–C44]#2	3.788	2.63	20.15	17.53	3.613	3.557

Symmetry transformations: (**4**) #3: −*x* + 1, −*y*, *z* + 1; #2: −*x*, −*y*, −*z* + 1. (**7**) #3: −*x* + 1, −*y* + 1, −*z* + 2. (**9**) #2: *x* + 1, *y*, *z*.
[a] Centroid–centroid distance.
[b] Dihedral angle between the ring planes.
[c] Angle between the centroid vector Cg(*I*)···Cg(*J*) and the normal to the plane *I*.
[d] Angle between the centroid vector Cg(*I*)···Cg(*J*) and the normal to the plane *J*.
[e] Perpendicular distance of Cg(*I*) on ring plane *J*.
[f] Perpendicular distance of Cg(*J*) on ring plane *I*.

Table 5
Selected bond lengths [Å] and angles [°] for [Zn(4,6-CF_3MepymS)$_2$(bipy)] (**9**).

Zn(1)–N(6)	2.083(3)	S(1)–C(1)	1.738(4)
Zn(1)–N(5)	2.116(3)	S(2)–C(7)	1.739(5)
Zn(1)–S(2)	2.2819(13)	Zn(1)–S(1)	2.2964(12)
N(6)–Zn(1)–N(5)	78.30(13)	N(6)–Zn(1)–S(1)	102.55(10)
N(6)–Zn(1)–S(2)	121.92(10)	N(5)–Zn(1)–S(1)	118.81(11)
N(5)–Zn(1)–S(2)	104.42(10)	S(2)–Zn(1)–S(1)	123.10(5)

a: #3: $x-1$, y, z.

3. Results and discussion

3.1. Preparation

Zinc complexes of general formula [Zn(RpymS)$_2$] (R = 4,6-Me_2,5-Et; 4-CF_3; 4,6-CF_3,Me) were easily prepared in reasonable yields by a simple one-step electrochemical method [29]. Mixed complexes with 2,2′-bipyridine or 1,10-phenanthroline were also obtained by addition of the corresponding coligand to the cell. The compounds are air-stable and moderately soluble in non-polar organic solvents but are soluble in dimethyl sulfoxide and *N*,*N*′-dimethylformamide.

The electrochemical efficiency, defined as the amount of metal dissolved per Faraday of charge, was in all cases close to 0.5 mol F^{-1}. This fact, together with the evolution of hydrogen at the cathode, is compatible with the occurrence of the following electrode reactions.

$$\text{Cathode}: \text{RpymSH} + e^- \rightarrow \text{RpymS}^- + 1/2\ H_2$$

$$\text{Anode}: \text{Zn} \rightarrow \text{Zn}^{2+} + 2e^-$$

$$\text{Overall}: \text{Zn} + 2\text{RpymSH} \rightarrow [\text{Zn(RpymS)}_2]$$

$$\text{Zn} + 2\text{RpymSH} + \text{L} \rightarrow [\text{Zn(RpymS)}_2\text{L}]$$

where L is 2,2′-bipyridine or 1,10-phenanthroline.

For the complexes [Zn(4,6-Me_2,5-EtpymS)$_2$(MeOH)] (**4**), [Zn(4-CF_3pymS)$_2$(phen)] (**7**) and [Zn(4,6-CF_3MepymS)$_2$(bipy)] (**9**) crystals suitable for X-ray diffraction studies were obtained.

3.2. Crystallographic studies

In all cases the crystal structure consists of discrete molecular species. This fact shows that the presence of an additional coligand inhibits the polymerization of the compound, as found by X-ray diffraction of zinc complexes with only heterocyclic thiones as ligands. For example, [Zn(pymS)$_2$] [30] and [Zn(4,6-Me_2pymS)$_2$] [31] are polymeric.

3.2.1. Crystal and molecular structure of [Zn(4,6-Me_2,5-EtpymS)$_2$(MeOH)] (**4**)

A perspective view of compound **4** is shown in Fig. 1 together with the atomic labelling scheme used. Selected bond lengths

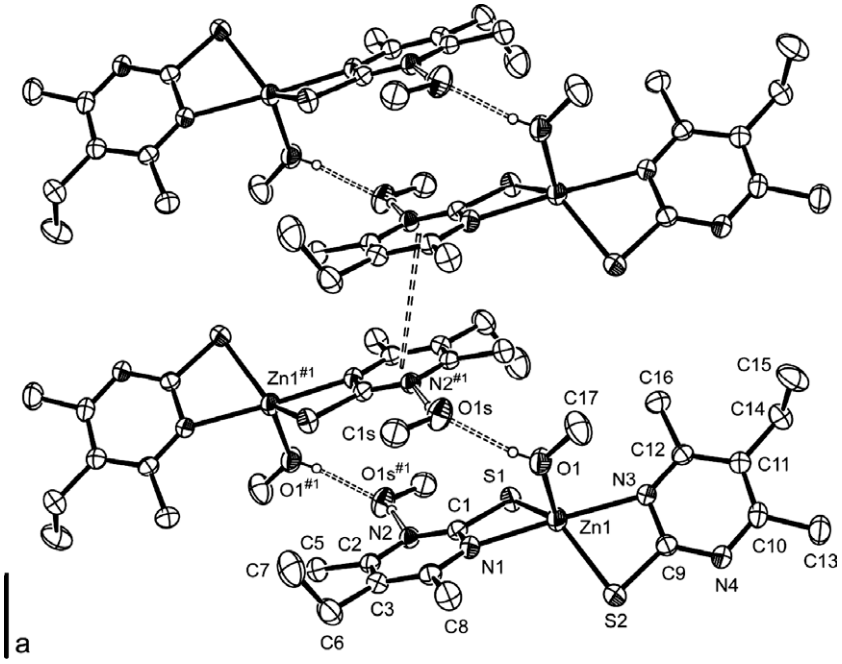


Fig. 1. Crystal structure of [Zn(4,6-Me_2,5-EtpymS)$_2$(MeOH)] (**4**) and a view of different kinds of intermolecular interactions.

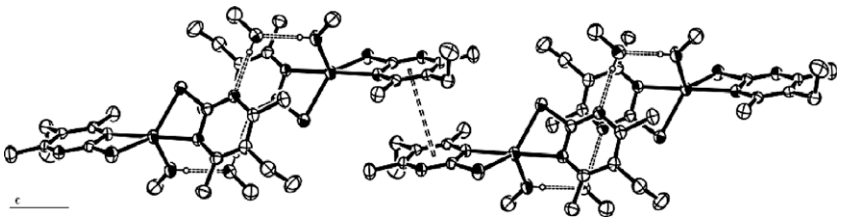


Fig. 2. A view of O–H···N interactions and π-stacking between pyrimidine rings in (**4**).

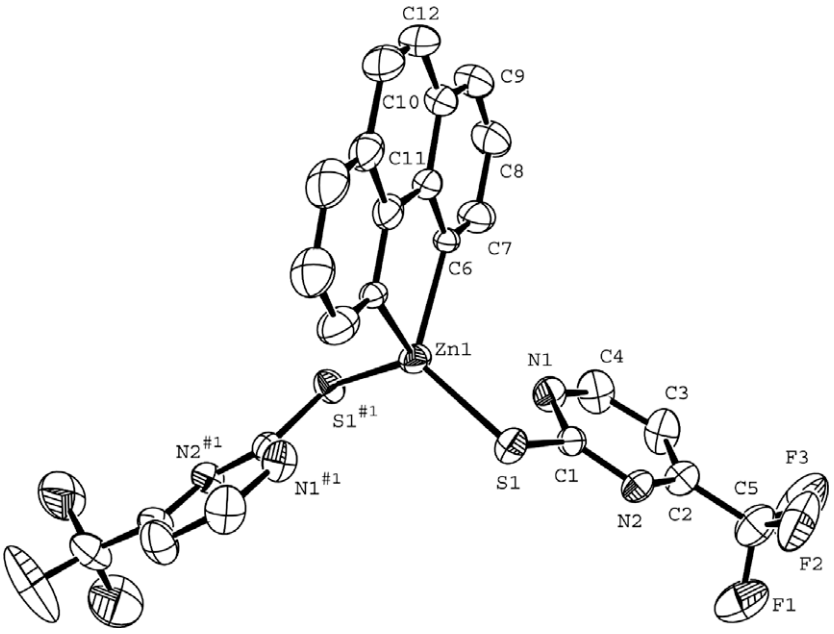


Fig. 3. Crystal structure of [Zn(4-CF_3pymS)$_2$(phen)] (**7**). The hydrogen atoms have been omitted for clarity.

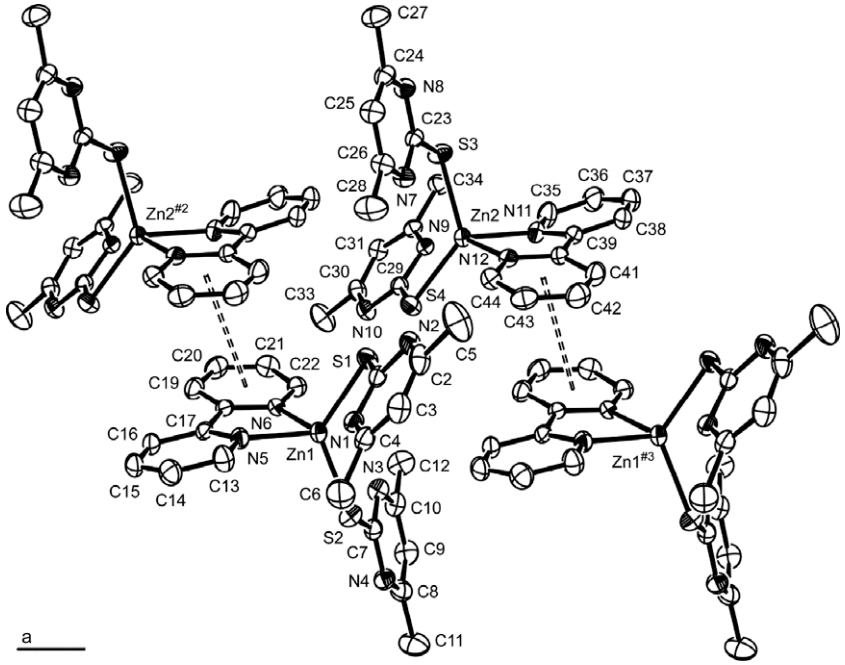


Fig. 4. Crystal structure of [Zn(4,6-CF_3MepymS)$_2$(bipy)] (**9**) and a view of π-stacking between bipyridine rings in **9**. The hydrogen atoms have been omitted for clarity.

and angles are given in Table 2. Crystallographic data are reported in Table 1.

The crystal structure consists of discrete molecular species in which the metal atom is coordinated by one methanol molecule and by two anionic pyrimidine-2-thionato ligands, which act in a bidentate manner (S,N); the other nitrogen atom of each pyrimidine-2-thionato ligand is not coordinated. Analysis of the shape-determining bond angles, using the geometrical parameter τ [$\tau = (\beta - \alpha)/60$], [32] gives a value of 0.77 and suggests that the zinc atoms are in a distorted [ZnN_2OS_2] trigonal bipyramidal environment. The nitrogen atoms are located in axial positions and the equatorial plane is described by two sulfur atoms from the pyrimidine-2-thionato ligands and the oxygen atom from the methanol molecule. The zinc atom is practically on the best plane defined by the donor atoms of the equatorial plane, with the deviation being only 0.028(1) Å. The distortion of the regular trigonal bipyramidal geometry is mainly due to the small bite of the thionato ligands, whose N(3)–Zn(1)–S(2) and N(1)–Zn(1)–S(1) chelate angles are 69.51(10)° and 69.31(10)°, respectively, which deviate significantly from 90°. These deviations produce bond angle values that are quite different from the expected ones. Thus, the N(1)–Zn(1)–S(2) and N(3)–Zn(1)–S(1) bond angles are 108.20(10) and

111.40(9)°, respectively, which are significantly different from 90° (the corresponding ideal value). However, the bond angles O(1)–Zn(1)–N(1) and O(1)–Zn(1)–N(3) [89.53(13) and 92.29(13)°] are very close to the ideal value (90°).

The angles described by atoms in equatorial positions should be close to 120°; the angles involving oxygen atoms [114.99(12)° and 113.40(12)°] are smaller than the ideal value (120°) but the S(2)–Zn(1)–S(1) bond angle is somewhat larger, 131.53(5)°. This is due to the steric requirements of the pyrimidine ligands. All of these facts do not significantly affect the N(1)–Zn(1)–N(3) bond angle [177.54(11)°], which is very close to the ideal value of 180°.

A comparison of the metal–ligand bond distances in complexes **4**, **7** and **9** shows that these are dependent on the coordination number of the metal, and this in turn depends on the monodentate or chelating nature of the thionato ligand. The Zn–S bond lengths in **4** [2.3318(19) and 2.377(2) Å] are greater than the average values [2.2892(13), 2.2929(13) and 2.3117(6) Å, respectively] found for the corresponding distances in the tetracoordinated complexes **7**, **9** and [Zn(5-CF_3pyS)$_2$(bipy)] [33] and are significantly shorter than those reported in the hexacoordinated complexes [Zn(3-CF_3pyS)$_2$(phen)] [2.5602(19) and 2.4770(19) Å] and [Zn(3-CF_3pyS)$_2$(bipy)] [2.5607(7) and 2.4781(7) Å] [33]. This fact is undoubtedly due to the coordination number in complex **4** being intermediate between four and six. However, these distances are quite similar to those found in other pentacoordinated zinc complexes that contain pyrimidine-2-thionato as a ligand; 2.347(2) and 2.369(2) Å in [Zn(4,6-Me_2pymS)$_2$(py)] [34] or 2.369(6) and 2.319(2) Å in [Zn(4,6-Me_2pymS)$_2$], [31] with the latter compound consisting of polymeric chains.

The Zn–N_{pymS} bond lengths [2.196(3) and 2.235(3) Å] are similar to those found in the above hexacoordinated complexes of zinc(II) with pyridine 2-thionato complexes [average values, 2.190(5) and 2.202(2) Å] and are also similar to those in the pentacoordinated complex [Zn(4,6-Me_2pymS)$_2$(py)] [2.241(5) Å] [34]. The fifth coordination position in this complex is occupied by a methanol molecule, which is quite usual for zinc coordination compounds [35–42]. The value for the Zn–O bond length [2.058(4) Å] is within the range reported for other pentacoordinated zinc complexes containing methanol as a solvate [1.950–2.078 Å] [36–42]. The pyrimidine portion of each thionato ligand is essentially planar, with the largest deviation from the least squares plane being 0.061(2) Å and the deviations of the sulfur atoms being 0.030(5) Å for S(1) and 0.021(5) Å for S(2) from the plane of the pyrimidine group that is bound.

3.2.2. Crystal packing and intermolecular interactions of **4**

In this complex the pyrimidine-2-thionato ligands do not exactly mimic the dianionic NS_2 environment of the zinc centre in LADH, but the presence in this complex of suitably positioned methanol molecules enables the formation of a hydrogen bond (see Fig. 1) between the alcoholic proton of the zinc-bound methanol molecule and the methanol molecule of crystallization [O(1)···O(1s) 2.617(5) Å; O(1)–H(1)···O(1s) 172(6)°]. This type of short hydrogen bonding interaction involving the zinc-bound methanol mimics the hydrogen-bonding network involving Ser_{48} in LADH [O(Ser_{48})···O(alcohol) = 2.6 Å] [43], which is responsible for the proton transfer from the active site of the enzyme to the solvent; this situation has been observed in the X-ray structures of other systems that have been used to model aspects of the active site chemistry of LADH [40,41].

Complex **4** also shows a wide variety of intra- and intermolecular interactions. For example, the molecule of crystallization involved in the aforementioned interaction with the coordinated methanol molecule also establishes an O–H···N interaction with the non-coordinated nitrogen of one of the pyrimidines of a neighbouring complex which is related to the first molecule through an inversion centre [O(1s)···N(2) 2.786(5) Å; O(1s)–H(1s)···N(2) 174(5)°]. At the same time, and due to symmetry requirements, this neighbouring complex establishes the same interactions as the original complex. In this way, associations of the type {[Zn(4,6-Me_2,5-EtpymS)$_2$(MeOH)]$_2$(MeOH)$_2$} are formed and these have an inversion centre. A view of this group is shown in Fig. 1 and the hydrogen bonding interactions are also indicated. In addition, the pyrimidine rings involved in the classical hydrogen bonding establish "parallel displaced" π-stacking interactions with equivalent rings in neighbouring groups. These interactions occur along the crystallographic *a* axis and are shown in Fig. 1. The interaction data (Table 3) show that this is a weak interaction (Cg···Cg > 3.8 Å, slip angles beta, gamma > 25°) [44]. At the same time a weaker π-stacking interaction is established between the pyrimidine rings not involved in classical hydrogen bonding. This interaction is "parallel displaced" in nature [45]. These interactions are propagated along the crystallographic *c* axis (Fig. 2). The interaction data (Table 3) show that this is a weak interaction, albeit slightly stronger than the π-stacking interaction that occurs along the *a* axis (vide supra).

3.2.3. Crystal and molecular structure of Zn[(4-CF_3pymS)$_2$(phen)] (**7**) and Zn[(4,6-CF_3MepymS)$_2$(bipy)] (**9**)

Perspective views of the molecular structures of **7** and **9** are shown in Figs. 3 and 4, respectively, together with the labelling schemes used. Crystallographic data are reported in Table 1 and a selection of bond distances and angles are given in Tables 4 and 5.

In both cases the structures consist of discrete molecular species and the difference in comparison to **4** is that in **7** and **9** the zinc atom is tetracoordinated. The metal is coordinated by one phenanthroline (**7**) or bipyridine (**9**) molecule, and by two anionic pyrimidine-2-thionato binding the metal through the sulfur atom only while the nitrogen atoms of the pyrimidine ligands are not coordinated; the distance from the nitrogen to the zinc atom is 2.855(4) Å in the phen complex and 2.778(4) and 3.224(4) Å in the bipy complex. These values are larger than those observed in other zinc complexes containing heterocyclic donor nitrogen ligands [2.085–2.291 Å] [46,47]. These distances are also significantly longer than the sum of the covalent radii of zinc and nitrogen but are in the order of the sum of the van der Waals radii (2.94 Å) [48]. Therefore, we consider that the Zn–N distances indicate a very weak contact.

The geometry around the metal atom is best described as a distorted tetrahedral [ZnS_2N_2] environment. This distortion is due to the small bite of the bipyridine, N–Zn–N = 78.30(13)°, or of the phenanthroline, N–Zn–N = 79.0(2)°, which results in secondary deviations of the other perinuclear angles from the ideal value of 109°. Thus the bond angles in these compounds are in the range 123.10(5)–78.30(13)° for the zinc environment.

There are no significant differences between the values reported for Zn–S bond lengths: 2.2819(13) and 2.2964(12) Å for the complex with bipy and 2.2929(13) Å for the phen complex. However, these distances are shorter than those reported for zinc pyridine-2-thionato complexes (hexacoordinated and pentacoordinated) and are also shorter than those found in another tetracoordinated zinc complex [2.3117(6) Å] [33].

The distances involving the metal and the nitrogen atoms of the phenanthroline [2.119(4) Å] in **7** or bipyridine [average value 2.100(3) Å] in **9** are in the expected range for zinc complexes containing this type of chelating nitrogen ligands [49]. In both compounds the Zn–N and Zn–S distances are very similar to those found in [Zn(S-*p*-tolyl)$_2$phen] [50] which in an EXAFS study has been used as a model for the zinc centre of Transcription Factor IIIA (TFIIIA) [51]; this raises the possibility that **7** and **9** might also be considered as models for this protein.

The 2,2′-bipyridine, 1,10-phenthroline and pyrimidine rings are planar [maximum deviation 0.015(3) Å]. In compound **7**, the sulfur atom is out of the plane of the pyrimidine ring to which is attached [0.081(6) Å]. However, in **9** one of the sulfur atoms, S(2), is approximately in the plane of the pyrimidine rings to which it is bound [0.006(6) Å] but S(1) is out of the plane of the pyrimidine ring to which is attached [0.1124(5) Å]. The S–C bond lengths, which are between 1.724(4) and 1.739(5) Å, are similar to those found in other complexes with pyrimidine-2-thionato derivatives, a fact that suggests that this ligand is coordinated in a form that is closer to the thionato than the thione.

*3.2.4. Crystal packing and intermolecular interactions in **7** and **9***

In the packing of compound **7**, the phenanthroline units establish π-stacking interactions between one another and these interactions occur along the *c* axis. The π-stacking interactions occur between phenanthrolines belonging to contiguous chains, which intercalate between the phenanthrolines of another chain. These interactions connect chains to one another, leading to interactions in the BC plane. Each phenanthroline unit is involved in two identical "parallel displaced" π-stacking interactions. These interactions are established between lateral rings of each phenanthroline molecule, as shown in Fig. 5 (the fluorine and hydrogen atoms not involved in the interactions have been removed for the sake of clarity). The values for these interactions (Table 3) show that the interaction is strong.

The bipyridine units in **9** establish a rather strong "parallel displaced" π-stacking interaction (Table 3) with other bipyridine units in symmetry inequivalent complexes. These interactions connect pairs of compound molecules that are arranged along the crystallographic *a* axis, as shown in Fig. 4.

3.3. IR spectroscopy

The IR spectra of the complexes do not show the band observed in the pyrimidine-2-thionato ligands at 3200–3000 cm^{-1}, which is attributed to ν(N–H) stretching. This difference in the spectra indicates that deprotonation of the NH group occurs during the electrochemical synthesis and that the ligand is coordinated in the anionic thionato form in the complex. This conclusion is also supported by the shift to lower wavenumbers of the strong bands for ν(C=C) and ν(C=N), which appear at 1600–1550 and 1570–1525 cm^{-1}, respectively, in the free ligands [52]. In the spectra of the bipy and phen complexes, in addition to the bands described above, the spectra contain bands at around 758 and 735 cm^{-1} and 1510, 850 and 730 cm^{-1}, which are typical of coordinated 2,2′-bipyridine [53] and 1,10-phenanthroline [53,54], respectively.

3.4. NMR spectroscopy

The room temperature ^{1}H NMR spectra of the complexes do not contain the signal attributable to the –NH hydrogen, which appears in the free ligand at δ = 14.40–13.00 ppm. The absence of this signal is a result of deprotonation of the ligand during the electrolytic process. The signals of all of the protons of the pyrimidine ring, methyl or methylene groups (see Section 2), are slightly shifted compared to those in the free ligands by the coordination of the pyrimidine-2-thionato ligand.

The ^{1}H NMR spectra of [Zn(RpymS)$_2$(bipy)] and [Zn(RpymS)$_2$(phen)] also show signals assignable to the hydrogens of the additional ligand. These signals undergo small shift with respect to the free ligand and these changes provide evidence for the coordination of the additional ligands to the metal atom through nitrogen atoms [55,56].

The ^{13}C NMR spectra of the complexes contain the signals for the different carbon atoms (see Section 2). The spectra of the complexes containing the ligand 4,6-CF_3MepymSH show that doubling observed in the free ligand of the signals for C_2, C_6, CF_3 and CH_3, has disappeared and this shows that, in solution, the ligand is coordinated to the metal in the thionato form only. In complexes where the –CF_3 group is a substituent in the heterocyclic ring, the signals of the corresponding carbon appear as a quadruplet because of coupling with fluorine atoms.

3.5. Mass spectrometry

All of the complexes were also characterized by mass spectrometry using the positive-ion FAB technique and 3-nitrobenzyl alcohol (NBA) as matrix. The FAB spectra of [Zn(4,6-Me_2EtpymS)$_2$], [Zn(4,6-CF_3MepymS)$_2$], and [Zn(4,6-CF_3MepymS)$_2$(phen)] show the molecular ion with the appropriate isotope distribution, as well as peaks due to the fragments generated by the loss of one of the thionato ligands. In the former case, the peak due to the loss of the 1,10-phenanthroline is also observed at m/z = 263. The peak due to the loss of one of the thionato ligands is observed in the spectra of most of the complexes.

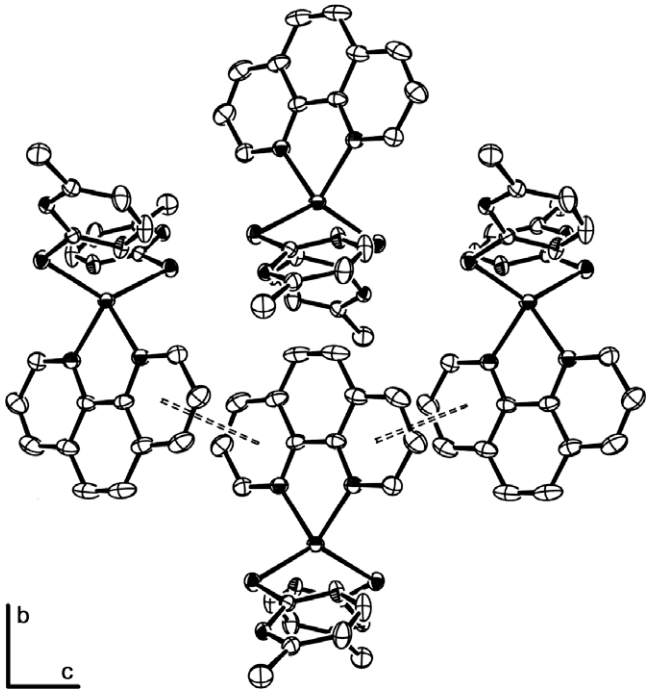


Fig. 5. A view of π stacking interactions in **7**.

4. Conclusion

In this paper, we report the electrochemical synthesis of a series of zinc complexes with pyrimidine-2-thionato derivatives as well as the synthesis of their adducts with *N,N* donors (bipy and phen). The thionato ligands differ in the nature, position and number of substituents in the heterocyclic ring.

At present we are unable to explain the different behaviour of the thionato ligands. Two different coordination modes (bidentate chelating and monodentate) are reported in this work. For Zn(4,6-Me_2,5-EtpymS)$_2$(MeOH)] the metal centre is in a ZnN_2S_2O environment, which describes a distorted bipyramidal trigonal. In the adducts with bipy and phen the zinc atom is in a highly distorted tetrahedral ZnN_2S_2 environment.

Acknowledgements

This work was supported by the Ministerio de Ciencia y Tecnologia (Spain) (Grant CTQ2006-05298) and by the Xunta de Galicia (Spain) (Grant PGIDIT07PXIB-203038PR).

Appendix A. Supplementary data

CCDC 701184, 701183 and 701182 contain the supplementary crystallographic data for **4**, **7** and **9**. These data can be obtained of charge via http://www.ccdc.cam.ac.uk/conts/retrieving.html, or from the Cambridge Crystallographic Data Centre, 12 Union Road, Cambridge, CB2 IEZ, UK, fax: (+44)-1223-336-033 or e-mail deposit@ccdc.cam.ac.uk.

References

[1] I.G. Dance, J. Am. Chem. Soc. 102 (1980) 3445.
[2] H. Eklund, C.-I. Bränden, in: T.G. Spiro (Ed.), Zinc Enzymes, Wiley, New York, 1983, p. 124.
[3] J.P. Klinman, Crit. Rev. Biochem. 10 (1981) 39.
[4] R.G. Matthews, Acc. Chem. Res. 34 (2001) 681.
[5] V.N. Krishnamurthy, K.V. Neglowara, P.L. Narasumha, B. Praphulla, Br. J. Pharmacol. Chemother. 31 (1967) 1.
[6] B. Rosenberg, L. van Camp, Nature 222 (1969) 385.
[7] B. Rosenberg, L. van Camp, Cancer Res. 30 (1970) 1799.
[8] P. Kamalakannan, D. Venkappayya, T. Balasubramanian, J. Chem. Soc., Dalton Trans. (2002) 3381.
[9] P. Kamalakannan, D. Venkappayya, in: Proceedings of the 37th Annual Conventions of Chemists, ING-OP-03, Harwar, 2000.
[10] P. Kamalakannan, D. Venkappayya, J. Inorg. Biochem. 90 (2002) 22.
[11] S.M. Kupchan, D.C. Fessler, M.A. Eakin, T.J. Giacobbe, Science 168 (1970) 376.
[12] K.H. Lee, T. Ibuka, R.Y. Wu, Chem. Pharm. Bull. 22 (1974) 2206.
[13] D.H. Petering, W.E. Antholine, L.A. Saryan, in: M. Dekker (Ed.) Anticancer, Interferon Agents, New York, 1984 (Chapter 7).
[14] A.C. Skapski, K.A. Woode, Acta Cryst. B 35 (1979) 59.
[15] M.J. Kendrick, M.T. May, M.J. Plishka, K.D. Robinson, in: Ellis Horwood (Ed.), Metals in Biological Systems, Chichester, UK, 1992.
[16] B.L. Barnett, H.C. Kretschmar, F.A. Hartman, Inorg. Chem. 16 (1977) 1834.
[17] D.M.L. Goodgame, I. Jeeves, G.A. Leach, Inorg. Chim. Acta 39 (1980) 247.
[18] Eric S. Raper, Coord. Chem. Rev. 165 (1997) 475.
[19] A. Rodríguez, J.A. García-Vázquez, A. Sousa-Pedrares, J. Romero, A. Sousa, Inorg. Chem. Commun. 6 (2003) 619.
[20] A. Rodríguez, A. Sousa-Pedrares, J.A. García-Vázquez, J. Romero, A. Sousa, Eur. J. Inorg. Chem. (2005) 2242.
[21] A. Rodríguez, A. Sousa-Pedrares, J.A. García-Vázquez, J. Romero, A. Sousa, Eur. J. Inorg. Chem. (2007) 1444. references therein.
[22] R. Battistuzzi, G. Peyronel, Spectrochim. Acta 36A (1980) 113.
[23] A. Rodríguez, J.A. García-Vázquez, A. Sousa-Pedrares, J. Romero, A. Sousa, J. Organomet. Chem. 689 (2004) 557. and references therein.
[24] J.A. García-Vázquez, J. Romero, A. Sousa, Coord. Chem. Rev. 193-195 (1999) 691.
[25] R. Battistuzzi, G. Peyronel, Transit. Metal Chem. 3 (1978) 345.
[26] G.M. Sheldrick, SADABS: Program for Absorption Correction Using Area Detector Data, University of Göttingen, Germany, 1996.
[27] SHELX97 [Includes SHELXS97, SHELXL97, CIFTAB]. Programs for Crystal Structure Analysis (Release 97-2). G.M. Sheldrick, Institüt für Anorganische Chemie der Universität, Tammanstrasse 4, D-3400 Göttingen, Germany, 1998.
[28] ORTEP3 for Windows L.J. Farrugia, J. Appl. Crystallogr. 30 (1997) 565.
[29] D.G. Tuck, Pure Appl. Chem. 51 (1979) 2005.
[30] A. Eichhöfer, G. Buth, Eur. J. Inorg. Chem. (2005) 4160.
[31] M.L. Godino-Salido, M.D. Gutiérrez-Valero, R. López Garzón, Inorg. Chim. Acta 221 (1994) 177.
[32] A.W. Addison, T.N. Rao, J. van Reedijk, J. van Rijn, G.C. Verschoor, J. Chem. Soc., Dalton Trans. (1984) 1349.
[33] A. Sousa Pedrares, J. Romero, J.A. García-Vázquez, M.L. Duran, I. Casanova, A. Sousa, Dalton Trans. (2003) 1379.
[34] R. Castro, J.A. García-Vázquez, J. Romero, A. Sousa, W. Hiller, J. Strähle, Polyhedron 13 (1994) 273.
[35] S. Akine, T. Taniguchi, T. Saiki, T. Nabeshima, J. Am. Chem. Soc. 128 (2006) 15765.
[36] J. Gradinaru, A. Fomi, V. Druta, S. Zecchin, S. Quici, N. Garbalau, Inorg. Chem. 46 (2007) 884.
[37] J.P. Holland, F.I. Algibirhio, H.M. Betts, P.D. Bonnitcha, P. Burke, M. Cristilleb, G.C. Churchill, A.R. Cowley, J.R. Dilworth, P.S. Donnelly, J.C. Green, J.M. Peach, S.R. Vasudevan, J.E. Warren, Inorg. Chem. 46 (2007) 465.
[38] B. Bauer-Siebanlist, F. Meyer, E. Farkas, D. Vidovic, S. Dechert, Chem.-Eur. J. 11 (2005) 4349.
[39] M. Doring, M. Ciesielski, O. Walter, H. Gorls, Eur. J. Inorg. Chem. (2002) 1615.
[40] L.M. Berreau, M.M. Makowska-Grzyska, A.M. Arif, Inorg. Chem. 40 (2001) 2212.
[41] M.M. Makowska-Grzyska, P.C. Jeppson, R.A. Allred, A.M. Arif, L.M. Berreau, Inorg. Chem. 41 (2002) 4872.
[42] A.W. Kleij, M. Kuil, M. Lutz, D.M. Tooke, A.L. Spek, P.C.J. Kamer, P.W.N.M. van Leeuwen, J.N.H. Reek, Inorg. Chim. Acta 359 (2006) 1807.
[43] S. Ramaswamy, H. Eklund, B.V. Plapp, Biochemistry 38 (1994) 13951.
[44] T. Dorn, C. Janiak, K. Abu-Shandi, Cryst. Eng. Commun. 7 (2005) 633. and references therein.
[45] C. Janiak, J. Chem. Soc., Dalton Trans. (2000) 3885.
[46] M.L. Durán, J. Romero, J.A. García-Vázquez, R. Castro, A. Castiñeiras, A. Sousa, Polyhedron 10 (1991) 197.
[47] (a) C. Jubert, A. Machamedou, J. Marrot, J.P. Barbier, J. Chem. Soc., Dalton Trans. (2001) 1230;
(b) M. Brand, H. Vahrenkamp, Inorg. Chim. Acta 308 (2000) 97;
(c) M. Mikuriya, K. Jian, S. Ikemi, T. Kawahashi, H. Tsutsumi, Bull. Chem. Soc. Jpn. 71 (1998) 2161.
[48] A. Bondi, J. Phys. Chem. 68 (1964) 441.
[49] (a) D.T. Corwin Jr., S.A. Koch, Inorg. Chem. 27 (1988) 493;
(b) R. Castro, J.A. García-Vázquez, J. Romero, A. Sousa, C.A. McAuliffe, R. Pritchard, Polyhedron 12 (1993) 2241.
[50] T.L. Cremers, D.R. Bloomquist, R.D. Willet, G.A. Crosby, Acta Cryst. B36 (1980) 3097.
[51] G.P. Diakun, L. Fairall, A. Klug, Nature (London) 324 (1986) 698.
[52] E. Spiner, J. Chem. Soc. (1960) 1237.
[53] A.A. Schilt, R.C. Taylor, J. Inorg. Nucl. Chem. 9 (1959) 211.
[54] R.G. Inskeep, J. Inorg. Nucl. Chem. 24 (1963) 763.
[55] (a) S. Castellano, H. Gunther, S. Ebersole, J. Phys. Chem. 69 (1965) 4166;
(b) H.E. Mabrouk, D.G. Tuck, J. Chem. Soc., Dalton Trans. (1988) 2539.
[56] (a) S. Yamazaki, Polyhedron 4 (1985) 1915;
(b) T.A. Annan, R.K. Chadha, D.G. Tuck, K.D. Watson, Can. J. Chem. 65 (1987) 2670.

Polyhedron 28 (2009) 2249–2257

Contents lists available at ScienceDirect

Polyhedron

journal homepage: www.elsevier.com/locate/poly

Preparation, crystal structures and magnetic properties of three thiocyanato-bridged copper(II) complexes with 2,2′-biimidazole or 2-(2′-pyridyl)imidazole as terminal ligands

José Carranza [a], Jorunn Sletten [b,*], Francesc Lloret [c], Miguel Julve [c,*]

[a] Facultad de Ciencias Químicas, Universidad Autónoma de Zacatecas, Jardín Juárez s/n, 98000 Zacatecas, Mexico
[b] Department of Chemistry, University of Bergen, Allégaten 41, N-5007 Bergen, Norway
[c] Departament de Química Inorgànica/Instituto de Ciencia Molecular (ICMol), Universitat de València, Polígono La Coma s/n, 46980 Paterna (València), Spain

ARTICLE INFO

Article history:
Received 24 November 2008
Accepted 2 April 2009
Available online 10 April 2009

Keywords:
Crystal structures
Copper(II) complexes
Thiocyanate complexes
Magnetic properties
Polynuclear complexes

ABSTRACT

The synthesis, crystal structures and variable temperature magnetic investigation of three new thiocyanato-bridged copper(II) complexes with 2,2′-biimidazole (H_2bim) or 2-(2′-pyridyl)imidazole) (pyim) as coligands, $\{[Cu(H_2bim)_2][Cu(H_2bim)(NCS)_2(SCN)_{0.6667}(NO_3)_{0.3333}]_2\}\cdot 2H_2O$ (**1**), $[Cu(H_2bim)(NCS)_2]_n$ (**2**) and $[Cu(pyim)(NCS)_2]_n$ (**3**) are reported. Complex **1** contains centrosymmetric trinuclear species where central $[Cu(2)(H_2biim)_2]^{2+}$ cations and peripheral $[Cu(1)(H_2biim)(NCS)_2(SCN)]^-$ anions are linked through single end-to-end thiocyanato bridges. Complexes **2** and **3** are made up of neutral zigzag chains of copper(II) ions linked by single (**2**) and double (**3**) end-to-end thiocyanato bridges. A bidentate H_2bim ligand (**2**) or pyim (**3**) and a terminal N-thiocyanate group (**2**) complete the coordination spheres around each copper atom. The values of the intramolecular (**1**) and intrachain (**2** and **3**) copper–copper separations are 5.6143(5) (**1**), 5.6744(3) (**2**) and 6.0797(11) Å (**3**). Magnetic susceptibility measurements for **1**–**3** in the temperature range 1.9–295 K show the occurrence of weak intramolecular (**1**) and intrachain (**2** and **3**) antiferromagnetic interactions [$J = -0.10$ (**1**), -0.24 (**2**) and -0.03 cm^{-1} (**3**), the Hamiltonians used being $\hat{H} = -J(\hat{S}_1\cdot\hat{S}_2 + \hat{S}_2\cdot\hat{S}_3)$ (**1**) and $H = -J\sum_i(\hat{S}_i\cdot\hat{S}_{i+1})$ (**2** and **3**)]. The magnitude and nature of these magnetic interactions are discussed in the light of the respective structures and they are compared with those reported for related systems.

© 2009 Elsevier Ltd. All rights reserved.

1. Introduction

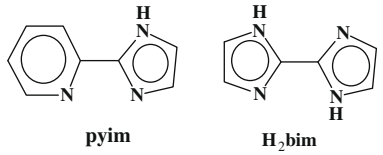
Aromatic nitrogen heterocycles such as 2,2′-biimidazole (H_2bim) or 2-(2′-pyridyl)imidazole (pyim) (see Scheme 1) have in common the bidentate and bridging (under deprotonation) coordination modes in their metal complexes, the neutral character, the presence of aromatic rings that make possible the π–π stacking and their good donor character in hydrogen bonding interactions. All these characteristics are very important with regard to the development and exploration of rational synthetic strategies leading to metal-containing extended supramolecular motifs [1,2]. Concerning this last point, the hydrogen bonded 2,2′-biimidazolate transition metal complexes as a tool of crystal engineering of extended coordination compounds has illustrated the versatility and potentiality of these precursors [3]. In fact, a quite large number of discrete complexes and polymeric species based on association in one, two or three dimensions (*nD* with $n = 1$–3) with H_2bim-containing metal species has been described [2–14]. Another point to be outlined concerns the good number of studies devoted to the synthesis and biological activity of tin(IV) and platinum(II) compounds of H_2bim and its derivatives that have been published [15].

As far as the related pyim ligand is concerned, its coordination chemistry is more limited than that of H_2bim, most likely due to the fact that the yield for this molecule in the more recent preparative method is only *ca.* 33% [16]. It deserves to be noted that the first structural report of a pyim-containing metal complex was published only in 2002 and it concerned the copper(II) chain $\{[Cu(pyim)(\mu\text{-}1,5\text{-}dca)]NO_3\}_n$ (dca = dicyanamide) [17]. Since then, other structures of copper(II) [6b,18], zinc(II) [19], iron(II) [20], manganese(II) [21], vanadium(IV) [22], rhenium(III/IV) [23] and ruthenium(II) [24] complexes as well as those of two heterobimetallic compounds [25] were determined. Apart from the interest in the possibilities of the pyim ligand as a builder of supramolecular arrays through coordinative bonds and hydrogen bonding, the magneto-structural studies on the iron(II)–pyim complexes have revealed the occurrence of the spin-crossover phenomenon [16,20a]. This fact makes this ligand very appealing in research fields such as molecular magnetism and materials science.

In the context of our current magneto-structural studies on polynuclear complexes, we have investigated the complex

* Corresponding authors.
E-mail addresses: jorunn.sletten@kj.uib.no (J. Sletten), miguel.julve@uv.es (M. Julve).

0277-5387/$ - see front matter © 2009 Elsevier Ltd. All rights reserved.
doi:10.1016/j.poly.2009.04.001



Scheme 1.

formation of the related H_2bim or pyim ligands with copper(II) in the presence of thiocyanate as a coligand. The trinuclear complex $\{[Cu(H_2bim)_2][Cu(H_2bim)(NCS)_2(SCN)_{0.6667}(NO_3)_{0.3333}]_2\} \cdot 2H_2O$ (**1**) and the chain compounds $[Cu(H_2bim)(NCS)_2]_n$ (**2**) and $[Cu(pyim)(NCS)_2]_n$ (**3**) were obtained and their preparation, crystal structure and magnetic properties are detailed herein.

2. Experimental

2.1. Materials

Copper(II) nitrate trihydrate and potassium thiocyanate were purchased from commercial sources and used as received. The ligands H_2bim and pyim were prepared by following previously reported methods [16,26]. Elemental analysis (C, H, N, S) were carried out by the Microanalytical Service of the Universidad Autónoma de Madrid.

2.2. Preparation of the complexes

2.2.1. $\{[Cu(H_2bim)_2][Cu(H_2bim)(NCS)_2(SCN)_{0.6667}(NO_3)_{0.3333}]_2\} \cdot 2H_2O$ (**1**) and $[Cu(H_2bim)(NCS)_2]_n$ (**2**)

Solid H_2bim (0.040 g, 0.313 mmol) was poured into an aqueous solution (150 cm^3) of $Cu(NO_3)_2 \cdot 3H_2O$ (0.150 g, 0.625 mmol) and then an aqueous solution (50 cm^3) containing KNCS (0.120 g, 1.25 mmol) was added dropwise under continuous stirring. X-ray quality deep green plate-like (**1**) and polyhedral (**2**) crystals were grown from the resulting green solution after one month by slow evaporation at room temperature. They were separated manually, washed with a small amount of cold water and dried on filter paper. The yields are 20% (**1**) and 75% (**2**). These percentages are practically interchanged when the starting Cu(II):H_2bim:NCS^- molar ratio is 1:1:2 [*ca.* 70% (**1**) and 20% (**2**)] (yields based on of the H_2bim ligand). *Anal.* Calc. for $C_{29.33}H_{28}Cu_3N_{22}O_4S_{5.33}$ (**1**): C, 31.61; H, 2.51; N, 27.66; S, 15.35. Found: C, 31.49; H, 2.46; N, 27.51; S, 15.25%. *Anal.* Calc. for $C_8H_6CuN_6S_2$ (**2**): C, 30.62; H, 1.91; N, 26.77; S, 20.44. Found: C, 30.51; H, 1.88; N, 26.70; S, 20.28%.

2.2.2. $[Cu(pyim)(NCS)_2]_n$ (**3**)

Single crystals of **3** as green polyhedra were grown by slow diffusion in an H-shaped tube of aqueous solutions containing KNCS (0.0408 g, 0.50 mmol) in one arm and a mixture of $Cu(NO_3)_2 \cdot 3H_2O$ (0.060 g, 0.25 mmol) and pyim (0.036 g, 0.25 mmol) in the other arm. The two arms were carefully filled with water and the whole was allowed to diffuse at room temperature. The crystals were collected after 20 days, they were washed with a small mount of cold water and dried on filter paper. The yield was *ca.* 80%. *Anal.* Calc. for $C_{10}H_7CuN_5S_2$ (**3**): C, 36.98; H, 2.16; N, 21.55; S, 19.75. Found: C, 36.87; H, 2.12; N, 21.20; S, 19.64%.

2.3. Physical techniques

IR spectra (4000–400 cm^{-1}) were recorded on a Bruker IF S55 spectrophotometer with samples prepared as KBr pellets. Variable-temperature (1.9–295 K) magnetic susceptibility measurements on polycrystalline samples were carried out with a Quantum Design SQUID susceptometer using an applied magnetic field of 1000 G over the whole temperature range. The complex $(NH_4)_2Mn(SO_4)_2 \cdot 6H_2O$ was used as a susceptibility standard. Diamagnetic corrections for the constituent atoms were estimated from Pascal's constants [27] as -525×10^{-6} (**1**), -147×10^{-6} (**2**) and -157×10^{-6} cm^3 mol^{-1} (**3**). A value of 60×10^{-6} cm^3 mol^{-1} was used for the temperature-independent paramagnetism of the copper(II) ion.

2.4. X-ray data collection and structure refinement

Diffraction data were collected with a Bruker-AXS SMART 2 K CCD area detector diffractometer at 293 (**1** and **2**) and 153 K (**3**). Crystal parameters and refinement results are listed in Table 1. The three structures were solved by direct methods and they were refined by full-matrix least-squares based on F^2, including all reflections. In the case of compound **1** the electron density maps

Table 1
Crystal data and structure refinement for $\{[Cu(H_2bim)_2][Cu(H_2bim)(NCS)_2(SCN)_{0.6667}(NO_3)_{0.3333}\} \cdot 2H_2O$ (**1**), $[Cu(H_2bim)(NCS)_2]_n$ (**2**) and $[Cu(pyim)(NCS)_2]_n$ (**3**).

	1	2	3
Empirical formula	$C_{29.33}H_{28}Cu_3N_{22}O_2S_{5.33}$	$C_8H_6CuN_6S_2$	$C_{10}H_7CuN_5S_2$
Formula weight	1114.20	313.85	324.87
Temperature (K)	293	293	153
λ (Å)	0.71073	0.71073	0.71073
Space group	$P\bar{1}$	$P2_1/c$	Cc
a (Å)	7.3602(4)	9.5176(5)	7.8972(11)
b (Å)	9.8917(6)	16.4831(8)	14.975(2)
c (Å)	15.8359(9)	7.6488(4)	10.4944(14)
α (°)	78.652(2)		
β (°)	83.0370(10)	99.9880(10)	95.140(3)
γ (°)	72.4100(10)		
V (Å^3)	1075.18(11)	1181.75(10)	1236.1(3)
Z	1	4	4
ρ (Mg m^{-3})	1.721	1.764	1.746
μ (mm^{-1})	1.794	2.186	2.091
Max. 2θ (°)	55.0	64.1	52.0
Reflections collected	8128	10 930	3929
Independent reflections [R_{int}]	4943 [0.0264]	3825 [0.0197]	1855 [0.0480]
Reflections with $I > 2\sigma(I)$	3302	3016	1504
Data/restraints/parameters	4943/0/278	3825/0/154	1855/0/164
Goodness-of-fit, S, on F^2	1.064	1.074	1.066
R [$I > 2\sigma(I)$]	0.0463	0.0298	0.0664
R_w [$I > 2\sigma(I)$]	0.1150	0.0776	0.1701

clearly indicated that disorder is present at the site of one of the terminal thiocyanato groups. Initially, models with two orientations of the thiocyanato group were tested (S- and N-coordinated, respectively), but the residual electron density was still high, and suggested the presence of a four-atom group, rather than a rotated three-atom group as the minor component. As copper(II) nitrate had been used in the synthetic procedure, the presence of nitrate at this site would be possible. Eventually the best fit was obtained for a disordered model in which an S-coordinated thiocyanato group is present in 2/3 of the unit cells and a nitrate in 1/3 of the cells. Both disordered groups were refined as rigid groups with idealized geometry. In case of compound **3** systematic extinctions are compatible with space groups *Cc* or *C2/c*. Structure refinement in the centrosymmetric space group, with Cu on the twofold axis, revealed that a disordered model, not only for the pyim group, but also for Cu and thiocyanate, had to be invoked. After conversion to the non-centrosymmetric space group, *Cc*, refinement of an ordered model resulted. A pseudo twofold axis and a pseudo centre of symmetry are present in the structure due to the similarity and positions of the five- and six-membered rings of the pyim ligands. For all three compounds non-hydrogen atoms, except those in the disordered region of **1**, were anisotropically refined. All hydrogen atoms were clearly seen in electron difference Fourier maps. Those bound to carbon and nitrogen were included at idealized positions whereas those bound to water oxygen in **1** were included at positions found in the electron difference map, and all hydrogen atoms were refined according to the riding model.

Table 2
Selected bond distances (Å) and angles (°) for $\{[Cu(H_2bim)_2][Cu(H_2bim)(NCS)_2(SCN)_{0.6667}(NO_3)_{0.3333}\}\cdot 2H_2O$ (**1**).[a]

Copper coordination spheres			
Cu(1)–N(5)	1.942(3)	Cu(1)–S(31)	2.804(2)
Cu(1)–N(6)	1.944(3)	Cu(2)–N(9)	2.014(3)
Cu(1)–N(1)	1.995(3)	Cu(2)–N(7)	2.025(3)
Cu(1)–N(3)	2.006(3)	Cu(2)–S(1)	3.0357(11)
Cu(1)–O(42)	2.277(7)		
N(5)–Cu(1)–N(6)	93.02(14)	N(6)–Cu(1)–S(31)	101.21(13)
N(5)–Cu(1)–N(1)	92.60(12)	N(1)–Cu(1)–S(31)	84.25(10)
N(6)–Cu(1)–N(1)	171.19(14)	N(3)–Cu(1)–S(31)	91.19(10)
N(5)–Cu(1)–N(3)	164.94(14)	O(42)–Cu(1)–S(31)	14.44(16)
N(6)–Cu(1)–N(3)	91.87(13)	N(9a)–Cu(2)–N(9)	180.00
N(1)–Cu(1)–N(3)	81.03(12)	N(9)–Cu(2)–N(7)	82.01(11)
N(5)–Cu(1)–O(42)	94.51(18)	N(9)–Cu(2)–N(7a)	97.99(11)
N(6)–Cu(1)–O(42)	89.3(2)	N(7)–Cu(2)–N(7a)	180.00
N(1)–Cu(1)–O(42)	97.04(19)	S(1)–Cu(2)–N(7)	88.44(8)
N(3)–Cu(1)–O(42)	99.79(18)	S(1)–Cu(2)–N(9)	94.38(8)
N(5)–Cu(1)–S(31)	101.80(11)	S(1)–Cu(2)–S(1a)	180.00
Thiocyanato groups			
S(1)–C(7)	1.637(4)	N(5)–C(7)	1.146(4)
S(2)–C(8)	1.618(4)	N(6)–C(8)	1.145(5)
C(7)–N(5)–Cu(1)	166.8(3)	N(6)–C(8)–S(2)	178.9(4)
C(8)–N(6)–Cu(1)	164.7(4)	C(7)–S(1)–Cu(2)	94.14(13)
N(5)–C(7)–S(1)	179.2(3)		

Hydrogen bonds[a]

D	H	A	D···A (Å)	H···A (Å)	D–H···A (°)
N(2)	H(2)	O(42b)[b]	2.717(19)	1.86	172
N(4)	H(4)	O(41b)[b]	2.96(4)	2.20	148
N(8)	H(8)	O(1)	2.836(4)	2.04	153
N(10)	H(10)	O(1)	3.003(4)	2.25	147
N(2)	H(2)	S(31b)[b]	3.319(4)	2.49	163
N(4)	H(4)	N(31b)[b]	3.00(4)	2.20	155
O(1)	H(22)	S(2c)	3.340(3)	2.54	146
O(1)	H(23)	N(31d)[b]	3.04(4)	2.11	159

[a] Symmetry transformation used to generate equivalent atoms: (a) $-x, -y+1, -z+1$; (b) $1+x, y, z$; (c) $-x, 1-y, -z$; (d) $x, 1+y, z$.
[b] These atoms belong to the disordered groups.

Data collection and data reduction were done with the SMART and SAINT programs [28]. Absorption corrections were carried out using the SADABS routine [29]. All other calculations were performed with the SHELXS-97, SHELXL/PC and XP programs [30]. Selected bond distances and angles are listed in Tables 2–4.

Table 3
Selected bond distances (Å) and angles (°) for $[Cu(H_2bim)(NCS)_2]_n$ (**2**).[a]

Copper coordination sphere			
Cu(1)–N(5)	1.9490(16)	Cu(1)–N(1)	2.0146(14)
Cu(1)–N(6)	1.9604(17)	Cu(1)–S(1a)	2.6744(6)
Cu(1)–N(3)	2.0032(14)		
N(5)–Cu(1)–N(6)	94.16(7)	N(3)–Cu(1)–N(1)	80.75(6)
N(5)–Cu(1)–N(3)	168.16(7)	N(5)–Cu(1)–S(1a)	98.34(6)
N(6)–Cu(1)–N(3)	92.38(7)	N(6)–Cu(1)–S(1a)	96.91(6)
N(5)–Cu(1)–N(1)	90.70(6)	N(3)–Cu(1)–S(1a)	90.65(5)
N(6)–Cu(1)–N(1)	166.02(7)	N(1)–Cu(1)–S(1a)	95.34(4)
Thiocyanato groups			
S(1)–C(7)	1.6312(18)	N(5)–C(7)	1.145(2)
S(2)–C(8)	1.6320(19)	N(6)–C(8)	1.141(2)
C(7)–S(1)–Cu(1b)	97.57(7)	N(5)–C(7)–S(1)	178.62(18)
C(7)–N(5)–Cu(1)	170.47(16)	N(6)–C(8)–S(2)	178.2(2)
C(8)–N(6)–Cu(1)	173.60(19)		

N–H···S contacts

D	H	A	D···A (Å)	H···A (Å)	D–H···A (°)
N(2)	H(2)	S(1d)	3.3309(15)	2.78	123
N(2)	H(2)	S(2c)	3.4647(17)	2.81	134
N(4)	H(4)	S(2e)	3.3912(16)	2.65	145

[a] Symmetry transformations used to generate equivalent atoms: (a) $x, -y+1/2, z-1/2$; (b) $x, -y+1/2, z+1/2$; (c) $-x, -y, 1-z$; (d) $1-x, -0.5+y, 1.5-z$; (e) $-x, -0.5+y, 0.5-z$.

Table 4
Selected bond distances (Å) and angles (°) for $[Cu(pyim)(NCS)_2]_n$ (**3**).[a]

Copper coordination sphere			
Cu(1)–N(4)	1.925(11)	Cu(1)–N(2)	2.014(9)
Cu(1)–N(5)	1.987(10)	Cu(1)–S(1a)	3.171(3)
Cu(1)–N(1)	2.001(11)	Cu(1)–S(2b)	3.177(4)
N(4)–Cu(1)–N(5)	97.0(3)	N(1)–Cu(1)–S(1a)	111.0(3)
N(4)–Cu(1)–N(1)	162.2(4)	N(2)–Cu(1)–S(1a)	79.3(3)
N(5)–Cu(1)–N(1)	92.2(5)	N(4)–Cu(1)–S(2b)	87.6(3)
N(4)–Cu(1)–N(2)	94.2(4)	N(5)–Cu(1)–S(2b)	91.8(3)
N(5)–Cu(1)–N(2)	161.2(3)	N(1)–Cu(1)–S(2b)	76.8(3)
N(1)–Cu(1)–N(2)	81.4(3)	N(2)–Cu(1)–S(2b)	103.8(3)
N(4)–Cu(1)–S(1a)	84.9(3)	S(1a)–Cu(1)–S(2b)	172.08(11)
N(5)–Cu(1)–S(1a)	86.7(3)		
Thiocyanato groups			
S(1)–C(9)	1.639(15)	N(4)–C(9)	1.159(13)
S(2)–C(10)	1.654(12)	N(5)–C(10)	1.097(12)
C(9)–S(1)–Cu(1b)	104.2(5)	C(10)–N(5)–Cu(1)	168.3(9)
C(10)–S(2)–Cu(1a)	103.9(4)	N(4)–C(9)–S(1)	178.3(11)
C(9)–N(4)–Cu(1)	165.9(9)	N(5)–C(10)–S(2)	179.4(10)
		N(1)–C(6)–N(3)	103.2(12)
C(3)–C(4)–C(5)	114.1(12)	C(5)–C(6)–N(3)	138.0(13)
N(2)–C(5)–C(4)	125.8(13)	C(8)–C(7)–N(1)	112.8(11)
N(2)–C(5)–C(6)	113.7(11)	C(7)–C(8)–N(3)	106.5(12)
C(4)–C(5)–C(6)	120.4(13)	N(4)–C(9)–S(1)	178.3(11)
N(1)–C(6)–C(5)	118.7(12)	N(5)–C(10)–S(2)	179.4(10)

N–H···S and C–H···S contacts[a]

D	H	A	D···A (Å)	H···A (Å)	D–H···A (°)
N(3)	H(31)	S(1c)	3.714(10)	2.92	151
C(7)	H(7)	S(1d)	3.699(13)	2.82	155
C(8)	H(8)	S(2e)	3.868(14)	2.93	171

[a] Symmetry transformations used to generate equivalent atoms: (a) $x, -y, z-1/2$; (b) $x, -y, z+1/2$; (c) $-0.5+x, 0.5-y, -0.5+z$; (d) $-1+x, -y, -0.5+z$; (e) $-0.5+x, 0.5+y, z$.

3. Results and discussion

3.1. Synthesis and IR characterization

Compounds **1**–**3** have been obtained by reacting copper(II) nitrate and potassium thiocyanate with H_2bim (**1** and **2**) or pyim (**3**) as coligands. **1** is a trinuclear species whereas **2** and **3** are chain compounds all of them being neutral. The electroneutrality in this family is achieved by the coordination of thiocyanate either as a terminal [through the nitrogen (**1** and **2**) and sulfur (**1**)] or bridging [single (**1** and **2**) and double (**3**) end-to-end coordination mode] ligand, H_2bim and pyim adopting the bidentate coordination mode. Curiously, in the case of **1** the nitrate is also present as a terminal ligand. The low solubility in water of **1** and **2** accounts for their coprecipitation, but either compound may become the major product by modifying starting Cu(II):H_2bim:NCS^- molar ratio. In the light of previous studies of metal complexes with H_2bim or pyim as ligands [3,31], it is clear that the possibility of their deprotonation in **1**–**3** deserves to be investigated further. Most likely, this deprotonation would allow to overcome their insolubility and it would afford different species. As widely shown for the coordinated H_2bim, the release of the imidazole-hydrogen from the coordinated pyim in the presence of a base, would allow the coordination of the free imidazolate nitrogen to a metal ion to yield imidazolate-bridged polynuclear compounds. Interestingly, only a limited number of metal complexes containing deprotonated pyim is cited and their structures remain unknown [31].

Dealing with the IR spectra of **1**–**3**, the most relevant information concerns the high frequency region. The presence of the coordinated H_2bim (**1** and **2**) or pyim (**3**) is evidenced by the N–H [3130 (**1**), 3122 (**2**) and 3265 cm^{-1} (**3**)] and C–H [multiplet in the range 3100–2700 (**1** and **2**) and 3090–2750 cm^{-1} (**3**)] stretchings. It deserves to be noted that the N–H and C–H stretching vibrations of the free H_2bim and pyim molecules appear as multiplets in the region 3200–2500 cm^{-1}. The region of the ν_{CN} stretching band of the thiocyanate is very illustrative in the present family because of the shift towards higher frequency values (this band appears at 2053 cm^{-1} for the free KNCS) and the number of peaks: a triplet at 2112, 2086 and 2055 cm^{-1} for **1**, a doublet at 2116 and 2090 cm^{-1} for **2** and a strong absorption at 2115 cm^{-1} with a shoulder at 2124 cm^{-1} for **3**. According to the literature [32–35], the the ν_{CN} stretching occurs close to 2053 cm^{-1} when it exhibits the N-bonded coordination mode whereas in complexes containing the S-bonded thiocyanate, this value is near 2100 cm^{-1} and in the case of end-to-end bridging (M–NCS–M), this vibrational frequency is higher than 2100 cm^{-1}. These spectral data are in agreement with the coordination modes of the thiocyanate ligand in the crystal structures of the present series of complexes [terminal thiocyanato-N (**1** and **2**) or -S (**1**) and end-to-end bridging thiocyanato (**2** and **3**)] (see below).

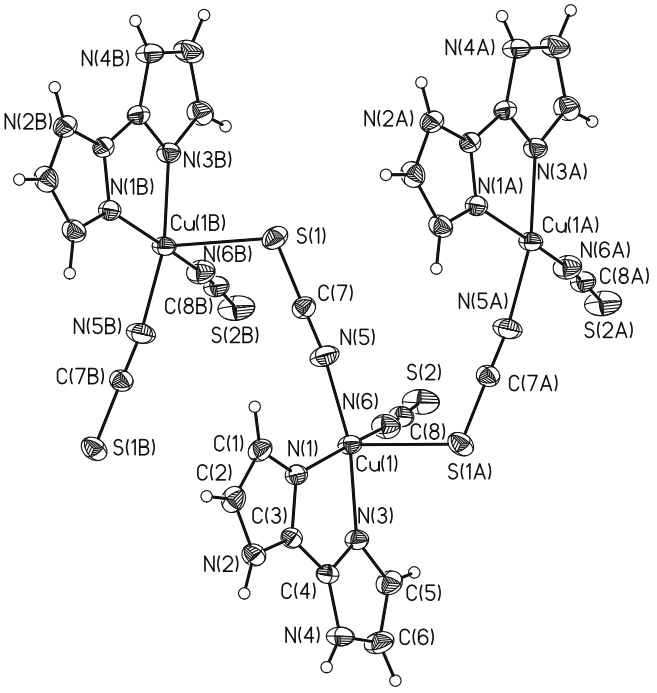


Fig. 2. Chain structure of **2**. Thermal ellipsoids are plotted at the 30% probability level. Symmetry code: (a) $x, 0.5 - y, -0.5 + z$; (b) $x, 0.5 - y, 0.5 + z$.

3.2. Description of the structures

3.2.1. $\{[Cu(H_2bim)_2][Cu(H_2bim)(NCS)_2(SCN)_{0.6667}(NO_3)_{0.3333}]_2\} \cdot 2H_2O$ (*1*)

The crystal structure of **1** is formally built of $[Cu(H_2bim)_2]^{2+}$ and $[Cu(H_2bim)(NCS)_2(SCN)]^-$ ions ($[Cu(H_2bim)(NCS)_2(NO_3)]^-$ ions in the minor site; see below) and water of hydration. One cation and two anions are connected through single end-to-end out-of-plane thiocyanato bridges to form a trinuclear entity (Fig. 1). The copper atom of the cation is situated at a crystallographic inversion

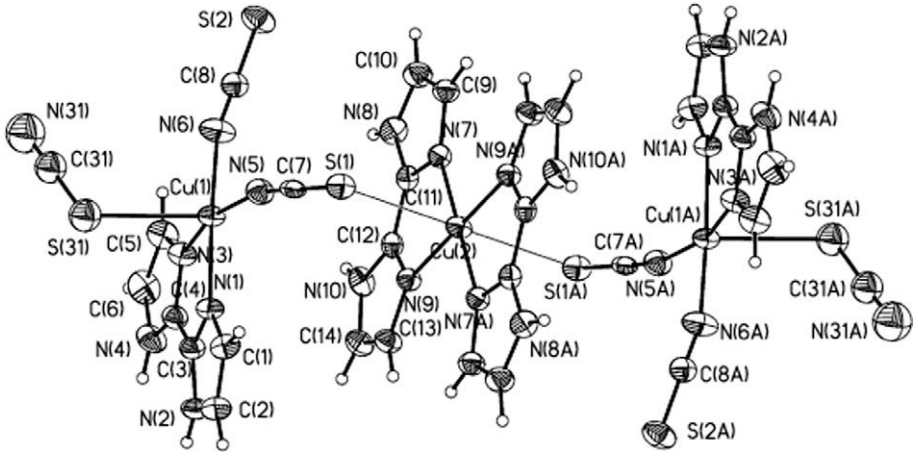


Fig. 1. The trinuclear unit in compound **1**. Only the major component of the disordered axial ligand on Cu(1) is shown. Thermal ellipsoids are plotted at the 30% probability level.

centre, and it is bound to four H_2bim nitrogen atoms in a rhombic planar arrangement [Cu(2)–N(7) = 2.025(3) Å and Cu(2)–N(9) = 2.014(3) Å]. In addition there are semi-coordinated weak axial Cu–S interactions [Cu(2)–S(1) = 3.0357(11) Å] to thiocyanato groups which are N-bound at the anion site. The copper atom of the anion [Cu(1)] has a distorted square pyramidal coordination sphere, the equatorial plane being defined by four nitrogen atoms, two from H_2bim, [Cu(1)–N(1) = 1.995(3) Å and Cu(1)–N(3) = 2.006(3) Å], one from the bridging thiocyanate [Cu(1)–N(5) = 1.942(3) Å], and one from a terminal thiocyanate [Cu(1)–N(6) = 1.944(3) Å]. The disordered thiocyanato/nitrato group resides in the apical site; the major site (occupancy 0.6667) through S-coordinated thiocyanate [Cu(1)–S(31) = 2.804(2) Å] and the minor site (occupancy 0.3333) across O-coordinated nitrate [Cu(1)–O(42) = 2.277(7) Å]. The plane of Cu(1) has a significant tetrahedral distortion, the maximum atomic deviation being 0.071 Å, and the copper atom is displaced 0.172 Å from this plane in the direction of the apical ligand. The equatorial plane of Cu(2) is exactly planar. Each of the imidazole rings is essentially planar, the dihedral angles between the two rings within a H_2bim molecule are 4.6° and 4.1°. These values compare well with that observed in the free H_2bim molecule (1.2°) [36]. The values of the inter-ring C(11)–C(12) and C(3)–C(4) bond distances of the two bidentate H_2bim ligands in **1** [1.431(5) and 1.439(5) Å, respectively] are similar to those found for the free [1.423(8) Å] [36] and coordinated biimidazole [1.447(3) and 1.442(5) Å in the complexes $[Cu(H_2bim)(C_2O_4)(H_2O)]\cdot H_2O$ and $[Cu(H_2bim)_2(H_2O)](NO_3)_2$, respectively] [6b,d]. The Cu(1)···Cu(2) distance within the trinuclear entity is 5.6143(5) Å whereas the shortest intermolecular copper–copper separation is 7.2046(6) Å [Cu(1)···Cu(2e), (e) referring to the unit cell translation $x, y-1, z$]. The neutral trinuclear units are interlinked through hydrogen bonds involving the imidazole, thiocyanate, nitrate and water molecules (see end of Table 2). To our knowledge this is the first report on a trinuclear thiocyanato-bridged copper(II) complex.

3.2.2. $[Cu(H_2bim)(NCS)_2]_n$ (**2**)

This compound features a chain structure with single out-of-plane, end-to-end thiocyanato bridges (Fig. 2). The copper atom has a distorted square pyramidal coordination sphere, the equatorial plane being defined by four nitrogen atoms, two from the chelating H_2bim group [Cu(1)–N(1) = 2.0146(14) Å, Cu(1)–N(3) = 2.0032(14) Å], one from the bridging thiocyanate group [Cu(1)–N(5) = 1.9490(16) Å], and one from the terminal thiocyanate [Cu(1)–N(6) = 1.9604(17) Å]. The sulfur atom of bridging thiocyanate resides in the apical position [Cu(1)–S(1a) = 2.6744(6) Å, (a) referring to the *c*-glide symmetry operation $x, 0.5-y, -0.5+z$]. The equatorial plane at the copper atom has a slight tetrahedral distortion (maximum atomic deviation of 0.033 Å), and the copper

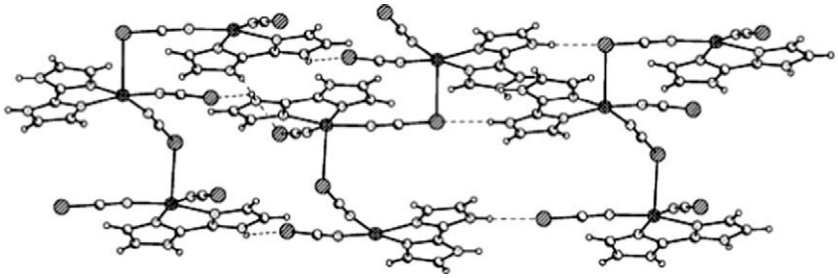


Fig. 3. Section of packing in compound **2**. Three neighbour chains are included. The N–H···S contacts listed in Table 3 are indicated by dashed lines.

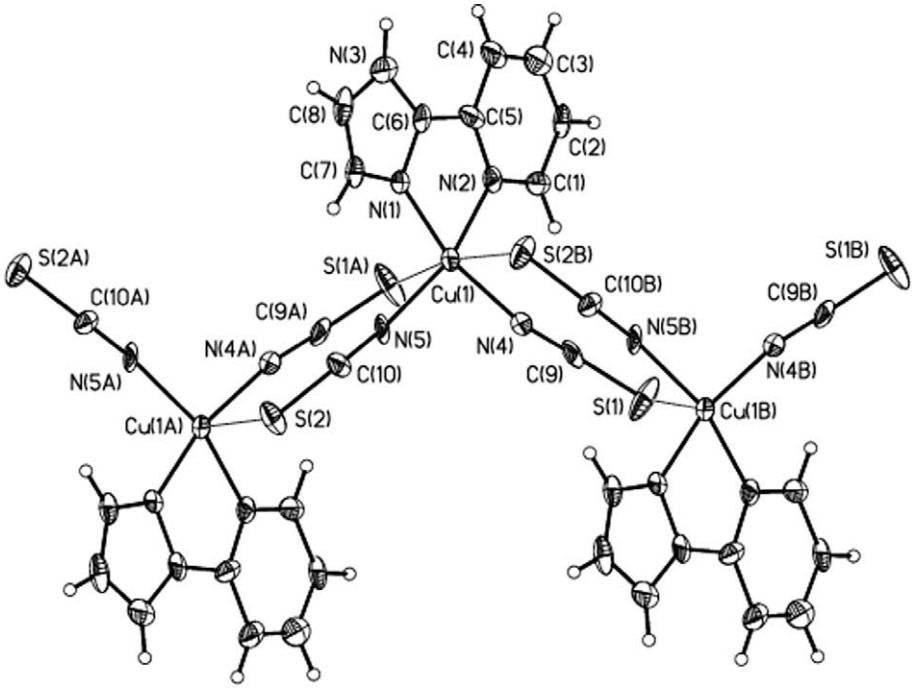


Fig. 4. Section of the chain structure in **3**. Thermal ellipsoids are plotted at the 30% probability level. Symmetry code: (a) $x, -y, -0.5+z$; (b) $x, -y, 0.5+z$.

atom is displaced by 0.188 Å from the mean equatorial plane towards the apical ligand. The individual imidazole rings are essentially planar and the dihedral angle between the two rings is 6.7°. The value of the inter-ring C(3)–C(4) bond distance of the bidentate H_2bim ligand is 1.438(2) Å. The chains are linked through weak N–H···S interactions (see end of Table 3 and Fig. 3) and van der Waals forces. The intra-chain Cu(1)···Cu(1a) distance is 5.6744(3) Å, a value which is somewhat longer then the shortest interchain metal–metal distance [5.4824(5) Å for Cu(1)··· Cu(1c); symmetry code: (c) $-x, -y, 1-z$].

3.2.3. $[Cu(pyim)(NCS)_2]_n$ (**3**)

The building block of this structure is the neutral [Cu(pyim)$(NCS)_2$] moiety with chelating pyim [Cu(1)–N(1) = 2.001(11) Å and Cu(1)–N(2) = 2.014(9) Å] and two thiocyanato nitrogen atoms [Cu(1)–N(4) = 1.925(11) Å and Cu(1)–N(5) = 1.987(10) Å)] coordinating in the equatorial plane of the copper atom. These units are connected into a chain through double, out-of-plane end-to-end thiocyanato bridges where the sulfur atoms form weak axial interactions with copper [Cu(1)–S(1a) = 3.171(3) Å and Cu(1)–S(2b) = 3.177(4) Å; (a) and (b) referring to symmetry operations $x, -y, -0.5+z$ and $x, -y, 0.5+z$, respectively] (Fig. 4). The equatorial plane of the copper atom has a pronounced tetrahedral distortion (maximum atomic deviation is 0.302 Å), the metal atom being situated close to the averaged plane (atomic deviation 0.004 Å). Each ring of the pyim ligand is essentially planar and the dihedral angle between the two rings is only 1.5°. The small deviation from planarity of the pyim molecule is in agreement with the significant double bond character of the inter-ring C(5)–C(6) bond [1.415(13) Å]. The bond distances and angles of the pyim ligand in **3** are similar to those observed in other pyim-containing copper(II) complexes [6b,17,18,25b]. Parallel chains in the crystal are linked through N–H···S and C–H···S type interactions (see end of Table 4) creating a three-dimensional network (Fig. 5). The intra-chain Cu(1)···Cu(1a) distance is 6.0797(11) Å whereas the shortest interchain metal–metal separation is 7.6758(12) Å [Cu(1)···Cu(1f); symmetry code: (f) $0.5+x, 0.5-y, 0.5+z$].

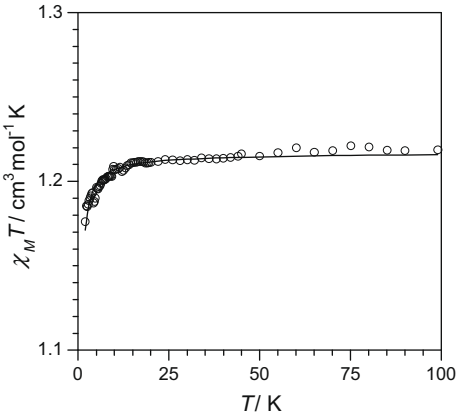


Fig. 6. Temperature dependence of the $\chi_M T$ product for **1**. The solid line is the best-fit curve through Eq. (1) (see text).

3.2.4. Magnetic properties

The thermal dependence of the $\chi_M T$ product for **1**–**3** [χ_M is the magnetic susceptibility per three (**1**) and one (**2** and **3**) copper(II) ions] is shown in Figs. 6 (**1**) and 7 (**2** and **3**). At room temperature, $\chi_M T$ is equal to 1.22 (**1**), 0.418 (**2**) and 0.407 cm^3 mol^{-1} K (**3**). These values are as expected for three (**1**) and one (**2** and **3**) magnetically isolated spin doublets. A Curie law behaviour is observed for the three compounds upon cooling from room temperature down to 90 (**2**), 15 (**1**) and 10 K (**3**). A small decrease of $\chi_M T$ is observed in the lower temperature range to reach minimum values of 0.373 (**2**), 1.175 (**1**) and 0.398 cm^3 mol^{-1} K (**3**) at 1.9 K. These features indicate the occurrence of very weak intramolecular (**1**) and intrachain (**2** and **3**) antiferromagnetic interactions.

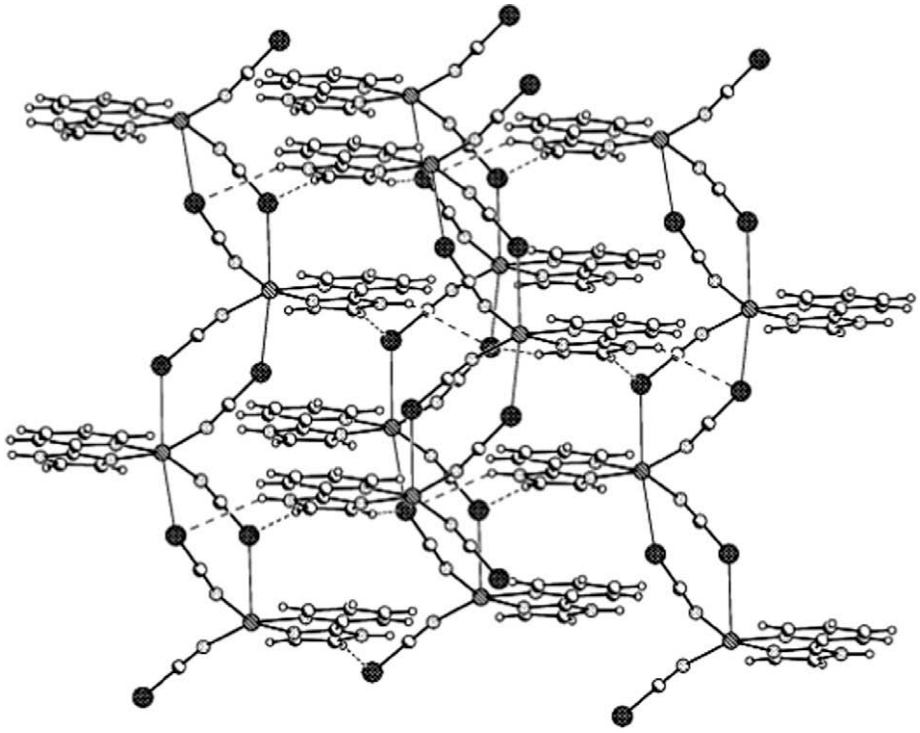


Fig. 5. Packing of chains in **3**. Four chains are shown, running vertical. N–H···S and C–H···S interactions between chains are indicated.

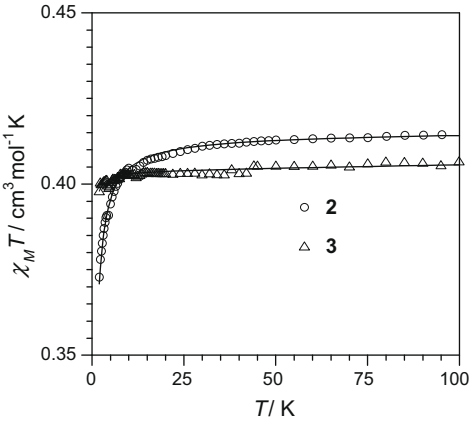


Fig. 7. Temperature dependence of the $\chi_M T$ product for **2** (△) and **3** (○). The solid lines are the best-fit curves through Eq. (2) (see text).

In agreement with the trinuclear structure of **1**, its magnetic susceptibility data were analyzed through the expression [Eq. (1)]

$$\chi_M = N\beta^2 g^2/4kT\{[1+\exp(J/kT)+10\exp(3J/2kT)]/[1+\exp(J/kT)+2\exp(3J/2kT)]\} \quad (1)$$

where N, β, g, k and T have their usual meaning and J is the exchange coupling between the peripheral and central copper(II) ions after the isotropic Hamiltonian $\hat{H} = -J[(\hat{S}_1 \cdot \hat{S}_2) + (\hat{S}_2 \cdot \hat{S}_3)]$ with $\hat{S}_1 = \hat{S}_2 = \hat{S}_3 = 1/2$. Best-fit parameters for **1** through Eq. (1) are $J = -0.10\ cm^{-1}$, $g = 2.08$ and $R = 1.1 \times 10^{-5}$ where R is the agreement factor defined as $\sum_i[(\chi_M T)_{obs(i)} - (\chi_M T)_{calc(i)}]^2/\sum_i[(\chi_M T)_{obs(i)}]^2$.

Given the one-dimensional structure of **2** and **3**, their magnetic data were analyzed through the numerical expression for a uniform chain of local spin doublets [Eq. (2)] [37]

$$\chi_M = (N\beta^2 g^2/kT)[(0.25+0.074975x+0.075235x^2)/(1.0+0.9931x+0.172135x^2+0.757825x^3)] \quad (2)$$

which is derived from the isotropic Hamiltonian $\hat{H} = -J\sum_i \hat{S}_i \cdot \hat{S}_{i+1}$ where $x = |J|/kT$ and J is the exchange coupling constant describing the magnetic interaction between the two nearest-neighbour spin doublets. Best-fit parameters through Eq. (2) leads to the following values: $J = -0.24\ cm^{-1}$, $g = 2.10$ and $R = 2.1 \times 10^{-5}$ for **2** and $J = -0.03\ cm^{-1}$, $g = 2.08$ and $R = 2.8 \times 10^{-5}$ for **3**.

The information available in the literature concerning the magnetic properties of structurally characterized single- and double-thiocyanato-bridged copper(II) complexes is quite limited and a summary of relevant magneto-structural data is listed in Table 5. One can see there that the magnetic coupling is weak and either ferro- or antiferromagnetic in nature. The observed weak antiferromagnetic couplings in **1**–**3** are hence in line with the previous magnetic data on related complexes. All these compounds have in common the end-to-end coordination mode of the thiocyanato bridge linking one equatorial position at one copper atom with the apical one of the adjacent copper. Taking our compounds as suitable examples, the weakness of the magnetic interaction can be easily understood having in mind the intramolecular (**1**) and intrachain (**2** and **3**) out-of-plane exchange pathways through the single (**1** and **2**) and double (**3**) thiocyanato bridges which

Table 5
Selected magneto-structural data for single- and double-$\mu_{1,5}$-thiocyanato-bridged copper(II) complexes.

Compound[a]	Nucleus	Geometry[b]	Cu–N (Å)	Cu–S (Å0	Cu–N–C (°)	Cu–S–C (°)	$d_{Cu\cdots Cu}$[c] (Å)	J[d] (cm^{-1})	Reference
Single end-to-end thiocyanato bridge									
$[CuL^1(NCS)_2]_n$	1D	dsp	1.959_{eq}	2.771_{ax}	146.5	97.6	5.599	~0	[44]
$[Cu(dach)(NCS)_2]_n$	1D	dsp	1.959_{eq}	2.769_{ax}	169.1	90.3	5.27	~0	[45]
1	trimer	dsp	1.942_{eq}		166.8		5.614	−0.10	this work
		eo		3.0357_{ax}		94.14			
[Cu(pebch)(NCS)]	1D	dsp	1.965_{eq}	2.711_{ax}	160.0	97.01	5.806	−0.23	[47]
2	1D	dsp	1.949_{eq}	2.674_{ax}	170.5	97.6	5.674	−0.24	this work
$[Cu(NCS)_2(dpk\cdot MeOH)]_n$	1D	eo	1.969_{eq}	2.837_{ax}	164.4	100.6	5.994	−0.3	[39]
[Cu(dmapb)	1D	dsp	1.954_{eq}	2.806_{ax}	173.2	111.3	6.268	−0.57	[48]
$[Cu(bpy)(NCS)_2]_n$	2D	eo	1.956_{eq}	3.030_{ax}*	169.0	99.2*	5.98*	−1.01[e]	[46]
		dsp	1.950_{eq}*	2.728_{ax}	166.6*	97.9			
$[Cu(mpsme)(NCS)]_n$	1D	dsp	1.926_{eq}	2.7445_{ax}	173.7	96.6	5.749	−1.73	[49]
$[Cu(daco)(NCS)_2]$	1D	dsp	2.005_{eq}	2.644_{ax}	161.5	91.9	5.293	+1.04	[50]
Double end-to-end thiocyanato bridges									
α-$[Cu(dmtp)_2(NCS)_2]_2$	dimer	dsp	1.953_{eq}	2.886_{ax}	167.7	95.2	5.552	~0	[41a]
3	1D	dsp	1.956_{eq}*	3.174_{ax}*	167.1*	104.1*	6.080	−0.03	this work
$[Cu(bpy)(NCS)_2]_n$	1D	eo	2.012_{eq}	3.239_{ax}	165.1(3)	104.7(3)	6.114	−0.13	[42]
$[Cu(bpym)(NCS)_2]_n$	1D	eo	1.941_{eq}	3.174_{ax}	165.0	83.1	5.328	−0.6	[38]
$[Cu(NCS)_2(dpk\cdot MeOH)]_n$	dimer	eo	1.945_{eq}	2.852_{ax}	171.9	91.2	5.389	−0.9	[39]
$[Cu(H_2O)(dpp)(NCS)_2]_2\cdot 2H_2O$	dimer	eo	1.956_{eq}	3.065_{ax}	161.3	86.3	5.371	−1.0	[34]
$[CuL^2(NCS)]_2$	dimer	dsp	1.995_{eq}	2.952_{ax}	164.1	102.6	5.863	−1.7	[40]
$[Cu(medpt)(NCS)]_2(ClO_4)_2$	dimer	dsp	2.016_{eq}*	2.722_{ax}*	164.2*	94.7*	5.486*	−1.8	[51]
β-$[Cu(dmtp)_2(NCS)_2]_2$	dimer	dsp	2.205_{ax}	2.413_{eq}	142.8	99.2	5.369	~+1	[41b]
$[Cu(ept)(NCS)]_2(ClO_4)_2$	dimer	eo	1.946_{eq}	2.978_{ax}	171.4	90.6	5.462	+1.3	[43]
$[Cu(Me_5dien)_2(NCS)_2]_2(ClO_4)_2$	dimer	dsp	1.943_{eq}	2.678_{ax}	164.4	99.8	5.575	+1.6	[43]
$[Cu(Et_3dien)(NCS)]_2(ClO_4)_2$	dimer	eo	1.978_{eq}	2.758_{ax}	169.0	99.82	5.718	+7.7	[43]

[a] *Abbreviations used:* L^1, 2-methylamino-5-pyridin-2-yl-1,3,4-oxadiazole; dach, 1,4-diazacycloheptane; dpk, di-2-pyridyl-ketone; dmtp, 5,7-dimethyl[1,2,4]triazolo[1,5-*a*]pyrimidine; bpy, 2,2′-bipyridine; bpym, 2,2′-bipyrimidine; dpp, 2,3bis(2-pyridyl)pyrazine; L^2, *N*-(3-aminopropyl)salicylaldimine; ept, *N*-(2-aminoethyl)-1,3-propanediamine; Me_5dien, 1,1,4,7,7-pentamethyldiethylenetriamine; Et_3dien, 1,4,7-triethyldiethylenetriamine; pebch, 1-(2-pyridyl)ethylidene) benzenecarbohydrazonate; mpsme, 6-methyl-2-formylpyridine-*S*-methyldithiocarbazate; daco, 1,5-diazacyclooctane; dmapb, 3-(dimethylamineethylimino)-1-phenylbutenolate; medpt, 3,3′-diamino-*N*-methyldipropylamine.
[b] Copper environment: eo, elongated octahedral; dsq, distorted square pyramidal.
[c] Metal–metal separation through the thiocyanato bridge.
[d] Magnetic coupling.
[e] This value is obtained through a simple Bleaney–Bowers expression for two interacting spin doublets.
* Average values.

are involved. The magnetic orbital on each copper(II) ion in this series is roughly defined by the short equatorial bonds around the copper atom. Given that the spin density in the axial positions is very weak, the overlap between the two parallel magnetic orbitals is very small. Under these conditions, the exchange coupling is expected to be very weak, and either ferro- (case of accidental orthogonality which is strongly dependent on the value of the angle at the apical bridging atom) or antiferromagnetic. In spite of the long axial Cu–S bond length and the large intramolecular copper–copper separation in the complexes listed in Table 5, some of them show a significant, although weak, magnetic interaction. This must be due to the diffuse character of the sulfur orbitals. The low ability of the thiocyanato ligand to mediate magnetic interactions through the out-of-plane pathway is also comparable with that of other pseudohalide ligands such as azido and cyanato [52], and it contrasts with the greater efficiency when the thiocyanate links the equatorial positions of two adjacent copper(II) ions, as in the dinuclear complex $[Cu(Hmtpo)(H_2O)(NCS)_2]_2$ (Hmtpo = 4*H*,7*H*-5-methyl-7-oxo[1,2,4]triazolo[1,5-*a*]pyrimidine) where $J = -148.2$ cm^{-1} [53]. In this latter case, the good overlap between the coplanar magnetic orbitals of each copper(II) ion accounts for the important antiferromagetic interaction observed.

4. Conclusions

The use of the thiocyanate group in combination with the blocking imidazole type ligands H_2bim or pyim has led to the preparation of three polynuclear copper(II) complexes: a trinuclear species (**1**) and two one-dimensional compounds (**2** and **3**). Different coordination modes and a different number of thiocyanate bridges are present in this series, illustrating once more the versatility of this ligand in its coordinating behaviour and the difficulty to predict it. In the three cases, the thiocyanate adopts the end-to-end bridging mode [single (**1** and **2**) and double (**3**)] linking one equatorial position of one copper atom with an apical position at the adjacent copper. The intramolecular (**1**) and intrachain (**2** and **3**) magnetic couplings are weak and antiferromagnetic in line with the scarce data from previous magneto-structural studies on related species.

Supplementary data

CCDC 697116, 697117 and 697118 contain the supplementary crystallographic data for **1**, **2** and **3**, respectively. These data can be obtained free of charge via http://www.ccdc.cam.ac.uk/conts/retrieving.html, or from the Cambridge Crystallographic Data Centre, 12 Union Road, Cambridge CB2 1EZ, UK; fax: (+44) 1223-336-033; or e-mail: deposit@ccdc.cam.ac.uk.

Acknowledgements

Thanks are due to the Ministerio Español de Ciencia y Tecnología (Project CTQ2007-61690) for financial support. One of us (J.C.) acknowledges the Mexican Government for funding through the PROMEP Programme.

References

[1] (a) R. Atencio, K. Biradha, T.L. Hennigar, K.M. Poirier, K.N. Power, C.M. Seward, N.S. White, M.J. Zaworotko, Cryst. Eng. 1 (1998) 203;
(b) A.J. Blake, N.R. Champness, P. Hubberstey, W.-S. Li, M.A. Whitersbay, M. Schröeder, Coord. Chem. Rev. 183 (1999) 117;
(c) S.R. Batten, B.F. Hoskins, P. Robson, Chem. Eur. J. 6 (2000) 156;
(d) A.M. Beatty, CrystEngCommun. 3 (2001) 243.
[2] (a) M. Takodoro, K. Isobe, H. Uekusa, Y. Ohashi, J. Toyoda, K. Tashiro, K. Nakasuji, Angew. Chem., Int. Ed. 38 (1999) 95;
(b) L. Öhrström, K. Larsson, S. Borg, S.T. Norberg, Chem. Eur. J. 7 (2001) 4805;
(c) J. Cancela, M.J.G. Garmendia, M. Quirós, Inorg. Chim. Acta 313 (2001) 156;
(d) R. Atencio, M. Chacón, T. González, A. Briceño, G. Agrifoglio, A. Sierraalta, Dalton Trans. (2004) 505.
[3] M. Tadokoro, K. Nakasuji, Coord. Chem. Rev. 198 (2000) 205.
[4] (a) I.G. Dance, A.S. Abushamleh, H.A. Goodwin, Inorg. Chim. Acta 43 (1980) 217;
(b) D. Boinnard, P. Cassoux, V. Petrouleas, J.M. Savarialut, J.P. Tuchagues, Inorg. Chem. 29 (1990) 4114;
(c) M.A. Martínez-Lorente, F. Dahan, Y. Sanakis, V. Petrouleas, A. Bousseksou, J.P. Tuchagues, Inorg. Chem. 34 (1995) 5346.
[5] (a) A.D. Mighell, C.W. Reimann, F.A. Mauer, Acta Crystallogr. B25 (1969) 60;
(b) M. Takodoro, T. Shiomi, K. Isobe, K.K. Nakasuji, Inorg. Chem. 40 (2001) 5476;
(c) B.B. Ding, Y.Q. Weng, Z.W. Mao, C.K. Lam, X.M. Chen, B.H. Ye, Inorg. Chem. 44 (2005) 8836;
(d) Y.R. Zhong, M.L. Cao, H.J. Mo, B.H. Ye, Cryst. Growth Des. 8 (2008) 2282.
[6] (a) S.H. Liu, C.C. Su, Polyhedron 15 (1996) 1141;
(b) J. Carranza, C. Brennan, J. Sletten, B. Vangdal, P. Rillema, F. Lloret, M. Julve, New J. Chem. 27 (2003) 1775;
(c) R. Atencio, K. Ramírez, J.A. Reyes, T. González, P. Silva, Inorg. Chim. Acta 358 (2005) 520;
(d) R.L. Sang, L. Xu, Polyhedron 25 (2006) 2167;
(e) R. Sang, L. Xu, Acta Crystallogr. E61 (2006) m793;
(f) A.K. Ghosh, D. Ghoshal, E. Zangrando, N.R. Chaudhuri, Polyhedron 26 (2007) 4195.
[7] (a) C. Kirchner, B. Krebs, Inorg. Chem. 26 (1987) 3569;
(b) B.H. Ye, F. Xue, G.Q. Xue, L.N. Ji, T.C.W. Mak, Polyhedron 18 (1999) 1785;
(c) L.M. Gruia, F.D. Rochon, A.L. Beauchamp, Inorg. Chim. Acta 360 (2007) 1825.
[8] (a) K. Larsson, L. Öhrström, CrystEngCommun. 5 (2003) 222;
(b) L.M. Gruia, F.D. Rochon, A.L. Beauchamp, Can. J. Chem. 84 (2006) 949.
[9] (a) K. Larsson, L. Öhrström, CrystEngCommun. 6 (2004) 354;
(b) B.H. Ye, B.B. Ding, Y.Q. Weng, X.M. Chen, Cryst. Growth Des. 5 (2005) 801;
(c) S. Li, S.B. Wang, F.L. Zhang, K. Tang, Acta Crystallogr. E64 (2008) m76.
[10] (a) C.A. Hester, H.L. Collier, R.G. Baughman, Polyhedron 15 (1996) 4255;
(b) R.L. Sang, L. Xiu, Inorg. Chim. Acta 359 (2006) 525.
[11] C.A. Hester, R.G. Baughman, H.L. Collier, Polyhedron 16 (1997) 2893.
[12] (a) M.P. García, A.M. López, M.A. Esteruelas, F.J. Lahoz, L.A. Oro, J. Chem. Soc., Chem. Commun. (1998) 793;
(b) K.K. Kamar, L.R. Falvello, P.E. Fanwick, J. Kim, S. Goswami, Dalton Trans. (2004) 1827.
[13] (a) S.W. Kaiser, R.B. Saillant, W.M. Butler, P.G. Rasmusen, Inorg. Chem. 15 (1976) 2681;
(b) S.W. Kaiser, R.B. Saillant, W.M. Butler, P.G. Rasmusen, Inorg. Chem. 15 (1976) 2688.
[14] (a) S. Fortin, A.L. Beauchamp, Inorg. Chem. 39 (2000) 4886;
(b) J. Martínez-Lillo, D. Armentano, G. De Munno, N. Marino, F. Lloret, M. Julve, J. Faus, CrystEngCommun. 10 (2008) 1284.
[15] (a) M.J. Bloemink, H. Engelking, S. Karentzopoulos, B. Krebs, J. Reedijk, Inorg. Chem. 35 (1996) 619;
(b) P. Alvarez-Boo, J.S. Casas, M.D. Couce, E. Freijanes, A. Furlani, V. Scarcia, J. Sordo, U. Russo, M. Varela, Appl. Organomet. Chem. 11 (1997) 963;
(c) J.S. Casas, A. Castiñeiras, Y. Parajó, M.L. Pérez-Parallé, A. Sánchez-González, J. Sordo, Polyhedron 22 (2003) 1113;
(d) Y. Parajó, J.L. Arolas, V. Moreno, A. Sánchez-González, J. Sordo, R. de Llorens, F.X. Avilés, J. Lorenzo, Inorg. Chim. Acta 362 (2008) 946.
[16] K.A. Reeder, E.V. Dose, L.J. Wilson, Inorg. Chem. 17 (1978) 1071.
[17] J. Carranza, C. Brennan, J. Sletten, F. Lloret, M. Julve, J. Chem. Soc., Dalton Trans. (2002) 3164.
[18] (a) A. Morsali, A. Ramazani, M. Babaee, F. Jamali, F. Gouranlou, H. Arjmandfar, A. Yanovsky, J. Coord. Chem. 56 (2003) 455;
(b) C. Yuste, D. Armentano, N. Marino, L. Cañadillas-Delgado, F.S. Delgado, C. Ruiz-Pérez, D.P. Rillema, F. Lloret, M. Julve, Dalton Trans. (2008) 1583.
[19] D.X. Zhu, Y.Q. Lan, Y.M. Fu, Z.M. Su, Acta Crystallogr. E62 (2006) m3479.
[20] (a) G.S. Matouzenko, G. Molnar, N. Bréfuel, M. Perrin, A. Bouseksou, S.A. Borshch, Chem. Mater. 15 (2003) 550;
(b) B.A. Leita, B. Moubaraki, K.S. Murray, J.P. Smith, Polyhedron 24 (2005) 2165.
[21] J. Carranza, M. Julve, J. Sletten, Inorg. Chim. Acta 361 (2008) 2499.
[22] X.Y. Yu, S.H. Cai, Z. Chen, J. Inorg. Biochem. 99 (2005) 1945.
[23] (a) T.I.A. Gerber, E. Hosten, P. Mayer, Z.R. Tshentu, J. Coord. Chem. 59 (2006) 243;
(b) J. Martínez-Lillo, D. Armentano, G. De Munno, J. Faus, Polyhedron 27 (2008) 1447.
[24] H. Mishra, R. Mukherjee, J. Orgnomet. Chem. 691 (2006) 3545.
[25] (a) L. Zhang, Y.Y. Ge, F. Peng, M. Du, Inorg. Chem. Commun. 9 (2006) 486;
(b) J. Martínez-Lillo, D. Armentano, G. De Munno, F. Lloret, M. Julve, J. Faus, Dalton Trans. (2008) 40.
[26] B.F. Fieselman, D.N. Hendrickson, G.D. Stucky, Inorg. Chem. 17 (1978) 2078.
[27] A. Earnshaw, Introduction to Magnetochemistry, Academic Press, London and New York, 1968.
[28] (a) SMART, Version 5.054, Data Collection Software, Bruker AXS Inc., Madison, Wisconsin, USA, 1999; (b) SAINT, Version 6.02a, Data Integration Software, Bruker AXS Inc., Madison, Wisconsin, USA, 2001.
[29] G.M. Sheldrick, SADABS, Version 2.03, Bruker AXS Inc., Madison, Wisconsin, USA, 2000.

[30] (a) G.M. Sheldrick, Acta Crystallogr., Sect. A 46 (1990) 467;
(b) G.M. Sheldrick, SHELXTL/PC, Version 6.12, Bruker AXS Inc., Madison, Wisconsin, USA, 1998;
(c) G.M. Sheldrick, XP, Version 5.1, Bruker AXS Inc., Madison, Wisconsin, USA, 1998.
[31] (a) B. Chiswell, F. Lions, B.S. Morris, Inorg. Chem. 3 (1964) 110;
(b) F. Holmes, K.M. Jones, E.G. Torrible, J. Chem. Soc. (1961) 4790.
[32] K. Nakamoto, Infrared and Raman Spectra of Inorganic and Coordination Compounds, 4th Ed., Wiley Interscience, New York, 1986.
[33] (a) J.S. Haynes, A. Kostikas, J.R. Sams, A. Simopoulos, R.C. Thompson, Inorg. Chem. 26 (1987) 2630;
(b) B. Zurowska, J. Mrozinski, M. Julve, F. Lloret, A. Maslejova, W. Sawka-Dobrowolska, Inorg. Chem. 41 (2002) 1771.
[34] H. Grove, M. Julve, F. Lloret, P.E. Kruger, K.W. Törnroos, J. Sletten, Inorg. Chim. Acta 325 (2001) 115.
[35] R.deA. Farani, W.M. Teles, C.B. Pinheiro, K.J. Guedes, K. Krambrock, M.I. Yoshida, L.F.C. de Oliveira, F.C. Machado, Inorg. Chim. Acta 361 (2008) 2045.
[36] D.T. Cromer, R.R. Ryan, C.B. Storm, Acta Crystallogr., Sect. C 43 (1987) 1435.
[37] W.E. Estes, D.P. Gavel, W.E. Hatfield, D. Hodgson, Inorg. Chem. 17 (1978) 1415.
[38] M. Julve, M. Verdaguer, G. De Munno, J.A. Real, G. Bruno, Inorg. Chem. 32 (1993) 795.
[39] Z.E. Serna, R. Cortés, M.K. Urtiaga, M.G. Barandika, L. Lezama, M.I. Arriortua, T. Rojo, Eur. J. Inorg. Chem. (2001) 865.
[40] S. Banerjee, M.G.B. Drew, C.Z. Lu, J. Tercero, C. Diaz, A. Gosh, Eur. J. Inorg. Chem. (2005) 2376.
[41] (a) M.B. Cingi, A.M.M. Manfredi, A. Tiripicchio, J.G. Haasnoot, J. Reedijk, Inorg. Chim. Acta 72 (1983) 81;
(b) J.G. Haasnoot, W.L. Driessen, J. Reedijk, Inorg. Chem. 23 (1984) 2803.
[42] C. Diaz, J. Ribas, N. Sanz, X. Solans, M. Font-Bardía, Inorg. Chim. Acta 286 (1999) 169.
[43] R. Vicente, A. Escuer, E. Peñalba, X. Solans, M. Font-Bardía, Inorg. Chim. Acta 255 (1997) 7.
[44] P. Gómez-Saiz, J. García-Tojal, F.J. Arnáiz, M.A. Maestro, L. Lezama, T. Rojo, Inorg. Chem. Commun. 6 (2003) 558.
[45] N.K. Karan, S. Mitra, T. Matsushita, V. Gramlich, G. Rosair, Inorg. Chim. Acta 332 (2002) 87.
[46] S. Ferlay, G. Francese, H.W. Schmalle, S. Decurtins, Inorg. Chim. Acta 286 (1999) 108.
[47] S. Sen, S. Mitra, D.L. Hughes, G. Rosair, C. Desplanches, Polyhedron 26 (2007) 1740.
[48] P. Talukder, A. Datta, S. Mitra, G. Rosair, M.S. El Fallah, J. Ribas, Dalton Trans. (2004) 4161.
[49] M.A. Ali, A.H. Mirza, R.J. Fereday, R.J. Butcher, J.M. Fuller, S.C. Drew, L.R. Gahan, G.R. Hanson, B. Moubaraki, K.S. Murray, Inorg. Chim. Acta 358 (2005) 3937.
[50] Z.-D. Wang, W. Han, F. Bian, Z.-Q. Liu, S-P. Yan, D.-Z. Liao, Z.-H. Jiang, P. Cheng, J. Mol. Struct. 733 (2005) 125.
[51] F.A. Mautner, R. Vicente, S.S. Massoud, Polyhedron 25 (2006) 1673.
[52] J. Carranza, J. Sletten, F. Lloret, M. Julve, J. Mol. Struct. 890 (2008) 31. and references therein.
[53] J.A.R. Navarro, M.A. Romero, J.M. Salas, M. Quirós, E.R.T. Tiekink, Inorg. Chem. 36 (1997) 4988.

Polyhedron 28 (2009) 2258–2262

Contents lists available at ScienceDirect

Polyhedron

journal homepage: www.elsevier.com/locate/poly

Synthesis, molecular and crystal structure of a new dicarbonylruthenium(II) complex containing a xantphos dioxide chelating ligand

Biswajit Deb, Dipak Kumar Dutta *

Materials Science Division, North-East Institute of Science and Technology (CSIR), Jorhat-785 006, Assam, India

ARTICLE INFO

Article history:
Received 3 March 2009
Accepted 3 April 2009
Available online 11 April 2009

Keywords:
Crystal structure
Ruthenium
Carbonyl complex
Xantphos dioxide
Chelating ligand

ABSTRACT

The reaction of xantphos dioxide (O∩O) with the polynuclear precursor $[Ru(CO)_2Cl_2]_n$ to give the mononuclear complex $[Ru(CO)_2Cl_2(O\cap O)]$(**1**) is reported together with single crystal X-ray structure analyses of both the free ligand and the ruthenium complex. The synthesized compounds have also been characterized by elemental analyses, IR and NMR (^1H, ^{31}P and ^{13}C) spectroscopy. The ligand O∩O crystallizes with lattice water molecules in a triclinic system with space group $P\bar{1}$ whereas the complex **1** crystallizes in an orthorhombic system with space group $P2_12_12_1$. Each mononuclear unit of O∩O and **1** is stabilized in their solid state through non-covalent (C–H···O, C–H···Cl and C–H···π) interactions to develop an extended three-dimensional network structure. The complex **1** exhibits an interesting intramolecular O···O interaction between one of the P═O groups and backbone O leading to different electron donacity of two P═O groups to the metal centre.

© 2009 Elsevier Ltd. All rights reserved.

1. Introduction

The assembly of mononuclear and polynuclear organometallic complexes in the solid state is governed by a balance between non-directional close packing forces and directional interactions between metal atoms or charged groups [1]. The intermolecular interactions acting among the molecules in their solid state plays an important role to understand the solid state properties of organometallic compounds as both physical (conductivity, diffusion, magnetic susceptibility, reorientation and second harmonic generation) and chemical (solid state reactivity, racemisation, resolution) properties of a compound depend on the ways in which the molecules are organized in the crystal and on the forces which hold them together [2]. The two major types of interactions employed by chemists to engineer supramolecules with predefined dimensions (1D, 2D and 3D), are metal ligand bonding and hydrogen bonding. In addition to strong (O–H···O) and weak (C–H···O) hydrogen bonds; halogen bonds (C–X···O) and weak (C–H···π) interactions have also been well characterized and exploited to playing an important role in crystal engineering and organometallic structures [3–7]. The metallosupramolecules thus generated have attracted attention in recent years due to their applications in diverse areas such as catalysis, optoelectronics, gas storage, ion exchange, molecular recognition and magnetism [8–21]. To develop such extended network structures, an appropriate ligand should be chosen, which on complexation with metal ions forms 'supramolecular glue' resulting in polymeric network. As a part of our continuing research activity [22–26], herein we report the synthesis, structure and self-aggregation of oxygen functionalised robust backbone ditertiary phosphine like xantphos [9,9-dimethyl-4,5-bis(diphenyl phosphino)xanthene] and its ruthenium(II) carbonyl complex.

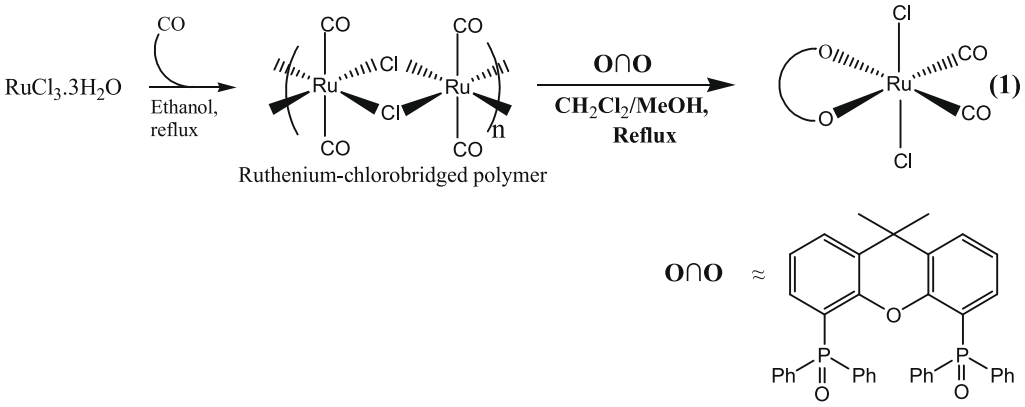
2. Results and discussion

The rigid backboned xantphos dioxide (O∩O) reacts with the polymeric precursor $[Ru(CO)_2Cl_2]_n$ in 1:1 molar ratio to afford hexa-coordinated mononuclear complex $[Ru(CO)_2Cl_2(O\cap O)]$ (**1**) (Scheme 1). The IR spectra of **1** show two equally intense ν(CO) bands at around 1973 and 2049 cm^{-1} attributing the presence of two terminal carbonyl groups only (Fig. 1). The ν(P–O) band of **1** at 1187 cm^{-1} is about 6 cm^{-1} lower than that of the free ligand (ν(P–O) = 1193 cm^{-1}) revealing the coordination to metal through O-donor. The ^{13}C NMR spectrum of **1** shows only one signal for the two non-equivalent carbonyl carbons as broad singlet at around δ 195 ppm. The ^{31}P NMR spectra of **1** exhibit only one sharp signal indicating the presence of a single isomer.

The ligand O∩O and its metal complex **1** have been structurally characterized by single crystal X-ray diffraction. The crystal information for the two compounds is summarized in Table 1. The ligand O∩O crystallizes with lattice water molecules in a triclinic system with space group $P\bar{1}$. The asymmetric unit of O∩O, shown in Fig. 2 consists of three xantphos dioxide moieties along with three disorder water molecules. The two P═O groups of each molecule form strong hydrogen bonds with one water molecule. The

* Corresponding author. Tel.: +91 376 2370081; fax: +91 376 2370011.
E-mail address: dipakkrdutta@yahoo.com (D.K. Dutta).

0277-5387/$ - see front matter © 2009 Elsevier Ltd. All rights reserved.
doi:10.1016/j.poly.2009.04.004



Scheme 1. Synthesis of complex **1**.

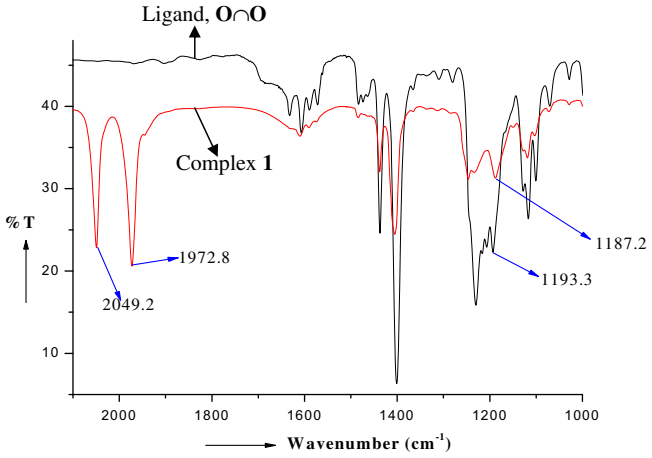


Fig. 1. IR spectra of the ligand (O∩O) and complex **1**.

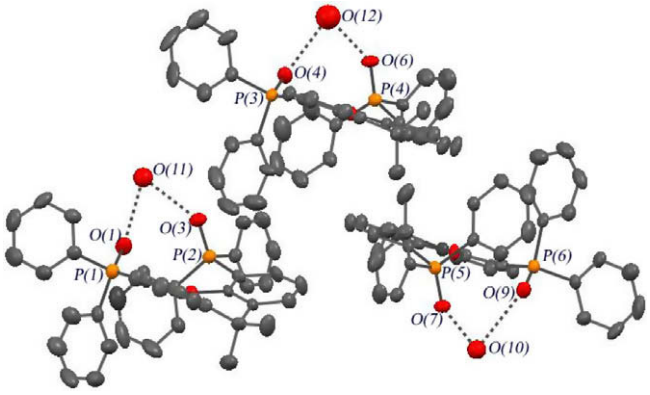


Fig. 2. Asymmetric structure of the ligand xantphos dioxide (O∩O). Hydrogen atoms are omitted for clarity.

Table 1
Crystallographic data for O∩O and **1**.

	O∩O	**1**
Empirical formula	$C_{117}H_{96}O_{12}P_6$	$C_{41}H_{32}Cl_2O_5P_2Ru$
Formula weight	1879.76	838.64
T (K)	293	293
λ (Å)	0.71073	0.71075
Cryst. Syst.	triclinic	orthorhombic
Space group	$P\bar{1}$	$P2_12_12_1$
Z	2	8
a (Å)	15.4027(5)	9.7437(19)
b (Å)	17.4463(6)	19.395(4)
c (Å)	20.3994(7)	20.072(4)
α (°)	71.715(2)	90
β (°)	70.483(2)	90
γ (°)	80.705(2)	90
μ(Mo Kα) mm^{-1}	0.174	1.377
Reflections collected	6675	7773
Flack parameter		0.01(3)
*R*1 (observed data)	0.0575(4211)	0.0461(7368)
wR_2 (all data)	0.1645(6675)	0.1399(7773)

average value of P═O bond length is found to be 1.48 Å (Table 2). The compound O∩O forms a three-dimensional network structure by extending infinitely via strong intermolecular C–H···O and C–H···π interactions as shown in Fig. 3. As indicated in both Figs. 3 and 4, water molecules are trapped into the network by the ligand O∩O through intermolecular hydrogen bonding by bridging each molecule of xantphos dioxide generating solvent stabilized three-dimensional network [O(3)···O(11) 2.722(3); O(1)···O(11) 2.776(2); H(49)···O(11) 2.676(1); H(63)···O(11) 2.708(2); H(47A)···O(11) 2.508(3) etc.] (Table 3). The compound loses water molecule on activating the sample at 100 °C for 1 h and this solvent loss is accompanied by the loss of transparency of the crystals. An X-ray powder diffraction analysis revealed that the solvent loss is accompanied by the loss of crystallinity, and indeed, no diffraction peaks were observed for the bulk sample.

The complex **1** crystallizes in an orthorhombic system with space group $P2_12_12_1$ where the Ru atom is situated at the centre of an octahedral environment formed by two O donors, two CO and two Cl atoms. The selected bond lengths and bond angles are presented in Table 2. The X-ray crystal structure (Fig. 5) reveals that the two Cl atoms are *trans* to each other, whereas the CO groups which are *cis* to each other are situated at the positions *trans* to two O donors. The two CO groups, two O donors and Ru metal are located in the same plane. The ligand O∩O forms a chelate (bite angle O2–Ru1–O1, 85.39) through O, O donor and forms a ten member distorted ring structure. The O1–Ru1–O2 plane is inclined by an angle 102° to the plane of the backbone of xantphos ligand. As a result of this folded structure, there appears a close intramolecular (O(1)···O(5) [2.905(4) Å, Fig. 5] interaction between the O atom of ligand backbone and one of the O atoms of P═O group of the chelating ligand. This type of O···O interaction is not commonly observed though the O–O short contact between two carbonyl groups is documented in literature [3]. The effect of the O···O interaction in **1** is reflected in CO bond order which is consistent with their corresponding Ru–C bond lengths (Table 2). The influence of O(1) *trans* to C(41) at the metal centre is less than that

Table 2
Selected bond distances (Å) and angles (°) for compounds O∩O and **1**.

Ligand O∩O					
P(1)–O(1)	1.476(4)	P(2)–O(3)	1.479(4)	P(5)–O(7)	1.484(4)
P(6)–O(9)	1.475(4)	P(4)–O(6)	1.478(4)	P(3)–O(4)	1.476(5)
Complex **1**					
P(1)–O(1)	1.491(3)	O(1)– Ru(1)	2.118(3)	P(2)–O(2)	1.487(3)
O(2)–Ru(1)	2.118(3)	Ru(1)– Cl(1)	2.3796(17)	Ru(1)–Cl(2)	2.3739(13)
Ru(1)–C(40)	1.833(7)	C(40)– O(4)	1.129(10)	Ru(1)–C(41)	1.931(7)
C(41)–O(3)	0.973(9)				
Cl(1)–Ru(1)–Cl(2)	176.59(5)	O(1)–Ru(1)–O(2)	85.39(12)		
C(40)–Ru(1)–O(2)	176.7(2)	C(41)–Ru(1)–O(1)	172.3(2)		
C(40)–Ru(1)–C(41)	89.1(3)				

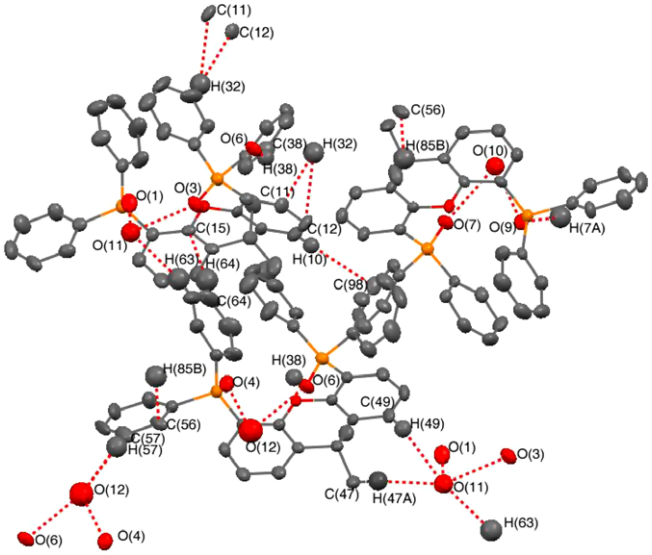


Fig. 3. Intermolecular short contacts in the molecule O∩O. All the hydrogen atoms except those involved in hydrogen bonding have been omitted for clarity.

of O(2) trans to C(42), which may be due to O(1)···O(5) interaction. Because of the weak Ru–O interaction in the former, the electron density increases on the metal centre in the latter case resulting in more dπ-electrons to the antibonding π^* orbital of the CO and hence decreases the Ru–C bond length and consequently reduces the C–O bond order (increases C–O bond length). The longer bond length of Ru1–C41 (1.931(7) Å) than Ru1–C40 (1.833(7) Å) indicates a weaker interaction in the former and is therefore likely to dissociate more easily.

The complex **1** exhibit some interesting intermolecular interactions involving shorter distances than the sum of van der Waals radii (Fig. 6). The interactions between these molecules are presented by dotted lines and summarized in Table 4. The molecules are connected by weak hydrogen bondings between H atoms of the phenyl ring of xantphos ligand and O atom of CO group (C–H···OC) and Cl atom (C–H···Cl) of the adjacent molecules [C(23)–H(23)···Cl(2) 2.763(4) Å, C(36)–H(36)···Cl(2) 2.879(4) Å, C(12)–H(12)···O(4) 2.582(7) Å and C(35)–H(35)···O(3) 2.704(6) Å]. In addition to these hydrogen bondings, intermolecular C–H···π interactions between H atoms of xantphos ligand and the phenyl ring of these molecules [C(30)–H(30)···C(33) 2.812(7) Å, C(8)–H(8)···C(24) 2.822(5) Å, and C(32)–H(32)···C(11) 2.832(8) Å] are also observed in their solid

Table 3
Significant intermolecular interactions in the crystal O∩O.

D–H···A	H···A/Å	D···A/Å	(D–H···A)/°
C(64)–H(64) ··C(15)^{i}	2.749(8)	3.670(1)	170.2(1)
C(38)–H(38) ··O(6)^{ii}	2.394(1)	3.242(2)	151.6(2)
C(47)–H(47A) ··O(11)^{i}	2.508(3)	3.463(9)	174.1(2)
C(57)–H(57) ··O(12)^{i}	2.377(9)	3.182(1)	144.6(1)
C(49)–H(49) ··O(11)^{i}	2.676(1)	3.532(7)	153.5(7)
C(63)–H(63) ··O(11)^{iii}	2.708(2)	3.626(5)	169.6(1)
O(1) ··O(11)^{iv}		2.776(2)	
O(3) ··O(11)^{iv}		2.722(3)	
O(4) ··O(12)^{v}		2.692(1)	
O(6) ··O(12)^{v}		2.726(1)	
O(7) ··O(10)^{i}		2.869(6)	
O(9) ··O(10)^{i}		2.860(2)	

Symmetry operators are (i) *x*, *y*, *z* (ii) 1−*x*, 1−*y*, 1−*x* (iii) 1 + *x*, *y*, *z* (iv) 1−*x*, *y*, (v) 1−*x*, −*y*, 1−*z*.

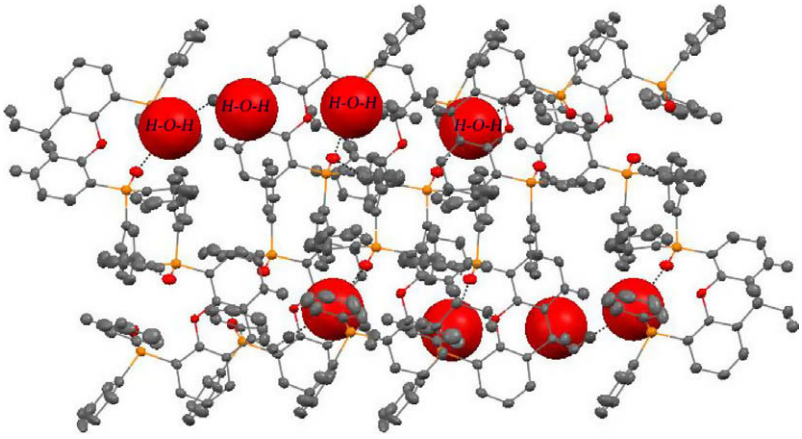


Fig. 4. 3-D network structure of O∩O containing water molecules inside the network when viewed down the *c*-axis.

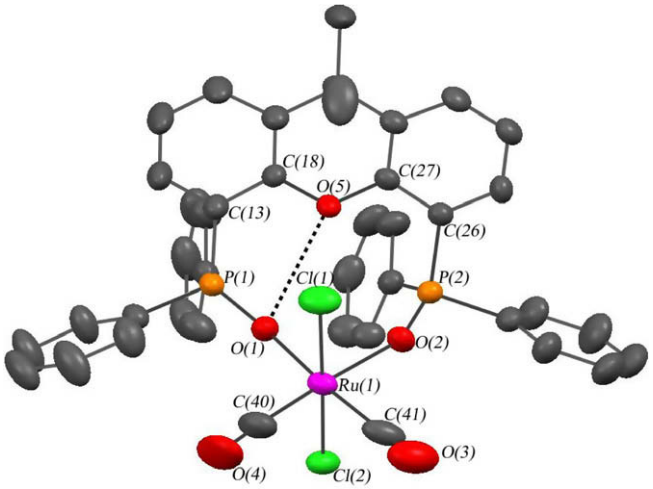


Fig. 5. X-ray crystal structure of **1**. Hydrogen atoms have been omitted for clarity.

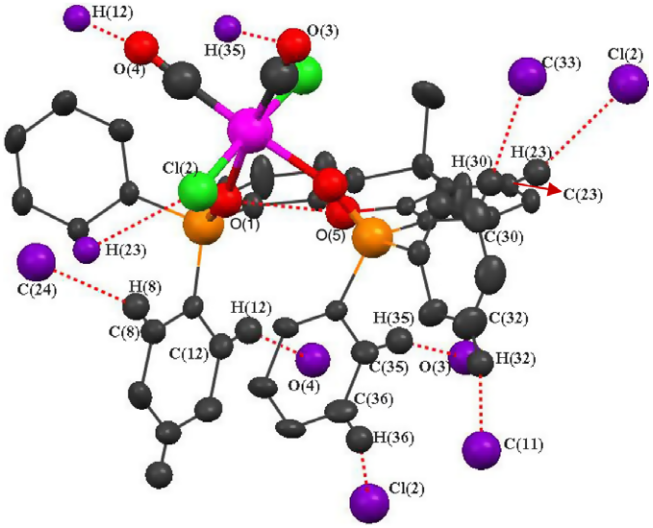


Fig. 6. Intermolecular short contacts in **1**. The atoms involved in short contact (only a few selective interactions) from surrounding molecules have been designated by dotted lines.

Table 4
Significant intermolecular interactions in the complex **1**.

D–H ··A	H ··A/Å	D ··A/Å	(D–H ··A)/°
C(23)–H(23) ··Cl(2)^{i}	2.763(4)	3.519(4)	138.9(4)
C(36)–H(36) ··Cl(2)^{i}	2.879(4)	3.729(8)	152.6(2)
C(12)–H(12) ··O(4)^{ii}	2.582(7)	3.369(9)	142.8(1)
C(35)–H(35) ··O(3)^{ii}	2.704(6)	3.519(9)	146.7(7)
C(30)–H(30) ··C(33)^{iii}	2.812(7)	3.740(8)	175.6(2)
C(8)–H(8) ··C(24)^{iv}	2.822(5)	3.679(3)	153.7(1)
C(32)–H(32) ··C(11)^{v}	2.832(8)	3.633(9)	149.9(5)
O(1) ··O(5)^{vi}		2.905(4)	

Symmetry operators are (i) $-x$, $-1/2+y$, $1.5-z$ (ii) $-1+x$, y, z (iii) $1/2+x$, $1/2-y$, $2-z$ (iv) $-x$, $1/2+y$, $1.5-z$ (v) $-1/2-x$, $1-y$, $1/2+z$ (vi) x, y, z.

state. All these results demonstrate the extended three-dimensional network structure as shown in Fig. 7 which exhibits high thermal stability (>300 °C). This result infers that the intermolecular interactions of one mononuclear unit of **1** with the adjacent members have a profound effect on overall thermal stability of the network.

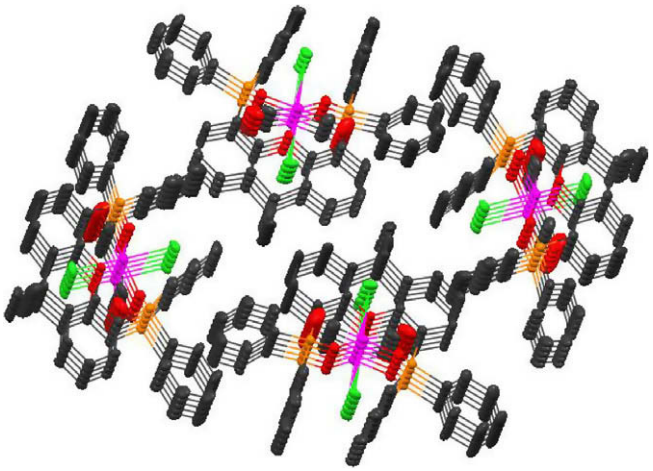


Fig. 7. 3D stacked structure of **1** stabilized by weak hydrogen bonding. Hydrogen atoms are omitted for clarity.

3. Experimental

3.1. General

All operations were carried out under nitrogen atmosphere. All solvents were distilled under N_2 prior to use. $RuCl_3 \cdot xH_2O$ was purchased from M/S Arrora Matthey Ltd., Kolkata, India. The ligand xantphos was purchased from M/S Aldrich, USA and used without further purification. H_2O_2 was obtained from Ranbaxy, New Delhi, India and estimated before use.

Elemental analyses were performed on a Perkin–Elmer 2400 elemental analyzer. IR spectra (4000–400 cm^{-1}) were recorded on KBr discs in a Perkin–Elmer system 2000 FT-IR spectrophotometer. The ^{1}H, ^{13}C and ^{31}P NMR spectra were recorded in $CDCl_3$ solution on a Bruker DPX-300 Spectrometer and chemical shifts were reported relative to $SiMe_4$ and 85% H_3PO_4 as internal and external standards, respectively. Thermal analyses of the complexes were carried out using a thermal analyzer (TA instrument, Model STD 2960 simultaneous DTA–TGA) in presence of N_2 atmosphere with a heating rate of 10 °C/min.

3.2. Synthesis of xantphos dioxide (O∩O)

The ligand xantphos dioxide was synthesized by oxidation of xantphos with H_2O_2 following the literature protocol [27].

IR (KBr, cm^{-1}): 1193 [ν(P–O)]. ^{1}H NMR ($CDCl_3$, ppm): δ 6.74–7.74 (m, 30H, Ph), 2.17 (s, 6H, CH_3). ^{13}C NMR ($CDCl_3$, ppm): δ 153.10–124.1 (Ar), δ 32.3, 34.9 (CH_3). $^{31}P\{^{1}H\}$ NMR ($CDCl_3$, ppm): δ 30.95 [s, P(v)]. *Anal.* Calc for $C_{39}H_{32}O_3P_2$: C, 74.40; H, 5.08. Found: C, 73.98; H, 5.09%.

3.3. Synthesis of the starting complex $[Ru(CO)_2Cl_2]_n$

The starting complex $[Ru(CO)_2Cl_2]_n$ was prepared by passing CO through a refluxing solution of $RuCl_3 \cdot 3H_2O$ in ethanol for about 24 h [28–31].

3.4. Synthesis of $[Ru(CO)_2Cl_2(O\cap O)]$ (**1**)

$[Ru(CO)_2Cl_2]_n$ (0.877 mmol, 200 mg) was dissolved in methanol (10 cm^3) and xantphos dioxide (0.877 mmol, 536 mg) was dissolved in dichloromethane (10 cm^3). Both the solutions were mixed together and refluxed for 4 h. The solvent was removed and washed with diethyl ether. The resulting reddish yellow

compound was recrystallised from dichloromethane/*n*-hexane to give the complex '**1**' (640 mg, 87%)

IR (KBr, cm^{-1}): 2049, 1973 [ν(CO)]. 1187 [ν(P–O)]. ^1H NMR ($CDCl_3$, ppm): δ 6.53–7.92 (m, 30H, Ph), 1.74 (s, 3H, CH_3), 1.82 (s, 3H, CH_3). ^{13}C NMR ($CDCl_3$, ppm): δ 152.78–122.13 (Ar), δ 33.59, 34.20 (CH_3), 195.64 (CO). $^{31}P\{^1H\}$ NMR ($CDCl_3$, ppm): δ 41.96 [s, P(v)]. Anal. Calc for $C_{41}H_{32}Cl_2O_5P_2Ru$: C, 57.40; H, 3.73. Found: C, 56.85; H, 3.65%.

3.5. X-ray structural analysis

Single crystals of O∩O and **1** were grown by layering a CH_2Cl_2 solution of O∩O and **1** with *n*-hexane. The intensity data of O∩O and **1** were collected on Bruker Smart–CCD and Rigaku Saturn CCD, respectively with Mo Kα radiation (λ = 0.71073 Å). The structures were solved with SHELXS-97 [32] and refined by full-matrix least squares on F^2 using SHELXL-97 computer program [33]. Hydrogen atoms were idealized by using the riding models.

Powder XRD spectra of the compound O∩O were recorded on a Bruker AXS D8 ADVANCE from 2 to 80 °C at 4° min^{-1} with a step size of 0.02° using Cu Kα source (λ = 1.54 Å). Samples were prepared as front-coated packed powders in aluminium sample holders.

4. Conclusion

In this paper, the synthesis of ruthenium(II) carbonyl complex (**1**) containing a xantphos dioxide chelating ligand along with the structural characterization of the ligand (O∩O) and its ruthenium complex (**1**) have been carried out. The compound O∩O forms a three-dimensional network structure by extending infinitely via strong intermolecular C–H···O and C–H···π interactions by bridging each molecule of xantphos dioxide with water molecules to generate a solvent stabilized architecture. The ligand O∩O reacts with $[Ru(CO)_2Cl_2]_n$ to afford hexa-coordinated Ru(II) complex **1**, which generates three dimensional rigid network via intermolecular C–H···O, C–H···Cl and C–H···π interactions resulting in high thermal stability (>300 °C). The complex **1** exhibit an interesting intramolecular O···O interactions leading to different electron donacity of two P═O groups to the metal centre.

Acknowledgement

The authors are grateful to Dr. P.G. Rao, Director, North-East Institute of Science and Technology (CSIR), Jorhat, Assam, India, for his kind permission to publish the work. Thanks are also due to DST, New Delhi for a financial support (Grant: SR/S1/IC-05/2006). The author B. Deb (JRF) is grateful to CSIR for providing the fellowship.

Appendix A. Supplementary data

CCDC 683610 and 707430 contain the supplementary crystallographic data (O∩O) and (**1**). These data can be obtained free of charge via http://www.ccdc.cam.ac.uk/conts/retrieving.html, or from the Cambridge Crystallographic Data Centre, 12 Union Road, Cambridge CB2 1EZ, UK; fax: (+44) 1223-336-033; e-mail: deposit@ccdc.cam.ac.uk.

References

[1] D. Braga, F. Grepioni, K. Biradha, V.R. Pedireddy, G.R. Desiraju, J. Am. Chem. Soc. 117 (1995) 3157.
[2] G.R. Desiraju, Crystal Engineering: The Design of Organic Solids, Elsevier, Amsterdam, 1989.
[3] J.S.Y. Wong, Y.J. Gu, L. Szeto, W.T. Wong, Cryst. Eng. Commun. 10 (2008) 29.
[4] U. Rychlewska, B. Warzajits, Acta Crystallogr., Sect. B 56 (2000) 833.
[5] B. Venkataramanan, M.A. Saifudin, V. Jagadese, V. Suresh, Cryst. Eng. Commun. 6 (2004) 284.
[6] J. Bernstein, R.E. Davis, L. Shimoni, N.L. Chang, Angew. Chem., Int. Ed. 34 (1995) 1555.
[7] C.F. Wang, Z.Y. Zhu, Z.X. Zhang, Z.X. Chen, X.G. Zhou, Cryst. Eng. Commun. 9 (2007) 35.
[8] A.S. Kumbhar, M.S. Deshpande, R.J. Butcher, Cryst. Eng. Commun. 10 (2008) 1520.
[9] D. Braga, Chem. Commun. (2003) 2751.
[10] K. Biradha, Cryst. Eng. Commun. 5 (2003) 374.
[11] G.R. Desiraju, Chem. Commun. (2005) 2995.
[12] G.A. Jeffery, in: An Introduction to Hydrogen Bonding, Wiley, Chichester, 1997.
[13] M. Eddaoudi, J. Kim, N. Rosi, D. Vodak, J. Wachter, M.O. Keeffee, O.M. Yaghi, Science 295 (2002) 469.
[14] D.N. Dybtsev, H. Chun, S.H. Yoon, D. Kim, K. Kim, J. Am. Chem. Soc. 126 (2004) 32.
[15] C. Boskovic, E.K. Brechin, W.E. Streib, K. Folting, J.C. Bollinger, D.N. Hendrickson, G. Christou, J. Am. Chem. Soc. 124 (2002) 3725.
[16] M.E. Davis, Nature 417 (2002) 813.
[17] M. Eddaoudi, H. Li, O.M. Yaghi, J. Am. Chem. Soc. 122 (2000) 1391.
[18] M. Shu, C. Tu, W. Xu, H. Jin, J. Sun, Cryst. Growth Des. 6 (2006) 1890.
[19] C.D. Wu, A. Hu, L. Zhang, W. Lin, J. Am. Chem. Soc. 127 (2005) 8940.
[20] B. Chen, F.R. Fronczek, A.W. Maverick, Inorg. Chem. 43 (2004) 8209.
[21] D.K. Kumar, A. Das, P. Dastidar, Cryst. Growth Des. 7 (2007) 205.
[22] D.K. Dutta, J.D. Woollins, A.M.Z. Slawin, D. Konwar, P. Das, M. Sharma, P. Bhattacharyya, S.M. Aucott, Dalton Trans. (2003) 2674.
[23] D.K. Dutta, J.D. Woollins, A.M.Z. Slawin, D. Konwar, M. Sharma, P. Bhatacharyya, S.M. Aucott, J. Organomet. Chem. 691 (2006) 1229.
[24] P. Chutia, M. Sharma, P. Das, N. Kumari, J.D. Woollins, A.M.Z. Slawin, D.K. Dutta, Polyhedron 22 (2003) 2725.
[25] D.K. Dutta, P. Chutia, J.D. Woollins, A.M.Z. Slawin, Inorg. Chim Acta 359 (2006) 877.
[26] B. Deb, B.J. Sarmah, B.J. Borah, D.K. Dutta, Spectrochim. Acta, Part A 72 (2009) 339.
[27] J. Fawcett, A.W.G. Platt, S. Vickers, M.D. Ward, Polyhedron 23 (2004) 2561.
[28] M.L. Berch, A. Davison, J. Inorg. Nucl. Chem. 35 (1973) 3763.
[29] R. Colton, R.H. Farthing, Aust. J. Chem. 20 (1967) 1283.
[30] R.J. Irving, J. Chem. Soc. (1956) 2879.
[31] M.J. Cleare, W.P. Griffith, J. Chem. Soc. A (1969) 372.
[32] G.M. Sheldrick, SHELXS 97, Program for the Solution of Crystal Structure, University of Gottingen, Germany, 1997.
[33] G.M. Sheldrick, SHELXL 97, Program for the Refinement of Crystal Structure, University of Gottingen, Germany, 1997.

Polyhedron 28 (2009) 2263–2267

Contents lists available at ScienceDirect

Polyhedron

journal homepage: www.elsevier.com/locate/poly

Preparation of PbO nanocrystals via decomposition of lead oxalate

Masoud Salavati-Niasari [a,b,*], Fatemeh Mohandes [b], Fatemeh Davar [a,b]

[a] Department of Chemistry, Faculty of Science, University of Kashan, Kashan, P.O. Box 87317-51167, Islamic Republic of Iran
[b] Institute of Nano Science and Nano Technology, University of Kashan, Kashan, P.O. Box 87317-51167, Islamic Republic of Iran

ARTICLE INFO

Article history:
Received 13 October 2008
Accepted 7 April 2009
Available online 21 April 2009

Keywords:
PbO nanocrystals
Thermal decomposition
Inorganic materials
Chemical synthesis

ABSTRACT

The present study reports the preparation and characterization of PbO nanocrystals obtained via a thermal decomposition route. The PbO nanocrystals were synthesized using lead oxalate powder as a precursor. Nanostructured products were investigated by means of XRD, TEM, FT-IR and XPS. The XRD results indicate that tetragonal phase β-PbO with a particle size of about 30–45 nm was obtained when the intermediate precipitate was calcined at 500 °C.

© 2009 Elsevier Ltd. All rights reserved.

1. Introduction

The synthesis of nanomaterials is an increasingly active area [1,2]. Nanostructured materials have attracted the attention of researchers not only by their unique chemical and physical properties but also by their potential application in many fields, which has stimulated the search for new synthetic methods for these materials. These materials consist of small grains with sizes below 100 nm.

Lead oxide (PbO), an important industrial material, has been widely applied in storage batteries, gas sensors, pigments and paints [3,4]. PbO has two polymorphic forms and a wide band gap: red α-PbO, stable at low temperature, and yellow β-PbO, stable at high temperature [5], and the α-PbO → β-PbO phase transition occurs at about 490 °C. However, the high temperature yellow form can exist even at room temperature.

In recent years, increased attention has been focused on the synthesis of PbO nanostructures. Pan et al. [6] synthesized PbO nanowires through electron beam irradiation on PbO_2 nanobelts. Jia and Gao [7] synthesized β-PbO nanorods with diameters ranging from 40 to 120 nm and lengths up to 500 nm, via the hydrothermal method in the presence of citrate. Xia and coworkers [8] synthesized PbO by the one-step solid state reaction of a Pb(II) compound with NaOH at room temperature.

One type of method to prepare nanosized PbO is thermal decomposition. Ma et al. [9] prepared nanometer-sized PbO by pyrogenetic decomposition of lead carbonate synthesized by chemical precipitation. Jiang et al. [10] prepared PbO nanowires via calcining lead glycolate nanowires that were synthesized by heating lead acetate in ethylene glycol. Nanosized PbO particles were prepared by thermal decomposition of lead hydroxycarbonate synthesized under microwave irradiation by Yang and coworkers [11]. Chen et al. [2] prepared PbO nanocrystals by thermal decomposition of $Pb(OH)_2$.

Recently, metal coordination complexes or organometallic compounds as precursors for the preparation of inorganic nanomaterials have been widely studied as they represent an important interface between synthetic chemistry and materials science. Complexation is a popular method of modifying ligands in the original precursor solution, and carboxylic acids or their salts are the most frequently used complexing agents. Nathan et al. [12] used citric acid as a chelating agent for the preparation of NiO nanostructures to induce molecular level mixing of the dissociated metal ions dissolved in the solution. Gajbhiye et al. [13] reported that by using cobalt acetylacetonate as a precursor, Co nanoparticles with the smallest size are synthesized compared to cobalt acetate. This is because of the chelate effect in the $[Co(acac)_2]$ complex.

Considering the reaction of the chelating agent, we suggest that oxalate anions coordinated to the Pb ions in $Pb(NO_3)_2$ inhibit the agglomeration of metal cations and decrease the particle size of the PbO nanoparticles. As far as we are aware, the use of lead oxalate for the production of lead oxide nanoparticles has not been reported. Therefore, we chose lead oxalate as a lead precursor. Recently, our group reported the synthesis of metal oxide nanoparticles via thermal decomposition of a novel precursor [14–19]. Herein, we report a facile method for the synthesis of PbO nanocrystals by thermolysis of lead (II) oxalate $[Pb(O_4C_2)]$ in the coordinating solvent oleylamine and with triphenylphosphine (TPP).

* Corresponding author. Address: Department of Chemistry, Faculty of Science, University of Kashan, Kashan, P.O. Box 87317-51167, Islamic Republic of Iran. Tel.: +98 361 5555333; fax: +98 361 5552935.
E-mail address: salavati@kashanu.ac.ir (M. Salavati-Niasari).

0277-5387/$ - see front matter © 2009 Elsevier Ltd. All rights reserved.
doi:10.1016/j.poly.2009.04.009

2. Experiment

2.1. Characterization

XRD patterns were recorded by a Rigaku D-max C III, X-ray diffractometer using Ni-filtered Cu Kα radiation (λ = 1.5406 Å). Elemental analysis was obtained from a Carlo ERBA Model EA 1108 analyzer. Transmission electron microscopy (TEM) images were obtained on a Philips EM208 transmission electron microscope with an accelerating voltage of 200 kV. Fourier transform infrared (FT-IR) spectra were recorded on a Shimadzu Varian 4300 spectrophotometer in KBr pellets. X-ray photoelectron spectroscopy (XPS) of the as-prepared products was measured on an ESCA-3000 electron spectrometer with non-monochromatized Mg Kα X-ray radiation as the excitation source. Thermogravimetric analysis (TG) was carried out using a thermal gravimetric analysis instrument (Shimadzu TGA-50H) with a flow rate of 20.00 ml/min and a heating rate of 10 °C min^{-1} in air from room temperature to 500 °C.

2.2. Synthesis of lead oxalate

All the chemical reagents used in our experiments were of analytical grade and were used as received without further purification. Lead (II) oxalate, [$Pb(O_4C_2)$], as a precursor was synthesized according to this procedure: lead (II) nitrate $Pb(NO_3)_2$ (2 mmol) was dissolved in 10 ml of distilled water to form a homogeneous solution. A stoichiometric amount of potassium oxalate dissolved in an equal volume of distilled water was added dropwise to the above solution under magnetic stirring. The solution was stirred for about 30 min and a white precipitate was isolated which was washed with water and ethanol several times to remove potassium nitrate as a by-product. The white precipitate of lead oxalate was dried at 50 °C. The reaction equation of the synthesis of lead oxalate is shown in Eq. (1). The [$Pb(O_4C_2)$] was characterized by elemental analysis, FT-IR, powder X-ray diffraction (XRD) and thermogravimetric analysis (TGA). *Anal.* Calc. for [$Pb(O_4C_2)$]: C, 8.14; Pb, 70.18. Found: C, 8.07; Pb, 70.10%.

$$Pb(NO_3)_{2(aq)} + K_2C_2O_4 \cdot H_2O_{(aq)} \rightarrow [Pb(O_4C_2)]_{(s)} + 2KNO_{3(aq)} \quad (1)$$

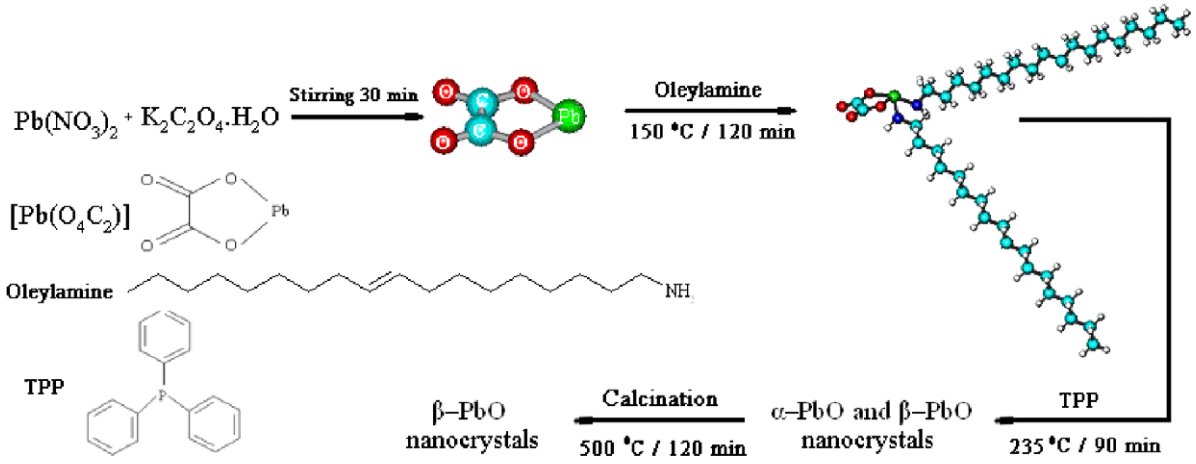
2.3. Synthesis of PbO nanocrystals

The current synthetic procedure is a modified version of the method developed by Hyeon et al. for the synthesis of nanocrystals [20]. The synthetic pathway is shown in Scheme 1. First, the [$Pb(O_4C_2)$]–oleylamine complex was prepared by the reaction 0.5 g of [$Pb(O_4C_2)$] and 7 ml of oleylamine. The mixed solution was placed in a 50 ml two-necked distillation flask and heated up to 150 °C for 2 h. In this step, metal nuclei are formed during the heat treatment in the presence of oleylamine. In the second step, the resulting metal-complex solution was injected into 5 g of triphenylphosphine (TPP) at 235 °C. Upon heating at 235 °C, the color of the reaction solution changed from white to dark orange, which indicates the short burst of nucleation. The dark orange solution was aged at 235 °C for 90 min, and then cooled to room temperature. The light red nanocrystals were precipitated by adding excess ethanol to the solution and then they were separated by centrifugation. The final product was washed with ethanol for at least three times to remove impurities. The product could easily be re-dispersed in non-polar organic solvents, such as hexane or toluene. The synthesized nanocrystals were characterized by XRD, TEM, FT–IR and XPS.

3. Results and discussion

The TG curve of [$Pb(O_4C_2)$] is shown in Fig. 1. There is only one weight loss step in the temperature range 250–330 °C. The weight loss at 250–330 °C may be ascribed to the decomposition of the oxalate. The weight loss is about 25.00%, which is close to the theoretical value (24.39 wt%). This weight loss is due to the decomposition of lead oxalate to lead oxide because the oxidation number of the lead ions is constant during the thermal decomposition process. Fig. 2 shows the XRD patterns of the lead oxalate precursor (a), intermediate precipitate (b) and PbO nanocrystals (c). The XRD pattern of lead oxalate in Fig. 2a can be indexed to the anorthic cell reported for lead oxalate (JCPDS No. 14-0803, a = 6.091 Å, b = 6.978 Å, c = 50557 Å). No significant impurities such as KNO_3 (JCPDS No. 15-0607) were observed, which indicates that pure lead oxalate was obtained. The intermediate precipitate contains a mixture of red and yellow PbO nanocrystals (α and β) formed through the thermal decomposition of lead oxalate in the presence of oleylamine and TPP. All of the reflections of the XRD pattern in Fig. 2b can be indexed to the orthorhombic lattice of PbO (α-PbO, JCPDS No. 35-1482, marked with "*") and the tetragonal lattice of PbO (β-PbO, JCPDS No. 01-0824, "♦"). The average crystallite size (D_c) of the PbO nanocrystals is 35 nm, which was calculated using the Debey–Scherrer Eq. (2) from the major diffraction peaks of the corresponding β-PbO (1 0 1) and α-PbO (1 1 1) [21],

$$D_c = \frac{K\lambda}{\beta \cos\theta} \quad (2)$$



Scheme 1. Schematic diagram illustrating the formation of PbO nanocrystals.

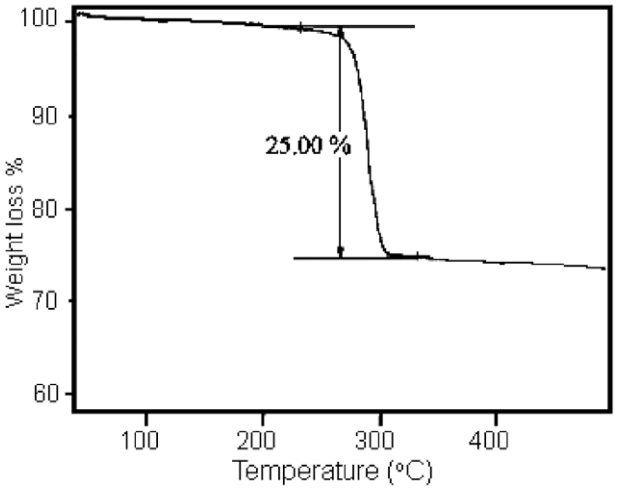


Fig. 1. TGA plot for the decomposition of the lead oxalate precursor.

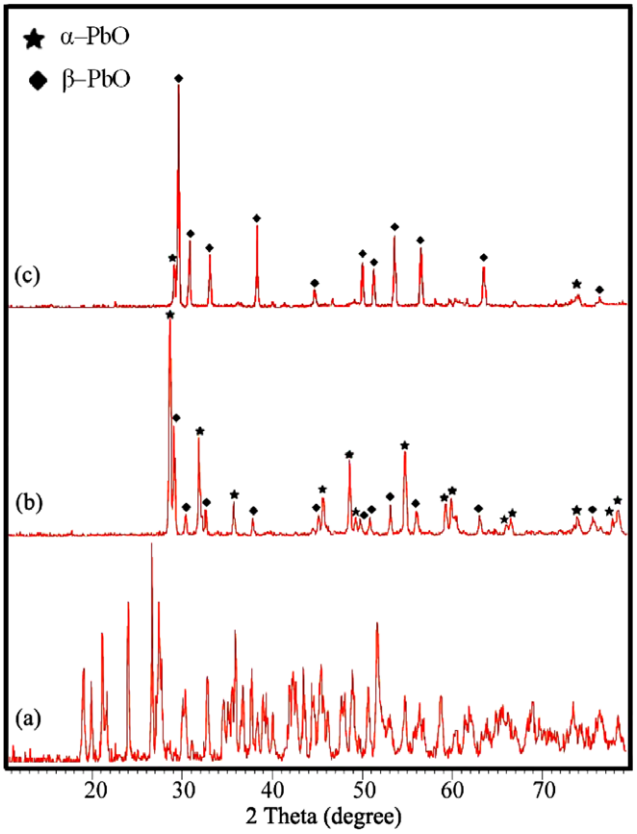


Fig. 2. XRD patterns of the obtained (a) lead oxalate precursor, (b) intermediate product (α-PbO and β-PbO) and (c) β-PbO nanocrystals.

where β is the breadth of the observed diffraction line at its half-intensity maximum, K is the so-called shape factor, which usually takes a value of about 0.9, and λ is the wavelength of the X-ray source used in the XRD. In order to change α-PbO into stable β-PbO, the intermediate precipitate was calcined at 500 °C for 2 h. The XRD pattern of β-PbO nanocrystals is shown in Fig. 2c. In this pattern, two reflection peaks of α-PbO with very low intensity are still observed, which can be removed at a higher calcination temperature but the particle size of the nanocrystals increases by increasing the temperature. The particle size of β-PbO nanocrystals calculated from the major diffraction peak of the corresponding β-PbO (1 0 1) using the Debey–Scherrer equation is 45 nm. All XRD results of the PbO nanocrystals, such as reflection peak (*h k l*), its corresponding full width at half maximum (FWHM) and theta positions, are listed in Tables 1 and 2 (Fig. 2b and c). Several peaks of the corresponding β-PbO have not been marked with *h k l* values (refer JCPDS No. 01-0824).

TEM images of β-PbO nanocrystals are shown in Fig. 3a and b. The images indicate that the PbO powder consists of nanometric particles with diameters of 30–45 nm, which is in agreement with the XRD results. The SAED pattern (Fig. 3c) indicates that the β-PbO nanocrystals are single crystals.

FT-IR spectroscopy is a useful tool to help understand the functional group behavior of any organic molecule. The infrared spectra of free TPP (a), oleylamine (b), lead oxalate (c) and β-PbO nanocrystals (d) are shown in Fig. 4. As shown in Fig. 4a, the peaks corresponding to the P–Ph stretching at 1710 cm^{-1}, the bending mode of the phenyl group γ(=CH) at 742 $cm^{-1}$and υ (benzene ring) at 697 cm^{-1} can be seen. In the IR spectrum of oleylamine (Fig. 4b) two sharp bands at 2925 and 2855 cm^{-1} are attributed to the asymmetric CH_2 stretch and the symmetric CH_2 stretch, respectively [22]. The rocking and bending mode of the methylene group $\omega(CH_2)$ is seen at 1270 cm^{-1}. The IR spectrum of $[Pb(O_4C_2)]$ is shown in Fig. 4c. The very weak broad absorption band around 3446 cm^{-1} corresponds to the ν_{O-H} stretching vibrations of water molecules [23]. This observation provides evidence for the presence of a small amount of water absorption on the surface of $Pb(O_4C_2)$ after handling. The double absorption peaks that appear at 1645 and 1610 cm^{-1} are due to the asymmetric vibrations of the carbonyl group and the absorption peaks at 1369 and 1287 cm^{-1} are assigned to $\nu_{s(C-O)+\delta(OC=O)}$ modes. Two distinct peaks at 776 and 508 cm^{-1} are attributed to the out-of-plane bending mode of water and O–C–O in-plane bending mode of oxalate, respectively [24], which indicate the formation of $[Pb(O_4C_2)]$. In the IR spectrum of lead oxalate, no peak appears at 1384 cm^{-1}, which is a typical absorbance of nitrate anions, indicating the lack of nitrate anions in the lead oxalate [25]. In the FT-IR spectrum of the β-PbO nanocrystals (Fig. 4d) a new peak appears at 451 cm^{-1}, which is assigned to the Pb–O bond.

Table 1
XRD results of Fig. 2b.

No.	Pos. (°2Th.)	FWHM (°2Th.)	(*h k l*)
1	28.8619	0.1771	(1 1 1) α
2	29.3221	0.2362	(1 0 1) β
3	30.5552	0.1771	β
4	32.0535	0.2362	(2 0 0) α
5	32.8648	0.1771	β
6	35.9716	0.2362	(0 0 2) α
7	38.0094	0.1771	β
8	45.3588	0.1771	(2 0 0) β
9	45.8372	0.2362	(2 2 0) α
10	48.7898	0.2362	(2 0 2) α
11	49.4727	0.1771	(2 2 1) α
12	50.0082	0.2362	(2 0 1) β
13	51.0335	0.2362	β
14	53.3110	0.2362	(2 1 1) β
15	54.9376	0.2952	(3 1 1) α
16	56.2369	0.3542	β
17	59.4584	0.2362	(2 2 2) α
18	60.0836	0.1771	(1 3 3) α
19	63.2407	0.2362	(2 1 2) β
20	66.1873	0.2362	(4 0 0) α
21	66.7499	0.2952	(0 4 0) α
22	74.1012	0.2362	(3 3 1) α
23	75.8592	0.4723	(0 0 4) β
24	77.9702	0.1771	(4 0 2) α
25	78.5910	0.2160	(3 1 3) α

Table 2
XRD results of Fig. 2c.

No.	Pos. (°2Th.)	FWHM (°2Th.)	(*h k l*)
1	28.7708	0.1771	(1 1 1) α
2	29.2655	0.1771	(1 0 1) β
3	30.4928	0.2362	β
4	32.7673	0.2362	β
5	37.9928	0.2362	β
6	45.2768	0.1771	(2 0 0) β
7	50.0093	0.2362	(2 0 1) β
8	50.9592	0.2362	β
9	53.2647	0.2952	(2 1 1) β
10	56.1978	0.2362	β
11	63.1587	0.2952	(2 1 2) β
12	74.0211	0.2362	(3 3 1) α
13	75.9755	0.4320	(0 0 4) β

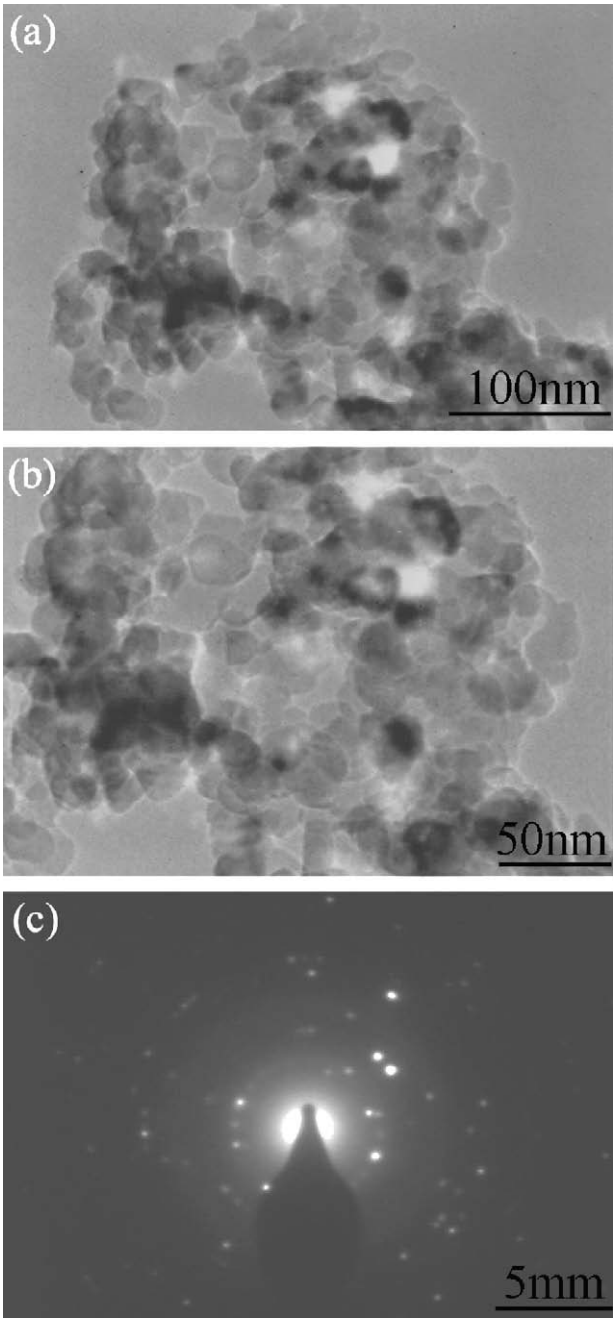


Fig. 3. (a and b) TEM images and (c) SAED pattern of the β-PbO nanocrystals.

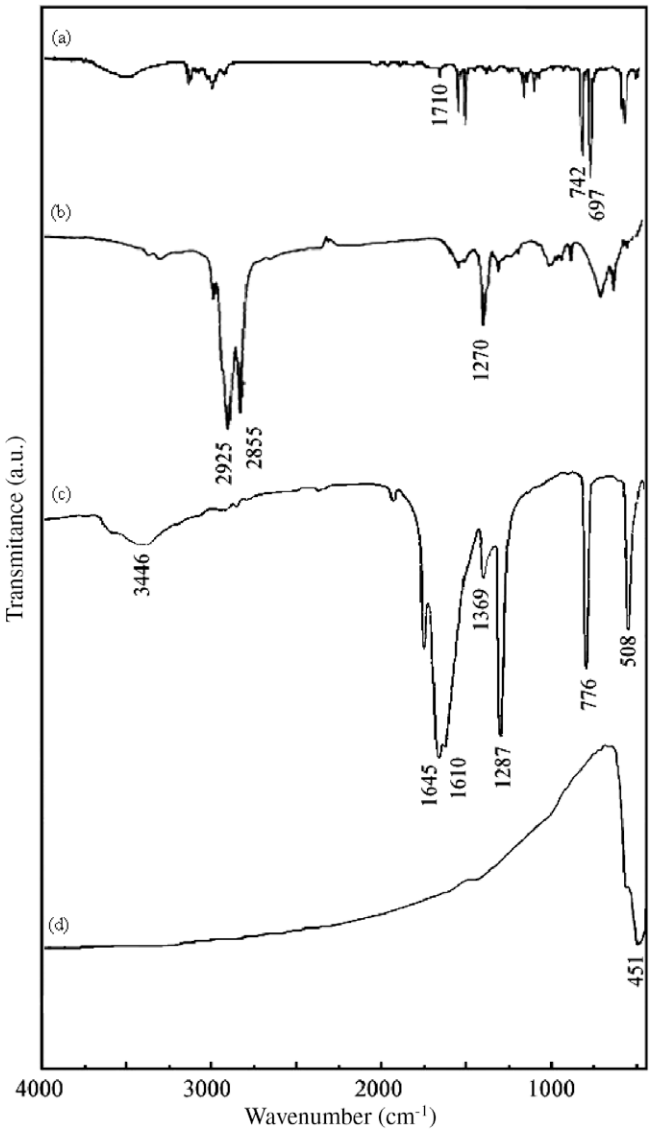


Fig. 4. FT-IR spectra of (a) TPP, (b) oleylamine (c) lead oxalate and (d) PbO nanocrystals.

In order to further prove the formation of PbO, the products were characterized by X-ray photoelectron spectroscopy (XPS). Fig. 5 shows the XPS of the as-synthesized samples. The XPS gives a binding energy of Pb 4f7/2 for the obtained product of 138.7 eV [26]. The O 1s spectrum shows a peak at 529.8 eV, approximately equal to the literature value of 530.9 eV for O 1s in PbO [2,27]. A full survey scan did not reveal any other element peaks. The results are agreeable to the data for PbO in the literature [26].

In order to prepare nanosized materials, they need to be coated with organic surfactants to prevent them from irreversible aggregation. TPP has been widely used in the synthesis of phosphine-stabilized gold or other metal nanoparticles. The phenyl groups in TPP can provide greater steric hindrance than the straight-chained alkyl groups such as tributylphosphine and trioctylphosphine, to control the size of the metal nanoparticles [28]. Lagunas et al. [29] found that Lewis bases such as trioctylphosphine oxide (TOPO) can accelerate the thermal decomposition of carbonyl species, and oleic acid plays a role of modulating the rate of decarbonylation. Oleylamine, similar to oleic acid, is chemically bonded to the surface of the metals through N atoms. TPP plus oleylamine are employed as a stabilizer to control the particle growth.

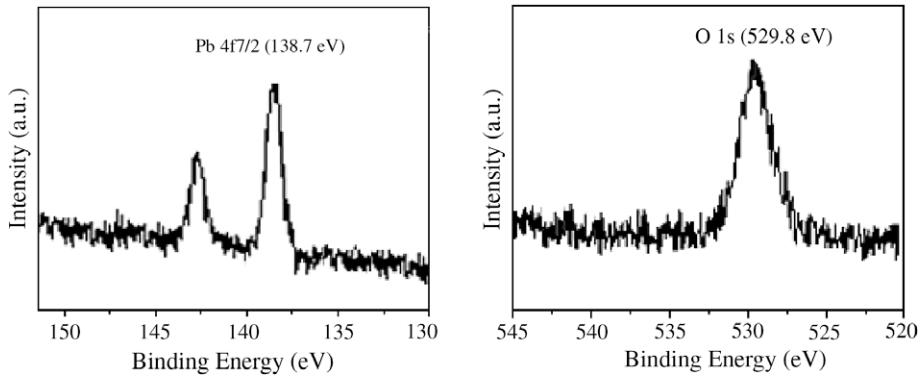


Fig. 5. XPS spectra of Pb 4f and O 1s of the PbO nanocrystals.

Table 3
Preparation of PbO nanocrystals under different conditions.

Sample	Capping agent	Temperature (°C)	Time	Product	Particles size (nm)
1		650	6 h	β-PbO	55
2	Oleylamine	150	120 min	α-PbO and [$Pb(O_4C_2)$]	45–60
3	Oleylamine + TPP	235	90 min	α-PbO and β-PbO	35
4	Oleylamine + TPP	500	120 min	β-PbO	30–45

In order to study the effect of TPP and oleylamine on the phase and particle size of PbO, different conditions were used to prepare the PbO nanoparticles (Table 3). According to previous reports, the stable phase β-PbO is obtained at high temperature [5]. Therefore, lead oxalate was calcined at 500 and 600 °C for 2 h. The XRD results showed that there is still an amount of α-PbO in the products. Although by increasing the temperature the particle size of PbO increases, a mixture of α- and β-PbO was exchanged into pure β-PbO at 650 °C. β-PbO with a particle size of about 55 nm and irregular shapes was obtained by calcining [$Pb(O_4C_2)$] at 650 °C for 6 h (sample 1). We decided to use a suitable solvent for the preparation of PbO with a small particle size at a lower temperature. So 0.5 g [$Pb(O_4C_2)$] and 5 ml oleylamine, (sample 2), were mixed and heated at 150 °C for 2 h. In this process, α-PbO and [$Pb(O_4C_2)$] with particle sizes of 45–60 nm were obtained. In order to prepare PbO nanocrystals without lead oxalate, the procedure mentioned in the experimental section including oleylamine and TPP, was carries out (sample 3). If sample 2 is compared to sample 3, it can be seen that by using of oleylamine and TPP, PbO nanocrystals (35 nm) without starting materials are obtained in a shorter time. In addition, pure β-PbO nanocrystals were obtained by calcination of sample 3 at 500 °C for 2 h (sample 4). By comparing samples 4–1, it was found that pure β-PbO with a smaller size is synthesized in the presence of TPP and oleylamine at a lower temperature and in a shorter time. After all, TPP as a Lewis base in the presence of oleylamine can accelerate the thermal decomposition of lead oxalate, so the thermal decomposition process occurs in a shorter time and nanoparticles with the smallest size are produced.

4. Conclusion

In summary, we have demonstrated the synthesis of α-PbO and β-PbO nanocrystals from lead oxalate powders via a thermal decomposition process. The controlled experimental results showed that oleylamine and triphenylphosphine (TPP) as the solvent and capping agent in the chemical process play an important role in the formation of pure products. This method is introduced as an inexpensive, fast, reproducible process for the large-scale synthesis of PbO nanocrystals.

Acknowledgement

Authors are grateful to the Council of the University of Kashan for providing financial support to undertake this work.

References

[1] C.D. Keating, M.J. Natan, Adv. Mater. 45 (2003) 451.
[2] L.J. Chen, S.M. Zhang, Z.S. Wu, Z.J. Zhang, H.X. Dang, Mater. Lett. 59 (2005) 3119.
[3] P. Veluchamy, M. Sharon, M. Shimizu, H. Minoura, J. Electroanal. Chem. 365 (1994) 179.
[4] S. Ghasemi, M.F. Mousavi, M. Shamsipur, H. Karami, Ultrason. Sonochem. 15 (2008) 448.
[5] L. Zhang, F. Guo, X. Liu, J. Cui, Y.T. Qian, J. Cryst. Growth 280 (2005) 575.
[6] Z.W. Pan, Z.R. Dai, Z.L. Wang, Appl. Phys. Lett. 14 (2002) 309.
[7] B. Jia, L. Gao, Mater. Chem. Phys. 100 (2006) 351.
[8] J. Li, L.Y. Gong, X. Xia, Yingyonghuaxue 18 (2001) 264.
[9] F.G. Ma, Z.Q. Shao, L.Y. Song, H.M. Tan, Hechenghuaxue 9 (2001) 449.
[10] X.C. Jiang, Y.L. Wang, T. Herricks, Y. Xia, J. Mater. Chem. 14 (2004) 695.
[11] S. Li, W. Yang, M. Chen, J. Gao, J. Kang, Y. Qi, Mater. Chem. Phys. 90 (2005) 262.
[12] T. Nathan, A. Aziz, A.F. Noor, S.R.S. Prabaharan, J. Solid. State. Electrochem. 12 (2008) 1003.
[13] N.S. Gajbhiye, S. Sharma, A.K. Nigam, R.S. Ningthoujam, Chem. Phys. Lett. 466 (2008) 181.
[14] M. Salavati-Niasari, F. Davar, M. Mazaheri, Mater. Lett. 62 (2008) 1890.
[15] M. Salavati-Niasari, F. Davar, M. Mazaheri, Polyhedron 27 (2008) 3467.
[16] M. Salavati-Niasari, F. Davar, Mater. Lett. 63 (2009) 441.
[17] M. Salavati-Niasari, F. Davar, N. Mir, Polyhedron 27 (2008) 3514.
[18] M. Salavati-Niasari, F. Davar, Z. Fereshteh, Chem. Eng. J. 146 (2009) 498.
[19] M. Salavati-Niasari, Z. Fereshteh, F. Davar, Polyhedron 28 (2009) 126.
[20] T. Hyeon, S.S. Lee, J. Park, Y. Chung, H.B. Na, J. Am. Chem. Soc. 123 (2001) 12798.
[21] R. Jenkins, R.L. Snyder (Eds.), Chemical Analysis: Introduction to X-ray Powder Diffractometry, John Wiley and Sons Inc., New York, 1996, p. 90.
[22] H.T. Yang, C.M. Shen, Y.G. Wang, Y.K. Su, T.Z. Yang, H.J. Gao, Nanotechnology 15 (2004) 70.
[23] K. Nakamoto, Infrared Spectra of Inorganic and Coordination Compound, 4th ed., Chemical Industry Press, Beijing, 1991.
[24] J.-M. Ouyang, H. Zheng, S.-P. Deng, J. Cryst. Growth 293 (2006) 118.
[25] Y. Hou, H. Kondoh, M. Shimojo, T. Kogure, T. Ohta, J. Phys. Chem. B 109 (2005) 19094.
[26] W.E. Morgan, J.R. Vanwazer, J. Phys. Chem. 77 (1973) 96.
[27] D.S. Zingg, D.M. Hercules, J. Phys. Chem. 82 (1978) 1992.
[28] H.T. Yang, Y.K. Su, C.M. Shen, T.Z. Yang, H.J. Gao, Surf. Interface Anal. 36 (2004) 155.
[29] A. Lagunas, C. Jimeno, D. Font, L. Solà, M.A. Pericàs, Langmuir 22 (2006) 3823.

Polyhedron 28 (2009) 2268–2276

Contents lists available at ScienceDirect

Polyhedron

journal homepage: www.elsevier.com/locate/poly

Synthesis, characterization, aggregation and thermal properties of a novel polymeric metal-free phthalocyanine and its metal complexes

Ahmet Bilgin [a,*], Çiğdem Yağcı [a], Ufuk Yıldız [b], Ersel Özkazanç [c], Erdoğan Tarcan [c]

[a] Department of Science Education, University of Kocaeli, 41380 Kocaeli, Turkey
[b] Department of Chemistry, University of Kocaeli, 41380 Kocaeli, Turkey
[c] Department of Physics, University of Kocaeli, 41380 Kocaeli, Turkey

ARTICLE INFO

Article history:
Received 13 January 2009
Accepted 10 April 2009
Available online 3 May 2009

Keywords:
Aggregation
Bisphthalonitrile
Electrical conductivity
Polymeric phthalocyanine

ABSTRACT

A novel polymeric metal-free phthalocyanine (M = 2H) and its metal complexes (M = Zn, Cu, Co and Ni) were prepared by the tetramerization reaction of 3,6,9-Tris(*p*-tolylsulfonyl)-1,11-bis(3,4-dicyanophenoxy)-3,6,9-triazaundecane **5** with the appropriate materials. The electrical conductivities of the metal-free phthalocyanine and the metal complexes, measured in air, were found to be $\sim 10^{-6}$–10^{-5} S m^{-1}. The aggregation property of the zinc complex **7** was investigated with Ni^{2+}, Cu^{2+}, Co^{2+}, Pb^{2+}, Cd^{2+} and Ag^{+} cations. Thermal analysis of the polymers were done by differential scanning calorimetry (DSC) and thermal gravimetric analysis (TGA) at a heating rate of 10 °C min^{-1} under a nitrogen atmosphere. All the novel compounds were characterized by using elemental analysis, UV–Vis, FT–IR, NMR and MS spectral data and DSC, DTA/TG techniques.

© 2009 Elsevier Ltd. All rights reserved.

1. Introduction

Phthalocyanines (Pcs) consisting of a planar macrocycle with an 18 π-electron system have been extensively studied due to their unique optical, electronic, catalytic and structural properties [1]. There has been growing interest in the use of phthalocyanines in a variety of new technological fields such as semiconductor devices [2], electrochromic display devices [3], liquid crystals [4], Langmuir–Blodgett films [5], catalysts [6], gas sensors [7–9] and as photosensitizers in photodynamic therapy of cancer [10].

Polymeric phthalocyananines are also very interesting since they belong to a class of π-conjugated semiconductor polymers, which offer a unique combination of properties. Being discovered in the 1950s, polymeric phthalocyanine remains an enigmatic material and many of its intrinsic properties are known rather insufficiently [11–13]. Polymeric phthalocyanines were mainly prepared via polycyclotetramerization reactions of bifunctional monomers such as aromatic tetracarbonitriles, various oxy-, arylenedioxy- and alkylenedioxy-bridged diphthalonitriles, and other nitriles or tetracarboxylic acid derivatives in the presence of metal salts or metals [11,12,14–16]. The electrical properties of polymeric phthalocyanines are of interest because of their conjugated structure and stability against light, heat, moisture and air. Hence polymeric phthalocyanines are suitable candidates for use as environmentally stable electrically conductive materials [14–16]. Their structural similarity to chlorophyll has also made them useful for applications in artificial solar cells [17]. The ion-binding ability of phthalocyanines containing homo- and hetero-donor atoms in peripheral substituent groups is receiving considerable attention in view of their effect on the aggregation of the molecules. After polymerization reactions, polymeric phthalocyanines will have many donor atoms and thus high metal binding ability.

Recently, several types of monomeric and polymeric phthalocyanines with various functional groups have been synthesized by our group. These phthalocycanines have peripheral substituents with several macrocyclic or podand units [15,16,18–22].

In the present work, we describe the synthesis and characterization of a novel polymeric metal-free phthalocyanine and metal complexes containing peripherally long triazadioxa derivatives which may allow the new functionalized materials to be of importance in the preparation of analytical chemicals such as new kinds of heavy metal extraction agents. We have examined the electrical conductivities of the polymers in air atmosphere. The aggregation properties of the polymer **7** and the thermal properties of all the polymers were investigated.

2. Experimental

2.1. Materials

Phosphorus pentoxide (P_2O_5), *p*-toluenesulfonyl chloride, diethylenetriamine, ethylene carbonate, potassium hydroxide, methanol, activated carbon, celite, 1,8-diazabicyclo[5.4.0]-undec-7-ene (DBU), ethanol, 1-pentanol, dimethylformamide (DMF), tetrahydrofuran (THF), chloroform, dichloromethane, petroleum ether,

* Corresponding author. Tel.: +90 262 3032438; fax: +90 262 3032403.
E-mail address: abilgin@kocaeli.edu.tr (A. Bilgin).

0277-5387/$ - see front matter © 2009 Elsevier Ltd. All rights reserved.
doi:10.1016/j.poly.2009.04.026

quinoline, sulfuric acid, hydrochloric acid, pyridine, acetone, sodium thiosulfate, acetonitrile, sodium carbonate, dioxane, *n*-hexane, lithium, glacial acetic acid, silica gel, ammonia, $MgSO_4$, $CoCl_2{\cdot}6H_2O$, $NiCl_2{\cdot}6H_2O$, $Cu(Ac)_2{\cdot}H_2O$ and $Zn(Ac)_2{\cdot}2H_2O$ were received from Merck and used as supplied. Potassium carbonate was received from Merck and used after drying in oven at 250 °C for 36 h. All organic solvents were dried and purified by the usual methods. 4-Nitrophthalonitrile was synthesized as described in the literature [23]. *N*,*N*′,*N*″-Tris(*p*-tolylsulfonyl)diethylene-triamine was synthesized according to the literature [24].

2.2. Measurements

Melting points of the compounds were determined with an electrothermal melting point apparatus and were uncorrected. ^{1}H NMR spectra were measured on a Bruker AMX 400 MHz NMR spectrometer in DMSO-d_6 with Me_4Si as an internal reference. ^{13}C NMR spectra were recorded on a Bruker AMX 100 MHz NMR spectrometer with DMSO-d_6 as the solvent and with Me_4Si as an internal reference. Transmission IR spectra of the samples were obtained on a FT–IR spectrophotometer (Shimadzu FT–IR-8201 PC) with the samples in KBr pellets. Optical spectra in the UV–Vis region were recorded with a model Shimadzu 1601 UV–Vis spectrometer using 10 mm pathlength cuvettes at room temperature. For the electrical measurements, the surfaces of the samples were covered with silver paste to form electrodes. The dielectric permittivity and AC conductivity of the samples were performed between 100 Hz and 1 MHz frequency range at room temperature by using a LCR meter (Agilent 4284A). Mass spectra were measured on a Micromass LCT Mass spectrometer. Elemental analyses were performed on a CHNS-932 LECO elemental analyzer. The metal contents of the metallophthalocyanine polymers were determined with a Unicam 929 AA spectrophotometer. Differential thermal analysis was performed on a TGA Q600 TA instrument under nitrogen (100 mL/min) atmosphere with a heating rate of 10 °C/min in the temperature range 30–700 °C. Differential scanning calorimetry (DSC) was performed on a Perkin Elmer Jade DSC under nitrogen atmosphere with a heating rate of 10 °C/min over the temperature range 50–700 °C.

2.3. Preparation of 3,6,9-Tris(p-tolylsulfonyl)-3,6,9-triazaundecane-1,11-diol (**3**)

A three-necked, round bottomed flask equipped with a mechanical stirrer and reflux condenser was charged with compound **1** (4.35 g, 7.5 mmol), ethylene carbonate (**2**) (1.5 g, 17.05 mmol) and finely powdered potassium hydroxide (0.016 g, 0.29 mmol). The stirred mixture was heated at 165 °C for 5 h under an inert nitrogen atmosphere. The reaction mixture was then allowed to cool to 90 °C, and 10 mL of ethanol was added through the condenser as rapidly as possible. 0.15 g of activated carbon was added to the solution and refluxed for 30 min. The temperature was then increased to 120 °C and the suspension was stirred for 30 min longer, and filtered through Celite. Water (10 mL) was added dropwise to the stirred solution, but no precipitate was observed. The reaction mixture was extracted with chloroform (5 × 35 mL). After drying on $MgSO_4$, the solvent was evaporated. The product **3** was a viscous brown liquid. After dissolving in toluene, the solution was kept in a refrigerator and the precipated colorless solid product that subsequently formed was filtered. The final product **3** was dried over P_2O_5 *in vacuo* at 50 °C.

Yield: 4.41 g (89%). M.p.: 104–105 °C. R_f: 0.43 (Chloroform:petroleum ether 7:3). *Anal.* Calc. $C_{29}H_{39}N_3O_8S_3$ (653.82): C, 53.27; H, 6.01; N, 6.43; S, 14.71. Found: C, 53.49; H, 6.27; N, 6.17; S, 14.94%. FT–IR (KBr, cm^{-1}): 3390 (O–H), 3068–3030 (Aromatic =CH), 2944–2882 (–CH_2–), 1599 (C=C), 1494, 1456, 1332 (SO_2), 1261, 1160 (SO_2), 1089–1001 (CH_2O–), 909, 812, 717, 645, 552. ^{1}H NMR (DMSO-d_6), δ (ppm): 7.74–7.67 (d, 6H, Ar*H*), 7.45–7.36 (d, 6H, Ar*H*), 4.87 (br. s, 2H, OH), 3.60–3.18 (m, 16H, NCH_2, OCH_2) 2.42 (s, 3H, ArCH_3), 2.40 (s, 6H, ArCH_3). ^{13}C NMR (DMSO-d_6), δ (ppm): 143.9, 143.6, 135.7, 135.4, 129.8, 127.4, 126.9 (Ar*C*), 59.9 (*C*H_2OH), 49.8, 49.3, 49.1 (*C*H_2N), 21.5 (*C*H_3), 21.3 (*C*H_3). MS (ES$^+$), *m/z*: 676.2 [M+Na]$^+$.

2.4. Preparation of 3,6,9-Tris(p-tolylsulfonyl)-1,11-bis(3,4-dicyanophenoxy)-3,6,9-triazaundecane (**5**)

3,6,9-Tris(*p*-tolylsulfonyl)-3,6,9-triazaundecane-1,11-diol (**3**) (4.41 g, 6.75 mmol) and 4-nitrophthalonitrile (**4**) (2.36 g, 13.50 mmol) were dissolved in 10 mL of dry DMF in a 100 mL three-necked flask and the mixture was stirred at room temperature under an inert atmosphere and degassed three times. Then temperature was increased to 50 °C. Finely powdered K_2CO_3 (2.83 g, 20.25 mmol) was added to the solution in eight equal potions at 30 min intervals. The reaction mixture was stirred at 50 °C for 6 days. The reaction was monitored by a thin layer chromatography ($CHCl_3$:MeOH, 7:3). At the end of this period, the mixture was cooled and poured into ice (100 g), and mixed for 4 more hours. The precipitate that formed was filtered and washed with water and EtOH. After recrystallization from MeOH, the obtained product **5** was dried over P_2O_5 in a vacuum oven at 50 °C to yield a light yellow powder.

Yield: 5.38 g (88%). M.p.: 138–139 °C. *Anal.* Calc. $C_{45}H_{43}N_7O_8S_3$ (906.06): C, 59.65; H, 4.78; N, 10.82; S, 10.62. Found: C, 59.42; H, 5.02; N, 10.60; S, 10.97%. FT–IR (KBr, cm^{-1}): 3086–3043 (Aromatic =CH), 2980–2880 (aliphatic CH_2), 2232 (C≡N), 1599 (aromatic –C=C–), 1564, 1493, 1458, 1339–1308 (SO_2), 1256 (Ar–OCH_2), 1157 (SO_2), 1089, 979, 814, 719, 699, 646, 549. ^{1}H NMR (DMSO-d_6), δ (ppm): 8.21 (d, 2H, Ar*H*), 8.01 (d, 2H, Ar*H*), 7.96 (s, 2H, Ar*H*), 7.69–7.54 (m, 6H, Ar*H*), 7.38–7.26 (m, 6H, Ar*H*), 4.21 (br. s, 4H, ArOCH_2), 3.53 (br. s, 4H, NCH_2CH_2OAr), 3.33–3.18 (m, 8H, NCH_2CH_2NCH_2CH_2N), 2.38 (s, 3H, ArCH_3), 2.35 (s, 6H, ArCH_3). ^{13}C NMR (DMSO-d_6), δ (ppm): 161.9, 145.1, 143.2, 135.3, 134.9, 131.2, 130.4, 128.7, 127.5, 119.8, 118.6, 117.2, 115.4 (CN), 114.9 (CN), 107.8, 69.6 (*C*H_2OAr), 52.6, 49.7, 49.3, 21.4, 20.9. MS (ES$^+$), *m/z*: 907.2 [M+H]$^+$, 751.1 [M-Ts]$^+$.

2.5. Preparation of polymeric metal-free phthalocyanine (**6**)

A mixture of **5** (0.906 g, 1.0 mmol), *n*-pentanol (5.0 mL) and 1,8-diazabicyclo[5,4,0] undec-7-ene (DBU) (0.15 mL, 0.16 g, 1.0 mmol) was placed in a standard Schlenk tube under nitrogen atmosphere and degassed two times. Then temperature was increased to 160 °C. The reaction mixture was stirred at 160 °C for 18 h. After the reaction mixture was cooled to room temperature, ethyl alcohol (10 mL) was added dropwise and mixed for half an hour. The dark green precipitate was filtered and washed with MeOH and diethyl ether. The dark green product **6** was dried at 50 °C under vacuum over P_2O_5.

Yield: 0.78 g (86%). M.p.: >300 °C. *Anal.* Calc. $(C_{180}H_{174}N_{28}O_{32}S_{12})_n$ (3626.25) (for (for nitrile end groups): C, 59.62; H, 4.84; N, 10.82; S, 10.61. Found: C, 53.49; H, 6.27; N, 6.17; S, 14.94%. FT–IR (KBr, cm^{-1}): 3294 (N–H), 3063 (Aromatic =CH), 2928–2866 (aliphatic CH_2), 2225 (C≡N), 1629 (C=N), 1604 (aromatic –C=C–), 1549, 1460, 1337 (SO_2), 1227 (Ar–OCH_2), 1153 (SO_2), 1087, 1035 (N–H), 810, 708, 648, 538.

2.6. Preparation of polymeric zinc and copper complexes (**7**, **8**)

A mixture of compound **5** (0.906 g, 1.0 mmol), zinc acetate dihydrate (0.114 g, 0.5 mmol) or cupric acetate monohydrate (0.100 g, 0.50 mmol) and amyl alcohol (5 mL) was put in a standard

Schlenk tube and the temperature was increased to 90 °C. DBU (0.15 mL, 1.0 mmol) was added dropwise to the suspension at the same temperature. Then the temperature was increased to 160 °C and the reaction was stirred at 160 °C for 18 h under a nitrogen atmosphere. After the reaction mixture was cooled to room temperature, ethanol (10 mL) was added and mixed for 30 min. The crude products were collected by filtration and washed with methanol, DMF, water and acetone. The final green **7** and dark green **8** products were dried under vacuum over P_2O_5 at 50 °C.

*2.6.1. Compound **7***

Yield: 0.98 g (96.1%). M.p.: >300 °C. *Anal.* Calc. $(C_{180}H_{176}N_{24}O_{40}S_{12}Zn)_n$ (3765.61): C, 57.41; H, 4.71; N, 8.93; S, 10.22; Zn, 1.74. Found: C, 57.72; H, 4.46; N, 8.65; S, 10.47; Zn, 1.95%. FT–IR (KBr, cm^{-1}): 3402 (imide N–H), 3057 (Aromatic =CH), 2928–2864 (CH_2), 1770 (sym. C=O), 1718 (asym. C=O), 1645 (–C=N–), 1601 (Aromatic –C=C–), 1487, 1456, 1395, 1334 (SO_2), 1222 (Ar-OCH_2), 1155 (SO_2), 1085–1043, 940, 810, 715, 650, 543.

*2.6.2. Compound **8***

Yield: 0.92 g (91.5%). M.p.: >300 °C. *Anal.* Calc. $(C_{180}H_{176}N_{24}O_{40}S_{12}Cu)_n$ (3763.78): C, 57.44; H, 4.71; N, 8.93; S, 10.22; Cu, 1.69. Found: C, 57.72; H, 4.53, N, 9.27; S, 10.49; Cu, 1.46%. FT–IR (KBr, cm^{-1}): 3386 (imide N–H), 3064 (Aromatic =CH), 2951–2824 (CH_2), 1772 (sym. C=O), 1714 (asym. C=O), 1645 (–C=N–), 1607 (Aromatic –C=C–), 1510, 1454, 1400, 1340 (SO_2), 1229 (Ar-OCH_2), 1157 (SO_2), 1089–1018, 954, 814, 718, 646, 548.

*2.7. Preparation of polymeric cobalt and nickel complexes (**9**, **10**)*

A mixture of compound **5** (0.906 g, 1 mmol), dry quinoline (3 mL) and $CoCl_2{\cdot}6H_2O$ (0.120 g, 0.5 mmol) or $NiCl_2{\cdot}6H_2O$ (0.122 g, 0.5 mmol) was charged in a standard Schlenk tube and degassed several times with nitrogen. The reaction mixture was treated at 210–220 °C for 18 h under a nitrogen inert atmosphere. After 18 h of refluxing, the reaction mixture was cooled to room temperature and then 10 mL of ethanol was added to the mixture slowly and stirred for 30 min. The obtained green **9** and dark green **10** products were filtered off. The crude products were washed with water, MeOH and diethyl ether. The final products (**9** and **10**) were dried under vacuum over P_2O_5 at 50 °C.

*2.7.1. Compound **9***

Yield: 1.0 g (97.4%). M.p.: >300 °C. *Anal.* Calc. $(C_{180}H_{176}N_{24}O_{40}S_{12}Co)_n$ (3759.17): C, 57.51; H, 4.72; N, 8.94; S, 10.23; Co, 1.57. Found: C, 57.29; H, 4.93; N, 8.65; S, 10.42; Co, 1.74%. FT–IR (KBr, cm^{-1}): 3368 (imide N–H), 3048 (Aromatic =CH), 2953–2729 (CH_2), 1770 (sym. C=O), 1719 (asym. C=O), 1640 (–C=N–), 1598 (Aromatic –C=C–), 1474, 1325 (SO_2), 1224 ($ArOCH_2$), 1126 (SO_2), 1084–1024, 984, 785, 735, 546.

*2.7.2. Compound **10***

Yield: 1.01 g (98.2%). M.p.: >300 °C. *Anal.* Calc. $(C_{180}H_{176}N_{24}O_{40}S_{12}Ni)_n$ (3758.92): C, 57.52; H, 4.72; N, 8.94; S, 10.23; Ni, 1.56. Found: C, 57.81; H, 4.97; N, 9.19; S, 9.87; Ni, 1.83%. FT–IR (KBr, cm^{-1}): 3437 (imide N–H), 3053 (Aromatic =CH), 2926–2731 (CH_2), 1768 (sym. C=O), 1721 (asym. C=O), 1654 (–C=N–), 1604 (Aromatic –C=C–), 1533, 1489, 1460, 1341 (SO_2), 1234 ($ArOCH_2$), 1155 (SO_2), 1089–1020, 991, 810, 723, 651, 546.

*2.8. The conversion of cyano end groups of the polymeric metal-free phthalocyanine into imido groups (**6a**)*

A sample of compound **6** (150 mg) was dissolved in a minimum volume of H_2SO_4 (96 wt.-%) at room temperature. After 3–4 h of stirring, the reaction mixture was filtered. The filtered part was poured into excess amount of ice-water mixture. The dark green crude product was washed with distilled water until the residue washing water was neutral. Then the final product **6a** was washed with ethanol, diethyl ether and dried under vacuum over P_2O_5 at 50 °C.

Yield: 118 mg (78.7%). M.p.: >300 °C. *Anal.* Calc. $(C_{180}H_{178}N_{24}O_{40}S_{12})_n$ (3702.25) (for imide end groups): C, 58.40; H, 4.85; N, 9.08; S, 10.39. Found: C, 58.17; H, 4.59; N, 9.43; S, 10.68%. FT–IR (KBr, cm^{-1}): 3380 (imide N–H), 3275 (N–H), 3056 (Aromatic =CH), 2938–2740 (CH_2), 1774 (sym. C=O), 1720 (asym. C=O), 1627 (–C=N–), 1600 (Aromatic –C=C–), 1565, 1458, 1345 (SO_2), 1230 ($ArOCH_2$), 1163 (SO_2), 1086, 1035 (N–H), 964, 815, 730, 648, 540.

2.9. Metal analysis of the polymeric metal complexes

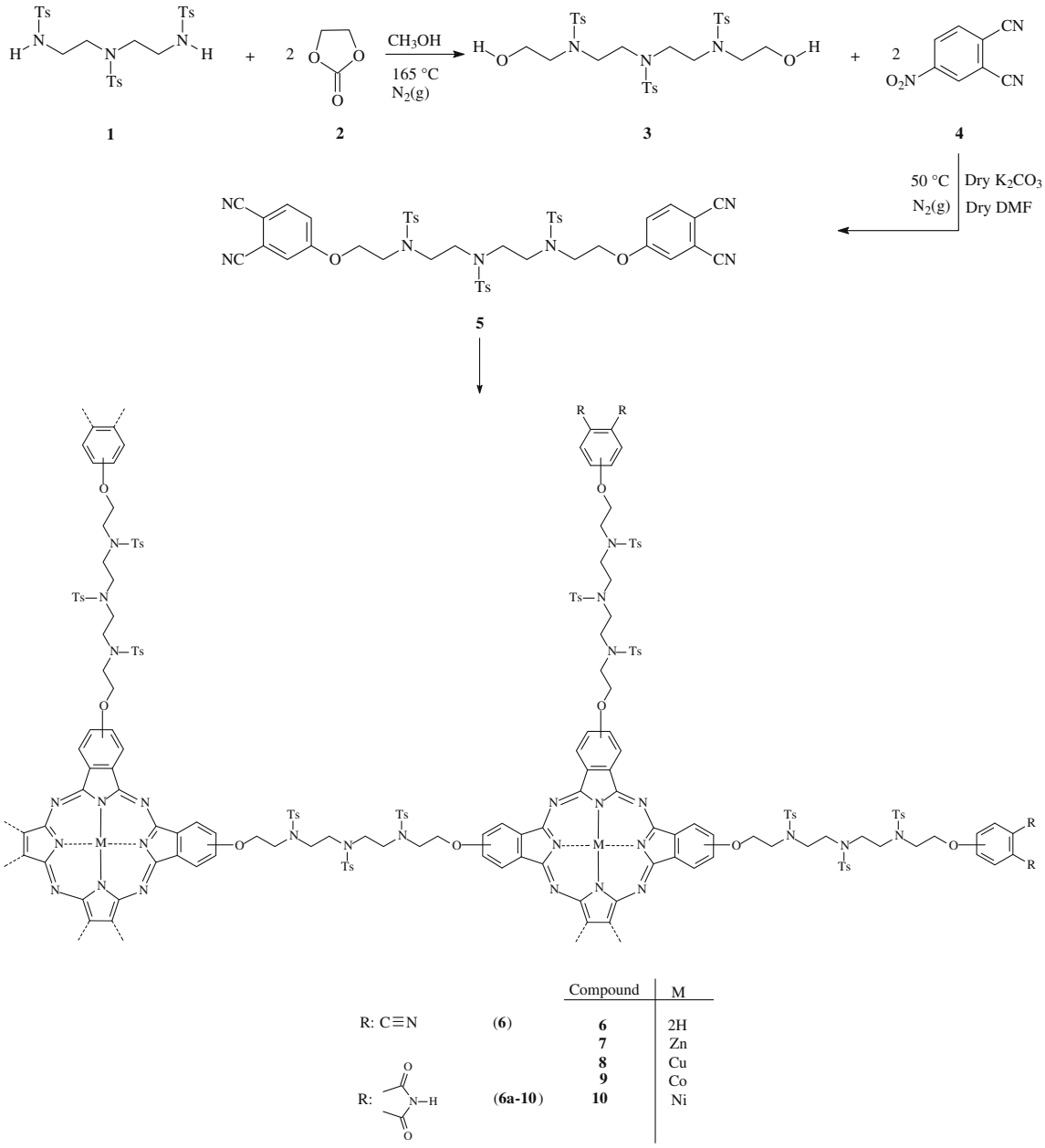
A sample of the polymeric metal complexes (**7**–**10**) (10 mg) was added into concentrated sulfuric acid (2.5 mL) and concentrated nitric acid (3.5 mL). The mixture was heated for 2 h at 160 °C in an oil-bath. The solution was firstly digested in conc. HCl acid solution and then diluted with deionize water (500 mL). The determination of metal ions was conducted by atomic absorption measurements.

3. Results and discussion

The synthesis of the 3,6,9-Tris(*p*-tolylsulfonyl)-3,6,9-triazaundecane-1,11-diol (**3**) was performed by starting with *N*,*N*′,*N*″-Tris(*p*-tolylsulfonyl)diethylenetriamine **1** (Scheme 1). Compound **1** was synthesized as described in the literature [24]. Elemental analysis and mass spectral data of **3** were satisfactory: 676.2 $[M+Na]^+$. Compound **3** was characterized by NMR and IR spectroscopy techniques. In the ^1H NMR (DMSO-d_6) spectrum of **3**, the NH group of **1** had disappeared, as expected, and a new signal at $\delta = 4.87$ (br. s, 2H, OH) appeared. The proton-decoupled ^{13}C NMR spectrum of **3** indicates the presence of the corresponding carbon atoms at $\delta = 59.9$ (CH_2OH) and 49.8 (CH_2N). The IR spectrum of **3** was easily verified with the disappearance of N–H and the presence of O–H stretching vibrations at 3390 cm^{-1}. The difference between the IR spectra of **3** and **1** is clear from the absence of characteristic vibrations such as N–H.

3,6,9-Tris(*p*-tolylsulfonyl)-1,11-bis(3,4-dicyanophenoxy)-3,6,9-triazaundecane (**5**) was prepared by the reaction of 4-nitrophthalonitrile and **3** in the presence of K_2CO_3 in dry DMF. Final purification of the bisphthalonitrile derivative by recrystallization afforded **5**, for which elemental analysis and ES^+ mass spectral data were satisfactory *m/z*: 907.2 $[M+H]^+$, 751.1 $[M-Ts]^+$. In the ^1H and ^{13}C NMR spectra of **5**, the OH groups of compound **3** disappeared and nitrile carbon atoms appeared as expected. The disappearance of O–H and the presence of the C≡N functional group at 2232 cm^{-1} in the IR spectrum of compound **5** confirm the formation of the desired compound **5**.

The metal-free phthalocyanine polymer **6** was synthesized by heating a mixture of **5**, DBU and amyl alcohol in a Schlenk tube. Model compound **6a**, containing phthalocyanine units and suitable imido end groups, was prepared to use its characteristic data for analysis of the polymerization degree. The cyano end groups of the metal-free phthalocyanine were converted into imido end groups by treating **6** with conc. H_2SO_4, and **6a** was obtained. The IR spectrum of polymer **6** is slightly broadened and reduced in intensity, which can be attributed to the difficulty in grinding the sample to a small particle size and the polymeric structure. The peaks at 3294 and 1035 cm^{-1} are the characteristic metal-free phthalocyanine N–H stretching and pyrrole ring vibration bands. A weak –C=N– absorption at 1629 cm^{-1} was detected. Elemental



Scheme 1. Synthesis of bisphthalonitrile **5** and polymers **6**–**10**.

Table 1
Wavelength and absorption coefficients of the UV-Vis spectra of the polymers.

Compound	M	Solvent	λ (nm)/(log ε)	Ratio[a] UV-Vis
(**6**)	2H	Pyridine	704(4.29) 674(4.28) 648(4.12) 616(4.02) 396(4.03) 334(4.39)	1.02
		H_2SO_4	888(3.92) 828(3.98) 731(3.19) 499(3.37) 307(4.05) 242(4.60)	1.17
(**7**)	Zn	Pyridine	684(4.24) 618(3.71) 358(4.07) 310(3.69)	0.87
		H_2SO_4	828(3.86) 733(2.26) 523(2.73) 311(3.57) 219(4.26)	1.10
(**8**)	Cu	Pyridine	682(4.13) 618(3.83) 346(3.98) 305(3.79)	0.92
		H_2SO_4	834(4.06) 738(2.91) 515(1.52) 307(3.56) 240(4.21)	1.04
(**9**)	Co	Pyridine	676(4.22) 615(3.89) 333(4.35) 314(4.36)	1.03
		H_2SO_4	812(4.13) 723(3.71) 503(2.75) 301(4.51) 242(4.60)	1.11
(**10**)	Ni	Pyridine	676(4.26) 624(4.12) 330(4.26) 314(4.37)	1.02
		H_2SO_4	812(4.21) 722(3.35) 503(2.66) 414(3.23) 308(4.17) 240(4.12)	0.98

[a] Intensity ratio of absorption B bands at λ = 219–334 nm and Q bands at λ = 676–888 nm ($C = 1.0 \times 10^{-4}$ g/L in H_2SO_4 and 1.0×10^{-4} g/L in pyridine).

analysis was satisfactory. In the IR spectra for **6a**, the disappearance of the peak at 2225 cm^{-1} due to the cyano groups of **6** and the appearance of new peaks at ~1774–1720 cm^{-1} due to imido groups supports the conversion of the cyano groups into imido groups.

The transition metal complexes (**7–10**) were prepared from the bisphthalonitrile compound **5** and the corresponding metal salt in the appropriate solvent (Scheme 1). The IR spectra of the metal complex polymers (**7–10**) are very similar, except for the metal-free phthalocyanine polymer **6**. The metal-free phthalocyanine polymer showed an N–H stretching band at 3294 and 1035 cm^{-1} due to the inner core [25]. These bands disappear in the spectra of the metal complex polymers. These bands are especially beneficial for characterization of metal-free phthalocyanine polymers, as there is little frequency dependence on the ring substitution and they are not overlapped by strong bisphthalonitrile monomer absorptions [14–16]. The end groups of the metal-free phthalocyanine polymer were cyano groups (2225 cm^{-1}), while the end groups of the metal complex polymers were imido groups (~1772–1714 cm^{-1}). The existence of imido groups in the case of the metal complex polymers was attributed to the presence of moisture during the work-up and the hydrated metal salts. There was little shift to longer wavelength numbers in most of the IR bands of the metal complexes with respect to the metal-free analogues [14–16,26]. The spectra of the complexes are quite complex and reveal many metal-independent ligand absorptions, and metal-N vibrations were expected to appear at 400–100 cm^{-1}, but they were not detected using KBr pellets [27]. The elemental analyses of the metal free (**6**, **6a**) and metal complex polymers (**7–10**) were satisfactory.

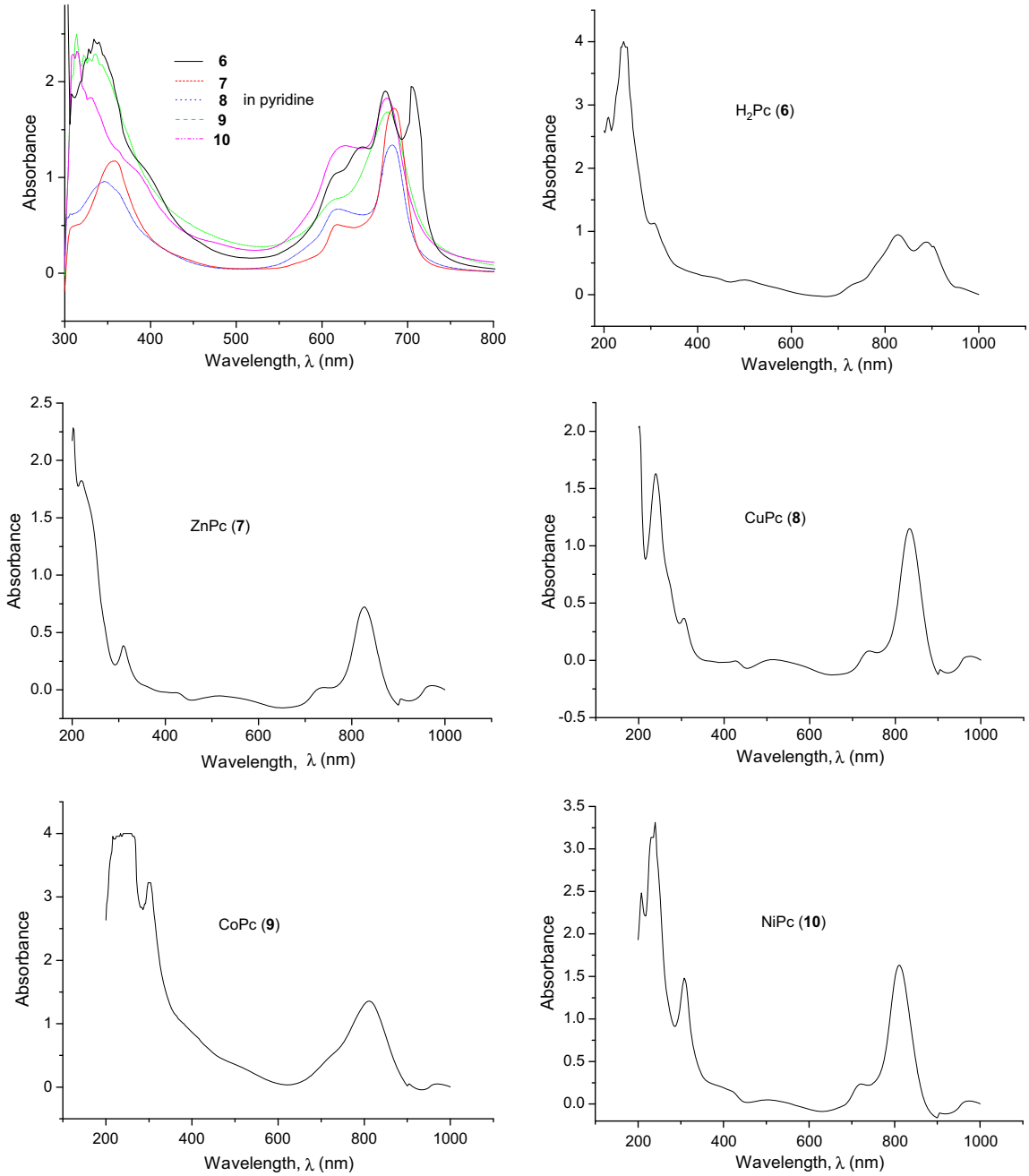


Fig. 1. UV–Vis spectra of polymers (**6–10**) in pyridine ($C = 1.0 \times 10^{-4}$ g/L) and in H_2SO_4 ($C = 1 \times 10^{-4}$ g/L).

It is very difficult to determine the molecular weight of polymeric phthalocyanines because of their poor solubility in common organic solvents. One possible procedure to determine the degree of polymerization is IR spectroscopy, by comparison of the intensity of the end cyano groups to other ring vibrations. This method has been applied to only a few cases [28,29]. We determined the degree of polymerization after converting the cyano end groups of the metal-free phthalocyanine polymer into imido end groups, due to the relatively good intensity of C=O imide groups to nitrile groups. After this, the ratios of the absorption intensities of (Ar–O–C) (etheric groups) of the polymers (~1230 cm^{-1}) to asym. C=O groups of the imides (~1714 cm^{-1}) were calculated [compound/$\log_{10} I_{1230}/I_{1714}$: **6a**/0.52, **7**/1.84, **8**/1.23, **9**/1.57, **10**/1.14]. The polymerization degrees follow the order: **7** > **9** > **8** > **10** > **6a**. On the other hand, the IR spectrum of **6** shows a low degree of polymerization due to the high intensity of the nitrile groups.

The metal-free phthalocyanine **6** and the metal complexes (**7–10**) gave the typical UV–Vis absorption spectra of phthalocyanines (Table 1). As can be seen in Table 1, there is a shoulder at the slightly higher energy side for polymeric metal-free phthalocyanine and the metal complexes. The presence of shoulders in the UV–Vis spectra of the polymers corresponds to aggregated or non-aggregated species in conc. sulfuric acid and pyridine. The metal-free phthalocyanine polymer (**6**) decomposes slowly by hydrolysis in conc. H_2SO_4, which is demonstrated by a decrease of the absorption coefficient at longer wavelengths and also the color of the solution turns from green to brown with time. However the metal complex polymers (**7–10**) were more stable in conc. sulfuric acid than the metal-free polymer and there was no color change in the case of the metal complexes even after a day. When going from organic solvents to concentrated H_2SO_4, the long-wave absorption band underwent a significant bathochromic shift, which was due to weak protonation of the phthalocyanine ring at the *meso* nitrogen atoms. The intensity of these absorptions also decreased. The UV–Vis spectrum of **6** was obtained in pyridine and conc. H_2SO_4. The electronic absorption spectra of (**6–10**) in pyridine and H_2SO_4 at room temperature are shown in Fig. 1. There was a single Q band for **7–10** while there was a split Q-band, as expected, and two strong bands in the visible region for **6** [30]. The split Q-band, which is characteristic for metal-free phthalocyanines, was observed at λ_{max} 705 and 674 nm, with shoulders at 647 and 617 nm, for (**6**) indicating the monomeric species; monomeric species with D_{2h} symmetry show two intense absorptions at around 700 nm [30,31]. On the other hand, such split-Q band absorptions are due to a $\pi\pi^*$ transition of this fully conjugated 18π electron system [32]. In the case of a H_2SO_4 solution of **6**, the primary band in the visible region was broadened and shifted to longer wavelength (182 nm). In all cases the intensities in the UV (Soret band transition) and vis (Q-band transition) spectra were $I_{UV}/I_{Vis} \leqslant 1$ (Table 1). This result can be attributed to the absence of poly(isoindolinine) co-units in all of the polymeric metal complexes (**7–10**).

UV–Vis titrations were performed with several heavy metal cations (Ni^{2+}, Cu^{2+}, Co^{2+}, Pb^{2+}, Cd^{2+}, Zn^{2+} and Ag^{+}) to investigate the metal-binding capabilities of complex **7** with triaza-dioxa long peripheral substituents. Firstly, we clarified whether methanol has any effect or not on the visible spectrum of **7**. For this purpose, different amounts of methanol were added to a solution of **7** in pyridine. There was only a little change in the intensities of the Q-bands in the visible absorption spectra of **7** with increasing the amounts of methanol, due to the increasing polarity. Then different concentrations of metal salt (e.g. $AgNO_3$, $NiCl_2{\cdot}6H_2O$, $Co(NO_3)_2{\cdot}6H_2O$, $Pb(NO_3)_2$, $Zn(CH_3COO)_2{\cdot}2H_2O$, $Cd(NO_3)_2{\cdot}4H_2O$ and $CuCl_2{\cdot}2H_2O$) solutions in methanol (1.0×10^{-4} M) were added to the solution of the zinc complex **7** in pyridine (1.0×10^{-4} g/L). When we added Ni^{2+}, Cu^{2+} and Co^{2+} solutions to the zinc complex solution, the Q band of **7** broadened and shifted to the low-wavelength region. The addition of Ni^{2+}, Cu^{2+} and Co^{2+} solutions caused a dramatic change due to aggregation in the visible spectrum of **7** (Fig. 2). The increasing interactions between the polymer chains due to the intermolecular complexation through triazadioxa peripheral units with Ni^{2+}, Cu^{2+}, Co^{2+} ions forms sandwich type complexes and causes the new absorption bands. The new bands can be attributed to the presence of dimeric and oligomeric phthalocyanine species. Further addition of Ni^{2+}, Cu^{2+} and Co^{2+} solutions caused no observable effect. On the other hand, when solutions of Pb^{2+}, Cd^{2+}, Zn^{2+} and Ag^{+} were added, the intensity of the bands at 684 and 618 nm gradually decreased without any shift and no optical change was observed (Fig. 3). The decrease in the intensity

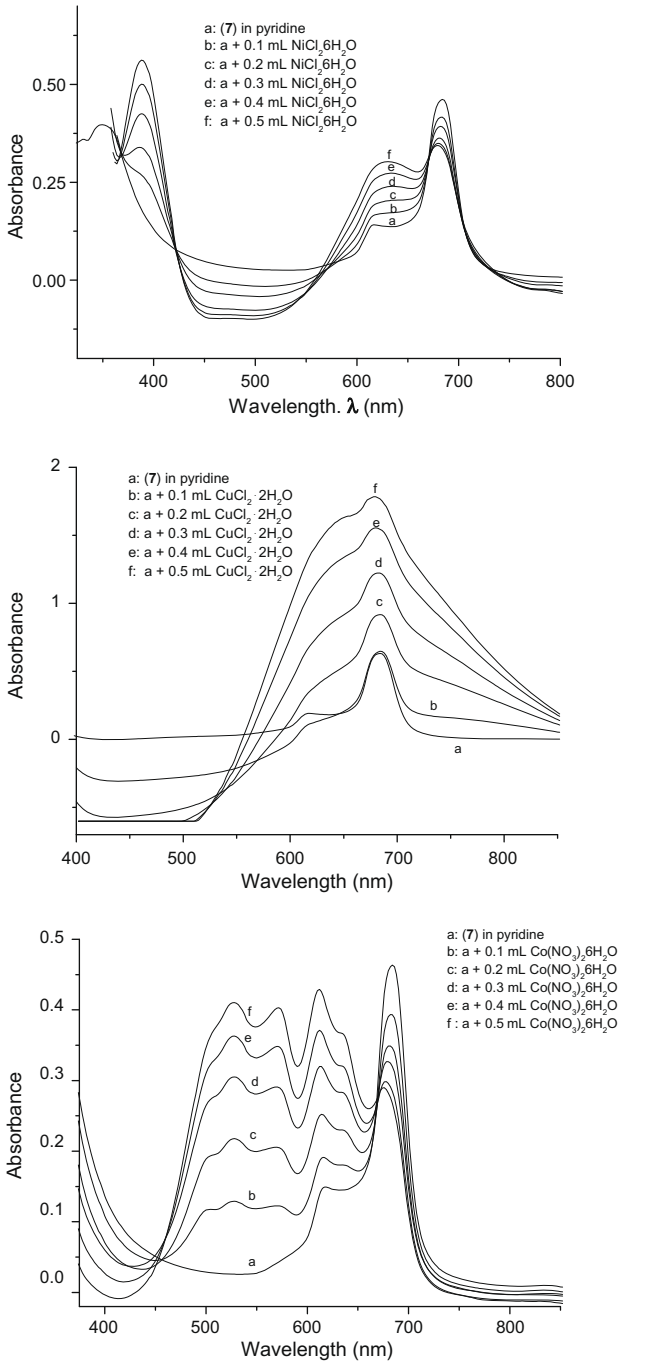


Fig. 2. Changes in the visible spectra of **7** in pyridine ($C = 1.0 \times 10^{-4}$ g/L) after the addition of $NiCl_2{\cdot}6H_2O$, $CuCl_2{\cdot}2H_2O$ and $Co(NO_3)_2{\cdot}6H_2O$ solutions in methanol ($C = 1.0 \times 10^{-4}$ M).

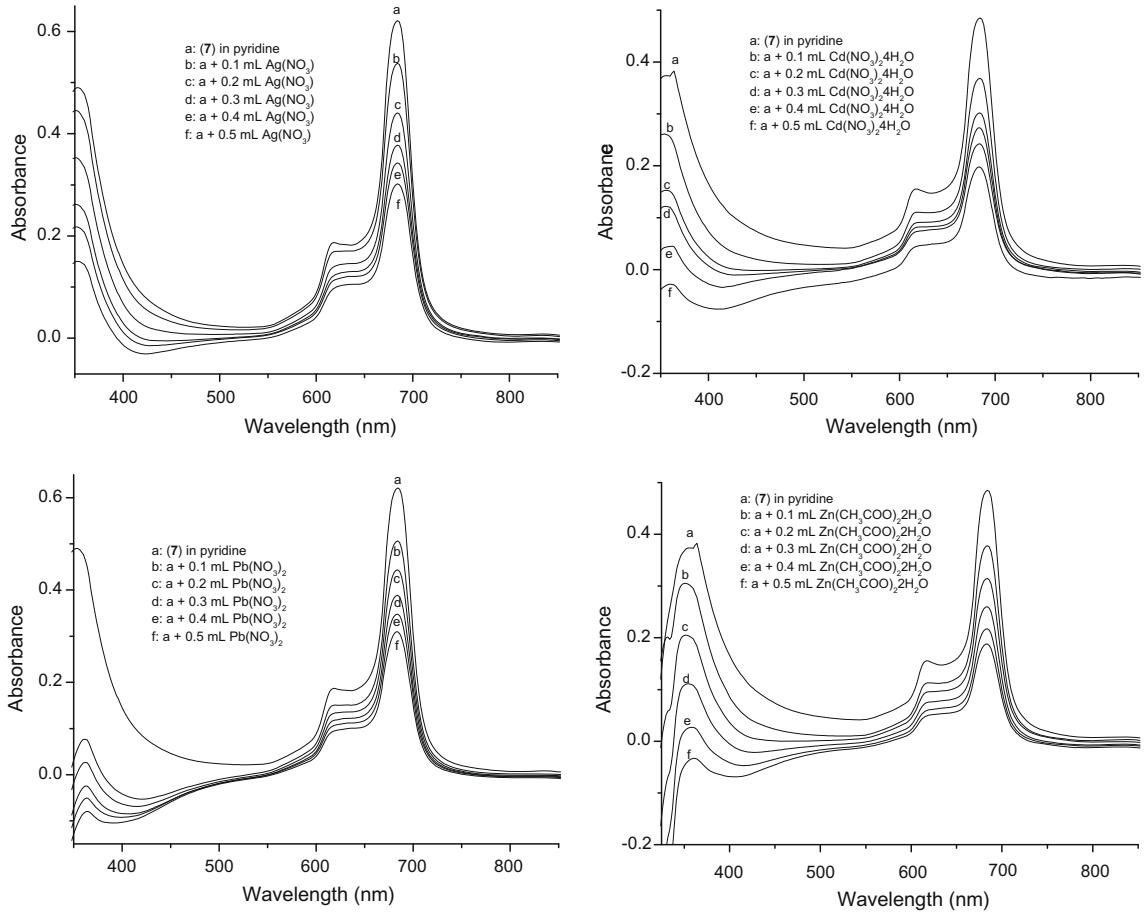


Fig. 3. Changes in the visible spectra of **7** in pyridine ($C = 1.0 \times 10^{-4}$ g/L) after the addition of $AgNO_3$, $Pb(NO_3)_2$, $Cd(NO_3)_2{\cdot}4H_2O$ and $Zn(CH_3COO)_2$ solutions in methanol ($C = 1.0 \times 10^{-4}$ M).

of the bands can be attributed to the dilution effect and the very weak or non-coordination of the N and O atoms to Pb^{2+}, Cd^{2+}, Zn^{2+} and Ag^{+} ions, thus leaving the $Pb(NO_3)_2$, $Cd(NO_3)_2{\cdot}4H_2O$, $Zn(CH_3COO)_2{\cdot}2H_2O$ and $AgNO_3$ units only loosely coordinated via oxygen and nitrogen donors.

The powder samples of the polymeric metal-free phthalocyanine and metal complexes were pressed in the form of pellets of 10 mm diameter and thickness ranging from 1 to 3 mm for AC conductivity measurements. The surfaces of the polymers were covered with silver paste to form electrodes. Then, the capacitance and the dielectric loss factor of each sample were measured between 10 kHz and 1 MHz frequency range at room temperature

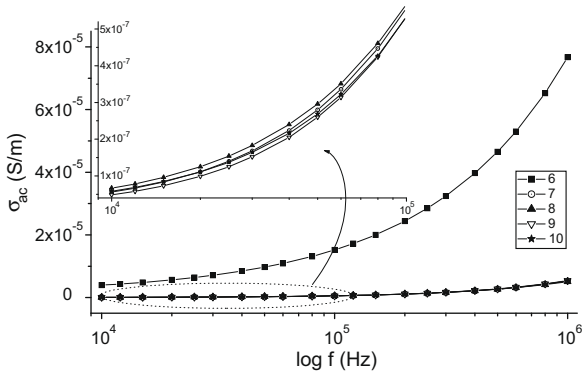


Fig. 4. The frequency versus AC conductivity of polymers (**6**–**10**) at room temperature.

Table 2
Thermal properties of the polymers.

Polymer	M	Tg	Initial decomposition temperature in °C	Main decomposition temperature in °C
6	2H	42	360	417
7	Zn	51	336	395
8	Cu	50	358	378
9	Co	56	310	371
10	Ni	45	341	367

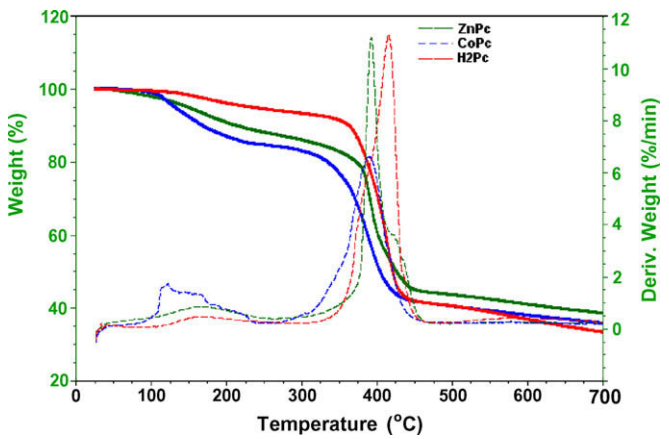


Fig. 5. DTA/TG thermograms of H_2Pc (**6**), ZnPc (**7**) and CoPc (**9**).

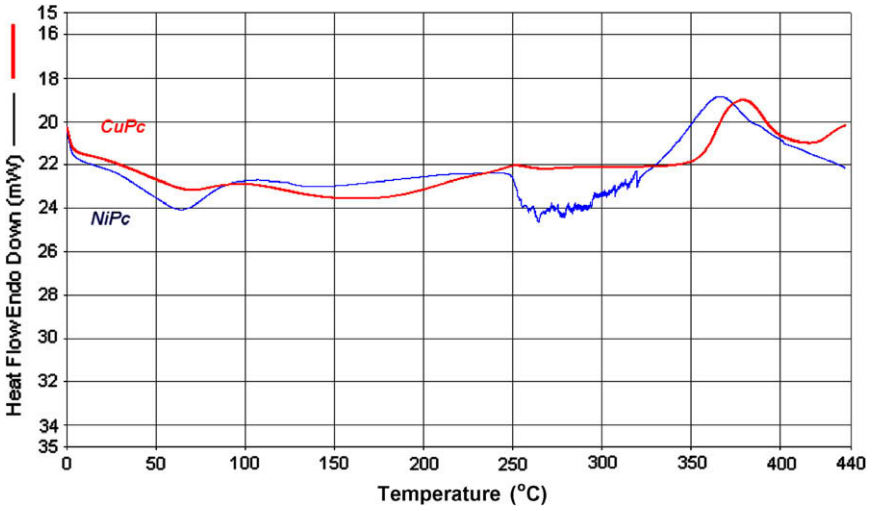


Fig. 6. DSC thermograms of CuPc (**8**) and NiPc (**10**).

by using a LCR meter (Agilent 4284A). From the measured values of the dielectric permittivity and the dielectric loss factor, the AC conductivity was calculated. The conductivity values correspond to those of semi-conductive materials encountered in most of the substituted phthalocyanine derivatives [33]. The dielectric permittivity of the samples was calculated using the relation;

$$C = \frac{\varepsilon_0 \varepsilon_r A}{d}$$

where C is the capacitance of the sample, ε_0 is the permittivity of air, A is the surface area of the sample, d is the thickness of the sample and ε_r is the dielectric permittivity of the sample. The frequency versus AC conductivity graph was plotted at room temperature and is depicted in Fig. 4. From the figure, it can be seen that the value of the AC conductivity does not show a clear variation at lower frequencies at room temperature. That is, there is no appreciable variation in AC conductivity of the polymers at low frequencies (<10^5 Hz), above 10^5 Hz, there is a rapid increase with frequency. This is in accordance with the theory of AC conduction in amorphous materials, which predicts that for polaron transport or other hopping modes, the AC conductivity will increase monotonically with the increased frequency of the applied field. The AC conductivity, dielectric permittivity, and dielectric loss can be related by the following equation;

$$\sigma_{AC} = 2\pi f \varepsilon_0 \varepsilon_r \tan\delta$$

where ε_0 is the permittivity of air, ε_r is the dielectric permittivity of the sample, f is the frequency and tan δ is the dielectric loss [34]. On the other hand, the AC conductivity of the metal-free polymer was higher than those of the metal complexes. This can be due to the oxygen-susceptible NH group of the metal-free polymer **6**. The NH groups should be partially oxidized in air. In the metal complexes, the NH groups were no longer sensitive to O_2 after complexation with transition metal ions [17].

Thermal properties of the metal-free and metal complex polymers were investigated by DSC and DTA/TG. The phthalocyanine polymers are resistant to thermal oxidation [35]. The DTA and DSC curves exhibit exothermic changes for all polymers in the region investigated [36], the curves do not show melting points. No obvious correlation between the transition metal ion in the phthalocyanine ring and the corresponding main decomposition temperatures could be established, while the initial decomposition temperature decreased in the order: **6** > **8** > **10** > **7** > **9** (Table 2). The higher stability of **6** as compared with the polymeric metal complexes (**7**–**10**) could obviously be traced to the interaction of the polar nitrile groups in the solids. DSC and DTA/TG thermograms of all the polymers can be seen in Figs. 5 and 6. The glass transitions were found as 42, 51, 50, 56 and 45 °C for **6**, **7**, **8**, **9** and **10**, respectively. All samples showed a weight loss below 200 °C, probably due to volatiles evaporation (N_2, O_2, CO_2 and H_2O) or low temperature degradation of unstable chemical fragments in the samples. At higher temperatures, between 350 and 400 °C, the main degradation step is visible, with a weight lost of about 43–54% for all samples. All the adsorbed gases and decomposed groups in the samples were identified by MS as: 17 (NH_3), 18 (H_2O), 28 (N_2), 32 (O_2) and 44 (CO_2) below 200 °C, 27 (HCN), 44 (CO_2) and 91 (toluene) above 400 °C.

4. Conclusion

We have presented the synthesis and characterization of the new bisphthalonitrile **5** and polymeric metal-free (**6**) phthalocyanine and metal complexes (**7**–**10**) with diazatrioxa peripheral units. The polymers (**6**–**10**) were prepared using a bisphthalonitrile monomer and the appropriate precursors. No obvious correlation between the transition metal ion in the phthalocyanine ring and the corresponding main decomposition temperatures could be established. The electrical conductivities of the polymeric materials measured in air at room temperature and were found to be 10^{-6}–10^{-5} S m^{-1} in air. The polymeric zinc complex **7** had a clear aggregation tendency with the addition of Ni^{2+}, Cu^{2+} and Co^{2+} solutions. On the other hand, there was no shift or optical change with the addition of Pb^{2+}, Cd^{2+}, Zn^{2+} and Ag^{+} solutions.

Acknowledgements

This study was supported by the Scientific and Technical Research Council of Turkey (TUBITAK), Project No. TBAG-2453(104T065) (Ankara, Turkey).

References

[1] M. Hanack, H. Heckmann, R. Polley, in: E. Schaumann (Ed.), Houben-Weyl Methods of Organic Chemistry, fourth ed., vol. E 9d, Georg Thieme Verlag, Stuttgart, 1998, p. 717.
[2] J. Simon, P. Bassoul, Design of Molecular Materials: Supramolecular Engineering, VCH, Weinheim, 2000.
[3] D. Schlettwein, D. Wohrle, N.I. Jaeger, J. Electrochem. Soc. 136 (1989) 2882.
[4] J. Simon, C. Sirlin, Pure Appl. Chem. 61 (1989) 1625.

[5] M.J. Cook, N.B. McKeown, J.M. Simmons, A.J. Thomson, M.F. Daniel, K.J. Harrison, R.M. Richardson, S.J. Roser, J. Mater. Chem. 1 (1991) 121.
[6] O.L. Kaliya, E.A. Lukyanets, G.N. Vorozhtsov, J. Porphyrins Phthalocyanines 3 (1999) 592.
[7] F. Hacıvelioğlu, M. Durmuş, S. Yeşilot, A.G. Gürek, A. Kılıç, V. Ahsen, Dyes Pigments 79 (2008) 14.
[8] X. Ding, S. Shen, Q. Zhou, H. Xu, Dyes Pigments 40 (1999) 187.
[9] Z. Odabaş, A. Altındal, B. Salih, M. Bulut, Ö. Bekaroğlu, Tetrahedron Lett. 48 (2007) 6326.
[10] J.E. van Lier, in: D. Kessel (Ed.), Photodynamic Therapy of Neoplastic Diseases, vol. 1, CRC Press, Boca Raton, FL, 1990.
[11] YuA Kokshorov, A.I. Sherle, A.N. Tikhonov, Synth. Met. 149 (2005) 19.
[12] D. Wöhrle, Macromol. Rapid Commun. 22 (2001) 68.
[13] N.B. McKeown, J. Matter. Chem. 10 (2000) 1979.
[14] D. Wöhrle, U. Marose, R. Knoop, Makromol. Chem. 186 (1985) 2209.
[15] A. Bilgin, Ç. Yağcı, U. Yıldız, Macromol. Chem. Phys. 206 (2005) 2257.
[16] A. Bilgin, A. Mendi, U. Yıldız, Polymer 47 (2006) 8462.
[17] J. Simon, J.J. Andre, in: J.M. Lehn, C.W. Rees (Eds.), Molecular Semiconductors, Springer-Verlag, Berlin, 1985, p. 136.
[18] A. Bilgin, Ç. Yağcı, A. Mendi, U. Yıldız, Polyhedron 26 (2007) 617.
[19] A. Bilgin, Y. Gök, Supramol. Chem. 18 (2006) 491.
[20] A. Bilgin, B. Ertem, Y. Gök, Supramol. Chem. 17 (2005) 277.
[21] A. Bilgin, Ç. Yağcı, A. Mendi, U. Yıldız, J. Appl. Polym. Sci. 110 (2008) 2115.
[22] A. Bilgin, B. Ertem, Y. Gök, Eur. J. Inorg. Chem. (2007) 1703.
[23] G.J. Young, W. Onyebuagu, J. Org. Chem. 55 (1990) 2155.
[24] T.J. Atkins, J.E. Richman, W.F. Oettle, Org. Synth. 58 (1978) 86.
[25] A.W. Snow, J.R. Griffith, N.P. Marullo, Macromolecules 17 (1984) 1614.
[26] D. Wöhrle, E. Preuβner Makromol. Chem. 186 (1985) 2189.
[27] K. Nakomato, Infrared Spectra of Inorganic and Coordination Compounds, second ed., Wiley, New York, 1970.
[28] D. Wöhrle, B. Schulte, Makromol. Chem. 189 (1988) 1167.
[29] D. Wöhrle, R. Benters, O. Suvorova, G. Schnurpfeil, N. Trombach, T. Bogdahn-Rai, J. Porphyrins Phthalocyanines 4 (2000) 491.
[30] İ. Özçeşmeci, A.İ. Okur, A. Gül, Dyes Pigments 75 (2007) 761.
[31] E.A. Cuellar, T.J. Marks, Inorg. Chem. 20 (1981) 3766.
[32] Y. Gök, H. Kantekin, A. Bilgin, D. Mendil, İ. Degirmencioğlu, Chem. Commun. 3 (2001) 285.
[33] G. Gümüş, R.Z. Öztürk, V. Ahsen, A. Gül, Ö. Bekaroğlu, J. Chem. Soc., Dalton Trans. 16 (1992) 2485.
[34] S. Saravanan, C.J. Mathai, M.R. Anantharaman, S. Venkatachalam, P.V. Prabhakaran, J. Appl. Polym. Sci. 91 (2004) 2529.
[35] A.D. Delman, J.J. Kelly, A.A. Stein, F.B. Simms, Thermal analysis, Proceedings of the International Conference 2nd, vol. 1, Academic Press, New York, 1969, p. 539.
[36] H. Shirai, K. Kobayashi, Y. Takemae, A. Suzuki, O. Hirabaru, N. Hojo, Makromol. Chem. 180 (1979) 2073.

Polyhedron 28 (2009) 2277–2283

Contents lists available at ScienceDirect

Polyhedron

journal homepage: www.elsevier.com/locate/poly

Novel thiourea derivatives of α-amino acids and their oxorhenium(V) complexes

Jennifer Schroer, Ulrich Abram *

Institute of Chemistry and Biochemistry, Freie Universität Berlin, Fabeckstr. 34-36, D-14195 Berlin, Germany

ARTICLE INFO

Article history:
Received 1 March 2009
Accepted 10 April 2009
Available online 21 April 2009

Keywords:
Rhenium complexes
Thiourea ligands
Amino acids
Structure determination

ABSTRACT

N-[(Dialkylamino)(thiocarbonyl)]benzimidoyl chlorides react with α-amino acid esters under formation of the corresponding *N*-[(dialkylamino)(thiocarbonyl)]benzamidines. Derivatives with glycine ethylester, HL(GlyOEt), cysteine methylester and S-benzyl protected cysteine ethylester, HL(S-Bzl-CysOEt), were prepared and isolated in crystalline form. The reaction with cysteine methylester yields the corresponding sulfur-bridged dimeric compound $\{HL(CysOMe)\}_2$.

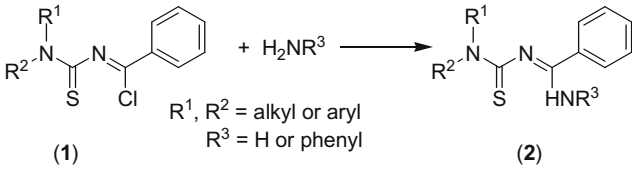
Starting from $[ReOCl_3(PPh_3)_2]$, complexes of these new ligands could be obtained in two different coordination modes: monodentate coordination by only the thiourea sulfur atom or S,N,O tridentate coordination after ester hydrolysis.

© 2009 Elsevier Ltd. All rights reserved.

1. Introduction

Besides many applications in catalysis, the coordination chemistry of rhenium is of interest with respect to potential applications as radiopharmaceuticals. The β^--emitting rhenium nuclides ^{186}Re and ^{188}Re are under investigation for use in radioimmunotherapy [1]. Furthermore, the coordination chemistry of rhenium is in many cases comparable to its lighter homologue technetium, which is the workhorse in diagnostic nuclear medicine [2]. Nevertheless, the labeling of biomolecules such as peptides or proteins with radioactive metal isotopes still remains a challenge in the development of new radiopharmaceuticals. For this purpose, ligand systems, which form stable complexes with the metal ions and can readily be used for the formation of bioconjugates are of high interest.

Since the first report about *N*-[(dialkylamino)(thiocarbonyl)]benzimidoyl chlorides (**1**) in 1982 [3,4], the coordination chemistry of many bidentate *N*-[(dialkylamino)(thiocarbonyl)]-benzamidines (**2**), which can readily be obtained by reactions of the chlorides with ammonia or aniline, with various metals like Ni, Pt, Cu, Ag, Au, Tc or Re has been extensively studied [5].



(**1**) (**2**)

Recently, we extended the chemistry of *N*-[(dialkylamino)(thiocarbonyl)]benzamidines to tridentate ligands and studied the coordination behavior of this novel ligand family with rhenium and technetium [6].

Here, we describe the synthesis and structural characterization of *N*-[(diethylamino)(thiocarbonyl)]benzamidines with glycine ester, L-cysteine ester, and some derivatives as well as their reactions with $[ReOCl_3(PPh_3)_2]$.

2. Results and discussion

2.1. Preparation of the ligands

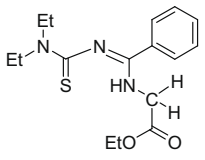
The amino acid derivatives of **2** were prepared following the general route of Hartmann et al. [4] starting from **1** with $R^1 = R^2$ = ethyl. *N*-[(diethylamino)(thiocarbonyl)]benzimidoyl chloride was exposed to glycine ethylester or L-cysteine methylester in absolutely dry acetone at 0 °C in the presence of triethyl amine. After filtration from a colorless precipitate, which is $(NHEt_3)Cl$, the glycine derivative HL(GlyOEt) was isolated in good yields, while oxidation was observed in the case of cysteine and only the disulfide $\{HL(CysOMe)\}_2$ could be isolated. Similar reactions have been undertaken before with the amino acids leucine, valine and glycine, but the glycine derivative could not be isolated as a pure solid, and the reaction products of metal salts with the leucine and valine derivatives have not been structurally characterized [7].

The crude HL(GlyOEt) was recrystallized from $CHCl_3$, which gave slightly yellow, almost colorless crystals. The infrared spectrum of the product exhibits a strong band at 1750 cm^{-1} due to the carbonyl function of the amino acid ester, and a strong band at 3245 cm^{-1} due to the vibration of the NH group. Its ^{1}H NMR spectrum is characterized by a set of well separated quartets for the methylene protons and one triplet for each methyl group. This indicates a hindered rotation around the CN bond of the

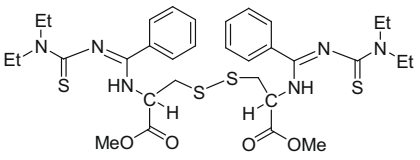
* Corresponding author. Tel.: +49 30 838 54002; fax: +49 30 838 52676.
E-mail address: abram@chemie.fu-berlin.de (U. Abram).

0277-5387/$ - see front matter © 2009 Elsevier Ltd. All rights reserved.
doi:10.1016/j.poly.2009.04.012

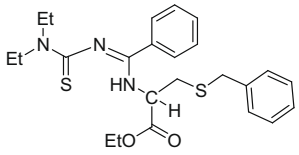
diethylamino group. The compound crystallizes in the orthorhombic space group $P2_12_12_1$ with one molecule in the asymmetric unit. The molecular structure of HL(GlyOEt) is shown in Fig. 1, selected bond lengths and angles are summarized in Table 1. The data confirm hindered rotation around the CN bonds because of mesomeric effects. The bonds N21–C2, C2–N3 and N3–C4 possess partially double bond character, as has already been reported previously for similar ligands [5].



HL(GlyOEt)



{HL(CysOMe)}$_2$



HL(S-Bzl-CysOEt)

The infrared spectrum of {HL(CysOMe)}$_2$ shows strong bands for the NH vibration at 3325 cm^{-1} and for the carbonyl group at 1740 cm^{-1}. The dimeric structure of this compound could be elucidated by X-ray crystallography (Fig. 2) and the ESI-TOF mass spectrum, which shows the molecular peak with one proton at 705 *m*/*z*. Selected bond lengths and angles are given in Table 1. The formation of a dimer is not unexpected under these reaction conditions and it should be possible to prevent this by working under completely oxygen free conditions. With regard to planed reactions with ^{188}Re and/or ^{99m}Tc under 'radiopharmaceutical reaction conditions', that means highly diluted aqueous solutions and aerobic conditions, we decided to choose another approach and protected the thiol by a benzyl group.

The reaction of benzimidoyl chloride with S-benzyl protected cysteine ethylester in the presence of triethylamine as a supporting base leads to the product HL(S-Bzl-CysOEt) in good yields. The infrared spectrum of the ligand shows clearly the stretching vibration of the NH bond at 3385 cm^{-1} and an additional band for the carbonyl group at 1725 cm^{-1}. The ^{1}H NMR spectrum of this compound also reveals the hindered rotation around the CN bonds by well separated signals for the methylene and methyl groups. Also for this compound the mesomeric effects are confirmed by X-ray crystallography. The structure is shown in Fig. 3, and the values of the selected bond lengths and angles clearly show the partial double bond character for the CN bonds C2–N21, C2–N3 and C4–N5, while the bond length of 1.288(2) Å for C3–N4 reveals a stronger double bond character.

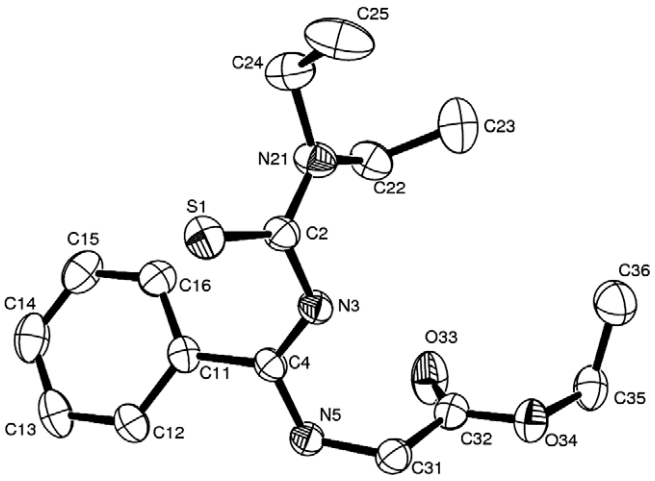


Fig. 1. Ellipsoid representation [15] of HL(GlyOEt). Thermal ellipsoids represent 50% probability. H atoms have been omitted for clarity.

Table 1
Selected bond lengths (Å) and angles (°) in HL(GlyOEt), {HL(CysOMe)}$_2$ and HL(S-Bzl-CysOEt).

	HL(GlyOEt)	{HL(CysOMe)}$_2$	HL(S-Bzl-CysOEt)
S1-C2	1.692(2)	1.673(4)	1.678(2)
N21-C2	1.349(3)	1.345(4)	1.338(2)
C2-N3	1.369(2)	1.385(4)	1.388(3)
N3-C4	1.297(2)	1.291(4)	1.288(2)
C4-N5	1.348(2)	1.344(4)	1.344(2)
N5-C31	1.436(2)	1.448(4)	1.440(3)
C32-O33	1.192(3)	1.184(5)	1.205(3)
C32-O34	1.333(2)	1.338(4)	1.316(3)
S1-C2-N21	123.8(2)	124.7(3)	124.3(2)
S1-C2-N3	121.4(2)	121.4(3)	120.9(2)
C2-N3-C4	124.6(2)	122.5(3)	123.5(2)
N3-C4-N5	118.2(2)	118.0(3)	118.8(2)
C4-N5-C31	121.0(2)	119.9(3)	122.0(2)
C31-C32-O33	124.9(2)	125.9(3)	121.3(2)
C31-C32-O34	125.3(2)	108.7(3)	114.0(2)
N5-C31-C41		111.3(3)	109.4(2)
C31-C41-S42		114.2(3)	112.9(2)

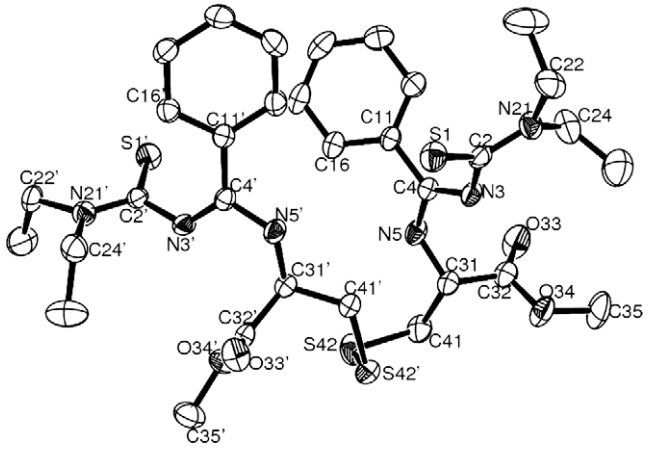


Fig. 2. Ellipsoid representation [15] of {HL(CysOMe)}$_2$. Thermal ellipsoids represent 50% probability. H atoms have been omitted for clarity.

2.2. Synthesis of the rhenium complexes

The reaction of equimolar amounts of [$ReOCl_3(PPh_3)_2$] and HL(GlyOEt) in dry acetone gave a deep green solution, from which a green powder was isolated after removal of the solvent and washing the residue with diethylether. After recrystallisation from acetonitrile/toluene, green needles were obtained, which were suitable for X-ray crystallography. The infrared spectrum of the crystalline compound reveals a medium band at 3350 cm^{-1}, which indicates that the ligand is still protonated and does mutually not coordinate via the nitrogen atom. The vibration of the Re=O double bond is found at 985 cm^{-1}. The ^{1}H NMR spectrum of the complex reveals one multiplet and one triplet for the methyl groups and

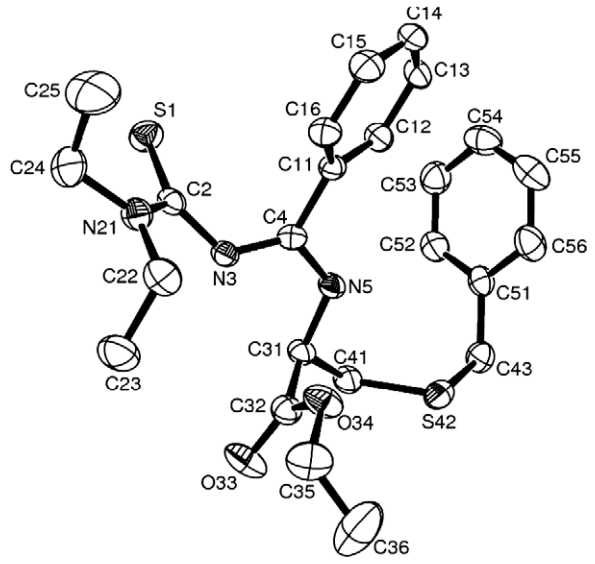


Fig. 3. Ellipsoid representation [15] of HL(S-Bzl-CysOEt). Thermal ellipsoids represent 50% probability. H atoms have been omitted for clarity.

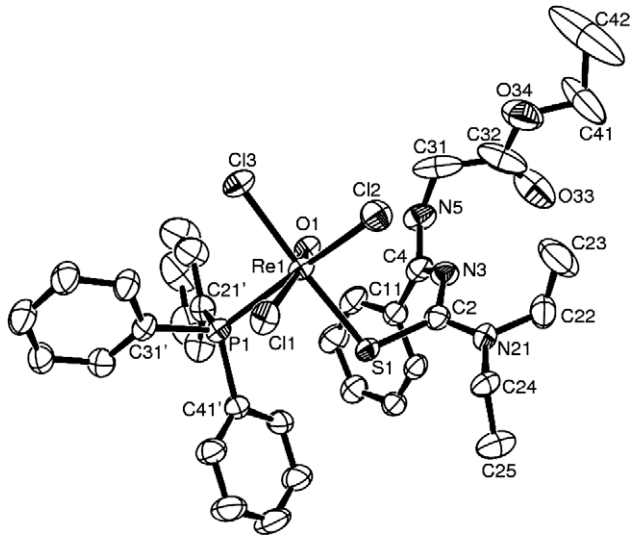


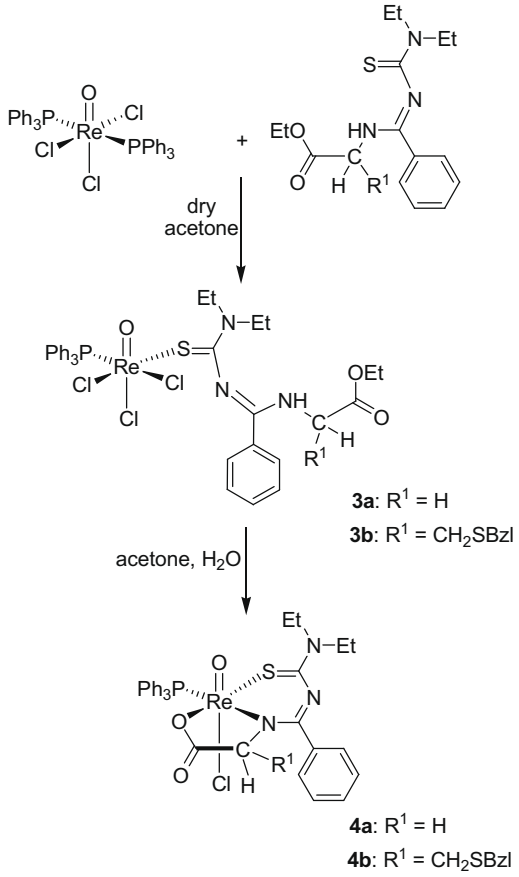
Fig. 4. Ellipsoid representation [15] of $[ReOCl_3(HL(GlyOEt))(PPh_3)]$. Thermal ellipsoids represent 50% probability. H atoms have been omitted for clarity.

four separated signals for four different methylene groups, suggesting hindered rotation of the diethylamino group as has been discussed for the uncoordinated benzamidine. The molecular structure of the complex is shown in Fig. 4 and confirms the composition of the compound as $[ReOCl_3\{HL(GlyOEt)\}(PPh_3)]$ (**3a**) and the monodentate coordination of the ligand by the sulfur atom S1. The complex crystallizes in the monoclinic space group *C*2/*c*. The rhenium atom is coordinated octahedrally by one triphenylphosphine, three facially coordinated chloro ligands, an oxo ligand and the monodentate coordinated, neutral HL(GlyOEt). Selected bond lengths and angles are given in Table 2. They suggest some delocalization of electron density within the thiourea unit. The C=S double bond is elongated and the C–N bonds are shortened with respect to values obtained for the uncoordinated compounds and for other rhenium complexes with thiourea [8]. The monodentate coordination pattern is very unusual for this type of *N*-(dialkylamino)(thiocarbonyl)benzamidines, particularly when the

Table 2
Selected bond lengths (Å) and angles (°) in $[ReOCl_3\{HL(GlyOEt)\}(PPh_3)]$ (**3a**) and $[ReOCl_3\{HL(S\text{-}Bzl\text{-}CysOEt)\}(PPh_3)]$ (**3b**).

	3a	3b
Re1-O1	1.666(5)	1.670(9)
Re1-Cl1	2.481(2)	2.460(3)
Re1-Cl2	2.368(2)	2.365(3)
Re1-Cl3	2.416(2)	2.396(3)
Re1-P1	2.485(2)	2.483(3)
Re1-S1	2.3364(2)	2.385(3)
S1-C2	1.769(7)	1.76(2)
C2-N21	1.323(9)	1.30(2)
C2-N3	1.329(9)	1.35(2)
N3-C4	1.313(9)	1.28(2)
C4-N5	1.356(9)	1.33(2)
O1-Re1-Cl1	163.5(2)	165.8(3)
P1-Re1-Cl2	166.76(6)	171.3(2)
S1-Re1-Cl3	169.44(6)	166.4(2)
Cl1-Re1-Cl2	89.16(7)	92.0(2)
Cl1-Re1-Cl3	87.75(6)	86.3(2)

coordination behavior of the metal ions allows chelate formation. There are only a few reports about Au and Ag complexes and one Tc complex with such ligands with exclusive sulfur coordination [5f,5g,5l].



The same pattern of reactivity is found for the reaction of $[ReOCl_3(PPh_3)_2]$ with HL(S-Bzl-CysOEt) in dry acetone and the neutral rhenium(V) complex $[ReOCl_3\{HL(S\text{-}Bzl\text{-}CysOEt)\}(PPh_3)]$ (**3b**) with a monodentate coordinated HL(S-Bzl-CysOEt) ligand is formed, as is shown in Fig. 5. Selected bond lengths and angles are compared with the corresponding values of **3a** in Table 2. They suggest similar bonding situations for both compounds.

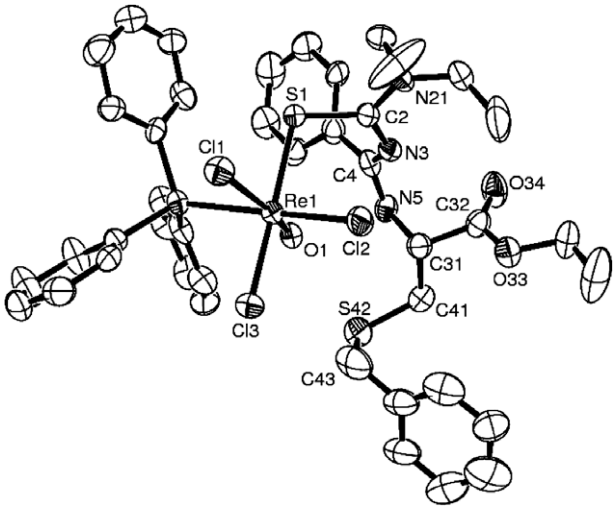


Fig. 5. Ellipsoid representation [15] of [$ReOCl_3${HL(S-BzlCysOEt)}(PPh_3)]. Thermal ellipsoids represent 50% probability. H atoms have been omitted for clarity.

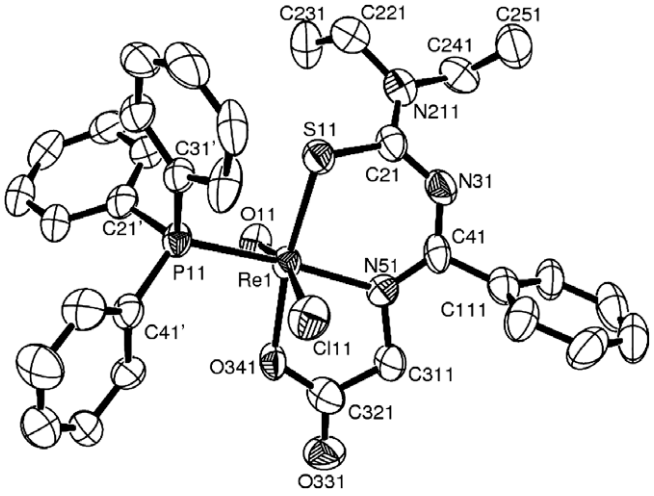


Fig. 6. Ellipsoid representation [15] of [ReOCl(LGly)(PPh_3)]. Thermal ellipsoids represent 50% probability. H atoms have been omitted for clarity.

Our attempts to deprotect the thiol groups in HL(S-Bzl-CysOEt) or **3b** by standard procedures, in order to increase the chelating power of the ligand, failed. The thiocarbonyl unit did not resist the deprotection conditions and decomposition of the non-coordinated HL(S-Bzl-CysOEt) as well as of **3b** occurred, and no defined products could be isolated. Compounds **3a** and **3b** are stable as solids and in solution of dry and aprotic solvents. Addition of water to a solution of **3a**, however, resulted in an immediate change of color from deep green to orange-red, and a compound of the composition [ReOCl{L(Gly)}(PPh_3)] (**4a**) could be isolated after removal of the solvent. Compound **4a** can also be prepared from the crude reaction mixture of the synthesis of **3a** in moderate yields, simply by the addition of some drops of water.

The infrared spectrum of **4a** indicates deprotonation of the organic ligands by the absence of an NH vibration and the band of the carbonyl group is shifted by 60 cm^{-1} with regard to the corresponding band in **3a**. This is a strong hint towards a coordination via the the oxygen atom. The ^1H NMR spectrum of this compound reveals a set of four well separated signals for the methylene protons of the diethyl group. The methyl groups are characterized by two well separated triplets, but there are no more signals of the ester group. The ready hydrolysis of the ester and the subsequent rearrangement of the coordination sphere of the rhenium atom is confirmed by the X-ray crystal structure of the product.

The compound crystallizes in the triclinic space group $P\bar{1}$ with two complex molecules and co-crystallized solvent in the asymmetric unit. Fig. 6 shows the molecular structure of **4a**, selected bond lengths and angles are summarized in Table 3. The thiocarbamoylbenzamidinate acts in the product as a doubly deprotonated, tridentate, equatorially coordinated S,N,O ligand. The rhenium atom has a distorted octahedral coordination environment with the chloro ligand *trans* to the oxo oxygen. The general bonding situation inside the chelating ligand can best be described as an extended π-system with delocalized electron density inside the chelate ring, but also including the C–N bond of the diethylamino group. The C–N bonds inside this system are almost equal as has been observed for other metal complexes with *N*-[(dialkylamino)(thiocarbonyl)]benzamidines before [5,6]. The consequence of such a bonding mode is a comparably rigid structure, which favours a planar coordination and, thus, does obviously not allow a facial coordination of $LGly^{2-}$ in the compound under study.

A similar ester hydrolysis and ligand rearrangement is observed for compound **3b**. Recrystallization of the complex from a mixture of acetone and water results in a yellow–brown solid of [ReOCl{L(S-Bzl-Cys)}(PPh_3)] (**4b**). The infrared spectrum of this compound does not show any band which can be assigned to the NH vibration which indicates deprotonation and coordination via the nitrogen atom. The band of the carbonyl function is shifted by about 50 cm^{-1} with respect to **3b**. The ^1H NMR spectrum of the product shows two triplets for the methyl groups and four multiplets for the four methylene protons of the diethylamino group, but no more signals for the ester group. The ^{31}P NMR spectrum in DMSO exhibits a peak at 23.1 ppm for coordinated triphenylphosphine.

Table 3
Selected bond lengths (Å) and angles (°) in [ReOCl(LGly)(PPh_3)] (**4a**).*

Re1-O11	1.680(7)/1.683(7)	C21-N211	1.31(2)/1.30(2)
Re1-Cl11	2.444(3)/2.443(3)	C21-N31	1.33(2)/1.36(1)
Re1-S11	2.325(3)/2.331(3)	N31-C41	1.34(2)/1.31(1)
Re1-N51	2.040(8)/2.041(9)	C41-N51	1.34(2)/1.34(1)
Re1-O341	2.069(8)/2.035(8)	C321-O331	1.23(2)/1.21(2)
Re1-P11	2.476(3)/2.492(3)	C321-O341	1.30(2)/1.30(1)
S11-C21	1.77(2)/1.76(1)		
O11-Re1-Cl11	164.4(3)/167.0(2)	Re1-S11-C21	101.9(4)/103.9(4)
O11-Re1-S11	100.3(3)/99.4(3)	S11-C21-N31	122.0(9)/122.7(9)
O11-Re1-N51	107.1(3)/108.2(4)	C21-N31-C41	127.8(9)/129.1(9)
O11-Re1-O341	89.3(3)/90.1(3)	N31-C41-N51	127(1)/128(1)
O11-Re1-P11	92.2(2)/92.2(2)	C41-N51-Re1	126.6(7)/126.9(7)
S11-Re1-N51	92.5(3)/93.1(2)	N51-C311-C321	112.2(9)/111.5(9)
N51-Re1-O341	80.1(3)/80.4(3)	C311-C321-O341	117(1)/119(1)
O341-Re1-P11	99.7(2)/95.0(2)	C321-O341-Re1	116.6(7)/118.7(7)
P11-Re1-S11	84.79(9)/88.34(9)		

* Values for two crystallographically independent molecules.

Ester hydrolysis during the coordination to a rhenium center has already been observed by Seifert et al. [9]. The reaction of mercaptoacetic acid ester with (Ph_4As)[$ReOCl_4$] seems to be pH-dependent. The hydrolysis of the ester group under acidic conditions was in this case faster than in neutral solution. However, Angelici et al. [10] made the observation that during the metal-catalyzed hydrolysis of ethyl valinate-*N*,*N*-diacetic acid and ethyl leucinate-*N*,*N*-diacetic acid and the forming of neutral complexes the pH value is not of importance. In our case, we could also make the latter observation. While the complexes **3** are stable in solution even after addition of HCl, the color of the solution immediately turns from green to orange–brown after addition of water. This supports the conclusion that the addition of water changes the coordination sphere of the complex (most probably by the exchange of a chloro

ligand) and the proton transfer to the ester is a secondary step. Metal catalysis is also indicated by the fact that HL(GlyOEt) and HL(S-Bzl-CysOEt) do not hydrolyze under the same conditions.. A detailed mechanism, however, cannot be formulated with the present results.

3. Conclusions

Novel ligands derived from *N*-[(diethylamino)(thiocarbonyl)]benzimidoyl chloride and α-amino acid esters can readily be prepared as stable solids. Surprisingly, they react with [$ReOCl_3(PPh_3)$] in dry acetone only as monodentate, neutral ligands via the thiocarbonyl unit. Addition of water, however, results in an immediate hydrolysis of the ester function and the formation of complexes with tridentate S,N,O ligands. This is the result of a remarkably mild, metal-induced saponification of amino acid esters and guides the way to new ligand systems of this type also for the chemistry of technetium. The metal-catalyzed hydrolysis allows the convenient synthesis of ester-protected ligand systems which are activated by the presence of the metal ion and water.

4. Experimental

[$ReOCl_3(PPh_3)_2$] [11] and $Et_2NCSNCClPh$ [3] were prepared by literature procedures. The acetone was dried over P_4O_{10} and distilled under argon.

Infrared spectra were measured as KBr pellets on a Shimadzu FTIR-spectrometer 8300. ESI-TOF mass spectra were measured on an Agilent 6210 ESI-TOF. FAB^+ mass spectra were recorded with a TSQ (Finnigan) instrument using nitrobenzyl alcohol as matrix. Elemental analyses were determined using a Heraeus (vario EL) elemental analyzer. The found hydrogen values of most of the rhenium complexes are significantly too low. This seems to be a systematic problem probably caused by some hydride formation during the combustion process and does not refer to impure samples. Reference samples have been checked by high resolution mass spectrometry. ^1H and $^{31}P\{^1H\}$ NMR spectra were taken with a JEOL 400 MHz multinuclear spectrometer.

4.1. Synthesis of HL(GlyOEt)

A solution of $Et_2NCSNCClPh$ (1 g, 4 mmol) in 20 ml of dry acetone was cooled to 0 °C and glycine ethylester hydrochlorid (560 mg, 4 mmol) was added. Triethylamine (1.5 ml, 10 mmol) dissolved in 5 ml of dry acetone was dropped to the suspension during a period of 30 min. The mixture was vigorously stirred for 3 h at room temperature and filtered from the precipitated triethylamine hydrochloride. The solvent was removed in vacuum and the residue was redissolved in 10 ml THF. After filtration from a small amount of insoluble solid, the mixture was brought to dryness again and the oily residue was dissolved in 2 ml chloroform and kept at 4 °C. The product crystallized upon standing overnight as pale yellow crystals. They were filtered off and washed with a small amount of diethylether. The obtained single crystals were suitable for X-ray crystallography. Yield: 880 mg (60%). *Anal.* Calc. for $C_{16}H_{23}N_3O_2S$: N, 13.1; C, 59.8; H, 7.2; S, 9.4. Found: N, 12.8; C, 59.8; H, 6.9; S, 9.4%. IR (ν_{max}, cm^{-1}): 3245 (st), 3050 (w), 2980 (m), 2930 (m), 2869 (w), 1750 (st), 1620 (st), 1575 (m), 1535 (m), 1480 (m), 1455 (w), 1420 (m), 1405 (w), 1350 (w), 1270 (m), 1195 (st), 1120 (m), 1055 (w), 995 (m), 885 (m), 785 (st), 700 (st), 600 (m). ^1H NMR (δ, $CDCl_3$): 1.15 (t, 3H, CH_3), 1.16 (t, 3H, CH_3), 3.55 (q, 2H, CH_2), 3.84 (q, 2H, CH_2), 4.09 (s, 2H, CH_2), 4.15 (q, 2H, CH_2), 7.30-7.43 (m, 5H, $CH_{aromatic}$) ppm. +ESI-MS: *m/z* 322 $M+H^+$, 344 $M+Na^+$.

4.2. Synthesis of {HL(CysOMe)}$_2$

The compound was prepared from $Et_2NCSNCClPh$ (515 mg, 2 mmol) and L-cysteine methylester hydrochlorid (344 mg, 2 mmol) following the procedure given for HL(GlyOEt) with the exception that the reaction mixture was heated under reflux for 1 h and the oily residue was crystallized from MeOH. Yield: 210 mg (31%). *Anal.* Calc. for $C_{32}H_{44}N_6O_6S_4$: N, 11.9; C, 54.5; H, 6.3; S 18.2. Found: N, 11.7; C, 54.5; H, 5.9; S, 18.1%. IR (ν_{max}, cm^{-1}): 3405 (w), 3325 (st), 3050 (w), 2965 (m), 2930 (m), 2870 (w), 1745 (st), 1740 (st), 1625 (st), 1575 (m), 1535 (m), 1480 (st), 1420 (st), 1375 (m), 1310 (m), 1255 (st), 1215 (m), 970 (m), 900 (m), 780 (m), 725 (w), 700 (m), 605 (m), 495 (m). ^1H NMR (δ, $CDCl_3$): 1.17 (t, 6H, CH_3), 1.18 (t, 6H, CH_3), 3.33 (m, 24H, 2·CH_2), 3.58 (m, 4H, 2·CH_2), 3.74 (s, 6H, 2·OCH_3), 3.78 (m, 4H, 2···CH_2), 3.93 (m, 2H, 2·CH), 7.30–7.43 (m, 10H, $CH_{aromatic}$) ppm. ESI-MS: *m/z* 705 $M+H^+$.

4.3. Synthesis of HL(S-Bzl-CysOEt)

The compound was prepared from $Et_2NCSNCClPh$ (258 mg, 1 mmol) and L-(S-benzyl)cysteine ethylester hydrochlorid (276 mg, 1 mmol) as described for HL(GlyOEt). The oily residue was crystallized by slow evaporation of a 1:1 (v/v) mixture of CH_2Cl_2 and MeOH. Yield: 340 mg (79%). *Anal.* Calc. for $C_{24}H_{31}N_3O_2S_2$: N, 9.2; C, 63.0; H, 6.8; S 14.0. Found: N, 9.0; C, 63.0; H, 6.7; S, 14.2%. IR (ν_{max}, cm^{-1}): 3385 (st), 3040 (w), 2975 (m), 2925 (m), 1725 (st), 1620 (st), 1575 (w), 1515 (m), 1480 (st), 1420 (m), 1375 (w), 1300 (w), 1275 (st), 1255 (st), 1195 (m), 1140 (m), 1075 (m), 1030 (m), 1010 (w), 900 (w), 855 (w), 765 (w), 725 (w), 700 (m), 620 (w). ^1H NMR (δ, $CDCl_3$): 1.10 (t, 3H, CH_3), 1.13 (t, 3H, CH_3), 1.21 (t, 3H, CH_3), 3.30–3.60 (m, 4H, 2·CH_2,), 3.65 (s, 2H, CH_2), 3.75 (m, 2H, CH_2), 3.89 (m, 1H, CH), 4.13 (q, 2H, CH_2), 7.15–7.40 (m, 10H, $CH_{aromatic}$) ppm. +ESI-MS: *m/z* 485 $M+H^+$, 480 $M+Na^+$, 496 $M+K^+$.

4.4. Synthesis of [$ReOCl_3${HL(GlyOEt)}(PPh_3)] (**3a**)

HL(GlyOEt) (66 mg, 0.2 mmol) was dissolved in 5 ml of dry acetone and added to a suspension of [$ReOCl_3(PPh_3)_2$] (166 mg, 0.2 mmol) in 15 ml of dry acetone. After heating under reflux for 6 h, the solid was completely dissolved and a dark green solution was formed. The solvent was removed to dryness under reduced pressure and the residue was treated with 20 ml diethylether and kept overnight at 4 °C. During this time, a dark green solid precipitated, which was filtered off and recrystallized from acetonitrile/toluene. Yield: 75 mg (48%). *Anal.* Calc. for $ReC_{34}H_{38}N_3O_3SPCl_3$: N, 4.7; C, 45.8; H, 4.3; S 3.6. Found: N, 5.2; C, 44.9; H, 2.8; S, 4.0%. IR (ν_{max}, cm^{-1}): 3350 (m), 3055 (m), 2980 (m), 2930 (w), 2875 (w), 1755 (m), 1590 (st), 1560 (st), 1520 (st), 1480 (m), 1435 (st), 1410 (w), 1350 (w), 1315 (w), 1195 (m), 1130 (w), 1095 (m), 1025 (w), 985 (m), 870 (w), 785 (w), 745 (m), 696 (st), 530 (st), 515 (m). ^1H NMR (δ, DMSO-d_6): 1.21 (m, 6H, 2·CH_3), 1.39 (t, 3H, CH_3), 3.63 (q, 2H, CH_2,), 3.73 (q, 2H, CH_2), 4.14 (q, 2H, CH_2), 4.24 (bs, 2H, CH_2), 7.38–7.63 (m, 10H, $CH_{aromatic}$), 9.86 (s, 1H, NH) ppm. ^{31}P NMR (δ, DMSO): 23.1 ppm.

4.5. Synthesis of [$ReOCl_3${HL(S-Bzl-CysOEt)}(PPh_3)] (**3b**)

HL(S-Bzl-CysOEt) (46 mg, 0.1 mmol) in 5 ml acetone was added to a suspension of [$ReOCl_3(PPh_3)_2$] (83 mg, 0.1 mmol) in 5 ml acetone. The reaction mixture was stirred at room temperature until the solid was completely dissolved and the solution became dark green. The solvent was removed under reduced pressure and the obtained residue was redissolved in 20 ml diethylether by slight warming. Green crystals, which were suitable for X-ray crystallog-

Table 4
X-ray structure data collection and refinement parameters.

	HL(GlyOEt)	{HL(CysOMe)}$_2$	HL((S-Bzl)CysOEt)	**3a**·0.25 toluene	**4a**·0.25 CH_3CN·0.125 H_2O	**3b**·0.5·O(C_2H_5)$_2$
Formula	$C_{16}H_{23}N_3O_2S$	$C_{32}H_{44}N_6O_4S_4$	$C_{24}H_{31}N_3O_2S_2$	$C_{35.75}H_{40}N_3O_3SPCl_3Re$	$C_{32.5}H_{32.75}N_{3.25}O_{3.13}$ SPClRe	$C_{44}H_{51}N_3O_{3.5}S_2PCl_3Re$
M_w	321.43	704.97	457.64	915.34	803.55	1065.58
Crystal system	orthorhombic	orthorhombic	orthorhombic	monoclinic	triclinic	monoclinic
a (Å)	9.388(1)	7.721(1)	10.868(1)	35.012(3)	9.056(1)	10.416(1)
b (Å)	12.539(1)	20.264(2)	13.756(1)	14.516(1)	19.342(2)	19.908(2)
c (Å)	14.310(1)	23.525(2)	16.401(1)	18.104(2)	20.354(2)	12.988(1)
α (°)	90	90	90	90	104.50(1)	90
β (°)	90	90	90	113.54(1)	97.72(1)	109.83(1)
γ (°)	90	90	90	90	102.19(1)	90
V (Å^3)	1684.5(3)	3681.0(7)	2452.0(4)	8435(2)	3307.1(6)	2533.5(4)
Space group	$P2_12_12_1$	$P2_12_12_1$	$P2_12_12_1$	$C2/c$	$P\bar{1}$	$P2_1$
Z	4	4	4	8	4	2
D_c (g cm^{-3})	1.267	1.272	1.240	1.442	1.614	1.397
μ (mm^{-1})	0.203	0.301	0.242	3.193	3.904	2.709
Absorption correction	none	none	none	integration	integration	integration
$T_{min.}/T_{max.}$				0.5571/0.6958	0.3634/0.7171	0.7005/0.8450
No. of reflections	34 236	33 605	18 432	32 047	46 351	20 131
No. of independent	4555	9952	6590	11 377	12 982	13 575
No. parameters	200	416	280	455	790	517
R_1/wR_2	0.0586/0.1603	0.0475/0.0894	0.0431/0.0763	0.0521/0.1033	0.0596/0.1254	0.0529/0.1300
Goodness-of-fit (GOF)	0.851	1.287	0.824	0.872	0.971	0.960
Deposit number	CCDC 721754	CCDC 721755	CCDC 721756	CCDC 721757	CCDC 721759	CCDC 721758

raphy was obtained by slow cooling of the solution. Yield: 52 mg (51%). *Anal.* Calc. for $ReC_{40}H_{40}N_3O_3S_2PCl$: N, 4.1; C, 49.1; H, 4.5; S 6.2. Found: N, 3.7; C, 49.5; H, 3.6; S, 5.6%. IR (ν_{max}, cm^{-1}): 3230 (w), 3135 (w), 3050 (m), 2965 (m), 2905 (w), 2870 (w), 1745 (st), 1560 (st), 1526 (st), 1480 (m), 1435 (m), 1365 (m), 1305 (m), 1270 (w), 1215 (m), 1180 (m), 1095 (m), 1018 (w), 980 (m), 775 (w), 745 (m), 695 (st), 530 (m), 510 (m). ^{1}H NMR (δ, acetone-d_6): 1.11 (t, 3H, CH_3), 1.17–1.55 (m, 6H, 2·CH_3), 2.60–2.90 (m, 2H, CH_2,), 3.40 (q, 2H, CH_2), 3.65–4.19 (m, 6H, 3 CH_2), 4.89 (m, 1H, CH), 7.00–7.70 (m, 25 H, $CH_{aromatic}$), 8.14 (m, 1H, NH) ppm. ^{31}P NMR (δ, acetone-d_6): −35.0 ppm.

4.6. Synthesis of [ReOCl(LGly)(PPh_3)] (**4a**)

(a) The green solid, which was obtained as a crude product during the synthesis of **3a**, was dissolved in acetone. After addition of a few drops of water, the color of the solution immediately turned from green to orange–red. Slow evaporation of the acetone/water mixture gave orange–red crystals of X-ray quality. Yield: 36 mg (47%).

(b) Compound **3a** (90 mg, 0.1 mmol) was dissolved in acetone. A few drops of water were added to the green solution, which resulted in an immediate change of the color and forms an orange–red solution. Slow evaporation gave orange–red crystals. Yield: 39 mg (49%).

Anal. Calc. for $ReC_{32}H_{32}N_3O_3SPCl$: N, 4.9; C, 48.6; H, 2.9; S 4.0. Found: N, 4.9; C, 48.8 H, 2.9; S, 4.1%. IR (ν_{max}, cm^{-1}): 3055 (m), 2975 (m), 2930 (w), 2870 (w), 1695 (st), 1525 (st), 1435 (st), 1390 (st), 1350 (m), 1330 (m), 1275 (m), 1225 (w), 1190 (w), 1145 (w), 1075 (m), 970 (st), 930 (w), 775 (w), 750 (m), 695 (m), 530 (m), 505 (w). ^{1}H NMR (δ, DMSO-d_6): 1.15 (t, 3H, CH_3), 1.27 (t, 3H, CH_3), 3.63 (q, 2H, CH_2), 3.73 (q, 2H, CH_2), 3.75 (m, 2H, CH_2), 4.14 (q, 2H, CH_2), 4.24 (bs, 2H, CH_2), 7.38–7.63 (m, 10H, $CH_{aromatic}$), 9.86 (s, 1H, NH) ppm. ^{31}P NMR (δ, DMSO): 23.1 ppm. +ESI-MS: m/z 756 M-Cl$^+$.

4.7. Synthesis of [ReOCl{L(S-Bzl-Cys)}(PPh_3)] (**4b**)

HL(S-Bzl-CysOEt) (46 mg, 0.1 mmol) in 5 ml acetone was added to a suspension of [$ReOCl_3(PPh_3)_2$] (83 mg, 0.1 mmol) in 5 ml acetone. The reaction mixture was stirred at room temperature until the solid was completely dissolved and the solution was deep green. After addition of 5 ml H_2O, the color of the solution turned from green to yellow–orange. Slow evaporation of the solvent gave a yellow precipitate. Yield: 35 mg (37%). *Anal.* Calc. for $ReC_{42}H_{46}N_3O_3S_2PCl_3$: N, 4.5; C, 51.8; H, 4.35; S 6.9. Found: N, 4.3; C, 50.5; H, 2.7; S, 6.3 IR (ν_{max}, cm^{-1}): 3055 (m), 2975 (m), 2930 (w), 1695 (st), 1525 (st), 1435 (st), 1355 (st), 1330 (m), 1290 (w), 1255 (w), 1190 (w), 1145 (w), 1095 (m), 1070 (m), 1000 (w), 970 (m), 770 (w), 750 (w), 695 (st), 530 (m), 510 (w). ^{1}H NMR (δ, DMSO-d_6): 1.23 (t, 3H, CH_3), 1.29 (t, 3H, CH_3), 2.55 (m, 1H, CH_2), 2.75 (dd, 1H, CH_2), 3.07 (d, 1H, CH_2), 3.23 (d, 1H, CH_2), 3.56 (m, 1H, $CH_{2,\ ethyl}$), 3.91 (m, 1H, $CH_{2,\ ethyl}$), 4.04 (m, 1H, $CH_{2,\ ethyl}$), 4.26 (m, 1H, $CH_{2,\ ethyl}$), 5.04 (dd, 1H, CH), 7.01–7.70 (m, 25H, $CH_{aromatic}$) ppm. ^{31}P NMR (δ, DMSO): 23.6 ppm.

4.8. X-ray structure determinations

The intensities for the X-ray determinations were collected on a STOE IPDS automated single crystal diffractometer with Mo Kα radiation. The structures were solved by direct methods using SIR 92 [12] or Patterson SHELXS-86 [13] or SHELXS-97 [13]. Subsequent Fourier-difference map analyses gave the position of the non-hydrogen atoms. Refinement was performed using SHELXL-97 [13]. Hydrogen atom positions were calculated for idealized positions and treated with the 'riding model' option of SHELXL.

The compound **3a** crystallized with a disordered quarter molecule of toluene per asymmetric unit. Another area of diffuse electron density (counting for an overall amount of 115 electrons) was located near the center of inversion and could not be refined as discrete solvent molecules. It has therefore been removed from the electron density map by the program SQUEEZE [14] Crystal data and more details of the data collections and refinements are contained in Table 4.

Appendix A. Supplementary data

CCDC 721754, 721755, 721756, 721757 and 721758 contain the supplementary crystallographic data for HL(GlyOEt), {HL(CysOMe)}$_2$, HL((S-Bzl)CysOEt), 3a·0.25 toluene and 3b·0.5·O(C_2H_5)$_2$. These data can be obtained free of charge via http://www.ccdc.cam.ac.uk/conts/retrieving.html, or from the Cambridge Crystallographic Data Centre, 12 Union Road, Cambridge CB2 1EZ, UK; fax: (+44) 1223-336-033; or e-mail: deposit@ccdc.cam.ac.uk.

References

[1] U. Abram, in: J.A. McCleverty, T.J. Meyer (Eds.), Rhenium, Comprehensive Coordination Chemistry, vol. II, Elsevier, Amsterdam, 2004, p. 271.
[2] R. Alberto, in: J.A. McCleverty, T.J. Meyer (Eds.), Technetium, Comprehensive Coordination Chemistry, vol. II, Elsevier, Amsterdam, 2004, p. 127.
[3] (a) L. Beyer, R. Widera, Tetrahedron Lett. 32 (1982) 1881;
(b) L. Beyer, J. Hartung, Tetrahedron 40 (1984) 405.
[4] H. Hartmann, L. Beyer, E. Hoyer, J. Prakt. Chem. 320 (1978) 647.
[5] (a) J. Hartung, G. Weber, L. Beyer, R. Szargan, Z. Anorg. Allg. Chem. 523 (1985) 153;
(b) R. del Campo, J.J. Criado, E. Garcia, M.R. Hermosa, A. Jimenez-Sanchez, J.L. Manzano, E. Monte, E. Rodriguez-Fernandez, F. Sanz, J. Inorg. Biochem. 89 (2002) 74;
(c) W. Hernandez, E. Spodine, R. Richter, K.-H. Hallmeier, U. Schröder, L. Beyer, Z. Anorg. Allg. Chem. 629 (2003) 2559;
(d) U. Schröder, R. Richter, L. Beyer, J. Angulo-Cornejo, M. Lino-Pacheco, A. Guillen, Z. Anorg. Allg. Chem. 629 (2003) 1051;
(e) E. Guillon, I. Dechamps-Olivier, A. Mohamadou, J.P. Barbier, Inorg. Chim. Acta 268 (1998) 13;
(f) R. Richter, U. Schröder, M. Kampf, J. Hartung, L. Beyer, Z. Anorg. Allg. Chem. 623 (1997) 1021;
(g) U. Braun, J. Sieler, R. Richter, B. Hettich, A. Simon, Z. Anorg. Allg. Chem. 557 (1988) 134;
(h) U. Abram, R. Münze, J. Hartung, L. Beyer, R. Kirmse, K. Köhler, J. Stach, H. Behm, P.T. Beurskens, Inorg. Chem. 28 (1989) 834;
(i) U. Abram, R. Hübener, Inorg. Chim. Acta 206 (1993) 23;
(j) J. Sieler, R. Richter, L. Beyer, O. Lindqvist, L. Anderson, Z. Anorg. Allg. Chem. 41 (1984) 515;
(k) F. Yaoting, L. Huije, H. Honwei, Z. Zhengmin, Z. Qinghuan, Z. Linpin, C. Fenghong, J. Coord. Chem. 65 (2000) 50;
(l) H. Braband, U. Abram, J. Organomet. Chem. 689 (2004) 2066.
[6] H.H. Nguyen, J. Grewe, J. Schroer, B. Kuhn, U. Abram, Inorg. Chem. 47 (2008) 5136.
[7] (a) L. Beyer, J.J. Criado, E. Garcia, F. Lessmann, M. Medarde, R. Richter, E. Rodriguez, Tetrahedron 52 (1996) 6233;
(b) J.J. Criado, E. Rodriguez-Fernandez, E. Garcia, M.R. Hermosa, E. Monte, J. Inorg. Biochem. 60 (1998) 113.
[8] (a) U. Abram, S. Abram, R. Alberto, S. Schibli, Inorg. Chim. Acta 248 (1996) 193;
(b) D. Gambino, L. Otero, E. Kremer, E.O. Piro, E.E. Castellano, Polyhedron 16 (1997) 2263;
(c) D. Gambino, E. Kremer, E.J. Baran, A. Mombru, L. Suescun, R. Mariezcurrena, M. Kieninger, O.N. Ventura, Z. Anorg. Allg. Chem. 625 (1999) 813.
[9] S. Seifert, A. Hoepping, K. Klostermann, H. Spies, B. Johannsen, Appl. Radiat. Isot. 48 (1997) 943.
[10] R.J. Angelici, B.E. Leach, J. Am. Chem. Soc. 90 (1968) 2499.
[11] N.P. Johnson, C.J.L. Lock, G. Wilkinson, Inorg. Synth. (1967) 145.
[12] A. Altomare, G. Cascarano, C. Giacovazzo, A. Guagliardi, J. Appl. Crystallogr. 26 (1993) 343.
[13] (a) G.M. Sheldrick, Acta Crystallogr., Sect. A 46 (1990) 467;
(b) G.M. Sheldrick, SHELX97 – A Programme Package for the Solution and Refinement of Crystal Structures, University of Göttingen, Germany, 1997.
[14] A.L. Spek, Acta Crystallogr., Sect. A 46 (1990) C34.
[15] L.J. Farrugia, J. Appl. Crystallogr. 30 (1997) 565.

Polyhedron 28 (2009) 2284–2286

Contents lists available at ScienceDirect

Polyhedron

journal homepage: www.elsevier.com/locate/poly

Functionalised β-diketone assisted self-assembly of a hexanuclear yttrium oxo-hydroxo cluster

Ananda Kumar Jami, Pilli V.V.N. Kishore, Viswanathan Baskar *

School of Chemistry, University of Hyderabad, Hyderabad 500046, India

ARTICLE INFO

Article history:
Received 9 March 2009
Accepted 12 April 2009
Available online 6 May 2009

Keywords:
Yttrium clusters
Self-assembly
Functionalised β-diketones
Oxo-hydroxo bridges
Synthesis and structural elucidation

ABSTRACT

The reaction of $YCl_3{\cdot}6H_2O$ with *ortho*-hydroxydibenzoylmethane (HO-DBMH) in a 1:2 ratio, in methanol and in the presence of excess triethylamine as a base yielded a yellow precipitate which on crystallization from toluene or benzene /hexane afforded pale yellow block-like crystals. Single crystal X-ray diffraction of **1** revealed the formation of an interesting hexanuclear yttrium oxo-hydroxo cluster $[Y_6(O\text{-}DBM)_6(HO\text{-}DBM)_4(\mu_3\text{-}OH)_2(MeOH)_4]$; the core resembles a butterfly framework flanked by a lanthanide atom on each side. Ten phenolic β-diketone ligands are present in the cluster, which bridge the metal centers in both chelating and chelating-bridging fashions.

© 2009 Elsevier Ltd. All rights reserved.

1. Introduction

Multinuclear metal clusters, in particular lanthanide based clusters, have generated a huge amount of interest in recent years owing to their wide ranging applications from precursors to magnetic materials to catalysis [1–13]. Traditionally, lanthanide oxo-hydroxo clusters have been synthesized either by controlled hydrolysis of air and moisture sensitive lanthanide precursors [14–16] or by slow deprotonation of the coordinated water molecules of hydration in lanthanum salts like $LnCl_3{\cdot}xH_2O$, in the presence of suitable ligands by addition of a base [17–19]. β-Diketones have been used as ligands extensively to synthesize a large number of lanthanide clusters whose solid state structures vary from tetra- to tetra decanuclear forms [17–23]. Although β-diketones have been investigated in detail for their ligating ability towards lanthanides and their solid state structures are well understood, the use of functionalized β-diketones [24] and in particular phenolic β-diketones [25,26] as ligands towards lanthanides are rare. In this paper, we present the synthesis and structural characterization of a hexanuclear cluster of yttrium and using HO-DBMH as a ligand. The single crystal X-ray characterization technique revealed the formation of a novel hexanuclear yttrium cluster, $[Y_6(O\text{-}DBM)_6(HO\text{-}DBM)_4(\mu_3\text{-}OH)_2(MeOH)_4]$ (**1**).

2. Experimental

Yttrium trichloride hexahydrate was synthesized from the corresponding oxide by neutralizing with conc. HCl, followed by evaporation to dryness. The ligand 1-(2-hydroxyphenyl)-3-phenyl-1,3-propanedione was prepared according to the literature method [27]. Triethylamine and the solvents were used as purchased from commercial sources without further purification. Elemental analyses were carried out with a FLASH EA series 1112 CHNS analyzer. IR spectra were recorded on a JASCO-5300 FT-IR spectrophotometer (using KBr pellets). The ^1H solution NMR spectrum was recorded on a BRUCKER DRX 400 instrument. Single crystal X-ray data was collected at 298(2) K on a BRUKER SMART APEX CCD area detector system [λ(Mo Kα) = 0.71073 Å] with a graphite monochromator, and the data were reduced using SAINTPLUS. The structure was solved using SHELXS-97 and refined using SHELXS-97 [28,29]. All non hydrogen atoms were refined anisotropically, except for the carbon and oxygen atom of a methanol solvent molecule (C_{81}–O_{32}) which was refined isotropically. As the solvents of crystallization, methanol and water molecules, were heavily disordered, the hydrogen atoms were not fixed for the solvents of crystallization found in **1**.

2.1. Synthesis

The ligand, 1-(2-hydroxyphenyl)-3-phenyl-1,3-propanedione (H0-DBMH) (0.470 g, 1.96 mmol) and $YCl_3{\cdot}6H_20$ (0.30 g, 0.98 mmol) were dissolved in methanol (20 ml). Triethylamine (0.39 g, 3.92 mmol) was slowly added to the above reaction mixture and stirred for 12 h at room temperature. The pale yellow precipitate that formed was filtered, washed with methanol (5 ml)

* Corresponding author. Tel.: +91 40 66794825; fax: +91 40 23012460.
E-mail addresses: vbsc@uohyd.ernet.in, baskarviswanathan@gmail.com (V. Baskar).

0277-5387/$ - see front matter © 2009 Elsevier Ltd. All rights reserved.
doi:10.1016/j.poly.2009.04.035

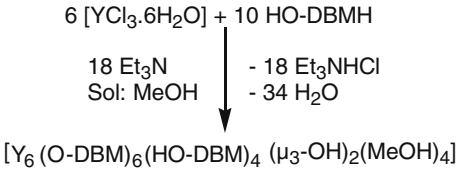
and air dried. Further the precipitate was dissolved in toluene (15 ml) and stirred for 20 min, at which point the solution was again filtered. Slow evaporation of toluene at room temperature yielded yellow crystals of **1** in 78% yield (0.39 g). The crystals lost the solvent of crystallization rapidly and turned opaque. Better quality crystals suitable for single crystal X-ray diffraction studies were obtained by slow evaporation of **1** from benzene (*Caution*: Benzene is a class A carcinogen and should be used with the proper precautions) or by a benzene/hexane diffusion method after a week. Elemental analysis for $C_{154}H_{122}O_{36}Y_6$: *Anal.* calcd. C 60.01, H 3.99; found: C 60.04, H 3.95. IR(KBr, cm^{-1}): 3580(m) (ν OH), 3057(m), 1597(s) (ν CO), 1547(w), 1516(s) (ν C–C), 1483(m), 1392(m), 1296(m), 1248(s), 1203(m), 1138(m), 1024(m), 941(m), 860(m), 756(s), 719(m), 696(m), 625(s), 584(m), 520(m). ^{1}H NMR ($CDCl_3$) δ (ppm): 2.65 (s, Me/coordinated solvent methanol), 4.54 (s, CH), 6.54–8.02 (m, Ph), 11.60 (broad peak, phenolic OH).

3. Results and discussion

The synthetic methodology used for the preparation of **1** was adopted from recent literature reports [17–19]. Hydrated yttrium chloride and the ligand, *ortho*-hydroxydibenzoylmethane (HO-DBMH) were dissolved in methanol (20 ml) in a ratio 1:2, and triethylamine (excess) was added dropwise to the stirred reaction mixture (Scheme 1). Halfway through the addition of the base, a yellow precipitate was obtained. The reaction mixture was stirred further for a period of 12 h and filtered to isolate the precipitate.

The precipitate was then washed thoroughly with methanol to remove the unreacted starting materials and the product was air dried. Pale yellow block-like crystals were obtained after a week by slow diffusion of hexane into a toluene or benzene solution of **1** at room temperature. The products were characterized by standard analytical and spectroscopic techniques. The IR spectrum of **1** shows a peak corresponding to a C–O stretch at around 1597 cm^{-1}. A broad peak at 3580 cm^{-1} can be attributed to the presence of an OH group in the product. The ^{1}H NMR spectrum of **1** in $CDCl_3$ shows a multiplet centered around 6.54–8.02 ppm, corresponding to the aromatic groups of the phenolic β-diketone ligand.

The solid state structure of **1** was established by single crystal X-ray diffraction. The crystallographic data is given in Table 1. Although we could crystallize **1** from both toluene and benzene solutions by slow diffusion of hexane at room temperature, only the crystals isolated from benzene were of sufficiently good quality for single crystal X-ray diffraction analysis, in spite of several attempts to isolate good quality crystals of **1** from toluene (*Caution*: Benzene is a class A carcinogen and should be used with the proper precautions). The neutral cluster **1** crystallises in the triclinic space group $P\bar{1}$. The core of the cluster consists of six yttrium centers connected through oxo and hydroxo bridges. A sheath of organic groups encapsulates the metal oxo-hydroxo core enabling the product to dissolve in a wide range of organic solvents like chloroform, dichloromethane, benzene and toluene. The hexanuclear metal core can be visualized in the following manner; a central butterfly core (consisting of four yttriums) flanked by a yttrium metal on each side (Fig. 1).



Scheme 1.

The yttrium atoms that make up the butterfly core are eight-coordinate and the peripheral yttriums are seven-coordinate. The central butterfly core is held together by two μ3-OH bridges, similar to the ones found in the tetranuclear structures of ytterbium and lutetium reported recently [20]. The yttrium to oxygen bond distances (2.254–2.436 Å) and the Y–O–Y bond angles (95.44–111.12°) fall in the ranges reported in the literature [17–19]. Selected bond lengths and bond angles are given in Table 2.

Ten phenolic β-diketone ligands are found coordinated to the metal centers in **1**, displaying varying modes of binding.

Six of these ligands are in the dianionic $[O–DBM]^{2-}$ form, while the other four are monoanionic $[OH–DBM]^-$. The six dianionic $[O–DBM]^{2-}$ ligands are found wrapped around the central butterfly

Table 1
Crystallographic data for **1**.

Formula	$C_{164}H_{192}O_{66}Y_6$
Formula weight	3752.64
Crystal system	triclinic
Space group	$P\bar{1}$
a (Å)	15.8562(9)
b (Å)	16.2774(9)
c (Å)	19.7466(11)
α (°)	99.3220(10)
β (°)	93.9730(10)
γ (°)	95.9110(10)
V (Å^3)	4983.3(5)
Z	1
D_{calcd} (Mg m^{-3})	1.250
μ (Mo-α) (mm^{-1})	1.805
T (K)	298
Data/restraints/parameters	19686/0/1055
Goodness-of-fit on F^2	0.965
Final R indices [$I > 2\sigma(I)$]	$R_1 = 0.0802$, w$R_2 = 0.2123$
R indices (all data)	$R_1 = 0.2057$, w$R_2 = 0.2719$
Largest difference in peak and hole (e Å^{-3})	1.086 and −0.501

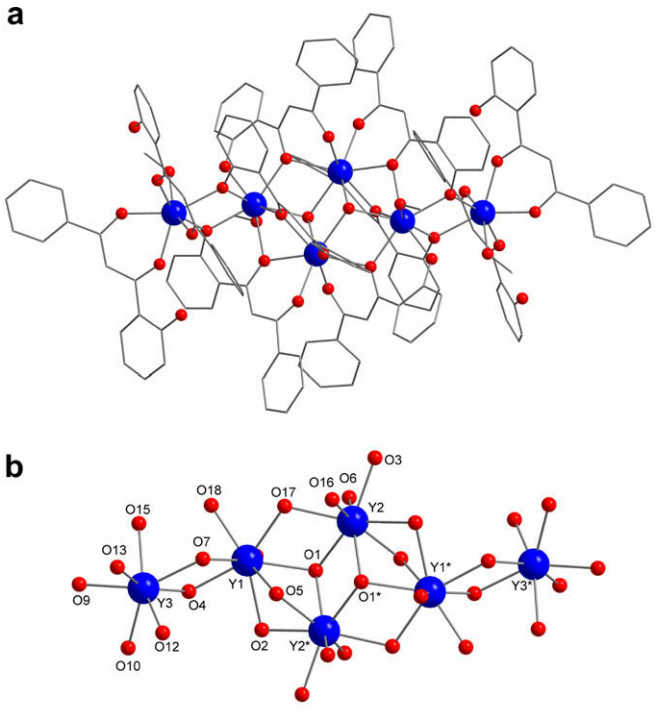


Fig. 1. (a) Solid state structure of **1**; hydrogen atoms and solvents of crystallization are omitted for clarity (b) the yttium oxo core of the cluster **1** omitting carbon and hydrogen atoms.

Table 2
Selected bond lengths (Å) and bond angles (°) in **1**.

Bond lengths		Bond angles	
Y1–O1	2.362(6)	Y1–O1–Y2	109.34(21)
Y2–O1	2.391(5)	Y1–O17–Y2	111.12(21)
Y1–O2	2.435(5)	Y1–O2–Y2*	95.44(17)
Y2*–O2	2.421(5)	Y1–O5–Y2*	96.41(17)
Y1–O5	2.436(5)	Y1–O1–Y2*	100.65(19)
Y2*–O5	2.382(6)	Y1–O4–Y3	111.02(24)
Y1–O17	2.361(5)	Y1–O7–Y3	110.57(24)
Y2–O17	2.355(5)	Y2–O1–Y2*	108.66(21)
Y1–O18	2.276(7)		
Y1–O7	2.276(6)		
Y1–O4	2.299(5)		
Y2–O16	2.272(6)		
Y2–O6	2.254(7)		
Y2–O3	2.274(6)		
Y3–O4	2.277(6)		
Y3–O7	2.313(5)		
Y3–O15	2.248(7)		
Y3–O10	2.253(6)		
Y4–O9	2.266(6)		
Y3–O13	2.239(7)		
Y3–O15	2.358(7)		

core, displaying both chelating and chelating-bridging modes of binding. The oxygens of the β-diketone part of the ligand chelate to the central dimeric core of the butterfly unit. Further, one of the oxygen atoms of the β-diketone part of each ligand also bridges to a third yttrium metal atom (so does the symmetry related oxygen) leading to the formation of the central butterfly framework observed in **1**. This core is linked to the peripheral metal centres through the phenoxide groups, which act as bridging ligands, leading to the formation of a hexanuclear cluster. Each of the peripheral yttrium centers are further chelated to two monoanionic OH-DBM ligands. The varying modes of binding found in **1** are depicted in Chart 1. Interestingly, other than the central metal dimer of the butterfly unit, all the other metal centers are coordinated to a methanol solvent molecule to saturate their coordination spheres.

It is of interest to mention here that a subtle change in the stoichiometry of the reactants can lead to isolation of interesting new structures in the solid-state. In a recent report, reaction of hydrated lanthanum nitrate with H0-DBMH in methanol as solvent followed by addition of triethylamine as a base in the ratio 1:3:3 has led to the isolation of mononuclear complexes of lanthanides where the phenolic part of the ligand is essentially non-coordinating [25]. In the present case, however, where the stoichiometry of the metal/ligand/base is 1:2:4, hexanuclear clusters have been isolated wherein the phenolic oxygen from the ligand acts as a bridging group in a μ-2 fashion (Chart 1). Hence a small change in the stoichiometry of the ligand and base (a slight excess) has had a dramatic change in the coordination chemistry of the ligand, leading to the isolation of a novel hexanuclear cluster. Similar observations, wherein a subtle change in the stoichiometry or the nature of solvents/base used in a reaction lead to dramatic variations in the structure of the resultant cluster, are widely reported for transition metal clusters [30,31], whereas they are a rarity in the case of rare earths. This observation opens up further interesting possibilities as far as the coordination chemistry of the ligand towards lanthanide metals is concerned.

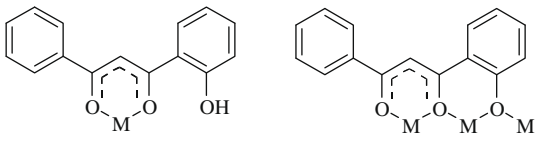


Chart 1.

4. Conclusion

We have been successful in synthesizing a hexanuclear yttrium oxo-hydroxo cluster using a phenolic β-diketone as a ligand. The hexanuclear framework reported here is quite unique and we believe that changing yttrium to other paramagnetic lanthanides, like dysprosium or gadolinium, will lead to the generation of paramagnetic lanthanide oxo-hydroxo clusters possessing interesting magnetic properties. Work is currently under progress in this direction.

Supplementary data

CCDC 721333 contains the supplementary crystallographic data for **1**. These data can be obtained free of charge via http://www.ccdc.cam.ac.uk/conts/retrieving.html, or from the Cambridge Crystallographic Data Centre, 12 Union Road, Cambridge CB2 1EZ, UK; fax: (+44) 1223-336-033; or e-mail: deposit@ccdc.cam.ac.uk.

Acknowledgements

VB thanks the Department of Science and Technology, New Delhi, India for financial support under the SERC-Fast track scheme. We thank Dr. P. Raghavaiah for useful discussions in crystallography.

References

[1] R. Sessoli, H.L. Tsai, A.R. Schake, S. Wang, J.B. Vincent, K. Folting, D. Gatteschi, G. Christou, D.N. Hendrickson, J. Am. Chem. Soc. 115 (1993) 1804.
[2] R. Sessoli, D. Gatteschi, A. Caneschi, M.A. Novak, Nature 365 (1993) 141.
[3] B. Moulton, M.J. Zaworotko, Chem. Rev. 101 (2001) 1629.
[4] A. Móller, P. Kögerller, Coord. Chem. Rev. 182 (1999) 3.
[5] R.E.P. Winpenny, Chem. Soc. Rev. 27 (1998) 447.
[6] C. Benelli, D. Matteeschi, Chem. Rev. 102 (2002) 2369.
[7] Y.-Z. Zheng, Y. Lan, C.E. Anson, A.K. Powell, Inorg. Chem. 47 (2008) 10813.
[8] X. Gu, D. Xue, Inorg. Chem. 46 (2007) 3212.
[9] P.-H. Lin, T.J. Burchell, R. Clérac, M. Murugesu, Angew. Chem., Int. Ed. 47 (2008) 1.
[10] G. Abbas, Y. Lan, G. Kostakis, C.E. Anson, A.K. Powell, Inorg. Chim. Acta. 361 (2008) 3494.
[11] B. Hussain, D. Savard, T.J. Burchell, W. Wernsdorfer, M. Murugesu, Chem. Commun. (2009) 1100.
[12] M.T. Gamer, Y. Lan, P.W. Roesky, A.K. Powell, R. Clérac, Inorg. Chem. 47 (2008) 6581.
[13] P.W. Roesky, G. Canseco-Melchor, A. Zulys, Chem. Commun. (2004) 738.
[14] Z. Zheng, Chem. Commun. (2001) 2521.
[15] A. Babai, A.V. Mudring, Z. Anorg. Allg. Chem. 632 (2006) 1956.
[16] M.R. Bürgstein, H. Berberich, P.W. Roesky, Chem. Eur. J. 7 (2001) 3078.
[17] V. Baskar, P.W. Roesky, Z. Anorg. Allg. Chem. 631 (2005) 2782.
[18] S. Datta, V. Baskar, H. Li, P.W. Roesky, Eur. J. Inorg. Chem. (2007) 4216.
[19] V. Baskar, P.W. Roesky, J. Chem. Soc., Dalton Trans. (2006) 676.
[20] L.G. Hubert-Pfalzgraf, L. Cauro-Gamet, A. Brethon, S. Daniel, P. Richard, Inorg. Chem. Commun. 10 (2007) 143.
[21] G. Xu, Z.-M. Wang, Z. He, Z. Lu, C.-S. Liao, C.-H. Yan, Inorg. Chem. 41 (2002) 6802.
[22] P.C. Andrews, T. Beck, C.M. Forsyth, B.H. Fraser, P.C. Junk, M. Massi, P.W. Roesky, J. Chem. Soc., Dalton Trans. (2007) 5651.
[23] R. Wang, D. Song, S. Wang, Chem. Commun. (2002) 368.
[24] P.C. Andrews, G.B. Deacon, R. Frank, B.H. Fraser, P.C. Junk, J.G. MacLellan, M. Massi, B. Moubaraki, K.S. Murray, M. Silberstein, Eur. J. Inorg. Chem. (2009) 744.
[25] S. Tanase, M. Viciano-Chumillas, Jan M.M. Smits, R. de Gelder, J. Reedijk, Polyhedron 28 (2009) 457.
[26] E.W. Ainscough, A.M. Brodie, R.J. Cresswell, J.M. Waters, Inorg. Chim. Acta 277 (1998) 37.
[27] T.S. Wheeler, Org. Synth. 32 (1952) 72.
[28] G.M. Sheldrick, SHELXS-97, Program of Crystal Structure Solution, University of Göttingen, Germany, 1997.
[29] G.M. Sheldrick, SHELXS-97, Program of Crystal Structure Refinement, University of Göttingen, Germany, 1997.
[30] T. Taguchi, T.C. Stamatatos, K.A. Abboud, C.M. Jones, K.M. Poole, T.A. O'Brien, G. Christou, Inorg. Chem. 47 (2008) 4095.
[31] E.I. Tolis, M. Helliwell, S. Langley, J. Raftery, R.E.P. Winpenny, Angew. Chem., Int. Ed. 42 (2003) 3804.

Polyhedron 28 (2009) 2287–2293

Contents lists available at ScienceDirect

Polyhedron

journal homepage: www.elsevier.com/locate/poly

Crystal structures of (azido)(pentamethylcyclopentadienyl)iridium(III) complexes containing various types of bidentate ligands

Takayoshi Suzuki [a,b,*], Mai Kotera [b], Asuka Takayama [a], Masaaki Kojima [a]

[a] Department of Chemistry, Faculty of Science, Okayama University, Okayama 700-8530, Japan
[b] Department of Chemistry, Graduate School of Science, Osaka University, Toyonaka 560-0043, Japan

ARTICLE INFO

Article history:
Received 16 January 2009
Accepted 14 April 2009
Available online 21 April 2009

Keywords:
Iridium(III) azido complexes
Crystal structures
8-Quinolylphosphine
2-Pyridylphosphine
2-(2-Pyridyl)benzimidazolate

ABSTRACT

Several (azido)iridium(III) complexes having a pentamethylcyclopentadienyl (Cp^*) group, $[Cp^*Ir(N_3)_2(Ph_2Ppy\text{-}\kappa P)]$ (**1**: Ph_2Ppy = 2-diphenylphosphinopyridine), $[Cp^*Ir(N_3)(Ph_2Ppy\text{-}\kappa P,\kappa N)]CF_3SO_3$ (**2**), $[Cp^*Ir(N_3)(dmpm)]PF_6$ (**3**: dmpm = bis(dimethylphosphino)methane), $[Cp^*Ir(N_3)(Ph_2Pqn)]PF_6{\cdot}CH_3OH$ (**4**·CH_3OH: Ph_2Pqn = 8-diphenylphosphinoquinoline), and $[Cp^*Ir(N_3)(pybim)]$ (**5**: Hpybim = 2-(2-pyridyl)benzimidazole) have been prepared and their crystal structures have been analyzed by X-ray diffraction. In complex **1**, the Ph_2Ppy ligand is only coordinated via the P atom (-κP), while in **2** it acts as a bidentate ligand through the P and N atoms (-$\kappa P,\kappa N$) to form a four-membered chelate ring. Comparing the structural parameters of the chelate ring in **2** with those of a similar five-membered chelate ring formed by Ph_2Pqn in **4**, it became apparent that the angular distortion in the Ph_2Ppy-$\kappa P,\kappa N$ ring was remarkable, although the Ir–P and Ir–N bonds in the Ph_2Ppy-$\kappa P,\kappa N$ ring were not elongated very much from the corresponding bonds in the Ph_2Pqn-$\kappa P,\kappa N$ ring. In the pybim complex **5**, the five-membered chelate ring was coplanar with the pyridine and benzimidazolyl rings. With the related (azido)iridium(III) complexes analyzed previously, comparison of the structural parameters of the Ir–N_3 moiety in $[Cp^*Ir^{III}(N_3)(L\text{–}L')]^{+/0}$ complexes reveals an anomalous feature of the 2,2′-bipyridyl (bpy) complex, $[Cp^*Ir(N_3)(bpy)]PF_6$.

© 2009 Elsevier Ltd. All rights reserved.

1. Introduction

Recently, the investigation of transition-metal azido complexes has been revived because they often show interesting chemical reactivities and physical properties [1–4]. For example, photolysis of some azido complexes results in higher-valent metal nitrido complexes, which have the potential for further nitrogen-atom (or imino-group) transfer reactions [2]. The *crick* reactions of azido complexes with nitriles or alkynes via 1,3-dipolar cycloaddition, which affords the corresponding tetrazolato or triazolato complexes, are also attractive for the creation of new functional compounds [3]. Furthermore, the azido-bridged dinuclear complexes or cluster compounds are of current interest in studies of supramolecular architecture and the development of molecular magnetic materials [4]. We have also investigated the photochemical reactivities of (azido)iridium(III) complexes with a $Cp^*Ir^{III}(N_3)$ ($Cp^* = \eta^5\text{-}C_5Me_5$) fragment, and found a novel nitrogen-atom insertion reaction on photolysis of $[Cp^*Ir(N_3)(R_2dtc$, 2-Spy, or 2-Sqn)] (R_2dtc^- = *N,N*-dialkyldithiocarbamate; 2-Spy^- = 2-pyridinethiolate; 2-Sqn^- = 2-quinolinethiolate) complexes (Scheme 1) [5–7]. This interesting reaction seems to be attributable to the highly strained chelate ring and the stability of the Ir–S bond of the above dithiocarbamato or thiolato ligands. On the other hand, it is also known that some Cp^*Ir^{III} complexes having phosphines or imidazolates often exhibit interesting structural features and novel reactivities [8–11]. Therefore, the related $Cp^*Ir^{III}(N_3)$ complexes bearing 2-diphenylphosphinopyridine (Ph_2Ppy), 8-diphenylphosphinoquinoline (Ph_2Pqn), bis(diphenyl- or dimethylphosphino)methane (dppm or dmpm), as well as 2-(2-pyridyl)benzimidazolate ($pybim^-$) (L–L′: Scheme 2) may be possible candidates for similar or other fascinating reactions. Here, we have prepared such complexes of $[Cp^*Ir^{III}(N_3)(L\text{–}L')]^{+/0}$, and their molecular structures and chemical reactivities were compared, together with the analogous complexes characterized previously in our group [5,7,12,13].

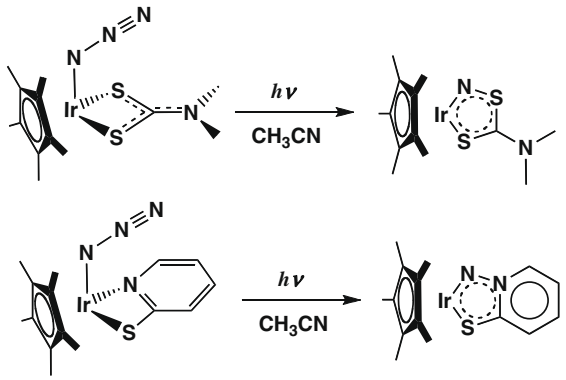
2. Experimental

2.1. Preparation of complexes

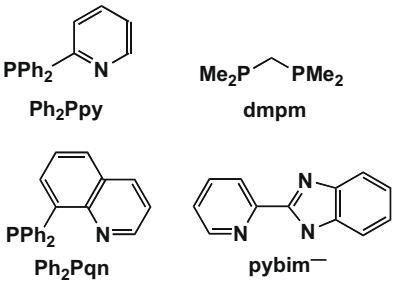
The diazidoiridium(III) complex, $[Cp^*Ir(N_3)_2]_2$ [12], and the phosphines, Ph_2Ppy [14] and Ph_2Pqn [15], were prepared by the literature methods. The ligands, dmpm and 2-(pyridyl)benzimidazole (Hpybim), were purchased from Aldrich Co. Ltd.

* Corresponding author. Address: Department of Chemistry, Faculty of Science, Okayama University, Okayama 700-8530, Japan. Tel./fax: +81 86 251 7900.
E-mail address: suzuki@cc.okayama-u.ac.jp (T. Suzuki).

0277-5387/$ - see front matter © 2009 Elsevier Ltd. All rights reserved.
doi:10.1016/j.poly.2009.04.010



Scheme 1.



Scheme 2.

Caution! The AgN_3 resulting from the preparation of complex **2** is potentially explosive. Although we had no severe experience in our laboratory, all experiments handling the precipitated AgN_3 should be performed with the greatest care.

*2.1.1. [Cp*Ir(N$_3$)$_2$(Ph$_2$Ppy-κP)] (**1**)*

A methanol solution (6 cm^3) of Ph_2Ppy (135 mg, 0.57 mmol) was added with stirring to a solution of $[Cp^*Ir(N_3)_2]_2$ (236 mg, 0.287 mmol) in a mixture of dichloromethane and methanol (1:1, 4 cm^3), affording a yellow–brown precipitate in a few minutes. The reaction mixture was concentrated (to ca. 5 cm^3) under reduced pressure, and the resulting precipitate was collected by filtration. The crude product was washed with methanol (1 cm^3) and diethyl ether (3 cm^3), and recrystallized from a mixture of dichloromethane and methanol to give orange platelet crystals. Yield: 244 mg (63%). *Anal.* Calc. for $C_{27}H_{29}IrN_7P$: C, 48.06; H, 4.33; N, 14.53%. Found: C, 47.91; H, 4.28; N, 14.41%. ^1H NMR (CD_2Cl_2, 303 K): δ 1.44 (d, J_{HP} = 2.4 Hz, Cp*, 15H), 7.10–7.57 (m, Ph and py, 13H), 8.70 (dq, J_{HH} = 31.9 and 0.9 Hz, 6-py, 1H).

*2.1.2. [Cp*Ir(N$_3$)(Ph$_2$Ppy-κP,κN)]O$_3$SCF$_3$ (**2**)*

A methanol solution (3 cm^3) of $Ag(O_3SCF_3)$ (97 mg, 0.38 mmol) was added dropwise with stirring to an orange solution of **1** (255 mg, 0.378 mmol) in dichloromethane (2 cm^3). The mixture was stirred in the dark at room temperature for 18 h, and the resulting white precipitate (AgN_3) was filtered off. The precipitate was washed successively with acetonitrile (5 cm^3), methanol (5 cm^3) and dichloromethane (5 cm^3), and the filtrate and all washings were combined. The mixture was evaporated to dryness under reduced pressure, and the orange residue was dissolved in hot methanol (50 °C, 3 cm^3). After removal of undissolved impurities by filtration, the filtrate was allowed to stand in a refrigerator overnight, affording yellow–brown prismatic crystals. Yield: 226 mg (76%). *Anal.* Calc. for $C_{28}H_{29}F_3IrN_4O_3PS$: C, 43.02; H, 3.74; N, 7.17%. Found: C, 43.09; H, 3.79; N, 7.14%.

The corresponding PF_6 salt (**2′**) was prepared similarly using $AgPF_6$, instead of $Ag(O_3SCF_3)$.

*2.1.3. [Cp*Ir(N$_3$)(dmpm)]PF$_6$ (**3**)*

The ligand, dmpm (26 mg, 1.9 mmol) was added dropwise by syringe to a red suspension of $[Cp^*Ir(N_3)_2]_2$ (400 mg, 0.972 mmol) in methanol (10 cm^3) under a dinitrogen atmosphere. The reaction mixture was stirred at room temperature for 30 min and evaporated to dryness under reduced pressure. The residue was washed with Et_2O (10 cm^3 × 3), and then dissolved in methanol (2 cm^3) under air. A saturated methanol solution containing NH_4PF_6 (800 mg, 4.9 mmol) was added to the filtered methanol solution. The mixture was allowed to stand for 30 min to afford a pale yellow precipitate, which was collected by filtration, washed with methanol (1 cm^3) and Et_2O (3 cm^3), and dried in vacuo. The crude product was dissolved in a mixture of acetonitrile and methanol (1:1), and Et_2O vapor was diffused into the filtered solution to give yellow crystals of **3**. Yield: 432 mg (69%). *Anal.* Calc. for $C_{15}H_{29}F_6IrN_3P_3$: C, 27.69, H, 4.49; N, 6.46%. Found: C, 27.93; H, 4.47; N. 6.33%. ^1H NMR (CD_3CN, 303 K): δ 1.66 (virtual t, $^1J_{HP} + {}^3J_{HP}$ = 6.6 Hz, PMe, 6H), 1.83 (virtual t, $^1J_{HP} + {}^3J_{HP}$ = 6.2 Hz, PMe, 6H), 1.93 (s, Cp*, 15H), 3.49 (q, J_{HP} and J_{HH} = 15.9 Hz, CH_2, 1H), 4.68 (dt, J_{HP} = 15.6, J_{HH} = 10.5 Hz, CH_2, 1H).

*2.1.4. [Cp*Ir(N$_3$)(Ph$_2$Pqn)]PF$_6$ (**4**)*

Ph_2Pqn (74.8 mg, 0.239 mmol) was added to a suspension of $[Cp^*Ir(N_3)_2]_2$ (96.5 mg, 0.117 mmol) in methanol (5 cm^3), and the mixture was stirred at room temperature for 8 h. A methanol solution (3 cm^3) of NH_4PF_6 (137 mg, 0.839 mmol) was added to the resulting orange solution, affording an immediate precipitation. The precipitate was filtered off, washed with methanol (2 cm^3), and dried in vacuo. The crude product was recrystallized from acetonitrile/methanol to form orange platelet crystals. Yield: 171 mg (88%). *Anal.* Calc. for $C_{31}H_{31}F_6IrN_4P_2$: C, 44.98; H, 3.77; N, 6.77%. Found: C, 44.68; H, 3.93; N, 6.95%. ^1H NMR (CD_3CN, 303 K) δ 1.56 (d, J_{HP} = 2.4 Hz, Cp*).

*2.1.5. [Cp*Ir(pybim)(N$_3$)] (**5**)*

A methanol solution (3 cm^3) of Hpybim (46.7 mg, 0.239 mmol) and $NaOCH_3$ (13.8 mg, 0.255 mmol) was added to a suspension of $[Cp^*Ir(N_3)_2]_2$ (103.5 mg, 0.126 mmol) in a mixture of dichloromethane and methanol (2:1, 3 cm^3). The mixture was stirred at room temperature for 8 h and concentrated to ca. 1 cm^3 by a flow of dinitrogen. The resulting yellow precipitate was collected by filtration and dried in vacuo. Yield: 109.4 mg (77%). *Anal.* Calc. for $C_{22}H_{23}IrN_6$: C, 46.88; H, 4.11; N, 14.91%. Found: C, 46.50; H, 4.21; N, 14.88%. Yellowish orange platelet crystals suitable for the X-ray diffraction study were obtained from a mixture of dichloromethane and methanol.

2.2. Measurements

Proton NMR spectra were acquired on a JEOL EX270 or a Varian Mercury 300 spectrometer; chemical shifts were referenced to the residual ^1H NMR signals of the deuterated solvent and are reported versus TMS. Infrared spectra were measured on a JASCO FT/IR FT-550 spectrophotometer using Nujol mulls.

2.3. Crystallography

The X-ray diffraction data were obtained at −73(2) °C on a Rigaku R-axis rapid imaging plate detector with a graphite-monochromated Mo Kα radiation (λ = 0.71073 Å). A suitable crystal was mounted with a cryoloop and flash-cooled by cold dinitrogen stream. Data were processed by the Process-Auto program package [16a], and absorption corrections were made by the numerical

Table 1
Crystal data of complexes.

Compound	**1**	**2**	**3**	**4**·CH_3OH	**5**
Formula	$C_{27}H_{29}IrN_7P$	$C_{28}H_{29}F_3IrN_4O_3PS$	$C_{15}H_{29}F_6IrN_3P_3$	$C_{32}H_{35}F_6IrN_4OP_2$	$C_{22}H_{23}IrN_6$
FW	674.74	781.78	650.52	859.78	563.66
T/(K)	200(2)	200(2)	200(2)	200(2)	200(2)
Crystal system	monoclinic	monoclinic	monoclinic	monoclinic	monoclinic
Space group, *Z*	$P2_1/a$, 4	$P2_1/a$, 4	$P2_1/c$, 4	$P2_1/c$, 4	$P2_1/n$, 4
a/(Å)	17.5522(7)	10.0102(5)	8.7472(9)	8.6711(4)	8.2833(5)
b/(Å)	8.6997(4)	28.3235(12)	16.771(2)	14.3015(6)	16.2409(10)
c/(Å)	17.5992(8)	10.5269(5)	15.705(2)	26.485(1)	14.4564(9)
β/(°)	99.063(1)	96.222(2)	91.949(3)	93.975(1)	98.113(2)
V/(Å^3)	2653.8(2)	2967.0(2)	2302.7(5)	1843.3(13)	1925.3(2)
D_x/(Mg m^{-3})	1.689	1.750	1.876	1.743	1.945
μ(Mo Kα)/(mm^{-1})	5.135	4.680	6.061	4.240	6.957
T_{min}, T_{max}	0.427, 0.628	0.455, 0.604	0.377, 0.582	0.417, 0.484	0.337, 0.543
R_{int}	0.033	0.030	0.065	0.048	0.042
Reflection/parameter ratio	6056/331	4196/227	5182/263	7475/416	4398/268
R_1 [$F_o^2 > 2\sigma(F_o^2)$]	0.019	0.019	0.068	0.033	0.025
wR_2 (all reflection)	0.042	0.082	0.228	0.082	0.058
Goodness of fit	1.046	1.183	1.177	1.080	1.125

method from the crystal shapes [16b]. The structures were solved by the direct method using SIR2004 [17a], and refined on F^2 (with all independent reflections) using SHELXL97 [17b]. All non-H atoms were refined anisotropically, and H atoms were introduced at the positions calculated theoretically and treated with riding models. For the compound **3**, the positions of the F atoms of PF_6^- were severely disordered but no satisfactory model could be found. Therefore, the reported result was an artificially distorted structure for this anion. All calculations were carried out using the CRYSTAL STRUCTURE software package [16c].

Crystal data are collected in Table 1.

3. Results and discussion

3.1. 2-Diphenylphosphinopyridine (Ph_2Ppy) complexes

Kollipara et al. have recently reported the syntheses of $[Cp^*IrCl_2(Ph_2Ppy)]$, $[Cp^*IrCl(Ph_2Ppy)_2]PF_6$ and $[Cp^*IrCl(Ph_2Ppy)]PF_6$, as well as the crystal structures of the first two complexes having monodentately P-coordinated ligands (Ph_2Ppy-κP) [18]. Similar to their synthetic procedure and to the preparative method for $[Cp^*Ir(N_3)_2(napy\text{-}\kappa N)]$ (napy = 1,8-naphthyridine) [12], a stoichiometric reaction of $[Cp^*Ir(N_3)_2]_2$ and Ph_2Ppy (1:2 mole ratio) in a mixture of dichloromethane and methanol afforded an orange crystalline product of $[Cp^*Ir(N_3)_2(Ph_2Ppy)]$ (**1**) in 63% yield.

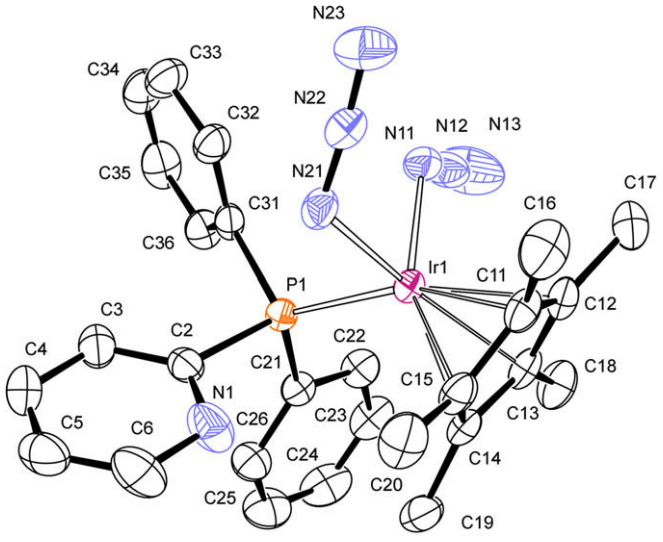


Fig. 1. An ORTEP view (50% probability level, hydrogen atoms omitted) of $[Cp^*Ir(N_3)_2(Ph_2Ppy\text{-}\kappa P)]$ (**1**).

The molecular structure of **1** determined by single-crystal X-ray analysis is illustrated in Fig. 1, which revealed the monodentate coordination mode of Ph_2Ppy through the P atom. In this analysis, three six-membered rings bound to the P atom, i.e., two phenyl and one pyridyl rings, were not distinguishable from one another, and the N atom of Ph_2Ppy could not be specified [19,20]. We tentatively assigned the N atom to the atom that was closest to Ir among the six possible atoms. Even under this assumption, the Ir1···N1 distance was 3.537(2) Å, which is far from being a bonding interaction. The structure of the "$Cp^*Ir(Ph_2Ppy)$" moiety in **1** is very similar to that in $[Cp^*IrCl_2(Ph_2Ppy\text{-}\kappa P)]$ [18]; the Ir–P bond lengths in **1** (2.3060(6) Å) and in the dichloro complex (2.299(2) Å) are comparable. Also, the "$Cp^*Ir(N_3)_2$" moiety corresponds well to that in $[Cp^*Ir(N_3)_2(napy\text{-}\kappa N)]$ [9]. The Ir–N(N_3) bonds in **1**, 2.112(3) and 2.129(2) Å, are comparable to those of the napy complex, 2.114(7) and 2.126(7) Å. The bending coordination mode and the intraligand structural parameters of the coordinated N_3^- ligands are also quite similar to those of the napy complex (see: Table 2).

The ligand, Ph_2Ppy, has the potential to form a four-membered chelate ring [21]. However, unlike the related bis(phosphino)methanes (dmpm or dppm; vide infra) and thiolates (2-Spy^- or 2-Sqn^-), a simple reaction of Ph_2Ppy with $[Cp^*Ir(N_3)_2]_2$ in a mixture of dichloromethane and methanol did not give the chelate complex. Kollipara et al. reported the formation of a chelate complex by the reaction of Ph_2Ppy and $[Cp^*IrCl_2]_2$ in methanol [18]. Here, to obtain a pure sample in high yield, we have utilized the reaction of complex **1** with a stoichiometric amount of $Ag(O_3SCF_3)$ or $AgPF_6$ for the preparation of $[Cp^*Ir(N_3)(Ph_2Ppy)](O_3SCF_3$ or $PF_6)$ (**2** or **2′**). The chelate coordination mode of Ph_2Ppy-$\kappa P,\kappa N$ was confirmed by X-ray analysis (Fig. 2). The Ir1–P1 bond length in **2** (2.3159(9) Å) is nearly the same as that in **1** (monodentately P-coordinated Ph_2Ppy complex). The Ir1–N1 bond length and the chelate bite angle of P1–Ir1–N1 in **2** are 2.125(3) Å and 67.40(8)°, respectively. These values are comparable to those in the corresponding 2-Spy complex (Ir–N = 2.111(4) Å, S–Ir–N = 67.0(1)°) [22] and 2-Sqn complex (Ir–N = 2.131(5) Å, S–Ir–N = 66.6(2)°) [7]. We expected, therefore, that the chelate Ph_2Ppy complex **2** would be stable, similar to the 2-Spy and 2-Sqn complexes. However, it was found that complex **2** was labile in acetonitrile solution.

Fig. 3 depicts the variable-temperature (−20–40 °C) ^1H NMR spectra of $[Cp^*Ir(N_3)(Ph_2Ppy)]PF_6$ (**2′**) in acetonitrile-d_3 (ca.

Table 2
Comparison of the structural parameters (Å, °) of the $Cp^*Ir^{III}(N_3)$ moiety and the vibration frequency, $\nu(N_3)$ (cm^{-1}).

Complex	Ir–C	Ir–N_α	Ir–N_α–N_β	N_α–N_β	N_α–N_β–N_γ	N_β–N_γ	$\nu(N_3)$
1	2.180(2)–2.223(2)	2.112(2)	118.7(2)	1.201(3)	176.7(3)	1.149(4)	2025
		2.129(2)	117.4(2)	1.198(3)	175.0(3)	1.153(3)	
2	2.171(3)–2.210(3)	2.108(3)	121.6(2)	1.202(4)	176.3(4)	1.151(5)	2036
3	2.170(12)–2.285(10)	2.113(13)	117.9(10)	1.230(17)	177.6(18)	1.155(18)	2035
4·CH_3OH	2.168(4)–2.244(4)	2.122(3)	120.5(3)	1.195(5)	175.8(5)	1.151(6)	2035
5	2.152(4)–2.186(3)	2.115(3)	124.3(3)	1.188(5)	174.4(4)	1.155(5)	2034
$[Cp^*Ir(N_3)_2(napy)]$	2.146(9)–2.185(8)	2.114(7)	124.5(6)	1.193(10)	176.4(9)	1.140(10)	2034
		2.126(7)	120.5(4)	1.180(10)	176.4(10)	1.170(10)	
$[Cp^*Ir(N_3)(bpy)]PF_6$	2.145(7)–2.179(7)	2.230(6)	116.4(6)	1.025(12)	172.3(10)	1.282(15)	2022
$[Cp^*Ir(Me_2dtc)(N_3)]$	2.159(7)–2.179(5)	2.120(6)	122.5(5)	1.197(8)	176.3(8)	1.157(9)	2030
$[Cp^*Ir(2\text{-}Sqn)(N_3)]$	2.144(6)–2.172(5)	2.132(6)	127.3(4)	1.178(7)	175.4(7)	1.127(7)	2035
	2.156(6)–2.174(6)	2.091(6)	124.2(5)	1.205(8)	175.3(7)	1.169(8)	
$[Cp^*Ir(8\text{-}Sqn)(N_3)]$	2.160(4)–2.197(4)	2.136(3)	120.5(3)	1.200(5)	175.9(5)	1.153(5)	2029
$[\{Cp^*Ir(N_3)\}_2(\mu\text{-}Hbimt)_2]$	2.155(5)–2.198(5)	2.109(4)	122.4(4)	1.181(6)	175.7(7)	1.158(7)	2036
	2.162(7)–2.202(7)	2.134(4)	118.1(4)	1.199(6)	176.3(6)	1.155(6)	2042[sh]

sh: Shoulder

0.05 mol dm^{-3}, prepared under a dinitrogen atmosphere). At 40 °C the Cp* resonance was observed as a broad signal around d 1.6. On cooling, this signal separated into two broad resonances with different intensities. At −20 °C both resonances were detected as sharp doublets at δ 1.51 and 1.64, with an intensity ratio of 4:1. The doublet resonances are indicative of the existence of an Ir–P bond, and, therefore, the two species in solution are assumed to be the chelate and the monodentately P-coordinated Ph_2Ppy complexes (Scheme 3). This results indicate that complex **2′** exists as an equilibrium mixture because of the dissociation of the Ir–N(py) bond in acetonitrile-d_3. Such a dissociation would be favorable for a N-atom insertion reaction, because the reaction of $[Cp^*Ir(N_3)(2\text{-}Spy)]$ was initiated by the photochemical cleavage of the Ir–N(py) bond [6]. However, photochemical or thermal reaction of an acetonitrile-d_3 solution of complex **2′** gave a complicated mixture of unidentified products, in which there was no lower-field shifted ^1H NMR resonance diagnostic for the two-legged piano stool structure of $Cp^*Ir^{III}(L\text{–}L')$-type complexes [5–7]. It has also been reported [23] that photolysis of $[Cp^*Ir(N_3)_2(PPh_3)]$ gave $[Cp^*Ir(H)(Ph_2PC_6H_4\text{-}\kappa P,\kappa C)]$, presumably via a "$Cp^*Ir^I(PPh_3)$" transient species formed by homoleptic cleavage of two Ir–$N(N_3)$ bonds. Thus, the present reactions might be caused by the undesirable thermal or photoreduction of the iridium(III) azido complex.

As mentioned above, the Ir–N(py) bond length and the chelate bite angle of complex **2** were comparable to those of $[Cp^*Ir(N_3)(2\text{-}Spy \text{ or } 2\text{-}Sqn)]$, while the solution behavior, i.e., the lability of the Ir–N(py) bond, was obviously different. To elucidate the reason for the different behavior from the structural point of view, we have also analyzed the crystal structures of the related complexes bearing dmpm and Ph_2Pqn.

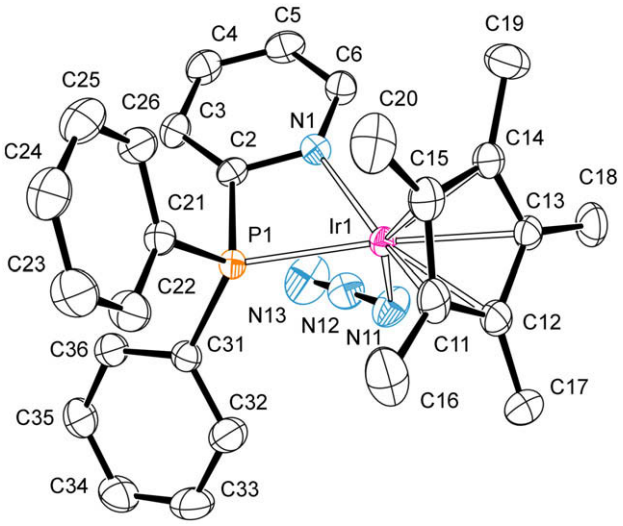


Fig. 2. An ORTEP view (50% probability level, hydrogen atoms omitted) of the cation in $[Cp^*Ir(N_3)(Ph_2Ppy\text{-}\kappa P,\kappa N)]O_3SCF_3$ (**2**).

3.2. Bis(dimethylphosphino)methane (dmpm) complex

It has been reported that particular Pt^{II}–dppm complexes of the form $[Pt(CH_2X)_2(dppm\text{-}\kappa^2P,P)]$ (X = Cl, Br, or I) demonstrated a fascinating chelate-ring expansion reaction by insertion of a CH_2

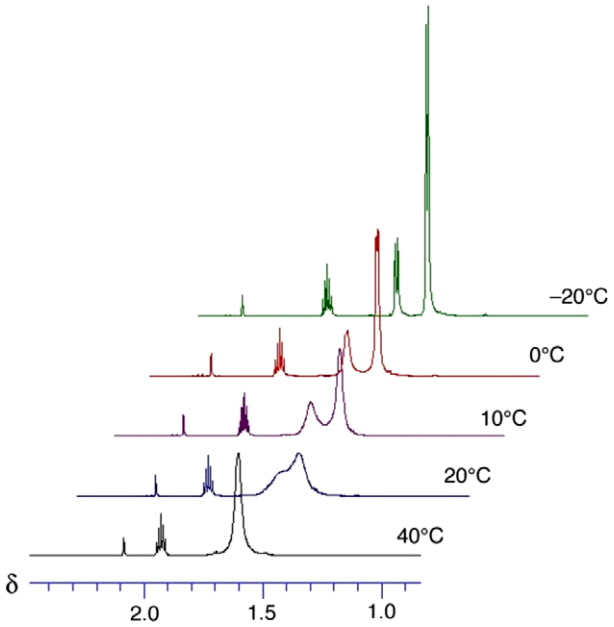
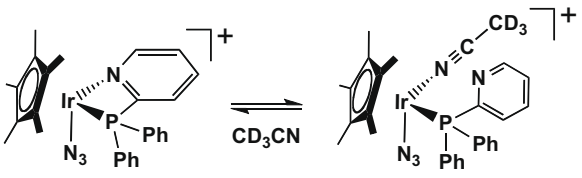


Fig. 3. Variable-temperature ^1H NMR spectra in the Cp* region of $[Cp^*Ir(N_3)(Ph_2Ppy\text{-}\kappa P,\kappa N)]PF_6$ (**2′**) in CD_3CN.



Scheme 3.

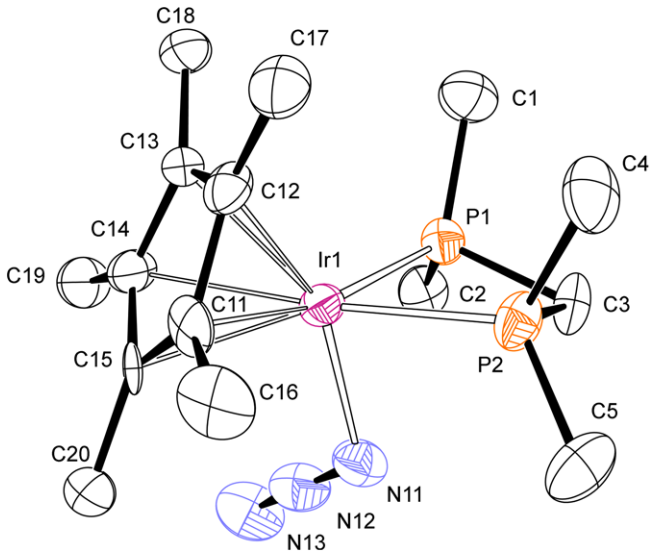


Fig. 4. An ORTEP view (50% probability level) of the cation in $[Cp^*Ir(N_3)(dmpm)]PF_6$ (**3**).

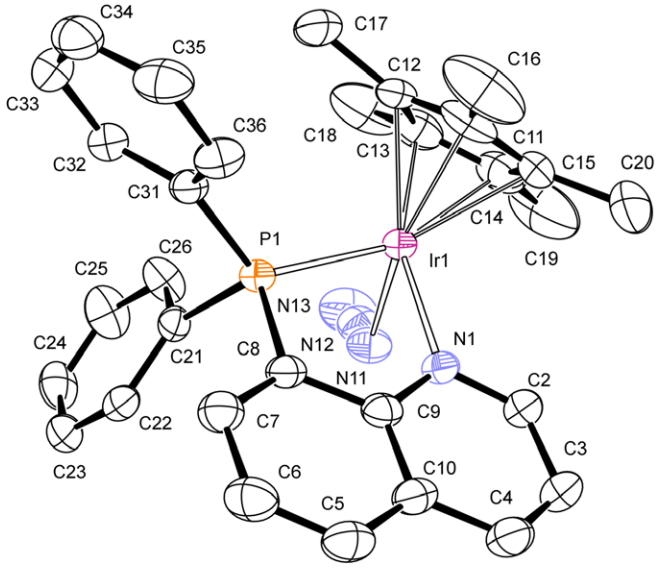


Fig. 5. An ORTEP view (50% probability level, hydrogen atoms omitted) of the cation in $[Cp^*Ir(N_3)(Ph_2Pqn)]PF_6{\cdot}CH_3OH$ (**4**·CH_3OH).

group into a Pt–P bond [24], which is somewhat related to a N-atom insertion reaction. Thus, we thought it might be interesting to investigate the structures and reactivities of the bis(phosphino)methane complexes of $[Cp^*Ir(N_3)(P–P)]PF_6$ (P–P = dppm or dmpm). These complexes were prepared in good yields by reaction of $[Cp^*Ir(N_3)_2]_2$ and the phosphines in methanol, followed by isolation of the PF_6 salts on addition of NH_4PF_6. We have also prepared the CF_3SO_3, BF_4 and BPh_4 salts of the dppm complexes, but none of them deposited suitable crystals for an X-ray diffraction study. Instead, we have determined the crystal structure of $[Cp^*Ir(N_3)(dmpm)]PF_6$ (**3**). The molecular structure with a four-membered chelate ring was confirmed, as illustrated in Fig. 4. The chelate bite angle, P1–Ir1–P2, of dmpm in complex **3** is 71.0(1)°, which is larger than those of Ph_2Ppy in complex **2**, 67.40(8)°. The Ir1–P1–C3 and Ir1–P2–C3 angles in **3** are 93.3(5) and 95.7(4)°, respectively, which are larger than the Ir1–P1–C2 angle in **2,** 85.9(1)°. These angular differences indicate clearly that the steric strain effects are more severe in the Ph_2Ppy chelate than in the dmpm chelate. It is also notable that two Ir–P bonds of complex **3** showed a large numerical deviation, Ir1–P1 2.344(4) versus Ir1–P2 2.282(3) Å, but we cannot account for this unusual feature at present.

Unlike the Ph_2Ppy chelate in complex **2**, the four-membered chelate rings in the dppm and dmpm complexes were stable in acetonitrile solution. When acetonitrile-d_3 solutions of the dppm and dmpm complexes were photolyzed by a high-pressure Hg lamp under a dinitrogen atmosphere at temperature below 0 °C, the ^1H NMR spectra of the resulting solutions indicated the formation of a complicated mixture of unidentified products. Similar to the case of Ph_2Ppy complex **2**, there was no lower-field shifted resonance diagnostic for Cp^*Ir^{III} complexes with a two legged piano stool structure. However, most of the Cp^* resonances became doublets (*cf.* the reactant complexes showed a triplet), because of coupling to the single P nucleus. This may suggest that a N-atom insertion could have taken place on photolysis.

3.3. 8-Diphenylphosphinoquinoline (Ph_2Pqn) complex

To clarify the structural features of the Ph_2Ppy chelate ring in complex **2**, the corresponding Ph_2Pqn complex was prepared and characterized by X-ray diffraction analysis for comparison. The complex, $[Cp^*Ir(N_3)(Ph_2Pqn)]PF_6$ (**4**), was obtained in nearly quantitative yield, and deposited orange prismatic crystals with a methanol molecule of crystallization, **4**·CH_3OH. The molecular structure of the cation in **4**·CH_3OH revealed by the X-ray diffraction study is shown in Fig. 5.

The chelate bite angle of Ph_2Pqn (P1–Ir1–N1) in complex **4** is 81.25(9)°, which is comparable to those in the other Ph_2Pqn complexes determined previously [21,25], but much larger than that of Ph_2Ppy in complex **2**, 67.40(8)°. The five-membered chelate ring is almost planar, and coplanar with the quinolyl ring. The deviations of atoms Ir1 and P1 from the least-square quinolyl ring plane are only 0.246(4) and 0.177(4) Å, respectively. The Ir1–P1–C8 angle in the chelate ring is 102.2(1)°, which is a little smaller than the ideal tetrahedral angle, but is normal for the coordinated phosphines. All bond angles around N1 are nearly 120°. These values indicate that the chelate coordination of Ph_2Pqn forms a strain-free planar five-membered ring. The Ir1–P1 and Ir1–N1 bond lengths in **4** are 2.294(1) and 2.115(3) Å, respectively, which are comparable to those in $[Cp^*Ir(8\text{-}Sqn)(N_3)]$ (Ir–N 2.104(3) Å), $[Cp^*IrCl(8\text{-}MeSqn)]PF_6$ (Ir–N 2.094(3) Å) [26], and the Ph_2Ppy complex **2** (vide supra). It is surprising that the Ir–P and Ir–N bonds in the highly strained four-membered Ph_2Ppy chelate ring elongate only by 0.02 and 0.01 Å, respectively, while the bond angles in the Ph_2Ppy ring show severe deviation from the ideal values: P–Ir–N 67.40(8)°, Ir–P–C 85.4(1)°, and Ir–N–C 106.3(2)°. This observation suggests that the primary reason for the dissociation of the Ir–N(py) bond of the Ph_2Ppy complex **2** in solution must be an angular strain in the four-membered chelate ring. In other words, even the bond lengths are seemingly comparable, the coordination bond in the strained chelate ring is remarkably weak and easy to dissociate in solution to relieve the steric strain.

In the crystal structure of **4**·CH_3OH, there was a stacking interaction between the quinolyl rings with a neighboring molecule, forming a dimer unit. The distance between the planes is ~3.6 Å. This stacking interaction is the most remarkable difference from the crystal structure of the Ph_2Ppy complex **2**.

3.4. 2-(2-Pyridyl)benzimidazolato (pybim) complex

In a series of studies we are investigating the molecular structures and photochemical reactivities of (azido)iridium(III) complexes containing various kinds of bidentate coligands, $[Cp^*Ir^{III}(N_3)(L–L')]^{+/0}$. Previously, we have reported the crystal

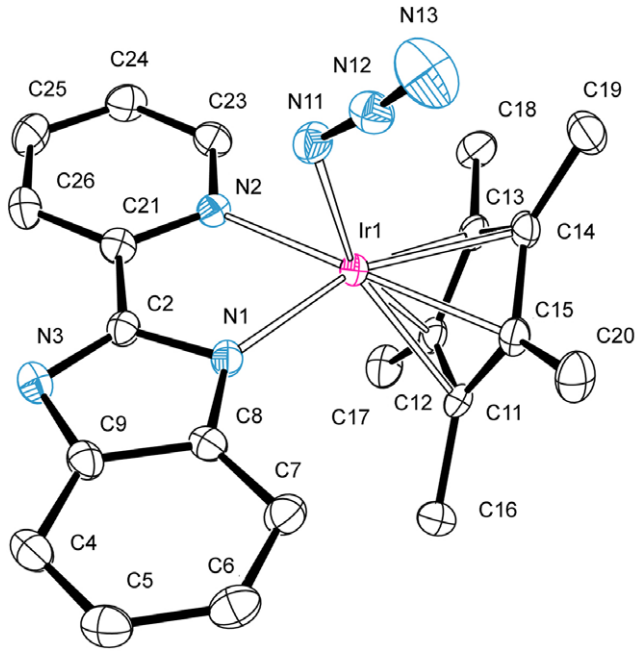


Fig. 6. An ORTEP view (50% probability level, hydrogen atoms omitted) of $[Cp^*Ir(N_3)_2(pybim)]$ (**5**).

structure of $[Cp^*Ir(N_3)(bpy)]PF_6$ [13], which showed an interesting 1,3-dipolar cycloaddition reaction in acetonitrile to form 5-methyltetrazolato complexes [20]. Furthermore, it has also been revealed that 2-pyridyl and 2-benzimidazolyl groups exhibited a different coordination behavior, at least when they were incorporated into bidentate thiolato ligands, i.e., 2-pyridinethiolate (2-Spy$^-$) and benzimidazole-2-thiolate (Hbimt$^-$) [7]. Thus, to compare directly the molecular structures between the bpy and pybim$^-$ complexes, we have prepared and characterized the pybim complex, $[Cp^*Ir(N_3)(pybim)]$ (**5**).

Complex **5** was obtained from $[Cp^*Ir(N_3)_2]_2$ and Na(pybim) as yellow–orange crystals in 77% yield. The molecular structure determined by X-ray analysis is shown in Fig. 6. As expected, the anionic pybim$^-$ ligand formed a planar five-membered chelate ring, which is coplanar with the pyridine and benzimidazolate rings. The chelate bite angle (N1–Ir1–N11) is 76.5(2)°, which is comparable to that of bpy in $[Cp^*Ir(N_3)(bpy)]PF_6$, 76.8(2)° [13]. The Ir1–N2(py) bond length in **5**, 2.139(3) Å, is longer than the Ir–N(bpy) bonds in the above bpy complex, 2.086(5) and 2.097(5) Å. The Ir–N1(bim) bond in **5** is 2.087(3) Å, which is remarkably shorter than the Ir1–N2(py) bond and comparable to the Ir–N(bim) bond length in a dinuclear 2-benzimidazolethiolato (Hbimt$^-$) complex of $[\{Cp^*Ir(N_3)\}_2(\mu\text{-Hbimt})_2]\cdot CH_3OH$, 2.098(4) Å [7]. Because the N ligator in the anionic benzimizadolate ring is more basic than that in the neutral pyridine ring, the bim-*N* donor would give a stronger σ-bonding interaction with an Ir^{III} center than the py-*N* does. When the bite angle of the ligands, N–E, are compared in $[Cp^*Ir^{III}(N_3)(N\text{–}E)]^{0/+}$ having a planar five-membered chelate ring, the angle increases in the order (N–E =) pybim$^-$ ≈ bpy < Ph_2Pqn < 8-Sqn$^-$. The same order was observed in the Ir–E bond lengths: Ir–N(pybim) 2.087(3) ≈ Ir–N(bpy) 2.092(7) < Ir–P(Ph_2Pqn) 2.294(1) < Ir–S (8-Sqn) 2.366(1) Å.

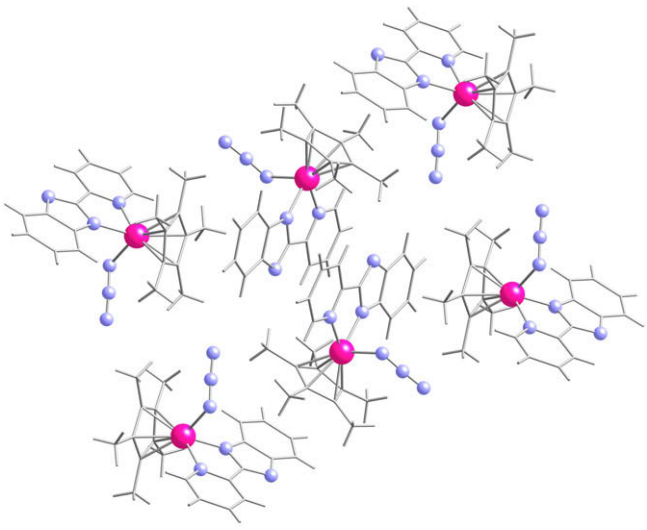


Fig. 7. A stacking diagram of the pybim complexes in the crystal.

The crystal structure of **5** exhibited a characteristic packing diagram. As seen in Fig. 7, a planar pybim ring is stacked with the other pybim ring in a neighboring molecule and a Cp* ring in another molecule. The interplanar distances between the planes are ~3.4 Å. In the crystal structure of $[Cp^*IrCl(Hpyim)]PF_6$ (Hpyim = 2-(2-pyridyl)imidazole) [9], a similar stacking interaction between a pair of Hpyim ligand planes was observed, in addition to the hydrogen-bonding interaction between the im-H group and the coordinated Cl$^-$ ligand. However, in the present complex **5** the N3 atom of the pybim ligand was free from coordination or hydrogen-bonding interaction.

3.5. Comparison of the structural parameters of the $Cp^*Ir^{III}(N_3)$ moiety

The structural parameters of the $Cp^*Ir^{III}(N_3)$ moiety in the complexes determined in the previous and present studies are collected in Table 2. The Ir–C bond lengths of the complexes analyzed previously were in the range of 2.14–2.20 Å. However, some of the Ir–C bonds in complexes **1**–**4** are slightly longer than 2.20 Å (up to 2.29 Å). A detailed examination revealed that the elongated Ir–C bonds are all *trans* to the phosphino donor group(s). Thus, it is concluded that the Ir–C bonds of the Cp* group are also affected by the strong *trans* influence of the phosphines.

The parameters associated with the Ir–N_3 moiety are very similar among the complexes listed in Table 2, except for the bpy complex of $[Cp^*Ir(N_3)(bpy)]PF_6$. Namely, in most (azido)iridium(III) complexes the Ir–N_α bond lengths are in the range 2.09–2.14 Å and the Ir–N_α–N_β bond angles are in the range 117–127°. The coordinated azido ligands are nearly linear (N_α–N_β–N_γ 174–177°), with longer N_α–N_β (1.18–1.23 Å) bonds than N_β–N_γ (1.13–1.17 Å) bonds. In contrast, in $[Cp^*Ir(N_3)(bpy)]PF_6$ all of the parameters for the Ir–N_3 moiety are outside the above ranges. In particular, the Ir–N_α bond is strikingly long at 2.230(6) Å, and the N_α–N_β bond (1.025(12) Å) is remarkably shorter than the N_β–N_γ bond (1.282(15) Å). Consistent with the differences in these structural parameters, the $\nu(N_3)$ stretching frequency of the bpy complex, 2022 cm^{-1}, is observed at a slightly lower frequency than those of the other complexes (Table 2). At this time, we cannot explain these exceptional observation for the bpy complex, but they could give an important insight into the different reactivity of the bpy complex from the others [25].

4. Conclusion

In this study, the crystal structures of five (azido)iridium(III) complexes bearing potentially bidentate ligands (L–L′) have been determined and their structural parameters have been discussed, together with those of the related complexes analyzed previously. Comparing the parameters of the four-membered chelate ring

formed by Ph_2Ppy (in complex **2**) with those of the five-membered chelate ring of the related phosphine–imine-type hybrid ligand Ph_2Pqn (in complex **4**), it became apparent that the Ph_2Ppy ring was highly strained as indicated by the smaller bond angles, but the Ir–P/N coordination bond lengths were comparable to those in the strain-free Ph_2Pqn chelate ring. Although the Ir–N bond and the Ir–N–C angle in the Ph_2Ppy complex **2** are similar to those in the 2-Spy and 2-Sqn complexes analyzed previously [6,22], complex **2** exhibits a dissociation equilibrium of the Ir–N(py) bond in acetonitrile solution.

The pybim complex showed an interesting molecular and crystal structure. The ligand, $pybim^-$, forms a planar five-membered chelate ring with an extended π-delocalized system, and the pybim plane shows a stacking interaction with the neighboring pybim and Cp^* planes to give a characteristic packing structure of the crystal. Furthermore, the Ir–N(bim) bond is shorter than the Ir–N(py) bond, because of the stronger electron-donating properties of the benzimidazole moiety.

We have also examined the photochemical and thermal reactivities of the complexes described in this study, but they showed a complicated mixture of unidentified products.

Supplementary data

CCDC 711474, 711475, 711476, 711477, and 711478 contain the supplementary crystallographic data for **1, 2**, **3**, **4**·CH_3OH, and **5**, respectively. These data can be obtained free of charge via http://www.ccdc.cam.ac.uk/conts/retrieving.html, or from the Cambridge Crystallographic Data Centre, 12 Union Road, Cambridge CB2 1EZ, UK; fax: (+44) 1223-336-033; or e-mail: deposit@ccdc.cam.ac.uk.

Acknowledgement

This work was supported by Grant-in-Aid for Scientific Research No. 20550064 from the Ministry of Education, Culture, Sports, Science, and Technology, Japan.

References

[1] J. Šima, Coord. Chem. Rev. 250 (2006) 2325.
[2] (a) J.F. Berry, E. Bill, E. Bothe, S.D. George, B. Mienert, F. Neese, K. Wieghardt, Science 312 (2006) 1937;
(b) J. Du Bois, C.S. Tomooka, J. Hong, M.E. Carreira, Acc. Chem. Res. 30 (1997) 364.
[3] (a) H.C. Kolb, M.G. Finn, K.B. Sharpless, Angew. Chem., Int. Ed. 40 (2001) 2004;
(b) M. Obata, A. Kitamura, A. Mori, C. Kameyama, J.A. Czaplewska, R. Tanaka, I. Kinoshita, T. Kusumoto, H. Hashimoto, M. Harada, Y. Mikata, T. Funabiki, S. Yano, Dalton Trans. (2008) 3292;
(c) S. Mukhopadhyay, J. Lasri, M.A.J. Charmier, M.F.C. Guedes da Silva, A.J.L. Pombeiro, Dalton Trans. (2007) 5297.
[4] (a) H.-B. Xu, B.-W. Wang, F. Pan, Z.-M. Wang, S. Gao, Angew. Chem., Int. Ed. 46 (2007) 7388;
(b) T.-F. Liu, D. Fu, S. Gao, Y.-Z. Zhang, H.-L. Sun, G. Su, Y.-J. Liu, J. Am. Chem. Soc. 125 (2003) 13976;
(c) J. Carranza, C. Brennan, J. Sletten, J.M. Clemente-Juan, F. Lloret, M. Julve, Inorg. Chem. 43 (2003) 8716;
(d) M. Habib, T.K. Marmakar, G. Aromi, J. Ribas-Ariño, H.-K. Fun, S. Chantrapromma, S.K. Chandra, Inorg. Chem. 47 (2008) 4109.
[5] T. Suzuki, A.G. Dipasquale, J.M. Mayer, J. Am. Chem. Soc. 125 (2003) 10514.
[6] Y. Sekioka, S. Kaizaki, J.M. Mayer, T. Suzuki, Inorg. Chem. 44 (2006) 8173.
[7] M. Kotera, Y. Sekioka, T. Suzuki, Inorg. Chim. Acta 361 (2008) 1479.
[8] (a) V. Pons, D.M. Heinekey, J. Am. Chem. Soc. 125 (2003) 8428;
(b) K.-I. Fujita, M. Nakamura, R. Yamaguchi, Organometallics 20 (2001) 100.
[9] K. Pachhunga, B. Therrien, K.A. Kreisel, G.P.A. Yap, M.R. Kollipara, Polyhedron 26 (2007) 3638.
[10] M. Albrecht, T. Scheiring, T. Sixt, W. Kaim, J. Organomet. Chem. 596 (2000) 84.
[11] K. Yamanari, R. Ito, S. Yamamoto, T. Konno, A. Fuyuhiro, M. Kobayashi, R. Arakawa, Dalton Trans. (2003) 380.
[12] T. Suzuki, Inorg. Chim. Acta 359 (2006) 2431.
[13] T. Suzuki, Acta Crystallogr., Sect. E 61 (2005) m488.
[14] A. Maisonnet, J.P. Farr, M.M. Olmstead, C.T. Hunt, A.L. Balch, Inorg. Chem. 21 (1982) 3961.
[15] R.D. Feltham, H.G. Metzer, J. Organomet. Chem. 33 (1971) 347.
[16] (a) PROCESS-AUTO, Automatic Data Acquisition and Processing Package for Imaging Plate Diffractometer, Rigaku Corporation, Akishima, Tokyo, Japan, 1998.;
(b) T. Higashi, SHAPE, Program to obtain Crystal Shape using CCD Camera, Rigaku Corporation, Tokyo, Japan, 1999.;
(c) CRYSTAL STRUCTURE Ver. 3.6.0, Crystal Structure Analysis Package, Rigaku and Rigaku/MSC, Akishima, Tokyo, Japan and The Woodlands, TX, USA, 2000–2004.
[17] (a) M.C. Burla, R. Caliandro, M. Camalli, B. Carrozzini, G.L. Cascarano, L. De Caro, C. Giacovazzo, G. Polidori, R. Spagna, SIR2004, 2005.;
(b) G.M. Sheldrich, SHELXL97, University of Göttingen, Göttingen, Germany, 1997.
[18] P. Covindaswamy, P. Carroll, Y.A. Mozharivskyj, M.R. Kollipara, J. Chem. Sci. 118 (2006) 319.
[19] M. Kotera, Y. Sekioka, T. Suzuki, Inorg. Chem. 47 (2008) 3498.
[20] M. Rashidi, K. Kamali, M.C. Jennings, R.J. Puddephatt, J. Organomet. Chem. 690 (2005) 1600.
[21] T. Suzuki, T. Kuchiyama, S. Kishi, S. Kaizaki, M. Kato, Bull. Chem. Soc. Jpn. 75 (2002) 2433.
[22] Y. Sekioka, T. Suzuki, Bull. Chem. Soc. Jpn. 79 (2006) 1897.
[23] D.A. Freedman, K.R. Mann, Inorg. Chem. 30 (1991) 836.
[24] N.W. Alcock, P.G. Pringle, P. Bergamini, S. Sostero, O. Traverso, J. Chem. Soc., Dalton Trans. (1990) 1553.
[25] T. Suzuki, Bull. Chem. Soc. Jpn. 77 (2004) 1869.
[26] S. Ye, W. Kaim, M. Albrecht, F. Lissner, T. Schleid, Inorg. Chim. Acta 357 (2004) 3325.

Polyhedron 28 (2009) 2294–2300

Contents lists available at ScienceDirect

Polyhedron

journal homepage: www.elsevier.com/locate/poly

Preparation and reactivity of the heterobimetallic ReIr face-shared bioctahedral compounds $Cp^*Ir(\mu\text{-}Cl)_3Re(CO)_3$ and $Cp^*Ir(\mu\text{-}SC_6H_4Me\text{-}4)_3Re(CO)_3$: X-ray diffraction structures and redox behavior

Xiaoping Wang [a,*], Casey Hammons [b], Michael G. Richmond [b,*]

[a] Neutron Scattering Science Division, Oak Ridge National Laboratory, Oak Ridge, TN 37831-6460, United States
[b] Department of Chemistry, University of North Texas, Denton, TX 76203, United States

ARTICLE INFO

Article history:
Received 22 December 2008
Accepted 15 April 2009
Available online 3 May 2009

Keywords:
Rhenium–iridium compounds
Halide-bridged compounds
Sulfido-bridged compounds
Heterobimetallic compounds
X-ray crystallography

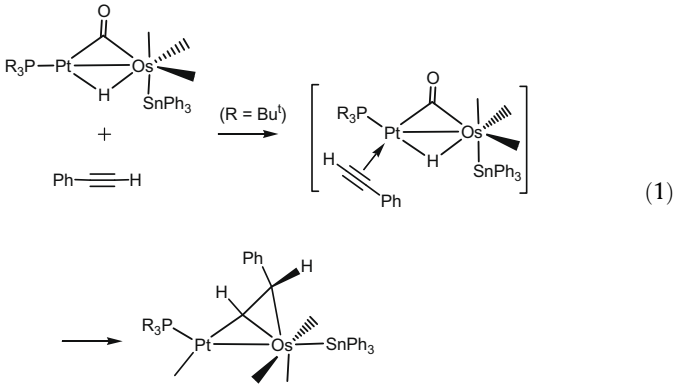
ABSTRACT

Thermolysis of the dinuclear compound $[Cp^*IrCl_2]_2$ (**1**) with $ClRe(CO)_5$ (**2**) leads to the formation of the confacial bioctahedral compound $Cp^*Ir(\mu\text{-}Cl)_3Re(CO)_3$ (**3**) in high yield. Whereas the substitution of the chloride ligands in **3** is observed on treatment with excess *p*-methylbenzenethiol to furnish the sulfido-bridged compound $Cp^*Ir(\mu\text{-}SC_6H_4Me\text{-}4)_3Re(CO)_3$ (**4**), **3** undergoes fragmentation upon reaction with tertiary phosphines [PPh_3 and $P(OMe)_3$] to furnish the mononuclear compounds Cp^*IrCl_2P and *fac*-$ClRe(CO)_3P_2$. Both **3** and **4** have been isolated and fully characterized in solution by IR and ^1H NMR spectroscopies, and their solid-state structures have been established by X-ray crystallography. The redox properties of **3** and **4** have been explored by cyclic voltammetry, and the results are discussed relative to extended Hückel MO calculations.

© 2009 Elsevier Ltd. All rights reserved.

1. Introduction

The catalysis of organic reactions using dinuclear mixed-metal compounds remains under active investigation, with synergistic bimetallic participation in C–H and C–C bond activation processes promoting altered product distributions relative to the corresponding homometallic systems [1]. An undisputed paradigm of cooperative bimetallic reactivity involving alkyne coordination and insertion into a metal–hydride bond has recently been demonstrated by Adams et al. in the case of the mixed-metal compound $HOsPt(CO)_4(SnPh_3)(PBu^t_3)$. Eq. (1) shows this particular reaction, and control experiments and MO calculations confirm the fact that the platinum metal serves as the initial site for alkyne coordination, leading to a weakened Os–H bond, which in turn facilitates the ensuing alkyne insertion and formation of the vinylidene species $OsPt(CO)_4(SnPh_3)(PBu^t_3)[\mu - HC_2(H)Ph]$ [2]. The role played by heterobimetallic species in Fischer–Tropsch chemistry, alkyl and CO insertion reactions, alkyne and alkene hydrogenations, and the reversible reduction of hydronium ions to H_2 by FeNi hydrogenases continues to receive attention, and the mechanistic insight afforded by the mixed-metal species in these different reactions cannot be underscored in terms of modeling heterogeneous catalysts and biological processes [3].



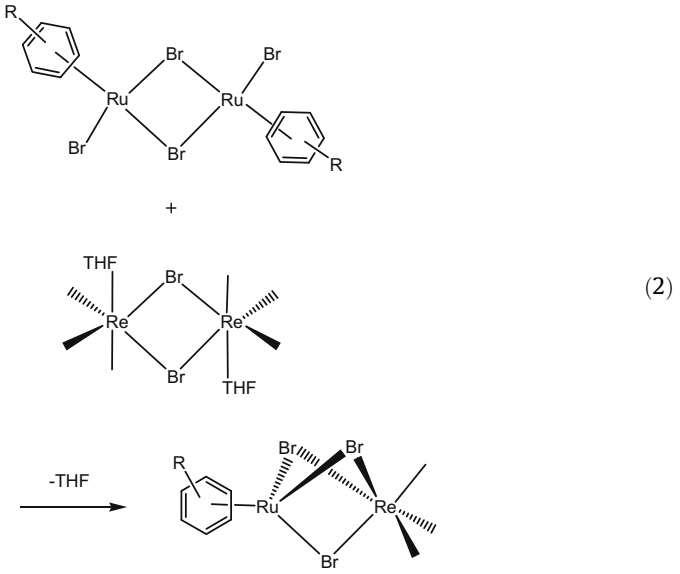
(1)

Severin and co-workers have shown that heterobimetallic compounds based on a $M(\mu\text{-}X)_3M'$ architecture can serve as highly active catalyst precursors in Oppenauer-type oxidations of alcohols and atom-transfer radical addition (ATRA) reactions to alkenes [4]. Accordingly, the directed synthesis of new heterobimetallic systems is warranted if a full understanding of the cooperative synergism between dissimilar metals is to be unraveled in the above catalytic reactions. Severin has outlined several different synthetic methodologies that may be employed in the synthesis of $M(\mu\text{-}X)_3M'$ compounds, with the union of a halide-containing compound and a "lightly activated" or weakly bound solvent com-

* Corresponding authors. Tel.: +1 940 565 3548; fax: +1 940 565 4318 (M.G. Richmond).
E-mail addresses: wangx@ornl.gov (X. Wang), cobalt@unt.edu (M.G. Richmond).

0277-5387/$ - see front matter © 2009 Elsevier Ltd. All rights reserved.
doi:10.1016/j.poly.2009.04.023

plex providing a clean route that leads to the formation of a plethora of different M(μ-X)$_3$M′ derivatives [5]. An elegant example demonstrating this concept involves the synthesis of (η^6-arene)Ru(μ-Br)$_3$Re(CO)$_3$ (where arene = benzene, cymene, 1,3,5-Et$_3$C$_6$H$_3$) from the reaction of [(η^6-arene)RuBr$_2$]$_2$ with [ReBr(THF)(CO)$_3$]$_2$, as depicted in Eq. (2). Here the formal loss of THF and splitting of the halide bridges in the latter dimer afford the mononuclear rhenium species "BrRe(CO)$_3$" that is readily scavenged by the donating halide ligands associated with the (η^6-arene)RuBr$_2$ fragment. The driving force for this and related reactions is entropically driven, and the formation of new bridging metal–halogen bonds in the binuclear RuRe product compensates for the loss of the weakly bound THF molecules.



(2)

Recently, we reported our results on the synthesis of the chlorine-bridged compound (η^6-cymene)Ru(μ-Cl)$_3$Re(CO)$_3$ from [(η^6-cymene)RuCl$_2$]$_2$ and ClRe(CO)$_5$. Here we capitalized on known lability of the CO groups in the latter reagent to generate the unsaturated species "ClRe(CO)$_4$" under thermal and photochemical activation, which in turn reacts with the starting ruthenium dimer to furnish the observed heterobimetallic end-product [6]. The trapping of an *in situ* generated unsaturated species upon loss of CO represents an alternative protocol for the preparation of M(μ-X)$_3$M′ compounds. Herein we present our data on the synthesis and physical characterization of Cp*Ir(μ-Cl)$_3$Re(CO)$_3$ (**3**) and the corresponding sulfido-bridged product Cp*Ir(μ-SC$_6$H$_4$Me-4)$_3$Re(CO)$_3$ (**4**). Preliminary reactions between **3** and phosphine ligands support the fragmentation of the starting heterobimetallic compound to mononuclear species.

2. Experimental

2.1. General

The starting materials [Cp*IrCl$_2$]$_2$[7] and ClRe(CO)$_5$[8] used in the synthesis of **3** were prepared by established literature procedures. The chemicals IrCl$_3$·*x*H$_2$O (Engelhard), Re$_2$(CO)$_{10}$ (Pressure Chemical), and *p*-methylbenzenethiol (Aldrich) were used as received, while the pentamethylcyclopentadiene employed in the synthesis of **1** was prepared from 2-bromo-2-butenes (isomeric mixture) [9], the latter which was purchased from Aldrich. The reaction solvents were either distilled from an appropriate drying agent under argon using Schlenk techniques or obtained from an Innovative Technology solvent purification system. All distilled solvents were stored in Schlenk storage vessels equipped with high-vacuum Teflon stopcocks [10]. The combustion analysis on **3** was performed by Atlantic Microlab, Norcross, GA.

The reported IR data were recorded on a Nicolet 6700 FT-IR spectrometer, while all ^{1}H spectra were recorded at 500 MHz on a Varian VXR-500 spectrometer. The ESI-APCI mass spectrum of **4** was recorded at the UC San Diego mass spectrometry facility in the positive ionization mode.

2.2. Synthesis of Cp*Ir(μ-Cl)$_3$Re(CO)$_3$ from the thermolysis of [Cp*IrCl$_2$]$_2$ with ClRe(CO)$_5$

To 10 mg (0.013 mmol) of **1** in a 100 mL Schlenk round-bottom flask under argon flush was added 20 mL of CH$_2$Cl$_2$, followed by 9.1 mg (0.025 mmol) of **2**. The solution was then heated at reflux over night and allowed to cool to room temperature, at which time TLC analysis revealed the consumption of the latter starting material and a large spot at the origin of the TLC plate belonging to the desired compound **3**. The solvent was removed under vacuum and the residue recrystallized from a minimum amount of CH$_2$Cl$_2$/benzene to yield **3** as a golden-yellow solid in 91% yield (16 mg). IR (CH$_2$Cl$_2$): υ(CO) 2037 (s), 1919 (s, broad) cm^{-1}. ^{1}H NMR (CDCl$_3$): δ 1.90 (s, Cp*). *Anal.* Calc. for C$_{13}$H$_{15}$Cl$_3$IrO$_3$Re·1/8C$_6$H$_6$: C, 23.12; H, 2.21. Found: C, 22.87; H, 2.22%.

2.3. Synthesis of Cp*Ir(μ-SC$_6$H$_4$Me-4)$_3$Re(CO)$_3$ from **3** and *p*-methylbenzenethiol

To a 250 mL Schlenk round-bottom flask was added 50 mg (0.071 mmol) of **3**, followed by the addition of 50 mL of toluene via cannula. The slurry was stirred for several minutes to ensure complete dissolution of **3**, after which time 35 mg (0.28 mmol; slight excess) of *p*-methylbenzenethiol was added in one portion and the contents heated at reflux for 1.5 h. TLC analysis of the crude reaction solution in CH$_2$Cl$_2$/hexane (1:9) revealed the presence of the desired product **3** as a bright yellow spot at R_f = 0.86, along with a trace amount of an orange spot at R_f = 0.80 ascribed to Cp*Ir(μ-Cl)(μ-SC$_6$H$_4$Me-4)$_2$Re(CO)$_3$ and some material that remained at the origin. **3** was subsequently isolated by column chromatography over silica gel using the aforementioned mobile phase in 64% yield (44 mg). IR (CH$_2$Cl$_2$): υ(CO) 2012 (s), 1902 (s, broad) cm^{-1}. ^{1}H NMR (CDCl$_3$): δ 1.30 (s, 15 H, Cp*), 2.32 (s, 9 H, Me-4), 7.06 (d, 6 H, ^3J = 8 Hz, aryl), 7.61 (d, 6 H, ^3J = 8 Hz, aryl). ESI-MS (*m*/*z*): 988.97 [**3**+Na]$^+$, 845.01 [**3**-SC$_6$H$_4$-Me-*p*]$^+$.

2.4. X-ray crystallographic data

Single crystals of **3** and **4**·1/2CH$_2$Cl$_2$ suitable for diffraction analysis were grown from CH$_2$Cl$_2$ solutions containing each compound that had been layered with hexane. The X-ray data for **3** and **4**·1/2CH$_2$Cl$_2$ were collected on an APEX II CCD-based diffractometer at 100(2) K. The frames were integrated with the available APEX2 [11] software package using a narrow-frame algorithm, and the structures were solved and refined using the SHELXTL program package [12]. Each molecular structure was checked using PLATON [13], and all nonhydrogen atoms were refined anisotropically. The hydrogen atoms in **3** and **4**·1/2CH$_2$Cl$_2$ were assigned calculated positions and allowed to ride on the attached carbon heavy atom. The refinement for **3** converged at R = 0.0534 and R_w = 0.1575 for 3179 independent reflection with $I > 2\sigma(I)$, with convergence values for **4**·1/2CH$_2$Cl$_2$ obtained at R = 0.0181 and R_w = 0.0374 for 7729 independent reflection with $I > 2\sigma(I)$. The X-ray data and processing parameters are reported in Table 1, with selected bond distances and angles quoted in Table 2.

Table 1
X-ray crystallographic data and processing parameters for **3** and **4**·1/2CH_2Cl_2.

Compound	**3**	**4**·1/2CH_2Cl_2
Crystal system	monoclinic	triclinic
Space group	$P2(1)/n$	$P\bar{1}$
a (Å)	9.622(1)	10.037(2)
b (Å)	14.776(2)	12.102(2)
c (Å)	12.045(2)	15.679(3)
α (°)		75.35(3)
β (°)	90.003(1)	84.78(3)
γ (°)		73.06(3)
V (Å^3)	1712.6(4)	1762.3(6)
Molecular formula	$C_{13}H_{15}Cl_3IrO_3Re$	$C_{34.5}H_{37}ClIrO_3ReS_3$
Formula weight	611.86	1009.67
Formula units per cell (Z)	4	2
$D_{calc.}$ (Mg/m^3)	2.730	1.903
λ (Mo Kα) (Å)	0.71073	0.71073
μ (mm^{-1})	15.296	7.489
Absorption correction	semi-empirical from equivalents	semi-empirical from equivalents
Absorption correction factor	0.6243/0.1928	0.1772/0.1197
Total reflections	15508	21693
Independent reflections	3179	7729
Data/restraints/parameters	3179/78/197	7729/4/416
R_1[a] [$I \geqslant 2\sigma(I)$]	0.0534	0.0181
wR_2[b] (all data)	0.1575	0.0374
Goodness-of-fit (GOF) on F^2	1.167	1.095
$\Delta\rho$(max), $\Delta\rho$(min) (e/Å^3)	3.174, −3.866	0.774, −0.768

[a] $R_1 = \Sigma\|F_o\| - \|F_c\|/\Sigma\|F_o\|$.
[b] $R_2 = \{\Sigma[w(F_o^2 - F_c^2)^2]/\Sigma[w(F_o^2)^2]\}^{1/2}$.

Table 2
Selected bond distances (Å) and angles (°) in **3** and **4**·1/2CH_2Cl_2.

Compound **3**			
Bond distances			
Re(1)–C(13)	1.89(2)	Re(1)–C(11)	1.90(2)
Re(1)–C(12)	1.92(2)	Re(1)–Cl(1)	2.504(4)
Re(1)–Cl(2)	2.510(5)	Re(1)–Cl(3)	2.512(4)
Ir(1)–Cl(1)	2.439(4)	Ir(1)–Cl(2)	2.452(4)
Ir(1)–Cl(3)	2.461(4)	Ir(1)–centroid[a]	1.7663(5)
Bond angles			
C(13)–Re(1)–C(11)	86.3(8)	C(13)–Re(1)–C(12)	88.4(8)
C(11)–Re(1)–C(12)	87.7(8)	Ir(1)–Cl(1)–Re(1)	85.1(1)
Ir(1)–Cl(2)–Re(1)	84.7(1)	Ir(1)–Cl(3)–Re(1)	84.4(1)
O(1)–C(11)–Re(1)	178(2)	O(2)–C(12)–Re(2)	177(2)
O(3)–C(13)–Re(3)	176(2)		
Compound **4**·1/2CH_2Cl_2			
Bond distances			
Re(1)–C(3)	1.910(3)	Re(1)–C(2)	1.924(3)
Re(1)–C(1)	1.926(3)	Re(1)–S(3)	2.515(1)
Re(1)–S(2)	2.5030(9)	Re(1)–S(1)	2.509(1)
Ir(1)–S(3)	2.3973(9)	Ir(1)–S(2)	2.403(1)
Ir(1)–S(1)	2.406(1)	Ir(1)–centroid[b]	1.8058(1)
Bond angles			
C(3)–Re(1)–C(2)	90.3(1)	C(3)–Re(1)–C(1)	90.0(1)
C(2)–Re(1)–C(1)	92.3(1)	S(2)–Re(1)–S(3)	75.73(3)
S(1)–Re(1)–S(3)	75.70(3)	S(2)–Re(1)–S(1)	76.68(3)
S(3)–Ir(1)–S(2)	79.83(3)	S(3)–Ir(1)–S(10	79.85(3)
S(2)–Ir(1)–S(1)	80.56(4)		

[a] Mean Ir(1)–C distance for the Cp^* carbons C(1)–C(5).
[b] Mean Ir(1)–C distance for the Cp^* carbons C(4)–C(8).

2.5. Electrochemical studies

The reported cyclic voltammetry data were recorded on a PAR Model 273 potentiostat/galvanostat, equipped with positive feedback circuitry to compensate for *i*R drop. The homemade three-electrode cell that was employed allowed the cyclic voltammograms to be recorded under oxygen- and moisture-free conditions. A platinum disk (area = 0.0079 cm^2) was utilized as the working and auxiliary electrode, and the reference electrode utilized a silver wire as a quasi-reference electrode. The reported potential data were standardized against the formal potential of the $Cp^*_2Fe/Cp^*_2Fe^+$ (internally added) redox couple, taken to have $E_{1/2} = -0.20$ V [14].

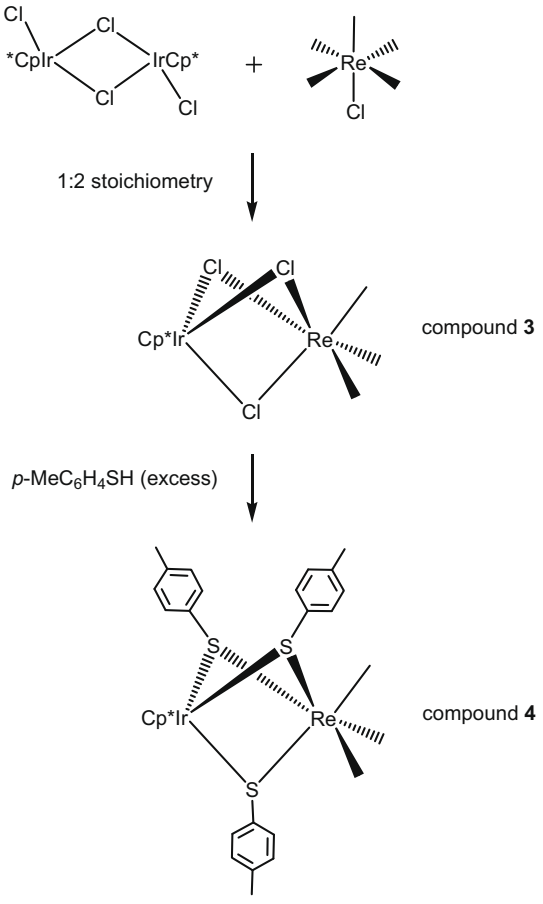
2.6. Extended Hückel MO calculations

The extended Hückel calculations reported here were carried out using the original program developed by Hoffmann and Lipscomb [15], as modified by Mealli and Proserpio [16]. The weighted H_{ij}'s contained in the program were used in the calculations, and the input Z-matrices for **3** and **4** were constructed from the available X-ray data, with the predefined CACAO packaged Cp moiety replacing the Cp* ligand in each compound and methyl groups substituted for the *p*-tolyl groups in **4**.

3. Results and discussion

3.1. Syntheses and X-ray diffraction structure of $Cp^*Ir(\mu\text{-}Cl)_3Re(CO)_3$ (**3**)

Thermolysis of **1** and **2** (equimolar in metal) in refluxing CH_2Cl_2 furnishes the new heterobimetallic compound **3**, as assessed by IR and NMR analysis of the reaction solution before formal work-up; heating **1** and **2** in either 1,2-dichloroethane or toluene also affords **3** without complications. Scheme 1 shows the reaction leading to **3**. Compound **3** could not be purified by column chromatography employing traditional supports such as silica gel and alumina because of the irreversible binding of **3** to the chromatographic sup-



Scheme 1.

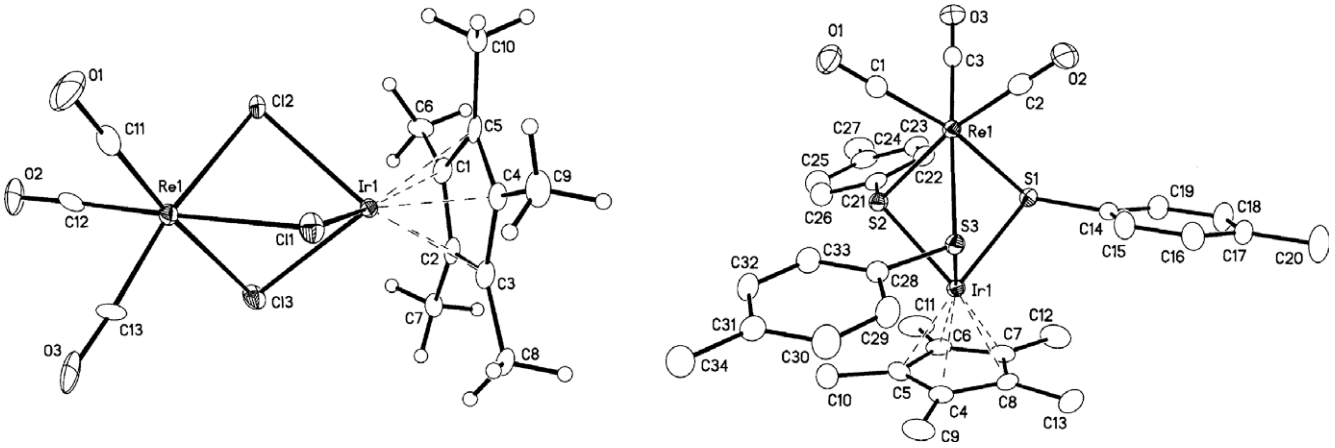


Fig. 1. Thermal ellipsoid plot of **3** (left) and **4**·1/2CH_2Cl_2 (right) showing the thermal ellipsoids at the 50% probability level. The accompanying solvent molecule in the latter structure has been omitted for clarity.

ports, necessitating the use of recrystallization in order to purify **3**. Isolated yields of **3** ranged from good to excellent and were readily achieved through recrystallization of the crude reaction material using the non-coordinating solvents CH_2Cl_2 and benzene. **3** was isolated as an air-stable golden-yellow solid, and samples of **3** maintained under argon did not exhibit any visible sign of decomposition over the course of several months; however, exposure of **3** to atmospheric moisture led to the slow decomposition of **3**. This same decomposition was noticeably accelerated by directly treating **3** with water, consistent with the reactive nature of the halide bridging ligands in related M(μ-Cl)$_3$M′ dimers and formation of hydrolysis-derived species representing a significant decomposition manifold [17].

CO dissociation in $XRe(CO)_5$ has been shown to be facile and facilitated by the ancillary halide ligand, facts experimentally established by different research groups over three decades ago [18]. Essentially quantitative yields of **3** may also be achieved by making use of the lability of the CO groups in **2** in the presence of the weak donor solvent MeCN. The *cis* labilization exerted by the chloride ligand in **2** leads to facile loss of *cis* CO groups and the *in situ* generation of the "lightly activated" compound *fac*-$ClRe(CO)_3(MeCN)_2$.[19] Moreover, the thermolysis of **2** has been kinetically studied and found to proceed by a rapid first-order process involving dissociative CO loss, exhibiting a $t_{1/2}$ ca. 25 min at 60 °C [20]. Reaction of the *in situ* generated *fac*-$ClRe(CO)_3(MeCN)_2$ with **1** then gives the desired product **3**.[1] The proposed reaction sequence was verified by a control experiment between independently synthesized *fac*-$ClRe(CO)_3(MeCN)_2$ and **1**, which afforded **3** in >90% yield. Finally, **3** may be synthesized by a photochemical route employing near-UV irradiation (366 nm). Loss of CO in **2** upon optical excitation leads to the unsaturated intermediate $ClRe(CO)_4$ [21], which in turn is free to react with **1**, followed by an accompanying redistribution of a Cp^*IrCl_2 fragment.

3 was characterized by IR and ^{1}H NMR spectroscopies, combustion analysis, and X-ray crystallography. The IR spectrum exhibits two terminal carbonyl stretching bands for the Re–CO groups at 2037 and 1919 cm^{-1} consistent with the idealized C_{3v} symmetry displayed by the $Re(CO)_3$ moiety, while the ^{1}H NMR spectrum reveals a single resonance at δ 1.90 for the Cp^* ligand. Fig. 1 shows the solid-state structure of **3** and reveals a molecular motif predicated on a triply bridged confacial bioctahedral geometry, where the three chlorines function as the common face-sharing ligands. Assuming the occupation of three coordination sites by the Cp^* ligand, each metal center in **3** is formally six-coordinate and electronically saturated according to the Effective Atomic Number (EAN) rule when the bridging chlorides are treated as 3e-donating ligands. The structure of **3** is analogous to the bromine-bridged derivative $Cp^*Ir(\mu\text{-}Br)_3Re(CO)_3$ prepared by Severin and co-workers [22], and represents the only heterobimetallic ReIr derivative containing face-sharing chlorine ligands on file with the Cambridge Structural Data Center [23]. The internuclear Re(1)···Ir(1) distance of 3.3424(8) Å in **3** precludes any significant metal–metal bonding when contrasted with the Re–Ir single-bond lengths of 2.8081(6), 2.9013(6), and 2.8519(2) Å reported for the heterobimetallic compounds $Cp^*(CO)Ir(\mu\text{-}CO)_2Re(CO)Cp^*$, $[ReIr(CO)_3Cp^*(\eta^5\text{-}7\text{-}CB_{10}H_{11}]$, and $[Cp^*Ir(PMe_3)(\mu\text{-}S)_2Re(NC_6H_3Me_2\text{-}2,6)_2]$, respectively [24]. The structural absence of a metal–metal bond in **3** has, in fact, been theoretically confirmed in related $L_3M(\mu\text{-}X)ML_3$ compounds by extended Hückel MO calculations [25]. Here the tethering of the d^6-$[CpIr]^{2+}$ and d^6-$[Re(CO)_3]^+$ fragments by three chloride ligands (Cl^-) gives rise to a filled set of low-energy d orbitals incapable of metal–metal bonding.[2] The Re–Cl distances range from 2.504(4) Å [Re(1)–Cl(1)] to 2.5123(4) Å [Re(1)–Cl(3)] and display a mean distance of 2.509 Å, while the slightly shorter Ir–Cl distances range from 2.439(4) Å [Ir(1)-Cl(1)] to 2.461(4) Å [Ir(1)–Cl(3)] and reveal a mean length of 2.484 Å. Both sets of metal–halides distances are in excellent agreement with the mean Re–Cl and Ir–Cl bond distances tabulated by Orpen et al.[26]. The remaining bond distances and angles are unremarkable and require no comment.

3.2. Syntheses and X-ray diffraction structure of $Cp^*Ir(\mu\text{-}SC_6H_4Me\text{-}4)_3Re(CO)_3$ (**4**)

Due to the interest in functionalized dendrimers and star-shaped molecules based on $M_2(\mu\text{-}SR)_3$ cores, we next explored the functionalization of **3** with *p*-methylbenzenethiol [27]. Facile substitution of the three chloride ligands in **3** by *p*-methylbenzenethiol (slight excess) is observed in refluxing toluene to afford

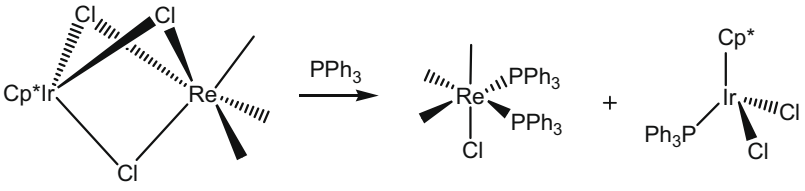
[1] A control experiment (^{1}H NMR) involving the reaction of MeCN with **1** was conducted to explore the formation of the solvated species $Cp^*IrCl_2(MeCN)$ which, in principal, could then undergo reaction with *fac*-$ClRe(CO)_3(MeCN)_2$ to furnish **3**. While no direct NMR evidence for the MeCN-induced fragmentation of **1** was observed, our data do not rule out a small equilibrium concentration (<5%) of the ligand-substitution product $Cp^*IrCl_2(MeCN)$.

[2] The formal union of two d^6-ML_3 moieties is net non-bonding because of the filled t_{2g} set of orbitals belonging to each metal. Inclusion of bridging ligands having π character does not change the situation due to the existence of the appropriate symmetry-adopted linear combination orbitals (SALCs) that negate any net bonding between the metal centers.

the sulfido-bridged compound **4** as the major product, along with a trace amount of material whose spectroscopic properties were indicative of the bis-substituted sulfido-bridged species $Cp^*Ir(\mu\text{-}Cl)(\mu\text{-}SC_6H_4Me\text{-}4)_2Re(CO)_3$. This latter material was examined for its reactivity with added *p*-methylbenzenethiol and found to give **4**. Whereas **3** was unstable with respect to chromatographic supports, **4** could be readily purified by column chromatography over silica gel. **4** was characterized in solution by IR spectroscopy, which revealed two strong υ(CO) bands at 2013 and 1902 cm^{-1} consistent with the *A* and *E* symmetry bands belonging to the *fac*-$Re(CO)_3$ moiety. The observed ca. 20 cm^{-1} shift to lower frequency of each carbonyl band in **4** vis-a-vis the υ(CO) bands in **3** is consistent with the presence of the stronger σ donating sulfido ligands in the former compound. The ^{1}H NMR spectrum of **4** exhibited two high-field resonances at δ 1.30 and 2.32 that are readily ascribed to the Cp^* and *p*-Me moieties, respectively, with the aryl hydrogens at δ 7.06 and 7.61 exhibiting a classic AX pattern having a $J/\Delta\delta$ value of 0.03. Finally, the ESI mass spectrum of **4** displayed two prominent peaks at *m/z* 988.97 and 845.01 that are attributed to a pseudo-molecular ion for [**3**+Na]$^+$ and the loss of a single sulfido ligand for [**3**-SC_6H_4-Me-*p*]$^+$, respectively, consistent with the formulated structure. The unequivocal identity of **4**, as the CH_2Cl_2 solvate, was subsequently established by X-ray diffraction analysis. The thermal ellipsoid plot of **4** in Fig. 1 establishes the presence of the three bridging sulfido groups and the local octahedral coordination about the Re(1) and Ir(1) centers. **4** is unique insomuch as it represents, to our knowledge, the first structurally characterized sulfido-bridged heterobimetallic ReIr compound exhibiting a confacial bioctahedral geometry. The overall molecular structure is identical to that of **3**, and the internuclear Re(1)···Ir(1) distance of 3.3718(7) Å is elongated by 0.030 Å compared to the corresponding distance found in **3**. The formation of **4** in near quantitative yield, along with the collective spectroscopic and mass spectral data, confirm the fact that metal redistribution to give the homometallic products $[Cp^*Ir(\mu\text{-}SR)_3IrCp^*]^+$ and $[(OC)_3Re(\mu\text{-}SR)_3Re(CO)_3]^-$ is not an important manifold in the reaction involving **3** with added thiol [28].

3.3. Reaction of **3** with tertiary phosphines

The reactivity of **3** with various phosphines was next explored by NMR spectroscopy, with the synthesis of ligand-substituted derivatives possessing an intact heterobimetallic $Ir(\mu\text{-}Cl)_3Re$ core as our targeted goal. To our knowledge, no reports exist for the reaction of such halide-bridged mixed-metal systems and phosphine donor ligands. **3** reacts rapidly with a slight excess of added PPh_3 (ca. 3.1 equiv. per **3** employed), leading to the disruption of the starting chloride-bridged dimer and formation of the known mononuclear compounds *fac*-$ClRe(CO)_3(PPh_3)_2$ and $Cp^*IrCl_2(PPh_3)$, as depicted in Eq. (3) [29]. Similar reactivity was found when an excess of $P(OMe)_3$ was employed in the reaction with **3**, with the corresponding compounds *fac*-$ClRe(CO)_3[P(OMe)_3]_2$ and Cp^*IrCl_2 $[P(OMe)_3]$ observed by NMR spectroscopy.

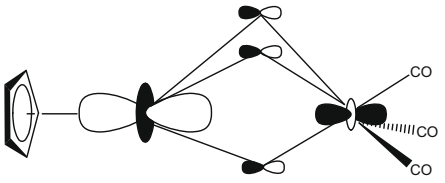


(3)

The reaction of **3** with the rigid bidentate phosphine 4,5-bis(diphenylphosphino)-4-cyclopenten-1,3-dione (bpcd) was also probed by ^{31}P NMR spectroscopy, given our longstanding interest in the coordination chemistry and activation of this particular ligand by polynuclear metal clusters [30]. As in the above reactions with monodentate phosphines, rapid fragmentation of **3** is observed upon treatment with a measured amount of bpcd (1:2 ratio), with new ^{31}P resonances recorded at δ 22.28 and −26.91 that are readily assignable to the known chelated rhenium compound *fac*-$ClRe(CO)_3$(bpcd) (cf.: δ 22.29) and the ionic compound [Cp^*IrCl(bpcd)][Cl], respectively [31,32]. The latter product is assumed to derive from chloride loss upon ring-closure of the pendent phosphine in the intermediate species $Cp^*IrCl_2(\eta^1\text{-bpcd})$. Having established the lability of **3** in phosphine-promoted fragmentation reactions, further substitution studies were abandoned.

3.4. Redox properties and MO data for **3** and **4**

The electrochemical properties of **3** and **4** were next investigated the cyclic voltammetry at platinum electrodes in THF at room temperature using 0.2 M TBAP as the supporting electrolyte. The CV of **3** when examined at a scan rate of 250 mV/s over the potential range of 1.5 to −1.5 V revealed a diffusion-controlled irreversible oxidation at $E_p^a = 1.42$ V [33]. The nature of the orbital associated with this oxidation wave in **3** was established by MO analysis of the model complex $CpIr(\mu\text{-}Cl)_3Re(CO)_3$ at the extended Hückel level. The energy level of the HOMO in **3** was computed to be −11.52 eV by extended Hückel MO calculations, and the HOMO is best described as an antibonding Re–Ir orbital that is largely iridium based and formed from the overlap of metal d_{z2} and chlorine p_z orbitals, as depicted below.[3] The general orbital composition of the HOMO in **3** is similar to the a_2" HOMO reported by Hoffmann and co-workers for a series of homobimetallic $L_3M(\mu\text{-}X)_3ML_3$ compounds [25,34]. Finally, the computed Mulliken reduced overlap population (ROP) of −0.095 between the two metal centers in **3** reinforces the absence of any net bonding between the two metal centers.



HOMO (-11.52 eV)

[3] The HOMO in the model compound $CpIr(\mu\text{-}Cl)_3Re(CO)_3$ consists of significant atomic contributions from the iridium (84%) and rhenium (4%) centers, and the three bridging chlorines (collectively 8%). Here the three in-phase linear combination of p_z chlorine orbitals are situated antisymmetric relative to a twofold rotation axis defined by the metal atoms.

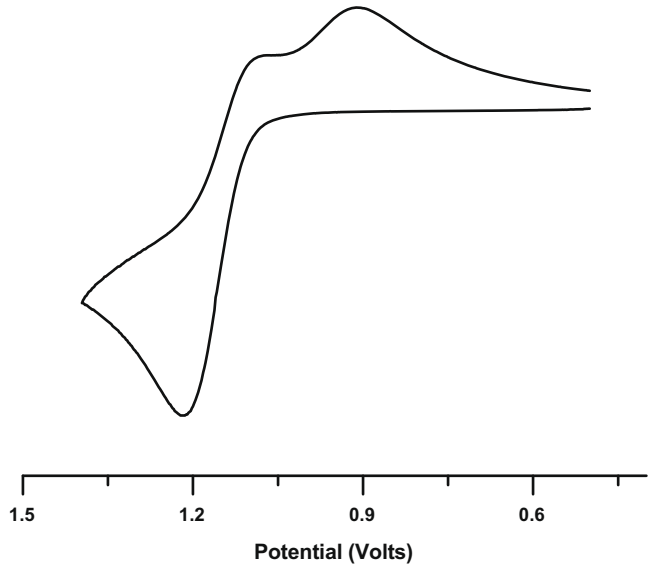


Fig. 2. Anodic scan cyclic voltammogram of **4** (ca. 10^{-3} M) in THF containing 0.2 M TBAP at 0.25 V/s at room temperature.

Examination of **4** by CV, in a manner identical to that of **3**, also revealed the presence of an irreversible oxidation wave at $E_p^a = 1.22$ V, in addition to a return cathodic wave at $E_p^c = 0.74$ V as depicted in Fig. 2. The redox behavior for **4** is not unlike the irreversible oxidation properties displayed by several tris(sulfido)-bridged Ru_2 and Rh_2 compounds prepared by Chérioux et al. [35] The identity of the HOMO in **4** was verified by extended Hückel MO calculations on the model compound $CpIr(\mu\text{-}SMe)_3Re(CO)_3$, where an energy of −11.51 eV was computed and an orbital composition analogous to **3** found.[4] The ROP value of −0.071 computed for the Ir and Re centers in $CpIr(\mu\text{-}SMe)_3Re(CO)_3$ is consistent with a structure where the bridging sulfido ligands act as simple tethering agents and do not promote metal–metal bonding.

4. Conclusions

The syntheses, X-ray diffraction structures, and electrochemical properties of the new mixed-metal compounds **3** and **4** have been presented and discussed. Whereas the halide-bridged compound **3** exhibits fragmentation upon reaction with phosphine ligands, treatment of **3** with added *p*-methylbenzenethiol furnishes the corresponding sulfido-bridged ReIr heterobimetallic compound **4**. Future work will probe the sequential metathesis of the chlorine ligands in **3** with suitable hydride and alkyl reagents in connection with our chemical and catalytic interests on the cooperative activation and formation of C–H and C–C bonds at structurally defined bimetallic ensembles.

Supplementary data

CCDC 709012 and 709013 contain the supplementary crystallographic data for **3** and **4**·1/2CH_2Cl_2. These data can be obtained free of charge via http://www.ccdc.cam.ac.uk/conts/retrieving.html, or from the Cambridge Crystallographic Data Centre, 12 Union Road, Cambridge CB2 1EZ, UK; fax: (+44) 1223-336-033; or e-mail: deposit@ccdc.cam.ac.uk.

[4] The atomic orbital contributions to the antibonding HOMO in $CpIr(\mu\text{-}SMe)_3Re(CO)_3$ consist of Ir (80%) and Re (3%) d_{z^2} character and sulfur (collectively 15%) p_z character.

Acknowledgment

Generous and continued financial support from the Robert A. Welch Foundation (Grant B-1093-MGR) is much appreciated.

References

[1] R.D. Adams, F.A. Cotton (Eds.), Catalysis by Di- and Polynuclear Metal Cluster Complexes, Wiley-VCH, New York, 1998.
[2] R.D. Adams, B. Captain, L. Zhu, J. Am. Chem. Soc. 128 (2006) 13672.
[3] (a) B.D. Rowsell, R. McDonald, M. Cowie, Organometallics 23 (2004) 3873;
(b) J.M. Thomas, B.F.G. Johnson, R. Raja, G. Sankar, P.A. Midgley, Acc. Chem. Res. 36 (2003) 20;
(c) E. Iglesia, S.L. Soled, R.A. Fiato, G.H. Via, J. Catal. 143 (1993) 345;
(d) P. Braunstein, M. Knorr, T. Stährfeldt, J. Chem. Soc., Chem. Commun. (1994) 1913;
(e) S.A. Reed, M.C. White, J. Am. Chem. Soc. 130 (2008) 3316;
(f) T. Shima, T. Ichikawa, H. Suzuki, Organometallics 26 (2007) 6329;
(g) D.J. Evans, C.J. Pickett, Chem. Soc. Rev. 32 (2003) 268;
(h) Z. Li, Y. Ohki, T. Tatsumi, J. Am. Chem. Soc. 127 (2005) 8950;
(i) J.C. Fontecilla-Camps, Nature 373 (1995) 580.
[4] (a) A.C. da Silva, H. Piotrowski, P. Mayer, K. Polborn, K. Severin, Eur. J. Inorg. Chem. (2001) 685;
(b) L. Quebatte, R. Scopelliti, K. Severin, Angew. Chem., Int. Ed. 43 (2004) 1520.
[5] (a) A.C. da Silv, H. Piotrowski, P. Mayer, K. Polborn, K. Severin, J. Chem. Soc., Dalton Trans. (2000) 2960;
(b) K. Severin, Chem. Eur. J. 8 (2002) 1515;
(c) L. Quebatte, R. Scopelliti, K. Severin, Eur. J. Inorg. Chem. (2006) 231.
[6] S.W. Hunt, X. Wang, M.G. Richmond, J. Chem. Crystallogr. (2009), in press.
[7] C. White, A. Yates, P.M. Maitlis, Inorg. Synth. 29 (1990) 228.
[8] S.P. Schmidt, W.C. Trogler, F. Basolo, Inorg. Synth. 28 (1990) 161.
[9] R.S. Threlkel, J.E. Bercaw, J. Organomet. Chem. 136 (1977) 1.
[10] D.F. Shriver, The Manipulation of Air-Sensitive Compounds, McGraw-Hill, New York, 1969.
[11] APEX2 Version 2.14, Bruker Advanced Analytical X-ray Systems Inc., Copyright 2007, Madison, WI.
[12] SHELXTL Version 6.14, Bruker Advanced Analytical X-ray Systems Inc., Copyright 2003, Madison, WI.
[13] PLATON – A Multipurpose Crystallographic Tool, Utrecht University, Utrecht, The Netherlands, A.L. Spek, 2006.
[14] M.F. Ryan, D.E. Richardson, D.L. Lichtenberger, N.E. Gruhn, Organometallics 13 (1994) 1190.
[15] (a) R. Hoffmann, W.H. Lipscomb, J. Chem. Phys. 36 (1962) 2179;
(b) R. Hoffmann, J. Chem. Phys. 39 (1963) 1397.
[16] C. Mealli, D.M. Proserpio, J. Chem. Ed. 67 (1990) 399.
[17] E.G. Fidalgo, L. Plasseraud, H. Stoeckli-Evans, G. Süss-Fink, Inorg. Chem. Commun. 4 (2001) 308.
[18] (a) F. Zingales, M. Graziani, F. Faraone, U. Belluco, Inorg. Chim. Acta 1 (1967) 17;
(b) M.F. Farona, K.L. Kraus, Inorg. Chem. 7 (1970) 1700;
(c) J.D. Atwood, T.L. Brown, J. Am. Chem. Soc. 97 (1975) 3380.
[19] (a) For reports describing the utility of *fac*-$ClRe(CO)_3(MeCN)_2$ as a starting material in ligand substitution reactions, see: M. Harmjanz, I.M. Piglosiewicz, B.L. Scott, C.L. Burns, Inorg. Chem. 43 (2004) 642;
(b) G. Pereiras-Gabián, E.M. Vázquez-López, U. Abram, Z. Anorg. Allg. Chem. 630 (2004) 1665;
(c) J. Granifo, Polyhedron 18 (1999) 1061.
[20] (a) For kinetic studies related to CO loss and the facile coordination of external ligands by the unsaturated species "$ClRe(CO)_4$", see: D.A. Brown, R.T. Sane, J. Chem. Soc. A (1971) 2088;
(b) M.J. Blandamer, J. Burgess, S.J. Cartwright, M. Dupree, J. Chem. Soc., Dalton Trans. (1976) 1158.
[21] (a) P.M. Treichel, J.P. Williams, J. Organomet. Chem. 135 (1977) 39;
(b) M.M. Glezen, A.J. Lees, J. Am. Chem. Soc. 110 (1988) 3892.
[22] A.C. da Silva, H. Piotrowski, P. Mayer, K. Polborn, K. Severin, J. Chem. Soc., Dalton Trans. (2000) 2960.
[23] As of the CSD Version 5.30, November 2008.
[24] (a) J.-M. Zhuang, R.J. Batchelor, F.W.B. Einstein, R.H. Jones, R. Hader, D. Sutton, Organometallics 9 (1990) 2723;
(b) J.C. Jeffery, P.A. Jelliss, L.H. Rees, F.G.A. Stone, Organometallics 17 (1998) 2258;
(c) K. Arashiba, Y. Tanabe, Y. Ishii, Chem. Lett. 36 (2007) 622.
[25] R.H. Summerville, R. Hoffmann, J. Am. Chem. Soc. 101 (1979) 3821.
[26] A.G. Orpen, L. Brammer, F.H. Allen, O. Kennard, D.G. Watson, R. Taylor, J. Chem. Soc., Dalton Trans. (1989) S1.
[27] (a) F. Chérioux, C.M. Thomas, B. Therrien, G. Süss-Fink, Chem. Eur. J. 8 (2002) 4377;
(b) F. Chérioux, B. Therrien, G. Süss-Fink, Eur. J. Inorg. Chem. (2003) 1043.
[28] (a) For reports on the synthesis and structural details of $[Cp^*Ir(\mu\text{-}SR)_3IrCp^*]^+$ and $[(OC)_3Re(\mu\text{-}SR)_3Re(CO)_3]^-$ derivatives, see: F. Takagi, H. Seino, Y. Mizobe,

M. Hidai, Can. J. Chem. 79 (2001) 632;
(b) Z. Tang, Y. Nomura, Y. Ishii, Y. Mizobe, H. Hidai, Inorg. Chim. Acta 267 (1998) 73;
(c) F. Takagi, H. Seino, M. Hidai, Y. Mizobe, J. Chem. Soc., Dalton Trans. (2002) 3603;
(d) R. Mattes, H. Weber, J. Organomet. Chem. 178 (1979) 191;
(e) S.E. Nefedov, A.A. Pasynskii, I.L. Eremenko, G.A. Papoyan, L.I. Rubinshtein, A.I. Yanovsky, Y.T. Struchkov, Russ. J. Inorg. Chem. 38 (1993) 76;
(f) M.J. Calhorda, M.A.A.F.de C.T. Carrondo, A.R. Dias, V. Félix, A.M. Galvão, M.H. Garcia, P.M. Matias, M.J. Villa de Brito, J. Organomet. Chem. 453 (1993) 231.

[29] (a) The unequivocal identity of the quoted reaction products was also verified by their independent synthesis, using standard methodology. The *in situ* generated phosphine-substituted Ir and Re compounds exhibited NMR (^{1}H and ^{31}P) and IR (in the case of the rhenium products) spectral data identical with the data obtained from the reaction between **3** and added ligand. For pertinent literature references, see: E.W. Abel, G. Wilkinson, J. Chem. Soc. (1959) 1501;
(b) M. Freni, D. Giusto, P. Romiti, J. Inorg. Nucl. Chem. 33 (1971) 4093;
(c) J.W. Kang, K. Moseley, P.M. Maitlis, J. Am. Chem. Soc. 91 (1969) 5970.

[30] (a) H. Shen, S.A. Bott, M.G. Richmond, Organometallics 14 (1995) 4625;
(b) W.H. Watson, G. Wu, M.G. Richmond, Organometallics 25 (2006) 930;
(c) W.H. Watson, B. Poola, M.G. Richmond, J. Organomet. Chem. 691 (2006) 5579;
(d) S.G. Bott, H. Shen, S.-H. Huang, M.G. Richmond, J. Organomet. Chem. 693 (2008) 2327.

[31] W.H. Watson, S. Kandala, M.G. Richmond, J. Chem. Crystallogr. 36 (2006) 71.

[32] (a) For reactivity examples and spectroscopic data on related $[Cp^{*}IrCl(P\text{-}P)]^{+}$ derivatives, see: J.R. Berenguer, M. Bernechea, J. Forniés, J. Gómez, E. Lalinde, Organometallics 21 (2002) 2314;
(b) H. Brunner, I. Grau, M. Zabel, Organometallics 23 (2004) 3788.

[33] Electrochemical reversibility was determined via the ususal methods, see: A.J. Bard, L.R. Faulkner, Electrochemical Methods, Wiley, New York, 1980.

[34] For a report on related M_2L_6 species displaying similar orbital properties, see: D.M. Hoffman, R. Hoffmann, C.R. Fisel, J. Am. Chem. Soc. 104 (1982) 3858.

[35] F. Chérioux, B. Therrien, S. Sadki, C. Comminges, G. Süss-Fink, J. Organomet. Chem. 690 (2005) 2365.

Polyhedron 28 (2009) 2301–2305

Contents lists available at ScienceDirect

Polyhedron

journal homepage: www.elsevier.com/locate/poly

Increasing the antibacterial activity of gallium(III) against *Pseudomonas aeruginosa* upon coordination to pyridine-derived thiosemicarbazones

Jeferson G. da Silva [a], Lucas S. Azzolini [a], Solange M.S.V. Wardell [b], James L. Wardell [a], Heloisa Beraldo [a,*]

[a] Departamento de Química, Universidade Federal de Minas Gerais, Av. Antonio Carlos 6627, Pampulha, 31270-901 Belo Horizonte, MG, Brazil
[b] Departamento de Síntese Orgânica, Farmanguinhos – Fiocruz, Instituto de Tecnologia em Fármacos, Far-Manguinhos, FIOCRUZ, CEP 21041-250 Rio de Janeiro, RJ, Brazil

ARTICLE INFO

Article history:
Received 3 November 2008
Accepted 15 April 2009
Available online 24 April 2009

Keywords:
Thiosemicarbazones
Gallium(III) complexes
Antibacterial
Pseudomonas aeruginosa

ABSTRACT

Reaction of *N*(4)-phenyl-2-formylpyridine thiosemicarbazone (H2Fo4Ph), *N*(4)-phenyl-2-acetylpyridine thiosemicarbazone (H2Ac4Ph) and *N*(4)-phenyl-2-benzoylpyridine thiosemicarbazone (H2Bz4Ph) with gallium nitrate gave $[Ga(H2Fo4Ph)_2](NO_3)_3$ (**1**), $[Ga(2Ac4Ph)_2]NO_3$ (**2**) and $[Ga(2Bz4Ph)_2]NO_3$ (**3**). In all complexes coordination of the thiosemicarbazone via the N_{py}–N–S chelating system occurs. In **1** the thiosemicarbazone acts as a neutral ligand while in **2** and **3** the ligand is anionic. Upon slow diffusion of **2** in DMSO $[Ga(2Ac4Ph)_2]NO_3{\cdot}DMSO$ (**2a**) was formed. The crystal structure of **2a** was determined. Upon coordination the antibacterial activity of both gallium and thiosemicarbazones against *Pseudomonas aeruginosa* significantly increases.

© 2009 Elsevier Ltd. All rights reserved.

1. Introduction

Indiscriminate antibiotic use both in humans and animals results in the emergence of resistance to several drugs, as in the case of clinical isolates of the bacterium *Pseudomonas aeruginosa* and other microorganisms [1,2]. New agents are needed because conventional antibiotics generally work poorly in chronic infections. A key factor accounting for this is that the infecting organisms live in biofilms, surface-associated bacterial communities encased in a polymeric matrix. Physiological changes inherent to biofilm growth make bacteria resistant to killing by the immune system and antibiotics [2].

Iron metabolism is a major vulnerability for infecting bacteria. In fact, in almost all pathogens, Fe is essential for growth and the functioning of key enzymes, and is required in various metabolic and DNA-synthetic pathways. Free Fe levels are extremely low *in vivo* due to multiple host defenses that sequester Fe, and this is a potent restriction to both acute and chronic infection [2]. The chemical behavior of gallium(III) is close to that of iron(III), in terms of its electric charge, ion diameter, and coordination number. Many biological systems are unable to distinguish gallium(III) from iron(III) [2,3]. Ga can disrupt Fe-dependent processes because, unlike iron(III), gallium(III) cannot be reduced, and sequential oxidation and reduction are critical for many of Fe's biological functions [2]. The literature reports the use of Ga as a strategy to disrupt bacterial Fe metabolism in *P. aeruginosa*. Ga was able to inhibit *P. aeruginosa* growth and prevent biofilm formation, and showed bactericidal activity [2].

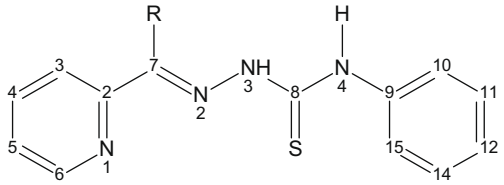
Coordination of gallium(III) to organic ligands could improve the antimicrobial action of Ga by increasing its lipophilicity and bioavailability [4]. In addition, by the use of appropriate ligands, metal–ligand synergism could occur.

Thiosemicarbazones and their metal complexes present wide pharmacological versatility and their applications as antitumoral, antiviral and antimicrobial agents have been extensively investigated [5]. Although, thiosemicarbazones are well known for their ability to form complexes with iron(II) and iron(III), the literature reports few works on their complexes with gallium(III) [6,7].

In previous works we demonstrated that coordination to copper(II) could be a strategy for antimicrobial dose reduction of *N*(4)-tolyl- thiosemicarbazones derived from 2-formylpyridine, 2-acetylpyridine and 2-benzoylpyridine [8,9]. In this work we investigated the effect of coordination to gallium(III) on the antibacterial activity of *N*(4)-phenyl-2-formylpyridine thiosemicarbazone (H2Fo4Ph), *N*(4)-phenyl-2-acetylpyridine thiosemicarbazone (H2Ac4Ph) and *N*(4)-phenyl-2-benzoylpyridine thiosemicarbazone (H2Bz4Ph) (see Fig. 1) against the *gram*-negative bacilli *P. aeruginosa*. Since Ga proved to exhibit antibacterial activity against *P. aeruginosa* [2], the effect of coordination with thiosemicarbazones on the antimicrobial activity of Ga has been evaluated as well. To our knowledge this is the first investigation on the antibacterial activity of Ga complexes with thiosemicarbazones.

* Corresponding author. Tel.: +55 31 3409 5740; fax: +55 31 3409 5700.
E-mail address: hberaldo@ufmg.br (H. Beraldo).

0277-5387/$ - see front matter © 2009 Elsevier Ltd. All rights reserved.
doi:10.1016/j.poly.2009.04.022



R = H (in H2Fo4Ph), CH_3 (in H2Ac4Ph) or Ph (in H2Bz4Ph)

Fig. 1. Generic representation for *N*(4)-phenyl-2-pyridine-derived thiosemicarbazones.

2. Experimental

2.1. Materials and measurements

All common chemicals were purchased from Aldrich and used without further purification. The thiosemicarbazones were prepared according to standard procedures [10].

Partial elemental analyses were performed on a Perkin Elmer CHN 2400 analyzer. An YSI model 31 conductivity bridge was employed for molar conductivity measurements. Infrared spectra were recorded on a Perkin Elmer FT-IR Spectrum GX spectrometer using nujol mulls between CsI plates. NMR spectra were obtained with a Bruker DPX-200 Avance (200 MHz) spectrometer using DMSO-d_6 as the solvent and TMS as internal reference.

2.2. Synthesis of gallium(III) complexes with N(4)-phenyl-2-formylpyridine thiosemicarbazone, N(4)-phenyl-2-acetylpyridine thiosemicarbazone and N(4)-phenyl-2-benzoylpyridine thiosemicarbazone

The gallium(III) complexes were obtained by refluxing, for 3 h, an ethanol solution (25 mL) of the desired thiosemicarbazone (2 mmol) with gallium nitrate in 2:1 ligand-to-metal molar ratio. The resulting solids were filtered off then washed with ethanol followed by diethyl ether, and dried *in vacuo*.

2.2.1. Bis[N(4)-phenyl-2-formylpyridinethiosemicarbazone]-gallium(III) nitrate [Ga(H2Fo4Ph)$_2$](NO$_3$)$_3$ (**1**)

Yellow solid. *Anal.* Calc. for $C_{26}H_{24}GaN_{11}O_9S_2$: C, 40.64; H, 3.15; N, 20.05. Found: C, 40.98; H, 3.21; N, 20.25%. FW: 768.39 g mol^{-1}. IR (CsI/nujol, cm^{-1}): ν(C=N) 1608, ν(C=S) 760, ν(NO$_3$) 1421, 1320, ρ(py) 613, ν(Ga–N$_{azometh.}$) 441, ν(Ga–S) 320, ν(Ga–N$_{py}$) 232. ^{1}H RMN [200 MHz, DMSO-d_6, δ (ppm)] main signals: 12.52 [s, 1H, N(3)H]; 10.47 [s, 1H, N(4)H]; 8.82 [d, 1H, H(6)]; 8.55 [d, 1H, H(3)]; 8.38 [t, 1H, H(4)]; 8.24 [s, 1H, H(7)]; 7.82 [t, 1H, H(5)]. ^{13}C RMN [200 MHz, DMSO-d_6, δ (ppm)] main signals: 176.7 [C(8)=S]; 148.4 [C(2)]; 144.7 [C(6)]; 143.1 [C(4)]; 138.5 [C(9)]; 135.6 [C(7)=N]; 125.7 [C(5)]; 124.3 [C(3)]. Λ_M = 190.94 Ω^{-1} cm^2 mol^{-1} in DMF. Yield 69%.

2.2.2. Bis[N(4)-phenyl-2-acetylpyridinethiosemicarbazonato]-gallium(III) nitrate [Ga(2Ac4Ph)$_2$]NO$_3$ (**2**)

Yellow solid. *Anal.* Calc. for $C_{28}H_{26}GaN_9O_3S_2$: C, 50.16; H, 3.91; N, 18.80. Found: C, 50.13; H, 3.75; N, 18.50%. FW: 670.42 g mol^{-1}. IR (CsI/nujol, cm^{-1}): ν(C=N) 1600, ν(C=S) 764, ν(NO$_3$) 1424, 1332, ρ(py) 621, ν(Ga–N$_{azometh.}$) 443, 438, ν(Ga–S) 343, 339, ν(Ga–N$_{py}$) 216. ^{1}H RMN [200 MHz, DMSO-d_6, δ (ppm)] main signals: 10.25 [s, 1H, N(4)H]; 8.36 [d, 1H, H(6)]; 8.11 [d, 1H, H(3)]; 8.30 [dt, 1H, H(4)]; 8.11 [d, 1H, H(3)] 7.68 [t, 1H, H(5)]; 2.95 [s, 3H, H(15)]. ^{13}C RMN [200 MHz, DMSO-d_6, δ (ppm)] main signals: 171.5 [C(8)=S]; 151.1 [C(2)]; 145.1 [C(6)]; 144.6 [C(7)=N]; 142.8 [C(4)]; 142.4 [C(3)]; 139.5 [C(9)]; 128.3 [C(5)]; 125.2 [C(3)]. Λ_M = 75.57 Ω^{-1} cm^2 mol^{-1} in DMF. Yield 78%.

2.2.3. Bis[N(4)-phenyl-2-benzoylpyridinethiosemicarbazonato]-gallium(III) nitrate [Ga(2Bz4Ph)$_2$]NO$_3$ (**3**)

Orange solid. *Anal.* Calc. for $C_{38}H_{30}GaN_9O_3S_2$: C, 57.44; H, 3.81; N, 15.87. Found: C, 57.48; H, 3.84; N, 16.12%. FW: 794.56 g mol^{-1}. IR (CsI/nujol, cm^{-1}): ν(C=N) 1597, ν(C=S) 760, ν(NO$_3$) 1423, 1331, ρ(py) 616, ν(Ga–N$_{azometh.}$) 437, 432, ν(Ga–S) 344, 337, ν(Ga–N$_{py}$) 205. ^{1}H RMN [200 MHz, DMSO-d_6, δ (ppm)] main signals: 10.43 [s, 1H, N(4)H]; 8.34 [d, 1H, H(6)]; 8.25 [t, 1H, H(4)]; 7.71 [d, 1H, H(3)]; 7.57 [d, 1H, H(5)] 7.68 [t, 1H, H(5)]; 2.95 [s, 3H, H(15)]. ^{13}C RMN [200 MHz, DMSO-d_6, δ (ppm)] main signals: 172.3 [C(8)=S]; 149.1 [C(2)]; 145.2 [C(6)]; 144.7 [C(7)=N]; 142.7 [C(4)]; 142.4 [C(3)]; 139.2 [C(9)]; 130.7 [C(5)]; 126.2 [C(3)]. Λ_M = 50.78 Ω^{-1} cm^2 mol^{-1} in DMF. Yield 73%.

As shown by crystal structure determinations (see Section 3.3) upon dissolution of complex **2** in DMSO conversion to bis[*N*(4)-phenyl-2-acetylpyridine thiosemicarbazonato]gallium(III) nitrate DMSO solvate, [Ga(2Ac4Ph)$_2$]NO$_3$·DMSO (**2a**) occurred.

2.3. Crystallography

Data were obtained at 120 K with Mo Kα radiation by means of the Enraf Nonius KappaCCD area detector diffractometer of the EPSRC crystallographic service, based at the University of Southampton. Data collection was carried out under the control of the program COLLECT [11] and data reduction and unit cell refinement

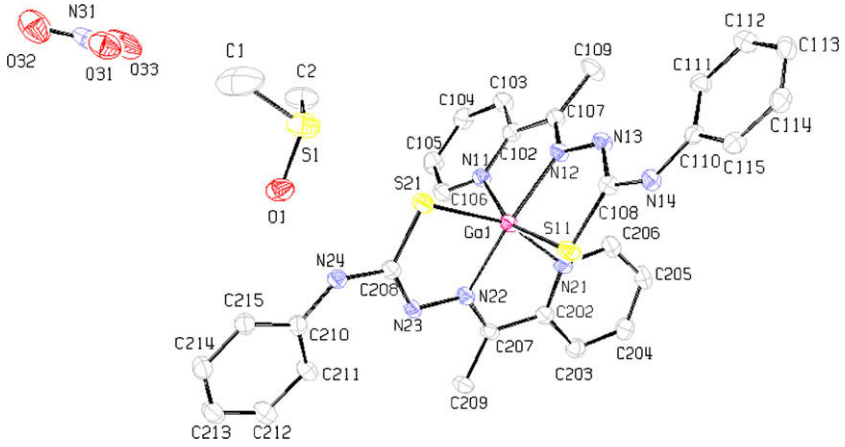


Fig. 2. Atom arrangement and atom numbering scheme for molecule of [Ga(2Ac4Ph)$_2$]NO$_3$·DMSO (**2a**). For purposes of clarity, the hydrogen atoms have been omitted. Probability ellipsoids are drawn at the 50% level. Hydrogens on nitrogens are drawn as spheres of arbitrary radii.

were achieved with the COLLECT [11] and DENZO programs [12]. The program ORTEP-3 for Windows [13] was used in the preparation of Fig. 2 and SHELXL-97 [14] and PLATON [15] in the calculation of molecular geometry. The structure was solved by direct methods using SHELXS-97 [16] and fully refined by means of the program SHELXL-97 [14]. Difference map peaks provided positions for the hydrogen atoms of the NH groups for which the coordinates, along with isotropic displacement parameters, were fully refined. All other hydrogen atoms were placed initially in calculated positions. Crystal data and structure refinement details are listed in Table 1.

2.4. Antibacterial activity

Antibacterial activity was evaluated by minimum inhibitory concentration (MIC) using the macro dilution test [17–20]. *P. aeruginosa* (ATCC 27853) stored in Brain Heart Infusion (BHI) broth was subcultured for testing in the same medium and grown at 37 °C. Then the bacterial cells were suspended, according to the McFarland protocol in saline solution [19], to produce a suspension of about 10^5 CFU mL^{-1} (colony-forming units per mL). Serial dilutions of the test compounds, previously dissolved in dimethyl sulfoxide (DMSO), were prepared in test tubes to final concentrations of 512, 256, 128, 64, 32, 16, 8, 4, 2, and 1 μg mL^{-1}; 100 μL of a 24-h-old-inoculum was added to each tube. The MIC, defined as the lowest concentration of the test compound which inhibits the visible growth after 20 h, was determined visually after incubation for 20 h at 37 °C. Tests using tetracycline hydrochloride and DMSO as controls were carried out in parallel. All tests were performed in triplicate with full agreement between results.

3. Results and discussion

Microanalyses and molar conductivity data suggest the formation of $[Ga(H2Fo4Ph)_2](NO_3)_3$ (**1**), $[Ga(2Ac4Ph)_2]NO_3$ (**2**) and $[Ga(2Bz4Ph)_2]NO_3$ (**3**). In complex **1** the thiosemicarbazone acts as a neutral ligand while in **2** and **3** it is attached to the metal centre in the anionic form.

Table 1
Crystal data and structure refinement for $[Ga(2Ac4Ph)_2]NO_3$·DMSO (**2a**).

Identification code	**2a**
Empirical formula	C_{30} H_{32} Ga N_9 O_4 S_3
Formula weight	748.55
Temperature	120(2) K
Wavelength	0.71073 Å
Crystal system	orthorhombic
Space group	Pbac
Unit cell dimensions	a = 15.4610(2) Å, α = 90° b = 20.7393(2) Å, β = 90° c = 20.1822(2) Å, δ = 90°
Volume	6471.43(12) $Å^3$
Z	8
Density (calculated)	1.537 Mg/m^3
Absorption coefficient	1.096 mm^{-1}
F(0 0 0)	3088
Crystal size	0.08 × 0.08 × 0.05 mm
θ Range for data collection	2.99°–27.54°
Index ranges	$-20 \leqslant h \leqslant 20$; $-25 \leqslant k \leqslant 26$; $-26 \leqslant l \leqslant 26$
Reflections collected	95 045
Independent reflections	7431 [R_{int} = 0.0652]
Reflections observed (>2σ)	6010
Data Completeness	0.996
Absorption correction	none
Refinement method	full-matrix least-squares on F^2
Data/restraints/parameters	7431/4/432
Goodness-of-fit on F^2	1.066
Final R indices [$I > 2\sigma(I)$]	R_1 = 0.0628, wR_2 = 0.1515
R indices (all data)	R_1 = 0.0815, wR_2 = 0.1663
Largest diff. in peak and hole	3.235 and −1.250 e $Å^{-3}$

3.1. Infrared Spectra

The vibrations attributed to ν(C=N) at 1600–1588 cm^{-1} in the spectra of the free thiosemicarbazones shift to 1608–1597 cm^{-1} in the spectra of the complexes, in agreement with coordination via the azomethine nitrogen [8–10,21].

The ν(C=S) absorption is observed at 774 cm^{-1} in the spectrum of H2Fo4Ph. This absorption shifts to 760 cm^{-1} in the spectrum of **1**, according to coordination of a thione sulfur. In the spectra of H2Ac4Ph and H2Bz4Ph the ν(C=S) absorption is found at 801 and 798 cm^{-1}, respectively, and it shifts to 764 and 760 cm^{-1} in the spectra of **2** and **3**, in agreement with coordination of a thiolate sulfur [21,22].

The in-plane deformation mode of the pyridine ring at 599–583 cm^{-1} in the spectra of the uncomplexed thiosemicarbazones shifts to 621–613 cm^{-1} in complexes **1–3**, suggesting coordination of the hetero-aromatic nitrogen [21–23].

Absorptions at 1424–1421 cm^{-1} and 1331–1320 cm^{-1} were attributed to vibrations of the nitrate group as counter-ion in the spectra of all complexes [24]. New absorptions at 443–432 cm^{-1}, 344–337 cm^{-1} and 240–205 cm^{-1} were attributed to ν(Ga–N), ν(Ga–S) and ν(Ga–N_{py}), respectively [6].

Hence, the infrared data suggest coordination of the thiosemicarbazones via the N_{py}–N–S chelating system in the all cases.

3.2. NMR Spectra

The ^{1}H and ^{13}C NMR assignments for the gallium(III) complexes in DMSO-d_6 are reported in Section 2.2. The ^{1}H resonances were attributed based on chemical shifts, multiplicities and coupling constants. The carbon type (C, CH) was determined by using DEPT135 experiments. The assignments of the protonated carbons were made by 2D heteronuclear-correlated experiments (HMQC) using delay values which correspond to ^1J(C, H).

In the ^{1}H NMR spectra of the free thiosemicarbazones the signals of N(3)–H were found in the δ 13.14–10.63 range. Only one signal of N(3)–H at δ 12.07 and at δ 10.67 was found for H2Fo4Ph and H2Ac4Ph, respectively, which is consistent with hydrogen bonding to the oxygen of DMSO and with the presence of the thiosemicarbazones in the *E* configuration [10]. The lower frequency signal for the acetyl derivative is probably due to the gamma gauche effect of the methyl group attached to C7 which makes N(3)–H less acidic [25]. Two signals at δ 10.63 and δ 13.14 were observed for H2Bz4Ph, suggesting the presence of the *E* and *Z* configurational isomers, respectively. In the first N(3)–H is hydrogen-bonded to DMSO and in the second N(3)–H is hydrogen-bonded to the hetero-aromatic nitrogen [10]. Again the gamma gauche effect of the phenyl group makes N(3)–H of the phenyl derivative less acidic in comparison to that of the formyl thiosemicarbazone [25].

In the ^{1}H NMR spectra of the gallium(III) complexes only one signal was observed for each hydrogen. In **1** the signal for N(3)–H at δ 12.52 indicates that the thiosemicarbazone remains protonated after coordination. The absence of the signal for N(3)–H in the spectra of **2** and **3** is in agreement with the presence of an anionic thiosemicarbazone in both cases. Upon coordination with formation of complexes **1–3** the pyridine hydrogens undergo significant shifts, indicating complexation through the hetero-aromatic nitrogen [10,21].

In the ^{13}C NMR spectrum the signals of C(7)=N and the pyridine carbons shift significantly upon coordination and formation of **1–3**, in accordance with complexation through the imine nitrogen and the hetero-aromatic nitrogen. The C(8)=S signal undergoes a small shift after formation of **1**, in accordance with the coordination of a thione sulfur. Upon formation of complexes **2** and **3** significant shifts were observed for the signals of C(8)=S, in accordance with coordination of a thiolate sulfur. The NMR data suggest tridentate

Table 2
Selected Bond lengths (Å) and angles (°) for $[Ga(2Ac4Ph)_2]NO_3{\cdot}DMSO$ (**2a**).

Bond lengths			
Ga(1)–N(11)	2.122(3)	Ga(1)–N(21)	2.127(3)
Ga(1)–N(12)	2.058(3)	Ga(1)–N(22)	2.048(3)
Ga(1)–S(11)	2.377(1)	Ga(1)–S(21)	2.377(1)
S(11)–C(108)	1.743(4)	S(21)–C(208)	1.747(4)
N(13)–C(108)	1.327(5)	N(23)–C(208)	1.322(5)
N(12)–N(13)	1.371(4)	N(22)–N(23)	1.373(4)
N(12)–C(107)	1.300(5)	N(22)–C(207)	1.291(5)
C(102)–C(107)	1.473(5)	C(202)–C(207)	1.476(5)
N(11)–C(102)	1.355(5)	N(21)–C(202)	1.343(5)
Angles			
N(11)–C(102)–C(107)	115.4(3)	N(21)–C(202)–C(207)	115.2(4)
N(12)–C(107)–C(102)	115.1(4)	N(22)–C(207)–C(202)	115.1(3)
C(107)–N(12)–N(13)	118.3(3)	C(207)–N(22)–N(23)	118.3(3)
C(108)–N(13)–N(12)	113.4(3)	C(208)–N(23)–N(22)	113.6(3)
N(13)–C(108)–S(11)	126.6(3)	N(23)–C(208)–S(21)	126.7(3)
C(108)–S(11)–Ga(1)	95.0(1)	C(208)–S(21)–Ga(1)	94.4(1)
C(102)–N(11)–Ga(1)	113.7(3)	C(202)–N(21)–Ga(1)	113.9(3)
N(13)–N(12)–Ga(1)	123.1(2)	N(23)–N(22)–Ga(1)	122.9(2)
C(107)–N(12)–Ga(1)	118.2(3)	C(207)–N(22)–Ga(1)	118.8(3)
N(12)–Ga(1)–N(11)	77.2(1)	N(22)–Ga(1)–N(21)	76.9(1)
N(11)–Ga(1)–S(11)	158.6(1)	N(21)–Ga(1)–S(21)	158.81(9)
N(12)–Ga(1)–S(11)	81.81(9)	N(22)–Ga(1)–S(21)	82.3(1)
N(12)–Ga(1)–S(21)	108.0(1)	N(22)–Ga(1)–S(11)	103.7(1)
N(11)–Ga(1)–S(21)	93.4(1)	N(21)–Ga(1)–S(11)	91.6(1)
N(12)–Ga(1)–N(21)	92.4(1)	N(22)–Ga(1)–N(11)	96.3(1)
N(11)–Ga(1)–N(21)	85.5(1)	N(22)–Ga(1)–N(12)	168.0(1)
S(11)–Ga(1)–S(21)	96.75(4)		

coordination through the N_{py}–N–S system in all cases. Hence, in complexes **1–3** the thiosemicarbazone adopts the *E* configuration [10,21,22].

3.3. X-ray Crystallography

Attempts to crystallize complex **2** from DMSO solution led to the isolation of $[Ga(2Ac4Ph)_2]NO_3{\cdot}DMSO$ (**2a**). The atom arrangements and atom numbering scheme for molecule **2a** are shown in Fig. 2. Selected geometric parameters are listed in Table 2.

In **2a** the gallium(III) cation is in a distorted octahedral environment. The sulfur atoms are in a *cis* arrangement, with a S(11)–Ga–S(21) angle of 96.75(4)° and *trans* to the pyridinyl nitrogen atoms. Distortion from an ideal octahedral arrangement mainly arises from the small N–Ga–N and N–Ga–S chelate bite angles, which are very close to 80° (see Table 2).

The free thiosemicarbazone crystallizes in the *EE* conformation [26]. A twisting of approximately 180° in the N3–C8 bond of the thiosemicarbazone to match the steric requirements of tridentate coordination was evidenced. Therefore, in complex **2a** the ligand adopts the *EZ* conformation. Hence some angles undergo significant changes on complexation. The C8–N3–N2 angle goes from 118.89° in H2Ac4Ph [26] to 113.4(3)° and 113.6(3)° in **2a**; N3–C8–S1 goes from 119.68° in H2Ac4Ph [26] to 126.6(3)° and 126.7(3)° in **2a**.

Table 3
Hydrogen bonding parameters (Å,°) for $[Ga(2Ac4Ph)_2]NO_3{\cdot}DMSO$ (**2a**).

D–H···A	D–H	H···A	D···A	D–H···A
N(14)–H(14)–O(1)^{i}	0.896(14)	2.005(15)	2.873(4)	163(4)
N(24)–H(24)–O(1)	0.900(14)	2.051(16)	2.931(5)	166(4)

Symmetry operations: *i*: 1/2 + *x*, 1/2-*y*, -*z*.

There is a slight shortening of the bond distance between Ga and the imine nitrogen (2.058(3) and 2.048(3) Å) compared to the distance between Ga and the hetero-aromatic nitrogen (2.122(3) and 2.127(3) Å). Similar feature was observed in the gallium complex with 2-acetylpyridine *N*(4)-dimethylthiosemicarbazone, with Ga–N_{imine} bond distances (2.033(2) and 2.038(2) Å) longer than the Ga–N_{py} bond distances (2.131(2) and 2.114(2) Å) [6]. By contrast, in the case of the complex with acetylpyrazine *N*,*N*-dimethylthiosemicarbazone the Ga–N_{py} bond distances (2.036(2) and 2.037(2) Å) are shorter than the Ga–N_{imine} bond distances (2.141(2) and 2.164(2)Å) [7].

The expected lengthening of the C8–S1 bonds from 1.677 Å in H2Ac4Ph [26] to 1.743(4) and 1.747(4) Å in **2a**, and shortening of the N3–C8 bonds from 1.358 Å in H2Ac4Ph [26] to 1.327(5) and 1.322(5) Å in **2a** were observed. Therefore the C8–S1 bond changes from a double to a predominantly single bond whereas N3–C8 acquires some double bond character.

Of interest, DMSO solvate is hydrogen bonded via oxygen to N(14)–H(14)^{i} and N(24)–H(24). Details are listed in Table 3 (see Fig. 3) [symmetry code: *i*: 1/2 + *x*, 1/2 − y, −z].

3.4. Antibacterial activity

Table 4 lists the minimum inhibitory concentration (MIC) against the growth of *P. aeruginosa* (ATCC 27853) for the thiosemicarbazones and their gallium(III) complexes, together with values obtained for tetracycline hydrochloride as positive control, and for gallium nitrate.

The values of MIC were 736 μM (H2Fo4Ph), 269 μM (H2Ac4Ph) and 111 μM (H2Bz4Ph), indicating that the C7-substituent affects the antibacterial activity. Gallium nitrate showed a poor effect in the studied strain. Upon coordination to gallium(III) a significant increase in the activities of both Ga (up to fifteen fold) and the thiosemicarbazones (up to ten-fold) was observed, with values of MIC

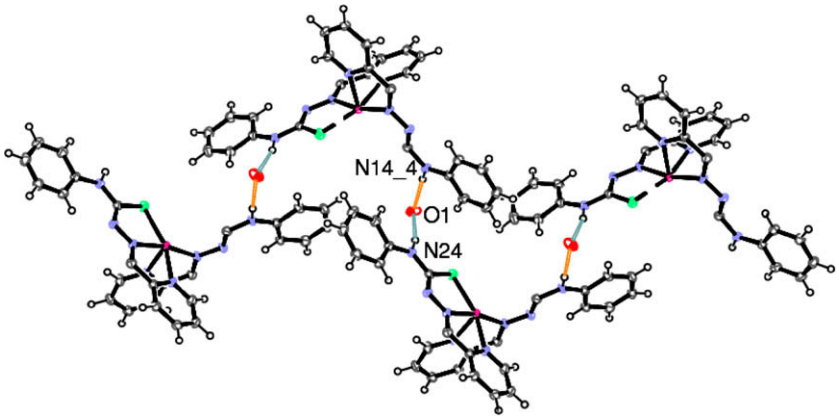


Fig. 3. Hydrogen bonding of $[Ga(2Ac4Ph)_2]NO_3{\cdot}DMSO$ (**2a**) formed by solvent molecule and N–Hs. For purposes of clarity, anion and methyl carbons of cation were omitted.

Table 4
Minimum Inhibitory Concentration (MIC) against *P. aeruginosa* ATCC 27853 for *N*(4)-phenyl-2-formylpyridine thiosemicarbazone (H2Fo4Ph), *N*(4)-phenyl-2-acethylpyridine thiosemicarbazone (H2Ac4Ph) and *N*(4)-phenyl-2-benzoylpyridine thiosemicarbazone (H2Bz4Ph), their gallium(III) complexes, gallium nitrate and tetracycline hydrochloride.

Compounds	MIC (μmol L^{-1})
H2Fo4Ph	736
$[Ga(H2Fo4Ph)_2](NO_3)_3$ (**1**)	75
H2Ac4Ph	269
$[Ga(2Ac4Ph)_2]NO_3$ (**2**)	42
H2Bz4Ph	111
$[Ga(2Bz4Ph)_2]NO_3$ (**3**)	47
Gallium nitrate	667
Tetracycline hydrochloride	24

in the 75–42 μM range for complexes **1–3**, which were of the same order of magnitude as the value of MIC determined for tetracycline.

As already mentioned, Ga has been used as a strategy to disrupt bacterial Fe metabolism in *P. aeruginosa* [2]. In the present case the activity of Ga was substantially enhanced upon coordination to the thiosemicarbazones. Therefore the thiosemicarbazones were probably able to successfully deliver the metal to the bacterial cell. Changes of lipophilicity upon complexation could explain such effect. Metal-ligand synergism could also occur particularly in the cases of complexes **2** and **3**.

4. Conclusions

The foregoing results suggest that coordination of Ga to thiosemicarbazones could be an interesting strategy for enhancing both metal and ligand activities and that thiosemicarbazones could function as vehicles for increasing Ga bioavailability. Moreover, since thiosemicarbazones are in general poorly active against *gram*-negative bacteria [5], coordination to Ga could be an efficient strategy to broaden their spectrum of antibacterial action.

Supplementary data

CCDC 701075 contains the supplementary crystallographic data for **2a**. These data can be obtained free of charge via http://www.ccdc.cam.ac.uk/conts/retrieving.html, or from the Cambridge Crystallographic Data Centre, 12 Union Road, Cambridge CB2 1EZ, UK; fax: (+44) 1223-336-033; or e-mail: deposit@ccdc.cam.ac.uk.

Acknowledgements

This work was supported by CNPq and Instituto do Milênio-Inovação e Desenvolvimento de Novos Fármacos e Medicamentos (IMINOFAR, Proc. CNPq 420015/05-1).

References

[1] A. Valentin, R. Le Guennec, E. Rodriguez, J. Reynes, M. Mallie, J.M. Bastide, Antimicrob. Agents Chemother. 40 (1996) 1342.
[2] Y. Kaneko, M. Thoendel, O. Olakanmi, B.E. Britigan, P.K. Singh, J. Clin. Invest. 117 (2007) 877.
[3] L. Benstein, Pharmacol. Rev. 50 (1998) 665. and references therein.
[4] P. Collery, B. Keppler, C. Madoulet, B. Desoize, Crit. Rev. Onc. Hemat. 42 (2002) 283.
[5] H. Beraldo, D. Gambino, Mini-Rev. Med. Chem. 4 (2004) 159.
[6] V.B. Arion, M.A. Jakupec, M. Galanski, P. Unfried, B.K. Keppler, J. Inorg. Biochem. 91 (2002) 298.
[7] C.R. Kowol, R. Berger, R. Eichinger, A. Roller, M.A. Jakupec, P.P. Schmidt, V.B. Arion, B.K. Keppler, J. Med. Chem. 50 (2007) 1254.
[8] I.C. Mendes, J.P. Moreira, A.S. Mangrich, S.P. Balena, B.L. Rodrigues, H. Beraldo, Polyhedron 26 (2007) 3263.
[9] I.C. Mendes, J.P. Moreira, N.L. Speziali, A.S. Mangrich, J.A. Takahashi, H. Beraldo, J. Braz. Chem. Soc. 17 (2006) 1571.
[10] A.P. Rebolledo, G.M. de Lima, L.N. Gambi, N.L. Speziali, D.F. Maia, C.B. Pinheiro, J.D. Ardisson, M.E. Cortes, H. Beraldo, Appl. Organomet. Chem. 17 (2003) 945.
[11] R.W.W. Hooft, COLLECT, Nonius BV, Delft, The Netherlands, 1998.
[12] C.W. Carter Jr., R.M. Sweet (Eds.), Methods in Enzymology, Macromolecular Crystallography Part A, Academic Press, New York, 1997. p. 307.
[13] L.J. Farrugia, J. Appl. Cryst. 32 (1999) 837.
[14] G.M. Sheldrick, SHELXL-97. Program for Crystal Structure Refinement, University of Göttingen, Germany, 1997.
[15] A.L. Spek, J. Appl. Cryst. 36 (2003) 7.
[16] G.M. Sheldrick, SHELXS-97. Program for the Solution of Crystal Structures, University of Göttingen, Germany, 1997.
[17] E.J.L. Lana, F. Carazza, J.A.J. Takahashi, Agric. Food Chem. 54 (2006) 2053.
[18] J.C.P. Resende, M.A. Resende, Mycoses 42 (1999) 641.
[19] National Committee for Clinical Laboratory Standards. Methods for Dilution Antimicrobial Susceptibility Tests for Bacteria That Grow Aerobically; Approved Standard – Sixth Edition. NCCLS Document M7-A6 (ISBN 1-56238-486-4). NCCLS, 940 West Valley Road, Suite 1400, Wayne, Pennsylvania 19087-1898, USA, 2003.
[20] Clinical and Laboratory Standards Institute. Performance Standards for Antimicrobial Susceptibility Testing; Fifteenth Informational Supplement. CLSI document M100-S15 (ISBN 1-56238-556-9). Clinical and Laboratory Standards Institute, 940 West Valley Road, Suite 1400,Wayne, Pennsylvania 19087-1898, USA, 2005.
[21] A.P. Rebolledo, M. Vieites, D. Gambino, O.E. Piro, E.E. Castellano, C.L. Zani, E.M. Souza-Fagundes, L.R. Teixeira, A.A. Batista, H. Beraldo, J. Inorg. Biochem. 99 (2005) 698.
[22] I.C. Mendes, J.P. Moreira, J.D. Ardisson, R.G. Santos, P.R.O. Silva, I. Garcia, A. Castiñeiras, H. Beraldo, Eur. J. Med. Chem. 43 (2008) 1454.
[23] D.X. West, J.S. Ives, J. Krejci, M.M. Salberg, T.L. Zumbahlen, G.A. Bain, A.E. Liberta, Polyhedron 14 (1995) 2189.
[24] K. Nakamoto, Infrared and Raman Spectra of Inorganic and Coordination Compounds, forth ed., Wiley, New York, 1986.
[25] H. Beraldo, W.F. Nacif, D.X. West, Spectrochim. Acta, Part A 57 (2001) 1847.
[26] E. Bernejo, A. Castiñeiras, R. Domingues, C. Maichle-Moessmer, J. Straehle, D.X. West, Z. Anorg. Allg. Chem. 625 (1999) 961.

Polyhedron 28 (2009) 2307–2312

Contents lists available at ScienceDirect

Polyhedron

journal homepage: www.elsevier.com/locate/poly

Synthesis, properties and crystal structures of volatile β-ketoiminate Pd complexes, precursors for palladium chemical vapor deposition

G.I. Zharkova, P.A. Stabnikov *, I.A. Baidina, A.I. Smolentsev, S.V. Tkachev

Nikolaev Institute of Inorganic Chemistry, Siberian Division of Russian Academy of Sciences, Pr. Lavrentiev 3, Novosibirsk 630090, Russia

ARTICLE INFO

Article history:
Received 14 November 2008
Accepted 27 February 2009
Available online 17 March 2009

Keywords:
β-Ketoimine
Palladium
Crystal structure
Thermolysis
Volatility

ABSTRACT

The β-aminovinylketone ligands $CH_3C(NH_2)CHC(O)CH_3$ (**1**) and $CH_3C(NHCH_3)CHC(O)CH_3$ (**2**) were synthesized from 2,4-pentandione by amination with a water solution of the appropriate amine in toluene at room temperature. The reactions of **1** and **2** with the $PdCl_2$ salt in amine medium gave the volatile chelate metal complexes $Pd[CH_3C(NH)CHC(O)CH_3]_2$ (**3**) and $Pd[CH_3C(NCH_3)CHC(O)CH_3]_2$ (**4**). The obtained compounds were identified by elemental analysis, ^1H and ^{13}C NMR, IR-spectroscopy and were characterized by TGA and a single-crystal X-ray diffraction study. In compounds **3** and **4**, the Pd atom has a square coordination environment Pd O_2N_2.

© 2009 Elsevier Ltd. All rights reserved.

1. Introduction

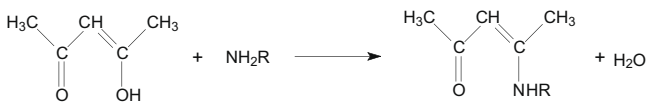
An important practical implementation of volatile metal compounds concerns the preparation of metal films by the chemical vapor deposition method (MO CVD) [1–3]. Volatile molecular β-diketonates and β-ketoiminates of palladium(II) are the most adequate precursors for the preparation of palladium films [4,5]. β-Ketoimine is an analogue of β-diketone with one oxygen atom substituted by an NH- or NR-group. Metal β-diketonates and β-ketoiminates, having the same substituents in the ligand, possess similar volatility [6]. The first offer, however, an advantage over the latter because of the lower oxygen content in the molecule which decreases the substrate oxidation process upon the preparation of a metal film. Besides, replacing two oxygen atoms in the chelate with nitrogen improves the thermal stability of the complexes compared to the O–O-chelate analogues [7], and this renders them the most suitable for application in CVD. Metal ketoiminates, however, have been studied and applied to a lesser degree than metal diketonates because of the hampered availability of β-ketoimines compared to β-diketones. Upon the synthesis of metal complexes with these ligands, ketoimines need to be prevented from undergoing saponification. Unlike Pd(II) β-diketonates, which are rather well studied and reported in [8–11], Pd complexes based on enamineketones are less studied. Structural studies of fluorinated Pd(II) β-ketoiminates are known in the literature [5,7,12]. The synthesis of the palladium β-ketoiminate, $Pd(ki)_2$, is given in Ref. [13]. A crystallographic study performed in Ref. [14] suggests that this compound is isostructural to the complexes $Cu(ki)_2$ and $Ni(ki)_2$. The complete solution of the crystal structure of $Pd(ki)_2$ is unavailable in the literature and in Structure Databases to date.

This paper reports the synthesis, properties and structures of two β-aminovinylketones: 4-amino-3-penten-2-one – $CH_3C(NH_2)$-$CHC(O)CH_3$ (Hki) (**1**) and 4-methylamino-3-penten-2-one – $CH_3C(NHCH_3)CHC(O)CH_3$ (Hmki) (**2**), as well as of two volatile Pd(II) complexes with these ligands: $Pd[CH_3C(NH)CHC(O)CH_3]_2$, $Pd(ki)_2$ (**3**) and a new complex $Pd[CH_3C(NCH_3)CHC(O)CH_3]_2$, $Pd(mki)_2$ (**4**). The crystal structures of compounds **1**–**4** are studied for the first time.

2. Results and discussion

2.1. Synthesis and structural characterization of *1* and *2*

There are many techniques for the synthesis of β-aminovinylketones, including the condensation of β-diketones with amines [15–18]. To prepare the ligands, we have used a simple method [19]. The ligands 4-amino-3-penten-2-on (**1**) and 4-methylamino-3-penten-2-on (**2**) were obtained from 2,4-pentandione (Hacac) following the scheme:



where R = H (**1**), CH_3 (**2**).

* Corresponding author. Tel.: +7 3833309556; fax: +7 3833309489.
E-mail address: stabnik@che.nsk.su (P.A. Stabnikov).

0277-5387/$ - see front matter © 2009 Elsevier Ltd. All rights reserved.
doi:10.1016/j.poly.2009.02.043

A mixture of acetylacetone (Hacac) with a concentrated aqueous amine solution, and toluene in a 1:1:1 volume ratio was used. This mixture was stirred in a closed vessel for 12 h. The enaminoketones, isolated from toluene, were purified by sublimation in a vacuum. This procedure allowed us to obtain the (N,O)-ligands **1** and **2** in a high yield. Chemical analysis confirmed the presence of one nitrogen atom in each of the ligands. With the general similarity of the IR spectra of enaminoketones, the spectrum of **1** shows a strong wide band over the 3334 cm^{-1} range, which is associated with valence ν(N–H) vibrations [20].

The synthesized β-aminovinylketones, 4-amino-3-penten-2-one (**1**) and 4-methylamino-3-penten-2-one (**2**), may be represented as three tautomeric structures, similar to that we discussed earlier for 2,2,6,6-tetramethyl-3-amino-4-hepten-5-one [21] with an oxygen in the ketone or enol form. The ^1H and ^{13}C NMR spectra of solutions of **1** and **2** in $CDCl_3$ unambiguously reveal that the given compounds, as all other enaminoketones, exist in the solution predominantly in the carbonyl form [16]. Also we assume the formation of an intramolecular hydrogen bond between the proton of the RNH-group and the oxygen atom (Fig. 1). In the ^1H NMR spectra, the broad signal near 10 ppm corresponds to this hydrogen atom of the (RN···H···O–) moiety.

An X-ray structure study revealed that the ligand Hki (**1**) has a molecular structure, which consists of isolated molecules (Fig. 2a). In the structure, there are two crystallographically independent molecules of approximately the same geometry. Not taking into account the hydrogen atoms of the methyl groups, the molecules are planar to within 0.02 Å and the angle between the normals to the planes of two independent molecules is 50.8°. The average length of the O–C bonds (1.256 Å) is less than that of the N–C bonds (1.326 Å) by 0.07 Å. The difference in the corresponding values of C–C_γ is no more than 0.03 Å, and the average value of the terminal C–C_{Methyl} bonds is 1.501 Å. The deviations of the bond angles on the carbon atoms from 120° are no more than 3.6°. The molecules are linked by N–H···O bonds with N···O and H···O equal to 2.86 and 1.95 Å, respectively.

The compound Hmki (**2**) crystallizes as colorless transparent plates, which tend to twin, resulting in the high *R*-value. Structure **2** is of the molecular type and is built up of ligand hydrogen-bonded molecules (Fig. 2b). The molecule is practically planar, since all non-hydrogen atoms are located in the same plane to within 0.013 Å. The O–C bond length (1.247 Å) is shorter than that of N–C (1.337 Å) by 0.09 Å; the corresponding C–C bonds are 1.396 Å and the C(1)–C(3)–C(4) bond angle is 124.5°. The terminal C–C and N–C bonds are 1.512 and 1.454 Å, respectively. In the structure, the molecules are hydrogen-bonded into planar centrosymmetric dimers, which form the (1 2 1) layers with d = 3.44 Å, and the N–H···O bonds are 2.99 (2.28) Å.

2.2. Synthesis and structure characterization of $Pd[CH_3C(NH)CHC(O)CH_3]_2$ (**3**) and $Pd[CH_3C(NCH_3)CHC(O)CH_3]_2$ (**4**)

For the synthesis of the β-ketoiminate complexes $Pd(ki)_2$ (**3**) and $Pd(mki)_2$ (**4**), we have used a new procedure based on the interaction between the $PdCl_2$ salt and the ligand HL (where HL is Hki (**1**) or Hmki (**2**)) in the corresponding amine medium, according to the following scheme:

$$PdCl_2 \xrightarrow{\text{excess } NH_2R\ (solv)} [Pd(NH_2R)_4]Cl_2 \xrightarrow{+2HL,\ pH\ 8-9} PdL_2,$$

where R = H or CH_3.

The reaction occurs via an intermediate stage, with the formation of the colorless $[Pd(NH_2R)_4]Cl_2$ complex, which subsequently reacts with the ligand. The intermediate complex is stable only in alkaline media and is readily converted into the sparingly soluble *trans*-$[Pd(NH_2R)_2Cl_2]$ at the lower pH of the solution. Therefore for the chelate of the palladium complex to be obtained in high yield, the reaction conditions should rule out the formation of the sparingly soluble $[Pd(NH_2R)_2Cl_2]$, whose precipitation withdraws the palladium from the reaction and lowers the yield of the target product.

The IR spectrum of complex **3** shows a band for the N–H vibrations at 3284 cm^{-1} [20]. The lack of this band in the spectrum of compound **4** confirms indirectly the presence of the N–CH_3 bond in this compound. This data and elemental analyses results confirm the successful preparation of the palladium complexes **3** and **4**.

The structure of the complex $Pd(ki)_2$ (**3**) is of the molecular type and comprises the isolated complexes, shown in Fig. 3. There are two crystallographically independent complexes with similar structures. The Pd(1) complex lies on a two-fold axis, and the Pd(2) complex has 2 2 2 symmetry. The O and N atoms are statistically located in the same position with 0.5 occupancy that is, the complexes are simultaneously *cis*- and *trans*-isomers. The Pd–O (N)

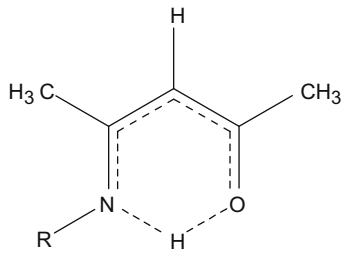


Fig. 1. Supposed tautomeric form of enaminoketones in solution (R = H, CH_3).

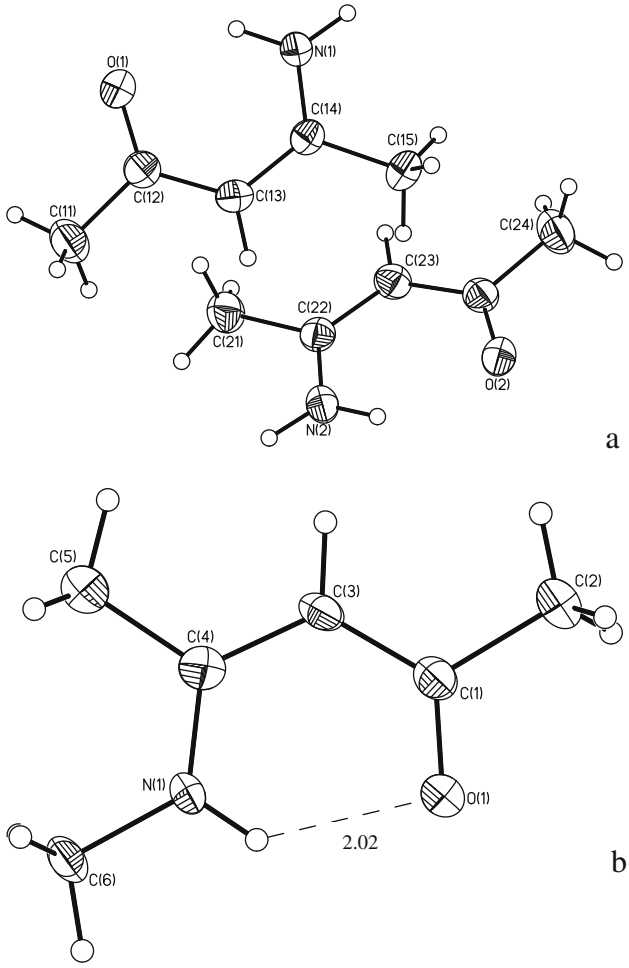


Fig. 2. ORTEP drawing of enaminoketone molecules: a – **1**, b – **2**.

bond lengths are similar, within the measuring error, with an average value of 1.984 Å, and the average value of the chelate O–Pd–N angles is 92.8°. In metal cycles, the average values of the O (N)–C, C–C_γ and C–C_{Methyl} bonds are 1.305, 1.389 and1.506 Å, respectively. The angles of bending of the cycles along the O (N)···O (N) line are no more than 1.9°, hence the molecules in the complexes, except the terminal hydrogen atoms, are practically planar, to within 0.073 Å. The angle between the normals to the planes of the two independent palladium complexes is 58.8°. Fig. 5a shows the general packing of the molecules along the *z*-axis. In the structure, the molecules of the complexes are packed into one-dimensional associates (ribbons), as if located on the 6_3 pseudoaxes with Pd···Pd distances of 5.67 and 5.74 Å. Such ribbons form the (0 1 1) layers with $d = 7.52$ Å. The intermolecular interactions between the layers are determined by the H···H contacts over the 2.37–2.63 Å range.

In the Pd(mki)$_2$ complex (**4**), the Pd atom has a square coordination of two oxygen and two nitrogen atoms (Fig. 4). The difference between the Pd–O (1.972 Å) and Pd–N (2.041 Å) bond lengths is 0.07 Å and the chelate O–Pd–N angle is 92.4°. In the metal cycles, the N–C and O–C bonds are practically equal, and the C–C and C–C_γ bonds differ by 0.07 Å. The molecule of the complex, not taking into account the hydrogen atoms, is planar to within 0.03 Å, and the angle of bending of the metal cycles along the O···N line is 4.6°. The C–C_{Methyl} and N–C_{Methyl} separations are 1.51 and 1.47 Å, respectively. Fig. 5b shows the molecule packing in the crystal along the *a*-axis. All the complexes are identically oriented and packed along the *x*-axis with a minimal Pd···Pd distance of 6.077 Å (the "*a*" parameter). We can also isolate the $(\bar{1}\,\bar{1}\,1)$ layers in the complexes with the interlayer distance $d = 3.59$ Å. The hydrogen atoms of the methyl groups alone emerge at the outer surfaces of the layers, and the molecule skeleton of the non-hydrogen atoms lies fully in the layer plane. The shortest contacts to the methyl groups of the neighboring complexes, which complete the Pd coordination, are Pd···C (H) 4.10 (2.92) Å.

*2.3. Thermogravimetric study (TG) of Pd[$CH_3C(NH)CHC(O)CH_3$]$_2$ (**3**) and Pd[$CH_3C(NCH_3)CHC(O)CH_3$]$_2$ (**4**)*

The TG study was performed under a helium flow up to 350 °C. To perform a comparative analysis of the volatility and thermal stability of the Pd(ki)$_2$ (**3**) and Pd(mki)$_2$ (**4**) complexes and the comparison with the (O,O)-chelate analogue, the TG curves for the Pd complex with acetylacetone, Pd(acac)$_2$, obtained under the same conditions, are given in Fig. 6. Among the considered palladium(II) complexes, complex **4** is the most volatile. A loss of the mass of this complex through sublimation is only ~90% owing to partial decomposition. This is also true for the other ketoiminate complex **3**, with a significant thermal stability but lesser volatility as compared to its O,O chelate analogue, Pd(acac)$_2$. The thermal

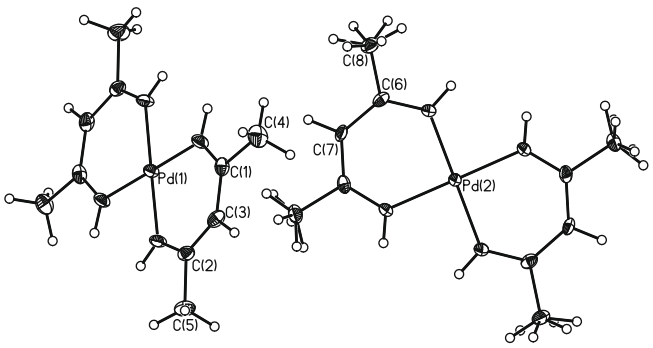


Fig. 3. The structure of the palladium(II) β-ketoiminate complexes in compound **3**.

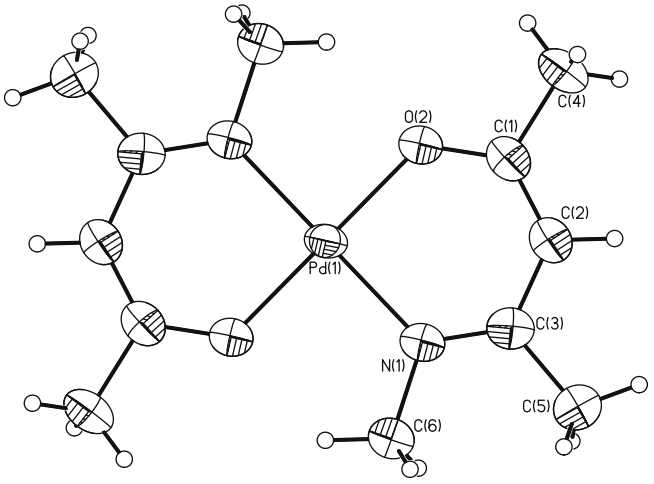


Fig. 4. ORTEP drawing of the palladium (II) β-methylketoiminate (**4**).

analysis of the Pd ketoiminates showed that replacing the NH group with the NCH_3 group in the chelate significantly increased the volatility of Pd(mki)$_2$ (**4**).

3. Concluding remarks

The ligands $CH_3C(NH_2)CHC(O)CH_3$ (**1**) and $CH_3C(NHCH_3)CHC(O)CH_3$ (**2**) were synthesized from 2,4-pentandione by amination with a water solution of the appropriate amine in toluene at room temperature. Pd[$CH_3C(NH)CHC(O)CH_3$]$_2$ (**3**) and Pd[$CH_3C(NCH_3)CHC(O)CH_3$]$_2$ (**4**) have been synthesized in water amine solutions. The obtained compounds have been identified by elemental analysis, ^{1}H and ^{13}C NMR, IR-spectroscopy, and were characterized by TGA and a single-crystal X-ray diffraction study. A crystallographic analysis has shown that metal complexes (**3**) are isostructural to β-ketoiminate complexes of Cu(II) and Ni(II).

4. Experimental

4.1. General considerations

Hacac (2,4-pentandione) of 99% purity (Merck) was used without pretreatment. Commercially available $PdCl_2$, aqueous ammonia and methylamine of adequate purity were used. The synthesis of Hki (**1**) and Hmki (**2**) was carried out according to Ref. [19].

Ligands **1** and **2**, and complexes Pd(ki)$_2$ (**3**), Pd(mki)$_2$ (**4**) and Pd(acac)$_2$ have been purified by vacuum sublimation in a gradient tube oven ($P \sim 10^{-2}$ Torr, $T = 50$–250 °C). Elemental analysis was performed with a Carlo-Erba 1106 (Italy) device. Infrared spectra were measured in KBr pellets, with the use of a Scimitar FTS2000 spectrometer. NMR spectra were recorded on a Bruker MSL300 spectrometer; chemical shifts were referenced to the proton impurity of the NMR solvent (^{1}H) or to the NMR solvent (^{13}C). The thermal analysis was performed in an Ar flow at a heating rate of 10 K/min (~1–3 mg samples) using a NETZSCH TG 209 F1 device.

X-ray intensity data were collected on a Bruker X8Apex CCD diffractometer at 150 K using standard techniques (ω- and φ-scans of narrow frames) and corrected for absorption effects (SADABS). The structures were solved by direct methods and refined by full-matrix least-squares on F^2 using the SHELX97 program set (Bruker AXS Inc., 2004) [22]. Crystallographic data and details of single-crystal diffraction experiments for compounds **1**–**4** are given in Table 1. All non-hydrogen atoms were refined anisotropically. The hydrogen atoms of CH_3 groups were calculated by geometrical methods. Selected bond lengths and angles are in Tables 2 and 3.

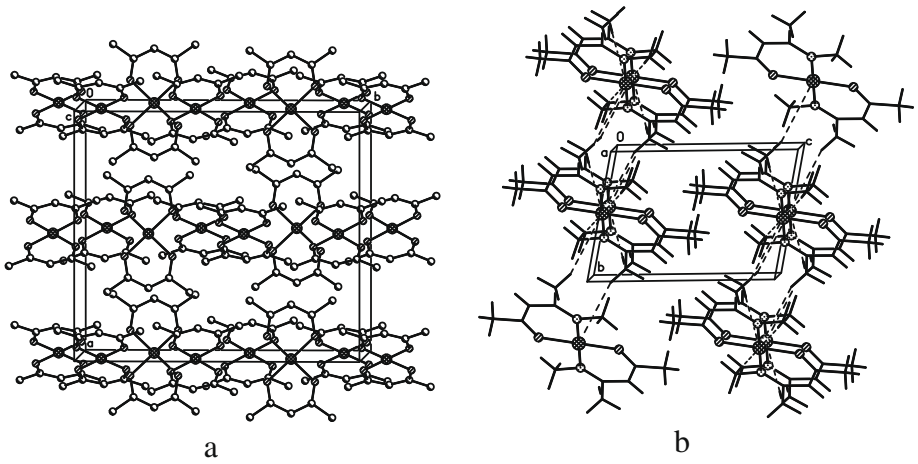


Fig. 5. Projection of the crystal packing of compounds **3** – (a) and **4** – (b).

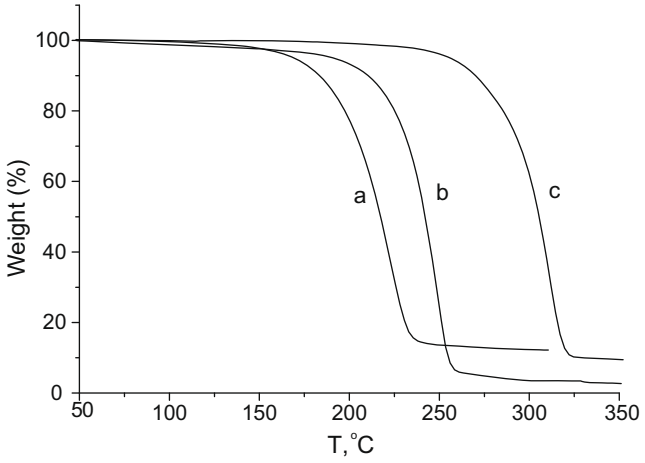


Fig. 6. TGA profiles for a – $Pd(mki)_2$ (**4**); b – $Pd(acac)_2$; c – $Pd(ki)_2$ (**3**).

4.2. Synthesis of $CH_3C(NH_2)CHC(O)CH_3$ ligand (*1*)

About 10 ml of acetylacetone, 10 ml of toluene, and 10 ml of 25% aqueous solution of ammonia were cooled to 5 °C and were mixed. The reaction mixture was kept in the closed vessel at room temperature for 12 h. Then the aqueous layer was isolated and washed with 25 ml toluene twice. The toluene solutions were combined, evaporated to 20 ml, and cooled to 0–5 °C. The white ketoimine precipitate, resulting from the cooled solution, was filtered off. A small amount of ketoimine was also isolated upon the evaporation. The crude product was separated on a rotary evaporator and recrystallized from heptane after cooling in a refrigerator. White crystals of pure ligand were obtained after sublimation in a vacuum (T = 150 °C, $P = 10^{-2}$ Torr). Yield ~ 60%. *Anal.* Calc. for C_5H_9NO: C, 60.58; H, 9.15; N, 14.13. Found: C, 60.39; H, 9.53; N, 14.45%.

^1H and ^{13}C NMR spectra in $CDCl_3$ solution indicate that the compound exists in the ketone form, giving a structure with an intramolecular hydrogen bond, shown in Fig. 1. ^1H NMR (300 MHz, 25 °C, ppm): 1.89 [s, $(CH_3)CN$]; 2.02 [s, $(CH_3)CO$]; 4.97 (s, CH); 5.0 (br, s, HNH); 9.7 (br, s, HNH–O). ^{13}C NMR{^1H} (75.4 MHz, 25 °C, ppm): 22.8 [s, $(CH_3)CN$]; 29.8 [s, $(CH_3)CO$]; 96.4 (s, CH); 160.7 (s, C–N); 196.9 (s, C=O).

IR (cm^{-1}): 3334 (vs), 3174 (vs), 2972 (s), 2907 (m), 2922 (m), 1619 (vs), 1537 (vs), 1414 (s), 1356 (s), 1290 (vs), 1196 (s), 1106 (m), 1019 (m), 989 (m), 931 (w), 896 (m), 749 (m), 629 (s), 554 (vw), 483 (vw), 396 (w). M.p.: 43–44 °C.

4.3. Synthesis of $CH_3C(HNCH_3)CHC(O)CH_3$ ligand (*2*)

Ligand **2** was prepared according to the above described procedure from acetylacetone (10 ml), toluene (10 ml) and a saturated 25% aqueous solution of methylamine (10 ml). The reagents were cooled to 5 °C and poured together with stirring. Then all the procedures for ligand **1** were followed. The crude product was separated on a rotary evaporator and recrystallized from heptane after cooling in a refrigerator. White crystals were obtained after sublimation in a vacuum (T = 120 °C, $P = 10^{-2}$ Torr). Yield ~ 80%. *Anal.* Calc. for $C_6H_{11}NO$: C, 63.68; H, 9.80; N, 12.38. Found: C, 63.46; H, 9.51; N, 12.61%.

^1H and ^{13}C NMR spectra in $CDCl_3$ solution indicate that the compound exists in the ketone form, giving a structure with intramolecular hydrogen bonds as shown in Fig. 1. ^1H NMR (300 MHz, 25 °C, ppm): 1.89 [s, $(CH_3)CN$]; 1.94 [s, $(CH_3)CO$]; 2.92 [d, $(CH_3)NH$, $^4J_{HH}$ = 5.3]; 4.91 (s, CH); 10.65 [br, s, $(CH_3)NH$–O]. ^{13}C NMR{^1H} (75.4 MHz, 25 °C, ppm): 19.2 [s, $(CH_3)CN$]; 29.3 [s, $(CH_3)CO$]; 29.9 [s, $(CH_3)N$]; 95.8 (s, CH); 164.0 (s, C–N); 195.1 (s, C=O).

IR (cm^{-1}): 3165 (vw), 3076 (vw), 2995 (vw), 2937 (vw), 1612 (vs), 1569 (vs), 1521 (s), 1461 (m), 1436 (s), 1352 (s), 1293 (vs), 1195 (m), 1071 (s), 1015 (m), 968 (m), 930 (w), 823 (s), 731 (s), 648 (w), 555 (vw), 532 (w), 393 (w). M.p.: 39–40 °C.

4.4. Synthesis of $Pd[CH_3C(NH)CHC(O)CH_3]_2$ (*3*)

A $PdCl_2$ sample (1 g, 5.6 mmol) was placed in an ammonia solution (25 ml of water and 25 ml of concentrated ammonia solution) and heated on a water bath until the salt completely dissolved and a colorless solution was obtained (the pH should be kept at a highly alkaline level). Then, ligand **1** (2.22 g, 22.4 mmol) dissolved in water (20 ml) was added to the solution. The pH of the reaction mixture decreases with the reaction time. The chelate complex $Pd(ki)_2$ (**3**) started to form slowly at pH 8–9, and the reaction was continued for at least 5 h. The precipitate was filtered off, washed with water, dried in air, and dissolved in benzene. The product isolated from benzene was purified by vacuum sublimation (T = 200 °C, $P = 10^{-2}$ Torr). Yield 1.1 g (65%). The $Pd(ki)_2$ complex is a yellow crystalline powder. The compound begins to decompose slowly at 245 °C. *Anal.* Calc. for $C_{10}H_{16}N_2O_2Pd$: C, 39.68; H, 5.33; N, 9.26. Found: C, 39.52; H, 5.18; N, 9.45%.

Table 1
Crystal data and structure refinement for **1**, **2**, **3** and **4**.

Empirical formula	C_5H_9NO (**1**)	$C_5H_{11}NO$ (**2**)	$C_{10}H_{16}N_2O_2Pd$ (**3**)	$C_{12}H_{20}N_2O_2Pd$ (**4**)
Formula weight	99.13	113.16	302.65	330.70
T (K)	293(2)	173(2)	150(2)	206.(2)
Wavelength (Å)	0.71073	0.71073	0.71073	0.71073
Crystal system	monoclinic	triclinic	orthorhombic	triclinic
Space group	$P2_1/c$	$P\bar{1}$	$Ccca$	$P\bar{1}$
Unit cell dimensions				
a (Å)	9.2227(18)	6.203(3)	15.0418(7)	6.077(2)
b (Å)	10.049(2)	6.948(5)	17.1568(7)	6.999(2)
c (Å)	12.911(3)	9.149(4)	13.2223(6)	9.155(4)
α	90	70.78(2)	90	93.730(12)
β (°)	98.22(3)	7231(5)	90	106.336(9)
γ	90	64.38(3)	90	112.576((9)
V (Å^3)	1184.3	329/6(3)	3412.3(3)	338.4(2)
Z	8	1	12	1
$D_{(calc)}$ (g/cm^3)	1.112	1.140	1.767	1.623
Absorption coefficient (mm^{-1})	0.078	0.078	1.614	1.364
F(0 0 0)	4326	124	1824	168
θ range for data collection (°)	2.23–27.14	2.40–2568	2.37–28.29.	2.36–25.68
Reflections collected	8471	2025	12 856	2065
Independent reflections	2614 [R_{int} = 0.0312]	1132 [R_{int} = 0.0218]	2102 [R_{int} = 0.0393]	1146 [R_{int} = 0.0224]
Completeness to θ = 25.00° (%)	99.8	90.3	98.9	89.6
Refinement method	full-matrix least-squares on F^2	full-matrix least-squares on F^2	full-matrix least-squares on F^2	full-matrix least-squares on F^2
Data/restraints/parameters	2614/0/199	11.32/0/77	2102/0/107	11 462/0/82
Goodness-of-fit (GOF) on F^2	1.033	1.726	0.991	1.121
Final R indices [$I > 2\sigma(I)$]	R_1 = 0.0434, wR_2 = 0.1177	R_1 = 0.1016, wR_2 = 0.2884	R_1 = 0.0300, wR_2 = 0.0676	R_1 = 0.0460, wR_2 = 0.1270
R indices (all data)	R_1 = 0.0711, wR_2 = 0.1283	R_1 = 0.1108, wR_2 = 0.2945	R_1 = 0.0842, wR_2 = 0.0757	R_1 = 0.0461, wR_2 = 0.1271

Table 2
Selected bond lengths (Å) and angles (°) for **1** and **2**.

Compound **1**				Compound **2**	
O(1)–C(12)	1.2590(17)	O(1)–C(12)–C(13)	123.15(13)	O(1)–C(1)	1.247(4)
N(1)–C(14)	1.3269(18)	O(1)–C(12)–C(11)	118.42(13)	N(1)–C(4)	1.337(3)
N(2)–C(22)	1.3253(18)	C(13)–C(12)–C(11)	118.43(14)	N(1)–C(6)	1.454(3)
O(2)–C(24)	1.2538(17)	C(14)–C(13)–C(12)	123.73(13)	C(5)–C(4)	1.494(4)
C(11)–C(12)	1.506(2)	N(1)–C(14)–C(13)	122.55(13)	C(4)–C(3)	1.396(4)
C(12)–C(13)	1.4119(19)	N(1)–C(14)–C(15)	116.42(13)	C(2)–C(1)	1.531(4)
C(13)–C(14)	1.3855(19)	C(13)–C(14)–C(15)	121.02(13)	C(3)–C(1)	1.396(4)
C(14)–C(15)	1.4998(18)	N(2)–C(22)–C(23)	122.88(13)	C(4)–N(1)–C(6)	125.3(3)
C(21)–C(22)	1.495(2)	N(2)–C(22)–C(21)	116.74(13)	N(1)–C(4)–C(3)	121.8(3)
C(22)–C(23)	1.3849(19)	C(23)–C(22)–C(21)	120.35(13)	C(4)–C(3)–C(1)	124.5(3)
C(23)–C(24)	1.4108(19)	C(22)–C(23)–C(24)	123.60(13)	O(1)–C(1)–C(3)	123.9(2)
C(24)–C(25)	1.504(2)	O(2)–C(24)–C(23)	123.55(12)	O(1)–C(1)–C(2)	117.4(3)
		O(2)–C(24)–C(25)	118.20(13)		
		C(23)–C(24)–C(25)	118.23(14)		

Table 3
Selected bond lengths (Å) and angles (°) for **3** and **4.**

Compound **3**				Compound **4**	
Pd(1)–O,N(2)	1.982(3)	O,N(2)#1–Pd(1)–O,N(1)	179.44(15)	Pd(1)–O(2)	1.972(5)
Pd(1)–O,N(1)	1.984(3)	O,N(2)–Pd(1)–O,N(1)	92.75(11)	Pd(1)–N(1)	2.041(5)
Pd(2)–O,N(3)	1.987(3)	O,N(3)#4–Pd(2)–O,N(3)	178.5(2)	O(2)–C(1)	1.292(9)
O,N(1)–C(1)	1.298(5)	O,N(3)#3–Pd(2)–O,N(3)	92.79(15)	N(1)–C(3)	1.295(9)
O,N(2)–C(2)	1.312(5)	C(1)–O(1)–Pd(1)	125.3(3)	N(1)–C(6)	1.479(8)
C(1)–C(3)	1.388(6)	C(2)–O(2)–Pd(1)	125.1(3)	C(1)–C(2)	1.345(11)
C(1)–C(4)	1.511(5)	O(1)–C(1)–C(3)	125.2(4)	C(1)–C(4)	1.514(10)
C(2)–C(3)	1.395(6)	O(2)–C(2)–C(3)	124.7(4)	C(3)–C(2)	1.420(10)
C(2)–C(5)	1.496(5)	C(1)–C(3)–C(2)	126.(9)	C(3)–C(5)	1.512(10)
O,N(3)–C(6)	1.305(4)	C(6)–O(3)–Pd(2)	124.9(2)	O(2)–Pd(1)–N(1)	92.4(2)
C(6)–C(7)	1.384(4)	O(3)–C(6)–C(7)	124.7(3)	C(1)–O(2)–Pd(1)	125.1(4)
C(6)–C(8)	1.512(5)	C(6)–C(7)–C(6)#3	127.7(5)	C(3)–N(1)–Pd(1)	124.2(4)
				O(2)–C(1)–C(2)	126.2(6)
				N(1)–C(3)–C(2)	123.5(6)
				C(1)–C(2)–C(3)	128.3(7)

The symmetry operators used for the generation of the equivalent atoms: #1 $-x+1, y, -z+1/2$; #2 $-x, y, -z+1/2$; #3 $x, -y+1/2, -z+1/2$; #4 $-x, -y+1/2, z$.

IR(cm^{-1}): 3284 (vs), 2988 (vw), 2915 (vw), 1597 (vs), 1512 (vs), 1460 (s), 1435 (s), 1377 (vs), 1349 (vs), 1221 (s), 1179 (s), 1023 (m), 934 (s), 792 (m), 761 (m), 710 (vw), 677 (m), 654 (m), 473 (s), 445 (vw).

4.5. Synthesis of $Pd[CH_3C(NCH_3)CHC(O)CH_3]_2$ (**4**)

This complex was prepared according to the above described procedure for complex (**3**) from $PdCl_2$ (1 g, 5.6 mmol) and ligand **2** (2.54 g, 22.4 mmol) in 20 ml water. The yield of the sublimed product was 1.3 g (70%). The $Pd(mki)_2$ complex is a pale yellow crystalline powder. The compound begins to decompose slowly at 195 °C. *Anal.* Calc. for $C_{12}H_{20}N_2O_2Pd$: C, 43.58; H, 6.10; N, 8.47. Found: C, 43.37; H, 6.24; N, 8.24%.

^1H and $^{13}C\{^1H\}$ NMR spectra in $CDCl_3$ indicate that compound **4** exists in solution mainly as one of the two possible isomers, but the second one forms slowly in the solution on standing. ^1H NMR (300 MHz, 25 °C, ppm): 1.89 [s, $(CH_3)CN$]; 1.94 [s, $(CH_3)CO$]; 2.99 [s, $(CH_3)N$]; 4.83 (s, CH). ^{13}C NMR$\{^1H\}$ (75.4 MHz, 25 °C, ppm): 22.3 [s, $(CH_3)CN$]; 24.2 [s, $(CH_3)CO$]; 36.7 [s, $(CH_3)N$]; 99.2 (s, CH); 164,4 (s, C–N); 173.6 (s, C═O).

IR(cm^{-1}): 3356 (vw), 2991 (vw), 2910 (vw), 1591(s), 1573 (s), 1513 (vs), 1459 (s), 1391 (vs), 1273 (m), 1223 (m), 1134 (w), 1021 (m), 1004 (m), 951 (m), 862 (vw), 757 (m), 731 (w), 693 (vw), 653 (vw), 615 (vw), 467 (w), 405 (vw).

Acknowledgement

The authors thank Mrs. Tamara Yudanova for her help in translation of the paper from Russian.

Appendix A. Supplementary material

CCDC 704729-704732 contains the supplementary crystallographic data for **1**–**4**, respectively. These data can be obtained free of charge via http://www.ccdc.cam.ac.uk/conts/retrieving.html, or from the Cambridge Crystallographic Data Centre, 12 Union Road, Cambridge CB2 1EZ, UK; fax: (+44) 1223-336-033; or e-mail: deposit@ ccdc.cam.ac.uk.

References

[1] T.H. Baum, P.B. Comita, Thin Solid Films 218 (1992) 80.
[2] T.T. Kodas, M.J. Hampden-Smith, The Chemistry of Metal CVD, VCH, Weinheim, Germany, 1994.
[3] I.K. Igumenov, J. Physique IV 5 (1995) C5-489.
[4] I.K. Igumenov, G.I. Zharkova, I.A. Baidina, P.A. Stabnikov, P.P. Semyannikov, et al., Electochem. Soc. Proc. (2005–09) (2005) 675.
[5] Yan-Hsiu Liu, Yi-Ching Cheng, Yung-Liang Tung, Yun Chi, Yao-Lun Chen, Chao-Shiuan Liu, Shie-Ming Pengb, Gene-Hsiang Leeb, J. Mater. Chem. 13 (2003) 135.
[6] P.A. Stabnikov, I.A. Baidina, S.V. Sysoev, N.S. Vanina, N.B. Morozova, I.K. Igumenov, J. Struct. Chem. 44 (2003) 1054.
[7] G.I. Zharkova, I.A. Baidina, S.A. Gromilov, I.K. Igumenov, Koord. Khim. 24 (1998) 117.
[8] N.YanaseY. Nakamura, S. Kavaguchi, Inorg. Chem. 19 (1980) 1575.
[9] S. Okeya, Sh. Ooi, K. Matsumoto, Y. Nakamura, Bull. Chem. Soc. Jpn. 54 (1981) 1085.
[10] Y. Otani, Y. Nakamura, S. Kavaguchi, S. Okeya, Bull. Chem. Soc. Jpn. 55 (1982) 1467.
[11] G.I. Zharkova, I.K. Igumenov, N.M. Tyukalevskay, Koord. Khim. 14 (1988) 67.
[12] I.A. Baidina, G.I. Zharkova, N.V. Pervukhina, et al., J. Struct. Chem. 45 (2004) 678.
[13] T.J. McGee, J.L. Walter, Spectrosc. Lett. 11 (1978) 765.
[14] G.E. Gurr, Inorg. Chem. 3 (1964) 614.
[15] S.C. McGeachin, Can. J. Chem. 46 (1968) 1903.
[16] J.V. Greenhill, Chem. Soc. Rev. 6 (1977) 277.
[17] M.E.F. Braibante, H.S. Braibante, L. Missio, A. Andricopulo, Synthesis (1994) 898.
[18] D.V. Baxter, K.G. Caulton, W.-C. Chiang, M.H. Chisholm, V.F. DiStasi, S.G. Dutremez, K. Folting, Polyhedron 20 (2001) 2589.
[19] D.G. Norton, V.E. Haury, et al., Org. Chem. 19 (1954) 1054.
[20] A.J. Gordon, R.A. Ford, The Chemist's Companion, Handbook of Practical Data, Techniques and References, New York, 1972.
[21] P.A. Stabnikov, G.I. Zharkova, I.A. Baidina, S.V. Tkachev, V.V. Krisyuk, I.K. Igumenov, Polyhedron 26 (2007) 4445.
[22] Bruker AXS Inc. (2004). APEX2 (Version 1.08), SAINT (Version 7.03), SADABS (Version 2.11) and SHELXTL (Version 6.12), Bruker Advanced X-ray Solutions, Madison, Wisconsin, USA.

Polyhedron 28 (2009) 2313–2320

Contents lists available at ScienceDirect

Polyhedron

journal homepage: www.elsevier.com/locate/poly

Synthesis and characterization of new bis(diphenylphosphino)aniline ligands and their complexes: X-ray crystal structure of palladium(II) and platinum(II) complexes, and application of palladium(II) complexes as pre-catalysts in Heck and Suzuki cross-coupling reactions

Murat Aydemir [a], Feyyaz Durap [a], Akın Baysal [a,*], Osman Akba [a], Bahattin Gümgüm [a], Saim Özkar [b], Leyla Tatar Yıldırım [c]

[a] Dicle University, Department of Chemistry, TR-21280 Diyarbakır, Turkey
[b] Middle East Technical University, Department of Chemistry, TR-06531 Ankara, Turkey
[c] Hacettepe University, Department of Engineering Physics, Beytepe, TR-06800 Ankara, Turkey

ARTICLE INFO

Article history:
Received 9 March 2009
Accepted 10 April 2009
Available online 4 May 2009

Keywords:
Aminophosphine
Complexes
Crystal structures
Catalysis
Heck reaction
Suzuki coupling

ABSTRACT

Two new bis(diphenylphosphino)isopropylphenylamines, $(PPh_2)_2N\text{-}C_6H_4\text{-}CH(CH_3)_2$, having the isopropyl substituent at the carbon atom 2 (**1**) or 4 (**2**), were prepared by the aminolysis of chlorodiphenylphosphine with isopropyl substituted aniline at the *ortho*- or *para*-position, respectively, under anaerobic conditions. Oxidation of **1** and **2** with either aqueous hydrogen peroxide, elemental sulfur or grey selenium in thf gave the corresponding oxides, sulfides and selenides $(Ph_2P{=}E)_2N\text{-}C_6H_4\text{-}CH(CH_3)_2$, where E = O, S or Se, respectively. The palladium and platinum complexes $[M\{(Ph_2P)_2N\text{-}C_6H_4\text{-}CH(CH_3)_2\}Cl_2]$ (M = Pd, Pt) and the copper complex $[Cu\{(Ph_2P)_2N\text{-}C_6H_4\text{-}CH(CH_3)_2\}_2]PF_6$ were isolated from the reaction of the bis(phosphino)anilines with $MCl_2(cod)$ or $[Cu(CH_3CN)_4]PF_6$, respectively. The new compounds were characterized by NMR, IR spectroscopy and elemental analysis. Furthermore, the solid-state structures of two representative complexes were determined using single crystal X-ray diffraction analysis. The compounds of palladium (**1d**) and platinum (**1e**), both mononuclear complexes, crystallize in the monoclinic $P2_1/c$ space group. In both compounds the metal ion has a distorted square–planar coordination geometry. The structural properties of complexes **1d** and **1e** in the solid state are very similar. The palladium complexes were also tested for their catalytic activities in C–C coupling reactions.

© 2009 Elsevier Ltd. All rights reserved.

1. Introduction

Tertiary phosphines have long been used in the design and synthesis of transition metal complexes with catalytic properties [1–3], especially with late transition metals like nickel, rhodium, ruthenium, palladium and platinum [4] that can be used as highly active catalysts in industrially important reactions such as allylic alkylation [5–8], amination [9–11], the Heck reaction [12–20], Suzuki coupling [21–25], hydroformylation [26–29], and hydrogenation of olefins [30–33]. In particular, palladium complexes containing phosphine ligands serve as highly active catalysts for the straightforward formation of carbon–carbon bonds [34–37]. Compounds containing phosphorus–nitrogen direct bonds have been known for many years and their chemistry has been of considerable interest because of their applications in increasingly diverse fields [38,39]. The applications of chelating bis(phosphino)amine ligands is widespread in organometallic chemistry and in homogeneous catalysis as these ligands can be used for fine tuning the activity and selectivity of the catalyst [40]. A variety of PNP and related diphosphine ligands, specially in combination with Cr(III) compounds, were reported to be very active and efficient catalysts for ethylene tri- and tetramerization [41–44]. Bis(phosphino)amines display their versatility by exhibiting different coordination behavior when the donor–acceptor properties are altered by incorporating a substituent at the ligand backbone [45]. Synthesis and coordination chemistry of bis(phosphino)anilines have also been studied in some detail [46,47]. It has been shown that coordination of bis(phosphino)anilines to transition metal ions occurs mainly via the phosphorus centers due to the low basicity of the amine nitrogen, attributable to the P–N π interaction between the phosphorus d_π and nitrogen p_π orbitals [48].

Herein, we report the synthesis of two new bis(diphenylphosphino)anilines by the aminolysis of chlorodiphenylphosphine with isopropyl substituted aniline at the *ortho*- or *para*-positions and the corresponding oxides, sulfides and selenides as well as their complexes with selected transition metal ions (Cu^+, Pd^{2+} and Pt^{2+}). The

* Corresponding author. Tel.: +90 412 2488550x3175; fax: +90 412 2488039.
E-mail address: akinb@dicle.edu.tr (A. Baysal).

0277-5387/$ - see front matter © 2009 Elsevier Ltd. All rights reserved.
doi:10.1016/j.poly.2009.04.033

compounds were isolated from the reaction mixture by crystallization and fully characterized using elemental analysis, FT-IR, multinuclear NMR spectroscopy. The solid-state structures of two of the products were established by single crystal X-ray diffraction analyses. We also report on the catalytic activities of the palladium(II) complexes as pre-catalysts in the Heck and Suzuki coupling reactions.

2. Results and discussion

2.1. Synthesis and characterization

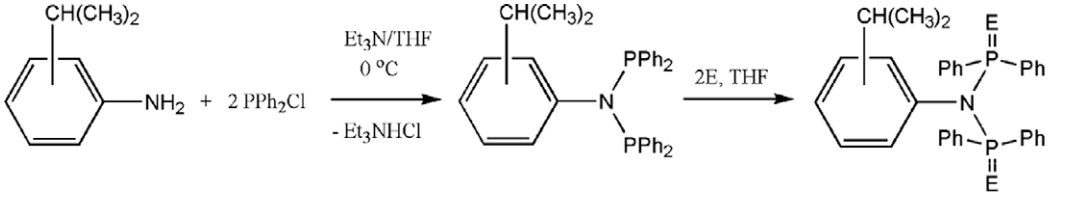
N,*N*-bis(diphenylphosphino)isopropylanilines $(PPh_2)_2N$-C_6H_4-$CH(CH_3)_2$, having the isopropyl substituent at the carbon 2 (**1**) or 4 (**2**) were easily prepared from the reaction of *o*-H_2N-C_6H_4-$CH(CH_3)_2$ or *p*-H_2N-C_6H_4-$CH(CH_3)_2$, respectively, with two equivalents of chlorodiphenylphosphine in the presence of triethylamine in thf solution at 0 °C (Scheme 1). Although the existence of compound **1** has been reported by Killian et al., neither the experimental procedure for the preparation nor characterization data is available [49]. Hence, the synthesis and full characterization of compound **1** will be reported herein for the first time. Compounds **1** and **2** were isolated as white solids in high yields (87% and 85%, respectively) under anaerobic conditions. Attempts to prepare *N*,*N*-bis(diphenylphosphino)-2,6-diisopropylaniline did not succeed, may be due to the steric repulsion between the two isopropyl groups and phenyl rings of the phosphine.

In the ^{1}H NMR spectra, both **1** and **2** show multiplets for the aromatic H-atoms in the regions 6.75–7.53 and 6.58–7.39 ppm, respectively. The CH signal of the isopropyl group is at 2.99 ppm for **1** and 2.76 ppm for **2**. The methyl groups of the isopropyl substituent give doublets at 0.75 and 1.15 ppm for **1** and **2**, respectively. The ^{31}P–{^{1}H} NMR spectra of **1** and **2** show a single resonance at 62.2 and 68.5 ppm, respectively, in line with the values previously observed for similar compounds [50,51]. The ^{13}C NMR spectra of the compounds give four signals for the phenyl carbon atoms, two signals for the isopropyl groups, and six or four signals for the aniline ring in **1** or **2**, respectively.

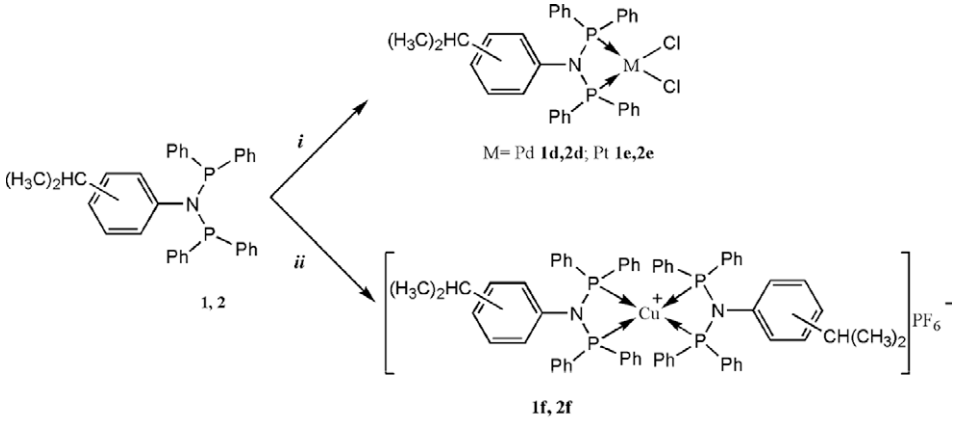
Oxidation of **1** and **2** with aqueous hydrogen peroxide or elemental sulfur or selenium in thf gave the corresponding oxides (**1a**, **2a**), sulfides (**1b**, **2b**), and selenides (**1c**, **2c**), respectively (Scheme 1).

Oxidation of both **1** and **2** using aqueous H_2O_2 was very rapid even at ambient temperature. However, the reaction with elemental sulfur or selenium had to be carried out at elevated temperatures, as expected because elemental sulfur and selenium are weaker oxidizing agents than hydrogen peroxide, especially towards phosphorus atoms with bulky phenyl groups [52–55]. The ^{31}P–{^{1}H} NMR spectra display one singlet for each of **1a** and **2a** (23.9 and 24.2 ppm) and **1b** and **2b** (68.5 and 68.9 ppm), suggesting that the two phosphorus atoms are chemically equivalent in these compounds. The ^{31}P NMR signals of **1c** and **2c** are also singlets, but they are accompanied by selenium satellites at 67.8 ppm ($^1J(^{31}P–^{77}Se) = 787$ Hz) and 67.3 ppm ($^1J(^{31}P–^{77}Se) = 792$ Hz), respectively.

In the reaction of [M(cod)Cl_2] (M = Pd, Pt; cod = 1,5-cyclooctadiene) with one equivalent of **1** or **2** in thf solution, cod is replaced by *N*,*N*-bis(diphenylphosphino)isopropylaniline as a bidentate ligand, yielding the respective [M{$(Ph_2P)_2N$-C_6H_4-$CH(CH_3)_2$}Cl_2] complexes **1d**, **2d**, **1e**, **2e** (M = Pd, Pt, respectively). The reaction of $[Cu(CH_3CN)_4]PF_6$ with two equivalents of **1** or **2** gives the expected complexes [Cu{$(Ph_2P)_2N$-C_6H_4-$CH(CH_3)_2$}$_2$]PF_6 **1f** or **2f**, respectively. Both reactions are summarized in Scheme 2. The ^{31}P–{^{1}H} NMR spectra of **1d** and **2d** exhibit a single resonance at 37.9 and 38.5 ppm, respectively, which are within the range expected for structurally similar complexes [56–58]. The phosphorus reso-



Scheme 1. Syntheses of *N*,*N*-bis(diphenylphosphino)isopropylanilines by the aminolysis reaction of H_2N-C_6H_4-$CH(CH_3)_2$ with Ph_2PCl (**1**: 2-$CH(CH_3)_2$; **2**: 4-$CH(CH_3)_2$) and oxidation of **1** and **2** with aqueous H_2O_2 (**1a**, **2a**), elemental sulfur (**1b**, **2b**) and grey selenium (**1c**, **2c**).



Scheme 2. Reactions of aminophosphines **1** and **2** with [M(cod)Cl_2] (M = Pd, Pt) and $[Cu(CH_3CN)_4]PF_6$ in thf.

Table 1
Crystal data and experimental details of the structural analysis of dichloro{*N*,*N*-bis(diphenylphosphino)-2-isopropyl aniline}palladium(II) **(1d)** and dichloro{*N*,*N*-bis(diphenylphosphino)-2-isopropyl aniline}platinum(II) **(1e)**.

	1d	**1e**
Empirical formula	$[(Ph_2P)_2N\text{-}(C_6H_4)\text{-}2\text{-}CH(CH_3)_2PdCl_2]\cdot(C_2H_5)_2O$	$[(Ph_2P)_2N\text{-}(C_6H_4)\text{-}2\text{-}CH(CH_3)_2PtCl_2]\cdot(C_2H_5)_2O$
Formula weight	754.97	843.63
Crystal system	monoclinic	monoclinic
Space group	$P2_1/c$	$P2_1/c$
Unit cell dimensions		
a (Å)	12.1266(10)	12.170(2)
b (Å)	14.028(2)	14.167(5)
c (Å)	21.617(2)	21.552(2)
β (°)	101.744(7)	101.610(11)
Volume (Å^3)	3600.3(7)	3639.7(15)
Z	4	4
D_{calc} (Mg/m^3)	1.393	1.539
Absorption coefficient (mm^{-1})	0.782	4.119
F(0 0 0)	1552	1680
h, k, l ranges	$-14 \rightarrow 15$, $-17 \rightarrow 0$, $-26 \rightarrow 0$	$-14 \rightarrow 15$, $-17 \rightarrow 0$, $-26 \rightarrow 0$
Reflections collected/unique	7483–7284 [R_{int} = 0.0356]	7580/7377 [R_{int} = 0.0432]
Refinement on F^2	$w = 1/[\sigma^2F_0^2 + 20.0701P)^2 + 0.0000P]$, $P = (F_0^2 + 2F_c^2)/3$	$w = 1/[\sigma^2F_0^2 + 20.0447P)^2 + 2.3P = (F_0^2 + 2F_c^2)/3$
Parameters/restrains	400/3	401/1
Goodness of fit (GOF) on F^2	0.99	1.025
R indices [$I > 2\sigma(I)$]	R_1 = 0.0432, wR_2 = 0.1046	R_1 = 0.0315, wR_2 = 0.0764
R indices [all data]	R_1 = 0.1023, wR_2 = 0.1237	R_1 = 0.0572, wR_2 = 0.0839
$(\Delta/\sigma)_{max}$	0.001	0.002
Largest difference in peak and hole (e/Å^3)	0.865 and −0.508	1.39 and −1.674

nances of **1d** and **2d** are shifted to lower frequencies by ca. 24 and 30 ppm, respectively, compared to the free ligands. The $^{31}P\text{–}\{^1H\}$ NMR spectra of complexes **1e** and **2e** show a singlet at δ 23.6 and 20.5 ppm, respectively, accompanied by platinum satellites. The large $^1J(^{135}Pt\text{–}^{31}P)$ coupling constants of 3325 and 3310 Hz for **1e** and **2e**, respectively, are indicative of a *cis* arrangement of phosphines around a platinum(II) center [59]. The $^{31}P\text{–}\{^1H\}$ NMR chemical shifts of **1f** and **2f** are also within the expected range, 89.4 and 87.6 ppm, respectively, for structurally similar complexes [43,54,60,61]. The phosphorus resonances of complexes **1f** and **2f** show a coordination shift to higher frequencies by ca. 27 and 19 ppm, respectively, compared to those of the free ligands.

Single crystals of $[Pd\{(Ph_2P)_2N\text{-}C_6H_4\text{-}2\text{-}CH(CH_3)_2\}Cl_2]$ (**1d**) and $[Pt\{(Ph_2P)_2N\text{-}C_6H_4\text{-}2\text{-}CH(CH_3)_2\}Cl_2]$ (**1e**) suitable for X-ray diffraction studies were obtained by slow diffusion of diethylether into a solution of the complexes in dichloromethane. Both complexes were crystallized as 1:1 solvent adducts and the crystallographic data of $[Pd\{(Ph_2P)_2N\text{-}C_6H_4\text{-}2\text{-}CH(CH_3)_2\}Cl_2]\cdot(C_2H_5)_2O$ and $[Pt\{(Ph_2P)_2N\text{-}C_6H_4\text{-}2\text{-}CH(CH_3)_2\}Cl_2]\cdot(C_2H_5)_2O$ are listed in Tables 1 and 2 for **1d** and **1e**. A perspective view of the molecules is given in Fig. 1.

These two crystal structures are isomorphous. The key bond lengths and angles of complexes **1d** and **1e** in the solid state are very similar, with minimal structural differences due to the relocation of the isopropyl groups. The coordination geometry around the Pd and Pt atoms is distorted square–planar, involving two P and two Cl atoms. In the coordination environment, the Pd–P and Pt–P bond lengths are 2.2045(11)–2.2068(10) and 2.1925(12)–2.1936(12) Å, respectively. The Pd–Cl and Pt–Cl coordination bond lengths are 2.3600(11)–2.3553(11) and 2.3462(13)–2.3510(13) Å, respectively. The coordination bond lengths of the Pt atom are slightly smaller than the Pd atom. The palladium(II) complex **1d** and the platinum(II) complex **1e** have coordination angles around the Pd and Pt atoms in the range 71.93(4)–96.96(5)° and 72.52(4)–97.36(5)°, respectively. Despite the difference of the two metal atoms, the P–Pd–P angle and P–Pt–P angles are close to each other (71.93(4)° and 72.52(4)°, respectively). The fact that these angles are much smaller than the ideal value of 90° in a regular square planar geometry can be attributed to the strain in the diphosphine ligands: the bite distance in these ligands is obviously small. Indeed, the P1···P2 distances are 2.5908(14) Å for Pd complex and 2.5942(16) Å for Pt complex. The Pd and Pt atoms are at distance of 0.0538(3) and

Table 2
Selected bond lengths (Å) and bond angles (°) for the solid state structure of **1d** and **1e**. M = Pd and Pt, respectively.

	1d	**1e**		**1d**	**1e**
M–P1	2.2045(11)	2.1925(12)	P1–M–P2	71.93(4)	72.52(4)
M–P2	2.2068(10)	2.1936(12)	Cl1–M–Cl2	96.96(5)	92.92(5)
M–Cl1	2.3600(11)	2.3462(13)	P1–M–Cl1	167.26(4)	97.15(5)
M–Cl2	2.3553(11)	2.3510(13)	P1–M–Cl2	95.37(4)	169.76(5)
P1–N	1.722(3)	1.719(4)	P2–M–Cl1	95.62(4)	169.55(5)
P2–N	1.710(3)	1.724(4)	P2–M–Cl2	167.14(4)	97.36(5)
P1–C1	1.797(4)	1.799(5)	P1–N–P2	98.02(16)	97.82(17)
P1–C7	1.794(5)	1.808(5)	M–P1–N	94.68(11)	94.71(12)
P2–C13	1.795(4)	1.798(5)	M–P2–N	94.96(11)	94.53(12)
P2–C19	1.799(4)	1.809(4)	C25–N–P1	126.2(3)	126.6(3)
P1···P2	2.5908(14)	2.5942(16)	C25–N–P2	127.6(3)	127.5(3)
N–C25	1.459(5)	1.454(5)			

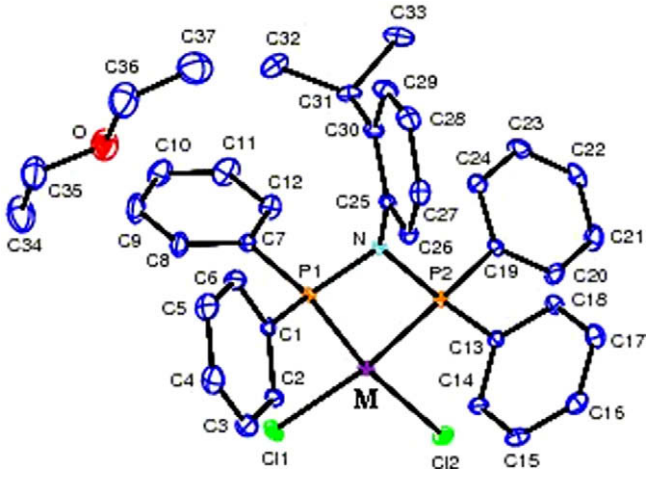


Fig. 1. ORTEP drawing of the compounds **1d** and **1e** with the atomic numbering scheme. H atoms have been omitted for clarity, where M = Pd and Pt, respectively.

0.0341(3) Å, respectively from the basal plane defined by the atoms Cl1, Cl2, P1, P2.

The P–N bond distances of palladium complex **1d** [1.722(3) and 1.710(3) Å] are very similar to those of platinum complex **1e** [1.724(4) and 1.719(4) Å]. They are within the expected ranges in comparison to similar structures [52–54,58]. The aromatic rings in the molecules, as expected, have the usual bond lengths and angles.

It is interesting to note that compounds **1d** and **1e** crystallized under similar conditions, both forming 1:1 adduct with solvent molecules. To get information about the conformation of the complexes **1d** and **1e**, dihedral angles between the neighboring square planes in the molecule were calculated with PARST [62]. Some dihedral angles between the planes around the coordination sphere and phenyl rings (Fig. 2) are given in Table 3. The title molecule is not planar but the phenyl rings are essentially planar.

2.2. The Heck coupling reactions

The palladium complexes **1d** and **2d** were tested as catalysts in one of the most important C–C bond forming processes in synthetic organic chemistry, known as the Heck reaction, the palladium-catalyzed coupling of aryl/vinyl halides with olefins [63,64]. After optimizing the reaction conditions, we carried out the coupling reactions of several substrates with styrene. We found that the use of 0.01 mmol of palladium complexes (**1d** and **2d**) with two equivalents of K_2CO_3 in dioxane at 85 °C led to the best conversion. A control experiment indicated that the coupling reaction does not occur in the absence of **1d** or **2d**. Under these optimum conditions, a wide range of arylbromides bearing electron-donating or electron-withdrawing groups (*p*-bromoacetophenone, *p*-bromobenzaldehyde, *p*-bromobenzene, *p*-bromoanisole and *p*-bromotoluene) react with styrene giving the coupled products in high yields (Table 4).

2.3. The Suzuki coupling reactions

The palladium complexes **1d** and **2d** were tested as catalysts in the Suzuki reaction of aryl/vinyl halides with boronic acid, which is one of the most efficient methods for C–C bond formation [65]. Following optimization experiments, we found that the use of 0.01 mmol of the palladium complexes (**1d** and **2d**) with Cs_2CO_3 as the base at 75 °C in dioxane appeared to provide the highest yield. We initially tested the catalytic activity of the complexes (**1d** and **2d**) for the coupling of *p*-bromoacetophenone with phenylboronic acid and the control experiments showed that the coupling reaction does not occur in the absence of the catalyst. Under these conditions, *p*-bromoacetophenone, *p*-bromobenzaldehyde, *p*-bromobenzene, *p*-bromoanisole and *p*-bromotoluene react cleanly with phenylboronic acid giving high yields of the products (Table 5).

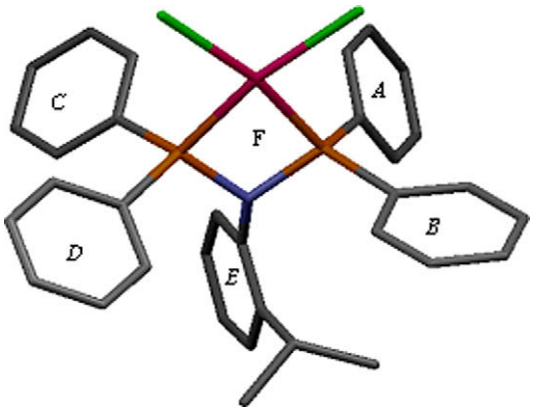


Fig. 2. Conformation of the compounds **1d** and **1e**.

Table 3
Dihedral angles between defined planes of the compounds **1d** and **1e**.

Plane 1	Plane 2	Dihedral angle (°) **1d**	Dihedral angle (°) **1e**
P1/M/P2	Cl1/M/Cl2	3.69(5)	2.31(4)
P1/M/P2	P1/N/P2	6.6(2)	6.7(2)
A	B	61.3(2)	59.9(2)
C	D	64.2(2)	64.9(2)
E	F	77.1(1)	77.1(1)

Notes: Planes A–F are involving the atoms as given (Fig. 2): A: C1/C2/C3/C4/C5/C6, B: C7/C8/C9/C10/C11/C12, C: C13/C14/C15/C16/C17/C18, D: C19/C20/C21/C22/C23/C24, E: C25/C26/C27/C28/C29/C30, F: Pt/P1/N/P2. M = Pd, Pt.

3. Experimental

All reactions and manipulations were performed under argon atmosphere using standard Schlenk techniques unless otherwise stated. Ph_2PCl, 2-isopropylaniline and 4-isopropylaniline were purchased from Fluka and were used as received. Solvents were dried using the appropriate reagents and distilled prior to use. The starting materials $[MCl_2(cod)]$ (M = Pd, Pt, cod = 1,5-cyclooctadiene) [66,67] and $[Cu(CH_3CN)_4]PF_6$ [68] were prepared according to the literature procedures. Infrared spectra were recorded from KBr pellets in the range 4000–400 cm^{-1} on a Mattson 1000 ATI UNICAM FT-IR spectrometer. NMR spectra were recorded on a Bruker AC 400 spectrometer (400.1 MHz for ^1H, 100.6 MHz for ^{13}C, and 162.0 MHz ^{31}P). Microanalysis was carried out on a Fisons EA 1108 CHNS-O instrument. GC analyses were performed on a HP 6890 N Gas Chromatograph equipped with a capillary column (5% biphenyl, 95% dimethylsiloxane) (30 m × 0.32 mm × 0.25 μm).

3.1. General procedure for the synthesis of N,N-bis(diphenylphosphino) isopropylanilines $[(Ph_2P)_2N\text{-}(C_6H_4)\text{-}CH(CH_3)_2]$ (**1**, **2**)

Ph_2PCl (1.63 g, 7.40 mmol) was added slowly to a solution of 2- or 4-isopropylaniline (0.50 g, 3.70 mmol) and Et_3N (0.75 g, 7.40 mmol) in thf (20 mL) at 0 °C. The resulting white suspension was stirred for 1 h and precipitated triethylamine hydrochloride was removed by filtration through a sintered Schlenk tube. The solution was evaporated to dryness under reduced pressure and white solids of **1** or **2** were obtained.

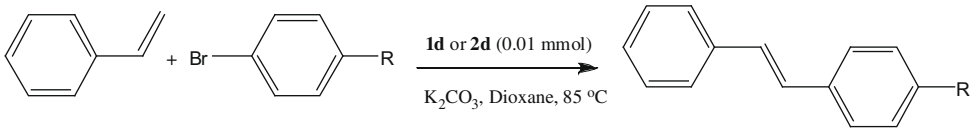
3.1.1. N, N-bis(diphenylphosphino)-2-isopropylaniline $[(Ph_2P)_2N\text{-}(C_6H_4)\text{-}2\text{-}CH(CH_3)_2]$ (**1**)

Yield: 1.62 g, 87%; M.p. 129–131 °C; ^1H NMR (400 MHz, [D]$CHCl_3$, 25 °C, TMS): 6.75–7.53(m, 24H, Ar–H), 2.99(m, 1H, $CH(CH_3)_2$, 0.75(d, ^3J(H–H) = 6.4 Hz, 6H, –$CH(CH_3)_2$); ^{13}C NMR (100 MHz, [D]$CHCl_3$, 25 °C, TMS): 146.3, 139.7, 134.9, 132.5, 131.4, 130.5, 128.5, 127.8, 126.6, 125.8 (C_{arm}); 27.5 (–$CH(CH_3)_2$); 23.6 (–$CH(CH_3)_2$); $^{31}P\{^1H\}$ NMR (162 MHz, [D]$CHCl_3$, 25 °C, 85% H_3PO_4): 62.2 (s); IR (KBr pellet, ν cm^{-1}): 901 (PNP), 1432 (PPh); Elemental *Anal.* Calc. for $C_{33}H_{31}NP_2$: C, 78.71; H, 6.21; N, 2.78. Found: C, 78.46; H, 5.97; N, 2.59%.

3.1.2. N, N-bis(diphenylphosphino)-4-isopropylaniline $[(Ph_2P)_2N\text{-}(C_6H_4)\text{-}4\text{-}CH(CH_3)_2]$ (**2**)

Yield: 1.58 g, 85%; M.p. 103–105 °C; ^1H NMR (400 MHz, [D]$CHCl_3$, 25 °C, TMS): 6.58–7.39(m, 24H, Ar–H), 2.76(m, 1H, $CH(CH_3)_2$, 1.15(d, ^3J(H–H) = 7.2 Hz, 6H, –$CH(CH_3)_2$); ^{13}C NMR (100 MHz, [D]$CHCl_3$, 25 °C, TMS): 145.8, 139.6, 133.3, 131.3, 128.9, 128.5, 127.9, 126.2 (C_{arm}); 33.5 (–$CH(CH_3)_2$); 24.0 (–$CH(CH_3)_2$); $^{31}P\{^1H\}$ NMR (162 MHz, [D]$CHCl_3$, 25 °C, 85%

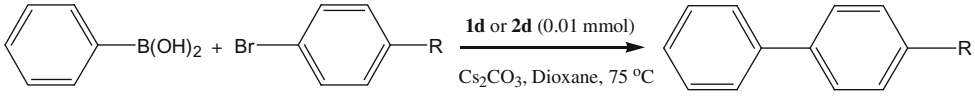
Table 4
The Heck coupling reactions of aryl bromides with styrene[a].



Entry	R	Catalyst	Yield (%)[b]	TOF (h^{-1})
1	$COCH_3$	**1d**	95.42	63.6
2	$COCH_3$	**2d**	93.25	62.2
3	CHO	**1d**	97.12	64.8
4	CHO	**2d**	94.08	62.7
5	H	**1d**	88.77	59.2
6	H	**2d**	74.93	49.9
7	OCH_3	**1d**	69.28	46.2
8	OCH_3	**2d**	57.95	38.6
9	CH_3	**1d**	76.53	51.0
10	CH_3	**2d**	69.26	46.2

[a] *Reaction conditions:* 1.0 mmol of R-C_6H_4Br-*p*, 1.5 mmol of styrene, 2.0 mmol K_2CO_3, 0.01 mmol Pd complex, dioxane (3 mL).
[b] Purity of compounds was checked by NMR and yields are based on aryl bromide, all reactions were monitored by GC, temperature 85 °C, 1.5 h. TOF = (mol product/mol Cat) x h−1.

Table 5
The Suzuki coupling reactions of aryl bromides with phenylboronic acid[a].



Entry	R	Catalyst	Yield (%)[b]	TOF (h^{-1})[c]
1	$COCH_3$	**1d**	94.06	94.1
2	$COCH_3$	**2d**	91.72	91.7
3	CHO	**1d**	98.46	98.5
4	CHO	**2d**	95.12	95.1
5	H	**1d**	85.80	85.8
6	H	**2d**	88.35	88.4
7	OCH_3	**1d**	70.45	70.5
8	OCH_3	**2d**	67.08	67.1
9	CH_3	**1d**	73.57	73.6
10	CH_3	**2d**	61.79	61.8

[a] *Reaction conditions:* 1.0 mmol of R-C_6H_4Br-*p*, 1.5 mmol of phenylboronic acid, 2.0 mmol Cs_2CO_3, 0.01 mmol Pd complex, dioxane (3 mL).
[b] Purity of compounds was checked by NMR and yields are based on aryl bromide, all reactions were monitored by GC, temperature 75 °C, 1 h.
[c] TOF = (mol product/mol Cat) x h^{-1}.

H_3PO_4): 68.5 (s); IR (KBr pellet, ν cm^{-1}): 906 (PNP), 1438 (PPh); Elemental *Anal.* Calc. for $C_{33}H_{31}NP_2$: C, 78.71; H, 6.21; N, 2.78. Found: C, 78.62; H, 6.02; N, 2.64%.

3.2. General procedure for the synthesis of the chalcogenides

3.2.1. N,N-bis(diphenyloxophosphino)isopropylanilines [$(Ph_2P(O))_2N$-(C_6H_4)-$CH(CH_3)_2$] (**1a**, **2a**)

A thf solution (10 mL) of *N*,*N*-bis(diphenylphosphino)isopropyl aniline (0.20 g, 0.40 mmol) and aqueous H_2O_2 (30% w/w, 0.08 mL) was stirred for 2 h at room temperature. The solution was filtered through Celite to remove a small amount of insoluble material. The filtrate was concentrated in vacuo to ca. 1–2 mL and addition of *n*-hexane (10 mL) gave **1a** and **2a** as white solids which were collected by suction filtration.

3.2.2. N,N-bis(diphenyloxophosphino)-2-isopropylaniline [$(Ph_2P(O))_2N$-(C_6H_4)-2-$CH(CH_3)_2$] (**1a**)

Yield: 0.16 g, 75%; M.p. 202–204 °C; ^{1}H NMR (400 MHz, [D]$CHCl_3$, 25 °C, TMS): 6.98–7.71(m, 24H, Ar–H), 3.59(m, 1H, C*H*$(CH_3)_2$), 0.65(d, ^3J(H–H) = 6.4 Hz, 6H, –CH(C*H*$_3)_2$); ^{13}C NMR (100 MHz, [D]$CHCl_3$, 25 °C, TMS): 149.2, 134.6, 134.2, 133.1, 132.6, 132.2, 131.9, 128.3, 127.7, 125.9 (C_{arm}); 27.8 (–*C*H$(CH_3)_2$); 23.9 (–CH$(CH_3)_2$). ^{31}P–{^{1}H} NMR (162 MHz, [D]$CHCl_3$, 25 °C, 85% H_3PO_4): 23.9 (s); IR (KBr pellet, ν cm^{-1}): 908 (PNP), 1448 (PPh), 1216 (PO); Elemental *Anal.* Calc. for $C_{33}H_{31}NO_2P_2$: C, 74.01; H, 5.83; N, 2.62. Found: C, 73.81; H, 5.72; N, 2.46%.

3.2.3. N,N-bis(diphenyloxophosphino)-4-isopropylaniline [$(Ph_2P(O))_2N$-(C_6H_4)-4-$CH(CH_3)_2$] (**2a**)

Yield: 0.18 g, 85%; M.p. 124–126 °C; ^{1}H NMR (400 MHz, [D]$CHCl_3$, 25 °C, TMS): 6.97–7.81(m, 24H, Ar–H), 3.56(m, 1H, C*H*$(CH_3)_2$), 0.75(s, 6H, –CH(C*H*$_3)_2$); ^{13}C NMR (100 MHz, [D]$CHCl_3$, 25 °C, TMS): 149.3, 134.1, 133.2, 132.6, 131.6, 128.5, 127.8, 125.6 (C_{arm}); 27.8 (–*C*H$(CH_3)_2$); 24.1 (–CH$(CH_3)_2$); ^{31}P–{^{1}H} NMR (162 MHz, [D]$CHCl_3$, 25 °C, 85% H_3PO_4): 24.2 (s); IR (KBr pellet, ν cm^{-1}): 910 (PNP), 1446 (PPh), 1199 (PO); Elemental *Anal.* Calc. for $C_{33}H_{31}NO_2P_2$: C, 74.01; H, 5.83; N, 2.62. Found: C, 73.67; H, 5.48; N, 2.43%.

3.2.4. N,N-bis(diphenylthiophosphino)isopropylanilines [$(Ph_2P(S))_2N$-(C_6H_4)-$CH(CH_3)_2$] (**1b**, **2b**)

To a solution of **1** or **2** (0.20 g, 0.40 mmol) in thf (10 mL), S_8 (0.025 g, 0.80 mmol) was added and this mixture was refluxed

for 4 h. The solution was filtered through Celite while hot to remove a small amount of insoluble material. The filtrate was concentrated in vacuo to ca. 1–2 mL and addition of *n*-hexane (15 mL) gave **1b** and **2b** as light yellow solids which were collected by suction filtration.

*3.2.5. N,N-bis(diphenylthiophosphino)-2-isopropylaniline [(Ph$_2$P(S))$_2$N-(C$_6$H$_4$)-2-CH(CH$_3$)$_2$] (**1b**)*

Yield: 0.17 g, 75%; M.p. 149–151 °C; ^{1}H NMR (400 MHz, [D]CHCl$_3$, 25 °C, TMS): 6.90–8.05(m, 24H, Ar–H), 3.54(m, 1H, C*H*(CH$_3$)$_2$), 0.69(d, ^3J(H–H) = 6.8 Hz, 6H, –CH(C*H*$_3$)$_2$); ^{13}C NMR (100 MHz, [D]CHCl$_3$, 25 °C, TMS): 151.0, 136.5, 134.7, 134.0, 133.7, 132.2, 131.3, 128.4, 127.4, 125.0 (C$_{arm}$); 28.3 (–*C*H(CH$_3$)$_2$); 24.6 (–CH(*C*H$_3$)$_2$); ^{31}P–{^{1}H} NMR (162 MHz, [D]CHCl$_3$, 25 °C, 85% H$_3$PO$_4$): 68.5 (s); IR (KBr pellet, ν cm^{-1}): 905 (PNP), 1440 (PPh), 650 (PS); Elemental *Anal.* Calc. for C$_{33}$H$_{31}$NS$_2$P$_2$: C, 69.82; H, 5.50; N, 2.47. Found: C, 69.61; H, 5.31; N, 2.38%.

*3.2.6. N,N-bis(diphenylthiophosphino)-4-isopropylaniline [(Ph$_2$P(S))$_2$N-(C$_6$H$_4$)-4-CH(CH$_3$)$_2$] (**2b**)*

Yield: 0.19 g, 84%: M.p. 189–191 °C; ^{1}H NMR (400 MHz, [D]CHCl$_3$, 25 °C, TMS): 6.72–8.10(m, 24H, Ar–H), 2.59(m, 1H, C*H*(CH$_3$)$_2$), 0.99(s, 6H, –CH(C*H*$_3$)$_2$); ^{13}C NMR (100 MHz, [D]CHCl$_3$, 25 °C, TMS): 147.8, 136.1, 133.6, 132.9, 132.4, 131.3, 127.5, 125.9 (C$_{arm}$); 33.4 (–*C*H(CH$_3$)$_2$); 23.7 (–CH(*C*H$_3$)$_2$); ^{31}P–{^{1}H} NMR (162 MHz, [D]CHCl$_3$, 25 °C, 85% H$_3$PO$_4$): 68.9 (s); IR (KBr pellet, ν cm^{-1}): 906 (PNP), 1446 (PPh), 694 (PS); Elemental *Anal.* Calc. for C$_{33}$H$_{31}$NS$_2$P$_2$: C, 69.82; H, 5.50; N, 2.47. Found: C, 69.68; H, 5.36; N, 2.36%.

*3.2.7. N,N-bis(diphenylselenophosphino)isopropylanilines [(Ph$_2$P(Se))$_2$N-(C$_6$H$_4$)-CH(CH$_3$)$_2$] (**1c**, **2c**)*

Grey Se (0.063 g, 0.8 mmol) was added to a solution of **1** or **2** (0.20 g, 0.40 mmol) in thf (10 mL) and this mixture was refluxed for 1 h. The solution was filtered through Celite while hot to remove a small amount of insoluble material. The filtrate was concentrated in vacuo to ca. 1–2 mL and addition of *n*-hexane (15 mL) gave **1c** and **2c** as light yellow solids which were collected by suction filtration.

*3.2.8. N,N-bis(diphenylselenophosphino)-2-isopropylaniline [(Ph$_2$P(Se))$_2$N-(C$_6$H$_4$)-2-CH(CH$_3$)$_2$] (**1c**)*

Yield: 0.21 g, 80%; M.p. 240–242 °C; ^{1}H NMR (400 MHz, [D]CHCl$_3$, 25 °C, TMS): 6.88–8.04(m, 24H, Ar–H), 3.53(m, 1H, C*H*(CH$_3$)$_2$), 0.70(d, ^3J(H–H) = 6.8 Hz, 6H, –CH(C*H*$_3$)$_2$); ^{13}C NMR (100 MHz, [D]CHCl$_3$, 25 °C, TMS): 151.2, 136.8, 134.6, 134.4, 132.8, 131.6, 130.5, 127.8, 127.5, 125.0 (C$_{arm}$); 28.4 (–*C*H(CH$_3$)$_2$); 24.9 (–CH(*C*H$_3$)$_2$); ^{31}P–{^{1}H} NMR (162 MHz, [D]CHCl$_3$, 25 °C, 85% H$_3$PO$_4$): 67.8, J(PSe) = 786.6 Hz; IR (KBr pellet, ν cm^{-1}): 891 (PNP), 1438 (PPh), 563 (PSe); Elemental *Anal.* Calc. for C$_{33}$H$_{31}$NSe$_2$P$_2$: C, 59.92; H, 4.72; N, 2.12. Found: C, 59.62; H, 4.43; N, 2.01%.

*3.2.9. N,N-bis(diphenylselenophosphino)-4-isopropylaniline [(Ph$_2$P(Se))$_2$N-(C$_6$H$_4$)-4-CH(CH$_3$)$_2$] (**2c**)*

Yield: 0.22 g, 84%: M.p. >300 °C (dec.); ^{1}H NMR (400 MHz, [D]CHCl$_3$, 25 °C, TMS): 6.71–8.15(m, 24H, Ar–H), 2.60(m, 1H, C*H*(CH$_3$)$_2$), 1.00(d, ^3J(H–H) = 6.8 Hz, 6H, –CH(C*H*$_3$)$_2$); ^{13}C NMR (100 MHz, [D]CHCl$_3$, 25 °C, TMS): 147.6, 136.0, 134.3, 133.4, 132.8, 131.4, 127.5, 125.9 (C$_{arm}$); 33.4 (–*C*H(CH$_3$)$_2$); 23.6 (–CH(*C*H$_3$)$_2$); ^{31}P–{^{1}H} NMR (162 MHz, [D]CHCl$_3$, 25 °C, 85% H$_3$PO$_4$): 67.3, J(PSe) = 792 Hz; IR (KBr pellet, ν cm^{-1}): 917 (PNP), 1446 (PPh), 542 (PSe); Elemental *Anal.* Cal. for C$_{33}$H$_{31}$NSe$_2$P$_2$: C, 59.92; H, 4.72; N, 2.12. Found: C, 59.72; H, 4.57; N, 1.98%.

3.3. General procedure for the synthesis of the complexes

*3.3.1. Dichloro{N,N-bis(diphenylphosphino)isopropylaniline}palladium(II) (**1d**, **2d**)*

A solution of [PdCl$_2$(cod)] (0.227 g, 0.795 mmol) and **1** or **2** (0.40 g, 0.795 mmol) in thf (20 mL) was stirred for 2 h. The volume was concentrated in vacuum to ca. 1–2 mL and addition of diethyl ether (15 mL) gave **1d** and **2d** as yellow solids which were collected by suction filtration and dried in vacuum.

*3.3.2. Dichloro{N,N-bis(diphenylphosphino)-2-isopropylaniline} palladium(II) (**1d**)*

Yield: 0.44 g, 81%; M.p. 249–251 °C; ^{1}H NMR (400 MHz, [D]CHCl$_3$, 25 °C, TMS): 6.78–7.85(m, 24H, Ar–H), 2.57(m, 1H, C*H*(CH$_3$)$_2$), 0.31(d, ^3J(H–H) = 6.4 Hz, 6H, –CH(C*H*$_3$)$_2$); ^{13}C NMR (100 MHz, [D]CHCl$_3$, 25 °C, TMS): 147.4, 136.4, 134.8, 134.4, 132.4, 130.6, 130.4, 129.9, 128.6, 126.6 (C$_{arm}$); 28.7 (–*C*H(CH$_3$)$_2$); 23.8 (–CH(*C*H$_3$)$_2$); ^{31}P–{^{1}H} NMR (162 MHz, [D]CHCl$_3$, 25 °C, 85% H$_3$PO$_4$): 37.9 (s); IR (KBr pellet, ν cm^{-1}): 890 (PNP), 1438 (PPh); Elemental *Anal.* Calc. for C$_{33}$H$_{31}$NP$_2$PdCl$_2$: C, 58.21; H, 4.59; N, 2.06. Found: C, 57.94; H, 4.43; N, 1.83%.

*3.3.3. Dichloro{N,N-bis(diphenylphosphino)-4-isopropylaniline} palladium(II) (**2d**)*

Yield: 0.48 g, 89%; M.p. 250–252 °C; ^{1}H NMR (400 MHz, [D]CHCl$_3$, 25 °C, TMS): 6.79–7.85(m, 24H, Ar–H), 2.58(m, 1H, C*H*(CH$_3$)$_2$), 0.3(d, ^3J(H–H) = 6.0 Hz, 6H, –CH(C*H*$_3$)$_2$); ^{13}C NMR (100 MHz, [D]CHCl$_3$, 25 °C, TMS): 147.3, 138.1, 134.8, 134.4, 132.1, 130.0, 128.7, 126.6 (C$_{arm}$); 28.9 (–*C*H(CH$_3$)$_2$); 23.8 (–CH(*C*H$_3$)$_2$); ^{31}P–{^{1}H} NMR (162 MHz, [D]CHCl$_3$, 25 °C, 85% H$_3$PO$_4$): 38.5 (s); IR (KBr pellet, ν cm^{-1}): 892 (PNP), 1447 (PPh); Elemental *Anal.* Calc. for C$_{33}$H$_{31}$NP$_2$PdCl$_2$: C, 58.21; H, 4.59; N, 2.06. Found: C, 57.84; H, 4.37; N, 1.93%.

*3.3.4. Dichloro{N,N-bis(diphenylphosphino)isopropylaniline} platinum(II) (**1e**, **2e**)*

A solution of [PtCl$_2$(cod)] (0.298 g, 0.795 mmol) and **1** or **2** (0.40 g, 0.795 mmol) in thf (20 mL) was stirred for 2 h. The volume was concentrated in vacuum to ca. 1–2 mL and addition of diethyl ether (15 mL) gave **1e** and **2e** as white solids which were collected by suction filtration and dried in vacuum.

*3.3.5. Dichloro{N,N-bis(diphenylphosphino)-2-isopropylaniline} platinum(II) (**1e**)*

Yield: 0.52 g, 85%; M.p. 294–296 °C; ^{1}H NMR (400 MHz, [D]CHCl$_3$, 25 °C, TMS): 6.75–7.81(m, 24H, Ar–H), 2.63(m, 1H, C*H*(CH$_3$)$_2$), 0.30(d, ^3J(H–H) = 6.8 Hz, 6H, –CH(C*H*$_3$)$_2$); ^{13}C NMR (100 MHz, [D]CHCl$_3$, 25 °C, TMS): 147.7, 139.3, 134.6, 134.2, 132.2, 130.6, 130.2, 129.8, 127.4, 126.4 (C$_{arm}$); 28.9 (–*C*H(CH$_3$)$_2$); 23.8 (–CH(*C*H$_3$)$_2$); ^{31}P–{^{1}H} NMR (162 MHz, [D]CHCl$_3$, 25 °C, 85% H$_3$PO$_4$): 23.6, J(PtP) = 3325 Hz; IR (KBr pellet, ν cm^{-1}): 893 (PNP), 1440 (PPh); Elemental *Anal.* Calc. for C$_{33}$H$_{31}$NP$_2$PtCl$_2$: C, 51.51; H, 4.06; N, 1.82. Found: C, 51.24; H, 3.82; N, 1.69%.

*3.3.6. Dichloro{N,N-bis(diphenylphosphino)-4-isopropylaniline} platinum(II) (**2e**)*

Yield: 0.55 g, 90%; M.p. >250 °C (dec.); ^{1}H NMR (400 MHz, [D]CHCl$_3$, 25 °C, TMS): 6.40–7.81(m, 24H, Ar–H), 2.66(m, 1H, C*H*(CH$_3$)$_2$), 0.31(d, ^3J(H–H) = 6.8 Hz, 6H, –CH(C*H*$_3$)$_2$); ^{13}C NMR (100 MHz, [D]CHCl$_3$, 25 °C, TMS): 147.0, 137.6, 134.3, 133.1, 132.2, 130.1, 128.0, 126.6 (C$_{arm}$); 30.8 (–*C*H (CH$_3$)$_2$); 25.6 (–CH(*C*H$_3$)$_2$); ^{31}P–{^{1}H} NMR (162 MHz, [D]CHCl$_3$, 25 °C, 85% H$_3$PO$_4$): 20.5, J(PtP): 3310 Hz; IR (KBr pellet, ν cm^{-1}): 892 (PNP),

1438 (PPh); Elemental *Anal.* Calc. for $C_{33}H_{31}NP_2PtCl_2$: C, 51.51; H, 4.06; N, 1.82. Found: C, 51.29; H, 3.94; N, 1.73%.

3.3.7. Bis[N,N-bis(diphenylphosphino)isopropylaniline]copper(I) hexafluorophosphates (**1f**, **2f**)

To a solution of $[Cu(CH_3CN)_4]PF_6$ (0.148 g, 0.398 mmol) in thf (15 mL) was added compound **1** or **2** (0.40 g, 0.795 mmol), and the resulting solution was stirred for 1 h. The volume was concentrated in vacuum to ca. 1–2 mL and addition of diethyl ether (15 mL) gave **1f** and **2f** as white solids which were collected by suction filtration and dried in vacuum.

3.3.8. Bis[N,N-bis(diphenylphosphino)-2-isopropylaniline]copper(I) hexafluorophosphate (**1f**)

Yield: 0.41 g, 85%; M.p. 179–181 °C; ^{1}H NMR (400 MHz, [D]$CHCl_3$, 25 °C, TMS): 7.11–7.57(m, 24H, ArH), 2.60(m, 1H, C*H*$(CH_3)_2$), 0.10(d, ^3J(H–H):6.4 Hz, 6H, –$CH(CH_3)_2$); No ^{13}C NMR spectrum was obtained due to the low solubility of the complex in all common solvents; ^{31}P–{^{1}H} NMR (162 MHz, [D]$CHCl_3$, 25 °C, 85% H_3PO_4): 89.4, PF_6: −144.3, $J(PF_6)$ = 712 Hz; IR (KBr pellet, ν cm^{-1}): 898 (PNP), 1446 (PPh); Elemental *Anal.* Calc. for $C_{66}H_{62}N_2P_5F_6Cu$: C, 65.21; H, 5.14; N, 2.30. Found: C, 64.96; H, 4.95; N, 2.18%.

3.3.9. Bis[N,N-bis(diphenylphosphino)-4-isopropylaniline]copper(I) hexafluorophosphate (**2f**)

Yield: 0.38 g, 79%; M.p. 181–183 °C; ^{1}H NMR (400 MHz, [D]$CHCl_3$, 25 °C, TMS): 6.77–7.52(m, 24H, ArH), 2.72(br, 1H, C*H*$(CH_3)_2$), 1.10(s, 6H, –$CH(CH_3)_2$); No ^{13}C NMR spectrum was obtained due to the low solubility of the complex in all common solvents; ^{31}P–{^{1}H} NMR (162 MHz, [D]$CHCl_3$, 25 °C, 85% H_3PO_4): 87.6, PF_6: −144.3, $J(PF_6)$ = 712 Hz; IR (KBr pellet, ν cm^{-1}): 908 (PNP), 1439 (PPh); Elemental *Anal.* Calc. for $C_{66}H_{62}N_2P_5F_6Cu$: C, 65.21; H, 5.14; N, 2.30. Found: C, 65.02; H, 4.97; N, 2.19%.

3.4. General procedure for the Heck coupling reaction

Heck coupling reactions were conducted as follows: the bisphosphinoamine–palladium complexes (**1d** or **2d**) (0.01 mmol), arylbromide (1.0 mmol), styrene (1.5 mmol), K_2CO_3 (2.0 mmol) and 1,4-dioxane (3 mL) were placed in a Schlenk tube and the mixture was heated to 85 °C for 1.5 h. The progress of the reaction was monitored by GC. Upon completion, the mixture was cooled, and the product extracted with ethyl acetate/hexane (1:5), filtered through a pad of silica gel with copious washing, concentrated and purified by flash chromatography on silica gel. The purity of the compounds was checked by NMR and GC, and yields are based on arylbromide.

3.5. General procedure for the Suzuki coupling reaction

Suzuki coupling reactions were conducted as follows: the bisphosphinoamine–palladium complexes (**1d** or **2d**) (0.01 mmol), arylbromide (1.0 mmol), phenylboronic acid (1.5 mmol), Cs_2CO_3 (2.0 mmol) and 1,4-dioxane (3 mL) were placed in a small Schlenk tube and the mixture was heated at 75 °C for 1 h. The progress of the reaction was monitored by GC. Upon completion, the mixture was cooled, the product extracted with ethyl acetate/hexane (1:5), filtered through a pad of silica gel with copious washing, concentrated and purified by flash chromatography on silica gel. The purity of the compounds was checked by NMR and GC, and yields are based on arylbromide.

3.6. X-ray diffraction structure analyses

To determine the crystal structures of **1d** and **1e**, X-ray diffraction data were collected at room temperature using an Enraf-nonius CAD4 diffractometer with graphite monochromated Mo Kα radiation using the $w/2\theta$ scan mode. The lattice parameters and their estimated standard deviations were determined from a least-squares analysis using 25 centered reflections in the range 9.86–17.99° for the Pd complex and 10.15-17.98° for the Pt complex by using CAD4 Express [69]. Data reduction was carried out using XCAD 4 [70]. The structures were solved by the direct method using the solution program SHELXS97 and refined on F_0^2 using SHELXS97 [71]. In both complexes, all non-hydrogen atoms were refined, first with isotropic and then with anisotropic thermal parameters by full matrix least squares. The hydrogen atom of the CH group in the 2-isopropyl aniline ligand was taken from a difference Fourier map. All other hydrogen atoms were positioned geometrically with C–H = 0.93, 0.97 and 0.96 Å for aromatic, methylene and methyl H, and constrained to ride on their parent atoms, with $U_{iso}(H) = xU_{eq}(C)$, where $x = 1.5$ for methyl H, and $x = 1.2$ for others H atoms. Results of the X-ray structure determination are given in Tables 1–3 for **1d** and **1e**, and the ORTEP [72] drawings of the molecules are shown in Fig. 1.

4. Conclusion

In conclusion, two new bis(diphenylphosphino)amines and their oxides, sulfides and selenides have been prepared. In addition, both compounds show similar coordination properties towards Cu, Pd and Pt. The Pd complexes exhibit high catalytic activity in the Heck and Suzuki cross-coupling reactions. The procedure for carrying out the catalytic reactions is quite simple and efficient towards various aryl bromides and does not require an induction period. Based on these findings, it can be postulated that **1d** and **2d** offer some distinctive advantages in the C–C coupling reactions compared to other palladium/aminophosphine systems [20,50,55,64].

5. Supplementary data

CCDC 694356 and 69455 contain the supplementary crystallographic data for **1d** and **1e**. These data can be obtained free of charge via http://www.ccdc.cam.ac.uk/conts/retrieving.html, or from the Cambridge Crystallographic Data Centre, 12 Union Road, Cambridge CB2 1EZ, UK; fax: (+44) 1223-336-033; or e-mail: deposit@ccdc.cam.ac.uk.

Acknowledgements

Partial support from Turkish Academy of Sciences, Dicle University (Project number: DÜAPK 05-FF-27) and Hacettepe University (Scientific Research Department, Project number: 04A602004) are gratefully acknowledged.

References

[1] T. Appleby, J.D. Woollins, Coord. Chem. Rev. 235 (2002) 121.
[2] P. Bhattacharrya, J.D. Woollins, Polyhedron 14 (1995) 3367.
[3] N. Fey, J.N. Harvey, G.C. Lloyd-Jones, P. Murray, A.G. Orpen, R. Osborne, M. Purdie, Organometallics 27 (2008) 1372.
[4] F. Majoumo-Mbe, P. Lönnecke, E.V. Novikova, G.P. Belov, E. Hey-Hawkins, J. Chem. Soc., Dalton Trans. (2005) 3326.
[5] M. Bourghida, M. Widhalm, Tetrahedron: Asymmetry 9 (1998) 1073.
[6] Y. Wang, H. Guo, K.L. Ding, Tetrahedron: Asymmetry 11 (20) (2000) 4153.
[7] Y. Wang, X. Li, K.L. Ding, Tetrahedron Lett. 43 (2002) 159.

[8] T. Mino, Y. Tanaka, Y. Yabusaki, D. Okumara, M. Sakamoto, T. Fujita, Tetrahedron: Asymmetry 14 (2003) 2503.
[9] S. Urgaonkar, J.G. Verkade, Tetrahedron 60 (2004) 11837.
[10] S. Urgaonkar, J.G. Verkande, Adv. Synth. Catal. 346 (2004) 611.
[11] S.L. Parisel, L.A. Adrio, A.A. Pereira, M.M. Perez, J.M. Vila, K.K. Hii, Tetrahedron 61 (2005) 9822.
[12] M.T. Reetz, G. Lohmer, R. Schwickardi, Angew. Chem., Int. Ed. Engl. 36 (1997) 1526.
[13] K.R. Reddy, K. Surekha, G.H. Lee, S.M. Peng, S.T. Lui, Organometallics 19 (13) (2000) 2637.
[14] I.P. Beletskaya, A.V. Cheprakov, Chem. Rev. 100 (8) (2000) 3009.
[15] A. Mansour, M. Portnony, Tetrahedron Lett. 44 (2003) 2195.
[16] D.P. Catsoulacos, B.R. Steele, G.A. Heropoulos, M. Micha-Screttas, C.G. Screttas, Tetrahedron Lett. 44 (2003) 4575.
[17] X.-L. Hou, D.X. Dong, K. Yuan, Tetrahedron: Asymmetry 15 (2004) 2189.
[18] D.L. Zotto, E. Zangrando, W. Baratta, A. Felluga, P. Martinuzzi, P. Rigo, Eur. J. Inorg. Chem. (2005) 4707.
[19] O. Akba, F. Durap, M. Aydemir, A. Baysal, B. Gümgüm, S. Özkar, J. Organomet. Chem. 694 (5) (2009) 731.
[20] M. Aydemir, A. Baysal, G. Öztürk, B. Gümgüm, Appl. Organomet. Chem. 23 (2009) 108.
[21] M.L. Clarke, D.J. Cole-Hamilton, J.D. Woollins, J. Chem. Soc., Dalton Trans. (2001) 2721.
[22] T. Schareina, R. Kepme, Angew. Chem., Int. Ed. Engl. 41 (2002) 1521.
[23] S. Urgaonkar, M. Nagarajan, J.G. Verkade, Tetrahedron Lett. 43 (2002) 8921.
[24] J. Cheng, F. Wang, J.-H. Xu, Y. Pan, Z. Zhang, Tetrahedron Lett. 44 (2003) 7095.
[25] F. Bellina, A. Carpita, R. Rossi, Synthesis 15 (2004) 2419.
[26] C. Abu-Gnim, I. Amer, J. Organomet. Chem. 516 (1996) 235.
[27] C. Saluzzo, J. Breuzard, S. Pellet-Rostaing, M. Vallet, F.L. Guyader, M. Lemaire, J. Organomet. Chem. 643 (2002) 98.
[28] J. Andriev, P. Richard, J.M. Camus, R. Poli, Inorg. Chem. 41 (5) (2002) 3876.
[29] E.J. Zijp, J.I. Van der Vlugt, D.M. Tooke, A.L. Spek, D. Vogt, J. Chem. Soc., Dalton Trans. 3 (2005) 512.
[30] R.W. Guo, A.J. Lough, R.H. Morris, D.T. Song, Organometallics 23 (23) (2004) 5524.
[31] C. Blanc, F. Agbossou-Niedercorn, G. Nowogrocki, Tetrahedron: Asymmetry 15 (2004) 2159.
[32] Y. Xing, J.S. Chen, Z.R. Dong, Y.Y. Li, J.X. Gas, Tetrahedron Lett. 47 (2006) 4501.
[33] B. Pugin, H.U. Blaser, Adv. Synth. Catal. 348 (2006) 1743.
[34] S. Demir, İ. Özdemir, B. Çetinkaya, Appl. Organomet. Chem. 20 (2006) 254.
[35] İ. Özdemir, M. Yiğit, E. Çetinkaya, B. Çetinkaya, Appl. Organomet. Chem. 20 (2006) 187.
[36] B. Punji, G. Ganesamoorthy, M.S. Balakrishna, J. Mol. Catal. A 259 (2006) 78.
[37] R.B. Bedford, S.L. Welch, Chem. Commun. (2001) 129.
[38] F.R. Hartley, The Chemistry of Organophosphorus Compounds, Wiley, Manchester, 1990. p. 1.
[39] N.N. Greenwood, A. Earnshaw, Chemistry of Elements, Pergamon Press, Oxford, 1984. p. 619.
[40] M.S. Balakrishna, R. Panda, D.C. Smith Jr., A. Kalamn, S.P. Nolan, J. Organomet. Chem. 599 (2000) 159.
[41] A. Bollmann, K. Blann, J.T. Dixon, F.M. Hess, E. Killian, H. Maumela, D.S. McGuinness, D.H. Morgan, A. Nevelling, S. Otto, M. Overett, A.M.Z. Slawin, P. Wasserscheid, S. Kuhlmann, JACS 126 (2004) 14712.
[42] L.E. Bawen, D.F. Wass, Organometallics 25 (2006) 555.
[43] A. Jabri, P. Crewdson, S. Gambarotta, I. Korobkov, R. Duchateav, Organometallics 25 (2006) 715.
[44] S. Teo, Z. Weng, T.S.A. Hor, Organometallics 27 (2008) 4188.
[45] M.S. Balakrishna, K. Ramaswamy, R.M. Abhyankar, J. Organomet. Chem. 560 (1998) 131.
[46] K.G. Gaw, M.B. Smith, A.M.Z. Slawin, New J. Chem. 24 (2000) 429.
[47] N. Biricik, F. Durap, B. Gumgum, Z. Fei, R. Scopelliti, Transition Met. Chem. 32 (7) (2007) 877.
[48] M. Necas, M.R.J. Foreman, J. Marek, J.D. Woollins, J. Novosad, New J. Chem. 25 (2001) 1256.
[49] E. Killian, K. Blann, A. Bollmann, J.T. Dixon, S. Kuhlmann, M.C. Mavmela, H. Maumela, D.H. Morgan, P. Nongodlwana, M.J. Overett, M. Pretorius, K. Höfener, P. Wasserscheid, J. Mol. Catal. A 270 (2008) 214.
[50] M. Aydemir, A. Baysal, B. Gümgüm, J. Organomet. Chem. 693 (2008) 3810.
[51] N. Biricik, F. Durap, C. Kayan, B. Gümgüm, Heteroatom Chem. 18 (6) (2007) 613.
[52] Z. Fei, I. Neda, H. Thönnessen, P.G. Jones, R. Schmutzler, Phosphorus, Sulfur, Silicon Relat. Elem. 131 (1997) 1.
[53] Z. Fei, H. Thönnessen, P.G. Jones, R. Schmutzler, Z. Anorg. Allg. Chem. 625 (1999) 1732.
[54] Z. Fei, Y. Lu, M. Freytag, P.G. Jones, R. Schmutzler, Z. Anorg. Allg. Chem. 626 (2000) 969.
[55] N. Biricik, F. Durap, C. Kayan, B. Gümgüm, N. Gürbüz, İ. Özdemir, W.H. Ang, Z. Fei, R. Scopelliti, J. Organomet. Chem. 693 (2008) 2693.
[56] H.L. Milton, M.V. Wheatley, A.M.Z. Slawin, J.D. Woollins, Inorg. Chem. Commun. 7 (10) (2004) 1106.
[57] Z. Fei, W.H. Ang, D. Zhao, R. Scopelliti, P.J. Dyson, Inorg. Chim. Acta 359 (2006) 2635.
[58] F. Durap, N. Biricik, B. Gümgüm, S. Özkar, W.H. Ang, Z. Fei, R. Scopelliti, Polyhedron 27 (2008) 196.
[59] A.M.Z. Slawin, J.D. Woollins, Q. Zhang, J. Chem. Soc., Dalton Trans. (2001) 621.
[60] A.M.Z. Slawin, H.L. Milton, J. Wheatley, J.D. Woollins, Polyhedron 23 (2004) 3125.
[61] A.M.Z. Slawin, J. Wheatley, J.D. Woollins, Phosphorus, Sulfur, Silicon Relat. Elem. 179 (4–5) (2004) 991.
[62] M. Nardelli, J. Appl. Cryst. 28 (1995) 659.
[63] A.F. Littke, G.C. Fu, Angew. Chem., Int. Ed. Engl. 41 (2002) 4176.
[64] B. Gümgüm, N. Biricik, F. Durap, İ. Özdemir, N. Gürbüz, W.H. Ang, P.J. Dyson, Appl. Organomet. Chem. 21 (2007) 711.
[65] İ. Özdemir, S. Yaşar, S. Demir, B. Çetinkaya, Heteroatom Chem. 16 (7) (2005) 557.
[66] D. Drew, J.R. Doyle, Inorg. Synth. 13 (1972) 47.
[67] J.X. McDermott, J.F. White, G.M. Whitesides, J. Am. Chem. Soc. 98 (1976) 6521.
[68] G.J. Kubas, Inorg. Synth. 19 (1979) 90.
[69] CAD-4 Express Software, Version 1.1, Enraf-Nonius, Delft, The Netherlands, 1993.
[70] K. Horms, S. Wocadlo, XCAD-4, Program for Processing CAD-4 Diffractometer Data, University of Marburg, Germany, 1995.
[71] G.M. Sheldrick, SHELXS97 and SHELXL97, Program for Crystal Structure Sulution and Refinement, University of Göttingen, Germany, 1997.
[72] L.J. Farrugia, J. Appl. Cryst. 30 (1997) 565.

Polyhedron 28 (2009) 2321–2328

Contents lists available at ScienceDirect

Polyhedron

journal homepage: www.elsevier.com/locate/poly

Synthesis and characterization of 18- and 20-membered hexaaza macrocycles containing pyridine manganese(II) complex nanoparticles dispersed within nanoreactors of zeolite-Y

Masoud Salavati-Niasari *

Institute of Nano Science and Nano Technology, University of Kashan, Kashan, P.O. Box 87317-51167, Islamic Republic of Iran
Department of Chemistry, University of Kashan, Kashan, P.O. Box 87317-51167, Islamic Republic of Iran

ARTICLE INFO

Article history:
Received 7 December 2008
Accepted 16 April 2009
Available online 23 April 2009

Keywords:
Complex nanoparticles
Hexaaza
Macrocycle
Manganese(II)
Zeolite encapsulation

ABSTRACT

Manganese(II) complexes of [18]py_2N_4: 3,6,14,17,23,24-hexaazatricyclo[17.3.1.1^{8,12}]tetracosa-1(23),2,6,8(24),9,11,13,17,19,21-decane; [20]py_2N_4: 3,7,15,19,25,26-hexaazatricyclo[19.3.1.1^{9,13}]hexacosa-1(25),2,7,9(26),10,12,14,19,21,23-decaene; Bzo_2[18]py_2N_4: 3,10,18,25,31,32-hexaazapentacyclo[25.3.1.1.^{12,16}.0^{4,9}.0^{19,24}]dotriaconta 1(31),2,4(9),5,7,10,12(32),13,15,17,19,21,23,25,29-hexadecane and Bzo_2[18]py_2N_4: 2,10,16,24,30,32-hexaazapentacyclo[23.3.1.1^{4,8}.1^{1,1,15}1^{18,22}otriaconta-1(29),2,4,6,8(32),9,11,13,15(31),16,18(30),19,21,23,25,27-hexadecane have been encapsulated in the nanopores of zeolite-Y by the template condensation reaction. Mn(II) complexes with macrocyclic ligand were entrapped in the nanocavity of zeolite-Y by a two-step process in the liquid phase: (i) the adsorption of [bis(diamine)manganese(II)]; [Mn(diamine)$_2$]$^{2+}$@NaY; in the supercages of the zeolite, and (ii) in situ condensation of the manganese(II) precursor complex with 2,6-diacetylpyridine. The new complex nanoparticles entrapped in the nanoreactor of zeolite-Y have been characterized by FT-IR, diffuse reflectance (DRS), X-ray photoelectron (XPS), thermal analysis, UV–Vis spectroscopic techniques, X-ray diffraction (XRD) and elemental analysis as well as by nitrogen adsorption.

© 2009 Elsevier Ltd. All rights reserved.

1. Introduction

Complex nanoparticles entrapped in the nanoreactors of zeolite-Y are fascinating class of materials, which have attracted wide spread attention in basic science as well as in technology development. Zeolites are endowed with a unique physical and chemical characterization, which offers opportunities to manipulate active sites microenvironment. They are even compared with the catalytic antibodies and metallo-enzymes and hence they are often referred to as zeozymes [1]. Some of the prominent physical characteristics of zeolites are their ruggedness to temperature and pressure and their ability to recognize, discriminate and organize molecules with less than 0.1 nm levels precision at the active sites [2]. Moreover, non-corrosive, environmentally friendly and economically viable nature of the zeolite-catalyzed reactions have provided the opportunity for the development of various industrial processes such as fluid catalytic cracking, hydrocracking, isomerization and oxidation.

Zeolites are crystalline aluminosilicates whose internal voids are formed by cavities and channels of strictly regular dimensions and of different sizes and shapes. In particular, the pore structure of Y zeolite consists of almost spherical 1.3 nm cavities interconnected tetrahedrally through smaller apertures of 0.74 nm diameter. The metal complex can be easily accommodated inside the supercages of Y zeolite [3–19]. The large internal surface area and void volumes with extremely narrow pore size distribution as well as functional centres homogeneously dispersed over the surface make nanoporous solids highly active materials. Over the last decades, there has been a dramatic increase in the synthesis, characterization and application of novel nanoporous materials [20].

In this paper, I report the synthesis and characterization of manganese(II) complexes of 18- and 20-membered hexaaza macrocyclic ligand; [18]py_2N_4: 3,6,14,17,23,24-hexaazatricyclo[17.3.1.1^{8,12}]tetracosa-1(23),2,6,8(24),9,11,13,17,19,21-decane; [20]py_2N_4: 3,7,15,19,25,26-hexaazatricyclo[19.3.1.1^{9,13}]hexacosa-1(25),2,7,9(26),10,12,14,19,21,23-decaene; Bzo_2[18]py_2N_4 : 3,10,18,25,31,32-hexaazapentacyclo[25.3.1.1.^{12,16}.0^{4,9}.0^{19,24}]dotriaconta 1(31),2,4(9),5,7,10,12(32),13,15,17,19,21,23,25,29-hexadecane; Bzo_2[18]py_2N_4: 2,10,16,24,30,32-hexaazapentacyclo[23.3.1.1^{4,8}.1^{1,1,15}1^{18,22}otriaconta-1(29),2,4,6,8(32),9,11,13,15(31),16,18(30),19,21,23,25,27-hexadecane; encapsulated within the nanopores of zeolite-Y by the template condensation of 2,6-diacetylpyridine and [bis(diamine)manganese(II)]; [Mn([18]py_2N_4)]$^{2+}$@NaY, [Mn([20]

* Address: Department of Chemistry, University of Kashan, Kashan, P.O. Box 87317-51167, Islamic Republic of Iran. Tel.: +98 361 5555333; fax: +98 361 5552930.
E-mail address: salavati@kashanu.ac.ir

0277-5387/$ - see front matter © 2009 Elsevier Ltd. All rights reserved.
doi:10.1016/j.poly.2009.04.018

$py_2N_4)]^{2+}$@NaY, $[Mn(Bzo_2[18]py_2N_4)]^{2+}$@NaY and $[Mn(Bzo_2[20]$-$py_2N_4)]^{2+}$@NaY; shown in Schemes 1 and 2.

2. Experimental

2.1. Chemical and starting materials

Caution: Although no problems were encountered during the course of this work, attention is drawn to the potentially explosive nature of perchlorates.

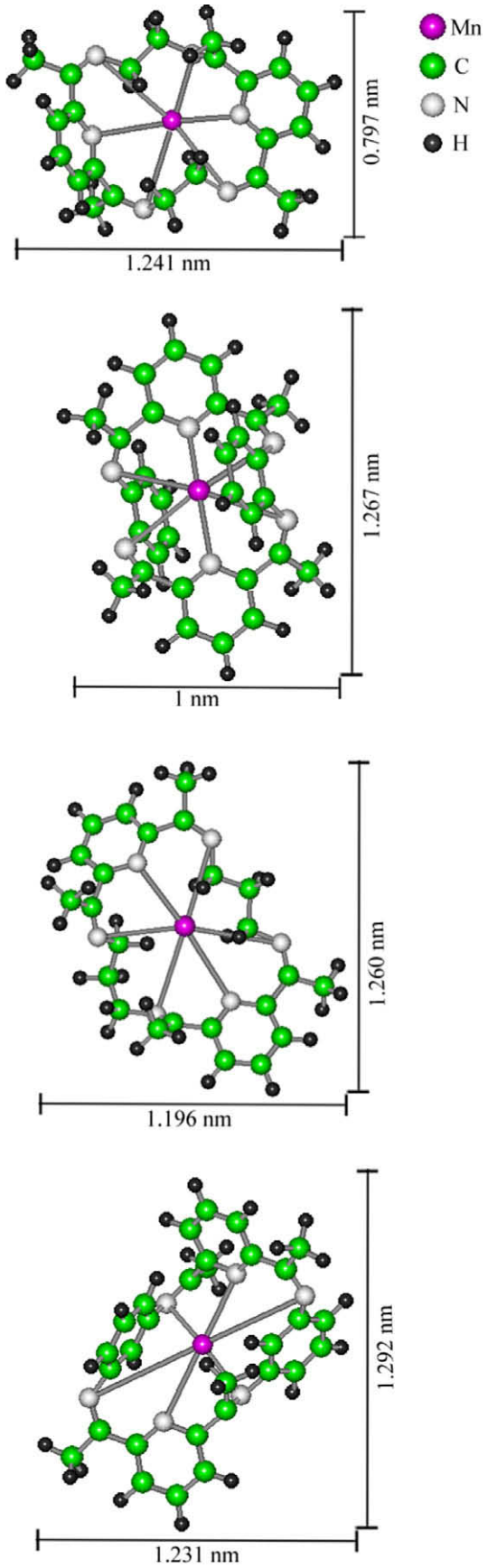
2,6-Diacetylpyridine, 1,2-diaminoethane, 1,3-diaminepropane, 1,2-diaminobenzene, 1,3-diaminobenzene, $MnCl_2{\cdot}6H_2O$ and $LiClO_4{\cdot}3H_2O$ were commercial products obtained from Alfa and Aldrich, and were used without further purifications. The solvents used were of reagent grade and were purified by usual methods. NaY with the Si:Al ratio of 2.53 was purchased from Aldrich (Lot No. 67812). The complex "$[Mn(diamine)_2](ClO_4)_2$" was prepared according to a similar reported procedure [21]. Hexaaza macrocyclic ligands ($[18]py_2N_4$, $[20]py_2N_4$, $Bzo_2[18]py_2N_4$ and $Bzo_2[20]$-py_2N_4) were prepared by following the procedures reported in Ref. [22].

2.2. Physical measurements

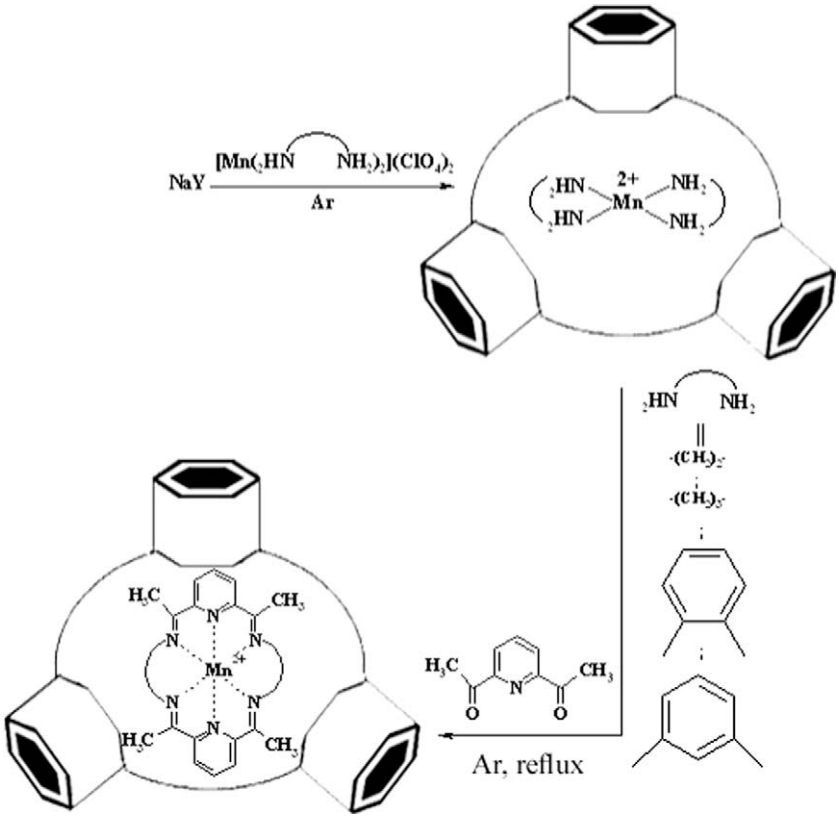
FT-IR spectra were recorded on Shimadzu Varian 4300 spectrophotometer in KBr pellets. The electronic spectra of the neat complexes were taken on a Shimadzu UV–Vis scanning spectrometer (Model 2101 PC). Diffuse reflectance spectra (DRS) were registered on a Shimadzu UV/3101 PC spectrophotometer in the range 1500–200 nm, using MgO as a reference. The elemental analysis (carbon, hydrogen and nitrogen) of the materials was obtained from Carlo ERBA Model EA 1108 analyzer. XRD patterns were recorded by a Rigaku D-max C III, X-ray diffractometer using Ni-filtered Cu Kα radiation. Nitrogen adsorption measurements were performed at 77 K using a Coulter Ofeisorb 100CX instrument. The samples were degassed at 150 °C until a vacuum better than 10^{-3} Pa was obtained. Micropore volumes were determined by the *t*-method, a "monolayer equivalent area" was calculated from the micropore volume [23,24]. The amounts of metallocomplexes encapsulated in zeolite matrix were determined by the elemental analysis and by subtracting the amount of metallocomplex left in the solutions after the synthesis of the materials as determined by UV–Vis spectroscopy, from the amount taken for the synthesis. Atomic absorption spectra (AAS) were recorded on a Perkin–Elmer 4100–1319 Spectrophotometer using a flame approach, after acid (HF) dissolution of the known amounts of the zeolitic material and SiO_2 was determined by gravimetric analysis. XPS (small area X-ray photoelectron spectroscopy) data were recorded with the PHI-5702 Multi-Technique System, Power Source by Mg Kα line and Ag 3d5/2 FWHM 6 0.48 eV. Thermogravimetric-differential thermal analysis (TG-DTA) was carried out using a thermal gravimetric analysis instrument (Shimadzu TGA-50H) with a flow rate of 20.0 mL min^{-1} and a heating rate of 10 °C min^{-1}. FAB mass spectra were recorded on a Kratos MS50TC spectrometer. Distance for as-prepared complexes was calculated by HyperChem (HyperChem is an exceptional molecular modelling programme).

2.3. Preparation of $[Mn([18]py_2N_4)]^{2+}$, $[Mn([20]py_2N_4)]^{2+}$, $[Mn(Bzo_2[18]py_2N_4)]^{2+}$ and $[Mn(Bzo_2[20]py_2N_4)]^{2+}$

To a stirred methanol solution (500 ml) of $[Mn(diamine)_2]$-$(ClO_4)_2$ (42.07 mmol; diamine = 1,2-diaminoethane (2.53 g), 1,3-diaminopropane (3.11 g), 1,2-diaminobenzene (4.54 g) or 1,3-diaminobenzene (4.54 g)) was slowly added 2,6-diacetylpyridine (13.69 g, 84.20 mmol) under nitrogen atmosphere. The mixture was heated at reflux for 12 h until a dark yellow solution resulted.



Scheme 1. 18- and 20-membered hexaaza macrocyclic manganese(II) complexes.



Scheme 2. Encapsulation manganese(II) complex nanoparticles of 18- and 20-membered hexaaza macrocyclic within nanoreactors of zeolite-Y.

The solution was cooled to room temperature and was filtered to remove manganese hydroxide. Excess perchloric acid or lithium perchlorate dissolved in methanol was added to the filtrate, and the mixture was kept in the refrigerator until a deep yellow solid was formed. The deep yellow solid was filtered, washed with diethyl ether and air-dried. The products were crystallized from hot methanol.

2.4. Preparation of $[Mn(diamine)_2]^{2+}$@NaY

To a stirred methanol solution of NaY (4 g) was added 0.37 g of [bis(diamine)manganese(II)] perchlorate (diamine = 1,2-diaminoethane, 1,3-diaminopropane, 1,2-diaminobenzene or 1,3-diaminobenzene) suspended in 100 ml of methanol and was then refluxed for 8 h under Ar atmosphere. The light yellow solid consisting of $[Mn(diamine)_2]^{2+}$ denoted as $[Mn(diamine)_2]^{2+}$@NaY was collected by filtration, washed with ethanol. The resulted zeolites were Soxhlet extracted with ethanol (for 4 h) and then with chloroform (for 3 h) to remove excess unreacted diamine and any Mn(II) complexes adsorbed onto the external surface of the zeolite crystallites. The resulting light yellow solids were dried at 60 °C under vacuum for 24 h.

2.5. Preparation of complex nanoparticles entrapped in the nanopores of zeolite-Y

To a stirred methanol suspension (100 ml) of $[Mn(diamine)_2]^{2+}$@NaY (2 g) was slowly added 2,6-diacetylpyridine (under Ar atmosphere). The mixture was heated under reflux condition for 24 h until a pale yellow suspension resulted. The solution was filtered and the resulting zeolites were Soxhlet extracted with chloroform (for 4 h) and then with ethanol (for 4 h) to remove excess unreacted products from amine–ketone condensation and any manganese(II) complexes adsorbed onto the external surface of the zeolite crystallites. The resulting pale yellow solids were dried at 70 °C under vacuum for 12 h. The remaining [bis(diamine)manganese(II)] ions in zeolite were removed by exchanging with aqueous 0.1 M NaCl solutions. The stability of the encapsulated complex nanoparticles was checked after the reaction by UV–Vis and possible leaching of the complex was investigated by UV–Vis in the reaction solution after filtration of the zeolite. The amounts of Mn(II) complexes encapsulated in zeolite matrix were determined by the elemental analysis and by subtracting the amount of Mn(II) complex left in the solutions after the synthesis of the materials as determined by UV–Vis spectroscopy, from the amount taken for the synthesis.

3. Results and discussion

Hexaaza macrocyclic manganese(II) complexes were prepared by reacting 2 equiv. of 2,6-diacetylpyridine and 1 equiv. of $[Mn(diamine)_2]^{2+}$ (Scheme 1). It was observed that the 18- and 20-membered hexaaza macrocyclic product obtained from the reaction was largely affected by the molar ratio of the reactants. The complexes are soluble in dimethylformamide (DMF) and dimethylsulfoxide (DMSO), but are insoluble in common organic solvents and water. They are thermally stable up to ~250 °C. The complexes are extremely stable in the solid state and in solution and are relatively stable against ligand dissociation even in highly acidic solutions. The analytical data of the metal chelates are given in Table 1, which show that chelates may be represented by the formula $[Mn([18]py_2N_4)](ClO_4)_2$, $[Mn([20]py_2N_4)](ClO_4)_2$, $[Mn(Bzo_2[18]py_2N_4)](ClO_4)_2$ and $[Mn(Bzo_2[20]py_2N_4)](ClO_4)_2$. The measurements of molar conductance in DMF show that these chelates are 1:2 electrolytes. The tests for anions are positive directly without decomposing the chelates showing their presence outside

Table 1
Elemental analysis, vibrations parameters and some physical properties for ligands and 18- and 20-membered hexaaza macrocyclic manganese(II) complexes.

Complex	Calculated (Found)					Λ_M[a], Ω^{-1} (cm^2 mol^{-1})	μ_{eff} (MB)	IR (KBr, cm^{-1})			d ↔ d (nm; ε, l mol^{-1} cm^{-1})	[Mn–ClO_4]$^+$	[M-2ClO_4–H]$^+$
	%C	%H	%N	C/N	%Mn			υ(C=N)	υ(py)	υ(ClO_4^{-1})			
[18]py_2N_4	70.56 (70.34)	7.00 (6.89)	22.4 (22.60)	3.14 (3.11)				1620	1590				
[Mn([18]py_2N_4)](ClO_4)$_2$	42.06 (41.88)	4.17 (4.06)	13.38 (13.50)	3.14 (3.10)	8.74 (8.60)	346	6.01	1615	1593	1080, 625	560 (47) 400 (50) 344 (65) 312 (160)	529	428
[20]py_2aneN_4	71.61 (71.42)	7.51 (7.40)	20.88 (21.00)	3.43 (3.40)				1618	1598				
[Mn([20]py_2N_4)](ClO_4)	43.92 (43.78)	4.61 (4.52)	12.80 (12.96)	3.43 (3.38)	8.37 (8.22)	335	5.96	1613	1600	1086, 624	562 (50) 402(57) 345 (69) 314 (169)	557	456
Bzo_2[18]py_2N_4	76.57 (76.38)	5.57 (5.43)	17.86 (17.98)	4.29 (4.24)				1630	1601				
[Mn(Bzo_2[18]py_2N_4)](ClO_4)	49.74 (49.59)	3.62 (3.51)	11.60 (11.80)	4.29 (4.20)	7.58 (7.44)	342	5.94	1625	1604	1085, 623	558 (43) 397(48) 342 (63) 310 (158)	625	524
Bzo_2[20]py_2N_4	76.57 (76.40)	5.57 (5.45)	17.86 (17.90)	4.29 (4.27)				1635	1603				
[Mn(Bzo_2[20]py_2N_4)](ClO_4)	49.74 (49.62)	3.62 (3.54)	11.60 (11.78)	4.29 (4.21)	7.58 (7.46)	340	5.93	1632	1605	1083, 622	563 (42) 404(53) 347 (66) 316 (166)	625	524

[a] In acetonitrile solutions.

the coordination sphere. The molecular formulae of the complexes have been assigned on the basis of the results of their elemental analyses and the molecular ion peaks in the mass spectra (Table 1).

Synthesis of hexaaza manganese(II) complex nanoparticles encapsulated in the nanocavity of zeolite-Y involves two steps: (i) exchange of $[Mn(diamine)_2]^{2+}$ (diamine = 1,2-diaminoethane, 1,3-diaminopropane, 1,2-diaminobenzene or 1,3-diaminobenzene) ions with NaY in methanol solution and (ii) reaction of $[Mn(diamine)_2]^{2+}$@NaY with excess 2,6-diacetylpyridine in methanol where 2,6-diacetylpyridine slowly enters into the nanocavity of zeolite-Y due to its template nature and interacts with [bis(diamine)manganese(II)] ions. Soxhlet extraction using ethanol and chloroform finally purified the impure complexes. The remaining uncomplexed metal ions in zeolite were removed by exchanging with an aqueous 0.01 M NaCl solution. As one extra anionic ligand would be required to balance the overall charges on the Mn(II), Cl^- of NaCl used during exchanged process fulfills this requirement. Thus, the formula of manganese(II) complex may be written as $[Mn([18]py_2N_4)]^{2+}$@NaY, $[Mn([20]py_2N_4)]^{2+}$@NaY, $[Mn(Bzo_2[18]py_2N_4)]^{2+}$@NaY, $[Mn(Bzo_2[20]py_2N_4)]^{2+}$@NaY. The percentage of metal contents determined before and after encapsulation by inductively coupled plasma (ICP) along with their expected formula is presented in Table 2. As crude mass was extracted with methanol, the metal ion content found after encapsulation is only due to the presence of metal complexes in the nanopores of the zeolite-Y. The molecular formulae of the complex nanoparticles are based on the neat complexes $[Mn([18]py_2N_4)]^{2+}$, $[Mn([20]py_2N_4)]^{2+}$, $[Mn(Bzo_2[18]py_2N_4)]^{2+}$ and $[Mn(Bzo_2[20]py_2N_4)]^{2+}$Y which have also been prepared and characterized.

The C, H, N analysis results of the neat manganese(II) complex nanoparticles showed close similarity to the theoretical values. The molecular formulae of the hexaaza complexes have been assigned on the basis of the results of their elemental analyses. A preliminary identification of the metal complexes was made on the basis of their IR spectra, which exhibited no bands characteristic of free primary amine, thus supporting the proposed macrocyclic

Table 2
Chemical composition, d ↔ d transition and IR stretching frequencies (as KBr pellets) of 18- and 20-membered hexaaza macrocyclic manganese(II) complex nanoparticles encapsulated in the nanoreactor of zeolite-Y.

Sample	C (%)	H (%)	N (%)	C/N	Si (%)	Al (%)	Na (%)	Mn (%)	Si/Al	$\nu_{C=N}$ (cm^{-1})	d ↔ d (nm)
NaY					21.76	8.60	7.50		2.53		
Mn(II)@NaY					22.08	8.73	3.34	2.58	2.53		
$[Mn([18]py_2N_4)]^{2+}$@NaY	4.86	1.78	1.60	3.03	21.00	8.30	5.32	2.29	2.53	1617	558, 400, 343, 312
$[Mn([20]py_2N_4)]^{2+}$@NaY	4.90	1.82	1.52	3.22	20.95	8.28	5.30	2.27	2.53	1614	560, 401, 344, 312
$[Mn(Bzo_2[18]py_2N_4)]^{2+}$@NaY	5.03	1.88	1.23	4.09	20.85	8.24	5.28	2.24	2.53	1627	557, 395, 342, 308
$[Mn(Bzo_2[20]py_2N_4)]^{2+}$@NaY	5.01	1.90	1.24	4.03	20.87	8.25	5.25	2.25	2.53	1634	562, 403, 345, 414

skeleton (Scheme 1). The manganese contents of the materials were estimated by dissolving the known amounts of the materials in conc. HCl and from these solutions, the manganese contents were estimated by using atomic absorption spectrometry (AAS). The chemical compositions (Tables 1 and 2) confirmed the purity and stoichiometry of the neat and encapsulated complexes. The chemical analyses of the samples revealed the presence of organic matter with a C/N ratio roughly similar to that for neat complexes. In Table 2 the mol ratios Si/Al obtained by chemical analysis for zeolites are presented. The Si and Al contents in Mn(II)@NaY and the nanocomposite materials were almost in the same ratio as in the parent zeolite. This indicates little changes in the zeolite framework due to the absence of de-alumination in metal ion exchange. The parent NaY zeolite has Si/Al molar ratio of 2.53 which corresponds to a unit cell formula $[Na_{56}[(AlO_2)_{56}(SiO_2)_{136}]$. The unit cell formula of metal-exchanged zeolites showed a manganese dispersion of 11.4 moles per unit cell $(Na_{33.8}Mn_{11.4}[(AlO_2)_{56}(SiO_2)_{136}].n\text{-}H_2O)$. The analytical data of each complex indicated Mn:C:N molar ratios almost close to those calculated for the mononuclear structure. The excess amount of un-reacted complex can be removed with NaCl solution.

The IR spectra of all the complexes do not exhibit any bands in the region at *ca.* 3400–3200 cm^{-1}, which is the characteristic frequency of the free $-NH_2$ group. There is no absorption ~1600–1700 cm^{-1} due to the free carbonyl group [25]. The absence of stretching and bending vibrations of the (C–O) group at *ca.* 1525 and 1280 cm^{-1} substantiates the absence of this group [26]. The strong bands appearing as doubles at *ca.* 1610–1640 cm^{-1} may be assigned to υ(C=N) vibrations and point towards the coordinated azomethine groups [27,28]. Therefore, it is clear from the IR spectra that both the NH_2 groups of diamine have condensed with both the carbonyl groups of 2,6-diacetylpyridine to give rise to an N_6 arrangement of four azomethines and two pyridine nitrogen atoms equally suitable for coordination. 2,6-Disubstituted pyridine derivatives show various bands at *ca.* 1585–1615, 1570–1590, 1455–1490 and at *ca.* 1440–1445 cm^{-1} can be assigned to four υ(C=C) skeletal frequencies and designated as bands I, II, III and IV of pyridine rings, respectively [27–29]. The spectra also exhibit a ring breathing mode at *ca.* 990 cm^{-1}, an out-of-plane (C–H) deformation at *ca.* 800 cm^{-1}, an in-plane (C–C) deformation at *ca.* 615 cm^{-1} and an out-of-plane (C–C) deformation at *ca.* 405 cm^{-1}, respectively. The two strong bands at *ca.* 785 and 740 cm^{-1} are assigned to γ(C–H) and ø(C–C) vibrations [30], respectively.

The spectra of the chelates exhibit a downward shift in the location of bands I, II, III and IV. The bands at *ca.* 990 cm^{-1} disappear and are replaced by a band at *ca.* 1015–1025 cm^{-1}.The band assigned γ(C–C) splits into two at *ca.* 725 and 740 cm^{-1}, while γ(C–H) appears at *ca.* 785 cm^{-1} as a single band. These changes point towards the involvement of the pyridine nitrogen in coordination. Furthermore, the bands assignable to an in-plane (C–C) deformation (~605 cm^{-1}) and an out-of-plane (C–C) deformation (~410 cm^{-1}) undergo an upward shift to 15–20 cm^{-1} in the spectra of chelates, which is consistent with the coordination of pyridine-nitrogen to the metal atom [31]. This mode of coordination is further supported by the far-IR spectra of complexes. In the spectra of complexes under study, a strong band at *ca.* 1615 cm^{-1} with a shoulder at *ca.* 1610 cm^{-1} may be assigned to symmetric and anti-symmetric stretching modes of the azomethine linkage [32] and the frequency concerned with the υ(C=N) stretching mode shifted to a lower range by 2–5 cm^{-1}, with a marginal loss of the intensity of the band. This lowering may be taken as an indication of the coordination of the nitrogen of the azomethine group to the metal atom [33]. The appearance of one band at *ca.* 1080 and 625 cm^{-1} assignable to Cl_4^- stretching and bending modes, respectively, is found in the perchlorate complexes of manganese(II). The position of these bands is compatible with the ionic perchlorate group [34].

The far-IR spectra of the complexes show various bands in various regions assignable to pyridine ring and metal-nitrogen vibrations. The spectra of the complexes derived from 2,6-diacetylpyridine and diamine show bands at *ca.* 415 and 600 cm^{-1}, assignable to (C–C) out-of-plane and (C–C) in-plane deformations. The vibrations suffer significant shift towards higher frequencies and support pyridine-nitrogen coordination to the metal atom [35]. The spectra also exhibit various bands in the region at *ca.* 260-280 cm^{-1}. In this region the various vibrations observed are at *ca.* 260–270, 265–274 and 275–280 cm^{-1} and these may be assigned to υ(Mn–py) stretching vibrations, respectively [36]. The far-IR spectra also show various bands at *ca.* 430–495 cm^{-1}, which implies $\upsilon_{(Mn-N)}$ (azomethine) vibrational modes and confirms the involvement of the azomethine nitrogen.

IR spectroscopy provided information on the integrity of the encapsulated complexes, as well as the crystallinity of the host zeolite. The IR bands of all encapsulated complexes were weak due to their low concentration in the zeolite. Mn(II) complexes encapsulated in the zeolite cages did not show any significant shift in C=N stretching modes. I did not notice any appreciable changes in the frequencies of Mn complexes after incorporation into zeolite matrix. The major FT-IR bands of the encapsulated complexes are tabulated in Table 2. All metal complexes encapsulated zeolites exhibit band around 1140, 1035, 960, 780 and 740 cm^{-1} due to zeolite framework. No significant broadening or shift of the structure-sensitive zeolite vibrations at 1130 cm^{-1} (due to the asymmetric T–O stretch) on encapsulation of metal complexes indicates that there is no significant expansion of the zeolite nanocavities or dealumination during the encapsulation process. This further indicates that the structure of metal complexes fit nicely within the cavity of the zeolite.

The magnetic moment measurements of the manganese(II) complexes at room temperature are in the range 5.93–6.01 BM (Table 1), corresponding to five unpaired electrons. Electronic spectra of Mn(II) complexes exhibit four weak intensity absorption bands, in the range 560 nm (ε = 47 l mol^{-1} cm^{-1}), 400 nm (ε = 50 l mol^{-1} cm^{-1}), 344 nm (ε = 65 l mol^{-1} cm^{-1}) and 312 nm (ε = 160 l mol^{-1} cm^{-1}). These bands may be assigned to the transitions: $^6A_1g \rightarrow {}^4T_1g$ (^4G), $^6A_1g \rightarrow {}^4Eg$, ^4A_1g (^4G), $^6A_1g \rightarrow {}^4Eg$ (^4D) and $^6A1\,g \rightarrow {}^4T_1g$ (^4P), respectively (Table 1). When the complex

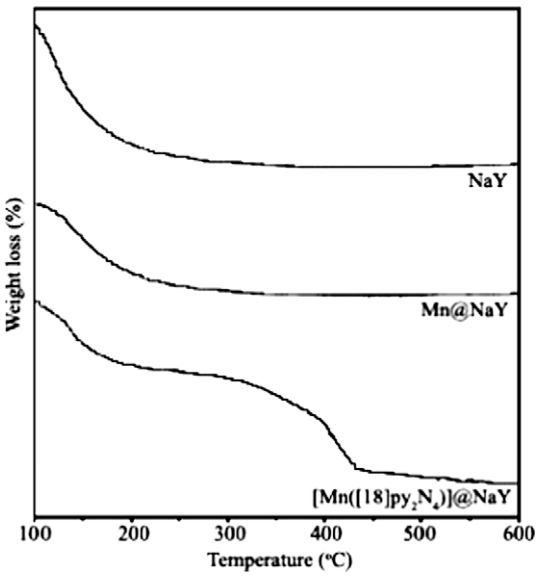


Fig. 1. TGA profiles of NaY, Mn@NaY and $[Mn([18]py_2N_4)]^{2+}$@NaY.

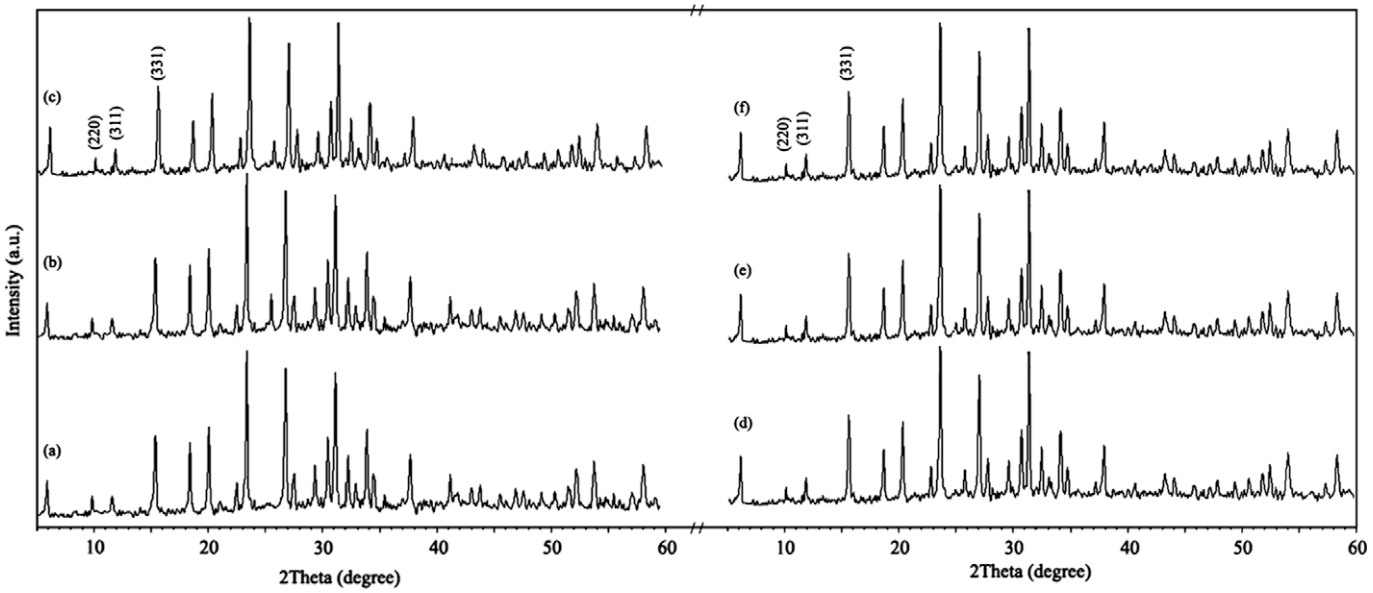


Fig. 2. XRD patterns of (a) NaY, (b) Mn@NaY, (c) $[Mn([18]py_2N_4)]^{2+}$@NaY, (d) $[Mn([20]py_2N_4)]^{2+}$@NaY, (e) $[Mn(Bzo_2[18]py_2N_4)]^{2+}$@NaY, (f) $[Mn(Bzo_2[20]py_2N_4)]^{2+}$@NaY.

nanoparticles were encapsulated in zeolite-Y, the d ↔ d band shifted again to the higher energy side. The stability of the complexes increases apparently when they are encapsulated in zeolite-Y. The position of the d ↔ d band corresponds to a octahedral geometry for macrocyclic manganese(II) complex nanoparticles [37].

The TGA profile of one of the representative nanocomposite material, $[Mn([18]py_2N_4)]^{2+}$@NaY is given in Fig. 1. The thermal decomposition of all these materials occurs in two steps. The endothermic loss in the first step starts shortly after increasing the temperature above 150 °C and continues until the loss of all intrazeolite water. The exothermic loss in the two steps, as expected, occurs in a wide temperature range (200–500 °C) and is due to the slow decomposition of the chelating ligand. A very small weight percentage loss indicates the presence of only small amount of metal complex insertion in the cavity of the zeolite. This is in agreement with the low percentage of metal content estimated by atomic absorption spectrometer. As shown in Fig. 1, the decomposition of encapsulated complexes occurred at high temperature, so the encapsulated complexes are stable than the neat complexes [38–41].

The X-ray powder diffraction (XRD) patterns of NaY, Mn(II)@-NaY and encapsulated complexes along with simple complexes "$[Mn([18]py_2N_4)]^{2+}$" were recorded at 2θ values between 5° and 60° to study the crystallinity and to ensure encapsulation (Fig. 2). The XRD patterns of manganese exchanged zeolite and their respective encapsulated complexes are essentially similar to that of NaY, though a slight change in the intensity of the bands has been noticed. The relative peak intensities of the 220, 311 and

Table 3
Surface area and pore volume data of 18- and 20-membered hexaaza macrocyclic manganese(II) complex nanoparticles encapsulated in nanopores of zeolite-Y.

Sample	Surface area[a] (m^2/g)	Pore volume[b] (cm^3/g)
NaY	545	0.31
Mn(II)@NaY	535	0.30
$[Mn([18]py_2N_4)]^{2+}$@NaY	324	0.12
$[Mn([20]py_2N_4)]^{2+}$@NaY	316	0.11
$[Mn(Bzo_2[18]py_2N_4)]^{2+}$@NaY	285	0.07
$[Mn(Bzo_2[20]py_2N_4)]^{2+}$@NaY	276	0.06

[a] Surface area is the "monolayer equivalent area" calculated as explained in Refs. [23,24].
[b] Calculated by the *t*-method.

Table 4
Curve fitting data of the XPS spectra in the Si 2p, Al 2p, Na 1s, Mn 2p3/2, C 1s, O 1s and N 1s bands of the samples.

Sample	Binding energy (eV)								
	Si (2p)	Al (2p)	Na (1s)	Mn (2p3/2)	C (1s)	O (1s)	N (1s)	Si/Al[a]	2p3/2 and 2p1/2 separation (eV)
NaY	103.5	75.1	1072.6		285.0	531.0		2.60	
Mn(II)@NaY	103.5	75.1	1072.6	639.9	285.0	532.5		2.57	
					285.0, 286.5		400.1	2.41	
$[Mn([18]py_2N_4)]^{2+}$@NaY	103.5	75.1	1074.0	640.5		532.6			13.3
					286.9, 289.4		402.3		
					285.0, 286.5		400.1	2.40	
$[Mn([20]py_2N_4)]^{2+}$@NaY	103.5	75.1	1074.1	640.3		532.6			13.1
					286.9 289.4		402.3		
					285.0, 286.9		400.6	2.39	
$[Mn(Bzo_2[18]py_2N_4)]^{2+}$@NaY	103.5	75.1	1074.3	640.6		532.7			13.7
					289.5, 289.1		402.3		
					285.0, 286.9		400.6		
$[Mn(Bzo_2[20]py_2N_4)]^{2+}$@NaY	103.5	75.1	1074.3	640.4		532.7		2.39	13.2
					289.5, 289.1		402.3		

[a] Amount of the elements determined by XPS analysis of the samples.

331 reflections have been thought to be correlated to the locations of cations. In zeolite-Y, the order of peak intensity is in the order: $I_{331} \gg I_{220} > I_{311}$, while in encapsulated complexes, the order of peak intensity became $I_{331} \gg I_{311} > I_{220}$. The difference indicates that the ion-exchanged Mn^{2+}, which substitutes at the location of Na^{+}, undergoes rearrangement during complexation. These observations indicate that the framework of the zeolite has not undergone any significant structural changes during the incorporation of the materials, i.e. the crystallinity of zeolite-Y is preserved during encapsulation. This clearly suggests the presence of metal complexes in zeolite matrix. X-ray diffraction indicated that zeolites with good crystallinity can be obtained during the encapsulation of manganese(II) complexes by the template condensation reaction.

The surface area and pore volume of the materials are presented in Table 3. The encapsulation of $[Mn([18]py_2N_4)]^{2+}$, $[Mn([20]py_2N_4)]^{2+}$, $[Mn(Bzo_2[18]py_2N_4)]^{2+}$ and $[Mn(Bzo_2[20]py_2N_4)]^{2+}$ complexes in zeolite reduced the adsorption capacity and the surface area of the zeolite. The lowering of the pore volume and surface area indicated the presence of complexes ($[Mn([18]py_2N_4)]^{2+}$, $[Mn([20]py_2N_4)]^{2+}$, $[Mn(Bzo_2[18]py_2N_4)]^{2+}$, $[Mn(Bzo_2[20]py_2N_4)]^{2+}$) within the zeolite nanocages and not on the external surface.

The presence of the complex in NaY was supported by XPS analysis. All modified NaY samples revealed the presence of oxygen, sodium, silicon and aluminum from the zeolite lattice in their XPS resolution spectra. The bands typical of the Mn(II)–py_2N_4 complex, scarcely visible because of their low loading, were identified in the Mn $2p_{3/2}$ and N 1s region. The bulk (Table 1) and the surface Si/Al (Table 4) atomic ratios of NaY and of modified samples were similar, which indicates that dealumination does not occur during the encapsulation procedure. The binding energies of the elements detected by XPS are summarized in Table 4. The most intense bands identified are due to the zeolite structure, in the Si 2p region a band at 103.5 eV typical for Si atoms with different chemical environments, such as SiO_4 and terminal Si–OH groups. In the Al 2p region a band at 75.1 eV from the tetrahedral AlO_4 groups and a symmetrical large band at 531.0 eV from the O 1s region, and finally a band in the Na 1s region at 1072.6 eV were also observed (Table 4).

As seen from Table 4, the amount of surface manganese is very similar to the that of bulk manganese content (Table 1), which suggests that the Mn(II)–py_2N_4 complexes are homogeneously distributed throughout the NaY crystals. The medium binding energy values for Mn 2p3/2 are different before and after encapsulation, which indicates the change in environment of the manganese upon coordination with the py_2N_4 ligand. Before coordination the medium binding energy of Mn 2p3/2 value was 639.9 eV (Mn(II)@NaY) and after the complex encapsulation the value is 640.5 eV, $[Mn([18]py_2N_4)]^{2+}$@NaY; 640.3 eV, $[Mn([20]py_2N_4)]^{2+}$@NaY; 640.6 eV, $[Mn(Bzo_2[18]py_2N_4)]^{2+}$@NaY and 640.4 eV, $[Mn(Bzo_2[20]py_2N_4)]^{2+}$@NaY (Table 4). These results confirm the same manganese coordination sphere for the complex when free or encapsulated within NaY zeolite and that the host matrix environment does not affect the valence state of the metal atom of the complex.

The high resolution C 1s spectrum of encapsulated complexes shows an asymmetric band centred at 285.0 eV that can be deconvoluted into three individual bands (Table 4). The three bands at high energy were also observed in the starting material and are presumably due to the presence of some contamination. The band at 289.0 eV is attributed to the aromatic carbons of the py_2N_4 ligand. The encapsulated complexes and the free complex samples exhibit a band centred at 400.1 and 402.3 eV in the N 1s region, due to the contribution of nitrogen atoms of the ligand (Fig. 3).

Fig. 3 shows the Mn 2p core levels of neat and encapsulated complexes. Manganese remains in the 2+ oxidation state in both

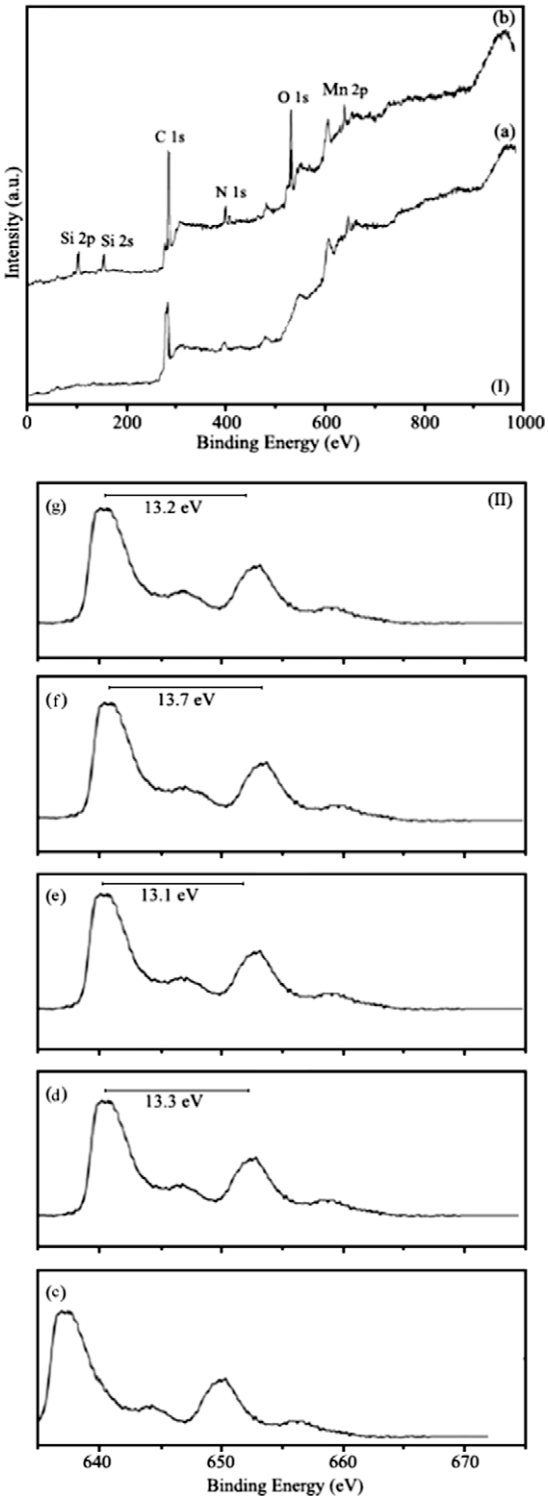


Fig. 3. XPS spectra of (I) (a), $[Mn([18]py_2N_4)](ClO_4)_2$; (b), $[Mn([18]py_2N_4)]^{2+}$@NaY. (II) XPS Mn 2p2/3 of (c), $[Mn([18]py_2N_4)](ClO_4)_2$; (d), $[Mn([18]py_2N_4)]^{2+}$@NaY; (e), $[Mn([20]py_2N_4)]^{2+}$@NaY; (f), $[Mn(Bzo_2[18]py_2N_4)]^{2+}$@NaY; (g), $[Mn(Bzo_2[20]py_2N_4)]^{2+}$@NaY.

the neat and encapsulated complexes and it matches well with the reported values for similar systems [42]. There is a strong increase in satellite intensity for Mn 2p levels and a large energy gap (13.1–13.7 eV) between them is observed from encapsulated complex, which results in higher stability than in neat complex. Table 4 lists out the relevant parameters for Mn complexes.

4. Conclusion

The octahedral hexaaza complex nanoparticles; [Mn-([18]py_2N_4)]$^{2+}$, [Mn([20]py_2N_4)]$^{2+}$, [Mn(Bzo_2[18]py_2N_4)]$^{2+}$ and [Mn(Bzo_2[20]py_2N_4)]$^{2+}$; have been encapsulated in the nanocavity of zeolite by template condensation between pre-entrapped; [bis(diamine)manganese(II)] (diamine = 1,2-diaminoethane, 1,3-diaminopropane, 1,2-diaminobenzene, 1,3-diaminobenzene), [Mn(N–N)$_2$]$^{2+}$@NaY; complexes with 2,6-diacetylpyridine. This strategy appears to be effective for the encapsulated of Mn(II) complexes with 18- and 20-membered hexaaza macrocycle ligands derived from [Mn(N–N)$_2$]$^{2+}$@NaY, as template condensation in the nanocavity is still possible and no unreacted [Mn(N–N)$_2$]$^{2+}$ ions were detected. Furthermore, the spectroscopic data suggest that the encapsulated complex nanoparticle experience very little distortion in the supercage and that the chemical ligation to the zeolite surface is minimal.

Acknowledgement

The author is grateful to Council of University of Kashan for providing financial support to undertake this work.

References

[1] C.R. Jacob, S.P. Varkey, P. Ratnasamy, Appl. Catal. A: Gen. 168 (1998) 353.
[2] P.C.H. Mitchel, Chem. Ind. 6 (1991) 308.
[3] M. Salavati-Niasari, Inorg. Chem. Commun. 9 (2006) 628.
[4] M.R. Maurya, S.J.J. Titinchi, S. Chand, J. Mol. Catal. A: Chem. 214 (2004) 257.
[5] M. Salavati-Niasari, F. Davar, Inorg. Chem. Commun. 9 (2006) 263.
[6] M. Salavati-Niasari, F. Davar, Inorg. Chem. Commun. 9 (2006) 304.
[7] M. Salavati-Niasari, J. Mol. Catal. A: Chem. 245 (2006) 192.
[8] I.W.C.E. Arends, R.A. Sheldon, Appl. Catal. A: Gen. 212 (2001) 175.
[9] M. Salavati-Niasari, Chem. Lett. 34 (2005) 1444.
[10] M. Salavati-Niasari, J. Mol. Catal. A: Chem. 229 (2005) 159.
[11] P.P. Knops-Gerrits, F. Thibault-Starzyk, P.A. Jacobs, Stud. Surf. Sci. Catal. 84 (1994) 1411.
[12] D. Chatterjee, A. Mitr, J. Mol. Catal. A: Chem. 144 (1999) 363.
[13] M. Salavati-Niasari, Chem. Lett. 34 (2005) 244.
[14] M. Salavati-Niasari, Inorg. Chem. Commun. 8 (2005) 174.
[15] M. Salavati-Niasari, Inorg. Chem. Commun. 7 (2004) 963.
[16] M. Salavati-Niasari, J. Mol. Catal. A: Chem. 217 (2004) 87.
[17] K.J. Balkus Jr., A.K. Khanrnamedova, K.M. Dixon, F. Bedioui, Appl. Catal. A: Gen. 143 (1996) 159.
[18] R.F. Parton, I.F.J. Vankelecom, M.J.A. Casselman, C.P. Bezoukhanova, J.B. Uytterhoeven, P.A. Jacobs, Nature 370 (1994) 541.
[19] G. Li, L. Chen, J. Bao, T. Li, F. Mei, Appl. Catal. A: Gen. 346 (2008) 134.
[20] A.K. Cheetham, G. Ferey, T. Loiseau, Angew. Chem., Int. Ed. 38 (1999) 3268.
[21] J. Basset, G.H. Denney, G.H. Jeffery, J. Mendham, Vogel's Textbook of Quantitative Inorganic Analysis, Wiley, New York, 1987. p. 429.
[22] R.W. Stotz, R.C. Stoufer, Chem. Commun. (1970) 1682.
[23] S.W. Wang, H. Everett, R.A.W. Haul, L. Moscou, R.A. Pierotti, J. Rouquerol, T. Siemieniewska, Pure Appl. Chem. 57 (1985) 603.
[24] A. Lineares-Solano, Textural characterization of porous carbons by physical adsorption of gases, in: J.L. Figueiredo, J.A. Moulijn (Eds.), Carbon and Coal Gasification, M. Nijhoff, M.A. Dordrecht, 1986. p. 137.
[25] M. Tsuboi, Bull. Chem. Soc. Jpn. 25 (1952) 385.
[26] K. Nakamoto, Infrared Spectra of Inorganic and Coordination Compounds, 2nd ed., Wiley Interscience, New York, 1970.
[27] V.B. Rana, J.N. Gurtu, M.P. Teotia, J. Inorg. Nucl. Chem. 42 (1980) 331.
[28] V.B. Rana, D.P. Singh, P. Singh, M.P. Teotia, Trans. Met. Chem. 6 (1981) 1982.
[29] D.P. Singh, V.B. Rana, Polyhedron 14 (1995) 2901.
[30] W.J. Gilbert, L.T. Taylor, J.G. Dillard, J. Am. Chem. Soc. 95 (1973) 2477.
[31] N.S. Gill, H.J. Kingdom, Aust. J. Chem. 19 (1966) 2197.
[32] L.T. Taylor, R.D. Patton, Inorg. Chim. Acta 8 (1974) 191.
[33] C.N.R. Rao, Chemical Application of Infrared Spectroscopy, Academic Press, New York, 1963.
[34] D.M. Adams, Metal-Ligand and Related Vibrations, Arnold, London, 1967.
[35] J.R. Ferraro, Low Frequency Vibrations of Inorganic and Coordination Compounds, Plenum Press, New York, 1971.
[36] R.J.H. Clark, C.S. Williams, Inorg. Chem. 4 (1965) 350.
[37] A.B. Lever, Inorganic Electronic Spectroscopy, 2nd ed., Elsevier, New York, 1968.
[38] R. Abraham, K.K.M. Yusuff, J. Mol. Catal. A: Chem. 198 (2003) 175.
[39] A. Romero, A. Garrido, A. Nieto-Márquez, P. Sánchez, A. de Lucas, J.L. Valverde, Micropor. Mesopor. Mater. 110 (2008) 318.
[40] T.M. Salama, I.O. Ali, H.A. Gumaa, Micropor. Mesopor. Mater. 113 (2008) 90.
[41] K.J. Balkus, M. Eissa Jr., R. Lavado, Stud. Surf. Sci. Catal. 94 (1995) 713.
[42] M. Salavati-Niasari, S.N. Mirsattari, M. Bazarganipour, Polyhedron 27 (2008) 3653.

Polyhedron 28 (2009) 2329–2334

Contents lists available at ScienceDirect

Polyhedron

journal homepage: www.elsevier.com/locate/poly

Interaction of Cu-dipeptide complexes with Calf Thymus DNA and antiproliferative activity of [Cu(ala-phe)] in osteosarcoma-derived cells

Gianella Facchin [a], Eduardo Kremer [a], Daniel A. Barrio [b], Susana B. Etcheverry [b], Antonio J. Costa-Filho [c], María H. Torre [a,*]

[a] Química Inorgánica, DEC, Facultad de Química, Gral. Flores 2124, CC1157 Montevideo, Uruguay
[b] Bioquímica Patológica, Facultad de Ciencias Exactas, Universidad Nacional de La Plata, 47 y 115 (1900) La Plata, Argentina
[c] Grupo de Biofísica Sérgio Mascarenhas, Instituto de Física de São Carlos, Universidade de São Paulo, C.P. 369, 13560 São Carlos (SP), Brazil

ARTICLE INFO

Article history:
Received 18 September 2008
Accepted 22 April 2009
Available online 3 May 2009

Keywords:
Cu(II)complexes
DNA-interaction
EPR
CD
Osteosarcoma

ABSTRACT

In this work the study of Calf Thymus DNA interaction with several Cu(L-dipeptide) complexes was reported. The binding stoichiometry (Cu(mmol)/DNAmol base) was determined and in an attempt to clarify the binding mode, EPR and CD experiments were performed. All the studied complexes interacted with DNA, in a more selective way than $[Cu(H_2O)_6]^{2+}$, being the [Cu(ala-phe)] the complex with the highest interaction. The EPR experiments suggested that the monomeric species formed in solution were coordinated through a nitrogen atom of the DNA bases (inner-sphere binding) and the CD studies showed structural changes upon the DNA–complex interaction. Besides, the ratio Cu(mmol)/DNAmol base obtained by the binding stoichiometry experiments was close to that found by EPR and CD determinations. The effect on cell proliferation determined by the crystal violet bioassay on UMR106 rat osteosarcoma-derived cells showed that the [Cu(ala-phe)] complex exerted an antiproliferative action against this tumor line.

© 2009 Elsevier Ltd. All rights reserved.

1. Introduction

The interaction of metal complexes with nucleic acids and their constituents has been a subject of interest in bioinorganic chemistry, especially since the discovery of cisplatin and their analogues. These studies have been useful for the development and the comprehension of the activity of new chemotherapeutic agents designed for the treatment of numerous diseases [1–3]. Many of these chemotherapeutic agents act by inhibition of the synthesis of the deoxyribonucleic acid (DNA), a natural target due to its predominant role in cellular replication. One way to achieve this inhibition is by direct DNA binding in either a noncovalent interaction by intercalation, groove-face binding or external electrostatic binding or a covalent interaction due to an outer-sphere or inner-sphere binding and (or consecutive) strand breakage [4,5].

In particular, in the search for new drugs the proposal that complexes based on essential metals may be less toxic than those with non essential ones led to the study of copper based drugs, some of them having an important cytotoxic effect [6–8]. Consequently, active copper compounds and their interaction with DNA have attracted great interest [5,9–11]. These studies have mostly used methods that focus on changes in the DNA structure as electronic absorption titration, fluorescence spectroscopy, viscosity measurements and circular dichroism, among others. For instance, chemotherapeutic copper complexes with polypyridil ligands showed an important interaction with DNA as intercalators as determined by UV–Vis and circular dichroism (CD) spectroscopies and viscosity [3]. Moreover, Sarkar's group studied the DNA interaction of Cu(II) complexes with piroxicam and meloxicam (anti-inflammatory drugs) which exhibited anticancer activity by UV–Vis and circular dichroism (CD) spectroscopies. They showed that their complexes bind strongly to DNA-backbone possibly with intercalation [12].

On the other hand, there is much less work using methods based on properties related to the metal ion. In this area relevant studies were performed by Chikira's group that provided information on the binding of copper complexes with amino acids or peptides to DNA fibers by electronic paramagnetic resonance (EPR) [13–20].

As a part of our research on metal-based drugs we have studied several copper complexes with oligopeptides as potential antitumoral agents encouraged by the antecedents in the literature [21,22]. In particular, we have synthesized and structurally characterized in solid state and in water solution a series of copper complexes with dipeptides [23–30] and analysed their magnetic interactions [31,32].

Due to these previously reported antecedents and with the aim of obtaining structural information about the interaction of DNA with copper-dipeptide complexes we explored changes in the environment of the copper ion and in the DNA upon coordination.

* Corresponding author. Tel.: +598 2 9249739; fax: +598 2 9241806.
E-mail address: mtorre@fq.edu.uy (M.H. Torre).

0277-5387/$ - see front matter © 2009 Elsevier Ltd. All rights reserved.
doi:10.1016/j.poly.2009.04.029

In particular, the study of the DNA interaction with several Cu(L-dipeptide) complexes previously characterized by our research group was performed. Several dipeptides commercially available were selected in an effort to include ligands with inverted sequences of aminoacids and to cover a series containing aminoacids with different sizes. The aim of this selection was to perform a screening that provides structural information useful for biggest systems. Firstly, the direct quantification of the amount of copper bound to the DNA (binding stoichiometry) was measured. Secondly, EPR experiments were made with the complex that presented the best binding stoichiometry and with two complexes that presented medium interaction, in order to test whether there was any change in the Cu(II) coordination sphere when binding to the DNA. CD technique was used to explore the distortion introduced in the DNA structure upon binding with complexes or the distortion in the Cu(dipeptide) complexes.

Besides, to evaluate potential pharmacological activity of the complexes, a cell proliferation assay on UMR106 rat osteosarcoma-derived cells was performed.

2. Materials and methods

2.1. Synthesis of the complexes and analytical characterization

The copper (II) complexes with L-dipetides (SIGMA) ala-ala, ala-val, ala-ile, ala-leu, ala-thr, ala-phe, ala-tyr, phe-ala, phe-leu, phe-phe, val-phe, val-gly were obtained and characterized as described previously [26,27,29,30].

Table 1 summarizes the stoichiometry and analytical data for the Cu(II) complexes. Elemental analysis was performed with a CARLO ERBA EA 1108 equipment.

2.2. Spectroscopic measurements

Electronic absorption spectra of aqueous solution samples were recorded on a Milton Roy Spectronic 3000 spectrophotometer, using 1-cm path length quartz cells.

The copper concentration was measured by atomic absorption spectroscopy using a Perkin–Elmer 5000 instrument, with a Photron lamp for copper analysis, at 325 nm with air/acetylene flame.

X-band (9.5 GHz) EPR measurements were carried out on frozen aqueous solutions using a Varian E109 spectrometer and cavity with 100 kHz field modulation. The measurements were performed at N_2 liquid temperature. The *g*-values were obtained from spectral simulations using the QPOW program [33].

The CD spectra were recorded using a Jasco 720 instrument in a 1-cm path length quartz cell, in the 200–300 nm range.

2.3. Determination of the stoichiometry of the interaction Cu(II)dipeptide–DNA

The technique used in order to determine the stoichiometry of the interaction of the complexes with DNA was adapted from Mahnken et al. [34]. An aqueous solution of Calf Thymus DNA (SIGMA) (c.a. 1.7 mg/mL, 1 mL) was allowed to react with an aqueous solution of Cu-dipeptide (c.a. 1 mM, 1 mL) for 24 h at 37 °C.

The DNA was precipitated afterwards by addition of absolute ethanol (4 mL) and an aqueous solution of NaCl (2 M, 0.2 mL), and it was centrifuged (30 min at 50 rpm). The supernatant was discarded. The precipitate was dissolved in 2 mL of H_2O. This process was repeated three times. DNA and copper concentrations were monitored in the final solution. DNA concentration was determined at 260 nm using $\varepsilon_M = 6000\ M^{-1}\ cm^{-1}$. Copper concentration was measured by atomic absorption spectroscopy as described in Section 2.1. The solubility of the complexes was checked in the conditions of the precipitation of the DNA. The interaction was expressed as the ratio: Cu(mmol)/DNA(mol base).

2.4. Cu(II)dipeptide–DNA binding: characterization by EPR measurements

The EPR spectra of an aqueous solution of Calf Thymus DNA (SIGMA, 2.45 mg/mL) in presence of increasing amounts of copper complexes were recorded. The dilution scheme for each Cu(II) complex covered a 10–500 μM range, while the concentration of the DNA solution varied from 500 to 700 μM in DNA bases (pH 7). After each addition of copper complex the mixture was allowed to mix for 15 min at room temperature and then an aliquot was frozen at N_2 liquid temperature in order to register the EPR spectrum.

2.5. Cu(II)dipeptide–DNA binding: characterization by CD measurements

The CD spectra of an aqueous solution of Calf Thymus DNA (SIGMA) in presence of increasing amounts of copper complexes were recorded. The dilution scheme for each Cu(II) complex covered a 0.5–5 μM range, while the concentration of the DNA solution (DNA concentration was determined at 260 nm using $\varepsilon_M = 6000$) remained approximately constant at 50 μM in DNA bases (pH 7). As the data were obtained in excess of DNA, the total molar concentration remained nearly constant in all the spectra of each complex. This enabled us to perform a Job analysis of the data at 218 nm in order to estimate a binding constant for DNA–[Cu-peptide] [35].

Table 1
Stoichiometry, code and analytical data for the Cu(II) complexes.

Complex code	Complex stoichiometry	%C		%N		%H	
		Calc.	Exp.	Calc.	Exp.	Calc.	Exp.
1	$[Cu(ala\text{-}ala)]\cdot 2H_2O$	27.93	27.57	10.86	10.41	5.40	4.89
2	[Cu(ala-val)]	38.44	38.40	11.21	11.15	5.60	5.66
3	[Cu(ala-ile)]	40.94	40.85	10.61	10.55	6.06	6.18
4	$[Cu_3(ala\text{-}leu)_3(H_2O)_3(CO_3)]\cdot PF_6\cdot H_2O$	31.40	32.23	7.85	8.17	5.54	6.09
5	$[Cu(ala\text{-}thr)]\cdot {}^1/_2H_2O$	32.22	32.30	10.74	10.66	4.98	5.05
6	$[Cu(ala\text{-}phe)]\cdot {}^1/_2H_2O$	48.35	48.15	9.40	9.30	4.70	4.81
7	$[Cu(ala\text{-}tyr)]\cdot H_2O$	43.40	43.33	8.44	8.54	4.82	4.98
8	$[Cu(phe\text{-}ala)]\cdot {}^1/_2H_2O$	46.93	47.12	9.13	9.19	4.89	4.23
9	[Cu(phe-leu)]	53.01	53.21	8.24	8.52	5.93	6.26
10	[Cu(phe-phe)]	57.82	57.42	7.49	7.57	4.85	4.76
11	[Cu(val-phe)]	51.60	51.96	8.60	8.71	5.57	6.01
12	[Cu(val-gly)]	35.67	35.92	11.88	11.96	5.13	5.58

2.6. Cell proliferation assay

Due to the fact that [Cu(ala-phe)] presented the higher interaction with DNA, it was selected to study the antiproliferative activity. The effect of the copper salt and [Cu(ala-phe)] complex over the cell proliferation was study in a model of osteoblastic tumoral UMR106 cells.

UMR106 rat osteosarcoma-derived cells were grown in DMEM supplemented with 100 U/ml penicillin, 100 μg/ml streptomycin and 10% (v/v) serum bovine fetal (FBS) at 37 °C, 5% CO_2. When 70–80% confluence was reached, cells were subcultured using 0.1% trypsin 1 mM EDTA in Ca^{2+}–Mg^{2+} free phosphate buffered saline (PBS) (11 mM KH_2PO_4, 26 mM Na_2HPO_4, 115 mM NaCl, pH: 7.4). For experiments, cells were grown in 24-well plates. When cells reached 70% confluence, the monolayers were washed twice with DMEM and were incubated in different conditions according to the experiment.

A mitogenic bioassay was carried out as described by Okajima with some modifications [36].

Briefly, cells were grown in 48-well plates. When cells reached 60% confluence, the monolayers were washed twice with serum-free DMEM and were incubated with different concentrations of $CuSO_4$ or Cu-complex. The monolayers were washed with PBS buffer and fixed with 5% glutaraldehyde/PBS at room temperature for 10 min. Then, they were stained with 0.5% crystal violet/25% methanol for 10 min. After that, the dye solution was discarded and the plate was washed with water and dried. The dye taken up by the cells was extracted using 0.5 ml/well 0.1 M glycine/HCl buffer, pH 3.0/30% methanol and transferred to test tubes. Absorbance was read at 540 nm after a convenient sample dilution [37].

3. Results and discussion

3.1. Determination of the stoichiometry of the interaction Cu(II)dipeptide–DNA

The results of the binding stoichiometry of Cu(II)dipeptide–DNA are shown in Table 2. As shown in Table 2, the stoichiometry of binding depends on the complex, from what it is possible to assume that it is the Cu(II)dipeptide complex, and not only the free copper ion that interacts with DNA. The $[Cu(H_2O)_6]^{2+}$ complex interacts with DNA at a higher extent (>150 (mmol)/DNA(mol base)), probably in a less selective way interacting also with phosphate groups due to the positive charge.

All the studied complexes showed interaction, in a lower, and possibly more selective way than Cu(II) aqua ion. The extent of the interaction depended on the dipeptide ligand. The [Cu(ala-phe)] complex presented the highest binding stoichiometry while the rest of the series [Cu(ala-X)] (X = different aminoacids) showed significantly lower values. Besides, the interaction of [Cu(phe-ala)] was almost four times smaller than that of the [Cu(ala-phe)]. It might be possible that the phenyl ring (without substituents) in the second aminoacid is important in the interaction when the first aminoacid is alanine. Another observation is that in the complexes with a voluminous first aminoacid in the dipeptide ligand the interaction with DNA seems to be disfavoured. This is the case of [Cu(phe-ala)], [Cu(phe-leu)], [Cu(phe-phe)], [Cu(val-phe)] and Cu(-val-gly)].

Based on these results, [Cu(ala-phe)] that presented the best binding stoichiometry and [Cu(ala-val)] and [Cu(val-phe)] that presented medium interaction, were chosen for carrying out EPR and CD experiments with the aim to obtain structural information of the interaction.

Table 2
Binding stoichiometry expressed as Cu(mmol)/DNA(mol base).

Complex number	Complex stoichiometry	Cu(mmol)/ DNA(mol base)
1	$[Cu(ala\text{-}ala)]\cdot 2H_2O$	11
2[a]	[Cu(ala-val)][a]	9
3[a]	[Cu(ala-ile)][a]	14
4	$[Cu_3(ala\text{-}leu)_3(H_2O)_3(CO_3)]\cdot PF_6\cdot H_2O$	20
5	$[Cu(ala\text{-}thr)]\cdot {}^1/_2H_2O$	14
6[a]	[Cu(ala-phe)][a]	42
7	$[Cu(ala\text{-}tyr)]\cdot H_2O$	10
8	$[[Cu(phe\text{-}ala)]\cdot {}^1/_2H_2O$	11
9[a]	[Cu(phe-leu)][a]	13
10[a]	[Cu(phe-phe)][a]	2
11	[Cu(val-phe)]	8
12	[Cu(val-gly)]	10

[a] Previously reported [38].

3.2. Cu(II)dipeptide–DNA binding: EPR measurements

EPR experiments were carried out with solutions of the complexes [Cu(ala-phe)], [Cu(ala-val)], and [Cu(val-phe)]. Moreover, EPR spectra of DNA solution in presence of increasing concentrations of the Cu-dipeptide complexes were also recorded (see Section 2.3). The Fig. 1 shows the EPR spectra of a solution of free [Cu(ala-phe)] and solutions of this complex in presence of DNA at various mmol Cu(ala-phe)/mol bases DNA ratios. Besides, the spectral simulations are included in Fig. 1. Similar results were obtained studying the spectra of [Cu(ala-val)], and [Cu(val-phe)] in presence of DNA.

[Cu(ala-phe)] (Fig. 1A) in frozen solution presented an EPR spectrum characteristic of coupled Cu(II) ions with a single resonance around $g \sim 2$ ($H \sim 310$ mT) [30,39,40] whereas the spectrum of the Cu(ala-phe) complex with DNA at low mmol Cu(ala-phe)/DNA mol bases ratios (Fig. 1B) is the typical spectrum of

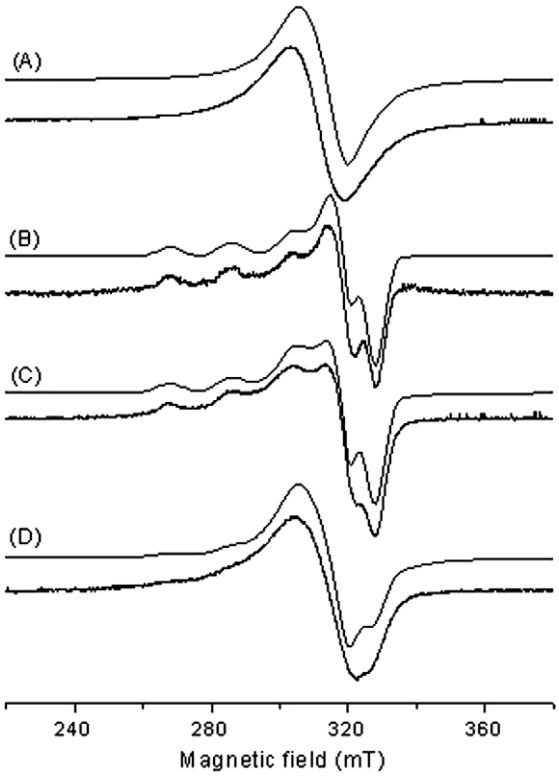


Fig. 1. Experimental (lower trace) and simulated (upper trace) X-band EPR spectra of a frozen solution of: (A) [Cu(ala-phe)] and [Cu(ala-phe)] in presence of DNA at (B) 30, (C) 110, and (D) 500 mmol Cu(ala-phe)/DNA mol bases.

monomeric Cu(II) complexes where the four hyperfine lines arising from the interaction of the $S = 1/2$ electron spin with the $I = 3/2$ copper nucleus are observed. This result showed that, at low Cu-dipeptide per DNA ratios (low copper complex levels), the magnetically coupled structure of the Cu-dipeptide complex is lost due to the coordination of the Cu-dipeptide monomer with the DNA molecule. The g values obtained from simulations of the spectrum at low mmol Cu(ala-phe)/mol bases DNA are: $g_{//} = 2.217$, $g_{\perp} = 2.048$, $A_{//} = 550$ MHz and $A_{\perp} = 35$ MHz.

With the aim to obtain structural information Peisach's proposal was used [19,41]. The magnitude of $A_{//}$ and $g_{//}$ was interpolated in the Peisach graph and the nature of the coordinating atoms in the equatorial plane was assigned. Our $A_{//}$ and $g_{//}$ values are similar to those reported for Cu(II) coordinated through three N atoms and one O atom (N3O).

Fig. 2 shows the Cu(II) environment in solution as presented in our previous work [38].

As shown in Fig. 2, in the free complex Cu(II) is coordinated through two N atoms and two O atoms in the equatorial plane. After the interaction with DNA, the EPR spectra suggest that the copper ion is equatorially coordinated through three N atoms and one O atom. This behaviour would show that one O atom from the copper environment is replaced by one N from a DNA base (inner-sphere binding).

When the Cu-dipeptide per DNA ratios increases (Fig. 1C and D) a spectrum of coupled Cu(II) ions appears superposed to the monomeric signal. The spectra in Figs. 1C and D could only be satisfactorily simulated when two spectral components were included in the fitting protocol using the QPOW program: the spectrum of the polymeric species (Cu(ala-phe) alone) and the spectrum of the monomeric specie (Cu(ala-phe) bonded to DNA), described above.

The existence of two spectral components supports the hypothesis that the DNA is able to bind only a small amount of Cu(dipeptide), and the remaining Cu(dipeptide) exists as free complex in solution (not coordinated to the DNA).

3.3. Cu(II)dipeptide–DNA binding: characterization by CD measurements

Circular dichroism experiments were carried out with [Cu(ala-phe)], [Cu(ala-val)] and [Cu(val-phe)] in (a) copper complex solutions and (b) copper complex solutions in presence of DNA. The aim of these experiments was to confirm the interaction and determine whether the DNA or the Cu(dipeptide) complex experimented structural changes due to the Cu(dipeptide)–DNA interaction.

(a) The spectra of aqueous solutions of the Cu(dipeptide) complexes were registered at increasing concentrations. As an example, the inset of Fig. 3 shows the spectra of Cu(ala-phe) complex. As expected, the ellipticity at 218 nm (maximum wavelength) linearly increases with the concentration, as shown Fig. 3, with a molar ellipticity of 765 M^{-1} cm^{-1}. Similar results were obtained for the complex [Cu(val-phe)] (molar ellipticity at 218 nm: 1190 M^{-1} cm^{-1}) while complex [Cu(ala-val)] does not show any significant ellipticity at 218 nm (15 M^{-1} cm^{-1}).

(b) The spectra of a DNA solution in presence of increasing concentrations of Cu(dipeptide) complexes were registered. Fig. 4 shows the spectra obtained for the [Cu(ala-phe)]–DNA system. Similar results were obtained with the [Cu(val-phe)] complex.

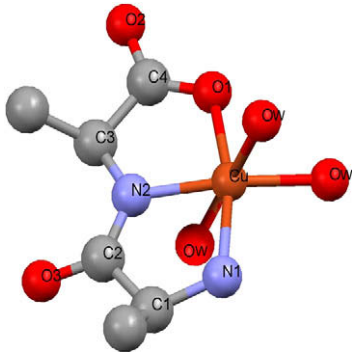


Fig. 2. Scheme of the Cu(II) environment of the Cu-dipeptide complexes in solution.

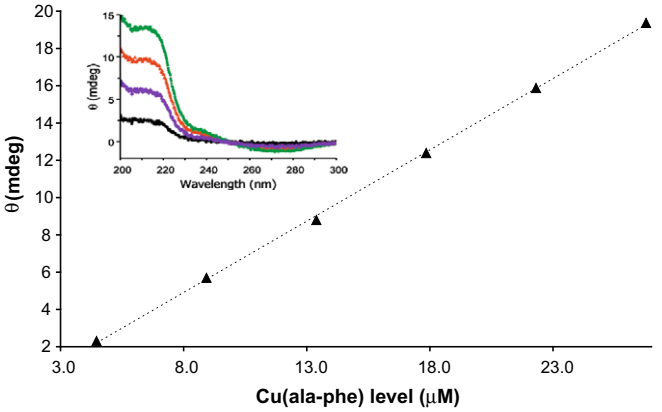


Fig. 3. Ellipticity of [Cu(ala-phe)] at 218 nm *vs.* concentration. Inset: CD spectra of [Cu(ala-phe)].

Fig. 4 presents the ellipticity of the system at 218 nm *versus* [Cu(ala-phe)] concentration.

It can be observed that the ellipticity at 218 nm does not increase linearly with the [Cu(ala-phe)] concentration, as would be expected if there were no interaction between the [Cu(ala-phe)] complex and the DNA. At low Cu(dipeptide) concentration (that is, low mmol [Cu(ala-phe)]/mol bases DNA ratio) the ellipticity almost does not increase with the increment of the Cu(dipeptide) concentration. As the ratio is increased, the ellipticity increases, showing a molar ellipticity similar to that of the free Cu(dipeptide) complex. This may be explained considering that at low mmol

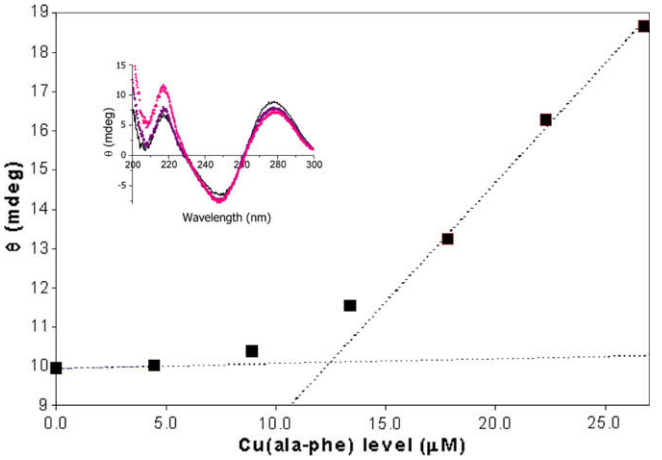


Fig. 4. Ellipticity of the [Cu(ala-phe)]-DNA system at 218 nm *vs.* [Cu(ala-phe)] concentration. Inset: selected CD spectra of DNA and DNA in presence of [Cu(ala-phe)] (with mmol [Cu(ala-phe)]/mol bases DNA ratios from 5 to 55).

[Cu(ala-phe)]/mol bases DNA ratio all the Cu(dipeptide) complex added is bonded to the DNA. The coordination with DNA induces structural changes with the consequently quenching of the complex ellipticity. As the mmol Cu(dipeptide)/mol bases DNA ratio is increased, the DNA is not more able to bind the Cu(dipeptide) complex, therefore the system behaves as if there were no interaction between the excess of Cu(dipeptide) complex and the DNA. In the Cu(dipeptide) concentration range of 8.9–13.4 μM (where we observed the slope change), the Cu(mmol)/DNA(mol base) ratio is 18–32 mmol Cu/DNA (mol base). Although the binding stoichiometry presented in Section 3.1 (42 Cu(mmol)/DNA(mol base)) is not included in this range it is still comparable and supports the proposal of the DNA saturation.

In the case of the [Cu(ala-val)] complex the results are different from the previous ones, as shown in Fig. 5.

As the complex has a very low molar ellipticity at 218 nm, the ellipticity of a solution of DNA with increasing concentrations of [Cu(ala-val)] should slightly increase at this wavelength. On the contrary, a decrease in the signal at 218 nm was observed. This result shows that the molar ellipticity of the DNA decreases in presence of [Cu(ala-val)], as previously reported for metallic complexes which bind to DNA [41]. This behaviour suggests a structural change in the DNA. It is possible that in the case of the complex [Cu(ala-phe)] there is also a decrease in the molar ellipticity of the DNA, which is masked by the decrease in the ellipticity of the complex bounded to the DNA.

In relation to the binding constant, the obtained values for [Cu(ala-phe)] and [Cu(val-phe)] were 1.2×10^4 and $5.9 \times 10^3\ M^{-1}$, respectively. These results are of the same order that the corresponding ones for complexes with biological activity reported in the bibliography [42,43].

The spectra of [Cu(ala-val)] does not show enough differences to estimate a binding constant.

3.4. Cell proliferation assay

The obtained results are shown in Fig. 6. As can be seen from the figure, at concentrations lower than 50 μM, the complex do not exert any inhibition on cell proliferation since no differences *versus* basal results could be observed. At higher doses, the complexes and the copper salt caused different inhibition of cell growth in a dose response manner. [Cu(ala-phe)] showed the greatest cell proliferation inhibition at the highest concentration (500 μM) where 45% cell survival could be detected when the osteosarcoma cells were incubated with this complex.

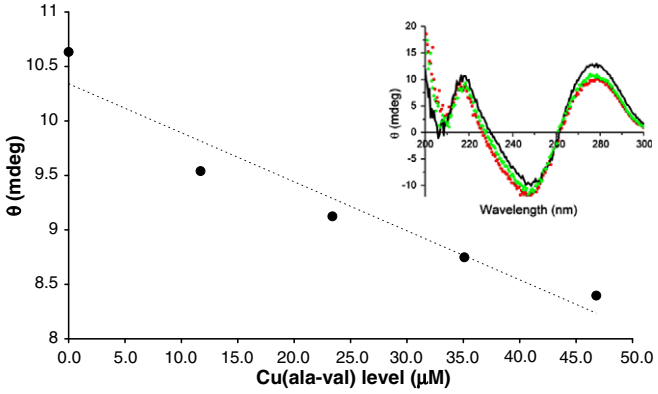


Fig. 5. Ellipticity of the [Cu(ala-val)]/DNA system at 218 nm *vs.* [Cu(ala-val)] concentration. Inset: selected CD spectra of DNA and DNA in presence of [Cu(ala-val)] (with mmol Cu(ala-val)/mol bases DNA ratios from 20 to 100).

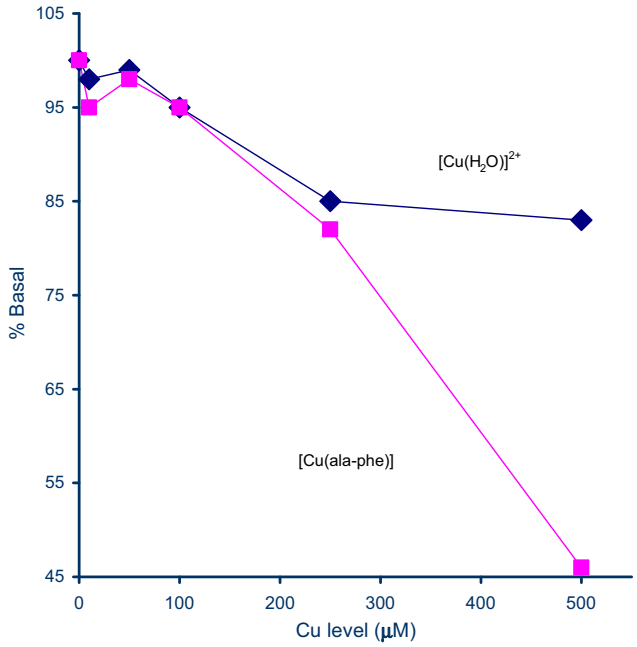


Fig. 6. Cell proliferation experiments with UMR106 after the treatment with [Cu(ala-phe)] and copper salt.

4. Conclusions

This work provided information about the interaction of a series of Cu(dipeptide) complexes with Calf Thymus DNA using different methodologies. All the studied complexes showed interaction, in a lower, and possibly more selective way than Cu(II) aqua ion. The extent of the interaction depended on the dipeptide ligand.

Interestingly, the EPR and CD studies suggested that the DNA binds a fixed amount of the Cu(dipetide) complex (which is coordinated to the bases of the DNA) up to saturation. Moreover, the systems start to show saturation at a mmol Cu(dipeptide)/mol bases DNA ratio close to that obtained in the binding stoichiometry values.

The inhibitory effect caused by [Cu(ala-phe)] on cell proliferation in the cultures of UMR106 osteoblasts is encouraging for future studies on the bioactivity of this complex with other tumoral cell lines since it may have potential application as antitumoral agent.

Acknowledgements

The authors thank CSIC, PEDECIBA Química (Uruguayan organisations), AMSUD-Pasteur and CNPq for financial support. SBE and DAB are members of the Carrera del Investigador, CONICET, Argentina and they are indebted with CONICET and UNLP for the financial support for the biological studies.

References

[1] N. Farrell, Compr. Coord. Chem. II 9 (2003) 809.
[2] R.A. Delgado, A. Anzellotti, Mini Rev. Med. Chem. 4 (2004) 159.
[3] M. Navarro, E.J. Cisneros-Fajardo, A. Sierralta, M. Fernández-Mestre, P. Silva, D. Arrieche, E. Marchan, J. Biol. Inorg. Chem. 8 (2003) 401.
[4] N. Farrell, Transition Metal Complexes as Drugs and Chemoterapeutic Agents, Kluwer Academic Publishers Group, Dordrecht, 1989.
[5] J. Liu, T. Zhang, T. Lu, L. Qu, H. Zhou, Q. Zhang, L. Ji, J. Inorg. Biochem. 91 (2002) 269.
[6] A.D. Vizcaya-Ruíz, A. Rivero-Muller, L. Ruíz-Ramírez, G.E.N. Kass, L.R. Kelland, R.M. Orr, M. Dobrota, Toxicol. In Vitro 14 (2000) 1.

[7] A. Marín-Hernández, I. Gracia-Mora, L. Ruiz-Ramírez, R. Moreno-Sánchez, Biochem. Pharm. 65 (2003) 1979.
[8] Y.W. Jeong, K.S. Kim, J.Y. Oh, J.C. Park, J.H. Bang, S.W. Choi, J.C. Lee, J. Microbiol. Biotechnol. 13 (2003) 394.
[9] P. Lugo-Ponce, D.R. McMillin, Coord. Chem. Rev. 208 (2000) 169.
[10] M. Lainé, F. Richard, E. Tarnaud, C. Bied-Charreton, C. Verchére-Béaur, J. Biol. Inorg. Chem. 9 (2004) 550.
[11] H. Li, X. Le, D. Pang, H. Deng, Z. Xu, Z. Lin, J. Inorg. Biochem. 99 (2005) 2240.
[12] S. Roy, R. Banerjee, M. Sarkar, J. Inorg. Biochem. 100 (2006) 1320.
[13] W. Harada, T. Nojima, A. Shibayama, H. Ueda, H. Shindo, M. Chikira, J. Inorg. Biochem. 64 (1996) 273.
[14] M. Chikira, M. Inoue, R. Nagane, W. Harada, H. Shindo, J. Inorg. Biochem. 66 (1997) 131.
[15] R. Nagane, M. Chikira, M. Oumi, H. Shindo, W.E. Antholine, J. Inorg. Biochem. 78 (2000) 243.
[16] R. Nagane, T. Koshigoe, M. Chikira, E.C. Long, J. Inorg. Biochem. 83 (2001) 17.
[17] M. Chikira, Y. Tomizawa, D. Fukita, T. Sugizaki, N. Sugawara, T. Yamazaki, A. Sasano, H. Shindo, M. Palaniandavar, W. Antholine, J. Inorg. Biochem. 99 (2002) 163.
[18] R. Nagane, T. Koshigoe, M. Chikira, J. Inorg. Biochem. 93 (2003) 204.
[19] T. Hirohama, A. Chiba, M. Chikira, Y. Fuji, J. Inorg. Biochem. 98 (2004) 371.
[20] M. Chikira, J. Inorg. Biochem. 102 (2008) 1016.
[21] E. Kimoto, H. Tanaka, J. Gyotoku, F. Morishige, L. Pauling, Cancer Res. 43 (1983) 824.
[22] L. Pickart, M. Thaler, Nature 288 (1980) 715.
[23] A. Cuevas, I. Viera, M.H. Torre, E. Kremer, S.B. Etcheverry, E.J. Baran, Acta Farm. Bonaerense 17 (1998) 213.
[24] A. Cuevas, I. Viera, M.H. Torre, E. Kremer, E. Baran, Afinidad 475 (1998) 183.
[25] A. Cuevas, I. Viera, M.H. Torre, E. Kremer, S.B. Etcheverry, E.J. Baran, Afinidad 482 (1999) 263.
[26] G. Facchin, M.H. Torre, E. Kremer, O.E. Piro, E.E. Castellano, E.J. Baran, Z. Naturforsch. 55b (2000) 1157.
[27] G. Facchin, M.H. Torre, E. Kremer, O. Piro, E.E. Castellano, E.J. Baran, J. Inorg. Biochem. 89 (2002) 174.
[28] G. Facchin, M.H. Torre, I. Viera, E. Kremer, E.J. Baran, in: L. Khassanova, P. Collery, I. Maymard, Z. Khassanova, J. Étienne (Eds.), Metal Ions in Biology and Medicine, vol. 7, John Libbey Eurotext, Paris, 2002, pp. 11–14.
[29] G. Facchin, M.H. Torre, E. Kremer, E.J. Baran, A. Mombrú, H. Pardo, M.P. Araujo, A.A. Batista, A.J. Costa-Filho, Inorg. Chim. Acta 355 (2003) 408.
[30] G. Facchin, E. Kremer, E.J. Baran, E.E. Castellano, O.E. Piro, J. Ellena, A.J. Costa-Filho, M.H. Torre, Polyhedron 25 (2006) 2597.
[31] E.D. Viera, N.M.C. Casado, G. Facchin, M.H. Torre, A.J. Costa-Filho, R. Calvo, Inorg. Chem. 45 (2006) 2942.
[32] J. Sanchiz, C. Kremer, M.H. Torre, G. Facchin, E. Kremer, E.E. Castellano, J. Ellena, J. Mol. Struct. 797 (2006) 179.
[33] R.L. Belford, M.J. Nilges, in: Computer Simulation of Powder Spectra in EPR Symposium 21st Rocky Mountain Conference, Denver, 1979.
[34] R.E. Mahnken, M.A. Billadeau, E.P. Nikonowicz, H. Morrison, J. Am. Chem. Soc. 114 (1992) 9253.
[35] P. Job, Ann. Chim. 9 (1928) 113.
[36] T. Okajima, K. Nakamura, H. Zhang, N. Ling, T. Tanabe, T. Yasuda, R.G. Rosenfeld, Endocrinology 130 (1992) 2201.
[37] A.M. Cortizo, S.B. Etcheverry, Mol. Cell. Biochem. 145 (1995) 97.
[38] G. Facchin, E. Kremer, O.R. Nascimento, A.J. Costa-Filho, J. Ellena, M.H. Torre, in: P. Collery, I. Maynard, T. Theophanides, L. Khassanoca, T. Collery (Eds.), Metal Ions in Biology and Medicine, vol. 10, John Libbey Eurotext, Paris, 2008, pp. 140–145.
[39] A. Bencini, D. Gatteschi, EPR of Exchange Coupled Systems, Springer-Verlag, Berlin, 1990.
[40] A.J. Costa-Filho, O.R. Nascimento, R. Calvo, J. Phys. Chem. B 108 (2004) 9549.
[41] J. Peisach, W.E. Blumberg, Arch. Biochem. Biophys. 165 (1974) 691.
[42] E. Froehlich, A. Gupta, J. Provencher-Mandeville, E. Asselin, J. Bariyanga, G. Berube, H. Tajmir-Riahi, DNA Cell Biol. 28 (1) (2009) 1.
[43] M. Navarro, A. Betancourt, C. Hernández, E. Marchán, J. Brazil Chem. Soc. 19 (7) (2008) 1355.

Polyhedron 28 (2009) 2335–2340

Contents lists available at ScienceDirect

Polyhedron

journal homepage: www.elsevier.com/locate/poly

Optical properties of binuclear zinc (II) macrocyclic complexes derived from 4-methyl-2,6-diformylphenol and 1,2-diaminobenzene

Verónica Paredes-García [a,*], D. Venegas-Yazigi [b], A. Cabrera [c], P. Valencia-Gálvez [c], M. Arriagada [a], D. Ruiz-Leon [c], N. Pizarro [d], A. Zanocco [c], Evgenia Spodine [c,*]

[a] Departamento de Química, Universidad Tecnológica Metropolitana, Santiago, Chile
[b] Departamento de Química de los Materiales, Facultad de Química y Biología, Universidad de Santiago de Chile, Santiago, Chile
[c] Facultad de Ciencias Químicas y Farmacéuticas, Universidad de Chile, Casilla 233, Olivos-Independencia-Santiago, Chile
[d] Departamento de Ciencias Químicas, Facultad de Ecología y Recursos Naturales, Universidad Andres Bello, Santiago, Chile

ARTICLE INFO

Article history:
Received 30 January 2009
Accepted 22 April 2009
Available online 3 May 2009

Keywords:
Zinc macrocyclic complexes
Optical properties

ABSTRACT

In this work, we present the synthesis and optical study of the binuclear zinc(II) macrocyclic complexes, derived from 4-methyl-2,6-diformylphenol and 1,2-diaminobenzene (H_2L). Two zinc macrocyclic complexes with different anions were prepared and characterized: $[Zn_2LCl_2]\cdot H_2O$ (**1**) and $[Zn_2L](NO_3)_2$ (**2**).

The complexes are emissive, both in the solid state and in solution at room temperature. Spectroscopic properties of the macrocyclic complexes were investigated using stationary and time resolved methods in solutions of dimethylsulfoxide (DMSO), and in solid state. DMSO solutions show two emission bands centered at 480 and 521 nm for complex (**1**), and at 527 nm with a shoulder at 480 nm for (**2**). The emission spectra of these compounds in solid state show a red shifted band, presenting the maxima at 565 nm for (**1**) and 575 nm for (**2**). The emission lifetimes for these compounds are very short, viz. 650 and 480 ps for macrocycles (**1**) and (**2**), respectively.

© 2009 Elsevier Ltd. All rights reserved.

1. Introduction

The rich chemistry of complexes of dicompartmental ligands binding two metals has been applied to the investigation of magnetic exchange interactions between these centres, the stabilisation of mixed valence species and the activation of small molecules [1–7]. Besides, macrocycles derived from 4-methyl-2,6-diformylphenol and 1,2-diaminobenzene are studied since they show a high electronic delocalisation due to the planar structure that they present.

Luminescent metal complexes are gaining significant attention as sensors and probes in view of their applications in light emitting diodes (LEDs), biomedical analyses, fluorescence imaging and possibly in cancer phototherapy [8]. For example, metal complexes are promising luminescent materials for their applications as LEDs, owing to their ability to enhance, shift and quench luminescent emission of organic ligands by metal coordination. Many polynuclear zinc(II) compounds exhibit promising luminescent properties, especially those with ligands containing heteroaromatic rings, since the metal centres enhance the fluorescence of the aromatic moieties. Therefore, they are currently of interest in the development of fluorescent materials [9–11].

The zinc(II) macrocyclic complexes, derived from 4-methyl-2,6-diformylphenol and 1,2-diaminobenzene were prepared and characterized. We herein report an optical study of the binuclear macrocyclic compounds shown in Scheme 1.

2. Experimental

The reagents and solvents employed were used as received without further purification. Elemental analyses (C,H,N) were determined with a Perkin–Elmer elemental analyzer. The percentage of zinc was determined by atomic absorption with a Perkin–Elmer equipment, model 1100B. The FT-IR spectra were recorded from KBr pellets in the range 4000–400 cm^{-1} on a Bruker-IFS 28 spectrophotometer. The low frequency region, from 400–200 cm^{-1}, was recorded on a Bruker Vector 22 spectrophotometer. Micro-Raman spectra for (**1**) and (**2**) were recorded on Renishaw systems 2000, using laser excitation at 785 nm. All measurements were made in a back-scattering geometry, using a spatial resolution of 1 μm^2; the laser beam had circular polarization and laser powers of 10%. Single point spectra were recorded with 10 s accumulation times. In order to reduce the high fluorescence showed by the zinc macrocyclic complexes, the sample was deposited over a glass covered with gold nanoparticles in terms to get an enhanced Raman signal. The diffuse reflectance UV–Vis spectra were recorded using a Perkin–Elmer Lambda 20 UV–Vis spectrophotometer equipped with a Labsphere RSA-PE-20 diffuse reflectance

* Corresponding authors. Tel.: +562 978 2862; fax: +562 978 2868 (E. Spodine).
E-mail addresses: vpg@manquehue.net (V. Paredes-García), espodine@uchile.cl (E. Spodine).

0277-5387/$ - see front matter © 2009 Elsevier Ltd. All rights reserved.
doi:10.1016/j.poly.2009.04.027

accessory. Magnesium oxide was used as reference and the spectra were recorded in the range 1.5–6.0 eV at room temperature. Reflectance measurements were converted to absorption spectra using the Kubelka–Munk function $F(R_\infty)$. Solution absorption spectra were recorded on a Unicam-UV3 spectrophotometer.

Solution fluorescence spectra in DMSO were performed on a Spex Fluorolog 2τ2 spectrophotometer. Fluorescence lifetime measurements were performed using Time-Correlated Single Photon Counting (TCSPC) technique [12]. Approximately 100 femtosecond excitation pulses with tunable wavelength (360–470 nm) were generated by doubling the fundamental frequency of a modelocked Ti:sapphire laser (Spectraphysics Tsunami) pulses in β-barium borate crystal. The laser repetition rate was reduced to 2 MHz by a home-made acousto-optical pulse picker in order to avoid saturation of the chromophore. TCSPC system is equipped with an ultrafast microchannel plate photomultiplier tube detector (Hamamatsu R3809U-51) and an electronics board (Becker and Hickl SPC-630), and has instrument response time less than 50 ps. Triggering signal for the TCSPC board was generated by sending a small fraction of the laser beam onto a fast (400 MHz bandwidth) Si photodiode (Thorlabs Inc.). Fluorescence signal was dispersed in Acton Research SPC-300 monochromator after passing through a pump blocking, long wavelength-pass, autofluorescence-free, interference filter (Omega Filters, ALP series). The monochromator is equipped with a CCD camera (Roper Scientific PIXIS-400B) allowing for monitoring of the fluorescence spectrum. Fluorescence transients were not deconvolved with the instrument response function since their characteristic time-constants were much longer than the width of the system response to the excitation pulse.

Emission spectra in solid state at room temperature were recorded using a Perkin–Elmer LS55 UV/Visible spectrometer. The solid sample were prepared by mixing the complexes with an inert silicone, and deposited on a quartz sample slice.

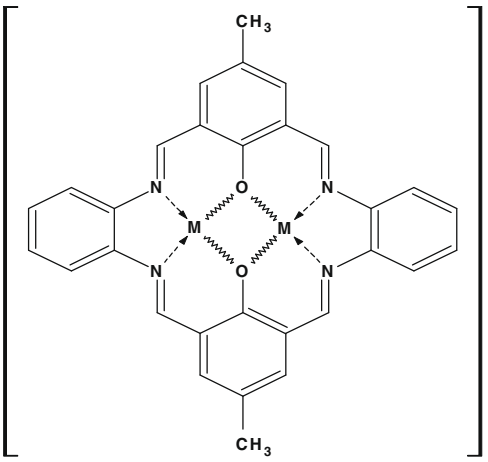
Thermogravimetric analyses (TGA) were performed from room temperature to 800 °C, under argon with a heating rate of 10 °C min^{-1}, using a Netzsch thermogravimetric analyzer, model 209-F1.

2.1. Synthesis of the partially reduced macrocyclic ligand derived from 4-methyl-2,6-diformylphenol and 1,2-diaminobenzene. (H_2L': 7,16-dihydroxy-6′,13′-dimethyl-1,4,10,13-tetraaza-tetrabenzo[2,3-a;6,7,8-f,a;11,12-a;15,16,17-f,a]cyclooctadeca-2,6,9,11,15,18-hexaene)

The template reaction, using Mg^{2+} or H^+ ions as template agents, was done by reacting under reflux 2-hydroxy-5-methyl-1,3-benzenedicarbaldehyde with 1,2-diaminobenzene in boiling methanol. The isolated macrocyclic ligand (**H_2L'**) was the partially reduced amino-imine compound, which was characterized by elemental analyses, ^{1}H NMR and FT-IR spectroscopy. The tetraimine ligand was not obtained with these synthetic conditions. *Anal.* Calc for H_2L' ($C_{30}H_{28}N_4O_2$): C, 75.61; N, 11.76; H, 5.92. Found: C, 74.55; N, 11.61; H, 5.97%. ^{1}H NMR: s: 2.31 (6H, methyl); d: 4.42 (4H, methylene); s: 6.32 (2H, amine); m: 6.75–7.27 (12H, aromatic); s: 8.60 (2H, azomethine); s: 13.5 ppm (2H, OH). FT-IR: ν_{N-H} = 3406 cm^{-1}; $\nu_{C=N}$ = 1617 cm^{-1}.

2.2. Synthesis of $M_2LX_2{\cdot}nH_2O$ (H_2L: 7,16-dihydroxy-6′,13′-dimethyl-1,4,10,13-tetraaza-tetrabenzo[2,3-a;6,7,8-f,a;11,12-a;15,16,17-f,a]cyclooctadeca-2,4,6,9,11,13,15,18-octaene); M = Zn(II), X = Cl (1); X = NO_3 (2)

The synthesis of the zinc(II) tetraimine macrocyclic compounds was achieved in a step by step synthesis. Initially 2-hydroxy-5-methyl-1,3-benzenedicarbaldehyde (1.84 mmol, 0.300 g) was refluxed for 3 h with $MX_2{\cdot}nH_2O$ (1.84 mmol, 0.250 g for X = Cl^- or 0.480 g for X = NO_3^-) in 2-propanol (40 mL), under an inert atmosphere (N_2). The dinuclear metal aldehydate complex was formed, and was used as the precursor for the formation of the macrocyclic compound. 1,2-Diaminobenzene (1.84 mmol, 0.199 g) dissolved in 2-propanol (10 mL) was added drop by drop to the 2-propanol solution of the precursor, and was left at ambient temperature with stirring for 90 min.; the macrocyclic complex $M_2LX_2{\cdot}nH_2O$ precipitated as a brick-red solid. The solid was first washed with acetone and then with methanol, and the purity was verified by column chromatography. *Anal.* Calc. for (**1**) ($C_{30}H_{24}N_4O_3Cl_2Zn_2$): C, 52.20; N, 8.12; H, 3.50; Zn, 18.95. Found: C, 52.6; N, 8.0; H, 3.7, Zn, 18.6%. *Anal.* Calc. for (**2**) ($C_{30}H_{22}N_6O_8Zn_2$): C, 49.68; N, 11.59; H, 3.06; Zn, 18.04. Found: C, 49.8; N, 11.2; H, 3.2; Zn, 18.1%.



1=Zn(II), Cl^- 2=Zn(II), NO_3^-

Scheme 1.

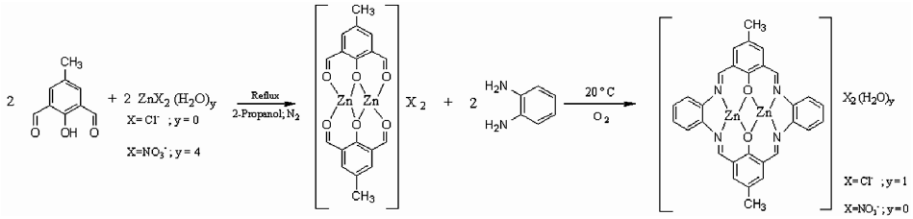
The zinc(II) macrocyclic complexes (**1**) and (**2**) were also synthesized by an alternative synthetic route, which involves a solvent free mechanochemical synthesis. Complexes (**1**) and (**2**) were obtained without any applied heating. The metal salts (2 mmol) and 2-hydroxy-5-methyl-1,3-benzenedicarbaldehyde (2 mmol) were mixed by grinding in a porcelain mortar for 10 min, till a strong yellow color of the solid was observed. Later, 1,2-diaminobenzene (2 mmol) was added to the reacting mixture, and this was also ground; a brick-red solid was obtained within a few minutes. The analyses gave the same percentage values, and the infrared spectra presented the same absorption bands as those obtained for the complexes synthesized by the traditional procedure.

3. Results and discussion

3.1. Syntheses

The reaction of dicarbonyl compounds with diamines is much more complicated than the simple Schiff condensation of mono carbonyl compounds with amines [13]. Moreover, the Schiff condensation with macrocyclic closure is usually obtained by a template reaction, in which metal ions [14] or anions of protic acids [15] are used as template agents. The introduction of a template agent is the most reliable method to prevent the formation of oligomers, and assures the presence of the macrocyclic compound.

In order to avoid the abnormal condensation of 2,6-diformyl-4-methylphenol with 1,2-diaminobenzene, accompanied with the reduction of two *trans* C=N double bonds of the macrocycle [16], the aldehydate dinuclear complex was formed, before the diamine was added. The final template formation of the dinuclear zinc(II) macrocyclic complexes was done in the presence of oxygen, in order to avoid any further reduction process (see Scheme 2).



Scheme 2.

3.2. Thermogravimetric analyses

Thermal behaviour of the $[Zn_2LCl_2]\cdot H_2O$ macrocyclic complex (**1**) shows a weight loss in several steps. At 115 °C an experimental weight loss of 2.6% is found and it can be associated with the weight loss of one water molecule (calculated value is 2.6%). The temperature at which the water molecule is lost in (**1**) permits to infer that it is not coordinated to the metal ion. There is a second weight loss at 335 °C which corresponds to 9.8%; this correlates well with the calculated value for the loss of two chlorides, with a weight loss of 10%. Above this temperature a gradual loss of weight is recorded, associated with the thermal decomposition of the sample (Fig. 1Sa).

In the case of the nitrate complex $[Zn_2L](NO_3)_2$ (**2**) the thermal behaviour is characterized by a weight loss at 430 °C, corresponding to a 15.9%, which correlates with the loss of two nitrate ions (calculated value is 17.1%). The weight loss above 430 °C is associated with the thermal decomposition of the sample (Fig. 1Sb).

No single crystals of compounds (**1**) and (**2**), suitable for X-ray diffraction were obtained. Due to the low solubility of these macrocyclic compounds in most of the organic solvents, the ^{1}H NMR spectra were recorded in DMSO-d^6. However, the recorded spectra presented low resolution, which precluded the assignment of the signals. Therefore the proposed structures of the two complexes are written considering the above information. The proposed geometry around the zinc ion can be defined as square base pyramid for (**1**) and square planar for (**2**) (see Scheme 3).

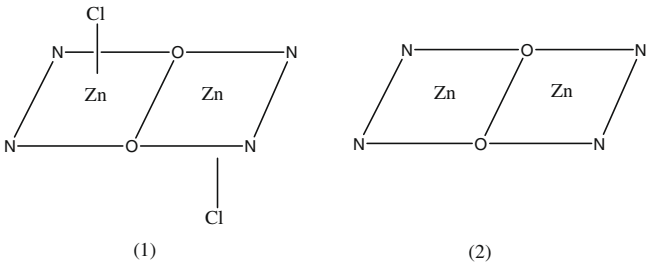
Literature data shows that for zinc, the most common coordination numbers are five and six. Several N_2O_2X pentacoordinated zinc(II) complexes are found in the literature, where the apical position of the first coordination sphere is occupied by a chlorine atom [17–20]. An example of a pentacoordinated zinc(II) species with a monodentate nitrate ligand is given by Tandon et al. [21] Even though the zinc square planar compounds are scarce, literature data show that square planar zinc(II) complexes can be found for Schiff base species with a N_2O_2 first coordination sphere [22–25].

3.3. Spectroscopy

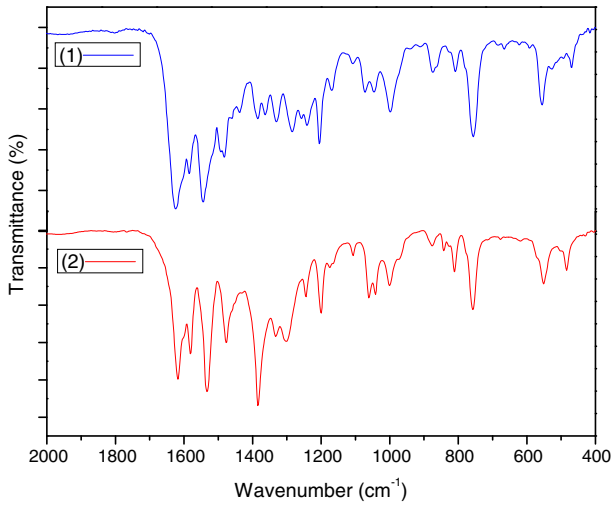
3.3.1. Infrared and Raman spectra

Fig. 1 shows the infrared and Raman spectra for (**1**) and (**2**). The IR spectra of both macrocyclic complexes show the fundamental vibration bands of the ligand; the stretching bands corresponding to νC=N appear at 1623 and 1618 cm^{-1}, the stretching vibration of νC=C at 1544 and 1535 cm^{-1}, νC–O$_{Ph}$ at 1330 and 1298 cm^{-1}, and the bending vibration of aromatic rings νC–H at 755 and 758 cm^{-1} for (**1**) and (**2**), respectively [26]. Furthermore, the macrocyclic complex $[Zn_2L](NO_3)_2$ presents a sharp and intense band at 1384 cm^{-1}, which corresponds to a ionic nitrate ion. When the nitrate ion is coordinated to a zinc ion, the infrared spectrum presents an absorption band at ca. 1750 cm^{-1}, band which is absent in the spectrum of the studied macrocyclic complex, suggesting the ionic nature of the nitrate ion.

On the other hand, the absence in the spectrum of the band around 1700 cm^{-1}, characteristic of the carbonyl group indicates the formation of the macrocyclic complex [27], which is in agree-



Scheme 3.



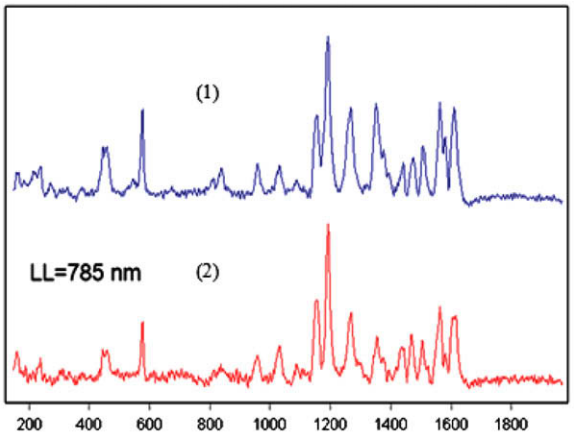


Fig. 1. Above: FT-IR Spectra of macrocyclic complexes, $[Zn_2LCl_2]\cdot H_2O$ (**1**), $[Zn_2L](NO_3)_2$ (**2**); below: Raman spectra, $[Zn_2LCl_2]\cdot H_2O$ (**1**) and $[Zn_2L](NO_3)_2$ (**2**).

ment with similar published data for these types of macrocyclic complexes.

Micro-Raman measurements are shown in Table 1. Characteristic fundamental vibrational modes observed in the Raman spectrum between 1000 and 1600 cm^{-1} are frequently used to study morphological structure. The measured samples show the typical C–H bending, C=C ring stretching and C=N bands for all complexes in this region, confirming the FT-IR assignments. Between 200 and 600 cm^{-1}, Zn–O, Zn–N stretching bands and some macrocycle and ring deformations appear, which are not well defined in the FT-IR spectra. Complex (**1**) presents a band at 285 cm^{-1} which can be assigned to the M–Cl stretching mode, while in the spectrum of complex (**2**) this band is absent [28,29].

3.3.2. Electronic spectra

The visible spectra of macrocyclic compounds (**1**) and (**2**) are depicted in Fig. 2. The absorption spectra of these dinuclear compounds in pure dimethylsulfoxide solution show two transitions at 422 nm ($1.7 \times 10^4\ M^{-1}\ cm^{-1}$) and 450 nm ($1.5 \times 10^4\ M^{-1}\ cm^{-1}$) for (**1**) and 416 nm ($2.9 \times 10^4\ M^{-1}\ cm^{-1}$) and 450 nm ($2.0 \times 10^4\ M^{-1}\ cm^{-1}$) for (**2**) in the visible region (Fig. 2a). The absorption bands, centred approximately at 420 and 450 nm for the zinc complexes may be assigned to the spin allowed MLCT $d \rightarrow \pi^*$ transition [26d], due to the relatively high extinction coefficient.

If the spectra are recorded in a mixture of DMSO:H_2O (3:2), changes are observed in the shape of the spectra, reaching a similar pattern for both complexes (Fig. 2b). This effect can be attributed to a change in the first coordination sphere of the complex cations (Scheme 4). In DMSO solution it is possible to propose that the chloride ions are acting as ligands, inside of the first coordination sphere for (**1**), while the nitrate anions are simple counterions for (**2**) and do not form part of the first coordination sphere (Scheme 4a). When a mixture of DMSO:H_2O is used, the water molecules are able to promote the substitution of the coordinated chloride ions, achieving both complexes a similar first coordination sphere (Scheme 4b).

The diffuse reflectance spectrum for (**1**) is shown in Fig. S2. This $[Zn_2LCl_2]\cdot H_2O$ macrocycle possesses an optical band gap of 2.1 eV, which is identical with the one corresponding to (**2**), and can be associated to the metal to ligand charge transfer process.

Table 1
Assignment of Raman bands (cm^{-1}) for $[Zn_2LCl_2]\cdot H_2O$ (**1**).

Wavenumber	FWHM	Relative intensity	Assignment
173	17	13	Zn–O stretching
196	17	8	Zn–N stretching
230		Shoulder	Macrocycle deformation
250	10	8	Macrocycle deformation
285	20	8	Zn–Cl stretching
459	18	22	Ring deformation
474	16	19	Ring deformation
590	9	22	Ring deformation
824	23	9	C–H bending
854	20	15	C–H bending
975	15	15	C–H bending
1047	22	17	C–H bending
1106	18	6	C–H bending
1172	19	48	C–H bending
1209	22	100	Ring stretching + C–H bending
1284	27	72	Ring stretching + C–H bending
1371	19	36	Ring stretching
1388		Shoulder	Ring stretching
1459	17	16	Ring stretching
1494	17	22	C=N stretching
1529	17	27	C=N stretching
1585	19	54	C=C ring stretching
1603	9	15	C=C ring stretching

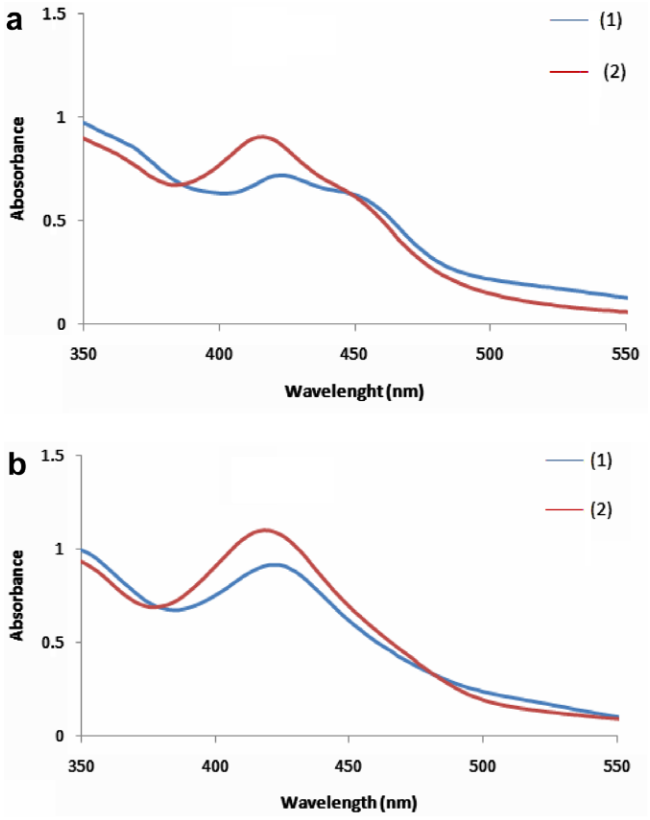
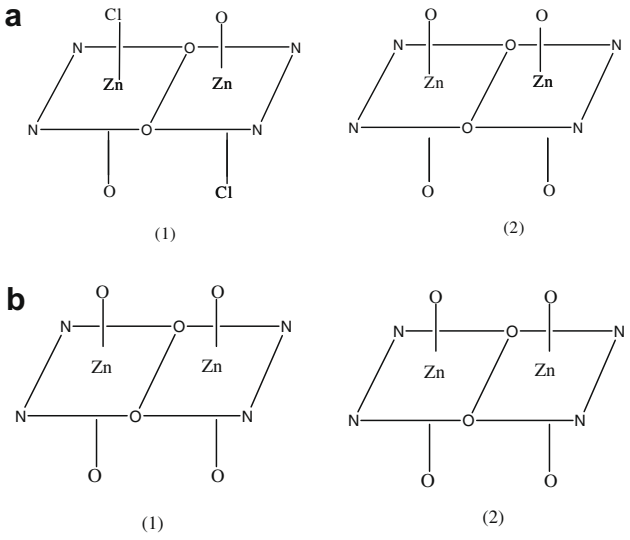


Fig. 2. UV–Vis Spectra of $[Zn_2LCl_2]\cdot H_2O$ (**1**) and $[Zn_2L](NO_3)_2$ (**2**) in (a) DMSO and (b) DMSO:H_2O (3:2).



Scheme 4.

The complexes are emissive both in the solid state and in solution at room temperature (RT). Spectroscopic properties of the macrocyclic complexes were investigated using stationary and time resolved methods in solutions of dimethylsulfoxide (DMSO) and in solid state. When the DMSO solutions of the macrocyclic complexes (**1**) and (**2**) are irradiated with a wavelength of 422 and 420 nm, respectively, a green emission can be observed with bands centred at 480 and 521 nm for complex (**1**), and at 527 nm with a shoulder at 480 nm for (**2**) (Fig. 3). It can be observed that

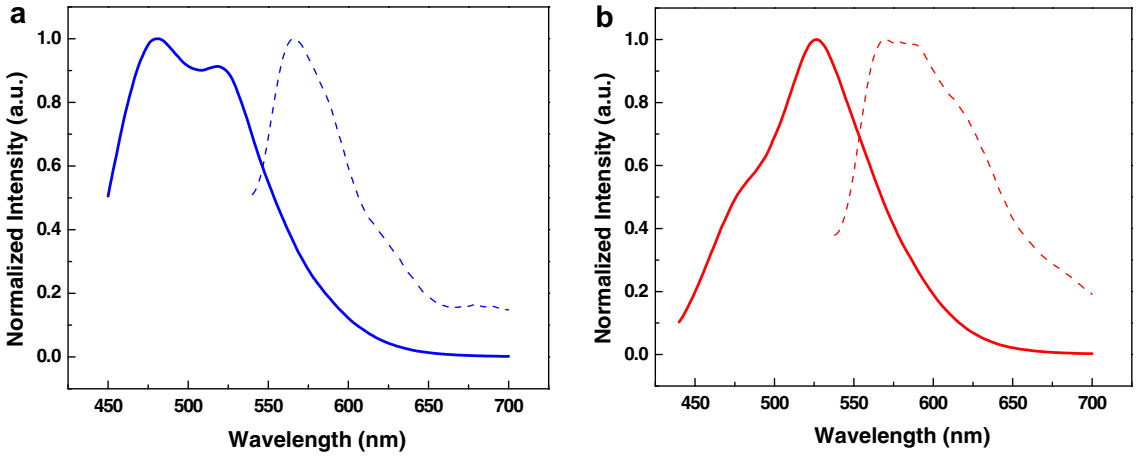


Fig. 3. Emission spectra of the macrocycles in DMSO solution (——) and solid state (– – – –). (a) $[Zn_2LCl_2]\cdot H_2O$ (**1**); (b) $[Zn_2L](NO_3)_2$ (**2**).

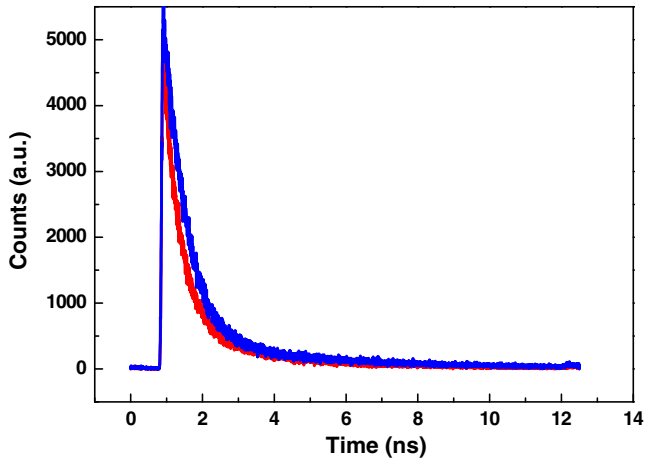


Fig. 4. Time resolved emission decay for $[Zn_2LCl_2]\cdot H_2O$, (**1**) (blue line) and $[Zn_2L](NO_3)_2$, (**2**) (red line) in DMSO solution at 545 and 550 nm, respectively, following excitation at 425 nm. (For interpretation of the references to color in this figure legend, the reader is referred to the web version of this article.)

macrocyclic complex (**1**) shows the highest energy of emission. The fluorescent emission may originate from the metal to ligand emission excited state. The emission is broad and structureless, which rules out a ligand centred nature of the emission, which would induce prominent vibrational structure, and makes it consistent with a charge transfer nature of the excited state [30].

The solid-state photoluminiscent spectra of the macrocyclic complexes (**1**) and (**2**) are depicted in Fig. 3. The emission spectra of these compounds in solid state compared with those in DMSO solutions show a red shifted band at 565 nm (**1**) and 575 nm (**2**). Red shifting of emission maxima can be observed for most fluorescent compounds in the solid state, probably due to π–π stacking of the aromatic rings in the molecules [31]. Comparing the solution with the solid emission spectra, it is possible to infer that the solvent destroys the π–π interactions, and thus the energy of the transition is increased in solution.

Time-resolved luminescent measurements allowed us to follow the intensity of the emission of the macrocycle after a laser excitation pulse at 425 nm. Fig. 4 shows the monoexponential intensity decays for the emission of the zinc macrocycles. The emission wavelengths used were chosen in order to minimize the signal–noise ratio. The emission lifetimes for these compounds are very short, viz. 650 and 480 ps for macrocycles (**1**) and (**2**), respectively. The lifetime difference could be explained in terms of the different coordination sphere for both macrocycles (see Scheme 4). Longer lifetimes have been reported for similar binuclear zinc macrocycles; however the involved transitions were assigned to a ligand centred emission [32] or from an excited state centred on the acceptor in a donor–acceptor system [33].

4. Conclusions

Two zinc macrocyclic complexes with different anions were prepared and characterized: $[Zn_2LCl_2]\cdot H_2O$ (**1**) and $[Zn_2L](NO_3)_2$ (**2**).

The infrared, Raman and electronic spectroscopic data were used to define the coordination of the anions; the chloride ions inside the first coordination sphere for (**1**) and the nitrate ions as simple counteranions for (**2**). The influence of the first coordination sphere on the fluorescent properties was shown to be important, being the emission lifetime for (**1**) longer than for (**2**).

Due to fact that the title compounds present emission at 500 nm, being thermally stable and insoluble in several solvents, they might be promising candidates for further applications as green light emitting materials.

Acknowledgments

The authors acknowledge FONDAP 11980002 and FONDECYT 1080318 grants for financial support. Professor R. Aroca (University of Windsor, Canada) and Professor A. Cheetham (Materials Research Laboratory, University of California, Santa Barbara, USA) for laboratory facilities. DRL thanks CONICYT for a Post-doctoral position, and PVG thanks 21061162 doctoral grant.

Appendix A. Supplementary data

Supplementary data associated with this article can be found, in the online version, at doi:10.1016/j.poly.2009.04.027.

References

[1] P.A. Vigato, S. Tamburini, Coord. Chem. Rev. 248 (2004) 1717.
[2] D. Venegas-Yazigi, S. Cortés, V. Paredes-García, O. Pena, A. Ibáñez, R. Baggio, E. Spodine, Polyhedron 25 (2006) 2072.
[3] A.E. Martell, J. Perutka, D. Kong, Coord. Chem. Rev. 216–217 (2001) 55.
[4] S. Brooker, T.C. Davidson, S.J. Hay, R.J. Kelly, D.K. Kennepohl, P.G. Plieger, B. Moubarak, K.S. Murray, E. Bill, E. Bothe, Coord. Chem. Rev. 216–217 (2001) 3.
[5] S. Brooker, Coord. Chem. Rev. 222 (2001) 33.
[6] V. Beckman, S. Brooker, Coord. Chem. Rev. 245 (2003) 17.

[7] W. Radecka-Paryzek, V. Patroniak, J. Lisowski, Coord. Chem. Rev. 249 (2005) 2156.
[8] P. Jiang, Z. Guo, Coord. Chem. Rev. 248 (2004) 205.
[9] B. Dutta, P. Bag, U. Flörke, K. Nag, Inorg. Chem. 44 (2005) 147.
[10] U.W. Grummt, E. Birckner, E. Klemm, D.A.M. Egbe, B. Heise, J. Phys. Org. Chem. 13 (2000) 112.
[11] R.F. Hu, J. Zhang, Y. Kang, Y.G. Yao, Inorg. Chem. Commun. 8 (2005) 828.
[12] W. Becker, Advanced Time-correlated Single Photon Counting Techniques, Springer-Verlag, New York, 2005.
[13] N.E. Borisova, M.D. Reshetova, Yu.A. Ustynyuk, Chem. Rev. 107 (2007) 46.
[14] N.E. Borisova, Yu.A. Ustynyuk, M.D. Reshetova, G.G. Aleksandrov, I.L. Eremenko, I.I. Moiseev, Russ. Chem. Bull. Int. Ed. 53 (2004) 340.
[15] J.L. Sessler, M.R. Jonson, V. Lynch, J. Org. Chem. 52 (1987) 4394.
[16] N.E. Borisova, M.D. Reshetova, Yu.A. Ustynyuk, Russ. Chem. Bull. Int. Ed. 53 (2004) 181.
[17] A. Tamilselvi, M. Nethaji, G. Mugesh, Chem. Eur. J. 12 (2006) 7797.
[18] A.J. Atkins, D. Black, R.L. Finn, A. Marin-Becerra, A.J. Blake, L. Ruiz-Ramirez, W.-Sh. L, M. Schroeder, Dalton Trans. (2003) 1730.
[19] S.R. Korupoju, N. Mangayarkarasi, S. Armeenrunishe, E. Valente, P.S. Zacharias, J. Chem. Soc. Dalton Trans. (2000) 2845.
[20] L.E. Breyfogle, C.K. Williams, V.G. Young Junior, M.A. Hillmyer, W.B. Tolman, Dalton Trans. (2006) 928.
[21] S.S. Tandon, S. Chauder, L.K. Thompson, Inorg. Chim. Acta 300 (2000) 683.
[22] (a) C.B. Wu, Acta Crystallogr. E 60 (2004) m1580;
(b) Z.-X. Li, X.-L. Zhang, Acta Crystallogr. E 60 (2004) m1017.
[23] H.-N. Hou, Acta Crystallogr. E 61 (2005) m1197.
[24] H.-J. Xu, Z.-D. Liu, L.-Q. Sheng, Acta Crystallogr. E 62 (2006) m2695.
[25] Y.-Q. Liu, X.-R. Zeng, Q.-Y. Luo, Y.-P. Xu, Acta Crystallogr. E 63 (2007) m2396.
[26] (a) K. Nakamoto, Infrared and Raman Spectra of Inorganic and Coordination Compounds, John Wiley & Sons Inc., New York, 1986;
(b) N. Raman, J. Dhaveethu-Raja, A. Saktivel, J. Chem. Sci. 119 (2007) 303;
(c) J. Vanco, J. Marek, Z. Travnicek, E. Racanska, J. Muselík, O. Svajlenová, J. Inorg. Biochem. 102 (2008) 595;
(d) D.N. Kumar, B.S. Garg, Spectrochim. Acta A 64 (2006) 141.
[27] R.R. Gagne, C.L. Spiro, J.T. Smith, J. Am. Chem. Soc. 103 (1981) 4073.
[28] M.F. Abo El-Ghar, N.T. Abdel-Ghain, Y. Badr, O.M. El-Borady, ISESCO Sci. Technol. Vision 3 (2007) 58.
[29] B. Simó, L. Perelló, R. Ortiz, A. Castineiras, J. Latorre, E. Canton, J. Inorg. Biochem. 81 (2000) 275.
[30] J.P. Collin, I.M. Dixon, J.P. Sauvage, J.A.G. Williams, F. Barigelletti, L. Flamini, J. Am. Chem. Soc. 121 (1999) 5009.
[31] (a) Q. Su, Q.L. Li, X.M. Liu, Y. Mu, Polyhedron 26 (2007) 5053;
(b) H. Yersin, A. Vogler, Photochemistry and Photophysics of Coordination Compounds, Springer, Berlin, 1987;
(c) B. Valeur, Molecular Fluorescence Principles and Application, Wiley-VCH, Weinheim, 2002.
[32] L.B. Picraux, A.L. Smeigh, D. Guo, J.K. McCusker, Inorg. Chem. 44 (2005) 7846.
[33] M. Soler, J.K. McCusker, J. Am. Chem. Soc. 130 (2008) 4708.

Polyhedron 28 (2009) 2341–2346

Contents lists available at ScienceDirect

Polyhedron

journal homepage: www.elsevier.com/locate/poly

A reversible solid–solid phase transition $Z' = 1$ to $Z' = 6$ in [Ni(OAc)(**PNP^{tBu}**)]OTf

Martin Lutz [a,*], Jarl Ivar van der Vlugt [b], Dieter Vogt [c], Anthony L. Spek [a]

[a] Bijvoet Center for Biomolecular Research, Crystal and Structural Chemistry, Faculty of Science, Utrecht University, Padualaan 8, 3584CH Utrecht, The Netherlands
[b] van 't Hoff Institute for Molecular Sciences, Laboratory for Supramolecular and Homogeneous Catalysis, University of Amsterdam, Nieuwe Achtergracht 166, 1018 WV Amsterdam, The Netherlands
[c] Schuit Institute of Catalysis, Laboratory of Homogeneous Catalysis, Department of Chemistry and Chemical Engineering, Eindhoven University of Technology, P.O. Box 513, 5600 MB Eindhoven, The Netherlands

ARTICLE INFO

Article history:
Received 16 January 2009
Accepted 23 April 2009
Available online 3 May 2009

Keywords:
Phase transition
Symmetry change
Disorder–order
Pincer complex
Nickel complex

ABSTRACT

At ambient temperature, the complex [Ni(OAc)(**PNP^{tBu}**)]OTf has one independent molecule in the asymmetric unit of the crystal structure with very large anisotropic displacement parameters. During cooling a fully reversible solid–solid phase transition occurs at a discrete temperature in the range 210–230 K. The low-temperature phase has six independent, well ordered molecules in the asymmetric unit. The $P2_1/a$ space group symmetry of the high-temperature phase changes to $P2_1/n$ for the low-temperature phase and the *c*-axis increases by a factor of six. The acetate ligand is shown to be coordinated in a η^1-fashion through one of the oxygen atoms, with the sterically encumbered, tridentate **PNP^{tBu}** ligand completing the square planar geometry around the Ni^{II} ion. The synthesis and full characterization of the complex is reported.

© 2009 Elsevier Ltd. All rights reserved.

1. Introduction

Crystal structures with more than one independent molecule of the same species in the asymmetric unit ($Z' > 1$) are a curiosity for several decades and still relatively rare. There are interesting discussions still ongoing about the origin of this phenomenon [1]. Obviously, crystallization temperature and kinetics play an important role as well as the crystallization conditions (from solution by cooling or solvent evaporation, from the melt, or from the gas phase by sublimation). The central question under discussion is, whether a compound packed in a crystal structure with $Z' > 1$ should always have a more stable polymorph with $Z' = 1$, which only has to be sought.

Not only crystallization can lead to structures with $Z' > 1$, such structures can also be the result of solid–solid phase transitions. Here, the high Z' structures are frequently the ordered low-temperature phase, while the high-temperature phase with a lower Z' value shows signs of large thermal motion or disorder. The α-phase of the trivalent metal acetylacetonates $M^{III}(acac)_3$ of manganese [2], aluminum [3] and chromium [4] are isostructural at room temperature with $Z' = 1$, but at low-temperature they show different symmetries with $Z' = 2$, 3, or 6. Other examples are the divalent crown ether complexes $[M^{II}(H_2O)_2(15\text{-crown-}5)](NO_3)_2$, where Z' depends on the metal as well as on the measurement temperature [5].

The high Z' structure after a phase transition that is presented in this publication was found in an organometallic compound of a late transition metal. These compounds containing tridentate, pincer ligands continue to attract major attention [6]. Most examples of such ligands formally exist as monoanionic frameworks [7], but more recently neutral analogues have also gained interest [8]. Amidst that class of ligands, those derived from 2,6-lutidine have been studied intensely, in part because of the non-innocent character of the ligand framework, which has allowed for unusual cooperativity of the metal and the ligand, in particular for both fundamental coordination chemistry studies [9] and catalytic applications [10] (Scheme 1).

Recently, we applied the neutral (pseudo-)pincer ligand **PNP^{tBu}** [11] to construct a number of Cu^{I} complexes, wherein the potentially tridentate ligand but rather acted as a flexidentate ligand with hemilabile coordination of the pyridine N-atom [12]. More recently, we decided to explore the non-innocent character of the PNP-backbone in combination with its coordination to Ni^{II} and were able to selectively synthesize several thiolate and alkyl complexes [13]. During these investigations, we required the corresponding Ni(**PNP^{tBu}**)-acetato complex as a potential starting material.

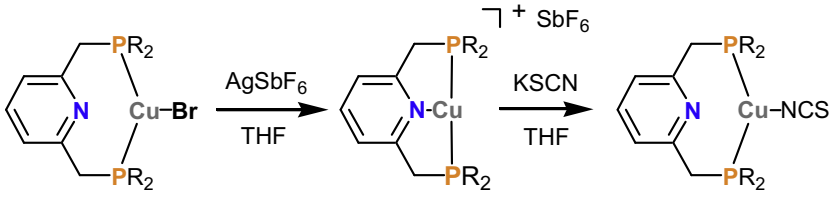
2. Experimental

2.1. General

Solvents were purified by established procedures. Starting materials were purchased from commercial sources and used as

* Corresponding author. Tel.: +31 30 253 3902; fax: +31 30 253 3940.
E-mail address: m.lutz@uu.nl (M. Lutz).

0277-5387/$ - see front matter © 2009 Elsevier Ltd. All rights reserved.
doi:10.1016/j.poly.2009.04.031



Scheme 1. Hemilabile coordination of the pyridine N-atom of **PNP^{tBu}** whilst coordinated to Cu^{I}.

received. IR spectra (ATR reflectance mode) were recorded with a Nicolet Avatar 360 FT-IR, NMR spectra were recorded with a Varian 200 spectrometer at room temperature (^{1}H: 200 MHz, ^{13}C: 50 MHz, ^{31}P: 80 MHz) and calibrated to the residual proton and carbon signals of the solvent (^{1}H) or an external solution of 85% aqueous H_3PO_4 (^{31}P{^{1}H}). **PNP^{tBu}** was synthesized according to a literature procedure [11,12].

2.2. Synthesis of complex *1*, *[Ni(PNP^{tBu})(OAc)]OTf*

To a solution of **PNP^{tBu}** (395.5 mg, 1.00 mmol) in THF/CH_2Cl_2 (1:1 v/v; 80 mL) was added $Ni(OAc)_2 \cdot 4H_2O$ (248.8 mg, 1.00 mmol), together with NaOTf (172.1 mg, 1.00 mmol) and 4 Å molecular sieves. The resultant orange-red suspension was stirred for 16 h before being filtered. After removal of solvent *in vacuo*, recrystallization of the red solid yielded orange-red crystals by slow diffusion of pentane into a THF-solution (476.9 mg, 0.72 mmol, 72%). ^{31}P NMR (80.9 MHz, acetone-d_6): δ 49.1. ^{1}H NMR (200 MHz, acetone-d_6): δ 7.99 (t, J_1 = 7.0 Hz, 1H, *p*-ArH), 7.56 (d, J_1 = 7.0 Hz, 2H, *m*-ArH), 3.91 (m, 4H, –CH_2–), 1.76 (s, OCOCH_3), 1.57 (vt, J_1 = 7.0 Hz, 36H, ^{t}Bu). IR (ATR, cm^{-1}): *v* 1631, 1604, 1566, 1467.

2.3. X-ray crystal structure determinations

The crystal structures of **1a** and **1b** were determined on the same crystal. Intensities were measured on a Nonius KappaCCD diffractometer with rotating anode (graphite monochromator, λ = 0.71073 Å). Integration was performed with Eval15 [14] (structure **1a**) or Eval14 [15] (structure **1b**). For **1a** a non-reduced setting of the cell parameters was used for comparison with **1b**. The program SADABS [16] was used for absorption correction and scaling. The structures were solved with Direct Methods using the program SHELXS-97 [17] and refined with SHELXL-97 [17] against F^2 of all reflections. Non-hydrogen atoms were refined with anisotropic displacement parameters. All hydrogen atoms were introduced in calculated positions and refined with a riding model. The orientations of the methyl groups were refined successfully. Geometry calculations and checking for higher symmetry was performed with the PLATON program [18]. Further details are given in Table 1.

2.4. Temperature dependent unit cell determinations

The temperature dependent unit cell determinations were performed on a Nonius KappaCCD diffractometer with a different crystal than the collection of the complete datasets for the structure determination. To minimize apparatus errors, the CCD detector was kept fixed during the experiment. The Phi/Phi–Chi routine was used to obtain accurate positions of the reflections [19] and the cell parameters were re-determined after every temperature change and refined with the program PEAKREF [20]. The crystal was cooled from 290 to 110 K in steps of 20 K with a rate of 360 K/h and then warmed up to 290 K with the same steps and rate. The orientation matrix of the low-temperature phase was taken as starting point for all unit cell determinations.

Table 1
Details of the X-ray crystal structure determinations.

	1a	**1b**
Formula	$[C_{25}H_{46}NNiO_2P_2](CF_3O_3S)$	$[C_{25}H_{46}NNiO_2P_2](CF_3O_3S)$
Fw	662.35	662.35
Crystal color	orange-red	orange-red
Crystal size (mm^3)	0.48 × 0.42 × 0.15	0.48 × 0.42 × 0.15
T (K)	240(2)	110(2)
Crystal system	monoclinic	monoclinic
Space group	$P2_1/a$ (number 14)	$P2_1/n$ (number 14)
a (Å)	30.1361(4)	30.3953(5)
b (Å)	14.1476(3)	13.9346(2)
c (Å)	8.1084(3)	47.7404(7)
β (°)	113.680(1)	114.231(1)
V (Å^3)	3165.96(13)	18438.8(5)
Z	4	24
Z′	1	6
D_x (g/cm^3)	1.390	1.432
μ (mm^{-1})	0.832	0.857
Absorption corruption method	multi-scan [16]	multi-scan [16]
Absorption corruption range	0.76–0.88	0.71–0.88
$(\sin\theta/\lambda)_{max}$ (Å^{-1})	0.65	0.59
Number of reflections (measurement/unique)	35816/7280	139943/32176
Number of reflection ($I > 2\sigma(I)$)	5482	20792
Parameters/restraints	365/0	2185/0
*R*1/*wR*2 (I>2σ(I))	0.0664/0.1858	0.0463/0.0885
*R*1/*wR*2 (all reflections)	0.0864/0.2039	0.0941/0.1045
S	1.067	1.028
$\rho_{min/max}$ (e/Å^3)	−0.79/1.05	−0.39/0.61

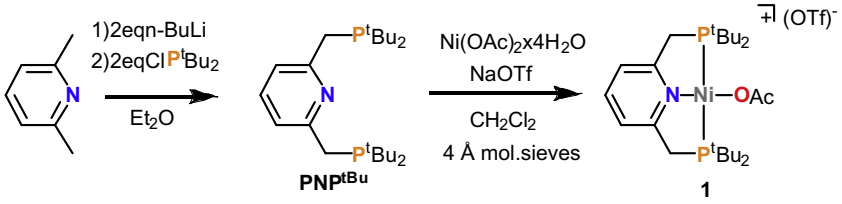
3. Results and discussion

3.1. Synthesis

Complex **1** is prepared in a straightforward manner by the stoichiometric reaction of $Ni(OAc)_2 \cdot 4H_2O$ and **PNP^{tBu}** in CH_2Cl_2, together with one equiv NaOTf and 4 Å molecular sieves, as a red solid. The ^{31}P NMR spectrum showed a singlet at δ 49.1, while the presence of the acetate co-ligand was corroborated by virtue of a triplet at δ 1.76 in the ^{1}H NMR spectrum. The IR spectrum showed bands at *v* 1631 and 1467 cm^{-1} for the acetato fragment, together with two bands at 1604 and 1566 cm^{-1} for the coordinated **PNP^{tBu}** ligand. Recrystallization from THF-pentane yielded orange-red single crystals (Scheme 2).

3.2. Molecular structure

The molecular structure of **1** is discussed on the basis of **1b**, which is a well ordered structure, while **1a** shows signs of disorder. The Ni^{II} center is four coordinated with a slightly distorted square



Scheme 2. Synthesis of complex **1** starting from commercially available 2,6-lutidine.

Table 2
Selected bond lengths (Å), angles and torsion angles (°) for **1a** at 240 K and the six independent molecules of **1b** at 110 K.

	1a	**1b**					
		1	2	3	4	5	6
Ni1–P1	2.2254(10)	2.2061(10)	2.2116(10)	2.2081(10)	2.2145(10)	2.2120(10)	2.2148(10)
Ni1–P2	2.2293(10)	2.2613(10)	2.2441(10)	2.2381(10)	2.2389(10)	2.2405(10)	2.2273(10)
Ni1–N1	1.924(3)	1.925(3)	1.922(3)	1.925(3)	1.922(3)	1.922(3)	1.929(3)
Ni1–O1	1.854(3)	1.865(2)	1.866(2)	1.864(2)	1.863(2)	1.860(2)	1.862(2)
C24–O1	1.264(6)	1.289(4)	1.282(4)	1.279(4)	1.275(4)	1.285(4)	1.289(4)
C24–O2	1.218(7)	1.224(4)	1.223(4)	1.222(4)	1.222(4)	1.218(4)	1.217(4)
P1–Ni1–N1	86.83(10)	86.35(9)	86.23(9)	86.24(9)	86.35(8)	86.91(8)	87.25(9)
P2–Ni1–N1	87.26(10)	87.13(9)	86.43(9)	87.00(9)	86.70(8)	86.51(8)	86.35(9)
P1–Ni1–O1	91.51(9)	90.12(7)	91.46(7)	90.80(7)	91.83(7)	91.08(7)	91.89(7)
P2–Ni1–O1	94.42(9)	97.29(7)	95.98(7)	95.96(7)	95.00(7)	96.01(7)	93.90(7)
P1––Ni1–P2	174.06(4)	170.30(4)	172.55(4)	173.23(4)	173.04(4)	172.20(4)	172.60(4)
Ni1–O1–C24	127.7(4)	123.0(2)	123.9(2)	125.7(2)	125.8(2)	124.6(2)	129.8(2)
O1–C24–O2	124.2(5)	125.0(4)	125.3(3)	125.3(4)	125.4(3)	125.5(4)	125.7(3)
P1–Ni1–O1–C24	102.0(3)	113.7(2)	111.9(2)	108.3(2)	103.9(3)	104.0(2)	100.4(3)
N1–C1–C6–P1	11.7(9)	−29.2(3)	15.9(4)	17.3(4)	13.8(4)	−24.9(4)	−21.5(4)
N1–C5–C15–P2	23.4(6)	38.0(4)	31.2(4)	26.4(4)	26.8(4)	36.5(4)	−13.5(4)

planar geometry with cis angles between 86.23(9)° and 97.29(7)° in **1b** (Table 2). The coordination environment is formed by the neutral **PNP^{tBu}** ligand and one oxygen atom of the anionic carboxylate ligand leading to an overall single positive charge of the complex (Fig. 1). The second oxygen of the carboxylate is not coordinated (the Ni–O2 distances are 3.059(2)–3.223(2) Å in **1b**). The five atoms of the metal coordination plane are nearly coplanar with the pyridine ring with interplanar angles of 9.36(12)–11.24(13)° in **1b**. This is in contrast with the bent shape of the corresponding cationic three-coordinated Cu^{I} complexes [12], where the interplanar angles are between 34.40(11)° and 44.09(7)°. The P–Ni–P angles in **1b** are between 170.30(4)° and 173.23(4)°, which is much higher than in corresponding second- or third row square planar complexes with **PNP^{tBu}**. This reflects the direct influence of the ionic radius and the flexibility range of the ligand skeleton.

The overall single positive charge of the metal complex is balanced by a non-coordinated triflate anion per formula unit. The shortest intermolecular distance of a triflate oxygen to a nickel center in **1b** is 6.017(3) Å, but there are weak intermolecular C–H···O and C–H···F interactions with the triflate as acceptor. The corresponding C···O and C···F distances are 3.173(5)–3.564(4) and 3.204(4)-3.453(5) Å, respectively, with C–H···O and C–H···F angles of 124–170° and 124–154°.

The main difference between the molecular structures of **1a** at 240 K and **1b** at 110 K are the displacement ellipsoids. A rigid-body analysis of the metal complex in **1a** using the program THMA11 [21]

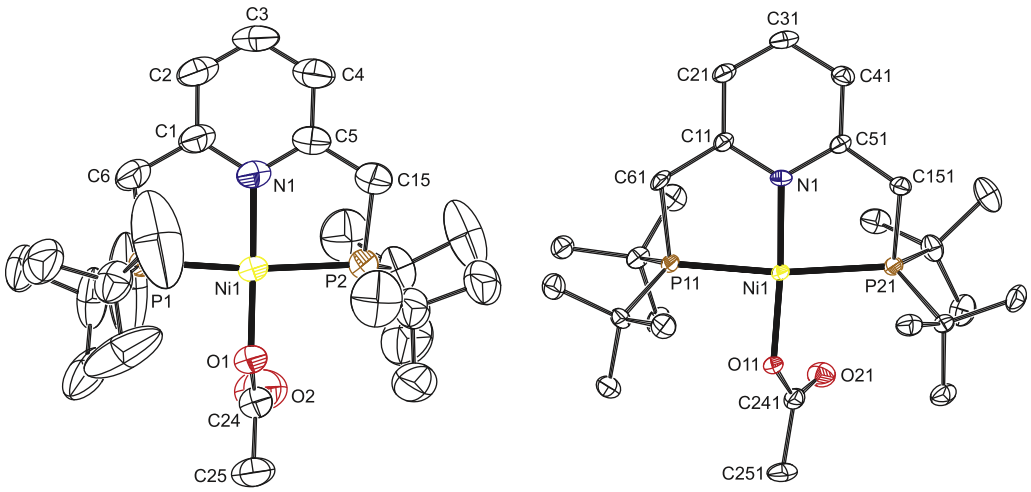


Fig. 1. Displacement ellipsoid plots of **1a** at 240 K (left) and one of the six independent molecules of **1b** at 110 K (right), drawn at the 50% probability level. Hydrogen atoms and triflate anions are omitted for clarity.

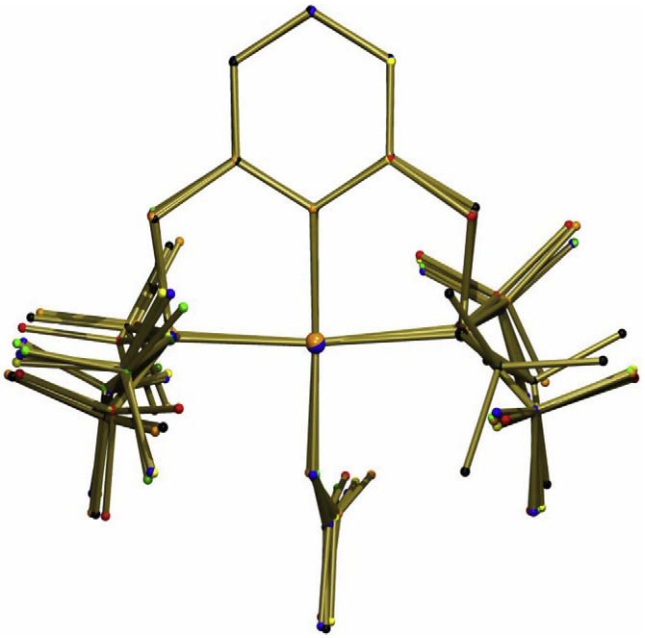


Fig. 2. Quaternion fit [24] of the six independent molecules in **1b** based on the atoms of the metal coordination environment and the pyridine ring. The calculation was performed with the program PLATON [18].

results in a very high R value of 0.554 [$R = (\Sigma(U_{obs} - U_{calc})^2/\Sigma(U_{obs})^2)^{1/2}$], which indicates that the displacement parameters of the molecule cannot be described with a rigid body model. The largest deviations from the rigid body model are in the *tert*-butyl groups at P1 (Fig. S1 [23], Supplementary data). Large deviations are also observed in the *tert*-butyl groups at P2, the benzylic carbon C6, and the non-coordinated acetate oxygen O2. The rigid body fit of the six independent molecules of **1b** is significantly better with R values between 0.213 and 0.363.

The main differences between the six independent molecules in **1b** are the orientations of the *tert*-butyl groups at phosphorus P1 (Fig. 2). These differences correspond to the large displacement ellipsoids in **1a**, which contains only one independent molecule in the asymmetric unit and can thus be considered as disordered average structure of **1b**. The puckering of the five-membered chelate rings in **1b** also differs: in four molecules the N–C–C–P torsion angles have an equal sign, in two molecules they have an opposite sign. In other words: four molecules have a local twofold symmetry, two molecules have a local mirror symmetry. Both of these different puckering modes are rather common in metal pincer complexes [22] and the change between local twofold and local mirror symmetry obviously has only a small energy barrier.

3.3. Symmetry change during the phase transition

Crystal structure **1a** at 240 K is described in a non-reduced setting of the cell parameters in space group $P2_1/a$, which is a non-standard setting of $P2_1/c$. This setting simplifies the comparison with **1b** at 110 K. The reduction of the cell parameters of **1a** can be obtained by applying transformation matrix $\mathbf{T_1} = (-1, 0, -2/0, -1, 0/0, 0, 1)$, which keeps the space group $P2_1/a$.

Applying transformation matrix $\mathbf{T_2} = (0, 0, 1/-2, 0, -3/0, -1, 0)$ with a determinant of 2 on **1a** will generate a C-centered pseudo-orthorhombic cell with $\alpha = \beta = 90°$ and $\gamma = 90.122(1)°$, but the associated orthorhombic Laue symmetry is not fulfilled by the reflection intensities ($R_{int} = 0.546$). No indications for pseudo-orthorhombic twinning were detected during data integration or structure refinement.

If transformation matrix $\mathbf{T_3} = (1, 0, 0/0, 1, 0/0, 0, 6)$ with a determinant of 6 is applied on the cell parameters of **1a**, the low-temperature cell of **1b** is generated. The corresponding operation with respect to the symmetry operations and the atomic coordinates involves matrix $\tilde{\mathbf{T}}_3^{-1} = (1, 0, 0/0, 1, 0/0, 0, 1/6)$. Before the application of $\tilde{\mathbf{T}}_3^{-1}$ the unit cell, symmetry operations and atomic coordinates must be expanded in c-direction by a factor of 6 resulting in 24 symmetry operations. After the application of $\tilde{\mathbf{T}}_3^{-1}$ only four symmetry operations have translational components of 0 and ½, consistent with space group $P2_1/n$ (space group of **1b**). The other 20 symmetry operations have translational components of 1/6 and 1/3 and do not belong to $P2_1/n$. By structural changes related to the phase transition these 20 symmetry operations become only approximate.

The phase transition keeps the point group (in German: "*Kristallklasse*") intact and only changes the translation symmetry. It can therefore be classified as *klassengleich*. Projections of the molecular packing of **1a** and **1b** in the crystal are depicted in Fig. 3. The crystal structure consists of alternating layers of

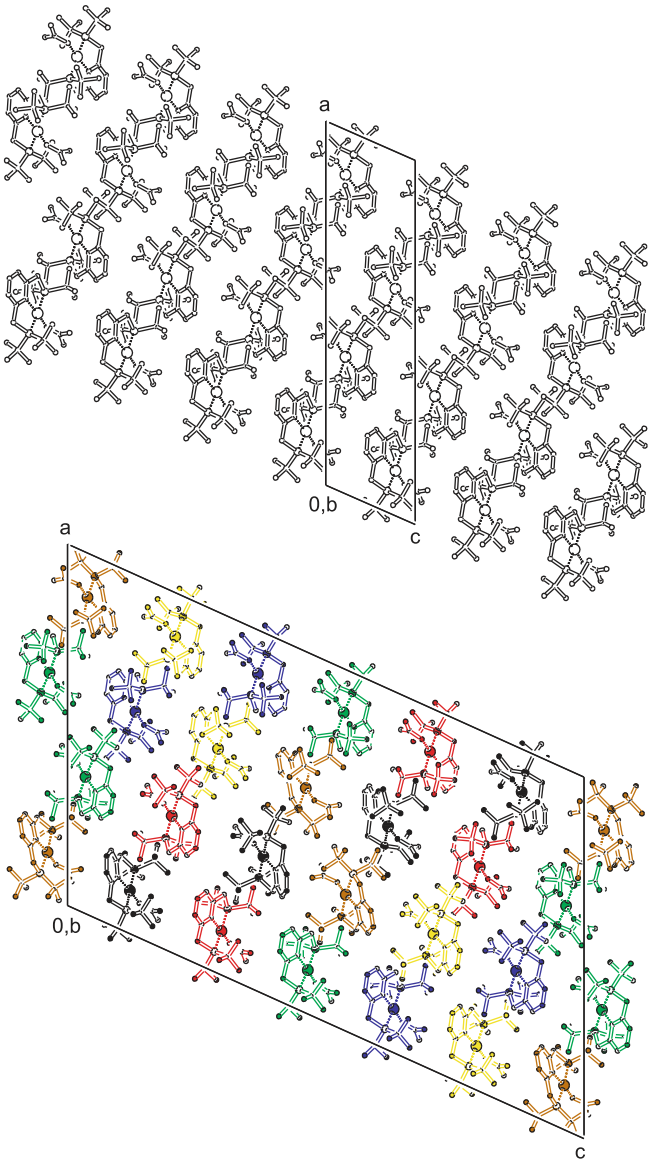


Fig. 3. Packing in the crystals of **1a** at 240 K (top) and **1b** at 110 K (bottom). View along the crystallographic b-axis. Independent molecules are drawn in different colors. Hydrogen atoms and triflate anions are omitted for clarity.

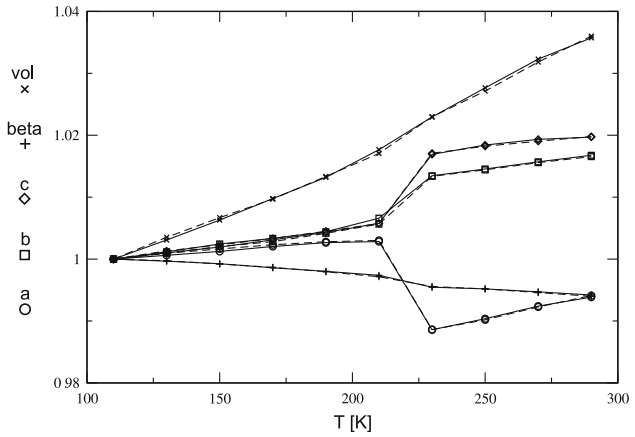


Fig. 4. Temperature dependence of the unit cell parameters normalized to those at 110 K. In the range 230-290 K the values of the *c*-axis were multiplied by a factor of 6. This multiplication was also taken into account for the calculation of the volume. The cooling curves are drawn as straight lines, the warming curves as dashed lines. Between 110 and 210 K and between 230 and 290 K the behavior is assumed linear. The lines between 210 and 230 K only indicate the discontinuity; the exact temperature of the phase change was not determined.

[Ni(OAc)(**PNP^{tBu}**)] cations and triflate anions parallel to the (2, 0, −1) plane (**1a**) or the (1, 0, −3) plane (**1b**). The only noteworthy intermolecular interactions are the above mentioned C–H···O and C–H···F bonds.

3.4. Temperature dependent unit cell parameters

The unit cell parameters of **1** have been determined by cooling from 290 to 110 K and warming up again to 290 K (see Section 2). The behavior is linear between 290 and 230 K, has a discontinuity between 230 and 210 K and then again linear between 210 and 110 K (Fig. 4). We assume that a phase transition occurs at a discrete temperature in the range between 230 and 210 K. The temperature of 240 K for the data collection of **1a** was chosen above this discontinuity in order to obtain the pure high-temperature phase.

1b at 110 K has a higher density (1.432 g/cm^3) than **1a** at 240 K (1.390 g/cm^3), which is a consequence of the discontinuity in the volume curve (Fig. 4); extrapolations of the volume of **1b** to 240 K would result in a density of 1.406 and 1.407 g/cm^3 for the cooling and warming curves, respectively. The better packing in **1b** can also be seen in the packing index [25] of 69.6%, compared to 66.9% in **1a**. In the case of polymorphic compounds with large Z' it has been discussed that the structures should be metastable [1], which would mean a relatively low density. In the present case of a disorder–order phase transition the density of the high Z' structure is higher than in the low Z' structure. The phase transition in **1** is fully reversible, as can be seen by comparing the cooling and the warming curves (Fig. 4).

For all unit cell changes in the ranges 290–230 and 210–110 K strain tensors have been calculated in the (Cartesian) crystal-physical coordinate system [26]. All eigenvalues of the tensors are positive in these temperature ranges, which means a triaxial positive thermal expansion.

3.5. Crystal defects of the low-temperature phase

The X-ray reflections of **1a** at 240 K have a normal profile (Fig. S2, Supplementary data) and a relatively small mosaicity of 0.25° has been assumed for the integration of the intensities. The crystal is well aligned in the center of the X-ray beam. After cooling to 110 K (**1b**) the reflections were found to be split. This splitting of the reflections is best described by two orientation matrices, which are related by a 0.42° rotation about a non-crystallographic axis. Additionally, both crystal fragments are no longer in the center of the X-ray beam. Integration of the intensity was performed with Eval14 [15] using a large enough contour around the split peak and summing all intensity within the contour based on the *background-peak-background* method. If the crystal is warmed to 240 K again, the splitting of the peaks disappears and the structure refined from these data is identical to **1a**.

3.6. Description of the low-temperature phase as modulated structure

In Fig. 2 the six independent molecules of **1b** were fitted on each other, taking into account the molecular geometry and ignoring the packing of the molecules in the crystal. The packing can be seen, if the transformation matrix $\mathbf{T_3}^{-1}$ is applied to the cell parameters and $\tilde{\mathbf{T}}_3$ to the coordinates of **1b** (Fig. S3, Supplementary data). Here, the deviations not only concern the conformations of the *tert*-butyl groups but affect all atoms and these deviations are very large. The Ni-atoms differ by up to 1.29 Å, the P-atoms up to 1.27 Å, the N-atoms up to 1.44 Å. The largest difference is between equivalent atoms of C18 and C22 in *tert*-butyl groups with 2.51 and 2.50 Å, respectively.

This very strong modulation of the atomic positions can also be seen in the intensity statistics of the reflections (Table S1, Supplementary data). While the substructure reflections with $l = 6n$, which correspond to **1a** at 240 K, are significantly stronger, the superstructure reflections with $l = 6n \pm m$, which are absent in **1a**, are still very strong due to the very strong modulation.

As a consequence of this intensity statistics the refinement of **1b** as a commensurate modulated structure in the four-dimensional space group $P2_1/a(\alpha 0 \gamma)0s$ appears not advisable. For such a refinement the reflections would have to be re-indexed with a six times smaller *c*-axis and a *q*-vector = 0, 0, 1/6.

The superstructure refinement in the three-dimensional space group $P2_1/a$ presented in this study is very stable. The data/parameter ratio is 14.7 and there are no correlation matrix elements larger than 0.608.

4. Conclusions

The free energy of a crystal has contributions from enthalpy and entropy [27]. On a qualitative level it can be stated that disorder increases the contribution of the entropy, while an optimal packing increases the contribution of the enthalpy. In many cases of solid–solid phase transitions the high-temperature phase shows signs of disorder and the low-temperature phase is well ordered [28]. In nearly all cases the high-temperature phase has higher symmetry, which is broken during cooling.

The present results confirm these simple theories, but it interesting to see how large the changes are, as well in the molecular conformation as in the crystal packing. Differences up to 2.51 Å are found between equivalent positions of non-hydrogen atoms of the six independent molecules of **1b** as a consequence of different puckering of the chelate-rings. From these huge changes we may conclude that the model of the average structure of **1a** is only approximate and does not cover all disorder features of this structure. The large structural changes during the phase transition will cause enormous stress, which is the probable reason for the crystal defects observed in the X-ray diffraction images of **1b**.

Acknowledgement

This work was supported by the Council for the Chemical Sciences of the Netherlands Organization for Scientific Research

(NWO-CW), including a VENI Innovation grant (to J.I.v.d.V.). We acknowledge A.M.M. Schreurs for fruitful discussions and the preparation of Fig. S2.

Appendix A. Supplementary data

CCDC 716696 and 716697 contain the supplementary crystallographic data for (**1a**) and (**1b**). These data can be obtained free of charge via http://www.ccdc.cam.ac.uk/conts/retrieving.html, or from the Cambridge Crystallographic Data Centre, 12 Union Road, Cambridge CB2 1EZ, UK; fax: (+44) 1223-336-033; or e-mail: deposit@ccdc.cam.ac.uk. Supplementary data associated with this article can be found, in the online version, at doi:10.1016/j.poly.2009.04.031.

References

[1] (a) G.R. Desiraju, Cryst. Eng. Commun. 9 (2007) 91;
(b) K.M. Anderson, J.W. Steed, Cryst. Eng. Commun. 9 (2007) 328.
[2] S. Geremia, N. Demitri, J. Chem. Educ. 82 (2005) 465.
[3] L.S. von Chrzanowski, M. Lutz, A.L. Spek, Acta Crystallogr. C 63 (2007) m129.
[4] L.S. von Chrzanowski, M. Lutz, A.L. Spek, Acta Crystallogr. C 63 (2007) m377.
[5] (a) X. Hao, M.A. Siegler, S. Parkin, C.P. Brock, Cryst. Growth Des. 5 (2005) 2225;
(b) M.A. Siegler, X. Hao, S. Parkin, C.P. Brock, Acta Crystallogr. B 64 (2008) 738.
[6] (a) C. Crocker, R.J. Errington, R. Markham, C.J. Moulton, K.J. Odell, B.L. Shaw, J. Am. Chem. Soc. 102 (1980) 4373;
(b) M. Albrecht, G. van Koten, Angew. Chem., Int. Ed. 40 (2001) 3750;
(c) J.T. Singleton, Tetrahedron 59 (2003) 1837;
(d) J. Zhao, A.S. Goldman, J.F. Hartwig, Science 307 (2005) 1080;
(e) A.S. Goldman, A.H. Roy, Z. Huang, R. Ahuja, W. Schinski, M. Brookhart, Science 312 (2006) 257;
(f) M. Gagliardo, D.J.M. Snelders, P.A. Chase, R.J.M. Klein Gebbink, G.P.M. van Klink, G. van Koten, Angew. Chem., Int. Ed. 45 (2007) 8558;
(g) H. Nishiyama, Chem. Soc. Rev. 36 (2007) 1133.
[7] (a) Besides the 'common' pincer ligands with alkyl- and phenyl as the building block, several other classes have been developed over the years, see: M.D. Fryzuk, P.A. MacNeill, S.J. Rettig, A.S. Secco, J. Trotter, Organometallics 1 (1982) 918;
(b) S. Nemeh, R.J. Flesher, K. Gierling, C. Maichle-Mössmer, H.A. Mayer, W.C. Kaska, Organometallics 17 (1998) 2003;
(c) J.C. Peters, S.B. Harkins, S.D. Brown, M.W. Day, Inorg. Chem. 40 (2001) 5083;
(d) E.J. Farrington, E.M. Viviente, B.S. Williams, G. van Koten, J.M. Brown, Chem. Commun. (2002) 308;
(e) L.C. Liang, Coord. Chem. Rev. 250 (2006) 1152;
(f) Z. Csok, O. Vechorkin, S.B. Harkins, R. Scopelliti, X. Hu, J. Am. Chem. Soc. 130 (2008) 8156;
(g) N.P. Mankad, E. Rivard, S.B. Harkins, J.C. Peters, J. Am. Chem. Soc. 127 (2005) 16032;
(h) P. Sangtrirutnugul, T.D. Tilley, Organometallics 27 (2008) 2223.
[8] (a) S. Hillebrand, B. Bartkowska, J. Bruckmann, C. Krüger, M.W. Haenel, Tetrahedron Lett. 39 (1998) 813;
(b) C.L. Foster, C.A. Kilner, M. Thornton-Pett, M.A. Halcrow, Polyhedron 21 (2002) 1031;
(c) S. Ekici, M. Nieger, R. Glaum, E. Niecke, Angew. Chem. Int. Ed. 42 (2003) 435;
(d) H.M. Lee, J.Y. Zeng, C.-H. Hu, M.-T. Lee, Inorg. Chem. 43 (2004) 6822;
(e) A. Hayashi, M. Okazaki, F. Ozawa, R. Tanaka, Organometallics 26 (2007) 5246;
(f) D. Pugh, A.A. Danopoulos, Coord. Chem. Rev. 251 (2007) 610;
(g) B. Benito-Garagorri, K. Kirchner, Acc. Chem. Res. 41 (2008) 201.
[9] (a) G. Vasapollo, C.F. Nobile, A. Sacco, J. Organomet. Chem. 296 (1988) 435;
(b) G. Müller, M. Klinga, M. Leskelä, B. Rieger, Z. Anorg. Allg. Chem. 628 (2002) 2839;
(c) R.J. Trovitch, E. Lobkovsky, P.J. Chirik, Inorg. Chem. 45 (2006) 7252;
(d) M. Feller, E. Ben-Ari, T. Gupta, L.J.W. Shimon, G. Leitus, Y. Diskin-Posner, L. Weiner, D. Milstein, Inorg. Chem. 46 (2007) 10479;
(e) D. Vuzman, E. Poverenov, L.J.W. Shimon, Y. Diskin-Posner, D. Milstein, Organometallics 27 (2008) 2627.
[10] (a) C. Hahn, P. Morvillo, A. Vitagliano, Eur. J. Inorg. Chem. (2001) 419;
(b) M.E. Cucciolito, A. D'Amora, A. Tuzi, A. Vitagliano, Organometallics 26 (2007) 5216;
(c) S.M. Kloek, D.M. Heinekey, K.I. Goldberg, Angew. Chem., Int. Ed. 46 (2007) 4736;
(d) C. Gunanathan, Y. Ben-David, D. Milstein, Science 317 (2007) 790;
(e) B.M. Cochran, F.E. Michael, J. Am. Chem. Soc. 130 (2008) 2786.
[11] (a) M. Kawatsura, J.F. Hartwig, Organometallics 20 (2001) 1960;
(b) D. Hermann, M. Gandelman, H. Rozenberg, L.J.W. Shimon, D. Milstein, Organometallics 21 (2002) 812.
[12] J.I. van der Vlugt, E.A. Pidko, D. Vogt, M. Lutz, A.L. Spek, A. Meetsma, Inorg. Chem. 47 (2008) 4442.
[13] J.I. van der Vlugt, M. Lutz, E.A. Pidko, D. Vogt, A.L. Spek, Dalton Trans. (2009) 1016.
[14] X. Xian, A.M.M. Schreurs, L.M.J. Kroon-Batenburg, Acta Crystallogr. A 62 (2006) s92.
[15] A.J.M. Duisenberg, L.M.J. Kroon-Batenburg, A.M.M. Schreurs, J. Appl. Cryst. 36 (2003) 220.
[16] G.M. Sheldrick, SADABS: Area-Detector Absorption Correction, Version 2008/1, Universität Göttingen, Germany.
[17] G.M. Sheldrick, Acta Crystallogr. A 64 (2008) 112.
[18] A.L. Spek, J. Appl. Cryst. 36 (2003) 7.
[19] A.J.M. Duisenberg, R.W.W. Hooft, A.M.M. Schreurs, J. Kroon, J. Appl. Cryst. 33 (2000) 893.
[20] A.M.M. Schreurs, PEAKREF, Utrecht University, The Netherlands, 2008.
[21] V. Schomaker, K.N. Trueblood, Acta Crystallogr. B 54 (1998) 507.
[22] C.A. Kruithof, H.P. Dijkstra, M. Lutz, A.L. Spek, R.J.M. Klein Gebbink, G. van Koten, Organometallics 27 (2008) 4928.
[23] W. Hummel, J. Hauser, H.B. Bürgi, J. Mol. Graphics 8 (1990) 214.
[24] A.L. Mackay, Acta Crystallogr. A 40 (1984) 165.
[25] A.I. Kitajgorodskij, Molecular Crystals and Molecules, Academic Press, New York, 1973.
[26] Y. Ohashi, in: R.M. Hazen, L.W. Finger (Eds.), Comparative Crystal Chemistry, Wiley-Interscience, Chichester, 1982, pp. 91–102.
[27] M.T. Dove, Structure and Dynamics: An Atomic View of Materials, Oxford University Press, Oxford, 2003.
[28] F.H. Herbstein, Crystalline Molecular Complexes and Compounds, vol. 2, Oxford University Press, Oxford, 2005.

Polyhedron 28 (2009) 2347–2354

Contents lists available at ScienceDirect

Polyhedron

journal homepage: www.elsevier.com/locate/poly

Mixed-ligand complexes with *trans*-1-(2-pyridyl)-2-(4-pyridyl)ethylene terminal and different aromatic polycarboxyl linkers: Synergistic modulation of metallosupramolecular architectures *via* coordinative and secondary interactions

Qian Yu, Cheng-Peng Li, Zhi-Hui Zhang, Miao Du *

College of Chemistry and Life Science, Tianjin Key Laboratory of Structure and Performance for Functional Molecule, Tianjin Normal University, Tianjin 300387, PR China

ARTICLE INFO

Article history:
Received 19 November 2008
Accepted 28 April 2009
Available online 19 May 2009

Keywords:
Supramolecular complex
trans-1-(2-Pyridyl)-2-(4-pyridyl)ethylene (bpe)
Polycarboxyl ligand
Secondary interaction
Crystal engineering

ABSTRACT

A series of Co^{II}, Ni^{II}, and Cu^{II} complexes with *trans*-1-(2-pyridyl)-2-(4-pyridyl)ethylene (bpe) and various polycarboxyl co-ligands have been prepared under general condition and characterized by IR, elemental analysis, and TG-DTA techniques. Single-crystal X-ray diffraction indicates that these complexes display multifarious binuclear, 1-D, and 2-D coordination motifs in virtue of the bridging polycarboxyl building blocks, in which the bpe ligand uniformly adopts the unidentate coordination by using its 4-pyridyl group. Remarkably, higher-dimensional extended networks are further formed with the aid of additional secondary interactions based on bpe (such as H-bonding and π–π stacking). These results demonstrate that bpe is a reliable bifunctional tecton to construct diverse supramolecular architectures *via* synergistic effect of multiple intermolecular interactions.

© 2009 Elsevier Ltd. All rights reserved.

1. Introduction

The development of metallosupramolecular complexes based on crystal engineering strategy is of significant success in recent years, which provides a rational junction between aesthetics of the crystalline materials and their physicochemical properties [1–8]. From the viewpoint of supramolecular chemistry, the information of a predesigned ligand could be read by the metal ion in the assembled process according to the coordination algorithm to define the primary architecture [9–13]. Moreover, the secondary intermolecular non-covalent interactions such as H-bonding and aromatic stacking do play a key role in structural assembly [14–19], which however are difficult to control at the present time. In this regard, dipyridyl- and polycarboxyl-type ligands have been illustrated to be reliable building blocks for the construction of such metallosupramolecular systems [20–22].

In this context, we have demonstrated that *trans*-1-(2-pyridyl)-2-(4-pyridyl)ethylene (bpe) is a potential bifunctional ligand [23] to be readily involved in different intermolecular interactions due to the distinct steric effect of the terminal pyridyl groups. Generally, the 4-pyridyl ring prefers to coordinate with the metal ion, whereas the 2-pyridyl group has a tendency to serve as the H-bonding acceptor. Significantly, this characteristic can be applied to direct the photocycloaddition of such metallosupramolecular complexes in solid state to give new coordination species [24]. As a continuation of our efforts on this interesting project, we will describe herein the preparation, crystal structures, and thermal properties of five Co^{II}, Ni^{II}, and Cu^{II} complexes constructed from bpe and different aromatic polycarboxyl co-ligands (see Chart 1) such as benzene-1,3,5-tricarboxylic acid (H_3btc), benzene-1,2,4,5-tetracarboxylic acid (H_4btec), isophthalic acid (H_2ip), and terephthalic acid (H_2tp). The results undoubtedly reveal that structural diversity of these supramolecular solids is dominated by the interplay of both coordinative and multiple secondary interactions.

2. Experimental

2.1. Materials and general methods

All reagents and solvents were commercially available and used as received. Fourier transform (FT) IR spectra (KBr pellets) were recorded on an AVATAR-370 (Nicolet) spectrometer. Elemental analyses were carried out on a CE-440 (Leemanlabs) analyzer. Thermogravimetric and differential thermal analysis experiments were performed in the temperature range of 25–800 °C (heating rate: 10 °C/min) on a Rigaku standard TG-DTA analyzer under N_2 atmosphere with an empty Al_2O_3 crucible as the reference.

2.2. Synthesis of complexes **1**–**5**

2.2.1. $[Co(Hbtc)(bpe)_2]_n$ (**1**)

A CH_3OH (10 mL) solution of H_3btc (21 mg, 0.1 mmol) was mixed with an aqueous solution (10 mL) of $Co(NO_3)_2{\cdot}6H_2O$

* Corresponding author. Tel./fax: +86 22 23766556.
E-mail address: dumiao@public.tpt.tj.cn (M. Du).

0277-5387/$ - see front matter © 2009 Elsevier Ltd. All rights reserved.
doi:10.1016/j.poly.2009.04.049

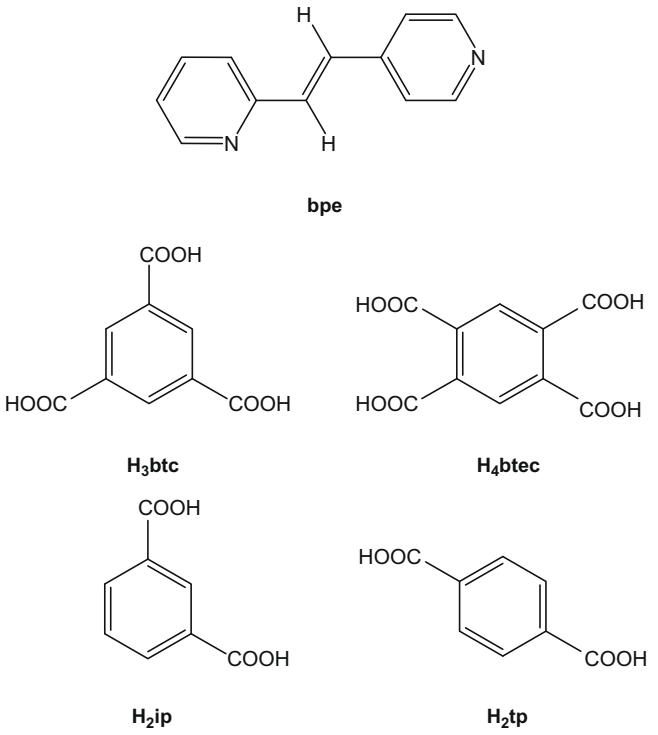


Chart 1.

(29 mg, 0.1 mmol) under stirring, to which a CH_3OH (5 mL) solution of bpe (18 mg, 0.1 mmol) was added. The resulting solution was filtered and left to stand under ambient condition. Red lamellar crystals of **1** suitable for X-ray diffraction were obtained upon slow evaporation of the solvents after a period of two weeks in 48% yield (15 mg, based on bpe). *Anal.* Calc. for $C_{33}H_{24}CoN_4O_6$: C, 62.76; H, 3.83; N, 8.87%. Found: C, 62.91; H, 3.74; N, 9.03%. IR (cm^{-1}): 3425b, 1691m, 1614vs, 1560s, 1432s, 1376s, 1220w, 1103w, 967m, 815m, 767m, 721m, 546m.

2.2.2. $[Co_2(btec)(bpe)_2(H_2O)_8](CH_3OH)_2(H_2O)_4$ (**2**)

The same synthetic method as that for **1** was used except that H_3btc was replaced by H_4btec (25 mg, 0.1 mmol), producing red block crystals of **2** in 58% yield (29 mg, based on bpe). *Anal.* Calc. for $C_{36}H_{54}Co_2N_4O_{22}$: C, 42.70; H, 5.37; N, 5.53%. Found: C, 42.43; H, 5.18; N, 5.41%. IR (cm^{-1}): 3416b, 1611vs, 1561vs, 1377s, 1139w, 1013m, 816m, 684w, 541m.

2.2.3. $[Ni(ip)(bpe)_2(H_2O)_2]_2(CH_3OH)(H_2O)_3$ (**3**)

The same synthetic method as that for **1** was used except that $Co(NO_3)_2{\cdot}6H_2O$ and H_3btc were replaced by $Ni(ClO_4)_2{\cdot}6H_2O$ (37 mg, 0.1 mmol) and H_2ip (17 mg, 0.1 mmol), respectively. Blue prism crystals of **3** were obtained in 51% yield (17 mg, based on bpe). *Anal.* Calc. for $C_{65}H_{66}Ni_2N_8O_{16}$: C, 58.58; H, 4.99; N, 8.41%. Found: C, 58.73; H, 5.15; N, 8.30%. IR (cm^{-1}): 3419b, 1610vs, 1546vs, 1472m, 1433s, 1386vs, 1221m, 1151w, 1073w, 1021m, 970w, 818m, 747s, 713m, 658w, 546m.

2.2.4. $\{[Ni(tp)(bpe)_2(H_2O)_2](CH_3OH)(H_2O)_2\}_n$ (**4**)

The same synthetic method as that for **1** was used except that $Co(NO_3)_2{\cdot}6H_2O$ and H_3btc were replaced by $Ni(ClO_4)_2{\cdot}6H_2O$ (37 mg, 0.1 mmol) and H_2tp (17 mg, 0.1 mmol), respectively. Green block crystals of **4** were produced in 43% yield (15 mg, based on bpe). *Anal.* Calc. for $C_{33}H_{36}NiN_4O_9$: C, 57.33; H, 5.25; N, 8.10%. Found: C, 57.53; H, 5.12; N, 8.23%. IR (cm^{-1}): 3414b, 1667w, 1593vs, 1497w, 1428m, 1379vs, 1153w, 1098w, 977m, 881m, 808m, 751s, 676w, 551s.

2.2.5. $\{[Cu(ip)(bpe)_2](H_2O)_4\}_n$ (**5**)

The same synthetic procedure as that for **1** was used except that $Co(NO_3)_2{\cdot}6H_2O$ and H_3btc were replaced by $Cu(ClO_4)_2{\cdot}6H_2O$ (37 mg, 0.1 mmol) and H_2ip (17 mg, 0.1 mmol), respectively. Green block crystals of **5** were produced in 45% yield (15 mg, based on bpe). *Anal.* Calc. for $C_{32}H_{32}CuN_4O_8$: C, 57.87; H, 4.86; N, 8.44%. Found: C: 57.58; H, 4.68; N, 8.76%. IR (cm^{-1}): 3427b, 1619vs, 1560s, 1367vs, 1221w, 1080w, 969w, 818m, 752m, 544m.

2.3. X-ray crystallography

Single-crystal X-ray diffraction data for **1**–**5** were collected on a Bruker Apex II CCD diffractometer at 296(2) K with Mo Kα radiation (λ = 0.71073 Å). There was no evidence of crystal decay during data collection. Semi-empirical absorption corrections were applied using SADABS and the program SAINT was used for integration of the diffraction profiles [25]. The structures were solved by direct methods using the SHELXS program of the SHELXTL package and refined with SHELXL [26]. The final refinement was performed by full-matrix least-squares methods on F^2 with anisotropic thermal parameters for all non-H atoms. In general, hydrogen atoms attached to carbon were generated geometrically with assigned isotropic thermal

Table 1
Crystallographic data and structural refinement summary for complexes **1–5**.

	1	**2**	**3**	**4**	**5**
Formula	$C_{33}H_{24}CoN_4O_6$	$C_{36}H_{54}Co_2N_4O_{22}$	$C_{65}H_{66}Ni_2N_8O_{16}$	$C_{33}H_{36}NiN_4O_9$	$C_{32}H_{32}CuN_4O_8$
M	631.49	1012.69	1332.68	691.36	664.16
Crystal size (mm)	0.18 × 0.15 × 0.04	0.28 × 0.26 × 0.22	0.21 × 0.18 × 0.16	0.25 × 0.22 × 0.20	0.18 × 0.14 × 0.12
Crystal system	triclinic	triclinic	monoclinic	triclinic	monoclinic
Space group	$P\bar{1}$	$P\bar{1}$	*C*2/c	$P\bar{1}$	$P2_1/c$
a (Å)	10.094(4)	8.7695(6)	21.908(2)	9.209(2)	15.116(5)
b (Å)	12.516(4)	9.9359(6)	21.335(2)	9.744(2)	11.177(4)
c (Å)	12.983(5)	14.2879(9)	14.869(1)	11.310(2)	20.068(7)
α (°)	109.117(5)	75.219(1)	90	73.139(2)	90
β (°)	93.146(5)	76.777(1)	108.352(1)	89.748(2)	110.649(6)
γ (°)	105.765(4)	67.959(1)	90	73.642(2)	90
V (Å^3)	1472.7(9)	1103.4(1)	6596.4(9)	928.6(3)	3173(2)
Z	2	1	4	1	4
D_{calc} (g cm^{-3})	1.424	1.524	1.342	1.236	1.391
μ (mm^{-1})	0.635	0.839	0.643	0.575	0.745
F(0 0 0)	650	528	2784	362	1380
Parameters	398	291	448	232	406
R indices [$I > 2\sigma(I)$]	0.0669, 0.1168	0.0361, 0.0893	0.0414, 0.1195	0.0447, 0.1460	0.0681, 0.1502
Goodness-of-fit on F^2	0.985	1.064	1.047	1.038	0.998

Table 2
Selective bond lengths (Å) and angles (°) for complexes **1–5**.

1			
Co1–O1	2.249(4)	Co1–O2	2.132(4)
Co1–O3A	2.012(4)	Co1–O4B	2.036(4)
Co1–N2	2.150(5)	Co1–N3	2.148(5)
O1–Co1–O2	59.8(1)	O1–Co1–O3A	151.8(2)
O1–Co1–O4B	91.6(2)	O1–Co1–N2	92.9(2)
O1–Co1–N3	87.2(2)	O2–Co1–O3A	92.2(2)
O2–Co1–O4B	151.3(2)	O2–Co1–N2	93.6(2)
O2–Co1–N3	90.3(2)	O3A–Co1–O4B	116.1(2)
O3A–Co1–N2	92.8(2)	O3A–Co1–N3	89.2(2)
O4B–Co1–N2	89.8(2)	O4B–Co1–N3	85.8(2)
N2–Co1–N3	175.5(2)		
2			
Co1–O1	2.144(2)	Co1–O5	2.076(2)
Co1–O6	2.105(2)	Co1–O7	2.052(2)
Co1–O8	2.132(2)	Co1–N1	2.161(2)
O1–Co1–O5	91.10(7)	O1–Co1–O6	89.74(7)
O1–Co1–O7	88.62(7)	O1–Co1–O8	90.31(7)
O1–Co1–N1	173.75(7)	O5–Co1–O6	85.60(7)
O5–Co1–O7	175.80(7)	O5–Co1–O8	88.07(7)
O5–Co1–N1	92.87(8)	O6–Co1–O7	90.21(7)
O6–Co1–O8	173.67(7)	O6–Co1–N1	95.36(8)
O7–Co1–O8	96.12(8)	O7–Co1–N1	87.76(8)
O8–Co1–N1	85.01(7)		
3			
Ni1–O1	2.051(2)	Ni1–O3A	2.046(2)
Ni1–O5	2.108(2)	Ni1–O6	2.123(2)
Ni1–N1	2.108(2)	Ni1–N3	2.087(2)
O1–Ni1–O3A	87.92(7)	O1–Ni1–O5	91.93(7)
O1–Ni1–O6	179.46(7)	O1–Ni1–N1	86.53(8)
O1–Ni1–N3	89.86(8)	O3A–Ni1–O5	178.62(7)
O3A–Ni1–O6	91.87(7)	O3A–Ni1–N1	86.66(8)
O3A–Ni1–N3	88.74(8)	O5–Ni1–O6	88.28(8)
O5–Ni1–N1	94.70(8)	O5–Ni1–N3	89.88(8)
O6–Ni1–N1	92.97(8)	O6–Ni1–N3	90.63(8)
N1–Ni1–N3	174.25(9)		
4			
Ni1–O1	2.040(2)	Ni1–O3	2.084(2)
Ni1–N1	2.116(3)		
O1–Ni1–O3	91.52(9)	O1–Ni1–N1	90.5(1)
O3–Ni1–N1	87.2(1)		
5			
Cu1–O1	1.965(4)	Cu1–O3B	2.280(4)
Cu1–O4A	1.950(4)	Cu1–N1	2.037(5)
Cu1–N3	2.012(5)		
O1–Cu1–O3B	90.0(2)	O1–Cu1–O4A	157.7(2)
O1–Cu1–N1	87.6(2)	O1–Cu1–N3	92.7(2)
O3B–Cu1–O4A	111.4(2)	O3B–Cu1–N1	86.5(2)
O3B–Cu1–N3	95.6(2)	O4A–Cu1–N1	87.6(2)
O4A–Cu1–N3	91.4(2)	N1–Cu1–N3	177.9(2)

Symmetry codes for **1**: A = $-x+1, -y+1, -z$; B = $x-1, y, z$; for **2**: A = $-x+1, -y+1, -z+1$; for **3**: A = $-x+3/2, -y+1/2, -z+2$; for **4**: A = $-x+1, -y+1, -z$; for **5**: A = $x, -y+1/2, z-1/2$; B = $-x+1, y-1/2, -z+1/2$. The symmetry codes also correspond to those in Fig. 1a to Fig. 5a.

parameters, and those of oxygen were first located in difference Fourier syntheses and then treated as riding. Notably, most of hydrogen atoms of the lattice methanol and water in **3–5** were not located. One bpe ligand in **3** was treated by using a disorder model with the central —CH=CH— fragment adopting two different locations. Further details for crystallographic data and refinement conditions are listed in Table 1. Selected bond distances and angles are shown in Table 2 and hydrogen bonding geometries are listed in Table 3.

3. Results and discussion

3.1. Synthesis and general characterization

All complexes described here were similarly prepared by direct assembly of the ligands with the corresponding metal salt in water–methanol at ambient condition. In each case, an approximate metal/ligand composition of 1: 1: 1 (M: bpe: H_3btc/H_4btec/H_2ip/H_2tp) was utilized for the starting materials. However, the resulting complexes are found to have the stoichiometric ratios of 2: 2: 1 for **2** and 1: 2: 1 for others in order to achieve the charge balance. The compositions of all complexes were confirmed by microanalysis, IR, and X-ray single-crystal diffraction techniques. As for the IR spectra, the broad bands centered at *ca.* 3400 cm^{-1} indicate the O—H stretching of carboxyl (for **1**) or solvents (for **2–5**). In the IR spectra of **2–5**, the absence of characteristic absorption bands of carboxyl suggests the complete deprotonation of the polycarboxyl ligands. As a result, the antisymmetric and symmetric stretching vibrations of carboxylate appear in the range of 1593–1619 and 1367–1386 cm^{-1}, respectively. It should be noted that the coexistence of both carboxyl and carboxylate groups is observed in **1**, with the characteristic IR absorption peaks occurring at 1691, 1614, and 1376 cm^{-1}, respectively.

Table 3
Hydrogen bonding geometries in the crystal structures of complexes **1–4**.

D–H···A	D···A (Å)	H···A (Å)	D–H···A (°)	Symmetry code
1				
O5–H5···N1	2.614	1.80	171	$-x+1, -y+1, -z+1$
2				
O5–H5A···O4	2.712	1.87	173	$x+1, y, z$
O5–H5B···N2	2.781	1.94	171	$x, y-1, z$
O6–H6A···O3	2.777	1.98	155	$-x+1, -y, -z+1$
O6–H6B···O3	2.784	1.95	165	$x+1, y, z$
O7–H7A···O1	2.736	1.90	169	$-x+1, -y, -z+1$
O7–H7B···O9	2.724	1.89	165	$-x+1, -y+1, -z+1$
O8–H8A···O10	2.768	1.93	170	
O8–H8B···O2	2.598	1.76	170	
O9–H9···O4	2.714	1.91	165	$-x+1, -y, -z+1$
O10–H10A···O11	2.666	1.91	147	$x, y-1, z$
O11–H11B···O5	3.109	2.45	135	$x-1, y+1, z$
3				
O5–H5A···O2	2.583	1.78	158	
O5–H5B···O7	2.774	1.99	152	$-x+1, y, -z+1/2$
O6–H6A···O4	2.627	1.83	156	$-x+3/2, -y+1/2, -z$
O6–H6B···O6	2.984	2.23	148	$-x+1, y, -z-1/2$
O7–H7A···O4	2.847	2.00	174	$-x+3/2, -y+1/2, -z+1$
O7–H7B···O5	2.900	2.06	167	$x, -y+1, z+1/2$
4				
O3–H3B···O2	2.672	1.87	157	
O3–H3A···N2	2.865	2.02	179	$-x+1, -y, -z$

3.2. Structural analysis of *1–5*

3.2.1. $[Co(Hbtc)(bpe)_2]_n$ (*1*)

In complex **1**, each Co^{II} ion is six-coordinated and exhibits a distorted octahedral geometry (see Fig. 1a), in which four oxygen donors from three different Hbtc anions constitute the equatorial plane and a pair of nitrogen atoms from two bpe ligands occupy the axial sites with the N2–Co1–N3 angle of 175.5(2)°. For benzene-1,3,5-tricarboxylic acid, two carboxyl groups thereof are deprotonated and bind to Co^{II} in chelating and bridging modes, respectively. Thus, the Hbtc anionic components interlink the Co^{II} centers to result in a 1-D coordination motif along [1 0 0] with dimeric $[Co(COO)]_2$ subunits, in which the Co···Co separation is 4.174(1) Å. As expected, the bpe ligands serve as unidentate terminals using their 4-pyridyl nitrogen donors and decorate the 1-D patterns along two sides as pendants (see Fig. 1b). Notably, each uncoordinated 2-pyridyl N1 atom of bpe is hydrogen bonded to the carboxyl group of Hbtc and such interchain O5–H5···N1 interactions extend the 1-D arrays into a 2-D layered network (see Fig. 1c and Table 3). Moreover, such layers are arranged in an interdigitated fashion to result in a 3-D supramolecular architecture, which is sustained by interlayer aromatic stacking interactions be-

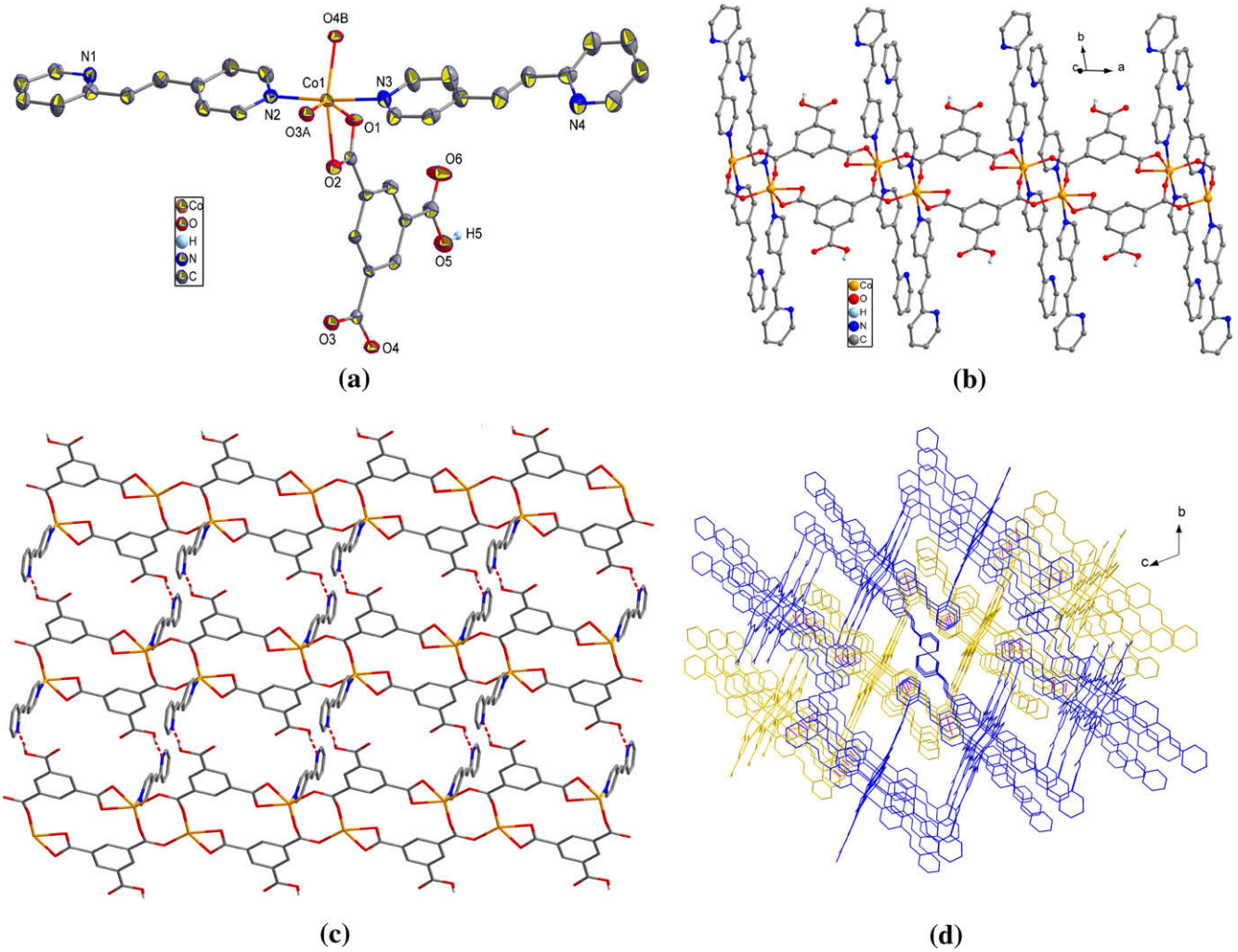


Fig. 1. (a) A portion view of **1** showing the coordination environment of Co^{II}. Displacement ellipsoids are drawn at the 30% probability level. (b) 1-D polymeric coordination motif in **1**. (c) A perspective view of the layered network in **1** constructed *via* O–H···N interactions between the 1-D coordination arrays (the irrelative bpe ligands are omitted for clarity). (d) 3-D supramolecular lattice of **1** viewed along [1 0 0], showing interlayer π–π stacking interactions as pink broken lines.

Table 4
Structural parameters of aromatic stacking interactions in the crystal structures of complexes **1**, **2**, and **5**.

Ring (1)	Ring (2)	$d_{C(1)-C(2)}$ (Å)[a]	$d_{C(1)-R(2)}$ (Å)[b]	$d_{C(2)-R(1)}$ (Å)[b]	θ (°)[c]
Complex ***1***					
C1–C2–C3–C4–C5–N1	C8–C9–C10–C11–C12–N2	3.67	3.47	3.30	9.5
Complex ***2***					
C13–C14–C15–C16–C17–N2	C13–C14–C15–C16–C17–N2	3.50	3.42	3.42	0
Complex ***5***					
C13–C14–C15–C16–C17–N3	C20–C21–C22–C23–C24–N4	3.97	3.79	3.70	4.0

[a] The distance between the centers of two pyridyl rings involved in aromatic stacking.
[b] The distance from the center of one pyridyl ring to the other pyridyl plane involved in aromatic stacking.
[c] The dihedral angle between the two pyridyl rings involved in aromatic stacking.

tween the bpe components (see Fig. 1d and Table 4). Very small interspace is found in this structure with a volume of 80.9 $Å^3$ (5.5% of the unit cell volume).

3.2.2. $[Co_2(btec)(bpe)_2(H_2O)_8](CH_3OH)_2(H_2O)_4$ (**2**)

The replacement of H_3btc with H_4btec in the reaction process leads to the formation of a distinct dinuclear complex **2**. Each Co^{II} center in **2** is surrounded by one N atom of bpe, one O atom of btec, and four aqua molecules, forming a distorted octahedron with the axial O1–Co1–N1 angle of 173.74(7)°. Interestingly, the fully deprotonated btec anion links two adjacent Co^{II} ions (Co···Co = 11.619(7) Å) by using two unidentate carboxylate groups to constitute a centrosymmetric binuclear entity (see Fig. 2a). These binuclear motifs are further extended by multiple O–H···O bonds between the water ligands and carboxylate groups (O5–H5A···O4, O6–H6A···O3, O6–H6B···O3, O7–H7A···O1, and O8–H8B···O2, see Table 3 for details) to result in a 2-D network (see Fig. 2b). In addition, each "free" 2-pyridyl nitrogen of bpe is also hydrogen bonded to the water ligand to afford an intralayer O5–H5B···N2 interaction. Further investigation of the crystal pack-

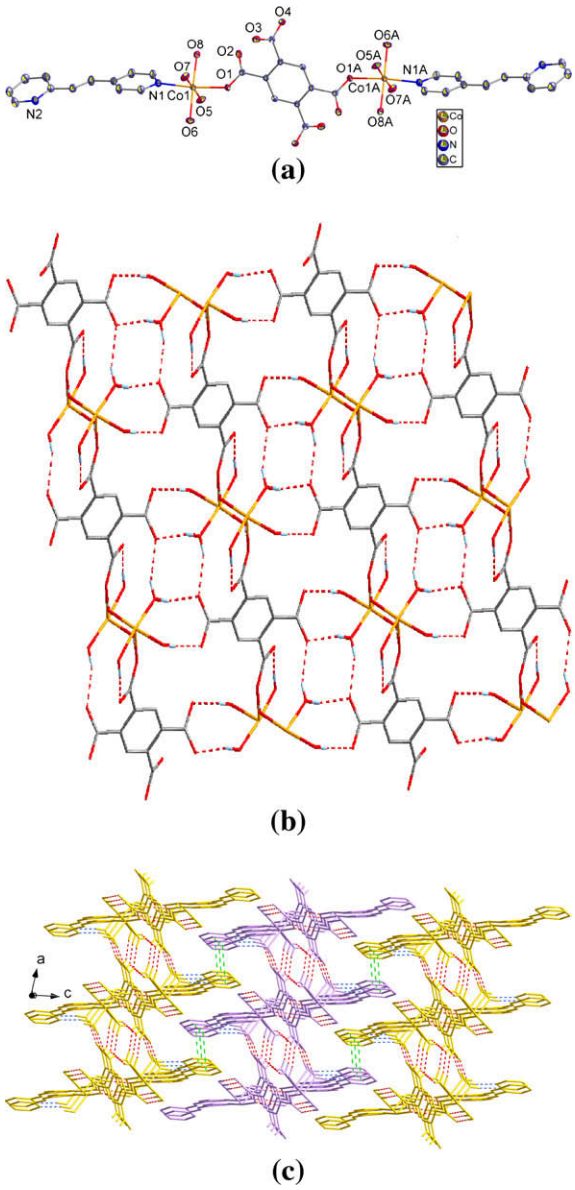


Fig. 2. (a) Molecular structure of the dinuclear coordination unit of **2**. Displacement ellipsoids are drawn at the 30% probability level. (b) A perspective view of the layered network in **2** constructed *via* O–H···O bonds between the dimeric motifs (the bpe ligands are omitted for clarity). (c) Packing diagram of **2** viewed along [0 1 0] with omitting the lattice solvents (the red and blue broken lines indicate the O–H···O and O–H···N hydrogen bonding and the green ones represent the aromatic stacking).

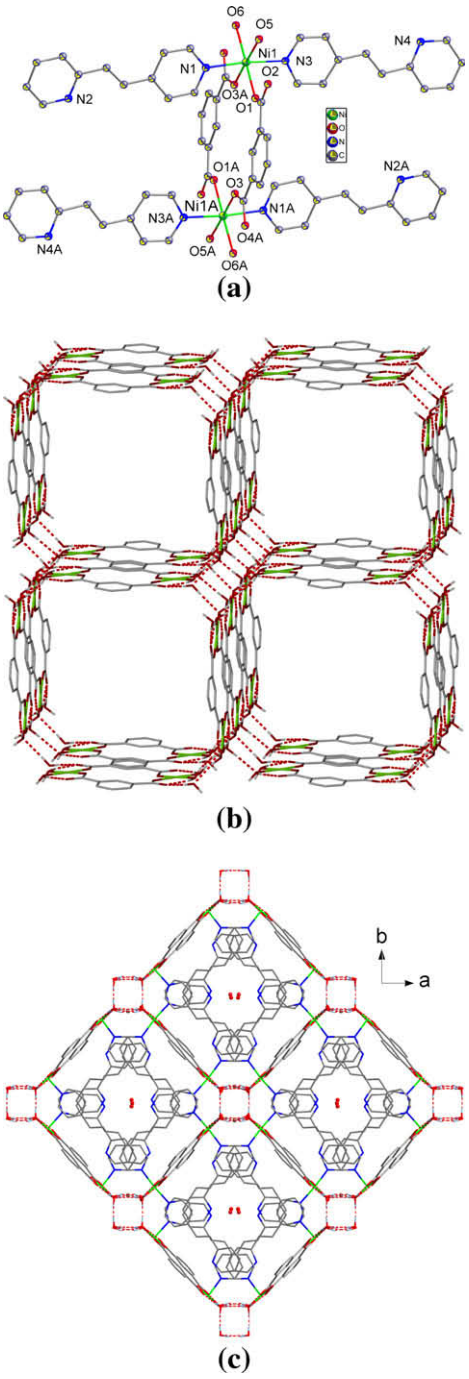


Fig. 3. (a) Molecular structure of the dinuclear coordination unit of **3**. Displacement ellipsoids are drawn at the 30% probability level. (b) 3-D supramolecular network in **3** linked *via* O–H···O bonds between the dinuclear units and lattice water molecules (the bpe ligands are omitted for clarity). (c) Packing diagram of **3** viewed along [0 0 1].

ing indicates that these 2-D patterns adopt a similar interdigitated packing to that in **1** with the presence of significant interlayer π–π stacking interactions (see Fig. 2c and Table 4). Furthermore, the included lattice water and methanol molecules are found to interact with the 2-D motifs by means of multiple O–H···O bonds such as O7–H7B···O9, O8–H8A···O10, O9–H9···O4, O10–H10A···O11, and O11–H11B···O5 (see Table 3 for details), which consolidate the 3-D supramolecular lattice of **2**.

3.2.3. *[Ni(ip)(bpe)$_2$(H$_2$O)$_2$]$_2$(CH$_3$OH)(H$_2$O)$_3$* (**3**)

In the structure of **3**, each octahedral Ni^{II} ion is six-coordinated by four O atoms from two ip and two aqua ligands as well as a pair of N atoms from the terminal bpe ligands (Fig. 3a). Two symmetry related Ni^{II} centers are doubly bridged by the ip ligands (Ni···Ni = 7.779(1) Å) to result in a bimetallic macrocyclic motif decorated by four unidentate bpe pendants, which is different from the linear binuclear array of **2**. Both carboxylate groups of ip are unidentate and as a result, intramolecular O5–H5A···O2 and O6–H6A···O4 bonds are found between the aqua ligands and uncoordinated carboxylate oxygen atoms. Significantly, the binuclear complexes are linked *via* O6–H6B···O6 interactions to afford 1-D zigzag arrays and each lattice water molecule of O7 serves as a trifurcate bridging (O5–H5B···O7, O7–H7A···O4, and O7–H7B···O5, see Table 3 for details) to interconnect the 1-D arrays, resulting in a 3-D reticular framework (see Fig. 3b). In this open network,

the void cavities are mostly occupied by the protrudent bpe ligands in a staggered fashion and thus, only small channels constituted by the bpe ligands are found (395.3 Å^3, 6.0% of the unit cell volume) to accommodate the lattice water guests (see Fig. 3c). The methanol solvents are located within the interstice between the water molecules of O5, O6, and O7. Even now, very small potential solvent-accessible void (113.4 Å^3, 1.7% of the unit cell volume) is found for the overall 3-D lattice. It should be noted that each uncoordinated 2-pyridyl N2 atom of bpe is hydrogen bonded to the included lattice water of O9 (N···O = 2.840 Å) and no aromatic stacking interaction is observed in this case.

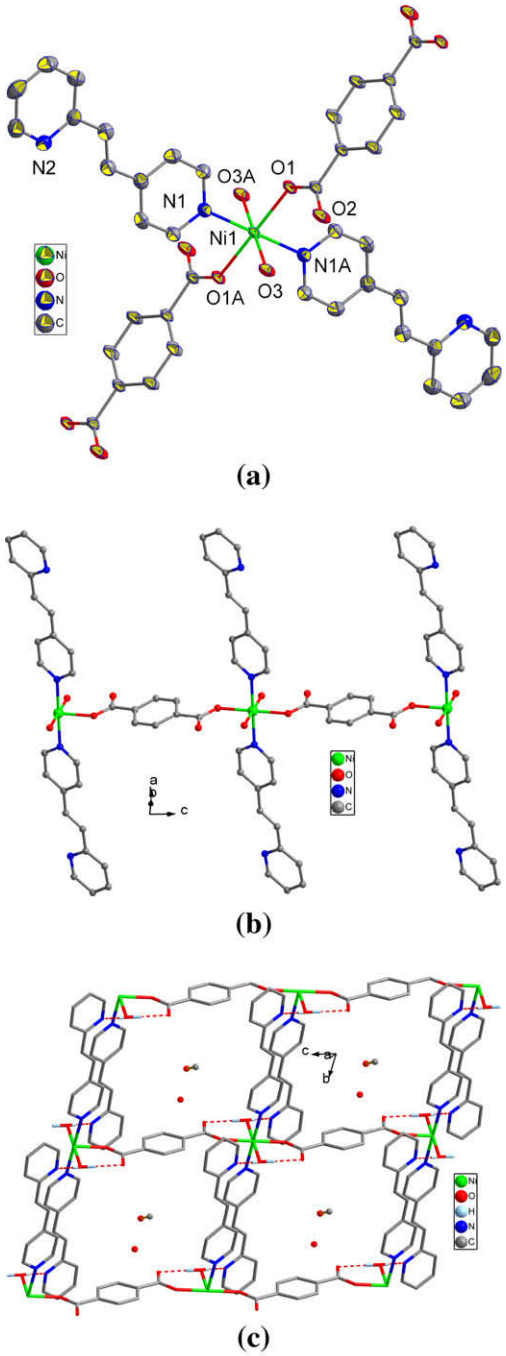


Fig. 4. (a) A portion view of **4** showing the coordination geometry of Ni^{II}. Displacement ellipsoids are drawn at the 30% probability level. (b) 1-D fishbone-like coordination motif in **4**. (c) A perspective view of the layered network in **4** with the inclusion of lattice solvents.

*3.2.4. $\{[Ni(tp)(bpe)_2(H_2O)_2](CH_3OH)(H_2O)_2\}_n$ (**4**)*

Each Ni^{II} ion in **4** lying at the inversion center is ligated by two unidentate carboxylate oxygen atoms, two 4-pyridyl nitrogen donors as well as a pair of water molecules to compose a NiN_2O_4 octahedral sphere (Fig. 4a). As a result, the adjacent Ni^{II} ions are connected by the tp dianionic bridges to afford a 1-D linear chain along [0 0 1] with the Ni···Ni distance of 11.310(2) Å, which is also decorated by bpe at both sides in an approximately perpendicular mode to result in a fishbone-like motif (see Fig. 4b). Intrachain O3–H3B···O2 bond between the water ligand and adjacent uncoordinated carboxylate oxygen is found. And of further importance, interchain O3–H3A···N2 contacts (see Table 3 for details) between the water ligands and 2-pyridyl N atoms further extend the 1-D arrays into a 2-D supramolecular layer along the *bc* plane, within

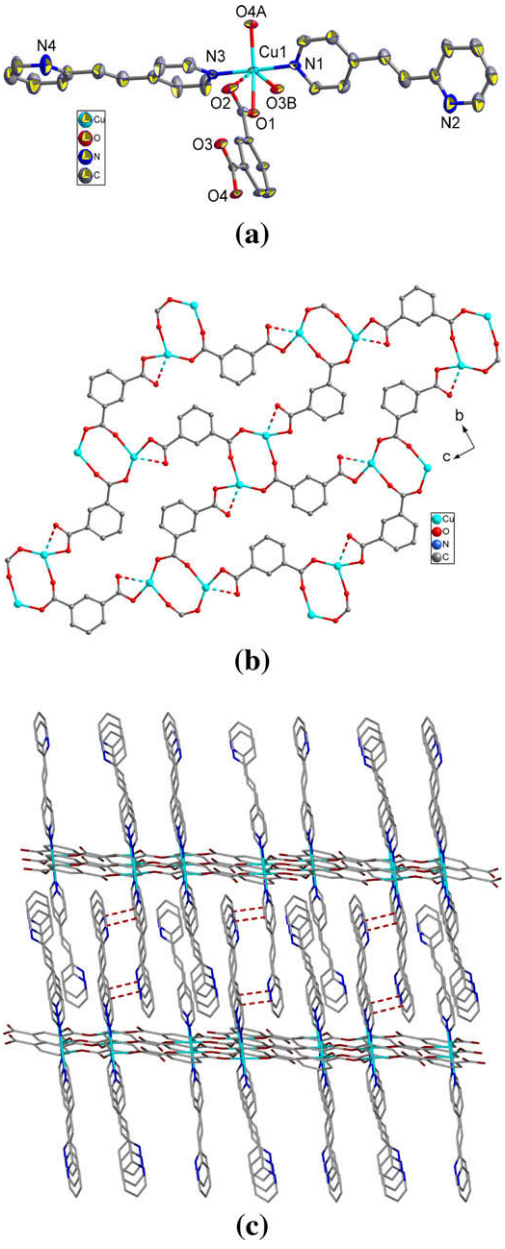


Fig. 5. (a) A portion view of **5** showing the coordination geometry of Cu^{II}. Displacement ellipsoids are drawn at the 30% probability level. (b) 2-D coordination sheet in **5** (the bpe ligands are omitted for clarity). (c) Packing diagram of **5** viewed along [0 1 0], showing interlayer π–π stacking as brown broken lines (the lattice water molecules are omitted for clarity).

which the lattice water and methanol molecules are included (see Fig. 4c). These 2-D arrays show a parallel packing mode along the [1 0 0] direction and no aromatic stacking interaction is found in this structure, which has very small solvent-accessible areas with a volume of 60.7 Å^3 (6.5% of the unit cell volume).

3.2.5. $\{[Cu(ip)(bpe)_2](H_2O)_4\}_n$ (**5**)

As depicted in Fig. 5a, each Cu^{II} ion in **5** is surrounded by three carboxylate oxygen donors from different ip and two 4-pyridyl nitrogen atoms from two bpe. The local coordination sphere of Cu^{II} can be described as a distorted square-pyramid with the τ value of 0.33 [27], in which the axial site is occupied by O3B. In addition, there exists a weak Cu1···O2 contact with the distance of 2.757(5) Å. Each ip ligand is coordinated to three Cu^{II} ions *via* the carboxylate groups and in this way, the adjacent Cu^{II} centers are connected by the bridging ip ligands to form a 2-D sheet (see Fig. 5b). In this 2-D pattern, each Cu^{II} center and ip ligand can be regarded as the equivalent three-connecting nodes to result in a 4.8^2 topology (**fes** net) [28]. On the other hand, if the bimetallic $[Cu_2(COO)_2]$ subunits (Cu···Cu = 4.459(2) Å) are considered as nodes, such a 2-D motif can be simplified to a familiar 4^4 topology (**sql** net). As expected, the bpe pendants around the 2-D arrays facilitate their interdigitated stacking mode and the resulting 3-D supramolecular lattice is sustained by interlayer aromatic stacking contacts (see Fig. 5c and Table 4) between the pyridyl rings of bpe. Furthermore, the lattice water molecules are located within the interlayer voids with the formation of water···water interactions and there also exist secondary contacts such as N2···O7 (2.816 Å) and N4···O8 (3.074 Å) between the 2-pyridyl nitrogen of bpe and lattice water.

3.3. Structural assembly of **1**–**5** via multiple supramolecular interactions

It is noteworthy that high-dimensional supramolecular assembly may be rationally designed *via* synergistic effect of multiple intermolecular interactions. In the structures of **1**–**5**, a variety of coordination motifs from discrete dinuclear species (for **2** and **3**) to infinite 1-D (for **1** and **4**) and 2-D (for **5**) arrays are formed. This structural discrepancy can be ascribed to the different bridging functions of the polycarboxyl building blocks (e.g. **1** versus **2** or **3** versus **4**) as well as the coordination tendencies of the metal ions (e.g. **3** versus **5**). On the other hand, all bpe ligands in these complexes are uniformly unidentate coordination by using the 4-pyridyl nitrogen and serve as the end-capping segments to decorate the coordination motifs. Of further importance, the coordination-unfavored 2-pyridyl group of bpe is always involved in the formation of O–H···N bonds with carboxyl (for **1**) or water (for **2**–**5**). Additionally, aromatic stacking interactions (see Table 4) are also observed between the pyridyl groups of bpe in complexes **1**, **2**, and **5**. Moreover, the solvent molecules especially water show the H-bonding activity in most of these structures. As a result, a variety of supramolecular networks that display distinct propagating and packing features are constructed under the regulation of both coordinative and secondary interactions. This investigation further confirms that the application of a bifunctional tecton (such as bpe here) is a practicable approach for the assembly of supramolecular coordination solids.

3.4. Thermal stability of complexes **1**–**5**

All complexes are air stable and their thermal stability was investigated by thermogravimetric (TG) and differential thermal analysis (DTA) experiments (see Fig. S1 in Supplementary Information for TG-DTA curves). Complex **1** is thermally stable to 228 °C, where the weight loss occurs and ends at 443 °C. Accordingly, an intensive exothermic peak is observed at 421 °C in DTA. The TG curve of **2** shows the first weight loss of 14.03% (calculated: 13.44%) from 59 to 118 °C, corresponding to the exclusion of all lattice aqua and methanol molecules (an endothermic peak at 94 °C in DTA). The residual coordination framework starts to decompose until heating to 216 °C and ends at 407 °C with an endothermic and an exothermic peaks at 243 and 408 °C in DTA. The resulting residue holds a weight of 24.07% of the total sample and seems to be $CoCO_3$ (calculated: 23.49%). In the TG curve of **3**, the weight loss of 5.54% in the range of 96–145 °C indicates the elimination of all lattice solvents (calculated: 6.45%) with an endothermic peak at 116 °C in DTA. Pyrolysis of the residuary component occurs upon heating to 169 °C and stops at 476 °C with two exothermic peaks at 380 and 447 °C in the DTA curve. As for **4**, the first weight loss of 12.51% in the TG curve (41–168 °C) suggests the release of all lattice solvents and one coordination water (calculated: 12.44%). Accordingly, an endothermic peak is found at 73 °C in DTA. Decomposition of the residual framework supervenes upon further heating to 191 °C and ends at 596 °C with an exothermic peak at 429 °C in DTA. The final residual solid has a weight of 11.00% of the total sample and seems to be nickel oxide (calculated: 10.80%). The TG curve of **5** displays a weight loss of 2.90% from room temperature to 133 °C, corresponding to the release of one lattice aqua molecule (calculated: 2.71%) with an endothermic peak at 78 °C in DTA. Upon further heating to 188 °C, a series of weight losses are observed in the TG curve, which end at 473 °C (three exothermic peaks at 262, 287, and 458 °C in DTA).

4. Conclusion

In this work, five novel metallosupramolecular complexes based on a bifunctional tecton bpe and different polycarboxyl co-ligands are presented. These complexes display discrete (dinuclear), 1-D, and 2-D coordination patterns through the polycarboxyl linkers, which are further extended in virtue of the predictable secondary interactions based on bpe to form diverse high-dimensional architectures. That is to say, the synergistic effect of multiple intermolecular contacts (coordination force as well as H-bonding and aromatic stacking) is critical to direct such network materials. These results provide further insights into the design and assembly of crystalline supramolecular solids and more systematic studies on this perspective are ongoing.

Acknowledgements

This work was financially supported by the National Natural Science Foundation of China (No. 20671071), Program for New Century Excellent Talents in University (No. NCET-07-0613), and Tianjin Normal University.

Appendix A. Supplementary data

CCDC 707850, 707851, 707852, 707853 and 707854 contain the supplementary crystallographic data for complexes **1**–**5**. These data can be obtained free of charge via http://www.ccdc.cam.ac.uk/conts/retrieving.html, or from the Cambridge Crystallographic Data Centre, 12 Union Road, Cambridge CB2 1EZ, UK; fax: (+44) 1223-336-033; or e-mail: deposit@ccdc.cam.ac.uk.

Supplementary data associated with this article can be found, in the online version, at doi:10.1016/j.poly.2009.04.049.

References

[1] S.R. Batten, R. Robson, Angew. Chem., Int. Ed. 37 (1998) 1460.
[2] M.W. Hosseini, Acc. Chem. Res. 38 (2005) 313.
[3] M. Du, C.-P. Li, X.-J. Zhao, Q. Yu, CrystEngComm 9 (2007) 1011.

[4] H.W. Roesky, M. Andruh, Coord. Chem. Rev. 236 (2003) 91.
[5] C.-Q. Wan, X.-D. Chen, T.C.W. Mak, CrystEngComm 10 (2008) 475.
[6] B. Moulton, M.J. Zaworotko, Chem. Rev. 101 (2001) 1629.
[7] X.-D. Chen, M. Du, T.C.W. Mak, Chem. Commun. (2005) 4417.
[8] R.-Q. Zou, H. Sakurai, Q. Xu, Angew. Chem., Int. Ed. 45 (2006) 2542.
[9] J.-M. Lehn, Science 260 (1993) 1762.
[10] B.-H. Ye, M.-L. Tong, X.-M. Chen, Coord. Chem. Rev. 249 (2005) 545.
[11] M. Du, X.-J. Jiang, X.-J. Zhao, Inorg. Chem. 45 (2006) 3998.
[12] M.-L. Tong, Y.-M. Wu, J. Ru, X.-M. Chen, H.-C. Chang, S. Kitagawa, Inorg. Chem. 41 (2002) 4846.
[13] H.-L. Sun, S. Gao, B.-Q. Ma, G. Su, S.R. Batten, Cryst. Growth. Des. 5 (2005) 269.
[14] D. Braga, L. Brammer, N.R. Champness, CrystEngComm 7 (2005) 1.
[15] G.R. Desiraju, J. Chem. Soc., Dalton Trans. (2000) 3745.
[16] C. Janiak, J. Chem. Soc., Dalton Trans. (2000) 3885.
[17] C.B. Aakeröy, A.M. Beatty, B.A. Helfrich, Angew. Chem., Int. Ed. 40 (2001) 3240.
[18] B.R. Bhogala, P.K. Thallapally, A. Nangia, Cryst. Growth. Des. 4 (2004) 215.
[19] Z.-B. Wang, H.-F. Zhu, M. Zhao, Y.-Z. Li, T. Okamura, W.-Y. Sun, H.-L. Chen, N. Ueyama, Cryst. Growth. Des. 6 (2006) 1420.
[20] D.-F. Sun, R. Cao, Y.-Q. Sun, W.-H. Bi, X.-J. Li, Y.-Q. Wang, Q. Shi, X. Li, Inorg. Chem. 42 (2003) 7512.
[21] X.-L. Wang, C. Qin, E.-B. Wang, Cryst. Growth. Des. 6 (2006) 439.
[22] S.C. Manna, S. Konar, E. Zangrando, K. Okamoto, J. Ribas, N.R. Chaudhuri, Eur. J. Inorg. Chem. (2005) 4646.
[23] M. Du, C.-P. Li, X.-J. Zhao, CrystEngComm 8 (2006) 552.
[24] Y. Hill, A. Briceno, Chem. Commun. (2007) 3930.
[25] Bruker AXS, SAINT Software Reference Manual, Madison, WI, 1998.
[26] G.M. Sheldrick, SHELXTL NT Version 5.1. Program for Solution and Refinement of Crystal Structures, University of Göttingen, Germany, 1997.
[27] A.W. Addison, T.N. Rao, J. Reedijk, J. Van Rijn, G.C. Verschoor, J. Chem. Soc., Dalton Trans. (1984) 1349.
[28] N.W. Ockwig, O. Delgado-Friedrichs, M. O'Keeffe, O.M. Yaghi, Acc. Chem. Res. 38 (2005) 176 (and reference cited therein).

Polyhedron 28 (2009) 2355–2358

Contents lists available at ScienceDirect

Polyhedron

journal homepage: www.elsevier.com/locate/poly

Ambient temperature imidazolium-based ionic liquids with tetrachloronickelate(II) anions

M. Brett Meredith, C. Heather McMillen, Jonathan T. Goodman, Timothy P. Hanusa *

Department of Chemistry, Vanderbilt University, Nashville, Tennessee 37235, United States

ARTICLE INFO

Article history:
Received 21 January 2009
Accepted 28 April 2009
Available online 6 May 2009

Keywords:
Ionic liquid
Nickel
Viscosity
Imidazolium
Thermal stability

ABSTRACT

Deep blue tetrachloronickelate(II) salts of 1-alkyl-3-methylimidazolium cations $[C_n mim]^+$ with intermediate chain lengths (n = 5, 7, 8 and an n = 4/6 mixture) have been prepared from imidazolium chlorides and $NiCl_2$. They are liquid at ambient temperatures (ca. 20 °C) and above, and display viscosities and thermal stability comparable to related $[BF_4]^-$ compounds. The similarities may reflect the compensating effects of the dinegative charge of the $[NiCl_4]^{2-}$ ion and its larger size.

© 2009 Elsevier Ltd. All rights reserved.

1. Introduction

In the past several decades, the chemistry of room temperature ionic liquids (RTILs) has expanded markedly as these compounds have become better understood and more broadly applied in academic and commercial settings [1]. Their unique properties, including large liquid temperature ranges, negligible vapor pressure, and adjustable viscosity and basicity, have stimulated uses as 'designer solvents' [2–4], in electrochemistry [5–7], and in catalysis [8]. A substantial part of their attractiveness stems from the discovery of air- and moisture-stable RTILs with main group anions such as $[PF_6]^-$ [9], $[BF_4]^-$ [10], $[(CF_3SO_2)_2N]^-$ [11], and $[CF_3SO_2]^-$ [11]. Metal-containing anions from across the periodic table have also been incorporated into ionic liquids, and they also can possess air- and moisture-stability; among these are zinc, tin, and iron-containing $[MCl_x]^-$ anions associated with various choline-derived cations [12]. In comparison with commonly used main group monoanions, metal-containing anions offer the possibility of more highly charged species (e.g., $[LnX_6]^{3-}$) [13] and additional variations in geometries (e.g., tetrahedral and square planar $[MX_4]^{2-}$ species) [14–16].

Nickel-based anions have a long history of use in ionic liquids. Osteryoung investigated the solubility of $NiCl_2$ in chloroaluminate melts, and determined that the predominant nickel containing species was $[NiCl_4]^{2-}$, although several additional ions were also detected [17]. Imidazolium-based Ni-containing salts $[C_n mim]_2[NiCl_4]$ (n = 2 (mp = 92–93 °C) [18]; 4 (mp = 55–58 °C) [15]; 12–18 (mp = 50–75 °C) [19]) were later prepared by other workers; crystal structures for the compounds with n = 2 and 4 demonstrated the existence of extensive cation-anion hydrogen-bonding. Pyridinium-based Ni-containing salts $[C_n py]_2[NiCl_4]$ (n = 12, 14, 16, 18) were investigated by Seddon and coworkers, who found all of them to be mesogenic solids with melting points ranging from 80–88 °C [19]. Abbott found that a choline-derived nickel chloride salt had a melting point above 100 °C [12]; it thus falls outside the conventional definition of RTILs (mp < 100 °C) [20].

In a search for nickel-containing ionic liquids that would be fluid at ambient temperatures (ca. $\geqslant$ 20 °C), and which might be useful in film formation or electrochemical applications [5], we have investigated the use of imidizolium cations with pendant alkyl chains of intermediate length, roughly C_5–C_{10}. This region has been previously identified as one in which compounds with low melting points are often found, as the hydrogen bonding that contributes to the high melting points of $[C_{(n \leqslant 4)}mim]$-based RTILs is disrupted, but the dispersion forces between longer chains that cause $[C_{(n \geqslant 10)}mim]$-based compounds to exhibit mesogenic characteristics have yet to become dominant [9,10].

In this work we outline the synthesis of several imidazolium RTILs that incorporate tetrachloronickelate anions and are liquid at 25 °C. The composition, viscosity and thermal behavior of these compounds was investigated.

2. Results and discussion

2.1. Synthesis of compounds

The mixture of the alkyl imidazolium chlorides with hydrated nickel(II) chloride results in dark blue liquids containing the $[NiCl_4]^{2-}$ anion (Eq. (1)).

* Corresponding author. Tel.: +1 615 322 4667; fax: +1 615 343 1234.
E-mail address: t.hanusa@vanderbilt.edu (T.P. Hanusa).

0277-5387/$ - see front matter © 2009 Elsevier Ltd. All rights reserved.
doi:10.1016/j.poly.2009.04.037

$$2[C_n\text{mim}]\text{Cl} + \text{NiCl}_2(\text{H}_2\text{O})_6 \rightarrow 2[C_n\text{mim}]_2[\text{NiCl}_4] + 6\text{H}_2\text{O} \quad (1)$$

The water can be removed by heating under vacuum. When $n = 5$, the originally mobile liquid forms an opaque aqua-colored gel after several days at room temperature. When $n = 7$ or 8, or for the mixed cation species with $n = 4$, $n = 6$, the compounds remain transparent blue liquids indefinitely. The previously described $[C_2\text{mim}]^+$ and $[C_4\text{mim}]^+$ salts of $[\text{NiCl}_4]^{2-}$, in contrast, have melting points of 92–93 °C [18] and 56 °C [15], respectively [21]. The salts reported here are hygroscopic, and deliberate addition of water causes them to turn green, but the blue color will be regenerated on heating under vacuum.

2.2. Viscosity measurements

The viscosities of the nickelate salts were measured from 23–60 °C (the exact range varied with the cation), and the available viscosities closest to 25, 30 and 40 °C are given in Table 1. Not surprisingly, the two longer-chained salts with $[C_7\text{mim}]^+$ and $[C_8\text{mim}]^+$ cations have higher viscosities at a given temperature than do those with shorter chains; e.g., the viscosity of the $[C_8\text{mim}]^+$ salt is between 40% and 60% greater than for the $[C_5\text{mim}]^+$ analogue. Below 30 °C, the viscosity of the mixed $[C_4\text{mim}][C_6\text{mim}][\text{NiCl}_4]$ species (which could be considered to have an "average" chain length of C_5) tracks closely with that of the single-chained $[C_5\text{mim}]_2[\text{NiCl}_4]$ salt. Above that temperature, the viscosities start to diverge, and values for the mixed imidazolium salt stay roughly 15% below that of the single. The effect of mixed cations on the viscosities of ionic liquids is not well studied (cf. the relative rarity of viscosity measurements in systems with mixed anions [12,22,23]), so that it is not clear how typical the behavior of $[C_4\text{mim}][C_6\text{mim}][\text{NiCl}_4]$ is.

Table 1
Representative values for substituted imidazolium $[\text{NiCl}_4]^{2-}$, $[\text{PF}_6]^-$, $[\text{BF}_4]^-$ salts.

Ionic liquid	T (°C)	η (cP)	Ref.
$[C_5\text{mim}]_2[\text{NiCl}_4]$	24.9	125	This work
$[C_5\text{mim}]_2[\text{NiCl}_4]$	30.2	76	This work
$[C_5\text{mim}]_2[\text{NiCl}_4]$	40.2	33	This work
$[C_7\text{mim}]_2[\text{NiCl}_4]$	26.3	178	This work
$[C_7\text{mim}]_2[\text{NiCl}_4]$	30.1	116	This work
$[C_7\text{mim}]2[\text{NiCl}_4]$	40.0	49	This work
$[C_8\text{mim}]2[\text{NiCl}_4]$	27.7	144	This work
$[C_8\text{mim}]2[\text{NiCl}_4]$	30.2	109	This work
$[C_8\text{mim}]2[\text{NiCl}_4]$	40.0	50	This work
$[C_8\text{mim}][\text{PF}_6]$	30	452	[24]
$[C_8\text{mim}][\text{BF4}]$	30	82	[25]
$[C_4\text{mim}][C_6\text{mim}][\text{NiCl}_4]$	25.1	122	This work
$[C_4\text{mim}][C_6\text{mim}][\text{NiCl}_4]$	30.0	70	This work
$[C_4\text{mim}][C_6\text{mim}][\text{NiCl}_4]$	40.0	30	This work
$[C_4\text{mim}][\text{PF}_6]$	30	204	[24]
$[C_4\text{mim}][\text{BF}_4]$	30	91.4	[24]
$[C_6\text{mim}][\text{PF}_6]$	30	363	[24]
$[C_6\text{mim}][\text{BF}_4]$	30	177	[24]

Although the data are still limited, at similar temperatures the $[\text{NiCl}_4]^{2-}$ salts appear to have viscosities considerably less than that observed for $[\text{PF}_6]^-$ salts, and similar to or slightly greater than $[\text{BF}_4]^-$ salts [24,25]. The last point is somewhat surprising, considering that the dianionic charge on the $[\text{NiCl}_4]^{2-}$ ion might be expected to strengthen coulombic attractions and hence to increase viscosity. On the other hand, the larger size of $[\text{NiCl}_4]^{2-}$ compared to $[\text{BF}_4]^-$ (with effective radii of ca. 2.9 Å versus 2.1 Å, respectively) [26] should weaken such interactions, and serve as a compensating influence. It is worth noting that the viscosity of the mixed $[C_4\text{mim}][C_6\text{mim}][\text{NiCl}_4]$ salt is comparable to that of $[C_4\text{mim}]_2[\text{BF}_4]$, underscoring the potential viscosity lowering ability of mixed cations.

Plots of the complete data sets (Fig. 1) indicate slightly non-Arrhenius behavior for the ionic liquids at higher temperatures. Nevertheless, a fit of the data to an Arrhenius-like equation that expresses the energy of activation for viscous flow (Eq. (2)),

$$\eta = \eta_0 e^{E_\eta/RT} \quad (2)$$

for which E_η is the energy of action for viscous flow, and η_0 is a constant, is very good for all four liquids ($r^2 > 0.99$). The E_η values (Table 2) cluster around 65–69 kJ mol^{-1}, without an obvious correlation with the chain length. These are near the value of 55.7 kJ mol^{-1} determined for the RTIL [choline][Zn_2Cl_5] [12], but are roughly four times higher than the average of 17 ± 3 kJ mol^{-1} found for various RTILs with more common anions ($[\text{BF}_4]^-$, $[\text{PF}_6]^-$, $[\text{Tf}_2\text{N}]^-$, $[\text{Tf}_2\text{C}]^-$), even when the cations are hydroxy-substituted, and thus capable of engaging in hydrogen bonding [27].

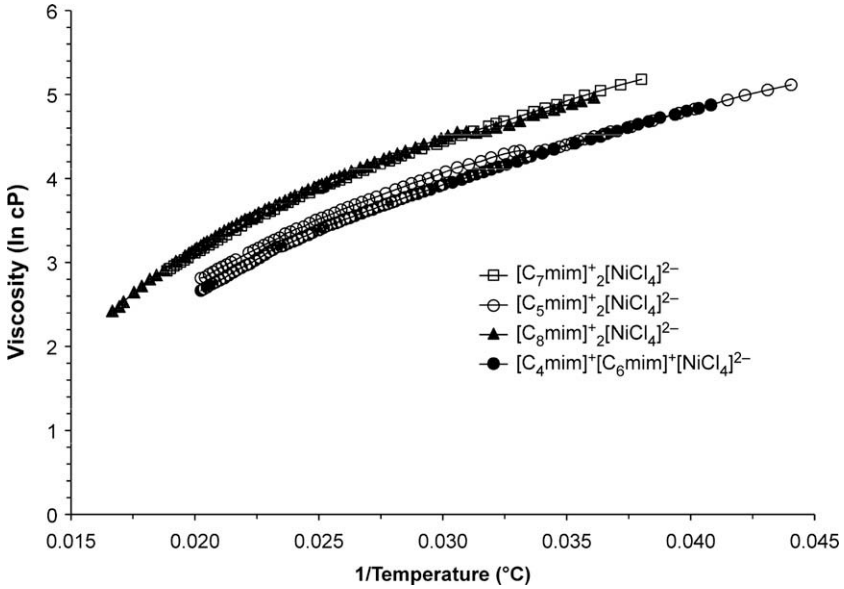


Fig. 1. Viscosity of imidazolium $[\text{NiCl}_4]^{2-}$ salts as a function of temperature.

Table 2
Energy of activation for viscous flow of tetrachloronickelate salts.

Compound	$E\eta$ (kJ mol^{-1})	r^2
$[C_5mim]_2[NiCl_4]$	65.6	0.997
$[C_7mim]_2[NiCl_4]$	67.8	0.998
$[C_8mim]_2[NiCl_4]$	64.6	0.995
$[C_4mim][C_6mim][NiCl_4]$	68.7	0.996

2.3. Thermal behavior

The thermal stabilities of imidazolium salts have been studied under various conditions, and have been found to have more dependence on anion type than cation size [24]. The three single-chain $[C_nmim]_2[NiCl_4]$ salts were investigated with scanning TGA, and all were found to decompose in a similar, multistep manner. A TGA scan for $[C_7mim]_2[NiCl_4]$ is presented in Fig. 2. Onset of decomposition (2% weight loss) under N_2 occurs just above 300 °C, and approximately two-thirds of the mass is gone by 430 °C, which corresponds to the loss of both imidazolium cations. Such volatilization temperatures are typical for imidazolium salts [28], but determination of the exact temperature and rate at which decomposition occurs is a non-trivial matter [29]. With imidazolium salts, whether decomposition occurs in a single or in multiple steps varies with the anion; $[C_1mim][PF_6]$ decomposes in a single step, for example, but $[C_1mim][BF_4]$ (like the tetrachloronickelate liquids) does so in several steps [30].

Continued heating of $[C_7mim]_2[NiCl_4]$ eventually leads to a constant weight near 690 °C, with a residual mass of 14%. This value does not correspond to the presence of completely reduced nickel or nickel chloride alone. To investigate this point further, a sample of $[C_7mim]_2[NiCl_4]$ was placed in a tube furnace at 700 °C for 1 h under N_2. After the sample cooled, powder XRD analysis on the resulting metallic-appearing film indicated the presence of both elemental nickel and $NiCl_2$; given this information, the residual weight in the TGA experiment corresponds to a Ni:$NiCl_2$ ratio of 3:1. Other modifications to the anion could make the decomposition to nickel alone more likely [31].

2.4. Conclusions

The strategy of using imidiazolium cations with intermediate chain lengths to produce ambient temperature ionic liquids is successful with $[NiCl_4]^{2-}$ anions. Despite the latters' dinegative charge, the viscosity and thermal properties of the resulting liquids are similar to related $[BF_4]^-$-based species. The nickelate-based liquids could provide useful substrates for electrochemical studies and metal deposition reactions.

3. Experimental

3.1. General considerations

Organic and inorganic starting materials were reagent grade from Acros or Strem Chemical and used as received. The preparation of 1-butyl-3-methylimidazolium chloride ($[C_4mim]Cl$), 1-pentyl-3-methylimidazolium chloride ($[C_5mim]Cl$), 1-hexyl-3-methylimidazolium chloride ($[C_6mim]Cl$), 1-heptyl-3-methylimidazolium chloride ($[C_7mim]Cl$), and 1-octyl-3-methylimidazolium chloride ($[C_8mim]Cl$) followed literature procedures [32].

Viscosity data were obtained on a Cambridge Applied Systems Viscolab 400 Viscometer fitted with heating tape. All thermal measurements were carried out on an Instrument Specialist TGA-1000 instrument. Elemental analyses were performed by the University of Illinois Microanalytical Laboratory, Desert Analytics (Tucson, AZ), or at the Micro-Mass Facility, University of California, Berkeley (Berkeley, CA).

3.2. Preparation of bis(1-pentyl-3-methylimidazolium) tetrachloronickelate(II), $[C_5mim]_2[NiCl_4]$

1-Pentyl-3-methylimidazolium chloride (5.26 g, 27.9 mmol) and $NiCl_2(H_2O)_6$ (3.31 g, 13.9 mmol) were placed in a 50 mL round bottom flask equipped with a magnetic stirring bar. The flask was flushed with N_2 and the reaction was allowed to stir at 80 °C for 18 h. The reaction was removed from heat and allowed to cool to room temperature. The solution was dried under vacuum at 95 °C to afford a dark blue liquid (6.24 g, 88%). *Anal.* Calc. for $C_{18}H_{34}Cl_4N_4Ni$: C, 42.64; H, 6.76; N, 11.05. Found: C, 39.31; H, 6.38; N, 10.19%. Although individual percentage values are low, the C:H:N values are in nearly exact molar ratios (18.0:34.8:4.0), suggesting that combustion was incomplete.

3.3. Preparation of bis(1-heptyl-3-methylimidazolium) tetrachloronickelate(II), $[C_7mim]_2[NiCl_4]$

1-Heptyl-3-methylimidazolium chloride (4.29 g, 19.8 mmol) and $NiCl_2(H_2O)_6$ (2.35 g, 9.89 mmol) were placed in a 100 mL

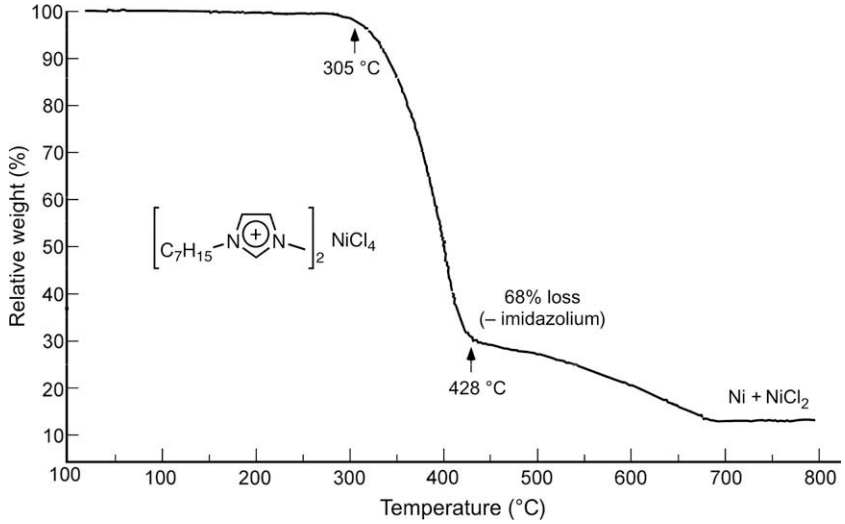


Fig. 2. Thermal behavior of $[C_7mim]_2[NiCl_4]$ under N_2 (20° min^{-1}). The arrow at 305 °C marks the decomposition onset.

round bottom flask equipped with a magnetic stirring bar. The flask was flushed with N_2 and the reaction was allowed to stir at 80 °C for 17 h. The reaction was removed from heat and allowed to cool to room temperature. The solution was dried under vacuum at 95 °C to afford a dark blue liquid (4.65 g, 83%). *Anal.* Calc. for $C_{22}H_{42}Cl_4N_4Ni$: C, 46.93; H, 7.52; N, 9.95. Found: C, 46.04; H, 7.57; N, 9.80%.

3.4. Preparation of bis(1-octyl-3-methylimidazolium) tetrachloronickelate(II), $[C_8mim]_2[NiCl_4]$

1-Octyl-3-methylimidazolium chloride (4.54 g, 19.7 mmol) and $NiCl_2(H_2O)_6$ (2.34 g, 9.84 mmol) were placed in a 100 mL round bottom flask equipped with a magnetic stirring bar. The flask was flushed with N_2 and the reaction was allowed to stir at 90 °C for 9 h. The reaction was removed from heat and allowed to cool to room temperature. The solution was dried under vacuum at 90 °C for 2 h to afford a dark blue liquid (5.17 g, 89%). *Anal.* Calc. for $C_{24}H_{46}Cl_4N_4Ni$: C, 48.72; H, 7.84; N, 9.48. Found: C, 47.91; H, 7.90; N, 9.38%.

3.5. Preparation of (1-butyl-3-methylimidazolium)(1-hexyl-3-methylimidazolium) tetrachloronickelate(II), $[C_4mim][C_6mim][NiCl_4]$

1-Butyl-3-methylimidazolium chloride (2.25 g, 12.9 mmol), 1-hexyl-3-methylimidazolium chloride (2.61 g, 12.9 mmol), and $NiCl_2(H_2O)_6$ (3.06 g, 12.9 mmol) were placed in a 100 mL round bottom flask equipped with a magnetic stirring bar. The flask was flushed with N_2 and the reaction was allowed to stir at 90 °C for 23 h. The reaction was removed from heat and allowed to cool to room temperature. The solution was dried under vacuum at 100 °C to afford a dark blue liquid (5.97 g, 91%).

Acknowledgment

We thank the Petroleum Research Fund, administered by the American Chemical Society, for support of this research.

References

[1] N.V. Plechkova, K.R. Seddon, Chem. Soc. Rev. 37 (2008) 123.
[2] T. Welton, Chem. Rev. 99 (1999) 2071.
[3] I. Newington, J.M. Perez-Arlandis, T. Welton, Org. Lett. 9 (2007) 5247.
[4] N.V. Plechkova, K.R. Seddon, Ionic liquids: designer solvents for green chemistry, in: A. Perosa, F. Zecchini, P. Tundo (Eds.), Methods and Reagents for Green Chemistry: An Introduction, John Wiley and Sons, Hoboken, NJ, 2007.
[5] M.-J. Deng, I.W. Sun, P.-Y. Chen, J.-K. Chang, W.-T. Tsai, Electrochim. Acta 53 (2008) 5812.
[6] T.-I. Leong, I.W. Sun, M.-J. Deng, C.-M. Wu, P.-Y. Chen, J. Electrochem. Soc. 155 (2008) F55.
[7] D.-X. Zhuang, M.-J. Deng, P.-Y. Chen, I.W. Sun, J. Electrochem. Soc. 155 (2008) D575.
[8] P. Wasserscheid, W. Keim, Angew. Chem., Int. Ed. 39 (2000) 3772.
[9] C.M. Gordon, J.D. Holbrey, A.R. Kennedy, K.R. Seddon, J. Mater. Chem. 8 (1998) 2627.
[10] J.D. Holbrey, K.R. Seddon, J. Chem. Soc., Dalton Trans. (1999) 2133.
[11] P. Bônhote, A.-P. Dias, N. Papageorgiou, K. Kalyanasundaram, M. Grätzel, Inorg. Chem. 35 (1996) 1168.
[12] A.P. Abbott, G. Capper, D.L. Davies, R. Rasheed, Inorg. Chem. 43 (2004) 3447.
[13] K. Binnemans, Chem. Rev. 107 (2007) 2592.
[14] M.S. Sitze, E.R. Schreiter, E.V. Patterson, R.G. Freeman, Inorg. Chem. 40 (2001) 2298.
[15] C. Zhong, T. Sasaki, A. Jimbo-Kobayashi, E. Fujiwara, A. Kobayashi, M. Tada, Y. Iwasawa, Bull. Chem. Soc. Jpn. 80 (2007) 2365.
[16] R.E.D. Sesto, T.M. McCleskey, A.K. Burrell, G.A. Baker, J.D. Thompson, B.L. Scott, J.S. Wilkes, P. Williams, Chem. Commun. (2008) 447.
[17] R.J. Gale, B. Gilbert, R.A. Osteryoung, Inorg. Chem. 18 (1979) 2723.
[18] P.B. Hitchcock, K.R. Seddon, T. Welton, J. Chem. Soc., Dalton Trans. (1993) 2639.
[19] C.J. Bowlas, D.W. Bruce, K.R. Seddon, Chem. Commun. (1996) 1625.
[20] J.D. Holbrey, R.D. Rogers, Physicochemical properties of ionic liquids: melting points and phase diagrams, in: P. Wasserscheid, T. Welton (Eds.), Ionic Liquids in Synthesis, Wiley-VCH, Weinheim, 2008.
[21] The melting points of the single-chain liquids were below 0 °C, but attempts to measure the exact temperatures with DSC were unsuccessful.
[22] J.S. Wilkes, J.A. Levisky, R.A. Wilson, C.L. Hussey, Inorg. Chem. 21 (1982) 1263.
[23] J.R. Sanders, E.H. Ward, C.L. Hussey, J. Electrochem. Soc. 133 (1986) 325.
[24] J.G. Huddleston, A.E. Visser, W.M. Reichert, H.D. Willauer, G.A. Broker, R.D. Rogers, Green Chem. 3 (2001) 156.
[25] L.C. Branco, J.N. Rosa, J.J.M. Ramos, C.A.M. Afonso, Chem. Eur. J. 8 (2002) 3671.
[26] D.M.P. Mingos, A.L. Rohl, J. Chem. Soc., Dalton Trans. (1991) 3419.
[27] H. Jin, B. O'Hare, J. Dong, S. Arzhantsev, G.A. Baker, J.F. Wishart, A.J. Benesi, M. Maroncelli, J. Phys. Chem. B 112 (2008) 81.
[28] B.K.M. Chan, N.-H. Chang, M.R. Grimmett, Aust. J. Chem. 30 (1977) 2005.
[29] K.J. Baranyai, G.B. Deacon, D.R. MacFarlane, J.M. Pringle, J.L. Scott, Aust. J. Chem. 57 (2004) 145.
[30] D.M. Blake, L. Moens, D. Rudnicki, H. Pilath, J. Sol. Energy Eng. 128 (2006) 54.
[31] In preliminary experiments, the reaction of 1-heptyl-3-methylimidazolium iodide and NiI_2 was used to prepare $[C_7mim]_2NiI_4$. The dark red liquid was heated to 700 °C for 30 min under N_2. Powder XRD indicated that the residue consisted only of elemental nickel; a Scherrer analysis of peak widths suggested an average particle size of 44 nm.
[32] J.G. Huddleston, R.D. Rogers, Chem. Commun. (1998) 1765.

Polyhedron 28 (2009) 2359–2370

Contents lists available at ScienceDirect

Polyhedron

journal homepage: www.elsevier.com/locate/poly

Trends in *ortho*-carboranes 1-X-2-R-1,2-$C_2B_{10}H_{10}$ (R = Ph, Me) bearing an *exo*-CN-bonded substituent group (X = NO, N=NR′ or NHR″)

Mark A. Fox [a,*], Richard J. Peace [a], William Clegg [b], Mark R.J. Elsegood [b,1], Kenneth Wade [a,*]

[a] Chemistry Department, Durham University Science Laboratories, South Road, Durham DH1 3LE, UK
[b] School of Chemistry, Newcastle University, Newcastle Upon Tyne NE1 7RU, UK

ARTICLE INFO

Article history:
Received 19 December 2008
Accepted 30 April 2009
Available online 8 May 2009

Keywords:
Carborane
Amine
Nitroso
Benzene
Cluster
π-Bonding

ABSTRACT

The preparation and crystal structures of four *ortho*-carboranyl-nitrogen compounds, PhCb^{o}N=N(C_6H_4Me-4) (**1**), PhCb^{o}NHNH(C_6H_4Me-4) (**2**), MeCb^{o}NHNHPh (**3**) and PhCb^{o}NHOH (**4**) (Cb^o = 1,2-$C_2B_{10}H_{10}$; nitrogen groups at cage carbon C1, Ph or Me at C2), the last as a 1,4-dioxane solvate, are reported. Comparisons of their structures with those of other *ortho*-carboranyl-nitrogen systems studied earlier reveal further correlations between their cage C–C and *exo*-C–N bond distances and bond orders. Substituent orientations and bond distances (cage C1–C2, *exo*-C1–N) in RCb^{o}NHR″ systems (R = Ph or Me at C2) are consistent with dative π-bonding from a nitrogen lone pair into the cage carbon *p*-AO otherwise responsible for cage C1–C2 σ bonding. Their C1–C2 bond distances are remarkably sensitive to the planar (sp^2) or pyramidal (sp^3) nature of the NHR″ group. The N=O and N=NR′ residues in RCb^{o}X prefer to be orientated in plane with the cage C1–C2 in contrast to the RCb^{o}NHR″ systems. Correlations between their cage C–C and *exo*-C–N bond distances and the ^{11}B NMR chemical shifts of their antipodal boron atoms reflect the π-bonding characteristics of the nitrogen substituent.

© 2009 Elsevier Ltd. All rights reserved.

1. Introduction

The remarkable capacity of π-donor substituents, attached to carbon atoms of an *ortho*-carborane C_2B_{10} cage, to influence cage C1–C2 bond lengths was first detected some two decades ago [1] with the structural characterisation of the proton sponge salt of the anion PhCb^{o}O$^-$, (Cb^o = 1,2-$C_2B_{10}H_{10}$; O$^-$ at cage carbon C1, Ph at C2) followed by many related studies [2,3–7] on *ortho*-carboranes containing thiolato and phosphino groups. However, this area has only recently been documented systematically by experimental and computational studies on systems RCb^{o}X and XCb^{o}X in which X is a potential π-donor such as NH_2, OH, SH or anions derived therefrom by deprotonation [8,9]. *Exo*-C=X π-bonding in these systems between the cage carbon atom and substituent X involves a tangentially oriented *p*-AO on carbon that would otherwise be involved in cage bonding, and C1–C2 bond lengthening will occur if the *p*-AO used for *exo*-C=X π-bonding is the *p*-AO that in *ortho*-carborane itself is involved in C1–C2 σ-bonding (AO = atomic orbital; Fig. 1).

The extent to which the cage C1–C2 bond is affected by *exo* π-bonding will therefore depend on the orientation of the substituent in the *exo*-CN systems explored here. Though many *ortho*-carborane derivatives with *exo*-C–N bonds are known, only three structural studies have been carried out elsewhere to our knowledge: the first was on a rhenium complex ^{i}PrCb^{o}N$_2$Re(CO)$_4$ [10], which contains a 6-membered –Re–N=N–C–B–H– ring in which the metal atom is attached to one nitrogen atom and to a boron-attached hydrogen; the second was on a hydrazocarborane, HCb^{o}NRNHR (R = $CO_2{}^t$Bu) [11], which contains an intramolecular cage C–H···O hydrogen bond [12]; and the third was on a zirconium complex, PhN$_3$Cb^{o}ZrCp$_2$ [13], which contains a 3-membered ZrN_2 ring. All three systems thus contain intramolecular interactions that influence the orientation about nitrogen at C1 with respect to the cage C1–C2 bond.

In 2004, we reported the crystal structures of PhCb^{o}NH$_2$ and the adduct PhCb^{o}NH$_2$·OP(NMe$_2$)$_3$ which revealed six independent molecules with C1–C2 bond distances ranging between 1.74 and 1.85 Å [8]. We also reported improved syntheses of *ortho*-carborane nitroso derivatives RCb^{o}NO and dicarboranylamines (RCb^o)$_2$NH (R = Ph, Me) and discussed their structures, which in the case of the secondary amines (and amides [(RCb^o)$_2$N]$^-$ derived therefrom) showed significant cage distortion (C1–C2 bond lengthening) attributable to *exo*-C=N π-bonding [14–16]. To supplement these studies, we have carried out a synthetic, spectroscopic, structural and computational investigation of the compounds

* Corresponding authors.
E-mail addresses: m.a.fox@durham.ac.uk (M.A. Fox), kenneth.wade@durham.ac.uk (K. Wade).
[1] Present address: Chemistry Department, Loughborough University, Loughborough, Leicestershire LE11 3TU, UK.

0277-5387/$ - see front matter © 2009 Elsevier Ltd. All rights reserved.
doi:10.1016/j.poly.2009.04.041

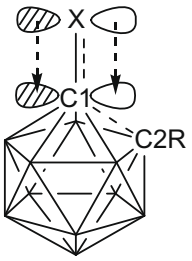


Fig. 1. Orbitals involved in the *exo* π-bonding for RCb^{o}X where X is a π-donating group and R is not a donor group.

RCb^{o}X (R = Ph, Me; X = NNR′, NHNHR′, NHOH; R′ = Ph or C_6H_4Me-4), and further spectroscopic and computational studies on systems with X = NH_2, NO, NHCb^{o}R and [NCb^{o}R]$^-$, which have revealed hitherto unremarked characteristics and trends in *ortho*-carborane systems RCb^{o}X containing *exo*-CN units, which we report here.

2. Results and discussion

In this section, we outline the synthetic procedures used to prepare the new compounds, and describe their structures. We then explore the structural, bonding and spectroscopic characteristics of *ortho*-carboranyl-nitrogen systems RCb^{o}N═O, RCb^{o}N═NR′ and RCb^{o}NHR′′ in general, including both the new systems and those previously characterised [8,14]. We also compare the structural and bonding relationships of these 3D pseudoaromatic cages with 2D aromatic ring analogues.

2.1. Synthetic aspects

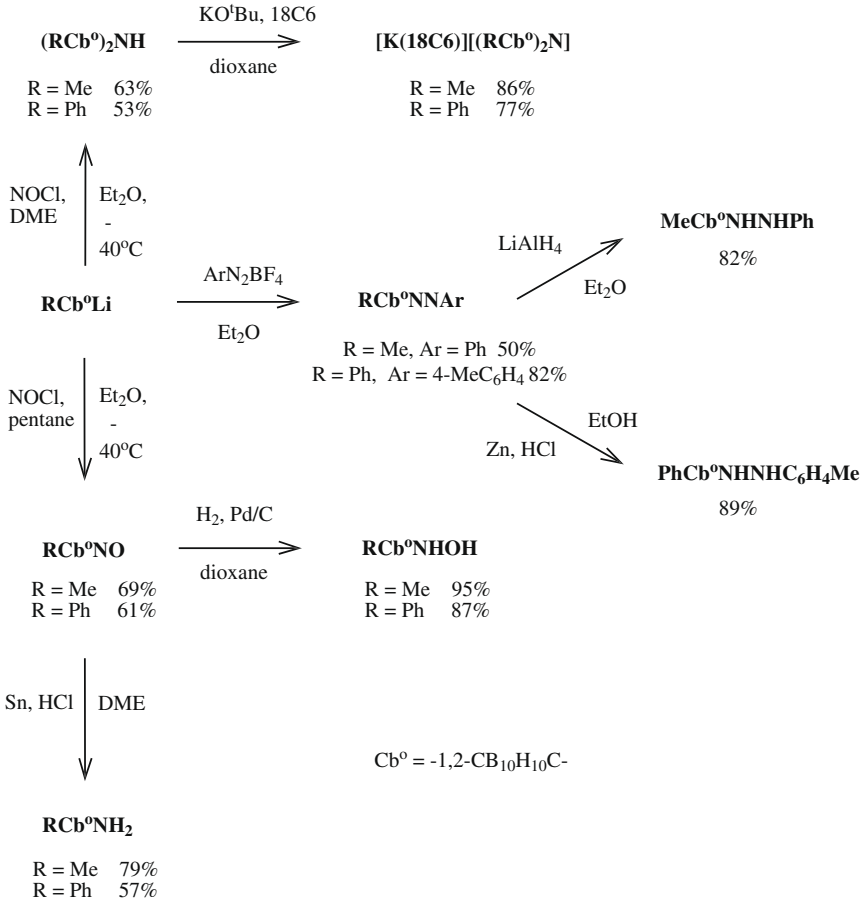
Scheme 1 summarises the experimental procedures used for the syntheses of the carboranes investigated in this definitive study. Synthetic methods that have not been reported in our earlier papers [8,14] are described in detail in Section 4. The azocarboranes were synthesised using a reported literature procedure [17]. The reductions of the nitroso-carboranes RCb^{o}NO with hydrogen using a palladium/carbon catalyst gave the known [18,19] hydroxylamines RCb^{o}NHOH in high yields. High-yield reductions of the azocarboranes RCb^{o}NNAr to the hydrazines RCb^{o}NHNHAr were carried out here using the reducing agents $LiAlH_4$ and Zn/HCl.

2.2. Structural aspects: new experimentally determined structures

2.2.1. The azo-carborane PhCb^{o}N$_2$(C_6H_4Me-4) (**1**) and hydrazo-carboranes PhCb^{o}NHNH(C_6H_4Me-4) (**2**) and MeCb^{o}NHNHPh (**3**)

The crystal structures of these three compounds were determined by X-ray diffraction (for details, see Section 4). Their molecular structures are illustrated in Figs. 2 and 3.

The structures of the azo-carborane (**1**) and its hydrazo analogue (**2**) (Fig. 2) are similar, differing significantly, and as expected, only in the bond lengths and angles in the region of their –N═N– and –N(H)N(H)– units. Their NN links, at 1.250(2) in (**1**) and 1.409(2) Å in (**2**), are of normal length for double and single bonds, respectively, between nitrogen atoms. The CNN bond angles, at both ends of the N(1)–N(2) links, appear not to differ between the two ends (implying that the link to the carboranyl residue resembles that to the aryl group in both **1** and **2**) nor between **1** and **2**, suggesting both **1** and **2** contain sp^2-hybridised



Scheme 1. Routes to carboranyl-nitrogen derivatives.

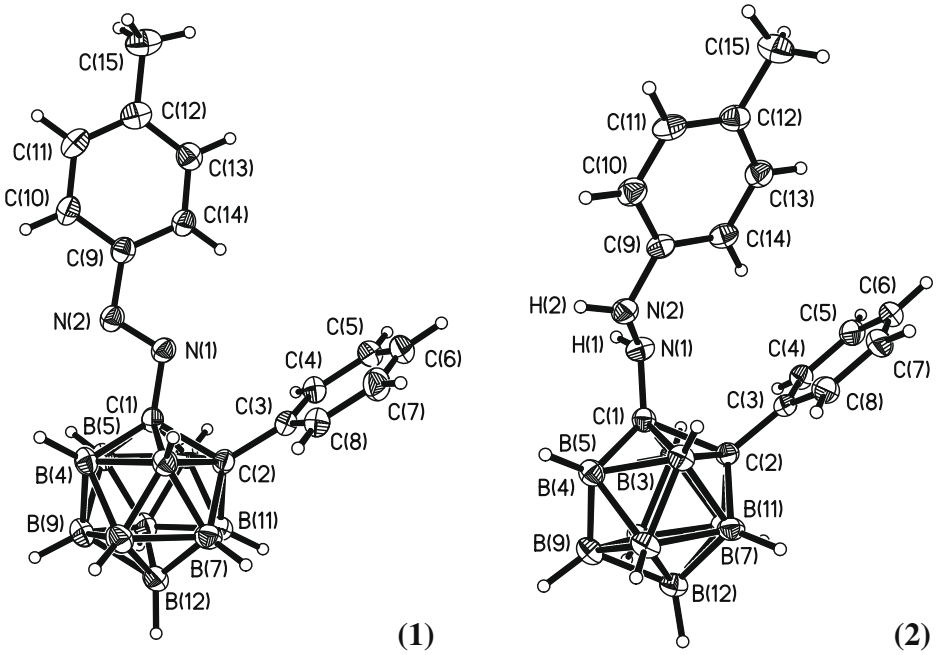


Fig. 2. Molecular structures of PhCb^{o}N$_2$C$_6$H$_4$Me (**1**) and PhCb^{o}NHNHC$_6$H$_4$Me (**2**). Selected bond distances (Å) and angles (°) for (**1**): N(1)–N(2) 1.250(2); N(2)–C(9) 1.428(3); C(2)–C(3) 1.509(3); N(1)–N(2)–C(9) 112.88(15); N(1)–N(2)–C(9)–C(14) 15.3(3). For (**2**): N(1)–N(2) 1.409(2); N(2)–C(9) 1.421(3); C(2)–C(3) 1.497(3); N(1)–N(2)–C(9) 115.73(16); N(1)–N(2)–C(9)–C(14) −25.7(3).

nitrogen atoms. In both **1** and **2**, the phenyl substituent on C(2) lies in a plane roughly perpendicular to the N(1)–C(1)–C(2) plane, as would be expected not only on steric grounds (to keep it away from the substituent on C(1)), but also as this is the orientation that optimises π-donation from ring to cage and causes *ca.* 0.03 Å C1–C2 bond lengthening [20–23].

The orientations of the azo and hydrazo substituents on C(1), however, differ significantly. In **1**, the azo N(1)–N(2)–C(9) unit lies in the N(1)–C(1)–C(2) plane, as in the nitroso carborane PhCb^{o}NO studied previously [14]. In **2**, the hydrazo N(1)–N(2)–C(9) unit is twisted out of the C(1)–C(2)–C(3) plane, clearly not on steric grounds, but to an extent that significantly ensures that the lone pair on N(1) lies in that plane. The view of **2** in Fig. 2 shows the *ortho* hydrogen atom on C(14) lying over, and attracted to, the π-cloud of the phenyl group on C(2), with an H···centroid distance of 2.65 Å, and this attraction is likely to be responsible for the orientation of the tolyl group.

The molecular structure of compound **3**, MeCb^{o}NHNHPh, shown in Fig. 3, differs from that of **2** in the orientation of the aryl-hydrazo group, away from the methyl substituent on C(2). However, the local geometry about N(1) resembles that in **2** in ensuring that the lone pair on N(1) lies in the N(1)–C(1)–C(2) plane.

2.2.2. The hydroxylamino-carborane PhCb^{o}NHOH (*4*)

The molecular structure of this compound (Fig. 4) was determined by single-crystal studies on a dioxane hemisolvate of composition PhCb^{o}NHOH·0.5dioxane. The orientations of both substituents on the carborane cage were found to resemble those already discussed for compounds **2** and **3**, and are in line with those found previously for PhCb^{o}NH$_2$ [8]. The phenyl group in **4** lies roughly perpendicular to the N(1)–C(1)–C(2) plane, and the HNOH

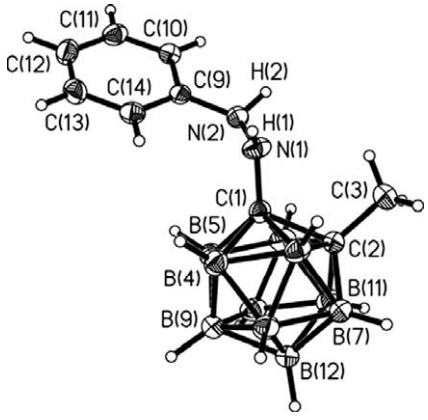


Fig. 3. Molecular structure of MeCb^{o}NHNHPh (**3**). Selected bond distances (Å) and angles (°): N(1)–N(2) 1.395(2), N(2)–C(9) 1.405(2), C(2)–C(3) 1.511(2), N(1)–N(2)–C(9) 119.17(13), N(1)–N(2)–C(9)–C(14) −19.0(2).

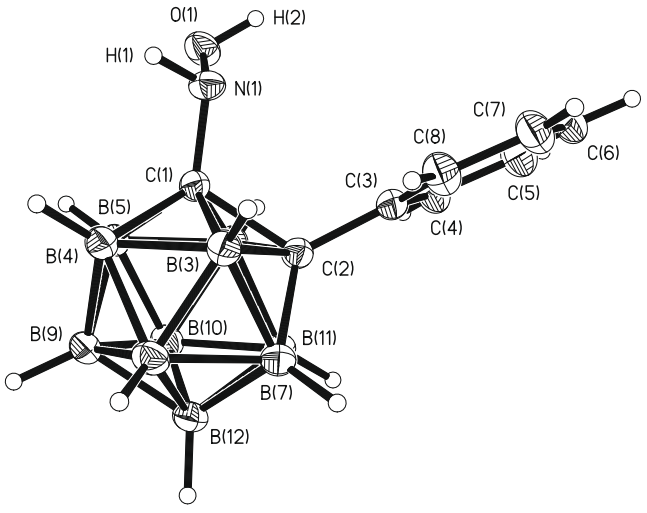


Fig. 4. Molecular structure of PhCb^{o}NHOH (**4**). The dioxane molecule in the crystal structure is not shown. Selected bond distances (Å): N(1)–O(1) 1.435(2); C(2)–C(3) 1.506(3).

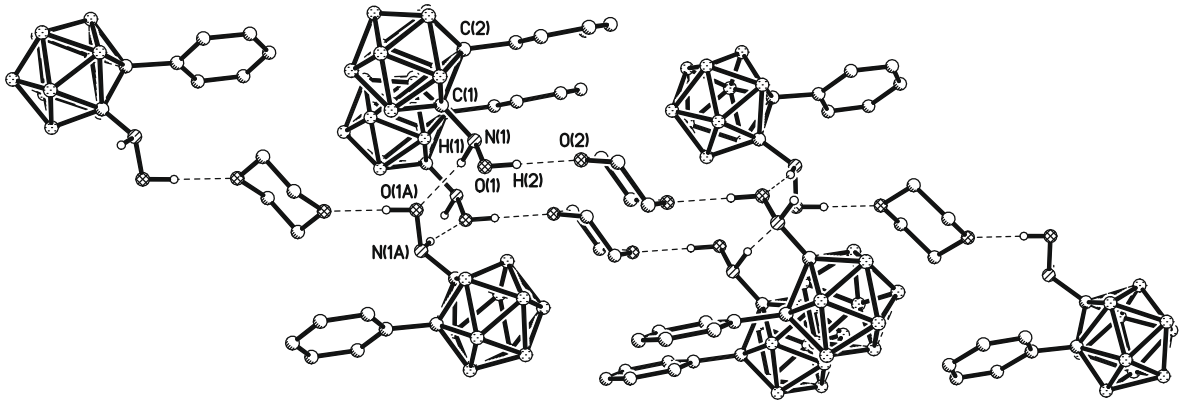


Fig. 5. Supramolecular structure of PhCb^{o}NHOH·0.5dioxane. Selected intermolecular distances (Å) and angles (°): O(1)···O(2) 2.752(2), N(1)···O(1A) 3.209(2), O(1)–H(2)···O(2) 177(3), N(1)–H(1)···O(1A) 167(2). [O(1A) is generated from O(1) by screw-axis symmetry].

unit is oriented away from the phenyl group, like the HNNHR unit in **2**, implying that the lone pair on the nitrogen lies in the N(1)–C(1)–C(2) plane. In the crystal structure, intermolecular N–H···O hydrogen-bonding interactions between the hydroxylamino units link the molecules into (PhCb^{o}NHOH)$_n$ chains, which in turn are interlinked by N–OH···O hydrogen bonds to both oxygen atoms of the dioxane molecules (Fig. 5).

2.3. Structural aspects: general characteristics of RCb^{o}N systems

The structures of the four compounds **1**–**4** described above, together with the four in our previous paper [14] [PhCb^{o}NO, (PhCb^o)$_2$NH, (MeCb^o)$_2$NH and the anion (PhCb^o)$_2$N$^-$] and the amine PhCb^{o}NH$_2$ characterised earlier [8], provide a useful data bank from which to deduce some common characteristics of *ortho*-carboranyl-nitrogen systems. These include preferred orientations of the *exo*-nitrogen substituent with respect to the carborane cage, and systematic complementary trends in their *exo*-C(1)–N(1) and cage C(1)–C(2) bond distances; as the former shorten, the latter lengthen.

The compounds we have studied are of two formula types, RCb^{o}NHR″ and RCb^{o}N=Z. Their structures are shown in Figs. 6 and 7. The nitroso- and azo-carboranes PhCb^{o}N=O and PhCb^{o}N=N(C$_6$H$_4$Me-4) are of the latter type [14]. All of the other compounds are of the former type, including the anion (PhCb^o)$_2$N$^-$ in which the lone pair left on deprotonation of the parent amine can be regarded as occupying the site vacated by proton.

Figs. 6 and 7 show the NHR″ and N=Z units in their preferred orientations about the *exo*-C(1)–N(1) bond with respect to the carborane cage, with the substituents R″ or Z leaning away from the substituent R (Ph or Me) on the other cage carbon atom C(2). This orientation not only minimises steric non-bonding repulsive interactions between the groups on C(1) and C(2), but aligns the lone pair of electrons on the *exo*-nitrogen atom on C(1) in the C(2)–C(1)–N(1) plane for RCb^{o}NHR″, the alignment best suited for dative π-bonding from the nitrogen lone pair into the *p*-AO on C(1) responsible for cage C(1)–C(2) σ-bonding, as shown in Fig. 6.

The extent to which *exo*-dative C=N π-bonding donation from the NHR″ group occurs (and whether it does so at the expense of cage C(1)–C(2) σ-bonding) can be inferred from the experimental C(1)–C(2) and C(1)–N(1) distances in Table 1, in which compounds are listed in the order of their increasing cage C(1)–C(2) distances, which matches the sequence of decreasing C(1)–N(1) distances. Table 1 includes also torsion angles C(2)–C(1)–N(1)–Z/R″, which reveal that these compounds show some departures from the preferred orientations shown in Figs. 6 and 7; bond angles C(2)–C(1)–N(1), which show expected deviations from a normal angle of 121.7° for an *exo*-bond on a regular icosahedron; and the C(1)–N(1)–Z/R″ bond angles at nitrogen, which for species RCb^{o}NHR″ would be 120° for an ideal trigonal planar coordination at nitrogen (sp^2) and 109° for pyramidal nitrogen (sp^3). The data in Table 1 include the four distinct molecules of PhCb^{o}NH$_2$ in the asymmetric unit of the crystal structure and for the two distinct molecules of this same species in its hydrogen-bonded adduct with hexamethylphosphoramide, PhCb^{o}NH$_2$·HMPA [8].

The range over which cage C(1)–C(2) bond distances vary in Table 1 (1.677(2)–1.995(3) Å, i.e. 0.32 Å) is more than twice the range over which *exo*-C=N distances vary (1.490(2)–1.345(4) Å i.e. 0.15 Å), because the former are fractional-order bonds becoming progressively weaker as the table is descended, whereas the latter

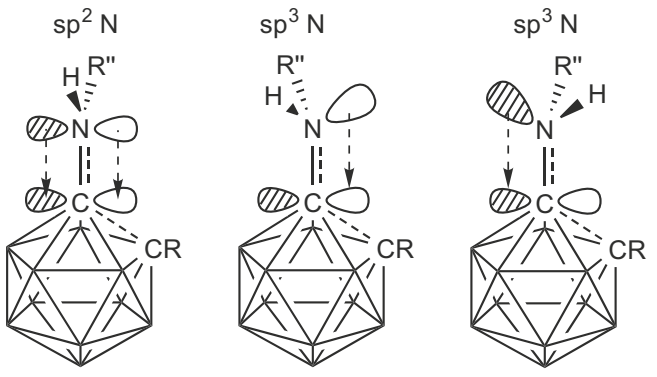


Fig. 6. Preferred orientations in RCb^{o}NHR″ systems. The cage acts as a π-acceptor.

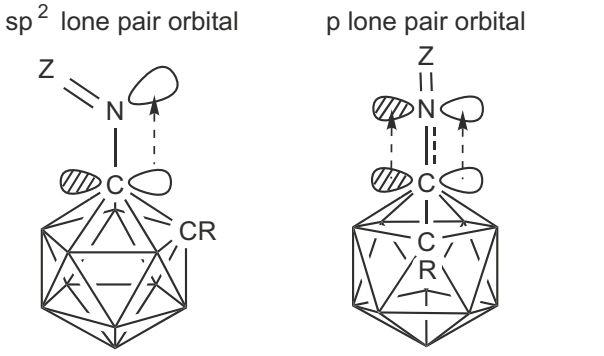


Fig. 7. Preferred orientation in RCb^{o}N=Z systems (Z = O, NR′). The cage *may* act as a π-donor.

Table 1
X-ray-determined trends: the optimum torsion angle C(2)–C(1)–N(1)–Z/R′′ to align the p-orbital lone pair of sp^2-hybridised nitrogen with the cage C(1)–C(2) bond is 90° for compounds RCb^{o}NHR′′, and to align the sp^2-orbital lone pair of sp^2-hybridised nitrogen with the cage C(1)–C(2) bond is 180° for compounds RCb^{o}N=Z. HMPA = OP(NMe$_2$)$_3$.

X		C(1)–C(2) (Å)	C(1)–N(1) (Å)	C(2)–C(1)–N(1) (°)	C(1)–N(1)–Z/R′′ (°)	C(2)–C(1)–N(1)–Z/R′′ (°)	C(1)–C(2)–C(Ph)–C(Ph) (°)	Reference
PhCb^{o}X								
NO		1.677(2)	1.490(2)	112.1(2)	113.0(2)	164.7	82.4	[14]
N=NC$_6$H$_4$Me		1.694(2)	1.443(2)	111.3(1)	112.8(2)	178.2	75.5	This work
NHOH		1.737(3)	1.423(3)	115.7(2)	110.7(2)	101.6	86.5	This work
NH$_2$ (4)	A	1.745(3)	1.391(3)	119.3(2)			69.9	[8]
	B	1.765(3)	1.403(3)	115.9(2)			91.2	
	C	1.774(3)	1.404(3)	119.8(2)			64.1	
	D	1.785(3)	1.392(2)	118.5(2)			76.7	
NHNHC$_6$H$_4$Me		1.778(3)	1.401(2)	115.2(2)	116.4(2)	105.9	83.4	This work
NHCb^{o}Ph		1.794(3)	1.404(2)	117.3(2)	132.0(2)	92.4	70.1	[14]
		1.799(3)	1.404(2)	116.9(2)		97.6	73.9	
NH$_2$·HMPA (2)	A	1.818(8)	1.360(8)	116.1(6)			59.3	[8]
	B	1.853(8)	1.363(9)	114.9(5)			81.8	
[NCb^{o}Ph]$^-$		1.980(3)	1.355(4)	118.8(2)	127.0(2)	90.3	53.6	[14]
		1.995(3)	1.345(4)	118.8(2)		89.0	53.2	

	C(1)–C(2) (Å)	C(1)–N(1) (Å)	C(2)–C(1)–N(1) (°)	C(1)–N(1)–Z/R′′ (°)	C(2)–C(1)–N(1)–Z/R′′ (°)	Reference
MeCb^{o}X						
NHCb^{o}Me	1.748(4)	1.409(4)	117.3(2)	131.1(2)	95.0	[14]
	1.752(4)	1.410(4)	117.0(2)	131.1(2)	94.7	
NHNHPh	1.770(2)	1.388(2)	115.9(1)	118.8(1)	104.1	This work

Table 2
Observed bond distances (Å) and calculated bond orders.

X	C(1)–C(2)	Bond order	C(1)–N(1)	Bond order	π-Bond order
PhCb^{o}X					
NO	1.677(2)	0.605	1.490(2)	0.921	0.056
N=NAr	1.694(2)	0.590	1.444(2)	0.998	0.070
NHOH	1.737(3)	0.539	1.423(3)	1.025	0.073
NHNHAr	1.778(3)	0.485	1.401(2)	1.044	0.104
NHCb^{o}Ph	1.798(3)	0.453	1.404(2)	1.038	0.124
NH$_2$ (C)	1.774(3)	0.456	1.404(3)	1.102	0.143
NH$_2$·HMPA (av)	1.835(8)	0.396	1.362(8)	1.146	0.185
[NCb^{o}Ph]$^-$	1.987(3)	0.235	1.350(4)	1.295	0.357
MeCb^{o}X					
NHCb^{o}Me (av)	1.750(4)	0.506	1.410(4)	1.026	0.113
NHNHPh	1.770(2)	0.486	1.387(2)	1.057	0.128

range in bond order from single to multiple. To aid comparison within the series, AM1 calculations have been carried out using the atomic coordinates determined by X-ray diffraction, without further optimisation. Selected bond distances and orders, with corresponding σ and π contributions, are given in Table 2.

The data in Table 2 show the correlation between the cage C(1)–C(2) and *exo*-C(1)–N(1) bond orders expected from their lengths. The bond orders of the cage C···C bonds decrease as those of the *exo*-C(1)–N(1) bonds increase. The range over which the C(1)–C(2) bond orders vary (from 0.61 in PhCb^{o}NO to 0.24 in the anion (PhCb^o)$_2$N$^-$) is comparable to that over which the *exo*-C(1)–N bond orders vary (from 0.92 to 1.30), and is itself worthy of comment. Because icosahedral carborane clusters are held together by only 13 skeletal electron pairs spread around their 30 edge 'bonds', the average cage edge bond order will be 0.43 (13/30). The cage carbon–carbon bond in *ortho*-carborane HCb^{o}H itself has an order some 50% in excess of this because the carbon atoms are more electronegative than their boron neighbours and so attract a greater share of the electrons available. The data in Table 2 show that the cage C(1)–C(2) bond order has been reduced to about this average icosahedral value of 0.43 in the amine PhCb^{o}NH$_2$, and to roughly half this value in the anion (PhCb^o)$_2$N$^-$.

In our discussion of bond lengths and bond order so far, we have concentrated on the cage C(1)–C(2) and *exo*-C(1)–N(1) bonds. This is because these are the only bonds in these systems PhCb^{o}X whose lengths and orders change significantly and systematically with X, as illustrated by the data in Table 3, which lists the experimental lengths of all the 2-centre links in the immediate environment of C(1); Fig. 8 illustrates that pentagonal pyramidal environment. From Table 3 it is clear that, although there are minor variations between compounds in the measured lengths of C(1)–B(3/6), C(1)–B(4,5), C(2)–B(3,6), B(3,6)–B(4,5) and B(4)–B(5), these variations cannot be regarded as systematic or significant.

However, on closer inspection, the C1–C2 bond lengths determined cannot simply be explained by the orientation of the π-donating groups. For example, the two compounds **2** and **3** contain similar C1–C2 bond lengths of *ca.* 1.77 Å even though it is generally accepted that the phenyl group lengthens the bond by *ca.* 0.03–0.05 Å compared to the methyl group due to the steric and/or electronic effect(s) of the former [24,25]. The difference of 0.04 Å for the C1–C2 bond lengths in **2** and **4** is significant even though the orientations of the nitrogen groups are similar. There are six distinct PhCb^{o}NH$_2$ molecular geometries experimentally determined, with C1–C2 bond lengths ranging from 1.745 to 1.853 Å (see Table 1) – a difference of 0.11 Å, which cannot be explained solely by the orientation of the amine group.

2.4. Structural aspects: computational studies

Optimised geometries of carboranes at the MP2/6-31G* level of theory have been shown to be in excellent agreement with experimental geometries determined by gas-phase electron diffraction

Table 3
Interatomic distances (Å) for compounds PhCb^{o}X.

X	C1–C2	C1–N	C1–B3/6	C1–B4/5	C2–B3/6	B3/6–B4/5	B4–B5
H [26,27]	1.643(1)		1.713(1)	1.695(1)	1.733(1)	1.776(1)	1.781(1)
NO	1.677(2)	1.490(2)	1.706(2)	1.703(2)	1.740(2)	1.786(3)	1.779(3)
NNAr	1.694(2)	1.443(2)	1.716(3)	1.703(3)	1.738(3)	1.780(3)	1.784(3)
NHOH	1.737(3)	1.423(3)	1.721(3)	1.701(3)	1.732(3)	1.779(3)	1.781(3)
NHNHAr	1.778(3)	1.401(2)	1.719(3)	1.708(3)	1.736(3)	1.786(3)	1.784(3)
NH_2 (av)	1.767(3)	1.396(3)	1.715(4)	1.698(4)	1.722(4)	1.780(4)	1.775(4)

[28–30] and X-ray crystallography [8,12,20,31,32]. Earlier, we had carried out computations on model geometries of HCb^{o}X with π-donor groups (X = OH, NH^-, NH_2 and CH_2^-) to investigate the effect of orientation of these groups on the C1–C2 bond length; in these computations a planar configuration (sp^2) was assumed for NH_2 [8]. The effect of a pyramidal form (sp^3) at a nitrogen π-donor group on the C1–C2 bond or the effect of π-acceptor groups on the cage geometry had not been investigated previously. Here, data for the systems HCb^{o}X where X = N═O, N═NH, NHOH, NH_2 and $NHNH_2$ in various possible orientations (indicated by their torsion angles) are listed in Table 4. The pyramidal or planar configurations of the nitrogen atom N1 attached to C1 for NHR″ groups were also examined.

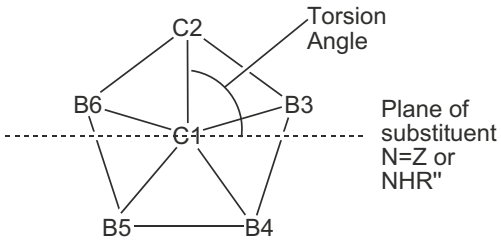


Fig. 8. The pentagonal pyramidal environment about C1.

The model carboranes with Π-acceptor groups, NO and NNH, prefer to be oriented in plane (0° and 180°) with the C1–C2 bond, as opposed to being oriented perpendicular to the C1–C2 bond, with an energy difference of *ca.* 4 kcal mol^{-1} (Fig. 8). The reasons for a slight preference for 0° orientations over 180° orientations in these models are cage C–H···X bond interactions [12]. Energetically, the hydroxylamino (NHOH) group clearly favours the pyramidal form (sp^3 N) over the planar form (sp^2 N) irrespective of the orientation. There is no strong preference for one orientation over another for the NHOH group. The substituents NO, NNH and NHOH (with sp^3 N) have little orientational influence on the *ortho*-carborane cage geometry.

By contrast, the models containing the NH_2 groups are similar in energy irrespective of whether the nitrogen atom N1 is planar (sp^2) or pyramidal (sp^3) in configuration (Fig. 7). However, the 90° orientations are energetically favourable and are expected for a π-donor group –NHR″ to be oriented to align the donor p-orbital with the C1–C2 bond for maximum overlap. The model HCb^oNH_2 has four geometries within a range of 2.9 kcal mol^{-1} in energy but their C1–C2 bond distances vary from 1.623 to 1.713 Å, a difference of 0.09 Å, attributable to the orientations and the sp^2 or sp^3 configuration about the nitrogen atom. Similar observations are found for the model carborane containing the $NHNH_2$ group.

Table 4
Selected bond lengths (Å) and energies of MP2-optimised geometries of HCb^{o}X where torsion angles for C2–C1–N–Z/R″ are fixed at 0, 90 and 180° (a = N–H away from C1, t = N–H towards C1).

X		N1–Z/R″	C1–N1	C1–C2	C1–B3/6	C1–B4/5	Energy (au)	Relative *E* (kcal mol^{-1})
NO	0	1.230	1.491	1.621	1.713	1.691	−459.79796	0.0
	90	1.227	1.514	1.618	1.716	1.689	−459.79160	4.1
	180	1.228	1.493	1.617	1.711	1.692	−459.79740	0.2
NNH	0	1.265	1.455	1.634	1.716	1.694	−439.98786	0.0
	90	1.265	1.468	1.621	1.725	1.693	−439.98075	4.7
	180	1.265	1.457	1.624	1.715	1.698	−439.98616	1.1
NHOH(sp^3)	0	1.445	1.450	1.631	1.712	1.693	−460.99182	0.0
	90(a)	1.440	1.441	1.635	1.727	1.699	−460.99040	0.1
	90(t)	1.437	1.434	1.665	1.723	1.697	−460.98922	1.7
	180	1.441	1.452	1.620	1.731	1.699	−460.98794	2.6
NHOH(sp^2)	0	1.396	1.397	1.609	1.749	1.704	−460.97107	13.0
	90	1.397	1.377	1.739	1.720	1.700	−460.97564	10.0
	180	1.394	1.396	1.607	1.756	1.706	−460.96728	15.6
NH_2(sp^3)	0	1.019	1.430	1.640	1.731	1.700	−386.01371	4.1
	90(a)	1.017	1.422	1.651	1.722	1.702	−386.01982	0.0
	90(t)	1.015	1.412	1.675	1.725	1.700	−386.01982	0.0
	180	1.020	1.434	1.623	1.732	1.701	−386.01650	2.2
NH_2 (sp^2)	0	1.007	1.396	1.612	1.752	1.705	−386.00656	8.9
	90	1.008	1.383	1.713	1.718	1.703	−386.01552	2.9
$NHNH_2$(sp^3)	0	1.417	1.442	1.636	1.728	1.701	−441.16414	3.9
	90(a)	1.420	1.429	1.654	1.725	1.701	−441.16998	0.0
	90(t)	1.416	1.414	1.703	1.724	1.699	−441.16752	1.6
	180	1.428	1.445	1.623	1.736	1.701	−441.16800	1.3
$NHNH_2$(sp^2)	0	1.389	1.406	1.612	1.748	1.705	−441.15795	8.0
	90	1.399	1.386	1.731	1.721	1.701	−441.16639	2.4
	180	1.395	1.403	1.611	1.755	1.706	−441.15887	7.4

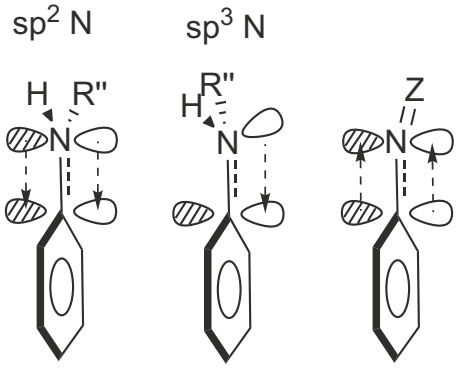


Fig. 9. Preferred orientations in PhNHR′′ and PhN=Z systems.

There are parallels here between carborane chemistry and aromatic ring chemistry, where substituents that can act as π-donors or π-acceptors adopt orientations that maximise interaction with the π-system of the aromatic ring (Fig. 9) provided that steric factors do not rule out the preferred orientations of substituents NO, NNH, NHOH, NH_2 and $NHNH_2$ when attached to a benzene ring. Selected bond distances and relative energies from computational data on these benzene derivatives for the two orientations, planar (0°) and perpendicular (90°), at the MP2/6-31G* level of theory are listed in Table 5. For the acceptor groups NO and NNH, the coplanar form is energetically preferred over the perpendicular form by 8.9 and 5.1 kcal mol^{-1}, respectively, but the orientation has little influence on the ring geometries [33]. The NHOH group strongly favours the pyramidal (sp^3) configuration over the planar (sp^2) form energetically, but small energy and geometry differences between the two orientations are found for the sp^3 form. The amino NH_2 group does not have a strong energetic preference for the sp^2 or sp^3 form but has a notable orientational effect on the C–N bond, with distances of 1.381 Å for the sp^2 N geometry in plane with the C1–C2 bond (0°) and 1.435 Å for the sp^3 N geometry perpendicular to the C1–C2 bond (90°) [34]. The ring geometry, however, remains largely unaffected by the C–N bond variations. The orientation of the $NHNH_2$ group has a similar effect on the geometry and energies as the orientation of the NH_2 group. Preferred orientations determined computationally for PhNNH and $PhNHNH_2$ are in accord with the orientations of the aromatic rings in the experimental structures for **1**, **2** and **3**.

Table 5
Selected bond lengths (Å) and energies of MP2-optimised geometries of PhX where torsion angles for C2–C1–N–Z/R′′ are fixed at 0 and 90°.

X		N1–Z/R′′	C1–N1	C1–C2	Relative energy (kcal mol^{-1})
NO	0	1.244	1.443	1.399	0.0
	90	1.243	1.460	1.394	8.9
NNH	0	1.272	1.433	1.399	0.0
	90	1.270	1.441	1.395	5.1
NHOH(sp^3)	0	1.440	1.432	1.399	0.0
	90	1.465	1.434	1.398	1.5
NHOH(sp^2)	0	1.395	1.378	1.403	7.5
	90	1.412	1.408	1.403	16.9
NH_2(sp^3)	0	1.014	1.409	1.403	0.0
	90	1.019	1.435	1.401	2.4
NH_2(sp^2)	0	1.007	1.381	1.405	1.2
	90	1.005	1.416	1.403	9.2
$NHNH_2$(sp^3)	0	1.410	1.404	1.404	0.0
	90	1.449	1.432	1.401	1.8
$NHNH_2$(sp^2)	0	1.396	1.386	1.404	2.4
	90	1.403	1.415	1.402	12.4

The geometries of PhCb^{o}X and MeCb^{o}X were also computed at the MP2/6-31G* level of theory. Comparisons shown in Table 6 reveal very good agreements between the selected geometric parameters for optimised and experimental geometries in all cases. The NHR′′ groups, as discussed for the model carboranes, are particularly intriguing: the sp^3 N form is more stable than the sp^2 N form in these groups. However, for the NH_2 group the energy difference between the geometries containing sp^3 N and sp^2 N groups is small (less than 3 kcal mol^{-1}), which indicates that both forms could coexist in the solid and solution states where intermolecular interactions come into play. The computed C1–C2 distances of 1.743 and 1.813 Å for the sp^3 N and sp^2 N PhCb^oNH_2 geometries, respectively, and their energies, are in broad agreement with the observation of six distinct PhCb^oNH_2 molecules with C(1)–C(2) bond distances of 1.745–1.853 Å (see Table 1) in the crystal structure.

For compounds with NHNHR′ groups, **2** and **3**, the relative energies between their sp^3 N and sp^2 N geometries are slightly larger at *ca.* 4.0 kcal mol^{-1}, but comparison of the bond parameters of experimental geometries with sp^3 N optimised geometries are poor. The experimental geometry for **3** is in much better agreement with the sp^2 N optimised geometry of MeCb^{o}NHNHPh, whereas the experimental geometry for **2** lies between the two optimised geometries (sp^2 N and sp^3 N) of PhCb^o$NHNHC_6H_4Me$. As for PhCb^oNH_2, these geometries depend on intermolecular interactions such as crystal packing forces. This subtle difference in the sp^2/sp^3 N character results in similar C1–C2 bond distances found experimentally for **2** and **3**. The pyramidal sp^3 N form is clearly favoured in energy for the PhCb^{o}NHOH geometry and in accord with the experimental geometry found for **4**.

The optimised and experimental geometries for the dicarboranylamines (PhCb^o)$_2$NH and (MeCb^o)$_2$NH are in excellent agreement and their planar nitrogen atoms are clearly sp^2 in character. Optimised geometries for some methyl analogues, where no experimental structures were determined, reveal geometries and trends similar to the experimental and optimised geometries for the phenyl analogues.

2.5. Experimental and computed NMR trends

The ^{11}B NMR spectra of polyhedral borane clusters such as carboranes provide a rich source of information provided that signals can be assigned with confidence. At the simplest level, the number of different boron sites in a molecule, deduced from the number of resonances, helps identify isomers. Of more importance in the present context is the 'antipodal effect' in icosahedral carborane chemistry [35–39], whereby the NMR shift of the boron atom directly opposite a substituted cage carbon atom is sensitive to the nature of the substituent. In *ortho*-carborane derivatives RCb^{o}X, bearing substituents X and R on carbon atoms 1 and 2, respectively, the resonances of the atoms opposite (B12 and B9, respectively) respond to the corresponding substituent, particularly if that substituent is a π-donor [2,8]. For the present series of compounds RCb^{o}X, where X is a nitrogen π-donor, the antipodal shift is expected to be related to the degree of *exo* π-bonding, and hence to *exo*-C1–N1 and cage C1–C2 bond lengths.

For such a comparison to be made the ^{11}B NMR shift for the antipodal atom (^{11}B δ-B12) must be reliably assigned. Although the two peaks corresponding to B9 and B12 are readily identified from the peak intensities it is impossible to assign each unambiguously without assumptions being made. One of these peaks appears at approximately the same shift in all compounds. This therefore can be assigned to B9, antipodal to the Ph or Me group in PhCb^{o}X and MeCb^{o}X, respectively. This peak would be expected to change little in these series of compounds as the substituent on C2, i.e. the Me or Ph group, remains unchanged. ^{11}B NMR shifts for B9 and B12 have been assigned on this basis (see Table 7).

Table 6
Comparison of selected computed and experimental geometric parameters (Å and °) for RCb°X systems. Experimental values are shown in italics.

X		C1–C2	C1–N1	C2–C1–N1	C1–N1–X/R″	Angle sum at N	Relative energy (kcal mol^{-1})
PhCb°X							
H		1.636					
		1.643(1)					
NO		1.671	1.490	112.1	111.6		
		1.677(2)	*1.490(2)*	*112.1(2)*	*113.0(2)*		
N=NC$_6$H$_4$Me		1.679	1.441	111.1	111.3		
		1.694(2)	*1.444(2)*	*111.3(1)*	*112.8(2)*		
NHOH	sp^3	1.719	1.430	113.5	110.6	322.4	0.0
	sp^2	1.828	1.367	116.2	120.9	360.0	8.3
		1.737(3)	*1.423(3)*	*115.7(2)*	*110.7(2)*	*324.7*	
NHCb°Ph		1.790	1.401	115.9	132.3	360.0	
		1.798(3)	*1.404(2)*	*117.3(2)*	*132.0(2)*	*360.0*	
NHNHC$_6$H$_4$Me	sp^3	1.727	1.424	116.4	117.4	335.4	0.0
	sp^2	1.830	1.379	119.1	120.5	360.0	4.2
		1.778(3)	*1.401(2)*	*115.2(2)*	*116.4(2)*	*342.4*	
NH$_2$	sp^3	1.743	1.411	114.5		332.7	0.0
	sp^2	1.813	1.374	117.0		360.0	2.6
		1.767(3)	*1.396(3)*	*118.4(2)*		*344.3*	
[NCb°Ph]$^-$		1.977	1.353	118.7	126.2		
		1.987(3)	*1.355(4)*	*118.8(2)*	*127.0*		
MeCb°X							
H		1.630					
NO		1.638	1.488	112.5	111.9		
N=NPh		1.644	1.444	112.2	110.9		
NHOH	sp^3	1.696	1.427	115.4	113.2		0.0
	sp^2	1.774	1.374	118.2	120.7		6.0
NHCb°Me		1.748	1.406	117.3	132.3	360.0	
		1.750(4)	*1.410(4)*	*117.2(2)*	*131.1(2)*	*359.8*	
NHNHPh	sp^3	1.737	1.448	114.5	119.9	338.9	0.0
	sp^2	1.764	1.384	117.9	121.6	360.0	3.8
		1.770(2)	*1.387(2)*	*115.9(1)*	*118.8(1)*	*355.4*	
NH$_2$	sp^3	1.683	1.420	114.9		330.0	0.0
	sp^2	1.770	1.379	118.0		360.0	2.7
[NCb°Me]$^-$		1.886	1.358	118.7	126.2		

Table 7
Comparison of selected experimental (in $CDCl_3$) and computed NMR shifts (ppm) for RCb°X systems. Calculated values are in italics.

X	δ(B12)		δ(B12H)		δ(C1)		δ(C2)	
PhCb°X								
H [8]	−1.2	*−1.2*	2.46	*3.09*	60.1	*57.7*	76.5	*78.5*
NO	−2.0	*0.2*	2.67	*3.34*	114.1	*125.1*	81.3	*84.1*
N=NC$_6$H$_4$Me	−4.2	*−2.4*	2.57	*3.18*	98.8	*103.8*	81.7	*83.0*
NHOH[a]	−5.5	*−4.5*	2.38	*3.00*	98.4	*101.0*	86.5	*87.8*
NHCb°Ph	−5.8	*−5.1*	2.28	*2.86*	94.4	*95.7*	90.3	*92.5*
NHNHC$_6$H$_4$Me[b]	−6.8	*−6.0*	2.32	*2.85*	102.3	*105.3*	90.0	*91.3*
NH$_2$[b]	−8.3	*−7.8*	2.18	*2.80*	96.3	*98.1*	87.7	*92.2*
[NCb°Ph]$^-$[c]	−12.6	*−13.6*	1.72	*2.08*	129.5	*125.4*	89.8	*95.5*
MeCb°X								
H [40]	−1.7	*0.0*	2.31	*3.05*	61.5	*58.6*	70.4	*70.5*
NO	−2.4	*0.4*	2.50	*3.29*	111.4	*120.2*	73.3	*74.6*
N=NPh	−4.2	*−2.6*	2.40	*3.07*	95.7	*97.9*	73.9	*73.8*
NHOH[a]	−6.1	*−5.8*	2.24	*2.83*	94.5	*96.6*	78.6	*81.8*
NHCb°Me	−6.4	*−6.0*	2.22	*2.78*	90.9	*93.0*	81.8	*84.0*
NHNHPh[b]	−7.1	*−6.5*	2.16	*2.81*	96.7	*98.9*	80.9	*82.2*
NH$_2$[b]	−9.4	*−8.4*	1.98	*2.90*	91.1	*92.5*	78.9	*81.0*
[NCb°Me]$^-$[c]	−13.7	*−14.4*	1.59	*1.99*	120.0	*119.1*	87.0	*90.8*

[a] Computed shifts for sp^3 geometry.
[b] Computed shifts averaged for both sp^2 and sp^3 geometries.
[c] Observed values in CD_3CN.

The antipodal shift increases as π-bonding increases, displayed by the graph of the B12 shift vs experimental C–N bond lengths (Fig. 10). This is in agreement with previous work showing that such shifts are related to electron donation to the cluster. Hence the ^{11}B NMR data give an indication of degree of *exo* π-bonding and this can be used to assess such effects in compounds which have not been structurally characterised.

The shifts of the BH protons revealed by ^{1}H{^{11}B} NMR can be assigned using ^{1}H–^{11}B HETCOR or ^{1}H{^{11}B selective} experiments. The ^{1}H shifts of the hydrogen atoms bonded to the antipodal boron show the same relationship with the C–N bond length as the ^{11}B shifts of B12, decreasing frequency of the antipodal hydrogen with increased π-bonding to the cage suggesting increased shielding. The ^{13}C shifts of the cage carbon atoms C1 and C2, however, are

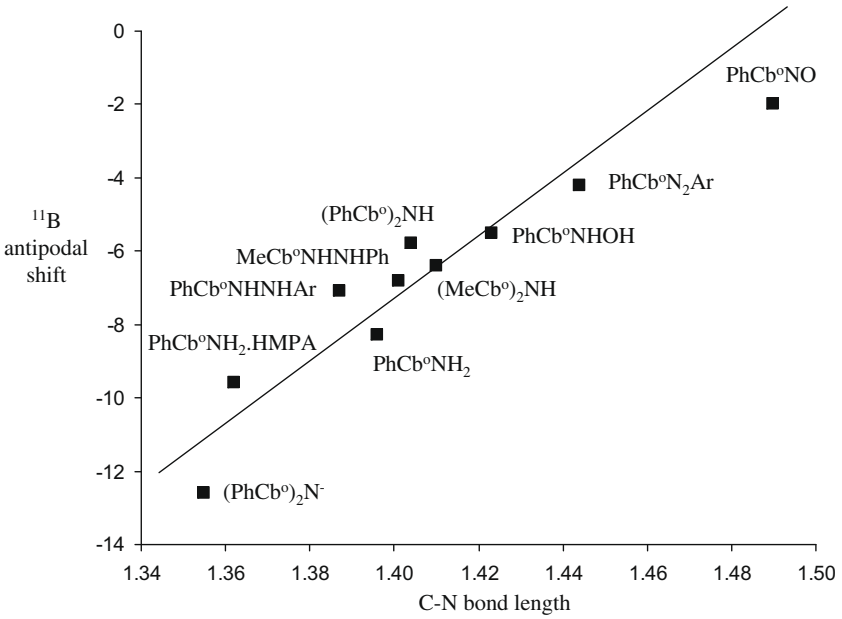


Fig. 10. Correlation between the observed ^{11}B shift of B12 (ppm) and the experimental C(1)–N(1) bond length (Å).

not simply related to the *exo*-C–N π-bonding effects. Calculated NMR chemical shifts on MP2-optimised geometries are in very good agreement with observed shifts and trends as shown in Table 7.

3. Conclusions

In this paper we have reported the crystallographically derived molecular structures and ^{11}B, ^{13}C and ^{1}H NMR spectra of four new *ortho*-carboranyl-nitrogen compounds PhCb^{o}N=N(*p*-tolyl) (**1**), PhCb^{o}NHNH(*p*-tolyl) (**2**), MeCb^{o}NHNHPh (**3**) and PhCb^{o}NHOH (**4**) (Cb^o = 1,2-$C_2B_{10}H_{10}$). Together with other carboranyl-nitrogen systems RCb^{o}X reported earlier, these provide a useful data bank from which the general structural, bonding and NMR characteristics of such systems can be discerned. Their structures show how dative *exo*-C=N *p*-bonding from the substituent to the cage is reflected in shortening of the *exo*-C–N bond (as it gains multiple character) and lengthening of the cage C1–C2 bond (as it loses bond order) to an extent that reflects the π-donor power of the substituent, the orientation of the CN group and the sp^2 or sp^3 character of the nitrogen atom for the NHR″ group, which are seen from computational studies to be important. The ^{11}B NMR chemical shift of the boron atom antipodal to the substituent also provides a guide to the π-donor power of X.

4. Experimental

All air-sensitive manipulations were carried out under dry, oxygen-free N_2. Stirring refers to use of a magnetic stirrer. Hexanes were distilled over Na. 1,2-Dimethoxyethane (DME) was dried by reflux and distillation over potassium; ether refers to diethyl ether dried, where appropriate, over sodium. Ether solutions were dried over magnesium sulfate and evaporated near room temperature. 1-Methyl-*ortho*-carborane [41] and 1-phenyl-*ortho*-carborane [42] were prepared by literature methods and dried by sublimation at 0.01 mm Hg. 1-Nitroso-2-methyl-*ortho*-carborane and 1-nitroso-2-phenyl-*ortho*-carborane were made as described elsewhere [14]. Benzenediazonium tetrafluoroborate and 4-methylbenzenediazonium tetrafluoroborate salts were made using a general literature method [43].

Melting points were measured in capillary tubes with an Electrothermal 9200 heating block. Infrared spectra were recorded from KBr discs on Perkin–Elmer 1600 series FTIR or Perkin–Elmer 1720X FTIR spectrometers and ultraviolet spectra with a Shimadzu UV 1201. Elemental carbon, hydrogen and nitrogen analyses were performed using Exeter Analytical CE-440 or Carlo Erba Strumentazione EA Model 1106 instruments. Mass spectra (MS) were recorded on a VG Micromass 7070E instrument under EI conditions at 70 eV. Values of M show the isotope range $^{10}B_n$ to $^{11}B_n$ including a ^{13}C contribution if observed. NMR spectra were measured using Varian Unity-300 (^{1}H, ^{11}B, ^{13}C), Bruker AM250 (^{1}H, ^{13}C), Bruker Avance 400 (^{1}H, ^{11}B, ^{13}C) and/or Varian Inova 500 (^{1}H, ^{11}B) instruments. All chemical shifts are reported in δ (ppm) and coupling constants in Hz. ^{1}H NMR spectra were referenced to residual protio impurity in the solvent ($CDCl_3$, 7.26 ppm). ^{13}C NMR spectra were referenced to the solvent resonance ($CDCl_3$, 77.0 ppm). ^{11}B NMR spectra were referenced externally to $Et_2O{\cdot}BF_3$, δ = 0.0 ppm. Peak assignments of cage boron and hydrogen atoms were determined with the aid of 2D ^{11}B{^{1}H}–^{11}B{^{1}H} COSY, selective ^{1}H{^{11}B} and ^{1}H–^{11}B correlation spectra.

4.1. Preparation of azocarboranes (modification of a reported [17] method)

A solution of the substituted lithiocarborane was prepared by the addition of butyllithium (5.05 ml, 2.5 M in hexanes) to a solution of the starting carborane (0.0127 mol) in diethyl ether (100 ml) at 0 °C. The solution was warmed to ambient temperature with stirring for 30 min. The diazonium salt was added as a solid over a period of 30 min and stirred overnight to give a cloudy red solution. Water was added and the organic layer was separated and washed with water. The organic layer was dried and evaporated to leave a brown residue. This was recrystallised from hexane to give orange crystals of the azocarborane.

1-Methyl-2-phenylazo-*ortho*-carborane, 1.78 g (50%), M.p. 122.5–123.5 °C (lit. [17] 121–122 °C). *Anal.* Calc. for $C_9H_{18}B_{10}N_2$: C, 41.2; H, 6.9; N, 10.7. Found: C, 41.1; H, 7.0; N, 10.6%. IR ν_{max} (KBr) [cm^{-1}]: 3062w (aryl CH), 2926w (methyl CH), 2640m, 2615s, 2582s, 2574s, 2550s (BH), 1497s, 1451s, 1205s, 1157s, 1072s, 1019s, 768s, 728s, 683s, 419s. ^{1}H{^{11}B} NMR ($CDCl_3$), δ:

7.81 (d, 2H, *ortho*-phenyl CH), 7.58 (t, 1H, *para*-phenyl CH), 7.52 (d, 2H, *meta*-phenyl CH), 2.50 (s, 2H, H8,10), 2.40 (s, 5H, BH including H12), 2.30 (s, 3H, CH_3), 2.20 (s, 3H, BH); $^{11}B\{^1H\}$ NMR ($CDCl_3$), δ: −4.2 (1B, B12), −6.4 (1B, B9), −10.6 (8B); ^{13}C NMR ($CDCl_3$), δ: 151.2 (C_6H_5 *ipso*), 133.5 (d of t, $^1J_{CH}$ 161 Hz, $^2J_{CH}$ 8 Hz, C_6H_5 *para*), 129.4 (d of d, $^1J_{CH}$ 161 Hz, $^2J_{CH}$ 8 Hz, C_6H_5 *ortho*), 123.6 (d of t, $^1J_{CH}$ 161 Hz, $^2J_{CH}$ 6 Hz, C_6H_5 *meta*), 95.7 (C1), 73.9 (C2), 22.5 (q, $^1J_{CH}$ 132 Hz, CH_3).

1-Phenyl-2-(4-methylphenyl)azo-*ortho*-carborane, 2.77 g (82%), M.p. 90–91 °C. *Anal.* Calc. for $C_{15}H_{22}B_{10}N_2$: C, 53.3; H, 6.5; N, 8.3. Found: C, 53.1; H, 6.8; N, 8.1%. MS (EI$^+$, *m*/*z*) 91 (C_6H_4Me); 216–221 [PhCb]$^+$; IR ν_{max} (KBr) [cm^{-1}]: 3052w (aryl CH), 2922w (methyl CH), 2642m, 2603s, 2566s (BH), 1600s, 1500s, 1489s, 1472s, 1446s, 1157s, 1071s, 1026s, 827s, 810s, 802s, 752s, 688s. $^1H\{^{11}B\}$ NMR ($CDCl_3$), δ: 7.70 (d, 2H, *ortho* C_6H_5), 7.42 (t, $^3J_{HH}$ 8 Hz, 1H, *para* C_6H_5), 7.34 (t, $^3J_{HH}$ 8 Hz, 2H, *meta* C_6H_5), 7.35 (d, $^3J_{HH}$ 8 Hz, 2H, *meta* C_6H_4Me), 7.17 (d, $^3J_{HH}$ 8 Hz, 2H, *ortho* C_6H_4Me), 3.00 (s, 2H, BH), 2.63 (s, 2H, BH), 2.57 (s, 3H, BH), 2.44 (s, 1H, BH), 2.37 (s, 3H, CH_3), 2.34 (s, 2H, H9,12); $^{11}B\{^1H\}$ NMR ($CDCl_3$), δ: −4.2 (2B, B9,12), −11.0 (8B); ^{13}C NMR ($CDCl_3$), δ: 149.1 (C–N), 144.4 (*C*–CH_3), 131.1 (*ortho* C_6H_5), 130.5 (*ipso* C_6H_5), 130.2 (*para* C_6H_5), 129.8, 128.2 (aryl CH); 123.5 (*C*HCN), 98.8 (C1), 81.7 (C2), 21.6 (CH_3).

4.2. Preparation of hydrazocarboranes

Lithium aluminium hydride, $LiAlH_4$, (0.3 g, 8 mmol), was added to a solution of 1-methyl-2-phenylazo-*ortho*-carborane (0.50 g, 1.91 mmol) in diethyl ether (20 ml) and the mixture stirred for 20 h. Wet diethyl ether was added, followed by water (10 ml) and dilute HCl until the cloudy solution became clear. The organic layer was washed with water (2 × 50 ml), dried and evaporated to leave a pale yellow solid. This was recrystallised from hot hexane to yield colourless crystals of 1-methyl-2-phenylhydrazo-*ortho*-carborane (0.41 g, 82%). M.p. 142–144 °C (lit. [17] 143–144 °C). *Anal.* Calc. for $C_9H_{20}B_{10}N_2$: C, 40.9; H, 7.6; N, 10.3. Found: C, 40.7; H, 7.8; N, 10.3%. MS (EI$^+$, *m*/*z*) [M]$^+$ 260–267; 264 (100); IR ν_{max} (KBr) [cm^{-1}]: 3360, 3322 (NH), 3125 (phenyl CH), 2933 (methyl CH), 2615s, 2580s, 2559s (BH), 1601, 1497, 1454m, 1251m, 1019m, 754s, 696 m. $^1H\{^{11}B\}$ NMR ($CDCl_3$), δ: 7.24 (t, $^3J_{HH}$ 7 Hz, 2H, *meta* C_6H_5), 6.90 (t, $^3J_{HH}$ 7 Hz, 1H, *para* C_6H_5), 6.85 (d, $^3J_{HH}$ 8 Hz, 2H, *ortho* C_6H_5), 5.68 (s, 1H, NH), 4.89 (s, 1H, NH), 2.52 (s, 2H, H8,10), 2.23 (s, 3H, BH), 2.16 (s, 3H, BH), 2.09 (s, 3H, CH_3), 2.05 (s, 2H, BH); $^{11}B\{^1H\}$ NMR ($CDCl_3$), δ: −6.1 (1B, B9), −7.1 (1B, B12), −11.0 (4B), −11.8 (4B); ^{13}C NMR ($CDCl_3$), δ: 147.3 (C_6H_5 *ipso*), 129.3 (d, $^1J_{CH}$ 158 Hz, C_6H_5), 121.0 (d, $^1J_{CH}$ 160 Hz, C_6H_5), 113.0 (d of t, $^1J_{CH}$ 156 Hz, C_6H_5), 96.7 (C1), 80.9 (C2), 22.1 (q, $^1J_{CH}$ 130 Hz, CH_3).

The compound 1-phenyl-2-(4-methylphenyl)azo-*ortho*-carborane (0.73 g) was dissolved in 20 ml of ethanol. Zinc dust (3.5 g) was added and 20 ml conc HCl added dropwise. The solution was stirred overnight, becoming colourless. It was poured into water (200 ml), giving a white precipitate. The solid was extracted with diethyl ether (3 × 50 ml). The organic layer was washed with water, dried and evaporated. The residue was recrystallised from hexane to give pale yellow crystals of 1-phenyl-2-(4-methylphenyl)hydrazo-*ortho*-carborane (0.65 g, 89%). M.p. 148–149.5 °C. *Anal.* Calc. for $C_{15}H_{24}B_{10}N_2$: C, 52.8; H, 7.0; N, 8.2. Found: C, 53.0; H, 7.0; N, 8.1%. MS (EI$^+$, *m*/*z*) [M]$^+$ 336–343; 340 (100); IR ν_{max} (KBr) [cm^{-1}]: 3312s (NH), 3120, 3105 (aryl CH), 2950 (methyl CH), 2663s, 2628s, 2550s (BH), 1514s, 1262m, 814s, 689s. $^1H\{^{11}B\}$ NMR ($CDCl_3$), δ: 7.69 (d, $^3J_{HH}$ 8 Hz, 2H, *ortho* C_6H_5), 7.53 (t, $^3J_{HH}$ 8 Hz, 1H, *para* C_6H_5), 7.40 (t, $^3J_{HH}$ 8 Hz, 2H, *meta* C_6H_5), 6.82 (d, $^3J_{HH}$ 8 Hz, 2H, *meta* C_6H_4Me), 6.17 (d, $^3J_{HH}$ 8 Hz, 2H, *ortho* C_6H_4Me), 5.28 (br,s, 1H, NH), 4.83 (s, 1H, N*H*Ar), 2.83 (s, 2H, H3,6), 2.59 (s, 2H, BH), 2.41 (s, 3H, BH incl H9), 2.32 (s, 1H, H12), 2.21 (s, 3H, CH_3), 2.14 (s, 2H, H8,10); $^{11}B\{^1H\}$ NMR ($CDCl_3$), δ: −3.9 (1B, B9), −6.8 (1B, B12), −10.6 (4B), −12.6 (4B); $^{13}C\{^1H\}$ NMR ($CDCl_3$), δ: 144.9 (*C*–CH_3), 131.8, 129.5, 128.8 (aryl CH); 131.0 (*ipso* C_6H_5), 130.5 (*para* C_6H_5), 130.1 (C–N), 112.5 (*C*HCN), 102.3 (C1), 90.0 (C2), 20.4 (CH_3).

4.3. Preparation of carboranylhydroxylamines

The methyl nitrosocarborane (0.22 g) was dissolved in 10 ml of *p*-dioxane, 5% Pd/C (40 mg) added and the solution degassed by a freeze-pump–thaw process. Hydrogen was admitted and its uptake measured using a standard hydrogenation apparatus. Twenty-five milliliters of hydrogen was consumed over a period of 6 h. The solution was filtered and evaporated to leave a white solid (210 mg, 95%), M.p. 253–255 °C (lit. [19] 256–258 °C). *Anal.* Calc. for $C_{15}H_{24}B_{10}N_2$: C, 19.1; H, 7.9; N, 7.4. Found: C, 19.4; H, 8.1; N, 6.2%. MS (EI$^+$, *m*/*z*) [M]$^+$ 185–192; 189 (100); IR ν_{max} (KBr) [cm^{-1}]: 3340, 3290 (NH,OH), 2914 (methyl CH), 2579s (BH), 1254s, 1116s, 1080m, 870s. $^1H\{^{11}B\}$ NMR ($CDCl_3$), δ: 5.94 (s, 1H, NH), 5.39 (s, 1H, OH), 2.46 (s, 2H, H3,6), 2.24 (s, 3H, BH), 2.22 (s, 1H, BH), 2.18 (s, 2H, BH), 2.05 (s, 2H, H8,10), 2.02 (s, 3H, CH_3); $^{11}B\{^1H\}$ NMR ($CDCl_3$), δ: −6.1 (2B, B9,12), −10.9 (4B), −11.7 (4B); $^{13}C\{^1H\}$ NMR ($CDCl_3$), δ: 94.5 (C1), 78.6 (C2), 21.6 (CH_3).

A larger-scale preparation was used for the phenyl analogue to afford 3.37 g (87%) from 3.86 g of the nitroso compound, M.p. 95–96 °C, (lit. [18] 98–99 °C). *Anal.* Calc. for $C_{15}H_{24}B_{10}N_2$: C, 38.2; H, 7.2; N, 5.4. Found: C, 38.3; H, 6.8; N, 5.6%. MS (EI$^+$, *m*/*z*) [M]$^+$ 247–255; 251 (100); IR ν_{max} (KBr) [cm^{-1}]: 3532, 3463, 3280 (NH,OH), 3061 (phenyl CH), 2574s (BH), 1493m, 1446s, 1071s, 1003s, 689s. $^1H\{^{11}B\}$ NMR ($CDCl_3$), δ: 7.70 (d, 2H, *ortho* C_6H_5), 7.47 (t, 1H, *para* C_6H_5), 7.40 (t, 2H, *meta* C_6H_5), 5.69 (s, 1H, NH), 5.09 (s, 1H, OH), 2.83 (s, 2H, H3,6), 2.53 (s, 2H, BH), 2.42 (s, 3H, BH), 2.38 (s, 1H, H12), 2.17 (s, 2H, H8,10); $^{11}B\{^1H\}$ NMR ($CDCl_3$), δ: −3.8 (1B, B9), −5.7 (1B, B12), −10.6 (4B), −12.1 (4B); $^{13}C\{^1H\}$ NMR ($CDCl_3$), δ: 131.3, 130.8 (para C), 130.0 (ipso C), 129.1, 98.4 (C1), 86.5 (C2).

4.4. Preparation of methyl-ortho-carboranyl amine

The compound 1-nitroso-2-methyl-*ortho*-carborane (1.50 g) was dissolved in dimethoxyethane (25 ml) and tin powder (1.50 g) was added. Concentrated HCl (25 ml) was added dropwise and the solution stirred for 15 min, after which time the blue colour had disappeared. The solution was heated to reflux for 3 h, cooled to room temperature and diluted with diethyl ether (100 ml). The solution was washed with water (3 × 50 ml), dried and evaporated. The white residue was sublimed to yield 1-amino-2-methyl-*ortho*-carborane (1.10 g, 79%), M.p. 301–302 °C (lit. [19] 302–303 °C). *Anal.* Calc. for $C_3H_{15}B_{10}N$: C, 20.8; H, 8.7; N, 8.1. Found C, 20.9; H, 9.0; N, 7.1%. MS (EI): M, 169–176 ($C_3H_{15}B_{10}N$ = 173). I.R. (cm^{-1}): 3306, 3219br (NH), 2939w (methyl CH), 2671s, 2634s, 2602s, 2580s (BH), 1491m, 1451m, 1221m, 1079s, 1026m, 1002m, 864m, 809m, 764s, 700s. $^1H\{^{11}B\}$ NMR ($CDCl_3$): 3.00 (2H, s, H4,5), 2.99 (2H, NH_2), 2.41 (2H, H7,11), 2.20 (1H, H9), 2.04 (3H, CH_3), 2.02 (2H, H3,6), 1.98 (1H, H12), 1.95 (2H, H8,10), ^{11}B NMR ($CDCl_3$): −5.5 (1B, d, B9), −9.4 (1B, d, B12), −9.8 (2B, d, B4,5), −10.6 (4B, d, B3,6,7,11), −12.5 (2B, d, B8,10). $^{13}C\{^1H\}$ NMR ($CDCl_3$): 91.1 (C1), 78.9 (C2), 21.1 (CH_3).

4.5. Crystal structure determinations

Crystals of the compounds **1**–**4** were examined on Bruker SMART (**3**) and Stoe STADI4 (**1**, **2**, **4**) diffractometers with Mo Kα radiation (λ = 0.71073 Å; Cu Kα with λ = 1.54184 Å for **1**) at 160 K. Crystal data and other information are given in Table 8. Standard methods and software were employed, including refine-

Table 8
Crystal data and refinement information for compounds **1**–**4**.

Compound	**1**	**2**	**3**	**4**
Formula	$C_{15}H_{22}B_{10}N_2$	$C_{15}H_{24}B_{10}N_2$	$C_9H_{20}B_{10}N_2$	$C_8H_{17}B_{10}NO{\cdot}½C_4H_8O_2$
M	338.5	340.5	264.4	295.38
Crystal system	monoclinic	monoclinic	monoclinic	monoclinic
Space group	*C*2/*c*	$P2_1/c$	$P2_1/n$	$P2_1/c$
a (Å)	28.695(6)	11.753(6)	8.6912(11)	12.394(1)
b (Å)	7.071(2)	7.617(4)	15.568(2)	6.714(1)
c (Å)	19.008(5)	21.899(13)	11.5680(15)	19.498(2)
β (°)	96.34(3)	104.74(6)	96.576(3)	94.30(2)
V (Å^3)	3833.2(17)	1895.9(18)	1554.9(3)	1617.9(3)
Z	8	4	4	4
Data collected	6424	4051	8134	4131
Unique data	2992	3329	3099	2846
R_{int}	0.046	0.049	0.056	0.031
Refined parameters	246	252	271	217
R (on *F*, $F^2 > 2\sigma$)	0.053	0.049	0.049	0.048
R_w (on F^2, all data)	0.154	0.137	0.126	0.134
Minimum, maximum electron density (e Å^{-3})	0.25, −0.23	0.24, −0.21	0.23, −0.20	0.25, −0.21

ment on all F^2 values [44]; no absorption corrections were applied, and no structural disorder was found.

5. Computational

AM1 [45,46] calculations were carried out on crystallographically determined geometries using MOPAC2002 (Version 2.40) within the CACHE 6.1 program for Windows [47]. *Ab initio* computations were carried out with the GAUSSIAN 03 package [48]. All model geometries of HCb^{o}X and PhX with fixed torsion angles for C2–C1–N–R/X listed in Tables 4 and 5, respectively, were optimised initially at the HF/6-31G* level of theory followed by the MP2/6-31G* level of theory. The geometries of PhCb^{o}X and MeCb^{o}X listed in Table 6 were optimised at the HF/6-31G* level of theory either with no symmetry constraints (and confirmed by frequency calculations to be a true minimum) or with the nitrogen atom N1 constrained to a planar configuration. These geometries were then optimised at the MP2/6-31G* level of theory.

Calculated NMR shifts at the GIAO-B3LYP/6-311G* level were obtained from these MP2-optimised geometries. Theoretical ^{11}B chemical shifts at the GIAO-B3LYP/6-311G*//MP2/6-31G* level were referenced to B_2H_6 (16.6 ppm [49]) and converted to the usual $BF_3{\cdot}OEt_2$ scale: $\delta(^{11}B) = 102.83 - \sigma(^{11}B)$. The ^{13}C and ^{1}H chemical shifts were referenced to TMS: $\delta(^{13}C) = 179.81 - \sigma(^{13}C)$; $\delta(^1H) = 32.28 - \sigma(^1H)$. Agreements between observed and calculated (B3LYP/6-311G*//MP2/6-31G* level) ^{11}B and ^{13}C NMR shifts generated from optimised geometries are generally very good for carboranes [50–54]. Agreements between observed and calculated ^{1}H NMR shifts in carboranes are often not as good due to a narrow ppm range (*ca.* 12 ppm) and substantial solvent effects on ^{1}H shift measurements [40].

Supplementary data

CCDC 704893, 704894, 704895 and 704896 contain the supplementary crystallographic data for **1**, **2**, **3** and **4**. These data can be obtained free of charge via http://www.ccdc.cam.ac.uk/conts/retrieving.html, or from the Cambridge Crystallographic Data Centre, 12 Union Road, Cambridge CB2 1EZ, UK; fax: (+44) 1223-336-033; or e-mail: deposit@ccdc.cam.ac.uk.

Acknowledgements

EPSRC is gratefully acknowledged for funding (M.A.F., R.J.P., W.C.). We thank Durham University for access to its High Performance Computing facility.

References

[1] D.A. Brown, W. Clegg, H.M. Colquhoun, J.A. Daniels, I.R. Stephenson, K. Wade, J. Chem. Soc., Chem. Commun. (1987) 889.
[2] R. Coult, M.A. Fox, W.R. Gill, K. Wade, W. Clegg, Polyhedron 11 (1992) 2717.
[3] R. Kivekäs, R. Sillanpää, F. Teixidor, C. Viñas, R. Nuñez, Acta Crystallogr., Sect. C 50 (1994) 2027.
[4] R. Kivekäs, R. Sillanpää, F. Teixidor, C. Viñas, R. Nuñez, Acta Crystallogr., Sect. C 51 (1995) 1864.
[5] R. Kivekäs, F. Teixidor, C. Viñas, R. Nuñez, Acta Crystallogr., Sect. C 51 (1995) 1868.
[6] J.M. Oliva, C. Viñas, J. Mol. Struct. 556 (2000) 33.
[7] J. Llop, C. Viñas, J.M. Oliva, F. Teixidor, M.A. Flores, R. Kivekäs, R. Sillanpää, J. Organomet. Chem. 657 (2002) 232.
[8] L.A. Boyd, W. Clegg, R.C.B. Copley, M.G. Davidson, M.A. Fox, T.G. Hibbert, J.A.K. Howard, A. Mackinnon, R.J. Peace, K. Wade, Dalton Trans. (2004) 2786.
[9] J.M. Oliva, N.L. Allan, P.v.R. Schleyer, C. Viñas, F. Teixidor, J. Am. Chem. Soc. 127 (2005) 13547.
[10] A.I. Yanovskii, Y.T. Struchkov, V.N. Kalinin, A.V. Usatov, L.I. Zakharkin, Koord. Khim. 8 (1982) 240.
[11] J.F. Valliant, O.O. Sogbein, P. Morel, P. Schaffer, K.J. Guenther, A.D. Bain, Inorg. Chem. 41 (2002) 2731.
[12] M.A. Fox, A.K. Hughes, Coord. Chem. Rev. 248 (2004) 457.
[13] L. Deng, H.S. Chan, Z. Xie, J. Am. Chem. Soc. 127 (2005) 13774.
[14] M.A. Fox, J.A.H. MacBride, R.J. Peace, W. Clegg, M.R.J. Elsegood, K. Wade, Polyhedron 28 (2009) 789.
[15] M.A. Fox, J.A.H. MacBride, R.J. Peace, K. Wade, J. Chem. Soc., Dalton Trans. (1998) 401.
[16] L.A. Boyd, H.M. Colquhoun, M.G. Davidson, M.A. Fox, W.R. Gill, P.L. Herbertson, T.G. Hibbert, J.A.H. MacBride, R.J. Peace, G.P. Rivers, K. Wade, Spec. Publ. R. Soc. Chem. 201 (1997) 289.
[17] V.N. Kalinin, G.G. Zhigareva, L.I. Zakharkin, Synth. Inorg. Met.-Org. Chem. 2 (1972) 105.
[18] L.I. Zakharkin, V.N. Kalinin, Dokl. Akad. Nauk SSSR 164 (1965) 577.
[19] L.I. Zakharkin, G.G. Zhigareva, Zh. Obshch. Khim. 45 (1975) 1293.
[20] E.S. Alekseyeva, M.A. Fox, J.A.K. Howard, J.A.H. MacBride, K. Wade, Appl. Organomet. Chem. 17 (2003) 499.
[21] M. Tsuji, J. Org. Chem. 69 (2004) 4063.
[22] I.V. Glukhov, K.A. Lyssenko, A.A. Korlyukov, M.Y. Antipin, Faraday Discuss. 135 (2007) 203.
[23] I.V. Glukhov, M.Y. Antipin, K.A. Lyssenko, Eur. J. Inorg. Chem. 7 (2004) 1379.
[24] ZG. Lewis, A.J. Welch, Acta Crystallogr., Sect. C 49 (1993) 705.
[25] T.D. McGrath, A.J. Welch, Acta Crystallogr., Sect. C 51 (1995) 646.
[26] R.L. Thomas, G.M. Rosair, A.J. Welch, Acta Crystallogr., Sect. C 52 (1996) 1024.
[27] I.V. Glukhov, K.A. Lyssenko, A.A. Korlyukov, M.Y. Antipin, Russ. Chem. Bull. 54 (2005) 547.
[28] D. Hnyk, J. Holub, M. Hofmann, P.v.R. Schleyer, H.E. Robertson, D.W.H. Rankin, J. Chem. Soc., Dalton Trans. (2000) 4617.
[29] D. Hnyk, D.W.H. Rankin, Dalton Trans. (2009) 585.
[30] M.A. Fox, R. Greatrex, A. Nikrahi, P.T. Brain, M.J. Picton, D.W.H. Rankin, H.E. Robertson, M. Bühl, L. Li, R.A. Beaudet, Inorg. Chem. 37 (1998) 2166.
[31] M. Buhl, P.v.R. Schleyer, J. Am. Chem. Soc. 114 (1992) 477.
[32] M.A. Fox, A.E. Goeta, A.K. Hughes, A.L. Johnson, J. Chem. Soc., Dalton Trans (2002) 2132.
[33] D.A. Fletcher, B.G. Gowenlock, K.G. Orrell, J. Chem. Soc., Perkin Trans. 2 (1998) 798.
[34] M. Barfield, P. Fagerness, J. Am. Chem. Soc. 119 (1997) 8699.
[35] S. Heřmánek, J. Plešek, V. Gregor, B. Štibr, J. Chem. Soc., Chem. Commun. (1977) 561.
[36] S. Heřmánek, D. Hnyk, Z. Havlas, J. Chem. Soc., Chem. Commun. (1989) 1859.

[37] M. Bühl, P.v.R. Schleyer, Z. Havlas, D. Hnyk, S. Heřmánek, Inorg. Chem. 30 (1991) 3107.
[38] S. Heřmánek, Chem. Rev. 92 (1992) 325.
[39] S. Heřmánek, Inorg. Chim. Acta 289 (1999) 20.
[40] E.S. Alekseyeva, A.S. Batsanov, L.A. Boyd, M.A. Fox, T.G. Hibbert, J.A.K. Howard, J.A.H. MacBride, A. Mackinnon, K. Wade, Dalton Trans. (2003) 475.
[41] M.F. Hawthorne, T.D. Andrews, P.M. Garrett, E.P. Olsen, M. Reintjes, F.N. Tebbe, L.F. Warren, P.A. Wegner, D.C. Young, Inorg. Synth. 10 (1967) 91.
[42] P.T. Brain, J. Cowie, D.J. Donohoe, D. Hnyk, D.W.H. Rankin, D. Reed, B.D. Reid, H.E. Robertson, A.J. Welch, M. Hofmann, P.v.R. Schleyer, Inorg. Chem. 35 (1996) 1701.
[43] A. Roe, Organic Reactions, vol. 5, Wiley, New York, 1949.
[44] G.M. Sheldrick, Acta Crystallogr., Sect. A 64 (2008) 112.
[45] M.J.S. Dewar, E.G. Zoebisch, E.F. Healy, J.J.P. Stewart, J. Am. Chem. Soc. 107 (1985) 3902.
[46] M.J.S. Dewar, C. Jie, E.G. Zoebisch, Organometallics 7 (1988) 513.
[47] CACHE 6.1.1 for Windows, Fujitsu Ltd., Chiba, Japan, 2003.
[48] GAUSSIAN 03, Revision C.02, M.J. Frisch, G.W. Trucks, H.B. Schlegel, G.E. Scuseria, M.A. Robb, J.R. Cheeseman, J.A. Montgomery Jr., T. Vreven, K.N. Kudin, J.C. Burant, J.M. Millam, S.S. Iyengar, J. Tomasi, V. Barone, B. Mennucci, M. Cossi, G. Scalmani, N. Rega, G.A. Petersson, H. Nakatsuji, M. Hada, M. Ehara, K. Toyota, R. Fukuda, J. Hasegawa, M. Ishida, T. Nakajima, Y. Honda, O. Kitao, H. Nakai, M. Klene, X. Li, J.E. Knox, H.P. Hratchian, J.B. Cross, C. Adamo, J. Jaramillo, R. Gomperts, R.E. Stratmann, O. Yazyev, A.J. Austin, R. Cammi, C. Pomelli, J.W. Ochterski, P.Y. Ayala, K. Morokuma, G.A. Voth, P. Salvador, J.J. Dannenberg, V.G. Zakrzewski, S. Dapprich, A.D. Daniels, M.C. Strain, O. Farkas, D.K. Malick, A.D. Rabuck, K. Raghavachari, J.B. Foresman, J.V. Ortiz, Q. Cui, A.G. Baboul, S. Clifford, J. Cioslowski, B.B. Stefanov, G. Liu, A. Liashenko, P. Piskorz, I. Komaromi, R.L. Martin, D.J. Fox, T. Keith, M.A. Al-Laham, C.Y. Peng, A. Nanayakkara, M. Challacombe, P.M.W. Gill, B. Johnson, W. Chen, M.W. Wong, C. Gonzalez, J.A. Pople, GAUSSIAN, Inc., Wallingford, CT, 2004.
[49] T.P. Onak, H.L. Landesman, R.E. Williams, J. Phys. Chem. 63 (1959) 1533.
[50] M.A. Fox, A.K. Hughes, J.M. Malget, J. Chem. Soc., Dalton Trans. (2002) 3505.
[51] A.R. Turner, H.E. Robertson, K.B. Borisenko, D.W.H. Rankin, M.A. Fox, Dalton Trans. (2005) 1310.
[52] P.v.R. Schleyer, J. Gauss, M. Bühl, R. Greatrex, M.A. Fox, J. Chem. Soc., Chem. Commun. (1993) 1766.
[53] I.D. Mackie, H.E. Robertson, D.W.H. Rankin, M.A. Fox, J.M. Malget, Inorg. Chem. 43 (2004) 5387.
[54] A.S. Batsanov, M.A. Fox, A.E. Goeta, J.A.K. Howard, A.K. Hughes, J.M. Malget, J. Chem. Soc., Dalton Trans. (2002) 2624.

Polyhedron 28 (2009) 2371–2376

Contents lists available at ScienceDirect

Polyhedron

journal homepage: www.elsevier.com/locate/poly

Ni(II) complexes of stereo-isomeric hexazamacrocyclic ligands derived from 2,6-diacetylpyridine

M. del Carmen Fernández-Fernández [b], Rufina Bastida [b,*], Alejandro Macías [b], Paulo Pérez Lourido [a], Laura Valencia [a,*]

[a] Departamento de Química Inorgánica, Facultad de Química, Universidad de Vigo, 36310 Vigo, Pontevedra, Spain
[b] Departamento de Química Inorgánica, Universidad de Santiago de Compostela, Avenida de las Ciencias s/n 15782, Santiago de Compostela, La Coruña, Spain

ARTICLE INFO

Article history:
Received 18 April 2009
Accepted 30 April 2009
Available online 8 May 2009

Keywords:
Nickel(II) complex
Azamacrocyclic ligand
X-ray crystal structure

ABSTRACT

The nitrate and perchlorate Ni(II) complexes of the stereo-isomeric hexazamacrocyclic ligands L^1(3,6,14,17,23,24-hexaazatricyclo[17.3.1.18,12]tetracosa-1(23),8,10,12(24),19,21-hexaene,2,7,13,18-tetramethyl) and L^2 (3,7,15,19,25,26-hexaazatricyclo[19.3.1.19,13]hexacosa-1(25),9,11,13(26),21,23-hexaene,2,8,14,20-tetramethyl) derived from 2,6-diacetylpyridine have been synthesized and characterized by microanalysis, LSI-MS, conductivity measurements, IR, UV–Vis spectroscopy and magnetic studies. Crystal structures of $L^1{\cdot}2H_2O$ as well as of the complexes $[NiL^1](ClO_4)_2$ and $[NiL^2](NO_3)_2$ have been determined. The X-ray studies show the presence of mononuclear endomacrocyclic complexes with the metal ion coordinated to all the nitrogen donor atoms from the macrocyclic framework in a N6 core. The geometry around the metal ions can be described as distorted octahedral. The nitrate and perchlorate anions do not coordinate to the metal ions, but they are involved in intermolecular interactions through hydrogen bonds to the amine groups of the macrocyclic ligands.

© 2009 Elsevier Ltd. All rights reserved.

1. Introduction

Azamacrocyclic ligands have been extensively investigated during the past decades [1] mainly due their ability to form complexes with different metal ions or anionic species [2–6] with considerable potential in areas such as catalysis, modelling of metalloenzyme activity, molecular recognition [7]. The presence of pyridine groups in the macrocyclic framework offering the possibility of obtain highly stable metal complexes have been the subject of numerous investigations in recent years [8–10]. The cavity size, the rigidity and the donor type of the macrocycle is important in governing the host–guest interactions and the selectivity of metal ions [11,12].

This paper is an extension of the investigation of our research group about the structure–function relationships in the complexation behavior of transitional and post-transitional metal ions with azamacrocyclic ligands derived from 2,6-diformylpyridine or 2,6-diacetylpyridine and different diamine moieties [13–18]. In this case, we have tried to explore if the variety of the size of the macrocyclic framework can be adequate for the coordination of more than one metal ions into the macrocyclic cavity, giving rise to di- or polynuclear endomacrocyclic complexes.

In this way, we present the nitrate and perchlorate Ni(II) complexes with two different reduced hexaazamacrocycle ligands: the hexaaza 18-membered (L^1) and the hexaaza 20-membered (L^2) (Scheme 1). The intermolecular interactions through hydrogen bonds between the nitrate and perchlorate counter ions and amine groups in crystal structures are also studied.

2. Experimental

2.1. Chemical and starting materials

2,6-Diacetylpyridine, 1,2-ethanediamine, 1,3-diaminepropane, barium(II) chloride dihydrated and nickel(II) hydrated nitrate and perchlorate salts were commercial products obtained from Alfa and Aldrich, and were used without further purifications. The solvents used were of reagent grade and purified by usual methods.

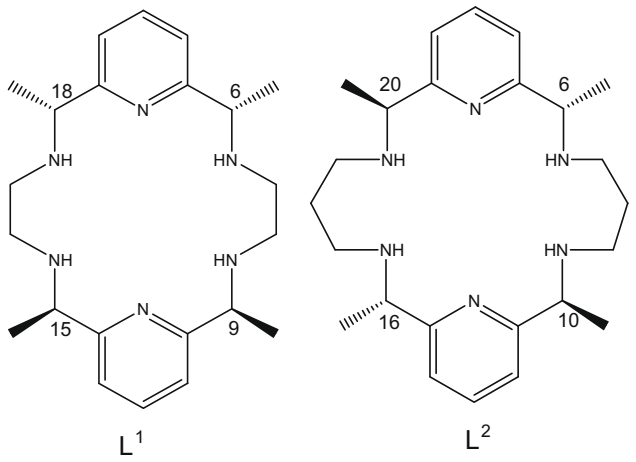
Caution: Although no problems were encountered during the course of this work, attention is drawn to the potentially explosive nature of perchlorates.

2.2. Synthesis of macrocyclic ligands

The ligands L^1 and L^2 were obtained following the method described previously [17,18] by sodium borohydride reduction of

* Corresponding authors. Address: Departamento de Química Inorgánica, Facultad de Química, As Lagoas-Marcosende, 36310 Vigo, Pontevedra, Spain. Tel.: +34 986 812607; fax: +34 986813797 (L. Valencia), Departamento de Química Inorgánica, Facultad de Química, Avenida de las Ciencias s/n, 15782 Santiago de Compostela (La Coruña), Spain. Tel.: +34 981 591076; fax: +34 981597525 (R. Bastida).
E-mail addresses: qibastid@usc.es (R. Bastida), qilaura@uvigo.es (L. Valencia).

0277-5387/$ - see front matter © 2009 Elsevier Ltd. All rights reserved.
doi:10.1016/j.poly.2009.04.042



Scheme 1.

the result of a barium(II) template condensation of 2,6-diacetylpyridine and 1,2-ethanediamine (L^1) or 1,3-diaminepropane (L^2).

2.3. Synthesis of metal complexes – general procedure

The reactions were carried out in 1:1 metal:ligand molar ratio in all cases. The appropriate metal salt (0.25 mmol) was dissolved in acetonitrile (10 ml) and added to a stirred solution of the macrocyclic ligand (0.25 mmol) in acetonitrile (20 ml). The solution was stirred for 2 h and concentrated in a rotary evaporator until *ca.* 5–6 ml. The products obtained were filtered off, dried and recrystallized in acetonitrile.

2.3.1. $[NiL^1](NO_3)_2$

Anal. Calc. for $C_{22}H_{34}N_8O_6Ni$ (MW: 564.7): C, 46.7; H, 6.0; N, 19.8. Found: C, 46.4; H; 6.2; N, 19.6%. Yield: 57%. IR (KBr, cm^{-1}): 3234 [ν(N–H)], 1606, 1477, 1448 [ν(C=N)py and ν(C=C)], 1382 [$\nu(NO_3^-)$]. LSI-MS (m/z): 440 $[NiL^1]^{2+}$. Λ_M/Ω^{-1} cm^2 mol^{-1}(in CH_3CN): 235 (2:1). Colour: green. Magnetic moment: 3.3 B.M.

2.3.2. $[NiL^1](ClO_4)_2$

Anal. Calc. for $C_{22}H_{34}N_6O_8Cl_2Ni$ (MW: 639.7): C, 41.3; H, 5.3; N, 13.1. Found: C, 41.2; H, 5.1; N, 12.9%. Yield: 63%. IR (KBr, cm^{-1}): 3296 [ν(N–H)], 1608, 1579, 1461 [ν(C=N)py and ν(C=C)], 1100, 624 [$\nu(ClO_4^-)$]. LSI-MS (m/z): 440 $[NiL^1]^{2+}$. Λ_M/Ω^{-1} cm^2 mol^{-1}(in CH_3CN): 284 (2:1). Colour: green. Magnetic moment: 3.1 B.M.

2.3.3. $[NiL^2](NO_3)_2$

Anal. Calc. for $C_{24}H_{40}N_8O_6Ni$ (MW: 594.7): C, 48.4; H, 6.7; N, 18.8. Found: C, 48.5; H, 6.8; N, 19.0%. Yield: 73%. IR (KBr, cm^{-1}): 3215 [ν(N–H)], 1605, 1583, 1477 [ν(C=N)py and ν(C=C)], 1383 [$\nu(NO_3^-)$]. LSI-MS (m/z): 471 $[NiL^2]^{2+}$. Λ_M/Ω^{-1} cm^2 mol^{-1}(in CH_3CN): 275 (2:1). Colour: green. Magnetic moment: 3.2 B.M.

2.3.4. $[NiL^2](ClO_4)_2$

Anal. Calc. for $C_{24}H_{40}N_6O_8Cl_2Ni$ (MW: 669.7): C, 43.0; H, 6.0; N, 12.5. Found: C, 43.2; H, 6.1; N, 12.3%. Yield: 62%. IR (KBr, cm^{-1}): 3271 [ν(N–H)], 1600, 1583, 1467 [ν(C=N)py and ν(C=C)], 1089, 624 [$\nu(ClO_4^-)$]. LSI-MS (m/z): 471 $[NiL^2]^{2+}$. Λ_M/Ω^{-1} cm^2 mol^{-1}(in CH_3CN): 280 (2:1). Colour: green. Magnetic moment: 3.1 B.M.

2.4. Physical measurements

Elemental analyses were performed in a Carlo–Erba EA microanalyser. Infra-red spectra were recorded as KBr discs on a Bruker IFS-66 V spectrophotometer. LSI-MS were recorded using a Micromass Autospec spectrometer with 3-nitrobenzyl alcohol as the matrix. Conductivity measurements were carried out in 10^{-3} mol dm^{-3} acetonitrile solutions at 20 °C using a WTW LF3 conductivimeter. Solid state electronic spectra were recorded on a Hitachi 4-3200 spectrophotometer using $MgCO_3$ as reference. Magnetic studies were determined at 298 K on a vibration sample magnetometer (VSM) Digital Measurement System 1660 with a magnetic field of 5000 G.

2.5. X-ray data collection, structure determination and refinement

The details of the X-ray crystal structure solution and refinement are given in Table 1. Measurements were made on a MACH3 Enraf Nonius for $L^1{\cdot}2H_2O$ and on a Bruker SMART CCD Area Detector for $[NiL^1](ClO_4)_2$ and $[NiL^2](NO_3)_2$. All data were corrected for Lorentz and polarization effects. For $L^1{\cdot}2H_2O$ a semi-empirical absorption correction (φ-scan) was made [19], whilst an empirical absorption correction was applied for $[NiL^1](ClO_4)_2$ and $[NiL^2](NO_3)_2$ [20]. Complex scattering factors were taken from the program package SHELXTL[1]. The structures were solved by direct methods, which revealed the position of all non-hydrogen atoms. All the structures were refined on F^2 by a full-matrix least-squares procedure using anisotropic displacement parameters for all non-hydrogen atoms [21]. Hydrogen atoms were included in calculated positions and refined in riding mode for $[NiL^1](ClO_4)_2$ and located on a difference electron density map and refined with isotropic displacement parameters for $L^1{\cdot}2H_2O$ and $[NiL^2](NO_3)_2$.

3. Results and discussion

The ligands L^1 and L^2 have been obtained by reduction of the tetraiminic barium(II) complexes, giving an isomeric mixture of the corresponding saturated macrocycle. Previously, we also reported the X-ray data of the nitrate salt of the diprotonated 6S,9S,15R,18R-*meso* form of the ligand L^1 [17].

In this case, the crude isomeric mixture of the protonated ligand L^1 was treated with a water solution of NaOH, extracted with chloroform and recrystallised in acetonitrile to give crystals suitable for X-ray diffraction of the 6S,9S,15S,18S-*meso* form of the ligand, $L^1{\cdot}2H_2O$.

The molecular structure of $L^1{\cdot}2H_2O$ together with the atomic numbering scheme adopted and selected bond distances and angles are shown in Fig. 1. The X-ray data are listed in Table 1. The structure does not differ much from that previously found for $[H_2L^1](NO_3)_2{\cdot}3H_2O$.

The crystal belongs to the triclinic $P\bar{1}$ space group with bond lengths and angles falling within the normal ranges. The asymmetric unit is comprised by two independent half molecules of the ligand. As in the protonated $[H_2L^1](NO_3)_2{\cdot}3H_2O$, the macrocyclic ligand has a markedly stepped conformation and the four amine nitrogen atoms of each molecule are coplanar, but in this case the pyridine rings are parallel-dihedral angle of 28.73° in $[H_2L^1](NO_3)_2{\cdot}3H_2O^-$ and the dihedral angle between the plane containing one of the pyridine ring and the plane determined by the four aliphatic nitrogen atoms is 61.18° for one molecule and 55.96° for the other −61.2° in $[H_2L^1](NO_3)_2{\cdot}3H_2O$. No intra- or intermolecular π,π-stacking interactions between pyridine rings have been observed in the structure, but some intermolecular interactions through hydrogen bonds between amine groups and water molecules are present in the crystal lattice: [O2W–H2W···N3_$1 = 1.995(1) Å; 168.8(1)°] ($1 $-x + 1$, $-y + 1$, $-z + 1$);

[1] SHELXTL version. An integrated system for solving and refining crystal structures from diffraction data (Revision 5.1), Bruker AXS LTD.

Table 1
Crystal data and structure refinement for $L^1 \cdot 2H_2O$, $[NiL^1](ClO_4)_2$ and $[NiL^2](NO_3)_2$.

	$L^1 \cdot 2H_2O$	$[NiL^1](ClO_4)_2$	$[NiL^2](NO_3)_2$
Empirical formula	$C_{22}H_{38}N_6O_2$	$C_{22}H_{34}Cl_2NiN_6O_8$	$C_{24}H_{38}NiN_8O_6$
Formula weight	418.58	640.16	593.33
Temperature (K)	293(2)	120(2)	120(2)
Wave length (Å)	1.54184	0.71073	0.71073
Crystal system	triclinic	orthorhombic	monoclinic
Space group	$P\bar{1}$	*Aba*2	*P*21/*c*
Unit cell dimensions			
a (Å)	10.961(5)	13.780(17)	13.865(6)
b (Å)	10.952(5)	38.990(5)	14.339(7)
c (Å)	90.315(5)	15.653(19)	13.165(6)
α (°)	90.104(5)		
β (°)	10.970(5)		90.173(8)
γ (°)	111.111(5)		
Volume (Å^3)	1228.5(10)	8409(17)	2617(2)
Z	2	12	4
D_{calc} (Mg/m^3)	1.132	1.517	1.506
Absorption coefficient (mm^{-1})	0.591	0.939	0.798
F(0 0 0)	456	4008	1256
Crystal size (mm)	0.25 × 0.24 × 0.16	0.39 × 0.27 × 0.25	0.57 × 0.35 × 0.34
θ Range for data collection (°)	4.03–74.92	1.04–26.38	1.42–26.44
Index ranges	$-12 \leqslant h \leqslant 13$, $-13 \leqslant k \leqslant 0$, $-13 \leqslant l \leqslant 0$	$0 \leqslant h \leqslant 17$, $0 \leqslant k \leqslant 48$, $-19 \leqslant l \leqslant 19$	$-17 \leqslant h \leqslant 17$, $0 \leqslant k \leqslant 17$, $0 \leqslant l \leqslant 16$
Reflections collected	5349	35 307	5546
Independent reflections (R_{int})	5075 (0.0126)	8497 (0.0598)	5318 (0.0238)
Completeness to θ =	99.9% (74.92°)	99.3% (26.38°)	98.6% (26.44°)
Absorption correction	semi-empirical (φ-scan)	empirical (SADABS)	empirical (SADABS)
Maximum and minimum transmission	0.9109 and 0.8657	0.7992 and 0.7110	0.7731 and 0.6591
Refinement method	full-matrix least-squares on F^2	full-matrix least-squares on F^2	full-matrix least-squares on F^2
Data/restraints/parameters	5075/0/308	8497/1/531	5318/0/373
Goodness-of-fit on F^2	1.022	1.025	1.030
Final *R* indices [$I > 2\sigma(I)$]	$R_1 = 0.0696$, $wR_2 = 0.1866$	$R_1 = 0.0699$, $wR_2 = 0.1701$	$R_1 = 0.0495$, $wR_2 = 0.1261$
R indices (all data)	$R_1 = 0.1091$, $wR_2 = 0.2128$	$R_1 = 0.1351$, $wR_2 = 0.2151$	$R_1 = 0.0713$, $wR_2 = 0.1364$
Largest difference in peak and hole (e Å^{-3})	0.605 and −0.222	0.632 and −0.654	0.759 and −0.622

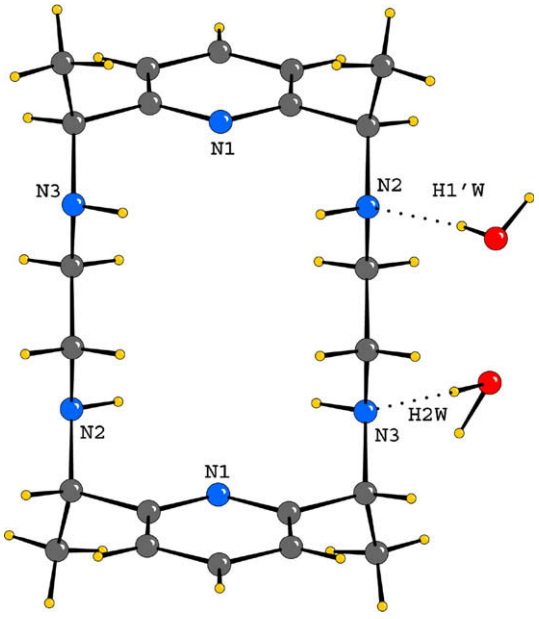


Fig. 1. Crystal structure of the ligand $L^1 \cdot 2H_2O$. Selected bond lengths (Å) and angles (°): C(12)–N(4)#1 1.342(3), C(16)–N(4) 1.345(3), C(1)–N(1)#2 1.351(3); C(5)–N(1) 1.347(3); C(6)–N(2) 1.445(4); C(7)–N(2) 1.475(3); C(9)–N(3) 1.466(3); N(1)#2–C(1)–C(2) 121.7(3); N(1)#2–C(1)–C(8) 116.1(3); N(1)–C(5)–C(4) 122.5(2); N(1)–C(5)–C(6) 115.7(3); N(2)–C(7)–C(9) 109.6(2); N(3)–C(8)–C(11) 109.9(2); N(3)–C(8)–C(1) 113.0(2); N(3)–C(9)–C(7) 109.9(2); C(6)–N(2)–C(7) 113.0(2); C(8)–N(3)–C(9) 112.7(2). Symmetry transformations used to generate equivalent atoms: #1 $-x+2,-y+1,-z+2$; #2 $-x+1,-y+2,-z+1$.

[O1W–H1W···N5_$2 = 2.080(1) Å; 167.9(1)°] ($2 $x-1$, $+y$, $+z$);
[O1W–H1'W···N2_$3 = 2.003(1) Å; 163.8(1)°] ($3 x, $+y-1$, $+z$).

The coordination ability of the hexaazamacrocyclic ligands L^1 and L^2 towards hydrated nitrate and perchlorate salts of Ni(II) in 1:1 metal:ligand molar ratio was studied.

The complexes $[NiL^1](NO_3)_2$ and $[NiL^1](ClO_4)_2$ were synthesized starting from the 6S,9S,15R,18R-*meso* form of the ligand L^1. However, $[NiL^2](NO_3)_2$ and $[NiL^2](ClO_4)_2$, were obtained starting from the isomeric mixture of L^2. All the complexes have been characterized by microanalysis, LSI-MS, conductivity measurements, IR, UV–Vis spectroscopy and magnetic studies. The complexes $[NiL^1](ClO_4)_2$ and $[NiL^2](NO_3)_2$ were also characterized by X-ray diffraction.

3.1. Crystal structures of metal complexes

By slow concentration of an acetonitrile solution of the corresponding complexes, crystals suitable for X-ray diffraction of $[NiL^1](ClO_4)_2$ and $[NiL^2](NO_3)_2$ were obtained.

One and a half structurally similar $[NiL^1]^{2+}$ cations, together with three perchlorate anions are present in the asymmetric unit of the crystal structure of $[NiL^1](ClO_4)_2$. The atomic numbering scheme adopted of one of $[NiL^1]^{2+}$ cations, together with selected bond distances and angles is shown in Fig. 2a. X-ray data are listed in Table 1.

The Ni(II) ion is sited in the middle of the macrocyclic cavity, endomacrocyclic coordinated in a distorted octahedral geometry with a N6 core arising from coordination by the six donor nitrogen atoms from the macrocyclic framework. The equatorial plane can be considered by the amine nitrogen atoms [N2–N3–N5–N6, rms 0.474, for Ni(1) and N8–N9–N8#–N9#, rms 0.478 for Ni(2)], with the Ni(II) atoms at 0.0059 and 0.0114 Å from that planes, respectively. The axial positions are occupied by the pyridine nitrogen atoms (N1 and N4 atoms for Ni1 and N7, N10 for Ni2).

The structure shows a 'twist-wrap' conformation, typical of this kind of ligand, where the macrocycle adopts a helical shape with

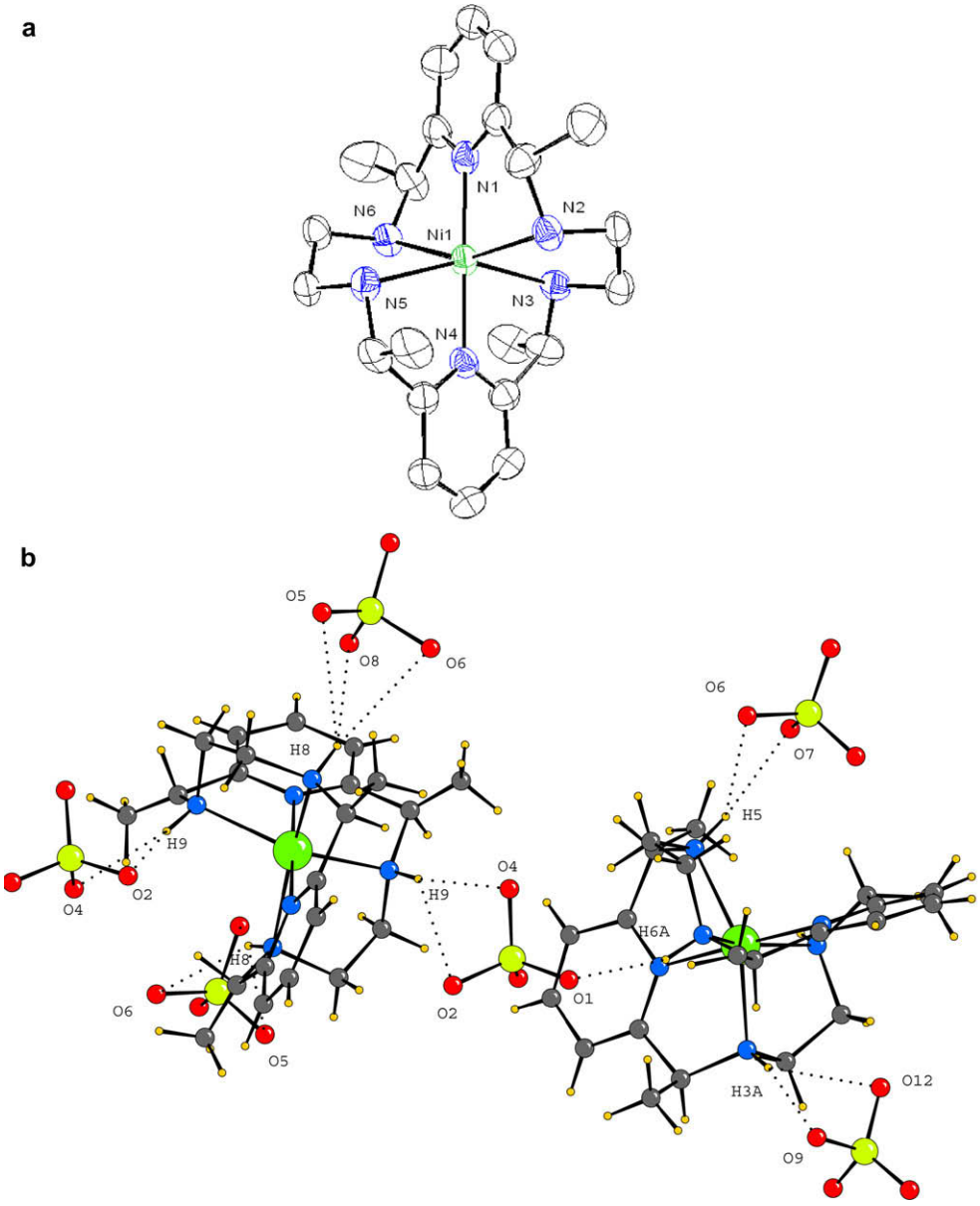


Fig. 2. (a) Crystal structure of $[NiL^1]^{2+}$ cation. Selected bond lengths (Å) and angles (°): N(1)—Ni(1) 2.016(8); N(2)—Ni(1) 2.147(7); N(3)—Ni(1) 2.144(8); N(4)—Ni(1) 2.005(8); N(5)—Ni(1) 2.171(8); N(6)—Ni(1)2.110(8); N(4)—Ni(1)—N(1) 178.5(3); N(4)—Ni(1)—N(6) 102.7(3); N(1)—Ni(1)—N(6) 76.8(3); N(4)—Ni(1)—N(3) 77.3(3); N(1)—Ni(1)—N(3) 101.4(3); N(6)—Ni(1)—N(3) 101.7(3); N(4)—Ni(1)—N(2) 102.7(3); N(1)—Ni(1)—N(2) 77.7(3); N(6)—Ni(1)—N(2) 154.6(3); N(3)—Ni(1)—N(2) 83.5(3); N(4)—Ni(1)—N(5) 77.0(3); N(1)—Ni(1)—N(5) 104.4(3); N(6)—Ni(1)—N(5) 83.6(3); N(3)—Ni(1)—N(5) 154.3(3); N(2)—Ni(1)—N(5) 102.6(3). (b) Crystal lattice structure of $[NiL^1](ClO_4)_2$ complex showing some intermolecular hydrogen bonding between perchlorate anions and amine groups.

the two pyridine rings oriented at 67.43° and 69.88° relative to each other for Ni1 and Ni2, respectively. The angle between the pyridinic nitrogen atoms and the metal ion [N1–Ni1–N4, 178.5(3)° for Ni1 and N7–Ni1–N10 180.00(9)° for Ni2], shows that the macrocycle is not folded.

The pyridine groups provide the shortest bond to the Ni(II) atoms [2.016(8) and 2.005(8) Å for Ni1; 2.006(11) and 2.046(12) Å for Ni2]. The bond lengths of the secondary amine groups are in the range 2.171(8)–2.110(8) Å for Ni1 and 2.152(8)–2.127(8) Å for Ni2, not markedly different from those reported previously with similar macrocyclic ligands [22,23]. The perchlorate ions are not coordinated to the metal centers, but they are involved in intermolecular interactions through hydrogen bonds with some of the amine groups of the macrocyclic ligand (Fig. 2b): [N5–H5···O6 = 2.918(10) Å; 126(1)°], [N5–H5···O7 = 2.207(10) Å; 173(1)°], [N8–H8···O5 = 2.822(10) Å; 124(1)°], [N8–H8···O6 = 2.741(10) Å; 153(1)°], [N8–H8···O8 = 2.485(10) Å; 151(1)°], [N9–H9···O2 = 2.984(10) Å; 141(1)°], [N9–H9···O3 = 2.843(10) Å; 127(1)°], [N9–H9···O4 = 2.324(10) Å; 167(1)°], [N6–H6A···O1 = 2.238(10) Å; 150(1)°], [N2–H2A···O10_$1 = 2.666(20) Å; 150(1)°], [N2–H2A···O11_$1 = 2.397(10) Å; 142(1)°], [N3–H3A···O12_$2 = 2.490(20) Å; 142(1)°], [N3–H3A···O9_$2 = 2.684(20) Å; 170(1)°], [N3–H3A···O10_$2 = 2.787(20) Å; 128(1)°]. $1 $x - 1, +y, +z$; $2 $-x + 1, -y + 1/2 + 1, +z - 1/2$.

The reaction between the isomer mixture of L^2 with $Ni(NO_3)_2 \cdot 6H_2O$ gave rise to adequate crystals for X-ray studies. The solution of the crystal structure reveals the presence of a Ni(II) nitrate complex of the 6R,10R,16R,20R-*meso* form of the ligand L^2. The molecular X-ray structure of $[NiL^2](NO_3)_2$ with the atomic numbering scheme adopted, together with selected bond distances and angles is shown in Fig. 3a. The details of the X-ray crystal structure solution and refinement are given in Table 1. The

asymmetric unity is consistent with the cation $[NiL^2]^{2+}$ and two well-separated nitrate anions. The X-ray analysis confirms the presence of mononuclear endomacrocyclic complex, where the metal ion is also six coordinated by all the donor nitrogen atoms from the macrocyclic backbone, in a distorted octahedral geometry. The equatorial plane can be also formed by the amine nitrogen atoms [N2–N3–N5–N6, rms 0.4131] and the distance between the nickel ion and that plane is 0.0056 Å. The axial positions are occupied by the pyridine nitrogen atoms, N1 and N4.

The structure also shows a 'twist-wrap' conformation with the two pyridine rings oriented at 88° relative to each other. The angle between the pyridinic nitrogen atoms and the metal ion [N1–Ni–N4, 178.38(14)°], shows that the macrocycle is not folded.

The pyridine groups also provide the shortest bond to the Ni atom [2.029(3) and 2.022(3) Å]. The bond lengths of the secondary amine groups vary from 2.126(4) to 2.145(3) Å, not markedly different from that described above for $[NiL^1](ClO_4)_2$. The nitrate ions are not coordinated to the metal center, but they are involved in intermolecular interactions through hydrogen bonds with the amine nitrogen atoms (Fig. 3b): [N2–H2N···O6N = 2.904(1) Å; 174(1)°], [N3–H3N···O1N = 3.057(1) Å; 156(1)°], [N3–H3N···O3N = 3.344(1) Å; 147(1)°], [N5–H5N···N2N = 3.640(1) Å; 154(1)°], [N5–H5N···O5N = 3.060(1) Å; 164(1)°], [N5–H5N···O6N = 3.486 (1) Å; 136(1)°], [N6–H6N···O3N = 2.939(1) Å; 175(1)°].

Inter- or intramolecular π,π-stacking interactions between the pyridine rings are not observed.

3.2. Spectroscopic and magnetic studies

Elemental analysis are consistent with the presence of mononuclear Ni(II) complex in all cases.

The IR spectra of the complexes (KBr discs) show that the ν(C=N) vibration band of the pyridine groups are shifted to higher wavenumber than in the free ligand suggesting the coordination to the metal atom [24]. The secondary amine stretches around 3300 cm^{-1} in the free ligands are shifted suggesting also the coordination to the metal ion. The IR spectra of the nitrate and perchlorate complexes feature absorptions attributable to ionic nitrate (1383 cm^{-1}) and perchlorate (1100 cm^{-1}). The lack of splitting of these bands indicates that there is no coordination of these groups

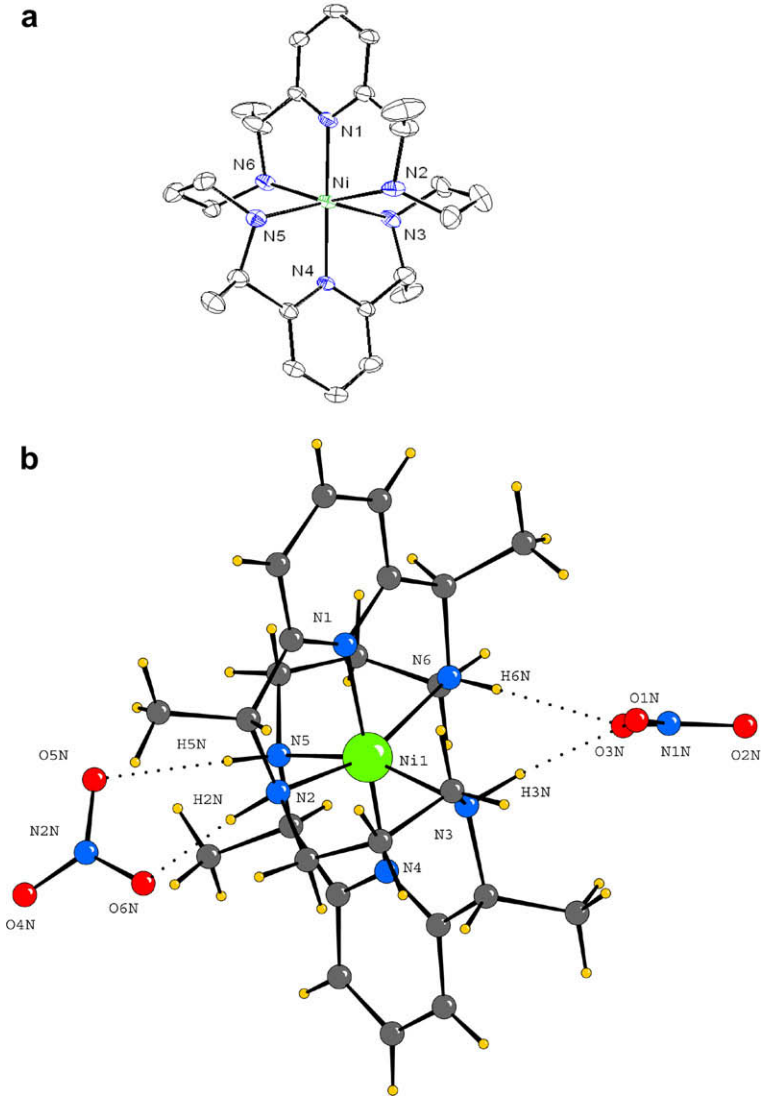


Fig. 3. (a) Crystal structure of $[NiL^2]^{2+}$ cation. Selected bond lengths (Å) and angles (°): Ni—N(4) 2.022(3); Ni—N(1) 2.029(3); Ni—N(2) 2.126(4); Ni—N(5) 2.142(3); Ni—N(6) 2.142(4); Ni—N(3) 2.145(3); N(4)—Ni—N(1) 178.38(14); N(4)—Ni—N(2) 98.70(16); N(1)—Ni—N(2) 79.90(15); N(4)—Ni—N(5) 78.89(12); N(1)—Ni—N(5) 100.36(13); N(2)—Ni—N(5) 94.22(15); N(4)—Ni—N(6) 103.26(16); N(1)—Ni—N(6) 78.14(15); N(2)—Ni—N(6) 158.04(13); N(5)—Ni—N(6) 90.30(15); N(4)—Ni—N(3) 78.65(12); N(1)—Ni—N(3) 102.12(13); N(2)—Ni—N(3) 90.38(15); N(5)—Ni—N(3) 157.51(13); N(6)—Ni—N(3) 93.62(16). (b) Crystal lattice structure of $[NiL^2](NO_3)_2$ complex showing some intermolecular hydrogen bonding between nitrate anions and amine groups.

to the metal centers as has been demonstrated by the X-ray analysis of $[NiL^1](ClO_4)_2$ and $[NiL^2](NO_3)_2$ [25,26].

Also, molar conductivity data, measured at room temperature using acetonitrile as solvent, showed the presence of ionic counterions, since they are in the range reported in that solvent for 2:1 [27].

The LSI mass spectra of the complexes show peaks according to the mononuclear nature of the complexes.

The reflectance spectra of all complexes show three bands at *ca.* 9804 (ν_1), 16502 (ν_2) and 28571 cm^{-1} (ν_3). These bands are attributable to the $^3T_{2g} \leftarrow {}^3T_{2g}$, $^3T_{1g}(F) \leftarrow {}^3T_{2g}$ and $^3T_{1g}(P) \leftarrow {}^3T_{2g}$ transitions, respectively, and are indicative of octahedral Ni(II) compounds [28,29].

The value of the room temperature magnetic moments of the compounds [3.1 – 3.3 B.M.] lies within the range usually observed for octahedral Ni(II) complexes [30].

4. Conclusion

The nitrate and perchlorate Ni(II) complexes of the potential neutral hexadentate N_6 donor macrocyclic ligands, L^1 and L^2, have been synthesized in acetonitrile. The crystal structure of $L^1{\cdot}2H_2O$ as well as of $[NiL^1](ClO_4)_2$ and $[NiL^2](NO_3)_2$ complexes have been also determined. All the complexes are mononuclear with the metal ion endomacrocyclicly coordinated by the six donor nitrogen atoms from the macrocyclic framework in a N6 core. The coordination geometry can be considered as distorted octahedral. The nitrate and perchlorate anions are no coordinated to the metal ions, but both anions are involved in intermolecular interactions through hydrogen bond with some amine groups of the ligands.

5. Supplementary data

CCDC 728059, 728060 and 728061 contain the supplementary crystallographic data for $L^1{\cdot}2H_2O$, $[NiL^1](ClO_4)_2$ and $[NiL^2](NO_3)_2$. These data can be obtained free of charge via http://www.ccdc.cam.ac.uk/conts/retrieving.html, or from the Cambridge Crystallographic Data Centre, 12 Union Road, Cambridge CB2 1EZ, UK; fax: (+44) 1223-336-033; or e-mail: deposit@ccdc.cam.ac.uk.

Acknowledgements

We thank Xunta de Galicia (PGIDIT07PXIB209039PR) and Universidade de Vigo (1Z80564102) for financial support. Intensity measurements were performed at the Unidade de Raios X. RIAIDT, University of Santiago de Compostela, Spain.

References

[1] A. Bianchi, M. Micheloni, P. Paoletti, Coord. Chem. Rev. 110 (1991) 17. and references therein.
[2] R.M. Izatt, J.S. Bradshaw, S.A. Nielsen, J.D. Lamb, J.J. Christensen, D. Sen, Chem. Rev. 85 (1985) 271.
[3] K.B. Mertes, J.M. Lehn, in: G. Wilkinson (Ed.), Comprehensive Coordination Chemistry, Pergamon, Oxford, 1987, p. 915.
[4] J.M. Lehn, Angew. Chem., Int. Ed. Engl. 27 (1988) 89.
[5] K.E. Krakowiak, J.S. Bradshaw, D.J. Zamecka-Krakowiak, Chem. Rev. 89 (1989) 929.
[6] J.S. Bradshaw, Aza-Crown Macrocycles, Wiley, New York, 1993.
[7] P. Guerriero, S. Tamburini, P.A. Vigato, Coord. Chem. Rev. 139 (1995) 17. and references therein.
[8] E.C. Constable, M.G.B. Drew, G. Forsyth, M.D. Ward, J. Chem. Soc., Chem. Commun. (1988) 1450.
[9] D.E. Fenton, R.W. Matthews, M. McPartlin, B.P. Murphy, I.J. Scowen, P.A. Tasker, J. Chem. Soc., Chem. Commun. (1994) 1391.
[10] L.H. Bryant Jr., A. Lachgar, K.S. Coates, S.C. Jackels, Inorg. Chem. 33 (1994) 2219.
[11] L.F. Lindoy, The Chemistry of Macrocyclic Ligands Complexes, Cambridge Universitu Press, Cambridge, UK, 1989.
[12] J.-M. Lehn, Supramolecular Chemistry, VCH, Weinheim, 1995.
[13] L. Valencia, J. Martínez, A. Macías, R. Bastida, R.A. Carvalho, C.F.G.C. Geraldes, Inorg. Chem. 41 (2002) 5300.
[14] S. Gonzalez, L. Valencia, R. Bastida, D.E. Fenton, A. Macias, A. Rodríguez, J. Chem. Soc., Dalton Trans. (2002) 3551.
[15] L. Valencia, R. Bastida, M. del C. Fernández-Fernández, A. Macias, M. Vicente, Inorg. Chim. Acta 25 (2005) 2618.
[16] J. Martinez-Sanchez, R. Bastida, A. Macias, P. Perez-Lourido, L. Valencia, Polyhedron 25 (2006) 3495.
[17] M. del C. Fernández-Fernández, R. Bastida, A. Macias, P. Perez-Lourido, L. Valencia, Z. Anorg. Allg. Chem. 633 (2007) 747.
[18] M. del C. Fernández-Fernández, R. Bastida, A. Macias, P. Perez-Lourido, L. Valencia, Polyhedron 26 (2007) 5317.
[19] A.C.T. North, D.C. Phillips, F.S. Mathews, Acta Crystallogr., Sect. A 42 (1986) 351.
[20] G.M. Sheldrick, SADABS, Program for Empirical Absorption Correction of Area Detector Data, University of Göttingen, Germany, 1996.
[21] G.M. Sheldrick, SHELXTL 97. Program for the Refinement of Crystal Structures, University of Göttingen, Germany, 1997.
[22] L. Branco, J. Costa, R. Delgado, M.G.B. Drew, V. Felix, B.J. Goodfellow, J. Chem. Soc., Dalton Trans. (2002) 3539.
[23] F. Li, R. Delgado, J. Costa, M.G.B. Drew, V. Felix, Dalton Trans. (2005) 82.
[24] N.S. Gill, R.H. Nuttall, D.E. Scaife, D.W. Sharp, J. Inorg. Nucl. Chem. 18 (1961) 79.
[25] M.F. Rosenthal, J. Chem. Educ. 50 (1973) 331.
[26] A.J. Hathaway, A.E. Underhill, J. Chem. Soc. (1961) 3091.
[27] W.J. Geary, Coord. Chem. Rev. 7 (1971) 81.
[28] W.J. Eilbeck, F. Holmes, A.E. Underhill, J. Chem. Soc. (A) 5 (1967) 757.
[29] J. Reedijk, T.M. Mulder, J.A. Smit, Inorg. Chim. Acta 13 (1975) 219.
[30] B.N. Figgis, Introduction to Ligand Fields, Interscience, New York, 1967.

Polyhedron 28 (2009) 2377–2384

Contents lists available at ScienceDirect

Polyhedron

journal homepage: www.elsevier.com/locate/poly

Novel rhenium(III) complexes with the picolinate ligand: Synthesis, spectroscopic investigations, X-ray structures and DFT calculations for $[ReX_2(pic)(PPh_3)_2]$ complexes

B. Machura [a,*], M. Wolff [a], R. Kruszynski [b], J. Mroziński [c], J. Kusz [d]

[a] Department of Crystallography, Institute of Chemistry, University of Silesia, 9th Szkolna St., 40-006 Katowice, Poland
[b] Department of X-ray Crystallography and Crystal Chemistry, Institute of General and Ecological Chemistry, Lodz University of Technology,116 Żeromski St., 90-924 Łódź, Poland
[c] Faculty of Chemistry, Wroclaw University, F. Joliot-Curie 14 St., 50-383 Wrocław, Poland
[d] Institute of Physics, University of Silesia, 4th Uniwersytecka St., 40-006 Katowice, Poland

ARTICLE INFO

Article history:
Received 24 March 2009
Accepted 1 May 2009
Available online 23 May 2009

Keywords:
Keywords
Rhenium complexes
Picolinate ligand
X-ray
Electronic structure
DFT calculations, magnetic measurement

ABSTRACT

The paper presents a combined experimental and computational study of novel rhenium(III) complexes with the picolinate ligand – $[ReCl_2(pic)(PPh_3)_2]$ (**1**) and $[ReBr_2(pic)(PPh_3)_2]$ (**2**). Both complexes **1** and **2** have been characterised spectroscopically and structurally (by single-crystal X-ray diffraction). Complex **1** has been additionally studied by magnetic measurement. The magnetic behavior is characteristic of a mononuclear d^4 low-spin octahedral Re(III) complex ($^3T_{1g}$ ground state) and arises because of the large spin–orbit coupling ($\zeta = 2500\ cm^{-1}$), which gives a diamagnetic ground state. DFT and time-dependent (TD)DFT calculations have been carried out for complex **1**, and UV–vis spectra of the $[ReX_2(pic)(PPh_3)_2]$ compounds have been discussed on this basis.

© 2009 Elsevier Ltd. All rights reserved.

1. Introduction

The coordination chemistry of rhenium is a field of current growing interest from various viewpoints. The attention of scientists concentrates on synthetic aspects, structural, physicochemical properties and reactivity, as well as on topics with an applied character such as the development of radiotherapeutic cancer agents, nitrogen fixation and catalysis [1]. The ^{186}Re (1.07 MeV β-emitter, $t_{1/2}$ 90 h) and ^{188}Re (2.12 MeV β-emitter, $t_{1/2}$ 17 h) isotopes are among the most attractive isotopes for applications in targeted radionuclide therapy [2,3].

Diazenido and dinitrogen rhenium complexes are important in view of their significance in the field of nitrogen fixation [4–6]. Methyltrioxorhenium is one of the most versatile catalysts for olefin oxidation reactions, aldehyde olefination and olefin metathesis [7,8]. The *mer, trans*-$[ReOCl_3(PPh_3)_2]$ and its derivatives catalyze the oxidation of sulfides to sulfoxides, thiols to disulfides and catalyze oxygen-transfer from sulfoxides to phosphines [8]. The $[ReOCl_2(O–N)(PPh_3)]$ chelates with pyridinecarboxylate ligands exhibit a remarkable catalytic activity for the conversion of ethane to a mixture of propionic and acetic acids in a single-pot process [9]. The $[CH_3ReO(pic)_2]$ complex is an active precursor in olefin oxidation and forms epoxides in a two-phase H_2O_2–H_2O/CH_2Cl_2 system [10].

Generally, chelation of nitrogenous π-acidic ligands to Re^VO facilitates the oxygen atom transfer to oxophilic substrates *via* electron withdrawal from the metal [11]. In this context, the design, synthesis and reactivity of oxorhenium complexes has become the aim of several laboratories, including ours.

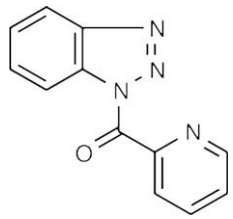
Previously, we investigated the reactivity of $[ReOX_3(EPh_3)_2]$ (X = Cl, Br; E = P or As) oxorhenium(V) species towards 1,10-phenanthroline and 5,6-diphenyl-3-(2-pyridyl)-1,2,4-trazine. The products of these reactions include both Re(V) oxocomplexes – $[ReOCl_3(phen)]$ and Re(III) compounds – $[ReCl_2(phen)(PPh_3)_2](ReO_4)\cdot\frac{1}{2}H_2O$, $[ReCl_3(OPPh_3)(dppt)]$ [12,13]. In this report we focus on the examination of the reactions of $[ReOX_3(PPh_3)_2]$ with 1-(2-pyridylcarbonyl)benzotriazole. Potentially, 1-(2-pyridylcarbonyl)benzotriazole can bind to the metal center ion *via* one of two modes: either through the two nitrogen atoms located in the pyridine and triazole rings or through one pyridyl nitrogen and the carbonyl oxygen (Scheme 1).

The reactions of $[ReOX_3(PPh_3)_2]$ with 1-(2-pyridylcarbonyl)benzotriazole lead to novel Re(III) $[ReX_2(pic)(PPh_3)_2]$ complexes (Scheme 2).

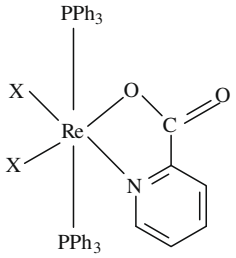
The 1-(2-pyridylcarbonyl)benzotriazole hydrolyzes in the reaction with $[ReOX_3(PPh_3)_2]$, and the formed picolinic acid coordinates to the rhenium ion. With much higher yield, however,

* Corresponding author.
E-mail addresses: basia@ich.us.edu.pl (B. Machura), rafal.kruszynski@p.lodz.pl (R. Kruszynski), jmroz@wchuwr.chem.uni.wroc.pl (J. Mroziński).

0277-5387/$ - see front matter © 2009 Elsevier Ltd. All rights reserved.
doi:10.1016/j.poly.2009.05.032



Scheme 1. Structure of 1-(2-pyridylcarbonyl)benzotriazole.



Scheme 2. Structure of $[ReCl_2(pic)(PPh_3)_2]$; X = Cl for **1** and X = Br for **2**.

$[ReCl_2(pic)(PPh_3)_2]$ (**1**) and $[ReBr_2(pic)(PPh_3)_2]$ (**2**) were isolated from the reactions of $[ReOX_3(PPh_3)_2]$ with picolinic acid in the presence of PPh_3 in ethanol.

The molecular orbital diagram of **1** has been calculated with the density functional theory (DFT) method. Currently the density functional theory (DFT) is commonly used to examine the electronic structure of transition metal complexes. It meets with the requirements of being accurate, easy to use and fast enough to allow the study of relatively large molecules of transition metal complexes [14]. The electronic spectrum of **1** has been discussed on the basis of the time-dependent DFT calculations. Recent studies have supported the TDDFT method to be applicable for open- and closed-shell 5d-metal complexes (including rhenium complexes), giving good assignments of the experimental spectra [15–17].

2. Experimental

2.1. General procedure

The reagents used in the syntheses were commercially available and were used without further purification. The $[ReOX_3(PPh_3)_2]$ complexes were prepared according to the literature methods [18]. IR spectra were recorded on a Nicolet Magna 560 spectrophotometer in the spectral range 4000–400 cm^{-1} with the samples in the form of KBr pellets. Electronic spectra were measured on a spectrophotometer Lab Alliance UV–vis 8500 in the range 1000–180 nm in acetonitrile solution. Elemental analyses (C, H, N) were performed on a Perkin–Elmer CHN-2400 analyzer. The ^1H NMR spectrum was obtained in d_6-DMSO using a Bruker Avance 400 spectrometer.

2.2. Preparation of $[ReCl_2(pic)(PPh_3)_2]$ (**1**)

2.2.1. Method A

$[ReOCl_3(PPh_3)_2]$ (0.50 g, 0.6 mmol) was added to 1-(2-pyridylcarbonyl)benzotriazole (0.135 g, 0.6 mmol) in ethanol (100 ml) and the reaction mixture was refluxed for 4 h. The resulting reaction mixture was reduced in volume to ~10 ml and allowed to cool to room temperature. An orange crystalline precipitate of **1** was filtered off and dried in air. Yield 55%.

2.2.2. Method B

$ReOCl_3(PPh_3)_2$] (0.50 g, 0.6 mmol) was added to picolinic acid (0.075 g, 0.61 mmol) and PPh_3 (0.30 g, 1.15 mmol) in ethanol (100 ml) and the reaction mixture was refluxed for 4 h. The resulting reaction mixture was reduced in volume to ~10 ml and allowed to cool to room temperature. An orange crystalline precipitate of **1** was filtered off and dried in air. Yield 80%.

IR (KBr; ν/cm^{-1}): 1697 (vs) ν_{asymCO_2}; 1616 (m) and 1596 (w) ν_{CN} and $\nu_{C=C}$; 1288(s) ν_{asymCO_2}.

Anal. Calc. for $C_{42}H_{34}Cl_2NO_2P_2Re$: C, 55.82; H, 3.79; N, 1.55%. Found: C, 55.61; H, 3.56; N, 1.72%.

2.3. Preparation of $[ReBr_2(pic)(PPh_3)_2]$ (**2**)

A procedure similar to that for $[ReCl_2(pic)(PPh_3)_2]$ was used with $[ReOBr_3(PPh_3)_2]$ (0.50 g, 0.52 mmol) and 1-(2-pyridylcarbonyl)benzotriazole (0.12 g, 0.53 mmol) in method A, and $[ReOBr_3(PPh_3)_2]$ (0.50 g, 0.52 mmol), picolinic acid (0.068 g, 0.55 mmol) and PPh_3 (0.29 g, 1.10 mmol) in method B.

IR (KBr; ν/cm^{-1}): 1684 (vs) ν_{asymCO_2}; 1608 (m) and 1586 (w) ν_{CN} and $\nu_{C=C}$; 1281(s) ν_{asymCO_2}.

Anal. Calc. for $C_{42}H_{34}Br_2NO_2P_2Re$: C, 50.82; H, 3.45; N, 1.41%. Found: C, 50.59; H, 3.32; N, 1.34%.

2.4. Crystal structure determination and refinement

The X-ray intensity data of **1** and **2** were collected on a KM-4-CCD automatic diffractometer equipped with a CCD detector and graphite monochromated Mo Kα radiation (λ = 0.71073 Å) at room temperature. Details concerning crystal data and refinement are given in Table 1. Lorentz, polarization and absorption corrections [19] were applied. The structures were solved by the Patterson method and subsequently completed by difference Fourier recycling. All the non-hydrogen atoms were refined anisotropically using the full-matrix, least-squares technique. The hydrogen atoms were treated as "riding" on their parent carbon atoms and assigned isotropic temperature factors equal to 1.2 times the value of equivalent temperature factor of the parent atom. SHELXS97 [20], SHELXL97 [21] and SHELXTL [22] programs were used for all the calculations. Atomic scattering factors were those incorporated in the computer programs.

2.5. Computational details

The gas phase geometry of **1** was optimized without any symmetry restrictions in the singlet and triplet ground-states with the DFT method using the hybrid B3LYP functional of GAUSSIAN-03 [23–25]. The calculations were performed using the ECP basis set LANL2DZ [26] with an additional *d* and *f* function with the exponent α = 0.3811 and α = 2.033 [27] for rhenium and the standard 6-31G basis set for the other atoms. For chloride, oxygen, nitrogen and phosphorous atoms, diffuse and polarization functions were added [28–33]. The vibrations in the calculated vibrational spectrum of **1** were real, thus the geometry corresponds to a true energy minimum.

The electronic spectrum of **1** was calculated with the TDDFT method, and the solvent effect (acetonitrile) was simulated using the polarizable continuum model with the integral equation formalism (IEF-PCM) [34–37].

2.6. Magnetic measurement

Magnetic measurements of **1** in the temperature range 1.8–300 K were performed using a Quantum Design SQUID-based MPMSXL-5-tpe magnetometer. The superconducting magnet was generally operated at a field strength ranging from 0 to 5 T.

Table 1
Crystal data and structure refinement for complexes **1** and **2**.

	1	**2**
Empirical formula	$C_{42}H_{34}Cl_2NO_2P_2Re$	$C_{42}H_{34}Br_2NO_2P_2Re$
Formula weight	903.74	992.66
Temperature (K)	293.0(2)	100(2)
Wavelength (Å)	0.71073	0.71073
Crystal system	orthorhombic	orthorhombic
Space group	Abm2	Abm2
Unit cell dimensions		
a (Å)	9.3610(2)	9.3877(2)
b (Å)	25.0585(10)	24.7704(8)
c (Å)	15.8943(6)	15.8178(3)
Volume, Å^3	3728.4(2)	3678.23(17)
Z	4	4
Density (calculated) (Mg/m^3)	1.610	1.793
Absorption coefficient (mm^{-1})	3.526	5.601[1]
F(000)	1792	1936
Crystal size, mm	0.004 × 0.006 × 0.093	0.052 × 0.056 × 0.34
θ Range for data collection (°)	1.63–25.04	3.06–25.03
Index ranges	$-11 \leqslant h \leqslant 11$ $-29 \leqslant k \leqslant 29$ $-15 \leqslant l \leqslant 18$	$-11 \leqslant h \leqslant 11$ $-29 \leqslant k \leqslant 29$ $-18 \leqslant l \leqslant 11$
Reflections collected	18 291	12 642
Independent reflections	3131 (R_{int} = 0.0583)	2347 (R_{int} = 0.0243)
Completeness to 2θ (%)	100	99.7
Max. and min. transmission	0.990 and 0.971	0.751 and 0.688
Data/restraints/parameters	3131/1*/244	2347/1*/244
Absolute structure parameter	−0.022(9)	0.002(6)
Goodness-of-fit on F^2	1.088	1.042
Final *R* indices [$I > 2(I)$]	R1 = 0.0292 wR2 = 0.0609	R1 = 0.0147 wR2 = 0.0349
R indices (all data)	R1 = 0.0379 wR2 = 0.0777	R1 = 0.0152 wR2 = 0.0349
Largest difference in peak and hole (e Å^{-3})	1.288 and −0.869	0.632 and −0.452

[*] Restraint of floating origin.

Measurements were made at a magnetic field of 0.5 T. Corrections are based on subtracting the sample-holder signal and the contribution χ_D estimated from Pascal constants equals -499×10^{-6} cm^{3}mol^{-1} for complex **1**. The effective magnetic moment was calculated from the equation, $\mu_{eff} = 2.83(\chi_M T)^{1/2}$ (*B.M.*).

3. Results and discussion

The $[ReCl_2(pic)(PPh_3)_2]$ (**1**) and $[ReBr_2(pic)(PPh_3)_2]$ (**2**) complexes were first isolated from the reactions of $[ReOX_3(PPh_3)_2]$ (X = Cl or Br) with 1-(2-pyridylcarbonyl)benzotriazole in ethanol. Although mechanism of the reaction has not been examined in detail, two reaction courses can be supposed.

The first one is thought to occur *via* reduction of $[ReOX_3(PPh_3)_2]$ by triphenylphosphine and coordination of 1-(2-pyridylcarbonyl)benzotriazole to the Re(III) center. After the coordination of 1-(2-pyridylcarbonyl)benzotriazole to the Re(III) ion, hydrolysis of 1-(2-pyridylcarbonyl)benzotriazole occurs and the picolinic acid formed coordinates to the Re(III) ion to give $[ReCl_2(pic)(PPh_3)_2]$, whereas the benzotriazole remains uncoordinated. The oxygen atom transfer is believed to proceed *via* initial nucleophilic attack on the Re≡O π^* orbitals, and many instances of formation of phosphine oxides from Re^VO and tertiary phosphines can be given [11,38,39]. The starting oxo complex is synthesised using a large excess of triphenylphosphine and it can be impure with PPh_3. The $[ReCl_3(L\text{-}L)(PPh_3)]$ complex with coordinated 1-(2-pyridylcarbonyl)benzotriazole (L-L) has not been isolated from the reaction, but many instances of the formation of $[ReCl_3(L\text{-}L)(PPh_3)]$ in related syntheses can be given [11,38,39].

The second probable reaction model involves hydrolysis of 1-(2-pyridylcarbonyl)benzotriazole, coordination of the picolinate ligand to Re(V), formation of $[ReOCl_2(pic)(PPh_3)_2]$ and subsequent reduction of $[ReOCl_2(pic)(PPh_3)_2]$ to $[ReCl_3(pic)(PPh_3)_2]$. The low yield of $[ReX_2(pic)(PPh_3)_2]$ in the reactions of $[ReOX_3(PPh_3)_2]$ with 1-(2-pyridylcarbonyl)benzotriazole results from an insufficient amount of PPh_3.

With a much higher yield, compounds **1** and **2** were isolated from the reactions of $[ReOX_3(PPh_3)_2]$ with picolinic acid in the presence of PPh_3. In this case, similar reaction models can be postulated. The more probable one seems to involve coordination of the picolinate ligand to Re(V), formation of $[ReOCl_2(pic)(PPh_3)_2]$ and subsequent reduction of $[ReOCl_2(pic)(PPh_3)_2]$ to $[ReCl_3(pic)(PPh_3)_2]$. It has been previously proven that $[ReOCl_3(PPh_3)_2]$ easily reacts with picolinic acid to give $[ReOCl_2(pic)(PPh_3)]$ [9]. However, the other reaction course involving reduction of Re(V) to Re(III) followed by coordination of picolinate ion to the Re(III) is also possible.

The IR spectra of **1** and **2** show features comparable to those of mononuclear picolinato species [40]. The bands assigned to $\nu_{sym}(CO_2)$ and $\nu_{as}(CO_2)$ appear at 1697 and 1288 cm^{-1} for **1**, and 1984 and 1281 cm^{-1} for **2**. The value of $\Delta\nu(CO_2) = \nu_{as}(CO_2) - \nu_s(CO_2)$, equal to ≈400 cm^{-1} for the $[ReX_2(pic)(PPh_3)_2]$ compounds, confirms a unidentate coordination mode of the carboxylate group. Characteristic bands corresponding to the ν(CN) and ν(C=C) modes of the *pic* ligand appear in the range 1620–1550 cm^{-1} [41]. The absence of the strong ν(Re=O) band at ~980 cm^{-1} is a clear indication that there is no oxo-Re(V) starting material left in the samples of **1** and **2**.

The proton spectrum of **1** shows features comparable to those of mononuclear Re(III) with tertiary phosphines. The ^{1}H NMR signals of **1** are relatively narrow due to short electron-spin relaxation time of the Re(III) center, but the signals are spread over the ppm range [42]. The *ortho* protons of two PPh_3 coordinated molecules appear as a doublet at 12.02 ppm, and they are downfield from the *meta* and *para* protons (8.5–8.7 ppm). The three protons of the picolinate ion appear as a triplet at 10.15 ppm and two doublets at 7.13 and 6.81 ppm, respectively.

3.1. Crystal structures

A definite proof for the structure is provided by the X-ray diffraction results. The crystallographic data of the complexes **1** and **2** are summarized in Table 1. The $[ReX_2(pic)(PPh_3)_2]$ complexes are isostructural, crystallise in the orthorhombic Abm2 space group (No. 39) with rhenium, halogen and all the picolinate anion atoms located on the special position *c* with site symmetry m. Thus both the polyhedron $ReCl_2NO$ base and picolinate anion are planar by symmetry.

The short intra- and intermolecular contacts, which can be classified as weak hydrogen bonds [43,44], are gathered in Table 2. The

Table 2
Hydrogen bonds for **1** and **2**.

D–H···A	D–H	H···A	D···A	D–H···A
1				
C(2)–H(2)···Cl(1)	0.93	2.66	3.479(8)	147.9
C(18)–H(18)···O(1)	0.93	2.36	3.105(10)	136.9
C(23)–H(23)···Cl(2)	0.93	2.80	3.378(11)	121.7
2				
C(2)–H(2)···Br(1)	0.93	2.71	3.548(4)	149.8
C(18)–H(18)···O(1)	0.93	2.31	3.068(4)	138.9
C(23)–H(23)···Br(2)	0.93	2.83	3.450(6)	125.2
C(20)–H(20)···Br(2)#1	0.93	2.83	3.615(6)	142.4
C(22)–H(22)···O(2)#2	0.93	2.54	3.320(7)	141.5
C(23)–H(23)···Br(1)#3	0.93	2.77	3.488(6)	135.1

Symmetry transformations used to generate equivalent atoms: #1 −1 + *x*, *y*, *z*; #2 −*x*, *y*, 1/2 + *z*; #3 1−*x*, *y*, 1/2 + *z*.

hydrogen bonding scheme in the both structures is similar due to the isostructurality, however, in **2** some more short contacts exist due to the larger radius of the Br atom. The planar, in the range of experimental error, phenyl rings of the PPh_3 ligands are inclined at 62.4(3), 71.3(3), 81.5(3)° in **1** and at 61.23(3), 71.98(4), 81.25(3)° in **2**. The O–C═O bonds of the carboxylate groups show significant delocalization in both structures (the C(24)–O(1) distances are 1.264(18) and 1.292(8) Å, and the C(24)–O(2) distances are 1.22(2) and 1.248(9) Å, respectively, in **1** and **2**).

The molecular structure of **1** is presented in Fig. 1, and selected bond distances and angles of **1** and **2** are collected in Tables 3 and 4, respectively. The $[ReX_2(pic)(PPh_3)_2]$ complexes show a distorted octahedral geometry about Re with bidentate N,O donors of the picolinato ligand, two halide ions arranged in *cis* geometry and two PPh_3 molecules in *trans* arrangement.

The bond lengths and angles of **1** and **2** do not differ significantly from the expected values for related mononuclear rhenium complexes [9]. The Re–Cl(1) bond *trans* to N is far longer than the Re–Cl(2) bond *trans* to O, indicating a *structural trans* effect of the pyridine ring.

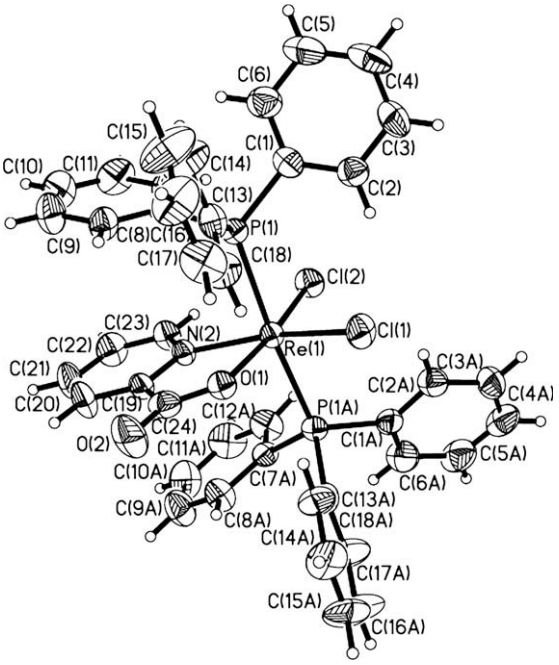


Fig. 1. The molecular structure of **1**.

Table 4
The experimental and optimized bond lengths [Å] and angles [°] for **2**.

Bond lengths	Experimental	Bond angles	Experimental
Re(1)–O(1)	2.044(4)	O(1)–Re(1)–N(2)	76.20(15)
Re(1)–N(2)	2.131(5)	O(1)–Re(1)–Br(2)	170.51(12)
Re(1)–Br(1)	2.5205(6)	N(2)–Re(1)–Br(2)	94.31(14)
Re(1)–Br(2)	2.4906(6)	O(1)–Re(1)–Br(1)	85.44(12)
Re(1)–P(1)	2.4530(8)	N(2)–Re(1)–Br(1)	161.65(14)
		Br(2)–Re(1)–Br(1)	104.04(3)
		O(1)–Re(1)–P(1)	93.99(2)
		N(2)–Re(1)–P(1)	90.93(3)
		Br(2)–Re(1)–P(1)	86.06(3)
		Br(1)–Re(1)–P(1)	90.34(3)
		P(1)–Re(1)–P(1)#1	172.03(5)

3.2. Magnetic properties

The magnetic properties of **1**, in the form μ_{eff} versus T (μ_{eff} is the effective magnetic moment) is shown in Fig. 2. The rhenium(III) complex shows a room temperature magnetic moment of 1.68 B.M. The magnetic moment of the solid is temperature dependent between 300 and 1.8 K and the value of the $\chi_M T$ product decreases on lowering the temperature. This behavior is characteristic of mononuclear d^4 low-spin pseudo-octahedral Re(III) complexes ($^3T_{1g}$ ground state) [45–54] and arises because of the large spin–orbit coupling ($\zeta = 2500\ cm^{-1}$ [55]), which gives a diamagnetic ground state. It seems that at room temperature, in accordance

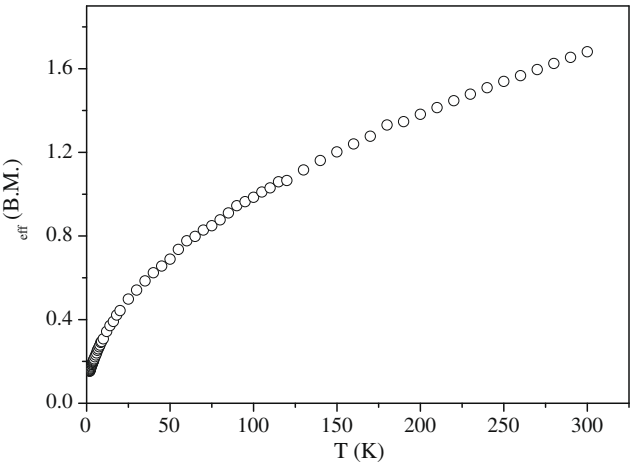


Fig. 2. Plots of experimental effective magnetic moment μ_{eff} (○) vs. temperature for **1**.

Table 3
The experimental and optimized bond lengths [Å] and angles [°] for **1**.

Bond lengths	Experimental	Optimized	Bond angles	Experimental	Optimized
Re(1)–O(1)	2.039(9)	1.941	O(1)–Re(1)–N(2)	75.6(3)	76.20
Re(1)–N(2)	2.143(10)	2.082	O(1)–Re(1)–Cl(2)	169.7(3)	168.47
Re(1)–Cl(1)	2.395(3)	2.503	N(2)–Re(1)–Cl(2)	94.1(3)	92.27
Re(1)–Cl(2)	2.347(3)	2.442	O(1)–Re(1)–Cl(1)	87.6(3)	95.51
Re(1)–P(1)	2.4572(16)	2.481	N(2)–Re(1)–Cl(1)	163.3(3)	171.71
			Cl(2)–Re(1)–Cl(1)	102.66(15)	96.02
			O(1)–Re(1)–P(1)	93.15(6)	91.16
			N(2)–Re(1)–P(1)	91.01(7)	94.46
			Cl(2)–Re(1)–P(1)	86.94(7)	89.72
			Cl(1)–Re(1)–P(1)	89.90(9)	85.61
			P(1)–Re(1)–P(1)#1	173.68(10)	171.09
			O(1)–Re(1)–P(1)#1	93.15(6)	91.70
			N(2)–Re(1)–P(1)#1	91.01(8)	94.46
			Cl(2)–Re(1)–P(1)#1	86.94(7)	89.72
			Cl(1)–Re(1)–P(1)#1	89.90(9)	85.61

Table 5
The energy and character of the selected molecular orbitals with α and β spins for **1**.

	MOs with α spin		MOs with β spin	
	E (eV)	Character	*E* (eV)	Character
HOMO−5	−6.818	$\pi(PPh_3)$	−6.849	$\pi(PPh_3)$, π(Cl)
HOMO−4	−6.779	$\pi(PPh_3)$	−6.820	$\pi(PPh_3)$
HOMO−3	−6.396	π(Cl), n(P) $\pi(PPh_3)$, d_{xz}(Re)	−6.809	$\pi(PPh_3)$
HOMO−2	−6.139	d_{xz}(Re), π(Cl), π(pic)	−6.776	$\pi(PPh_3)$
HOMO−1	−5.821	d_{xy}(Re), π(Cl), π(pic)	−6.342	π(Cl), n(P) $\pi(PPh_3)$
HOMO	−5.818	d_{yz}(Re), π(Cl), π(pic)	−5.298	d_{yz}(Re), π(Cl), π(pic)
LUMO	−2.048	π^*(pic)	−3.148	π^*(Re–Cl), π^*(pic)
LUMO +1	−1.246	π^*(pic)	−2.482	π^*(Re–Cl), π^*(pic)
LUMO+2	−1.028	d^2_z, $\pi^*(PPh_3)$	−1.932	π^*(pic), d_{yz}
LUMO+3	−0.969	$\pi^*(PPh_3)$, d^2_z	−1.239	π^*(pic)
LUMO+4	−0.900	$\pi^*(PPh_3)$	−0.995	$\pi^*(PPh_3)$
LUMO+5	−0.811	$\pi^*(PPh_3)$	−0.891	$\pi^*(PPh_3)$

with Boltzmann's distribution, the higher magnetic state is populated, and it is depopulated with temperature lowering, and a decrease of the magnetic moment is observed.

The magnetization indicates a value of only 0.001 B.M. at 5 T. The magnetization of the sample confirms that the ground state is diamagnetic and the rhenium(III) compound is of a very high purity.

3.3. Geometry optimisation

The gas phase geometry of **1** was optimized in the triplet and singlet states using the DFT method with the B3LYP functional. The total energy of the triplet state is 5.8 kcal/mol smaller in comparison with the singlet state. The optimized geometric parameters of the triplet state are gathered in Table 3. Generally, the predicted bond lengths and angles are in agreement with the values based upon the X-ray crystal structure data, and the general trends observed in the experimental data are well reproduced in the calculations. The largest differences are found for the Re–Cl bond distances. This may come from the basis sets which are approximated to a certain extent or may indicate the influence of the crystal packing on the values of the experimental bond lengths. The theoretical calculations do not consider the effects of chemical environment. However, a similar elongation of the rhenium–chlorine bond lengths (up to 0.25 Å) in the B3LYP with different basis sets has been found in other rhenium–chlorine complexes [56].

3.4. Molecular orbitals

The energies and characters of several of the highest occupied and lowest unoccupied molecular orbitals of **1** are presented in Table 5. Among the highest occupied MOs of **1**, the largest numbers constitute π orbitals of the phenyl rings with a contribution from the Cl atoms. The three highest molecular orbitals with α-spin can be represented as a combination of π^*_{Re-Cl} and π_{pic}, with predominant involvement of the former component. The HOMO orbital, with β-spin, has the same character. The LUMO+1 and LUMO+3 β orbitals of **1** are also to a large extent formed by rhenium d_π atomic orbitals (d_{xz}, d_{yz} or d_{xy}). Among the lowest unoccupied MOs of **1**, the most are constituted of π^* orbitals of the *pic* and phenyl rings. The

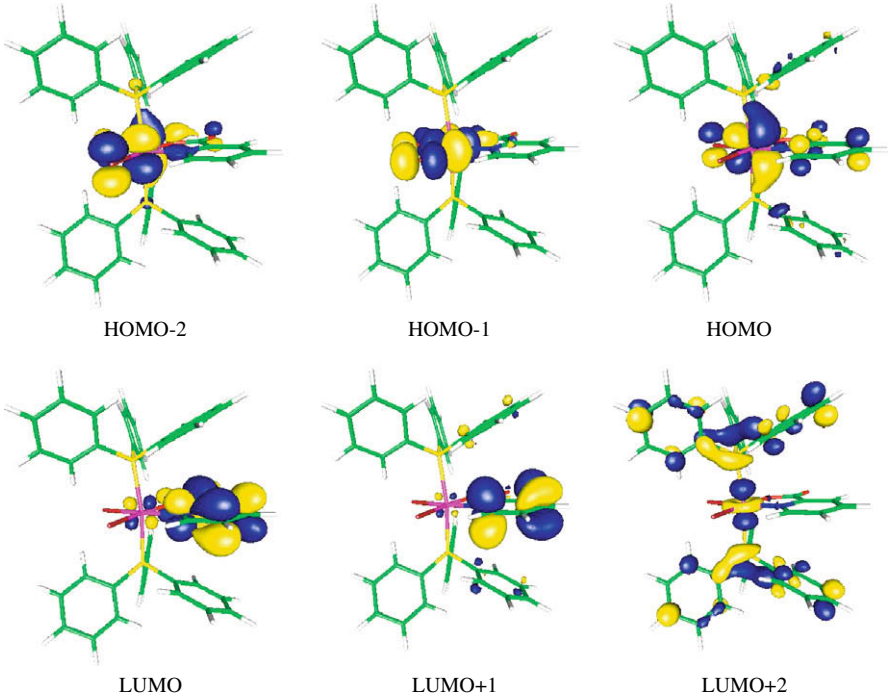


Fig. 3. The selected HOMO and LUMO orbitals with α-spin for **1**.

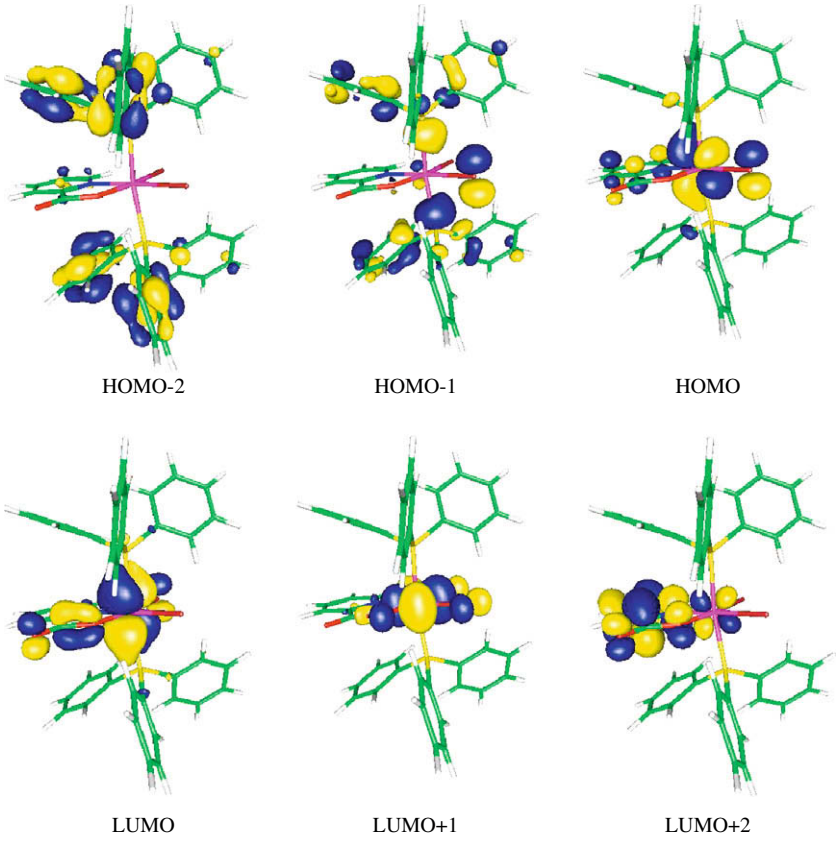


Fig. 4. The selected HOMO and LUMO orbitals with β-spin for **1**.

LUMO and LUMO+1 with α-spin and LUMO+2 and LUMO+3 with β-spin have π^*(pic) character. The π^* phenyl ring orbitals of the triphenylphosphine ligands participate in the higher unoccupied orbitals. The contours of the selected occupied and unoccupied molecular orbitals of **1** with α-spin and β-spin are presented in Figs. 3 and 4, respectively.

3.5. Electronic spectra

The experimental and calculated electronic spectra of **1** are presented in Fig. 5. Each calculated transition is represented by a gaussian function $y = ce^{-bx^2}$ with the height (c) equal to the oscillator strength and b equal to 0.04 nm^{-2}. The electronic spectrum of **2** is very similar in terms of the position, intensity and shape of the bands in the whole region 1000–180 nm; with maxima at 514.1, 458.8, 341.4, 251.5 and 201.7 nm.

Table 6 presents the most important spin-allowed triplet–triplet electronic transitions calculated with the TDDFT method, assigned to the observed absorption bands of **1**. For the high energy part of the spectrum, only transitions with oscillator strengths larger than 0.020 are listed in Table 6. The investigated complex is of a large size; the numbers of basis functions are equal to 832. The calculated electron transitions (1 1 0) do not comprise all the experimental absorption bands; the UV–vis spectrum was calculated to ~270 nm. Thus the shortest wavelength experimental bands of **1** are not assigned to the calculated transitions; some additional intraligand and interligand transitions are expected to be found at higher energies in the calculations for **1**.

The assignment of the calculated orbital excitations to the experimental bands was based on an overview of the contour plots and relative energy to the HOMO and LUMO involved in the electronic transitions.

In the 350–600 nm region, complex **1** displays multiple transitions of moderate intensity in the form of peaks and shoulders.

The low-energy absorption band of **1** originates from the transitions between HOMO-1, HOMO, LUMO and LUMO+2 with β-spin. As can be seen from Fig. 4, the β HOMO−1 is composed of ligand (chloride and triphenylphosphine) orbitals, β HOMO is delocalized on the central ion and ligands, and β LUMO and β LUMO+2 are

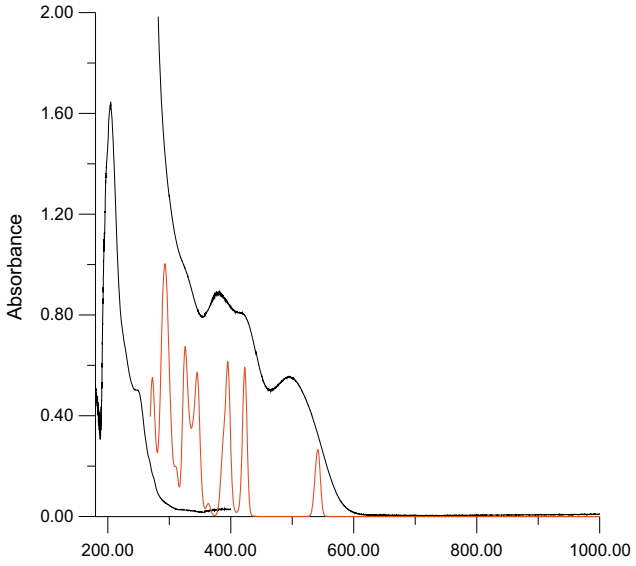


Fig. 5. The experimental (black) and calculated (red) electronic absorption spectra of a solution of **1** in acetonitrile. (For interpretation of the references to colour in this figure legend, the reader is referred to the web version of this article.)

Table 6
The energy and molar absorption coefficients of experimental absorption bands and the electronic transitions calculated with the TDDFT method for **1**.

The most important orbital excitations	Character	Calculated			Experimental Λ (nm) (E [eV]) ε
		λ (nm)	E (eV)	f	
H(β) → L+2(β) H-1(β) → L(β)	d/π(Cl)/π(pic) → π*(pic)/d n(P)/π(PPh_3)/π(Cl) → d/π*(pic)	542.6	2.28	*0.0145*	510.5 (2.43) 3600
H-1(β) → L(β) H(β) → L+2(β)	n(P)π(PPh_3)/π(Cl) → d/π*(pic) d/π(Cl)/π(pic) → π*(pic)/d	537.8	2.31	*0.0067*	
H(α) → L(α)	d/π(Cl)/π(pic) → π*(pic)	422.7	2.93	*0.0389*	427.7 (2.90) 5350
H-2(α) → L(α)	d/π(Cl)/π(pic) → π*(pic)	395.4	3.14	*0.0383*	379.3 (3.27) 6150
H-2(α) → L(α) H(β) → L+3(β)	d/π(Cl)/π(pic) → π*(pic)	388.0	3.20	*0.0162*	
H(α) → L+2(α) H(α) → L+11(α)	d/π(Cl)/π(pic) → d/π*(PPh_3)	345.9	3.58	*0.0296*	328.2 (3.78) 6650
H(β) → L+5(β) H(α) → L+1(α)	d/π(Cl)/π(pic) → π*(PPh_3) d/π(Cl)/π(pic) → π*(pic)	325.2	3.81	*0.0273*	
H-2(α) → L+1(α)	d/π(Cl)/π(pic) → π*(pic)	300.4	4.13	*0.0100*	247.9 (5.00) 87 000
H(α) → L+3(α)	d/π(Cl)/π(pic) → π*(PPh_3)/d	297.0	4.17	*0.0100*	
H(β) → L+9(β) H-5(α) → L(α)	d/π(Cl)/π(pic) → π*(PPh_3) π(PPh_3) → π*(pic)	295.9	4.19	*0.0154*	
H-14(β) → L+1(β)	π(Cl) → d	291.9	4.25	*0.0146*	
H-3(β) → L+2(β)	π(PPh_3) → π*(pic)/d	288.9	4.29	*0.0179*	
					204.8 (6.05) 270 000

ε – Molar absorption coefficient [$dm^3\ mol^{-1}\ cm^{-1}$].
f – Oscillator strength.
H – Highest occupied molecular orbital.
L – Lowest unoccupied molecular orbital.

formed from d_{Re} orbitals and π^*-bonding orbitals of the picolinate ligand. Accordingly, these transitions can be seen as delocalized MLLCT (*Metal–Ligand-to-Ligand CT*) transitions.

The transitions assigned to the experimental bands at 427.7 and 379.3 nm can be seen as mixed Re → π*(pic) (*Metal–Ligand Charge Transfer*; *LMCT*) and π(Cl)/π(pic) → π*(pic) (*Ligand–Ligand Charge Transfer*; *LLCT*) transitions. The experimental absorption band at 328.2 nm is mainly attributed to the d/π(Cl)/π(pic) → d/π*(PPh_3) transition, whereas the transitions assigned to the experimental band at 247.9 are mainly of *LLCT* character.

4. Conclusions

This work is an extension of our previous research on the reactivity of [$ReOX_3(PPh_3)_2$] towards N–O and N–N chelating ligands. 1-(2-Pyridylcarbonyl)benzotriazole does not coordinate to the rhenium ion. Hydrolysis of 1-(2-pyridylcarbonyl)benzotriazole in the reaction with the oxo-complexes occurs and picolinic acid binds to the Re center to give the [$ReX_2(pic)(PPh_3)_2$] complexes (X = Cl, Br). The studied compounds were synthesized for the first time. Their structures were definitively proven by X-ray diffraction measurements and confirmed by spectroscopic analysis. The magnetic measurements, NMR and UV–vis studies confirm that the [$ReX_2(pic)(PPh_3)_2$] complexes are typical mononuclear d^4 low-spin octahedral Re(III) complexes. In the visible region the [$ReX_2(pic)(PPh_3)_2$] complexes display multiple transitions of moderate intensity in the form of peaks and shoulders. The TDDFT/PCM calculations show that these transitions can be seen as delocalized MLLCT (Metal–Ligand-to-Ligand CT) transitions.

Supplementary data

CCDC 724894 and 724895 contain the supplementary crystallographic data for $C_{42}H_{34}Cl_2NO_2P_2Re$ and $C_{42}H_{34}Br_2NO_2P_2Re$. These data can be obtained free of charge via http://www.ccdc.cam.ac.uk/conts/retrieving.html, or from the Cambridge Crystallographic Data Centre, 12 Union Road, Cambridge CB2 1EZ, UK; fax: (+44) 1223-336-033; or e-mail: deposit@ccdc.cam.ac.uk.

Acknowledgements

The GAUSSIAN-03 calculations were carried out in the Wrocław Centre for Networking and Supercomputing, WCSS, Wrocław, Poland, http://www.wcss.wroc.pl, under calculational Grant No. 51/96.

References

[1] U. Abram, in: J.A. McCleverty, T.J. Meyer (Eds.), Comprehensive Coordination Chemistry, second ed., vol. 5, Elsevier, 2003, pp. 271–402 (Chapter 5.3).
[2] J.R. Dilworth, S.J. Parrott, Chem. Soc. Rev. 27 (1998) 43.
[3] P. Blower, J. Chem. Soc., Dalton Trans. (2006) 1705.
[4] R.L. Richards, Coord. Chem. Rev. 154 (1996) 83.
[5] M.D. Fryzuk, S.A. Johnson, Coord. Chem. Rev. 200–202 (2000) 379.
[6] A.J.L. Pombeiro, M.F.C. Guedes da Silva, R.A. Michelin, Coord. Chem. Rev. 218 (2001) 43.
[7] F.E. Kühn, A. Scherbaum, W.A. Herrmann, J. Organomet. Chem. 689 (2004) 4149.
[8] G.S. Owens, J. Arias, M.M. Abu-Omar, Catalysis Today 55 (2000) 317.
[9] A.M. Kirillov, M. Haukka, M.V. Kirillova, A.J.L. Pombeiro, Adv. Synth. Catal. 347 (2005) 1435.
[10] A. Deloffre, S. Halut, L. Salles, J.-M. Brégeault, J.R. Gregorio, B. Denise, H. Rudler, J. Chem. Soc., Dalton Trans. (1999) 2897.
[11] S. Bhattacharyya, I. Chakraborty, B.K. Dirghangi, A. Chakravorty, Chem. Commun. (2000) 1813.
[12] B. Machura, R. Kruszynski, M. Jaworska, J. Kłak, J. Mroziński, Polyhedron 25 (2006) 2537.
[13] B. Machura, R. Kruszynski, J. Kusz, J. Kłak, J. Mroziński, Polyhedron 26 (2007) 4427.
[14] H. Chermette, Coord. Chem. Rev. 178–180 (1998) 699.
[15] M.C. Aragoni, M. Arca, T. Cassano, C. Denotti, F.A. Devillanova, F. Isaia, V. Lippolis, D. Natali, L. Niti, M. Sampietro, R. Tommasi, G. Verani, Inorg. Chem. Commun. 5 (2002) 869.
[16] P. Romaniello, F. Lelj, Chem. Phys. Lett. 372 (2003) 51.
[17] P. Norman, P. Cronstrand, J. Ericsson. Chem. Phys. 285 (2002) 207.
[18] G. Rouschias, G. Wilkinson, J. Chem. Soc. A (1966) 465.
[19] (a) CrysAlis RED, Oxford Diffraction Ltd., Version 1.171.29.2.;
(b) STOE and Cie, X-RED. Version 1.18. STOE & Cie GmbH, Darmstadt, Germany, 1999.
[20] G.M. Sheldrick, Acta Cryst. A46 (1990) 467.
[21] G.M. Sheldrick, SHELXL97. Program for the Refinement of Crystal Structures, University of Gttingen, Germany, 1997.

[22] G.M. Sheldrick, SHELXTL: release 4.1 for Siemens Crystallographic Research Systems, 1990.
[23] Gaussian 03, Revision D.01, M. J. Frisch, G. W. Trucks, H. B. Schlegel, G. E. Scuseria, M. A. Robb, J. R. Cheeseman, J. A. Montgomery, Jr., T. Vreven, K. N. Kudin, J. C. Burant, J. M. Millam, S. S. Iyengar, J. Tomasi, V. Barone, B. Mennucci, M. Cossi, G. Scalmani, N. Rega, G. A. Petersson, H. Nakatsuji, M. Hada, M. Ehara, K. Toyota, R. Fukuda, J. Hasegawa, M. Ishida, T. Nakajima, Y. Honda, O. Kitao, H. Nakai, M. Klene, X. Li, J. E. Knox, H. P. Hratchian, J. B. Cross, V. Bakken, C. Adamo, J. Jaramillo, R. Gomperts, R. E. Stratmann, O. Yazyev, A. J. Austin, R. Cammi, C. Pomelli, J. W. Ochterski, P. Y. Ayala, K. Morokuma, G. A. Voth, P. Salvador, J. J. Dannenberg, V. G. Zakrzewski, S. Dapprich, A. D. Daniels, M. C. Strain, O. Farkas, D. K. Malick, A. D. Rabuck, K. Raghavachari, J. B. Foresman, J. V. Ortiz, Q. Cui, A. G. Baboul, S. Clifford, J. Cioslowski, B. B. Stefanov, G. Liu, A. Liashenko, P. Piskorz, I. Komaromi, R. L. Martin, D. J. Fox, T. Keith, M. A. Al-Laham, C. Y. Peng, A. Nanayakkara, M. Challacombe, P. M. W. Gill, B. Johnson, W. Chen, M. W. Wong, C. Gonzalez, J. A. Pople, Gaussian, Inc., Wallingford CT, 2004.
[24] A.D. Becke, J. Chem. Phys. 98 (1993) 5648.
[25] C. Lee, W. Yang, R.G. Parr, Phys. Rev. B 37 (1988) 785.
[26] P.J. Hay, W.R. Wadt, J. Chem. Phys. 82 (1985) 299.
[27] K. Eichkorn, F. Weigend, O. Treutler, R. Ahlrichs, Theor. Chem. Acc. 97 (1997) 119.
[28] W.J. Hehre, R. Ditchfield, J.A. Pople, J. Chem. Phys. 56 (1972) 2257.
[29] P.C. Hariharan, J.A. Pople, Theoret. Chimica Acta 28 (1973) 213.
[30] M.M. Francl, W.J. Petro, W.J. Hehre, J.S. Binkley, M.S. Gordon, D.J. DeFrees, J.A. Pople, J. Chem. Phys. 77 (1982) 3654.
[31] T. Clark, J. Chandrasekhar, P.v.R. Schleyer, J. Comp. Chem. 4 (1983) 294.
[32] R. Krishnam, J.S. Binkley, R. Seeger, J.A. Pople, J. Chem. Phys. 72 (1980) 650.
[33] P.M.W. Gill, B.G. Johnson, J.A. Pople, M.J. Frisch, Chem. Phys. Lett. 197 (1992) 499.
[34] M.T. Cances, B. Mennucci, J. Tomasi, J. Chem. Phys. 107 (1997) 3032.
[35] M. Cossi, V. Barone, B. Mennucci, J. Tomasi, Chem. Phys. Lett. 286 (1998) 253.
[36] B. Mennucci, J.Tomasi, J. Chem. Phys. 106 (1997) 5151.
[37] M. Cossi, G. Scalmani, N. Rega, V. Barone, J. Chem. Phys. 117 (2002) 43.
[38] I. Chakraborty, S. Bhattacharyya, S. Banerjee, B.K. Dirghangi, A. Chakravorty, J. Chem. Soc., Dalton Trans. (1999) 3747.
[39] S. Sengupta, J. Gangopadhyay, A. Chakravorty, J. Chem Soc., Dalton Trans. (2003) 4635.
[40] A. Deloffre, S. Halut, L. Salles, J.-M. Brégeault, J.R. Gregorio, B. Denise, H. Rudler, J. Chem. Soc., Dalton Trans. (1999) 2897.
[41] K. Nakamoto, Infrared and Raman Spectra of Inorganic and Coordination Compounds, fourth ed., Wiley-Interscience, New York, 1986.
[42] C. Pearson, A.L. Beauchamp, Inorg. Chim. Acta 237 (1995) 13.
[43] G.A. Jeffrey, W. Saenger, Hydrogen Bonding in Biological Structures, Springer-Verlag, 1994.
[44] G.R. Desiraju, T. Steiner, The Weak Hydrogen Bond in Structural Chemistry and Biology, Oxford University Press, 1999.
[45] B. Machura, R. Penczek, R. Kruszyński, J. Kłak, J. Mroziński, J. Kusz, Polyhedron 26 (2007) 4833.
[46] J.E. Fergusson, Coord. Chem. Rev. 1 (1966) 459.
[47] B.N. Figgis, J. Lewis, Prog. Inorg. Chem. 6 (1964) 37.
[48] B.N. Figgis, Introduction to Ligand Field, Wiley-Interscience, New York, 1966. p. 248.
[49] J. Chatt, G.J. Leigh, D.M.P. Mingos, E.W. Randall, D. Shaw, J. Chem. Soc., Chem. Commun. (1968) 419.
[50] H.P. Gunz, G.J. Leigh, J. Chem. Soc. (1971) 2229.
[51] B. Coutinho, J.R. Dilworth, P. Jobanputra, R.M. Thompson, S. Schmidt, J. Strähle, C.M. Archer, J. Chem. Soc., Dalton Trans (1995) 1663.
[52] M. Hirsch-Kuchma, T. Nicholson, A. Davison, W.M. Davis, A.G. Jones, Inorg. Chem. 36 (1997) 3237.
[53] C.A. McConnachie, E.I. Stiefel, Inorg. Chem. 36 (1997) 6144.
[54] C. Pearson, A.L. Beauchamp, Can. J. Chem. 75 (1997) 220.
[55] A. Earnshaw, B.N. Figgis, J. Lewis, R.D. Peacok, J. Chem. Soc. (1961) 3132.
[56] Psaroudakis, K. Mertis, D.G. Liakos, E.D. Simandiras, Chem. Phys. Lett. 369 (2003) 490.

Polyhedron 28 (2009) 2385–2390

Contents lists available at ScienceDirect

Polyhedron

journal homepage: www.elsevier.com/locate/poly

3D-supramolecular copper(I) cyanide coordination polymers through hydrogen bonding

Safaa El-din H. Etaiw *, Said A. Amer, Mohamed M. El-bendary

Chemistry Department, Faculty of Science, Tanta University, Tanta 31527, Egypt

ARTICLE INFO

Article history:
Received 2 March 2009
Accepted 1 May 2009
Available online 19 May 2009

Keywords:
Copper cyanide
Supramolecular coordination polymer
Acetylpyridine
Hydrogen bonding

ABSTRACT

The reactions of $K_3[Cu(CN)_4]$, 3-acetylpyridine (3-Acpy) or 4-acetylpyridine (4-Acpy) in the presence of Me_3SnCl in H_2O/acetonitrile media at room temperature afford the 3D-supramolecular coordination polymers $(SCPs)_\infty{}^3[Cu_2CN(\mu\text{-}CN)\cdot(3\text{-}Acpy)_2]$ **1** and $_\infty{}^3[Cu_2CN(\mu\text{-}CN)\cdot(4\text{-}Acpy)_2]$ **2**. The structures of **1** and **2** consist of Cu_2CN building blocks which are connected by CN groups, forming 1D-zig-zag chains. Each chain is bonded to another chain by hydrogen bonding into a 2D-layer, which is further stacked in an interwoven mode by π–π stacking interactions and hydrogen bonds in **1** and **2**, as well as Cu···Cu interactions in **1**, to create supramolecular 3D-network structures. The high dimensional topologies of **1** and **2** result mainly from extensive hydrogen bonding and π–π stacking. The long wavelength absorption band at 400–420 nm in the electronic spectra of **1** and **2** is assigned to a CT from copper(I) to the Acpy ligand. Compound **2** exhibits strong luminescence at 485 and 527 nm, corresponding to MLCT and metal-centered transitions, respectively.

© 2009 Elsevier Ltd. All rights reserved.

1. Introduction

There has been much interest in recent years in the design and synthesis of supramolecular coordination polymers, due to their intriguing structural motifs and potential applications in luminescence, conduction, magnetism, ion exchange, gas adsorption, catalysis and biology [1–19]. Recent work has focused on the copper(I) cyanide system because of the known versatility of $Cu(CN)_n$ structural motifs in accommodating various ligands, and Cu(I) compounds have rich fluorescent properties [20–25]. In addition, copper(I) cyanide has shown promise in the assembly of a zeolitic-type framework [26–29] and as a precursor in the synthesis of $YBa_2Cu_3O_{7-x}$ superconductors [30].

The structure and properties of a number of copper(I) cyanide coordination polymers containing nitrogen bases have been reported previously [20,21,31–39]. However, a limited number of copper(I) cyanide coordination polymers incorporating unidentate pyridine bases have been studied [40–42]. $[CuCN(py)_2]$ and $[(CuCN)_2(2\text{-}mpy)_2]$ are single-stranded polymers, with successive copper atoms linked by single linear cyanide bridges with four- or three-coordinate $\mu_2Cu(CN)_2$ or $\mu Cu(CN)_2$ copper environments [40–42]. Also, $[(CuCN)_2(4\text{-}mpy)_3]$ is a one dimensional polymer containing the familiar linear polymeric –Cu(CN)Cu(CN)Cu(CN)– array in which the Cu(1) atom has one pyridine base attached and the Cu(2) atom has two base nitrogen atoms. On the other hand, $[Cu_2(CN)(IN)(HIN)]_n$ (IN: isonicotinate) is based on fused chair-shaped $[Cu_6(\mu\text{-}HIN)_2(\mu\text{-}(IN)_2(\mu\text{-}(CN)_2]$ hexagons, which form a triple interpenetrated 2D-ligand to metal coordinative bonding network and simultaneously a triple interpenetrated 3D-hydrogen bonding network [43].

Extending the previous essays, Cu(I)CN:3/4Acpy adducts have been crystallized from a H_2O/CH_3CN solution containing Me_3SnCl. Acetylpyridine compounds can be considered as versatile ligands for the construction of novel metal–organic frameworks. The *N*-pyridinic and the acetyl groups should allow not only multiple metal coordination, but also supramolecular interactions via hydrogen bonding. Two distinct complexes have been obtained for which single crystals have been isolated and subjected to single crystal X-ray studies.

2. Experimental

All chemicals and solvents used in this study were of analytical grade, supplied by Aldrich or Merck and were used as received, except $K_3[Cu(CN)_4]$ which was prepared in the laboratory according to the literature [44,45]. Microanalyses (C, H, N) were carried out with a Perkin Elmer 2400 automatic elemental analyzer. The IR spectra were recorded on a Perkin Elmer 1430 Ratio Recording Infrared Spectrophotometer as KBr discs. Electronic absorption spectra as solid matrices were measured on a Shimadzu (UV-310PC) spectrometer. Fluorescent spectra as solid matrices were measured with a Perkin Elmer (LS 50 B) spectrometer.

* Corresponding author. Tel.: +20222601379.
E-mail address: Safaaetaiw@hotmail.com (Safaa El-din H. Etaiw).

0277-5387/$ - see front matter © 2009 Elsevier Ltd. All rights reserved.
doi:10.1016/j.poly.2009.05.028

2.1. Synthesis of $[(CuCN)_2{\cdot}(L)_2]$ [L = 3-Acpy, 4-Acpy] (**1**, **2**)

A solution of 90 mg (0.3 mmol) of $K_3[Cu(CN)_4]$ in 30 mL H_2O was added, under gentle stirring, to a solution of 189 mg (0.95 mmol) of Me_3SnCl in 10 mL H_2O and 0.1 mL (0.916 mmol) of 3-acetylpyridine (3-Acpy) (for **1**) or 4-acetylpyridine (4-Acpy) (for **2**) in 20 mL acetonitrile, and after one week yellow needle or yellow prismatic crystals started growing from the initially clear solution. After filtration, washing with a small cold quantity of H_2O and acetonitrile and over night drying, about 40 mg (75% referred to $K_3[Cu(CN)_4]$) of yellow crystals **1** or about 50 mg (83.3% referred to $K_3[Cu(CN)_4]$) of yellow crystals **2** were obtained. All attempts for the synthesis of **1** and **2** at room temperature in the absence of Me_3SnCl were unsuccessful.

Anal. Calc. for **1** ($C_{16}H_{14}N_4O_2Cu_2$): C, 45.5; H, 3.3; N, 13.2. Found: C, 45.2; H, 3.1; N, 13.1%.

Anal. Calc. for **2** ($C_{16}H_{14}N_4O_2Cu_2$): C, 45.5; H, 3.3; N, 13.2. Found: C, 45.2; H, 3.2; N, 13.1%.

2.2. Single crystal structure determination

Structural measurements for **1** and **2** were performed on a Kappa CCd Enraf Nonius FR 90 four cycle geniometer with graphite monochromatic Mo Kα radiation {[λ Mo Kα] = 0.71073 Å} at 25 ± 2 °C. All structures were resolved using direct methods and all of the non-hydrogen atoms were located from the initial solution or from subsequent electron density difference maps during the initial stages of the refinement. After locating all of the non-hydrogen atoms in each structure, the models were refined against F^2, first using isotropic and finally using anisotropic thermal displacement parameters. The positions of the hydrogen atoms were then calculated and refined isotropically, and then the final cycle of refinements was performed. The cyano groups of all structures were ordered unless otherwise stated. Crystallographic data for **1** and **2** are summarized in Table 1. Selected bond distances and bond angles are given in Tables 2 and 4. The C13 and N11 atoms of the two bridging cyanide groups in **2** are centrosymmetric and were modelled as disordered over a pair of sites of equal occupancy. The disorder of these cyano groups in the asymmetric unit of **2** reflects the observation that *Rw* remains constant upon adopting a C atom or N atom at these sites.

Table 1
Crystal data for **1** and **2**.

	1	**2**
Empirical formula	$C_{16}H_{14}N_4O_2Cu_2$	$C_{16}H_{14}N_4O_2Cu_2$
Formula weight (g/mol)	421.406	421.406
T (K)	298	298
Crystal system	monoclinic	monoclinic
Space group	$P21/c$	$C2/c$
a (Å)	12.0343(9)	18.3689(3)
b (Å)	9.0576(6)	17.0722(7)
c (Å)	7.5298(4)	14.3451(6)
α (°)	90.00	90.00
β (°)	90.469	129.960(3)
γ (°)	90.00	90.00
V (Å^3)	820.73(9)	3448.2(2)
Z	2	8
μ(Mo Kα) (mm^{-1})	2.59	2.48
Calculated density (g cm^{-3})	1.584	1.624
Goodness-of-fit (GOF) on F^2	1.312	2.662
F(0 0 0)	394	1695
R indices [$I > 3\sigma(I)$] R_1/wR_2]	0.034/0.064	0.040/0.072
R indices(all data)	0.057/0.068	0.094/0.081
R_{int}	0.026	0.029
Data/restraints/parameters	983/0/109	1827/0/207

Table 2
Bond lengths (Å) and bond angles (°) of **1**.

Cu1–N2	2.098(2)	N2–Cu1–N4	99.66(9)
Cu1–N4	1.940(2)	N2–Cu1–C6	119.22(11)
Cu1–C6	1.881(3)	N4–Cu1–C6	134.40(12)
C7–C9	1.481(5)	Cu1–N2–C5	122.6(2)
N4–C6	1.147(4)	Cu1–N2–C11	148.81(14)
O3–C7	1.217(4)	Cu1–N2–C12	120.2(2)
C7–C10	1.494(4)	Cu1–N4–C6	163.4(2)
Cu1–N4^{iv}	3.024(2)	Cu1^{i}–C6–N4	173.9(3)
Cu1–C6^{v}	2.790(3)	O9–H9C–N4	136.26(3)
Cu1–Cu1^{i}	4.9068(3)	N2–C5^{vi}	3.641(3)
Cu1–Cu1^{iii}	2.9580(7)	N2–C6^{iv}	3.434(4)
N4–H5	2.714(2)	N2–C6^{v}	3.324(4)

Symmetry codes: (i) $x-1,1/2-y,1/2+z$; (ii) $-1-x,1/2+y,3/2-z$, (iii) $x-1/2,1/2-y,1/2-z$; (iv) $1/2+x,y,1/2-z$; (v) $1/2+x,1/2-y,1/2-z$.(vi) $x,1/2-y,1/2+z$.

3. Results and discussion

The room temperature reactions of the ternary adducts $K_3[Cu(CN)_4]$, Me_3SnCl and L (L = (3-Acpy) or (4-Acpy)) afford yellow crystals of the tin free $[Cu_2(CN)_2{\cdot}(3\text{-Acpy})_2]$, **1** and $[Cu_2(CN)_2{\cdot}(4\text{-Acpy})_2]$, **2**. There are two abnormal features in these reactions: they proceed at room temperature producing significant amounts of single-phase products and they result exclusively in the formation of the tin free assemblies **1** and **2**, in spite of the presence of Me_3SnCl to produce, as was expected, zeolitic-type SCP. The room temperature products of **1** and **2** can be considered as novel SCPs that may be compared with those prepared by hydrothermal reactions for $[Cu_2(CN)_2{\cdot}L]$ [46–48] or otherwise with those prepared recently by using atmospheric aqueous reflux reactions, $[Cu_2(CN)_2{\cdot}(L)]$ and $[(CuCN)_3{\cdot}(L)]$ [49]. Such room temperature reactions avoid the substantial drawbacks of hydrothermal syntheses (including small reaction scales, modest yields and mixed products) or the open reflux reactions (including long time and relatively high temperature). On the other hand, in the absence of Me_3SnCl, the reaction does not proceed and consequently no product is formed under the used experimental conditions. The presence of Me_3SnCl seems to be essential for the reaction to proceed thermodynamically at room temperature, a point which needs further investigation. However, it is known that the Me_3SnCl molecule has a weak Sn···Cl bond, since the non-polar trimethyltin(IV) units are bridged to the chlorine atoms by unequal, and relatively large, (2.430 and 3.269 Å) distances [50]. In this case, one might suggest that this may cause decomposition of the tetrahedral $[Cu(CN)_4]^{-3}$ anion to different $(Cu)_n(CN)_m$ fragments which are readily assembled with the other reactants in solution to produce the thermodynamically more stable SCP. The Me_3SnCl may form, in this case, the more stable Me_3SnCN, since the Sn–C or the Sn–N bond distances of the ordered C–N–Sn–N–C or even N–C–Sn–C–N chains are in the range of 2.49 ± 0.02 Å [51], or it may form the $(Me_3Sn)_2$ dimer. Nevertheless, it is quite clear that Me_3SnCl plays an important role in the formation of the different topologies of the SCPs of Cu(I)CN and heterocyclic ligands [52].

3.1. Crystal structure of $[Cu_2(CN)_2{\cdot}(3\text{-Acpy})_2]$, **1**

The asymmetric unit of **1** comprises half of the formula unit, it involves one crystallographically distinct copper(I) atom, which has an identical symmetry operation, one ordered cyanide group and one 3-Acpy ligand (Fig. 1). The X-ray analysis reveals that the structure of **1** displays a 1D-extended corrugated chain of $(CuCN)_n$ with the 3-Acpy ligand attached to every Cu atom (Fig. 2). The coordination geometry of the Cu(1) atom can be described as distorted trigonal planar, and it is coordinated by two cyano groups (N–Cu1–C) and one 3-Acpy ligand. The angles of

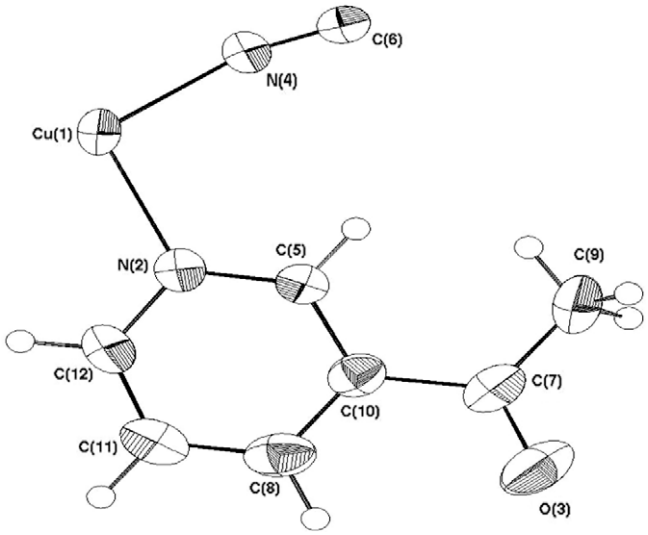


Fig. 1. An ORTEP plot showing the asymmetric unit of **1** with the atom labelling scheme.

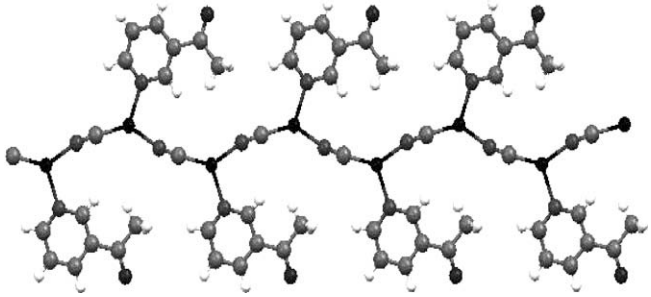


Fig. 2. A 1D-extended chain of CuCN in **1** along the *a*-axis.

the trigonal structure deviate largely from 120° (Table 2) due to the pyramidalization of the trigonal structure around the Cu atom which is caused by close Cu–C6 (2.791 Å), Cu–N4 (3.024 Å) or Cu–Cu (2.959 Å) contacts. Alternatively, the structure of **1** can be considered to consist of Cu_2CN building blocks which are connected by the CN group forming a one dimensional zig-zag chain with the 3-Acpy ligands, which are nearly parallel (ca: 1.19°), located above and below the chain. This one dimensional zig-zag chain is bonded to another chain by hydrogen bonds between the oxygen atoms of 3-Acpy in one chain and the hydrogen atoms of 3-Acpy in another chain, organizing these chains into a two dimensional layer (O3–H11 = 2.512 Å) (Fig. 3).

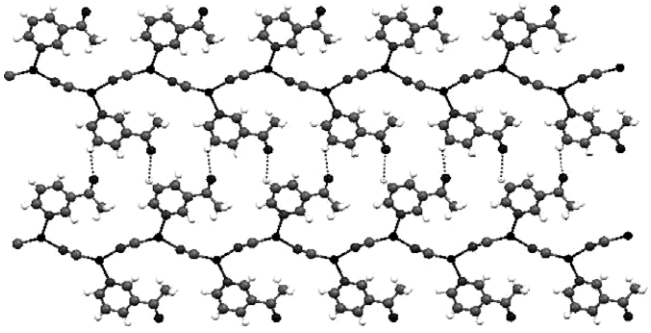


Fig. 3. A view of the hydrogen bonds between two adjacent chains along the *b*-axis in **1**.

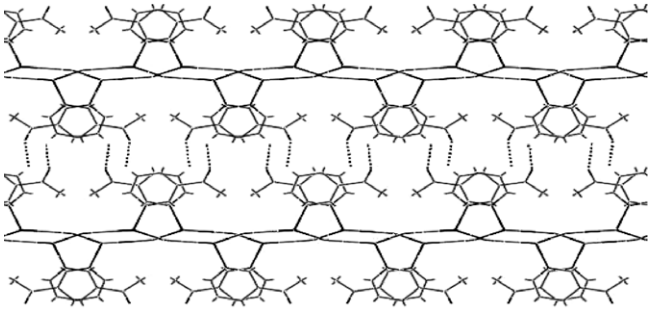


Fig. 4. A packing diagram of **1** showing π–π stacking and hydrogen bonds along the *c*-axis.

Table 3
Hydrogen bond lengths (Å) and bond angles (°) in **1**.

N4–H9A	3.154(2)	C9–H9A···N4	116.68
O3–H8^{ii}	3.127(3)	C8–H8^{ii}···O3	102.58
N4–H9C	2.934(2)	C9–H9C···N4	136.26
O3–H8^{i}	2.888(2)	C8–H8^{i}···O3	114.33
N4–H5	2.714(2)	C5–H5···N4	116.08
O3–H11^{i}	2.512(3)	C11–H11^{i}···O3	131.00

Symmetry codes: (i) $-1-x,1/2+y,3/2-z$; (ii) $-x,1-y,-z$.

The two dimensional layers of **1** are close packed in a parallel fashion along the *c*-axis, while the 3-Acpy planes are stacked in an interwoven mode along the *c*-axis (Fig. 4) causing π–π stacking interactions (ca: 3.58 Å) [53]. In addition, hydrogen bonds between the layers, ca: 2.513–3.127 Å (Table 3) create a supramolecular 3D-network structure containing channels with separation distances in the range 2.959–4.906 Å (Fig. 5). These corrugated layers are also stacked along the *b*-axis, and they are interconnected mainly by Cu–Cu interactions; Cu–Cu = 2.959 Å [54–58], and metal–π interactions between the Cu ions from one chain and the pyridine rings from the adjacent layer; 2.791 Å. In view of the recent discussions of cuprophilic interactions [49,59–61], one might suggest that the weak Cu–Cu interaction seems to be realistic according to a detailed quantum chemical study focused on pairs of $Cu^{I}XY$ systems, as experimentally determined Cu–Cu distances of convincing examples in favour of cuprophilic attraction are usually longer than 2.70 Å, [59–61]. Thus, the value of 2.959 Å falls within the range of cuprophilic interactions. All these interactions, especially hydrogen bonds and the cuprophilic interaction, play an important role in constructing the 3D-network structure of **1**.

3.2. Crystal structure of $[Cu_2(CN)_2{\cdot}(4\text{-Acpy})_2]$, **2**

The structure of the organotin-free product **2** seems to be different from the prototype compound **1**. The asymmetric unit of **2** involves not only two copper centers, Cu(1) and Cu(2), and two cyanide groups, but also two organic ligands; 4-Acpy (Fig. 6). One 4-Acpy (N3,O4) ligand is coordinated to Cu1 while the other

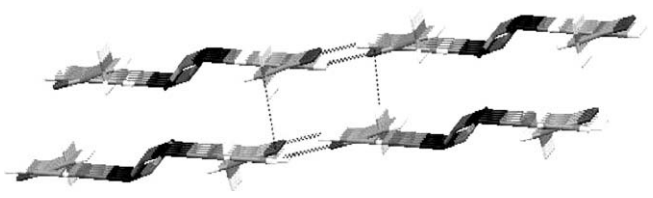


Fig. 5. A packing diagram showing the hydrogen bonds and channels in **1** along the *b*-axis.

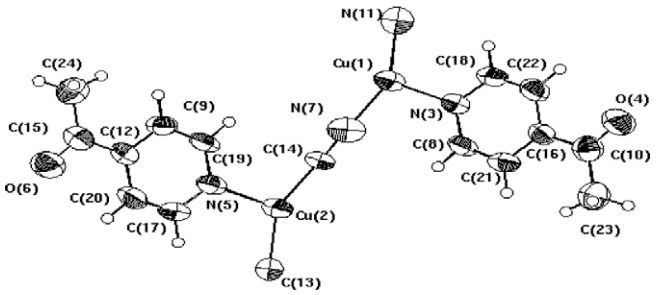


Fig. 6. An ORTEP plot showing the asymmetric unit of **2** with the atom labelling scheme.

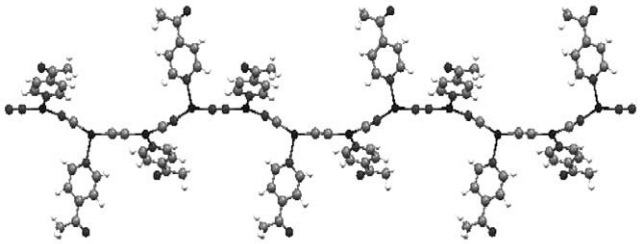


Fig. 7. 1D-puckered chain of 2 in the ac-plane with the 4-Acpy ligands tilted out of the plane on both sides of the chain by 66.48°.

4-Acpy (N5,O6) is coordinated to Cu2 in a unique fashion in that the two ligands have two different planes with an angle equal to 66.48° (Fig. 7). The cyanide group (C14N7) is ordered, exhibiting a Cu–C distance of 1.853 Å and Cu–N distance of 1.896 Å, while the other cyanide group (C13N11) is disordered (Table 4).

Each of Cu1 and Cu2 is coordinated to two cyanide groups and one 4-Acpy ligand, forming a distorted trigonal configuration. Three coordination is a characteristic feature not only of Cu(I) cyanide structures such as $KCu(CN)_2$ [62], $NaCu(CN)_2{\cdot}2H_2O$ [63] and $K[Cu_2(CN)_3]{\cdot}H_2O$ [64], but also of cyanohalides [65] and cyano amine structures [66]. The angles of the trigonal structure deviate largely from 120° (Table 4) due to the pyramidalization of the trigonal structure around the Cu atoms, which is caused by close Cu–C or Cu–N contacts in the range 2.991–3.039 Å (Table 4).

The structure of **2** consists of Cu_2CN building blocks which are connected by CN groups forming a 1D-puckered chain, while the 4-Acpy ligands intermingle on both sides of the chain in a unique way (Fig. 7). The lengths of the Cu1–N3 and Cu2–N5 bonds are

Table 4
Bond lengths (Å) and bond angles (°) of **2**.

Cu1–N3	2.105(2)	N3–Cu1–N7	105.85(9)
Cu1–N7	1.895(2)	N3–Cu1–N11	105.72(8)
Cu1–N11	1.860(2)	N7–Cu1–N11	148.06(9)
Cu2–N5	2.099(2)	N5–Cu2–C13	105.94(8)
Cu2–C13	1.885(2)	N5–Cu2–C14	106.39(9)
Cu2–C14	1.855(2)	C13–Cu2–C14	147.34(9)
N7–C14	1.150(3)	Cu1–N3–C8	121.9(2)
$N11–N11^{i}$	1.177(4)	Cu1–N3–C18	121.6(2)
$C13–C13^{ii}$	1.132(4)	Cu2–N5–C17	122.3(2)
C10–C16	1.493(4)	Cu2–N5–C19	122.1(2)
O4–C10	1.215(3)	Cu1–N7–C14	169.0(2)
C10–C23	1.492(4)	Cu1–N11–C11	175.71(2)
C12–C15	1.498(4)	Cu2–C13–N13	174.16
O6–C15	1.207(3)	$Cu2–C13^{ii}$	3.014(2)
C15–C24	1.480(4)	Cu1–C18	3.039(6)
$Cu1–N11^{i}$	3.036(2)	$Cu1–Cu1^{i}$	4.8934(6)
Cu2–N7	2.991(2)	$Cu2–Cu2^{ii}$	4.8957(6)

Symmetry codes: (i) $x-1,1/2-y,1/2+z$; (ii) $-1-x,1/2+y,3/2-z$.

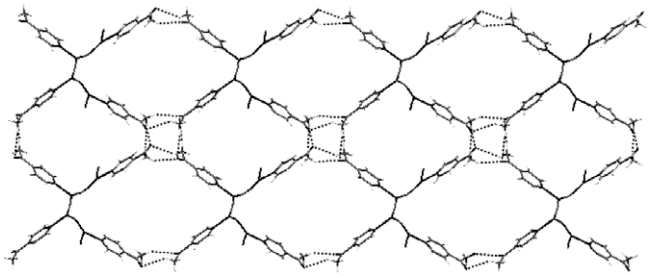


Fig. 8. A view of the hydrogen bonds between two adjacent chains along the *b*-axis in **2**.

Table 5
Hydrogen bond lengths (Å) and bond angles (°) in **2**.

O6–H23C	2.704(2)	C23–H23C···O6	146.68
O6–H24B	2.628(2)	C24–H24B···O6	169.18
O6–H8	2.628(2)	C8–H8···O6	129.32
O6–H21	2.8022)	C21–H21···O6	122.53
O4–H23B	2.617(2)	C23–H23B···O4	168.59
O4–H24C	2.717(2)	C24–H24C···O4	145.93
O4–H19	2.673(2)	C19–H19···O4	129.86

2.105 and 2.099 Å, respectively which are in the usual range reported for the prototype compounds [40–42]. Alternatively the structure can be viewed as two N11–Cu1–N7–C14–Cu2 sub-building blocks connected by the disordered cyanide group (C13–N13), forming the main building blocks of the structure **2**, along with two 4-Acpy ligands located on both sides of the chain. On the other hand, the shape of the puckered chain looks like a fan with four arms that have two different lengths, 6.404 and 8.697 Å. This main building block can propagate along the *b*-axis via hydrogen bondings where the repeating main building blocks are connected by the O4···H24C bond; 2.717 Å, O6···H23C bond; 2.704 Å, O6···H24B bond; 2.628 Å, and O4···H23B bond; 2.617 Å (Fig. 8, Table 5) and along the *a*-axis via the second disordered cyanide group forming a 2D-network structure. Alternatively, the main building block forms down the projection of the *c*-axis zig-zag $(CuCN)_4$ chain with two 4-Acpy ligands above the chain while the other two 4-Acpy ligands are locate underneath the chain, creating a cavity with dimensions of 9.659 × 12.725 Å, which is capable of accommodating two 4-Acpy ligands of another building block (Fig. 9). It is worth mentioning that there are no kinds of interactions; hydrogen bonding or π–π stacking, between the fragments of the main

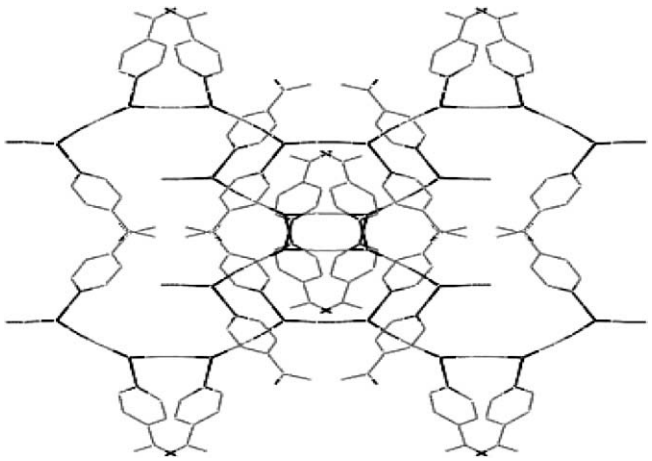


Fig. 9. A 3D-network showing cavities in **2** along the *c*-axis.

Table 6
The wavenumbers (cm^{-1}) of different vibrational modes of **1** and **2**.

No.	Compound	$\nu_{(CH)}$ (arom.)	$\nu_{(CH)}$ (aliph.)	$\nu_{(C\equiv N)}$	$\nu_{(C=O)}$	$\nu_{(C=N)}$ and $\nu_{(C=C)}$ (arom.)	δ_{CH} of L	γ_{CH} of L
1	$[Cu_2(CN)_2{\cdot}(3\text{-Acpy})_2]$	3093m 3000w	2921m	2112s	1683s	1583s–1477m	1420s	697s 653s
2	$[Cu_2(CN)_2{\cdot}(4\text{-Acpy})_2]$	3035m	2921m	2126s 2041m	1698s	1601s–1551s 1486m	1415s	779s 758s

s = strong, m = medium, w = weak.

building blocks. However, in spite of the shape of the structure of the main building blocks down the projection of the *c*-axis looking like a circle, it forms an open framework at the methyl groups along any other axes. The distance between two Cu1 atoms in this presented circle is 13.47 Å. The extended structure of **2** is interwoven, creating polygon structures which connect the main building blocks, forming a 3D-network structure. This polygon structure is formed via the O4 and O6 atoms which form hydrogen bonds with the hydrogen atoms of the pyridine ring (H8, H19), and of the acetyl groups, O4···H19 = 2.673 Å, O6···H8 = 2.681 Å, O6···H24B = 2.628 Å, as well as Cu(I) contacts; Cu2–C13 = 3.014 Å (Table 5). It worth mentioning that there is no Cu–Cu interaction, since the shortest Cu–Cu distances are Cu2–Cu2 = 5.828 Å, Cu1–Cu2 = 6.967 Å and Cu1–Cu1 = 8.541 Å, while the distance between the chains along the *a*-axis are Cu1–Cu2 = 11.264 Å, C14–C14 = 10.386 Å and N7–N7 = 11.703 Å.

3.3. Infrared spectra of *1* and *2*

The IR spectra of **1** and **2** exhibit bands characteristic of the $(CuCN)_n$ fragment and the unidentate ligand; (3-Acpy, 4-Acpy) (Table 6). The bands at 3035–3093, 3000, 2921, 1415–1420, 653–697 and 779–758 cm^{-1} are attributed to $\nu_{CH(arom.)}$, $\nu_{CH(aliph.)}$, δ_{CH} and γ_{CH} of the Acpy ligands in the IR spectra of **1** and **2**, respectively. These bands are shifted to lower wavenumbers than the vibrational frequencies of the free ligands due to the formation of hydrogen bonds between the hydrogen atoms of the ligands and the other donor sites of the $(CuCN)_n$ fragment [67]. On the other hand, the bands at 1583–1601, 1551 and 1477–1486 cm^{-1} are attributed to $\nu_{C=N}$ and $\nu_{C=C}$ of Acpy ligands in **1** and **2**, respectively. These bands exhibit small shifts to lower wavenumbers compared to those of the free Acpy ligands, supporting the coordination of 3-Acpy and 4-Acpy to the Cu(I) sites.

Also, the IR spectra of **1** and **2** show a strong band at 1683–1698 cm^{-1} which can be assigned to $\nu_{C=O}$. This band is shifted to a lower wavenumber than the vibration frequency of the carbonyl group of the free ligands due to the formation of hydrogen bonds.

It is worth mentioning that the $\nu_{C\equiv N}$ bond of **1** and **2** is different from that of $K_3[Cu(CN)_4]$, which is potentially used as one of the adducts for forming **1** and **2**. The $\nu_{C\equiv N}$ band of $K_3[Cu(CN)_4]$ appears at 2081 cm^{-1}. It is obvious that the structures of **1** and **2** are quite different from that of $K_3[Cu(CN)_4]$, but it does contain the $(CuCN)_n$ fragment. The presence of two $\nu_{C\equiv N}$ IR absorption bands in the spectrum of **2** at 2126 and 2041 cm^{-1} supports the presence of two different cyanide groups; one is ordered while the other is disordered. On the other hand, the presence of only one $\nu_{C\equiv N}$ IR absorption band in the spectrum of **1** at 2112 cm^{-1} supports the presence of one ordered cyanide group.

It is worth mentioning that **1** and **2** are associated with non-linearly bridging cyanide groups as their stretching frequencies lie close to that of the genuine salt [68,69].

3.4. Electronic absorption and emission spectra of *1* and *2*

The electronic absorption spectra of **1** and **2** display absorption bands for 3-Acpy and 4-Acpy at 260–280, 300–310 and 400–420 nm. The band at 260 nm corresponds to the $^1L_b \leftarrow {}^1A$ transition in pyridine, which resembles that of benzene. The band at 280 nm is due to the π–π^* transitions within the acetyl moiety. On the other hand, the band observed at 310 and 300 nm in the spectra of **1** and **2,** respectively, can be assigned to n–π^* transitions of the acetyl moiety. The long wavelength absorption band at 400–420 nm can be assigned to a CT from the copper(I) to the Acpy ligand. The band is red shifted on going from **1** to **2**. The emission spectra of free 3-Acpy and 4-Acpy do not show any emission bands under the used experimental conditions, however, **2** exhibits strong luminescence at 485 and 527 nm (Fig. 10). The high energy emission band is due to a metal-to-ligand charge transfer (MLCT), where the electron is transferred from the Cu(I) center to the unoccupied π^*–orbital of the 4-Acpy ligand, while the low-energy emission may be ascribed to metal-centered transitions of the type $3d^{10} \rightarrow 3d^9\,4s^1$ and $3d^{10} \rightarrow 3d^9\,4p^1$ on the Cu(I) center. Compound **1** does not exhibit any luminescence properties under the used experimental conditions.

4. Discussion

These results reinforce the observation that the cyanide group is an effective bridging ligand which can link together two copper centers; μ_2-1,2-CN. The cyanide group is a popular bridging ligand for the construction of the solid state structures, and appears to be a potentially useful synthon for crystal engineering to obtain supramolecular materials with valuable physical and chemical properties. In spite of the fact that **1** and **2** are tin free compounds, the presence of Me_3SnCl has an important role for the synthesis of copper(I) cyanide SCPs at room temperature, since such SCPs are usually produced by solvothermal reactions. Supramolecular coordination polymers with the same composition do not necessary have the same structure. In spite of the stoichiometry of **1** and **2**

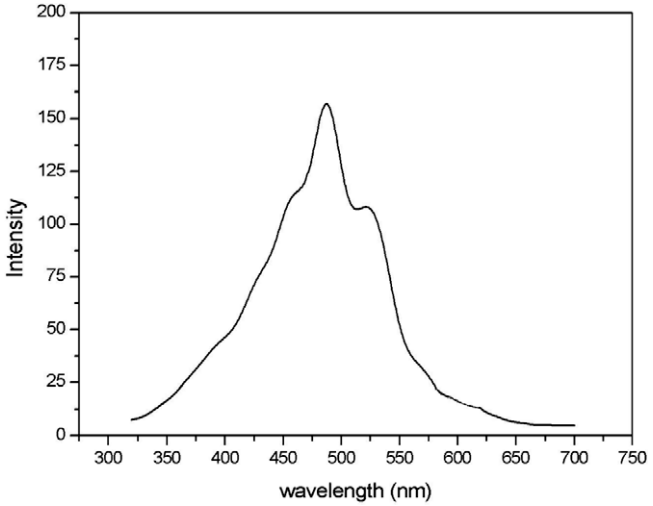


Fig. 10. Solid-state emission spectrum of **2** upon excitation at 350 nm.

being the same, the 3D-network of **1** is created by hydrogen bonding, π–π stacking and Cu···Cu interactions while the 2D-layers of **2** form a non-interpenetrating 3D-network via hydrogen bonging. The acetyl group plays an essential role in the formation of hydrogen bonding to generate 3D-network structures. For comparison, substituted pyridine adducts of copper(I) cyanide have shown considerable capacity for steric control of the coordination environment of copper by variation of the substitution pattern of the base [40–42]. The arrays of $[CuCN(py)_2]$, $[(CuCN)_2(2\text{-mpy})_2]$ and $[(CuCN)_2(4\text{-mpy})_3]$ are low dimensional single-stranded polymers, comprising a sequence of copper(I) atoms linked by single end-coordinated cyanides, with one or two pyridine ligands appended, with associated copper atom coordination numbers of three or four. No hydrogen bonds are observed in these polymers. On the other hand, replacing the methyl group by an acid group affords the three dimensional interpenetrated $[Cu_2(CN)(IN)(HIN)]_n$ polymer. 2D-layers are formed by interpenetrated $[Cu_6(CN)_2(C_6H_4\text{-}NO_2)_2(C_6H_4NO_2H)_2]$ hexagons stacked by short hydrogen bonds. Each independent 2D-network is hydrogen bonded to only one of the three independent networks of an adjacent layer, to give a 3D-supramolecular architecture. Cuprophilic interactions and π–π stacking are avoided in the network, leaving the combination of coordination and hydrogen bonds to be responsible for the formation of the triple interpenetrated 3D supramolecular material with relatively high thermal stability [43]. In the structures of **1** and **2**, the acetyl groups are also capable of creating 3D-networks via hydrogen bonding. Thus, it is clear that the organic ligands may be introduced as structural components of composite inorganic–organic materials and used to propagate high dimensional-topologies. In this case the hydrogen bonds play an essential role in constructing 3D-topologies exhibiting more flexible networks which should open a very concrete way to porous materials.

Supplementary data

CCDC 191302 and 191303 contain the supplementary crystallographic data for **1** and **2**. These data can be obtained free of charge via http://www.ccdc.cam.ac.uk/conts/retrieving.html, or from the Cambridge Crystallographic Data Centre, 12 Union Road, Cambridge CB2 1EZ, UK; fax: (+44) 1223-336-033; or e-mail: deposit@ccdc.cam.ac.uk.

References

[1] C.N.R. Rao, S. Natarajan, R. Vaidhyanathan, Angew. Chem., Int. Ed. 43 (2004) 1466.
[2] A. Erxleben, Coord. Chem. Rev. 246 (2003) 203.
[3] G.V. Oshovsky, D.N. Reinhoudt, W. Verboom, Angew. Chem., Int. Ed. 46 (2007) 2366.
[4] O.M. Yaghi, M. O'Keeffe, N.W. Ockwig, H.K. Chae, M. Eddaoudi, J. Kim, Nature 423 (2003) 705.
[5] R. Custelcean, B.A. Moyer, Eur. J. Inorg. Chem. (2007) 1321.
[6] L. Pan, D.H. Olson, L.R. Ciemnolonski, R. Heddy, J. Li, Angew. Chem., Int. Ed. 45 (2006) 616.
[7] S.-L. Zheng, X.-M. Chen, Aust. J. Chem. 57 (2004) 703.
[8] C. Janiak, J. Chem. Soc., Dalton Trans. (2003) 2781.
[9] U. Mueller, M. Schubert, F. Teich, H. Puetter, K. Schierle-Arndt, J. Pastré, J. Mater. Chem. 16 (2006) 626.
[10] D. Maspoch, D. Ruiz-Molina, J. Veciana, Chem. Soc. Rev. 36 (2007) 770.
[11] D. Maspoch, D. Ruiz-Molina, J. Veciana, J. Mater. Chem. 14 (2004) 2713.
[12] S.R. Batten, K.S. Murray, Coord. Chem. Rev. 246 (2003) 103.
[13] G. Férey, Chem. Soc. Rev. 37 (2008) 191.
[14] S. Bureekaew, S. Shimomura, S. Kitagawa, Sci. Technol. Adv. Mat. 9 (2008) Art. No. 014108.
[15] T. Korzeniak, K. Stadnicka, R. Pelka, M. Balanda, K. Tomala, K. Kowalski, B. Sieklucka, Chem. Commun. (2005) 2939.
[16] R.-Q. Zou, H. Sakurai, Q. Xu, Angew. Chem., Int. Ed. 45 (2006) 2542.
[17] L. Yi, B. Ding, B. Zhao, P. Cheng, D.Z. Liao, S.P. Yan, Z.H. Jiang, Inorg. Chem. 43 (2004) 33.
[18] J.M. Zheng, S.R. Batten, M. Du, Inorg. Chem. 44 (2005) 3371.
[19] P.V. Bernhardt, F. Bozoglián, B.P. Macpherson, Manuel Martíınez, Coord. Chem. Rev. 249 (2005) 1902.
[20] X. He, C.Z. Lu, D.Q. Yuan, S.M. Chen, J.T. Chen, Eur. J. Inorg. Chem. 11 (2005) 2181.
[21] S.W. Liang, M.X. Li, M. Shao, Z.X. Miao, Inorg. Chem. Commun. 9 (2006) 1312.
[22] H.A. Habib, A. Hoffmann, H.A. Hoppe, G. Steinfeld, C. Janiak, Inorg. Chem. 48 (2009) 2166.
[23] S.-W. Liang, M.-X. Li, M. Shao, X. He, J. Mol. Struct. 875 (2008) 17.
[24] H. Wang, M.-X. Li, M. Shao, X. He, Polyhedron 26 (2007) 5171.
[25] L.S. Wen, H. Xiang, S. Min, L.M. Xing, J. Coord. Chem. 61 (2008) 2999.
[26] B.F. Hoskins, R. Robson, J. Am. Chem. Soc. 112 (1990) 1546.
[27] A.K. Brimah, E. Siebel, R.D. Fischer, N.A. Davies, D.C. Apperley, R.K. Harris, J. Organomet. Chem. 475 (1994) 85.
[28] L.C. Brousseau, D. Williams, J. Kouvetakis, M. O'Keefe, J. Am. Chem. Soc. 119 (1997) 6292.
[29] C. Zhang, G. Jin, Y. Xu, H.-K. Fun, X. Xin, Chem. Lett. (2000) 502.
[30] N.A. Khan, N. Baber, M. Zafar Iqbal, M. Mazhar, Chem. Mater. 5 (1993) 1283.
[31] E. Colacio, R. Kivekas, F. Lloret, M. Sunberg, J.S. Varela, M. Bardaji, A. Laguna, Inorg. Chem. 41 (2002) 5141.
[32] J.M.D. Vera, J.M. Moreno, E. Colacio, Inorg. Chim. Acta 357 (2004) 611.
[33] L. Triscikova, I. Potocnak, J. Chomic, P. Baran, Transition Met. Chem. 31 (2006) 504.
[34] H. Mao, C. Zhang, C. Xu, H. Zhang, X. Shen, B. Wu, Y. Zhu, Q. Wu, H. Wang, Inorg. Chim. Acta 358 (2005) 1934.
[35] X. He, C.Z. Lu, C.D. Wu, L.J. Chen, Eur. J. Inorg. Chem. 12 (2006) 2491.
[36] D.J. Chestnut, A. Kusnetzow, R.R. Birge, J. Zubieta, Inorg. Chem. 38 (1999) 2663.
[37] D.J. Chesnut, J. Zubieta, Chem. Commun. (1998) 1707.
[38] Xiong-Bin Chen, Bin Chen, Yi-Zhi Li, Xiao-Zeng You, Appl. Organomet. Chem. 21 (2007) 777.
[39] O. Teichert, W.S. Sheldrick, Z. Anorg. Allg. Chem. 626 (2000) 1509.
[40] G.A. Bowmaker, C. Pettinari, B.W. Skelton, N. Somers, N.A. Vigar, A.H. White, Z. Anorg. Allg. Chem. 633 (2007) 415.
[41] G.A. Bowmaker, K.C. Lim, B.W. Skelton, A.H. White, Z. Naturforsch 59 (2004) 1264.
[42] J.C. Dyason, P.C. Healy, L.M. Engelhardt, C. Pakawatchai, V.A. Patrick, A.H. White, J. Chem Soc., Dalton Trans. (1985) 839.
[43] P. Amo-Ochoa, P.J. Sanz Miguel, O. Castillo, F. Zamora, CrystEngComm 9 (2007) 987.
[44] J.W. Eastes, W.M. Burgess, J. Am. Chem. Soc. 64 (1942) 1187.
[45] J.W. Eastes, W.M. Burgess, J. Am. Chem. Soc. 64 (1942) 2715.
[46] S.J. Hibble, A.M. Chippindal, Z. Anorg. Allg. Chem. 631 (2005) 542.
[47] D.J. Chesnut, D. Plewak, J. Zubieta, J. Chem. Soc., Dalton Trans. (2001) 2567.
[48] Y.-N. Chi, F.-Y. Cui, Y.-Q. Xu, C.-W. Hu, Eur. J. Inorg. Chem. (2007) 4375.
[49] T.A. Tronic, K.E. deKrafft, M.J. Lim, A.N. Ley, .R.D. Pike, Inorg. Chem. 46 (2007) 8897.
[50] J.L. Lefferts, K.C. Molly, M.B. Hossain, D. Vander Helen, J.J. Zuckerman, J. Organomet. Chem. 240 (1982) 349.
[51] P. Avalle, R.K. Harris, Hilka Hanika-Hiedl, R. Dieter Fisher, Solid State Sci. 6 (2004) 1069.
[52] H.H. Heidl, S.E.H. Etaiw, M.Sh. Ibrahim, A.S.B. El-din, R.D. Fischer, J. Organomet. Chem. 684 (2003) 329. and references therein.
[53] C. Janiak, J. Chem. Soc., Dalton Trans. (2000) 3885.
[54] P.K. Mehrotra, R. Hoffmann, Inorg. Chem. 17 (1978) 2187.
[55] K.M. Merz, R. Hoffmann, Inorg. Chem. 27 (1988) 2120.
[56] N. Kuganathan, J.C. Green, Chem. Commun. (2008) 2432.
[57] P.C. Ford, E. Cariati, J. Bourassa, Chem. Rev. 99 (1999) 3625. and references therein.
[58] P.C. Ford, A. Vogler, Acc. Chem. Res. 26 (1993) 220.
[59] J.M. Goodwin, P.-C. Chiang, M. Brynda, K. Penkina, M.M. Olmstead, T.E. Patten, J. Chem. Soc., Dalton. Trans. (2007) 3086.
[60] A. Sundararaman, L.N. Zakharov, A.L. Rheingold, F. Jäkle, Chem. Commun. (2005) 1708.
[61] H.L. Hermann, G. Boche, P. Schwedtfeger, Chem. Eur. J. 7 (2001) 333.
[62] D.T. Cromer, J. Phys. Chem. 61 (1957) 1388.
[63] C. Kappenstien, R.P. Hugel, Inorg. Chem. 16 (1977) 250.
[64] D.T. Cromer, A.C. Larson, Acta Crystallogr. 15 (1962) 397.
[65] G.A. Bowmaker, H. Hartl, V. Vraban, Inorg. Chem. 39 (2000) 4548.
[66] F.B. Stocker, T.P. Staeve, C.M. Rienstra, D. Britton, Inorg. Chem. 38 (1999) 984.
[67] A. Spalleti, G. Cruciani, U. Mazzucato, J. Mol. Struct. 612 (2002) 339.
[68] A. Bonardi, C. Carini, C. Pelizzi, G. Pelizzi, G. Predieri, P. Tarasconi, Organomet. Chem. 401 (1991) 283.
[69] A.M.A. Ibrahim, J. Organomet. Chem. 556 (1998) 1.

Polyhedron 28 (2009) 2391–2396

Contents lists available at ScienceDirect

Polyhedron

journal homepage: www.elsevier.com/locate/poly

Pyrazine control of the solid-state supramolecular chemistry of zinc phthalocyanine

Jan Janczak *, Ryszard Kubiak

Institute of Low Temperature and Structure Research, Polish Academy of Sciences, PO Box 1410, 50-950 Wrocław, Poland

ARTICLE INFO

Article history:
Received 3 April 2009
Accepted 1 May 2009
Available online 8 May 2009

Keywords:
Zinc phthalocyanine
Pyrazine
Coordination compounds
Supramolecular complexes
Thermal stability
Crystal structure

ABSTRACT

Crystals of monoaxially coordinated T-shaped and H-shaped supramolecular zinc(II) phthalocyaninato complexes with pyrazine are obtained. In both types of molecules the central Zn atom of ZnPc complexes with pyrazine exhibits 4 + 1 coordination. The Zn atom is equatorially coordinated by four isoindole N atoms of Pc macrocycle and axially by N atom of pyrazine molecule. The interaction of the central Zn atom of ZnPc with the axial N atom of pyrazine leads to a deviation of Zn from the centre of cavity by 0.371(2) Å in the T-shaped complex and by 0.296(2) Å in the H-shaped complex. Thermogravimetric analysis of the crystals exhibits three slopes down, corresponding to the loss in succession of solvated pyrazine molecules, than the loss of ligated pyrazine molecules from the T-shaped complex and the finally the loss of the bridged pyrazine molecule from the H-shaped complex. Finally the thermal processing leads to the β-ZnPc as residue. The UV–Vis spectrum taken in solution shows the batochromic shift in the polar solvent like α-chloronaphthalene in relation to the spectrum in non-polar solvent like benzene.
© 2009 Elsevier Ltd. All rights reserved.

1. Introduction

The syntheses of the metallophthalocyaninate complexes and studies of their properties are still of interest since compounds of this family exhibit many technologically important features [1–4]. One of the useful methods of the MPc's functionalization is their transformative or non-transformative recrystallization in organic solvents. For many MPc's including the zinc phthalocyanine too, the complexes, formed with solvents composed of monodentate N-donating molecules, are well studied and also their single crystal X-ray structures are known [5–10]. This is not so good in the case of the potentially N-bidentately additive molecules like pyrazine (pyz).

The first experimental results on the products of the metallophthalocyanines recrystallization in pyrazine were published just for the ZnPc–pyz system 40 years ago [13]. For this binary system the existence of the only one uniform new phase, with the 2(ZnPc):3(pyz) molar composition was established. However its crystalline structure reminded unexplored.

Later, Hanack and coworkers [12–15] published various experimental results for Fe(II), Co(II) and Ru(II) phthalocyanine systems with pyz. These experiments have shown that depending on the processing conditions used, the FePc, or CoPc or RhPc can form two kinds of compounds with pyrazine, composed appropriately of monomeric or linearly polymerized, pyrazine bridged, molecules. For monomers as well as for polymers the central M(II) ion of MPc complexes exhibits the 4 + 2 coordination, i.e. it is equatorially coordinated by four N-isoindole atoms of the Pc macroring and bis-axially coordinated by two pyz units. It corresponds with the experimentally determined M(II)Pc:pyz units relations, being 1:2 for monomers and close approximately to 1:1 for polymers. The formation of the polymer illustrates Scheme 1.

We are supposing however, that the 2ZnPc:3pyz composition of the crystalline phase cannot be composed of the uniform molecules formed from ZnPc and pyz molecules arranged and connected in such a simple way as shown in Scheme 2.

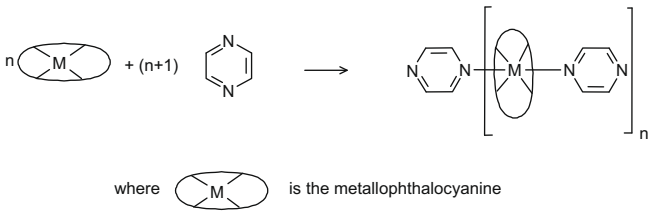
This statement may be supported by the literature data concerning the coordinativity of the zinc ion being in the ZnN_4 chromophore, which indicate that only monoaxial coordination of the relative ZnPc complex with pyz should be expected [10,16]. If so, the ZnPc should at the most be able to form only two different units with pyz as shown in Scheme 3.

In consequence the 2ZnPc:3pyz crystalline phase, independently if it is composed of one kind of such units, or both of them, requires the presence of the additive pyz units in the solid-state. Besides it means that in the ZnPc–pyz system, in contrast to the FePc or CoPc-pyz systems, the polymerization should not be possible.

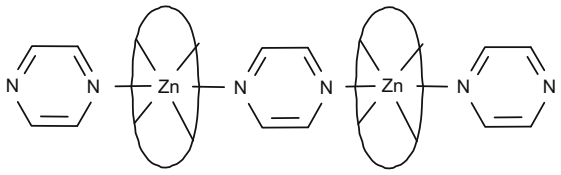
To revise the idea, and in particular to verify how the building blocks of the 2ZnPc:3pyz phase are arranged in the solid state we decided to obtain the crystalline sample of the 2ZnPc:3pyz phase, as well as to investigate the role of pyrazine in controlling the solid-state supramolecular chemistry of ZnPc and the crystal growth.

* Corresponding author.
E-mail address: j.janczak@int.pan.wroc.pl (J. Janczak).

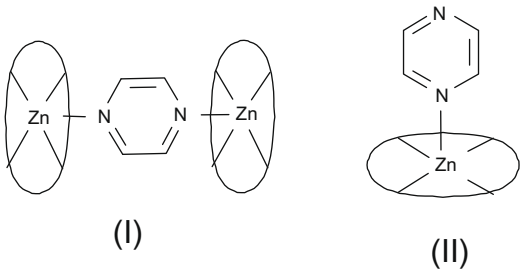
0277-5387/$ - see front matter © 2009 Elsevier Ltd. All rights reserved.
doi:10.1016/j.poly.2009.05.003



Scheme 1.



Scheme 2.



Scheme 3.

2. Experimental

2.1. Preparation and growing of the crystals

The ZnPc and pyz (both obtained from Aldrich), taken at the weight proportion 1:10, were mixed together and next portioned on to the samples, of ca. 1.5 g in mass each. The individual samples were degassed and sealed off in the glass ampoule, ca. 10 cm in length. Next, each of the ampoules was annealed at selected temperature by one-two days in a slightly inclined position.

2.1.1. 2(ZnPc):3(pyz), phase I

The annealing of ampoules at the temperature between the range of 70–150 °C leads to formation of the 2(ZnPc):3(pyz) crystalline phase I. When in the suspension the crystals of phase I were clearly seen, the inclination of the ampoule was reversed and the ampoule was heated again. This allowed to flow off the excessive pyz liquids away from the crystals, which were remained in the opposite part of the ampoule. The samples made of the crystalline phase I were controlled by X-ray dispersive spectroscopic and X-ray powder diffraction methods. The results were in agreement with the experimental data reported earlier [11]. However, the violet single crystals suitable for the X-ray single crystal analysis were selected from the sample processed at 110 °C. The ampoules processed at 70, 90 or 150 °C gave microcrystalline product of phase I. enable to obtain the crystals since the crystals of ZnPc:pyz = 2:3 are stable.

2.1.2. β-ZnPc, phase II

When the samples of the ZnPc/pyz mixture were processed at 190 °C or higher temperature, the effective behaviour of pyz is no longer as ligating but as transporting medium. In the result above the suspension in the free ampoule volume, the violet well developed prysmatic β-ZnPc crystals are growing (Fig. 1). For one of such single crystals the X-ray diffraction data were collected, giving the high quality structural data.

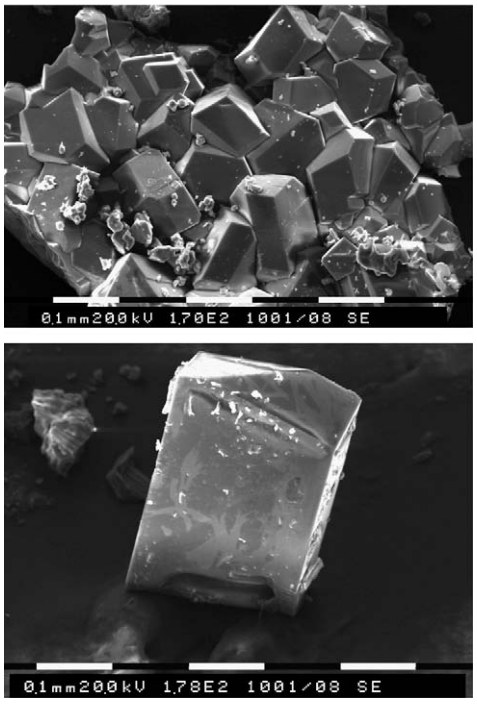


Fig. 1. Crystals of β-ZnPc obtained at 190 °C in the ZnPc-pyrazine system.

2.2. UV–Vis spectroscopic measurements

Measurements of the electronic spectra were carried out at room temperature using a Varian Cary 5E UV–Vis–NIR spectrometer. The UV–Vis spectra were recorded for the phase I as well as for the phase II in polar (α-chloronaphthalene, DMF) and non-polar solvents (benzene, cyclohexane) in 0.5 cm quartz cell.

2.3. Thermal measurements

Thermal analysis was carried out on a Lines L81 thermobalance apparatus with Pt crucibles. Powdered Al_2O_3 has been used as a reference. The measurements have been performed under static air atmosphere on heating from room temperature to 300 °C at the heating rate of 5 °C min^{-1}.

2.4. X-ray powder diffraction measurements

The purified started metallophthalocyanines as well as the rest of the samples left after thermogravimetric analyses were measured on a STOE powder diffractometer equipped with a linear position detector (PSD) [17] using Cu $K\alpha_1$ radiation (λ = 1.540562 Å) at room temperature.

2.5. X-ray data collection and structure determination

A violet single crystal of 2(ZnPc):3(pyz) having edges of 0.34 × 0.27 × 0.22 mm was measured on a KUMA KM-4 CCD diffractometer with graphite monochromatized Mo Kα (λ = 0.71073 Å) radiation at room temperature. The final unit cell parameters were refined by least-squares methods on the basis of 2342 reflections. 32203 reflections (14111 independent, 8608

Table 1
Crystallographic data and final refinement parameters for 2(ZnPc):3(pyz) crystal.

Chemical formula	$C_{76}H_{44}N_{22}Zn_2$
Molecular weight	1396.07
T (K)	295(2)
Crystal system	triclinic
Space group	$P\bar{1}$ (no. 2)
Unit cell dimensions	
a, b, c (Å)	12.047(2), 15.258(3), 17.742(4)
α, β, γ (°)	76.53(1), 88.59(1), 81.72(1)
V (Å^3)	3138.3(11)
Z	2
D_{obs} (measured by flotation)/g cm^{-3}	1.47
$D_{calc.}$ (g cm^{-3})	1.477
Radiation, Mo Kα (Å)	0.71073
Absorption coefficient (μ/mm^{-1})	0.83
Minimum and maximum transmission factors	0.765 and 0.838
Refinement on F^2	
R [$F^2 > 2\sigma(F^2)$][a]	0.041
wR (F^2 all reflections)[b]	0.088
Goodness-of-fit (Gof), S	1.01
Residual electron density, $\Delta\rho_{max}$, $\Delta\rho_{min}$ (e Å^{-3})	+0.56, −0.49

[a] $R = \Sigma||F_o| - ||F_c||/\Sigma F_o$.
[b] $wR = \{\Sigma[w(F_o^2 - F_c^2)^2]/\Sigma wF_o^4\}^{1/2}$; $w^{-1} = [\sigma^2(F_o^2) + (0.0296P)^2]$ where $P = (F_o^2 + 2F_c^2)/3$.

observed with $I > 2\sigma(I)$, $R_{int} = 0.037$) were measured up to 56.3° in 2θ covering over 98% of the Ewald sphere. Data collections were made using the CRYSALIS CCD program [18], integration and scaling of the reflections were performed with CRYSALIS Red program [18]. Face-indexed absorption corrections were carried out using the SHELXTL program [19]. The structure was solved by direct methods using the SHELXS-97 and refined using the SHELXL-97 program [20]. Fourier maps gave the positions of the zinc(II) and most of the nitrogen and carbon atoms of the phthalocyaninato rings. The remaining atoms were located from difference Fourier synthesis. The hydrogen atoms of the phenyl rings were located from the $\Delta\rho$ maps and in final cycles of calculations they were refined with riding model. The H atoms of the solvated pyrazine molecules were set isotropic with thermal parameters 20% greater than the equivalent isotropic displacement parameter of the carbon atom. The final differences Fourier map showed no peaks of chemical significance. The largest peaks on the final $\Delta\rho$ map were +0.56 and −0.49 e Å^{-3}. Details of the data collection parameters, crystallographic data and final agreement parameters are collected in Table 1.

3. Results and discussion

3.1. Synthesis and equilibrium in solution

When the procedure described in the Section 2.1 is carried out in the temperature range of 90–150 °C the crystalline product has always the 2(ZnPc):3(pyz) composition. However, the single crystals suitable for the full X-ray analysis were obtained when the ampoule was processed at 110 °C. At this temperature the prolonged heating enable to obtained crystals of ZnPc:pyz = 2:3 composition that are stable (Fig. 2). When the ampoule containing the crystalline 2(ZnPc):3(pyz) product was prolonged heated at 190 °C or at higher temperature, the 2(ZnPc):3(pyz) crystals appear decomposed, since the Zn–N(pyz) bond become broken liberating the pyrazine molecules. Simultaneously the liberated ZnPc molecules interact with each other initialising the growth of the pure β-ZnPc crystals, which after prolonged heating leads to the well-developed good quality prismatic crystals (Fig. 1). When the ampoule with the β-ZnPc crystals was heated again at the temperature between 90 and 150 °C, the pyrazine interacts with the β-ZnPc forming

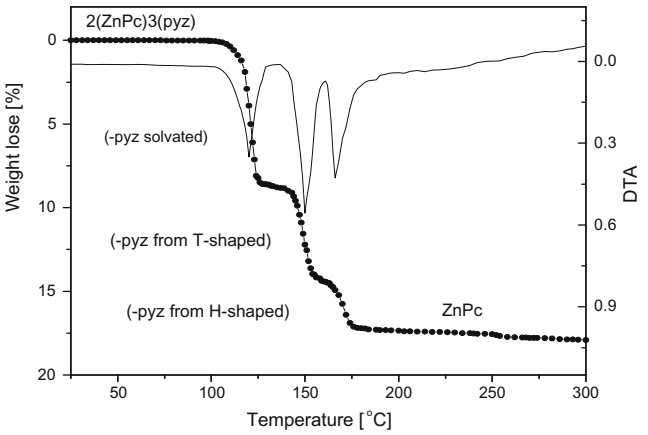


Fig. 2. Thermograms for the crystalline phase of 2(ZnPc):3(pyz). Speed rate 5 °C min^{-1}.

again the 2(ZnPc):3(pyz) crystals. Thus the formation of the solid-state supramolecular crystalline 2(ZnPc):3(pyz) phase is reversible and can be controlled by the annealing temperature. The 2(ZnPc):3(pyz) crystals are relatively soluble in 1-chloronaphthalene, quinoline, pyridine and other N-donating solvents, and slightly soluble in benzene, DMSO and CH_2Cl_2. Contact of 2(ZnPc):3(pyz) crystals with dilute acids lead to the demetallation, yielding metal-free phthalocyanine (H_2Pc) in the α-form, which was identified by X-ray powder diffraction method [21].

3.2. Thermal measurement and analysis

The obtained crystalline 2(ZnPc):3(pyz) phase is relatively stable up to about 120 °C (Fig. 2). Above this temperature the solvated pyrazine molecules are released (weight loss ~8.5%) yielding a mixture of the H- and T-shaped supramolecular complexes. These complexes loss the ligated pyrazine at ~150 and ~170 °C. First, at lower temperature (150 °C), the T-shaped complex losses the ligated pyrazine molecule, and next, at temperature higher by about 20 °C, the H-shaped complex releases the bridged pyrazine molecule, since the respective weight losses are ~5.7% and ~2.8%. The calculated weight losses for the thermal decomposition of the 2(ZnPc):3(pyz) phase are: 8.60% (solvated pyz), 14.33% (solvated + ligated pyz in the T-shaped complex) and 17.19% (solvated + ligated T-shaped + bridged H-shaped complexes) and they are in agreement with the experimental results (Fig. 2). The thermogravimetric experiment clearly shows that the H-shaped supramolecular complex is more stable than the T-shaped complex. Although, the axial Zn–$N_{(pyz)}$ bond in the T-shaped complex is stronger (2.178(2) Å) than in the H-shaped complex (2.207(2) Å), due to the bridging effect the H-shaped complex is more stable. The differential thermal curve indicates three distinct endothermic deflection peaks appearing during thermal decomposition of the 2(ZnPc):3(pyz) crystals. The thermal decomposition of the 2(ZnPc):3(pyz) phase leads to the β-ZnPc as was identified by the X-ray powder diffraction method. The TG analysis is fully consistent with the preparation procedure which shows that the 2(ZnPc):3(pyz) crystalline phase can be obtained only at the middle temperature range of 70–150 °C. However, the good quality single crystals suitable for the X-ray analysis were obtained at 110 °C, below the first steep of decomposition (see Fig. 2).

3.3. Stereochemistry and supramolecular arrangement

A single X-ray analysis of the 2(ZnPc):3(pyz) crystal revealed the formation of a supramolecular structure. The crystal of the

phase I is built up of two different types of supramolecular complexes and the pyrazine as solvent molecules. One of them is H-shaped supramolecular complex and the second one is T-shaped. In both types of the supramolecular ZnPc-derivatives the Zn(II) atom exhibits the 4 + 1 coordination. It is equatorially coordinated by four isoindole N atoms of Pc macrocycle and axially by the N-ring atom of ligated pyrazine molecule. In the H-shaped complex both N-ring atoms of pyrazine molecule are ligated to two ZnPc molecules. Thus in the H-shaped complex the pyrazine molecule is a bridging molecule developing the centrosymmetric supramolecular dimeric structure (Fig. 3a). In T-shaped ZnPc complex the pyrazine molecule coordinates only one ZnPc molecule (Fig. 3b). In both supramolecular complexes each Zn(II) center is pentacoordinated forming a distorted square pyramid. The phthalocyaninate(2-) macroring in both supramolecular ZnPc-complexes, H-shaped and T-shaped, is not strictly planar due to the interactions of the Zn-center with axial pyz molecule. Interaction between the N-ring atom of pyz molecule, with a lone-pair of electrons, and positively charged Zn(II)-center of ZnPc molecules leads to deviation of Zn(II) from the N_4-isoindole plane by 0.296(2) Å in the H-shaped supramolecular dimeric complex and by 0.371(2) Å in the T-shaped monomer. As a result of the interaction of Zn(II) with the axially ligated pyrazine molecule, the planar Pc ligand as found in the β-ZnPc adopts a saucer shaped form in the T-shaped complex, while in the H-shaped supramolecular dimeric complex the two isoindole rings of Pc on the diagonal are bent upward and the other two are bent downward in respect to the N_4-isoindole plane. Thus in the H-shaped supramolecular complex the Pc rings exhibit approximately the S_4 symmetry. In the T-shaped complex the greatest deviations of the non-H atoms from the N_4-isoindole plane are observed for the outermost carbon atoms: C3B-C6B, 0.167(2)–0.275(2) Å; C11B-C14B, 0.209(2)–0.295(2) Å; C19B-C22B, 0.106(2)–0.247(2) Å and C27B-C30B, 0.141(2)–0.215(2) Å, while in the H-shaped the greatest upward deviations are observed for C5 and C6 (0.123(2) and 0.141(2) Å) and for C20 and C21 (0.258(2) and 0.295(2) Å) while the downward deviations are observed for C13 and C14 (−0.047(2) and −0.112(2) Å) and for C28 and C29 (−0.179(2) and −0.176(2) Å). In both supramolecular complexes the greatest deviations of the carbon atoms from the N_4-isoindole plane of Pc ring correlate well with the orientation of the bridged (in H-shaped) or axially ligated (in T-shaped) pyrazine molecule, which is almost perpendicular to the N_4-isoindole plane of respective Pc rings (84.8(1)° in H-shaped and 87.2(1)° in the T-shaped). The pyrazine ring is oriented by the H atoms in the orto position in relation to N atoms of the isoindole rings showing the greatest deviation from the N_4-isoindole plane of Pc ring. The equatorial Zn–N bonds in the H-shaped supramolecular complex ranging from 1.997(2) to 2.005(2) Å are slightly shorter than those in the T-shaped complex (2.009(2)–2.012(2) Å), while the opposite relation is observed in the axial Zn–N(pyz) bonds, longer in H-shaped and shorter in T-shaped (Table 2). Thus the interaction of pyrazine molecule with one ZnPc molecule with the formation of T-shaped complex is stronger than the interaction with two ZnPc molecules with the formation of the H-shaped supramolecular complex. The strength of the axial Zn–N(pyz) interaction is also evidenced by the displacement of Zn(II) from the N_4-isoindole plane of Pc ring. The displacement values of Zn(II) in these H- and T-shaped complexes are in the normal range observed in the 4 + 1 coordinated ZnPc-derivatives [10,22–26]. In the H-shaped supramolecular complex the Pc rings are parallel to each other and are separated by a distance of 7.763(3) Å (the N_4–N_4 distance).

The arrangement of the H- and T-shaped supramolecules in the crystal is mainly determined by the π–π interactions between the aromatic Pc macrorings. Strong π–π interaction is common feature in the structures of phthalocyanine and its metal complexes, and determines their crystal structures. The π–π interactions also play an important role in association of metallophthalocyanines in solution [27,28]. The H-shaped supramolecules are arranged in the back-to-back fashion forming stacks almost parallel to [1 0 0] direction with the distance of 3.341(2) Å between the N_4-planes

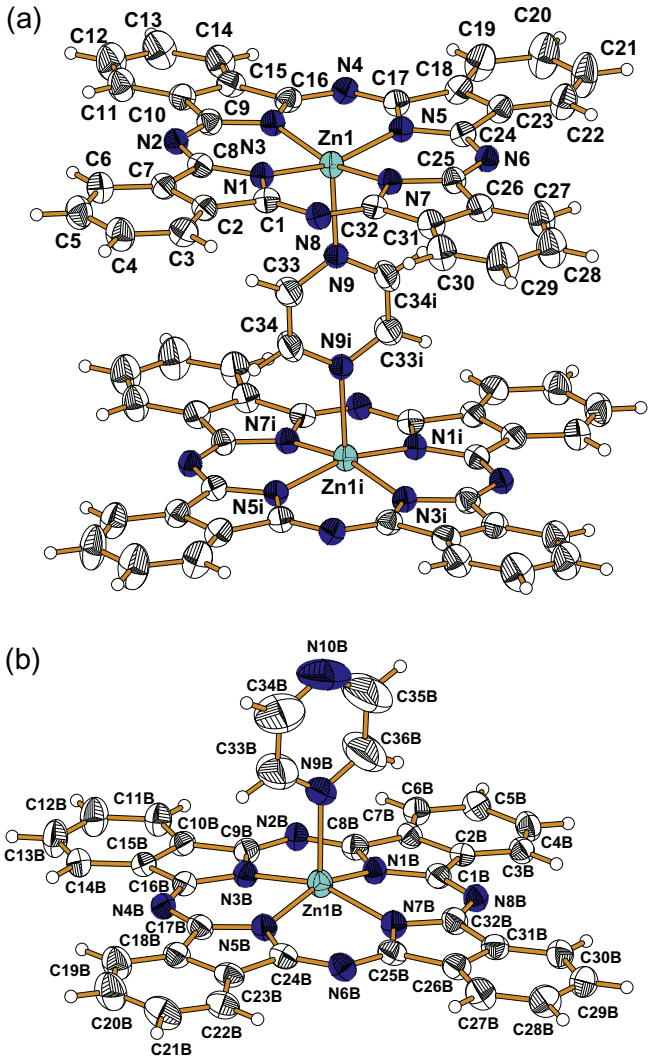


Fig. 3. Molecular structure of H-shaped (a) and T-shaped (b) supramolecular complex of ZnPc with the labelling scheme. Displacement ellipsoids are shown at the 50% probability level. H atoms are shown as spheres with arbitrary radii. Symmetry code: $i = 1 - x, 2 - y, 1 - z$.

Table 2
Selected geometrical parameter of H- and T-shaped supramolecular complexes (Å, °).

H-shaped complex		T-shaped complex	
Zn1–N1	1.997(2)	Zn1B–N1B	2.009(2)
Zn1–N3	1.999(2)	Zn1B–N3B	2.010(2)
Zn1–N5	2.003(2)	Zn1B–N5B	2.012(2)
Zn1–N7	2.005(2)	Zn1B–N7B	2.012(2)
Zn1–N9	2.207(2)	Zn1B–N9B	2.178(2)
N1–Zn1–N3	88.90(9)	N1B–Zn1B–N3B	88.04(9)
N1–Zn1–N5	163.13(9)	N1B–Zn1B–N5B	159.15(9)
N1–Zn1–N7	87.98(9)	N1B–Zn1B–N7B	87.61(9)
N3–Zn1–N5	88.45(9)	N3B–Zn1B–N5B	88.13(9)
N3–Zn1–N7	162.89(9)	N3B–Zn1B–N7B	158.26(9)
N5–Zn1–N7	89.67(9)	N5B–Zn1B–N7B	88.40(9)
N9–Zn1–N1	102.93(9)	N9B–Zn1B–N1B	102.95(10)
N9–Zn1–N3	98.32(9)	N9B–Zn1B–N3B	100.53(10)
N9–Zn1–N5	93.95(9)	N9B–Zn1B–N5B	97.89(10)
N9–Zn1–N7	98.78(9)	N9B–Zn1B–N7B	101.20(10)

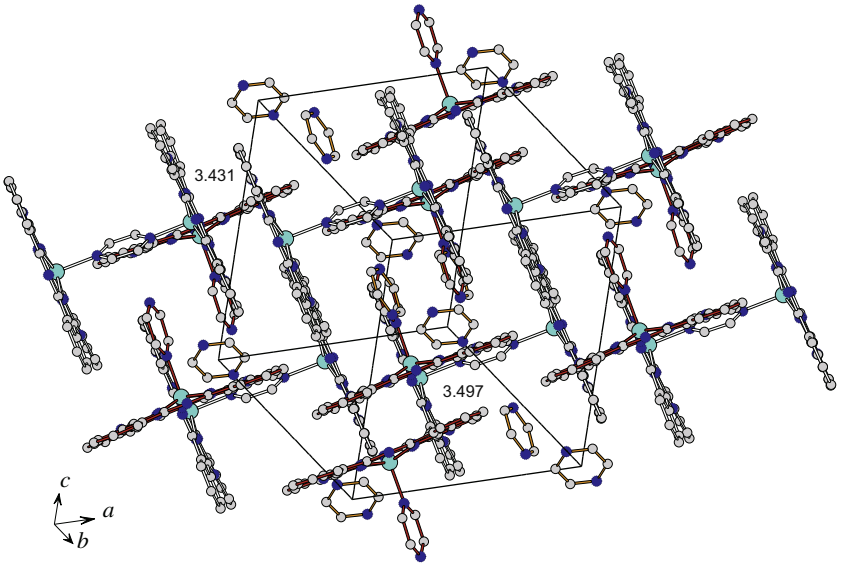


Fig. 4. View of the arrangement of H- and T-shaped molecules in the unit cell.

of Pc macrorings. The T-shaped molecules are also arranged in the back-to-back fashion with the distance between the N_4-planes of 3.497(2) Å. The back-to-back oriented T-shaped molecules form layers parallel to (0 2 0) crystallographic plane, while the H-shaped supramolecules form layers almost parallel to (0 0 2) crystallographic plane (Fig. 4). Thus the overlap of the Pc ligands in the solid state of the phase I is characteristic of the (4 + 1)-Zn-phthalocyaninate complexes. Scheidt and Lee examined the overlap in neutral, structurally characterized metal-porphyrinate complexes and discovered that the distribution of the lateral shift of the ligands is trimodal rather than continuous [29]. The values appear to be ~1.5 Å for clusters with strong π–π overlap, at ~3.5 Å with intermediate π–π overlap and at ~6.5 Å with weak overlap. The back-to-back overlap, in this crystal with distances of 3.341(2) Å in H-shaped and 3.397(2) Å in T-shaped supramolecular ZnPc-complexes, represents an intermediate interaction between the π-aromatic Pc-ligands. However, owing to the saucer-shape of Pc ligand in T-shaped complex or diagonally deformed up and downward in H-shaped, the mean inter-planar separation between the back-to-back overlapped dimers (~3.28 Å in H-shaped and 3.37 Å in T-shaped) is nearly midway between the sum of the C-atom van der Waals radii of the π ring system (~3.4 Å) and the distance at which the steric interactions between the π ring system becomes predominantly repulsive (~3.08 Å) [30]. Thus the π–π stabilization of the solid state arrangement is evident and the π–π interactions play important role in the supramolecular arrangement and the packing pattern. Both back-to-back oriented H-shaped and T-shaped supramolecular complexes in the crystal are almost perpendicular, the N_4-planes of Pc rings of the H-shaped complex form an angles of 93.7(1)° with the N_4-plane of Pc of the T-shaped complex. The pyrazine molecules are located in the holes between the mutually arranged H- and T-shaped molecules. One of them is located around an inversion center at the origin of the unit cell and is almost parallel to (0 0 1) crystallographic plane, while to other pyrazine molecule is located between the Pc rings of the H-shaped molecule and is almost parallel to the Pc rings (the dihedral angle of pyrazine plane and plane of Pc ring is equal to ~17.5°). Since in H-shaped complex the Pc rings are apart by 7.767(3) Å, the pyrazine molecules are located between the phenyl rings (C18–C23/$C2^i$–$C7^i$ and C2–C7/$C18^i$–$C23^i$, $i = 1 - x, 2 - y, 1 - z$), while between the other phenyl rings (C10–C15/$C25^i$–$C30^i$ and $C10^i$–$C15^i$/C25–C30) is located the coordinated pyrazine molecule of the T-shaped complex. This arrangement of the H- and T-shaped molecules and the pyrazine solvated molecules indicates that besides the π–π interactions between the back-to-back oriented H-shaped and T-shaped supramolecular units, the π–π interactions between the solvated pyrazine molecules and the phenyl rings of Pc macrorings are also significant factor stabilising the supramolecular arrangement and the crystal packing.

3.4. UV–Vis spectroscopy

To investigate further the structure of the 2(ZnPc):3(pyz) species in solution, the electronic absorption spectra in polar and non-polar solvents were recorded. The absorption spectra of the 2:3 complexes in both polar (1-chloronaphthalene) and non-polar solvents (benzene) are very similar (Fig. 5) and characterize the ZnPc with a single pyz in axial position. They both show characteristic well-developed intense Q band, assigned from HOMO (A_{1a} ground state) to LUMO (E_u, the first excited state) transition, and the broad B-Soret band, and they are in agreement with the spectrum of ZnPc published by A.B.P. Lever [31]. As can be seen from Fig. 5 the spectra exhibit characteristic splitting of the Q band due to the vibronic coupling in the excited state, which was well

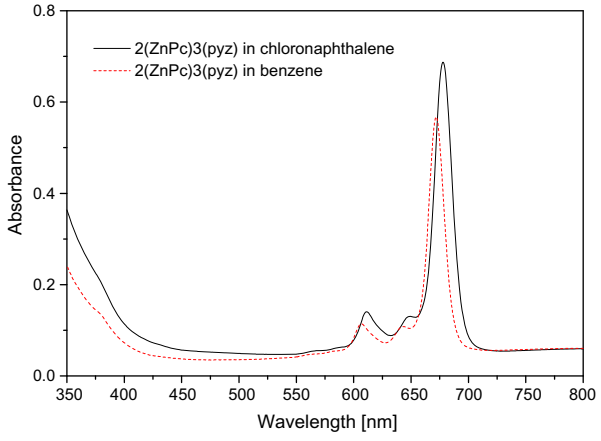


Fig. 5. Electronic absorption spectra of 2(ZnPc):3(pyz) in chloronaphthalene (solid line) and in benzene (doted line).

described in the literature [32–35]. However, the spectrum taken in benzene is blue shifted (~10 nm) in the relation to that taken in α-chloronaphthalene. The difference in the wavelength of the absorption in benzene or in α-chloronaphthalene is a consequence of different solvents (solvent effect). A similar correlation is observed in other polar and non-polar solvents. What seems also important, we did not notice any time dependence of the spectra, as it was in the cause of iron phthalocyanine–pyz system [14].

4. Conclusion

The experiment performed with the ZnPc–pyz system confirms a presence of the stable supramolecular 2(ZnPc):3(pyz) phase in which the three various molecules, ZnPc(pyz), $(ZnPc)_2$(pyz) and pyz constitute the solid-state phase. The results indicate also on the peculiar feature of the zinc cation, which being in the essentially planar ZnN_4 moiety, is capable to only monoaxial coordination of the electron donating ligand molecules. It is also interesting, that the high quality ZnPc crystals can be grown when in the ZnPc–pyz system the annealing temperature is set to the value exceeding the ZnN_4–Npyz attraction force, roughly 200 °C.

Appendix A. Supplementary data

CCDC 725910 contains the supplementary crystallographic data for this paper. These data can be obtained free of charge via http://www.ccdc.cam.ac.uk/conts/retrieving.html, or from the Cambridge Crystallographic Data Centre, 12 Union Road, Cambridge CB2 1EZ, UK; fax: (+44) 1223-336-033; or e-mail: deposit@ccdc.cam.ac.uk.

References

[1] C.C. Leznoff, A.B.P. Lever (Eds.), Phthalocyanines: Properties and Applications, vol. 2, VCH Publishers, New York, 1993.
[2] C.C. Leznoff, A.B.P. Lever (Eds.), Phthalocyanines: Properties and Applications, vol. 3, VCH Publishers, New York, 1994.
[3] C.C. Leznoff, A.B.P. Lever (Eds.), Phthalocyanines: Properties and Applications, vol. 4, VCH Publishers, New York, 1996.
[4] P. Gregory, J. Porphyrins Phthalocyanines 4 (2000) 432.
[5] L.H. Vogt, A. Zalkin, D.H. Templeton, Inorg. Chem. 6 (1967) 1725.
[6] F. Cariati, F. Morazzoni, C. Busetto, J. Chem. Soc., Dlaton Trans. 9 (1978) 1018.
[7] J. Janczak, R. Kubiak, Polyhedron 21 (2002) 265.
[8] J. Janczak, R. Kubiak, Inorg. Chim. Acta 342 (2003) 64.
[9] J. Janczak, R. Kubiak, M. Śledź, H. Borrmann, Y. Grin, Polyhedron 22 (2003) 2689.
[10] R. Kubiak, J. Janczak, M. Śledź, E. Bukowska, Polyhedron 26 (2007) 4179.
[11] T. Kobayashi, N. Uyeda, E. Suito, J. Phys. Chem. 72 (1968) 2246.
[12] O. Schneider, M. Hanack, Angew. Chem., Int. Ed. 19 (1980) 392.
[13] J. Metz, M. Hanack, New J. Chem. 5 (1991) 541.
[14] O. Schneider, M. Hanack, Chem. Ber. 116 (1983) 2088.
[15] W. Kobel, M. Hanack, Inorg. Chem. 25 (1986) 103.
[16] Q. Zeng, D. Wu, C. Wang, J. Lu, B. Ma, C. Shu, H. Ma, Y. Li, C. Bai, Cryst. Eng. Commun. 7 (2005) 243.
[17] WinXPow Software Manual, STOE and GmbH, Darmstadt, Germany, 1997.
[18] CRYSALIS CCD and CRYSALIS Red program, Ver. 171.31.8, Oxford Diffraction Poland, Wrocław, Poland, 2006.
[19] G.M. Sheldrick, SHELXTL, Siemens Analytical X-ray Instruments Inc., Madison, WI, USA, 1990.
[20] G.M. Sheldrick, SHELXS97, SHELXL97, Programs for Crystal Structure Solution and Refinement, University of Göttingen, Göttingen, Germany, 1997.
[21] J. Janczak, Pol. J. Chem. 74 (2000) 157.
[22] T. Kobayashi, T. Ashida, N. Uyeda, E. Suito, M. Kakudo, Bull. Chem. Soc. Jpn. 44 (1971) 2095.
[23] A. Geiss, H. Vahrenkamp, Inorg. Chem. 39 (2000) 4029.
[24] T. Fuukuda, S. Homma, N. Kobayashi, Chem. Eur. J. 11 (2005) 5205.
[25] S.Y. Al-Raqa, M.J. Cook, D.L. Hughes, Chem. Commun. (2003) 62.
[26] H. Haas, S.X. Liu, A. Neels, S. Decurtins, Eur. J. Org. Chem. (2006) 5467.
[27] D.S. Terekhov, K.J.M. Nolan, C.R. McArthur, C.C. Leznoff, J. Org. Chem. 61 (1996) 3034.
[28] H. Isago, D.S. Terekhov, C.C. Leznoff, J. Porphyrins Phthalocyanines 1 (1997) 135.
[29] W.R. Scheidt, Y.L. Lee, Struct. Bond. 64 (1987) 1.
[30] L. Pauling, The Nature of the Chemical Bond, 3rd ed., Coronell University Press, Ithaca, 1960. p. 260.
[31] A.B.P. Lever, Adv. Inorg. Radiat. 7 (1965) 27.
[32] A.J. McHugh, M. Gouterman, C. Weiss, Theor. Chim. Acta 24 (1972) 346.
[33] W.R. Browett, M.J. Stillman, Inorg. Chim. Acta 49 (1981) 69.
[34] T. Nykong, Z. Gasyna, M.J. Stillman, Inorg. Chem. 26 (1987) 1087.
[35] M.P. Donzello, C. Ercolani, A.A. Gaberkon, E.V. Kudrik, M. Meneghetti, G. Marcolongo, C. Rizzoli, P.A. Stuzin, Chem. Eur. J. 9 (2003) 4009.

Polyhedron 28 (2009) 2397–2402

Contents lists available at ScienceDirect

Polyhedron

journal homepage: www.elsevier.com/locate/poly

Synthesis, characterization and antimicrobial activity of Ni(II) and Zn(II) complexes with N',N'^2-bis[(1*E*)-1-(2-pyridyl)ethylidene]propanedihydrazide. Crystal structures of two highly solvated bimetallic complexes of Ni(II)

Tamara R. Todorović [a], Urszula Rychlewska [b], Beata Warżajtis [b], Dušanka D. Radanović [c], Nenad R. Filipović [d], Ivana A. Pajić [a], Dušan M. Sladić [a], Katarina K. Anđelković [a,*]

[a] Faculty of Chemistry, University of Belgrade, Studentski trg 12-16, 11000 Belgrade, Serbia
[b] Faculty of Chemistry, A. Mickiewicz University, Grunwaldzka 6, 60-780 Poznań, Poland
[c] Institute of Chemistry, Technology and Metallurgy, University of Belgrade, Njegoševa 12, P.O. Box 815, 11000 Belgrade, Serbia
[d] Faculty of Agriculture, University of Belgrade, Nemanjina 6, 11000 Belgrade-Zemun, Serbia

ARTICLE INFO

Article history:
Received 20 March 2009
Accepted 1 May 2009
Available online 8 May 2009

Keywords:
Malonic acid dihydrazide derivative
Ni(II) and Zn(II) complexes
X-ray analysis
Antimicrobial activity

ABSTRACT

The bimetallic $[Ni_2(H_2L2)_2](ClO_4)_4$ (**1**), $[Ni_2(HL2)(H_2L2)](ClO_4)_3$ (**2**) and $[Zn_2(H_2L2)_2](BF_4)_4$ (**3**) complexes (H_2L2 = N',N'^2-bis[(1*E*)-1-(2-pyridyl)ethylidene]propanedihydrazide) were synthesized and characterized. The structure of complexes (**1**) and (**2**) was established by X-ray analysis. NMR spectroscopy was used for the characterization of complex (**3**). The complexes (**1**) and (**2**) were obtained from the same synthetic reaction and two crystal types of these complexes have been isolated during the fractional crystallization process.

In complex (**1**) each Ni(II) ion is coordinated with two NNO donor atom sets from two H_2L2 ligands forming an octahedral geometry. Similarly, in complex (**2**) the octahedral geometry of each Ni(II) ion is attained by coordination of two NNO donor atom sets, one from the neutral and the other from the mono-anionic form of the ligand. The antimicrobial activity of the ligand and complexes is also presented.

© 2009 Elsevier Ltd. All rights reserved.

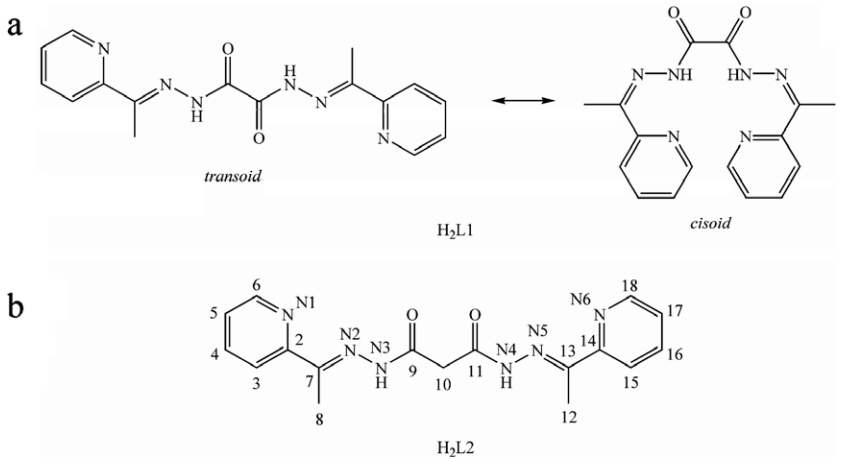
1. Introduction

For the past years one line of our research has been dedicated to complexes of polydentate dihydrazone ligands with adjacent coordination pockets, predominantly condensation derivatives of 2-acetylpyridine and oxalic or malonic acid dihydrazide [1,2]. Dihydrazone type ligands display a versatile behavior in metal coordination. Occupation of all possible coordination sites depends on the nature of the central metal atom, conformational flexibility of the ligand as well as on the presence of other species capable to compete for coordination pockets. Oxalic dihydrazide based ligands, like N',N'^2-bis[(1*E*)-1-(2-pyridyl)ethylidene]ethanedihydrazide (H_2L1, Scheme 1a), are capable to bind more than one metal center. In the reaction with $Cu(AcO)_2{\cdot}H_2O$ binuclear complex with L1 was obtained [3], where the ligand in its *transoid* orientation binds two metal centers through oxamido type bridges in bis-tridentate mode. With $Ni(BF_4)_2{\cdot}6H_2O$ formation of tetranuclear complex, with fully occupied coordination sites of HL1, is favoured [4]. However, use of $Ni(AcO)_2{\cdot}4H_2O$ afforded formation of neutral mononuclear Ni(II) complex where L1 in its *cisoid* orientation is coordinated as tetradentate via only the nitrogen atoms, with no involvement of the central oxalic fragment [3]. On the other hand, it was shown that H_2L1 is hydrolytically unstable, which is not so uncommon for ligands derived from condensation reactions. Decomposition of H_2L1 by hydrolysis at the hydrazide moiety occurs in a reaction with $Cu(NO_3)_2{\cdot}3H_2O$ or $Cu(ClO_4)_2{\cdot}6H_2O$ in aqueous methanol, affording formation of the binuclear Cu(II) complex with 2-acetylpyridine hydrazone in which oxalate ion bridges two metal centers [5]. Similarly, hydrolysis of H_2L1 takes place in the reaction with $Fe(ClO_4)_3{\cdot}6H_2O$ in water with concomitant reduction of Fe(III) to Fe(II) by oxalic fragment affording formation of mononuclear Fe(II) complex with 2-acetylpyridine hydrazone [1]. In contrast, with structurally similar dihydrazone ligand, N',N'^2-bis[(1*E*)-1-(2-pyridyl)ethylidene]propanedihydrazide (H_2L2, Scheme 1b), which is more flexible in comparison to H_2L1, the hydrolysis does not take place. In mononuclear octahedral Fe(III) complex, H_2L2 is coordinated through nitrogen atoms from both coordination pockets [1], while it binds two metal centers in bis-tridentate fashion in Cd(II) complex [2].

Oxalic and malonic based dihydrazones and their complexes showed versatile biological activities [2,6]. Evaluation of cytotoxic activity of H_2L1 and H_2L2 on HeLa (human cervix carcinoma cells) and B16 (murine melanoma) tumor cell lines showed that these ligands were more active in comparison to other acyl hydrazones of 2-acetylpyridine [6], while heptacoordinated binuclear Cd(II)

* Corresponding author. Tel.: +381 11 3336 737; fax: +381 11 3282 750.
E-mail address: kka@chem.bg.ac.rs (K.K. Anđelković).

0277-5387/$ - see front matter © 2009 Elsevier Ltd. All rights reserved.
doi:10.1016/j.poly.2009.05.002



Scheme 1.

complex with H_2L2 showed cytotoxic activity in low micromolar range [2].

As a continuation of the investigation of coordination behavior of flexible 2-acetylpyridine based dihydrazone ligands, the present work reports synthesis and characterization of Ni(II) and Zn(II) complexes with H_2L2 and evaluation of the biological activity of the synthesized compounds.

2. Experimental

2.1. General remarks

2-Acetylpyridine (99+%), malonic acid dihydrazide (97%), Ni-$(ClO_4)_2{\cdot}6H_2O$ (purum p.a. $\geq$ 98.0%), and $Zn(BF_4)_2{\cdot}6H_2O$ were obtained from Aldrich. All solvents (ethanol, *N*,*N*-dimethylformamide, diethyl ether, acetonitrile, dimethyl sulfoxide) were reagent grade and used without further purification. IR spectra were recorded on the Perkin–Elmer FT-IR 1725X spectrometer using the KBr-pellet technique in the region 4000–400 cm^{-1}. Electronic absorption spectra were recorded on a GBC UV–visible Cintra 6 Spectrometer. The NMR spectra were performed on Bruker Avance 500 equipped with broad-band direct probe. All spectra were measured at 298 K. The Zn(II)–H_2L2 complex was characterized on the basis of NMR spectroscopy results: 1D (^1H, ^{13}C), 2D COSY (Correlation Spectroscopy) and 2D ROESY (Rotational Frame Nuclear Overhauser Effect Spectroscopy) spectra, as well as 2D ^1H–^{13}C heteronuclear correlation spectra. Chemical shifts are given on δ scale relative to tetramethylsilane (TMS) as internal standard for ^1H and ^{13}C.

2.2. Synthesis of N′,N′²-bis[(1E)-1-(2-pyridyl)ethylidene]propanedihydrazide (H_2L2)

The ligand H_2L2 was prepared as described previously [1] by condensation reaction of 2-acetylpyridine and malonic acid dihydrazide in water with a few drops of conc. HCl (pH $\sim$ 4.5). IR (KBr-pellet, cm^{-1}): 3190 (w), 3089 (w), 3006 (w), 1662 (vs), 1626 (m), 1580 (s), 1460 (m), 1430 (m), 1378 (m), 1227 (m), 1152 (m), 1084 (w), 991 (w), 784 (s), 726 (s), 662 (m), 623 (m), 560 (m), 483 (m), 404 (m). ^1H NMR (500.26 MHz, DMSO-d_6): δ = 2.32 (s, 6H, H–C8═H–C12), 4.09 (s, 2H, H–C10), 7.33 (t, 2H, H–C5═H–C17, ^3J = 5.0 Hz, ^3J = 1.5 Hz), 7.58 (dt, 2H, H–C4═H–C16, ^3J = 7.5 Hz, ^3J = 1.5 Hz), 7.97 (d, 2H, H–C3═H–C15, ^3J = 7.5 Hz), 8.56 (d, 2H, H–C6═H–C18, ^3J = 5.0 Hz), 10.86 (bs, 2H, H–N3═H–N4). ^{13}C NMR (125.79 MHz, DMSO-d_6): δ = 11.93 (C8═C12), 40.70 (C10), 119.79 (C6═C18), 123.79 (C5═C17), 136.20 (C4═C16), 148.56 (C3═C15), 155.00 (C9═C11), 163.88 (C2═C14), 170.31 (C7═C13).

2.3. Synthesis of Ni(II) complexes with H_2L2 ligand

Into a solution of $Ni(ClO_4)_2{\cdot}6H_2O$ (0.22 g, 0.59 mmol) in EtOH (20 mL), the ligand H_2L2 (0.20 g, 0.59 mmol) was added. After refluxing the suspension for 1 h, an olive-green precipitate was filtered off and washed with cold EtOH and ether. The precipitate was dissolved in DMSO and after two days of slow diffusion of EtOH vapour, green crystals of complex **(1)** were obtained, and taken out of the solution. Seven days later, from the same mother liquid, after slow diffusion of EtOH vapour, brown crystals of complex **(2)** were obtained. The crystals of **(1)** and **(2)** were separated by fractional crystallization. Both crystals were unstable in air. X-ray diffraction measurements for **(1)** and **(2)** were performed on crystals mounted in a LithoLoop immediately after taking from the mother liquid and flash-cooled on a diffractometer.

(1): After filtration, green crystals were washed with cold water and ethanol, and dried in vacuo. The data listed below reflects the product obtained after drying. IR (KBr-pellet, cm^{-1}): 3105 (w), 3000 (w), 2921 (w), 2742 (w), 1629 (w), 1599 (s), 1538 (s), 1472 (m), 1362 (m), 1219 (m), 1171 (m), 1077 (vs), 1001 (vs), 954 (s), 779 (s), 744 (m), 694 (m), 619 (vs), 570 (m), 519 (m), 461 (m), 414 (w).

(2): After filtration, brown crystals were washed with cold water and ethanol, and dried in vacuo. The data listed below reflects the product obtained after drying. IR (KBr-pellet, cm^{-1}): 3106 (w), 2925 (w), 2745 (w), 1598 (s), 1541 (s), 1511 (vs), 1464 (s), 1374 (s), 1263 (w), 1221 (s), 1174 (m), 1071 (vs), 1003 (vs), 952 (s), 780 (s), 745 (m), 705 (m), 618 (vs), 569 (s), 519 (s), 460 (s), 414 (m).

2.4. Synthesis of Zn(II) complex with H_2L2 ligand

Into the solution of $Zn(BF_4)_2{\cdot}6H_2O$ (0.20 g, 0.59 mmol) in EtOH (20 mL), the ligand H_2L2 (0.20 g, 0.59 mmol) was added. After refluxing the suspension for 1 h, a white precipitate was separated, filtered off and washed with cold EtOH and ether. The precipitate was dissolved in DMSO and after two days of slow diffusion of EtOH vapour, white crystals of complex **(3)** were obtained. The crystals were unstable in air, therefore the data listed below reflects the product obtained after washing crystals of **(3)** with cold water and ethanol, and drying in vacuo. IR (KBr-pellet, cm^{-1}):

3442 (w), 3268 (w), 1631 (m), 1600 (s), 1525 (s), 1475 (m), 1444 (w), 1352 (m), 1209 (s), 1184 (m), 1106 (s), 1025 (vs), 784 (s), 748 (w), 692 (w), 666 (w), 640 (w), 590 (w), 562 (m), 517 (m), 454 (m), 410 (m). ^{1}H NMR (500.26 MHz, DMSO-d_6): δ = 2.32 (s, 6H, H–C8=H–C12), 4.00 (s, 2H, H–C10), 7.34 (t, 2H, H–C4=H–C16, ^3J = 7.5 Hz), 7.36 (t, 2H, H–C5=H–C17, ^3J = 5.0 Hz), 8.03 (d, 2H, H–C6=H–C18, ^3J = 5.0 Hz), 8.57 (d, 2H, H–C3=H–C15, ^3J = 7.5 Hz), 11.02 (bs, 2H, H–N3=H–N4). ^{13}C NMR (125.79 MHz, DMSO-d_6): δ = 12.16 (C8=C12), 40.96 (C10), 120.09 (C3=C15), 124.06 (C5=C17), 136.46 (C4=C16), 148.59 (C6=C18), 154.83 (C9=C11), 163.88 (C2=C14), 170.42 (C7=C13).

2.5. X-ray analysis

For X-ray measurements the crystals were mounted in a loop containing some amount of solvent and flash-cooled on a diffractometer to 130 (**1**) and 100 (**2**) K. The intensity data were measured with a KM4CCD kappa-geometry diffractometer using graphite monochromated Mo Kα radiation (λ = 0.71073 Å) [7] and the temperature of the samples was controlled with an Oxford Instruments Cryosystem cold-nitrogen-gas blower. The intensity data were corrected for Lp effects as well as for absorption [7]. The structures were solved by direct methods using SHELXS97 [8] and refined by least-squares techniques with SHELXL97 [8]. In (**1**) all hydrogen atoms have been placed at calculated positions, including the ethanol hydrogen, the location of which was made possible by the use of the AFIX 147 instruction of SHELXL [8]. In (**2**) only hydrogen atoms connected to carbon atoms have been placed at calculated positions, while those attached to the nitrogen atoms have been located on subsequent difference Fourier maps. In (**2**) only three out of four possible N–H hydrogens (belonging to two crystallographically independent ligands) have been located, which could be interpreted as an indication of the partial deprotonation of one of the two ligands. That the absence of the hydrogen atom in the vicinity of N33 was not accidental was further confirmed by a detailed analysis of the complex geometry and intermolecular interactions (*vide infra*).

During the process of the crystal structure refinement the H atom positions were refined in a so called "riding model" with constraints on the C–H, N–H and O–H bond lengths and isotropic displacement parameters. Both crystal structures contain significant amount of solvent (DMSO, ethanol, diethyl ether) molecules, which together with perchlorate anions are the source of severe crystal disorder.

In (**1**) only the complex cation, one perchlorate group, two DMSO molecules and one ethanol molecule were readily discernable; the remainder of the structure appeared considerably disordered, which included three out of four perchlorate anions as well as DMSO and ethanol solvent molecules. The disordered parts of the structure were refined with restraints on 1,2 and 1,3 distances (DFIX instructions). The disorder model for two of the perchlorate groups was such that two sites were identified for one of the perchlorate oxygen atoms (i.e. O11 and O11a, and O13 and O13a). These perchlorate anions were refined with positional restraints and with anisotropic displacement parameters for all but the disordered oxygen atoms. The remaining perchlorate anion was highly disordered with all four oxygen atoms occupying three different sites with 0.53, 0.25 and 0.22 occupancy ratio. All its oxygen atoms were refined isotropically. Two disordered DMSO molecules were also refined isotropically. At the final stages of the structure solution it appeared evident that the investigated crystal contains, besides four perchlorate anions, four DMSO molecules and an ethanol molecule, some other solvent molecules not easily recognizable. All these molecules were situated in-between cationic layers, roughly parallel to the (1 0 0) lattice planes. Eventually, we have modeled this residual electron density as coming from a half of a DMSO molecule and a fraction of an ethanol molecule but the molecules were so disordered that numerous attempts to resolve multiple sites were unsuccessful. Therefore, we have removed these molecules from the model and used the SQUEEZE [9] program to account for the presence of these solvent molecules. The atom list does not contain the atoms of the residual solvent molecules.

The model of the crystal structure of (**2**) that came out from the numerous attempts to account for the presence of the residual electron density, contained in the asymmetric unit one bimetallic cluster, three perchlorate groups, three DMSO molecules and severely disordered ethanol and/or diethyl ether molecules. The solvent molecules concentrated in channels and hydrogen bonded to the complex cations. One of the three DMSO molecules was disordered with two methyl groups occupying three sites with 0.86, 0.82 and 0.32 occupancies. The disorder of ethanol and diethyl ether solvent molecules could not be properly modeled, therefore these molecules were removed from the atom list and the program SQUEEZE [9] was used to account for their presence. Again the contribution of these additional solvent molecules has been treated by the SQUEEZE program [9] globally, hence the atom list does not contain atoms constituting these remaining solvent molecules.

Siemens computer graphics program [10] was used to prepare Figs. 1 and 2. The crystal data for (**1**) and (**2**) and the parameters of data collection are summarized in Table 1.

2.6. Antimicrobial activity

All the synthesized compounds were screened for their antibacterial activity against gram positive bacteria *Staphylococcus aureus* ATCC 25923, *Micrococcus lysodeikticus* ATCC 4698, *Bacillus subtilis* ATCC 6633 and gram negative bacteria *Escherichia coli* ATCC 35218 *in vitro* using cup plate agar diffusion method. Solid medium used for this study was the nutrient agar (Torlak, Belgrade), pH 7.3. The medium was autoclaved for 15 min. The suspension of a bacterial culture in sterile isotonic saline solution (0.5 mL) was added to 10 mL of agar which was melted and cooled. Agar was poured onto the sterile petri dishes with a swirling motion to form an agar layer of uniform thickness. The plate was left undisturbed until the agar solidified. Small wells (8 mm in diameter) were punched in agar layer. The solutions of synthesized compounds (1 mg/100 μL of DMSO and 100 μL DMSO for control) were poured into the wells. The amount of standard antibiotic was 10 μg/disk. The zones of inhibition were measured in mm after incubation at 37 °C for 24 h. Antifungal activity was determined in the same way as antibacterial activity on Sabouraud dextrose agar (Torlak, Belgrade; pH

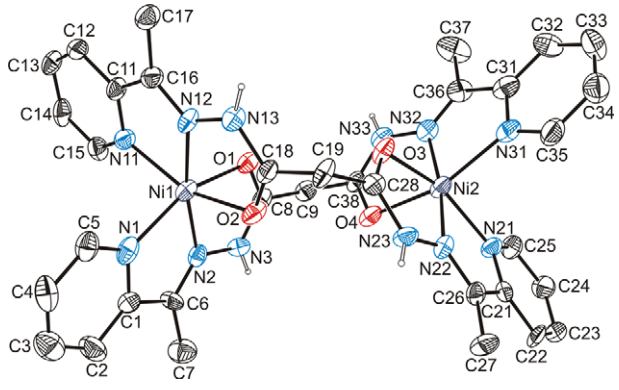


Fig. 1. View of the bimetallic complex cation of (**1**). Displacement ellipsoids drawn at 40% probability level. For clarity, hydrogen atoms bonded to carbon atoms have been omitted. The hydrogen atoms attached to the nitrogen atoms have been displayed to illustrate the neutral (uncharged) form of the malonic acid dihydrazide ligand.

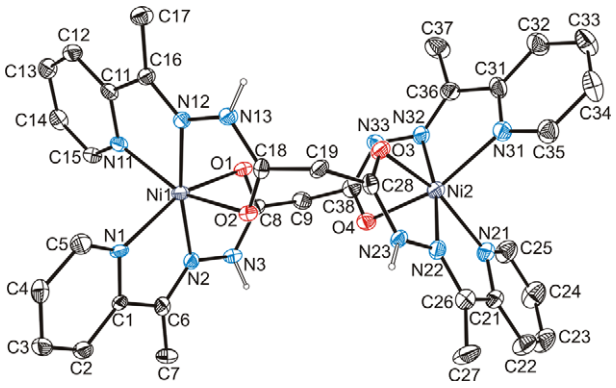


Fig. 2. View of the bimetallic complex cation of (**2**). Displacement ellipsoids drawn at 40% probability level. For clarity, hydrogen atoms bonded to carbon atoms have been omitted. The hydrogen atoms attached to the nitrogen atoms have been displayed to illustrate the monodeprotonated (monoanionic) form of the malonic acid dihydrazide ligand.

5.6) against the *Candida albicans* strain ATCC 24433. The amount of standard antimicotic was 10 μg/disk.

3. Results and discussion

3.1. General

By the fractional crystallization from DMSO/EtOH solution of the precipitate, obtained in the reaction of H_2L2 with $Ni(ClO_4)_2\cdot 6H_2O$ in EtOH, two different Ni(II) complexes were separated as green **(1)** and brown **(2)** crystals. Both crystals lose crystalline form when exposed to air, the brown ones being more stable. Complex **(2)** is soluble in MeCN, DMF and DMSO already at room temperature, and partially soluble in hot MeOH. When complex **(1)** is dissolved in either MeCN, DMF or DMSO the color of the solution almost instantly changes from green to brown. Furthermore, from the solution obtained by dissolution of green crystals, both complexes of Ni(II), green and brown ones, were obtained. The complex (**1**) crystallized first. The proposed mechanism for the formation of complex (**2**) starting from complex (**1**) is given in Eq. (1). As mentioned above, upon dissolution of complex **(1)** in DMSO the color of the solution rapidly changed from green to brown. The electronic absorption spectrum of this brown solution is practically the same in the shape and position of the absorption maximum as that of complex **(2)** (Supplementary data Fig. S1). This supports the assumption that complex **(1)** easily converts into the more stable complex **(2)**. The three spin allowed absorption bands ($^3A_{2g} \rightarrow {}^3T_{2g}(F)$; $^3A_{2g} \rightarrow {}^3T_{1g}(F)$ and $^3A_{2g} \rightarrow {}^3T_{1g}(P)$) are expected for Ni(II) complexes when the noncubic field components are small compared with the approximately cubic field components. However, in the electronic absorption spectrum of complex **(2)** only one asymmetric band occurs in the near infrared region at 854 nm. The absorption bands that are expected to appear in the visible and UV region are most probably masked with more intense charge transfer bands or by transitions within the ligands.

By the reaction of $Zn(BF_4)_2\cdot 6H_2O$ and H_2L2 ligand Zn(II) complex, which forms unstable white crystals soluble in MeCN, DMF and DMSO, was obtained.

$$\begin{aligned} &[Ni_2(H_2L2)_2]^{4+} \leftrightarrows [Ni_2(H_2L2)(solvent)]^{4+} + H_2L2 \\ &2H_2L2 \leftrightarrows HL2^- + H_3L2^+ \\ &[Ni_2(H_2L2)(solvent)]^{4+} + HL2^- \leftrightarrows [Ni_2(HL2)(H_2L2)]^{3+} \end{aligned} \quad (1)$$

Table 1
Crystal data.

	(1)	**(2)**
Crystal data		
Chemical formula	$C_{44}H_{66}Cl_4N_{12}Ni_2O_{25}S_4$	$C_{40}H_{53}Cl_3N_{12}Ni_2O_{19}S_3$
M_r	1550.55	1325.89
Cell setting, space group	triclinic, *P*-1	triclinic, *P*-1
Temperature (K)	130 (2)	100 (2)
a, *b*, *c* (Å)	15.9701 (5), 16.0803 (7), 16.9448 (5)	14.5164 (3), 15.7449 (4), 16.1039 (4)
α, β, γ (°)	69.646 (3), 81.811 (3), 61.609 (4)	63.241 (2), 79.428 (2), 82.553 (2)
V (Å^3)	3587.7 (2)	3226.10 (13)
Z	2	2
D_x (Mg m^{-3})	1.435	1.365
Radiation type	Mo Kα	Mo Kα
μ (mm^{-1})	0.87	0.88
Crystal form, color	plate, green	needle, brown
Crystal size (mm)	0.70 × 0.15 × 0.01	0.30 × 0.10 × 0.10
Data collection		
Diffractometer	kuma KM4CCD κ-geometry diffractometer	kuma KM4CCD κ-geometry diffractometer
Data collection method	ω scans	ω scans
Absorption correction	multi-scan (based on symmetry-related measurements)	multi-scan (based on symmetry-related measurements)
T_{min}	0.476	0.779
T_{max}	0.958	0.916
Number of measured, independent and observed reflections	28592, 12638, 5543	25574, 11379, 6721
Criterion for observed reflections	$I > 2\sigma(I)$	$I > 2\sigma(I)$
R_{int}	0.067	0.035
θ_{max} (°)	25.0	25.0
Refinement		
Refinement on	F^2	F^2
$R[F^2 > 2\sigma(F^2)]$, $wR(F^2)$, *S*	0.071, 0.194, 0.96	0.044, 0.123, 0.96
Number of reflections	12638 reflections	11379 reflections
Number of parameters	813	717
H-atom treatment	constrained to parent site	constrained to parent site
Weighting scheme	calculated $w = 1/[\sigma^2(F_o^2) + (0.0929P)^2]$ where $P = (F_o^2 + 2F_c^2)/3$	calculated $w = 1/[\sigma^2(F_o^2) + (0.0661P)^2]$ where $P = (F_o^2 + 2F_c^2)/3$
$(\Delta/\sigma)_{max}$	0.001	0.001
$\Delta\rho_{max}$, $\Delta\rho_{min}$ (e Å^{83})	0.83, −0.80	0.91, −0.54

3.2. Description of the crystal structures

The ligand H_2L2 used in the synthesis of complexes (**1**) and (**2**) contains eight donor atoms: six nitrogens and two oxygens. It has the ability to coordinate in a neutral, mono or dianionic form. Views of the cationic moieties of complexes (**1**) and (**2**) are shown in Figs. 1 and 2, respectively, and Ni(II) coordination geometry is listed in Table 2. As can be seen from these Figures, cationic moieties in both complexes are binuclear. Each complex cation is built of two ligands, each acting as bis tridentate (N_2O) bridging two metal centers. This results in octahedral environment around each Ni(II) center. The planes formed by the five atoms constituting the two O,N,N-chelates coordinated to one metal center are mutually perpendicular with dihedral angles of 83.6 and 82.5° in (**1**), and 83.7, and 85.6° in (**2**). The intramolecular Ni···Ni distance in (**1**) equal to 6.029(1) Å is quite long, with twelve bond connections between the metal centers. The corresponding distance in (**2**) is only slightly shorter and amounts to 5.983(1) Å. What differs the two complex cations is the form of the ligands. While in (**1**) both ligand molecules are present in a neutral form, so the total charge of the complex cation is balanced by four perchlorate groups, in (**2**) one of the ligands is present in a neutral and one in a monoanionic (singly deprotonated) form, so the charge of this complex cation in balanced by three perchlorate groups. Structural arguments for this finding are as follows. Inspection of bond lengths and angles (Table 2) reveals that in complex (**2**) they are different around and in the vicinity of the N33 nitrogen atom, and the coordinated oxygen atom O4 than around the other nitrogen and oxygen atoms. Of the four Ni–O bonds three are nearly identical, with the mean value 2.11(2) Å and one (Ni–O4) is by 0.05 Å shorter, indicating coordination to the deprotonated enolic oxygen. Moreover, the valence angle on the unprotonated nitrogen N33 amounts to 108.4(3)°, while the mean of the other three angles is 113.4(2)°, the difference being 5.0°. Differences in other bond lengths within the three protonated (average values) and one unprotonated O,N chelate ring in complex cation (**2**) range from 0.011 Å (for N–N bonds) to 0.030 Å (for C–O bonds). Differences in valence angles spread from 0.5° (for N–Ni–O angles) to 4.3° (for O–C–N angles). Further support for the presence of one deprotonated ligand in the complex cation (**2**) comes from the inspection of the hydrogen bonding pattern (Table 3). It reveals that the environment of N33 nitrogen is different from the environment of the remaining nitrogen atoms (N3, N13, N23) of which each acts as strong hydrogen bond donor to three different DMSO molecules.

The average Ni–N and Ni–O bonds in (**1**) amount to 2.04 (5) and 2.108(5) Å. The shortest coordinate bond is to the central nitrogen atom (N2, N12, N22, N32). As a rule, the coordinate bonds to the oxygen atoms are longer than to the nitrogen atoms. Strong

Table 2
Selected bond distances and valence angles.

	(1)	(2)		(1)	(2)
Bond distances (Å)					
Ni1–N1	2.085(5)	2.075(3)	Ni2–N21	2.087(6)	2.067(3)
Ni1–N2	1.983(5)	1.989(3)	Ni2–N22	1.995(5)	1.997(3)
Ni1–N11	2.056(6)	2.067(3)	Ni2–N31	2.079(5)	2.087(3)
Ni1–N12	2.012(5)	1.988(3)	Ni2–N32	1.986(5)	1.976(3)
Ni1–O1	2.101(4)	2.092(3)	Ni2–O3	2.111(4)	2.124(3)
Ni1–O2	2.110(4)	2.112(2)	Ni2–O4	2.112(4)	2.063(2)
Valence angles (°)					
N1–Ni1–N2	77.6(2)	77.96(12)	N21–Ni2–N22	78.3(2)	77.62(13)
N1–Ni1–N11	94.82(19)	93.57(12)	N21–Ni2–N31	93.57(19)	96.34(13)
N1–Ni1–N12	109.1(2)	107.36(12)	N21–Ni2–N32	106.5(2)	109.40(13)
N1–Ni1–O1	155.04(18)	155.44(11)	N21–Ni2–O3	155.50(19)	154.92(12)
N1–Ni1–O2	93.78(17)	93.68(10)	N21–Ni2–O4	96.05(17)	92.19(11)
N2–Ni1–N11	108.7(2)	108.56(12)	N22–Ni2–N31	109.2(2)	107.45(12)
N2–Ni1–N12	171.0(2)	171.61(12)	N22–Ni2–N32	172.1(2)	170.34(13)
N2–Ni1–O1	77.45(18)	77.48(11)	N22–Ni2–O3	77.2(2)	77.31(11)
N2–Ni1–O2	96.17(18)	95.93(11)	N22–Ni2–O4	95.43(18)	95.49(11)
N11–Ni1–N12	77.3(2)	77.95(12)	N31–Ni2–N32	77.13(19)	78.84(13)
N11–Ni1–O1	93.98(18)	94.70(11)	N31–Ni2–O3	93.63(18)	91.89(11)
N11–Ni1–O2	154.92(18)	155.41(11)	N31–Ni2–O4	154.93(19)	156.74(11)
N12–Ni1–O1	95.64(17)	96.98(11)	N32–Ni2–O3	97.94(18)	95.41(11)
N12–Ni1–O2	77.59(18)	77.46(11)	N32–Ni2–O4	77.95(18)	77.92(11)
O1–Ni1–O2	87.97(16)	88.32(9)	O3–Ni2–O4	87.10(15)	89.40(10)

Table 3
Hydrogen bond parameters.

	D–H (Å)	D···A (Å)	H···A (Å)	D–H···A (°)	Symmetry operations on A
(1)					
N3–H3A···O24	0.88	2.729(10)	1.900(6)	156.4(4)	
N13–H13A···O23	0.88	2.713(8)	1.858(5)	163.6(4)	$x+1, y, z$
N23–H23A···O21	0.88	2.678(7)	1.824(5)	163.0(4)	$x+1, y, z$
N23–H23A···O21A	0.88	2.779(14)	1.950(14)	156.4(6)	$x+1, y, z$
N33–H33A···O22	0.88	2.649(11)	1.790(10)	164.4(6)	$x, y+1, z$
N33–H33A···O22A	0.88	2.730(12)	1.906(13)	155.2(6)	$x, y+1, z$
O1E–H1E···O19	0.85	2.973(8)	2.123(6)	179.4(4)	$-x+1, -y+1, -z+1$
(2)					
N3–H3···O1S	1.003	2.735(6)	1.754(4)	164.9(2)	$x, y+1, z$
N13–H13···O3S	0.998	2.670(4)	1.691(3)	166.0(2)	
N23–H23···O2S	0.989	2.709(4)	1.726(3)	172.7(2)	

Table 4
Antimicrobial effects of the investigated compounds.

Compound	Inhibition zone diameter[a] (mm)				
	E. coli	*S. aureus*	*M. lysodeikticus*	*B. subtilis*	*C. albicans*
Control (DMSO)	n.a.[b]	n.a.	n.a.	n.a.	n.a.
H_2L2	16.0	16.0	n.a.	n.a.	n.a.
(**2**)	n.a.	12.0	n.a.	10.0	n.a.
(**3**)	16.0	11.0	20.0	14.0	9.0
$Ni(ClO_4)_2{\cdot}6H_2O$	n.a.	9.0	12.0	10.0	8.0
$Zn(BF_4)_2{\cdot}6H_2O$	11.0	12.0	16.0	9.0	8.0
Ampicillin	18.0	26.0	33.0	15.0	n.t.[c]
Nystatin	n.t.	n.t.	n.t.	n.t	21.0

[a] Including diameter of well (8 mm).
[b] n.a. – not active.
[c] n.t. – not tested.

hydrogen-bonding interactions exist between oxygen atoms belonging to the four DMSO molecules and the protonated nitrogen atoms (N3, N13, N23 and N33). These H-bonding interactions are summarized in Table 3.

3.3. Spectroscopic characterization

In the IR spectrum of the ligand H_2L2 the most intense band is amide band I [ν(C=O)] at 1662 cm^{-1}, and the band of ν(C=N) at 1580 cm^{-1} is also prominent. In the spectra of complexes (**1**) and (**2**) relative intensities and positions of the bands ν(C=O) and ν(C=N) are different. In the spectrum of (**1**) ν(C=O) is at the lower wave number (1629 cm^{-1}) and becomes weaker than the band ν(C=N) at 1599 cm^{-1}. In the spectrum of complex (**2**) the intensity of the carbonyl band is even weaker, so that it becomes a shouder on the ν(C=N) band. This is a consequence of deprotonation of the hydrazide nitrogen, so that, due to electron delocalization, C=O bond acquires partial single bond character, and the C–N bond partial double bond character. This is in accordance with shorter C–N bond length in the complex (**2**) in comparison to the corresponding bond lengths in part of complex (**2**) in which deprotonation did not occur. The most intense band in both complexes (**1**) and (**2**) is the band corresponding to perchlorate anion, at 1077 cm^{-1} and 1071 cm^{-1} in (**1**) and (**2**), respectively. In the Zn(II) complex (**3**) there is the same pattern of bands as in complex (**1**). In the spectrum of (**3**), the most intense band is at 1025 cm^{-1} due to tetrafluoroborate anion.

Preliminary X-ray results of the highly solvated Zn(II)–H_2L2 complex showed the coordination number six of dinuclear Zn(II) complex. However, ^{1}H NMR spectrum of the Zn complex in DMSO-d_6 solution indicates dissociation of the complex affording the free ligand and the dinuclear Zn complex, with one molecule of the ligand bridging two Zn atoms, the remaining coordination sites being occupied by solvent molecules. This conclusion is based on two series of signals in the ratio 1:1, one corresponding to the free ligand, and the other to the coordinated ligand. In the complex itself there are no prominent changes of chemical shifts upon complexation. It is noteworthy that hydrazide moieties are not deprotonated (signal at 11.02 ppm).

3.4. Antimicrobial activity evaluation

The results of the determination of antimicrobial activity of the ligand, the complexes (**2**) and (**3**), as well as the simple metal salts are presented in Table 4. The complex (**3**) showed activity against all tested microorganisms, while complex (**2**) was active against some strains of Gram positive bacteria only.

4. Conclusion

It was demonstrated that the investigated ligand forms unstable, highly solvated bimetallic complexes with Ni(II) cations. Two crystal types of these complexes have been isolated during the fractional crystallization process. They differ in both the crystal color and the stability. The less stable green crystals convert slowly to brown crystals while being kept in the solution. Once taken from the solution they decompose rapidly. It was shown that the apparent changes in crystal color signal a process of deprotonation of the hydrazide derived ligand and a consequent loss of a perchlorate anion.

The studied complexes (**2**) and (**3**) showed antimicrobial activity.

Acknowledgement

This work was supported by the Ministry of Science and Technological Development of the Republic of Serbia (Grant 142026).

Appendix A. Supplementary data

CCDC 717998 and 717999 contains the supplementary crystallographic data for (**1**) and (**2**). These data can be obtained free of charge via http://www.ccdc.cam.ac.uk/conts/retrieving.html, or from the Cambridge Crystallographic Data Center, 12 Union Road, Cambridge CB2 1EZ, UK; fax: (+44) 1223-336-033; or e-mail: deposit@ccdc.cam.ac.uk. Supplementary data associated with this article can be found, in the online version, at doi:10.1016/j.poly.2009.05.002.

References

[1] K. Anđelković, D. Sladić, A. Bacchi, G. Pelizzi, N. Filipović, M. Rajković, Transition Met. Chem. 30 (2005) 243.
[2] N.R. Filipović, A. Bacchi, M. Lazić, G. Pelizzi, S. Radulović, D.M. Sladić, T.R. Todorović, K.K. Anđelković, Inorg. Chem. Commun. 11 (2008) 47.
[3] S. Sen, C.R. Choudhury, P. Talukder, S. Mitra, M. Westerhausen, A.N. Kneifel, C. Desplanches, N. Daro, J.-P. Sutter, Polyhedron 25 (2006) 1271.
[4] L. Zhao, V. Niel, L.K. Thompson, Z. Xu, V.A. Milway, R.G. Harvey, D.O. Mille, C. Wilson, M. Leech, J.A.K. Howard, S. Heath, Dalton Trans. (2004) 1446.
[5] T.L. Kelly, V.A. Milway, H. Grove, V. Niel, T.S.M. Abedin, L.K. Thompson, L. Zhao, R.G. Harvey, D.O. Miller, M. Leech, A.E. Goeta, J.A.K. Howard, Polyhedron 24 (2005) 807.
[6] M. Lazić, S. Radulović, T. Todorović, D. Sladić, Ž. Tešić, K. Anđelković, Mater. Sci. Forum 495 (2006) 513.
[7] Oxford Diffraction CrysAlis CCD and CrysAlisRED including ABSPACK, Oxford Diffraction, Oxfordshire, England.
[8] G.M. Sheldrick, Acta Crystallogr., Sect. A: Found. Crystallogr. 64 (2008) 112.
[9] P. Van der Sluis, A.L. Spek, Acta Crystallogr., Sect. A: Found. Crystallogr. 46 (1990) 194.
[10] XP, Siemens Analytical X-ray Instruments Inc. Madison, Wisconsin, USA, 1990.

Polyhedron 28 (2009) 2403–2410

Contents lists available at ScienceDirect

Polyhedron

journal homepage: www.elsevier.com/locate/poly

Stabilities and coordination modes of methionine in copper(II) mixed-ligand complexes with ethylenediamine, diethylenetriamine or N, N, N′, N″, N″-pentamethyldiethylenetriamine in aqueous solution

Barbara Kurzak [a,*], Anna Kamecka [b], Katarzyna Bogusz [b], Julia Jezierska [c], Agnieszka Woźna [b]

[a] Faculty of Chemistry, University of Opole, Oleska 48, 45-052 Opole, Poland
[b] Institute of Chemistry, University of Podlasie, 3-Maja 54, 08-110 Siedlce, Poland
[c] Faculty of Chemistry, University of Wrocław, F. Joliot-Curie14, 50-383 Wrocław, Poland

ARTICLE INFO

Article history:
Received 9 April 2009
Accepted 1 May 2009
Available online 8 May 2009

Keywords:
Copper(II) complexes
Mixed-ligand complexes
Amino acids
EPR
Vis spectroscopy
Potentiometry
Equilibria
Stability constants
Polyamines
Five-coordinate complexes

ABSTRACT

Solution equilibrium studies on the Cu(II)–polyamine–methionine ternary systems (polyamine: ethylenediamine (en), diethylenetriamine (dien), N,N,N′,N″,N″-pentamethyldiethylenetriamine (Me_5dien)) have been performed by pH-potentiometry, UV–Vis spectrophotometry and EPR methods. The obtained results suggest the formation of the mixed-ligand complexes with $[Cu(A)(Met)]^+$ stoichiometry in all studied systems. Our spectroscopic results indicate the tetragonal geometry for $[Cu(en)(Met)]^+$, the geometry slightly deviated from square pyramidal for $[Cu(dien)(Met)]^+$ and strongly deviated from square pyramidal towards trigonal bipyramidal for the $[Cu(Me_5dien)(Met)]^+$ species. The coordination modes in these mixed-ligand complexes are discussed.

© 2009 Elsevier Ltd. All rights reserved.

1. Introduction

From 20 natural amino acids, which are the building blocks of proteins, eight are essential and cannot be produced by the human body, among them is methionine. Containing sulphur, it helps to prevent disorder of the hair, skin and nails, to lower the cholesterol levels by increasing the liver's production of lecithin and to reduce fat build-up in the liver and body [1].

On the other hand, the ferrocenylmethyl substituted L-methionine (together with L-asparagine) derived ligands and their copper(II) complexes [2,3] receive attention as owing to their redox properties, as electrochemical sensor design, and due to their ability to coordinate weakly Cu(II) at axial position through thioether group.

Chakravarty and coworkers [4–10] are involved in the development of the chemistry of non-porphyrinic low molecular weight copper-based complexes as new photoactive DNA cleaving agents. They [11] showed that although the amino acid (A) or heterocyclic base (B) are individually cleavage inactive, their ternary copper(II) complexes "A–Cu(II)–B" revealed efficient photoinduced DNA cleavage ability. One of them is the ternary copper(II) complex containing L-methionine as a photosensitizer and N,N-donor planar phenanthroline bases as DNA groove binders. They were observing a dramatic shift of the photoactive wavelength to the PDT window on complexation of L-methionine to the d^9-copper(II) ion.

The investigation of sulfur atom containing ligands for copper complexes receives attention from bioinorganic chemistry as well as coordination chemistry. Cysteine–thiolate–copper interactions are important in electron-transfer protein centers [12] and sulfide–copper interactions as a Cu_4–S cluster occur in the enzyme nitrous oxide reductase [13,14]. Thioether methionine–copper interactions occur in the type 1 "blue" electron-transfer proteins [15,16] but also at the active site of certain monooxygenases which effect substrate C–H bond activation and oxygenation chemistry. Thus, an area of research interest is to shed further light on copper redox chemistry in the presence of thioether groups (as models for protein methionine residues) directed toward oxidative chemistry, i.e., emphasizing Cu^+/O_2 or Cu^{2+}/H_2O_2 reactions (but this problem is out of the scope of our interest).

The important role of mixed-ligand complexes in different systems is beyond question. Thus, these types of complexes are our continuous inspiration to assemble data on formation, stability and structure and on the mutual influence of two ligands derived

* Corresponding author.
E-mail address: bkurzak@gmail.com (B. Kurzak).

0277-5387/$ - see front matter © 2009 Elsevier Ltd. All rights reserved.
doi:10.1016/j.poly.2009.05.001

from amino acids (hydroxamic acids) or amino acids and different polyamines bound to the same metal ion [17–26], (selected papers). In this paper we report the results of the studies on molecular structures and reactivity of the mixed-ligand copper(II) complexes of simple polyamines and methionine.

2. Experimental

2.1. Materials

Ethylenediamine dihydrochloride (en 2HCl) and diethylenetriamine (dien) were purchased from Sigma–Aldrich Chemical Co, N,N,N′,N″,N″-pentamethyldiethylenetriamine (Me_5dien) from Fluka and D,L-methionine was obtained from Reanal (Hungary). All ligands were of analytical grade and were used without further purification. The exact concentrations of the ligand stock solutions used for potentiometric measurements were determined by the Gran's method [27]. Copper(II) chloride solution was purchased from Merck as a Titrisol concentrate for the preparation of standard solutions. The concentration of the metal ion stock solution was standardized by complexometric ethylenediaminetetraacetate (EDTA) titration. Carbonate-free potassium hydroxide solution (the titrant) was prepared and standardized against a standard potassium hydrogen phthalate solution. All solutions were prepared with deionized water. The formulae of the fully protonated form of the ligands used in this study are shown in Scheme 1.

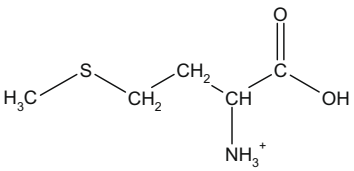
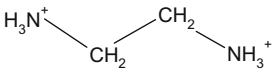
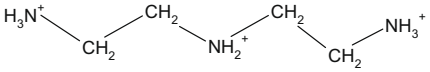
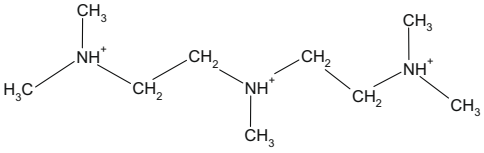
2.2. Potentiometric measurements

The stability constants of the proton and copper(II) complexes were determined by pH-metric titration of 5 cm^3 samples in aqueous solutions. All the measurements were carried out at 0.2 mol dm^{-3} ionic strength (KCl) and 25.0 ± 0.1 °C using a constant-temperature water-bath. The titrations were performed with carbonate-free KOH solution of known concentration (ca. 0.2 mol dm^{-3}) under argon atmosphere over the pH range 2.0 ≈ 11.0 or until precipitation occurred. For the binary systems the ligand concentration was 4×10^{-3} or 8×10^{-3} mol dm^{-3} (because of precipitation the ligand concentration for the Cu^{2+}–Met system was 1, 2 or 4×10^{-4} mol dm^{-3}). The metal ion to ligand ratios were 1:1, 1:2, 1:4 and 1:8.

For the ternary systems the ratios of copper(II):en/dien/Me_5dien:Met were 1:1:1, 1:1:2, 1:2:1 and 1:2:2. Titrations were made on samples containing the copper(II) ion at 4×10^{-3} mol dm^{-3} prepared from $CuCl_2$ salt. The values of stability constants of the complexes formed in the binary systems were kept constant during calculating the potentiometric data of the ternary systems.

The pH-metric titrations were carried out with a Radelkis Op-208/1 instrument equipped with a combination pH electrode (SINGLE PORE, Hamilton) and an ABU-80 autoburette (Radiometer).The electrode system was calibrated by periodic titrations of HCl solution (7.5×10^{-3} mol dm^{-3} in KCl) against standard KOH solution as described earlier [26]. The pH-metric results were used to establish the stoichiometry of the species and to calculate the stability constants of the species formed in the ternary systems. The equilibrium calculations were performed by the HYPERQUAD 2006 computer program [28]. The reported standard deviations were calculated by assuming random errors.

The charges of the complexes have been omitted in the text and tables. However, for clarity, it should be mentioned here that the fully deprotonated form of amino acid (Met) is L^- while the amines (en), (dien) or (Me_5dien) are neutral.

Ligands	Abreviation
 D,L-methionine	$[H_2L]^+$
 ethylenediamine	$[H_2\text{-en}]^{2+}$
 dietylenotriamina	$[H_3\text{-dien}]^{3+}$
 N,N,N',N'',N''-pentamethyldiethylenetriamine	$[H_3\text{-}Me_5\text{dien}]^{3+}$

Scheme 1.

2.3. UV/Vis spectroscopy

A BECKMAN DU68 spectrophotometer and 2-cm quartz cells were used to record the electronic absorption spectra in the visible range at room temperature. The spectra were recorded digitally (0.5 nm step) in the range of 200–900 nm. The metal ion concentration prepared from $CuCl_2$ salt was 4×10^{-3} mol dm^{-3} for Vis and 1×10^{-4} mol dm^{-3} for UV. For the ternary systems copper(II):en:Met, copper(II):dien:Met and copper(II):Me_5dien:Met the concentration ratios were 1:2:1, 1:1:2 and 1:2:1, respectively. The concentration ratios of the reagents were chosen in order to achieve as high as possible concentration of the mixed-ligand species and to get the lowest concentration of the [Cu(Met)$_2$] species that precipitates in the solution. The measurements were carried out in water at different pH values, using 1, 2 or 3 cm path length quartz cuvettes. The net ligand-field absorption band of each mixed-ligand species was extracted from the absorption spectra applying the procedure described in Ref. [20].

2.4. EPR spectroscopy

Electron paramagnetic resonance (EPR) spectra were performed on a Bruker 300E X-band spectrophotometer equipped with a Bruker NMR gaussmeter ER 035M and a Hewlett–Packard frequency counter HP 5350B at 77 K in water/ethyleneglycol (4:1 v/v) solution. The EPR parameters were calculated by computer simulation of the experimental spectra using Bruker's WIN-EPR SIMFONIA Software Version 1.25. The metal ion concentration and the metal ion to ligands molar ratios were the same as those used in the electronic absorption spectra.

3. Results and discussion

3.1. Acidity of the ligands and Cu^{2+}-complexation for the binary systems

The values of the protonation constants for the studied ligands and the stability constants of the complexes formed in the binary systems were re-determined under the same experimental conditions as those applied for the ternary systems. The obtained results for the ligands [19,22,25,29] and for the binary systems Cu^{2+}–en [30–32], Cu^{2+}–dien [20,22], Cu^{2+}–Me_5dien [23,29,30] and Cu^{2+}–Met [19,30,33–35] are in good agreement with the literature data.

The fully protonated form of en contains two dissociable protons (H_2L^{2+}), one at each amino group $-NH_3^+$, while dien and Me_5dien (H_3L^{3+}) are able to release three protons in the whole pH range. Met (H_2L^+) has two dissociable protons that dissociate off the ligand in the measurable pH range. The carboxylic function is depro-

Table 1
Cumulative formation constants (logβ), derived equilibrium constants (log K) and characteristic parameters for the stability of complexes formed in the ternary systems Cu^{2+}–amine (en, dien or Me_5dien)–D,L-methionine at 25 °C and I = 0.2 mol dm^{-3} (KCl). (Charges are omitted for simplicity).

Nr	Assignments	System Cu^{2+}–A–Met; (A = en, dien or Me_5dien)		
		Cu^{2+}–en–Met	Cu^{2+}–dien–Met	Cu^{2+}–Me_5dien–Met
1	logβ[Cu(A)(Met)]	17.33 (1)	19.46 (1)	16.79 (1)
2	log $K_{[Cu(A)(Met)]}$; [Cu(A)]+Met ⇌ [Cu(A)(Met)][a]	6.75	3.45	4.32
3	log$K_{[Cu(A)(Met)]}$ − p$K_{NH_3^+}$ − pK_{COOH}	−4.59	−7.89	−7.02
4	χ^2	10.89	11.13	11.47
5	σ	4.15	9.3	4.04
6	Δlog K[b]	−1.01	−4.31	−3.44
7	log$X$	0.66	3.89	

[a] log$K_{[Cu(A)(Met)]}$ = log$\beta_{[Cu(A)(Met)]}$-log$\beta_{[Cu(A)]}$; log$\beta_{[Cu(en)]}$ = 10.58, log$\beta_{[Cu(en)2]}$ = 19.73 [32], log$\beta_{[Cu(dien)]}$ = 16.01, log$\beta_{[Cu(dien)2]}$ = 20.76 [22], log$\beta_{[Cu(Me5dien)]}$ = 12.47 [23], log$\beta_{[Cu(Met)]}$ = 7.76, log$\beta_{[Cu(Met)2]}$ = 14.27, pK_{COOH} = 2.22 and p$K_{NH_3^+}$ = 9.12 [19].
[b] $\Delta \log K = \log \beta_{[M(A)(Met)]} - (\log \beta_{[M(A)]} + \log \beta_{[M(Met)]})$.

Table 2
Vis and EPR spectral parameters of the copper(II) complexes.

Species	EPR						Coordination mode	Vis
	g_{iso}	A_{iso} (10^{-4} cm^{-1})	$g_{\|\|}$	$A_{\|\|}$ (10^{-4} cm^{-1})	$g_\perp$	$A_\perp$ (10^{-4} cm^{-1})		λ_{max} (nm) ε (dm^3 mol^{-1} cm^{-1})
[Cu(Met)]$^+$	2.153	59	2.314	171	2.068	15	{NH_2, COO^-}	700 (53)
[Cu(α-Ala)]$^+$	2.153	57	2.318	167	2.065	10	{NH_2, COO^-}	690
[Cu(α-Ala)$_2$]	2.119	65	2.252	187	2.058	14	2 x {NH_2, COO^-}	618 (56)
[Cu(en)]$^{2+}$ (Ref. [25])	2.138	68	2.283	183	2.060	14	{NH_2, NH_2}	666 (39)
[Cu(en)$_2$]$^{2+}$ (Ref. [25,41])	2.100	86	2.207	198	2.040	20	2 × {NH_2, NH_2}	549 (71)
[Cu(en)(α-Ala)]$^+$ (Ref. [41])			2.230	190	2.051	18	{NH_2, NH_2}; {NH_2, COO^-}	580 (58)
[Cu(en)(Met)]$^+$			2.234	193	2.050	21	{NH_2, NH_2}; {NH_2, COO^-}	582 (72)
[Cu(dien)]$^{2+}$ (Ref. [20,41])			2.234	192	2.055	20	{NH_2, NH, NH_2}	614 (78)
	g_z	g_x	g_y	A_z (10^{-4} cm^{-1})	A_x (10^{-4} cm^{-1})	A_y (10^{-4} cm^{-1})		
[Cu(dien)(α-Ala)]$^+$ (Ref. [41])	2.217	2.054	2.043	190	30	15	{NH_2, NH, NH_2}; {NH_2, COO^-}	635 (106)
[Cu(dien)(Met)]$^+$	2.215	2.054	2.044	193	29	14	{NH_2, NH, NH_2}; {NH_2, COO^-}	635 (107)
[Cu(Me_5dien)]$^{2+}$ (Ref. [26])	2.240	2.065	2.050	183	29	14	{$N(CH_3)_2$,$N(CH_3)$,$N(CH_3)_2$}	665 (225)
	g_1	g_2	g_3	A_1 (10^{-4} cm^{-1})	A_2 (10^{-4} cm^{-1})	A_3 (10^{-4} cm^{-1})		
[Cu(Me_5dien)(α-Ala)]$^+$ (Ref. [41])	2.208	2.138	2.007	135	20	62	{$N(CH_3)_2$,$N(CH_3)$,$N(CH_3)_2$}; {NH_2, COO^-}	777 (275)
[Cu(Me_5dien)(Met)]$^+$	2.205	2.140	2.008	132	20	61	{$N(CH_3)_2$,$N(CH_3)$,$N(CH_3)_2$}; {NH_2, COO^-}	784 (294)

tonated in the acidic pH range, whereas the amino group dissociates in the basic solution [19].

In the Cu^{2+}–Met system the complexation process starts at pH 2.5. $[Cu(Met)]^+$ is predominant species in the solution in the pH range about 4–5. A further increase in pH leads to the $[Cu(Met)_2]$ complex formation. This is accompanied by the changes in d–d transition energies. The values of λ_{max} received at the maximum concentration of the $[Cu(Met)]^+$ (700 nm) and $[Cu(Met)_2]$ (λ_{max} = 623 nm) species are very similar to these found for $[Cu(\alpha\text{-ala})]^+$ (690 nm) and $[Cu(\alpha\text{-ala})_2]$ (λ_{max} = 618 nm), respectively [36]. Furthermore, the EPR parameters of the spectra observed for the $[Cu(Met)]^+$ species at pH 3.3 in the liquid and frozen solution are close to those observed for $[Cu(\alpha\text{-ala})]^+$ at pH 4.68 (Table 2). This data indicate that the amino nitrogen atom and the carboxylate oxygen are the major binding sites in both species $[Cu(\alpha\text{-ala})]^+$ and $[Cu(Met)]^+$. Such coordination mode without the involvement of the thioether sulfur of Met in the coordination to the copper(II) ions was also postulated on the basis of the IR spectra [35]. Although there is a wide range of studies focused on Cu^{2+} binding to a variety of peptides containing methionyl residue that revealed the possibility of S–Cu^{2+} interaction [24,37–39], methionine itself was reported to act as a tridentate ligand for copper(II) ions only at low temperatures and at low pH values [40].

3.2. Cu^{2+}-complexation for the ternary systems

The four-component equilibria can be described as:

$$pM + q(A) + r(Met) + sH \rightleftharpoons M_p(A)_q(Met)_rH_s$$

where *p*, *q*, *r* and *s* are the stoichiometric coefficients corresponding to the metal ion, Cu^{2+}, A (A = en, dien or Me_5dien), Met, and H, respectively; charges are omitted for simplicity.

The overall formation constants are defined as:

$$\beta_{pqrs} = [M_p(A)_q(Met)_rH_s]/[M]^p[(A)]^q[(Met)]^r[H]^s$$

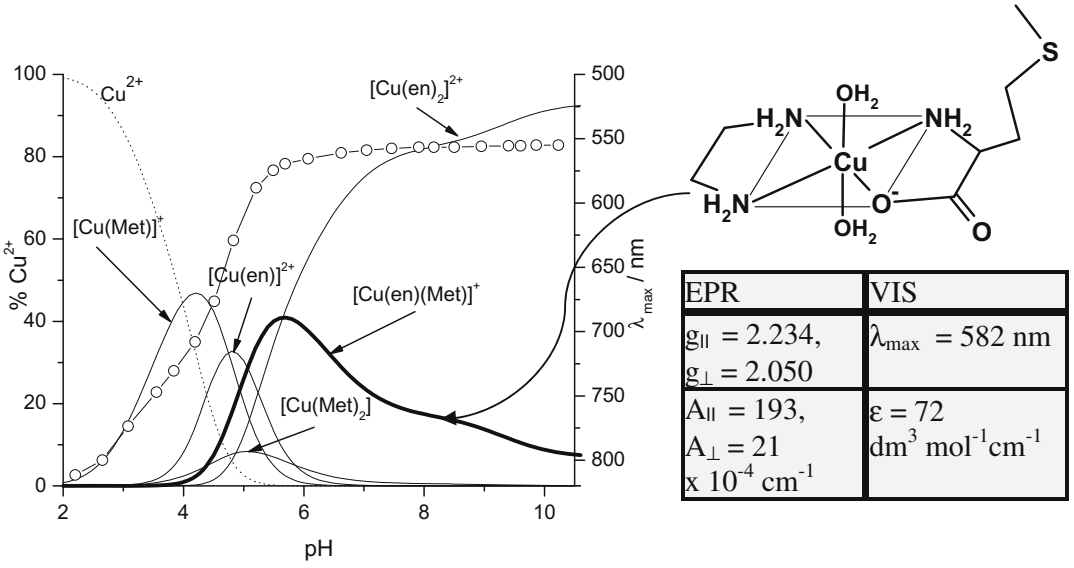
The equilibrium models for ternary systems and corresponding stability constants giving the best fits of the pH-metric titration curves are presented in Table 1. According to these data, only one type of mixed-ligand species with stoichiometry $[Cu(A)Met]^+$ is formed in all ternary systems.

The binding strength between Met and copper(II) ions in the presence of polyamine can be evaluated from the computed values β_{pqrs} according to the equation: $\log K_{Cu(A)Met} = \log\beta_{Cu(A)Met} - \log\beta_{Cu(A)}$ (Table 1 row 2). The derived equilibrium constant, $K_{Cu(A)Met}$, shows how tightly Met is bound to the simple $[Cu(A)]^{2+}$ complex. Similarly as it was observed for the ternary systems of the same polyamines and L-histidine in copper(II) solution, the stepwise stability constants of the mixed-ligand species involving tridentate dien and Me_5dien are much lower than for the species containing bidentate en [41].

The relative stability of $[M(A)(Met)]^+$ can be expressed in terms of $\Delta\log K$ parameter (the constant due to $[M(A)] + [M(Met)] \rightleftharpoons [M(A)(Met)] + M$ equilibrium). It can be seen that, $\Delta\log K$ is equal to −1.01 for $[Cu(en)(Met)]^+$ and is very low for $[Cu(dien)(Met)]^+$ (−4.31) and for $[Cu(Me_5dien)(Met)]^+$ (−3.44). It is known that the statistical value of $\Delta\log K$ depends on the geometry of the complex and for the distorted octahedral coordination sphere of Cu^{2+} with two different bidentate ligands was deduced as −0.9 [42,43]. The distinctly lower values observed in the case of mixed-ligand complexes with dien or Me_5dien are most likely caused by lower than six coordination number of Cu^{2+} [42,43].

It is also possible to calculate the $\log X_{M(A)(Met)}$ values (the constant due to $[M(A)_2] + [M(Met)_2] \rightleftharpoons 2[M(A)(Met)]$ equilibrium, (Table 1 row 7). In the ternary systems of dien the formation of mixed-ligand complexes is especially favoured (0.6) [44]. For the $[Cu(Me_5dien)(Met)]^+$ mixed-ligand species the $\log X_{M(A)(L)}$ value cannot be calculated, since the complex with 1:2 metal to ligand ratio is not formed in the Cu^{2+}–Me_5dien binary system [23]. It could be noticed that the $\log X_{M(A)(L)}$ value for the system with dien is distinctly higher than that for the system with en. The same effect was observed for the ternary systems with L-histidine and simple polyamines [41].

The species distribution curves for the Cu^{2+}–en–Met system at 1:2:1 molar ratio as a function of pH presented in Fig. 1 indicate that under these experimental conditions the $[Cu(en)(Met)]^+$ mixed-ligand species starts to form above pH 4 and reaches the maximum concentration at pH 6. Below this pH value the simple species with Met and H_2O are formed. The EPR spectrum at pH 4.1 is very similar to the spectrum observed for the Cu^{2+}–Met binary system in an acid solution (see above) and changes distinctly at



EPR	VIS
$g_{\|\|} = 2.234$, $g_\perp = 2.050$	$\lambda_{max} = 582$ nm
$A_{\|\|} = 193$, $A_\perp = 21$ x 10^{-4} cm^{-1}	$\varepsilon = 72$ $dm^3\ mol^{-1}cm^{-1}$

Fig. 1. Species distribution curves as a function of pH and variations of visible absorption maximum wavelength (circle) for the Cu^{2+}–en–Met ternary system at 1:2:1 molar ratio; $c_{Cu^{2+}} = 4 \times 10^{-3}$ mol dm^{-3}.

pH 4.8. At this pH the concentration of the $[Cu(Met)]^+$ species decreases but the $[Cu(en)]^{2+}$ species increases in the solution. Two patterns of copper hyperfine splitting of parallel orientation in EPR spectrum corresponding to the equilibrium between $[Cu(Met)]^+$ and $[Cu(en)]^{2+}$ (Table 2) are observed. In the pH range 5–6 a new spectrum appeared. It was obtained as separate by subtraction of the EPR signals from the equilibrial $[Cu(en)]^{2+}$ and $[Cu(en)_2]^{2+}$ species (with suitable contribution) present also in the Cu–en–Met ternary system at pH 5.6. The parameters of this new spectrum $g_{||} = 2.234$, $A_{||} = 193 \times 10^{-4}$ cm^{-1} (Fig. 1), should be assigned to the mixed-ligand species $[Cu(en)(Met)]^+$ predicted at this pH range (the concentration ca. 40%). Its parameters are very similar to those corresponding to the mixed-ligand species formed by en and α-Ala with copper(II) ions $[Cu(en)(\alpha\text{-Ala})]^+$ (Table 2). In addition, the energy of d-d transition (Figs. 1 and 2) for the $[Cu(en)(Met)]^+$ species is almost the same as for $[Cu(en)(\alpha\text{-Ala})]^+$ (Table 2). Furthermore, the expected S(thioether) → Cu(II) charge transfer (CT) band is not observed in the UV region for this ternary system. The existence of such CT transition around 320–360 nm is generally a good indication of thioether coordination [38,45,46]. This spectroscopic data indicate the formation of (NH_2,NH_2) and (NH_2,COO^-) chelates in the plane of $[Cu(en)(Met)]^+$ without the involvement of the sulphur atom in the metal ion coordination (Fig. 1).

The calculated concentrations of the copper(II) complex species formed in the Cu^{2+}–dien–Met system, with 1:1:2 molar ratio, reveal that complexation of $[Cu(dien)]^{2+}$ by Met begins above pH 6 and reaches the maximum concentration at pH 9 Fig. 3a. The formation of mixed-ligand species is preceded mainly by the appearance of simple complexes with Met and dien. At pH 3.3 three patterns of copper hyperfine splitting in EPR spectrum corresponding to equilibrium between $[Cu(dien)]^{2+}$ ($g_{||} = 2.234$, $A_{||} = 195 \times 10^{-4}$ cm^{-1}), $[Cu(Met)]^{2+}$ ($g_{||} = 2.312$, $A_{||} = 172 \times 10^{-4}$ cm^{-1}) and Cu^{2+}_{aqua} ($g_{||} = 2.42$, $A_{||} = 132 \times 10^{-4}$ cm^{-1}) are observed. As pH of the solution increases, the concentrations of $[Cu(Met)]^{2+}$ and Cu^{2+}_{aqua} decrease and about pH 5.5 the spectrum of the $[Cu(dien)]^{2+}$

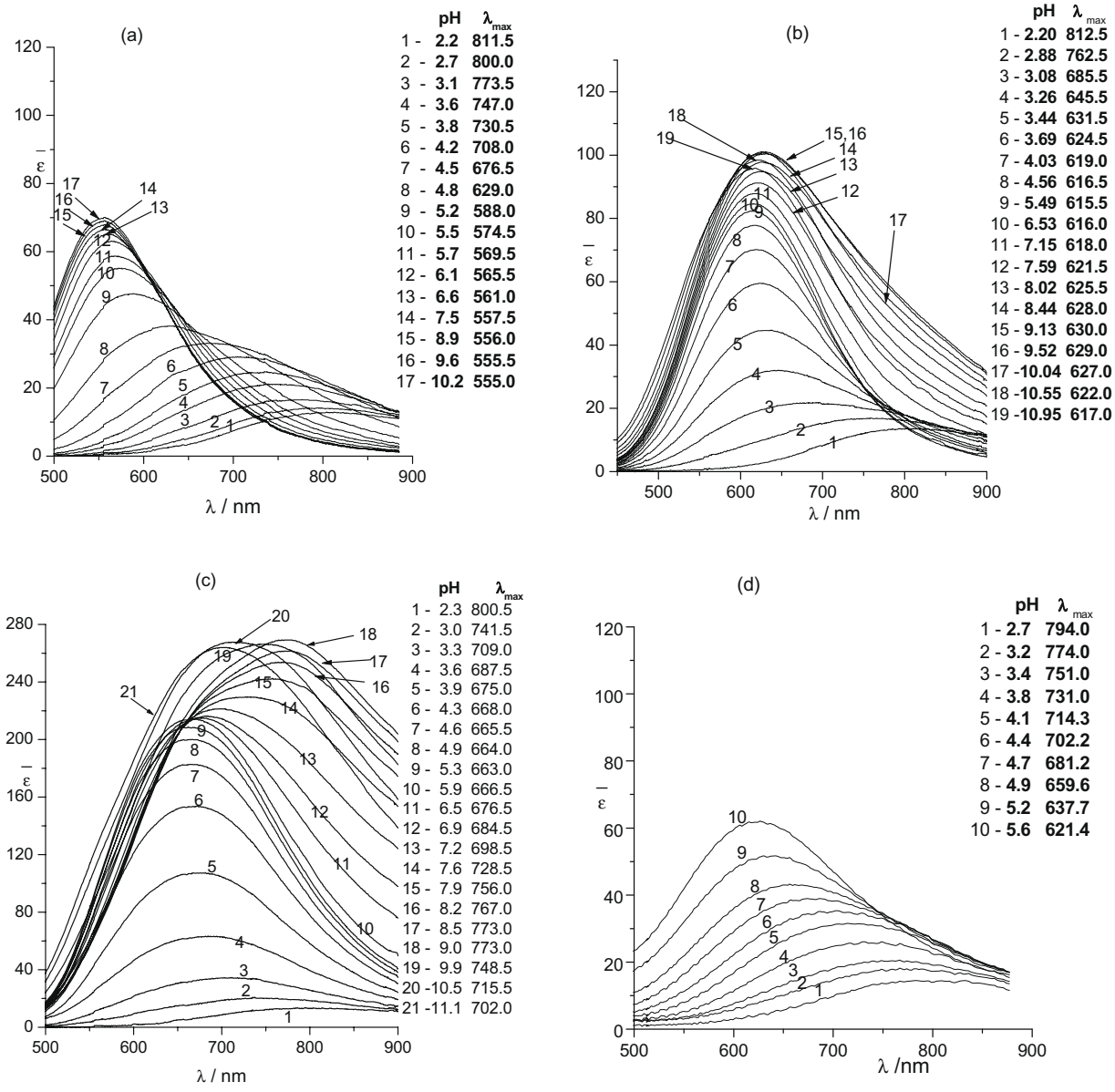


Fig. 2. pH-varied absorption spectra of the Cu^{2+}–en–Met system at 1:2:1 molar ratio (a), Cu^{2+}–dien–Met system at 1:1:2 molar ratio (b), Cu^{2+}–Me_5dien–Met system at 1:2:1 molar ratio (c) $c_{Cu^{2+}} = 4 \times 10^{-4}$ mol dm^{-3}, 2 cm cells), Cu^{2+}–Met system at 1:8 molar ratio (d) ($cCu^{2+} = 4 \times 10^{-4}$ mol dm^{-3}, 10 cm cell).

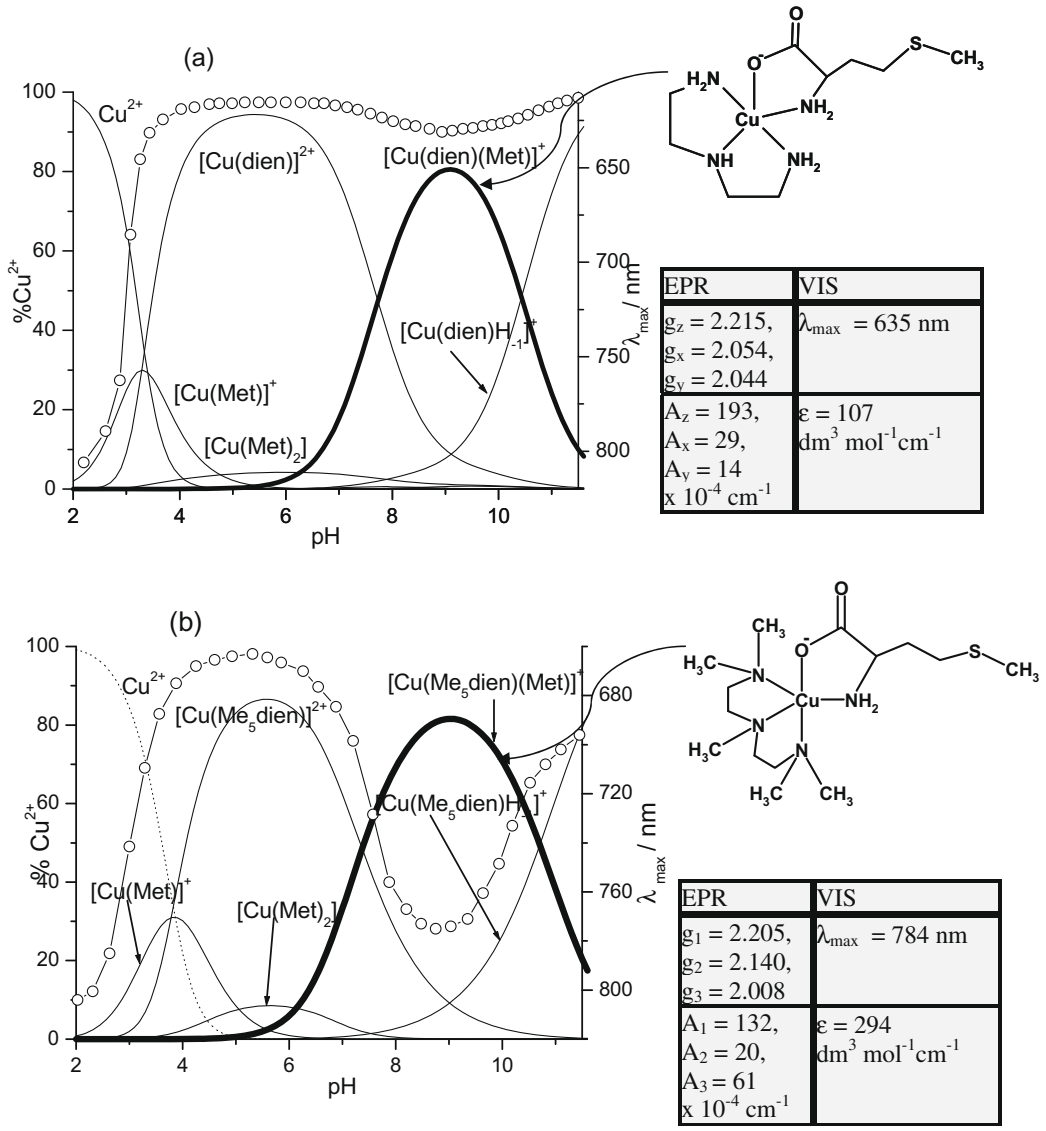


Fig. 3. Species distribution curves as a function of pH and variations of visible absorption maximum wavelength (circle) for the Cu^{2+}–dien–Met system at 1:1:2 molar ratio (a) and Cu^{2+}–Me_5dien–Met system at 1:2:1 molar ratio (b); $c_{Cu^{2+}} = 4 \times 10^{-3}$ mol dm^{-3}.

complex is only observed as dominant. In the pH range 7.5–10.5 a distinct change of EPR spectral feature could be noticed. A new spectrum is apparently different from that observed for Cu^{2+}–dien and should be ascribed to the predominant at this pH range mixed-ligand species $[Cu(dien)(Met)]^+$ (Fig. 3a). The spectral parameters calculated for this species (Table 2) are consistent with those corresponding to a five-coordinate species formed by α-alanine and dien in the copper(II) frozen solution (Table 2). So, Met similarly to α-Ala, completes the coordination number to five by binding amine nitrogen in Cu^{2+} plane and carboxylic oxygen in axial position. The presence of a weak rhombic distortion suggests that the geometry is slightly deviated from square pyramidal towards trigonal bipyramidal [47]. The effect of the $[Cu(dien)(Met)]^+$ species formation is also observed in the electronic spectral changes (Figs. 2b and 4d). From the comparison between the species distribution curves (Fig. 3a) and pH-varied absorption spectra of the Cu^{2+}–dien–Met system (Fig. 2b) the red shift of visible absorption maximum wavelength (circle in Fig. 3a) may be observed indicating the formation and decay of the mixed-ligand species. Its isolated electronic absorption spectrum at pH 9.1 (Fig. 4) demonstrates a characteristic of the five-coordinate complexes asymmetry [22,41]. The energy of d–d transition for $[Cu(dien)(Met)]^+$ (Fig. 3a) is almost identical to that stated for $[Cu(dien)(\alpha\text{-Ala})]^+$ (Table 2). Furthermore, a comparison of relative stability constants for mixed-ligand complexes of Met and α-Ala strongly confirms the proposed coordination mode. The relative stability constants, $\log K_{Cu(dien)(L)} - pK_{NH_3^+} - pK_{COOH}$, which takes into account the difference in the basicity of coordinating amino and carboxylic groups, for the ternary system with α-Ala (−7.89; [48]) is the same as this calculated for $[Cu(dien)(Met)]^+$ (Table 1). It suggests the same, ({NH_2, NH, NH_2}{NH_2, COO^-}, coordination mode, independently on amino-acid Fig. 3a).

The concentration distribution curves for the Cu^{2+}–Me_5dien–Met system together with the variations of visible absorption maximum wavelength are presented in Fig. 3b. It can be seen, that up to pH 7 the simple species with Me_5dien or Met are mainly formed. The EPR spectrum observed at pH 3.8 in the frozen solution of this ternary system corresponds to the existence of the equilibrium between $[Cu(Me_5dien)]^{2+}$, $[Cu(Met)]^+$ (see above) and $[Cu(H_2O)_6]^{2+}$ species. The increasing contribution of the $[Cu(Me_5dien)]^{2+}$ complex dominant between pH 5.0–6.0 is accompanied by a change of the recorded EPR spectra. The EPR parameters of the spectra ob-

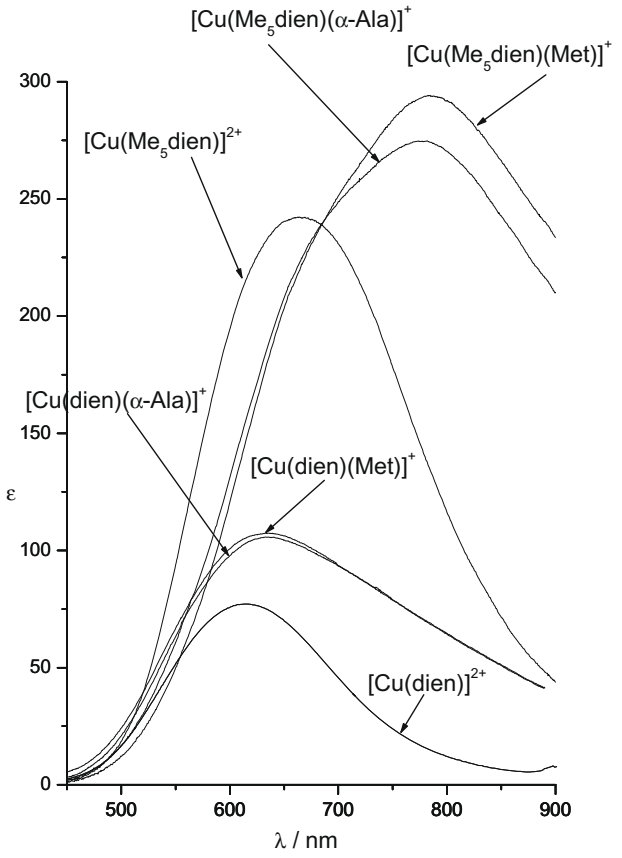


Fig. 4. Distribution-corrected absorption spectra for the $[Cu(dien)(Met)]^+$, $[Cu(dien)(\alpha\text{-Ala})]^+$, $[Cu(Me_5dien)(Met)]^+$, $[Cu(Me_5dien)(\alpha\text{-Ala})]^+$, $[Cu(Me_5dien)]^{2+}$, $[Cu(dien)]^{2+}$ species.

served in this pH range ($g_z = 2.238$, $g_x = 2.065$, $g_y = 2.050$ and $A_z = 185$, $A_x = 24$, $A_y = 14 \times 10^{-4}$ cm^{-1}) resemble quite closely those obtained for $[Cu(Me_5dien)]^{2+}$ (Table 2).

The $[Cu(Me_5dien)(Met)]^+$ species starts to form above pH 6 and reaches maximum concentration (ca. 80%) at pH ~9 (Fig. 3b). The pH-varied absorption spectra of Cu^{2+}-Me_5dien-Met ternary system are different from those for both Cu^{2+}–Me_5dien [26] and Cu^{2+}–Met binary systems (Figs. 3c and 2d). In addition, the pH dependence of λ_{max} in the visible spectra collected for the Cu^{2+}–Me_5dien–Met system clearly shows a significant red shift (the value of λ_{max} increases from 664 at pH ca. 5.5 to 775 nm at pH ca. 9 and then starts to decrease) which parallels the formation and decay of the $[Cu(Me_5dien)(Met)]^+$ species. This effect clearly indicates the structural change around the copper(II) ion and transition from a six to distorted five-coordination geometry while going from the simple to mixed-ligand species [20,22,23,26,41]. Moreover, the energy of d–d transition for $[Cu(Me_5dien)(Met)]^+$ (Figs. 3b and 4), is similar to those for five-coordinate mixed-ligand species containing Me_5dien and other α-amino acids [48], e.g. $[Cu(Me_5dien)(\alpha\text{-Ala})]^+$ (Fig. 4 and Ref. [41]). Similarly, the relative stability constants, $\log K_{Cu(Me_5dien)(L)} - pK_{NH_3^+} - pK_{COOH}$, calculated for the ternary system with α-Ala (−6.89; [48]) is close to this for the $[Cu(Me_5dien)(Met)]^+$ species (Table 1). These spectroscopic and potentiometric facts imply that the coordination modes in $[Cu(Me_5dien)(\alpha\text{-Ala})]^+$ and $[Cu(Me_5dien)(Met)]^+$ mixed-ligand species are the same, most probably without any interaction of the thioether sulfur of Met with Cu^{2+} ion (Fig. 3b).

The EPR measurements provide further information on the lack of the interaction between copper(II) and the sulfur atom. The values of the hyperfine splitting constants A and g parameters which are calculated from the separated EPR spectrum of the $[Cu(Me_5dien)(Met)]^+$ mixed-ligand species in frozen solution (Fig. 3b) are very close to these obtained for $[Cu(Me_5dien)(\alpha\text{-Ala})]^+$ (Table 2), $[Cu(Me_5dien)(\text{L-proline})]^+$ or $[Cu(Me_5dien)(\text{L-valine})]^+$ [48]. Thus, it can be concluded that geometry of the $[Cu(Me_5dien)(Met)]^+$ species is strongly deviated from square pyramidal towards trigonal bipyramidal, similarly as it was observed for other mixed-ligand species with Me_5dien due to the dominant bulky effect of two methyl substituents at each nitrogen atoms [23,26,29,41,48].

4. Conclusion

In the studied copper(II)-polyamine-Met ternary systems, the potentiometric, VIS and EPR results support the formation of the mixed-ligand complexes with $[Cu(A)(Met)]^+$ stoichiometry. The coordination in the $[Cu(en)(Met)]^+$ species, which reaches the maximum concentration at pH 6, is most likely realised by $\{NH_2, NH_2\}$ of en and $\{NH_2, COO^-\}$ of Met in the equatorial plane without the involvement of the sulphur atom in the copper(II) ion coordination. For the $[Cu(dien)(Met)]^+$ species, which predominates in basic solution, the geometry slightly deviated from square pyramidal is postulated. In this mixed-ligand species the binding of Cu^{2+} in the equatorial plane is realised by three amine nitrogens of dien and the amine nitrogen of Met whereas the carboxylic oxygen completes the coordination sphere at the axial position ($\{NH_2$, NH, $NH_2\}\{NH_2, COO^-\}$). The coordination mode in the $[Cu(Me_5dien)(Met)]^+$ species is the same as in the case of $[Cu(dien)(Met)]^+$, most probably without any interaction of the thioether sulfur of Met, but the geometry of this mixed-ligand species is strongly deviated from square pyramidal towards trigonal bipyramidal due to the dominant bulky effect of two methyl substituents at each nitrogen atoms.

Acknowledgment

We would like to express our gratitude to Ms. Jadwiga Kędzierska for her technical assistance in the EPR measurements.

References

[1] M. Usami, H. Ohyanagi, S. Ishimoto, S. Nishimatsu, T. Ueda, Y. Saitoh, Pub. Med. 15 (1991) 540.
[2] A. Hess, J. Sehnert, T. Weyhermiiller, N. Metzler-Nolte, Inorg. Chem. 39 (2000) 5437.
[3] S.C. Sahoo, M. Ray, Dalton Trans. 44 (2007) 5148.
[4] S. Dhar, D. Senapati, P.K. Das, P. Chattopadhyay, M. Nethaji, A.R. Chakravarty, J. Am. Chem. Soc. 125 (2003) 12118.
[5] S. Dhar, A.R. Chakravarty, Inorg. Chem. 42 (2003) 2483.
[6] S. Dhar, D. Senapati, P.A.N. Reddy, P.K. Das, A.R. Chakravarty, Chem. Commun. (2003) 2452.
[7] A.M. Thomas, M. Nethaji, A.R. Chakravarty, J. Inorg. Biochem. 98 (2004) 1087.
[8] P.A.N. Reddy, B.K. Santra, M. Nethaji, A.R. Chakravarty, J. Inorg. Biochem. 98 (2004) 377.
[9] A.M. Thomas, A.D. Naik, M. Nethaji, A.R. Chakravarty, Inorg. Chim. Acta 357 (8) (2004) 2315.
[10] A.M. Thomas, A.D. Naik, M. Nethaji, A.R. Chakravarty, Indian J. Chem. 43A (2004) 691.
[11] A.K. Patra, S. Dhar, M. Nethaji, A.R. Chakravarty, Dalton Trans. 7 (2005) 896.
[12] Y. Lu, Electron Transfer: Cupredoxins, in: L. Que Jr., W.B. Tolman (Eds.), Bio-Coordination Chemistry, vol. 8, Elsevier Ltd., Oxford, UK, 2004, p. 91.
[13] P. Chen, S.I. Gorelsky, S. Ghosh, E.I. Solomon, Angew. Chem., Int. Ed. 43 (32) (2004) 4132.
[14] Y. Lee, A.A.N. Sarjeant, K.D. Karlin, Chem. Commun. 6 (2006) 621.
[15] E.I. Solomon, R.K. Szilagyi, S.D. George, L. Basumallick, Chem. Rev. 104 (2) (2004) 419.
[16] D.B. Rorabacher, Chem. Rev. 104 (2) (2004) 651.
[17] B. Kurzak, H. Kozłowski, E. Farkas, Coord. Chem. Rev. 114 (1992) 169.
[18] K. Kurzak, B. Kurzak, E. Matczak-Jon, M. Hoffmann, Spectrosc. Lett. 29 (7) (1996) 1307.
[19] B. Kurzak, E. Matczak-Jon, M. Hoffmann, J. Coord. Chem. 43 (1998) 243.
[20] B. Kurzak, D. Kroczewska, J. Jezierska, Polyhedron 17 (1998) 1831.
[21] B. Kurzak, A. Kamecka, K. Kurzak, J. Jezierska, P. Kafarski, Polyhedron 17 (25–26) (1998) 4403.

[22] B. Kurzak, K. Bogusz, D. Kroczewska, J. Jezierska, Polyhedron 20 (2001) 2627.
[23] D. Kroczewska, K. Bogusz, B. Kurzak, J. Jezierska, Polyhedron 21 (2002) 295.
[24] B. Kurzak, A. Woźna, J. Jezierska, M. Jeżowska-Bojczuk, W. Szczepanik, P. Kafarski, Polyhedron 23 (2004) 1939.
[25] B. Kurzak, A. Kamecka, K. Bogusz, J. Jezierska, Polyhedron 26 (2007) 4223.
[26] B. Kurzak, A. Kamecka, K. Bogusz, J. Jezierska, Polyhedron 26 (2007) 4345.
[27] G. Gran, Acta Chem. Scand. 4 (1950) 559.
[28] P. Gans, A. Sabatini, A. Vacca, Talanta 43 (1996) 1739.
[29] D. Kroczewska, B. Kurzak, J. Jezierska, Polyhedron 25 (2006) 678.
[30] G. Brookes, L.D. Pettit, J. Chem. Soc., Dalton Trans. (1977) 1918.
[31] A. Odani, O. Yamauchi, Inorg. Chim. Acta 93 (1984) 13.
[32] B. Kurzak, D. Kroczewska, J. Coord. Chem. 34 (1995) 67.
[33] I. Sovago, G. Petocz, J. Chem. Soc., Dalton Trans. (1987) 1717.
[34] G. Berthon, Pure Appl. Chem. 67 (1995) 1117.
[35] A. Stanila, A. Marcu, D. Rusu, M. Rusu, L. Dawid, J. Mol. Struct. 834–836 (2007) 364.
[36] B. Kurzak, K. Bogusz, unpublished results.
[37] T. Kowalik-Jankowska, A. Kiss, I. Sovado, H. Kozłowski, Pol. J. Chem. 68 (1994) 1993.
[38] K. Varnagy, B. Boka, I. Sovago, D. Sanna, P. Marras, G. Micera, Inorg. Chim. Acta 275–276 (1998) 440.
[39] L. Xiao, M. Jouini, B.T. Fan, G. Lapluye, J. Huet, J. Chem. Soc., Dalton Trans. (1990) 1137.
[40] H. Kozlowski, T. Kowalik, Inorg. Nucl. Chem. 14 (1978) 201.
[41] B. Kurzak, A. Kamecka, K. Bogusz, J. Jezierska, Polyhedron 27 (2008) 2952.
[42] H. Sigel, Angew. Chem. 87 (1975) 391.
[43] H. Sigel, Angew. Chem. Int. Ed. Engl. 14 (1975) 394.
[44] H. Sigel (Ed.), Metal Ions in Biological Systems, vol. 2, Marcel Dekker, Inc., New York, 1973.
[45] J.V. Dagdigian, V. McKee, C.A. Reed, Inorg. Chem. 21 (1982) 1332.
[46] A.W. Addison, P.J. Burke, K. Henrick, T.N. Rao, E. Sinn, Inorg. Chem. 22 (1983) 3645.
[47] N. Azuma, Y. Kohno, K. Izshizu, T. Takakuwa, S. Tsuboyama, K. Tsuboyama, K. Kobayashi, T. Sakurai, Inorg. Chim. Acta 215 (1994) 109.
[48] T. Murakami, K. Murata, Y. Ishikawa, Inorg. Chim. Acta 244 (1996) 51.

Polyhedron 28 (2009) 2411–2417

Contents lists available at ScienceDirect

Polyhedron

journal homepage: www.elsevier.com/locate/poly

4-Diphenylphosphinosydnone imines as bidentate ligands

Valeriy N. Kalinin [a,*], Sergey N. Lebedev [a], Il'ia A. Cherepanov [a], Ivan A. Godovikov [a], Konstantin A. Lyssenko [a], Evamarie Hey-Hawkins [b]

[a] A.N. Nesmeyanov Institute of Organoelement Compounds, Russian Academy of Sciences, Vavilov Str. 28, Moscow 119991, Russian Federation
[b] Department of Inorganic Chemistry, Universitat Leipzig, Johannisallee 29, D-04103 Leipzig, Germany

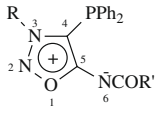
ARTICLE INFO

Article history:
Received 31 March 2009
Accepted 16 April 2009
Available online 7 May 2009

Keywords:
Sydnone imines
Mesoionic heterocycles
P,N-donor bidentate ligands
Palladium complexes
Crystal structure

ABSTRACT

The synthesis and characterization of new 3-substituted-4-diphenylphosphinosydnone imines (1,2,3-oxadiazolium-imines-5) are reported.



(R= ^{n}Bu, NMe_2 ; R'= Me, ^{t}Bu, Ph, CF_3)

These compounds react with $[PdCl_2(MeCN)_2]$ in MeCN to afford monomeric *cis*-P,N-coordinated palladium complexes.

© 2009 Elsevier Ltd. All rights reserved.

1. Introduction

The synthesis and application of phosphorus ligands, especially for the cases where the phosphorus ligand contains another coordinating functionality, are of considerable interest [1]. By introducing the second donor atom (N, S, O, Se, As, P) into the ligand it is possible to obtain bidentate ligands with donor centers of different donor capability and steric properties. The use of a heterocyclic moiety as a part of the ligand system has attracted great attention in recent years. In this paper we report the synthesis of new type of bidentate ligand containing a mesoionic moiety.

The first attempt to prepare such complexes based on sydnones was described in [2]. 4-Phosphino derivatives of sydnones, **1**, were chosen as the subject of the investigation. It was suggested by the authors that the exocyclic oxygen atom, bearing a negative charge, of the sydnone ring can act as a second donor center. However, the reaction of 3-(4-methoxyphenyl)-4-(ditertbutylphosphino)-sydnone **1** (R = –OMe) with $PdCl_2$ in EtOH gave the cyclometallation product, **2**. The cyclometallation process does not occur in the absence of a donor substituent at the 3 position of the phenyl group (Scheme 1). In this case, only the formation of the bis(phosphine) complex **3** is observed.

Sydnone imines, **4** in Fig. 1, are nitrogen analogues of sydnones and their exocyclic nitrogen atom also bears a significant negative charge [3]. However, the electron donating properties of the exocyclic nitrogen atom in sydnone imines are substantially stronger than those of the oxygen atom in sydnones. Sydnone imines, in contrast to sydnones, form salts with strong acids. The pK_a values for sydnone imines **4** vary from 2.5 to 4.6, depending on the substituents [4,5]. In addition, sydnone imines **4** react with methyl iodide to give the quaternary ammonium salt of the exocyclic nitrogen [5,6].

4-Phosphino substituted derivatives of sydnone imines, **5** in Fig. 1, should be more prone to act as bidentate ligands than their sydnone analogues (**1** in Scheme 1). Thus, coordination of **5** to transition metals could give rise to chelated complexes, **6** in Fig. 1.

2. Results and discussion

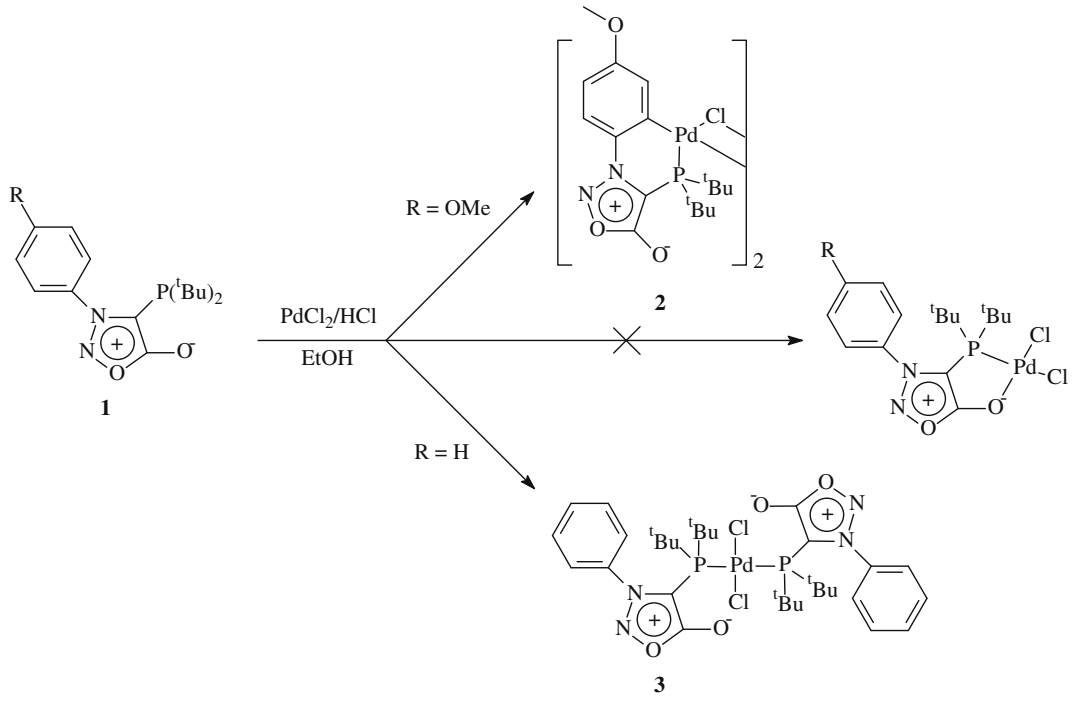
2.1. Synthesis of 4-diphenylphosphinosydnone imines

To synthesize new 4-diphenylphosphino derivatives of the sydnone imines **5** we have used the reaction of 4-lithium derivatives of sydnone imines [7] with diphenylphosphine chloride (Scheme 2, Table 1). Both the lithiation of sydnone imines and the addition of Ph_2PCl were carried out at the temperatures below −90 °C. At higher temperatures the formation of large amounts of decomposition products was observed, especially at the lithiation stage. Furthermore, both *n*-BuLi and Ph_2PCl must be slowly added to the reaction mixture to avoid overheating of the solution.

The 3-substituted-4-diphenylphosphinosydnone imines obtained belong to the class of hemilabile ligands, which contain both soft and hard donor atoms. The π-acceptor character of the phosphorus atom can stabilize a metal center in a low oxidation state, while the π-donor ability of the nitrogen atom makes the metal atom more susceptible to oxidative addition reactions.

* Corresponding author. Tel.: +7 499 135 9314.
E-mail address: vkalin@ineos.ac.ru (V.N. Kalinin).

0277-5387/$ - see front matter © 2009 Elsevier Ltd. All rights reserved.
doi:10.1016/j.poly.2009.04.038



Scheme 1.

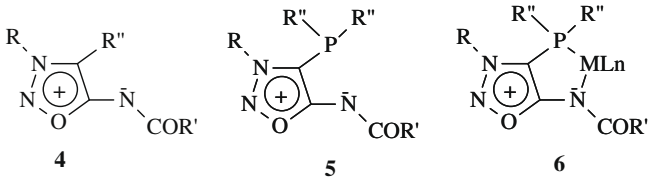
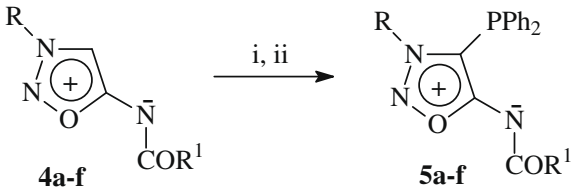


Fig. 1. Starting materials, ligands and target complexes.



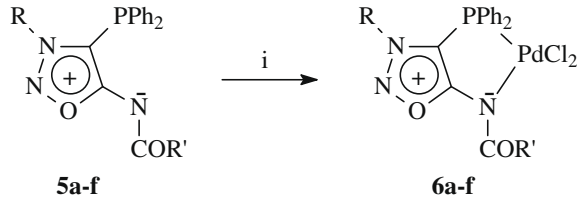
Scheme 2. (i) 1 equiv. *n*-BuLi, THF, −90 °C and (ii) 1 equiv. Ph_2PCl, −90 °C → r.t (slowly).

Table 1
Synthesis of 3-substituted-4-diphenylphosphinosydnone imines.

Compound	R	R_1	Yield, %
5a	*n*-Bu	Me	67
5b	*n*-Bu	Ph	80
5c	*n*-Bu	CF_3	56
5d	*n*-Bu	*t*-Bu	86
5e	Me_2N	Me	75
5f	Me_2N	Ph	70

2.2. Bidentate coordination chemistry of 3-substituted-4-diphenylphosphinosydnone imines

Treatment of the 4-diphenylphosphinosydnone imine **5a** with $[PdCl_2(MeCN)_2]$ in MeCN resulted in the formation of only one product, **6a** (Scheme 3). According to the X-ray structural data of complex **6a**, the ligand coordinates with palladium by P(1) and N(6) atoms forming the five-membered metallocycle (Fig. 2).



Scheme 3. (i) $[PdCl_2(MeCN)_2]$, MeCN.

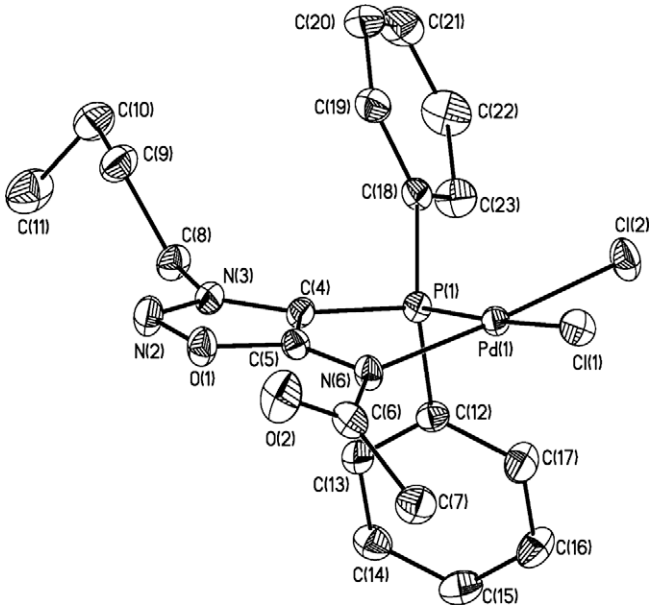


Fig. 2. General view of compound **6a**, atoms represented by 50% thermal ellipsoids.

Table 2
Synthesis of palladium complexes of 3-substituted-4-diphenylphosphinosydnone imines.

Compound	R	R_1	Yield,%
6a	*n*-Bu	Me	90
6b	*n*-Bu	Ph	85
6c	*n*-Bu	CF_3	53
6d	*n*-Bu	*t*-Bu	85
6e	Me_2N	Me	83
6f	Me_2N	Ph	95

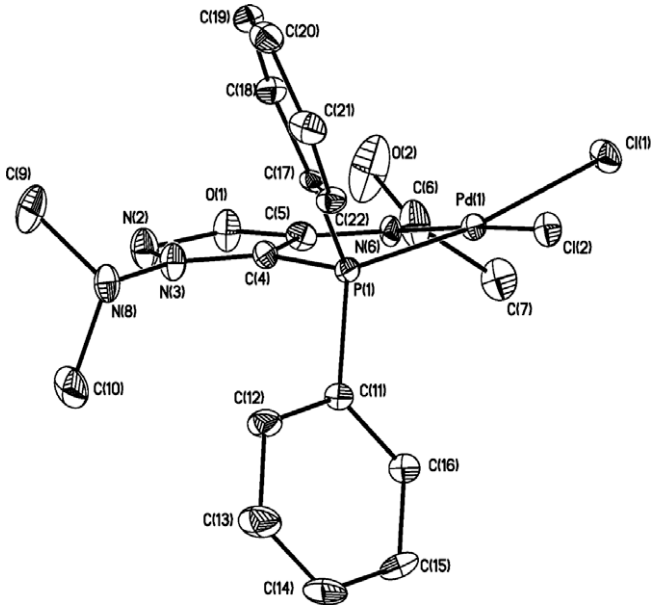


Fig. 3. General view of the complex **6e**, atoms represented by 50% thermal ellipsoids.

Very similar results were obtained in the case of phosphines **5b–f** (Scheme 3, Table 2).

The electron donating ability of N(6) in **5** is high. Even the presence of such electron-withdrawing groups as trifluoroacetyl (**5c**) does not prevent the formation of the chelate complex with palladium, although the yield of the product is low.

It should be noted that for compounds **5e** and **5f**, the dimethylamino group could provide an alternative coordination site. Nevertheless, the X-ray study of **6e** shows that the reactions of these compounds with $[PdCl_2(MeCN)_2]$ in MeCN give rise only to complexes in which the ligand acts as a bidentant ligand bound to palladium by the P(1) and N(6) atoms. (Fig. 3).

Despite the certain differences in the geometry of the ligands, the geometrical parameters of the two complexes **6a** and **6e** are similar (see Table 3). In both complexes the coordination of palladium is close to planar, with a slight tetrahedral distortion. The angles between the planes Pd(1)P(1)N(6) and Pd(1)Cl(1)Cl(2) are equal to 3.0(1)° and 8.5(1)° in **6a** and **6e**, respectively. The bite angles N(6)Pd(1)P(1) in both complexes are almost equal (87.13(9)° and 88.5(1)°). The five-membered metallocycles in **6a** and **6e** are characterized by an envelope conformation, with a deviation of the Pd(1) atom from the plane C(4)C(5)P(1)N(6) of 0.54 Å in **6a** and 0.32 Å in **6e**. In turn, the angles of bend along the P(1)···N(6) line in the complexes **6a** and **6e** are 20.5° and 12.2°. Despite the different substituents at N(3), the bond lengths of the metallocycles in **6a** and **6e** are almost the same. Comparing the geometrical parameters of the sydnone imine ring, one can conclude that the introduction of the Me_2N group leads to a slight shortening of the N(3)–C(4) bond, considerable shortening of the C(5)–N(6) and an increase of the N(6)–C(6) bond length.

Table 3
Selected bond lengths (Å) and angles (°) for the compounds **6a**, **6e** and **5e**.

Parameter	**6a**	**6e**	**5e**
Bond lengths			
Pd(1)–Cl(1)	2.361(1)	2.351(1)	
Pd(1)–Cl(2)	2.286(1)	2.282(1)	
Pd(1)–P(1)	2.232(1)	2.224(1)	
Pd(1)–N(6)	2.096(3)	2.104(4)	
P(1)–C(4)	1.796(4)	1.785(5)	1.811(2)
O(1)–N(2)	1.395(4)	1.390(5)	1.382(2)
O(1)–C(5)	1.364(4)	1.366(6)	1.391(2)
N(2)–N(3)	1.295(5)	1.301(6)	1.300(2)
N(3)–C(4)	1.356(5)	1.337(6)	1.349(2)
C(4)–C(5)	1.391(5)	1.394(6)	1.409(2)
C(5)–N(6)	1.323(5)	1.310(6)	1.296(2)
N(6)–C(6)	1.414(5)	1.435(6)	1.380(2)
N(3)–N(8)		1.428(5)	1.410(2)
Bond angles			
P(1)–Pd(1)–N(6)	87.1(1)	88.5(1)	
Cl(1)–Pd(1)–Cl(2)	92.16(5)	91.84(5)	
N(2)–O(1)–C(5)	109.2(3)	109.3(3)	110.2(1)
O(1)–N(2)–N(3)	104.9(3)	103.7(3)	103.4(1)
N(2)–N(3)–C(4)	114.2(3)	116.1(4)	116.8(1)
N(3)–C(4)–C(5)	104.9(3)	103.6(4)	103.5(1)
C(4)–C(5)–O(1)	106.8(3)	107.2(4)	105.9(1)

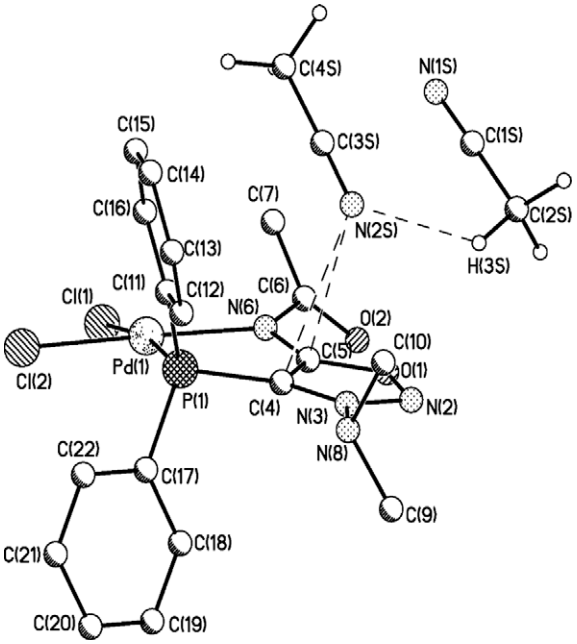


Fig. 4. The fragment of crystal packing illustrating the interaction of complex **6e** with acetonitrile molecules.

It should be mentioned that two solvate acetonitrile molecules in the crystal of **6e** are assembled into a dimer *via* the shortened C(1S)···C(3S) (3.344(3) Å) and N(2S)···H(3S) (2.51 Å) contacts (Fig. 4). In addition to the above contacts, one of the acetonitrile molecules participates in rather rare N···π binding with the mesoionic cycle, with a shortening of the N(2S)···C(4) and N(2S)···C(5) distances to 3.114(4) and 3.128(4) Å, respectively.

In order to analyze the influence of the complex formation on the distribution of bond lengths in the mesoionic moiety, we also performed an X-ray diffraction study of **5e** (Fig. 5). A comparison of the geometries of the free ligand **5e** and its complex **6e** shows that the coordination of N(6) to palladium causes the conjugation

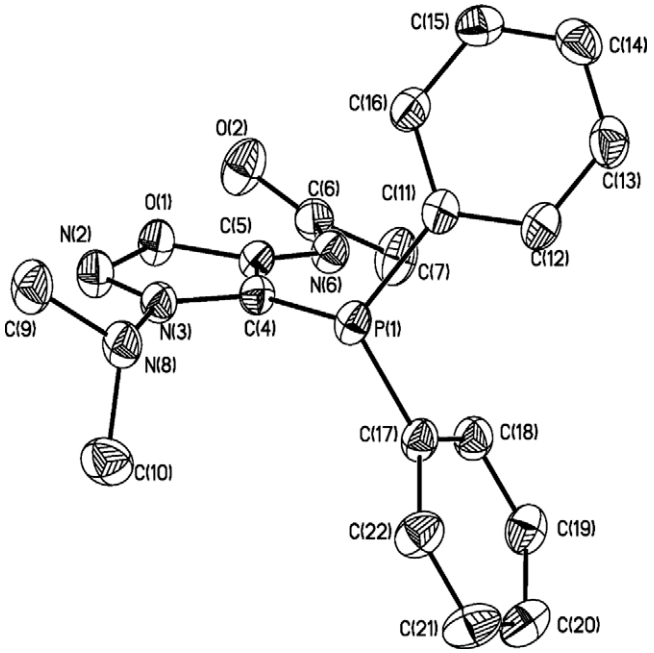


Fig. 5. General view of compound **5e**, atoms represented by 50% thermal ellipsoids.

of the N(6) atom with the π-system of the mesoionic ring and C=O group to decrease. As a result, the O(1)–C(5) bond in **5e** is considerably longer and the C(5) atom of the cycle deviates from the O(1)N(2)N(3)C(4) plane by 0.06 Å.

An analysis of IR spectra of the free ligands and the corresponding palladium complexes shows that the coordination of the mesoionic fragment by palladium atom gives no significant variation of the vibration spectrum character. The characteristic C=O and C=N bond vibrations of the mesoionic fragment are slightly blue shifted by 10–20 cm^{-1}.

The character of the chemical bonding in the mesoionic cycle, as well as the conjugation with the amide group, has been analyzed on the basis of a DFT calculation (m052x/6-311G(d,p)) of the molecule **5a** [8]. The obtained geometry is rather close to those observed in the complexes **6a** and **5e**. In particular, the C(5)–N(6) and C(6)–N(6) bond lengths are equal to 1.288 and 1.396 Å. An examination of the chemical bonding in **5a** has been performed within the "Atoms in Molecules" theory [9]. First of all, it should be noted that the charges obtained by integration over the atomic basins indicate that the most negative value is observed for the N(6) atom (−1.17 e). For comparison, the charge of the N(3) atom is significantly lower than those of the N(6) and N(8) atoms, which are −0.4 and −0.62 e. The total charge of the mesoionic cycle is close to zero (−0.02 e). According to the ellipticity values (ε) (the ratio of the Hessian eigenvalues in the critical points of the corresponding bonds), the mesoionic cycle is characterized by a significant contribution of π-character. Indeed, the maximum value of ε is observed for the N(2)–N(3) bond (0.41), while the minimum one – for the C(5)–O(1) bond (0.29). Both bonds formed by the N(6) atom are also characterized by substantial contributions of the π-component, with the ellipticity values being 0.20 and 0.30 for the N(6)–C(5) and N(6)–C(6) bonds, respectively.

The $^{31}P\{^1H\}$ NMR spectra of the obtained complexes show the variation of the chemical shift of the phosphorus atom (Table 4) upon complex formation.

2.2.1. Conclusion

In this work, the first representatives of 4-phosphorus substituted sydnone imines have been synthesized. It was shown that that these molecules can serve as hemilabile bidentante ligands and coordinate to a palladium atom by the phosphorus and exocyclic nitrogen N(6) atoms. The charge distribution in the mesoinic fragment was analyzed by DFT calculations, while the peculiarities of the geometries for the complexes were investigated by means of X-ray diffraction analysis. The presence of such a zwitterionic group as sydnone imine, which is unusual for palladium complexes, can provide them with rather unusual catalytic properties.

Table 4
$^{31}P\{^1H\}$ NMR parameters for the compounds **5a–f** and **6a–f**.

Compound	Chemical shifts (ppm) for compounds **5a–f**	Chemical shifts (ppm) for compounds **6a–f**
a	−35.91	−7.44
b	−35.89	−15.50
c	−35.84	13.48
d	−36.26	10.07
e	−35.83	−5.85
f	−35.81	−5.77

3. Experimental

3.1. General

Unless otherwise indicated, all the reactions were performed in a dry argon atmosphere. The starting sydnone imines **4a–b** [10], **4c** [11], **4d** [12], **4e** [13] and **4f** [6] were prepared according to the described procedures. All commercially available reagents were used without further purification. IR spectra were recorded from KBr pellets in the range 4000–400 cm^{-1} on a Nicolet Magna-IR 750 FT-IR spectrophotometer. ^1H NMR spectra were recorded on a Bruker Avance-400 spectrometer operating at a frequency of 400.13 MHz. ^{31}P NMR spectra were recorded on a Bruker Avance-400 spectrometer operating at a frequency of 161.98 MHz. Elemental analyses for C, H and N were performed on a Carlo Erba Elemental Analyzer – 1106 automatic analyzer. Melting points were determined with an electrically heated Gallenkamp apparatus.

3.2. Preparations

*3.2.1. N6-acetyl-3-butyl-4-diphenylphosphinosidnonimine (**5a**)*

To a solution of N6-acetyl-3-butylsidnonimine (0.5 g, 2.73 mmol) in THF (50 ml) at −90 °C, a 1.6 M solution of *n*-BuLi in hexane (1.9 ml, 3.00 mmol) was added. The solution was stirred for 10 min at the same temperature. Then chlorodiphenylphosphine (0.55 g, 3.13 mmol) was added. Reaction mixture was stirred for 10 min at the same temperature and then it was heated to room temperature. The solvent was removed under reduced pressure and the residue was dissolved in ethyl acetate, filtered through a layer of Al_2O_3 (2 × 3 cm) and washed away with ethyl acetate. The solvent was removed under reduced pressure and the residue was crystallized from a mixture of ether and hexane. Yield: 0.67 g (67%). M.p. 94–95 °C. *Anal.* Calc. for $C_{20}H_{22}N_3O_2P$ (367.39): C, 65.39; H, 6.04; N, 11.44. Found: C, 65.20; H, 6.50; N, 11.83%. IR data (KBr-pellet, cm^{-1}): 2960w, 2780w, 1660s, 1570vs, 1430m, 1250w, 1090m, 999m, 815w, 747w, 528m. ^1H NMR (DMSO-d_6): δ 0.76–0.80 (m, 3H, $CH_3CH_2CH_2CH_2$), 1.12–1.28 (m, 2H, $CH_3CH_2CH_2CH_2$), 1.81–1.87 (m, 2H, $CH_3CH_2CH_2CH_2$), 1.95 (s, 3H, $COCH_3$), 4.75–4.79 (m, 2H, $CH_3CH_2CH_2CH_2$), 7.28–7.45 (m, 6H, *p*-C_6H_5 + *m*-C_6H_5), 7.50–7.54 (m, 4H, *o*-C_6H_5). $^{31}P\{^1H\}$ NMR (DMSO-d_6): δ −35.91 (s).

*3.2.2. N6-benzoyl-3-butyl-4-diphenylphosphinosidnonimine (**5b**)*

The title compound was prepared in the same way as compound **5a**, starting from **4b** (2 g, 8.16 mmol), 5.6 ml of a 1.6 M solution of *n*-BuLi in hexane (8.98 mmol) and 1.7 ml of chlorodiphenylphosphine (9.38 mmol). Yield 2.8 g (80%). M.p. 107–108 °C. *Anal.* Calc.

for $C_{25}H_{24}N_3O_2P$ (429.46): C, 69.92; H, 5.63; N, 9.78. Found: C, 69.32; H, 5.89; N, 9.50%. IR data (KBr-pellet, cm^{-1}): 3052vw, 2959vw, 2874vw, 1635s, 1571vs, 1432m, 1312m, 1240m, 1207m, 1090m, 989s, 814w, 735w, 695m, 533w. ^1H NMR (DMSO-d_6): δ 0.74–0.81 (m, 3H, $CH_3CH_2CH_2CH_2$), 1.11–1.29 (m, 2H, CH_3CH_2-CH_2CH_2), 1.86–1.89 (m, 2H, $CH_3CH_2CH_2CH_2$), 4.84–4.87 (m, 2H, $CH_3CH_2CH_2CH_2$), 7.19–7.26 (m, 2H, *o*-($NCOC_6H_5$)), 7.29–7.43 (m, 6H, *p*-$(C_6H_5)_2P$ + *m*-$(C_6H_5)_2P$), 7.45–7.48 (m, 3H, *p*-($NCOC_6H_5$) + *m*-($NCOC_6H_5$)), 7.54–7.62 (m, 4H, *o*-$(C_6H_5)_2P$). $^{31}P\{^1H\}$ NMR (DMSO-d_6): δ −35.89 (s).

3.2.3. N6-trifluoroacetyl-3-butyl-4-diphenylphosphinosidnonimine (**5c**)

The title compound was prepared in the same way as compound **5a** starting from **4c** (0.7 g, 2.95 mmol), 2.1 ml of a 1.6 M solution of *n*-BuLi in hexane (3.39 mmol) and 0.63 ml of chlorodiphenylphosphine (3.54 mmol). Yield 0.7 g (56%). M.p. 125–126 °C. *Anal.* Calc. for $C_{20}H_{19}F_3N_3O_2P$ (421.36): C, 57.01; H, 4.55; N, 9.97. Found: C, 57.25; H, 5.01; N, 9.21%. IR data (KBr-pellet, cm^{-1}): 3052vw, 2963vw, 2874vw, 1653s, 1568vs, 1435w, 1202m, 1165s, 1132m, 1017m, 866w, 747w, 696w. ^1H NMR (DMSO-d_6): δ 0.77–0.81 (m, 3H, $CH_3CH_2CH_2CH_2$), 1.24–1.30 (m, 2H, $CH_3CH_2CH_2CH_2$), 1.84–1.91 (m, 2H, $CH_3CH_2CH_2CH_2$), 4.88–4.91 (m, 2H, CH_3CH_2-CH_2CH_2), 7.33–7.41 (m, 6H, *p*-C_6H_5 + *m*-C_6H_5), 7.52–7.56 (m, 4H, *o*-C_6H_5). $^{31}P\{^1H\}$ NMR (DMSO-d_6): δ −35.84 (s).

3.2.4. N6-trimethylacetyl-3-butyl-4-diphenylphosphinosidnonimine (**5d**)

The title compound was prepared in the same way as compound **5a** starting from **4d** (1.0 g, 4.44 mmol), 3.0 ml of a 1.6 M solution of *n*-BuLi in hexane (4.89 mmol) and 0.92 ml of chlorodiphenylphosphine (5.10 mmol). Yield 1.56 g (86%). M.p. 104–105 °C. *Anal.* Calc. for $C_{23}H_{28}N_3O_2P$ (409.47): C, 67.47; H, 6.89; N, 10.26. Found: C, 67.30; H, 7.01; N, 10.63%. IR data (KBr-pellet, cm^{-1}): 3059w, 2956w, 2867w, 1634s, 1601vs, 1579s, 1475w, 1435m, 1383w, 1313w, 1172m, 1109w, 999m, 744w, 692w, 515vw. ^1H NMR (DMSO-d_6): δ 0.77–0.92 (m, 12H, $CH_3CH_2CH_2CH_2$ + $C(CH_3)_3$), 1.20–1.27 (m, 2H, $CH_3CH_2CH_2CH_2$), 1.83–1.91 (m, 2H, CH_3CH_2-CH_2CH_2), 4.80–4.83 (m, 2H, $CH_3CH_2CH_2CH_2$), 7.34–7.36 (m, 6H, *p*-C_6H_5 + *m*-C_6H_5), 7.51–7.54 (m, 4H, *o*-C_6H_5). $^{31}P\{^1H\}$ NMR (DMSO-d_6): δ −36.26 (s).

3.2.5. N6-acetyl-3-dimethylamino-4-diphenylphosphinosidnonimine (**5e**)

The title compound was prepared in the same way as compound **5a** starting from **4e** (2.5 g, 14.70 mmol), 10.0 ml of a 1.6 M solution of *n*-BuLi in hexane (16.20 mmol) and 3.0 ml of chlorodiphenylphosphine (16.90 mmol). Yield 3.9 g (75%). M.p. 126–127 °C *Anal.* Calc. for $C_{18}H_{19}N_4O_2P$ (354.35): C, 61.01; H, 5.40; N, 15.81. Found: C, 60.59; H, 6.00; N, 15.20%. IR data (KBr-pellet, cm^{-1}): 2785w, 2459w, 1671s, 1580vs, 1435s, 1390w, 1265w, 1150m, 1121m, 1032w, 725m, 699m, 555w. ^1H NMR (DMSO-d_6): δ 1.86 (s, 3H, $COCH_3$), 3.07 (s, 6H, $(CH_3)_2N$), 7.35–7.37 (m, 6H, *m*-C_6H_5 + *p*-C_6H_5), 7.52–7.56 (m, 4H, *o*-C_6H_5). $^{31}P\{^1H\}$ NMR (DMSO-d_6): δ −35.83 (s.).

3.2.6. N6-benzoyl-3-dimethylamino-4-diphenylphosphinosidnonimine (**5f**)

The title compound was prepared in the same way as compound **5a** starting from **4f** (2.0 g, 8.60 mmol), 5.9 ml of a 1.6 M solution of *n*-BuLi in hexane (9.50 mmol) and 1.8 ml of chlorodiphenylphosphine (9.90 mmol). Yield 2.5 g (70%). M.p. 123–124 °C. *Anal.* Calc. for $C_{23}H_{21}N_4O_2P$ (416.42): C, 66.34; H, 5.08; N, 13.45. Found: C, 65.99; H, 5.22; N, 13.25%. IR data (KBr-pellet, cm^{-1}): 3040w, 2878vw, 1620s, 1550vs, 1430m, 1340m, 1255m, 1140w, 1000m, 750w, 532w. ^1H NMR (DMSO-d_6): δ 3.15 (s, 6H, $(CH_3)_2N$), 7.22–7.27 (m, 2H, *o*-($NCOC_6H_5$)), 7.33–7.42 (m, 6H, *p*-$(C_6H_5)_2P$ + *m*-$(C_6H_5)_2P$), 7.57–7.65 (m, 7H, *p*-($NCOC_6H_5$) + *m*-($NCOC_6H_5$) + *o*-$(C_6H_5)_2P$). $^{31}P\{^1H\}$ NMR (DMSO-d_6): δ −35.81 (s).

3.2.7. N6-acetyl-3-butyl-4-diphenylphosphinosidnonimine palladium dichloride (**6a**)

To a solution of N6-acetyl-3-butyl-4-diphenylphosphinosidnonimine **5a** (0.5 g, 1.36 mmol) in CH_3CN (10 ml), $[PdCl_2(MeCN)_2]$ (0.35 g, 1.36 mmol) was added. The solution was stirred for 30 min at room temperature. The solvent was removed under reduced pressure and the residue was crystallized from a mixture of CH_3CN and ether. Yield: 0.67 g (90%). M.p. 214 °C (dec.). *Anal.* Calc. for $C_{20}H_{22}Cl_2N_3O_2PPd$ (544.71): C, 44.10; H, 4.07; N, 7.71. Found: C, 44.29; H, 4.52; N, 7.13%. IR data (KBr-pellet, cm^{-1}): 3052w, 2964w, 2900w, 1671s, 1585vs, 1422m, 1377w, 1265w, 1080m, 1002m, 837w, 768w, 540w. ^1H NMR (DMSO-d_6): δ 0.57–0.60 (m, 3H, $CH_3CH_2CH_2CH_2$), 1.00–1.07 (m, 2H, $CH_3CH_2CH_2CH_2$), 1.26–1.29 (m, 2H, $CH_3CH_2CH_2CH_2$), 2.47 (s, 3H, $COCH_3$), 4.16–4.20 (m, 2H, $CH_3CH_2CH_2CH_2$), 7.63–7.64 (m, 4H, *m*-C_6H_5), 7.73–7.76 (m, 2H, *p*-C_6H_5) 7.98–8.03 (m, 4H, *o*-C_6H_5). $^{31}P\{^1H\}$ NMR (DMSO-d_6): δ −7.44 (s).

3.2.8. N6-benzoyl-3-butyl-4-diphenylphosphinosidnonimine palladium dichloride (**6b**)

The title compound was prepared in the same way as compound **6a** starting from **5b** (0.2 g, 0.475 mmol) and $[PdCl_2(MeCN)_2]$ (0.12 g, 0.475 mmol). Yield 0.25 g (85%). M.p. 194 °C (dec.). *Anal.* Calc. for $C_{25}H_{24}Cl_2N_3O_2PPd$ (606.78): C, 49.49; H, 3.99; N, 6.93. Found: C, 49.10; H, 4.20; N, 6.55%. IR data (KBr-pellet, cm^{-1}): 3059vw, 2963vw, 2874vw, 1656s, 1568vs, 1431m, 1257m, 1169vw, 1098w, 1013m, 747w, 688m. ^1H NMR (DMSO-d_6): δ 0.63–0.75 (m, 3H, $CH_3CH_2CH_2CH_2$), 1.05–1.16 (m, 2H, $CH_3CH_2CH_2CH_2$), 1.50–1.63 (m, 2H, $CH_3CH_2CH_2CH_2$), 4.05–4.18 (m, 2H, $CH_3CH_2CH_2CH_2$), 7.18–7.25 (m, 2H, *o*-($NCOC_6H_5$)), 7.29–7.43 (m, 3H, *p*-($NCOC_6H_5$) + *m*-($NCOC_6H_5$)), 7.52–7.65 (m, 6H, *p*-$(C_6H_5)_2P$ + *m*-$(C_6H_5)_2P$), 8.04–8.21 (m, 4H, *o*-$(C_6H_5)_2P$). $^{31}P\{^1H\}$ NMR (DMSO-d_6): δ −15.50 (s).

3.2.9. N6-trifluoroacetyl-3-butyl-4-diphenylphosphinosidnonimine palladium dichloride (**6c**)

The title compound was prepared in the same way as compound **6a** starting from **5c** (0.2 g, 0.475 mmol) and $[PdCl_2(MeCN)_2]$ (0.12 g, 0.475 mmol). Yield 0.15 g (53%). M.p. 190 °C (dec.). *Anal.* Calc. for $C_{20}H_{19}Cl_2F_3N_3O_2PPd$ (598.68): C, 40.12; H, 3.20; N, 7.02. Found: C, 40.32; H, 3.05; N, 6.89%. IR data (KBr-pellet, cm^{-1}): 3050vw, 2963vw, 2877vw, 1665s, 1571vs, 1440w, 1220m, 1140m, 1120w, 1030m, 869vw, 758w, 675w. ^1H NMR (DMSO-d_6): δ 0.70–0.74 (m, 3H, $CH_3CH_2CH_2CH_2$), 1.11–1.18 (m, 2H, $CH_3CH_2CH_2CH_2$), 1.52–1.67 (m, 2H, $CH_3CH_2CH_2CH_2$), 4.48–4.57 (m, 2H, $CH_3CH_2CH_2CH_2$), 7.53–7.59 (m, 4H, *m*-C_6H_5), 7.63–7.67 (m, 2H, *p*-C_6H_5), 8.09–8.17 (m, 4H, *o*-C_6H_5). $^{31}P\{^1H\}$ NMR (DMSO-d_6): δ 13.48 (s).

3.2.10. N6-trimethylacetyl-3-butyl-4-diphenylphosphinosidnonimine palladium dichloride (**6d**)

The title compound was prepared in the same way as compound **6a** starting from **5d** (0.5 g, 1.22 mmol) and $[PdCl_2(MeCN)_2]$ (0.32 g, 1.22 mmol). Yield 0.61 g (85%). M.p. 204 °C (dec.). *Anal.* Calc. for $C_{23}H_{28}Cl_2N_3O_2PPd$ (586.79): C, 47.08; H, 4.81; N, 7.16. Found: C, 46.95; H, 5.11; N, 7.64%. IR data (KBr-pellet, cm^{-1}): 2963w, 2874vw, 1723m, 1619vs, 1568m, 1479w, 1435m, 1095m, 1006m, 751w, 688w, 529m. ^1H NMR (DMSO-d_6): δ 0.69–0.77 (m, 12H, $CH_3CH_2CH_2CH_2$ + $C(CH_3)_3$), 1.11–1.16 (m, 2H, $CH_3CH_2CH_2CH_2$), 1.61–1.68 (m, 2H, $CH_3CH_2CH_2CH_2$), 4.59–4.69 (m, 2H, CH_3CH_2-CH_2CH_2), 7.48–7.65 (m, 6H, *p*-C_6H_5 + *m*-C_6H_5), 7.95–8.05 (m, 4H, *o*-C_6H_5). $^{31}P\{^1H\}$ NMR (DMSO-d_6): δ 10.07 (s.).

Table 5
Crystal data and structure refinement parameters for **5e**, **6a** and **6e**.

	5e	6a	6e
Formula	$C_{18}H_{19}N_4O_2P$	$C_{20}H_{22}Cl_2N_3O_2PPd$	$C_{22}H_{25}Cl_2N_6O_2PPd$
Formula weight	354.34	544.68	613.75
T (K)	120	153	153
Crystal system	triclinic	monoclinic	monoclinic
Space group	$P\bar{1}$	$P2_1/c$	$P2_1/n$
Z (Z′)	2 (1)	4 (1)	4 (1)
a (Å)	8.0945(12)	8.6676(17)	10.487(3)
b (Å)	9.6967(15)	14.121(3)	14.694(3)
c (Å)	11.3273(17)	18.115(4)	17.440(5)
α (°)	87.477(3)	90.00	90.00
β (°)	83.704(3)	97.97(3)	97.02(2)
γ (°)	89.965(3)	90.00	90.00
V (Å^3)	882.9(2)	2195.8(8)	2667.3(12)
d_{calc} (g cm^{-3})	1.333	1.648	1.528
μ (cm^{-1})	1.75	11.83	9.86
F(0 0 0)	372	1096	1240
$2\theta_{max}$ (°)	56	56	50
Reflections collected	7805	6509	4988
Independent reflections	4184	5281	4717
Observed reflections [$I > 2\sigma(I)$]	3183	4865	3184
Number of parameters	229	265	316
R_1	0.0489	0.0549	0.0411
wR_2	0.1210	0.1381	0.1016
Goodness-of-fit (GOF)	1.004	1.092	0.922
$\Delta\rho_{max}/\Delta\rho_{min}$ (e Å^{-3})	0.388/−0.261	1.265/−1.446	1.395/−0.976

*3.2.11. N6-acetyl-3-dimethylamino-4-diphenylphosphinosidnonimine palladium dichloride (**6e**)*

The title compound was prepared in the same way as compound **6a** starting from **5e** (0.5 g, 1.40 mmol) and [$PdCl_2(MeCN)_2$] (0.37 g, 1.40 mmol). Yield 0.62 g (83%). M.p. 195 °C (dec.). *Anal.* Calc. for $C_{18}H_{19}Cl_2N_4O_2PPd$ (531.67): C, 40.66; H, 3.60; N, 13.34. Found: C, 40.99; H, 3.82; N, 13.11%. IR data (KBr-pellet, cm^{-1}): 3052vw, 2926vw, 1693s, 1579s, 1557vs, 1435s, 1361w, 1213s, 1106m, 999w, 747w, 688m, 526m. ^{1}H NMR (DMSO-d_6): δ 2.36 (s, 3H, $COCH_3$), 2.80 (s, 6H, $(CH_3)_2N$), 7.55–7.62 (m, 4H, *m*-C_6H_5), 7.68–7.79 (m, 2H, *p*-C_6H_5), 7.98–8.02 (m, 4H, *o*-C_6H_5). ^{31}P{^{1}H} NMR (DMSO-d_6): δ −5.85 (s).

*3.2.12. N6-benzoyl-3-dimethylamino-4-diphenylphosphinosidnonimine palladium dichloride (**6f**)*

The title compound was prepared in the same way as compound **6a** starting from **5f** (0.5 g, 1.20 mmol) and [$PdCl_2(MeCN)_2$] (0.31 g, 1.20 mmol). Yield 0.68 g (95%). M.p. 189–190 °C (dec.). *Anal.* Calc. for $C_{23}H_{21}Cl_2N_4O_2PPd$ (593.75): C, 46.53; H, 3.56; N, 9.44. Found: C, 46.08; H, 3.28; N, 9.23%. IR data (KBr-pellet, cm^{-1}): 3052vw, 1639s, 1597vs, 1571s, 1446m, 1350w, 1279w, 1246m, 1158w, 1098m, 991m, 751w, 725w, 537w. ^{1}H NMR (DMSO-d_6): δ 3.20 (s, 6H, $(CH_3)_2N$), 7.19–7.26 (m, 2H, *o*-($NCOC_6H_5$)), 7.28–7.43 (m, 6H, *p*-($NCOC_6H_5$) + *m*-($NCOC_6H_5$)), 7.51–7.66 (m, 6H, *p*-$(C_6H_5)_2P$ + *m*-$(C_6H_5)_2P$)), 8.05–8.23 (m, 4H, *o*-$(C_6H_5)_2P$). ^{31}P{^{1}H} NMR (DMSO-d_6): δ −5.77 (s).

4. X-ray diffraction analysis

Crystals suitable for the X-ray diffraction analysis were obtained by slow evaporation from MeCN solutions. X-ray diffraction experiments of **5e** were carried out with a Bruker SMART 1000 CCD diffractometer (Mo Kα) = 0.71073 Å, ω-scans) at 110 K, while for **6a** and **6e** they were carried out with a Syntex P21 diffractometer (Mo Kα) = 0.71073 Å, ω-scans) at 153 K. The structures were solved by the direct method and refined by full-matrix least-squares against F^2 in anisotropic approximation for non-hydrogen atoms. The analysis of the Fourier density synthesis has revealed a disorder of the oxygen atom O(2) in **6e** over two positions with occupancies of 0.78 and 0.22. The positions of the hydrogen atoms were calculated. Crystal data and structure refinement parameters for **5e, 6a** and **6e** are given in Table 5. All calculations were performed using the SHELXTL software [14].

Supplementary data

CCDC 723513, 723514, and 723515 contain the supplementary crystallographic data for **5e**, **6a**, and **6e**. These data can be obtained free of charge via <http://www.ccdc.cam.ac.uk/conts/retrieving.html>, or from the Cambridge Crystallographic Data Center, 12 Union Road, Cambridge CB2 1EZ, UK; fax: (+44) 1223-336-033; or e-mail: deposit@ccdc.cam.ac.uk.

Acknowledgements

Authors thank the Russian Foundation for Basic Research (grant no. 09-03-00603-a) and the International Science and Technology Center (grant ISTC G-1361) for financial support.

References

[1] (a) G. Chelucci, G. Orrù, G.A. Pinna, Tetrahedron 59 (2003) 499;
(b) P. Braunstein, J. Organomet. Chem. 689 (2004) 3953;
(c) S.E. Angell, C.W. Rogers, Y. Zhang, M.O. Wolf, W.E. Jones Jr., Coord. Chem. Rev. 250 (2006) 1829.
[2] (a) L. Shao-Tao, C.H. Sheng, L. Lin-Shun, W. Ju-Chun, Organometallics 16 (1997) 1803;
(b) L. Shao-Tao, C.H. Sheng, L. Lin-Shun, W. Ju-Chun, J. Organomet. Chem. 610 (2000) 1.
[3] (a) C.G. Newton, C.A. Ramsden, Tetrahedron 38 (1982) 2967;
(b) Uspehi Khimii 49 (1980) 64.
[4] V.G. Yashunskii, L.E. Holodov, O.I. Samoilova, Chem. Commun. 30 (1965) 4257.
[5] V.G. Yashunskii, O.I. Samoilova, L.E. Holodov, Zur. Obsh. Him. 34 (1964) 2050.
[6] K. Masuda, T. Kamiya, I. Imashira, T. Kaneko, Chem. Pharm. Bull. Jpn. 19 (1971) 72.
[7] (a) I.A. Cherepanov, V.N. Kalinin, Mendeleev Commun. (2000) 181;
(b) I.A. Cherepanov, N.V. Egorova, K.B. Martinovich, V.N. Kalinin, Doklady Chem. 374 (2000) 175.
[8] M.J. Frisch, G.W. Trucks, H.B. Schlegel, G.E. Scuseria, M.A. Robb, J.R. Cheeseman, V.G. Zakrzewski, J.A. Montgomery, R.E. Stratmann, J.C. Burant, S. Dapprich, J.M. Millam, A.D. Daniels, K.N. Kudin, M.C. Strain, O. Farkas, J. Tomasi, V. Barone, M. Cossi, R. Cammi, B. Mennucci, C. Pomelli, C. Adamo, S. Clifford, J. Ochterski, G.A. Petersson, P.Y. Ayala, Q. Cui, K. Morokuma, D.K. Malick, A.D. Rabuck, K. Raghavachari, J.B. Foresman, J. Cioslowski, J.V. Ortiz, A.G. Baboul, B.B. Stefanov,

G. Liu, A. Liashenko, P. Piskorz, I. Komaromi, R. Gomperts, R.L. Martin, D.J. Fox, T.A. Keith, M.A. Al-Laham, C.Y. Peng, A. Nanayakkara, M. Challacombe, P.M.W. Gill, B. Johnson, W. Chen, M.W. Wong, J.L. Andres, C. Gonzalez, M. Head-Gordon, E.S. Replogle, J.A. Pople, Gaussian 98, Revision A.9, Gaussian Inc., Pittsburgh, PA, 1998.
[9] R.F.W. Bader , Atoms in Molecules. A Quantum Theory, Clarendron Press, Oxford, 1990.
[10] H.U. Daeniker, J. Druey, Helv. Chim. Acta 95 (1962) 2441.
[11] V.G. Yashunskii, L.E. Holodov, S.A. Zotova, Zur. Vseros. Him. Obsh. Im. D.I. Mendeleeva (1964) 105.
[12] Z.A. Oloviannikova, B.I. Briantsev, I.S. Slusarenko, V.G. Yashunskii, Him. Het. Soed. (1975) 1198.
[13] M. Gotz, K. Grozinger, J. Het. Chem. 7 (1970) 123.
[14] G.M. Sheldrick, SHELXTL-97, Version 5.10, Bruker AXS Inc., Madison, WI, USA.

Polyhedron 28 (2009) 2418–2430

Contents lists available at ScienceDirect

Polyhedron

journal homepage: www.elsevier.com/locate/poly

A study of nerve agent model organophosphonate binding with manganese-A_2B-corrole and -A_2B_2-porphyrin systems

Kibong Kim [a,b], Inkoo Kim [a], Nilkamal Maiti [a,b,1], Seong Jung Kwon [a], Daniela Bucella [c], Olga A. Egorova [a,b], Yoon Sup Lee [a], Juhyoun Kwak [a], David G. Churchill [a,b,*]

[a] Department of Chemistry and School of Molecular Science (BK 21), Korea Advanced Institute of Science and Technology (KAIST), 373-1 Guseong-dong, Yuseong-gu, Daejeon 305-701, Republic of Korea
[b] Molecular Logic Gate Laboratory, Korea Advanced Institute of Science and Technology (KAIST), 373-1 Guseong-dong, Yuseong-gu, Daejeon 305-701, Republic of Korea
[c] Department of Chemistry, Columbia University, 3000 Broadway, New York, New York 10027, USA

ARTICLE INFO

Article history:
Received 15 February 2009
Accepted 16 April 2009
Available online 24 April 2009

Keywords:
A_2B-corrole
trans-A_2B_2-porphyrin
Manganese
Organophosphonate
Nerve agent sensing
UV–Vis titrations
Cyclic voltammetry
Model nerve agent
Binding study

ABSTRACT

Herein the synthesis and binding studies of novel *trans*-A_2B-corrole and *trans*-A_2B_2-porphyrin derivatives are presented in comparing manganese(III)-organophosphonate (OP) binding (e.g., $M^{n+} \leftarrow O{=}PR(OR)_2$) capabilities. H_3(PFP-VC) [PFP-VC = 5,15-di(pentafluorophenyl)-10-(3-vinylphenyl)corrolate] was synthesized by way of literature procedures and was characterized by a variety of 2-D NMR spectroscopic techniques and single-crystal X-ray diffraction. These compounds represent the first example of 3-vinyl-phenyl-containing meso-substituted corroles or porphyrins. Mn(PFP-VC) (**3**) was treated separately with $(CH_3CH_2O)_2P{=}O(C_3H_6NMe_2)$, $(C_4H_9O)_2P{=}O(Me)$, $(C_2H_5O)_2P{=}O(CH_2COCH_3)$, $(CH_3CH_2O)_2P{=}O(Me)$, to give 1:1 adducts, as determined by UV–Vis spectroscopy (Job Plot), giving a *red* shift; $Ph_3P{=}O$, was also found to bind, but very weakly. The *trans*-A_2B_2-porphyrin analogue Mn(PFP-VP) (**4**) was also prepared by way of a literature procedure; related binding studies gave 1:1 organophosphonate-Mn(PFP-VP) adducts (Job Plot). A clean *blue* shift occurred for the Mn-porphyrins at higher organophosphonate loadings (K_a values: 6.7 (0.9)–11.9 (0.4) M^{-1}). DFT geometry optimizations of $O{=}P(OMe)_2Me$ binding and formal Mn–O or P–O cleavage products in the unsubstituted *neutral* Mn-corrolato and -porphyrinato systems with a range of metal-based spin states revealed greatest stability in formal phosphoryl oxygen binding (energies: 11–13 kcal/mol) for the Mn-corrole (*singlet*); the Mn-porphyrin (*sextet*) was also quite stable.
© 2009 Elsevier Ltd. All rights reserved.

1. Introduction

Macrocyclic polypyrroles are motifs of great ubiquity, constituting a range of both synthetic metal complexes and natural systems (i.e., hemoglobin, corrin and chlorophylls) (Fig. 1). Of note, the porphyrin sub-class is crucial in oxygen-atom transfer [1], and in analyte binding (e.g., O_2), with the ability to host a variety of Lewis bases in forming important adducts in biology. Corroles, members of a currently greatly expanding class of contracted porphyrin, are gaining greater visibility through the sub-field's major contributors: Gross [2], Gryko [3,4], Kadish [5,6], and Paolesse [7]. Corroles differ from porphyrins in two important ways: they possess one direct pyrrole–pyrrole bond in place of one methine (C–H) linkage, and they are *tri*valent instead of divalent. This difference allows for metal-corrolato species to possess a likeness to Nature's hemes through their aromaticity on one hand, and a corrin-like structural cavity that bears a *tri*valent cavity instead of a monovalent core (Fig. 1) on the other hand. These features enable a stabilization of transition metal ions in valence states [8] that are systematically higher than those known in the respective porphyrins.

Through the study of transition metal coordination chemistry, adequate control of complex color, electronics, sterics, and molecular geometry can, in theory, be imparted, especially through the use of a rigid delocalized ligand corrole or porphyrin frame. A delocalized and rigid frame may also be fluorogenic. Mn-corrolato species, however, do not appear to be promising in this respect. Thus, to determine whether a porphyrin or corrole framework, or both, is of utility in the optical or otherwise sensing of organophosphonate is the goal of these solution studies. Since our primary focus here is on nerve agent model [O=P] oxygen metal ion binding, we also undertook theoretical calculations to fully determine M-corrole $O{=}P(OR)_2R$ binding energies using model systems. Understanding the features and substitutions that enhance, or detract from, the binding capabilities of metalloporphyrin derivatives are essential in the rational development of these systems as detection platforms in hazardous analyte sensing. Generally, metallocorroles

* Corresponding author.
E-mail address: dchurchill@kaist.ac.kr (D.G. Churchill).
[1] Present address: Midnapore College, Midnapore, Paschim Medinipur, West Bengal 721101, India. Tel.: +82 42 350 2845; fax: +82 42 350 2810.

0277-5387/$ - see front matter © 2009 Elsevier Ltd. All rights reserved.
doi:10.1016/j.poly.2009.04.020

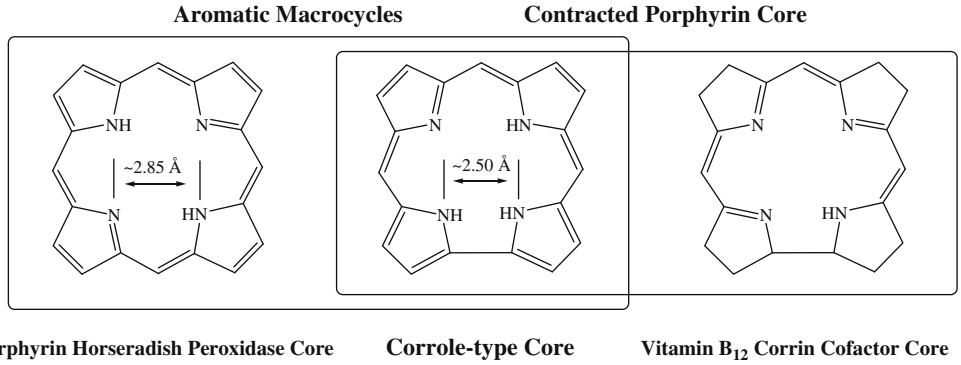


Fig. 1. A comparison of the macrocyclic porphyrin, corrole and corrin (vitamin B_{12} cofactor) frames. Note: the left and middle structures are the basis of geometry optimization calculations, illustrated below in Figs. 11 and 12.

and metalloporphyrins show some promise as selective analyte sensing platforms. Corroles have been explored as CO sensors of sufficient selectivity when testing with competitive analytes such as O_2 and N_2. The nature of the metal (e.g., Co^{3+}) as well as corrole substitution play essential parts in the Lewis acidity of the metal center [9], which is the sensing core. Metallocorroles also have good reproducibility and stability over a term of months as "electronic noses." In a related report, there was no loss of corrole "monomer" from a thin layer array over a four-week period of continual use [10]. Precedent for related metallo*porphyrin*-based sensors comes from reports by Di Natale and coworkers [11–13]. Porphyrin derivatives have also been the subject of computational efforts in the context of analyte selectivity [14–17].

The types of analytes we chose to study here are organophosphonates, relatives of the extremely deadly organophosphonate nerve agents (Fig. 2). While there have been significant efforts to fully decontaminate all stockpiles, undertaken in good faith to abide by the time-table set forth by the Chemical Weapons Convention (CWC), there are still significant amounts of organophosphonate-based chemical weapons in North America as well as in Eurasia that, to date await complete destruction and remediation. This impetus, along with potential terrorist agent development and use, support the need for continued investigations into improved real-time sensing devices [17].

Cyclic polypyrrole ligand-based sensing platforms may be able to efficiently and selectively mediate in techniques such as piezoelectric crystal sorption detection which are the centerpiece of portable and growingly reliable nerve agent detection/discernment. The possibility of metallocorroles serving in nerve agent detection and decontamination is suggestive from results reported by Gross and coworkers in which $Ph_3P{=}O$ forms an adduct with Mn(III)tpfcorrolato; this adduct can also be formed from the manganyl [Mn=O] species upon addition of PPh_3 [18]. The crystal structure in which triphenylphosphine oxide is coordinated to tris-pfp-Mn-corrole [19a,19b] can be compared to one in which there exists a free Mn(III)corrolato center [19c].

Mn-corrole-based organophosphonate nerve agent sensing can be explored in a variety of ways. Our approach involved preparing closely related Mn-corrolates that bear stability imparted from the pentafluorophenyl groups but that also contain a 10-position *meso*-aryl group that contains an attachment point. We were able to develop the corrole and the related porphyrin system for comparison. We also go further here theoretically, in determining how oxygen binding of organophosphonate nerve agent mimics, and how the phosphoryl oxygen can formally migrate from the Mn=O group; this can be treated theoretically (*vide infra*). While organophosphonates have different electronic and steric properties as the simpler $Ph_3P{=}O$ molecule [19], we can look at a variety of organophosphonate species: $(CH_3CH_2O)_2P{=}O(C_3H_6NMe_2)$, $(C_4H_9O)_2P{=}O(Me)$, $(C_2H_5O)_2P{=}O(CH_2COCH_3)$, $(CH_3CH_2O)_2P{=}O(Me)$, $Ph_3P{=}O$ (Fig. 2), and other analytes with compounds **3** or **4** (Scheme 1) [20].

In terms of the preparative chemistry of corroles, extremely practical pathways to A_2B-corroles have been reported by Gryko and coworkers [3,4]. Thus, we have prepared *meso*-thienyl-A_2B-corroles species with the well-known C_6F_5-substitution, and also the 3-vinylphenyl substitution which may facilitate chemisorption *via* sulfhydryl groups of functionalized surfaces [21]. We have also prepared the analogous porphyrin system to compare analyte binding in two closely related systems.

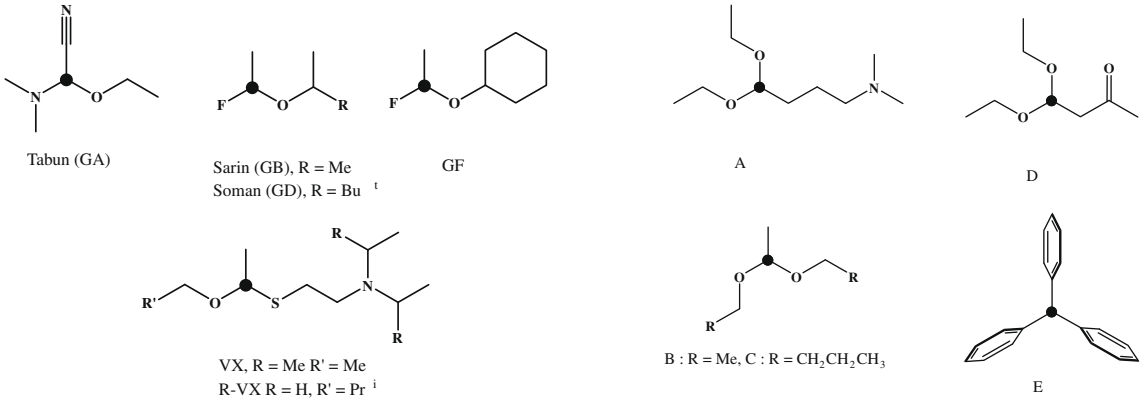
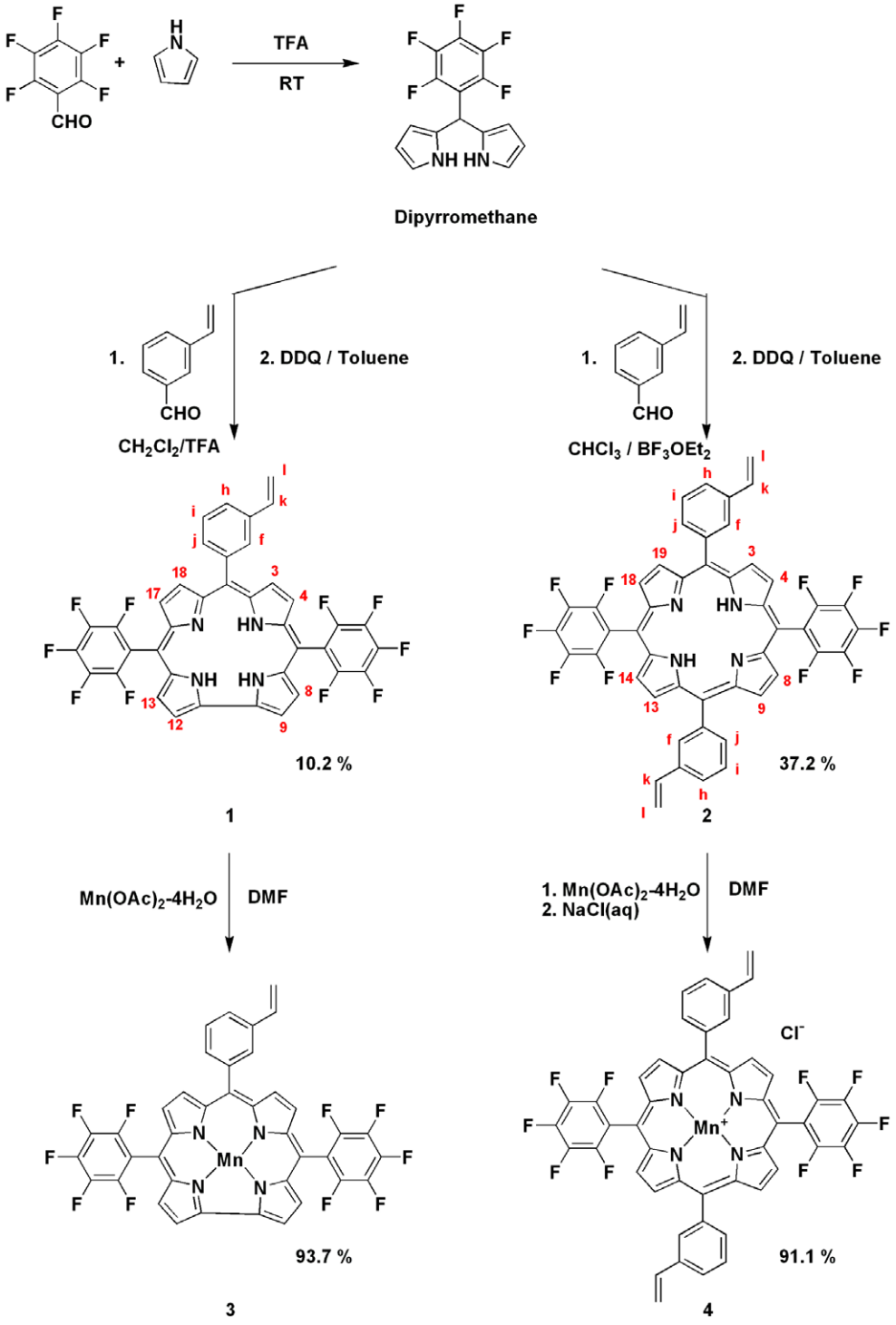


Fig. 2. ● = [O=P] group. (*left*) Common organophosphate nerve agents. G- and V-type chemical warefare (nerve) agents. (*right*) Phosphorus-containing molecules used in this study.



Scheme 1. The synthesis of corroles and porphyrins and their products of metallation reported herein. Percent yields are included next to each molecule. The crystallographic report of **1** appears below.

2. Results and discussion

2.1. Synthesis and characterization

Corrole preparation began with the generation of dipyrromethane prepared by the literature method of Lindsey and coworkers [22] involving the condensation of pyrrole and aldehyde. The synthesis of A_2B corroles were adapted from well-known literature reports [23,4], which begins with the dipyrromethane and involves the addition of benzaldehyde derivative followed by oxidation, usually effected by DDQ. We have previously reported 2- and 3-thienyl-dipyrromethanes [24a] as well as meso-substituted A_3-corroles that were prepared analogously as reported previously in *Polyhedron* [24b]. While the A_2B_2 porphyrin (Compound **2**) can sometimes be satisfactorily isolated as a by-product in the corrole-generating reaction above [25a], this species was prepared using more optimal conditions in accordance with a previously reported literature method [25b] to give a microcrystalline sample of

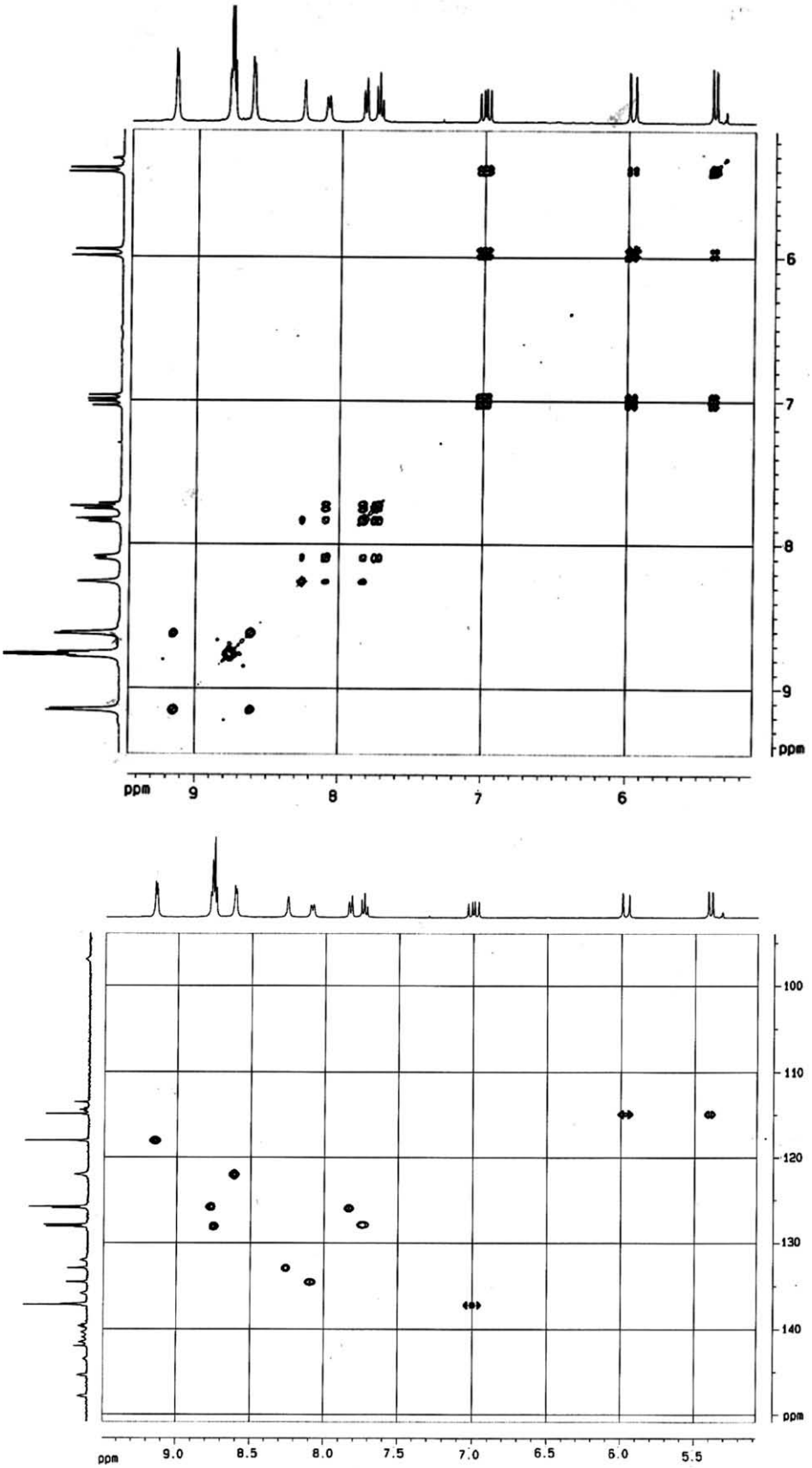


Fig. 3. (*top*) The aromatic portion of the ^{1}H–^{1}H COSY NMR spectrum showing all C–H protons, and (*bottom*) ^{1}H–^{13}C HMQC NMR spectrum showing all carbon resonances, for H_3(PFP-VC).

the species formulated as the Mn(III)porphyrinato chloride (**4**) [25c]. Thus, a solid of compound **2** was obtained through recrystallization in 37% yield (See Section 4). Suitability of this as an oxygen-atom transfer catalyst has been previously reported [20b,20d].

Characterization of the new compounds **1**–**4** reported herein was made mainly by spectroscopic techniques: ^{1}H NMR, ^{13}C NMR and UV–Vis spectroscopic studies (e.g., Fig. 3 and Supporting Information) as well as CV measurements. We also relied on 2-D NMR spectra, which are used conveniently because of the fully unsaturated nature of Compounds **1** and **2** which have resonances gathered in the aromatic region (5–9 ppm). The substitution (as in Compound **2**) as well as other corrole features give rise to clearly assignable cross-peaks in 2-D NMR spectra such as the ^{1}H–^{1}H COSY and ^{1}H–^{13}C HMQC NMR spectra of H_3(PFP-VC) provided in Fig. 3. For mass spectrometry, the presence of the expected species comes from the inspection of isotopic clusters centered at calculated values for complexes **1**–**4** (Supporting Information). Additional characterization is provided by single-crystal X-ray diffraction for compound **1**, presented below.

2.2. UV–Vis spectroscopic detection of organophosphonate via titrations in CH_2Cl_2

While fluorescence characteristics of corroles can be intense and unique, incorporation of Mn^{3+} renders the complexes non-fluorescent. Thus, herein we rely on UV–Vis absorption spectroscopic changes. Electronic absorption spectra of Mn(PFP-VC) (**3**) and Mn(PFP-VP) (**4**) with different organophosphonate species bearing various binding atoms will be presented in this section. Detailed titrimetric spectra are provided in Figs. 4–6 for Mn corroles and Figs. 7 and 8 for Mn-porphyrins. These trials all show a diminution in the Soret band at 411 nm when Compound **3** is used. A new band at 473–483 nm grows in as indicated by a label in each figure. Triphenyl phosphine was also tested as an analyte; it also has the capacity to bind through its (lone) oxygen atom, and, along with the sterics and rigidity of the phenyl groups, does so less efficiently, as shown by comparatively smaller changes in the spectrum (Supporting Information). This is surprising in light of the fact that a crystal structure of a closely related adduct is known. It is interesting to note that other, possibly better binding, phosphorus oxide species were *not* studied as of yet in this context.

A determination of ligand-to-metal complex stoichiometry in this reaction mixture was performed by the method of continuous variation. Titrimetric trials for A–D (Fig. 2) were performed, as shown e.g., in Fig. 4, in which a portion of Mn(PFP-VC) in dichloromethane was titrated by $(CH_3CH_2O)_2P{=}O(C_3H_6NMe_2)$ (**A**). Clear growth of new bands appear at 473 and 634 nm. The $(CH_3CH_2O)_2P{=}O(C_3H_6NMe_2)$ species is interesting in that there is a pendant amino group in virtually the same place as that seen for VX (Fig. 2), relative to the central phosphorus [26,27]. The next titration involved $(C_2H_5O)_2P{=}O(CH_2COCH_3)$ which afforded new bands in the electronic absorption spectra at 483 and 631 nm. The $(CH_3CH_2O)_2P{=}O(Me)$ species gave bands at 481 and 635 nm. Finally, $(C_4H_9O)_2P{=}O(Me)$ gave bands at 481 and 631 nm (Supporting Information). For these four species (Figs. 4–6, and S14) the Job plots involving the method of continuous variation were prepared; in all these cases (Insets of Figs. 4–6, and S14), the maximum peak at a mole fraction of ~0.5 is indicative that the solution stoichiometry is the expected 1:1 ligand-to-metal binding ratio. This is in accordance with the notion that the organophosphonate species will bind mainly through the phosphoryl [O=P] oxygen atom. The possibility of its binding through other heteroatoms, albeit more weakly, will not be considered herein.

There may be some concern that the Mn corrolato system valence state may change during, or prior to, analyte binding in light of (i) Mn^{4+} being an air stable metallocorrolate oxidation state and (ii) the involvement of stabilizing axial ligation [25e]. Importantly, to support our formulated Mn valence states, EPR spectroscopy for the $Ph_3P{=}O$ adduct of the Mn(tpf)corrolato species reported by Gross et al., reveals a Mn(III) ($S = 2$) metal center [19a]. This characterization excludes the possibility for the Mn(II) "radical cation" species [25d] and also for a Mn(IV) center. Compound **3** differs from the Mn(tpf)corrolato species only by the 10-position aryl group in which a 3-vinyl phenyl group replaces a pentafluorophenyl group. This small substitution will unlikely change the chemistry dramatically. Further experimental support that we do *not*

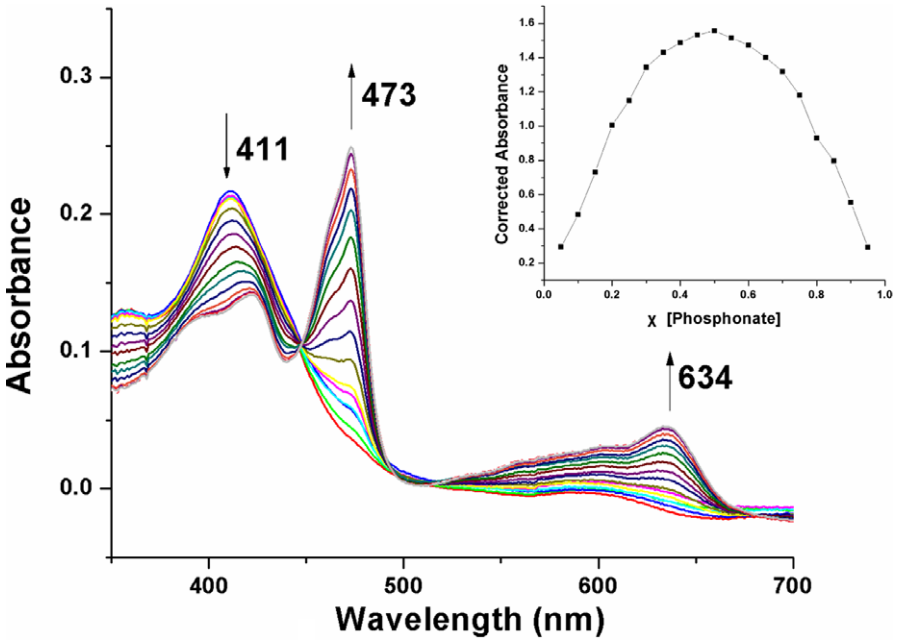


Fig. 4. Electronic absorption spectra of Mn(PFP-VC) [4.69×10^{-6} M] treated in dichloromethane with $(CH_3CH_2O)_2P{=}O(C_3H_6NMe_2)$ [5.06×10^{-3} M] (10–50 (by 10), 100–650 (by 50) μL). Inset: Job Plot for a (binary) mixture of **3** with $(CH_3CH_2O)_2P{=}O(C_3H_6NMe_2)$ showing a 1:1 stoichiometric correspondence.

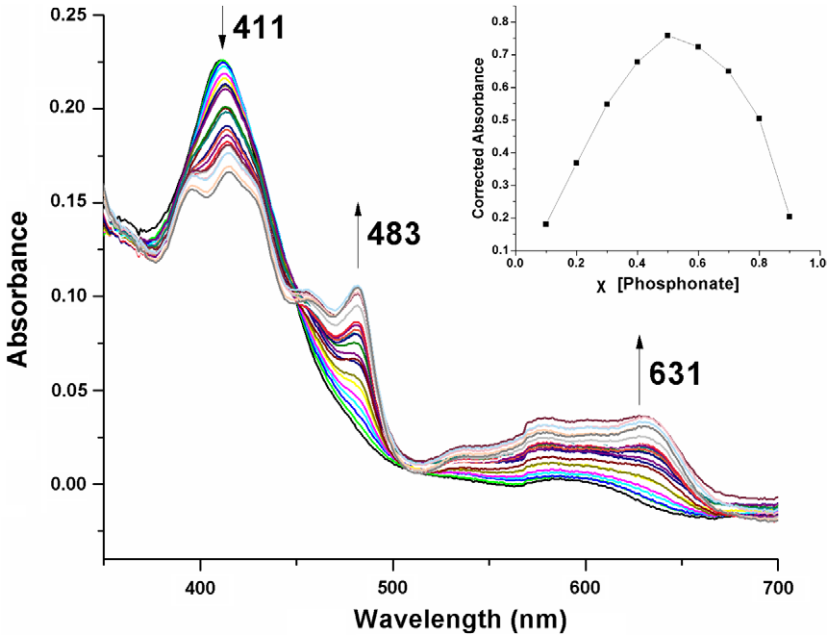


Fig. 5. Electronic absorption spectra of Mn(PFP-VC) [4.69×10^{-6} M] in the presence of various amounts (50–1100 (by 50) μL) of $(C_2H_5O)_2P{=}O(CH_2COCH_3)$ [1.51 M] in dichloromethane. Inset: Job plot for a binary mixture of **3** with $(C_2H_5O)_2P{=}O(CH_2COCH_3)$.

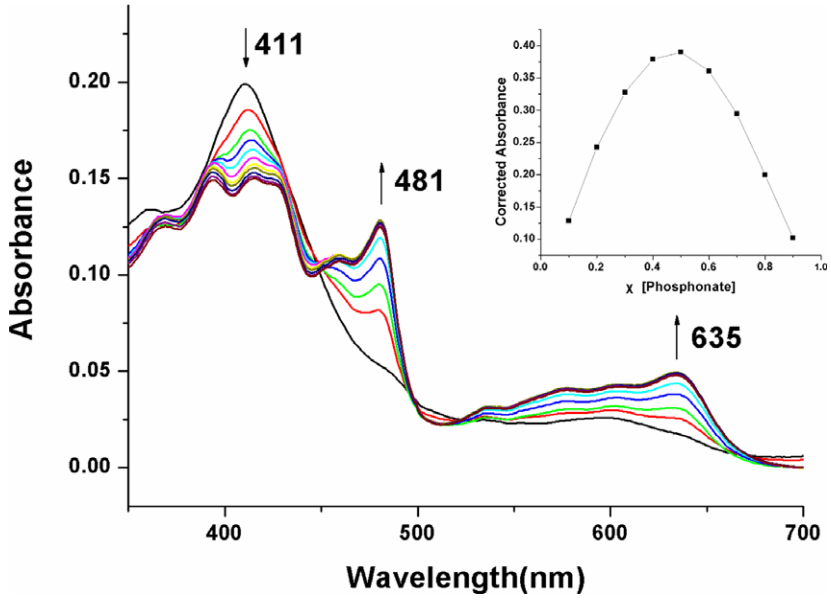


Fig. 6. Electronic absorption spectra of Mn(PFP-VC) [4.69×10^{-6} M] in the presence of various amounts (50–500 (by 50) μL) of $(CH_3CH_2O)_2P{=}O(Me)$ [2.74 M] in dichloromethane. Inset: Job Plot for a binary mixture of **3** with $(CH_3CH_2O)_2P{=}O(Me)$.

access *reduced* Mn-corrolato forms comes from the fact that electro-reduced forms of Mn(III) are unstable towards solvents, i.e., methylene chloride [25e], especially in the absence of a clear reductant. Additional support for Mn(III)corrolato ones comes from an analogous corrolazine compound reported by Goldberg and coworkers in which a shoulder at 722 nm in the UV–Vis spectrum is assigned to the Mn(III)O=PPh_3 adduct [19b]. In terms of Mn-corrole coordination, the Mn(III) species may exist in solution with one more axial MeCN. To further delve into the particulars of the valence state as well as a consideration of substrate/anion binding, we can turn to electrochemical studies discussed below that introduces a detailed report by Kadish and coworkers [25f] who have addressed how to best assign the valence state of the metal ion under various conditions [8].

We also studied the related binding for the *porphyrin* compound Mn(PFP-VP) with $(C_4H_9O)_2P{=}O(Me)$, $(C_2H_5O)_2P{=}O(CH_2COCH_3)$, and $(CH_3CH_2O)_2P{=}O(Me)$. These analytes were used in UV–Vis titrimetric trials whose results are plotted in Figs. 7 and 8 (and Supporting Information). All four assays give rise to clear changes compared to those of the Mn-corrole cases in that the Soret band undergoes moderate diminution and blue shifting only to give a new band in the range of 450–460 nm. While there is a clean spectral change, a much greater amount of analyte was required to effect this optical change than was needed in the corrole case, thus,

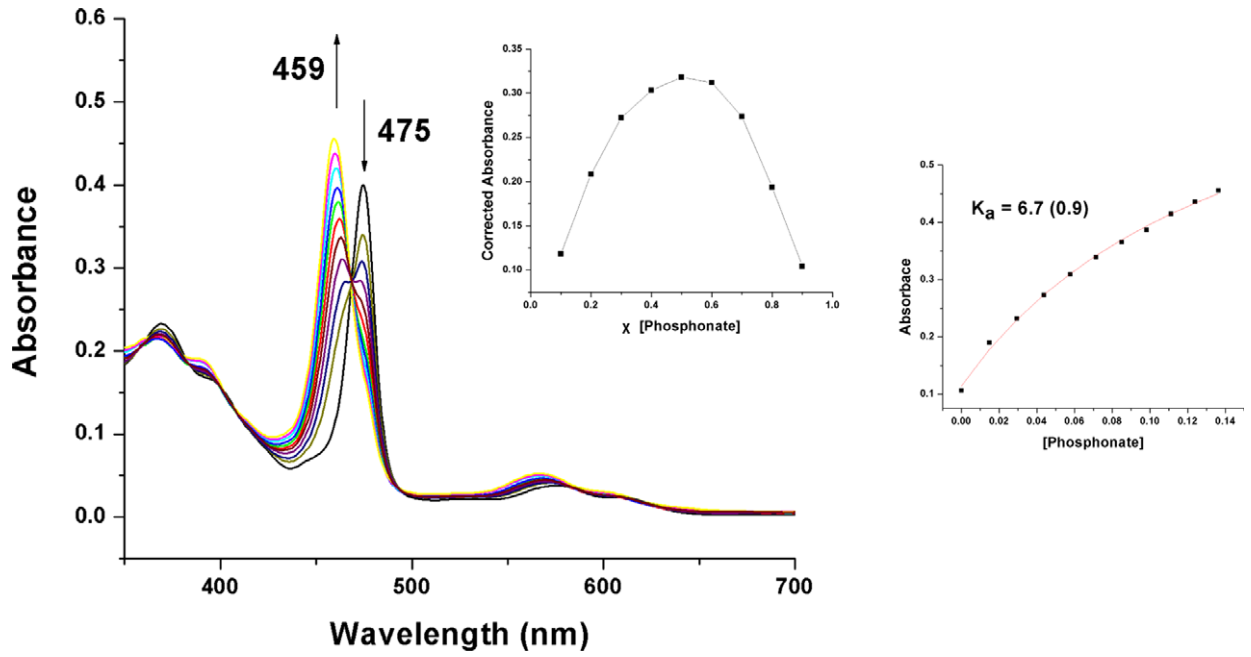


Fig. 7. Electronic absorption spectra of Mn(PFP-VP) [5.00×10^{-6} M] in dichloromethane upon titration with various amounts of $(C_2H_5O)_2P{=}O(CH_2COCH_3)$ [1.50 M] (20–200 (by 20) μL). Inset: Job Plot for a binary mixture of **4** with $(C_2H_5O)_2P{=}O(CH_2COCH_3)$.

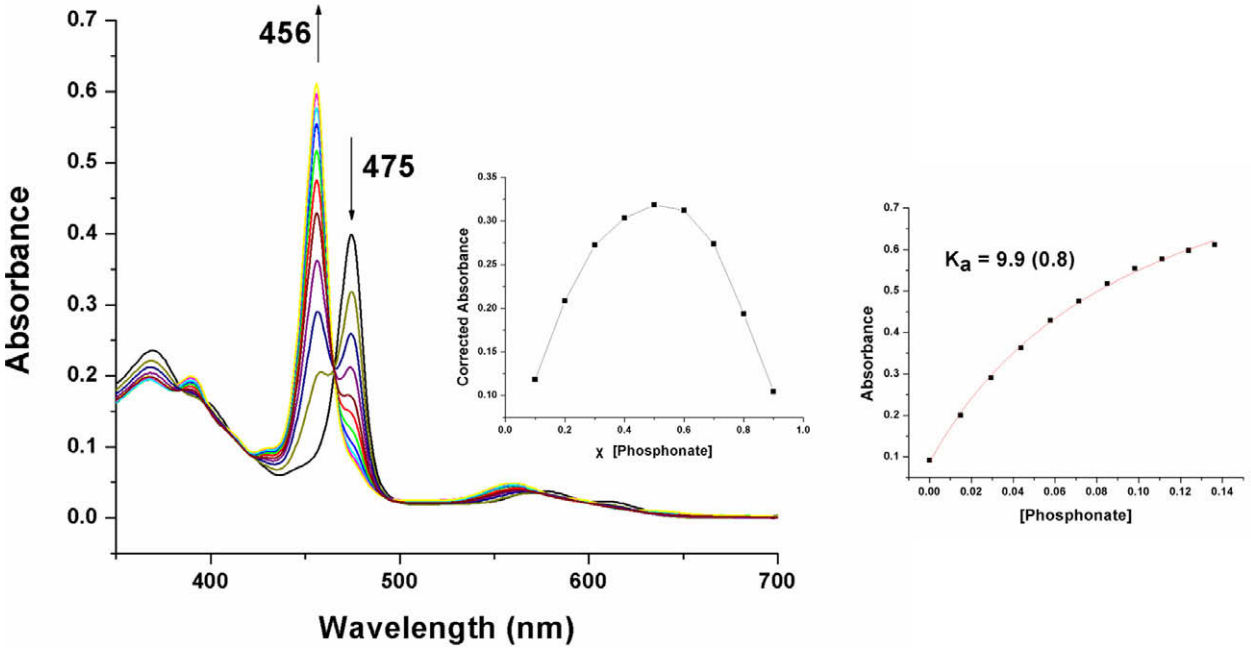


Fig. 8. Electronic absorption spectra of Mn(PFP-VP) [5.00×10^{-6} M] in dichloromethane in the presence of various amounts of $(C_2H_5O)_2P{=}O(Me)$ [1.50 M] (20–200 (by 20) μL). Inset: Job Plot for a binary mixture of **4** with $(C_2H_5O)_2P{=}O(Me)$.

these porphyrin-based systems are obviously less sensitive and less impressive as a potential sensing platform in the context of organophosphonates. This is in line with the tendency for a more in-plane metal ion in which a larger deviation from the [N_4] plane may encourage stronger analyte binding. The binding constants (K_a) values were measured by way of an equation reported by Valeur et al. [32] and are provided below as insets (Figs. 7 and 8). The binding constant for $(C_2H_5O)_2P{=}O(CH_2COCH_3)$ is 6.7 (0.9) M^{-1}; that for $(C_2H_5O)_2P{=}O(Me)$ is 9.9 (0.8) M^{-1}; and, that for $(C_4H_9O)_2P{=}O(Me)$ is 11.9 (0.4) M^{-1}.

As in the corrole case, we believe that this porphyrin system maintains an unchanged valence state upon binding. We should note, however, that a similarity in blue shifting pattern occurs for Mn=O formation. The oxo-Mn-(*meso*-tetrakis-2,3,5,6,-tetrafluoro-*N*,*N*,*N*-trimethyl-4-aniliniumyl)porphyrinato species (427 nm) gives a band at for the Mn(III)-porphyrinato at ~450 nm, upon

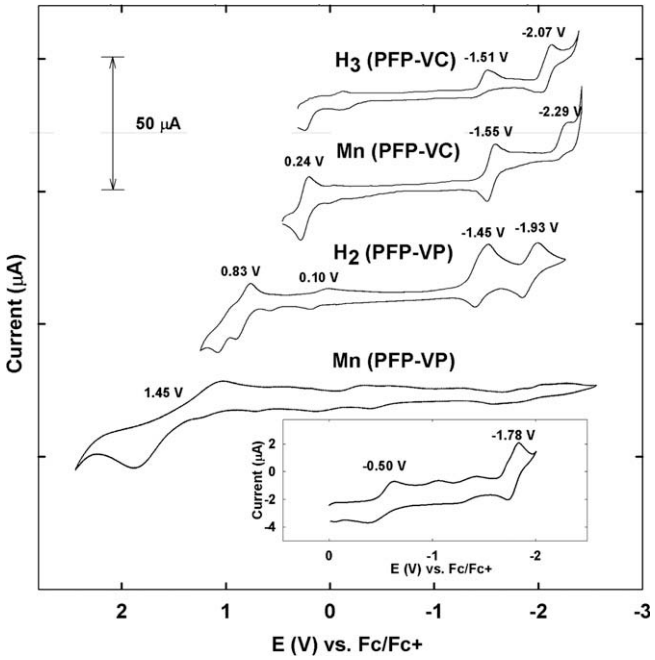


Fig. 9. Cyclic voltammetry data for compounds **1–4**, [3.0 mM], respectively, at room temperature in benzonitrile. Refer to Section 4 for further details. Half-wave potentials and peak potentials for **1–4** in benzonitrile. The inset is from a measurement of compound **4** at 1.0 mM.

carbamazepine epoxidation (10,11-position oxidation) [25c]. Thus further determinations for our porphyrin species will need to be made through future work.

2.3. Cyclic voltammetry (CV)

Electrochemistry often enables for the useful assignment of metal and ligand oxidations and affords a look at an analysis of the state of the M^{n+} of the metal complex, especially when considering transition metal ions such as manganese. A variety of recent reports of Mn-corrolates are available [25f]. The cyclic voltammograms have been obtained for compounds **1–4** and are provided below in Fig. 9. The cyclic voltammograms which include half-wave potentials/peak potentials (versus Ag/Ag^+ or Fc/Fc^+ or SCE) were obtained in PhCN. As revealed by the CV curve in Fig. 9, the reduction potentials for **3** are −1.55 and −2.29 V (versus SCE). This value is very similar to the reduction potentials of −1.51 and −2.07 V (versus SCE) for the metal free corrole **1** and has been assigned as corrole-centered reductions. The oxidation potential for **3** (0.24 V versus SCE) is assigned to the metal center, and is less than that for the Mn(tpf)corrole (0.71 V versus SCE), indicating **3** is more easily oxidized than the Mn(tpf)corrole [28]. A comparison to Mn(Mes_2Ph)corrole can also be made (Table 1). This species has been studied in considerable detail and has a variety of reduction and oxidation potentials depending on the solvent and axial anion coordination which are similar when in non aqueous media [25f].

Data was also obtained for the porphyrin-based species **2** and **4** (Scheme 1). For the free-base porphyrin, the first reduction occurs at −1.45, and −1.93 V, and the oxidization values occur at 0.10 and 0.83 V. For the Mn(III)-porphyrin chloride species, the first small $E_{1/2}$ reduction occurs at −0.50 with another occurring out at −1.78 V (Inset, Fig. 9); a broad $E_{1/2}$ of oxidation exists at 1.45 V.

2.4. Structural characterization of compound *1*

We also provide herein the crystal structure of 5,15-bis(pentafluorophenyl)-10-(3-vinylphenyl)corrole (**1**) (Fig. 10). The molecular structure of **1** confirms the presence of the vinyl moiety found also naturally in hemes; it points down and is suggestive of a clear surface anchoring group [21]. This serves as the first structural example of molecule with a 3-vinyl-phenyl dipyrrin/dipyrromethane fragment. There exists a plausible hydrogen bonding network between pairs of molecules as well (Supporting Information). Crystallographic packing structures provided for this structural solution separately along all three axes have been prepared (Supporting Information).

2.5. DFT calculations on bare corrole and porphyrin model systems

To try to understand the differences between neutral [28b] Mn–corrole and Mn–porphyrin organophosphonate binding and related transformations, we undertook DFT calculations using an unsubstituted corrole or porphyrin, oxygen atom, and the requiste phospho*nate*/*-ite* fragments. While calculations have previously been undertaken in trying to understand porphyrin M=O species, the details of M–O–P interactions are particularly informative in the present context. Electronic energies and geometries for formal M–O and P–O bond cleavage products for various metal-based spin states are illustrated in Figs. 11 and 12. The spin states in the corrole case were the singlet, triplet and quintet. Going from the bench-mark "Compound I"-like metal oxo species [1,29] the differences in energies in the middle section and those on the left represent the energy of formal O–M cleavage, whereupon the O-atom formally migrates from the metal to the phosphorus atom of the phospon*ite* ($POMe_2Me$). Going from the middle set to the right side set (in Fig. 11) formally signifies the attachment of the phosphine atom to the manganyl O-atom. This atom then becomes engaged as the donor atom in a Lewis base adduct with the metal center. The presence of the O=P bond, as well as a favorable dative interaction of ~10 kcal/mol gives this species (for the singlet) the lowest energy state. How the O-atom rearranges from an $X_2(L)$ donor to an L-type donor is a very interesting point for later consideration. A similar profile exists for the neutral Mn-porphyrinato and its derivatives (Fig. 12). Herein, the doublet, quartet, and sextet spin states were calculated. A much higher energy profile for the

Table 1
A comparison of reduction and oxidation potentials of **3** and related compounds Mn(Mes_2Ph)-corrole and Mn(tpf)corrole in various solvents.

	Solvent	3rd ox. (V)	2nd ox. (V)	1st ox. (V)	1st red. (V)
Mn(Mes_2Ph-Corrole) [25f]	CH_2Cl_2	–	1.00	0.32 (0.03)[b]	–
Mn(Mes_2Ph-Corrole) [25f]	PhCN	1.83[a]	1.07	0.45 (0.12)[b]	−1.36, −1.64
Mn(Mes_2Ph-Corrole) [25f]	Pyridine	–	–	0.42	−1.46
Mn(tpf)Corrole [28]	CH_2Cl_2	–	–	0.71	–
Compound **3** [*this article*]	PhCN	–	–	0.24	−1.55, −2.29

All values referenced to the SCE except for **3** which was reported versus the ferrocene/ferrocenium ion redox couple.; SCE = (Fc/Fc^+) + 0.40 V; $(Fc/Fc^+) = (Ag/Ag^+) - 0.092$ V; $E_{1/2}$ TBAP = tetrabutylammonium perchlorate.

[a] Scan rate 0.1 V/s.

[b] Extra peaks are due to the varation of axial ligation. A dash indicates an unreported or unobtainable value.

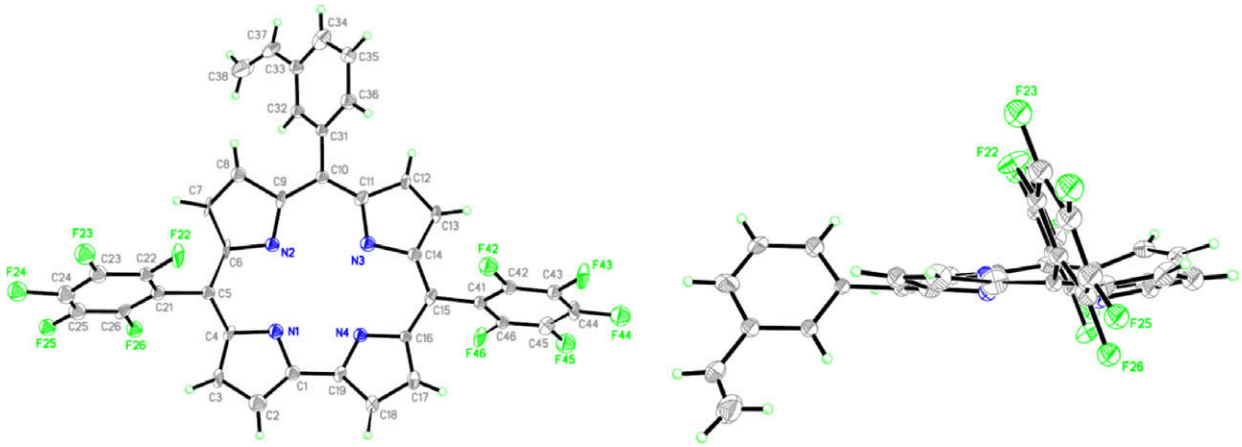


Fig. 10. Top and side views of **1** (CCDC 684999). Hydrogens are retained for clarity. X-ray diffraction study parameters: chemical formula $C_{39}H_{18}F_{10}N_4$, fw 732.14, Space group $P\bar{1}$, a = 10.077(13) Å, b = 13.359(18) Å, c = 14.907(19) Å, α = 113.113 (17)°, β = 90.83(3)°, γ = 105.165(17)°, V = 1766(4) Å^3, Z = 4, μ = 0.121 (mm^{-1}), R_1 = 0.2094, wR_2 = 0.4016 {$R_1 = (\Sigma||F_o| - |F_c||)/\Sigma|F_o|$; $wR_2 = [(\Sigma(F_o^2 - F_c^2)^2)/\Sigma w(F_o^2)^2]^{1/2}$}, ρ_{calcd} = 1.404 (mg/m^3), Temp = 243(2).

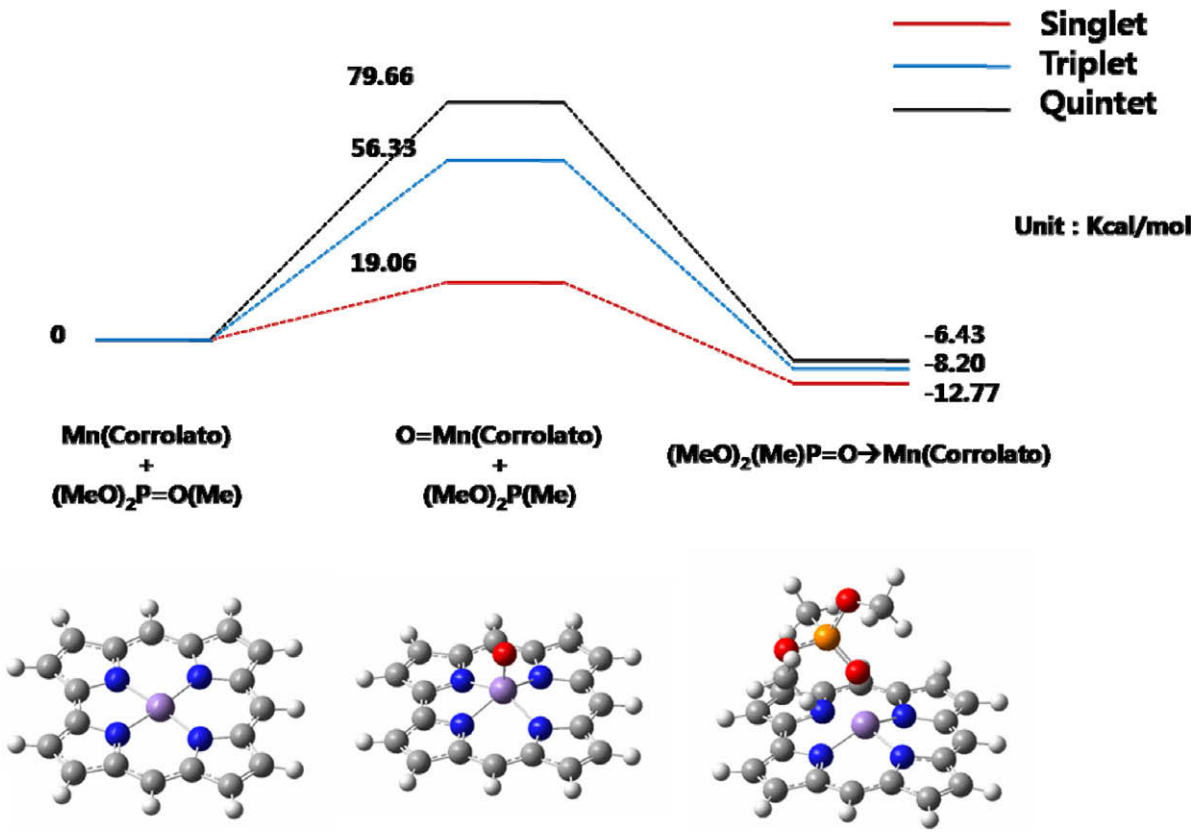


Fig. 11. Relative energies and geometries for three neutral manganese(III) corrolato species.

terminal oxo-derivative is evident, when compared to the corrolato counterpart. The oxo-intermediate is lowest for the doublet spin state; but the sextet actually "edges out" the doublet as the lowest energy species as the phosphonate adduct (right side set in Fig. 12). Clearly, the P═O will never oxidize the manganese in either the corrole or porphyrin case; and this obviously drives phosphine oxidation catalysis; how phosph*onites* might oxidize or *de*-oxidize in the context of nerve agent sensing and remediation is "food for thought." These calculations help in approaching or understanding the opportunities, and limitations of catalytic decontamination of organophosphonate-based chemical warefare agents. Structurally, the Mn–O–P angle in the Mn(pfp)corrolato is 158.6° and the metal exists 0.29 Å above the [N_4] mean plane [19a], the calculated Mn–O–P angles and manganese atom "out-of-plane" distances in these model systems depend on the spin state and are provided in Table 2 comparison for both the corrole and porphyrin adducts.

3. Conclusion

In this report we have described the preparation, characterization, and dynamics of new A_2B-corrole, *trans*-A_2B_2-porphyrin, and their manganese complexes. To our knowledge, this is the first

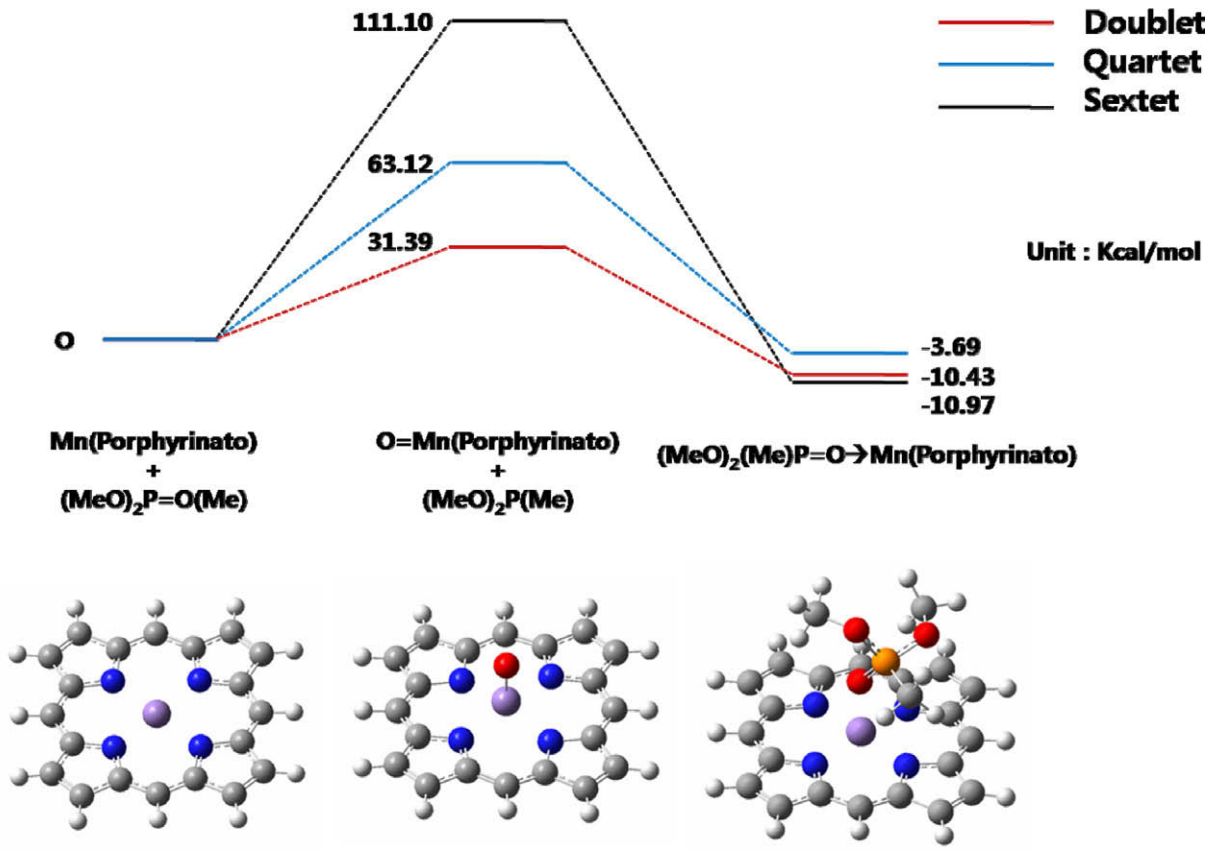


Fig. 12. Relative energies and geometries for three neutral manganese(II) porphyrinato species.

Table 2
Geometrical features in the calculated structures of Mn-porphyrinato and -corrolato species.

Mn-corrole multiplicity	Distance of Mn and [N_4] mean plane	Mn-corrole multiplicity	Mn–O–P angle
Singlet	0.54 Å	singlet	141.1°
Triplet	0.47 Å	triplet	136.3°
Quintet	0.36 Å	quintet	140.6°
Mn-porphyrin multiplicity		Mn-porphyrin multiplicity	
Doublet	0.29 Å	doublet	139.8°
Quartet	0.38 Å	quartet	141.1°
Sextet	0.11 Å	sextet	139.8°

determination of OP sensing capabilities of metallocorroles and metalloporphyrins. Also this is the first report of a *meso* 3-vinylphenyl substituted polypyrrole species. The synthesis for the metallocorroles and metalloporphyrin species is adapted from the literature. We undertook detailed NMR spectral characterization and obtained the structure of the free-base corrole (**1**) through the use of single-crystal X-ray diffraction. We probed the possibility of selective sensing of nerve agent model organophosphonate species. The bonding of organophosphonate to the Mn^{n+} center is supported by the strong responses in the UV–Vis spectrum upon analyte titration. This technique gave quantification of 1:1 binding for the Mn(PFP-VC)corrole (**3**) (PFP-VC = 5,15-di(pentafluorophenyl)-10-(3-vinylphenyl)corrolate) with $(CH_3CH_2O)_2P{=}O(C_3H_6NMe_2)$, $(C_4H_9O)_2P{=}O(Me)$, $(C_2H_5O)_2P{=}O(Me)$, and $(CH_3COCH_2)P{=}O(OC_2H_5)_2$. The titrimetric data allows for the calculated K_a values in the case of the [Mn(PFP-VP)][Cl] which ranged from 6.7 to 11.9 M^{-1}. These studies confirm 1:1 binding through the use of Job plots for compound **4** as well. Cyclic voltammetry of compounds was acquired for **1**-**4**; the values of the Mn(PFP-VC)corrole can be compared to those for Mn(Mes_2Ph)corrolato that appear in a recent report from Kadish and coworkers [25f]. Modeling of $O{=}P(OMe)_2Me$ binding and formal M–O or P–O cleavage products in bare neutral Mn-corrole and -porphyrins with different metal-based spin states was undertaken. These efforts revealed the effect of $(MeO)_2P{=}O(Me)$ phosphoryl O-atom binding using three different metal-based spin states. Regarding the minimum bare corrole/porphyrin organophosphonate binding energies, greater stability occurred for the Mn-corrole (singlet) and the Mn-porphyrin (sextet) than for other spin states studied. From this data, we can support that the corrole is a more sensitive platform for organophosphonate sensing and has a possibility to optically detect organophosphonate on at least the *micro*molar level because of clear changes that occur in the UV–Vis spectrum. This sensitivity is probably inadequate for current nerve agent applications as a stand-alone method, however. But it is hoped that this report will enable various further studies, especially in realm of nanoscience, and with respect to piezoelectric studies in which the response involves acoustic signals of mass differences, not optical signals. Also, these compounds can be studied in the presence of a variety of decomposition products (CN^-, F^-, phosphonic acids) that could be present under real "battlefield" conditions. Future studies, may include catalysis with these species [20b]; also an expansion

of this same analyte binding can be made to the related manganese-corrolazines.

4. Experimental

4.1. General considerations

All reagents and solvents herein were of analytical grade and used as received from reliable commercial sources. The reagents 3-vinylbenzaldehyde, DMF, TFA, DDQ, $F_3B{\cdot}OEt_2$, $Mn(OAc)_2{\cdot}4H_2O$ were purchased from Aldrich, USA; pentafluorophenylcarboxaldehyde was acquired from TCI, Japan; toluene, dichloromethane, and chloroform were acquired from Merck [30]. Dipyrromethane was prepared by literature report [22]. The synthetic procedures for A_2B corroles and their metallocorroles were adapted from the literature [23]. All solvents used for NMR spectral analysis were purchased commercially and were of spectroscopic grade. ^{1}H NMR spectra were measured in $CDCl_3$ or CD_2Cl_2 with Bruker Avance 300 and 400 MHz spectrometers. Spectral signals were calibrated by the *protio* impurity of the deuterated solvent. Infrared spectra were recorded with a Bruker Equinox 55 spectrophotometer; UV–Vis spectra were obtained with a JASCO V-503 UV–Vis spectrometer. A Vario EL III CHNS elemental analyzer was used in obtaining microanalysis values. High resolution MALDI mass spectrometry was performed by the staff of the research supporting team at KAIST on a VG AUTOSPEC ULTIMA with a trisector double focusing magnetic sector analyzer at a resolution of 80 000.

4.2. Preparation of 5,15-bis(pentafluorophenyl)-10-(3-vinylphenyl) corrole [H_3(PFP-VC)], (**1**)

A mixture of 5-(pentafluorophenyl)dipyrromethane (5.13 g, 16.4 mmol) and 3-vinylbenzaldehyde (1.04 mL, 8.2 mmol) and a dichloromethane solution of TFA (80 μL), were dissolved in 800 mL dichloromethane. The reaction mixture was stirred for 12 h. DDQ (4.47 g, 19.6 mmol) in toluene was added dropwise over several minutes accompanied by vigorous stirring, which continued for 15 additional minutes. The volume of the reaction mixture was then reduced and the mixture was filtered through a pad of silica (silica gel, CH_2Cl_2:hexane = 1:1), followed by column chromatography (silica gel, CH_2Cl_2:hexane 1:4) which ultimately gave a dark green solid. This compound was further purified by preparative TLC to give pure corrole, H_3(PFP-VC) (613 mg, 10.2%). MALDI-TOF: m/z $[M+H]^+$: 733.137 (calc); 733.791 (obs). ^{1}H NMR(δ, CD_2Cl_2): 9.15 (d, J_{H-H} = 4.17 Hz, $2H_{3,18}$), 8.76 (m, $4H_{8,9,12,13}$), 8.62 (d, J_{H-H} = 3.98 Hz, $2H_{4,17}$), 8.26 (s, $1H_f$), 8.09 (d, J_{H-H} = 7.22 Hz, $1H_j$), 7.83 (d, J_{H-H} = 7.86 Hz, $1H_h$), 7.74 (t, J_{H-H} = 7.58 Hz, $1H_i$), 7.00 (dd, J_{H-H} = 17.60, 10.94, $1H_k$), 5.97 (d, J_{H-H} = 17.56, $1H_{l\text{-}trans}$), 5.40 (d, J_{C-H} = 10.98, $1H_{l\text{-}cis}$). ^{13}C-NMR: 147.87, 145.42, 143.49, 141.96, 141.52, 140.96, 140.37, 139.66, 137.19 (t, $^1J_{C-H}$ = 82.6 Hz, C_k), 135.88, 134.54 (d, $^1J_{C-H}$ = 159.9 Hz, C_j), 132.93 (d, $^1J_{C-H}$ = 164.3 Hz, C_f), 132.01, 128.11 (d, $^1J_{C-H}$ = 173.2 Hz, $C_{8,13}$), 127.91 (d, $^1J_{C-H}$ = 159.5, C_i), 125.97 (d, $^1J_{C-H}$ = 147.6 Hz, C_h), 125.81 (d, $^1J_{C-H}$ = 172.0 Hz, $C_{9,12}$), 122.02 (d, ^1J = 170.1 Hz, $C_{4,17}$), 118.06 (dd, ^1J = 173.1 Hz, 3.5 Hz, $C_{3,18}$), 114.93 (dd, ^1J = 159.7 Hz, 6 Hz, C_l), 114.47, 113.543. ν_{N-H} (KBr): 3421 cm^{-1}.

4.3. Preparation of 5,15-bis(pentafluorophenyl)-10,20-bis(3-vinylphenyl)porphyrin [H_2(PFP-VP)] (**2**)

5-(Pentafluorophenyl)dipyrromethane (0.50 g, 1.6 mmol) and 3-(vinylphenyl)benzaldehyde (0.20 mL, 1.6 mmol) were added to a portion of chloroform (160 mL); $BF_3{\cdot}OEt_2$ (65 μL) was then added dropwise to this reaction mixture. The reaction mixture was stirred for 1 h at RT; DDQ (0.27 g, 1.2 mmol) in toluene was then added slowly. After 1 h, the reaction mixture was filtered through a silica gel pad followed by purification via silica gel column chromatography (CH_2Cl_2: hexane = 1: 1) which gave a purple solution. This solution was then evaporated to give a purple solid (247 mg, 37.2%). ^{1}H NMR ($CDCl_3$): δ 8.97 (d, J_{H-H} = 4.8 Hz, $H_{3,9,13,19}$), 8.80 (d, J_{H-H} = 4.8 Hz, $H_{4,8,14,18}$), 8.26 (s, $2H_f$), 8.11 (d, J_{H-H} = 7.5 Hz, $2H_j$), 7.86 (d, J_{H-H} = 7.9 Hz, $2H_h$), 7.73 (t, J_{H-H} = 7.6, $2H_i$), 6.99 (dd, J_{H-H} = 17.6, 10.9 Hz, $2H_k$), 5.96 (d, J_{H-H} = 17.5, $2H_{l\text{-}trans}$), 5.42 (d, J_{H-H} = 11.0, $2H_{l\text{-}cis}$), −2.82 (s, $2H_{N-H}$). MALDI-TOF: m/z $[M+H^+]$ 847.184 (calc); 847.666 (obs). ν_{N-H} (KBr): 3321 cm^{-1}. *Anal.* Calc. for $C_{48}H_{24}N_4F_{10}$: C, 68.09; H, 2.86; N, 6.62. Found: C, 66.99; H, 2.91; N, 6.46%.

4.4. Preparation of 5,15-bis(pentafluorophenyl)-10-(3-vinylphenyl) corrolate manganese(III) [Mn(PFP-VC)] (**3**)

A small round-bottom flask was charged with 15 mL of dry DMF, H_3(PFP-VC) (0.05 g, 0.068 mmol), and $Mn(OAc)_2{\cdot}4H_2O$ (0.05 g, 0.20 mmol) and was heated to reflux for 20 minutes. The complete consumption of H_3(PFP-VC) was confirmed through the use of TLC assaying. The reaction mixture was then allowed to cool to room temperature after which time the solvent was removed under reduced pressure. The resulting residue was purified by silica gel column chromatography (1:1, hexane:ethyl acetate) to give pure Mn(PFP-VC). The yield was 50.0 mg (94%). MALDI-TOF: m/z (M^+): 784.052 (calc); 784.215 (obs). *Anal.* Calc. for $C_{39}H_{15}N_4F_{10}Mn$: C, 59.71; H, 1.93; N, 7.14. Found: C, 59.66; H, 3.04; N, 6.08%. λ_{max} (log ε/(M^{-1} cm^{-1})): 601 (3.56); 411 (4.60) [soret band]; 356 (4.47).

4.5. Preparation of 5,15-bis(pentafluorophenyl)-10,20-bis(3-vinylphenyl)porphyrinato manganese(III) [Mn(PFP-VP)] chloride (**4**)

H_2(PFP-VP) (85 mg, 0.1 mmol) and manganese acetate tetrahydrate (101 mg, 0.41 mmol) were dissolved in DMF (10 mL). The reaction mixture was refluxed for 1 h, and was then allowed to cool to room temperature. A TLC assay revealed no trace of free-base porphyrin. The reaction mixture was then placed into a NaCl aqueous solution containing a portion of ice, which allowed a green precipitate to form. This solid was isolated by filtration and dried affording a (green) solid formulated as the mono-chloride **4** (85.1 mg, 91.1%). MALDI-TOF: m/z ($M-Cl^+$) 899.107 (calc), 899.427 (obs). λ_{max} (log ε/(M^{-1} cm^{-1})): 609 (3.68); 576 (3.88); 475 (4.90) [Soret band]; 396 (4.52); 369 (4.67).

4.6. X-ray structural determination of compound **1**

A single crystal of **1** was mounted on a goniometer and data were collected on a Bruker P4 diffractometer equipped with a SMART CCD detector using graphite-monochromated Mo Kα radiation (λ = 0.71073 Å). The structure was solved using direct methods and standard difference map techniques, and was refined by full-matrix least-squares procedures on F^2 with SHELXTL (version 5.10). Cell parameters were determined and refined by the SMART program [31a]. Data reduction was performed by using SAINT software [31a]. The data were corrected for Lorentz and polarization effects. An empirical absorption correction was applied using the SADABS program [31b]. The structures were solved by direct methods using the program SHELXS-97 [31c] and refined by full matrix least-squares calculations (F2) by using the SHELXL-97 software [31d]. All non-H atoms were refined anisotropically against F^2 for all reflections. All hydrogen atoms were placed at their calculated positions and refined isotropically. Crystal data, data collection and refinement parameters are summarized in the caption of Fig. 10.

4.7. Modeling of analyte binding

For non-linear fitting, we have used Eq. (1) [32,33] to determine 1:1 stoichiometry in our Mn-corrole and Mn- porphyrin systems.

$$A = A_0 + \frac{A_{\lim} - A_0}{2c_0}\left[c_0 + c_M + \frac{1}{K_s} - \left[\left(c_0 + c_M + \frac{1}{K_s}\right)^2 - 4c_0c_M\right]^{1/2}\right] \quad (1)$$

The parameters are as follows: A = absorbance, C_0 = concentration of corrole or porphyrin; K_s = binding constant, C_M = concentration of organophosphonate analyte, A_0 = absorbance of corrole or porphyrin; A_{lim} = absorbance when analyte is bound completely.

4.8. Cyclic voltammetry (CV)

Measurements were carried out with a BAS 100B instrument (Bioanalytical Systems, Inc). A three-electrode system was used consisting of a gold disk working electrode, a platinum wire counter electrode, and an Ag/Ag^+ electrode (MF-2062 kit, Bioanalytical Systems, Inc.) as the reference electrode. The Ag/Ag^+ contained 0.1 M tetrabutylammonium perchlorate (TBAP) and 0.01 M $AgNO_3$ in benzonitrile. In 0.1 M TBAP, the $E_{1/2}$ of the ferrocene/ferrocenium ion couple was taken to be 0.067 V versus Ag/Ag^+ in benzonitrile. The values in electrochemical experiments are reported versus the ferrocene/ferrocenium ion [29] redox couple.

4.9. Computational details

The GAUSSIAN 03 program was used for all calculational work [34]. All geometries were processed *in silico* in the gas phase at 0 K. The following protocol was used for all calculations: (i) input geometries were derived from the crystallographic structures provided herein where possible, or by careful modification of closely related geometries and invoking chemical intuition. (ii) Density functional theory (DFT) geometry optimizations were performed using B3LYP hybrid functional with the LACVP* (double zeta) basis set. The basis set used the Lanl2DZ effective core potential (ECP) for the manganese atom, and 6-31G(d) for all other atoms.

Acknowledgements

D.G.C. acknowledges support from the Korea Science and Engineering Foundation (KOSEF) Grant (No. R01-2008-000-12388-0), funded by the Korean Government (MOST). Professor Y.S.L. and I.K. (Quantum Chemistry Laboratory) gratefully acknowledge (i) financial support from the Korea Science and Engineering Foundation (Nos. R01-2007-000-11015-0, R11-2007-012-03001-0) and (ii) computational time from the supercomputing center of KISTI. Professor Gerard Parkin (Department of Chemistry, Columbia University) facilitated the X-ray diffraction study of Compound **1**. MALDI-TOF analyses were obtained with the help of the KAIST research supporting team. Hack Soo Shin is gratefully acknowledged for his help in acquiring NMR data. Dr. Raj Chakrabarti (former NIH Postdoctoral fellow at the Departments of Chemistry at M.I.T. & Columbia University) is acknowledged for helpful discussions during his visit to KAIST (July, 2005). Teresa Lindstead (Cambridge, England) is thanked for her assistance in filing our crystallographic data (CCDC 684999).

Appendix A. Supplementary data

CCDC 684999 contains the supplementary crystallographic data for this paper. These data can be obtained free of charge via www.ccdc.cam.ac.uk/conts/retrieving.html, or from the Cambridge Crystallographic Data Centre, 12 Union Road, Cambridge CB2 1EZ, UK; fax: (+44) 1223-336-033; or e-mail: deposit@ccdc.cam.ac.uk.

Supplementary data associated with this article can be found, in the online version, at doi:10.1016/j.poly.2009.04.020.

References

[1] B. Meunier, Heme-peroxidases, in: J.A. McCleverty, T.J. Meyer (Eds.), Comprehensive Chemistry II, vol. 8, 2004, p. 261.
[2] I. Aviv, Z. Gross, Chem. Commun. (2007) 1987.
[3] D.T. Gryko, B. Koszarna, Org. Biomol. Chem. 1 (2003) 350.
[4] D.T. Gryko, Chem. Commun. (2000) 2243.
[5] E. VanCaemelbecke, S. Will, M. Autret, V.A. Adamian, J. Lex, J.P. Gisselbrecht, M. Gross, E. Vogel, K.M. Kadish, Inorg. Chem. 35 (1996) 184.
[6] M. Autret, S. Will, E. Vancaemelbecke, J. Lex, J.P. Gisselbrecht, M. Gross, E. Vogel, K.M. Kadish, J. Am. Chem. Soc. 116 (1994) 9141.
[7] (a) S. Nardis, D. Monti, R. Paolesse, Mini-Rev. Org. Chem. 2 (2005) 355;
(b) S. Nardis, F. Mandoj, R. Paolesse, F.R. Fronczek, K.M. Smith, L. Prodi, M. Montalti, G. Battistini, Eur. J. Inorg. Chem. (2007) 2345.
[8] G. Parkin, J. Chem. Educ. 83 (5) (2006) 791.
[9] J.-M. Barbe, G. Canard, S. Brandes, F. Jerome, G. Dubois, R. Guilard, Dalton Trans. (2004) 1208.
[10] R. Czolk, Sens. Actuators B B30 (1996) 61.
[11] R. Paolesse, C. Di Natale, A. Macagnano, F. Sagene, M.A. Scarselli, P. Chiaradia, V.I. Troitsky, T.S. Berzina, A. D'Amino, Langmuir 15 (1999) 1268–1274.
[12] C. Di Natale, C. Goletti, R. Paolesse, M. Drago, A. Macagnano, A. Mantini, V.I. Troitsky, T.S. Berzina, M. Cocco, A. D'Amico, Sens. Actuators B B57 (1999) 183.
[13] A. D'Amico, C. Di Natale, A. Macagnano, F. Davide, A. Mantini, E. Tarizzo, R. Paolesse, T. Boschi, Biosens. Bioelectron. 13 (1998) 711.
[14] (a) T.A. Romanova, O.V. Kravchenko, I.I. Morgulis, A.A. Kuzubov, P.O. Krasnov, P.V. Avramov, Koord. Khim. 30 (2004) 403;
(b) S. Han, K. Cho, J. Ihm, Phys. Rev. E: Stat. Phys., Plasmas, Fluids 19 (1999) 2218.
[15] R. Zwaans, J.H. van Lenthe, D.H.W. den Boer, Theochem 339 (1995) 153.
[16] J.W. Grate, S.N. Kaganove, Strongly Hydrogen-Bond Acidic Polymer and Methods of Making and Using, US Patent 6015,869, January 2000.
[17] D.A. Atwood, D.G. Churchill, "Destruction and detection of chemical warfare agents", Chem. Rev., cr-2008-00223w, in preparation.
[18] Z. Gross, G. Golubkov, L. Simkhovich, Angew. Chem., Int. Ed. 39 (2000) 4045.
[19] (a) J. Bendix, H.B. Gray, G. Golubkov, Z. Gross, Chem. Commun. (2000) 1957;
(b) The report by D.P. Goldberg on corrolazines is particulary relevant to the discussion herein:B.S. Mandimutsira, B. Ramdhanie, R.C. Todd, H. Wang, A.A. Zareba, R.S. Czernuszewicz, D.P. Goldberg, J. Am. Chem. Soc. 124 (2002) 15170;
(c) S. Licoccia, E. Morgante, R. Paolesse, F. Polizio, M.O. Senge, E. Tondello, T. Boschi, Inorg. Chem. 36 (1997) 1564.
[20] (a) Preliminary presentations of portions of this work include two poster presenations: K. Kim, N. Maiti, D.G. Churchill, Abstracts of Papers, 235th ACS National Meeting, New Orleans, LA, United States, April 6–10, 2008, INOR-192.;
(b) K. Kim, N. Maiti, D.G. Churchill, Abstracts of Papers, 234th ACS National Meeting, Boston, MA, United States, August 19–23, 2007, INOR-660.;
(c) D.G. Churchill, N. Maiti, S.H. Choi, Metallocorrole catalyst produced by substituting 3-vinyl phenyl group from a corrole compound and a method for producing the same, Repub. Korean Kongkae Taeho Kongbo (2007), CODEN: KRXXA7 KR 2007049466 A 20070511 CAN 147:475473 AN 2007:1191159 (Note, the first two authors were erroneously listed as David, G.C. and Nilkamal, M.).;
(d) Oxygen-atom transfer catalysis has previously been explored with Compound **3**: N. Maiti, K. Kim, B. Meka, D.G. Churchill, unpublished results, 2005–2007.
[21] D.L. Pilloud, C.C. Moser, K.S. Reddy, P.L. Dutton, Langmuir 14 (1998) 4809.
[22] B.J. Littler, M.A. Miller, C.H. Hung, R.W. Wagner, D.F. O'Shea, P.D. Boyle, J.S. Lindsey, J. Org. Chem. 64 (1999) 1391.
[23] D.T. Gryko, B. Koszarna, Synthesis (2004) 2205.
[24] (a) N. Maiti, J. Lee, Y. Do, H.S. Shin, D.G. Churchill, J. Chem. Crystallogr. 35 (2005) 949;
(b) N. Maiti, J. Lee, S.J. Kwon, J. Kwak, Y. Do, D.G. Churchill, Polyhedron 25 (2006) 1519.
[25] [a] The isolation of the porphyrin from the corrole reaction involves preparative TLC. This however would favor migration of Mn(II) which is not ionic; as the Mn(II) migrates on silica in air, it may decompose and become the oxo (manganyl) species (ligand oxidation may also occur). The Mn(II) species however, is less stable than the [Mn(III)Cl] porphyrin species which can be more completely synthesized as chloride salt as discussed herein and reported previously.;
(b) R.D. Jones, D.A. Summerville, F. Basolo, J. Am. Chem. Soc. 100 (1978) 4416;
(c) While the formulation of the porphyrin is Mn(III), it is well known that upon appropriate oxidant, the preparation can be made for Mn(IV) (e.g., using ^{t}BuOOH) and Mn(V) (e.g., using H_2O_2):W. Nam, I. Kim, M.H. Lim, H.J. Choi, J.S. Lee, H.G. Jang, Chem. Eur. J. 8 (2002) 2067;
(d) D. Turner, M.J. Gunter, Inorg. Chem. 33 (1994) 1406;
(e) Z. Ou, C. Erben, M. Autret, S. Will, D. Rosen, J. Lex, E. Vogel, K.M. Kadish, J. Porphyrins Phthalocyanines 9 (2005) 398;

(f) J. Shen, M.E. Ojaimi, M. Chkounda, C.P. Gros, J.-M. Barbe, J. Shao, R. Guilard, K.M. Kadish, Inorg. Chem. 47 (2008) 7717. See references herein for previous electrochemical studies of a variety of Mn corroles, e.g., octaethyl substituted corrole-based systems.

[26] I. Bandyopadhyay, M.J. Kim, Y.S. Lee, D.G. Churchill, J. Phys. Chem. A 110 (2006) 3655.

[27] It is thought that a carefully positioned carboxylic acid or related group could effect secondary *N*-binding of this analyte in the context of selective VX binding.

[28] (a) G. Golubkov, J. Bendix, H.B. Gray, A. Mahammed, I. Goldberg, A.J. DiBilio, Z. Gross, Angew. Chem., Int. Ed. 40 (2001) 2132;
[b] An Mn(III) porphyrinato would require the use of an anion for electroneutrality; this was not pursued in these calculations. The point of this work was to seek an understanding of the diversity of the various spin states, which was done through the analysis of neutral systems. A Mn(III)porphyrinato species would be more electron deficient at the metal center (on average) and this would be expected to *strengthen* the organophosphonate dative interaction.

[29] (a) M.K. Tse, Z. Zhang, K.S. Chan, Chem. Commun. (1998) 1199;
(b) A.E. Meier-Callahan, H.B. Gray, Z. Gross, Inorg. Chem. 39 (2000) 3605;
(c) H.-Y. Chao, D.G. Churchill, J. Chem. Educ. 85 (2008) 1210;
(d) O.A. Egorova, O.G. Tsay, S. Khatua, J.O. Huh, D.G. Churchill, Inorg. Chem, in press.

[30] With regards to laboratory safety, a useful description of some common laboratory chemical explosion hazards has been prepared: D.G. Churchill, J. Chem. Educ. 83 (2006) 1798.

[31] [a] SMART and SAINT, Area Detector Software Package and SAX Area Detector Integration Program; Bruker Analytical X-ray, Madison, WI, 1997.;
[b] SADABS, Area Detector Absorption Correction Program; Bruker Analytical X-ray: Madison, WI, 1997.;
[c] G.M. Sheldrick, SHELXS-97 program for crystal structure determination, Acta Crystallogr. A46 (1990) 467–473.;
[d] G. Sheldrick, SHELXL-97, Universität Göttingen, Göttingen, Germany, 1999.

[32] B. Valeur, J. Pouget, J. Bourson, M. Kaschke, N.P. Ernsting, J. Phys. Chem. 96 (1992) 6545.

[33] ORIGIN 6.1, Windows-Based Scientific Graphing and Data Analysis Software, OriginLab Co. Northampton, MA, USA.

[34] GAUSSIAN 03: M.J. Frisch et al., Gaussian Inc., Wallingford CT, 2004 (see Supplementary Supporting Information for complete citation).

Polyhedron 28 (2009) 2431–2435

Contents lists available at ScienceDirect

Polyhedron

journal homepage: www.elsevier.com/locate/poly

Synthesis and characterization of rhenium carbonyltrifluoroacetate complexes with phosphites, phosphonites and phosphinites

Sandra Bolaño, Jorge Bravo *, Jesús Castro, Soledad García-Fontán, María C. Rodríguez

Departamento de Química Inorgánica, Universidade de Vigo, Campus Universitario, E-36310 Vigo, Spain

ARTICLE INFO

Article history:
Received 26 February 2009
Accepted 19 April 2009
Available online 12 May 2009

Keywords:
Carbonyls
Rhenium
Phosphites
Phosphonites
Phosphinites

ABSTRACT

The rhenium(I) complexes $[Re(O_2CCF_3)(CO)_3(L)]$ (**1**) and $[Re(O_2CCF_3)(CO)_2LL']$ ($L = Ph_2POCH_2CH_2OPPh_2$; $L' = PPh_n(OR)_{3-n}$; R = Me, Et; $n = 0–2$) (**2a–f**) have been synthesised by the reaction of the parent bromo derivatives with AgO_2CCF_3. These compounds have been characterized by microanalysis, IR, NMR, mass spectrometry and, in the cases of **1** and **2a**, by X-ray diffraction. The metal is in a distorted octahedral environment with the trifluoroacetate ligand acting in a monodentate manner.

© 2009 Elsevier Ltd. All rights reserved.

1. Introduction

Transition metal carbonyl complexes are widely studied in chemistry because they have many different applications ranging from catalysts [1] to biochemistry [2]. Many properties of the complexes, such as redox potential of the metal centre, lability of the ligands, etc., are related to the synergistic effects of σ and π bonds between the metal centre and the CO ligands [3]. On the other hand, phosphines are also very common ligands with tuneable electronic properties that allow them to mimic those of CO ligands. Moreover, the possibility of modifying their steric properties explains their wide use in many coordination compounds. Replacement of the R groups from PR_3 compounds by OR groups to form mixed phosphites ($PR_n(OR)_{3-n}$; $n = 0–2$) modifies the electronic character of the ligand, enhancing its π-acceptor character and reducing its σ-donor behaviour [4]. These changes, in turn, modify the properties of the metal complex. We are interested in analysing the properties of carbonyl complexes that bear mono- and bidentate mixed phosphites and we have previously reported on the properties of $[ReX(CO)_3L]$ [5] and $[ReBr(CO)_2LL']$ [6] (X = Br, OTf; L = diphosphinite; L′ = mixed phosphite). Substitution of the bromo ligand by the potentially bidentate OTf ligand, did not produce relevant differences on the properties of the complex. Thus, we report here the carbonyl rhenium complexes $[Re(O_2CCF_3)(CO)_3(L)]$ and $[Re(O_2CCF_3)(CO)_2LL']$ ($L = Ph_2POCH_2CH_2OPPh_2$; $L' = PPh_n(OR)_{3-n}$; R = Me, Et; $n = 0–2$) bearing the more basic trifluoroacetate ligand to investigate its influence on the properties of the new complexes.

2. Experimental

2.1. General methods and instrumentation

All experimental manipulations were carried out under an argon atmosphere using Schlenk techniques. Solvents were purified by conventional procedures [7] and distilled prior to use. The complexes $[ReBr(CO)_3(L)]$ and $[ReBr(CO)_2LL']$ ($L = Ph_2POCH_2CH_2OPPh_2$; $L' = PPh_n(OR)_{3-n}$, R = Me, Et; $n = 0–2$) were prepared by previously described methods [6].

The ^1H, $^{31}P\{^1H\}$, $^{13}C\{^1H\}$ and $^{19}F\{^1H\}$ NMR (δ in ppm) spectra were obtained on a Bruker ARX-400 spectrometer operating at frequencies of 400, 161, 100 and 376 MHz, respectively. ^1H and $^{13}C\{^1H\}$ chemical shifts are referred to internal TMS. $^{19}F\{^1H\}$ and $^{31}P\{^1H\}$ chemical shifts are reported with respect to $CFCl_3$ and 85% H_3PO_4, respectively, with downfield shifts considered positive. Infrared spectra were recorded as KBr discs on a Bruker VECTOR IFS28 FT spectrophotometer. Mass spectra were recorded in the LSIMS (FAB^+), Cs^+ mode on a Micromass Autospec M instrument, using 3-nitrobenzyl alcohol as the matrix material. The conductivity values of 10^{-3} mol dm^{-3} solutions of the complexes in $MeNO_2$ at 25 °C were measured with a Crison GLP 32 conductimeter. Elemental analyses (C, H) were performed using a Fisons EA-1108 microanalyzer. Melting points were determined on a GallenKamp MFB-595 and are uncorrected.

2.2. Synthesis of the complexes

AgO_2CCF_3 was added to a dichloromethane solution of the precursor complex $[ReBr(CO)_2(X)(L)]$ (X = CO or L′) in a 1.5:1 molar

* Corresponding author. Tel.: +34 986 812 275; fax: +34 986 813 798.
E-mail address: jbravo@uvigo.es (J. Bravo).

0277-5387/$ - see front matter © 2009 Elsevier Ltd. All rights reserved.
doi:10.1016/j.poly.2009.04.045

ratio. The mixture was heated under reflux for 2–3 h and the AgBr formed was removed from the resulting grey suspension by filtration through Celite. In the case of complex **1**, the concentration of the resulting solution afforded an oil, which was triturated with diethyl ether (5 mL) to give a beige solid. This solid was filtered off, washed with diethyl ether (2 × 3 mL), dried under vacuum and recrystallised from a mixture of CH_2Cl_2/diethyl ether. In the case of compounds **2**, white solids were obtained and these were recrystallised from a mixture of CH_2Cl_2/hexane.

2.2.1. [Re(O$_2$CCF$_3$)(CO)$_3$(L)] (**1**)

AgO_2CCF_3 (42.4 mg, 0.192 mmol) was added to a solution of [ReBr(CO)$_3$(L)] (100 mg, 0.128 mmol) in dichloromethane (20 mL). Yield ⩾ 58%. M.p. 211 °C. $\Lambda_{M(nitromethane)}$ = 3.5 Ω^{-1} cm^2 mol^{-1}. *Anal.* Calc. for $C_{31}H_{24}O_7P_2F_3Re$: C, 45.7; H, 3.0. Found: C, 46.0; H, 3.1%. IR (cm^{-1}) ν_{CO}: 2041, 1967, 1932; $\nu_{asym(OCO)}$: 1692, $\nu_{sym(OCO)}$: 1420. ^{1}H NMR ($CDCl_3$, ppm): δ 7.56–7.21 (m, 20H, Ph), 4.33–4.07 (m, 4H, –CH_2CH_2–). $^{31}P\{^1H\}$ NMR ($CDCl_3$, ppm): δ 116.5 (s). $^{19}F\{^1H\}$ NMR ($CDCl_3$, ppm): δ −74.8 (s). $^{13}C\{^1H\}$ NMR (CD_2Cl_2, ppm): δ 66.5 (s, br, –CH_2–), 114.7 (q, J_{CF} = 288 Hz, CF_3), 128.8–138.3 (Ph), 162.2 (qt, J_{CF} = 37 Hz, J_{CP} = 2 Hz, O_2CCF_3), 191.2 (m, 2CO *cis* to O_2CCF_3), 191.5 (t, J_{CP} = 7 Hz, CO *trans* to O_2CCF_3).

2.2.2. [Re(O$_2$CCF$_3$)(CO)$_2$(L)(L′)] (**2**)

AgO_2CCF_3 (33 mg, 0.15 mmol) was added to [ReBr(CO)$_2$LL′] (0.1 mmol) in CH_2Cl_2 (20 mL).

Compound **2a**, L′ = P(OMe)$_3$: Yield ⩾ 37%. M.p. 202 °C. $\Lambda_{M(nitromethane)}$ = 3.0 Ω^{-1} cm^2 mol^{-1}. *Anal.* Calc. for $C_{33}H_{33}O_9P_3F_3Re$: C, 43.6; H, 3.7. Found: C, 43.4; H, 3.7%. FAB MS: *m*/*z* (referred to the most abundant isotopes): 910 (48.5%) [M]; 882 (35.7%) [M−CO]; 797 (100%) [M−O_2CCF_3]; 758 (95.6%) [M−CO−L′]; 645 (6.0%) [M−CO−L′−O_2CCF_3]. IR (cm^{-1}) ν_{CO}: 1962, 1882; $\nu_{asym(OCO)}$: 1697; $\nu_{sym(OCO)}$: 1418. ^{1}H NMR ($CDCl_3$, ppm): δ 7.64–7.19 [m, 20H, Ph (L)], 4.50 (m, 1H, –CH_2CH_2–), 4.00 (m, 3H, –CH_2CH_2–), 3.39 [d, 9H, J_{HP} = 10 Hz, –CH_3 (L′)]. $^{31}P\{^1H\}$ NMR ($CDCl_3$, ppm) (see Scheme 1 for labelling): δ 115.2 (dd, J_{AB} = 33 Hz, J_{BC} = 299 Hz, P_B), 118.2 (dd, J_{AC} = 32 Hz, P_A), 124.3 (dd, P_C). $^{19}F\{^1H\}$ NMR ($CDCl_3$, ppm): δ −75.1 (s).

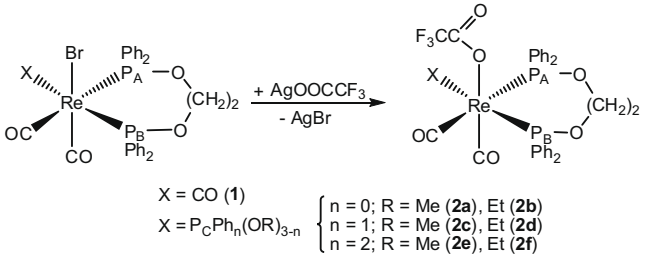
Compound **2b**, L′ = P(OEt)$_3$: Yield ⩾ 36%. M.p. 190 °C. $\Lambda_{M(nitromethane)}$ = 2.9 Ω^{-1} cm^2 mol^{-1}. *Anal.* Calc. for $C_{36}H_{39}O_9P_3F_3Re$: C, 45.4; H, 4.2. Found: C, 45.2; H, 4.1%. FAB MS: *m*/*z* (referred to the most abundant isotopes): 952 (58.5%) [M]; 924 (52.7%) [M−CO]; 839 (99.9%) [M−O_2CCF_3]; 758 (100%) [M−CO−L′]; 645 (6.2%) [M−CO−L′−O_2CCF_3]. IR (cm^{-1}) ν_{CO}: 1975, 1876; $\nu_{asym(OCO)}$: 1696; $\nu_{sym(OCO)}$: 1410. ^{1}H NMR ($CDCl_3$, ppm): δ 7.66–7.19 [m, 20H, Ph (L)], 4.50 (m, 1H, –CH_2CH_2–), 4.20–3.80 [m, 3H, –CH_2CH_2–(L)], 3.76 [m, 6H, –CH_2–(L′)], 1.01 [t, 9H, J_{HH} = 7 Hz, –CH_3(L′)]. $^{31}P\{^1H\}$ NMR ($CDCl_3$, ppm) (see Scheme 1 for labelling): δ 114.6 (dd, J_{AB} = 49 Hz, J_{BC} = 308 Hz, P_B), 119.1 (dd, J_{AC} = 32 Hz, P_A), 119.9 (dd, P_C). $^{19}F\{^1H\}$ NMR ($CDCl_3$, ppm): δ −74.9 (s).

Compound **2c**, L′ = PPh(OMe)$_2$: Yield ⩾ 28%. M.p. 182 °C. $\Lambda_{M(nitromethane)}$ = 3.2 Ω^{-1} cm^2 mol^{--1}. *Anal.* Calc. for $C_{38}H_{35}O_8P_3F_3Re$: C, 47.7; H, 3.7. Found: C, 48.1; H, 3.7%. FAB MS: *m*/*z* (referred to the most abundant isotopes): 956 (42.0%) [M]; 928 (45.9%) [M−CO]; 843 (88.7%) [M−O_2CCF_3]; 758 (100%) [M−CO−L′]; 645 (5.0%) [M−CO−L′−O_2CCF_3]. IR (cm^{-1}) ν_{CO}: 1974, 1877; $\nu_{asym(OCO)}$: 1697; $\nu_{sym(OCO)}$: 1403. ^{1}H NMR ($CDCl_3$, ppm): δ 7.64–7.26 [m, 25H, Ph (L+L′)], 4.54 [m, 1H, –CH_2CH_2–(L)], 4.06 [m, 2H, –CH_2CH_2–(L)], 3.94 [m, 1H, –CH_2CH_2–(L)], 3.40 [d, 3H, J_{HP} = 11 Hz, –CH_3(L′)], 3.31 [d, 3H, J_{HP} = 11 Hz, –CH_3 (L′)]. $^{31}P\{^1H\}$ NMR ($CDCl_3$, ppm) (see Scheme 1 for labelling): δ 116.3 (dd, J_{AB} = 34 Hz, J_{BC} = 251 Hz, P_B), 117.8 (dd, J_{AC} = 33 Hz, P_A), 143.9 (dd, P_C). $^{19}F\{^1H\}$ NMR ($CDCl_3$, ppm): δ −74.8 (s).

Compound **2d**, L′ = PPh(OEt)$_2$: Yield ⩾ 59%. M.p. 177 °C. $\Lambda_{M(nitromethane)}$ = 4.1 Ω^{-1} cm^2 mol^{-1}. *Anal.* Calc. for $C_{40}H_{39}O_8P_3F_3Re$: C, 48.8; H, 4.00. Found: C, 48.7; H, 3.95%. FAB MS: *m*/*z* (referred to the most abundant isotopes): 984 (43.9%) [M]; 956 (46.2%) [M−CO]; 871 (82.6%) [M−O_2CCF_3]; 758 (100%) [M−CO−L′]; 645 (3.9%) [M−CO−L′−O_2CCF_3]. IR (cm^{-1}) ν_{CO}: 1993, 1888; $\nu_{asym(OCO)}$: 1694; $\nu_{sym(OCO)}$: 1406. ^{1}H NMR ($CDCl_3$, ppm): δ 7.76–7.16 [m, 25H, Ph (L+L′)), 4.55 [m, 1H, –CH_2CH_2–(L)], 4.05 [m, 1H, –CH_2CH_2–(L)], 3.88 [m, 2H, –CH_2CH_2–(L)], 3.40–3.70 [m, 4H, –CH_2–(L′)], 1.07 [t, 3H, J_{HH} = 7 Hz, –CH_3 (L′)], 1.00 [t, 3H, J_{HH} = 7 Hz, –CH_3 (L′)]. $^{31}P\{^1H\}$ NMR ($CDCl_3$, ppm) (see Scheme 1 for labelling): δ 115.4 (dd, J_{AB} = 37 Hz, J_{BC} = 269 Hz, P_B), 118.6 (dd, J_{AC} = 33 Hz, P_A), 138.2 (dd, P_C). $^{19}F\{^1H\}$ NMR ($CDCl_3$, ppm): δ −74.8 (s).

Compound **2e**, L′ = PPh$_2$(OMe): Yield ⩾ 40%. M.p. 174 °C. $\Lambda_{M(nitromethane)}$ = 3.5 Ω^{-1} cm^2 mol^{-1}. *Anal.* Calc. for $C_{43}H_{37}O_7P_3F_3Re$: C, 51.5; H, 3.7. Found: C, 51.4; H, 3.7%. FAB MS: *m*/*z* (referred to the most abundant isotopes): 1003 (11.7%) [M+1]; 974 (7.7%) [M−CO]; 889 (32.2%) [M−O_2CCF_3]; 758 (100%) [M−CO−L′]; 645 (7.6%) [M−CO−L′−O_2CCF_3]. IR (cm^{-1}) ν_{CO}: 1973, 1872; $\nu_{asym(OCO)}$: 1695; $\nu_{sym(OCO)}$: 1406. ^{1}H NMR ($CDCl_3$, ppm): δ 7.65–7.19 [m, 30H, Ph (L+L′)], 4.31 [m, 1H, –CH_2CH_2–(L)], 3.91 [m, 3H, –CH_2CH_2–(L)], 2.88 [t, 3H, J_{HP} = 6 Hz, –CH_3(L′)]. $^{31}P\{^1H\}$ NMR ($CDCl_3$, ppm) (see Scheme 1 for labelling): δ 115.2 (d_{app}, J_{app} = 33 Hz, P_B+P_C), 117.2 (t_{app}, P_A). $^{19}F\{^1H\}$ NMR ($CDCl_3$, ppm): δ −75.0 (s).

Compound **2f**, L′ = PPh$_2$(OEt): Yield ⩾ 44%. M.p. 170 °C. $\Lambda_{M(nitromethane)}$ = 3.2 Ω^{-1} cm^2 mol^{-1}. *Anal.* Calc. for $C_{44}H_{39}O_7P_3F_3Re$: C, 52.0; H, 3.97. Found: C, 49.2; H, 3.97%. FAB MS: *m*/*z* (referred to the most abundant isotopes): 1017 (31.5%) [M+1]; 988 (11.1%) [M−CO]; 903 (65.3%) [M−O_2CCF_3]; 758 (100%) [M−CO−L′]; 645 (3.8%) [M−CO−L′−O_2CCF_3]. IR (cm^{-1}) ν_{CO}: 1979, 1881; $\nu_{sym(OCO)}$: 1693; $\nu_{asym(OCO)}$: 1408. ^{1}H NMR ($CDCl_3$, ppm): δ 7.75–7.16 [m, 30H, Ph (L+L′)], 4.46 [m, 1H, –CH_2CH_2–(L)], 4.03–3.89 [m, 3H, –CH_2CH_2–(L)], 3.23 [m, 2H, –CH_2–(L′)], 0.81 [t, 3H, J_{HH} = 7 Hz, –CH_3 (L′)]. $^{31}P\{^1H\}$ NMR ($CDCl_3$, ppm) (see Scheme 1 for labelling): δ 113.8 (m, P_B+P_C), 117.5 (t_{app}, J_{app} = 32 Hz, P_A). $^{19}F\{^1H\}$ NMR ($CDCl_3$, ppm): δ −75.0 (s).



Scheme 1.

2.3. X-ray crystallography

Single crystals of compounds **1** and **2a** were mounted on a glass fibre and studied on a Bruker Smart CCD area-detector diffractometer using graphite-monochromated Mo Kα radiation (λ = 0.71073 Å). The crystal parameters and experimental details for data collection are summarized in Table 1. Absorption corrections were carried out using SADABS [8]. The structures were solved with the OSCAIL program [9] by the Patterson method and refined by full-matrix least-squares based on F^2 [10]. All non-hydrogen atoms were refined with anisotropic displacement parameters. The hydrogen atoms were included in idealised positions and refined with isotropic displacement parameters. Atomic scattering factors and anomalous dispersion corrections for all atoms were taken from the International Tables for X-ray Crystallography [11]. Details of crystal data and structural refinement are given in Table 1.

Table 1
Crystal data and structure refinement for compounds **1** and **2a**.

	1	**2a**
Empirical formula	$C_{62}H_{48}F_6O_{14}P_4Re_2$	$C_{33}H_{33}F_3O_9P_3Re$
Formula weight	1627.28	909.70
Crystal size (mm)	0.67 × 0.39 × 0.12	0.22 × 0.08 × 0.07
T (K)	293(2)	293(2)
Wavelength (Å)	0.71073	0.71073
Crystal system	triclinic	monoclinic
Space group	$P\bar{1}$	$P2_1/c$
a (Å)	10.1231(5)	12.0956(10)
b (Å)	17.9762(9)	17.4771(15)
c (Å)	18.5233(9)	17.1160(14)
α (°)	67.5350(10)	90
β (°)	87.8420(10)	90.309(2)
γ (°)	89.5730(10)	90
V (Å^3)	3112.7(3)	3618.2(5)
Z	2	4
Density (calc.) (Mg/m^3)	1.736	1.670
μ (mm^{-1})	4.070	3.557
F(0 0 0)	1592	1800
θ Range for data collection (°)	2.01–28.01	1.67–17.99
Index ranges	$-13 \leqslant h \leqslant 11$, $-23 \leqslant k \leqslant 23$, $-20 \leqslant l \leqslant 24$	$-10 \leqslant h \leqslant 10$, $-11 \leqslant k \leqslant 15$, $-13 \leqslant l \leqslant 14$
Reflections collected	18 666	8412
Independent reflections (R_{int})	13 127(0.0762)	2468(0.0660)
Reflections observed (>2σ)	9663	1767
Data completeness	0.871	0.990
Max. and min. transmission	1.000 and 0.234	1.000 and 0.719
Data/restraints/parameters	13 127/0/793	2468/0/445
Goodness-of-fit on F^2	0.961	0.771
Final R indices [I>2$\sigma(I)$]	R_1 = 0.0681, wR_2 = 0.1721	R_1 = 0.0282, wR_2 = 0.0435
R indices (all data)	R_1 = 0.0853, wR_2 = 0.1819	R_1 = 0.0551, wR_2 = 0.0480
Largest difference in peak and hole (e Å^{-3})	4.241 and −3.922	0.309 and −0.355

3. Results and discussion

3.1. Synthesis

The bromo complexes [ReBr(CO)$_3$(L)] [5a] and [ReBr(CO)$_2$LL′] [6] [L = $Ph_2POCH_2CH_2OPPh_2$, L′ = $PPh_n(OR)_{3-n}$ n = 0–2] reacted with an excess of AgO_2CCF_3 in refluxing dichloromethane to give [Re(O_2CCF_3)(CO)$_3$L] (**1**) and [Re(O_2CCF_3)(CO)$_2$LL′] (**2**), respectively, as beige (**1**) or white (**2**) solids (Scheme 1). The new complexes are air-stable in the solid state and in solution at room temperature, and were characterized by elemental analysis, IR spectroscopy, mass spectrometry and, in the cases of compounds **1** and **2a**, by X-ray diffraction. Conductivity measurements on nitromethane solutions of the compounds show values that are consistent with non-electrolyte behaviour, in agreement with the coordination of the trifluoroacetate anion to the rhenium atom. The compounds were also studied in solution by NMR spectroscopy.

3.2. Description of the structures

3.2.1. [Re(O_2CCF_3)(CO)$_3$(L)] (*1*)

An ORTEP [12] drawing of the two molecules in the asymmetric unit, along with the numbering scheme adopted, is shown in Fig. 1. Selected bond lengths and bond angles are listed in Table 2. The asymmetric unit contains two different molecules with identical formulae. Both consist of a rhenium(I) atom coordinated in an octahedral arrangement by three *facially* disposed carbonyl ligands, two phosphorus atoms of the chelating phosphinite ligand $Ph_2POCH_2CH_2OPPh_2$, and an oxygen atom of a trifluoroacetate ion acting as a monodentate ligand. The main differences between the two molecules in the asymmetric unit are: (i) the seven-membered chelate ring adopts a twisted boat conformation [13] in molecule 1 whereas it adopts a twisted chair conformation [13] in molecule 2; (ii) the chelate angles are 86.5(1)° [Re(1)] and 90.0(1)° [Re(2)]; (iii) molecule 1 has surrounding Re(1) parameters that are more distorted from the ideal octahedral geometry than those for molecule 2; (iv) the orientation of the carboxylate moiety [C–CO_2] is different in the two molecules, being directed towards the bisector of the two CO ligands in molecule 1 [torsion angles 38.3(4) and 52.8(4)°] and almost parallel to one of them [torsion angle 1.3(6)°] and perpendicular to the other in molecule 2.

The Re–P bond lengths span from 2.431(2) to 2.456(2) Å, a narrower range than that found in the closely related triflato complex [Re(OSO_2CF_3)(CO)$_3$(L)] [5b]. The Re–C bond lengths range from 1.87(1) to 2.00(1) Å, and they are similar to those of the triflato complex [5b]. The Re–C bond distances *trans* to the phosphorus atoms are, on average, 0.08 Å longer than that *trans* to the oxygen atom, a greater but comparable difference, than that observed for the triflato complex (0.06 Å) [5b]. Those values are also in a comparable range to that found for other *fac*-tricarbonyl Re(I) complexes bearing related diphosphinite ligands [5c].

The trifluoroacetate group acts as a monodentate ligand in a similar way to other rhenium(I) compounds bearing this group as a ligand [14]. The OCO angle (∼129°) and the O–C bond lengths of the carboxylate moiety (1.20–1.23 Å), which are near to the ionic limit (1.250 Å) as defined by Hocking and Hambley [15], are indicative of a high ionic character (>90%) for the carboxylate–rhenium interaction.

3.2.2. [Re(O_2CCF_3)(CO)$_2$(L){P(OMe)$_3$}] (*2a*)

An ORTEP [12] drawing of the molecule, along with the numbering scheme adopted, is shown in Fig. 2. Selected bond lengths and bond angles are listed in Table 3. The compound consists of a rhenium(I) atom coordinated by two *cis* carbonyl ligands, two phosphorus atoms of the chelating bidentate phosphinite ligand $Ph_2POCH_2CH_2OPPh_2$, another phosphorus atom from a trimethylphosphite ligand and an oxygen atom of a trifluoroacetate group, which acts as a monodentate ligand. This arrangement results in an octahedral arrangement around the metal atom. The three phosphorus atoms are in meridional positions. The Re–C

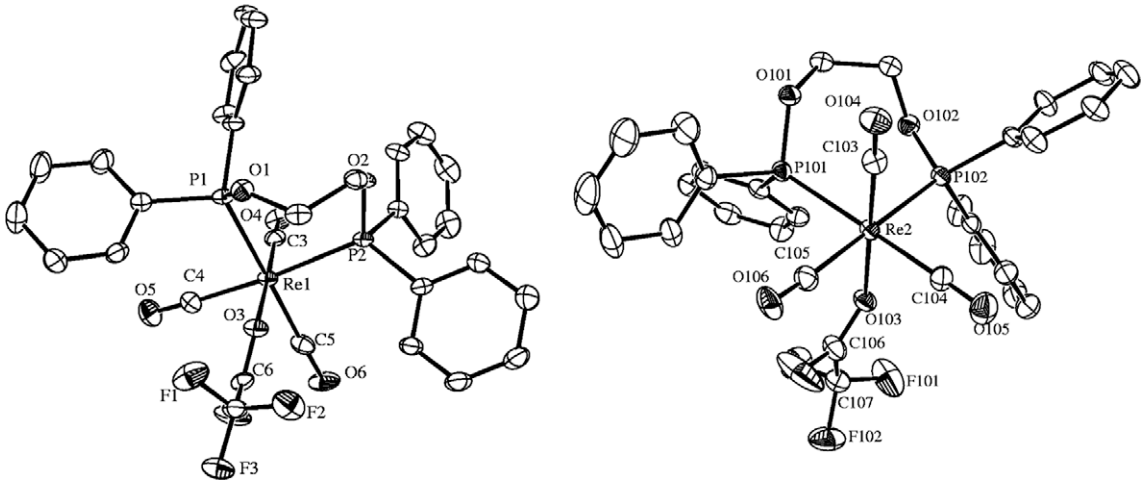


Fig. 1. Molecular structure of molecules 1 (left) and 2 (right) of compound **1**.

bond distances are 1.864(12) and 1.914(13) Å, with the shorter one corresponding to that *trans* to the trifluoroacetate ion. The bidentate phosphinite ligand shows two different Re–P bond lengths, 2.402(3) and 2.467(3) Å, with the shorter one corresponding to that *trans* to the phosphite ligand. The geometrical parameters for the trifluoroacetate ligand are similar to those observed for **1** and are consistent with its monodentate behaviour. The *cis* angles range from 82.2(2) to 95.9(4)°. It is noteworthy that the most distorted values are those of the trifluoroacetate ligand, probably due to the steric requirements of the phenyl groups of the bidentate phosphinite ligand in the direction of the position occupied by the trifluoromethyl group. In fact, the carboxylate moiety of the trifluoroacetate ligand is not parallel to any other ligand, but is directed towards the free space between a carbonyl and the phosphite ligand with very different torsion angles: 21.8(4)° with the carbonyl ligand and 69.9(3)° with the phosphite ligand [vectors defined as O(4)–O(3) versus Re–O(2) and Re–P(3)]. The seven-membered chelate ring adopts a twisted boat conformation [13] with a chelate P(1)–Re–P(2) angle of 87.8(1)°.

Table 2
Selected bond lengths [Å] and angles [°] for compound **1**.

Re(1)–C(3)	1.874(10)	Re(2)–C(103)	1.909(10)
Re(1)–C(4)	1.981(11)	Re(2)–C(104)	1.937(10)
Re(1)–C(5)	1.954(11)	Re(2)–C(105)	1.999(11)
Re(1)–P(1)	2.456(2)	Re(2)–P(101)	2.449(2)
Re(1)–P(2)	2.433(2)	Re(2)–P(102)	2.431(2)
Re(1)–O(3)	2.175(6)	Re(2)–O(103)	2.185(7)
C(3)–O(4)	1.179(11)	C(103)–O(104)	1.123(12)
C(5)–O(6)	1.150(12)	C(105)–O(106)	1.115(12)
C(4)–O(5)	1.106(12)	C(104)–O(105)	1.137(12)
O(3)–C(6)	1.214(11)	O(103)–C(106)	1.218(13)
O(7)–C(6)	1.230(12)	O(107)–C(106)	1.205(16)
C(3)–Re(1)–C(5)	89.6(4)	C(103)–Re(2)–C(105)	88.1(5)
C(3)–Re(1)–C(4)	87.1(4)	C(103)–Re(2)–C(104)	91.9(4)
C(3)–Re(1)–P(1)	96.5(3)	C(103)–Re(2)–P(102)	92.5(3)
C(5)–Re(1)–C(4)	90.5(4)	C(104)–Re(2)–C(105)	88.6(4)
C(5)–Re(1)–O(3)	91.2(3)	C(105)–Re(2)–O(103)	93.5(4)
C(4)–Re(1)–O(3)	91.7(3)	C(104)–Re(2)–O(103)	89.4(4)
C(3)–Re(1)–P(2)	88.5(3)	C(103)–Re(2)–P(101)	86.5(3)
C(5)–Re(1)–P(2)	92.3(3)	C(105)–Re(2)–P(101)	89.7(3)
O(3)–Re(1)–P(1)	82.76(17)	O(103)–Re(2)–P(102)	85.81(19)
O(3)–Re(1)–P(2)	92.64(19)	O(103)–Re(2)–P(101)	92.3(2)
C(4)–Re(1)–P(1)	91.2(3)	C(104)–Re(2)–P(102)	91.7(3)
P(2)–Re(1)–P(1)	86.50(8)	P(102)–Re(2)–P(101)	90.00(8)
C(4)–Re(1)–P(2)	174.8(3)	C(104)–Re(2)–P(101)	177.7(3)
C(3)–Re(1)–O(3)	178.6(3)	C(103)–Re(2)–O(103)	178.0(3)
C(5)–Re(1)–P(1)	173.7(3)	C(105)–Re(2)–P(102)	179.2(3)

3.3. Spectroscopic studies

The IR spectrum of compound **1** shows three strong ν(CO) bands that are characteristic of the *fac*-Re^{I}(CO)$_3$ fragment [16] at 2041, 1967 and 1932 cm^{-1}. These bands are displaced to higher wavenumbers with respect to the precursor complex [ReBr(CO)$_3$(L)] [5a], in agreement with a minor electronic back-donation of the

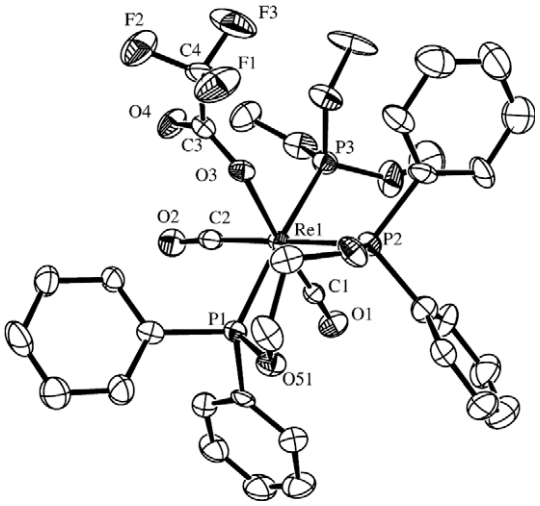
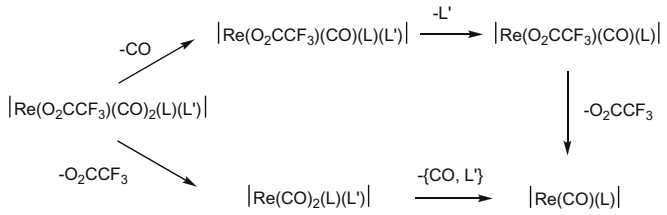


Fig. 2. Molecular structure of compound **2a**.

Table 3
Selected bond lengths [Å] and angles [°] for compound **2a**.

Re(1)–C(1)	1.864(12)	Re(1)–C(2)	1.914(13)
Re(1)–O(3)	2.175(8)	Re(1)–P(3)	2.362(3)
Re(1)–P(1)	2.402(3)	Re(1)–P(2)	2.467(3)
C(1)–O(1)	1.174(11)	C(2)–O(2)	1.164(12)
O(3)–C(3)	1.264(13)	O(4)–C(3)	1.218(13)
C(1)–Re(1)–C(2)	86.7(5)	C(1)–Re(1)–O(3)	175.0(4)
C(2)–Re(1)–O(3)	95.9(4)	C(1)–Re(1)–P(3)	87.2(3)
C(2)–Re(1)–P(3)	91.2(3)	O(3)–Re(1)–P(3)	88.5(2)
C(1)–Re(1)–P(1)	88.8(3)	C(2)–Re(1)–P(1)	90.2(3)
O(3)–Re(1)–P(1)	95.4(2)	P(3)–Re(1)–P(1)	175.71(11)
C(1)–Re(1)–P(2)	95.4(4)	C(2)–Re(1)–P(2)	177.1(4)
O(3)–Re(1)–P(2)	82.2(2)	P(3)–Re(1)–P(2)	90.95(11)
P(1)–Re(1)–P(2)	87.79(11)		



Scheme 2. Fragmentation pathways for compounds **2a**–**f**.

rhenium atom to the CO ligands due to the replacement of Br by the trifluoroacetate ligand. Similarly, the IR spectra of compounds **2** display two strong ν(CO) bands, characteristic of *cis*-dicarbonyl compounds [6,17], and these are also displaced to higher energy with respect to the [ReBr(CO)$_2$(L)(L′)] compounds [6]. On the other hand, compounds **1** and **2** display a strong band at 1692–1697 cm^{-1} and a medium band at 1403–1418 cm^{-1} due to the asymmetric and symmetric modes of the carboxylate group of the O_2CCF_3 ligand [18]. The energy difference between the two bands is related to the coordination type of the carboxylate ligand and, in our case, this is in accordance ($\sim$290 cm^{-1}) with a monodentate behaviour of the ligand in all the complexes [19]. The X-ray diffraction studies of complexes **1** and **2a** confirm this behaviour.

The ^{1}H NMR spectrum of compound **1** does not show any relevant differences compared with that of the precursor. However, the ^{31}P{^{1}H} NMR spectrum of **1** shows a singlet at a lower field (δ = 116.5 ppm) than that of the precursor (δ = 105.3 ppm), as expected because of the electron-withdrawing characteristics of the trifluoromethyl group. In the case of compounds **2**, the ^{1}H NMR signals of the –CH_2CH_2– group of the bidentate phosphinite ligand (which appear as three multiplets with intensities 1:1:2 in the spectra of the parent bromide complexes), are two multiplets with intensities 1:3, except for compounds **2c** and **2d** in which they appear as three 1:2:1 and 1:1:2 multiplets, respectively. In all cases, these multiplets span in a similar but narrower region than those of the bromide precursors. On the other hand, the signals of the OR groups of the monodentate mixed-phosphite ligands, are similar to those of the parent bromide complexes but slightly upfield shifted. Compounds **2a**–**d** display ^{31}P{^{1}H} NMR spectra that are consistent with an ABM spin system (three double doublets), but compounds **2e**–**f** show signals corresponding to ABC and A_2B spin systems [20], respectively, reflecting the similarity between the P nuclei of both bidentate and monodentate phosphinite ligands. In all cases the signals are shifted downfield when compared to their bromide analogues. These shifts are consistent with the IR data discussed above and are in accordance with the presence of the more electron-withdrawing trifluoroacetate group, which reduces the rhenium π-back-donation to the phosphorus ligands. The mass spectra of compounds **2a**–**f** show, in all cases, five sets of peaks (see Section 2) displaying the rhenium isotope pattern. This allows us to propose possible fragmentation pathways for these compounds that would give rise to the identified fragments (Scheme 2).

The most abundant peak is, in all cases (except for **2a** – although in this case its abundance is also very high, 95.6%), that at m/z = 758, corresponding to loss of a carbonyl and the monodentate L′ ligand.

4. Conclusions

The synthesis and structural characterization of trifluoroacetatecarbonylrhenium(I) complexes bearing different mono- and bidentate mixed-phosphite ligands are described. The new complexes were prepared by the reaction of the parent bromo-complexes with silver trifluoroacetate. All the complexes were studied by spectroscopic techniques and, in the cases of complexes **1** and **2a**, structures in the solid state were determined by X-ray diffraction. In all cases the trifluoroacetate ligand behaves in a monodentate manner.

Supplementary data

CCDC 719369 and 719370 contains the supplementary crystallographic data for compounds **1** and **2a**, respectively. These data can be obtained free of charge via http://www.ccdc.cam.ac.uk/conts/retrieving.html, or from the Cambridge Crystallographic Data Centre, 12 Union Road, Cambridge CB2 1EZ, UK; fax: (+44) 1223-336-033; or e-mail: deposit@ccdc.cam.ac.uk.

Acknowledgements

Financial support from the Xunta de Galicia (Project PGIDT04PXIC31401PN) and the Spanish Ministry of Education (Project BQU2003-06783) is gratefully acknowledged. We thank the University of Vigo CACTI services for collecting X-ray data and recording NMR spectra.

References

[1] T.G. Spiro, M.Z. Zgierski, P.M. Kozlowski, Coord. Chem. Rev. 219–221 (2001) 923.
[2] T.G. Spiro, I.H. Wasbotten, J. Inorg. Biochem. 99 (2005) 34.
[3] C. Elschenbroich, in: Organometallics, third ed., Wiley-VCH, Weinheim, 2006.
[4] (a) C.A. Tolman, Chem. Rev. 77 (1977) 313;
(b) M.M. Rahaman, H.Y. Liu, K. Eriks, A. Prock, W.P. Giering, Organometallics 8 (1981) 1.
[5] (a) S. Bolaño, J. Bravo, R. Carballo, S. García-Fontán, U. Abram, E.M. Vázquez-López, Polyhedron 18 (1999) 1431;
(b) M.C. Rodríguez, J. Bravo, E. Freijanes, E. Oñate, S. García-Fontán, P. Rodríguez-Seoane, Polyhedron 23 (2004) 1045;
(c) S. Bolaño, J. Bravo, J. Castro, S. García-Fontán, M.C. Marín, P. Rodríguez-Seoane, J. Organomet. Chem. 690 (2005) 4945.
[6] F. Fernández-García, S. Bolaño, R. Carballo, S. García-Fontán, J. Bravo, Polyhedron 20 (2001) 2675.
[7] D.D. Perrin, W.L.F. Armarego, Purification of Laboratory Chemicals, third ed., Butterworth and Heinemann, Oxford, 1988.
[8] G.M. Sheldrick, SADABS. An Empirical Absorption Correction Program for Area Detector Data, University of Göttingen, Germany, 1996.
[9] P. McArdle, J. Appl. Cryst. 28 (1995) 65.
[10] G.M. Sheldrick, SHELX-97, Program for the Solution and Refinement of Crystal Structures, University of Göttingen, Germany, 1997.
[11] International Tables for X-ray Crystallography, vol. C, Kluwer, Dordrecht, 1992.
[12] L.J. Farrugia, J. Appl. Cryst. 30 (1997) 565.
[13] E.L. Eliel, S.H. Wilen, Stereochemistry of Organic Compounds, Wiley, New York, 1994. p. 764.
[14] (a) A. Egli, K. Hegetschweiler, R. Alberto, U. Abram, R. Schibli, R. Hedinger, V. Gramlich, R. Kissner, P.A. Schubiger, Organometallics 16 (1997) 1833;
(b) S.J. Dossett, M. Green, M.F. Mahon, J.M. McInnes, C. Vaughan, J. Chem. Soc., Dalton Trans. (1997) 3671;
(c) F. Tisato, F. Refosco, A. Moresco, G. Bandoli, A. Dolmella, C. Bolzati, Inorg. Chem. 34 (1995) 1779;
(d) S. Feracin, T. Buergi, V.I. Bakhmutov, I. Eremenko, E.V. Vorontsov, A.B. Vimenits, H. Berke, Organometallics 13 (1994) 4194.
[15] R.K. Hocking, T.W. Hambley, Inorg. Chem. 42 (2003) 2833.
[16] L.H. Staal, A. Oskam, K. Vrieze, J. Organomet. Chem. 170 (1979) 235.
[17] G. Albertin, S. Antoniutti, S. Garcia-Fontán, R. Carballo, F. Padoan, J. Chem. Soc., Dalton Trans. (1998) 2071.
[18] K. Nakamoto, Infrared and Raman Spectra of Inorganic and Coordination Compounds, fifth ed., John Wiley and Sons, 1997.
[19] (a) D.H. Gibson, Y. Ding, R.L. Miller, B.A. Sleadd, M.S. Mashuta, J.F. Richardson, Polyhedron 18 (1999) 1189;
(b) G.B. Deacon, R.J. Phillips, Coord. Chem. Rev. 33 (1980) 227.
[20] P.H.M. Budzelaar, gNMR Version 4.1, Cherwell Scientific Limited, Oxford, 1999.

Polyhedron 28 (2009) 2436–2442

Contents lists available at ScienceDirect

Polyhedron

journal homepage: www.elsevier.com/locate/poly

Synthesis, crystal structures and magnetic behaviors of two dicyanamide bridged di- and polynuclear complexes of cobalt(II) derived from 2,4,6-tris(2-pyridyl)1,3,5-triazine and imidazole

Anamika Das [a], Christoph Marschner [b], Joan Cano [c,d], Judith Baumgartner [b], Joan Ribas [c], M. Salah El Fallah [c,*], Samiran Mitra [a,*]

[a] Department of Chemistry, Jadavpur University, Raja S.C. Mallik Road, Kolkata, West Bengal 700032, India
[b] Institut für Anorganische Chemie, Technische Universität Graz, Austria
[c] Departament de Química Inorgànica, Universitat de Barcelona, Martí i Franquès, 1-11, 08028-Barcelona, Spain
[d] Centre de Recerca en Química Teórica, Universitat de Barcelona, Institució Catalana de Recerca i Estudis Avançats (ICREA), Spain

ARTICLE INFO

Article history:
Received 27 February 2009
Accepted 20 April 2009
Available online 3 May 2009

Keywords:
Cobalt(II)
Tptz
Dca
Imz
Magnetic property

ABSTRACT

Two new dicyanamido-bridged di- and polynuclear complexes of Co(II), $[Co(dca)(tptz)(H_2O)]_2 \cdot 2(ClO_4)$ (**1**) and $[Co(dca)_2(imz)_2]_n$ (**2**) [dca, dicyanamide; tptz, 2,4,6-tris(2-pyridyl)1,3,5-triazine; and imz, imidazole] have been synthesized and characterized structurally, as well as magnetically. The X-ray single crystal structure determination of complex **1** shows that two symmetry related octahedral Co(II) ions are separated by dca ligand and other coordination sites are satisfied by tptz and aquo ligands. Each dinuclear unit is associated with each other by intramolecular hydrogen bonding interactions, giving rise to a 1D chain structure. On the other hand complex **2** is a 1D coordination polymer having $[Co(II)(imz)_2]$ units connected by double bridging dca ligands. These 1D chains interact through face-to-face π–π stacking interactions of the imz rings extending the dimensionality to a 2D supramolecular network. The variable temperature (300–2 K) magnetic measurements of both compounds reveal that dicyanamide exhibits a weak antiferromagnetic interaction between the metal centers.

© 2009 Elsevier Ltd. All rights reserved.

1. Introduction

In the past few decades, tremendous progress has been made in supramolecular chemistry. A large number of beautiful and functional supramolecular architectures have been constructed, starting with well-defined building blocks via self-assembly process [1–4]. In this process, the small molecular building blocks that recognizes each other through direction specific molecular interactions such as coordination bonds, hydrogen bond, π–π stacking and C–H–π interaction etc. to form the extended architecture [5]. The particular attractive is the novel type of structural motifs, like honeycomb, grid, interdigitation, different degree of interpenetration, three dimensional channels are obtained depending upon the metal ions and organic linkers with different tunable properties [1–5]. One strategy to build an extended network is to utilize certain features of the bridging ligands, such as azide, [6] dicyanamide [7], carboxylate [8] and different neutral organic spacer [9] having versatile binding modes, conformational flexibility and the ability to form non-covalent interactions [10].

Among the abovementioned bridging ligand, dca acts as a remarkable building blocks for the construction of various functional coordination architectures such as discrete mononuclear, dinuclear, as well as 1D chains, tubes, or ladders, 2D sheets and 3D supramolecular networks, when terminal or bridging coligands (L) are introduced to form M–dca–L system having important magnetic property [11–16]. The different coordination modes of dca such as terminal, bidentate, tridentate and unusual μ_4-dca towards metal ions plays an important role for the construction of extended architecture [7].

The magnetic properties of polynuclear architecture depend on the nature of the paramagnetic metal center *i.e.* the spin state, the dimensionality of the system and on the type of bridging ligands. Although dca can mediate only weak interactions between paramagnetic metal centers and a few multidimensional dca bridged compounds exhibit long-range ferromagnetic ordering [7]. Among the first row transition metal ions containing an unpaired electron, the magnetic properties of Co(II) complexes are interesting and are affected by the several factors such as single-ion effects, spin–orbit coupling, distortion from regular stereochemistry, electron delocalization, crystal field mixing of the excited states into the ground

* Corresponding authors. Tel.: +91 33 2668 2017; fax: +91 33 2414 6414 (S. Mitra).
E-mail addresses: christoph.marschner@tugraz.at (C. Marschner), baumgartner@tugraz.at (J. Baumgartner), salah.elfallah@qi.ub.es (M.S. El Fallah), smitra_2002@yahoo.com (S. Mitra).

0277-5387/$ - see front matter © 2009 Elsevier Ltd. All rights reserved.
doi:10.1016/j.poly.2009.04.024

state etc. [17]. Thus, the interpretation of these magnetic results is challenging. To date, the synthesis of high spin polynuclear Co(II) complexes and their magnetic study at low temperature have been reported by several groups [18,19]. In contrast, there are only a few examples of structurally as well as magnetically characterized dca bridged discrete dinuclear compounds [15,16].

In this paper, we report the synthesis, structural characterizations and hence magnetic properties of two cobalt coordination compounds $[Co(dca)(tptz)(H_2O)]_2{\cdot}2(ClO_4)$ (**1**), $[Co(dca)_2(imz)_2]_n$ (**2**) [where dca = dicyanamide; tptz = 2,4,6-tris(2-pyridyl)1,3,5-triazine; and imz, imidazole]. Here, dca is used as a bridging ligand and coordination environment is varied by N-donor ligands *i.e.* tptz for complex **1**, and imz for complex **2**. In complex **1**, two symmetry related Co(II) atoms are separated through nitrile nitrogen atoms of dca ligand and tptz act as a chelating ligand. Each dinuclear unit is connected to each other by H-bonding forming 1D stair-case like structure. To the best of our knowledge this is the first example of dinuclear Co(II) complex bridged by dca ligand. Whereas complex **2** is a doubly end-to-end dca bridged 1D coordination polymer with trans coordinated imz ligands. The overall structure is stabilized by face-to-face π–π stacking and H-bonding interactions arising among the imz ligands. Variable temperature magnetic study of these complexes reveals weak antiferromagnetic coupling between the metal centers.

2. Experimental

2.1. Physical techniques

Elemental analyses were carried out using a Perkin–Elmer 2400 II elemental analyzer. Infrared spectra were recorded on a Perkin–Elmer RX I FT-IR spectrophotometer using KBr pellets. Magnetic measurements were carried out in the "Servei de Magnetoquímica Universitat de Barcelona" on polycrystalline sample with a Quantum Design MPMS SQUID susceptometer operating at a magnetic field of approximately 1000 G between 2 and 300 K. The diamagnetic corrections were evaluated from Pascal's constants for all the constituent atoms.

2.2. Materials

High-purity 2,4,6-tris(2-pyridyl)-1,3,5-triazine and imidazole were purchased from the Aldrich Chemical Co. Inc. and used without further purification. High purity sodium dicyanamide was obtained from Fluka. All other chemicals were of AR grade.

Caution: Perchlorate salts are potentially explosive in the presence of organic compounds. Only a small amount of the materials should be prepared and handled with care.

2.3. Syntheses

2.3.1. Synthesis of $[Co(dca)(tptz)(H_2O)]_2{\cdot}2(ClO_4)$ (**1**)

A methanolic solution of tptz (0.5 mmol, 0.15 g) was added to an aqueous solution (5 mL) of $Co(ClO_4)_2{\cdot}6H_2O$ (1 mmol, 0.365 g) and sodium dicyanamide (2 mmol, 0.17 g) with continuous stirring for about 20 min. The resulting solution was filtered and the filtrate was kept at room temperature. After five days, orange crystals suitable for X-ray diffraction were obtained from the filtrate. Yield 84%. *Anal.* Calc. for **1** $C_{40}H_{28}Co_2N_{18}O_22(ClO_4)$: C, 43.33; H, 2.34; N, 22.75. Found: C, 43.35; H, 2.33; N, 22.71%.

2.3.2. Synthesis of $[Co(dca)_2(imz)_2]_n$ (**2**)

An aqueous solution (5 mL) of $CoCl_2{\cdot}6H_2O$ (1 mmol, 0.237 g) and sodium dicyanamide (2 mmol, 0.17 g) were mixed with constant stirring. Then an ethanolic solution of imidazole (1 mmol, 0.06 g) was added to the solution and stirred for about 30 min at room temperature. After three days, pink crystals suitable for X-ray diffraction were obtained from the filtrate. Yield 95%. *Anal.* Calc. for **2** $C_{10}H_8CoN_{10}$: C, 36.67; H, 2.44; N, 42.78. Found: C, 36.26; H, 2.45; N, 42.75%.

2.3.3. X-ray data collection and structure refinement

Single crystal X-ray diffraction study for **1** was carried out on a Bruker Smart Apex CCD diffractometer using graphite-monochromatizd Mo Kα radiation (0.71073 Å). The data were corrected for absorption by using the multi-scans program SADABS [20]. The structure was solved by direct and difference Fourier methods and refined by full-matrix least-squares on F^2 using SHELXL-97 [21] and SHELXS-97 program package [22], respectively. The single crystal data of complex **2** were collected on Enraf Nonius, CAD4 diffractometer and the structure was solved by direct methods and subsequently refined by full-matrix least-squares procedures on F^2 with allowance for anisotropic thermal motion of all non-hydrogen atoms employing the WINGX package with the relevant programs SIR-97 [23] and SHELXL-97 [22]. All non-hydrogen atoms were refined with anisotropic displacement parameters. The hydrogen atoms were placed geometrically and refined with isotropic thermal parameters. All calculations were carried out using PLATON and ORTEP-32 programs [24,25]. The unit-cell parameters, crystal system, space group and refinement details are summarized in Table 1.

3. Results and discussion

3.1. Infrared spectra

Complexes **1** and **2** display strong absorption bands at 2280, 2242 and 2162 cm^{-1}, respectively, which correspond to the ν(CN) of dca ligand [7]. The large shift towards high frequencies, compared with these of free dca (2232, 2179 cm^{-1}) confirmed that dca bridged between the metal centers. In complex **1**, the bands in the region 1645–1390 cm^{-1} and 950–900 cm^{-1} are observed

Table 1
Crystal data and structure refinements of **1** and **2**.

Sample	**1**	**2**
Empirical formula	$C_{40}H_{28}Co_2N_{18}O_2{\cdot}2(ClO_4)$	$C_{10}H_8CoN_{10}$
M	1107.55	327.19
Crystal system	triclinic	monoclinic
Space group	$P\bar{1}$ (No.2)	$P21/c$ (No.14)
a (Å)	7.7755(16)	6.5800(10)
b (Å)	10.577(2)	14.1540(10)
c (Å)	13.985(3)	7.395(2)
α (°)	70.55(3)	90
β (°)	79.30(3)	94.920(10)
γ (°)	82.02(3)	90
V (Å)	1062	686.2(2)
Z	2	2
$\lambda_{Mo\ K\alpha}$ (Å)	0.71073	0.71069
D_c [g cm^{-3}]	1.732	1.584
μ (mm^{-1})	0.992	2.758
F(0 0 0)	560	3328
θ Range (°)	1.6–24.7	2.4–26.3
Total data	7409	2759
Unique data	3548	2571
Observed data [$I > 2\sigma(I)$]	2838	1017
Nref; Npar	3548;333	257;1135
R[a]	0.0521	0.0575
R_w[b]	0.1167	0.2033
R_{int}	0.045	0.129
$\Delta\rho_{max.}$ (e^- $Å^{-3}$)	0.91	0.55
$\Delta\rho_{min.}$ (e^- $Å^{-3}$)	−0.40	−0.83

[a] $R = \sum(|F_o - F_c|)/\sum|F_o|$.
[b] $R^w = \{\sum[w(|F_o - F_c|)^2]/\sum[w|F_o|^2]\}^{1/2}$.

due to the C–N and C–C stretching and bending modes of the coordinated tptz ligand [26]. Besides this, IR spectrum of complex **1** shows absorption bands in the region of 3552–3200 cm^{-1} and 1160–1085 cm^{-1} which clearly indicate the presence of crystal water and perchlorate moiety respectively. Apart from this complex **2** a strong absorption band is observed in the range 1270–750 cm^{-1}, which may be assigned as C–C, C–N stretching and bending modes of the coordinated imz ligand.

3.2. Description of the crystal structures

3.2.1. Crystal structure of $[Co(dca)(tptz)(H_2O)]_2{\cdot}2(ClO_4)$ **1**

The ORTEP diagram of **1** (Fig. 1) shows that this is a discrete dinuclear complex where two symmetry related Co(II) atoms are separated by two dca anions in an end-to-end fashion. Each asymmetric unit contain one cobalt(II) atom which is octahedrally coordinated by three nitrogen atoms of tptz ligand, two nitrogen atoms of dca ligands and one oxygen atoms of aqua ligand. The equatorial coordination sites are composed by two nitrogen atoms (N7, N8) of bridging dca, one oxygen atom (O1) of coordinated water molecule and one nitrogen (N1) atom of central triazine ring whereas the axial coordination sites are occupied by two pyridyl nitrogen atoms (N4, N5) of tptz ligand with bond angle between them 147.30(12). Between Co-N(tptz) and Co-N(dca) bond distances (2.087(3)–2.196(3) and 2.030(4)–2.108(4) Å, respectively) the former is significantly larger. The cobalt···cobalt separation within dinuclear unit is 7.377(1) Å and comparable to similar type of $[Cd(dca)(tptz)(H_2O)]_2{\cdot}2(ClO_4)$ system [27]. The deviation from ideal octahedral geometry is reflected by bond length and angles given in Table 2.

Each dimer is connected to each other by H-bonding forming a stair-case 1D chain running along the crystallographic *a* axis (Fig. 2). The uncoordinated nitrogen atom (N6) of pyridyl ring of tptz ligand and coordinated water (H15w···N6, 2.22(6) Å, Table 3) play a role in the formation of this type of architecture. The two perchlorate counter anions present in the crystal lattice balance the electronic charge of the complex and also involved in H-bonding with coordinated water molecule (Table 3).

3.2.2. Crystal structure of $[Co(dca)_2(imz)_2]_n$ **2**

The molecular structure of **2** displays 1D polymeric pattern built up by cobalt ions, pairs of bridging dca and imz ligands (Fig. 3). The asymmetric unit contain one cobalt(II) atom which is coordinated through three nitrogen atoms coming from two bridging dca and one imz ligand, respectively. For symmetry reasons, the nitrogen atom N3, N4 and its symmetry related counter parts lie in the equatorial plane along with the cobalt atom whereas imz nitrogen atom (N1) and its symmetry related counter part lie in the trans-axial position with bond angle between them 180°. The Co–N(nitrile) bond distances of 2.161(2) and 2.164(3) Å are slightly higher than that involving the imz of 2.101(2) Å and those are comparable to similar type of $[Mn(dca)_2(im)_2]_n$ system where as im = imidazole [28]. The slight deviation from ideal octahedral geometry is due to the equatorial bond lengths and angles (Table 4). Similar to **1** here, dca anions coordinate through the nitrile nitrogen atoms and span the metals at 7.395(1) Å corresponding to the length of the crystallographic *c* axis. The metal–metal separation through the dca anions is in good agreement with the distance of 7.370 (1) Å found in the anionic dicyanamidometallate ladder–like 1D polymer $[(Ph_4As)_2\{Co_2(dca)_6(H_2O)\}{\cdot}H_2O\ CH_3OH]_n$ [29]. An interesting Hbonding network is formed by the amide nitrogen atom of the bridging dca ligands with the hydrogen atom of the secondary amine of imz ligands of a neighbouring unit (N2–H2, 0.86; H2···N5, 2.13 Å, Table 3) that leads to a supramolecular 2D arrangement. Similar type of hydrogen bonding interactions are also observed in $Co(biz)_2(dca)_2$ (biz = 2,2′biimidazole) system, where 1D chain structure is formed [30]. This 2D arrangement is further stabilized by face-to-face π–π stacking interactions arising among the imz rings and the chains are interlocked at a distance of 3.851(2) Å which is shown in Fig. 4.

Table 2
Selected bond lengths (Å) and bond angles (°) for **1**.

Co1–O1	2.168(3)	Co1–N1	2.087(3)
Co1–N4	2.176(3)	Co1–N5	2.196(3)
Co1–N7	2.108(4)	Co1–N8	2.030(4)
O1–Co1–N1	83.75(12)	O1–Co1–N4	89.64(12)
O1–Co1–N5	86.40(12)	O1–Co1–N7	173.10(13)
O1–Co1–N8	87.43(13)	N1–Co1–N4	73.53(12)
N1–Co1–N5	73.77(12)	N1–Co1–N7	102.71(13)
N1–Co1–N8	170.50(14)	N4–Co1–N5	147.30(12)
N4–Co1–N7	94.51(13)	N4–Co1–N8	110.02(13)
N5–Co1–N7	93.02(13)	N5–Co1–N8	102.22(14)
N7–Co1–N8	85.97(14)		

3.3. Magnetic study and magneto-structural correlation of **1** and **2**

The magnetic property of complex **1** in the form of $\chi_M T$ versus *T* plot (χ_M is the molar magnetic susceptibility for two Co(II) ions) is shown in Fig. 5. The value of $\chi_M T$ at 300 K is 6.019 $cm^3\ K\ mol^{-1}$ which is greater than that expected for two isolated spin-only ions ($\chi_M T$ = 3.74 $cm^3\ K\ mol^{-1}$ for two isolated $S = 3/2$ ions) indicating that an important orbital contribution is involved. The $\chi_M T$ value of complex **1** is continuously decreased from room temperature to 4.41357 $cm^3\ K\ mol^{-1}$ at 20 K. The shape of these curves until 20 K can indicate not only antiferromagnetic coupling but also

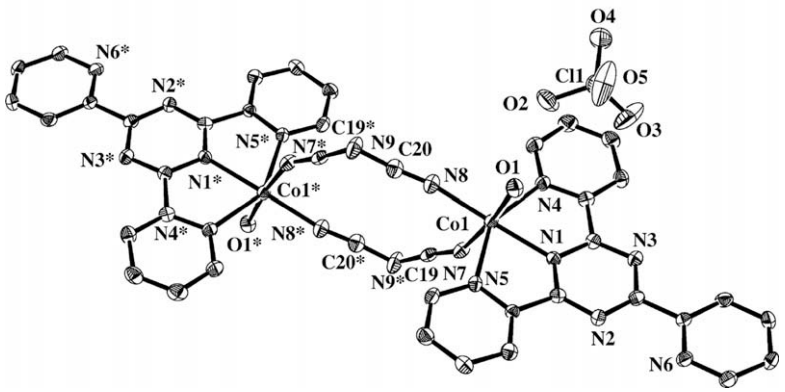


Fig. 1. ORTEP diagram (40% thermal ellipsoids) of **1** with atom labeling scheme. (Hydrogen atoms are removed for clarity.)

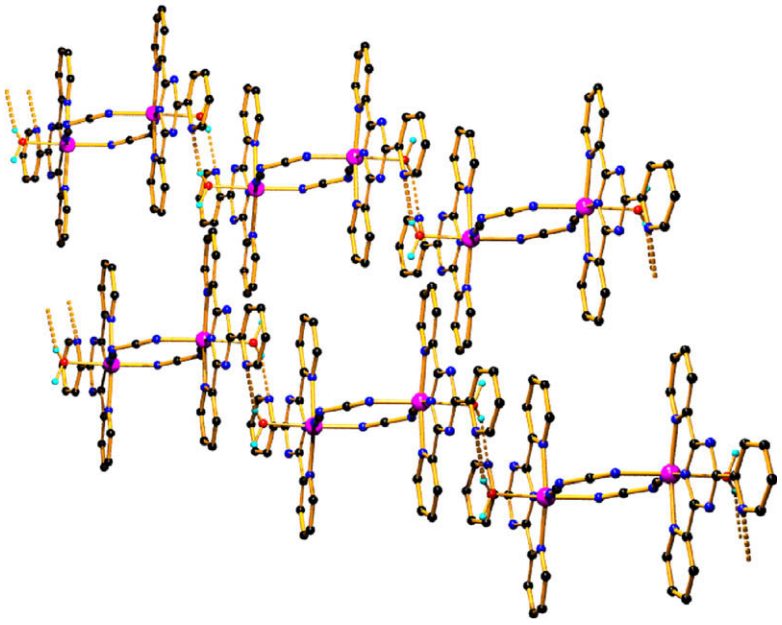


Fig. 2. H-bonded 1D chain structure of **1**. Perchlorate moieties are omitted for clarity.

spin–orbit coupling as typically observed for octahedral Co(II) ions. At low temperatures, there are significant differences in $\chi_M T$ values applying small magnetic fields which indicates the presence of a small amount of ferromagnetic or canted antiferromagnetic-ordered impurities, like α- or β-[Co(dca)$_2$] [7]. This feature (presence of magnetic ordered impurities) is very frequent in most of the Co–dca–L derivatives [18] and all calculations given below refer to the sample with the smallest amount of impurities.

On the other hand, for many years, the Lines' theory has been utilized to obtain the exchange coupling in dinuclear and trinuclear Co(II) complexes [31]. In this theory, it is assumed a perfect octahedral high-spin Co(II) complex where the single-ion excited states are well separated (>9000 cm^{-1}) from the ground state and can be neglected. The $^4T_{1g}$ ground state is split into a sextet, a quartet and a Kramers' doublet by spin–orbit coupling. The eigen values and eigen functions have been found by the diagonalization of the operator given in

$$H = -\frac{3}{2}\kappa\lambda\, L \cdot S$$

where κ and λ are the orbital reduction factor and the spin–orbit coupling parameters, respectively. The occurrence of the factor $-3/2$ is due to the analogy between the matrix elements of L within the $^4T_1$ state and that of the $-3/2L$ between the p functions. Applying Lines' formula to fit the magnetic data for dinuclear Co(II) complexes, the poor results are obtained. This is due to the lack of consideration of typical distortion with regard to the perfect octahedral geometry. Herrera et al. [32] have adapted a new method to solve this problem in mononuclear systems assuming axial distortion. In this case, the triplet orbital $^4T_{1g}$ ground state splits into a singlet $^4A_2$ and a doublet ^4E levels with a Δ energy gap.

The Hamiltonian involving the spin–orbit coupling, axial distortion and Zeeman interaction is given in

$$H = -A\kappa\lambda L \cdot S + \Delta\left[L_z^2 - \frac{1}{3}L(L+1)\right] + \mu_B(-A\kappa L + g_e S)H$$

where A, is the general factor that corresponds to 3/2 factor in Lines-equation. The factor A in the frame of T and P term isomorphism, which allows us to distinguish between the matrix elements of the orbital angular momentum operator calculated with the wave function of the ground $^4T_{1g}$ term with those calculated with P term basis. In the weak crystal field limit ($B \gg \Delta q$), $c = 0$ and $A = 1.5$ whereas in the strong crystal field limit ($B \ll \Delta q$), $c = -1/2$

Table 3
Hydrogen bonding interactions (Å, °) for **1** and **2**.

Complex	D–H···A	D–H	H···A	D···A	∠D–H···A
1	O1–H15.···N6^i	0.77(6)	2.22(6)	2.947(5)	159(7)
	O1–H14···O2	1.07(6)	1.67(6)	2.736(4)	172(5)
2	N2–H2···N5^i	0.8600	2.1300	2.942(4)	158.00

Symmetry code: i = 1–x, 1–y, –z for **1** and i = 2–x, –1/2 + y, 1/2–z for **2**.

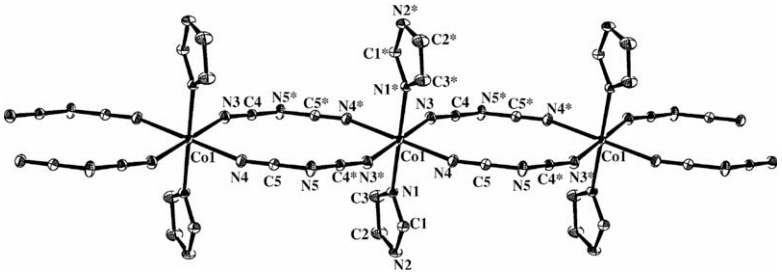


Fig. 3. The coordination environment of Co(II) ions in **2** with atom labeling scheme, thermal ellipsoids are shown in 40% probability. (Hydrogen atoms are removed for clarity.)

Table 4
Selected bond lengths (Å) and bond angles (°) for **2**.

Co1–N1	2.101(2)	Co1–N3	2.161(2)
Co1–N4	2.164(3)	Co1–N1*	2.101(2)
Co1–N3*	2.161(2)	Co1–N4*	2.164(3)
N1–Co1–N3	89.53(9)	N1–Co1–N4	89.86(9)
N1–Co1–N1*	180.00	N1–Co1–N3*	90.47(9)
N1–Co1–N4*	90.14(9)	N3–Co1–N4	89.59(9)
N1*–Co1–N3	90.47(9)	N3–Co1–N3*	180.00
N3–Co1–N4*	90.41(9)	N1*–Co1–N4	90.14(9)
N3*–Co1–N4	90.41(9)	N4–Co1–N4*	180.00
N1*–Co1–N3*	89.53(9)	N1*–Co1–N4*	89.86(9)
N3*–Co1–N4*	89.59(9)		

* Symmetry code: 1−*x*, −*y*, 1−*z*.

and $A = 1$. No analytical expression for the magnetic susceptibility, which depends on A, κ, λ and Δ can be derived. The values of these parameters have to be determined through numerical matrix diagonalization [31]. Although not yet fully developed in the literature about Co(II) dinuclear complexes, the mononuclear system can be extrapolated to a dinuclear one, introducing the J coupling parameter between the two pure $S = 3/2$ states [32]. In Fig. 6, we illustrate this new situation. Now, instead of four parameters A, κ, λ and Δ we will deal with five parameters A, κ, λ, D and J_{Co-Co}, respectively. The values of these parameters have to be determined, again through numerical matrix diagonalization and FORTRAN program adapted to do these calculations which has been performed by one of us [32]. The best-fit values found using the experimental data for $T > 25$ K were: $A\kappa = 1.36$, $\Delta = 430\ cm^{-1}$; $J_{L-S} = -163.5\ cm^{-1}$ with $R = 4.4 \times 10^{-4}$. Taking into account that $A\kappa = 1.36$ and $J_{L-S} = A\kappa\lambda$ the real λ value in this complex will be $-120\ cm^{-1}$ (λ for the free ion is $-180\ cm^{-1}$). As it is shown in the Fig. 5, the calculated curve matches well the experimental data in the temperature range 28–300 K. At $T < 25$, the magnetic data deviate from the calculated curve due to the presence of a small amount of ferromagnetic or canted antiferromagnetic-ordered impurities. Consequence of this, we cannot determine the exchange pathways J_{Co-Co} between the Co(II) atoms, which normally manifested in this range of temperatures. The field dependence of the reduced molar magnetization, $M/N\beta$, at 2 K (Fig. 7), shows a saturation value at 50 *kOe* (2.29 $N\beta$ per cobalt(II) ion). The extrapolated saturation value is ca. 4.58 $N\beta$, lie slightly above the expected value for two Co(II) centers.

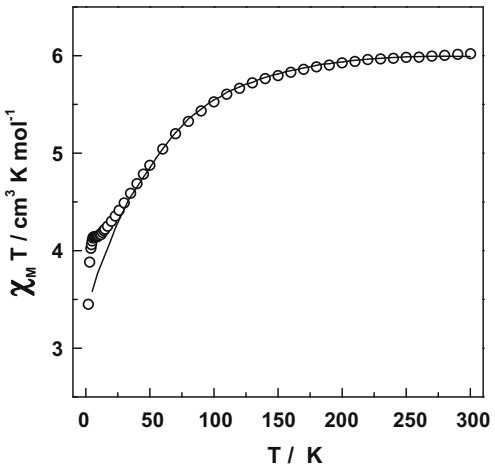


Fig. 5. Plot of the $\chi_M T$ vs T for complex **1**. Solid line represents the best fit obtained according to the method described in the text.

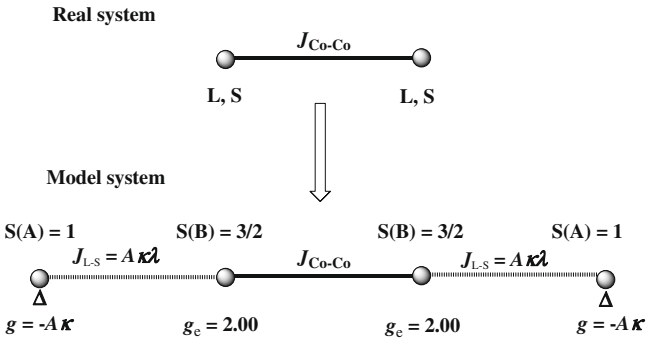


Fig. 6. Schematic representation of the spin–orbit coupling and exchange coupling parameter (J_{Co-Co}) in a dinuclear Co(II) complex.

Although for a Co(II) the ground term is $^4T_{1g}$ ($L = 1$; $S = 3/2$) the experimental $N\beta$ value at 2 K does not correspond to three unpaired electrons, because at this low temperature only the $J = 1/2$ doublet ($M_J = \pm 1/2$) is populated behaving, thus, as an effective spin $S' = 1/$

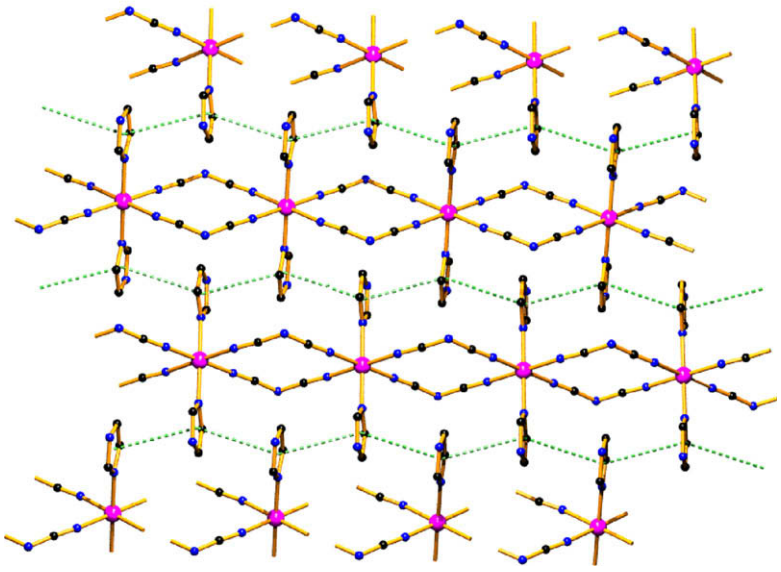


Fig. 4. Crystal packing of complex **2** showing three adjacent π interacting polymeric chains. (Hydrogen atoms are removed for clarity.)

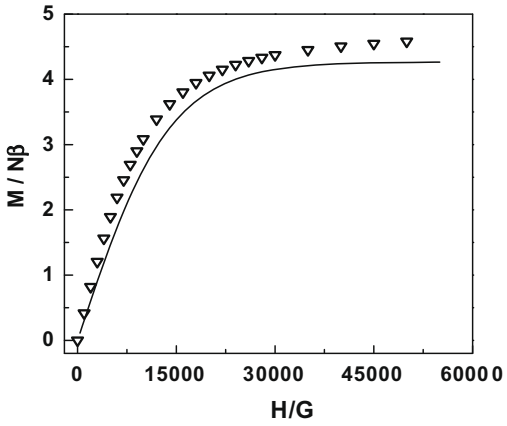


Fig. 7. Plot of the reduced magnetization ($M/N\beta$) for **1** at 2 K (for two cobalt(II) ions). Solid line represents the Brillouin formula for two Co(II) ions isolated with $S = 1$, $T = 2$ K and $A\kappa = 1.36$.

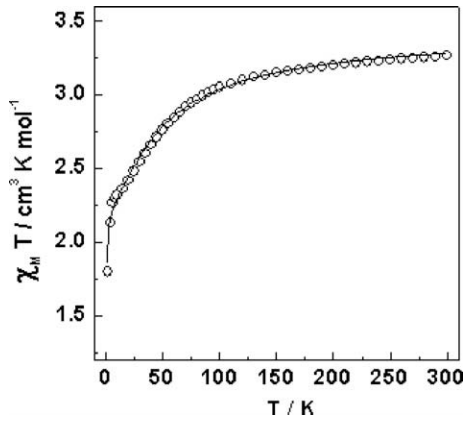


Fig. 8. Plot of $\chi_M T$ vs T of polycrystalline complex of **2**. Solid line corresponds to the best fit (see text).

2 with $g = (10 + 2A\kappa)/3$ [33]. The noticeable Δ (distortion) parameter agrees with the great distortion created by the chelated dca and tptz ligands (N7–Co–N8 angle = 85.9° and N5–Co–N4 = 147.3°, instead of 90° and 180° for a regular octahedron).

The magnetic properties of complex **2**, in the form of $\chi_M T$ versus T plot (χ_M is the molar magnetic susceptibility for one Co(II) ion) is shown in Fig. 8. The value of $\chi_M T$ at 300 K is 3.26 $cm^3\ K\ mol^{-1}$, which is large than that expected for spin-only case ($\chi_M T = 1.87\ cm^3\ K\ mol^{-1}$ K, $S = 3/2$). The $\chi_M T$ values are continuously decreased from room temperature to 1.795 $cm^3\ K\ mol^{-1}$ at 2 K. The global feature is characteristic of weak antiferromagnetic interactions. The small polynuclear systems can also be fitted through sophisticated computer programs, based on full diagonalization methods at low temperature region (where the effective spin $S' = 1/2$) [35,36]. One-dimensional systems of Co(II) atoms are frequently associated with anisotropic Ising systems, and they can be fitted in the low temperature zone assuming an effective spin $S' = 1/2$ [37]. Rueff et al. [38] have proposed a phenomenological approach for some low-dimensional Co(II) systems that allows to have an estimate the strength of the antiferromagnetic exchange interactions. They have postulated the phenomenological equation:

$$\chi_M T = A\exp(-E_1/kT) + B\exp(-E_2/kT)$$

in which $A + B$ equals the Curie constant [≈2.8–3.4 $cm^3\ mol^{-1}$ K for octahedral cobalt(II) ions], and E_1, E_2 represent the "activation energies" corresponding to the spin–orbit coupling and the antiferromagnetic exchange interaction, respectively. This equation adequately describes the spin–orbit coupling, which results in a splitting between discrete levels, and the exponential low-temperature divergence of the susceptibility. Very good results have been reported in one- and two-dimensional Co(II) complexes [39]. An important experimental feature in almost all octahedral Co(II) complexes is that $\chi_M T$ (or μ_{eff}) values at room temperature are greater than one isolated spin-only ion ($\chi_M T = 1.87\ cm^3\ mol^{-1}$ K for a $S = 3/2$ ion), indicating that an important orbital contribution is involved. Typical values of $\chi_M T$ (or μ_{eff}) are 2.75–3.4 $cm^3\ mol^{-1}$ K (4.7–5.2 μ_β) [32]. Lower values at r.t. indicate perturbation from ideal octahedral geometry [40]. An estimated J value has been calculated using the two exponential Rueff expression, mentioned above, which is suitable for any temperature greater than the possible T_c [34,35]. The fit values obtained with this procedure are: $A + B = 3.43\ cm^3\ K\ mol^{-1}$, ($A = 1.05$ and $B = 2.38$) which perfectly agrees with those given in the literature for the Curie constant ($C \approx 2.8$–$3.4\ cm^3\ K\ mol^{-1}$), $E_1/k = 46.71$ K, is of the same magnitude than those reported by Rueff et al. for several one- and two-dimensional Co(II) complexes [38]. As for the value found for the antiferromagnetic exchange interaction, it is very week ($E_2/k = 0.500$ K), corresponding to $J = -1.0$ K (=$-0.7\ cm^{-1}$) according to the Ising chain approximation, $\chi_M T \propto exp(J/2kT)$. The small J value is compatible with double $\mu_{1,5}$-dca bridge ligand which always give almost negligible coupling parameters [18]. Thus we can conclude that complex **2** behaves as a one-dimensional system which is weakly magnetically coupled by dca ligand and also intramolecular π–π interactions.

4. Conclusions

In this paper, we present structural and magnetic aspects of two novel dca bridged Co(II) complexes having two different coligands, namely tptz and imz. Complex **1** is a dinuclear Co(II) system extended to 1D chain through intermolecular H-bonding interactions. To the best of our knowledge, this is the first reported dicyanamido-bridged dinuclear Co(II) complex. In fact, dca bridged dinuclear complexes are few in literature, since dca has a strong tendency to form polynuclear structure. Probably, the bulkiness of the tptz ligand prevents the dinuclear moiety to propagate in a polynuclear fashion. Complex **2** is a 1D chain interlocked by face-to-face π–π stacking interactions to generate a 2D sheet. The magnetic behaviors of both the high-spin Co(II) complexes exhibit weak antiferromagnetic coupling. Further scope of this work aims at synthesis and study of different properties of various dca bridged complexes varying metal centers, as well as coligands.

Supplementary data

CCDC 697126 and 697128 contain the supplementary crystallographic data for **1** and **2**. These data can be obtained free of charge via http://www.ccdc.cam.ac.uk/conts/retrieving.html, or from the Cambridge Crystallographic Data Centre, 12 Union Road, Cambridge CB2 1EZ, UK; fax: (+44) 1223-336-033; or e-mail: deposit@ccdc.cam.ac.uk.

Acknowledgments

Anamika Das is grateful to the Council of Scientific and Industrial Research, New Delhi, for providing a Research Associate ship to her. This work is also supported by AICTE New Delhi and by grants given by the Spanish (CTQ2006-01759, CTQ2006-03949) and Catalan (2005SGR-00593) governments.

References

[1] N.L. Rosi, J. Eckert, M. Eddaoudi, D.T. Vodak, J. Kim, M. O'Keeffe, O.M. Yaghi, Science 300 (2003) 1127.
[2] B. Moulton, M.J. Zaworotko, Chem. Rev. 101 (2001) 1629.
[3] H.-B. Yang, N. Das, F. Huang, A.M. Hawkridge, D.C. Muddiman, P.J. Stang, J. Am. Chem. Soc. 128 (2006) 10014.
[4] C. Janiak, Dalton Trans. (2003) 2781.
[5] G.R. Desiraju, Acc. Chem. Res. 29 (1996) 441.
[6] A. Das, G.M. Rosair, M.S. El Fallah, J. Ribas, S. Mitra, Inorg. Chem. 45 (2006) 3301.
[7] S.R. Batten, K.S. Murray, Coord. Chem. Rev. 246 (2003) 103.
[8] A. Majumder, V. Gramlich, G.M. Rosair, S.R. Batten, J.D. Masuda, M.S. El Fallah, J. Ribas, J.P. Sutter, C. Desplanches, S. Mitra, Cryst. Growth Des. 6 (2006) 2355.
[9] S.A. Barnett, N.R. Champness, Coord. Chem. Rev. 246 (2003) 145.
[10] A. Das, G. Pilet, D. Luneau, M.S. El Fallah, J. Ribas, S. Mitra, Inorg. Chim. Acta 358 (2005) 4581.
[11] J.L. Manson, A.M. Arif, C.D. Incarvito, L.M.-L. Sands, A.L. Rheingold, J.S. Miller, J. Solid State Chem. 145 (1999) 369.
[12] E. Colacio, F. Lloret, I.B. Maimoun, R. Kivekas, R. Sillanpaa, J. Suárez-Varela, Inorg. Chem. 42 (2003) 2720.
[13] P.M. van der Werff, S.R. Batten, P. Jensen, B. Moubaraki, K.S. Murray, J.D. Cashion, Cryst. Growth Des. 4 (2004) 503.
[14] G.A. van Albada, M.G. van der Horst, I. Mutikainen, U. Turpeinen, J. Reedijk, Inorg. Chem. Commun. 10 (2007) 1014.
[15] D. Ghoshal, A.D. Jana, T.K. Maji, G. Mostafa, Inorg. Chim. Acta 359 (2006) 690.
[16] G.Y. Hsu, P. Mishra, S.C. Cheng, H.-H. Wei, S. Mohanta, Polyhedron 25 (2006) 3393.
[17] B.N. Figgis, M.A. Hitchman, Ligand Field Theory and Its Applications, Wiley-VCH, New York, 2000.
[18] D. Ghoshal, G. Mostafa, T.K. Maji, E. Zangrando, T.-H. Lu, J. Ribas, N. Ray Chaudhuri, New J. Chem. 28 (2004) 1204.
[19] B.L. Li, X.Y. Wang, X. Zhu, S. Gao, Y. Zhang, Polyhedron 26 (2007) 5219.
[20] G.M. Sheldrick, SADABS, University of Göttingen, Göttingen, Germany, 1996.
[21] G.M. Sheldrick, SHELXL-97, Program for Refinement of Crystal Structures, University of Göttingen, Germany, 1997.
[22] G.M. Sheldrick, SHELXS-97, Program for Refinement of Crystal Structures, University of Göttingen, Germany, 1997.
[23] A. Altomare, M.C. Burla, M. Camalli, G.L. Cascarano, C. Giacovazzo, A. Guagliardi, A.G.G. Moliterni, G. Polidori, R. Spagna, J. Appl. Crystallogr. 32 (1999) 115.
[24] A.L. Spek, J. Appl. Crystallogr. 36 (2003) 7.
[25] L.J. Farrugia, J. Appl. Crystallogr. 30 (1997) 565.
[26] K. Nakamoto, Infrared and Raman Spectra of Inorganic and Coordination Compounds, fourth ed., Wiley-Interscience, New York, 1986.
[27] A. Majumder, G. Pilet, M.T.G. Rodriguez, S. Mitra, Polyhedron 25 (2006) 2550.
[28] S. Koner, S. Dalai, J. Ribas, M.G.B. Drew, E. Zangrando, N. Ray Chaudhuri, Inorg. Chim. Acta 357 (2004) 4208.
[29] P.M. van der Werff, S.R. Batten, P. Jensen, B. Moubaraki, K.S. Murray, E.H.-K. Tan, Polyhedron 20 (2001) 1129.
[30] A. Mohamadou, G.A.V. Albada, H. Kooijman, B. Wieczorek, A.L. Spek, J. Reedjik, New J. Chem. 27 (2003) 983.
[31] M.E. Lines, J. Chem. Phys. 55 (1971) 2977.
[32] J.M. Herrera, A. Bleuzen, Y. Dromzée, M. Julve, F. Lloret, M. Verdaguer, Inorg. Chem. 42 (2003) 7052.
[33] J. Cano, VPMAG Package, B.1 Revision, University of Valencia, 2003.
[34] R.L. Carlin, Magnetochemistry, Springer-Verlag, Berlin, 1986.
[35] E. Coronado, M. Drillon, P.R. Nutgeren, L.J. De Jongh, D. Beltran, J. Am. Chem. Soc. 110 (1988) 3907.
[36] MAGPACK Program: J.J. Borrás-Almenar, J.M. Clemente-Juan, E. Coronado, B.S. Tsukerblat, Inorg. Chem. 38 (1999) 6081.
[37] J.J. Borrás-Almenar, J.M. Clemente-Juan, E. Coronado, B.S. Tsukerblat, J. Comput. Chem. 22 (2001) 985.
[38] J.-M. Rueff, N. Masciocchi, P. Rabu, A. Sironi, A. Skoulios, Eur. J. Inorg. Chem. (2001) 2843.
[39] J.-M. Rueff, N. Masciocchi, P. Rabu, A. Sironi, A. Skoulios, Chem. Eur. J. 8 (2002) 1813.
[40] S.G. Telfer, T. Sato, R. Kuroda, J. Lefebvre, D.B. Leznoff, Inorg. Chem. 43 (2004) 421.

Polyhedron 28 (2009) 2443–2449

Contents lists available at ScienceDirect

Polyhedron

journal homepage: www.elsevier.com/locate/poly

Synthesis and X-ray crystallographic studies of Ni (II) and Cu (II) complexes of [5-(4-pyridyl)-1,3,4] oxadiazole-2-thione/thiol formed by transformation of N-(pyridine-4-carbonyl)-hydrazine carbodithioate in the presence of ethylenediamine

N.K. Singh [a,*], M.K. Bharty [a], R. Dulare [a], R.J. Butcher [b]

[a] Department of Chemistry, Banaras Hindu University, Varanasi 221005, India
[b] Department of Chemistry, Haward University, Washington, DC 20059, USA

ARTICLE INFO

Article history:
Received 16 December 2008
Accepted 21 April 2009
Available online 3 May 2009

Keywords:
Oxadiazole complexes
Nickel(II) and Copper(II) complexes
Mixed ligand complexes
Supramolecular architecture

ABSTRACT

The reaction of $[M(H_2L)_2]$ [M = Ni(II) Cu(II)] ($K^+H_2L^-$ = N-(pyridine-4-carbonyl)-hydrazine carbodithioate) with excess of ethylenediamine (en) gave mixed ligand complexes $[Ni(en)_2(4\text{-pytone})_2]$ (4-pytone = 5-(4-pyridyl)-1,3,4-oxadiazole-2-thione), and $[Cu(en)_2](4\text{-pytol})_2{\cdot}H_2O$ (4-pytol = 5-(4-pyridyl)-1,3,4-oxadiazole-2-thiol). The metal complexes have been characterized with the aid of elemental analyses, IR, magnetic susceptibility and single crystal X-ray studies. Complexes (**1**) and (**2**) crystallize in monoclinic system, space group $P_{1\ 21}/n_1$ and C_2/c, respectively. The ligand after cyclization is present in the deprotonated thiol form in the Cu(II) complex where it is ionically bonded through sulfur. In the Ni(II) complex (**1**) bonding of the ligand take place through oxadiazole nitrogen and the ligand exists as the thione form.
© 2009 Elsevier Ltd. All rights reserved.

1. Introduction

N-Aroyl dithiocarbazates and their salts could be converted to 1,3,4-oxadiazole derivatives, which are biologically important molecules [1,2]. The oxadiazole molecules act as spacer via coordination, hydrogen bonding and show intermolecular cooperative interaction [3]. Oxadiazole derivatives, which belong to an important group of heterocyclic compounds, have been the subject of extensive study in the recent past. Numerous reports have highlighted their chemistry and uses [1,3]. Oxadiazole derivatives show diverse biological activities, such as anti-tuberculostatic, antiinflamatory, analgesic, antipyretic and anticonvulsant [4,5]. Although some work have been reported on the metal complexes of 5-phenyl-1,3,4-oxadiazole-2-thione [6,7], 5-(4-pyridyl)-1,3,4-oxadiazole-2-thione [8–13], 5-(3-pyridyl)-1,3,4-oxadiazole-2-thione [14] and 5-(2-pyridyl)-1,3,4-oxadiazole-2-thione [15]. Since 1,3,4-oxadiazole-2-thiones are biologically active compounds; information about their 3-dimensional structures may be of great interest for rational drug design. 1,3,4-oxadiazole-2-thione consists of an equilibrium mixture of its thione and thiol forms [16–19], therefore it will be of interest to investigate the bonding mode of oxadiazole in their complexes. In view of this, we have prepared and characterized the complexes of 5-(4-pyridyl)-1,3,4-oxadiazole-2-thione/thiol formed after cyclization of the Ni(II) and Cu(II) complexes of N-(pyridine-4-carbonyl)-hydrazine carbodithioate in the presence of ethylenediamine which acts as a coligand.

2. Experimental

2.1. Materials and methods

Commercial reagents were used without further purification and all experiments were carried out in open atmosphere. Isonicotinic acid hydrazide (Sigma–Aldrich), CS_2 (S D Fine Chemicals, India) and KOH (Qualigens) were used as received. All the solvents were purchased from Merck Chemicals, India, and used after purification.

2.2. Preparations of potassium [N′-(pyridine-4-carbonyl)-hydrazine carbodithioate [$K^+(H_2L)^-$]]

The potassium N-(pyridine-4-carbonyl)-hydrazine carbodithioate (Fig. 1) was prepared by adding CS_2 (1.5 ml, 0.2 mmol) dropwise to a suspension of isonicotinic acid hydrazide (2.7 g, 20 mmol) in methanol (20 ml) in the presence of potassium hydroxide (1.2 g, 20 mmol). The reaction mixture was stirred continuously for 30 min and the yellow solid [$K^+(H_2L)^-$] which separated was filtered, washed with EtOH and dried. Yield: 77%. mp: 578K. ^{1}H NMR (DMSO-d_6, δ ppm): 10.60 (*s*, 2H, NH), 8.65,7.85

* Corresponding author. Tel.: +91 5422318529.
E-mail address: nksingh@bhu.ac.in (N.K. Singh).

0277-5387/$ - see front matter © 2009 Elsevier Ltd. All rights reserved.
doi:10.1016/j.poly.2009.04.030

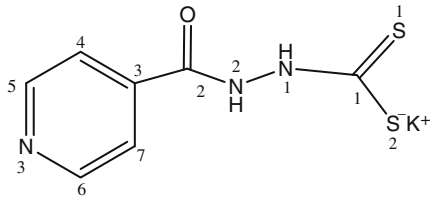


Fig. 1. [N-(pyridine-4-carbonyl)-hydrazine carbodithioate $[K^+(H_2L)^-]$.

(*m*,4H, pyridine ring). ^{13}C NMR (DMSO-d_6, δ ppm): 201.05(>C=S), 163.90(>C=O), 131.77(C3), 150.56(C6), 140.27(C5), 121.01(C4), 118.63(C7). IR (KBr, cm^{-1}): ν(NH) 3289m, 3182m; ν(C=O) 1676s; ν (N–N) 1062s; ν (C=S) 993s; pyridine ring 667. *Anal.* Calc. for $C_7H_6N_3OS_2K$ (251.36): C, 33.45; H, 2.41; N, 16.72; S, 25.51. Found: C, 33.40; H, 2.35; N, 16.76; S, 25.45%.

2.3. Preparation of [Ni (en)$_2$(4-pytone)$_2$] (**1**)

Freshly prepared potassium N-(pyridine-4-carbonyl)-hydrazine carbodithioate $[(K^+(H_2L)^-]$ (0.500 g, 2 mmol) was dissolved in water (20 ml) and an aqueous solution of $Ni(OAc)_2{\cdot}4H_2O$ (0.250 g, 1 mmol) was added to the above solution and stirred for 15 min. The brown solid which separated was filtered, washed with methanol–water mixture (50:50) and dried in vacuo. A methanol solution (10 ml) of ethylenediamine (0.30 ml, 4 mmol) was added to the methanol suspension of the above compound and after shaking for a few minutes the resulting clear brown solution was filtered and kept for crystallization. Brown single crystals of (**1**) suitable for an X-ray analysis were obtained by slow evaporation of its methanol solution over a period of 10 days, mp.535 K, yield 62%. *Anal.* Calc. For $C_{18}H_{24}Ni\ N_{10}O_2S_2$: C, 40.39; N, 26.17; H, 4.52; S, 11.98%. Found: C, 40.30; N, 26.25; H, 4.40; S, 11.86% .IR data (KBr, cm^{-1}); ν(NH) 3322, 3256m, ν(C=N) 1604; ν (C–O–C) 1274w; ν(N–N)1085; ν(C=S) 953m; ν(Ni–N) 524w. μ_B = 2.90 BM. UV–Vis Spectrum (λ_{max} Nujol, cm^{-1}): 12545, 18940, 25575, 29500.

2.4. Preparation of [Cu(en)$_2$] (4-pytol)$_2{\cdot}H_2O$ (**2**)

$Cu(OAc)_2{\cdot}H_2O$ (0.200 g, 1 mmol) and freshly prepared potassium N-(pyridine-4-carbonyl)-hydrazine-carbodithioate $[K^+(H_2L)^-]$ were dissolved separately in 15–20 ml water, mixed together and stirred for 30 min. The black solid which separated was filtered, washed successively with methanol–water mixture (50:50) and finally with methanol. A methanol solution (10 ml) of ethylenediamine (0.30 ml, 4 mmol) was added to the methanol suspension of the above compound and stirred for 1 h. A clear dark blue solution was obtained which was filtered and kept for crystallization. Dark blue needle shaped single crystals of (**2**) suitable for an X-ray analysis were obtained by slow evaporation of the above solution over a period of 8 days, mp.461 K, yield 55%. *Anal.* Calc. For $C_{18}H_{26}CuN_{10}O_3S_2$: C, 38.73; N, 25.09; H, 4.69; S, 11.49. Found: C, 38.65; N, 25.15; H, 4.56; S, 11.35%. IR data (KBr, cm^{-1}); ν(OH) 3415, ν(NH) 3254, 3101m, ν(C=N) 1605s; ν(C–O–C) 1283w; ν(N–N) 1053s; ν(C–S) 827m; ν(Cu–N) 479w. μ_B = 1.81 BM. UV–Vis Spectrum (λ_{max} Nujol, cm^{-1}): 17635, 26665, 28410.

2.5. Physical measurements

Carbon, hydrogen and nitrogen contents were estimated on a Carlo Erba 1108 model microanalyser. Magnetic susceptibility measurements were performed at room temperature on a Cahn Faraday balance using Hg $[Co(NCS)_4]$ as the calibrant. Electronic spectra were recorded on a SHIMADZU 1700 UV–Vis spectrophotometer as Nujol mull [20]. IR spectra were recorded in the 4000–400 cm^{-1} region as KBr pellets on a Varian Excalibur 3100-FT IR spectrophotometer. ^{1}H and ^{13}C NMR spectra were recorded in d_6-DMSO on a JEOL AL 300 FT NMR spectrometer using TMS as an internal reference.

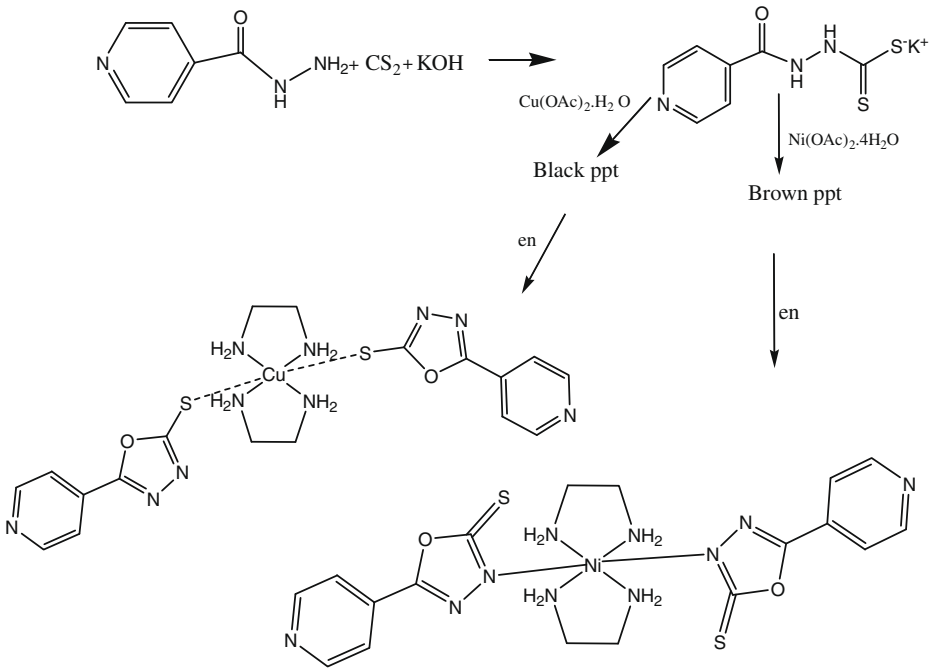
3. Crystal structure determination

Data for the structures **1** and **2** were obtained at 295(2) and 298(2) K, on an Oxford Gemini and a Bruker three-circle diffracto-

Table 1
Crystallographic data for complexes (**1**) and (**2**).

Parameters	[Ni(en)$_2$(pot)$_2$]	[Cu(en)$_2$](pot)$_2{\cdot}H_2O$
Empirical formula	$C_{18}H_{24}N_{10}NiO_2S_2$	$C_{18}H_{26}N_{10}CuO_3S_2$
Formula weight	535.30	558.15
Crystal system	monoclinic	monoclinic
Space group	$P_{1\ 21}/n_1$	C_2/c
T (K)	295(2)	298(2)
λ, Mo Kα (Å)	0.71073	0.71073
a (Å)	10.9076(8)Å	22.7599(9)
b (Å)	10.2048(7)	16.6418(6)
c (Å)	11.9871(7)	16.6377(11)
β (°)	114.048(8)	130.78
V, (Å3)	1218.47(14)	4771.8(4)
Z	2	8
ρ_{calcd} (mg/m^3)	1.459	1.554
μ (mm^{-1})	1.004	1.133
F(0 0 0)	556	2312
Crystal size(mm^3)	0.55 × 0.49 × 0.37	0.44 × 0.38 × 0.15
θ Range for data collections, (°)	4.71–32.56	1.70–27.40
Index ranges	$-16 \leqslant h \leqslant 16$, $-15 \leqslant k \leqslant 15$, $-17 \leqslant l \leqslant 17$	$-29 \leqslant h \leqslant 29$, $-19 \leqslant k \leqslant 21$, $-21 \leqslant l \leqslant 21$
No. of reflections collected	20 879	23 154
No. of independent reflections (R_{int})	4104 (0.0461)	5424 (0.0227)
No. of data/restrains/parameters	4104/0/151	5424/0/351
Goodness-of-fit on F^2	1.081	1.042
R_1[a], wR_2[b] [$I > 2\sigma$(I)]	0.0429, 0.0982	0.0341, 0.0879
R_1[a], wR_2[b] (all data)	0.0863, 0.1253	0.0453, 0.0964
Largest difference in peak/hole (e.Å^{-3})	0.992, −0.660	1.074, −0.549

[a] $R_1 = \Sigma||F_o|-|F_c||\Sigma|F_o|$.
[b] $R_2 = [\Sigma w(|F_o^2|-|F_c^2|)^2/\Sigma w|F_o^2|^2]^{1/2}$.



Scheme 1. Preparation of the ligand and the complexes.

metre, respectively equipped with a SMART 6000 CCD diffractometre using a graphite mono-chromated Mo Kα (λ = 0.71073 Å) radiation source (Table 1). The structure was solved by direct methods (SHELXL-97) and refined against all data by full matrix least-square on F^2 using anisotropic displacement parameters for all non-hydrogen atoms. All hydrogen atoms were included in the refinement at geometrically ideal position and refined with a riding model [21,22].

The MERCURY and DIAMOND packages were used for molecular graphics [23,24]. Crystal structure diagrams were generated by use of the ORTEP-3 for windows program [25].

4. Results and discussion

The potassium salt of N-acyl hydrazine carbodithioate generates 1, 3, 4 oxadiazole-2-thione/ thiol (4-pytone/4-pytol) in neutral and alkaline medium, respectively by an internal ring closure reaction via desufurization [26]. The elemental analyses and physical measurements of complexes **1** and **2** indicated that both hydrazinic hydrogens from [-C(O)NHNHC(S)S$^-$-] moiety and one sulfur atom were missing from the resulting complexes. The compounds (**1**) and (**2**) were obtained by shaking [M(H_2L)$_2$] with a methanol solution of ethylenediamine taken in 1:4 molar ratio. The Scheme 1 depicts the formation of the complexes which contains 4-pytone/ 4-pytol as the ligand and ethylenediamine as coligand. The compounds (**1**) and (**2**) are insoluble in ethanol and chloroform but are soluble in MeOH, DMF and DMSO and melt at 535 and 461 K, respectively.

4.1. IR spectra

The IR spectrum of the ligand N-(pyridine-4-carbonyl)-hydrazine carbodithioate in KBr shows absorptions due to the stretching modes of NH (3289m, 3182m cm^{-1}), C=O (1676 cm^{-1}), CS

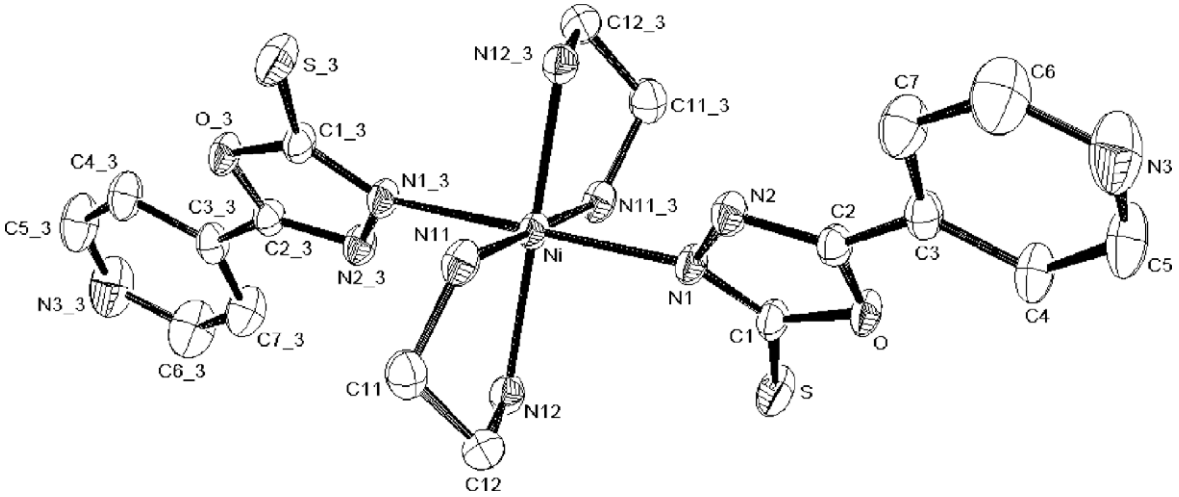


Fig. 2. Ortep plot of [Ni(en)$_2$(4-pytone)$_2$] showing atomic numbering scheme with ellipsoid of 30% probability.

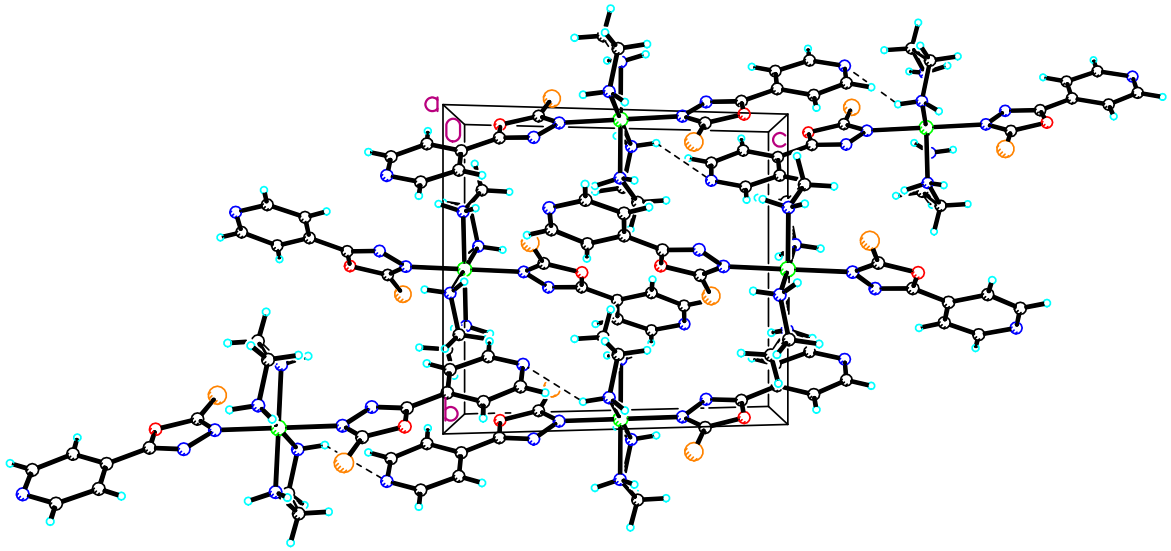


Fig. 3. Crystal packing of $[Ni(en)_2(pytone)_2]$ showing weak van der Walls' interactions.

(993 cm^{-1}), N–N (1062 cm^{-1}). The pyridine ring vibrations are observed at 985 and 693 cm^{-1}. The IR spectra of complexes (**1**) and (**2**) show bands in the region of 3320–3100 cm^{-1} due to the N–H stretching vibrations of en which are shifted to lower frequency than those encountered in the free en [27]. A negative shifts in ν(NH) and appearance of a new band near 520 cm^{-1} due to ν(M–N) suggests formation of a chelate. A negative shift of 166 cm^{-1} in ν(C=S) in complex (**2**) indicates conversion of C=S bond to C–S. In the complex (**1**), ν(C=S) shows a very little negative shift showing that the exocyclic sulfur is not participating in bonding but can be attributed to the involvement of sulfur in hydrogen bonding with NH_2 hydrogen of ethylenediamine. The new peaks appearing in the region of 1610–1600 cm^{-1} due to ν(C=N) (endocyclic) and ν(C–O–C)1285–1270 cm^{-1} suggest cyclization of the dithiolate moiety to 1,3,4-oxadiazole-2-thione via desulfurization. The IR data are thus consistent with the presence of an 1, 3, 4-oxadiazole moiety in compounds **1** and **2** [28].

4.2. Electronic spectra and magnetic moment

$[Cu(en)_2](4\text{-pytol})_2{\cdot}H_2O$ shows a magnetic moment of 1.81 BM, which indicates the presence of one unpaired electron. The presence of a broad band around 17635 cm^{-1} assigned to the envelope of the $^2B_1g \rightarrow {}^2A_1g$, ^2B_2g and ^2Eg transitions suggests a square planar geometry for the complex. Two other high energy bands observed at 26665 and 28410 cm^{-1}may be assigned to intraligand/charge transfer transitions. A magnetic moment of 2.90 BM for $[Ni(en)_2(4\text{-pytone})_2]$ and the presence of two bands at 12545 and 18940 cm^{-1} assigned to the $^3A_2g \rightarrow {}^3A_1g(F)$ (υ_1) and $^3T_1g(P)$ (υ_2) transitions, respectively, suggest a distorted octahedral geometry for the complex. Other two bands observed at 25575 and 29500 cm^{-1} may like wise be assigned to intraligand/charge transfer transitions [29].

4.3. Crystal structure description of complex (*1*)

Fig. 2 shows a ORTEP plot of $[Ni(en)_2(4\text{-pytone})_2]$ with the atomic numbering scheme. The elements of the structure are joint to each other in the crystal packing (Fig. 3) by means of an extended system of H-bonds where hydrogen belonging to the en are participating in the structure. The monomeric unit $[Ni(en)_2(4\text{-pytone})_2]$ possesses a centrosymmetry nickel at the inversion center. Its coordination environment is fulfilled by two axial (4-pytone) anions at trans position to each other, each bonded through oxadiazole nitrogen atom and the four equatorial sites are occupied by the two bidentate N, N′ ethylenediamine. The bonding of two en designated as, Ni–N(11) has a distance of 2.102(2) Å and that of Ni–N(12) occurs at a distance of 2.095(2) Å involve two five membered chelate rings C_2N_2Ni with bite angle of 82.71(9)°, and represent a major deviation from the octahedral geometry (Table 2). The geometry and bonding parameters within the en molecule agree with those of related compounds, e.g. Ni [trans $(L)_2$ $(en)_2$] {L = N-(5-chlorouracilato)} [30], isothiocyanato [31] and salicylato [32]. Weak intermolecular N–H···N interaction between pyridine nitrogen and NH_2 hydrogen atoms and N–H···S interaction stabilize the structure of compound **1**, (Table 4). The two N···S distances of 3.422(2) and 3.514(2) Å (Table 4) are close to the mean N···S distance reported for NH···S hydrogen bonds by Shrinivashan and Chacko [33]. The arrangement of the mono-

Table 2
Interatomic distances (Å) and angles (°) for $[Ni(en)_2(4\text{-pytone})_2]$.

Nickel coordination sphere			
Ni–N(12)#1	2.095(2)	N(12)#1–Ni–N(1)#1	90.16(8)
Ni–N(11)#1	2.102(2)	N(12)–Ni–N(1)#1	89.84(8)
Ni–N(1)#1	2.1217(16)	N(11)#1–Ni–N(1)#1	89.54(7)
		N(11)–Ni–N(1)#1	90.46(7)
		N(1)#1–Ni–N(1)	180.00(5)
Ethylenediamine			
N(11)–C(11)	1.467(4)	N(12)#1–Ni–N(11)#1	82.71(9)
N(12)–C(12)	1.475(4)	N(12)–Ni–N(11)#1	97.29(9)
C(11)–C(12)	1.511(4)	N(11)#1–Ni–N(11)	180.00(9)
Oxadiazole ring			
S–C(1)	1.679(3)	C(2)–O–C(1)	104.49(17)
O–C(2)	1.353(3)	C(1)–N(1)–N(2)	108.53(17)
O–C(1)	1.381(2)	C(1)–N(1)–Ni	132.37(15)
N(1)–C(1)	1.314(3)	N(2)–N(1)–Ni	118.97(13)
N(1)–N(2)	1.402(3)	C(2)–N(2)–N(1)	105.43(19)
N(2)–C(2)	1.285(3)	N(1)–C(1)–O	108.6(2)
C(2)–C(3)	1.462(3)	N(1)–C(1)–S	130.82(17)
		O–C(1)–S	120.55(17)
		N(2)–C(2)–O	112.95(19)
		N(2)–C(2)–C(3)	128.6(2)
		O–C(2)–C(3)	118.45(19)

Table 3
Interatomic distances (Å) and angles (°) for $[Cu(en)_2](4\text{-pytol})_2{\cdot}H_2O$.

Copper coordination sphere			
Cu(1)–N(2A)#1	2.0044(19)	N(2A)#1–Cu(1)–N(2A)	180.000(1)
Cu(1)–N(1A)#1	2.0063(18)	N(2A)#1–Cu(1)–N(1A)#1	84.62(9)
		N(2A)–Cu(1)–N(1A)#1	95.38(9)
		N(1A)–Cu(1)–N(1A)#1	180.0
Ethylenediamine			
N(1A)–C(1A)	1.466(3)	C(1A)–N(1A)–Cu(1)	110.30(15)
N(2A)–C(2A)	1.476(3)	C(2A)–N(2A)–Cu(1)	107.14(15)
C(1A)–C(2A)	1.498(4)	N(1A)–C(1A)–C(2A)	109.59(19)
		N(2A)–C(2A)–C(1A)	108.2(2)
Oxadiazole ring			
Cu(1)–N(2A)	2.0044(19)	C(6C)–O(1C)–C(7C)	103.21(16)
S(1C)–C(7C)	1.696(2)	C(6C)–N(1C)–N(2C)	106.51(18)
O(1C)–C(6C)	1.358(2)	C(7C)–N(2C)–N(1C)	107.32(18)
O(1C)–C(7C)	1.384(2)	N(1C)–C(6C)–O(1C)	112.73(18)
N(1C)–C(6C)	1.277(3)	N(1C)–C(6C)–C(1C)	127.7(2)
N(1C)–N(2C)	1.400(3)	O(1C)–C(6C)–C(1C)	119.60(18)
N(2C)–C(7C)	1.299(3)	N(2C)–C(7C)–O(1C)	110.23(18)
N(3C)–C(3C)	1.325(4)	N(1C)–C(7C)–S(1C)	129.96(17)
		O(1C)–C(7C)–S(1C)	119.81(16)

Table 4
Hydrogen bond parameters for $[Ni(en)_2(4\text{-pytone})_2]$ [Å and °].

D–H···A	d(D–H)	d(H···A)	d(D···A)	<(DHA)
N(11)–H(11C)···N(3)[b]	0.90	2.51	3.255(3)	140.0
N(11)–H(11C)···N(2)	0.90	2.62	3.198(3)	122.9
N(11)–H(11D)···S[a]	0.90	2.65	3.422(2)	143.7
N(12)–H(12C)···N(2)a	0.90	2.64	3.217(3)	122.6
N(12)–H(12D)···S	0.90	2.76	3.514(2)	141.9

[a] −x, −y + 1, −z.
[b] −x, −y + 1, −z + 1.

meric $[Ni(en)_2(4\text{-pytone})_2]$ units in the two dimensional architecture along the a axis provide a supramolecular network (Fig. 4).

4.4. Crystal structure description of complex (*2*)

Fig. 5 shows a molecular structure of compound **2** with the atom labeling scheme and weak Cu···S interaction. The crystallographic asymmetric unit consists of the complex cations $[Cu(en)_2]^{2+}$ and the 1, 3, 4-oxadiazole thiolate (4-pytol) anions. The complex cation consists of two ethylenediamine molecules which chelate Cu(II) in equatorial positions and two ionically bonded 1, 3, 4-oxadiazole -2-thiolate anions. The Cu–N distances are in the range (2.004–2.006 Å) (Table 3) which is normal for the Cu–N amine coordination. The bite angles for the CuC_2N_4 five membered rings are 84.62(9)° and 95.38(9)° indicating a substantial distortion in the molecule. Similar geometrical parameters for the coordination sphere have been reported for other diaquabis (ethylenediamine) Cu(II) salts [34,35]. Each $[Cu(en)_2]^{+2}$ forms a

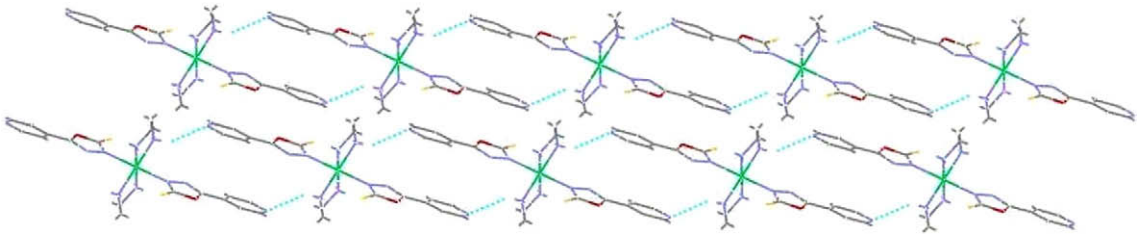


Fig. 4. The metal organic framework of $[Ni(en)_2(4\text{-pytone})_2]$ along a axis leading to supramolecular architecture.

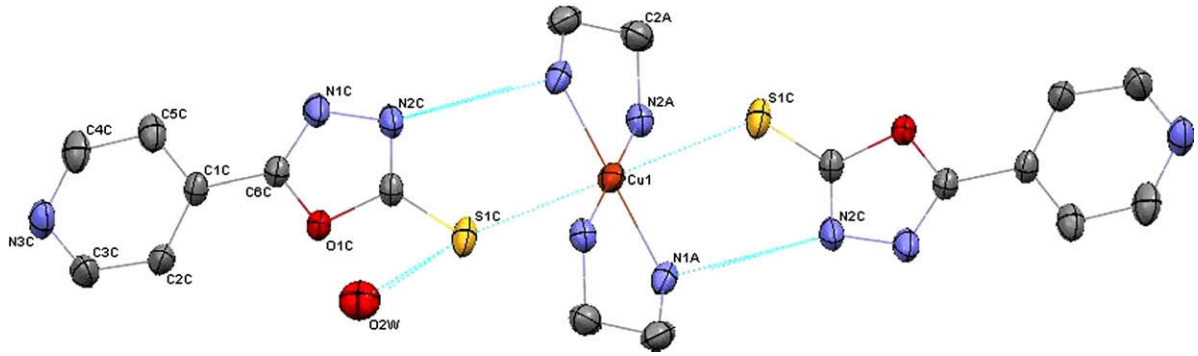


Fig. 5. Molecular structure of $[Cu(en)_2](4\text{-pytol})_2{\cdot}H_2O$ with the atom labeling scheme and showing weak Cu···S interaction.

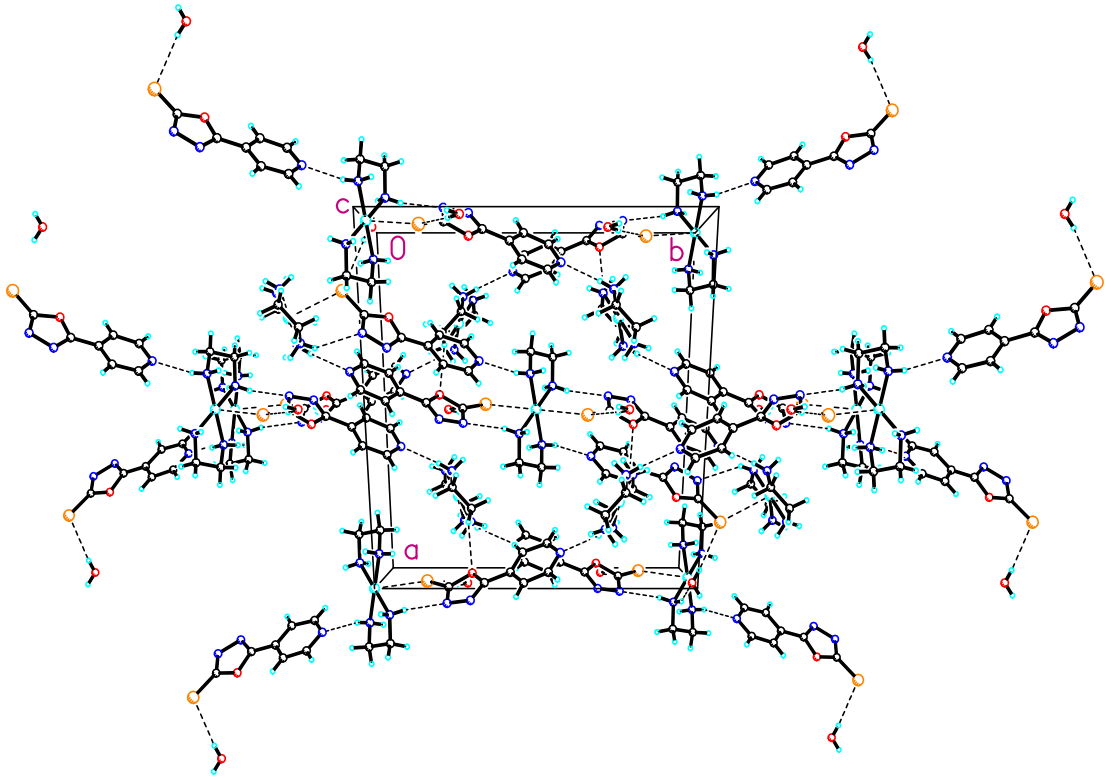


Fig. 6. Crystal packing of $[Cu(en)_2](4\text{-pytol})_2{\cdot}H_2O$ showing non-covalent interactions.

Table 5
Hydrogen bond parameters for $[Cu(en)_2]$ $(pytol)_2{\cdot}H_2O$ [Å and °].

D–H···A	d(D–H)	d(H···A)	d(D···A)	<(DHA)
O(1W)–H(1W)···S(1D)[a]	0.75(3)	2.64(3)	3.3695(18)	168(4)
O(2W)–H(2W)···S(1C)	0.83(3)	2.49(3)	3.310(2)	172(4)
N(1A)–H(1A1)···N(2C)	0.79(3)	2.29(3)	3.020(3)	153(3)
N(1A)–H(1A2)···O(1W)	0.81(3)	2.37(3)	3.114(2)	153(3)
N(2A)–H(2A1)···N(3D)	0.84(3)	2.21(3)	3.024(3)	166(3)
N(1B)–H(1B1)···N(2D)[b]	0.77(3)	2.47(3)	3.125(3)	144(3)
N(1B)–H(1B2)···O(2W)[a]	0.84(3)	2.65(3)	3.241(2)	129(3)
N(2B)–H(2B2)···N(3C)	0.79(3)	2.22(3)	2.982(3)	165(2)

[a] $x + 1/2, y + 1/2, z$.
[b] $x + 1/2, y + 3/2, z$.

pair of intermolecular Cu···S interaction with a distance of 3.09 Å which is well within the distance of 3.2 Å for the sum of van der Waals' radii of Cu and S [36] and greater than Cu–S covalent bond [37]. The Cu(II) in D_{2h} symmetry is bonded to four nitrogen atoms of en groups which offer interesting hydrogen bonding packing. The elements of the structure are joint to each other in the crystal packing (Fig. 6) by means of an extended system of H-bonds where hydrogen belonging to the en are participating in the structure. The hydrogen bonding parameters are listed in Table 5. A close cavity is formed by the weak N–H···O and O–H···S interactions (Fig. 7). In the solid state the complex is stabilized via intermolecular N–H···N interaction between oxadiazole nitrogen atoms and NH_2 hydrogen atoms as well as pyridine nitrogen atoms and NH_2 hydrogen atoms. The O–H···S interaction takes place between thiol sulfur and hydrogen atoms of the water molecule as well as weak N–H···O interaction between the oxygen atoms of the water molecule and hydrogen atoms (NH_2) of en. The two pyridine rings are almost parallel (<ACB = 89.63) but displaced with respect to each other. The displacement as measured by the angle formed between the ring centroids AB and the ring normal BC to the pyridine plane

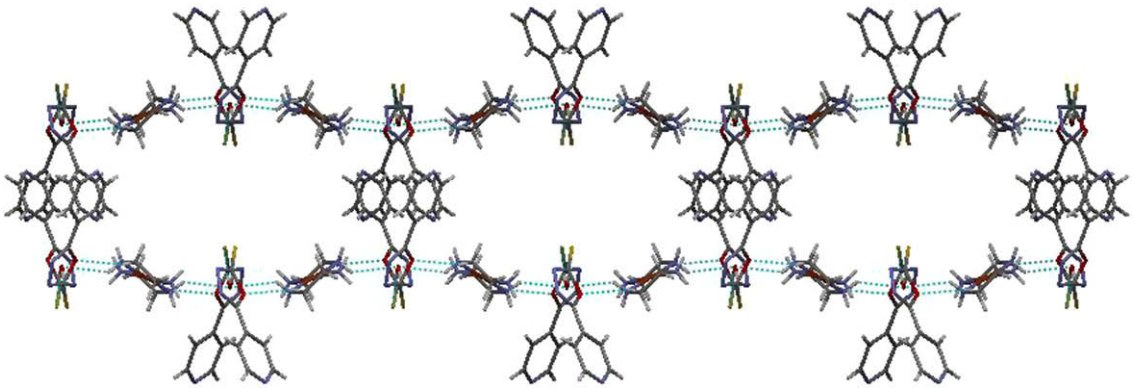


Fig. 7. Closed cavity formed by weak N–H···O and O–H···S interactions in complex **2**.

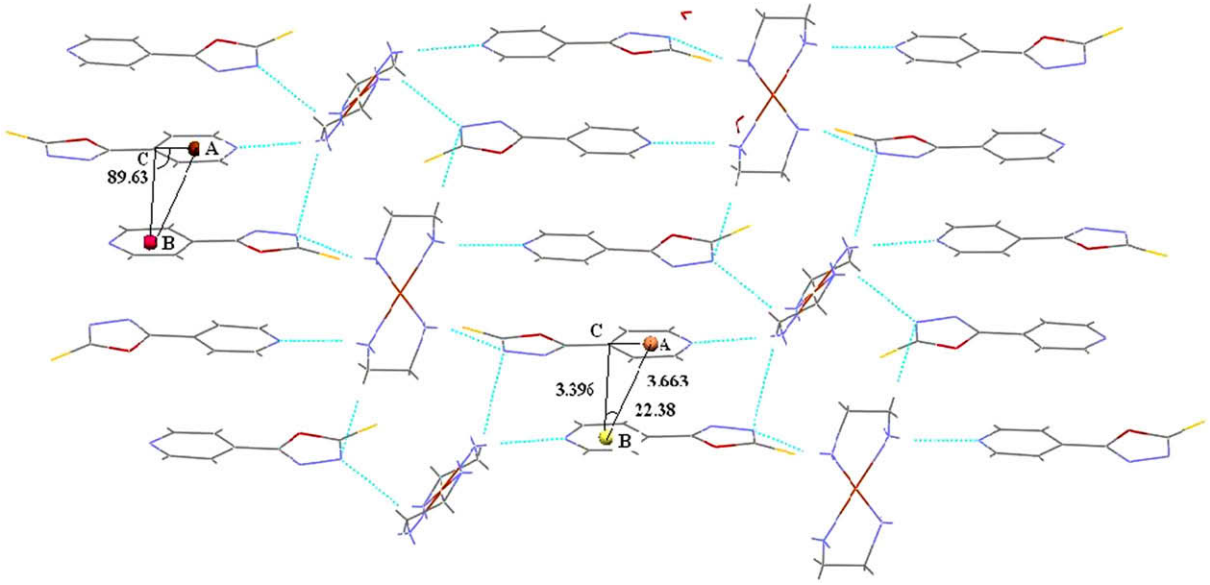


Fig. 8. π–π stacking and relative shift between two pyridine ring centroids in complex **2**.

shown in Fig. 8 was found to be 0.257 Å with a displacement angle of 22.38° and the ring centroids contacts (Cg···Cg) of 3.663 Å is well within the reported range [38].

5. Conclusions

We have reported here the synthesis and crystal structure of new Ni(II) and Cu(II) complexes of 5-(4-pyridyl)-1,3,4-oxadiazole-2-thione/thiol having ethylenediamine as the coligand. The formation of a five membered C_2N_2M chelate ring with en is the common feature in both the complexes. Different bonding behavior of the ligand is clearly seen in complexes (**1**) and (**2**). The structure of the complex **1** is stabilized through weak intermolecular N–H···S, and N–H···N, hydrogen bonding and **2** is stabilized via weak O–H···S, N–H···N and a π–π stacking between the pyridine ring centroids.

Supplementary data

CCDC 686805 and 686806 contains the supplementary crystallographic data for $[Ni(en)_2(4\text{-pytone})_2]$ (**1**) and $[Cu(en)_2](4\text{-pytol})_2{\cdot}H_2O$ (**2**). These data can be obtained free of charge via http://www.ccdc.cam.ac.uk/conts/retrieving.html, or from the Cambridge Crystallographic Data Centre, 12 Union Road, Cambridge CB2 1EZ, UK; fax: (+44) 1223-336-033; or e-mail: deposit@ccdc.cam.ac.uk.

References

[1] A. Hetzheim, K. Mockel, Adv. Heterocycl. Chem. 7 (1966) 183.
[2] B.L. Sharma, S.K. Tandon, Pharmazic 39 (H-12) (1984) 858.
[3] M. Du, X.-J. Zhao, J. Mol. Struct. 694 (2004) 235.
[4] K. Potts, in: A.R. Katritzky, Ch. Rees (Eds.), Comprehensive Heterocyclic Chemistry, vol. 6, Pergamon Press, 1984, p. 427.
[5] Y.D. Kulkarni, A. Rowhani, J. Indian Chem. Soc. 66 (1989) 492.
[6] P. Tripathi, A. Pal, V. Jancik, A.K. Pandey, J. Singh, N.K. Singh, Polyhedron 26 (2007) 2597.
[7] O.H. Amin, L.J. Al-Hayaly, S.A. Al-Jibori, T.A.K. Al-Allaf, Polyhedron 23 (2004) 2013.
[8] Z.-H. Zhang, Y.-L. Tian, Y.-M. Guo, Inorg. Chim. Acta 360 (2007) 2783.
[9] Z.-H. Zhang, C.-P. Li, G.-M. Tang, Y.-L. Tian, Y.-M. Guo, Inorg. Chem. Commun. 11 (2008) 326.
[10] Y.-T. Wang, G.-M. Tang, W.-Y. Ma, W.-Z. Wan, Polyhedron 26 (2007) 782.
[11] M. Du, Z.-H. Zhang, X.-J. Zhao, Q. Xu, Inorg. Chem. 45 (2006) 5785.
[12] Y.-T. Wang, G.-M. Tang, Inorg. Chem. Commun. 10 (2007) 53.
[13] H.-X. Xu, J.P. Ma, R.-Q. Huang, Y.-B. Dong, Acta Crystallogr., Sect. E 61 (2005) m2462.
[14] M. Singh, R.J. Butcher, N.K. Singh, Polyhedron 27 (2008) 3151.
[15] Y.-T. Wang, G.-M. Tang, Z.-W. Qiang, Polyhedron 26 (2007) 4542.
[16] K. Obi, A. Kojima, H. Fukuda, K. Hirai, Bioorg. Med. Chem. Lett. 5 (1995) 2777.
[17] L. Mishra, M.K. Said, H. Itokawa, K. Takeya, Bioorg. Med. Chem. 3 (9) (1995) 1241.
[18] S.P. Suman, S.C. Bahel, J. Indian Chem. Soc. 56 (1979) 712.
[19] D.A. Charistos, G.V. Vagenas, L.C. Tzavellas, C.A. Tsoleridis, N.A. Rodios, J. Heterocyclic Chem. 31 (1994) 1593.
[20] R.H. Lee, G. Griswold, H. Kleinberg, Inorg. Chem. 3 (1964) 1278.
[21] G.M. Sheldrick, Acta Crystallogr., Sect. A 46 (1990) 467.
[22] G.M. Sheldrick, SHELXL-97, Program For of Crystal Structure Refinement, University of Gottingen, Germany, 1997.
[23] I.J. Bruno, J.C. Cole, P.R. Edgington, M. Kessler, C.F. Macrae, P. McCabe, J. Pearson, R. Taylor, Acta Crystallogr., Sect. B 58 (2002) 389.
[24] K. Brandenburg, H. Putz, DIAMOND, Version 3.0, University of Bonn, Germany, 2004.
[25] L.J. Farrugia, J. Appl. Crystallogr. 30 (1997) 565.
[26] K.S. Siddiqi, F. Rafat, S.H. Kar, Synth. React. Inorg. Metal-Org. Chem. 34 (2004) 93.
[27] P. Molina, A. Tarraga, A. Espinosa, Synthesis (1998) 690.
[28] G.S. Patricia, G.T. Javier, A.M. Miguel, J. Arnaiz Francisco, R. Teofilo, Inorg. Chem. 41 (2002) 1345.
[29] A.B.P. Lever, Inorganic Electronic Spectroscopy, 2 ed., Elsevier, Amsterdam, 1984.
[30] A. Terron, A.G. Rosa, J.J. Fiol, S. Amengual, M.B. Oliver, R.M. Totaro, M.C. Apella, E. Molins, I. Mata, J. Inorg. Biochem. 98 (2004) 632.
[31] P.J. Squattrito, T. Iwamoto, S.-I. Nishikiori, Chem. Commun. (1996) 2665.
[32] H. Icbudak, H. Olmez, O.Z. Yesilel, F. Arslan, P. Naumov, G. Jovanovski, A.R. Ibrahim, A. Usman, H.-K. Fun, S. Chantrapromma, S.W. Ng, J. Mol. Struct. 657 (2003) 255.
[33] R. Shrinivasan, K.K. Chacko, Conformation of Biopolymers, vol. 2, Academic press, New York, 1967.
[34] J. Emsely, M. Arif, P.A. Bates, M.H. Hursthouse, Chem. Commun. (1998) 1387.
[35] P. Gomez-Romero, G.B. Jameson, J.J. Borras-Almenar, E. Escriva, E. Coronado, D. Beltran, J. Chem. Soc., Dalton Trans. (1988) 274.
[36] A.J. Bondi, Phys. Chem. 68 (1964) 441.
[37] D.W. Bennett, T.A. Siddiquee, D.T. Haworth, M. Das, J. Chem. Crystallogr. 34 (12) (2004).
[38] C. Janiak, J. Chem. Soc., Dalton Trans. (2000) 3885.

Polyhedron 28 (2009) 2450–2458

Contents lists available at ScienceDirect

Polyhedron

journal homepage: www.elsevier.com/locate/poly

Formation of nanoporous and non-porous organic–inorganic hybrid materials incorporating α-Keggin phosphotungstate anion: X-ray crystal structure of a 3D polymeric complex $[\{Na_6(C_9H_5O_6)_3(H_2O)_{15}\}\{PW_{12}O_{40}\}]_\infty$ with a 'Ball-in-Bowl' type molecular structure

Geeta Hundal [a,b,*], Young Kyu Hwang [a], Jong-San Chang [a,*]

[a] Catalysis Center for Molecular Engineering, Korea Research Institute of Chemical Technology (KRICT), P.O. Box 107, Yuseong, Daejeon 305600, Republic of Korea
[b] Department of Chemistry, Guru Nanak Dev University, Amritsar 143 005, India

ARTICLE INFO

Article history:
Received 11 March 2009
Accepted 21 April 2009
Available online 3 May 2009

Keywords:
MOFs
Keggin
Encapsulation
Nanoporous and non-porous material

ABSTRACT

Two different synthetic approaches to prepare inclusion complexes of Keggin anion $[PW_{12}O_{40}]^{3-}$ and $[Cu_3(BTC)_2(H_2O)_3]_n$ (also known as HKUST-1) have resulted in the formation of two different materials $[Cu_3(C_9H_3O_6)_2(H_2O)_3]_2Na_3PW_{12}O_{40}{\cdot}nH_2O$ (**1**) and $[Na_6(BTC\text{-}H_2)_3(H_2O)_{15}][PW_{12}O_{40}]$ (**2**). Compound **1** is a thermally stable, nanoporous material with a type 1 adsorption isotherm. It contains the well-known MOF material $[Cu_3(BTC)_2(H_2O)_3]_n$ with half of its pores occupied by the guest Keggin anion. The second product **2** is a crystalline, 3D coordination polymer with a composition of $[Na_6(BTC\text{-}H_2)_3(H_2O)_{15}][PW_{12}O_{40}]$ (where BTC-H_3 stands for 1,3,5-benzene-tricarboxylic acid) and is a non-porous, highly water soluble and thermally unstable material. The compound **1** was prepared hydrothermally using precursors of HKUST-1 and $Na_3[(PW_{12}O_{40})]$ whereas **2** was obtained at room temperature from aqueous solutions containing $[Cu_3(BTC)_2(H_2O)_3]_n$ and $Na_3[(PW_{12}O_{40})]$ salts. The molecular structure of **2** is unique and features two distinct elements: an anionic Keggin ion $[PW_{12}O_{40}]^{3-}$ and a "bowl type" hexameric $[Na_6(C_9H_5O_6)_3(H_2O)_{15}]^{3+}$ macrocation which is formed by coordination of Na^+ ions by $(BTC\text{-}H_2)^-$ anions and water molecules. The macrocation extends in three dimensions due to Y type $(BTC\text{-}H_2)^-$ to form a porous MOF offering triangular voids. In this framework the globular Keggin ions support themselves above these voids by coordinating to Na^+ ions and render it completely nonporous. The complex has an unusual structure in the sense that the polyoxoanion is coordinated to $[Na_6(C_9H_5O_6)_3(H_2O)_{15}]^{3+}$ ions by using the three terminal oxygen atoms in a single M_3O_{13} triplet, when each one of them is also bridging between two Na^+ ions. In the crystal structure the POM anion is encapsulated by six octahedrally disposed $(BTC\text{-}H_2)^-$ moieties. H-bonding interactions among water molecules produce supramolecular water hexamers and dimers.

© 2009 Published by Elsevier Ltd.

1. Introduction

Polyoxometalates (POMs) have received great attention because of their amazing electronic versatility and structural diversity [1–3] which enables them to have largest number of potential applications than any other class of cluster compounds [4–9]. Out of the various approaches which have been used to arrange or link POM building blocks to obtain solid-state materials with extended structures, coordination to the metal ion has been the most common one, owing to the sufficient charge density at the surface oxygen atoms of these POMs. In this regard, mostly *d*-block [10–19] and *f*-block [20–25] metal ions and sometimes *p*-block metal ions [26,27] have been used as linkers for assisting organization of POMs. The *s*-block elements [28–31] have received much less attention. At the same time the well-known Keggin POMs, though are amply used with coordination complexes to produce 0D to 2D materials [32–35] but the process of assembling them into 3D frameworks is still in its budding stage [36–38] which may be attributed to the steric requirements and the deficient charge density at their surfaces. On the other hand, simple incorporation of Keggin anions into various nanoporous materials like silica, zeolites and MCM-41, has been reported in literature to improve their catalytic properties by enhancing their surface area [39–41]. However, there are only a few examples known for assimilation of polyoxometalate anions into organic/inorganic hybrids [42–44]. The inclusion of these anions into MOF materials

* Corresponding authors. Address: Catalysis Center for Molecular Engineering, Korea Research Institute of Chemical Technology (KRICT), P.O. Box 107, Yuseong, Daejeon 305600, Republic of Korea.
E-mail addresses: geetahundal@yahoo.com (G. Hundal), jschang@krict.re.kr (J.-S. Chang).

0277-5387/$ - see front matter © 2009 Published by Elsevier Ltd.
doi:10.1016/j.poly.2009.04.025

[45–54] is highly selective and depends on the respective sizes of the accessible pores and that of the anionic species. Many new materials are thus expected to form as inclusion complexes and their formation may also depend on synthetic methods and materials being used. The latter may turn out to be an important but unexplored aspect so far.

In this pursuit we chose a combination of well-known polyoxometalate anion $[PW_{12}O_{40}]^{3-}$ and MOF material $Cu_3(BTC)_2(H_2O)_3{\cdot}xH_2O$. The latter, named as HKUST-1, is one of the first robust metal-organic framework (MOF) materials with a microporous structure that is reminiscent of zeolite frameworks [55]. The HKUST-1 is one of the highly cited MOFs because it has a large surface area, high pore volume, high chemical stability, high Lewis acidity and lability of coordinated water molecules. These properties enable it to be a potential candidate for adsorption, gas storage applications and catalysis [56]. A hydrothermal reaction at 120 °C between the Keggin and precursor compounds of $[Cu_3(BTC)_2(H_2O)_3]_n$ produced a Keggin-encapsulated polymeric open framework **1** similar to the one whose crystal structure has been earlier reported [44] by Yang et al. who prepared the compound by a different method. However, a room temperature synthesis carried by us, produced an entirely new ternary, 3D non-porous polymeric complex **2** consisting of Na, BTC and Keggin ions. Herein we present the synthesis of both the compounds, characterize **1** by powder XRD, IR and make a first time report of its thermal and adsorption characteristics *vis-à-vis* the parent MOF. We also wish to report here the X-ray crystal structure of the inorganic/organic hybrid $[Na_6(C_9H_5O_6)_3(H_2O)_{15}][PW_{12}O_{40}]$ **2**. Whereas **1** serves as an example of much less studied case of simple incorporation of Keggin anion into nanoporous HKUST-I, **2** stands for one of the rare examples of a unique, 3D extended non-porous network involving Keggin and Na^+ ions. Both materials have metal-BTC framework encapsulating the Keggin anions and differ basically in constitution from a porous $\{Mo_6\}_2$-based hybrid framework which offers chiral channels occupied by BTC molecules, instead [57].

Table 1
Crystal data and structure refinement for pwabtc.

Identification code	pwabtc
Empirical formula	$C_{27}H_{45}Na_6O_{73}PW_{12}$
Formula weight	3912.74
T (K)	296(2)
λ (Å)	0.71073
Crystal system	rhombohedral
Space group	$R3m$
Unit cell dimensions	$a = 21.350(5)$ Å, $\alpha = 90°$ $b = 21.350(5)$ Å, $\beta = 90°$ $c = 13.717(5)$ Å, $\gamma = 120°$
V (Å3)	5415(3)
Z	3
D_{calc} (Mg/m)	3.600
M (mm^{-1})	19.226
$F(0\,0\,0)$	5280
Crystal size (mm^3)	$0.2 \times 0.1 \times 0.1$
θ Range for data collection	1.85–28.33°
Index ranges	$-27 \leqslant h \leqslant 28, -28 \leqslant k \leqslant 28, -17 \leqslant l \leqslant 18$
Reflections collected	19 075
Independent reflections (R_{int})	3240 (0.0321)
Completeness to $\theta = 28.33°$	100.0%
Absorption correction	semi-empirical from equivalents
Maximum and minimum transmission	0.1294 and 0.0862
Refinement method	full-matrix least-squares on F^2
Data/restraints/parameters	3240/3/205
Goodness-of-fit on F^2	1.030
Final R indices [$I > 2\sigma(I)$]	$R_1 = 0.0218$, $wR_2 = 0.0534$
R indices (all data)	$R_1 = 0.0228$, $wR_2 = 0.0537$
Absolute structure parameter	0.032(14)
Largest difference in peak and hole	0.869 and −0.923 e Å^{-3}
CCDE number	699004

2. Experimental

2.1. General experimental

Powder X-ray diffraction patterns of all samples were obtained by a Rigaku diffractometer (D/MAX IIIB, 2 kW) using Ni-filtered Cu Kα-radiation (40 kV, 30 mA, $\lambda = 1.5406$ Å) and a graphite crystal monochromator. The crystal size and morphology were examined using a scanning electron microscope (SEM, JEOL JSM-840A). Thermogravimetric analyses (TGA) were performed with TA instrument model, TGA Q500 V6.7 with 10° C/min in N_2 atmosphere, on samples which were placed in a chamber having saturated NH_4Cl vapor for 24 h. The BET analyses were performed with N_2 adsorption–desorption isotherms at liquid nitrogen temperature (77 K) after dehydration under vacuum at 423 K for 12 h using Micromeritics Tristar 3000. The specific surface areas were evaluated using the Brunauer–Emmett–Teller (BET) method in the p/p_0 range of 0.05–0.2. IR spectra were recorded as KBr pellets on a Nicolet Magna-560 IR spectrophotometer.

2.2. Synthesis of $[Cu_3(C_9H_3O_6)_2(H_2O)_3]_2Na_3PW_{12}O_{40}{\sim}40{\cdot}H_2O$ (*1*)

To a 1:1 (w:w) mixture of water:ethanol (15 ml) added 1–2 drops of concentrated nitric acid to make its pH between 1.5 and 2.0. Added 0.210 g (1 mmol) of BTC-H_3 and 0.437 g (1.82 mmol)

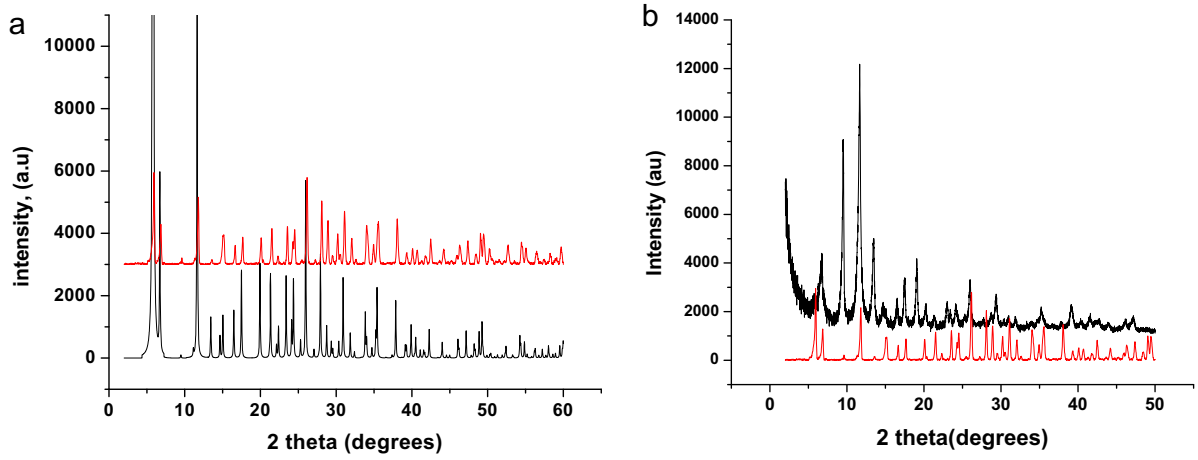


Fig. 1. Comparison of the XRD of (a) **1** (red) with that generated from the known crystal structure [44] (b) **1** (red) with $[Cu_3(BTC)_2(H_2O)_3$ (black). (For interpretation of the references to color in this figure legend, the reader is referred to the web version of this article.)

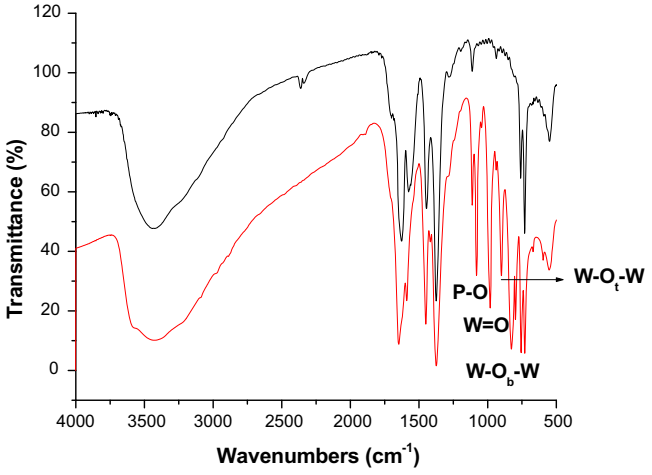


Fig. 2. A comparison of FT-IR of $[Cu_3(BTC)_2(H_2O)_3]$ (black) and **1** (red). (For interpretation of the references to color in this figure legend, the reader is referred to the web version of this article.)

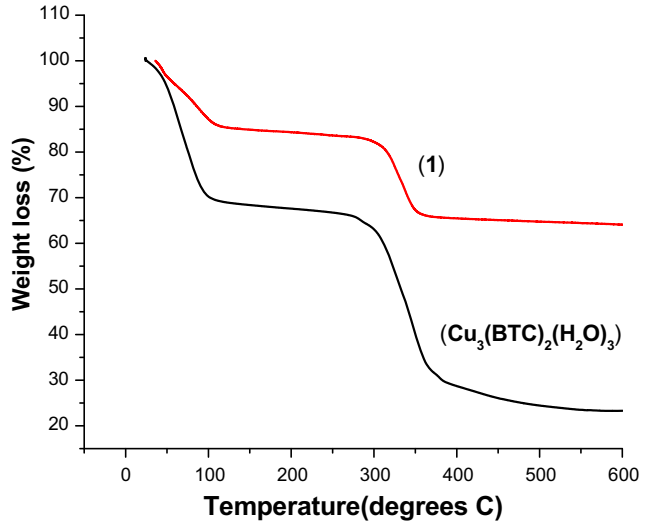


Fig. 3. A comparison of the TGA curves of $[Cu_3(BTC)_2(H_2O)_3]$ and **1**. (For interpretation of the references to color in this figure legend, the reader is referred to the web version of this article.)

of $Cu(NO_3)_2{\cdot}3H_2O$. Stirred the reaction mixture for 5 min and checked the pH which was ~1.5. Added anhydrous $Na_3[PW_{12}O_{40}]$ 2.948 g (1 mmol), stirred the mixture for 2 min and then transferred it to the autoclave Teflon reactor and heated at 120 °C for 12 h. Turquoise blue colored precipitates obtained were then filtered and washed with water many times and dried at 100 °C for 4–5 h. Yield 78% (based on W). *Anal.* Calcd. for $C_{36}H_{62}Cu_6Na_3O_{89}PW_{12}$ (partially dehydrated): H, 1.34; C, 9.38; O, 30.91; Cu, 8.27; Na, 1.49%. Found: H, 1.48; C, 9.10; O, 29.13; Cu, 7.53; Na, 1.29%. IR (cm^{-1}) ν_{OH} 3400, ν_{asym} and $\nu_{sym\ -COO}$ at 1648, 1450 and 1376, ν_{P-O} 1081, $\nu_{W=O}$ 981, ν_{W-Ot-W} 900, ν_{W-Ob-W} 829,795. The total number of water molecules were deduced from the TGA data.

2.3. Synthesis of $[Na_6(C_9H_5O_6)_3(H_2O)_{15}][PW_{12}O_{40}]$ (**2**)

For preparation of **2**, 0.950 g of $[Cu_3BTC_2]$ [56] and 3.50 g of $Na_3[PW_{12}O_{40}]$ were dissolved in 30 ml of deionized water preadjusted to pH 1.5 by adding a few drop of 1 M HNO_3 in it. The reaction mixture was stirred for 5 min, filtered and kept for slow evaporation at room temperature. Colorless, block type crystals appeared in the turquoise blue colored solution after several days (yield 38%). The mother liquor evaporated later on to give a turquoise blue powder of unknown composition. All attempts to prepare the compounds from direct reaction of $Na_3PW_{12}O_{40}$ with BTC-H_3 ended up in the crystallization $Na_3PW_{12}O_{40}$ itself, which may be due to the high acidity of $[PW_{12}O_{40}]^{3-}$ at this pH which suppresses the ionization of BTC-H_3. The presence of BTC as a pre-complexed ligand with Cu(II) ion somehow helps in the formation of the above-mentioned complex, with a much reduced extent of ionization, of course. *Anal.* Calc. for $C_{27}H_{45}Na_6O_{73}PW_{12}$: H, 1.15; C, 8.28;

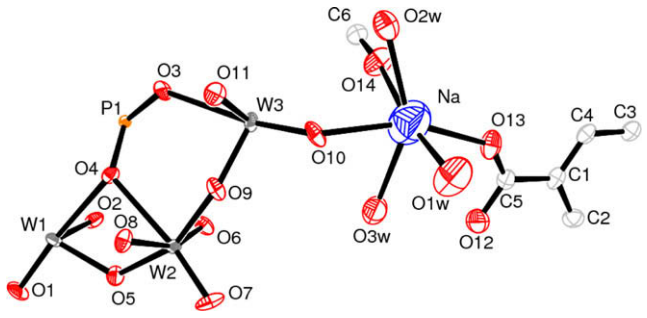


Fig. 5. An ORTEP diagram of the asymmetric unit.

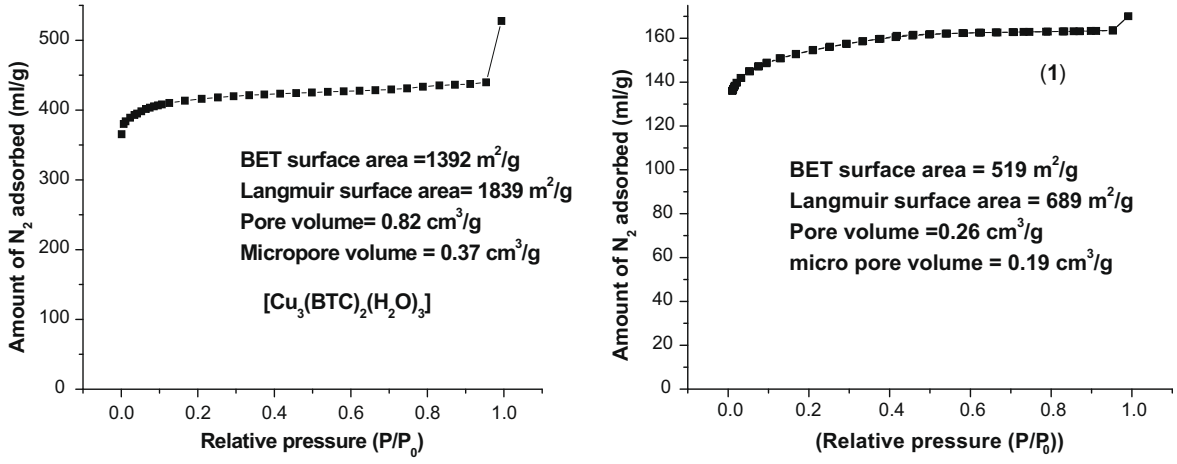


Fig. 4. Showing N_2 adsorption isotherms for $[Cu_3(BTC)_2(H_2O)_3]$ and **1**. (For interpretation of the references to color in this figure legend, the reader is referred to the web version of this article.)

O, 29.84; Na, 3.52. Found (for the crystals): H, 1.27; C, 8.40; O, 27.62; Na, 2.84%. IR (KBr, cm^{-1}) 3448 (ν_{O-H}), 1724 ($\nu_{C=O}$), 1273 (ν_{C-O}), 1620, 1403 ($\nu_{COO\ asym}$,ν_{COOsym}), 1080 ($\nu_{P-O\ asym}$), 981 ($\nu_{W=O\ asym}$), 923, 815 ($\nu_{W-Oc-W\ asym}$ and $\nu_{W-Oe-W\ asym}$) (Fig S1, Supporting data). The compound is thermally unstable, starts decomposing with effect from 27 °C and looses all organic compo-

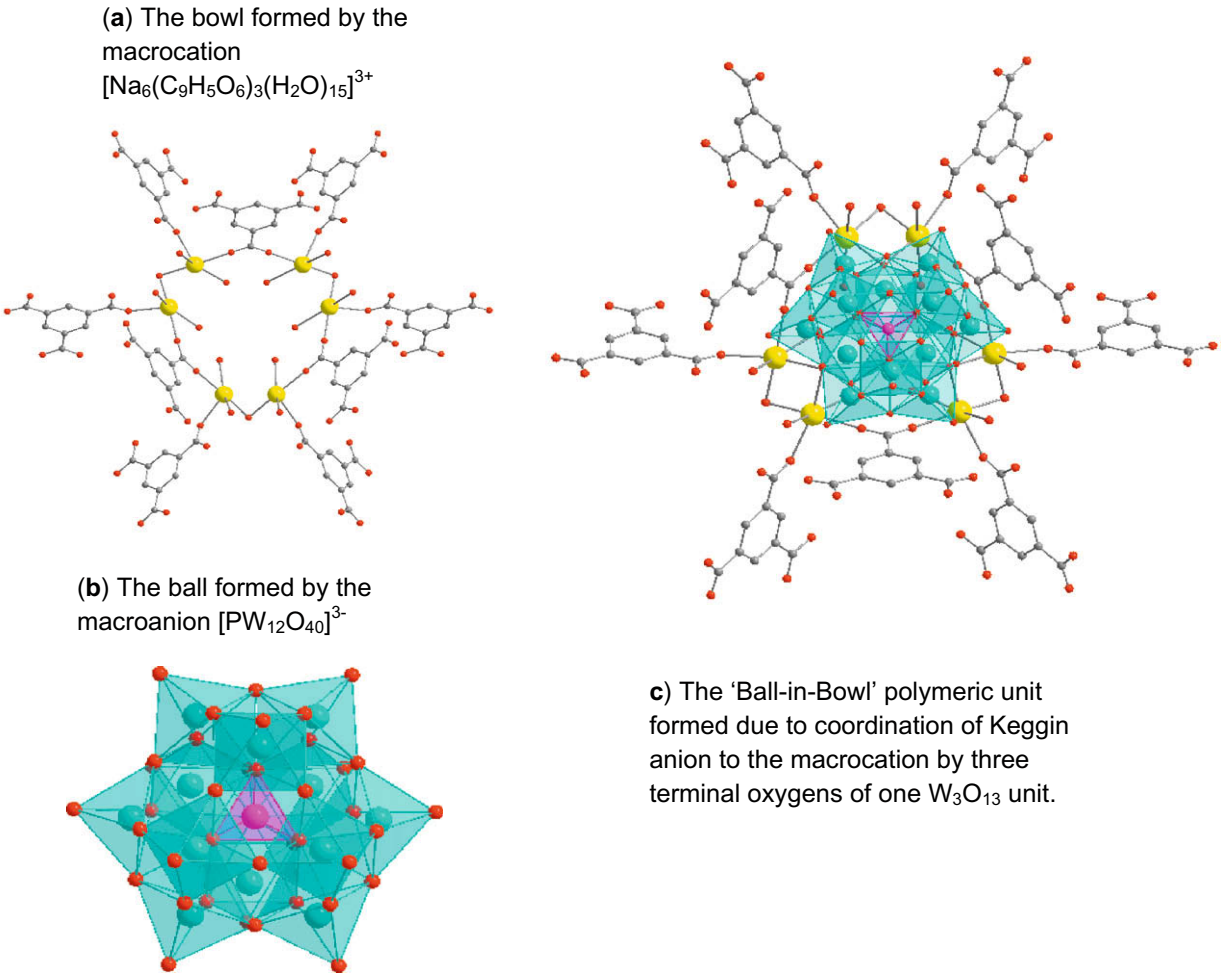


Fig. 6. Showing a ball-n-sticks, top view of two units (a) and (b) which join to form the basic repeat unit (c) in the extended polymer. C (grey), Na (yellow), O (red), W (cyan), P (purple). (For interpretation of the references to color in this figure legend, the reader is referred to the web version of this article.)

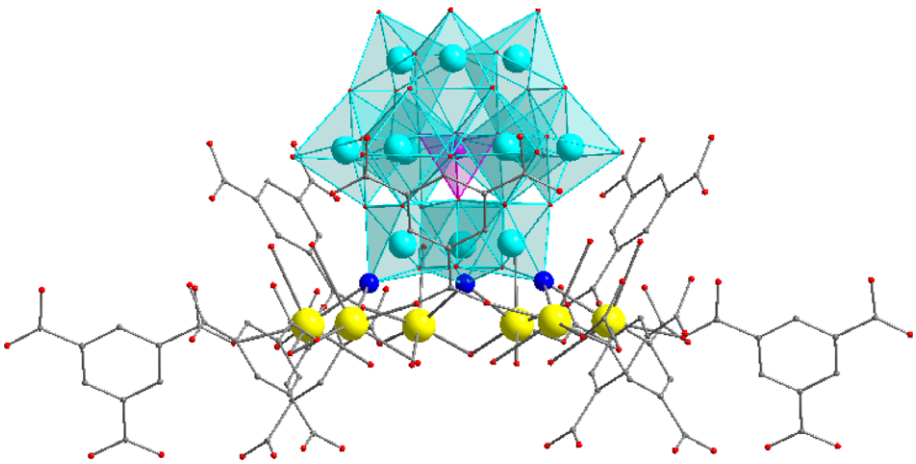


Fig. 7. A side view of the repeat unit of the extended polymer, Na^+ ions (yellow) and O_t O10 (blue) are shown in ball-n-stick representation, O (red), C (grey), W (cyan), P (purple). (For interpretation of the references to color in this figure legend, the reader is referred to the web version of this article.)

nents and water upto 300 °C (Fig S2, Supporting data) with only 10% weight loss.

2.4. Single crystal X-ray diffraction studies

One of the above-mentioned colorless crystals was used for data collection on a Bruker SMART CCD diffractometer at room temperature with Mo Kα radiation. Table 1 gives the important cell and refinement parameters. The data were reduced correcting for Lorentz and polarization and absorption corrections, in a non-centrosymmetric space group R3 m. A total of 19 075 reflections were collected out of which 3240 (R_{int} = 0.032) were unique and 3138 were considered observed ($I > 2\sigma(I)$). The structure was solved by direct methods and refined on F^2 by full-matrix least-squares refinement methods using SHELXL97 program. The distinction between $-COO^-$ and –COOH groups was made on the basis of their bond lengths (C5–O12 1.332(10), C5–O13 1.223(10), C6–O14 1.257(8) Å) which correspond to a C–O single and C═O double bond between C5–O12 and C5–O13, respectively, whereas C6–O14 and C6–O14^{i} (i = $-x + y + 1, y, z$) are equal due to symmetry restrictions, corresponding to a delocalized partial double bond. The presence of both protonated and deprotonated carboxylates is also evident in IR spectra due to peaks at 1724, 1273, 1620 and 1403 cm^{-1} [57]. During refinements O2W water molecule showed disorder in terms of high thermal parameter. The disorder could be resolved by splitting O2W at two atomic positions with partial site occupancies of 0.56 and 0.44 and a common U_{iso} parameter. All non-hydrogen atoms, including O2W were refined anisotropically. Hydrogen atoms of the water molecules were located from difference Fourier synthesis. Their positional parameters were refined initially but in the final cycles they were not refined and were assigned an isotropic thermal parameter of 0.05. The O–H distances to the disordered O2W were fixed at 1.02(2) Å. All other hydrogens were fixed geometrically with U_{eq} set at 1.2U_{eq} of their carrier atoms. The Flack's parameter value of 0.03(1) indicates that the absolute configuration is correct. The final cycle of refinement for 205 parameters, 3 restraints gave GOF = 1.030, R_1 = 0.0218, wR_2 = 0.0534 for observed reflections and R_1 = 0.0228, wR_2 = 0.0537 for all reflections. In the final difference map, the deepest hole was −0.923 e Å^3 and the highest peak was 0.869 e Å^3. A platon check of the cif shows two 'A' level alerts which need some comment: the first of them is ratio U_{eq}(max)/U_{eq}(min) = 4.89 (highest 0.0850 for O1W and lowest 0.0174 for O4) being high for O element, since there are different types of oxygens for example both terminal and bridging of Keggin anion, terminal oxygens of BTC and also of solvent water molecules so high value of this ratio is not surprising. The second alert is regarding a high U_{eq} of Na atom as compared to its neighbors. The Na atom has a U_{eq} of 0.125 which is slightly on the higher side but is not unacceptable (values of this order are routinely seen during crystal structure solutions) and owing to the small U_{eq} of different types of coordinating O atoms around it, this value seems to be higher. However, there is no chance of it being wrongly labeled as is evident from the EDAX of the compound (Fig S3, Supporting data) which clearly shows the presence of Na in it.

3. Results and discussion

The phase **1** was characterized by IR, TGA, powder XRD methods. The XRD powder pattern of **1** matches with that generated for the already reported complex [44] $[Cu_3(BTC)_2(H_2O)_3]_4[\{(CH_3)_4N\}_2(HPW_{12}O_{40})]$ as shown in Fig. 1a, the small differences in intensities for some reflections in Fig. 1a may be attributable to the cations being different (Na^+ verus $(CH_3)_4N^+$) in the two compounds. In comparison to XRD pattern of $[Cu_3(BTC)_2(H_2O)_3$ (Fig 1b) there are significant differences in the intensities but not their Bragg positions. A comparison of the IR spectra of **1** with that of $[Cu_3(BTC)_2(H_2O)_3]$ clearly shows the presence of the Keggin ion $[PW_{12}O_{40}]^{3-}$ in it due to appearance of strong peaks at ν_{P-O} 1081, $\nu_{W=O}$ 981, ν_{W-Ot-W} 900, ν_{W-Ob-W} 829,795 cm^{-1} which are absent in HKUST-1 (see Fig. 2).

The thermal stability of **1** was studied using TGA and is compared to that of HKUST-1 (Fig. 3), which again shows that **1** is different than the latter. The first step in the curves is associated with the loss of water molecules [56] and second is attributable to the disintegration of the metal-organic structure. The as-synthesized, sample **1** shows a continuous weight loss of (16.5%) up to a temperature <100 °C corresponding to a theoretical loss of 16.3% due to 45 water molecules, both coordinated and in the lattice. A second weight loss (17.7%), starting at ~270 °C disintegrates the metal-organic structure with a calculated loss of 17.4% due to a

Table 2
Some important bond lengths [Å] and angles [°].

Na–O1W	2.282(13)	W2–O6	1.883(2)
Na–O2W	2.587(16)	W2–O9	1.922(5)
Na–O3W	2.801(12)	W2–O7	1.678(5)
O13–Na	2.417(10)	W2–O8	1.923(3)
O14–Na	2.298(10)	W3–O3	2.427(6)
O10–Na	2.448(11)	W3–O9	1.874(5)
Na–Na^{i}	3.096(18)	W3–O10	1.704(8)
O1W–Na^{i}	2.282(13)	W3–O11	1.934(4)
O10–Na^{i}	2.448(11)	O11–W3^{ii}	1.934(4)
P1–O3	1.561(12)	W1–O2^{ii}	1.894(2)
P1–O4	1.523(7)	W1–O5^{iv}	1.922(5)
P1–O4^{ii}	1.523(7)	W3–O9^{i}	1.874(5)
P1–O4^{iii}	1.523(7)	W3–O11^{iii}	1.934(4)
W1–O1	1.699(8)	O2–W1^{iii}	1.894(2)
W1–O2	1.894(2)	O3–W3^{ii}	2.427(6)
W1–O4	2.455(7)	O3–W3^{iii}	2.427(6)
W1–O5	1.922(5)	O4–W2^{iv}	2.432(5)
W2–O4	2.432(5)	O6–W2^{i}	1.883(2)
W2–O5	1.909(5)	O8–W2^{iv}	1.923(3)
O1W–Na–O14	170.9(6)	O7–W2–O6	102.4(3)
O1W–Na–O13	78.4(4)	O7–W2–O5	102.7(3)
O14–Na–O13	98.4(4)	O6–W2–O5	89.7(3)
O1W–Na–O10	97.6(4)	O7–W2–O9	101.6(3)
O14–Na–O10	88.4(4)	O6–W2–O9	85.7(3)
O13–Na–O10	158.0(5)	O5–W2–O9	155.6(2)
O1W–Na–O2W	111.7(6)	O7–W2–O8	101.9(3)
O14–Na–O2W	63.0(4)	O6–W2–O8	155.7(3)
O13–Na–O2W	124.4(5)	O5–W2–O8	86.5(3)
O10–Na–O2W	77.3(5)	O9–W2–O8	87.9(3)
O1W–Na–O3W	92.4(5)	O7–W2–O4	171.6(3)
O2W–Na–O3W	147.0(5)	O6–W2–O4	84.3(3)
O14–Na–O3W	95.5(4)	O5–W2–O4	71.9(2)
O13–Na–O3W	81.0(3)	O2–W1–O4	83.5(3)
O10–Na–O3W	77.5(3)	O5^{iv}–W1–O4	71.16(18)
O4^{ii}–P1–O4^{iii}	110.0(3)	O5–W1–O4	71.15(18)
O4^{ii}–P1–O4	110.0(3)	O9–W2–O4	83.8(2)
O4^{iii}–P1–O4	110.0(3)	O8–W2–O4	71.7(2)
O4^{ii}–P1–O3	108.9(3)	O10–W3–O9^{i}	102.9(3)
O4^{iii}–P1–O3	108.9(3)	O10–W3–O9	102.9(3)
O4–P1–O3	108.9(3)	O9^{i}–W3–O9	87.1(3)
O1–W1–O2^{ii}	104.5(3)	O10–W3–O11	100.5(3)
O1–W1–O2	104.5(3)	O9^{i}–W3–O11	156.6(3)
O2^{ii}–W1–O2	85.9(4)	O9–W3–O11	89.0(3)
O1–W1–O5^{iv}	01.0(3)	O10–W3–O11^{iii}	100.5(3)
O2^{ii}–W1–O5^{iv}	88.6(3)	O9^{i}–W3–O11^{iii}	89.0(3)
O2–W1–O5^{iv}	154.5(3)	O9–W3–O11^{iii}	156.6(3)
O1–W1–O5	101.0(3)	O11–W3–O11^{iii}	85.5(5)
O2^{ii}–W1–O5	154.5(3)	O10–W3–O3	169.8(4)
O2–W1–O5	88.6(3)	O9^{i}–W3–O3	84.3(2)
O5^{iv}–W1–O5	85.8(3)	O9–W3–O3	84.3(2)
O1–W1–O4	169.0(3)	O11–W3–O3	72.3(3)
O2^{ii}–W1–O4	83.5(3)	O11^{iii}–W3–O3	72.3(3)

I: $-y + 1, -x + 1, z$; ii: $-y + 1, x - y, z$; iii: $-x + y + 1, -x + 1, z$; iv: $x, x - y, z$.

complete transformation into 6 molecules of CuO and one of $Na_3[PW_{12}O_{40}]$, per formula unit.

A SEM image of **1** (Fig S4, Supporting data) shows that the compound is homogeneous and crystalline in nature with octahedron shaped crystals having large particle size (av. $\geqslant$20 μm). To compare the permanent porosity of **1** with $[Cu_3(BTC)_2(H_2O)_3]$ we have obtained the N_2 adsorption–desorption isotherms of the purified samples at −196 °C after evacuation at 150 °C for 12 h. The nitrogen physiosorption isotherms (Fig. 4) for both compounds are of type I, however the BET surface area of **1** 519 m^2/g and a total pore volume of 0.26 cm^3/g are much smaller than those found for $[Cu_3(BTC)_2(H_2O)_3]$ by us and others [56]. A considerable decrease (~62%) in the surface area indicates that a large amount of Keggin anions get accumulated within the pores of the MOF material, which is consistent with the results of the reported crystal structure for the compound [44] which shows that alternate pores of the MOF are occupied by the Keggin anion. Such a decrease in surface area and percentage loss of weight in TGA has been seen in the case of an inclusion complex of another Keggin polyanion $K_7[PW_{11}O_{40}]\cdot nH_2O$ in the porous MIL-101 MOF [42].

A solid state UV–Vis absorption spectrum of **1** compared to $[Cu_3(BTC)_2(H_2O)_3]$ (Fig S5, Supporting data) shows that both of them exhibit an intense CT band centered at 472 nm (21 186 cm^{-1}) and another weak, very broad band centered at 700 nm (14 388 cm^{-1}). The latter is considered to be the *d*–*d* band typical of copper(II) carboxylate complexes [58] and shows a lot of vibrational fine structure in it. There is no significant shift in the spectra of the two compounds which indicates that incorporation of Keggin into $[Cu_3(BTC)_2(H_2O)_3]$ has not altered the immediate coordination sphere of the metal ion and in turn also supports its inclusion in the pores of the MOF only.

3.1. X-ray crystal structure of compound **2**

An ORTEP diagram of the asymmetric unit is shown in Fig. 5. The solid state structure of the polymer comprises of two components i.e. a macrocation $[Na_6(C_9H_5O_6)_3(H_2O)_{15}]^{3+}$ and the Keggin anion $[PW_{12}O_{40}]^{3-}$ as shown in Fig. 6. The hexameric macrocation is formed by the self-assembly of three dimeric $[Na_2(C_9H_5O_6)(H_2O)_5]^+$ units. In the dimeric unit each Na^+ ion is terminally bound by two water molecules (O2W, O3W) and carbonyl oxygen O13 of one of the protonated carboxylic groups of BTC-H_2. Third water molecule O1W bridges between two Na^+ ions in the dimer. Three such dimeric units are then joined to form a hexameric macrocation due to bridging bidentate coordination by the only deprotonated carboxylic group O14–C6–O14^i from three $[BTC\text{-}H_2]^-$ anions (i = $-x + y + 1, y, z$). The Na^+ ions in this hexameric, a puckered bowl shaped macrocation, are in turn coordinated to three terminally bonded, W=O (O_t) oxygens, O10 of the Keggin anion. The unusual feature here is that the Keggin anion $[PW_{12}O_{40}]^{3-}$ is coordinated to Na^+ ions via these three O_t oxygens O10 which belong to a single W_3O_{13} triplet and each O10 is bridging between two Na^+ ions of the dimeric unit, conforming the threefold symmetry of the lattice. Such coordination of a Keggin ion, through O_t of one M_3O_{13} triplet has only been seen in the molecular complex [{Na(dibenzo-18-crown-6)(MeCN)}$_3${$PMo_{12}O_{40}$}] [59] but to the best of our knowledge, they have never been found in a bridging coordination mode at the same time. This type of coordination places the globular Keggin anion like a "golf ball on a Tee" in the bowl of macrocation as shown in the top view (Fig. 6) and side view (Fig. 7).

The $[PW_{12}O_{40}]^{3-}$ unit has a classical α-Keggin type geometry, which consists of a central PO_4 tetrahedron surrounded by 12 WO_6 octahedrons (Fig. 6), present in the four W_3O_{13} groups. No

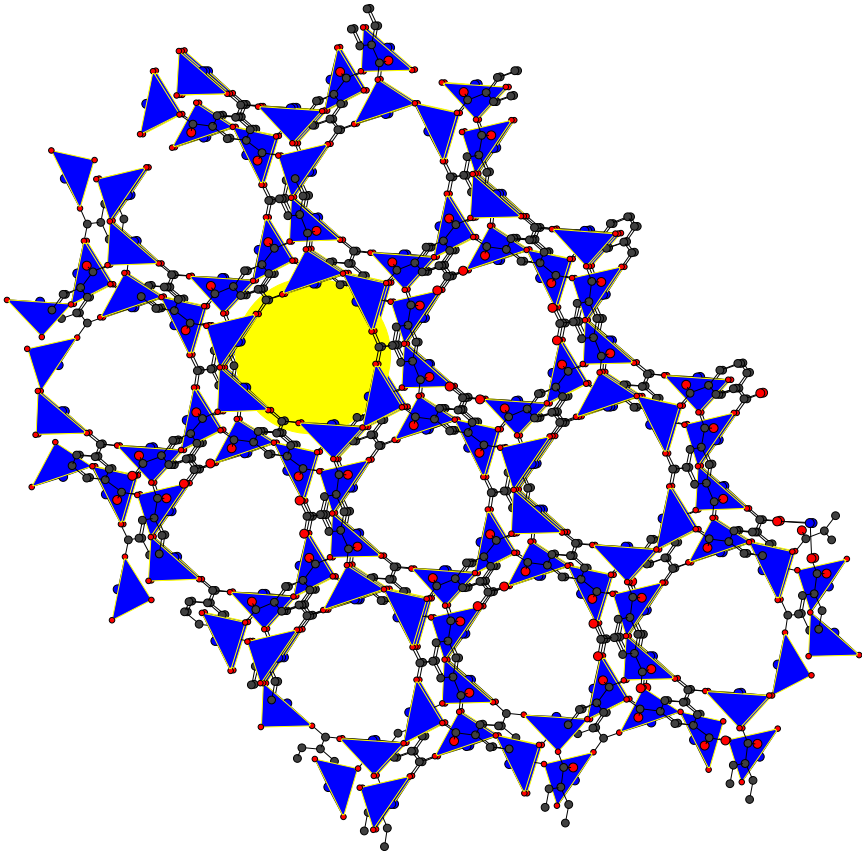


Fig. 8. Showing extended MOF formed by self-assembly of $[Na_6(C_9H_5O_6)_3(H_2O)_{15}]^{3+}$ cations. The Keggin anion and hydrogen atoms have been removed to show the channels and triangular voids (yellow dummy atom) down the *c* axis, Na octahedra (blue), C (black), O (red). (For interpretation of the references to color in this figure legend, the reader is referred to the web version of this article.)

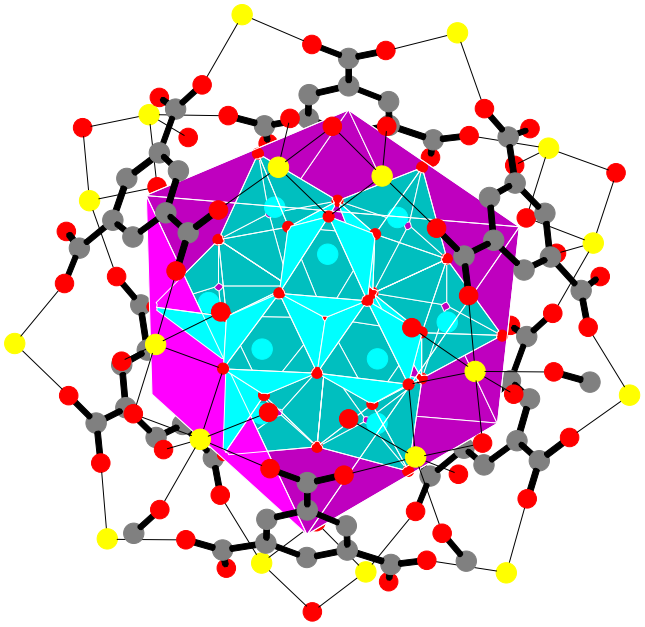


Fig. 9. Showing a Keggin anion encapsulated in an octahedral space (purple) created by six BTC anions, down the *c* axis, C (black), Na (yellow), W (cyan), O(red). (For interpretation of the references to color in this figure legend, the reader is referred to the web version of this article.)

disorder was seen in the anion unlike that reported earlier for same anion [29] and other similar anions containing α-Keggin structures [33,60–64]. The P–O distances 1.523(7), 1.561(12) Å fall in the range 1.52(2)–1.58(2) Å reported earlier [65]. The oxygen atoms are divided according to their different coordination environments into three groups, O_t (W=O), O_b (W–O–W) and O_c (P–O–W). The average observed distances (Table 2) in these categories 1.693(7), 1.909(4) and 2.441(7) Å, respectively, fall in the ranges 1.660(18)–1.719(17), 1.81(2)–1.935(16) and 2.33(3)–2.46(3) Å found [33,65] earlier.

The coordination polyhedrons around Na^+ ions in each dimeric unit may be defined as distorted, edge sharing octahedrons. A Na···Na interaction is present at 3.096(18) Å to augment this distortion. The Na–O bond lengths vary from the shortest Na–O1W 2.282(13) to the longest Na–O3W 2.801 Å. The three *trans* O–Na–O angles are O1W–Na–O14 170.9(6), O13–Na–O10 158.0(5) and O2W–Na–O3W 147.0(5), with the latter being largely responsible for the distortion, as discussed later. The coordination to Na^+ ions by the terminal oxygens of polyoxometalate anions has been seen in many crystals [59,66] Such interactions are most common for Na^+ ion than any other alkali metal ion with a coordination number of six, including the water molecules.

The self-assembly of three dimeric units via BTC forming a hexameric macrocation coupled with the Y type, four coordinating BTC ligand creates a 3D network with channels running down the *c* axis (Fig. 8). Each channel presents an equilateral triangular void with side being 8.2 Å (C6···C6^{i} i = −x + y, 2 − *x*,*z*). The Keggin anion sits on these triangular voids using three terminal oxygens of a single W_3O_{13} triplet like a tripod stand.

Although the 12 terminal oxygens of Keggin anion are in the same environment but this uneven distribution of the Keggin ion over the macrocation, using the three terminal oxygens like a 'Tee' may be attributed to the complementarity of the void. The shape and size of the void is tailor made to hold the Keggin anion in this position, just above the cavity totally in compliance with the threefold symmetry of the molecular and crystal system. In the extended 3D structure of the MOF each Keggin anion finds itself enclosed in a capsule created by six octahedrally disposed $(BTC\text{-}H_2)^-$ ligands (Fig. 9) with diagonal and edge (centroid to centroid) distances of 13.15 and 10.26 Å, respectively.

The 3D coordination polymer is further stabilized by an extensive network of strong H-bonding interactions. Looking down the channel axis i.e. parallel to the *c* axis, the three terminal oxygens O10 and O1 lie in a plane parallel to it and the remaining six terminal oxygens O7 are in a perpendicular plane. Unlike the three symmetry related O_t oxygens, O10 of Keggin anion which are coordinated to the macrocation from below, the O_t oxygens O1 at the other end are doubly H-bonded to six O2W water molecules belonging to the macrocation lying above it (Fig. 10a). Thus the molecules are stacked one above the other along the *c* axis due to alternate coordinating and H-bonding interactions. The six O2W water molecules have moved inside towards the triangular cavity to facilitate strong H-bonding interactions among them. This decreases ∠O3W–Na–O2W to 147° and distorts the coordination polyhedron around Na^+ ion as mentioned above. The driving force for this distortion is the formation of a H-bonded hexamer of O2W water molecules as described below. Each O2W water molecule in the dimeric $[Na_2(C_9H_5O_6)(H_2O)_5]^+$ entity is held at a O···O non-bonding distance of 2.39(3) Å (O2W···O2W^{vi}) and 3.30(3) Å (O2W···O2W^{iii}) (Table 3) from its counterparts in the adjacent and in the same dimer, respectively. Apparently ∠O2W–H21···O2W^{vi} is quite small (73°(2)) and H21···O2W^{vi} (2.48 Å) is

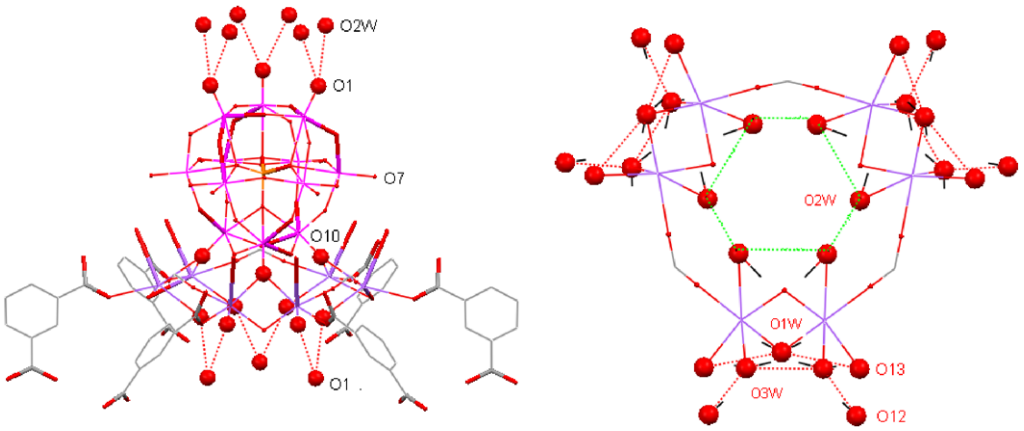


Fig. 10. (a) (Left) shows O2W···O1 H-bonding interactions and O10–Na coordinate bonds responsible for stacking along *c* axis. (b) (Right) shows a supramolecular water hexamer of O2W and dimer of O3W due to H-bonding. O (red), C (grey), W (pink), P (yellow), Na (blue). One carboxylate group from each $(BTC\text{-}H_2)$ ligand has been removed for clarity. (For interpretation of the references to color in this figure legend, the reader is referred to the web version of this article.)

Table 3
Showing important H-bonding interactions.

D–H···A	D···A	H···A	D–H···A
O12–H12···O3W	2.756(8)	1.96	162
O1W–H1W···O13	2.973(12)	2.44	120
O1W–H1W···O12^{i}	3.734(18)	2.92	157
O3W–H31W···O7	3.260(11)	2.31	163
O3W–H32W···O10	3.299(9)	2.89	105
O3W–H31W···O13^{ii}	3.233(10)	2.58	124
O3W–H32W···O3W^{iii}	2.884(13)	2.00	144
O2W–H22···O10	3.138(19)	2.27	125
O2W–H21···O12^{i}	3.186(14)	2.69	121
O2W–H22···O2W^{iii}	3.297(29)	2.62	113
O2W–H21···O1^{iv}	2.923(17)	2.19	150
O2W–H21···O1^{v}	2.923(17)	2.19	150

(i) $-y+1/3+1,+x-y+2/3+1,+z-1/3$; (ii) $-x+y-1/3,-x+1/3+1,+z+1/3$; (iii) $-x+y,+y,+z$; (iv) $x,+y,+z-1$; (v) $x,+x-y+2,+z-1$; (vi) $-x+y+1,+y,+z$.

longer than O2W···O2W^{vi} to call it a O2W–H21···O2W^{vi} H-bond. But considering that O2W is a disordered molecule (only atom of higher partial occupancy being used in H-bond calculations), position of H-atoms is not unambiguous and most importantly owing to the short O2W···O2W^{vi} distance, it is reasonable to consider that there exists a H-bond between O2W···O2W.^{vi} This interaction coupled with O2W–H22···O2W^{iii} H-bond creates a supramolecular water hexamer (Fig. 10b) out of O2W molecules. This water hexamer serves as a base of the bowl type $[Na_6(C_9H_5O_6)_3(H_2O)_{15}]^{3+}$ hexameric macrocation and coordinates to the six Na^+ ions in it. Apart from this O2W is intramolecularly H-bonded to O10 and donates H-bond to carboxylic O12 also, hence forming links between Keggin anion and BTC-H_2 ligand. The second terminally bonded water molecule O3W is self H-bonded to its counterpart in the dimeric unit $[Na_2(C_9H_5O_6)(H_2O)_5]^+$ thus producing a supramolecular water dimer. It also acts as a H-bond donor towards carbonyl O13 and terminal oxygens O7 and O10 of the Keggin ion and accepts a H-bond from the carboxylic O12. The bridging water molecule O1 W is acting as a H-bond donor to O13.

4. Conclusions

In conclusion, a hydrothermal synthesis of an inclusion complex from HKUST-I and Keggin anion $[PW_{12}O_{40}]^{3-}$ results in encapsulation of the guests in half of the pores of the nanoporous MOF forming **1**. Whereas a room temperature attempt to do the same has resulted in dissociation of the HKUST-1 nanoporous material, leading to a novel 3D extended network involving Na, BTC-H_2 and Keggin ions and is non-porous in nature. The inorganic/organic porous hybrid is formed by coordination assembly of Na^+, partially deprotonated $[BTC\text{-}H_2]^-$ anion and water molecules where the pores are completely occupied by the Keggin ions which reside on top of them. The Keggin ions are not diffused into the cavities in the hybrid material but rather form coordination bonds with Na^+ ions through three terminally bonded oxygens from one W_3O_{13} triplet which are also bridging between two Na^+ ions at the same time. This is a unique coordination mode of the Keggin ion, to the best of our knowledge and forms one of the lesser known alkali metal linked POM having 3D structures. Extensive H-bonding interactions result in the formation of supramolecular water hexamers and dimers in the crystal structure.

Acknowledgement

This work was supported by Ministry of Knowledge Economy (MKE) through the Research Center for Nanocatalysts and partially Korea Research Council Industrial Science and Technology (ISTK) through the Institutional Research Program. Dr. Geeta Hundal gratefully acknowledges KOFST for awarding Brain Pool fellowship at KRICT, South Korea.

Appendix A. Supplementary data

CCDC 699004 contains the supplementary crystallographic data for **2**. These data can be obtained free of charge via http://www.ccdc.cam.ac.uk/conts/retrieving.html, or from The Cambridge Crystallographic Data Centre, 12 Union Road, Cambridge CB2 1EZ, UK; fax: (+44) 1223-336-033; or e-mail: deposit@ccdc.cam.ac.uk. Supplementary data associated with this article can be found, in the online version, at doi:10.1016/j.poly.2009.04.025.

References

[1] M.T. Pope, A. Müller, Polyoxometalate Chemistry: From Topology via Self-Assembly to Applications, Kluwer, Dordrecht, The Netherlands, 2001.
[2] T. Yamase, M.T. Pope, Polyoxometalate Chemistry for Nano-Composite Design, Kluwer, Dordrecht, The Netherlands, 2002.
[3] L. Xu, M. Lu, B.B. Xu, Y.G. Wei, Z.H. Peng, D.R. Powell, Angew. Chem., Int. Ed. 41 (2002) 4129.
[4] D.G. Kurth, P. Lehmann, D. Volmer, A. Muller, D. Schwahn, J. Chem. Soc., Dalton Trans. (2000) 3989.
[5] P. Mialane, A. Dolbecq, J. Marrot, E. Riviere, F. Secheresse, Chem. Eur. J. 11 (2005) 1771.
[6] I.M. Botto, D.A. Barrio, M.G. Egusquizza, C.I. Cabello, A.M. Cortizo, S.B. Etcheverry, Met. Ion. Biol. Med. 7 (2002) 159.
[7] X. Wang, J. Liu, J. Li, Y. Yang, J. Liu, B. Li, M.T. Pope, J. Inorg. Biochem. 94 (2003) 279.
[8] T. Ruether, V.M. Hultgren, B.P. Timco, B.P.A.M. Bond, W.R. Jackson, A.G. Wedd, J. Am. Chem. Soc. 125 (2003) 10133.
[9] C.L. Hill, Comprehensive Coordination Chemistry II, in: J.A. McClerverty, T.J. Meyer (Eds.), Elsevier Lrd., Oxford, UK, 2004.
[10] C.-M. Liu, D.-Q. Zhang, M. Xiong, D.-B. Zhu, Chem. Commun. (2002) 1416.
[11] J.-Y. Niu, Q. Wu, J.-P. Wang, J. Chem. Soc., Dalton Trans. (2002) 2512.
[12] W.-M. Bu, L. Ye, G.-Y. Yang, J.-S. Gao, Y.-G. Fan, M.-C. Shao, J.-Q. Xu, Inorg. Chem. Commun. 4 (2001) 1.
[13] M.I. Khan, J. Solid State Chem. 152 (2000) 105.
[14] D.J. Chesnut, D. Hagrman, P.J. Zapf, R.P. Hammond, R. Laduca, R.C. Haushalter, J. Zubieta, J. Coord. Chem. Rev. 192 (1999) 73.
[15] A. Müller, M. Koop, P. Schiffels, H. Bögge, J. Chem. Soc., Chem. Commun. (1997) 1715.
[16] J.R.D. Debord, R.C. Haushalter, L.M. Meyer, D.J. Rose, P.J. Zapf, J. Zubieta, Inorg. Chim. Acta 256 (1997) 165.
[17] I. Loose, M. Bösing, R. Klein, B. Krebs, R.P. Schultz, B. Scharbert, Inorg. Chim. Acta 263 (1997) 99.
[18] S. Reinoso, P. Vitoria, J.M. Gutiérrez-Zorrilla, L. Lezama, L.S. Felices, J.I. Beitia, Inorg. Chem. 44 (2005) 9731.
[19] S.T. Zheng, J. Zhang, G.Y. Yang, Angew. Chem., Int. Ed. 47 (2008) 3909.
[20] R.N. Devi, J. Zubieta, Inorg. Chim. Acta 332 (2002) 72.
[21] V. Shivaiah, P.V.N. Reddy, L. Cronin, S.K. Das, J. Chem. Soc., Dalton Trans. (2002) 3781.
[22] (a) M. Sadakane, M.H. Dickman, M.T. Pope, Angew. Chem. 112 (2000) 3036; (b) M. Sadakane, M.H. Dickman, M.T. Pope, Angew. Chem., Int. Ed. 39 (2000) 2914.
[23] P. Mialane, L. Lisnard, A. Mallard, J. Marrot, E. Antic-Fidancev, P. Aschehoug, D. Vivien, F. Sécheresse, Inorg. Chem. 42 (2003) 2102.
[24] P. Mialane, A. Dolbecq, F. Sécheresse, Chem. Commun. (2006) 3477.
[25] J.-Y. Niu, M.-L. Wei, J.-P. Wang, D.-B. Dang, Eur. J. Inorg. (2004) 160.
[26] J. Fischer, I. Ricard, R. Weiss, J. Am. Chem. Soc. 98 (1976) 3050.
[27] B. Botar, T. Yamase, E. Ishikawa, Inorg. Chem. Commun. 3 (2000) 579.
[28] M. McCann, K. Maddock, C. Cardin, M. Convery, V. Quillet, Polyhedron 13 (1994) 835.
[29] N. Honma, K. Kusaka, T. Ozeki, Chem. Commun. (2002) 2896.
[30] S. Manikumari, V. Shivaiah, S.K. Das, Inorg. Chem. 41 (2002) 6953.
[31] X. Chen, S. Lin, L. Chen, X. Chen, C. Liu, J. Chen, L. Yang, Inorg. Chem. Commun. 10 (2007) 1285.
[32] A. Dolbecq, P. Mialane, L. Lisnard, J. Marrot, F. Sécheresse, Chem. Eur. J. 9 (2003) 2914.
[33] M.X. Li, J. Du, J.-P. Wang, J.-Y. Niu, Inorg. Chem. Commun. 10 (2007) 1391. and references [11–20] therein.
[34] M. Nyman, F. Bonhomme, T.M. Alam, M.A. Rodriguez, B.R. Cherry, J.L. Krumhansl, T.M. Nenoff, A.M. Sattler, Science 297 (2002) 996.
[35] P.Q. Zheng, Y.P. Ren, L.S. Long, R.B. Huang, L.S. Zheng, Inorg. Chem. 44 (2005) 1190.
[36] F.X. Liu, C. Marchal-Roch, P. Bouchard, J. Marrot, J.P. Simonato, G. Herve, F. Sécheresse, Inorg. Chem. 43 (2004) 2240.
[37] H.-Y. An, E.-B. Wang, D.-R. Xiao, Y.-G. Li, Z.-M. Su, L. Xu, Angew. Chem. Int. Ed. 45 (2006) 904.

[38] L. Lisnard, A. Dolbecq, P. Mialane, J. Marrot, F. Sécheresse, Inorg. Chim. Acta 357 (2004) 845.
[39] T. Okuhara, N. Mizuno, M. Misono, Adv. Catal. 41 (1996) 113.
[40] I.V. Kozhevnikov, A. Sinnema, R.J.J. Jansen, H. van Bekkum, Catal. Lett. 30 (1995) 241.
[41] S.R. Mukai, T. Masuda, I. Ogino, K. Hashimoto, Appl. Catal. A 165 (1997) 219.
[42] G. Férey, C. Mellot-Draznicks, C. Serre, E. Millange, J. Dutour, S. Surblé, I. Margiolaki, Science 309 (2005) 2040.
[43] A. Müller, S.K. Das, P. Kögerler, H. Bögge, M. Schmidtmann, E. Krickemeyer, W. Preetz, Angew. Chem., Int. Ed. Engl. 39 (2000) 3414.
[44] L. Yang, H. Naruke, T. Yamase, Inorg. Chem. Commun. 6 (2003) 1020.
[45] C. Serre, F. Millange, S. Surblé, G. Férey, Angew. Chem., Int. Ed. 43 (2004) 6285.
[46] L. Pan, X. Huang, J. Li, Y. Wu, N. Zheng, Angew. Chem., Int. Ed. 38 (1999) 2638.
[47] M.C. Hong, Y.J. Zhao, W.P. Su, R. Cao, M. Fujita, Z.Z. Zhou, S.C. Albert, J. Am. Chem. Soc. 122 (2000) 4819.
[48] O.M. Yaghi, H. Li, C. Davis, D. Richardson, T.L. Groy, Acc. Chem. Res. 31 (1998) 474.
[49] K.T. Holman, A.M. Pivovar, J.A. Swift, M.D. Ward, Acc. Chem. Res. 34 (2001) 107.
[50] B. Moultonand, M.J. Zaworotko, Chem. Rev. 101 (2001) 1629.
[51] M. Eddaoudi, J. Kim, N. Rosi, D. Vodak, J. Wachter, M. O'Keeffe, O.M. Yaghi, Science 295 (2002) 469.
[52] N.W. Ockwig, O. Delgado-Friedrichs, M. O'Keeffe, O.M. Yaghi, Acc. Chem. Res. 38 (2005) 176.
[53] O.M. Yaghi, M. O'Keeffe, N.W. Ockwig, H.K. Chae, M. Eddaoudi, J. Kim, Nature 423 (2003) 705.
[54] C.J. Kepert, T.J. Prior, M.J. Rosseinsky, J. Am. Chem. Soc. 122 (2002) 5158.
[55] S.S.-Y. Chui, S.M.-F. Lo, J.P.H. Charmant, A.G. Orpen, I.D. Williams, Science 283 (1999) 1148.
[56] Y.-K. Seo, G. Hundal, I.T. Jang, Y.K. Hwang, C.-H. Jun, J.-S. Chang, Micropor. Mesopor. Mater. (2008), doi:10.1016/j.micromeso.2008.10.035 and references [18–27] therein.
[57] C. Streb, D.-L. Long, L. Cronin, Chem. Commun. (2007) 471.
[58] A.B.P. Lever, Inorganic Electronic Spectroscopy, Elsevier, Amsterdam, 1968.
[59] W. You, E. Wang, Y. Xu, Y. Li, L. Xu, C. Hu, Inorg. Chem. 40 (2001) 5468.
[60] X. Lu, R. Zhong, S. Liu, Y. Liu, Polyhedron 16 (1997) 3865.
[61] J. Peng, E.B. Wang, Y.S. Zhou, J. Chem. Soc., Dalton Trans. (1998) 3865.
[62] R. Neier, C. Trojanowski, R. Mattes, J. Chem. Soc., Dalton Trans. (1995) 2521.
[63] H.T. Evans, M.T. Pope, Inorg. Chem. 23 (1984) 501.
[64] P.L. Maguerés, L. Ouahab, S. Golhen, D. Grandjean, O. Pena, J.C. Jegaden, C.J. Gomez-Garcia, P. Delhaés, Inorg. Chem. 33 (1994) 5180.
[65] W. You, E. Wang, H. Zhang, L. Xu, Y. Wang, J. Mol. Struct. 554 (2000) 141.
[66] B. Hedman, R. Strandberg, Acta Crystallogr., Sect. B 35 (1979) 278. and references therein.

Polyhedron 28 (2009) 2459–2465

Contents lists available at ScienceDirect

Polyhedron

journal homepage: www.elsevier.com/locate/poly

Structures of Co, Pd and Ni complexes with iminopyridine ligands having an hydroxymethyl or acrylate pendant group

Junpei Kuwabara [1], Daisuke Takeuchi, Kohtaro Osakada *

Chemical Resources Laboratory, Tokyo Institute of Technology, 4259 Nagatsuta, Midori-ku, Yokohama 226-8503, Japan

ARTICLE INFO

Article history:
Received 16 March 2009
Accepted 23 April 2009
Available online 21 May 2009

Keywords:
Iminopyridine ligand
Palladium
Cobalt
Nickel
Aqua complex

ABSTRACT

Co(II), Pd(II) and Ni(II) complexes with iminopyridine ligands have different coordination structures in the solid state, depending on the metal, pendant group of the pyridyl ring and recrystallization conditions. The iminopyridine ligand having an acrylate group, Ar–N=CH-2,6-C_5H_3N–CH_2–OCO–CH=CH_2 (**L**^{1}: Ar = 2,6-diisopropylphenyl), forms a Co(II) complex whose metal center has a trigonal pyramidal coordination with two chloride ligands and an *N,N'*-bidentate ligand **L**^{1}. Both **L**^{1} and the iminopyridine ligand with a CH_2OH pendant on the pyridyl ring, Ar–N=CH-2,6-C_5H_3N–CH_2–OH (**L**^{2}: Ar = 2,6-diisopropylphenyl), coordinate to the $PdCl_2$ moiety, giving complexes with a square–planar coordination. The reaction of **L**^{1} with [$NiBr_2(H_2O)_3$] and recrystallization of the products forms crystals which contain mono- and dinuclear complexes with aqua ligands and the *N,N'*-bidentate ligand. **L**^{2} is coordinated to the Ni(II) center as an *N,N',O*-tridentate ligand. Recrystallization of the products of the reaction of **L**^{2} with [$NiBr_2(H_2O)_3$] with and without excess H_2O in the solution yields crystals of the cationic octahedral complex with two aqua ligands [$NiBr(H_2O)_2$(**L**^{2})]Br and the neutral square pyramidal complex [$NiBr_2$(**L**^{2})], respectively.

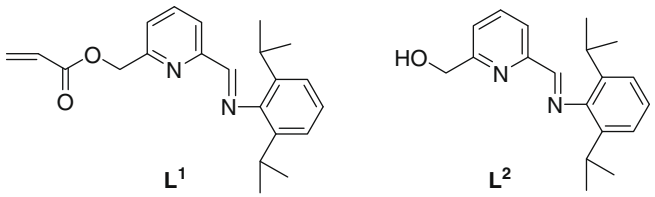
© 2009 Elsevier Ltd. All rights reserved.

1. Introduction

Iminopyridine derivatives have been extensively employed as ligands of transition metal complexes. The aromatic ligands whose conformation is fixed by coordination to a metal center act as a mesogen of liquid crystalline molecules, and Cu complexes with such ligands are expected to be liquid crystalline materials [1]. Iminopyridine ligands provide convenient building blocks of supramolecules, partly because ligands with various functional groups can be obtained easily by simple condensation reactions of amines and 2-formylpyridine derivatives, forming a new C=N bond [2–4]. Introduction of a polar hydroxy group on the iminopyridine ligand allows the formation of supramolecular assemblies with the molecules having a hydrogen-bond acceptor group, via hydrogen bonds [3,4]. Catalysis is another important research topic for transition metal complexes with iminopyridine ligands [5]. In particular, bis(imino)pyridine complexes of Fe and Co exhibit high activity for olefin polymerization [6,7]. Recently, we reported the synthesis of heterobimetallic complexes having Co, Pd and Ni metal centers and iminopyridine ligands, and their unique behavior as catalysts for polymerization [8]. During the study, we characterized mononuclear Co(II), Pd(II) and Ni(II) complexes which were prepared as intermediates for dinuclear complexes, and found different coordination modes of the ligand depending on the metal and the ligand. Herein, we report the syntheses and crystal structures of Co(II), Pd(II) and Ni(II) complexes having iminopyridine ligands with hydroxy or acrylate groups, and the interaction between the metal centers and these groups in the crystalline state.

2. Results and discussion

Iminopyridine ligands having an acrylate group, Ar–N=CH-2,6-C_5H_3N–CH_2–OCO–CH=CH_2 (**L**^{1}; Ar = 2,6-diisopropylphenyl) [8], and a hydroxy group, Ar–N=CH-2,6-C_5H_3N–CH_2–OH (**L**^{2}), were synthesized by the condensation reactions of 2,6-diisopropylaniline with the corresponding aldehyde (Chart 1). The reaction of

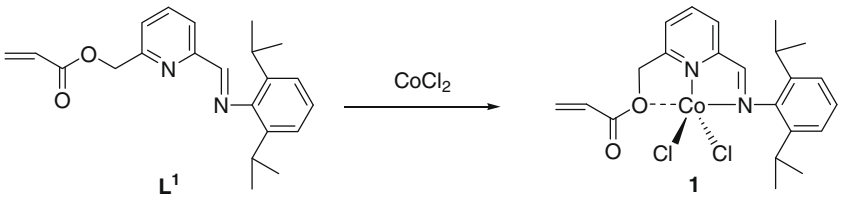


L^1 **L**^{2}

Chart 1.

* Corresponding author. Fax: +81 45 924 5224.
E-mail address: kosakada@res.titech.ac.jp (K. Osakada).
[1] Present address: Tsukuba Research Center for Interdisciplinary Materials Science (TIMS), Graduate School of Pure and Applied Science, University of Tsukuba, 1-1-1 Tennoudai, Tsukuba 305-8573, Japan.

0277-5387/$ - see front matter © 2009 Elsevier Ltd. All rights reserved.
doi:10.1016/j.poly.2009.04.050



Scheme 1.

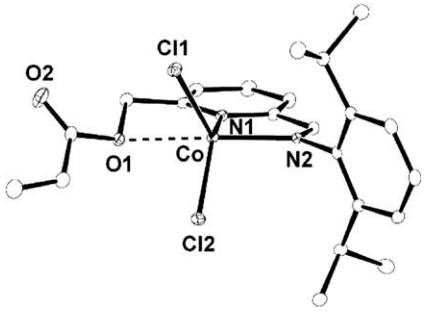


Fig. 1. ORTEP drawing of **1** with thermal ellipsoids shown at the 30% probability level. Hydrogen atoms are omitted for clarity.

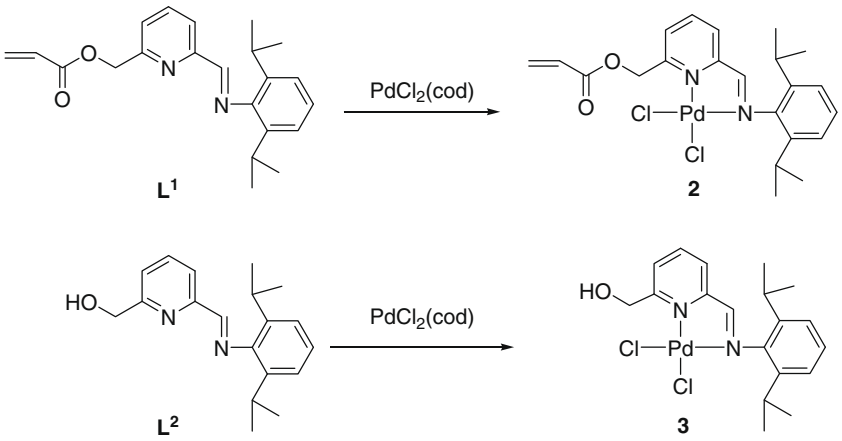
L^{1} with $CoCl_2$ afforded the Co-iminopyridine complex **1** (Scheme 1). The crystal structure of **1** is shown in Fig. 1. Table 1 summarizes selected bond parameters. Sum of the N1–Co–Cl1, N1–Co–Cl2 and Cl1–Co–Cl2 angles (353.46°) is close to 360°, and the coordination is recognized to be distorted trigonal pyramidal with the N2 atom at the apical position. The ether oxygen atom (O1) of the acrylate group seems to occupy the remaining apical site by a weak interaction with the Co center, with a distance of 2.690 Å. The Zr–Co bimetallic complex, with a similar coordination of the iminopyridine to Co, has a slightly longer Co–O distance (2.774 Å). Co complexes with acetyl- or ester-substituted iminopyridine ligands have a penta-coordinated structure with coordination of the carbonyl group (Co–O lengths = 2.327 and 2.374 Å) [9,10]. The bond parameters around Co are similar between $CoCl_2$(Ar–N=CH-2,6-C_5H_3N–CO–CH_3) (Ar = 2,6-diisopropylphenyl) and **1**, with the exception of the short Co–O bond in the former complex.

The reactions of **L**^{1} and **L**^{2} with [$PdCl_2$(cod)] (cod = 1,5-cyclooctadiene) afforded complexes **2** and **3**, respectively (Scheme 2). Fig. 2 shows the crystal structures of the Pd complexes with the *N*,*N*′-bidentate iminopyridine ligands. Each Pd center has a distorted square–planar geometry without any remarkable interaction with the acrylate or hydroxy pendant group. The square

Table 1
Selected bond distances (Å) and angles (°) for complexes **1–5b**.

	1 (M=Co, X=Cl)	**2** (M=Pd, X=Cl)	**3** (M=Pd, X=Cl)	**4a** (M=Ni, X=Br)	**4b** (M=Ni, X=Br)	**5a** (M=Ni, X=Br)	**5b** (M=Ni, X=Br)
M–X1	2.2420(6)	2.2819(6)	2.302(2)	2.4408(5)	2.5085(6)	2.3935(7)	2.4690(7)
M–X2	2.2290(7)	2.2625(7)	2.258(2)	2.4296(5)	2.4338(6)	2.4134(9)	
M–N1	2.063(2)	2.121(2)	2.096(7)	2.094(3)	2.078(3)	2.005(3)	2.006(2)
M–N2	2.105(2)	2.009(2)	2.021(6)	2.025(3)	2.043(3)	2.135(3)	2.127(3)
M–O1						2.137(4)	2.248(2)
M–O2							2.049(3)
M–O3				2.107(3)			2.089(2)
X1–M–X2	113.13(2)	86.61(2)	86.99(9)	139.55(2)	144.94(2)	107.86(3)	
X1–M–N1	129.51(6)	101.86(5)	101.0(2)	91.97(9)	89.10(9)	150.7(2)	172.8(1)
X1–M–N2	100.44(5)	175.33(6)	172.3(2)	108.70(9)	104.70(9)	102.33(9)	106.23(9)
X2–M–N1	110.82(6)	171.43(5)	172.0(2)	93.95(9)	91.40(8)	100.8(1)	
X2–M–N2	117.66(5)	91.12(6)	92.0 (2)	111.73(9)	109.97(9)	100.6(1)	
N1–M–N2	79.66(7)	80.53(8)	80.1(3)	80.0(2)	80.7(2)	77.9(2)	79.2(2)

In the case of **4b** (dimer complex), X1, X2, N1 and N2 indicate Br3, Br4, N3 and N4, respectively.



Scheme 2.

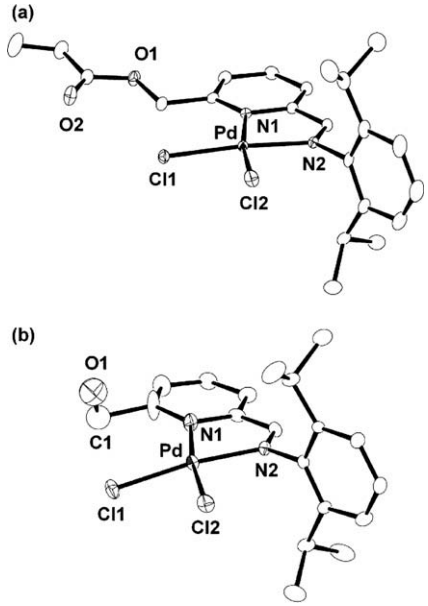


Fig. 2. ORTEP drawing of (a) **2** and (b) **3**·1.5$CHCl_3$ with thermal ellipsoids shown at the 30% probability level. Hydrogen atoms are omitted for clarity. Hydrogen atoms and solvating $CHCl_3$ molecules are omitted for clarity.

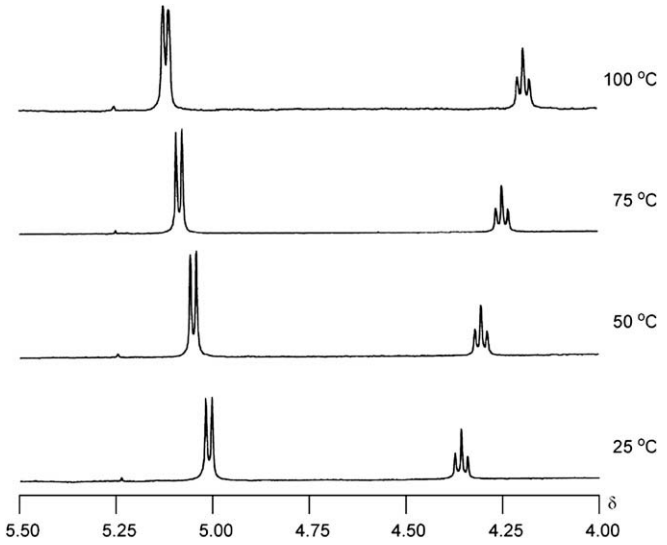
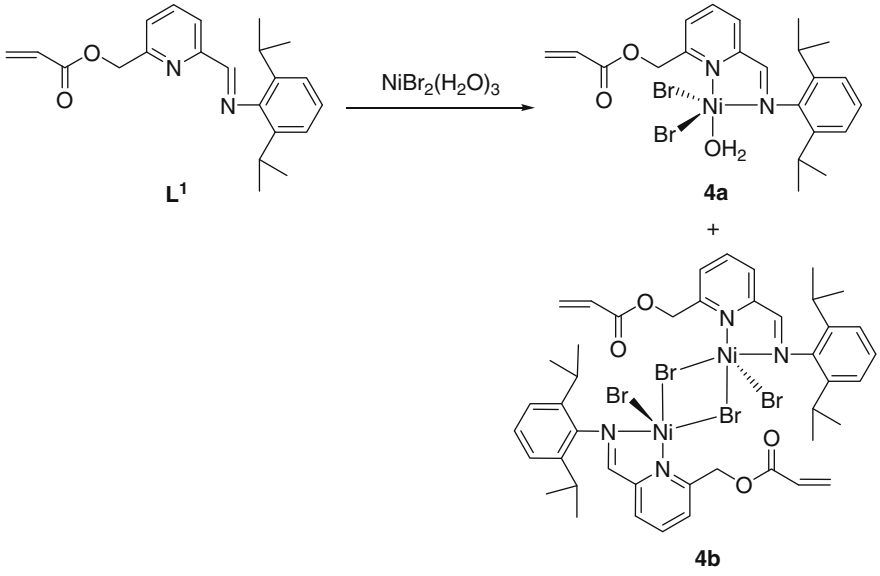


Fig. 3. ^1H NMR spectra of the hydroxymethyl region of **3** at 25–100 °C in $C_2D_2Cl_4$ (8.2 mM).

plane is orthogonally-oriented to the 2,6-diisopropylphenyl group owing to the sterically bulky isopropyl groups [6,7]. The CH_2–OH bond is orientated towards the Cl ligand with the distance Cl1–O1 = 3.046 Å, which indicates intramolecular hydrogen bonding in the crystal structure (Fig. 2b). The ^1H NMR spectrum of **3** (25 °C, $CDCl_3$) exhibits a triplet (J_{HH} = 8 Hz) assigned to the OH hydrogen at 4.67 ppm, which is at a much lower magnetic field than that of $\mathbf{L^2}$. Appearance of H–H coupling between the OH and CH_2 hydrogen of **3**, as well as the shift of the OH peak position, upon coordination of the ligand suggests Pd–Cl···H–O intramolecular hydrogen bonding in solution [11–13]. Fig. 3 shows the variable temperature ^1H NMR spectra of **3** in $ClCD_2CD_2Cl$. The triplet signal of the OH hydrogen shifts downfield by ca 0.17 ppm on raising the temperature from 25 to 100 °C. The OH and CH_2 hydrogen signals became somewhat broadened at 100 °C. The temperature-dependent change of the spectra may also suggest O–H···Cl hydrogen bonds in solution.

Elemental analysis of the product from the reaction of $\mathbf{L^1}$ and $[NiBr_2(H_2O)_3]$ indicates the formation of the aqua complex, $[NiBr_2(H_2O)L^1]$ (**4a**) [8], but X-ray crystallography of the crystals obtained from $CHCl_3$ revealed the presence of **4a** and a dinuclear complex with two bridging Br ligands, $[NiBr(\mu\text{-}Br)L^1]_2$, (**4b**) in a 1:1 ratio (Scheme 3). Fig. 4 shows the structure of the mononuclear and dinuclear complexes contained in the crystal lattice. Complex **4a** undergoes partial dissociation of the aqua ligand to yield the anhydrous dinuclear complex **4b** during the recrystallization. Chart 2 lists the penta-coordinated Ni(II) complexes with two Br, one aqua and one iminopyridine ligand, similar to **4a** [14,15]. The coordination of **4a** resembles that of a complex with an iminopyridine ligand with a methyl group next to the pyridine group (right in Chart 2), although the other complex (left) has different ligand positions. The reaction of an iminopyridine ligand with $[NiBr_2(dme)]$ (dme = 1,2-dimethoxyethane) gives dinuclear com-



Scheme 3.

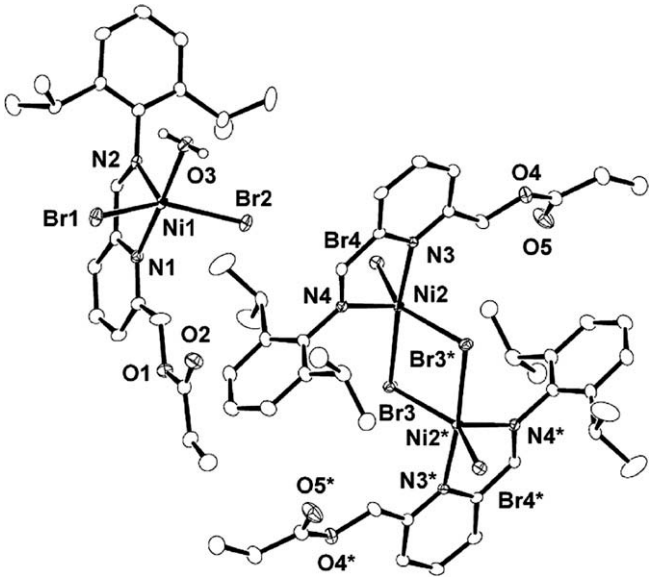


Fig. 4. ORTEP drawing of **4a** and **4b** with thermal ellipsoids shown at the 30% probability level. Hydrogen atoms except for O–H hydrogens are omitted for clarity. Atoms with asterisks are crystallographically equivalent to those having the same number without asterisks.

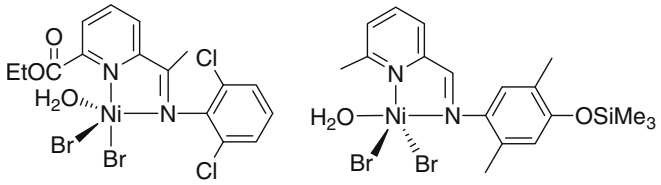


Chart 2.

plexes with two bridging Br ligands (Chart 3) [16,17]. In the crystal structures of **4a** and **4b**, the acrylate group of the ligand does not interact with the Ni(II) centers.

The reaction of the ligand with the CH_2OH pendant, $\mathbf{L^2}$, with $[NiBr_2(H_2O)_3]$ yielded a Ni complex, **5a**, having an *N,N′,O*-coordination (Scheme 4). The crystal structure of **5a** shows a five-coordinate square pyramidal geometry with a Br atom (Br2) at the apical position (Fig. 5a). The Ni center lies 0.43 Å out of the basal plane composed of the N1, N2, Br1 and O1 atoms. A similar *N,N′,O*-coordination was observed in Ni(II) complexes with Ar–N=CCH_3-2,6-C_5H_3N–$COCH_3$ (Ar = 2,6-diisopropylphenyl) and Ar–N=CCH_3-2,6-C_5H_3N–$COOCH_2CH_3$ (Ar = 2,6-dimethylphenyl) [10,14], which have longer Ni–O bonds (2.334 and 2.402 Å) than that of **5a** (2.137 Å) (Chart 4). Recently, Gibson and co-workers reported a Fe(II) complex with a similar ligand to $\mathbf{L^2}$, Ar–N=CCH_3-2,6-C_5H_3N–$C(CH_3)_2OH$

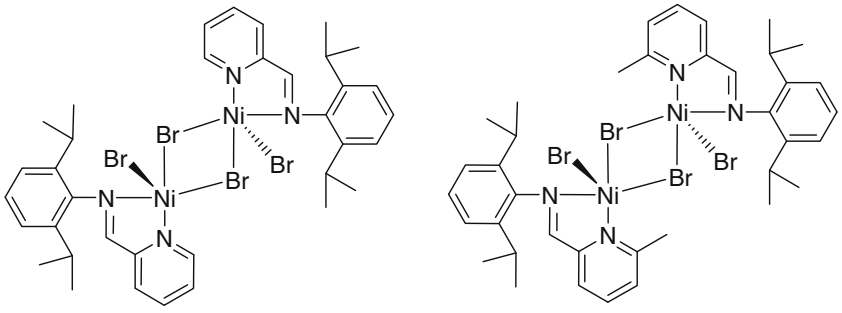
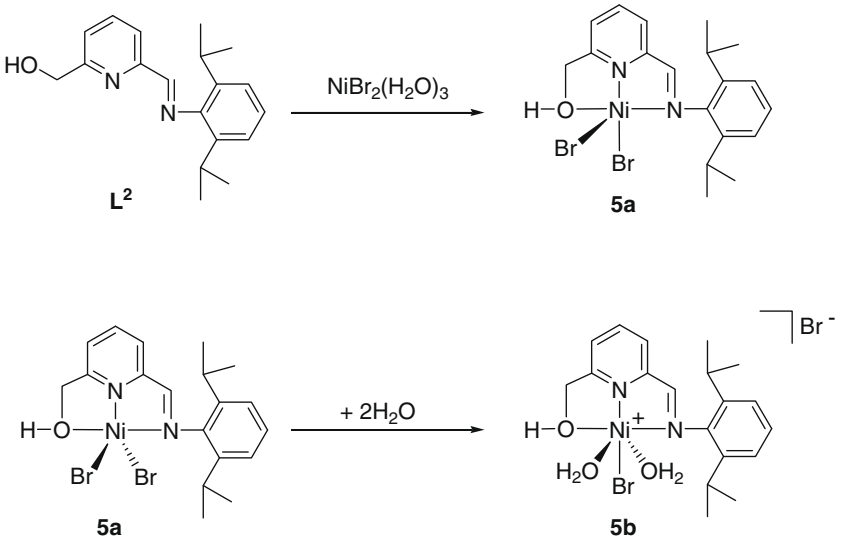


Chart 3.



Scheme 4.

(Ar = 2,6-diisopropylphenyl), in which the OH group is coordinated to Fe with a Fe–O bond distance of 2.173 Å (Chart 4) [18]. The bond length of the Ni and imine nitrogen (N2) is 0.13 Å longer than that of Ni and the pyridine nitrogen (N1). In contrast, **4a** and **4b** have shorter Ni–imine bonds than Ni–pyridine bonds. Therefore, coordination of the hydroxy group is likely to elongate the Ni–imine bond due to the *trans* influence of the O-ligand [19,20]. Other Ni-iminopyridine complexes with *N,N',O*-tridentate coordination have Ni–imine bonds approximately 0.1 Å longer than the Ni–pyridine bonds (Chart 4) [10,14,18]. Recrystallization of **5a** in the presence of an excess amount of H_2O caused dissociation of a Br ligand, resulting in the formation of the cationic aqua complex **5b** (Fig. 5b). The structure has a distorted octahedral geometry with two aqua ligands at *trans* positions. In analogy to **5a**, **5b** has longer Ni–imine bonds (2.127 Å) than Ni–pyridine bonds (2.006 Å). A similar replacement of a Br ligand with an aqua ligand was reported in a Ni(II) complex with the bidentate diphenyl(dipyrazolyl)methane ligand [21].

Intermolecular hydrogen bonding was observed in the aqua complexes **4a** and **5b**, as shown in Fig. 6. In the structure of **4a**, the short distance of H1···Br1* (2.596 Å) and the angle of H1–Br1*–Ni* (105.8°) indicate hydrogen bonding [22]. The distance H2···O2* (2.451 Å) is also related to an intermolecular interaction, although the non-linear O3–H2–O2* bonding (139.8°) suggests that the contribution of the H2–O2* hydrogen bond is minor. The structure of **5b** shows that H1 in the hydroxy group and H2 in the aqua ligand have an interaction with the free Br anion (Br2)

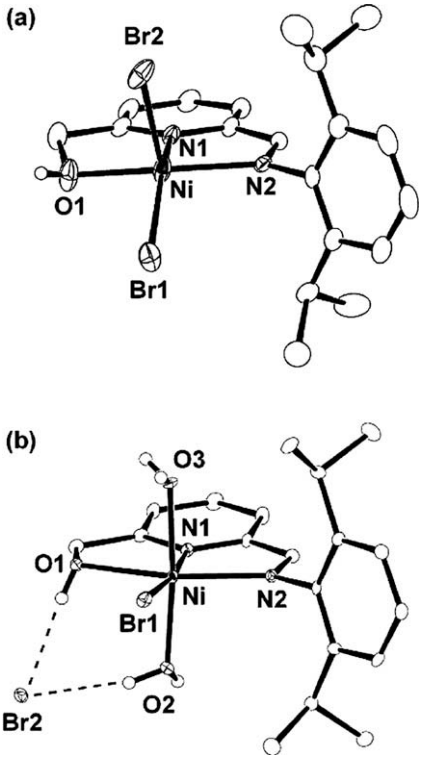


Fig. 5. ORTEP drawing of (a) **5a**·C_4H_8O and (b) **5b**·C_4H_8O with thermal ellipsoids shown at the 30% probability level. Hydrogen atoms except for O–H hydrogens and solvating THF molecules are omitted for clarity.

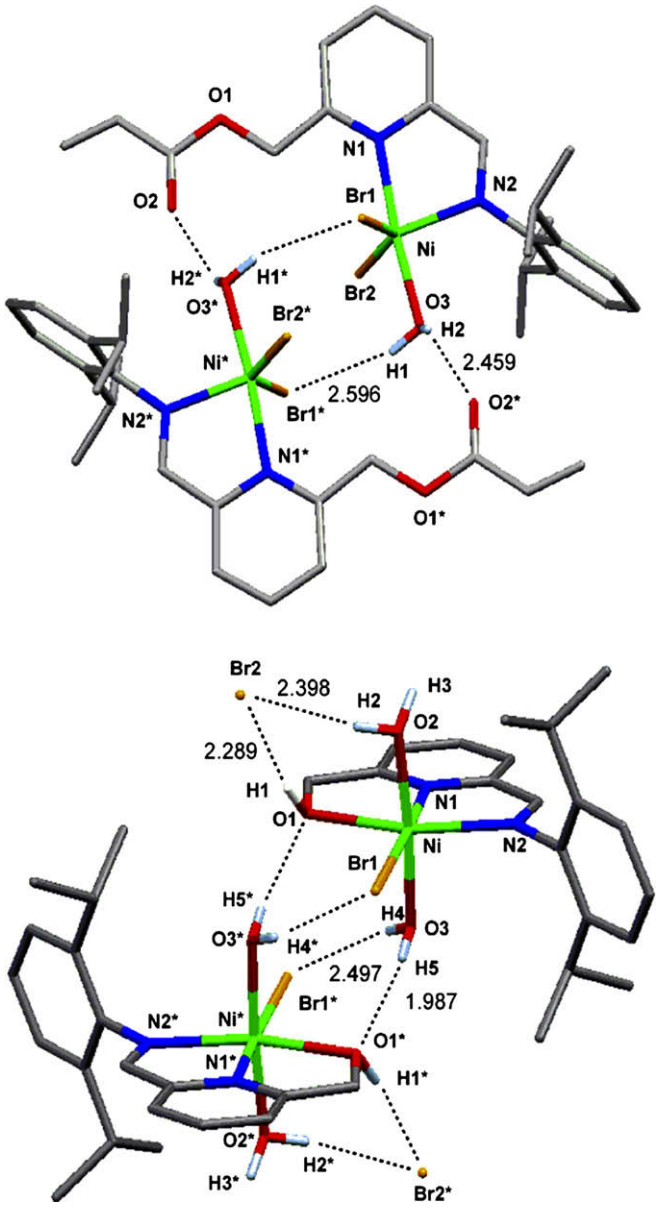


Fig. 6. Association of (a) **4a** and (b) **5b** via hydrogen bonding. Hydrogen atoms except for O–H hydrogens and solvating THF molecules are omitted for clarity. Selected angles for **4a** (°): H1–Br1*–Ni* 105.7, O3–H1–Br1* 160.2, O3–H2–O2* 138.9, Ni–O3–Br1* 102.8, Ni–O3–O2* 138.6. Selected angles for **5b** (°): H4–Br1*–Ni 86.1, O1–H1–Br2 177.4, O2–H2–Br2 160.2, O3–H4–Br1* 155.5, O3–H5–O1* 150.9, Ni–O1–Br2 105.8, Ni–O2–Br2 105.8, Ni–O3–Br1* 120.6, Ni–O3–O1* 125.7.

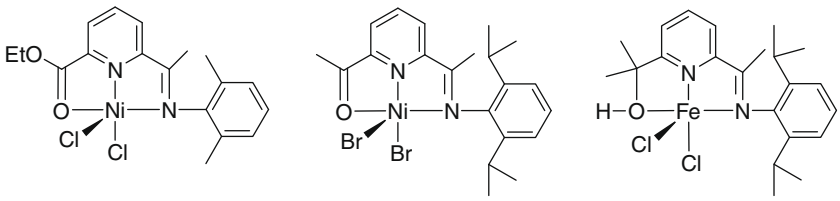


Chart 4.

with distances of 2.289 and 2.398 Å, respectively. The other aqua ligand shows hydrogen bonding with the Br1* and O1* atoms in the neighboring molecule in the crystal packing.

3. Conclusions

The crystal structures of iminopyridine complexes with an acrylate or a hydroxy pendant group were revealed by single-crystal X-ray diffraction studies. The weak interaction of the acrylate pendant group to the metal center was observed only in the case of the Co(II) complex. Coordination of the carbonyl oxygen atoms is unfavorable partly because it requires the formation of unstable 7-membered metallacycles. In the iminopyridine complexes with an hydroxy pendant group (**L²**), the ligand coordinates to the Ni(II) center in an *N,N′,O*-tridentate coordination fashion. Since coordination of an aqua ligand to Ni(II) caused the dissociation of the Br ligand in the presence of the coordinated hydroxy group, the coordination of the hydroxy group is presumably stronger than that of Br because of the chelate effect.

4. Experimental

4.1. General

6-Hydroxymethyl-2-pyridinecarboxaldehyde [23], $[PdCl_2(cod)]$ [24], **1** (green solid), **2** (yellow solid) and **4** (orange solid) were prepared according to the literature methods [8]. $[NiBr_2{\cdot}(H_2O)_3]$ and other chemicals were used as received from commercial suppliers. NMR spectra (^1H and $^{13}C\{^1H\}$) were recorded on Varian Mercury 300 and JEOL JNM LA-500 spectrometers. Elemental analyses were carried out with a Yanaco MT-5 CHN autocorder.

4.2. Synthesis of 2-hydroxymethyl-6-[(2,6-diisopropylphenyl)iminomethyl]pyridine (**L²**)

A mixture of 6-hydroxymethyl-2-pyridinecarboxaldehyde (141.0 mg, 1.0 mmol), 2,6-diisopropylaniline (0.200 mL, 1.1 mmol) and acetic acid (1 drop) in EtOH (3 mL) was stirred for 14 h at room temperature. After the volatiles were evaporated under reduced pressure, the residue was washed with hexane (2 mL × 4) and dried under reduced pressure to give 2-hydroxymethyl-6-[(2,6-diisopropylphenyl)iminomethyl]pyridine as a pale yellow solid (275.6 mg, 90%). *Anal.* Calc. for $C_{19}H_{24}N_2O$: C, 76.99; H, 8.16; N, 9.45. Found: C, 76.30; H, 7.99; N, 9.30%. ^1H NMR (300 MHz, $CDCl_3$): δ 8.31 (s, 1H, N=C*H*), 8.19 (d, 1H, J^3 = 8 Hz, C*H* in pyridyl group), 7.78 (t, 1H, J^3 = 8 Hz, C*H* in pyridyl group), 7.38 (d, 1H, J^3 = 8 Hz, C*H* in pyridyl group), 7.20–7.11 (m, 3H, C*H* in aromatic group), 4.85 (s, 2H, CH_2), 3.90 (br, 1H, O*H*), 2.96 (quint, 2H, J^3 = 7 Hz, C*H*), 1.18 (d, 12H, J^3 = 7 Hz, CH_3). $^{13}C\{^1H\}$ NMR (75 MHz, $CDCl_3$): δ162.9 (s, N=*C*H), 159.2 (s, *ipso*), 153.8 (s, *ipso*), 148.6 (s, *ipso*), 137.7 (s, *C*H in pyridyl group), 137.4 (s, *ipso*), 124.8 (s, *C*H in pyridyl group), 123.3 (s, *C*H in aromatic group), 122.4 (s, *C*H in aromatic group), 120.1 (s, *C*H in pyridyl group), 64.2 (s, CH_2), 28.2 (s, *C*H), 23.7 (s, CH_3).

4.3. Synthesis of dichloro{2-hydroxymethyl-6-[(2,6-diisopropylphenyl)iminomethyl]pyridine}palladium(II) (**3**)

A mixture of 2-hydroxymethyl-6-[(2,6-diisopropylphenyl)iminomethyl]pyridine (68.0 mg, 0.23 mmol) and $[PdCl_2(cod)]$ (65.3 mg, 0.23 mmol) in THF (20 mL) was stirred for 12 h at room temperature. After the volatiles were evaporated under reduced pressure, the residue was extracted with THF. Crystallization from THF/Et_2O gave **3** as yellow solid (91.9 mg, 78%). *Anal.* Calc. for $C_{19}H_{24}N_2OCl_2Pd$: C, 48.17; H, 5.11; N, 5.91; Cl, 14.97. Found: C, 47.92; H, 5.32; N, 5.92; Cl, 15.38% ^1H NMR (300 MHz, $CDCl_3$): δ8.17 (t, 1H, J^3 = 8 Hz, C*H* in pyridyl group), 8.07 (s, 1H, N=C*H*), 7.84 (d, 1H, J^3 = 8 Hz, C*H* in pyridyl group), 7.80 (d, 1H, J^3 = 8 Hz, C*H* in pyridyl group), 7.36 (t, 1H, J^3 = 8 Hz, C*H* in aromatic group), 7.20 (d, 2H, J^3 = 8 Hz, C*H* in aromatic group), 5.15 (d, 2H, J^3 = 8 Hz, CH_2), 4.67 (t, 1H, J^3 = 8 Hz, O*H*), 3.31 (double quartet, 2H, J^3 = 7 Hz, C*H*), 1.41 (d, 6H, J^3 = 7 Hz, CH_3), 1.14 (d, 6H, J^3 = 7 Hz, CH_3). The low solubility of the complex made it impossible to obtain a $^{13}C\{^1H\}$ NMR spectrum.

Table 2
Crystal data and details of structure refinement of complexes **1–5b**.

	1	**2**	**3**·1.5$CHCl_3$	**4**	**5a**·C_4H_8O	**5b**·C_4H_8O
Chemical formula	$C_{22}H_{26}Cl_2CoN_2O_2$	$C_{22}H_{26}Cl_2N_2O_2Pd$	$2C_{19}H_{24}Cl_2N_2OPd{\cdot}3CHCl_3$	$C_{44}H_{54}Br_4N_4Ni_2O_5$	$C_{19}H_{24}Br_2N_2NiO{\cdot}C_4H_8O$	$C_{19}H_{28}Br_2N_2NiO_3{\cdot}C_4H_8O$
Formula weight	480.30	527.77	1303.55	1155.95	587.03	623.06
Crystal system	Monoclinic	Orthorhombic	Orthorhombic	Monoclinic	Monoclinic	Triclinic
Space group	$P2_1/c$ (No. 14)	$P2_12_12_1$ (No. 19)	$P2_12_12$ (No. 18)	$P2_1/c$ (No. 14)	$P2_1/n$ (No. 14)	$P\bar{1}$ (No. 2)
a (Å)	9.200(2)	12.022(3)	12.435(2)	10.216(2)	9.468(2)	9.9948(4)
b (Å)	15.087(2)	12.905(3)	21.765(2)	22.678(3)	13.707(3)	10.1121(4)
c (Å)	16.460(3)	14.881(4)	9.974(2)	20.599(3)	19.654(5)	13.9053(5)
α (°)						78.734(2)
β (°)	91.980(3)			97.398(2)	93.247(4)	85.777(2)
γ (°)						76.073(2)
V (Å^3)	2283.3(6)	2308.7(9)	2699.6(5)	4733(1)	2547(1)	1337.27(1)
Z	4	4	2	4	4	2
μ (cm^{-1})	10.054	10.552	13.463	42.294	39.299	37.520
F(0 0 0)	996	1072	1304	2328	1192	636
D_{calc}, (g cm^{-3})	1.397	1.518	1.604	1.622	1.531	1.547
Crystal size (mm)	0.40 × 0.12 × 0.10	0.20 × 0.20 × 0.20	0.45 × 0.20 × 0.12	0.20 × 0.17 × 0.15	0.12 × 0.10 × 0.10	0.50 × 0.15 × 0.15
Exposure rate sec. (°)	20.0	10.0	40.0	80.0	80.0	60.0
Number of date	16 961	15 716	20 296	34 856	18 884	13 241
Number of unique date	5070	5194	6161	10 775	5771	6040
Number of used reflections ($I > 2\sigma(I)$)	4249	5076	5848	8917	3832	4635
Number of variables	263	263	243	541	276	310
R ($I > 2\sigma(I)$)	0.042	0.026	0.085	0.049	0.057	0.044
R (All reflections)	0.054	0.027	0.088	0.065	0.088	0.065
R_W (All reflections)	0.113	0.068	0.230	0.118	0.168	0.128
Goodness-of-fit (GOF)	1.07	1.13	1.07	1.13	1.08	1.11

4.4. Synthesis of dibromo{2-hydroxymethyl-6-[(2,6-diisopropylphenyl)iminomethyl]pyridine}nickel(II) (**5a**)

$[NiBr_2{\cdot}(H_2O)_3]$ (54.5 mg, 0.20 mmol) was added to a solution of 2-hydroxymethyl-6-[(2,6-diisopropylphenyl)iminomethyl]pyridine (59.3 mg, 0.20 mmol) in THF (10 mL). After stirring at room temperature for 18 h, the solvent was reduced under vacuum. Et_2O was added to the solution to cause the separation of **5a** as an orange solid (68.9 mg, 67%). *Anal.* Calc. for $C_{19}H_{24}Br_2N_2Ni{\cdot}C_4H_8O$: C, 47.06; H, 5.49; N, 4.77; Br, 27.22. Found: C, 46.91; H, 5.52; N, 4.77; Br, 27.26%.

4.5. Synthesis of bisaqua(bromo){2-hydroxymethyl-6-[(2,6-diisopropylphenyl) iminomethyl]pyridine}nickel(II) bromide (**5b**)

Complex **5a** (19.1 mg, 0.037 mmol) was stirred in a mixture of THF and H_2O (30/1) for 20 h. After the solution was dried with $MgSO_4$, the solvent was slowly evaporated to cause the separation of **5b** as green crystals (11.5 mg, 59%). *Anal.* Calc. for $C_{19}H_{28}Br_2N_2O_3Ni{\cdot}C_4H_8O$: C, 44.34; H, 5.82; N, 4.50; Br, 25.65. Found: C, 44.12; H, 6.06; N, 4.40; Br, 25.63%.

4.6. Crystal structure determination

Intensity data were collected on a Rigaku Saturn CCD area detector or a Rigaku R-AXIS Rapid diffractometer with Mo Kα radiation. Crystals of **1–5b** suitable for an X-ray diffraction study were mounted on glass capillary tubes. Crystallographic data and details of refinement of the complexes are summarized in Table 2. A full matrix least-squares refinement was used for non-hydrogen atoms with the anisotropic thermal parameters method by the SHELXL-97 program. In the structure of **3**·1.5$CHCl_3$, disordered $CHCl_3$ molecules, C1 and O1 atoms were refined isotropically. The positional parameters for O–H hydrogen atoms, except for those in **3**·1.5$CHCl_3$, were refined isotropically, but other hydrogens were located by assuming an ideal geometry and were included in the structure calculation without further refinement of the parameters [25].

Supplementary data

CCDC 719682, 719683, 719684, 719685, 719686, 719687 contains the supplementary crystallographic data for **1**, **2**, **3**, **4**, **5a** and **5b**, respectively. These data can be obtained free of charge via http://www.ccdc.cam.ac.uk/conts/retrieving.html, or from the Cambridge Crystallographic Data Centre, 12 Union Road, Cambridge CB2 1EZ, UK; fax: (+44) 1223-336-033; or e-mail: deposit@ccdc.cam.ac.uk.

Acknowledgements

This work was supported by the Ministry of Education, Science, Sports and Culture, Japan and by a 21st Century COE program "Creation of Molecular Diversity and Development of Functionalities". J. K. acknowledges a JSPS Research Fellowship for a Young Scientist.

References

[1] R. Ziessel, L. Douce, A. El-ghayoury, A. Harriman, A. Skoulios, Angew. Chem., Int. Ed. 39 (2000) 1489.
[2] D.A. Leigh, P.J. Lusby, S.J. Teat, A.J. Wilson, J.K.Y. Wong, Angew. Chem., Int. Ed. 40 (2001) 1538.
[3] A. Lavalette, F. Tuna, G. Clarkson, N.W. Alcock, M.J. Hannon, Chem. Commun. (2003) 2666.
[4] R. Ziessel, P. Nguyen, Synthesis (2005) 223.
[5] S. Mori, M. Nambo, L.C. Chi, J. Bouffard, K. Itami, Org. Lett. 10 (2008) 4609.
[6] S.D. Ittel, L.K. Johnson, M. Brookhart, Chem. Rev. 100 (2000) 1169.
[7] G.J.P. Britovsek, V.C. Gibson, B.S. Kimberley, P.J. Maddox, S.J. McTavish, G.A. Solan, A.J.P. White, D.J. Williams, Chem. Commun. (1998) 849.
[8] J. Kuwabara, D. Takeuchi, K. Osakada, Chem. Commun. (2006) 3815.
[9] B.Y. Su, J.S. Zhao, Polyhedron 25 (2006) 3289.
[10] F.A.R. Kaul, G.T. Puchta, G.D. Frey, E. Herdtweck, W.A. Herrmann, Organometallics 26 (2007) 988.
[11] M. Svensson, U. Bremberg, K. Hallman, I. Csregh, C. Moberg, Organometallics 18 (1999) 4900.
[12] B. Bernet, A. Vasella, Helv. Chim. Acta 83 (2000) 995.
[13] B. Hoffmann, B. Bernet, A. Vasella, Helv. Chim. Acta 85 (2002) 265.
[14] X. Tang, W.H. Sun, T. Gao, J. Hou, J. Chen, W. Chen, J. Organomet. Chem. 690 (2005) 1570.
[15] J.M. Benito, E. de Jesús, F.J. de la Mata, J.C. Flores, R. Gómez, P. Gómez-sal, Organometallics 25 (2006) 3876.
[16] T.V. Laine, M. Klinga, M. Leskelä, Eur. J. Inorg. Chem. (1999) 959.
[17] T.V. Laine, U. Piironen, K. Lappalainen, M. Klinga, E. Aitola, M. Leskelä, J. Organomet. Chem. 606 (2000) 112.
[18] V.C. Gibson, C. Redshaw, G.A. Solan, A.J.P. White, D.J. Williams, Organometallics 26 (2007) 5119.
[19] T.G. Appleton, H.C. Clark, L.E. Manzer, Coord. Chem. Rev. 10 (1973) 335.
[20] P.L. Holland, M.E. Smith, R.A. Andersen, R.G. Bergman, J. Am. Chem. Soc. 119 (1997) 12815.
[21] N. Baho, D. Zargarian, Inorg. Chem. 46 (2007) 7621.
[22] G. Aullón, D. Bellamy, L. Brammer, E.A. Bruton, A.G. Orpen, Chem. Commun. (1998) 653.
[23] Y. Okuyama, H. Nakano, C. Kabuto, E. Nozawa, K. Takahashi, H. Hongo, Heterocycles 58 (2002) 457.
[24] D. Drew, J.R. Doyle, Inorg. Synth. 13 (1972) 47.
[25] International Tables for X-ray Crystallography, vol. 4, Kynoch: Birmingham, UK, 1974.

Polyhedron 28 (2009) 2466–2472

Contents lists available at ScienceDirect

Polyhedron

journal homepage: www.elsevier.com/locate/poly

Cu(II) coordination polymers incorporating 3-aminopyridine and flexible aliphatic dicarboxylate ligands: Synthesis, structure and magnetic properties

Nina Lah [a,*], Rodolphe Clérac [b,c]

[a] University of Ljubljana, Faculty of Chemistry and Chemical Technology, Aškerčeva 5, 1000 Ljubljana, Slovenia
[b] CNRS, UPR 8641, Centre de Recherche Paul Pascal (CRPP), Equipe "Materiaux Moléculaires Magnétiques", 115 Avenue du Dr. Albert Schweitzer, Pessac F-33600, France
[c] Université de Bordeaux, UPR 8641, Pessac F-33600, France

ARTICLE INFO

Article history:
Received 10 March 2009
Accepted 23 April 2009
Available online 15 May 2009

Keywords:
Copper(II)
Coordination polymer
Dicarboxylate
Magnetic properties
Crystal engineering

ABSTRACT

The synthesis, structural chemistry and magnetic properties of a series of new Cu(II) polymers with α,ω-dicarboxylic acids (sebacic (H_2seb), suberic (H_2sub), succinic (H_2suc) and adipic (H_2adip)) and 3-aminopyridine (3-apy) are described: $[Cu(Hsub)_2(3\text{-apy})_2{\cdot}2CH_3OH]_n$ (**1**); $[Cu(Hseb)_2(3\text{-apy})_2{\cdot}4CH_3OH]_n$ (**2**); $[Cu(Hsuc)_2(3\text{-apy})_2]_n$ (**3**); $[Cu(adip)(3\text{-apy})_2]_n{\cdot}n(H_2adip)$ (**4**). All four compounds feature a bis-monodentate bridging mode of the coordinated dicarboxylate moiety. Compounds **1** and **2** exhibit linear chains, whereas compound **3** shows two-dimensional structure. The 3-apy ligand acts as terminal ligand in **1**–**3**. Compound **4** contains a doubly deprotonated adipate ($adip^{2-}$) that connects Cu centers into linear chains. Additionally, 3-apy acts as a bridge in **4,** resulting in the formation of parallel two-dimensional layers distant enough to host neutral molecules of adipic acid. Magnetic susceptibility measurements of compounds **1** and **3** show Curie law behavior indicating that the $S = 1/2$ Cu(II) spin carriers are magnetically well isolated by the dicarboxylate ligands.

© 2009 Elsevier Ltd. All rights reserved.

1. Introduction

The interest in research concerning coordination polymers remains high because of their capabilities in catalysis, selective separation processes, light-to-energy conversion, etc. [1]. The construction of the multicomponent system represents an important step in the development of novel molecular and supramolecular materials. For systems in which cationic metal nodes are connected, the emphasis lies in the choice of bridging ligands as critical elements for successful design. Prominent among the organic ligands used to construct extended structures are carboxylates, providing not only the necessary charge balance to permit construction of numerous neutral frameworks but also the ability to connect metal cations in a variety of coordination modes [2]. The coordination versatility can be enhanced by choosing bi- and multi-functional ligands that contain more than one carboxylate group (di-, tri- and polycarboxylates). For example, the oxalate ion ($C_2O_4^{2-}$), the first from a series of aliphatic dicarboxylates, has proved to be a versatile bridging species for the controlled assembly of 1D, 2D and 3D inorganic architectures and its coordination chemistry is well documented [3]. On the opposite, the coordination polymers based on longer aliphatic α,ω-dicarboxylates have received less attention. While the structural rigidity of oxalate units can have its advantage, higher homologs contain flexible alkyl chains which by their conformational freedom offer a greater degree of structural diversity. Recently, we have been investigating the Cu(II) coordination compounds of longer aliphatic monocarboxylates [4]. Along these lines, with a view to prepare novel coordination polymers, we have turned our attention to study the coordination behavior of aliphatic α,ω-dicarboxylates in combination with additional pyridine type ligand, namely 3-aminopyridine (3-apy) (Scheme 1). Besides the endocyclic N-atom that usually coordinates to metal center, 3-apy contains the additional functionality at the position 3: an amino group. Since the coordination compounds containing 3-apy as the additional linker are poorly documented, we have primarily set up to investigate the coordination chemistry of Cu/α,ω-dicarboxylates/3-apy system and determine: (i) the coordination geometry of the copper ion, (ii) which binding motif is preferred for carboxylate coordination, and (iii) whether the amino N atom on 3-apy can contribute to the coordination of the copper ion in any way.

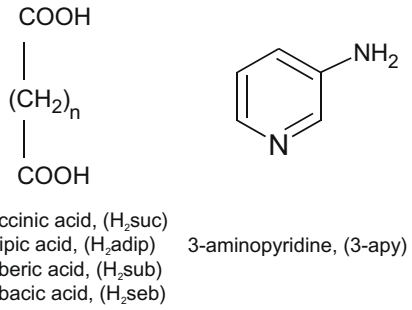
2. Experimental

2.1. General procedures and materials

All manipulations were carried out under ambient conditions by using commercial grade solvents: Chemicals were used as received (Aldrich) without further purifications.

* Corresponding author. Tel.: +386 1 2419 114; fax: +386 1 2419 220.
E-mail address: nina.lah@fkkt.uni-lj.si (N. Lah).

0277-5387/$ - see front matter © 2009 Elsevier Ltd. All rights reserved.
doi:10.1016/j.poly.2009.04.047



Scheme 1. Ligands discussed in this work.

2.2. Synthesis

2.2.1. $[Cu(Hsub)_2(3\text{-}apy)_2{\cdot}2CH_3OH]_n$ (**1**)

$CuBr_2$ (0.12 g) was dissolved in methanol (15 mL) and suberic acid (0.73 g) was added while heating and stirring. Upon the addition of 3-aminopyridine ligand (0.44 g) the solution became dark green. Green block-shaped crystals precipitated after standing one week at 4 °C with high yield (>90%). *Anal.* Calc. for $C_{28}H_{46}CuN_4O_{10}$: C, 50.78; H, 7.00; N, 8.46. Found: C, 50.85; H, 7.12; N, 8.55%.

2.2.2. $Cu(Hseb)_2(3\text{-}apy)_2{\cdot}4CH_3OH]_n$ (**2**)

$CuBr_2$ (0.12 g) was dissolved in methanol (12 mL). Sebacic acid (0.80 g) was added while heating and stirring. Upon the addition of 3-aminopyridine (0.45 g) the solution became dark green. Green block-shaped crystals precipitated with high yield (90%) after standing two weeks at 4 °C. *Anal.* Calc. for $C_{34}H_{62}CuN_4O_{12}$: C, 52.19; H, 7.99; N, 7.16. Found: C, 52.28; H, 7.70; N, 7.30%.

2.2.3. $[Cu(Hsuc)_2(3\text{-}apy)_2]_n$ (**3**)

$CuBr_2$ (0.12 g) was dissolved in methanol (17 mL). Succinic acid (0.55) g was added while heating and stirring. Upon the addition of 3-aminopyridine ligand (0.44 g) the color of the solution changed to dark green. On cooling slowly to ambient temperature, green crystalline product precipitated overnight. *Anal.* Calc. for $C_{18}H_{22}CuN_4O_8$: C, 44.49; H, 4.56; N, 11.53. Found: C, 44.55; H, 4.54; N, 11.58%.

2.2.4. $[Cu(adip)(3\text{-}apy)_2]_n{\cdot}n(H_2adip)$ (**4**)

$CuBr_2$ (0.12 g) was dissolved in methanol (13 mL). Adipic acid (0.23 g) was added while heating and stirring. Upon the addition of 3-aminopyridine ligand the color of the solution changed from brown to dark green. Slow cooling of the solution to 4 °C gave grass-green crystals with high yield (61%). $C_{22}H_{30}CuN_4O_8$: C, 48.75 H, 5.58; N, 10.34. Found: C, 48.50 H, 5.69; N, 10.43%.

2.3. Physical measurements

Elemental analyses were measured at the Faculty of Chemistry and Chemical Technology, University of Ljubljana with a Perkin–Elmer 240 C, H, N analyzer. Infrared spectra were recorded with a Perkin–Elmer Spectrum 100 FT-IR spectrometer using the Specac Golden Gate Diamond ATR as a solid sample support. The spectra for all studied compounds are contained in the Supplementary data. Magnetic susceptibility measurements were obtained with the use of a Quantum design SQUID MPMS-XL magnetometer. Measurements were performed on finely ground crystalline samples: 51.36 mg (**3**) and 30.49 mg (**1**) over the temperature range 1.8–300 K. The magnetic data were corrected for the sample holder, and the diamagnetic contributions. The presence of ferromagnetic impurities has been systematically checked by measuring the magnetization as a function of the field at 100 K. No presence of ferromagnetic impurities was detected for both samples. Physical characterizations of **2** and **4** have not been possible because of the high instability in air.

2.4. Crystallography

Single-crystal X-ray data were collected on a Nonius Kappa CCD diffractometer with graphite monochromated Mo Kα radiation (λ = 0.71073 Å) at 150 K. Data reduction and integration were performed by DENZO-SMN software package [5]. The structures were solved by direct methods implemented in the SHELX-97 package and refined by a full-matrix least-squares method on F^2 against all reflections using the same program [6]. Hydrogen atoms were placed in geometrically calculated positions and were refined using a riding model, except those of the protonated carboxylic groups, which were found in a Fourier difference map and freely refined in all the reported structures. The 3-apy molecule is disordered over two positions in compounds **1** and **2**. The disorder was successfully modeled resulting in the partial occupancies of 0.5868 (0.4132) and 0.7290 (0.271) for compounds **1** and **2**, respectively. Crystallographic data are listed in Table 1. Figures depicting the structures were prepared by ORTEP3 [7], SHELXTL [8] and CRYSTALMAKER [9].

3. Results and discussion

Polymeric compounds are formed from the reaction of $CuBr_2$ with dicarboxylic acids: succinic (suc), adipic (adip), suberic (sub), and sebacic (seb) in the presence of 3-aminopyridine (3-apy) in methanol. Despite the approximately equivalent synthetic conditions, the structures of the isolated products differ significantly. For the comprehensible and comparative purposes, the structures are described in the order of increasing complexity, starting with isostructural one-dimensional polymers of suberic and sebacic acid and continuing with two-dimensional structures of succinic and adipic acid.

3.1. Structural description

3.1.1. One-dimensional polymers: $[Cu(Hsub)_2(3\text{-}apy)_2{\cdot}2\ CH_3OH]_n$ (**1**) and $[Cu(Hseb)_2(3\text{-}apy)_2{\cdot}4CH_3OH]_n$ (**2**)

The overall geometries are similar in both compounds, hence only the features of compound **1** will be described. The atom labeling scheme pertains to both structures, thus the comparison of the structural data is possible through the inspection of Table 2. A basic building unit as found in **1** is depicted in Fig. 1. Copper ion, located at the inversion center, is coordinated by two suberato ligands with the preserved hydroxylic group ($Hsub^-$) and two neutral 3-apy molecules. The $Hsub^-$ anions are bound with their carboxylate moieties to copper center in a monodentate manner with the Cu–O11 distance being 1.9722(13) Å. The remaining carboxylate oxygen O12 does not participate in the coordination (Cu–O12 > 3.2 Å). 3-Apy molecules complete the square-planar coordination with their endocyclic N-atoms at a distance of 2.0015(17) Å. The tendency of copper ions to accept additional ligands at the apical sites of the basal coordination plane and thus complete the octahedral coordination leads to the assembly of the above described monomeric units. The assembly takes place through the protonated carboxylic group of the dicarboxylate moiety, namely through the hydroxyl oxygen atom (O21). O21 from the adjacent building unit occupies the axial position with the Cu1–O21 ($-x+1, -y, -z$) distance being 2.5218(15) Å. Infinite chains that propagate along the *ac* diagonal are thus formed (Fig. 2). Intrachain Cu centers are separated by 13.2243(4) Å. There is no covalent bonding between the chains. The 3-apy molecules protrude from both sides of the chains perpendicular to the direction of their

Table 1
Crystallographic data for compounds **1**–**4**.

	1	**2**	**3**	**4**
Empirical formula	$C_{28}H_{46}CuN_4O_{10}$	$C_{34}H_{62}CuN_4O_{12}$	$C_{18}H_{22}CuN_4O_8$	$C_{22}H_{30}CuN_4O_8$
Formula weight	662.24	782.42	485.94	542.04
Space group	$P\bar{1}$	$P\bar{1}$	$P2_1/c$	$P\bar{1}$
Z	1	1	2	1
T (K)	150	150	150	150
a (Å)	8.9763(3)	8.8026(1)	9.1494(2)	6.5407(2)
b (Å)	9.0880(3)	9.3813(1)	7.5833(1)	9.8108(2)
c (Å)	10.0090(4)	12.4325(2)	14.3728(3)	10.3024(3)
α (°)	92.370(1)	83.151(1)		113.931(5)
β (°)	91.873(1)	85.476(1)	92.813(9)	99.232(5)
γ (°)	93.345(2)	87.767(1)		99.090(5)
V (Å^3)	813.91(5)	1015.72(2)	996.02(3)	577.92(3)
μ (Mo Kα) (mm^{-1})	0.729	0.598	1.152	1.002
D_{calc} (g cm^{-3})	1.351	1.279	1.620	1.557
$\Delta\rho_{min,max}$ (e Å^{-3})	−0.642, 0.628	−0.659, 1.125	−0.427. 0.418	−0.507, 0.515
Goodness-of-fit	1.054	1.017	1.062	1.054
R_1[a], wR_2[b] [$I > 2\sigma(I)$]	0.0472, 0.0928	0.0490, 0.1274	0.0295, 0.0737	0.0344, 0.0737

[a] $R_1 = \sum ||F_o| - |F_c|| / \sum |F_o|$.
[b] $wR_2 = \{[w(F_o^2 - F_c^2)^2] / \sum [wF_o^2]\}^{1/2}$.

Table 2
Selected bond lengths (Å) and angles (°) for compounds **1** and **2**.

1		**2**	
Cu1–O11	1.9722(13)	Cu1–O11	1.9642(15)
Cu1–N1	2.0015(17)	Cu1–N1	1.9965(19)
Cu1–O21[a]	2.5218(15)	Cu1–O21	2.5798(17)
Cu1–Cu1[b]	13.2243(4)	Cu1–Cu1[b]	15.7898(2)
O11–Cu1–N1	89.67(6)	O11–Cu1–N1	89.56(7)
O11–Cu1–O21[a]	89.15(5)	O11–Cu1–O21[b]	91.10(6)
N1–Cu1–O21[a]	90.27(6)	N1–Cu1–O21[b]	88.95(7)

[a] $-x+1, -y, -z$.
[b] $x-1, y, z-1$.

propagation and are involved (through the noncoordinated NH_2 groups) in H-bonding with noncoordinated O atoms of the neighboring carboxylato moieties. Additionally, solvated methanol molecules are located between the chains and kept in the structure by H-bonds in both structures. The polyhedral view of the structure **1** is presented in Fig. 3.

3.1.2. Two-dimensional $[Cu(Hsuc)_2(3\text{-apy})_2]_n$ (**3**)

The basic building unit of **3** is similar to those of compounds **1** and **2**. The Cu atom, located at the inversion center is coordinated by two hydrogensuccinato ($Hsuc^-$) anions and two neutral 3-apy ligands (Fig. 4). The coordination of 3-apy takes place through

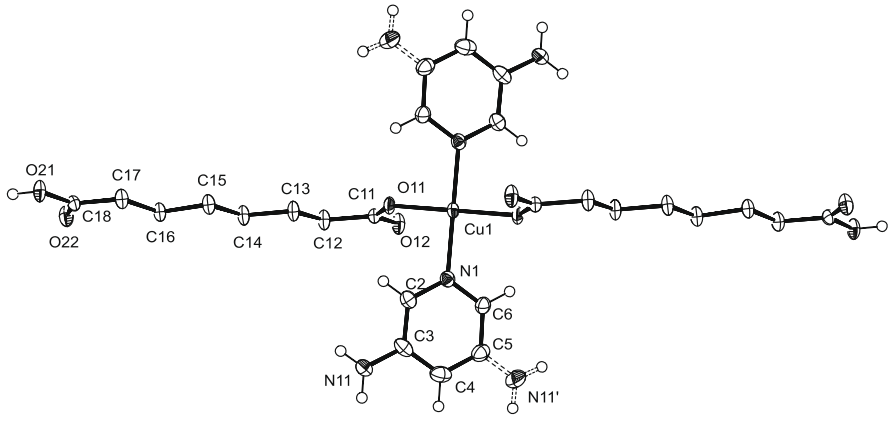


Fig. 1. An ORTEP view of a building unit of **1** with the thermal ellipsoids drawn at 50% probability level. Only the atoms of the asymmetric unit are labeled. The bonds of the disordered amino group (N11′) are drawn as dashed lines.

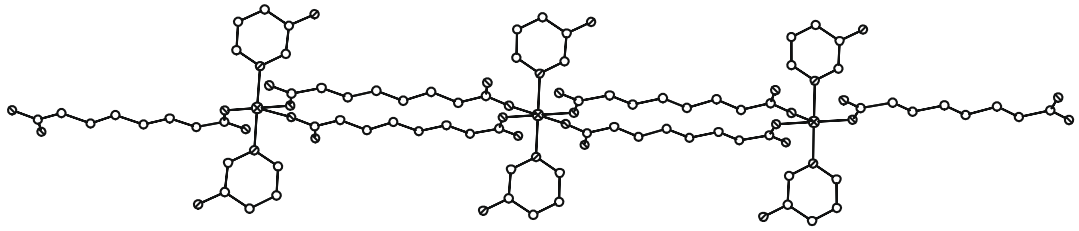


Fig. 2. The one-dimensional linear chain of **1**.

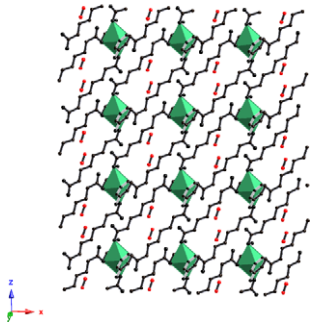


Fig. 3. A packing diagram of **1**, showing the arrangement of solvate methanol molecules between the linear chains.

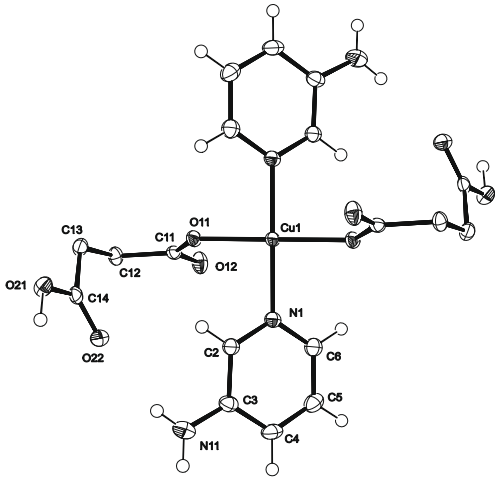


Fig. 4. An ORTEP view of a building unit of **3** with the thermal ellipsoids drawn at 50% probability level. Only the atoms of the asymmetric unit are labeled.

the endocyclic N atom with the Cu1–N1 distance of 1.9990(13) Å, whereas the $Hsuc^-$ is coordinated to Cu atom through one of the oxygen atoms of the deprotonated carboxylate group (Cu1–O11 2.0109(11) Å). The two remaining apical coordination sites are occupied by oxygen atoms from protonated carboxylic groups belonging to symmetry related hydrogensuccinato ligands (Cu1–O21 at $-x+2, y-0.5, -z+0.5$ 2.4636(11) Å) resulting in a distorted octahedral geometry around the copper center. Basic geometrical parameters are listed in Table 3. By contrast to the above described structures (compounds **1** and **2**), the mononuclear units are bridged by bis-monodentate dicarboxylic ligands to form two-dimensional layers perpendicular to *a* axis (Fig. 5). The difference could be ascribed to the conformation of the alkyl chain of the dicarboxylate unit. While the suberic and sebacic acid chains are in fully extended all *trans* conformations and as such facilitate chain

Table 3
Selected bond lengths (Å) and angles (°) for compound **3**.

Cu1–N1	1.9990(13)
Cu1–O11	2.0109(11)
Cu1–O21[a]	2.4636(11)
Cu1–Cu1[b]	8.12533(14)
N1–Cu1–O11	90.23(5)
N1–Cu1–O21[a]	89.93(5)
O11–Cu1–O21[b]	91.52(4)

[a] $-x+2, y-0.5, -z+0.5$.
[b] $-x+2, y+0.5, -z+0.5$

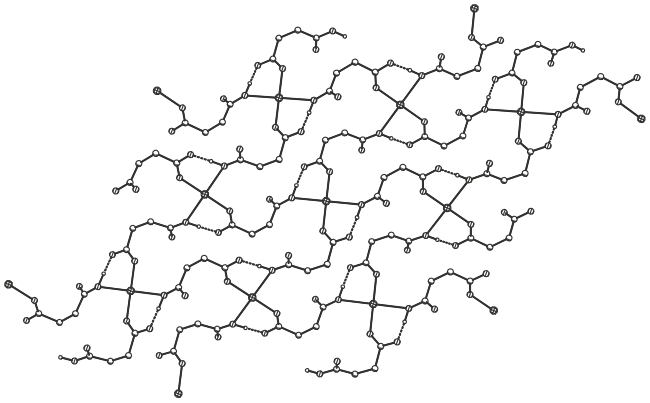


Fig. 5. Two-dimensional layer in **3** formed through bridging $Hsuc^-$ anions and supported by strong O–H···O hydrogen bonds, indicated as dashed lines. The coordinated 3-apy molecules have been omitted for clarity.

structure, the succinic acid in **3** adopt gauche orientation through the rotation around C12–C13 single bond (C11–C12–C13–C14 torsion angle of −77.9°). The geometrical requirements of the bridging succinate ligand thus enforce the formation of layers rather than chains. The formation of two-dimensional structure is further stabilized by strong hydrogen bonds of O–H···O type between the protonated and deprotonated carboxylic oxygen atoms of the two neighboring anions within the layer. No covalent interactions were observed between the layers, instead the crystal structure is stabilized by H-bonds of N–H···O type as well as through face-to-face π–π stacking interactions of the pyridine rings between the layers. The Cu–Cu separation within the same layer is 8.12533(14) Å, while the distance between the parallel layers equals the dimension of the unit cell edge *a*. The polyhedral view of **3** along the *c* axis is illustrated in Fig. 6.

3.1.3. Two-dimensional inclusion compound $[Cu(adip)(3\text{-}apy)_2]_n \cdot n(H_2adip)$ (**4**)

Unlike the complexes of suberic, sebacic and succinic acid which all contained monoprotonated dicarboxylic acid, the compound **4** contains adipic acid in its two forms: doubly deprotonated anion ($adip^{2-}$) and fully protonated molecule (H_2adip). Only the $adip^{2-}$ anion participates in coordination to the metal center. To fulfill a charge balance condition the overall stoichiometry should necessary be changed. Namely, the complex contains only one $adip^{2-}$ ligand per Cu^{2+} ion. Despite this requirement, the basic building unit is similar to those observed in the previously described compounds, while the necessary condition is achieved

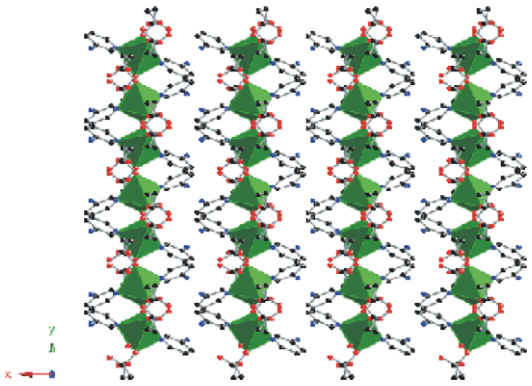


Fig. 6. A packing diagram of **3**, showing the arrangement of 2D layers, with 3-apy molecules dangling from the layers on both sides.

through the symmetry of the building unit (Fig. 7). The copper atom lies on an inversion center and is coordinated by two 3-apy molecules through endocyclic N atoms (Cu–N1 2.0209(14) Å). The $adip^{2-}$ anion is coordinated to the copper center in monodentate mode through one of the oxygen atoms (Cu1–O11 1.9746(12) Å). Only one half of the $adip^{2-}$ anion belongs to the asymmetric unit; the second half of the ligand is generated through the inversion center located at the midpoint of the alkyl chain. Consequently, the symmetry restrictions are reflected in the nature of Cu–Cu connectivity. $Adip^{2-}$ acts as a bis-monodentate bridging ligand that connects monomeric units into infinite chains along *b* axis. Four coordination sites of each copper atom are thus occupied: two by pyridine N atoms and two by O atoms from the dicarboxylate moieties. Surprisingly, the remaining two coordination sites are occupied by exocyclic 3-apy nitrogen atom of the amino group from the adjacent building unit at a longer distance (Cu1–N11 at $-x, -y+1, -z+1$ 2.6406(15) Å). The two-dimensional layers parallel to *ab* are thus formed (Fig. 8). The separation between the Cu centers bridged by 3-apy is 6.5407(2) Å, whereas the separation of those connected through dicarboxylate moiety equals the dimension of the unit cell edge *b*. In addition, the crystal contains adipic acid molecules captured between these polymeric layers (Fig. 9). The neutral H_2adip molecules lie on an inversion center located in the middle of the aliphatic chain, thus the asymmetric unit contains only half of the molecule. The "guest" molecule is kept in the structure by strong hydrogen bonds of O–H···O type as well as with hydrogen bonds of N–H···O type (see Table 4 for details).

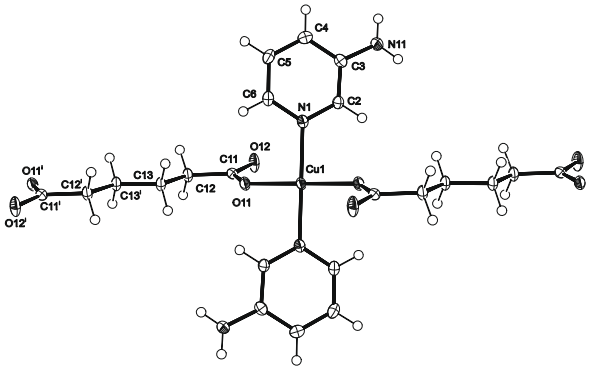


Fig. 7. An ORTEP view of a building unit of **4** with the thermal ellipsoids drawn at 50% probability level.

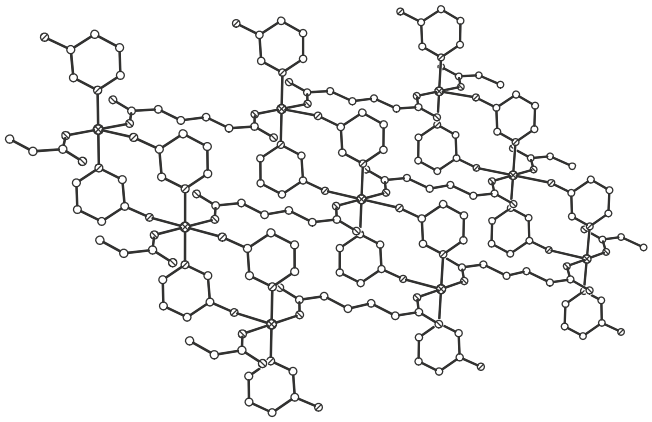


Fig. 8. Two-dimensional layers in **4**, showing the role of 3-apy as a bridging ligand.

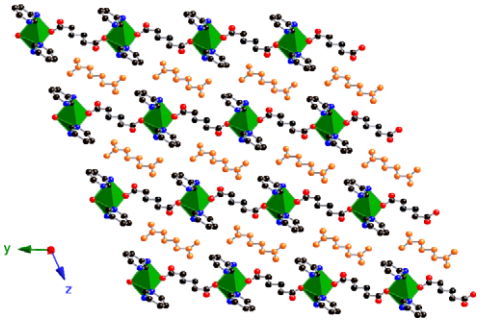


Fig. 9. A packing diagram of **4**, showing the arrangement of neutral adipic acid molecules between the 2D layers of $[Cu(adip^{2-})(3\text{-apy})_2]_n$ composition.

Table 4
Selected bond lengths (Å) and angles (°) for compound **4**.

Cu1–O11		1.9746(12)
Cu1–N1		2.0209(14)
Cu1–N11[a]		2.6406(15)
Cu1–Cu1[b]		6.5407(2)
Cu1–Cu1[c]		9.8108(3)
Hydrogen bonds	**D···A**	**DHA angle**
N11–H11a···O12[a]	2.847(2)	149.7
N11–H11b···O12′[b]	3.018(2)	140.3
O11′–H1···O12[d]	2.562(2)	178.3

[a] $-x, -y+1, -z+1$.
[b] $x-1, y, z$.
[c] $x, y-1, z$.
[d] $x, y-1, z-1$.

3.2. Comments on the dicarboxylate ligation

It has to be noted, that the majority of the copper complexes with dicarboxylate ligands have polymeric structures. Only few examples of structures with discrete entities are known [10]. One feature is common to all these discrete structures; they all contain additional bifunctional N-ligands (i.e. 1,10-phenantroline, 2,2-bipyridine, etc.) that by chelation occupy two coordination sites and are large enough to prevent further interactions in the directions to polymer formation. As shown above, all here reported complexes have polymeric structure that is achieved through the bridging binding mode of the dicarboxylate moiety. The compounds **1–3** contain only partially deprotonated dicarboxylato ligands, while in **4** the coordinated ligand is fully deprotonated. Interestingly, the carboxylate binding motif is uniform, irrespective of the ionization state of the dicarboxylate moiety: both terminal functional groups are coordinated to metal centers in monodentate mode with only one of the two O atoms of each carboxylate group participating in coordination. This is not unprecedented, though not very frequently observed. In most of the reported copper complexes with saturated aliphatic dicarboxylates at least one of the carboxylate ends adopt *syn–syn* chelating mode, while the second end adopts either chelating, monodentate or monoatomic bridging arrangement.[1] It is worth noting that the related system with oxalate as the first from the homologous series of α,ω-dicarboxylates and aminopyridines has already been investigated [11]. However, the structures of none of the reported complexes resemble those

[1] A search through the CSD reveals that the frequency of the structures of Cu(II) complexes comprising linear aliphatic dicarboxylates is decreasing with the increasing number of carbon atoms of the alkyl chain. Namely, only three structures with sebacic, and six structures with suberic acid are reported, while the search gave 30 hits for complexes with adipic acid and 77 hits for complexes with succinic acid.

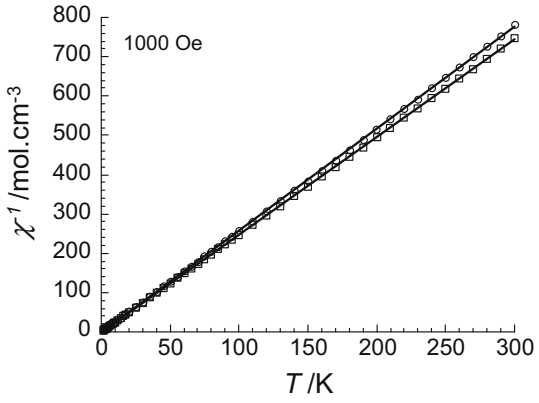


Fig. 10. Temperature dependence of the inverse of the susceptibility (□ defined as M/H per Cu^{II} metal ions) at 1000 Oe for **1** (○) and **3** (□).

reported in this work: Cu(II) centers are joined by bis-bidentate oxalato ligands.

3.3. Comments on the aminopyridine coordination

Simple neutral amino substituted pyridines (2-aminopyridine, 3-aminopyridine, 4-aminopyridine) have been used in copper coordination chemistry before. A survey through CSDB [12] for Cu coordination compounds comprising aminopyridine as the ancillary ligand gave 21, 15 and 26 hits for compounds with 2-, 3- and 4-apy, respectively. Although the amino group is a potential electron donor, there have been no structures reported with 2-apy or 4-apy as a bridging ligand; all compounds contain aminopyridine as a terminal ligand, coordinated through endocyclic nitrogen atom only. The engagement of both N atoms of the 3-apy ligand in compound **4** is rather rare, but not an exceptional phenomenon: among 15 reported Cu complexes comprising 3-apy, only one structures is known where 3-apy adopt a bridging role with both functional groups engaged in the coordination to the copper center [13].

3.4. Magnetic properties

While **2** and **4** are too unstable to be studied by magnetic measurements, the magnetic susceptibility (χ) of compounds **1** and **3** has been investigated. As shown in Fig. 10, the plot of $1/\chi$ versus T for both compounds in the 1.8–300 K temperature range reveals a linear dependence that extrapolate to zero at $T = 0$ K. This type of thermal property is known as a Curie Law and is expected for magnetically well-isolated spins. This result is not surprising considering the crystal structure described above. In both compounds, the dicarboxylate ligands arrange the magnetic Cu(II) sites far apart in space preventing any significant magnetic interactions. It is worth mentioning that the Curie constants deduced from the linear fit of the $1/\chi$ T experimental data are $C = 0.39$ and 0.40 cm^3 K/mol for **1** and **3**, respectively. These Curie constants are in very good agreement with the presence of an $S = ½$ Cu(II) spin with g factors of 2.03(2) and 2.07(2) for **1** and **2**.

4. Concluding remarks

In conclusion, we have illustrated by the examples the richness of the Cu(II) chemistry generated by dicarboxylato ligands acting as bridges. Cu(II) ion possesses centrosymmetric distorted octahedral geometry in all the complexes addressed in this work. Furthermore, they all feature uniform dicarboxylate binding motif; a bis-monodentate coordination seems to be preferred, regardless of the ionization state of the dicarboxylate moiety. The ability of aminopyridine ligand to participate in bridging with its amino group adds new dimensions and deserves further investigations. Studies to discern the generality of our observations to other aliphatic α,ω-dicarboxylates and aminopyridines are in progress.

Acknowledgements

The work was supported by the Slovenian Ministry of Higher Education, Science and Technology through grant P1-175-103, the CNRS, The University of Bordeaux, MAGMANet (NMP3-CT-2005-515767), and the Conseil Régional d'Aquitaine.

Appendix A. Supplementary data

CCDC 720545, 720546, 720547 and 720548 contain the supplementary crystallographic data for compounds **1**, **2**, **3** and **4**, respectively. These data can be obtained free of charge via http://www.ccdc.cam.ac.uk/conts/retrieving.html, or from the Cambridge Crystallographic Data Centre, 12 Union Road, Cambridge CB2 1EZ, UK; fax: (+44) 1223-336-033; or e-mail: deposit@ccdc.cam.ac.uk. Supplementary data associated with this article can be found, in the online version, at doi:10.1016/j.poly.2009.04.047.

References

[1] (a) For example, see: M. Eddaoudi, H.L. Li, O.M. Yaghi, J. Am. Chem. Soc. 122 (2000) 1391;
(b) S. Noro, S. Kitagawa, M. Kondo, K. Seki, Angew. Chem., Int. Ed. Engl. 39 (2000) 2082;
(c) J.L.C. Rowsell, O.M. Yaghi, Micropor. Mesopor. Mater. 73 (2004) 3;
(d) X. Lin, J. Jia, P. Hubberstey, M. Schröder, N.R. Champness, Cryst. Eng. Commun. 9 (2007) 438;
(e) A.K. Cheetham, C.N.R. Rao, R.K. Feller, Chem. Commun. (2006) 4780;
(f) B. Moulton, M.J. Zaworotko, Chem. Rev. 101 (2001) 1629;
(g) G. Ferey, Chem. Soc. Rev. 37 (2008) 191;
(h) S. Kitagawa, R. Matsuda, Coord. Chem. Rev. 251 (2007) 2490;
(i) A.Y. Robin, K.M. Fromm, Coord. Chem. Rev. 250 (2006) 2127;
(j) S. Bureekaew, S. Shimomura, S. Kitagawa, Sci. Technol. Adv. Mater. 9 (2008) (Art. No. 014108).
[2] (a) For example, see: N. Guillou, C. Livage, G. Férey, Eur. J. Inorg. Chem. (2006) 4963;
(b) S. Kitagawa, R. Kitaura, S. Noro, Angew. Chem., Int. Ed. Engl. 43 (2004) 2334;
(c) C.N.R. Rao, S. Natarajan, R. Vaidhyanathan, Angew. Chem., Int. Ed. Engl. 43 (2004) 1466;
(d) N.L. Rosi, J. Kim, M. Eddaoudi, B.L. Chen, M. O'Keeffe, O.M. Yaghi, J. Am. Chem. Soc. 127 (2005) 1504;
(e) S.M. Hawxwell, H. Adams, L. Brammer, Acta Crystallogr., Sect. B 62 (2006) 808;
(f) A.K. Ghosh, D. Ghoshai, E. Zangrando, J. Ribas, N.R. Chaudhuri, Inorg. Chem. 46 (2007) 3057;
(g) L. Rajput, K. Biradha, Polyhedron 27 (2008) 1248;
(h) C.D. Ene, F. Tuna, O. Fabelo, C. Ruiz-Pérez, A.M. Madalan, H.W. Roesky, M. Andruh, Polyhedron 27 (2008) 574;
(i) J. Pasan, F.S. Delgado, Y. Rodriguez-Martin, M. Hernandez-Molina, C. Ruiz-Perez, J. Sanchiz, F. Lloret, M. Julve, Polyhedron 22 (2003) 2143.
[3] (a) M. Pilkington, S. Decurtins, in: J.A. McCleverty, T.J. Meyer (Eds.), Comprehensive Coordination Chemistry II, vol. 7, Elsevier, University of Bern, Switzerland, 2004, p. 214;
(b) C.N.R. Rao, S. Natarajan, A. Chouhury, S. Neeraj, R. Vaidhyanathan, Acta Crystallogr., Sect. B 57 (2001) 1;
(c) O. Castillo, A. Luque, J. Sertucha, P. Roman, F. Lloret, Inorg. Chem. 39 (2000) 6142.
[4] (a) N. Lah, G. Giester, J. Lah, P. Šegedin, I. Leban, New J. Chem. 25 (2001) 753;
(b) N. Lah, J. Koller, G. Giester, P. Šegedin, I. Leban, New J. Chem. 26 (2002) 933;
(c) N. Lah, P. Šegedin, I. Leban, Struct. Chem. 13 (2002) 357;
(d) N. Lah, I. Leban, Acta Crystallogr., Sect. E 61 (2005) m835.
[5] Z. Otwinowski, W. Minor, Methods Enzymol. 276 (1996) 307.
[6] G.M. Sheldrick, SHELX97, Program for Crystal Structure Solution and Refinement, University of Göttingen, Germany, 1997.
[7] L.J. Farrugia, J. Appl. Crystallogr. 36 (2003) 7.
[8] G.M. Sheldrick, SHELXTL, version 6.12, Bruker Analytical X-ray Systems Inc., Madison, WI, 2000.

[9] CRYSTALMAKER for Windows, version 1.4.5, CrystalMaker Software Ltd., Oxfordshire, UK, 2007.
[10] (a) For example, see: M. McCann, J.F. Cronin, M. Devereux, G. Ferguson, Polyhedron 14 (1995) 2379;
(b) M. Devereux, M. McCann, J.F. Cronin, G. Ferguson, V. McKee, Polyhedron 18 (1999) 2141.
[11] O. Castillo, A. Luque, P. Román, F. Lloret, M. Julve, Inorg. Chem. 40 (2001) 5526.
[12] F.H. Allen, Acta Crystallogr., Sect. B 58 (2002) 380 (CSD version 5.30, November 2008 update).
[13] H.-Y. He, L.-G. Zhu, Acta Crystallogr., Sect. E 62 (2006) m198.

Polyhedron 28 (2009) 2473–2479

Contents lists available at ScienceDirect

Polyhedron

journal homepage: www.elsevier.com/locate/poly

Syntheses, structures and electrochemistry of manganese(III) complexes derived from *N*,*N*′-*o*-phenylenebis(3-ethoxysalicylaldimine): Efficient catalyst for styrene epoxidation

Samit Majumder [a], Susanta Hazra [a], Supriya Dutta [b], Papu Biswas [c,*], Sasankasekhar Mohanta [a,*]

[a] Department of Chemistry, University of Calcutta, 92 Acharya Prafulla Chandra Road, Kolkata 700 009, India
[b] Department of Inorganic Chemistry, Indian Association for the Cultivation of Science, Kolkata 700 032, India
[c] Department of Chemistry, Bengal Engineering and Science University, Shibpur, Howrah 711 103, India

ARTICLE INFO

Article history:
Received 10 February 2009
Accepted 24 April 2009
Available online 4 May 2009

Keywords:
Manganese(III) compounds
X-ray diffraction
Hydrogen bonds
Cyclic voltammetry
Styrene epoxidation

ABSTRACT

Syntheses, characterizations, electrochemistry and catalytic properties for styrene epoxidation of three manganese(III) compounds $[Mn^{III}L^1(H_2O)(MeOH)](ClO_4)$ (**1**) $[Mn^{III}L^1(N_3)(H_2O)]\cdot dmf$ (**2**) $[Mn^{III}L^1(Cl)(H_2O)]$ (**3**) derived from the Schiff base compartmental ligand *N*,*N*′-*o*-phenylenebis(3-ethoxysalicylaldimine) (H_2L^1) are reported. The three compounds are characterized by elemental analyses, IR, mass and UV–Vis spectra and conductance values. Single crystal X-ray structures of **1** and **2** have been determined. The structures of **1** and **2** show that these are mononuclear compounds having a salen type structure. In both structures, a dinuclear species is formed by bifurcated hydrogen bonding involving coordinated water molecule. The coordination of chloride in **3** is shown by conductance measurements. The compounds have also been characterized by UV–Vis and mass spectroscopic studies. Cyclic voltammetric and square wave voltammetric studies of the three compounds reveal that these undergo Mn(III)/Mn(II) reduction reversibly with the order of the ease of reduction as **3** > **2** > **1**. This order has been explained proposing the composition of active species in solution. Catalytic properties for epoxidation of styrene by all the three complexes using PhIO and NaOCl as oxidant have been studied. The order of both the styrene conversion and styrene epoxidation using the three title compounds is **3** > **1** > **2**. Again, it has been observed that more efficient conversion and epoxidation take place when PhIO is used as oxidant.

© 2009 Elsevier Ltd. All rights reserved.

1. Introduction

Over the past few decades extensive studies have been made on the chemistry of manganese(III) complexes derived from Schiff base type ligands due to their important role in several metalloenzymes [1] and to understand their catalytic activities in many organic reactions [2–6].

The recent development of bioinorganic manganese chemistry has been stimulated by the involvement of manganese ions in many biological systems [1]. Manganese can exist in various oxidation states ranging from 0 to +7 in different complexes [7]. This property has been utilized by the living systems in the manganese containing enzymes that are involved in many diverse Redox functions. Manganese plays an important role in metalloenzymes such as catalase [8], superoxide dismutase [9], and photosystem II of green plants [10,11]. These proteins perform biological functions in different ways; disproportionation of H_2O_2 (psuedocatalase from *Lactobacillus planatrum*), dismutation of superoxide anion O_2^{2-} (superoxide dismutase), and involvement of oxomanganese entity as the key element of the oxygen evolving complex (OEC) which performs the light-induced oxidation of water into dioxygen, may be mentioned as some of the examples.

An important aspect of Mn(III) salen type complexes is their catalytic role in various organic reactions as catalysts. Synthetic metalloporphyrins and manganese(III) salen complexes are among the most efficient catalysts for the epoxidation of unfunctionalized olefins with high selectivities and yield. Epoxidation of olefins catalyzed by manganese(III) salen complexes has been studied extensively since Kochi and coworkers described in 1986 that they are highly effective, chemoselective, and stereoselective catalysts [12a]. At the beginning of the last decades, Jacobsen and Katsuki groups independently reported that manganese(III) complexes derived from the Schiff base ligand possessing a chiral center may be used as highly enantioselective catalyst [4–6]. The synthetic accessibility of the manganese(III)–Schiff base complexes from readily available and inexpensive precursors constitutes one of the vital attractive features. The salen type ligand system is easily obtainable from the condensation reaction between diamines and salicyldehyde derivatives and optimal selectivity can be achieved by

* Corresponding authors. Fax: +91 709 737 3316 (P. Biswas), tel.: +91 33 23508386; fax: +91 33 23519755 (S. Mohanta).
E-mail addresses: biswaspapu@rediffmail.com (P. Biswas), sm_cu_chem@yahoo.co.in (S. Mohanta).

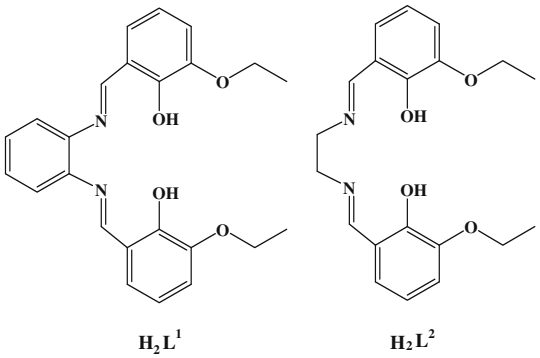
0277-5387/$ - see front matter © 2009 Elsevier Ltd. All rights reserved.
doi:10.1016/j.poly.2009.04.034

tuning the catalyst's steric and electronic properties [5]. Numerous salen type ligands have been prepared and utilized to investigate steric, electronic, and overall structural effects on the catalytic activity of manganese(III) center. Thus, manganese(III) complexes derived from salen type ligands can be used as laboratory and industrial homogeneous catalysts in the epoxidation of unfunctionalised alkenes using iodosylbenzene, sodium hypochlorite, hydrogen peroxide and alkyl hydroperoxides as the oxygen sources. The mechanism of the oxygen transfer from the intermediate oxo-metallic species to the olefin as well as the spin state of the intermediate oxo-metallic species, which exists possibly in a higher oxidation state, are still debatable issues [4,13]. Nevertheless, the [O = Mn(V) – salen Cl] species has been identified directly by mass spectroscopy [14] and indirectly by nuclear magnetic resonance spectroscopy [15] when iodosylbenzene was used as the oxygen source. Recently it has been reported that the mechanism and consequently the products depend on several factors like olefin [16], oxidant, counter-ion, structure of the Schiff base ligand, oxygen donor and added Lewis base [13b,17].

Using compartmental Schiff base ligands obtained on condensation of 3-ethoxysalicylaldehyde and diamines, a few 3d [18,19], 3d–3d [19] and 3d–4f [20] compounds have been previously reported. It has been observed that the $O(phenoxo)_2O(ethoxy)_2$ compartments of the mononuclear fragments derived from *N*,*N*′-*o*-phenylenebis(3-ethoxysalicylaldimine) [19b] (H_2L^1; Chart 1) and *N*,*N*′-ethylenebis(3-ethoxysalicylaldimine) [19a] (H_2L^2; Chart 1) are potential host sites for water molecules by forming bifurcated hydrogen bonds. Interesting examples of mononuclear inclusion products [18,19] and mononuclear–dinuclear cocrystals [19], resulted due to the hydrogen bonding interactions involving water and O_4 compartment, have been observed in complexes containing copper(II) in the salen-type cavity [19]. It will therefore be interesting to explore the inclusion phenomenon in complexes keeping other 3d metal ions in the salen type compartments. Manganese complexes will be additionally interesting for the scope of their catalytic properties. It may also be mentioned that manganese complexes are good members to enlighten the electrochemical aspects due to the possibility of various oxidation states of this metal center. We report here the syntheses, characterizations including single crystal X-ray structures of two complexes, electrochemistry, and catalytic roles for olefin epoxidation of three manganese(III) complexes derived from *N*,*N*′-*o*-phenylenebis(3-ethoxysalicylaldimine) (H_2L^1; Chart 1).

2. Experimental

Caution! Perchlorate and azide complexes of metal ions are potentially explosive. Only a small amount of material should be prepared, and it should be handled with caution.



H_2L^1 H_2L^2

Chart 1. Chemical structures of the Schiff base ligands H_2L^1 and H_2L^2.

2.1. Materials and physical methods

The Schiff base ligand H_2L^1 was prepared by 2:1 condensation of 3-ethoxysalicylaldehyde and *o*-phenylenediamine in methanol. Iodosylbenzene (PhIO) was prepared by the hydrolysis of iodobenzene diacetate [21]. Styrene and styrene oxide were purchased from Aldrich and used in epoxidation experiment without further purification. The styrene oxide was used as standard sample in GC analysis. All the other reagents and solvents were purchased from commercial sources and used as received.

Elemental (C, H, and N) analyses were performed on a Perkin–Elmer 2400 II analyzer. IR spectra were recorded in the region 400–4000 cm^{-1} on a Perkin–Elmer RXIFT spectrophotometer with samples as KBr disks. Magnetic susceptibility measurements of **1**–**3** at 300 K were carried out with a Sherwood Scientific Co., UK magnetic susceptibility balance. Electronic spectra were obtained with Hitachi U-3501 spectrophotometer. The electrospray ionization mass spectra were recorded on a Micromass Qtof YA 263 mass spectrometer. Molar conductivities (Λ_M) of 1 mM solution in dmf of complexes **1**–**3** were measured at 25 °C with a Systronics conductivity bridge. The electrochemical measurements of these complexes were performed at 25 °C under nitrogen atmosphere using a Bioanalytical Systems BAS 100B electrochemical analyzer. The concentration of the supporting electrolyte tetrabutylammonium perchlorate (TBAP) was 0.1 M, while that of complex was 1 mM. Cyclic voltammetric (CV) and square wave voltammetric (SWV) measurements were carried out with three-electrode assembly comprising a glassy carbon disk working electrode, platinum auxiliary electrode and an aqueous Ag/AgCl reference electrode (290 mV versus NHE). IR compensation was made automatically during each run. Under the experimental conditions used, the $E_{1/2}$ value of the ferrocene/ferrocenium couple was 420 mV in *N*,*N*-dimethylformamide. GC experiments were performed with Agilent 6890N Network GC systems.

2.2. Syntheses of the complexes

2.2.1. $[Mn^{III}L^1(H_2O)(MeOH)](ClO_4)$ (**1**)

To a stirred suspension of H_2L^1 (0.404 g, 1.00 mmol) in methanol (15 mL) was dropwise added a methanol solution (5 mL) of manganese(II) perchlorate hexahydrate (0.254 g, 1.00 mmol). After a few minutes a brown precipitate started to deposit. This was dissolved by adding the requisite amount of acetonitrile. After one hour stirring, the solution was filtered and the filtrate was kept for slow evaporation. The diffraction quality red crystals that deposited over a period of a few days were collected by filtration and washed with methanol (516 mg, 85%). *Anal.* Calc. for $C_{25}H_{28}N_2O_{10}ClMn$ (606.89): C, 49.48; H, 4.65; N, 4.62. Found: C, 49.52; H, 4.72; N, 4.75%. IR (KBr): ν = 3413(m) ν (H2O), 1594(s) ν (C=N), 1110(vs), 619(w) ν (ClO_4) cm^{-1}. MS(ESI+): *m*/*z*: 457 $[C_{24}H_{22}N_2O_4Mn]^+$. UV–Vis (dmf, λ_{max}/nm (ε/M^{-1} cm^{-1})): 410 (15 960), 307 (23 910). μ_{eff} = 4.76 BM.

2.2.2. $[Mn^{III}L^1(N_3)(H_2O)]\cdot dmf$ (**2**)

A solution of **1** (0.303 g, 0.50 mmol) in methanol (30 mL) was heated under reflux and to this hot solution was added an aqueous solution (5 mL) of sodium azide (0.130 g, 2.00 mmol). After a few minutes a dark brown precipitate started to deposit. The reflux was continued for 2 h and then after cooling the deposited solid was collected by filtration, washed with methanol and air dried. Recrystallization by diffusing diethylether into a dimethylformamide solution of the crude product yielded red crystals of diffraction quality (192 mg, 65%). $C_{27}H_{31}N_6O_6Mn$ (590.52): C, 54.92; H, 5.29; N, 14.23. Found: C, 54.85; H, 5.35; N, 14.40%. IR (KBr): ν = 3440(m) ν (H_2O), 1596(s) ν (C=N), 2028(vs) ν (N_3), 1660(m) ν (amide, dmf) cm^{-1}. MS(ESI+) *m*/*z*: 457 $[C_{24}H_{22}N_2O_4Mn]^+$. UV–Vis

(dmf, λ_{max}/nm (ε/M^{-1} cm^{-1})): 412 (17 440), 307 (26 100). μ_{eff} = 4.72 BM.

2.2.3. $[Mn^{III}L^1(Cl)(H_2O)]$ (**3**)

To a stirred solution of H_2L^1 (0.404 g, 1.00 mmol) in acetonitrile (15 mL) was dropwise added a methanol solution (5 mL) of manganese(II) chloride tetrahydrate (0.198 g, 1.00 mmol). Immediately an orange-red precipitate started to deposit. This was dissolved by adding the requisite amount of methanol. After one hour stirring, the solution was filtered and the filtrate was kept for slow evaporation. After two days, the compound that deposited was collected by filtration and washed with acetonitrile. Recrystallization from methanol–acetonitrile mixture yielded dark red colored crystalline compound (383 mg, 75%). *Anal.* Calc. for $C_{24}H_{24}N_2O_5ClMn$ (510.86): C, 56.43; H, 4.74; N, 5.48. Found: C, 56.34; H, 4.72; N, 5.62%. IR (KBr): ν = 3440(s) ν (H_2O), 1599(vs) ν (C=N). MS(ESI+) m/z: 457 $[C_{24}H_{22}N_2O_4Mn]^+$. UV–Vis (dmf, λ_{max}/nm (ε/M^{-1} cm^{-1})): 412 (13 240), 305 (22 840). μ_{eff} = 4.60 BM.

2.3. Crystal structure determination of $[Mn^{III}L^1(H_2O)(MeOH)](ClO_4)$ (**1**) and $[Mn^{III}L^1(N_3)(H_2O)]$·dmf (**2**)

The crystallographic data of these two compounds are summarized in Table 1. Intensity data of **1** and **2** were collected at 293 K and 296 K, respectively, on a Bruker-APEX II SMART CCD diffractometer using graphite-monochromated Mo Kα radiation (λ = 0.71073 Å). For data processing and absorption correction the packages SAINT [22] and SADABS [22] were used. The structure was solved by direct and Fourier methods and refined by full-matrix least-squares based on F^2 using SHELXTL [23] and SHELXL-97 [24] packages. The non hydrogen atoms were refined anisotropically. For **1**, H(26), H(27) and H(28) have been located, while the other hydrogen atoms have been placed at geometrical positions with fixed thermal parameters. Three perchlorate oxygens are disordered over two sites and modeled accordingly. In the case of **2**, H(28) and H(29) have been located, while the other hydrogen atoms are placed at geometrical positions with fixed thermal parameters. The dimethylformamide molecule in compound **2** is highly disordered and difficult to model. Therefore it was eliminated using the SQUEEZE facility of PLATON [25]. The final least-squares refinements ($R1$) based on $I > 2\sigma(I)$ converged to 0.0454 and 0.0339 for **1** and **2**, respectively.

Table 1
Crystal data for (**1**) and (**2**).

	1	**2**
Formula	$C_{25}H_{28}N_2O_{10}ClMn$	$C_{24}H_{24}N_5O_5Mn$
Molecular weight	606.89	517.42
Crystal color	red	red
Crystal system	triclinic	monoclinic
Space group	$P\bar{1}$	$P21/c$
a (Å)	9.714(3)	12.4275(15)
b (Å)	11.971(4)	15.5031(19)
c (Å)	13.107(7)	15.1470(19)
α (°)	112.859(12)	90.00
β (°)	102.587(12)	105.190(3)
γ (°)	102.570(8)	90.00
V (Å^3)	1291.0(9)	2816.3(6)
Z	2	4
D_{calc} (g cm^{-3})	1.561	1.220
μ (mm^{-1})	0.677	0.507
T (K)	293(2)	296(2)
F(0 0 0)	628	1072
2θ	3.58–51.36	3.40–56.66
Index ranges	$-11 \leqslant h \leqslant 11$	$-16 \leqslant h \leqslant 16$
	$-13 \leqslant k \leqslant 14$	$-20 \leqslant k \leqslant 20$
	$-15 \leqslant l \leqslant 15$	$-20 \leqslant l \leqslant 16$
Reflections collected	12 918	39 902
Independent reflections	4837	6935
Parameters refined	394	326
Goodness-of-fit (Gof) F^2	0.933	0.998
R_1[a]/wR_2[b] ($I > 2a(7)$)	0.0454/0.1295	0.0339/0.0899
R_1[a]/wR_2[b] (all data)	0.0624/0.1455	0.0498/0.0946
Residuals (e A^{-3})	0.536/0.756	0.270/0.244

[a] $R_1 = [\Sigma||F_o| - |F_c||/\Sigma|F_o|]$.
[b] $wR_2 = [\Sigma w(F_o^2 - F_c^2)^2/\Sigma wF_o^4]^{1/2}$.

2.4. General method for styrene epoxidation

The epoxidation reactions were carried out at room temperature in acetonitrile under nitrogen atmosphere with constant stirring. The composition of the reaction mixture was 2.00 mmol of styrene, 2.00 mmol of chlorobenzene (internal standard), 0.10 mmol of Mn(III) complex (catalyst) and 2.00 mmol iodosylbenzene or sodium hypochlorite (oxidant) in 5.00 mL freshly distilled acetonitrile. When the oxidant was sodium hypochlorite, the solution was buffered to pH 11.2 with NaH_2PO_4 and NaOH [26]. The composition of reaction medium was determined by GC with styrene and styrene epoxide quantified by the internal standard method (chlorobenzene). All other products detected by GC were mentioned as others. For each complex the reaction time for maximum epoxide yield was determined by withdrawing periodically 0.1 mL aliquots from the reaction mixture and this time was used to monitor the efficiency of the catalyst on performing at least two independent experiments. Blank experiments with each oxidant and using the same experimental conditions except catalyst were also performed.

3. Results and discussion

3.1. Syntheses and characterization

Reaction of manganese(II) perchlorate and H_2L^1 produces the mononuclear manganese(III) complex $[Mn^{III}L^1(H_2O)(MeOH)](ClO_4)$ (**1**). Similarly, reaction of manganese(II) chloride and H_2L^1 produces the mononuclear manganese(III) complex $[Mn^{III}L^1(Cl)(H_2O)]$ (**3**). Clearly, aerial oxidation of manganese(II) to manganese(III) and metal assisted deprotonation of the phenolic moieties take place during the formation of **1** and **3**. As will be described below, the X-ray structure of **1** shows that the water and methanol molecules are coordinated to the metal center, while perchlorate exists as a counter anion in this molecule. The reaction of $[Mn^{III}L^1(H_2O)(MeOH)](ClO_4)$ (**1**) with sodium azide produces the compound $[Mn^{III}L^1(N_3)(H_2O)]$·dmf (**2**). As will be described below, the azide in this molecule is coordinated to the metal center. The molar conductivity (Λ_M) of **1** (80 Ω^{-1} cm^2 M^{-1}) is consistent with the values expected for 1:1 electrolytes (72–90 Ω^{-1} cm^2 M^{-1}) [27]. The poor conductivity of complexes **2** and **3** (ca. 10 Ω^{1} cm^2 M^{-1}) indicate that azide and chloride ion in these complexes are coordinated to the metal center and are not dissociated by dmf molecules in solution. The characteristic imine stretching of the complexes **1**, **2**, and **3** is observed at 1594, 1596 and 1599 cm^{-1} as a strong or very strong signal. The perchlorate vibrations in **1** takes place as a very strong and a weak signals at 1110 and 619 cm^{-1}, respectively. Appearance of two bands at 2028 and 1660 cm^{-1} indicates the presence of azide and dmf, respectively, in **2**. The IR spectra of the complexes **1**, **2** and **3** exhibit one medium or strong absorption at 3413, 3440 and 3440 cm^{-1} due to the coordinated water molecule. In contrast to the weak and broad water stretching observed in most of the crystal hydrates, the water stretching signal in the title compounds are medium or strong and sharp. As will be seen, the water molecule of one mononuclear unit forming bifurcated hydrogen bonds in the O_4 compartment of another molecule. It has been observed previously that separation of symmetric and

asymmetric stretching of encapsulated water molecule takes place in mononuclear copper(II) complexes derived from H_2L^1 and H_2L^2. In these copper(II) complexes, the water molecule is noncoordinated and highly encapsulated. The bifurcated hydrogen of the coordinated water molecule in **1**–**3** can not restrict the vibration in large extent. However, the vibration is partially restricted so that the signal becomes sharper with medium or strong intensity. The composition of **1**, **2** and **3** was further verified by electrospray ionization mass spectroscopy (ESI-MS positive). The ESI-MS spectra of all the three complexes in acetonitrile exhibits one peak at $m/z = 457$, which is assignable to $C_{24}H_{22}N_2O_4Mn^+$ (100%) cation. The UV–Vis spectra of the three complexes exhibit two bands at ca. 410 nm and 306 nm which can be assigned to phenolate→manganese(III) charge transfer and manganese(III)→imine ($d\rightarrow\pi^*$) metal to ligand charge transfer transitions, respectively. The observed magnetic moment at 300 K of **1**, **2** and **3** is 4.76, 4.72 and 4.60 B. M., respectively, indicating that the manganese(III) center in the title compounds exists in high spin state.

3.2. Description of the structure of $[Mn^{III}L^1(H_2O)(MeOH)](ClO_4)$ (**1**) and $[Mn^{III}L^1(N_3)(H_2O)]\cdot dmf$ (**2**)

The crystal structures of cationic part of **1** and **2** are shown in Figs. 1 and 2, respectively, while the bond lengths and angles around the coordination environment of these two complexes are listed in Tables 2 and 3, respectively. The structures show that both are mononuclear compound of manganese(III) having the metal center in the salen-type cavity of $[L^1]^{2-}$. The metal center in **1** and **2** is hexacoordinated. In **1**, the remaining two sites are occupied by one water molecule and one methanol molecule, while one water molecule and one azide anion occupy the remaining two coordination positions in the case of **2**. The charge of the compound **1** is balanced by a perchlorate anion. There is one dimethylformamide (dmf) molecule in **2** as solvent of crystallization.

The coordination environment of the metal ions in both **1** and **2** is slightly distorted tetragonal. The two phenolate oxygen atoms (O(1) and O(2)) and the two imine nitrogen atoms (N(1) and N(2)) define the basal plane. The average deviation (0.0007 Å for **1** and 0.024 Å for **2**) of the donor centers and the displacement (0.014 Å for **1** and 0.071 Å for **2**) of the metal center from the least-squares O(1)O(2)N(1)N(2) plane indicate that the N_2O_2 cavity

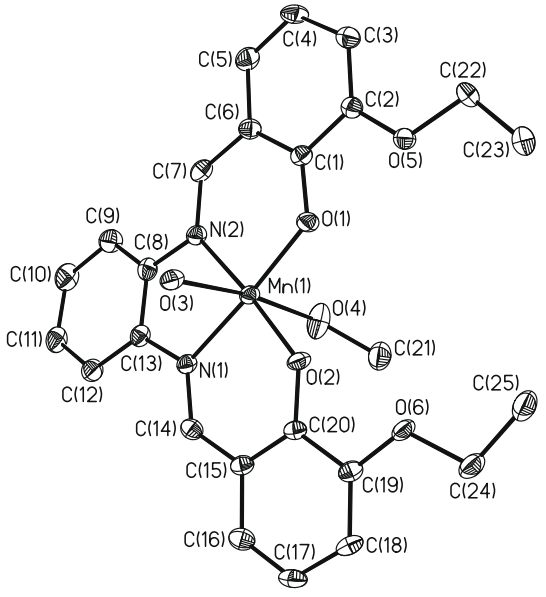


Fig. 1. Crystal structure of the cation of $[Mn^{III}L^1(H_2O)(MeOH)](ClO_4)$ (**1**).

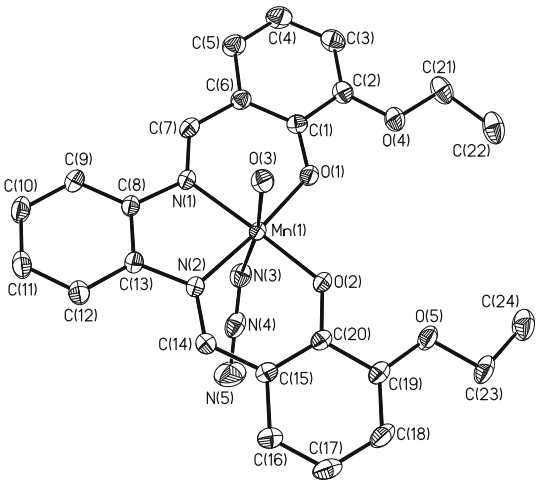


Fig. 2. Crystal structure of $[Mn^{III}L^1(N_3)(H_2O)]\cdot dmf$ (**2**).

Table 2
Selected bond lengths (Å) and angles (°) of (**1**).

Mn(1)–O(1)	1.882(2)
Mn(1)–O(2)	1.871(2)
Mn(1)–N(1)	1.998(2)
Mn(1)–N(2)	1.982(3)
Mn(1)–O(3)	2.235(2)
Mn(1)–O(4)	2.261(3)
O(3)–Mn(1)–O(4)	173.45(11)
O(1)–Mn(1)–N(1)	175.13(9)
O(2)–Mn(1)–N(2)	175.17(9)
O(3)–Mn(1)–O(1)	93.53(10)
O(3)–Mn(1)–O(2)	89.86(10)
O(3)–Mn(1)–N(1)	87.40(10)
O(3)–Mn(1)–N(2)	90.69(10)
O(4)–Mn(1)–O(1)	91.79(10)
O(4)–Mn(1)–O(2)	86.13(10)
O(4)–Mn(1)–N(1)	87.62(10)
O(4)–Mn(1)–N(2)	92.87(10)
O(1)–Mn(1)–O(2)	92.03(9)
O(1)–Mn(1)–N(2)	92.73(9)
O(2)–Mn(1)–N(1)	92.76(9)
N(1)–Mn(1)–N(2)	82.47(10)

Table 3
Selected bond lengths (Å) and angles (°) of (**2**).

Mn(1)–O(1)	1.8856(10)
Mn(1)–O(2)	1.8782(10)
Mn(1)–N(1)	1.9887(12)
Mn(1)–N(2)	1.9896(12)
Mn(1)–O(3)	2.3114(13)
Mn(1)–N(3)	2.1896(14)
N(3)–N(4)	1.180(2)
N(4)–N(5)	1.163(2)
O(3)–Mn(1)–N(3)	171.81(5)
O(1)–Mn(1)–N(2)	174.65(4)
O(2)–Mn(1)–N(1)	172.44(5)
O(3)–Mn(1)–O(1)	91.24(5)
O(3)–Mn(1)–O(2)	89.37(5)
O(3)–Mn(1)–N(2)	85.78(5)
O(3)–Mn(1)–N(1)	84.75(5)
N(3)–Mn(1)–O(1)	95.31(5)
N(3)–Mn(1)–O(2)	95.28(5)
N(3)–Mn(1)–N(2)	87.29(5)
N(3)–Mn(1)–N(1)	90.03(5)
O(1)–Mn(1)–O(2)	92.19(4)
O(1)–Mn(1)–N(1)	92.67(5)
O(2)–Mn(1)–N(2)	92.22(5)
N(2)–Mn(1)–N(1)	82.64(5)

affords an almost perfect plane to the metal center. The axial positions of the metal center in **1** are occupied by the water and methanol oxygens (O(3) and O(4), respectively), while one water oxygen (O(3)) and one azide nitrogen (N(3)) occupy the axial positions in the case of **2**. In the basal plane, the metal–ligand bond distances involving the imine nitrogens (**1**: Mn(1)–N(1) = 1.998(2) Å, Mn(1)–N(2) = 1.982(3) Å. **2**: Mn(1)–N(1) = 1.98887(12) Å, Mn(1)–N(2) = 1.9896(12) Å) are slightly greater than the bond lengths involving phenoxo oxygens (**1**: Mn(1)–O(1) = 1.882(2) Å, Mn(1)–O(2) = 1.871(2) Å. **2**: Mn(1)–O(1) = 1.8856(10) Å, Mn(1))–O(2) = 1.8782(10) Å). As expected due to Jahn–Teller distortion of high spin manganese(III), the bond distances involving the axial water and methanol oxygen atoms in **1** (Mn(1)–O(3) = 2.235(2) Å, Mn(1)–O(4) = 2.261(3) Å) as well as involving water oxygen and azide nitrogen in **2** (Mn(1)–O(3) = 2.3114(13) Å, Mn(1)–N(3) = 2.1896(14) Å) significantly longer than the bond lengths involving the basal atoms. The *transoid* angles (**1**: 173.45(11)°, 175.13(9)°, and 175.17(9)°. **2**: 171.81(5)°, 174.65(4)°, and 172.44(5)°) and the *cisoid* angles (**1**: 82.47(10)–93.53(10)°. **2**: 82.64(5)–95.31(5)°) deviate slightly from the ideal values.

As shown in Figs. 3 and 4, each of the two hydrogen atoms of the coordinated water molecule ($H_2O(3)$) in both the compounds **1** and **2** forms bifurcated hydrogen bonds with one phenoxo and one ethoxy oxygen atoms of a symmetry related mononuclear molecule resulting in the formation of self-assembled dinuclear species. The geometries of the hydrogen bonds are summarized in Table 4. The ranges of the donor–acceptor contacts in **1** and **2** are 2.897–2.982 Å and 2.929–3.022 Å respectively, indicating that the hydrogen bonds responsible for the formation of dinuclear self-assembly may be considered as strong. Another interesting structural feature of compounds **1** and **2** is the presence of relatively strong π–π interaction. The aromatic ring C(1)C(2)C(3)C(4)C(5)C(6) of one molecule interacts with an aromatic ring (C(15A)C(16A)-C(17A)C(18A)C(19A)C(20A) for **1** and C(15B)C(16B)C(17B)C-(18B)C(19B)C(20B) for **2**) of a symmetry related molecule (A, $1-x$, $1-y$, $1-z$; B, $1-x$, $-y$, $1-z$). The distance between the two centroids is 3.622 and 3.696 Å, respectively, for **1** and **2**. The combined effect of hydrogen bonding and π–π interaction result

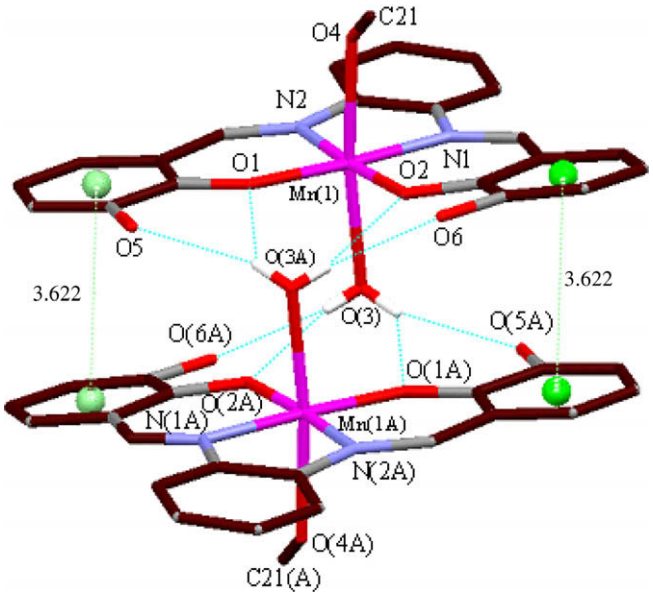


Fig. 3. Perspective view to demonstrate the bifurcated hydrogen bonds by coordinated water in $[Mn^{III}L^1(H_2O)(MeOH)](ClO_4)$ (**1**) resulting in the formation of self-assembled dinuclear aggregate. Some atoms have been omitted for clarity.

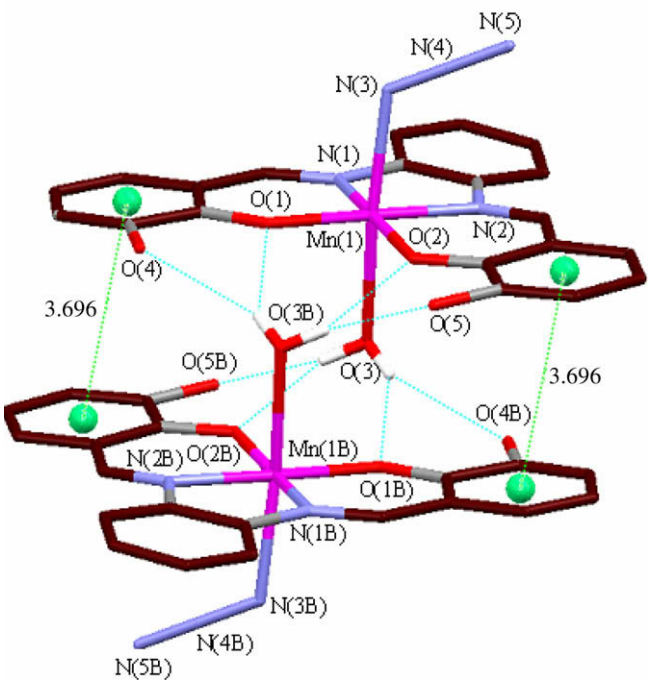


Fig. 4. Perspective view to demonstrate the bifurcated hydrogen bonds by coordinated water in $[Mn^{III}L^1(N_3)(H_2O)]\cdot dmf$ (**2**) resulting in the formation of self-assembled dinuclear aggregate. Some atoms have been omitted for clarity.

the mononuclear manganese(III) molecules are self-assembled to dinuclear species [28].

3.3. Electrochemistry

The electrochemical measurements have been carried out for complexes **1**–**3** in dmf. The results obtained in these measurements are summarized Table 5. All these complexes show only one reversible peak due to Mn(III)/Mn(II) couple. The cyclic voltammogram of the complexes **1**, **2** and **3** are shown in Figs. S1–S3 (in Supplementary Informations) respectively. The $E_{½}$ values of the Redox couples for **1**, **2** and **3** are $E_{½}$ = 90, 105 and 165 mV, respectively, while the ΔE_p values the couples are 70, 70, and 75 mV, respectively. The ΔE_p values for all the three complexes clearly indicate the reversible nature of the reduction process. The complimentary Redox potentials obtained from square wave voltammetry (SWV) is also given in the Table 5. The order of the $E_{½}$ values in **1**, **2**, and **3** indicates that the order of the feasibility of the reduction of manganese(III) center in the three complexes are **3** > **2** > **1**. Therefore, the order of the relative extent of the accumulation of negative charge on manganese(II) center in solution is **1** > **2** > **3**. The structures of the inner sphere of the complexes **1**, **2**

Table 4
Geometries (distances in (Å) and angles in (°)) of hydrogen bonds in (**1**) and (**2**). Symmetry codes: A, $1-x$, $1-y$, $1-z$; B, $1-x$, $-y$, $1-z$.

Compound	D–H···A	D···A	H···A	D–H···A
1	O(3)–H(26)···O(1A)	2.982	2.320	138.2
	O(3)–H(26)···O(5A)	2.950	2.202	151.8
	O(3)–H(27)···O(2A)	2.926	2.389	141.4
	O(3)–H(27)···O(6A)	2.897	2.304	152.8
2	O(3)–H(28)···O(2B)	2.929	2.316	134.0
	O(3)–H(28)···O(5B)	2.973	2.222	156.7
	O(3)–H(29)···O(1B)	2.988	2.319	145.9
	O(3)–H(29)···O(4B)	3.022	2.348	146.8

Table 5
Electrochemical measurements[a] of **1**–**3** in dmf.

Complex	$E_{1/2}$ (mV)		ΔE_p[b] (mV)
	CV	SWV	
1	90	90	70
2	105	100	70
3	165	170	75

[a] All the potentials are against Ag/AgCl reference electrode and scan rate in all cases is 100 mV s^{-1} for cyclic voltammogram.
[b] For cyclic voltammogram.

and **3** in solid state are $[Mn^{III}L^1(H_2O)(MeOH)]^+$, $[Mn^{III}L^1(N_3)(H_2O)]$ and $[Mn^{III}L^1(Cl)(H_2O)]$, respectively. Evidently, in contrast to methanol in **1**, there are coordinated anions in **2** and **3**. Therefore, if the compositions in solution are same as in solid state, the reduction of the metal center should be easier in **1** than that in **2** or **3**. However, the reverse order is observed indicating the change of composition of the inner sphere in solution. As already discussed, azide and chloride in **2** and **3** are not substituted by solvent molecules in dmf solutions and therefore the active species of **1**, **2**, and **3** to undergo reduction may be considered to be $[Mn^{III}L^1(dmf)_2]$, $[Mn^{III}L^1(dmf)(N_3)]$ and $[Mn^{III}L^1(dmf)Cl]$, respectively. In that case, due to the presence of two dmf, there is a possibility of the accumulation of relatively more negative charge on the metal center in **1** resulting in the less positive $E_{½}$ value. It also seems that azide in **2** accumulates more negative charge on the metal center in **2** than that by chloride in **3**.

3.4. Epoxidation of styrene by complexes *1*, *2* and *3*

Epoxidation of styrene was carried out at room temperature with manganese(III) complexes, **1**, **2**, and **3**, as the catalysts and PhIO and NaOCl as oxidants. The deep red color of the solutions containing the Mn(III) complexes and the substrate was intensified after the addition of oxidant indicating the formation of oxo-metallic intermediates of the catalysts [4]. After completion of oxidation reaction of the alkene, the solution regains its initial color which suggests that the regeneration of the catalysts takes place. Because of the insolubility of the iodosylarenes in common organic solvents, we did not attempt to determine the rate law [29]. The percentage of conversion of styrene, selectivity for styrene oxide, yield of styrene oxide for each complex and reaction time to obtain maximum yield using both the oxidants are given in Table 6.

The data in Table 6 reveals that catalyst **3** converts styrene most efficiently in presence of both the oxidants. Nevertheless, all the catalysts are selective towards the formation of styrene epoxide despite of the formation of by-products which have been identified by GC-MS as benzaldehyde, phenylacetaldehyde, styrene epoxide derivative, alcohols etc. From the data it is also clear that complex **3** also exhibits the highest efficiency for styrene epoxide yield.

When the reactions are carried out with PhIO, styrene conversions were 87%, 80% and 95% for catalysts **1**, **2** and **3**, respectively.

Table 6
Epoxidation of styrene catalyzed by complexes **1**–**3** in acetonitrile.

Complex	Time(h)	Oxidant	Conversion (%)	Epoxide yield (%)	Selectivity (%)	
					Epoxide	Other
1	2.5	PhIO	87	74	85	15
	2	NaOCl	71	58	82	18
2	2.5	PhIO	80	65	81	19
	4	NaOCl	68	52	76	24
3	1.5	PhIO	95	87	92	8
	2	NaOCl	90	77	85	15

With NaOCl as oxidant, styrene conversion dropped to 71%, 68% and 90% for **1**, **2** and **3**, respectively. It is evident that from Table 6 that between NaOCl and PhIO, later acts as a better oxidant with respect to both styrene conversion and styrene epoxide selectivity. Figs. 5 and 6 show bar diagrams for the epoxidation of the styrene using PhIO and NaOCl as oxidant, respectively.

It is relevant to compare the catalytic performance of the title complexes with that of the current "best" systems. Kochi and coworker reported epoxide yields of 50-75% for the epoxidation of various types of olefins, including substituted styrenes, stilbenes, and cyclic and acyclic alkenes, within 15 min at ambient temperatures in acetonitrile using PhIO as the oxidant and several substituted Mn(III)–salen complexes as catalysts [12a]. Recently Silva et al. reported styrene epoxide yield ranging from 22.5% to 85.7% in presence of NaOCl as oxidant and from 71.2% to 98.3% in presence of PhIO as oxidant by using a number of manganese(III)–Schiff base complexes in acetonitrile [12b]. Evidently, as the epoxide yields for the title complexes range between 65 and 87% using PhIO as oxidant and between 52% and 77% using NaOCl as oxidant, the title

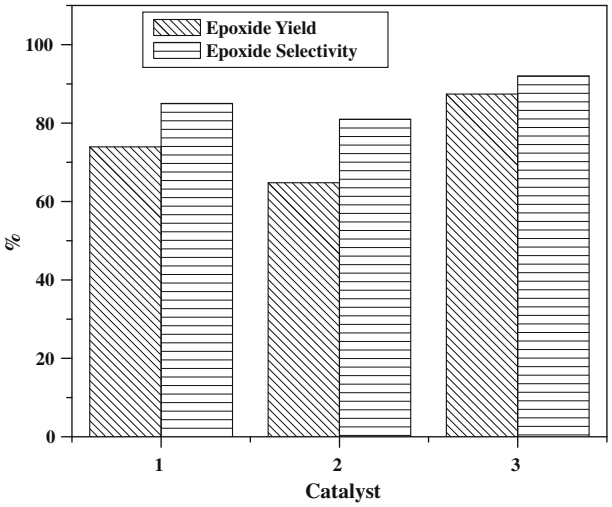


Fig. 5. Bar diagram showing the catalytic activity of complexes **1**–**3** with styrene in CH_3CN using PhIO as oxidant.

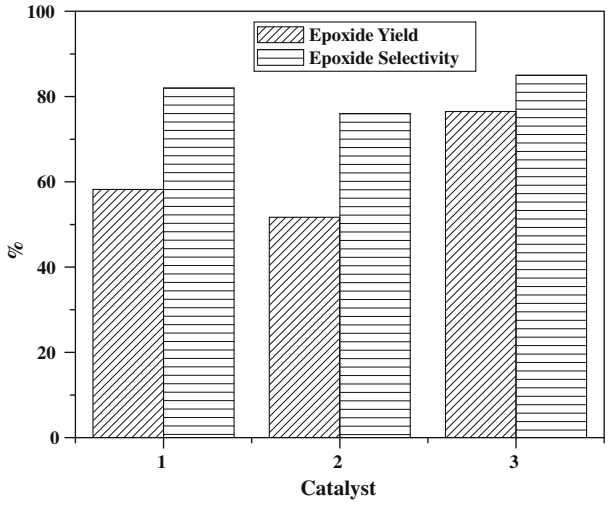


Fig. 6. Bar diagram showing the catalytic activity of complexes **1**–**3** with styrene in CH_3CN using NaOCl as oxidant.

compounds can be included in the family of "best" catalysts reported so far.

4. Conclusions

One aim of the present investigation is to explore the possibility of inclusion properties of water molecule in the O_4 compartment of the complexes of 3d metal ions, other than copper(II), derived from H_2L^1. It has been also observed that the combined effect of hydrogen bonding and $\pi-\pi$ interaction result the mononuclear manganese(III) molecules are self-assembled to dinuclear species. Another aim of the present study is to enlighten the electrochemical behavior of manganese complexes. It has been observed that the expected trend of the ease of reduction does not take place in the present series. However, the observation has been tentatively explained proposing the active species in solution. The final aim of this investigation is to explore the catalytic properties for styrene epoxidation by new manganese complexes. In parallel with our anticipation, the title compounds catalyze both the styrene conversion and epoxidation efficiently.

Acknowledgements

Financial support from the Department of Science and Technology, Government of India (Project No.: SR/S1/IC-12/2008) is gratefully acknowledged. S. Majumder, S. Hazra, and S. Dutta are thankful to Council for Scientific and Industrial Research, Government of India for providing Fellowship. Crystallography was performed at the DST, India-funded National Single Crystal Diffractometer Facility at the Department of Inorganic Chemistry, IACS, Kolkata.

Appendix A. Supplementary data

CCDC 715118 and 715119 contain the supplementary crystallographic data for **1** and **2**. These data can be obtained free of charge via http://www.ccdc.cam.ac.uk/conts/retrieving.html, or from the Cambridge Crystallographic Data Centre, 12 Union Road, Cambridge CB2 1EZ, UK; fax: (+44) 1223-336-033; or e-mail: deposit@ccdc.cam.ac.uk. Supplementary data associated with this article can be found, in the online version, at doi:10.1016/j.poly.2009.04.034.

References

[1] E.J. Larson, V.L. Pecoraro, in: V.L. Pecoraro (Ed.), Manganese Redox Enzymes, VCH Publisher, Inc., New York, 1992, p. 1.
[2] K.A. Jørgensen, Chem. Rev. 89 (1989) 431.
[3] M.J. Gunter, P. Turner, Coord. Chem. Rev. 108 (1991) 115.
[4] E.N. Jacobsen, in: I. Ojima (Ed.), Catalytic Asymmetric Synthesis, VCH, Weinheim, 1993, p. 159.
[5] (a) T. Katsuki, Coord. Chem. Rev. 140 (1995) 189;
(b) T. Katsuki, J. Mol. Catal. A: Chem. 113 (1996) 87.
[6] T. Katsuki, in: I. Ojima (Ed.), Catalytic Asymmetric Synthesis, 2nd ed., Wiley, New York, 2000, p. 287.
[7] F.A. Cotton, G. Wilkinson, Advanced Inorganic Chemistry, 5th ed., Wiley, New York, 1980.
[8] (a) Y. Kono, I. Fridovich, J. Biol. Chem. 258 (1983) 6015;
(b) W.F. Beyer Jr., I. Fridovich, Biochemistry 24 (1985) 6460.
[9] R.H. Holm, P. Kennepohl, E.I. Solomon, Chem. Rev. 96 (1996) 2239.
[10] V.K. Yachandra, K. Sauer, M.P. Klein, Chem. Rev. 96 (1996) 2927.
[11] A.W. Rutherford, A. Boussac, Science 303 (2004) 1782.
[12] (a) K. Srinivas, P. Michand, J.K. Kochi, J. Am. Chem. Soc. 108 (1986) 2309;
(b) A.R. Silva, C. Freire, B.de. Castro, New J. Chem. 28 (2004) 253.
[13] (a) C.T. Dalton, K.M. Ryan, V.M. Wall, C. Bousquet, D.G. Gilheany, Top. Catal. 5 (1998) 75;
(b) W. Adam, K.J. Roschmann, C.R. Saha-Möller, D. Seebach, J. Am. Chem. Soc. 124 (2002) 5068.
[14] D. Feichtinger, D.A. Plattner, Angew. Chem., Int. Ed. 36 (1997) 1718.
[15] K.P. Bryliakov, D.E. Babushin, E.P. Talsi, J. Mol. Catal. A: Chem. 158 (2000) 19.
[16] E.N. Jacobsen, M.H. Wu, in: A. Pfaltz, E.N. Jacobsen, H. Yamamoto (Eds.), Comprehensive Asymmetric Catalysis, vol. 2, Springer-Verlag, Berlin, 1999, p. 649.
[17] K.A. Campbell, M.R. Lashley, J.K. Wyatt, M.H. Nant, R.D. Britt, J. Am. Chem. Soc. 123 (2001) 5710.
[18] (a) G. Hoshina, M. Tsuchimoto, S. Ohba, Bull. Chem. Soc. Jpn. 73 (2000) 369;
(b) D. Cunningham, J.F. Gallagher, T. Higgins, P. McArdle, J. McGinley, M. O'Gara, J. Chem. Soc., Dalton Trans. (1993) 2183;
(c) J.R. Zamian, E.R. Dockal, G. Castellano, G. Oliva, Polyhedron 14 (1995) 2411;
(d) I.-C. Hwang, K. Ha, Z. Kristallogr. New Cryst. Struct. 221 (2006) 363.
[19] (a) M. Nayak, R. Koner, H.-H. Lin, U. Flörke, H.-H. Wei, S. Mohanta, Inorg. Chem. 45 (2006) 10764;
(b) M. Nayak, S. Hazra, P. Lemoine, R. Koner, C.R. Lucas, S. Mohanta, Polyhedron 27 (2008) 1201.
[20] (a) R. Koner, H.-H. Lin, H.-H. Wei, S. Mohanta, Inorg. Chem. 44 (2005) 3524;
(b) R. Koner, G.-H. Lee, Y. Wang, H.-H. Wei, S. Mohanta, Eur. J. Inorg. Chem. (2005) 1500.
[21] H. Saltzman, J.G. Sharefkin, Organic Syntheses Collect, vol. V, Wiley, New York, 1973.
[22] G.M. Sheldrick, SAINT (Version 6.02), SADABS (Version 2.03), Bruker AXS Inc., Madison, Wisconsin, 2002.
[23] G.M. Sheldrick, SHELXTL (Version 6.10), Bruker AXS Inc., Madison, Wisconsin, 2002.
[24] G.M. Sheldrick, SHELXL-97: A Program for Crystal Structure Solution, University of Göttingen, Göttingen, Germany 1997.
[25] A.L. Spek, PLATON, A Multipurpose Crystallographic Tool, University of Utrecht, Utrecht, The Netherlands, 2008.
[26] W. Zhang, E.N. Jacobsen, J. Org. Chem. 56 (1991) 2296.
[27] W.J. Geary, Coord. Chem. Rev. 7 (1971) 81.
[28] (a) M.R. Bermejo, A. Castiñeiras, J.C. Garcia-Monteagudo, M. Rey, A. Sousa, M. Watkinson, C.A. McAuliffe, R.G. Pritchard, R.L. Beddoes, J. Chem. Soc., Dalton Trans. (1996) 2935;
(b) N. Aurangzeb, C.E. Hulme, C.A. McAuliffe, R.G. Pritchard, M. Watkinson, M.R. Bermejo, A. Garcia-Deibe, M. Rey, J. Sanmartin, A. Sousa, J. Chem. Soc., Chem. Commun. (1994) 1153.
[29] (a) B.C. Schardt, C.L. Hill, Inorg. Chem. 22 (1983) 1563;
(b) R.E. White, Inorg. Chem. 26 (1987) 3916.

Polyhedron 28 (2009) 2480–2486

Contents lists available at ScienceDirect

Polyhedron

journal homepage: www.elsevier.com/locate/poly

New metal–organic architectures of cobalt(II), nickel(II) and zinc(II) with tripodal ligand 5-(1H-imidazol-4-ylmethyl)aminoisophthalic acid

Jing Xu [a], Zheng-Shuai Bai [a], Taka-aki Okamura [b], Man-Sheng Chen [a], Wei-Yin Sun [a,*], Norikazu Ueyama [b]

[a] Coordination Chemistry Institute, State Key Laboratory of Coordination Chemistry, School of Chemistry and Chemical Engineering, Nanjing National Laboratory of Microstructures, Nanjing University, Nanjing 210093, China
[b] Department of Macromolecular Science, Graduate School of Science, Osaka University, Toyonaka, Osaka 560 0043, Japan

ARTICLE INFO

Article history:
Received 23 March 2009
Accepted 24 April 2009
Available online 3 May 2009

Keywords:
Cobalt(II) complex
Nickel(II) complex
Zinc(II) complex
Hydrothermal reaction
Metal–organic framework
Topology

ABSTRACT

Four new coordination polymers $\{[Ni(HL)(H_2O)]\cdot H_2O\}_n$ (**1**), $\{[Co(HL)(H_2O)]\cdot H_2O\}_n$ (**2**), $\{[Co(HL)]\cdot 4H_2O\}_n$ (**3**) and $\{[Zn(HL)]\cdot 2H_2O\cdot 0.5C_2H_5OH\}_n$ (**4**) [H_3L = 5-(1H-imidazol-4-ylmethyl)aminoisophthalic acid] have been synthesized under hydrothermal conditions and characterized by single-crystal X-ray diffraction analyses. Complexes **1** and **2** display (3, 3)-connected 2D network with (4, 8^2) topology. While **3** and **4** exhibit a binodal (3, 6)-connected 2D network with a Schläfli symbol $(4^3)_2(4^6, 6^6, 8^3)$. The complexes **1**–**4** show remarkable thermal stability and **4** exhibits blue fluorescence with maximum emission at 413 nm upon excitation at 362 nm in the solid state at room temperature. In addition, the magnetic measurements of **3** indicate that there are antiferromagnetic interactions between the neighboring Co(II) centers.

© 2009 Elsevier Ltd. All rights reserved.

1. Introduction

The rational design and synthesis of metal–organic frameworks (MOFs) have been of great interest in recent years in materials science and chemical research because they may provide a new strategy for achieving solid functional materials with potential applications in the areas of catalysis, gas storage, magnetism and optics [1–10]. Obviously the nature of the coordination sites, conformation, flexibility of organic ligands as well as the geometric preference, potential properties of the metal centers affected the structure and property of the final MOFs greatly. Over the past decades, there are varied examples of metal–organic coordination frameworks obtained by using imidazole-based ligands, for example 1,3,5-tris(1-imidazolyl)benzene, 1,3,5-tris(imidazol-1-ylmethyl)-2, 4,6-trimethylbenzene, 2,4,6-tris[4-(imidazol-1-ylmethyl)phenyl]-1, 3,5-triazine [11–16]. Such ligands were designed and used to investigate the influence of bridging ligand on formation and structure of supramolecular architectures, and MOFs with a broad range of structures including cage, one-dimensional (1D) tube, two-dimensional (2D) network, three-dimensional (3D) non-interpenetrating or interpenetrating frameworks have been reported [11–16]. On the other hand, MOFs with carboxylate-containing ligands are of increasing interest since the carboxylate groups can adopt varied coordination modes such as monodentate, bis-monodentate, chelating, and as a result diverse structures can be obtained [17–19].

In this study, we have designed a new carboxylate and imidazole containing ligand, namely 5-(1H-imidazol-4-ylmethyl)aminoisophthalic acid (H_3L), which has remarkable features as following: (a) the two carboxylate groups can be partially or completely deprotonated by tuning the reaction pH and thus different bridging and coordination modes could be expected in the formation of MOFs; (b) the flexible arms of H_3L can adopt varied conformations which would further generate diverse architectures; (c) the introduced aromatic and the imidazole groups can offer additional π–π and hydrogen bonding interactions to further consolidate the structure [20–22]. Herein, the syntheses, structure characterization and properties of four MOFs $\{[Ni(HL)(H_2O)]\cdot H_2O\}_n$ (**1**), $\{[Co(HL)(H_2O)]\cdot H_2O\}_n$ (**2**), $\{[Co(HL)]\cdot 4H_2O\}_n$ (**3**), and $\{[Zn(HL)]\cdot 2H_2O\cdot 0.5C_2H_5OH\}_n$ (**4**) are reported.

2. Experimental

2.1. Materials and measurements

All commercially available solvents and starting materials were used as received without further purification. FT-IR spectra were recorded on a Bruker Vector22 FT-IR spectrophotometer using KBr disks. Elemental analyses were taken on a Perkin–Elmer 240C elemental analyzer. The luminescent spectra for the solid samples were recorded at room temperature on an Aminco

* Corresponding author. Tel.: +86 25 83593485; fax: +86 25 8331 4502.
E-mail address: sunwy@nju.edu.cn (W.-Y. Sun).

0277-5387/$ - see front matter © 2009 Elsevier Ltd. All rights reserved.
doi:10.1016/j.poly.2009.04.032

Bowman Series 2 spectrophotometer with xenon arc lamp as the light source. In the measurements of the emission and excitation spectra, the pass width was 5.0 nm. All the measurements were carried out under the same conditions. Thermogravimetric analyses (TGA) were performed on a TGA V5.1A Dupont 2100 instrument heating from room temperature to 700 °C under N_2 with a heating rate of 20 °C/min. The magnetic susceptibilities in the temperature range of 1.8–300 K were measured on a Quantum Design MPMS7 SQUID magnetometer in a field of 2000 Oe. Diamagnetic corrections were made with Pascal's constants for all samples.

2.2. Synthesis of the ligand 5-(1H-imidazol-4-ylmethyl)aminoisophthalic acid (H_3L)

Ligand H_3L was prepared by reaction of imidazole-4-carboxaldehyde (0.96 g, 10 mmol) and 5-aminoisophthalic acid (1.81 g, 10 mmol) in methanol, followed by sodium borohydride reduction. The resulting white crystalline solid was obtained with a yield of 80% (2.1 g). IR (KBr, cm^{-1}): 3377 (s), 3168 (s), 1710 (ms), 1671 (ms), 1611 (s), 1525 (s), 1470 (ms), 1384 (s), 1338 (ms), 1299 (s), 1268 (m), 1210 (s), 813 (ms), 756 (s), 733 (m), 667 (s).

2.3. Synthesis of the complexes

2.3.1. Synthesis of{[Ni(HL)(H_2O)]·H_2O}$_n$ (**1**)

A mixture of H_3L (0.026 g, 0.10 mmol), $Ni(NO_3)_2{\cdot}6H_2O$ (0.029 g, 0.10 mmol), NaOH (0.10 mmol), CH_3CN (2 mL) and H_2O (8 mL) was kept in a 15 mL Teflon liner autoclave at 140 °C for 3 days. After the mixture was cooled to room temperature, green platelet crystals of complex **1** were collected with a yield of 46%. *Anal.* Calc. for $C_{12}H_{13}NiN_3O_6$ (**1**): C, 40.70; H, 3.70; N, 11.87. Found: C, 40.52; H, 3.67; N, 11.79%. IR (KBr pellet, cm^{-1}): 3423 (s), 1628 (ms), 1616 (ms), 1552 (s), 1532 (s), 1445 (s), 1415 (s), 1380 (s), 1353 (ms), 798 (m), 781 (m), 727 (s).

2.3.2. Syntheses of {[Co(HL)(H_2O)]·H_2O}$_n$ (**2**) and {[Co(HL)]·4H_2O}$_n$ (**3**)

A mixture of H_3L (0.026 g, 0.10 mmol), $Co(ClO_4)_2{\cdot}6H_2O$ (0.036 g, 0.10 mmol), C_2H_5OH (3 mL) and aqueous sodium bicarbonate solution (0.04 M, 5 mL) was kept in a 15 mL Teflon liner autoclave at 120 °C for 3 days. After the mixture was cooled to room temperature, pink platelet crystals of complex **2** and purple block crystals of **3** were collected with a yield of 24% and 37%, respectively. *Anal.* Calc. for $C_{12}H_{13}CoN_3O_6$ (**2**): C, 40.69; H, 3.70; N, 11.86. Found: C, 40.99; H, 3.41; N, 11.87%. IR (KBr pellet, cm^{-1}): 3284 (s), 1616 (s), 1556 (s), 1475 (ms), 1417 (s), 1349 (s), 1282 (ms), 1024 (m), 786 (s), 722 (s), 620 (m). *Anal.* Calc. for $C_{12}H_{17}CoN_3O_8$ (**3**): C, 36.94; H, 4.39; N, 10.77. Found: C, 36.99; H, 4.31; N, 10.81. IR (KBr pellet, cm^{-1}): 3419 (s), 1618 (ms), 1570 (s), 1425 (s), 1384 (s), 1324 (ms), 1076 (m), 785 (s), 725 (s), 616 (m).

2.3.3. Synthesis of {[Zn(HL)]·2H_2O·0.5C_2H_5OH}$_n$ (**4**)

A mixture of H_3L (0.026 g, 0.10 mmol), $Zn(NO_3)_2{\cdot}6H_2O$ (0.030 g, 0.10 mmol), NaOH (0.10 mmol), C_2H_5OH (2 mL) and H_2O (8 mL) was kept in a 15 mL Teflon liner autoclave at 120 °C for 3 days. After the mixture was cooled to room temperature, colorless platelet crystals of complex **4** were collected with a yield of 44%. *Anal.* Calc. for $C_{13}H_{16}ZnN_3O_{6.5}$ (**4**): C, 40.70; H, 4.20; N, 10.95. Found: C, 40.74; H, 4.16; N, 10.87%. IR (KBr pellet, cm^{-1}): 3320 (s), 3142 (w), 1619 (s), 1572 (s), 1422 (s), 1364 (s), 782 (s), 727 (m), 621 (m).

2.4. Crystal structure determination

Crystallographic data of **1** and **2** were collected at 293 K on a Bruker SMART CCD system equipped with monochromated Mo Kα radiation (λ = 0.71073 Å) using ω–φ scan technique. The data integration and empirical absorption corrections were carried out by SAINT programs [23]. The structures were solved by direct methods (SHELXS-97) [24]. All the non-hydrogen atoms were refined anisotropically on F^2 by full-matrix least-squares techniques using the SHELXL-97 crystallographic software package [25]. The hydrogen atoms of water molecules in **1** and **2** and H1 in **1** were located from difference Fourier maps, and the other hydrogen atoms were generated geometrically. Crystallographic data for complexes **3** and **4** were carried out on a Rigaku RAXIS-RAPID Imaging Plate diffractometer at 200 K, using graphite-monochromated Mo Kα radiation (λ = 0.71075 Å). The structures of **3** and **4** were solved by direct

Table 1
Crystallographic data for **1**–**4**.

Complex	**1**	**2**	**3**	**4**
Formula	$C_{12}H_{13}N_3O_6Ni$	$C_{12}H_{13}N_3O_6Co$	$C_{12}H_{17}N_3O_8Co$	$C_{13}H_{16}N_3O_{6.5}Zn$
Formula weight	353.96	353.18	390.22	383.67
Crystal system	monoclinic	monoclinic	triclinic	triclinic
Space group	$P2_1/n$	$P2_1/n$	$P\bar{1}$	$P\bar{1}$
a (Å)	11.6336(15)	11.6065(18)	9.165(4)	9.224(4)
b (Å)	8.7105(12)	8.7508(13)	9.203(4)	9.281(4)
c (Å)	14.0802(18)	14.206(2)	10.097(4)	10.138(4)
α (°)	90.00	90.00	63.229(14)	74.495(13)
β (°)	105.263(3)	105.219(4)	74.541(12)	62.672(14)
γ (°)	90.00	90.00	83,034(16)	83.385(15)
Volume (Å^3)	1376.5(3)	1392.3(4)	732.9(5)	742.9(5)
Z	4	4	2	2
T (K)	293(2)	293(2)	200	200
μ (Mo Kα), (cm^{-1})	14.44	12.67	12.22	16.935
D_{calcd}, (g/m^3)	1.708	1.690	1.768	1.715
F(0 0 0)	728	724	402	394
Reflections collected	6885	7321	5516	7008
Unique reflections	2558	2736	2562	3363
Goodness-of-fit (Gof)	1.054	0.909	1.116	1.015
R_{int}	0.0632	0.0794	0.1501	0.0982
R_1 ($I > 2\sigma(I)$)	0.0632	0.0622	0.1372	0.0522
wR_2 ($I > 2\sigma(I)$)	0.1093[a]	0.0832[b]	0.3755[c]	0.1277[d]
Residues (e/Å^3)	−0.522, 0.636	−0.632, 0.500	−0.799, 1.677	−0.932, 1.163

[a] $w = 1/[\sigma^2(F_0)^2 + (0.0348P)^2]$, where $P = (F_0^2 + 2F_c^2)/3$.
[b] $w = 1/[\sigma^2(F_0)^2 + (0.0050P)^2]$, where $P = (F_0^2 + 2F_c^2)/3$.
[c] $w = 1/[\sigma^2(F_0)^2 + (0.1851P)^2 + 8.5171P]$, where $P = (F_0^2 + 2F_c^2)/3$.
[d] $w = 1/[\sigma^2(F_0)^2 + (0.0611P)^2]$, where $P = (F_0^2 + 2F_c^2)/3$.

methods with SIR92 [26] and expanded using Fourier techniques [27]. All the non-hydrogen atoms were refined anisotropically on F^2 by full-matrix least-squares methods. All the hydrogen atoms except those of water molecules and H1 in **3** and **4** were generated geometrically and refined isotropically using the riding model, while the H1 in **3** and **4** were located from difference Fourier maps directly. Atoms of ethanol (C71, C72 and O7) in complex **4** are disordered with occupancy of 0.5. All calculations were performed using the TEXSAN crystallographic software package of Molecular Structure Corporation [28]. Details of the crystal parameters, data collection and refinements for **1**–**4** are summarized in Table 1. Selected bond lengths and angles for **1**–**4** are listed in Table 2.

Table 2
Selected bond lengths (Å) and angles (°) for **1**–**4**.

1[a]			
Ni(1)–N(11)#1	2.010(4)	Ni(1)–O(3)#2	2.012(3)
Ni(1)–O(5)	2.041(3)	Ni(1)–O(2)	2.130(3)
Ni(1)–O(1)	2.132(3)	Ni(1)–N(1)#1	2.181(4)
N(11)#1–Ni(1)–O(3)#2	173.1(2)	N(11)#1–Ni(1)–O(5)	89.6(2)
O(3)#2–Ni(1)–O(5)	90.5(1)	N(11)#1–Ni(1)–O(2)	94.9(2)
O(3)#2–Ni(1)–O(2)	91.8(2)	O(5)–Ni(1)–O(2)	105.7(1)
N(11)#1–Ni(1)–O(1)	93.0(2)	O(3)#2–Ni(1)–O(1)2	88.5(1)
O(5)–Ni(1)–O(1)	167.1(1)	O(2)–Ni(1)–O(1)	61.5(1)
N(11)#1–Ni(1)–N(1)#1	81.2(2)	O(3)#2–Ni(1)–N(1)#1	91.9(2)
O(5)–Ni(1)–N(1)#1	93.7(2)	O(2)–Ni(1)–N(1)#1	160.2(1)
O(1)–Ni(1)–N(1)#1	99.2(1)		
2[b]			
Co(1)–O(3)#1	2.023(4)	Co(1)–N(11)#2	2.041(4)
Co(1)–O(5)	2.080(3)	Co(1)–O(2)	2.163(4)
Co(1)–O(1)	2.169(3)	Co(1)–N(1)#2	2.275(4)
O(3)#1–Co(1)–N(11)#2	172.0(2)	O(3)#1–Co(1)–O(5)	89.7(1)
N(11)#2–Co(1)–O(5)	89.6(2)	O(3)#1–Co(1)–O(2)	93.5(2)
N(11)#2–Co(1)–O(2)	94.4(2)	O(5)–Co(1)–O(2)	106.5(1)
O(3)#1–Co(1)–O(1)	89.3(1)	N(11)#2–Co(1)–O(1)	93.2(2)
O(5)–Co(1)–O(1)	167.0(1)	O(2)–Co(1)–O(1)	60.6(1)
O(3)#1–Co(1)–N(1)#2	92.5(2)	N(11)#2–Co(1)–N(1)#2	79.6(1)
O(5)–Co(1)–N(1)#2	93.4(1)	O(2)–Co(1)–N(1)#2	159.2(1)
O(1)–Co(1)–N(1)#2	99.6(1)		
3[c]			
Co(1)–O(2)#1	2.020(9)	Co(1)–N(11)#2	2.05(1)
Co(1)–O(1)	2.060(8)	Co(1)–O(4)#3	2.114(9)
Co(1)–O(3)#3	2.249(9)	Co(1)–N(1)#2	2.37(1)
O(2)#1–Co(1)–N(11)#2	104.3(4)	O(2)#1–Co(1)–O(1)	102.4(3)
N(11)#2–Co(1)–O(1)	100.8(4)	O(2)#1–Co(1)–O(4)#3	94.4(4)
N(11)#2–Co(1)–O(4)#3	155.5(4)	O(1)–Co(1)–O(4)#3	90.4(4)
O(2)#1–Co(1)–O(3)#3	152.4(3)	N(11)#2–Co(1)–O(3)#3	98.0(4)
O(1)–Co(1)–O(3)#3	89.0(4)	O(4)#3–Co(1)–O(3)#3	60.1(4)
O(2)#1–Co(1)–N(1)#2	84.2(4)	N(11)#2–Co(1)–N(1)#2	76.7(4)
O(1)–Co(1)–N(1)#2	173.3(4)	O(4)#3–Co(1)–N(1)#2	89.6(4)
O(3)#3–Co(1)–N(1)#2	85.3(4)		
4[d]			
Zn(1)–O(4)#1	2.006(2)	Zn(1)–N(11)	2.011(3)
Zn(1)–O(1)#2	2.020(3)	Zn(1)–O(3)#3	2.029(3)
Zn(1)–O(2)#2	2.466(3)		
O(4)#1–Zn(1)–N(11)	106.5(1)	O(4)#1–Zn(1)–O(1)#2	97.3(1)
N(11)–Zn(1)–O(1)#2	145.0(1)	O(4)#1–Zn(1)–O(3)#3	106.4(1)
N(11)–Zn(1)–O(3)#3	102.9(1)	O(1)#2–Zn(1)–O(3)#3	94.3(1)
O(4)#1–Zn(1)–O(2)#2	152.2(1)	N(11)–Zn(1)–O(2)#2	92.3(1)
O(1)#2–Zn(1)–O(2)#2	57.5(1)	O(3)#3–Zn(1)–O(2)#2	88.4(1)

[a] Symmetry transformations used to generate equivalent atoms: #1: $-x+3/2$, $y-1/2$, $-z+1/2$, #2: $x-1/2$, $-y+3/2$, $z-1/2$.
[b] Symmetry transformations used to generate equivalent atoms: #1: $x+1/2$, $-y+3/2$, $z+1/2$, #2: $-x+3/2$, $y+1/2$, $-z+3/2$.
[c] Symmetry transformations used to generate equivalent atoms: #1: $-x+1$, $-y$, $-z$, #2: $x-1$, y, z, #3: $-x+1$, $-y$, $-z+1$.
[d] Symmetry transformations used to generate equivalent atoms: #1: $-x$, $-y+1$, $-z+1$, #2: $-x$, $-y+1$, $-z+2$, #3: x, $y+1$, z.

3. Results and discussion

3.1. Syntheses of the complexes

Hydrothermal methods were employed in this work for the preparation and crystal growth of the title complexes, furthermore, pH value of the reaction plays a key role in the formation of coordination polymers with open frameworks, especially in those with carboxylate-containing ligands. Although different bases such as NaOH, $NaHCO_3$, triethylamine with different molar ratio of ligand to base were used in the preparation of complexes **1** and **4** to deprotonate the H_3L, only the addition of NaOH to the ligand with molar ratio 1:1 was successful and led to the formation of suitable single crystals of **1** and **4**. In the case of **2** and **3**, only the addition of $NaHCO_3$ solution with molar ratio 2:1 to the ligand was successful and suitable single crystals of **2** and **3** were obtained.

3.2. Crystal structures of complexes *1*–*4*

3.2.1. $\{[Ni(HL)(H_2O)]\cdot H_2O\}_n$ (*1*) and $\{[Co(HL)(H_2O)]\cdot H_2O\}_n$ (*2*)

Complexes **1** and **2** crystallize in the same monoclinic $P2_1/n$ space group with similar cell parameters (Table 1), and the results of X-ray crystallographic analysis indicate that they are isomorphous and isostructural. Thus, as a typical example, only the structure of **2** is described here in detail. The asymmetric unit of **2** consists of one Co(II) atom, one HL^{2-} ligand, one coordinated and one non-coordinated water molecule. As depicted in Fig. 1a, each Co(II) atom is six coordinated with a distorted octahedral geometry by two nitrogen atoms from one HL^{2-} ligand in a chelating mode, three oxygen atoms from two carboxylate groups of two different HL^{2-} ligands and one oxygen atom from a coordinated water molecule. The Co–O and Co–N bond lengths are in the range of 2.02(4)–2.17(3) Å and 2.04(4)–2.28(4) Å, respectively as listed in Table 2. On the other hand, each HL^{2-} ligand in **2** connects three Co(II) atoms through the Co–O and Co–N coordination interactions. Each carboxylate group coordinates with one metal atom, and one imidazole-nitrogen together with the amine-nitrogen chelate one Co(II) atom. The coordination modes of the HL^{2-} ligand appeared in **1**–**4** are summarized in Scheme 1. It is noticeable that two carboxylate groups of HL^{2-} ligand in **2** have different coordination fashion, one adopts a bidentate chelating mode and the other one acts a monodentate (Scheme 1a). The imidazole ring of the flexible arm is nearly perpendicular to the central benzene ring since the dihedral angel between them is 89.99°.

In complex **2**, the Co(II) atoms are linked together by the carboxylate groups from HL^{2-} ligands to form an infinite 1D zigzag chain if the Co–N connections are neglected. The 1D chains are further linked together through the Co–N coordination leading to the formation of a 2D network (Fig. 1b). As described above, each Co(II) is surrounded by three HL^{2-} ligands and each HL^{2-} ligand links three Co(II) atoms. Thus, both Co(II) atom and HL^{2-} ligand can be considered as 3-connected nodes in a ratio of 1:1 in **2**. Therefore, the complex **2** exhibits a (3, 3)-connected 2D network with a $(4, 8^2)$ topology as clearly shown in Fig. 1c. The 2D layers packed together through C–H···O and N–H···O hydrogen bonding interactions and face-to-face π–π interactions between imidazole ring planes with the centroid–centroid separation of 3.60 Å resulting a 3D framework (Fig. 1d).

3.2.2. $\{[Co(HL)]\cdot 4H_2O\}_n$ (*3*)

It is interesting that complexes **2** and **3** with different structure were obtained simultaneously by the same reaction (see Section 2). The asymmetric unit of **3** consists of one Co(II) atom and one HL^{2-} ligand. Fig. 2a shows the coordination environment of the Co(II) atom in **3**. The Co(II) center with octahedral coordination geometry is six coordinated by four carboxylic oxygen atoms from three different HL^{2-} ligands with Co–O bond distances ranging from 2.02(9)

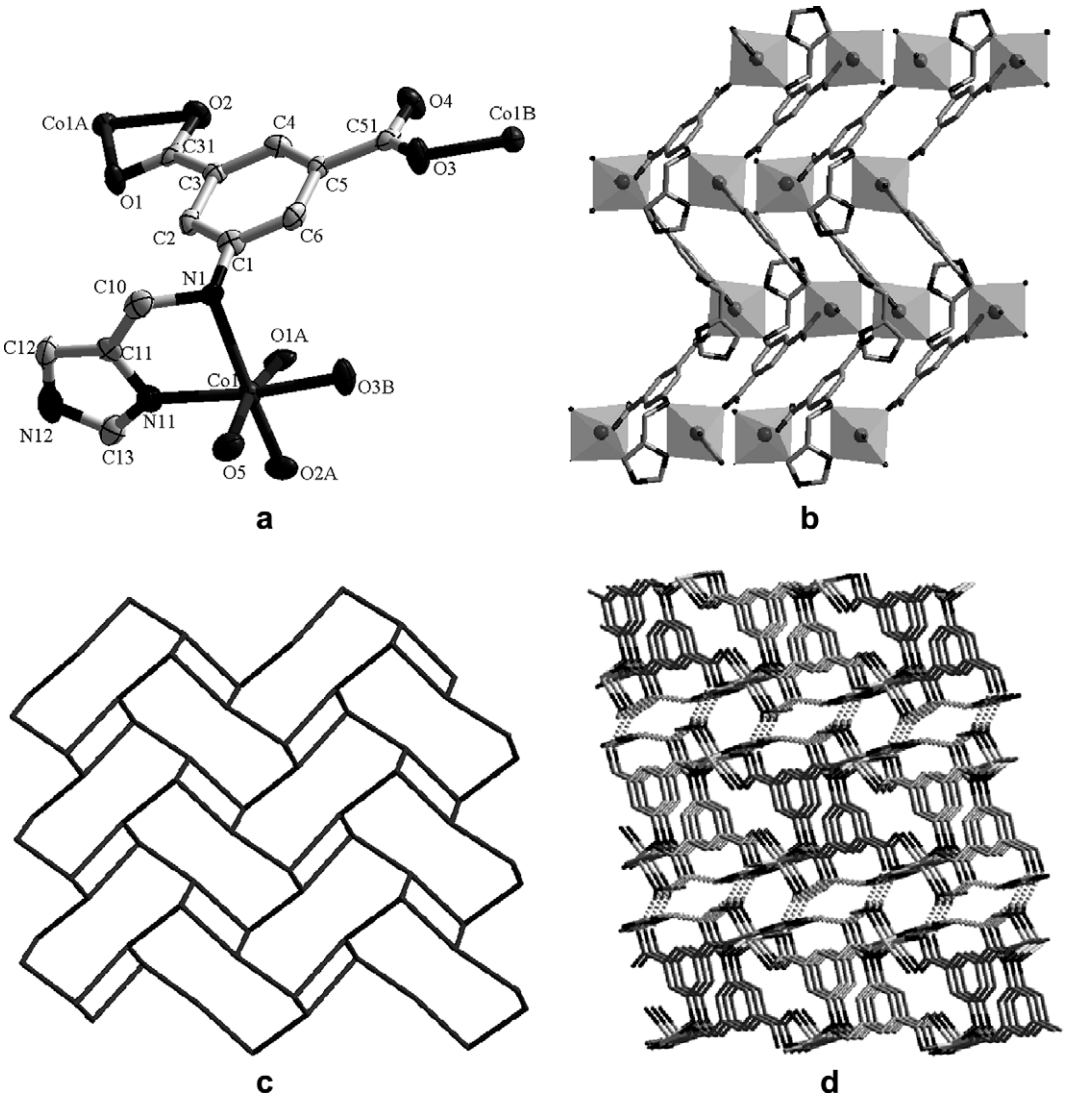
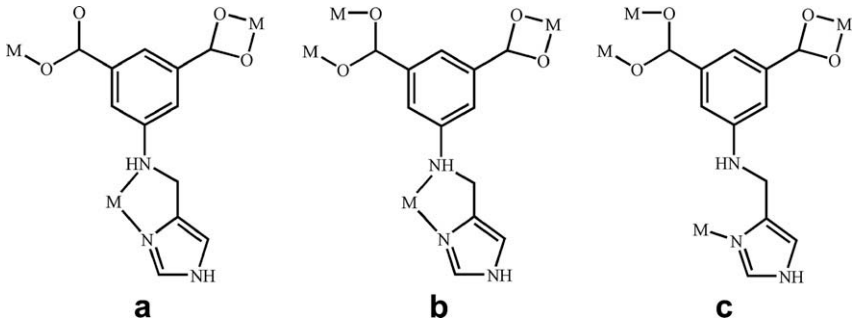


Fig. 1. (a) Coordination environment of Co(II) in **2** with the ellipsoids drawn at the 30% probability level, hydrogen atoms were omitted for clarity. (b) Polyhedral representation of the 2D layer structure of complex **2**. (c) (4, 8^2) topological grid in **2**. (d) 3D framework of **2** linked by hydrogen bonds indicated by dashed line.



Scheme 1. Coordination modes of HL^{2-} ligand.

to 2.25(9) Å and two nitrogen atoms from another HL^{2-} ligand with Co1–N bond lengths of 2.37(1) and 2.05(1) Å (Table 2). Each HL^{2-} ligand acts as a 4-connector to link four Co(II) atoms in complex **3** (Scheme 1b), which is different from that in complex **2** (and also **1**), one of the carboxylate group is coordinated with one Co(II) atom through a bidentate chelating mode, while the other one adopts a *syn-syn* μ_2-η^1:η^1 bridge to link two metal atoms forming a second building unit (SBU) of $Co_2(COO)_2$, the imidazole group without protonation coordinates to one Co(II) atom with the amine nitrogen via a chelating mode. Therefore, a 2D network is formed (Fig. 2b) through such connection of the HL^{2-} ligands.

In order to better identify the nature of the structure of complex **3**, suitable connectors should be confirmed by using the topological approach [29–31]. The net topology can be simplified by just

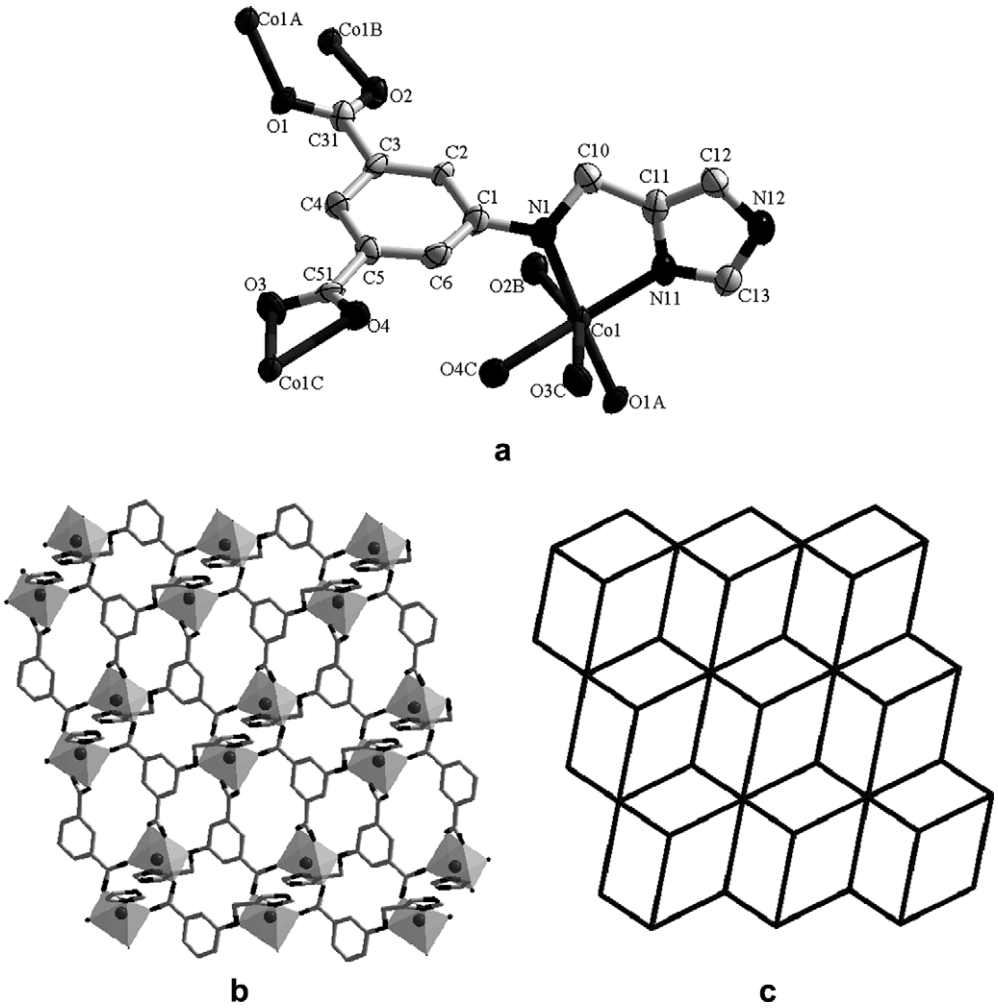


Fig. 2. (a) Coordination environment of Co(II) in **3** with the ellipsoids drawn at the 30% probability level, hydrogen atoms were omitted for clarity. (b) Polyhedral representation of the 2D layer structure in **3**. (c) A binodal (3, 6)-connected 2D network of complex **3**.

considering $Co_2(COO)_2$ units and HL^{2-} ligands. As discussed above, each HL^{2-} ligand can be considered as a three-connecting node since it links three $Co_2(COO)_2$ units. On the other hand, each $Co_2(COO)_2$ unit links six HL^{2-} ligands which can be regarded as a six-connecting node. Thus the topology of **3** is a binodal (3, 6)-connected 2D network (Fig. 2c) with a Schläfli symbol of $(4^3)_2(4^6, 6^6, 8^3)$. The long Schläfli notation is [4·4·4] for the 3-connected HL^{2-} nodes and $[4{\cdot}4{\cdot}4{\cdot}4{\cdot}4{\cdot}4{\cdot}6_2{\cdot}6_2{\cdot}6_2{\cdot}6_2{\cdot}6_2{\cdot}6_2{\cdot}8_8{\cdot}8_8{\cdot}8_8]$ for 6-connected $Co_2(COO)_2$ nodes, respectively.

3.2.3. $\{[Zn(HL)]\cdot 2H_2O\cdot 0.5C_2H_5OH\}_n$ (**4**)

Complex **4** also crystallizes in the triclinic $P\bar{1}$ space group with similar cell parameters to those of **3** (Table 1), and the single crystal X-ray crystallographic analysis confirmed that **3** and **4** have almost the same network structure. The difference between **3** and **4** is the coordination environment of the metal center and the coordination mode of the HL^{2-} ligand (Scheme. 1c). In complex **4**, the Zn(II) atom with a distorted square–pyramidal coordination geometry was bounded by four oxygen atoms from three HL^{2-} ligands and one nitrogen atom from the another ligand (Fig. 3a), however, no coordination of the amine nitrogen was found in **4**, which is different from that in **3**. Another difference between **3** and **4** is that solvent ethanol molecules were found in **4**, while there only are water molecules in **3**. There are also N–H···O hydrogen bonding interactions and face-to-face π–π interactions with centroid–centroid distance of 3.58 Å between the imidazole ring planes which makes **4** a 3D supramolecular framework (Fig. 3b).

3.3. Properties

3.3.1. Thermal properties

Thermalgravimetric analyses (TGA) were carried out to examine the thermal stabilities of complexes **1**–**4** by heating to 700 °C under flowing N_2. As shown in Fig. 4, complex **1** lost two water molecules in the temperature range of 40–210 °C with a weight loss of 10.7% (calculated: 10.2%), the decomposition of the residue was observed at ca. 370 °C and the final percentage weight (observed 20.8%) at the end of the decomposition of the complex is in accordance with the formation of NiO (calculated: 21.1%). The TGA curve of **2** showed a weight loss between 75 and 110 °C, corresponding to the loss of two water molecules (10.1% weight loss observed; 10.2% calculated). The decomposition of the residue was observed at ca. 270 °C, and the total weight loss of 77.2% indicates the completely decomposition to give Co_2O_3 (calculated: 76.5%). The TGA curve of **3** shows that the first weight loss of 18.4% (calculated: 18.5%) between 30 and 140 °C corresponds to the loss of the four lattice water molecules. The decomposition of the residue was observed at ca. 425 °C and the final percentage weight (observed 22.0%) at the end of the decomposition of the complex is in accordance with the formation of Co_2O_3 (calculated: 21.3%). The TGA

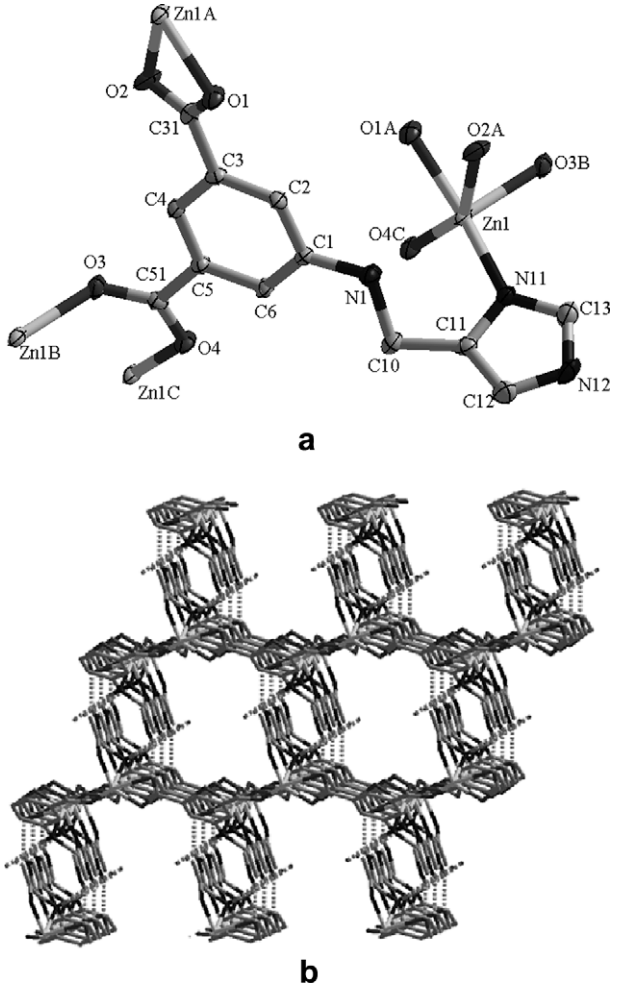


Fig. 3. (a) Coordination environment of Zn(II) in **4** with the ellipsoids drawn at the 30% probability level, hydrogen atoms were omitted for clarity. (b) 3D framework of **4** linked by hydrogen bonding shown by dashed line.

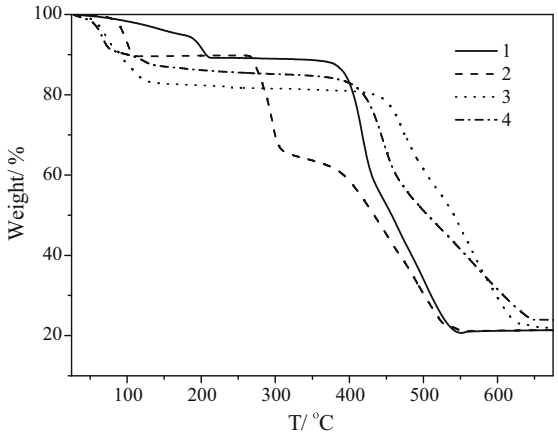


Fig. 4. The TGA curves of complexes **1**–**4**.

curve of **4** displayed two main steps of weight losses: the first step completed the loss of the ethanol molecule at 50 °C (6.0% weight loss observed; 6.1% calculated). The second step occurred between 70 and 180 °C with the loss of two lattice water molecules (9.2% weight loss observed; 9.4% calculated). The framework collapsed in the temperature range 390–645 °C, and the residual percentage

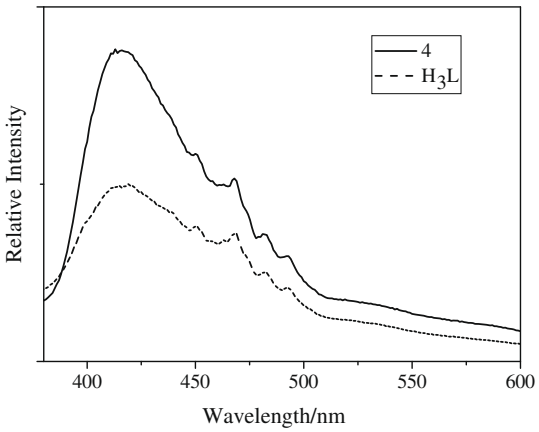


Fig. 5. The emission spectra of **4** and H_3L ligand.

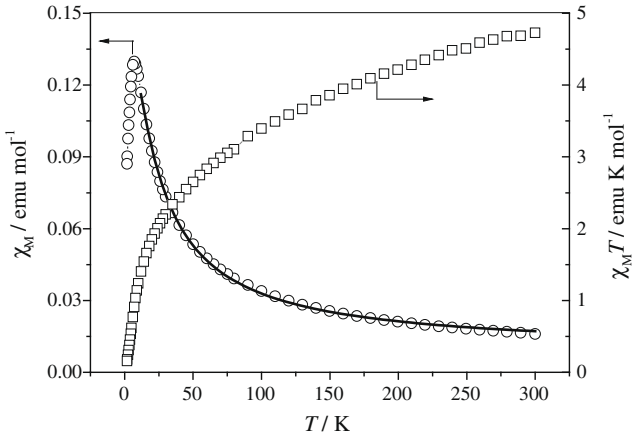


Fig. 6. The χ_M and $\chi_M T$ vs. T plots for **3** (the solid line shows the best fit to the model).

weight (observed 23.9%) at the end of the decomposition of the complex is in accordance with the formation of ZnO (calculated: 21.3%). All these results indicate that complexes **1**–**4** have high thermal stability.

3.3.2. Luminescent properties

Inorganic–organic hybrid coordination complexes, especially with d^{10} metal centers, have been investigated for fluorescence properties owing to their potential applications as luminescent materials [32–34]. Thus the luminescent spectra of complex **4** as well as free H_3L ligand were investigated in the solid state at room temperature. As shown in Fig. 5, complex **4** exhibits an intense broad photoluminescence with maximum emission at 413 nm upon excitation at 362 nm, which is close to the emission at 419 nm of the free H_3L ligand under the same conditions. Therefore the emission observed in **4** is attributed to the π–π^* intraligand photoluminescence due to its resemblance to that of H_3L ligand, and the enhancement and slight red-shift of **4** compared to that of the free ligand probably result from the fact that the coordination of Zn(II) ions increases the ligand conformational rigidity and thus reduces the loss of energy by thermal vibrational decay [35–37].

3.3.3. Magnetic property

The temperature dependent magnetic measurements of **3** were carried out ranging from 1.8 to 300 K with an applied field of 2 K Oe. As depicted in Fig. 6, the χ_M curve increases when the compound is cooled until a maximum is reached at 7 K with a value

of 0.13 emu mol^{-1} and then decreases rapidly, which is the nature of antiferromagnetic coupling between Co(II) ions [38]. The observed $\chi_M T$ value is 4.727 emu K mol^{-1} at room temperature, which is higher than the spin-only resulting from the orbital contribution of the octahedral Co(II) ions [39]. As the temperature decreases, the value of $\chi_M T$ decreases gradually, indicating the occurrence of dominant antiferromagnetic interactions within the neighboring Co(II) ions connected through the carboxylate groups. In order to get an estimate of the strength of the antiferromagnetic exchange interaction, one may use the following simple phenomenological equation: $\chi T = A\exp(-E_1/kT) + B\exp(-E_2/kT)$ [40], where $A + B$ equals the Curie constant, and E_1, E_2 hold for the "activation energies" corresponding to the spin–orbital and the antiferromagnetic exchange interaction, respectively. The best fit parameters $A + B = 3.23$ emu K mol^{-1} and $E_1/k = 88.56$ K are consistent with those given in the literature for Curie constant ($C \approx 2.8$–3.4 emu K mol^{-1}) and for the effect of spin–orbit coupling and site distortion (E_1/k of the order of +100 K) [40]. The $-E_2/k$ value is -10.24 K, corresponding to antiferromagnetic exchange interaction of $J = -20.48$ K with in the Ising chain approximation ($\chi T \propto \exp(+J/2kT)$).

4. Conclusions

Four new coordination polymers have been synthesized under hydrothermal conditions by using a new imidazol- and carboxylate-containing ligand 5-(1H-imidazol-4-ylmethyl)aminoisophthalic acid. TGA data showed that complexes **1**–**4** have high thermal stability and luminescent measurements showed that complex **4** exhibits blue fluorescence in the solid state at room temperature, the magnetic study of **3** indicates that there are antiferromagnetic interactions between the neighboring Co(II) centers. The varied coordination modes of the ligand found in present work prove that the ligand is a useful building block in the construction of new MOFs.

Acknowledgments

This work was financially supported by the National Natural Science Foundation of China (Grant Nos. 20731004 and 20721002) and the National Basic Research Program of China (Grant No. 2007CB925103).

Appendix A. Supplementary data

CCDC 723273, 723274, 723275 and 723276 contain the supplementary crystallographic data for **1**, **2**, **3** and **4**. These data can be obtained free of charge via http://www.ccdc.cam.ac.uk/conts/retrieving.html, or from the Cambridge Crystallographic Data Centre, 12 Union Road, Cambridge CB2 1EZ, UK; fax: (+44) 1223-336-033; or e-mail: deposit@ccdc.cam.ac.uk.

References

[1] J.L.C. Rowsell, O.M. Yaghi, Angew. Chem., Int. Ed. 46 (2005) 4670.
[2] N.L. Rosi, J. Eckert, M. Eddaoudi, D.T. Vodak, J. Kim, M. O'Keeffe, O.M. Yaghi, Science 300 (2003) 1127.
[3] S. Kitagawa, R. Kitaura, S. Noro, Angew. Chem., Int. Ed. 43 (2004) 2334.
[4] O.M. Yaghi, M. O'Keeffe, N.W. Ockwing, H.K. Chae, M. Eddaoudi, J. Kim, Nature 423 (2003) 705.
[5] C. Janiak, J. Chem. Soc., Dalton Trans. (2003) 2781.
[6] D. Maspoch, D.R. Molinaa, J. Veciana, Chem. Soc. Rev. 36 (2007) 770.
[7] S.L. Zheng, M.L. Tong, X.M. Chen, Coord. Chem. Rev. 246 (2003) 185.
[8] N.R. Champness, J. Chem. Soc., Dalton Trans. (2006) 877.
[9] A.Y. Robin, K.M. Fromm, Coord. Chem. Rev. 250 (2006) 2127.
[10] C. Kepert, Chem. Commun. (2006) 695.
[11] H.K. Liu, W.Y. Sun, D.J. Ma, K.B. Yu, W.X. Tang, Chem. Commun. (2000) 591.
[12] W.Y. Sun, J. Fan, T.-a. Okamura, J. Xie, K.B. Yu, N. Ueyama, Chem. Eur. J. 7 (2001) 2557.
[13] J. Fan, H.F. Zhu, T.-a. Okamura, W.Y. Sun, W.X. Tang, N. Ueyama, Inorg. Chem. 42 (2003) 158.
[14] J. Fan, B. Sui, T.-a. Okamura, W.Y. Sun, W.X. Tang, N. Ueyama, J. Chem. Soc., Dalton Trans. (2002) 3868.
[15] S.Y. Wan, Y.T. Huang, Y.Z. Li, W.Y. Sun, Micropor. Mesopor. Mater. 73 (2004) 101.
[16] W. Zhao, Y. Song, T.-a. Okamura, J. Fan, W.Y. Sun, N. Ueyama, Inorg. Chem. 44 (2005) 3330.
[17] S.S.Y. Chui, S.M.F. Lo, J.P.H. Charmant, A.G. Orpen, I.D. Williams, Science 283 (1999) 1148.
[18] Z.H. Zhang, Y. Song, T.-a. Okamura, Y. Hasegawa, W.Y. Sun, N. Ueyama, Inorg. Chem. 45 (2006) 2896.
[19] R.Q. Zou, H. Sakurai, Q. Xu, Angew. Chem., Int. Ed. 45 (2006) 2542.
[20] T. Steiner, Angew. Chem., Int. Ed. 41 (2002) 48.
[21] C. Janiak, J. Chem. Soc., Dalton Trans. (2000) 3885.
[22] M. Nishio, Cryst. Eng. Commun. 6 (2004) 130.
[23] SAINT, Program for Data Extraction and Reduction, Bruker AXS, Inc., Madison, WI, 2001.
[24] G.M. Sheldrick, SHELXS-97, Program for the Solution of Crystal Structures, University of Göttingen, Germany, 1997.
[25] G.M. Sheldrick, SHELXL-97, Program for Refinement of Crystal Structures, University of Göttingen, Germany, 1997.
[26] SIR92: A. Altomare, M.C. Burla, M. Camalli, M. Cascarano, C. Giacovazzo, A. Guagliardi, G. Polidori, J. Appl. Cryst. 27 (1994) 435.
[27] DIRFID-94: P.T. Beurskens, G. Admiraal, G. Beurskens, W.P. Bosman, R. de Gelder, R. Israel, J.M.M. Smits, The DIRFID-94 Program System, Technical Report of the Crystallography Laboratory; University of Nijmegen, Nijmegen, The Netherlands, 1994.
[28] TEXSAN: Crystal Structure Analysis Package, Molecular Structure Corporation, The Woodlands, TX, 1999.
[29] N.W. Ockwig, O. Delgado-Friederichs, M. O'Keeffe, O.M. Yaghi, Acc. Chem. Res. 38 (2005) 176.
[30] O.M. Yaghi, H. Li, C. Davis, D. Richardson, T.L. Groy, Acc. Chem. Res. 31 (1998) 474.
[31] S.R. Batten, R. Robson, Angew. Chem., Int. Ed. 37 (1998) 1461.
[32] A. Vogler, H. Kunkely, Coord. Chem. Rev. 250 (2006) 1622.
[33] R.Q. Fan, D.S. Zhu, Y. Mu, G.H. Li, Y.L. Yang, Q. Su, S.H. Feng, Eur. J. Inorg. Chem. (2004) 530.
[34] L. Wen, Y. Li, Z. Lu, J. Lin, C. Duan, Q. Meng, Cryst. Growth. Des. 6 (2006) 530.
[35] U.H.F. Bunz, Chem. Rev. 100 (2000) 1605.
[36] W. Wang, H. Schmider, Q. Wu, Y.S. Zhang, S. Wang, Inorg. Chem. 39 (2000) 2397.
[37] Y.B. Chen, J. Zhang, J.K. Cheng, Y. Kang, Z.J. Li, Y.G. Yao, Inorg. Chem. Commun. 7 (2004) 1139.
[38] J.I. Vlugt, S. Demeshko, S. Dechert, D. Meyer, Inorg. Chem. 47 (2008) 1576.
[39] J.M. Rueff, N. Masciocchi, P. Rabu, A. Sironi, A. Skoulios, Chem. Eur. J. 8 (2002) 1813.
[40] R.L. Carlin, Magnetochemistry, Springer-Verlag, Berlin, Heidelberg, 1986.

Polyhedron 28 (2009) 2487–2493

Contents lists available at ScienceDirect

Polyhedron

journal homepage: www.elsevier.com/locate/poly

Syntheses, spectral, thermal and structural characterization of dinuclear and polynuclear copper(II) orotate complexes, $[Cu_2(HOr)_2(H_2O)_4]$ and $[Cu(\mu\text{-}HOr)(ba)_2]_n$

Mustafa Serkan Soylu [a], Okan Zafer Yeşilel [b,*], Bünyamin Karabulut [c], Orhan Büyükgüngör [c]

[a] Department of Physics, Faculty of Arts and Sciences, Giresun University, 28100 Giresun, Turkey
[b] Department of Chemistry, Faculty of Arts and Sciences, Eskişehir Osmangazi University, 26480 Eskişehir, Turkey
[c] Department of Physics, Faculty of Arts and Sciences, Ondokuz Mayıs University, 55139 Kurupelit, Samsun, Turkey

ARTICLE INFO

Article history:
Received 6 January 2009
Accepted 27 April 2009
Available online 19 May 2009

Keywords:
Butylamine complex
Copper(II) complex
Orotato complex

ABSTRACT

The novel *catena-poly-μ*-orotatobis(butylamine)copper(II), $[Cu(\mu\text{-}HOr)(ba)_2]_n$ (**1**), and diaqua(orotato)copper(II), $[Cu_2(HOr)_2(H_2O)_4]$ (**2**), complexes have been prepared and characterized by elemental analysis, magnetic measurements, FT-IR spectroscopy, EPR spectroscopy, thermal analysis and X-ray diffraction. Both complexes crystallize in the monoclinic space group, $C2/c$ in **1** and $P2_1/n$ in **2**. In the complexes, the copper(II) ion is chelated by a deprotonated pyrimidine nitrogen atom and a carboxylate oxygen atom of the orotate. While the coordination sphere around Cu(II) is completed by two N atoms from butylamine groups and a carboxylic O atom in the axial position from a neighboring molecule in **1**, the square-planar environment of Cu(II) is completed by two water atoms and one axial position is occupied by the carbonyl oxygen atom from the symmetry related molecule in **2**. The coordination sphere should be described as a square pyramid and (4+1)-geometry in **1** and **2**, respectively. While complex **1** shows a polymeric arrangement, compound **2** has a dimeric arrangement. The non-covalent Cu(II)-π binding force is very important for stabilizing the crystal structure of **2**. The thermal decomposition of the complexes has been predicted by the help of thermal analysis (TG, DTG and DTA).

© 2009 Elsevier Ltd. All rights reserved.

1. Introduction

The design and synthesis of coordination polymers have received much attention in coordination chemistry because of their interesting potential applications [1,2]. In order to prepare ideal coordination polymers, the key lies in the design and selection of the bridging ligands. Heterocyclic carboxylates have been extensively used to design polynuclear complexes [1–5]. In the present work, we selected the potentially interesting orotic acid (1,2,3,6-tetrahydro-2,6-dioxo-4-pyrimidine carboxylic acid, vitamin B13, H_3Or) and the orotate anions (H_2Or^- and HOr^{2-}) which are interesting multidentate ligands and they can coordinate through the nitrogen atoms of the pyrimidine ring, the carbonyl oxygen and the carboxyl oxygen atoms. Although the literature lists many reports on the coordinating presences of the orotate moiety in metal complexes [6–14], polymeric orotate complexes of copper(II) with neutral ligands are not known. The first copper(II)–orotate complex, $[Cu(HOr)(NH_3)_2]$ [8], and the first polymeric Cu(II)–orotate complexes, $[Cu(HOr)(H_2O)_2]_n$ [9], were reported by Mutikainen and Ha et al. in 1980 and 1999, respectively. X-ray structures of other monomeric Cu(II)–orotate complexes, $[Cu(HOr)(phen)]$ [10], $[Cu(HOr)(H_2O)(en)]\cdot H_2O$ [11], $[Cu(HOr)(tea)]\cdot H_2O$ [12], $[Cu(HOr)(bipy)(H_2O)]\cdot H_2O$ [13], (phen = 1.10-phenanthroline, en = ethylenediamine, tea = triethanolamine, bipy = 2,2′-bipyridine), *cis*-$[Cu(orotato)(NH_3)_2]$ and $[Cu(orotato)(H_2O)_4]\cdot H_2O$ [14], have been studied.

In the present paper, we describe the syntheses, spectroscopic (IR and EPR), thermal studies (TG, DTG, DTA) and crystal structures of the first mixed-ligand polymeric orotate complex of copper(II) with butylamine, μ-orotatobis(butylamine)copper(II), $[Cu(\mu\text{-}HOr)(ba)_2]_n$ (**1**), and the bis[diaqua(orotato)copper(II)] complex, $[Cu_2(HOr)_2(H_2O)_4]$ (**2**).

2. Experimental

2.1. Syntheses of complexes

2.1.1. $[Cu(\mu\text{-}HOr)(ba)_2]_n$ (**1**)

A solution of *n*-butylamine (0.30 g, 4 mmol) in water (5 mL) was added dropwise to a stirring solution of $[Cu(HOr)(H_2O)_2]$ (0.51 g, 2 mmol) in water (20 mL). The solution was heated to 50 °C in a temperature-controlled bath and refluxed with stirring for 5 h at 50 °C. The reaction mixture was then cooled to room temperature. Dark blue crystals were formed, filtered and washed with 10 mL of cold water, and then dried in air. *Anal.* Calc. for $C_{13}H_{24}N_4O_4Cu$: C, 42.91; H, 6.65; N, 15.40. Found: C, 42.88; H, 6.67; N, 15.58%. IR (KBr pellet, cm^{-1}): 3450(m), 3415(s), 3320(m), 2970(m),

* Corresponding author. Tel.: +90 2222393750.
E-mail address: yesilel@ogu.edu.tr (O.Z. Yeşilel).

0277-5387/$ - see front matter © 2009 Elsevier Ltd. All rights reserved.
doi:10.1016/j.poly.2009.04.048

2801(m), 1697(s), 1676(s), 1637(s), 1475(m), 1400(m), 1334(w), 1033(w), 956(w), 773(w), 597(w). μ-eff (298 K): 1.41 B.M.

2.1.2. [CuHOr(H_2O)$_2$] (**2**)

A solution of $Cu(CH_3COO)_2{\cdot}H_2O$ (0.80 g, 4 mmol) in water (20 mL) was added dropwise to a solution of orotic acid hydrate (0.63 g, 4 mmol) in pyridine (20 mL) with stirring at 60 °C. The mixture was refluxed with stirring for 2 h at 60 °C in a temperature-controlled bath, and then solution was cooled to room temperature. Violet crystals were formed, filtered and washed with 10 mL of water, and then dried in air. *Anal.* Calc. for $C_5H_6N_2O_6Cu$: C, 23.68; H, 2.38; N, 11.04. Found: C, 23.69; H, 2.41; N, 10.98%. IR (KBr pellet, cm^{-1}): 3519(s), 3317(s), 3180(s), 2977(s), 2811(s), 1660(vs, b), 1477(m), 1411(m), 1373(m), 1267(m), 1140(w), 1020(m), 891(m), 843(w), 802(s), 771(s), 713(m). μ-eff (298 K): 1.64 B.M.

2.2. Materials and measurements

All chemicals used were analytical reagents and commercially purchased. IR spectra were obtained with a Bruker Tensor 27 FT-IR spectrometer using KBr pellets in the 4000–400 cm^{-1} range. Elemental analysis for C, H and N were performed using a Carlo Erba 1106 microanalyzer. Magnetic susceptibility measurements at room temperature were performed using a Sherwood Scientific MXI model Gouy magnetic balance. A Perkin–Elmer Diamond TG/DTA thermal analyzer was used to record simultaneous TG, DTG and DTA curves in a static air atmosphere at a heating rate of 10 $Kmin^{-1}$, in the temperature range 20–600 °C, using platinum crucibles.

The EPR spectra were recorded using a Varian E-109C model X-band spectrometer. The magnetic field modulation frequency was 100 kHz and the microwave power was around 10 mW.

2.3. Crystallographic analyses

X-ray diffraction data for compounds **1** and **2** were collected at 293 (2) K on a Stoe IPDS diffractometer. Data collection: Stoe X-AREA [15]. Cell refinement: Stoe X-AREA [15]. Data reduction: Stoe X-RED [15]. The structures were solved by direct methods using the program SHELXS-97 [16] with anisotropic thermal parameters for all non-hydrogen atoms. All non-hydrogen atoms were refined anisotropically by full-matrix least-squares methods, using SHELXL-97 [17]. All hydrogen atoms for **1** were positioned geometrically and refined by a riding model with U_{iso} 1.2 or U_{iso} 1.5 times that of the attached atoms. The butylamine group shows two-positioned orientation disorder, the final site-occupancy factors for N(3)A–N(4)A/C(6)A–C(13)A being 38.4(6)% and 61.6(6)%. Restrains were applied to the water hydrogens to the idealized geometry for **2**. Other hydrogen atoms for **2** were positioned geometrically and refined by a riding model with U_{iso} 1.2 times that of the attached atoms. Molecular drawings were obtained using ORTEP-III for WINDOWS [18] and DIAMOND (demonstrated version) [19]. The crystal data and the refinement details of **1** and **2** are given in Table 1.

3. Results and discussion

3.1. IR spectra

The IR spectrum of **2** shows a strong band at 3519 cm^{-1} due to the O–H stretching vibrations of the H_2O ligand. The intense bands at 3450 and 3415 cm^{-1} are attributed to the NH_2 vibration of the butylamine ligand. The bands at *ca.* 3320 cm^{-1} are attributed to the ν(NH) vibrations of the orotato ligands. The relatively weak bands between 3180 and 2801 cm^{-1} can be assigned to both aromatic CH and aliphatic CH_2 stretching vibrations of the HOr and ba ligands, respectively. The position of the characteristic stretching modes of the carbonyl of the orotate moiety can be used to characterize the coordination mode of this ligand to metal ions. Carbonyl stretching bands of orotic acid were observed at 1729 and 1719 cm^{-1} for [$\nu_{C=O(acid)} + \nu_{C(2)=O}$], and 1700 and 1653 cm^{-1} for [$\nu_{C(6)=O} + \nu_{ring} + \nu_{C=C}$] [20]. These bands were shifted to 1697, 1676 and 1637 cm^{-1} in **1** and show a broad-strong absorption band at 1660 cm^{-1} due to overlapping of the two bands in **2**. The weak bands at 453 and 607 cm^{-1} are due to Cu–N and Cu–O stretching vibrations, respectively. From the IR spectra of **1** and **2**, it can be assumed that the orotate ligand is coordinated to the Cu(II) ions as a tridentate ligand through the N atom of the pyrimidine ring and two carboxyl O atoms (O_{acid}, N, O_{acid}).

Table 1
Crystal data and structure refinement parameters for (**1**) and (**2**).

	1	**2**
Empirical formula	$C_{13}H_{24}N_4O_4Cu$	$C_5H_6N_2O_6Cu$
Formula weight	363.90	253.66
T (K)	293 (2)	293 (2)
Wavelength (Å) (Mo Kα)	0.71073	0.71073
Crystal system	monoclinic	monoclinic
Space group	$C2/c$	$P2_1/n$
a (Å)	34.193 (4)	7.1905 (9)
b (Å)	6.964 (5)	7.5771 (6)
c (Å)	14.748 (1)	15.126 (2)
β (°)	107.963 (8)	100.802 (9)
V (Å^3)	3341 (2)	809.5 (2)
Z	8	2
Absorption coefficient (mm^{-1})	1.33	2.71
D_{calc} (Mg m^{-3})	1.447	2.081
Crystal size (mm)	0.35 × 0.25 × 0.06	0.32 × 0.30 × 0.19
θ Range for data collection (°)	2.2–26	2.7–27.9
Measured reflections	8528	5620
Independent reflections	2939	1899
Absorption correction	integration Stoe X-RED [15]	
Refinement method	full-matrix least-squares on F^2	
R_{int}	0.047	0.032
Final R indices [$I > 2\sigma(I)$]	R_1 = 0.0568, wR_2 = 0.1576	R_1 = 0.0347, wR_2 = 0.0967
Final R indices (all data)	R_1 = 0.0765, wR_2 = 0.1713	R_1 = 0.0397, wR_2 = 0.0994
Goodness-of-fit on F^2	1.036	1.112
$\Delta\rho_{max}$ (eÅ^{-3})	0.55	0.54
$\Delta\rho_{min}$(eÅ^{-3})	−0.7	−0.7

3.2. Thermal analyses

3.2.1. Complex **1**

The first stage between 213 and 264 °C (DTA_{max} = 201, 213 and 264 °C) corresponds to the loss of two ba ligands (found 40.65, calcd. 41.19%). The following stages between 286 and 431 °C are related to the consecutive decomposition of the orotate ligand with exothermic effects (found 40.81, calcd. 40.55%). The final solid product of thermal decomposition was identified as CuO (found 81.46, calcd. 79.07%).

3.2.2. Complex **2**

The complex is decomposed in three stages and thermally stable up to 288 °C. The first stage between 288 and 338 °C is related to the dehydration and decarboxylation of the orotate ligand (DTG_{max} = 324 °C). In the temperature range of 338–409 °C, the following second and third stages involve the consecutive decomposition of the uracil ligand by exothermic effects (DTG_{max} = 368, 388 °C). The final decomposition product, namely CuO, was identified by IR spectroscopy.

3.3. Crystal structures

3.3.1. $[Cu(\mu\text{-}HOr)(ba)_2]_n$ (**1**)

A view of **1** and its atom-numbering scheme is shown in Fig. 1. Selected bond lengths and bond angels are given in Table 2. The crystallographic analyses reveal that the crystal structure of **1** is a one-dimensional wave-like polymer chain along the *b*-axis. The central metal ion adopts a distorted square pyramidal coordination sphere and is bound by two N atoms [N(3) and N(4)] from two butylamine ligands, an orotate dianion *via* the carboxylate oxygen O(4) and N(1), and a carboxylic O atom from a neighboring orotato ligand. Atoms N(1) and O(4) are bonded to Cu(1) to form a five-membered chelate ring [N(1)–Cu(1) = 2.003 (4) Å and O(4)–Cu(1) = 1.958 (3) Å]. All the N–Cu–N, N–Cu–O and O–Cu–O bond angles deviate significantly from 90° to 180°, presumably as a result of the steric constraints arising from the shape of the ligands.

The $M–O_{HOr}$ distances are 2.4243(12) Å for $Cu(1)–O(3)^{i}$ (i: $0.5 - x$, $0.5 + y$, $0.5 - z$) and 1.958(3) Å for Cu(1)–O(4). In this conformation, the HOr^{2-} ligand links two metal centers in a μ-bridging mode and each metal center connects two HOr^{2-} ligands to form one-dimensional chain along the *b*-axis (Fig. 2), in which metal atoms possess an 'S' shape with the $Cu–Cu^{i}$ (i: $0.5 - x$, $0.5 + y$, $0.5 - z$) distance being 5.4213(17) Å.

The orotate ligand in the complex is essentially planar (r.m.s. deviation is 0.0297 Å). Of all the N–C bonds in the uracil ring of the orotate ligand, N(1)–C(1) [1.368(5) Å] and N(1)–C(4) [1.353(6) Å] are the shortest. This indicates a significant π-electron delocalization within the C(3)–C(4)–N(1)–C(1) skeleton.

It should be noted that different kinds of hydrogen bonds are observed between the chains: (i) hydrogen bonding between the amino H atom of the HOr ligand and the coordinated carboxylic oxygen [N(2)···O(4): 3.017(5) Å], (ii): hydrogen bonding between the amino H atoms of butylamine ligands and the coordinated

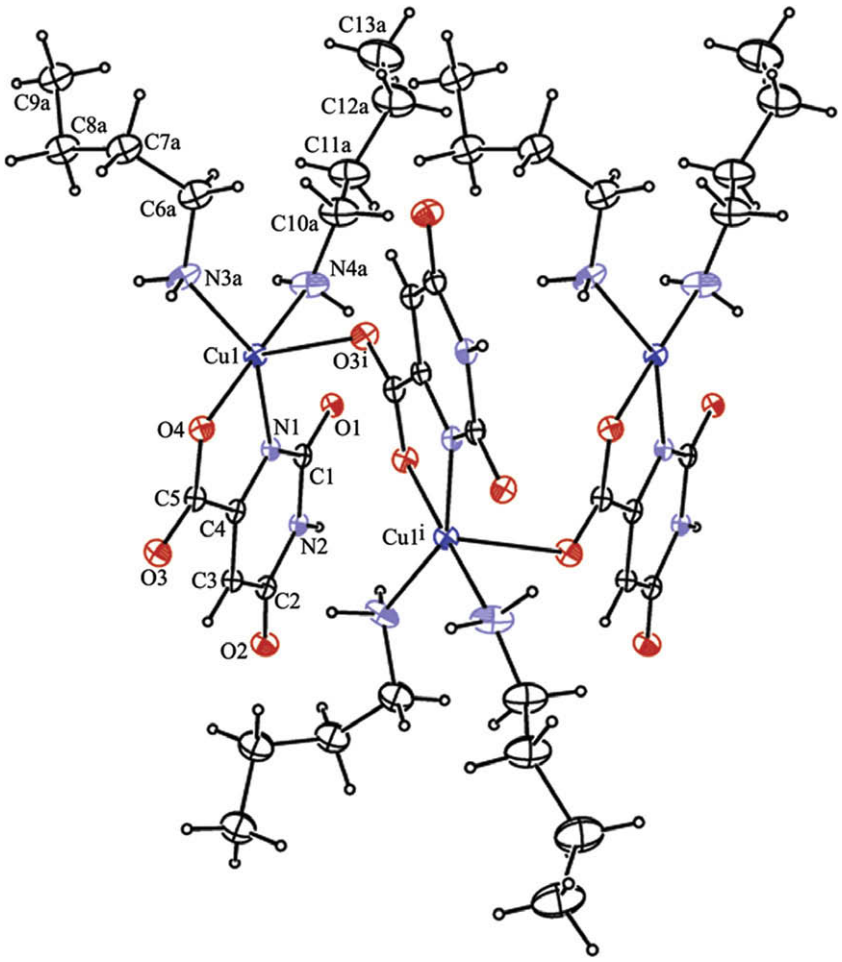


Fig. 1. ORTEP III view of $[Cu(\mu\text{-}HOr)(ba)_2]_n$ with the atom-numbering scheme (20% probability ellipsoids). The disordered part of the atoms has been omitted for clarity [i:$1/2 - x$, $-1/2 + y$, $1/2 - z$].

Table 2
Comparison of bond distances and angles (Å, °).

Selected atoms	1	2	[9]
Cu1–N1	2.003(4)	1.994(2)	1.975(2)
Cu1–O4	1.958(3)	1.956(2)	1.948(2)
Cu1–O6		1.995(3)	1.944(2)
Cu1–O5		1.959(3)	1.941(2)
Cu1–O2^{i}		2.919(3)	
N1–C1	1.368(5)	1.360(4)	1.354(2)
N1–C4	1.353(6)	1.362(4)	1.371(2)
N2–C1	1.384(6)	1.382(4)	1.376(2)
O1–C1	1.226(5)	1.232(4)	1.249(2)
O2–C2	1.233(6)	1.232(4)	1.241(2)
O3–C5	1.228(6)	1.229(4)	1.232(2)
O4–C5	1.270(6)	1.283(4)	1.278(2)
C2–N2	1.373(6)	1.362(4)	1.376(3)
C2–C3	1.431(6)	1.434(4)	1.430(3)
C3–C4	1.357(6)	1.354(4)	1.355(3)
C4–C5	1.520(6)	1.508(4)	1.512(3)
O3–C5–O4	125.9(4)	125.2(3)	125.5(2)
O5–Cu1–O6		90.70(12)	
O4–Cu1–N1	82.47(14)	82.54(9)	83.57(6)
O5–Cu1–N1		96.70(11)	
O4–Cu1–O6		90.06(11)	88.03(7)
C1–N1–Cu1	129.9(3)	129.7(2)	
C4–N1–Cu1	111.8(3)	112.16(19)	
O4–Cu1–N1–C4	3.6(3)	2.3(2)	
O4–Cu1–N1–C1	176.7(4)	177.6(3)	
N1–Cu1–O4–C5	−4.4(3)	0.9(2)	
Cu1–O4–C5–O3	−174.4(4)	176.6(3)	
Cu1–O4–C5–C4	4.2(5)	−3.7(3)	

Symmetry code: (i): $2-x, 1-y, 1-z$.

carbonyl oxygen [N(3B)···O(1): 2.884(8) Å] and the uncoordinated carbonyl oxygen [N(4B)···O(2): 3.337(14) Å]. As a result of all these interactions, each chain is linked to other chains by the hydrogen-bonding interactions. The layers are further linked by C–H···O hydrogen bonds lying on the *bc* planes. There is also a weak intramolecular hydrogen bond (N–H···O) (Table 3).

3.3.2. $[Cu_2(HOr)_2(H_2O)_4]$ (**2**)

Complex **2** crystallizes in the monoclinic crystal system. A view of the molecule and its atom-numbering scheme are shown in Fig. 3. Selected bond lengths and bond angels are given in Table 2. Ha et al. [9] determined the crystal and molecular structure of the polymeric $[Cu(orotato)(H_2O)_2]_n$ complex, but it should be emphasized that in contrast to the polymeric complex of $[Cu(orotato)(H_2O)_4]_n$ [14] and $[Cu(orotato)(H_2O)_2]_n$ [9], compound **2** has a dimeric form of two $[Cu(HOr)(H_2O)_2]$ molecules.

Table 3
Hydrogen bonding interactions in **1**.

D–H···A	d(D–H) (Å)	d(H···A) (Å)	d(D···A) (Å)	∠ (DHA) (°)
N2–H2···O4^{i}	0.86	2.16	3.017 (5)	171
N3B–H3B1···O1^{ii}	0.90	2.04	2.897 (12)	159
N4B–H4B1···O2^{iii}	0.90	2.52	3.204 (13)	134
N4B–H4B2···O1	0.90	1.92	2.772 (12)	157
C6B–H6B1···O2^{iv}	0.97	2.52	3.146 (17)	122

Symmetry codes: (i) $x, -y+2, z-1/2$; (ii) $-x+1/2, y+5/2, -z+1/2$; (iii) $-x+1/2, -y+5/2, -z$; (iv) $-x+1/2, -y+3/2, -z$.

Square-planar copper(II) has a tendency to extend its coordination sphere to five, the so-called (4+1)-coordination geometry, or to six (4+2) or (4+1+1) geometries. In the present compound, the copper(II) ion is in distorted square pyramidal coordination sphere, which is extended to five (4+1) by an intermolecular *exo*-acid oxygen atom O(2), and it is also bound by the deprotonated N(1) nitrogen atom and the O(4) carboxylate oxygen atom of the bidentate orotate ligand. Two water oxygen atoms (O(5) and O(6)) complete the distorted square-planar environment around Cu(II). The N(1) and O(4) atoms are bonded to Cu(1) to form a five-membered chelate ring in **2** [N(1)–Cu(1) = 1.994(2) (3) Å and O(4)–Cu(1) = 1.956(2) Å]. The carbonyl O2 atom from a neighboring molecule occupies the axial coordination site [Cu(1)–O(2)^{i} = 2.9193(2) Å; i: $2-x, 1-y, 1-z$].

The orotato ligand is slightly deviated from planarity (the r.m.s. deviation is 0.6998 Å), the largest deviation from the mean plane is 1.0571 (2) Å for the O(4) atom. Of all the N–C bonds in the uracil ring of the orotato ligand, N(1)–C(1) [1.360(4) Å] and N(1)–C(4) [1.362(4) Å] are the shortest. This indicates that there is significant π-electron delocalization within the C(3)–C(4)–N(1)–C(1) skeleton. The bond distances and bond angles in the ring are consistent with those found in [9] (comparison in Table 2).

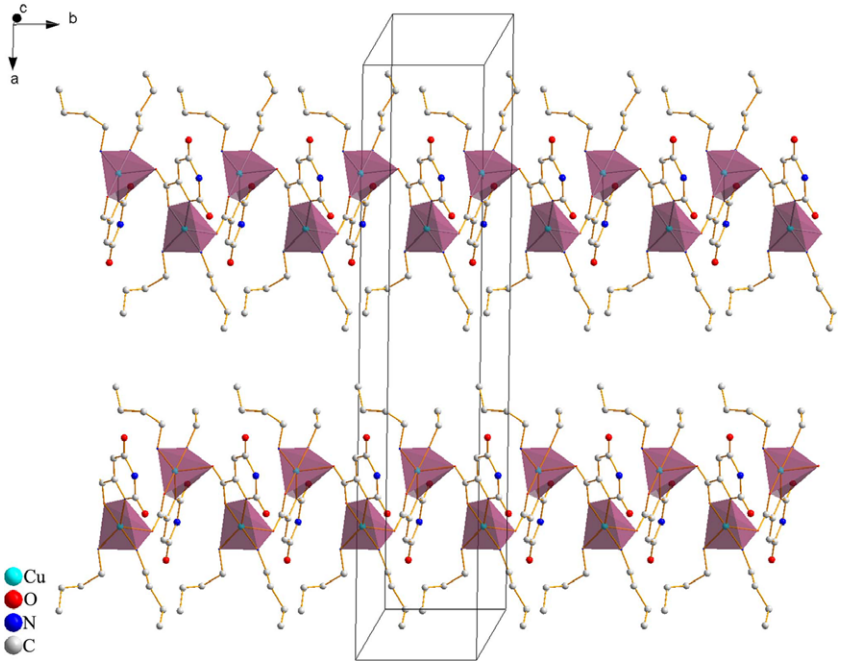


Fig. 2. Polyhedral representation of polymeric $[Cu(\mu\text{-}HOr)(ba)_2]_n$ molecules. Distorted octahedral are shaded dark. All H atoms and the disordered part of the atoms have been omitted for clarity.

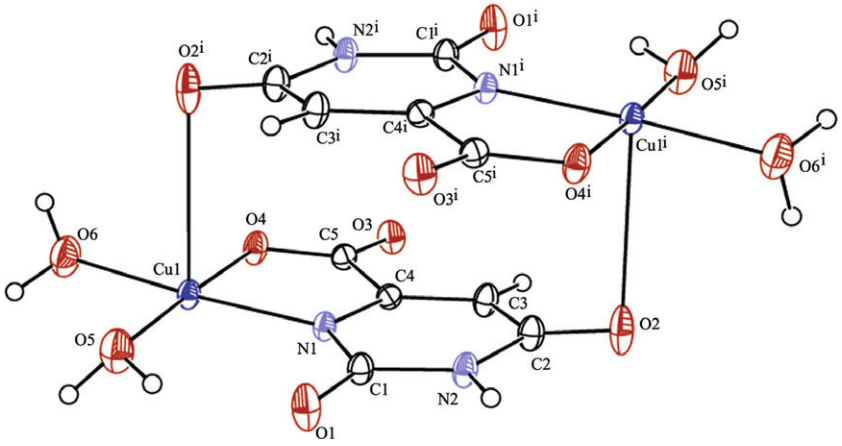


Fig. 3. ORTEP III view of $[Cu_2(HOr)_2(H_2O)_4]$ with the atom-numbering scheme (20% probability ellipsoids). The disordered part of the atoms has been omitted for clarity [i: $2-x, 1-y, 1-z$].

The stability of the columns is further enhanced by the formation of extensive intermolecular hydrogen bonds (indicated by dashed lines). Molecules of complex **2** are linked by a pair of Watson–Crick type hydrogen bonds, involving the O2═C2 and N2–H2 groups of each uracil ring, with a N2···O2^{iv} distance of 2.862(4) Å and N2–H2···O2^{iii} angle of 176° (the symmetry codes are listed under Table 4). A very similar type of intermolecular hydrogen bonding was reported before with the corresponding N···O distances of 2.83 Å [21] and 2.860(2) [14]. O_{water}–H···O intermolecular hydrogen bonds are also effective in **2** (Table 4). All these intermolecular interactions result in the formation of a two-dimensional network (Fig. 4). There is also an intramolecular O5–H5a···O1 hydrogen bond formed between the water hydrogen atom and the carbonyl oxygen atoms of the orotate ligand.

Table 4
Hydrogen bonding interactions in **2**.

D–H···A	*d*(D–H) (Å)	*d*(H···A) (Å)	*d*(D···A) (Å)	∠(DHA) (°)
O5–H5A···O1	0.838 (10)	2.07 (3)	2.776 (4)	142 (4)
O5–H5A···O2^{i}	0.838 (10)	2.58 (4)	3.068 (4)	118 (4)
O5–H5B···O3^{ii}	0.842 (10)	2.21 (3)	2.928 (4)	143 (4)
N2–H2···O2^{iii}	0.86	2.00	2.862 (4)	176
O6–H6A···O1^{iv}	0.844 (10)	2.52 (3)	3.239 (4)	143 (5)
O6–H6B···O3^{ii}	0.842 (10)	2.48 (3)	3.250 (4)	152 (5)

Symmetry codes: (i) $x-1/2, -y+3/2, z-1/2$; (ii) $x-1/2, -y+1/2, z-1/2$; (iii) $-x+2, -y+2, -z+1$; (iv) $x, y-1, z$.

Of greater interest is the Cu–π axial interaction which contributes to the crystal packing by forming an infinite chain of dimers. It is suggested that the π-type interaction between the chelated Cu^{2+} cation and the aromatic compounds can play a significant role in biological systems, e.g. in the active sites of copper enzymes. The Cu(II)···Cg^{ii} distance of 3.557(1) Å is close to the van der Waals contacts between the stacking bases in DNA (Fig. 5) [Cg = N1–C1–N2–C2–C3–C4 (uracil ring)]. It should be emphasized that the O2^{i}–Cu–Cg^{ii} angle deviates from linearity [151.9(6)°, (i) $2-x, 1-y, 1-z$; (ii) $1-x, 1-y, 1-z$]. Michalska et al. reported the same interaction in *cis*-$[Cu(HOr)(NH_3)_2]$ with the parameters Cu–X^{ii} (X = centroid, Cg) distance of 3.293(9) Å and O2^{i}–Cu–X^{ii} angle of 169.6(1)°. It is interesting that in the crystal structure of $[Cu(HOr)(en)(H_2O)]\cdot H_2O$, reported by Icbudak et al. [11], the vertical distance between the copper atom and the uracil ring is between 3.156 and 3.274 Å (private communication).

π–π stacking interactions between uracil rings have been observed in other Cu(II) complexes with orotic acid derivatives, the

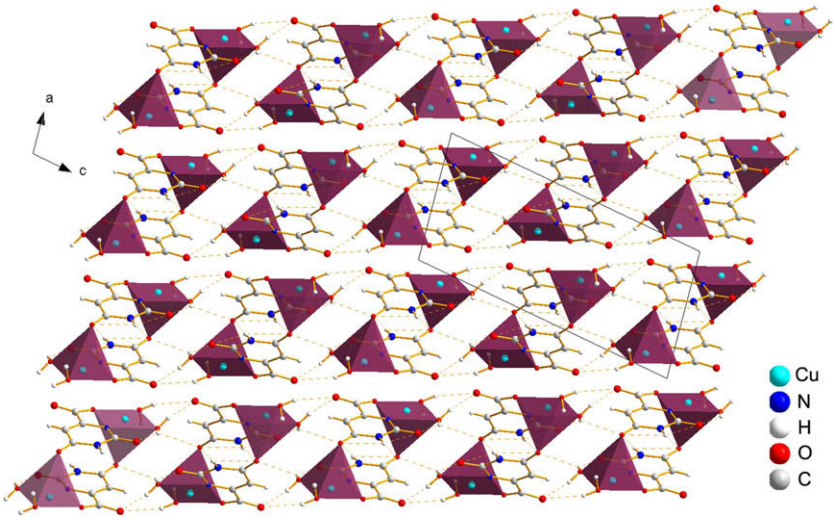


Fig. 4. A stereoscopic packing in the crystal of $[Cu_2(HOr)_2(H_2O)_4]$ (**2**) displaying the distorted square octahedral environment around the copper ions. Hydrogen bonds are indicated by dashed lines.

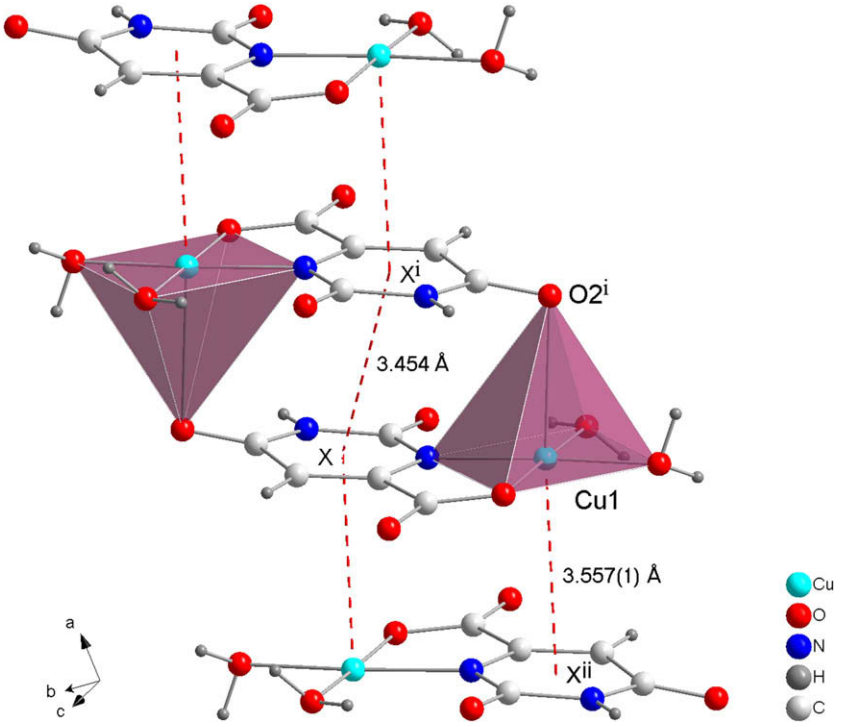


Fig. 5. The view of the dimer unit of $[Cu_2(HOr)_2(H_2O)_4]$ showing the axial Cu–O2^i bonds and Cu(II)···X (X = centroid, Cg) interactions (dashed lines). The π···π interaction is also shown. Symmetry codes are as follows: (i) $2-x, 1-y, 1-z$; (ii) $1-x, 1-y, 1-z$.

distance between partially overlapping uracil rings varies from 3.250(3) Å in the mononuclear $[Cu(5\text{-fluoroorotato})(NH_3)(H_2O)]$ complex [22] to 3.40 Å in the diamine(5-nitroorotato)copper(II) hydrate [23]. The same effect is found in **2** between the uracil rings, with the parameters shown in Fig. 5.

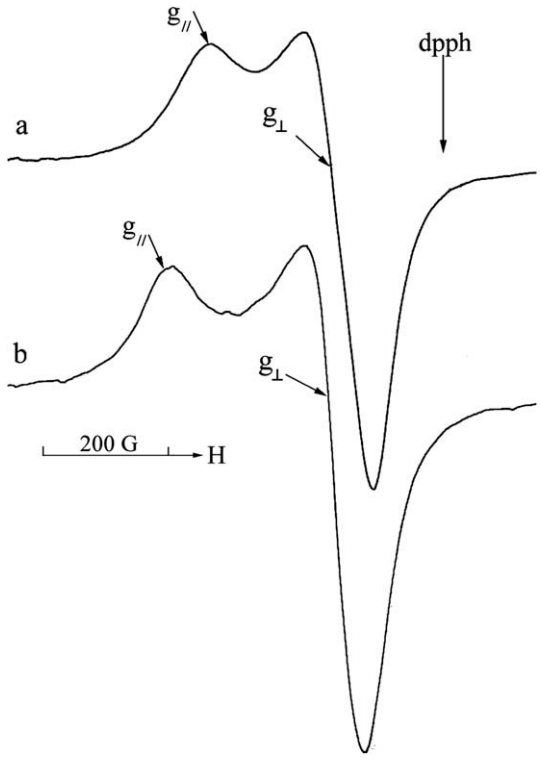


Fig. 6. Powder EPR spectra at room temperature (a) $[Cu(\mu\text{-HOr})(ba)_2]_n$ and (b) $[Cu_2(HOr)_2(H_2O)_4]$.

3.4. EPR investigations

The powder EPR spectra of the complexes **1** and **2** at room and liquid nitrogen temperature were recorded (Fig. 6). As can be seen from Fig. 6, only one $g_{\parallel}$ and one $g_{\perp}$ component were obtained due to the influence of the exchange interaction, which makes the hyperfine lines smaller. The g parameters were calculated, giving $g_{\parallel} = 2.197$, $g_{\perp} = 2.089$ and $g_{\parallel} = 2.232$, $g_{\perp} = 2.092$ for **1** and **2**, respectively. The g values are in the order of $g_{\parallel} > g_{\perp} > g_e$ (free electron g value, $g_e = 2.0023$). Considering these values, together with the observed characteristic $g_{\parallel}$ and $g_{\perp}$ values for Cu(II) complexes, it can be concluded that the paramagnetic center is axially symmetric.

4. Conclusions

We have successfully synthesized and characterized the novel *catena-poly*-μ-orotatobis(butylamine)copper(II), $[Cu(\mu\text{-HOr})(ba)_2]_n$ (**1**), and bis[diaqua(orotato)copper(II)], $[Cu_2(HOr)_2(H_2O)_4]$ (**2**), complexes. To our surprise, complex **1** is thermally stable up to about 288 °C, despite the water molecules contain within it. The presence of Cu^{2+}/Cu^{+} centers is mainly responsible for the oxidase activity of copper-containing enzymes and proteins, e.g. galactose oxidase (GAO) and ceruloplasmin (C_p). The experimental study on **2** has revealed the great importance of the non-covalent Cu(II)–π binding force between the chelated Cu^{2+} ion and the uracilate ligand. The powder EPR spectrum shows clearly that the paramagnetic center symmetry of the two complexes in the crystals is axial.

Supplementary data

CCDC 653990 and 653991 contain the supplementary crystallographic data for **1** and **2**. These data can be obtained free of charge via http://www.ccdc.cam.ac.uk/conts/retrieving.html, or from the

Cambridge Crystallographic Data Centre, 12 Union Road, Cambridge CB2 1EZ, UK; fax: (+44) 1223 336 033; or e-mail: deposit@ccdc.cam.ac.uk.

References

[1] M. Kondo, T. Okubo, A. Asami, S. Noro, T. Yoshitomi, S. Kitagawa, T. Ishii, H. Matsuzaka, K. Seki, Angew. Chem., Int. Ed. Engl. 38 (1999) 1433.
[2] G. Beobide, O. Castillo, A. Luque, U. Garcia-Coucerio, J.P. Garcia-Teran, P. Roman, Inorg. Chem. 45 (2006) 5367.
[3] H. Yin, S.X. Liu, Polyhedron 26 (2007) 3103.
[4] X.H. Li, Q. Shi, M.L. Hu, H.P. Xiao, Inorg. Chem. Commun. 7 (2004) 912.
[5] J.Z. Zou, Z. Xu, W. Chen, K.L. Lo, X.Z. You, Polyhedron 18 (1999) 1507.
[6] D.J. Darenbourg, D.L. Larkins, J.H. Reibenspies, Inorg. Chem. 37 (1998) 6125.
[7] S.T. James, D.M.P. Mingos, X. Xu, A.J.P. White, D.J. Williams, J. Chem. Soc., Dalton Trans. (1998) 1335.
[8] I. Mutikainen, P. Lumme, Acta Crystallogr., Sect. B 36 (1980) 2233.
[9] T.T.B. Ha, A.M. LarsonneurGalibert, P. Castan, J. Jaud, J. Chem. Crystallogr. 29 (1999) 565.
[10] X. Li, R. Cao, W. Bi, D. Sun, M. Hong, Acta Crystallogr., Sect. E 59 (2003) m228.
[11] H. İçbudak, H. Ölmez, O.Z. Yeşilel, F. Arslan, P. Naumov, G. Jovanovski, A.R. Ibrahim, A. Usman, H.K. Fun, S. Chantrapromma, S.W. Ng, J. Mol. Struct. 657 (2003) 255.
[12] H. Olmez, H. Icbudak, O.Z. Yeşilel, C. Arici, D. Ulku, Z. Kristallogr. 219 (2004) 300.
[13] O.Z. Yeşilel, H. Olmez, H. Icbudak, O. Büyükgüngör, Z. Naturforsch. 60b (2005) 1138.
[14] D. Michalska, K. Hernika, R. Wysokiński, B. Morzyk-Ociepa, A. Pietraszko, Polyhedron 26 (2007) 4303.
[15] Stoe & Cie, X-AREA (version 1.18) and X-RED32 (version 1.04), Stoe & Cie, Darmstadt, Germany, 2002.
[16] G.M. Sheldrick, SHELXS-97, Program for Crystal Structure Determination, University of Göttingen, Germany, 1997.
[17] G.M. Sheldrick, SHELXL-97, Program for the Refinement of Crystal Structures, University of Göttingen, Germany, 1993.
[18] L.J. Farrigua, J. Appl. Crystallogr. 30 (1997) 565.
[19] K. Brandenburg, DIAMOND, Demonstrated Version, Crystal Impact GbR, Bonn, Germany, 2005.
[20] A. Hernanz, F. Billes, I. Bratu, R. Navarro, Biopolymers 57 (2000) 187.
[21] K. Hoogsteen, Acta Crystallogr. 16 (1963) 28.
[22] A.G. Schneider, H.W. Schmalle, F. Arod, E. Dubler, J. Inorg. Biochem. 89 (2002) 227.
[23] P. Arrizabalaga, P. Castan, F. Dahan, Inorg. Chem. 22 (1983) 2245.

Polyhedron 28 (2009) 2494–2502

Contents lists available at ScienceDirect

Polyhedron

journal homepage: www.elsevier.com/locate/poly

Various coordination architectures constructed from *N*-[(carboxyphenyl)-sulfonyl]glycine: Structural variation *via* ligand isomerism effects and metal-directed assembly

Lu-Fang Ma [a], Li-Ya Wang [a,*], Shu-Hui Chen [a,b], Hong-Wei Hou [b], Stuart R. Batten [c]

[a] College of Chemistry and Chemical Engineering, Luoyang Normal University, Luoyang 471022, PR China
[b] Department of Chemistry, Zhengzhou University, Zhengzhou 450001, PR China
[c] School of Chemistry, Monash University, Victoria 3800, Australia

ARTICLE INFO

Article history:
Received 14 December 2008
Accepted 30 April 2009
Available online 10 May 2009

Keywords:
N-[(4-carboxyphenyl)-sulfonyl]glycine
N-[(3-carboxyphenyl)-sulfonyl]glycine
Crystal structure
Magnetic properties

ABSTRACT

Using Cu(II), Mn(II) or Co(II) salt and the flexible ligands, *N*-[(4-carboxyphenyl)-sulfonyl]glycine (H_3L_1) and *N*-[(3-carboxyphenyl)-sulfonyl]glycine (H_3L_2), a series of new coordination polymers, $[Mn(phen)(H_2O)_4][HL_1]$ (**1**), $[Co_3(L_1)_2(bipy)_3(H_2O)_6]_n{\cdot}8nH_2O$ (**2**), $[Cu_4(L_1)_2(OH)_2(bipy)_4]_n{\cdot}12nH_2O$ (**3**), $[Na(H_2L_1)(H_2O)]_n$ (**4**), $[Mn_2(HL_2)_2(dpe)_3(H_2O)_2]_n{\cdot}ndpe$ (**5**), (phen = 1,10-phenanthroline, bipy = 4,4′-bipyridine, dpe = 1,2-di(4-pyridyl)ethylene), varying from 0D to 3D, have been synthesized and structurally characterized. Compound **1** has a $[Mn(phen)(H_2O)_4]^{2+}$ cation and a HL_1^{2-} anion. Compound **2** features a new 1D triple chain, based on octahedral cobalt atoms bridged by bipy molecules and terminally coordinated by two H_3L_1 ligands. Compound **3** has a 2D layered structure, constructed from new alternating chains where H_3L_1, hydroxyl and water molecules simultaneously act as bridging ligands. Compound **4** possesses a bilayer structure in which two adjacent layers are pillared by H_3L_1 ligands into a 2D bilayer network. Compound **5** is a unique 3D coordination polymer in which each Mn center binds two *trans*-located dpe molecules. The thermal stability as well as magnetic properties of **5** was also studied. This work and our previous work indicate that the positional isomer of the anionic *N*-[(carboxyphenyl)-sulfonyl]glycine is important in the construction of these network structures, which are also significantly regulated by the metal centers.

© 2009 Elsevier Ltd. All rights reserved.

1. Introduction

The rational design and assembly of inorganic coordination polymers or metal–organic frameworks has received remarkable attention and has developed rapidly in recent years. Being easily and efficiently synthesized from relatively simple subunits, these complexes exhibit fascinating structural topologies and potential applications as functional materials [1–4]. However, the control of dimensionality is still a major challenge in the design and synthesis of organic–inorganic frameworks because the final structure is frequently modulated by various factors such as solvent medium, the geometry of metal ions, coordination character of the organic ligand, temperature, metal–ligand ratio, template and counterion [5]. Among these factors, the selection of appropriate metal ions and organic ligands is often the key in the construction of complexes. Metal ions, and in particular their radii and coordination geometry determine the bridging pattern and coordination modes of the organic ligands, and thus the overall structures of the complexes. In the crystal engineering, the employment of ligand isomers as the organic component is an effective way to investigate the effect of the ligand geometry. Usually, ligand isomers having similar structures but different coordination modes would lead to different structural motifs, such as seen for benzenedicarboxylates. Benzenedicarboxylate anions have three structural isomers (phthalate, isophthalate and terephthalate) with different angles between the two carboxylato groups, which may exhibit different geometric effects on the construction of coordination polymers [6]. To date, a variety of metal organic frameworks have been reported, however, systematic studies of the isomeric effect on the generation of such coordination frameworks are surprisingly rare [7]. With this in mind, one crucial aim of this work was to explore the effect of two isomers on the structural assembly. This may provide further insights in designing new hybrid crystalline materials.

Furthermore, amino acid is one of the most important biological ligands. Recently, amino acids with flexible coordination modes have been utilized to construct metal–organic supramolecular networks [8]. To date, a number of Ln-amino acid and transition metal–amino acid complexes with mononuclear, binuclear or chain structural motifs have been synthesized [9]. Several reports of polynuclear transition metal clusters or various 3d–4f high-nuclearity clusters with different structural motifs have also

* Corresponding author. Tel.: +86 0379 65523593; fax: +86 0379 65511205.
E-mail address: wlya@lynu.edu.cn (L.-Y. Wang).

0277-5387/$ - see front matter © 2009 Elsevier Ltd. All rights reserved.
doi:10.1016/j.poly.2009.04.044

reported [10]. However, reports of metal complexes of amino acids with high dimensional structures are rare [11]. This may be due to deprotonated amino acids preferring to chelate metal centers through their amine N and carboxylic O atoms to form five-membered rings which prevent extension into high dimensional structures. In order to overcome this problem, our research has focused on designing a new versatile ligand which contains both carboxylate and amino acid groups by introduction of an aromatic carboxylato group at its amino group.

We have recently used such a multifunctional amino acid derivative, namely *N*-[(3-carboxyphenyl)-sulfonyl]glycine, to create a series of unusual metal–organic frameworks [12,13]. In comparison to benzenedicarboxylic acids, *N*-[(3-carboxyphenyl)-sulfonyl]glycine not only contains two bridging carboxylato moieties but also possesses another two potential coordination sites, i.e., the nitrogen atom and oxygen atoms of the sulfonate groups. This asymmetric geometry may produce beautiful new structural motifs and useful functional properties. To further probe the influence of systematic variations of ligand structures and metal ions on the overall molecular architectures, we extend the building blocks from the bent *N*-[(3-carboxyphenyl)-sulfonyl]glycine to its quasi-linear isomer *N*-[(4-carboxyphenyl)-sulfonyl]-glycine to explore the isomeric effect on network assembly. Herein, the synthesis and X-ray crystal structures of eight coordination networks, including our previous reported $[Mn_2(HL_2)_2(phen)_4]_n{\cdot}8nH_2O$ (**6**), $[Co_3(L_2)_2(bipy)_2(H_2O)_6]_n{\cdot}2nCH_3OH{\cdot}8nH_2O$ (**7**) and $[Ca(H_2O)_4Cu_2(bipy)_2(L_2)_2]_n{\cdot}4nH_2O$ (**8**), formed by Cu^{2+}, Mn^{2+}, Co^{2+} salts with H_3L_1 and H_3L_2 are reported (See Schemes 1 and 2). The influence of ligand isomerism and metal ions on the final structures of the assemblies is discussed.

2. Experimental

2.1. Materials and instruments

All reagents used in the syntheses were of analytical grade. Elemental analyses for carbon, hydrogen and nitrogen atoms were performed on a Vario EL III elemental analyzer. The infrared spectra (4000–600 cm^{-1}) were recorded by using KBr pellet on an Avatar™ 360 E.S.P.IR spectrometer. The crystal structure determination was performed on a Bruker SMART APEX II CCD diffractometer equipped with graphite-monochromatized Mo Kα radiation (λ = 0.71073 Å). Thermogravimetric analyses (TG) were carried out on a STA449C integration thermal analyzer. The PXRD patterns were recorded with a Rigaku D/Max 3III diffractometer with a scanning rate of four degrees per minute. Variable-temperature magnetic susceptibilities were measured using a MPMS-7 SQUID magnetometer.

2.2. Synthesis of N-[(4-carboxyphenyl)-sulfonyl]glycine

To a solution of glycine (2.25 g, 0.03 mol) in NaOH 2 M (30 mL), 4-(chlorosulfonyl)benzoic acid (6.78 g, 0.03 mol) was added. The mixture was stirred at room temperature for 2 h, and the aqueous solution was then acidified to pH 4 with 6 M hydrochloric acid, upon which a white solid derivative began to crystallize at once with a yield of about 60%. *Anal.* Calc. for $C_9H_9NO_6S$: C, 41.70; H, 3.50; N, 5.40. Found: C, 41.79; H, 3.62; N, 5.58%. IR: 3287s, 1718s, 1432s, 1171m, 753m, 1336s, 897m.

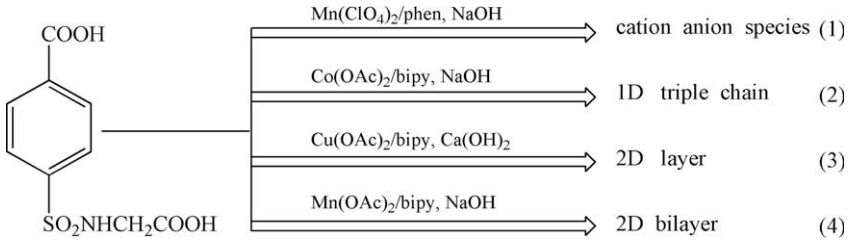
2.3. Preparation of ***1*–*5***

2.3.1. $[Mn(phen)(H_2O)_4][HL_1]$ (***1***)

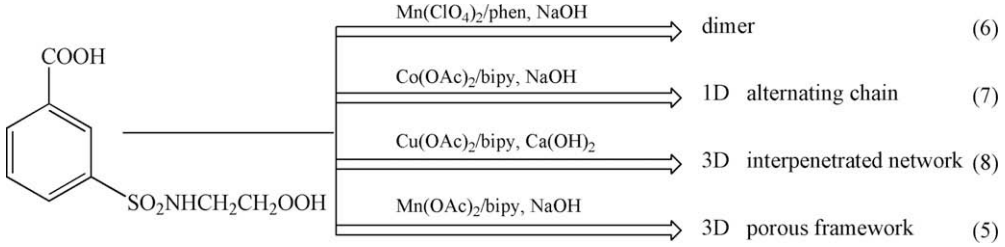
A mixture of $Mn(ClO_4)_2 \cdot 6H_2O$ (0.16 g, 0.5 mmol) and H_3L_1 (0.26 g, 1 mmol) was stirred into 15 mL of water. The pH was then adjusted to *ca.* 5 with 1 M NaOH. A solution of phen (0.21 g, 1 mmol) in ethanol (3 mL) was then added. The reaction mixture was heated on a water bath for 10 h at 70 °C, and then filtered. The yellow crystals were separated from the mother liquor by slow evaporation at room temperature after 4 weeks. *Anal.* Calc. for $C_{21}H_{23}MnN_3O_{10}S$: C, 44.69; H, 4.11; N, 7.44. Found: C, 44.51; H, 4.19; N, 7.50%. IR: 3413s, 1676s, 1411s, 1167m, 729m, 1345s, 851m.

2.3.2. $[Co_3(L_1)_2(bipy)_3(H_2O)_6]_n{\cdot}8nH_2O$ (***2***)

A mixture of $Co(OAc)_2{\cdot}4H_2O$ (0.13 g, 0.5 mmol) and H_3L_1 (0.13 g, 0.5 mmol) was stirred into 15 mL of water, and then refluxed for *ca.* 1 h. The pH was then adjusted to *ca.* 6 with 1 M NaOH. A solution of bipy (0.04 g, 0.25 mmol) in methanol (3 mL) was then



Scheme 1. Summary of the products obtained from the reactions of metal ions and H_3L_1.



Scheme 2. Summary of the products obtained from the reactions of metal ions and H_3L_2.

added. The reaction mixture was heated on a water bath for 10 h at 70 °C, and then filtered. The red crystals were separated from the mother liquor by slow evaporation at room temperature after 2 weeks. *Anal.* Calc. for $C_{48}H_{64}Co_3N_8O_{26}S_2$: C, 40.89; H, 4.58; N, 7.94. Found: C, 40.76; H, 4.67; N, 7.81%. IR: 3412s, 1684s, 1567s 1427s, 1127s, 1160m, 725m, 1396s, 864m.

2.3.3. $[Cu_4(L_1)_2(OH)_2(bipy)_4]_n \cdot 12nH_2O$ (**3**)

Complex **3** was synthesized using a procedure analogous to that of **2** except that $Cu(OAc)_2 \cdot H_2O$ was used instead of $Co(OAc)_2 \cdot 4H_2O$ and 1.2 mmol $Ca(OH)_2$ was added. Blue crystals were produced after 3 weeks. *Anal.* Calc. for $C_{29}H_{35}Cu_2N_5O_{13}S$: C, 42.44; H, 4.30; N, 8.53. Found: C, 42.56; H, 4.26; N, 8.68%. IR: 3415s, 1695s, 1427s, 1159m, 706m, 1332 s, 864m.

2.3.4. $[Na(H_2L_1)(H_2O)]_n$ (**4**)

An aqueous methanol solution of $Mn(OAc)_2 \cdot 4H_2O$ (0.12 g, 0.5 mmol), H_3L (0.13 g, 0.5 mmol) and bipy (0.04 g, 0.25 mmol) was stirred for 6 h at room temperature and then filtered. The pH was then adjusted *ca.* 6 with 1 M NaOH. The filtrate was allowed to stand for 1 week. The colorless crystals obtained were suitable for X-ray analysis. Yield: 26%. *Anal.* Calc. for $C_9H_{10}NNaO_7S$: C, 36.13; H, 4.37; N, 4.68. Found: C, 36.21; H, 3.52; N, 4.61%. IR: 3423s, 1714s, 1417s, 1109s, 1157m, 721m, 1362s, 814m.

2.3.5. $[Mn_2(HL_2)_2(dpe)_3(H_2O)_2]_n \cdot ndpe$ (**5**)

Complex **5** was synthesized in a procedure analogous to that of **4** except that dpe and H_3L_1 were used instead of bipy and H_3L_2. Yield: 35%. *Anal.* Calc. for $C_{66}H_{56}Mn_2N_{10}O_{14}S_2$: C, 57.13; H, 4.07; N, 10.10. Found: C, 57.01; H, 3.93; N, 9.98%. IR: 3423s, 1597s, 1420s, 1161m, 731m, 1389s, 857m.

2.4. Crystallographic data collection and structures determination

Single-crystals of **1–5** were put on a Bruker SMART APEX II CCD diffractometer equipped with a graphite monochromated Mo Kα radiation (λ = 0.71073 Å) at room temperature. The structures were solved by direct methods with SHELXS-97. A full-matrix least-squares refinement on F^2 was carried out using SHELXL-97. The crystallographic data and selected bond lengths and angles for **1–5** are listed in Table 1 and Table S1, Supplementary data. Hydrogen bonds parameters in **1–5** are listed in Table S2.

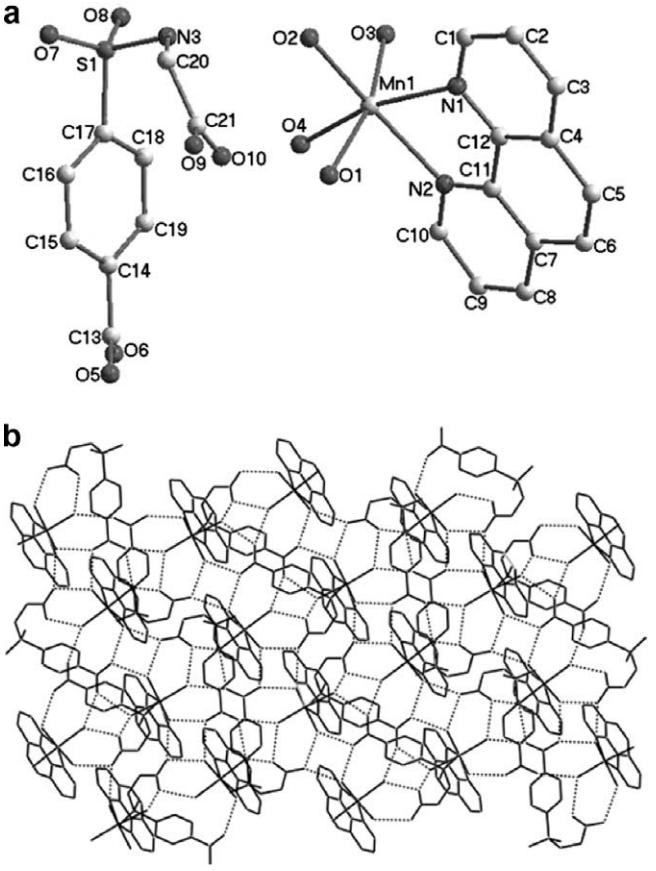


Fig. 1. (a) Molecular structure of **1**. (b) View of the 2D supramolecular system of **1** showing the cyclic intramolecular hydrogen bonding interactions.

3. Results and discussion

3.1. Description of the structures

3.1.1. $[Mn(phen)(H_2O)_4][HL_1]$ (**1**)

As shown in Fig. 1a, the unit of **1** contains a $[Mn(phen)(H_2O)_4]^{2+}$ cation and a HL_1^{2-} anion. The Mn(II) ion is six-coordinated

Table 1
Crystallographic data for complexes **1–5**.

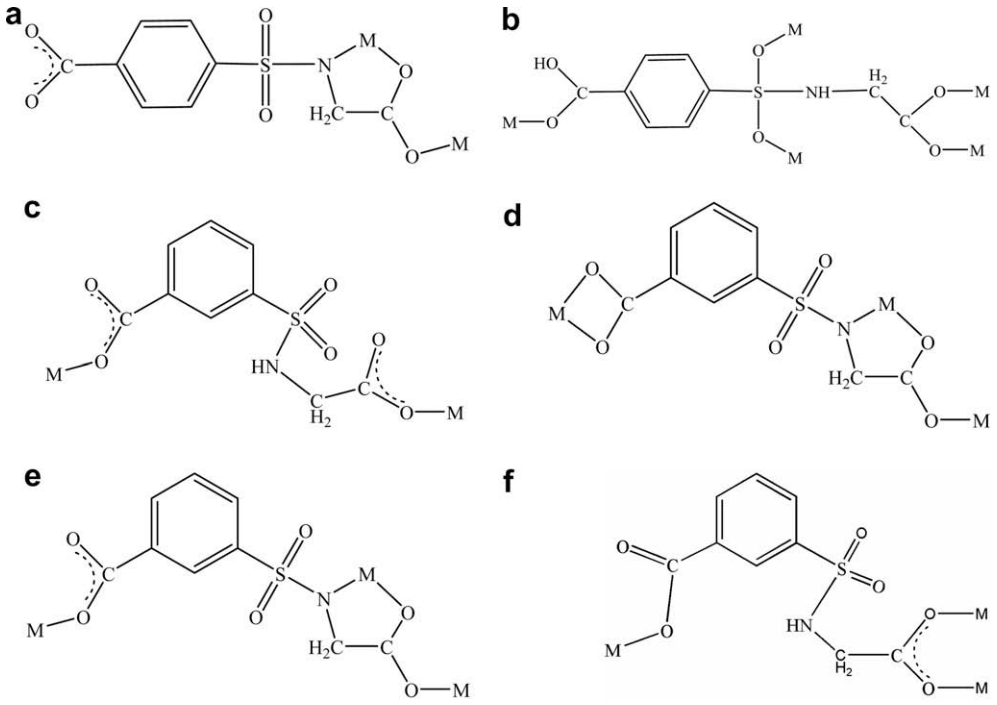
Compounds	1	2	3	4	5
Formula	$C_{21}H_{23}MnN_3O_{10}S$	$C_{48}H_{64}Co_3N_8O_{26}S_2$	$C_{29}H_{35}Cu_2N_5O_{13}S$	$C_9H_{10}N$ Na O_7 S	$C_{66}H_{56}Mn_2N_{10}O_{14}S_2$
M_r	564.42	1409.98	820.76	299.23	1387.21
T (K)	291(2)	291(2)	291(2)	291(2)	293(2)
Crystal system	monoclinic	monoclinic	monoclinic	triclinic	monoclinic
Space group	*C*2/*c*	*C*2/*c*	*P*2/*n*	$P\bar{1}$	*C*2/*c*
Unit cell dimensions					
a (Å)	23.228(5)	24.906(2)	16.948(3)	5.5061(11)	37.011(3)
b (Å)	13.909(3)	14.9985(12)	11.144(2)	7.6378(16)	8.5952(7)
c (Å)	15.045(3)	17.3262(14)	17.273(3)	14.332(3)	26.729(2)
α (°)				79.301(2)	
β (°)	100.134(2)	117.199(10)	99.373(3)	88.416(2)	129.231(10)
γ (°)				75.341(2)	
V (Å^3)	4784.7(17)	5756.5(8)	3218.9(11)	572.8(2)	6586.5(10)
Z	8	4	4	2	4
ρ (g cm^{-3})	1.567	1.627	1.694	1.735	1.399
F(0 0 0)	2328	2916	1688	308	2864
Goodness-of-fit	1.043	1.023	1.028	1.040	1.052
Crystal size (mm^3)	0.33 × 0.29 × 0.22	0.27 × 0.17 × 0.15	0.18 × 0.07 × 0.07	0.26 × 0.24 × 0.13	0.33 × 0.26 × 0.25
R_1, wR_2 [$I > 2\sigma(I)$]	0.0292, 0.0725	0.0330, 0.0795	0.0559, 0.1273	0.0326, 0.0856	0.0667, 0.1854
R_1, wR_2 (all data)	0.0361, 0.0773	0.0435, 0.0861	0.1029, 0.1521	0.0394, 0.0903	0.0857, 0.2039
Largest difference in peak and hole (e Å^{-3})	0.246, −0.304	0.523, −0.506	0.774, −0.907	0.289, −0.428	1.734, −0.464

(MnN_2O_4) and the coordination polyhedron is a distorted octahedral geometry. The bond lengths of Mn1–O are in the range of 2.1451(13)–2.2070(13) Å. The phen molecule chelating to the Mn(II) ion with Mn1–N1 and Mn1–N2 bond distances of 2.3010(16) and 2.2738(15) Å, respectively. It is notable that even though HL_1^{2-} does not coordinate to the metal atoms, it plays an important templation role in the crystallization process of compound **1**. Each HL_1^{2-} group is involved in significant intermolecular hydrogen bonding interactions with coordinated water molecules through its two carboxylato groups. Finally, these cation–anion species are organized into a two-dimensional supramolecular architecture (Fig. 1b). The bond lengths and angles of the hydrogen bonding are in the range of 2.658(2)–2.8088(19) Å and 157.8–175.2°, respectively. By comparison, the previously reported $[Mn_2(HL_2)_2(phen)_4]_n{\cdot}8nH_2O$ (**6**) which displays a binuclear unit and further forms the 2D supramolecular structure through unique π–π stacking and hydrogen bonding interactions [13]. This structural discrepancy may arise from the different coordination modes displayed by the HL_1^{2-} and HL_2^{2-} ligands. The HL_1^{2-} acts as a bridging ligand in **6** (Scheme 3c) while HL_2^{2-} does not coordinate at all in **1**.

3.1.2. $[Co_3(L_1)_2(bipy)_3(H_2O)_6]_n{\cdot}8nH_2O$ (**2**)

Complex **2** crystallizes in the space group *C*2/*c*. As illustrated in Fig. 2a, the asymmetric unit contains three Co(II) ions, two L_1^{3-} anions, three bipy, six coordinated water and eight lattice water molecules. The L_1^{3-} ligands use the nitrogen atom and one carboxylato oxygen atom from the glycinato group to chelate one Co atom, while the remaining carboxylato oxygen atom from the glycinato group coordinates to another Co atom. The two carboxylato oxygen atoms of the $C_6H_5COO^-$ group are free, as shown in Scheme 3a. There are two crystallographically independent cobalt atoms, one of which (Co2) lies on a center of symmetry, while the other (Co1) lies on a general position. The geometries around the Co(II) ions are both distorted octahedra, giving rise to a [4+2] type of configuration. Co1 is coordinated by two carboxylato oxygen atoms from two L_1^{3-} ligands and two water molecules in the equatorial plane and two nitrogen atoms of bipy at the axial sites. Co2 is surrounded by one carboxylato oxygen atom, one nitrogen atom from a L_1^{3-} ligand and two water molecules in the equatorial plane and two nitrogen atoms of bipy in the axial position. The Co–O_{L1} and Co–N_{bipy} bond lengths are in agreement with those reported for carboxylate and bipy-containing Co(II) complexes. One inner Co1 atom and two outer Co2 atoms are bridged by single carboxylato group in a *syn–anti* mode to form a linear trinuclear cluster with an adjacent Co···Co distance of 5.736 Å. The similar carboxylato bridged linear trinuclear Co(II) complexes $[Co_3(O_2CMe)_6(bpy)_2]$, $[Co_3(O_2CPh)_6(base)_2]$, $[Co_3(O_2C(C_6H_4NO_2)_6(base)_2)]$ and $[Co_3(O_2CMe)_8]$ have also been reported in the literatures [14–16]. The trinuclear clusters in **2** are connected to each other through bipy bridges to give rise to a new 1D triple infinite chain extending along the *b*-axis (Fig. 2b), which is different from those of the known 1D polymers with linear chain [17], zigzag chain [18], helical chain [19], ladder chain [20], double-stranded chain [21] and 1D double chain motifs [22]. To the best of our knowledge, this is the first example of a 1D triple chain complex containing amino acid-type and linear trinuclear metal arrangements.

In addition, there exist aromatic ring stacking interactions in the trinuclear unit between benzene rings of L_1^{3-} ligands and pyridine rings of bipy, with the centroid to centroid distance being 3.77 Å and a dihedral angle of 4.16°. These π–π stacking interactions encourage the L_1^{3-} ligands to alternately decorate two sides of the 1D triple chain. Extensive hydrogen bonds between coordinated water molecules and lattice water molecules are also formed, which reinforce the intra- and inter-chain linkages, and result in the formation of a 3D extended framework. In **2**, the two types of weak interactions, namely hydrogen bonds and aromatic ring stacking interactions, play an important role in the self-assembly and stabilization of the supramolecular structure. Notably, a related compound $[Co_3(L_2)_2(bipy)_2(H_2O)_6]_n{\cdot}2nCH_3OH{\cdot}8nH_2O$ (**7**) is obtained by using H_3L_2 under similar conditions, however, this structure shows a 1D alternating chain with $[CoL(H_2O)]_2^{2-}$ binuclear and $[Co(bipy)_2(H_2O)_4]^{2+}$ mononuclear units along the *a*-direction [12]. Furthermore, the coordination mode of L_2^{3-} in **7** (Scheme 3d) is different from that of L_1^{3-} in **2**.



Scheme 3.

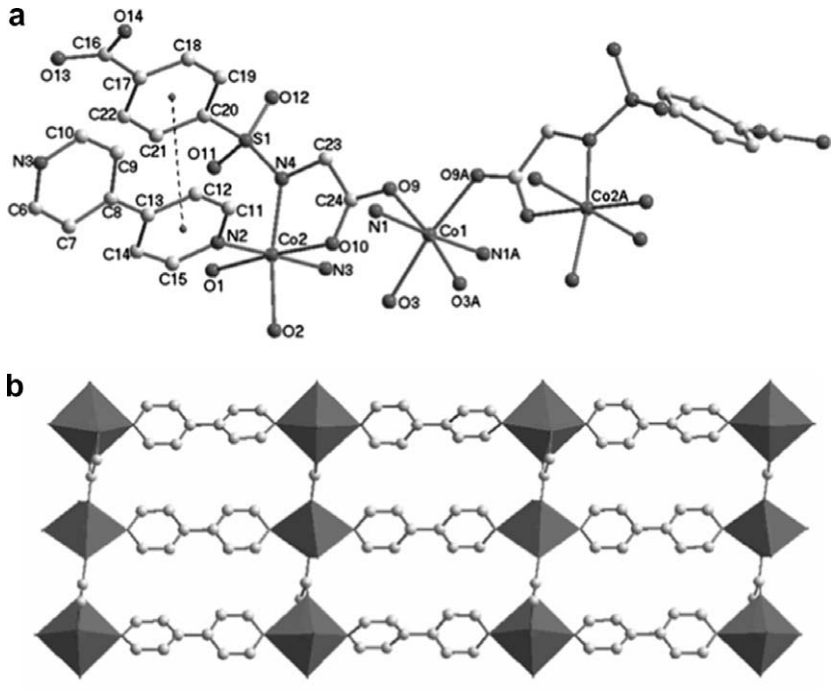


Fig. 2. (a) A perspective view of the discrete Co_3 cluster, hydrogen atoms and lattice water molecules are omitted for clarity. (b) The 1D triple polymeric chain architecture in **2**, the L_1^{3-} ligands are omitted for clarity.

*3.1.3. $[Cu_4(L_1)_2(OH)_2(bipy)_4]_n \cdot 12nH_2O$ (**3**)*

It can be seen from Fig. 3a that **3** contains tetranuclear Cu(II) units. Each tetranuclear unit is composed of four Cu(II) ions, two L_1^{3-} ligands, and two OH^- groups. There are also twelve intercalated water molecules per tetramer. Within the tetramer, there are three kinds of crystallographically independent Cu(II) ions with different coordination environments in the unit. Cu1 and Cu2 are bridged by one L_1^{3-} ligand and Cu2 and Cu3 are bridged by a hydroxyl group with distances of 5.374 and 3.369 Å between Cu1/Cu2 and Cu2/Cu3, respectively. The geometry of Cu1 can be considered as a distorted octahedral geometry with a $[N_4O_2]$ coordination sphere. The four equatorial coordination sites are occupied by N1, N2, N7 and N7A. Two oxygen atoms (O2, O2A) from two different glycinato groups occupy the axial coordination sites. The axial bond lengths (Cu1–O2, 2.354(4) Å) are considerably longer than the equatorial bond lengths (Cu(1)–N(7) = 2.013(4), Cu(1)–N(1) = 2.031(6), Cu(1)–N(2) = 2.079(6) Å) leading to the distortion from regular octahedral geometry. Cu2 is four-coordinated by one bridging carboxylato oxygen atom, two nitrogen atoms from different bipy ligands and one bridging hydroxyl group with a $[N_2O_2]$ coordination sphere. The Cu2–$O7_{OH}$ (1.917(4) Å) distance is shorter than that of Cu2–$O1_{L1}$ (1.969(4) Å), but the Cu2–N distances (Cu2–N3 = 2.045(4), Cu2–N4 = 2.042(4) Å) are the same within error. The Cu3 ion is coordinated by two bridged hydroxyl groups (O7, O7A) and two bipy nitrogen atoms (N5, N6) to form a square planar geometry. The Cu–O and Cu–N bond distances are 1.932(4), 2.039(6) and 2.050(6) Å, respectively.

The asymmetric unit in **3** forms uniform tetranuclear cycles ($Cu_1Cu_2Cu_3Cu_2$). The tetranuclear units are then connected together by the coordination bonds between oxygen atoms from the glycinato groups and Cu(II) ions to form a new $\cdots Cu_1Cu_2Cu_3Cu_2Cu_1Cu_2Cu_3Cu_2 \cdots$ 1D chain. These 1D chains are further interconnected by bipy ligands to generate a 2D wave-like rectangular grid layer along the *a*-axis, as shown in Fig. 3b and c.

It is interesting that the aromatic ring containing C(4) atom is almost parallel to the related pyridine ring containing N(1) atom in a tetranuclear unit. (the dihedral angle between two planes was *ca.* 12.13°) with a close intramolecular separation of *ca.* 3.83 Å. The stacking interactions encourage the L_1^{3-} ligands to lie alternatively above and below the 2D planes, and further extensive hydrogen bonds exist between coordinated water and lattice water molecules between the adjacent 2D layers, generating an overall 3D network. The structure of **3** is different from that of $[Ca(H_2O)_4Cu_2(bipy)_2(L_2)_2]_n \cdot 4nH_2O$ (**8**), which has a 2-fold 3D interpenetrating network where Cu atoms are joined by bipy to generate a 1D zigzag chain [12]. Every L_2^{3-} ligand adopts a tetradentate bridging mode to link one Ca and two Cu atoms in **8** (Scheme 3e) while L_1^{3-} acts as a tridentate bridging mode to link two Cu atoms forming a uniform chain in **3**.

*3.1.4. $[Na(H_2L_1)(H_2O)]_n$ (**4**)*

Single-crystal X-ray structural analysis shows that **4** is a bilayer structure in which two single layers are linked by H_2L_1 ligands to generate a 2D bilayer framework. Each sodium is primarily coordinated by two oxygen atoms [Na(1)–O(5), 2.4514(18); Na(1)–O(6), 2.4290(17) Å] from two different glycinato groups, two oxygen atoms [Na(1)–O(3), 2.4996(17); Na(1)–O(4), 2.4818(17) Å] from sulfonate groups, one oxygen atom from a carboxylato group of H_2L_1 [Na(1)–O(2), 2.4137(17) Å] and one oxygen atom from a water molecule [Na(1)–O(7), 2.491(2) Å] to furnish a distorted octahedral geometry (Fig. 4a). Unlike compounds **1–3**, oxygen atoms from both sulfonate groups and $C_6H_5COO^-$ groups coordinate to metal ions. The $H_2L_1^-$ ligand in **4** acts as a pentadentate ligand, as shown in Scheme 3b, where two carboxylato oxygen atoms from the glycinato group adopt a *syn–anti* bridging mode, while the other two oxygen atoms from the sulfonate group exhibit a *syn–syn* bridging mode, and the carboxylate from the $C_6H_5COO^-$ group adopts a monodentate coordination mode. Thus, each $H_2L_1^-$ ligand links five sodium atoms and each sodium center interacts with five $H_2L_1^-$ ligands.

On the basis of these connection modes, pairs of Na(1) centers are doubly bridged by oxygen atoms from glycinato and sulfonate groups to form an eight-membered ring with a Na···Na separation of 5.506 Å. These dinuclear units are arranged uniformly to form a

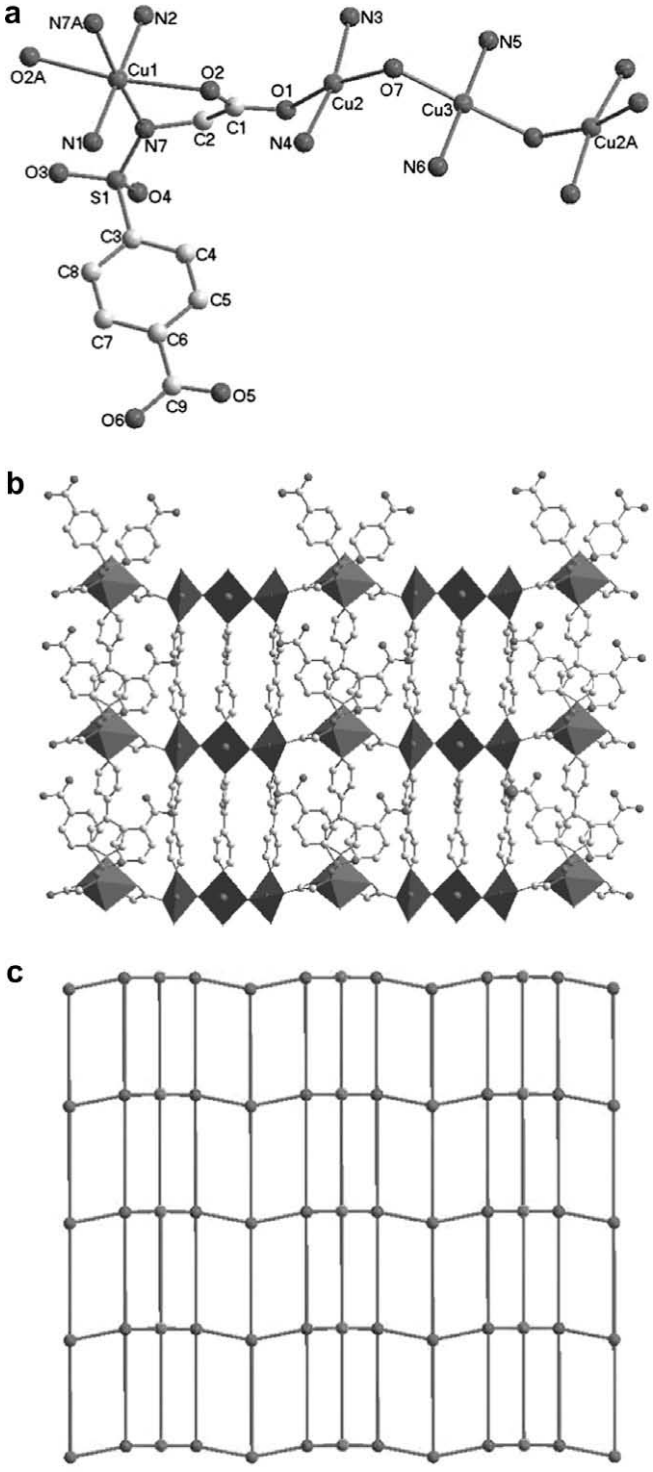


Fig. 3. (a) The coordination environment of a tetranuclear Cu(II) unit in **3**, hydrogen atoms, lattice water molecules and coordinated bipy are omitted for clarity. (b) 2D layer of **3** constructed from the 1D chain. (c) Schematic representation of a 2D layer structure.

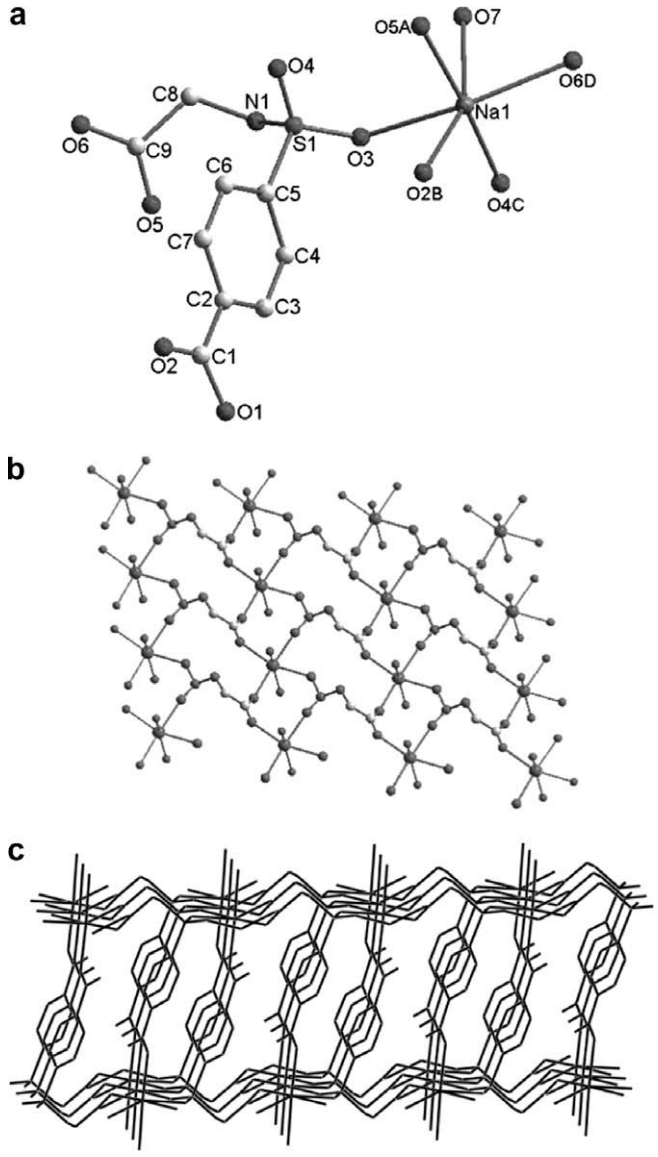


Fig. 4. (a) The local coordination environment of Na ion with atomic numbering scheme in **4**. (b) Perspective view of the single Na–H_3L sheet; (c) Side view along the *a*-axis showing bilayer motif in **4**.

1D chain. These chains are linked by $-SO_2NHCH_2COO-$ groups to build a 2D layer (Fig. 4b). Interestingly, the 2D layers are linked by $H_2L_1^-$ to generate a new 2D bilayer framework with a distance of 10.899 Å (based on Na...Na) between the two single layers (Fig 4c). The adjacent 2D bilayers are further linked to each other by O–H···O hydrogen bonds [O(7)–H(2W)···O(7A), 2.845(6) Å; O(7)–H(1W)···O(6), 2.992(3); O(1)–H(1)···O(5), 2.569(2) Å] to complete the final 3D supramolecular architecture. This is, to our knowledge, the first example of bilayer architecture assembled by alkali metal with amino acid derivatives.

3.1.5. $[Mn_2(HL_2)_2(dpe)_3(H_2O)_2]_n \cdot ndpe$ (5)

The fundamental building unit of **5** is composed of two Mn(II) cations, two monodentate coordinated dpe, one μ_2-dpe, two HL_2^{2-} anions, two coordinated water molecules and one guest dpe molecule. The coordinated and uncoordinated dpe molecules are disordered over two sites. For clarity, only one of these sites is shown in Fig. 5. The dpe molecules exist in three types of coordination modes (monodentate, bis-monodentate and uncoordinate) in **5**, which is unusual in the construction of polycarboxylate and dpe polymers. Each Mn center exhibits a distorted octahedral geometry with two pyridyl nitrogen atoms from two dpe ligands in the axial positions, and four oxygen atoms in the equatorial plane composed of three oxygen atoms from three HL_2^{2-} ligands and one from coordinated water molecule. The Mn–O bond distances fall in the range of 2.120(3)–2.189(2) Å, and the Mn–N bond distances are 2.296(3) and 2.304(3) Å, respec-

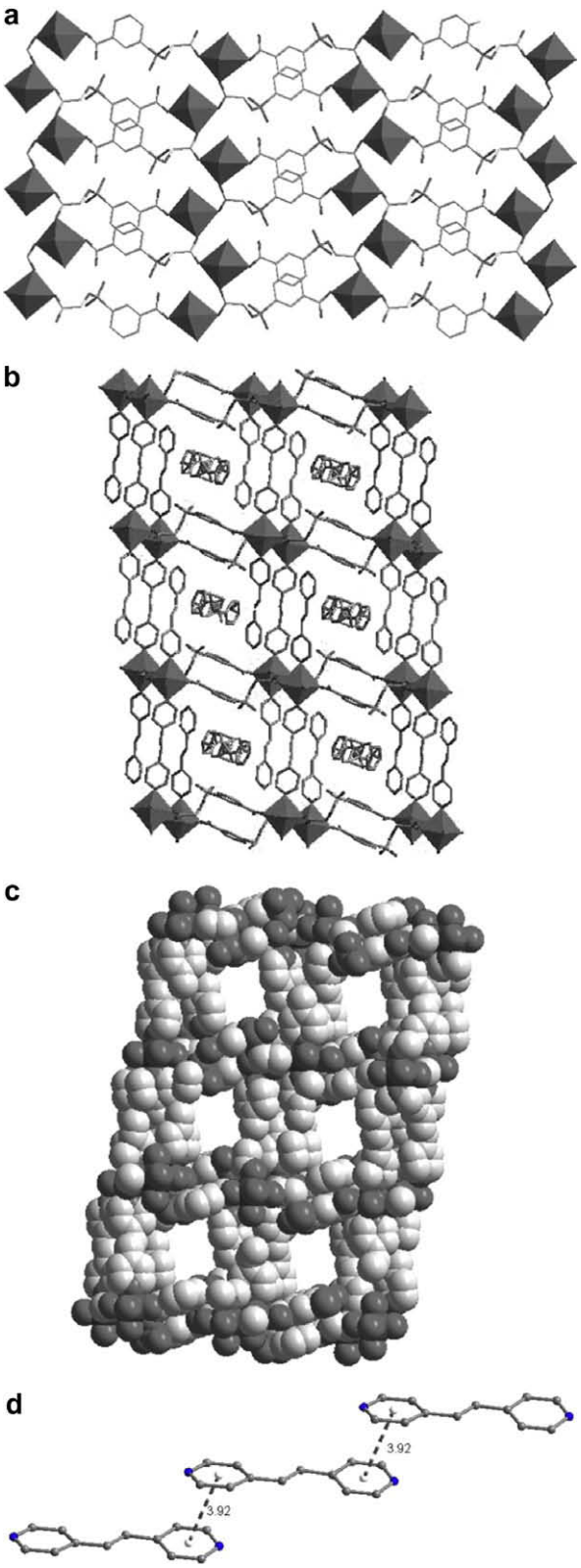


Fig. 5. (a) 2D sheets bridged by HL_2^{2-} molecules. (b) View of the channels formed by the 3D network. (c) Space-filling model of **5** as viewed down the *b*-axis (disordered guest dpe molecules are omitted for clarity). (d) A view of the 1D supramolecular dpe chain constructed by the intermolecular π–π aromatic stacking interactions.

tively. The HL_2^{2-} ligand displays both monodentate and bis-monodentate bridging coordination modes in the assemblies, as shown in Scheme 3f. In addition, two HL_2^{2-} ligands bridge two Mn(II) ions to form a 22-membered ring and another four Mn(II) ions and four HL_2^{2-} ligands form a 30-membered ring. Therefore, a $[Mn(HL_2)(H_2O)]_\infty$ layer is formed through an alternating arrangement of the 22- and 30-membered rings (Fig. 5a). The resulting 2D sheets are pillared by dpe to generate an overall 3D framework in which free disordered dpe are encapsulated as guest molecules (Fig. 5b and c). The adjacent dpe molecules in the channels stack along the *b*-axis through π–π stacking interactions through the pyridine rings to form a 1D supramolecular chain (Fig. 5d). Each Mn center binds two *trans*-located dpe molecules. One is a terminal dpe which lies in the interlayer region and the other is a bridging dpe which lies alternatively between the 2D planes to link the 2D layers into a 3D framework.

3.2. Structural diversity of *1*–*8*

It is noteworthy that a variety of framework structures can be achieved on the basis of the choice of the *N*-[(carboxyphenyl)-sulfonyl]glycine isomers. The slight positional differences of the carboxylato groups between these two isomers may lead to significant geometric diversification of the resulting coordination polymers. We have successfully isolated and characterized eight coordination polymers containing Mn, Co, Cu, Na and Ca centers varying from 0D to 3D. These results illustrate the isomeric effect of the bridging ligands on coordination polymers. In **1–8**, these isomers exhibit several coordination patterns as illustrated in Scheme 3, in which the glycinato and carboxylato groups can adopt the unidentate, chelating and bridging modes. Thus, the variation of the *N*-[(carboxyphenyl)-sulfonyl]glycine isomers used in the assembled process has a significant role in the structural diversity shown by **1–8**. Secondly, the N-donor auxiliary ligands are good connectors in mediating and constructing MOFs with specific structure. In this study, phen, bipy and dpe with different conformations and flexibility were used to investigate their influence on the structure of the complexes. The steric hindrance of the phen molecule may contribute to the formation of the discrete units of complexes **1** and **6**, while the introduction of the bipy and dpe leads to the polymeric structures of complexes **2**, **3**, **5**, **7** and **8**.

On the other hand, the choice of metal centers may also have a significant effect on the binding fashions of the *N*-[(carboxyphenyl)-sulfonyl]glycine isomers as well as the resultant extended networks of **1–8**. For *N*-[(4-carboxyphenyl)-sulfonyl]glycine/bipy systems containing **2** and **3**, two coordination modes of H_3L_1 are observed, and interestingly, two different types of 1D triple chain or 2D layer frameworks are generated depending on the metal centers Co or Cu. The structures of **7** and **8** are also metal-controlled, and notably, Co^{2+}-based complex **7** shows an alternating chain while a unique 3D interpenetrating architecture is formed in the case of mixed Ca^{2+} and Cu^{2+} in **8**. This is consistent with the fact that the radius of Cu^{2+} and Ca^{2+} ions are larger than that of Co^{2+} ion. This result indicates that the choice of metal ion has a significant effect on these polymeric structures as well as the binding modes of the ligands.

3.3. Thermal stability

Thermogravimetric experiments were conducted to study the thermal stability of **5**, which is an important parameter for porous metal–organic framework materials (Fig. S1, Supplementary data). The TGA curve for **5** suggests that the first weight loss of 16.37% in the region of 30–275 °C corresponds to the loss of two coordinated water and one guest dpe per formula unit (calculated 15.59%), which is also in agreement with the results of elemental analysis. The residual framework starts to decompose beyond 300 °C with a series of complicated weight losses and does not stop until heating ends at 550 °C. In principle, TGA measurements alone cannot

be used to determine the stability of an open structure since it may collapse without a notable change in the weight. As shown in Fig. 6, the peak positions of the simulated and experimental XRPD patterns for **5** are in agreement with each other, demonstrating the good phase purity of **5**. XPRD measurements at different temperatures (Fig. 6) show that after heating at 275 °C, the spectra are similar to the original one, suggesting its crystalline nature is still maintained after removing the guest dpe molecules.

3.4. Magnetic properties

The magnetic susceptibilities, χ_M, of **5** were measured in the 2–300 K temperature range, and shown as $\chi_M T$ and χ_M versus T plots in Fig. 7. The experimental $\chi_M T$ value of **5** at room temperature is 4.18 cm^3 K mol^{-1} per Mn(II) ion, close to the spin value expected for an uncoupled high-spin Mn(II) ion (4.38 cm^3 K mol^{-1}). The temperature dependence of the reciprocal susceptibilities ($1/\chi_M$) of **5** obeys the Curie–Weiss law above 5 K with $\theta = -2.1$ K, $C = 4.59$ cm^3·K/mol, $R = 4.9 \times 10^{-5}$, which indicates that antiferromagnetic interactions are operative in **5**. According to the structure of **5**, it could be presumed that the main magnetic interactions between the metal centers might happen between two carboxylate bridged Mn(II) ions, whereas the superexchange interactions between Mn(II) ions through the HL_2^{2-} and dpe bridges can be ignored because of the long length of the HL_2^{2-} and dpe ligands. The magnetic susceptibility data were fitted assuming that the carboxylate bridges Mn(II) ions to form a uniform chain with an exchange constant J, and then dpe and HL_2^{2-} connect the chains to form a 3D structure with an exchange constant zJ'. The susceptibility data were thus approximately analyzed by a chain mode of spin $S = 5/2$ [23,24]. The least-squares analysis of magnetic susceptibilities data led to $J = -0.18$ cm^{-1}, $g = 2.04$, $zJ' = -0.04$ cm^{-1} and $R = 1.65 \times 10^{-4}$, The J value indicates a weakly antiferromagnetic interaction between the nearest Mn(II) ions bridged by H_3L_1.

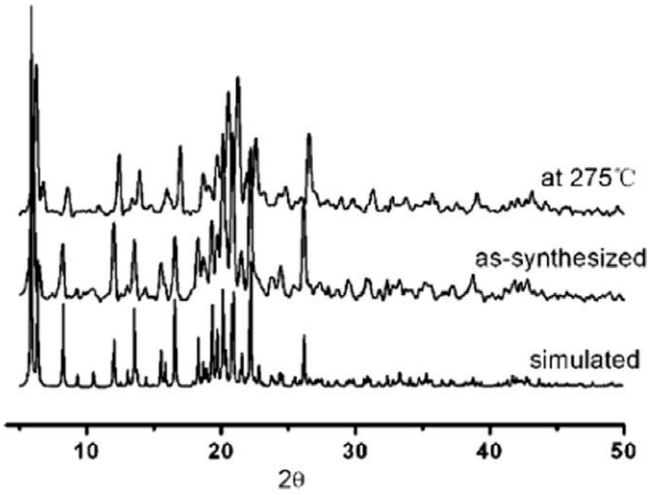


Fig. 6. Comparison of XRPD patterns of the simulated pattern from the single-crystal structure determination, the as-synthesized and the product after heating at 275 °C for **5**.

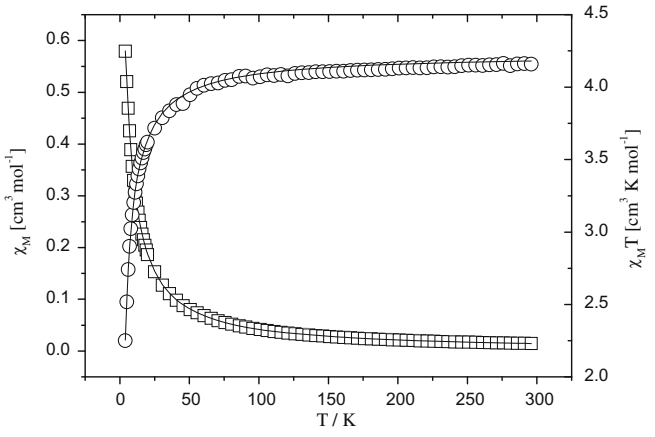


Fig. 7. Temperature dependence of $\chi_M T$ and χ_M for **5**. The solid line represents the theoretical values based on Eq. (1) described in the text.

4. Conclusions

In summary, we have successfully synthesized eight new complexes by using two versatile ligands, *N*-[(4-carboxyphenyl)-sulfonyl]glycine and its isomer *N*-[(3-carboxyphenyl)-sulfonyl] glycine. Their structures range from a 0D cation–anion species to a 3D network with different structural motifs and this result demonstrates that ligand isomers and metal centers have a tuning effect upon the motifs of the resultant structures. Subsequent work will be focused on the construction of new polymers by using these two isomers or other related amino acid derivatives as basic building units.

Acknowledgements

This work was supported by the Natural Science Foundation of China (Nos. 20471046 and 20771054) and Henan tackle key problem of science and technology (Nos. 072102270030 and 072102270034) and the Foundation of Education Committee of Henan province (Nos. 2006150017 and 2008A150018).

Appendix A. Supplementary data

CCDC 659934–659937, 675251 contain the supplementary crystallographic data for **1**–**5**. These data can be obtained free of charge via http://www.ccdc.cam.ac.uk/conts/retrieving.html, or from the Cambridge Crystallographic Data Centre, 12 Union Road, Cambridge CB2 1EZ, UK; fax: +44 1223 336 033; or e-mail: deposit@ccdc.cam.ac.uk.

Supplementary data associated with this article can be found, in the online version, at doi:10.1016/j.poly.2009.04.044.

References

[1] (a) Y. Su, S.Q. Zang, Y.Z. Li, H.Z. Zhu, Q.J. Meng, Cryst. Growth Des. 7 (2007) 1277;
(b) S. Leninger, B. Olenyuk, P.J. Stang, Chem. Rev. 100 (2000) 853;
(c) O.M. Yaghi, M. O'Keeffe, N.W. Ockwing, H.K. Chae, M. Eddaoudi, J. Kim, Nature 423 (2003) 705;
(d) S. Horike, R. Matsuda, D. Tanaka, M. Mizuno, K. Endo, S. Kitagawa, J. Am. Chem. Soc. 128 (2006) 4222;
(e) M. Dinca, A.F. Yu, J.R. Long, J. Am. Chem. Soc. 128 (2006) 8904;
(f) M. Du, Z.H. Zhang, X.G. Wang, L.F. Tang, X.J. Zhao, CrystEngCommun. 10 (2008) 1855;
(g) X.D. Chen, H.F. Wu, X.H. Zhao, X.J. Zhao, M. Du, Cryst. Growth Des. 7 (2007) 124.
[2] (a) B.F. Abrahams, S.R. Batten, H. Hamit, B.F. Hoskins, R. Robson, Angew. Chem., Int. Ed. Engl. 35 (1996) 1690;
(b) B. Zhao, H.L. Gao, X.Y. Chen, P. Cheng, W. Shi, D.Z. Liao, S.P. Yan, Z.H. Jiang, Chem. Eur. J. 12 (2006) 149;
(c) M. Tominaga, S. Tashiro, M. Aoyagi, M. Fujita, Chem. Commun. (2002) 2038;
(d) R.J. Hill, D.L. Long, N.R. Champness, P. Hubberstey, M. Schroder, Acc. Chem. Res. 38 (2005) 335;
(f) X.M. Gao, D.S. Li, J.J. Wang, F. Fu, Y.P. Wu, H.M. Hu, J.W. Wang, CrystEngCommun. 10 (2008) 479.
[3] (a) J. Yang, Q. Yue, G.D. Li, J.J. Cao, G.H. Li, J.S. Chen, Inorg. Chem. 45 (2006) 2857;
(b) N.L. Rosi, J. Eckert, M. Eddaoudi, D.T. Vodak, J. Kim, M. O'Keeffe, O.M. Yaghi,

Science 300 (2003) 1127;
(c) S. Kitagawa, R. Kitaura, S.I. Noro, Angew. Chem., Int. Ed. Engl. 43 (2004) 2334;
(d) S.R. Batten, K.S. Murray, Coord. Chem. Rev. 246 (2003) 103;
(e) X.D. Chen, H.F. Wu, M. Du, Chem. Commun (2008) 1296;
(f) M. Du, X.J. Jiang, X.J. Zhao, Chem. Commun. (2005) 5521;
(g) M. Du, C.P. Li, X.J. Zhao, Cryst. Growth Des. 6 (2006) 335.
[4] (a) S.C. Zimmerman, M.S. Wendland, N.A. Rakow, I. Zharov, K.S. Suslick, Nature 418 (2002) 399;
(b) L. Carlucci, G. Ciani, D.M. Proserpio, Coord. Chem. Rev. 246 (2003) 247;
(c) M.L. Tong, S. Kitagawa, H.C. Chang, M. Ohba, Chem. Commun. (2004) 418;
(d) R.Q. Zou, H. Sakurai, Q. Xu, Angew. Chem., Int. Ed. Engl. 45 (2006) 2542.
[5] (a) S.A. Barnett, N.R. Chempness, Coord. Chem. Rev. 246 (2003) 145;
(b) S. Leininger, B. Olenyuk, P.J. Stang, Chem. Rev. 100 (2000) 853;
(c) B.J. Holliday, C.A. Mirkin, Angew. Chem., Int. Ed. Engl. 40 (2001) 2023;
(d) G.F. Swiegers, T.J. Malefetse, Chem. Rev. 100 (2000) 3483;
(e) M. Eddaoudi, D.B. Moler, H. Li, B. Chen, T.M. Reineke, M. O'Keeffe, O.M. Yaghi, Acc. Chem. Res. 34 (2001) 319;
(f) H.W. Roesky, M. Andruh, Coord. Chem. Rev. 236 (2003) 91;
(g) S.R. Batten, J. Solid State Chem. 178 (2005) 2475.
[6] (a) B.H. Ye, B.B. Ding, Y.Q. Weng, X.M. Chen, Cryst. Growth Des. 5 (2005) 801;
(b) M. Du, X.J. Jiang, X.J. Zhao, Inorg. Chem. 46 (2007) 3984.
[7] (a) H.X. Zhang, B.S. Kang, A.W. Xu, Z.N. Chen, Z.Y. Zhou, A.S.C. Chan, K.B. Yu, C. Ren, J. Chem. Soc., Dalton Trans. (2001) 2559;
(b) C.B. Ma, C.N. Chen, Q.T. Liu, D.Z. Liao, L.C. Li, L.C. Sun, New J. Chem. 27 (2003) 890.
[8] (a) B.Q. Ma, D.S. Zhang, S. Gao, T.Z. Jin, C.H. Yan, G.X. Xu, Angew. Chem., Int. Ed. Engl. 39 (2000) 3644;
(b) E.V. Anokhina, A.J. Jacobson, J. Am. Chem. Soc. 126 (2004) 3044;
(c) W.H. Bi, N. Mercier, N. Louvain, M. Latroche, Eur. J. Inorg. Chem. (2006) 4225;
(d) B.Y. Lou, F.L. Jiang, B.L. Wu, D.Q. Yuan, M.C. Hong, Cryst. Growth Des. 6 (2006) 989.
[9] (a) N. Ohata, H. Masuda, O. Yamauchi, Angew. Chem., Int. Ed. Engl. 35 (1996) 531;
(b) H. Masuda, A. Odani, T. Yamazaki, T. Yajima, O. Yamauchi, Inorg. Chem. 32 (1993) 1111.
[10] (a) A.H. Abu-Nawwas, J. Cano, P. Christian, T. Mallah, G. Rajaraman, S.J. Teat, R.E.P. Winpenny, Y. Yukawa, Chem. Commun. (2004) 314;
(b) H. Strasdeit, I. Busching, S. Behrends, W. Saak, W. Barklage, Chem. Eur. J. 7 (2001) 1133;
(c) J.J. Zhang, T.L. Sheng, S.Q. Xia, G. Leibeling, F. Meyer, S.M. Hu, R.B. Fu, C.X. Xiang, X.T. Wu, Inorg. Chem. 43 (2004) 5472;
(d) J.J. Zhang, S.M. Hu, L.M. Zheng, X.T. Wu, Z.Y. Fu, J.C. Dai, W.X. Du, H.H. Zhang, R.Q. Sun, Chem. Eur. J. 8 (2002) 367.
[11] (a) J.J. Zhang, T.L. Sheng, S.M. Hu, S.Q. Xia, G. Leibeling, F. Meyer, Z.Y. Fu, L. Chen, R.B. Fu, X.T. Wu, Chem. Eur. J. 10 (2004) 3963;
(b) H.Y. An, E.B. Wang, D.R. Xiao, Y.G. Li, Z.M. Su, L. Xu, Angew. Chem., Int. Ed. Engl. 45 (2006) 904.
[12] L.F. Ma, L.Y. Wang, X.K. Huo, Y.Y. Wang, Y.T. Fan, J.G. Wang, S.H. Chen, Cryst. Growth Des. 8 (2008) 620.
[13] L.F. Ma, Y.Y. Wang, L.Y. Wang, J.Q. Liu, Y.P. Wu, J.G. Wang, Q.Z. Shi, S.M. Peng, Eur. J. Inorg. Chem. (2008) 693.
[14] B.H. Ye, X.M. Chen, F. Xue, L.N. Ji, T.C.W. Mak, Inorg. Chim. Acta 299 (2000) 1.
[15] J. Catterick, P. Thronton, J. Chem. Soc., Dalton Trans. (1976) 1634.
[16] R.A. Reynolds III, W.R. Dunham, D. Coucouvanis, Inorg. Chem. 37 (1998) 1232.
[17] (a) H.J. Choi, M.P. Suh, Inorg. Chem. 38 (1999) 6309;
(b) M.C. Hong, Y.J. Zhao, W.P. Su, R. Cao, M. Fujita, Z.Y. Zhou, A.S.C. Chan, Angew. Chem., Int. Ed. Engl. 39 (2000) 2468;
(c) A.Y. Robin, K.M. Fromm, H. Goesmann, G. Bernardinelli, CrystEngCommun. 5 (2003) 405.
[18] (a) J.L. Manson, T. Lancaster, L.C. Chapon, S.J. Blundell, J.A. Schlueter, M.L. Brooks, F.L. Pratt, C.L. Nygren, J.S. Qualls, Inorg. Chem. 44 (2005) 989;
(b) A.J. Blake, N.R. Champness, P. Hubberstey, W.S. Li, M.A. Withersby, M. Schroder, Coord. Chem. Rev. 183 (1999) 117;
(c) M.B. Zaman, M.D. Smith, D.M. Ciurtin, H.C. Zur Loye, Inorg. Chem. 41 (2002) 4895.
[19] (a) K. Biradlha, C. Seward, M.J. Zaworotko, Angew. Chem., Int. Ed. Engl. 38 (1999) 492;
(b) T. Ezuhara, K. Endo, Y. Aoyama, J. Am. Chem. Soc. 121 (1999) 3279;
(c) K.M. Fromm, J.L. Sagué Doimeadios, A.Y. Robin, Chem. Commun. (2005) 4548;
(d) W.W. Ellis, M. Schmitz, A.A. Arif, P.J. Stang, Inorg. Chem. 39 (2000) 2547;
(e) M.C. Hong, W.P. Su, R. Cao, M. Fujita, J.X. Lu, Chem. Eur. J. 6 (2000) 427.
[20] (a) B.M. Wells, C.P. Landee, M.M. Turnbull, F.F. Awwadi, B. Twamley, J. Mol. Catal. A 228 (2005) 117;
(b) L. Carlucci, G. Ciani, D.M. Proserpio, Chem. Commun. (1999) 449;
(c) P. Losier, M.J. Zaworotko, Angew. Chem., Int. Ed. Engl. 35 (1996) 2779.
[21] (a) J.H. Zhou, Y.F. Peng, Y.P. Zhang, B.L. Li, Y. Zhang, Inorg. Chem. Commun. 7 (2004) 1181;
(b) R. Bronisz, Inorg. Chim. Acta 340 (2002) 215.
[22] L.F. Ma, Y.F. Wang, L.Y. Wang, J.G. Wang, X. Feng, Z. Anorg. Allg. Chem. 632 (2006) 675.
[23] W. Hiller, J. Strähle, A. Datz, M. Hanack, W.E. Hatfield, L.W. Haar, P. Gütlich, J. Am. Chem. Soc. 106 (1984) 329.
[24] C.J. O' Connor, Prog. Inorg. Chem. 29 (1982) 203.

Polyhedron 28 (2009) 2503–2509

Contents lists available at ScienceDirect

Polyhedron

journal homepage: www.elsevier.com/locate/poly

Intramolecular amide → imine reduction in higher valent rhenium complexes stabilized by arylimido coligand: Rate studies and effect of reductants

Jaydip Gangopadhyay [a,*], Suparna Banerjee [b], Jiu-Tong Chen [c], Can-Zhong Lu [c]

[a] Department of Chemistry, St. Paul's C.M. College, University of Calcutta, 33/1 Raja Rammohan Roy Sarani, Kolkata 700009, India
[b] Department of Chemistry, Uluberia College, University of Calcutta, Howrah 711315, India
[c] The State Key Laboratory of Structural Chemistry, Fujian Institute of Research on the Structure of Matter, The Chinese Academy of Sciences, Suzhou, Fujian 350002, PR China

ARTICLE INFO

Article history:
Received 12 February 2009
Accepted 30 April 2009
Available online 8 May 2009

Keywords:
Amide complex
Outward OAT
Reduction
Imine derivative
Kinetics

ABSTRACT

The present work deals with the imidorhenium(V) complexes of type $[ReCl_3(NC_6H_4Y\text{-}p)(L)]$, with Y = OCH_3(**1d**), CH_3(**1c**), H(**1b**), Cl(**1a**) where L is the pyridylimine Schiff base ligand obtained from facile condensation of pyridine-2-carboxaldehyde and *p*-phenylenediamine. Structural authentication of one representative (**1d**) reveals meridional disposition of three Cl atoms around the metal center in a distorted octahedral $ReCl_3N_3$ coordination environment. Re–$N^{pyridine}$ bond lying trans to Re≡NC_6H_4Y-*p* motif is lengthened by ~0.2 Å compared to Re–N^{imine} bond and is attributed to *trans* influence of imide nitrogen. The complexes, **1** are reactive towards dilute aqueous nitric acid furnishing amide bound hexavalent rhenium complexes, **2**. Six lines EPR spectra have been recorded for **2** in solution phase at ambient condition ($g_{iso} \sim 1.945$, $A_{av} \sim 493$ G) and magnetic susceptibility measurement indicates strong orbital coupling consistent with one electron paramagnetic nature (~1.45 μ_B). Re^{VI}/Re^{V} responses for **1** appear at higher potential (~0.95 V) that those observed for **2** (~0.12 V). Type **2** complexes are reduced (low Re^{VI}/Re^{V} reduction potential, +0.15 V) by $N_2H_5^+$ and NH_3OH^+ species under mild condition to regenerate **1**. The reduction with $N_2H_5^+$ is nearly five times faster than NH_3OH^+. Rate study suggests an associative pathway ($\Delta H^{\neq}$ = 11.61 kcal mol^{-1}, $\Delta S^{\neq}$ = −31.22 eu using $N_2H_5^+$ and $\Delta H^{\neq}$ = 10.74 kcal mol^{-1}, $\Delta S^{\neq}$ = −37.30 eu using NH_3OH^+) for amide → imine transformation. No such analogous amide → imine conversion has yet been achieved in metal free environment, accentuating the exclusive electronic role of variable metal valence. Further, the oxo complex, **6** does not exhibit intramolecular ligand oxidation suggesting decisive electronic role of the coligands (oxo/arylimido) in stabilizing higher metal valence.

© 2009 Elsevier Ltd. All rights reserved.

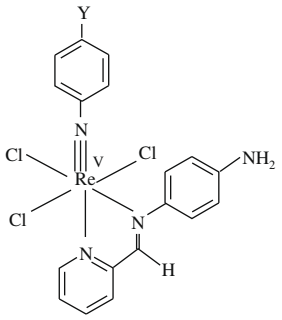
1. Introduction

Higher valent rhenium complexes have spurred interest owing to active participation as catalysts in various molecular transformations featuring key changes like functionality conversion [1], derivatization [2], cyclisation [3,4], oxygen atom transfer [5–7] in the products. Most of the oxygen atom transfer reactions between organic molecules characterizing the red-ox functional pairs like sulphide–sulphoxide; sulphoxide–sulphone; phosphine–phosphine oxide do not proceed at reasonable rates at normal temperature even recognized as thermodynamically favourable. To overcome the kinetic sluggishness, middle and late transition metals multiply bonded to heteroatom coligands have long been successfully employed [8–10] for oxidation of small molecules. Metal bound oxo → dioxo, phosphine → phosphine oxide transformations and metal catalysed sulphide → sulphoxide; pyridine oxide → pyridine; phosphine → phosphine oxide conversions mediated through oxygen atom transfer phenomenon have been authenticated in rhenium chemistry [11–21]. Moreover, abiological molecular oxotransferase incorporating $Re^{V}O$ motif has been established as useful catalyst to successfully accomplish reductions of stable inorganic moieties like ClO_4^-, NO_3^-, NO [22].

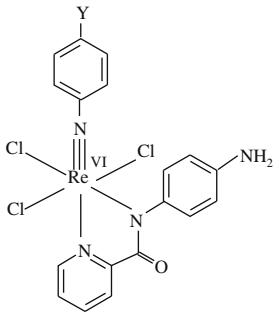
Structure-reactivity correlation reveals the prevalence of multiply bonded oxo (O^{2-}) coligand to the higher valent metal in the promising catalysts. Our programme focuses on the study of redox related organic functionality pair conversion assisted by imido (NR^{2-}) bonded higher valent rhenium complexes. Herein, we report ligand centered oxygen atom abstraction followed by reduction providing access to route of

* Corresponding author.
E-mail address: gjaydip@rediffmail.com (J. Gangopadhyay).

0277-5387/$ - see front matter © 2009 Elsevier Ltd. All rights reserved.
doi:10.1016/j.poly.2009.04.040



1



2

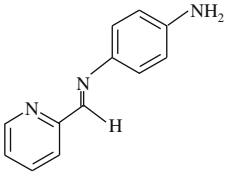
facile amide → imine conversion in secondary metal coordination sphere. The amide chelated imidorhenium(VI) complexes (**2**) were prepared by oxidation of imine bound imidorhenium(V) complexes (**1**) with dilute HNO_3. Complexes of type **2**, on reaction with either $N_2H_5^+$ or NH_3OH^+ undergoes outward oxygen atom transfer and reduced to the imine complex **1**. This observation is unprecedented in the sense of mobilizing a metal bound amide function (most inactive carboxylic acid derivative) to participate in electronic and geometrical changes resulting in the generation of reduced imine form.

The syntheses, representative structure determination of **1**, metal redox and spectroscopic properties of complexes are reported. The kinetic behaviour of outward oxygen atom transfer has been studied and a viable mechanism consistent with the experimental findings and kinetics is proposed.

2. Results and discussion

2.1. Synthesis

Facile condensation of pyridine-2-carboxaldehyde and *p*-phenylenediamine in a 1:1 molar ratio respectively, afforded a neutral condensate, N-p-aminophenyl-2-pyridinecarboxaldimine **L**, which has been employed as a bidentate ligand in the present



L, $C_{12}H_{11}N_3$

work. The violet coloured complexes **1**, $[Re(NC_6H_4Y\text{-}p)Cl_3L]$ (Y = Cl(**1a**), H(**1b**), CH_3(**1c**), OCH_3(**1d**)) are formed in good yields upon reacting $[Re(NC_6H_4Y\text{-}p)Cl_3(PPh_3)_2]$ with L in 1:1.5 molar ratio in benzene under reflux followed by chromatographic work up of the reaction mixture. In the product, two *trans* oriented PPh_3 groups are being substituted by the ligand L, Eq. (1).

$$[Re^{V}(NC_6H_4Y)Cl_3(PPh_3)_2] + L \rightarrow [Re^{V}(NC_6H_4Y)Cl_3(L)] + 2PPh_3 \quad (1)$$

1 reacts smoothly with aqueous nitric acid [23] in acetonitrile solution at room temperature under stirring condition resulting yellow picolinamide complexe (**2**). The feasibility of the reverse reaction **2** → **1** has been scrutinized with different reducing agents and successfully carried out using nitrogenous reagents like hydrazine sulphate (Eq. (2)) and hydroxylamine hydrochloride (Eq. (3)) at mild condition in acetonitrile medium.

$$[Re^{VI}(NC_6H_4Y)Cl_3(C_{12}H_{10}N_3O)] + 3N_2H_5^+ \rightarrow [Re^{V}(NC_6H_4Y)Cl_3(C_{12}H_{11}N_3)] + \frac{3}{2}N_2 + 3NH_4^+ + H_2O \quad (2)$$

$$4[Re^{VI}(NC_6H_4Y)Cl_3(C_{12}H_{10}N_3O)] + 6NH_3OH^+ \rightarrow 4[Re^{V}(NC_6H_4Y)Cl_3(C_{12}H_{11}N_3)] + 3N_2O + 6H^+ + 7H_2O \quad (3)$$

2.2. Magnetic moment, NMR and EPR spectra

The type **1** complexes are diamagnetic corresponding to low spin $5d^2$ electronic configuration and the effective magnetic moment data of complexes **2** confirm the presence of one unpaired electron ($5d^1$, $s = 1/2$) in a pseudo-octahedral environment although the magnetic moments are significantly lower (**2a**, 1.42 μ_B; **2b**, 1.45 μ_B; **2c**, 1.46 μ_B; **2d**, 1.47 μ_B) than the spin only value. The lowering could be attributed to appreciable orbital coupling [24] as encountered in other hexavalent rhenium species.

The type **1** complexes uniformly exhibit well separated NMR signals in solution consistent with diamagnetism. However, amide complexe (**2**) display paramagnetically shifted relatively broad peaks lacking well resolved spin-spin structures. The type **2** complexes are EPR active (Fig. 1, Table 1) in fluid solution at room temperature and display well resolved spectra consisting of six isotropic hyperfine lines due to the interaction of the unpaired electron with the nuclear spin of both rhenium isotopes ($I = 5/2$; ^{185}Re, 37.07%; ^{187}Re, 62.93%). The isotopic fine structure has not been resolved because of the small difference (1%) in the two nuclear quadrupole moments. There is a systematic increase in the separation between the adjacent hyperfine lines on going from lower to higher fields due to the second order effects [25]. The range of this variable hyperfine

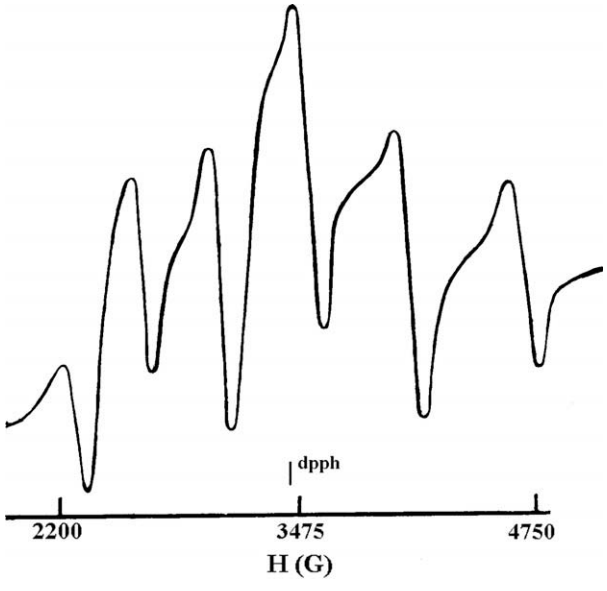


Fig. 1. EPR diagram of Complex **1d** in solution phase at 9.1 GHz and 298 K.

Table 1
EPR data for **2** at 298 K in dichloromethane-benzene (1:1) solution.

Complexes	Center field g	A (G, average)
2a	1.939	488
2b	1.945	492
2c	1.948	498
2d	1.957	496

spacing spans the domain 360-640 G, consistent with very high oxidation state (+VI) of the metal. Centre field g values and average hyperfine splitting A for the complexes fall in the ranges 1.939–1.957 and 488–498 G, respectively. Well resolved sextet EPR spectra in solution at ambient temperature are relatively rare for Re(VI) owing to the comparatively large line width followed by significant overlapping and only broad signals [26–28] are usually observed. However, Re(VI) complexes of type $[ReNX_4]^-$ (X = Cl, Br and NCS) follow similar spectral characteristics [29] at room temperature.

The spectra of **2** in a frozen (77 K) dichloromethane/toluene glass become axial and are characterized with individual g-tensors ~1.92 ($g_{||}$) and ~1.98 ($g_{\perp}$). The observed g inequality is consistent with a tetragonally distorted octahedral geometry. The hyperfine components due to the $g_{||}$ resonance (reference axis, Re≡NAr), especially the outer components have been resolved to a satisfactory extent whereas the components corresponding to $g_{\perp}$ absorptions overlap considerably. This observation corroborates that the rhombic field is not strong enough to split the perpendicular absorption into individual tensors (g_{xx} and g_{yy}). The separations between $g_{||}$ hyperfine lines are unequal and gradually increases towards higher field. It is noteworthy that the separations between $g_{||}$ hyperfine structures are larger (350–800 G) than those in isotropic solution (360–640 G) and the inter spacing between $g_{\perp}$ components are correspondingly smaller.

2.3. UV–visible and IR spectra

The electronic spectra for type **1** and **2** complexes were recorded in dichloromethane solution at room temperature. The Re^V chelates (**1**) display a relatively weak transition near 750 nm related to $5d_{xy} \rightarrow d_{yz}, d_{xz}$ excitation. Well separated moderately intense second band appeared at about 540 nm, presumably LMCT ($\pi_{Cl} \rightarrow Re^V$) in origin. Another highly intense band near 350 nm could be ascribed to bound aldimine based internal CT transition. Spectra of **2** are characterized with two peaks in higher energy (535 and 350 nm) and disappearance of lowest energy peak.

All IR spectra of **1** and **2** exhibit two primary N–H stretching modes near 3350 and 3280 cm^{-1} as sharp doublets for the asymmetric and symmetric vibrations, respectively. The strong bands observed in the range 1590–1610 cm^{-1} are assigned to C=N stretch and red shift of this azomethine absorption by ~25 cm^{-1} from free ligand to the complexes suggests weak π–accepting property of the coordinated ligand. Two Re–Cl stretches were observed in the region 320–340 cm^{-1}, consistent with *mer*-$ReCl_3$ motif for both types of complexes. Picolinamide bound complexes (**2**) uniformly exhibit another characteristic band near 1640 cm^{-1} for C=O function of the ligand.

2.4. Structure

The X-ray structure of **1d** has been determined. Molecular view, atom numbering scheme are presented in Fig. 2 and selected bond parameters are collected in Table 2.

The $ReCl_3$ fragment is uniformly disposed in a meridional fashion in the distorted octahedral complex. The Cl1, Cl2, Cl3 and N2 atoms define a good equatorial plane (mean deviation ~0.01 Å) from which the metal atom is displaced towards the imide nitrogen N4 by 0.30 Å. The five membered chelate ring (Re, N1, C5, C6 and N2) along with the pyridine moiety constitute a satisfactory plane (md < 0.02 Å) with which the p-aminophenyl group of the ligand L is obliquely oriented (dihedral angle ~70°). Trans influence of imido nitrogen (N4) is reflected in the Re–N1 bond length (2.236 Å), longer by about 0.19 Å compared to normal Re–N2 length (2.045 Å). The Re–N4 length, 1.714(3) Å and Re–N4–C13 angle, 173.9(2)° are consistent with the triply bonded ($\sigma^2\ \pi^4$), more or less linear arylimidorhenium ($Re^V{\equiv}NC_6H_4Y$) motif [30,31].

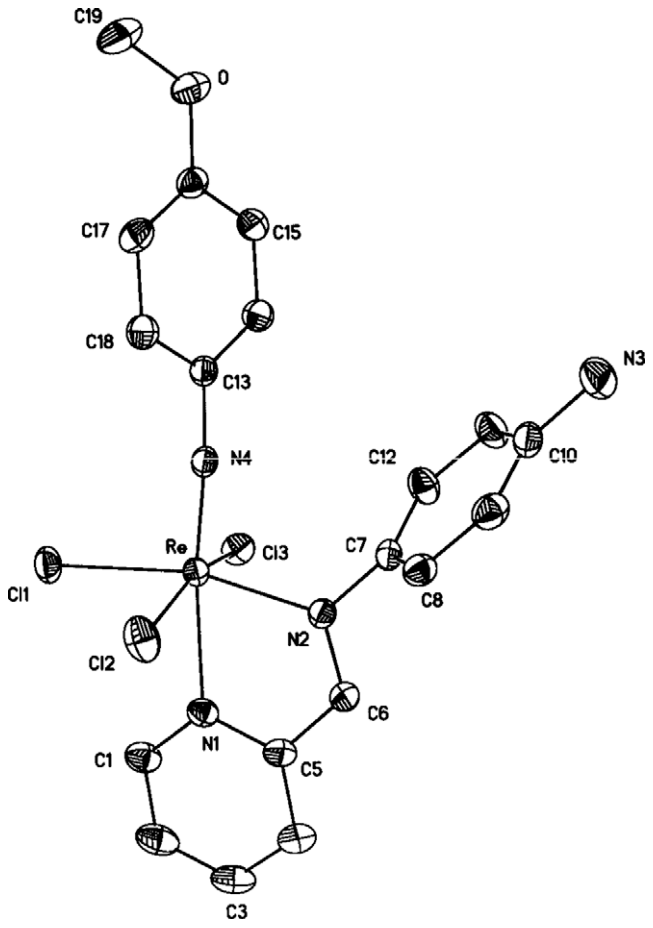


Fig. 2. A perspective view (25% probability thermal ellipsoids) and atom labeling scheme of **1d**. Hydrogen atoms have been omitted for clarity.

Table 2
Selected bond distances (Å) and angles (°) for **1d**.

Distances			
Re–N(4)	1.714(3)	Re–N(2)	2.045(2)
Re–N(1)	2.236(3)	Re–Cl(2)	2.3813(10)
Re–Cl(1)	2.3826(9)	Re–Cl(3)	2.3856(9)
Angles			
N(4)–Re–N(2)	98.63(11)	N(4)–Re–N(1)	173.01(10)
N(2)–Re–N(1)	74.85(10)	N(4)–Re–Cl(2)	99.72(9)
N(2)–Re–Cl(2)	87.34(7)	N(1)–Re–Cl(2)	82.69(7)
N(4)–Re–Cl(1)	96.51(8)	N(2)–Re–Cl(1)	164.81(7)
N(1)–Re–Cl(1)	90.09(7)	Cl(2)–Re–Cl(1)	88.83(4)
N(4)–Re–Cl(3)	95.56(9)	N(2)–Re–Cl(3)	91.71(7)
N(1)–Re–Cl(3)	82.29(7)	Cl(2)–Re–Cl(3)	164.66(4)
Cl(1)–Re–Cl(3)	88.12(3)		

Molecular packing reveals that one Cl atom of a molecule underwent two weak Cl···H contacts (2.829 and 2.898 Å) with two other proton donor molecules oriented in a nearly parallel manner to the acceptor. The donor fragments are linked through O···H interaction (2.461 Å) to form a trimeric assembly and the pattern is extended inside the lattice. Apart from the said interactions, the stability of the trimer is partly imparted from π–π stacking force operating between arylimido and aminophenyl groups (centroid···centroid distance – 3.885 Å) of two donor molecules.

2.5. Electrochemistry

All the two families are electroactive in acetonitrile solution at platinum electrode. The reduction potential data are collected in

Table 3
Cyclic voltammetric formal potentials at 298 K in acetonitrile solvent (TEAP, supporting electrolyte) at a platinum working electrode.[a,b,c,d]

Complex **1**	$E_{½}$ (Re^{VI}/Re^{V}),V (ΔE_p, mV)	Complex **2**	$E_{½}$,V (ΔE_p, mV)	
			Re^{VI}/Re^{V}	Re^{VII}/Re^{VI}
1a	1.02 (80)	**2a**	0.16(80)	1.58(80)
1b	0.97(85)	**2b**	0.13(80)	1.54(85)
1c	0.95(80)	**2c**	0.11(85)	1.52(85)
1d	0.91(80)	**2d**	0.08(80)	1.48(80)

[a] Scan rate 50 mVs^{-1}.
[b] $E_{½} = ½ (E_{pa} + E_{pc})$, where E_{pa} and E_{pc} are anodic and cathodic peak potentials, respectively.
[c] $\Delta E_p = E_{pa} - E_{pc}$.
[d] Reference electrode SCE.

Table 4
Rate constants and activation parameters[a] for the conversion **2**→**1** in acetonitrile using $[N_2H_5^+]$.[b,c]

T (K)	$[N_2H_5^+]$, M	10^3 k_{obsd}, s^{-1}	10^3k_2, $M^{-1}s^{-1}$
299	1.11	2.84	2.63(0.02)
	1.67	4.33	
	2.22	5.74	
296	1.11	2.30	2.13(0.03)
	1.67	3.49	
	2.22	4.68	
293	1.11	2.04	1.77(0.04)
	1.67	3.06	
	2.22	4.02	
288	1.11	1.19	1.21(0.04)
	1.67	1.88	
	2.22	2.54	
283	1.11	0.72	0.82(0.03)
	1.67	1.21	
	2.22	1.64	

[a] $\Delta H^{\neq}$ = 11.61 (0.59) kcal mol^{-1} and $\Delta S^{\neq}$ = −31.22 (2.4) eu.
[b] The initial concentration of **2** is 2.5×10^{-4} M.
[c] Least squares deviations are given in parentheses.

Table 5
Rate constants and and Activation parameters[a] for the conversion **2**→**1** in acetonitrile using $[NH_3OH^+]$.[b,c]

T (K)	$[NH_3OH^+]$, M	10^3 k_{obsd}, s^{-1}	10^3k_2, $M^{-1}s^{-1}$
299	1.11	0.54	0.53(0.04)
	1.67	0.89	
	2.22	1.13	
296	1.11	0.50	0.44(0.03)
	1.67	0.71	
	2.22	0.99	
293	1.11	0.42	0.37(0.01)
	1.67	0.61	
	2.22	0.83	
288	1.11	0.25	0.26(0.02)
	1.67	0.37	
	2.22	0.54	
283	1.11	0.15	0.18(0.03)
	1.67	0.24	
	2.22	0.35	

[a] $\Delta H^{\neq}$ = 10.74 (0.62) kcal mol^{-1} and $\Delta S^{\neq}$ = −37.30 (2.1) eu.
[b] The initial concentration of **2** is 2.5×10^{-4} M.
[c] Least squares deviations are given in parentheses.

Table 3. The type **1** complexes display well-defined quasi-reversible anodic peak (peak to peak separation ~ 80 mV) near 0.95 V versus SCE. The response is tentatively assigned to the oxidation of Re^{V} to Re^{VI} and relevant to the redox reaction $\mathbf{1^+ + e \rightarrow 1}$. The potential increases with the increase in electron withdrawing power of Y (OCH_3 < CH_3 < H < Cl) and the observed trend follows usual Hammett order. The picolinamide complexes of type **2** exhibit two successive quasi-reversible (peak to peak separation ~ 80 mV) one electron signals near 0.15 and 1.50 V for Re(VI)/Re(V) and Re(VII)/Re(VI) couples respectively (Eq. (4)).

$$\mathbf{2} + \mathbf{e} \rightarrow \mathbf{2^-} \quad (4a)$$

$$\mathbf{2^+} + \mathbf{e} \rightarrow \mathbf{2} \quad (4b)$$

Lowering of reduction potential for Re^{VI}/Re^{V} couple by a substantial margin of ~0.8 V for type **2** complexes compared to that of **1** indicates superior stabilization of amide bound hexavalent rhenium in the former species [32]. Like **1**, type **2** complexes also exhibit substitution effect at Y of arylimido moiety in a usual manner.

2.6. Reduction kinetics

In order to understand the kinetic behaviour of amide → imine reduction, the progress of the reaction was monitored by spectrophotometry in acetonitrile solution. The conversion **2** → **1** was characterized by the increase in absorbance at 535 nm in the temperature interval 283–299 K. The second order rate constants at different temperatures and activation parameters for the reaction using $N_2H_5^+$ are collected in Table 4. Under pseudo-first order condition (excess hydrazine), the rates are found to be proportional to the concentration of amide complex **2** (Rate = k_{obsd} [2]), as evident from the linear plots of $-\ln(A_\alpha - A_t)$ versus time t at different hydrazine concentrations under variable temperatures. The plot between any set of k_{obsd} values and used hydrazine concentrations at any recorded temperature is linear in nature and the corresponding slope gives the second order rate constant k_2 as stated in Eq. (5). First order dependence of **2** and

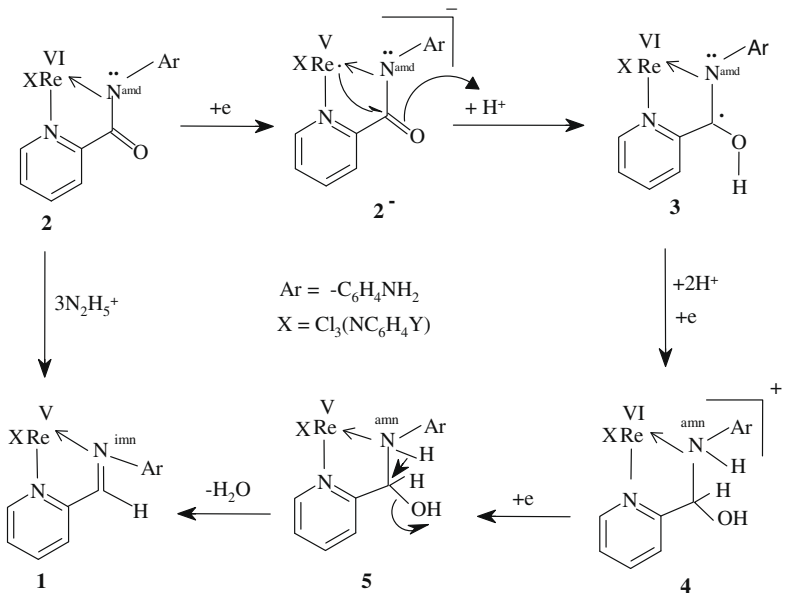
$$\text{Rate} = k_2[\mathbf{2}][\mathbf{N_2H_5^+}](\mathbf{k_{obsd}} = \mathbf{k_2}[\mathbf{N_2H_5^+}]) \quad (5)$$

hydrazine on rate implies that the oxygen atom transfer reaction proceeds through the rate determining step involving close association ($\Delta S^{\neq}$ = −31.22 eu) of hexavalent metal amide substrate and the reducing agent.

The rate of reduction of **2** by $N_2H_5^+$ was found to be nearly five times faster than that measured with NH_3OH^+ (Table 5) at all recorded temperatures. The difference in rates can be reconciled by considering higher reducing ability of $N_2H_5^+$ (higher oxidation potential) over NH_3OH^+ (lower oxidation potential).

2.7. Reaction model

N_2H_4 has the unique ability to act as either one electron or multi electron (two and four) donor reducing agent depending on the reaction condition and nature of the oxidant. The number of proton and electron equivalents transferred from each equivalent of $N_2H_5^+$ is a requisite for the proposition of reduction mechanism. Isolation of ammonium salt from the products of **2** → **1** conversion is consistent with one electron and one proton donor function of $N_2H_5^+$, relevant to half cell reaction, $N_2H_5^+ \rightarrow ½N_2 + NH_4^+ + H^+ + e$.



Scheme 1.

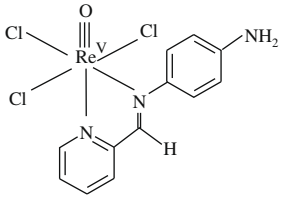
2 → **1** conversion does not involve nucleophilic attack of hydrazine instead outward transfer of oxygen atom from the bonded ligand occurs through proton assisted amide C=O labilisation. In attempt to extend the reaction model (Scheme 1), the initiation is thought to occur via fast metal reduction (low Re^{VI}/Re^{V} reduction potential, ~0.15 V) by $N_2H_5^+$ to form the anionic complex $\mathbf{2}^-$. Lower metal valence (+V) in $\mathbf{2}^-$ considerably decreases the Lewis acidity of the metal and expansion of radius upon reduction substantially weakens Re-amido nitrogen bonding.

These electronic changes in $\mathbf{2}^-$ promote internal electron transfer [33] from pentavalent metal to the amide function and augmented oxygen basicity arising there from induces proton capture [34] to generate the radical based reactive Re(VI) species, **3**. Such electron transfer events are facile in $\mathbf{2}^-$ containing comparatively electron rich Re^{V} centre rather than in **2** incorporating electron poor Re^{VI} metal. Subsequent reduction of amido carbon and nitrogen sites in **3** resulted cationic α-hydroxyamine intermediate, **4** [35–39]. Finally, **4** undergo metal reduction followed by dehydration to regenerate **1**. Elimination of water from **5** is driven by stronger Re^{V}-imine bonding, resulting from metal electron density delocalization over π^* framework of aldimine ligand. The proposed mechanism indicates stepwise utilization of three equivalents of proton and three equivalents of electron derived from three equivalents of $N_2H_5^+$ for the reduction of one equivalent of **2**. This observed reaction stoichiometry is in complete agreement with Eq. (2).

In support of the existence of transient reduced species $\mathbf{2}^-$, we performed constant potential exhaustive reduction of **2** at +0.30 V in dry acetonitrile solvent under deareated condition. The coulomb count ratio suggests an almost quantitative one electron reduction of **2** to form stereoretentive Re^{V} analogue ($\mathbf{2}^-$), evident from the virtually superposable cyclic voltammogram of the electrogenerated species $\mathbf{2}^-$ (anodic scan) with that of **2** (cathodic scan). Attempts to isolate $\mathbf{2}^-$ did not succeed. Such an analogous transformation of N-substituted amide to imine has not yet been documented in metal free condition. Appreciable π-delocalisation in free amide makes amido oxygen feebly basic hindering the protonation step and no scope for induced electron transfer halts the successive stages of the transformation. Hence, the concerned **2** → **1** conversion is entirely metal regulated in electronic sense via easy accession of variable metal valence as required in different steps.

2.8. Coligand effect on intramolecular oxidation

π-acidic Re^{V} ion can be stabilized with the help of π-donor oxo and arylimido coligands. The scrutiny of imine → amide conversion in the Re^{V}-oxo complex (**6**), $[Re^{V}OCl_3L]$ can help us to understand role of electronic effect of coligands exerted on oxidation process. With the aim to investigate, we prepared the concerned oxo complex and allowed to react with aqueous HNO_3 under the same condition. The reaction was only ended up with no observable colour change and no isolation of the corresponding amide product. The observation implies that the Re^{VI} ion is better stabilized by arylimido



6

group compared to the oxo coligand. This is attributed to superior π-donor ability of arylimido group (NAr^{2-}) over oxo (O^{2-}) to efficiently stabilize the Re^{VI} centre as attested from the higher oxidation potential of oxo complex, **6** (1.55 V) than the imido complexes, **1** (~0.95 V) and the lower electronegativity of nitrogen than oxygen. Significantly high oxidation potential for the oxo complex renders the rhenium metal inactive for initial oxidation to promote imine → amide oxidation. Moreover, coulometric oxidation of $[Re^{V}OCl_3L]$ in dry acetonitrile solvent afforded no tractable Re^{VI} product which suggests that the Re^{VI} analogue is only stable in cyclic voltammetric short time scale.

3. Conclusion

Reported pyridylimine chelated type **1** imidorhenium(V) complexes are active towards inward oxygen atom transfer reaction in dilute nitric acid medium affording pyridylamide bound hexavalent rhenium analogues, **2**. Low Re^{VI}/Re^{V} potential for **2** provides the opportunity to scrutiny the reductive susceptibility with nitroge-

nous reducing agents like hydrazine sulphate and hydroxylamine hydrochloride. Rate measurements for **2**→**1** conversion reveal an associative pathway and on that basis reaction mechanism is proposed. The reduction mode explains the role of variable metal valence in proton mediated structural changes of the bound amide ligand in **2**. The oxo complex (**6**) does not respond to such imine→amide oxidation owing to considerably high metal oxidation potential.

Electroactive complexes of type **2** display Re^{VI}/Re^{V} and Re^{VII}/Re^{VI} voltammetric signals near ~0.1 and ~1.6 V in contrast to only one Re^{VI}/Re^{V} couple (~0.95 V) for **1**. The appearance of Re^{VII}/Re^{VI} response for **2** implies superior stabilizing effect of amide group for higher valent rhenium species. Type **2** complexes uniformly exhibit one electron paramagnetism and display well-resolved six lines EPR spectra at room temperature in solution.

4. Experimental

4.1. Materials and physical measurements

The starting materials $[Re(NC_6H_4Y)Cl_3(PPh_3)_2]$ [40] and $[ReOCl_3(PPh_3)_2]$ [41] and the ligand L [42] were synthesized by reported standard methods. All other chemicals were of reagent grade and used as received. Solvents were dried and distilled prior to use. The IR spectra were recorded on KBr pellets with a Perkin–Elmer FT-IR spectrometer. A Perkin–Elmer 2400 II elemental analyzer was used for microanalysis. The electronic spectra and kinetic studies were done using Hitachi U-3501 spectrophotometer fitted with thermostated cell compartments. Electrochemical measurements were performed using a PAR model Versastat-2 electrochemical analyzer, with a platinum working electrode. The supporting electrolyte was tetraethylammonium perchlorate (TEAP), and the potentials were referenced to saturated calomel electrode (SCE) without junction correction. X-band EPR spectra in solution and frozen glass states were recorded using a Bruker 300E spectrometer. Magnetic susceptibilities were measured on a PAR 155 vibrating sample magnetometer.

4.2. Preparation of complexes

4.2.1. Synthesis of $[Re^{V}(NC_6H_4Y)Cl_3(C_{12}H_{11}N_3)]$, 1

The same general procedure was used to synthesize the above complexes from $[Re^{V}(NC_6H_4Y)Cl_3(PPh_3)_2]$. Procedural details are given for one representative case (**1d**). Yields varied in the range 80–85%.

To a green suspension of $[Re^{V}(NC_6H_4Y)Cl_3(PPh_3)_2]$ (190 mg, 0.20 mmol) in 30 ml of benzene was added 60 mg (0.30 mmol) of L in 10 ml of benzene, and the mixture was heated to reflux for 2 h, affording a violet solution. The solvent was then removed under reduced pressure, and the dark mass thus obtained was subjected to chromatography on a silica gel column (25 × 1 cm, 60–120 mesh). Excess ligand and phosphine was eluted with benzene. A violet band was then eluted with benzene-acetonitrile (20:1) mixture. Solvent removal form the eluate under reduced pressure afforded $[Re^{V}(NC_6H_4OCH_3)Cl_3(L)]$, **1d** as a violet solid. Yield: 106 mg (82%). *Anal.* Calc. for $C_{19}H_{18}Cl_3N_4ORe$: C, 37.35; H, 2.95; N, 9.17. Found: C, 37.30; H, 2.98; N, 9.13. UV–vis (λ_{max}, nm (ε, M^{-1} cm^{-1}), CH_2Cl_2 solution): 735 (1500); 540 (7500); 325 (13200). IR (cm^{-1}): 320, 335 (Re–Cl), 1595 (C=N). ^1H NMR [δ (*J*/Hz), $CDCl_3$ solution]: L, 9.41(H(1), d, 5.5); 6.84 (H(2), t, 7.5); 7.98 (H(3), t, 8.4); 7.34 (H(4), d, 7.7); 6.41(H(6), s); 7.45–7.55 (H(8,9,11,12), m); 16.06 (NH_2, s); $NC_6H_4OCH_3$, 7.08 (2H(o), d, 5.3); 7.13 (2H(m), d, 5.4); 3.99 (OCH_3, s).

1c: *Anal.* Calc. for $C_{19}H_{18}Cl_3N_4Re$: C, 38.35; H, 3.03; N, 9.42. Found: C, 38.31; H, 2.99; N, 9.37. UV–vis (λ_{max}, nm (ε, M^{-1} cm^{-1}), CH_2Cl_2 solution): 735 (1500); 540 (7500); 330 (13400). IR (cm^{-1}): 325, 335 (Re–Cl), 1595 (C=N). ^1H NMR [δ (*J*/Hz), $CDCl_3$ solution]: L, 9.40(H(1), d, 5.5); 6.86 (H(2), t, 7.4); 7.96 (H(3), t, 8.2); 7.33 (H(4), d, 7.3); 6.41(H(6), s); 7.46–7.57 (H(8,9,11,12), m); 16.08 (NH_2, s); $NC_6H_4CH_3$, 7.06 (2H(o), d, 5.5); 7.15 (2H(m), d, 5.4); 4.04 (CH_3, s).

1b: *Anal.* Calc. for $C_{18}H_{16}Cl_3N_4Re$: C, 37.21; H, 2.75; N, 9.65. Found: C, 37.23; H, 2.78; N, 9.63. UV–vis (λ_{max}, nm (ε, M^{-1} cm^{-1}), CH_2Cl_2 solution): 735 (1500); 540 (7500); 325 (13300). IR (cm^{-1}): 320, 335 (Re–Cl), 1600 (C=N). ^1H NMR [δ (*J*/Hz), $CDCl_3$ solution]: L, 9.42(H(1), d, 5.5); 6.85 (H(2), t, 7.5); 7.99 (H(3), t, 8.1); 7.35 (H(4), d, 7.2); 6.40(H(6), s); 7.45–7.50 (H(8,9,11,12), m); 16.05 (NH_2, s); NC_6H_5, 7.09 (2H(o), d, 5.9); 7.13 (2H(m), t, 6.6); 7.19 (1H(p), t, 6.3).

1a: *Anal.* Calc. for $C_{18}H_{15}Cl_4N_4Re$: C, 35.12; H, 2.44; N, 9.10. Found: C, 35.17; H, 2.41; N, 9.06. UV–vis (λ_{max}, nm (ε, M^{-1} cm^{-1}), CH_2Cl_2 solution): 735 (1500); 540 (7600); 325 (13200). IR (cm^{-1}): 320, 335 (Re–Cl), 1595 (C=N). ^1H NMR [δ (*J*/Hz), $CDCl_3$ solution]: L, 9.39(H(1), d, 5.8); 6.83 (H(2), t, 7.5); 7.97 (H(3), t, 8.2); 7.34 (H(4), d, 7.4); 6.42(H(6), s); 7.44–7.53 (H(8,9,11,12), m); 16.06 (NH_2, s); NC_6H_4Cl, 7.05 (2H(o), d, 5.8); 7.12 (2H(m), d, 5.6).

4.2.2. Synthesis of $[Re^{VI}(NC_6H_4Y)Cl_3(C_{12}H_{10}N_3O)]$, 2

The same general method was used to prepare the above complexes from $[Re^{V}(NC_6H_4Y)Cl_3(C_{12}H_{11}N_3)]$, **1**. Procedural details are given for one representative case (**2d**). Yields are in the range 75–80%.

One hundred and two milligrams (0.17 mmol) of **1d** was dissolved in 25 ml acetonitrile, and 4.5 ml 1(N) nitric acid (acidity ~0.15 N) was added. The violet solution was stirred for 1 h, during which the colour turned yellowish brown. Solvent evaporation yields dark brown product. The mass thus obtained was thoroughly washed with cold water to remove adherent nitric acid and finally dried in vacuum over fused $CaCl_2$. Yield: 80 mg (77%). *Anal.* Calc. for $C_{19}H_{17}Cl_3N_4O_2Re$: C, 36.45; H, 2.72; N, 8.95. Found: C, 36.40; H, 2.75; N, 8.99. UV–vis (λ_{max}, nm (ε, M^{-1} cm^{-1}), CH_2Cl_2 solution): 535 (1600); 355 (12200). IR (cm^{-1}): 320, 335 (Re–Cl), 1595 (C=N), 1635 (C=O).

2c: *Anal.* Calc. for $C_{19}H_{17}Cl_3N_4ORe$: C, 37.41; H, 2.79; N, 9.19. Found: C, 37.45; H, 2.75; N, 9.22. UV–vis (λ_{max}, nm (ε, M^{-1} cm^{-1}), CH_2Cl_2 solution): 535 (1600); 355 (12000). IR (cm^{-1}): 320, 335 (Re–Cl), 1595 (C=N), 1635 (C=O).

2b: *Anal.* Calc. for $C_{18}H_{15}Cl_3N_4ORe$: C, 36.27; H, 2.52; N, 9.40. Found: C, 36.30; H, 2.57; N, 9.33. UV–vis (λ_{max}, nm (ε, M^{-1} cm^{-1}), CH_2Cl_2 solution): 535 (1600); 355 (12300). IR (cm^{-1}): 325, 335 (Re–Cl), 1595 (C=N), 1635 (C=O).

2a: *Anal.* Calc. for $C_{18}H_{14}Cl_4N_4ORe$: C, 34.28; H, 2.22; N, 8.89. Found: C, 34.32; H, 2.25; N, 8.81. UV–vis (λ_{max}, nm (ε, M^{-1} cm^{-1}), CH_2Cl_2 solution): 535 (1500); 355 (12400). IR (cm^{-1}): 320, 330 (Re–Cl), 1595 (C=N), 1635 (C=O).

4.2.3. Synthesis of 1 from 2

4.2.3.1. Hydrazine method. To a yellow–brown solution of **2** (125 mg, 0.20 mmol) in acetonitrile (25 ml) was added hydrazine sulphate (91 mg, 0.70 mmol) in 10 ml solvent. It was then stirred for 1.5 h at room temperature whereupon the solution gradually turned violet. The solvent was removed from the resulting solution under reduced pressure. The obtained violet mass (**1**) was washed with cold water to free adhered hydrazine and dried in vacuum over fused $CaCl_2$. Yield: 100 mg (82%).

4.2.3.2. Hydroxylamine method. To a yellow–brown solution of **2** (125 mg, 0.20 mmol) in acetonitrile (25 ml) was added hydroxylamine hydrochloride (28 mg, 0.40 mmol) in 5 ml solvent. It was then stirred for 8 h at room temperature. The solvent was removed from the resulting solution under reduced pressure. The obtained

Table 6
Crystallographic data for **1d**.

Complex	**1d**
Formula	$C_{19}H_{18}Cl_3N_4ORe$
M	610.92
System	monoclinic
Space group	P2(1)/c
a (Å)	9.123(2)
b (Å)	15.961(3)
c (Å)	15.333(3)
α (°)	90
β (°)	106.19(3)
γ (°)	90
V (Å^3)	2144.1(7)
Z	4
D (mg m^{-3})	1.893
T (K)	293(2)
μ (mm^{-1})	6.058
Independent reflections	5954
R_{int}	0.0410
Collected reflections	27807
$R1$, $wR2$ [$I > 2\sigma(I)$]	0.0251, 0.0516

violet mass (**1**) was washed with cold water to free adhered hydrazine and dried in vacuum over fused $CaCl_2$. Yield: 104 mg (84%).

*4.2.4. Synthesis of [$Re^VOCl_3(C_{12}H_{11}N_3)$], **6***

To a green solution of [$ReOCl_3(PPh_3)_2$] (208 mg, 0.25 mmol) in 30 ml of dichloromethane was added 60 mg (0.30 mmol) of L in 10 ml of dichloromethane, and the mixture was stirred for 20 min, affording a pink solution. The volume of the solvent was then reduced to one fifth under reduced pressure, and excess of n-hexane was added into it. It causes precipitation of the pink complex and the solution was then filtered. The pink product was collected by filtration and washed twice with diethyl ether. The mass was finally dried in vacuum over fused $CaCl_2$. The pink mass is unstable on silica gel column and can not be isolated by chromatography. Yield: 111 mg (88%). *Anal.* Calc. for $C_{12}H_{11}Cl_3N_3ORe$: C, 28.56; H, 2.18; N, 8.33. Found: C, 28.49; H, 2.24; N, 8.26. IR (cm^{-1}): 320, 335 (Re–Cl), 1595 (C=N), 998 (Re≡O).

4.3. X-ray crystallography

Dark violet single crystals of **1d** were obtained by slow diffusion of solvent pair (dichloromethane/hexane) at room temperature. Data were collected at $T = 293(2)$ K on a Siemens SMART CCD area-detector diffractometer equipped with graphite monochromated Mo Kα radiation ($\lambda = 0.71073$ Å, rotating anode source) in the range $1.88° = \theta = 30.55°$. All the data were corrected for Lorentz polarization and absorption [43]. The structure was generated by direct methods using SHELXS-97 [44] followed by successive Fourier synthesis and refined by full matrix least squares based on F^2 with SHELXL-97 [45]. Anisotropic displacement parameters were assigned to all non-hydrogen atoms. Significant crystal data are listed in Table 6. The crystallographic data have been deposited to CCDC.

Supplementary data

CCDC 673975 contains the supplementary crystallographic data for **1d**. These data can be obtained free of charge via http://www.ccdc.cam.ac.uk/conts/retrieving.html, or from the Cambridge Crystallographic Data Centre, 12 Union Road, Cambridge CB2 1EZ, UK; fax: (+44) 1223-336-033; or e-mail: deposit@ccdc.cam.ac.uk.

Acknowledgement

We thank the University Grants Commission (UGC), India for financial support.

References

[1] B.D. Sherry, A.T. Radosevich, F.D. Toste, J. Am. Chem. Soc. 125 (2003) 6076.
[2] E.A. Ison, E.R. Trived, R.A. Corbin, M.M. Abu-Omar, J. Am. Chem. Soc. 127 (2005) 15374.
[3] Y. Koninobu, Y. Nishina, C. Nakagawa, K. Takai, J. Am. Chem. Soc. 128 (2006) 12376.
[4] Y. Kuninobu, A. Kawata, K. Takai, J. Am. Chem. Soc. 127 (2005) 13498.
[5] M.M. Abu-Omar, E.H. Appelman, J.H. Espenson, Inorg. Chem. 35 (1996) 7751.
[6] E.A. Ison, J.E. Cessarich, G. Du, P.E. Fanwick, M.M. Abu-Omar, Inorg. Chem. 45 (2006) 2385.
[7] L.D. McPherson, M. Drees, S.I. Khan, T. Strassner, M.M. Abu-Omar, Inorg. Chem. 43 (2004) 4036.
[8] J.M. Mayer, Acc. Chem. Res. 31 (1998) 441.
[9] R.H. Holm, Chem. Rev. 87 (1987) 1401.
[10] D.E. Wigley, Prog. Inorg. Chem. 42 (1994) 239.
[11] J. Dixon, J.H. Espenson, Inorg. Chem. 41 (2002) 4727.
[12] Y. Wang, Inorg. Chem. 41 (2002) 2266.
[13] G. Lente, X. Shan, I.A. Guzei, J.H. Espenson, Inorg. Chem. 39 (2000) 3572.
[14] G. Lente, J.H. Espenson, Inorg. Chem. 39 (2000) 4197.
[15] B. Domereq, M. Fourmique, Eur. J. Inorg. Chem. 40 (2001) 1625.
[16] G.D.J. Correia, A. Domingos, I. Santos, Eur. J. Inorg. Chem. 39 (2000) 1523.
[17] P. Klufers, O. Krotz, M. Obberger, Eur. J. Inorg. Chem. 41 (2002) 1919.
[18] J.C. Bryan, R.E. Stenkemp, T.H. Tulip, J.M. Mayer, Inorg. Chem. 26 (1987) 2283.
[19] J. Gangopadhyay, S. Sengupta, S. Bhattacharyya, I. Chakraborty, A. Chakravorty, Inorg. Chem. 41 (2002) 2616.
[20] S. Sengupta, J. Gangopadhyay, A. Chakravorty, Dalton Trans. (2003) 4635.
[21] I. Chakraborty, S. Bhattacharyya, S. Banerjee, B.K. Dirghangi, A. Chakravorty, J. Chem. Soc., Dalton Trans. (1999) 3747.
[22] M.M. Abu-Omar, Chem. Commun. (2003) 2102.
[23] B.K. Dirghangi, M. Menon, S. Banerjee, A. Chakravorty, Inorg. Chem. 36 (1997) 3595.
[24] L.A. de Learie, R.C. Haltiwanger, C.G. Pierpont, Inorg. Chem. 26 (1987) 817.
[25] A. Abragam, B. Bleaney, Electron Paramagnetic Resonance of Transition Ions, Clarendon, Oxford, England, 1970.
[26] J. Baldas, J.F. Boas, J. Bonnyman, J.R. Pilbrow, G.A. Williams, J. Am. Chem. Soc. 107 (1985) 1886.
[27] J.F. Gibson, K. Mertis, G. Wilkinson, J. Chem. Soc., Dalton Trans. (1975) 1093.
[28] J.H. Holloway, J.B. Raynor, J. Chem. Soc., Dalton Trans. (1975) 737.
[29] U. Abram, M. Braun, S. Abram, R. Kirmse, A. Voigt, J. Chem. Soc., Dalton Trans. (1998) 231.
[30] W.A. Nugent, B.L. Haymore, Coord. Chem. Rev. 31 (1980) 123.
[31] G.V. Goeden, B.L. Haymore, Inorg. Chem. 22 (1983) 157.
[32] G. Lyashenko, V. Jancik, A. Pal, R.H. Irmev, N.C. Mosch-Zanetti, Dalton Trans. (2006) 1294.
[33] H. Taube, Electron Transfer Reactions of Complex Ions in Solution, New York, Academic Press, 1973.
[34] S. Pal, S. Pal, J. Chem. Soc., Dalton Trans. (2002) 2102.
[35] G. Bandoli, T.I.A. Gerber, R. Jacobs, J.G.H. Du Preez, Inorg. Chem. 33 (1994) 178.
[36] V. Katovic, S.C. Vergez, D.H. Busch, Inorg. Chem. 16 (1977) 1716.
[37] D.H. Busch, J.C. Bailer, J. Am. Chem. Soc. 78 (1956) 1137.
[38] C.M. Harris, E.D. Mckenzie, Nature 196 (1962) 670.
[39] L.A. Tyler, M.M. Olmstead, P.K. Mascharak, Inorg. Chem. 40 (2001) 5408.
[40] J. Chatt, J.D. Garforth, N.P. Johnson, G.A. Rowe, J. Chem. Soc. (1964) 1012.
[41] G.W. Parshall, Inorg. Synth. 17 (1977) 110.
[42] G. Bhar, H. Thamlitz, Z. Anorg. Allg. Chem. 282 (1955) 3.
[43] G.M. Sheldrick, SADABS, Absorption Correction Program, University of Gottingen,, Germany, 1996.
[44] G.M. Sheldrick, SHELXS-97, University of Gottingen, Germany, 1997.
[45] G.M. Sheldrick, SHELXL-97, University of Gottingen, Germany, 1997.

Polyhedron 28 (2009) 2510–2516

Contents lists available at ScienceDirect

Polyhedron

journal homepage: www.elsevier.com/locate/poly

The synthesis, thermal and photophysical properties of phenoxycyclotriphosphazenyl-substituted cyclic and polymeric phosphazenes

Bünyemin Çoşut, Ferda Hacıvelioğlu, Mahmut Durmuş, Adem Kılıç, Serkan Yeşilot *

Department of Chemistry, Gebze Institute of Technology, P.O. Box 141, Gebze 41400, Kocaeli, Turkey

ARTICLE INFO

Article history:
Received 28 February 2009
Accepted 1 May 2009
Available online 19 May 2009

Keywords:
Cyclophosphazene
Polyphosphazene
^{31}P NMR
Thermal stability
Fluorescence

ABSTRACT

An hydroxyl substituted hexa(phenoxy)cyclotriphosphazene (**3**) is reacted with hexachlorocyclotriphosphazene, $N_3P_3Cl_6$, octachlorocyclotetraphosphazene, $N_4P_4Cl_8$ and poly(dichlorophosphazene), $(Cl_2P{=}N)_n$, to give cyclic compounds (**4** and **5**) and a polymeric compound (**6**). The newly synthesised compounds have been fully characterised by elemental analysis, MALDI-TOF mass spectrometry, gel permeation chromatography (**6**), FT-IR, ^{1}H, ^{13}C and ^{31}P NMR spectroscopy. The thermal stability and fluorescence spectral properties of all these novel compounds have been investigated. It was found that the thermal stability and fluorescence spectral properties of cyclic compounds **4** and **5** are superior to those of compound **6**.

© 2009 Elsevier Ltd. All rights reserved.

1. Introduction

Cyclic and polymeric phosphazenes are an important class of inorganic heterocyclic ring systems in basic and applied science [1,2]. They are usually prepared by nucleophilic substitution reactions of alkoxides, aryloxides or amines on halocyclophosphazenes or high polymers [3–5], and their physical and chemical properties can be tailored via the appropriate substituted groups on the phosphorus atoms [6]. The design of materials containing cyclotriphosphazenyl groups have attracted attention because of their special properties, such as thermal stability, catalytic properties, electrical conductivity, liquid crystal and biomedical activity [7–9]. The thermal stability and flame resistance of polyphosphazenes that bear aryloxy side groups are especially well documented, and aryloxyphosphazene polymers have been developed commercially as foams for electrical, heat, and sound insulation [10–12]. Cyclotriphosphazenes have also been investigated as flame retardant additives for organic polymers [13]. Compositions that contain cyclotriphosphazenes or polyphosphazenes with commercial polymers are relatively easy to prepare, and flame retardant poly(urethane) [14], poly(methylmethacrylate) [15], polystyrene [16] and various other polymers [17] have been produced in this way.

Luminescent compounds are attracting much current research interest because of their many applications, including emitting materials for organic light emitting diodes, light harvesting materials for photocatalysis and fluorescent sensors for organic or inorganic analysers [18]. Cyclophosphazenes serve many advantageous purposes for useful luminescent materials for electroluminescent devices. For example, substituted cyclic phosphazenes are very stable and do not breakdown under very aggressive chemical conditions. Also the functional groups are projected above and below the cyclophosphazene plane and thus produce a rigid spherical core from which to grow the dendrons of interest. Therefore there has been considerable interest, recently, in fluorescent compounds based on cyclic phosphazene cores [19] or cyclolinear polymers with cyclotriphosphazene units [20] for the development of electroluminescent devices.

In phosphazene chemistry, there are many examples of organic or inorganic side group bearing cyclophosphazenes or polyphosphazenes [3–5]. However, there are limited examples of cyclophosphazenes and polyphosphazenes [21,22] or organic polymers [23,24] that bear an organic group substituted cyclophosphazene ring as the side group. Hence, we report the synthesis and characterisation of cyclophophazenes and polyphosphazene bearing hexaphenoxycyclotriphosphazenenyl groups, shown in Fig. 1. The thermal stability and fluorescence spectral properties of the cyclophosphazene compounds **4** and **5** are compared with compound **6**. The fluorescence quantum yields and lifetimes of these compounds are also investigated.

2. Experimental

2.1. Materials

Hexachlorocyclotriphosphazene(trimer) and octachlorocyclotetraphosphazene (Otsuka Chemical Co., Ltd.) were purified by

* Corresponding author. Tel.: +90 262 6053137; fax: +90 262 6053101.
E-mail address: yesil@gyte.edu.tr (S. Yeşilot).

0277-5387/$ - see front matter © 2009 Elsevier Ltd. All rights reserved.
doi:10.1016/j.poly.2009.05.027

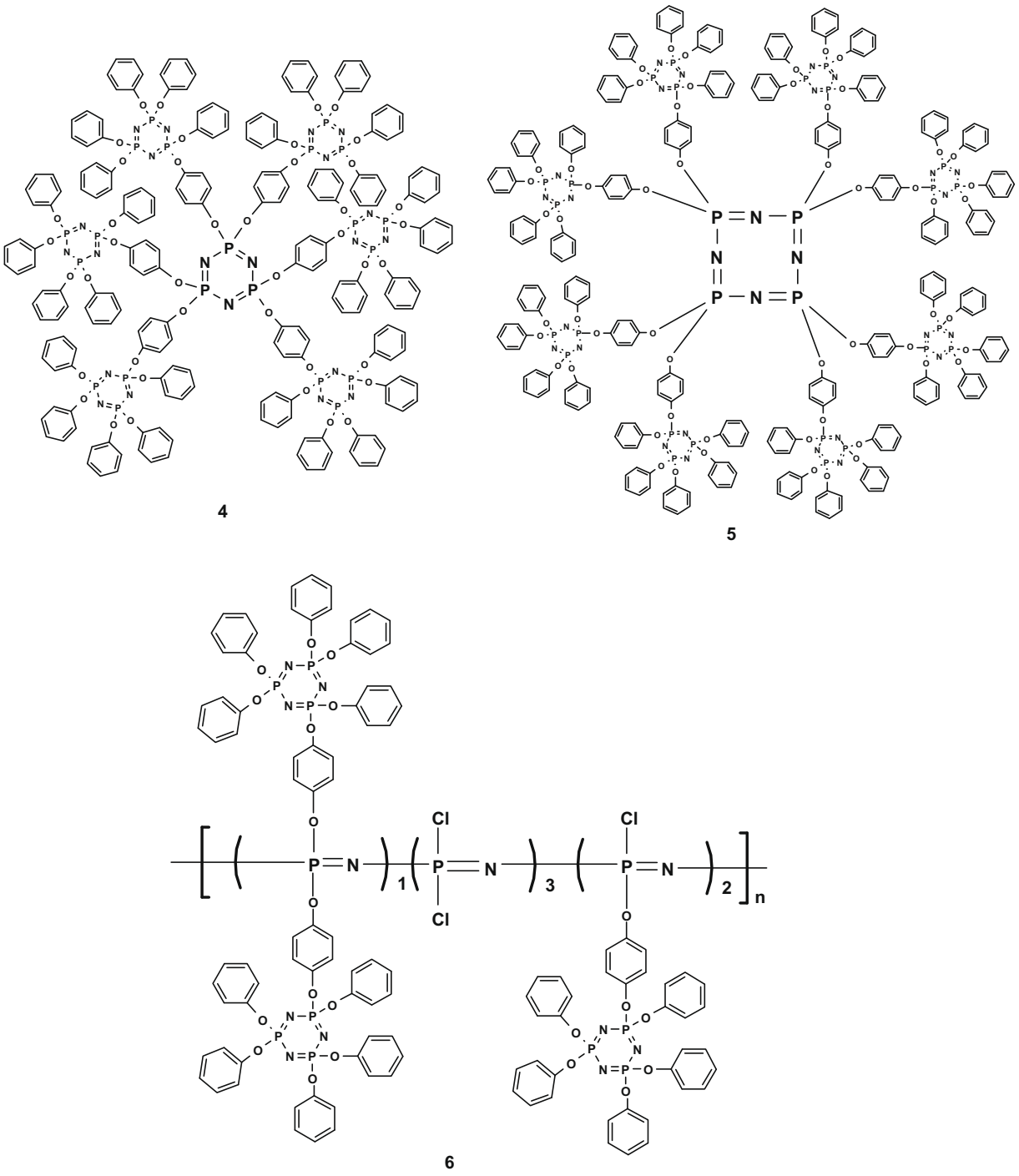


Fig. 1. Structures of the cyclic and polymeric phosphazenes **4–6**.

fractional crystallization from *n*-hexane. The crystallised hexachlorocyclotriphosphazene was further purified by vacuum sublimation before the ring opening polymerisation and only 60% of the material was allowed to be sublimed. The deuterated solvents ($CDCl_3$ and toluene) for NMR spectroscopy and the following chemicals were obtained from Merck: cyclohexene, ethanol, phenol, $Pd(OH)_2$, Cs_2CO_3, NaH, acetone, triethylamine, silica gel 60, tetrahydrofuran. 1,8,9-Anthracenetriol for the MALDI matrix was obtained from Fluka. All other reagents and solvents were reagent grade quality and obtained from commercial suppliers.

2.2. Equipment

Elemental analyses were carried out using a Thermo Finnigan Flash 1112 Instrument. UV/Vis spectra were recorded with a Shimadzu 2001 UV Pc spectrophotometer. Fluorescence excitation and emission spectra were recorded on a Varian Eclipse spectrofluoremeter using 1 cm pathlength cuvettes at room temperature. Infrared spectra were recorded on a Bio-Rad FTS 175C FT-IR spectrophotometer using KBr dyes. Mass spectra were acquired in linear modes with an average of 50 shots on a Bruker Daltonics Microflex mass spectrometer (Bremen, Germany) equipped with

a nitrogen UV–Laser operating at 337 nm. Gel permeation chromatography was performed with an Agilent 1100 series GPC system equipped with CHEMSTATION software with the addition of a GPC Add On to calculate the average molecular weights (*Mw* and *Mn*) against a polystyrene standard. The glove box (Plas Labs. 855-AC \ 220) was equiped with spectrograde N_2. Analytical thin layer chromatography (TLC) was performed on silica gel plates (Merck, Kieselgel 60, 0.25 mm thickness) with F_{254} indicator. Column chromatography was performed on silica gel (Merck, Kieselgel 60, 230–400 mesh; for 3 g crude mixture, 100 g silica gel was used in a column of 3 cm in diameter and 60 cm in length) and preparative thin layer chromatography was performed on silica gel 60 P F_{254}. ^{1}H, ^{13}C and ^{31}P NMR spectra were recorded in $CDCl_3$ and toluene-d_7 solutions on a Varian 500 MHz spectrometer. Thermal properties of compounds were investigated on a Mettler Toledo TGA/SDTA 851 Thermogravimetric Analysis (TGA) and Differential Scanning Calorimeter DSC 821^e (DSC) equipped with METTLER TOLEDO STAR^e software at a heating rate of 10 °C min^{-1} under nitrogen flow (50 ml min^{-1}).

2.3. Fluorescence quantum yields and lifetimes

Fluorescence quantum yields (Φ_F) were determined by the comparative method (Eq. (1)) [25],

$$\Phi_F = \Phi_F(\mathrm{Std})\frac{F.A_{\mathrm{Std}}.\eta^2}{F_{\mathrm{Std}}.A.\eta^2_{\mathrm{Std}}} \quad (1)$$

where F and F_{Std} are the areas under the fluorescence emission curves of the samples (**4**, **5** and **6**) and the standard, respectively. A and A_{Std} are the respective absorbance of the samples and standard at the excitation wavelengths, respectively. The refractive indices of the solvents were employed in calculating the fluorescence quantum yields in different solvents. 2-Aminopyridine (in 0.1 M H_2SO_4) ($\Phi_F = 0.60$) [26] was employed as the standard. Both the samples and standard were excited at the same wavelength. The molar concentration of compound **6** was calculated on the basis of the molecular mass of the repeating unit. The concentration of the solutions at the excitation wavelength was fixed at 1×10^{-5} mol dm^{-3}. Natural radiative (τ_0) life times were determined using the PHOTOCHEMCAD program which uses the Strickler–Berg equation [27]. The fluorescence lifetimes (τ_F) were evaluated using Eq. (2).

$$\Phi_F = \frac{\tau_F}{\tau_0} \quad (2)$$

2.4. Synthesis

The 1,1,3,3,5-pentaphenoxy-5-chlorocyclotriphosphazatriene (**1**) [28], compounds (**2**, **3**) [29] and poly(dichlorophosphazene) [30] were prepared and purified according to the literature procedures.

2.5. Synthesis of compound *4*

The trimer $N_3P_3Cl_6$ (0.048 g, 0.141 mmol) and compound **3** (0.60 g, 0.84 mmol) were dissolved in dry THF (10 ml) under an argon atmosphere. After stirring for 15 min. at 40 °C, dry and finely powdered caesium carbonate (0.291 g, 0.9 mmol) was added portionwise over 15 min. with efficient stirring. The reaction mixture was stirred under an argon atmosphere at 80 °C for 24 h. The reaction mixture filtered, the volatile materials were evaporated under vacuum and the product was purified by preparative TLC on silica gel using hexane: THF (1:1) as the eluent. Compound **4** is a highly viscous oil; Yield: 0.351 g (57%). (*Anal.* Calc. for $C_{216}H_{174}N_{21}O_{42}P_{21}$ (4386): C, 59.15; H, 4.00; N, 6.71. Found: C, 58.75; H, 4.08; N, 6.60%). ^{1}H NMR ($CDCl_3$) δ = 11.85–12.08 (m, 174H, ArCH). $\{^1H\}^{13}C$ NMR ($CDCl_3$) δ = 137.62 (ArC), 128.84 (ArCH), 127.95 (ArC), 125.07 (ArCH), 77.5 (ArCH). $\{^1H\}^{31}P$ NMR (toluene-d_7) δ = 10.41 [m, 4P, > $P(OPh)_2$, B_2], 10.77 [m,2P > P(OPh)(OPhO),A], 10.1[s,1P, >PR_2, C_3]; $^2J_{P,P}$ = 90.88 Hz. MS (MALDI-TOF) *m*/*z* (%):4387 (100) $[M+H]^+$.

2.6. Synthesis of compound *5*

Octachlorocyclotetraphosphazene(tetramer), $N_4P_4Cl_8$, (0.06 g, 0.126 mmol) and compound **3** (0.72 g, 1.02 mmol) were dissolved in dry THF (10 ml) under an argon atmosphere. After stirring for 15 min. at 40 °C, dry and finely powdered caesium carbonate (0.39 g, 1.2 mmol) was added portionwise over 30 min with efficient stirring. The reaction mixture was stirred under an argon atmosphere at 80 °C for 48 h. The reaction mixture was filtered, the volatile materials were evaporated under vacuum and the product was purified by preparative TLC on silica gel using hexane: THF (1:1) as the eluent. Compound **5** is a highly viscous oil; Yield: 0.324 g (44%). (Anal. Calc. for $C_{288}H_{232}N_{28}O_{56}P_{28}$ (5848): C, 59.15; H, 4.00; N, 6.71. Found: C, 59.25; H, 4.08; N, 6.61%). ^{1}H NMR ($CDCl_3$) δ = 6.68–7.29 (m, 232H, ArCH). $\{^1H\}^{13}C$ NMR ($CDCl_3$) δ = 147.50 (ArC), 136.01 (ArCH), 128.49 (ArC), 125.76 (ArCH), 121.13 (ArCH). $\{^1H\}^{31}P$ NMR (toluene-d_7) δ = 9.83 [m,4P, >$P(OPh)_2$,B_2], 10.11 [m,2P, >P(OPh)(OPhO),A], −11.21[s,1P, >PR_2,X_4]; $^2J_{P,P}$ = 89.78 Hz. MS (MALDI-TOF) *m*/*z* (%):5849 (100) $[M+H]^+$.

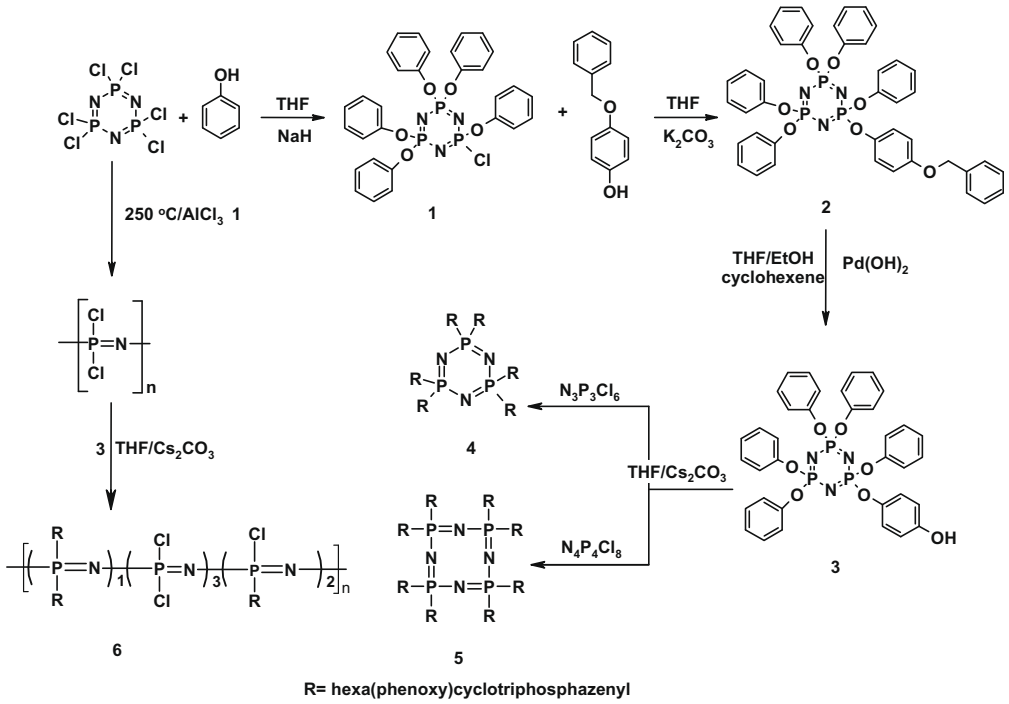
2.7. Synthesis of compound *6*

Compound **3** (0.7 g, 1 mmol) was added to a THF solution of poly(dichlorophosphazene) [38 mg, 0.32 mmol (based on $NPCl_2$)] in 7 ml THF, under a nitrogen atmosphere. Then dry and finely powdered caesium carbonate (0.27 g, 1.27 mmol) was added quickly to the reaction mixture with efficient stirring, as an HCl acceptor. The reaction mixture was stirred under a nitrogen atmosphere at room temperature for 24 h and then refluxed for 7 days. The reaction mixture was then cooled to room temperature and poured into concentrated HCl (10 ml). The soluble materials were filtered off and the remaining polymer (**6**) was washed with water (2 × 100 ml) and ethanol (2 × 50 ml), and then dried in a vacuum oven for 8 h at 60 °C. Compound **6** is white amorphous material; Yield: 0.27 g (51%) (*Anal.* Calc. for $[C_{144}H_{116}Cl_8N_{18}O_{28}P_{18}]_n$: C, 51.05; H, 3.45; N, 7.44. Found: C, 50.67; H, 3.48; N, 7.41%). $\{^1H\}^{31}P$ NMR ($CDCl_3$) δ = 9.75 [br.s,∼12P, >$P(OPh)_2$ and >P(OPh)(OPhO)], −17.6 [br.s,∼3P, $Cl_2P{=}N$], −20.3 [br.s,∼2P, $RClP{=}N$],−20.8 [br.s,∼1P, $R_2P{=}N$] (GPC): $Mw = 4.95 \times 10^5$, $Mn = 1.56 \times 10^5$.

3. Results and discussion

3.1. Synthesis and characterisation

The synthetic route for the compounds presented in this work is shown in Scheme 1. Compound **1** was synthesised [28] by the reaction of phenol with trimer $N_3P_3Cl_6$, in the presence of NaH in THF. Compound **1** was reacted with 4-benzyloxyphenol in the presence of K_2CO_3 in THF to obtain compound **2**. The 4-benzyloxyphenoxy unit of compound **2** was converted to a 4-hydroxyphenoxy group with cyclohexene in a mixture of THF/ethanol, in the presence of $Pd(OH)_2$ as a catalyst to give compound **3** in good yield (90%), as reported in our earlier work [29]. Compounds **4** and **5** were obtained from nucleophilic displacement reactions of **3** with $N_3P_3Cl_6$ or $N_4P_4Cl_8$ under an argon atmosphere with caesium carbonate as the base. The products were purified by preparative TLC on silica gel using hexane:THF (1:1) as the eluent. The conventional methods



Scheme 1. Chemical structure and synthetic pathway of **1–6**.

[31,32] of thermal ring opening polymerisation of the trimer yields a high molecular weight (>l0^6) polymer, but for subsequent substitution reactions careful purification procedures are required to remove the unreacted trimer and partially crosslinked polymer. Sohn and coworkers described another ring opening polymerisation method of the trimer which gives relatively lower molecular weight (10^4–10^5) poly(dichlorophosphazene) with almost quantitative yield, and can be used without purification for subsequent substitution reactions [30]. Thus poly(dichlorophosphazene) was prepared via the ring opening polymerisation of the trimer in a sealed tube at 250 °C in the presence of $AlCl_3$ as a catalyst, as described in the literature procedure [30]. The average molecular weight of the prepared poly(dichlorophospazene) was 1.02×10^5, and the polydispersity index was 3.38, as determined by GPC {^{31}P NMR($CDCl_3$) $\delta = -17.6$ [s,1P,($Cl_2P{=}N$)]} and the total impurities, including starting material (trimer), tetramer and other oligomers, was less than 3%. Thus compound **3** was added a THF solution of poly(dichlorophosphazene) under a nitrogen atmosphere in a glove box with caesium carbonate, which was used as the base.

The new compounds were characterised by FT-IR, ^{1}H, ^{13}C and ^{31}P NMR, mass spectrometry and elemental analysis. All the results were consistent with the predicted structures, as shown in the experimental section. The FT-IR spectra feature peaks at around 1200 cm^{-1} (br) (P═N), 960 cm^{-1} (P–O) for a phosphazene ring and aromatic C–H stretching around 3200–3400 cm^{-1}, as expected [33]. The elemental analysis results and the mass spectral data for the newly synthesised cyclic compounds **4** and **5** were consistent with the assigned formulations. The mass spectra of these compounds were obtained by MALDI-TOF spectrometry. Many different MALDI matrices were investigated to find intense molecular ion peaks and low fragmentation. 1,8,9-Anthracenetriol MALDI matrix yielded the best MALDI-MS spectra. The MS spectra of **4** and **5** provided definitive characterisation. The peak group representing the protonated molecular ion of the **4** was observed at 4387 Da (Fig. 3s a) and the protonated molecular ion peak were observed at 5849 Da for **5** (Fig. 3s b). The average molecular weight and polydispersity index (PDI) of the polymer (**6**), determined by gel permeation chromatography, was 4.95×10^5 and 3.17, respectively. This large PDI value of compound (**6**) was an expected result because it originated from the preparation method of the starting polymer (PDI: 3.38). In particular, ^{31}P NMR spectra of **4** and **5** were analysed in two different spin systems as $(AB_2)_6C_3$ and $(AB_2)_8X_4$. The proton-decoupled ^{31}P NMR spectrum of **4** has the expected AB_2 and C_3 spin system parts, shown in Fig. 2. The resonances belonging to phenoxy substituted phosphorous atoms for the AB_2 pattern were observed at ca. 10.41 ppm for >P(OPh)$_2$ and at ca. 10.77 ppm for >P(OPh)(OPhOX) (X = trimer core). The resonance belonging to the trimer core phosphorus at ca. 10.1 ppm is observed in a C_3 spin system, yielding a single peak as expected. The proton-decoupled ^{31}P NMR spectrum of **5** has the expected AB_2 and X_4 spin system parts shown in Fig. 3. The resonances belonging to the phenoxy substituted phosphorous atoms for the AB_2 pattern were observed at ca. 9.83 ppm for >P(OPh)$_2$ and at ca. 10.11 ppm for >P(OPh)(OPhOX) (X = tetramer core). The resonance belonging to the tetramer core phosphorus at −11.21 ppm was observed in a X_4 spin system, yielding a single peak as expected [34]. The magnitude of $^2J_{(PP)}$ for the cyclic compounds **4**

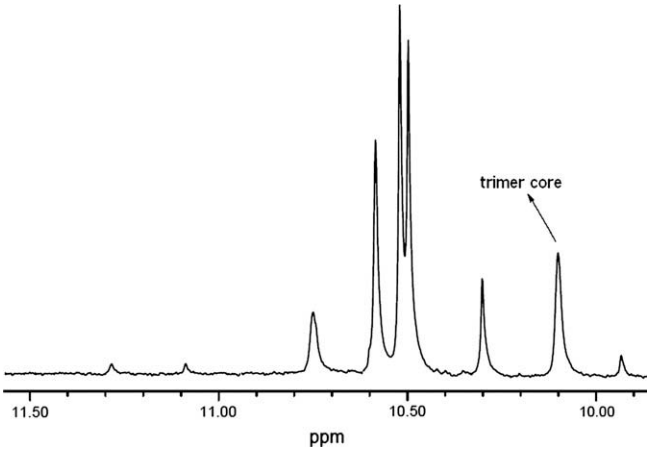


Fig. 2. Proton-decoupled ^{31}P NMR spectrum of **4** in toluene-d_7 solution.

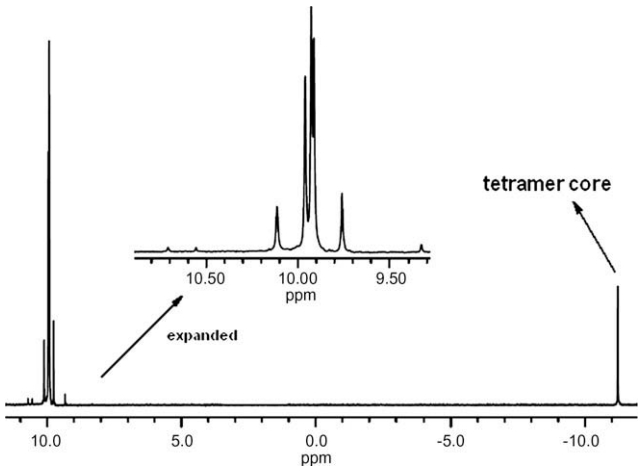


Fig. 3. Proton-decoupled ^{31}P NMR spectrum of **5** in toluene-d_7 solution.

and **5** have very similar coupling constants, 90.88 and 89.78 Hz, respectively. The integration of the AB_2 part to the remaining singlet of the proton-decoupled ^{31}P NMR spectra of cyclic compounds **4** and **5** gave a 6:1 phosphorus ratio that confirms the suggested structures. The structural characterisation of compound **6** was determined by ^{31}P NMR spectroscopy. The progress of the reaction was investigated by the removal of small aliquots and diluting them approximately one to one with deuterated chloroform. The ^{31}P NMR results are given in the Supplementary information in Fig. 1s. In the reaction of poly(dichlorophosphazene) with compound **3** there are three possible species, $NPCl_2$, NPClR and NPR_2 belong to the macromolecular phosphazene chain. The narrow singlet of poly(dichlorophosphazene) at −17.6 ppm broadens at the start of the reaction (Fig. 1s a and b). Approximately at −20.3 ppm there is a broad resonance that has been assigned to NPClR, that appears after 5 h room temperature reaction. After 24 h reaction at room temperature, the results are similar to the previous ^{31}P NMR spectrum, which is shown in Fig. 1s b. The reaction continued on refluxing and a broad resonance at approximately −20.8 ppm appeared after 1 h, which has been assigned to NPR_2 (Fig. 1s). On further reflux of up to 5 h, the intensities of the broad resonances at −17.6 and −20.3 ppm decrease whilst the intensity of the broad resonance at −20.8 ppm increases (Fig. 1s c and d). On the other hand, there is a broad singlet which belongs to the side units, at approximately 9.6 ppm, which shows increasing intensity with the reaction progress (Fig. 1s b–d). Further refluxing up to 7 days did not change the results and the ^{31}P NMR spectrum is similar to Fig. 1s d. The ^{31}P NMR spectrum of the isolated polymer (**6**) after 7 days reflux is given in Fig. 2s. The ^{31}P NMR spectrum of compound **6** (Fig. 2s) shows four groups of peaks; a broad singlet at 9.75 ppm belonging to the phosphorus atoms of the side unit, as expected, and an additional three broad peaks at −17.6 ($Cl_2P{=}N$), −20.3 (RClP=N) and −20.8 ppm ($R_2P{=}N$), belonging to the phosphorus atoms of the macromolecular polymer chain. The integration of the proton-decoupled ^{31}P NMR spectrum of the isolated polymer (Fig. 2s) gave approximately a 12:3:2:1 phosphorus ratio. Thus the repeating unit of compound **6** was suggested to be $[(NP(OR)_2)_1(NPORCl)_2(NPCl_2)_3]_n$.

3.2. Thermal properties

The glass transition temperatures (T_g) of all the compounds were clearly detected by differential scanning calorimetry (DSC) from −40 to 100 °C with a heating rate of 10 °C/min under nitrogen flow. The T_g of all the new phosphazene compounds (**4–6**) are represented in Table 1 and the DSC thermograms are given in the Supplementary information in Fig. 4s.

Table 1
Thermal properties and molecular weights of **4**, **5** and **6**.

Compound	T_g (°C)	T_d (°C)	*Mw*	*Mn*	Char yield (%)
4	26.2	422	4387	4387	33.3
5	24.5	445	5849	5849	64.6
6[a]	28.7	396	4.95×10^5	1.56×10^5	59.8

[a] Molecular weight determined by GPC.

Phosphazenes are attractive compounds due to their higher thermal stability and flame retardancy properties when compared to their organic homologues. Owing to the excellent thermal stability and char yield performance, aryloxy substituted polyphosphazene has attracted interest for its potential application in flame retardants [35]. For such reasons we have investigated the thermal stability of the compounds **4** and **5**, and compared the results with polymer **6** by determining the weight loss of a sample upon linearly increasing the temperature by conventional TGA at 10 °C/min up to 700 °C under nitrogen flow. According to the TGA thermograms of compounds **4–6** (Fig. 5s), they exhibit very good thermal stability with decomposition temperatures (T_d) in the range 396–445 °C (see Table 1). The decomposition onset temperatures (T_{on}) of compounds **4**,**5** and polymer **6** are 396, 423 and 347 °C, and the char yields reaches 33.3%, 64.6% and 59.8% at 700 °C, respectively. The increase of T_d from compound **4** to **5** can be explained by the increasing substitution degree of the cyclophosphazene chain. However, the partially substituted polymer **6** has a lower T_d (396 °C) when compared with **4** and **5**. This is an expected result with the depolymerisation effect of the unsubstituted P–Cl groups on the polymer chain overriding the thermal stability [36]. On the other hand, polyaryloxyphosphazenes always contains unreacted chlorine atoms based on the rigidity and the steric hindrance of the aryloxy nucleophiles. Therefore, if they are used as a flame retardant, poisonous gases are released, which limits their further application [36]. Therefore aryloxycyclophosphazenes are more useful candidates for flame retardant additives to organic polymers [35]. As a result, the high char yields and T_d values of these novel phosphazene compounds (**4**, **5**) make them good flame retardants in theory [37], and we can clearly say that the cyclic derivatives **4** and **5** have excellent thermal properties because of their high purity against the polymeric analogue **6**.

3.3. Ground state electronic absorption and fluorescence spectra

The absorption and fluorescence spectra of the phosphazene derivatives were measured in dichloromethane with dilute solutions of 1×10^{-5} mol dm^{-3} upon excitation at 260 nm. Absorption bands were observed for compounds **4** and **5** at 260 and 270 nm, and 230, 260 and 270 nm for polymer **6** (Fig. 4). The trend in absorption maximum amongst the phosphazene compounds is polymeric phosphazene derivative (**6**) > tetrameric core phosphazene derivative (**5**) > trimeric core phosphazene derivative (**4**), according to the number of phenol groups (Fig. 4). Fig. 5 shows the fluorescence emission spectra for the studied phosphazene compounds. Fluorescence emission peaks were observed at around 298 nm for all the compounds in dichloromethane. The cyclic phosphazene derivatives (**4** and **5**) showed higher fluorescence emission behaviour than the polymeric phosphazene derivative (**6**). When comparing between the cyclicphosphazenes, the tetrameric core phosphazene compound (**5**) showed higher fluorescence emission than the trimeric core phosphazene compound (**4**). Fig. 5 indicates that the cyclic phosphazenes compounds (**4**, **5**) are more fluorescent than the polymeric analogue (**6**). In contrast to the absorption spectra, the fluorescence emission is

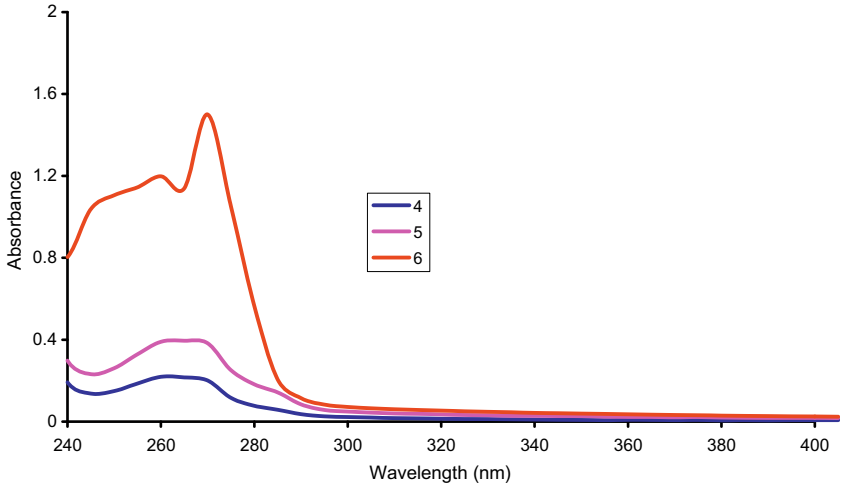


Fig. 4. The absorption spectra of **4**, **5** and **6** in dichloromethane. Concentration: 1×10^{-5} mol dm^{-3}.

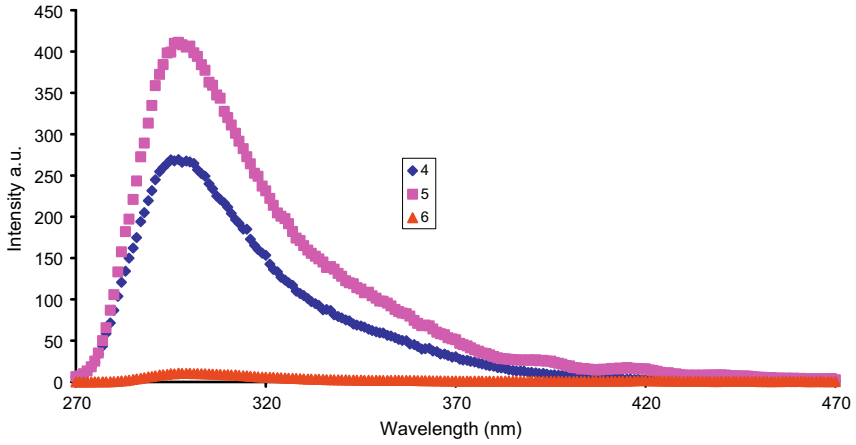


Fig. 5. The fluorescence emission spectra of **4**, **5** and **6** in dichloromethane. Concentration: 1×10^{-5} mol dm^{-3}. Excitation wavelength: 260 nm.

not related to the number of the phenol groups. We suggest that the arrangement of substituents is more effective than the number of substituents for the fluorescence emission behaviour of these compounds. This can be explained by non-covalent π–π interactions between the phenol groups. Crystal structure analysis of hexaphenoxycyclotriphosphazene has shown [38] that the six phenoxy groups reach almost perpendicularly above and below the nearly planar cyclotriphosphazene core. This structural features make it possible for the three phenoxy groups to be located on the same side of the $(PN)_3$ plane and the centroid–centroid distance of two phenyl groups are very close to the normal π–π stacking contact. This type of non-covalent π–π interaction can explain the higher fluorescence behaviour of the cyclic phosphazene compounds when compared to a polymeric phosphazene compound which is substituted with the same group. It can also support that the partially (unsubstituted PCl_2 groups on the polymer chain) substituted polymer **6** has reduced non-covalent π–π interactions. According to these results, the cyclic phosphazenes are more suitable candidates than the polymeric analogues for some applications such as organic light emitting devices.

3.4. Fluorescence quantum yields and lifetimes

The fluorescence quantum yields (Φ_F) of the phosphazene derivatives were measured in dichloromethane, and 2-aminopyridine in 0.1 M H_2SO_4 solution was used as the standard. The refractive indexes of the solvents were used for calculations of Φ_F. All the compounds were excited at 260 nm. The fluorescence quantum yield values are: 0.16 for **4**, 0.18 for **5** and 0.00033 for **6** in dichloromethane. The cyclic phosphazene derivatives (**4** and **5**) showed approximately 500 times larger Φ_F values than the polymeric phosphazene derivative (**6**). When we made a comparison between the cyclic phosphazenes, the tetrameric core phosphazene compound (**5**) showed a slightly higher fluorescence quantum yield than the trimeric core phosphazene compound (**4**). It can be explained that the non-covalent π–π interactions between the aryloxy groups on the cyclophosphazene core compounds have caused the higher fluorescence quantum yield values of the cyclophosphazene core compounds when compared to the polymeric phosphazene compound. The fluorescence lifetime refers to the average time a molecule stays in its excited state before fluorescing, and its value is directly related to that of Φ_F; i.e. the longer the lifetime, the higher the quantum yield of fluorescence. Any factor that shortens the fluorescence lifetime of a fluorophore indirectly reduces the value of Φ_F. Such factors include internal conversion and intersystem crossing. As a result, the nature and the environment of a fluorophore determine its fluorescence lifetime. The fluorescence lifetimes (τ_F) of phosphazene compounds were calculated using the Strickler–Berg equation [26]. A good correlation has been found between the experimental and the theoretically determined lifetimes for the unaggregated molecules [39]. Thus, we suggest that the values obtained using this equation

are an appropriate measure of the fluorescence lifetimes. The fluorescence lifetime (τ_F) values are: 0.14 ns for **4**, 0.32 ns for **5** and 0.00003 ns for **6** in dichloromethane. The τ_F values for the cyclic-phosphazene derivatives (**4** and **5**) are approximately 10000 times larger than the polymeric phosphazene derivative (**6**). A comparison between the cyclophosphazenes **4** and **5** shows the tetrameric core phosphazene compound (**5**) has a longer fluorescence lifetime value (τ_F) than the trimeric cored phosphazene compound (**4**) in dichloromethane. The rate constants for the fluorescence (k_F) and radiative lifetime (τ_0) were also measured for the synthesised phosphazene compounds in this study. The rate constants for fluorescence (k_F) values are: 1.11×10^9 for **4**, 0.57×10^9 for **5** and 12.0×10^9 for **6**, and the radiative lifetime (τ_0) values are: 0.89 ns for **4**, 1.76 ns for **5** and 0.083 ns for **6** in dichloromethane. The cyclophosphazene compounds **4** and **5** showed lower the rate constants for fluorescence (k_F) and showed longer radiative lifetime (τ_0) values when compared to the polymeric phosphazene derivative (**6**).

4. Conclusion

In summary, we have synthesised novel hexa(phenoxy)cyclotriphosphazenyl substituted cyclic and polymeric phosphazene compounds (**4–6**) for the first time. All the compounds were fully characterised by standard spectroscopic techniques. The thermal stability and fluorescence spectral properties of all the compounds were investigated. It was found that compounds **4** and **5** have higher thermal stability and fluorescence behaviour when compared with the polymeric phosphazene analogue (**6**). We suggest that the non-covalent π–π interactions between the phenoxy groups have resulted in the higher fluorescence behaviour of the cyclic phosphazene compounds when compared to the polymeric phosphazene compound. Thus, it can be suggested that cyclic phosphazenes are more suitable candidates than the polymeric analogue for some industrial applications such as flame retardant additives to polymers or light emitting electroluminescent devices.

Acknowledgement

We thank the Gebze Institute of Technology (GIT) Research Fund for partial financial support.

Appendix A. Supplementary data

Supplementary data associated with this article can be found, in the online version, at doi:10.1016/j.poly.2009.05.027.

References

[1] J.E. Mark, H.R. Allcock, R. West, Inorganic Polymers, Prentice Hall, Englewood Cliffs, NJ, 1992.
[2] I. Manners, Angew. Chem., Int. Ed. Engl. 35 (1996) 1602.
[3] H.R. Allcock, Phosphorus–Nitrogen Compounds, Academic Press, New York, 1972 (Chapters 6 and 7).
[4] C.W. Allen, Chem. Rev. 91 (1991) 119.
[5] R. de Jaeger, M. Gleria, Prog. Polym. Sci. 23 (1998) 179.
[6] M. Gleria, R. De Jaeger (Eds.), Phosphazenes: A World Wide Insight, Nova Science Publishers, New York, 2004.
[7] H.R. Allcock, Chemistry and Applications of Polyphosphazenes, Wiley Interscience, New York, 2003.
[8] H.R. Allcock, E.H. Klingenberg, Macromolecules 28 (1995) 4351.
[9] R.E. Singler, R. Willingham, C. Noel, C. Friedrich, L. Bosio, E. Atkins, Macromolecules 24 (1991) 510.
[10] R.L. Dieck, E.J. Quinn, US Patent 4,055.520, 1977.
[11] K.A. Reynard, S.H. Rose, US Patent 3,883.451, 1975.
[12] W.B. Mueller, S.D. Landry, US patent 4,870.113, 1989.
[13] W.K. Huang, J.-T. Yeh, K.J. Chen, K.N. Chen, J. Appl. Polym. Sci. 79 (2001) 662.
[14] G.F. Levchik, Y.V. Grigoriev, A.I. Balabanovich, S.V. Levchik, M. Klatt, Polym. Int. 49 (2000) 1095.
[15] B.L. Denq, Y.S. Hu, W.Y. Chiu, L.W. Chen, Y.S. Chid, Polym. Degrad. Stab. 57 (1997) 269.
[16] B.L. Denq, W.Y. Chiu, L.W. Chen, C.Y. Lee, Polym. Degrad. Stab. 57 (1997) 26l.
[17] R. Liu, X. Wang, Polym. Degrad. Stab. 95 (2009) 1.
[18] N. Chattopadhyay, B. Haldar, A. Mallick, S. Sengupta, Tetrahedron Lett. 46 (2005) 3089.
[19] H.J. Bolink, S.G. Santamaria, S. Sudhakar, C. Zhen, A. Sellinger, Chem. Commun. 67 (2008) 618.
[20] J. Xu, C.L. Toh, K.L. Ke, J.J. Li, C.M. Cho, X. Lu, E.W. Tan, C. He, Macromolecules 41 (24) (2008) 9624.
[21] H.R. Allcock, D.C. Ngo, Macromolecules 25 (1992) 2802.
[22] V. Maraval, A.M. Caminade, J.P. Majoral, J.C. Blais, Angew. Chem., Int. Ed. 42 (2003) 1822.
[23] H.R. Allcock, W.R. Laredo, E.C. Kellam, R.V. Morford, Macromolecules 34 (2001) 787.
[24] S.T. Fei, R.M. Wood, D.K. Lee, D.A. Stone, H.L. Chang, H.R. Allcock, J. Memb. Sci. 320 (2008) 206.
[25] S. Fery-Forgues, D. Lavabre, J. Chem. Ed. 76 (1999) 1260.
[26] R. Rusakowicz, A.C. Testa, J. Phys. Chem. 72 (1968) 2680.
[27] H. Du, R.A. Fuh, J. Li, A. Corkan, J.S. Lindsey, Photochem. Photobiol. 68 (1998) 141.
[28] D. Dell, B.W. Fitzsimmons, R.A. Shaw, J. Chem. Soc. (1965) 4070.
[29] F. Hacıvelioğlu, M. Durmuş, S. Yeşilot, A.G. Gürek, A. Kılıc, V. Ahsen, Dyes Pigments 79 (2008) 14.
[30] Y.S. Sohn, Y.H. Cho, H. Baek, O.S. Jung, Macromolecules 28 (1995) 7566.
[31] H.R. Allcock, R.L. Kugel, J. Am. Chem. Soc. 87 (1965) 4216.
[32] R.E. Singler, N.S. Schneider, G.L. Hagnauer, Polym. Eng. Sci. 15 (1975) 321.
[33] H.R. Allcock, J. Am. Chem. Soc. 86 (1964) 2591.
[34] S.S. Krishnamurthy, M. Woods, Annu. Rep. NMR Spectrosc. 19 (1987) 175.
[35] P. Potin, R.D. Jaeger, Eur. Polym. J. 27 (1991) 341.
[36] B.X. Huang, L. Yın, Z.X. Tang, Sci. China, Ser. B-Chem. 51 (1) (2008) 46.
[37] A.F. Van, K.D.W. Van, J. Polym. Sci.: Polym. Phys. Ed. 10 (1972) 2423.
[38] W.C. Marsh, J. Trotter, J. Chem. Soc. A 1 (1971) 169.
[39] N.K. Suhling, D. Phillips, J. Porphyrins Phthalocyanines 6 (2002) 373.

Polyhedron 28 (2009) 2517–2521

Contents lists available at ScienceDirect

Polyhedron

journal homepage: www.elsevier.com/locate/poly

Synthesis, characterization and crystal structure of a dioxomolybdenum(VI) complex with a N,O type bidentate Schiff base ligand as a catalyst for homogeneous oxidation of olefins

Mojtaba Bagherzadeh [a,*], Reza Latifi [a], Laleh Tahsini [a], Vahid Amani [a], Arkady Ellern [b], L. Keith Woo [b]

[a] Chemistry Department, Sharif University of Technology, Tehran, P.O. Box 11155-3615, Iran
[b] Chemistry Department, Iowa State University, Ames, Iowa 50011-3111, USA

ARTICLE INFO

Article history:
Received 10 December 2008
Accepted 5 May 2009
Available online 22 May 2009

Keywords:
Molybdenum(VI)
Schiff base
TBHP
Catalytic epoxidation
Olefin

ABSTRACT

The synthesis of a Mo(VI) Schiff base complex, *cis*-[MoO_2{(4,6-bis(*tert*-butyl)-2-{(benzyl)iminomethyl}-phenolate)$_2$}], *cis*-[$MoO_2(L)_2$] where L = 4,6-bis(*tert*-butyl)-2-{(benzyl)iminomethyl}phenol, derived from benzylamine and 3,5-di-*tert*-butylsalycilaldehyde is reported. Full characterization of this complex was accomplished with elemental analyses, spectroscopic studies (NMR, IR and electronic) and X-ray structure analysis. This complex was tested as a catalyst for the homogeneous oxidation of olefins. The Mo(VI) complex is catalytically active for the epoxidation of aliphatic substrates at 80 °C, yielding the epoxide as the sole product in yields up to 100% and turnover numbers up to 5000. Under the optimized conditions styrene was oxidized in an 81% conversion to produce styrene oxide, benzaldehyde, and acetophenone.
© 2009 Elsevier Ltd. All rights reserved.

1. Introduction

As molybdenum is widely available to biological systems, the coordination chemistry of Mo(VI) has aroused considerable interest in view of its biochemical significance [1–4]. Apart from nitrogenases, where molybdenum can be a component of the multinuclear active sites [5], there are a number of mononuclear molybdenum enzymes that are often referred to as oxomolybdenum enzymes [2,3]. The latter can be divided into two groups: enzymes from the first group catalyze the oxidative hydroxylation of aldehydes and aromatic heterocycles in reactions that necessarily involve the cleavage of a C–H bond [2,3,6]. Mononuclear enzymes from the second group catalyze proper oxygen atom transfer reactions to or from an available electron lone pair of the substrates [7]. The present view of these enzymes indicates that the formal oxidation state of the molybdenum center cycles between 4+ and 6+ during the catalysis. The two-electron oxygen atom transfer seems to be the relevant mechanism in understanding the chemical role of enzymatic reactions. In order to mimic biological systems, a number of dioxomolybdenum complexes have been synthesized and characterized [8–27]. Molybdenum Schiff base complexes continue to serve as one of the most important models of molybdoenzymes due to their preparative accessibility [28–37].

Moreover, a broad variety of molybdenum complexes are highly active catalysts for olefin epoxidation in the homogeneous phase. Molybdenum catalysts are commercially applied to the production of propylene oxide using *tert*-butyl hydrogen peroxide (TBHP) as the oxidant [38]. TBHP as an oxidant has good thermal stability and is relatively easy to handle [38]. Furthermore, the by-product of the reaction, *tert*-butyl alcohol, is easy to separate by distillation and can be recycled or used for other industrial processes. This paper investigates the synthesis, spectral and structural characterization of a *cis*-dioxomolybdenum complex of a bidentate 4,6-bis(*tert*-butyl)-2-{(benzyl)iminomethyl}phenol Schiff base ligand. The oxo-transfer reaction from *cis*-[$MoO_2(L)_2$] to olefins is also reported.

2. Experimental

2.1. Materials and instrumentations

All of the reagents were supplied by Merck and Fluka, and were employed without further purification. IR spectra were recorded on a Unicam Matson 1000 FT-IR paragon 1000 spectrophotometer. ^{1}H NMR spectra of the ligand and the complex were recorded on a Bruker FT-NMR 500 MHz spectrometer using $CDCl_3$ and $(CD_3)_2SO$ as solvents. The electronic spectra were recorded on a CARY 100 Bio UV–Vis spectrophotometer. Elemental analyses (C, H and N) were performed using a Heraeus Elemental Analyzer CHN–O-Rapid (Elementar-Analysensysteme, GmbH).

* Corresponding author. Tel.: +98 21 66165354; fax: +98 21 66012983.
E-mail address: bagherzadehm@sharif.edu (M. Bagherzadeh).

0277-5387/$ - see front matter © 2009 Elsevier Ltd. All rights reserved.
doi:10.1016/j.poly.2009.05.036

2.2. Synthesis of cis-[MoO_2(4,6-bis(tert-butyl)-2-{(benzyl)iminomethyl}phenolate)$_2$], cis-[$MoO_2(L)_2$]

To a solution of 3,5-di-*tert*-butylsalicyldehyde [39] (1 mmol) in 25 mL methanol was added a solution of 1 mmol benzylamine in 15 mL methanol, and the reaction mixture was heated at reflux for 1 h. Then a methanolic solution of 0.5 mmol of $MoO_2(acac)_2$ [40] (15 mL) was added dropwise under stirring. The solution color changed to deep yellow and after 5 min yellow crystals of *cis*-[MoO_2(4,6-bis(*tert*-butyl)-2-{(benzyl)iminomethyl}phenolate)$_2$] started to precipitate. After the reflux was continued for 30 min, the product was filtered and washed with methanol (82% yield). X-ray quality crystals were obtained after recrystallization from a ethanol:chloroform (1:1) solvent mixture. Elemental *Anal.* Calc. for *cis*-[$MoO_2(L)_2$] ($C_{44}H_{56}MoN_2O_4$, FW = 772.85): C, 68.38; H, 7.30; N, 3.62. Found: C, 68.40; H, 7.31; N, 3.60%. Selected IR frequencies (KBr disk, cm^{-1}): 1622 (C=N), 1560, 1454, 1437, 1392, 1358, 1269, 1247. Electronic absorption spectrum in CH_3OH λ (nm) ($\varepsilon(M^{-1}\,cm^{-1})$): 342 (21122), 267 (76281), 240 (90424). ^1H NMR (500 MHz, DMSO-d_6, δ): 1.35 (s, 18H), 1.44 (s, 18H), 4.52 (d, 2H), 4.92 (d, 2H), 7.08 (m, 6H), 7.27 (m, 6H), 7.59 (d, 2H), 8.05 (s, 2H).

2.3. Single crystal X-ray diffraction

The crystal data of the title compound and the parameters of data collection are summarized in Table 1. A yellow transparent crystal was selected under ambient conditions. The crystal was mounted and centered in the X-ray beam using a video camera. The crystal evaluation and data collection were performed at 173 K on a Bruker CCD-1000 diffractometer with Mo Kα (λ = 0.71073 Å) radiation and a detector to crystal distance of 5.03 cm. The initial cell constants were obtained from three series of ω scans at different starting angles. Each series consisted of 30 frames collected at intervals of 0.3° in a 10° range about ω with an exposure time of 20 s per frame. The obtained reflections were successfully indexed by an automated indexing routine built in the SMART program. The final cell constants were calculated from a set of strong reflections from the actual data collection.

The data were collected using the full sphere routine by collecting four sets of frames with 0.3° scans in ω with an exposure time 20 s per frame. This dataset was corrected for Lorentz and polarization effects. The absorption correction was based on fitting a function to the empirical transmission surface as sampled by multiple equivalent measurements [41] using SADABS software [42]. The systematic absences in the diffraction data were consistent for the space group *C2/c* [42], and yielded chemically reasonable and computationally stable results of refinement. The positions of almost all the non-hydrogen atoms were found by direct methods. The remaining atoms were located in an alternating series of least-squares cycles and difference Fourier maps. All non-hydrogen atoms were refined in full-matrix anisotropic approximation. All hydrogen atoms were placed in the structure factor calculation at idealized positions and were allowed to ride on the neighboring atoms with relative isotropic displacement coefficients. The ORTEP diagram was drawn at the 50% probability level. Hydrogen atoms were omitted for clarity. The resulting CIF file has been tested with PLATON [43] software.

Table 1
Crystal data and structure refinement for *cis*-[$MoO_2(L)_2$].

Formula	$C_{44}H_{56}MoN_2O_4$
Formula weight	772.85
T (K)	173(2)
Crystal system	monoclinic
Space group	*C2/c*
Crystal size/mm	0.50 × 0.20 × 0.15
a (Å)	24.76(3)
b (Å)	6.631(7)
c (Å)	26.09(3)
α (°)	90
β (°)	108.83(3)
γ (°)	90
V (Å^3)	4054(7)
Z	4
$D_{calcd.}$ (g cm^{-1})	1.266
θ Ranges for data collection	1.97–23.26
F(0 0 0)	1632
Absorption coefficient (mm^{-1})	0.366
Index range h, k, l	−26 → 27, −7 → 7, −28 → 28
Data collected	10 011
Unique data (R_{int})	2905(0.0772)
Parameters, restrains	237, 0
Final R_1, wR_2 (Obs. data)	0.0628, 0.1538
Final R_1, wR_2 (All data)	0.0994, 0.1836
Goodness of fit on F^2 (S)	0.963
Largest difference in peak and hole (e Å^3)	0.927, −1.080

2.4. Catalytic experiments

In a typical catalytic experiment, TBHP (1 mmol) was added to a solution of olefin (1 mmol), chlorobenzene (1 mmol) as an internal standard and *cis*-[$MoO_2(L)_2$] (2×10^{-4} mmol) in 1,2-dichloroethane (0.5 mL). The mixture was stirred at 80 °C under air and the course of the reaction was monitored using gas chromatography (Agilent Technologies Instruments 6890N, equipped with a capillary column (19019J-413 HP-5, 5% Phenyl Methyl Siloxane, Capillary 60.0 m × 250 μm × 1.00 μm) and a flame ionization detector). Assignments of products were made by comparison with authentic samples. All the reactions were run at least in duplicate.

3. Results and discussion

3.1. Crystal structure of cis-[$MoO_2(L)_2$]

The molecular structure of *cis*-[$MoO_2(L)_2$], crystal data and structure refinement are shown in Fig. 1 and Table 1, respectively. The selected bond distances and angles that are reported in Table 2 are in a good accord with those previously observed in analogous complexes with the MoO_2 moiety [16,18,44]. Like many other dioxomolybdenum(VI) complexes with nitrogen-donor-containing

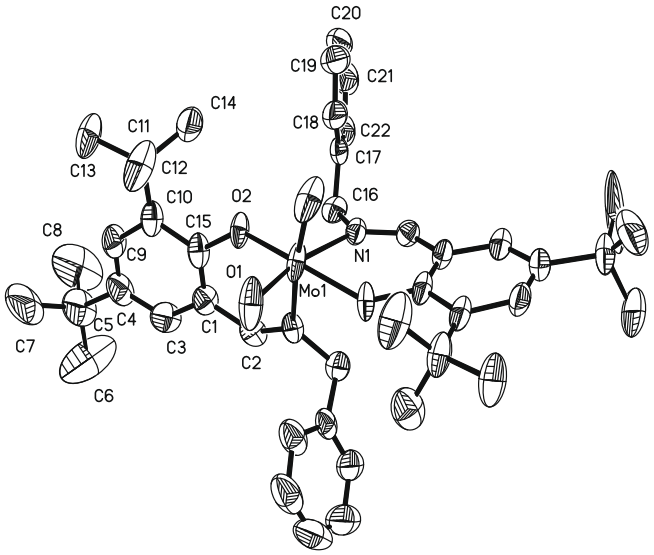


Fig. 1. An ORTEP view of the structure of *cis*-[MoO_2\{(4,6-bis(*tert*-butyl)-2-{(benzyl)iminomethyl}phenolate)$_2$\}], *cis*-[$MoO_2(L)_2$].

Table 2
Selected bond lengths (Å) and angles (°) for *cis*-[MoO(L)$_2$].

O(1)–Mo–O(1)#1	107.65(12)	O(2)–Mo–N(1)	84.19(7)
O(1)–Mo–O(2)	96.70(9)	O(2)#1–Mo–N(1)	79.98(7)
O(1)#1–Mo–O(2)	95.06(9)	N(1)–Mo–N(1)#1	75.14(10)
O(2)–Mo–O(2)#1	160.00(8)	C(2)#1–N(1)–Mo	123.37(13)
O(1)–Mo–N(1)	163.44(6)	C(16)–N(1)–Mo	121.18(12)
O(1)#1–Mo–N(1)	88.69(9)	C(15)–O(2)–Mo	135.22(10)
Mo–O(1)	1.7030(18)	Mo–N(1)	2.315(2)
Mo–O(2)	1.943(2)		

Symmetry transformations used to generate equivalent atoms: (#1) $-x+2$, y, $-z+3/2$.

bidentate ligands, this compound adopts a distorted octahedral geometry with the N atoms trans to the terminal oxo groups [16,18,44]. In the complex each of the Schiff base ligands behaves in a monoanionic bidentate manner, bonded to the *cis*-MoO_2^{2+} ion through the phenolic oxygen atom and an imine nitrogen atom. The O–Mo–O angle is significantly larger than 90°, which is expected due to a larger repulsion between oxygen atoms with short Mo–O bonds [16,31,37,45,46]. The O=Mo=O angle (107.65(12) Å) for *cis*-[MoO_2(L)$_2$] is typical for *cis*-dioxomolybdenum(VI) complexes [31,37,45,46]. The Mo=O distances are also as short as 1.7030(18) Å, as commonly observed for terminal oxygen atoms. These bonds are of double-bond character.

3.2. Catalytic oxidation of olefins

The catalytic performance of *cis*-[MoO_2(L)$_2$] was first studied in the homogeneous epoxidation of cyclooctene, used as a model substrate, and *tert*-butyl hydrogen peroxide as the oxygen donor. In a series of control experiments we evaluated the influence of several solvents. Epoxide conversion was found to be dependent on the solvent. For the given solvents in Table 3, benzene, toluene and 1,2-dichloroethane (DCE) produce the highest yields and the catalytic activity is the best when DCE is used as the solvent (100% conversion). With molar ratios of 1:5000:5000 for catalyst:substrate:oxidant at 80 °C as the optimized condition, a turnover number (TON) of up to 5000 can be achieved.

In this study, an attempt was also made to investigate the effect of temperature. The temperature-dependent curves for the yield of cyclooctene oxide in Fig. 2 show the epoxide yield is very low at lower temperatures (30 °C). Catalytic reactions run at higher temperatures led to a significant increase in the product yield. For example, at 50 °C, the *cis*-[MoO_2(L)$_2$] complex shows a moderate activity, reaching cyclooctene oxide yields of 74% for 1 h reaction time (Fig. 2). However, the activity increases considerably with an increase in temperature, so that at 70 and 80 °C, yields of 89% and 100% can be obtained, respectively.

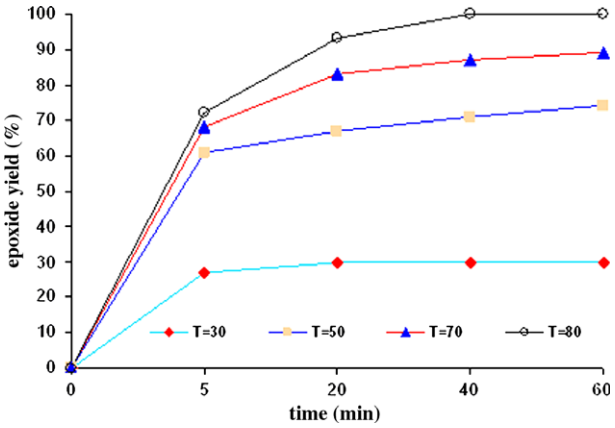


Fig. 2. Temperature effect on the epoxidation of cyclooctene with TBHP in the presence of *cis*-[MoO_2(L)$_2$].

This study was further extended to the catalytic epoxidation of several linear and cyclic olefins using *cis*-[MoO_2(L)$_2$] (Table 4). Generally the epoxide yields and selectivities were very good for aliphatic substrates, with the best epoxide yield and selectivity being obtained for cyclohexene in a short reaction time (Table 4, entry 1). The catalytic activity tends to decrease as the olefin becomes less electron rich, so that the lowest epoxide yields were obtained for styrene, α-methylstyrene and indene (Table 4, entries 10–12). Moreover, the present catalytic system was highly selective for the epoxide for all substrates except for styrene with benzaldehyde and acetophenone, and α-methylstyrene with acetophenone as side products. The relatively low activity for epoxidation of styrene, α-methylstyrene and indene does not seem to be caused by catalyst decomposition, since an increase in the reaction time for epoxidation of styrene leads to a significant increase in the conversion (Table 4, entry 10). It is worth pointing out that the *cis*-[MoO_2(L)$_2$] complex is quite stable under the oxidation reaction conditions. The significantly improved oxidation yield of styrene at higher reaction times can be good evidence for this stability (Table 4, entry 10).

In general, the mechanisms proposed for *t*-BuOOH-based epoxidation of olefins with Mo^{VI} complexes are heterolytic in nature, involving coordination of the oxidant to the metal center. The Lewis acidity of the Mo center increases the oxidizing power of the peroxo group and the olefin is subsequently deoxidized by nucleophilic attack on an electrophilic oxygen atom of the coordinated *tert*-butyl peroxide [47]. Spectroscopic and computational methods applied to molybdenum dioxo and oxodiperoxo complexes support a reaction mechanism involving an activation state formed between the complex, oxidant and olefin (Scheme 1) [48,49]. In this process, in higher conversions, the catalytic reaction may be prone to auto-retardation by coordination of the co-product *tert*-butanol to the molybdenum complex. *tert*-Butanol can compete with TBHP for coordination to the molybdenum center and form an inactive species that leads to the decreasing reaction rate [48]. Similarly, for complex *cis*-[MoO_2(L)$_2$], the initial reaction rates are much higher than those observed later in the reactions (Table 3 entries 5 and 9, and Fig. 3).

Previously, many systems have reported the oxidation of olefins by various transition metal complexes, such as Mn, V and Ru

Table 3
The effect of various solvents on the epoxidation of cyclooctene with TBHP using *cis*-[MoO_2(L)$_2$].[a]

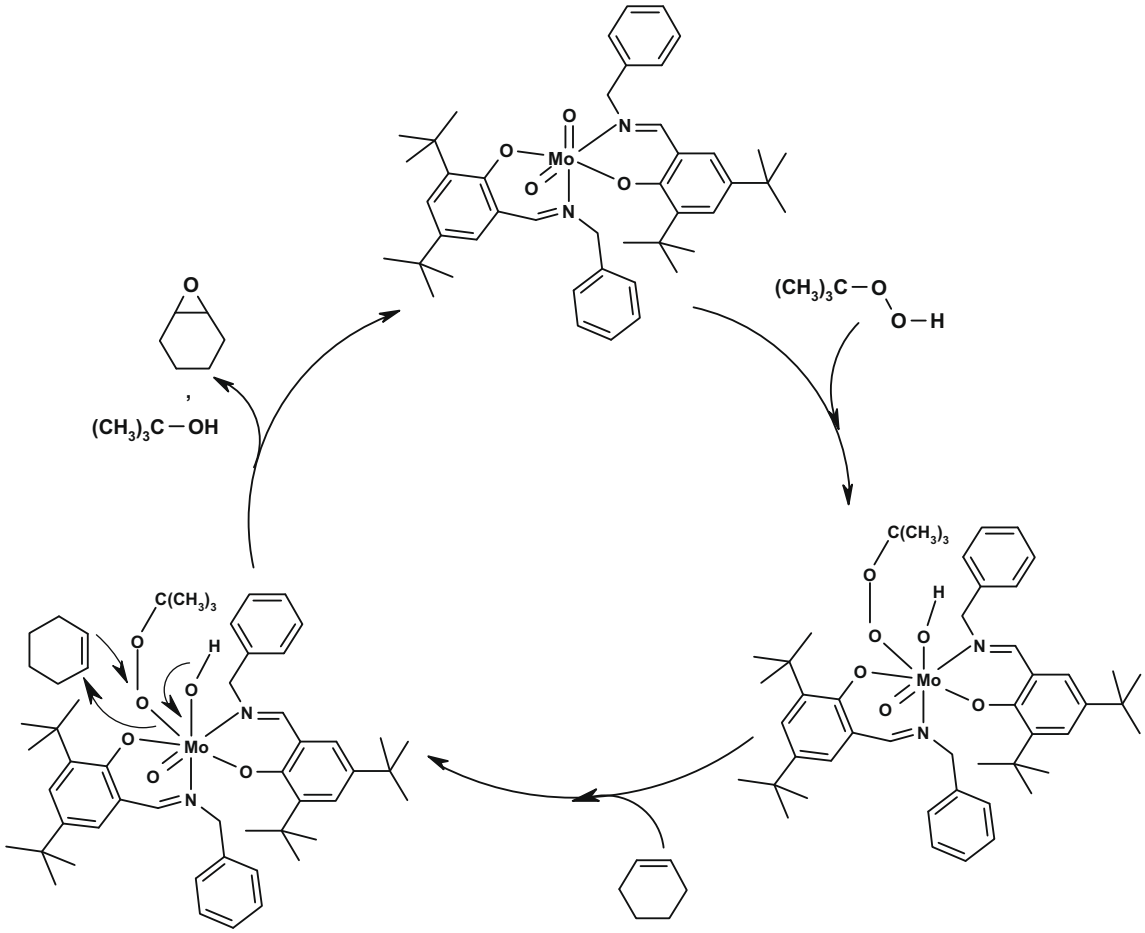
Entry	Solvent	Conversion[b]	Time	TON[d]
1	*n*-Hexane	92[c]	1 h	4600
2	*n*-Nonane	79	1 h	3950
3	Ethanol	95[c]	1 h	4750
4	*n*-Butanol	84	1 h	4200
5	*tert*-Butanol	32	5 min	1600
		64	20 min	3200
		80	40 min	4000
		89	1 h	4450
6	Benzene	98	1 h	4900
7	Chlorobenzene	89	1 h	4450
8	Toluene	98	1 h	4900
9	1,2-Dichloroethane	83	5 min	4150
		95	20 min	4750
		100	40 min	5000

[a] *Conditions:* The molar ratios for using catalyst:cyclooctene:oxidant are 1:5000:5000. The reactions were run for 1 h at 80 °C.
[b] GC yields based on the starting olefin.
[c] The reactions were run at reflux temperature.
[d] Turnover number (TON) = mol of epoxide per mol of catalyst.

Table 4
cis-[$MoO_2(L)_2$] complex catalyzed epoxidation of different olefins by TBHP at 80 °C.[a]

Entry	Substrate	Conversion[b]	Selectivity to epoxide	Time	TON[c]
1	Cyclohexene	100	100	20 min	5000
2	1-Methylcyclohexene	100	100	30 min	5000
3	Cyclooctene	100	100	40 min	5000
4	2-Cyclohexen-1-ol	90	97	1 h	4365
5	2-Cyclohexen-1-one	35	90	150 min	1575
6	α-Terpineol	61	100	70 min	3050
7	1-Heptene	89	100	1 h	4450
8	1-Octene	90	100	160 min	4500
9	*trans*-2-Octene	94	100	80 min	4700
10	Styrene	54	39	1 h	1053
		81	35	160 min	1417
11	α-Methylstyrene	64	30	170 min	960
12	Indene	48	100	70 min	2400

[a] *Conditions:* The molar ratios for using catalyst:olefin:TBHP are 1:5000:5000.
[b] GC yields based on the starting olefin.
[c] Turnover number (TON) = mol of epoxide per mol of catalyst.



Scheme 1. Proposed mechanism for epoxidation of cyclohexene with TBHP catalyzed by *cis*-[$MoO_2(L)_2$].

[50,51]. The complexes of these metals with Schiff base ligands have shown efficient catalytic activity for epoxidation, but the reaction times are usually long and are accompanied with low turnover numbers. Generally the present catalytic system, *cis*-[$MoO_2(L)_2$]/TBHP/DCE, has the following advantages in the oxidation of olefins: (i) reasonably low reaction time for the oxidation of aliphatic olefins, (ii) completely selective oxidation of aliphatic olefins to the corresponding epoxides, (iii) high turnover numbers of up to 5000, and (iv) easy preparation method of the catalyst.

4. Conclusions

The molybdenum complex, *cis*-[MoO_2(4,6-bis(*tert*-butyl)-2-{(benzyl)iminomethyl}phenolate)$_2$], was synthesized by the reaction of a bidentate Schiff base with $MoO_2(acac)_2$. This complex is employed as a novel catalyst for the epoxidation of alkenes with *tert*-butylhydroperoxide in DCE. In this study, we demonstrated that *cis*-[MoO_2(4,6-bis(*tert*-butyl)-2-{(benzyl)iminomethyl}phenolate)$_2$] promotes highly the catalytic epoxidation reaction associ-

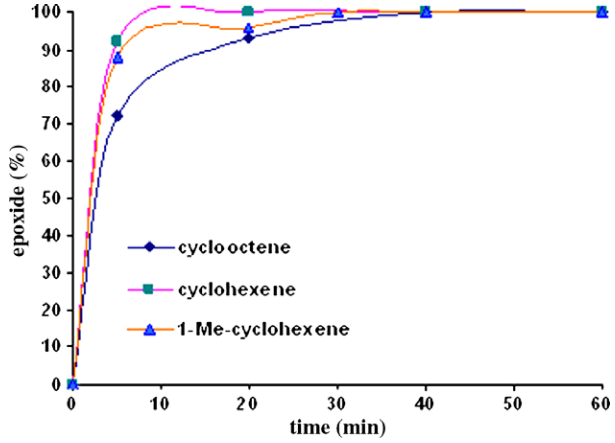


Fig. 3. Conversion profiles of epoxidation using *cis*-[$MoO_2(L)_2$] with TBHP.

ated with TBHP as the oxidant (epoxide yield and TON of up to 100% and 5000% respectively). Moreover, the epoxide yields show that the efficiency of the catalytic system is strongly dependent on the temperature, and the best yields were achieved at 80 °C.

Supplementary data

CCDC 675718 contains the supplementary crystallographic data for this paper. These data can be obtained free of charge via http://www.ccdc.cam.ac.uk/conts/retrieving.html, or from the Cambridge Crystallographic Data Centre, 12 Union Road, Cambridge CB2 1EZ, UK; fax: (+44) 1223-336-033; or e-mail: deposit@ccdc.cam.ac.uk.

Acknowledgments

M.B. thanks the Research Council of Sharif University of Technology for financially support of this work and L.K.W. thanks the National Science Foundation for partial funding of this work.

References

[1] Molybdenum and Tungsten: Their Roles in Biological Processes; A. Sigel, H. Sigel, Eds.; Metal Ions in Biological Systems 39; Marcel Dekker: New York, 2002.
[2] M.M. Abu-Omar, A. Loaiza, N. Hontzeas, Chem. Rev. 105 (2005) 2227.
[3] R. Hille, Chem. Rev. 96 (1996) 2757.
[4] R. Hille, Trends Biochem. Sci. 27 (2002) 360.
[5] J.B. Howard, D.C. Rees, Chem. Rev. 96 (1996) 2965.
[6] R.C. Bray, in: P.D. Boyer (Ed.), The Enzymes, vol. 12, Academic Press, New York, 1975, p. 299.
[7] R.H. Holm, Chem. Rev. 87 (1987) 1401.
[8] A.J. Burke, Coord. Chem. Rev. 252 (2008) 170.
[9] Y.L. Wong, D.K.P. Ng, H.K. Lee, Inorg. Chem. 71 (2002) 5276.
[10] J.A. Brito, H. Teruel, G. Muller, S. Massou, M. Gomez, Inorg. Chim. Acta 361 (2008) 2740.
[11] A. Jimtaisong, R.L. Luck, Inorg. Chem. 45 (2006) 10391.
[12] J.M. Mitchell, N.S. Finney, J. Am. Chem. Soc. 123 (2001) 862.
[13] J.C. Alonso, P. Neves, M.J.P. da Silva, S. Quintal, P.D. Vaz, C. Silva, A.A. Valente, P. Ferreira, M.J. Calhorda, V. Felix, M.G.B. Drew, Organometallics 26 (2007) 5548.
[14] H. Yang, H. Wang, C. Zhu, J. Org. Chem. 72 (2007) 10029.
[15] J.H. Enemark, J.J.A. Cooney, J.J. Wang, R.H. Holm, Chem. Rev. 104 (2004) 1175.
[16] K. Kandasamy, H.B. Singh, R.J. Butcher, J.P. Jasinski, Inorg. Chem. 43 (2004) 5704.
[17] S.M. Bruno, B. Monteiro, M.S. Balula, F.M. Pedro, M. Abrantes, A.A. Valente, M. Pillinger, P.R. Claro, F.E. Kuhn, I.S. Goncualves, J. Mol. Catal. A: Chem. 260 (2006) 11.
[18] M. Bagherzadeh, L. Tahsini, R. Latifi, A. Ellern, L. Keith Woo, Inorg. Chim. Acta 361 (2008) 2019.
[19] I. Luobeznova, M. Raizman, I. Goldberg, Z. Gross, Inorg. Chem. 45 (2006) 386.
[20] W.S. Liu, R. Zhang, J.S. Huang, C.M. Che, S.M. Peng, J. Organomet. Chem. 634 (2001) 34.
[21] C.C.L. Pereira, S.S. Balula, F.A.A. Paz, A.A. Valente, M. Pillinger, J. Klinowski, I.S. Goncualves, Inorg. Chem. 46 (2007) 8508.
[22] S.K. Maiti, K.M. Abdul Malik, S. Gupta, S. Chakraborty, A.K. Ganguli, A.K. Mukherjee, R. Bhattacharyya, Inorg. Chem. 45 (2006) 9843.
[23] G. Lyashenko, G. Saischek, A. Pal, R.H. Irmer, N.C.M. Zanetti, Chem. Commun. (2007) 701.
[24] J.A. Brito, M. Gomez, G. Muller, H. Teruel, J.C. Clinet, E. Dunach, M.A. Maestro, Eur. J. Inorg. Chem. (2004) 4278.
[25] S. Das, T. Bhowmick, T. Punniyamurthy, D. Dey, J. Nath, M.K. Chaudhuri, Tetrahedron Lett. 44 (2003) 4915.
[26] S.K. Maiti, K.M.A. Malik, R. Bhattacharyya, Inorg. Chem. Commun. 7 (2004) 823.
[27] E.P. Carreiro, G.Y. En, A.J. Burke, Inorg. Chim. Acta 359 (2006) 1519.
[28] S.M. Bruno, S.S. Balula, A.A. Valente, F.A.A. Paz, M. Pillinger, C. Sousa, J. Klinowski, C. Freire, P.R. Claro, I.S. Goncualves, J. Mol. Catal. A: Chem. 270 (2007) 185.
[29] J.M. Sobczak, J.J. Ziolkowski, Appl. Catal. A: Gen. 248 (2003) 261.
[30] X.Y. Wang, H.C. Shi, C. Sun, Z.G. Zhang, Tetrahedron 60 (2004) 10993.
[31] J. Liimatainen, A. Lehtonen, R. Sillanpaa, Polyhedron 19 (2000) 1133.
[32] M.M. Farahani, F. Farzaneh, M. Ghandi, J. Mol. Catal. A: Chem. 248 (2006) 53.
[33] M.M. Farahani, F. Farzaneh, M. Ghandi, Catal. Commun. 8 (2007) 6.
[34] A. Syamal, M.R. Maurya, Coord. Chem. Rev. 95 (1989) 183.
[35] K. Ambroziak, R. Pelech, E. Milchert, T. Dziembowska, Z. Rozwadowski, J. Mol. Catal. A: Chem. 211 (2004) 9.
[36] N.R. Pramanik, S. Ghosh, T.K. Raychaudhuri, S. Ray, R.J. Butcher, S.S. Manda, Polyhedron 23 (2004) 1595.
[37] S.N. Rao, K.N. Munshi, N.N. Rao, M.M. Bhadbhade, E. Suresh, Polyhedron 18 (1999) 2491.
[38] J.M. Bregeault, J. Chem. Soc., Dalton Trans. (2003) 3289.
[39] L. Deng, E.N. Jacobsen, J. Org. Chem. 57 (1992) 4320.
[40] G.J.J. Chen, J.W. McDonald, W.E. Newton, Inorg. Chem. 15 (1976) 2612.
[41] R.H. Blessing, Acta Crystallogr., Sect. A 51 (1995) 33.
[42] All software and sources of the scattering factors are contained in the SHELXTL (version 5.1) program library (G. Sheldrick, Bruker Analytical X-Ray Systems, Madison, WI).
[43] A.L. Spek, J. Appl. Crystallogr. 36 (2003) 7.
[44] W.A. Herrmann, J.J. Haider, J. Fridgen, G.M. Lobmaier, M. Spiegler, J. Organomet. Chem. 603 (2000) 69.
[45] T. Glowiak, L. Jerzykiewicz, J.M. Sobczak, J.J. Ziolkowski, Inorg. Chim. Acta 356 (2003) 387.
[46] K. Nakajima, M. Yokoyama, T. Kane, M. Kojima, Inorg. Chim. Acta 282 (1998) 209.
[47] C.D. Nunes, A.A. Valente, M. Pillinger, J. Rocha, I.S. Goncualves, Chem. Eur. J. 9 (2003) 4380.
[48] F.E. Kuhn, M. Groarke, E. Bencze, E. Herdtweck, A. Prazeres, A.M. Santos, M.J. Calhorda, C.C. Romao, I.S. Goncualves, A.D. Lopes, M. Pillinger, Chem. Eur. J. 8 (2002) 2370.
[49] W.R. Thiel, J. Eppinger, Chem. Eur. J. 3 (1997) 696.
[50] (a) G. Huang, S. Liu, Y. Guo, A. Wang, J. Luo, C. Cai, Appl. Catal. A: Gen. 358 (2009) 173;
(b) S.T. Castamana, S. Nakagakia, R.R. Ribeiroa, K.J. Ciuffib, S.M. Drechsel, J. Mol. Catal. A: Chem. 300 (2009) 89.
[51] (a) D. Chatterjee, Coord. Chem. Rev. 252 (2008) 176;
(b) K.C. Gupta, A.K. Sutar, Coord. Chem. Rev. 252 (2008) 1420.

Polyhedron 28 (2009) 2522–2530

Contents lists available at ScienceDirect

Polyhedron

journal homepage: www.elsevier.com/locate/poly

Synthesis and surface chemistry of nano silver particles

Revathi Janardhanan, Murugan Karuppaiah, Neha Hebalkar, Tata Narsinga Rao *

International Advanced Research Center for Powder Metallurgy and New Materials, Balapur PO, Hyderabad 500005, India

ARTICLE INFO

Article history:
Received 29 September 2008
Accepted 5 May 2009
Available online 23 May 2009

Keywords:
Nano silver
Gluconic acid
Diethyl amine
Chemical synthesis

ABSTRACT

In this report, we present a simple wet chemical route to synthesize nano-sized silver particles, and their surface properties are discussed in detail. Silver nano particles of the size 40–80 nm are formed in the process of oxidation of glucose to gluconic acid by amine in the presence of silver nitrate, and the gluconic acid caps the nano silver particle. The presence of gluconic acid on the surface of nano silver particles was confirmed by XPS and FTIR studies. As the nano silver particle is encapsulated by gluconic acid, there was no surface oxidation, as confirmed by XPS studies. The nano silver particles have also been studied for their formation, structure, morphology and size using UV–Visible spectroscopy, XRD and SEM. Further, the antibacterial properties of these nano particles show promising results for *E. Coli*. The influence of the alkaline medium towards the particle size and yield was also studied by measuring the pH of the reaction for DEA, NaOH and Na_2CO_3.

© 2009 Elsevier Ltd. All rights reserved.

1. Introduction

Metal nano particles have attracted a great deal of attention in recent years due to their optical, physical and chemical properties that differentiates them from bulk material properties. Hence they find wide application in various fields like catalysis, photonics, optoelectronics, information storage, antibacterial applications, etc. Silver powders, having ultra fine and uniformly distributed particle size, are of considerable use in the electronics industry as thick film conductors in integrated circuits due to their unique properties such as high electrical and thermal conductivity, high resistance to oxidation. Recently a method was perfected for using nano silver particles in inkjet printing that could see circuits get even smaller and cheaper [1]. Apart from electronic applications, it has been known for centuries that silver has bactericidal properties. Silver is a safe and effective bactericidal metal because it is non-toxic to animal cells and highly toxic to bacteria such as *Escherchia coli* (*E. coli*) and *Staphylococcus aureas* [2,3]. Silver based compounds have been used in recent years to prevent bacterial growth in applications such as burn care [4]. Silver doped polymer fabrics, catheters and polyurethane are well known for their antibacterial functionality [2,5]. Colloidal silver [6,7], nano silver coated fabric [8], nano silver metal oxide granules [9] and nano silver coated ceramic materials [10] are used for antibacterial applications. Nano silver in the form of powders as well as suspensions, due to the high surface to volume ratios, has been used in the above said applications as it enables the loading of small quantities of silver and thus makes the product cost effective. Researchers around the world are trying to produce nanosized mono dispersed powders by different methods. Pluym et al. prepared nano silver powders by the technique of spray pyrolysis, with the production at a rate of 1–2 g/h [11], but the silver particles tend to be agglomerated, irregular shaped, and hollow due to solvent evaporation.

There are several aqueous based chemical methods [12–23] reported in the literature to produce nano silver. While most of these reports deal with inorganic bases such as NaOH and Na_2CO_3 to control the pH to above 9, the contamination of silver with metals ions will cause limitations in specific applications such as electronics, and hence organic bases are required in the nano silver synthesis, as reported by Hsu and co-worker [23]. The same group used organic bases such as triethyl amine and pyridine for contamination-free silver nanoparticles, useful for micro-interconnects, that cure at relatively lower temperatures. Chaki et al. used a non-aqueous single-phase preparation of Ag clusters from silver benzoate using triethylamine as the organic base [12]. In both the organic base related studies, they have used external capping agents for stabilizing the powders or suspensions. In all the cases, the stability and antibacterial activity are dependent on the surface chemistry of the silver produced. For example, Kvítek et al. [24] have reported a SDS stabilized nano silver suspension to have better dispersion and antibacterial action. The best condition for high performance of nano silver, for either electronic or antibacterial applications, is that the particles should contain minimum or no capping agents so that the maximum surface is available for antibacterial action or sintering at low temperatures. Apart from the contamination issues, we have also found that the yield of the nano silver in the reduction reaction depends on the strength of the base.

* Corresponding author. Fax: +91 40 24442699.
E-mail address: tata@arci.res.in (T.N. Rao).

0277-5387/$ - see front matter © 2009 Elsevier Ltd. All rights reserved.
doi:10.1016/j.poly.2009.05.038

In the present work, we have synthesised silver nanoparticles by an aqueous chemical method with an organic base and with no external capping agents, and carried out surface chemistry studies and compared the properties, such as stability and yield, with those obtained with inorganic bases, NaOH and Na_2CO_3. We made an attempt to synthesize nano silver colloids using a lower concentration of the reactants that could be stable for a few weeks without any surfactant. Nano silver colloids prepared in the absence of surfactant using inorganic bases such as NaOH and Na_2CO_3 settle down immediately. Hence we tried to explore the possibility of using an organic base, diethyl amine, that provides a good yield and low particle size in the absence of a protective agent. It is interesting to explore the surface chemistry of the nano silver particles that confirms the capping by gluconic acid, which prevents the oxidation/sulfidisation of the nano silver particle as confirmed by XPS studies. The suspensions made in this work using diethyl amine were found to be stable for nine months. The merits of this method are that it is a room temperature process with glucose as a reducing agent, which also modifies the surface after undergoing oxidation to stabilize the suspension without the requirement of other

Table 1
Details of the reaction parameters used in the silver nanoparticles synthesis, corresponding size of the particles measured from the SEM micrographs and λ_{max} observed for nano silver suspensions.

S. No.	Concentration of $AgNO_3$ (mM)	Concentration of glucose (mM)	Concentration of DEA (mM)	λ_{max} (nm)	Powder/suspension	Particle size from SEM (±10 nm)
S1	5	5	115	432	suspension	65
S2	3	5	115	426	suspension	45
S3	3	5	77	436	suspension	75
S4	3	5	23	464	suspension	85
S5	100	50	58		powder	110
S6	100	50	87		powder	94
S7	100	50	115		powder	63
S8	50	40	58		powder	72
S9	100	40	58		powder	238
S10	300	40	58		powder	630

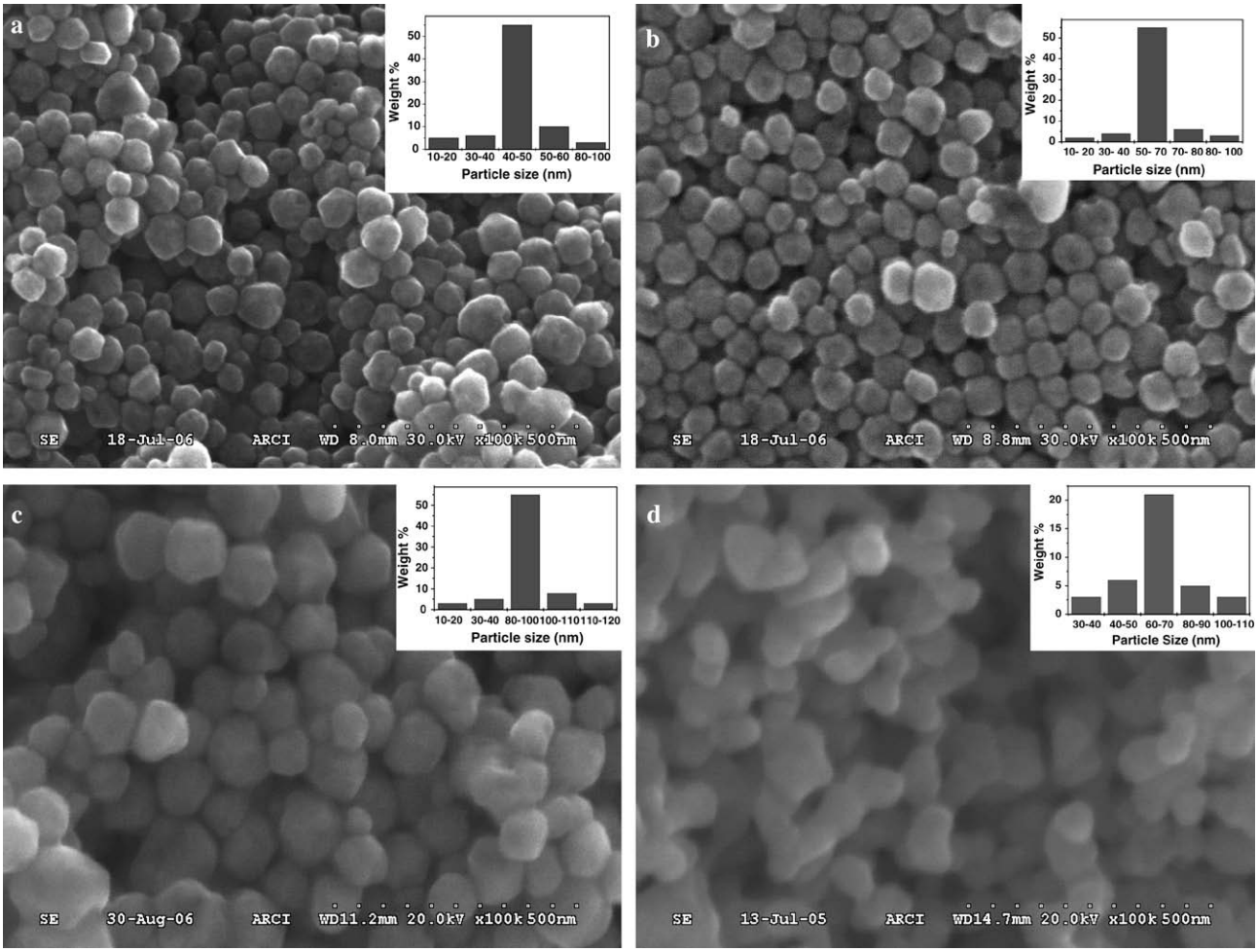


Fig. 1. SEM of silver nanoparticles (a) S2 (b) S3 (c) S4 (d) S7; inset shows the measured particle size distribution from the micrograph.

external capping or stabilizing agent. The resulting nano silver exhibit high antibacterial activity and is also useful for electronic interconnecting applications.

2. Experimental

2.1. Preparation of the nano silver suspension and powders

Analytical grade of silver nitrate (Ultrafine Chemicals), glucose, diethyl amine, sodium carbonate and sodium hydroxide (Qualigens) were used as starting materials. The different concentrations of aqueous solutions of silver nitrate and glucose solutions were mixed together and stirred to obtain a homogeneous solution. An aqueous solution of diethyl amine (DEA) of a pre-decided molarity was added to it quickly and stirred vigorously. Similar experiments were done with sodium carbonate and sodium hydroxide. The color of the solution changed to black, brown and then finally a light green colored precipitate was obtained for higher concentrations S5–S10. After decanting and washing repeatedly 2 to 3 times with distilled water, the precipitate was collected and dried in air at 50–60 °C. The final pale green colored dried powder was subjected to further characterization and antibacterial tests. The details of the reaction parameters for DEA are given in Table 1. For the samples S1–S4 low concentrations of reactants were used and suspensions were obtained which were stable for a few weeks when prepared using DEA in contrast to NaOH and Na_2CO_3, which settled immediately.

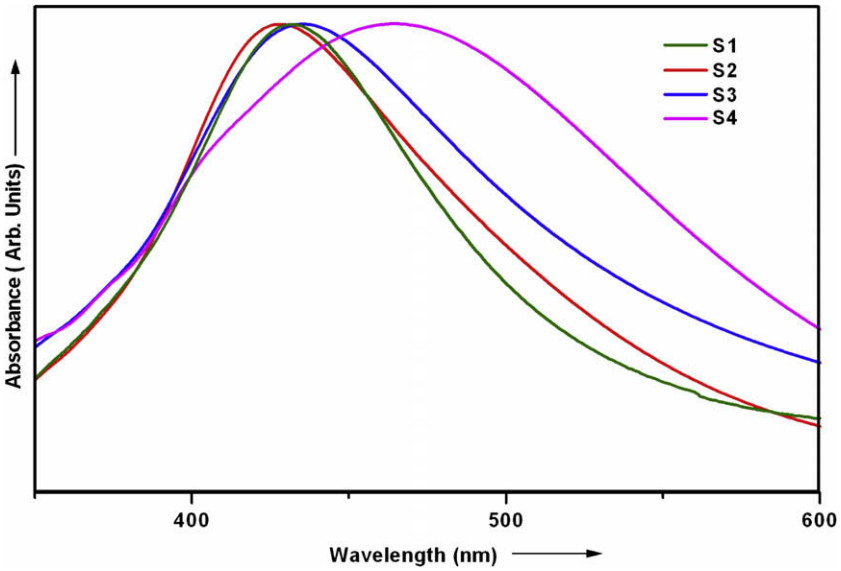


Fig. 2. UV–Visible absorption spectra for silver nanoparticles for samples S1, S2, S3 and S4.

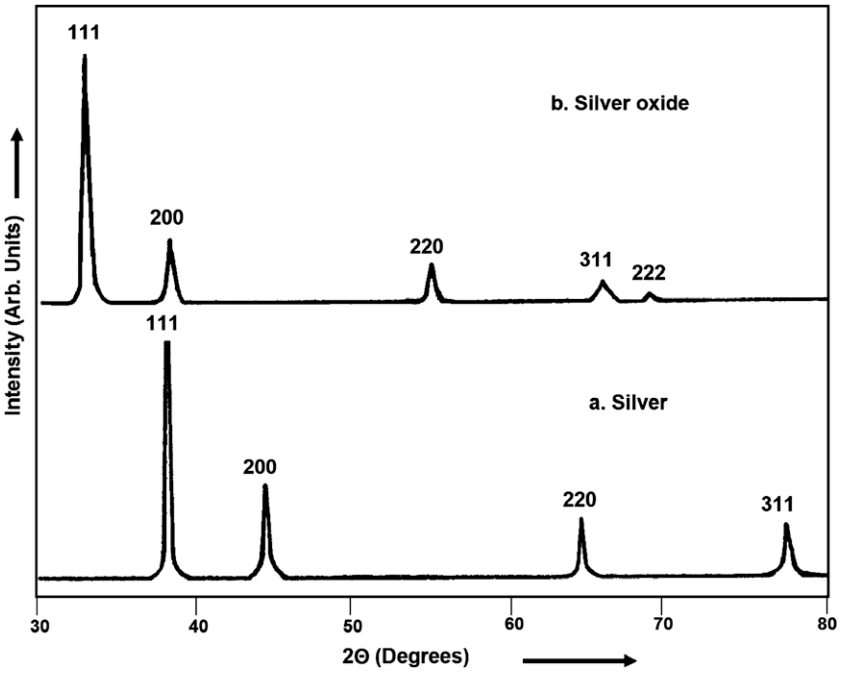


Fig. 3. XRD of (a) silver nanoparticles and (b) silver oxide particles.

To understand the exact role of glucose, the reactions were also performed without addition of glucose, keeping all the other reaction parameters the same. In these reactions, a black colored powder was collected as the end product. When the reactions were done without amine, the rate of reaction was found to be very slow and after 24 h the color of the solution changed to light brown. Silver nano particles thus prepared were in the form of either stable suspensions or powders, depending on the reactant concentrations as mentioned in Table 1.

2.2. Characterization of the nano silver powders

The powders obtained under the various conditions were characterized using different techniques. The particles were tested for their optical absorption property using a PELambda 650, Perkin–Elmer UV–Visible spectrometer, to ensure the formation of nano silver. The suspensions were tested as prepared. The powdered samples were prepared by dispersing them in water using stirring and sonication. The powdered samples were subjected to X-ray diffraction (XRD) studies on a Bruker AXS D8 Advanced XRD to understand their structure. The morphology, size and shape of the particles were obtained using an Hitachi Scanning Electron Microscope equipped with EDAX. A drop of nano silver suspension or dispersed nano silver powders in water was placed on the carbon tape on an aluminum stub and dried. Fourier Transform Infra Red (FTIR) spectroscopy was performed on a THERMO Nicolet Nexus 740 spectrometer. The powdered samples were mixed with KBr and pelletized at 1000 psi pressure. X-ray photoelectron spectroscopy (XPS) measurements were obtained on a KRATOS-AXIS 165 instrument equipped with dual aluminum–magnesium anodes using Mg Kα radiation. The X-ray power supply was run at 15 kV and 5 mA. The pressure of the analysis chamber during the scan was 10^9 Torr. The peak positions were based on calibration with respect to the C 1s peak at 284.6 eV. The obtained XPS spectra were fitted using a non-linear square method with the convolution of Lorentzian and Gaussian functions after polynomial background subtraction from the raw data.

2.3. Antibacterial test

Nutrient agar was poured on two disposable sterilized Petri dishes and was allowed to solidify. To understand the antibacterial activity of the nano silver powder, 0.1 gm of nano silver powder was mixed with 1 ml of *E. coli* bacterial water containing 170 CFU/ml. One milliliter of the *E. coli* bacterial water containing 170 CFU/ml was streaked on one agar plate and 1 ml of the bacterial water mixed with nano silver powder was streaked on the other plate and it was spread uniformly. Plates were incubated at 37 °C for 24 h. Growth of the colonies of bacteria was observed.

A zone of inhibition test was done on the nano silver coated plastic. The nano silver powder was ultrasonicated in acetone for 5 min and it was spin-coated on the plastic at 500 rpm. Nutrient agar was poured on two Petri dishes. The nano silver powder coated plastic and uncoated plastic were placed in the two Petri dishes and then the Nutrient agar was allowed to solidify. 1 ml of 170 cfu/ml concentrated *E. coli* bacterial water was streaked on the two Petri dishes. The plates were incubated at 37 °C for 24 h and then the zone of inhibition was observed.

3. Results and discussion

The silver mirror test is commonly used to detect the presence of an aldehyde group in an organic compound. Here excess ammo-

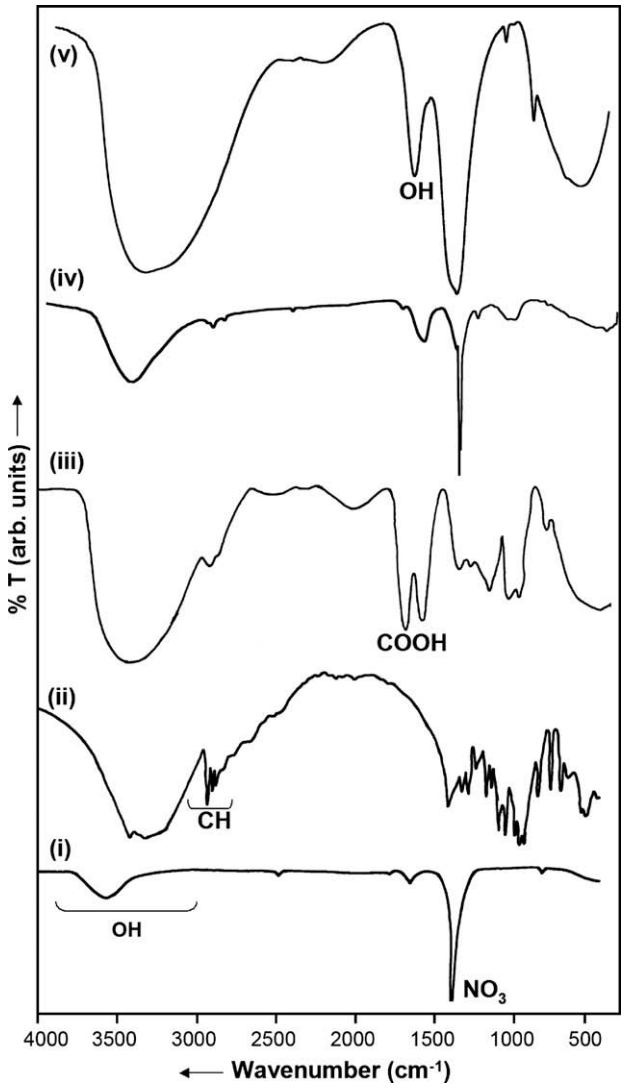


Fig. 4a. FTIR spectra for (i) silver nitrate (ii) glucose (iii) gluconic acid (iv) silver nanoparticles (v) silver oxide particles.

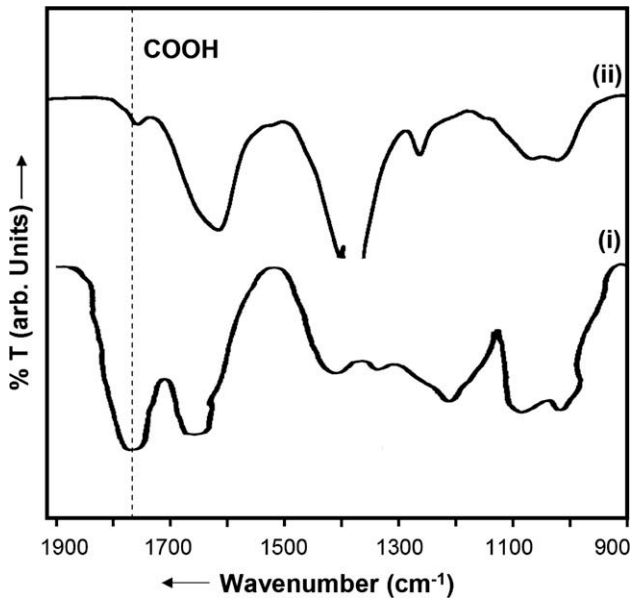


Fig. 4b. Enlarged FTIR spectra for (i) gluconic acid and (ii) resolved spectrum of silver nanoparticles in the wavenumber range 1900–900 cm^{-1}.

nia and silver nitrate are reacted in the presence of the aldehyde which oxidizes to form carboxylic acid and release silver, which deposits on the glass container wall to give silver mirror. The general reaction can be written as:

$$RCHO + 2Ag(NH_3)_2OH \rightarrow RCOONH_4 + 2Ag + 3NH_3 + H_2O \quad (1)$$

Following this reaction, the process was modified to get silver nano particles. Glucose was used as an aldehyde and an amine was used in the place of ammonia. The proposed reaction mechanism for this reaction is very similar to that of the silver mirror test. When the amine is dissolved in water, it withdraws hydrogen ions by leaving hydroxyl ions in solution. The hydrated amine ion further reacts with silver nitrate to form a complex of silver. The remaining hydroxyl ions oxidize the aldehyde group here in glucose to form gluconic acid and an electron is released in the process. This electron reduces the silver complex to get metallic silver. The DEA acts as a catalyst. The reactions can be written as follows:

$$NH(C_2H_5)_2 + H_2O \rightarrow {}^{+}NH_2(C_2H_5)_2 + {}^{-}OH \quad (2)$$

$$R\text{-}CHO + 2{}^{-}OH \rightarrow R\text{-}COOH + H_2O + 2e^{-} \quad (3)$$

$$Ag^{+} + e^{-} \rightarrow Ag^{0} + 2NH(C_2H_5)_2 \quad (4)$$

$$R = (CHOH)_4CH_2OH$$

Some reactions were carried out in the absence of glucose to confirm its exact role in the silver formation. It was observed that the absence of glucose in the reaction produces silver oxide (Ag_2O) instead of metallic silver. Here the silver complex formed with amine in presence of hydroxyl ions produces silver hydroxide which converts into silver oxide as:

$$2AgOH \rightarrow Ag_2O + H_2O \quad (5)$$

Although glucose is a known reducing agent, its activity on silver nitrate was observed to be very weak in the absence of amine, and both reactants remain unreacted for many hours. Yan et al., modified a fabric by using a similar process and deposited silver by heating the fabric [8]. To investigate the effect of the concentration of the precursors towards the particle size of the nano silver, different studies were performed by varying the concentrations of glucose, silver nitrate and diethyl amine, as mentioned in Table 1. The particle size was measured from SEM images and also from XRD data by calculating the average particle size using the Scherror formula, and both were found to be in agreement.

The $AgNO_3$:glucose molar ratio was changed from 1:0.5 to 1:2. The concentration of glucose did not show much influence on the particle size, but was found to be very essential to form metallic silver nano particles, without which an oxide is formed as shown in reaction (4), indicating the role of glucose as a reducing agent.

The concentration of silver nitrate is one of the most important factors that decide the particle size. As the concentration of silver nitrate is increased from 3 to 300 mM, correspondingly the particle size increases from 40 to 630 nm and grows towards bulk silver. The concentration of DEA was found to be another size controlling factor. In the case of S2–S4 (suspensions) as DEA the concentration is decreased from 115 to 23 mM, the particle size increases from 40 to 100 nm, as mentioned in Table 1. In the case of S5–S7 (powders) the increasing concentration of DEA shows a decrease in the average particle size from 110 to 63 nm.

The scanning electron micrograph and particle size distribution for the samples S2, S3 and S4 are shown in Fig. 1a–c. Nearly spherical particles are seen with a maximum number of particles in the size range of 40–50 nm, 50–70 nm and 80–100 nm for samples S2, S3 and S4, respectively. The sharp boundaries of the particles clearly show non-agglomeration of particles even after drying, indicating that some factor is controlling and maintaining the nano

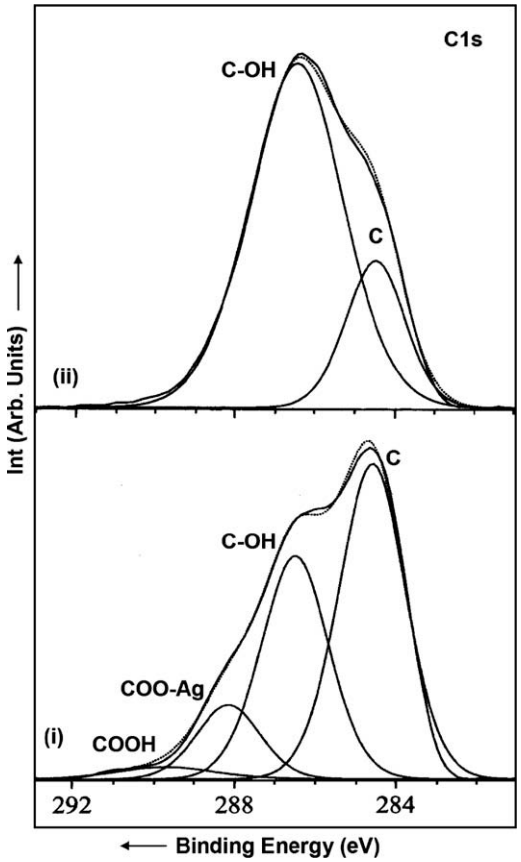


Fig. 5a. XPS core-lever spectra of C 1s for (i) silver and (ii) silver oxide particles.

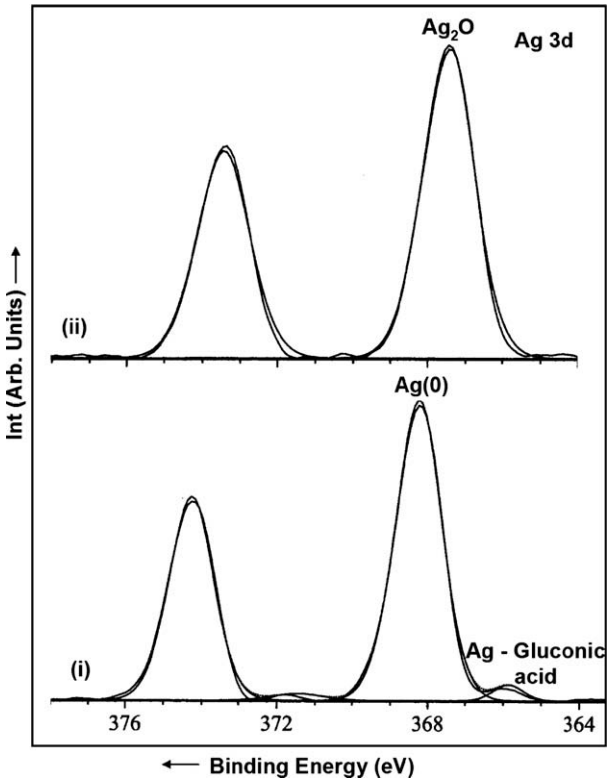


Fig. 5b. XPS core-level spectra for Ag 3d in (i) silver and (ii) Ag_2O particles.

size of the silver particles. Fig. 1d shows a typical micrograph for a powder sample (S7) used for XPS and FTIR studies. Here the particles in the size range of 60–70 nm are seen to be somewhat agglomerated as at some places necking between the particles is observed. This is obvious for nano powders prepared using higher concentrations of precursors and dried in air at 50–60 °C.

The change in the particle size also reflected in the optical absorption studies. The λ_{max} values observed in the UV–Visible absorption studies for samples S1, S2, S3 and S4 are depicted in Fig. 2. The samples S1 and S2 show a blue shift in λ_{max}, which is at 432 and 426 nm, respectively. The decrease in the silver nitrate concentration has resulted in a smaller particle size. The sample S3 and S4 were prepared with smaller concentrations of DEA as compared to S2 and show λ_{max} at 433 and 464 nm, respectively, as shown in Fig. 2. It clearly shows a red shift in λ_{max} from S2 to S4 with the decreasing concentration of DEA, and a decrease in the FWHM with an increase in concentration of DEA. The powder samples did not show any clear absorption peaks in UV–Visible range. This may be due to the agglomeration of the particles, observed in the SEM.

Typical XRD spectra are given in Fig. 3a and b for silver and silver oxide, respectively. The powdered silver nanoparticles show a cubic structure showing peaks at 2θ: 38.1 (1 1 1), 44.2 (2 0 0), 64.4 (2 2 0) and 77.472(3 1 1), which match exactly with the standard data. Fig. 3b shows the spectra for particles prepared in the absence of glucose. It shows the cubic phase of Ag_2O, which is in good agreement with the literature [25].

It was very interesting to understand the formation of nano particles with the change in reactant concentrations. This was possible only when the particles were studied by FTIR, to understand the remains of the organic molecules, if any, after completion of the reaction. The surface properties of the nano silver particles, studied using XPS, throw some light about their size controlling factors.

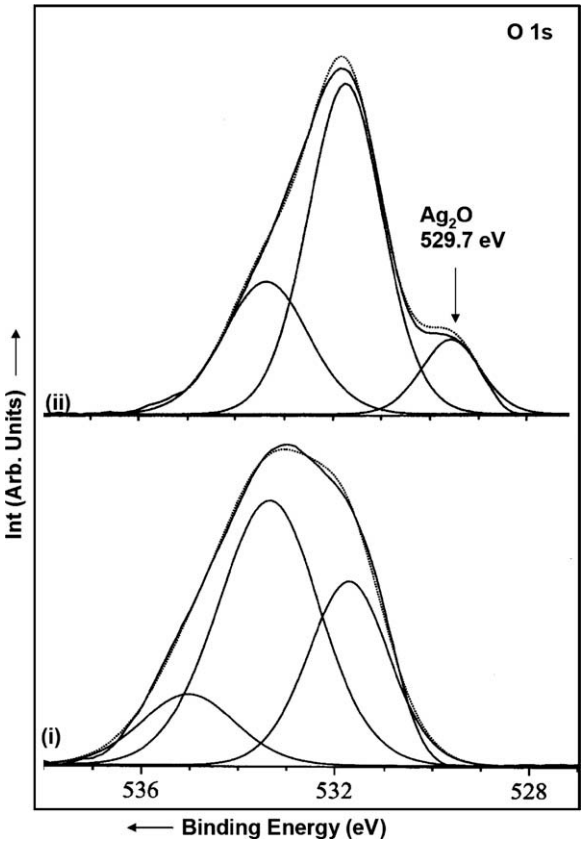


Fig. 5c. XPS core-level spectra for O 1s in (i) silver and (ii) silver particles.

Fig. 4ai–v shows the FTIR spectra recorded for silver nitrate, glucose, gluconic acid, silver nanoparticles and silver oxide nanoparticles, respectively. The attempt made here is to do only a qualitative study. The IR spectrum for the silver nanoparticles (Fig. 4aiv) shows various peaks. The peaks at 3423 and 1605 cm^{-1} are very broad and strong, and can be assigned to the hydroxyl groups [25], either from glucose/gluconic acid, from adsorbed moisture or both. A prominent and very sharp peak is observed at 1384 cm^{-1} which was concluded to be due to the nitrate ions when compared with the FTIR spectrum for silver nitrate, as shown in Fig. 4ai. Some other smaller peaks present at 1740, 1400, 1250, 1100 and 1039 cm^{-1} were also observed. These peaks are absent in the silver oxide IR spectrum (v), which shows major peaks at 3380, 1651 and 1382 cm^{-1}, and are due to the OH group [26], adsorbed moisture and nitrate impurities, respectively. As explained in reaction (4), the gluconic acid is produced by oxidation of glucose and it may be present in the sample. Hence these IR peaks were also compared with the glucose and gluconic acid peaks. The smaller peaks in nano silver do not match with those of glucose (Fig. 4aii) but they match with many features in gluconic acid. The FTIR spectrum of gluconic acid (i) and the resolved spectrum for nano silver powder (ii) was compared in the wave number region from 900 to 1900 cm^{-1}, as depicted in Fig. 4b. The gluconic acid shows peaks at 1740, 1638, 1412, 1230, 1100, 1036 and 875 cm^{-1}. Almost all these peaks match with those for the nano silver sample. Thus a small amount of gluconic acid remains in the sample even after repetitive washings of the silver precipitate.

Fig. 5ai shows the core-level spectrum for C 1s for the nano silver powder. The broad peak can be fitted to four different components at binding energies 289.7, 288.1, 286.5 and 284.6 eV. The peak at 284.6 eV is mostly due to the carbon present on the sample surface due to handling [27]. This peak was observed in all samples. While discussing the other two components, it is necessary to consider the gluconic acid molecule, the presence of which

Table 2
Comparison of sodium carbonate, diethyl amine and sodium hydroxide.

	pK_b	Yield (%)	Particle size (nm)
Sodium carbonate	4.67	96	45
Diethyl amine	3	90	55
Sodium hydroxide	0.2	71	50

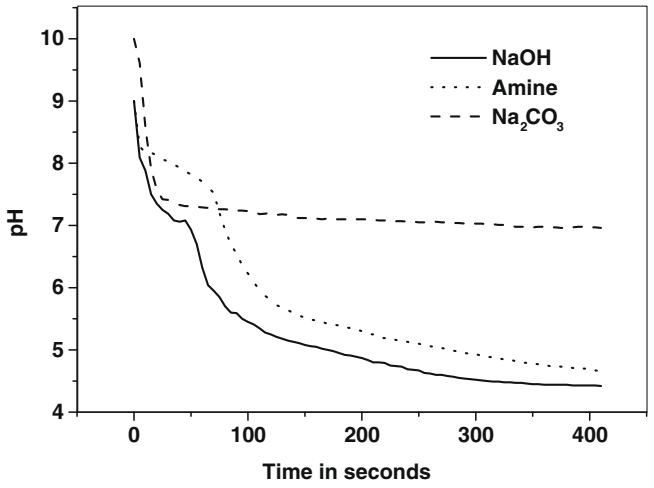
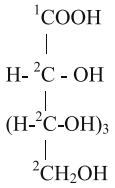


Fig. 6. Photograph of antibacterial test (a) control (b) control with nano silver particles (c) control with uncoated plastic and (d) control with nano silver coated plastic.

was observed in the FTIR studies. In one gluconic acid molecule, depending on the functional groups attached, there are two types of carbons in the atomic ratio 1:5, as numbered below.



The carbon in carboxylic group shows a binding energy at 289 ± 2 eV [28]. The component at 288.1 eV is due to C-1, which is a carboxylic group. Here the shift is observed towards a lower binding energy. This is in good agreement with the literature, where carboxylic groups attached to a metal particle like Co, Cu show a binding energy shift to 288.1 eV [29]. Also the standard data available for silver acetate shows a XPS peak for carbon at 288.1 eV [30,31]. It has been shown that the carboxylic acid group binds to silver surface in the case where citrate is used as the reducing agent. In this case, it was shown that two carboxylic groups of the citrate bind to the Ag surface, having the third group normal to the surface, which make the Ag particle charged, and that is responsible for the electrostatic stability [32]. However in the present case only one carboxylic acid is available on gluconic acid that is likely to bind with the Ag surface. The capping of the silver particle controls the grain growth but does not provide charge to the particles. The peak at 286.5 eV is due to C-2 (the carbon with OH groups) [33,34]. The intensities of the corresponding XPS peaks are fairly in agreement with the atomic ratio of these carbons in the molecule. A very small component at 289.7 eV may be due to some non-bonded gluconic acid. The C 1s spectrum was also recorded for silver oxide powders where only two components were observed, at 284.5 and 286.5 eV, as shown in Fig. 5aii. The former peak is due to a carbon impurity. The latter peak was unexpected and may be due to some unknown carbon contamination, as no C–O bond is possible in this sample.

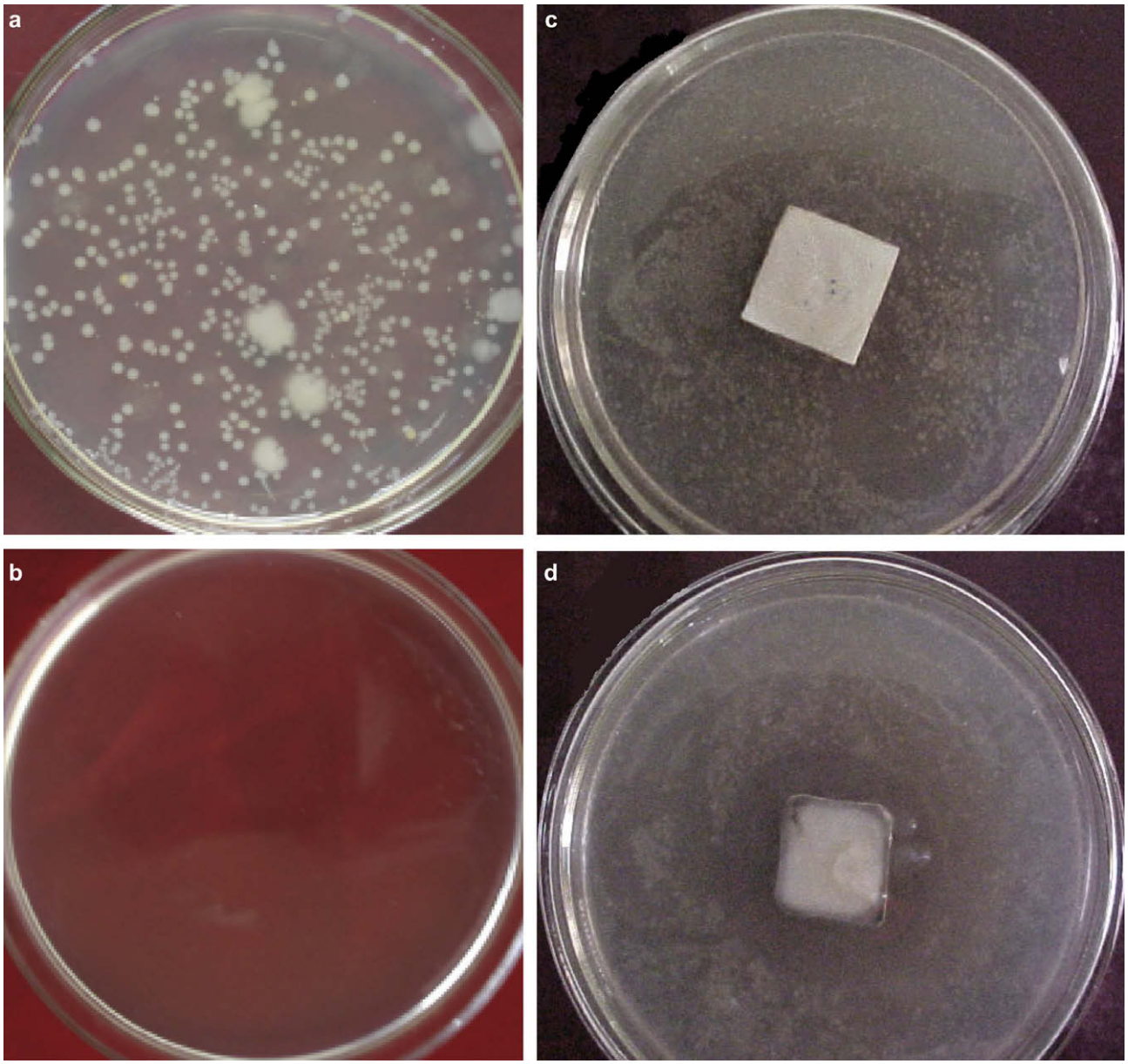


Fig. 7. pH of the reaction for NaOH, DEA and Na_2CO_3.

The core-level spectrum for Ag 3d, shown in Fig. 5bi, is fitted in two components, one is major and the second is very small in the% concentration ratio of (96:4). The peak at 368.2 eV is clearly due to metallic silver [25,35]. A surprising small peak shifted to lower binding energy at 365.8 eV may be due to the surface silver atoms surrounded by the six carbon chain of gluconic acid molecules. Unlike in the silver nanoparticles, silver oxide nanoparticles show only one peak at a binding energy of 367.4 eV, which is a characteristic for Ag_2O, as shown in Fig. 5bii.

Fig. 5c–i shows the core-level spectra for O 1s in the case of silver nanoparticles. It shows a broad peak which can be deconvoluted into three peaks at 535.0, 533.4 and 531.7 eV. The first peak can be assigned to the adsorbed water [36]. The component at 533.4 can be correlated to either C–O or C–OH present in the gluconic acid molecules [37–39]. The peak at 531.7 eV was observed in all samples, and can be attributed to adsorbed oxygen on the surface as an impurity in the form of either atomic oxygen or in the hydroxyl form [40]. Some of its contribution can also be due to organometallic oxygen. Hoof et al studied Co and Cu bonded with organic molecules and found the binding energy of O 1s at 531.6 eV [29]. Here if the silver atoms on the surface of the nanoparticles are bonded with carboxylic ions, the oxygen from the carboxylic group may show a binding energy at 531.7 eV. The peculiar peak of silver oxide at 529.6 eV, as shown in Fig. 5cii, is observed in the case of the silver oxide nanoparticles, but is absent in the silver nanoparticles. Other than the oxide peak, the silver oxide nanoparticles show two components at 533.3 and 531.7 eV, which can be attributed to hydroxyl groups which may be present on the surface of the oxide particles and surface adsorbed oxygen, respectively. This clearly tells us that the surface of the silver nanoparticles does not have any oxide layer as it is protected by gluconic acid molecules.

The reducing ability of aldehyde is dependant on the pH. As already mentioned, if only glucose is added the reduction rate is very slow at room temperature because of the low pH. We tried to explore the influence of different alkaline medium towards the particle size and yield of nano silver powder. The pK_b values, yield and particle size of nano silver powder for NaOH, Na_2CO_3 and DEA are listed in Table 2. The changes in the pH of the solution for NaOH, Na_2CO_3 and DEA are shown in Fig. 6.

The yield of the nano silver powder was found in increase with a decrease in the pK_b value. The lower the pK_b value, the stronger is the basicity of the alkaline medium. Under highly alkaline conditions, the aldehyde functional group in glucose gets converted to a ketone [41]. As ketones are weak reducing agents when compared with aldehydes, the yield of the nano silver prepared by sodium hydroxide ($pK_b = 0.2$) is less when compared with DEA and Na_2CO_3 [14,42]. The reaction mechanism is the same in each case. Gluconic acid formed as a by-product in the reaction acts as a capping agent. This imparts a negative charge on the surface, which was confirmed by immediate adsorption of negatively charged silver particles on the anion exchange resin Amberlite IRA 400 [43].

From all these results, the inference that can be drawn is like this. As mentioned in Table 1, an increase in concentration of DEA reduces the size of nano silver particle. As discussed earlier, the amine in aqueous solution forms a hydrated ion and hydroxy ions are left in the solution which in turn oxidizes glucose to form gluconic acid. If the concentration of amine is greater then the number of hydroxy ions are present is greater and the amount of gluconic acid formed also increases. These gluconic acid molecules present on the surface of the nano particles may act as a particle size controlling factor. So in turn the amine concentration is determining the size of the particles for a particular set of concentrations of silver nitrate and glucose, as mentioned in Table 1 (S2–S4). It is very easy to understand the increase in the size of particles with the concentration of $AgNO_3$, due to the increase in the ratio of available gluconic acid to silver particles. In the given set of conditions in Table 1, by increasing the concentration of glucose, the size remains unaffected as the glucose to gluconic acid conversion in the presence of amine is a size controlling factor and not just the glucose concentration. Just by changing the molar ratio of reactants, we can get a stable nano silver suspension or powder.

The reactions for samples S5–S10 can be scaled up to a total volume of 5 liters, which can yield 45–50 gm of nano silver powder which is quiet a substantial yield.

The powders of nano silver were tested for antibacterial properties on *E. coli*. The effect of the silver nano particles on *E. coli* is shown in the photograph in Fig. 6 for sample S7. The number of *E. coli* has been reduced by a considerable number because of the antibacterial action of the nano silver particles, whereas growth was observed in the control, as shown in Fig. 7a and b, respectively. The zone of inhibition observed for the nano silver powder coated plastic confirms the antibacterial action of the nano silver particles, whereas there was no zone of inhibition for the uncoated plastic, as shown in Fig. 7c and d, respectively. These observations clearly indicate the antibacterial properties of nano silver. It is interesting to observe that, although the nanoparticles contain traces of gluconic acid on the surface, as is evident from the XPS analysis, the surface of the nano silver particle is still available for efficient antibacterial activity.

4. Conclusions

The present work reveals a simple, cost effective wet chemical synthetic route to form nano silver powders. Silver nano particles are formed in a simple oxidation–reduction reaction in diethyl amine, glucose and silver nitrate. A blue shift in λ_{max} observed for an increase in the diethyl amine concentration in samples S2–S4 was found to be the size controlling factor. Detailed surface analysis studies using XPS and FTIR revealed the presence of gluconic acid that encapsulates the nano silver particle. The negative charge on the surface due to the presence of gluconic acid was confirmed by anion exchange resin. The antibacterial studies show very high activity against *E. coli*. This process of producing large scale silver nano powders with highly efficient antibacterial properties is certainly going to increase its commercial value and widen the application range.

Acknowledgement

Authors would like to thank Dr. B. Sreedhar, IICT, Hyderabad for providing the XPS and FTIR facility.

References

[1] Hsien-Hsueh Lee, Kan-Sen Chou, Nanotechnology 16 (2005) 2436.
[2] U. Klueh, V. Wagner, S. Kelly, A. Johnson, J.D. Bryers, J. Biomed. Mater. Res. 53 (2000) 621.
[3] G. Zhao, S.E. Stevens, Biometals 11 (1998) 27.
[4] H.J. Klasen, Burns 26 (2000) 117.
[5] J.W. Cho, J.H. So, Mater. Lett. 60 (2006) 2653.
[6] J. Yan, J. Cheng, US 2003/0185889 A1, 2003.
[7] R. Prucek, L. Kvitek, Chemica 43 (2004) 59.
[8] J. Yan, J. Cheng, US Patent No. 0190851 A1, 2003.
[9] J. Yan, J. Cheng, US Patent No. 6379712B1, 2002.
[10] S. Kawasumi, M. Yamada. M. Honma, US Patent No. 5824267, 1998.
[11] T.C. Pluym, Q.H. Powell, A.S. Gurav, T.L. Ward, T.T. Kodas, L.M. Wang, H.D. Glicksman, J. Aerosol. Sci 24 (1993) 383.
[12] N.K. Chaki, S.G. Sudrik, H.R. Sonawane, K. Vijaymohanan, Chem. Commun. (2002) 76.
[13] N.R. Jana, L. Gearheart, C.J. Murphy, Chem. Commun. (2001) 617.
[14] K.-S. Chou, C.-Y. Ren, Mater. Chem. Phys. 64 (2000) 241.
[15] H.S. Zhou, T. Wada, H. Sasabe Komiyama, Appl. Phys. Lett. 68 (1996) 1288.
[16] P.Y. Lim, R.S. Liu, P.L. She, C.F. Hung, H.C. Shih, Chem. Phys. Lett. 420 (2006) 304.
[17] H. Katsuki, S. Komarneni, J. Mater. Res. 18 (2003) 747.
[18] Y. Sun, B. Gates, B. Mayers, Y. Xia, Nano Lett. 2 (2002) 165.

[19] M.J. Rosemary, T. Pradeep, J. Colloid Interface Sci. 268 (2003) 81.
[20] S. Mandal, S. Arumugam, R. Pasricha, M. Sastry, Bull. Mater. Sci. 28 (2005) 503.
[21] M. Starowicz, B. Stypula, J. Banaś, Electrochem. Commun. 8 (2006) 227.
[22] Y. Dai, T. Deng, S. Jia, L. Jin, F. Lu, J. Membr. Sci. 281 (2006) 685.
[23] S.L.-C. Hsu, R.-T. Wu, Mater. Lett. 61 (2007) 3719.
[24] L. Kvítek, A. Panáek, J. Soukupová, M. Kolář, R. Veeřová, R. Prucek, M. Holecová, R. Zbořil, J. Phys. Chem. C 112 15 (2008) 5825.
[25] X.-Y. Gao, S.-Y. Wang, J. Li, Y.-X. Zheng, R.-J. Zhang, P. Zhou, Y.-M. Yang, L.-Y. Chen, Thin Solid Films 455–456 (2004) 438.
[26] H.H. Willard, L.L. Merritt Jr., J.A. Dean, F.A. Settle, in: Instrumental Methods of Analysis, CBS Publishers and Distributors, Delhi, 1986, p. 290
[27] H. Estrade-Szwarckopf, B. Rousseau, J. Phys. Chem. Solids 53 (1992) 419.
[28] U. Gelius, P.F. Heden, J. Hedman, B.J. Lindberg, R. Manne, R. Nordberg, C. Nordling, K. Siegbahn, Phys. Scripta 2 (1970) 70.
[29] D.L. Hoof, D.G. Tisley, R.A. Walton, J. Chem. Soc., Dalton Trans. (1973) 200.
[30] J.S. Hammond, J.W. Holubka, J.E. Devries, R.A. Duckie, Corros. Sci. 21 (1981) 239.
[31] P.V. Kamat, M. Flumiani, G.V. Hartland, J. Phys. Chem. B 102 (1998) 3123.
[32] L.J. Gerenser, J. Vac. Sci. Technol. A 8 (1990) 3682.
[33] K. Wagener, C. Batich, B. Kirsch, S. Wanigatunga, J. Polym. Sci. Part A 27 (1989) 2625.
[34] A. Hozumi, M. Inagaki, N. Shirahata, Appl. Surf. Sci. 252 (2006) 6111.
[35] John F. Moulder, William F. Stickle, Peter E. Sobol, Kenneth D. Bomben, Handbook of X-ray Photoelectron Spectroscopy, Perkin–Elmer Corporation, Physical Electronics Division, 1992.
[36] P.D. Schulze, S.L. Shaffer, R.L. Hance, D.L. Utley, J. Vac. Sci. Technol. A 1 (1983) 97.
[37] G. Barth, R. Linder, C. Bryson, Surf. Interf. Anal. 11 (1988) 307.
[38] B.M. DeKoven, P.L. Hagans, Appl. Surf. Sci. 27 (1986) 199.
[39] T. Ohta, M. Yamada, H. Kuroda, Bull. Chem. Soc. Jpn. 47 (1974) 1158.
[40] C.M. Worley, M.D. Vannet, G.L. Ball, W.E. Moddeman, Surf. Interf. Anal. 10 (1987) 273.
[41] L. Finar, Organic Chemistry Volume 1: The Fundamental Principles, Longman Singapore Publishers, Singapore, 1990. p. 514.
[42] L. Kvítek, R. Prucek, A. Paná ek, R. Novotný, J. Hrbá, R. Zbo il, J. Mater. Chem. 15 (2005) 1099.
[43] S. Panigrahi, S. Kundu, S.K. Ghosh, S. 'Nath, S. Praharaj, S. Basu, T. Pal, Polyhedron 25 (2006) 1263.

Polyhedron 28 (2009) 2531–2536

Contents lists available at ScienceDirect

Polyhedron

journal homepage: www.elsevier.com/locate/poly

Calorimetric measurements of diluted spin crossover complexes $[Fe_xM_{1-x}(btr)_2(NCS)_2]\cdot H_2O$ with M^{II} = Zn and Ni

Aurelian Rotaru [a,b], Marinela M. Dîrtu [c], Cristian Enachescu [b], Radu Tanasa [b], Jorge Linares [a,*], Alexandru Stancu [b], Yann Garcia [c,1]

[a] Groupe d'Etude de la Matière Condensée (GEMaC), CNRS-UMR 8635, UVSQ, 78035 Versailles Cedex, France
[b] Department of Physics, Alexandru Ioan Cuza University, 700506 Iasi, Romania
[c] Unité de Chimie des Matériaux Inorganiques et Organiques, Département de Chimie, Université Catholique de Louvain, Place L. Pasteur 1, 1348 Louvain-la-Neuve, Belgium

ARTICLE INFO

Article history:
Received 5 January 2009
Accepted 20 April 2009
Available online 15 May 2009

Keywords:
Spin crossover
Ising-like model
FORC diagram
Calorimetric measurements

ABSTRACT

Motivated by the application of the First Order Reversal Curve (FORC) technique to obtain a distribution of like spin domains in the spin crossover complexes $[Fe_xM_{1-x}(btr)_2(NCS)_2]\cdot H_2O$ with M^{II} = Zn and Ni, we have performed Differential Scanning Calorimetry (DSC) experiments. We have measured the heat capacity in the heating and cooling modes and then calculated the enthalpy and the entropy variations at the phase transition. In the framework of an Ising-like model, we have converted the experimental thermal hysteresis into terms of physical parameters related to these compounds. We have also performed a statistical analysis of these parameters and concluded that the correlation between them increases with the dilution degree of these spin crossover complexes.

© 2009 Elsevier Ltd. All rights reserved.

1. Introduction

Spin crossover (SCO) solids [1] are attractive molecular compounds containing transition metals with the electronic configuration $3d^{4-7}$ that are switchable between two states with different optical, magnetic, vibrational and volume properties: respectively the low-spin (LS) state and the high-spin (HS) state. The large majority of the known SCO complexes, prepared as nanoparticles, powder, crystallites or single crystals, are based on Fe(II,III) ions. A few examples of SCO complexes with cobalt(II,III), manganese(II,III) or chromium(II) have also been synthesised [2]. A thermally induced entropy driven spin transition can occur from the stable LS state at low temperatures to the HS state at higher temperatures. If the interactions of elastic origin between the spin changing molecules are strong enough, cooperative phenomena occur in steep phase transitions, accompanied by a hysteresis loop whose width depends on the intensity of these interactions.

In this paper, we study the behavior of solid solutions of the coordination polymer $[Fe(btr)_2(NCS)_2]\cdot H_2O$ (btr = 4,4′-bis-1,2,4-triazole) [3] that has a 2D network structure. The iron atom is related in a plane to four btr ligands and to two isothiocyanato groups in *trans* positions. The btr ligands of two consecutive planes are linked by hydrogen bonding to a non-coordinated water molecule. This compound displays a hysteretic and complete spin transition below room temperature [3], as shown in Fig. 1, under the form of the temperature dependence of the HS molar fraction, γ_{HS}. It is possible to obtain isomorphous compounds by replacing the iron ion by other transition metals such as nickel, cobalt, copper or zinc [4–7] which, contrary to the iron ion, exist only under one spin state. One thus can obtain a solid solution of the formula $[Fe_xM_{1-x}(btr)_2(NCS)_2]\cdot H_2O$, with M^{II} = Co, Cu, Ni, Zn. The strength of the ligand field determines the bistable character of the complex, and the presence of the thermal hysteresis loop is a signature of a first order phase transition. However, the progressive dilution [8] of a cooperative system isolates more and more the SCO molecules and the interactions can become insufficient [9,10] to favor a cooperative behavior; the hysteresis loop disappears and the transition becomes continuous. Above a threshold value, $x \geqslant 0.40$, the hysteresis loop was observed to collapse for the isostructural systems $[Fe_xM_{1-x}(btr)_2(NCS)_2]\cdot H_2O$ where the dilution metal M^{II} = Co or Ni [11,12]. As the dilution increases, the transition is shifted to lower temperatures and the HS state is further stabilized. The thermal hysteresis loops, derived from magnetic measurements, for different concentrations of Zn atoms in $[Fe_xZn_{1-x}(btr)_2(NCS)_2]\cdot H_2O$ are reported in Fig. 1. In the mean-field description, the "effective" interaction in a diluted system is proportional to the number of SCO neighbors, i.e. to the composition parameter x. We note a decrease of the hysteresis width as x increases, but the steepness and shape of the hysteresis loop is preserved.

Besides the magnetic and optical measurements [13], Mössbauer [13] and Raman spectroscopy [14], and calorimetric

* Corresponding author. Tel.: +33 139254661; fax: +33 139254652.
E-mail addresses: jlinares@physique.uvsq.fr (J. Linares), yann.garcia@uclouvain.be (Y. Garcia).
[1] Tel.: +32 1047 2826; fax: +32 1047 2330.

0277-5387/$ - see front matter © 2009 Elsevier Ltd. All rights reserved.
doi:10.1016/j.poly.2009.04.046

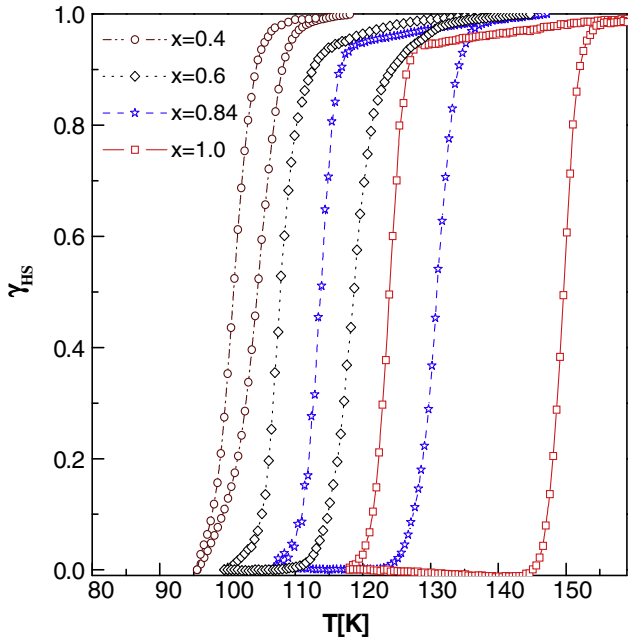


Fig. 1. $[Fe_xZn_{1-x}(btr)_2(NCS)_2]\cdot H_2O$ for different dilution degrees ($x = 1$; 0.84; 0.6; 0.4) [15].

(heat capacity) measurements [13,15] are among the most commonly used methods to quantitatively evaluate the spin state. They make it possible to determine, besides the transition temperatures, relevant thermodynamic quantities such as the enthalpy ΔH and entropy changes ΔS associated to the spin transition. Typical values for the enthalpy change are between 10 and 20 kJ/mol, while the entropy change is normally between 50 and 80 J/mol/K [16].

Martin et al. [4] have studied, some time ago, the effect of dilution on the SCO behavior of $[Fe_xM_{1-x}(btr)_2(NCS)_2]\cdot H_2O$, using magnetic and calorimetric measurements for M = Co^{II} and Ni^{II}. In this paper, we complete this series with further calorimetric measurements on the Zn diluted system (M = Zn), and correct the thermodynamic data provided for the Ni diluted system that were only reported in the heating mode [4]. Simulated hysteresis loops using an Ising-like model, including new experimental parameters, are presented and a comparison with the previous simulated data [17,18] is provided.

2. Experimental

The diluted samples were prepared according to [4]. The calorimetric measurements were carried out in a $He_{(g)}$ atmosphere using a Perkin–Elmer DSC Pyris 1 instrument equipped with a cryostat and operating down to 100 K. The purge gas was $N_{2(g)}$. Temperatures and enthalpies were calibrated over the temperature range 100–300 K using the solid/solid and liquid/solid transitions of pure cyclopentane (⩾99%, Acros) (Table S1). The calibration sample was introduced in an aluminum pan and hermetically sealed using an encapsulating press. The calibration was made at a scan rate of 2 and 5 K/min using 47(2) mg and 49(1) mg of cyclopentane, respectively. The characteristic temperatures, which were assigned to the crystal/crystal transitions of cyclopentane, were obtained by the extrapolation of the onset peak temperatures [19]. An empty aluminum pan, identical to the one used for the sample, was used as a reference to obtain a reliable baseline. The system produces or uptakes energy in order to keep the temperature of the compound identical to the reference. This energy difference between two resistances (in mW) is transformed by PYRIS™ DSC Software 7.0 in specific heat C_p (J mol^{-1} K^{-1}). This function is plotted as a function of temperature of the sample and enables the transition temperature to be obtained, together with the associated changes of enthalpy and entropy of the transition. These temperatures were determined by taking into account T_{max} of the peaks.

Differential scanning measurements of the samples were carried out at a scan rate of 2 and 5 K/min, in the warming and cooling modes. 33.6 mg of each sample were encapsulated at room temperature in aluminum pans and hermetically sealed. The samples were maintained at room temperature for 5 min in order to allow the system to equilibrate, and were further cooled down from 298 to 110 K (or 100 K depending on the sample) with different scan rates. The samples were maintained at the lowest temperature for 5–10 min to reach equilibrium, followed by a similar scanning mode as on cooling between 110 K and room temperature. Each experiment was carried out twice to check the reproducibility.

3. Results and discussions

In Figs. 2 and 3 the DSC profiles of $[Fe_xM_{1-x}(btr)_2(NCS)_2]\cdot H_2O$ (M = Zn, Ni) in the cooling (a) and heating modes (b) related to the same mass (33.6 mg) for different dilution degrees, obtained between 100 and 160 K, at a rate of 5 K/min, are presented. Exothermic and endothermic peaks are observed on cooling and warming respectively. As the dilution ratio increases, the peak amplitude decreases, as expected. Less data are provided for the Zn diluted system ($x \geqslant 0.7$) due to the working temperature range of our instrument. A summary of our measurements is given in Tables 1 and 2. The calorimetric measurements agree reasonably well with those observed from magnetic measurements [18]. The small differences in transition temperatures $T_{1/2}$ between DSC and magnetic data have their origin in the different rates at which the experiments were carried out.

In the thermograms, the enthalpy change corresponds to the peak area. The enthalpy change ΔH related to the conversion of 1mol of [Fe] mononuclear entities according to the relationship $\Delta H = \Delta H_{exp} M_x / x$, where ΔH_{exp} is the experimental value of the enthalpy change related to the mass unit of the sample, has been calculated directly from the DSC measurement. The evolution of ΔH with x is shown in Fig. 4. For the $[Fe_xNi_{1-x}(btr)_2(NCS)_2]\cdot H_2O$ system, the enthalpy change variation is constant above $x \geqslant 0.8$ and decreases below that value, whereas for the $[Fe_xZn_{1-x}(btr)_2(NCS)_2]H_2O$ system, ΔH decreases more effectively as the dilution ratio increases. A hysteresis is observed in the variation of the enthalpy change in the heating and cooling modes, this one being larger for the system diluted with Ni than for the system diluted with Zn.

The relevant entropy changes ΔS near the transition temperature were determined from $\Delta S = \Delta H / T_{1/2}$. The entropy changes for both systems in the cooling and heating modes are shown in Fig. 5. Similarly, as x decreases, ΔS decreases, and no significant hysteresis effect is observed except for $x \geqslant 0.85$.

The thermodynamic values obtained for the enthalpy change variation are systematically smaller than those obtained by Martin et al. [4], but no comparison is possible for the heat capacity since no C_p values were reported. Our thermodynamic parameters were used for simple simulations in the frame of an Ising-like model, presented in the next section.

3.1. Simple simulations using some of the values of ΔH and ΔS

One remarkable model for the description of such bistable systems is the Ising-like model, which describes the interaction of two-level units, with energy levels having different energies and degeneracies. However, it permits the description of most of the

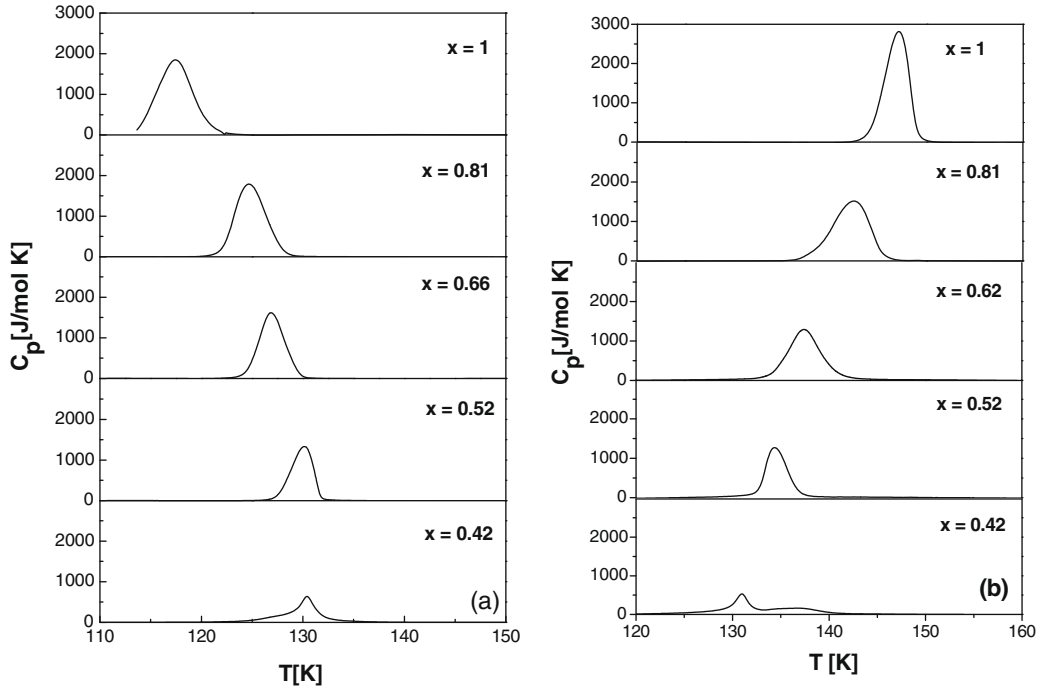


Fig. 2. Heat capacity profiles for $[Fe_xNi_{1-x}(btr)_2(NCS)_2]\cdot H_2O$ recorded on cooling (a) and warming (b) modes ($x = 1$; 0.81; 0.66; 0.52; 0.42), clearly evidencing a hysteresis effect.

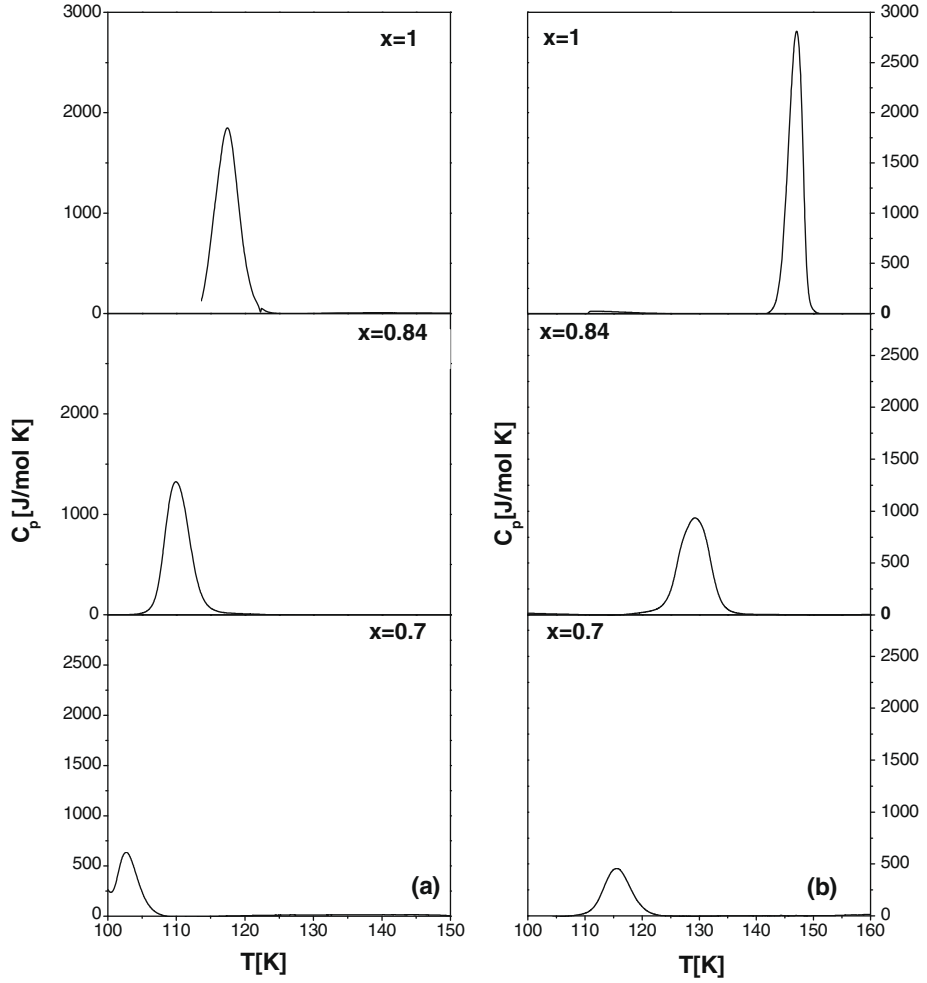


Fig. 3. Heat capacity profiles for $[Fe_xZn_{1-x}(btr)_2(NCS)_2]\cdot H_2O$ recorded on cooling (a) and warming (b) modes ($x = 1$; 0.84; 0.7), clearly evidencing a hysteresis effect.

Table 1
Summary of the calorimetric measurements for $[Fe_xNi_{1-x}(btr)_2(NCS)_2]\cdot H_2O$.

Formula	Mode	$T_{1/2}$ [K]	Integration interval [K]	ΔH [J/mol]	$\Delta H/x$ [J/mol]	ΔS [J/mol/K]
$[Fe(NCS)_2(btr)_2]\cdot H_2O$	heating	147	142–152	8947	8947	58.7
$[Fe(NCS)_2(btr)_2]\cdot H_2O$	cooling	117.4	113.6–123.7	8036	8036	68.0
$[Fe_{0.81}Ni_{0.19}(NCS)_2(btr)_2]\cdot H_2O$	heating	142.5	133.8–148.6	7183	8868	50.4
$[Fe_{0.81}Ni_{0.19}(NCS)_2(btr)_2]\cdot H_2O$	cooling	124.7	118.7–134	6610	8160	53.0
$[Fe_{0.66}Ni_{0.34}(NCS)_2(btr)_2]\cdot H_2O$	heating	137.4	121.7–143.8	5722	8669	41.6
$[Fe_{0.66}Ni_{0.34}(NCS)_2(btr)_2]\cdot H_2O$	cooling	126.8	120.7–132,5	4943	7490	39.0
$[Fe_{0.52}Ni_{0.48}(NCS)_2(btr)_2]\cdot H_2O$	heating	134.4	125.7–150	3853	7409	28.7
$[Fe_{0.52}Ni_{0.48}(NCS)_2(btr)_2]\cdot H_2O$	cooling	130.1	125.5–134.5	3505	6740	26.9
$[Fe_{0.42}Ni_{0.58}(NCS)_2(btr)_2]\cdot H_2O$	heating	131	122.2–152.2	2584	6152	19.7
$[Fe_{0.42}Ni_{0.58}(NCS)_2(btr)_2]\cdot H_2O$	cooling	130.5	117.7–140.7	2172	5171	16.6

Table 2
Summary of the calorimetric measurements on $[Fe_xZn_{1-x}(btr)_2(NCS)_2]\cdot H_2O$.

Formula	Mode	$T_{1/2}$ [K]	Integration interval [K]	ΔH [J/mol]	$\Delta H/x$ [J/mol]	ΔS [J/mol/K]
$[Fe(NCS)_2(btr)_2]\cdot H_2O$	heating	147	142–152	8947	8947	58.7
$[Fe(NCS)_2(btr)_2]\cdot H_2O$	cooling	117.4	113.6–123.7	8036	8036	68.0
$[Fe_{0.84}Zn_{0.16}(NCS)_2(btr)_2]\cdot H_2O$	heating	129.2	114–146	6236	7423	48.3
$[Fe_{0.84}Zn_{0.16}(NCS)_2(btr)_2]\cdot H_2O$	cooling	110	102–121	5851	6965	53.2
$[Fe_{0.7}Zn_{0.3}(NCS)_2(btr)_2]\cdot H_2O$	heating	115.5	108.7–125.1	3767	5381	32.6
$[Fe_{0.7}Zn_{0.3}(NCS)_2(btr)_2]\cdot H_2O$	cooling	102.8	102–109	3425	4892	33.3

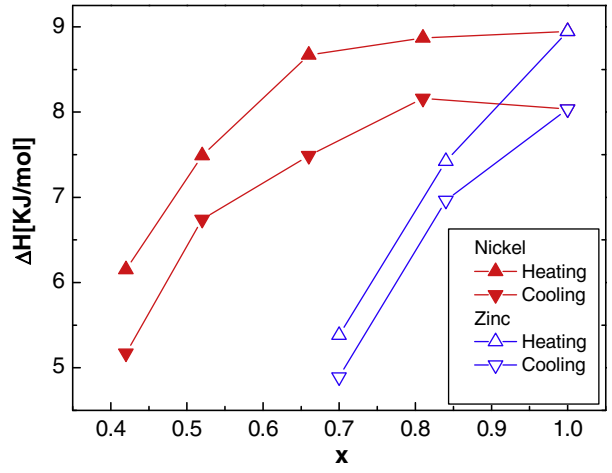


Fig. 4. Evolution of ΔH for $[Fe_xM_{1-x}(btr)_2(NCS)_2]\cdot H_2O$ (M^{II} = Ni, Zn).

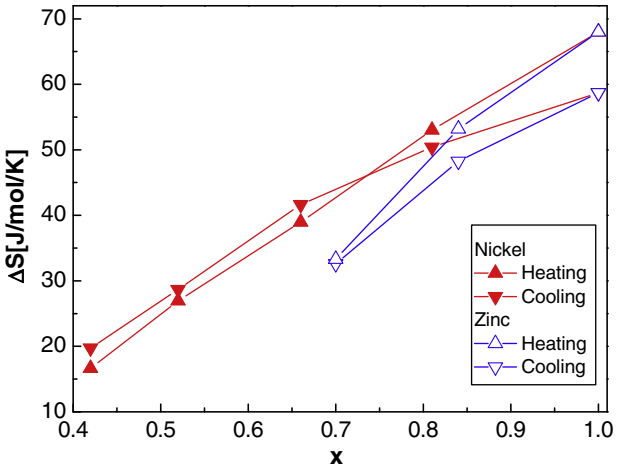


Fig. 5. Evolution of ΔS for $[Fe_xM_{1-x}(btr)_2(NCS)_2]\cdot H_2O$ (M^{II} = Ni, Zn).

quasi-static properties of the SCO compounds with amazing success. The degeneracy ratio, $g = g_{HS}/g_{LS}$, is related to the entropy variation during the total conversion $\Delta S = R \ln g$, which can be determined from calorimetric measurements. The g value may be quite large (up to a few thousands because it involves both the spin degeneracies and the density of vibrational states). The Ising-like model was used for the description of static properties as well as for dynamical properties of SCO compounds [20].

The Ising Hamiltonian writes:

$$H = \frac{\Delta}{2}\sum_i \hat{\sigma}_i - \sum_{\langle i,j\rangle} J_{i,j}\hat{\sigma}_i\hat{\sigma}_j, \tag{1}$$

with fictitious spins $\hat{\sigma}$, with eigenvalues +1 in the HS state and −1 in the LS state. We shall use $\langle i,j\rangle$ to denote the sum over the nearest neighbor spins, and the reference sign for a cooperative interaction, favoring spin like states, is $J_{i,j} > 0$ with $\Delta = E(HS) - E(LS)$, being the energy gap. The Ising equivalent form involves a temperature-dependent energy gap accounting for the degeneracy ratio:

$$H = \frac{\Delta_{eff}(T)}{2}\sum_i \hat{\sigma}_i - \sum_{\langle i,j\rangle} J_{i,j}\hat{\sigma}_i\hat{\sigma}_j, \tag{2}$$

with:

$$\Delta_{eff} = \Delta - k_B T \ln g. \tag{3}$$

The equilibrium temperature $T_{1/2}$, for which $\gamma_{HS} = \gamma_{LS} = 1/2$, corresponds to a null effective field, irrespective of the interactions:

$$T_{1/2} = \Delta_{eff}/k_B \ln g. \tag{4}$$

Assuming that all sites are equivalent, the mean field treatment is performed as usual, so that the one-site mean field Hamiltonian can be written as:

$$H = \frac{\Delta_{eff}}{2}\hat{\sigma} - J\hat{\sigma} < \hat{\sigma} >, \tag{5}$$

where $< \sigma >= m$ is the "fictitious magnetization", that can be written as:

$$< \hat{\sigma} >= m = \tan h\left(\frac{2Jm + TS - \Delta}{2}\right). \tag{6}$$

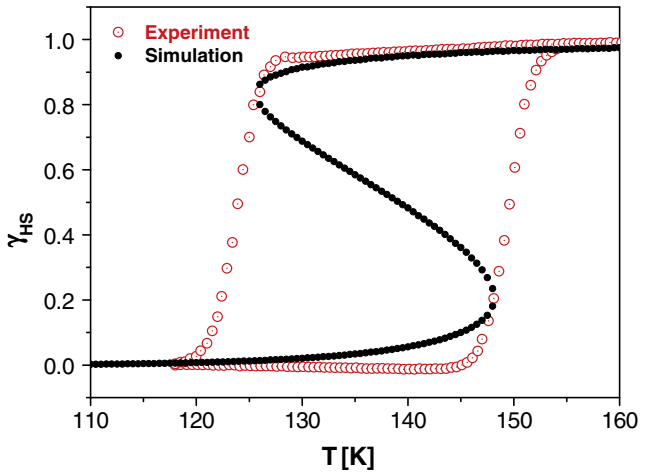


Fig. 6. Temperature variation of the HS fraction obtained for $[Fe(btr)_2(NCS)_2]\cdot H_2O$.

Fig. 6 presents a comparison between the experimental and computed temperature variation of the HS fraction obtained for $[Fe(btr)_2(NCS)_2]\cdot H_2O$. The values of the parameters used in these calculations are: J = 113K; $g = 2040$ ($< \Delta S > = 61.27 Jmol^{-1}K^{-1}$), $\Delta = 1021.35K$ ($< \Delta H > = 8491.5 Jmol^{-1}$).

3.2. Distribution of physical parameters derived from the FORC diagram

One important characteristic of SCO compounds is determined by the intensity of the elastic interactions inside the system. In the case of weak interactions, the reversible spin conversion between HS and LS states is gradual and characterized mainly by the transition temperature $T_{1/2}$ corresponding to equal amounts of HS and LS molecules ($\gamma_{HS} = 0.5$). If the interactions overpass a threshold value, the transition becomes abrupt and the system undergoes a first order phase transition with hysteresis, a desirable property in most of the potential applications in displays and data recording devices [21–23]. The hysteresis is described in most of the situations by $T_{1/2}$ of both heating and cooling modes. As hysteresis is a complicate non-linear phenomenon, using only two parameters appears to be insufficient to describe it fully.

The idea that in spin-transition solids the molecules are organized in domains, including molecules in the same spin state, has been proposed by Sorai and Seki [24]. They consider that the molecules are organized in domains with a certain critical size, succeeding in this way to predict the critical size that should have a domain in order to present a first order phase transition, which is characteristic for a transition accompanied by hysteresis. Over the past few years, the existence of such like spin domains were pointed out from experimental data, namely the observation of minor hysteresis loops for thermal, pressure and light-induced thermal transitions [25–27], X-ray diffraction [28] and neutron Laue scattering on single crystals [29]. In order to evidence the elastic domain distribution, the experimental First-order Reversal Curve (FORC) diagram method was suggested [18,30,31]. The method, applied initially to study the magnetic interactions in geological samples [32], is based on measuring a set of First Order Reversal Curves (FORC). To measure a FORC, one should saturate the sample in the HS (or LS) state followed by reducing (or increasing) temperature to a specific value, usually denoted as reversal temperature, T_r. From this point, the temperature is increased (or decreased) back to saturation and the HS molecules fraction is measured, being a function of two variables: reversal and actual temperatures. The interior area of the hysteresis loop is systematically covered by a set of these FORCs, selecting between 20 and 30 reversal temperatures. In the final step of the method, one has to calculate the mixed derivative of $\gamma_{HS}(T, T_r)$, also known as a FORC distribution. The contour plot of the FORC distribution is named a FORC diagram. Even if this experimental procedure is more time consuming compared to a classical major hysteresis loop measurement, the FORC diagram provides the experimentalist with a wealth of physical information which makes the method attractive. However, the FORC diagram in the switching temperature plane does not provide directly the physical information needed for the characterization of the spin transition material.

Unfortunately, temperature is not the best parameter to characterize the properties and the behavior of SCO materials. An elegant solution to this situation was to convert the FORC diagram from the temperature plane to a physical parameters plane [18]. The Ising-like model modified for SCO systems was an ideal tool for the conversion, and the detailed procedure is described in Ref. [18,33]. The main elements, the energy gap between the LS and HS states, Δ, and the interaction parameter, J, were correlated with the critical temperatures. In our previous work [18], the degeneracy ratio of HS and LS was overestimated since we approximated by using calorimetrical data obtained for another transition metal ion (Co^{II}) [5].

Here, we calculate the distribution of physical parameters for $[Fe(btr)_2(NCS)_2]\cdot H_2O$ and for a diluted one ($x = 0.84$, M = Zn) using

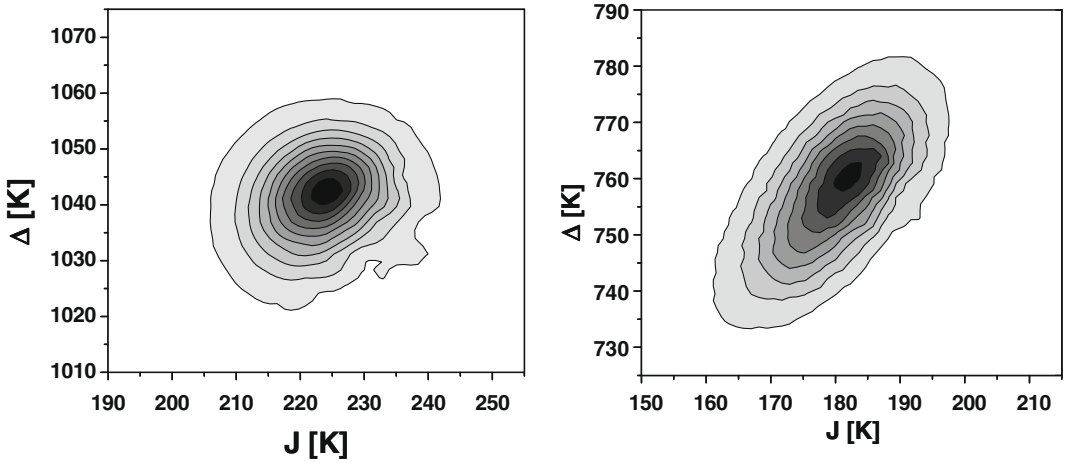


Fig. 7. The $P(\Delta, J)$ distributions of the undiluted system (left) and the mixed crystal system $Fe_{0.84}Zn_{0.16}(NCS)_2(btr)_2]\cdot H_2O$ (right) determined from the FORC data.

Table 3
Statistical analysis of the diagrams from Fig. 7.

x	$\bar{\Delta}$ (K)	$\sigma(\Delta)$ (K)	$\bar{J}$ (K)	$\sigma(J)$ (K)	$r_{\Delta J}$	$\bar{\Delta}$ (K)	$\sigma(\Delta)$ (K)	$\bar{J}$ (K)	$\sigma(J)$ (K)	$r_{\Delta J}$
0.8	1028	14.5	195	10.4	0.56	756	9.6	180	7.1	0.63
1.0	1225	8.8	235	8.3	0.16	1041	6.3	223	6.2	0.20

as the input degeneracy for Ising model the values determined from the calorimetric measurement presented above, i.e. $g = 2040$ for $x = 1.0$ and $g = 445$ for $x = 0.84$. The distributions obtained are presented in Fig. 7 and the statistical parameters that characterize them are reported in Table 3, on the right hand side. On the left hand side, one can find the averages $\bar{\Delta}$, $\bar{J}$, dispersions $\sigma(\Delta)$, $\sigma(J)$ and correlation $r_{\Delta J}$, as listed in Ref. [18].

We observed that even if the degeneracy was overestimated, the shape of the physical parameters diagrams did not suffer major modifications; the pure compound has a round shape distribution and the diluted one is more close to an ellipse. If we compare the results from a quantitative perspective, all the values obtained with our recently reliable degeneracy are smaller than in our initial study. The energy gap Δ was overestimated by 35% in the case of $x = 0.8$ compared with 17% for the non-diluted sample. If we refer to interactions, the modifications are below 8%. The only parameter that presents an opposite behavior is the correlation between Δ and J.

4. Conclusion

We have performed DSC measurements in the heating and cooling modes for a spin crossover compound $[Fe_xM_{1-x}(btr)_2(NCS)_2]\cdot H_2O$ (M^{II} = Ni, Zn) for pure and diluted cases. The heat capacity is dissymmetrical, for the pure compound $C_{p,heating} > C_{p,cooling}$ while for diluted compounds the situation is reversed $C_{p,heating} < C_{p,cooling}$. Entropy changes and the degeneracy ratio between HS and LS have been calculated from the experimental thermodynamical data and then we have applied the FORC technique in order to obtain the distribution of spin like domains on these compounds. We have also performed a statistical analysis on these distributions and found that the correlations between Δ and J increases with the dilution degree.

Acknowledgments

We acknowledge financial support from FSR-UCL, IAP-VI (P6/17) INANOMAT, FNRS (FRFC), Agence Universitaire de la Francophonie (Ref. 63-13PS818), the program PHC/BRANCUSI, the COSIF for allowing us to purchase a DSC cryostat, and Tournesol 2007 for allowing regular exchanges between Versailles and Louvain-la-Neuve. The researchers from "Al. I. Cuza" University are indebted to a CNCSIS-IDEI FASTSWITCH grant.

Appendix A. Supplementary data

Supplementary data associated with this article can be found, in the online version, at doi:10.1016/j.poly.2009.04.046.

References

[1] P. Gütlich, H. Goodwin, Top. Curr. Chem. 233 (2004) 1.
[2] Y. Garcia, P. Gütlich, Top. Curr. Chem. 234 (2004) 49.
[3] W. Vreugdenhil, J.H. Diemen, R. Graaff, J.G. Haasnoot, J. Reedijk, A.M. Hraan, O. Kahn, J. Zarembowitch, Polyhedron 9 (1990) 2971.
[4] J.P. Martin, J. Zarembowitch, A. Dworkin, J.G. Haasnoot, E. Codjovi, Inorg. Chem. 33 (1994) 2617.
[5] J.P. Martin, J. Zarembowitch, A. Bousseksou, A. Dworkin, J.G. Haasnoot, F. Varret, Inorg. Chem. 33 (1994) 6325.
[6] W. Vreugdenhil, J.G. Haasnoot, O. Kahn, P. Thuery, J. Reedijk, J. Am. Chem. Soc. 109 (1987) 5272.
[7] C. Enachescu, H. Constant-Machado, E. Codjovi, J. Linares, K. Boukheddaden, F. Varret, J. Phys. Chem. Solids 62 (2001) 1409.
[8] H. Spiering, E. Meissner, H. Köppen, E.W. Müller, P. Gütlich, Chem. Phys. 68 (1982) 65.
[9] J. Wajnflasz, R. Pick, Journal de Physique 32 (1971) C1.
[10] C.P. Slichter, H.G. Drickamer, J. Chem. Phys. 56 (1972) 2142.
[11] H. Constant-Machado, J. Linares, F. Varret, J.G. Haasnoot, J.P. Martin, J. Zarembowitch, A. Dworkin, A. Bousseksou, J. Phys. I France 6 (1996) 1203.
[12] H. Constant-Machado, A. Stancu, J. Linares, F. Varret, IEEE Trans. Magn. 34 (1998) 2213.
[13] P. Gütlich, Y. Garcia, H. Spiering, in: J.S. Miller, M. Drillon (Eds.), Magnetism: From Molecules to Materials IV, Wiley, VCH, 2003, p. 271.
[14] J.H. Takemoto, J.H. Hutchinson, Inorg. Nucl. Chem. Lett. 8 (1972) 769.
[15] M. Sorai, Bull. Chem. Soc. Jpn. 74 (2001) 2223.
[16] E. König, Struct. Bonding 76 (1991) 51.
[17] R. Tanasa, C. Enachescu, A. Stancu, E. Codjovi, J. Linares, F. Varret, J. Opt. Adv. Mater. 6 (2004) 551.
[18] R. Tanasa, C. Enachescu, A. Stancu, E. Codjovi, J. Linares, F. Varret, J. Haasnoot, Phys. Rev. B 71 (2005) 014431.
[19] J.G. Aston, H.L. Fink, S.C. Schimann, J. Am. Chem. Soc. 65 (1943) 341.
[20] M. Nishino, K. Boukheddaden, S. Miyashita, F. Varret, Phys. Rev. B 72 (2005) 064452.
[21] O. Kahn, J. Krober, C. Jay, Adv. Mater. 4 (1992) 718.
[22] O. Kahn, C.J. Martinez, Science 279 (1998) 44.
[23] Y. Garcia, V. Ksenofontov, P. Gütlich, Hyperfine Interactions 139 (2002) 543.
[24] M. Sorai, S. Seki, J. Phys. Soc. Japan 33 (1972) 575.
[25] E.W. Müller, H. Spiering, P. Gütlich, J. Chem. Phys. 79 (1983) 1439.
[26] H. Constant-Machado, A. Stancu, J. Linares, F. Varret, IEEE Transactions on Magnetics 34 (1998) 2213 Part 2.
[27] C. Enachescu, R. Tanasa, A. Stancu, E. Codjovi, J. Linares, F. Varret, Physica B 343 (2004) 15.
[28] S. Pillet, J. Hubsch, C. Lecomte, Eur. Phys. J. B49 (2006) 265.
[29] F. Varret, K. Boukheddaden, A. Goujon, B. Gillon, G.J. McIntyre, Zeit. Krist. 223 (2008) 250.
[30] C. Enachescu, R. Tanasa, A. Stancu, F. Varret, J. Linares, E. Codjovi, Phys. Rev. B 72 (2005) 054413.
[31] R. Tanasa, A. Stancu, E. Codjovi, J. Linares, F. Varret, J.F. Letard, J. Appl. Phys. 103 (2008) 07b905.
[32] C.R. Pike, A.P. Roberts, K.L. Verosub, J. Appl. Phys. 85 (1999) 6660.
[33] R. Tanasa, PhD Thesis, University of Versailles, 2006

Polyhedron 28 (2009) 2537–2544

Contents lists available at ScienceDirect

Polyhedron

journal homepage: www.elsevier.com/locate/poly

Oxidative DNA cleavage by copper ternary complexes of 1,10-phenanthroline and ethylenediamine-sulfonamide derivatives

Andreea Bodoki [a], Adriana Hangan [a], Luminita Oprean [a], Gloria Alzuet [b], Alfonso Castiñeiras [c], Joaquín Borrás [b,*]

[a] Department of Inorganic Chemistry, Iuliu Hatieganu University of Medicine and Pharmacy, Cluj-Napoca, Romania
[b] Department of Inorganic Chemistry, University of Valencia, Burjassot (Valencia), Spain
[c] Department of Inorganic Chemistry, University of Santiago de Compostela, Santiago de Compostela, Spain

ARTICLE INFO

Article history:
Received 31 March 2009
Accepted 5 May 2009
Available online 15 May 2009

Keywords:
Ternary Cu(II) complexes
Phenanthroline
Sulfonamide derivatives
Oxidative DNA cleavage

ABSTRACT

Ternary copper(II) complexes (**1**–**3**) of 1,10-phenanthroline and ethylenediamine-R-sulfonamide derivatives (R = benzene, toluene and naphthalene rings) have been synthesized and characterized with the aid of X-ray diffraction and spectroscopic and electrochemical techniques. The crystal structures of the complexes show that the coordination polyhedron around copper(II) is distorted square planar. Both 1,10-phenanthroline and ethylenediamine-R-sulfonamide act as bidentate ligands. The three structures are stabilized by π–π stacking interactions. The interaction of the complexes with calf thymus DNA has been investigated by thermal denaturation studies which indicated that DNA was stabilized in the presence of the compounds. The increase in DNA stability induced by the complexes follows the order: **3** > **2** > **1**. All three complexes were found to be very efficient agents of plasmid DNA cleavage in the presence of ascorbate as reducing agent. Mechanistic studies of the DNA cleavage process performed with radical scavengers show that the reactive oxygen species involved in the DNA damage are the hydroxyl radical, singlet oxygen-like species, the superoxide and hydrogen peroxide.

© 2009 Elsevier Ltd. All rights reserved.

1. Introduction

The success of cisplatin and other platinum anticancer drugs has stimulated a renaissance of inorganic medicinal chemistry and the search for complexes of other transition metals with interesting biological properties [1,2]. The continuous demand for new anticancer drugs has addressed chemotherapeutic research based on the use of essential metalloelements [3] since potential drugs developed in this way may be less toxic and more prone to exhibit antiproliferative activity against tumors. In this context, copper(II) and its complexes play an important role as suitable species for antiproliferative tests [4,5].

In recent years, there has been substantial interest in the rational design of novel transition metal complexes which bind and cleave duplex DNA with high sequential or structural selectivity [6–8]. An approach to the discovery of new metallodrugs involves binding an organic compound of known therapeutic value to a metal-containing fragment; this results in a metal–drug synergism in which the metal acts as a carrier and stabilizer for the drug until it reaches its target, while at the same time the organic drug carries and protects the metal preventing side reactions in its transit toward a second target of biological action [9]. Such combined effects may result in an important enhancement of the activity of the drug and the opening of new mechanism of action, such as when the well-known breast cancer drug tamoxifen is coordinated to iron (Ferrocifen) [10]. The use of transition metal complexes as artificial nucleases is an area of extensive research due to the diverse structural features and reactivity of such complexes [11,12].

For the past several years, our group has worked on the synthesis of copper–sulfonamide complexes in order to obtain novel antitumor agents. These complexes are especially attractive as anticancer agents because several substituted sulfonamides have been found to arrest the cell cycle, causing apoptosis in the M phase [13]. In this context, we have described the nuclease activity of several copper–sulfonamide complexes [14–21]. In the present paper, we report three new copper ternary complexes of substituted *N*-sulfonamides derived of ethylenediamine (Chart 1) and 1,10-phenanthroline. 1,10-Phenanthroline is a versatile ligand able to chelate copper to give mono-phen or bis-phen copper complexes at the oxidation state I or II [22]. In the presence of hydrogen peroxide, the $Cu^{I}(phen)_2$ complex efficiently cleaves DNA by oxidative attack on deoxyribose units in the DNA minor groove [23,24]. The presence of two organic ligands with biological properties and, on the other hand, the known nuclease ability of copper(II) complexes in the presence of reducing agents may lead to the development of new products with remarkable antitumoral properties.

* Corresponding author. Fax: +34 963544960.
E-mail address: Joaquin.Borras@uv.es (J. Borrás).

0277-5387/$ - see front matter © 2009 Elsevier Ltd. All rights reserved.
doi:10.1016/j.poly.2009.05.017

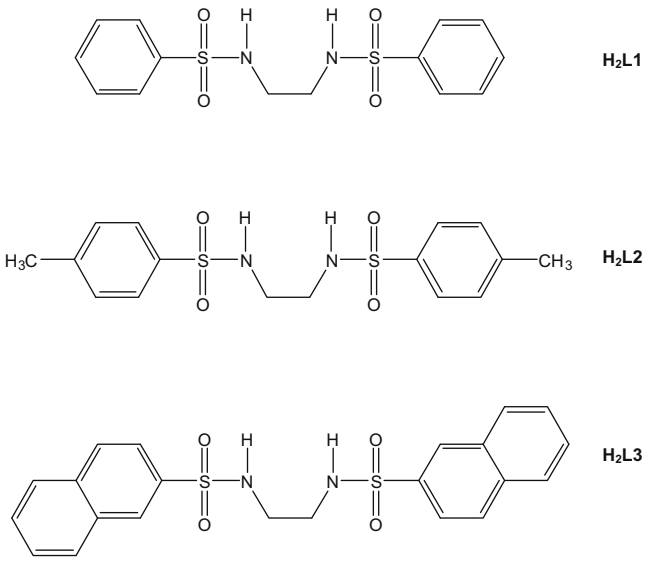


Chart 1. Scheme of the ligands.

2. Experimental

2.1. Materials and physical measurements

Reagents and solvents were commercially available (Sigma) in high purity and used as received. Plasmid pUC18 (0.25 μg/μL, 750 μM in nucleotides) in TE (tris 10 mM and EDTA 1 mM, pH 8.0) was purchased from Roche Diagnostics, Germany. CT-DNA (type XV) was from Sigma. Solutions of the metal complexes and other reagents for strand scission experiments were prepared fresh daily.

Elemental analyses (C, N, H, S) were performed on a Carlo Erba AAS instrument. Infrared spectra were recorded with a Mattson Satellite FT-IR spectrophotometer from 4000 to 400 cm^{-1} on KBr disks. Diffuse reflectance spectra (nujol mulls) of the complexes were performed on a Shimadzu 2101-PC UV–Vis spectrophotometer. UV–Vis spectra of the complex solutions were recorded with an HP 8453 instrument. Fast atom bombardment (FAB) mass spectra were obtained with a VG Autospec spectrometer with 3-nitrobenzyl alcohol as matrix. ESI mass (+ mode) analyses were performed on a Bruker Esquire 3000 plus LC-MS system. Electronic Paramagnetic Resonance (EPR) spectra of ground crystals were collected at the X-band frequency at room temperature with a Bruker ELEXSYS spectrometer. Cyclic voltammetry experiments were performed in a single compartment cell with a three-electrode system on a PAR 273A potentiostat/galvanostat. The working and auxiliary electrodes were platinum, and the reference electrode was Ag/AgCl. The supporting electrolyte was tetrabutylammonium perchlorate. Solutions of the complexes were deoxygenated by purging with nitrogen for 15 min prior to measurement.

2.2. Synthesis of the ligands

2.2.1. N,N′-(Ethane-1,2-diyl)dibenzenesulfonamide (H_2L1) and N,N′-(ethane-1,2-diyl)dinaphthalene-2-sulfonamide (H_2L3)

A solution containing 1 g of ethylenediamine (16.6 mmol) and 34 mmol of benzenesulfonylchloride (6.0 g) (for H_2L1) or naphthalenesulfonylchloride (7.7 g) (for H_2L3) in 6 mL of pyridine was heated at reflux for 10 h. The mixture was added to 10 mL of cold water and stirred for several minutes. The resulting solid was recrystallized from ethanol.

Anal. Calc. for $C_{14}H_{16}N_2S_2O_4$ (H_2L1) (340.06): C, 49.40; H, 4.74; N, 8.23; S, 18.84. Found: C, 49.35; H, 4.73; N, 8.27; S, 19.13%. Yield: 85%. IR (KBr) (ν_{max}/cm^{-1}): 3321, 3273 (N–H); 1324, 1157 (SO_2). FAB: m/z^+ 341 $[H_2L1 + H]^+$.

Anal. Calc. for $C_{22}H_{20}N_2S_2O_4$ (H_2L3) (440.09): C, 59.98; H, 4.58; N, 6.36; S, 14.56. Found: C, 59.32; H, 4.55; N, 6.36; S, 14.15%. Yield: 75%. IR (KBr) (ν_{max}/cm^{-1}): 3282 (N–H); 1336, 1156 (SO_2). FAB: m/z^+ 441 $[H_2L3 + H]^+$.

2.2.2. N,N′-(Ethane-1,2-diyl)bis(4-methylbenzenesulfonamide) (H_2L2)

This compound was obtained and characterized as previously reported [25].

2.3. Synthesis of [Cu(L1)(phen)] (**1**), [Cu(L2)(phen)]·H_2O (**2**) and [Cu(L3)(phen)](**3**)

0.5 mmoles of the ligand were dissolved in 30 mL of methanol (H_2L1 or H_2L2) or in a mixture of 35 mL methanol and 10 mL *N*,*N*′-dimethylformamide (H_2L3). To this solution were then added 2 mL of a methanolic solution of KOH (0.5 M) and 0.25 mmol of $Cu(CH_3COO)_2{\cdot}H_2O$. Separately, another solution was prepared by dissolving 0.5 mmol of 1,10-phenanthroline (phen) in 25 mL of methanol and then added dropwise under continuous stirring to the solution containing the ligand and the Cu(II) salt. The final green reaction mixture was stirred for an hour at 30 °C and was then left to stand at room temperature. Slow evaporation of this resulting solution provided well-developed blue crystals of the compounds that were suitable for X-ray diffraction.

Anal. Calc. for $C_{26}H_{22}CuN_4S_2O_4$ (**1**) (582.15): C, 53.64; H, 3.81; N, 9.62; S, 11.02. Found: C, 53.18; H, 3.94; N, 9.12; S, 11.18%. Yield: 72%. IR (KBr) (ν_{max}/cm^{-1}): 1269, 1135 $\nu(SO_2)$. Diffuse reflectance (λ_{max}, nm): 396 ($\pi \rightarrow \pi^*$), 590, 740sh (d–d). UV–Vis (λ_{max}, nm) in DMF: 386 ($\varepsilon = 1440\ M^{-1}\ cm^{-1}$), 627 ($\varepsilon = 305\ M^{-1}\ cm^{-1}$), ESI^+ mass spectra in DMF: m/z^+ 582.0 $[1+H]^+$.

Anal. Calc. for $C_{28}H_{28}CuN_4S_2O_5$ (**2**) (628.22): C, 53.53; H, 4.49; N, 8.92; S, 10.21. Found: C, 53.92; H, 4.32; N, 8.89; S, 10.24%. Yield: 65%. IR (KBr) (ν_{max}/cm^{-1}): 1266, 1133 $\nu(SO_2)$. Diffuse reflectance (λ_{max}, nm): 400 ($\pi \rightarrow \pi^*$), 590, 740sh (d–d). UV–Vis (λ_{max}, nm) in DMF: 386 ($\varepsilon = 1680\ M^{-1}\ cm^{-1}$), 623 ($\varepsilon = 265\ M^{-1}\ cm^{-1}$), ESI^+ mass spectra in DMF: m/z^+ 610.1 $[2\text{-}H2O+H]^+$.

Anal. Calc. for $C_{34}H_{26}CuN_4S_2O_4$ (**3**) (682.28): C, 59.85; H, 3.84; N, 8.21; S, 9.40. Found: C, 59.74; H, 3.89; N, 8.19; S, 9.32%. Yield: 76%. IR (KBr) (ν_{max}/cm^{-1}): 1279, 1122 $\nu(SO_2)$. Diffuse reflectance (λ_{max}, nm): 400 ($\pi \rightarrow \pi^*$), 630 (d–d). UV–Vis (λ_{max}, nm) in DMF: 629 ($\varepsilon = 215\ M^{-1}\ cm^{-1}$), ESI^+ mass spectra in DMF: m/z^+ 718.9 **3**+$2H_2O$+H]$^+$.

2.4. X-ray crystallography

A crystal of compound **1** (blue prismatic), compound **2** (blue needle) or compound **3** (blue plate) was mounted on a glass fiber and used for data collection. Crystal data were collected at 100.0(1) K, using a Bruker X8 Kappa APEXII diffractometer. Graphite monochromated Mo Kα radiation ($\lambda = 0.71073$ Å) was used throughout. The data were processed with APEX2 [26] and corrected for absorption using SADABS (transmissions factors: 1.000–0.099) [27]. The structure was solved by direct methods using the program SHELXS-97 [28] and refined by full-matrix least-squares techniques against F^2 using SHELXL-97 [29]. Positional and anisotropic atomic displacement parameters were refined for all nonhydrogen atoms. Hydrogen atoms were located in difference maps and included as fixed contributions riding on attached atoms with isotropic thermal parameters 1.2 times those of their carrier atoms. Criteria of a satisfactory complete analysis were the ratios of rms shift to standard deviation less than 0.001 and no significant features in final difference maps. Atomic scattering factors were from "International Tables for Crystallography" [30]. Molecular graphics were from PLATON [31] and SCHAKAL [32]. A summary of the crystal

data, experimental details and refinement results for the three complexes are listed in Table 1.

2.5. DNA-melting experiments

DNA-melting experiments were carried out by monitoring the absorption spectrum between 1000 and 200 nm of CT-DNA (50 μM base pairs) at different temperatures in both the absence and the presence of the ligands or the complexes in a ratio of 2.5:1 DNA to complex. Measurements were performed with an Agilent 8453 UV–Vis spectrophotometer equipped with a Peltier temperature controlled sample cell and driver (Agilent 89090A). Solutions containing the ternary complexes (**1**–**3**) and CT-DNA in borate buffer, pH 8 (1 mM borate, 2 mM NaCl) was stirred continuously and heated with a temperature increase of 1 °C min^{-1}. The temperature interval studied ranged from 25 to 90 °C. The melting point was obtained with the first derivative using the Savitsky–Golay algorithm.

2.6. pUC18 DNA cleavage

A typical reaction for complexes was undertaken by mixing 7 μL of 0.05 M borate buffer (pH 8.0), 1 μL of pUC18 (0.25 μg/μL), 6 μL of a solution of the tested complex at increasing concentrations to obtain final concentrations between 3 and 12 μM and 6 μL of ascorbate, in a 1000-fold molar excess relative to the concentration of the complex in borate buffer (0.05 M, pH 8.0). The mixtures were allowed to stand at 37 °C for 60 min, after which, 3 μL of a loading buffer solution consisting of 0.25% bromophenol blue, 0.25% xylene cyanole, and 30% glycerol was added. The solution was then subjected to electrophoresis on a 0.8% agarose gel in 0.5 × TBE buffer (0.045 M tris(hydroxymethyl)aminomethane (tris), 0.045 M boric acid, and 1 mM EDTA) containing 2 μL/100 mL of a solution of ethidium bromide (10 mg/mL) at 80V for about 2 h. The gel was photographed using a TDI Gel Printer Plus system.

To test for the presence of reactive oxygen species (ROS) generated during strand scission, reactive oxygen intermediate scavengers were added alternatively to the reaction mixtures. These scavengers were DMSO (0.4 M), *tert*-butyl alcohol (0.4 M), sodium formate (0.4 M), 1,4-diazabicyclo[2,2,2]octane (DABCO) (0.4 M), 4, 5-dihydroxy-1,3-benzenedisulfonic acid (Tiron) (0.1 M) and catalase (10 μg/mL, 650 U/mL). Assays in the presence of the minor groove binder distamycin (8 μM) and major groove binder methyl green (3 μM) or the copper(I) stabilizer neocuproine, at different concentrations (12, 120 and 240 μM) were also performed. Samples were treated as described above.

3. Results and discussion

3.1. Crystal structures of the complexes *1*–*3*

Figs. 1–3 show the molecular structure of complexes **1**–**3** respectively with the atomic labeling scheme adopted. The relevant structural parameters for the compounds are listed in Table 2. The crystal structures of compounds **1**–**3** consist of a discrete monomeric copper(II) species surrounded by two N atoms belonging to a phenanthroline molecule and two sulfonamido N atoms of the dideprotonated *N*-sulfonamide ligands in a distorted square-planar geometry.

Both, the dideprotonated sulfonamide ligand ($L1^{2-}$, $L2^{2-}$ or $L3^{2-}$) and the 1,10-phenanthroline, act as bidentate forming five-membered rings with the metal ion. The Cu–Nphen distances which range from 1.992(5) Å to 2.024(5) Å are similar to those reported for copper–phenanthroline complexes [33]. The Cu–Nsulfonamidato bond lengths lie in the range from 1.947(4) Å to 1977(5) Å and are normal distances for copper–sulfonamidato complexes [25]. The N–Cu–N angles that describe the coordination polyhedron [82.13(19)–104.67(19)° in **1**, 81.99(15)–103.64(15)° in **2** and 81.67(18)–103.30(2)° in **3**] deviate significantly from 90°. In all complexes, the smaller angle corresponds to that formed by the copper ion and the two phenanthroline nitrogen atoms, as a consequence of the constrained geometry of the phen rings [34–36].

The distortion of the square-planar geometry (commonly known as tetrahedrality) can be determined from the angle subtended by two planes, each encompassing the copper and two adjacent atoms. The tetrahedrality values of 46.46°, 34.0° and

Table 1
Crystal and structure refinement data for complex **1**, complex **2** and complex **3**.

	Complex 1	Complex 2	Complex 3
Empirical formula	$C_{26}H_{22}CuN4O_4S_2$	$C_{28}H_{28}CuN_4O_5S_2$	$C_{34}H_{26}CuN_4O_4S_2$
Formula weight	582.14	628.20	682.25
T (K)	100 (2)	100 (2)	100 (2)
Wavelength (Å)	0.71073	0.71073	0.71073
Crystal system, space group	monoclinic, $P2_1/c$ (number 14)	triclinic, $P\bar{1}$ (number 2)	monoclinic, $P2(1)/n$ (number 14)
a (Å)	7.2144(9)	7.4589(8)	10.1370(3)
b (Å)	30.913(4)	10.7390(13)	11.1709(3)
c (Å)	10.7325(15)	17.7483(17)	25.9632(8)
α (°)	90.000	106.147(7)	90.000
β (°)	94.576(7)	92.209(7)	100.637(2)
γ (°)	90.000	96.264(8)	90.000
V ($Å^3$)	2385.9(5)	1353.9(3)	2889.54(15)
Z, calculated density (Mg m^{-3})	4, 1.621	2, 1.541	4, 1.568
Absorbtion coefficient (mm^1)	1.134	1.008	0.950
F(000)	1196	650	1404
Crystal size (mm)	0.11 × 0.03 × 0.08	0.37 × 0.07 × 0.04	0.22 × 0.20 × 0.10
θ range for data collection (°)	1.32–26.48	1.99–25.68	1.60–27.88
Limiting indices	$-9 \leqslant h \leqslant 8$	$-9 \leqslant h \leqslant 9$	$-13 \leqslant h \leqslant 13$
	$0 \leqslant k \leqslant 38$	$-13 \leqslant k \leqslant 12$	$0 \leqslant k \leqslant 14$
	$0 \leqslant l \leqslant 13$	$0 \leqslant l \leqslant 21$	$0 \leqslant l \leqslant 34$
Reflections collected/unique	45124/4893	17555/5119	36832/6896
	[R_{int} = 0.1249]	[R_{int} = 0.0812]	[R_{int} = 0.0318]
Data/restraints/parameters	4893/0/334	5119/0/361	6896/0/361
Completeness to θ = 26.48 (%)	99.2	99.9	100
Final R indices [$I > 2\sigma(I)$]	R_1 = 0.0756, wR_2 = 0.1840	R_1 = 0.0694, wR_2 = 0.1770	R_1 = 0.0887, wR_2 = 0.2366
R indices (all data)	R_1 = 0.1163, wR_2 = 0.2038	R_1 = 0.0900, wR_2 = 0.1879	R_1 = 0.1089, wR_2 = 0.2514

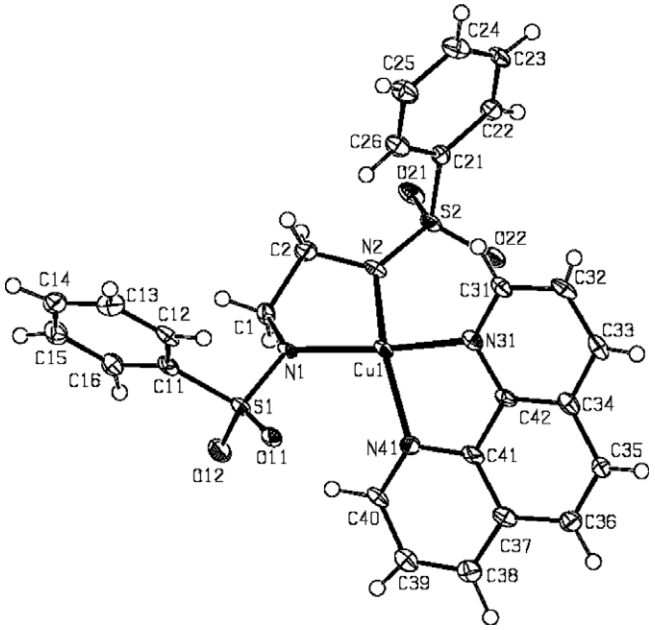


Fig. 1. ORTEP view of [Cu(L1)(phen)] (**1**).

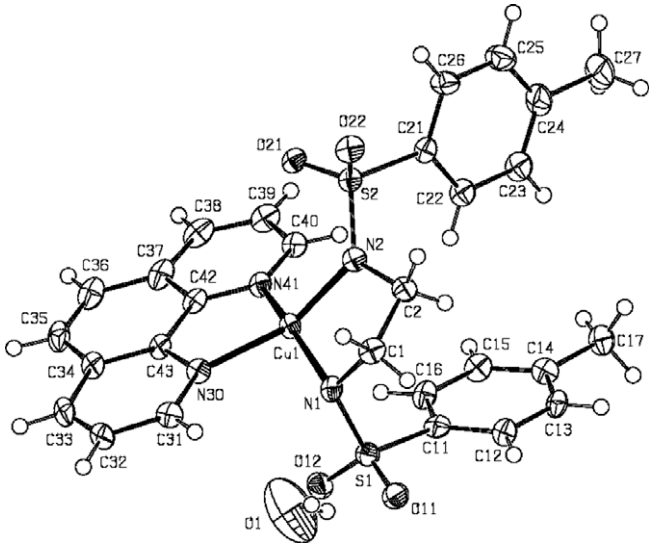


Fig. 2. ORTEP drawing of complex [Cu(L2)(phen)]·H_2O (**2**).

28.70° for **1**, **2** and **3**, respectively indicates that the copper ion adopts a significant distorted square-planar geometry. This distortion can be attributed to the presence of two bidentate ligands.

One remarkable aspect to be considered in the crystal structures of the compounds is the presence of the π–π stacking interactions which are similar for complexes **1** and **2** and have different characteristics for complex **3**. The structures of complexes **1** and **2** are stabilized by π–π interactions brought on by intermolecular parallel π–π stacking between the phenanthroline rings belonging to adjacent complex molecules (Fig. 4) [33,34,36,37]. The geometric parameters characterizing these interactions are summarized in Tables 3 and 4. In addition, the structure of complex **2** is stabilized by an intermolecular hydrogen bond of moderate strength [38] formed between the O(1) of a water molecule and the O(11) of the sulfonamide group [O(1)···O(11), 2.841(7) Å, O(1)–H(10B)···O(11), 168.1°].

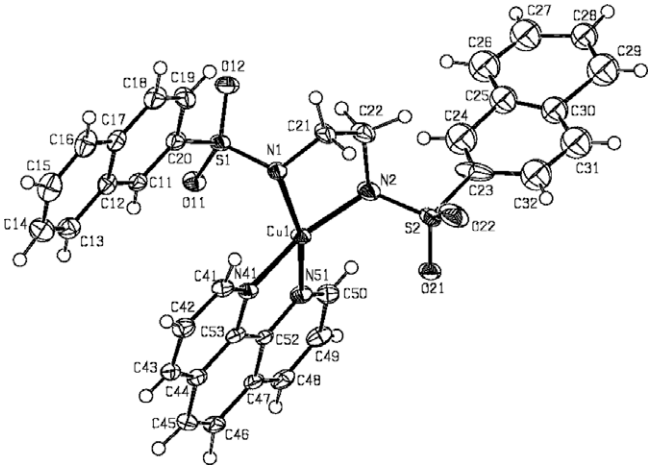


Fig. 3. ORTEP view of [Cu(L3)(phen)] (**3**).

Complex **3** presents strong π–π stacking interactions involving the phenanthroline molecules, the "Cu chelate" (the chelate ring formed by the copper atom and the coordinated phenanthroline, Cu1–N41–C53–C52–N51) and the naphthalene rings. Phen–phen and phen–"Cu chelate" interactions occur between neighboring complex molecules. Additional phen–naphthalen interactions occur between the resulting pairs and adjacent complex molecules, giving rise to 2D frameworks, parallel to *ac* plane (Fig. 5). The geometric parameters for these π–π interactions are summarized in Table 5. These π–π interactions are similar to those reported for other copper complexes of 1,10-phenanthroline [39,40].

3.2. Spectroscopic properties

All the complexes present the same infrared spectrum pattern. As for the sulfonamide group, the bands assigned to $\nu(SO_2)_{as}$ and $\nu(SO_2)_s$ vibrations are slightly shifted to lower frequencies with respect to those of the uncoordinated ligands. In general, the IR spectra are similar to those observed for other copper *N*-sulfonamide derivatives [17,41] with the modifications noted above being mainly due to ligand deprotonation at the sulfonamide group. In addition, the spectrum of the complex exhibits new bands at 1428, 1254, and 850 cm^{-1}, which are assigned to the characteristic vibrations of the coordinated phenanthroline molecules [42,43].

The diffuse reflectance spectra of complexes **1** and **2** exhibit a d–d maximum at 590 nm and a shoulder at about 740 nm while that of complex **3** shows a broad d–d maximum centered at about 630 nm. These bands correspond to ligand field transitions of distorted square planar complexes with CuN_4 chromophores [44]. The spectra of DMF solutions of complexes **1–3** show the same maxima at 630 nm, thus suggesting that all three compounds contain the same chromophore in solution. The shift of the d–d band position with respect to that in the diffuse reflectance spectra is probably a consequence of the coordination of solvent molecules. These results are in agreement with those obtained from the ESI experiments which show that the copper(II), a sulfonamidate ligand, and a phenanthroline species exist as a whole entity.

The EPR spectrum of the complex **1** (Fig. 6) is slightly rhombic. The EPR parameters obtained by simulation [45] are: $g_x = 2.042$, $g_y = 2.063$ and $g_z = 2.233$. For systems with $g_z > g_y > g_x$ the ratio $R = (g_y - g_x)/(g_z - g_y)$ indicates the ground state of the complex [46]. The *R* value of 0.12 for **2** suggests than the unpaired electron of copper(II) is in the d_{x2-y2} orbital. The EPR spectra of the complexes **2** and **3** are axial with the following EPR parameters $g_{||} = 2.218$ and 2.210 and $g_\perp = 2.057$ and 2.050, respectively. The $g_{||} > g_\perp$ indicates a mainly copper(II) d_{x2-y2} ground state.

Table 2
Selected bond lengths (Å) and angles (°) for complexes **1**–**3**.

Complex 1		Complex 2		Complex 3	
Cu(1)–N(1)	1.952(5)	Cu(1)–N(1)	1.950(4)	Cu(1)–N(1)	1.947(4)
Cu(1)–N(2)	1.972(5)	Cu(1)–N(2)	1.951(4)	Cu(1)–N(2)	1.977(5)
Cu(1)–N(31)	1.992(5)	Cu(1)–N(41)	1.997(4)	Cu(1)–N(41)	2.005(5)
Cu(1)–N(41)	2.024(5)	Cu(1)–N(30)	2.012(4)	Cu(1)–N(51)	2.015(4)
N(1)–Cu(1)–N(2)	83.59(19)	N(1)–Cu(1)–N(2)	85.53(15)	N(1)–Cu(1)–N(2)	85.04(19)
N(1)–Cu(1)–N(31)	157.43(19)	N(1)–Cu(1)–N(41)	160.56(16)	N(1)–Cu(1)–N(41)	96.28(19)
N(2)–Cu(1)–N(31)	104.03(19)	N(2)–Cu(1)–N(41)	103.04(15)	N(2)–Cu(1)–N(41)	162.0(2)
N(1)–Cu(1)–N(41)	104.67(19)	N(1)–Cu(1)–N(30)	97.93(15)	N(1)–Cu(1)–N(51)	159.36(19)
N(2)–Cu(1)–N(41)	143.21(19)	N(2)–Cu(1)–N(30)	154.24(15)	N(2)–Cu(1)–N(51)	103.3(2)
N(31)–Cu(1)–N(41)	82.13(19)	N(41)–Cu(1)–N(30)	81.99(15)	N(41)–Cu(1)–N(51)	81.67(18)

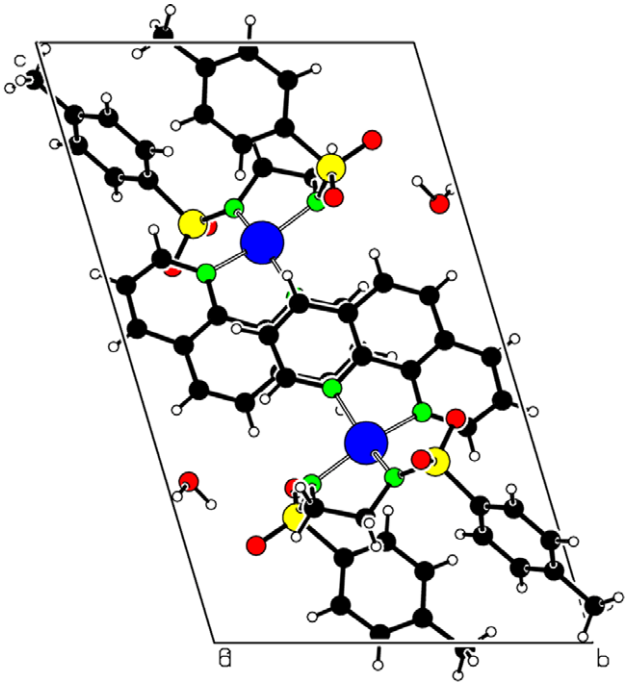


Fig. 4. Crystal packing of complex **1** showing the π–π interactions.

Table 3
Geometric parameters for π–π stacking (Å/°) in complex **1**.

π–π stacking	d_{c-c}	α	β	γ	$d_{\perp}$[Cg(*I*)–P(*J*)]	$d_{\perp}$[Cg(*J*)–P(*I*)]
Phen–phen						
Cg(4)–Cg(4)[a]	3.7505	0.00	29.52	29.52	3.264	3.264
Cg(4)–Cg(4)[b]	3.6682	0.00	27.56	27.56	3.252	3.252

d_{c-c}: distance between ring centroids; *a*: dihedral angle between the rings *I* and *J*; β, γ: slipping angles; $d_{\perp}$[Cg(*I*)–P(*J*)] and $d_{\perp}$[Cg(*J*)–P(I)]: perpendicular distance of Cg(4) on the ring Cg(4)[a] or Cg(4)[a].

[a] 1 − *x*, −*y*, 2 − *z*.

[b] 2 − *x*, −*y*, 2 − z. Cg(4): N41–C40–C39–C38–C36–C41.

Table 4
Geometric parameters for π–π stacking (Å/°) in complex **2**.

π–π stacking	d_{c-c}	α	β	γ	$d_{\perp}$[Cg(*I*)–P(*J*)]	$d_{\perp}$[Cg(*J*)–P(*I*)]
Phen–phen						
Cg(3)–Cg(3)[a]	3.7923	0.00	29.27	29.27	3.308	3.308
Cg(3)–Cg(3)[b]	3.6765	0.00	25.35	25.35	3.323	3.323

d_{c-c}: distance between ring centroids; *a*: dihedral angle between the rings *I* and *J*; β, γ: slipping angles; $d_{\perp}$[Cg(*I*)–P(*J*)] and $d_{\perp}$[Cg(*J*)–P(*I*)]: perpendicular distance of Cg(3) on the ring Cg(3)[a] or Cg(3)[b].

[a] 2 − *x*, 1 − *y*, 1 − *z*.

[b] 1 − *x*, 1 − *y*, 1−*z*. Cg(3): N30–C31–C32–C33–C34–C43.

3.3. Cyclic voltammetry experiments

The electrochemical profiles of the complexes were studied in DMF by cyclic voltammetry in the range of 1.0 to −1.0 V. In the three cases, the voltammograms show irreversible redox processes with one cathodic peak at −0.108 V, −0.144 V and −0.103 V for **1**–**3**, respectively (versus NHE) (Fig. S1). All the redox processes are clearly irreversible suggesting that the copper(I) species decompose at higher potential. The reduction peaks indicate that the stability of the copper(II) complex decreases as follows: **2** > **1** ≈ **3**.

3.4. Thermal denaturation studies

Since DNA is the primary pharmacological target of many antitumor compounds [47], the interaction between DNA and metal complexes is of paramount importance in understanding the mechanism of tumor inhibition for the treatment of cancer. Thus, the binding of the ligands and the complexes **1**–**3** to CT-DNA was studied by measuring changes in the melting temperature (T_m) of DNA that characterizes the transition from a double-stranded nucleic acid to a single stranded one [48]. The melting curves for complex **1** and the CT DNA are shown in Fig. 7. The three compounds produced a large increase in T_m (T_m = 50.8 °C for CT-DNA; T_m = 62.7, 64.6 and 69.9 °C for **1**, **2** and **3**, respectively) when the concentration ratio of DNA to complex is 2.5:1, which indicates a strong metal complex–DNA interaction that stabilizes the native DNA conformation [49]. The considerable increase of the melting temperature of DNA produced by the compounds is also indicative of an intercalative binding mode involving the phenanthroline molecule. The stronger interaction of complex **3** may be the result of the presence of a naphthalene ring in the sulfonamide ligand, which reinforces its DNA-binding propensity by stacking interaction. Moreover, our results reveal that the sulfonamide ligands have not significant effect on T_m of CT-DNA, suggesting that the free sulfonamides do not interact with the nucleic acid (data not shown).

3.5. Cleavage of pUC18 DNA

The DNA endonucleolytic cleavage, activated by metal ions, has been of interest to researchers [50]. Transition metal-mediated radical production may result in an efficient DNA cleavage. DNA cleavage is controlled by relaxation of the supercoiled circular form of pUC18 into the nicked circular and linear forms. When circular plasmid DNA is run in horizontal gel using electrophoresis, the fastest migration will be observed for the supercoiled form (Form I). If one strand is cleaved, the supercoils will relax to produce a slower-moving open circular form (Form II). If both strands are cleaved, a linear form (Form III) that migrates in between will be generated.

The ability of complexes **1**–**3** to cleave DNA was investigated by means of gel electrophoresis with supercoiled pUC18 in 0.05 M borate buffer (pH 8.0) and with ascorbate activation. Control

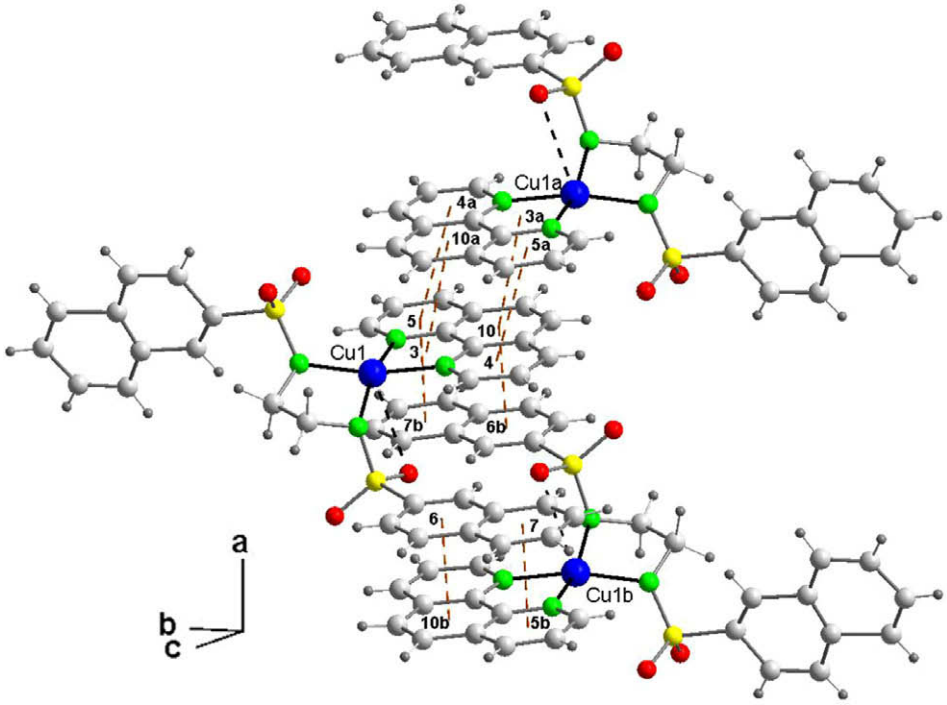


Fig. 5. Portion of the crystal packing of complex **3** showing the π–π interactions and the scheme of numeration of the rings.

experiments with $CuCl_2$ were also carried out under the same experimental conditions. All the complexes were found to exhibit nuclease activity (Fig. 8) and were more effective at higher concentrations. At 9 μM the complexes were able to transform almost completely Form I into Form II. At 12 μM the compounds induced complete degradation of the supercoiled Form I to yield open circular (Form II) and linear DNA (Form III) (lanes 10, 11 for complex **1**, lanes 14, 15 for complex **2** and lanes 18, 19 for complex **3**).

Neither the copper salt with ascorbate (lane 4) nor the copper complexes without ascorbate at the maximum concentration assayed (lanes 5, 6 and 7, respectively) yields significant strand scission, proving that both the copper complex and the ascorbate are required for the efficient DNA cleavage. Even though active, the three complexes exhibit lower nucleolytic efficiency as compared to that of the bis(*o*-phenanthroline)copper(II) complex, a well-known and very efficient chemical nuclease. Thus, at 12 μM $[Cu(phen)_2]^{2+}$ induces the conversion of DNA into small linear fragments and a considerable smear appears (lane 20).

Table 5
Geometric parameters for π–π stacking (Å/°) in complex **3**.

π–π stacking	d_{C-C}	α	β	γ	$d_{\perp}$[Cg(*I*)–P(*J*)]	$d_{\perp}$[Cg(*J*)–P(*I*)]
Phen–phen						
Cg(4)–Cg(10)[a]	3.5623	0.42	15.95	16.17	3.421	3.425
Cg(5)–Cg(4)[a]	3.7297	1.01	23.69	22.73	3.440	3.415
Phen–"Cu chelate [Cg(3)]"						
Cg(3)–Cg(4)[a]	3.9296	2.86	31.04	28.29	3.460	3.367
Cg(3)–Cg(10)[a]	3.6940	2.66	21.74	20.79	3.454	3.431
Phen–naphthalene						
Cg(5)–Cg(6)[b]	3.8765	2.39	29.06	31.31	3.313	3.389
Cg(5)–Cg(7)[b]	3.5505	0.32	19.49	19.65	3.344	3.347
Cg(6)–Cg(10)[b]	3.5820	1.60	19.03	18.83	3.390	3.386

d_{C-C}: distance between ring centroids; *a*: dihedral angle between the rings *I* and *J*; β, γ: slipping angles; $d_{\perp}$[Cg(*I*)–P(*J*)] and $d_{\perp}$[Cg(*J*)–P(*I*)]: perpendicular distance of Cg(*I*) on the ring Cg(*J*)[a] or Cg(*J*)[b].

[a] 1 − *x*, 1 − *y*, −*z*.

[b] 1 − *x*, 1 − *y*, −*z*. Cg(3): Cu1–N41–C53–C52–N51; Cg(4): N41–C41–C42–C43–C44–C53; Cg(5): N51–C50–C49–C48–C47–C52; Cg(6): C11–C12–C17–C18–C19–C20; Cg(7): C12–C13–C14–C15–C16–C17; Cg(10): C44–C45–C46–C47–C52–C53.

3.6. DNA cleavage mechanism

We used different inhibiting reagents to study various aspects of the mechanism of pUC18 DNA cleavage induced by the complexes with ascorbate activation (Figs. 9 and 10).

The reduction of the copper(II) complexes during the DNA cleavage process was evaluated by adding neocuproine, a ligand that strongly chelates copper(I), to the reaction mixtures. The

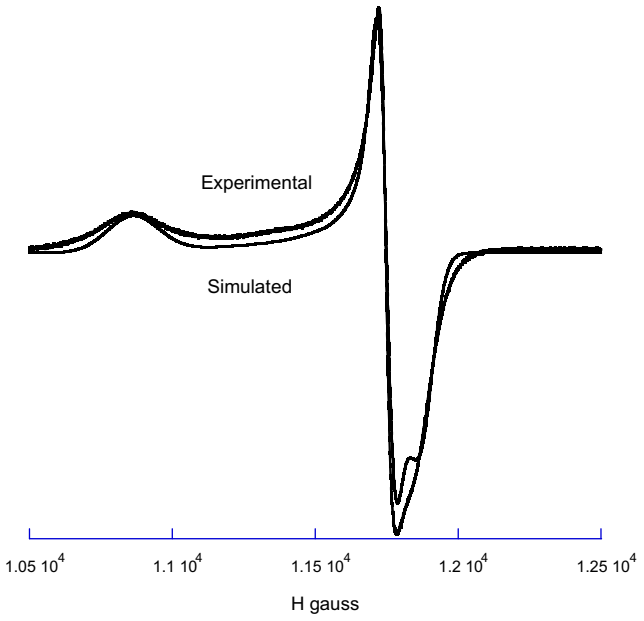


Fig. 6. X-band polycrystalline powder EPR spectrum of complex **1**.

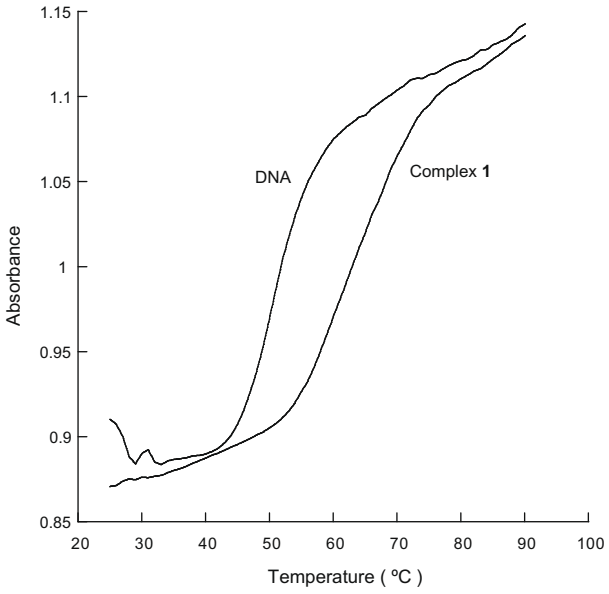


Fig. 7. Thermal denaturation curves of complex **1** and calf thymus DNA.

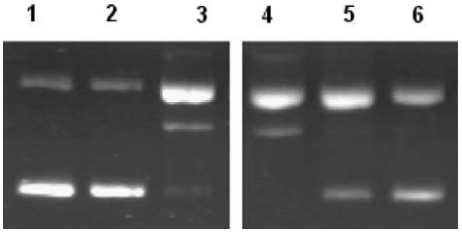


Fig. 9. Agarose gel electrophoresis of pUC18 plasmid treated with 12 μM complex **2** and 12 mM ascorbate in the presence of increasing concentrations of neocuproine. Incubation time: 1 h (37 °C). Lane 1: supercoiled DNA; lane 2: supercoiled DNA + ascorbate; lane 3: **2** without inhibitor; lane 4: **2** + neocuproine (12 μM); lane 5: **2** + neocuproine (120 μM); lane 6: **2** + neocuproine (240 μM).

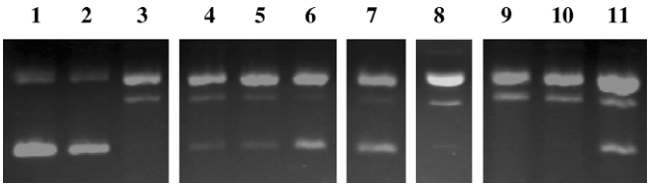


Fig. 10. Agarose gel electrophoresis of pUC18 plasmid treated with 12 μM complex **3** and 12 mM ascorbate in the presence of potential inhibitors. Incubation time: 1 h (37 °C). Lane 1: supercoiled DNA; lane 2: supercoiled DNA + ascorbate; lane 3: **3** without inhibitor; lane 4: **3** + DMSO (0.4 M); lane 5: **3** + *tert*-butyl alcohol (0.4 M); lane 6: **3** + sodium formiate (0.4 M); lane 7: **3** + DABCO (0.4 M); lane 8: **3** + Tiron (0.1 M); lane 9: **3** + distamycin (8 μM); lane 10: **3** + methyl green (3 μM); lane 11: **3** + catalase (6.5 units).

effect of neocuproine on the DNA cleavage induced by the complexes was tested at different concentrations. Results for complex **2** are shown in Fig. 9. The addition of neocuproine at a concentration equivalent to that of the compound (12 μM) (lane 4) did not attenuate the DNA cleavage; however higher concentrations of neocuproine (120 and 240 μM) (lanes 5 and 6) clearly inhibit the DNA strand scission mediated by **2** which indicates that Cu(I) is formed in the DNA damage reaction. Complexes **1** and **3** exhibit a similar behavior (data not shown). Generation of a Cu(I) complex induced in the presence of ascorbate was expected to lead to the activation of dioxygen that, in turn, could produce the intermediate or intermediates responsible for plasmid DNA strand scission. If the reaction follows a Fenton-like mechanism, several possible intermediates could be formed, depending on the number of electrons transferred from the complex to O_2. The possible intermediates are superoxide anion (O_2^-), hydrogen peroxide (H_2O_2) or hydroxyl radical (·OH). The three-electron reduced species, hydroxyl radical, is a well-accepted oxidant of DNA both free in solution and coordinated to a metal complex [50]. The presence of free diffusible radicals can be ascertained through their competitive reduction due to additional hydrogen-atom donors in the reaction mixture. Thus, we used several radical scavengers that might inhibit the DNA scission induced in the presence of the title Cu(II) complexes. Data for complex **3** are shown in Fig. 10. Complexes **1** and **2** presented the same behavior. The DNA breakdown mediated by complex **3** was clearly inhibited in the presence of the hydroxyl radical scavengers DMSO, *tert*-butyl alcohol and sodium formiate (lanes 4–6), indicating that the freely diffusible hydroxyl radical is one of the intermediates involved in the DNA scission process. The addition of DABCO decreased the cleavage efficiency of the compound (lane 7), which suggests the involvement of singlet oxygen-like entities in the DNA damage. The DNA cleavage was attenuated in the presence of Tiron (lane 8) as a consequence of the involvement of superoxide in the DNA scission. The significant reduction in the ability of the complex to cleave DNA in the presence of catalase (lane 11) implies that hydrogen peroxide is necessary for the breakdown of DNA. The cleavage is oxidative in nature as the enzyme catalase, which lowers solution concentrations of hydrogen peroxide, inhibited the cleavage reaction. From these results we concluded that a Cu(I) complex, the hydroxyl radical, singlet oxygen-like species, the superoxide, and hydrogen peroxide are the active species involved in the DNA cleavage induced by **3**. A metal bound species similar to that proposed for the $[Cu(phen)_2]^{2+}$, often formulated as $[CuOH]_2^+$ or $[CuO]^+$, remains a possibility [12,50]. A cupric superoxo (Cu^{II}–O_2^-) or cupric hydroperoxo (Cu^{II}–OOH) such as that suggested for peptidylglycine monooxygenase and dopamine β-hydroxylase may also serve as the active O_2-derived species [51–53].

In the presence of the minor groove binder distamycin and major groove binder methyl green (lanes 9 and 10, Fig. 10), no

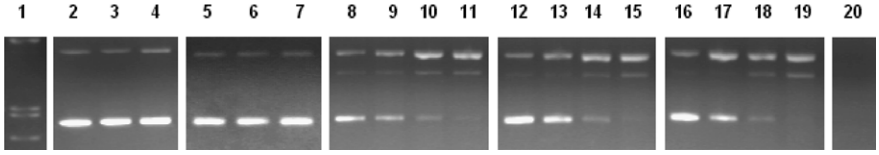


Fig. 8. Agarose gel electrophoresis of pUC18 plasmid DNA, in the presence of the complexes **1**–**3** or $CuCl_2$, with or without ascorbate activation. Incubation time: 1 h (37 °C). Lane 1: λDNA/EcoRI + Hind III Marker; lane 2: supercoiled DNA; lane 3: supercoiled DNA + ascorbate 12 mM; lane 4: 12 μM $CuCl_2$ + 12 mM ascorbate; lane 5: 12 μM **1** without ascorbate; lane 6: 12 μM **2** without ascorbate; lane 7: 12 μM **3** without ascorbate; lane 8: 3 μM **1** + 3mM ascorbate; lane 9: 6 μM **1** + 6 mM ascorbate; lane 10: 9 μM **1** + 9 mM ascorbate; lane 11: 12 μM **1** + 12 mM ascorbate; lane 12: 3 μM **2** + 3 mM ascorbate; lane 13: 6 μM **2** + 6mM ascorbate; lane 14: 9 μM **2** + 9 mM ascorbate; lane 15: 12 μM **2** + 12 mM ascorbate; lane 16: 3 μM **3** + 3mM ascorbate; lane 17: 6 μM **3** + 6 mM ascorbate; lane 18: 9 μM **3** + 9 mM ascorbate; lane 19: 12 μM **3** + 12 mM ascorbate; lane 20: 12 μM $[Cu(phen)_2]^{2+}$ + 12 mM ascorbate.

apparent inhibition of DNA damage was observed, a finding that implies a lack of interaction of the complexes through the grooves.

4. Conclusions

Ternary copper(II) complexes with ethylenediamine-R-sulfonamide derivatives and phenanthroline have been prepared and structurally characterized with the aid of X-ray crystallography. Their interaction with DNA has been studied with the aid of T_m measurements, which have indicated an intercalative mode of binding between DNA base pairs. The complexes act as efficient chemical nucleases upon ascorbate activation. The participation of hydrogen peroxide, hydroxyl radical, superoxide anion and singlet-oxygen-like entities in the scission process mediated by the compounds suggests a mechanism pathway involving a Fenton or a Haber–Weiss reaction. Results indicate that these compounds can be used as potential chemotherapeutical agents, although further investigations need to be carried out.

Acknowledgements

G.A., J.B. acknowledge financial support from the Spanish Comisión Interministerial de Ciencia y Tecnología (CTQ2007-63690/BQU). A.C. thanks CICYT (CTQ2006-15329-C02/BQU) for financial support. A.B., A.H., L.O. thank the Romanian Autoritatea Nationala pentru Cercetare Stiintifica (research Grant PN II 61-003) for financial support.

Appendix A. Supplementary data

CCDC 722483, 722484 and 722485 contains the supplementary crystallographic data for **1**, **2** and **3**. These data can be obtained free of charge via http://www.ccdc.cam.ac.uk/conts/retrieving.html, or from the Cambridge Crystallographic Data Centre, 12 Union Road, Cambridge CB2 1EZ, UK; fax: (+44) 1223-336-033; or e-mail: deposit@ccdc.cam.ac.uk. Supplementary data associated with this article can be found, in the online version, at doi:10.1016/j.poly.2009.05.017.

References

[1] A. Sigel, H. Sigel (Eds.), Metal Ions in Biological Systems, vol. 41, Marcel Dekker, New York, 2004.
[2] A. Sigel, H. Sigel (Eds.), Metal Ions in Biological Systems, vol. 42, Marcel Dekker, New York, 2004.
[3] J.R.J. Sorenson, Free Rad. Biol. Med. 13 (1992) 593.
[4] J.R.J. Sorenson, Prog. Med. Chem. 26 (1989) 437.
[5] N. Farrell (Ed.), Transition Metal Complexes as Drugs and Chemotherapeutic Agents, Kluwer Academic, Dordrecht, 1989, p. 143 (Chapter 6).
[6] B.H. Geierstanger, M. Marksich, P.B. Dervan, D.E. Wemmer, Science 266 (1994) 646.
[7] C. Liu, J. Zhou, Q. Li, L. Wang, Z. Liao, H.J. Xu, Inorg. Biochem. 75 (1996) 233.
[8] G. Patviel, J. Bernadou, B. Meunier, Angew. Chem., Int. Ed. Engl. 34 (1995) 746.
[9] R.A. Sánchez-Delgado, A. Anzelloti, Mini Rev. Med. Chem. 4 (2004) 23.
[10] R.H. Fish, G. Jaouen, Organometallics 22 (2003) 2166.
[11] P.B. Dervan, Science 232 (1986) 464.
[12] D.S. Sigman, A. Mazumder, M.D. Perrin, Chem. Rev. 93 (1993) 2295.
[13] T. Owa, H. Yoshino, T. Okauchi, K. Yoshimatsu, Y. Ozawa, N.H. Sugi, T. Nagasu, N. Koyanagi, K. Kitoh, J. Med. Chem. 42 (1999) 3789.
[14] M. González-Álvarez, G. Alzuet, J. Borrás, B. Macías, A. Castiñeiras, Inorg. Chem. 42 (2003) 2992.
[15] M. González-Álvarez, G. Alzuet, J. Borrás, M. Pitié, B. Meunier, J. Biol. Inorg. Chem. 8 (2003) 644.
[16] B. Macías, I. García, M.J. Villa, M. González-Álvarez, J. Borrás, A. Castiñeiras, J. Inorg. Biochem. 96 (2003) 367.
[17] R. Cejudo, G. Alzuet, M. González-Álvarez, J.L. García-Gimenez, J. Borrás, M. Liu-González, J. Inorg. Biochem. 100 (2006) 70.
[18] M. González-Álvarez, G. Alzuet, L. del Castillo-Agudo, J. Borrás, M. Liu-González, Eur. J. Inorg. Chem. 19 (2006) 3823.
[19] B. Macías, M.V. Villa, B. Gómez, J. Borrás, G. Alzuet, M. González-Álvarez, A. Castiñeiras, J. Inorg. Biochem. 101 (2007) 444.
[20] M. González-Alvarez, G. Alzuet, J. Borrás, L. del Castillo-Agudo, J.M. Montejo-Bernardo, A. Gutiérrrez-Rodríguez, S. García-Granda, J. Biol. Inorg. Chem. 13 (2008) 1249.
[21] J.L. García-Gimenez, G. Alzuet, M. González-Alvarez, M. Liu-González, A. Castiñeiras, J. Borrás, J. Inorg. Biochem. 103 (2009) 243.
[22] B.R. James, R.J.P. Williams, J. Chem. Soc. (1961) 2007.
[23] L.E. Marshall, D.R. Graham, K.A. Reich, D.S. Sigman, Biochemistry 20 (1981) 244.
[24] J.M. Veal, K. Merchant, R.L. Rill, Biochemistry 30 (1991) 1132.
[25] J. Sanchez-Piso, J.A. García-Vazquez, J. Romero, M.I. Durán, A. Sousa-Pedrares, E. Labisbal, O.R. Nascimento, Inorg. Chim. Acta 328 (2002) 111.
[26] Bruker, APEX2 Software, Bruker AXS Inc. V2.0-1, Madison, Wisconsin, USA, 2005.
[27] G.M. Sheldrick, SADABS. Program for Empirical Absorption Correction of Area Detector Data, University of Goettingen, Germany, 1997.
[28] G.M. Sheldrick, Acta Crystallogr. A46 (1990) 467.
[29] G.M. Sheldrick, SHELXL-97. Program for the Refinement of Crystal Structures, University of Goettingen, Germany, 1997.
[30] A.J.C. Wilson, International Tables for Crystallography, vol. C, Kluwer Academic Publishers, Dordrecht, The Netherlands, 1995.
[31] A.L. Spek, PLATON. A Multipurpose Crystallographic Tool, Utrecht University, Utrecht, The Netherlands, 2003.
[32] E. Keller, SCHAKAL-97. A Computer Program for the Graphic Representation of Molecular and Crystallographic Models, University of Freiburg i. Br, Germany, 1997.
[33] S. Zhang, Y. Zhu, C. Tu, H. Wei, Z. Yang, L. Lin, J. Ding, J. Zhang, Z. Guo, J. Inorg. Biochem. 98 (2004) 2099.
[34] R.N. Patel, N. Singh, K.K. Shukla, J. Niclós-Gutiérrez, A. Castiñeiras, V.G. Vaidyanathan, Spectrochimica Acta, Part A 62 (2005) 261.
[35] S.M. Morehouse, H. Suliman, D. Nguyen, Inorg. Chim. Acta 297 (2000) 411.
[36] Z.D. Matovic, G. Pelosi, S. Lanelli, G. Ponticelli, D.D. Radanovic, D.J. Radanovic, Inorg. Chim. Acta 268 (1998) 221.
[37] M. Kuwabara, C. Yoon, T.E. Goyne, T. Thederahn, D.S. Sigman, Biochemistry 25 (1986) 7401.
[38] G.A. Jefrey, Introduction to Hydrogen Bonding, Oxford University Press, Oxford, 1997.
[39] E. Dubler, U.K. Häring, K.H. Scheller, P. Baltzer, H. Sigel, Inorg. Chem. 23 (1984) 3785.
[40] J.L. García-Giménez, G. Alzuet, M. González-Alvarez, A. Castiñeiras, M. Liu-González, J. Borrás, Inorg. Chem. 46 (2007) 7178.
[41] L. Gutiérrez, G. Alzuet, J.A. Real, J. Borrás, A. Castiñeiras, Eur. J. Inorg. Chem. (2002) 2094.
[42] M.L. Calatayud, J. Sletten, M. Julve, I. Castro, J. Mol. Struct. 741 (2005) 121.
[43] J. Yang, J.-F. Ma, D.-M. Wu, L.-P. Guo, J.-F. Liu, J. Mol. Struct. 657 (2003) 333.
[44] L. Gutiérrez, G. Alzuet, J. Borrás, M. Liu-González, F. Sanz, A. Castiñeiras, Polyhedron 20 (2001) 703.
[45] WINEPR Simphonia 1.25 Bruker Analytic Gmbh, Kalrsruhe, FRG, 1994.
[46] M.F. El-Shazly, A. El-Dissowky, T. Salem, M. Osman, Inorg. Chim. Acta 40 (1980) 1.
[47] A.G. Quiroga, J.M. Pérez, I. López-Solera, E.I. Montero, J.R. Masaguer, C. Alonso, C. Navarro-Raninger, J. Inorg. Biochem. 69 (1998) 275.
[48] E.T. Tselepi-Kalouli, N. Katsaros, J. Inorg. Biochem. 37 (1989) 271.
[49] A. Silvestri, G. Barone, G. Ruisi, D. Anselmo, S. Riela, V.T. Liveri, J. Inorg. Biochem. 101 (2007) 841.
[50] W.K. Pogozelski, T.D. Tullius, Chem. Rev. 98 (1998) 1017.
[51] J.P. Klinman, Chem. Rev. 96 (1996) 2541.
[52] N.J. Blackburn, F.C. Rhames, R. Ralle, S. Jaron, J. Biol. Inorg. Chem. 5 (2000) 341.
[53] S.T. Prigge, R.E. Mains, B.A. Eiper, L.M. Amzel, Cell Mol. Life Sci. 57 (2000) 1236.

Polyhedron 28 (2009) 2545–2554

Contents lists available at ScienceDirect

Polyhedron

journal homepage: www.elsevier.com/locate/poly

Early transition metal derivatives stabilised by the phenylenediamido 1,2-$C_6H_4(NCH_2tBu)_2$ ligand: Synthesis, characterisation and reactivity studies: Crystal structures of [Ta{1,2-$C_6H_4(NCH_2tBu)_2$}$_2$Cl] and [Zr{(1,2-$C_6H_4(NCH_2tBu)_2$}(NMe_2)(μ-NMe_2)]$_2$

Vanessa Tabernero [a], Tomás Cuenca [a,*], Marta E.G. Mosquera [a,1], Carmen Ramírez de Arellano [b,1]

[a] Departamento de Química Inorgánica, Universidad de Alcalá, Campus Universitario, 28871 Alcalá de Henares, Spain
[b] Departamento de Química Orgánica, Universidad de Valencia, 46100 Valencia, Spain

ARTICLE INFO

Article history:
Received 2 March 2009
Accepted 7 May 2009
Available online 2 June 2009

Keywords:
Titanium
Zirconium
Tantalum
Diamido

ABSTRACT

Li_2[1,2-$C_6H_4(NCH_2tBu)_2$] reacts with one equiv of [$TiCl_4(THF)_2$] in refluxing toluene to give the chelate compound [Ti{1,2-$C_6H_4(NCH_2tBu)_2$}Cl_2(THF)] (**1**), isolated as a black product, while the reaction of the dilithio diamido salt with one equiv of [$ZrCl_4(THF)_2$] in refluxing toluene affords the dinuclear zirconium derivative [Zr{1,2-$C_6H_4(NCH_2tBu)_2$}Cl(THF)(μ-Cl)]$_2$ (**2**), obtained as an orange solid. Treatment of the dilithio diamido salt with $TaCl_5$ in a 2:1 molar ratio in toluene yields [Ta{1,2-$C_6H_4(NCH_2tBu)_2$}$_2$Cl] (**3**) as a red product. The reaction of 1,2-$C_6H_4(NHCH_2tBu)_2$ with [$Zr(NMe_2)_4$] in toluene at room temperature affords the dinuclear zirconium complex [Zr{1,2-$C_6H_4(NCH_2tBu)_2$}(NMe_2)(μ-NMe_2)]$_2$ (**4**). The dibenzyl derivative [Ti{1,2-$C_6H_4(NCH_2tBu)_2$}(CH_2Ph)$_2$] (**5**) is obtained by the reaction of **1** with 2 equiv of Mg(CH_2Ph)Cl at −78 °C. Compound **1** reacts with the lithium amide reagent LiN($SiMe_3$)$_2$ to afford [Ti{1,2-$C_6H_4(NCH_2tBu)_2$}Cl{N($SiMe_3$)}] (**6**). The μ-oxo titanium derivative [(Ti{1,2-$C_6H_4(NCH_2tBu)_2$}{CH_2Ph})$_2$(μ-O)] **7** is precipitated when compound **5** is maintained in solution. The tendency of these compounds to coordinate donor ligands and their reactivity with Lewis acid reagents are described. All compounds were analytically and spectroscopically characterised and the molecular structures of the diamine 1,2-$C_6H_4(NHCH_2tBu)_2$ and the complexes **3** and **4** were established by single-crystal X-ray diffraction studies. The lack of correlation between the degree of metallacycle folding and phenylene ring distortion is observed in the solid state structures. The performance of precursors **1**, **3** and **5** were evaluated in ethylene polymerisation upon activation with B(C_6F_5)$_3$, methylaluminoxane (MAO) and sMAO as cocatalysts, with very modest activities.

© 2009 Elsevier Ltd. All rights reserved.

1. Introduction

In recent years olefin polymerisation investigations have focused on the development of non-Cp based catalysts giving rise to previously unknown polymerisation behaviours and new polyolefin materials [1].

Bis(phenoxido-imino) group 4 metal complexes and titanium and zirconium derivatives with chelating diamido ligands [2,3] are currently receiving considerable attention, largely because of their potential use as homogeneous catalyst precursors for the α-olefin polymerisation process [4]. Chelating diamido ligands are versatile in view of the large number of possible available substituents attached to the nitrogen atoms [5]. Corresponding group 5 metal complexes are less active in polymerisation, so they have not been widely studied as potential catalysts for olefin polymerisation, although they are more tolerant of functionalised olefin monomers [6,7].

We are interested in the synthesis and chemical behaviour of MCp′(LL)X derivatives (Cp′ = substituted or unsubstituted η^5-cyclopentadienyl ring; LL = chelating diamido [8–10] and dialkoxo [11–13] ligands). The synthesis and characterisation of new chloro diamido complexes of titanium and zirconium $MCp^{R'}$[1,2-$C_6H_4(NR)_2$]Cl [M = Ti, Zr; $Cp^{R'}$ = η^5-C_5H_5, η^5-$C_5(CH_3)_5$, η^5-$C_5H_4(SiMe_3)$; R = *n*Pr, Np] have been described [8–10]. These complexes were tested as potential catalysts for ethylene and styrene polymerisation after activation with MAO. In this context, we report here a series of dichloro titanium, zirconium and chloro tantalum complexes bearing the bulky diamido ligand [1,2-$C_6H_4(NCH_2tBu)_2$]$^{2-}$ not supported by a cyclopentadienyl ring. The presence of the ligand [1,2-$C_6H_4(NCH_2tBu)_2$]$^{2-}$ in the metal

* Corresponding author. Tel.: +34 91 8854655; fax: +34 91 8854683.
E-mail addresses: tomas.cuenca@uah.es (T. Cuenca), martaeg.mosquera@uah.es (M.E.G. Mosquera), Carmen.Ramirezdearellano@uv.es (C.R. de Arellano).
[1] Correspondence concerning the crystallography data should be addressed to these authors.

0277-5387/$ - see front matter © 2009 Elsevier Ltd. All rights reserved.
doi:10.1016/j.poly.2009.05.055

environment not only provides the delicate electronic balance and electronic relief to the Lewis acidic metal centre on account of its electron rich nitrogen atoms, but the bulky neopentyl substituents also render enough steric protection to the electrophilic metal centre.

2. Results and discussion

The synthesis of *N*,*N*′-alkyl 1,2-phenylenediamines 1,2-$C_6H_4(NHR)_2$ [R = $CH_2CH_2CH_3$ (*n*Pr), CH_2tBu (Np)] has been reported [8] in three steps, lithiation of the corresponding primary 1,2-phenylenediamine, reaction with the appropriate acyl chloride and reduction using $LiAlH_4$. However, no crystallographic data were published. In the course of the present study, the solid state structure of the compound 1,2-$C_6H_4(NHCH_2t$Bu$)_2$ has been confirmed by single-crystal X-ray diffraction (Fig. 1). Crystals suitable for the X-ray diffraction were obtained from methanol at room temperature. The angles around the nitrogen atom show the expected values for a geometry consistent with secondary amine species [14].

The addition of Li*n*Bu to a stirred suspension of the diamine 1,2-$C_6H_4(NHCH_2t$Bu$)_2$ in cold hexane resulted in the immediate deposition of the corresponding lithium salt, which further reacts in toluene with $[MCl_4(THF)_2]$ (M = Ti, Zr) or $TaCl_5$. This strategy allows the preparation of a series of titanium, zirconium and tantalum chloro derivatives synthesized by a metathesis reaction (Scheme 1). Reaction of Li_2[1,2-$C_6H_4(NCH_2t$Bu$)_2$] with one equiv of $[TiCl_4(THF)_2]$ in refluxing toluene produces the chelate compound [Ti{1,2-$C_6H_4(NCH_2t$Bu$)_2$}Cl_2(THF)] (**1**) isolated as a black product. According to literature precedents [15–17], the initial formation of a bis-diamido compound [Ti{1,2-$C_6H_4(NCH_2t$Bu$)_2$}$_2$] could be suggested, which quickly should undergo an exchange reaction with the remaining $[TiCl_4(THF)_2]$ to give complex **1**. The THF coordination seems to be the driving force for this process since it avoids the possibility of metal reduction that sometimes occurs during conventional $TiCl_4$ metathesis reactions. Treatment of the dilithio diamido salt with $[ZrCl_4(THF)_2]$ in refluxing toluene affords the dinuclear zirconium derivative [Zr{1,2-C_6H_4(NCH$_2t$Bu$)_2$}Cl(THF)(μ-Cl)]$_2$ (**2**), obtained as an orange solid. The reaction of Li_2[1,2-$C_6H_4(NCH_2t$Bu$)_2$] with $ZrCl_4$ or $[ZrCl_4(THF)_2]$ in a molar ratio of 2:1 and the ligand redox reactivity of the corresponding coordinated zirconium complexes have been recently described [18]. The standard procedure described for group 4 metal complexes was also used for tantalum. Thus, when the dilithio diamido salt reacts with $TaCl_5$ in 2:1 molar ratio in toluene, formation of [Ta{1,2-$C_6H_4(NCH_2t$Bu$)_2$}$_2$Cl] (**3**) as a red product is observed immediately.

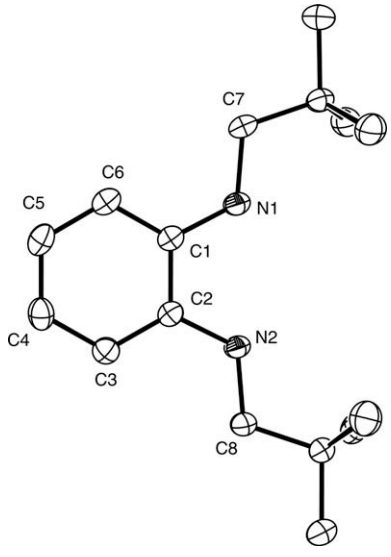


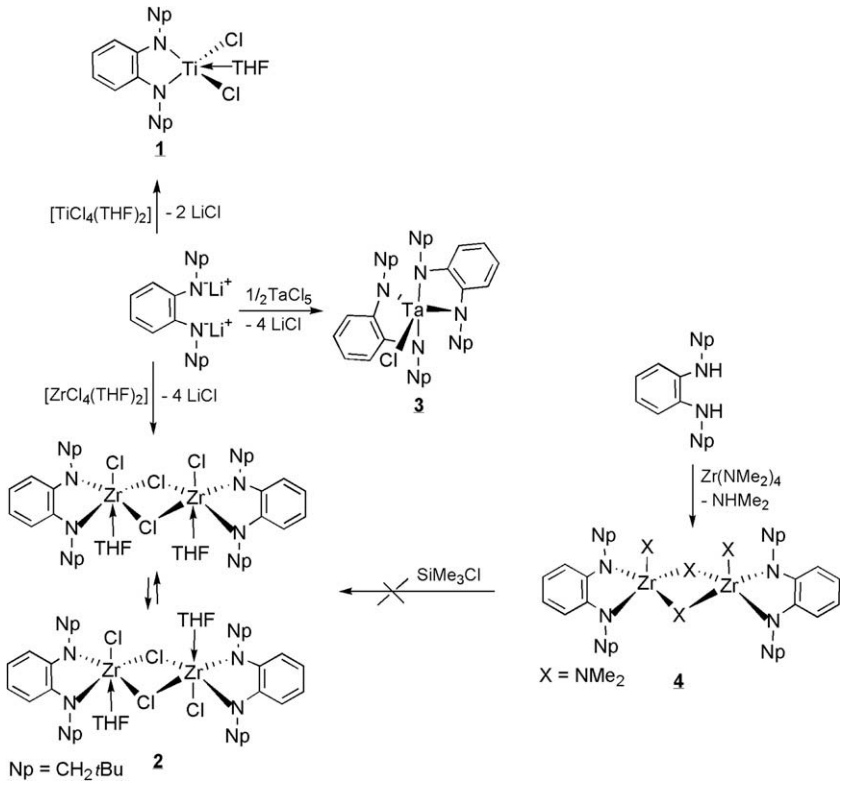
Fig. 1. ORTEP view of 1,2-$C_6H_4(NHCH_2t$Bu$)_2$ with 30% probability ellipsoids, hydrogen atoms have been omitted for clarity. Selected interatomic distances (Å) and angles (°): C(8)–N(2) = 1.457(2), C(2)–N(2) = 1.418(2), C(1)–C(2) = 1.418(2), C(2)–C(3) = 1.391(2), C(3)–C(4) = 1.400(2), C(4)–C(5) = 1.378(3), C(5)–C(6) = 1.400(3), C(1)–C(6) = 1.396(2), N(1)–C(7) = 1.454(2), N(1)–C(1) = 1.409(2), C(8)–N(2)–C(2) = 119.53(14), C(7)–N(1)–C(1) = 121.06(15).

Complexes **1–3** are air and moisture sensitive in solution and in the solid state, although they can be stored unaltered for weeks under an inert atmosphere. The complexes were characterised by the usual analytical and spectroscopic methods (NMR spectra for different solvents are given in the Section 5 as consequence for resolution and assignment). The elemental analysis value found for **2** was inaccurate, caused by small amounts of LiCl in the mixture, which could not be removed. The molecular structure of **3** has been confirmed by single-crystal X-ray diffraction.

The formulation of **1** was based on NMR and analytical data in accordance with analogous complexes [19]. We suggest a five coordinate titanium centre in which the metal atom is surrounded by two chlorine atoms, the diamido chelating ligand and a molecule of coordinated THF to stabilise the final product. The ^{1}H NMR spectra (C_6D_6 or $CDCl_3$, 25 °C) are indicative of a C_{2v} symmetry and exhibits the expected signals assigned to the resonances arising for the phenylenediamido ligand, two signals for the phenyl ring, one signal for the methylenic and one singlet for the *tert*-butyl protons. The ^{1}H NMR spectra also indicate one coordinated THF molecule (δ 4.01 and 1.93 versus δ 3.76 and 1.85 for the free THF molecule in $CDCl_3$). Similar results were also observed in the ^{13}C NMR spectra under the same conditions. However, attempts to grow crystals of this product were unsuccessful.

The resonances observed in the NMR spectra at room temperature for the zirconium complex **2** in C_6D_6 or $CDCl_3$ broaden to a greater degree than those observed for the titanium species **1**. On the basis of the structural properties for the titanium compound **1** and the comparable amido compound **4**, we propose for **2** a dinuclear structure connected by two chlorine atoms comparable to that found in similar diamido complexes [20–24]. As in analogous compounds, in this structural disposition each zirconium centre must adopt an octahedral coordination surrounded by terminal diamido, one chloro and one THF ligand, with two chlorine atoms located in bridge positions. Variable temperature ^{1}H NMR studies were investigated for this compound. Resonances for the THF ligand are observed in the spectra at 40 °C. Upon cooling the sample to −70 °C all proton resonances sharpened and the data are consistent with the presence of two products (see Section 5). These spectroscopic observations suggest that at room temperature two rapidly interconverting forms are present in solution. These two forms are separated (with a 1:1 integrating ratio) at low temperature and would have the two diamido ligands and the two bridging chlorine atoms in the equatorial plane and the terminal THF and the chloro substituents in the *cis* or *trans* axial positions, respectively (Scheme 1).

We thought that problems for the spectroscopic characterisation of **2** might be eliminated by using an alternative synthetic route through amine elimination. The reaction of 1,2-C_6H_4(NHCH$_2t$Bu$)_2$ with $[Zr(NMe_2)_4]$ in toluene at room temperature affords the dinuclear zirconium complex [Zr{1,2-C_6H_4(NCH$_2t$Bu$)_2$}(NMe$_2$)(μ-NMe$_2$)]$_2$ (**4**) as a yellow solid in high yield (Scheme 1). The ^{1}H NMR spectra (C_6D_6 or $CDCl_3$, 25 °C) of **4** display three resonances for the NMe_2 fragments coordinated to the zirconium centre: one signal at δ 2.93 for six protons and two singlets at δ 2.85 and 1.55 (C_6D_6) integrating for three protons each one. The CH_2 attached to nitrogen atoms appears diastereotopic as doublets of an AB spin system. This spectroscopic pattern can be explained



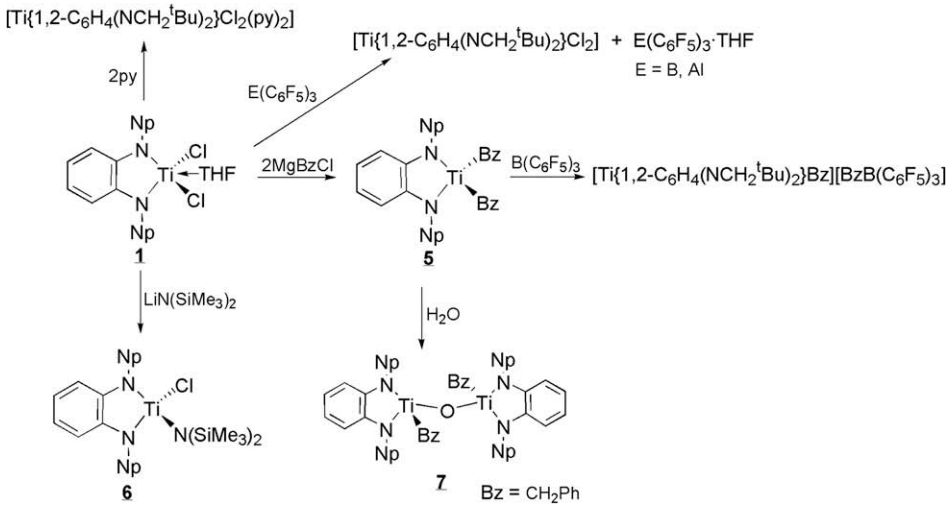
Scheme 1. Synthesis of titanium, zirconium and tantalum phenylenediamido complexes.

by considering the complex as a dinuclear species connected through two NMe_2 units. The geometry at the zirconium atoms should be described as a distorted square pyramid with the NMe_2 fragment occupying axial positions and two NMe_2 units bridging the two metal centres. An indication of this conformation is provided by the proton resonance of the methyl groups positioned on the bridging amido ligand: two of which appear at δ 2.85, with the others at δ 1.55. Such a highfield shift would be expected if these methyl groups were positioned towards the phenylene ring and experience the influence of its magnetic anisotropy. On heating the sample, coalescence of the methyl signals of the NMe_2 is observed at 70 °C, indicating rapid positional equilibration of the NMe_2 moieties on the NMR timescale. For this process we have obtained Gibbs activation energy values ($\Delta G^{\#}$) of 65 ± 0.8 kJ/mol at 343 K. Similar results were also observed in the ^{13}C NMR spectra under the same conditions. The unequivocal arrangement of metal atoms in this complex has been established by X-ray diffraction studies (see *infra*). Addition of THF to C_6D_6 solutions of **4** did not reveal any tendency of THF coordination even upon heating the sample to 100 °C (in a Young's Teflon valve NMR tube). The lack of coordination could be ascribed to the crowded environment around zirconium which decreases the Lewis acidity at the metal and hinders THF approaching. The conversion of the amido compound **4** to the chloro derivative **2** was tried by using $SiMe_3Cl$ as a chloro transfer reagent, but a mixture of unidentified products was obtained.

The ^1H NMR spectra (C_6D_6 or CD_2Cl_2, 25 °C) of complex **3** show one signal for the CH_2 protons attached to the nitrogen atoms and two multiplets for the aromatic protons, indicating the presence of a molecule in solution that exhibits equivalent phenylenediamido fragment ligands in contrast to the molecular disposition observed in the solid state by X-ray diffraction studies (see *infra*). This fact prompted us to carry out structural investigations in solution. However, on cooling the sample to −70 °C unambiguous correlations could not be established and a clear resolution of the signals was not observed.

The coordinated THF molecule in **1** is labile and tends to dissociate from the titanium centre in the presence of a donor ligand. Conversion of **1** to [Ti{1,2-$C_6H_4(NCH_2tBu)_2$}$Cl_2(py)_2$] was studied by NMR spectroscopy and occurs immediately at room temperature after adding free pyridine to a solution of **1** in $CDCl_3$ (Scheme 2). The NMR data show pyridine coordination [25] of two molecules with three broadened peaks at δ 9.62, 8.00 and 7.62 assigned to the coordinated pyridine and two multiplets at δ 3.76 and 1.85 due to free liberated THF, suggesting a six coordinated geometry around the titanium atom. The spectroscopic signals are broadened and the methylene resonances are not observed in the spectra, which indicate a coordination environment that is fluxional on the NMR timescale. Reactions of **1** with Lewis acids such as $E(C_6F_5)_3$ (E = B, Al) in $CDCl_3$ were monitored by NMR spectroscopy and show the abstraction of the coordinated THF to form [Ti{1,2-$C_6H_4(NCH_2tBu)_2$}Cl_2], concomitant with the formation of the adduct $E(C_6F_5)_3$·THF (Scheme 2). In a similar way, treatment of **2** with $B(C_6F_5)_3$ gives a CD_2Cl_2 solution in which the presence of a mixture of the species "Zr[1,2-$C_6H_4(NCH_2tBu)_2$]Cl_2" and $B(C_6F_5)_3$·THF is spectroscopically detected. We can conclude that the tendency of the titanium compound **1** and the zirconium complex **2** to coordinate donor ligands such as pyridine or THF reflects their acidic nature and the accessibility of the metal centre, and prompted us to investigate the polymerisation behaviour of this compound along with the reaction of the alkyl derivatives with different cocatalysts.

Methylation of **1** with MgMeCl in ether at −78 °C gave an unstable, intractable and unresolved mixture of products with a regrettably uninformative ^1H NMR spectrum. Due to the unexpected poor behaviour of the methyl ligand to create a stable coordination environment at the titanium centre, the use of voluminous ligands was explored to stabilise the alkyl compounds. The dibenzyl



Scheme 2. Reactions of the titanium phenylenediamido compound **1**.

derivative [Ti{1,2-$C_6H_4(NCH_2tBu)_2$}Bz_2] (**5**) (Bz = CH_2Ph) was obtained by the reaction in toluene of **1** with 2 equiv of MgBzCl in THF solution at −78 °C (Scheme 2). Recrystallisation from hexane at −30 °C affords, after filtration, higher purity material as a red oil. The ^1H NMR spectrum of **5** indicates that THF dissociation has occurred. The data are consistent with a compound with a degree of high symmetry. The four equivalent methylene protons in the "CH_2N" linkage appear as a singlet. The two equivalent benzyl ligands exhibit a singlet resonance integrating for four protons for the methylenic protons and three sets of *o*-, *m*-, and *p*-phenyl resonances. The expected signals for the phenylenediamido ligand are also observed. Complex **1** reacted readily with the lithium amide reagent $LiN(SiMe_3)_2$ to afford [Ti{1,2-$C_6H_4(NCH_2tBu)_2$}Cl{$N(SiMe_3)$}] (**6**) (Scheme 2). Thermolysis of **6** was carried out in the attempt to eliminate $SiMe_3Cl$ and to generate an imido [25] derivative, but after heating an NMR sample at 80 °C for 12 h only a mixture of unidentified products was observed.

When compound **5** is maintained in solution (toluene or hexane), the oxo derivative [(Ti{1,2-$C_6H_4(NCH_2tBu)_2$}{CH_2Ph})$_2$(μ-O)] **7** (Scheme 2) precipitates as red crystals, indicating the extreme sensitivity of **5** to moisture and confirming the formation of a benzyl derivative in the alkylating reaction of **1**. All attempts to obtain this product as a single and pure substance by controlled hydrolysis of **5** were unsuccessful with only a mixture of free amine and unidentified products being obtained. The molecular structure of **7** has been determined by X-ray diffraction methods although the crystals studied gave X-ray diffraction data of poor quality (Fig. 2).[2]

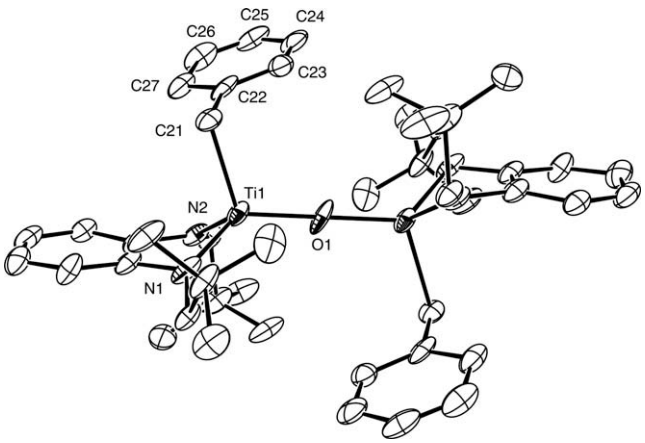


Fig. 2. X-ray thermal ellipsoid plot of **7** (30% probability level) showing the labelling scheme (hydrogen atoms have been omitted for clarity).

Compound **2** was treated with various alkylating reagents under different reaction conditions. However, all the attempts proved unfruitful and uninformative broad signals were observed in the corresponding NMR spectra.

Addition of $B(C_6F_5)_3$ to a solution of **5** in C_6D_6 at room temperature affords a cationic species, which was characterised by ^1H, ^{13}C and ^{19}F NMR spectroscopy. The NMR spectra featured downfield benzyl resonances assigned to a cationic-electron deficient benzyl titanium derivative. From these spectroscopic data, we propose the formation of the ionic [Ti{1,2-$C_6H_4(NCH_2tBu)_2$}Bz][$BzB(C_6F_5)_3$] species (Scheme 2). The large difference (4.5 ppm) between *p*-F and *m*-F chemical shifts of the [$BzB(C_6F_5)_3$]$^-$ anion suggests a strong interaction between the anion and the titanium centre, as observed for related cationic species [26–28]. The relative solubility of this complex in benzene is also consistent with its zwitterionic character. The same electrophilic reaction was tested and observed in CD_2Cl_2 at low temperature (−70 °C) and the spectroscopic study reveals that the abstraction reaction was facile even at this temperature. No reaction was observed when the tantalum complex **3** was reacted with $LiB(C_6F_5)_4$ in an attempt to form a cationic species from which activation of *t*Bu groups attached to nitrogen atoms due to the electronic deficiency could be enforced.

Given our interest in the polymerisation chemistry of diamido [9] or dialkoxo [11,12] early metal complexes, we undertook preliminary studies on α-olefin polymerisation and the complexes **1**, **3** and **5** were tested as catalysts for ethylene polymerisation in the presence of $B(C_6F_5)_3$, methylaluminoxane (MAO) and sMAO (MAO used as an $AlMe_3$-free solid) [29] as cocatalysts. The dichloro complex **1** and the dibenzyl compound **5** showed very low activity (≈10 Kg PE/mol_{cat} atm h). These activities are much lower than those of the best know non-cyclopentadienyl group 4 metal com-

[2] Crystal data for **7**: $C_{46}H_{66}N_4OTi_2$, M_r = 786.83, crystal size 0.39 × 0.34 × 0.22 mm^3, Triclinic, space group $P\bar{1}$, a = 9.915(5) Å, b = 11.342(6) Å, c = 11.626(11) Å, α = 70.75(4)°, β = 86.79(6)°, γ = 65.67(4)°, V = 1119.9(13) $Å^3$, Z = 1, ρ_{calcd} = 1.167 Mg m^{-3}, μ = 0.393 mm^{-1}, Mo Kα radiation (λ = 0.71073 Å). Data collection was performed at 200(2) K on a Nonius KappaCCD single crystal diffractometer. Reflections collected/unique 13251/3902 [R_{int} = 0.8802]. The final cycle of full matrix least-squares refinement based on 3902 reflections and 242 parameters converged to final values of $R_1(F^2 > 2\sigma(F^2))$ = 0.1853, $wR_2(F^2 > 2\sigma(F^2))$ = 0.4554, $R_1(F^2)$ = 0.2648, $wR_2(F^2)$ = 0.5446). Largest diff. peak/hole 0.879/−1.484 e$Å^{-3}$.

plexes such as McConville's titanium compounds [30], but are similar to other related complexes [31,32]. GPC results are indicative of polyethylenes that have very broad polydispersities (Mw/Mn values of 4–6) [9,31]. DSC measurements of the polymers show melting temperatures (T_m) for the polymers produced that are typical of high density polyethylene. These results may be a consequence of the gradual generation of low active Ti active species upon losing the diamido ligand from these diamido titanium precursors. It is a general observation that the complexes containing the *n*Pr amido ligand show higher polymerisation activities compared with the Np derivatives [8], suggesting that the activity is highly influenced by the steric effect [33] at the titanium centre caused by the *n*-propyl or neopentyl substituents at the nitrogen atom of the diamido ligand. Similar cases of strongly bulky substituents influencing catalytic polymerisation activity have been observed for related amidinate complexes [34,35]. The non-metallocene tantalum diamido complex **3** has no site for two alkyls, one of which is required for the propagation and the other of which is the source of cationic formation, and it was inactive in ethylene polymerisation.

3. Crystal structures of [Ta{1,2-$C_6H_4(NCH_2tBu)_2$}$_2$Cl] (3) and [Zr{(1,2-$C_6H_4(NCH_2tBu)_2$}(NMe_2)(μ-NMe_2)]$_2$ (4)

Red single crystals of **3**·C_6D_6 were grown in a saturated C_6D_6 solution at room temperature and the molecular structure established by X-ray diffraction studies. Selected bond lengths and angles for the structure are listed in Table 1. The molecular structure shows the tantalum atom bonded to a chlorine atom and two chelating phenylenediamido ligands (Fig. 3). In the crystal, the compound presents a twofold axis along the Ta–Cl bond. The coordination geometry of the Ta(V) centre can be described as a distorted trigonal bipyramid [36]. The Ta, Cl, N(2) and N(2)^i (i: $-x+1, y, -z+3/2$) atoms are in exactly the same plane, defining the trigonal bipyramidal equatorial plane. The N(1) and the N(1)^i atoms occupy the trigonal bipyramidal axial positions with a N(1)–Ta–N(1)^i angle of 167.37(10)°. Both N(1) and N(2) coordinated nitrogen atoms are essentially planar with a sum of angles of 359.5° and 354.7°, respectively. Ta–Cl [2.4123(8) Å] bond lengths compare well with related Ta(V) complexes [10]. Compound **3** is almost isostructural to the previously reported bisphenylenediamido Nb(V) complex [Nb{4,5-Me_2-1,2-$C_6H_2(NSiMe_3)_2$}$_2$Cl] [37].

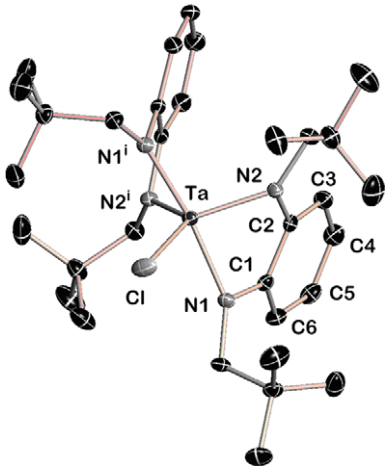


Fig. 3. X-ray thermal ellipsoid plot of **3** (50% probability level) showing the labelling scheme (i: $-x+1, y, -z+3/2$, hydrogen atoms have been omitted for clarity).

Table 1
Selected bond distances (Å) and angles (°) for complexes **3**·C_6D_6 and **4**.[a]

Compound **3**·C_6D_6			
Ta–N(1)	2.0108(18)	N(2)–Ta–N(2)[b]	108.11(10)
Ta–N(2)	1.9733(17)	N(2)–Ta–N(1)[b]	103.44(7)
Ta–Cl	2.4123(8)	N(2)–Ta–N(1)	84.07(7)
Ta–C(1)	2.588(2)	N(1)[b]–Ta–N(1)	167.37(10)
Ta–C(2)	2.559(2)	N(2)–Ta–Cl	125.95(5)
N(1)–C(1)	1.412(3)	N(1)–Ta–Cl	83.69(5)
N(2)–C(2)	1.417(3)	C(1)–N(1)–C(11)	119.70(17)
C(1)–C(6)	1.411(3)	C(1)–N(1)–Ta	96.67(12)
C(1)–C(2)	1.424(3)	C(11)–N(1)–Ta	143.17(14)
C(2)–C(3)	1.408(3)	C(2)–N(2)–C(21)	121.18(17)
C(3)–C(4)	1.383(3)	C(2)–N(2)–Ta	96.63(13)
C(4)–C(5)	1.397(3)	C(21)–N(2)–Ta	136.93(14)
C(5)–C(6)	1.377(3)		
Compound ***4***			
N(7)–Zr(1)	2.024(5)	C(1)–N(1)–C(17)	119.6(5)
N(1)–Zr(1)	2.085(5)	C(1)–N(1)–Zr(1)	102.7(4)
N(2)–Zr(1)	2.120(5)	C(17)–N(1)–Zr(1)	136.4(5)
N(5)–Zr(1)	2.274(5)	C(2)–N(2)–C(13)	120.1(5)
N(6)–Zr(1)	2.349(5)	C(2)–N(2)–Zr(1)	103.9(4)
N(8)–Zr(2)	2.037(5)	C(13)–N(2)–Zr(1)	135.2(4)
N(3)–Zr(2)	2.087(5)	C(8)–N(3)–C(18)	118.7(5)
N(4)–Zr(2)	2.118(5)	C(8)–N(3)–Zr(2)	101.0(3)
N(5)–Zr(2)	2.366(5)	C(18)–N(3)–Zr(2)	138.5(4)
N(6)–Zr(2)	2.283(5)	C(7)–N(4)–C(23)	123.0(5)
C(1)–Zr(1)	2.761(7)	C(7)–N(4)–Zr(2)	102.8(3)
C(2)–Zr(2)	2.808(6)	C(23)–N(4)–Zr(2)	133.0(4)
C(7)–Zr(1)	2.742(6)	C(38)–N(5)–C(37)	107.9(5)
C(8)–Zr(1)	2.795(5)	C(38)–N(5)–Zr(1)	114.7(4)
N(1)–C(1)	1.410(10)	C(37)–N(5)–Zr(1)	108.9(4)
N(2)–C(2)	1.400(9)	C(38)–N(5)–Zr(2)	111.6(4)
N(3)–C(8)	1.423(8)	C(37)–N(5)–Zr(2)	114.1(4)
N(4)–C(7)	1.414(8)	Zr(2)–N(5)–Zr(1)	99.69(17)
		C(40)–N(6)–C(39)	107.3(6)
		C(40)–N(6)–Zr(2)	112.7(4)
		C(39)–N(6)–Zr(2)	108.8(4)
		C(40)–N(6)–Zr(1)	114.1(5)
		C(39)–N(6)–Zr(1)	113.8(4)
		Zr(1)–N(6)–Zr(2)	99.94(18)

[a] E.s.d's are given in parentheses.
[b] Symmetry transformation used to generate equivalent atoms $-x+1, y, -z+3/2$.

The related chelating diamido ligands and the Ta atom form a "TaN_2C_2" metallacycle that is bent through the N···N axis (N(1)–Ta–N(2) and N(1)–C(1)–C(2)–N(2) planes dihedral angle of 52.05(9)°). The "TaN_2C_2" metallacycle structural parameters indicate that the phenylenediamido ligand is bonded to the metal in a η^4 fashion showing σ^2,π-enediamido behaviour [38]. This type of σ^2-*N*,*N*′-π-phenylenediamido coordination allows the donation of electron density from the phenylene ring to the metal and should quench the electrophilicity of Ta(V). Similar structural features have been reported for analogous X-ray structures of chelating phenylenediamido group 5 metal complexes found in the CSD [39]. Thus, the Ta(V) complexes [Ta(η^5-C_5Me_5){1,2-C_6H_4(NSiPr^i_3)$_2$}Cl_2], [Ta{η^5-1,3-$C_5H_3(SiMe_3)_2$}{1,2-$C_6H_4(NSiMe_3)_2$}Cl_2], and the Nb(V) derivative [Nb{4,5-Me_2-1,2-$C_6H_2(NSiMe_3)_2$}$_2$Cl] present sp^2 planar coordinated N atoms and are bent through the N···N axis "MN_2C_2" (M = metal) metallacycles (dihedral angle range 53.8–58.7°) [40,41]. The Ta–C(1) and Ta–C(2) bond lengths [2.588(2) and 2.559(2) Å, respectively] for compound **3** are in good agreement with π-bonding involving the C_{ipso} atoms at the phenylene ring. Slightly shorter Ta–C bond lengths (range 2.40–2.54 Å) are present in the previously described phenylenediamido Ta(V) complexes with a σ^2,π-enediamido type of coordination [40,41]. Rather short Ta–N bond lengths [1.9733(17) and 2.0108(18) Å] are observed in the molecular structure of **3**, consistent with a significant p_π–d_π contribution, similar to that found for other amido groups bound to tantalum [40–43]. The 1,2-$C_6H_4(NCH_2tBu)_2$ phenylenediamido ring is distorted with the carbon–carbon bond distances ranging from the longest bond for C(1)–C(2) (1.424(3) Å) to both C(3)–C(4) and

C(5)–C(6) as the shortest bonds (1.383(3), 1.377(3) Å), while the N–C_{ipso} distances (1.412(3) and 1.417(3) Å) are consistent with single bond formulation.

Yellow single crystals of **4** suitable for X-ray diffraction studies, grown in a saturated hexane solution at −40 °C, were used to unequivocally establish the molecular structure of this complex, shown in Fig. 4. Selected bond distances and angles for the structure are listed in Table 1. This compound crystallised as an enantiomeric pure isomer due to conformation chirality arising from the relative disposition of the phenylene rings in the solid state. By contrast, C_2-symmetry is inferred for **4** in solution as deduced from the NMR spectroscopic data.

The environment around each Zr atom is approximately square pyramidal with one of the NMe_2 ligands in the axial position. The zirconium atoms are not located in the planar base of the square pyramid, as distances of 0.728 Å from the Zr(2) to the N(4)N(3)N(6)N(5) plane and 0.726 Å from Zr(1) to the N(5)N(6)N(1)N(2) plane were measured. There is a central Zr(1)N(5)N(6)Zr(2) core that appears puckered (Zr(2)N(6)Zr(1) 99.94(18)°, Zr(2)N(5)Zr(1) 99.69(17)°). In this central unit, the Zr–N bond lengths range from 2.274(5) to 2.366(5) Å and the endocyclic angles at N(5) or N(6) are wider than those at Zr(1) or Zr(2). Within the molecule, the Zr–N bond lengths vary significantly, ranging from 2.024(5) to 2.366(5) Å, with the longest length corresponding to the bridging ligands (N(5) and N(6)) and the shortest to the distances between the metal and the terminal NMe_2 groups. This feature can be related to the degree of donation from the respective amido ligand to the metal centre, indicating a p_π–d_π bonding contribution for the amido moieties closer to it [18,30,44]. In addition, the sum of the angles around the nitrogen atoms in those groups (N(1), N(2), N(3) and N(4)) are essentially planar, with a tetrahedral disposition for the bridging N(5) and N(6) atoms.

As observed in **3**, and in similar structures reported for group 4 eneamido complexes [45,46], the "Zr[$C_6H_4(NCH_2tBu)$]" metallacycle is folded along the N···N axis (41.88° and 43.83° dihedral angles between the NZrN and NCCN planes). The "ZrN_2C_2" metallacycle's structural parameters indicate that the phenylenediamido ligands are bonded to the metal in a η^4 fashion showing a σ^2,π-enediamido manner [38]; the Zr–C_{ipso} bond distances [2.742(6)–2.808(6) Å range] are also in good agreement with π-bonding involving C_{ipso} atoms at the phenylene ring.

Analysis of the η^2-*N*,*N*′-phenylenediamido ligand's geometrical parameters reported in the CSD for group 4 and 5 metal complexes has been performed [8,10,37,40,41,47–50]. Bent and planar "MN_2C_2" metallacycles with wide folding through the N···N axis degree range have been reported (0–58° N-metal-N/N–C_{ipso}–C_{ipso}–N dihedral angle range) [51]. As should be expected, short M–C_{ipso} distances correspond to highly bent metallacycles and long M–C_{ipso} distances are found for planar or slightly bent metallacycles, with very few exceptions. The N–C_{ipso} bond lengths are in the 1.33–1.46 Å range for both group 4 and 5 η^2-phenylenediamido metal complexes. Furthermore, in the analysed complexes the phenylene ring is distorted, showing a long C_{ipso}–C_{ipso} bond length (range 1.41–1.47 Å) and two short ring bond lengths, generally corresponding to C(3)–C(4) and C(5)–C(6) (a range of 1.35–1.39 Å is observed in compound **3**, although in compound **4** the shortest bond length corresponds to C(4)–C(5) with values of 1.372(17) Å in one ring and 1.345(13) Å in the other one). Surprisingly, we have found that a distortion of the phenylene ring is present for both bent and planar "MN_2C_2" metallacycles and it seems not to depend on the degree of metallacycle folding. The absence of a direct correlation for the degree of metallacycle folding and phenylene ring distortion could imply that the phenylenediamido ligand ring distortion is not related to the π-coordination of the ligand.

4. Conclusions

In summary, we report the synthesis of early metal complexes stabilised by coordination of the $[1,2\text{-}C_6H_4(NCH_2tBu)_2]^{2-}$ ligand that are fully characterised by various methods. Direct reaction of $Li[1,2\text{-}C_6H_4(NCH_2tBu)_2]$ with $[TiCl_4(THF)_2]$ or $TaCl_5$ in toluene gives the monomeric derivatives in reasonable yield, while dimeric complexes were obtained for zirconium. The results indicate that monomeric titanium and tantalum complexes require the presence of additional Lewis base molecules to stabilise the final product. Reactions of the titanium compounds with Lewis acids show the abstraction of the coordinated Lewis base. Voluminous alkyl ligands are required to stabilise the alkyl compounds and the dibenzyl derivative $[Ti\{1,2\text{-}C_6H_4(NCH_2tBu)_2\}Bz_2]$ can be obtained.

η^2-Phenylenediamido group 4 and 5 metal complexes show distorted phenylene rings with the C_{ipso}–C_{ipso} bond length as the longest length and generally the two conjugated C–C bonds as

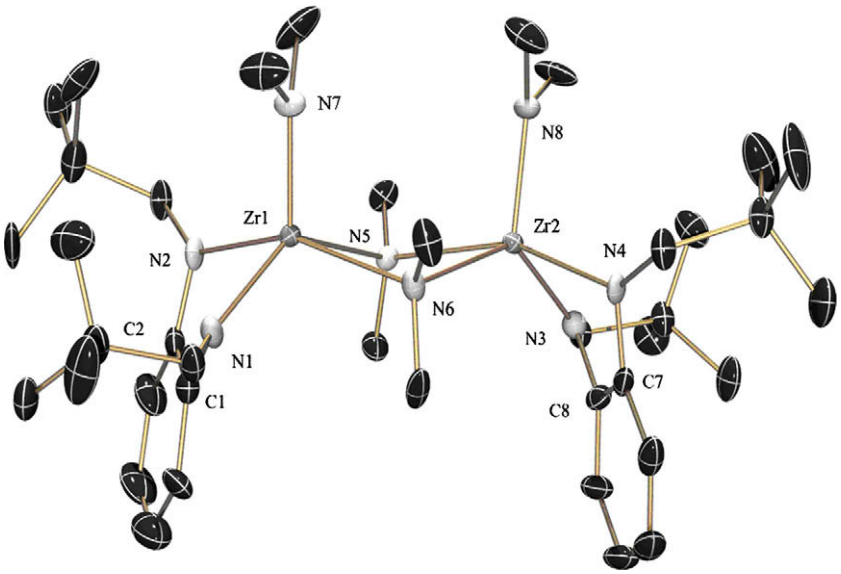


Fig. 4. X-ray thermal ellipsoid plot of **4** (30% probability level) showing the labelling scheme (hydrogen atoms have been omitted for clarity).

the shortest lengths. However, the direct correlation for the degree of metallacycle folding and phenylene ring distortion could imply that the phenylenediamido ligand ring distortion is not related to the π-coordination of the ligand.

5. Experimental

5.1. General considerations

All manipulations were performed with rigorous exclusion of oxygen and moisture under argon using Schlenk and high-vacuum line techniques or in a glove box model MO40-2. Solvents were predried by standing over activated 4 Å molecular sieves and then purified by distillation under argon before use by employing the appropriate drying/deoxygenated agent. Deuterated solvents were degassed by several freeze–thaw cycles and stored in ampoules equipped with Young's Teflon valves over activated 4 Å molecular sieves. C, H and N microanalyses were performed on a Perkin–Elmer 2400 microanalyzer. NMR spectra were recorded on a Bruker AV400 (^{1}H NMR at 400.13 MHz, ^{13}C NMR at 100.60 MHz and ^{19}F NMR at 376.40 MHz) spectrometer and chemical shifts were referenced to $SiMe_4$ via the ^{13}C resonances and the residual protons (^{1}H) of the deuterated solvent, while ^{19}F resonance were measured relative to external $CFCl_3$. Spectra were recorded at 25 °C unless otherwise stated. Li*n*Bu (1.6 M in hexane solution), MgMeCl (3 M in THF), MgBzCl (2 M in THF), pyridine, $LiN(SiMe_3)_2$ and $TaCl_5$ were purchased from Aldrich. $Br(C_6F_5)$ was purchased from ABCR. MAO, 30 wt% solution in toluene was received from Crompton GmbH. Compounds $[TiCl_4(THF)_2]$ [52], $[ZrCl_4(THF)_2]$ [52], $B(C_6F_5)_3$ [53–56], $Al(C_6F_5)_3{\cdot}0.5C_7H_8$ [7] and $[Zr(NMe_2)_4]$ [57], were synthesized following established procedures.

Polymerisation grade ethylene was used as received. Ethylene polymerisation was carried out in a glass reactor with magnetic stirring. The polymerisation solvent (toluene) was dried by refluxing over sodium-benzophenone and distilled before use in an inert atmosphere. MAO (Witco 10%) was used as a solution in toluene. Melting temperatures of the polymers were measured by differential scanning calorimetry (DSC) on a Perkin Elmer DSC6 instrument.

5.2. Synthesis of [Ti{1,2-$C_6H_4(NCH_2tBu)_2$}Cl_2(THF)] (**1**)

Li*n*Bu (1.6 M in hexane, 4.02 mmol, 2.5 mL) was slowly added to a suspension of 0.500 g (2.01 mmol) of 1,2-$C_6H_4(NHCH_2tBu)_2$ in hexane (50 mL) at −78 °C. The reaction mixture was warmed to room temperature over 4 h and a white precipitate of Li_2[1,2-$C_6H_4(NCH_2tBu)_2$] was formed with evolution of butane. The desired amount of the lithium salt (0.296 g, 1.14 mmol) and 0.380 g of $[TiCl_4(THF)_2]$ (1.14 mmol) were introduced in a Young's ampoule and toluene (50 mL) was charged at −78 °C. A red–brown suspension was immediately obtained. After 2 h, the reaction mixture was heated at reflux for 12 h. After cooling, all volatiles of the dark solution were removed under vacuum and the black product was extracted into hexane. Recrystallisation with cold hexane afforded the product identified as [Ti{1,2-$C_6H_4(NCH_2tBu)_2$}Cl_2(THF)] **1**, as a black solid (0.268 g, 0.613 mmol, 54% yield). *Anal.* Calc. for $C_{20}H_{34}N_2Cl_2OTi$ (436.98 g/mol): C, 54.92; H, 7.77; N, 6.40. Found: C, 54.56; H, 8.59; N, 6.73%. ^{1}H NMR (400 MHz, C_6D_6, 25 °C): δ 7.36 (m, 2H, Ph), 7.07 (m, 2H, Ph), 4.25 (s, 4H, CH_2), 3.74 (m, 2H, THF), 1.26 (m, 2H, THF), 0.85 (s, 18H, *t*Bu). ^{1}H NMR (400 MHz, $CDCl_3$, 25 °C): δ 7.54 (m, 2H, Ph), 7.24 (m, 2H, Ph), 4.31 (s, 4H, CH_2), 4.01 (m, 2H, THF), 1.93 (m, 2H, THF), 0.82 (s, 18H, *t*Bu). ^{13}C{^{1}H} NMR (100.60 MHz, C_6D_6, 25 °C): δ 126.0, 115.7 (Ph), 123.9 (*ipso*-Ph), 71.0 (CH_2), 66.9 (THF), 36.0 (*ipso*-*t*Bu), 28.9 (*t*Bu), 25.4 (THF).

5.3. Synthesis of [Zr{1,2-$C_6H_4(NCH_2tBu)_2$}Cl(THF)(μ-Cl)]$_2$ (**2**)

The same procedure described for **1** using 0.300 g (1.15 mmol) of Li[1,2-$C_6H_4(NCH_2tBu)_2$] and 0.435 g of $[ZrCl_4(THF)_2]$ (1.15 mmol) gives [Zr{1,2-$C_6H_4(NCH_2tBu)_2$}Cl(THF)(μ-Cl)]$_2$ **2**, obtained as an orange product which was washed with hexane (0.673 g, 0.700 mmol, 61% yield). The elemental analysis value found for **2** was inaccurate, caused by small amounts of LiCl in the mixture, which could not be removed. ^{1}H NMR (400 MHz, C_6D_6, 25 °C): δ 6.94 (br, 2H, Ph), 6.68 (br, 2H, Ph), 3.87 (br, 4H, CH_2), 1.08 (s, 18H, *t*Bu). ^{1}H NMR (400 MHz, $CDCl_3$, 25 °C): δ 6.98 (br, 4H, Ph), 3.94 (br, 4H, CH_2), 0.89 (s, 18H, *t*Bu), THF resonances not observed. ^{1}H NMR (400 MHz, $CDCl_3$, 40 °C): δ 6.92 (br, 2H, Ph), 6.75 (br, 2H, Ph), 3.87 (br, 4H, CH_2), 3.89 (br, 2H, THF), 1.15 (m, 2H, THF), 1.07 (s, 18H, *t*Bu). ^{13}C{^{1}H} NMR (100.60 MHz, $CDCl_3$, 25 °C): δ 128.3, 114.7 (Ph), 74.0 (THF), 60.7 (*C*H_2N), 36.6 (*ipso*-*t*Bu), 25.5 (THF), 28.1 (*t*Bu), *ipso*-Ph not observed. ^{1}H NMR (400 MHz, CD_2Cl_2, −70 °C): **isomer A**: δ 6.98 (m, 2H, Ph), 6.86 (m, 2H, Ph), 4.00 (d, *J* = 14.4 Hz, 2H, AB spin system, CH_2), 3.34 (d, *J* = 14.4 Hz, 2H, AB spin system, CH_2), 4.31 (br, 2H, THF), 2.02 (m, 2H, THF), 0.92 (s, 18H, *t*Bu); **isomer B**: δ 6.37 (m, 2H, Ph), 6.30 (m, 2H, Ph), 4.30 (br, 2H, CH_2), 3.70 (br, 2H, CH_2), 4.40 (br, 2H, THF), 2.02 (m, 2H, THF), 0.92 (s, 18H, *t*Bu). ^{13}C{^{1}H} NMR (100.60 MHz, CD_2Cl_2, −70 °C): **isomer A**: δ 125, 116 (Ph), 75.0 (THF), 60 (*C*H_2N), 27 (THF), 28 (*t*Bu), *ipso* of Ph and *ipso* of *t*Bu not observed; **isomer B:** δ 119, 112 (Ph), 75.0 (THF), 58 (*C*H_2N), 27(THF), 30 (*t*Bu), *ipso* of Ph and *ipso* of *t*Bu not observed.

5.4. Synthesis of [Ta{1,2-$C_6H_4(NCH_2tBu)_2$}$_2$Cl] (**3**)

The same procedure described for **1** using 0.207 g (0.79 mmol) of Li[1,2-$C_6H_4(NCH_2tBu)_2$] and 0.14 g of $TaCl_5$ (0.40 mmol) gives [Ta{1,2-$C_6H_4(NCH_2tBu)_2$}$_2$Cl] **3** as a red solid (0.130 g, 0.183 mmol, 46% yield). *Anal.* Calc. for $C_{32}H_{52}N_4ClTa$ (709.18 g/mol): C, 54.19; H, 7.33; N, 7.89. Found: C, 54.32; H, 7.09; N, 7.73%. ^{1}H NMR (400 MHz, C_6D_6, 25 °C): δ 7.01 (m, 4H, Ph), 6.79 (m, 4H, Ph), 4.68 (s, 8H, CH_2), 0.71 (s, 36H, *t*Bu). ^{1}H NMR (400 MHz, CD_2Cl_2, 25 °C): δ 7.08 (m, 4H, Ph), 6.97 (m, 4H, Ph), 4.03 (s, 8H, CH_2), 0.75 (s, 36H, *t*Bu). ^{13}C{^{1}H} NMR (100.60 MHz, C_6D_6, 25 °C): δ 137.8 (*ipso*-Ph), 129.3, 119.2 (Ph), 66.9 (*C*H_2N), 30.1 (*ipso*-*t*Bu), 28.4 (*t*Bu).

5.5. Synthesis of [Zr{1,2-$C_6H_4(NCH_2tBu)_2$}(NMe_2)(μ-NMe_2)]$_2$ (**4**)

A solution of 0.185 g (0.75 mmol) of 1,2-$C_6H_4(NHCH_2tBu)_2$ was added to 0.20 g of $Zr(NMe_2)_4$ (0.74 mmol) in toluene (50 mL). The solution was maintained at room temperature for 16 h and gradually became golden yellow. The volatiles were evaporated and hexane was added. The solution was set at −30 °C for 12 h and a microcrystalline yellow powder precipitated. The solid was isolated by filtration and dried in vacuum. Recrystallisation with cold hexane led to the product identified as [Zr{1,2-$C_6H_4(NCH_2tBu)_2$}(N-Me_2)(μ-NMe_2)]$_2$ **4** (0.495 g, 0.581 mmol, 78% yield). *Anal.* Calc. for $C_{40}H_{76}N_8Zr_2$ (850.84 g/mol): C, 56.46; H, 8.93; N, 13.16. Found: C, 56.10; H, 9.01; N, 13.20%. ^{1}H NMR (400 MHz, C_6D_6, 25 °C): δ 6.99 (m, 2H, Ph), 6.90 (m, 2H, Ph), 3.88 (d, 2H, *J* = 13.2 Hz, AB spin system, CH_2), 3.65 (d, 2H, *J* = 13.2 Hz, AB spin system, CH_2), 2.93 (s, 6H, N*Me*$_2$), 2.85 (s, 3H, N*Me*$_2$), 1.55 (s, 3H, N*Me*$_2$), 0.87 (s, 18H, *t*Bu). ^{1}H NMR (400 MHz, $CDCl_3$, 25 °C): δ 6.85 (m, 2H, Ph), 6.67 (m, 2H, Ph), 3.82 (d, 2H, *J* = 13.4 Hz, AB spin system, CH_2), 3.60 (d, 2H, *J* = 13.4 Hz, AB spin system, CH_2), 3.09 (s, 6H, N*Me*$_2$), 3.03 (s, 3H, N*Me*$_2$), 1.45 (s, 3H, N*Me*$_2$), 0.71 (s, 18H, *t*Bu). ^{13}C{^{1}H} NMR (100.60 MHz, C_6D_6, 25 °C): δ 135.1 (*ipso*-Ph), 120.1, 115.8 (Ph), 60.6 (*C*H_2N), 44.4, 43.2, 42.05 (N*Me*$_2$), 35.2 (*ipso*-*t*Bu), 28.8 (*t*Bu). ^{13}C{^{1}H} NMR (100.60 MHz, $CDCl_3$, 25 °C): δ 136.1 (*ipso*-Ph) 118.9, 115.2 (Ph), 60.4 (*C*H_2N), 44.1, 43.3, 42.3 (N*Me*$_2$), 35.3 (*ipso*-*t*Bu), 28.8 (*t*Bu).

5.6. [Ti{1,2-$C_6H_4(NCH_2tBu)_2$}$Cl_2(py)_2$]

Pyridine was added at room temperature into a Teflon-valved NMR tube containing a chloroform-d (0.5 mL) solution of [Ti{1,2-$C_6H_4(NCH_2tBu)_2$}Cl_2(THF)]. The reaction mixture turned brown and the ^1H and ^{13}C NMR spectra were obtained, showing the formation of [Ti{1,2-$C_6H_4(NCH_2tBu)_2$}$Cl_2(py)_2$]. ^1H NMR (400 MHz, $CDCl_3$, 25 °C): δ 9.62 (br, 4H, py), 8.00 (br, 2H, py), 7.62 (br, 4H, py), 6.36 (m, 2H, Ph), 5.88 (m, 2H, Ph), 0.75 (s, 18H, *t*Bu), CH_2 protons not observed.

5.7. Reaction of [Ti{1,2-$C_6H_4(NCH_2tBu)_2$}Cl_2(THF)] with $B(C_6F_5)_3$ or $Al(C_6F_5)_3$

In a glovebox, chloroform-d or benzene-d_6 (0.5 mL) was added at room temperature to a Teflon-valved NMR tube containing the solid mixture of [Ti{1,2-$C_6H_4(NCH_2tBu)_2$}Cl_2(THF)] and $B(C_6F_5)_3$. The ^1H and ^{13}C NMR spectra obtained showed the formation of [Ti{1,2-$C_6H_4(NCH_2tBu)_2$}Cl_2] with $B(C_6F_5)_3$·(THF) also present. **[Ti{1,2-$C_6H_4(NCH_2tBu)_2$}Cl_2]**: ^1H NMR (400 MHz, C_6D_6, 25 °C): δ 7.34 (m, 2H, Ph), 7.00 (m, 2H, Ph), 4.16 (s, 4H, CH_2), 0.75 (s, 18H, *t*Bu). ^1H NMR (400 MHz, $CDCl_3$, 25 °C): δ 7.64 (m, 2H, Ph), 7.31 (m, 2H, Ph), 4.29 (s, 4H, CH_2), 0.86 (s, 18H, *t*Bu). $^{13}C\{^1H\}$ NMR (100.60 MHz, C_6D_6, 25 °C): δ 129.0, 116.0 (Ph), 67.8 (CH_2), 35.8 (*ipso*-*t*Bu), 28.6 (*t*Bu), *ipso*-Ph not observed. **$B(C_6F_5)_3$·(THF)**: ^1H NMR (400 MHz, C_6D_6, 25 °C): δ 3.23 (m, 2H, OCH_2), 0.85 (m, 2H, CH_2). ^1H NMR (400 MHz, $CDCl_3$, 25 °C): δ 4.25 (m, 2H, OCH_2), 2.13 (m, 2H, CH_2). $^{13}C\{^1H\}$ NMR (100.60 MHz, C_6D_6, 25 °C): δ 75.7 (THF), 25.4 (THF). ^{19}F NMR (376.40 MHz, $CDCl_3$, 25 °C): δ −128.7 (broad, *o*-C_6F_5), −143.7 (broad, *p*-C_6F_5), −160.7 (broad, *m*-C_6F_5). ^{19}F NMR (376.40 MHz, C_6D_6, 25 °C): δ −131.6 (broad, *o*-C_6F_5), −152.6 (broad, *p*-C_6F_5), −161.8 (broad, *m*-C_6F_5).

A similar procedure using [Ti{1,2-$C_6H_4(NCH_2tBu)_2$}Cl_2(THF)] and $Al(C_6F_5)_3$ gives a mixture of the same compound [Ti{1,2-$C_6H_4(NCH_2tBu)_2$}Cl_2] and $Al(C_6F_5)_3$.(THF). **$Al(C_6F_5)_3$·(THF)**: ^{19}F NMR (376.40 MHz, $CDCl_3$, 25 °C): δ −123.2 (s broad, *o*-C_6F_5), −151.7 (s broad, *p*-C_6F_5), −161.0 (s broad, *m*-C_6F_5).

5.8. Reaction of [Zr{1,2-$C_6H_4(NCH_2tBu)_2$}Cl(THF)(μ-Cl)]$_2$ (**2**) with $B(C_6F_5)_3$

In a glovebox, dichloromethane-d_2 (0.5 mL) was added via a syringe at room temperature to a Teflon-valved NMR tube containing the solid [Zr{1,2-$C_6H_4(NCH_2tBu)_2$}Cl(THF)(μ-Cl)]$_2$ and $B(C_6F_5)_3$. The ^1H and ^{13}C NMR spectra were obtained showing formation of "Zr[1,2-$C_6H_4(NCH_2tBu)_2$]Cl_2" with $B(C_6F_5)_3$·(THF) also present. **Zr[1,2-$C_6H_4(NCH_2tBu)_2$]Cl_2**: ^1H NMR (400 MHz, CD_2Cl_2, 25 °C): δ 7.21 (m, 2H, Ph), 7.17 (m, 2H, Ph), 4.05 (s, 4H, CH_2), 0.88 (s, 18H, *t*Bu). **$B(C_6F_5)_3$·(THF)**: ^1H NMR (400 MHz, CD_2Cl_2, 25 °C): δ 4.28 (m, 2H, OCH_2), 2.12 (m, 2H, CH_2). ^{19}F NMR (376.40 MHz, CD_2Cl_2, 25 °C): δ −132.1 (broad, *o*-C_6F_5), −154.6 (broad, *p*-C_6F_5), −162.9 (broad, *m*-C_6F_5).

5.9. Synthesis of [Ti{1,2-$C_6H_4(NCH_2tBu)_2$}Bz_2] (**5**)

A solution of **1** (0.250 g, 0.57 mmol) in toluene (50 mL) was cooled to −78 °C and a solution of $Mg(CH_2Ph)Cl$ in THF (2 M, 1.14 mmol, 0.57 mL) was added. The reaction immediately turned red. The mixture was warmed to room temperature and stirred for 5 h. The solvent was pumped off and subsequent extraction into hexane afforded a red oil, which was recrystallised from cold hexane giving the product identified as [Ti{1,2-$C_6H_4(NCH_2tBu)_2$}Bz_2] **5** (0.198 g, 0.416 mmol, 73% yield). *Anal.* Calc. for $C_{30}H_{40}N_2Ti$ (476.17 g/mol): C, 70.66; H, 8.40; N, 5.88. Found: C, 70.45; H, 8.51; N, 5.88%. ^1H NMR (400 MHz, C_6D_6, 25 °C): δ 7.26 (m, 2H, Ph), 7.15 (m, 2H, Ph), 6.99 (t, *J* = 7.2 Hz, CH_2Ph), 6.94 (t, *J* = 7.2 Hz, CH_2Ph), 6.86 (d, *J* = 7.2 Hz, CH_2Ph), 3.79 (s, 4H, CH_2), 2.40 (s, 4H, CH_2Ph), 0.71 (s, 18H, *t*Bu). ^1H NMR (400 MHz, CD_2Cl_2, 25 °C): δ 7.21 (m, 2H, Ph), 7.10 (m, 2H, Ph), 7.19 (t, *J* = 7.6 Hz, CH_2Ph), 6.94 (t, *J* = 7.6 Hz, CH_2Ph), 6.73 (d, *J* = 7.6 Hz, CH_2Ph), 3.84 (s, 4H, CH_2), 2.18 (s, 4H, CH_2Ph), 0.75 (s, 18H, *t*Bu). $^{13}C\{^1H\}$ NMR (100.60 MHz, C_6D_6, 25 °C): δ 128.7 (*ipso*-Bz), 129.3, 127.2, 125.3 (Bz), 126.7, 115.5 (Ph), 123.1 (*ipso*-Ph), 81.02 (CH_2Ph), 64.6 (CH_2N), 34.6 (*ipso*-*t*Bu), 28.6 (*t*Bu). $^{13}C\{^1H\}$ NMR (100.60 MHz, CD_2Cl_2, 25 °C): δ 144.4 (*ipso*-Bz), 129.1, 126.8, 124.9 (Bz), 122.8, 115.3 (Ph), 80.4 (CH_2Ph), 64.7 (CH_2N), 34.8 (*ipso*-*t*Bu), 28.5 (*t*Bu), *ipso*-Ph not observed.

5.10. Synthesis of [Ti{1,2-$C_6H_4(NCH_2tBu)_2$}Cl{N(SiMe$_3$)}] (**6**)

Toluene (50 mL) was added to a mixture of **1** (0.200 g, 0.46 mmol) and Li[N(SiMe$_3$)]$_2$ (0.076 g, 0.46 mmol), at room temperature. The reaction immediately turned black. The mixture was stirred for 5 h. The solvent was pumped off and subsequent extraction into hexane afforded a black oil, which was recrystallised from cold hexane giving the product identified as [Ti{1,2-$C_6H_4(NCH_2tBu)_2$}Cl{N(SiMe$_3$)}] **6** (0.159 g, 0.325 mmol, 70% yield). *Anal.* Calc. for $C_{22}H_{44}N_3Si_2ClTi$ (489.5 g/mol): C, 53.95; H, 8.98; N, 8.57. Found: C, 53.98; H, 8.72; N, 8.36%. ^1H NMR (400 MHz, C_6D_6, 25 °C): δ 7.26 (m, 2H, Ph), 7.15 (m, 2H, Ph), 4.45 (d, *J* = 13.5 Hz, 2H, CH_2), 3.78 (d, *J* = 13.5 Hz, 2H, CH_2), 0.83 (s, 18H, *t*Bu), 0.15 (s, 18H, SiMe_3). $^{13}C\{^1H\}$ NMR (100.60 MHz, C_6D_6, 25 °C): δ 126.7, 115.5 (Ph), 123.1 (*ipso*-Ph), 67.7 (CH_2), 35.9 (*ipso*-*t*Bu), 28.6 (*t*Bu), 4.6 (SiMe_3).

5.11. Reaction of [Ti{1,2-$C_6H_4(NCH_2tBu)_2$}Bz_2] with $B(C_6F_5)_3$

About 0.010 g (21.0 mmol) of [Ti{1,2-$C_6H_4(NCH_2tBu)_2$}Bz_2] and 0.011 g (21.0 mmol) of $B(C_6F_5)_3$ were placed in a Teflon-valved NMR tube and C_6D_6 was added at room temperature (when the reaction was cooled to −78 °C in CD_2Cl_2, the solvent was vacuum transferred into the NMR tube that had previously been placed in a thermostat-controlled bath). The NMR spectrum was obtained immediately at the desired temperature. ^1H NMR (400 MHz, C_6D_6, 25 °C): δ 7.50 (m, 2H, Ph), 7.20–6.99 (m, 12H, Ph), 5.89 (t, *J* = 7.2 Hz, CH_2Ph), 5.77 (t, *J* = 7.2 Hz, CH_2Ph), 5.26 (d, *J* = 7.2 Hz, CH_2Ph), 4.15 (d, *J* = 12.8 Hz, 4H, CH_2), 3.64 (d, *J* = 13.2 Hz, 4H, CH_2), 3.89 (br, 4H, CH_2Ph), 2.70 (br, 4H, CH_2Ph), 0.56 (s, 18H, *t*Bu). ^{19}F NMR (376.40 MHz, C_6D_6, 25 °C): δ −130.4 (s broad, *o*-C_6F_5), −160.5 (s broad, *p*-C_6F_5), −165.0 (s broad, *m*-C_6F_5). ^1H NMR (400 MHz, CD_2Cl_2, −70 °C): δ 8.10 (m, 2H, Ph), 7.65 (m, 2H, Ph), 7.30 (t, *J* = 7.6 Hz, CH_2Ph), 7.19 (t, *J* = 7.2 Hz, CH_2Ph), 7.00–6.73 (Ph), 5.91 (d, *J* = 6.8 Hz, CH_2Ph), 4.60 (d, *J* = 13.2 Hz, 2H, CH_2), 4.16 (d, *J* = 13.2 Hz, 2H, CH_2), 2.81 (br, 4H, CH_2Ph), 2.72 (br, 4H, CH_2Ph), 0.77 (s, 18H, *t*Bu). ^{19}F NMR (376.40 MHz, CD_2Cl_2, 25 °C): δ −131.3 (s broad, *o*-C_6F_5), −165.0 (s broad, *p*-C_6F_5), −167.7 (s broad, *m*-C_6F_5).

5.12. Single-crystal X-ray structure determination of compounds 1,2-$C_6H_4(NHCH_2tBu)_2$, **3**·C_6D_6, and **4**

Relevant crystallographic data and details of the refinements for the structures are given in Table 2. Crystals of **3**·C_6D_6 were grown by slow evaporation of a C_6D_6 solution. Crystals suitable for X-ray diffraction were measured at 100(2) K on a Bruker SMART APEX diffractometer using graphite-monochromated Mo Kα radiation (λ = 0.71073 Å) and φ and ω scan modes. Crystal structures were solved by direct methods and all non-hydrogen atoms refined anisotropically on F^2 (program SHELXL-97) [58]. The deuterium atoms were located in a difference Fourier synthesis and refined with restrained C–D bond lengths. The methyl group hydrogen atoms were refined as rigid. Other hydrogen atoms were included

Table 2
Crystal data and structure refinement details for 1,2-$C_6H_4(NHCH_2tBu)_2$, **3**·C_6D_6, and **4**.

	1,2-$C_6H_4(NHCH_2tBu)_2$	**3**·C_6D_6	**4**
Formula	$C_{16}H_{28}N_2$	$C_{38}H_{52}ClD_6N_4Ta$	$C_{40}H_{38}N_4Zr$
FW	248.40	793.32	425.76
Color habit	red prism	orange prism	yellow stick
Crystal dimensions (mm^3)	2.9 × 2.5 × 1.8	0.09 × 0.07 × 0.06	0.44 × 0.38 × 0.36
Crystal system	monoclinic	monoclinic	orthorhombic
Space group	$P2_1/c$	$C2/c$	$P2_12_12_1$
a (Å)	11.3619(11)	13.6723(5)	13.438(5)
b (Å)	11.462(2)	15.6431(6)	16.869(8)
c (Å)	12.748(2)	18.5698(7)	20.570(2)
β (°)	97.557(15)	110.2660(10)	90
V ($Å^3$)	1645.8(4)	3725.8(2)	4663(3)
Z	4	4	4
T (K)	200(2)	100(2)	200(2)
D_{calcd} (g cm^{-3})	1.003	1.414	1.213
μ (mm^{-1})	0.058	3.052	0.481
F(0 0 0)	552	1616	1808
θ Range (°)	3.55–27.50	2.05–27.88	3.55–27.50
Number of reflections collected	36 908	25 468	82 570
Number of independent reflections/R_{int}	3772 [R_{int} = 0.078]	4316 [R_{int} = 0.0346]	10 663 [R_{int} = 0.0796]
Data/restraints/parameters	3772/0/172	4316/426/252	10 663/279/485
R_1/wR_2 ($I > 2\sigma(I)$)	R_1 = 0.0561, wR_2 = 0.1327	R_1 = 0.0221, wR_2 = 0.0494	R_1 = 0.0604, wR_2 = 0.1342
R_1/wR_2 (all data)	R_1 = 0.1206, wR_2 = 0.1559	R_1 = 0.0251, wR_2 = 0.0507	R_1 = 0.0786, wR_2 = 0.1424
Extinction coefficient	0.016(3)		0.0456(14)
Goodness-of-fit (GOF) (on F^2)	1.023	1.057	1.256
Difference in peak/hole (e $Å^{-3}$)	0.262 and −0.154	1.026 and −0.530	0.766 and −0.773

using a riding model. The deuterated benzene molecule is disordered over two sites. The programs use neutral atom scattering factors, $\Delta f'$ and $\Delta f''$ and absorption coefficients from the International Tables for Crystallography [59].

Suitable crystals of the diamine 1,2-$C_6H_4(NHCH_2tBu)_2$ and **4** were selected, manipulated under argon with perfluoropolyether and mounted on a glass fiber. The intensity data sets were collected at 200 K on a Bruker–Nonius KappaCCD diffractometer equipped with an Oxford Cryostream 700 unit. The structures were solved, using the WINGX package [60], by direct methods (SHELXS-97) and refined by least-squares against F^2 (SHELXL-97) [58]. All non-hydrogen atoms were anisotropically refined. In **4** C15, C30 and C32 were disordered in two positions, also, in **4** some SIMU and DELU restraints were applied. Hydrogen atoms were geometrically placed and left riding on their parent atoms, with the exception of the hydrogen atom on N(1) and N(2) for the diamine 1,2-$C_6H_4(NHCH_2tBu)_2$ that were found in the Fourier map and refined freely. Relevant crystallographic data and details of the refinements for the two structures are given in Table 2.

Acknowledgements

Financial support for this research by Dirección General de Investigación Científica y Técnica (Project MAT2007-60997), Comunidad Autónoma de Madrid: (Project S-0505-PPQ/0328-02) is gratefully acknowledged. C.R.A. thanks Consolider Ingenio 2010 (CSD2007-00006) and Generalitat Valenciana (GV07/087) for financial support.

Appendix A. Supplementary data

CCDC 710428, 711924 and 710429 contain the supplementary crystallographic data for (1,2-$C_6H_4(NHCH_2tBu)$ **2**, compound **3** and compound **4**. These data can be obtained free of charge via http://www.ccdc.cam.ac.uk/conts/retrieving.html, or from the Cambridge Crystallographic Data Centre, 12 Union Road, Cambridge CB2 1EZ, UK; fax: (+44) 1223-336-033; or e-mail: deposit@ccdc.cam.ac.uk.

Supplementary data associated with this article can be found, in the online version, at doi:10.1016/j.poly.2009.05.055.

References

[1] V.C. Gibson, S.K. Spitzmesser, Chem. Rev. 103 (2003) 283.
[2] F. Guèrin, D.H. McConville, J.J. Vittal, Organometallics 15 (1996) 5586.
[3] J.D. Scollard, D.H. McConville, J. Am. Chem. Soc. 118 (1996) 10008.
[4] J.F. Carpentier, A. Martin, D.C. Swenson, R.F. Jordan, Organometallics 22 (2003) 4999.
[5] G.J.P. Britovsek, V.C. Gibson, D.F. Wass, Angew. Chem., Int. Ed. Engl. 38 (1999) 428.
[6] K. Hakala, B. Lofgren, M. Polamo, M. Leskela, Macromol. Rapid Commun. 18 (1997) 635.
[7] S.G. Feng, G.R. Roof, E.Y.X. Chen, Organometallics 21 (2002) 832.
[8] V. Tabernero, T. Cuenca, E. Herdtweck, Eur. J. Inorg. Chem. (2004) 3154.
[9] V. Tabernero, T. Cuenca, Eur. J. Inorg. Chem. (2005) 338.
[10] V. Tabernero, C. Maestre, G. Jiménez, T. Cuenca, C.R. de Arellano, Organometallics 25 (2006) 1723.
[11] M. González-Maupoey, T. Cuenca, L.M. Frutos, O. Castano, E. Herdtweck, Organometallics 22 (2003) 2694.
[12] M. González-Maupoey, T. Cuenca, Organometallics 25 (2006) 4358.
[13] M. González-Maupoey, T. Cuenca, L.M. Frutos, O. Castaño, E. Herdtweck, B. Rieger, Eur. J. Inorg. Chem. (2007) 147.
[14] K. Nienkemper, G. Kehr, S. Kehr, R. Frohlich, G. Erker, J. Organomet. Chem. 693 (2008) 1572.
[15] S. Tinkler, R.J. Deeth, D.J. Duncalf, A. McCamley, Chem. Commun. (1996) 2623.
[16] Y.M. Jeon, J. Heo, W.M. Lee, T.H. Chang, K. Kim, Organometallics 18 (1999) 4107.
[17] L.C. Liang, Y.N. Chang, H.M. Lee, Inorg. Chem. 46 (2007) 2666.
[18] N.A. Ketterer, H.J. Fan, K.J. Blackmore, X.F. Yang, J.W. Ziller, M.H. Baik, A.F. Heyduk, J. Am. Chem. Soc. 130 (2008) 4364.
[19] R.R. Schrock, R. Baumann, S.M. Reid, J.T. Goodman, R. Stumpf, W.M. Davis, Organometallics 18 (1999) 3649.
[20] F.G.N. Cloke, P.B. Hitchcock, J.B. Love, J. Chem. Soc., Dalton Trans. (1995) 25.
[21] M. Polamo, M. Leskela, J. Chem. Soc., Dalton Trans. (1996) 4345.
[22] M. Polamo, M. Leskela, Acta Chem. Scand. 51 (1997) 44.
[23] C.H. Lee, Y.H. La, S.J. Park, J.W. Park, Organometallics 17 (1998) 3648.
[24] F.J. Schattenmann, R.R. Schrock, W.M. Davis, Organometallics 17 (1998) 989.
[25] N.A. Ketterer, J.W. Ziller, A.L. Rheingold, A.F. Heyduk, Organometallics 26 (2007) 5330.
[26] A.D. Horton, J. de With, A.J. van der Linden, H. van de Weg, Organometallics 15 (1996) 2672.
[27] A.D. Horton, J. deWith, Chem. Commun. (1996) 1375.
[28] J.M. Wright, C.R. Landis, M. Ros, A.D. Horton, Organometallics 17 (1998) 5031.
[29] I. Tritto, S.X. Li, M.C. Sacchi, G. Zannoni, Macromolecules 26 (1993) 7111.
[30] J.D. Scollard, D.H. McConville, S.J. Rettig, Organometallics 16 (1997) 1810.
[31] C. Lorber, B. Donnadieu, R. Choukroun, Organometallics 19 (2000) 1963.
[32] C.H. Lee, Y.H. La, J.W. Park, Organometallics 19 (2000) 344.
[33] R. Kleinschmidt, Y. Griebenow, G. Fink, Mol. Catal. A: Chem. 157 (2000) 83.
[34] J. Richter, F.T. Edelmann, M. Noltemeyer, H.G. Schmidt, M. Shmulinson, M.S. Eisen, J. Mol. Catal. A: Chem. 130 (1998) 149.
[35] S.J. Kim, I.N. Jung, B.R. Yoo, S.H. Kim, J.J. Ko, D.J. Byun, S.O. Kang, Organometallics 20 (2001) 2136.
[36] M. Talja, M. Polamo, Polyhedron 25 (2006) 3039.

[37] J.M. Decams, S. Danièle, L.G. Hubert-Pfalzgraf, J. Vaissermann, S. Lecocq, Polyhedron 20 (2001) 2405.
[38] K. Mashima, Y. Matsuo, K. Tani, Organometallics 18 (1999) 1471.
[39] A Search on the Cambridge Structural Database Version 5.29 Update Jan 2008, with 436384 Entries.
[40] K. Aoyagi, P.K. Gantzel, T.D. Tilley, Polyhedron 15 (1996) 4299.
[41] G.J. Pindado, M. Thornton-Pett, M. Bochmann, J. Chem. Soc., Dalton Trans. (1998) 393.
[42] M.H. Chisholm, J.C. Huffman, L.S. Tan, Inorg. Chem. 20 (1981) 1859.
[43] J.R. Clark, P.E. Fanwick, I.P. Rothwell, Organometallics 15 (1996) 3232.
[44] J.D. Scollard, D.H. McConville, J.J. Vittal, Organometallics 16 (1997) 4415.
[45] S.Y.S. Wang, K.A. Abboud, J.M. Boncella, J. Am. Chem. Soc. 119 (1997) 11990.
[46] T.M. Cameron, K.A. Abboud, J.M. Boncella, J. Chem. Soc., Chem. Commun. (2001) 1224.
[47] K. Aoyagi, P.K. Gantzel, K. Kalai, T.D. Tilley, Organometallics 15 (1996) 923.
[48] S. Daniele, P.B. Hitchcock, M.F. Lappert, P.G. Merle, J. Chem. Soc., Dalton Trans. (2001) 13.
[49] A.F. Heyduk, K.J. Blackmore, N.A. Ketterer, J.W. Ziller, Inorg. Chem. 44 (2005) 468.
[50] P.B. Hitchcock, Q.G. Huang, M.F. Lappert, X.H. Wei, M.S. Zhou, J. Chem. Soc., Dalton Trans. (2006) 2991.
[51] See Supplementary Material for all Discussed Parameters.
[52] L.E. Manzer, Inorg. Synth. 21 (1982) 135.
[53] A.G. Massey, F.G.A. Stone, A.J. Park, Proc. Chem. Soc. London (1963) 212.
[54] A.G. Massey, A.J. Park, J. Organomet. Chem. 2 (1964) 245.
[55] A.G. Massey, A.J. Park, J. Organomet. Chem. 5 (1966) 218.
[56] A. Sundararaman, F. Jäkle, J. Organomet. Chem. 681 (2003) 134.
[57] M.H. Chisholm, C.E. Hammond, J.C. Huffman, Polyhedron 7 (1988) 399.
[58] G.M. Sheldrick, SHELXL-97, Universität Göttingen, Göttingen, Germany, 1998.
[59] A.J.C. Wilson (Ed.), International Tables for Crystallography, vol. C, Tables 6.1.1.4, 4.2.6.8, and 4.2.4.2, Kluwer Academic Publishers, Dordrecht, The Netherlands, 1992.
[60] L.J. Farrugia, J. Appl. Cryst. 32 (1999) 837.

Polyhedron 28 (2009) 2555–2558

Contents lists available at ScienceDirect

Polyhedron

journal homepage: www.elsevier.com/locate/poly

Novel structurally characterized *o*-semiquinonato PCP-pincer nickel complexes

Konstantin A. Kozhanov *, Michael P. Bubnov, Nina N. Vavilina, Larisa Yu. Efremova, Georgy K. Fukin, Vladimir K. Cherkasov, Gleb A. Abakumov

G.A. Razuvaev Institute of Organometallic Chemistry, Russian Academy of Sciences, 603950 Nizhny Novgorod, Russia

ARTICLE INFO

Article history:
Received 29 January 2009
Accepted 8 May 2009
Available online 20 May 2009

Keywords:
Pincer complexes
o-Semiquinones
Nickel
X-ray diffraction

ABSTRACT

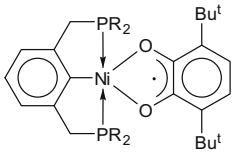
Structural study of dialkyl (PCP)-pincer *o*-semiquinonato nickel complexes indicated sloped relative positions of bi- and tri-dentate ligands. It became bright confirmation of propositions made on the base of their EPR spectra followed by molecular modelling.

© 2009 Elsevier Ltd. All rights reserved.

1. Introduction

Previously we have communicated about new class of the spin labelled nickel compounds: the *o*-semiquinonato nickel complexes with the pincer ligands [1,2]. The structural study of 3,6-di-*tert*-butyl-*o*-semiquinonato nickel with 2,6-bis-(diphenylphosphinomethyl)phenyl (**1**) indicates a distorted square–pyramidal geometry of the inner coordination core [1]. Difference of the ligands occupying *trans*-positions towards oxygen atoms of the semiquinone causes an asymmetrical distribution of the spin density inside the *o*-semiquinonato ligand. The molecular motion which swaps oxygens being in the base of the pyramid and which is responsible for redistribution of the spin density in the *o*-semiquinonato fragment was called "swing" oscillation (Scheme 1). Similar rearrangements in the metal coordination sphere can be found as a stage of certain pincer complexes-catalyzed reactions, such as Heck coupling [3,4].

Using of pincer ligand with alkyl substituents (such as *cyclo*-hexyl (Cy), *iso*-propyl (*i*-Pr)) at the phosphorus atoms causes a difference of spin density on the pincer phosphoruses [5]. The molecular motion which is responsible for redistribution of spin density between the phosphorus atoms we have called "fan" oscillation (Scheme 1). We supposed that the complexes with the pincer ligands having alkyl substituents (*cyclo*-hexyl and *iso*-propyl having no axial symmetry along the P-alkyl bond) should have sloped relative positions of the planes of semiquinonato and pincer ligands (Scheme 1). This configuration should result in different spin density on the pincer phosphorus atoms. Here we report on structural investigation of two complexes of such type (**2** and **3**). Comparative analysis of two novel structures with previously published **1**, together with EPR data and results of molecular modelling, is presented here as well.



1 - R = Ph,

2 - R = Cy,

3 - R = *i*-Pr

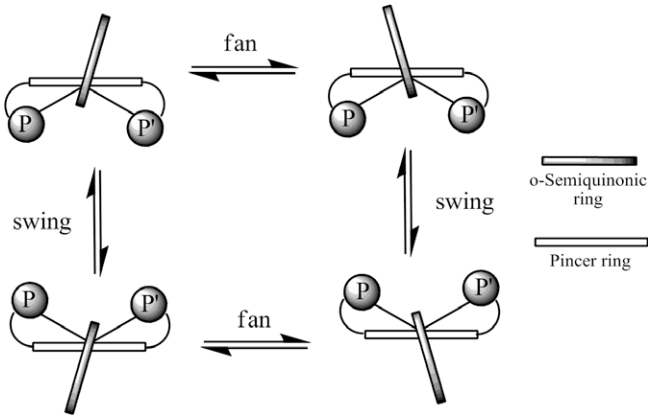
2. Results and discussion

Structural study of **1** was carried out earlier [1]. Complexes **2** and **3** were obtained as previously described [5]. Slow evaporation of their pentane solutions gave X-ray quality single crystals. The X-ray diffraction study has shown that the Ni atom has a distorted square–pyramidal coordination mode in all three complexes (Fig. 1). In general, the bonds lengths and the angles in the chelate cycle of coordinated *o*-semiquinone are typical for the anion-radical coordination mode (Table 1).

It should be noted that the differences between C1–O1 and C2–O2 bonds lengths in the chelate cycles of the *o*-semiquinones, which reflect the asymmetry of the spin density distribution, in **2** and **3** are essentially larger than the same difference in **1** (Δ = 0.0154 Å in **2** and 0.0243 Å in **3** against 0.0085 Å in **1**). It causes the difference between HFC constants on semiquinonic pro-

* Corresponding author. Tel.: +7 8314627682.
E-mail address: kostik@iomc.ras.ru (K.A. Kozhanov).

0277-5387/$ - see front matter © 2009 Elsevier Ltd. All rights reserved.
doi:10.1016/j.poly.2009.05.023

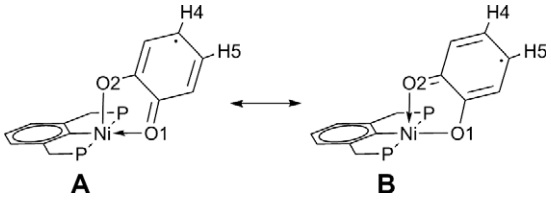


Scheme 1. "Swing" and "fan" oscillations (schematic view along basal O–Ni–C direction).

Table 1
Structural data of nickel-*o*-semiquinonato chelate cycles for complexes **1**, **2** and **3**.

Complex	1	2	3
Ni1–O1	1.9238(10)	1.9306(10)	1.9377(8)
Ni1–O2	2.0595(10)	2.0664(11)	2.2165(10)
C1–O1	1.2975(17)	1.3076(18)	1.3006(16)
C2–O2	1.2890(17)	1.2922(17)	1.2763(14)
O1–Ni1–O2	81.60(4)	81.16(3)	78.35(3)[a]

[a] Small deviation of the angle O1–Ni1–O2 in **3** comparing with the same one in **1** and **2** is the consequence of the elongation of the Ni1–O2 bond.



Scheme 2. Resonance structures responsible for hyperfine coupling with semiquinonic protons.

tons in EPR spectra of the complexes (a_{H4}/a_{H5} = 2.2/3.4 G in **1**, 2.2/3.6 G in **2** and 2.2/3.8 G in **3**) (Scheme 2, Table 2). It is known that spin density transfer from the *o*-semiquinone to the phosphorus magnetic nuclei of the pincer metallo-fragment can be realized by two independent mechanisms: by spin polarization of the σ-skeleton through Ni–O σ-bonds and by direct interaction of the group Ni–P orbitals with the corresponding oxygen p-orbitals containing unpaired electron. The last mechanism is quite more effective comparing with the first one, but its effectiveness strongly depends on the angles between Ni–P bonds and chelate plane of the *o*-semiquinone. Phosphorus HFC constant is larger when this angle is close to 90° [6,7]. Examination of inner coordination core describes that the angles P1–Ni1–O2 in the complexes **2** and **3** are close to right angle (89.39° in **2** and 87.86° in **3**) comparing with the P2–Ni1–O2 (124.54° in **2** and 111.03° in **3**) whereas in **1** both angles are closer one to another (115.70° and 101.58°). It is the reason of the larger difference between phosphorus HFC constants a_{P1}/a_{P2} for **2** and **3** comparing with the same value for **1** (a_{P1}/a_{P2} = 27.8/14.7 G in **2**, 25.3/15.7 G in **3** and 25.6/25.6 G in **1**). The angles P1–Ni1–O2 and P2–Ni1–O2 (both relative to O2) are especially preferred in examination of phosphorus HFC constants because O2 has an excess of spin density comparing with O1 [1]. The asymmetry of the spin density distribution inside the *o*-semiquinone follows from the difference of the bonds lengths in the chains Ni1–O1–C1 and Ni1–O2–C2 according to Scheme 2. The

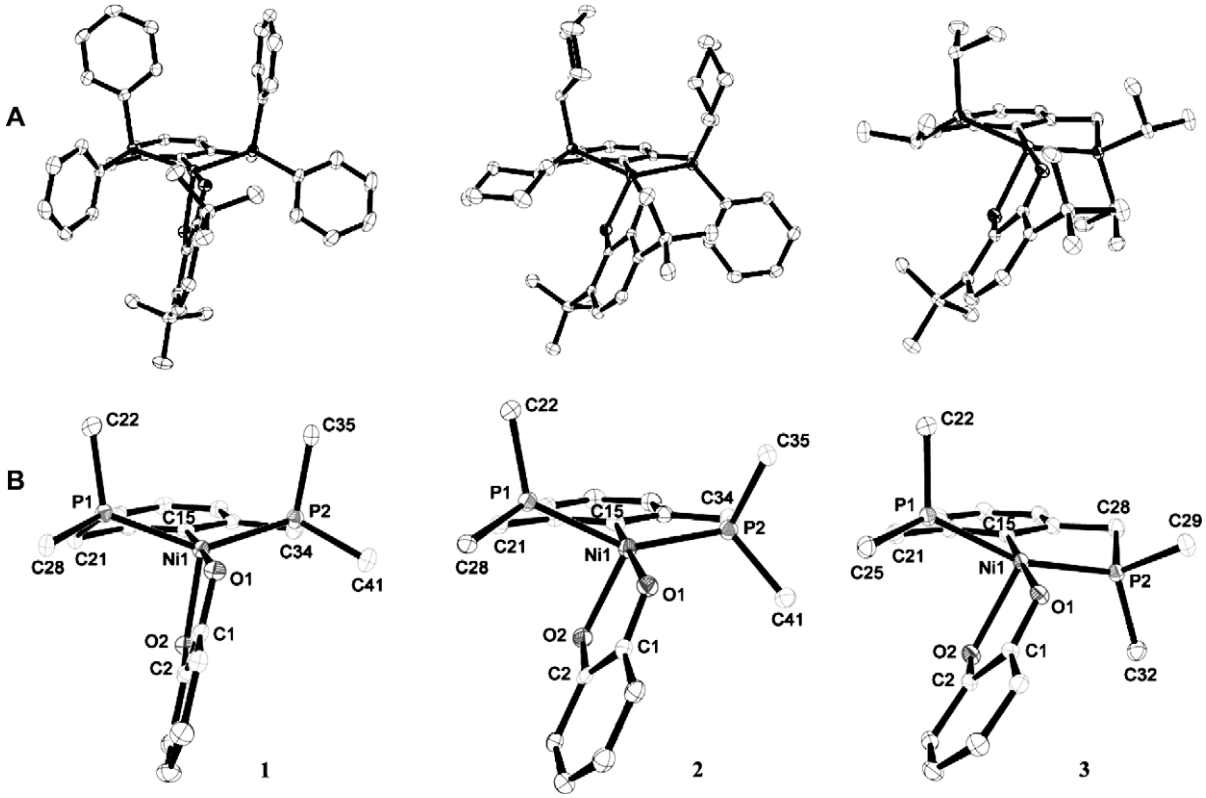


Fig. 1. ORTEP view of **1**–**3** with 50% thermal ellipsoids, hydrogen atoms are omitted for clarity. (a) With all substituents, (b) without substituents.

Table 2
Structure and EPR parameters for **1**–**3**: selected bond lengths (Å), angles (°) and HFC constants (G).

Complex	**1**[a]	**2**	**3**
X-ray			
Ni1–P1	2.1669(5)	2.2492(5)	2.1979(4)
Ni1–P2	2.1867(5)	2.1540(5)	2.1668(4)
Ni1–C15	1.9261(15)	1.9156(14)	1.9218(12)
C15–Ni1–O1	177.96(6)	173.26(5)	178.47(5)
C15–Ni1–O2	98.37(5)	95.58(5)	101.69(5)
P1–Ni1–O1	98.30(4)	101.98(3)	99.21(3)
P2–Ni1–O1	95.47(3)	92.65(3)	94.35(3)
P1–Ni1–O2	115.70(3)	89.39(3)	87.86(3)
P2–Ni1–O2	101.58(3)	124.54(3)	111.03(3)
EPR[b]			
a_{P1}	25.6	27.8	25.3
a_{P2}	25.6	14.7	15.7
a_{H4}	2.2	2.2	2.2
a_{H5}	3.4	3.6	3.8

[a] Cited from Ref. [1].
[b] Cited from Refs. [1,5].

chelate cycle of each complex can be presented as a sum of the resonance structures **A** and **B** which are responsible for appearing of spin density on the protons H4 and H5. The excess of spin density on the O2 means that the resonance structure **B** predominates over the structure **A**. (Moreover it is bright confirmed by difference of the HFC constants on semiquinonic protons.) As it was already mentioned, this predomination in complexes **3** and **2** is larger than the same one in **1**. This fact is additional reason of larger difference between phosphorus splitting constants in EPR spectra of **2** and **3** comparing with the same difference in spectra of **1**.

In general the examination of relative positions of *o*-semiquinonato and pincer ligands evidence that their planes are more sloped in complexes **2** and **3** comparing with **1**. The angles between the planes of the aromatic rings of the pincer ligands and the planes of the pseudo-aromatic rings of the *o*-semiquinones are: 75.64° for **1**, 60.87° for **2** and 50.79° for **3**.

However, conformation of **1** is sufficiently sloped, whereas the phosphorus HFC constants are equal. We have proposed that the crystal packing causes a distortion of the complex geometry. To neglect this factor we have provided the molecular modelling of **1**, **2** and **3** using obtained crystal data as starting model. The geometry optimization in general keeps the structures unchanged but it makes molecule of complex **1** virtually symmetrical with virtually equal angles between the phosphorus atoms and the *o*-semiquinonic plane. This fact is in accordance with the equivalence of the phosphorus HFC constants in **1**. On the contrary, the angles between the ligands planes in **2** and **3** remain different; moreover the configuration of **3** remains more sloped than configuration of **2**. This result is in a good agreement with the ratio a_{P1}/a_{P2} of the phosphorus HFC constants (Table 2).

The phosphorus units in all complexes have distorted tetrahedral geometry. The most distorted is P1 unit in **2** (the largest deviation of the angles from tetrahedral 109.5°: Ni1–P1–C21 96.43°; Ni1–P1–C22 125.62°). Five-membered pincer chelate cycles containing phosphorus are not planar in all three complexes. They are bent around the axis Ni···CH_2 (–CH_2– bridge connecting phosphorus with pincer aryl ring). In this aspect the pincer coordination mode in **3** differs from that one in **1** and **2**. In **1** and **2** the phosphorus atoms lie at one side out from the plane of pincer aryl whereas in **3** the phosphorus cycles are inversed around the Ni1–C15 axis and the phosphorus atoms are situated at the different sides relative to the pincer aryl plane (Scheme 3). So, the complexes **1** and **2** are in configuration **B**, whereas the compound **3** is in configuration **A**.

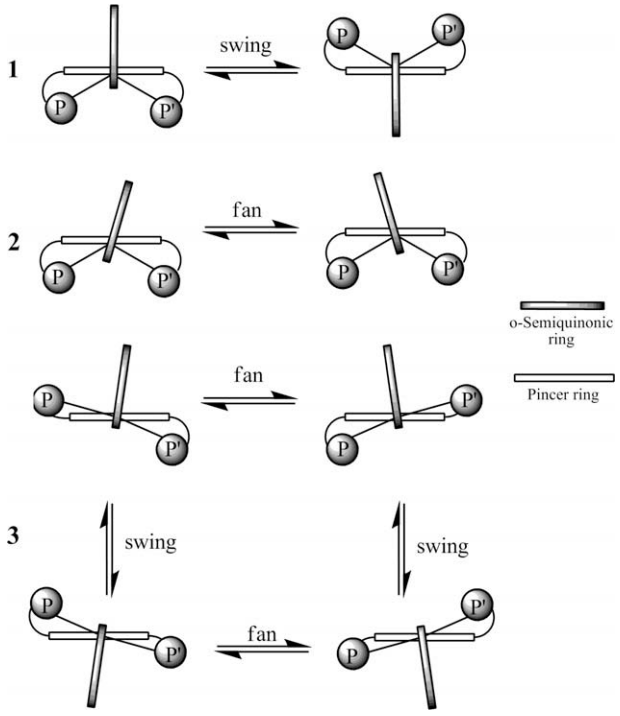


Scheme 3. Possible configurations of phosphoruses chelate cycles.

The examination of the structural data collected up to nowadays shows that the configuration **A** is preferable for the five-coordinated pincer nickel complexes having distorted square–pyramidal geometry. They exist in the configuration **B** only in the case of the sterically hindered ligand at the top of the pyramid [8]. It means that the chelate unit in complex **3** is not so sterically hindered as in **1** and **2**.

All compounds **1**, **2** and **3** detect the structural tautomerism [5]. It means that moving along reaction coordinate which corresponds to rotation of one ligand relatively another has two minima of energy. It was shown previously [5] that complexes **1** and **2** demonstrate "pure" "swing" and "fan" oscillations correspondingly whereas for complex **3** both kinds of them are observed. The analysis of the structural data and the molecular modelling results allows us to build up improved schemes of these oscillations (Scheme 4).

In the case of "swing" oscillations (Scheme 4) the origin of the barrier between the tautomers is clear. For all three compounds such motion requires at least the concerted rotation of all substituents at both phosphorus atoms (Fig. 1, Scheme 4). Additionally, for **1** and **2** the inversion of both pincer chelate cycles is necessary (Fig. 1, Scheme 4). Doubtlessly, both factors should depend on the bulkiness of the substituents at phosphoruses. So the barrier magnitude in the case of **2** should be considerably larger than that in the cases of **1** and **3**, and it explains the absence of the "swing" oscillations for **2** (Scheme 4). For example, no "swing" oscillations



Scheme 4. "Swing" and "fan" oscillations for **1**–**3** (schematic view along basal O–Ni–C direction).

were observed for analogous complex with the pincer ligand having *tert*-butyl substituents at the phosphorus [5].

In the case of symmetrical 3,6-di-*tert*-butyl-*o*-benzosemiquinone the "swing" tautomers do not differ. One "swing" tautomer can be converted into another one by the simple rotation of the molecule. In the case of asymmetrical *o*-semiquinones they become structural isomers [2,5]. In contrast to the "swing" ones, the "fan" tautomers are the enantiomers. In crystal cell of **1**, **2** and **3** both enantiomers ("fan" tautomers) are present. In the case of **1**, the sloped geometry in the crystal appears as a result of the crystal packing. The molecular modelling (in vacuum) detects that this molecule have a configuration with orthogonal ligands planes. Moreover, the orientations of the phenyl groups directed towards the *o*-semiquinonato ligand are close one to another. In the molecular modelling result their positions become virtually equivalent. So, in solution complex **1** should not have "fan" tautomers. Sloped position of the ligands planes in the cases of **2** and **3** itself can't be the reason of the appearing of the "fan" tautomerism. In order to understand the origin of the barrier between the enantiomers one should pay attention to the orientation of the alkyl substituents at the phosphorus atoms which are directed towards the *o*-semiquinonato ligand. One of them (left in Fig. 1) is virtually parallel to the *o*-semiquinonato plane in the case of **2** and have the methyl groups directed away from the *o*-semiquinone in the case of **3**; whereas the other one (right in Fig. 1) is virtually orthogonal to the *o*-semiquinonato plane in **2** and have methyls directed towards the *o*-semiquinonato plane in **3**. Thus, the "fan" motion of the *o*-semiquinonato ligand requires a concerted rotation of at least two alkyl substituents at the phosphorus atoms. It is evident that these local minima of the energy can appear only in the case of alkyl phosphorus substituents having no axial symmetry along the P-alkyl bond. Analogous complex having phenyl or *tert*-butyl substituents at phosphorus atoms have no "fan" tautomers according to EPR data [5].

3. Conclusion

Two novel *o*-semiquinonato PCP-pincer complexes were structurally characterized. Structural features of inner coordination cores are in a good agreement with EPR data obtained earlier. Sloped relative positions of *o*-semiquinonato and pincer ligands together with the absence of axis symmetry of alkyl substituents at phosphoruses (*cyclo*-hexyl and *iso*-propyl) create the conditions for appearing of "fan" motion of *o*-semiquinone relative to pincer ligand which was observed earlier by EPR.

4. Experimental

The synthesis of **2** and **3** was described earlier [5]. Their X-ray quality single crystals were obtained from pentane solution by slow evaporation. The data were collected on a SMART APEX diffractometer (graphite-monochromated, Mo Kα-radiation, ω- and θ-scan technique, $\lambda = 0.71073$ Å). The structures were solved by direct methods and were refined on F^2 using SHELXTL package. All non-hydrogen atoms were refined anisotropically. The hydrogen atoms in **2** were placed in calculated positions and were refined in the riding model. The hydrogen atoms in **3** were found from Fourier syntheses of electron density and were refined isotropically. SADABS was used to perform area-detector scaling and absorption corrections in **3**. Crystals of **2** were a twin therefore the TWINABS program (HKLF 5 format, MERG 0) was used and reflections were not merged.

4.1. Crystal data of complex **2**

$C_{46}H_{71}NiO_2P_2$; $M = 776.68$; $T = 100$ K; $\lambda = 0.71073$ Å; triclinic, space group $P\bar{1}$; $a = 10.8167(4)$ Å, $b = 11.1652(6)$ Å, $c = 19.0778(6)$ Å, $\alpha = 101.4930(10)°$, $\beta = 94.812(2)°$, $\gamma = 110.468(2)°$; $V = 2085.50(15)$ Å^3; $Z = 2$, $D_{Calc} = 1.237$ g sm^{-3}; $F(0\,0\,0) = 842$; θ(deg) 2.04–26.00; reflections collected: 16 368 unique: 16 368 ($R_{int} = 0.0000$); final R indices [$I > 2\sigma(I)$] $R_1 = 0.0428$, $wR_2 = 0.1096$; R indices (all data) $R_1 = 0.0614$, $wR_2 = 0.1174$.

4.2. Crystal data of complex **3**

$C_{34}H_{55}NiO_2P_2$; $M = 616.43$; $T = 100$ K; $\lambda = 0.71073$ Å; triclinic, space group $P\bar{1}$; $a = 10.8111(4)$ Å, $b = 11.7961(4)$ Å, $c = 15.4730(5)$ Å, $\alpha = 70.7220(10)°$, $\beta = 75.8570(10)°$, $\gamma = 62.9420(10)°$; $V = 1648.30(10)$ Å^3; $Z = 2$, $D_{Calc} = 1.242$ g sm^{-3}; $F(0\,0\,0) = 842$; θ(deg) 2.68–27.00; reflections collected: 15 315 unique: 7115 ($R_{int} = 0.0314$); final R indices [$I > 2\sigma(I)$] $R_1 = 0.0364$, $wR_2 = 0.0761$; R indices (all data) $R_1 = 0.0573$, $wR_2 = 0.0816$.

The molecular modelling was provided using "HYPERCHEM 8.0" software. The X-ray data were used as a starting model. The molecular mechanics "MM+" method with "bonds dipoles" options and all of force field components using "Fletcher–Reeves" algorithm was applied for geometry optimization.

Acknowledgements

The authors are grateful to RFBR (grant 06-03-32753-a), Russian President grant supporting young scientists (MK-2580.2007.3) and leading scientific schools (NSh-4182.2008.3) for financial support.

Appendix A. Supplementary data

CCDC 711098 and 711099 contain the supplementary crystallographic data for complexes **2** and **3**. These data can be obtained free of charge via http://www.ccdc.cam.ac.uk/conts/retrieving.html, or from the Cambridge Crystallographic Data Centre, 12 Union Road, Cambridge CB2 1EZ, UK; fax: (+44) 1223-336-033; or e-mail: deposit@ccdc.cam.ac.uk.

Supplementary data associated with this article can be found, in the online version, at doi:10.1016/j.poly.2009.05.023.

References

[1] K.A. Kozhanov, M.P. Bubnov, V.K. Cherkasov, G.K. Fukin, G.A. Abakumov, Chem. Commun. (2003) 2610.
[2] K.A. Kozhanov, M.P. Bubnov, V.K. Cherkasov, G.K. Fukin, G.A. Abakumov, Dalton Trans. (2004) 2957.
[3] J.T. Singleton, Tetrahedron 59 (2003) 1837.
[4] M.E. van der Boom, D. Milstein, Chem. Rev. 103 (2003) 1759.
[5] K.A. Kozhanov, M.P. Bubnov, V.K. Cherkasov, N.N. Vavilina, L.Yu. Efremova, O.I. Artyushin, I.L. Odinets, G.A. Abakumov, Dalton Trans. (2008) 2849.
[6] G.A. Razuvaev, V.K. Cherkasov, G.A. Abakumov, J. Organomet. Chem. 160 (1978) 361.
[7] V.I. Nevodchikov, G.A. Abakumov, V.K. Cherkasov, G.A. Razuvaev, J. Organomet. Chem. 214 (1981) 119.
[8] F.H. Allen, Acta Crystallogr., Sect. B 58 (2002) 380.

Polyhedron 28 (2009) 2559–2564

Contents lists available at ScienceDirect

Polyhedron

journal homepage: www.elsevier.com/locate/poly

Cyclopalladation of (*E*)-N-(2,6-dichlorobenzylidene)(naphthalen-1-yl)methanamine: Synthesis and X-ray molecular structure of [κ²-***N,C1***-η²-***C3,C4***-Pd{(PhC=CPh)$_2$–$C_{10}H_6$–CH_2–N=CH–(2,6-$Cl_2C_6H_3$)}Cl]·CH_2Cl_2

Joan Albert [a,*], Lucía D'Andrea [a], Graciela García [a], Jaume Granell [a], Abdelouahab Rahmouni [a], Mercè Font-Bardia [b], Teresa Calvet [b]

[a] Institut de Biomedicina, Departament de Química Inorgànica, Universitat de Barcelona, Martí i Franquès 1-11, 08028 Barcelona, Spain
[b] Departament de Cristal·lografia, Mineralogia i Dipòsits Minerals, Universitat de Barcelona, Martí i Franquès s/n, 08028 Barcelona, Spain

ARTICLE INFO

Article history:
Received 14 April 2009
Accepted 8 May 2009
Available online 20 May 2009

Keywords:
Cyclometallation
Palladium
Imine
Insertion
Alkyne

ABSTRACT

The reaction of equimolecular amounts of (*E*)-N-(2,6-dichlorobenzylidene)(naphthalen-1-yl)methanamine (**1**) and $Pd(OAc)_2$ in acetic acid at 60 °C for 24 h produced a selective palladation at the 2 position of the naphthyl group of **1**, which afforded the new acetato-bridged five-membered cyclopalladated dimer (μ-OAc)$_2$[(κ²-***C,N***-Pd{($C_{10}H_6$)–CH_2–N=CH–(2,6-$Cl_2C_6H_3$)}]$_2$ (**2**), in which the imines adopted the *Z* configuration. A metathesis reaction between **2** and LiCl exchanged the acetato ligands of **2** for chloro ligands. This produced the dinuclear cyclopalladated compound (μ-Cl)$_2$[κ²-***C,N***-Pd{($C_{10}H_6$)–CH_2–N=CH–(2,6-$Cl_2C_6H_3$)}]$_2$ (**3**), which consisted of a mixture of stereoisomers with imines in the *E* and *Z* configuration. Bridge-splitting reactions of the dimers **2** and **3** with py-d_5 and PPh_3 yielded the mononuclear compounds *trans*-***N,L***-[κ²-***C,N***-Pd{($C_{10}H_6$)–CH_2–N=CH–(2,6-$Cl_2C_6H_3$)}(X)(L)]; **4** (X = OAc, L = py-d_5), **5** (X = OAc, L = PPh_3), **6** (X = Cl, L = py-d_5), **7** (X = Cl, L = PPh_3), in which the imine ligands adopted the *Z* configuration. In addition, **3** reacted with diphenylacetylene, which afforded the mononuclear organopalladium compound [κ²-***N,C1***-η²-***C3,C4***-Pd{(PhC=CPh)$_2$–$C_{10}H_6$–CH_2–N=CH–(2,6-$Cl_2C_6H_3$)}Cl] (**8**). This compound derived from the insertion of two alkyne molecules into the C–Pd σ bonds of **3** and presented the imine ligand in a *Z* configuration. The crystal structure of **8**·CH_2Cl_2 has been determined.

© 2009 Elsevier Ltd. All rights reserved.

1. Introduction

Primary amines are the simplest of the N-donor ligands that can experience the cyclopalladation reaction [1]. In spite of this, methods for the direct cyclopalladation of some of these ligands have not been developed until quite recently [2]. Following these studies, the cyclo-platination, -ruthenation, -rhodation and -iridiation of some primary amines have been reported [3]. However, the cyclopalladation of primary amines remains a difficult task. For instance, in our current work on the cyclopalladation of primary amines [1,4], we were interested in obtaining cyclopalladated derivatives of the primary amine (naphthalen-1-yl)methanamine (**A** in Fig. 1) by direct cyclopalladation. The treatment of **A** with $Pd(OAc)_2$ in equimolecular amounts in toluene or acetic acid for different lengths of time and at varying temperatures did not produce the expected cyclopalladated derivative (**B** in Fig. 1) in acceptable yields and purity. These results contrast with the straightforward cyclopalladation reaction that (*R*)-1-(naphthalen-1-yl)ethanamine (**C** in Fig. 1) undergoes when it is treated with $Pd(OAc)_2$ in acetic acid, which produces its acetato-bridged five-membered cyclopalladated derivative (**D** in Fig. 1) [4b,5]. These results show that bulky substituents in the α position in relation to the heteroatom promote the cyclopalladation reaction. This is in accordance with previous reports [6].

We and other authors have introduced synthetic methods for the preparation by direct cyclopalladation of *exo*-cyclopalladated imines derived from benzylamines, 2-phenylethylamines, 2-phenylaniline, 2-*tert*-butyl-5-methoxy-phenylamine, and α-amino acids, such as phenylglicine and phenylalanine [7]. These compounds can be seen as protected cyclopalladated primary amines and α-amino acids; in the same way that *endo*-cyclopalladated imines have been treated as protected cyclopalladated aromatic ketones or aldehydes [8]. The *endo* and *exo* descriptors were initially introduced to differentiate between the structural isomers of *ortho*-cyclopalladated benzyl-benzylidene-amine (Fig. 2) [8]. However, the use of these descriptors has been extended to refer, in general, to cyclometallated imines with the C=N bond inside the metallacycle (*endo* cyclometallated imines) and outside the metallacycle (*exo* cyclometallated imines) [9].

In this paper, we report that the imine (*E*)-N-(2,6-dichlorobenzylidene)(naphthalen-1-yl)methanamine (**1**), which is easily

* Corresponding author. Tel.: +34 934039131; fax: +34 934907725.
E-mail address: joan.albert@qi.ub.es (J. Albert).

0277-5387/$ - see front matter © 2009 Elsevier Ltd. All rights reserved.
doi:10.1016/j.poly.2009.05.021

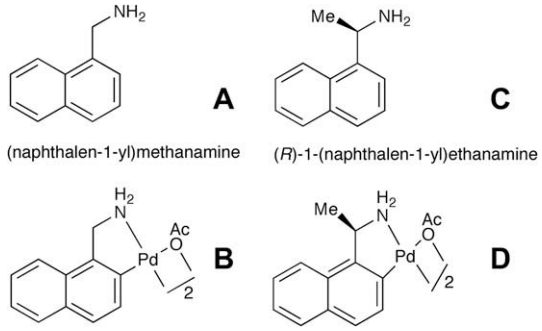


Fig. 1. Structural formula of compounds **A**–**D**.

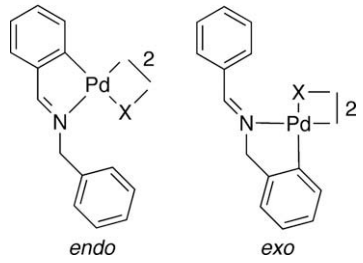


Fig. 2. *Endo* and *exo* structural isomers of cyclopalladated benzyl-benzylideneamine.

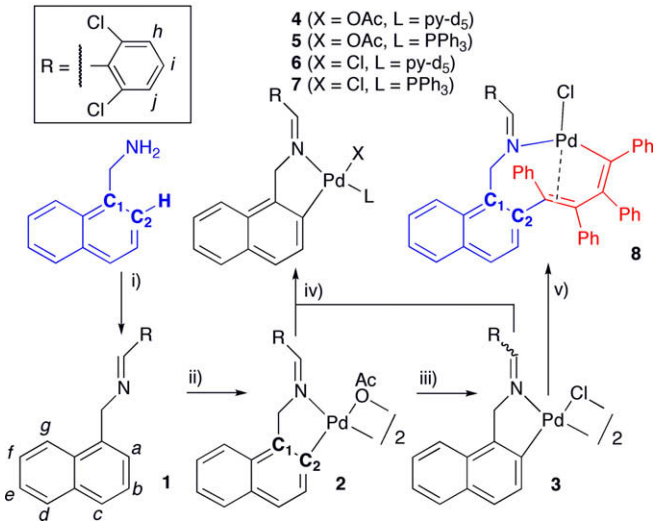
obtained by a condensation reaction between 2,6-dichlorobenzaldehyde and (naphthalen-1-yl)methanamine, reacts with $Pd(OAc)_2$ in acetic acid at 60 °C for 24 h to produce the new acetato-bridged *exo*-five-membered cyclopalladated dimer **2**. This new dimer is derived from the selective palladation of the 2 position of the naphthyl group of **1**. In addition, the chloro-bridged cyclopalladated derivative of **2** (compound **3**) reacts with diphenylacetylene to afford the mononuclear organopalladium compound [κ^2-***N,C1***-η^2-***C3,C4***-Pd{(PhC═CPh)$_2$–$C_{10}H_6$–CH_2–N═CH(2,6-$Cl_2C_6H_3$)}Cl], which results from the insertion of two alkyne molecules into the C–Pd σ bonds of **3**. These results are similar to those previously reported by us for the imine (*E*)-N-(2,6-dichlorobenzylidene)-1-phenylmethanamine [7i,10].

2. Results and discussion

Scheme 1 shows the new compounds prepared in this work and the labelling of the aromatic protons for the discussion that follows.

Imine **1** was prepared in high yield by a condensation reaction between 2,6-dichlorobenzaldehyde and (naphthalen-1-yl)methanamine. This compound was a pale yellow solid that was insoluble in ethanol and soluble in chloroform. It produced satisfactory elemental analysis, IR, DEPCI mass spectrum and ^{1}H NMR. The ^{1}H NMR of **1** showed a single set of signals, which indicated that it consisted of only one geometrical isomer in relation to the carbon–nitrogen double bond. ^{1}H–^{1}H COSY and NOESY experiments at 500 MHz enabled the assignation of almost all protons of **1**, and the cross-peak in the NOESY experiment between the CH═N and the CH_2 protons was indicative of an *E* configuration for imine **1**.

Treatment of equimolecular amounts of imine **1** and $Pd(OAc)_2$ in acetic acid at 60 °C for 24 h produced the new acetato-bridged *exo*-five-membered cyclopalladated dimer **2**, which was derived from the palladation of the 2 position of the naphthyl group of **1**. An alternative structure for compound **2**, with the 8 position of



Scheme 1. (i) 2,6-Dichlorobenzaldehyde, ethanol, reflux, 4h; (ii) $Pd(OAc)_2$, acetic acid, 60 °C, 24 h; (iii) LiCl, acetone, room temperature, 1 h 30 min; (iv) **4** and **6**: py-d_5, $CDCl_3$, room temperature. **5** and **7**: PPh_3, acetone, room temperature, 1 h; (v) diphenylacetylene, chloroform, reflux, 5 days.

the naphthyl group palladated and containing a six-membered metallacycle (Fig. 3), was discarded in view of the ^{31}P chemical shift of compounds **5** and **7**, 41.55 and 42.22 ppm, respectively. These shifts were in the range expected for mononuclear cyclopalladated compounds of general formula *trans*-***N,P***-[Pd(C,N)(X)(PPh_3)] (X = OAc, Cl, Br, I) that contain a five-membered pallacycle and a phenyl or naphthyl metallated carbon atom (42–40 ppm) [6a,7g,11]. The ^{31}P chemical shift of analogous compounds with a six-membered palladacycle appears in the interval 37–33 ppm [7a,d,f,12]. Furthermore, the X-ray molecular structure of compound **8** was in agreement with the proposed structure for **2**.

Compound **2** was a yellowish solid that was insoluble in acetic acid and soluble in chloroform. It afforded satisfactory elemental analysis, IR, positive ESI mass spectrum and ^{1}H NMR. In the IR spectrum, the asymmetric and symmetric stretchings of the carboxylic functions of **2** produced broad intense bands at 1568 and 1429 cm^{-1}, respectively, in accordance with the proposed bridging coordination mode of the acetato ligands of **2** [13]. The positive ESI mass spectrum produced intense signals corresponding to [(M/2)-OAc+acetonitrile]$^+$ and [(M/2)+Na]$^+$, which were consistent with the labile acetato-bridged dinuclear structure proposed for **2**. The most interesting features of the ^{1}H NMR at 300 MHz of **2** in $CDCl_3$ were the singlet produced by the methyl acetato protons and the AB spin system afforded by the CH_2 protons. These features were consistent with a *trans* folded structure with C_2 symmetry for **2**. Acetato-bridged cyclopalladated dimers usually present this structure, both in the solid state and in chloroform solution [14]. In addition, the coupling constant between the CH═N and the CH_2

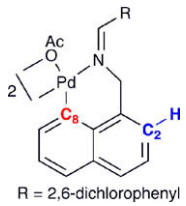


Fig. 3. An alternative structural isomer of **2**, which could be formed by direct cyclopalladation of imine **1**.

protons of 2.7 Hz was in agreement with the proposed *Z* configuration for the imine ligands of compound **2** [15]. Note the following: (i) in this paper the palladium atom is not taken into account to determine the *E* or *Z* configuration of the imine ligand in compounds **2**–**8**, and (ii) the coupling constant between the CH=N and CH_2 protons for the imine Ph–CH=N–CH_2–Ph (benzyl-benzylidene-amine), which adopts an *E* configuration, is *ca.* 1 Hz [15].

A metathesis reaction between **2** and LiCl yielded the expected chloro-bridged cyclopalladated dimer **3**. Compound **3** was a pale yellow solid that was soluble in chloroform. It afforded satisfactory elemental analysis, IR, positive MALDI-TOF mass spectrum and ^{1}H NMR. In the IR spectrum, the carbon–nitrogen double bond stretching appeared at 1635 cm^{-1}. The positive MALDI-TOF mass spectrum produced intense signals at $[M+(M/2)-Cl]^+$ and $[M-Cl]^+$, which were in agreement with the labile dimeric structure of compound **3** with bridging chloro ligands. The ^{1}H NMR at 400 MHz in $CDCl_3$ of compound **3** showed two methinic protons at 9.05 and 8.67 ppm and four signals for the CH_2 protons in the interval between 5.75 and 4.60 ppm. This suggests that compound **3** consisted of different stereoisomers with imines in the *Z* and *E* configuration [7g].

Bridge-splitting reactions of the cyclopalladated dimers **2** and **3** with py-d_5 and PPh_3 yielded the mononuclear cyclopalladated compounds **4**–**7**, which presented the py-d_5 or the PPh_3 ligand *trans* to the iminic nitrogen atom, in agreement with the antisymbiotic effect [16].

The mononuclear compounds **4** and **6** were prepared in an NMR tube, by treating $CDCl_3$ solutions of these compounds with py-d_5, and were not isolated. In both cases, a colour change of the initial yellow or pale yellow solution to a colourless solution indicated the quantitative transformation of the dimers **2** and **3** into the mononuclear compounds **4** and **6**. This was confirmed by the ^{1}H NMR at 400 MHz of the final colourless solutions, which were consistent with the quantitative formation of compounds **4** and **6**. The upfield shift of the *b* aromatic proton in relation to **1** was in agreement with a *trans* disposition of the py-d_5 and the iminic nitrogen [7g,17]. Furthermore, the downfield shift of the methinic proton in relation to **1** was indicative of a *Z* configuration of the imine ligand [7g]. Further evidence of the *Z* configuration of the imine ligands in compounds **4** and **6** was given by the coupling constant between the CH=N and CH_2 protons: 2.8 Hz for compound **4** and 2.4 Hz for compound **6** [15]. For compound **4**, the methyl protons of the acetato ligand appeared as a singlet at 1.97 ppm. This chemical shift was in accordance with an acetato ligand coordinated to a palladium(II) centre in a terminal mode [1,9a,15].

The mononuclear compounds **5** and **7** were obtained on a preparative scale and isolated. These compounds were pale yellow solids that were soluble in chloroform. They afforded satisfactory elemental analysis, IR, positive MALDI-TOF, and ^{1}H and ^{31}P{^{1}H} NMR spectra. In the IR spectrum, the q X-sensitive mode of the coordinated PPh_3 produced a medium intense band at *ca.* 1090 cm^{-1}. The carbon–nitrogen double bond stretching appeared at 1642 cm^{-1} for compound **5**, and 1652 cm^{-1} for compound **7**. For compound **5**, the asymmetric and symmetric stretchings of the carboxylic functions produced broad intense bands at 1604 and 1433 cm^{-1}, respectively, according to a unidentate mode of coordination for the acetato ligand [13]. In the positive MALDI-TOF experiment, both compounds gave an intense signal at $[M-X]^+$ (X = OAc for compound **5**, and X = Cl for compound **7**). This was in accordance with their structures, which contain labile terminal acetato and chloro ligands. In the ^{1}H NMR of compounds **5** and **7**, the upfield shift of the *b* proton in relation to **1**, and its coupling constant with the phosphorus *ca.* 6 Hz, were in accordance with a *trans* disposition between the phosphine ligand and the iminic nitrogen atom [7g]. The downfield shift of the methinic proton in relation to **1** was consistent with a *Z* configuration of their imine ligands. For compound **5**, the chemical shift of the methyl protons of the acetato ligand appeared as a singlet at 1.34 ppm. In addition, the ^{31}P chemical shifts of compounds **5** and **7** (41.55 ppm for compound **5**, and 42.22 ppm for compound **7**) were in the range expected for mononuclear cyclopalladated compounds of general formula *trans*-***N,P***-[Pd(C,N)(X)(PPh_3)] (X = OAc, Cl, Br, I) that contain a five-membered pallacycle and a phenyl or naphthyl metallated carbon atom (42–40 ppm) [6a,7g,11].

Interestingly, the chloro-bridged cyclopalladated dimer **3** reacted at reflux of chloroform with diphenylacetylene very slowly, but in a very clean reaction, which produced the mononuclear organopalladium compound **8**. This compound was derived from the insertion of two alkyne molecules into the C–Pd σ bonds of **3**. This is the third reported case of insertion of alkyne molecules into the C–Pd σ bond of a cyclopalladated compound that contains a palladated naphthyl group. Previously, (i) Pfeffer et al. [18] published the synthesis of *N*-methyl-benzo[d,e]quinolines and *N,N*-dimethyl-benzo[d,e]quinolinium salts by monoinsertion of internal alkynes into the C–Pd σ bond of *N,N*-dimethyl-1-aminonaphthalenes cyclopalladated derivatives, with the 8 position of the naphthyl group palladated (Fig. 4A I and II); and (ii) Nelson et al. [19] described the monoinsertion of dimethylacetylenedicarboxylate or diphenylacetylene into the C–Pd σ bond of *N,N*-dimethyl-α-(2-naphthyl)ethylamine cyclopalladated derivatives, with the 3 position of the naphthyl group palladated (Fig. 4A III). In addition, Beydoun et al. [20] reported a catalytic synthesis of *N*-methyl-benzo[d,e]quinolines by a reaction between 8-iodo-*N,N*-dimethyl-1-aminonaphthalene and internal alkynes, using a cyclopalladated compound as a precatalyst (Fig. 4B). These results and those described here show the potential of the cyclopalladation reaction in organic and organometallic synthesis, since starting from commercial naphthalene derivatives it allows the selective functionalisation of the 8, 3 and 2 positions of naphthyl groups.

Compound **8** was a yellow solid that was soluble in chloroform. It afforded satisfactory elemental analysis, IR, positive MALDI-TOF

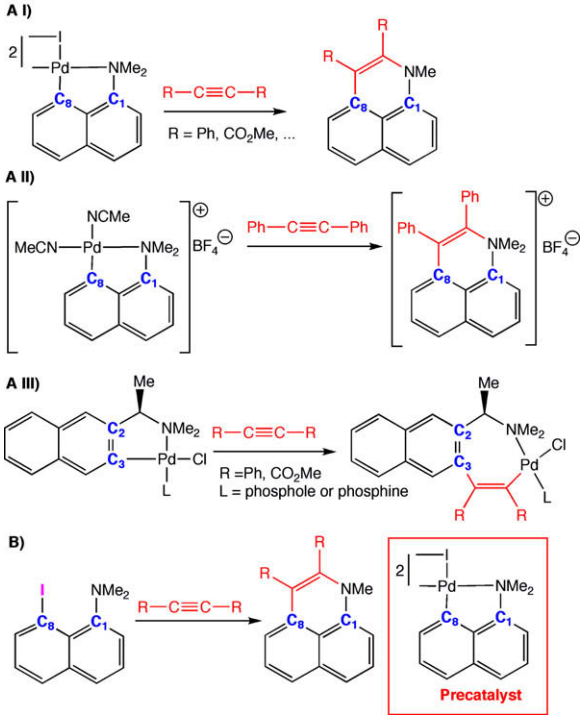


Fig. 4. (A) Previous reports on the insertion of alkynes into the C–Pd σ bond of cyclopalladated compounds containing a palladated naphthyl group: I and II) (Ref. [18]). III) (Ref. [19]). (B) A catalytic version of the stoichiometric reaction A I) (Ref. [20]).

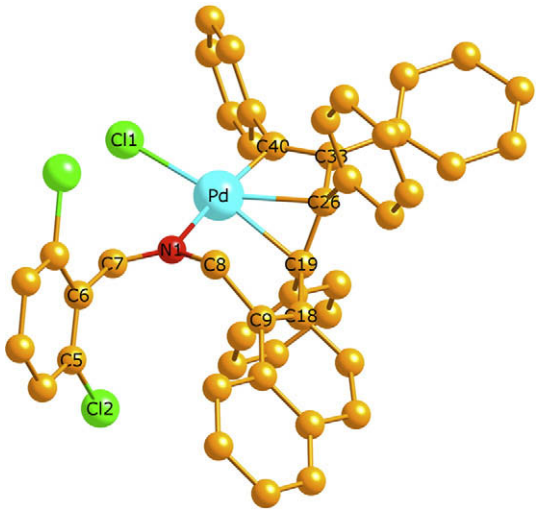


Fig. 5. X-ray molecular structure of compound **8**·CH_2Cl_2.

mass spectrum and ^{1}H NMR spectrum. In the IR spectrum, the stretching of the carbon–nitrogen double bond appeared at 1647 cm^{-1} and the positive MALDI-TOF produced an intense signal for $[M–Cl]^+$, according to the lability of the chloro ligand in compound **8**. In the ^{1}H NMR spectrum at 400 MHz, the most interesting features were the downfield shift of the methinic proton in relation to **1**, which suggested a *Z* configuration for the imine ligand [7g] and the AB spin system produced by the CH_2 protons, which was consistent with the lack of symmetry elements of molecule **8**. The structure of compound **8** was established by an X-ray diffraction study. Yellow crystals of the adduct **8**·CH_2Cl_2 suitable for the X-ray diffraction study were obtained by slow evaporation of the solvents of a solution of **8** in dichloromethane/methanol (1:1). Fig. 5 shows the X-ray molecular structure of compound **8**, and Table 1 gives selected distances and bond angles. The structure agrees with palladation of the 2 position of the naphthyl group of **1**, followed by a double insertion of diphenylacetylene into the Pd–C σ bonds of **3**. The molecule of **8** is chiral. The C19–C26–C33–C40 butadienyl fragment presents a *trans–cis* configuration and is η^2-κ^1 coordinated to palladium(II). Thus, this compound adopts the structure found in most organopalladium compounds derived from the insertion of two alkyne molecules into the C–Pd σ bonds of five- and six-membered cyclopalladated compounds, in which the resulting butadienyl fragment presents a *trans–cis* configuration and is η^2-κ^1 coordinated to palladium(II) [21].

Distances and angles around palladium(II) were within the normal range for this kind of organopalladium compound [10,22]. As expected, the carbon–carbon distance of the alkene unit coordinated η^2 to palladium(II) was larger than that of the alkene unit coordinated κ^1 to palladium(II): 1.407(1) and 1.331(4) Å, respectively. The alkene unit with an η^2 coordination mode did not deviate very much from planarity [torsion angle C18–C19–C26–C33 = −172.4(3)°]. In addition, the imine ligand adopted the *Z* configuration [torsion angle C8–N1–C7–C6 = −0.3(5)°]. The 2,6-dichlorophenyl group was almost perpendicular to the plane defined by the C7–N1–C8 atoms, which included the iminic function [torsion angle C5–C6–C7–N1 = 90.4(8)°]. The Pd–Cl [2.3195(15) Å] and Pd–N [2.139(3) Å] distances were shorter and longer respectively than the analogous distances in mononuclear cyclopalladated compounds of general formula *trans*-***N,P***-[Pd(C,N)Cl(phosphine)] [23]. This is due to the weaker *trans* influence of an η^2-coordinated alkene in relation to a metallated carbon atom, and to the stronger *trans* influence of a metallated carbon atom in relation to a phosphine ligand [24].

Work is in progress to find practical methods of deprotection of compounds **2**–**8** and to make more extensive the study of the reactivity of compounds **2** and **3** towards unsaturated molecules and electrophilic reagents.

As suggested by a reviewer, we studied the reaction between **3** and diphenylacetylene in a molar ratio **3**/diphenylacetylene = 1/2. The reaction was carried out in $CDCl_3$ at 60 °C and monitored by ^{1}H NMR over a period of 48 h. The ^{1}H NMR showed that the reaction solution was almost exclusively formed by compound **8** and the starting materials, compound **3** and diphenylacetylene.

3. Experimental

3.1. Instruments and reagents

Elemental analyses of C, H and N were performed with an Eager 1108 microanalyzer. Infrared spectra were recorded on a Nicolet Impact-400 spectrophotometer, using pressed discs of dispersed samples of compounds **1**–**8** in KBr. NMR experiments were recorded using Varian Inova 500, Varian Mercury 400, Varian Unity 300 and Bruker 250 instruments. Chemical shifts are reported in δ values (ppm) relative to $SiMe_4$ and coupling constants in Hz. The mass spectra were recorded with the following instruments: DEPCI with a ThermoFinnigan TRACE DSQ, using as reactive gas NH_3; Electrospray with a LC/MSD-TOF, using H_2O–CH_3CN 1:1 to introduce the sample; and MALDI-TOF$^+$ with a VOYAGER-DE-RP. All chemicals and solvents were of commercial grade and used as received.

3.2. Preparation of *1*

Twenty millimole of (naphthalen-1-yl)methanamine (3.144 g) and 20 mmol of 2,6-dichlorobenzaldehyde (3.502 g) were treated

Table 1
Selected bond distances (Å) and angles (°) for compound **8**·CH_2Cl_2.

Pd–C40	2.004(3)	C40–Pd–N1	172.57(11)	C9–C18–C19	128.0(3)
Pd–N1	2.139(3)	C40–Pd–C26	65.82(12)	C26–C19–C18	121.7(3)
Pd–C26	2.231(3)	N1–Pd–C26	106.82(11)	C26–C19–Pd	71.18(17)
Pd–C19	2.244(3)	C40–Pd–C19	86.28(12)	C18–C19–Pd	119.1(2)
Pd–Cl1	2.3195(15)	N1–Pd–C19	88.03(11)	C19–C26–C33	118.5(3)
Cl2–C5	1.732(5)	C26–Pd–C19	36.66(11)	C19–C26–Pd	72.17(17)
N1–C7	1.255(4)	C40–Pd–Cl1	95.17(10)	C33–C26–Pd	85.42(18)
N1–C8	1.470(4)	N1–Pd–Cl1	91.39(8)	C40–C33–C26	108.4(3)
C5–C6	1.362(5)	C26–Pd–Cl1	153.23(8)	C33–C40–Pd	100.1(2)
C6–C7	1.506(5)	C19–Pd–Cl1	167.98(8)		
C8–C9	1.529(5)	C7–N1–C8	121.0(3)		
C9–C18	1.358(5)	C7–N1–Pd	126.5(2)		
C19–C26	1.407(4)	C8–N1–Pd	112.1(2)		
C26–C33	1.513(4)	N1–C7–C6	126.5(3)		
C33–C40	1.331(4)	C18–C9–C8	120.7(3)		

at reflux of ethanol (30 mL) for 4 h. The resulting solution was allowed to cool to room temperature, whereupon most of imine **1** separated as a pale yellow powder, which was filtered and dried under vacuum. Yield: 5.589 g (89%). Characterization data: *Anal.* Calc. for $C_{18}H_{13}Cl_2N$: C, 68.81; H, 4.17; N, 4.46. Found: C, 68.37; H, 4.19; N, 4.53%. DEPCI (+) (NH_3 reactive gas): $[M + H]^+ = 315.1$ (calc. 314.0) (base peak). IR (cm^{-1}): 1642 st C=N. ^1H NMR 500 MHz ($CDCl_3$) (selected data): 8.55 (s, CH=N), 8.13 (d, H_g, $^3J_{HH} = 8.4$), 7.88 (d, H_d, $^3J_{HH} = 8.4$), 7.80 (d, H_c, $^3J_{HH} = 8.4$), 7.30 (d, H_h and H_j, $^3J_{HH} = 8.0$), 7.17 (t, H_i, $^3J_{HH} = 8.0$), 5.40 (s, CH_2).

3.3. Preparation of **2**

A suspension formed by 0.194 (0.86 mmol) of $Pd(OAc)_2$, 0.270 (0.86 mmol) of **1** and 20 mL of acetic acid was treated at 60 °C for 24 h. The resulting suspension was allowed to cool to room temperature, whereupon most of compound **2** separated as a yellow powder, which was filtered and dried under vacuum. Yield: 0.254 g (62%). Characterization data: *Anal.* Calc. for $C_{40}H_{30}Cl_4N_2O_4Pd_2$: C, 50.18; H, 3.16; N, 2.93. Found: C, 50.06; H, 3.14; N, 2.90%. IR (cm^{-1}): 1568 (st as. OAc), 1429 (st s. OAc). ESI-(+): Intense peaks at $[(M/2)\text{-OAc} + \text{acetonitrile}]^+ = 460.96$ (calc. 460.97) (base peak) and $[(M/2) + Na]^+ = 500.99$ (calc. 500.94). ^1H NMR 300 MHz ($CDCl_3$) (selected data): 8.48 (t, CH=N, $^4J_{HH} = 2.7$), 7.72 (d, 1H, aromatic, $^3J_{HH} = 7.8$), 7.38 (d, 1H, aromatic, $^3J_{HH} = 8.7$), 6.96 (d, 1H, aromatic, $^3J_{HH} = 8.4$), 4.74, 4.68, 4.46, 4.41 (AB spin system, CH_2), 2.25 (s, OAc).

3.4. Preparation of **3**

A suspension formed by 0.629 g (0.66 mmol) of **2**, 0.111 g (2.62 mmol) of LiCl and 20 mL of acetone was stirred at room temperature for 1 h 30 min. The resulting suspension was concentrated under vacuum and the residue was eluted through a silica gel column with a solution of methanol in chloroform in a 2–100 volume ratio. The yellow band was collected and concentrated under vacuum. Addition of diethyl ether (5 mL) to the residue led to the precipitation of **3** as a pale yellow powder, which was filtered and dried under vacuum. Yield: 0.424 g (71%). Characterization data: *Anal.* Calc. for $C_{36}H_{24}Cl_6N_2Pd_2$: C, 47.51; H, 2.66; N, 3.08. Found: C, 47.04; H, 2.68; N, 3.11%. MALDI-TOF (+) (matrix = 2,5-hydroxibenzoic acid): Intense peaks at $[M+(M/2)\text{-Cl}]^+ = 1329.9$ (calc. 1326.7) and $[M\text{–Cl}]^+ = 875.1$ (calc. 872.8) (base peak). IR (cm^{-1}): 1635 st C=N. ^1H NMR 400 MHz ($CDCl_3$) (selected data) (mixture of stereoisomers): 9.05 s, 8.67 s (CH=N); 5.75 s, 5.18 d $^4J_{HH} = 2.4$, 5.07 s, 4.60 s (CH_2).

3.5. Preparation of the $CDCl_3$ solutions of **4** and **6**

ca. 10 mg of **2** or **3** were treated with 0.7 mL of $CDCl_3$ and two drops of py-d_5. The formation of a colourless solution was an indication of the quantitative transformation of compound **2** or **3** into the mononuclear compounds **4** or **6**. Characterization data: Compound **4**: ^1H NMR 400 MHz ($CDCl_3$ + py-d_5) (selected data): 8.88 (t, CH=N, $^4J_{HH} = 2.8$), 6.32 (d, H_b, $^3J_{HH} = 8.4$), 5.19 (d, CH_2, $^4J_{HH} = 2.8$), 1.97 (s, OAc). Compound **6**: ^1H NMR 400 MHz ($CDCl_3$ + py-d_5) (selected data): 9.65 (t, CH=N, $^4J_{HH} = 2.4$), 7.73 (d, 1H, aromatic, $^3J_{HH} = 8.4$), 6.29 (d, H_b, $^3J_{HH} = 8.4$), 5.21 (d, CH_2, $^4J_{HH} = 2.8$).

3.6. Preparation of **5**

A suspension formed by 0.100 g (0.1 mmol) of **2**, 0.055 g (0.2 mmol) of PPh_3 and 10 mL of acetone was stirred at room temperature for 1 h. The resulting suspension was concentrated under vacuum and the residue was treated with 5 mL of acetone/diethyl ether (1/1). Compound **5** precipitated as a pale yellow solid, which was filtered and dried under vacuum. Yield: 0.078 g (50%). Characterization data: *Anal.* Calc. for $C_{38}H_{30}Cl_2NO_2PPd$: C, 61.60; H, 4.08; N, 1.89. Found: C, 61.40; H, 4.06; N, 1.85%. MALDI-TOF (+) (matrix = 2,5-hydroxibenzoic acid): Intense peak at $[M\text{-OAc}]^+ = 682.1$ (calc. 681.0) (base peak). IR (cm^{-1}): 1642 st C=N, 1604 (st as. OAc), 1433 (st s. OAc), 1090 q X-sensitive mode of the coordinated PPh_3 ligand. ^1H NMR 400 MHz ($CDCl_3$) (selected data): 8.85 (t, CH=N, $^4J_{HH} = 2.4$), 6.90 (d, H_c, $^3J_{HH} = 8.8$), 6.68 (dd, H_b, $^3J_{HH} = 8.4$, $^4J_{PH} = 6.0$), 5.32 (s, CH_2), 1.34 (s, OAc). $^{31}P\{^1H\}$ NMR 121.6 MHz ($CHCl_3$, inset $P(OMe)_3$ in CD_3COCD_3) = 41.55 s.

3.7. Preparation of **7**

A suspension formed by 0.106 g (0.11 mmol) of **3**, 0.061 g (0.23 mmol) of PPh_3 and 10 mL of acetone was stirred at room temperature for 1 h. The resulting solution was concentrated under vacuum and the residue was treated with 5 mL of diethyl ether. Compound **7** precipitated as a pale yellow powder, which was filtered and dried under vacuum. Yield: 0.098 g (62%). Characterization data: *Anal.* Calc. for $C_{36}H_{27}Cl_3NPPd$: C, 60.27; H, 3.79; N, 1.95. Found: C, 60.10; H, 3.82; N, 1.99%. MALDI-TOF (+) (matrix = dithranol): Intense peak at $([M\text{–Cl}]^+ = 682.2$ (calc. 681.0) (base peak). IR (cm^{-1}): 1652 st C=N, 1095 q X-sensitive mode of the coordinated PPh_3 ligand. ^1H NMR 400 MHz ($CDCl_3$) (selected data): 9.71 (q, CH=N, $^4J_{HH} \approx {}^4J_{PH} = 2.4$), 7.86–7.81 (m, 6H, o-$PPh_3$), 6.88 (d, H_c, $^3J_{HH} = 8.8$), 6.68 (dd, H_b, $^3J_{HH} = 8.8$, $^4J_{PH} = 6.4$), 5.36 (s, CH_2). $^{31}P\{^1H\}$ NMR 101.26 MHz ($CHCl_3$, inset $P(OMe)_3$ in CD_3COCD_3): 42.22 s.

3.8. Preparation of **8**

A suspension formed by 0.248 g (0.27 mmol) of **3**, 0.194 g (1.09 mmol) of diphenylacetylene and 20 mL of chloroform was subjected to reflux temperature for 5 days. The resulting yellow solution was concentrated under vacuum and the residue was eluted through a silica gel chromatographic column with a solution of methanol in chloroform in a 2–100 volume ratio. The yellow band was collected and concentrated under vacuum. Addition of diethyl ether (5 mL) to the residue produced the precipitation of **8** as a yellow powder which was filtered and dried under vacuum. Yield: 0.303 g (69%). Characterization data: *Anal.* Calc. for $C_{46}H_{32}Cl_3NPd$: C, 68.08; H, 3.97; N, 1.72. Found: C, 67.66; H, 3.87; N, 1.78%. MALDI-TOF (+) (matrix = 2,5-hydroxibenzoic acid): Intense peak at $[M\text{–Cl}]^+ = 775.7$ (calc.775.1) (base peak). IR (cm^{-1}): 1647 st C=N, 1595, 1576, 1561 st arCC. ^1H NMR 400 MHz ($CDCl_3$) (selected data): 8.97 (s, CH=N), 7.64 (d, H_h and H_j, $^3J_{HH} = 8.0$), 7.38 (t, H_i, $^3J_{HH} = 8.0$), 6.76 (d, 1H, aromatic, $^3J_{HH} = 8.0$), 5.16, 5.12, 3.86, 3.83 (CH_2, AB spin system).

3.9. Crystal structure

Crystals for the X-ray determination of **8**·CH_2Cl_2 were obtained by slow evaporation of a solution of **8** in dichloromethane/methanol (1/1). A prismatic crystal (0.1 × 0.1 × 0.2 mm) was selected and mounted on a MAR345 diffractometer with an image plate detector. Unit-cell parameters were determined from 1665 reflections ($3 < \theta < 31°$) and refined by the least-squares method. Intensities were collected with graphite monochromatised Mo Kα radiation. The structure was solved by Direct methods, using the SHELXS computer program [25]. It was refined by full-matrix least-squares method with the SHELXL97 computer program [26]. The minimised function was $\Sigma\ w\ ||Fo|^2 - |Fc|^2|^2$, where $w = [\sigma^2(I) + (0.0579P)^2 + 0.6694P]^{-1}$, and $P = (|Fo|^2 + 2|Fc|^2)/3$. f, f' and f'' were taken from International Tables of X-ray Crystallography [27]. All H atoms were computed and refined, using a riding model with an isotropic

Table 2
Crystallographic data for compound **8**·CH_2Cl_2.

Empirical formula	$C_{46}H_{32}Cl_3NPd{\cdot}CH_2Cl_2$
Formula weight	896.40
T (K)	293 (2)
Wavelength (Å)	0.71073
Crystal system, space group	triclinic, $\bar{P}$
Unit cell dimensions	
a (Å)	11.180(6)
b (Å)	12.987(4)
c (Å)	15.065(6)
α (°)	74.31(2)
β (°)	77.25(3)
γ (°)	84.70(3)
Volume (Å^3)	2052.7(15)
Z, calculated density (Mg/m^3)	2, 1.450
Absorption coefficient (mm^{-1})	0.812
F(0 0 0)	908°
Crystal size (mm)	0.2 × 0.1 × 0.1
θ Range for data collection	2.58–32.43
Limiting indices	$-16 \leqslant h \leqslant 16$ $-19 \leqslant k \leqslant 19$ $-22 \leqslant l \leqslant 22$
Reflections collected/unique	24289/12856 [R_{int} = 0.0628]
Completeness to θ = 25.00°	93.8%
Absorption correction	empirical
Max. and min. transmission	0.92 and 0.91
Refinement method	full-matrix least-squares on F^2
Data/restraints/parameters	12856/8/487
Goodness-of-fit on F^2	1.080
Final R indices [$I > 2\sigma(I)$]	$R1$ = 0.0574, $wR2$ = 0.1345
R indices (all data)	$R1$ = 0.0902, $wR2$ = 0.1457
Largest difference in peak and hole (e Å^3)	1.006 and −0.785

temperature factor equal to 1.2 times the equivalent temperature factor of the atoms that are linked to them. A summary of the crystallographic data is given in Table 2.

Supplementary data

CCDC 717397 contains the supplementary crystallographic data for **8**·CH_2Cl_2. These data can be obtained free of charge via http://www.ccdc.cam.ac.uk/conts/retrieving.html, or from the Cambridge Crystallographic Data Centre, 12 Union Road, Cambridge CB2 1EZ, UK; fax: (+44) 1223-336-033; or e-mail: deposit@ccdc.cam.ac.uk.

Acknowledgements

We are grateful to the Ministerio de Ciencia y Tecnología for financial support (Grant CTQ2006-02007/BQU), L.D. to the University of Barcelona for a BRD grant, G.G. to the MICINN for an undergraduated grant, and A.R. to the MAE for an AECID predoctoral grant.

References

[1] J. Albert, J. Granell, R. Tavera, Polyhedron 22 (2003) 287.
[2] J. Vicente, I. Saura-Llamas, Comments on Inorganic Chemistry 28 (2007) 39.
[3] (a) B. Calmuschi-Cula, U. Englert, Organometallics 27 (2008) 3124;
(b) J.-B. Sortais, N. Pannetier, A. Holuigue, L. Barloy, C. Sirlin, M. Pfeffer, N. Kyritsakas, Organometallics 26 (2007) 1856;
(c) A. Capapé, M. Crespo, J. Granell, M. Font-Bardia, X. Solans, Dalton Trans. (2007) 2030;
(d) R. Annunziata, S. Cenini, F. Demartin, G. Palmisano, S. Tollari, J. Organomet. Chem. 496 (1995) C1.
[4] (a) J. Albert, J. Granell, J. Zafrilla, M. Font-Bardia, X. Solans, J. Organomet. Chem. 690 (2005) 422;
(b) J. Albert, J.M. Cadena, J. Granell, Tetrahedron: Asymmetry 8 (1997) 991;
(c) J. Albert, J. Granell, A. Luque, J. Mínguez, R. Moragas, M. Font-Bardia, X. Solans, J. Organomet. Chem. 522 (1996) 87.
[5] E. Durán, E. Gordo, J. Granell, M. Font-Bardia, X. Solans, D. Velasco, F. López-Calahorra, Tetrahedron: Asymmetry 12 (2001) 1987.
[6] (a) V.V. Dunina, L.G. Kuz'mina, M.Yu. Kazakova, O.N. Gorunova, Y.K. Grishin, E.I. Kazakova, Eur. J. Inorg. Chem. (1999) 1029;
(b) V.V. Dunina, O.A. Zalevskaya, V.M. Potapov, Russ. Chem. Rev. 57 (1988) 250.
[7] (a) J. Albert, J.M. Cadena, A. González, J. Granell, X. Solans, M. Font-Bardia, Chem. Eur. J. 12 (2006) 887;
(b) J. Albert, J.M. Cadena, A. González, J. Granell, X. Solans, M. Font-Bardia, Chem. Commun. (2003) 528;
(c) B.D. Dangel, K. Godula, S.W. Youn, B. Sezen, D. Sames, J. Am. Chem. Soc. 124 (2002) 11856;
(d) J. Albert, J.M. Cadena, A. González, J. Granell, X. Solans, M. Font-Bardia, J. Organomet. Chem. 663 (2002) 277;
(e) S. Tollari, S. Cenini, C. Tunice, G. Palmisano, Inorganica Chimica Acta 272 (1998) 18;
(f) J. Albert, J. Granell, A. Luque, M. Font-Bardia, X. Solans, J. Organomet. Chem. 545 - 546 (1997) 131;
(g) J. Albert, J. Granell, J. Sales, M. Font-Bardia, X. Solans, Organometallics 14 (1995) 1393;
(h) H. Yang, M.A. Kan, K.M. Nicholas, J. Chem. Soc., Chem. Commun. (1992) 210;
(i) J. Albert, M. Gómez, J. Granell, J. Sales, X. Solans, Organometallics 9 (1990) 1405.
[8] P.W. Clark, S.F. Dyke, G. Smith, C.H.L. Kennard, J. Organomet. Chem. 330 (1987) 447.
[9] (a) J. Albert, L. D'Andrea, J. Granell, R. Tavera, M. Font-Bardia, X. Solans, J. Organomet. Chem. 692 (2007) 3070;
(b) M. Gómez, J. Granell, M. Martínez, Organometallics 16 (1997) 2539;
(c) R. Bosque, C. López, J. Sales, J. Organomet. Chem. 498 (1995) 147;
(d) J. Albert, R.M. Ceder, M. Gómez, J. Granell, J. Sales, Organometallics 11 (1992) 1536;
(e) M. Crespo, M. Martínez, J. Sales, X. Solans, M. Font-Bardia, Organometallics 11 (1992) 1288.
[10] J. Albert, J. Granell, J. Sales, X. Solans, J. Organomet. Chem. 379 (1989) 177.
[11] J. Albert, J.M. Cadena, J.R. Granell, X. Solans, M. Font-Bardia, Tetrahedron: Asymmetry 11 (2000) 1943.
[12] J. Albert, R. Bosque, J. Granell, R. Tavera, J. Organomet. Chem. 595 (2000) 54.
[13] K. Nakamoto, Infrared and Raman Spectra of Inorganic and Coordination Compounds, 5th ed., Wiley, New York, 1997.
[14] P.G. Evans, N.A. Brown, G.J. Clarkson, C.P. Newman, J.P. Rourke, J. Organomet. Chem. 691 (2006) 1251.
[15] J. Albert, R. Bosque, J. Granell, R. Tavera, Polyhedron 20 (2001) 3225.
[16] (a) J. Vicente, A. Arcas, D. Bautista, M.C. Ramírez de Arellano, J. Organomet. Chem. 663 (2002) 164;
(b) R. Navarro, E.P. Urriolabeitia, J. Chem. Soc., Dalton Trans. (1999) 4111;
(c) J. Vicente, A. Arcas, D. Bautista, P.G. Jones, Organometallics 16 (1997) 2127.
[17] A.D. Ryabov, L.G. Kuz'mina, V.A. Polyakov, G.M. Kazankov, E.S. Ryabova, M. Pfeffer, R. van Eldik, J. Chem. Soc., Dalton Trans. (1995) 999.
[18] (a) M. Pfeffer, N. Sutter-Beydoun, A. De Cian, J. Fischer, J. Organomet. Chem. 453 (1993) 139;
(b) F. Maassarani, M. Pfeffer, G. Le Borgne, Organometallics 6 (1987) 2029.
[19] N. Gül, J.H. Nelson, A.C. Willis, A.D. Rae, Organometallics 21 (2002) 2041.
[20] N. Beydoun, M. Pfeffer, Synthesis (1990) 729.
[21] (a) J. Dupont, M. Pfeffer (Eds.), Palladacycles. Synthesis, Characterization and Applications, Wiley-VCH, Weinheim, 2008;
(b) J. Dupont, C.S. Consorti, J. Spencer, Chem. Rev. 105 (2005) 2527;
(c) J. Spencer, M. Pfeffer, Adv. Metal-Organic Chem. 6 (1998) 103;
(d) M. Pfeffer, Pure Appl. Chem. 64 (1992) 335;
(e) M. Pfeffer, Recl. Trav. Chem. Pays-Bas 109 (1990) 567;
(f) A.D. Ryabov, Synthesis (1985) 233.
[22] J. Albert, L. D'Andrea, J. Granell, J. Zafrilla, M. Font-Bardia, X. Solans, J. Organomet. Chem. 692 (2007) 4895.
[23] (a) J.M. Vila, G. Alberdi, M.T. Pereira, M. Mariño, A. Fernández, M. López-Torres, R. Ares, Polyhedron 22 (2003) 241;
(b) M. López-Torres, A. Fernández, J.J. Fernández, A. Suárez, S. Castro-Juiz, M.T. Pereira, J.M. Vila, J. Organomet. Chem. 655 (2002) 127;
(c) A. Fernández, D. Vázquez-García, J.J. Fernández, M. López-Torres, A. Suárez, R. Mosteiro, J.M. Vila, J. Organomet. Chem. 654 (2002) 162.
[24] T.G. Appleton, H.C. Clark, L.E. Manzer, Coord. Chem. Rev. 10 (1973) 335.
[25] G.M. Sheldrick, SHELXS A program for Automatic Solution of Crystal Structure, University of Gottingen, Germany, 1997.
[26] G.M. Sheldrick, SHELX-97 A Program for Automatic Solution of Crystal Structure, University Gottingen, Germany, 1997.
[27] International Tables of X-ray Crystallography, vol. IV. Kynoch Press, Birmingham, UK, 1974, pp. 99–100, 149.

Polyhedron 28 (2009) 2565–2570

Contents lists available at ScienceDirect

Polyhedron

journal homepage: www.elsevier.com/locate/poly

Substituted pyridine coordinated *N,N-trans* and *N,N-cis* cyclopalladated complexes of (*S*)-4-*tert*-butyl-2-phenyl-2-oxazoline: Crystal structures, spectral study and catalysis of the decomposition of P═S pesticides

Zhong-Lin Lu [a,*], Xiao-Sheng Yang [a], Rui-Yao Wang [b], Hoong-Kun Fun [c], Suchada Chantrapromma [d]

[a] *Department of Chemistry, Beijing Normal University, Beijing 100875, PR China*
[b] *Department of Chemistry, Queen's University, Kingston, Ontario, Canada K7L 3N6*
[c] *X-ray Crystallography Unit, School of Physics, Universiti Sains Malaysia, 11800 USM, Penang, Malaysia*
[d] *Crystal Materials Research Unit, Department of Chemistry, Faculty of Science, Prince of Songkla University, Hat-Yai, Songkhla 90112, Thailand*

ARTICLE INFO

Article history:
Received 2 January 2009
Accepted 11 May 2009
Available online 20 May 2009

Keywords:
Palladacycles
Kinetics
Pestcides
Crystal structures

ABSTRACT

Three pyridine coordinated cyclopalladated complexes: (*S*)-chloro{2-[2-(4-*tert*-butyl)oxazolinyl]phenyl-*C,N*}(4-R-pyridine)palladium(II) (R = H, **2**; R = CF_3, **3**; R = NMe_2, **4**), have been synthesized and structurally characterized. While the crystal structure shows that **2** has a normal *N,N-trans*-conformation in the coordination sphere of palladium(II), **3** and **4** exhibit uncommon *N,N-cis*-conformations. From ^{1}H NMR measurements, the major coordination isomer in deuterated chloroform solution is *N,N-trans* configuration for three palladacycles. It was found that the three complexes catalyze effectively the methanolysis of the P═S pesticides including chiral thiophosphates but show different activity depending on the substituents of co-coordinated pyridine ring in **2**–**4**.

© 2009 Elsevier Ltd. All rights reserved.

1. Introduction

After the discovery of the first cyclometallated derivatives [1,2], many palladacycle compounds have been synthesized and their use widely applied in organic synthesis, organometallic catalysis, and new molecular materials [3–12]. In recent years, the research groups of Ryabov [13], Gabbaie [14], and Tao [15] have investigated the catalytic properties of palladacycles for the hydrolysis of organic thiophosphates and demonstrated their remarkable catalytic activities. However, there are some problems accompanying the catalytic hydrolytic degradation of pesticides, including poor aqueous solubility of both the metal catalysts and organic phosphate substrates and the fact that the anionic hydrolytic products can bind to the metal ions thereby curtailing further catalysis. As an alternative strategy in catalytic decomposition of organic phosphate pesticides and related chemical warfare (CW) agents, the catalytic methanolysis of various organic phosphates with lanthanide and transition metal ions and some of their metal complexes as well as palladacycles have been explored in recent years [16–19].

As a part of our interest in the catalytic degradation of thiophosphates, we report here the synthesis, structural characterization, and preliminary catalytic properties of three palladacycles containing the (*S*)-4-*tert*-butyl-2-phenyl-2-oxazoline ligand (see Scheme 1). We have found that the structures and catalytic activities of these palladacycles can be significantly modified by changing the electronic property of the substituents on the mono-dentate pyridine ring in **2**–**4**.

2. Results and discussion

2.1. X-ray structure studies of complexes 2–4

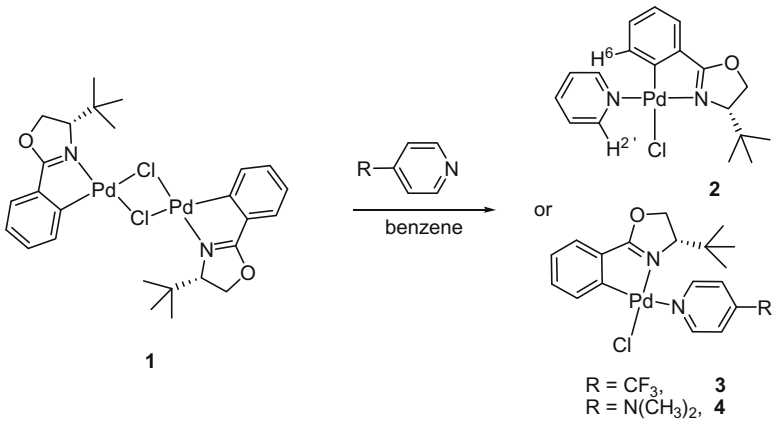
The crystal data for the data collection and refinement of **2**–**4** are given in Table 1. Selected bond lengths, bond angles and torsion angles are listed in Table 2. ORTEP diagrams of **2**–**4** at the 50% probability level are given in Figs. 1–3.

For complex **2**, the palladium atom displays the expected square planar coordination with the pyridine and oxazoline nitrogen atoms positioned *trans* to one another. The dihedral angle between the planes {C1/Pd/N1} and {N2/Pd/Cl1} is 5.83° which indicates that the coordination sphere is almost square planar. The bond lengths and bond angles of palladacycle fall within the range of the values reported for other cyclopalladated derivatives of oxazoline ligands and other palladacycle compounds with two nitrogen atoms in the *trans* position [20–22].

For complexes **3** and **4**, it can clearly be seen that the pyridine and oxazoline nitrogen atoms are in a *cis* position (see Figs. 2 and 3), which is not so common for the *ortho*-palladated complexes

* Corresponding author. Tel./fax: +86 10 58801804.
E-mail address: luzl@bnu.edu.cn (Z.-L. Lu).

0277-5387/$ - see front matter © 2009 Elsevier Ltd. All rights reserved.
doi:10.1016/j.poly.2009.05.030



1 2

Scheme 1.

Table 1
Experimental data for the X-ray diffraction study on complex **2–4**.

Complex	2	3	4
Formula	$C_{18}H_{21}ClN_2OPd$	$C_{19}H_{20}ClF_3N_2OPd$	$C_{19}H_{26}ClN_3OPd$
Formula weight	423.23	491.22	466.29
T (K)	180(2)	100.0(1)	293(2)
λ (Å)	0.71073	0.71073	0.71073
Space group	$P2(1)2(1)2(1)$	$P2(1)2(1)2(1)$	$P2(1)2(1)2(1)$
a (Å)	5.671(11)	9.5946(1)	9.6641(1)
b (Å)	12.002(2)	9.9297(1)	9.8777(1)
c (Å)	25.016(5)	20.4246(2)	20.8164(2)
α (°)	90	90	90
β (°)	90	90	90
γ (°)	90	90	90
V (Å$^{3)}$	1731.5(6)	1945.88(3)	1987.11(3)
Z	4	4	4
ρ (g cm^{-3})	1.631	1.677	1.559
μ (mm^{-1})	1.233	1.130	1.082
F(0 0 0)	860	984	952
Crystal size (mm)	0.35 × 0.30 × 0.25	0.25 × 0.25 × 0.25	0.35 × 0.19 × 0.14
θ (°)	1.63–24.55	2.28–37.50	1.96–35.95
Index ranges	$-6 \leqslant h \leqslant 6$, $-14 \leqslant k \leqslant 14$, $-29 \leqslant l \leqslant 29$	$-16 \leqslant h \leqslant 14$, $-16 \leqslant k \leqslant 16$, $-33 \leqslant l \leqslant 34$	$-15 \leqslant h \leqslant 10$, $-16 \leqslant k \leqslant 15$, $-34 \leqslant l \leqslant 34$
Reflections collected	9956	45 435	32 225
Independent reflections	3039 [R_{int} = 0.0183]	10 128 [R_{int} = 0.0373]	9359 [R_{int} = 0.0600]
Data/restraints/parameters	3039/0/292	10 128/0/324	9359/0/240
Goodness-of-fit (GOF) on F^2	1.000	1.018	1.035
Final R indices [$I > 2\sigma(I)$]	R_1 = 0.0142, wR_2 = 0.0145	R_1 = 0.0306, wR_2 = 0.0367	R_1 = 0.0418, wR_2 = 0.0609
Largest difference in peak and hole (e Å^{-3})	0.186 and −0.379	0.568 and −0.593	1.275 and −1.172

containing monodentate N or P ligands. The structure of **4** is quite different from the analog palladacycle compound (*S*)-chloro{2-[2-(4-*iso*-propyll)oxazolinyl]phenyl-*C*,*N*}(4-*N*,*N*-dimethylaminopyridine)palladium(II), which contains *iso*-propyl group on the oxazoline ring instead of *tert*-butyl group and has *N*,*N*-*trans* configuration in the coordination sphere of palladium atom. The *N*,*N*-*cis* configuration in *ortho*-palladated complexes is sometimes observed in solution by NMR, but the only other crystal structure of which we are aware is that of the palladacycle [Pd{$C_6H_4C(Me)$=$NC_{10}H_7$}Cl(4-Me-py)] ($C_{10}H_7$ = α-naphthyl) [23]. The torsion angles between the pyridine plane and the palladacycle plane (Pd/C1/C2/C7/N1) are 46.41° and 40.17° for complexes **3** and **4**, respectively. The effect of the strong donating phenyl ring on the pyridine can be observed since the σ-bound phenyl induces 0.142 and 0.118 Å elongation of the Pd–N (pyridine) bonds *trans* to it in **3** and **4**, respectively, compared with that in complex **2**. The Pd–Cl bonds in **3** and **4** are shorter by 0.074 and 0.067 Å than that in **2** since they are positioned to have less *trans* effect on the nitrogen donor. Another point of note is that the dihedral angles between the {C1/Pd/N1} and {N2/Pd/Cl1} planes are 8.89° and 7.93° in **3** and **4**, respectively. The maximum displacements of atom C1 are 0.121 and 0.109 Å in com-

Table 2
Selected bond lengths [Å], bond angles [°] and torsion angles [°] for **2–4**.

Parameter	2	3	4
Pd1–C1	1.991(2)	1.9940(15)	1.998(3)
Pd1–Cl1	2.3817(7)	2.3076(4)	2.315(2)
Pd1–N1	2.0351(17)	2.0611(12)	2.060(2)
Pd1–N2	2.0189(18)	2.1509(15)	2.137(2)
C1–Pd1–N1	81.20(8)	81.44(6)	81.05(10)
C1–Pd1–N2	92.38(8)	173.53(6)	173.04(12)
N1–Pd1–N2	171.49(7)	96.01(5)	96.86(9)
C1–Pd1–Cl1	177.78(6)	93.13(4)	92.72(8)
N2–Pd1–Cl1	81.88(5)	89.51(7)	89.78(6)
N1–Pd1–Cl1	91.37(5)	171.53(4)	172.48(7)
C1–Pd1–N2–C10	75.92(17)	−21.1(5)	148.5(7)
N1–Pd1–N2–C10	−35.2(6)	45.44(12)	−139.2(2)
Cl1–Pd1–N2–C14	−72.14(16)	43.86(12)	−141.9(2)

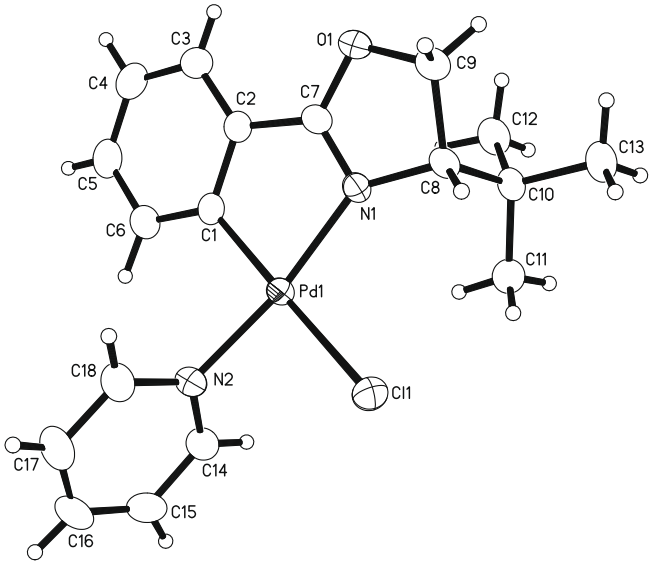


Fig. 1. Molecular structure of complex **2** showing the atom numbering. Displacement parameters are shown at the 50% level.

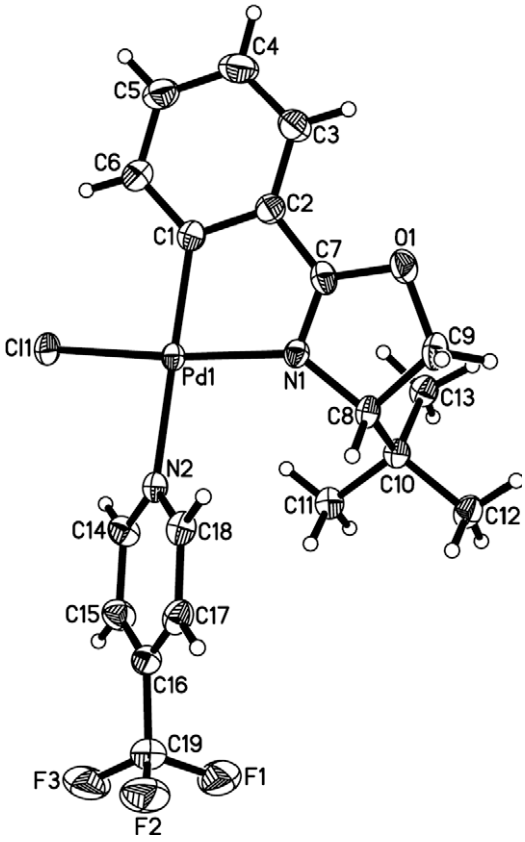


Fig. 2. Molecular structure of complex **3** showing the atom numbering. Displacement parameters are shown at the 50% level.

plexes **3** and **4**, which indicates that the palladium coordination spheres in these two complexes have significant tetrahedral distortions. The other structural features of complexes **3** and **4**, including conformation of the palladacycle and oxazoline rings, are similar to those of **2**.

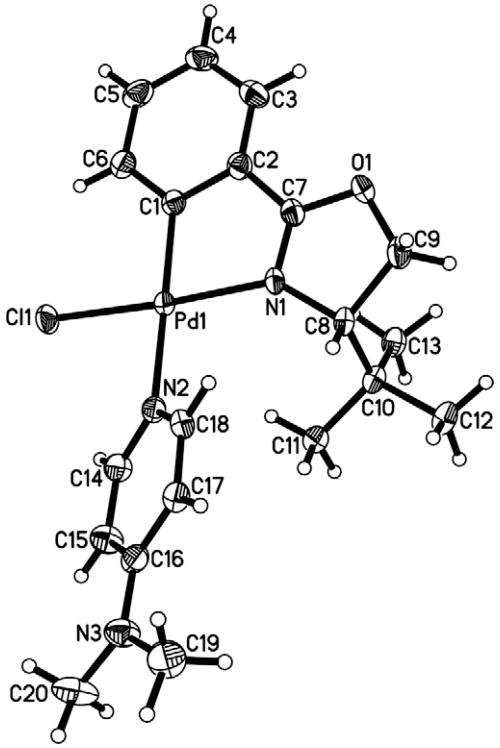


Fig. 3. Molecular structure of complex **4** showing the atom numbering. Displacement parameters are shown at the 50% level.

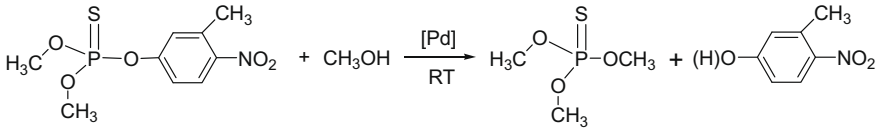
A question that might arise is "why complexes **3** and **4** have *N,N-cis* configuration while complex **2** has *N,N-trans* configuration?" The effects from electronic and steric factors of the mono-dentate pyridine ligands can be excluded, since all of three pyridine derivatives have almost the same sizes, and 4-dimethylamino- and 4-trifluoromethyl-substituent groups show opposite electronic effects. From NMR studies (see below), the majority coordination conformation is *N,N-trans* for all of three complexes. So for **2**, the molecular structure in the crystal is consistent with that in solution, while it may be that the thermodynamically stable *trans* isomers of **3** and **4** give way to a *cis* configuration in the solid state due to the more thermodynamically stable isomers in solution crystallizing out to form **3** and **4**. It can also be due to the stable packing of *tert*-butyloxazoline substituted palladacycle **4** *cis*-isomer during the crystallization, since the space group for **4** is $P2_12_12_1$, while the *iso*-propyl substituted (*S*)-chloro{2-[2-(4-*iso*-propyll)oxazolinyl]phenyl-*C,N*}(4-*N,N*-dimethylamino-pyridine)palladium(II) has a space group of $P2_1$ [22]. However the mechanism of how *trans* configuration in liquid state converts to *cis* isomer in solid state is still not clear from our knowledge.

To avoid the situation that the structure of **4** is due to the specific crystal sample, so eight more crystal samples were chosen to measure the cell parameters (see Supplementary data Table S1). It proved the cell parameters of all samples measured fall in the permitted error.

Furthermore XRD method was used to measure the powered sample of compound **4**. The result (see Supplementary data Table S2) indicated that the structure of **4** in the solid state is almost consistent with that from the X-ray single crystal analysis.

2.1.1. ^{1}H NMR spectra of complexes 2–4

For the palladacycle complexes with monodentate ligands, both *cis* and *trans* coordination isomers are observed in solution by NMR. The ^{1}H NMR spectra of **2**–**4** were recorded in $CDCl_3$, and



Scheme 2.

Table 3
Concentration dependence for the pseudo first-order rate constant of methanolysis of **5** promoted by **2–4** and corrected for buffer effects at [**5**] = 2.84×10^{-5} mol dm^{-3}, $^{s}_{s}$pH 10.80, triethylamine buffer, 25 °C.

[Pd] (mol dm^{-3}) × 10^5	k^{obs} (s^{-1} × 10)[a,b]		
	2	**3**	**4**
8.0	0.231 ± 0.008	1.53 ± 0.01	0.032 ± 0.001
6.0	0.227 ± 0.008	1.28 ± 0.05	0.0218 ± 0.0009
4.0	0.20 ± 0.01	0.93 ± 0.03	0.0170 ± 0.0007
2.0	0.141 ± 0.005	0.55 ± 0.03	0.0097 ± 0.0005
1.0	0.081 ± 0.003	0.32 ± 0.02	0.0053 ± 0.0002
0.5	0.0227 ± 0.008	0.101 ± 0.008	0.0023 ± 0.0001

[a] Rate constants determined at three different [buffer] from (1–3) × 10^{-3} mol dm^{-3}, and average values were used.
[b] Errors are calculated from standard deviation of the mean.

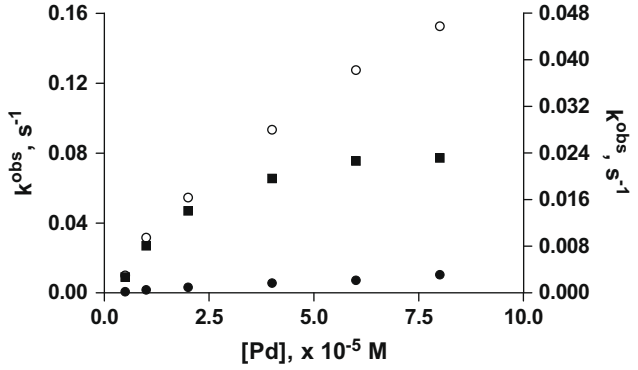


Fig. 4. Plot of k^{obs} vs. [Pd] for the methanolysis of **5** (2.84×10^{-5} M) at 25 °C, buffer triethylamine (1–3) × 10^{-3} M, $^{s}_{s}$pH 10.80. k^{obs} values of **2** (■) and **4** (●) are corresponding to the right *Y* axis, k^{obs} of **3** (○) is corresponding to the left *Y* axis.

showed the typical features of the *N,N-trans* conformation at first glance. The proton H^6 of the palladacycle ring is shifted upfield to δ 6.23, 6.21 and 6.44 ppm, respectively, for **2**–**4**. It is well known that the upfield shift of H^6 results from the shielding of pyridine ring which is at the *trans* position to the nitrogen in the palladacycle ligand and non-planar to phenyl ring [20]. Thus the palladium coordination geometry of palladacycle **3** and **4** in solution is quite different from those in crystal structures. Even using dissolved crystals of **3** and **4** in $CDCl_3$, the ^{1}H NMR spectra immediately showed the presence of upfield H^6 protons. For **4**, the chemical shift of the H^6 proton is almost the same as that in [Pd{C_6H_4C(Me)=NOH}(4-Me_2N-py)Cl], which exhibits *N,N-trans* conformation in solid state [20]. Thus the majority coordination conformation of palladacycle **4** in solution is *N,N-trans*. The detailed NMR spectra of **2**–**4** in different solvents such as CD_3OD, at different pH, and at different temperatures are undertaking and will be reported together with other palladacycles.

2.1.2. Catalytic activity

Preliminary work on methanolysis of the P=S pesticide fenitrothion **5** catalyzed by palladcycles **2**–**4** was investigated under buffered conditions (1–3 mM triethylamine, $^{s}_{s}$pH 10.80, *T* = 25 °C) (see Scheme 2). The concentration dependences of the methanolysis are listed in Table 3. It should be noticed that $^{s}_{s}$pH for neutral methanol is 8.4 [18], thus the $^{s}_{s}$pH 10.80 is not very strong basic in methanol.

All three palladacyles exhibit good catalytic activity but showed different concentration dependences (Fig. 4). Palladacyle **3** shows the highest activity with $k_2 = (2.2 \pm 0.1) \times 10^3$ M^{-1} s^{-1}, showing a little curvature at higher concentration. Compound **2** shows some saturation at the higher concentrations of the catalyst, while **4** shows good linearity but is the least active catalyst with a $k_2 = (0.039 \pm 0.001) \times 10^3$ M^{-1} s^{-1}. It can be seen that through

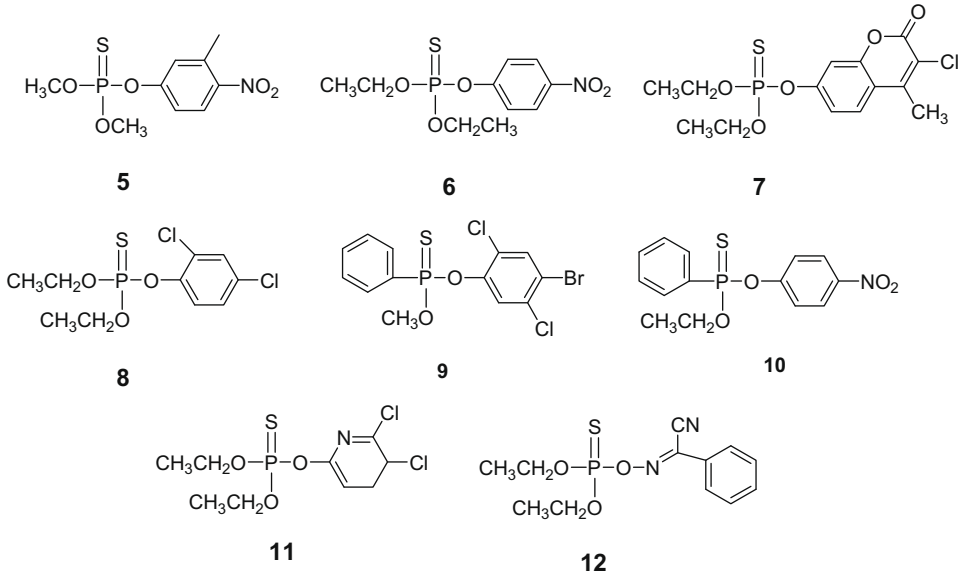


Fig. 5. Structures of the pesticides investigated in the catalytic methanolysis.

Table 4
Turnover experiments for the methanolysis of different phosphorothioate esters catalyzed by **2** at 0.05 M TEA, pH 10.80, 25 °C and ^{31}P NMR data of the substrates and product.

Phosphorothioate esters (mol dm^{-3})		TON	k^{obs} (s^{-1})	k_2^{obs} (dm^3 mol^{-1} s^{-1})	^{31}P NMR (δ/ppm)	
					Substrate	Product
5	2.0×10^{-3}	40[a]	$(2.0 \pm 0.3) \times 10^{-3}$	40.0	66.18	73.19
6	2.0×10^{-3}	40[a]	$(2.10 \pm 0.1) \times 10^{-3}$	42.0	66.18	69.60
7	3.9×10^{-3}	78[a]	$(2.53 \pm 0.3) \times 10^{-4}$	5.06	62.73	69.63
8	2.0×10^{-3}	40[a]	1.2×10^{-2}	240	63.29	69.63
9	2.6×10^{-4}	5.2[a]	3.22×10^{-2}	644	85.37	88.57
10	2.6×10^{-4}	5.2[a]	2.83×10^{-2}	566	88.85	90.92
11	5.0×10^{-4}	10[b]	$(4.3 \pm 0.3) \times 10^{-4}$	1.7	61.14	69.63
12	1.0×10^{-3}	20[a]	$(7.1 \pm 0.3) \times 10^{-2}$	284	68.45	69.63

[a] [**2**] = 5.0×10^{-5} mol dm^{-3}.
[b] [**2**] = 2.5×10^{-4} mol dm^{-3}.

changing the electronic property of the substituent on mono-dentate pyridine ligand, the activity of the palladacycles can be greatly modified (the activity of **3** is about 56 times of that of **4**).

The activity of **3** is comparable to those of palladacycles in hydrolysis of pesticides reported by Kazankov, Ryabov [13] and Gabbaie [14]. At 0.01 mM of palladacycle catalysts and $^{s}_{s}$pH 10.80, the $\tau_{1/2}$ of the decomposition of fenitrothion with **2**–**4** is 8.6, 2.2, and 130s, respectively, which afforded the acceleration by 7.7×10^6–4.5×10^8 folds compared to the methoxide catalyzed background reaction ($\tau_{1/2} \approx 10^9$ s) [18].

At the optimized condition, triethylamine buffer $^{s}_{s}$pH 10.80, T = 25 °C, the reactivity of **2** to the decomposition of different thiophosphates (Fig. 5) were screened with turnover numbers (see Table 4). The final products were confirmed with ^{1}H and ^{31}P NMR spectra. We tried to use the chiral palladacycles for the asymmetric methanolysis. It was found that the alkoholysis kinetics of racemic thiophosphates letophos **9** and EPN **10** by **2** are strictly first order, showing no evidence of any kinetically significant chiral discrimination under the experimental conditions.

3. Conclusion

Cleavage of the chloro-bridge in cyclopalladated dimer complex of (*S*)-4-*tert*-butyl-2-phenyl-2-oxazoline by different pyridine derivatives resulted in high yields of three mononuclear palladacycles: (*S*)-chloro{2-[2-(4-*tert*-butyl)oxazolinyl]phenyl-*C*,*N*}(4-R-pyridine)palladium(II) (R = H, **2**, R = CF_3, **3**; R = $N(CH_3)_2$, **4**). In the solid state, the palladacycle containing the pyridine ligand (**2**) exhibits a commonly observed *N*,*N*-*trans* conformation in the palladium(II) coordination sphere, while **3** and **4** show the uncommon *N*,*N*-*cis*-conformation. In solution, the majority conformation isomers are *N*,*N*-*trans* for three palladacycles. The catalytic effect of **2**–**4** in promoting the methanolysis of fenitrothion is related to the electronic properties of the substituents on pyridine ring, with the highest activity with the CF_3 derivative, followed by pyridine and then the dimethylamino group. At 0.01 mol dm^{-3} of **3** at $^{s}_{s}$pH 10.80 gives a $\tau_{1/2}$ = 2.2 s for methanolysis of **5**, which corresponds to 4.0×10^8-fold acceleration compared to the background reaction. The large accelerations provided to the decomposition of P═S pesticides by these and other easily prepared palladacycles including pincer ligands are under active investigation for the eventual development of efficient methods of decomposing P═S pesticides.

4. Experimental

4.1. Materials and methods

All organometallic syntheses were performed in a dried argon atmosphere. Solvents were dried by standard methods. The ligand, (*S*)-4-*tert*-butyl-2-phenyl-2-oxazoline, and corresponding chloro-bridged palladacycle dimer **1** were prepared as described [21] and were characterized by ^{1}H NMR. Pyridine, 4-trifluromethylpyridine, *N*,*N*-dimethylaminopyridine, and methanol (99.8% anhydrous) were purchased from Aldrich and used without further purification. $HClO_4$ (70% aqueous solution) was obtained from BDH.

Fenitrothion (**5**, *O*,*O*-dimethyl *O*-(3-methyl-4-nitrophenyl) phosphorothioate), parathion (**6**, *O*,*O*-diethyl *O*-(4-nitrophenyl) phosphorothioate), coumaphos (**7**, *O*-(3-chloro-4-methyl-2-oxo-2H-chromen-7-yl) *O*,*O*-diethyl phosphorothioate), dichlofenthion (**8**, *O*,*O*-diethyl-*O*-(2,4-dichlorophenyl) phosphorothioate), letophos (**9**, O-4-bromo-2,5-dichlorophenyl *O*-methyl phenylphosphonothioate), and EPN (**10**, *O*-ethyl *O*-4-nitrophenyl phenylphosphorothioate), were purchased from Chem Service Inc. Chlorpyrifos (**11**, *O*,*O*-diethyl-*O*-[3,5,6-trichloro-2-pyridyl]-phosphorothiate) and phoxim (**12**, α-[[(diethoxyphosphinthioyl) zoxy]imino]benzene-acetonitrile) are gifts, obtained from Beijing Yoloo Pesticide Company Ltd., China. All structures of these pesticides are given in Fig. 5.

Caution: All the phosphorus substrates described herein are acetylcholinesterase inhibitors, for compounds **5**–**12** with oral LD50 values of 250, 2, 16, 270, 43, 8, 82, and 300 mg kg^{-1} in rats [24], respectively. The preparations of compounds **2**–**4** require the use of benzene which should be handle with care.

^{1}H NMR spectra were determined at 400 MHz using a Bruker Avance-400 NMR spectrometer. In $CDCl_3$, ^{1}H NMR spectra were referenced to the C**H**Cl_3 peak at 7.25 ppm. ^{31}P NMR spectra were referenced to an external standard of 70% phosphoric acid in water, and up-field chemical shifts are negative. Mass-spectra were determined using a VG Quattro mass spectrophotometer equipped with an electrospray source. IR spectra were obtained on NaBr pellets and melting points were measured on a Fisher–Johns melting point apparatus.

4.1.1. Preparation of the complexes ***2–4***

4.1.1.1 General procedure. To a solution of 118 mg (0.172 mmol) of dimers **1** in benzene (20 ml) was added pyridine or a substituted pyridine (0.38 mmol, 2.2 eq.). The mixture was stirred at room temperature for 3 h and then filtered through Celite. The Celite was washed with another 20 ml of dichloromethane and the combined organic layers stripped of solvent by rotary evaporation under reduced pressure. The pale white solid residue was re-crystallized from a mixture of hexane and dichloromethane (ratio 5:1) to afford the desired compounds, yields are 76%, 80%, and 86%, respectively.

(S)-chloro{2-[2-(4-tert-butyl)oxazolinyl]phenyl-C,N}(pyridine)palladium(II) ***2***: IR (KBr, cm^{-1}): 3044 (m), 2961 (m), 2922 (m), 1618 (vs), 1589 (s), 1569 (s), 1480(s), 1447 (s), 1399 (vs), 1249 (s), 1136 (vs), 1094 (m), 919 (s), 762 (vs), 726 (vs), 694 (vs), 673 (s). m.p.: 240 °C.

^{1}H NMR (ppm, 400 MHz, $CDCl_3$): δ 8.91 (d, J = 8.0 Hz, $H^{2'}$, $H^{6'}$), 7.84 (m, $H^{4'}$), 7.43 (t, J = 6.0 Hz, $H^{3'}$, $H^{5'}$), 7.25 and 7.03 (m, H^3, H^4, H^5), 6.23 (d, J = 8.0 Hz, H^6), 4.77 (dd, J = 16 Hz, 4.0 Hz, OCH), 4.53 (t, J = 12 Hz, OCH), 4.20 (dd, J = 16 Hz and 4.0 Hz, NCH), 1.08 (s, $C(CH_3)_3$). MS (FAB): m/z 387.7 (M−Cl).

Anal. Calc. for $C_{18}H_{21}ClN_2OPd$ (Fw: 423.04): C, 51.06; H, 5.00; N, 8.38. Found: C, 51.36; H, 5.30; N, 8.08%.

(S)-chloro{2-[2-(4-tert-butyl)oxazolinyl]phenyl-C,N}(4-trifluromethylpyridine)palladium(II) ***3***: IR (KBr, cm^{-1}): 2959 (m), 1620 (vs), 1572(s), 1479(s), 1401(s), 1324 (m), 1254 (s), 1139 (s), 1096 (m), 1034 (m), 917 (s), 732 (s). m.p.: 235 °C.

^{1}H NMR (ppm, 400 MHz, $CDCl_3$): δ 9.14 (d, J = 8.0 Hz, $H^{2'}$ and $H^{6'}$), 7.65 (d, J = 8.0 Hz, $H^{3'}$ and $H^{5'}$), 7.27 and 7.04 (m, H^3, H^4 and H^5), 6.21 (d, J = 8 Hz, H^6), 4.74 (dd, J = 8.0 Hz, OCH), 4.53 (t, J = 8.0 Hz, OCH), 4.14 (dd, J = 8.0 Hz, NCH), 1.06 (s, $C(CH_3)_3$). ^{19}F NMR (ppm, 376.47 MHz, $CDCl_3$): δ −67.7. MS (FAB): m/z 455.78 (M−Cl).

Anal. Calc. for $C_{19}H_{20}ClF_3N_2OPd$ (Fw: 491.23): C, 46.41; H, 4.10; N, 5.70. Found: C, 46.21; H, 4.30; N, 5.35%.

(S)-chloro{2-[2-(4-tert-butyl)oxazolinyl]phenyl-C,N}(4-N,N-dimethylaminopyridine)palladium(II) ***4***: IR (KBr, cm^{-1}): 2961 (m), 2868 (m), 1619 (vs), 1534(s), 1460(s), 1397(s), 1386 (s), 1224 (s), 1135 (m), 1015 (s), 806 (s), 733 (s), 672 (m), 533 (m). m.p.: 226 °C (decomp.).

^{1}H NMR (ppm, 400 MHz, $CDCl_3$): δ 8.34 (d, J = 8.0 Hz, $H^{2'}$ and $H^{6'}$), 7.21 and 7.02 (m, H^3, H^4 and H^5), 6.50 (d, J = 8.0 Hz, $H^{3'}$ and $H^{5'}$), 6.44 (d, J = 8.0 Hz, H^6), 4.70 (dd, J = 8.0 Hz, OCH), 4.49 (t, J = 8.0 Hz, OCH), 4.15 (dd, J = 8.0 Hz and 4.0 Hz), 3.05 (s, 6H), 1.07 (s, 9H). MS (FAB): m/z 430.84 (M−Cl).

Anal. Calc. for $C_{20}H_{26}ClN_3OPd$ (Fw: 466.30): C, 51.52; H, 5.62; N, 9.01. Found: C, 51.32; H, 5.42; N, 8.70%.

4.1.2. X-ray crystal structure determination

Crystals suitable for diffraction measurements were prepared by diffusing *n*-hexane into a dichloromethane solution of the complex at room temperature.

Data collection of **2** was performed on a Bruker SMART CCD 1000 X-ray diffractometer and data were processed using the Bruker AXS Crystal Structure Analysis Package, Version 5.10 [25]. Neutral atom scattering factors were taken from Cromer and Waber [26]. The raw intensity data were integrated using the program SAINT-PLUS, which corrects for Lp and decay. Absorption corrections were applied using the program SADABS [27].

For **3** and **4**, data collection: APEX2 [28]; cell refinement: APEX2; data reduction: SAINT [28], programs used to solve structure: SHELXTL [29]; programs used to refine structure: SHELXTL; molecular graphics: SHELXTL, software prepare materials for publication: SHELTXL and PLATON [30]. Full structural details for each complex are given as Supplementary data.

*4.1.3. Catalytic methanolysis of fenitrothion (**5**) mediated by complexes **2–4***

The kinetics of decomposition of P═S pesticides were performed in methanol at the buffered condition, the detailed procedure was described in Ref. [19]. The concentration dependences for the methanolysis of **5** promoted by **2–4** were monitored using an OLIS-modified Cary 17 UV–Vis spectrophotometer (see Table 3 and Fig. 4). The plots of the k^{obs} values versus [Pd] indicate that these concentration dependent curves (see Fig. 4). The catalytic turnover experiments were performed for other P═S pesticides at the optimized condition (^s_spH 10.80, Table 4).

Acknowledgements

The authors gratefully acknowledge the financial assistance of Beijing Normal University, (107026), Beijing Municipal Commission of Education, and the Scientific Research Foundation for the Returned Overseas Chinese Scholars (213006), State Education of Ministry, China, and the Malaysian Government and Universiti Sains Malaysia for Research University Golden Goose Grant No. 1001/PFIZIK/811012. The authors thank the kind support and helpful discussion from Prof. R.S. Brown at Queen's University. The XRD data of 2 were measured by Prof. Xiao-Jing Yang at Beijing Normal University.

Appendix A. Supplementary data

CCDC 661287, 660754, and 660755 contain the supplementary crystallographic data for **2**, **3** and **4**, respectively. These data can be obtained free of charge via http://www.ccdc.cam.ac.uk/conts/retrieving.html, or from the Cambridge Crystallographic Data Centre, 12 Union Road, Cambridge CB2 1EZ, UK; fax: (+44) 1223-336-033; or e-mail: deposit@ccdc.cam.ac.uk. Supplementary data associated with this article can be found, in the online version, at doi:10.1016/j.poly.2009.05.030.

References

[1] A.A. Cope, R.W. Siekman, J. Am. Chem. Soc. 87 (1965) 3272.
[2] A.A. Cope, E.C. Friedrich, J. Am. Chem. Soc. 90 (1968) 909.
[3] J. Dupont, C.S. Consorti, J. Spencer, Chem. Rev. 105 (2005) 2527.
[4] W.A. Herrmann, V.P.W. Bohm, C.P. Reisinger, J. Organomet. Chem. 576 (1999) 23.
[5] I. Omae, Coord. Chem. Rev. 248 (2004) 995.
[6] J.T. Singleton, Tetrahedron 59 (2003) 1837.
[7] I.P. Beletskaya, A.V. Cheprakov, J. Organomet. Chem. 689 (2004) 4055.
[8] R.B. Bedford, C.S.J. Cazin, D. Hold, Coord. Chem. Rev. 248 (2004) 2283.
[9] M. Albrecht, G. van Koten, Angew. Chem., Int. Ed. 40 (2001) 3750.
[10] V.I. Sokolov, Pure Appl. Chem. 55 (1983) 1837.
[11] J.-Y. Li, Y.-J. Wu, Z.-X. Han, S. Jiang, Gaodeng Xuexiao Huaxue Xuebao 29 (2008) 1555.
[12] J.-Y. Li, A.J. Yu, Y.-J. Wu, Y. Zhu, C.-X. Du, H.-W. Yang, 26 (2007) 2629.
[13] G.M. Kazankov, V.S. Sergeeva, E.N. Efremenko, L. Alexandrova, S.D. Varfolomeev, A.D. Ryabov, Angew. Chem., Int. Ed. 39 (2000) 3117.
[14] M. Kim, A. Picot, F.P. Gabbaie, Inorg. Chem. 45 (2006) 5600.
[15] J.C. Tao, J. Jia, X.W. Wang, S.T. Zang, Chin. Chem. Lett. 13 (2002) 1170.
[16] J.S. Tsang, A.A. Neverov, R.S. Brown, J. Am. Chem. Soc. 125 (2003) 7602.
[17] J.S.W. Tsang, A.A. Neverov, R.S. Brown, Org. Biomol. Chem. 2 (2004) 3457.
[18] A.A. Neverov, R.S. Brown, Org. Biomol. Chem. 2 (2004) 2245.
[19] Z.L. Lu, A.A. Neverov, R.S. Brown, Org. Biomol. Chem. 3 (2005) 3379.
[20] A.D. Ryabov, G.M. Kazankov, A.K. Yatsimirsky, L.G. Kuz'mina, O.Y. Burtseva, N.V. Vvortsova, V.A. Polyakov, Inorg. Chem. 31 (1992) 3083.
[21] D.L. Peterson, K.J. Keuseman, N.A. Kataeva, L.G. Kuz'mina, J.A.K. Howard, V.V. Dunina, I.P. Smoliakova, J. Organomet. Chem. 654 (2002) 66.
[22] H.-M. Li, J.-G. Su, Z.-L. Lu, H.-K. Fun, S. Chantrapromma, Inorg. Chem. Commun. 11 (2008) 235.
[23] M. Pfeffer, N. Sutter-Beydoun, A. De Cian, J. Fisher, J. Organomet. Chem. 453 (1993) 139.
[24] M.E. van der Boom, D. Milstein, Chem. Rev. 103 (2003) 1759.
[25] Brucker, AXS Crystal Structure analysis Package Version 5.10 (SMART NT (Version 5.053), SAINT-PLUS (Version 6.01), SHELXTL (Version 5.1), Brucker AXS Inc., Madision, WI, USA, 1999.
[26] D.T. Cromer, J.T. Waber, International Tables for X-Ray Crystallography, Kynoch Press, Birmingham, UK, 1974.
[27] G.M. Sheldick, SADABS, Program for Area Detector Adsorption Correction, Institute of Inorganic Chemistry, University of Goettingen, Germany, 1996.
[28] Bruker, APEX2 (Version 1.27), SAINT (Version 7.12A) and SADABS (Version 2004/1), Bruker AXS Inc., Madison, Wisconsin, USA, 2005.
[29] G.M. Sheldrick, Acta Cryst. A64 (2008) 112.
[30] A.L. Spek, Acta Cryst. D65 (2009) 148.

Polyhedron 28 (2009) 2571–2578

Contents lists available at ScienceDirect

Polyhedron

journal homepage: www.elsevier.com/locate/poly

Synthesis, spectroscopic characterization, X-ray structure and DFT calculations of $[Re(CO)_3L_2Cl]$ (L = 1,2,4-triazolo-[1,5-a]pyrimidine)

B. Machura [a,*], M. Jaworska [b], P. Lodowski [b], J. Kusz [c], R. Kruszynski [d], Z. Mazurak [e]

[a] Department of Crystallography, Institute of Chemistry, University of Silesia, 9th Szkolna St., 40-006 Katowice, Poland
[b] Department of Theoretical Chemistry, Institute of Chemistry, University of Silesia, 9th Szkolna St., 40-006 Katowice, Poland
[c] Institute of Physics, University of Silesia, 4th Uniwersytecka St., 40-006 Katowice, Poland
[d] Department of X-ray Crystallography and Crystal Chemistry, Institute of General and Ecological Chemistry, Lodz University of Technology, 116 Żeromski St., 90-924 Łódź, Poland
[e] Polish Academy of Sciences, Centre of Polymer Chemistry, M. Sklodowskiej-Curie 34, Zabrze 41-819, Poland

ARTICLE INFO

Article history:
Received 17 April 2009
Accepted 12 May 2009
Available online 19 May 2009

Keywords:
Rhenium(I) carbonyl complexes
1,2,4-Triazolo-[1,5-a]pyrimidine
X-ray structure
Absorption and emission spectra
DFT and TDDFT calculations

ABSTRACT

The paper presents a combined experimental and computational study of novel tricarbonyl complex – *fac*-$[Re(CO)_3(tp)_2Cl]$ (tp = 1,2,4-triazolo-[1,5-a]pyrimidine). The compound has been characterized spectroscopically and structurally (by single-crystal X-ray diffraction). The absorption and emission spectra of the complex have been discussed on the basis of DFT and time-dependent (TD)DFT calculations.

© 2009 Elsevier Ltd. All rights reserved.

1. Introduction

The d^6 transition metal complexes with heteroaromatic ligands have been the subject of intense investigations for many years. The interest of researches has been attracted mostly by their unique photophysical and photochemical properties, crucial for numerous potential and already introduced practical applications. The most frequently studied compounds of this type are complexes containing the $Re(CO)_3^+$ fragment. The photobehaviour of such complexes may be discussed in terms of three types of excited states: (i) metal-to-ligand charge transfer (MLCT) states, (ii) ligand-to-ligand charge transfer (LLCT) states, (iii) intraligand (IL) states. The latter one appears to lie at rather high energies in these complexes, and they are of little photochemical importance. The excited states of these compounds are often sufficiently long-lived to become engaged in energy transfer reactions. Currently, several *fac*-$Re(CO)_3^+$ complexes are used as electroluminescent materials in OLED-type devices [1–12].

Furthermore, the excited states of the discussed complexes may be both strong reductants and oxidants. The high reactivity of the reduced species may be utilized in photocatalysis. For example, photoexcitation of $[Re(CO)_3(bipy)Cl]$ in the presence of triethylamine produces $[Re(CO)_3(bipy)Cl]^-$ which loses the chloride ligand. The further reaction with CO_2 results in the photocatalytic CO_2 reduction to CO [10].

The recent application of the *fac*-$Re(CO)_3^+$ complexes as diagnostic and therapeutic radiopharmaceuticals has resulted in an added increase in the interest of this group compounds [11,12].

Here, we present the synthesis, spectroscopic characterization, crystal and molecular structure of the $[Re(CO)_3(tp)_2Cl]$ tricarbonyl with 1,2,4-triazolo-[1,5-a]pyrimidine (tp).

The basic skeleton of 1,2,4-triazolo-[1,5-a]pyrimidine differs from the purine ring in having a pyrimidine nitrogen atom in a bridgehead position with disappearance of the acidic H-proton of the five-membered ring. Because of the similarity of both systems, coordination compounds of 1,2,4-triazolo-[1,5-a]pyrimidine and its derivatives can be considered as model systems for various naturally occurring metal coordination compounds. Complexes with bidentately coordinated 1,2,4-triazolo-[1,5-a]pyrimidine can act as model systems for adenine, whereas compounds with bridging 1,2,4-triazolo-[1,5-a]pyrimidine are specially suited for mimicking imidazolato bridges in model compounds for metalloproteins [13].

2. Experimental

2.1. General procedure

The reaction was performed under an argon atmosphere. The solvents were dried before use, using the appropriate drying

* Corresponding author.
E-mail addresses: basia@ich.us.edu.pl (B. Machura), mj@tc3.ich.us.edu.pl (M. Jaworska), rafal.kruszynski@p.lodz.pl (R. Kruszynski).

0277-5387/$ - see front matter © 2009 Elsevier Ltd. All rights reserved.
doi:10.1016/j.poly.2009.05.025

Table 1
Crystal data and structure refinement for $[Re(CO)_3(tp)_2Cl]$.

Empirical formula	$C_{13}H_8ClN_8O_3Re$
Formula weight	545.92
Temperature	200.0(3) K
Wavelength	0.71073 Å
Crystal system	monoclinic
Space group	$P2_1/n$
Unit cell dimensions	a = 6.7555(3) Å
	b = 16.7250(8) Å; β = 100.534(4)°
	c = 15.3266(8) Å
V	1702.50(14) Å^3
Z	4
$D_{calc.}$	2.130 Mg/m^3
Absorption coefficient	7.327 mm^{-1}
F(0 0 0)	1032
Crystal size	0.02 × 0.06 × 0.20 mm
θ range for data collection	2.97 to 25.05°
Index ranges	$-5 \leqslant h \leqslant 8$
	$-19 \leqslant k \leqslant 19$
	$-18 \leqslant l \leqslant 18$
Reflections collected	10611
Independent reflections	3007 [R(int) = 0.0291]
Completeness to 2θ	99.8%
Data/restraints/parameters	3007/0/235
Goodness of fit (GOF) on F^2	0.957
Final R indices [$I > 2\sigma(I)$]	R_1 = 0.0160
	wR_2 = 0.0321
R indices (all data)	R_1 = 0.0233
	wR_2 = 0.0327
Largest differential peak and hole	1.009 and −0.620 e Å^{-3}

reagents. $Re(CO)_5Cl$ and 1,2,4-triazolo-[1,5-a]pyrimidine (tp) were purchased from Aldrich, and used as received.

The IR spectrum was recorded on a Nicolet Magna 560 spectrophotometer in the spectral range 4000–400 cm^{-1} with the samples in the form of KBr pellets. The electronic spectrum was measured on a spectrophotometer Lab Alliance UV–Vis 8500 in the range 1000–200 nm in dichloromethane solution. Elemental analyses (C H N) were performed on a Perkin–Elmer CHN-2400 analyzer. Luminescence measurements were made on a Jobin-Yvon (SPEX) FLUOROLOG-3.12 spectrofluorometer at room temperature.

2.2. Preparation of $[Re(CO)_3(tp)_2Cl]$

$Re(CO)_5Cl$ (0.2 g, 0.55 mmol) and 1,2,4-triazolo-[1,5-a]pyrimidine (0.14 g, 1.16 mmol) in toluene (80 ml) were refluxed for 6 h. The resulting reaction mixture was allowed to cool to room temperature and reduced in volume to ~10 ml. The white solid was filtered off, washed with hexane, diethyl ether, and dried; yield 85%. Single crystals of complex $[Re(CO)_3(tp)_2Cl]$ were grown by the slow diffusion of diethyl ether into a solution of the complex dissolved in dichloromethane.

IR (KBr, cm^{-1}): ν_{CO} = 2019, 1907 and 1882 cm^{-1}; ν_{CN} and $\nu_{C=C}$ = 1621, 1532 and 1527 cm^{-1}. *Anal.* Calc. for $C_{13}H_8ClN_8O_3Re$: C, 28.60; H, 1.48; N, 20.53. Found: C, 28.16; H, 1.60; N, 20.95%.

2.3. Crystal structure determination and refinement

The crystal of $[Re(CO)_3(tp)_2Cl]$ was mounted on a KM-4-CCD automatic diffractometer equipped with a CCD detector, and used for data collection. X-ray intensity data were collected with graphite monochromated Mo Kα radiation (λ = 0.71073 Å) at temperature of 200.0(3) K, with ω scan mode. Details concerning crystal data and refinement are given in Table 1. Lorentz, polarization and empirical absorption correction using spherical harmonics implemented in SCALE3 ABSPACK scaling algorithm [14] were applied. The structure was solved by the Patterson method and subsequently completed by the difference Fourier recycling. All the non-hydrogen atoms were refined anisotropically using full-matrix, least-squares technique. The hydrogen atoms were found from difference Fourier synthesis and were refines as "riding" on their parent carbon atoms [d(C–H) = 0.93 Å] and assigned isotropic temperature factors equal 1.2 times the value of equivalent temperature factor of the parent carbon atom. SHELXS97 [15], SHELXL97 [16] and SHELXTL [17] programs were used for all the calculations. Atomic scattering factors were those incorporated in the computer programs.

2.4. Computational details

All calculations have been performed using the GAUSSIAN 03 [18] and TURBOMOLE [19] programs for electronic structure calculations. The geometry of the singlet ground state and the lowest triplet state of $[Re(CO)_3(tp)_2Cl]$ was optimized with the DFT method. The electronic spectrum was calculated with the TDDFT method [20]. The vertical excitation energies, together with the corresponding oscillator strengths, were calculated at the optimized structure of the ground electronic singlet and triplet states of the $[Re(CO)_3(tp)_2Cl]$. The calculations were carried out using hybrid B3LYP functional [21,22]. In the calculations the solvent effect was simulated using the polarizable continuum model (PCM) [23–26] and the Conductor-like Screening Model (COSMO) [27] with dichloromethane as solvent. The first of them was used in the GAUSSIAN calculations and the second one in the TURBOMOLE calculations. Two different basis sets have been used. The basis depicted as B1 consists of ECP LANL2DZ [28] basis set for rhenium with an additional d and f function with the exponent α = 0.3811 and α = 2.033 [29], respectively and B2 consists of ECP MWB60 [30] with an one additional f function with the exponent α = 0.48989. These basis sets were used in conjunction with the standard 6-31 + G** basis set for chloride, oxygen, carbon and nitrogen atoms [31–36] and the standard 6-31G basis set for hydrogen. The geometry of the several singlet and triplet excited states were optimized using TDDFT/B3LYP level of theory in the B2 basis. In the case of excited state geometry optimization the TURBOMOLE program was used.

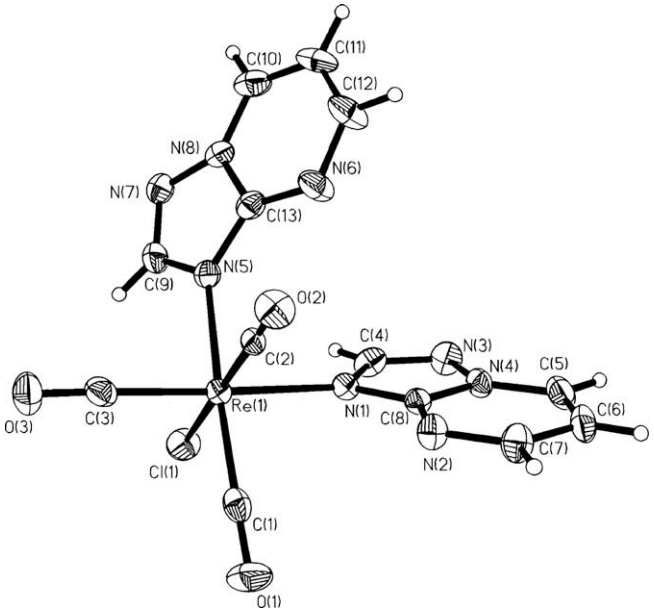


Fig. 1. Molecular structure of $[Re(CO)_3(tp)_2Cl]$.

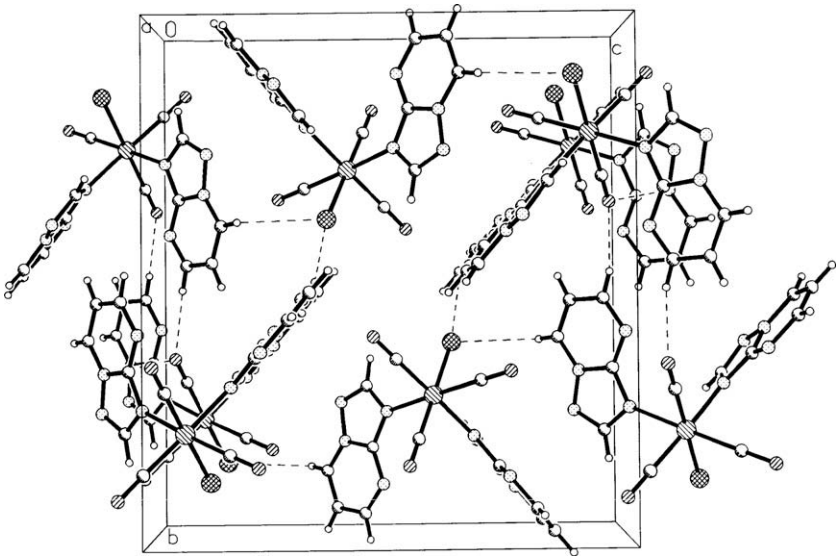


Fig. 2. Part of the molecular packing of the title compound, showing the intermolecular hydrogen bonds creating a net structure. Hydrogen bonds are indicated by dashed lines.

Table 2
The experimental and optimized bond lengths [Å] and angles [°] for $[Re(CO)_3(tp)_2Cl]$.

	Experimental	Optimized			Experimental	Optimized	
		B1	B2			B1	B2
Bond lengths				*Bond angles*			
Re(1)–C(1)	1.924(3)	1.921	1.925	C(2)–Re(1)–C(1)	90.13(13)	90.74	89.87
Re(1)–C(2)	1.893(3)	1.915	1.918	C(2)–Re(1)–C(3)	88.49(13)	90.30	89.47
Re(1)–C(3)	1.913(3)	1.918	1.924	C(3)–Re(1)–C(1)	91.05(13)	90.22	89.65
Re(1)–Cl(1)	2.4908(8)	2.546	2.544	C(1)–Re(1)–N(1)	91.20(11)	92.25	93.16
Re(1)–N(1)	2.191(2)	2.248	2.239	C(2)–Re(1)–N(1)	91.75(11)	93.86	93.93
Re(1)–N(5)	2.197(2)	2.256	2.248	C(3)–Re(1)–N(1)	177.74(11)	175.13	175.60
C(1)–O(1)	1.157(4)	1.161	1.166	N(1)–Re(1)–N(5)	84.08(9)	85.31	84.31
C(2)–O(2)	1.158(4)	1.166	1.168	N(1)–Re(1)–Cl(1)	86.15(7)	84.18	84.71
C(3)–O(3)	1.159(4)	1.162	1.167	C(1)–Re(1)–Cl(1)	92.28(9)	92.98	92.54
				C(2)–Re(1)–Cl(1)	176.84(9)	175.86	177.29
				C(3)–Re(1)–Cl(1)	93.52(10)	91.51	91.78
				C(1)–Re(1)–N(5)	173.94(11)	175.41	176.12
				C(2)–Re(1)–N(5)	93.81(11)	93.30	93.24
				C(3)–Re(1)–N(5)	93.66(11)	91.94	92.71
				N(5)–Re(1)–Cl(1)	83.63(7)	82.92	84.30
				O(1)–C(1)–Re(1)	178.1(3)	179.31	179.74
				O(2)–C(2)–Re(1)	178.4(3)	178.24	177.47
				O(3)–C(3)–Re(1)	178.7(3)	179.15	179.75

3. Results and discussion

3.1. Preparation and infrared data

The title complex was prepared by refluxing of $[Re(CO)_5Cl]$ with 1,2,4-triazolo-[1,5-a]pyrimidine in toluene. It was isolated as air-stable, microcrystalline solid, soluble in common organic solvents. The infrared spectrum of $[Re(CO)_3(tp)_2Cl]$ displays three bands in the carbonyl stretching region: a sharp intense band at 2019 cm^{-1} and two lower-energy bands 1907 and 1882 cm^{-1}. This pattern corresponds to three CO units in a *fac* arrangement [37]. The characteristic bands of the C=C and C=N stretching modes of 1,2,4-triazolo-[1,5-a]pyrimidine are observed in the range 1630–1500 cm^{-1} [38].

3.2. Crystal structure

The crystallographic data for the title complex are given in Table 1. The perspective drawing of $[Re(CO)_3(tp)_2Cl]$ with atomic numbering is shown in Fig. 1. The coordination geometry at the Re atom is a distorted octahedron with the three carbonyl ligands arranged in a facial fashion. The 1,2,4-triazolo-[1,5-a]pyrimidine ligands are monodentately coordinated via the nitrogen atom of the triazolo rings. The selected bond lengths and angles of $[Re(CO)_3(tp)_2Cl]$ are given in Table 2. The average Re–C(CO) bond distance is 1.91 Å, and the average Re–N bond distance is 2.194(1) Å. These values are within the range expected for such complexes [39]. The tp substituents are close to planarity (maxi-

Table 3
Hydrogen bonds for $[Re(CO)_3(tp)_2Cl]$ [Å] and [°].

D–H···A	*d*(D–H)	*d*(H···A)	*d*(D···A)	<(DHA)
C(5)–H(5)···Cl(1)#1	0.93	2.71	3.599(3)	160.3
C(7)–H(7)···N(3)#2	0.93	2.62	3.252(4)	126.1
C(9)–H(9)···Cl(1)	0.93	2.80	3.231(3)	109.5
C(10)–H(10)···Cl(1)#3	0.93	2.79	3.423(4)	126.0
C(12)–H(12)···O(2)#4	0.93	2.59	3.256(4)	129.3

Symmetry transformations used to generate equivalent atoms: #1 $-x-1/2, y-1/2, -z+1/2$; #2 $x+1, y, z$; #3 $x-1/2, -y+3/2, z-1/2$; #4 $-x, -y+1, -z$.

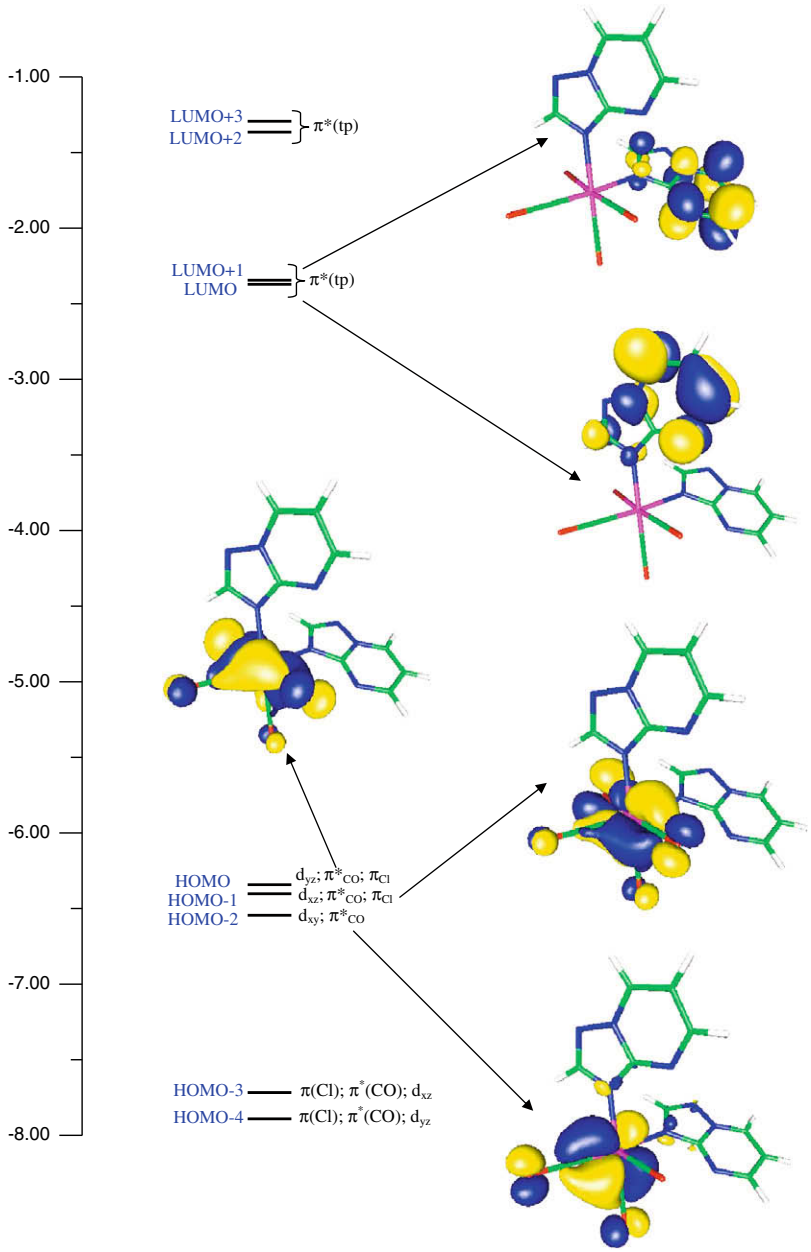


Fig. 3. The energy (eV), character and some contours of the occupied and unoccupied molecular orbitals of $[Re(CO)_3(tp)_2Cl]$.

mum deviation of 0.018(2) Å exist for C(4) atom in one of the planes and 0.029(3) for atom C(11) in second plane) and are inclined at 57.16(6)°. The rhenium atom derives 0.199(4) and 0.048(4) Å from above mentioned weighted least squares planes. In the structure can be found some short intermolecular interactions (Table 3), which can be classified as weak hydrogen bonds [40,41]. *Via* these interactions a semiinfinite three-dimensional net is created (Fig. 2).

3.3. Optimized geometry

The geometry of $[Re(CO)_3(tp)_2Cl]$ was optimized in a singlet state by the DFT method with the B3LYP functional in B1 and B2 bases. The optimized geometric parameters are gathered in Table 2. The calculated bond lengths and angles are in agreement with the values based upon the X-ray crystal structure data, and the general trends observed in the experimental data are well reproduced in the calculations. The optimized geometry parameters obtained in both bases, B1 and B2, are quite similar.

3.4. Electronic structure

The complex $[Re(CO)_3(tp)_2Cl]$ is a closed-shell structure. Its molecular orbital diagram with several occupied and virtual molecular orbital contours is presented in Fig. 3. The HOMO–LUMO gap equals to 3.97 eV. The low-lying virtual orbitals correspond mainly to π^*_{tp} and π^*_{CO}. The LUMO, LUMO+1, LUMO+2 and LUMO+5 are centered on the 1,2,4-triazolo-[1,5-a]pyrimidine ligand. The higher virtual orbitals are mainly delocalized among Re and carbonyls.

The three highest occupied molecular orbitals are predominately localized on the rhenium atom, corresponding to the $(5d_{xy})^2$ $(5d_{xz})^2$ $(5d_{yz})^2$ occupation of the central ion. However, ligand contributions are also important. All these orbitals have a

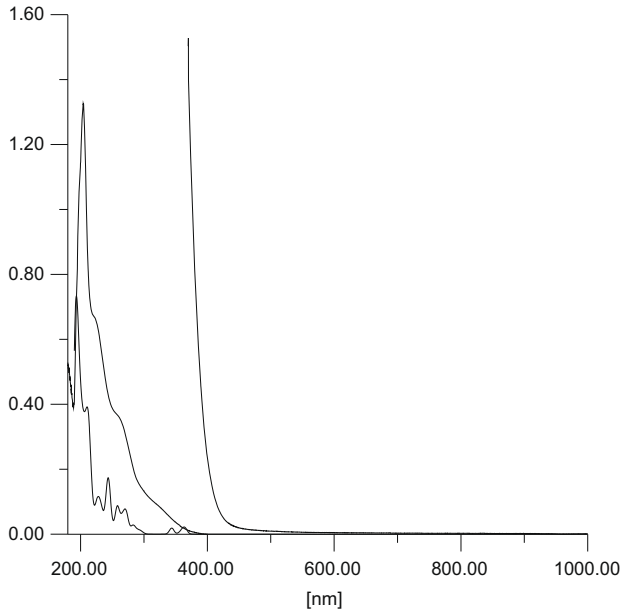


Fig. 4. The experimental and calculated electronic absorption spectra of $[Re(CO)_3(tp)_2Cl]$. Full line: the experimental spectrum measured in CH_2Cl_2. Blue dashed line: spectrum calculated in vacuum. Red dashed line: spectrum calculated in dichloromethane.

relatively considerable CO character. The HOMO-2 and HOMO-1 orbitals contain also an admixture of chloride p_π orbitals.

3.5. UV–Vis spectrum

The electronic absorption spectrum was measured at room temperature in dichloromethane, and the experimental absorption bands were assigned using the singlet excited states calculated with the time-dependent DFT method. The experimental and calculated electronic spectra of $[Re(CO)_3(tp)_2Cl]$ are compared in Fig. 4. Each calculated transition is represented by a GAUSSIAN function $y = ce^{-bx^2}$ with the height (c) equal to the oscillator strength and b equal to 0.04 nm^{-2}. As seen in the Fig. 4, TDDFT/PCM calculations well reproduce the absorption spectrum of $[Re(CO)_3(tp)_2Cl]$ measured in dichloromethane. The lowest allowed absorption band, which occurs at 3.54 eV, has been calculated at 3.39 eV.

Table 4 shows the spin-allowed singlet–singlet electronic transitions calculated with the TDDFT method for $[Re(CO)_3(tp)_2Cl]$. For the high energy part of the spectrum, only transitions with oscillator strengths larger than 0.020 are listed in Table 4. The assignment of the calculated transitions to the experimental bands is based on the criterion of the energy and oscillator strength of the calculated transitions.

The low-energy absorption band of $[Re(CO)_3(tp)_2Cl]$ originates in the transitions between three highest occupied molecular orbitals and two lowest unoccupied molecular orbitals. As can be seen from the Fig. 3, the HOMO-2, HOMO-1 and HOMO are delocalized on the whole $Re(CO)_3Cl$ unit, whereas the LUMO and LUMO+1 are completely centered on the tp ligand. Accordingly, these transitions can be seen as mixed Re → tp (MLCT) and Cl → tp (LLCT) or a delocalized MLLCT (metal–ligand-to-ligand CT) description can be used.

The experimental absorption bands at 269.8 and 227.6 nm are also attributed to *metal–ligand-to-ligand charge transfers*, whereas the lowest energy band originates in the inter- and intra-ligand (IL) transitions (Table 4).

Table 4
The energy and molar absorption coefficients of the experimental absorption bands and the singlet electronic transitions calculated with the TDDFT method and basis B1for $[Re(CO)_3(tp)_2Cl]$.

The most important orbital excitations	Character	λ [nm]	*E* [eV]	*f*	Experimental λ [nm] (*E*[eV]) ε
H → L	d/π(Cl) → π^*(tp)	365.6	3.39	*0.0087*	350.0.(3.54) 1520
H → L+1	d/π(Cl) → π^*(tp)	363.1	3.41	*0.0121*	
H-1 → L	d/π(Cl) → π^*(tp)	359.1	3.45	*0.0037*	
H-1 → L+1	d/π(Cl) → π^*(tp)	357.4	3.47	*0.0040*	
H-2 → L	d → π^*(tp)	344.2	3.60	*0.0108*	
H-2 → L+1	d → π^*(tp)	343.0	3.61	*0.0080*	
H-1 → L+4 H → L+2	d/π(Cl) → π^*(tp)	282.8	4.38	*0.0221*	269.8 (4.60) 13250
H-2 → L+2	d/π(Cl) → π^*(tp)	272.1	4.56	*0.0474*	
H-2 → L+3	d/π(Cl) → π^*(tp)	266.3	4.66	*0.0353*	
H-3 → L	π(Cl)/d → π^*(tp)	258.1	4.80	*0.0473*	
H-2 → L+5	d → π^*(CO)/ π^*(tp)	257.6	4.81	*0.0268*	
H-3 → L	π(Cl)/d → π^*(tp)				
H-5 → L+1	π(Cl) → π^*(tp)	243.6	5.09	*0.0755*	
H-6 → L	π(tp)/ π(Cl) → π^*(tp)	243.3	5.10	*0.0776*	
H → L+7	d/ π^*(Cl) → π^*(tp)/ π^*(CO)	230.6	5.38	*0.0278*	227.6 (5.45) 25650
H-2 → L+6	d → π^*(tp)	227.0	5.46	*0.0510*	
H → L+9	d → π^*(tp)/ π^*(CO)	222.9	5.56	*0.0292*	
H-1 → L+9	d/ π^*(Cl) → π^*(tp)/ π^*(CO)	216.3	5.73	*0.0360*	204.4 (6.07) 56000
H-10 → L+2	π(tp) → π^*(tp)	215.4	5.76	*0.0285*	
H → L+8	d/ π^*(Cl) → π^*(tp)/ π^*(CO)	213.4	5.81	*0.0256*	
H-3 → L+4	π(Cl)/d → π^*(tp)	212.7	5.83	*0.0996*	
H-2 → L+9	d/ π^*(Cl) → π^*(tp)/ π^*(CO)	211.6	5.86	*0.0526*	
H-3 → L+3	π(Cl)/d → π^*(tp)	210.6	5.89	*0.0357*	
H-4 → L+2	π(Cl)/d → π^*(tp)	209.9	5.91	*0.0489*	
H-3 → L+4	π(Cl)/d → π^*(tp)	207.9	5.96	*0.0484*	
H → L+10	d/π(Cl) → π^*(tp)	206.0	6.02	*0.0350*	
H-1 → L+10	d/π(Cl) → π^*(tp)	205.3	6.04	*0.0479*	
H-4 → L+3	π(Cl)/d → π^*(tp)	203.8	6.08	*0.0392*	
H-1 → L+10	d/π(Cl) → π^*(tp)	203.1	6.11	*0.0520*	
H-3 → L+5	π(Cl)/ d → π^*(tp)/ π^*(CO)	201.9	6.14	*0.0505*	
H-6 → L+2	π(tp)/ σ(Cl) → π^*(tp)	199.4	6.22	*0.0372*	
H-13 → L	π(tp) → π^*(tp)	198.6	6.24	*0.0509*	
H-12 → L	π(tp) → π^*(tp)	198.5	6.24	*0.0367*	
H-6 → L+2	π(tp)/ σ(Cl) → π^*(tp)	196.8	6.30	*0.0535*	
H-6 → L+3	π(tp)/ σ(Cl) → π^*(tp)	196.2	6.32	*0.0400*	
H-6 → L+3	π(tp)/ σ(Cl) → π^*(tp)	195.8	6.33	*0.0480*	
H-2 → L+11	d → π^*(tp)	195.2	6.35	*0.0300*	
H-6 → L+4	π(tp)/ σ(Cl) → π^*(tp)	194.7	6.37	*0.0630*	
H-8 → L+2	π(tp) → π^*(tp)	194.4	6.38	*0.0505*	
H-8 → L+2	π(tp) → π^*(tp)	192.9	6.43	*0.0575*	
H-7 → L+2	π(tp) → π^*(tp)	192.8	6.43	*0.0449*	
H-10 → L+3	π(tp) → π^*(tp)	192.3	6.45	*0.0345*	
H-5 → L+5	σ^*(Cl) → π^*(tp)/ π^*(CO)	191.5	6.48	*0.1131*	
H-9 → L+2	n(N) → π^*(tp)	191.2	6.49	*0.0801*	
H-8 → L+3	π(tp) → π^*(tp)	191.0	6.49	*0.0678*	
H-8 → L+3	π(tp) → π(tp)	190.3	6.51	*0.1117*	

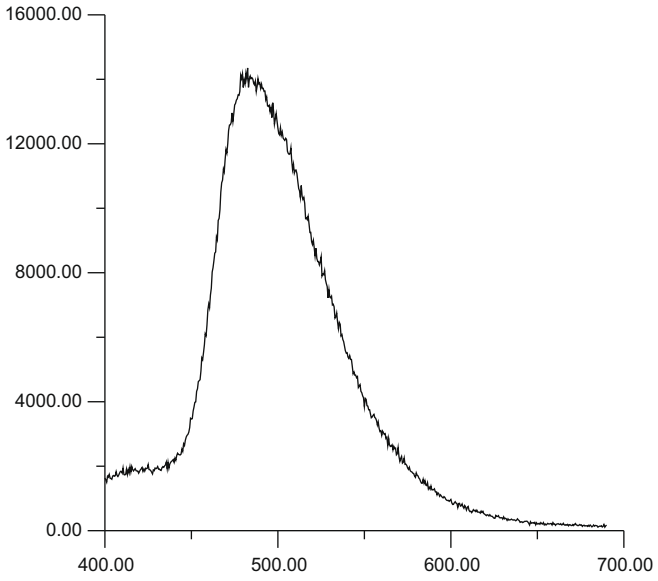


Fig. 5. The emission spectrum of $[Re(CO)_3(tp)_2Cl]$.

3.6. Emission spectrum

Emission properties of the title complex have been examined in the deaerated dichloromethane solution at room temperature. As indicated in Fig. 5, the title complex is a weak emitter. On the excitation at λ = 366 nm the emission is observed at λ_{max} = 482 nm. The peak is broad and structureless, in accordance with the ^{3}MLCT assignment of the emission for similar rhenium(I) tricarbonyl complexes [42].

The structure of several lowest singlet and triplet states was optimized for $[Re(CO)_3(tp)_2Cl]$ with the use of TURBOMOLE program in the B2 basis. The lowest triplet state was also optimized by the independent DFT calculations. The geometry obtained for the lowest triplet state was denoted T_1(A). The selected bond lengths and the calculated vertical emission energies are gathered in Table 5 for the optimized excited state structures. The values of bond lengths collected in the Table 5 shows that the rhenium–nitrogen and rhenium–chlorine bonds are shortened in the excited states, while rhenium–carbonyl bonds are elongated. The T_1(B) structure which has the longest Re–C(2) bond is described below. From the data in Table 5 it can be seen that the independent DFT optimization gives a higher emission energy than the TDDFT optimization. Both values are much smaller than the experimental emission energy. In the optimization of excited states geometry the geometry of the ground state was used as a starting guess. Since this may lead to a local minimum on the energy surface, we calculated the energy curves of lowest triplet along the metal–ligand bond stretching coordinates for all carbonyl and tp ligands. The remaining coordinates were optimized during such calculations. We located another minimum on the T_1 surface, denoted T_1(B) in Table 5. It has a long Re–C(2) bond of 2.14 Å comparing to that in T_1(A) equal to 1.97 Å, and it is of 7.4 kcal lower in energy than T_1(A). Both structures A and B are presented in Fig. 6, together with their singly occupied orbitals. In structure B a link between carbonyl carbon located trans to chlorine and a nitrogen atom from one tp ligand is formed, with d(C(2)–N(2)) = 1.45 Å. We calculated the energy curve along C2–N2 distance, changing stepwisely this parameter and optimizing the remaining ones. At each step we determined several singlet and triplet states by the TDDFT calculations. The resulting energy curves are presented in Fig. 7. On the left-hand side of Fig. 7 the energies of vertical singlet and triplet transitions were schematically depicted. The energy of the ground state (S0) in the T_1 geometry was also plotted in Fig. 7. There is an energy barrier of 5.9 kcal between A and B minima on T_1 curve. At the B minimum geometry the triplet state is lower in energy than the ground singlet state. The shape of the T_1 energy curve reveals that this state is nonemissive. Starting from T_1(A) minimum, which is close to the ground state geometry, the system passes over small energy barrier on T_1, and at geometry near to T_1(B) it reverts to the ground state through an intersystem crossing. From the second triplet state there is also a possibility of nonemissive return to the ground state through interaction with lowest triplet or singlet states. The luminescence most probably occurs from some higher triplet state, T_3–T_5, after intersystem crossing from the initially formed singlet excited state with a high oscillator strength. Such transition is calculated at 360 nm in the B2 basis. The emission energy calculated from states T_3, T_4 and T_5 (561 nm, 523 nm and 489 nm, Table 4) gives quite good agreement with the experimental data. From emissive state a reverse to a lower lying excited state is also possible and finally non-emissive return to the ground state. The radiative and nonradiative paths are depicted in Fig. 7 by solid and dashed green lines, respectively. Such a scheme is also in agreement with a weak emissive properties of $[Re(CO)_3(tp)_2Cl]$. As can be seen from the singly occupied MOs in Fig. 6 the T_1 state is of

Table 5
The vertical excitation energy of optimized lowest singlet and triplet states and bond lengths between Re and ligand atoms for $[Re(CO)_3(tp)_2Cl]$ in basis B2.

	Vertical excitation energy		r[Å] ($\Delta r = r_{Ex} - r_{GS}$)[c]					
	E (eV)	λ (nm)	Re(1)–C(1)	Re(1)–C(2)	Re(1)–C(3)	Re(1)–Cl(1)	Re(1)–N(1)	Re(1)–N(5)
Singlet states								
S_1	1.99	623.6	1.978 (0.053)	1.999 (0.081)	1.943 (0.019)	2.433 (−0.111)	2.205 (−0.034)	2.152 (−0.096)
S_2	2.16	574.0	1.980 (0.055)	1.995 (0.077)	1.951 (0.027)	2.428 (−0.116)	2.165 (−0.074)	2.212 (−0.036)
S_3	2.39	517.7	1.985 (0.060)	1.962 (0.044)	1.981 (0.057)	2.502 (−0.042)	2.153 (−0.086)	2.179 (−0.069)
S_4	2.40	516.2	1.972 (0.047)	1.991 (0.073)	1.962 (0.038)	2.431 (−0.113)	2.174 (−0.065)	2.189 (−0.059)
S_5	2.61	475.2	1.987 (0.062)	1.967 (0.049)	1.972 (0.048)	2.486 (−0.058)	2.173 (−0.066)	2.160 (−0.088)
Triplets states								
T_1(A)[a]	1.83	677.3	1.984 (0.059)	1.975 (0.057)	1.947 (0.023)	2.466 (−0.078)	2.200 (−0.039)	2.120 (−0.128)
T_1(A)[b]	2.06	601.9	1.996 (0.071)	1.974 (0.056)	1.955 (0.031)	2.466 (−0.078)	2.199 (−0.040)	2.112 (−0.136)
T_1(B)	−0.05		1.950 (0.025)	2.145 (0.227)	1.921 (−0.003)	2.467 (−0.077)	2.229 (−0.010)	2.220 (−0.028)
T_2	2.10	590.4	1.997 (0.072)	1.998 (0.080)	1.934 (0.010)	2.420 (−0.124)	2.176 (−0.063)	2.200 (−0.048)
T_3	2.21	561.5	1.975 (0.050)	1.979 (0.061)	1.955 (0.031)	2.473 (−0.071)	2.208 (−0.031)	2.148 (−0.100)
T_4	2.37	523.0	1.978 (0.053)	1.993 (0.075)	1.954 (0.030)	2.429 (−0.115)	2.174 (−0.065)	2.188 (−0.060)
T_5	2.53	489.1	1.968 (0.043)	1.978 (0.060)	1.973 (0.049)	2.471 (−0.073)	2.171 (−0.068)	2.185 (−0.063)

[a] Results from TDDFT optimization.
[b] Results from independent DFT optimization.
[c] Bond lengths differences between the excited and ground state optimized geometries (ground state geometry from Table 2).

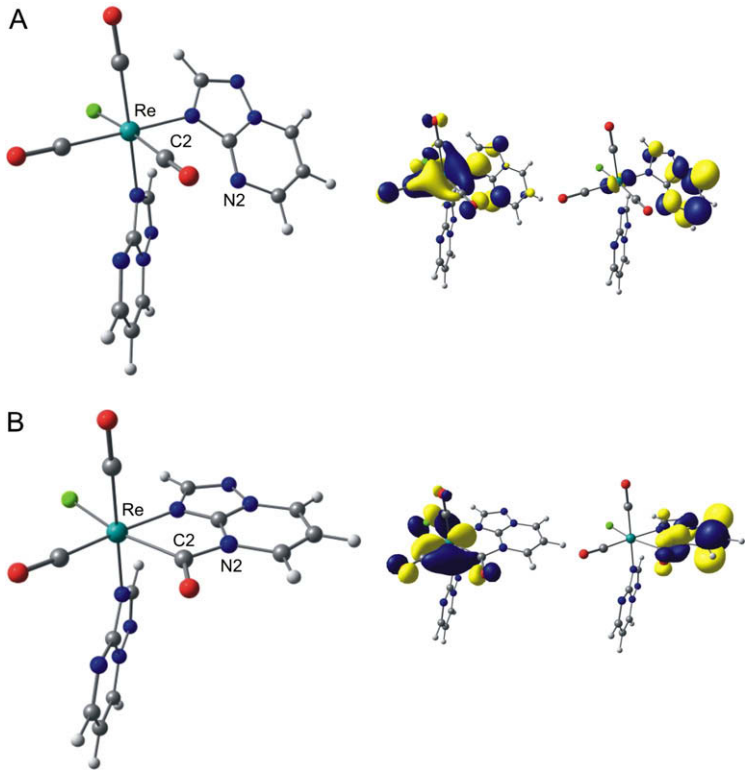


Fig. 6. Molecular structures and isosurface plots of singly occupied MOs for triplet states A and B.

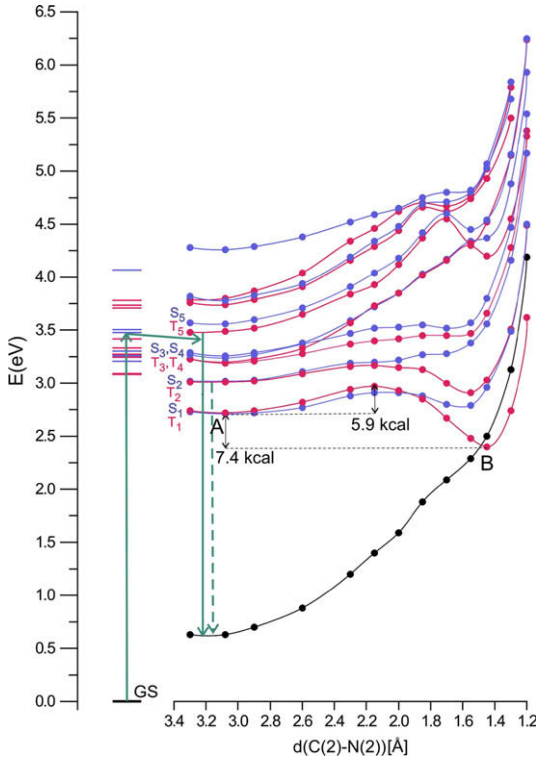


Fig. 7. The ground and excited states energy curves for $[Re(CO)_3(tp)_2Cl]$ as functions of C(2)–N(2) distance. Left –hand side – vertical excitations. Red lines denote triplet states, blue lines – singlet states. The solid green lines denote absorption and emission, the dashed green lines denote nonradiative deactivation.

MLCT character. The states T_2–T_5 are also of MLCT type, hence the calculations confirm that luminescence occurs from a MLCT state.

Supplementary data

CCDC 717905 contains the supplementary crystallographic data for $C_{13}H_8ClN_8O_3Re$. These data can be obtained free of charge via http://www.ccdc.cam.ac.uk/conts/retrieving.html, or from the Cambridge Crystallographic Data Centre, 12 Union Road, Cambridge CB2 1EZ, UK.

Acknowledgements

Crystallographic part was financed by funds allocated by the Ministry Science and Higher Education to the Institute of General and Ecological Chemistry, Technical University of Łódź.

The GAUSSIAN-03 calculations were carried out in the Wrocław Centre for Networking and Supercomputing, WCSS, Wrocław, Poland, http://www.wcss.wroc.pl, under calculational Grant No. 51/96. The TURBOMOLE calculations were carried out in the Academic Computer Centre CYFRONET of the University of Science and Technology in Cracow, ACC CYFRONET AGH, Kraków, Poland, http://www.cyfronet.pl, under Grant No. MNiSW/SGI3700/UŚląski/111/2007 and MNiSW/IBM_BC_HS21/UŚląski/111/2007.

References

[1] V. Balzani, A. Juris, M. Venturi, S. Campagna, S. Serroni, Chem. Rev. 96 (1996) 759.
[2] D.J. Stufkens, A. Vlček Jr., Coord. Chem. Rev. 177 (1998) 127.
[3] I.R. Farrell, A. Vlček Jr., Coord. Chem. Rev. 208 (2000) 87.
[4] A. Vogler, H. Kunkely, Coord. Chem. Rev. 200–202 (2000) 991.
[5] D.R. Striplin, G.A. Crosby, Coord. Chem. Rev. 211 (2001) 163.
[6] A. Vlček Jr., M. Busby, Coord. Chem. Rev. 250 (2006) 1755.
[7] A. Vlček Jr., S. Záliš, Coord. Chem. Rev. 251 (2007) 258.
[8] F. Li, G. Cheng, Y. Zhao, J. Feng, S. Liu, M. Zhang, Y. Ma, J. Shen, Appl. Phys. Lett. 83 (2003) 4716.
[9] P. Christensen, A. Hamnett, A.V.G. Muir, J.A. Timney, J. Chem. Soc., Dalton Trans. (1992) 1455.
[10] H. Hori, F.P.A. Johnson, K. Koike, K. Takeuchi, T. Ibusuki, O. Ishitani, J. Chem. Soc., Dalton Trans. (1997) 1019.

[11] S.S. Jurisson, J.D. Lydon, Chem. Rev. 99 (1999) 2205.
[12] W.A. Volkert, T.J. Hoffman, Chem. Rev. 99 (1999) 2269.
[13] J.M. Salas, M.A. Romero, M.P. Sánchez, M. Quirós, Coord. Chem. Rev. 193–195 (1999) 1119.
[14] CrysAlis RED, Oxford Diffraction Ltd., Version 1.171.
[15] G.M. Sheldrick, Acta Crystallogr., Sect. A 46 (1990) 467.
[16] G.M. Sheldrick, SHELXL97. Program for the Solution and Refinement of Crystal Structures, University of Göttingen, Germany (1997).
[17] G.M. Sheldrick, SHELXTL: release 4.1 for Siemens Crystallographic Research Systems (1990).
[18] GAUSSIAN 03, Revision D.01, M.J. Frisch, G.W. Trucks, H.B. Schlegel, G.E. Scuseria, M.A. Robb, J.R. Cheeseman, J.A. Montgomery, Jr., T. Vreven, K.N. Kudin, J.C. Burant, J.M. Millam, S.S. Iyengar, J. Tomasi, V. Barone, B. Mennucci, M. Cossi, G. Scalmani, N. Rega, G.A. Petersson, H. Nakatsuji, M. Hada, M. Ehara, K. Toyota, R. Fukuda, J. Hasegawa, M. Ishida, T. Nakajima, Y. Honda, O. Kitao, H. Nakai, M. Klene, X. Li, J.E. Knox, H.P. Hratchian, J.B. Cross, V. Bakken, C. Adamo, J. Jaramillo, R. Gomperts, R.E. Stratmann, O. Yazyev, A.J. Austin, R. Cammi, C. Pomelli, J.W. Ochterski, P.Y. Ayala, K. Morokuma, G.A. Voth, P. Salvador, J.J. Dannenberg, V.G. Zakrzewski, S. Dapprich, A.D. Daniels, M.C. Strain, O. Farkas, D.K. Malick, A.D. Rabuck, K. Raghavachari, J. B. Foresman, J. V. Ortiz, Q. Cui, A.G. Baboul, S. Clifford, J. Cioslowski, B.B. Stefanov, G. Liu, A. Liashenko, P. Piskorz, I. Komaromi, R.L. Martin, D.J. Fox, T. Keith, M.A. Al-Laham, C.Y. Peng, A. Nanayakkara, M. Challacombe, P.M.W. Gill, B. Johnson, W. Chen, M.W. Wong, C. Gonzalez, J.A. Pople, Gaussian, Inc., Wallingford CT, 2004.
[19] (a) R. Ahlrichs, M. Bär, M. Häser, H. Horn, C. Kölmel, Chem. Phys. Lett. 162 (1989) 165;
(b) O. Treutler, R. Ahlrichs, J. Chem. Phys. 102 (1995) 346;
(c) F. Furche, R. Ahlrichs, J. Chem. Phys. 117 (2002) 7433;
(d) F. Furche, D. Rappoport, Density functional methods for excited states: equilibrium structure and electronic spectra Chapter III of "Computational Photochemistry", in: M. Olivucci (Ed.), "Theoretical and Computational Chemistry", vol. 16, Elsevier, Amsterdam, 2005;
[e] TURBOMOLE has been designed by the Quantum Chemistry Group, University of Karlsruhe, Germany, since 1988. The following members of the group have made contributions: Reinhart Ahlrichs, Michael Bär, Hans-Peter Baron, Rüdiger Bauernschmitt, Stephan Böcker, Nathan Crawford, Peter Deglmann, Michael Ehrig, Karin Eichkorn, Simon Elliott, Filipp Furche, Frank Haase, Marco Häser, Christof Hättig, Arnim Hellweg, Hans Horn, Christian Huber, Uwe Huniar, Marco Kattannek, Andreas Köhn, Christoph Kölmel, Markus Kollwitz, Klaus May, Paola Nava, Christian Ochsenfeld, Holger Öhm, Holger Patzelt, Dmitrij Rappoport, Oliver Rubner, Ansgar Schäfer, Uwe Schneider, Marek Sierka, Oliver Treutler, Barbara Unterreiner, Malte von Arnim, Florian Weigend, Patrick Weis, Horst Weiss, <http://www.turbomole.com>.
[20] M.E. Casida, in: J.M. Seminario (Ed.), Recent Developments and Applications in Modern Density Functional Theory, Theoretical and Computational Chemistry, vol. 4, Elsevier, Amsterdam, 1996.
[21] A.D. Becke, J. Chem. Phys. 98 (1993) 5648.
[22] C. Lee, W. Yang, R.G. Parr, Phys. Rev. B 37 (1988) 785.
[23] M.T. Cances, B. Mennucci, J. Tomasi, J. Chem. Phys. 107 (1997) 3032.
[24] M. Cossi, V. Barone, B. Mennucci, J. Tomasi, Chem. Phys. Lett. 286 (1998) 253.
[25] B. Mennucci, J. Tomasi, J. Chem. Phys. 106 (1997) 5151.
[26] M. Cossi, G. Scalmani, N. Rega, V. Barone, J. Chem. Phys. 117 (2002) 43.
[27] A. Klamt, G. Schüürmann, J. Chem. Soc. Perkin Trans. 2 (5) (1993) 799.
[28] P.J. Hay, W.R. Wadt, J. Chem. Phys. 82 (1985) 299.
[29] K. Eichkorn, F. Weigend, O. Treutler, R. Ahlrichs, Theor. Chem. Acc. 97 (1997) 119.
[30] D. Andrae, U. Haussermann, M. Dolg, H. Stoll, H. Preuss, Theor. Chim. Acta 77 (1990) 123.
[31] W.J. Hehre, R. Ditchfield, J.A. Pople, J. Chem. Phys. 56 (1972) 2257.
[32] P.C. Hariharan, J.A. Pople, Theor. Chim. Acta 28 (1973) 213.
[33] M.M. Francl, W.J. Petro, W.J. Hehre, J.S. Binkley, M.S. Gordon, D.J. DeFrees, J.A. Pople, J. Chem. Phys. 77 (1982) 3654.
[34] T. Clark, J. Chandrasekhar, P.V.R. Schleyer, J. Comp. Chem. 4 (1983) 294.
[35] R. Krishnam, J.S. Binkley, R. Seeger, J.A. Pople, J. Chem. Phys. 72 (1980) 650.
[36] P.M.W. Gill, B.G. Johnson, J.A. Pople, M.J. Frisch, Chem. Phys. Lett. 197 (1992) 499.
[37] P.J. Giordano, M.S. Wrighton, J. Am. Chem. Soc. 101 (1979) 2888.
[38] K. Nakamoto, Infrared and Raman Spectra of Inorganic and Coordination Compounds, 4th ed., Wiley-Interscience, New York, 1986.
[39] F.H. Allen, Acta Crystallogr., Sect. B B58 (2002) 380.
[40] G.A. Jeffrey, W. Saenger, Hydrogen Bonding in Biological Structures, Springer-Verlag, 1994.
[41] G.R. Desiraju, T. Steiner, The Weak Hydrogen Bond in Structural Chemistry and Biology, Oxford University Press, 1999.
[42] R.J. Shaver, M.W. Perkovic, D.P. Rillema, C. Woods, Inorg. Chem. 34 (1995) 5446.

Polyhedron 28 (2009) 2579–2584

Contents lists available at ScienceDirect

Polyhedron

journal homepage: www.elsevier.com/locate/poly

Synthesis, characterization and spectroscopic properties of novel periphery – functionalized unsymmetrical porphyrazines containing mixed dithienylpyrrolyl and dimethylamino groups

Tomasz Goslinski [a,*], Andrew J.P. White [b]

[a] Department of Chemical Technology of Drugs, University of Medical Sciences, Grunwaldzka 6, 60-780 Poznan, Poland
[b] Department of Chemistry, Imperial College, London SW7 2AZ, UK

ARTICLE INFO

Article history:
Received 26 February 2009
Accepted 13 May 2009
Available online 21 May 2009

Dedicated to Professor Bozenna Golankiewicz.

Keywords:
Diketones
2,5-Di(2-thienyl)-1*H*-pyrrole derivatives
Linstead macrocyclization
Porphyrazine
Spectroscopy
Solvatochromic effect

ABSTRACT

Following our previous report on a novel class of C_4 symmetric porphyrazines bearing 2,5-dimethylpyrrolyl and methyl(3-pyridylmethyl)amino groups in the periphery, here we report the synthesis and characterization of unsymmetrical porphyrazines with peripheral 2,5-di(2-thienyl)pyrrolyl and dimethylamino groups that break the molecular C_4 symmetry. The porphyrazines were prepared *via* macrocyclization reactions of a dinitrile precursor. Variable-temperature ^{1}H NMR experiments, single crystal X-ray work and UV–Vis spectra in different solvents of the unsymmetrical magnesium porphyrazine provided information on the structural and electronic features of the entire macrocyclic system. A detailed discussion of the UV–Vis spectra in different solvents emphasizes the role played by the extended peripheral 2,5-di(2-thienyl)pyrrolyl substituent.

© 2009 Elsevier Ltd. All rights reserved.

1. Introduction

Porphyrazines (pzs) functionalized in the periphery form a distinct class of novel macrocycles, along with the functionalized porphyrins and phthalocyanines [1]. Peripherally modified pzs can be substituted in the β-positions with sulfur, oxygen and nitrogen residues or have rings bound to both β,β-positions, which results in significant modulation of their electrochemical and optical properties [2]. Porphyrazines have been investigated as sensitizers for photodynamic therapy [3], metal ion probes [4], precursors to optical, magnetic and conductive materials for nanotechnology, electrophotography, optical data recording systems, electronic devices, photovoltaic cells, fuel cells, and electrochromic displays [5–9].

Porphyrazines containing annulated 5-membered heteroarenes (4,5-thiazole, 2,3-thiophene, 1,2,5-selenodiazole) have found applications as synthetic precursors [1,10]. There is limited data on pzs possessing 5-membered heteroaromatic rings substituted directly to the β-position of the porphyrazine system. Bisthienylethenes with heterocyclic aryl groups and a coplanar binuclear porphyrazine bearing six bis-(trimethylthiophenyl) photochromic functionalities at the periphery, have become candidates for various applications including information storage, imaging devices and switches [10,11].

Lately, we have reported the synthesis and characterization of unsymmetrical porphyrazines with peripheral 2,5-dimethylpyrrolyl and methyl(3-pyridylmethyl)amino groups bearing interesting optical and electrochemical properties [12]. In this study, we decided to extend this work to the synthesis to novel porphyrazine systems with peripheral 2,5-di(2-thienyl)-1*H*-pyrrole and dimethylamino substituents. We were encouraged with the data on conductive polymers, derivatives of 2,5-di(2-thienyl)-1*H*-pyrrole, which have revealed electrical and optical properties of metals or semiconductors while retaining the attractive mechanical properties and processing advantages of polymers [13,14]. Similarly, π-excessive chromophores possessing a thienylpyrrolyl π-conjugated system acting as an auxiliary donor, attached to a functionalized benzimidazole electron-withdrawing heterocyclic group have shown excellent solvatochromic properties, high thermal stabilities and good molecular optical non-linearities [15].

2. Experimental

1,4-Di(2-thienyl)-1,4-butanedione (**2**) was prepared according to a literature procedure by the double Friedel–Crafts reaction be-

* Corresponding author. Tel.: +48 61 854 66 37; fax: +48 61 854 66 39.
E-mail address: tomasz.goslinski@ump.edu.pl (T. Goslinski).

0277-5387/$ - see front matter © 2009 Elsevier Ltd. All rights reserved.
doi:10.1016/j.poly.2009.05.033

tween thiophene and succinyl chloride, employing aluminium chloride as the Lewis acid catalyst in a one-step procedure with good yield [13,14].

2.1. Synthesis of 2-amino-3-[2,5-di(2-thienyl)-1H-pyrrol-1-yl]-(2Z)-butene-1,4-dinitrile (**3**)

A solution of diaminomaleonitrile (852 mg, 7.88 mmol), 1,4-di(2-thienyl)-butane-1,4-dione (1.97 g, 7.88 mmol) and trifluoroacetic acid (100 μL) in methanol (45 mL) was refluxed for 37 h. The reaction mixture was cooled down and most of the unreacted diketone crystallized to give white plates. The filtered solution was concentrated in vacuo. This material was chromatographed twice (hexane:EtOAc, 7:1–7:3) to give **3** (1.173 g, 46%) as small slightly yellow crystals: mp 200–202 °C, R_f 0.21 (hexane:EtOAc, 7:3). UV–Vis (CH_3OH): λ_{max}, nm (logε) 305 (4.43). IR (neat) cm^{-1} 3396, 3313, 3196, 2212 (CN), 1624, 1599, 1408, 1037, 776. ^1H NMR (400 MHz; DMSO-d_6): δ_H, ppm 8.30 (bs, 2H, NH_2), 7.56 (d, 2H, thienyl-H, ^3J = 4.0 Hz), 7.24 (d, 2H, thienyl-H, ^3J = 4.0 Hz), 7.15 (pt, 2H, thienyl-H, ^3J = 4.0 Hz), 6.66 (s, 2H, pyrrolyl-H). ^{13}C NMR (100 MHz; DMSO-d_6): δ_C, ppm 134.7, 132.8, 130.0, 128.2, 126.2, 125.1, 117.5, 113.2, 111.9, 87.9. HRMS (ES pos): m/z 323.0428 (calc. for $[M+H]^+$ 323.0425). *Anal.* Calc. for $C_{16}H_{10}N_4S_2$: C, 59.61; H, 3.13; N, 17.38. Found: C, 59.67; H, 3.08; N, 17.30%.

2.2. Synthesis of 2-(dimethylamino)-3-[2,5-di(2-thienyl)-1H-pyrrol-1-yl]-(2Z)-butene-1,4-dinitrile (**4**)

NaH (60% dispersion in mineral oil; 302 mg, 7.55 mmol) was suspended in THF (8 mL) at (−30 °C). Next **3** (486 mg, 1.51 mmol) in THF (5 mL) was added and stirred 30 min until the temperature raised to (−10 °C). Me_2SO_4 (358 μL, 3.78 mmol) was added dropwise to the solution for 1 h at (−10 °C) and then allowed to warm up slowly to room temperature (2 h) and stirring was continued for 21 h. Water (30 mL) was carefully added to the reaction mixture and then extracted with ethyl acetate (4 × 75 mL). The combined organic extracts were washed with water (2 × 50 mL), dried ($MgSO_4$), filtered and evaporated to dryness. This material was chromatographed (hexane:EtOAc, 7:3) to give **4** (404 mg, 76%) as orange crystals: mp 128–130 °C, R_f 0.25 (hexane:EtOAc, 7:3). UV–Vis (CH_3OH): λ_{max}, nm (logε) 317 (4.51). IR (neat): ν, cm^{-1} 3101, 2937, 2191 (CN), 1598, 1407, 1315, 1224, 1048, 786, 707. ^1H NMR (400 MHz; DMSO-d_6): δ_H, ppm 7.62 (d, 2H, thienyl-H, ^3J = 4.0 Hz), 7.35 (d, 2H, thienyl-H, ^3J = 4.0 Hz), 7.19 (pt, 2H, thienyl-H, ^3J = 4.0 Hz), 6.65 (s, 2H, pyrrolyl-H), 2.80 (s, 6H, $N(CH_3)_2$). ^{13}C NMR (100 MHz; DMSO-d_6): δ_C, ppm 135.1, 132.6, 132.4, 128.5, 126.8, 125.9, 118.6, 112.7, 111.5, 86.6, 42.1. HRMS (ES pos): m/z 351.0750 (calc. for. $[M+H]^+$ 351.0738). *Anal.* Calc. for $C_{18}H_{14}N_4S_2$: C, 61.69; H, 4.03; N, 15.99. Found: C, 61.76; H, 3.98; N, 15.93%.

2.3. {2,7,12,18-Tetrakis(dimethylamino)-3,8,13,17-tetrakis[2,5-di(2-thienyl)-1H-pyrrol-1-yl]porphyrazinato}magnesium (II) (**5**)

Mg turnings (36 mg, 1.50 mmol), a crystal of I_2, and 1-butanol (25 mL) were heated under reflux for 16 h. After the mixture was cooled to room temperature, dinitrile **4** (351 mg, 1.00 mmol) was added and the solution heated under reflux for a further 22 h. After being allowed to cool to room temperature, the dark green mixture was evaporated with toluene (2 × 50 mL). Next the mixture was dissolved in CH_2Cl_2 (250 mL), filtered through Celite and evaporated. Chromatography (CH_2Cl_2:CH_3OH, 25:1) was performed twice to give main product, porphyrazine **5** (84 mg, 24%) as a dark green solid: mp > 300 °C, R_f 0.39 (CH_2Cl_2:CH_3OH, 25:1). UV–Vis (CH_2Cl_2): λ_{max}, nm (logε) 348 (4.97), 440 (4.12), 524 (4.18), 727 (4.50). IR (neat): ν, cm^{-1} 3102, 2955, 2924, 2854, 1595, 1339, 1035, 762, 692. ^1H NMR (500 MHz; d_5-pyridine): δ_H, ppm 7.24 (2H, d, ^3J = 5.0 Hz), 7.13 (2H, s), 7.11 (2H, d, ^3J = 5.0 Hz), 7.03 (2H, d, ^3J = 5.0 Hz), 7.02 (s, 2H), 6.98 (d, 2H, ^3J = 5.0 Hz), 6.71 (s, 2H), 6.69 (d, 2H, ^3J = 5.0 Hz), 6.64 (s, 2H), 6.63 (m, 4H), 6.58 (2H, m), 6.57 (2H, m), 6.55 (2H, d, ^3J = 5.0 Hz), 6.42 (2H, t, ^3J = 5.0 Hz), 6.39 (2H, t, ^3J = 5.0 Hz), 3.59 (s, 6H), 3.48 (s, 6H), 3.41 (s, 6H), 3.18 (s, 6H). ^{13}C NMR (125 MHz; d_5-pyridine): δ_C, ppm 159.2, 158.0, 157.9, 154.1, 152.0, 152.0, 151.6, 151.3, 149.6[h], 149.2, 146.9, 145.7, 145.4, 145.2, 145.0, 144.2, 136.4, 136.3, 136.1, 136.1, 136.0, 135.6[h], 135.1, 134.7, 134.7, 134.3, 128.5, 128.3, 128.1, 128.1, 127.8, 127.7, 127.1, 127.0, 126.9, 124.9, 124.7, 124.1, 124.0, 123.5[h], 123.1, 112.4, 112.1, 110.0, 109.8, 109.5, 109.3, 108.5, 42.8, 42.6, 42.5, 42.3. MS (MALDI TOF): m/z 1426 $[M+H]^+$. Single crystals for X-ray analysis were grown at room temperature by slow evaporation of ethanol–chloroform (**5a**) and methanol–chloroform (**5b**, **5c**) mixtures.

*Crystal data for **5a**:* $C_{74}H_{62}MgN_{16}OS_8{\cdot}0.5H_2O$, M = 1481.19, triclinic, $P\bar{1}$ (no. 2), a = 13.9822(10) Å, b = 16.3084(7) Å, c = 18.5161(9) Å, α = 64.196(4)°, β = 72.889(5)°, γ = 67.092(6)°, V = 3461.5(4) Å^3, Z = 2, D_c = 1.421 g cm^{-3}, μ(Cu Kα) = 2.963 mm^{-1}, T = 173 K, very dark needles, Oxford Diffraction Xcalibur PX Ultra diffractometer; 10 825 independent measured reflections (R_{int} = 0.0611), F^2 refinement, R_1(obs) = 0.118, wR_2(all) = 0.404, 4886 independent observed absorption–corrected reflections [$|F_o| > 4\sigma(|F_o|)$, $2\theta_{max}$ = 126°], 939 parameters.

*Crystal data for **5b**:* $[C_{73}H_{60}MgN_{16}OS_8]_{0.5}[C_{72}H_{58}MgN_{16}OS_8]_{0.5}{\cdot}H_2O$, M = 1469.16, monoclinic, $P2_1/c$ (no. 14), a = 13.1879(3) Å, b = 15.7249(3) Å, c = 34.5102(9) Å, β = 91.079(2)°, V = 7155.4(3) Å^3, Z = 4, D_c = 1.364 g cm^{-3}, μ(Cu Kα) = 2.868 mm^{-1}, T = 173 K, very dark blocks, Oxford Diffraction Xcalibur PX Ultra diffractometer; 13 801 independent measured reflections (R_{int} = 0.0587), F^2 refinement, R_1(obs) = 0.130, wR_2(all) = 0.402, 5882 independent observed absorption–corrected reflections [$|F_o| > 4\sigma(|F_o|)$, $2\theta_{max}$ = 144°], 996 parameters.

*Crystal data for **5c**:* $C_{73}H_{60}MgN_{16}OS_8{\cdot}C_5$, M = 1518.21, monoclinic, $P2_1/c$ (no. 14), a = 13.28975(15) Å, b = 16.12306(19) Å, c = 34.8211(5) Å, β = 93.2910(12)°, V = 7448.86(16) Å^3, Z = 4, D_c = 1.354 g cm^{-3}, μ(Cu Kα) = 2.765 mm^{-1}, T = 173 K, very dark blocks, Oxford Diffraction Xcalibur PX Ultra diffractometer; 14 436 independent measured reflections (R_{int} = 0.0582), F^2 refinement, R_1(obs) = 0.114, wR_2(all) = 0.382, 7531 independent observed absorption–corrected reflections [$|F_o| > 4\sigma(|F_o|)$, $2\theta_{max}$ = 143°], 1082 parameters.

As the second product was isolated {2,7,12,17-tetrakis(dimethylamino)-3,8,13,18-tetrakis[2,5-di(2-thienyl)-1*H*-pyrrol-1-yl]porphyrazinato}magnesium (II) (**6**), which was unstable during drying at higher temperature. Chromatography (CH_2Cl_2:CH_3OH, 25:1) and (CH_2Cl_2) gave porphyrazine **6** (36 mg, 10%) as a green film: R_f 0.96 (CH_2Cl_2:CH_3OH, 25:1), R_f 0.44 (CH_2Cl_2). UV–Vis (CH_2Cl_2): λ_{max}, nm (logε) 350 (4.84), 424 (3.84), 534 (3.76), 742 (4.70). IR (neat): ν, cm^{-1} 3102, 2957, 2923, 2865, 1589, 1477, 1403, 1318, 1118, 1042, 860. ^1H NMR (400 MHz; d_5-pyridine): δ_H, ppm 7.13 (d, 8H, ^3J = 4.0 Hz), 7.05 (s, 8H), 6.59 (m, 16H), 3.42 (s, 24H). MS (MALDI TOF): m/z 1425 M^+.

2.4. 2,7,12,18-Tetrakis(dimethylamino)-3,8,13,17-tetrakis[2,5-di(2-thienyl)-1H-pyrrol-1-yl]porphyrazine (**7**)

In the dark, CF_3COOH (12 mL) was added to crude porphyrazine **5** (210 mg, 0.15 mmol), obtained after the macrocyclization reaction, and stirred for 30 min at room temperature. Next the solution was added to rapidly stirred ice-H_2O (150 mL) and neutralized with satd. $NaHCO_3$. Afterwards the brown–purple mixture was extracted with CH_2Cl_2 (5 × 300 mL) and evaporated to dryness. Chromatography (CH_2Cl_2) and (CH_2Cl_2–hexane, 1:1) gave porphyrazine **7** (17 mg, 8%) as a brown–violet film; R_f 0.48 (CH_2Cl_2–hexane, 1:1).

UV–Vis (CH_2Cl_2): λ_{max}, nm (logε) 336 (4.95), 432 (4.26), 509 (4.34), 679 (4.29), 752 (4.42). IR (neat): ν, cm^{-1} 3284, 3100, 2922, 2853, 1599, 1530, 1384, 1311, 1010, 841, 753, 687. ^1H NMR (500 MHz; d_5-pyridine): δ_H, ppm 7.26 (d, 2H, ^3J = 5.0 Hz), 7.16 (d, 2H, ^3J = 5.0 Hz), 7.08 (s, 1H), 7.01 (s, 1H), 7.00 (d, 2H, ^3J = 5.0 Hz), 6.98 (d, 2H, ^3J = 5.0 Hz), 6.83 (d, 2H, ^3J = 5.0 Hz), 6.67–6.74 (m, 14H), 6.63 (pt, 2H, ^3J = 5.0 Hz), 6.49 (pt, 2H, ^3J = 5.0 Hz), 6.46 (pt, 2H, ^3J = 5.0 Hz), 3.47 (s, 6H), 3.39 (s, 6H), 3.35 (s, 6H), 3.19 (s, 6H). ^{13}C NMR (125 MHz; d_5-pyridine): δ_C, ppm 159.2, 154.5, 154.2, 154.2, 152.7, 152.6, 151.9, 151.0, 148.8, 145.4, 145.2, 145.0, 144.2, 142.5, 140.4, 139.2, 138.4, 135.3, 134.7, 134.6, 134.3, 134.1, 128.4, 128.2, 128.1, 127.8, 127.6, 127.3, 127.3, 127.1, 126.4, 125.9, 125.7, 125.5, 125.2, 124.7, 124.6, 124.4, 123.9[h], 111.7, 110.3, 110.0, 109.8, 108.9, 107.0, 42.8, 42.7, 42.5, 42.5. MS (MALDI TOF): m/z 1403 $[M+H]^+$.

2.5. {2,7,12,18-Tetrakis(dimethylamino)-3,8,13,17-tetrakis[2,5-di(2-thienyl)-1H-pyrrol-1-yl]porphyrazinato}zinc (II) (**8**)

Dinitrile **4** (199 mg, 0.57 mmol), zinc acetate (53 mg, 0.29 mmol), 1,8-diazabicyclo[5.4.0]undec-7-ene (85 μL, 0.57 mmol) and 1-pentanol (2 mL) were heated at 130 °C for 20 h. After being allowed to cool to room temperature, the dark green–violet mixture was evaporated with toluene (2 × 50 mL) to dryness. Chromatography (hexane:EtOAc, 7:3) and (CH_2Cl_2 to CH_2Cl_2:CH_3OH, 200:1) gave the main product porphyrazine **8** (12.3 mg, 6%) as a dark green film (violet in solution): R_f 0.33 (CH_2Cl_2:CH_3OH, 200:1); R_f 0.53 (hexane:EtOAc, 7:3). UV–Vis (CH_2Cl_2): λ_{max}, nm (logε) 338 (5.05), 429 (4.17), 531 (4.19), 742 (4.52). IR (neat): ν, cm^{-1} 3102, 2957, 2927, 2859, 1725, 1595, 1410, 1287, 1125, 1039, 691. ^1H NMR (500 MHz; d_5-pyridine): δ_H, ppm 7.24 (d, 2H, ^3J = 5.0 Hz), 7.13 (d, 2H), 7.12 (s, 2H), 7.02 (2H, d, ^3J = 5.0 Hz), 7.01 (s, 2H), 6.98 (d, 2H, ^3J = 5.0 Hz), 6.72 (s, 2H), 6.70 (d, 2H, ^3J = 5.0 Hz), 6.65 (s, 2H), 6.64 (2H, d, ^3J = 5.0 Hz), 6.58 (m, 8H), 6.43 (pt, 2H, ^3J = 5.0 Hz), 6.41 (pt, 2H, ^3J = 5.0 Hz), 3.57 (s, 6H), 3.46 (s, 6H), 3.40 (s, 6H), 3.18 (s, 6H). ^{13}C NMR (125 MHz; d_5-pyridine): δ_C, ppm 159.2, 158.6, 157.9, 157.9, 153.9, 151.6, 147.8, 147.7, 146.5, 145.6, 145.2, 145.0, 144.7, 144.0, 134.4, 134.4, 134.0, 128.6, 128.2, 128.0, 127.9, 127.8, 127.6, 127.4, 126.9, 126.8, 126.8, 126.7, 125.5, 125.3, 125.1, 124.7, 124.4, 118.4, 117.0, 111.9, 111.7, 109.7, 109.6, 109.5, 109.3, 109.1, 42.5, 42.3, 42.2, 42.0. MS (MALDI TOF): m/z 1467 $[M+H]^+$.

3. Results and discussion

3.1. Synthesis

The Paal–Knorr reaction of diaminomaleonitrile **1** with 1,4-di(2-thienyl)-1,4-butanedione **2** was acid-catalysed (activation of the ketone functionality) using trifluoroacetic acid (TFA) in refluxing ethanol or methanol and led to the novel dinitrile system **3** after 37 h with moderate yield. Dinitrile **4** was easily synthesized from **3** using $(MeO)_2SO_2$/NaH in THF by a modification of the Sheppard's method [16]. The Linstead macrocyclization of **4** gave unsymmetrical magnesium porphyrazine **5** as the major product, accompanied by one isomer **6** [17]. Demetallation of **5** by removal of the magnesium ion with trifluoroacetic acid gave the free base porphyrazine **7** (Scheme 1). An identical pz system **8** with zinc (II) in the core was obtained, when the macrocyclization reaction of **4** was performed using $Zn(OAc)_2$ in pentanol with 1,8-diazabicyclo[5.4.0]undec-7-ene (DBU) as a base. All porphyrazines **5**–**8** were freely soluble in common organic solvents, thereby facilitating purification by column chromatography. Further recrystallization of **5** by slow evaporation of ethanol–chloroform or methanol–chloroform solutions led to crystals **5a**–**5c** suitable for single crystal X-ray analysis.

A previously performed macrocyclization reaction study using mixed 2,5-dimethylpyrrolyl-methyl(3-pyridylmethyl)amino maleonitrile led to C_4 symmetrical pz with an alternate order of substituents, whereas other isomers have only been isolated as the minor product [12]. Herein the dithienylpyrrolyl pz product **5** was surprisingly isolated as the main product and the symmetrical C_4 pz **6** possessing an alternate order of substituents appeared as a low-yielding and easily decomposing side product (see spectrum, Supplementary data). When a harsh method of macrocyclization adapted from the phthalocyanine approach was used ($Zn(OAc)_2$–DBU–pentanol), the pz **8** was isolated as the only reaction product [18]. Therefore the isolated products, **5** and **8**, possessing the disturbed order of substituents appear to be the only stable thermodynamically isomers.

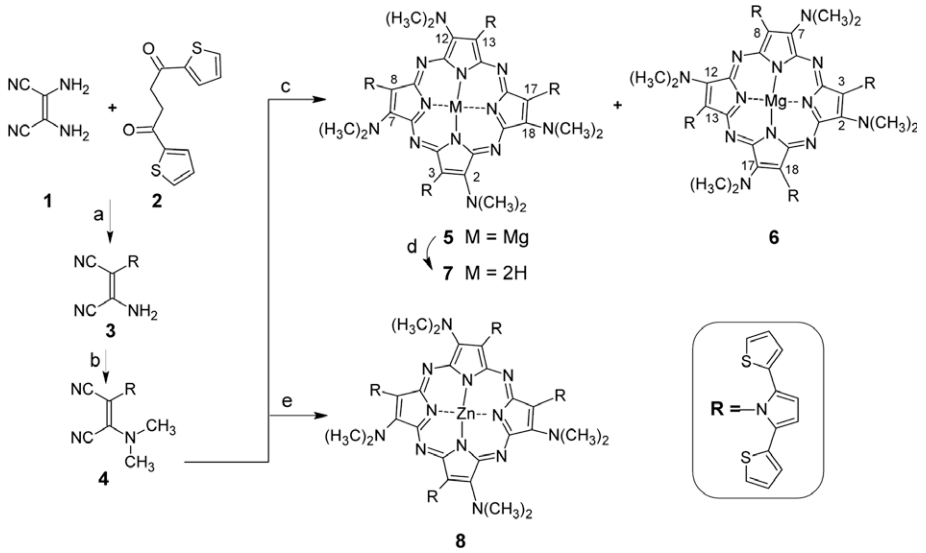
3.2. NMR studies

The asymmetry imposed by the non-alternate order of both peripheral substituents resulted in the non-equivalent signals. Both pzs: unsymmetrical **5** and C_4 symmetrical **6**, representing various isomers might be easily distinguished by ^1H and ^{13}C NMR spectra. Dimethylamino groups in the structure of pz **5** appear as four signals at 3.59, 3.48, 3.41, 3.18 ppm in ^1H NMR and at 42.8, 42.6, 42.5, 42.3 ppm in ^{13}C NMR, whereas in the structure of pz **6** as only one signal at 3.42 ppm in ^1H NMR and at 42.5 ppm in ^{13}C NMR. The 1H–1H COSY, HMQC and HMBC spectra in pz structure **5**, were necessary to resolve the connectivities within each substituted pyrrolyl fragment of the porphyrazine ring (Table 1S, Supplementary data).

In the variable-temperature ^1H NMR spectra resonances received from aromatic 2,5-di(2-thienyl)-1*H*-pyrrol-1-yl groups were found within the regions of: 6.92–7.35 and 6.53–6.79 ppm, whereas the resonances from $N(CH_3)_2$ groups appeared as four signals within the region of: 2.92–3.67 ppm at the temperature range studied (243 → 343 K) (Fig. 1). The sharp proton NMR signals of the 2,5-di(2-thienyl)-1*H*-pyrrol-1-yl group underwent minor shifts, whereas the multiplicity of the signals changed significantly, e.g. a multiplet observed at 6.40 ppm at 343 K changed to two triplets at 6.46 and 6.42 ppm at 243 K. All resonances grouped within the region of 6.92–7.18 ppm at 343 K shifted upfield to the region of 7.08–7.35 ppm at 243 K. The most significant changes were found for all pyrrolyl singlet signals belonging to the 2,5-di(2-thienyl)-1*H*-pyrrol-1-yl groups. When the temperature raised, two of them shifted downfield (from 6.62 to 6.79 and 6.53 to 6.73 ppm) and the other two shifted upfield (from 7.08 to 7.00 and 7.21 to 7.08 ppm). Additionally at 343 K some complex, cross-ring type, resonances were found. By contrast, the $N(CH_3)_2$ proton signals were well resolved at 343 K but when the temperature decreased to 243 K, upfield shifting and broadening of the signals at 2.92 and 3.27 ppm was found. This fact might be attributed to the steric hindrance between positions 3, 8 and 13 in the macrocyclic core, which implies slower rotation of differently shielded $N(CH_3)_2$ groups in positions 7 and 12 at lower temperatures. The ^1H NMR signals arising from the $N(CH_3)_2$ groups present in positions 2 and 18 are sharp singlets at all temperatures studied, as the periphery is relatively less crowded and there is no significant barrier to rotation for both groups.

3.3. X-ray study of **5**

The X-ray structures of the ethanol, mixed methanol/water (see Supplementary data) and methanol complexes of **5a**, **5b** and **5c** are very similar, as can readily be seen from Fig. 2. The most noticeable features of the three structures are the orientations of the peripheral ligands and the dishing of the ring. In each structure the dithienylpyrrolyl ligands are unsurprisingly oriented approximately orthogonal to the "plane" of the porphyrazine ring (*vide infra*) while



Scheme 1. Reagents and conditions: (a) CH_3OH, TFA, Δ, 37 h (46%); (b) Me_2SO_4, NaH, DMF, −30–20 °C, 24 h (76%); (c) $Mg(OnBu)_2$, *n*BuOH, Δ, 22 h (**5** – 24%, **6** – 10%); (d) TFA, 20 °C, 30 min (8%); (e) $Zn(OAc)_2$, DBU, *n*PeOH, 130 °C, 20 h (6%).

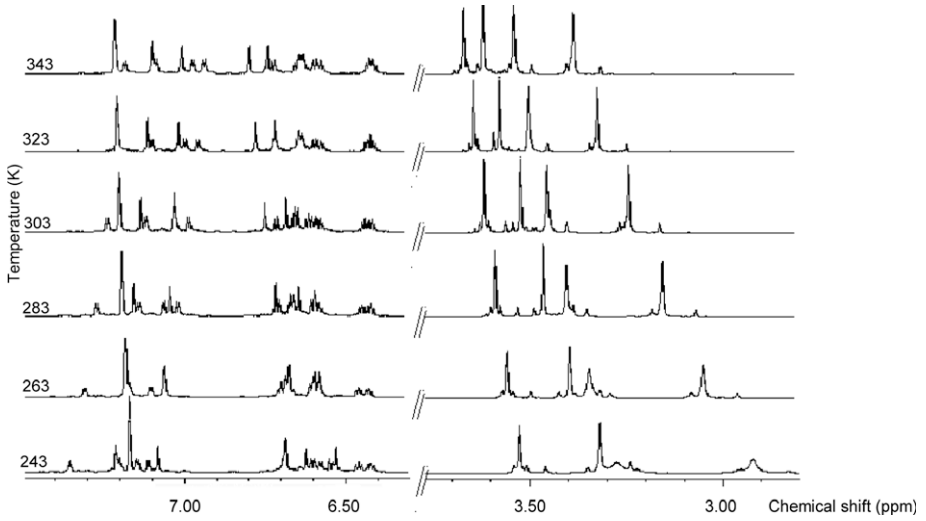


Fig. 1. Variable-temperature ^1H NMR spectra for **5** in pyridine-d_5.

the dimethylamine ligands are approximately parallel. The dishing of the porphyrazine rings can be quantified by considering the three "circles" of nitrogen atoms; the inner circle consists of the metal coordinated nitrogen atoms N(2), N(7), N(12) and N(17), the intermediate circle is comprised of the remaining four porphyrazine nitrogen atoms N(1), N(6), N(11) and N(16), and the peripheral circle consists of the eight nitrogen atoms N(21), N(36), N(39), N(54), N(57), N(72), N(75) and N(78), bound to the periphery of the porphyrazine ring. In the structure of **5a**, the magnesium lies ca. 0.49, 0.62 and 0.90 Å out of the inner, intermediate and peripheral circles respectively. The corresponding displacements for **5b** and **5c** are ca. 0.51, 0.62 and 0.80 Å and ca. 0.53, 0.66 and 0.88 Å, respectively. Also of note is the substitution pattern around the porphyrazine ring. Considering the periphery of the porphyrazine ring starting at N(1) and cycling round *via* N(6), N(11) and N(16), the ligand order in each complex is pyrrole–amine–pyrrole–amine–pyrrole–amine–amine–pyrrole, i.e. the "last" two ligands are reversed and thus break the potential molecular C_4 symmetry.

3.4. Spectroscopic and solvatochromic studies

The UV–Vis spectra of demetallated porphyrazine **7** exhibits an intense Soret band at 336 nm, Q-bands at 679 and 752 nm and an n–π^* transition at 509 nm. Alternatively, the precursor magnesium pz **5** and zinc pz **8** display intense Soret peaks at 348 and 338 nm and Q-band $\pi \rightarrow \pi^*$ transitions at 727 and 742 nm, respectively (Fig. 3). Q-band transitions of **5** and **8** are broad and complex, whereas in case of C_4 symmetrical isomer **6** the Q-band is sharp. Additionally for pzs **5** and **8**, less intense Soret bands at 440 and 429 nm, respectively, may be observed next to the intense Soret peaks. The resultant n–π^* transitions were visible for porphyrazines **5** and **8** as weak bands at 524 and 531 nm, respectively.

The UV–Vis spectroscopy was employed to evaluate the solvatochromic effects of **5**. In dichloromethane–methanol (1:1) solution pz **5** exhibits a Soret peak centred at 348 nm with a less intense Soret band at 442 nm and a broad Q-band at 723 nm, untypical for symmetrical metallated porphyrazine **6**, where a

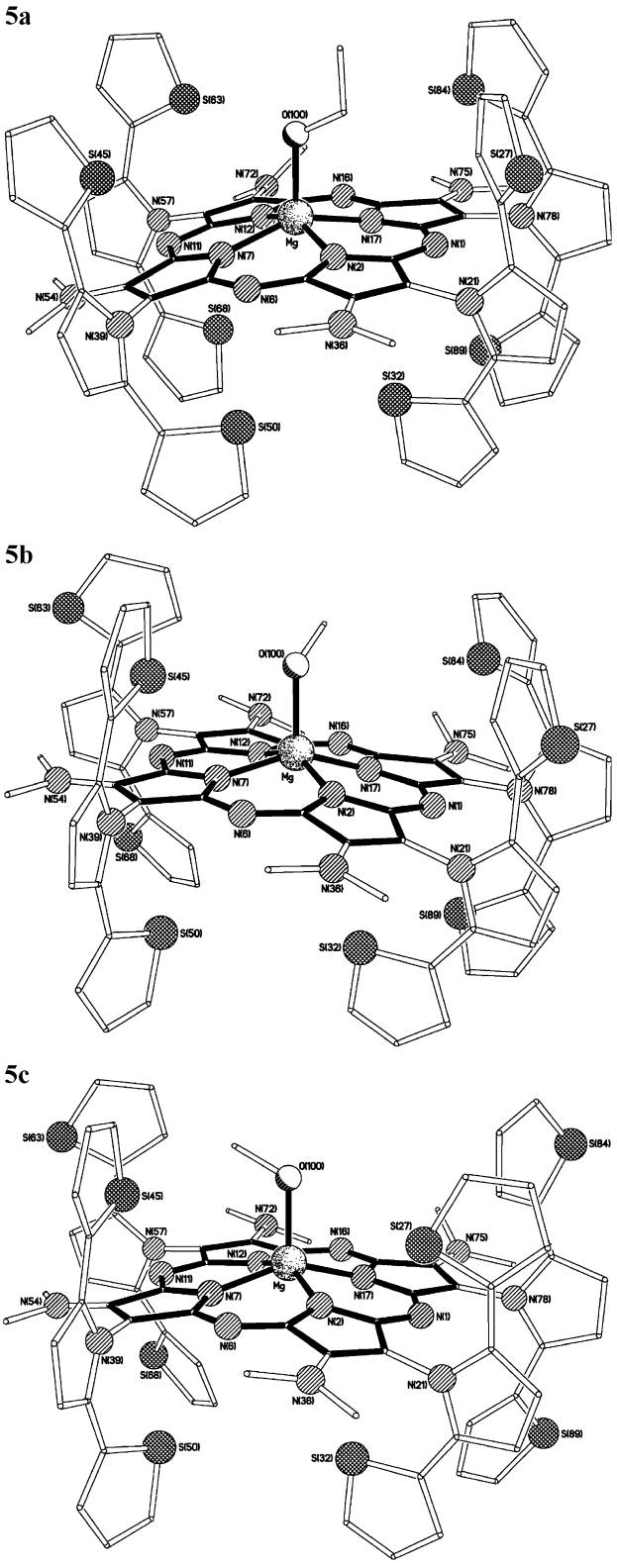


Fig. 2. The molecular structures of **5a**, **5b** and **5c**.

sharp and intense Q-band was found at 742 nm. The very weak peak at 516 nm was assigned to an n–π^* transition from the lone-pair of electrons on the external nitrogen atoms into a π^* ring orbital. It is obvious, that the solvent affects the photophysical and photochemical properties of pz **5**. However, changes observed for the novel 2,5-di(2-thienyl)pyrrolyl peripheral substituent present

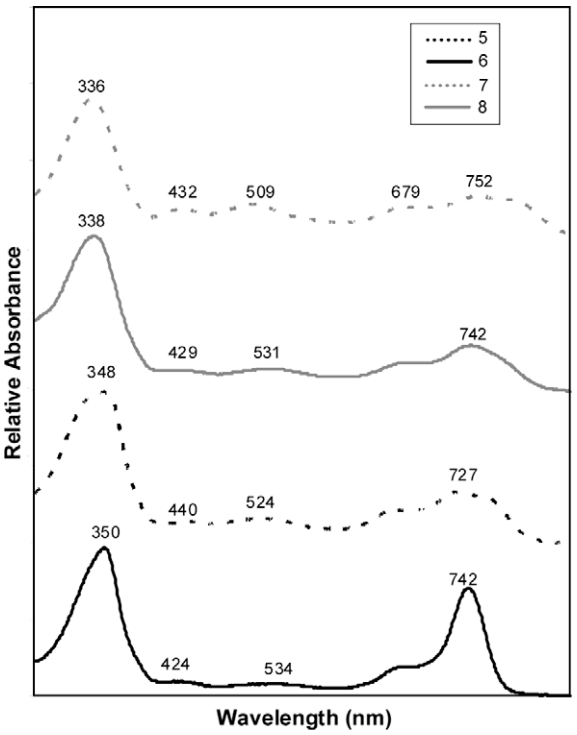
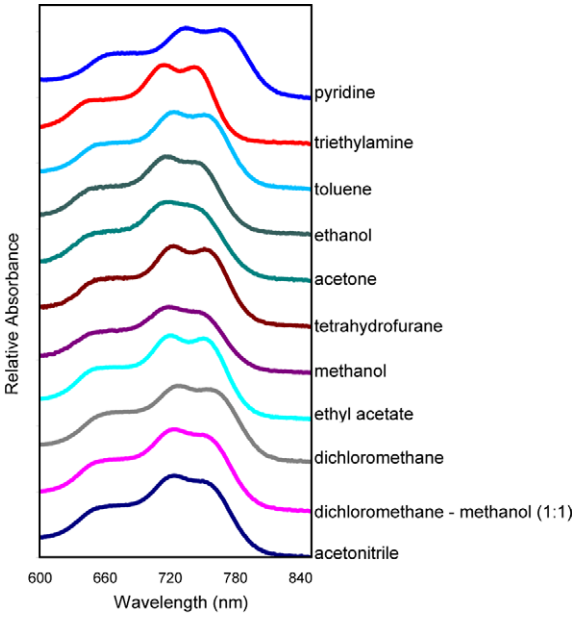


Fig. 3. Electronic absorption spectra of **5**–**8** in CH_2Cl_2:CH_3OH.



Solvent	Q-band (λ_{max}, nm)	Dipole moment (μ)	Refractive index (n_D)
methanol	719	1.70	1.328
acetonitrile	724	3.92	1.344
acetone	719	2.88	1.359
ethanol	718	1.69	1.3611
ethyl acetate	722, 750	1.78	1.372
triethylamine	714, 741	0.66	1.401
tetrahydrofurane	721, 751	1.75	1.407
dichloromethane	729, 753	1.60	1.445
toluene	727, 751	0.37	1.497
pyridine	734, 765	2.21	1.510

Fig. 4. The variation of the Q-band for **5** in various solvents (dipole moments and refractive indices [19,20].

in pz **5** are more significant than those for the previously described 2,5-dimethylpyrrolyl counterpart [12]. The absorption maximum of **5** in methanol, ethanol, acetone, acetonitrile are at the range 718–724 nm (Fig. 4). In triethylamine the Q-band of pz **5** exhibited the strongest hypsochromic shift at 714, 741 nm and an additional Q-band split was present. Whereas in pyridine, the strongest bathochromic shift and a split of the Q-band at 734 and 765 nm were observed. The Q-band split was also found in toluene, THF, ethyl acetate and dichloromethane. The long-wavelength maxima in the UV–Vis spectra of **5** were found to be sensitive to a change in the dielectric properties of the medium for coordinating solvents, with the magnitude of the red shift following the order ethanol < methanol < tetrahydrofurane < ethyl acetate < pyridine. The refractive index of the solvents triethylamine, acetone, tetrahydrofurane, toluene, dichloromethane and pyridine increased as the red shift of the Q-band increased. The largest red shift of the Q-band was observed in aromatic solvents, with the highest shift being observed for pyridine. Moreover, the Q-band split was observed only for solvents possessing refractive indices higher than 1.372. The presence of an additional band in the Q-region, indicating a loss of symmetry was explained in phthalocyanine systems by the distortion of the ring of the analyzed molecule. The position of the Q-band for pz system **5** in the range of solvents analyzed seems to result from both coordination and solvation [19,20].

4. Conclusion

Novel unsymmetrical pz bearing peripheral 2,5-di(2-thienyl)-1*H*-pyrrole and dimethylamino substituents were synthesized and characterized. The novel type of macrocyclic structure possesses an alternate order of substituents in three out of four fragments only. As a consequence, in the discussed structure, two dimethylamino groups and two dithienylpyrrolyl groups are in close vicinity. The asymmetry imposed by this non-alternate order of peripheral substituents, breaking C_4 symmetry, resulted in the non-equivalence of ^{1}H and ^{13}C NMR signals for all pz discussed. The X-ray structure of **5** revealed an almost perpendicular orientation of the bulky, dithienylpyrrolyl system to the core of the macrocycle.

The synthesis of this novel pz system was performed using both a Linstead macrocyclization and a $Zn(OAc)_2$-1,8-diazabicyclo[5.4.0]undec-7-ene – pentanol approaches. The unexpected direction of the reaction to unsymmetrical pzs **5** and **8** might be the result of their thermodynamic stability and thus instability of other kinetic isomers, which even if formed under the reaction conditions, are likely to decompose, similar to pz **6**.

As pz **5** exhibited significant solvatochromic changes in the UV–Vis spectrum in various solvents, the pzs described in this report are expected to find diverse applications as precursors to optical materials. The direction of this research will be continued and reported in due course.

Acknowledgements

This study was supported by the Polish Ministry of Science and Higher Education Grant No. N405 031 32/2052. T.G. thanks to the British Council and the Polish Ministry of Science and Higher Education for the opportunity to participate in the British-Polish Young Scientific Programme (YSP). T.G. thanks to Professor A.G.M. Barrett from Imperial College London for supporting his studies within the YSP programme.

Appendix A. Supplementary data

CCDC 713577, 713578 and 713579 contain the supplementary crystallographic data for **5a**, **5b** and **5c**, respectively. These data can be obtained free of charge *via* http://www.ccdc.cam.ac.uk/conts/retrieving.html, or from the Cambridge Crystallographic Data Centre, 12 Union Road, Cambridge CB2 1EZ, UK; fax: (+44) 1223-336-033; or e-mail: deposit@ccdc.cam.ac.uk. Supplementary data associated with this article can be found, in the online version, at doi:10.1016/j.poly.2009.05.033.

References

[1] M.S. Rodriguez-Morgade, P.A. Stuzhin, J. Porphyrins Phthalocyanines 8 (2004) 1129.
[2] S.L.J. Michel, S.M. Baum, A.G.M. Barrett, B.M. Hoffman, in: K.D. Karlin (Ed.), Progress in Inorganic Chemistry, vol. 50, J. Wiley & Sons, New York, 2001, pp. 473–590.
[3] E.G. Sakellariou, A.G. Montalban, H.G. Meunier, G. Rumbles, D. Phillips, R.B. Ostler, K. Suhling, A.G.M. Barrett, B.M. Hoffman, Inorg. Chem. 41 (2002) 2182.
[4] S.J. Lange, J.W. Sibert, A.G.M. Barrett, B.M. Hoffman, Tetrahedron 56 (2000) 7371.
[5] T. Goslinski, C. Zhong, M.J. Fuchter, C. Stern, A.J.P. White, A.G.M. Barrett, B.M. Hoffman, Inorg. Chem. 45 (2006) 3686.
[6] S.L.J. Michel, D.P. Goldberg, C. Stern, A.G.M. Barrett, B.M. Hoffman, J. Am. Chem. Soc. 123 (2001) 4741.
[7] D.H. Hochmuth, S.L. Michel, A.J.P. White, D.J. Williams, A.G.M. Barrett, B.M. Hoffman, Eur. J. Inorg. Chem. (2000) 593.
[8] A. Koca, M. Şahin, A. Gül, R.Z. Uslu, Monatsh. Chem. 133 (2002) 1135.
[9] B.J. Vesper, K. Salaita, H. Zong, C.A. Mirkin, A.G.M. Barrett, B.M. Hoffman, J. Am. Chem. Soc. 126 (2004) 16653.
[10] M.P. Donzello, C. Ercolani, P.A. Stuzhin, Coord. Chem. Rev. 250 (2006) 1530.
[11] Q. Luo, S. Cheng, H. Tian, Tetrahedron Lett. 45 (2004) 7737.
[12] T. Goslinski, E. Tykarska, W. Szczolko, T. Osmalek, A. Smigielska, S. Walorczyk, H. Zong, M. Gdaniec, B.M. Hoffman, J. Mielcarek, S. Sobiak, J. Porphyrins Phthalocyanines 13 (2009) 223.
[13] P.E. Just, K.I. Chane-Ching, P.C. Lacaze, Tetrahedron 58 (2002) 3467.
[14] A. Arslan, Ö. Türkarslan, C. Tanyeli, İ.M. Akhmedov, L. Toppare, Mater. Chem. Phys. 104 (2007) 410.
[15] R.M.F. Batista, S.P.G. Costa, M. Belsley, M.M.M. Raposo, Tetrahedron 63 (2007) 9842.
[16] R.W. Begland, D.R. Hartter, F.N. Jones, D.J. Sam, W.A. Sheppard, O.W. Webster, F.J. Weigert, J. Org. Chem. 39 (1974) 2341.
[17] R.P. Linstead, M. Whalley, J. Chem. Soc. (1952) 4839.
[18] J. Vacus, G. Memetzidis, P. Doppelt, J. Simon, Chem. Commun. (1994) 697.
[19] D.R. Lide (Ed.), CRC Handbook of Chemistry and Physics, 78th ed., CRC Press LLC, Boca Raton, 1997.
[20] A. Ogunsipe, D. Maree, T. Nyokong, J. Mol. Struct. 650 (2003) 131.

Polyhedron 28 (2009) 2585–2590

Contents lists available at ScienceDirect

Polyhedron

journal homepage: www.elsevier.com/locate/poly

Synthesis and structure of indenylnickel(II) chlorides bearing free *N*-heterocyclic carbene ligands and their catalysis for styrene polymerization

Ling-Zhi Xie, Hong-Mei Sun *, Dong-Mei Hu, Zhi-Hong Liu, Qi Shen, Yong Zhang

The Key Laboratory of Organic Synthesis of Jiangsu Province, College of Chemistry, Chemical Engineering and Materials Science, Soochow University, Suzhou 215123, PR China

ARTICLE INFO

Article history:
Received 20 March 2009
Accepted 18 May 2009
Available online 16 June 2009

Keywords:
N-heterocyclic carbene
Nickel(II) complexes
Indenyl
Styrene
Polymerization

ABSTRACT

The reaction of $(R\text{-}Ind)_2Ni$ (Ind = C_9H_7, indenyl) with an equivalent of a bulky aryl-substituted imidazolium salt in CH_2Cl_2/THF at 45 °C results in the corresponding *N*-heterocyclic carbene (NHC) indenylnickel(II) chloride of the type (R-Ind)Ni(L)Cl [R = 1-H, L = 1,3-bis(2,6-diisopropylphenyl)imidazol-2-ylidene (IPr), **1**; R = 1-Me, L = IPr, **2**] in high yield. Complexes **1** and **2** were characterized by elemental analysis, NMR spectroscopy and X-ray crystallography. The resulted NHC indenylnickel(II) complexes are capable of polymerizing styrene in the presence of $NaBPh_4$ to give atactic polystyrene with M_n values in the range of 10^4. The present studies show a close relationship between the structure and catalytic activity of the NHC indenylnickel(II) halides (including the previously reported indenylnickel(II) halides bearing alkyl-substituted NHC ligands), and complex **2** shows the highest catalytic activity. In comparison with its phosphine analogue (1-Me-Ind)Ni(PPh_3)Cl, complex **2** shows significant improvements in stability and catalytic performance.

© 2009 Elsevier Ltd. All rights reserved.

1. Introduction

During the past decade there has been increasingly interesting in the application of *N*-heterocyclic carbenes (NHCs) as a structure principle for developing late transition metal-based homogeneous catalysts [1–4]. In many types of catalytic processes, NHCs have been used as a valid alternative to the traditional phosphine ligands due to their unique and tunable steric and electronic properties [5–7]. The replacement of phosphine ligands with electron-rich NHC ligands could represent significant catalytic activity in most cases. For example, benzannulated NHC Ni(II) complexes of the general formula $Ni(NHC)_2Br_2$ exhibited much higher catalytic activity than their phosphine analogues, $Ni(PPh_3)_2Br_2$, in reductive Ullmann coupling reactions of aryl bromides [8].

However, in comparison with the intensively studied NHC complexes of palladium, a relatively small number of well-defined NHC nickel complexes have been reported to date. Only recently have NHC complexes of nickel garnered more attention and emerged as effective catalysts for a series of reactions, such as C–F bond [9] or C–H bond activation [10], C–C or C–N cross-coupling reactions [8,11–14], olefin dimerization [15,16], polymerizations [17–24], and so on. The $(NHC)_nNi(CO)_m$ system has been used as a model for the understanding of electronic and steric effects of NHCs [25,26], nevertheless, the principles regulating their structures and reactivities remain unclear. This prompted us to develop the free NHC-based indenylnickel(II) complexes.

In fact, although tertiary phosphine analogues of the type $(R\text{-}Ind)Ni(PR'_3)X$ (X = halide, alkyl, alkynyl, imidate, thiolate) have been reported, and include examples that are effective precatalysts for the oligomerization or polymerization of ethylene, styrene and alkynes, the dehydrogenative oligomerization or polymerization of phenylsilane [27], NHC indenylnickel(II) complexes have received little attention until our recent report on a one-step facile synthetic method, i.e. the direct reaction of the bis-indenyl Ni(II) complex of $(1\text{-}H\text{-}Ind)_2Ni$ with an alkyl-substituted imidazolium salt, for the synthesis of alkyl-substituted NHC indenylnickel(II) complexes (1-H-Ind)Ni(iPr)X (iPr = 1,3-diisopropylimidazole-2-ylidene) in high yields [28,29]. This procedure needs no extra steps for the isolation and purification of the corresponding *N*-heterocyclic carbene, and provides simple access to NHC Ni(II) complexes with polydentate co-ligands. Despite our investigation, there has only been one example reported so far that such NHC complexes could be synthesized by the reaction of $(R\text{-}Ind)Ni(PPh_3)X$ with free NHC, mentioned briefly in one review [27]. To explore a simple route to a large number of complexes in this family would be desirable.

Herein we described the extension of our methodology to the synthesis of indenylnickel(II) chlorides bearing sterically bulky aryl-substituted NHC ligands, (1-H-Ind)Ni(IPr)Cl [IPr = 1,3-bis(2,6-diisopropylphenyl)imidazol-2-ylidene, **1**) and its alkyl-substituted indenyl derivative (1-Me-Ind)Ni(IPr)Cl (**2**). The present investigation enlarges the list of analogous complexes already described [28,29], to such an extent that comparative studies of

* Corresponding author. Tel.: +86 512 65880330; fax: +86 512 65880305.
E-mail address: sunhm@suda.edu.cn (H.-M. Sun).

0277-5387/$ - see front matter © 2009 Elsevier Ltd. All rights reserved.
doi:10.1016/j.poly.2009.05.080

the relationship between their structures and catalytic activities in styrene polymerization may be possible. Their catalytic activities for styrene polymerization have also been compared to their tertiary phosphine analogues.

2. Experimental

2.1. General procedures

All manipulations were performed under pure argon with rigorous exclusion of air and moisture using standard Schlenk techniques. Solvents were distilled from Na/benzophenone ketyl under pure argon prior to use. Indene (Fluka) (dried over 4 Å molecular sieves) was distilled immediately before use. (1-H-Ind)$_2$Ni [28], (1-Me-Ind)$_2$Ni [30], 1,3-bis(2,6-diisopropylphenyl)imidazolium chloride (IPr·HCl [31], (1-H-Ind)Ni(iPr)X [iPr = 1,3-diisopropylimidazole-2-ylidene, X = Cl (**3**) and Br (**4**)] [28], (1-Me-Ind)Ni(PPh_3)Cl (**5**) [32] and CpNi(IPr)Cl (Cp = cyclopentadienyl, **6**) [33] were prepared by published methods. Elemental analysis was performed by direct combustion on a Carlo-Erba EA-1110 instrument. NMR ($CDCl_3$) spectra were measured on a Unity Inova-400 spectrometer at 25 °C, and were assigned by the assistance of 2D techniques (H–H correlation spectroscopy and C–H heteronuclear correlation spectroscopy). Molecular weight and molecular weight distribution were determined by gel-permeation chromatography (GPC) measurements calibrated to commercial polystyrene standards and performed on a PE PL-GPC50 apparatus with two PLgel 10 μm MIXED-B columns in THF (1.0 mL/min) at 40 °C.

2.2. Synthesis of (1-H-Ind)Ni(IPr)Cl (*1*)

A Schlenk flask was charged with 1,3-bis(2,6-diisopropylphenyl)imidazolium chloride (0.85 g, 2.00 mmol), CH_2Cl_2 (5 mL) and a stir bar. To this solution was added (1-H-Ind)$_2$Ni (0.57 g, 2.00 mmol) in 20 mL of THF via syringe at room temperature. The solution was stirred overnight at 45 °C, filtered and then evaporated to dryness. After being washed with hexane, the residue was extracted with hot toluene and recrystallized from concentrated toluene at −10 °C, yielding bright red crystals (0.32 g, 63%) suitable for elemental analysis and X-ray diffraction studies. M.p. 176–178 °C. *Anal.* Calc. for $C_{36}H_{43}ClN_2Ni$: C, 72.32; H, 7.25; N, 4.69. Found: C, 72.24; H, 7.43; N, 4.45%. ^{1}H NMR (400 MHz, $CDCl_3$, 25 °C): δ 1.05 (d, 12H, *Me*), 1.34 (d, 12H, *Me*), 2.65 (br, 1H, *H*3), 3.07 (br, 2H, C*H*Me$_2$), 4.44 (br, 2H, C*H*Me$_2$), 6.38 (s, 1H, *H*1), 6.62 (br, 2H, *H*5/*H*8 and *H*2), 7.01 (s, 2H, C*H*=C*H*), 7.35-7.57 (m, 9H, *H*5/*H*8, *H*6, *H*7 and *Ph*). ^{13}C NMR (100 MHz, $CDCl_3$, 25 °C): δ 23.1 (*Me*), 26.6 (*Me*), 29.0 (CHMe$_2$), 103.3 (*C*1), 118.1 and 118.2 (*C*2 and *C*5/*C*8), 124.7 and 125.5 (*m-Ph*, *C*6 and *C*7), 125.8 (C*H*=C*H*), 130.4 (*p-Ph*), 132.73 (*C*4 and *C*9), 136.8 (*o-Ph*), 146.7 (*ipso-Ph*), 175.4 ($C_{carbene}$); however, the assignment of some of these signals remains ambiguous, such as the resonance for *C*3 which is missing and should be presented at ca. 50.

2.3. Synthesis of (1-Me-Ind)Ni(IPr)Cl (*2*)

Following a procedure similar to the synthesis of **1**, (1-Me-Ind)$_2$Ni (0.62 g, 2.00 mmol) in 20 mL of THF was added to a solution of 1,3-bis(2,6-diisopropylphenyl)imidazolium chloride (0.85 g, 2.00 mmol) in CH_2Cl_2 (5 mL) at room temperature. After workup, dark red crystals (0.86 g, 70%) suitable for elemental analysis and X-ray diffraction studies were obtained from concentrated toluene at −10 °C. M.p. 206–207 °C. *Anal.* Calc. for $C_{37}H_{45}ClN_2Ni$: C, 72.62; H, 7.41; N, 4.58. Found: C, 72.31; H, 7.07; N, 4.47%. ^{1}H NMR (400 MHz, $CDCl_3$, 25 °C): δ 0.95 (m, 9H, *Me* and 1-*Me*-Ind), 1.15 (d, 6H, *Me*), 1.23 (d, 6H, *Me*), 1.39 (d, 6H, *Me*), 2.55 (br, 2H, C*H*Me$_2$), 3.17 (br, 2H, C*H*Me$_2$), 4.16 (s, 1H, *H*3), 5.65 (d, 1H, *H*5), 6.01 (s, 1H, *H*2), 6.29 (m, 1H, *H*6), 6.57 (d, 1H, *H*8), 6.77 (d, 1H, *H*7), 7.01 (s, 2H, C*H*=C*H*), 7.32-7.53 (m, 6H, *Ph*). ^{13}C NMR (100 MHz, $CDCl_3$, 25 °C): δ 12.2 (1-*Me*-Ind), 22.7 (*Me*), 23.6 (*Me*), 26.1 (*Me*), 27.0 (*Me*), 29.0 (CHMe$_2$), 58.1 (*C*3), 93.9 (*C*1), 103.8 (*C*2), 116.7 (*C*8), 117.0 (*C*5), 124.5 (*C*6), 124.6 (*m-Ph*), 125.5 (*C*7), 125.8 (CH=CH), 130.2 (*p-Ph*), 132.0 (*C*4), 134.0 (*C*9), 136.9 (*o-Ph*), 146.7 (*ipso-Ph*), 177.1 ($C_{carbene}$).

2.4. Structure determination

Suitable single crystals of **1** and **2** were sealed in a thin-walled glass capillary for X-ray structural analysis. Diffraction data were collected on a Rigaku Mercury CCD area detector at 193(2) K. The structures were solved by direct methods and refined by full-ma-

Table 1
X-ray crystallographic data for **1** and **2**.

	1	**2**
Empirical formula	$C_{36}H_{43}ClN_2Ni$	$C_{37}H_{45}ClN_2Ni$
Formula weight	597.88	611.91
Temperature (K)	193(2)	153(2)
λ (Mo Kα) (Å)	0.7107	0.7107
Crystal system	monoclinic	monoclinic
Space group	*p21/n*	*p21/n*
Unit cell dimensions		
a (Å)	9.8993(9)	10.3994(11)
b (Å)	19.239(2)	19.057(2)
c (Å)	16.883(1)	16.861(2)
β (°)	106.072(2)	105.843(2)
V (Å^3)	3089.7(5)	3214.9(6)
Z	4	4
D_{calc} (g cm^{-3})	1.285	1.264
Absorption coefficient (mm^{-1})	0.742	0.714
F(0 0 0)	1272	1304
Crystal size (mm^3)	0.30 × 0.20 × 0.15	0.25 × 0.25 × 0.07
$2\theta_{max}$ (°)	25.34	25.3
Reflections collections	30454	31317
Independent reflections	5642 (R_{int} = 0.0421)	5869 (R_{int} = 0.0717)
Goodness-of-fit on F^2	1.103	1.156
Final *R* indices [$I > 2\sigma(I)$]	0.0415	0.0598
R_w	0.0816	0.0985

Table 2
Select bond lengths (Å), angles (°) and structural parameters for **1** and **2**.

1		**2**	
Ni–Cl	2.1759(7)	Ni–Cl	2.1829(9)
Ni–C(10)	1.896(2)	Ni–C(11)	1.895(3)
Ni–C1	2.119(2)	Ni–C1	2.132(3)
Ni–C(2)	2.019(3)	Ni–C(2)	2.041(3)
Ni–C(3)	2.028(2)	Ni–C(3)	2.025(3)
Ni–C(4)	2.412(2)	Ni–C(4)	2.385(3)
Ni–C(9)	2.437(2)	Ni–C(9)	2.415(3)
C(1)–C(2)	1.394(4)	C(1)–C(2)	1.407(5)
C(1)–C(9)	1.442(3)	C(1)–C(9)	1.454(5)
C(2)–C(3)	1.421(4)	C(2)–C(3)	1.423(5)
C(3)–C(4)	1.465(4)	C(3)–C(4)	1.458(5)
C(4)–C(9)	1.421(3)	C(4)–C(9)	1.419(4)
C1–Ni–Cl	96.5(8)	C1–Ni–Cl	95.0(1)
C1–Ni–C3	66.3(1)	C1–Ni–C3	66.6(1)
C3–Ni–C10	102.6(1)	C3–Ni–C11	103.4(1)
C10–Ni–Cl	95.4(1)	C11–Ni–Cl	95.5(1)
ΔM-C (Å)[a]	0.35	ΔM-C (Å)[a]	0.32
HA (°)[b]	11.4	HA (°)[b]	10.1
FA (°)[c]	12.5	FA (°)[c]	11.4

[a] ΔM-C = 1/2[M-Cav(for C4, C5)] − 1/2[M-Cav(for C1, C3)].
[b] HA is the angle formed between the planes formed by the atoms C(1), C(2), C(3) and C(1), C(3), C(4), C(5).
[c] FA is the angle formed between the planes formed by the atoms C(1), C(2), C(3) and C(4), C(5), C(6), C(7), C(8), C(9).

trix least-squares procedures based on F^2. All non-hydrogen atoms were refined with anisotropic displacement coefficients. Hydrogen atoms were treated as idealized contributions. The structures were solved and refined using SHELXS-97 and SHELXL-97 programs, respectively. Crystal data, collection and main refinement parameters are given in Table 1. Selected bond lengths (Å) and angles (°) for **1** and **2** are given in Table 2.

2.5. A typical procedure for the polymerization of styrene

A typical procedure for the polymerization of styrene is given as follows. Under dry argon, complex **1** (12.0 mg, 0.02 mmol), $NaBPh_4$ (47.9 mg, 0.14 mmol), toluene (0.2 mL), and styrene (0.7 mL, 6.0 mmol) were added into a dry glass ampule in turn. Then, the sealed ampule was placed in a water bath held at 80 °C. After a definite reaction time, the polymerization was stopped by adding 1 mL of 5% HCl/ethanol. After evaporation of the solvent and unreacted monomer, the resultant polymer was dissolved in THF, followed by precipitation in 95% ethanol. After filtration, the white polymer was dried in vacuo at room temperature overnight. The polymer yield was determined gravimetrically.

3. Results and discussion

3.1. Synthesis and structural characterization of *1* and *2*

Focusing on the nickel-based system, the bulky aryl-substituted NHC complexes exhibit unusual stability or reactivity in certain instances [8,25,34]. So, as a continuation of our previous work on NHC indenylnickel(II) complexes, it was considered to test whether the reported imidazolium salts metathesis and indene elimination reaction [28–29] could also occur between 1,3-bis(2,6-diisopropylphenyl)imidazolium chloride (IPr·HCl) and $(1\text{-H-Ind})_2Ni$, to yield the corresponding bulky aryl-substituted NHC indenylnickel(II) complex. Thus, a 1:1 (in molar ratio) mixture of $(1\text{-H-Ind})_2Ni$ and IPr·HCl was stirred at 45 °C in CH_2Cl_2/THF overnight. This reaction worked smoothly from the change of color from red to dark red. After workup, the designed NHC complex **1** was isolated as dark red crystals in ca. 63% yield (Scheme 1). The proposed structure for **1** was first supported by elemental analysis and NMR spectroscopy. The ^1H NMR and ^{13}C NMR data indicated the presence of one indenyl group and one *N*-heterocyclic carbene group, respectively. Moreover, in the ^{13}C NMR spectrum, a singlet $C_{carbene}$ atom signal appears at δ 175.4 ppm, which resembles a clear downfield shift compared to the reported Ni(II) complexes of $\Delta\delta \sim 9$ ppm for (1-H-Ind)Ni(iPr)Cl (**3**, δ = 166.3 ppm) [28] or $\Delta\delta \sim 6$ ppm for CpNi(IPr)Cl (**6**, δ = 169.3 ppm) [33]. The identity of this complex is further confirmed by X-ray analysis. To further ascertain the versatility of this synthetic approach, the similar reaction of the alkyl-substituted bis-indenyl Ni(II) complex of $(1\text{-CH}_3\text{-Ind})_2Ni$ with the same imidazolium salt was tested in turn. The analogous chloride **2** was isolated as dark red crystals in ca. 70% yield by a similar procedure (Scheme 1). Elemental analysis, NMR spectroscopy and X-ray analysis confirmed the expected product composition. In its ^{13}C NMR spectrum, the singlet $C_{carbene}$ atom signal appears at δ 177.1 ppm, which is very close to that of **1**. These results demonstrated undoubtedly that the imidazolium salt metathesis and indene elimination is a valid synthetic route to a variety of NHC indenylnickel(II) complexes.

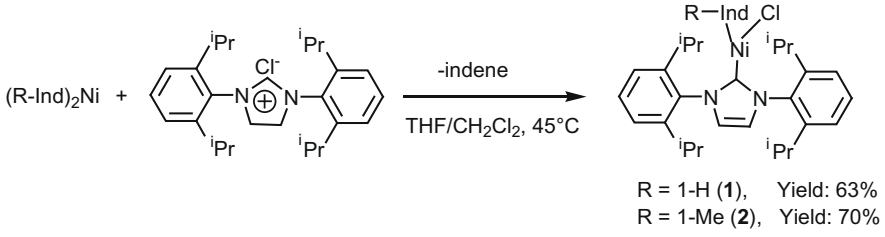
Compared with the alkyl-substituted NHC indenylnickel(II) complexes (1-H-Ind)Ni(iPr)Cl (iPr = 1,3-diisopropylimidazole-2-ylidene, **3**) [28], both **1** and **2** are much more thermally stable and melt at ca. 177 °C for **1** and ca. 206 °C for **2** (the melting point of **3** is 147 °C). Besides, they are also much less sensitive to air and moisture than complex **3**, and can even be kept unchanged in the open air for several hours in the solid state, compared to only a few minutes for complex **3** [28]. Additionally, it is worth mentioning that the tertiary phosphine analogues, $(1\text{-H-Ind})Ni(PPh_3)Cl$ [35] or $(1\text{-Me-Ind})Ni(PPh_3)Cl$ (**5**) [32], decompose immediately in open air.

3.2. Crystal structures of *1* and *2*

Crystals of **1** and **2** suitable for X-ray structure determination were grown from cold toluene solution. The crystallographic and measurement data are shown in Table 1, and selective bond lengths and angles are listed in Table 2. The molecular structures of these complexes are shown as ORTEP drawings in Figs. 1 (**1**) and 2 (**2**).

The molecular structures of **1** and **2** are similar, and both are monomeric in the solid state. The nickel atom is bonded to the indenyl group in a highly unsymmetric mode. The bond lengths of Ni–C1, Ni–C2 and Ni–C3 equal 2.119(2), 2.019(3) and 2.028(2) Å in **1** and 2.132(3), 2.041(3) and 2.025(3) Å in **2**, respectively, which are within the normal bonding distances, while the other two carbon atoms of the five-ring of the indenyl group (C4 and C9) are considerably further away (Ni–C4 = 2.412(2), Ni–C9 = 2.437(2) Å in **1**; Ni–C4 = 2.385(3), Ni–C9 = 2.415(3) Å in **2**). Such a highly unsymmetric mode of the indenyl ligand is not only very similar to the reported NHC indenylnickel(II) complexes [28–29] but also common in the family of the corresponding tertiary phosphine indenylnickel(II) complexes [27].

The Ni–Ind interaction could be quantitatively calculated by the main geometrical parameters such as (a) the slip value represented by ΔM-C and (b) the hinge and fold angles (HA and FA) representing the bending of the indenyl ligand at C1/C3 and C4/C9, respectively [28]. For example, ΔM-C values close to zero indicate little distortion from η^5 hapticity, whereas values above ca. 0.5 Å indicate nearly η^3 hapticity; HA values of ca. 14° or greater are associated with nearly trihapto cases. Here, in complex **1**, ΔM-C = 0.35 Å, HA = 11.4°, FA = 12.74°; and in complex **2**, ΔM-C = 0.32 Å, HA = 10.1°, FA = 11.4° (Table 2). These values led us to propose that the Ni–Ind bonding fashion here can be described as an intermediate hapticity between the η^5- and η^3-modes, which is somewhat similar to that found in $(1\text{-H-Ind})_2Ni$ (ΔM-C = 0.42 Å, HA = 13.9°, FA = 13.1°) [27]. However, the larger parameter values (ΔM-C, HA, and FA) for **1** indicated a more unsymmetric Ni–Ind interaction is present in **1**. This phenomenon that the methyl substituent on



Scheme 1. Synthesis of NHC indenylnickel(II) complexes of **1** and **2**.

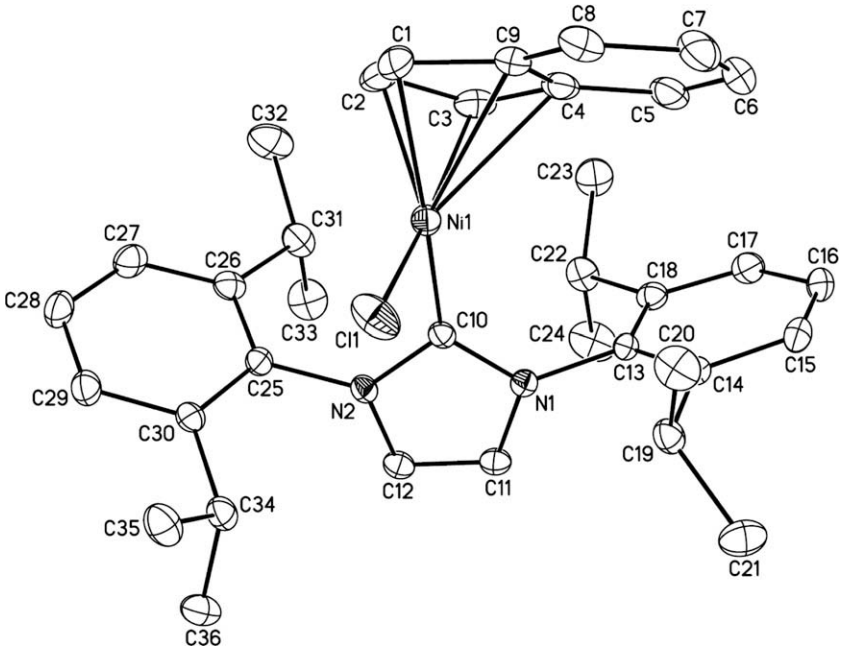


Fig. 1. The crystal structure of complex **1**.

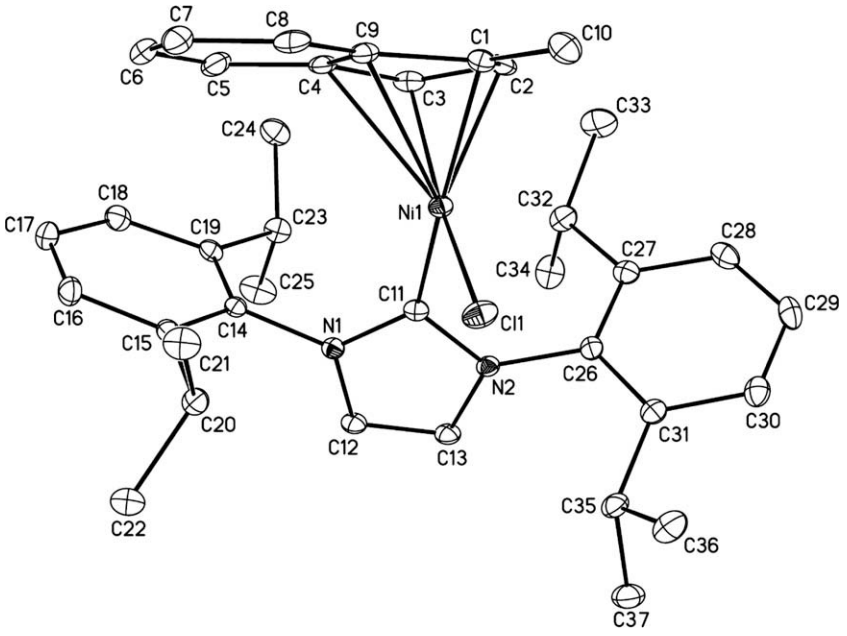


Fig. 2. The crystal structure of complex **2**.

the indenyl ligand of **2** leads to a less unsymmetric Ni-Ind interaction, i.e. represents a stronger Ni–Ind interaction, is very similar to the one found in its PPh_3-based analogous [32]. Furthermore, since the bond lengths of Ni–C1 and C2–C3 are longer than those of Ni–C3 and C1–C2 in **1** and **2**, respectively, it can be argued that the distortion in the hapticity of the indenyl ligand is not quite $\eta^5 \leftrightarrow \eta^3$ but rather $\eta^5 \leftrightarrow (\eta^1, \eta^2)$, i.e. the C1 = C2 occupy a single coordination site. In addition, the NMR data are also valuable in assessing the indenyl hapticity in solution [27]. For example, Zargarian has suggest that large chemical shift differences between H1 and H3 (>2 ppm) or C1 and C3 (>20 ppm) correlated well with a partial localization of bonding in the allyl moiety of the indenyl ligand in (I-H-Ind)Ni(PPh_3)Cl, since such a bonding type requires that C1 and C3 be quite different in terms of hybridization [35]. Herein we note that even if the assignment of these signals remains somewhat ambiguous, the H1 and H3 signals for **1** appear at 2.65 and 6.38 ppm, respectively, meanwhile the C1 and C3 signals for **2** appear at 58.1 and 93.3 ppm, respectively. The pairwise δ values are more than 3 ppm (H1/H3 in **1**) or 35 ppm (C1/C3 in **2**) apart, attesting to the greater sp^2 character of C1 in **1** and **2**, respectively [27].

Thus, the nickel atom is bonded to a Cl, $C_{carbene}$, C1, C2 and C3 of the indenyl group, to form a highly distorted square plane with C1 = C2 occupying a single coordination site (i.e. C1–C2 < C2–C3, Table 2). Such a coordinated fashion can be mainly attributed to the tendency of Ni(II) to avoid forming 18-electron complexes [27–28] and the unequal *trans* influences of the *N*-heterocyclic carbene and the halogen group [28]. Besides, as compared with 0.31 Å (ΔM-C), 12.1° (HA) and 9.1° (FA) reported for (1-H-Ind)Ni(iPr)Cl (**3**)

and 0.30 Å (ΔM-C), 12.3° (HA) and 9.5° (FA) reported for (1-H-Ind)Ni(iPr)Br (**4**) [28], the differences in these parameters among **1**, **2**, **3** and **4** demonstrate that the NHC ligand has a great influence on the Ni–Ind interaction presented in (R-Ind)Ni(NHC)X. The bulky IPr ligand possesses a more *trans* influence than the iPr ligand, which leads to a more unsymmetric Ni–Ind interaction. In addition, in comparison with the previously measured parameters for (I-H-Ind)Ni(PPh_3)Cl (i.e. ΔM-C = 0.26 Å) [35] and **5** (i.e. ΔM-C = 0.25 Å) [32], it is found that there is a more unsymmetric Ni–Ind interaction for NHC-based systems, which could be attributed to the stronger donor ability of the NHC ligand than that of PPh_3 [25] and a more unequal *trans* influences between the NHC ligand and the halogen group.

The Ni–$C_{carbene}$ bond lengths are almost the same for the two complexes (1.896(2) Å in **1** and 1.895(3) Å in **2**), and both are longer than that of 1.886(3) Å in **3** or 1.888(4) Å in **4** [28]. These data indicate that the ancillary ligand of (R-Ind)Ni(NHC)X, i.e. the indenyl moiety or the halogen atom has subtle effect on the Ni–$C_{carbene}$ interaction, meanwhile steric factor differences of the NHC ligands should be responsible for the weaker interaction between the nickel atom and the carbene carbon. Nevertheless, since alkyl-substituted NHCs are marginally more electron-donating than their aryl-substituted counterparts [25], it should be taken into account that small differences in donor capacities of NHC ligands may also play an important role in the Ni–$C_{carbene}$ interaction.

The Ni–Cl bond length of 2.1759(7) Å in **1** is slightly shorter than 2.1829(9) Å in **2**, and obviously shorter than that of 2.2025(7) Å in **3** [28]. The strongest Ni–Cl interaction in **1** might be a compensation for the weakening trend of the Ind–Ni interaction on going from **1** to **2** and then to **3**. Alternatively, a weakening trend of the Ni–Cl interaction is probably caused by the Cl–Ni π-donation [32]. However, it is well known that the X–M π-donation would destabilize d^8 complexes. In addition, the Ni–Cl distances in **1** or **2** are slightly shorter than that of 2.1822(7) Å in (I-H-Ind)Ni(PPh_3)Cl [35] or 2.1865(10) Å in **5** [32], respectively.

3.3. Catalytic activity of the free NHC indenylnickel(II) complexes for styrene polymerization

Previous studies had indicated that the neutral tertiary phosphine indenylnickel(II) complexes of (R-Ind)Ni(PR_3)X (X = halide) alone were inert toward the insertion of styrene, whereas the addition of proper amounts of $AgBPh_4$ (or $NaBPh_4$) and phosphine ligands led to the polymerization of styrene [36–41]. The role of $AgBPh_4$ (or $NaBPh_4$) was to abstract the halide ligand from these complexes, with the in situ formation of catalytically active cationic species, while addition of the phosphine ligand was needed to suppress the decomposition of the cationic species [27,39–41] unless the indenyl ligand tethered an amine moiety [36–38].

In the present paper, the catalytic activity of a series of free NHC indenylnickel(II) complexes for styrene polymerization has been investigated for the first time.[1] The preliminary results are listed in Table 3. The results show that the addition of a proper amount of $NaBPh_4$ is also necessary in the present case, which indicates that the present styrene polymerization also is catalyzed by the in situ generated electronically and coordinatively unsaturated species. For example, complex **1** alone shows no catalytic activity for styrene polymerization in toluene at 80 °C (Table 3, run 1), however, together with $NaBPh_4$, it shows considerable catalytic activity, i.e. 60% yield of polystyrene was obtained after 48 h polymerization (Table 3, run 2).

Table 3
Ni(II)-catalyzed homopolymerization of styrene.

Run	Initiator	$NaBPh_4$/[Ni]	t (h)	Yield (%)	$M_n \times 10^{-4}$	M_w/M_n
1	**1**	0	48	~0		
2	**1**	7	48	60	3.6	2.0
3	**2**	7	48	75	5.7	2.4
4	**3**	7	48	26	2.6	3.6
5	**4**	7	48	36	4.4	3.1
6[a]	**2**	7	48	33	3.3	2.6
7	**5**	7	48	24	0.4	2.4
8[a]	**5**	7	24	78	0.6	4.7
9	**6**	7	48	40	2.3	1.9

Conditions: styrene/[Ni] = 300:1 (molar ratio), toluene: 0.2 mL, T = 80 °C.
[a] $[NaBPh_4]/[Ni]/[PPh_3]$ = 7:1:1.

The influences of the indenyl ligand, the NHC ligand and the halide ligand on the catalytic activity of the corresponding Ni(II) complexes are investigated in turn. On the basis of the polymer yield, complex **2** shows the highest catalytic activity while complex **4** possess the lowest one (Table 3, runs 2–5). Meanwhile, the polystyrene with the highest number-average molecular weight (M_n = 57 000) was obtained with **2**. The diverse activities observed for these complexes may simply indicate that the catalytic active species remain ligated by the indenyl and carbene ligands, and the aryl-substituted NHC ligand together with the alkyl-substituted indenyl ligand are a benefit to enhance the catalytic activity of the NHC indenylnickel(II) complexes for the styrene polymerization. The difference in activity between **3** and **4** are probably due to their different thermal stabilities during the polymerization process [28,40].

All of the polymers obtained here are well soluble in THF and have very similar microstructures. Since a typical ^{13}C NMR spectrum ($CDCl_3$) of the obtained polystyrene shows characteristically broad signals of atactic polystyrene in the range of ca. 144–148 ppm [42], it is clear that the polystyrene obtained is an atactic polymer, which is very similar to those obtained by PPh_3-based indenylnickel(II) complexes [39–41] or by NHC-based cationic allylnickel(II) complexes [22].

It is worth noticing that the addition of a catalytic amount of other additives, i.e. PPh_3, is not necessary in the present case. For example, in the presence of one equivalent of PPh_3, the yield of polystyrene decreased greatly from 75% to 33% with a nearly half decrease of the number-average molecular weight (Table 3, runs 3 and 6). On the contrary, the addition of a catalytic amount of phosphine ligands is very necessary to styrene polymerization initiated by the phosphine analogues [39–41]. For example, in the absence of PPh_3, complex **5** shows a much lower catalytic activity, i.e. 24% yield of polystyrene with a relatively low number-average molecular weight (M_n = 4000) was obtained in the present conditions (Table 3, run 7). Notably, black powders appeared quickly in the glass ampule during this polymerization process, which indicated the decomposition of **5**. Otherwise, the addition of one equivalent of PPh_3 could efficiently suppress this decomposition and provide a much higher polymer yield (Table 3, run 8). Nevertheless, the polymer obtained still possesses a lower number-average molecular weight and a broadened molecular weight distribution. A similar phenomenon of decomposition was not observed in the styrene polymerization by NHC indenylnickel(II) complexes in the absence of PPh_3. The great difference of catalytic behaviors between the NHC indenylnickel(II) complexes and their tertiary phosphine analogues also indicates that the Ni center remains ligated by carbenes and the NHC ligands could provide a better coordination environment around the catalytic active Ni(II) species than the tertiary phophine ligands do in the indenylnickel(II) complexes.

Finally, the catalytic activity of CpNi(IPr)Cl (**6**) for the same polymerization has been investigated. As expect, its catalytic activity is lower than that of **1**, i.e. 40% yield of polystyrene was

[1] In one of our previous reports, i.e. Ref. [24], the catalytic activity of **4** for the polymerization of styrene had been mentioned briefly in comparison with the corresponding Ni(II) bromide containing an indenyl ligand tethered NHC moiety. However, we should point out that the reaction time of the styrene polymerization by **4** was incorrect, and it should be 48 h instead of the mentioned time of 24 h.

obtained after a 48 h polymerization (Table 3, run 9), which should be due to the so-called "indenyl effect" [32].

4. Conclusion

We have prepared two indenylnickel(II) complexes bearing a free bulky aryl-substituted NHC ligand via the reaction of the easily available metal precursor $(R\text{-}Ind)_2Ni$ and imidazolium salts. This procedure needs no extra step for the isolation and purification of the corresponding *N*-heterocyclic carbene, and could provide a valid synthetic route to a large number of NHC Ni(II) complexes containing polydentate ligands. The present work shows that the free NHC indenylnickel(II) halides are capable of polymerizing styrene in the presence of $NaBPh_4$, and a close relationship between their structures and catalytic activities is observed for the first time. The obtained results suggest that the presence of the bulky aryl-substituent on the NHC ligand, together with the alkyl-substituent on the indenyl ligand in these complexes, is of benefit not only to enhance their thermal/air stabilities but also to improve their catalytic activities. In comparison with the catalytic behaviors of PPh_3-based systems under the same conditions, the NHC-based ones show significant improvements in stability and catalytic performance. Further investigations focusing on developing the reactivity of NHC indenylnickel(II) complexes are in progress.

Supplementary data

CCDC 294978 and 665469 contain the supplementary crystallographic data for compounds **1** and **2**. These data can be obtained free of charge via http://www.ccdc.cam.ac.uk/conts/retrieving.html, or from the Cambridge Crystallographic Data Centre, 12 Union Road, Cambridge CB2 1EZ, UK; fax: (+44) 1223-336-033; or e-mail: deposit@ccdc.cam.ac.uk.

Acknowledgements

We thank the Chinese National Natural Science Foundation (Grant 20772089), the Department of Education of Jiangsu Province and the Key Laboratory of Organic Chemistry of Jiangsu Province for financial support.

References

[1] E.A.B. Kantchev, C.J. O'Brien, M.G. Organ, Angew. Chem., Int. Ed. 46 (2007) 2768.
[2] F. Glorius, *N*-Heterocyclic Carbenes in Transition Metal Catalysis, Springer-Verlag, Berlin, Germany, 2007.
[3] H. Clavier, S.P. Nolan, Annu. Rep. Prog. Chem., Sect. B 103 (2007) 193.
[4] F. Boeda, S.P. Nolan, Annu. Rep. Prog. Chem., Sect. B 104 (2008) 184.
[5] L. Cavallo, A. Correa, C. Costabile, H. Jacobsen, J. Organomet. Chem. 690 (2005) 5407.
[6] F.E. Hahn, Angew. Chem., Int. Ed. 45 (2006) 1348.
[7] N.M. Scott, H. Clavier, P. Mahjoor, E.D. Stevens, S.P. Nolan, Organometallics 27 (2008) 3181. and the references cited.
[8] H.V. Huynh, L.R. Wong, P.S. Ng, Organometallics 27 (2008) 2231. and the references cited.
[9] S. Kuhl, R. Schneider, Y. Fort, Adv. Synth. Catal. 345 (2003) 341.
[10] S. Caddick, F.G.N. Cloke, P.B. Hitchcock, A.K.de K. Lewis, Angew. Chem., Int. Ed. 43 (2004) 5824.
[11] K.. Matsubara, K. Ueno, Y. Koga, K. Hara, J. Org. Chem. 72 (2007) 5069, and the references cited.
[12] C.-H. Lee, W.-C. Ke, K.-T. Chan, C.-L. Lai, C.-H. Hu, H.M. Lee, Chem. Eur. J. 13 (2007) 582.
[13] Z.X. Xi, X.M. Zhang, W.Z. Chen, S.Z. Fu, D.Q. Wang, Organometallics 26 (2007) 6636.
[14] M.A. Schade, A. Metzger, S. Hug, P. Knochel, Chem. Commun. (2008) 3046.
[15] D.S. McGuinness, W. Mueller, P. Wasserscheid, K.J. Cavell, B.W. Skelton, A.H. White, U. Englert, Organometallics 21 (2002) 175.
[16] A.L. Mackinnon, M.C. Baird, J. Organomet. Chem. 683 (2003) 114.
[17] W. Buchowicz, A. Koziol, L.B. Jerzykiewicz, T. Lis, S. Pasynkiewicz, A. Pecherzewska, A. Pietrzykowski, J. Mol. Catal. A: Chem. 257 (2006) 118.
[18] J. Cámpora, L.O. De la Tabla, P. Palma, E. Álvarez, F. Lahoz, K. Mereiter, Organometallics 25 (2006) 3314.
[19] W.F. Li, H.M. Sun, M.Z. Chen, Q. Shen, Y. Zhang, J. Organomet. Chem. 693 (2008) 2047.
[20] X. Wang, S. Liu, G.X. Jin, Organometallics 23 (2004) 6002.
[21] B.E. Ketz, X.G. Ottenwaelder, R.M. Waymouth, Chem. Commun. (2005) 5693.
[22] S. Benson, B. Payne, R.M. Waymouth, J. Polym. Sci. A: Polym. Chem. 45 (2007) 3637.
[23] W.F. Li, H.M. Sun, M.Z. Chen, Z.G. Wang, D.M. Hu, Q. Shen, Y. Zhang, Organometallics 24 (2005) 5925.
[24] H.M. Sun, D.M. Hu, Y.S. Wang, Q. Shen, Y. Zhang, J. Organomet. Chem. 692 (2007) 903.
[25] S. Díez-González, S.P. Nolan, Coord. Chem. Rev. 251 (2007) 874.
[26] N.M. Scott, H. Clavier, P. Mahjoor, E.D. Stevens, S.P. Nolan, Organometallics 27 (2008) 3181.
[27] D. Zargarian, R. Giasson, Coord. Chem. Rev. 233–234 (2002) 157.
[28] H.M. Sun, Q. Shao, D.M. Hu, W.F. Li, Q. Shen, Y. Zhang, Organometallics 24 (2005) 331.
[29] D.M. Hu, H.M. Sun, Y.S. Wang, Q. Shen, F. Xue, Chin. J. Struct. Chem. 25 (2006) 1255.
[30] F.H. Köhler, Chem. Ber. 107 (1974) 570.
[31] L. Jafarpour, E.D. Stevens, S.P. Nolan, J. Organomet. Chem. 606 (2000) 49.
[32] T.A. Huber, M. Bayrakdarian, S. Dion, I. Dubuc, F. Bélanger-Gariépy, D. Zargarian, Organometallics 16 (1997) 5811.
[33] R.A. Kelly III, N.M. Scott, S. Díez-González, E.D. Stevens, S.P. Nolan, Organometallics 24 (2005) 3442.
[34] V. Ritleng, C. Barth, E. Brenner, S. Milosevic, M.J. Chetcuti, Organometallics 27 (2008) 4223.
[35] T.A. Huber, F. Bélanger-Gariépy, D. Zargarian, Organometallics 14 (1995) 4997.
[36] L.F. Groux, D. Zargarian, Organometallics 20 (2001) 3811.
[37] L.F. Groux, D. Zargarian, Organometallics 22 (2003) 3124.
[38] L.F. Groux, D. Zargarian, Organometallics 22 (2003) 4759.
[39] H.M. Sun, W.F. Li, X.Y. Han, Q. Shen, Y. Zhang, J. Organomet. Chem. 688 (2003) 132.
[40] W.F. Li, H.M. Sun, Q. Shen, Y. Zhang, K.B. Yu, Polyhedron 23 (2004) 1473.
[41] M. Jiménez-Tenorio, M.C. Puerta, I. Salcedo, P. Valerga, S.I. Costa, L.C. Silva, P.T. Gomes, Organometallics 23 (2004) 3139.
[42] N. Ishihara, T. Seimiya, M. Kuramoto, M. Uoi, Macromolecules 19 (1986) 2464.

Polyhedron 28 (2009) 2591–2598

Contents lists available at ScienceDirect

Polyhedron

journal homepage: www.elsevier.com/locate/poly

Synthesis, structure and DNA binding studies of mononuclear copper(II) complexes with mixed donor macroacyclic ligands, 2,6-bis({*N*-[2&3-(phenylselenato)alkyl]}benzimidoyl)-4-methylphenol

Vinay K. Verma [a,*], Ashish K. Asatkar [a], Tripti A. Jain [a], Santosh K. Tripathi [b], Rajendra Singh [c], Peter B. Hitchcock [d], Siddhi Nigam [e], Sushil K. Gupta [e]

[a] *Disha Institute of Management and Technology, Satya Vihar, Raipur, Chhattisgargh (C.G.) 492101, India*
[b] *Defence Materials and Stores Research & Development Establishment, Kanpur, India*
[c] *Defence Research and Development Organization, DRDO Bhawan, New Delhi, India*
[d] *Department of Chemistry, School of Life Sciences, University of Sussex, Brighton, UK*
[e] *School of Studies in Chemistry, Jiwaji University, Gwalior, India*

ARTICLE INFO

Article history:
Received 2 December 2008
Accepted 18 May 2009
Available online 6 June 2009

Keywords:
Selenium containing hybrid ligands
Copper(II) complexes
NMR
X-ray structure
DNA binding

ABSTRACT

Two new phenol based macroacyclic Schiff base ligands, 2,6-bis({*N*-[2-(phenylselenato)ethyl]}-benzimidoyl)-4-methylphenol (bpebmpH, **1**) and 2,6-bis({*N*-[3-(phenylselenato)propyl]}benzimidoyl)-4-methylphenol (bppbmpH, **2**) of the Se_2N_2O type have been prepared by the condensation of 4-methyl-2,6-dibenzoylphenol (mdbpH) with the appropriate (for specific reactions) phenylselenato(alkyl)amine. These ligands with Cu(II) acetate monohydrate in a 2:1 molar ratio in methanol form complexes of the composition $[(C_6H_2(O)(CH_3)\{(C_6H_5)C{=}N(CH_2)_nSe(C_6H_5)\}\{(C_6H_5)C{=}O\}_2Cu]$ (**3** ($n = 2$), **4** ($n = 3$)) with the loss of phenylselenato(alkyl)amine and acetic acid. In both these complexes, one arm of the ligand molecule undergoes hydrolysis, and links with Cu(II) in a bidentate (NO) fashion, as confirmed by single crystal X-ray crystallography of complex **3**. The selenium atoms do not form part of the copper(II) distorted square planar coordination sphere which has a *trans*-CuN_2O_2 core. The average Cu–N and Cu–O distances are, respectively, 1.973(3) and 1.898(2) Å. The N–Cu–N and O–Cu–O angles are, respectively, 167.4(11)° and 164.5(12)°. The compounds **1–4** have been characterized by elemental analysis, conductivity measurements, mass spectrometry, IR, electronic, ^1H and $^{77}Se\{^1H\}$ NMR spectroscopy and cyclic voltammetry. The interaction of complex **3** with calf thymus DNA has been investigated by a spectrophotometric method and cyclic voltammetry.

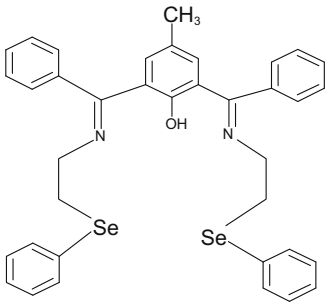
© 2009 Elsevier Ltd. All rights reserved.

1. Introduction

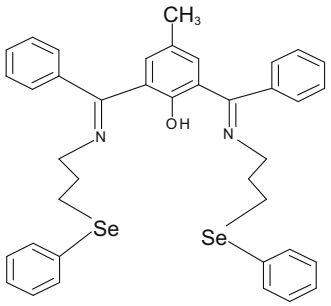
Ligands bearing variable donor functionalities such as O, S, N and P in their structural framework have been studied for several years and continue to be an area of active research for understanding the properties of donors that offer the opportunity to design metal complexes for specific purposes and applications [1–27]. The coordination chemistry of organochalcogen ligands containing 'hard' donor atoms (such as N and O) along with a 'soft' donor (Se or Te) is interesting because such a ligand framework can provide insight into competitive coordination behaviour between the 'hard' and 'soft' donors towards the metal center [28,29] and also stabilize low as well as high oxidation states of a metal atom. Such molecular systems may be important in transition metal catalyzed asymmetric synthesis [30,31] and as single source precursors in MOCVD processes [32–34]. Recently Khandelwal et al. have reported some pyridine based acyclic [35,36] and phenol based cyclic [37] Schiff bases. In fact, a number of polydentate ligands bearing N_3N_2, N_3O_2, N_3S_2 and NS_2P_2 are well documented and among them, a few of the systems have shown promising catalytic, biological, environmental and material properties [38–41]. We report herein the design and synthesis of a new (Se_2N_2O) molecular system (bpebmpH, **1** and bppbmpH, **2**), having both 'hard' and 'soft' donors in the ligand framework, and its reactivity towards Cu(II) ions. We also report our findings on a DNA binding study with one of the synthesized Cu(II) complexes.

* Corresponding author. Tel.: +91 771 4200292; fax: +91 771 4200110.
E-mail address: verma_vinay2002@rediffmail.com (V.K. Verma).

0277-5387/$ - see front matter © 2009 Elsevier Ltd. All rights reserved.
doi:10.1016/j.poly.2009.05.062



bpebmpH, 1



bppbmpH, 2

2. Experimental

All the chemicals used were of reagent grade. Solvents were purified by standard methods [42] and freshly distilled prior to use. The precursors 4-methyl-2,6-dibenzoylphenol (mdbpH) [43,44] and phenylselenato(alkyl) amine [45] were synthesized following the reported methods. Calf thymus DNA was obtained from Sigma and used as received. The sodium salt of CT-DNA was stored at 4 °C.

2.1. Physical measurements

Melting points of the compounds in the capillary tubes were recorded and are uncorrected. Elemental analyses were carried out on a Carlo-Erba Model DP 200 analyzer. The electrospray ion mass spectra (ESIMS) were recorded on a MICROMASS QUATTRO II triple quadrupole mass spectrometer. The solution was introduced into the ESI source through a syringe pump at the rate of 5 μL/min. The ESI capillary was set at 3.5 kV and the cone voltage was 40 V. The spectral print outs are the average of 6–8 scans. The ^{1}H NMR spectra were recorded on a Brucker AMX-400 FT NMR spectrophotometer in $CDCl_3$; the chemical shifts are recorded, relative to $SiMe_4$. The $^{77}Se\{^1H\}$ NMR spectra were recorded on the same instrument using Ph_2Se_2 as an external reference. Infrared spectra were recorded in the range 4000–400 cm^{-1} on a Nicolet Megna 750 FTIR spectrophotometer on a KBr disc. Electronic spectra were obtained with a Shimadzu UV-160A recording spectrophotometer.

2.1.1. Electrochemical measurements

Cyclic voltammetric measurements were carried out with an advanced electrochemical system, PARSTAT 2253 instrument equipped with a three-electrode system. The micro-cell model KO264 consisted of a glassy carbon working electrode, Pt wire as auxiliary electrode and a non-aqueous Ag/Ag^+ reference electrode with 0.1 M $AgNO_3$ in acetonitrile as the filling solution. Tetrabutylammonium perchlorate (0.1 M solution in CH_3CN) was used as the supporting electrolyte. Cyclic voltammograms with scan speeds of 50–350 mV/s were run in 10^{-4} M CH_3CN solution in a nitrogen atmosphere. Under these conditions the ferrocenium/ferrocene (fc^+/fc) couple shows a peak separation of 84 mV.

2.2. Synthesis of Schiff bases **1** and **2**

A solution of 4-methyl-2,6-dibenzoylphenol (mdbpH) (1.58 g, 5.0 mM) in dry acetonitrile (200 mL) was added drop-wise to a solution of the appropriate phenylselenato(ethyl)amine (2.0 g, 10.0 mM)/phenylselenato(propyl)amine (2.14 g, 10.0 mM) in acetonitrile (800 mL) in a 1:2 molar ratio respectively with stirring over a period of 7–8 h. The progress of the reaction was monitored by TLC. It took about 60 h for completion of the reaction. The organic solvent was removed under reduced pressure to obtain a viscous oily crude product. The product was purified by column chromatography (silica gel, 60–120 mesh, second fraction) using a solvent mixture of hexane:ethylacetate in 85:15 or 70:30 ratio. The characteristics of these compounds are given below.

2.2.1. 2,6-Bis({N-[2-(phenylselenato)ethyl]}benzimidoyl)-4-methylphenol(bpebmpH, **1**) [2,6-{$PhSe(CH_2)_2N{=}CPh\}_2C_6H_2$ (4-CH_3)(OH)]

Colour and state: yellow viscous liquid; yield: 2.48 g (73%). *Anal.* Calc. for $C_{37}H_{34}N_2OSe_2$: C, 65.29; H, 5.03; N, 4.11. Found: C, 65.23; H, 4.38; N, 4.08%. Positive ES–MS: *m/z* 683 [MH^+], 523, 500, 399, 158. FT IR (selected, cm^{-1}): *ν*(OH) 3450, *ν*(C=N) 1597, *ν*(C–O) 1252. UV–Vis λ_{max}/nm ($\varepsilon/M^{-1}\,cm^{-1}$) ($CH_3CN$): 391 ($PhO^- \rightarrow Ph$). ^{1}H NMR ($CDCl_3$, δ ppm): 15.90 (s, 1H, OH), 7.90–7.20 (m, 22H, C_6H_5 and C_6H_2), 3.47 (t, 4H, N–CH_2), 2.99 (t, 4H, Se–CH_2), 2.03 (s, 3H, CH_3). $^{77}Se\{^1H\}$ NMR ($CDCl_3$, δ ppm): 288.

2.2.2. 2,6-Bis({N-[3-(phenylselenato)propyl]}benzimidoyl)-4-methylphenol(bppbmpH, **2**) [2,6-{$PhSe(CH_2)_3N{=}CPh\}_2C_6H_2$ (4-CH_3)(OH)]

Colour and state: yellow viscous liquid; yield: 3.29 g (93%). *Anal.* Calc. for $C_{39}H_{38}N_2OSe_2$: C, 65.74; H, 5.37; N, 3.93. Found: C, 65.63; H, 5.31; N, 3.96%. Positive ES–MS: *m/z* 711 [MH^+], 553, 539, 514, 353, 158. FTIR (selected, cm^{-1}): *ν*(OH) 3416, *ν*(C=N) 1582, *ν*(C–O) 1253. UV–Vis λ_{max}/nm ($\varepsilon/M^{-1}\,cm^{-1}$) ($CH_3CN$): 390 ($PhO^- \rightarrow Ph$). ^{1}H NMR ($CDCl_3$, δ ppm): 15.90 (s, 1H, OH), 7.90–7.20 (m, 22H, C_6H_5 and C_6H_2), 3.40 (t, 4H, N–CH_2), 2.85 (t, 4H, Se–CH_2), 2.19 (q, 4 H, mid CH_2 (CH_2 between N–CH_2 and Se–CH_2)), 2.15 (s, 3H, CH_3). $^{77}Se\{^1H\}$ NMR ($CDCl_3$, δ ppm): 288.

2.3. Reactions of Schiff bases (**1**) and (**2**) with Cu(II)

A degassed solution of $Cu(OCOCH_3)_2.H_2O$ (0.10 g, 0.5 mM) in freshly distilled methanol (5 mL) was added to the degassed solution of the ligand *bpebmpH* (0.68 g, 1.0 mL)/*bppbmpH* (0.71 g, 1.0 mM) in dry methanol (15 mL) under an argon atmosphere. The reaction was carried out at room temperature with vigorous stirring. Precipitation of a green solid started almost immediately after mixing the reactants. After stirring the reaction mixture for 12 h, the precipitate thus obtained was filtered, washed with cold methanol and diethylether, and dried under vacuum. The characteristics of these complexes are given below.

2.3.1. Bis (2-[N-{2-(phenylselenato)ethyl}benzimidoyl]-6-benzoyl-4-methylphenolato)copper(II) (**3**) [(C_6H_2(O) (4-CH_3){PhC=N(CH_2)$_2$SePh}PhCO)$_2$.Cu]

Colour and state: dark green crystalline solid; yield: 0.42 g (79%). M.p.165 °C. *Anal.* Calc. for $C_{58}H_{48}N_2O_4Se_2Cu$: C, 65.81; H, 4.57; N, 2.64. Found: C, 65.12; H, 4.68; N, 2.51%. Positive ES–MS: *m/z* 1060 [MH^+]. FTIR (selected, cm^{-1}): *ν*(C=O) 1656, *ν*(C=N) 1531, *ν*(C–O) 1244, *ν*(Cu–N) 578, *ν*(Cu–O) 445. UV–Vis (nm) ($\varepsilon/M^{-1}cm^{-1}$)($CH_3CN$): 610 (167), 380 (10,080). ^{1}H NMR ($CDCl_3$, δ ppm): 7.90–7.20 (m, 34H, C_6H_5 and C_6H_2), 3.56 (t, 4H, N–CH_2), 3.05 (t, 4H, Se–CH_2), 2.07 (s, 3H, CH_3). Λ_M (10^{-3} M, CH_3CN, 298 K): 15 *S* cm^2 mol^{-1}.

2.3.2. Bis (2-[N-{3-(phenylselenato)propyl}benzimidoyl]-6-benzoyl-4-methylphenolato)copper(II) (**4**) [(C_6H_2(O)(4-CH_3) {PhC=N(CH_2)$_3$SePh}PhCO)$_2$.Cu)]

Colour and state: light green crystalline solid; yield: 0.29 g, (54%). M.p.176 °C. *Anal.* Calc. for $C_{60}H_{52}N_2O_4Se_2Cu$: C, 66.32; H, 4.82; N, 2.57. Found: C, 66.42; H, 4.61; N, 2.48%. Positive ES–MS: *m/z* 1088 [MH^+]. FTIR (selected, cm^{-1}): *ν*(C=O) 1657, *ν*(C=N)

1532, ν(C–O) 1244, ν(Cu–N) 569, ν(Cu–O) 445. UV–Vis (nm) (ε/M^{-1} cm^{-1}) (CH_3CN): 615 (170), 389 (10,100). ^1H NMR ($CDCl_3$, δ ppm): 7.90–7.20 (m, 34H, C_6H_5 and C_6H_2), 3.56 (t, 4H, N–CH_2), 2.85 (t, 4H, Se–CH_2), 2.19 (q, 4 H, mid-CH_2), 2.14 (s, 3H, CH_3). Λ_M (10^{-3} M, CH_3CN, 298 K): 70 S cm^2 mol^{-1}.

2.4. DNA binding studies

The experiments involving the interaction of the complex with CT-DNA were carried out in doubly distilled water buffer containing 5.0 mM Tris [Tris(hydroxymethyl)-aminomethane] and 50 mM NaCl and adjusted to pH 7.2 with hydrochloric acid. Solutions of CT-DNA gave ratios of absorbance at 260 and 280 nm of about 1.8–1.9, indicating that the DNA was free of protein contamination [46]. The DNA concentration per nucleotide was determined spectrophotometrically by employing a molar absorption coefficient of 6600 M^{-1} cm^{-1} at 260 nm after 1:100 dilution [47]. The complex was dissolved in 1% DMSO and 99% Tris–HCl buffer (5.0 mM Tris–HCl, 50 mM NaCl, pH 7.2) at a concentration of 3.0×10^{-5} M. An absorption titration was performed on 30 μmol L^{-1} compound by varying the concentration of nucleic acid. While measuring the absorption spectra, an equal amount of CT-DNA was added to both the compound solution and the reference solution to eliminate the absorbance of CT-DNA itself. Titration curves were constructed from the fractional change in absorption intensity as a function of DNA concentration. The intrinsic binding constant, K_b of the complex with CT-DNA was determined according to the following equation [48] through a plot of [DNA]/($\varepsilon_a - \varepsilon_f$) versus [DNA]/($\varepsilon_b - \varepsilon_f$)

$$[DNA]/(\varepsilon_a - \varepsilon_f) = [DNA]/(\varepsilon_b - \varepsilon_f) + 1/K_b(\varepsilon_b - \varepsilon_f), \quad (1)$$

where [DNA] is the concentration of DNA in base pairs, the apparent absorption coefficients ε_a, ε_f and ε_b correspond to A_{obsd}/[Cu], the extinction coefficient for the free copper complex and the extinction coefficient for the bound copper complex, respectively. In plots of [DNA]/($\varepsilon_a - \varepsilon_f$) versus [DNA]/($\varepsilon_b - \varepsilon_f$), K_b is given by the ratio of the slope to the intercept.

For the cyclic voltammetry, the supporting electrolyte was 50 mM NaCl, 5 mM Tris, pH 7.2 and an aqueous Ag/AgCl reference electrode with 3 M NaCl in saturated AgCl as the filling solution was used.

2.5. X-ray structure determination

Crystals of the complex 3 were grown as dark green needles by slow evaporation from the chloroform solution. Data were collected on a Nonius-Kappa CCD diffractometer and the structure solution and refinements were made by SHELXL-97 [49], as incorporated in the package WINGX [50]. Absorption corrections were made by MULTISCAN [51]. Non-hydrogen atoms were anisotropic and hydrogen atom positions were included in the riding mode. The ORTEP-3 program [52] was used to prepare the molecular drawings. Data collection parameters are given in Table 1. Selected bond lengths and angles are listed in Table 2.

Table 1
Crystal data and structure refinement for the copper complex **3**.

Empirical formula	$C_{58}H_{48}CuN_2O_4Se_2$
Formula weight	1058.44
T (K)	173(2)
Wavelength (Å)	0.71073
Crystal system	monoclinic
Space group	$P2_1/c$ (No. 14)
Unit cell dimensions	
a (Å)	9.4574(1)
b (Å)	32.4848(7)
c (Å)	15.7356(3)
α (°)	90
β (°)	5.842(1)
γ (°)	90
Volume (Å^3)	4809.21(15)
Z	4
Density (calculated) (Mg/m^3)	1.46
Absorption coefficient (mm^{-1})	2.02
F(0 0 0)	2156
Crystal size (mm^3)	0.25 × 0.20 × 0.05
θ Range for data collection (°)	3.45–26.02.
Index ranges	$-11 \leqslant h \leqslant 11$, $-36 \leqslant k \leqslant 40$, $-19 \leqslant l \leqslant 18$
Reflections collected	32 720
Independent reflections	9413 [R_{int} = 0.060]
Reflections with $I > 2\sigma(I)$	6496
Completeness to θ = 26.02°	99.0%
$T_{max.}$ and $T_{min.}$	0.7705 and 0.6207
Refinement method	full-matrix least-squares on F^2
Data/restraints/parameters	9413/0/606
Goodness-of-fit (GOF) on F^2	1.009
Final R indices [$I > 2\sigma(I)$]	R_1 = 0.050, wR_2 = 0.098
R indices (all data)	R_1 = 0.088, wR_2 = 0.112
Largest difference peak and hole (e Å^{-3})	0.99 and −1.09

Table 2
Selected bond lengths (Å) and bond angles (°) for compound **3**.

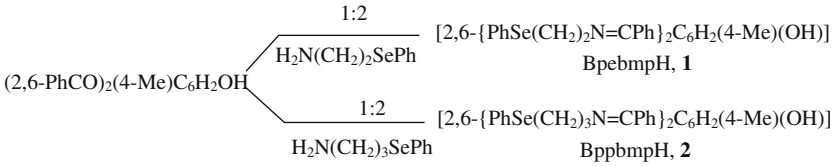
Bond lengths	
Cu–O(3)	1.884(2)
Cu–O(1)	1.913(2)
Cu–N(1)	1.973(3)
Cu–N(2)	1.974(3)
Se(1)–C(24)	1.925(4)
Se(1)–C(23)	1.938(4)
Se(2)–C(53)	1.913(4)
Se(2)–C(52)	1.949(4)
O(1)–C(1)	1.311(4)
O(2)–C(7)	1.217(4)
O(3)–C(30)	1.315(4)
O(4)–C(36)	1.220(4)
N(1)–C(15)	1.298(4)
N(1)–C(22)	1.479(4)
N(2)–C(44)	1.298(4)
N(2)–C(51)	1.485(4)
Bond angles	
O(3)–Cu–O(1)	167.38(11)
O(3)–Cu–N(1)	88.23(10)
O(1)–Cu–N(1)	89.35(11)
O(3)–Cu–N(2)	92.27(11)
O(1)–Cu–N(2)	93.35(11)
N(1)–Cu–N(2)	164.50(12)
C(22)–N(1)–Cu	116.8(2)
C(51)–N(2)–Cu	112.6(2)

3. Results and discussion

3.1. Ligand syntheses and characterization

The monoprotic hybrid macroacyclic ligands **1** and **2** were synthesized via a one step dipodal condensation of 4-methyl-2,6-dibenzoylphenol with the appropriate phenylselenato(alkyl)amine in a 1:2 molar ratio in acetonitrile (Scheme 1).

The condensation product is dependent on the reaction conditions. In a concentrated solution of reactants, only one carbonyl group of phenol condenses with the amine group of the phenylselenato(alkyl)amine to give rise to open-chain end-off unsymmetrical ($SeNO_2$) ligands, whereas in dilute solution both arms condense to yield symmetrical (Se_2N_2O) ligands in high yield along with some one arm condensed products. The open-chain end-off unsymmetrical ($SeNO_2$) type ligands are less soluble in the solvent, and therefore separate out first as a yellow solid powder. However following the experimental conditions, open-chain end-off



Scheme 1. Synthesis of ligands 1 and 2.

symmetrical (Se_2N_2O) macroacyclic ligands (**1**) and (**2**) were obtained in the pure form. Since the ligands (**1**) and (**2**) are obtained in good yield, after chromatographic workup, only these have been used for further characterization and complexation reactions.

The elemental analyses agreed well with their formulation. The ESI mass spectra of the ligands show the molecular ion peak along with typical isotopic patterns for selenium containing peaks. The molecular ion peak of these ligands corresponds to the condensation product of the precursors, 4-methyl-2,6-dibenzoylphenol with phenylselenato(ethyl)amine and phenylselenato(propyl)amine in a 1:2 molar ratio, respectively. The IR spectra of both ligands (**1**) and (**2**) show no N–H stretching frequency, suggesting that both the nitrogens are tertiary. The bands at 1597 cm^{-1} in **1** and 1581 cm^{-1} in **2** are attributable to ν(C=N). In addition, another band of low intensity appears in both the ligands at 1662 cm^{-1}, which may be due to ν(C=O). The appearance of this band may be due to presence of ethylacetate in traces, which was used as an eluent during the purification of the ligands by column chromatography. Further, a broad band appearing around 3450 in **1** and 3416 cm^{-1} in **2** due to ν(O–H) strongly suggests the presence of intramolecular hydrogen bonding between the phenolic hydrogen and azomethine nitrogen.

Intramolecular hydrogen bonding is also confirmed by significant deshielding of the phenolic (OH) proton signal by the order of 3.7 ppm as compared to 4-methyl-2,6-dibenzoylphenol (appears at δ 12.2 ppm) in their ^{1}H NMR spectra. The triplets due to N–CH_2 and Se–CH_2 protons in both ligands are appreciably shifted downfield as compared to the precursors 2- phenylselenato(ethyl)amine (δ 3.1 (t, 4H, N–CH_2), 2.9 (t, 4H, Se–CH_2)) and phenylselenato(propyl)amine (δ 2.9 (t, N–CH_2), 2.71 (t, Se–CH_2)). The appreciable deshielding in these proton signals along with the intensity ratios, as well as the disappearance of the –NH_2 signal [δ = 1.55 ppm {phenylselenato(ethyl)amine}, δ = 1.05 ppm {phenylselenato(propyl)amine}] suggest the condensation of the benzoyl oxygen of 4-methyl-2,6-dibenzoylphenol with the –NH_2 group of phenylselenato(alkyl)amine in a 1:2 molar ratio.

Structurally, this ligand framework is interesting as the presence of hetero (N, O, Se) donor sites could make it practical to design molecular complexes with a variety of coordination modes, depending on the nature of the central metal atom.

3.2. Synthesis and properties of complexes *3* and *4*

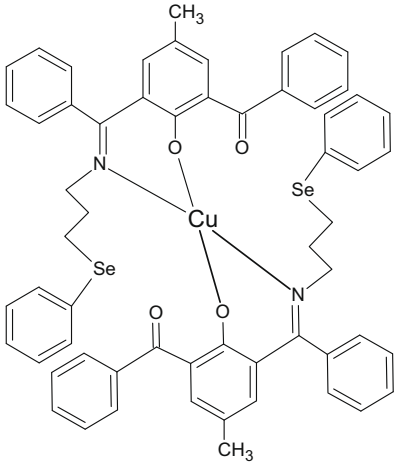
The reactivity of the selenium bearing ligands towards $Cu(OCOCH_3)_2H_2O$ has been studied by reacting them in a 2:1 molar ratio. The products obtained are found to have the composition $[(C_6H_2(O)(CH_3)\{(C_6H_5)C{=}N(CH_2)_nSe(C_6H_5)\}\{(C_6H_5)C{=}O\})_2Cu]$; n = 2, 3. The analytical data surprisingly suggests that one arm of the ligand is hydrolyzed at the C=N position, resulting in the release of the $PhSe(CH_2)_nNH_2$ moiety, whilst the other arm remains intact. The Cu(II) compounds are soluble in polar as well as non-polar solvents and are non-electrolytes.

The mass spectra of the Cu(II) complexes exhibit a molecular ion peak corresponding to a mass of double the partially hydrolyzed ligand plus one Cu(II) atom, suggesting the formation of complexes bearing a 2:1 ligand to metal stoichiometry. The ESIMS show a molecular ion peak with the typical isotopic patterns for selenium containing peaks.

In the infrared spectra of the Cu(II) complexes the absence of a ν(OH) absorption band suggests the combination of the phenolic proton with the CH_3COO^- ion of $Cu(OCOCH_3)_2H_2O$, and the linkage of the phenolic O with the Cu(II) ion. The combination of the phenolic proton of the ligand with the acetate group of $Cu(OCOCH_3)_2$-H_2O resulted in the release of water and the formation of CH_3COOH. The acid thus liberated probably catalyzes the hydrolysis of one arm of the ligand at the C=N position. Further, the ν(C=N) vibration is shifted to a lower frequency by ~50 cm^{-1}, suggesting the coordination of the azomethine N with Cu(II). However, the ν(C=O) band is found to be at almost the same position as in the precursor 4-methyl-2,6-dibenzoylphenol. This has been attributed to the non-involvement of the benzoyl O in coordination with the Cu(II) ion. Medium intensity bands, one in the 569–578 cm^{-1} region and one at 445 cm^{-1}, for both complexes can be assigned to ν(M–N) and ν(M–O), respectively [53,54].

The paramagnetic square planar Cu(II) complexes are expected to show three allowed absorption bands in the electronic spectra corresponding to the transitions: $e_g \rightarrow b_{1g}$ (d_{xz}, $d_{yz} \rightarrow d_{x2-y2}$), $a_{1g} \rightarrow b_{1g}$ ($d_{z2} \rightarrow d_{x2-y2}$), $b_{2g} \rightarrow b_{1g}$ ($d_{xy} \rightarrow d_{x2-y2}$) [55]. In the present investigation the Cu(II) complexes in CH_3CN show only one band in the 610–615 nm region before the charge transfer band takes over at higher energies. This band seems to have a major contribution from the $e_g \rightarrow b_{1g}$ transition, characteristic of a distorted square planar geometry [56].

The ^{1}H NMR spectra of the Cu(II) complexes do not show any phenolic proton signal, suggesting its displacement and coordination of the phenolic oxygen with Cu(II). Thus, based on the linkages in **3** and **4**, the partially hydrolyzed ligand molecules behave in a bidentate fashion and two molecules coordinate through the azomethine N and phenolic O atoms to one Cu(II) ion to give a N_2O_2 coordination sphere and forming two stable six membered rings around the Cu(II) ion. These binding modes are also confirmed by the X-ray crystal structure of complex **3**.



4

3.3. Crystal structure of complex **3**

The molecular structure of complex **3** is shown in Fig. 1. The two monoanionic ligands are bidentate, coordinating through the imino nitrogen and phenolic oxygen atoms, with both the nitrogen donors and the phenolic oxygen donors being *trans*. The copper coordination sphere is almost square planar, slightly distorted towards tetrahedral [O–Cu–O 167(11)°, N–Cu–N 164(12)°]. The Se atoms are not coordinated to Cu [Cu–Se 4.05, 4.82 Å]; they are on one side of the molecule and the phenol fragments are on the other side. There is no symmetry in the molecule as a whole. Both *cis* and *trans* complexes with the CuO_2N_2 core are known. The configuration is probably determined mainly by intraligand constraints e.g. chains linking N atoms or by steric interactions between the ligands. The latter effect probably accounts for the *trans* configuration here. The phenolic C–O distances in the complex [1.311(4) and 1.315(4) Å] are significantly shorter than that in mdbpH [1.360(4) Å] [43]. The average Cu–O and Cu–N bond lengths [1.898(2) and 1.973(3) Å, respectively] are similar to those in other *trans*-Schiff base complexes [57,58]. It is possible that the bond lengths in the *cis*-complexes are slightly longer [54] [Cu–N 1.964(2)–1.974(2) Å, Cu–O 1.926(2)–1.938(2) Å]. The Cu–N bonds in imino complexes, or where the rings are saturated, are longer [59–62]. One chelate ring, containing NO, is almost planar, with Cu slightly above the mean plane; the other ring is in a distorted boat configuration. The benzoyl O does not coordinate to the copper because the large Cu–N–CH_2CH_2SePh angle directs the ligand away from it [Cu–N1–C22 116.8(2)° and Cu–N2–C51 112.6(2)°, both wider than tetrahedral angles].

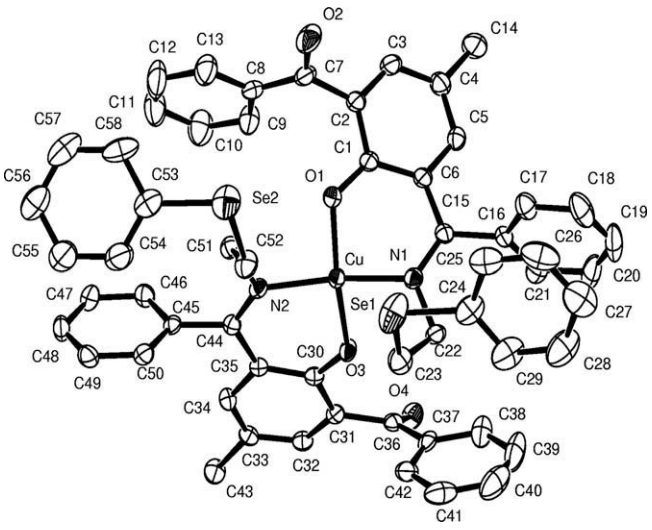


Fig. 1. Molecular structure of complex **3**.

Table 3
CV data of a 0.1 mM solution of the Schiff bases, bpebmpH **1** and bppbmpH **2** in CH_3CN/0.1 M NBu_4ClO_4 at a platinum electrode vs. Ag/0.1 M $AgNO_3$ at different scan rates.

Compound	Scan Rate	E_{pa} (V)	i_{pa} (μA)
bpebmpH **1**	100	0.760	28.40
	200	0.769	40.61
	300	0.784	49.45
	400	0.787	56.81
	500	0.793	62.83
bppbmpH **2**	100	0.559	1.570
	200	0.454	5.344
	300	0.589	6.399
	400	0.601	7.681
	500	0.634	9.366

3.4. Cyclic voltammetry

The electrochemical properties of the ligands and complexes were investigated by cyclic voltammograms (CV) in 0.1 M [NBu_4][ClO_4] in CH_3CN solution with 100–500 mV/s scan rates. All CV data were collected under a nitrogen atmosphere and potentials are reported with reference to Ag/0.1 M Ag^+. The results are summarized in Tables 3 and 4. The cyclic voltammograms of the ligands bpebmpH **1** and bppbmpH **2** (Fig. 2) exhibit an oxidation peak at

Table 4
CV data of a 0.1 mM solution of the complexes **3** and **4** in CH_3CN/0.1 M NBu_4ClO_4 at a platinum electrode vs. Ag/0.1 M $AgNO_3$ at different scan rates.

Complex	Scan Rate	E_{pa}(V)	i_{pa} (μA)	E_{pc}(V)	i_{pc} (μA)
Complex **3**	100	−0.962	5.585	−1.382	−26.20
	200	−0.374	15.27	−1.382	−49.54
	300	−0.386	22.49	−1.412	−73.99
	400	−0.374	30.56	−1.466	−99.47
	500	−0.374	42.78	−1.466	−119.70
Complex **4**	100	−0.872	5.109	−1.400	−18.98
	200	−0.326	20.54	−1.562	−62.19
	300	−0.296	29.10	−1.574	−79.46
	400	−0.278	40.23	−1.598	−89.64
	500	−0.254	51.40	−1.616	−108.10

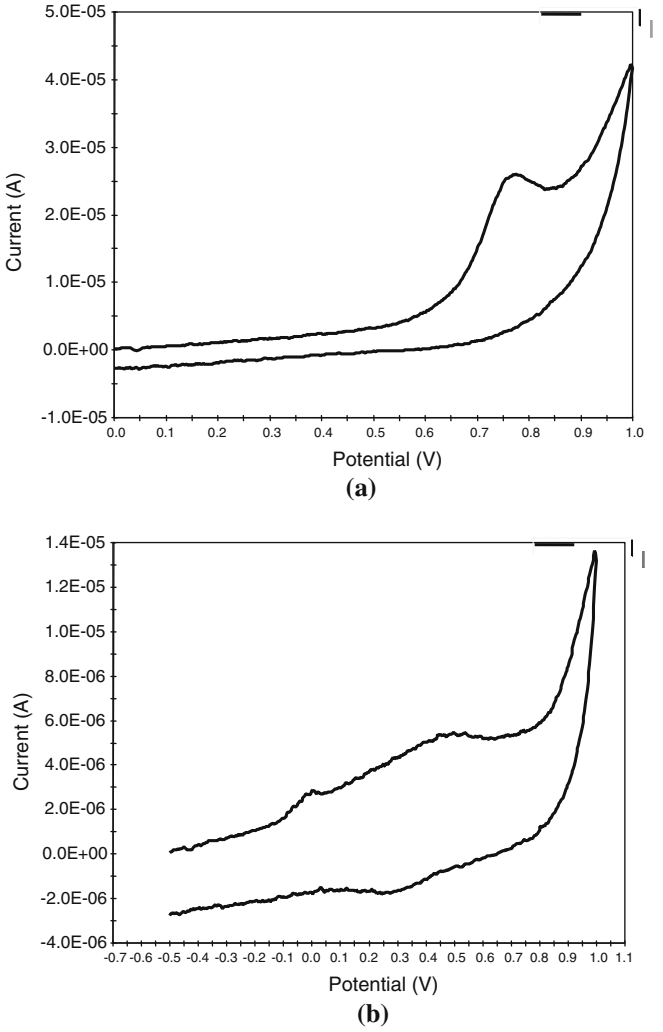


Fig. 2. Cyclic voltammograms of 0.1 mM solutions of the Schiff base bpebmpH **1** (a) and bppbmpH **2** (b) in CH_3CN/0.1 M NBu_4ClO_4 at a platinum electrode vs. Ag/0.1 M Ag^+ at 100 mV/s scan rate.

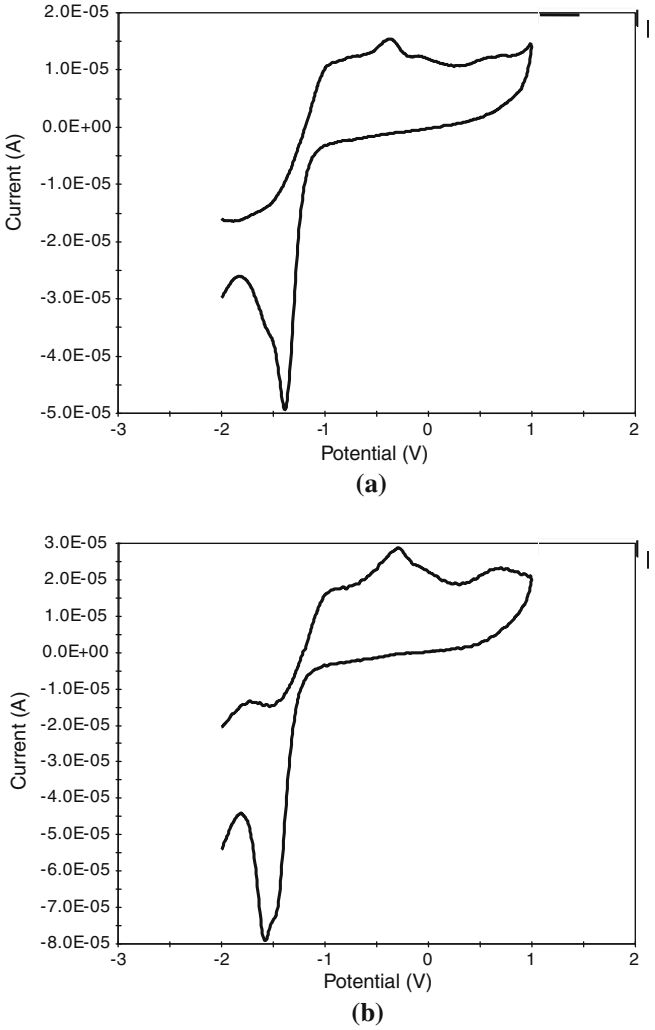


Fig. 3. Cyclic voltammograms of a 0.1 mM solution of complex **3** (a) and complex **4** (b) in CH_3CN/0.1 M NBu_4ClO_4 at a platinum electrode vs. Ag/0.1 M $AgNO_3$ at 200 mV/s scan rate.

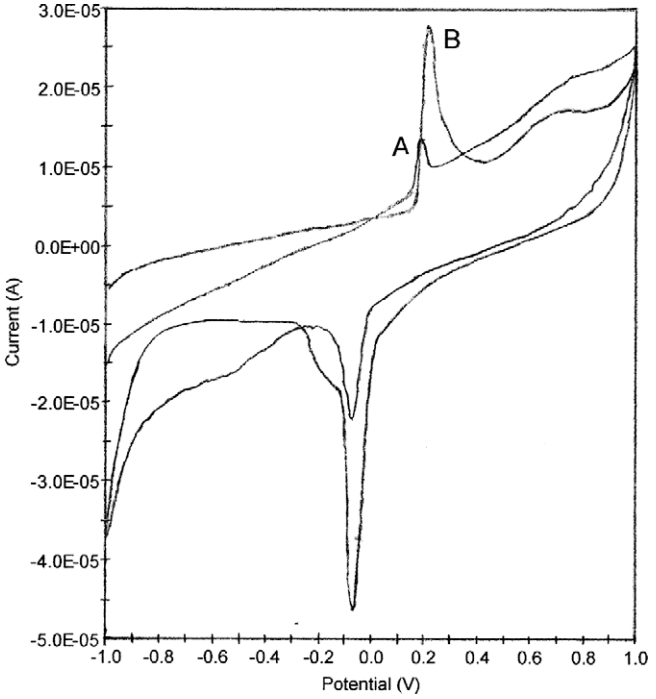


Fig. 5. Cyclic voltammograms of complex **3** (30 μM) in the absence (A) and the presence (B) of CT-DNA (30 μM) in 50 mM NaCl, 5 mM Tris, pH 7.2. Scan rate, 100 mV/s.

E_{pa} 0.778 and 0.567 V, respectively. The oxidation of **1** and **2** is electrochemically irreversible in spite of the strong intramolecular O–H···N hydrogen bond involving the phenol O and the imine N atoms. In the cyclic voltammograms of complexes **3** and **4** (Fig. 3), there is one oxidation peak (E_{pa} −0.494 (**3**), −0.405 V (**4**)) and one reduction peak (E_{pc} −1.422 (**3**), −1.550 V (**4**)). The reduction peaks for the complexes are due to Cu^{II} changing to Cu^{I}. The peak separation and current ratio between the related cathodic and anodic waves change with scan rate, indicating a quasi-reversible process. Free $Cu(CH_3COO)_2{\cdot}H_2O$ shows a different reduction

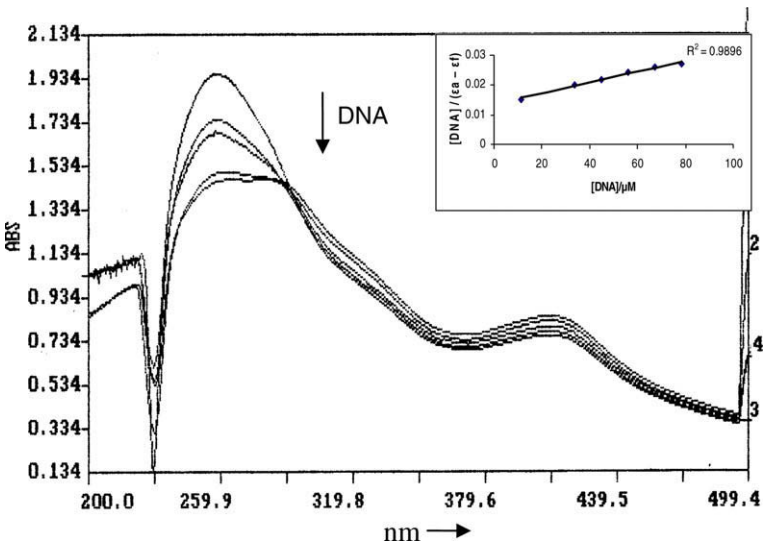


Fig. 4. Absorption spectra of complex **3** (30 μM) at 7.2 pH in the presence of increasing amounts of CT-DNA (0–80 μM). Inset: plot of [DNA]/($\varepsilon_a - \varepsilon_f$) vs. [DNA] for the titration of DNA with the Cu(II) complex **3**.

Table 5
Cyclic voltammetric behaviour of complex **3** in the presence of CT-DNA.

Scan rate (mV/s)	R	E_{pa}/V (i_{pa})/μA	E_{pc}/V (i_{pc})/μA	ΔE_p (mV)	$E^{\circ\prime}$ (V)	i_{pa}/i_{pc}
100	0	0.192 (13.75)	−0.068 (−22.34)	260	0.062	0.61
	30	0.224 (27.95)	−0.060 (−46.10)	284	0.082	0.61
	60	0.192 (27.66)	−0.032 (−42.63)	224	0.080	0.64
	90	0.196 (32.21)	−0.028 (−44.81)	224	0.084	0.71
	120	0.196 (32.31)	−0.032 (−45.03)	228	0.082	0.71
200	0	0.200 (24.52)	−0.076 (−33.31)	276	0.062	0.73
	30	0.240 (71.87)	−0.056 (−56.65)	296	0.092	1.26
	60	0.236 (62.85)	−0.064 (−67.44)	300	0.086	0.93
	90	0.228 (56.41)	−0.056 (−67.50)	284	0.086	0.84
	120	0.256 (88.62)	−0.052 (−65.38)	308	0.102	1.35

$\Delta E_p = (E_{pa} - E_{pc})$; $E^{\circ\prime} = 1/2(E_{pa} + E_{pc})$; complex 30 μM; R = [DNA]/[complex].
Supporting electrolyte: 50 mM NaCl + 5 mM Tris, pH 7.2; working electrode: Pt; reference electrode: Ag/AgCl.

peak at −0.707 V under similar conditions. The anodic peak potentials of the complexes are shifted to more negative values than that observed in the case of the ligand, which is in further conformity with the formation of a complex between the ligand and the Cu metal ion [63].

3.5. DNA binding properties of compound **3**

3.5.1. Absorption spectral studies

The application of electronic absorption spectroscopy is one of the most useful techniques for DNA binding studies [64]. Complex binding with DNA through intercalation usually results in hypochromism and bathochromism, due to the intercalative mode involving a strong stacking interaction between an aromatic chromophore and the DNA base pairs. The extent of the hypochromism commonly parallels the intercalative binding strength. The electronic absorption spectrum of complex **3** in 5 mM Tris–HCl/50 mM NaCl buffer exhibits bands around 408 and 264 nm. The band at 408 nm, arising from ligand-based transition, was used for the absorption spectral titration with CT-DNA. On incremental addition of DNA, the band shows only a small (6.0%) decrease in absorption accompanied by a small blue shift of 4 nm (Fig. 4). The binding constant K_b for the complex is found to be $1.46 \times 10^4\ M^{-1}$. These features are equivalent to those observed for the square planar Cu(II) complex Cu(*o*-VANAHE)$_2$ (*o*-VANAHE = 2(*o*-vanillinamine)-1-hydroxy-ethane; a bidentate Schiff base with a *trans*-CuN_2O_2 core) ($K_b = 7.3 \times 10^4\ M^{-1}$) [65]. The results suggest an association of the compound with DNA and it is also likely that this complex binds to the helix by intercalation [66].

3.5.2. Electrochemical studies

The cyclic voltammetric technique has been employed to study the interaction of the redox active Cu(II) complex with DNA in order to confirm the DNA bonding modes, suggested by the spectral studies. Typical CV behaviour of the copper complex in the absence (curve A) and presence (curve B) of CT-DNA is shown in Fig. 5. Summaries of the voltammetric results are given in Table 5. The cyclic voltammogram of complex **3** (v = 100 mV/s) in the absence of DNA featured the copper reduction of +2 to +1 at a cathodic peak potential, E_{pc}, of −0.068 V versus Ag/AgCl. Reoxidation of the +1 state occurred upon scan reversal at 0.192 V. The separation of the anodic and the cathodic peak potentials, ΔE_p, 260 mV (Table 5), indicates a quasi-reversible $1-e^-$ redox process. The formal potential, $E^{\circ\prime}$ (or voltammetric $E1/2$), taken as the average of E_{pc} and E_{pa}, was 0.062 V, in the absence of DNA. In presence of 30 μM DNA, at the same concentration of the complex, E_{pc} = −0.060 V and E_{pa} = 0.224 V. Thus, both the anodic and cathodic peak potentials shifted to more positive values versus a solution without DNA ($E^{\circ\prime}$ = 0.082 V). The value of ΔE_p in the presence of DNA was ca. 240 mV, showing that reversibility of the electron transfer process was maintained or even improved under these conditions. The apparent $E^{\circ\prime}$ shifted to more positive potentials by 20 mV in the presence of DNA. The peak current for reduction of the Cu(II) species, i_{pc}, decreased to 51% of that in the absence of DNA, for a solution with R = 30 (100 mV/s). The peak current for oxidation did not decrease under similar conditions. The ratio i_{pa}/i_{pc} was 0.61–0.71 with increasing R. Among the three kinds of binding modes for small molecules to DNA, Bard and coworkers [67] reported that if $E^{\circ\prime}$ shifted to a more negative value when small molecules interacted with DNA, the interaction mode was electrostatic binding. On the contrary, if $E^{\circ\prime}$ shifted to a more positive value, the interaction mode was intercalative binding. Thus, the observed results suggest that complex **3** interacts with DNA through an intercalative mode that involves a stacking interaction between the aromatic chromophore of the complex and the base pair of DNA.

4. Conclusions

In summary, two phenol based ligands **1** and **2** have been synthesized by dipodal condensation of 4-methyl-2,6-dibenzoylphenol with phenylselenato(alkyl)amine in acetonitrile in a 1:2 molar ratio respectively. The reaction of these ligands with Cu(II) metal ion revealed the cleavage of one arm of these ligands due to hydrolysis at the C=N position, leading to the release of the $PhSe(CH_2)_nNH_2$ (where n = 2, 3) moiety and the formation of a benzoyl group at one end. The partially hydrolyzed moiety of the ligands then forms complexes **3** and **4**, bearing a 2:1 ligand to metal stoichiometry in which two monoanionic ligands are bidentate coordinating through the azomethine N and phenolic O to one Cu(II) to give a N_2O_2 coordination sphere. Thus the phenolic proton of the ligand molecules is found to combine with the CH_3COO^- group of $Cu(OCOCH_3)H_2O$, liberating CH_3COOH. The structure of complex **3** revealed that the N_2O_2-donor sets of the two ligand fragments form a *trans*-distorted square planar configuration. Complex **3** shows binding with the helix of CT-DNA by intercalation.

5. Supplementary data

CCDC 706265 contains the supplementary crystallographic data for complex **3**. These data can be obtained free of charge via http://www.ccdc.cam.ac.uk/conts/retrieving.html, or from the Cambridge Crystallographic Data Centre, 12 Union Road, Cambridge CB2 1EZ, UK; fax: (+44) 1223-336-033; or e-mail: deposit@ccdc.cam.ac.uk.

Acknowledgements

We are grateful to the DRDO, New Delhi for financial assistance and for the award of a fellowship to A.A. We thank Dr. J. D. Smith, University of Sussex, UK and Prof. B.L. Khandelwal of DIMAT,

Raipur for discussion and IIT Kanpur for recording mass and NMR spectra.

References

[1] C.A. Schalley, A. Lützen, M. Albrecht, Chem. Eur. J. 10 (2004) 1072.
[2] M. Ruben, J. Rojo, F.J. Romero-Salguero, L.H. Uppadin, J.-M. Lehn, Angew. Chem. Int. Ed. 43 (2004) 3644.
[3] C.M. Hartshorn, P. Steel, Chem. Commun. (1997) 541.
[4] F.A. Cotton, C. Lin, C.A. Murillo, Acc. Chem. Res. 34 (2004) 759.
[5] C. Eschbaumer, U.S. Schubert, Angew. Chem. Int. Ed. 41 (2001) 2892.
[6] H.D. Selby, B.K. Ronald, Z. Zheng, Acc. Chem. Res. 36 (2003) 933.
[7] M. Fujita, K. Umemoto, M. Yoshizawa, N. Fujita, T. Kusukawa, B. Kumar, Chem. Commun. (2001) 509.
[8] C. Seel, F. Vögtle, Angew. Chem. Int. Ed. 31 (1992) 528.
[9] L. Brunsveld, B.J.B. Folmer, E.W. Meijer, R.P. Sijbesma, Chem. Rev. 101 (2001) 4071.
[10] F.A. Cotton, C. Lin, C.A. Murillo, Proc. Natl. Acad. Sci. USA 99 (2002) 4810.
[11] C.J. Kuehl, Y.K. Kryschenko, U. Radhakrishnan, S.R. Seidel, S.D. Huang, P.J. Stang, Proc. Natl. Acad. Sci. USA 99 (2002) 4932.
[12] M. Barboiu, J.-M. Lehn, Proc. Natl. Acad. Sci. USA 99 (2002) 5201.
[13] N.S. Oxtoby, A.J. Blake, N.R. Champness, C. Wilson, Proc. Natl. Acad. Sci. USA 99 (2002) 4905.
[14] A.J. Goshe, I.M. Steele, C. Ceccarelli, A.L. Rheingold, B. Bosnich, Proc. Natl. Acad. Sci. USA 99 (2002) 4823.
[15] M. Ohkita, M. Kawano, T. Suzuki, T. Tsuji, Chem. Commun. (2002) 3054.
[16] D.I. Schuster, J. Rosenthal, S. MacMahon, P.D. Jarowski, C.A. Alabi, D.M. Guldi, Chem. Commun. (2002) 2538.
[17] M. Hong, Y. Zhao, W. Su, R. Cao, M. Fujita, Z. Zhou, A.S.C. Chan, J. Am. Chem. Soc. 122 (2000) 4819.
[18] A.G. Bielejewska, C.E. Marjo, L.J. Prins, P. Timmerman, F. de Jong, D.N. Reinhoudt, J. Am. Chem. Soc. 123 (2001) 7518.
[19] L.J. Prins, K.A. Jolliffe, R. Hulst, P. Timmerman, D.N. Reinhoudt, J. Am. Chem. Soc. 122 (2000) 3617.
[20] L.J. Prins, E.E. Neuteboom, V. Paraschiv, M. Cregocalama, P. Timmerman, D.N. Reinhoudt, J. Org. Chem. Soc. 67 (2002) 4808.
[21] D.T. Vodak, K. Kim, L. Iordanidis, P.G. Rasmussen, A.J. Matzger, O.M. Yaghi, Chem. Eur. J. 9 (2003) 4197.
[22] P. Gamez, P.D. Hoog, O. Roubeau, M. Lutz, A.L. Driessen, A.L. Spek, J. Reedijk, Chem. Commun. (2002) 1488.
[23] A.J. Blake, N.R. Brooks, N.R. Champness, P.A. Cooke, A.M. Deveson, D. Fenske, P. Hubberstey, W.-S. Li, M. Schroder, J. Chem. Soc., Dalton Trans. (1999) 2103.
[24] H.K. Liu, W.-Y. Sun, D.-J. Ma, K.-B. Yu, W.-X. Tang, Chem. Commun. (2000) 591.
[25] M. Sasa, K. Tanaka, X. Bu, M. Shiro, M. Shionoya, J. Am. Chem. Soc. 123 (2001) 10750.
[26] R.D. Pike, B.D. Borne, J.T. Maeyer, A.L. Rheingold, Inorg. Chem. 41 (2002) 631.
[27] M.C. Carrion, A. Guerrero, F.A. Jalon, B.R. Manzano, A. de la Hoz, R.M. Claramunt, V. Milata, J. Elguero, Inorg. Chem. 41 (2003) 885.
[28] P.G. Jones, M. Carmen Ramirez de Arellano, J. Chem. Soc., Dalton Trans. (1996) 2713.
[29] C.O. Kienitz, C. Thone, P.G. Jones, Inorg. Chem. 35 (1996) 3990.
[30] Y. Nishibayashi, K. Segawa, J.D. Singh, S.I. Fukuzawa, K. Ohe, S. Uemura, Organometallics 15 (1996) 370.
[31] Y. Nishibayashi, J.D. Singh, Y. Arikawa, S. Uemura, M. Hidai, J. Organomet. Chem. 13 (1997) 531.
[32] Y. Cheng, T.J. Emge, J.G. Brennan, Inorg. Chem. 35 (342) (1996) 7339.
[33] M.L. Steigerwald, C.R. Sprinkle, J. Am. Chem. Soc. 109 (1987) 7200.
[34] W. Hirpo, S. Dhingra, A.C. Sutorik, M.G. Kanatzidis, J. Am. Chem. Soc. 115 (1993) 1597.
[35] J.D. Singh, M.D. Milton, B.L. Khandelwal, S. Karthikeyan, T.P. Singh, Phosphorus, Sulfur and Silicon 136–137 (1998) 299.
[36] J.D. Singh, M.S. Milton, G. Bhalla, B.L. Khandelwal, P. Kumar, T.P. Singh, R.J. Butcher, Phosphorus, Sulfur and Silicon 172 (2001) 223.
[37] S.K. Tripathi, B.L. Khandelwal, S.K. Gupta, Phosphorus, Sulfur and Silicon 177 (2002) 2285.
[38] T. Kawamoto, B.S. Hammes, R. Ostrander, A.L. Rheingold, A.S. Borovik, Inorg. Chem. 37 (1998) 3424.
[39] S. Brooker, T.J. Simpson, J. Chem. Soc. (1998) 1151.
[40] C.L. Merril, L.J. Wilson, T.J. Thamann, T.M. Loehr, N.S. Ferris, W.H. Woodruff, J. Chem. Soc. (1984) 2207.
[41] F.A. Chavez, C.V. Nguyen, M.M. Demstead, P. Mascharak, Inorg. Chem. 35 (1996) 6282.
[42] W.L.F. Armarego, D.D. Perrin, Purification of Laboratory Chemicals, fourth ed., Pergamon, Oxford, 1997.
[43] S.K. Gupta, P.B. Hitchcock, Y.S. Kushwah, Polyhedron 21 (2002) 1787.
[44] R.G. Hayter, F.S. Humiec, J. Inorg. Nucl. Chem. 26 (1964) 810.
[45] A. Khanna, A. Bala, B.L. Khandelwal, J. Organomet. Chem. 494 (1995) 199.
[46] J.J. Marmur, Mol. Biol. 3 (1961) 208.
[47] M.F. Reichmann, S.A. Rice, C.A. Thomas, P.J. Doty, J. Am. Chem. Soc. 76 (1954) 3047.
[48] A. Wolfe, G.H. Shimer, T. Meehan, Biochemistry 26 (1987) 6392.
[49] G.M. Sheldrick, Acta Crystallogr. A64 (2008) 112.
[50] L.J. Farrugia, J. Appl. Cryst. 32 (1999) 837.
[51] R.H. Blessing, Acta Crystallogr. 51a (1995) 33.
[52] L.J. Farrugia, J. Appl. Cryst. 30 (1997) 565.
[53] K. Nakamoto, Infrared and Raman Spectra of Inorganic and Coordination Compounds, fifth ed., Wiley, New York, 1997.
[54] Y.-P. Cai, C.-Y. Su, A.-W. Xu, B.-S. Kang, Y.-X. Tong, H.-Q. Liu, S. Jie, Polyhedron 20 (2001) 657.
[55] A.B.P. Lever, Inorganic Electronic Spectroscopy, second ed., Elsevier, Amsterdam, 1984.
[56] Y. Nishida, S. Kida, Bull. Chem. Soc. Jpn. 43 (1970) 3814.
[57] Y.-C. Shi, H.-M. Yang, H.-B. Song, Y.-H. Liu, Polyhedron 23 (2004) 1541.
[58] D.V. Baxter, K.G. Caulton, W.-C. Chiang, M.H. Chisolm, V.F. DiStasi, S.G. Dutremez, K. Folting, Polyhedron 20 (2001) 2589.
[59] D.L. Barber, S.J. Loeb, W.L. Martin, N.C. Payne, C.J. Willis, Inorg. Chem. 20 (1981) 272.
[60] S.J. Loeb, J.F. Richardson, C.J. Willis, Inorg. Chem. 22 (1983) 2736.
[61] H. Luo, P.E. Fanwick, M.A. Green, Inorg. Chem. 37 (1998) 1127.
[62] E. Lay, Y.-H. Song, Y.-C. Chiu, Y.-M. Lin, Y. Chi, A.J. Carty, S.-M. Peng, G.-H. Lee, Inorg. Chem. 44 (2005) 7226.
[63] D. Parker, E.S. Davies, C. Wilson, J. McMaster, Inorg. Chim. Acta 360 (2007) 203.
[64] J.K. Barton, J.J. Dannenberg, A.L. Raphael, J. Am. Chem. Soc. 106 (1984) 2172.
[65] L.-Z. Li, C. Xhao, T. Xu, H.-W. Ji, Y.-H. Yu, G.-Q. Guo, H. Chao, J. Inorg. Biochem. 99 (2005) 1076.
[66] K.E. Erkkila, D.T. Odom, J.K. Barton, Chem. Rev. 99 (1999) 2777.
[67] M.T. Carter, M. Rodriguez, A.J. Bard, J. Am. Chem. Soc. 111 (1989) 8901.

Polyhedron 28 (2009) 2599–2604

Contents lists available at ScienceDirect

Polyhedron

journal homepage: www.elsevier.com/locate/poly

Complexes of 3*d* metal ions of the Schiff-base, 4-hydroxy-*N*′-(4′-octadecyloxybenzylidene)benzohydrazide: Synthesis, spectral studies, crystal structure and magnetic interactions

Angad Kumar Singh [a], Sanyucta Kumari [a], K. Ravi Kumar [b], B. Sridhar [b], Miroslaw Wrzecion [c], Jerzy Mroziński [c], T.R. Rao [a,*]

[a] Department of Chemistry, Banaras Hindu University, Varanasi 221005, India
[b] Indian Institute of Chemical Technology, Hyderabad, India
[c] Faculty of Chemistry, University of Wrocław,14F Joliot-Curie, 50-383 Wroclaw, Poland

ARTICLE INFO

Article history:
Received 16 April 2009
Accepted 18 May 2009
Available online 27 May 2009

Keywords:
Mesogenic Schiff-base
Sq. pyramidal
Sq. planar
Anti-ferromagnetic and weak ferromagnetic interactions
Crystal structure and NMR and IR spectra

ABSTRACT

A novel hydrazide-based mesogenic (*nematic*) Schiff-base, 4-hydroxy-*N*′-(4′-octadecyloxybenzylidene)benzohydrazide, (Hhodbbh) (abbreviated as HL^3), was prepared and its structure studied by elemental analyses, mass, NMR and IR spectra and single crystal XRD (triclinic space group $P\bar{1}$ with $Z = 2$) techniques. The Schiff-base behaves as a non-deprotonated bi-dentate species in its metal complexes of the general formula, $[M(HL^3)_2](OAc)_2$ [M = Mn, Co, Ni, Cu and Zn]. The IR and NMR spectral data imply bonding of HL^3 species through amidic oxygen and azomethine nitrogen atoms. The Mn^{II} and Co^{II} complexes show gradual decrease in the $\chi_M T$ product with lowering of temperature and negative Weiss constants characteristic of anti-ferromagnetic interaction. The Mn^{II} complex shows magnetic hysteresis loops at 2.0 K.

© 2009 Elsevier Ltd. All rights reserved.

1. Introduction

Schiff-bases [1,2] play an important role in inorganic chemistry as they easily form stable complexes with most transition metal ions. The acid hydrazides, hydrazine derivatives and its metal complexes are known to exhibit a broad spectrum of biological, bactericidal and fungicidal activities and have great interest due to their analytical, industrial and pharmacological importance [3–5]. The chemistry of hydrazine derivatives has been investigated intensively in the last decade owing to their coordinative [3–5] and pharmacological activity [3–5] as well as their use in analytical chemistry as metal-extracting agents [5]. As a part of our investigation [6–10] on structural and spectroscopic studies of 3d metal complexes of a series of mesogenic organic Schiff-bases, we report here, the results of our investigations on synthesis, spectroscopic studies and crystal structure on a hydrazide-based mesogenic Schiff-base, 4-hydroxy-*N*′-(4′-octadecyloxybenzylidene)benzo-hydrazide (HL^3) and the corresponding 3d metal complexes.

2. Experimental

2.1. Starting materials

All reagents were purchased from commercial sources and used as received; 1-bromooctadecane, 4-hydroxybenzaldehyde and 4-hydroxybenzoic acid hydrazide are from Sigma–Aldrich, USA; all metal acetates and KOH are from Merck. The solvents received were dried using standard methods [11] when required.

2.2. Instrumentation

The ^{1}H NMR spectrum was recorded on a JEOL AL-300 MHz FT-NMR multinuclear spectrometer; C, H and N contents were microanalysed on an Elemental Vario EL III Carlo Erba 1108 analyser. Infrared spectra were recorded on a JASCO FT/IR (model-5300) spectrophotometer in the 4000–400 cm^{-1} region. The mass spectra were recorded on a JEOL SX-102 (EI/FAB) mass spectrometers. The UV–Vis spectra were recorded on a Shimadzu spectrophotometer, model, Pharmaspec, UV 1700. Magnetic susceptibility measurements were made at low temperature on a Quantum Design SQUID-based MPMSXL-5 type magnetometer. Single crystal X-ray data was collected at room temperature using a Bruker Smart Apex CCD diffractometer with graphite monochromated Mo Kα radiation ($\lambda = 0.71073$ Å) with ω method.

* Corresponding author. Tel.: +91 542 2307326; fax: +91 542 2368127.
E-mail address: drtrrao@gmail.com (T.R. Rao).

0277-5387/$ - see front matter © 2009 Elsevier Ltd. All rights reserved.
doi:10.1016/j.poly.2009.05.039

2.3. X-ray crystallographic data collection and refinement of the structure

X-ray data for the compound **HL^3** ***[aa85]*** was collected at room temperature. Preliminary lattice parameters and orientation matrices were obtained from four sets of frames. Unit cell dimensions were determined from the setting angles of 2854 reflections in the range of $2.43° < \theta < 23.79°$. Integration and scaling of intensity data was accomplished using the SAINT program [12]. The structure was solved by direct methods using SHELXS97 [13] and refinement was carried out by full-matrix least-squares technique using SHELXL97 [13]. Anisotropic displacement parameters were included for all non-hydrogen atoms. The N-bound H atom and O-bound H atom were located in a difference Fourier map and their positions and isotropic parameters were refined. All other hydrogen atoms were positioned geometrically and treated as riding atoms, with C–H distances in the range of 0.93–0.97 Å and with U_{iso}(H) values of $1.5U_{eq}$(C) for methyl hydrogen and $1.2U_{eq}$(C) for other hydrogen atoms.

2.4. Variable temperature magnetic susceptibility measurements

The magnetisation of the powdered samples was measured over the temperature range 1.8–300 K. The superconducting magnet was generally operated at a field strength ranging from 0 to 5 T and the sample measurements were made at a magnetic field 0.5 T as well as at the weak magnetic field of 25 and 50 Oe. The SQUID magnetometer was calibrated with a palladium rod sample. Corrections were based on subtracting the sample holder signal and the contribution χ_D [-862.6×10^{-6} cm^3 mol^{-1} for the Mn^{II} complex and -815.94×10^{-6} cm^3 mol^{-1} for the Co^{II} complex] was estimated using Pascal constants. The effective magnetic moment was calculated from the equation, $\mu_{eff} = 2.83(\chi_M T)^{1/2}$ (B.M.).

2.5. Synthesis and analysis

The synthesis of 4-hydroxy-*N*′-(4-(octadecyloxy)benzylidene)benzohydrazide (HL^3) (**2**) was achieved by proceeding through two major steps, *viz*., alkylation of 4-hydroxy benzaldehyde with *n*-octadecyl bromide, followed by Schiff-base formation. All the experimental details are given in Scheme 1.

[M(HL^3)$_2$(MeOH)$_n$](OAc)$_2$ (M = Mn, Co, Ni, Cu and Zn; *n* = 0 or 2) complexes were prepared by refluxing together hot dry chloroform solutions of the ligand, HL^3, (1.02 g, 2.0 mmol, in 30 mL) and the appropriate metal acetate (1.0 mmol, in 20 mL) for ~2 h at 70 °C. The solid complex that separated out in each case was filtered under suction and washed repeatedly with ethanol and dried over fused $CaCl_2$ in a desiccator.

2.5.1. Preparation of 4-octadecyloxybenzaldehyde (**1**)

Equimolar amounts of 1-bromo octadecane (30 mmol, 10.25 g), 4-hydroxy benzaldehyde (3.66 g, 30 mmol) and potassium bicarbonate (3.00 g, 30 mmol) were suspended in 200 mL of dried acetone and refluxed for ~24 h in presence of KI (0.1–0.2 g) as catalyst and filtered while hot to remove the insoluble solids, neutralised with dil. 6 N HCl and extracted twice with $CHCl_3$. The chloroform extracts were concentrated to obtain a purple solid which, in turn, was purified by column chromatography over SiO_2 (by eluting with a mixture of *n*-hexane and chloroform (v/v, 1/1)); evaporation of this purified extract finally yielded 4-octadecyloxybenzaldehyde in the form of a white solid; yield: 82% (9.20 g).

2.5.2. Synthesis of 4-hydroxy-*N*′-(4′-octadecyloxybenzylidene)benzohydrazide, HL^3 (**2**)

The ligand, 4-hydroxy-*N*′-(4-(octadecyloxybenzylidene)benzohydrazide was prepared by refluxing together absolute ethanolic solutions of 4-octadecyloxybenzaldehyde (14.96 g, 40 mmol in 100 mL) and 4-hydroxybenzoic acid hydrazide (6.08 g, 40 mmol, in 50 mL) for ~1 h in presence of few drops of acetic acid and leaving the solution over night in the flask closed with guard tube. The micro-crystalline cream coloured product was filtered off by suction, thoroughly washed with cold ethanol and recrystallised from a mixture of absolute ethanol and chloroform (1:2 v/v) and dried at room temperature; yield 13.34 g (85%) as a cream coloured solid; m.p. 200 °C. ^{1}H NMR (300 MHz; DMSO-*d*^{6}; Me_4Si at 25 °C, *J* (Hz), ppm) δ = 0.854 (t, $^3J_{H-H}$ = 6.9, 3H, –CH_3), 1.745–1.422 (m, 32H, –CH_2), 4.012 (t, $^3J_{H-H}$ = 6.9, 2H, –OCH_2), 6.845 (d, $^3J_{H-H}$ = 8.4, 1H, –$C_{3'}H/C_{5'}H$), 6.980 (d, $^3J_{H-H}$ = 7.8, 1H, –C_2H/C_6H), 7.614 (d, $^3J_{H-H}$ = 8.4,1H, –$C_{2'}H$), 7.784 (d, $^3J_{H-H}$ = 8.4,1H, –$C_3H/-C_5H$), 8.571 (s, 1H, –NCH), 9.944(s, 1H, –NH), 11.351 (br s, 1H, –OH); FAB Mass (*m*/*z*): 154 ((HO)C_6H_4CO–NH–NH_3^+, 20), 121((HO)$C_6H_4CO^+$, 45); IR(KBr, cm^{-1}): 3439_{br} ν(O–H)$_{phenol}$, 3250_s ν_s(N–H)$_{amide}$, 1647_s ν(>C=O)$_{amide-I}$, 1510 ν(N–H)$_{amide-II}$, 1606_w ν(C=N), 1249s ν(C–O)$_{phenol}$; *Anal.* Calc. for $C_{32}H_{48}N_2O_3$(508.74): C, 75.60; H, 9.45; N_2H_4, 6.30; N, 5.50. Found: C, 75.56; H, 9.37; N_2H_4, 6.27; N, 5.47%.

2.5.3. Synthesis of [Mn(HL^3)$_2$](OAc)$_2$

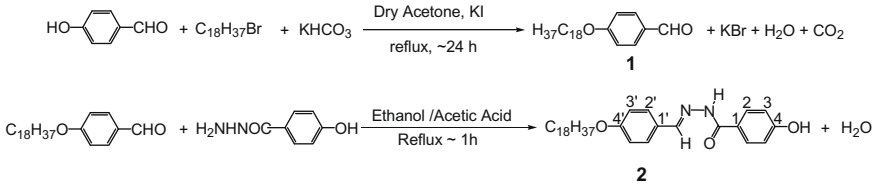
Yield 1.10 g (85%) as a brown coloured solid; m.p. 220 °C (decompose). FAB Mass (*m*/*z*): 1074 ([Mn(HL^3)$_2$]$^+$, 100), 121 ((HO)$C_6H_4CO^+$, 35); IR(KBr, cm^{-1}): 3443_{br} ν(O–H)$_{phenol}$, 3246_s ν_s(N–H)$_{amide}$, 1629_s ν(>C=O)$_{amide-I}$, 1507 ν(N–H)$_{amide-II}$, 1610s ν(ionic acetate), 1367_w ν(ionic acetate), 1552_w ν(C=N), 1244_s ν(C–O)$_{phenol}$; 479s ν(Mn–N), 449s ν(Mn–O). *Anal.* Calc. for $MnC_{68}H_{102}N_4O_{10}$ (1190.50): C, 68.60; N, 4.71; N_2H_4, 5.37; Mn, 4.61. Found: C, 68.22; N, 4.73; N_2H_4, 5.35; Mn, 4.57%.

2.5.4. Synthesis of [Co(HL^3)$_2$](OAc)$_2$

Yield 0.84 g (70%) as a cream coloured solid; m.p. 225 °C (decompose). IR(KBr, cm^{-1}): 3443_{br} ν(O–H)$_{phenol}$, 3242_s ν_s(N–H)$_{amide}$, 1633_s ν(>C=O)$_{amide-I}$, 1604_s ν(ionic acetate), 1370_w ν(ionic acetate), 1501 ν(N–H)$_{amide-II}$, 1572w ν(C=N), 1241s ν(C–O)$_{phenol}$; 475s ν(Co–N), 458s ν(Co–O); *Anal.* Calc. $CoC_{68}H_{102}N_4O_{10}$ (1194.49): C, 68.37; N, 4.69; N_2H_4, 2.68; Co, 4.93. Found: C, 68.39; N, 4.64; N_2H_4, 2.65; Co, 4.90%.

2.5.5. Synthesis of [Ni(HL^3)$_2$](OAc)$_2$

Yield 0.94 g (79%) as an orange coloured solid; m.p. 250 °C. ^{1}H NMR (300 MHz; DMSO-*d*^{6}; Me_4Si at 25 °C, *J* (Hz), ppm) δ = 0.863 (t, $^3J_{H-H}$ = 6.3, 3H, –CH_3), 1.780–1.260 (m, 32H, –CH_2), 4.031 (t, $^3J_{H-H}$ = 6.0, 2H, –OCH_2), 6.857 (d, 1H, –$C_{3'}H/C_{5'}H$), 6.990 (d, 1H,



Scheme 1. Reaction steps involved in the synthesis of 4-*octadecyloxy benzaldehyde* (**1**) and 4-hydroxy-*N*′-(4-(octadecyloxy)benzylidene)benzohydrazide (**2**) (HL^3).

–C_2H/C_6H), 7.790 (d, 1H, –C_3H/–C_5H), 8.228 (s, 1H, –NCH), 9.618 (s, 1H, –NH), 11.230 (br s, 1H, –OH); FAB Mass (*m*/*z*): 1074 ($[Ni(HL^3)_2]^+$, 30), 509 ($[HL^3]^+$, 35), 154 ($(HO)C_6H_4CO–NH–NH_3^+$, 100), 121($(HO)C_6H_4CO^+$, 40); IR(KBr, cm^{-1}): 3440_{br} ν(O–H)$_{phenol}$, 3245_s ν_s(N–H)$_{amide}$, 1631_s ν(>C=O)$_{amide\text{-}I}$, 1597_s ν(ionic acetate), 1369_w ν(ionic acetate), 1501 ν(N–H)$_{amide\text{-}II}$, 1562w ν(C=N), 1250s ν(C–O)$_{phenol}$; 478s ν(Ni–N), 451s ν(Ni–O); *Anal.* Calc. for $NiC_{68}H_{102}N_4O_{10}$ (1194.25): C, 68.39; N, 4.69; N_2H_4, 2.68; Ni, 4.91. Found: C, 68.36; N 4.65; N_2H_4, 2.65; Ni, 4.88%.

2.5.6. Synthesis of $[Cu(HL^3)_2](OAc)_2$

Yield 0.86 g (72%) as a yellowish-green solid; m.p. 270 °C (decompose). FAB Mass (*m*/*z*): 1081 ($[Cu(HL^3)_2]^+$, 75), 571 ($[Cu(HL^3)$, 100), 121($(HO)C_6H_4CO^+$, 50). IR(KBr, cm^{-1}): 3438_{br} ν(O–H)$_{phenol}$, 3246_s ν_s(N–H)$_{amide}$, 1634_s ν(>C=O)$_{amide\text{-}I}$, 1498 ν(N–H)$_{amide\text{-}II}$, 1604_s ν(ionic acetate), 1375_w ν(ionic acetate), 1575w ν(C=N), 1246s ν(C–O)$_{phenol}$; 485s ν(Cu–N), 455s ν(Cu–O); *Anal.* Calc. $CuC_{68}H_{102}N_4O_{10}$ (1199.70): C, 68.11; N, 4.67; N_2H_4, 2.67; Cu, 5.30. Found: C, 68.14; N 4.65; N_2H_4, 2.65; Cu, 5.28%.

2.5.7. Synthesis of $[Zn(HL^3)_2(MeOH)_2](OAc)_2$

Yield 13.34 g (70%) as a cream coloured solid; m.p. 200 °C. ^1H NMR (300 MHz; DMSO-d^6; Me_4Si at 35 °C, *J* (Hz), ppm) δ = 0.861 (t, $^3J_{H-H}$ = 6.9, 3H, –CH_3), 1.745–1.422 (m, 32H, –CH_2), 4.012 (t, $^3J_{H-H}$ = 6.9, 2H, –OCH_2), 6.845 (d, $^3J_{H-H}$ = 8.4, 1H, –C_3·H/C_5·H), 6.980 (d, $^3J_{H-H}$ = 7.8, 1H, –C_2H/C_6H), 7.614 (d, $^3J_{H-H}$ = 8.4,1H, –C_2·H), 7.784 (d, $^3J_{H-H}$ = 8.4,1H, –C_3H/–C_5H), 8.561 (s, 1H, –NCH), 9.898(s, 1H, –NH), 11.351 (br, 1H, –OH); FAB Mass (*m*/*z*): 1147 ($[Zn(HL^3)_2(MeOH)_2]^+$, 85), 1079 ($[Zn(HL^3)_2]^+$, 67), 121($(HO)C_6H_4$-CO^+, 49); IR(KBr, cm^{-1}): 3446_{br} ν(O–H)$_{phenol/MeOH}$, 3242_s ν_s(N–H)$_{amide}$, 1629_s ν(>C=O)$_{amide\text{-}I}$, 1501 ν(N–H)$_{amide\text{-}II}$, 1608_s ν(ionic acetate), 1367_w ν(ionic acetate), 1582w ν(C=N), 1244s ν(C–O)$_{phenol}$; 481s ν(Zn–N), 452s ν(Zn–O); *Anal.* Calc. for $ZnC_{70}H_{110}N_4O_{12}$ (1265.03): C, 66.46; N, 4.43; N_2H_4, 2.53; Zn, 5.17. Found: C, 66.48; N 4.47; N_2H_4, 2.50; Zn, 5.14%.

3. Results and discussion

3.1. Magnetic and spectral investigation

The cream coloured Schiff-base ligand (HL^3), **2**, is soluble in hot chloroform, DMSO, DMF and pyridine but insoluble in water, methanol, ethanol and acetonitrile; the orange-coloured Ni^{II} complex, $[Ni(HL^3)_2](OAc)_2$ is soluble in chloroform, and hot DMSO and DMF; $[Zn(HL^3)_2(MeOH)_2](OAc)_2$ is soluble in only hot/cold DMSO; all other complexes are soluble in pyridine. The electrical conductivity values measured in saturated DMSO solutions (concentration < 10^{-3} M) of the complexes (102–109 ohm^{-1} cm^2/mol) imply their ionic nature [14]. The Schiff-base as well as $[Ni(HL^3)_2](OAc)_2$ showed a *nematic* mesophase under a polarising microscope while none of the other metal complexes under present study were found to show any mesogenic behaviour. The structures and purity of the parent ligand and of the complexes were checked and confirmed by elemental analyses and IR, ^1H NMR and FAB mass spectra.

The colour and electronic spectral data of the present complexes are included in Table 1. The overall geometry around the metal ion has been assigned (Table 1) on the basis of the nature of the electronic spectra, the denticity of the ligand (*vide*. IR and NMR data) and the number of the ligands coordinated to the metal ion (*vide* elemental analyses) within the coordination sphere. The Mn^{II} complex gives rise to extremely weak bands in the electronic spectrum presumably in an octahedral environment (square-planar units polymerically connected with M–M bonding). The cream-coloured complex, $[Co(HL^3)_2](OAc)_2$, may be understood to have a square pyramidal geometry with M–M bonding [15] based on the electronic spectral transition, $^4E_g(T_{2g}(F)) \leftarrow {}^4E_g(T_{1g}(F))$. The electronic spectrum of the orange-coloured Ni^{II} complex shows a single transition at 407 nm which can be assigned to the transition, $^1B_{1g} \leftarrow {}^1A_{1g}$, in a square-planar environment of the metal ion [16]; the colour (orange) of the complex and its diamagnetic nature corroborate the proposed geometry [17]. The spectral features of the yellowish-green coloured complex, $[Cu(HL^3)_2](OAc)_2$, imply square pyramidal geometry (with M–M bonding) owing to the transition, $x^2 - y^2 \leftarrow xz, yz$ arising at 677 nm [16].

In the IR spectrum of HL^3 the broad absorptions centred at 3439 and 3250 cm^{-1} may be assigned to the ν(O–H)$_{phenolic}$ and ν_s(N–H)$_{amide}$ vibrations [18]; further, the strong bands occurring at 1647 and 1510 cm^{-1} may be assigned [18] to ν(>C=O)$_{amide\text{-}I}$ and ν(N–H)$_{amide\text{-}II}$ modes of the amide moiety and the band at 1606 cm^{-1} may be assigned to ν(C=N) absorption of the azomethine moiety; these bands are shifted to lower frequencies in the complexes indicating coordination through the O and N atoms of

Table 1
Colour and electronic spectral data[a] of complexes of HL^3.

Complex	Colour	d–d Transitions (nm)	Transition		Assignment
			Ground state(s)	Excited state(s)	
$[Mn(HL^3)_2](OAc)_2$	brown	319	$^6A_{1g}$	$^4E_g(D)$	octahedral, h.s. (M–M bonding)
$[Co(HL^3)_2](OAc)_2$	cream	911	^4E_g ($T_{1g}(F)$)	$^4E_g(T_{2g}(F))$	sq. py, h.s. (M–M bonding)
$[Ni(HL^3)_2](OAc)_2$	orange	407	$^1A_{1g}$	$^1B_{1g}$	sq. planar
$[Cu(HL^3)_2](OAc)_2$	yellowish-green	677	*xz*, *yz*	$x^2 - y^2$	sq. pyramidal (M–M bonding)

[a] Spectra recorded in solutions of DMSO/chloroform (1:1 v/v).

Table 2
Crystal data and structure refinement parameters of ligand, HL^3 ***[aa85]***.

Empirical formula	$C_{37}H_{53}N_3O_3$
Formula weight	587.82
Cell axes	
a (Å)	5.3220(9)
b (Å)	11.3921(19)
c (Å)	29.280(5)
Cell angles	
α (°)	82.490(3)
β (°)	89.741(3)
γ (°)	83.185(3)
Cell volume *V* (Å)^3	1747.4(5)
Crystal system	triclinic
Crystal size (mm)	19 × 15 × 0.08
T (K)	273(2)
Wavelength (Å)	0.71073
Space group	$P\bar{1}$
F(0 0 0)	640
D (Mg/m^3)	1.117
No form. unit *Z*	2
Absorption coefficient (mm^{-1})	0.070
Reflections collected/unique (R_{int})	16969/6152 (0.0291)
Completeness to θ = 25.00	99.6%
Absorption correction	none
Refinement method	full-matrix least-squares on F^2
Data/restraints/parameters	6152/0/397
H min, max	−6 6
K min, max	−13 13
L min, max	−34 34
θ min, max (°)	1.82 25.00
Goodness-of-fit on F^2	1.021
Final *R* indices [$I > 2\sigma(I)$]	R_1 = 0.0511, wR_2 = 0.1206
R indices (all data)	R_1 = 0.0886, wR_2 = 0.1400
Largest difference in peak and hole (e Å^{-3})	0.148 and −0.149

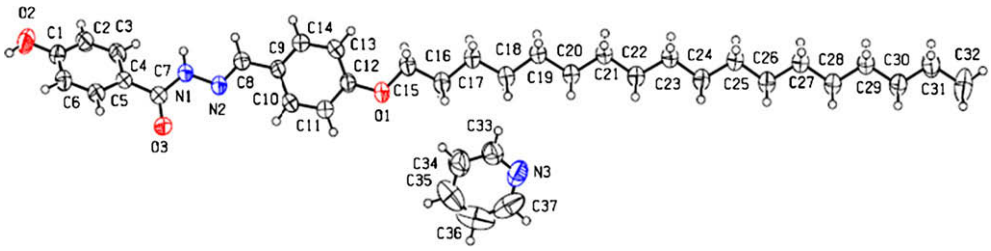


Fig. 1. Molecular structure and atomic labelling scheme of the HL^3 ***[aa85m]*** of 30% ellipsoid probability.

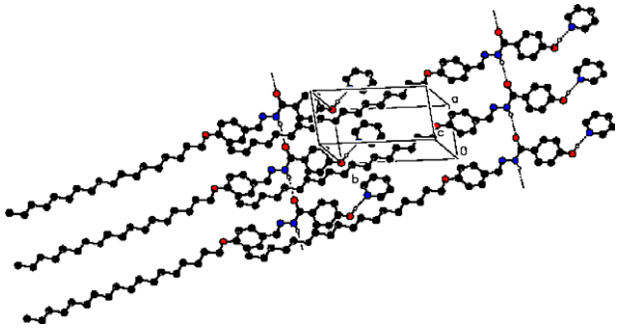


Fig. 2. Part of the packing diagram of HL^3 ***[aa85m]***, showing the N–H···O and O–H···N hydrogen bonded (dashed lines) chains running along *b*-axis.

Table 3
Hydrogen bonds geometry (Å, °) for the ligand HL^3 ***[aa85m]***.

D-H···A	*d*(D-H)	*d*(H···A)	*d*(D···A)	*d*(D-H···A)
O(2)-H(2A)···N(3)#1	0.91(2)	1.81(2)	2.701(2)	164(2)
N(1)-H(1 N)···O(3)#2	0.84(2)	2.32(2)	165(2)	3.130(2)

Symmetry transformations used to generate equivalent atoms: #1 $x+1, y-2, z$ #2 $x-1, y, z$.

the carbonyl and azomethine groups, respectively [19]; such coordination is further substantiated by the appearance of new bands in the complexes characteristic of ν(M–O) and ν(M–N) in the 449–458 and 475–485 cm^{-1} regions, respectively [20–22].

A comparison of the ^1H NMR spectral data of the ligand with those of the Ni^{II} and Zn^{II} complexes shows that (i) the phenolic-O*H* signal remains almost unaltered in the spectra (11.351, 11.230 and 11.351 ppm for the ligand and the complexes, respectively) and (ii) there is a significant shift in the peak positions of the –N=C*H* (from 8.571 of the ligand to 8.228 and 8.561 ppm) and –N–*H* signals (from 9.944 of the ligand to 9.618 and 9.898 ppm) in the spectra of the Ni^{II} and Zn^{II} complexes, respectively. These results imply bonding through the amidic oxygen and the azomethine nitrogen atoms of the ligand to the metal ions.

3.2. Crystal structure and molecular association

The ligand $\mathbf{HL^3}$ ***[aa85]*** crystallised in the triclinic space group, *viz*., $P\bar{1}$ with $Z=2$, respectively. The crystal data and structure refinement details for HL^3 are given in Table 2. The molecular structure, atomic labelling scheme and the packing diagrams of the ligand are as shown in Figs. 1 and 2. The details of the hydrogen-bonded geometry of HL^3 are tabulated in Table 3. The crystal structure of HL^3 is stabilised by both intra- and intermolecular O(2)-H(2A)···N(3) and N(1)–H(1N)···O(3) hydrogen bond interactions. One pyridine molecule is linked through O(2)–H(2A)···N(3) hydrogen bonds, thereby forming infinite hydrogen bonded network chain.

3.3. Variable temperature magnetic susceptibility measurements

The magnetic properties of Mn^{II} and Co^{II} complexes were determined over the temperature range, 1.8–300 K. Plots of magnetic susceptibility χ_M and $\chi_M T$ product versus T are given in Fig. 3. The experimental $\chi_M T$ values for Mn^{II} and Co^{II} complexes at room temperature are 2.52 $cm^3\,mol^{-1}\,K$ (4.50 B.M.) and 3.31 $cm^3\,mol^{-1}\,K$ (5.15 B.M.), respectively, while the corresponding values for isolated, not coupled spin carriers are 4.375 B.M. for Mn^{II} and 1.87 B.M. for Co^{II} ions. The $\chi_M T$ product undergoes minima and maxima with decrease of temperature in both the complexes; the values corresponding to the minima are

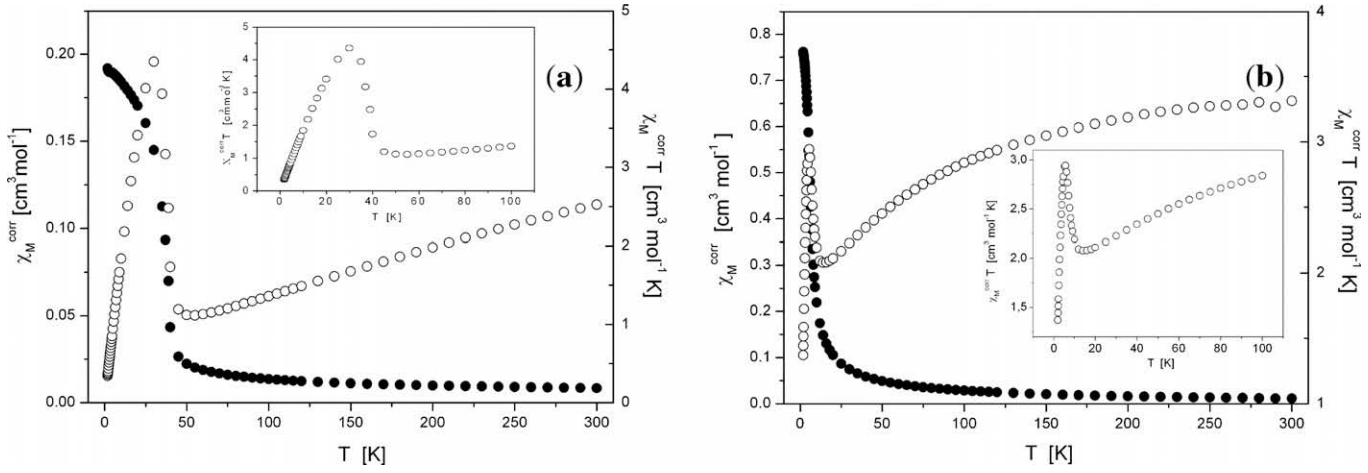


Fig. 3. Temperature dependence of χ_M(●) and $\chi_M T$ (○) versus T for Mn^{II} complex, and (b) Co^{II} complex.

1.11 $cm^3\ mol^{-1}\ K$ (2.99 B.M.) at 55 K in case Mn^{II} complex and 2.07 $cm^3\ mol^{-1}\ K$ (4.08 B.M.) at 14 K in the case of the Co^{II} complex while those of the maxima are 4.34 $cm^3\ mol^{-1}\ K$ (5.90 B.M.) at 30 K in the former complex and 2.94 $cm^3\ mol^{-1}\ K$ (4.86 B.M.) at 5.5 K in the latter. Following the maxima, the $\chi_M T$ values decrease with temperature up to 1.8 K to reach a minimum of 0.345 $cm^3\ mol^{-1}\ K$ (1.66 B.M.) in case of the Mn^{II} complex and 1.37 $cm^3\ mol^{-1}\ K$ (3.31 B.M.) in the Co^{II} complex.

Thus, the decrease of $\chi_M T$ value in the high-temperature region can be attributed to spin–orbit coupling effects [23] and/or anti-

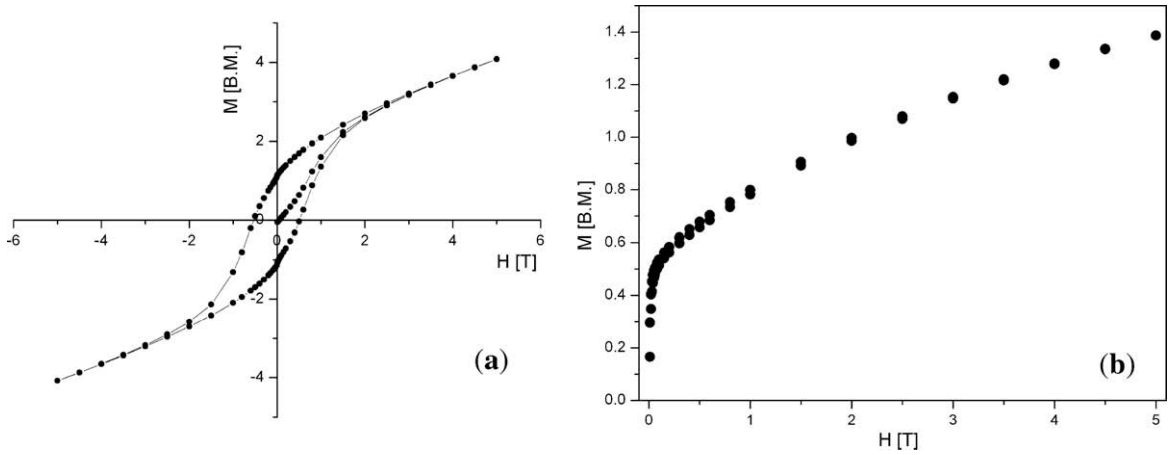


Fig. 4. Field dependence of the magnetisation at temperature 2 K for Mn^{II} complex (hysteresis loop) and (b) Co^{II} complex.

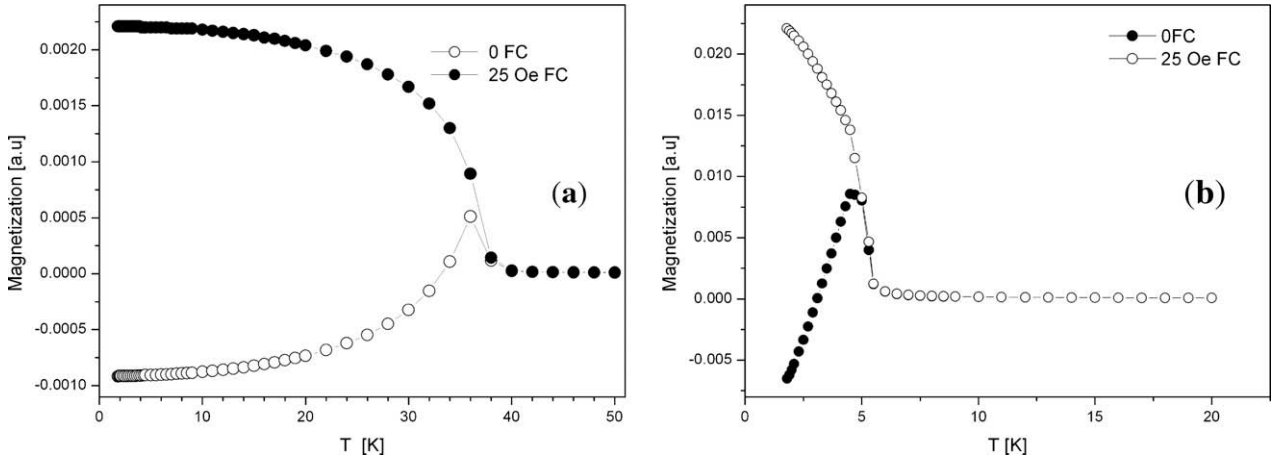


Fig. 5. Temperature dependence of magnetisation versus field (zero-field cooled and at 25 Oe field cooled versus T) for (a) Mn^{II} complex, and (b) Co^{II} complex.

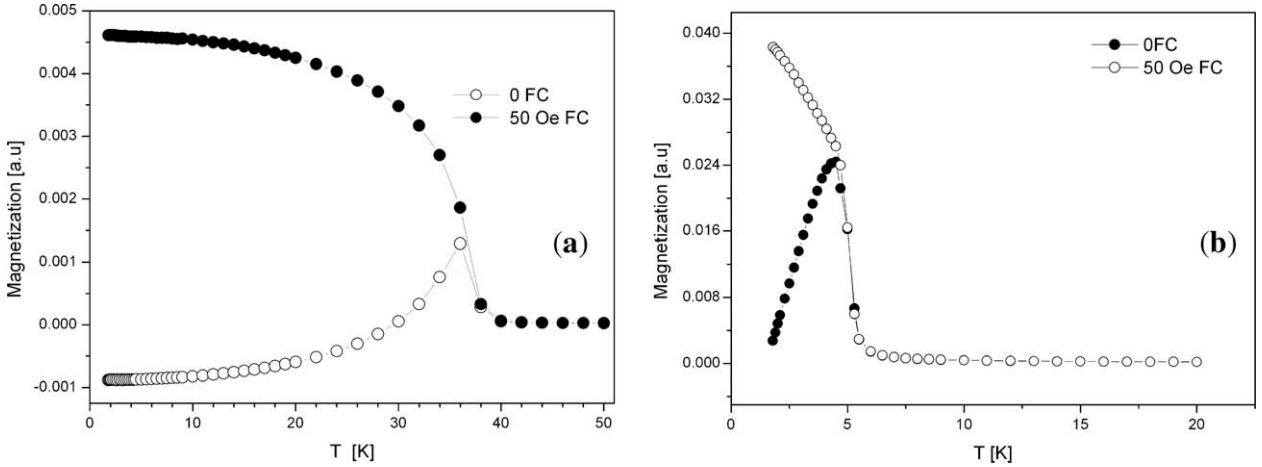


Fig. 6. Temperature dependence of magnetisation versus field (zero-field cooled and at 50 Oe field cooled versus *T*) for (a) Mn^{II} complex, and (b) Co^{II} complex.

ferromagnetic interactions, while the increase of $\chi_M T$ value in the low-temperature region is indicative of a weak ferromagnetic interaction between the two high-spin Mn^{II}/Co^{II} species [23]. Further, the data on the susceptibility values at Curie temperature and the Weiss constants (5.18 $cm^3 mol^{-1} K$, −321 K and 3.59 $cm^3 mol^{-1} K$ and −25.8 K for Mn^{II} and Co^{II} complexes) over the temperature range 150–300 K are consistent with the negative values of the Weiss constants implying presence of anti-ferromagnetic interactions in both the complexes at higher temperature range [24].

The variation of the magnetisation M versus magnetic field H at 2 K for the complexes is shown in Fig. 4; the ferromagnetic nature of the transition in the Mn^{II} complex is implied by the magnetic hysteresis loops at 2.0 K (Fig. 4a) (where the value of coercive field (H_c) = 0.5 T, the remnant magnetisation (M_r) = 1.02 B.M. and the upper limit of magnetisation is 4.08 B.M. at 5 T) which are characteristic of soft magnets [23]. In contrast, the corresponding curve of the Co^{II} complex is linear in the whole field range showing the magnetisation value of 1.38 B.M. at 5 T which is clearly smaller than the sum of two $S_{Co} = 3/2$ states of each Co^{II} ion but is consistent with the calculated one for two Co^{II} ions with an effective $S_{Co} = S_{eff} = 1/2$ state owing to the formation of ground Kramer′s doublet [23] due to the spin–orbit coupling interaction for each Co^{II} ion populated at 2.0 K. The ferromagnetic interaction of both the complexes in the low temperature range is further revealed by the temperature dependence of the field-cooled (FC) and the zero-field cooled (ZFC) magnetisation curves (Figs. 5 and 6). The FC curves, measured by cooling the samples within small fields of 25 and 50 Oe, increase sharply below the point of intersection with ZFC curve (40 ± 0.1 K in case of the Mn^{II} complex and 5 ± 0.1 K in case of the Co^{II} complex) and then saturate around 10.0 K in the case of the former.

4. Conclusions

The mesogenic (*nematic*) Schiff-base, 4-hydroxy-*N*′-(4′-octadecyloxybenzylidene)benzohydrazide, (HL^3) coordinates as a neutral bi-dentate species through amidic oxygen and azomethine nitrogen atoms to yield non-mesogenic complexes of the type, $[M(HL^3)_2](OAc)_2$, (M = Mn, Co, Cu and Zn) and a mesogenic Ni^{II} complex. The Mn^{II} and Co^{II} complexes show anti-ferromagnetic interaction and a weak ferromagnetic coupling at lower temperatures; further, the former complex shows magnetic hysteresis loops at 2.0 K.

Supplementary data

CCDC 685719 contains the supplementary crystallographic data for this paper. These data can be obtained free of charge via http://www.ccdc.cam.ac.uk/conts/retrieving.html, or from the Cambridge Crystallographic Data Centre, 12 Union Road, Cambridge CB2 1EZ, UK; fax: +44 1223 336 033; or e-mail: deposit@ccdc.cam.ac.uk.

Acknowledgements

We wish to acknowledge recording of FAB Mass spectra and elemental analyses at the Central Drug Research Institute, Lucknow, India. One of the authors, T.R. Rao, gratefully acknowledges the financial grant received from the University Grants Commission, New Delhi [vide Grant No. F.12-26/2003 (SR)] and the Department of Science & Technology, New Delhi [vide Grant No. SR/S1/IC-26/2004].

References

[1] A.B. Blake, J.R. Chipperfield, W. Hussain, R. Paschke, E. Sinn, Inorg. Chem. 34 (1995) 125;
R. Paschke, D. Balkow, E. Sinn, Inorg. Chem 41 (2002) 1949.
[2] S. Liebsch, M.A. Oakley, R. Paschke, E. Sinn, Inorg. Chem. Commun. 5 (2002) 525;
R. Paschke, S. Liebsch, C. Tschierske, M.A. Oakley, E. Sinn, Inorg. Chem. 42 (2003) 8230.
[3] M.B. Hursthouse, S.A.A. Jayaweera, A.J. Quick, J. Chem. Soc., Dalton Trans (1979) 79;
N.K. Sangwan, B.S. Verma, K.S. Dhindsa, Indian J. Chem. 25B (1986) 72;
A.A.T. Ramadan, M.A. Seada, E.N. Rizkalla, Talanta 30 (1983) 245.
[4] A. Haran, J. Gairin, G. Commenges, Inorg. Chim. Acta 46 (1980) 62;
H.M. El-Table, F.A. El-Saied, M.I. Ayad, Synth. React. Inorg. Met.-Org. Chem. 32 (2002) 1189.
[5] M. Gallego, M. Gareia-Varges, M. Valcaral, Analyst 104 (1979) 613;
S. Jayasree, K.K. Aravindkshan, J. Indian Chem. Soc. 71 (1994) 97.
[6] A.K. Singh, S. Kumari, K. Ravi Kumar, B. Sridhar, T.R. Rao, Polyhedron 27 (2008) 181.
[7] A.K. Singh, S. Kumari, K. Ravi Kumar, B. Sridhar, T.R. Rao, Polyhedron 27 (2008) 1937.
[8] A.K. Singh, S. Kumari, T.N. Guru Row, J. Prakash, K. Ravi Kumar, B. Sridhar, T.R. Rao, Polyhedron 27 (2008) 3710.
[9] N.V.S. Rao, M.K. Paul, T.R. Rao, A. Prasad, Liquid Crystals 29 (2002) 1243.
[10] T.R. Rao, A. Prasad, Synth. React. Inorg. Met.-Org. Chem. 35 (2005) 299.
[11] A. Weisberger, F.S. Praskver, in: Organic Solvents, International publishers Inc., New York, 1956, p. 1263.
[12] SMART and SAINT Software Reference manuals, Versions 6.28a & 5.625, Bruker Analytical X-ray Systems Inc., Madison, Wisconsin, USA, 2001.
[13] G.M. Sheldrick, SHELXS97 and SHELXL97, Programs for Crystal Structure Solution and Refinement, University of Gottingen, Germany, 1997.
[14] W.J. Geary, Coord. Chem. Rev. 7 (1971) 81.
[15] G. Singh, P.S.S.J. Shastry, R.K. Lonibala, T.R. Rao, Synth. Inorg. Met.-Org. Chem. 22 (1992) 1041.
[16] D. Nicholls, in: Comprehensive Inorganic Chemistry, vol. 31983, Pergamon Press, Oxford, p. 1109 (Chapter. 42).
[17] F.A. Cotton, G. Wilkinson, C.A. Murillo, M. Bochmann, in: Advanced Inorganic Chemistry, 6th Ed., 1999, p. 841.
[18] R.M. Silverstein, F.X. Webster, in: Spectroscopic Identification of Organic Compounds, 6th Ed., John-Wiley & Sons. Inc., New York, 2002, p. 82.
[19] P. Sousa, J.A.G. Vazquez, J.A. Masaquer, Transition Met. Chem. 9 (1984) 318.
[20] S.K. Agrawal, D.R. Tuflani, R. Gupta, S.K. Hajela, Inorg. Chim. Acta 129 (1987) 257.
[21] N. Saha, S. Sinha, Ind. J. Chem. 29 (1990) 292.
[22] K. Nakamoto, in: Infrared and Raman Spectra of Inorganic and Coordination Compounds, Wiley, New York, 1978.
[23] D. Cangussu, E.Pardo;M.C. Dul, R. Lescouëzec, P. Herson, Y. Journaux, E.F. Pedroso, L.M. Pereira Cynthia, H.O.Stumpf;M.C. Muñoz, R. Ruiz-García, J. Cano, M. Julve, F. Lloret, Inorg. Chim. Acta 361 (2008) 3394.
[24] P.W. Selwood, in: Magnetochemistry, 2nd Ed., Interscience Publishers, Inc., New York, 1956, p. 328.

Polyhedron 28 (2009) 2605–2610

Contents lists available at ScienceDirect

Polyhedron

journal homepage: www.elsevier.com/locate/poly

Heterobimetallic aluminium and zinc complex with *N*-arylanilido-imine ligand: Synthesis, structure and catalytic property for ring-opening polymerization of ε-caprolactone

Ai-Hong Gao, Wei Yao, Ying Mu *, Wei Gao, Ming-Tai Sun, Qing Su

State Key Laboratory for Supramolecular Structure and Materials, School of Chemistry, Jilin University, 2699 Qianjin Street, Changchun 130012, People's Republic of China

ARTICLE INFO

Article history:
Received 20 April 2009
Accepted 19 May 2009
Available online 23 May 2009

Keywords:
Aluminium
Zinc
Caprolactone

ABSTRACT

Treatment of a *N*-arylanilido-imine ligand [*ortho*-$C_6H_4(NHAr)CH{=}N]_2CH_2CH_2$ (Ar = 2,6-$Me_2C_6H_3$) (**L**H_2) with one equiv. of $AlMe_3$ affords a monometallic complex [$C_6H_4(NHAr)$–CH=N)]$CH_2CH_2(C_6H_4(NAr)CH{=}NAlMe_2)$ (**1**). The monometallic complex **1** reacts with one equiv. of $ZnEt_2$ to give a heterobimetallic complex [$C_6H_4(NAr)$–CH=NZnEt]$CH_2CH_2[C_6H_4(NAr)$–CH=$NAlMe_2]$ (**2**). Both complexes were characterized by ^1H and ^{13}C NMR spectroscopy and elemental analyses, and the molecular structures of **1** and **2** were determined by X-ray diffraction analysis. The complexes **1** and **2** both are efficient catalysts for ring-opening polymerization of ε-caprolactone in the presence of benzyl alcohol yielding polymers with narrow polydispersity values and complex **2** initiates the polymerization in a controllable manner.

© 2009 Elsevier Ltd. All rights reserved.

1. Introduction

In recent years, considerable efforts have been made to develop efficient catalysts for the ring-opening polymerization (ROP) of ε-caprolactone (CL), which has been a powerful tool for the synthesis of polyesters with controlled molecular weight and narrow molecular weight distribution [1–3]. So far, catalysts based on various metals such as magnesium [4–6], calcium [7,8], aluminium [9–16], titanium [17–20], iron [21,22], zinc [23–28], tin [29–31], and rare earth metal [32–35] have been reported. Among the reported catalysts, bimetallic complexes are relatively few. In some catalytic systems, bimetallic catalysts have been found to show cooperative effect and high catalytic activity. Coates and co-workers have suggested that the copolymerization of cyclohexene oxide/CO_2 by β-diketiminato Zn complexes takes place via a bimetallic Zn mechanism [36]. Lee et al. have also disclosed that the bimetallic anilido-imine zinc complexes show high activity for the copolymerization of cyclohexene oxide/CO_2 [37,38]. Recently we have reported several bimetallic anilido-imine Al or Zn complexes for the ROP of CL in the presence of BnOH [39]. To explore the cooperative effect of the metal centres, we have synthesized a new heterobimetallic complex containing Al and Zn metals with a ethylene bridged *N*-arylanilido-imine ligand. To the best of our knowledge, no heterobimetallic complex containing $AlMe_2$ and ZnEt groups has been reported so far. In the presence of BnOH, both complexes **1** and **2** were found to be efficient catalysts for the ROP of CL to give PCL, and the heterobimetallic complex **2** shows much higher catalytic activity in comparison to the monometallic complex **1**. Herein we report the synthesis and structure of the new monometallic aluminium complex [*o*-$C_6H_4(NHAr)CH{=}N]CH_2CH_2$ [*o*-$C_6H_4(NAr)CH{=}NAlMe_2$] (Ar = 2,6-$Me_2C_6H_3$) (**1**) and heterobimetallic Al/Zn complex [*o*-$C_6H_4(NAr)CH{=}NZnEt]CH_2CH_2[o$-$C_6H_4(NAr)$–CH=$NAlMe_2$] (**2**) as well as their catalytic property for the ROP of CL in the presence of BnOH.

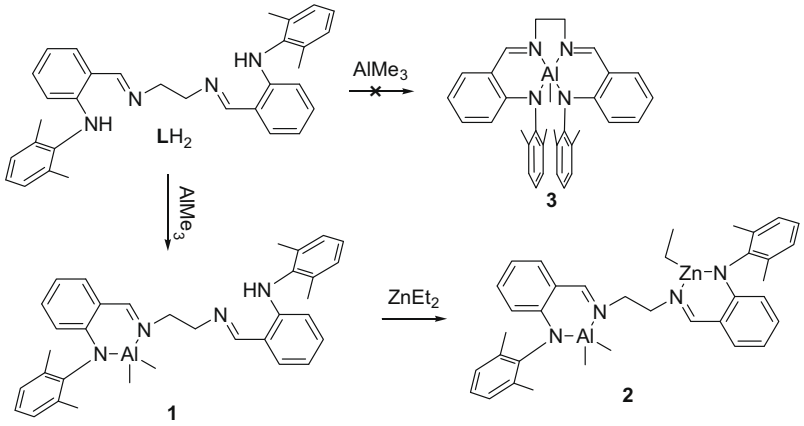
2. Results and discussion

2.1. Synthesis and characterization of complexes 1 and 2

The free *N*-arylanilido-imine ligand [*ortho*-$C_6H_4(NHAr)CH{=}N]_2CH_2CH_2$ (Ar = 2,6-$Me_2C_6H_3$) (**L**H_2) was synthesized according to the literature procedure [39]. The complexes **1**, **2** were synthesized as described in Scheme 1. Both complexes **1**, **2** were obtained in high yields in toluene by alkane elimination reaction. Reaction of the free ligand **L**H_2 with one equiv. of $AlMe_3$ did not give the expected pentacoordinate complex **3** even when the reaction mixture was heated to reflux for several days. However, pentacoordinate aluminium complexes supported by various tetracoordinate ligands were synthesized successfully [40,41]. The tetracoordinate complex **1** was instead obtained probably due to either the low reactivity of NH or the bulky substitutes of the ligand. Complex **1** was characterized by ^1H and ^{13}C NMR spectroscopy and elemental analyses. The ^1H NMR spectrum of **1** exhibits resonances at δ 8.06 and 8.45 for the two different imino N=CH protons, at δ 10.28 in the low field region for the unreacted NH proton, and at δ −0.84 in the high field region for $AlMe_2$ protons. The ^1H NMR analysis

* Corresponding author. Tel.: +86 431 85168376; fax: +86 431 85193421.
E-mail address: ymu@mail.jlu.edu.cn (Y. Mu).

0277-5387/$ - see front matter © 2009 Elsevier Ltd. All rights reserved.
doi:10.1016/j.poly.2009.05.037



Scheme 1. Synthetic procedure of complexes **1** and **2**.

demonstrates that only one of the two NH groups in the free ligand $\mathbf{L}H_2$ has reacted with $AlMe_3$ in the reaction. The heterobimetallic complex **2** was then prepared by the reaction of complex **1** with one equiv. of $ZnEt_2$ in toluene with heating at 80 °C for 12 h. The disappearance of the NH signal in complex **1** and the appearance of resonance for ZnEt protons in the high field region demonstrate the formation of the desired complex **2**.

2.2. X-ray crystal structural analysis

Crystals of complexes **1** and **2** suitable for X-ray crystal structure determination were grown from the mixture of CH_2Cl_2/hexane at −20 °C. Their molecular structures are shown in Figs. 1 and 2, respectively. Selected bond lengths and angles for **1** and **2** are given in Table 1. X-ray crystallographic analysis reveals that the Al centres in both complexes **1** and **2** adopt a distorted tetrahedral geometry and the Zn centre in complex **2** adopts a trigonal planar geometry. The Al and Zn centres in the two complexes are chelated by the imine and anilido nitrogen atoms of the bidentate ligand. In both complexes, the six-membered chelating ring is nearly planar, with the metal atom lying 0.1794 Å for **1**, 0.0199 Å (Al) and 0.0667 Å (Zn) for **2** out of the plane, respectively. The X-ray crystal structural analysis confirms the structure of complex **1** that contains only one aluminium centre and half of the ligand remains unreacted. The structural parameters of complex **1** are similar to those reported for related Al complexes with anilido-imine ligands [39,42], such as the Al–N distances and the torsion angles between

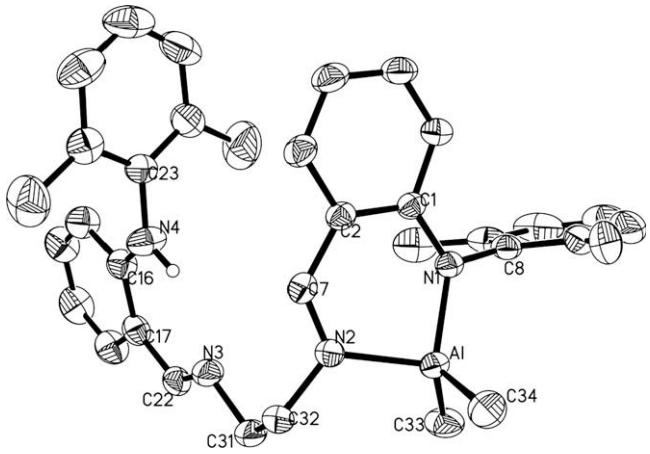


Fig. 1. X-ray structure of complex **1**, with all nonhydrogen atoms shown as 30% thermal ellipsoids.

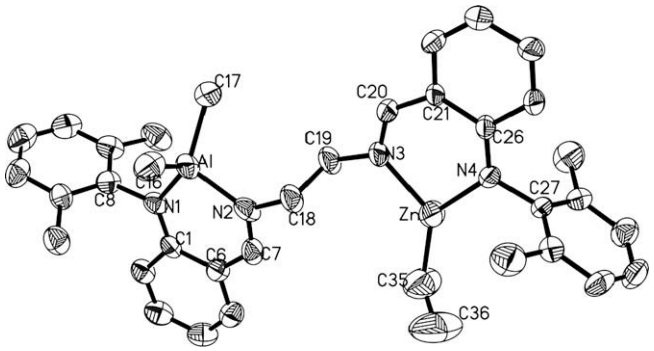


Fig. 2. X-ray structure of complex **2**, with all nonhydrogen atoms shown as 30% thermal ellipsoids.

Table 1
Selected bond lengths (Å) and angles (°) for complexes **1** and **2**.

*Complex **1***			
Al–N(1)	1.875(2)	N(1)–Al–C(33)	112.3(1)
Al–N(2)	1.940(2)	N(1)–Al–C(34)	116.4(1)
Al–C (33)	1.955(2)	N(2)–Al–C(33)	112.8(2)
Al–C (34)	1.964(3)	N(2)–Al–C(34)	103.4(2)
N(1)–C(1)	1.366(3)	C(33)–Al–C(34)	114.8(2)
N(2)–C(7)	1.294(3)	C(1)–N(1)–Al	124.8(1)
N(3)–C(22)	1.264(3)	C(8)–N(1)–Al	118.1(1)
N(4)–C(16)	1.373(3)	C(7)–N(2)–Al	121.5(2)
N(1)–Al–N(2)	95.0(8)	C(32)–N(2)–Al	120.7(2)
*Complex **2***			
Al–N(1)	1.866(5)	N(1)–Al–C(17)	115.3(3)
Al–N(2)	1.864(6)	N(2)–Al–C(16)	107.9(3)
Al–C (16)	2.010(8)	N(2)–Al–C(17)	111.0(3)
Al–C (17)	1.997(7)	C(16)–Al–C(17)	109.6(3)
N(1)–C(1)	1.351(8)	C(1)–N(1)–Al	127.1(4)
N(2)–C(7)	1.310(8)	C(8)–N(1)–Al	115.4(4)
N(1)–Al–N(2)	97.0(3)	C(7)–N(2)–Al	123.8(4)
N(1)–Al–C(16)	115.4(3)	C(18)–N(2)–Al	121.6(5)
Zn–N(3)	1.979(5)	N(3)–Zn–C(35)	128.7(4)
Zn–N(4)	1.907(5)	N(4)–Zn–C(35)	136.0(4)
Zn–C(35)	1.932(1)	C(19)–N(3)–Zn	118.2(5)
N(3)–C(20)	1.273(7)	C(20)–N(3)–Zn	121.7(4)
N(4)–C(26)	1.355(7)	C(26)–N(4)–Zn	126.3(4)
N(3)–Zn–N(4)	95.3(2)	C(27)–N(4)–Zn	113.8(3)

the six-membered chelating ring and the aromatic ring attached to the anilido nitrogen atom. In complex **2**, the structural data around the Al centre are quite different from those for known Al complexes with anilido-imine ligands [39,42]. The Al–N(1) (anilido) distance (1.866(5) Å) is close to the Al–N(2) (imine) distance

Table 2
Ring-opening polymerization of ε-CL initiated by complexes **1** and **2**.[a]

Entry	Catalyst	BnOH:M:CL	Time	*T* (°C)	Yield [b] (%)	DP_n [c]	M_n [d] × 10^3	M_w/M_n [d]
1	**1**	0:1:100	24 h	70	0	–	–	–
2	**2**	0:2:100	24 h	70	0	–	–	–
3	**1**	0.5:1:100	80 min	70	96.7	194	26.5	1.40
4	**1**	1:1:100	50 min	70	94.5	95	12.8	1.32
5	**1**	2:1:100	5.5 h	70	94.0	47	8.6	1.10
6	**2**	1:2:100	13 min	70	94.2	196	27.4	1.53
7	**2**	2:2:100	6 min	70	95.0	104	15.6	1.15
8	**2**	3:2:100	10 min	70	98.3	94	12.5	1.13
9	**2**	2:2:100	10 min	50	93.4	100	14.6	1.60
10	**2**	2:2:100	15 min	20	93.6	99	14.4	1.18
11	**2**	2:2:150	14 min	70	94.2	160	21.2	1.37
12	**2**	2:2:200	25 min	70	92.1	193	25.6	1.42
13	**2**	2:2:250	36 min	70	93.2	244	33.3	1.78
14	**2**	2:2:300	51 min	70	94.0	306	35.4	1.21

[a] Polymerization conditions: catalyst, 0.19 mmol; CL, 3.0 mol/L in toluene; a N_2 atmosphere.
[b] Isolated yield.
[c] The number-average degree of polymerization by ^{1}H NMR.
[d] Obtained from GPC analysis.

(1.864(6) Å) that is obviously shorter than normal Al–N values (1.870–1.963 Å) [39,42], and the imino C=N bond within the chelate ring does not retain its double bond character, being N(2)–C(7) 1.310(8) Å. These results, together with the fact that this six-membered chelating ring is nearly planar with the Al atom lying almost in the plane, imply better conjugation in this chelating ring. The N(1)–Al–N(2) angle (97.0(3)°) in complex **2** is bigger than that in complex **1** (95.0(8)°), while the C(16)–Al–C(17) angle (109.6(3)°) in complex **2** is smaller than the one in complex **1** (114.8(2)°). The structural parameters around the Zn centre in complex **2** are similar to those reported for related Zn complexes with anilido-imine ligands [39,43].

2.3. Ring-opening polymerization of ε-caprolactone

Complexes **1** and **2** were systematically investigated for the ROP of CL. Representative experimental results are summarized in Table 2. Both complexes show reasonable to good catalytic activities for the ROP of CL in the presence of BnOH, while no polymerization reaction takes place in the absence of BnOH (entries 1, 2). Under similar conditions, the catalytic activity of complex **2**/BnOH system is much higher than that of complex **1**/BnOH system. In comparison to the known catalyst systems, the catalytic activity of complex **1**/BnOH system is also lower than those of similar monometallic and bimetallic Al and Zn catalyst/BnOH systems, while the catalytic activity of complex **2**/BnOH system is higher than those of similar bimetallic Al catalyst/BnOH systems but lower than those of similar bimetallic Zn catalyst/BnOH systems [39]. These results imply that the catalytic activity of the Zn centre is much higher than the Al centre in **2**/BnOH catalyst system, which is in agreement with that the bond dissociation energy of Zn–O (284 kJ/mol) is much lower than that of Al–O (512 kJ/mol) [44]. The catalytic activity of the two catalyst systems is also dependent on the reaction temperature and increases upon elevating the reaction temperature from 20 to 70 °C.

The amount of BnOH has been found to be an important factor for affecting the catalytic activity of the catalyst system and controlling the molecular weight of the produced PCL [39,45]. In the present catalyst systems, the highest catalytic activity was observed with the BnOH/Al molar ratio being 1/1 for **1**/BnOH system, and the BnOH/metal molar ratio being about 2/2 for **2**/BnOH system. The reason why the BnOH/Al molar ratio of 1/1, instead of 2/1, for **1**/BnOH system shows the highest catalytic activity is not clear. For **1**/BnOH catalyst systems, the average degree of polymerization (DPn) of the obtained polymers (calculated by ^{1}H NMR) is close to the initial CL/BnOH molar ratio, and the number-averaged molecular weight (*M*n) of the polymers determined by gel permeation chromatography is proportional to the initial CL/BnOH molar ratio. Similar results have previously been reported for other initiator systems [45,46], which have been described as "immortal" polymerization. However, the DPn of the obtained polymers from **2**/BnOH catalyst system is obviously close to the CL/Zn molar ratio and the *M*n of the polymers is largely proportional to the CL/Zn molar ratio. A linear relationship between the *M*n and the CL/Zn molar ratio obtained from **2**/BnOH catalyst system is shown in Fig. 3, which is also indicative of "living" character of the polymerization process. Gel permeation chromatography (GPC) analysis of the obtained polymer samples indicates that the molecular weight distribution of the polymers produced by both catalyst systems is relatively narrow with the polydispersity indexes (PDI) ranging from 1.10 to 1.78. Based on these results, it seems that the Zn centre in **2**/BnOH catalyst system plays a major role in the catalyzed polymerization reaction while the polymerization occuring at the Al centre might be too slow to be taken into account.

^{1}H NMR spectroscopic analysis on the PCL samples shows that the polymer chain is capped with a benzyl ester group on one end and a hydroxylmethyl group on the other end. The ^{1}H NMR spectrum of a typical polymer sample is shown in Fig. 4, in which the

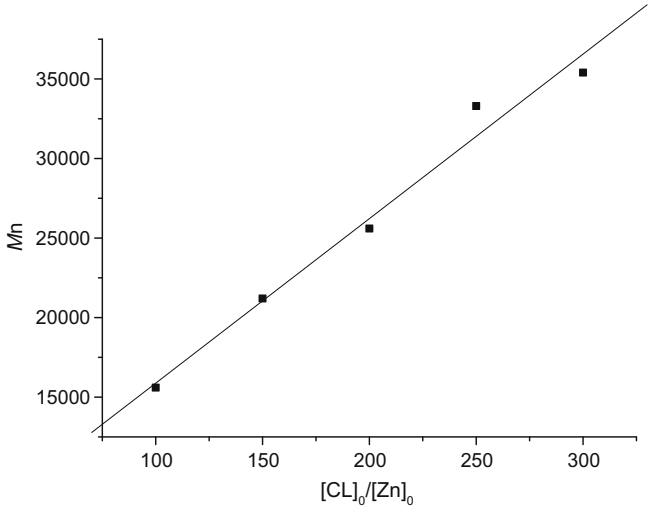


Fig. 3. The relationship between *M*n of the polymer and the initial mole ratio $[CL]_0/[Zn]_0$ for the polymerization of CL catalyzed by **2** and BnOH in toluene at 70 °C.

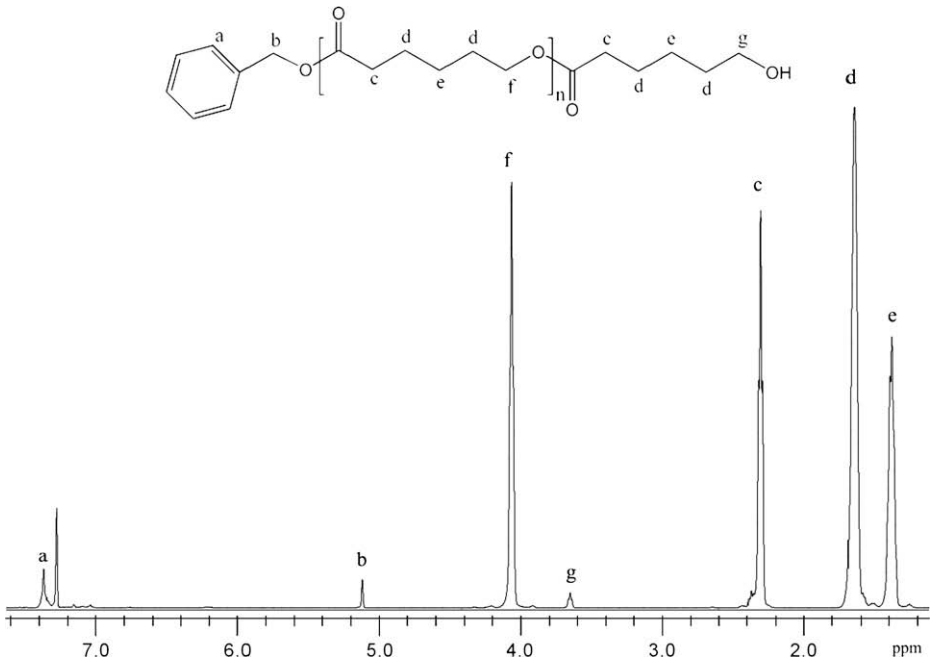


Fig. 4. ^{1}H NMR spectrum of a typical polymer sample.

signals of the methylene protons (c–f) at δ 2.33, 1.66, 1.40, 4.08, and the signals of the ending benzyl group (a, b) at δ 7.37 (ph) and 5.13 (CH_2) as well as the resonances of the terminal methylene protons (CH_2OH, g) at δ 3.67 all appear clearly. Hence, we deduce that BnOH reacts with the alkyl metal complexes to form metal benzyloxides as the catalytic active species. To further confirm that the metal benzyloxides form and act as the active catalysts in these systems, a reaction of complex **2** with BnOH (1:2) in $CDCl_3$ was monitored by ^{1}H NMR at room temperature. The ^{1}H NMR spectrum of the reaction mixture is shown in Fig. 5A. The disappearance of the resonances for protons of Zn*Et* and half of AlMe_2 in high field region and the appearance of the broad PhCH_2OM (M = Al and Zn) signals in the region of δ 4.3–4.6 demonstrate the formation of a bimetal dibenzyloxide complex. After CL was added to the above reaction mixture at room temperature, the formation of M–PCL–OCH_2Ph intermediates was clearly detected by ^{1}H NMR spectrum as shown in Fig. 5B, which indicates the benzyloxy metal complexes are indeed the catalytic active species. The ^{1}H NMR spectrum of the M–PCL–OCH_2Ph intermediates is quite similar to the one of the PCL sample as shown in Fig. 4. The remaining Al*Me* signal can still be seen at δ −0.80 after the polymer chains have been formed, which indicates that the Al–Me bond is stable to the ROP of CL.

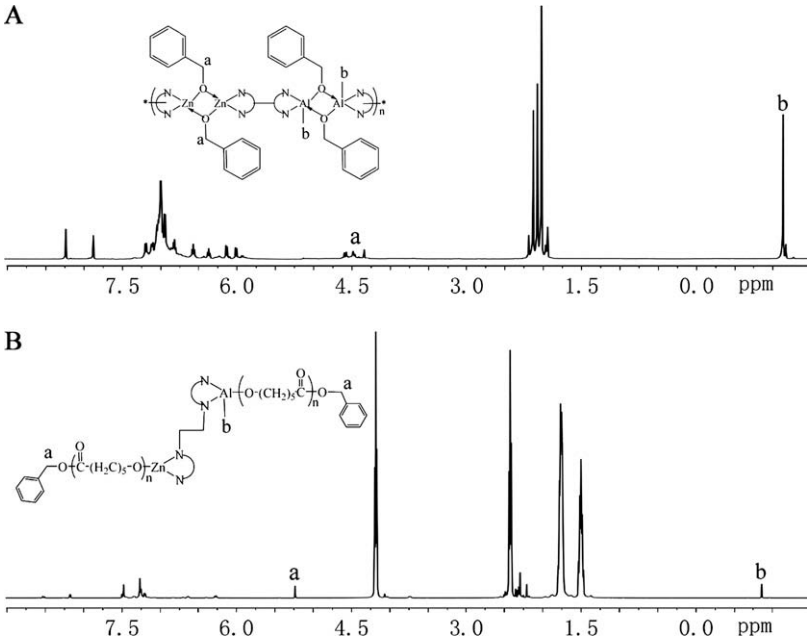


Fig. 5. ^{1}H NMR spectra of the reaction mixture of complex **2** with BnOH (1:2) in $CDCl_3$ (A) and the reaction mixture of complex **2**, BnOH and CL in $CDCl_3$ at room temperature (B).

Based on above results and discussion, the mechanism for the present polymerization systems is similar to the one proposed previously for the *N*-arylanilido-imine Al and Zn catalyst systems [39]. The metal benzyloxide complexes are the active catalysts which are produced by the reaction of the alkyl metal complexes with BnOH. The polymerization reaction takes place by repeated coordination of the CL monomer to the metal centres and insertion into the M–O bonds to form the polymerization intermediates LM–OP (where P refers to the polymer chain). The polymerization reaction stops when the monomer is totally consumed. Free polymers can be released by the addition of excess BnOH or acetic acid. BnOH acts as a co-initiator as well as a chain transfer regent (if there is excess BnOH) in the polymerization procedure.

3. Conclusion

In conclusion, mononuclear Al complex **1** and binuclear Al/Zn complex **2** supported by the *N*-arylanilido-imine ligand have been synthesized and fully characterized. The structures of the two complexes were determined by X-ray crystallography. Both complexes are efficient catalysts for the ring-opening polymerization of CL in the presence of BnOH. The catalytic activity of the binuclear complex **2**/BnOH system is much higher than that of the mononuclear Al complex **1**/BnOH system. Both catalyst systems produce PCL with narrow molecular weight distribution and capped with a benzyl ester group on one end and a hydroxylmethyl group on the other end. The ROP reaction of CL catalyzed by complex **2**/BnOH system takes place in a living fashion and the *M*n of the obtained polymers increases linearly with increase in the CL/Zn molar ratio. The formation and reaction of the metal benzyloxide complexes during the polymerization were confirmed by ^{1}H NMR spectroscopy.

4. Experimental

4.1. General procedures

All reactions were performed using standard Schlenk techniques in an atmosphere of high purity nitrogen or glove-box techniques. Toluene, hexane, THF were dried by refluxing over sodium and benzophenone and distilled under nitrogen prior to use. C_6D_6 was dried over activated 4 Å molecular sieves and vacuum-transferred to a sodium-mirrored air-free flask. $CDCl_3$, CH_2Cl_2 were dried over CaH_2 for 48 h and vacuum-transferred to an air-free flask. $AlMe_3$ and $ZnEt_2$ were purchased from Aldrich and used as received. ^{1}H and ^{13}C NMR spectra were measured using a Varian Mercury-300 NMR spectrometer or a Bruker AVANCE-500 NMR spectrometer. The elemental analysis was performed on a Perkin–Elmer 2400 analyzer. The GPC measurements were performed on a Waters-410 system using THF as the eluent (flow rate: 1 mL/min, at 35 °C). Molecular weights and molecular weight distributions were calculated using polystyrene as standard.

4.2. Synthesis of (C_6H_4(NHAr)–CH=N)CH_2CH_2(C_6H_4(NAr)CH=N$AlMe_2$) (**1**)

$AlMe_3$ (2.1 mL, 1.0 M in toluene, 2.1 mmol) was added to a solution of **L**H_2 (1.0 g, 2.1 mmol) in 20 mL of toluene at −78 °C. The reaction mixture was allowed to warm to room temperature and then stirred at 80 °C overnight, during which a clear yellow solution was formed. After removal of the solvent, the crude product was purified by recrystallization from a mixture of CH_2Cl_2/hexane to give the product as yellow crystalline solids (1.04 g, 93% yield). *Anal.* Calc. for $C_{34}H_{39}AlN_4$ (530.68): C, 76.95; H, 7.41; N, 10.56. Found: C, 76.90; H, 7.43; N, 10.58%. ^{1}H NMR (300 MHz, $CDCl_3$, 293 K): δ −0.84 (s, 6H, AlCH_3), 2.06 (s, 6H, CH_3), 2.17 (s, 6H, CH_3), 3.96 (s, 4H, NCH_2), 3.46 (m, 2H, NCH_2), 5.99–7.26 (m, 12H, Ph-*H*), 8.06 (s, 1H, C*H*=NAr), 8.45 (s, 1H, C*H*=NAr), 10.28 (s, 1H, N*H*). ^{13}C {1H} NMR (75 MHz, CDCl3, 293 K): δ −8.27, 18.58, 18.67, 56.84, 114.73, 114.99, 115.43, 116.01, 125.81, 126.43, 128.48, 128.64, 128.88, 129.06, 131.26, 133.84, 136.14, 136.79, 136.86, 142.46, 156.02, 165.63, 171.89.

4.3. Synthesis of (C_6H_4(NAr)CH=NZnEt)CH_2CH_2(C_6H_4(NAr)–CH=N$AlMe_2$) (**2**)

$ZnEt_2$ (1.9 mL, 1.0 M in toluene, 1.9 mmol) was added to a solution of 1 (1.0 g, 1.9 mmol) in 20 mL of toluene at −78 °C. The reaction mixture was allowed to warm to room temperature and then stirred at 80 °C overnight. After removal of the solvent, the crude product was purified by recrystallization from a mixture of CH_2Cl_2/hexane to give the product as yellow crystalline solids (1.07 g, 90% yield). Anal. Calc. for $C_{36}H_{43}AlN_4Zn$ (624.12): C, 69.28; H, 6.94; N, 8.98. Found: C, 69.27; H, 6.95; N, 8.97%. ^{1}H NMR (500 MHz, C_6D_6, 293 K): δ −0.11 (s, 6H, AlCH_3), 0.84 (q, 2H, ZnCH_2), 1.22 (t, 3H, $ZnCH_2CH_3$), 2.50 (s, 6H, CH_3), 2.53 (s, 6H, CH_3), 3.60 (s, 2H, NCH_2), 3.71 (s, 2H, NCH_2), 6.51–7.73 (m, 12H, Ph-*H*), 8.06 (s, 1H, C*H*=NAr), 8.13 (s, 1H, C*H*=NAr). 13C {1H} NMR (125 MHz, C_6D_6, 293 K): δ −1.00, 12.35, 14.30, 18.61, 18.65, 58.86, 60.85, 113.40, 114.58, 114.24, 114.69, 115.20, 117.16, 124.80, 126.04, 129.15, 129.37, 133.28, 135.02, 136.10, 136.69, 136.85, 137.70, 143.03, 147.92, 156.11, 156.58, 170.22, 170.92.

4.4. Polymerization of CL

In general, the polymerization experiments were performed as follows. To a rapidly stirred solution of CL in toluene (the amounts of CL and toluene were calculated based on the conditions given in Table 2), a solution of a catalyst (0.19 mmol) and appropriate amount of BnOH in toluene (3 mL) was added under a nitrogen atmosphere at the desired temperature. After the reaction mixture was stirred for a prescribed period or until the reaction mixture became very viscous and could not be stirred, the reaction was

Table 3
Crystal data and structural refinements details for complexes **1** and **2**.

	1	**2**
Formula	$C_{34}H_{39}AlN_4$	$C_{36}H_{43}AlN_4Zn$
Formula weight	530.67	624.09
Crystal system	triclinic	monoclinic
Space group	$P\bar{1}$	$P2(1)/n$
a (Å)	9.464(4)	16.063(3)
b (Å)	12.002(7)	9.0953(18)
c (Å)	15.337(7)	23.027(5)
α (°)	107.12(2)	90
β (°)	96.429(17)	92.69(3)
γ (°)	108.151(18)	90
V (Å^3)	1541.7(14)	3360.4(12)
Z	2	4
D_{calcd} (g cm^{-3})	1.143	1.234
F(0 0 0)	568	1320
θ Range for data collection (°)	3.25–27.48	3.00–27.48
Limiting indices	$-11 \leqslant h \leqslant 12$	$-20 \leqslant h \leqslant 20$
	$-15 \leqslant k \leqslant 15$	$-11 \leqslant k \leqslant 11$
	$-19 \leqslant l \leqslant 19$	$-29 \leqslant l \leqslant 29$
Data/restraints/parameters	6961/0/498	7613/0/380
Goodness-of-fit on F^2	1.085	1.022
Final R indices [$I > 2\sigma(I)$]	R_1[a] = 0.0614	R_1[a] = 0.0963
	wR_2[b] = 0.1720	wR_2[b] = 0.1920
R indices (all data)	R_1[a] = 0.0800	R_1[a] = 0.2462
	wR_2[b] = 0.1872	wR_2[b] = 0.2475
Largest difference in peak/hole (e Å^{-3})	0.816, −0.470	0.878, −0.502

[a] $R_1 = \sum||F_o| - |F_c||/\sum|F_o|$.
[b] $wR_2 = \{\sum[w(F_o^2 - F_c^2)^2]/\sum[w(F_o^2)^2]\}^{1/2}$.

quenched by the addition of excess acetic acid aqueous solution (1.0 N). The polymer was then precipitated by adding MeOH (100 mL) into the mixture, collected on a frit, washed with MeOH (3 × 10 mL) and dried in vacuo up to a constant weight.

4.5. Crystal structure determination

Single crystals of **1** and **2** suitable for X-ray structural analysis were obtained from CH_2Cl_2/hexane. Diffraction data were collected at 293 K on a Rigaku R-AXIS RAPID IP diffractometer equipped with graphite-monochromated Mo Kα radiation (λ = 0.71073 Å). Details of the crystal data, data collections, and structure refinements are summarized in Table 3. The structures were solved by direct methods and refined by full-matrix least-squares on F^2. All nonhydrogen atoms were refined anisotropically and the hydrogen atoms were included in idealized positions. All calculations were performed using the SHELXTL crystallographic software packages [47].

Supplementary data

CCDC 703678 and 703679 contains the supplementary crystallographic data for **1** and **2**. These data can be obtained free of charge via http://www.ccdc.cam.ac.uk/conts/retrieving.html, or from the Cambridge Crystallographic Data Centre, 12 Union Road, Cambridge CB2 1EZ, UK; fax: (+44) 1223-336-033; or e-mail: deposit@ccdc.cam.ac.uk.

Acknowledgment

This work was supported by the National Natural Science Foundation of China (Nos. 20674024 and 20772044).

References

[1] B.J. O'Keefe, M.A. Hillmyer, W.B. Tolman, J. Chem. Soc., Dalton Trans. (2001) 2215.
[2] A.C. Albertsson, I.K. Varma, Biomacromolecules 4 (2003) 1466.
[3] J. Wu, T.L. Yu, C.T. Chen, C.C. Lin, Coord. Chem. Rev. 250 (2006) 602.
[4] M.L. Shueh, Y.S. Wang, B.H. Huang, C.Y. Kuo, C.C. Lin, Macromolecules 37 (2004) 5155.
[5] L.F. Sánchez-Barba, D.L. Hughes, S.M. Humphrey, M. Bochmann, Organometallics 25 (2006) 1012.
[6] L.E. Breyfogle, C.K. Williams, V.G. Young, M.A. Hillmyer, W.B. Tolman, Dalton Trans. (2006) 928.
[7] Z.Y. Zhong, S. Schneiderbauer, P.J. Dijkstra, J. Feijen, Polym. Bull. (Berlin) 51 (2003) 175.
[8] Z.Y. Zhong, M.J.K. Ankoné, P.J. Dijkstra, C. Birg, M. Westerhausen, J. Feijen, Polym. Bull. (Berlin) 46 (2001) 51.
[9] R.C. Yu, C.H. Hung, J.H. Huang, H.Y. Lee, J.T. Chen, Inorg. Chem. 41 (2002) 6450.
[10] C.H. Huang, F.C. Wang, B.T. Ko, T.L. Yu, C.C. Lin, Macromolecules 34 (2001) 356.
[11] C.T. Chen, C.A. Huang, B.H. Huang, Macromolecules 37 (2004) 7968.
[12] L.M. Alcazar-Roman, B.J. O'Keefe, M.A. Hillmyer, W.B. Tolman, Dalton Trans. (2003) 3082.
[13] M.L. Hsueh, B.H. Huang, C.C. Lin, Macromolecules 35 (2002) 5763.
[14] S. Milione, F. Grisi, R. Centore, A. Tuzi, Organometallics 25 (2006) 266.
[15] A. Amgoune, L. Lavanant, C.M. Thomas, Y. Chi, R. Welter, S. Dagorne, J.F. Carpentier, Organometallics 24 (2005) 6279.
[16] N. Nomura, T. Aoyama, R. Ishii, T. Kondo, Macromolecules 38 (2005) 5363.
[17] J. Cayuela, V. Bounor-Legaté, P. Cassagnau, A. Michel, Macromolecules 39 (2006) 1338.
[18] M. Davidson, M.D. Jones, M.D. Lunn, M.F. Mahon, Inorg. Chem. 45 (2006) 2282.
[19] H. Wang, H.S. Chan, J. Okuda, Z.W. Xie, Organometallics 24 (2005) 3118.
[20] F. Gornshtein, M. Kapon, M. Botoshansky, M.S. Eisen, Organometallics 26 (2007) 497.
[21] B.J. O'Keefe, L.E. Breyfogle, M.A. Hillmyer, W.B. Tolman, J. Am. Chem. Soc. 124 (2002) 4384.
[22] M.Z. Chen, H.M. Sun, W.F. Li, Z.G. Wang, Q. Shen, Y. Zhang, J. Organomet. Chem. 691 (2006) 2489.
[23] D.A. Walker, T.J. Woodman, M. Schormann, D.L. Hughes, M. Bochmann, Organometallics 22 (2003) 797.
[24] H.Y. Chen, B.H. Huang, C.C. Lin, Macromolecules 38 (2005) 5400.
[25] Y. Sarazin, M. Schormann, M. Bochmann, Organometallics 23 (2004) 3296.
[26] Z.X. Wang, C.Y. Qi, Organometallics 26 (2007) 2243.
[27] B.H. Huang, C.N. Lin, M.L. Hsueh, T. Athar, C.C. Lin, Polymer 47 (2006) 6622.
[28] C.M. Silvernail, L.J. Yao, L.M.R. Hill, M.A. Hillmyer, W.B. Tolman, Inorg. Chem. 46 (2007) 6565.
[29] P. Lecomte, F. Stassin, R. Jér?me, Macrol. Symp. 215 (2004) 325.
[30] G. Deshayes, F.A.G. Mercier, P. Degée, I. Verbruggen, M. Biesemans, R. Willem, P. Dubois, Chem. Eur. J. 9 (2003) 4346.
[31] A. Kowalski, A. Duda, S. Penczek, Macromolecules 33 (2000) 689.
[32] A. Otero, J. Fernández-Baeza, A. Antiñolo, A. Lara-Sánchez, E. Martínez-Caballero, J. Tejeda, F.L. Sánchez-Barba, C. Alonso-Moreno, I. Isabel López-Solera, Organometallics 27 (2008) 976.
[33] H.T. Sheng, J.M. Li, Y. Zhang, Y.M. Yao, Q. Shen, Polyhedron 27 (2008) 1665.
[34] J.F. Wang, H.M. Sun, Y.M. Yao, Y. Zhang, Q. Shen, Polyhedron 27 (2008) 1977.
[35] W. Gao, D.M. Cui, X.M. Liu, Y. Zhang, Y. Mu, Organometallics 27 (2008) 5889.
[36] D. Moore, M. Cheng, E.B. Lobovsky, G.W. Coates, J. Am. Chem. Soc. 125 (2003) 11911.
[37] B.Y. Lee, H.Y. Kwon, S.Y. Lee, S.J. Na, S. Han, H. Yun, H. Lee, Y.W. Park, J. Am. Chem. Soc 127 (2005) 3031.
[38] T. Bok, H. Yun, B.Y. Lee, Inorg. Chem. 45 (2006) 4228.
[39] W. Yao, Y. Mu, A.H. Gao, W. Gao, L. Ye, Dalton Trans. (2008) 3199.
[40] Z.Y. Zhong, P.J. Dijkstra, J. Feijen, J. Am. Chem. Soc. 125 (2003) 11291.
[41] H.Z. Du, A.H. Velders, P.J. Dijkstra, Z.Y. Zhong, X.S. Chen, J. Feijen, Macromolecules 42 (2009) 1058.
[42] X.M. Liu, W. Gao, Y. Mu, G.H. Li, L. Ye, H. Xia, Y. Ren, S.H. Feng, Organometallics 24 (2005) 1614.
[43] D.J. Doyle, V.C. Gibson, A.J.P. White, Dalton Trans. (2007) 358.
[44] J.A. Dean, Lange's Handbook of Chemistry, 15th ed., McGraw-Hill, New York, 1999. p. 4.41.
[45] W. Yao, Y. Mu, A.H. Gao, Q. Su, Y.J. Liu, Y.Y. Zhang, Polymer 49 (2008) 2486.
[46] Z.Y. Zhong, P.J. Dijkstra, C. Birg, M. Westerhausen, J. Feijen, Macromolecules 34 (2001) 3863.
[47] G.M. Sheldrick, SHELXTL-97, Program for the Refinement of Crystal Structures, University of Gottingen, Germany, 1997.

Polyhedron 28 (2009) 2611–2618

Contents lists available at ScienceDirect

Polyhedron

journal homepage: www.elsevier.com/locate/poly

The C–H···Cl_2Cu(II) synthon in the structural direction and assembly of supramolecular complexes with the 3,3′-bis(2-benzimidazolyl)-2,2′-dipyridine ligand and its N-substituted derivatives

Bao-Ming Ji [a,*], Shao-Bin Miao [a,b], Dong-Sheng Deng [a], Chen-Xia Du [b,*]

[a] College of Chemistry and Chemical Engineering, Luoyang Normal University, Luoyang 471022, PR China
[b] Department of Chemistry, Zhengzhou University, Zhengzhou 450052, PR China

ARTICLE INFO

Article history:
Received 5 January 2009
Accepted 20 May 2009
Available online 14 June 2009

Keywords:
3,3′-Bis(2-benzimidazolyl)-2,2′-dipyridine
Crystal structure
Cu(II) complex
C–H···Cl and C–H···π interactions
Metallosupramolecular architecture

ABSTRACT

Three new Cu(II) supramolecular complexes [Cu($\mathbf{L_1}$)Cl_2]·2DMF (**1**), [Cu($\mathbf{L_2}$)Cl_2] (**2**) and [Cu($\mathbf{L_3}$)Cl_2]·DMF (**3**) ($\mathbf{L_1}$ = 3,3′-bis(2-benzimidazolyl)-2,2′-dipyridine, $\mathbf{L_2}$ = 3,3′- bis(N-ethyl-2-benzimidazolyl)-2,2′-dipyridine and $\mathbf{L_3}$ = 3,3′-bis(N-benzyl-2-benzimidazolyl)-2,2′-dipyridine) have been prepared and characterized by elemental analysis, IR spectra and single crystal X-ray diffraction. X-ray structural analysis of $\mathbf{L_1}$, $\mathbf{L_2}$·3.5H_2O and $\mathbf{L_3}$·H_2O indicates that all three ligands adopt the *trans* conformation with the two benzimidazole fragments located on opposite sides of the dipyridyl backbone. While in complexes **1**–**3**, all the ligands display the *cis* conformation and behave as bidentate chelating reagents to coordinate with Cu(II). The inorganic chloride ions always act as a reliable hydrogen bonded acceptor in these structures, and the resulting C–H···Cl_2Cu supramolecular synthons play a significant role in the formation and stabilization of the structures. Moreover, additional non-covalent interactions, such as C–H···π, are also identified to extend the discrete (0-D) or low-dimensional (1-D) motifs into high-dimensional architectures.

© 2009 Elsevier Ltd. All rights reserved.

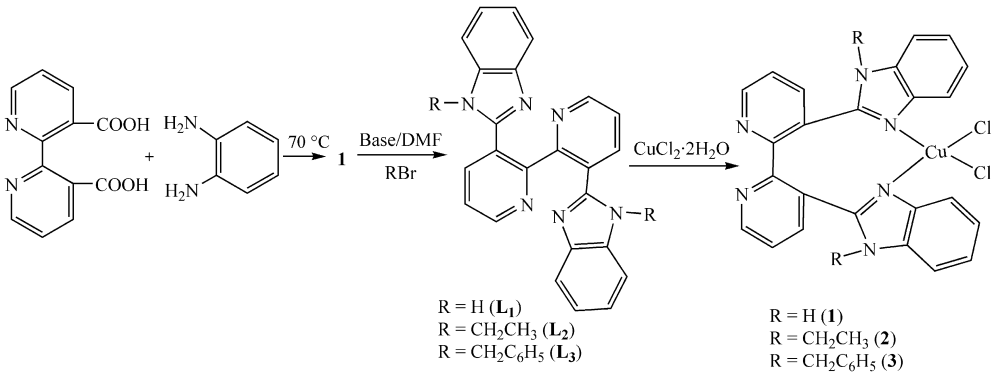
1. Introduction

As stated by Desiraju and Steiner, – there is a growing need to simultaneously assess different interactions and establish their hierarchy – and non-covalent interactions have received much interest in organic and inorganic crystal engineering [1–4]. One of the challenges of crystal engineering today is to clarify the relative roles of various synthons in crystal structures. In this regard, the role of X–H···Cl (X = O and N) and C–H···π interactions in the development of the supramolecular structures of hybrid organic/inorganic metal halides has recently received specific attention [5–7]. However, in this contribution, our interest in weak interactions has focused primarily on the so-called C–H···Cl inorganic supramolecular synthons and C–H···π interactions. To our delight, the previous studies have revealed that the formation of halide-involved hydrogen bonds in metal complexes depends on the coordination environments [8–11]. Moreover, the C–H···Cl contacts and charge–assisted (for strengthening non-covalent forces) terminal M–Cl bonds of chlorometallates have been found to play a decisive role in the formation of supramolecular architectures of crystalline solids [8,12–16]. Thus, it is significant to further explore the nature of such interactions by establishing appropriate chemical systems with a C–H donor for the acceptance of the chloride anion. To achieve this aim, one of the available strategies is to assemble metal chlorides with pre-designed receptors that can serve as proton donors. This idea has been reinforced by several recent works showing the potential utility of C–H···Cl–M hydrogen bonding (M = transition metal) in the self-assembly of tape- and sheet-shaped structures [17–20]. Another possible strategy is the choice of suitable organic ligands possessing one site for coordinating to the metal centers in well-defined geometries and the another site for non-covalent interactions.

In this context, we selected the ligand 3,3′-bis(2-benzimidazolyl)-2,2′-dipyridine ($\mathbf{L_1}$) and its N-substituted derivatives 3,3′-bis(N-ethyl-2-benzimidazolyl)-2,2′-dipyridine ($\mathbf{L_2}$) and 3,3′-bis(N-benzyl-2-benzimidazolyl)-2,2′-dipyridine ($\mathbf{L_3}$) as potential building blocks due to their bifunctional characters. In virtue of the free-rotation of the C–C bond, the two imino moieties of the bis-benzimidazolyl groups can coordinate to a metal ion to serve as the first coordination sphere and the acidic aromatic C–H groups may serve as the second coordination sphere to donate multifold hydrogen bonds with chloride anions [21,22]. In such a metal complex, the metallation of the ligand greatly enhances the electron-deficient character of the benzimidazolyl group, which will reinforce the C–H···Cl hydrogen bonding [23]. Furthermore, the substitution effect of the ligands may dramatically affect their coordination tendency [24], and it still remains a continuing challenge to prove

* Corresponding authors. Tel./fax: +86 37965523821 (B.-M. Ji).
E-mail addresses: lyhxxjbm@126.com (B.-M. Ji), dcx@zzu.edu.cn (C.-X. Du).

0277-5387/$ - see front matter © 2009 Elsevier Ltd. All rights reserved.
doi:10.1016/j.poly.2009.05.078



Scheme 1. Reaction pathways for synthesis of ligands L_1–L_3 and complexes **1**–**3**.

such an effect of the ligands on the formation of weak hydrogen bonding and further supramolecular frameworks. Herein, we will present the synthesis and characterization of two new ligands L_2 and L_3 as well as three copper(II) complexes **1**–**3** based on this series of ligands (see Scheme 1) to further illustrate the above-mentioned issues.

2. Experimental

2.1. Materials and instruments

2,2′-Bipyridyl-6,6′-dicarboxylic acid was prepared according to the procedure reported by Dholakia et al. [25], and the ligand L_1 was synthesized according to the literature method [24]. All other reagents were of commercial grade and were used as received. Elemental analyses (C, H, N) were carried out on a Flash 1112 elemental analyzer. FT-IR spectra (KBr pellet) were recorded in the range 4000–400 cm^{-1} on a Nicolet Avatar-360 spectrometer. ^1H NMR spectra were recorded on a Bruker DPX-400 spectrometer in DMSO with TMS as an internal standard.

2.2. Synthesis of 3,3′-bis(N-ethyl-2-benzimidazolyl)-2,2′-dipyridine (L_2)

Under N_2 atmosphere, a suspension of KOH (224 mg, 4 mmol) and 2,2′-bipyridyl-6,6′-dicarboxylic acid (776 mg, 2 mmol) in anhydrous DMF (20 mL) was stirred for 1 h at 70 °C. Then, bromoethane (4 mmol) was added. The mixture was heated at 70 °C for 12 h and then poured into ice. The product was purified by column chromatography using ethyl acetate/hexane (3:1) as the eluent. 610 mg, 67% yield. *Anal.* Calc. for $C_{28}H_{24}N_6$: C, 75.65; H, 5.44; N, 18.91. Found: C, 75.81; H, 5.36; N, 18.83%. Main IR bands (cm^{-1}): 1614w, 1557w, 1444m, 1392w, 767s, 744s. ^1H NMR (δ ppm): 8.32 (d, 2H, H_{Py}), 8.08 (d, 2H, H_{Py}), 7.57 (q, 2H, H_{Py}), 7.46 (d, 4H, H_{Ar}), 7.23 (d, 4H, H_{Py}), 4.18 (d, 4H, H_{CH_2}), 1.18 (d, 6H, H_{CH_3}).

2.3. Synthesis of 3,3′-bis(N-benzyl-2-benzimidazolyl)-2,2′-dipyridine (L_3)

Under N_2 atmosphere, a suspension of Na_2CO_3 (424 mg, 4 mmol) and 2,2′-bipyridyl-6,6′-dicarboxylic acid (776 mg, 2 mmol) in anhydrous DMF (20 mL) was stirred for 1 h at 70 °C. Then, benzyl bromide (4 mmol) was added. The mixture was heated at 70 °C for 24 h and then poured into ice. The product was purified by column chromatography using ethyl acetate/hexane (3:1) as the eluent. 732 mg, 64% yield. *Anal.* Calc. for $C_{38}H_{28}N_6$: C, 80.26; H, 4.96; N, 14.78. Found: C, 80.41; H, 5.15; N, 14.61%. Main IR bands (cm^{-1}): 1614w, 1558w, 1454m, 755s, 739s. ^1H NMR (δ ppm): 8.35 (d, 2H, H_{Py}), 7.93(d, 2H, H_{Py}), 7.35 (q, 2H, H_{Py}), 7.19–7.28 (m,18H, H_{Ar}), 5.56 (d, 4H, H_{CH_2}).

Table 1
Crystallographic data and structure refinement for ligands L_1–L_3.

Compound	L_1	L_2	L_3
Empirical formula	$C_{24}H_{16}N_6$	$C_{28}H_{31}N_6O_{3.5}$	$C_{38}H_{30}N_6O$
Formula weight	388.43	507.53	586.68
Crystal system	monoclinic	monoclinic	monoclinic
Space group	*P*(2)1/*n*	*C*/2*c*	*P*(2)1/*c*
a (Å)	7.9283(6)	18.463(3)	11.3010(8)
b (Å)	19.6324(14)	29.719(4)	12.7148(9)
c (Å)	12.6341(9)	13.6027(17)	21.8545(15)
α (°)	90	90	90
β (°)	97.3060(10)	130.699(2)	99.1460(10)
γ (°)	90	90	90
V (Å^3)	1950.6(2)	5658.6(13)	3100.3(4)
Z	4	8	4
D_C (g cm^{-3})	1.323	1.175	1.257
Absorption coefficient (mm^{-1})	0.083	0.080	0.078
F(0 0 0)	808	2096	1232
Reflections collected/unique [$R_{(int)}$]	10 112/3520 [0.0150]	12 418/6290 [0.0226]	11 414/5703 [0.0231]
Maximum and minimum transmission	0.9716 and 0.9598	0.9818 and 0.9640	0.9869 and 0.9745
Goodness-of-fit (GOF) (F^2)	1.053	1.032	1.012
R_1, wR_2 [$I > 2\sigma(I)$][a]	0.0358/0.0865	0.0769/0.2462	0.0428/0.0992
Largest difference in peak and hole (e Å^{-3})	0.139 and −0.206	0.701 and −0.223	0.188 and −0.133

[a] $R_1 = \sum||F_o| - |F_c||/\sum|F_o|$, $wR_2 = [\sum(F_o^2 - F_c^2)^2/\sum w(F_o^2)^2]^{1/2}$.

Table 2
Crystallographic data and structure refinement for complexes **1**–**3**.

	1	2	3
Empirical formula	$C_{30}H_{30}Cl_2CuN_8O_2$	$C_{28}H_{24}Cl_2CuN_6$	$C_{41}H_{35}Cl_2CuN_7O$
Formula weight	669.06	578.97	776.20
Crystal system	monoclinic	orthorhombic	monoclinic
Space group	*C*2/*c*	*Pbca*	*P*2(1)/*c*
a (Å)	24.1329(19)	16.1833(12)	16.348(4)
b (Å)	10.6704(9)	15.7301(12)	11.250(3)
c (Å)	14.6618(12)	20.6441(16)	20.534(5)
α (°)	90	90	90
β (°)	123.0190(10)	90	98.448(4)
γ (°)	90	90	90
V (Å^3)	3165.7(4)	5255.3(7)	3735.4(16)
Z	4	8	4
D_C (g cm^{-3})	1.404	1.464	1.380
Absorption coefficient (mm^{-1})	0.900	1.064	0.771
F(0 0 0)	1380	2376	1604
Reflections collected/unique [$R_{(int)}$]	8276/2916 [0.0163]	26 583/4882 [0.0413]	27 834/6936 [0.0239]
Maximum and minimum transmission	0.7932 and 0.6876	0.8883 and 0.6488	0.8899 and 0.7029
Goodness-of-fit (GOF) (F^2)	1.034	1.039	1.026
R_1, wR_2 [$I > 2\sigma(I)$][a]	0.0331/0.0923	0.0349/0.0820	0.0350/0.0943
Largest difference in peak and hole (e Å^{-3})	0.321 and −0.218	0.314 and −0.357	0.259 and −0.369

[a] $R_1 = \sum||F_o| - |F_c||/\sum|F_o|$, $wR_2 = [\sum(F_o^2 - F_c^2)^2/\sum w(F_o^2)^2]^{1/2}$.

2.4. Synthesis of [Cu(**L₁**)Cl₂]·2DMF (**1**)

A mixture of **L₁** (194.5 mg, 0.5 mmol) and $CuCl_2{\cdot}2H_2O$ (84.5 mg, 0.5 mmol) in DMF (10 mL) was stirred for 3 h at 60 °C. The solution was filtered and the filtrate was diffused by diethyl ether. After several days, single crystals suitable for X-ray analysis were obtained (269.0 mg, 80% yield). *Anal.* Calc. for $C_{30}H_{30}Cl_2CuN_8O_2$: C, 53.85; H, 4.52; N, 16.75. Found: C, 54.01; H, 4.62; N, 16.67%. Main IR bands (cm^{-1}): 1648s, 1593w, 1561, 1449s, 764s, 754s.

2.5. Synthesis of [Cu(**L₂**)Cl₂] (**2a**)

A mixture of **L₂** (250.2 mg, 0.5 mmol) and $CuCl_2{\cdot}2H_2O$ (84.5 mg, 0.5 mmol) in DMF (10 mL) was stirred for 3 h at 60 °C. The solution was filtered and the filtrate was diffused by diethyl ether. After several days, single crystals suitable for X-ray analysis were obtained (208.0 mg, 72% yield). *Anal.* Calc. for $C_{28}H_{24}Cl_2CuN_6$: C, 58.08; H, 4.18; N, 14.52. Found: C, 58.36; H, 4.32; N, 14.31%. Main IR bands (cm^{-1}): 1561m, 1475s, 1454s, 1436s, 1402s, 756s.

2.6. Synthesis of [Cu(**L₃**)Cl₂]·DMF (**3**)

A mixture of **L₃** (293.4 mg, 0.5 mmol) and $CuCl_2{\cdot}2H_2O$ (84.5 mg, 0.5 mmol) in DMF (10 mL) was stirred for 3 h at 60 °C. The solution was filtered and the filtrate was diffused by diethyl ether. After several days, single crystals suitable for X-ray analysis were obtained (291.0 mg, 75% yield). *Anal.* Calc. for $C_{41}H_{35}Cl_2CuN_7O$: C, 63.44; H, 4.54; N, 12.63. Found: C, 63.28; H, 4.34; N, 12.76%. Main IR bands (cm^{-1}): 1677s, 1454s, 763s, 734m.

2.7. X-ray crystallography

Intensity date were collected at 291(2) K on a Bruker APEX II CCD diffractometer with Mo Ka radiation (λ = 0.71073 Å). The structures were solved by direct methods and refined by full-matrix least-squares methods on F^2 with SHELXL-97 [26]. All non-hydrogen atoms were refined anisotropically, whereas hydrogen atoms were placed in geometrically calculated positions. Crystal data and structure refinements are summarized in Tables 1 and 2. Selected bond lengths and bond angles are given in Table 3.

Table 3
Selected bond lengths (Å) and bond angles (°) of compounds **L₁**–**L₃** and **1**–**3**.

L₁	N(1)–C(7)	1.3149(2)	N(5)–C(18)	1.3207(2)
L₂	C(1)–N(2)	1.315(4)	C(1A)–N(2A)	1.315(4)
L₃	N(1)–C(7)	1.314(2)	N(5)–C(25)	1.316(2)
1	Cu(1)–N(1)	1.9884(2)	Cu(1)–N(1A)	1.9884(2)
	Cu(1)–Cl(1)	2.2396(6)	Cu(1)–Cl(1A)	2.2395(6)
	N(1)–C(7)	1.325(2)	N(1A)–C(7A)	1.325(2)
	N(1)–Cu(1)–N(1A)	139.08(9)	N(1)–Cu(1)–Cl(1)	94.60(5)
	N(1)–Cu(1)–Cl(1A)	97.79(5)	Cl(1)–Cu(1)–Cl(1A)	144.06(4)
2	Cu(1)–N(1)	1.9895(2)	Cu(1)–N(5)	1.9969(2)
	Cu(1)–Cl(2)	2.2185(8)	Cu(1)–Cl(1)	2.2295(8)
	N(1)–C(7)	1.327(3)	N(5)–C(20)	1.324(3)
	N(1)–Cu(1)–N(5)	140.48(8)	N(1)–Cu(1)–Cl(2)	97.46(6)
	N(1)–Cu(1)–Cl(1)	94.42(6)	Cl(2)–Cu(1)–Cl(1)	142.25(4)
3	Cu(1)–N(3)	2.0132(2)	Cu(1)–N(5)	2.0244(2)
	Cu(1)–Cl(1)	2.2278(7)	Cu(1)–Cl(2)	2.2301(7)
	N(5)–C(25)	1.330(2)	N(3)–C(11)	1.336(3)
	N(3)–Cu(1)–N(5)	138.78(7)	N(3)–Cu(1)–Cl(1)	95.81(5)
	N(3)–Cu(1)–Cl(2)	98.86(5)	Cl(1)–Cu(1)–Cl(2)	138.19(3)

Symmetry codes: (A) 1 − *x*, *y*, 3 − *z*/2.

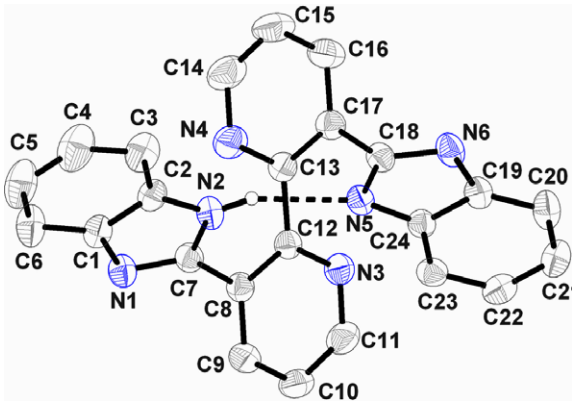


Fig. 1. Molecular structure of **L₁** showing the intramolecular N–H···N hydrogen bond.

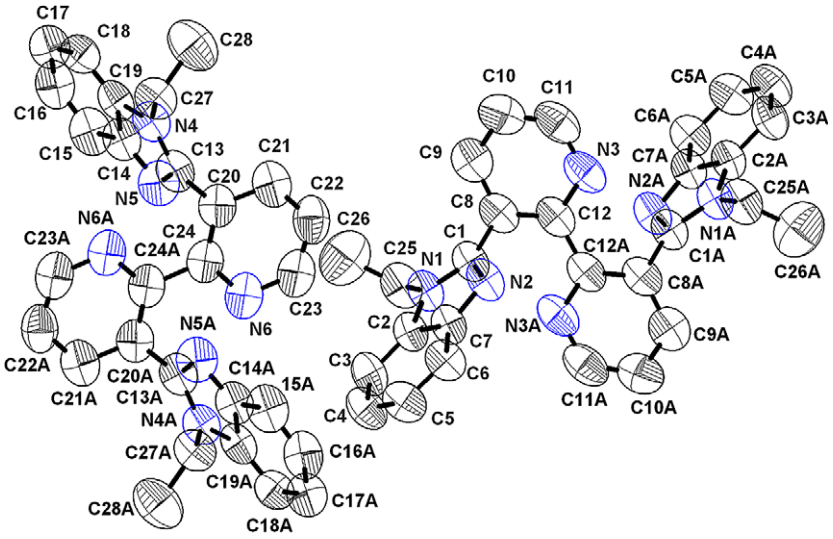


Fig. 2. Molecular structure of $\mathbf{L_2}\cdot 3.5H_2O$, omitting the lattice water molecules.

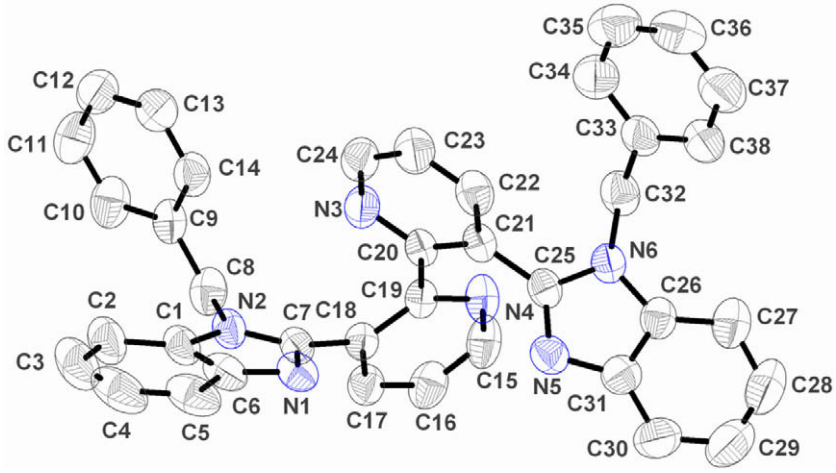


Fig. 3. Molecular structure of $\mathbf{L_3}\cdot H_2O$, omitting the lattice water molecules.

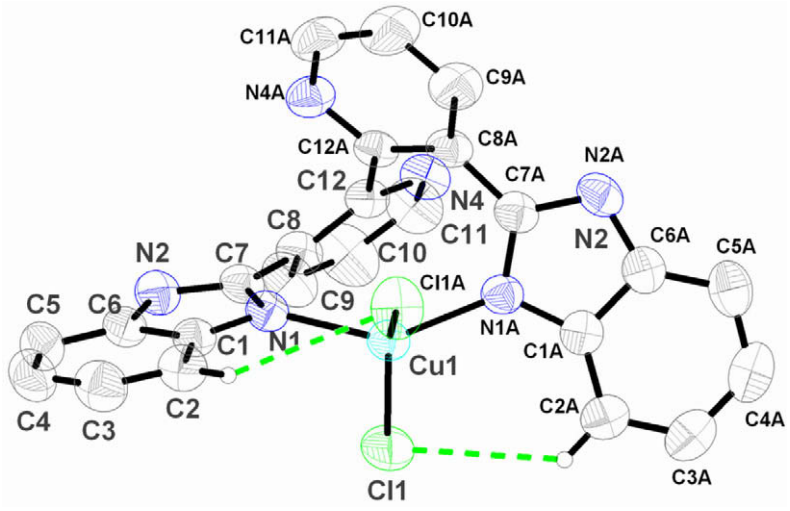


Fig. 4. Molecular structure of complex **1** showing two intramolecular C–H···Cl hydrogen bonds. DMF and irrelevant H atoms are omitted for clarity.

Table 4
Geometrical parameters of the secondary interactions.

Compound	H-bond	*d*(H-A) (Å)	*d*(D-A) (Å)	∠(DHA) (°)
L_1	N2–H2′···N5	2.110	2.9165(14)	156.2
	N6–H6′···N3^{i}	2.050	2.9063(15)	172.5
1	N2–H2···O1^{i}	1.74	2.596(4)	178
	C15–H15C···O1^{ii}	2.52	3.432(8)	158
	C10–H10···Cg3^{iii}	2.80	3.522(3)	135
	C10–H10···Cg1^{iiii}	2.89	3.702(3)	146
	C14′–H14E···Cg2^{iv}	2.99	3.712(9)	133
	C2–H2A···Cl1^{v}	2.87	3.547(4)	130
2	C17–H17···Cl1^{i}	2.810	3.674(3)	155
	C25–H25···Cl1	2.88	3.438(4)	120
	C5–H5···Cg6^{ii}	2.97	3.871(3)	163
	C9–H9B···Cg3^{iii}	2.98	3.771(3)	141
	C18–H18···Cg5^{iv}	2.75	3.548(3)	145
	C24–H24···Cg4^{v}	2.95	3.834(3)	160
3	C9–H9···Cl2^{i}	2.74	3.647(3)	164
	C16–H16···O1^{ii}	2.37	3.264(6)	160
	C20–H20···N2	2.38	3.265(4)	160
	C22–H22···Cl1^{iii}	2.78	3.682(3)	164
	C37–H37···Cg5 ^{iv}	2.81	3.655(4)	151
	C39′–H39F···Cg4^{v}	2.83	3.608(4)	139

Symmetry codes for **L_1**: (i) $-x+2, -y, -z+1$.
Symmetry codes for **1**: (i) $1/2-x, 1/2-y, 1-z$; (ii) $1/2-x, 3/2-y, 1-z$; (iii) $x, -y, -1/2+z$; (iv) $x, 1+y, z$; (v) $-x, y, 1/2-z$.
Rings for **1**: Cg1 (N1–C1–C6–N2–C7), Cg2 (N4–C11–C10–C9–C8–C12), Cg3 (C1–C6).
Symmetry codes for **2**: (i) $1/2-x, 1/2+y, z$; (ii) $1/2-x, y, -1/2+z$; (iii) $1-x, -y, -z$; (iv) $1/2-x, 1/2+y, z$; (v) $-1/2+x, y, 1/2-z$.
Rings for **2**: Cg3 (N3–C10–C11–C12–C13–C14), Cg4 (N4–C15–C16–C17–C18–C19), Cg5 (C1–C6), Cg6 (C21–C26).
Symmetry codes for **3**: (i) $-x, 1/2+y, 1/2-z$; (ii) $1-x, -1/2+y, 1/2-z$; (iii) $x, 1/2-y, -1/2+z$; (iv) $x, 1/2-y, 1/2+z$; (v) x, y, z.
Rings for **3**: Cg4 (N2–C6–C7–C8–C9–C10), Cg5 (C12–C17).

3. Results and discussion

3.1. Structural description of the ligands

The three ligands were prepared through the Phillips reaction [27], involving refluxing the aryl diamine with pyridine dicarboxylic acid, and the Ullmann coupling reaction [28] (see Scheme 1). Compound **L_1** is a polydentate ligand which has been previously reported [24,29]. In order to further investigate the molecular conformation of such ligands and the influence of the substituents, the crystal structures of **L_1**, **L_2**·3.5H_2O and **L_3**·H_2O have been determined. As shown in Figs. 1–3, all free ligands adopt the *trans* conformation in the solid state with the two benzimidazolyl groups on opposite sides of the 2,2′-dipyridine backbone, which is similar to that of other semi-rigid podal-type ligands such as bis(2-benzimidazolyl)biphenyl [30]. In each case, the flexibility of the ligand is provided by the torsional twist along the central C–C bond. The pyridyl–pyridyl and benzimidazole–benzimidazole dihedral angles in **L_1** (72.5° and 99.3°) are significantly larger than those in **L_2** or **L_3** (49.7° and 50.7° or 46.1° and 45.7°). This may be ascribed to the intramolecular N–H···N hydrogen bonds in **1**, which also consolidates the molecular conformation.

3.2. Structural description of complexes *1–3*

Ligands **L_1**, **L_2** and **L_3** are almost insoluble in diethyl ether at room temperature, however, they have good solubility in DMF. For the preparation of **1–3**, the two reaction components first were dissolved in DMF and stirred for 3 h at 60 °C, then the resulting solution was filtered and the filtrate was diffused by diethyl ether. After several days, single crystals of **1–3** were obtained.

The X-ray single crystal structure of [Cu(**L_1**)Cl_2]·2DMF (**1**) indicates that the coordination environment around Cu(II) is a distorted tetrahedron provided by one ligand **L_1** and two chloride ions, as depicted in Fig. 4. Interestingly, the ligand **L_1** in this case adopts the *cis* conformations with two benzimidazolyl groups on the same side of the dipyridyl skeleton, which is different from the *trans* style in the free ligand. The coordination motif in **1** is a discrete mononuclear molecule with the presence of intramolecular C–H···Cl contacts, as observed in other related systems [31,32]. In addition, C–H···π interactions (see Table 4) are also observed, in which the pyridyl rings are donors and the benzimidazoyl rings are acceptors. As a consequence, the discrete mononuclear units are assembled into a 3-D network (see Fig. 5). It should be noted that no intermolecular C–H···Cl hydrogen bonding is found in this structure. It must be pointed out that the DMF molecules are disordered over two sites and have been modelled with a 61.8(2):38.2(2) ratio. Interestingly, these disordered DMF molecules are trapped in the lattice by the formation of C–H···O hydrogen bonds (Table 4).

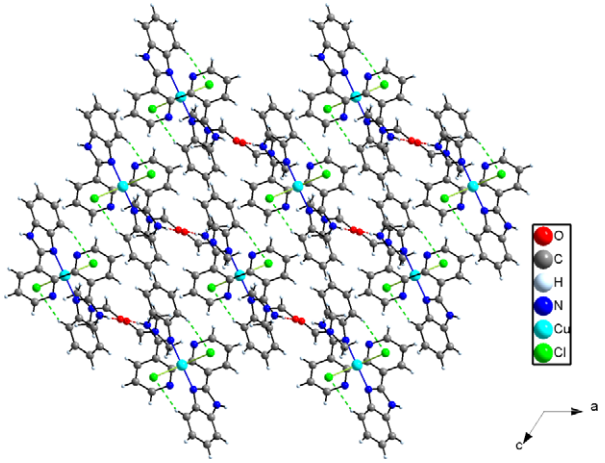


Fig. 5. View of the 3-D network of **1**. Intramolecular C–H···Cl hydrogen bonds are shown in green and C–H···O in red. (For interpretation of the references to colour in this figure legend, the reader is referred to the web version of this article.)

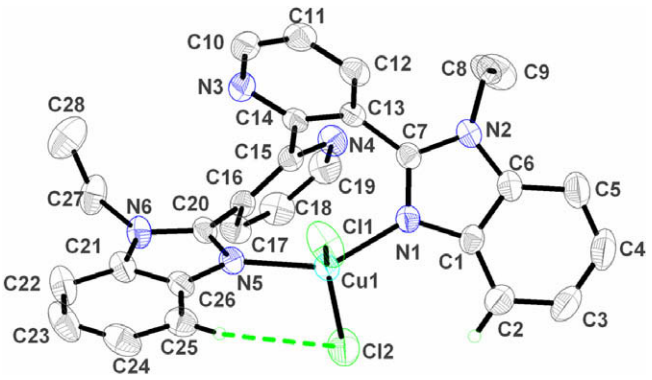


Fig. 6. Molecular structure of **2** showing one intramolecular C–H···Cl hydrogen bond. Irrelevant H atoms are omitted for clarity.

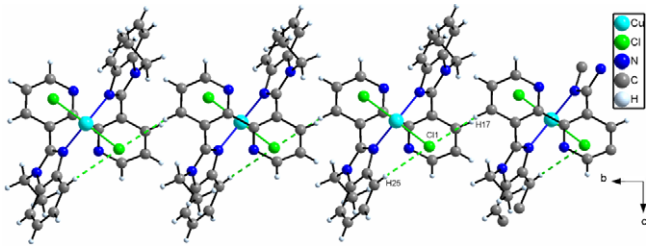


Fig. 7. 1-D chain in **2** along the *b* axis. The C–H···Cl hydrogen bonds are shown in green. (For interpretation of the references to colour in this figure legend, the reader is referred to the web version of this article.)

The structural analysis of [Cu(**L**$_2$)Cl$_2$] (**2**) reveals that each Cu(II) ion is coordinated by two nitrogen atoms from one **L**$_2$ ligand and two chloride ions to result in a distorted tetrahedral sphere, as in **1** (see Fig. 6). Unlike in **1**, there is only one intramolecular C–H···Cl bond in **2**. Moreover, the Cl1 ions are involved in intermolecular C–H···Cl interactions. The Cu–Cl1 bond of one molecule is linked with the pyridyl C–H of the adjacent molecule, and the C···Cl distance (3.674 Å) is in the normal range of C–H···Cl hydrogen bonding [9]. With this assembly, the [Cu(**L**$_2$)Cl$_2$] units are connected to each other to form a 1-D chain along the *b* axis (see Fig. 7). The 1-D chains are further assembled with the aid of C–H···π contacts to afford a 2-D layered structure along the *ac* plane. C–H···π contacts are established between the pyridyl and benzimidazolyl donors and acceptors (see Table 4). Furthermore, the layers are linked to each other by C–H···π interactions between the C-H donors of ethyl groups and the pyridyl rings, resulting in the final 3-D supramolecular lattice, as shown in Fig. 8. This results in the ethyl groups protruding out from the 1-D chains, and thus they are close to the adjacent pyridyl rings to effectively link the 2-D layers together.

As depicted in Fig. 9, the Cu(II) ion in **3** also displays a distorted tetrahedral geometry. In the crystal structure, the DMF molecules are also disordered over two sites and have been modelled with a 73.0(3):27.0(3) ratio. However, no intramolecular C–H···Cl interaction is found in this case**.** Instead, the chloride ions are only involved in intermolecular C–H···Cl interactions (Table 4). Thus, the [Cu(**L**$_3$)Cl$_2$] units are linked to each other via such secondary forces to produce a 1-D wave-like chain along the *c* axis (see Fig. 10). This stacking, with additional C–H···π secondary interactions between the phenyl donors and the acceptors of benzimidazolyl, leads to the formation of 2-D layered structures, which are eventually extended into a 3-D network (see Fig. 11). It should be noted that the DMF molecules are trapped in this lattice by C–H···O and C–H···π interactions (see Table 4).

3.3. Structural comparison of complexes *1*–*3*

The Cu(II) centers in complexes **1**–**3** adopt a similar distorted tetrahedral geometry, coordinating to two nitrogen atoms from the ligand and two chloride ions. In each case, the ligand acts as a bidentate chelator with four planar groups connected by three hinges. The two benzimidazole groups and Cu(II) form nine-membered chelating rings, which exhibit a twisted boat–boat conformation (see Fig. 12). Geometrical constraints within such a chelated ring cause the intra-ligand N–Cu–N angles to be 139.1° in **1**, 140.5° in **2** and 138.8° in **3**, which are significantly larger than those (92.6°) of a similar bis(benzimidazole) complex containing a seven-membered chelating ring [33]. Analysis of the Cu(II) coordination spheres in each complex reveals that the ligand binding ability in **1** and **2** is stronger than that in **3**, as indicated by their slightly shorter Cu–N bond distances (see Table 3). This result may be related to the conformational discrepancy of the ligands in **1–3**, which gives rise to different steric hindrance. Another outstanding feature is that the size and shape of the ligands have a significant effect on the formation of different C–H···Cl hydrogen bonding. As demonstrated by the above structural descriptions, the substituents of the ligands cause their distinct sizes, which in turn lead to the intra- or intermolecular C–H···Cl interactions. Furthermore, the ligand configuration will also be changed by the substituents, which may be reflected by the pyridyl–pyridyl and

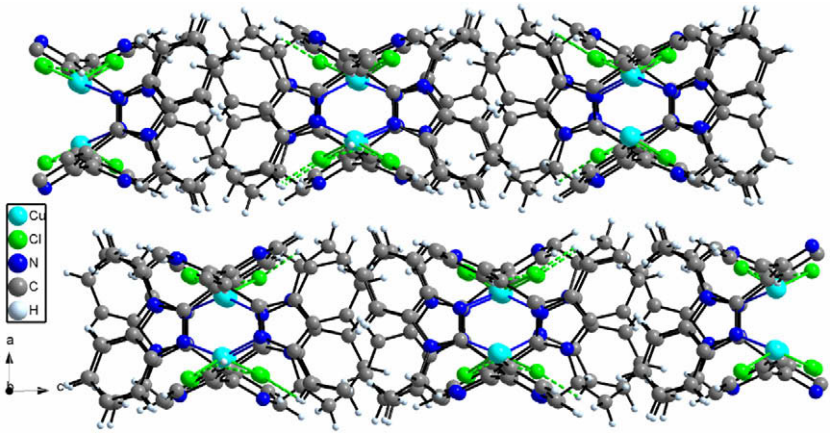


Fig. 8. View of the 3-D network containing 2-D layers in **2**. The C–H···Cl hydrogen bonds are shown in green. (For interpretation of the references to colour in this figure legend, the reader is referred to the web version of this article.)

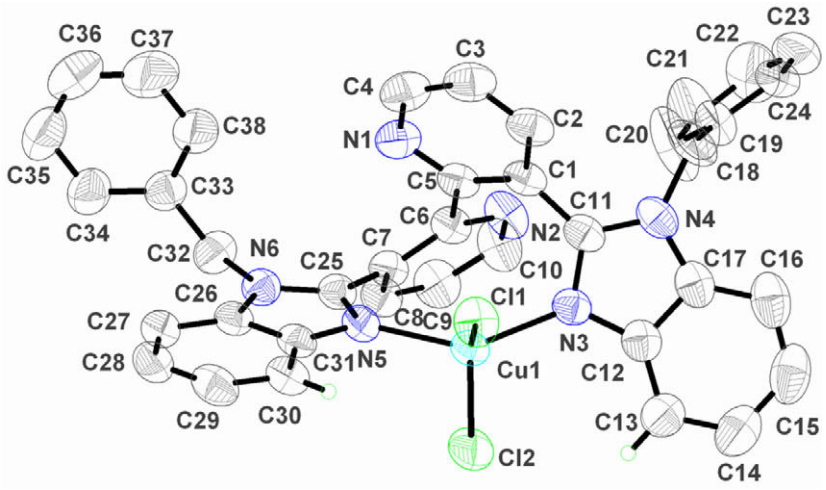


Fig. 9. Molecular structure of **3**. DMF and irrelevant H atoms are omitted for clarity.

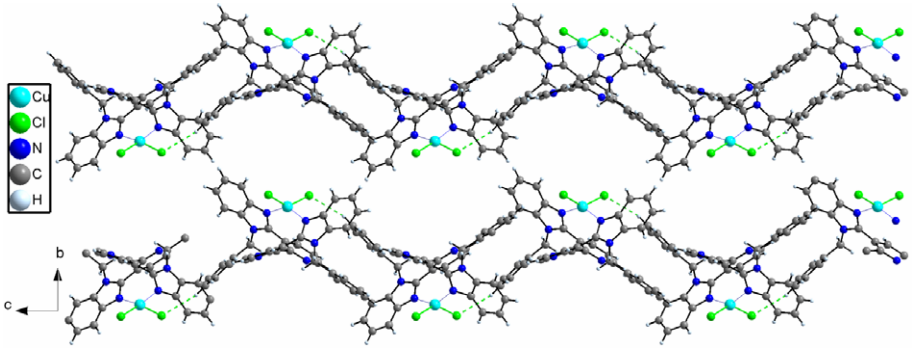


Fig. 10. 1-D chains in **3** along the *c* axis. Intermolecular C–H···Cl hydrogen bonds are shown in green. (For interpretation of the references to colour in this figure legend, the reader is referred to the web version of this article.)

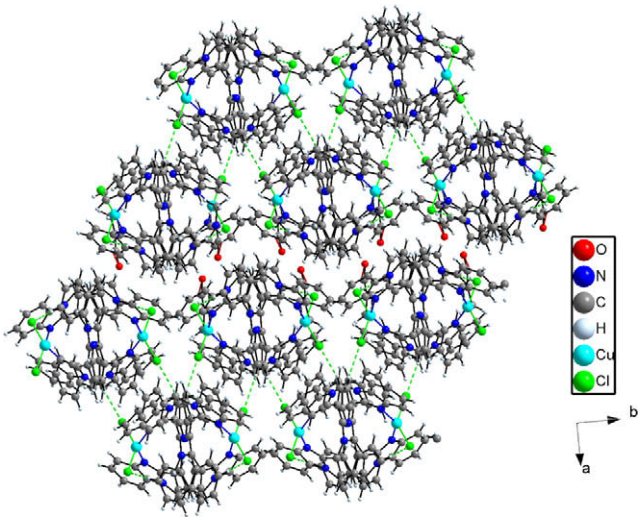


Fig. 11. View of the 3-D network of **3**. Intermolecular C–H···Cl hydrogen bonds are shown in green. (For interpretation of the references to colour in this figure legend, the reader is referred to the web version of this article.)

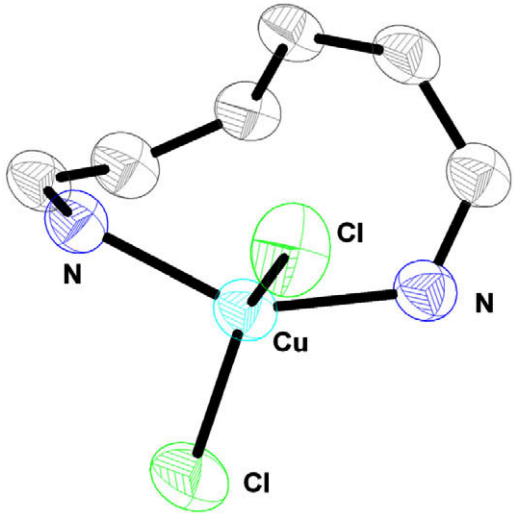


Fig. 12. The nine-membered chelated ring and the coordination spheres of Cu(II) in **1**–**3**.

benzimidazolyl–benzimidazolyl dihedral angles that are remarkably different in these structures (64.1° and 78.2° in **1**, 58.8° and 48.6° in **2**, and 50.8° and 62.0° in **3**). This will also affect the resultant hydrogen bonding modes.

3.4. The role of C–H···Cl and C–H···π interactions in the structural assembly

Detailed geometrical parameters for related secondary interactions are listed in Table 4. For C–H···Cl bonds, the H···Cl distances

range from 2.74 to 2.88 Å, being considerably shorter than the sum of van der Waals radii (2.95 Å), and the C–H···Cl angles range from 155° to 164°, falling in the normal range for C–H···Cl hydrogen bonds [14]. Further examination of the C–H···Cl contacts reveals two different types of hydrogen bonding patterns: linear (in **2** and **3**) and asymmetric bifurcated interactions (in **2**). Thus, while the ligands coordinate to Cu(II), diverse conformations that achieve these interactions are observed. In **1**, intramolecular C–H···Cl and C–H···π interactions are found, but not the intermolecular C–H···Cl type. This result may be due to the formation of linear intramolecular C–H···Cl interactions which causes a significant perturbation in the formation of intermolecular C–H···Cl interactions. This opinion can be further confirmed by the structural analysis of complexes **2** and **3**. That is, both intra and intermolecular C–H···Cl hydrogen bonds are found in **2**, and only an intermolecular C–H···Cl contact is formed in **3**. The difference in the hydrogen bonding modes results in their structural diversity. In **1**, the intramolecular C–H···Cl hydrogen bonding is preserved within the 0-D coordination motif, whereas in **2** and **3**, the intermolecular C–H···Cl hydrogen bonds lead to the formation of a 1-D chain array and a 2-D layer. Examination of the overall crystalline lattices of **1**–**3** shows that the 3-D packing largely depends on the accessibility of the pyridyl or phenyl rings in the supramolecular networks. This is particularly true for complex **3**, in which significant intermolecular C–H···Cl hydrogen bonds occur. In this case, the phenyl rings protrude out from the [Cu(**L$_3$**)Cl$_2$] units and are closer to the adjacent chloride ions. As a result, the intermolecular C–H···Cl hydrogen bonds effectively link the [Cu(**L$_3$**)Cl$_2$] units together. Except for the intermolecular C–H···Cl hydrogen bonds, the aggregation of these networks into the final architectures appears to be largely regulated by other weaker secondary interactions such as C–H···π interactions. This phenomenon is also observed in complexes **1** and **2**. The C–H···π contacts increase the dimensionality of the supramolecular architecture from 0-D to 3-D, and from 1-D to 3-D in **2**, as well as from 2-D to 3-D in **3**, which play a decisive role in the final structures.

4. Conclusion

The metallosupramolecular systems presented in this research demonstrate that the inorganic synthon C–H···Cl$_2$Cu(II) plays a significant role in the construction and stabilization of crystalline architectures. Interestingly, the size and shape of the ligand may have a remarkable effect on the formation of different intra- and/or intermolecular C–H···Cl hydrogen bonding. Furthermore, the overall higher-dimensional supramolecular networks for these complexes are modulated by the synergistic effect of the primary C–H···Cl hydrogen bonding and the complementary C–H···π interactions.

Supplementary data

CCDC 659366, 299930, 299931, 288137, 299933 and 288138 contain the supplementary crystallographic data for **L$_1$**, **L$_2$**·3.5H$_2$O, **L$_3$**·H$_2$O, **1**, **2** and **3**. These data can be obtained free of charge via http://www.ccdc.cam.ac.uk/conts/retrieving.html, or from the Cambridge Crystallographic Data Centre, 12 Union Road, Cambridge CB2 1EZ, UK; fax: (+44) 1223-336-033; or e-mail: deposit@ccdc.cam.ac.uk.

Acknowledgements

This work was supported by the National Natural Science Foundation of China (No. 20872057) and the Natural Science Foundation of Henan Province (No. 082300420040).

References

[1] G.R. Desiraju, Acc. Chem. Rev. 35 (2002) 565.
[2] L. Brammer, Chem. Soc. Rev. 33 (2004) 476.
[3] Z. Ciunik, G.R. Desiraju, Chem. Commun. (2001) 703.
[4] K. Aburaya, K. Nakano, K. Sada, N.G. Yoswathananont, M.S. Shigesato, I. Hisaki, N.S. Tohnai, M. Mikiji Miyata, Cryst. Growth Des. 8 (2008) 1013.
[5] P. Metrangolo, H. Neukirch, T. Pilati, G. Resnati, Acc. Chem. Res. 38 (2005) 386.
[6] M. Fourmigué, P. Batail, Chem. Rev. 104 (2004) 5379.
[7] F.F. Awwadi, R.D. Willett, B. Twamley, Cryst. Growth Des. 7 (2007) 624.
[8] G. Aullón, D. Bellamy, L. Brammer, E.A. Bruton, A.G. Orpen, Chem. Commun. (1998) 653.
[9] C.B. Aakeröy, T.A. Evans, K.R. Seddon, I. Pálinkó, New J. Chem. 23 (1999) 145.
[10] J.D. Dunitz, R. Taylor, Chem. Eur. J. 3 (1997) 89.
[11] I. Csöregh, T. Brehmer, P. Bombicz, E. Weber, Cryst. Eng. 4 (2001) 343.
[12] P.K. Thallapally, A. Nangia, CrystEngCommun 27 (2001) 1.
[13] D. Braga, F. Grepioni, New J. Chem. 22 (1998) 159.
[14] L. Brammer, J. Chem. Soc., Dalton Trans. (2003) 3145.
[15] R. Mukherjee, Coord. Chem. Rev. 203 (2000) 151.
[16] S. Singh, V. Mishra, J. Mukherjee, N. Seethalekshmi, R. Mukherjee, J. Chem. Soc., Dalton Trans. (2003) 3392.
[17] V. Balamurugan, M.S. Hundal, R. Mukherjee, Chem. Eur. J. 10 (2004) 1683.
[18] M. Freytag, P.G. Jones, Chem. Commun. (2000) 277.
[19] J.C. Mareque Rivas, L. Brammer, Inorg. Chem. 37 (1998) 4756.
[20] G.R. Lewis, A.G. Orpen, Chem. Commun. (1998) 1873.
[21] I.M. Gruia, F.D. Rohon, A.L. Beauchamp, Inorg. Chim. Acta 360 (2007) 1825.
[22] S. Fortin, P.I. Fabre, M. Dartiguenave, A.L. Beauchamp, J. Chem. Soc., Dalton Trans. (2001) 3520.
[23] D. Braga, S.M. Draper, E. Champeil, F. Grepioni, J. Organomet. Chem. 573 (1999) 73.
[24] S.B. Miao, B.M. Ji, C.X. Du, Chin. J. Struct. Chem. 26 (2007) 439.
[25] S. Dholakia, R.D. Gillard, F.L. Wimmer, Polyhedron 4 (1985) 791.
[26] G.M. Sheldrick, SHELXL-97, Program for Refinement of Crystal Structure, University of Göttingen, Germany, 1997.
[27] M.A. Phillips, J. Chem. Soc. (1928) 172.
[28] F. Ullmann, Chem. Ber. 36 (1903) 2382.
[29] K.L. Cheng, S.C. Sheu, G.H. Lee, Y.C. Lin, Y. Wang, T.I. Ho, Acta Crystallogr. C 53 (1997) 1238.
[30] R.T. Stibrany, M.V. Lobanov, H.J. Schugar, J.A. Potenza, Inorg. Chem. 43 (2004) 1472.
[31] X.F. Shi, Z.Y. Xing, L. Wu, W.Q. Zhang, Inorg. Chim. Acta 359 (2006) 603.
[32] T. Spaniel, H. Görls, J. Scholz, Angew. Chem., Int. Ed. 37 (1997) 1862.
[33] V. Broughton, G. Bernardinelli, A.F. Williams, Inorg. Chim. Acta 275 (1998) 279.

Polyhedron 28 (2009) 2619–2624

Contents lists available at ScienceDirect

Polyhedron

journal homepage: www.elsevier.com/locate/poly

New rhenium(I) compounds containing the donor–acceptor diphosphine ligands 2-(ferrocenylidene)-4,5-bis(diphenylphosphino)4-cyclopenten-1,3-dione (fbpcd) and 2-(3-ferrocenylprop-2-ynylidene)-4,5-bis(diphenylphosphino)4-cyclopenten-1,3-dione (fpbpcd): Electrochemical behavior, MO properties, and X-ray diffraction structure of *fac*-BrRe(CO)$_3$(fpbpcd)

Bhaskar Poola [a], Xiaoping Wang [b,*], Michael G. Richmond [a,*]

[a] Neutron Scattering Science Division, Oak Ridge, National Laboratory, Oak Ridge, TN 37831, United States
[b] Department of Chemistry, University of North Texas, Denton, TX 76203, United States

ARTICLE INFO

Article history:
Received 22 April 2009
Accepted 20 May 2009
Available online 28 May 2009

Keywords:
Rhenium(I) compounds
Diphosphine ligands
Redox chemistry
Crystal structure
MO calculations

ABSTRACT

Displacement of the labile THF molecules in BrRe(CO)$_3$(THF)$_2$ (**1**) by the diphosphine ligands 2-(ferrocenylidene)-4,5-bis(diphenylphosphino)4-cyclopenten-1,3-dione (fbpcd) and 2-(3-ferrocenylprop-2-ynylidene)-4,5-bis(diphenylphosphino)4-cyclopenten-1,3-dione (fpbpcd) yields the mononuclear compounds *fac*-BrRe(CO)$_3$(fbpcd) (**2**) and *fac*-BrRe(CO)$_3$(fpbpcd) (**3**), respectively. The new ligand fpbpcd ligand has been synthesized from 3-ferrocenylpropynal and the parent diphosphine ligand 4,5-bis(diphenylphosphino)-4-cyclopenten-1,3-dione (bpcd) through a Knoevenagel condensation. **2** and **3** have been isolated and fully characterized by IR and NMR spectroscopies (^{1}H and ^{31}P), ESI mass spectrometry, and X-ray diffraction analysis in the case of **3**. The electrochemical properties of compounds **2** and **3** have been examined by cyclic voltammetry, and the nature of the HOMO and LUMO levels in these systems has been confirmed by MO calculations at the extended Hückel level. The redox and MO data are discussed relative to the redox and orbital properties of related functionalized diphosphines based on the bpcd platform.

© 2009 Elsevier Ltd. All rights reserved.

1. Introduction

New inorganic and organometallic systems that can promote energy- and electron-transfer reactions are highly sought after as device components in optoelectronic applications, photosynthetic mimics, redox switches, and model systems for directional charge-transfer processes [1]. The synthesis and photophysical study of new luminescent organometallic complexes continue to command the attention of a diverse group of researchers. Many dyad and triad arrays possessing an energetically accessible LUMO typically give rise to long-lived charge-transfer species, a condition tantamount for the successful fabrication of photosynthetic and OLED devices [2]. While many derivatives exhibit a low-lying LUMO and promote long-lived charge separated species, the search for new systems with tunable LUMO levels remains a universal priority.

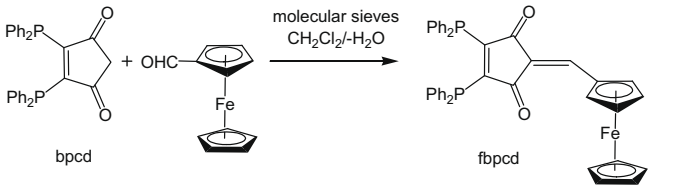
While diphosphine ligands are ubiquitous in transition-metal chemistry, only a few documented paradigms exist that display significant luminescent behavior [3]. Undoubtedly, the principal factor responsible for the disappointing photophysical data (i.e., efficient non-radiative decay) experimentally found in the overwhelming majority of diphosphine-substituted metal compounds is the absence of a low-lying π^* acceptor LUMO on the diphosphine ligand. The absence of an energetically accessible diphosphine LUMO radically changes the emissive behavior relative to those compounds containing an α-diimine or related heterocyclic ligand that possess a π^* LUMO that is localized on the ancillary heterocyclic residue [4].

Our groups maintain a longstanding interest in the synthesis and physical study of organometallic complexes containing the unsaturated diphosphine ligands 2,3-bis(diphenylphosphino) maleic anhydride (bma) and 4,5-bis(diphenylphosphino)-4-cyclopenten-1,3-dione (bpcd) [5,6]. These particular ligands are unique vis-á-vis the common diphosphine ligands dppm, (Z)-1,2-Ph$_2$PCH=CHPPh$_2$, and 1,2-bis(diphenylphosphino)benzene because both bma and bpcd exhibit a one-electron reduction at relatively low potential (<−1.1 V), with electron accession occurring at a π^*-based LUMO that is localized about the central platform ring [7]. The superb electron reservoir properties displayed by bma and bpcd have been shown to modulate ligand substitution in selected mononuclear compounds having electron counts in excess of 18e- [8].

* Corresponding authors. Tel.: +1 940 565 3548; fax: +1 940 565 4318 (M.G. Richmond).
E-mail addresses: wangx@ornl.gov (X. Wang), cobalt@unt.edu (M.G. Richmond).

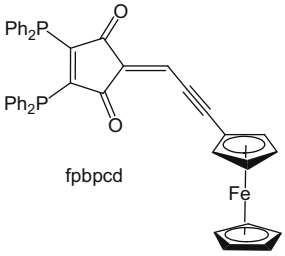
0277-5387/$ - see front matter © 2009 Elsevier Ltd. All rights reserved.
doi:10.1016/j.poly.2009.05.049

In our quest to prepare new, second-generation ligands based on bpcd, we have instituted Knoevenagel condensation reactions between bpcd and selected aldehydes [9]. Here the union of the bpcd platform with a redox-active appendage and/or light-harvesting moiety facilitates, in theory, the tuning of the HOMO–LUMO gap and emission properties in a given metal complex. We have successfully employed this concept in the synthesis of several new ligands [10], with Eq. (1) showing the reaction for the preparation of 2-(ferrocenylidene)-4,5-bis(diphenylphosphino)-4-cyclopenten-1,3-dione (fbpcd) [11]. The dynamic isomerization of this particular ligand has been investigated in the triosmium clusters 1,2-$Os_3(CO)_{10}$(fbpcd) and 1,2-$Os_3(CO)_{10}$(fbpcd) [11], and its redox properties have been recently reported in the case of the platinum(II) complex Pt(mnt)(fbpcd) [10b].



(1)

Given the importance of d^6 complexes in multicomponent redox relays [12], coupled with our interest in the coordination chemistry of the fbpcd ligand with different metal systems, we have prepared and examined the redox properties of the new rhenium(I) compound *fac*-BrRe(CO)$_3$(fbpcd) (**2**). The synthesis of the conjugated enyne derivative of fbpcd, whose structure is depicted below, and its use as a ligand in the synthesis of *fac*-BrRe(CO)$_3$(fpbpcd) (**3**) are also described herein.



2. Experimental

2.1. Materials and equipment

The $BrRe(CO)_5$ employed in the synthesis of $BrRe(CO)_3(THF)_2$ (**1**) was prepared from $Re_2(CO)_{10}$ [13]. **1** was prepared according to the published procedure and typically used within one week of preparation [14]. The bpcd ligand used in the synthesis of the title diphosphines fbpcd and fpbpcd was synthesized from 4,5-dichloro-4-cyclopenten-1,3-dione and Ph_2PSiMe_3 [15], with the former ferrocene-containing ligand prepared from ferrocenecarboxaldehyde and bpcd [11]. The acetylferrocene used in the preparation of 3-ferrocenylpropynal [16] was synthesized according the procedure of Parshall et al. [17]. $Re_2(CO)_{10}$ was purchased from Pressure Chemical Co., while the chemicals ferrocene, ferrocenecarboxaldehyde, hexachlorocyclopentadiene, and diethyl chlorophosphate were purchased from Aldrich Chemical Co. and used as received. The reaction and NMR solvents employed in these studies were distilled from an appropriate drying agent under argon using Schlenk techniques or obtained from an Innovative Technology solvent purification system. All distilled solvents were stored in Schlenk storage vessels equipped with high-vacuum Teflon stopcocks [18]. The tetra-*n*-butylammonium perchlorate (TBAP) electrolyte was purchased from Johnson Matthey Electronics and recrystallized from hexane/ethyl acetate and dried under vacuum for at least 36 h prior to use.

The IR spectra were recorded on a Nicolet 6700 FT–IR spectrometer in amalgamated NaCl cells capable of handling air-sensitive samples. The quoted ^1H and ^{31}P NMR spectral data were recorded at 500 and 201 MHZ, respectively, on a Varian VXR-500 spectrometer. The ^{31}P NMR spectra were collected in the proton-decoupled mode and the reported chemical shifts referenced to external H_3PO_4 (85%), taken to have δ=0. UV–Vis spectra for **2** and **3** were recorded on a Hewlett–Packard 8452A diode array spectrometer in Schlenk-modified 1.0 cm quartz UV–Vis cells. The ESI-APCI mass spectra were recorded at the University of the Pacific (**2**) and UNT (**3**) mass spectrometry facilities, respectively, in the positive ionization mode. The matrices employed for the collection of the mass spectra were MeOH (**2**) and MeCN/KI (**3**).

2.2. Synthesis of *fac*-BrRe(CO)$_3$(fbpcd) (**2**) from BrRe(CO)$_3$(THF)$_2$ (**1**) and fbpcd

To a small Schlenk tube under argon flush was charged 0.10 g (0.20 mmol) of **1** and 0.14 g (0.21 mmol) of fbpcd, followed the addition of 25 mL of CH_2Cl_2 via syringe. The solution was stirred at room temperature for 1 h and then examined by IR analysis, which revealed the consumption of **1** and the presence of the desired product. The volatiles were removed under vacuum and the crude residue recrystallized from toluene at −20 °C. **2** was isolated by filtration under argon as an air-sensitive, purple-blue solid in 95% yield (0.19 g). IR (CH_2Cl_2): ν(CO) 2040 (vs), 1966 (s), 1912 (s), 1720 (w, sym dione), 1676 (s, antisym dione) cm^{-1}. UV–Vis (CH_2Cl_2): λ_{max} 358 (ε=6100), 578 (ε=1500). ^1H NMR ($CDCl_3$): δ 4.19 (s, 5H, Cp), 4.81 (s, 1H, Cp), 4.85 (s, 1H, Cp), 4.98 (s, 1H, Cp), 5.35 (s, 1H, Cp), 7.36–7.91 (m, 21H, alkenyl and aryl). ^{31}P NMR ($CDCl_3$): δ 23.03 (d, $^3J_{P-P}$=11 Hz), 23.55 (s, $^3J_{P-P}$=11 Hz). ESI–MS: *m/z* 1033.59 for $[\mathbf{2}+Na]^+$ and 1012.90 for $[\mathbf{2}+H]^+$.

2.3. Synthesis of fpbpcd from bpcd and 3-ferrocenylpropynal

0.10 g (0.22 mmol) of bpcd and 51 mg (0.22 mmol) of 3-ferrocenylpropynal in 30 mL of a 5:1 mixture of CH_2Cl_2/MeOH were stirred in the presence of 3 Å molecular sieves for 48 hr at room temperature. The solution slowly acquired a green–blue color indicative of the condensation product fpbpcd, and TLC analysis using CH_2Cl_2 as an eluent confirmed the presence of trace amounts of the starting materials and a prominent green–blue streak belonging to the desired ligand (R_f = 0.5). The solution was filtered under argon and the volatiles removed under vacuum, after which the residue was washed with hexane to remove the unreacted bpcd and 3-ferrocenylpropynal. Yield of green–blue fpbpcd: 0.10 g (68%). Given the air sensitivity of the product and the poor quality NMR spectra obtained due to paramagnetic impurities, the fpbpcd ligand was characterized by IR spectroscopy and used directly in the next step. IR (CH_2Cl_2): ν(CO) 1715 (w, sym dione), 1674 (s, antisym dione) cm^{-1}.

2.4. Synthesis of *fac*-BrRe(CO)$_3$(fpbpcd) (**3**) from BrRe(CO)$_3$(THF)$_2$ (**1**) and fpbpcd

The synthesis of **3** followed the procedure outlined for **2**. Here 0.10 g (0.20 mmol) of **1**, 0.14 g (0.20 mmol) of fpbpcd, and 25 mL of CH_2Cl_2 were stirred at room temperature for 1 h. IR analysis at this point confirmed the presence of the desired product, after

which the solution was dried under vacuum to afford crude **3**. Recrystallization of **3** from toluene at −20 °C, followed by filtration under argon, gave **3** as an air-sensitive, green–blue solid in 91% (0.19 g). IR (CH_2Cl_2): ν(CO) 2041 (vs), 1967 (s), 1914 (s), 1729 (w, sym dione), 1687 (s, antisym dione) cm^{-1}. UV–Vis (CH_2Cl_2): λ_{max} 394 (ε = 12000), 608 (ε = 3800). ^1H NMR ($CDCl_3$): δ 4.27 (s, 5H, Cp), 4.54 (bs, 20H, Cp), 4.67 (bs, 2H, Cp), 6.80 (s, 1H, alkenyl), 7.15–7.81 (m, 2H, aryl). ^{31}P NMR ($CDCl_3$): δ 22.76 (d, $^3J_{P-P}$=12 Hz), 23.90 (s, $^3J_{P-P}$=12 Hz). ESI–MS: *m/z* 1073.13 for $[\mathbf{3}+K]^+$.

2.5. Electrochemical studies

The quoted cyclic voltammetric data were recorded on a PAR Model 273 potentiostat/galvanostat, equipped with positive feedback circuitry to compensate for *i*R drop. The cyclic voltammograms were recorded under oxygen- and moisture-free conditions in a homemade three-electrode cell. A platinum disk was utilized as the working and auxiliary electrode, and the reference electrode utilized a silver wire as a quasi-reference electrode, with the reported potential data standardized against the formal potential of the $Cp^*_2Fe/Cp^*_2Fe^+$ (internally added) redox couple, taken to have $E_{1/2}$=−0.20 V [19].

2.6. Extended Hückel MO calculations

The extended Hückel calculations on compounds **2** and **3** were carried out using the original program developed by Hoffmann [20], as modified by Mealli and Proserpio [21]. The weighted H_{ij}'s contained in the program were used in the calculations, and the input Z-matrices were constructed by using the available X-ray data for **3** and related compounds.

2.7. X-ray crystallographic data

Single crystals of $\mathbf{3}\cdot 1/2H_2O$ suitable for X-ray diffraction analysis were grown from an acetone solution containing **3** that had been layered with Et_2O. The X-ray data were collected on an APEX II CCD-based diffractometer at 100(2) K. The frames were integrated with the available APEX2 [22] software package using a narrow-frame algorithm, and the structure was solved and refined using the SHELXTL program package [23]. The molecular structure was checked using PLATON [24], and all nonhydrogen atoms were refined anisotropically. Except for the water solvent whose hydrogens were not located, all other hydrogen atoms were assigned calculated positions and allowed to ride on the attached carbon atom. The refinement for $\mathbf{3}\cdot 1/2H_2O$ converged at R = 0.0165 and $wR2$ = 0.0432 for 8316 independent reflection with $I > 2\sigma(I)$. The X-ray data and processing parameters are reported in Table 1, with selected bond distances and angles quoted in Table 2.

Table 1
X-ray crystallographic data and processing parameters for $\mathbf{3}\cdot 1/2H_2O$.

CCDC entry number	727855
Cryst system	triclinic
Space group	$P\bar{1}$
a (Å)	10.0766(3)
b (Å)	10.5463(4)
c (Å)	19.0710(7)
α (°)	92.612(1)
β (°)	101.511(1)
γ (°)	98.580(1)
V (Å^3)	1957.8(1)
Mol formula	$C_{44}H_{30}BrFeO_5P_2Re\cdot 1/2H_2O$
Formula weight	1043.60
Formula units per cell (Z)	2
D_{calcd} (Mg/m^3)	1.770
λ (Mo Kα) (Å)	0.71073
μ (mm^{-1})	4.610
Absorption correction	semi-empirical from equivalents
Absorption correction factor	0.8371/0.4042
Total reflections	23813
Independent reflections	8316
Data/res/parameters	8316/0/505
R_1[a] [$I \geqslant 2\sum(I)$]	0.0165
wR_2[b] (all data)	0.0432
GOF on F^2	1.103
$\Delta\rho$ (max), $\Delta\rho$ (min) (e/Å^3)	1.142, −0.503

[a] $R_1 = \sum ||F_o| - |F_c|| / \sum |F_o|$.
[b] $R_2 = \{\sum[w(F_o^2 - F_c^2)^2] / \sum[w(F_o^2)^2]\}^{1/2}$.

Table 2
Selected bond distances (Å) and angles (deg) in $\mathbf{3}\cdot 1/2H_2O$.

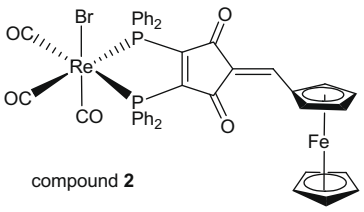
Bond distances			
Re(1)–C(1)	1.952(2)	Re(1)–C(2)	1.970(2)
Re(1)–C(3)	1.918(2)	Re(1)–Br(1)	2.6333(2)
Re(1)–P(1)	2.4373(6)	Re(1)–P(2)	2.4601(6)
C(4)–C(8)	1.349(3)	C(4)–C(5)	1.507(3)
C(7)–C(8)	1.513(3)	C(6)–C(7)	1.475(3)
C(5)–C(6)	1.478(3)	C(6)–C(33)	1.349(3)
C(33)–C(34)	1.405(3)	C(34)–C(35)	1.204(3)
C(35)–C(36)	1.419(3)	P(1)···P(2)	3.1810(8)
Fe(3)-centroid[a]	1.654(3)	Fe(3)-centroid[b]	1.660(3)
Bond angles			
C(2)–Re(1)–P(1)	173.17(7)	C(1)–Re(1)–P(2)	166.09(7)
P(1)–Re(1)–P(2)	81.01(2)	P(1)–Re(1)–Br(1)	88.89(1)
P(2)–Re(1)–Br(1)	80.29(2)	O(1)–C(1)–Re(1)	176.8(2)
O(2)–C(2)–Re(1)	179.6(3)	O(3)–C(3)–Re(1)	177.8(2)
C(33)–C(6)–C(7)	128.0(2)	C(33)–C(6)–C(5)	124.3(2)
C(6)–C(33)–C(34)	126.1(2)	C(35)–C(34)–C(33)	173.6(3)
C(34)–C(35)–C(36)	177.6(3)		

[a] Mean Fe(3)–C distance for the Cp carbons C(36)–C(40).
[b] Mean Fe(3)–C distance for the Cp carbons C(41)–C(45).

3. Results and discussion

3.1. Synthesis, spectroscopic data, and redox properties of *fac*-$BrRe(CO)_3$(fbpcd) (**2**)

Displacement of the THF ligands in $BrRe(CO)_3(THF)_2$ (**1**) by fbpcd is rapid and gives **2** in essentially quantitative yield as assessed by IR spectroscopy. While **2** may be isolated by column chromatography over silica gel, this leads to considerable material loss and oxidation of the ferrocene appendage, which in turn introduces unwanted paramagnetic impurities in the NMR sample. Alternatively, **2** could be isolated by recrystallization in toluene at low temperature in high yield, making this the preferred method of isolation. We would add that **2** may also be prepared by heating $BrRe(CO)_5$ in the presence of fbpcd but the yield of **2** is lower and the reaction is accompanied by decomposition, complicating the purification of the desired product. **2** is mildly air sensitive, especially in solution, but may be handled in the atmosphere for a short period of time. The structure of **2** is shown below.



compound **2**

2 was thoroughly characterized by IR, NMR, and UV–Vis spectroscopies, and mass spectrometry. The IR spectrum revealed terminal carbonyl stretching bands at 2041 (vs), 1967 (s), and 1914 (s) cm^{-1} characteristic of the signature *fac*-Re$(CO)_3$ moiety [25], in addition to two lower energy ν(CO) bands observed at 1729 (w) and 1687 (s) cm^{-1} ascribed to the vibrationally coupled symmetric and antisymmetric carbonyl stretching bands associated with the dione platform [26]. The ^{1}H NMR spectrum exhibited a 5H singlet at δ 4.19 for the unsubstituted Cp ring, with the alkenyl-substituted Cp ring displaying four 1H singlets at δ 4.81, 4.85, 4.98, and 5.35. The lone alkenyl hydrogen and the aromatic hydrogens appear as a set of overlapping resonances from δ 7.36–7.91. Two inequivalent ^{31}P resonances were observed in the ^{31}P NMR spectrum of **2** at δ 23.03 and 23.55 consistent with the formulated structure. The ESI mass spectrum of **2** revealed a strong molecular ion for the sodium-containing species [**2**+Na]$^+$ based on a *m/z* peak at 1033.59, along with a weak *m/z* peak at 1012.90 for [**2**+H]$^+$. Finally, the UV–Vis spectrum of **2** (Fig. 1) recorded in CH_2Cl_2 showed two featureless bands at 358 and 578 nm, whose assignments are ascribed to a $d\pi$(Re) → π^*(dione) MLCT and a charge-transfer-to-solvent (CTTS) transition involving the ferrocene and CH_2Cl_2, respectively [5a,27].

The redox properties of **2** were examined by cyclic voltammetry (CV) in CH_2Cl_2 containing 0.25 M TBAP as the supporting electrolyte. The CV of **2** (not shown) recorded over the potential range of 1.0 V to −1.0 V and at a scan rate of 250 mV/s revealed two diffusion-controlled waves at $E_{1/2}$ = 0.71 and −0.65 V belonging to 0/1$^+$ and 0/1$^-$ redox couples [28]. The site of the two redox waves was verified by extended Hückel MO calculations, which revealed HOMO and LUMO levels at −11.80 eV and −10.42 eV, respectively. The HOMO in **2** is best viewed as an iron-based d_{z2} orbital that is similar in nature to the a_{1g} HOMO found in ferrocene [29]. The computationally observed LUMO traces its parentage to the ψ_4 MO associated with the π system of dione ring, whose calculated energy and nodal pattern are in excellent agreement with those data reported for other bpcd-substituted compounds prepared by our groups [6a,10,30]. The relatively low energy of this π^* orbital renders it a superb electron reservoir and accounts nicely for the observed one-electron reduction found by CV.

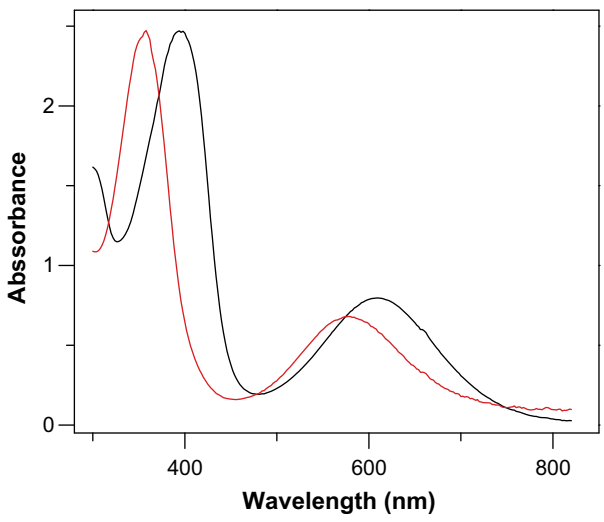


Fig. 1. UV–Vis spectra for **2** (red line; ca. 4e-4 M) and **3** (black line; ca. 2e-4 M) in CH_2Cl_2 solvent. The ordinate values displayed are for **2**, with **3** plotted alongside using arbitrary absorbance units.

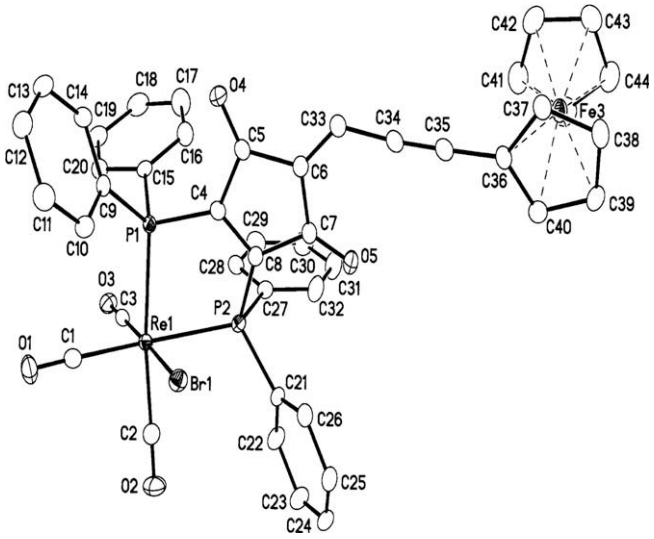
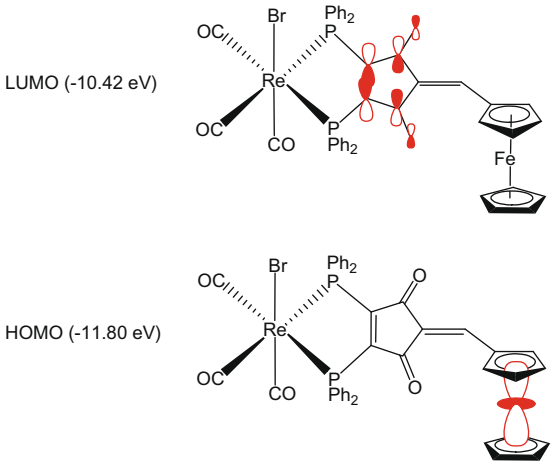


Fig. 2. Perspective view of **3** · 1/2H_2O showing the atom-numbering scheme. Displacement ellipsoids are drawn at the 50% probability level. The solvent molecule has been omitted for clarity.



3.2. Synthesis, spectroscopic data, and redox properties of *fac*-BrRe$(CO)_3$(fpbpcd) (**3**)

Knoevenagel condensation of 3-ferrocenylpropynal with an equimolar amount of bpcd in a solvent mixture composed of CH_2Cl_2/MeOH (5:1) in the presence of 3 Å molecular sieves, whose function is to absorb the liberated water, furnishes the new ligand 2-(3-ferrocenylprop-2-ynylidene)-4,5-bis(diphenylphosphino)4-cyclopenten- 1,3-dione (fpbpcd). Isolated yields of fpbpcd were on the order of ca. 70% for samples that were purified by recrystallization. The fpbpcd ligand exhibits a green–blue color and undergoes facile oxidation in solution upon exposure to oxygen, making characterization of the ligand by NMR spectroscopy problematic. The IR spectrum of the ligand revealed two ν(CO) bands at 1715 (w) and 1674 (s) for the kinematically coupled dione carbonyl groups consistent with the proposed structure.

Treatment of either BrRe$(CO)_5$ or **1** with a slight excess of fpbpcd affords the corresponding diphosphine-substituted compound **3**, whose structure is depicted below. As discussed earlier, reactions using **1** as a starting material were cleaner and afforded **3** in higher yields. **3** was isolated by recrystallization as a

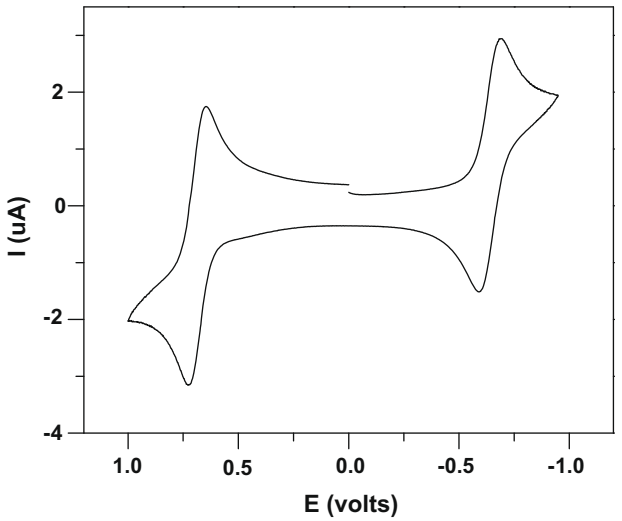
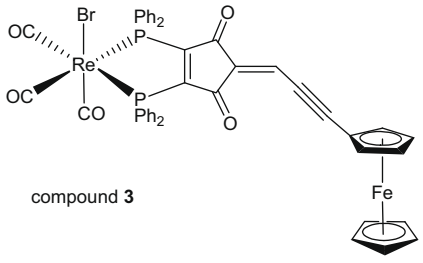


Fig. 3. Cathodic scan cyclic voltammogram of **3** (ca. 10^{-3} M and 0.25 V/s) in CH_2Cl_2 containing 0.25 M TBAP at room temperature.

green–blue solid and was characterized by a combination of IR, NMR, and UV–Vis spectroscopies, mass spectrometry, and X-ray diffraction analysis. The IR spectrum for **3** reveals terminal ν(CO) bands at 2041 (vs), 1967 (s), and 1914 (s) cm^{-1}, along with symmetric and antisymmetric dione ν(CO) bands at 1729 and 1687 cm^{-1}. These carbonyl frequencies relative to those recorded for **2** indicate that the electron-donating properties of the two diphosphine ligands are similar in magnitude. The UV–Vis spectrum (Fig. 1) shows a slight bathochromic shift of the two principal absorption bands compared to **2**, with maxima appearing at 394 nm and 608 nm. The spectroscopic assignments for these UV–Vis bands are assumed to be the same as those in **2** (*vide supra*). The ^{1}H NMR spectrum shows the cyclopentadienyl hydrogens at δ 4.27, 4.54, and 4.67 in a 5:2:2 integral ratio, and the lone vinyl hydrogen on the enyne chain appears as a singlet at δ 6.80. The aromatic hydrogens were observed as a multiplet from δ 7.15–7.81. The inequivalent phosphines in **3** appear as doublets in the ^{31}P NMR spectrum at δ 22.76 and 23.90 and exhibit a $^3J_{P-P}$ coupling of 12 Hz. The ESI mass spectrum recorded in MeCN/KI gave a strong molecular ion at *m/z* 1073.13 for $[\mathbf{3}+K]^+$ consistent with the formulated structure.



compound **3**

The unequivocal identity of **3** and the presence of the enyne linking moiety that serves to tether the bpcd and ferrocene groups were established by X-ray diffraction analysis. The solid-state structure of $\mathbf{3}\cdot 1/2H_2O$ is depicted in Fig. 2. The rhenium center is six-coordinate with the fpbpcd ligand situated *trans* to two of the three facial CO groups. The mean Re–P bond distance of 2.4487 Å and the bond angle of 81.01(2)° for the P(1)–Re(1)–P(2) linkage agree with those values reported for the octahedral rhenium(I) compounds *fac*-$BrRe(CO)_3$(bma) [5a], *fac*-$BrRe(CO)_3$(tbpcd) [10c], $ReCl_2[(Z)\text{-}Ph_2PCH{=}CHPPh_2]_2$ [31], and $ClRe(CO)_3$[3,4-Me_2-3′,4′- bis(diphenylphosphino)tetrathiafulvalene] [32]. The Re–CO bond distances range from 1.970(2) Å [Re(1)–C(2)] to 1.918(2) Å [Re(1)–C(3)] with the latter axial CO group displaying the shortest Re–CO bond distance. The Re(1)–Br(1) vector reveals a bond length of 2.6333(2) Å, whose value is in excellent agreement with the Re–Br distance found in the diphosphine-substituted compounds *fac*-$BrRe(CO)_3[\eta^2\text{-}(Ph_2PCH_2)_3CMe]$ [33], *fac*-$BrRe(CO)_3[Ph_2PO(CH_2)_2OPPh_2]$ [34], and *fac*-$BrRe(CO)_3$[1,2-$(HOCH_2P)_2C_6H_4$] [35]. The five-membered metallocyclic ring defined by the atoms Re(1)–P(2)–C(8)–C(4)–P(1) is distinctly non-planar and exhibits a fold angle of 29.49(4)° along the P(1) ··· P(2) hinge. The enyne carbons are nearly planar on basis of the observed torsion angle of ca. −165° for the C(6)–C(33)–C(34)–C(35) atoms. The remaining bond distances and angles are unremarkable and require no comment.

The cyclic voltammetric properties of **3** were examined in CH_2Cl_2 under conditions identical to those employed in the investigation of **2**. The CV of **3**, which is shown in Fig. 3, recorded over the potential range of 1.0 V to −1.0 V and at a scan rate of 250 mV/s revealed well-defined diffusion-controlled waves at $E_{1/2}$ = 0.68 and −0.65 V ascribed to $0/1^+$ and $0/1^-$ redox couples. These half-wave potentials are identical to those redox data recorded for **2**, suggesting identical HOMO and LUMO levels in the two different rhenium(I) products. This latter assumption was subsequently corroborated by extended Hückel MO calculations, which revealed HOMO and LUMO levels at −11.86 eV and −10.39 eV, respectively. The orbital composition of these important frontier molecular orbitals in **3** resembles the HOMO and LUMO levels computed for **2** and will not be reproduced here.

4. Conclusions

The new rhenium(I) compounds *fac*-$BrRe(CO)_3$(fbpcd) (**2**) and *fac*-$BrRe(CO)_3$(fpbpcd) (**3**) have been synthesized and their redox properties investigated by cyclic voltammetry. Both compounds exhibit well-defined $0/1^+$ and $0/1^-$ redox couples attributed to ferrocene oxidation and diphosphine reduction, respectively, with the HOMO and LUMO compositions in **2** and **3** corroborated by extended Hückel MO calculations. The π^*-based LUMO in compounds **2** and **3** is localized on the dione platform and remains unchanged to that found in the parent bpcd ligand. The selection of aldehydes more electron rich than ferrocenecarboxaldehyde will facilitate the tuning of the HOMO level in our bpcd-derived condensation products, and this aspect is under active investigation. Future time-resolved photophysical studies are planned and these data will be disseminated in due course.

5. Supplementary data

CCDC 727855 contains the supplementary crystallographic data for $\mathbf{3}\cdot 1/2H_2O$. These data can be obtained free of charge via http://www.ccdc.cam.ac.uk/conts/retrieving.html, or from the Cambridge Crystallographic Data Centre, 12 Union Road, Cambridge CB2 IEZ, UK; Fax: (+44) 1223-336-033; or email: deposit@ccdc.cam.ac.uk.

Acknowledgement

Continued financial support from the Robert A. Welch Foundation (Grant B-1093) is greatly appreciated. Prof. Andreas H. Franz (UP) and Ms. Nicole Ledbetter (UNT) are thanked for their expertise and help in recording the mass spectra for compounds **2** and **3**.

References

[1] (a) D.S. Tyson, C.R. Luman, X. Zhou, F.N. Castellano, Inorg. Chem. 40 (2001) 4063;
(b) C.J. McAdam, J.L. Morgan, B.H. Robinson, J. Simpson, P.H. Rieger, A.L. Rieger, Organometallics 22 (2003) 5126;
(c) J. Vicente, P. González-Herrero, M. Pérez-Cadenas, P.G. Jones, D. Bautista, Inorg. Chem. 44 (2005) 7200;
(d) K. Heinze, S. Reinhardt, Organometallics 26 (2007) 5406;
(e) S. Rau, D. Walther, J.G. Vos, Dalton Trans. (2007) 915;
(f) J. Zhang, P. Du, J. Schneider, P. Jarosz, R. Eisenberg, J. Am. Chem. Soc. 129 (2007) 7726.

[2] (a) S.-Y. Chang, J. Kavitha, J.-Y. Hung, Y. Chi, Y.-M. Cheng, E.Y. Li, P.-T. Chou, G.-H. Lee, A.J. Carty, Inorg. Chem. 46 (2007) 7064;
(b) C. Baik, W.-S. Han, Y. Kang, S.O. Kang, J. Ko, J. Organomet. Chem. 691 (2006) 5900;
(c) R. Saha, M.A. Qaium, D. Debnath, M. Younus, N. Chawdhury, N. Sultana, G. Kociok-Köhn, L.-L. Ooi, P.R. Raithby, M. Kijima, Dalton Trans. (2005) 2760.

[3] (a) V.W.W. Yam, W.K. Lee, T.F. Lai, J. Chem. Soc., Chem. Commun. (1993) 1571;
(b) Q.-H. Wei, G.-Q. Yin, L.-Y. Zhang, L.-X. Shi, Z.-W. Mao, Z.-N. Chen, Inorg. Chem. 43 (2004) 3484;
(c) I.O.A.J. Karttunen, S.P. Tunik, M. Haukka, S.I. Stanislav, A.S. Alexei, P.Y. Serdobintsev, M.A. Khodorkovskiy, T.A. Tapani, Inorg. Chem. 47 (2008) 9478.

[4] J.A. Zuleta, M.S. Burberry, R. Eisenberg, Coord. Chem. Rev. 97 (1990) 47.

[5] (a) For bma ligand studies, see: K. Yang, S.G. Bott, M.G. Richmond, Organometallics 13 (1994) 3788;
(b) K. Yang, S.G. Bott, M.G. Richmond, Organometallics 14 (1995) 2387;
(c) N.W. Duffy, R.R. Nelson, M.G. Richmond, A.L. Rieger, P.H. Rieger, B.H. Robinson, D.R. Tyler, J.C. Wang, K. Yang, Inorg. Chem. 37 (1998) 4849;
(d) S.G. Bott, K. Yang, M.G. Richmond, J. Organomet. Chem. 689 (2004) 791;
(e) S.G. Bott, K. Yang, M.G. Richmond, J. Organomet. Chem. 690 (2005) 3067;
(f) S.G. Bott, K. Yang, M.G. Richmond, J. Organomet. Chem. 691 (2006) 3771.

[6] (a) For bpcd ligand studies, see: H. Shen, S.G. Bott, M.G. Richmond, Organometallics 14 (1995) 4625;
(b) S.G. Bott, H. Shen, R.A. Senter, M.G. Richmond, Organometallics 22 (2003) 1953;
(c) W.H. Watson, G. Wu, M.G. Richmond, Organometallics 25 (2006) 930;
(d) W.H. Watson, S.G. Bodige, K. Ejsmont, J. Liu, M.G. Richmond, J. Organomet. Chem. 691 (2006) 3609;
(e) W.H. Watson, B. Poola, M.G. Richmond, J. Organomet. Chem. 691 (2006) 5579.

[7] (a) H.J. Becher, D. Fenske, M. Heymann, Z. Anorg. Allg. Chem. 475 (1981) 27;
(b) R. Meyer, D.M. Schut, K.J. Keana, D.R. Tyler, Inorg. Chim. Acta 240 (1995) 405.

[8] (a) F. Mao, D.R. Tyler, D. Keszler, J. Am. Chem. Soc. 111 (1989) 130;
(b) F. Mao, D.R. Tyler, M.R.M. Bruce, A.E. Bruce, A.L. Rieger, P.H. Rieger, J. Am. Chem. Soc. 114 (1992) 6418.

[9] For a report on Knoevenagel condensation reactions using 4,5-dichloro-4-cyclopenten-1,3-dione, the immediate precursor in the synthesis of the diphosphine ligand bpcd, see: R. Alfred, Z. Hellmut, Chem. Ber. 94 (1961) 1800.

[10] (a) S.W. Hunt, X. Wang, M.G. Richmond, J. Mol. Struct. 919 (2009) 34;
(b) B. Poola, S.W. Hunt, M.G. Richmond, Polyhedron 27 (2008) 3693;
(c) W.H. Watson, D. Wiedenfeld, A. Pingali, B. Poola, M.G. Richmond, Polyhedron 26 (2007) 3577;
(d) W.H. Watson, B. Poola, M.G. Richmond, J. Chem. Crystallogr. 36 (2006) 715.

[11] W.H. Watson, B. Poola, M.G. Richmond, Polyhedron 26 (2007) 3585.

[12] (a) P. Thanasekaran, R.-T. Liao, B. Manimaran, Y.-H. Liu, P.-T. Chou, S. Rajagopal, K.-L. Lu, J. Phys. Chem. A 110 (2006) 10683;
(b) R. Ziessel, A. Juris, M. Venturi, Inorg. Chem. 37 (1998) 5061;
(c) W.K. Chan, P.K. Ng, X. Gong, S. Hou, Appl. Phys. Lett. 75 (1999) 3920.

[13] S.P. Schmidt, W.C. Trogler, F. Basolo, Inorg. Synth. 28 (1990) 160.

[14] D. Vitali, F. Calderazzo, Gazz. Chim. Acta 102 (1972) 587.

[15] (a) D.T. Mowry, J. Am. Chem. Soc. 72 (1950) 2535;
(b) D. Fenske, H.J. Becher, Chem. Ber. 107 (1974) 117;
(c) D. Fenske, H.J. Becher, Chem. Ber. 108 (1975) 2155.

[16] G. Doisneau, G. Balavoine, T. Fillebeen-Khan, J. Organomet. Chem. 425 (1992) 113.

[17] P.J. Graham, R.V. Lindsey, G.W. Parshall, M.L. Peterson, G.M. Whitman, J. Am. Chem. Soc. 79 (1957) 3416.

[18] D.F. Shriver, The Manipulation of Air-Sensitive Compounds, McGraw-Hill, New York, 1969.

[19] M.F. Ryan, D.E. Richardson, D.L. Lichtenberger, N.E. Gruhn, Organometallics 13 (1994) 1190.

[20] (a) R. Hoffmann, W.H. Lipscomb, J. Chem. Phys. 36 (1962) 2179;
(b) R. Hoffmann, J. Chem. Phys. 39 (1963) 1397.

[21] C. Mealli, D.M. Proserpio, J. Chem. Ed. 67 (1990) 399.

[22] APEX2 Version 2.14, Bruker Advanced Analytical X-ray Systems, Inc. Copyright 2007, Madison, WI.

[23] G.M. Sheldrick, Acta Cryst. A64 (2008) 112.

[24] A.L. Spek, J. Appl. Cryst. 36 (2003) 7.

[25] C.M. Lukehart, Fundamental Transition Metal Organometallic Chemistry, Brooks/Cole Publishing Co., Monterey, CA, 1985.

[26] N.B. Coltrup, L.H. Daly, S.E. Wiberley, Introduction to Infrared and Raman Spectroscopy, Academic Press, New York, 1990.

[27] (a) G.L. Geoffroy, M.S. Wrighton, Organometallic Photochemistry, Academic Press, New York, 1979;
(b) Y. Yamaguchi, W. Ding, C.T. Sanderson, M.L. Borden, M.J. Morgan, C. Kutal, Coord. Chem. Rev. 251 (2007) 515.

[28] Electrochemical reversibility and electron stoichiometry were determined via the usual methods, see: P.H. Rieger, Electrochemistry, Chapman and Hall, New York, 1994.

[29] (a) Y.S. Sohn, D.N. Hendrickson, H.B. Gray, J. Am. Chem. Soc. 93 (1971) 3603;
(b) J.W. Lauher, R. Hoffmann, J. Am. Chem. Soc. 98 (1976) 1729.

[30] W.H. Watson, S. Kandala, M.G. Richmond, J. Chem. Crystallogr. 36 (2006) 813.

[31] M. Bakir, P.E. Fanwick, R.A. Walton, Polyhedron 6 (1987) 907.

[32] N. Avarvari, D. Martin, M. Fourmiqué, J. Organomet. Chem. 643–644 (2002) 292.

[33] D.H. Gibson, H. He, M.S. Mashuta, Organometallics 20 (2001) 1456.

[34] S. Bolano, J. Bravo, R. Carballo, S. Garcia-Fontan, E.M. Vazquez-Lopez, Polyhedron 18 (1999) 1431.

[35] R. Schibli, K.V. Katti, W.A. Volkert, C.L. Barnes, Inorg. Chem. 40 (2001) 2358.

Polyhedron 28 (2009) 2625–2634

Contents lists available at ScienceDirect

Polyhedron

journal homepage: www.elsevier.com/locate/poly

Five-coordinate pentafluorobenzothiolate osmium(IV) complexes $[Os(SC_6F_5)_4(P(C_6H_4X\text{-}4)_3)]$ (X = OCH_3, CH_3, F, Cl or CF_3): Solid and solution structural characterization

Maribel Arroyo [a,*], Consuelo Mendoza [a], Sylvain Bernès [b], Hugo Torrens [c], Hugo Morales-Rojas [d]

[a] Centro de Química del Instituto de Ciencias de la BUAP, Edificio 193, Complejo de Ciencias, Ciudad Universitaria, San Manuel 72571, Puebla, Pue., Mexico
[b] DEP, Facultad de Ciencias Químicas, UANL, Guerrero y Progreso S/N, Col. Treviño, 64570 Monterrey N.L., Mexico
[c] División de Estudios de Posgrado, Facultad de Química, UNAM, Cd. Universitaria, 04510 México D.F., Mexico
[d] Centro de Investigaciones Químicas, UAEM, Av. Universidad 1001. Col. Chamilpa, Cuernavaca, Morelos, Mexico

ARTICLE INFO

Article history:
Received 23 January 2009
Accepted 20 May 2009
Available online 27 May 2009

Keywords:
Five-coordinated osmium
Fluorinated thiolate ligands
Phosphane ligands
Variable temperature ^{19}F NMR

ABSTRACT

The reactions of OsO_4 with excess of HSC_6F_5 and $P(C_6H_4X\text{-}4)_3$ in ethanol afford the five-coordinate compounds $[Os(SC_6F_5)_4(P(C_6H_4X\text{-}4)_3)]$ where X = OCH_3 **1a** and **1b**, CH_3 **2a** and **2b**, F **3a** and **3b**, Cl **4a** and **4b** or CF_3 **5a** and **5b**. Single crystal X-ray diffraction studies of **1** to **5** exhibit a common pattern with an osmium center in a trigonal-bipyramidal coordination arrangement. The axial positions are occupied by mutually *trans* thiolate and phosphane ligands, while the remaining three equatorial positions are occupied by three thiolate ligands. The three pentafluorophenyl rings of the equatorial ligands are directed upwards, away from the axial phosphane ligand in the arrangement "3-up" (isomers **a**). On the other hand, $^{31}P\{^1H\}$ and ^{19}F NMR studies at room temperature reveal the presence of two isomers in solution: The "3-up" isomer (**a**) with the three C_6F_5-rings of the equatorial ligands directed towards the axial thiolate ligand, and the "2-up, 1-down" isomer (**b**) with two C_6F_5-rings of the equatorial ligands directed towards the axial thiolate and the C_6F_5-ring of the third equatorial ligand directed towards the axial phosphane. Bidimensional ^{19}F–^{19}F NMR studies encompass the two sub-spectra for the isomers **a** ("3-up") and **b** ("2-up, 1-down"). Variable temperature ^{19}F NMR experiments showed that these isomers are fluxional. Thus, the ^{19}F NMR sub-spectra for the "2-up, 1-down" isomers (**b**) at room temperature indicate that the two S-C_6F_5 ligands in the 2-up equatorial positions have restricted rotation about their C–S bonds, but this rotation becomes free as the temperature increases. Room temperature ^{19}F NMR spectra of **3** and **5** also indicate restricted rotation around the Os–P bonds in the "2-up, 1-down" isomers (**b**). In addition, as the temperature increases, the ^{19}F NMR spectra tend to be consistent with an increased rate of the isomeric exchange. Variable temperature $^{31}P\{^1H\}$ NMR studies also confirm that, as the temperature is increased, the **a** and **b** isomeric exchange becomes fast on the NMR time scale.

© 2009 Elsevier Ltd. All rights reserved.

1. Introduction

The first molecular polythiolate-complexes of ruthenium and osmium, $[M(SR)_4(CH_3CN)]$ (M = Ru, Os; R = C_6HMe_4-2,3,5,6 or $C_6H_2{}^iPr_3$-2,4,6), were reported by Koch and Millar in 1983 [1]. On these systems, the experimental M–S_{ax} bond length is substantially longer than the average of the Ru–S_{eq} bond length, as theoretically predicted for these diamagnetic low-spin d^4 complexes [2]. In these complexes two of the aromatic rings of equatorial thiolates are projected towards the axial CH_3CN ligand and the other one is directed towards the axial sulfur (arrangement "2-up, 1-down"). In addition, these compounds were the first examples of five-coordinate ruthenium and osmium complexes bearing a formal +4 oxidation state. In 1985, these authors reported [3] the rare carbonyl M^{IV} compounds, $[M(SR)_4(CO)]$, where the overall structure is similar to that of $[M(SR)_4(CH_3CN)]$, with the CO occupying an axial position in the trigonal-bipyramidal coordination arrangement, in contrast however the three equatorial thiolates are oriented in the direction of the CO (arrangement "3-up"). In a note, the authors remark the fact that the ^1H NMR spectra of all their $[M(SR)_4L]$ compounds are complex and thus, for example $[Ru(SC_6HMe_4\text{-}2,3,5,6)_4(CH_3CN)]$ in $CDCl_3$ exhibits five singlets between δ 6.6 and 7.2 ppm which are assigned to the aromatic protons of the thiolate ligands, ten singlets between δ 1.8 and 2.7 ppm which are assigned to the methyl groups of the thiolate ligands and two resonances at δ 1.0 and 0.89 ppm assigned to the CH_3CN ligand. The interpretation was that both the "3-up" isomer and the "2-up, 1-down" isomer are present in solution and that these two isomers are not interconverting rapidly on the NMR time scale due to a hindered rotation of the ligands at the Ru–S_{eq} bonds.

* Corresponding author. Tel.: +52 222 2295500x7293; fax: +52 222 2295551.
E-mail addresses: slarroyo@siu.buap.mx, slmarroyo@hotmail.com (M. Arroyo).

0277-5387/$ - see front matter © 2009 Elsevier Ltd. All rights reserved.
doi:10.1016/j.poly.2009.05.044

Other five-coordinate ruthenium and osmium compounds with these sterically hindered aromatic thiolate ligands were reported [4,5]. In 1992 [5], for one of the compounds "2-up, 1-down", the authors found out that rotation about the Ru^{IV}–S bonds and C–S bonds is not observed on the NMR time scale from room temperature to nearly 60 °C.

For a long time, we have also been involved in the synthesis and reactivity studies of five-coordinate Os^{IV}-polythiolate-complexes [6–12], of general formula $[OsX(SR_F)_3(PR_3)]$ (X = Cl, SR_F; SR_F = SC_6F_5, SC_6F_4H-4, SC_6H_4F-4, SC_6H_5; PR_3 = tertiary phosphane). Up to now, all members of these series -characterized by X-ray crystallography- have shown, invariably, the orientation "3-up" for the equatorial thiolates, probably because the axial tertiary phosphane hinders that a R_F group could lie near of such an axial position. In general the structures in solution, according to ^1H, ^{31}P and ^{19}F NMR spectra of some members of the series, are as expected if the solid-state structure is maintained in solution. Some compounds however, undergo a measurable isomerisation that had not been exhaustively investigated since generally only room temperature NMR spectra were available, and it was not possible to assign the isomers with certainty [7]. In fact, except for the "3-up" isomer, none other specific isomer had been accurately assigned in solution.

On the other hand, restricted rotation of polyfluoro-phenyl/alkyl groups has been observed in a variety of coordination and organometallic compounds [12–21]. For example $[Os(SC_6F_5)_3(SC_6F_4(SC_6F_5)$-2)] and $[Os(SC_6F_4H)_2(SOC_6F_3H)(PPh_3))]$ exhibited restricted rotation of groups C_6F_5 or C_6F_4H about their C–S bonds [12], whereas complexes $[IrCp^*\{(CF_2)_nCF_3\}(PMe_3)_2]^+$ (n = 1, 2, 3, 5, 7, 9, 11) exhibited restricted rotation about their Ir–C σ-bonds [13] and complex $[Pd(C_6F_5)_2(Me_2–TpzT)]$ (Me_2–TpzT = 2,4,6-tris(3,5-dimethylpyrazol-1-yl)-1,3,5-triazine) exhibited restricted rotation about its Pd–C_6F_5 bonds [15]. The corresponding fluxional processes can be accompanied by conformational changes in the molecules and dynamic ^{19}F NMR studies of fluoro-thiolate complexes, $[W(SC_6F_5)_3(CO)Cp]$ [20], have revealed that isomeric forms exist due to different orientations of the SC_6F_5 ligands and the isomers undergo exchange as a result of rotations about W–SC_6F_5 bonds.

We now report the structural characterization of the compounds $[Os(SC_6F_5)_4(P(C_6H_4X$-4)$_3)]$, where X = OCH_3 **1**, CH_3 **2**, F **3**, Cl **4** or CF_3 **5**, both in the solid-state by X-ray diffraction studies, and in solution by $^{31}P\{^1H\}$ and ^{19}F NMR investigation of structural changes depending of temperature. These fluorinated systems offer the possibility to distinguish clearly the structural details of these types of five-coordinated osmium(IV) molecules and their structural changes.

2. Results and discussion

The reactions of OsO_4 with excess of HSC_6F_5 and $P(C_6H_4X$-4)$_3$ in ethanol afford the pentacoordinated, diamagnetic compounds $[Os(SC_6F_5)_4(P(C_6H_4X$-4)$_3)]$ where X = OCH_3 **1**, CH_3 **2**, F **3**, Cl **4** or CF_3 **5**. A general preliminary information about the preparation of these compounds has been mentioned [9]. Pentafluorobenzenethiol is dissolved in ethanol and then osmium tetraoxide is added. The mixture quickly turns black, the phosphane is added and the mixture refluxed turning green/brown. In addition to the formation of $[Os(SC_6F_5)_4(P(C_6H_4X$-4)$_3)]$, the recently reported persulfurated complex, $[Os(SC_6F_5)_3(SC_6F_4(SC_6F_5)$-2)] [12] **6**, is present as an additional product of these reactions.

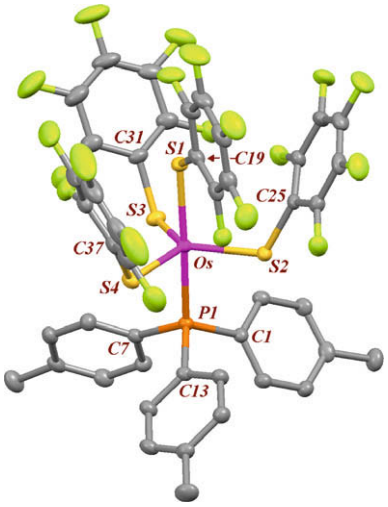


Fig. 1. Molecular structure of complex $[Os(SC_6F_5)_4(P(C_6H_4CH_3$-4)$_3)]$, **2a** [22]. H atoms have been omitted in the figure, and displacement ellipsoids are drawn at the 25% probability level.

The yields of **1**–**5** and **6** depend strongly on the relative proportion of phosphane ligand present always in excess to accomplish the required reduction of the osmium. Thus, the compound $[Os(SC_6F_5)_4(P(C_6H_4OCH_3$-4)$_3)]$ **1** is obtained in 70% yield when the molar ratio OsO_4:$P(C_6H_4OCH_3$-4)$_3$ is 1:6, while the yield drops down to only 9% when this ratio is 1:1.75. The formation of **6** depends just as well of this ratio.

The products were isolated by passage through a chromatographic column. These osmium(IV) diamagnetic complexes were characterized by elemental analyses, FAB^+-mass spectrometry, single crystal X-ray structure determinations and variable temperature $^{31}P\{^1H\}$ and ^{19}F NMR studies.

The FAB-mass spectra show low intensities signals of M^+ (X = Cl **4**) or $[M–H]^+$ (X = CF_3 **5**, F **3**, CH_3 **2**). A common high intensity signal on all the spectra is that corresponding to $[Os(SC_6F_5)_3(P(C_6H_4X$-4)$_3)]^+$. Also, peaks corresponding to $[P(C_6H_4X$-4)$_3)]^+$ and $[P(C_6H_4X$-4)$_2)]^+$ ions, with medium to high intensities are found on all FAB-mass spectra of compounds **1**–**5**.

The NMR studies show that each one of these products exists as a pair of isomers (**a**) and (**b**).

In the solid-state, compounds $[Os(SC_6F_5)_4(P(C_6H_4X$-4)$_3)]$ **1a**–**5a** share the trigonal-bipyramidal coordination geometry invariably observed for all Os^{IV} complexes formulated as $[OsX(SR_F)_3(PR_3)]$ (X = Cl, SC_6F_5, SC_6F_4H-4; SR_F = SC_6F_5, SC_6F_4H-4; PR_3 = tertiary phosphane) [6–8,10,11] (Fig. 1). The nature of the X substituent in the phosphane has none or little influence on the arrangement of ligands around the Os^{IV} ion. Axial positions are occupied by mutually *trans* thiolate and phosphane ligands, with S1–Os1–P1 angles in the short range 173.20(4)–177.23(4)°. Apparently there is no correlation between structural parameters and the *trans* influence of the phosphanes present in complexes **1a**–**5a**. Variations observed for Os1–S1 and Os1–P1 bond lengths are limited and virtually fall within the standard uncertainties for these parameters, 0.001–0.002 Å. Within experimental accuracy, any attempts to correlate phosphane basicity and solid-state structures would then be of questionable significance. Equatorial coordination sites are occupied by three thiolate ligands, with pentafluorophenyl groups

$$OsO_4 + HSC_6F_5(\text{excess}) + P(C_6H_4X\text{-}4)_3(\text{excess}) \xrightarrow{\text{Ethanol}} \underset{\textbf{1-5}}{[Os(SC_6F_5)_4(P(C_6H_4X\text{-}4)_3)]} + \underset{\textbf{6}}{[Os(SC_6F_5)_3(SC_6F_4(SC_6F_5)\text{-}2)]}$$

oriented away from the axial phosphane ligand, in the arrangement "3-up" (isomer **a**), in order to minimize the overall steric hindrance for peripheral phenyl rings in this molecule.

Although molecular structures are similar for all studied complexes, two points deserve to be commented. We previously reported that in the complex $[Os(SC_6F_5)_4(PPh_3)]$, which crystallizes with three crystallographically independent molecules in the asymmetric unit [10], the axial thiolate ligand gives rise to rotamers due to a non-restricted rotation about Os–S(*ax*) and S(*ax*)–C(*ipso*) σ-bonds. Similar results, although of limited extent, may be found among compounds **1a–5a** by inspecting the S(*eq*)–Os–S(*ax*)–C(*ipso*) torsion angles (Table 2). On the basis of these data, complexes **1a–5a** can be roughly classified in two groups: **1a–2a** (S4–Os–S1–C19 torsion angle close to 60°) and **3a–5a** (S4–Os–S1–C19 torsion angle close to 71°). This flexibility of orientation observed for the axial thiolate ligand is also present for the equatorial ligands, which experiment libration motions, particularly for S3-thiolate. Again, complexes **1a** and **2a** are differentiated from **3a–5a** (Fig. 2).

The second point of interest is about **3a**, which is the only member of this series crystallizing in a non-centrosymmetric achiral space group (*NA* crystal-structure type in the Flack's classification [23]). The measured crystal revealed to be a sample twinned by inversion, with components of the twin in the ratio 0.72(1):0.28(1) (see Section 4 and Fig. 2). A non-racemic mixture of configurations 0.72-*Λ*, 0.28-*Δ* was thus crystallized in the case of **3a** (the chiral axis is defined by P–Os bond). The other crystallized complexes of the series (**1a**, **2a**, **4a** and **5a**) are necessarily *Λ*,*Δ*-racemates, as they crystallize in centrosymmetric space groups (*CA* crystal-structure type in the Flack's classification [23]). In other words, **3a** in the solid-state represents an example of a co-crystallization associated with a partial spontaneous resolution. The factor promoting this resolution should probably be searched in crystallization conditions rather than in compound formulas or intermolecular interactions in the solid-sate. Single crystals were obtained either by crystallization from an acetone–ethanol solution of a powder sample, or directly by slow evaporation of chromatographed fractions (eluent: hexane-CH_2Cl_2) of the crude from the synthesis reactions. On the other hand, multiple crystal structure determinations on multiple crystallization crops would be necessary, in order to check if **3a** is systematically resolved in a more or less similar enantiomeric excess upon crystallization, and that such a resolution never occur for other complexes.

Although TLC for each of the products **1–5** shows only one spot, and in all the determined X-ray diffraction structures of these products the osmium center displays the same arrangement "3-up" for the equatorial thiolate ligands, the NMR studies show that each one of these products exists as the pair of isomers "3-up" (**a**) and "2-up, 1-down" (**b**) as depicted in the following scheme (Scheme 1).

The room temperature $^{31}P\{^1H\}$ NMR spectra of each product **1–5**, and the previously reported $[Os(SC_6F_5)_4(P(C_6H_5)_3)]$ [7] **7**, show two singlets suggesting the presence of two isomers. In all cases, the signal at low field corresponds to the more abundant isomer

Table 2
Selected torsion angles in compounds **1a–5a**.

δ (°)	1a	2a	3a	4a	5a
S2–Os–S1–C19	−61.3(2)	−64.9(2)	54.1(3)	−59.18(16)	−53.9(3)
S3–Os–S1–C19	−178.8(2)	178.2(2)	170.0(3)	−174.44(16)	−169.7(3)
S4–Os–S1–C19	62.9(2)	60.9(2)	−71.7(3)	71.08(16)	71.1(3)

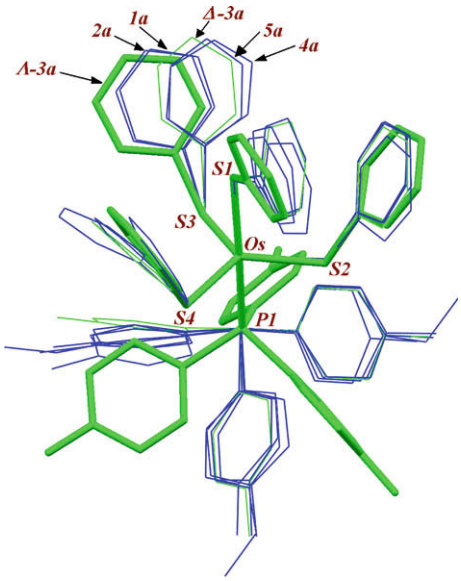
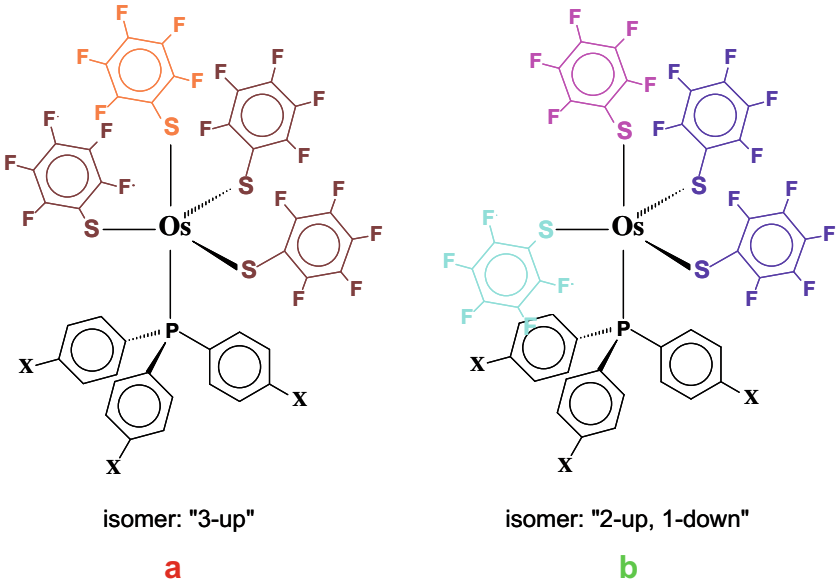


Fig. 2. A least-squares overlay [22] of molecular structures of complexes **1a–5a**. For the sake of clarity, F atoms of thiolate and of CF_3 groups, and all H atoms were omitted in the figure. The fit is carried out considering Os, P and S atoms (coordination sphere), while other atoms are free. In the case of complexes crystallizing in centrosymmetric space groups (blue bonds), *Δ* configuration has been arbitrarily selected. For **3a** (green bonds), both *Λ* and *Δ* configurations, forming a non-racemic mixture in the crystal, have been fitted.

Table 1
X-ray parameters.

Complex	**1a** (X = OCH_3)	**2a** (X = CH_3)	**3a** (X = F)	**4a** (X = Cl)	**5a** (X = CF_3)
Chemical formula	$C_{45}H_{21}F_{20}O_3OsPS_4$	$C_{45}H_{21}F_{20}OsPS_4$	$C_{42}H_{12}F_{23}OsPS_4$	$C_{42}H_{12}Cl_3F_{20}OsPS_4$	$C_{45}H_{12}F_{29}OsPS_4{\cdot}H_2O$
F_w	1339.03	1291.03	1302.93	1352.28	1470.97
Space group	$P\bar{1}$	$P2_1/c$	Pn	$P\bar{1}$	$P2_1/c$
a/Å	12.6081(13)	12.654(3)	11.2573(11)	11.9708(6)	12.3311(9)
b/Å	13.5869(12)	14.7363(19)	11.6399(12)	13.5087(6)	11.8013(8)
c/Å	14.4279(14)	25.476(3)	17.8021(16)	14.9035(8)	37.392(2)
α/°	92.608(5)	90.00	90.00	94.247(4)	90
β/°	96.775(8)	97.568(13)	104.753(7)	97.503(4)	96.414(6)
γ/°	97.287(7)	90.00	90.00	108.130(3)	90
V/Å^3	2429.9(4)	4709.3(15)	2255.8(4)	2253.90(19)	5407.4(6)
Z	2	4	2	2	4
μ/mm^{-1}	2.946	3.032	3.175	3.345	2.677
R_1, wR_2 [$I > 2\sigma(I)$][a]	0.0373, 0.0797	0.0385, 0.0864	0.0249, 0.0555	0.0370, 0.0663	0.0509, 0.1131
R_1, wR_2 (all data)[a]	0.0520, 0.0853	0.0583, 0.0961	0.0290, 0.0574	0.0636, 0.0746	0.0881, 0.1322
$D_{calc.}$/g cm^{-3}	1.830	1.821	1.918	1.993	1.807
T/°C	23(1)	23(1)	23(1)	23(1)	23(1)

[a] $R_1 = \frac{\sum||F_o|-|F_c||}{\sum|F_o|}$, $wR_2 = \sqrt{\frac{\sum w(F_o^2-F_c^2)^2}{\sum w(F_o^2)^2}}$.



Scheme 1.

Table 3
$^{31}P\{^{1}H\}$ NMR data in $CDCl_3$ at room temperature.

Product	Isomer a "3-up" δ(ppm)	Isomer b "2-up, 1-down" δ(ppm)	Integral ratio **a**/**b**
$[Os(SC_6F_5)_4(P(C_6H_4OCH_3\text{-}4)_3)]$ **1**	3.49	0.82	2.4
$[Os(SC_6F_5)_4(P(C_6H_4CH_3\text{-}4)_3)]$ **2**	5.34	2.83	2.0
$[Os(SC_6F_5)_4(P(C_6H_5)_3)]$ **7**	7.44	4.88	3.0
$[Os(SC_6F_5)_4(P(C_6H_4F\text{-}4)_3)]$ **3**	5.69	2.93	4.4
$[Os(SC_6F_5)_4(P(C_6H_4Cl\text{-}4)_3)]$ **4**	6.59	4.03	3.8
$[Os(SC_6F_5)_4(P(C_6H_4CF_3\text{-}4)_3)]$ **5**	8.52	6.08	4.4

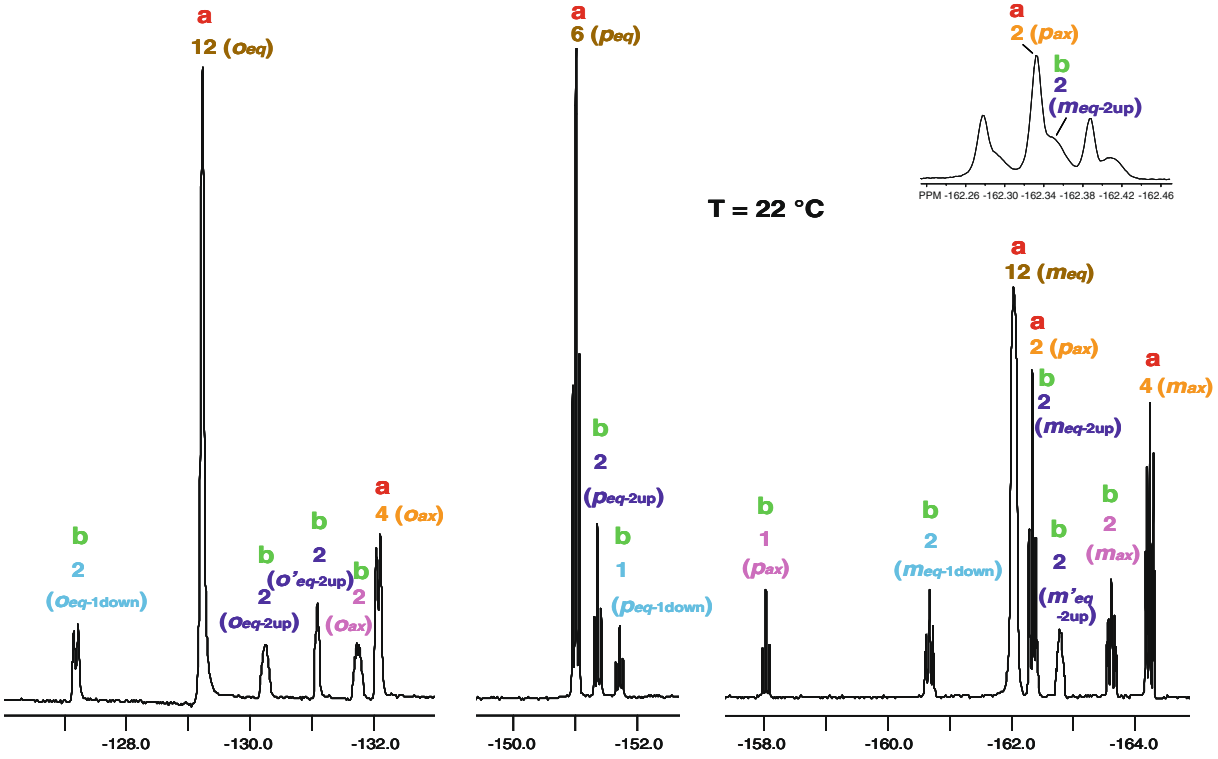


Fig. 3. ^{19}F NMR spectrum of $[Os(SC_6F_5)_4(P(C_6H_4CH_3\text{-}4)_3)]$ **2** at 22 °C in $C_6D_5CD_3$. The letter-labels identify the isomers: a, isomer "3-up"; b, isomer "2-up, 1-down". Numbers correspond to the relative integrals, which show that the ratio a/b is 2:1 in this product.

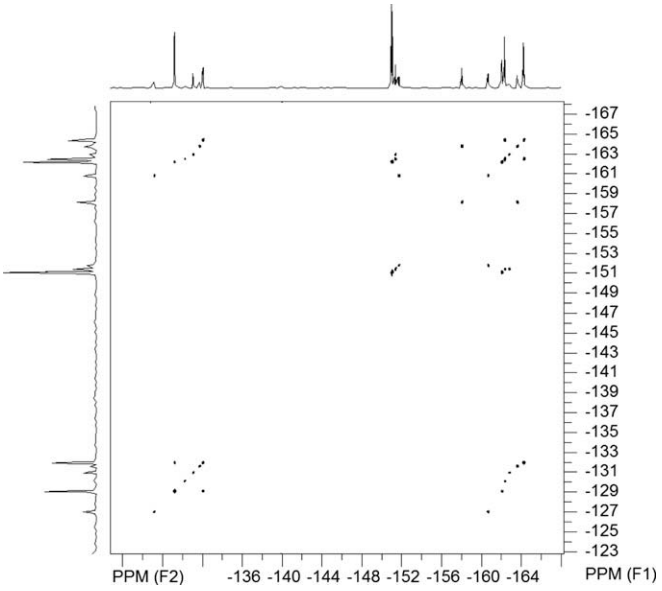


Fig. 4. $^{19}F–^{19}F$ COSY NMR spectrum of $[Os(SC_6F_5)_4(P(C_6H_4CH_3\text{-}4)_3)]$ **2** at 22 °C.

which, as deduced from the ^{19}F NMR studies below, is the "3-up" isomer (**a**). Table 3 indicates the relative abundances calculated from the $^{31}P\{^1H\}$ NMR spectra at room temperature, including the corresponding data from **7** for comparison purposes. These relative abundances are the same as those calculated from the ^{19}F NMR spectra.

Although the relative abundance of isomer **a** seems to growth with the electronegativity of the X substituent on the phosphane $P(C_6H_4X\text{-}4)_3$, the **a**/**b** ratio is probably a combination of electronic factors influencing the ability to undergo the required inversion of configuration at the sulfur atoms as well as solvent-complex interactions with the changing dipolar moments of the substituted phenyl rings.

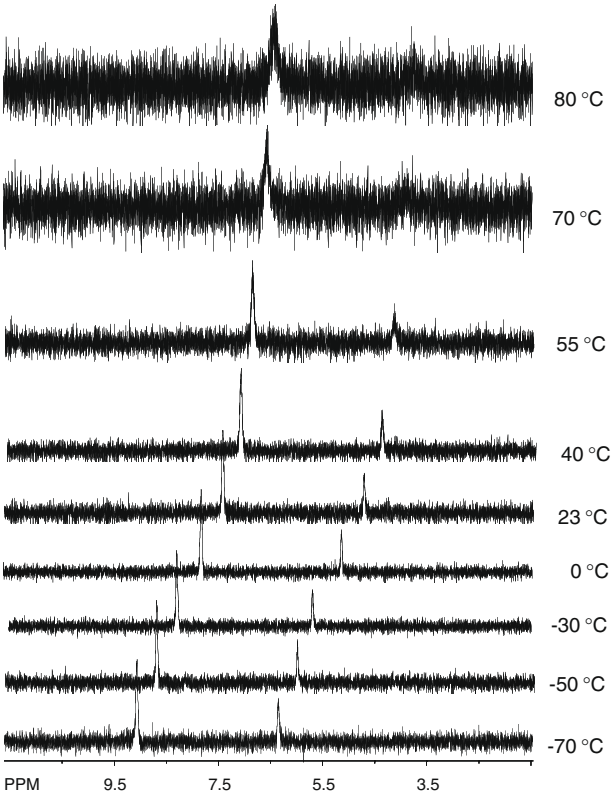


Fig. 6. Variable temperature $^{31}P\{^1H\}$ NMR spectra of $[Os(SC_6F_5)_4(P(C_6H_4CH_3\text{-}4)_3)]$ **2** in $C_6D_5CD_3$

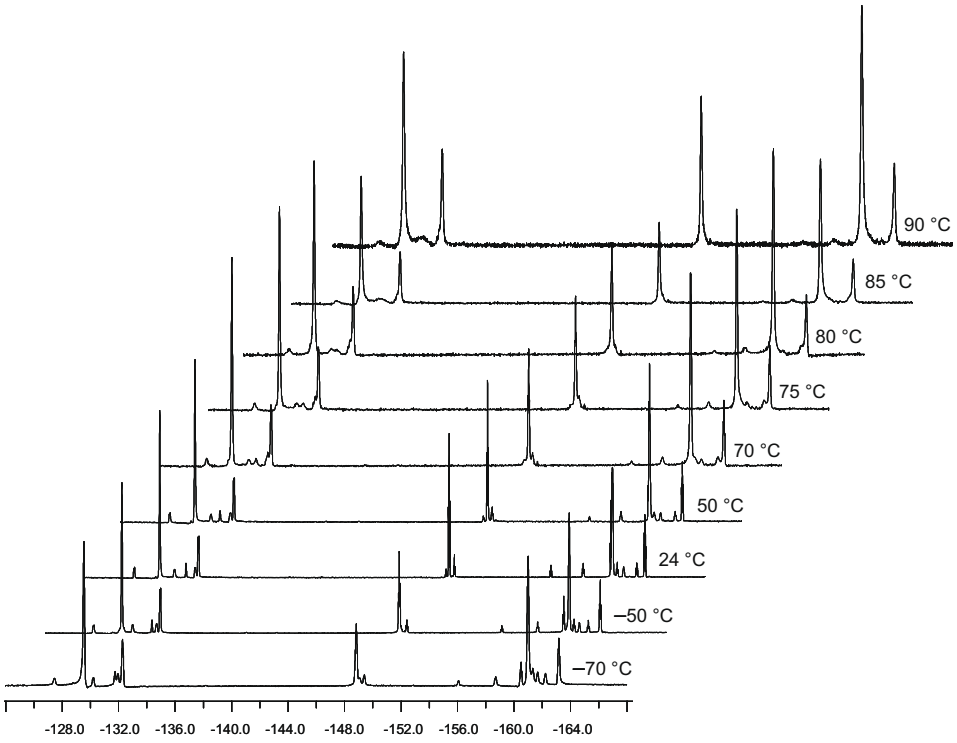


Fig. 5. Variable temperature ^{19}F NMR spectra of $[Os(SC_6F_5)_4(P(C_6H_4Cl\text{-}4)_3)]$ **4** in $C_6D_5CD_3$.

Room temperature ^{19}F NMR spectra of each product **1–5,** and the previously reported $[Os(SC_6F_5)_4(P(C_6H_5)_3)]$ [7,10] **7**, exhibit two independent sub-spectra, one for each of the isomers present in solution. $^{19}F–^{19}F$ NMR experiments were used to unambiguously identify each set of signals. The sub-spectrum of the isomer **a** "3-up" consists of two groups of signals with three absorptions each, corresponding to *ortho*, *para* and *meta*-fluorine atoms of C_6F_5 rings, at low, medium and high field, respectively [24,25]. One of these groups arises from the three equivalent equatorial thiolate ligands (A_2BC_2 spin system, relative integrals 6:3:6), and the second group from the axial thiolate ligand (another A_2BC_2 spin system, relative integrals 2:1:2). The sub-spectrum of the isomer **b** "2-up, 1-down" consists of three groups of signals: the group from one equatorial thiolate ligand in the orientation 1-down, which consists of three *ortho*, *para* and *meta* absorptions (A_2BC_2 spin system, relative integrals 2:1:2), the group from the two equatorial thiolate ligands in the orientation 2-up, which consists of five *ortho*, *ortho′*, *para*, *meta* and *meta′* signals (AA′BCC′ spin system, relative integrals 2:2:2:2:2), and the group of the axial thiolate ligand, which consists of three *ortho*, *para* and *meta* signals (A_2BC_2 spin system, relative integrals 2:1:2). The group of five signals from the two equatorial thiolate ligands in the orientation 2-up is consistent with two equivalent C_6F_5-groups restricted to rotate about their C–S bonds, where the two *ortho* (as well as *meta*) fluorine atoms in each ring are magnetically non-equivalent. Of course, the relative integrals between signals of isomer **a** and signals of isomer **b** are specific of each product. Fig. 3 shows the ^{19}F NMR spectrum at room temperature of the product **2** ($X = CH_3$), where the described assignments are illustrated whereas Fig. 4 shows the corresponding $^{19}F–^{19}F$ NMR spectrum.

For all "3-up" isomers, the room temperature $^{19}F–^{19}F$ NMR spectra show a significant magnetic coupling between $F_{ortho-equatorial}$ and $F_{ortho-axial}$ nuclei. These nuclei are eight bonds apart with a S–Os–S intermediate fragment and therefore, a conventional contact coupling mechanism is unlikely. On the other hand, the three equatorial thiolates on the "3-up" isomers form a bowl-like cavity which surrounds the axial thiolate with a very close spatial proximity to the *ortho* fluorine nuclei and therefore suggesting a through-space coupling mechanism.

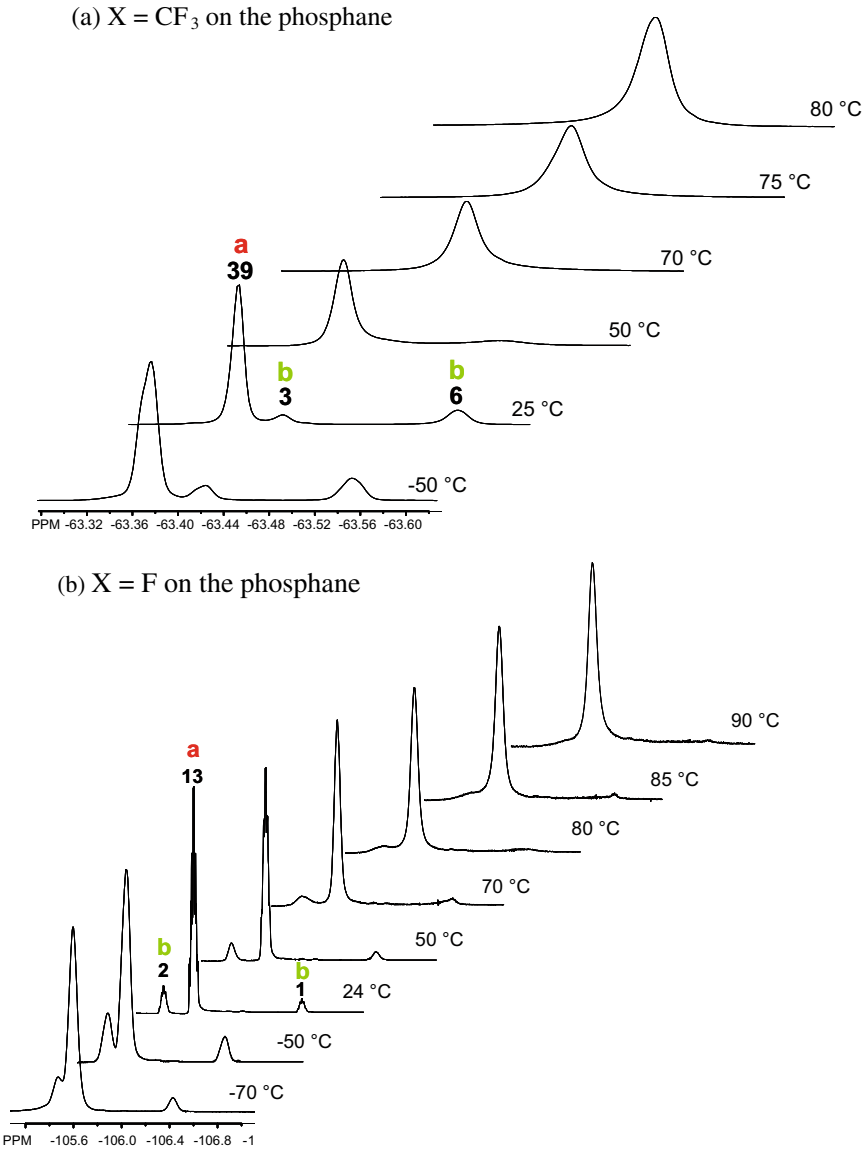


Fig. 7. Variable temperature ^{19}F NMR spectra on the phosphane–fluorine region of (a) $[Os(SC_6F_5)_4(P(C_6H_4CF_3\text{-}4)_3)]$ **5** and (b) $[Os(SC_6F_5)_4(P(C_6H_4F\text{-}4)_3)]$ **3** in $C_6D_5CD_3$; a corresponds to isomer "3-up" and b to isomer "2-up, 1-down". Numbers correspond to the relative integrals, which show that the ratio a/b is 4.4:1 in these products.

The ^{19}F NMR spectra of each product **1**–**5**, and **7**, registered from −80 °C to +90 °C, indicate that these products undergo fluxional processes in solution. Fig. 5 shows variable temperature ^{19}F NMR spectra of product **4** (X = Cl) in $C_6D_5CD_3$. In general, for isomers **b** "2-up, 1-down" in the series **1**–**5** and **7**, as the temperature is increased, the two *ortho* and *ortho*′ signals (relative intensities 2:2), from the two equivalent 2-up equatorial thiolates, broaden and eventually coalesce giving rise to a single *ortho* signal (intensity 4) at *ca.* 85–90 °C. The coalescence of the corresponding *meta* and *meta*′ signals follows a similar pattern, while at high temperatures the corresponding *para* absorption of these 2-up equatorial thiolate ligands exhibits chemical shift almost coincident with the *para* signal of the 1-down equatorial thiolate of the same isomer **b**, and with the *para* signal of the three 3-up equatorial thiolates of the isomer **a**. As the temperature is increased, the ^{19}F NMR spectra of **1**–**5**, and **7** tend to simplify until they resemble the spectra of the isomer **a**. The coalescence at high temperatures (85–90 °C) of the *ortho* and *ortho*′ signals from the two 2-up equatorial thiolates is consistent with free C–S bond rotations at these temperatures, with estimated $\Delta G^{\ddagger}$ values of 69–70 kJmol^{-1}. In addition, the tendency of both ^{19}F NMR sub-spectra of the isomers **a** and **b** (low temperatures) to merge into a single spectrum corresponding to the isomer **a** (high temperatures) suggests that a rapid conversion between isomers **a** and **b** occurs also and simultaneously. To investigate this process further, we have measured the $^{31}P\{^1H\}$ NMR spectra at variable temperature and found that, as the temperature is increased, both singlets from isomers **a** and **b** broaden and decrease in height, although at 80 °C (or inclusive 95 °C) their coalescence is still not completed (Fig. 6). This is a reversible process since the original spectra are obtained as the temperature is restored back. We conclude that two fluxional processes are being simultaneously observed: the C–S bond rotation of the two 2-up equatorial thiolates in the isomer **b** and the conversion between isomers **a** and **b** which involves inversion of configuration at the sulfur atoms.

Except for subtle differences in chemical shifts and some variations in the relative positions of the *para* and *meta* signals, the ^{19}F NMR spectra in the C_6F_5-region of these products **1**–**5** and **7** are all comparable.

In addition, the room temperature ^{19}F NMR spectrum of **5** (X = CF_3), in the CF_3-region of the phosphane ligand, exhibits: one singlet corresponding to equivalent CF_3 groups at the *para*-positions of the phenyl substituents of the phosphane in the isomer "3-up" **5a** and two singlets (relative integrals 3:6) corresponding to non-equivalent CF_3 groups of the phenyl substituents of the phosphane in the isomer "2-up, 1-down" **5b**. The corresponding spectrum of **3** (X = F) on the fluorine-region of the phosphane, also exhibits the same pattern of signals, corresponding to the *para*-fluorine nuclei in the phenyl substituents of the phosphane ligand of the isomers: **3a**: one doublet of triplets of triplets, corresponding to three equivalent C_6H_4F-4 substituents in this isomer, and **3b**: two doublets of triplets of triplets, relative integrals 2:1, corresponding to two equivalent C_6H_4F-4 rings plus another non-equivalent C_6H_4F-4 ring one in this isomer "2-up, 1-down". In each of these two products **3** or **5**, these additional signals at low field tend to coalesce into only one signal as the temperature increases (Fig. 7). The spectra of these two products **3** and **5** at low field corroborate the existence of the isomers "3-up" and "2-up, 1-down" in solution and show that, at low temperatures, the isomer "2-up, 1-down" exhibits restricted rotation of the osmium–phosphorous bond imposed by the pending thiolate ring giving rise to a system involving an unusual asymmetrical phosphane.

3. Conclusions

We report here the reactions of OsO_4 with HSC_6F_5 and $P(C_6H_4X\text{-}4)_3$ in ethanol to afford the five-coordinate compounds $[Os(SC_6F_5)_4(P(C_6H_4X\text{-}4)_3)]$ where X = OCH_3 **1a** and **1b**, CH_3 **2a** and **2b**, F **3a** and **3b**, Cl **4a** and **4b** or CF_3 **5a** and **5b**. Single crystal X-ray diffraction studies of **1**–**5** exhibit a common pattern with an osmium center in a trigonal-bipyramidal coordination arrangement with the axial positions occupied by mutually *trans* thiolate and phosphane ligands and the three C_6F_5-rings of the equatorial thiolate ligands directed towards the axial thiolate ligand (isomers **a** "3-up"). On the other hand, $^{31}P\{^1H\}$ and ^{19}F NMR studies at room temperature reveal accurately the presence of two isomers in solution: the "3-up" isomer (**a**) above mentioned, and the "2-up, 1-down" isomer (**b**) with two C_6F_5-rings of the equatorial ligands directed towards the axial thiolate and the C_6F_5-ring of the third equatorial ligand directed towards the axial phosphane. In addition, at low temperatures, the NMR studies reveal restricted rotations about specific bonds in the molecules. As the temperature increases, the ^{19}F and $^{31}P\{^1H\}$ NMR spectra tend to be consistent with an increased rate of these rotations about bonds in the isomers, as well as with an increased rate of the isomeric exchange.

4. Experimental

All reactions were carried out under argon atmospheres using conventional Schlenk-tube techniques. Thin-layer chromatography (TLC) (Merck, silica gel 60 F_{254}) was used to monitor the progress of the reactions under study with hexane–dichloromethane (4:1) as eluent. The starting materials: osmium tetraoxide, pentafluorobenzenethiol and phosphanes were used as received from Aldrich Chemical Co. and Strem. The products were separated by passage through a silica gel chromatographic column with hexanes–dichloromethane as eluent.

Melting points were obtained on a Fisher–Johns melting point apparatus and are uncorrected.

Infrared spectra were recorded on a 750 Nicolet Fourier Transform Magna-IR Spectrometer. The samples were prepared as KBr pellets. Data are expressed in wavenumbers (cm^{-1}) with relative intensities (vs = very strong, s = strong, m = medium, w = weak).

$^{31}P\{^1H\}$, ^{19}F, and COSY ^{19}F–^{19}F NMR spectra were recorded on a Varian Mercury VX400 spectrometer operating at 162 MHz, and 376 MHz, respectively. $^{31}P\{^1H\}$ NMR spectra were also recorded on a Varian Mercury VX300 spectrometer operating at 121 MHz. Chemical shifts are relative to H_3PO_4 $\delta = 0$ (^{31}P) and CCl_3F $\delta = 0$ (^{19}F), using $C_6D_5CD_3$ and $CDCl_3$ as solvents. The $\Delta G^{\ddagger}$ values reported in this paper have been calculated from variable temperature (VT) ^{19}F NMR data with the Eyring equation, estimating the rate constant at the coalescence temperature on the basis of the chemical shift difference at low temperature.

Positive ion FAB mass spectra were recorded on a Jeol JMS-SX102A mass spectrometer operated at an accelerating voltage of 10 kV. Samples were desorbed from a 3-nitrobenzyl alcohol (NOBA) matrix using 3 keV xenon atoms. Mass measurements in FAB are performed at a resolution of 3000 using magnetic field scans and the matrix ions as the reference material.

Elemental analyses were determined by Galbraith Laboratories Inc.

4.1. $[Os(SC_6F_5)_4(P(C_6H_4OCH_3\text{-}4)_3)]$ **1**

Pentafluorobenzenethiol (0.8 mL, 6.0 mmol) was dissolved in ethanol (15 mL), then osmium tetraoxide (0.25 g, 1.0 mmol) was added. The mixture rapidly turned black. $P(C_6H_4OCH_3\text{-}4)_3$ (0.62 g, 1.75 mmol) was added and the mixture refluxed for 4 h turning green. The solvent was distilled off under vacuum and the solid product was purified through a silica gel chromatographic column eluted with hexane–dichloromethane 4:1. Two fractions with compounds **1** and $[Os(SC_6F_5)_3(SC_6F_4(SC_6F_5)\text{-}2)]$ [12] **6** were separated

and dried under vacuum at room temperature for 4 h. Single crystals of **1** were obtained by slow evaporation of an acetone–ethanol solution of the compound.

[$Os(SC_6F_5)_4(P(C_6H_4OCH_3\text{-}4)_3)$] **1**. Green (0.12 g, 9%). *Anal.* Calc. for $C_{45}H_{21}F_{20}O_3OsPS_4$: C, 40.36; H, 1.58; S, 9.58. Found: C, 40.32; H, 1.66; S, 9.52%. Mp: 193 °C, decomposes. IR (KBr, cm^{-1}): $\nu_{thiolate}$ 1514(vs), 1486(vs), 1090(vs), 982(vs), 849(s); $\nu_{phosphane}$ 1593(s), 1567(w), 1502(vs), 1444(w), 1289(s), 1259(s), 1184(s), 1090(vs), 1026(w), 833(w), 800(w), 540(w). $^{31}P\{^1H\}$ NMR ($CDCl_3$, RT), δ(ppm): isomer "3-up", δ = 3.49 (s, 2.4P, 2.4(1P($C_6H_4OCH_3$-4)$_3$)); isomer "2-up, 1-down", δ = 0.82 (s, 1.0P, 1P($C_6H_4OCH_3$-4)$_3$). ^{19}F NMR ($C_6D_5CD_3$, RT), δ(ppm): isomer "3-up", δ = −129.24 (br s, 14.4F*o*, 2.4(3SC_6F_5-eq)), δ = −132.14 (d, 4.8F*o*, 2.4(1SC_6F_5-*ax*), $^3J_{Fo-Fm}$ = 23.32 Hz), δ = −150.99 (t, 7.2F*p*, 2.4(3SC_6F_5-*eq*), $^3J_{Fp-Fm}$ = 20.69 Hz), δ = −161.98 (br m, 14.4F*m*, 2.4(3SC_6F_5-*eq*)), δ = −162.44 (t, 2.4F*p*, 2.4(1SC_6F_5-*ax*), $^3J_{Fp-Fm}$ = 20.69 Hz), δ = −164.24 (m, 4.8F*m*, 2.4(1SC_6F_5-*ax*)); isomer "2-up, 1-down", δ = −127.05 (d, 2F*o*, 1SC_6F_5-*eq*-"1-down", $^3J_{Fo-Fm}$ = 25.96 Hz), δ = −130.27 (br s, 2F*o*, ½(2SC_6F_5)-*eq*-"2-up"), δ = −131.09 (br s, 2F*o*′, ½(2SC_6F_5)-*eq*-"2-up"), δ = −131.77 (m, 2F*o*, 1SC_6F_5-*ax*), δ = −151.32 (t, 2F*p*, 2SC_6F_5-*eq*-"2-up", $^3J_{Fp-Fm}$ = 19.18 Hz), δ = −151.37 (t, 1F*p*, 1SC_6F_5-*eq*-"1-down", $^3J_{Fp-Fm}$ = 19.18 Hz), δ = −158.16 (t, 1F*p*, 1SC_6F_5-*ax*, $^3J_{Fp-Fm}$ = 20.69 Hz), δ = −160.83 (m, 2F*m*, 1SC_6F_5-*eq*-"1-down"), δ = −162.30 (t, 2F*m*, ½(2SC_6F_5)-*eq*-"2-up", $^3J_{Fm-F}$ = 23.32 Hz), δ = −162.70 (br m, 2F*m*′, ½(2SC_6F_5)-*eq*-"2-up"), δ = −163.65 (m, 2F*m*, 1SC_6F_5-*ax*). FAB^+−MS {m/z (%) [fragment]}: 1141 (17) [M^+−(SC_6F_5)], 352 (8) [$P(C_6H_4OCH_3)_3^+$], 245 (14) [$P(C_6H_4OCH_3)_2^+$].

[$Os(SC_6F_5)_3(SC_6F_4(SC_6F_5)$-2)] [12] **6** (0.035 g, 3%).

When the starting quantities were: pentafluorobenzenethiol (0.8 mL, 6.0 mmol), osmium tetraoxide (0.25 g, 1.0 mmol) and P($C_6H_4OCH_3$-4)$_3$ (2.10 g, 6.0 mmol), complex **6** was not obtained and the only isolated complex was [$Os(SC_6F_5)_4(P(C_6H_4OCH_3\text{-}4)_3)$] **1** in 70% yield (0.94 g).

4.2. *[Os(SC$_6$F$_5$)$_4$(P(C$_6$H$_4$CH$_3$-4)$_3$)]* ***2***

The procedure is analogous to that for **1**: reflux time 3 h. Products **2** and **6**. Starting quantities: pentafluorobenzenethiol (0.8 mL, 6.0 mmol), osmium tetraoxide (0.25 g, 1.0 mmol), P($C_6H_4CH_3$-4)$_3$ (0.90 g, 2.95 mmol). Single crystals of **2** were obtained by slow evaporation of an acetone–ethanol solution of the compound.

[$Os(SC_6F_5)_4(P(C_6H_4CH_3\text{-}4)_3)$] **2**. Green (0.64 g, 50%). *Anal.* Calc. for $C_{45}H_{21}F_{20}OsPS_4$: C, 41.86; H, 1.64; S, 9.93. Found: C, 41.75; H, 1.71; S, 9.92%. Mp: 185 °C, decomposes. IR (KBr, cm^{-1}): $\nu_{thiolate}$ 1512(vs), 1488(vs), 1090(vs), 981(vs), 851(s); $\nu_{phosphane}$ 1488(vs), 1393(w), 1090(vs), 809(w), 631(w), 525(w), 512(w). $^{31}P\{^1H\}$ NMR ($CDCl_3$, RT), δ(ppm): isomer "3-up", δ = 5.34 (s, 2.0P, 2(1P($C_6H_4CH_3$-4)$_3$)); isomer "2-up, 1-down", δ = 2.83 (s, 1.0P, 1P($C_6H_4CH_3$-4)$_3$). ^{19}F NMR ($C_6D_5CD_3$, RT), δ(ppm): isomer "3-up", δ = −129.23 (br s, 12F*o*, 2(3SC_6F_5-*eq*)), δ = −132.07 (d, 4F*o*, 2(1SC_6F_5-*ax*), $^3J_{Fo-Fm}$ = 23.32 Hz), δ = −151.02 (t, 6F*p*, 2(3SC_6F_5-*eq*), $^3J_{Fp-Fm}$ = 20.69 Hz), δ = −162.04 (br s, 12F*m*, 2(3SC_6F_5-*eq*)), δ = −162.34 (t, 2F*p*, 2(1SC_6F_5-*ax*), $^3J_{Fp-Fm}$ = 20.69 Hz), δ = −164.24 (m, 4F*m*, 2(1SC_6F_5-*ax*)), isomer "2-up, 1-down", δ = −127.18 (d, 2F*o*, 1SC_6F_5-*eq*-"1-down", $^3J_{Fo-Fm}$ = 24.83 Hz), δ = −130.24 (br s, 2F*o*, ½(2SC_6F_5-*eq*-"2-up")), δ = −131.08 (br s, 2F*o*′, ½(2SC_6F_5-*eq*-"2-up")), δ = −131.74 (m, 2F*o*, 1SC_6F_5-*ax*), δ = −151.37 (t, 2F*p*, 2SC_6F_5-*eq*-"2-up", $^3J_{Fp-Fm}$ = 20.69 Hz), δ = −151.72 (t, 1F*p*, 1SC_6F_5-*eq*-"1-down", $^3J_{Fp-Fm}$ = 20.69 Hz), δ = −158.03 (t, 1F*p*, 1SC_6F_5-*ax*, $^3J_{Fp-Fm}$ = 20.69 Hz), δ = −160.67 (m, 2F*m*, 1SC_6F_5-*eq*-"1-down"), δ = −162.35 (t, 2F*m*, ½(2SC_6F_5-*eq*-"2-up"), $^3J_{Fm-F}$ = 22.57 Hz), δ = −162.79 (m, 2F*m*′, ½(2SC_6F_5-*eq*-"2-up")), δ = −163.61 (m, 2F*m*, 1SC_6F_5-*ax*). FAB^+−MS {m/z (%) [fragment]}: 1291 (2) [M^+−H], 1273 (4) [M^+−F], 1201 (1) [M^+−($C_6H_4CH_3$)], 1093 (51) [M^+−(SC_6F_5)], 911 (2) [M^+−(SC_6F_5)−2($C_6H_4CH_3$)], 893 (1) [M^+−2(SC_6F_5)−H], 304 (21) [$P(C_6H_4CH_3)_3^+$], 213 (17) [$P(C_6H_4CH_3)_2^+$].

[$Os(SC_6F_5)_3(SC_6F_4(SC_6F_5)$-2)] [12] **6** (0.035 g, 3%).

4.3. *[Os(SC$_6$F$_5$)$_4$(P(C$_6$H$_4$F-4)$_3$)]* ***3***

The procedure is analogous to that for **1**: reflux time 3 h. Products **3** and **6**. Starting quantities: pentafluorobenzenethiol (0.8 mL, 6.0 mmol), osmium tetraoxide (0.25 g, 1.0 mmol), P(C_6H_4F-4)$_3$ (0.81 g, 2.55 mmol). Single crystals of **3** were obtained by slow evaporation of a hexane–dichloromethane 4:1 solution of the compound.

[$Os(SC_6F_5)_4(P(C_6H_4F\text{-}4)_3)$] **3**. Brown (0.57 g, 44%). *Anal.* Calc. for $C_{42}H_{12}F_{23}OsPS_4$: C, 38.72; H, 0.93; S, 9.84. Found: C, 38.82; H, 0.97; S, 9.76%. Mp: 178 °C, decomposes. IR (KBr, cm^{-1}): $\nu_{thiolate}$ 1512(vs), 1491(vs), 1091(vs), 982(vs), 852(w); $\nu_{phosphane}$ 1592(w), 1491(vs), 1394(w), 1244(w), 1165(s), 1091(vs), 833(w), 530(w). $^{31}P\{^1H\}$ NMR ($CDCl_3$, RT), δ(ppm): isomer "3-up", δ = 5.69 (d, 4.4P, 4.4(1P(C_6H_4F-4)$_3$)); isomer "2-up, 1-down", δ = 2.93 (d, 1.0P, 1P(C_6H_4F-4)$_3$). ^{19}F NMR ($C_6D_5CD_3$, RT), δ(ppm): isomer "3-up", δ = −105.60 (dtt, 13.2F*p*, 4.4(1P(C_6H_4F-4)$_3$), $^3J_{Fp-Hm}$ = 5.70 Hz, $^4J_{Fp-Ho}$ = 3.99 Hz, $^5J_{Fp-P}$ = 2.14 Hz), δ = −129.29 (br s, 26.4F*o*, 4.4(3SC_6F_5-*eq*)), δ = −132.02 (d, 8.8F*o*, 4.4(1SC_6F_5-*ax*), $^3J_{Fo-Fm}$ = 23.32 Hz), δ = −150.04 (t, 13.2F*p*, 4.4(3SC_6F_5-*eq*), $^3J_{Fp-Fm}$ = 20.69 Hz), δ = −161.54 (br m, 26.4F*m*, 4.4(3SC_6F_5-*eq*)), δ = −161.65 (t, 4.4F*p*, 4.4(1SC_6F_5-*ax*), $^3J_{Fp-Fm}$ = 20.69 Hz), δ = −163.89 (m, 8.8F*m*, 4.4(1SC_6F_5-*ax*)), isomer "2-up, 1-down", δ = −105.34 (dtt, 2F*p*, 1P(C_6H_4F-4)$_3$, $^3J_{Fp-Hm}$ = 5.71 Hz, $^4J_{Fp-Ho}$ = 3.98 Hz, $^5J_{Fp-P}$ = 2.1 Hz), δ = −106.55 (dtt, 1F*p*, 1P(C_6H_4F-4)$_3$, $^3J_{Fp-Hm}$ = 5.7 Hz, $^4J_{Fp-Ho}$ = 3.9 Hz, $^5J_{Fp-P}$ = 2 Hz), δ = −127.23 (d, 2F*o*, 1SC_6F_5-*eq*-"1-down", $^3J_{Fo-Fm}$ = 24.83 Hz), δ = −130.34 (br s, 2F*o*, ½(2SC_6F_5)-*eq*-"2-up"), δ = −131.20 (br s, 2F*o*′, ½(2SC_6F_5)-*eq*-"2-up"), δ = −131.78 (m, 2F*o*, 1SC_6F_5-*ax*), δ = −149.92 (t, 1F*p*, 1SC_6F_5-*eq*-"1-down", $^3J_{Fp-Fm}$ = 20.69 Hz), δ = −150.38 (t, 2F*p*, 2SC_6F_5-*eq*-"2-up", $^3J_{Fp-Fm}$ = 20.69 Hz), δ = −157.29 (t, 1F*p*, 1SC_6F_5-*ax*, $^3J_{Fp-Fm}$ = 20.69 Hz), δ = −159.94 (m, 2F*m*, 1SC_6F_5-*eq*-"1-down"), δ = −161.87 (t, 2F*m*, ½(2SC_6F_5)-*eq*-"2-up", $^3J_{Fm-F}$ = 21.82 Hz), δ = −162.31 (br m, 2F*m*′, ½(2SC_6F_5)-*eq*-"2-up"), δ = −163.27 (m, 2F*m*, 1SC_6F_5-*ax*). FAB^+−MS {m/z (%) [fragment]}: 1303 (2) [M^+−H], 1285 (1) [M^+−F], 1209 (2) [M^+−(C_6H_4F)], 1105 (100) [M^+−(SC_6F_5)], 938 (3) [M^+−(SC_6F_5)−(C_6F_5)], 905 (3) [M^+−2(SC_6F_5)−H], 316 (68) [$P(C_6H_4F)_3^+$], 221 (58) [$P(C_6H_4F)_2^+$].

[$Os(SC_6F_5)_3(SC_6F_4(SC_6F_5)$-2)] [12] **6** (0.08 g, 7%).

4.4. *[Os(SC$_6$F$_5$)$_4$(P(C$_6$H$_4$Cl-4)$_3$)]* ***4***

Pentafluorobenzenethiol (0.8 mL, 6.0 mmol) was dissolved in ethanol (15 mL), then osmium tetraoxide (0.25 g, 1.0 mmol) was added. The mixture rapidly turned black. P(C_6H_4Cl-4)$_3$ (0.67 g, 1.82 mmol) was added and the mixture was stirred at room temperature for 9 h. The resulting solution was concentrated at *ca.* 50% under reduced pressure to give a brown precipitate. It was filtered off, washed with ethanol (15 mL) and hexane (15 mL) and dried under vacuum. Additional purification was necessary through a silica gel chromatographic column with hexane–dichloromethane 4:1 as eluent. Slow evaporation of the eluent affords brown crystals of **4**. With scope for increasing the yield of **4**, the filtrate was refluxed for 3 h giving a green product, **6**, which was also purified through a silica gel chromatographic column with hexane–dichloromethane 4:1 as eluent.

[$Os(SC_6F_5)_4(P(C_6H_4Cl\text{-}4)_3)$] **4**. Brown (0.14 g, 10%). *Anal.* Calc. for $C_{42}H_{12}Cl_3F_{20}OsPS_4$: C, 37.30; H, 0.89; S, 9.48. Found: C, 37.21; H, 0.95; S, 9.43%. Mp: 200 °C, decomposes. IR (KBr, cm^{-1}): $\nu_{thiolate}$ 1513(vs), 1483(vs), 1085(vs), 980(vs), 853(s); $\nu_{phosphane}$ 1483(vs), 1390(w), 1085(vs), 1013(w), 822(w), 749(w), 548(w), 503(w). $^{31}P\{^1H\}$ NMR ($CDCl_3$, RT), δ(ppm): isomer "3-up", δ = 6.59 (s, 3.8P,

3.8(1P(C_6H_4Cl-4)$_3$)); isomer "2-up, 1-down", δ = 4.03 (s, 1.0P, 1P(C_6H_4Cl-4)$_3$).^{19}F NMR ($C_6D_5CD_3$, RT), δ(ppm): isomer "3-up", δ = −129.25 (br s, 22.8F*o*, 3.8(3SC_6F_5-*eq*)), δ = −132.00 (d, 7.6F*o*, 3.8(1SC_6F_5-*ax*), $^3J_{Fo-Fm}$ = 24.45 Hz), δ = −149.82 (t, 11.4F*p*, 3.8(3SC_6F_5-*eq*), $^3J_{Fp-Fm}$ = 20.69 Hz), δ = −161.33 (t, 3.8F*p*, 3.8(1SC_6F_5-*ax*), $^3J_{Fp-Fm}$ = 20.69 Hz), δ = −161.43 (br m, 22.8F*m*, 3.8(3SC_6F_5-*eq*)), δ = −163.74 (m, 7.6F*m*, 3.8(1SC_6F_5-*ax*)), isomer "2-up, 1-down", δ = −127.43 (d, 2F*o*, 1SC_6F_5-*eq*-"1-down", $^3J_{Fo-Fm}$ = 23.32 Hz), δ = −130.30 (br s, 2F*o*, ½(2SC_6F_5)-*eq*-"2-up"), δ = −131.12 (br s, 2F*o*′, ½(2SC_6F_5)-*eq*-"2-up"), δ = −131.76 (m, 2F*o*, 1SC_6F_5-*ax*), δ = −149.60 (t, 1F*p*, 1SC_6F_5-*eq*-"1-down", $^3J_{Fp-Fm}$ = 20.31 Hz), δ = −150.20 (t, 2F*p*, 2SC_6F_5-*eq*-"2-up", $^3J_{Fp-Fm}$ = 20.69 Hz), δ = −157.06 (t, 1F*p*, 1SC_6F_5-*ax*, $^3J_{Fp-Fm}$ = 20.69 Hz), δ = −159.36 (m, 2F*m*, 1SC_6F_5-*eq*-"1-down"), δ = −161.78 (t, 2F*m*, ½(2SC_6F_5)-*eq*-"2-up", $^3J_{Fm-F}$ = 22.19 Hz), δ = −162.23 (br m, 2F*m*′, ½(2SC_6F_5)-*eq*-"2-up"), δ = −163.16 (m, 2F*m*, 1SC_6F_5-*ax*). FAB$^+$−MS {m/z (%) [fragment]}: 1352 (1) [M^+], 1333 (1) [M^+−F], 1153 (100) [M^+−(SC_6F_5)], 1241 (1) [M^+−(C_6H_4Cl)], 986 (2) [M^+−(SC_6F_5)−(C_6F_5)], 953 (2) [M^+−2(SC_6F_5)−H], 364 (13) [P(C_6H_4Cl)$_3^+$], 253 (18) [P(C_6H_4Cl)$_2^+$].

[Os(SC_6F_5)$_3$(SC_6F_4(SC_6F_5)-2)] [12] **6** (0.06 g, 5%).

4.5. [Os(SC_6F_5)$_4$(P($C_6H_4CF_3$-4)$_3$)] **5**

The procedure is analogous to that for **1**: reflux time 7 h. Products **5** and **6**. Starting quantities: pentafluorobenzenethiol (0.8 mL, 6.0 mmol), osmium tetraoxide (0.25 g, 1.0 mmol), P($C_6H_4CF_3$-4)$_3$ (1.00 g, 2.15 mmol). Slow evaporation of the eluent affords brown crystals of **5** and green crystals of **6**. Analyses and yields are as follow:

[Os(SC_6F_5)$_4$(P($C_6H_4CF_3$-4)$_3$)] **5**. Brown (0.13 g, 9%). *Anal.* Calc. for $C_{45}H_{12}F_{29}OsPS_4{\cdot}OH_2$: C, 36.74; H, 0.96; S, 8.72. Found: C, 36.49; H, 0.99; S, 8.73%. Mp: 166 °C, decomposes. IR (KBr, cm^{-1}): $\nu_{thiolate}$ 1512(vs), 1493(vs), 1090(vs), 983(vs), 856(s); $\nu_{phosphane}$ 1398(s), 1325(vs), 1177(s), 1135(s), 1063(vs), 1017(s), 839(s), 707(w), 600(w). ^{31}P{^{1}H} NMR ($CDCl_3$, RT), δ(ppm): isomer "3-up", δ = 8.52 (s, 4.4P, 4.4(1P($C_6H_4CF_3$-4)$_3$)); isomer "2-up, 1-down", δ = 6.08 (s, 1.0P, 1P($C_6H_4CF_3$-4)$_3$). ^{19}F NMR ($C_6D_5CD_3$, RT), δ(ppm): isomer "3-up", δ = −63.98 (s, 39.6F, 4.4(1P($C_6H_4CF_3$-4)$_3$)), δ = −129.19 (br s, 26.4F*o*, 4.4(3SC_6F_5-*eq*)), δ = −131.88 (d, 8.8F*o*, 4.4(1SC_6F_5-*ax*), $^3J_{Fo-Fm}$ = 22.83 Hz), δ = −149.15 (t, 13.2F*p*, 4.4(3SC_6F_5-*eq*), $^3J_{Fp-Fm}$ = 20.54 Hz), δ = −160.73 (t, 4.4F*p*, 4.4(1SC_6F_5-*ax*), $^3J_{Fp-Fm}$ = 20.65 Hz), δ = −161.07 (br s, 26.4F*m*, 4.4(3SC_6F_5-*eq*)), δ = −163.40 (m, 8.8F*m*, 4.4(1SC_6F_5-*ax*)), isomer "2-up, 1-down", δ = −64.01 (s, 3F, 1P($C_6H_4CF_3$-4)$_3$), δ = −64.15 (s, 6F, 1P($C_6H_4CF_3$-4)$_3$), δ = −127.51 (d, 2F*o*, 1SC_6F_5-*eq*-"1-down", $^3J_{Fo-Fm}$ = 22.68 Hz), δ = −130.23 (br s, 2F*o*, ½(2SC_6F_5)-*eq*-"2-up"), δ = −131.08 (br s, 2F*o*′, ½(2SC_6F_5)-*eq*-"2-up"), δ = −131.71 (m, 2F*o*, 1SC_6F_5-*ax*), δ = −148.55 (t, 1F*p*, 1SC_6F_5-*eq*-"1-down", $^3J_{Fp-Fm}$ = 20.99 Hz), δ = −149.51 (t, 2F*p*, 2SC_6F_5-*eq*-"2-up", $^3J_{Fp-Fm}$ = 20.20 Hz), δ = −156.42 (t, 1F*p*, 1SC_6F_5-*ax*, $^3J_{Fp-Fm}$ = 20.73 Hz), δ = −158.85 (m, 2F*m*, 1SC_6F_5-*eq*-"1-down"), δ = −161.42 (t, 2F*m*, ½(2SC_6F_5)-*eq*-"2-up", $^3J_{Fm-F}$ = 22.34 Hz), δ = −161.86 (br s, 2F*m*′, ½(2SC_6F_5)-*eq*-"2-up"), δ = −162.86 (m, 2F*m*, 1SC_6F_5-*ax*). FAB$^+$−MS {m/z (%) [fragment]}: 1453 (2) [M^+−H], 1435 (1) [M^+−F], 1255 (100) [M^+−(SC_6F_5)], 1088 (3) [M^+−(SC_6F_5)−(C_6F_5)], 1055 (3) [M^+−2(SC_6F_5)−H], 466 (35) [P($C_6H_4CF_3$)$_3^+$], 321 (13) [P($C_6H_4CF_3$)$_2^+$].

[Os(SC_6F_5)$_3$(SC_6F_4(SC_6F_5)-2)] [12] **6**. Green (0.28 g, 24%).

4.6. [Os(SC_6F_5)$_4$(P(C_6H_5)$_3$)] **7**

[Os(SC_6F_5)$_4$(P(C_6H_5)$_3$)] **7** was prepared as reported in a previous work [7] and its X-ray diffraction structure also reported [10]. ^{31}P{^{1}H} NMR ($CDCl_3$, RT), δ(ppm): isomer "3-up", δ = 7.44 (s, 3.0P, 3(1P(C_6H_5)$_3$)); isomer "2-up, 1-down", δ = 4.88 (s, 1.0P, 1P(C_6H_5)$_3$). ^{19}F NMR ($C_6D_5CD_3$, RT), δ(ppm): isomer "3-up", δ = −129.26 (br s, 18F*o*, 3(3SC_6F_5-*eq*)), δ = −132.13 (d, 6F*o*, 3(1SC_6F_5-*ax*), $^3J_{Fo-Fm}$ = 19.18 Hz), δ = −151.08 (t, 9F*p*, 3(3SC_6F_5-*eq*), $^3J_{Fp-Fm}$ = 20.69 Hz), δ = −162.30 (br s, 18F*m*, 3(3SC_6F_5-*eq*)) δ = −162.46 (t, 3F*p*, 3(1SC_6F_5-*ax*), $^3J_{Fp-Fm}$ = 20.69 Hz), δ = −164.50 (m, 6F*m*, 3(1SC_6F_5-*ax*)), isomer "2-up, 1-down", δ = −127.24 (d, 2F*o*, 1SC_6F_5-*eq*-"1-down", $^3J_{Fo-Fm}$ = 21.82 Hz), δ = −130.24 (br s, 2F*o*, ½(2SC_6F_5)-*eq*-"2-up"), δ = −131.20 (br s, 2F*o*′, ½(2SC_6F_5)-*eq*-"2-up"), δ = −131.80 (br s, 2F*o*, 1SC_6F_5-*ax*), δ = −151.26 (t, 1F*p*, 1SC_6F_5-*eq*-"1-down", $^3J_{Fp-Fm}$ = 21.82 Hz), δ = −151.44 (t, 2F*p*, 2SC_6F_5-*eq*-"2-up", $^3J_{Fp-Fm}$ = 20.69 Hz), δ = −158.06 (t, 1F*p*, 1SC_6F_5-*ax*, $^3J_{Fp-Fm}$ = 20.69 Hz), δ = −160.32 (m, 2F*m*, 1SC_6F_5-*eq*-"1-down"), δ = −162.62 (t, 2F*m*, ½(2SC_6F_5)-*eq*-"2-up", $^3J_{Fm-F}$ = 23.32 Hz), δ = −163.05 (br s, 2F*m*′, ½(2SC_6F_5)-*eq*-"2-up"), δ = −163.84 (m, 2F*m*, 1SC_6F_5-*ax*).

4.7. X-ray diffraction data

X-ray diffraction data for complexes **1a–5a** were measured on single crystals at 296(1) K, using a Bruker P4 diffractometer [26]. Data were corrected for absorption effects on the basis of ψ-scans (**1a–2a**) or crystal faces indexation (**3a–5a**). Essential X-ray data are given in Table 1, and details may be found in the deposited CIF, along with full geometric parameters. The structures were solved and refined using SHELXS97 and SHELXL97 software [27]. For **3a**, Wilson's statistics are in agreement with a non-centrosymmetric space group, and systematic extinction expected for a 2_1 axis is not observed, allowing to rule out space groups *P*2/*n* and *P*2$_1$/*n*. A refinement in space group *Pn* including 654 measured Friedel pairs (R_1 = 0.037) indicated a degree of twinning by inversion for the crystal. The fractional contribution of the inverted model was then refined, converging to *x* = 0.72(1) and R_1 = 0.025. For **5a**, each CF_3 groups of the phosphane ligand is disordered over two sites, by a rotation of *ca.* 60° about the C–CF_3 σ-bond. Site occupation factors for disordered F atoms were fixed to 1/2. In order to get a sensible geometry, C–F bond lengths were restrained to 1.31(1) Å and F...F separations within each disordered part were restrained to 2.09(2) Å. For disordered F atoms in each CF_3 group, U_{ij} displacement parameters were restrained to be similar with standard deviation of 0.04 Å^2, and to approximate to isotropic behavior. Complex **5a** crystallizes as a monohydrate, the lattice water molecule being disordered over two sites with occupancies 1/2. Drawings of Figs. 1 and 2 were made using the Mercury program [22].

Supplementary data

CCDC 716480, 716481, 716482, 716483, 716484 contains the supplementary crystallographic data for **1a–5a**. These data can be obtained free of charge via http://www.ccdc.cam.ac.uk/conts/retrieving.html, or from the Cambridge Crystallographic Data Centre, 12 Union Road, Cambridge CB2 1EZ, UK; fax: (+44) 1223-336-033; or e-mail: deposit@ccdc.cam.ac.uk.

Acknowledgments

We are grateful to CONACYT (27915E) and VIEP (ARCS-NAT-08-G) for financial support. SB acknowledges BUAP for the use of diffraction facilities.

References

[1] S.A. Koch, M. Millar, J. Am. Chem. Soc. 105 (1983) 3362.
[2] A.R. Rossi, R. Hoffmann, Inorg. Chem. 14 (1975) 365.
[3] M.M. Millar, T. O'Sullivan, N. de Vries, S.A. Koch, J. Am. Chem. Soc. 107 (1985) 3714.
[4] S.-L. Soong, J.H. Hain Jr., M. Millar, S.A. Koch, Organometallics 7 (1988) 556.
[5] S.P. Satsangee, J.H. Hain Jr., P.T. Cooper, S.A. Koch, Inorg. Chem. 31 (1992) 5160.

[6] A. Hills, D.L. Hughes, R.L. Richards, M. Arroyo, D. Cruz-Garritz, H. Torrens, J. Chem. Soc., Dalton Trans. (1991) 1281.
[7] M. Arroyo, J.A. Chamizo, D.L. Hughes, R.L. Richards, P. Román, P. Sosa, H. Torrens, J. Chem. Soc., Dalton Trans. (1994) 1819.
[8] M.-L. Abasq, C.J. Pickett, R.L. Richards, M. Arroyo, J.A. Chamizo, A. Calderón, P. Sosa, H. Torrens, Polyhedron 15 (1996) 3623.
[9] M. Arroyo, C. Mendoza, E. Mayoral, H. Torrens, R.L. Richards, Rev. Mex. Fís. 46 S2 (2000) 120.
[10] C. Mendoza, S. Bernès, M. Arroyo, Acta Crystallogr., Sect. C 62 (2006) m201.
[11] M. Cerón, M. Arroyo, S. Bernès, Acta Crystallogr., Sect. E 62 (2006) m2167.
[12] M. Arroyo, S. Bernès, M. Cerón, V. Cortina, C. Mendoza, H. Torrens, Inorg. Chem. 46 (2007) 4857.
[13] C.J. Bourgeois, H. Huang, R.B. Larichev, L.N. Zakharov, A.L. Rheingold, R.P. Hughes, Organometallics 26 (2007) 264.
[14] L.R. Falvello, J. Forniés, C. Fortuño, A. Martín, A.P. Martínez-Sariñena, Organometallics 16 (1997) 5849.
[15] M.C. Carrión, A. Guerrero, F.A. Jalón, B.R. Manzano, A. de La Hoz, Inorg. Chem. 42 (2003) 885.
[16] M. Arroyo, S. Bernès, J.L. Briansó, E. Mayoral, R.L. Richards, J. Rius, H. Torrens, J. Organomet. Chem. 599 (2000) 170.
[17] J. Forniés, M.A. Gómez-Saso, A. Martín, F. Martínez, B. Menjón, J. Navarrete, Organometallics 16 (1997) 6024.
[18] A. Gelling, M.D. Olsen, K.G. Orrell, A.G. Osborne, V. Sik, Inorg. Chim. Acta 264 (1997) 257.
[19] J.A. Casares, S. Coco, P. Espinet, Y.-S. Lin, Organometallics 14 (1995) 3058.
[20] W.A.W.A. Bakar, J.L. Davidson, W.E. Lindsell, K.J.W. McCullough, J. Chem. Soc., Dalton Trans. (1990) 61.
[21] W.A.W.A. Bakar, J.L. Davidson, W.E. Lindsell, K.J. McCullough, K.W. Muir, J. Chem. Soc., Dalton Trans. (1989) 991.
[22] C.F. Macrae, P.R. Edgington, P. McCabe, E. Pidcock, G.P. Shields, R. Taylor, M. Towler, J. van de Streek, J. Appl. Cryst. 39 (2006) 453.
[23] H.D. Flack, Helv. Chim. Acta 86 (2003) 905.
[24] A. Bertrán-Vila, J. García-Alejandre, E. Martin, P. Sosa, H. Torrens, Rev. Soc. Quím. Méx. 37 (4) (1993) 185.
[25] A. Bertrán-Vila, J. García-Alejandre, E. Martin, P. Sosa, H. Torrens, Chem. Abstr. 122 (1993) 329084j.
[26] XSCAnS (release 2.21) Users Manual, Siemens Analytical X-ray Instruments Inc., Madison, WI, USA, 1996.
[27] G.M. Sheldrick, Acta Crystallogr., Sect. A 64 (2008) 112.

Polyhedron 28 (2009) 2635–2640

Contents lists available at ScienceDirect

Polyhedron

journal homepage: www.elsevier.com/locate/poly

Zinc azaphthalocyanines with pyridin-3-yloxy peripheral substituents

Eva H. Mørkved [a,*], Trygve Andreassen [b], Per Bruheim [b]

[a] Norwegian University of Science and Technology, Department of Chemistry, N-7491 Trondheim, Norway
[b] Norwegian University of Science and Technology, Department of Biotechnology, N-7491 Trondheim, Norway

ARTICLE INFO

Article history:
Received 29 April 2009
Accepted 20 May 2009
Available online 21 June 2009

Keywords:
Zinc azaphthalocyanine
Tetrapyrazinoporphyrazine
Pyridin-3-yloxy
Dichlorobis(quinoline-N)zinc(II)

ABSTRACT

Phthalocyanines (Pc), which are peripherally substituted with pyridin-3-yloxy groups, have shown promise as sensitizers for photodynamic cancer therapy (PDT). Some aza-analogues (AzaPc) are reported here. Four monomers were synthesized, i.e. 5,6-di(pyridin-3-yloxy)pyrazine-2,3-dicarbonitrile, and three pyrazine-2,3-dicarbonitriles, substituted with pyridin-3-yloxy- in combination with H, Me and Ph groups. Cyclotetramerizations of these monomers with the reagent $Zn(quinoline)_2Cl_2$ yielded the targeted ZnAzaPcs in 20–40% yields.

The cyclotetramerizations were accompanied, and apparently initiated, by complexation between zinc(II) and the pyridin-3-yloxy groups attached to the pyrazine-dicarbonitriles. Two such zinc(II) complexes were isolated and characterized. Identifications of all new substances were primarily based on NMR spectra, where the pulse techniques COSY, NOESY, HSQC and HMBC were applied. Molecular ions of the ZnAzaPcs were determined by mass spectrometry (MALDI-TOF). The UV–Vis spectra of these macrocycles were as expected, with Q-band absorptions at 630–650 nm and molar extinction coefficients, ε, 70 000–100 000. Eight peripheral pyridin-3-yloxy groups induced a small blue shift of the Q-band, from 636 nm for unsubstituted ZnAzaPc, to 630 nm, whereas a red shifted Q-band at 650 nm resulted from the combination of phenyl and pyridin-3-yloxy substituents. Improved solubilities were observed for the unsymmetrical ZnAzaPcs compared to octa(pyridin-3-yloxy)ZnAzaPc.

© 2009 Elsevier Ltd. All rights reserved.

1. Introduction

Zinc phthalocyanines, ZnPc, with peripheral pyridin-3-yloxy substituents have been investigated previously and were found to be promising sensitizers for photodynamic therapy (PDT); by Wöhrle et al. [1–3] some years ago, and more recently by Vicente et al. [4]. Efficient PDT requires sensitizers with good solubility in polar solvents, strong UV–Vis Q-band absorption in the vicinity of 700 nm, and the ability to induce high production of singlet oxygen. The Q-bands of tetrapyrazinoporphyrazines, or azaphthalocyanines (AzaPc), are found at shorter wavelengths than for Pc, due to the increased number of nitrogen atoms in the macrocyclic skeleton. However, this may be compensated by introducing peripheral substituents, such as thien-2-yl or *t*-butylsulfanyl, which induce substantially red shifted AzaPc Q-bands [5–7]. The singlet oxygen quantum yields (Φ_Δ) for ZnAzaPcs are subject to similar variations, i.e. the lowest value ($\Phi_\Delta = 0.487$) was found for unsubstituted ZnAzaPc, and the highest value ($\Phi_\Delta = 0.672$) was found for tetra(*t*-butylsulfanyl)-tetra(thien-2-yl)ZnAzaPc [7].

The first aim of the present study is exploration of methods for the synthesis of octa(pyridin-3-yloxy)ZnAzaPc. An expected challenge for this cyclotetramerization is the known replacement of aryloxy substituents on pyrazine-dicarbonitriles by strong nucleophiles [8,9]. Consequently, the classical Linstead synthesis will not be suitable since metal alkoxides are used to induce cyclotetramerizations by this method.

Syntheses of similar ZnAzaPcs, substituted with pyridin-3-yloxy groups in combination with H, Me or Ph groups are expected to give a more detailed picture of this type of macrocycles. Characteristics of the ZnAzaPcs may indicate potential applications of these or similar compounds.

2. Experimental

2.1. Materials and methods

Electron impact (EI) mass spectra, or electron spray ionization (ESI) mass spectra were obtained of compounds **2**–**5** on a Finnigan MAT 95XL spectrometer, at 70 eV electron energy and 1.0 mA electron current for EI, and in positive mode for ESI on an Agilent 6210 Time of flight instrument, with MeOH + H_2O + AcOH/cap230 °C/3 kV. MALDI-TOF mass spectra of compounds **8** and **9** were recorded on a Bruker Ultraflex III MALDI-TOF-TOF mass spectrometer operated in TOF mode. Each sample was dissolved in pyridine, diluted with methanol (10× the volume of pyridine), spotted onto the target plate, airdried at ambient temperature and covered with the matrix solution which consisted of α-cyano-4-hydroxycin-

* Corresponding author. Tel.: +47 97 10 39 26; fax: +47 73 59 42 56.
E-mail address: eva.morkved@chem.ntnu.no (E.H. Mørkved).

0277-5387/$ - see front matter © 2009 Elsevier Ltd. All rights reserved.
doi:10.1016/j.poly.2009.05.060

namic acid, acetonitrile and trifluoroacetic acid. IR spectra were obtained on a Thermo Nicolet Nexus FT-IR spectrometer with a Smart Endurance reflexion cell. ^{1}H and ^{13}C NMR spectra were recorded on a Bruker Avance DPX 400 NMR spectrometer or on a Bruker Avance Digital 600 NMR spectrometer at 100.4, 399.65 or 600.18 MHz, respectively. Chemical shifts are given relative to internal tetramethyl silane (TMS) when $CDCl_3$ was used as solvent. Chemical shifts are calibrated relative to the DMSO signal at 2.50 ppm for ^{1}H, and 39.51 ppm for ^{13}C when DMSO-d_6 was used as solvent. The NMR pulse techniques COSY, NOESY, HSQC and HMBC were used to correlate ^{1}H and ^{13}C NMR signals for all new compounds. UV–Vis spectra were recorded on a Cary 50 UV–Vis spectrophotometer. Melting points were obtained on a Büchi 530 melting point apparatus and are uncorrected. Merck Kieselgel 60F 254 was used for thin layer chromatography (TLC) and Merck silica 63–200 μm was used for column chromatography. 3-Hydroxypyridine was obtained from Janssen Chimica. 5,6-Dichloropyrazine-2,3-dicarbonitrile, (**1**), was obtained as in [8,10], 5-chloropyrazine-2,3-dicarbonitrile (**3a**), as in [11], 5-chloro-6-methylpyrazine-2,3-dicarbonitrile (**3b**), and 5-chloro-6-phenylpyrazine-2,3-dicarbonitile (**3c**), were obtained as in [12].

2.2. Synthesis

2.2.1. Compounds **2**, **4a–c** and **5**

*2.2.1.1. General procedure for the synthesis of compounds **2** and **4**.* Triethylamine (4.3 mmol) was added dropwise to a stirred solution of **1** (2 mmol) and 3-hydroxypyridine (4.2 mmol) in acetone (20 ml), and the reaction mixture was stirred at ambient temperature for 4 h to give **2**. Stirred solutions of **3a–c** (2 mmol) and 3-hydroxypyridine (2.2 mmol) were treated dropwise with triethylamine (2.3 mmol) and were stirred at ambient temperature for 1 h to give **4a–c**. Triethylammonium chloride, which separated from all the reaction mixtures, was removed by filtration. The products **2**, **4a** and **4c** were chromatographed on silica with acetone, compound **4b** was eluted from a silica column with a 1:1 mixture of acetone and DCM.

*2.2.1.2. 5,6-Di(pyridin-3-yloxy)pyrazine-2,3-dicarbonitrile (**2**).* Yield of tan powder, 0.53 g (84%), m.p. 185–186 °C. ESIMS: *m/z* (% rel. int.) 300 (23.6), 316 (M, 100), 317 (M+1, 18.5). *Anal.* Calc. for $C_{16}H_9N_6O_2$: (M+H$^+$) 317.07812. Found: 317.0782. UV–Vis (DCM): λ_{max}, nm (ε, $M^{-1}\,cm^{-1}$) 275 (20 000). IR: ν, cm^{-1} 3070 (*CH* aromatic, w) 2239 (*CN*, w), 1543, 1440 (s), 1424 (s), 1358, 1232 (s), 1210, 1183, 1097, 1027, 951 (w), 925 (w), 852 (w), 833 (w), 799. ^{1}H NMR ($CDCl_3$): δ, ppm *pyridine*: 7.50 (2H, *H5*, dd, $J_{5,4}$ = 8.4 Hz, $J_{5,6}$ = 4.7 Hz), 7.67 (2H, *H4*, ddd, $J_{4,5}$ = 8.4 Hz, $J_{4,2}$ = 2.8 Hz, $J_{4,6}$ = 1.3 Hz), 8.63 (2H, *H2*, app. d, $J_{2,4}$ = 2.8 Hz), 8.66 (2H, *H6*, app.d, $J_{6,5}$ = 4.7 Hz). ^{13}C NMR ($CDCl_3$): δ, ppm 112.2 (*CN*), 124.3 (pyrazine *C2,C3*), 124.5 (pyridine *C5*), 129.0 (pyridine *C4*), 143.0 (pyridine *C2*), 147.9 (pyridine *C3*), 148.4 (pyridine *C6*), 150.7 (pyrazine *C5,C6*).

*2.2.1.3. 5-(Pyridin-3-yloxy)pyrazine-2,3-dicarbonitrile (**4a**).* Yield of tan powder, 0.37 g (83%), m.p. 103–104 °C. EIMS: *m/z* (% rel. int.). *Anal.* Calc. for $C_{11}H_5N_5O$: 223.04886. Found: 223.04862. UV–Vis (DCM): λ_{max}, nm (ε, $M^{-1}\,cm^{-1}$) 255 (17 000). IR: ν, cm^{-1} 3067 (*CH*, aromatic, w), 2244 (*CN*, w), 1556, 1528, 1426, 1361, 1338, 1205, 1187, 1107, 1023, 814, 702. ^{1}H NMR ($CDCl_3$): δ, ppm *pyridine:* 7.47 (1H, *H5*, ddd, $J_{5,4}$ = 8.4 Hz, $J_{5,6}$ = 4.7 Hz, $J_{5,2}$ = 0.8 Hz), 7.58 (1H, *H4*, ddd, $J_{4,5}$ = 8.4 Hz, $J_{4,2}$ = 2.8 Hz, $J_{4,6}$ = 1.4 Hz), 8.55 (1H, *H2*, dd, $J_{2,4}$ = 2.8 Hz, $J_{2,5}$ = 0.7 Hz), 8.64 (1H, *H6*, dd, $J_{6,5}$ = 4.7 Hz, $J_{6,4}$ = 1.5 Hz), *pyrazine:* 8.77 (1H, *H6* s). ^{13}C NMR ($CDCl_3$): δ, ppm 112.1, 112.7 (*CN* at pyrazine C2 and C3), 124.5 (pyridine *C5*), 127.5 (pyrazine *C2*), 128.8 (pyridine *C4*), 130.8 (pyrazine *C3*), 140.3 (pyrazine *C6*), 143.0 (pyridine *C2*), 147.8 (pyridine *C3*), 148.3 (pyridine C6), 159.2 (pyrazine *C5*).

*2.2.1.4. 5-(Pyridin-3-yloxy)-6-methylpyrazine-2,3-dicarbonitrile (**4b**).* Yield of a white powder, 0.36 g (77%), m.p. 127 °C. EIMS: *m/z* (% rel. int.) 209 (47.9), 222 (16.6), 223 (18.1), 237 (M, 100), 238 (13.6). *Anal.* Calc. for $C_{12}H_7N_5O$: 237.06451. Found: 237.06562. UV–Vis (DCM): λ_{max}, nm (ε, $M^{-1}\,cm^{-1}$) 265 (15 500). IR: ν, cm^{-1} 2239 (*CN*, w), 1544, 1477, 1387, 1215, 1190, 1098, 1022, 801, 710. ^{1}H NMR ($CDCl_3$): δ, ppm 2.83 (3H, CH_3, s), *pyridine:* 7.46 (1H, *H5*, ddd, $J_{5,4}$ = 8.4 Hz, $J_{5,6}$ = 4.7 Hz, $J_{5,2}$ = 0.8 Hz), 7.56 (1H, *H4*, ddd, $J_{4,5}$ = 8.4 Hz, $J_{4,2}$ = 2.8 Hz, $J_{4,6}$ = 1.4 Hz), 8.52 (1H, *H2*, dd, $J_{2,4}$ = 2.8 Hz, $J_{2,5}$ = 0.8 Hz), 8.62 (1H, *H6*, dd, $J_{6,5}$ = 4.7 Hz, $J_{6,4}$ = 1.4 Hz). ^{13}C NMR ($CDCl_3$): δ, ppm 20.1 (CH_3), 112.4, 113.0 (*CN* at pyrazine C2 and C3), 124.4 (pyridine *C5*), 126.7 (pyrazine *C3*), 128.3 (pyrazine *C2*), 129.1 (pyridine *C4*), 143.2 (pyridine *C2*), 148.06 (pyridine *C3*), 148.11 (pyridine *C6*), 151.7 (pyrazine *C6*), 158.0 (pyrazine *C5*).

*2.2.1.5. 5-(Pyridin-3-yloxy)-6-phenylpyrazine-2,3-dicarbonitrile (**4c**).* Yield of a white powder, 0.53 g (89%), m.p. 170–171 °C. EIMS: *m/z* (% rel. int.) 270 (100), 299 (M, 75), 300 (M+1, 12.4). *Anal.* Calc. for $C_{17}H_9N_5O$: 299.08071. Found: 299.00433. UV–Vis (DCM): λ_{max}, nm (ε, $M^{-1}\,cm^{-1}$) 340 (16 400), 300 (13 300). IR: ν, cm^{-1} 3050 (*CH*, aromatic, w), 2237 (*CN*, w), 1522, 1474, 1379, 1324, 1231, 1182, 1019, 839, 806, 765, 701, 685. ^{1}H NMR ($CDCl_3$): δ, ppm 7.48 (1H, pyridine *H5*, ddd, $J_{5,4}$ = 8.4 Hz, $J_{5,6}$ = 4.7, $J_{5,2}$ = 0.8 Hz), 7.59 (3H, overlap pyridine *H4* and phenyl *H3, H5*, m), 7.63 (1H, phenyl *H4*, m), 8.28 (2H, phenyl *H2, H6*, m), 8.55 (1H, pyridine *H2*, dd, $J_{2,4}$ = 2.8 Hz, $J_{2,5}$ = 0.8 Hz), 8.64 (1H, pyridine *H6*, dd, $J_{6,5}$ = 4.7 Hz, $J_{6,4}$ = 1.4 Hz). ^{13}C NMR ($CDCl_3$): δ, ppm 112.5 and 113.0 (*CN* at pyrazine *C2, C3*), 124.5 (pyridine *C5*), 127.3 and 127.6 (pyrazine *C2, C3*), 129.1 (phenyl *C3, C5*), 129.3 (pyridine *C4*), 130.1 (phenyl *C2, C6*), 131.8 (phenyl *C1*), 132.7 (phenyl *C4*), 143.3 (pyridine *C2*), 148.0 (pyrazine *C6*),148.1 (pyridine *C3*), 148.2 (pyridine *C6*), 156.9 (pyrazine *C5*).

*2.2.1.6. 5-(Propyl-1-oxy)pyrazine-2,3-dicarbonitrile (**5**).* A solution of **3a** (2 mmol, 0.33 g) in 1-propanol (15 ml) was heated under reflux for 144 h. The solvent was removed under reduced pressure, and the liquid residue was chromatographed on silica with DCM. A colourless oil, which crystallized upon cooling to −16 °C, was isolated by filtration with hexane. Yield 0.3 g (81%), m.p. 41–42 °C. EIMS: *m/z* (% rel. int.) 147 (93.5), 188 (M, 16.5). *Anal.* Calc. for $C_9H_8N_4O$: 188.0698. Found: 188.0701. ^{1}H NMR ($CDCl_3$): δ, ppm 1.07 (3H, t, $J_{3,2}$ = 7.4 Hz), 1.88 (2H, qt, $J_{2,3}$ = 7.4 Hz, $J_{2,1}$ = 6.7 Hz), 4.45 (2H, t, $J_{1,2}$ = 6.7 Hz), 8.45 (1H, s). ^{13}C NMR ($CDCl_3$): δ, ppm 10.3 (CH_3), 21.7 (CH_2), 71.0 (CH_2O), 112.9 (*CN* at pyrazine C2), 113.3 (*CN* at pyrazine C3), 125.1 (pyrazine *C2*), 131.2 (pyrazine *C3*), 140.7 (pyrazine *C6*), 160.4 (pyrazine *C5*).

*2.2.1.7. Reaction of **4a** with 1-propanol.* A solution of **4a** (1 mmol, 0.23 g) in 1-propanol (10 ml) was heated under reflux for 19 h. The solvent was removed under reduced pressure, and the liquid residue was chromatographed on silica. Compound **5** (0.2 mmol, 38 mg) was eluted from the column with DCM and was obtained as a white solid, m.p. 37–39 °C. TLC on silica gave R_f (DCM) = 0.55, as for compound **5** which had been obtained from **4a** and 1-propanol. A tan solid was eluted from the column with acetone and was isolated by filtration with diethyl ether and hexane. Yield 0.167 g (75%), m.p. 87–92 °C. TLC R_f (acetone) = 0.82, the same as for compound and **4a**.

2.2.2. Compounds **6** and **7**

2.2.2.1. Dichlorobis(quinoline-N)zinc(II) (Scheme 2). This compound, also referred to as Zn(quinoline)$_2$Cl$_2$, was prepared as in [13]. ^{1}H NMR (DMSO-d_6): δ, ppm 7.54 (2H, *H3*, dd, $J_{3,4}$ = 8.3 Hz, $J_{3,2}$ = 4.2 Hz), 7.61 (2H, *H6*, ddd, $J_{6,5}$ = 8.2 Hz, $J_{6,7}$ = 6.9 Hz, $J_{6,8}$ = 1.2 Hz), 7.77 (2H, *H7*, ddd, $J_{7,8}$ = 8.5 Hz, $J_{7,6}$ = 6.9 Hz, $J_{7,5}$ = 1.5 Hz), 7.99 (2H, *H5*, ddd, $J_{5,6}$ = 8.2 Hz, $J_{5,7}$ = 1.5 Hz, $J_{5,8}$ = 0.6 Hz), 8.04 (2H, *H8*,

dddd, $J_{8,7}$ = 8.5 Hz, $J_{8,6}$ = 1.2 Hz, $J_{8,4}$ = 0.9 Hz, $J_{8,5}$ = 0.6 Hz), 8.38 (2H, *H4*, ddd, $J_{4,3}$ = 8.3 Hz, $J_{4,2}$ = 1.8 Hz, $J_{4,8}$ = 0.9 Hz), 8.92 (2H, *H2*, dd, $J_{2,3}$ = 4.2 Hz, $J_{2,4}$ = 1.8 Hz). ^{13}C NMR (DMSO-d_6): δ, ppm 121.5 (*C3*), 126.6 (*C6*), 127.9 (*C10*), 128.1 (*C5*), 128.8 (*C8*), 129.5 (*C7*), 136.1 (*C4*), 147.6 (*C9*), 150.6 (*C2*)

2.2.2.2. Dichlorobis(pyridine-N)zinc(II) (Scheme 2). The crude product from a reaction of **4a** with excess Zn(quinoline)$_2$Cl$_2$ was sonicated with pyridine, which subsequently was removed under reduced pressure. The methanol extract from this reaction mixture gave some crystals, which were identified as dichlorobis(pyridine-N)zinc(II), apparently formed by an exchange of quinoline in dichlorobis(quinoline-N)zinc(II) with pyridine. M.p. 201–204 °C.

^{1}H NMR (DMSO-d_6): δ, ppm 7.41 (4H, m, *H3, H5*), 7.82 (2H, m, *H4*), 8.58 (4H, m, *H2, H6*). ^{13}C NMR (DMSO-d_6): δ, ppm 124.0 (*C3, C5*), 136.4 (*C4*), 149.5 (*C2, C6*).

*2.2.2.3. 5,6-Di(pyridin-3-yloxy)pyrazine-2,3-dicarbonitrile[ZnCl$_2$] complex (**6**).* A stirred mixture of **2** (0.6 mmol, 190 mg), Zn(quinoline)$_2$Cl$_2$ (0.5 mmol, 197 mg) and quinoline (0.3 ml) was flushed with nitrogen for 10 min, then heated at 175–180 °C for 20 min and cooled to ambient temperature. The dark reaction mixture was rinsed with diethyl ether, stirred with methanol (10 ml) for 30 min and then with acetone (15 ml) for 30 min. A pale gray–green solid was isolated by filtration. Yield 153 mg (56% for $C_{16}H_8N_6O_2ZnCl_2$, M = 452), m.p. ca. 345 °C decomp. UV–Vis (pyridine): 0.03 mg/ml: Trace of absorption at 630 nm, too strong absorption for measuring at 300 nm. IR: ν, cm^{-1} 3070 (*CH*, aromatic, w), 2240 (*CN*, w), 1614 (w), 1545, 1435 (s), 1361 (w), 1276 (w), 1236 (s), 1192 (w), 1104 (w), 1054, 1036 (w), 949 (w), 926 (w), 869 (w), 807, 692, 645, 618 (w). ^{1}H NMR (DMSO-d_6): δ, ppm 7.64 (2H, *H5*, dd, $J_{5,4}$ = 8.4 Hz, $J_{5,6}$ = 4.7 Hz), 7.89 (2H, *H4*, ddd, $J_{4,5}$ = 8.4 Hz, $J_{4,2}$ = 2.8 Hz, $J_{4,6}$ = 1.3 Hz), 8.62 (2H, *H6*, dd, $J_{6,5}$ = 4.7 Hz, $J_{6,4}$ = 1,2 Hz), 8.67 (2H, *H2*, d, $J_{2,4}$ = 2.7 Hz). ^{13}C NMR (DMSO-d_6): δ, ppm 113.5 (*CN*), 123.5 (pyrazine *C2, C3*), 125.1 (pyridine *C5*), 129.6 (pyridine *C4*), 142.9 (pyridine *C2*), 147.9 (pyridine *C6*), 148.2 (pyridine *C3*), 151.7 (pyrazine *C5, C6*).

Neither ^{1}H nor ^{13}C NMR signals, characteristic of quinoline, were found for this compound.

*2.2.2.4. 5-(Pyridin-3-yloxy)-6-methylpyrazine-2,3-dicarbonitrile[Zn (quinoline)Cl$_2$]complex (**7**).* Compound **4b** (0.84 mmol, 200 mg) and Zn(quinoline)$_2$Cl$_2$ (0.8 mmol, 315 mg) were ground together in a mortar, transferred to a round-bottomed flask, flushed with nitrogen, stirred and heated at 155 °C for 10 min. The dark solid was rinsed with diethyl ether, stirred with methanol (10 ml) for 24 h, and a dark solid, 175 mg, was isolated by filtration and rinsed with acetone on the filter. This solid was stirred with THF (15 ml) for 30 min, and a dark solid, 77 mg, was isolated by filtration. UV–Vis (pyridine): λ_{max}, nm (ε, M^{-1} cm^{-1}) 635 (66 000), 575 (19 000), 365 (55 000). A pale green solid, 90 mg, m.p. 217–221 °C (green melt) was obtained from the THF filtrate upon evaporation and trituration with a small amount of methanol.Yield of compound **7** ($C_{21}H_{14}N_6OZnCl_2$, M = 502), is ca. 20%. IR: ν, cm^{-1} 2238 (*CN*, w), 1541 (w), 1509 (w), 1480 (w), 1439 (w), 1395 (s), 1315, 1223, 133, 1101, 1052, 945, 823 (s), 788, 689 (s), 646 (w). ^{1}H NMR (DMSO-d_6): δ, ppm 2.72 (3H, C*H*$_3$, s), *pyridine:* 7.60 (1H, *H5*, ddd, $J_{5,4}$ = 8.4 Hz, $J_{5,6}$ = 4.7 Hz, $J_{5,2}$ = 0.8 Hz), 7.80 (1H, *H4*, ddd, $J_{4,5}$ = 8.4 Hz, $J_{4,2}$ = 2.8 Hz, $J_{4,6}$ = 1.4 Hz), 8.58 (1H, *H6*, dd, $J_{6,5}$ = 4.9 Hz, $J_{6,4}$ = 1.4 Hz), 8.59 (1H, *H2*, dd, $J_{2,4}$ = 2.7 Hz, $J_{2,5}$ = 0.7 Hz), *quinoline:* 7.54 (1H, *H3*, dd, $J_{3,4}$ = 8.3 Hz, $J_{3,2}$ = 4.2 Hz), 7.62 (1H, *H6,* ddd, $J_{6,5}$ = 8.1 Hz, $J_{6,7}$ = 6.9 Hz, $J_{6,8}$ = 1.3 Hz), 7.77 (1H, *H7*, ddd, $J_{7,8}$ = 8.4 Hz, $J_{7,6}$ = 6.9 Hz, $J_{7,5}$ = 1.5 Hz), 7.99 (1H, *H5*, ddd, $J_{5,6}$ = 8.2 Hz, $J_{5,7}$ = 1.5 Hz, $J_{5,8}$ = 0.6 Hz), 8.03 (1H, *H8*, dddd, $J_{8,7}$ = 8.4 Hz, $J_{8,6}$ = 1.3 Hz, $J_{8,4}$ = 0.9 Hz, $J_{8,5}$ = 0.6 Hz), 8.37 (1H, *H4*, ddd, $J_{4,3}$ = 8.3 Hz, $J_{4,2}$ = 1.8 Hz, $J_{4,8}$ = 0.9 Hz), 8.91 (1H, *H2*, dd, $J_{2,3}$ = 4.2 Hz, $J_{2,4}$ = 1.8 Hz). ^{13}C NMR (DMSO-d_6): δ, ppm 20.0 (C*H*$_3$), 113.6 (*CN*), 114.1 (*CN*), 125.7 (pyrazine *C3*),128.0 (pyrazine *C2*), 152.3 (pyrazine *C6*), 158.4 (pyrazine *C5*), 124.9 (pyridine *C5*), 129.61 (pyridine *C4*), 143.1 (pyridine *C2*), 147.6 (pyridine *C6*), 148.5 (pyridine *C3*), *quinoline*: 121.5 (*C3*), 126.6 (*C6*), 128.0 (*C10*), 128.1 (*C5*), 128.9 (*C8*), 129.59 (*C7*), 136.1 (*C4*), 147.7 (*C9*), 150.6 (*C2*).

*2.2.3. Compounds **8** and **9a–c***

*2.2.3.1. General procedure for the synthesis of compounds **8** and **9a–c**.* Compound **2** or **4** (1.0 mmol) and Zn(quinoline)$_2$Cl$_2$ (1.2 mmol) were ground in a mortar and transferred to a round-bottomed flask. The stirred reaction mixtures were flushed with nitrogen for 15 min at ambient temperature, then heated under nitrogen at 190–195 °C for 2.5 h (compound **2**) and at 170–175 °C for 1 h (compounds **4a–c**). The dark solids were rinsed with diethyl ether, stirred for 30 min at ambient temperature with methanol (25 ml), and then with THF (30 ml). Sonication of the solids with pyridine (10 ml), removal of the pyridine under reduced pressure, sonication with methanol (10 ml) and filtration, gave dark solids which were washed with acetone and THF. Compounds **8**, **9a** and **9c** were applied to silica columns with DMF:THF (1:1) and eluted with DMF:THF (1:10) and gradually increasing ratios of DMF until most colored material had been eluted. Compound **9b** was chromatographed on silica with pyridine. The solvents were removed under reduced pressure, diethyl ether was added to the dark solids, which were isolated by filtration and rinsed with acetone on the filter. The products were finally dried at 0.1 mm Hg for 3 h.

*2.2.3.2. [Octa(pyridin-3-yloxy)-(octazaphthalocyaninato)]zinc(II) (**8**).* Yield of a black solid 0.07 g (20%). UV–Vis (pyridine): λ_{max}, nm (ε, M^{-1} cm^{-1}) 630 (81 000), 575 (19 000), 375 (70 000), 315 (sh, 90 000). ^{1}H NMR (DMSO-d_6): δ, ppm *pyridine*: 7.86 (8H, *H5,* dd, $J_{5,4}$ = 8.2 Hz, $J_{5,6}$ = 4.9 Hz), 8.27 (8H, *H4,* ddd, $J_{4,5}$ = 8.2 Hz, $J_{4,2}$ = 3.0 Hz, $J_{4,6}$ = 1.3 Hz), 8.98 (8H, *H2*, m), 8.98 (8H, *H6*, m). ^{13}C NMR (DMSO-d_6): δ, ppm 124.9 (pyridine *C5*), 130.6 (pyridine *C4*), 142.0, 143.8 (pyridine *C2*), 147.5 (pyridine *C6*), 148.9, 149.4 (pyridine *C3*), 151.5 (probably pyrazine *C5, C6*). MS (MALDI-TOF) *m/z* 1329.168 [M+H$^+$]. *Anal.* Calc. for $C_{64}H_{32}N_{24}O_8Zn$: 1328.21 (M), $C_{64}H_{33}N_{24}O_8Zn$: 1329.21 (M+H$^+$). The expected isotopic pattern for zinc was found at *m/z* (calcd.% rel. int.) 1329.168 (100), 1330.168 (81), 1331.168 (91), 1332.168 (65), 1333.168 (67), 1334.168 (40), 1335.173 (16).

*2.2.3.3. [Tetra(pyridin-3-yloxy)-(octazaphthalocyaninato)]zinc(II) (**9a**).* Yield of a black shiny powder 0.053 g (22%). UV–Vis (pyridine): λ_{max}, nm (ε, M^{-1} cm^{-1}) 635 (91 000), 580 (20 000), 365 (66 000), 315 (sh, 69 000). ^{1}H NMR (DMSO-d_6): δ, ppm 9.4–9.3 (pyrazine *H6*), 9.1–8.9 (pyridine *H2*), 8.95–8.75 (pyridine *H6*), 8.6–8.3 (pyridine *H4*), 7.9–7.7 (pyridine *H5*). ^{13}C NMR (DMSO-d_6): δ, ppm 125–126 (pyridine *C5*), 129–130 (pyridine *C4*), 137–138 (pyrazine *C6*), 142–143 (pyridine *C2*), 146–147 (pyridine *C6*). MS (MALDI-TOF) *m/z* 957.104 [M+H$^+$]. *Anal.* Calc. for $C_{44}H_{20}N_{20}O_4Zn$: 956.13 (M), for $C_{44}H_{21}N_{20}O_4Zn$: 957.13 (M+H$^+$). The expected isotopic pattern for zinc was found at *m/z* (calcd.% rel. int.) 957.104 (100), 958.107 (57), 959.107 (74), 960.108 (44), 961.109 (54), 962.111 (25).

*2.2.3.4. [Tetra(pyridin-3-yloxy)-tetramethyl(octazaphthalocyaninato)]zinc(II) (**9b**).* Yield of a dark, blue/purple powder 0.1 g (39%). UV–Vis (pyridine): λ_{max}, nm (ε, M^{-1} cm^{-1}) 635 (122 000), 575 (27 000), 365 (91 000), 315 (sh, 91 200) (see Fig. 1). UV–Vis (DMSO): λ_{max}, nm (ε, M^{-1} cm^{-1}) 635 (70 000), 575 (18 000), 360 (53 000). ^{1}H NMR (DMSO-d_6): δ, ppm 3.3–3.0 (C*H*$_3$), 7.85–7.5 (pyridine *H5*),

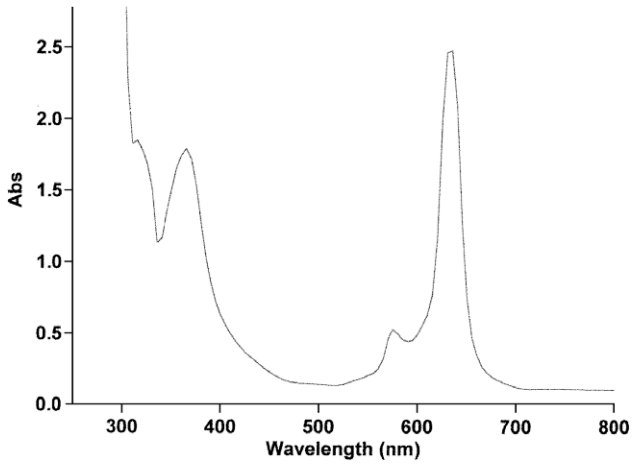


Fig. 1. UV–Vis absorption spectrum of compound **9b** dissolved in pyridine, concentration 0.002 mg/ml pyridine (3.55×10^{-5} M). Blue–green solution.

8.55–8.25 (pyridine *H4*), 8.95–8.75 (pyridine *H6*), 9.1–8.85 (pyridine *H2*). ^{13}C NMR (DMSO-d_6): δ, ppm 20–21 (CH_3), 124–125 (pyridine *C5)*, 129–130 (pyridine *C4*), 142–144 (pyridine *C2*), 146–147 (pyridine *C6*). MS (MALDI-TOF) *m/z* 1013.151 [M+H$^+$]. *Anal.* Calc. for $C_{48}H_{28}N_{20}O_4Zn$: 1012.19 (M), for $C_{48}H_{29}N_{20}O_4Zn$: 1013.19 (M+H$^+$). The expected isotopic pattern for zinc was found at *m/z* (calcd.% rel. int.) 1013.151 (100), 1014.151 (61), 1015.15 (77), 1016.153 (48), 1017.153 (56), 1018.159 (28).

*2.2.3.5. [Tetra(pyridin-3-yloxy)-tetraphenyl-(octazaphthalocyaninato)]zinc(II) (**9c**).* Yield of a dark blue powder 0.129 g, (41%). UV–Vis (pyridine): λ_{max}, nm (ε, $M^{-1}\,cm^{-1}$) 650 (101 000), 590 (25 000), 375 (94 000), 315 (sh, 97 000). ^{1}H NMR (DMSO-d_6): δ, ppm *phenyl*: 7.77 (*H4*), 7.78 (*H3,H5*), 8.58 (*H2, H6*), *pyridine*: 7.71 (*H5*), 8.39 (*H4*), 8.88 (*H2*), 8.90 (*H6*). All signals were broad, and no coupling constants could be determined. ^{13}C NMR (DMSO-d_6): δ, ppm *phenyl*: 128.4 (*C3, C5*), 130.0 (*C2, C6*), 130.1 (*C4*), *pyridine*: 124.5 (*C5*), 129.9 (*C4*), 143.1 (*C2*), 146.7 (*C6*). MS (MALDI-TOF) *m/z* 1261.260 [M+H$^+$]. *Anal.* Calc. for $C_{68}H_{36}N_{20}O_4Zn$: 1260.25 (M), for $C_{68}H_{37}N_{20}O_4Zn$: 1261.25 (M+H$^+$). The expected isotopic pattern for zinc was found at *m/z* (calcd.% rel. int.) 1261.260 (100), 1262.260 (84), 1263.260 (93), 1264.260 (66), 1265.261 (68), 1266.261 (41).

3. Results and discussion

3.1. Synthesis and characterization

3.1.1. Monomers *2, 4* and *5*

5,6-Di(pyridin-3-yloxy)pyrazine-2,3-dicarbonitrile (**2**) was obtained in 84% yield from a reaction of 5,6-dichloropyrazine-2,3-dicarbonitrile (**1**) with 3-hydroxypyridine and triethylamine in acetone at ambient temperature. Compounds **4a–c**, namely 5-(pyridin-3-yloxy)pyrazine-2,3-dicarbonitrile (**4a**), 5-(pyridin-3-yloxy)-6-methylpyrazine-2,3-dicarbonitrile (**4b**) and 5-(pyridin-3-yloxy)-6-phenylpyrazine-2,3-dicarbonitrile (**4c**), were obtained in good yields by the same procedure (Scheme 1).

In order to reveal potential instability of pyridin-3-yloxy substituted pyrazines **2** and **4** towards nucleophiles, compound **4a** was heated under reflux with propanol for 19 h. Chromatography of the product mixture separated unreacted **4a** (75%) from the reaction product 5-(1-propyloxy)pyrazine-2,3-dicarbonitrile (**5**), (20%). This product is identical to an authentic sample of **5** which was obtained from **3a** and 1-propanol (Scheme 1). Therefore, considering the weak nucleophilicity of 1-propanol compared to alkoxide ions, the use of metal alkoxides is ruled out for cyclotetramerizations of compounds **2** and **4**. This is in accordance with our previous experience with 5,6-di(phenoxy)pyrazine-2,3-dicarbonitrile [8]. Recently, the formation of a metal free AzaPc, obtained from prolonged heating in quinoline of di(aryloxy)pyrazine-2,3-dicarbonitrile, has been reported [9]. However, quinoline solutions of compounds **2** and **4** merely gave brown or black reaction mixtures after prolonged heating.

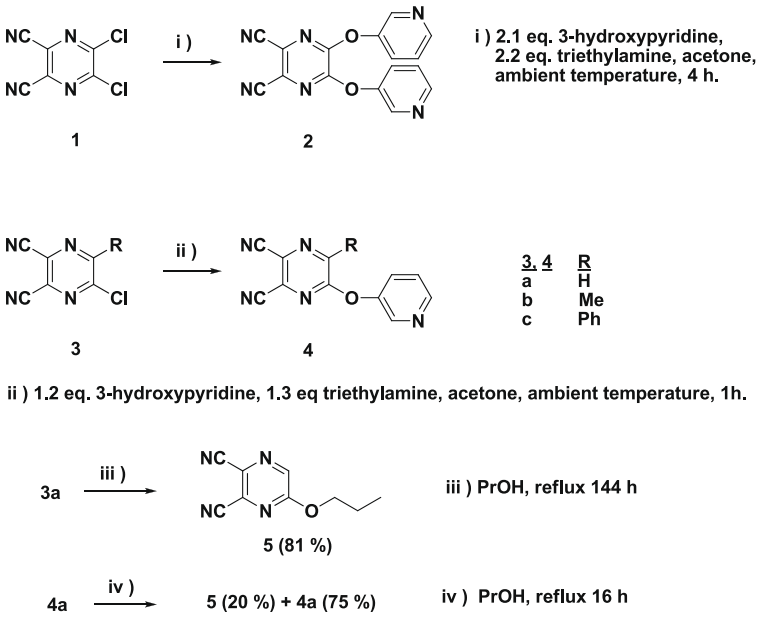
3.1.2. Reactions of compounds *2* and *4* with zinc(II) salts to form zinc complexes *6* and *7*

A known method for one-step syntheses of zinc(II) complexes of phthalocyanines and azaphthalocyanines is treatment of hot quinoline solutions of the monomers with zinc(II) acetate. This method was tested for cyclotetramerizations of compounds **2** and **4**, but resulted in extensive decomposition of these monomers.

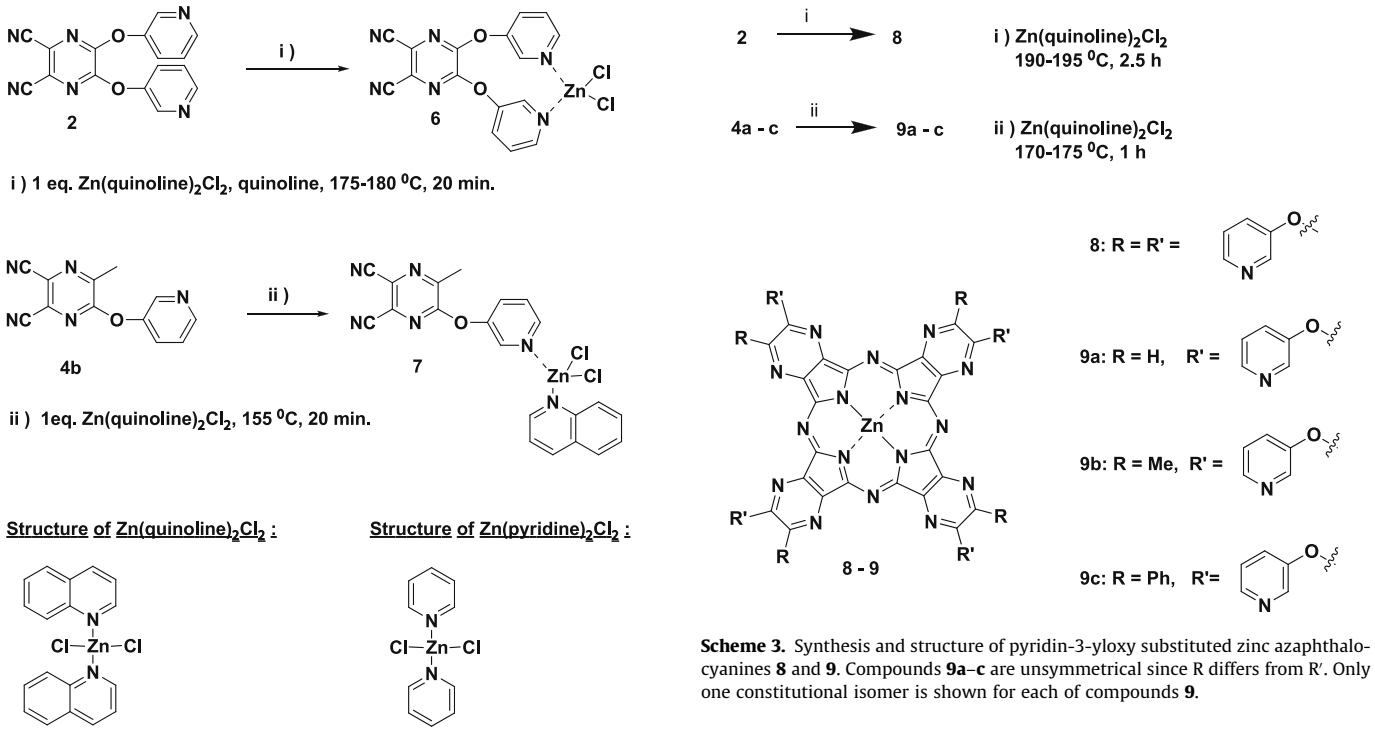
The salt Zn(quinoline)$_2$Cl$_2$, prepared from zinc(II) chloride and quinoline, has been used successfully for cyclotetramerizations of amino-substituted pyrazine-dicarbonitriles [13] and was tested in reactions with compounds **2** and **4**. At low temperatures, namely 1 h at 100 °C, or 15 min at 140 °C, no reaction was observed between equimolar amounts of Zn(quinoline)$_2$Cl$_2$ and **2**. However, a reaction at 180 °C for 20 min between a quinoline solution of **2** and 0.8 molar equivalents of Zn(quinoline)$_2$Cl$_2$ gave a pale blue–gray powder which was identified as 5,6-di(pyridin-3-yloxy)pyrazine-2,3-dicarbonitrile[ZnCl$_2$] complex (**6**). This complex is high melting and decomposes at approximately 345 °C. The suggested structure is shown in Scheme 2, together with the structure of Zn(quinoline)$_2$Cl$_2$. Identification of compound **6** is primarily based on NMR analysis, i.e. all hydrogen and carbon atoms were identified, and the integral of each hydrogen atom is in accord with structure **6**. The two cyano groups which are attached to the pyrazine ring were clearly identified as one signal at δ 113 ppm. The NMR spectra also exclude the presence of quinoline. However, the pale blue color and the UV–Vis spectrum of **6**, indicate the presence of a small amount of AzaPc **8**. Compound **6** was obtained in approximately 50% yield.

A similar reaction between equimolar amounts of **4b** and Zn(quinoline)$_2$Cl$_2$ at 155 °C for 10 min, gave 5-(pyridin-3-yloxy)-6-methylpyrazine-2,3-dicarbonitrile-[Zn(quinoline)Cl$_2$] complex (**7**) in approximately 20% yield. The structure of **7**, as shown in Scheme 2, would result from the replacement of one quinoline group of Zn(quinoline)$_2$Cl$_2$ with compound **4b**. The structure of **7** was confirmed by NMR analysis; the integrals for the methyl, pyridine and quinoline hydrogen atoms were as expected, and all the ^{1}H and ^{13}C NMR signals were accounted for and identified by the pulse techniques COSY, HSQC and HMBC.

The formations of compounds **6** and **7** strongly indicate that complexation between the pyridin-3-yloxy substituents and Zn(quinoline)$_2$Cl$_2$ is the initial reaction between this zinc complex and the monomers **2** or **4**. The electron withdrawing effect on the pyrazine moiety of **2** or **4** by zinc complexed to their pyridin-3-yloxy groups, is expected to promote the targeted cyclotetramerizations of **2** and **4**. However, purifications of these ZnAzaPcs necessarily involve destruction of the peripheral zinc-pyridin-3-yloxy complexes. These complexes will undoubtedly be weak, and excess pyridine is expected to be sufficiently nucleophilic to replace the pyridin-3-yloxy groups of these peripheral zinc complexes. A reaction of **4a** with excess Zn(quinoline)$_2$Cl$_2$ gave in fact some of the product Zn(pyridine)$_2$Cl$_2$ which has been known for many years [14,15]. The structure of Zn(pyridine)$_2$Cl$_2$ is shown in Scheme 2. We report both the NMR spectra of this compound and of Zn(quinoline)$_2$Cl$_2$ since these have not been reported earlier. The formation of Zn(pyridine)$_2$Cl$_2$ could either happen by exchange of quinoline in Zn(quinoline)$_2$Cl$_2$, or by replacement of **4a** in a complex analogous to **7**.



Scheme 1. Syntheses of pyrazine-2,3-dicarbonitriles substituted with pyridin-3-yloxy, methyl and phenyl groups.



Scheme 2. Reactions of pyrazine-2,3-dicarbonitriles **2** and **4b** with $Zn(quinoline)_2Cl_2$. Structures of $Zn(quinoline)_2Cl_2$ and $Zn(pyridine)_2Cl_2$.

Scheme 3. Synthesis and structure of pyridin-3-yloxy substituted zinc azaphthalocyanines **8** and **9**. Compounds **9a–c** are unsymmetrical since R differs from R′. Only one constitutional isomer is shown for each of compounds **9**.

3.1.3. Zinc azaphthalocyanines *8* and *9a–c*

The syntheses and structures of substituted ZnAzaPcs **8** and **9a–c** are shown in Scheme 3. Attempts to use dry zinc(II) acetate and quinoline for the synthesis of these compounds were unsuccessful; mostly dark tarry solids were obtained. Compounds **8** and **9** were prepared by dry condensations of monomers **2** or **4a–c** with $Zn(quinoline)_2Cl_2$, at 190–195 °C (compound **2**) or at 170–175 °C (compounds **4**). The peripheral complexations between the pyridin-3-yloxy substituents of monomers **2** and **4**, and $Zn(quinoline)_2Cl_2$, had to be taken into account when methods were considered for purification of macrocycles **8** and **9**. The crude products were separated from most of the unreacted zinc reagent by extraction with methanol and THF. In order to replace peripheral zinc attached to the pyridin-3-yloxy groups, the dark solids were sonicated with excess pyridine, which subsequently was removed under reduced pressure. The dark powders **8**, **9a** and **9c** were chromatographed on silica with THF mixed with DMF, whereas pyridine was used as eluent for compound **9b**. Compounds **8** and **9** were obtained in fair yields (20–40%). The symmetric monomer **2** affords only one macrocyclic isomer, namely **8**, but the monomers 4a–**c** are unsymmetric and consequently, four constitutional isomers of **9a–c** may be formed. The NMR spectra are in accordance with this, since the hydrogen signals of **8** are sharp and with well

defined coupling constants, whereas the corresponding signals of **9a–c** are broad and with unresolved splittings of the signals.

Mass spectrometry (MALDI-TOF) of compounds **8** and **9** showed the calculated molecular ions with the expected isotopic clusters characteristic of zinc. Due to low solubilities of these macrocycles, the compounds were dissolved in pyridine, diluted with methanol, then dried at ambient temperature before being covered with matrix and injected into the spectrometer.

UV–Vis spectra of unsubstituted ZnPc and ZnAzaPc show Q-bands at, respectively, 674 and 636 nm. This 38 nm blue shift for ZnAzaPc compared to ZnPc is ascribed to the additional nitrogen atoms in the AzaPc macrocycle.

Q-bands of compounds **8** and **9** are found at 630 nm (**8**), 635 nm (**9a**, **9b**) and 650 nm (**9c**). The UV–Vis spectrum of **9b** is shown in Fig. 1. Compared to unsubstituted ZnAzaPc, these data show that eight pyridin-3-yloxy groups of compound **8** induce a small blue shift (6 nm) of the Q-band, and four phenyl combined with four pyridin-3-yloxy substituents of **9c** induce a 14 nm red shift of the Q-band. These observations compare well with a reported Q-band at 645 nm for octa(aryloxy)ZnAzaPc where the peripheral substituents were bulky aryloxy groups [9]. A series of MgAzaPc substituted with alkoxy groups, has been reported as well, and the Q-bands were observed at 625 nm [8].

4. Conclusion

Peripheral pyridin-3-yloxy substituents complicate syntheses of the substituted ZnAzaPc compared to the corresponding ZnPc for several reasons. Strong nucleophiles easily replace the pyridin-3-yloxy groups attached to the starting monomers; i.e. the pyrazine-2,3-dicarbonitriles. Consequently the Linstead method for cyclotetramerization, which includes the use of metal alkoxides, must be excluded. Another known method, where diiminoimides are used as precursors for cyclotetramerizations, must be excluded as well, since the transformation of the dicarbonitriles to diiminoimides involves strong alkoxide ions.

We have found one successful direct synthesis of pyridin-3-yloxy substituted ZnAzaPc by using $Zn(quinoline)_2Cl_2$ as a reagent. However, these cyclotetramerizations are accompanied by peripheral complexation between the zinc(II) salt and the pyridin-3-yloxy substituents. Consequently purification of these ZnAzaPcs will be somewhat elaborate.

The electronic absorption spectrum of octa(pyridin-3-yloxy)ZnAzaPc, **8**, shows a Q-band which is blue shifted by 6 nm compared to unsubstituted ZnAzaPc, i.e. the pyridin-3-yloxy groups show insignificant substituent effects. The combination of phenyl and pyridin-3-yloxy substituents induce a Q-band at 650 nm, and this 14 nm red shift can be ascribed to the phenyl substituents.

The low solubility in organic solvents of ZnAzaPcs **8** and **9** combined with Q-bands far below 700 nm, make these compounds of little interest for use as sensitizers in PDT. However, the possibility of metal complexing of the peripheral pyridin-3-yloxy substituents is an interesting feature.

Acknowledgement

Lars Hagen is thanked for technical assistance with the MALDI-TOF analyses.

References

[1] D. Wöhrle, M. Eskes, K. Shigehare, A. Yamada, Synthesis (1993) 194.
[2] D. Wöhrle, N. Iskandar, G. Grashew, H. Sinn, E.A. Friedrich, W. Maier-Borst, J. Stern, P. Schlag, Photochem. Photobiol. 51 (1990) 351.
[3] U. Michelsen, H. Kliesch, G. Schnurpfeil, A.K. Sobbi, D. Wöhrle, Photochem. Photobiol. 64 (1996) 694.
[4] H. Li, T.J. Jensen, F.R. Fronczek, M.G.H. Vicente, J. Med. Chem. 51 (2008) 502.
[5] E.H. Mørkved, H. Ossletten, H. Kjøsen, J. Prakt. Chem. 342 (2000) 83.
[6] E.H. Mørkved, N.K. Afseth, P. Zimcik, J. Porphyr. Phthalocya. 11 (2007) 130.
[7] P. Zimcik, E.H. Mørkved, T. Andreassen, J. Lenco, V. Novakova, Polyhedron 27 (2008) 1368.
[8] E.H. Mørkved, H. Ossletten, H. Kjøsen, Acta Chem. Scand. 53 (1999) 1117.
[9] S. Maksheed, F. Ibrahim, C.G. Bezzu, N.B. McKeown, Tetrahedron Lett. 48 (2007) 7358.
[10] T. Suzuki, Y. Nagae, K. Mitsuhashi, J. Heterocycl. Chem. 23 (1986) 1419.
[11] A. Nakamura, T. Ataka, H. Segawa, Y. Takeuchi, T. Takematsu, Agric. Biol. Chem. 47 (1983) 1555.
[12] A. Nakamura, T. Ataka, H. Segawa, Y. Takeuchi, T. Takematsu, Agric. Biol. Chem. 47 (1983) 1561.
[13] E.H. Mørkved, N.K. Afseth, H. Kjøsen, J. Porphyr. Phthalocya. 10 (2006) 1301.
[14] D.P. Graddon, K.B. Heng, E.C. Watton, Aust. J. Chem. 19 (1966) 1801.
[15] W.L. Steffen, G.J. Palenik, Acta Crystallogr., Sect. B 32 (1976) 298.

Polyhedron 28 (2009) 2641–2648

Contents lists available at ScienceDirect

Polyhedron

journal homepage: www.elsevier.com/locate/poly

Novel coordination behavior of a pteridine-benzoylhydrazone ligand (BZLMH): Theoretical calculations, XRD structures and luminescence studies

Sonia B. Jiménez-Pulido, Fátima M. Linares-Ordóñez, Miguel N. Moreno-Carretero *

Departamento de Química Inorgánica y Orgánica, Facultad de Ciencias Experimentales, Campus Universitario "Las Lagunillas" (B3), Universidad de Jaén, 23071 Jaén, Spain

ARTICLE INFO

Article history:
Received 16 April 2009
Accepted 22 May 2009
Available online 6 June 2009

Keywords:
Crystal structure
Hydrazone
Lumazine
Pteridine
Metal complexes

ABSTRACT

The XRD structure and the influence of the conformation in the molecular orbitals of the pteridine-benzoylhydrazone ligand (BZLMH = benzoylhydrazone of 6-acetyl-1,3,7-trimethyllumazine, lumazine = (1*H*,3*H*)-pteridin-2,4-dione) have been studied. Complexes of BZLMH with nickel(II), zinc(II) and mercury(II) have been prepared and spectroscopically characterized by IR, NMR and fluorescence spectroscopy; also XRD studies have allowed to establish two different coordinative patterns in the complexes $[Ni_3(BZLMH)_3(OH)(H_2O)(CH_3CN)_2](ClO_4)_5 \cdot 2H_2O \cdot CH_3CN$ (**2**) and $[Zn(NO_3)(BZLMH)(H_2O)](NO_3)$ (**3**). Compound (**2**) is a trinuclear hydroxo-centered complex with a central hydroxo group bridging the three nickel(II) ions. The $[Ni_3(\mu_3\text{-}OH)]^{5+}$ core is planar with the benzoylhydrazone ligands coordinated in the bis-bidentate [O(4),N(5)]-[N(61),O(63)] mode. The zinc(II) compound displays a BPT coordination geometry in which the BZLMH ligand acts in a tridentate fashion using N(5), N(61) and O(63) donor atoms. Fluorescence spectroscopic properties of benzoylhydrazone (BZLMH) are studied and the fluorescence band shift and changes in intensity is modulated by complexation with different metal ions (Ni^{2+}, Zn^{2+} and Hg^{2+}), so the binding is signaled such a possible cause.

© 2009 Elsevier Ltd. All rights reserved.

1. Introduction

The metallochemistry of biomolecules has been largely focused on proteins amino acids, nucleic acids and carbohydrates [1–4]. In this setting, small coenzymes have received less recognition as ligands for metal centers; a lot of work in this area has consideration given to the chemistry and biological role of pteridines and underlying heterocyclic structures of coenzymatic constituents (pterins, lumazines, flavins) of some enzymes [5]. On the other hand, heterocyclic hydrazones constitute an important class of biologically active drugs which have attracted attention of medicinal chemists due to their wide ranging pharmacological properties like antifungal, antibacterial and anticonvulsant compounds [6–9], their metallochemistry being interesting since it is generally agreed that the complexes of some *3d* elements play an important role in biochemistry [10].

The correct choice of the ligands is fundamental due the properties of biological active molecules can be tailored to very specific conversions according to an appropriate design of them. To aid the rationally-based design, interesting general concepts have been developed. One of the most important is the ligand flexibility required for some reactions, whereas in other reactions higher selectivities and activities are obtained with more rigid ligand systems.

Once the N5–O4 coordination chemistry of unfunctionalized lumazines was extensively reported [11–13], we tried to expand it to polydentate behaviors by anchoring in the pyrazine ring substituents with both biological interest and coordination abilities. In this way, more versatile ligands such as a 6-acetyllumazine (DLMAceM) [14], its thiosemicarbazone derived ligand TSCLMH [15] and several lumazine 6-substituted azines [16] have been used, thus reporting new polydentate coordination behaviors including tri-, tetra- and doubly bidentate ones- quite different from the usual N5–O4 bidentate ligand-to-metal bonding found in metal-lumazine complexes. Furthermore, the ligand design has been extended introducing in the pyrazine ring the benzoylhydrazone substituent; this versatile branch, together with the pteridine one, allows a wide set of bonding-to-metal modes including from monodentate to polydentate bridging, the biological activities of many of these compounds being related to their metal chelating abilities [17]. Thus, in a previous paper [18], good results about both tri- and tetradentate behaviors of the hybrid benzoylhydrazone-pteridine ligand (BZLMH) has been already reported.

Here, the XRD structure of the BZLMH hybrid ligand is studied, this compound being into our knowledge the first reported hydrazone-derived from a pteridine moiety. Also, *ab initio* MO calculations have been carried out to characterize from the theoretical point of view the potential ligand-to-metal binding sites. Furthermore, some Ni(II), Zn(II) and Hg(II) complexes have been isolated and studied in order to establish the coordination behavior of BZLMH, in which the four available donors atoms (O4, N5, N61,

* Corresponding author. Tel.: +34 953212738; fax: +34 953211876.
E-mail address: mmoreno@ujaen.es (M.N. Moreno-Carretero).

0277-5387/$ - see front matter © 2009 Elsevier Ltd. All rights reserved.
doi:10.1016/j.poly.2009.05.061

O63) make it possible for the ligand to be bidentate, tridentate, tetradentate or doubly bidentate.

We have also focused this work to the study of luminescent properties of BZLMH ligand and above-described complexes because the luminescence of lumazine and benzoylhydrazone ligands are very well-known [15,19–25] and have been widely used to obtain fluorescent sensors. To place of rigid chromophoric framework in the ligand with a π-conjugation system can be an efficient method for obtaining new luminescent materials. In this work, we have tested the luminescent properties of the ligand BZLMH and related compounds, as well as the sensibility of the fluorescence to the presence of Ni(II), Zn(II) and Hg(II) ions.

2. Experimental

2.1. Materials and instrumentation

The pro-ligand 6-acetyl-1,3,7-trimethyllumazine was obtained according to the literature methods [26]; then, the multifunctional ligand BZLMH was synthesized as previously described [18]. Other starting compounds such as benzohydrazide, $Ni(ClO_4)_2 \cdot 6H_2O$, $Zn(NO_3)_2 \cdot 6H_2O$, $Hg(NO_3)_2 \cdot H_2O$ and $Hg(ClO_4)_2 \cdot 3H_2O$ are commercially available and reagent grade acetonitrile, ethanol and methanol were used without purification. Microanalyses were carried out with a Thermo Finnigan Flash EA 1112. The IR spectra were recorded between 4000 and 400 cm^{-1} using KBr pellets on a Perkin–Elmer 1760 FT-IR. The solution ^1H, ^{13}C NMR spectra and ^1H–^{15}N HMBC were recorded from DMSO-d_6 solution on Bruker Avance 400 and 500 spectrometers. The chemical shifts were referenced to residual solvent resonance external TMS in the ^1H and ^{13}C spectra and nitromethane in the ^1H–^{15}N HMBC. The mass spectra were performed on a Hewlett–Packard HP 5989GC/LC/MS apparatus. The UV-Vis spectra were recorded between 1200 and 250 nm with solid samples on a Perkin–Elmer Lambda 19, while fluorescence spectra were measured using a Varian Cary Eclipse machines.

2.2. Synthesis of complexes

Caution! Perchlorate salts are potentially explosive and should only be used in small quantities and handled with the necessary precautions.

2.2.1. $Ni(BZLMH)_2(ClO_4)_2 \cdot 3H_2O$ (**1**)

$Ni(ClO_4)_2 \cdot 6H_2O$ (183 mg, 0.5 mmol) and acetonitrile (10 mL) were put into a flask and stirred. BZLMH (183 mg, 0.5 mmol) solved in acetonitrile (15 mL) was added in one portion and the reaction mixture was stirred at 50 °C for 3 h. After that, we isolated a greenish powdered material (yield 30-35%).

Anal. Calc. for $C_{36}H_{42}N_{12}O_{17}Cl_2Ni$: C, 41.4; H, 4.1; N, 16.1. Found: C, 41.0; H, 4.3; N, 16.2; M, 1077.4. Main IR peaks (KBr, cm^{-1}): 3445 (ν(N–H), w), 1721, 1669 (ν(C=O). m, vs), 1621 ($\nu(C{=}N)_{azom}$, vs), 1553 (ν(C=N), m), 1459, 1292 (ν(C=C) + ν(C–N), m). UV–Vis [solid, λ (nm)]: 9500; 13700; 21300.

The slow evaporation for several weeks of resulting solution afforded a too small quantity of green crystals of $[Ni_3(BZLMH)_3(OH)(H_2O)(CH_3CN)_2](ClO_4)_5 \cdot 2H_2O \cdot CH_3CN$ (**2**); so, only XRD, IR and elemental analysis were performed. *Anal.* Calc. for $C_{60}H_{70}N_{21}O_{33}Cl_5Ni_3$: C, 36.6; H, 3.6; N, 14.9. Found: C, 36.1; H, 3.3; N, 14.5; M, 1965.6. Main IR peaks (KBr, cm^{-1}): 3402 (ν(N–H), w), 1730, 1641 (ν(CO), m, vs), 1614 ($\nu(C{=}N)_{azom}$, vs), 1560 (ν(C=N), s), 1465, 1296 (ν(C=C) + ν(C–N), m), 1022 (ν(N–N), w).

2.2.2. $[Zn(NO_3)(BZLMH)(H_2O)](NO_3)$ (**3**)

Compound **3** was prepared by similar reported method adding the BZLMH (183 mg, 0.5 mmol) ligand solved in acetonitrile to the $Zn(NO_3)_2 \cdot 6H_2O$ (149 mg, 0.5 mmol) solution in the same solvent. Orange crystals of this compound, suitable for X-ray diffraction, were grown at room temperature by diffusion of acetone into their acetonitrile solution (yield 55–60%).

Anal. Calc. for $C_{18}H_{20}N_8O_{10}Zn$: C, 37.7; H, 3.5; N, 19.5. Found: C, 37.3; H, 3.9; N, 19.4; M, 573.8. Main IR peaks (KBr, cm^{-1}): 3440, 3220 (ν(N–H), w), 1722, 1673 (ν(C=O), w, m), 1566 (ν(C=N), w), 1471, 1295 (ν(C=C) + ν(C–N), m), 1000 (ν(N–N), w). ^1H NMR data (δ, ppm, DMSO-d_6): 1.1 (12H, s, Me_4Si), 2.1 (3H, s, C(61)Me), 2.5 (3H, s, C(7)Me), 2.9 (3H, s, N(3)Me), 3.5 (3H, s, N(1)Me), 7.5 (2H, m, Ph), 7.9 (3H, m, Ph), 10.9 (1H, s, NH). ^{13}C NMR data (δ, ppm, DMSO-d_6): 14.8 (s, C(62)), 25.5 (s, C(71)), 28.4 (s, C(3)), 28.8 (s, C(1)), 123.9 (s, C(4A)), 128.1–131.5 (s, C_{arom}), 133.6 (s, C(6)), 144.8 (s, C(61)), 145.8 (s, C(1A)), 150.6 (s, C(2)), 157.1 (s, C(7)), 159.5 (s, C(4)). ^1H–^{15}N HMBC data (δ, ppm, DMSO-d_6): 120.1 (N(1)), 155.5 (N(3)), 170.2 (N(61)), 325.1 (N(5), N(8)), 365.1 ($MeNO_2$).

2.2.3. $Hg(NO_3)_2(BZLMH)$ (**4**)

To a stirred methanolic solution of BZLMH ligand (183 mg, 0.5 mmol) was added a solution of $Hg(NO_3)_2 \cdot H_2O$ (171 mg, 0.5 mmol) in methanol (10 mL) and the resulting yellow solution was stirred for 3 h. For this time a precipitated yellow compound was obtained (yield 55–60%).

Anal. Calc. for $C_{18}H_{18}N_8O_9Hg$: C, 31.3; H, 2.7; N, 16.2. Found: C, 31.1; H, 2.7; N, 16.0; M, 690.9. Main IR peaks (KBr, cm^{-1}): 3774, 3439 (ν(N–H), w), 1722, 1661 (ν(C=O), m, s), 1556 (ν(C=N), m), 1462, 1270 (ν(C=C) + ν(C–N), m), 1013 (ν(N–N), w). ^1H NMR data (δ, ppm, DMSO-d_6): 1.1 (12H, s, Me_4Si), 2.6 (3H, s, C(61)Me), 2.8 (3H, s, C(7)Me), 3.3 (3H, s, N(3)Me), 3.6 (3H, s, N(1)Me), 7.6 (2H, m, Ph), 7.9 (3H, m, Ph), 11.5 (1H, s, NH). ^{13}C NMR data (δ, ppm, DMSO-d_6): 15.3 (s, C(62)), 25.3 (s, C(71)), 28.5 (s, C(3)), 29.0 (s, C(1)), 123.7 (s, C(4A)), 127.6–131.9 (s, C_{arom}), 132.9 (s, C(6)), 144.5 (s, C(61)), 146.1 (s, C(1A)), 150.5 (s, C(2)), 158.0 (s, C(7)), 159.5 (s, C(4)), 199.0 (s, C(63)). ^1H–^{15}N HMBC data (δ, ppm, DMSO-d_6): 155.2 (N(3)), 300.2 (N(61)), 365.1 ($MeNO_2$).

2.2.4. $Hg(ClO_4)(BZLM)(BZLMH)$ (**5**)

A solution of BZLMH (183 mg, 0.5 mmol) in ethanol was added to a suspension of $Hg(ClO_4)_2 \cdot 3H_2O$ (227 mg, 0.5 mmol) in ethanol (10 mL). The mixture was stirred and heated for 3-4 h until the color of the solution turned to yellow and a precipitated compound was obtained (yield 25–30%).

Anal. Calc. for $C_{36}H_{35}N_{12}O_{10}ClHg$: C, 41.9; H, 3.4; N, 16.3. Found: C, 41.9; H, 3.4; N, 15.9; M, 1031.8. Main IR peaks (KBr, cm^{-1}): 3456 (ν(N–H), w), 1722, 1667 (ν(C=O), m, s), 1555 (ν(C=N), m), 1503, 1268 (ν(C=C) + ν(C–N), m). ^1H NMR data (δ, ppm, DMSO-d_6): 1.1 (12H, s, Me_4Si), 2.5 (3H, s, C(61)Me), 2.9 (3H, s, C(7)Me), 3.3 (3H, s, N(3)Me), 3.6 (3H, s, N(1)Me), 7.5 (2H, m, Ph), 7.9 (3H, m, Ph), 11.1 (1H, s, NH). ^{13}C NMR data (δ, ppm, DMSO-d_6): 14.9 (s, C(62)), 25.5 (s, C(71)), 28.4 (s, C(3)), 28.9 (s, C(1)), 123.8 (s, C(4A)), 127.5–131.7 (s, C_{arom}), 133.4 (s, C(6)), 144.7 (s, C(61)), 145.9 (s, C(1A)), 150.6 (s, C(2)), 157.2 (s, C(7)), 159.5 (s, C(4)), 166.5 (s, C(63)). ^1H–^{15}N HMBC data (δ, ppm, DMSO-d_6): 23.1 (N(1)), 155.4 (N(3)), 170.3 (N(61)), 295.3 (N(5), N(8)), 365.1 ($MeNO_2$).

2.3. XRD experimental details

Details of the crystallographic data collection and refinement parameters are given in Table 1. For compound $[Ni_3(BZLMH)_3(OH)(H_2O)(CH_3CN)_2](ClO_4)_5 \cdot 2H_2O \cdot CH_3CN$ (**2**), the perchlorate anions are disordered over two positions with a relative occupancy of 0.5. The CIF files have been deposited at the Cambridge Crystallographic Data Center and allocated the deposition numbers CCDC 650849, 650850, 650851.

Table 1
Crystal and structure refinement data.

	BZLMH	Compound **2**	Compound **3**
Empirical formula	$C_{18}H_{18}N_6O_3$	$Ni_3C_{60}H_{70}N_{21}O_{33}Cl_5$	$ZnC_{18}H_{20}N_8O_{10}$
Formula weight	366.24	1965.60	573.79
T (K)	293(2)	293(2)	290(3)
λ (Mo Kα) (Å)	0.71073	0.71073	0.71073
Crystal system	monoclinic	triclinic	monoclinic
Space group	$P2_1/c$	$P\bar{1}$	$P2_1/n$
a (Å)	12.670(1)	12.5456(1)	7.09(3)
b (Å)	8.3800(4)	15.5620(7)	18.100(1)
c (Å)	16.481(1)	21.0850(2)	16.961(8)
α (°)	90	88.722(6)	90
β (°)	97.675(7)	88.744(1)	91.160(1)
γ (°)	90	77.243(1)	90
Volume, (Å^3)	1734.2(2)	4013.3(2)	2177.0(1)
Z	4	2	4
D_x (Mg/m^3)	1.403	1.628	1.742
μ (mm^{-1})	0.100	0.963	1.205
F(0 0 0)	1384	2020	1164
Crystal size (mm)	1.51 × 1.15 × 0.31	0.35 × 0.20 × 0.15	0.26 × 0.14 × 0.10
Reflections collected (R_{int})	3605 (0.0359)	42801 (0.0578)	27797 (0.1819)
Goodness of fitness (Gof) on F^2	1.058	1.042	0.994
R_1/wR_2 ($I > 2\sigma(I)$)	0.0486/0.1541	0.0720/0.2126	0.0758/0.2055

The data were collected on a Nonius Kappa CCD diffractometer (graphite-monocromated Mo Kα radiation psi-scan technique, λ = 0.71073 Å) at room temperature. Empirical absorption correction (SADABS [27]) was applied. The structures were solved by SIR-04, expanded by Fourier-difference syntheses and refined with SHELXL-97, incorporated in WINGX 1.64 crystallographic collective package [28,29]. All non-hydrogen atoms were refined with anisotropic thermal parameters by full matrix least-squares procedures on F^2. Hydrogen atoms from methyl groups were placed in idealized positions, and treated using riding models; N–H hydrogens were found from difference map and refined isotropically. Graphics were obtained with PLATON [30].

2.4. Computational methods

Theoretical calculations were carried out on benzoylhydrazone of 6-acetyl-1,3,7-trimethyllumazine (BZLMH) by using *ab initio* methods with GAUSSIAN03 program package [31], as described previously [15].

3. Results and discussion

3.1. Ligand characterization: X-ray diffraction study and ab initio calculations

The significant IR bands of this ligand are close to those found in related compounds with lumazine and hydrazone derivatives. It exhibits a ν(N–H) in the 3222–3204 cm^{-1} region. The vibrational activity of carbonyl groups appears as two different bands located at 1698 and 1655 cm^{-1}, being the first one, weaker, being mainly due to ν(C(2)=O) whereas the second one it must be assigned to ν(C(4)=O) [14,15,32]. We also can observe a broad corresponding to the ν(C(63)=O) [32] (*ca.* 1708 cm^{-1}). The absorption bands located at 1603 cm^{-1} in the IR spectra of BZLMH are attributed to ν(C=N$_{azom}$) and the band at 1551 cm^{-1} for this organic ligand is assignable to ν(C=N) of pteridine ring. The infrared bands for ν(C=C) + ν(C–N) vibrations are located at 1451 and 1292 cm^{-1} [33,34].

In the ^{1}H NMR spectrum of BZLMH in DMSO-d$_6$ the *ortho* protons of benzenic framework show a broad signal at 7.9 ppm due to coupling with the remaining hydrogens of the ring. The hydrogens at *meta* and *para* positions appear being a multiplet (*ca.* 7.55 ppm) due to the strong coupling. The ^{13}C NMR and the ^{1}H–^{13}C NMR spectra allow us assign unequivocally the carbon signals of the ligand. In the ^{1}H–^{15}N NMR spectrum, we observed three different signals for the N(1), N(3) and N(62) nitrogens at 120, 155 and 295 ppm correlate with the hydrogen methyl groups C(1), C(3) and C(62), respectively, and a fourth broad signal for both N(5) and N(8) nitrogens atoms at 325 ppm, which could be explained by the similar environment in the pyrazine ring.

UV–Vis experiments for BZLMH showed three bands at 243, 282 and 341 nm assignable to $\pi \rightarrow \pi^*$ transitions [35] at pH of the ligand (pH 5.13). This experiment was also carried out at different pH values to obtain information about the ligand deprotonation, but not with extreme values of pH because the hydrolysis of hydrazone ligand takes place, possibly for the break of azometinic bond. To pH values between 3 and 4 we can observe some changes which we can assign to the possible behavior like a base of hydrazonic N(62).

The structure of BZLMH was also resolved by X-ray diffraction and included at this work for an unambiguous characterization (Fig. 1). The pteridine fragment shows similar geometry for other lumazine ligands, so pyrimidine and pyrazine rings are roughly planar with dihedral angle 1.39(9)°. On the other hand, the angle between the pteridine and the plane defined by the side chain in six position is 14°. The pteridine skeleton displays a C(2)=O(2) bond (1.213(2) Å) shorter than the C(4)=O(4) one (1.224(2) Å), as it is usual for related 2,6-dioxo heterocycles [36–41]. The rings are virtually planar, with average torsion angles of 1.4° and 1.5° (pteridine rings) and 1.6° (benzene ring). The benzene ring is angled by 41.7(1)° with the pteridine ring. The bonds distances near the donor atoms suggest the electronic delocalization in the chain C=N-NH-CO showing N(61)–N(62) (1.377 Å) and N(62)-C(63) (1.379 Å) bonds shorter than those expected for a single bond; this fact suggests the delocalization of the N(62) electron lone pair to the adjacent atoms. The bonds C(61)-N(61), N(61)–N(62) *y* N(62)–C(63) adopt the *EEZ* conformation.

The BZLMH molecules are packed *via* hydrogen bond resulting in helicoidal chains following the *b* axis through intermolecular interactions between the N(62)–H and oxygen atom of carbonylic group of pteridine in four position (N(62)–H(62)···O(4) (−*x*, ½ + *y*, ½−*z*)) [*d*(N(62)–O(4)) = 3.091(2) Å and (N(62)-H(62)···O(4)) = 173(2)°]). This arrangement is favoured by π-stacking interactions between the benzene ring and the pyrazine and pyrimidine rings of

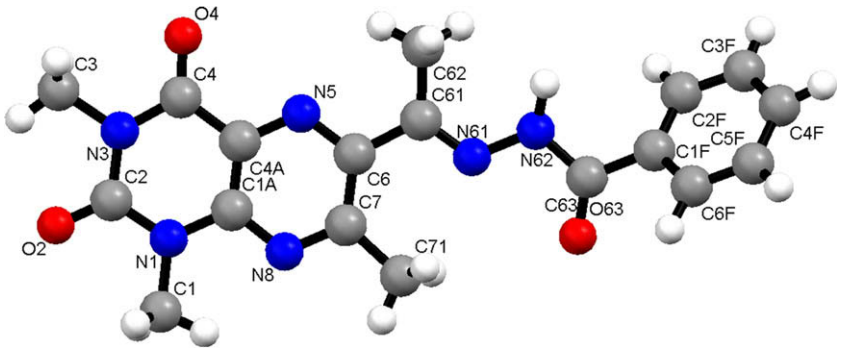


Fig. 1. The molecular structure for benzoylhydrazone of 6-acetyl-1,3,7-trimethyllumazine (BZLMH). Selected bond lengths/Å: O(63)–C(63) 1.211(3), O(2)–C(2) 1.213(2), O(4)–C(4) 1.224(2), C(6)–C(61) 1.491(3), N(61)–C(61) 1.277(3), N(61)–N(62) 1.377(2), N(62)–C(63) 1.379(3)). Selected bond angles/°: O(4)–C(4)–C(4A) 124.3(2), O(4)–C(4)–N(3) 121.2(2), N(61)–C(61)–C(6) 115.6(2), C(61)–N(61)–N(62) 119.7(2), N(61)–C(61)–C(62) 125.7(2), C(62)–C(61)–C(6) 118.7(2), N(61)–N(62)–C(63) 115.2(2), O(63)–C(63)–N(62) 122.6(2), N(62)–C(63)–C(1F) 115.4(2), O(63)–C(63)–C(1F) 122.0(2).

neighbouring molecules [42]. Data for these interactions are given in Table 2.

To elucidate the nature of the frontier orbitals in the BZLMH molecule, MO *ab inito* calculations were performed using two different optimized conformations *a* (C7–C6–C61–N61 torsion = 0.5°) and *b* (C7-C6-C61–N61 torsion = 180°) simulating the structural arrangements displayed in the metal-free and the complexed forms, respectively. The B3LYP/6-31G* MO results for BZLMH molecule (Table 3) shows the greater contributions to the HOMO (σ) are those from N(62) and N(61) atoms. Moreover, the HOMO-1 for both conformations is mainly localized over the carbonylic O(4) and (N8) atoms; finally, depending on the conformation *a* or *b*, this MO also exhibits contribution for carbonylic oxygen atom O(63) (*a* conformation) and N(5) atom (*b* conformation). The HOMO-2 seems to be mainly located over the carbonylic O(63) in both conformations. Also the LUMO's description is very similar, this fact being related with the structural similarity between them and the absence of electrons in this molecular orbital. With respect to the π-coordination, the data of Table 3 indicate this molecule can act in some extent as π-acceptor through the N(5) and N(8) atoms in *b* conformation. Therefore, we might state this ligand could show until four different coordinative behaviors: bidentate, tridentate, tetradentate or doubly bidentate ligand, through the O(4), N(5), N(61) and O(63) sites.

Accordingly, we have assembled the coordination capacity of hydrazone branch with that of the lumazine derivative, making available to the metal ligation two additional coordination sites (N(61) and O(63)) which could replace and/or extend the chelate properties of the original pterine ligand (N(5) and O4)). Thus, we have reacted BZLMH ligand with different metallic salts $Ni(ClO_4)_2 \cdot 6H_2O$, $Zn(NO_3)_2 \cdot 6H_2O$, $Hg(NO_3)_2 \cdot H_2O$ and $Hg(ClO_4)_2 \cdot 3H_2O$ in equimolar quantities, obtaining, as crystalline solids, the trinuclear green $[Ni_3(BZLMH)_3(OH)(H_2O)(CH_3CN)_2](ClO_4)_5 \cdot 2H_2O \cdot CH_3CN$ and the mononuclear orange $[Zn(NO_3)(BZLMH)(H_2O)](NO_3)$ compounds, in order to explore its coordination chemistry with particular emphasis on probing its possible binding modes.

Table 2
Intermolecular π-stacking parameters for BZLMH and $[Zn(NO_3)(BZLMH)(H_2O)](NO_3)$ (**3**).

Stacking parameters[a]	BZLMH	Zn-complex
	pyrimidine (c_1)–benzene (c_2)	
Av $d(\pi\text{-}\pi)$ Å	3.31	
$D(c_1\text{–}c_2)$ Å/α °	3.63/7.8	
$D(_\perp c_1\text{–}P_2)$ Å/β °	3.28/23.1	
$D(_\perp c_2\text{–}P_1)$ Å/γ °	3.33/25.1	
	pyrazine (c_1)–benzene (c_2)	
Av $d(\pi\text{-}\pi)$ Å	3.42	3.46
$D(c_1\text{–}c_2)$ Å/α °	3.60/6.5	3.64/4.4
$D(_\perp c_1\text{–}P_2)$ Å/β °	3.48/21.4	3.43/16.5
$D(_\perp c_2\text{–}P_1)$ Å/γ °	3.35/15.3	3.49/19.5

[a] c_i: Centroids of rings involved in π-interactions; P_i: Plane from c_i; α: angle between planes of both centroids; β and γ: slipping angles between the centroid–centroid vector and the normal to each stacked ring plane.

3.2. Crystallographic studies

3.2.1. Crystal structure of $[Ni_3(BZLMH)_3(OH)(H_2O)(CH_3CN)_2](ClO_4)_5 \cdot 2H_2O \cdot CH_3CN$ (**2**)

The structure of trinuclear nickel(II) compound (**2**) is given in Fig. 2. Selected bond distances and angles for (2) are listed in Table 4. This structure consists of a trinuclear hydroxo-centered nickel(II) complex. The three Ni(II) ions form an equilateral triangle with Ni–Ni distances at around 3.66 Å; the Ni-$O_{hydroxo}$ bond distances are about 2.15 Å and the angles are in the range 59.54–60.36°. The $[Ni_3(\mu_3\text{-}OH)]^{5+}$ core moiety is a strongly flattened tetrahedron being the $O_{hydroxo}$ atom 0.35 Å out of the plane formed by the metallic atoms. The Ni(II) centers show an octahedral environment, where each BZLMH molecule acts as doubly bidentate ligand binding to a nickel atom through O(4) and N(5) atoms and to another one by imine nitrogen atom (N(61)) and the benzoyl oxygen atom (O(63)). The Ni(1) and Ni(2) ions complete their coordination spheres with central $O_{hydroxo}$ and a acetonitrile molecule N-bonded to the metal, while Ni(3) ion bonds to $O_{hydroxo}$ and a water molecule (Fig. 3). The chelate rings Ni–O4–C4–C4A–N5 and Ni–N61–N62–C63–O63 show *trans* disposition, being angled by 20° to each other in the three octahedrons. Pteridine moieties are almost planar and they form angles of 4.7°, 5.2° and 3.9° with their chelates rings M–O4–C4–C4A–N5 for each Ni(1), Ni(2) and Ni(3) entity, respectively. In the trimeric Ni-complex, the benzoylhydrazone ligand displays a double-bidentate coordination mode like in the already reported dimeric Cu-TSCLMH complex [15] but the different conformational abilities of BZLMH and TSCLMH ligands could provide a feasible reason to justify the appearance of structures with different nuclearity.

We can observe some changes at pteridine-chain–phenyl angles, with respect to the free ligand, due each organic ligand is bonded to two different metal ions. The most significative change is produced at pteridine–phenyl angle, which shows values between 77° and 86° while at free ligand it was 41.4°. In addition to this, the coordination of BZLMH causes some differences with respect to metal-free structure: a small shortening (0.040–0.049 Å) in the N(62)–C(63) bond and a lengthening in the C(63)–O(63) bond (0.020–0.039 Å), which have also been observed in other complexes with related hydrazones [43]; bond lengths are as follows: N(62)–C(63) 1.336(7), 1.330(7) and 1.339(6) Å; C(63)–

Table 3
Atomic orbital contributions to the LUMO to HOMO-2 molecular orbitals of BZLMH (DFT 6-31G*).

MO	Conformation *a*		Conformation *b*	
	Energy, eV (symmetry[b])	Contribution[a]	Energy (eV) (symmetry[b])	Contribution[a]
HOMO-2	−7.044	O63: 0.298	−6.912	O63: 0.555
	(41% p_z)	C1F: 0.115	(σ)	N62: 0.145
		O4: 0.106		
HOMO-1	−6.969	O4: 0.175	−6.799	O4: 0.236
	(42% p_z)	N8: 0.131	(σ)	N5: 0.173
		O63: 0.123		N8: 0.104
HOMO	−6.129	N62: 0.181	−5.975	N62: 0.212
	(σ)	N1: 0.131	(π)	N1: 0.115
		N61: 0.114		N61: 0.110
LUMO	−2.044	N5: 0.285	−1.997	N5: 0.293
	(σ)	N8: 0.141	(π)	N8: 0.161

[a] The contribution of one atom is calculated as the sum of the squared coefficients of that atom AOs in the LCAO that defines the MO.
[b] orbitals with p_z component lower than 30% were considered σ, whereas those with this component higher than 70% were assumed as π.

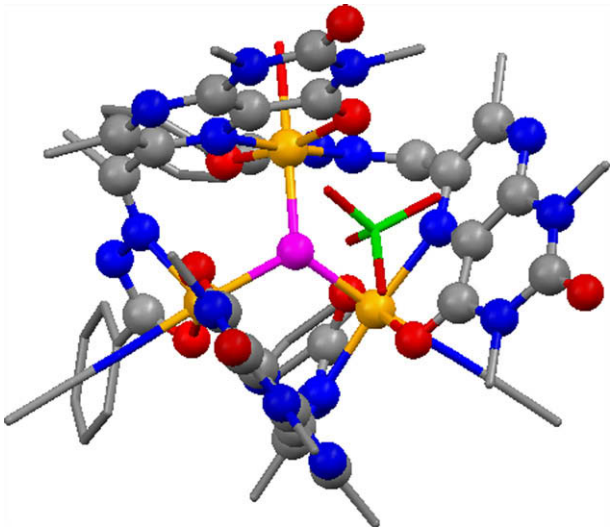


Fig. 2. The molecular structure of trimetallic cation $[Ni_3(BZLMH)_3(OH)(H_2O)(CH_3CN)_2]^{5+}$ at the compound **2** showing the perchlorate anion trapped inside. Ni atoms are coloured as orange and the central μ_3-OH oxygen atom is depicted as magenta; the other atoms are shown as usually. For clarity, neither hydrogen atoms nor atom labels are displayed.

O(63) 1.230(6), 1.242(6) and 1.249(6) Å. These facts confirm the geometry of the ligand could be described according the keto form with a small contribution of the enol form [17,44].

The crystal structure expands by eight hydrogen bonds which result in two chains extended along the *a* axis, with the involvement of three perchlorate groups. Two perchlorate groups are hydrogen-bonded to the ligand and water molecules, while the third one is captured inside the trimer unit, only connecting with the central hydroxo group.

3.2.2. Crystal structure of $[Zn(NO_3)(BZLMH)(H_2O)](NO_3)$ (**3**)

The molecular structure for Zn(II) compound (**3**) was also confirmed by X-ray diffraction methods. This structure is a bipyramidal trigonal zinc(II) having a tridentate BZLMH ligand (Fig. 4). Selected bond parameters are listed in Table 4. The ligand binds the metal ion *via* carbonyl oxygen atom O(63) and imine and pyrazine nitrogen atoms (N(61), N(5)); the nitrate O(1 N) and water O(1 W) ligands bring the coordination number to five. In this process, the benzoylhydrazone ligand forms two five-membered chelate rings and the chelate bite angles for both five membered rings are similar (N(5)–Zn–N(61) 72.2(2)° and N(61)-Zn-O(63) 74.1(2)°). As previously found in other metal complexes [44,45] the Zn-N(61) bond is shorter than Zn-N(5) bond, by *ca.* 0.109 Å. The two Zn–O(1N) and Zn-O(3N) bond distances also differ by 0.483 Å being the Zn–O(3N) significantly longer (2.513(8) Å), so this nitrate anion could be defined as a monodentate ligand. The shape of the polyhedra has been quantified using the Δ parameter proposed by Muetterties and Guggenberg [46]. The Δ values clearly assign slightly distorted bipyramidal trigonal for the coordination environment in this compound (Δ = 0.23).

Table 4
Metal-ligand bond distances (Å) and angles (°) in the crystal structures of (**2**) and (**3**).

Compound **2**					
Ni1–O63C	2.028	(4)	Ni2–O4B	2.101	(4)
Ni1–N2N	2.078	(5)	Ni2–N5B	2.114	(4)
Ni1–N61C	2.087	(4)	Ni2–O1H	2.150	(3)
Ni1–N5A	2.100	(4)	Ni3–O63B	2.011	(3)
Ni1–O4A	2.107	(4)	Ni3–O4C	2.085	(3)
Ni1–O1H	2.145	(2)	Ni3–N61B	2.100	(4)
Ni2–O63A	2.042	(4)	Ni3–O1W	2.106	(4)
Ni2–N61A	2.076	(4)	Ni3–N5C	2.118	(4)
Ni2–N1N	2.087	(5)	Ni3–O1H	2.143	(3)
O63C–Ni1–N2N	84.5	(2)	N1N–Ni2–N5B	88.6	(2)
O63C–Ni1–N61C	77.6	(2)	O4B–Ni2–N5B	79.5	(2)
N2N–Ni1–N61C	86.5	(2)	O63A–Ni2–O1H	94.5	(1)
O63C–Ni1–N5A	103.1	(2)	N61A–Ni2–O1H	97.3	(1)
N2N–Ni1–N5A	89.6	(2)	N1N–Ni2–O1H	175.3	(2)
N61C–Ni1–N5A	175.9	(2)	O4B–Ni2–O1H	95.1	(1)
O63C–Ni1–O4A	168.7	(2)	N5B–Ni2–O1H	86.8	(1)
N2N–Ni1–O4A	84.5	(2)	O63B–Ni3–O4C	169.6	(2)
N61C–Ni1–O4A	99.1	(2)	O63B–Ni3–N61B	77.6	(1)
N5A–Ni1–O4A	79.4	(2)	O4C–Ni3–N61B	101.6	(1)
O63C–Ni1–O1H	95.6	(1)	O63B–Ni3–O1W	86.4	(2)
N2N–Ni1–O1H	176.8	(2)	O4C–Ni3–O1W	83.3	(2)
N61C–Ni1–O1H	96.6	(1)	N61B–Ni3–O1W	88.0	(2)
N5A–Ni1–O1H	87.3	(1)	O63B–Ni3–N5C	99.9	(1)
O4A–Ni1–O1H	95.6	(1)	O4C–Ni3–N5C	80.2	(1)
O63A–Ni2–N61A	77.6	(2)	N61B–Ni3–N5C	175.6	(2)
O63A–Ni2–N1N	85.7	(2)	O1W–Ni3–N5C	88.3	(2)
N61A–Ni2–N1N	87.4	(2)	O63B–Ni3–O1H	97.1	(1)
O63A–Ni2–O4B	169.6	(2)	O4C–Ni3–O1H	93.2	(1)
N61A–Ni2–O4B	97.4	(2)	N61B–Ni3–O1H	96.2	(1)
N1N–Ni2–O4B	85.0	(2)	O1W–Ni3–O1H	175.1	(1)
O63A–Ni2–N5B	104.8	(2)	N5C–Ni3–O1H	87.7	(1)
N61A–Ni2–N5B	175.1	(2)			
Compound **3**					
Zn–O1W	1.979	(9)	Zn–O63	2.136	(1)
Zn–O1N	2.030	(9)	Zn–N5	2.211	(8)
Zn–N61	2.102	(7)			
O1W–Zn–O1N	140.5	(3)	N61–Zn–O63	74.2	(3)
O1W–Zn–N61	116.6	(3)	O1W–Zn–N5	95.8	(3)
O1N–Zn–N61	102.9	(3)	O1N–Zn–N5	94.3	(3)
O1W–Zn–O63	96.2	(3)	N61–Zn–N5	71.9	(3)
O1N–Zn–O63	96.3	(3)	O63–Zn–N5	146.0	(2)

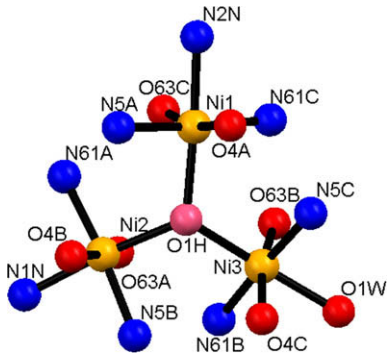


Fig. 3. Coordination environment for each Ni(II) ion in the $[Ni_3(BZLMH)_3(OH)(H_2O)(CH_3CN)_2](ClO_4)_5 \cdot 2H_2O{\cdot}CH_3CN$ complex.

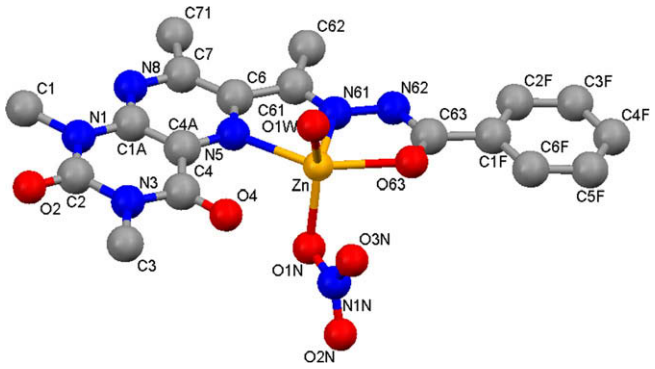


Fig. 4. Structure of the $[Zn(NO_3)(BZLMH)(H_2O)]^+$ cation (for clarity, hydrogen atoms were removed).

$[Zn(NO_3)(BZLMH)(H_2O)](NO_3)$ (**3**) is packed *via* hydrogen bonding in which perpendicular sheets to crystallographic *b* axis are formed by one hydrogen bond between the coordinated water molecule and the O(4) atom from carbonyl group (O(1W)–O(4) = 2.870 Å) and three intermolecular bonds (O(1W)-O(5N) = 2.810 Å (½ + *x*, ½−*y*, *z*−½); N(62)-O(4N) = 2.830 Å (1 + *x*, *y*, *z*); O(1W)–O(2N) = 2.801 Å (*x*−1, *y*, *z*)) between the water molecule and N(62)-H and oxygen atoms of both nitrates.

In addition to these interactions, a detailed analysis of the short aromatic ring-ring contacts (Table 2) (with centroid–centroid distances <6.0 Å and slipping angles β and $\gamma < 60°$) reveals the existence of π-stacking interactions [42] following the *a* axis. For symmetry reasons, such interaction (Fig. 5) is displayed by the parallel six-membered rings of pyrazine and phenyl of two adjacent $[Zn(NO_3)(BZLMH)(H_2O)]^+$ ions (symmetry code = ½ + ×, ½−*y*, *z*−½), with a centroid–centroid vector of 3.7 Å and slipping angles (between the centroid–centroid vector and the normal to each stacked plane) $\beta = 16.5°$ and $\gamma = 19.5°$ (angle between planes containing aromatic rings $\alpha = 4.4°$).

3.3. Spectral studies of the complexes

Spectral characterization of complexes was carried out by IR, NMR and UV–Vis spectroscopy. The significant IR bands of these complexes are close to those found in other compounds with lumazine and hydrazone derivatives. These exhibit a ν(N–H) in the 3800–3400 cm^{-1} region. The bands assignable to the C=N and C=O stretching vibrations are shifted with respect to their position in the spectra of uncoordinated BZLMH ligand. The vibrational activity of carbonyl groups appears as two bands. The higher (over 1700–1720 cm^{-1}) is mainly due to ν(C2=O) and the other one (*ca.* 1650–1670 cm^{-1}) must be assigned to ν(C4=O) [18]. In all complexes, both bands are shifted with respect to their position in the IR spectrum of the free ligand. The absorption bands located at 1603 cm^{-1} in the IR spectra of BZLMH are attributed to $\nu(C{=}N_{azom})$ and the band at 1553 cm^{-1} for this organic ligand is assignable to ν(C=N) of pteridine ring. These bands are shifted in the corresponding complexes, indicating the involvement of the N(5) and N(61) atoms in coordination to the metal ion.

The spectra of Ni(II) and Hg(II) perchlorate compounds also show a strong ν(Cl–O) band between 1100 and 1120 cm^{-1}, while Zn(II) and Hg(II) nitrate compounds displayed a strong band corresponding to ν(N–O) of the nitrate group at 1385 cm^{-1}.

The ligand BZLMH and its Zn(II) and Hg(II) complexes have well resolved ^1H, ^{13}C and ^1H–^{15}N spectra. In the ^1H NMR spectrum of the ligand, the N(62)–H proton appears at 10.99 ppm and also for Zn(II) complex. Other signals in the ^1H spectrum are the phenolic protons at 7.90 and 7.55 ppm and the signals due to the methyl groups at 3.54 (C(1)–H), 3.34 (C(3)–H), 2.92 (C(62)–H) and 2.50 (C(71)–H). The spectrum of the Zn(II) and Hg(II) complexes are similar to that of the uncomplexed ligand. The most notable differences are the upfield shift of the C(62)–H proton to 2.77 ppm for zinc complex (**3**). The C_{arom}, C6 and C62 signals of ^{13}C spectrum also show significant field shift together with the N(61) one in ^1H–^{15}N HMBC spectrum. These shifts are mainly resulting from an increased delocalization after coordination of imine nitrogen N(61) and carbonylic oxygen atoms O(63) to the zinc ion [33,34].

The main differences between the ^{13}C NMR spectra of ligand and nitrate and perchlorate mercury compounds are retrieved in the downfield shift of the C(7), C(1A) and C(6) for nitrate complex and C(7), C(6) for perchlorate complex. These shifts can be also justified by the involvement of the pyrazine and benzohydrazide donor atoms in the coordination of the Hg(II). In this way, the ^1H–^{15}N HMBC showed downfield shift for donor atom N(61) for Hg/NO_3 complex, while Hg/ClO_4 compound displayed upfield shift for N(5), N(8) and N(61) signals. These chemical shifts suggest bidentate coordination (N(5), N(61)) for Hg/ClO_4 complex and a tridentate coordination (N(5), N(61), O(63)) for Hg/NO_3 compound.

The UV–Vis absorption spectrum of $Ni(BZLMH)_2(ClO_4)_2 \cdot 3H_2O$ (**1**) compound exhibits the characteristic bands at 9500, 13700 and 21300 cm^{-1}, assignable to $^3T_{2g}(F) \leftarrow {}^3A_{2g}$, $^3T_{1g}(F) \leftarrow {}^3A_{2g}$, $^3T_{1g}(P) \leftarrow {}^3A_{2g}$ transitions in an idealized O_h symmetry. The position of the observed spectral bands permits to calculate the ligand field parameters, 10*Dq* (9500 cm^{-1}) and B (432 cm^{-1}). These results also agree with the expected octahedral environment for the Ni(II) complex in which N(5), N(61), O(63) tridentation of the ligand could be proposed. We might suggest that this compound may be a possible intermediate first formed and isolated as a solid compound that later evolves to afford the trimer nickel(II) compound (**2**).

3.4. Luminescence studies

Fluorescent transition-metal complexes containing rigid chromophoric ligands with π-conjugation system have been studied intensively because of their potential use. Moreover, to extend the π-conjugation only by synthesis and modification of organic composition may be difficult and tedious. Synthesis of inorganic/organic coordination complexes by using functional ligands and transition-metal centers can be an useful method to obtain new photoluminescent materials. In the current work, we try to obtain this kind of system with organic ligand (BZLMH) and complexes previously cited.

It is important to bear in mind that the luminescent properties of lumazine and benzoylhydrazone ligands are very well known and have been widely used in order to obtain fluorescent sensors [19–24]. Thus, we have borrowed this previous knowledge to study the luminescence of BZLMH ligand, a new lumazine derivative ligand incorporating the photochemically active benzoylhydrazide

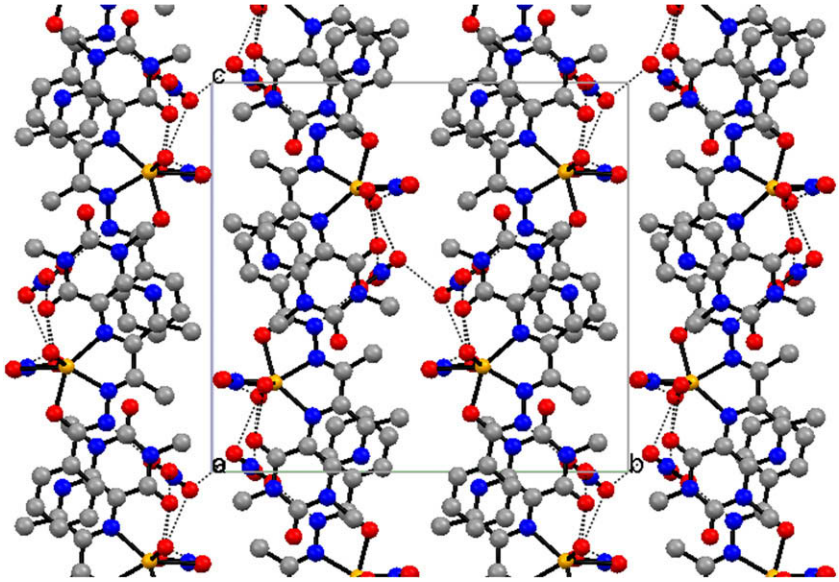


Fig. 5. View down the *a* axis of the H-bonds and π-stacking interactions in the structure of the Zn(II) complex (**3**).

group that could enhance the delocalization of π electrons. Moreover, this substituent could increase the fluorescence intensity of lumazine in BZLMH ligand possibly due to the internal photo induced ceto-enol tautomerism [19,47–50]. In this context, the fluorescence spectroscopy of BZLMH ligand and its nickel compound (**1**), monomeric zinc complex (**3**) and mercury (II) complexes (**4**) and (**5**) is described. Luminescence spectra were obtained using 10^{-3} M BZLMH and metal complexes solutions in DMSO (λ_{exc} = 420 nm).

The free ligand shows a strong luminiscence band centered at 492 nm while fluorescence intensity of Ni-complex (**1**) decreases by a factor of six and exhibits a band centered at 480 nm, which is 12 nm blue-shifted compared to the free ligand. In the same experiment performed with Zn(II) complex (**3**) a blue shift (11 nm) of the fluorescence band is observed (Fig. 6). In contrast with the results for nickel and zinc compound, Fig. 6 also shows enhancement and blue shift of fluorescence for mercury-nitrate (**4**) (λ_{max} = 465 nm) and mercury-perchlorate (**5**) (λ_{max} = 485 nm) complexes while uncomplexed ligand showed a luminescence band centered at 492 nm. Probably, the structures of mercury compounds (**4**) and (**5**) are different from that related Ni(II) and Zn(II) complexes and it could suggest that the ligand coordination mode in both mercury complexes makes the energy transfer from the Hg(II) ion to the ligand more effective than that in complexes with Ni(II) and Zn(II) [51]. On the other hand, if these data are compared with those already reported for the related TSCLMH ligand and complexes [15], a possible relation between the decrease of the fluorescence absorption and the metal-complexation through increasing polydentate modes could be pointed out, since, in general, from complexes with the tetra- or tridentate lumazine derivative bound to metal to those showing bidentate mode, an increase of the fluorescence signal can be observed.

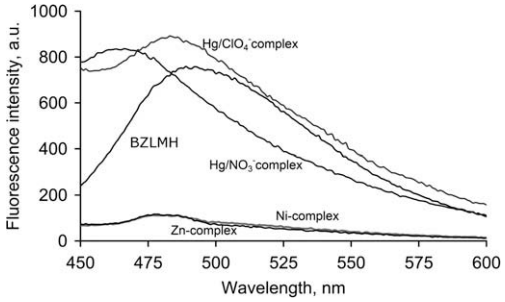


Fig. 6. Fluorescence spectra at room temperature (λ_{exc} = 420 nm) of BZLMH and Ni, Zn, Hg-complexes (DMSO 10^{-3} M).

4. Conclusions

We have studied the XRD crystal structure and the coordination behavior of BZLMH, in which the four possible donors atoms make it possible for the ligand to be tetradentate, tridentate, bidentate or doubly bidentate. In addition to the Rh(III) and Co(II) previously reported structures, the Ni(II) trimer and Zn(II) monomer structures presented here are new examples of the varied coordination chemistry of these hybrid ligands, forming a basis for future comparison with complexes of the same ligand with others metals and different geometry. The versatile coordinative behavior of BZLMH can be related with the rotational ability of both pteridine and benzoylhydrazone moieties to each other.

In this study, the sensibility of the BZLMH fluorescence to the presence of Ni(II), Zn(II) and Hg(II) ions has been found. The BZLMH system recently investigated show good affinity for Hg^{2+} due to the pronounced changes in photophysical properties such as emission wavelength and intensity of Hg(II) complexes. Keeping in mind the importance of Hg^{2+} ions as environmental pollutants, we think that these results are very interesting for future development and practical applications [52].

Supplementary data

CCDC 650849, 650850 and 650851 contains the supplementary crystallographic data for BZLMH, **2** and **3**. These data can be obtained free of charge via http://www.ccdc.cam.ac.uk/conts/retrieving.html, or from the Cambridge Crystallographic Data Centre, 12 Union Road, Cambridge CB2 1EZ, UK; fax: (+44) 1223-336-033; or e-mail: deposit@ccdc.cam.ac.uk.

Acknowledgements

Thanks are due to "Plan de Apoyo a la Investigación, al Desarrollo Tecnológico y a la Innovación de la Universidad de Jaén" (RFC/

PP2008/UJA_08_16_08) and Junta de Andalucía (FQM-273) for financial support. To M. Quirós-Olazábal, J. Cobo-Domingo and T. Peña-Ruiz for their valuable help.

References

[1] W. Kaim, B. Schewederski, O. Heilmann, F.M. Hornung, Coord. Chem. Rev. 182 (1999) 323.
[2] W. Kaim, B. Schwederski, Bioinorganic Chemistry, Wiley, Chichester, 1994.
[3] B. Lippert, BioMetals 5 (1992) 195.
[4] D.M. Whitfield, S. Stoijkowski, B. Sarkar, Coord. Chem. Rev. 122 (1993) 171.
[5] Y. Kim, Y. Kang, D. Baek, Bull. Korean Chem. Soc. 22 (2001) 141.
[6] H. Beraldo, W.F. Nacif, D.X. West, Spectrochim. Acta, Part A 57 (2001) 1847.
[7] J.R. Dimmock, R.N. Puthucode, J.M. Smith, M. Hetherington, J.W. Quail, U. Pugazhenthi, J. Med. Chem. 39 (1996) 3984.
[8] J.R. Dimmock, S.N. Pandeya, J.W. Quail, U. Pugazhenthi, T.M. Allen, G.I. Kao, Eur. J. Med. Chem. 30 (1995) 287.
[9] J.R. Dimmock, S.N. Pandeya, J.W. Quail, U. Pugazhenthi, T.M. Allen, G.I. Kao, Eur. J. Med. Chem. 30 (1995) 303.
[10] I.G. Eremenko, S.E. Nefedov, A.A. Sidorov, M.A. Golubnichaya, P.V. Danilov, V.N. Ikorskii, Y.G. Shevedenkov, V.M. Novotortsev, I.I. Moiseev, Inorg. Chem. 38 (1999) 3764.
[11] E.R. Acuña-Cueva, R. Faure, N.A. Illán-Cabeza, S.B. Jiménez-Pulido, M.N. Moreno-Carretero, M. Quirós-Olazábal, Inorg. Chim. Acta 342 (2003) 209.
[12] E.R. Acuña-Cueva, R. Faure, N.A. Illán-Cabeza, S.B. Jiménez-Pulido, M.N. Moreno-Carretero, M. Quirós-Olazábal, Inorg. Chim. Acta 351 (2003) 356.
[13] E.R. Acuña-Cueva, R. Faure, N.A. Illán-Cabeza, S.B. Jiménez-Pulido, M.N. Moreno-Carretero, M. Quirós-Olazábal, Polyhedron 22 (2003) 483.
[14] F. Hueso-Ureña, S.B. Jiménez-Pulido, M.P. Fernández-Liencres, M. Fernandez-Gómez, M.N. Moreno-Carretero, Dalton Trans. (2008) 6461.
[15] S.B. Jiménez-Pulido, F.M. Linares-Ordóñez, M.N. Moreno-Carretero, M. Quirós-Olazábal, Inorg. Chem. 47 (2008) 1096.
[16] I. Picón-Ferrer, F. Hueso-Ureña, N.A. Illán-Cabeza, S.B. Jiménez-Pulido, J.M. Martínez-Martos, M.J. Ramírez-Expósito, M.N. Moreno-Carretero, J. Inorg. Biochem. 103 (2009) 94.
[17] J. Patole, U. Sandbhor, S. Padhye, D.N. Deobagkar, C.E. Anson, A. Powell, Bioorg. Med. Chem. Lett. 13 (2003) 51.
[18] S.B. Jiménez-Pulido, F.M. Linares-Ordóñez, J.M. Martínez-Martos, M.N. Moreno-Carretero, M. Quirós-Olozábal, M.J. Ramírez Expósito, J. Inorg. Biochem. 102 (2008) 1677.
[19] B.D. Wang, Z.Y. Yang, T.R. Li, Bioorg. Med. Chem. 14 (2006) 6012.
[20] B. Tang, F. Han, G.Y. Zhang, Talanta 56 (2002) 603.
[21] C. Basu, S. Chowdhury, R. Banerjee, H. Stoeckli-Evans, S. Mukherjee, Polyhedron 26 (2007) 3617.
[22] R.M. Issa, A.A. Hassanein, I.M. El-Mehasseb, R.I.A. El-Wadoud, Spectrochim. Acta, Part A 65 (2006) 206.
[23] B.D. Wang, Z.Y. Yang, D.W. Zhang, Y. Wang, Spectrochim. Acta, Part A 63 (2006) 213.
[24] N. Saleh, A.M.M. Rawashdeh, Y.A. Yousef, Y.A. Al-Soud, Spectrochim. Acta, Part A 68 (2007) 728.
[25] G. Reibnegger, D. Fuchs, C. Murr, M.P. Dierich, W. Pfleiderer, H. Wachte, Free Rad. Biol. Med. 18 (1995) 515.
[26] Y. Kim, J. Kim, Y. Kang, J. Korean Chem. Soc. 43 (1999) 535.
[27] G.M. Sheldrick, SADABS 2.10, University of Göttingen, Germany, 2003.
[28] L.J. Farrugia, WINGX 1.70.01, University of Glasgow, 2005.
[29] G.M. Sheldrick, SHELX-97. A Program for the Solution of Crystal Structures from X-ray Data, University of Göttingen, Germany, 1997.
[30] A.L. Spek, PLATON. A Multipurpose Crystallographic Tool, Utrecht University, Utrecht, The Netherlands, 2003.
[31] M.J. Frisch, G.W. Trucks, H.B. Schlegel, G.E. Scuseria, M.A. Robb, J.R. Cheeseman, J.A. Montgomery, J.T. Vreven, K.N. Kudin, J.C. Burant, J.M. Millam, S.S. Iyengar, J. Tomasi, V. Barone, B. Mennucci, M. Cossi, G. Scalmani, N. Rega, G.A. Petersson, H. Nakatsuji, M. Hada, M. Ehara, K. Toyota, R. Fukuda, J. Hasegawa, M. Ishida, T. Nakajima, Y. Honda, O. Kitao, H. Nakai, M. Klene, X. Li, J.E. Knox, H.P. Hratchian, J.B. Cross, V. Bakken, C. Adamo, J. Jaramillo, R. Gomperts, R.E. Stratmann, O. Yazyev, A.J. Austin, R. Cammi, C. Pomelli, J.W. Ochterski, P.Y. Ayala, K. Morokuma, G.A. Voth, P. Salvador, J.J. Dannenberg, V.G. Zakrzewski, S. Dapprich, A.D. Daniels, M.C. Strain, O. Farkas, D.K. Malick, A.D. Rabuck, K. Raghavachari, J.B. Foresman, J.V. Ortiz, Q. Cui, A.G. Baboul, S. Clifford, J. Cioslowski, B.B. Stefanov, G. Liu, A. Liashenko, P. Piskorz, I. Komaromi, R.L. Martin, D.J. Fox, T. Keith, M.A. Al-Laham, C.Y. Peng, A. Nanayakkara, M. Challacombe, P.M.W. Gill, B. Johnson, W. Chen, M.W. Wong, C. González, J.A. Pople, GAUSSIAN 03, Revision C02, Gaussian, Inc., Wallingford CT, 2004.
[32] K. Nakamoto, Infrared and Raman Spectra of Inorganic and Coordination Compounds, 4th ed., Wiley, New York, 1997.
[33] N.C. Kasuga, K. Sekino, M. Ishikawa, A. Honda, M. Yokoyama, S. Nakano, N. Shimada, C. Koumo, K. Nomiya, J. Inorg. Biochem. 96 (2003) 298.
[34] G. Drutkowski, C. Donner, I. Schulze, P. Frohberg, Tetrahedron 58 (2002) 5317.
[35] H. Beraldo, D.X. West, Transition Met. Chem. 22 (1997) 294.
[36] E.R. Acuña-Cueva, R. Faure, S.B. Jiménez-Pulido, M.N. Moreno-Carretero, T. Peña-Ruiz, J. Mol. Struct. 697 (2004) 65.
[37] C. Enrique-Mirón, M. Quirós-Olozábal, M.A. Romero-Molina, J.M. Salas-Peregrín, M.P. Sánchez-Sánchez, F. Hueso-Ureña, M.N. Moreno-Carretero, J.D. Martín-Martos, J. Chem. Cryst. 24 (1994) 465.
[38] G. Ferguson, J.F. Gallagher, J.N. Low, R.A. Howie, F. Hueso-Ureña, M.N. Moreno-Carretero, Acta Crystallogr., Sect. C 49 (1993) 2162.
[39] J.N. Low, R.A. Howie, F. Hueso-Ureña, M.N. Moreno-Carretero, Acta Crystallogr., Sect. C 48 (1992) 145.
[40] J.N. Low, E. Cadoret, G. Ferguson, M.D. López, M.L. Quijano, A. Sánchez-Rodrigo, M. Nogueras-Montiel, Acta Crystallogr., Sect. C 51 (1995) 2141.
[41] M. Helliwell, A. Dinsmore, C.D. Garner, J.A. Joule, Acta Crystallogr., Sect. C 55 (1999) 254.
[42] C. Janiak, J. Chem. Soc., Dalton Trans. (2000) 3885.
[43] F. Hueso-Ureña, N.A. Illán-Cabeza, M.N. Moreno-Carretero, A.L. Peñas-Chamorro, R. Faure, Polyhedron 19 (2000) 689.
[44] M. Carcelli, S. Ianelli, P. Pelagatti, G. Pelizzi, Inorg. Chim. Acta 292 (1999) 121.
[45] L. Bresolin, R.A. Burrow, M. Hörner, E. Bermejo, A. Castiñeiras, Polyhedron 116 (1997) 3947.
[46] E.L. Muetterties, L.J. Guggenberg, J. Am. Chem. Soc. 96 (1974) 1748.
[47] W.E. Brewer, M.L. Martínez, P.T. Chou, J. Phys. Chem. 94 (1990) 1915.
[48] J.S. Stephan, C. Ríos-Rodriguez, K.H. Grellmann, K.A. Zachariasse, Chem. Phys. 186 (1994) 435.
[49] D. Sun, J. Fang, G. Yu, F. Ma, J. Mol. Struct. Teochem. 806 (2007) 105.
[50] R. Das, S. Mitra, D. Guha, S.J. Mukherjee, J. Lumin. 81 (1999) 61.
[51] C.H. Ye, H.L. Sun, X.Y. Wang, J.R. Li, D.B. Nie, J. Solid State Chem. 177 (2004) 3735.
[52] V. Amendola, L. Fabrizzi, F. Foti, M. Licchelli, C. Mangano, P. Pallavicini, A. Poggi, D. Sacchi, A. Taglietti, Coord. Chem. Rev. 250 (2006) 273.

Polyhedron 28 (2009) 2649–2654

Contents lists available at ScienceDirect

Polyhedron

journal homepage: www.elsevier.com/locate/poly

New series of platinum group metal complexes bearing η^5- and η^6-cyclichydrocarbons and Schiff base derived from 2-acetylthiazole: Syntheses and structural studies

Kota Thirumala Prasad [a], Gajendra Gupta [a], Anna Venkateswara Rao [a], Babulal Das [b], Kollipara Mohan Rao [a,*]

[a] Department of Chemistry, North Eastern Hill University, Shillong 793 022, India
[b] Department of Chemistry, Indian Institute of Technology, Guwahati, India

ARTICLE INFO

Article history:
Received 20 April 2009
Accepted 26 May 2009
Available online 2 June 2009

Keywords:
Arene
Cyclopentadienyl
2-Acetylthiazole azine
Ruthenium
Rhodium
Iridium

ABSTRACT

The mononuclear complexes $[(\eta^6\text{-arene})Ru(ata)Cl]PF_6$ {*ata* = 2-acetylthiazole azine; arene = C_6H_6 [(**1**)PF_6]; *p*-^{i}PrC_6H_4Me [(**2**)PF_6]; C_6Me_6 [(**3**)PF_6]}, $[(\eta^5\text{-}C_5Me_5)M(ata)]PF_6$ {M = Rh [(**4**)PF_6]; Ir [(**5**)PF_6]} and $[(\eta^5\text{-Cp})Ru(PPh_3)_2Cl]$ {η^5-Cp = η^5-C_5H_5 [(**6**)PF_6]; η^5-C_5Me_5 (Cp^*) [(**7**)PF_6]; η^5-C_9H_7 (indenyl); [(**8**)PF_6]} have been synthesised from the reaction of 2-acetylthiazole azine (*ata*) and the corresponding dimers $[(\eta^6\text{-arene})Ru(\mu\text{-Cl})Cl]_2$, $[(\eta^5\text{-}C_5Me_5)M(\mu\text{-Cl})Cl]_2$, and $[(\eta^5\text{-Cp})Ru(PPh_3)_2Cl]$, respectively. In addition to these complexes a hydrolysed product (**9**)PF_6, was isolated from complex (**4**)PF_6 in the process of crystallization. All these complexes are isolated as hexafluorophosphate salts and characterized by IR, NMR, mass spectrometry and UV–Vis spectroscopy. The molecular structures of [**2**]PF_6 and [**9**]PF_6 have been established by single-crystal X-ray structure analyses.

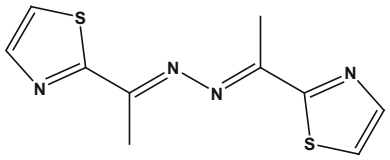
© 2009 Elsevier Ltd. All rights reserved.

1. Introduction

Recent interest in half- sandwich platinum group metal complexes with symmetrical Schiff bases come from the fact they can serve as synthetic models related to biological systems [1–7], as homogeneous catalysts in systems like [8–17], and supported chemical processes [18,19], and very recently as non-linear optical (NLO) materials [20,21]. Their attractiveness does also come from their preparative accessibility, their structural variability in addition to many of these novel ruthenium complexes combine an appropriate balance between the electronic and steric environment around the metal core.

Moreover, some of the nitrogen-donor ligands impart to the catalyst for good tolerance towards various organic functionalities, air, and moisture, thus widening the scope and limit's of their application. Of the above mentioned ligands, Schiff bases are of a great interest for creating new active and selective ruthenium catalytic systems [22,23]. There are few reports of half-sandwich Ru(II), Rh(III) and Ir (III) complexes with *N*,*N*-donor polypyridyl azine Schiff base ligands [24,25], but there are no reports with thiazole azine ligand in the literature. Complexes imparting other than pyridyl azine ligands are yet to be explored, in view of the fact that ring size and the substituents in the heterocyclic ring system significantly modifies the acidity and regulate the physical and chemical properties of the complexes [26,27]. The arene and cyclopentadienyl platinum group metal complexes containing thiazole azine ligand is being reported for the first time.

In the present communication we focus on the synthetic methodology applied for the development of homogeneous and immobilized half- sandwich ruthenium, rhodium and iridium complexes bearing Schiff base (*ata*) as a specific *N*,*N*-bidentate bridging ligand has shown below.



2-acetylthiazole azine *(ata)*

Ligand used in this study

2. Experimental

2.1. General remarks

All solvents were dried and distilled prior to use. Ruthenium trichloride trihydrate (Arora Matthey Ltd.), 2-acetylthiazole (Aldrich)

* Corresponding author. Tel.: +91 9436166937; fax: +91 364 2550486.
E-mail addresses: mohanrao59@gmail.com, kmrao@nehu.ac.in (K.M. Rao).

0277-5387/$ - see front matter © 2009 Elsevier Ltd. All rights reserved.
doi:10.1016/j.poly.2009.05.059

were purchased and used as received. $[(\eta^6\text{-}C_6H_6)Ru(\mu\text{-}Cl)Cl]_2$, $[(\eta^6\text{-}p\text{-}^iPrC_6H_4Me)Ru(\mu\text{-}Cl)Cl]_2$, $[(\eta^6\text{-}C_6Me_6)Ru(\mu\text{-}Cl)Cl]_2$ [28–30], $[(\eta^5\text{-}C_5Me_5)M(\mu\text{-}Cl)Cl]_2$ (M = Rh, Ir) [31–33], $[(\eta^5\text{-}C_5H_5)Ru(PPh_3)_2Cl]$ [34], $[(\eta^5\text{-}C_5Me_5)Ru(PPh_3)_2Cl]$, $[(\eta^5\text{-}C_9H_7)Ru(PPh_3)_2Cl]$ [33,35,36] and ligand *ata* [37,38] were prepared according to literature methods. NMR spectra were recorded on AMX-400 MHz spectrometer. Infrared spectra were recorded as KBr pellets on a Perkin–Elmer 983 spectrophotometer; elemental analyses of the complexes were performed on a Perkin–Elmer-2400 CHN/S analyzer. Mass spectra were obtained from ZQ mass spectrometer by ESI method. Absorption spectra were obtained at room temperature using a Perkin–Elmer Lambda 25 UV–Vis spectrophotometer.

2.2. Single crystal X-ray structure analyses

Crystals suitable for X-ray diffraction study for compound [**2**]PF_6 and [**4**]PF_6 were grown by slow diffusion of diethylether into dichloromethane solution of complexes [**2**]PF_6 and [**4**]PF_6, respectively. The bright orange crystals of compound [**2**]PF_6, the red color crystal of [**4**]PF_6 were mounted on a Stoe-Image Plate Diffraction system equipped with a ϕ circle goniometer, using Mo Kα graphite monochromated radiation (λ = 0.71073 Å) with ϕ range 0–200°, increment of 1.2°, D_{max}–D_{min} = 12.45–0.81 Å. X-ray intensity data were collected with Mo Kα graphite monochromatic radiation at 296 (2) K, with 0.3°ω scan mode and 10 second per frame. The intensity data were corrected for Lorentz and polarization effects. The structures were solved by direct methods using the program SHELXS-97 [39]. Refinement and all further calculations were carried out using SHELXL-97 [40]. The H-atoms were included in calculated positions and treated as riding atoms using the SHELXL default parameters. The non-H atoms were refined anisotropically, using weighted full-matrix least-squares on F^2. The data collection parameters and bond lengths and angles are presented in Tables 1 and 2, respectively. Figs. 1 and 2 were drawn with ORTEP [41].

2.3. General procedure for the preparation of the mononuclear complexes [**1**]PF_6–[**3**]PF_6

A mixture of $[(\eta^6\text{-arene})Ru(\mu\text{-}Cl)Cl]_2$ (arene = C_6H_6, p-$^iPrC_6H_4Me$ and C_6Me_6) (0.07 mmol), ligand *ata* (0.18 mmol) and 2.5 equivalents of NH_4PF_6 in dry methanol (15 ml) was stirred at room temperature for 6 h. The precipitate was separated by filtration, washed with cold methanol and diethyl ether to remove excess ligand and dried under vacuum.

Table 1
Crystallographic and structure refinement parameters for complexes.

Complex	[2]PF_6	[9]PF_6
Chemical formula	$C_{20}H_{24}ClF_6N_4PRuS_2$	$C_{15}H_{22}ClF_6N_3PRhS$
Crystal system	triclinic	triclinic
Space group	$P\bar{1}$	$P\bar{1}$
Crystal color and shape	plates, yellow	plates, redish yellow
Crystal size	0.45 × 0.30 × 0.18	0.36 × 0.28 × 0.18
a (Å)	7.8486 (4)	8.2601 (9)
b (Å)	12.9523 (7)	11.6219 (12)
c (Å)	13.4155 (8)	12.1958 (14)
α (°)	99.008 (3)	76.593 (7)°
β (°)	90.073 (3)	77.719 (7)°
γ (°)	98.780 (3)	78.838 (7)°
V (Å^3)	1330.74 (13)	1099.9 (2)
Z	2	2
T (K)	296 (2)	296 (2)
D_x (g /cm^3)	1.662	1.690
μ (mm^{-1})	0.97	1.12
Scan range (°)	1.54 < θ < 28.38	1.74 < θ < 28.08
Unique reflections	6542	4390
Reflections used [$I > 2\sigma(I)$]	5109	3402
R_{int}	0.037	0.043
Final R indices [$I > 2\sigma(I)$]	0.0406, wR_2 0.0943	0.0556, wR_2 0.1439
R indices (all data)	0.0563, wR_2 0.1013	0.0742, wR_2 0.1556
Goodness-of-fit (GOF)	1.022	1.098
Max., Min. $\delta\rho$ (e Å^{-3})	0.62, −0.62	0.76, −0.72

Table 2
Selected bond lengths (Å) and angles (°) for complexes [**1**]PF_6.and [**9**]PF_6.

[**1**]PF_6	Interatomoic distances		[**9**]PF_6
Ru–N1	2.087(3)	Rh–N1	2.097(4)
Ru–N2	2.104(2)	Rh–N2	2.136(5)
Ru–Cl1	2.406(8)	Rh–Cl1	2.396(15)
Ru–centroid (arene)	1.692	Rh–centroid (C_5 ring)	1.782
N2–N3	1.398(3)	N2–N3	1.369(6)
N1–C13	1.326(4)	N1–C13	1.318(7)
N2–C14	1.299(4)	N2–C11	1.292(7)
C13–C14	1.439(4)	C11–C13	1.458(8)
Angles			
N1–Ru–N2	75.58(10)	N2–Rh–N3	75.88 (17)
N1–Ru–Cl1	83.80(7)	N4–Rh–Cl1	84.25(13)
N2–Ru–Cl1	88.24(7)	N3–Rh–Cl1	87.88(13)
Ru1–N2–C14	119.10(2)	Rh1–N1–C13	114.13(4)
Ru1–N1–C13	114.39(2)	Rh1–N2–C11	117.59(4)

Calculated centroid of the C_6 or C_5 coordinated aromatic ring.

2.3.1. $[(\eta^6\text{-}C_6H_6)Ru(ata)Cl]PF_6$ ([**1**]PF_6)

Orange–yellow solid, yield 70 mg (79%): *Anal.* Calc. for $C_{16}H_{21}ClN_4S_2RuPF_6$ (609.5): C, 34.89; H, 3.84; N, 10.17. Found: C, 34.68; H, 3.98; N, 10.28%.

^{1}H NMR (CD_3CN, δ): 8.75 (d, 1H, J_{H-H} = 2.98 Hz), 8.52 (d, 1H, J_{H-H} = 3.20 Hz), 7.98 (d, 1H, J_{H-H} = 3.20 Hz), 7.62 (d, 1H, J_{H-H} = 3.2 Hz), 6. 50 (s, 6H), 2.56 (s, 3H, tz-Me), 2.47 (s, 3H, tz-Me); ESI-MS (m/z): 525.1 (100%) $[M-PF_6]^+$; IR (KBr, cm^{-1}): $\nu_{(P-F)}$ 844s; 1604, 1408, 558.

2.3.2. $[(\eta^6\text{-}p\text{-}^iPrC_6H_4Me)Ru(ata)Cl]PF_6$ ([**2**]PF_6)

Dark orange solid, yield 86 mg (89%): *Anal.* Calc. for $C_{20}H_{24}ClS_2N_4RuPF_6$ (651.5): C, 36.07; H, 3.63; N, 8.41. Found: C, 36.18; H, 3.68; N, 8.35%.

^{1}H NMR ($CDCl_3$, δ): 8.55 (d, 1H, J_{H-H} = 2.88 Hz), 8.06 (d, 1H, J_{H-H} = 3.20 Hz), 7.98 (d, 1H, J_{H-H} = 3.2 Hz), 7.71 (d, 1H, J_{H-H} = 2.80 Hz), 5.90 (d, 1H, J_{H-H} = 2.8 Hz, $Ar_{p\text{-}cy}$), 5.87 (d, H, J_{H-H} = 2.4 Hz, $Ar_{p\text{-}cy}$), 5.72 (d, 1H, J_{H-H} = 4 Hz, $Ar_{p\text{-}cy}$), 5.68 (d, 1H, J_{H-H} = 2.8 Hz, $Ar_{p\text{-}cy}$), 2.93 (sept, 1H, J_{H-H} = 4.4 Hz, $CH(CH_3)_2$), 2.56 (s, 3H, tz-Me), 2.47 (s, 3H, tz-Me), 2.28 (s, 3H, $Ar_{p\text{-}cy}$–Me), 1.26 (d, 3H, $CH(CH_3)_2$), 1.18 (d, 3H, $CH(CH_3)_2$); ESI-MS (m/z): 525.1 (100%) $[M-PF_6]^+$; IR (KBr, cm^{-1}): $\nu_{(P-F)}$ 844s; 1629, 1406, 763, 558.

2.3.3. $[(\eta^6\text{-}C_6Me_6)Ru(ata)Cl]PF_6$ ([**3**]PF_6)

Orange–yellow solid, yield 85 mg (88%): *Anal.* Calc. for $C_{22}H_{28}ClN_4S_2RuPF_6$ (694.1): C, 38.07; H, 4.07; N, 8.07. Found: C, 38.11; H, 4.18; N, 8.02%.

^{1}H NMR ($CDCl_3$, δ): 8.75 (d, 1H, J_{H-H} = 2.98 Hz), 8.52 (d, 1H, J_{H-H} = 3.20 Hz), 7.98 (d, 1H, J_{H-H} = 3.20 Hz), 7.62 (d, 1H, J_{H-H} = 3.2 Hz), 2.56 (s, 3H, tz-Me), 2.47 (s, 3H, tz-Me), 2.28 (s, 18H), ESI-MS (m/z): 549.14 (100%) $[M-PF_6]^+$; IR (KBr, cm^{-1}): $\nu_{(P-F)}$ 844s; 1624, 1437, 1409, 769, 558.

2.4. General Procedure for the preparation of the mononuclear complexes [**4**]PF_6 and [**5**]PF_6

A mixture of $[(\eta^5\text{-}C_5Me_5)M(\mu\text{-}Cl)Cl]_2$ (M = Rh, Ir) (0.07 mmol), ligand *ata* (0.15 mmol) and 2.5 equivalents of NH_4PF_6 in dry methanol (15 ml) was refluxed for 4 h. The reaction mixture was cooled over night at room temperature during this time dark yellow color crystalline compound formed. It was separated by filtration, washed with cold methanol and diethyl ether to remove excess ligand and dried under vacuum.

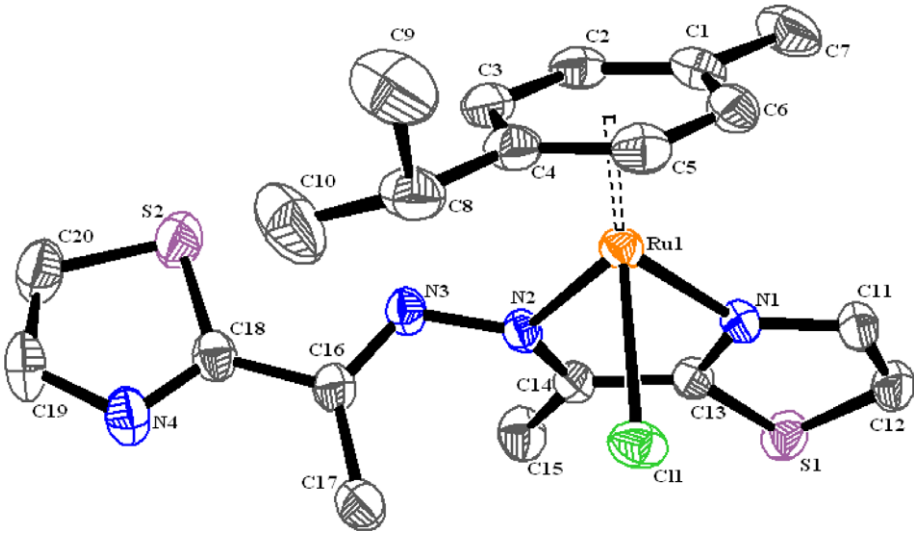


Fig. 1. Molecular structure of [**2**]PF_6 at 50% probability level. Hydrogen atoms, and hexafluorophosphate anion have been omitted for clarity.

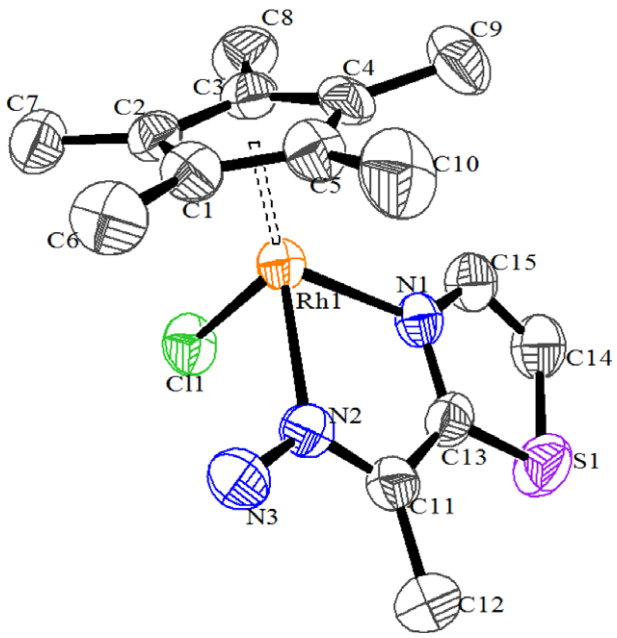


Fig. 2. Molecular structure of [**9**]PF_6 at 50% probability level. Hydrogen atoms and hexafluorophosphate anion have been omitted for clarity.

*2.4.1. [(η^5-C_5Me_5)Rh(ata)Cl]PF_6 ([**4**]PF_6)*

Dark yellow color, yield 86 mg (85%): *Anal.* Calc. for $C_{20}H_{25}ClN_4S_2RhPF_6$ (668.89): C, 35.91; H, 3.77; N, 8.38. Found: C, 36.00; H, 3.89; N, 8.29%.

^{1}H NMR (CD_3CN, δ): 8.33 (d, 1H, J_{H-H} = 5.58 Hz), 8.05 (d, 1H, J_{H-H} = 3.2 Hz), 7.82 (d, 1H, J_{H-H} = 2.8 Hz), 7.68 (d, 1H, J_{H-H} = 3.2 Hz), 2.57 (s, 3H, tz-Me), 2.50 (s, 3H, tz-Me), 1.77 (s, 15H, C_5Me_5); ESI-MS (*m*/*z*): 523.1 (100%) $[M-PF_6]^+$; IR (KBr, cm^{-1}): $\nu_{(P-F)}$ 845s; 1626, 1458, 759, 558.

*2.4.2. [(η^5-C_5Me_5)Ir(ata)Cl]PF_6 ([**5**]PF_6)*

Dark yellow color, yield 95 mg (84%): *Anal.* Calc. for $C_{20}H_{25}ClN_4S_2IrPF_6$ (818.21): C, 31.68; H, 3.32; N, 7.39. Found: C, 31.70; H, 3.48; N, 7.48%.

^{1}H NMR (CD_3CN, δ): 8.58 (d, 1H, J_{H-H} = 3.28 Hz), 8.26 (d, 1H, J_{H-H} = 3.26 Hz), 7.88 (d, 1H, J_{H-H} = 2.88 Hz), 7.68 (d, 1H, J_{H-H} = 3.24 Hz), 2.57 (s, 3H, tz-Me), 2.40 (s, 3H, tz-Me), 1.99 (s, 15H, C_5Me_5); ESI-MS (*m*/*z*): 613.18 (100%) $[M-PF_6]^+$; IR (KBr, cm^{-1}): $\nu_{(P-F)}$ 845s; 1631, 1495, 760, 558.

*2.5. General Procedure for the preparation of the mononuclear complexes [**6**]PF_6- [**8**]PF_6*

A mixture of [(η^5-Cp)Ru(PPh_3)$_2$Cl] (η^5-Cp = η^5-C_5H_5, η^5-C_5Me_5, η^5-C_9H_7) (0.1 mmol), ligand *ata* (0.12 mmol) and 1.5 equivalents of NH_4PF_6 in dry ethanol (15 ml) was refluxed for 10 h. It was changed to dark red color from dark yellow color. The solvent was evaporated on rotary evaporator and residue was dissolved in dichloromethane and filtered to remove ammonium chloride and filtrate was evaporated to 2 ml and excess hexane was added to induce dark color precipitate.

*2.5.1. [(η^5-C_5H_5)Ru(ata)(PPh_3)]PF_6 ([**6**]PF_6)*

Orange color, yield 60 mg (73%): *Anal.* Calc. for $C_{33}H_{30}N_4S_2RuP_2F_6$ (823.75): C, 48.12; H, 3.67; N, 6.80. Found: C, 48.11; H, 3.73; N, 6.75%.

^{1}H NMR ($CDCl_3$, δ) 8.52 (d, 1H, J_{H-H} = 2.80 Hz), 8.12 (d, 1H, J_{H-H} = 3.2 Hz), 7.77 (d, 1H, J_{H-H} = 3.2 Hz), 7.68 (d, 1H, J_{H-H} = 3.2 Hz), 7.46–7.23 (m, 15H), 4.57 (s, 5H, C_5H_5), 2.57 (s, 3H, tz-Me), 2.50 (s, 3H, tz-Me); ESI-MS (*m*/*z*): 678.78 (100%) $[M-PF_6]^+$; IR (KBr, cm^{-1}): $\nu_{(P-F)}$ 845s; 1626, 1458, 766, 558. ^{31}P {^{1}H} ($CDCl_3$): 49.34 ppm.

*2.5.2. [(η^5-C_5Me_5)Ru(ata)(PPh_3)]PF_6 ([**7**]PF_6)*

Orange color, yield 68 mg (76%): *Anal.* Calc. for $C_{38}H_{40}N_4S_2RuP_2F_6$ (893.88): C, 51.06; H, 4.51; N, 6.27. Found: C, 51.10; H, 4.62; N, 6.24%.

^{1}H NMR ($CDCl_3$, δ) 8.87 (d, 1H, J_{H-H} = 2.80 Hz), 8.52 (d, 1H, J_{H-H} = 3.2 Hz), 7.87 (d, 1H, J_{H-H} = 3.2 Hz), 7.79 (d, 1H, J_{H-H} = 3.2 Hz), 7.46–7.23 (m, 15H), 2.57 (s, 3H, tz-Me), 2.50 (s, 3H, tz-Me), 2.19 (s, 15H, C_5Me_5); ESI-MS (*m*/*z*): 748.88 (100%) $[M-PF_6]^+$; IR (KBr, cm^{-1}): $\nu_{(P-F)}$ 845s; 1621, 1479, 749, 558. ^{31}P {^{1}H} ($CDCl_3$): 48.54 ppm.

*2.5.3. [(η^5-C_9H_7)Ru(ata)(PPh_3)]PF_6 ([**8**]PF_6)*

Yellowish brown color, yield 66 mg (76%): *Anal.* Calc. for $C_{37}H_{35}N_4S_2RuP_2F_6$ (876.83): C, 50.68; H, 4.02; N, 6.39. Found: C, 50.61; H, 4.19; N, 6.34%.

^{1}H NMR ($CDCl_3$, δ) 8.52 (d, 1H, J_{H-H} = 2.80 Hz), 8.12 (d, 1H, J_{H-H} = 3.2 Hz), 7.77 (d, 1H, J_{H-H} = 3.2 Hz), 7.68 (d, 1H, J_{H-H} = 3.2 Hz), 7.46–7.23 (m, 20H), 4.87(t, 1H), 4.71 (d, 2H); 2.57 (s, 3H, tz-Me), 2.50 (s,

3H, tz-Me); ESI-MS (*m*/*z*): 731.87 (100%) $[M-PF_6]^+$; IR (KBr, cm^{-1}): $\nu_{(P-F)}$ 845s; 1629, 1468, 763, 558. $^{31}P\{^1H\}$ ($CDCl_3$): 54.42 ppm.

2.5.4. [(η^5-C_5Me_5)Rh(ata)Cl]PF_6 ([**9**]PF_6)*

The complex [**4**]PF_6 (50 mg, 0.074 mmol) was dissolved in 20 ml of dichloromethane in a small diameter test tube and layered with diethylether and it was sealed and kept at room temperature. Dark orange crystalline compound was observed after three days. The crystalline compound was separated by filtration and washed with diethylether and dried at room temperature.

Anal. Calc. for $C_{15}H_{22}ClF_6N_3PRhS$ (559.73): C, 32.19; H, 3.96; N, 7.51. Found: C, 32.00; H, 3.99; N 7.29%.

^1H NMR (CD_3CN, δ): 8.23 (d, 1H, J_{H-H} = 5.58 Hz), 7.89(d, 1H, J_{H-H} = 2.8 Hz), 4.78 (s, 2H, NH_2), 2.61 (s, 3H, tz-Me), (s, 15H, C_5Me_5); ESI-MS (*m*/*z*): 415.72 (100%) $[M-PF_6]^+$; IR (KBr, cm^{-1}): $\nu_{(P-F)}$ 845s; 759, 558, 1626, 1458, 2891.

3. Results and discussion

Mononuclear cationic arene ruthenium complexes having *ata* ligand viz., [(η^6-C_6H_6)Ru(*ata*)Cl]PF_6 [**1**]PF_6, [(η^6-*p*-^{i}PrC_6H_4Me)Ru(*ata*)Cl]PF_6 [**2**]PF_6, and [(η^6-C_6Me_6)Ru(*ata*)Cl]PF_6 [**3**]PF_6 (Scheme 1) have been expediently prepared by the reaction of arene ruthenium dimers [(η^6-arene)Ru(μ-Cl)Cl]$_2$ (arene = C_6H_6, *p*-^{i}PrC_6H_4Me, C_6Me_6) and two equivalents of 2-acetylthiazole azine (*ata*) in methanol at room temperature in the presence of NH_4PF_6. These complexes are isolated as hexafluorophosphate salts.

Similarly, the pentamethylcyclopentadienyl Rh and Ir dimers [(η^5-C_5Me_5)M(μ-Cl)Cl]$_2$ (M = Rh, Ir) with the 2-acetylthiazole azine (*ata*) ligand at 50 °C leads to the formation of the mononuclear cationic complexes [(η^5-C_5Me_5)Rh(*ata*)Cl]PF_6 [**4**]PF_6 and [(η^5-C_5Me_5)Ir(*ata*)Cl]PF_6 [**5**]PF_6 (Scheme 1) which are isolated as their hexafluorophosphate salts.

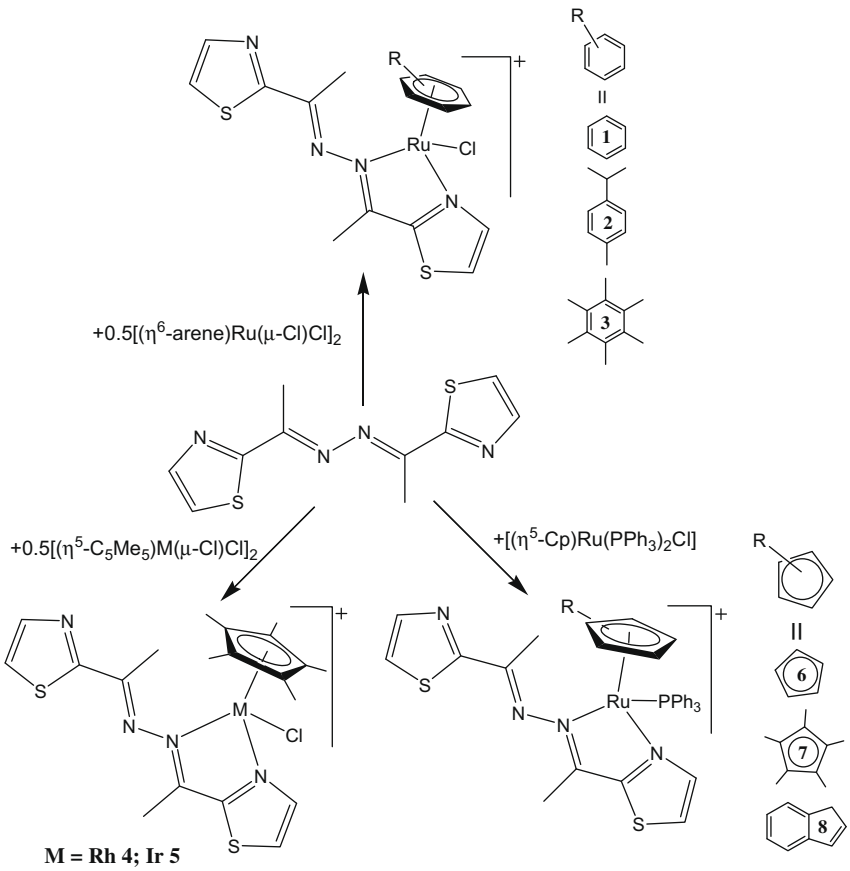
The cyclopentadienyl ruthenium triphenylphosphine complexes [(η^5-C_5H_5)Ru(PPh_3)$_2$Cl], [(η^5-C_5Me_5)Ru(PPh_3)$_2$Cl] and [(η^5-C_9H_7)Ru(PPh_3)$_2$Cl] with the 2-acetylthiazole azine (*ata*) ligand in methanol at 70 °C leads to the formation of the mononuclear cationic complexes [(η^5-C_5H_5)Ru(*ata*)PPh_3]PF_6 [**6**]PF_6, [(η^5-C_5Me_5)Ru(*ata*)PPh_3]PF_6 [**7**]PF_6 and [(η^5-C_9H_7)Ru(*ata*)PPh_3]PF_6 [**8**]PF_6 (Scheme 1) by replacement of one triphenylphosphine and chloride which are isolated as their hexafluorophosphate salts.

In order to prepare the dinuclear complexes we have used two fold metal-to-ligand or one fold metal to mononuclear complexes concentration, but we were not successful in either of the cases. This could be due to the steric strain from arene or pentamethylcyclopentadienyl ligands already present on metal atoms.

3.1. Characterization

The mononuclear complexes were fully characterized by IR, NMR (^1H and ^{31}P), and electronic spectroscopy. Analytical data of the complexes conformed well to their respective formulations. Further information about composition of the complexes has also been obtained from Mass spectrometry.

Infrared spectra of the ligand display an absorption band at 1606 cm^{-1} (*ata*) assignable to the C=N Bond, consistent with the fact that C=N stretching frequencies of Schiff bases appear in the range 1680–1603 cm^{-1} [42–44] and complexes display the same band at higher wave numbers and appeared around 1626 cm^{-1}. The bands associated with thiazole ring such as C=N and C=S appeared at about 1430 and 1406 cm^{-1}, these values are showing less wave numbers as compared to free ligand (1490 and 1417 cm^{-1}),



Scheme 1.

respectively. The shift in the position of $\nu_{C=N}$ of both azine and thiazole suggested that the coordination of the metal ion is through thiazole and azine of nitrogen and not through the thiazole sulfur. Strong band in the region 844 cm^{-1} have been assigned to counter ion PF_6.

The ^1H NMR spectrum of free ligand (*ata*) exhibit a characteristic set of three resonances for the thiazole ring protons and methyl protons of N=C–CH_3 group. Upon coordination with the metal atom, the mononuclear cationic complexes [**1**]PF_6 to [**5**]PF_6 exhibited six distinct resonances assignable to thiazolyl ring and N=C–CH_3 protons of the *ata* ligand indicating formation of mononuclear complexes. Besides these signals complexes [**1**]PF_6 and [**3**]PF_6 exhibit a singlet for the protons of the benzene ring and protons of the hexamethylbenzene at δ 6.50 and 2.28, respectively. Complex **2** exhibit a singlet at δ = 2.28 for methyl protons, a septet at δ = 2.82 for the CH proton of the isopropyl group. Interestingly we observe an unusual pattern for the diastereotopic methyl protons of the isopropyl group and diastereotopic CH protons of the *p*-cymene ligand showing two doublets at δ = 1.26–1.18, and four doublets in the range δ = 5.90–5.68 instead of one doublet and two doublets, respectively with reference to the starting precursor. This unusual pattern is due to the diastereotopic methyl protons of the isopropyl group and aromatic protons of the *p*-cymene ligand, since the ruthenium atom is stereogenic due to the coordination of four different ligand atoms and chiral nature of metal atom [45,46,52].

Complexes **[4]PF_6** and **[5]PF_6** exhibit a singlet for the methyl protons of the pentamethylcyclopentadienyl ligand at δ 1.77 and 1.99 ppm. Complexes **[6]PF_6** and **[7]PF_6** exhibit a singlet at δ 4.57 and 2.19 for the protons of cyclopentadienyl ligand and methyl protons of pentamethylcyclopentadienyl ligands respectively. Complex **[8]PF_6** exhibits a characteristic three sets of signals such as multiplet, triplet and doublet, for the protons of the indenyl ligand in the range of 7.46, 4.81 and 4.71, respectively. The protons of the triphenylphosphine ligand exhibit a multiplet at δ = 7.22 to 7.55.

The ^{31}P NMR spectra of complexes [**6**]PF_6, [**7**]PF_6, and [**8**]PF_6 showing down field shift compared to starting precursors viz. δ 49.34, 48.54, and 54.42 ppm, respectively. This down field chemical shift of phosphorus nucleus indicates the formation of cationic complexes.

3.2. Molecular structure presentation

The molecular structures of [(η^6-*p*-^{i}PrC_6H_4Me)Ru(*ata*)Cl]$^+$ (**2**) and [(η^5-C_5Me_5)Rh(*ata**)Cl]$^+$ (**9**) (*ata** = hydrolysed product of *ata*) (N($CH_2CH_2SCC(CH_3)$)N–NH_2) have been established by single-crystal X-ray analysis of their hexafluorophosphate salts. All the cationic complexes show a typical piano-stool geometry with the metal centre being coordinated by the arene/pentamethylcyclopentadienyl ligand, a terminal chloride and the chelating *ata*/*ata** ligand. The metal atom is in octahedral arrangement with two *cis*-nitrogen atoms of the *ata*/*ata** ligand acting as a bidentate chelating ligand through two neighbouring thiazole and azine nitrogen atoms. The molecular structures of complexes [**2**]PF_6 and [**9**]PF_6 are shown in Figs. 1 and 2, respectively, and bond lengths and angles are presented in Table 2.

In the mononuclear complexes [**2**]PF_6 and [**9**]PF_6 the metal to nitrogen bond distance (2.087(3), and 2.097(4) Å) of the thiazole is shorter than the corresponding azine N-metal distance (2.104(2) and 2.136(5) Å) which are comparable to those in [(η^6-C_6Me_6)RuCl–(C_5H_4N-2-CH=N=C_6H_4-p-NO_2)]PF_6 [47], [Ru(mes)Cl-{C_5H_4N-2-C(Me)=N(CHMePh)}]BF_4 [48], [(η^5-C_5Me_5)RhCl(C_5H_4N-2-CH=N=C_6H_4-*p*-NO_2)]BF_4 [49]. The Rh–N bond distance (2.097(4) and 2.136(5) Å) in [**9**]PF_6 is slightly longer than the corresponding distances of ruthenium complex **2** (2.104(3) Å), while the M–Cl [2.406(8) and 2.396(15)] bond lengths show no significant differences in both the cations and other reported values [50]. The N–M–N bond angles [75.58(10)° in **2** and 75.88(17)° in **9**] are similar to those in other reported complexes [(η^5-C_5Me_5)Ru(PPh_3)(C_5H_4N–CH=N–N=CH–C_5H_4N)]BF_4 and [(η^5-C_9H_7)Ru–(PPh_3)(C_5H_4N-2-CH=N=C_6H_4-*p*-NO_2)]PF_6 [75.90(2) and 75.53(8)°] [51].

The distances between the ruthenium atom and centroid of η^6-*p*-^{i}PrC_6H_4Me ring is 1.692 Å in complex [**2**]PF_6, whereas the distance betwen the rhodium atom and the centroid of the η^5-C_5Me_5 ring is 1.782 Å in complex [**9**]PF_6**.** These bond distances are comparable to those in the related complex cations [(η^6-*p*-^{i}PrC_6H_4Me)Ru(pyNp)Cl]PF_6 and [(η^5-C_5Me_5)Ir(pyNp)Cl]PF_6 (PyNp=2-(2-pyridyl)-1,8-naphthyridine) (1.68 and 1.79 Å) [52].

The solid state molecular structures of representative complexes have been presented in Figs. 1 and 2, respectively.

4. UV–Vis spectroscopy

Electronic absorption spectra of complexes [**1**]PF_6 to [**4**]PF_6 and [**6**]PF_6 and [**7**]PF_6 were acquired in acetonitrile, at 10^{-5} M concentration in the range 250–550 nm and spectral data are summarized in Table 3. The spectra of these complexes are characterized by two main features, viz., an intense ligand–localized or intra-ligand $\pi \rightarrow \pi^*$ transition in the ultraviolet region and metal-to-ligand charge transfer (MLCT) $d\pi(M) \rightarrow \pi^*$ (*ata*-ligand) bands in the visible region [53]. Since the low spin d^6 configuration of the mononuclear complexes provides filled orbitals of proper symmetry at the Ru(II), Rh(III) and Ir(III) centres, these can interact with low lying π^* orbitals of the ligands. All these complexes show an intense band in the region 310–320 nm and a low energy absorption band in the visible region 407–425 nm. The high intensity band in UV region is assigned to inter and intra-ligand π–π^* transitions [54,55],

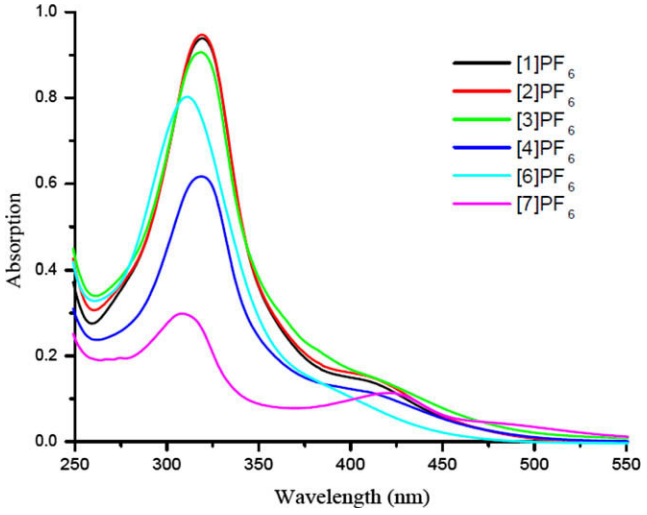


Fig. 3. UV–Vis electronic spectra of complexes in acetonitrile at 298 K.

Table 3
UV–Vis spectral data for selected complexes in acetonitrile at 298 K.

Sl. No.	Complex	λ_{max} (nm)/$\varepsilon \times 10^{-5}$ M^{-1} cm^{-1}
1	[(η^6-*p*-^{i}PrC_6H_4Me)Ru(*ata*)Cl]$^+$	320 (0.93) 412
2	[(η^6-C_6H_6)Ru(*ata*)Cl]$^+$	319(0.95) 415
3	[(η^6-C_6Me_6)Ru(*ata*)Cl]$^+$	319 (0.90) 420
4	[(η^5-C_5Me_5)Rh(*ata*)Cl]$^+$	310 (0.80) 413
6	[(η^5-C_5H_5)Ru(*ata*)PPh_3]$^+$	320 (0.61) 407
7	[(η^5-C_5Me_5)Ru(*ata*)PPh_3]$^+$	310 (0.29) 425

while the low energy absorption band in the visible region is assigned to metal-to-ligand charge transfer (MLCT) (t_{2g}–π^*). Electronic Spectra of these complexes are presented in Fig. 3.

5. Conclusions

In summary, in this work ligand *ata* reacted with series of arene and cyclopentadienyl ruthenium, rhodium and iridium complexes giving novel series of mononuclear complexes [**1**]PF_6 to [**8**] PF_6 in good yield, which are remarkably stable in air as well as in solution. In all these complexes, the metal is bonded with the major coordinated sites N1 and N2 and not with the other possible coordinated sites N1 and S1, where as our effort to make binuclear complexes by using other binding sites, i.e., N3 and N4 or N3 and S2 was not fruitful.

Acknowledgements

K. M. Rao thanks the Department of Science and Technology, New Delhi, (Sanction Order No. SR/S1/IC-11/2004) for financial support. We also thank the Sophisticated Analytical Instruments Facility (SAIF), NEHU, Shillong, for providing the NMR facility. The authors also acknowledge the reviewers for their helpful suggestions regarding results and discussion.

Appendix A. Supplementary data

CCDC 727807 and 727808 contain the supplementary crystallographic data for [**2**]PF_6 and [**9**]PF_6. These data can be obtained free of charge via http://www.ccdc.cam.ac.uk/conts/retrieving.html, or from the Cambridge Crystallographic Data Centre, 12 Union Road, Cambridge CB2 1EZ, UK; fax: (+44) 1223-336-033; or e-mail: deposit@ccdc.cam.ac.uk. Supplementary data associated with this article can be found, in the online version, at doi:10.1016/j.poly.2009.05.059.

References

[1] M. Calligaris, L. Randaccio, in: G. Wilkinson, R.D. Gillard, J.A. McCleverty (Eds.), Comprehensive Coordination Chemistry, Pergamon Press, Oxford, 1987, p. 715.
[2] Y.-G. Li, D.-H. Shi, H.-L. Zhu, H. Yan, S.W. Ng, Inorg. Chim. Acta 360 (2007) 2881.
[3] I. Rousso, N. Friedman, M. Sheves, M. Ottolenghi, Biochemistry 34 (1995) 12059.
[4] T. Baasov, M. Sheves, Biochemistry 25 (1986) 5249.
[5] A.J. Davenport, D.L. Davis, J. Fawcett, S.A. Garratt, D.R. Russell, J. Chem. Soc., Dalton Trans. (2000) 4432.
[6] J.W. Faller, J. Parr, Organometallics 19 (2000) 1829.
[7] H. Chen, J.A. Parkinson, S. Parsons, R.A. Coxall, R.O. Gould, P.J. Sadler, J. Am. Chem. Soc. 124 (2002) 3064.
[8] H. Chen, P.J. Sadler, D.I. Jodrell, Brit. J. Cancer 86 (2002) 1652.
[9] I. Ojima, Catalytic Asymmetric Syntheses, VCH Publishers, New York, 1993.
[10] D.M. Boghaei, S. Mohebi, Tetrahedron 58 (2002) 5357.
[11] C.R.K. Rao, H. Aneetha, B. Srinivas, P.S. Zacharias, A. Ramachandraiah, Polyhedron 13 (1994) 2659.
[12] B. De Clercq, F. Verpoort, Macromolecules 35 (2002) 8943.
[13] T. Opstal, F. Verpoort, Angew. Chem., Int. Ed. 42 (2003) 2876.
[14] T. Opstal, F. Verpoort, Synlett 6 (2002) 935.
[15] S.N. Pal, S. Pal, Inorg. Chem. 40 (2001) 4807.
[16] B. De Clercq, F. Verpoort, Adv. Synth. Catal. 34 (2002) 639.
[17] B. De Clercq, F. Lefebvre, F. Verpoort, Appl. Catal. A 247 (2003) 345.
[18] N.T.S. Phan, D.H. Brown, H. Adams, S.E. Spey, P. Styring, Dalton Trans. (2004) 1348.
[19] P. Styring, C. Grindon, C.M. Fisher, Catal. Lett. 77 (2001) 219.
[20] L. Rigamonti, F. Demartin, A. Forni, S. Righetto, A. Pasini, Inorg. Chem. 45 (2006) 10976.
[21] J. Gradinaru, A. Forni, V. Druta, F. Tessore, S. Zecchin, S. Quici, N. Garbalau, Inorg. Chem. 46 (2007) 884.
[22] K.C. Gupta, A.K. Sutar, Coord. Chem. Rev. 252 (2008) 1420.
[23] P.A. Vigato, S. Tamburini, Coord. Chem. Rev. 248 (2004) 1717.
[24] S.K. Singh, M. Chandra, D.S. Pandey, M.C. Puerta, P. Valerga, J. Organomet. Chem. 689 (2004) 3612.
[25] B. Mondal, V.G. Puranik, G.K. Lahiri, Inorg. Chem. 41 (2002) 5831.
[26] E.C. Constable, Coord. Chem. Rev. 93 (1989) 205.
[27] T. Yamamoto, Z. Zhou, T. Kanbara, M. Shimura, K. Kizu, T. Maruyama, T. Takamura, T. Fukuida, B. Lee, N. Ooba, S. Tomaru, T. Kurihara, T. Kaino, K. Kubota, S. Sasaki, J. Am. Chem. Soc. 118 (1996) 10389.
[28] M.A. Bennett, T.N. Huang, T.W. Matheson, A.K. Smith, Inorg. Synth. 21 (1982) 74.
[29] M.A. Bennett, T.W. Matheson, G.B. Robertson, A.K. Smith, P.A. Tucker, Inorg. Chem. 19 (1980) 1014.
[30] M.A. Bennett, A.K. Smith, J. Chem. Soc., Dalton Trans. (1974) 233.
[31] J.W. Kang, K. Moseley, P.M. Maitlis, J. Am. Chem. Soc. 91 (1969) 5970.
[32] R.G. Ball, W.A.G. Graham, D.M. Heinekey, J.K. Hoyano, A.D. McMaster, B.M. Mattson, S.T. Michel, Inorg. Chem. 29 (1990) 2023.
[33] C. White, A. Yates, P.M. Maitlis, Inorg. Synth. 29 (1992) 228.
[34] M.I. Bruce, N.J. Windsor, Aust. J. Chem. 30 (1977) 1601.
[35] M.I. Bruce, B.C. Hall, N.N. Zaitseva, B.W. Skelton, A.H. White, J. Chem. Soc., Dalton Trans. (1998) 1793.
[36] G. Consiglio, F. Morandini, Chem. Rev. 87 (1987) 761.
[37] Y.-B. Dong, L. Wang, J.-P. Ma, R.-Q. Huang, Inorg. Chem. 45 (2006) 9157.
[38] Y.-B. Dong, L. Wang, J.-P. Ma, X.-X. Zhao, D.-Z. Shen, R.-Q. Huang, Cryst. Growth Des. 6 (2006) 2475.
[39] M. Sheldrick, Acta Crystallogr. A46 (1990) 467.
[40] M. Sheldrick, SHELXL-97, University of Göttingen, Göttingen, Germany, 1999.
[41] L.J. Farrugia, J. Appl. Cryst. 30 (1997) 565.
[42] M. Calligaris, L. Randaccio, in: G. Wilkinson, R.D. Gillard, J.A. McCleverty (Eds.), Schiff Bases as Acyclic Polydentate Ligands in Comprehensive Coordination Chemistry, vol. 2, Pergamon Press, New York, 1987, p. 715.
[43] P.A. Vigato, S. Tanburini, Coord. Chem. Rev. 248 (2004) 1717.
[44] R.H. Molina, A. Mederos, in: J.A. McCleverty, T.J. Meyer (Eds.), Acyclic and Macrocyclic Schiff Base Ligands in Comprehensive Coordination Chemistry II, vol. 2, Pergamon Press, New York, 2004, p. 411.
[45] D.L. Davies, J. Fawcett, R. Krafczyk, D.R. Russell, K. Singh, Dalton Trans. (1998) 2349.
[46] D.L. Davies, O.A. Duaij, J. Fawcett, M. Giardiello, S.T. Hilton, D.R. Russell, Dalton Trans. (2003) 4132.
[47] R. Lalrempuia, K.M. Rao, P.J. Carroll, Polyhedron 22 (2003) 605.
[48] D.L. Davies, J. Fawcett, R. Krafczyk, D.R. Russell, J. Organomet. Chem. 545–546 (1997) 581.
[49] P. Govindaswamy, Y.A. Mozharivskyj, K.M. Rao, Polyhedron 24 (2005) 1710.
[50] A. Singh, M. Chandra, A.N. Sahay, D.S. Pandey, K.K. Pandey, S.M. Mobin, M.C. Puerta, P. Valerga, J. Organomet. Chem. 689 (2004) 1821.
[51] K.S. Singh, Y.A. Mozharivskyj, C. ThÖne, K.M. Rao, J. Organomet. Chem. 690 (2005) 3720.
[52] K.T. Prasad, B. Therrien, K.M. Rao, J. Organomet. Chem. 693 (2008) 3049.
[53] E. Binamira-Soriaga, N.L. Keder, W.C. Kaska, Inorg. Chem. 29 (1990) 3167.
[54] C.S. Araújo, M.G.B. Drew, V. Félix, L. Jack, J. Madureira, M. Newell, S. Roche, T.M. Santos, J.A. Thomas, L. Yellowlees, Inorg. Chem. 41 (2002) 2250.
[55] H. Deng, J. Li, K.C. Zheng, Y. Yang, H. Chao, L.N. Ji, Inorg. Chim. Acta 358 (2005) 3430.

Polyhedron 28 (2009) 2655–2660

Contents lists available at ScienceDirect

Polyhedron

journal homepage: www.elsevier.com/locate/poly

Kinetics of oxidation of quinol and ascorbic acid with the phen substituted semiquinone ligand, (5,6-dioxolene-1,10-phenanthroline-O,O), bound to the $Ru^{II}(bipy)_2$ moiety

Amit Mondal [a], Piyali De [a], Subrata Mukhopadhyay [a], Rupendranath Banerjee [a,*], Prasenjit Kar [b], Amilan D. Jose [b], Amitava Das [b,*]

[a] Department of Chemistry, Jadavpur University, Kolkata 700 032, India
[b] Central Salt and Marine Chemicals Research Institute (CSIR), Bhavnagar 364 002, India

ARTICLE INFO

Article history:
Received 25 March 2009
Accepted 27 May 2009
Available online 17 June 2009

Keywords:
Kinetics
Radicals
Phenanthrolinesemiquinone
Ascorbic acid
Quinol
Bipyridine

ABSTRACT

In 10% (v/v) $CH_3CN–H_2O$ media, the parent complex $[Ru(bpy)_2(sqphen)]^+$ (***I***$^+$) coexists with its conjugate acid $[Ru(bpy)_2(sqphenH)]^{2+}$ (HI^{2+}): $HI^{2+} \rightleftharpoons H^+ + I^+$; (deprotonation constant, $K_a^{ox} = 0.01$; (bpy = 2,2′-bipyridine; sqphen = 5,6-dioxolene-1,10-phenanthroline-O,O). Electrochemical reduction, and also chemical reductions with quinol and ascorbic acid, produced the corresponding catechol complex $[Ru(bpy)_2(catphen)]$ ($\boldsymbol{I}_R$), which also in solution coexists with its conjugate acid, $[Ru(bpy)_2(catphenH)]^+$ (HI_R^+) (deprotonation constant, $K_a^{red} = 0.002$). Progressive increase in [ascorbic acid] led to rate saturation, indicating adduct formation (formation constant, $Q = 990 \pm 80\ M^{-1}$). Added H^+, and also redox-innocent Lewis acid Zn^{2+}, increased $E_{1/2}$ but decreased the chemical reduction rates. Only an insignificant solvent isotope effect (k_{H_2O}/k_{D_2O}) was noted. An increased percentage of CH_3CN in the solvent also retards the rate. $[Ru(bpy)_2(sqphen)]^+$ (***I***$^+$) reacts at a much slower rate than $[Ru(bpy)_2sq]^+$ (sq = the unsubstituted semiquinone). Phen in the substituted ligand sqphen is known to become a much weaker base (sqphen < phen); O,O-coordination to the $Ru^{II}(bpy)$ center further lowers the basicity of sqphen. Catphen (O,O) in $\boldsymbol{I}_R$, produced on reduction of ***I***$^+$, is a stronger base than the O,O-coordinated sqphen in ***I***$^+$.

© 2009 Published by Elsevier Ltd.

1. Introduction

Transition metal complexes with organic radicals are receiving much current attention [1–5] because of their presence in the active sites of metalloproteins [3,4]. The best understood example is galactose oxidase which features a single Cu(II) ion coordinated to a modified tyrosyl-radical [1,2]. It is only due to this intricate bonding situation that the enzyme can perform the specific two-electron oxidation of alcohols to aldehydes. Metal complexes of dioxolenes and derivatives form another interesting group of metallo-radical complexes [6,7], often implicated in biology. Three randomly selected examples are: (a) Cr complexes of catecholamines [8], (b) V complexes with catechol-like ligands [9]; and (c) the group comprising of ubiquinone, semi-ubiquinone, menaquinone and their metal complexes [10–12].

In recent years, a large number of dioxolene complexes have been synthesized and subjected to detailed physicochemical studies [13–35] to understand the role of the metal centers and also to see the effect(s), if any, of structural modifications on such ligands. However, kinetic and mechanistic studies with metallo-radical complexes are scant. Consequently, many important mechanistic issues have not been addressed [36]. This is especially true with metal–dioxolenes.

In this backdrop, we report here the kinetics and mechanism of the reduction of the radical ligand sqphen in $[Ru(bpy)_2(sqphen)]^+$ (***I***$^+$, sqphen is 5,6-dioxolene-1,10-phenanthroline-O,O) with ascorbic acid and quinol to the corresponding catechol in $[Ru(bpy)_2(catphen)]$ ($\boldsymbol{I}_R$). We also have included some of our results on the same reaction induced electrochemically. This work enables a comparison of the reactivity of coordinated sqphen in ***I***$^+$ with that of semiquinone (sq) in $[Ru(bpy)_2(sq)]^+$ (Fig. 1), studied earlier [37].

We believe that the present work should lead to a better understanding of the effect(s), if any, structural modifications on the ligand might have, and should also shed some light on the possible role of the metal ion in modifying the physicochemical properties of the ligand.

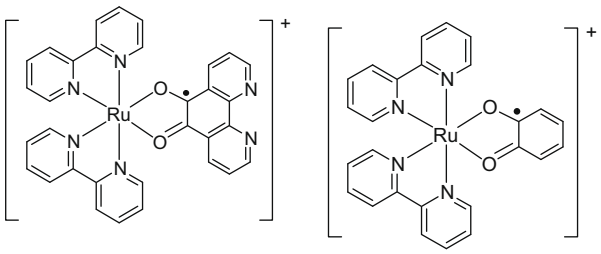
2. Experimental

2.1. Materials

The hexafluorophosphate salt $[Ru(bpy)_2(sqphen)](PF_6)$, (bpy = 2,2′-bipyridine) was prepared as reported [38] (yield: 55%). *Anal.*

* Corresponding authors. Tel.: +91 33 2555 1665; fax: +91 33 2414 6223 (R. Banerjee).
E-mail addresses: rupenju@yahoo.com (R. Banerjee), amitava@csmri.org (A. Das).

0277-5387/$ - see front matter © 2009 Published by Elsevier Ltd.
doi:10.1016/j.poly.2009.05.081



$[Ru(bpy)_2(sqphen)]^+$ ($\boldsymbol{I}^+$) $[Ru(bpy)_2(sq)]^+$

Fig. 1. Schematic drawing of the structures of $[Ru(bpy)_2(sqphen)]^+$ ($\boldsymbol{I}^+$) and $[Ru(bpy)_2(sq)]^+$.

Calc. for $RuC_{32}H_{22}N_6O_2PF_6$: C, 50.0; H, 2.86; N, 10.94. Found: C, 49.7; H, 3.0; N, 10.7%. FAB MS: *m/z* 768 (M^+, ~2%), 623 (M^+–PF_6, ~10%). IR (KBr, cm^{-1}): 1612, 1590 (C=C, C=N), 1448 (semiquinone stretching), 837 (PF_6^-). L-Ascorbic acid (G.R., E. Merck) was used as received. Care was taken to prevent oxidation and photodegradation of the L-Ascorbic acid by storing it in the dark when not in use. 1,4-Dihydroxybenzene (quinol, A.R., B.D.H) was crystallized from acetonitrile (25 g in 30 mL) under nitrogen, dried under vacuum, and stored at 0 °C [39]. Acetonitrile (G.R., E. Merck), used as a co-solvent, was purified by shaking with dilute aqueous sodium hydroxide, followed by washing successively with water, dilute acid and water. Water was removed partially by drying with sodium sulfate. This partially dried solvent was stirred with a small amount of P_2O_5. The solvent was decanted from the solid and fractionally distilled at atmospheric pressure (b.p. 81–82 °C). About one fifth of the acetonitrile was left in the distilling flask at the end of the distillation. The whole operation was carried out in an efficient fume cupboard.

2.2. Stoichiometry measurements

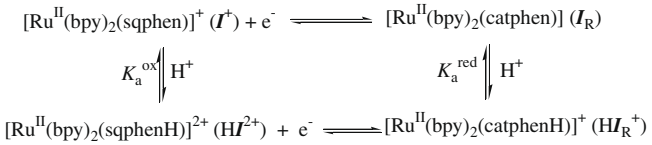
Spectrophotometric titration of the Ru^{II}-complex (0.10 mM) was conducted in 0.05 M $HClO_4$ for ascorbic acid and at pH 5.2 for quinol in 10% (v/v) CH_3CN–H_2O mixture; the ratio, T_C:T_R = was varied in the range 5:1–1:5 [T_C and T_R symbolize the total analytical concentration of the Ru^{II}-complex and the reducing agent, *R* respectively; *R* = H_2A for ascorbic acid and *R* = H_2Q for quinol].

2.3. Physical measurements and kinetics

Microanalyses (C, H, N) were performed using a Perkin–Elmer 4100 elemental analyzer. Electrochemical experiments were performed on a CH-660A (USA) electrochemical instrument using a conventional three-electrode cell assembly comprising saturated Ag/AgCl as the reference electrode and platinum as the working electrode. Ferrocene (Fc) was added at the end of each experiment as an internal standard. For all measurements, the Fc/Fc^+-couple appeared at 0.41 V (*versus* Ag/AgCl).

All solutions were prepared in doubly distilled, freshly boiled water. Kinetics were determined at 25.0 °C and at ionic strength *I* = 0.10 M, maintained with KCl in 10% (v/v) CH_3CN–H_2O media. The salt, $\boldsymbol{I}[PF_6]$ is sparingly soluble in water but dissolves in CH_3CN. Its initial dissolution in a few drops of CH_3CN followed by the addition of the necessary volume of H_2O provides an easy way to dissolve $\boldsymbol{I}[PF_6]$ in 10% (v/v) CH_3CN–H_2O media, as used in the kinetic studies.

Reactions with either ascorbic acid or quinol bleach the NIR absorption band of $\boldsymbol{I}^+$. Kinetics were monitored *in situ* in a thermostatted cell housing (CPS-240A) of a Shimadzu UV1601PC spectrophotometer, following the decrease in the absorbance for the peak (978 nm) of this band under first-order conditions ($T_R \gg T_C$).



Scheme 1. Various Ru(II)–dioxolene complexes coexisting in pH-dependent redox equilibria.

Reaction solutions were deaerated with argon gas prior to kinetic measurements.

3. Results and discussion

3.1. Protic equilibria

In 10% (v/v) CH_3CN–H_2O media and at pH 5.23, $\boldsymbol{I}^+$ exhibits a broad shoulder at ~610 nm (see Supplementary data, Fig. S1), at pH 5.23. A decrease in the media pH reversibly red shifts the shoulder to a lower energy and the changes were found to be reversible. The changes plausibly reflect the reversible protonation of the coordinated sqphen. The shoulder in question arises from an intra-ligand $\pi \rightarrow \pi^*$ charge transfer from bpy to sqphen [40]. Protonation stabilizes (lowers) the π^*-based LUMO of sqphen. Naturally, the shoulder arising out of a $\pi \rightarrow \pi^*$ charge transfer shifts to lower energy (see Supplementary data, Fig. S1). Acidification thus also eases electron addition to sqphen and turns $E_{1/2}$ for the sqphen/catphen couple in $\boldsymbol{I}^+$ more positive [38]. Addition of a redox-innocent Lewis acid, also shifts $E_{1/2}$ to a more positive potential. For example, $E_{1/2}$ increased from −0.285 V to −0.257 V (*versus* Fc^+/Fc couple) at pH 7 in the presence of 0.0032 M $Zn(ClO_4)_2$ (see Supplementary data, Fig. S2).

We employ the square scheme shown above to simulate the pH-dependent redox behavior (see Supplementary data, Fig. S2) of the complex (Scheme 1).

The scheme leads [40] to Eq. (1) (see Supplementary data)

$$E_{1/2} = E_0 - 0.059 \log\{(K_a^{ox} + [H^+])/(K_a^{red} + [H^+])\} \quad (1)$$

where K_a^{ox} and K_a^{red} are the acid dissociation constants for $H\boldsymbol{I}^{2+}$ and $H\boldsymbol{I}_R^+$ respectively.

The best-fit (Fig. 2, *r* = 0.98) of the $E_{1/2}$ *versus* $[H^+]$ data (see Supplementary data, Fig. S2) to Eq. (1) yielded K_a^{ox} = 0.01, K_a^{red} = 0.002 and a slope (=0.055) close to the theoretically expected value (0.059) for a one-electron transfer process. The sequence of deprotonation constants, $K_a^{ox} > K_a^{red}$, is expected because the reduced ligand (catphen in $\boldsymbol{I}_R$) bears a higher electron density and should deprotonate less readily. When compared with some analogous species, the order of protonation constants turns out to be: phen (9×10^4) [41] > sqphen (1.9×10^2) [42]; catphen in $\boldsymbol{I}_R$ (500) > sqphen in $\boldsymbol{I}^+$ (100).[1] Three aspects of this sequence seem important: (a) substitution of phen with sq makes phen a weaker base, (b) coordinated (O,O) sqphen is a weaker base than free sqphen, and (c) coordinated (O,O) sqphen is a weaker base than coordinated (O,O) catphen. These results indicate good electronic communication among the parts Ru^{II}, phen and sq of $\boldsymbol{I}^+$.

3.2. The reaction products

Addition of excess ascorbic acid (H_2A) or quinol (hydroquinone or 1,4-dihydroxybenzene, H_2Q) selectively bleaches the NIR band in $\boldsymbol{I}^+$. Selective bleaching of this MLCT band ($d_{Ru(II)} \rightarrow \pi^*_{sqphen}$) [38] strongly indicates selective reduction of the sqphen radical.

[1] For the best fit of the $E_{1/2}$ versus $[H^+]$ data, it requires $K_a^{ox} = 1.0 \times 10^{-2}$ M and $K_a^{red} = 2.0 \times 10^{-3}$ M whence $(K_a^{ox})^{-1}$ and $(K_a^{ox})^{-1}$ are, respectively, 100 M^{-1} and 500 M^{-1}.

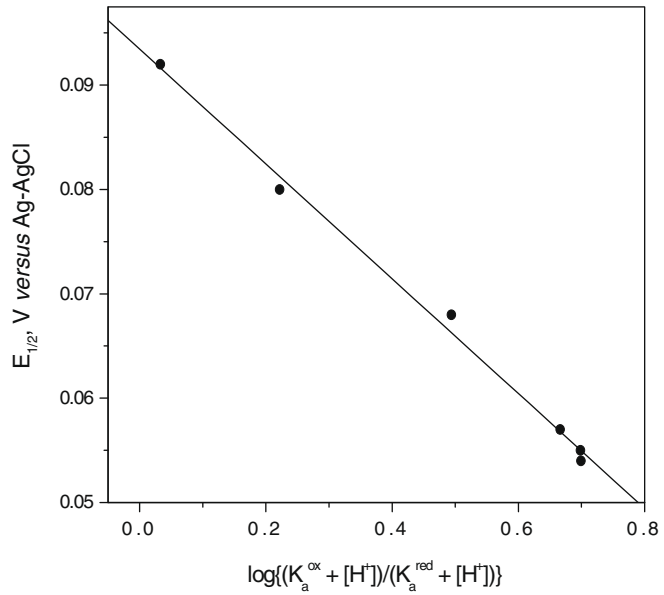


Fig. 2. $E_{1/2}$ vs. [H$^+$] data (black points) fitted to Eq. (1). The solid line presents the best-fit.

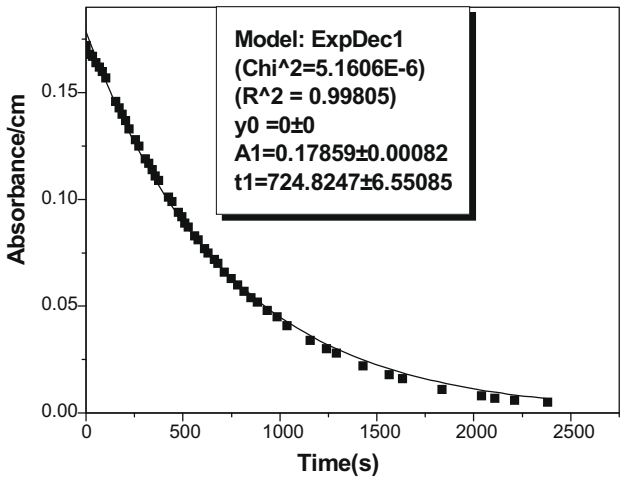


Fig. 3. A typical fit (solid curve) of absorbance vs. time data (black squares) to Eq. (3) for the ascorbate reaction in 10% (v/v) CH_3CN–H_2O media. T_C = 0.10 mM, T_{H2A} = 4.0 mM, I = 0.1 M, T = 25.0 °C.

Bleaching of this MLCT band leads to reduction of [Ru(bpy)$_2$(sqphen)]$^+$ ($\boldsymbol{I}^+$) to [Ru(bpy)$_2$(catphen)] ($\boldsymbol{I}_R$) and [Ru(bpy)$_2$(sqphenH)]$^{2+}$ (H$\boldsymbol{I}^{2+}$) to [Ru(bpy)$_2$(catphenH)]$^+$ (H$\boldsymbol{I}_R^+$). This is well-established in the literature [43–46].

Again, spectrophotometric titration curves (absorbance *versus* T_R) for both ascorbic acid and quinol yielded a break point at T_C:T_R = 2:1, indicating ascorbic acid and quinol are quantitatively oxidized respectively to dehydroascorbic acid and 1,4-benzoquinone (T_R and T_C being the analytical concentrations of the reducing agents and $\boldsymbol{I}^+$ respectively). One-electron reduction of $\boldsymbol{I}^+$ produces $\boldsymbol{I}_R$; but ascorbic acid is a two-electron donor. Therefore, the immediate product of the first act of electron transfer should be the radical species $H_2A^{\cdot+}$ or $A^{\cdot-}$. We anticipate that in the next step the ascorbate radical rapidly reduces another molecule of $\boldsymbol{I}^+$, leading to the final products – dehydroascorbic acid along with another molecule of $\boldsymbol{I}_R$. We studied the reactions of ascorbic acid in the range [H$^+$] = 0.01 – 0.10 M, where H$\boldsymbol{I}_R^+$ (pK_a^{red} = 2.7) is nearly exclusive in the final products (Eq. (2A)). In contrast, the products of the reactions with quinol in the pH range 5.40–7.22 ($\boldsymbol{I}_R$ formed exclusively), are two moles of $\boldsymbol{I}_R$ and one mole quinone (Eq. (2B)).

$$2I^+ + H_2A \rightarrow 2HI_R^+ + A \quad (2A)$$

$$2I^+ + H_2Q \rightarrow 2I_R + 2H^+ + Q \quad (2B)$$

3.3. Kinetics

All the reactions, under the experimental conditions, obeyed first-order kinetics (Eq. (3)), where the factor 2 at the right hand side appears due to the stoichiometry of the reactions

$$A_t = A_\infty + (A_0 - A_\infty)\exp(-2k_0t) \quad (3)$$

The absorbance (A_t)–time (t) data for more than four half-lives in each set of kinetics yielded an excellent fit to Eq. (3) (Fig. 3), whence the first-order rate constants (k_o) were evaluated. Tables 1 and 2 display some representative k_o values for the quinol and ascorbic acid reactions, extracted through such a fitting. Added H$^+$, and also Zn^{2+}, increases $E_{1/2}$ for the one-electron, reversible sqphen/catphen couple in $\boldsymbol{I}^+$ but retards its reduction with ascorbic acid and quinol (Tables 1 and 2). This observation is strong evidence against a pure outer-sphere reduction.

Table 1
Some representative first-order rate constants[a] (k_o) for the oxidation of quinol by $\boldsymbol{I}^+$.

pH	10^3 T_{H2Q} (M)	$10^4 k_0$ (s^{-1})
5.80	100	10.3
6.46	100	12.2
6.76	100	14.3
7.06	100	23.5
7.22	100	41.5
5.80	150	11.0
5.80	180	13.9
5.80	250	18.2
5.80	300	23.0
5.40	100	12.6[b1]
5.40	100	13.8[b2]

[a] 10% (v/v) CH_3CN–H_2O mixed media, ionic strength I = 0.10 M (KCl), T = 25.0 °C, [$\boldsymbol{I}^+$] = 0.10 mM.
[b1] In 50% D_2O.
[b2] In 89% D_2O.

3.4. Effect of D_2O on rate

Substitution of up to 89 mol% of D_2O for the solvent H_2O had only modest and opposite effects on the reaction rates for quinol (k_{H_2O}/k_{D_2O} = 1/1.34) and ascorbic acid (k_{H_2O}/k_{D_2O} = 1.38) [47]. Such small kinetic isotope effects are normally expected for simple electron transfer reactions [48]. Much more dramatic effects are usually observed when the electron transfer is coupled with the movement of a proton in equilibrium with solvent protons [36,49–51].

3.5. Effect of pH on rate

3.5.1. Reactions with quinol (H_2Q)

The observed first-order rate constants, k_o, for quinol oxidation were determined in the brief pH range 5.40–7.22; these reactions are is too slow below pH 5, but are too fast above pH 7.5. In the experimental pH range 5.40–7.22, $\boldsymbol{I}^+$ exclusively dominates over H$\boldsymbol{I}^{2+}$ (pK_a^{red} = 2.7), yet, k_o exhibits an inverse proton dependence (Fig. 4). Evidently, the inverse proton dependence arises from the rapid H_2Q/HQ^- equilibrium (Eq. (4); pK_a = 9.96) [52,53] and the expected greater kinetic activity of the conjugate base, HQ^- over the parent acid

Table 2
Some representative first-order rate constants[a] (k_0) for the oxidation of ascorbic acid by I^+.

pH	$10^3\ T_{H2A}$ (M)	$10^4 k_0$ (s^{-1})
2.00	1.0	4.0
2.00	2.0	4.6
2.00	3.0	6.3
2.00	4.0	6.7
2.01	4.0	5.5[b1]
2.01	4.0	4.8[b2]
1.70	4.0	6.9
1.52	4.0	6.8
1.40	4.0	5.8
1.30	4.0	5.7
1.22	4.0	4.7
1.15	4.0	4.0
1.00	4.0	2.4
1.52	4.0	5.3[c1]
1.52	4.0	4.9[c2]
1.52	4.0	4.1[c3]
1.52	4.0	2.8[d1]
1.52	4.0	2.3[d2]
1.52	4.0	1.8[d3]

[c(1–3)] In the presence of $[Zn^{2+}] = 0.005$, 0.01 and 0.20 M, respectively.
[d(1–3)] In presence of 20%, 30% and 40% (v/v) CH_3CN–H_2O, respectively.
[a] Unless stated otherwise, the reactions are carried out in 10% (v/v) CH_3CN–H_2O mixed media, ionic strength $I = 0.10$ M (KCl), $T = 25.0$ °C, $[I^+] = 0.10$ mM.
[b1] In 50% D_2O.
[b2] In 89% D_2O, in b1 and b2, pH meter readings were 1.61. Reported pH is pD = pH + 0.4.

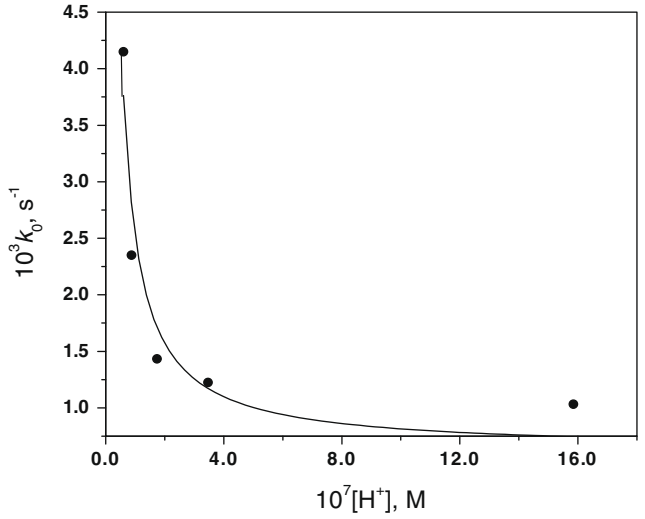


Fig. 4. Experimental k_o (solid circles) for the quinol redox fitted (smooth curve) to Eq. (7). $T_C = 0.10$ mM, $T_{H2Q} = 0.10$ M, $I = 0.1$ M, $T = 25.0$ °C, 10% (v/v) CH_3CN–H_2O media.

$$H_2Q \rightleftharpoons H^+ + HQ^-; \quad pK_a = 9.96 \tag{4}$$
$$I^+ + H_2Q \rightarrow \text{Products}; \quad k_1 \tag{5}$$
$$I^+ + HQ^- \rightarrow \text{Products}; \quad k_2 \tag{6}$$

Eq. (7) was derived from on Eqs. (4)–(6).

$$K_0 = (k_1[H^+] + k_2K_a)T_{H_2Q}/(K_a + [H^+]) \tag{7}$$

The observed first-order rate constants, k_o yielded an agreeable fit (Fig. 4) to Eq. (7). T_{H2Q} represents the total concentration of quinol. The best-fit of k_o to Eq. (7) yielded $k_1 = (6 \pm 2) \times 10^{-3}\ M^{-1}\ s^{-1}$ and $k_2 = (17 \pm 5)\ M^{-1}\ s^{-1}$, which shows that kinetically HQ^- is much more reactive than H_2Q.

3.5.2. Reaction with ascorbic acid (H_2A)

The kinetics of the reaction with ascorbic acid is measurable by the conventional technique only in acidic solutions where each of the four species, HI^{2+}, I^+, H_2A and HA^- might be kinetically significant. The following reaction scheme, Eqs. (8)–(13), is therefore drawn:

$$HI^{2+} \rightleftharpoons H^+ + I^+; \quad K_a^{ox} \tag{8}$$
$$H_2A \rightleftharpoons H^+ + HA^-; \quad K'_a \tag{9}$$
$$HI^{2+} + H_2A \rightarrow P; \quad k_1 \tag{10}$$
$$HI^{2+} + HA^- \rightarrow P; \quad k_2 \tag{11}$$
$$I^+ + H_2A \rightarrow P; \quad k_3 \tag{12}$$
$$I^+ + A^- \rightarrow P; \quad k_4 \tag{13}$$

Under the experimental conditions, $\{K'_a \ll [H^+]\ (0.01–0.10\ M)\}$, the scheme leads to Eq. (14) where T_{H2A} defines the total concentration of ascorbic acid.

$$k_o(K_a^{ox} + [H^+])\ [H^+] = \{k_1[H^+]^2 + (k_2K'_a + k_3K_a^{ox})[H^+] + k_4K'_aK_a^{ox}\}T_{H_2A} \tag{14}$$

A plot of the left hand side of Eq. (14) against $[H^+]$ (Fig. 5) yielded a fair straight line ($r > 0.97$) with finite slope = $(2.95 \pm 0.3) \times 10^{-5}\ M^{-1}\ s^{-1}$ $[= k_2K'_a + k_3K_a^{ox}) \cdot T_{H_2A}]$, but statistically insignificant intercept. The acid variation experiments therefore demonstrate the insignificance of the k_1 and k_4 paths and that only k_3 and/or k_2 path(s) is (are) contributing to the overall rate. Due to the proton ambiguity, individual contributions from the k_2 and k_3 paths cannot be evaluated. Nevertheless, not the conjugate acid form of an oxidant, but the conjugate base of the reductant is generally the better oxidant [54–57] and in many examples, HA^- has much greater kinetic activity over its parent acid H_2A. Therefore, the k_2 path ($HI^{2+} + HA^-$) should contribute more than the k_3 path ($I^+ + H_2A$). Moreover, as we see that the k_1 path ($HI^{2+} + H_2A$) has no contribution, it is expected that the k_3 path ($I^+ + H_2A$) also would not be operative as I^+ is expected to be less oxidizing than HI^{2+}. Using the literature data for $pK'_a = 4.03$ [58], and assuming no significant contribution from k_3, we estimated a value of 79 $M^{-1}\ s^{-1}$ as the upper limit for k_2.

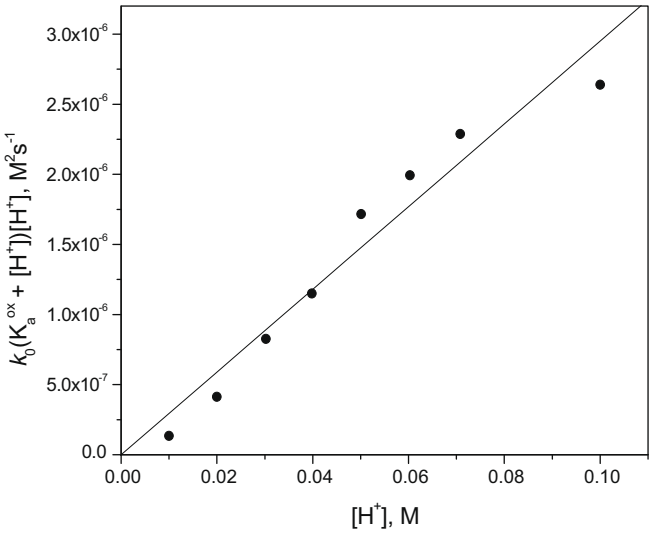


Fig. 5. Graphical verification of Eq. (14) and that the k_1 and k_4 paths contribute negligibly ($T_{H2A} = 4.0$ mM).

3.6. Effect of T_{H2A} and T_{H2Q} on k_o

A progressive increase in T_{H2A} tends to saturate k_o and the kinetics is not so simple as observed for quinol where no indication of rate saturation was observed, even at the highest [quinol] studied (Table 2). A double reciprocal plot between $1/k_o$ and $1/T_{H2A}$ was found to be fairly linear ($r = 0.978$), indicating a rapid adduct formation equilibrium with the formation constant $Q = 990 \pm 80\ M^{-1}$ prior to the rate step (Eq. (15)).

$$HI^{2+} + \text{Ascorbic acid} \overset{Q}{\rightleftharpoons} \text{Intermediate adduct} \overset{k}{\rightarrow} \text{products} \quad (15)$$

This Q value appears to be too large for a simple outer-sphere interaction [59] and suggests some kind of specific bonding, not mere electrostriction. Hydrogen-bonding with the two adjacent oxygen atoms from ascorbic acid (see Supplementary data Fig. S3) seems a distinct possibly [60–62].

The ascorbate anion is also notable for its unusually high rate of complex formation [63]. The high formation constant (Q) observed here may also be a consequence of a high formation rate, but relatively small dissociation rate for the adduct formed. Rate saturation was absent in the reactions with quinol; k_o increased linearly up to the maximum T_{H2Q} (0.30 M) studied.

3.7. Effect of solvent composition

λ_{max} for the $d_{Ru(II)} \rightarrow \pi^*_{sqphen}$ (SOMO) band (at the NIR) [38,64] of $\boldsymbol{I}^+$ blue- shifts from 978 nm to 930 nm on changing the solvent from 10% (v/v) CH_3CN–H_2O to neat acetonitrile. Presumably, the reduced solvent polarity (increased proportion of less polar CH_3CN in CH_3CN–H_2O mixture) destabilizes the singly occupied MO of the semiquinone and decreases the electron acceptance by this moiety. In agreement with this presumption, k_o for ascorbic acid decreased with an increased percentage of CH_3CN (20–40%; v/v) in the mixed CH_3CN–H_2O solvent (Table 2, d^{1-3}). However, decreased solvent polarity is also expected [65] to decrease K'_a and hence $[HA^-]$ (Eq. (9)). Such a decrease in the concentration of the more active form of the reductant may singly or additionally be a cause for the decreased k_o.

4. Conclusions

The protonated radical ligand, $sqphenH^+$ in $[Ru(bipy)_2(sqphen)]^+$ ($H\boldsymbol{I}^{2+}$) ($pK_a^{ox} = 2.0$) is a stronger acid than the one-electron reduced ligand $catphenH^+$ in $[Ru(bipy)_2(catphenH)]^+$ ($H\boldsymbol{I}_R^+$) ($pK_a^{red} = 2.7$). $E_{1/2}$ for the sqphen/catphen reduction couple increases on addition of H^+, and also Zn^{2+}, but either, when added, slow down the rate of the chemical reduction with ascorbic acid. A simple outer-sphere reaction is discarded as a possibility. Reductions with ascorbic acid redox indeed demonstrate an intermediate adduct formation. The solvent isotope effect is negligible and the electron transfer seems to proceed without proton movement at the rate-determining step. Sqphen in $[Ru(bipy)_2(sqphen)]^+$ is reduced at a rate much slower compared to the reduction of unsubstituted sq (semiquinone) in $[Ru(bipy)_2(sq)]^+$. This is plausibly because substitution with phen stabilizes sq through electron drainage from phen to sq via extended conjugation, and renders reduction difficult. Again, this same extended conjugation renders phen of sqphen less basic than phen itself. The sequence of basicity is: phen (9×10^4) [41] > sqphen (1.9×10^2) [42]; catphen in $\boldsymbol{I}_R$ $(500)^1$ > sqphen in $\boldsymbol{I}^+$ $(100)^1$ and shows that: (a) substitution of phen with sq makes phen a weaker base, (b) O,O-coordinated sqphen is a weaker base than free sqphen, and (c) coordinated (O,O) sqphen is a weaker base than coordinated (O,O) catphen. These results indicate good electronic communication among the parts Ru^{II}, phen and sq of $\boldsymbol{I}^+$.

Acknowledgments

Financial assistances received from the Council for Scientific and Industrial Research (New Delhi, Grant No. 01(2085)/06/EMR-II), award of a JRF to A. Mondal by the same agency and financial assistances received from the Department of Science and Technology (New Delhi, Grant No. SR/S1/IC-40/2007) are gratefully acknowledged.

Appendix A. Supplementary data

Supplementary data associated with this article can be found, in the online version, at doi:10.1016/j.poly.2009.05.081.

References

[1] B.A. Jadzewski, W.B. Tolman, Coord. Chem. Rev. 200 (2000) 633.
[2] P. Chaudhuri, K. Wieghardt, Prog. Inorg. Chem. 50 (2001) 151.
[3] H.S.A. Sigel, Metalloenzymes Involving Amino Acid Residue and Related Radicals, Marcel Dekker, New York, 1994.
[4] J. Stubbe, W.A. Van der Donk, Chem. Rev. 98 (1998) 705.
[5] G.C. Pierpont, C.W. Lange, Prog. Inorg. Chem. 41 (1994) 331.
[6] A. Dei, D. Gatteschi, C. Sangregorio, L. Sorace, Acc. Chem. Res. 37 (2004) 827.
[7] D.I. Pattison, M.J. Davies, A. Levina, N.E. Dixon, P.A. Lay, Chem. Res. Toxicol. 14 (2001) 500.
[8] P. Frank, K.O. Hodgson, Inorg. Chem. 39 (2000) 6018.
[9] P.R. Rich, Biochem. Biophys. Acta 768 (1984) 53.
[10] P. Mitchell, FEBS Lett. 59 (1975) 137.
[11] P. Mitchell, J. Theor. Biol. 62 (1976) 327.
[12] D.A. Saffarini, S.L. Blumerman, K.J. Mansoorbadi, J. Bacteriol. 184 (2002) 846.
[13] P. Chaudhuri, C.N. Verani, E. Bill, E. Bothe, T. Weyhermüller, K. Wieghardt, J. Am. Chem. Soc. 123 (2001) 2213.
[14] K. Shiren, K. Tanaka, Inorg. Chem. 41 (2002) 5912.
[15] H. Chun, C.N. Verani, P. Chaudhuri, E. Bothe, E. Bill, T. Weyhermüller, K. Wieghardt, Inorg. Chem. 40 (2001) 4157.
[16] H. Chun, T. Weyhermüller, E. Bill, K. Wieghardt, Angew. Chem., Int. Ed. 40 (2001) 2489.
[17] H. Chun, E. Bill, E. Bothe, T. Weyhermüller, K. Wieghardt, Inorg. Chem. 41 (2002) 5091.
[18] H.P. Chun, P. Chaudhuri, T. Weyhermüller, K. Wieghardt, Inorg. Chem. 41 (2002) 790.
[19] D. Herebian, E. Bothe, E. Bill, T. Weyhermüller, K. Wieghardt, J. Am. Chem. Soc. 123 (2001) 10012.
[20] D. Herebian, P. Ghosh, H. Chun, E. Bothe, T. Weyhermüller, K. Wieghardt, Eur. J. Inorg. Chem. (2002) 1957.
[21] P. Ghosh, E. Bill, T. Weyhermüller, F. Neese, K. Wieghardt, J. Am. Chem. Soc. 125 (2003) 1293.
[22] F. Neese, J. Phys. Chem. Solids 65 (2004) 781.
[23] D. Herebian, E. Bothe, F. Neese, T. Weyhermüller, K. Wieghardt, J. Am. Chem. Soc. 125 (2003) 9116.
[24] X.R. Sun, H. Chun, K. Hildenbrand, E. Bothe, T. Weyhermüller, F. Neese, K. Wieghardt, Inorg. Chem. 41 (2002) 4295.
[25] S. Bhattacharya, P. Gupta, F. Basuli, C.G. Pierpont, Inorg. Chem. 41 (2002) 5810.
[26] W. Kaim, M. Wanner, A. Knodler, S. Zalis, Inorg. Chim. Acta 337 (2002) 163.
[27] S. Frantz, H. Hartmann, N. Doslik, M. Wanner, W. Kaim, H.J. Kummerer, G. Denninger, A.L. Barra, C. Duboc-Toia, J. Fiedler, I. Ciofini, C. Urban, M. Kaupp, J. Am. Chem. Soc. 124 (2002) 10563.
[28] W. Kaim, A. Dogan, M. Wanner, A. Klein, I. Tiritiris, T. Schleid, D.J. Stufkens, T.L. Snoeck, E.J.L. McInnes, J. Fiedler, S. Zalis, Inorg. Chem. 41 (2002) 4139.
[29] C.G. Pierpont, Inorg. Chem. 40 (2001) 5727.
[30] C.G. Pierpont, Coord. Chem. Rev. 219 (2001) 415.
[31] C.G. Pierpont, Coord. Chem. Rev. 216 (2001) 99.
[32] M. Glockle, K. Hubler, H.J. Kummerer, G. Denninger, W. Kaim, Inorg. Chem. 40 (2001) 2263.
[33] G.A. Abakumov, V.K. Cherkasov, V.I. Nevodchikov, V.A. Kuropatov, G.T. Yee, C.G. Pierpont, Inorg. Chem. 40 (2001) 2434.
[34] C.G. Pierpont, A.S. Attia, Collect. Czech. Chem. Commun. 66 (2001) 33.
[35] B.S. Lim, D.V. Fomitchev, R.H. Holm, Inorg. Chem. 40 (2001) 4257.
[36] C. Costentin, Chem. Rev. 108 (2008) 2145.
[37] D. Ghosh, A.D. Shukla, R. Banerjee, A. Das, J. Chem. Soc., Dalton Trans. (2002) 1220.
[38] A.D. Shukla, A. Das, Polyhedron 19 (2000) 2605.
[39] R. Wolfenden, Y.-L. Liang, M. Matthews, R. Williams, J. Am. Chem. Soc. 109 (1987) 463.
[40] T. Fujihara, T. Wada, K. Tanaka, J. Chem. Soc., Dalton Trans. (2004) 645.
[41] H. Irving, D.H. Mellor, J. Chem. Soc. (1955) 3457.
[42] Y. Lei, F.C. Anson, J. Am. Chem. Soc. 117 (1995) 9849.
[43] G. Ramakrishna, D.A. Jose, K. Kumar, A. Das, H.N. Ghosh, J. Phys. Chem. B 110 (2006) 10197.
[44] D.A. Jose, A.D. Shukla, D.K. Kumar, B. Ganguly, A. Das, G. Ramakrishna, H.N. Ghosh, Inorg. Chem. 44 (2005) 2414.

[45] A.D. Shukla, B. White, H.C. Bajaj, A. Das, M.D. Ward, Inorg. Chim. Acta 285 (1999) 89.
[46] A.B.P. Lever, Inorganic Electronic Spectroscopy, Elsevier, Amsterdam, 1984.
[47] pH/pD scale is related as: pH = pD + 0.4. See, H.N.H. Irving, M.G. Miles, L.D. Petti, Anal. Chim. Acta 38 (1967) 475.
[48] J. Albery, in: E. Caldin, V. Gold (Eds.), Proton Transfer Reactions, Wiley, Interscience, New York, 1975. Chapter 9.
[49] M.C. Ghosh, J.W. Reed, R.N. Bose, E.S. Gould, Inorg. Chem. 33 (1994) 73.
[50] U. Roy Choudhury, S. Banerjee, R. Banerjee, J. Chem. Soc., Dalton Trans. (2000) 589.
[51] R.A. Binstead, T.J. Meyer, J. Am. Chem. Soc. 109 (1987) 3287.
[52] G.P. Laroff, R.W. Fessender, R.H. Schuler, J. Am. Chem. Soc. 94 (1972) 9062.
[53] A.A. Papina, Ph.D. Diss. ETH No. 16408, Swiss Federal Institute of Technology Zurich, Novosibirsk State University, 2005 (p. 124).
[54] M.B. Davies, Polyhedron 11 (1992) 285.
[55] S. Das, S. Mukhopadhyay, J. Chem. Soc., Dalton Trans. (2007) 2321.
[56] S. Das, J. Bhattacharyya, S. Mukhopadhyay, J. Chem. Soc., Dalton Trans. (2008) 6634.
[57] S. Das, S. Mukhopadhyay, Eur. J. Inorg. Chem. (2007) 4500.
[58] E. Pelizzetti, E. Mentasti, E. Pramauro, Inorg. Chem. 15 (1976) 2898.
[59] R.B. Jordan, Reaction Mechanisms of Inorganic and Organometallic Systems, Oxford University Press, 1991. p. 33.
[60] P. Martinez, D. Uribe, Z. Naturforsch B: Anorg. Chem., Org. Chem. 37B (1982) 1446.
[61] N. Nordenskiold, J. Kowalewski, N. Benetis, Inorg. Chim. Acta 56 (1981) L21.
[62] N. Benetis, K. Holmen, J. Kowalewski, L. Nordenskioeld, O. Wahlberg, Acta Chim. Scand. A35 (1981) 513.
[63] J. Xu, R.B. Jordan, Inorg. Chem. 29 (1990) 4180.
[64] T.E. Keys, R.J. Foster, P.M. Jayaweera, C.G. Coates, J.J. McGarvery, J.G. Vos, Inorg. Chem. 37 (1998) 5925.
[65] A. Frost, R.G. Pearson, Kinetics and Mechanism, 2nd ed., John Wiley and Sons, Inc., USA, 1961. p. 135.

Polyhedron 28 (2009) 2661–2666

Contents lists available at ScienceDirect

Polyhedron

journal homepage: www.elsevier.com/locate/poly

Novel heteroligand complexes of Co(II), Cu(II), Ni(II) and Mn(II) formed by 2,2′-dipyridyl or 1,10-phenanthroline and phosphortriamide ligands: Synthesis and structure

Kateryna E. Gubina [a,*], Oleg A. Maslov [b], Elizaveta A. Trush [a], Victor A. Trush [a], Vladimir A. Ovchynnikov [a], Svetlana V. Shishkina [c], Vladimir M. Amirkhanov [a]

[a] Department of Inorganic Chemistry, Kiev National Taras Shevchenko University, Vladimirskaya St. 64, Kiev 01033, Ukraine
[b] Analytical Laboratory "Agrotest", Stolichnoe St. 100, Kiev, 03045, Ukraine
[c] STC "Institute for Single Crystals", National Academy of Sciences of Ukraine, 60 Lenina Avenue, Kharkov 61001, Ukraine

ARTICLE INFO

Article history:
Received 21 January 2009
Accepted 1 June 2009
Available online 8 June 2009

Keywords:
Cobalt(II)
Manganese(II)
2,2′-Dipyridyl 1,10-phenanthroline
Carbacylamidophosphates
X-ray data

ABSTRACT

This paper presents examples of mixed-ligand Co(II), Cu(II), Ni(II) and Mn(II) complexes, with a distorted octahedral coordination geometry, with 2,2′-dipyridyl or 1,10-phenanthroline and phosphortriamide ligands. The complexes of the general type $ML_2{\cdot}Lig$ (where M = Co(II), Cu(II), Ni(II), Mn(II); $L^- = \{Cl_3C(O)NP(O)R_2\}^-$ (R = NHBz, $NHCH_2CHCH_2$, NEt_2); Lig = 2,2′-dipyridyl or 1,10-phenanthroline) were synthesised and characterised by means of X-ray diffraction, IR and UV–Vis spectroscopy. The phosphortriamide ligands are coordinated *via* oxygen atoms of phosphoryl and carbonyl groups involved in six-membered metal cycles. The additional ligands 2,2′-dipyridyl or 1,10-phenanthroline are coordinated to the central atom, forming five-membered cycles.

© 2009 Elsevier Ltd. All rights reserved.

1. Introduction

There has been significant growth in the field of coordination chemistry of carbacylamidophosphates over the last ten years. The main research interest concerns urea phosphate derivates of the type $[R^1_2NC(E)NHP(E)R^2_2]$ (E = O, S, Se; $R^1 = CCl_3$, Ar, $R^2 = CH_3$, Ar, C_2H_5), which have been studied as potential chelates to a range of late transition metals through both phosphorous and chalcogen donor atoms [1–3]. On the other hand, carbacylamidophosphates containing the structural frame [C(O)NHP(O)] of the above compounds have been known for a considerable time [4]. There has recently been a resurgence of interest in their coordination chemistry as a consequence of the steric control that this ligand system may impart compared to, for example, β-diketonates [5]. The especially interesting feature of carbacylamidophosphate ligands is the bidentate or μ^2-bidentate chelate character of their coordination to the central atom [6,7]. Carbacylamidophosphate complexes with the common formula $M(L)_2$ are neutral species with an unsaturated coordination sphere of metal ions that readily coordinate additional bidentate chelate donor groups like 2,2′-dipyridyl or 1,10-phenanthroline [8–10].

Investigations in this field are still actively in progress today. Thus, [11] reports the first example of a mixed-ligand Mn(II) complex $[Mn(acac)_2(bpy)]$ with a trigonal-prismatic coordination geometry with simple, bidentate ligands. Based on the very small energy differences for the calculated trigonal-prismatic and octahedral structures, it has been concluded that crystal packing effects must contribute significantly in determining the trigonal-prismatic structure of $[Mn(acac)_2(bpy)]$, even though our investigations confirm the common tendency to form a distorted octahedral coordination geometry for heteroligand Mn(II) and Co(II) complexes with the 2,2′-dipyridyl or 1,10-phenanthroline and phosphortriamidic ligands.

In this paper, we report the synthesis and study of heteroligand complexes of Co(II), Cu(II), Ni(II) and Mn(II) obtained from 2,2′-dipyridyl or 1,10-phenanthroline and the phosphortriamidic ligands N,N′-tetraethyl-N″-trichloracetylphosphorictriamide (R = $N(C_2H_5)_2$) [HL^1], N,N′-diallyl-N″-trichloracetylphosphorictriamide (R = $NHCH_2CHCH_2$) [HL^2] and N,N′-dibenzylamidol-N″-trichloracetylphosphorictriamide (R = NHBz) [HL^3].

2. Experimental

2.1. Synthesis

All chemicals were commercial products of reagent grade, used without further purification.

* Corresponding author. Tel.: +380 503107112; fax: +380 444942379.
E-mail address: katlig@univ.kiev.ua (K.E. Gubina).

0277-5387/$ - see front matter © 2009 Elsevier Ltd. All rights reserved.
doi:10.1016/j.poly.2009.06.004

Table 1
C, H, N analysis for the synthesised compounds.

Compound	M_w	Calc.			Found		
		C [%]	H [%]	N [%]	C [%]	H [%]	N [%]
$Co(L^1)_2$·Phen	944.41	40.70	5.34	11.86	40.47	5.5	11.8
$H(L^2)$	320.54	29.98	4.09	13.11	29.42	3.99	13.03
$Co(L^2)_2$·Phen	880.23	38.21	3.89	12.73	38.05	3.57	12.52
$Mn(L^2)_2$·Phen	876.24	38.38	3.91	12.79	37.94	3.79	12.53
$Ni(L^2)_2$·Phen	880.01	38.22	3.89	12.73	37.86	3.64	12.55
$Co(L^2)_2$·Dipy	856.21	36.47	4.00	13.09	35.91	3.85	12.97
$Mn(L^2)_2$·Dipy	852.22	36.28	3.98	13.02	36.01	3.73	12.92
$Cu(L^2)_2$·Dipy	860.82	36.64	4.02	13.15	36.19	3.92	13.05
$H(L^3)$	420.67	45.68	4.07	9.99	45.73	3.39	9.85
$Co(L^3)_2$·Phen	1080.48	48.91	3.92	5.92	48.24	3.72	5.92
$Cu(L^3)_2$·Phen	1085.09	48.70	3.90	5.90	48.07	3.75	5.76
$[Co(L^3)_2$·Dipy$]$·CH_3OH	1056.45	47.75	4.01	10.61	47.03	3.87	10.48

2.1.1. $H(L^1)$

N,N′-tetraethyl-N″-trichloroacetylphosphortriamide $H(L^1)$ was prepared by [12].

2.1.2. $H(L^2)$, $H(L^3)$

The syntheses of N,N′-diallyl-N″-trichloroacetylphosphorylamide $H(L^2)$ and N,N′-dibenzyl-N″-trichloroacetylphosphorylamide $H(L^3)$ were carried out according to the following general scheme:

$$CCl_3C(O)NHP(O)Cl_2 + 5H_2NR \rightarrow CCl_3C(O)NHP(O)(NHR)_2 \cdot RNH_2 + 2H_3NRCl,$$

$$R = CH_2CHCH_2, CH_2Ph.$$

The solution of the corresponding amine (250 mmol) in 30 ml of dry chloroform was placed into a four-neck round-bottomed flask (0.5 l) equipped with a condenser, mechanical stirrer, dropping funnel and thermometer, and it was then cooled to 0 °C. The dichloride of trichloroacetylamidophosphoric acid [13] 14.9 g (50 mmol) was dissolved in 150 ml of chloroform and slowly added to the previous amine solution, while stirring, over about 20 min. (The internal temperature was not allowed to rise above 5 °C). The stirring was continued for about 40 min. The resulting mixture, containing the ligand, $2H_3NRCl$ and excess of amine, was filtered off, the mother liquor was evaporated and the residue was treated with 100 ml of aqueous HCl (10%). The crude product, precipitated as a crude brown crystalline powder, was collected by filtration and recrystallised from aqueous 2-propanol (90% yield). The compounds were air stable, soluble in alcohols and hot acetone, and insoluble in non-polar aprotic solvents and water. M.p. (HL^2) = 85–87 °C. M.p. (HL^3) = 144–146 °C.

The sodium salts $[Na(L^1)]$, $[Na(L^2)]$ and $[Na(L^3)]$ were obtained from methanol solutions by treatment of the ligands with an equimolar ratio of sodium methoxide. All the salts were white fine-grained substances, soluble in alcohols and acetone, and insoluble in non-polar aprotic organic solvents.

2.1.3. $[Co(L^1)_2$·Phen$]$

A solution of $[NaL^1]$ (2 mmol) in methanol (10 ml) was added to a solution of hydrated cobalt (II) chloride or nitrate (1 mmol) in methanol (15 ml). The solution was then quenched with 30 ml of a 2-propanol solution of 1,10-phenanthroline 0.18 g (1 mmol), stirred under heating, and cooled, and the formed sodium chloride or nitrate was filtered off. After a while, orange crystals precipitated from the bleached solution. They were filtered, washed with cool

Table 2
Crystal data and structure refinement for $H(L^2)$, $[Co(L^1)_2$·Phen$]$, $[Mn(L^2)_2$·Dipy$]$ and $[Co(L^3)_2$·Dipy$]$·CH_3OH.

Identification code	$H(L^2)$	$[Co(L^1)_2$·Phen$]$	$[Mn(L^2)_2$·Dipy$]$	$[Co(L^3)_2$·Dipy$]$·CH_3OH
Empirical formula	$C_8H_{13}Cl_3N_3O_2P$	$C_{32}H_{48}Cl_6CoN_8O_4P_2$	$C_{26}H_{32}Cl_6MnN_8O_4P_2$	$C_{43}H_{44}Cl_6CoN_8O_5P_2$
Formula weight	320.53	942.35	850.18	1086.43
Temperature (K)	293(2)	293(2)	296(2)	296(2)
Wavelength, (Å)	0.71073	0.71073	0.71073	0.71073
Crystal system, space group	triclinic, $P\bar{1}$	monoclinic, $P2(1)/n$	monoclinic, $P2(1)/n$	triclinic, $P\bar{1}$
Unit cell dimensions				
a (Å)	10.96(1)	14.059(5)	11.0762	12.0902(2)
b (Å)	14.113(4)	17.425(5)	18.0392	18.6762(3)
c (Å)	20.296(5)	18.275(5)	19.9545(6)	24.6217(5)
α (°)	103.46(2)			108.26(1)
β (°)	100.04(1)	95.452(5)	102.485(2)	103.63(1)
γ (°)	103.3(1)			95.99(1)
Volume (Å^3)	2883.1(11)	4457(2)	3892.7(2)	5034.49(15)
Z, Calculated density, (g/cm^3)	8, 1.477	4, 1.404	4, 1.451	4, 1.433
Absorption coefficient, (mm^{-1})	0.740	0.860	0.875	0.774
F (0 0 0)	1312	1948	1732	2228
Crystal size (mm)	0.30 × 0.20 × 0.20	0.30 × 0.20 × 0.20	0.50 × 0.50 × 0.25	0.52 × 0.27 × 0.23
θ range for data collection (°)	2.94–30.00	1.62–25.00	1.95–26.29	1.20–26.46
Limiting indices	−15<=h<=14, −19<=k<=18, −28<=l<=28	0<=h<=16, 0<=k<=20, −21<=l<=21	−12<=h<=13, −20<=k<=21, −24<=l<=24	−11<=h<=15, −23<=k<=23, −30<=l<=29
Reflections collected/unique	24 224/15 830 [R_{int} = 0.0343]	8095/776 [R_{int} = 0.0286]	26 726/7797 [R_{int} = 0.0318]	38 724/20 096 [R_{int} = 0.0384]
Completeness to (%)	θ = 30.00 94.1	θ = 25.00 98.7	θ = 26.29 98.7	θ = 26.46 96.6
Absorption correction	none	semi-empirical from equivalents	SADABS	SADABS
Maximum and minimum transmission	0.9853 and 0.9781	0.8468 and 0.7824	0.8110 and 0.6688	0.8421 and 0.6891
Refinement method	Full-matrix least-squares on F^2			
Data/restraints/parameters	15 830/15/687	7764/1/478	7797/27/629	20 096/119/1135
Goodness-of-fit (Gof) on F^2	0.720	0.868	1.005	0.957
Final R indices [$I > 4\sigma(I)$]	R_1 = 0.0533, wR_2 = 0.1343	R_1 = 0.0537, wR_2 = 0.1427	R_1 = 0.0460, wR_2 = 0.1218	R_1 = 0.0609, wR_2 = 0.1485
R indices, (all data)	R_1 = 0.1504, wR_2 = 0.1568	R_1 = 0.1310, wR_2 = 0.1666	R_1 = 0.0799, wR_2 = 0.1357	R_1 = 0.1178, wR_2 = 0.1828
Largest differential peak and hole (e/Å^3)	0.485 and −0.329	0.798 and −0.705	0.437 and −0.550	1.028 and −0.509

Table 3
Main IR absorption bands and their assignments for the carbacylamidophosphate compounds, cm^{-1}.

Compound	ν(C=O)	ν(P=O)
$H(L^1)$	1725	1235
$Na(L^1)$	1625	1130
$H(L^2)$	1700	1215
$Na(L^2)$	1620	1110
$H(L^3)$	1710	1250
$Na(L^3)$	1643	1147
$Co(L^1)_2$·Phen	1630	1115
$Co(L^2)_2$·Phen	1590	1110
$Mn(L^2)_2$·Phen	1600	1130, 1110
$Ni(L^2)_2$·Phen	1600	1110
$Co(L^2)_2$·Dipy	1600	1120, 1100
$Mn(L^2)_2$·Dipy	1600	1130, 1100
$Cu(L^2)_2$·Dipy	1600	1160
$Co(L^3)_2$·Phen	1620	1130, 1100
$Cu(L^3)_2$·Phen	1580	1110, 1090
$[Co(L^3)_2$·Dipy$]\cdot CH_3OH$	1610	1100, 1070

2-propanol, and dried over $CaCl_2$ (yield 0.73 g (77%)). Single crystals of $[Co(L^1)_2$·Phen] were prepared by slow crystallization from 2-propanol–methanol (5:1) mixture. The complex as prepared is soluble in non-polar aprotic solvents, and is less soluble in acetone and cooled alcohols.

2.1.4. $[M(L^2)_2$·Phen] (M = Co; Mn; Ni) and $[M(L^2)_2$·Phen] (M = Co; Mn; Cu)

All of the complexes mentioned above were obtained according to the general procedures described previously, using the respective metals and sodium salts of the ligands (average yield 70–90%).

$[M(L^3)_2$·Phen] (M = Co; Cu) and $[Co(L^3)_2$·Dipy$]\cdot CH_3OH$. These complexes were obtained in the same manner as the complexes based on HL^2.

The compositions of the compounds obtained were proposed based on C, H, N analysis (Table 1).

2.2. Methods

2.2.1. UV–Vis spectroscopy, IR-spectroscopy

The IR spectra of the compounds were recorded on an UR-10 spectrometer in the range 400–4000 cm^{-1} (samples as KBr pellets). Electronic diffuse reflectance spectra were recorded on a SPECORD M-40 (Carl Zeiss, Jena) UV–Vis spectrometer. UV–Vis absorption spectra were measured at room temperature in absolute acetonitrile on a KSVU-23 "LOMO" spectrometer.

2.2.2. Crystallography

Crystallographic data for the compounds $H(L^2)$, $Co(L^1)_2$·Phen, $Mn(L^2)_2$·Dipy and $[Co(L^3)_2\cdot Dipy]\cdot CH_3OH$ are summarised in Table 2. All the above structures were solved by direct methods and refined by the full-matrix least-squares technique with anisotropic approximations for the main non-hydrogen atoms using the SHELXS97 and SHELXL97 programs. The data of the structures were corrected for Lorentz and polarization effects. The SADABS absorption correction was applied for $Mn(L^2)_2$·Dipy and $[Co(L^3)_2\cdot Dipy]\cdot CH_3OH$ [14].

2.2.3. $[HL^2]$, $[Co(L^1)_2$·Phen]

2.2.3.1. Crystal data. All crystallographic measurements were performed at room temperature on an "Xcalibur-3" diffractometer (Mo$K\alpha$ radiation, CCD-detector, graphite monochromator, ω-scans). The data for the both structures were corrected for Lorentz and polarization effects. The semi-empirical from equivalents absorption correction was applied.

2.2.4. $[Mn(L^2)_2\cdot Dipy]$, $[Co(L^3)_2\cdot Dipy]\cdot CH_3OH$

2.2.4.1. Crystal data. All crystallographic measurements for both compounds were performed at room temperature on a Bruker Smart Apex II diffractometer operating in the ω and φ scan modes. In the structure $[Mn(L^2)_2\cdot Dipy]$ the chlorine atoms of both CCl_3 groups C12Cl1–3 and C20Cl4–6 and carbon atoms C21–23 of terminal CH_2CHCH_2 group are disordered over three positions each, with multiplicities 0.50, 0.25, 0.25; 0.55, 0.20, 0.25 and 0.30, 0.50, 0.20, respectively. The atoms N7C13–15, N8C16–18 and C25–26 of other $—NCH_2CHCH_2$ groups are disordered over two positions each, with multiplicities 0.70, 0.30; 0.70, 0.30 and 0.50, 0.50, respectively. In the structure $[Co(L^3)_2\cdot Dipy]\cdot CH_3OH$ the chlorine atoms of the $C54Cl_3$ and $C70Cl_3$ groups are disordered over two positions each, with multiplicities 0.849, 0.151 and 0.457, 0.543, respectively. Hydrogen atoms were placed at calculated positions as a "riding" model in both structures.

3. Results and discussion

3.1. IR-Spectroscopy

The spectra of all the complexes reveal significantly lower frequencies of ν(PO) than those of their sodium salts, $\Delta\nu$(PO) = 10–50 cm^{-1}, reflecting the coordination *via* the phosphoryl oxygen atom (Table 3) [4,6]. In the case of the $Co(L^2)_2$·Phen and $Ni(L^2)_2$·Phen compounds, the position of the ν(PO) absorption band can be identified ambiguously. The ν(CO) values of the complexes are

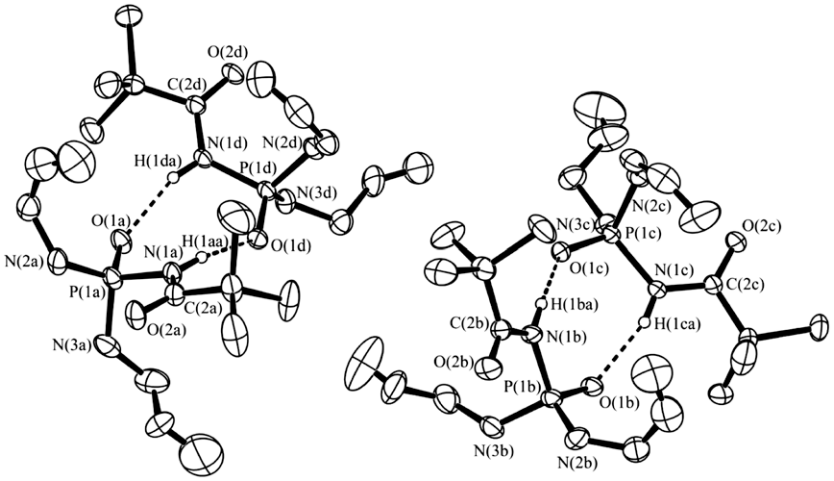


Fig. 1. Independent part of the N-(N′,N″-diallylaminophosphinyl)-trichloroacetamide (hydrogen atoms of allylamidic groups are omitted).

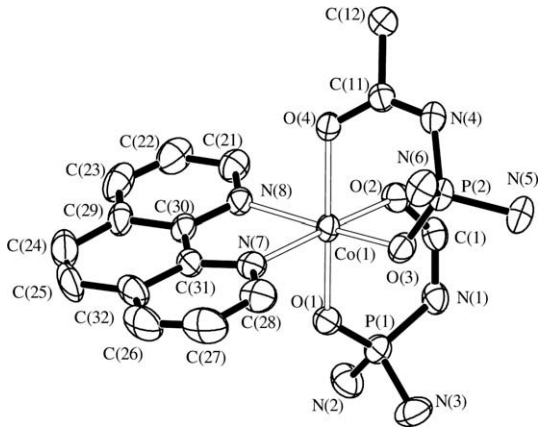


Fig. 2. Fragment of the structure of *bis*-N-(N′,N″-tetraethylaminophosphinyl)-trichloroacetamido–1,10-phenanthroline cobalt(II) (chlorine atoms, ethyl groups and protons are omitted).

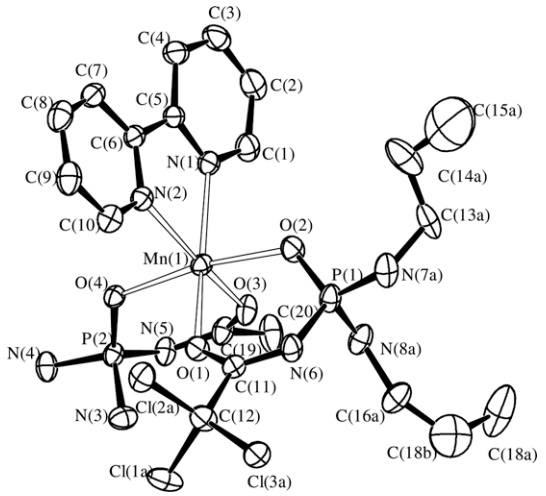


Fig. 3. Fragment of the structure of *bis*-N-(N′,N″-diallylaminophosphinyl)-trichloroacetamido-2,2′-dipyridyl manganese(II) (all protons, chlorine atoms in one molecule of ligand are omitted).

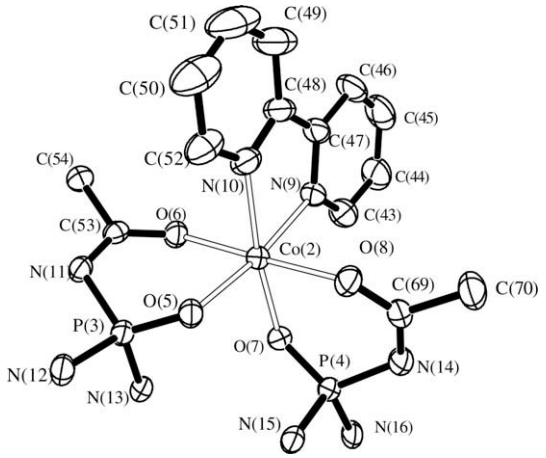


Fig. 4. Fragment of the structure of *bis*-N-(N′,N″-dibenzylaminophosphinyl)-trichloroacetamido-2,2′-dipyridyl cobalt(II) methanol solvate (chlorine atoms, benzyl groups and protons are omitted).

shifted to lower frequencies ($\Delta\nu$(CO) = 50–63 cm^{-1}). These facts can be explained by the fact that $(L^1)^-$, $(L^2)^-$ and $(L^3)^-$ display a bidentate coordination mode *via* the oxygen atoms of the phosphoryl and carbonyl groups, as in the deprotonated forms of the ligands. The absorption bands of dipyridyl and phenanthroline molecules in the IR spectra of the compounds are overlapped by the bands of the ligands or have low intensities.

3.2. UV–Vis Spectroscopy

The UV–Vis absorption spectra of the compounds $Co(L^2)_2$·Phen, $Ni(L^2)_2$·Phen, $Co(L^2)_2$·Dipy and $[Co(L^3)_2$·Dipy]·CH_3OH prove the octahedral environment of the metal atoms. Thus, in the absorption spectrum of $Co\{L\}_2$·Lig, a band corresponding to the transition $^4T_{1g}(P) \rightarrow {}^4T_{1g}$ is observed near 470 nm (for $Co(L^2)_2$·Phen – 465, 484.4 nm; for $Co(L^2)_2$·Dipy – 468, 483 nm; for $[Co(L^3)_2$·Dipy]·CH_3OH – 464, 484.4 nm) [15]. The transition $^4A_{2g} \rightarrow {}^4T_{1g}$ in the absorption spectrum of $Cu(L^3)_2$·Phen is very weak and appears as a peak near 670 nm. The transition $^3A_{2g} \rightarrow {}^3T_{1g}(^3F)$ is observed in the spectrum of the $Ni(L^2)_2$·Phen complex near 600 nm.

3.3. Description of the structures

We succeeded in confirming the conclusions about the structures of the obtained compounds (based on IR and UV–Vis spectroscopy data) by the results of full X-ray analysis of the compounds $Co(L^1)_2$·Phen, $Mn(L^2)_2$·Dipy and $[Co(L^3)_2$·Dipy]·CH_3OH. The geometry of the ligand HL^2 and the complexes, and the atom-labeling scheme are shown in Figs. 1–4. Selected bond lengths and angles are collected in Tables 4 and 5.

3.3.1. $H(L^2)$

The unique part of $H(L^2)$ consists of four molecules of ligands that are coupled into dimers by the H-bond function of the phosphoryl oxygen atoms. The hydrogen atoms of the amidic group form an eight-membered cycle (Fig. 1). The dimers are linked into polymer chains by means of hydrogen bonding with oxygen atoms of carbonyl groups and hydrogen atoms of allylamide groups. Table 4 lists the geometrical parameters of the hydrogen bonding for $H(L^2)$.

In the structure of $H(L^2)$, as in most carbacylamidophosphates [16], the carbonyl and phosphoryl groups are in *anti*-positions to each other. The phosphorus atom in the molecule of N,N′-diallyl-N″-trichloroacetylphosphortriamide has a slightly distorted tetrahedral configuration. The environment of the nitrogen atoms of the trichloroacetylamide group is practically planar. The P–N(1)

Table 4
Geometry of the hydrogen bonds for $H(L^2)$.

Donor (D)	Hydrogen atom (H)	Acceptor (A)	*d*, [Å]			Angle, [°]
			D–H	A···H	D···A	D–H···A
N1A	H1NA	O1D	0.86	2.01	2.813(3)	155.5
N2A	H2NA	O2A*	0.86	2.16	3.004(4)	165.7
N1B	H1NB	O1C	0.86	1.97	2.800(3)	161.3
N2B	H2NB	O2B**	0.86	2.20	3.031(4)	162.9
N1C	H1NC	O1B	0.86	2.06	2.891(3)	162.7
N2C	H2NC	O2C***	0.86	2.46	3.151(3)	137.4
N3C	H3NC	O1B****	0.86	2.30	3.045(4)	144.9
N1D	H1ND	O1A	0.86	2.02	2.853(3)	162.6
N2D	H2ND	O2D*****	0.86	2.39	3.095(3)	139.2
N3D	H3ND	O1A******	0.86	2.28	3.011(4)	143.6

Symmetry transformation used to generate equivalent atoms: * $-x, 1-y, -z$; ** $1-x, 1-y, 1-z$; *** $2-x, -y, 1-z$; **** $1-x, -y, 1-z$; ***** $1-x, -y, -z$; ****** $-x, -y, -z$.

Table 5
Selected bond lengths (Å) in the structures HL^2, $[Co(L^1)_2{\cdot}Phen]$, $[Mn(L^2)_2{\cdot}Dipy]$ and $[Co(L^3)_2{\cdot}Dipy]{\cdot}CH_3OH$.

	M–O(P)	M–O(C)	M–N	P=O	C=O	C–N$_{(cycle)}$	P–N$_{(cycle)}$	P–N$_{(term)}$
$[Co(L^1)_2{\cdot}Phen]$*	2.044(3)	2.094(3)	2.130(4)	1.494(3)	1.245(6)	1.292(7)	1.631(5)	1.634
	2.075(3)	2.097(3)	2.138(4)	1.491(4)	1.254(6)	1.286(6)	1.627(5)	
HL^1				1.475(1)	1.207(2)	1.338(3)	1.696(2)	1.622(2)
								1.631(2)
$[Mn(L^2)_2{\cdot}Dipy]$	2.115(2)	2.191(2)	2.256(2)	1.498(2)	1.260(3)	1.293(4)	1.642(3)	*
	2.147(2)	2.199(2)	2.264(2)	1.470(2)	1.259(3)	1.293(4)	1.638(3)	
$[Co(L^3)_2{\cdot}Dipy]$	2.066(3)	2.152(3)	2.110(4)	1.502(3)	1.254(5)	1.305(6)	1.644(4)	1.628(av)
$\cdot CH_3OH$	2.106(3)	2.118(3)	2.123(4)	1.502(3)	1.250(5)	1.298(5)	1.633(4)	
**	2.065(3)	2.146(3)	2.102(4)	1.505(3)	1.254(5)	1.311(6)	1.647(3)	
	2.074(3)	2.149(3)	2.113(4)	1.506(3)	1.265(5)	1.297(5)	1.640(4)	
HL^3				1.4806(14)	1.213(2)	1.355(2)	1.708(2)	1.630(2)
								1.631(2)
HL^2***				1.4663	1.2038	1.3458	1.6938	1.6074

* The bond lengths for P–N$_{(terminal)}$ in the structure are omitted because the carbon atoms of the terminal CH_2CHCH_2 group are disordered over 3 positions each.
** The unit cell consists of 2 independent molecules.
*** The unit cell consists of 4 independent molecules (the bond lengths are averaged).

distance of trichloroacetylamide (av. 1.6938 Å) is longer than the P–N distance in the allylamide group (1.6074 Å [17]).

The intramolecular distances between the carbonyl oxygen and phosphorus atoms (2.95 Å for molecule **A**, 2.96 Å for molecule **B**, 3.01 Å for molecule **C** and 3.04 Å for molecule **D**) are considerably shorter than the sum of Van der Waals radii (3.3 Å) (Fig. 1). This may be rationalised in terms of a strong attractive interaction between $P^{\delta+}$–$O^{\delta-}$. Similar contacts were found in $C_6H_5C(O)NHP(O)(OCH_3)_2$ [18] and $CCl_3C(O)NHP(O)[N(CH_2CH_2)_2O]_2$ [19], studied earlier.

3.3.2. $[Co(L^1)_2{\cdot}Phen]$, $[Mn(L^2)_2{\cdot}Dipy]$, $[Co(L^3)_2{\cdot}Dipy]{\cdot}CH_3OH$

The complexes $[Co(L^1)_2{\cdot}Phen]$, $[Mn(L^2)_2{\cdot}Dipy]$ and $[Co(L^3)_2{\cdot}Dipy]{\cdot}CH_3OH$ have a molecular structure. In all the complexes, the organic ligands are coordinated in the bidentate manner *via* oxygen atoms of phosphoryl and carbonyl groups, forming six-membered chelates (Figs. 2–4 respectively). The corresponding bond lengths M–O(P) for $[Co(L^1)_2{\cdot}Phen]$ and $[Co(L^3)_2{\cdot}Dipy]{\cdot}CH_3OH$ are in the 2.044–2.106 Å range (Table 5). The corresponding ranges of the carbonyl groups for these complexes are the longest ones, 2.094(3)–2.152(3) Å. In the case of $[Mn(L^2)_2{\cdot}Dipy]$, the similar bond lengths are rather longer 2.115(2) and 2.147(2) Å (for M–O(P)). Similarly, the M–O bond lengths for the carbonyl groups increase by an average of 0.06 Å. This fact can be explained by the stronger affinity of the phosphoryl group to metal ions than the carbonyl group.

The chelate (O)PNC(O) frames of all the phosphoryl ligands form planar six-membered rings with the central atom. A decrease in the P–N and C–N distances in the coordinated ligand compared to the free ligand (Table 5) and an increase in the P=O and C=O distances demonstrates the presence of π-conjugation in the chelate fragments.

The phosphorous atoms of the title compounds have a slightly distorted tetrahedral geometry. The maximum deviation is for the angle NPO, 114.3–115.9(5)°, which is involved in the formation of the six-membered chelate rings, whereas in the free ligands this angle is less than that in the tetrahedron and equals 105.40(9) for $H(L^1)$, 106.44° for $H(L^2)$ and 106.82(8) for $H(L^3)$ (Table 6). The carbonyl atom has a sp^2-character. The planar bidentate chelating dipyridyl and phenanthroline ligands are coordinated into

Table 6
The values of angles (°) involved in chelate fragments in the structures HL^2, $[Co(L^1)_2{\cdot}Phen]$, $[Mn(L^2)_2{\cdot}Dipy]$ and $[Co(L^3)_2{\cdot}Dipy]{\cdot}CH_3OH$.

	M–O–P	M–O–C	O-M-O$_{(cycle)}$	N-M-N	O–C–N	C–N–P	N–P–O
$[Co(L^1)_2{\cdot}Phen]$	127.2(1) 124.7(1)	127.3(3) 120.7(3)	88.6	77.8(1)	132.1	123.1	116.5
HL^1					125.8(3)	126.8(2)	105.40(9)
$[Mn(L^2)_2{\cdot}Dipy]$	123.17(1)	130.87(1)	83.81(8)	71.9(1)	130.9(5)	118.5(2)	116.19(1)
$[Co(L^3)_2{\cdot}Dipy]{\cdot}CH_3OH$	120.1	127.4	86.9	76.78(15)	131.5	116.8	114.3
**	118.8	126.1	87.8	76.96(18)	129.9	115.9	115.9
HL^3					125.3(2)	122.92(12)	106.82(8)
HL^2***					125.1	122.93	106.44

** The unit cell consists of 2 independent molecules.
*** The unit cell consists of 4 independent molecules (the bond lengths are averaged).

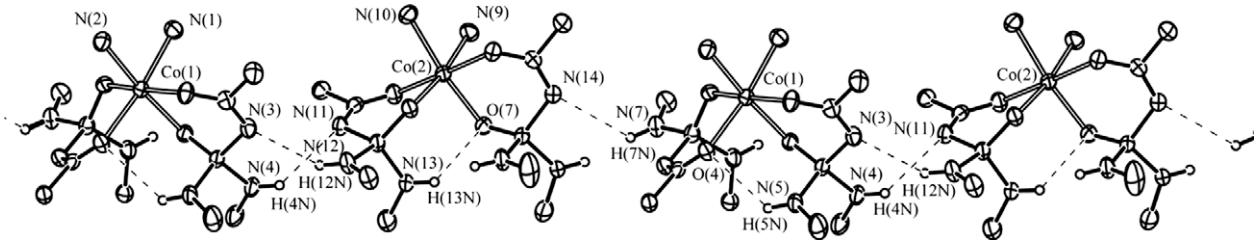


Fig. 5. System of H-bonds in the structure *bis*-N-(N′,N″-dibenzylaminophosphinyl)-trichloroacetamido-2,2′-dipyridyl cobalt(II) methanol solvate.

Table 7
Geometry of hydrogen bonds for $[Co(L^3)_2{\cdot}Dipy]{\cdot}CH_3OH$

Donor	Hydrogen	Acceptor	*d* (Å)			Angle (°)
(D)	atom (H)	(A)	D–H	A···H	D···A	D–H···A
O86	H86	O85	0.82	2.0848	2.860(1)	157.92
N5	H5N	O4	0.860(4)	2.5674	3.150(5)	125.90
N13	H13N	O7	0.860(4)	2.4836	3.068(6)	125.92
N4*	H4N*	N11	0.860(4)	2.7074	3.338(6)	131.32
N12*	H12N*	N3	0.861(4)	2.4722	3.219(5)	145.51
N7**	H7**	N14	0.860(4)	2.7192	3.315(6)	127.54

Symmetry transformation used to generate equivalent atom: * $1-x, 2-y, 1-z$; ** $1-x, 1-y, 1-z$.

five-membered rings. The coordination polyhedra in all the above structures are distorted octahedrons.

In the structure $[Co(L^3)_2{\cdot}Dipy]{\cdot}CH_3OH$ two types of irregular hydrogen bonds occur (Fig. 5). The parameters of all the hydrogen bonds are given in Table 7.

The complex molecules Co(1) and Co(2) are complementarily connected into dimer units by hydrogen atoms of the benzylamide group and nitrogen atoms of the chelate (H(4N)···N(11) and H(12N)···N(3)). Such units are associated by singular hydrogen bonds, which form between the free chelate nitrogen atom and benzylamide protons of the next unit, such as (N(14)···H(7N)).

4. Conclusion

In this contribution it has been shown that carbacylphosphotriamidic ligands, like β-diketonates, form stable coordination compounds of the composition $ML_2{\cdot}Lig$ (where M = Co(II), Mn(II); Cu(II), Ni(II), L = $\{Cl_3C(O)NP(O)R_2\}^-$ (R = $NHCH_2Ph$, $NHCH_2CHCH_2$, NEt_2); Lig = 2,2′-dipyridyl or 1,10-phenanthroline). Stable heteroligand complexes of Co(II) and Mn(II), with a distorted octahedral coordination geometry, have been realised. In the three structures studied, the organic ligands were coordinated *via* oxygen atoms of phosphoryl and carbonyl groups, forming six-membered cycles.

On the basis of X-ray studies, it was verified that the bond length M–O(P) in all the structures discussed is shorter than the M–O(C) bond length. This confirms the fact that the phosphoryl group has a greater affinity towards metal ions as compared to the carbonyl group.

For the first time in the chemistry of carbacylamidophosphates, intermolecular H-bonds with the participation of amidic protons and the coordinated phosphoryl oxygen of a neighboring ligand in the same complex molecule have been registered.

Supplementary data

CCDC 670292, 656940, 643803 and 643802 contains the supplementary crystallographic data for HL^2, $[Co(L^1)_2{\cdot}Phen]$, $[Mn(L^2)_2{\cdot}Dipy]$ and $[Co(L^3)_2{\cdot}Dipy]{\cdot}CH_3OH$, respectively. These data can be obtained free of charge via http://www.ccdc.cam.ac.uk/conts/retrieving.html, or from the Cambridge Crystallographic Data Centre, 12 Union Road, Cambridge CB2 1EZ, UK; fax: (+44) 1223-336-033; or e-mail: deposit@ccdc.cam.ac.uk.

References

[1] A.M.Z. Slawin, M. Wainwright, D. Woolins, New J. Chem. 24 (2000) 69.
[2] T.Q. Ly, J.D. Woolins, Coord. Chem. Rev. 176 (1998) 469.
[3] F.D. Sokolov, S.V. Baranov, D.A. Safin, F.E. Hahn, M. Kubiak, T. Pape, M. Babashkina, N. Zabirov, J. Galezowska, H. Kozlowski, R. Cherkasov, New J. Chem. 31 (2007) 1661.
[4] V.A. Ovchynnikov, V.M. Amirkhanov, A.A. Kapshuk, T.Yu. Sliva, T. Glowiak, H. Kozlowski, Z. Naturforsch. 53b (1998) 836.
[5] D.L. Kepert, Comprehensive coordination chemistry, in: G. Wilkinson (Ed.), Pergamon, Oxford, 1987, p. 61.
[6] E.A. Bundya, V.M. Amirkhanov, V.A. Ovchynnikov, V.A. Trush, K.V. Domasevitch, J. Sieler, V.V. Skopenko, Z. Naturforsch. 54 (1999) 1033.
[7] K.E. Gubina, V.A. Ovchynnikov, J. Swiatek-Kozlowska, V.M. Amirkhanov, T.Yu. Sliva, K.V. Domasevitch, Polyhedron 21 (2002) 963.
[8] A.N. Grigor'ev, A.Yu. Steblyanko, A.V. Goncharov, K.A. Potekhin, A.S. Batsanov, Yu.T. Struchkov, Russ. J. Inorg. Chem. 32 (1987) 706.
[9] A.Yu. Steblyanko, A.N. Grigor'ev, L.I. Martynenko, M.V. Reshetnyak, A.S. Batsanov, Yu.T. Struchkov, Russ. J. Inorg. Chem. 33 (1988) 1515.
[10] M.H. Dickman, Acta Crystallogr., Sect. C: Cryst. Struct. Commun. 55 (1999) 146.
[11] R. Gorkum, F. Buda, H. Kooijman, A.L. Spek, E. Bouwman, J. Reedijk, Eur. J. Inorg. Chem. (2005) 2255.
[12] V.M. Amirkhanov, V.A. Ovchynnikov, V.A. Trush, V.V. Skopenko, Russ. J. Org. Chem. 32 (1996) 376.
[13] A.V. Kirsanov, G.I. Derkach, Zh. Obshchei Khimii 26 (1956) 2631.
[14] G.M. Sheldirck, B. Blessing, Acta Cryst. A51 (1995) 33.
[15] A.B. Lever, Inorganic Electronic Spectroscopy, vol. 2, Moscow, 1987.
[16] V.M. Amirkhanov, V.A. Ovchynnikov, T. Glowiak, H. Kozlowski, Z. Naturforsch. 52b (1997) 1331.
[17] D.W.J. Cruickshank, J. Chem. Soc. (1961) 5486.
[18] V. Mizrahi, T.A. Modro, Cryst. Struct. Commun. 11 (1982) 627.
[19] V.A. Ovchynnikov, V.M. Amirkhanov, T.P. Timoshenko, T. Glowiak, H. Kozlowski, Z. Naturforsch. 53 b (1998) 481.

Polyhedron 28 (2009) 2667–2672

Contents lists available at ScienceDirect

Polyhedron

journal homepage: www.elsevier.com/locate/poly

Synthesis, crystal structure and properties of cobalt(II) and nickel(II) coordination polymers supported by functionalized dicarboxylate ligands

Yanhong Zhou, Li Guan, Hong Zhang *

Key Laboratory of Polyoxometalate Science of Ministry of Education, Department of Chemistry, Northeast Normal University, Changchun, Jilin 130024, China

ARTICLE INFO

Article history:
Received 10 May 2009
Accepted 3 June 2009
Available online 16 June 2009

Keywords:
Coordination polymers
Carboxylate ligands
Helical chain
Cobalt(II) and nickel(II)

ABSTRACT

Four new coordination polymers of cobalt(II) and nickel(II) with functionalized dicarboxylate ligands, namely, $[Co^{II}L^1(2,2'\text{-bpy})(H_2O)]$ (**1**), $[Ni^{II}L^1(2,2'\text{-bpy})(H_2O)]\cdot H_2O$ (**2**), $[Co^{II}_2(L^2)_2(2,2'\text{-bpy})_2(H_2O)]$ (**3**) and $[Ni^{II}_2(L^2)_2(2,2'\text{-bpy})_2(H_2O)]$ (**4**), where H_2L^1 = 2,5-dibenzoylterephthalic acid, H_2L^2 = 4,6-bis(4-methylbenzoyl) isophthalic acid and 2,2′-bpy = 2,2′-bipyridine, were synthesized and characterized by elemental analysis, IR spectra and thermogravimetric analysis. Complex **1** exhibits a zigzag chain with a C–H···π interaction between the phenyl ring proton and the phenyl ring of an adjacent chains to form a 2D supramolecular sheet. Complex **2** contains two helical chains which extend into 2D via a C–H···π interaction between the pyridine ring proton and the pyridine ring. Complexes **3** and **4** are isomorphous with helical chains that extend in the same direction and further link to one another by supramolecular forces into a 2D structure. Moreover, magnetic and luminescence properties have been investigated for **1** and **2**, respectively.

© 2009 Elsevier Ltd. All rights reserved.

1. Introduction

The design and synthesis of metal–organic frameworks (MOFs) are continuously attractive among coordination and material chemistry, not only due to the frequently novel motifs of their architectures but also their potential applications in gas storage, chemical separations, ion exchange, non-linear optics, magnetism and heterogeneous catalysis [1–17]. A great variety of interesting architectures have been reported including helix, brick wall, honeycomb, layer, ladder, grids, boxes and herringbone [18–26], of which helical coordination polymers are particularly attractive because of their fascinating structures and applications in many fields [27–34]. Although discrete helices and low-dimensional helical coordination polymers are now abundant, the assembly of such helical units into higher order networks is still a challenge.

In an attempt to construct helical frameworks, we choose functionalized dicarboxylate ligands to give birth to new complexes. So four new coordination polymers of Co(II) and Ni(II) were obtained by using benzoyl-substituted terephthalic acid (H_2L^1) and methylbenzoyl-substituted isophthalic acid (H_2L^2) (Chart 1) as ligands. The choice of these ligands was based on the following considerations: (1) Each ligand has six oxygen atoms potentially available for metal coordination; (2) the aromatic substituent may rotate around the central phenyl ring. This flexibility may be significant in realizing interesting structures; (3) the extended π-system of the substituted ligands, which are derived from terephthalic and isophthalic acid, may be useful for luminescent and/or magnetic properties of coordination polymers. In addition, in this work we also introduce 2,2′-bipyridine as an auxiliary ligand to control the structure and dimensionality of the resulting coordination polymers [35–37]. The synthesis and structural characterization of four new coordination polymers $[Co^{II}L^1(2,2'\text{-bpy})(H_2O)]$ (**1**), $[Ni^{II}L^1(2,2'\text{-bpy})(H_2O)]\cdot H_2O$ (**2**), $[Co^{II}_2(L^2)_2(2,2'\text{-bpy})_2(H_2O)]$ (**3**) and $[Ni^{II}_2(L^2)_2(2,2'\text{-bpy})_2(H_2O)]$ (**4**) are reported here. Furthermore, interesting luminescence and magnetic properties have been studied for complexes **1** and **2**, respectively.

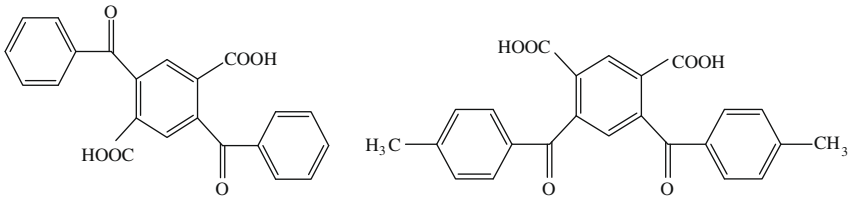
2. Experimental

2.1. Materials and physical measurements

Reagents were purchased commercially and were used without further purification. The ligands H_2L^1 and H_2L^2 were synthesized according to the literature method [38]. The FI-IR spectra were recorded using KBr pellets in the range 4000–400 cm^{-1} on a Mattson Alpha-Centauri spectrometer. Elemental analyses for C, H and N were performed on a Perkin–Elmer 2400 Elemental Analyzer. The thermal behaviors were studied by TGA on a Perkin–Elmer Thermal Analyzer under N_2 with a heating rate of 5 °C/min. The fluorescence spectrum for **2** was obtained using a Cary Eclipse luminescence spectrophotometer (VARIAN. USA). The temperature-dependent magnetic susceptibility of **1** was measured with crystalline samples on a Quantum Design MPMS XL-5 Squid magnetometer in a magnetic field of 1000 Oe under the temperature range 2–300 K.

* Corresponding author. Tel.: +86 431 85099372; fax: +86 431 85684009.
E-mail address: zhangh@nenu.edu.cn (H. Zhang).

0277-5387/$ - see front matter © 2009 Elsevier Ltd. All rights reserved.
doi:10.1016/j.poly.2009.06.022



H_2L^1 H_2L^2

Chart 1.

2.2. Synthesis

2.2.1. Synthesis of $[Co^{II}L^1(2,2'\text{-bpy})(H_2O)]$ (**1**)

To a mixture containing H_2L^1 (18.7 mg, 0.05 mmol), $Co(NO_3)_2{\cdot}6H_2O$ (0.73 mg, 0.025 mmol) and 20 mL H_2O, was added aqueous NaOH (0.05 M) to adjust the pH of the mixture to be 5.0, and then 2,2′-bpy (0.40 mg, 0.025 mmol) was added. The resulting mixture was stirred for 30 min and then filtered. Upon standing the filtrate for about a month, the purple-colored cube-shaped crystals were obtained, washed by H_2O and air-dried (yield: 54% based on $Co(NO_3)_2{\cdot}6H_2O$). *Anal.* Calc. for $C_{32}H_{21}CoN_2O_7$: C, 63.53; H, 3.47; N, 4.63. Found: C, 63.43; H, 3.6; N, 4.42%. IR (KBr, cm^{-1}): 1678s, 1594m, 1560m, 1395s, 1326m, 1246m, 1020w, 951w, 929w, 770s, 532s.

2.2.2. Synthesis of $[Ni^{II}L^1(2,2'\text{-bpy})(H_2O)]{\cdot}H_2O$ (**2**)

To a mixture containing H_2L^1 (18.7 mg, 0.05 mmol), $Ni(NO_3)_2{\cdot}6H_2O$ (0.72 mg, 0.025 mmol) and 20 mL H_2O, was added aqueous NaOH (0.05 M) to adjust the pH of the mixture to be 8.0, and then 2,2′-bpy (0.40 mg, 0.025 mmol) was added. The resulting mixture was stirred for 30 min and then transferred to a Teflon-lined stainless steel vessel (25 mL), sealed, heated to 160 °C and maintained at that temperature for 3 days, then finally cooled at a rate of 5 °C/h to room temperature. Blue-colored cube-shaped crystals were obtained, washed by H_2O and air-dried (Yield: 72% based on $Ni(NO_3)_2{\cdot}6H_2O$). *Anal.* Calc. for $C_{32}H_{23}NiN_2O_8$: C, 61.71; H, 3.7; N, 4.5. Found: C, 61.62; H, 3.85; N, 4.42%. IR (KBr, cm^{-1}): 1673s, 1660m, 1576m, 1552s, 1490w, 1353s, 1249s, 1026w, 772s, 634w, 521m.

2.2.3. Synthesis of $[Co^{II}_2(L^2)_2(2,2'\text{-bpy})_2(H_2O)]$ (**3**)

The pH of an aqueous solution containing H_2L^2 (20.2 mg, 0.05 mmol), $Co(NO_3)_2{\cdot}6H_2O$ (0.73 mg, 0.025 mmol) and 18 mL H_2O was adjusted with K_2CO_3 to 6.0, and then 2,2′-bpy (0.40 mg, 0.025 mmol) was added. The resulting mixture was stirred for 30 min, filtered, and then transferred to a Teflon-lined stainless steel vessel (25 mL), sealed, heated to 150 °C and maintained at that temperature for 4 days, then finally cooled at a rate of 5 °C/h to room temperature. This afforded purple-colored cube-shaped crystals of **3**, which were washed by H_2O and air-dried (Yield: 66% based on $Co(NO_3)_2{\cdot}6H_2O$). *Anal.* Calc. for $C_{68}H_{49}Co_2N_4O_{13}$: C, 65.39; H, 3.93; N, 4.49. Found: C, 65.28; H, 4.14; N, 4.30%. IR (KBr, cm^{-1}): 1657s, 1603s, 1582m, 1384s, 1260m, 920w, 896m, 768s, 738m, 655w, 506w.

2.2.4. Synthesis of $[Ni^{II}_2(L^2)_2(2,2'\text{-bpy})_2(H_2O)]$ (**4**)

Complex **4** was synthesized by starting with $Ni(NO_3)_2{\cdot}6H_2O$ (0.72 mg, 0.025 mmol) under similar conditions to **3**, except that the pH of the reaction mixture was 8.5. Blue-colored cube-shaped crystals of **4** were obtained (Yield 58% based on $Ni(NO_3)_2{\cdot}6H_2O$).

Table 1
Crystal data and structure refinement for complexes **1**–**4**.

Complex	**1**	**2**	**3**	**4**
Formula	$C_{32}H_{21}N_2O_7Co$	$C_{32}H_{23}N_2O_8Ni$	$C_{68}H_{49}N_4O_{13}Co_2$	$C_{68}H_{49}N_4O_{13}Ni_2$
fw	604.44	622.22	1247.97	1247.53
T (K)	293(2)	296(2)	296(2)	293(2)
λ (Å)	0.71069	0.71073	0.71073	0.71069
Crystal system	triclinic	monoclinic	monoclinic	monoclinic
Space group	$P\bar{1}$	$P2_1/c$	$P2_1/c$	$P2_1/c$
a (Å)	9.373(12)	13.9956(8)	16.0141(9)	15.852(12)
b (Å)	11.673(15)	20.7637(12)	17.5279(10)	17.539(13)
c (Å)	13.808(18)	10.2864(6)	22.2579(13)	22.255(17)
α (°)	75.243(2)	90.00	90.00	90.00
β (°)	75.941(2)	110.7600(10)	102.5850(10)	102.687(10)
γ (°)	71.844(2)	90.00	90.00	90.00
V (Å^3)	1366.1(3)	2795.2(3)	6097.5(6)	6036.4(8)
Z	2	4	4	4
Dc (g/cm^3)	1.469	1.474	1.359	1.373
μ (mm^{-1})	0.682	0.751	0.612	0.693
R_1[a] [$I > 2\sigma(I)$]	0.0356	0.0337	0.0389	0.0369
wR_2[b] [$I > 2\sigma(I)$]	0.0920	0.0941	0.0839	0.0831
R_1 (all data)	0.0428	0.0379	0.0805	0.0652
wR_2 (all data)	0.0953	0.0966	0.0965	0.0914
Goodness-of-fit	1.103	1.066	0.992	1.008
Transmission (max/min)	0.903/0.822	0.874/0.835	0.907/0.863	0.901/0.861
Δ/σ (max/min)	0.460/−0.269	0.746/−0.718	0.248/−0.262	0.331/−0.332
F(0 0 0)	620	1276	2572	2580

[a] $R_1 = \sum||F_o|-|Fc||/\sum|F_o|$.
[b] $wR_2 = \sum[w(F_o^2-Fc^2)2]/\sum[w(F_o^2)^2]^{1/2}$.

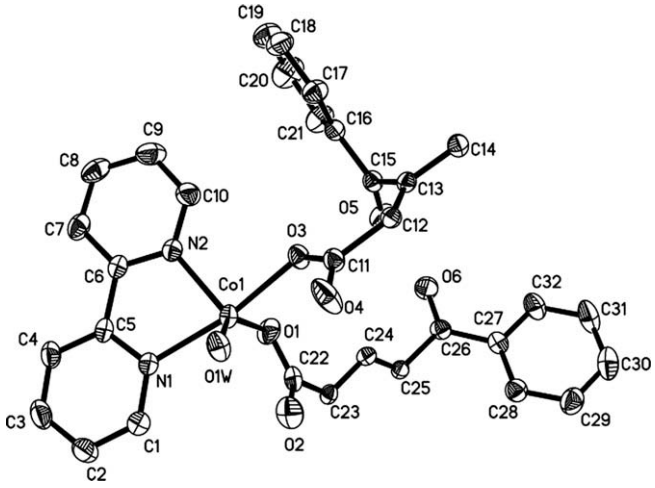


Fig. 1a. Coordination environment of Co atom in **1** with the ellipsoids draw at the 30% probability level, all hydrogen atoms are omitted for clarity.

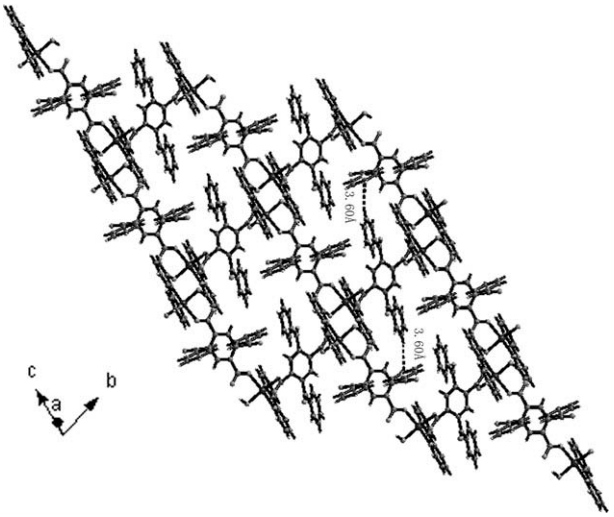


Fig. 1b. A view of a 2D diagram in **1** via C–H···π interactions.

Anal. Calc. for $C_{68}H_{49}Ni_2N_4O_{13}$: C, 65.41; H, 3.93; N, 4.49. Found: C, 65.32; H, 4.14; N, 4.30%. IR (KBr, cm^{-1}): 1658s, 1604s, 1579s, 1552s, 1490m, 1388s, 1042w, 896m, 769s, 739m, 571w, 413w.

2.3. X-ray crystallography

Single crystals of **1**–**4** were glued to a fiberglass for data collection on a SMART (Bruker, 2002) diffractometer equipped with Mo Kα radiation. Empirical absorption corrections were applied to the data using ABSCOR [39]. The structure was solved by the direct method followed by the difference Fourier method and refined by full-matrix least-squares on F^2 using the SHELXTL-97 package [40]. All non-hydrogen atoms were refined anisotropically, the hydrogen atoms of organic ligands and coordinated water were located geometrically. Due to the small crystallographic disorder for **2**, hydrogen atoms of the lattice water molecule were not located. The crystal data and structure refinements of **1**–**4** are summarized in Table 1 and selected bond lengths and angles are listed in the supplementaryinformation (S1 Table S1).

3. Results and discussion

3.1. Structure description

3.1.1. Structure description of *1*

Crystallographic analysis shows that complex **1** is an infinite zigzag chain coordination polymer. As shown in Fig. 1a, the Co atom is five-coordinate with two carboxylate O atoms (O1 and O3) of two different L^1 ligands, two N atoms (N1 and N2) of the chelating 2,2′-bpy and one O atom (O1 W) of the aqua ligand. The coordination geometry can be described as distorted trigonal bipyramidal with its equatorial plane defined by the O(1), N(2) and O(1 W) atoms; the axial positions are occupied by O(3) and N(1). The Co–O bond lengths, from 2.012(2) to 2.107(2) Å, and the Co–N bond lengths, from 2.086(2) to 2.131(2) Å, are within the normal range [41–43]. The two carboxylate groups show monodentate coordination (Scheme 1a) and the dihedral angles between the 1-, 4-carboxylate groups and their corresponding phenyl rings are both 173.26°. In the overall structure of **1**, units of $[Co(bpy)]^{2+}$ are connected by the bridging L^1 ligands to generate a zigzag chain with a pitch of 15.65 Å. Adjacent chains extend into

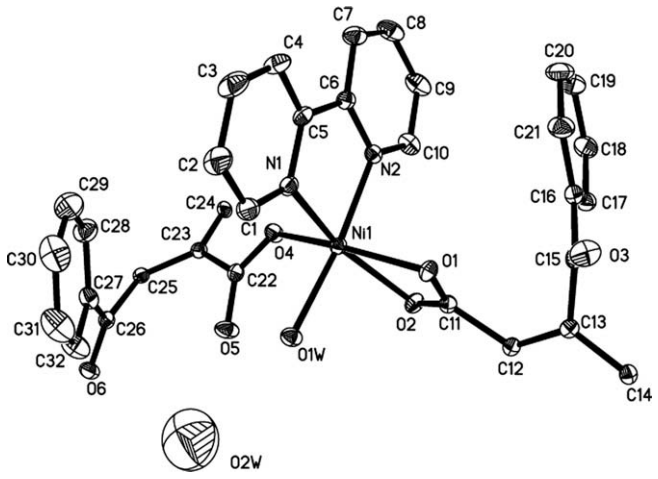
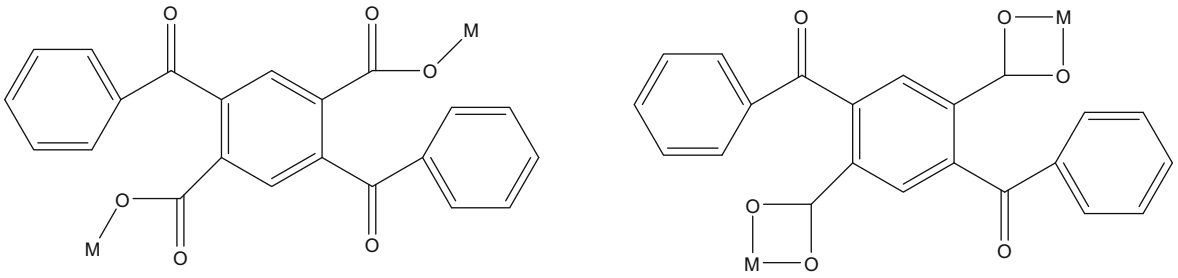


Fig. 2a. Coordination environment of the Ni atom in **2** with the ellipsoids draw at the 30% probability level, all hydrogen atoms are omitted for clarity.



Scheme 1. The L^1 ligand adopts two distinct coordination modes, namely bridging bis(mono-dentate) and chelating bisdentate coordination modes.

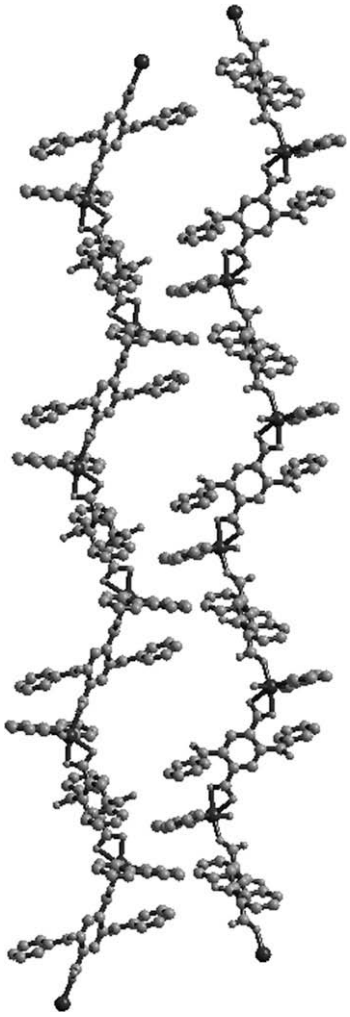


Fig. 2b. A perspective views of two infinite helical chains in **2**.

a 2D supramolecular sheet via a C–H···π interaction between the C–H moiety of the benzene rings in one chain and the benzene rings of adjacent chains (H···π 3.60 Å, C–H···π 146°, Fig. 1b).

3.1.2. Structure description of *2*

Crystallographic determination shows that there are two helical chains with opposite directions. In complex **2** the Ni atom is six-coordinate with a distorted octahedral geometry. The six-coordinate atoms are two N atoms of the 2,2′-bpy ligand (N1 and N2), two O atoms (O1 and O2) of a chelating carboxylate group, an O atom (O4) from the other monodentate carboxylate group of the L^1 ligand and an O atom (O1 W) of an aqua ligand (Fig. 2a). The average Ni–O and Ni–N bond lengths are 2.093(2) and 2.043(2) Å, respectively. The dihedral angles between the 1-, 4-carboxylate groups and their corresponding phenyl rings are both 145.89 (or 148.1)°. Doubly chelate (both carboxylate groups chelating) and doubly monodentate L^1 ligands alternate with the Ni atoms in complex **2** (Scheme 1a and b).

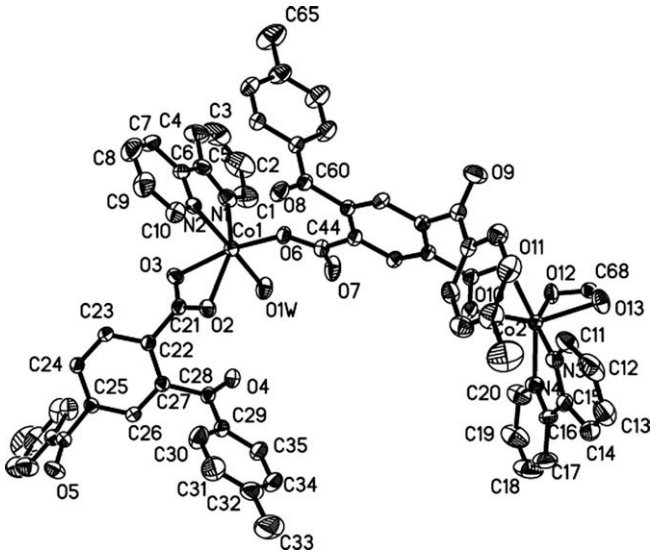


Fig. 3a. Coordination environment of the Co(1) and Co(2) atoms in **3** with the ellipsoids drawn at the 30% probability level, all hydrogen atoms are omitted for clarity.

It is clear from the above description that subtle differences exist in the coordination of the same ligand with Ni and Co ions. The combination of two twisted carboxylate groups and the rotated phenyl ring result in two strand chains in **2**, the two distinct chains coexist and are oppositely arranged via a C–H···π interaction (Fig. 2b). The $[Ni(bpy)]^{2+}$ units are joined by independent L^1 spacers to generate an infinite helical chain with a period of 20.09 Å. Those chains further extend into 2D via a C–H···π interaction between the pyridine ring proton and the pyridine ring of adjacent chains (H···π 3.18 Å, C–H···π 96°, Fig. 2c).

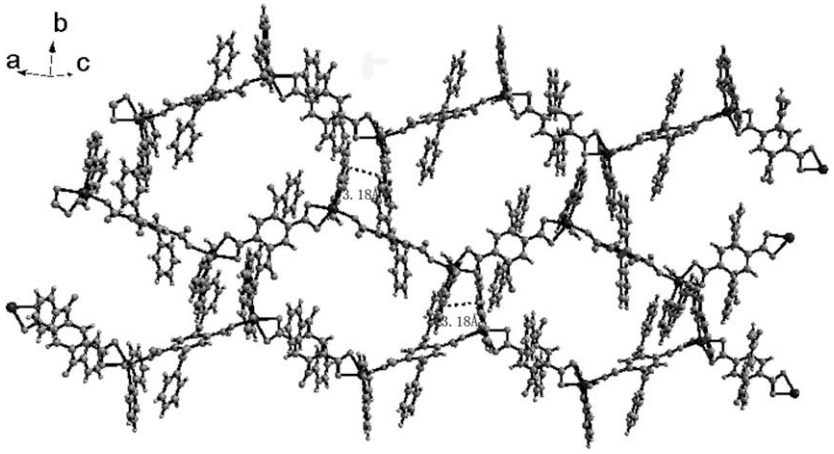
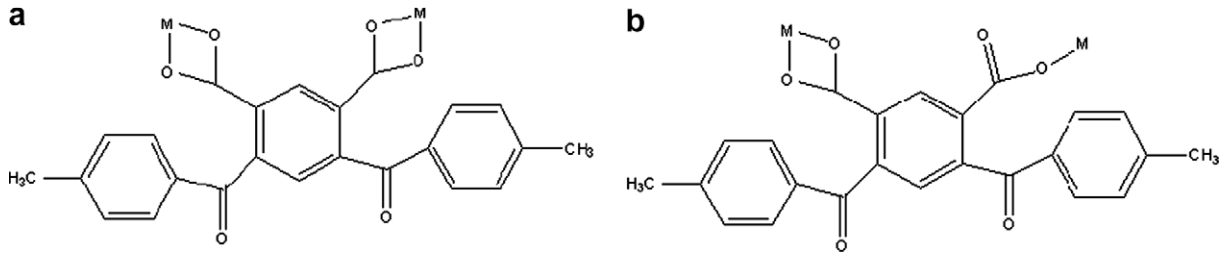


Fig. 2c. The perspective view of a 2D helical diagram in **2** via C–H···π interactions.



Scheme 2. The coordination modes of the deprotonated H_2L^2 ligand.

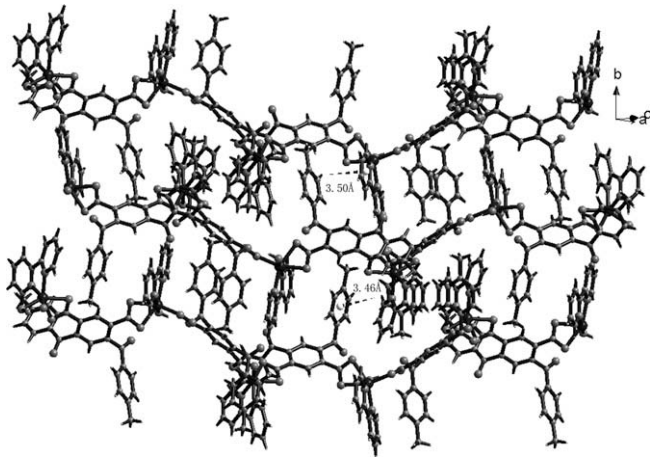


Fig. 3b. The 2D diagram of helical chain via C–H···π interactions in **3**.

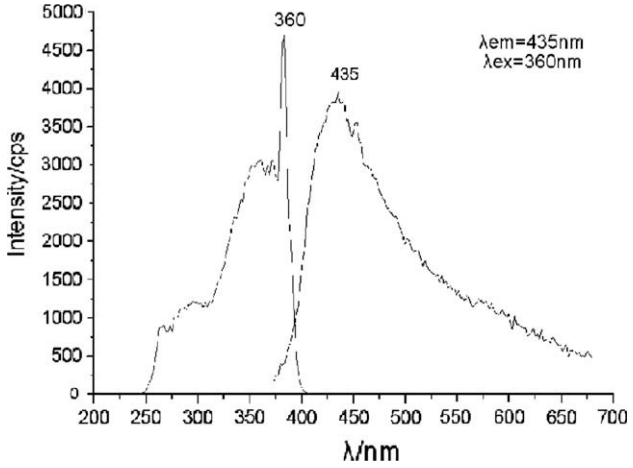


Fig. 4. Solid-state photoluminescent spectra of **2**.

*3.1.3. Structure description of **3** and **4***

Complex **3** is also a helical chain. As shown in Fig. 3a, there are two kinds of Co atoms (Co(1) and Co(2)) in **3**. The Co(1) is six-coordinate with a distorted octahedral geometry. The equatorial plane is defined by N(1), N(2), O(2) and O(1 W) atoms; the axial positions are occupied by O(3) and O(6) atoms (O(3)–Co(1)–O(6) 160.84(8)°). The Co(1)–O and Co(1)–N bond lengths are 2.024(2)–2.246(2) Å and 2.090(2)–2.100(2) Å, respectively. Co(2) is also six-coordinate, but the coordination polyhedron is more like a trigonal antiprism. In this complex Co(1) adopts the chelate-monodentate carboxylate groups coordination and Co(2) employs chelate carboxylate groups coordination (Scheme 2a and b) to afford an infinite helical chain with a period of 25.60 Å. These chains progress in one direction and further extend into a 2D supramolecular sheet via C–H···π interactions between the pyridine ring proton and a phenyl ring (H···π 3.50, 3.46 Å and C–H···π 117, 101°, Fig. 3b).

Complex **4** is isostructural with **3** but Ni atoms instead of Co atoms.

The different coordination polymers formed under slightly different reaction conditions, such as the pH is lower for **1** and **3** than for **2** and **4**, otherwise we can only obtain a precipitate not a crystalline product, which suggests that the assembly is sensitive to the synthetic conditions, including temperature (ambient or under hydrothermal conditions), pH and the nature of ligand and metal ion. At the same time, supramolecular forces also play an important role in constructing the MOFs.

3.2. Thermal analysis

The thermal stability of **1**–**4** were studied by TGA and are recorded in Fig. S1a–d (in the Supplementary data). For **1**, the weight loss incurred between 118 and 256 °C corresponds to the loss of the coordinated water molecule (Obsd. 3.01%, Calc. 2.98%). Subsequent weight loss from 300 to 402 °C is probably due to organic ligand decomposition (Obsd. 64.7%, Calc. 63.5%). The residue is Co_2O_3 (Obsd. 27.57%, Calc. 27.46%). For **2**, the TG curve exhibits three steps of weight loss. The first step is 2.84% from 100 to 140 °C and is possibly due to the loss of the water molecule of crystallization (Calc. 2.89%). The second weight loss is 2.99% in the temperature range 140–180 °C, ascribable to the loss of the aqua ligand (Calc. 2.89%). The third step from 200 to 400 °C is due to the decomposition of the organic ligand (Obsd. 65.71%, Calc. 61.71%). The remaining residue is probable NiO (Obsd. 13.62%, Calc. 12.05%). Complexes **3** and **4** are isomorphic with three steps of weight loss. For **3**, the first step is 1.40% in the temperature range 100–200 °C, corresponding to the loss of the coordinated

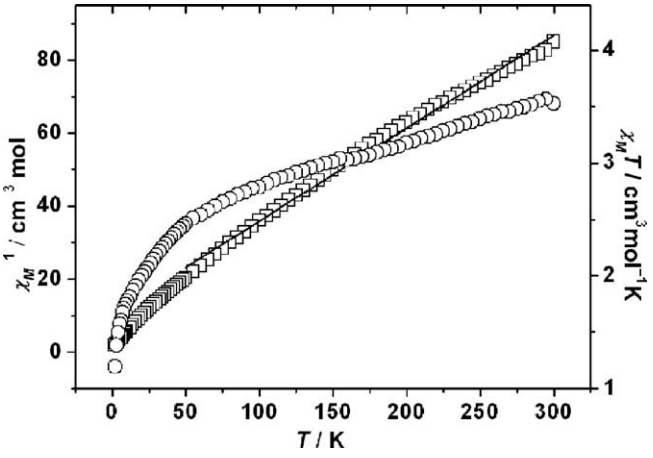


Fig. 5. Plots of the temperature dependence of $\chi_M T$ and $\chi_M{}^{-1}$ at 2–300 K.

water molecule (Calc. 1.44%). The second step is due to the release of the organic ligand in the temperature range 200–550 °C (Obsd. 64.17%, Calc. 65.38%), and the remaining weight (Obsd. 12.46%, Cacl. 13.30%) is assigned to Co_2O_3.

3.3. Luminescence properties

The solid-state luminescence of **2** was investigated. An intense emission at $\lambda em = 435$ nm upon excitation at $\lambda ex = 360$ nm (Fig. 4) was observed. The solid-state photoluminescence property of the free H_2L^1 ligand was analyzed (Fig. S2) in comparison. It is clear that the emission of **2** is blue shifted compared with the free H_2L^1 ligand, and this is assigned to an intraligand $\pi \rightarrow \pi^*$ transition and charge-transfer transition between the coordinated ligand and the metal center [44–47].

3.4. Magnetic properties

The magnetic properties of **1** were studied in the temperature range 2–300 K (Fig. 5). The $\chi_M T$ value at 300 K is 3.528 cm^3 K mol^{-1}, larger than the value for a spin-only $S = 3/2$ system (1.875 emu K mol^{-1}). This is expected as there is a significant first-order orbital contribution to the magnetic moment for a five-coordinate high spin cobalt(II) ion [48]. Upon lowering the temperature $\chi_M T$ decreases to 1.191 cm^3 K mol^{-1} at 2 K. The fitting of the curve for the $\chi_M{}^{-1}$ versus T plot to the Curie–Weiss law gives a good result in the temperature range of 50–300 K with $C = 3.931$ cm^3 K mol^{-1} and $\theta = -41.191$ K, consistent with the presence of an antiferromagnetic interaction in **1**.

4. Conclusions

In summary, $[Co^{II}L^1(2,2'\text{-bpy})(H_2O)]$ (**1**), $[Ni^{II}L^1(2,2'\text{-bpy})(H_2O)]\cdot H_2O$ (**2**), $[Co^{II}_2(L^2)_2(2,2'\text{-bpy})_2(H_2O)]$ (**3**) and $[Ni^{II}_2(L^2)_2(2,2'\text{-bpy})_2(H_2O)]$ (**4**), four new coordination polymers, were synthesized and characterized. In addition, magnetic and luminescence properties have been studied for **1** and **2**, respectively. It is anticipated that more metal–organic frameworks (MOFs) employing L^1, L^2 or other analogous ligands will be produced and possibly realized in functioned materials.

Acknowledgements

We gratefully acknowledge financial support by the NSF of China (20771023), 863 Program (2007AA03z218) and analysis and testing foundation of Northeast Normal University.

Appendix A. Supplementary data

CCDC 691998, 703442, 701829 and 702993 contain the supplementary crystallographic data for compounds **1**, **2**, **3** and **4**. These data can be obtained free of charge via http://www.ccdc.cam.ac.uk/conts/retrieving.html, or from the Cambridge Crystallographic Data Centre, 12 Union Road, Cambridge CB2 1EZ, UK; fax: (+44) 1223-336-033; or e-mail: deposit@ccdc.cam.ac.uk. Supplementary data associated with this article can be found, in the online version, at doi:10.1016/j.poly.2009.06.022.

References

[1] O.M. Yaghi, H. Li, C. Davis, D. Richardson, T.L. Groy, Acc. Chem. Res. 31 (1998) 474.
[2] D. Braga, F. Grepioni, G.R. Desiraju, Chem. Rev. 98 (1998) 1375.
[3] A.K. Cheetham, G. Férey, T. Loiseau, Angew. Chem., Int. Ed. 38 (1999) 3268.
[4] G.K.H. Shimizu, G.D. Enright, C.I. Ratcliffe, J.A. Ripmeester, Chem. Commun. (1999) 461.
[5] O.R. Evans, W.B. Lin, Inorg. Chem. 39 (2000) 2189.
[6] L. Pan, B.S. Finkel, X.Y. Huang, L. Jing, Chem. Commun. (2001) 105.
[7] R.-G. Xiong, J. Zhang, Z.-F. Chen, X.-Z. You, C.-M. Che, H.-K. Fun, J. Chem. Soc., Dalton Trans. (2001) 780.
[8] R.S. Raring, R. Lam, P.Y. Zavalij, J.K. Ngala, R.L. LaDuca, J.E. Greedan, J. Zubieta, Inorg. Chem. 41 (2002) 2124.
[9] R. Kitaura, K. Fujimoto, S.-I. Noro, M. Kondo, S. Kitagawa, Angew. Chem., Int. Ed. 41 (2002) 133.
[10] S.R. Batten, K.S. Murray, Coord. Chem. Rev. 246 (2003) 103.
[11] S. Kitagawa, R. Kitaura, S.-I. Noro, Angew. Chem., Int. Ed. 43 (2004) 2334.
[12] D. Bradshaw, J.B. Claridge, E.J. Cussen, T.J. Prior, M.J. Rosseinsky, Acc. Chem. Res. 38 (2005) 273.
[13] B.-H. Ye, M.-L. Tong, X.-M. Chen, Coord. Chem. Rev. 249 (2005) 545.
[14] A.Y. Robin, K.M. Fromm, Coord. Chem. Rev. 250 (2006) 2127.
[15] D.F. Sun, Y.X. Ke, D.J. Collins, G.A. Lorigan, H.C. Zhou, Inorg. Chem. 46 (2007) 2725.
[16] J.G. Vitillo, L. Regli, S. Chavan, G. Ricchiardi, G. Spoto, P.D.C. Dietzel, S. Bordiga, A. Zecchina, J. Am. Chem. Soc. 130 (26) (2008) 8386.
[17] C.Y. Sun, S.X. Liu, D.D. Liang, K.Z. Shao, Y.H. Ren, Z.M. Su, J. Am. Chem. Soc. 131 (2009) 1883.
[18] M.J. Zaworotko, Angew. Chem., Int. Ed. 39 (2000) 3052.
[19] O.M. Yashi, M. O'Keeffe, N.W. Ockwig, H.K. Chae, M. Eddaoudi, J. Kim, Nature 423 (2003) 705.
[20] M. Yoshizawa, Y. Takeyama, T. Kusukawa, M. Fujita, Angew. Chem., Int. Ed. 41 (2002) 1347.
[21] M. Albrecht, S. Dehn, R. Fröhlich, Angew. Chem., Int. Ed. 45 (2006) 2792.
[22] R.M. Yeh, K.N. Raymond, Inorg. Chem. 45 (2006) 1130.
[23] C.T. Yeung, H.L. Yeung, C.S. Tsang, W.Y. Wong, H.L. Kwong, Chem. Commun. (2007) 5203.
[24] R.W. Saalfrank, C. Spitzlei, A. Scheurer, H. Maid, F.W. Heinemann, F. Hampel, Chem. Eur. J. 14 (2008) 1472.
[25] K.Z. Shao, Y.H. Zhao, Y. Xing, Y.Q. Lan, X.L. Wang, Z.M. Su, R.S. Wang, Cryst. Growth Des. 8 (8) (2008) 2986.
[26] J.R. Li, D.J. Timmons, H.C. Zhou, J. Am. Chem. Soc. 131 (18) (2009) 6368.
[27] M. Albrecht, Chem. Rev. 101 (2001) 3457.
[28] C. Schmuck, Angew. Chem., Int. Ed. 42 (2003) 2448.
[29] M. Albrecht, Angew. Chem., Int. Ed. 44 (2005) 6448.
[30] B.F. Abrahams, P.A. Jackson, R. Robson, Angew. Chem., Int. Ed. 37 (1998) 2656.
[31] P.A. Maggard, C.L. Stern, K.R. Poeppilmeier, J. Am. Chem. Soc. 123 (2001) 7742.
[32] L. Han, M.C. Hong, Inorg. Chem. Commun. 8 (2005) 406.
[33] C. Kaes, M.W. Hosseini, C.E.F. Rickard, B.W. Skelton, A.H. White, Angew. Chem., Int. Ed. 37 (1998) 920.
[34] J.D. Ranford, J.J. Vittal, D.Q. Wu, X.D. Yang, Angew. Chem., Int. Ed. 38 (1999) 3498.
[35] K. Biradha, C. Seward, M.J. Zaworotko, Angew. Chem., Int. Ed. 38 (1999) 492.
[36] P. Lightfoot, A. Snedden, J. Chem. Soc., Dalton Trans. (1999) 3549.
[37] R. Kitaura, K. Seki, G. Akiyama, S. Kitagawa, Angew. Chem., Int. Ed. 42 (2003) 428.
[38] V.V. Korshak, S.V. Vinogradova, G.N. Melekhina, S.N. Salazkin, L.I. Komarova, P.V. Petrovskii, P.O. Okulevich, Bull. Acad. Sci. USSR Div. Chem. Sci. 25 (1976) 347.
[39] T. Highashi, ABSCOR-An Empirical Absorption Correction Based on Fourier Cofficient Fitting, Rigaku Corp., Tokyo, 1995.
[40] G.M. Sheldrick, SHELXS 97, Program for the Refinement of Crystal Structure, University of Gottingen, Germany, 1997.
[41] R.H. Groeneman, L.R. MacGillivray, J.L. Atwood, Inorg. Chem. 38 (1999) 208.
[42] D.F. Sun, R. Cao, Y.C. Liang, Q. Shi, W.P. Su, M.C. Hong, J. Chem. Soc., Dalton Trans. (2001) 2335.
[43] A.M. Baruah, A. Karmakar, J.B. Baruah, Polyhedron 26 (2007) 4479.
[44] K.A. Reeder, E.V. Dose, L.J. Wilson, Inorg. Chem. 17 (1978) 1071.
[45] B. Chiswell, F. Lions, B.S. Morris, Inorg. Chem. 3 (1964) 110.
[46] Y.-Q. Lan, Y.-M. Fu, K.-Z. Shao, Z.-M. Su, Acta Crystallogr., Sect. E 62 (2006) m2586.
[47] S.-L. Li, Y.-Q. Lan, J.-F. Ma, Y.-M. Fu, J. Yang, G.-J. Ping, J. Liu, Z.-M. Su, Cryst. Growth Des. 8 (2008) 1610.
[48] O. Kahn, Molecular Magnetism, VCH, Weinheim, Germany, 1993.

Polyhedron 28 (2009) 2673–2678

Contents lists available at ScienceDirect

Polyhedron

journal homepage: www.elsevier.com/locate/poly

Uranyl(VI) and lanthanum(III) thio-diglycolamides complexes: Synthesis and structural studies involving nitrate complexation

S.B. Deb [a], J.S. Gamare [b], S. Kannan [b,*], M.G.B. Drew [c]

[a] Radioanalytical Chemistry Division, Bhabha Atomic Research Centre, Mumbai 400085, India
[b] Fuel Chemistry Division, Bhabha Atomic Research Centre, Mumbai 400085, India
[c] Department of Chemistry, University of Readings, P.O. Box 224, Whiteknights, Reading, RG6 6AD, UK

ARTICLE INFO

Article history:
Received 28 April 2009
Accepted 3 June 2009
Available online 7 June 2009

Keywords:
Thio-diglycolamide
Coordination chemistry
Solvent extraction
Uranium(VI)
Lanthanum(III)
Crystal structure

ABSTRACT

New tri-functional ligands of the type $R_2NCOCH_2SCH_2CONR_2$ (where R = iso-propyl, *n*-butyl or iso-butyl) were prepared and characterized. The coordination chemistry of these ligands with uranyl and lanthanum(III) nitrates was studied by using the IR, ^{1}HNMR and elemental analysis methods. Structures for the compounds $[UO_2(NO_3)_2(^iPr_2NCOCH_2SCH_2CON^iPr_2)]$ $[UO_2(NO_3)_2(^iBu_2NCOCH_2SCH_2CON^iBu_2)]$, $[La(NO_3)_3(^iPr_2NCOCH_2SCH_2CON^iPr_2)_2]$ and $[La(NO_3)_3(^iBu_2NCOCH_2SCH_2CON^iBu_2)_2]$ were determined by single crystal X-ray diffraction. These structures show that the ligand acts as a bidentate chelating ligand and bonds through both the carbamoyl groups to the uranyl and lanthanum(III) nitrate groups. Solvent extraction studies show that the ligand can extract the uranyl ion from the nitric acid medium but does not show any ability to extract the americium (III) ion.

© 2009 Elsevier Ltd. All rights reserved.

1. Introduction

The coordination chemistry of actinide and lanthanide ions is not only very important for the development of new extractants for the separation and purification of actinide ions from irradiated nuclear fuel but also for the technology concerning the storage of highly radioactive waste materials [1–3]. Tri-functional diglycolamide ligands (Fig. 1a) show excellent extraction properties for trivalent actinide metal ions over the tetra or hexavalent actinide ions and extensive solvent extraction studies have been reported over the last 10 years [4,5]. The coordination chemistry of these ligands with lanthanide and actinide ions has been reported recently by us [6] and others [7,8] and shows that the ligand acts as a tridentate chelating ligand and bonds through both the carbamoyl oxygen and ethereal oxygen atoms to the metal centre. The replacement of ethereal oxygen by the CH_2 group in the glutaramide ligand (Fig. 1b) shows extraction for the hexavalent and tetravalent ions but not for the trivalent ions [9]. The coordination chemistry of glutaramide shows that it acts as a monodentate ligand and bridges uranyl nitrate in the solid state to form a linear polymeric chain arrangement [10]. The solvent extraction studies on tri-functional ligands having the "thio" group in place of the oxygen atom in diglycolamide (called thio-diglycolamide, Fig. 1c) reported by Sasaki et al. show extraction for hexavalent, tetravalent and trivalent actinides and lanthanides from the perchloric acid medium [11–13]. The observed distribution data show that its extraction properties are much superior to those of malanomides but poorer than those of diglycolamides. Sasaki et al. have proposed a tridentate mode of bonding for these ligands with the metal ion similar to those of diglycolamide ligands [13]. However, no structural work is reported to support this proposal. Since, the perchloric acid is no where used in the nuclear fuel reprocessing cycle, it is more relevant to carry out the extraction studies from nitric acid medium rather than that of perchloric acid. We report herein the synthesis of some new thio-diglycolamide ligands and their coordination chemistry with the uranyl and lanthanum(III) nitrates and their preliminary extraction studies with uranyl and americium(III) ions from nitric acid medium.

2. Experimental

2.1. General considerations

All the starting materials and other chemicals were reagent grade and were used as received. FTIR spectra were obtained on a JASCO-610 FTIR spectrometer and the samples were mounted as a nujol mull. The ^{1}H NMR spectra in $CDCl_3$, on a Bruker 500 MHz spectrometer and the peak positions are calibrated with respect to the internal residual solvent peaks. Elemental analyses were performed by the Analytical Chemistry Division of Bhabha Atomic Research Centre, Mumbai.

* Corresponding author. Tel.: +91 22 25594574; fax: +91 22 25505151.
E-mail address: skannan@magnum.barc.ernet.in (S. Kannan).

0277-5387/$ - see front matter © 2009 Elsevier Ltd. All rights reserved.
doi:10.1016/j.poly.2009.06.001

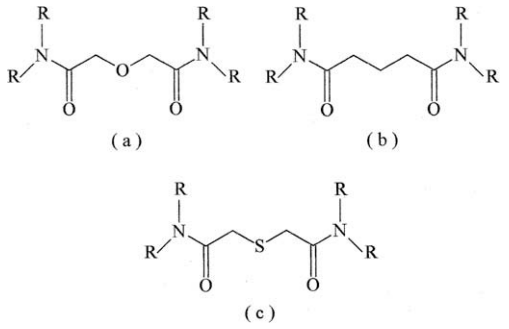


Fig. 1. (a) Diglycolamide, (b) glutaramide and (c) thio-diglycolamide.

2.2. Synthesis of $[(^iC_3H_7)_2NCOCH_2SCH_2CON\{(^iC_3H_7)_2]_2$ (**1**)

N,*N*-Di-isopropyl chloroacetamide (50 g, 0.279 mol) and $Na_2S{\cdot}9H_2O$ (34 g, 0.14 mol) in ethanol (100 mL) were refluxed for 24 h. The volume of the solution was reduced (50 mL) and ca. 300 mL of water was added. The viscous organic residue obtained was extracted with 100 mL of chloroform, dried over anhydrous sodium sulfate and filtered. Removal of the solvent yielded a pasty solid which was re-dissolved in hot hexane and filtered. The solution on slow evaporation yielded a pale yellow solid, which was filtered and washed with cold hexane and dried. Yield: 25 g (57%). Elemental *Anal.* Calc. for $[(^iC_3H_7)_2NCOCH_2SCH_2CON(^iC_3H_7)_2]$; $C_{16}H_{32}N_2O_2S$: C, 60.7; H, 10.1; N, 8.8. Found: C, 60.6; H, 9.9; N, 8.9%. IR (KBr, Nujol, ν/cm^{-1}): 1643 (CO). ^1H NMR (25 °C, $CDCl_3$, δ in ppm): 1.20 (d, 7.2 Hz, 12H, CH_3), 1.38 (d, 6.9 Hz, 12H, CH_3), 3.52 (s, 4H, SCH_2), 3.97 (m, 4H, CH).

2.3. Synthesis of $[(^iC_4H_9)_2NCOCH_2SCH_2CON(^iC_4H_9)_2]$ (**2**)

This was prepared similarly to **1** by taking $^iBu_2NCOCH_2Cl$ (10 g, 0.0486 mol) and $Na_2S{\cdot}9H_2O$ (5.5 g, 0.0229 mol). Yield: 95%. Elemental *Anal.* Calc. for $[(^iC_4H_9)_2NCOCH_2SCH_2CON(^iC_4H_9)_2]$; $C_{20}H_{40}N_2O_2S$: C, 64.5; H, 10.7; N, 7.5. Found: C, 64.1; H, 10.4; N, 8.0%. IR (KBr, Nujol, ν/cm^{-1}): 1640 (CO). ^1H NMR (25 °C, $CDCl_3$, δ in ppm): 0.89 (d, 6.5 Hz, 12H, CH_3), 0.92 (d, 7 Hz, 12H, CH_3), 1.91 (m, 2H, CH), 2.02 (m, 2H, CH), 3.14 (d, 8 Hz, 4H, NCH_2), 3.20 (d, 7.5 Hz, 4H, NCH_2), 3.52 (s, 4H, SCH_2).

2.4. Synthesis of $[(^nC_4H_9)_2NCOCH_2SCH_2CON\{(^nC_4H_9)_2]$ (**3**)

This was prepared similarly to **1** by taking Bu_2NCOCH_2Cl (25 g, 0.1216 mol) and $Na_2S{\cdot}9H_2O$ (14.5 g, 0.0604 mol). Yield: 89%. Elemental *Anal.* Calc. for $[(^nC_4H_9)_2NCOCH_2SCH_2CON(^nC_4H_9)_2]$, $C_{20}H_{40}N_2O_2S$: C, 64.5; H, 10.7; N, 7.5. Found: C, 64.2; H, 11.0; N, 7.7%. IR (KBr, Nujol, ν/cm^{-1}): 1639 (CO). ^1H NMR (25 °C, $CDCl_3$, δ in ppm): 0.91 (t, 7.5 Hz, 6H, CH_3), 0.94 (t, 7.5 Hz, 6H, CH_3), 1.31 (m, 8H, CH_2), 1.52 (m, 8H, CH_2), 3.27 (m, 8H, CH_2), 3.48 (s, 4H, SCH_2).

2.5. Synthesis of $[UO_2(NO_3)_2(^iC_3H_7)_2NCOCH_2SCH_2CON\{(^iC_3H_7)_2]$ (**4**)

To a solution of $(^iC_3H_7)_2NCOCH_2SCH_2CON(^iC_3H_7)_2$ (691 mg, 2.18 mmol) in chloroform, solid $[UO_2(NO_3)_2{\cdot}6H_2O]$ (502 mg, 1 mmol) was added and stirred for few minutes until all uranyl nitrate dissolves to give a clear solution. The solution was filtered and layered with iso-octane. The solution on slow evaporation deposited a pasty solid which was washed in di-isopropyl ether to remove the excess ligand and yield a fine yellow powder. The solution was filtered and the solid residue was washed in iso-propyl ether, hexane and dried. This crude product was crystallized from dichloromethane/iso-octane mixture as a yellow crystalline solid. Yield: 714 mg (92%). Elemental *Anal.* Calc. for $[UO_2(NO_3)_2(^iC_3H_7)_2NCOCH_2SCH_2CON(^iC_3H_7)_2]$; $C_{16}H_{32}N_4O_{10}SU$: C, 27.0; H, 4.5; N, 7.9. Found: C, 27.5; H, 4.9; N, 8.0%. IR (KBr, Nujol, ν/cm^{-1}): 1610, 1577 (CO), 927 (O=U=O). ^1H NMR (25 °C, CD_2Cl_2, δ in ppm): 1.51 (d,6.5 Hz, 24H, CH_3), 3.74 (br, 4H, SCH_2), 4.14 (m, 4H, CH).

2.6. Synthesis of $[UO_2(NO_3)_2(^iC_4H_9)_2NCOCH_2SCH_2C)N\{(^iC_4H_9)_2]$ (**5**)

This compound was prepared similarly to **4**, by taking $[(^iC_4H_9)_2NCOCH_2]_2S$ (750 mg, 2.016 mmol) and $[UO_2(NO_3)_2{\cdot}6H_2O]$ (502 mg, 1 mmol). The crude product was crystallized from chloroform/ dodecane mixture as a yellow crystalline solid. Yield: 738 mg (95.5%). Elemental *Anal.* Calc. for $[UO_2(NO_3)_2(^iC_4H_9)_2NCOCH_2SCH_2CON(^iC_4H_9)_2]$; $C_{20}H_{40}N_4O_{10}SU$: C, 31.3; H, 5.2; N, 7.3. Found: C, 30.9; H, 4.9; N, 7.1%. IR (KBr, Nujol, ν/cm^{-1}): 1610, 1579 (CO), 936 (O=U=O). ^1H NMR (25 °C, $CDCl_3$, δ in ppm): 1.01 (d, 7 Hz, 12H, CH_3), 1.10 (d, 6.5 Hz, 12H, CH_3), 2.17 (m, 2H, CH), 2.29 (m, 2H, CH), 3.45 (d, 7.5 Hz, 4H, NCH_2), 3.88 (s, 4H, SCH_2), 3.97 (d, 6.5 Hz, 4H, NCH_2).

2.7. Synthesis of $[UO_2(NO_3)_2(C_4H_9)_2NCOCH_2SCH_2CON(^nC_4H_9)_2]$ (**6**)

This was prepared similarly to **4**, by taking $[(^nC_4H_9)_2NC(O)CH_2]_2S$ (760 mg, 2.04 mmol) and $[UO_2(NO_3)_2{\cdot}6H_2O]$ (502 mg, 1 mmol). The crude product was crystallized from chloroform/iso-octane mixture as a yellow solid. Yield: 718 mg (93%). Elemental *Anal.* Calc. for $[UO_2(NO_3)_2(C_4H_9)_2NCOCH_2SCH_2CON(^nC_4H_9)_2]$; $C_{20}H_{40}N_4O_{10}SU$: C, 31.3; H, 5.2; N, 7.3. Found: C, 31.7; H, 5.5; N, 7.3%. IR (KBr, Nujol, ν/cm^{-1}): 1610, 1579 (CO), 929 (O=U=O). ^1H NMR (25 °C, $CDCl_3$, δ in ppm): 0.88 (t, 7.5 Hz, 6H, CH_3), 1.06 (t, 7.5 Hz, 6H, CH_3), 1.40 (br, 4H, CH_2), 1.49 (br, 4H, CH_2), 1.81 (br, 8H, CH_2), 3.57 (br, 4H, NCH_2), 3.80 (br, 4H, NCH_2), 3.98 (br, 4H, SCH_2).

2.8. Synthesis of $[La(NO_3)_3\{(^iC_3H_7)_2NCOCH_2SCH_2CON\{(^iC_3H_7)_2\}_2]$ (**7**)

To a chloroform solution of $[(^iC_3H_7)_2NC(O)CH_2]_2S$ (1.053 g, 3.33 mmol), $[La(NO_3)_3{\cdot}6H_2O]$ (476 mg, 1.09 mmol) was added and stirred till a clear solution is obtained. The solution was filtered and layered with iso-octane. The solution on slow evaporation yielded a white solid. This was washed with di-isopropyl ether, filtered, washed with hexane and finally dried to get a white powder. This powder was dissolved in hot ethanol and allowed to evaporate slowly at room temperature to give a white crystalline compound. Yield: 989 mg (93%). Elemental *Anal.* Calc. for $[La(NO_3)_3\{(^iC_3H_7)_2NCOCH_2SCH_2CON(^iC_3H_7)_2\}_2{\cdot}H_2O]$; $C_{32}H_{66}N_7O_{14}S_2La$: C, 39.4; H, 6.8; N, 10.0. Found: C, 40.1; H, 6.7; N, 10.3%. IR (KBr, Nujol, ν/cm^{-1}): 3534 (H_2O), 1610–1577 (br) (CO). ^1H NMR (25 °C, $CDCl_3$, δ in ppm): 1.26 (d, 7 Hz, 12H, CH_3), 1.41 (d, 6.5 Hz, 12H, CH_3), 1.64 (s, 4H, SCH_2), 3.99 (m, 4H, NCH).

2.9. Synthesis of $[La(NO_3)_3\{(^iC_4H_9)_2NCOCH_2SCH_2CON(^iC_4H_9)_2\}_2]$ (**8**)

This was prepared similarly to **7**, by taking $[(^iC_4H_9)_2NCOCH_2]_2S$ (684 mg, 1.83 mmol) and $[La(NO_3)_3{\cdot}6H_2O]$ (265 mg, 0.612 mmol). Yield: 622 mg (95%). Elemental *Anal.* Calc. for $[La(NO_3)_3\{(^iC_4H_9)_2NCOCH_2SCH_2CON(^iC_4H_9)_2\}_2]$; $C_{40}H_{80}N_7O_{13}S_2La$: C, 44.9; H, 7.4; N, 9.2. Found: C, 44.7; H, 7.9; N, 9.1%. IR (KBr, Nujol, ν/cm^{-1}): 1601–1580 (br) (CO). ^1H NMR (25 °C, $CDCl_3$, δ in ppm): 0.92 (d, 6.5 Hz, 12H, CH_3), 0.95 (d, 6.5 Hz, 12H, CH_3), 1.95 (m, 2H, CH), 2.04 (m, 2H, CH), 3.13 (d, 7.5 Hz, 4H, NCH_2), 3.22 (d, 7.5 Hz, 4H, NCH_2), 3.54 (s, 4H, SCH_2).

2.10. Synthesis of $[La(NO_3)_3\{(^nC_4H_9)_2NC(O)CH_2SCH_2C(O)N\{(^nC_4H_9)_2\}_2]$ (**9**)

This was prepared similarly to **7**, by taking $[(^nC_4H_9)_2NCOCH_2]_2S$ (1130 mg, 3.04 mmol) and $[La(NO_3)_3{\cdot}6H_2O]$ (438 mg, 1.01 mmol).

Yield: 985 mg (91%). Elemental *Anal.* Calc. for $[La(NO_3)_3\{(^nC_4H_9)_2N\text{-}COCH_2SCH_2CON(^nC_4H_9)_2\}_2]$; $C_{40}H_{80}N_7O_{13}S_2La$: C, 44.9; H, 7.4; N, 9.2. Found: C, 44.8; H, 7.6; N, 9.1%. IR (KBr, Nujol, ν/cm^{-1}): 1602–1580 (br) (CO).^{1}H NMR (25 °C, $CDCl_3$, δ in ppm): 0.95 (m, 12H, CH_3), 1.33 (m, 8H, CH_2), 1.57 (m, 8H, CH_2), 3.29 (m, 8H, CH_2), 3.49 (s, 4H, SCH_2).

2.11. ES-MS spectra

The electron spray ionization mass spectrometric detection of positive ions was performed using a MICROMASS-Q-TOF MICRO instrument. The samples **7** and **8** in CH_2Cl_2 were introduced with a syringe pump. Nitrogen was employed as both the drying and spraying gas with at source temperature of 90 °C. The cone voltage was set to 30 V, the voltage applied on the capillary was 1162 kV and sample solution flow rate was 5 μL min^{-1}. Spectra were recorded from m/z of 50 to 2000.

2.12. Solvent extraction studies

Distribution studies were performed by using a (0.2 M) solution of $[(^iC_4H_9)_2NCOCH_2SCH_2N(^iC_4H_9)_2]$ in chloroform, toluene or nitrobenzene with the 1 M HNO_3 as an aqueous phase spiked with ^{233}U or ^{241}Am tracers in a thermostated water bath for 1 h at 25 ± 0.1 C. Assay of organic and aqueous phases were done in duplicate by alpha counting using a dioxane based liquid scintillator for ^{233}U and gamma counting directly for the ^{241}Am. The distribution ratio (D) is defined as the ratio of the concentration of uranium in the organic phase to that of the aqueous phase.

2.13. X-ray diffraction studies of *4*, *5*, *7* and *8*

Data for the crystals **4**, **5**, **7** and **8** were measured with the Mo Kα radiation (λ = 0.71073 Å) using the MARresearch Image Plate System. The crystals were positioned at 70 mm from the Image Plate. Ninety-five frames were measured at 2° intervals with a counting time of 2 min. Data analysis was carried out with the XDS program [14]. The structures were solved using direct methods with the SHELXS program [15]. All non-hydrogen atoms in these structures were refined with anisotropic thermal parameters. The hydrogen atoms bonded to carbon atoms were included in the geometric positions and given thermal parameters equivalent to 1.2 times those of the atoms to which they attached. Empirical absorption corrections were carried out using the difabs program [16]. The structures were refined to convergence on F^2 using SHELXL [15]. Selected crystallographic data for **4**, **5**, **7** and **8** are summarized in Table 1.

3. Results and discussion

3.1. Synthesis of thio-diglycolamide ligands

Reaction of carbamoyl methyl chloride with sodium sulfide in ethanol yielded the corresponding thio-diglycolamide ligands. The IR spectra of all ligands show the presence of the carbamoyl group in the synthesized compounds. The ^{1}HNMR spectra show the expected peaks and multiplicities and integration. The CH_2 proton resonance appears at slightly up-field (δ = 3.52 ppm) with respect to the starting R_2NCOCH_2Cl (δ = 4.01 ppm) and the analogous diglycolamide $R_2NCOCH_2OCH_2CONR_2$ (δ = 5.7 ppm) [6] shows that the more electronegative chloride or oxygen is replaced by the less electronegative sulfur atom. The C, H, N analysis supports the expected stoichiometry for the compounds.

3.2. Uranyl complexes

Reaction of $[UO_2(NO_3)_2{\cdot}6H_2O]$ with the thio-glycolamide ligand in dichloromethane yielded compounds of the type $[UO_2(NO_3)_2(R_2NCOCH_2SCH_2CONR_2)]$. The IR spectra of **4**–**6** show that the water molecules from the starting compound $[UO_2(NO_3)_2{\cdot}6H_2O]$ are completely replaced by the thio-glycolamide ligand and that the ligand is bonded through both carbamoyl groups to the metal centre. The observed frequency differences for the carbamoyl groups ($\Delta\nu_{CO}$ = 30–60 cm^{-1}, where $\Delta\nu_{CO} = \nu_{CO(\text{free ligand})} - \nu_{CO(\text{complex})}$) are consistent with the supposition that the carbamoyl group is bonded to the uranyl group directly in the reported compounds. Similar differences are also observed in the compounds of amides with uranyl nitrate such as $[UO_2(NO_3)_2{\cdot}(^iC_3H_7CON\{^iC_4H_9\}_2)_2]$ [17] and $[UO_2(NO_3)_2(^iC_3H_7)_2NCOCH_2\text{-}CON(^iC_3H_7)_2]$ [18]. The ^{1}H NMR of the compounds show that the CH_2 protons are deshielded by ca. 0.3–0.4 ppm with respect to the free ligands. This shows clearly that ligands are also bonded to the metal centre in solution. The C, H and N analysis revealed that the metal to ligand ratio is 1:1 in all the compounds. Structures for the compounds $[UO_2(NO_3)_2[(^iPr_2NCOCH_2SCH_2CON^iPr_2)]$ and $[UO_2(NO_3)_2(^iBu_2NCOCH_2SCH_2CON^iBu_2)]$ were determined using X-ray diffraction methods and confirm the spectral and analysis results.

The structures of the compounds $[UO_2(NO_3)_2[(^iPr_2NCOCH_2\text{-}SCH_2CON^iPr_2)]$ and $[UO_2(NO_3)_2[(^iBu_2NCOCH_2SCH_2CON^iBu_2)]$ are

Table 1
Crystal and structural refinement details for **4**, **5**, **7** and **8**.

	4	5	7	8
Empirical formula	$C_{16}H_{32}N_4O_{10}SU$	$C_{20}H_{40}N_4O_{10}SU$	$C_{64}H_{132}N_{14}O_{27}S_4La_2$	$C_{40}H_{80}N_7O_{13}S_2La$
Formula weight	710.55	766.65	1947.91	1070.14
Crystal system	monoclinic	monoclinic	monoclinic	monoclinic
Space group	$P2_1/n$	$P2_1/c$	$P2_1/n$	$P2_1/n$
a (Å)	8.3175(3)	12.7013(5)	12.668(3)	9.8210(10)
b (Å)	16.9316(6)	12.6657(8)	23.760(3)	42.685(7)
c (Å)	18.8682(11)	10.3432(4)	15.163(3)	12.7543(19)
β (°)	94.159(5)	102.525(4)	90.241(17)	99.956(11)
Volume (Å^3)	2650.2(2)	2906.78(19)	4564.1(15)	5266.2(13)
Z (formula unit)	4	4	4	4
Calculated density (g cm^3)	1.781	1.752	1.417	1.350
Reflections collected/unique	16 990/7609	18 926/8418	32 098/13 168	34 477/15 208
Data/restraints/parameters	7690/0/279	8418/6/333	13 168/0/522	15 208/6/584
Goodness-of-fit (GOF) on F^2	1.105	1.126	0.779	1.223
Final R indices [$I > 2\sigma(I)$]	0.0577	0.0735	0.0544	0.1280
R indices (all data)	0.0826	0.0990	0.1544	0.1899

$W = 1/[\sigma^2(F_o^2) + (0.0405P)^2 + 17.8536P]$ for **4**, $W = 1/[\sigma^2(F_o^2) + (0.0319P)^2 + 48.2087P]$ for **5**, $W = 1/[\sigma^2(F_o^2) + (0.0343P)^2 + 0.0000P]$ for **7**, $W = 1/[\sigma^2(F_o^2) + (0.0409P)^2 + 66.2805P]$ for **8**, where $P = (F_o^2 + 2F_c^2)/3$.

shown in Figs. 2 and 3, respectively and the relevant bond lengths and angles are given in Table 2. These structures show that the thio-diglycolamide ligand bonds to uranyl nitrate in a bidentate chelating fashion through the carbamoyl oxygen atoms. They show further that the thio-ether group is un-coordinated in both these structures (U–S ≈ 4.8 Å). These structures are very similar to that of the uranyl nitrate–malonamide compound $[UO_2(NO_3)_2(^iC_3H_7)_2NCOCH_2CON(^iC_3H_7)_2]$ [18], in which the malonamide acts as a bidentate chelating ligand and bonds through both carbomoyl oxygen atoms. The coordination number around uranium(VI) is eight and the geometry is hexagonal bi-pyramidal. Four oxygen atoms from two nitrates and two oxygen atoms from the organic ligand form the planar hexagon. The two uranyl oxygen atoms occupy the axial positions. The observed U–O(amide) bond distances 2.352(4) and 2.374(5) Å in **4** and 2.358(6) and 2.385(5) Å in **5** are slightly shorter than the values observed in $[UO_2(NO_3)_2(^iC_3H_7)_2NCOCH_2CON(^iC_3H_7)_2]$ (2.41(2) Å) [18], $[UO_2(NO_3)_2Ph\{EtO\}POCH_2CONEt_2]$ (2.426(8) Å), $[UO_2(NO_3)_2Ph_2POCH_2CONEt_2]$ (2.404(5) Å) [19] and $[UO_2(NO_3)_2C_6H_5SOCH_2CON(C_4H_9)_2]$ (2.442(9) Å) [20] and comparable in magnitude with those observed in $[UO_2(NO_3)_2(C_5H_7N_2CH_2CO^iBu_2]$ (2.364(7)–2.377(9) Å) [21], $[UO_2(NO_3)_2(\text{tetrabutyl-glutaramide})]_n$ (2.37(2) Å) [10] and $[UO_2(NO_3)_2\cdot(^iC_3H_7CON\{^iC_4H_9\}_2)_2]$ (2.349(5) Å) [17]. The average U=O (1.757(5)–1.767(5) Å) and U–O(NO_3) (2.507(7)–2.526(7) Å) [10,17–21] bond distance are normal and agree well with the earlier reported uranyl nitrate neutral ligand compounds. As is apparent from Fig. 3, the butyl group bonded to N41 has high thermal motion. The interesting future of the structure is that the thio-glycolamide ligand acts as a bidentate chelating ligand, indeed the carbamoyl groups are connected by a three atom bridge CH_2–S–CH_2. However, the structure of the analogous glutaramide complex of uranyl nitrate $[UO_2(NO_3)_2(\text{glutaramide})]_n$ shows the bridging bidentate mode of bonding for the ligand, though the carbamoyl groups are also connected by a three atom bridge CH_2–CH_2–CH_2 [10]. The structure of the analogous diglycolamide ligand shows the tridentate chelating mode of bonding with the uranyl nitrate [6]. The structural studies clearly revealed that the nature of the complexes formed between the uranyl nitrate and bi-functional amide ligands is decided by the groups bridging the two carbamoyl (amide) groups. The eight-membered metallocyclic ring has the boat conformation with M–S distance of ≈4.8–4.9 Å in both structures. The structural studies revealed that the thio-glycolamide ligand behaves in a similar fashion to the malonamides in regards to its coordination behavior and not to the diglycolamides.

Table 2
Important bond distances (Å) and angles (°) for **4** and **5**.

4			
U(1)–O(1)	1.757(5)	U(1)–O(2)	1.758(4)
U(1)–O(11)	2.554(5)	U(1)–O(13)	2.484(5)
U(1)–O(21)	2.497(5)	U(1)–O(23)	2.496(5)
U(1)–O(31)	2.352(4)	U(1)–O(37)	2.374(5)
O(1)–U(1)–O(2)	179.1(2)	O(11)–U(1)–O(13)	50.32(15)
O(21)–U(1)–O(23)	51.03(17)	O(31)–U(1)–O(37)	70.95(17)
O(11)–U(1)–O(37)	63.49(17)	O(21)–U(1)–O(31)	65.40(16)
5			
U(1)–O(1)	1.765(6)	U(1)–O(2)	1.770(6)
U(1)–O(11)	2.546(7)	U(1)–O(13)	2.515(7)
U(1)–O(21)	2.518(7)	U(1)–O(23)	2.527(7)
U(1)–O(31)	2.358(6)	U(1)–O(37)	2.385(5)
O(1)–U(1)–O(2)	178.7(3)	O(11)–U(1)–O(13)	50.3(2)
O(21)–U(1)–O(23)	50.5(2)	O(31)–U(1)–O(37)	72.3(2)
O(11)–U(1)–O(37)	62.5(2)	O(23)–U(1)–O(31)	65.7(2)

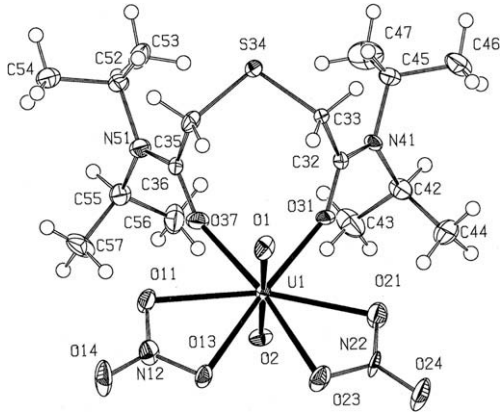


Fig. 2. Molecular structure of **4** (with 30% probability).

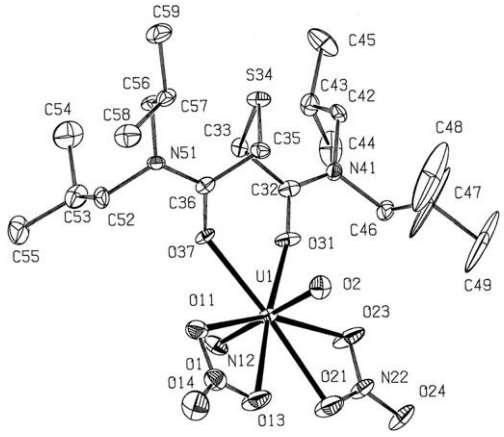


Fig. 3. Molecular structure of **5** (with 30% probability, hydrogen atoms omitted for clarity).

3.3. Lanthanum complexes

Reaction of $[La(NO_3)_3\cdot 6H_2O]$ with the thio-glycolamide ligand in ethanol yielded compounds of the type $[La(NO_3)_3[(R_2NCOCH_2SCH_2CONR_2)_2]$. The IR spectra of **7–9** show that the ligands are bonded through both the carbamoyl groups to the metal centre (Δ_{CO} = 30 cm^{-1}, $\Delta_{CO} = \nu_{CO(\text{free ligand})} - \nu_{CO(\text{complex})}$). The spectrum of **7** further shows a sharp peak at ca. 3534 cm^{-1} due to the presence of a water molecule in the solid state. The ^1H NMR spectra of **7–9** show the expected peak multiplicities and integrations. The spectra are very similar to those of free ligands without any deshielding of CH_2 protons, indicating that the ligands are weakly bonded to the metal nitrate in solution. This is further supported by the ES-MS of **7** and **8** which show peaks corresponding to the free ligands (LH^+, 100%) at 317.19 and 373.29, respectively for **2** and **3** and no peak corresponding to the complex **7** and **8** (see the Supplementary data). This shows that the compounds are dissociated in solution. The C, H and N analysis revealed that the metal to ligand ratio is 1:2 in the compounds in the solid state.

The structures for the compounds $[La(NO_3)_3(^iPr_2NCOCH_2SCH_2CON^iPr_2)_2\cdot(H_2O)]$ and $[La(NO_3)_3(^iBu_2NCOCH_2SCH_2CON^iBu_2)]$ were determined using X-ray diffraction methods and confirm the IR spectral and analysis results. The structures of the compounds $[La(NO_3)_3(^iPr_2NCOCH_2SCH_2CON^iPr_2)_2]$ (H_2O) and $[La(NO_3)_3[(^iBu_2NCOCH_2SCH_2CON^iBu_2)_2]$ are shown in Figs. 4 and 5, respectively and the relevant bond distances and angles are given in Table 3. These structures show that the thio-diglycolamide ligand bonds to lanthanum (III) nitrate in a bidentate chelating fashion through the

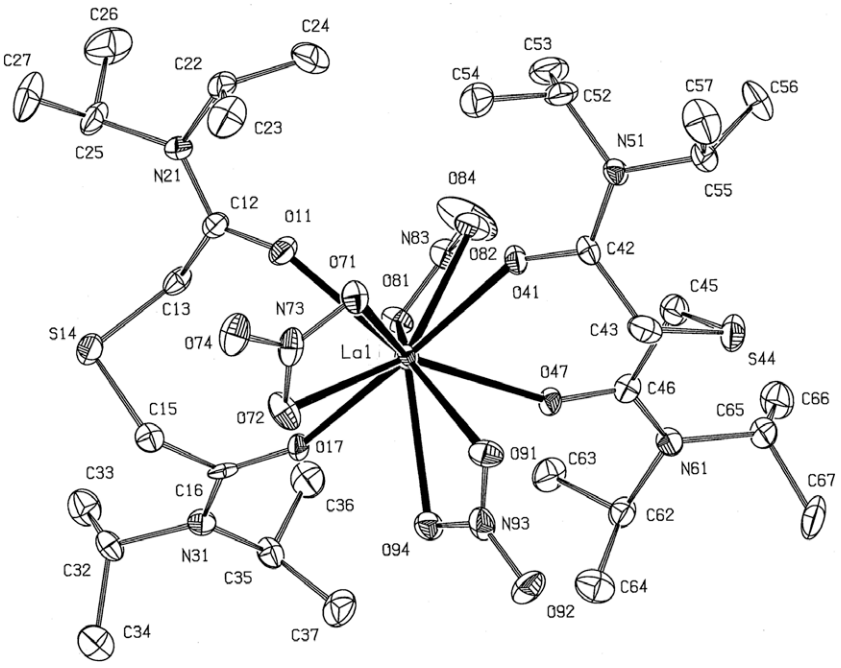


Fig. 4. Molecular structure of **7** (with 30% probability, hydrogen atoms omitted for clarity and water molecules are not shown).

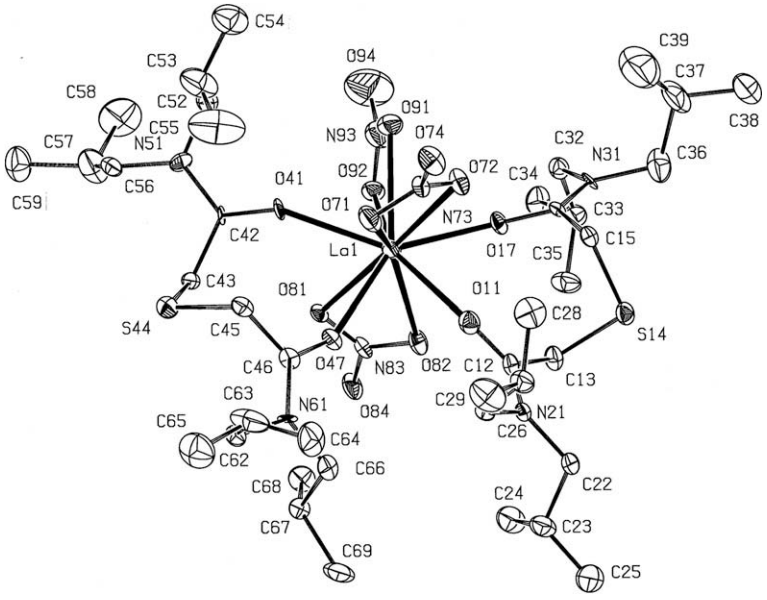


Fig. 5. Molecular structure of **8** (with 30% probability, hydrogen atoms omitted for clarity).

carbamoyl oxygen atoms. They show further that the thio-ether group is un-coordinated. These structures are very similar to those of lanthanide nitrate–malonamide compounds reported in the literature [22,23]. The coordination number around lanthanum(III) is ten and the geometry is a distorted bi-capped square-anti-prism. The average La–O(NO_3) (2.642(3) Å in **7** and 2.636(7) Å in **8**) [22–24] and La–O(amide) (2.537(3) Å in **7** and 2.500(8) Å in **8**) [22,23] bond distances are normal and comparable to those of the reported values. It is interesting to note that the structure of analogous diglycolamide shows the tridentate chelating mode of bonding with the lanthanide nitrate [6,7]. The structural studies revealed that the thio-glycolamide ligand behaves in a similar fashion to the malonamide ligands in its coordination behavior. The eight member metallocyclic ring has a boat conformation with La–S distances of ≈5.05–5.07 Å.

3.4. Solvent extraction studies

The distribution ratio for uranium and americium was determined with thio-glycolamide ligand **4** (0.2 M) in different diluents such as, chloroform, toluene, decanol and nitrobenzene from 1 M HNO_3 (Table 4). These data indicate that the thio-glycolamide ligand shows an appreciable extraction for uranium in both chloroform and toluene and poor extraction in decanol and nitrobenzene. It indicates clearly that the thio-diglycolamide is bonded to uranyl nitrate in solution (chloroform or toluene) and is responsible for

Table 3
Important bond distances (Å) and angles (°) for **7** and **8**.

7			
La(1)–O(11)	2.518(3)	La(1)–O(17)	2.554(3)
La(1)–O(81)	2.643(3)	La(1)–O(82)	2.678(3)
La(1)–O(91)	2.628(3)	La(1)–O(94)	2.611(3)
La(1)–O(71)	2.662(3)	La(1)–O(72)	2.632(3)
La(1)–O(41)	2.570(3)	La(1)–O(47)	2.509(3)
O(11)–La(1)–O(17)	77.89(10)	O(41)–La(1)–O(47)	77.38(9)
O(71)–La(1)–O(72)	48.80(10)	O(81)–La(1)–O(82)	47.84(9)
O(91)–La(1)–O(94)	48.94(10)	O(17)–La(1)–O(41)	176.68(10)
8			
La(1)–O(11)	2.500(8)	La(1)–O(17)	2.494(6)
La(1)–O(81)	2.678(6)	La(1)–O(82)	2.610(7)
La(1)–O(91)	2.651(7)	La(1)–O(92)	2.588(7)
La(1)–O(71)	2.628(8)	La(1)–O(72)	2.661(7)
La(1)–O(41)	2.478(7)	La(1)–O(47)	2.528(7)
O(11)–La(1)–O(17)	73.3(2)	O(41)–La(1)–O(47)	76.1(2)
O(71)–La(1)–O(72)	48.1(2)	O(81)–La(1)–O(82)	47.8(2)
O(91)–La(1)–O(92)	49.2(2)	O(72)–La(1)–O(81)	178.0(2)

Table 4
Distribution ratio (D) for U(VI) and Am(III) with **2** in different diluents.

Metal ion	Chloroform	Toluene	Decanol	Nitrobenzene
U(VI)	2.0	1.4	0.2	negligible
Am(III)	5.2×10^{-4}	3.1×10^{-4}	4.8×10^{-3}	negligible

Aqueous phase = 1 M HNO_3.

the extraction. This is supported by the observed ^{1}H NMR spectrum of the compound **5**, which shows a downfield shift for the CH_2 protons adjacent to the donor centres. The ligand did not show any extraction capability for Am(III) in all for diluents studied. It indicates that there is no bonding or only very week interaction between metal and ligand in all diluents studied. The ^{1}H NMR and ES-MS data for the chemically similar lanthanum compound **8** in chloroform supports this observation. The observed distribution data for uranyl and Am(III) from nitric acid medium in all the diluents clearly indicate that the thio-glycolamide behaves similar to that of glutaramide in its extraction behavior [9].

Our observed distribution data for Am(III) from nitric acid medium is completely different to those data reported by Sazaki et al. for a similar type of ligand, when the extraction was carried out from an non-complexing perchloric acid medium [11–13]. The observed extraction for Am(III) or Ln(III) from perchloric acid may be due the presence of strong bonding between thio-glycolamide and Am(III) in solution in the absence of the strongly complexing nitrate ion.

4. Conclusions

New class of tri-functional ligands thio-diglycolamide have been synthesized and their coordination chemistry with the uranyl and lanthanum(III) nitrates is studied. The structural studies revealed that the ligands behave similarly to those of malonamides in solid state. The solvent extraction studies from nitric acid medium show that thio-diglycolamide behaves similarly to those of glutaramides in solution.

Supplementary data

CCDC 725543, 725544, 725545 and 725543 contain the supplementary crystallographic data for **4**, **5**, **7** and **8**. These data can be obtained free of charge via http://www.ccdc.cam.ac.uk/conts/retrieving.html, or from the Cambridge Crystallographic Data Centre, 12 Union Road, Cambridge CB2 1EZ, UK; fax: (+44) 1223-336-033; or e-mail: deposit@ccdc.cam.ac.uk.

Acknowledgements

S.K. wishes to thank Dr. S.K. Aggarwal, Head, Fuel Chemistry and S.B.D wishes to thank Dr. R.L. Ramakumar, Head, Radioanalytical Chemistry for their supports. We wish to thank, the Head, Analytical Chemistry Division, BARC, for carbon, hydrogen and nitrogen analysis, the Head, National NMR facilities, TIFR, Mumbai for NMR spectra. We also wish to thank the EPSRC (UK) and the University of Reading for funds for the Image Plate system.

References

[1] L.R. Morss, N.M. Edelstein, J. Fuger, J.J. Katz, The Chemistry of the Actinide and Transactinide Elements, Springer, Netherlands, 2006.
[2] C.J. Burns, M.P. Neu, H. Boukhalfa, K.E. Gutowshi, N.J. Bridges, R.D. Rogers, in: J.A. McCleverty, T.J. Meyer, G.F.R. Parkin (Eds.), Comprehensive Coordination Chemistry II, vol. 3, Elsevier, Oxford, 2004, p. 189.
[3] M. Ephritikhine, Dalton Trans. (2006) 2501.
[4] Y. Sasaki, Z.X. Zhu, Y. Sugo, T. Kimura, J. Nucl. Sci. Technol. 44 (2007) 405.
[5] Z.X. Zhu, Y. Sasaki, H. Suzuki, S. Suzki, T. Kimura, Anal. Chim. Acta 527 (2004) 163.
[6] S. Kannan, M.A. Moody, C.L. Barnes, P.B. Duval, Inorg. Chem. 47 (2008) 4691.
[7] K. Matloka, A. Gelis, M. Regalbuto, G. Vandegrift, M.J. Scott, Dalton Trans. (2005) 3719.
[8] G. Tian, J. Xu, L. Rao, Angew. Chem., Int. Ed. 44 (2005) 6200.
[9] M.C. Carbonnel, C. Musikas, Solvent Extr. Ion Exch. 7 (1989) 1007.
[10] P. Charpin, M. Lance, M. Nierlich, D. Vigner, Acta Crystallogr., Sect. C 43 (1987) 442.
[11] Y. Sasaki, G.R. Choppin, Anal. Sci. 12 (1996) 225.
[12] Y. Sasaki, G.R. Choppin, J. Radioanal. Nucl. Chem. 222 (1997) 271.
[13] Y. Sasaki, S. Tachimori, Solvent Extr. Ion Exch. 20 (2002) 21.
[14] W. Kabsch, J. Appl. Crystallogr. 21 (1988) 916.
[15] G.M. Sheldrick, Acta Crystallogr., Sect. A 64 (2008) 112.
[16] N. Walker, D. Stuart, Acta Crystallogr., Sect. A 39 (1983) 158.
[17] S. Kannan, S.B. Deb, J.S. Gamare, M.G.B. Drew, Polyhedron 27 (2008) 2257.
[18] G.J. Lumetta, B.K. McNamara, B.M. Rapko, R.L. Sell, R.D. Rogers, G. Broker, J.E. Hutchison, Inorg. Chim. Acta 309 (2000) 103.
[19] L.J. Caudle, E.N. Duesler, R.T. Paine, Inorg. Chim. Acta 110 (1985) 91.
[20] S. Kannan, K.V. Chetty, V. Venugopal, M.G.B. Drew, Dalton Trans. (2004) 3604.
[21] S. Kannan, J.S. Gamare, K.V. Chetty, M.G.B. Drew, Polyhedron 27 (2007) 3810.
[22] P. Thuery, M. Nierlich, M.C. Charbonnel, C.D. Auwer, J.P. Dognon, Polyhedron 18 (1999) 3599.
[23] P. Byers, M.G.B. Drew, M.J. Hudson, N.S. Isaacs, C. Madic, Polyhedron 13 (1994) 349.
[24] M. Lees, A.W.G. Platt, Inorg. Chem. 42 (2003) 4673.

Polyhedron 28 (2009) 2679–2683

Contents lists available at ScienceDirect

Polyhedron

journal homepage: www.elsevier.com/locate/poly

Seeking new metalloligands: Synthesis and reactivity of palladacycles with pyridine and pyrimidine rings

Jesús J. Fernández [a,*], Nina Gómez-Blanco [a], Alberto Fernández [a], Digna Vázquez-García [a], Margarita López-Torres [a], José M. Vila [b,*]

[a] Departamento de Química Fundamental, Universidad de La Coruña, E-15071 La Coruña, Spain
[b] Departamento de Química Inorgánica, Universidad de Santiago de Compostela, E-15782 Santiago de Compostela, Spain

ARTICLE INFO

Article history:
Received 14 January 2009
Accepted 5 May 2009
Available online 12 May 2009

Keywords:
Palladium
Metallation
Phosphines
Metalloligands

ABSTRACT

Treatment of the Schiff base ligands 4-(NC_5H_4)$C_6H_4C(H)$=N[2′-$(OH)C_6H_4$] **(a)**, 3,5-($N_2C_4H_3$)$C_6H_4C(H)$=N[2′-(OH)-C_6H_4] **(b)** and 3,5-($N_2C_4H_3$)$C_6H_4C(H)$ =N[2′-(OH)-5′-$^tBuC_6H_3$] **(c)** with palladium (II) acetate in toluene gave the poly-nuclear cyclometallated complexes [Pd{4-(NC_5H_4)$C_6H_3C(H)$=N[2′-$(O)C_6H_4$]}]$_4$ **(1a)**, [Pd{3,5-($N_2C_4H_3$)$C_6H_3C(H)$=N[2′-(O)-C_6H_4]}]$_4$ **(1b)** and [Pd{3,5-($N_2C_4H_3$)$C_6H_3C(H)$=N[2′-(O)-5′-$^tBuC_6H_3$]}]$_4$ **(1c)** respectively, as air stable solids, with the ligand acting as a terdentate [C,N,O] moiety after deprotonation of the –OH group. Reaction of the cyclometallated complexes with triphenylphosphine gave the mononuclear species [Pd{4-(NC_5H_4)$C_6H_3C(H)$ =N[2′-$(O)C_6H_4$]}(PPh_3)], **(2a)**, [Pd{3,5-($N_2C_4H_3$)$C_6H_3C(H)$=N[2′-$(O)C_6H_4$]}(PPh_3)], **(2b)** and [Pd{3,5-($N_2C_4H_3$)$C_6H_3C(H)$=N[2′-(O)-5′-$^tBuC_6H_3$)}(PPh_3)], **(2c)** in which the polynuclear structure has been cleaved and the coordination of the ligand has not changed [C,N,O]. When the cyclometallated complexes **1b** and **1c** were treated with the diphosphines $Ph_2P(CH_2)_4PPh_2$ (dppb), $Ph_2PC_5H_4FeC_5H_4PPh_2$ (dppf) and $Ph_2P(CH_2)_2PPh_2$ (*t*-dppe) in a 1:2 molar ratio the dinuclear cyclometallated complexes [{Pd[3,5-($N_2C_4H_3$)$C_6H_3C(H)$=N{2′-$(O)C_6H_4$}]}$_2$(μ-$Ph_2P(CH_2)_4PPh_2$)], **(3b)**, [{Pd[3,5-($N_2C_4H_3$)$C_6H_3C(H)$ =N{2′-(O)-5′-$^tBuC_6H_3$}]}$_2$(μ-$Ph_2P(CH_2)_4PPh_2$)], **(3c)**, [{Pd[3,5-($N_2C_4H_3$)$C_6H_3C(H)$=N{2′-$(O)C_6H_4$}]}$_2$(μ-$Ph_2P(\eta^5$-$C_5H_4)Fe(\eta^5$-$C_5H_4)PPh_2$)], **(4b)**, [{Pd[3,5-($N_2C_4H_3$-$C_6H_3C(H)$=N{2′-(O)-5′-$^tBuC_6H_3$}]}$_2$(μ-$Ph_2P(\eta^5C_5H_4)Fe(\eta^5C_5H_4)$P-$Ph_2$)], **(4c)** and [{Pd[3,5-($N_2C_4H_3$)C_6H_3-C(H)=N{2′-(O)-5′-$^tBuC_6H_3$}]}$_2$(μ-$Ph_2P(CH$=$CH)PPh_2$)], **(5c)** were obtained as air stable solids.

© 2009 Elsevier Ltd. All rights reserved.

1. Introduction

The chemistry of cyclometallated transition metal complexes has attracted much attention in past decades. They are usually classified according to the metal, to the donor atom, or to chelate ring size; by far the most well-studied examples are five-membered palladacycles [1]. They exhibit a good number of applications which range from the use as chiral auxiliaries [2], as building blocks for molecular architectures of higher complexity [3] or as compounds with interesting mesogenic [4] and luminescent and electronic properties [5], as well as their potential use in medicine and biology [6] and in catalytic and synthetic processes [7].

We have been interested in palladium(II) and platinum(II) cyclometallated complexes derived from [C,N,X] (X = O, S) terdentate ligands. Those derived from [C,N,S] thiosemicarbazones [8–13] or from Schiff bases with phenolate oxygen atoms [14–17] show tetranuclear structures, with eight- membered Pd_4X_4 cores (X = O, S), bearing two different types of P–X bonds: $P–X_{chelating}$ and $P–X_{bridging}$, which bind the ligand tightly to the metal centre. More recently, we have shown that reaction of the tetranuclear tetramers derived from thiosemicarbazones (X=S) with bis(diphenylphosphino)methane caused cleavage of the tetranuclear structure to give new mononuclear complexes in which the phosphine is monodentate, where one phosphorus atom is uncoordinated. These complexes represent a new class of bidentate [*P*,*S*] chelating metalloligands capable of coordinating a second metal centre and, therefore, may be used as building blocks in the construction of polynuclear structures [18].

On the other hand, ligands with pyridine and pyrimidine rings have been extensively studied as building blocks in the construction of supramolecular assemblies [19–27]. We reasoned that the combination of the unusual structure shown by the cyclometallated tetramers with ligands containing pyridine o pyrimidine rings could result in a new type of metalloligands with potential applications in the construction of supramolecular aggregates, and these results are presented herein.

2. Results and discussion

For the convenience of the reader the compounds and reactions are shown in Schemes 1 and 2. The compounds described in this

* Corresponding authors. Fax: +34 981 167065 (J.J. Fernández), tel.: +34 981 563100x14255; fax: +34 981 595012 (J.M. Vila).
E-mail addresses: qiluaafl@udc.es (J.J. Fernández), josemanuel.vila@usc.es (J.M. Vila).

0277-5387/$ - see front matter © 2009 Elsevier Ltd. All rights reserved.
doi:10.1016/j.poly.2009.05.005

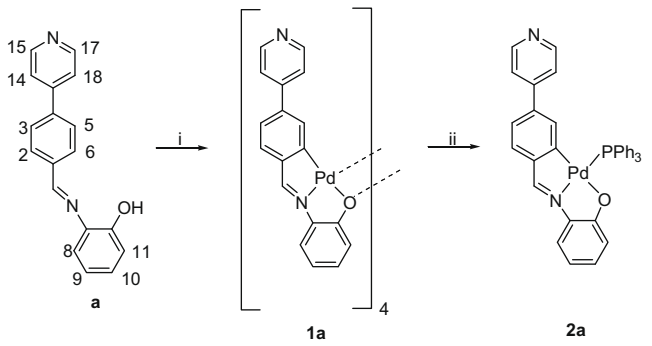
paper were characterised by elemental analysis (C, H, N) and by IR and by ^{1}H, ^{31}P–{^{1}H} spectroscopy and, in part, FAB mass spectrometry (data in Section 3).

Reaction of the Schiff base ligands **a**, **b** and **c** with palladium (II) acetate in toluene at 60 °C gave [Pd{4-(NC$_5$H$_4$)C$_6$H$_3$C(H)=N[2′-(O)C$_6$H$_4$]}]$_4$, **1a**, [Pd{3,5-(N$_2$C$_4$H$_3$)C$_6$H$_3$C(H)=N[2′-(O)-C$_6$H$_4$]}]$_4$, **1b** and [Pd{3,5-(N$_2$C$_4$H$_3$)C$_6$H$_3$C(H)=N[2′-(O)-5′-^{t}BuC$_6$H$_3$]}]$_4$, **1c**, respectively, as air stable solids. The IR spectra showed the shift of the ν(C=N) stretch toward lower wavenumbers, as compared to the free ligand, due to N-coordination of the imine [28,29]. The absence of the ν(O–H) band (present in the spectra of the free ligands at 3415, **a**, 3336, **b** and 3226, **c**, cm^{-1}) was in accordance with loss of the –OH proton. The absence of ν(COO) bands in the IR spectra precludes the formation of the compounds as the typical dinuclear species with bridging acetate ligands, as found earlier when using palladium (II) acetate as the metal salt. Unfortunately the insolubility of **1a**, **1b** and **1c** precluded their characterization in solution. Nevertheless, the characterization of their phosphine derivatives, *vide infra*, unambiguously established metallation at the phenyl ring through the position adjacent to the imino group. However, the tetrameric nature of the complexes has not been unequivocally determined. The tetranuclear disposition of similar complexes have been described by us [14,16,17] and others [15,30]; their spectra and reactivity were similar to the one shown by **1a**, **1b** and **1c**, however, only the FAB-mass spectra **1c** showed the expected molecular ion whilst **1a** and **1b** spectra showed peaks corresponding to 2/3 and 1/2, respectively of the mass expected for a tetramer. Consequently, the tetranuclear formulation given here for complexes **1a**, **1b** and **1c** is only tentative.

Treatment **a**, **b** and **c** with PPh$_3$ in 1:4 molar ratio afforded the mononuclear complexes [Pd{4-(NC$_5$H$_4$)C$_6$H$_3$C(H)=N[2′-(O C$_6$H$_4$]}-(PPh$_3$)] **2a**, [Pd{3,5-(N$_2$C$_4$H$_3$)C$_6$H$_3$C(H) =N-[2′-(O)C$_6$H$_4$]}(PPh$_3$)] **2b**, and [Pd{3,5-(N$_2$C$_4$H$_3$)C$_6$H$_3$C(H)=N[2′-(O)-5′-^{t}BuC$_6$H$_3$)}-(PPh$_3$)] **2c**. The proton resonances were unequivocally assigned (see Section 3). The spectra showed the absence of the signal corresponding to *H6* consequent on Pd–C bond formation. The H5 resonance was coupled to the ^{31}P nucleus, with ^4J(PH) *ca.* 4 Hz, and to H3 [^3J(H3H5) = 1.7 Hz]. The signal assigned to HC=N was as a doublet by coupling to the ^{31}P nucleus with ^4J(PH) *ca.* 10 Hz. In the ^{31}P–{^{1}H} spectra the phosphorus resonance was a singlet *ca.* δ34.5 ppm, in agreement with a phosphorus *trans* to nitrogen arrangement [14,16,17,31–34]. The signals assigned to the H5 and H14, H18 protons were strongly shifted to lower frequency, as compared to the uncoordinated ligands due to shielding of phosphine phenyl rings. We have previously observed similar shifts in related complexes, confirming the relative *trans* disposition of the nitrogen atom and the phosphine ligand [14,16,9]. The H15, H17 protons in **2a** and H16 in **2b** and **2c** were also affected by the shielding but to a lesser extent. Coordination of the palladium atom trough the C=N nitrogen, was confirmed by the shift to lower wavenumbers of the ν(C=N) band, as compared to the free ligand [14,16,17,27,28]. Absence of the ν(OH) band in the IR spectra and of the O*H* resonance in the ^{1}H NMR spectra was in agreement with the presence of a phenolate oxygen bonded to the palladium atom [14,16,17]. These findings were observed for the remaining compounds and shall not be discussed further (see Section 3). The mass FAB spectra showed the cluster of peaks characteristic of the [M]$^+$ fragment at 640, **2a**, 641, **2b**, and 697, **2c**, uma.

Reaction of **1b–1c** with the diphosphines, dppb, *trans*-dppe and dppf in 1:2 molar ratio gave the dinuclear cyclometallated complexes [{Pd[3,5-(N$_2$C$_4$H$_3$)C$_6$H$_3$C(H)=N{2′-(O)C$_6$H$_4$}]}$_2$(μ-Ph$_2$P-(CH$_2$)$_4$PPh$_2$)] **3b**, [{Pd[3,5-(N$_2$C$_4$H$_3$)C$_6$H$_3$C(H)=N{2′-(O)-5′-^{t}BuC$_6$-H$_3$}]}$_2$(μ-Ph$_2$P(CH$_2$)$_4$PPh$_2$)] **3c**, [{Pd[3,5-(N$_2$C$_4$H$_3$)C$_6$H$_3$C(H)=N{2′-(O)C$_6$H$_4$}]}$_2$-(μ-Ph$_2$P(η^5-C$_5$H$_4$)Fe(η^5-C$_5$H$_4$)PPh$_2$)] **4b**, [{Pd[3,5-(N$_2$-C$_4$H$_3$)C$_6$H$_3$C(H)=N{2′-(O)-5′-^{t}BuC$_6$H$_3$}]}$_2$(μ-Ph$_2$P(η^5C$_5$H$_4$)Fe-(η^5C$_5$H$_4$)P-Ph$_2$)] **4c** and [{Pd[3,5-(N$_2$C$_4$H$_3$)C$_6$H$_3$C(H)=N{2′-(O)-5′-^{t}BuC$_6$H$_3$}]}$_2$(μ-PPh$_2$(*trans*-(CH)$_2$)PPh$_2$)] **5c**, as air stable solids (see Section 3). Again, as with **2b** and **2c**, the spectroscopic data confirm the proposed structures for **1b** and **1c**. Thus, the most noticeable characteristics were the absence of the ν(OH) band and the shift to lower wavenumbers of the ν(C=N) band in the IR spectra; and in the ^{1}H NMR spectra, absence of the H6 resonance and coupling of the H5 and *H*C=N protons to the ^{31}P nucleus, as a consequence of the coordination of the diphosphine. In the ^{31}P–{^{1}H} NMR spectra only one singlet was assigned for the two equivalent nuclei; accordingly, only one set of signals was observed for the two equivalent metallated moieties, in accordance with the symmetric nature of the dinuclear complexes. The mass FAB spectra of the complexes showed the set of peaks corresponding to the [MH]$^+$ ions with the expected isotopic pattern.

As for reactivity of complex **1a** with the aforementioned diphosphines, although the IR data seemed similar to that of the **b** and **c** derivatives, the products were to insoluble for NMR characterization and their mass spectra did not show the expected peaks for the molecular ions; thus, their isolation was not pursued further.



Scheme 1. (i) Pd(OAc)$_2$, toluene; (ii) PPh$_3$ (chloroform, 4:1 molar ratio).

3. Experimental

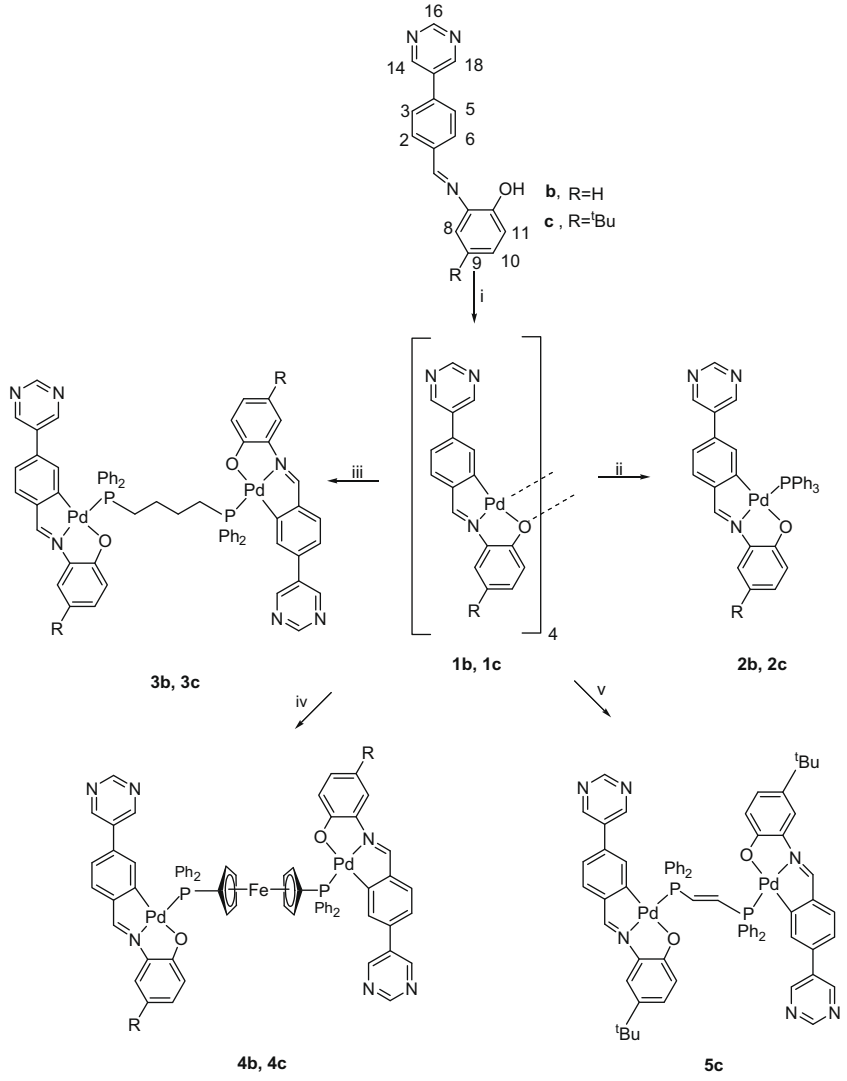
3.1. General procedures

Solvents were purified by standard methods [35]. Chemicals were reagent grade. The phosphines PPh$_3$, Ph$_2$P(CH=CH)PPh$_2$ (*trans*-dppe), Ph$_2$P(CH$_2$)$_4$PPh$_2$ (dppb) and Ph$_2$PC$_5$H$_4$FeC$_5$H$_4$PPh$_2$ (dppf) were purchased from Aldrich-Chemie. Microanalyses were carried out using a Carlo Erba Elemental Analyzer, Model 1108. IR spectra were recorded as KBr discs on a Perkin–Elmer 1330. NMR spectra were obtained as CDCl$_3$ and CD$_3$SOCD$_3$ solutions and referenced to SiMe$_4$ (^{1}H) or 85% H$_3$PO$_4$ (^{31}P–{^{1}H}) and were recorded on a BRUKER AV-300F or BRUKER AC-500F spectrometers. All chemical shifts were reported downfield from standards. The FAB mass spectra were recorded using a Quatro mass spectrometer with a Cs ion gun; 3-nitrobenzyl alcohol was used as the matrix.

4. Syntheses

4.1. Preparation of 4-(NC$_5$H$_4$)C$_6$H$_4$C(H)=N[2-(OH)C$_6$H$_4$] (a)

4-(NC$_5$H$_4$)C$_6$H$_4$COH (0.508 g, 2.77 mmol) was added to a solution of 2-aminophenol (0.305 g, 2.79 mmol) in 50 cm^3 of dry chloroform. The solution was heated under reflux in a Dean-Stark apparatus for 8 h. After cooling to room temperature the chloroform was removed to give a yellow solid. Yield 99%. *Anal.* calc. C$_{18}$H$_{14}$N$_2$O requires C, 78.8; H, 5.1; N, 10.2. Found: C, 78.9; H, 5.1; N, 10.1%. IR: ν(O–H), 3415sh cm^{-1}; ν(C=N), 1600s, m cm^{-1}. RMN ^{1}H (300 MHz, CDCl$_3$, δ



Scheme 2. (i) $Pd(OAc)_2$ (toluene); (ii) PPh_3 (chloroform, **2b**, acetone, **2c**, 4:1 molar ratio); (iii) dppb (acetone, **3b**, chloroform, **3c**, 2:1 molar ratio); (iv) dppf (chloroform **4b**, acetone, **4c**, 2:1 molar ratio); (v) *t*-dppe, (acetone, 2:1 molar ratio).

ppm, *J* Hz): δ = 8.77 [s, 1H, *HC*=N); 8.72 (d, 2H, H15,H17, ^3J(H14H15) = 6.1 Hz]; 8,68 (s, br, 1H, –OH/ resonance taken from a spectrum recorded in DMSO-d^6); 8.05 [d, 2H, H2,H6 ó H3,H5, ^3J(H2H3) = 8.3 Hz]; 7.77 [d, 2H, H3,H5 or H2,H6, ^3J(H2H3) = 8.3 Hz]; 7,57 [d, 2H, H14, H18, ^3J(H14H15) = 6.1 Hz]; 7.35 [dd, 1H, H8, ^3J(H8H9) = 8.2 Hz, ^4J(H8H10) = 1.4 Hz], 7.26 [m, 1H, H10, ^3J(H9H10) = ^{3}J(H10H11) = 8.2 Hz; ^4J(H8H10) = 1.4 Hz]; 7,04 [dd, 1H, H11, ^3J(H10H11) = 8.2 Hz, ^4J(H9H11) = 1.3 Hz]; 6.94 [m, 1H, H9, ^3J(H8H9) = ^3J(H9H10) = 8.2 Hz, ^4J(H9H11) = 1.3 Hz].

Ligands **b** and **c** were prepared similarly as yellow solids.

3,5-($N_2C_4H_3$)C_6H_4C(H)=N[2′-(OH)-C_6H_4] (b). Yield 95%. *Anal.* calc. $C_{17}H_{13}N_3O$ requires C, 74.2; H, 4.8; N, 15.3. Found: C, 74.2; H, 4.9; N, 15.4%. IR: ν(O–H), 3336s cm^{-1}; ν(C=N), 1621s cm^{-1}. RMN ^{1}H (300 MHz, $CDCl_3$, δ ppm, *J* Hz): δ = 9.26 (s, 1H, H16); 9.08 (s, br 1H, –OH/ resonance taken from a spectrum recorded in DMSO-d^6); 9.02 (s, 2H, H14, H18); 8.77 (s, 1H, HC=N); 8.08 [d, 2H, H3, H5 or H2, H6, ^3J(H2H3) = 8.2 Hz]; 7.72 [d, 2H, H3, H5 or H2, H6, ^3J(H2H3) = 8.2 Hz]; 7.35 [dd, 1H, H8, ^3J(H8H9) = 7.8 Hz, ^4J(H8H10) = 1.4 Hz]; 7.23 [m, 1H, H10, ^3J(H9H10) = ^3J(H10H11) = 7.8 Hz, ^4J(H8H10) = 1,4 Hz]; 7.05 [dd, 1H, H11, ^4J(H8H10) = 7.8 Hz, ^4J(H9H11) = 1.2 Hz]; 6.94 [m, 1H, H9, ^3J(H8H9) = ^3J(H9H10) = 7.8 Hz, ^4J(H9H11) = 1.2 Hz].

3,5-($N_2C_4H_3$)C_6H_4C(H)=N[2′-(OH)-5′-^{t}BuC_6H_3] (c). Yield 80%. *Anal.* calc. $C_{21}H_{21}N_3O$ requires C, 76.1; H, 6.4; N, 12.7. Found: C, 76.2; H, 6.5; N, 12.7%. IR: ν(O–H), 3226sh, m cm^{-1}; ν(C=N), 1622m cm^{-1}. RMN ^{1}H (300 MHz, $CDCl_3$, δ ppm, *J* Hz): δ = 9.25 (s, 1H, H16); 9.01 (s, 2H, H14, H18); 8.89 (s, br 1H, –OH/resonance taken from a spectrum recorded in DMSO-d^6); 8.76 (s, 1H, HC=N); 8.07 [d, 2H, H3, H5 or H2, H6, ^3J(H2H3) = 8.3 Hz]; 7.70 [d, H3,H5 or H2, H6, ^3J(H2H3) = 8.3 Hz]; 7.34 [d, 1H, H8, ^4J(H8H10) = 2.2 Hz]; 7.27 [dd, 1H, H10, ^3J(H10H11) = 8.5 Hz, ^4J(H8H10) = 2,2 Hz]; 6.97 [d, 1H, H11, ^3J(H10H11) = 8.5 Hz], 1.35 (s, 9H, ^{t}Bu).

4.2. Preparation of [Pd{4-(NC_5H_4)C_6H_3C(H)=N[2-(O)C_6H_4]}]$_4$ (1a)

A pressure tube containing 4-(NC_5H_4)C_6H_4C(H)=N[2′-(OH)C_6H_4] (0.125 g, 0.456 mmol), palladium acetate (0.101 g, 0.452 mmol) and 20 cm^3 of dry toluene was sealed under argon. The resulting mixture was heated at 60 °C for 24 h. After cooling to room temperature the resulting violet solid was filtered off and dried under vacuum. Yield 26%. *Anal.* calc. $C_{72}H_{48}N_8O_4Pd_4$ requires C, 57.1; H, 3.2; N, 7.4. Found: C, 57.0; H, 3.1; N, 7.3%. IR: ν(C=N), 1579sh, cm^{-1}. FAB-MS: *m*/*z* = 1136.1 $[(3/4M)H]^+$.

Compounds **1b** and **1c** were prepared similarly as violets solids.

[Pd{3,5-($N_2C_4H_3$)C_6H_3C(H)=N[2′-(O)-C_6H_4]}]$_4$ (1b). Yield 43%. *Anal.* calc. $C_{68}H_{44}N_{12}O_4Pd_4$ requires C, 53.8; H, 2.9; N, 11.1. Found: C, 53.7; H, 2.7; N, 11.2%. IR: ν(C=N), 1590s cm^{-1}. FAB-MS: m/z = 760.0 [(M/2)H]$^+$.

[Pd{3,5-($N_2C_4H_3$)C_6H_3C(H)=N[2′-(O)-5′-^{t}BuC_6H_3]}]$_4$ (1c) Yield 21%. *Anal.* calc. $C_{84}H_{76}N_{12}O_4Pd_4$ requires C, 57.9; H, 4.4; N, 9.6. Found: C, 57.8; H, 4.5; N, 9.7%. IR: ν(C=N), 1580m cm^{-1}. FAB-MS: m/z = 1741.2 [M]$^+$; 871.3 [(M/2)H]$^+$.

4.3. Preparation of [Pd{4-(NC_5H_4)C_6H_3C(H)=N[2-(O)C_6H_4]}(PPh_3)] (2a)

PPh_3 (16 mg, 0.015 mmol) was added to a suspension of **1a** (24 mg, 0.016 mmol) in chloroform (20 cm^3). The mixture was stirred for 72 h and the solvent removed to give a violet solid which was recrystallized from dichloromethane/hexane. Yield 68%. *Anal.* calc. $C_{36}H_{27}N_2OPPd$ requires C, 67.5; H, 4.3; N, 4.4. Found: C, 67.6; H, 4.3; N, 4.5%. IR: ν(C=N), 1537sh cm^{-1}. ^{1}H NMR (300 MHz, $CDCl_3$): δ = 8.38 [d, 2H, H15,H17, ^3J(H14H15) = 5.9 Hz]; 7.98 [d, 1H, *H*C=N, ^4J(PH) = 10.1 Hz], 7.22 [d,1H, H2, ^3J(H2H3) = 7.7 Hz]; 7.12 [dd, 1H, H8, ^3J(H8H9) = 8.0 Hz, ^4J(H8H10) = 1.5 Hz]; 7.10 [dd, 1H, H3, ^3J(H2H3) = 7.7 Hz, ^4J(H3H5) = 1.7 Hz]; 6.97 [m, 1H, H10, ^3J(H10H11) = 8.5 Hz, ^3J(H9H10) = 7.1 Hz, ^4J(H8H10) = 1.5 Hz]; 6.65 [d, 2H, H14, H18, ^3J(H14H15) = 5.9 Hz]; 6.54 [dd, 1H, H11, ^3J(H10H11) = 8.5 Hz, ^4J(H9H11) = 1,0 Hz]; 6.42 [dd, 1H, H5, ^4J(PH5) = 3.8 Hz, ^4J(H3H5) = 1.7 Hz]; 6.37 (t, 1H, H9). ^{31}P–{^{1}H} NMR (121.49 MHz, $CDCl_3$, δ ppm) 34.60s. FAB-MS: m/z = 640.1 [M]$^+$.

Compounds **2b** and **2c** were prepared as violets solids following a similar procedure to that used for **2a**, but using reaction times of 24 h and acetone as solvent in the case of **2c**.

[Pd{3,5-($N_2C_4H_3$)C_6H_3C(H)=N[2′-(O)C_6H_4]}(PPh_3)] (2b). Yield 71%. *Anal.* calc. $C_{35}H_{26}N_3OPPd$ requires C, 65.5; H, 4.1; N, 6.5. Found: C, 65.6; H, 4.3; N, 6.4%. IR: ν(C=N), 1583m cm^{-1}. ^{1}H NMR (300 MHz, $CDCl_3$): δ = 9.03 (s, 1H, H16); 8.13 (s, 2H, H14, H18); 7.98 [d, 1H, *H*C=N, ^4J(PH) = 10 Hz]; 7.24 [d, 1H, H2, ^3J(H2H3) = 7.7 Hz], 7.12 [dd, 1H, H8, ^3J(H8H9) = 8.0 Hz, ^4J(H8H10) = 1.4 Hz]; 7.05 [dd, 1H, H3, ^3J(H2H3) = 7.7 Hz, ^4J(H3H5) = 1.7 Hz]; 6.97 [m, 1H, H10, ^3J(H10H11) = 8.3 Hz, ^3J(H9H10) = 8 Hz, ^4J(H8H10) = 1.4 Hz]; 6.54 [dd, 1H, H11, ^3J(H10H11) = 8.3 Hz, ^4J(H9H11) = 0.9 Hz]; 6.38 [t, 1H, H9, ^3J(H8H9) = ^3J(H9H10) = 8 Hz, ^4J(H9H11) = 0.9 Hz]; 6.28 [dd, 1H, H5, ^4J(PH5) = 3.7 Hz, ^4J(H3H5) = 1.7 Hz]. ^{31}P–{^{1}H} NMR (121.49 MHz, $CDCl_3$, δ ppm) 34.46s. FAB-MS: m/z = 641.1 [M]$^+$.

[Pd{3,5-($N_2C_4H_3$)C_6H_3C(H)=N[2′-(O)-5′-^{t}BuC_6H_3)}(PPh_3)] (2c). Yield 67%. *Anal.* calc. $C_{39}H_{34}N_3OPPd$ requires C, 67.1; H, 4.9; N, 6.0. Found: C, 67.2; H, 4.8; N, 6.1%. IR: ν(C=N), 1580m cm^{-1}. ^{1}H NMR (300 MHz, $CDCl_3$): δ = 9.02 (s, 1H, H16); 8.14 (s, 2H, H14, H18); 7.98 [d, 1H, HC=N, ^4J(PH) = 10.2 Hz], 7.23 [d, 1H, H2, ^3J(H2H3) = 7.7 Hz]; 7.07–7.02 (m, 3H, H3, H8, H10); 6.48 [d, 1H, H11, ^3J(H10H11) = 8,6 Hz]; 6.25 [dd, 1H, H5, ^4J(PH5) = 3.7 Hz, ^4J(H3H5) = 1.7 Hz]; 1.27 (s, 9H, ^{t}Bu). ^{31}P–{^{1}H} NMR (121.49 MHz, $CDCl_3$, δ ppm) 34.46s. FAB-MS: m/z = 697.2 [M]$^+$.

4.4. Preparation of [{Pd[3,5-($N_2C_4H_3$)C_6H_3C(H)=N{2-(O)C_6H_4}]}$_2$(μ-$Ph_2P(CH_2)_4PPh_2$)] (3b)

$Ph_2P(CH_2)_4PPh_2$ (11.3 mg, 0.013 mmol) was added to a suspension of **1b** (21.0 mg, 0.014 mmol) in acetone (20 cm^3). The mixture was stirred for 72 h and the solvent removed to give a violet solid which was recrystallized from acetone/hexane. Yield 65%. *Anal*calc. $C_{62}H_{50}N_6O_2P_2Pd_2$ requires C, 62.8; H, 4.2; N, 7.1. Found: C, 62.9; H, 4.1; N, 7.2%. IR: ν(C=N), 1583s cm^{-1}. ^{1}H NMR (300 MHz, $CDCl_3$): δ = 9.02 (s, 1H, H16); 8.15 (s, 2H, H14, H18); 7.95 [d, 1H, *H*C=N, ^4J(PH) = 1000 Hz]; 7.18 [d, 1H, H2, ^3J(H2H3) = 7.8 Hz]; 7.09 [dd, 1H, H8, ^3J(H8H9) = 8.3 Hz, ^4J(H8H10) = 1.5 Hz]; 7.01 [dd, 1H, H3, ^3J(H2H3) = 7.8 Hz, ^4J(H3H5) = 1.6 Hz]; 6.91 (m, 1H, H10); 6.38–6.34 [m, 2H, H9, H11]; 6.29 [m, 1H, H5, ^4J(PH5) = 3.5 Hz, ^4J(H3H5) = 1.6 Hz]. ^{31}P–{^{1}H} NMR (121.49 MHz, $CDCl_3$, δ ppm) 30.22s. FAB-MS: m/z = 1186.1 [MH]$^+$.

Compounds **3c, 4b, 4c and 5c** were obtained as violet solids following a similar procedure to the one described for **3b** but using the appropriate phosphine.

[{Pd[3,5-($N_2C_4H_3$)C_6H_3C(H)=N{2′-(O)-5′-^{t}BuC_6H_3}]}$_2$(μ-$Ph_2P(CH_2)_4PPh_2$)] (3c). Yield 47%. *Anal.* calc. $C_{70}H_{66}N_6O_2P_2Pd_2$ requires C, 64.8; H, 5.1; N, 6.5. Found: C, 64.6; H, 5.3; N, 6.4%. IR: ν(C=N), 1578m cm^{-1}. ^{1}H NMR (300 MHz, $CDCl_3$): δ = 9.01(s, 1H, H16); 8.15 (s, 2H, H14, H18); 7.91 [d, 1H, *H*C=N, ^4J(PH) = 10.1 Hz]; 7.18 [d, 1H, H2, ^3J(H2H3) = 7.7 Hz]; 7.05 [d, 1H, H8, ^4J(H8H10) = 2.3 Hz]; 7.00 [dd, 1H, H3, ^3J(H2H3) = 7.7 Hz, ^4J(H3H5) = 1.8 Hz]; 6.98 [dd, 1H, H10, ^3J(H10H11) = 8.8 Hz, ^4J(H8H10) = 2.3 Hz]; 6.33 [d, 1H, H11, ^3J(H10H11) = 8.8 Hz]; 6.27 [dd, 1H, H5, ^4J(PH5) = 3.7 Hz, ^4J(H3H5) = 1.8 Hz]; 1.28 (s, 9H, ^{t}Bu). ^{31}P–{^{1}H} NMR (121.49 MHz, $CDCl_3$, δ ppm) 30.33s. FAB-MS: m/z = 1298.2 [MH]$^+$.

[{Pd[3,5-($N_2C_4H_3$)C_6H_3C(H)=N{2′-(O)C_6H_4}]}$_2$(μ-$Ph_2P(\eta^5$-$C_5H_4)Fe(\eta^5$-$C_5H_4)PPh_2$)] (4b). Yield 65%. *Anal.* calc. $C_{68}H_{50}N_6O_2P_2$-$FePd_2$ requires C, 62.2; H, 3.8; N, 6.4. Found: C, 62.4; H, 3.9; N, 6.5%. IR: ν(C=N), 1582s cm^{-1}. ^{1}H NMR (300 MHz, $CDCl_3$): δ = 9.02 (s, 1H, H16); 8.07 (s, 2H, H14, H18); 7.91 [d, 1H, HC=N, ^4J(PH) = 10.4 Hz]; 7.22 [d, 1H, H2, ^3J(H2H3) = 7.7 Hz]; 7.09-7.03 (m, 2H, H3, H8); 6.95 (m, 1H, H10); 6.56 (d, 1H, H11); 6.32 (t, 1H, H9); 6.21 [m, 1H, H5, ^4J(PH5) = 3.8 Hz, ^4J(H3H5) = 1.4 Hz]. ^{31}P–{^{1}H} NMR (121.49 MHz, $CDCl_3$, δ ppm) 24.56s. FAB-MS: m/z = 1314.1 [MH]$^+$.

[{Pd[3,5-($N_2C_4H_3$)C_6H_3C(H)=N{2′-(O)-5′-^{t}BuC_6H_3}]}$_2$(μ-$Ph_2P(\eta^5C_5H_4)Fe(\eta^5C_5H_4)$-$PPh_2$)] (4c). Yield 69%. *Anal.* calc. $C_{76}H_{66}N_6O_2P_2FePd_2$ requires C, 64.0; H, 4.7; N, 5.9. Found: C, 64.2; H, 4.5; N, 5.8%. IR: ν(C=N), 1584m cm^{-1}. ^{1}H NMR (300 MHz, $CDCl_3$): δ = 9,01 (s, 1H, H16); 8.07 (s, 2H, H14, H18); 7.94 [d, 1H, HC=N, ^4J(PH) = 10,5 Hz]; 7.22 [d, 1H, H2, ^3J(H2H3) = 7.8 Hz]; 7.06–7.01 [m, 3H, H3, H8, H10); 6.50 (d, 1H, H11, ^3J(H10H11) = 8.6 Hz]; 6.19 [m, 1H, H5, ^4J(PH5) = 3.8 Hz, ^4J(H3H5) = 1.6 Hz]; $(CH)_{ferrocene}$ = 5.19–4.32 (m, 4H); 1.28 (s, 9H, ^{t}Bu). ^{31}P–{^{1}H} NMR (121.49 MHz, $CDCl_3$, δ ppm) 24.67s. FAB-MS: m/z = 1426.2 [MH]$^+$.

[{Pd[3,5-($N_2C_4H_3$)C_6H_3C(H)=N{2′-(O)-5′-^{t}BuC_6H_3}]}$_2$(μ-Ph_2P(CH=CH)PPh_2)] (5c). Yield 89%. *Anal*calc. $C_{68}H_{62}N_6O_2P_2Pd_2$ requires C, 64.3; H, 4.9; N, 6.6. Found: C, 64.3; H, 4.8; N, 6.7%. IR: ν(C=N), 1579m cm^{-1}. ^{1}H NMR (300 MHz, $CDCl_3$): δ = 9.00 (s, 1H, H16); 8.14 (s, 2H, H14, H18); 7.92 [d, 1H, *H*C=N, ^4J(PH) = 10,1 Hz]; 7.19 [d, 1H, H2, ^3J(H2H3) = 7.8 Hz]; 7.08 [d, 1H, H8, ^4J(H8H10) = 2.3 Hz], 7.05–7.00 (m, 2H, H3, H10); 6.41 [d, 1H, H11, ^3J(H10H11) = 9.4 Hz]; 6.22 (m, 1H, H5); 1.29 (s, 9H, ^{t}Bu) ppm. ^{31}P–{^{1}H} NMR (121.49 MHz, $CDCl_3$, δ ppm) 30.96s. FAB-MS: m/z = 1268.2 [MH]$^+$.

Acknowledgments

We thank the Ministerio de Ciencia e Innovación (Projects CTQ2006-15621-C02-02/BQU, CTQ2006-15621-C02-01/BQU), the Xunta de Galicia and the Universidad de la Coruña for financial support.

References

[1] (a) J. Dehand, M. Pfeffer, Coord. Chem. Rev. 18 (1976) 327;
(b) M.I. Bruce, Angew. Chem., Int. Ed. Engl. 16 (1977) 73;
(c) I. Omae, Coord. Chem. Rev. 28 (1979) 97;
(d) I. Omae, Chem. Rev. 79 (1979) 287;
(e) I. Omae, Coord. Chem. Rev. 32 (1980) 235;
(f) I. Omae, Coord. Chem. Rev. 42 (1982) 245;
(g) E.C. Constable, Polyhedron 3 (1984) 1037;
(h) I.P. Rothwell, Polyhedron 4 (1985) 177;

(i) Y. Wu, S. Huo, J. Gong, X. Cui, L. Ding, K. Ding, C. Du, Y. Liu, M. Song, J. Organomet. Chem. 637–639 (2001) 27;
(j) M. Albrecht, G. van Koten, Angew. Chem., Int. Ed. 40 (2001) 3750;
(k) I. Omae, Coord. Chem. Rev. 248 (2004) 995;
(l) F. Mohr, S.H. Priver, S.K. Bhargava, M.A. Bennett, Coord. Chem. Rev. 250 (2006) 1851.
[2] (a) S.B. Wild, Coord. Chem. Rev. 166 (1997) 291;
(b) J. Albert, J.M. Cadena, J.R. Granell, X. Solans, M. Font-Bardia, Tetrahedron: Asymmetry 11 (2000) 1943;
(c) S.P. Flanagan, R. Goddard, P.J. Guiry, Tetrahedron 61 (2005) 9808;
(d) L. Tang, Y. Zhang, L. Ding, Y. Li, K.-F. Mok, W.-C. Yeo, P.-H. Leung, Tetrahedron Lett. 48 (2007) 33.
[3] (a) W.T.S. Huck, R. Hulst, P. Timmerman, F.C.J.M. van Veggel, D.N. Reinhoudt, Angew. Chem., Int. Ed. Engl. 36 (1997) 1006;
(b) J.R. Hall, S.J. Loeb, G.K.H. Shimizu, G.P.A. Yap, Angew. Chem., Int. Ed. 37 (1998) 121;
(c) W.T.S. Huck, L.J. Prins, R.H. Fokkers, N.M.M. Nibbering, F.C.J.M. van Veggel, D.N. Reinhoudt, J. Am. Chem. Soc. 120 (1998) 6240;
(d) R.F. Carina, A.F. Williams, G. Bernardinelli, Inorg. Chem. 40 (2001) 1827;
(e) M. López-Torres, A. Fernández, J.J. Fernández, A. Suárez, S. Castro-Juiz, S. Vila, M.T. Pereira, Organometallics 20 (2001) 1350;
(f) M.Q. Slagt, D.A.P. van Zwieten, A.J.C.M. Moerkerk, R.J.M. Klein Gebbink, G. van Koten, Coord. Chem. Rev. 248 (2004) 2275;
(g) W. Lu, V.A.L. Rpy, C.-M. Che, Chem. Commun. (2006) 3972;
(h) M. Gagliardo, G. Rodríguez, H.H. Dam, M. Lutz, A.L. Spek, R.W.A. Havenith, P. Coppo, L. De Cola, F. Hartl, G.P.M. van Klink, G. van Koten, Inorg. Chem. 45 (2006) 2143.
[4] (a) M. Marcos, in: J.L. Serrano (Ed.), Metallomesogens. Synthesis, Properties and Applications, VCH, Weinheim, 1996;
(b) D. Pucci, G. Barneiro, A. Bellusci, A. Crispini, M. Ghedini, J. Organomet. Chem. 691 (2006) 1138.
[5] (a) S.-W. Lai, T.-C. Cheung, M.C.W. Chan, K.-K. Cheung, S.-M. Peng, C.-M. Che, Inorg. Chem. 39 (2000) 255;
(b) B. Ma, P.I. Djurovich, M.E. Thompson, Coord. Chem. Rev. 249 (2005) 1501;
(c) M. Ghedini, I. Aiello, A. Crispini, A. Golemme, M. La Deda, D. Pucci, Coord. Chem. Rev. 250 (2006) 1373;
(d) M.L.S. Lowry, S. Bernhard, Chem. Eur. J. 12 (2006) 7970;
(e) L.-L. Wu, C.-H. Yang, I.-W. Sun, S.-Y. Chu, P.-C. Kao, H.-H. Huang, Organometallics 26 (2007) 2017;
(f) S.C.F. Kui, I.H.T. Sham, C.C.C. Cheung, C.-W. Ma, B. Pan, N. Zhu, C.M. Che, W.-F. Fu, Chem. Eur. J. 13 (2007) 417.
[6] (a) A. Habtemariam, B. Watchman, B.S. Potter, R. Palmer, S. Parsons, A. Parkin, P.J. Sadler, J. Chem. Soc., Dalton Trans. (2001) 1306;
(b) T. Okada, I.M. El-Mehasseb, M. Kodaka, T. Tomohiro, K. Okamoto, H. Okuno, J. Med. Chem. 44 (2001) 4661;
(c) A. Gómez-Quiroga, C. Navarro-Ranninger, Coord. Chem. Rev. 248 (2004) 119;
(d) J. Ruiz, J. Lorenzo, L. Sanglas, N. Cutillas, C. Vicente, M.D. Villa, F.X. Avilés, G. López, V. Moreno, J. Pérez, D. Bautista, Inorg. Chem. 45 (2006) 6347.
[7] (a) J. Dupont, M. Pfeffer, J. Spencer, Eur. J. Inorg. Chem. (2001) 1917;
(b) V. Ritleng, C. Sirlin, M. Pfeffer, Chem. Rev. 102 (2002) 1731;
(c) M.E. van der Boom, D. Milstein, Chem. Rev. 103 (2003) 1759;
(d) J. Dupont, C.S. Consorti, J. Spencer, Chem. Rev. 105 (2005) 2527;
(e) H.-Y. Thu, W.-Y. Yu, C.-M. Che, J. Am. Chem. Soc. 128 (2006) 9048;
(f) R. Huang, K.H. Shaugnessy, Organometallics 25 (2006) 4105;
(g) M. Weck, C.W. Jones, Inorg. Chem. 46 (2007) 1865;
(h) R. Johansson, O.L. Wendt, Dalton Trans. (2007) 488;
(i) I. Omae, J. Organomet. Chem. 692 (2007) 2608.
[8] J.M. Vila, M.T. Pereira, J.M. Ortigueira, M. López-Torres, D. Lata, M. Graña, A. Suárez, J.J. Fernández, A. Fernández, J. Chem. Soc., Dalton Trans. (1999) 4193.
[9] D. Vázquez-García, A. Fernández, J.J. Fernández, M. López-Torres, A. Suárez, J.M. Ortigueira, J.M. Vila, H. Adams, J. Organomet. Chem. 595 (2000) 199.
[10] A.G. Quiroga, J.M. Perez, I. Lopez-Solera, J.R. Masaguer, A. Luque, P. Roman, A. Edwards, C. Alonso, C. Navarro-Ranninger, J. Med. Chem. 41 (1988) 1399.
[11] A. Amoedo, M. Graña, J. Martínez, T. Pereira, M. López-Torres, A. Fernández, J.J. Fernández, J.M. Vila, Eur. J. Inorg. Chem. (2002) 613.
[12] A. Amoedo, L.A. Adrio, J.M. Antelo, J. Martínez, M.T. Pereira, A. Fernández, J.M. Vila, Eur. J. Inorg. Chem. (2006) 3016.
[13] J. Martínez, L.A. Adrio, J.M. Antelo, J.M. Ortigueira, M.T. Pereira, J.J. Fernández, A. Fernández, J.M. Vila, J. Organomet. Chem. 691 (2006) 2721.
[14] A. Fernández, D. Vázquez-García, J.J. Fernández, M. López-Torres, A. Suárez, S. Castro-Juiz, J.M. Vila, New J. Chem. 26 (2002) 105.
[15] C. López, A. Caubet, S. Pérez, X. Soláns, M. Font-Bardía, J. Organomet. Chem. 681 (2003) 82.
[16] J.J. Fernández, A. Fernández, D. Vázquez-García, M. López-Torres, A. Suárez, J.M. Vila, Polyhedron 26 (2007) 4567.
[17] J.J. Fernández, A. Fernández, D. Vázquez-García, M. López-Torres, A. Suárez, A. Suárez, N. Gómez-Blanco, J.M. Vila, Eur. J. Inorg. Chem. (2007) 5408.
[18] J. Martínez, M.T. Pereira, I. Buceta, G. Alberdi, A. Amoedo, J.J. Fernández, M. López-Torres, J.M. Vila, Organometallics 22 (2003) 5581.
[19] A. Weisman, M. Gozin, H. Kraatz, D. Milstein, Inorg. Chem. 35 (1996) 1792.
[20] M. Chas, D. Abella, V. Blanco, E. Pía, G. Blanco, A. Fernández, C. Platas-Iglesias, C. Peinador, J.M. Quintela, Chem. Eur. J. 13 (2007) 8572.
[21] K. Suzuki, M. Kawano, S. Sato, M. Fujita, J. Am. Chem. Soc. 129 (2007) 10652.
[22] I.S. Chun, J.A. Kwon, H.J. Yoon, M.N. Bae, J. Hong, O. Jung, Angew. Chem., Int. Ed. 46 (2007) 4960.
[23] M. Ferrer, A. Gutiérrez, M. Mounir, O. Rossell, E. Ruiz, A. Rang, M. Engeser, Inorg. Chem. 46 (2007) 3395.
[24] P. Thanasekaran, R.T. Liao, Y.H. Liu, T. Rajendran, S. Rajagopal, K.L. Lu, Coord. Chem. Rev. 249 (2005) 1085.
[25] G.F. Swiegers, T.J. Malefetse, Coord. Chem. Rev. 225 (2002) 91.
[26] M. Fujita, M. Tominaga, A. Hori, B. Therrien, Acc. Chem. Res. 38 (2005) 369.
[27] F. Wurthner, C.C. You, C.R. Saha-Moller, Chem. Soc. Rev. 33 (2004) 133.
[28] H. Onoue, I. Moritani, J. Organomet. Chem. 43 (1972) 431.
[29] H. Onoue, K. Minami, K. Nakagawa, Bull. Chem. Soc. Jpn. 43 (1970) 3480.
[30] C.L. Chen, Y.H. Liu, S.M. Peng, S.T. Liu, J. Organomet. Chem. 689 (2004) 1806.
[31] P.S. Pregosini, R.W. Kuntz, ^{31} P and^{13} C-NMR of transition metal phosphine complexes, in: P. Diehl, E. Fluck, R. Kosfeld (Eds.), NMR Basic Principles and Progress, vol. 16, Springer, Berlin, 1979.
[32] J. Albert, J. Granell, J. Sales, M. Font-Bardía, X. Solans, Organometallics 14 (1995) 1393.
[33] R. Bosque, J. Granell, J. Sales, M. Font-Bardía, X. Solans, J. Organomet. Chem. 453 (1994) 147.
[34] J.M. Vila, M. Gayoso, M.T. Pereira, M. López-Torres, G. Alonso, J.J. Fernández, J. Organomet. Chem. 445 (1993) 287.
[35] D.D. Perrin, W.L.F. Armarego, Purification of Laboratory Chemicals, 4th ed., Butterwort-Heinemann, 1996.

Polyhedron 28 (2009) 2684–2692

Contents lists available at ScienceDirect

Polyhedron

journal homepage: www.elsevier.com/locate/poly

Coordination networks constructed with supramolecular synthon R_X–C≡C⊃Ag_n (n = 4, 5; R_X = halophenyl)

Siegfried M.J. Wang, Thomas C.W. Mak *

Department of Chemistry and Centre of Novel Functional Molecules, The Chinese University of Hong Kong, Shatin, New Territories, Hong Kong SAR, China

ARTICLE INFO

Article history:
Received 11 March 2009
Accepted 5 May 2009
Available online 13 May 2009

Keywords:
Coordination network
Halogen···halogen
Silver–ethynide
Silver···halogen
Supramolecular synthon

ABSTRACT

Eight new silver(I) double salts: $AgL^1{\cdot}2AgCF_3COO$ (**1**), $AgL^1{\cdot}3AgNO_3$ (**2**), $2AgL^2{\cdot}5AgCF_3COO{\cdot}2CH_3CN{\cdot}H_2O$ (**3**), $4AgL^3{\cdot}6AgCF_3COO{\cdot}5CH_3CN$ (**4**), $4AgL^4{\cdot}6AgCF_3COO{\cdot}5CH_3CN$ (**5**), $2AgL^5{\cdot}4AgCF_3COO{\cdot}NC(CH_2)_4CN$ (**6**), $2AgL^5{\cdot}4AgCF_3COO{\cdot}2CH_3CN$ (**7**) and $AgL^6{\cdot}2CF_2(CF_2COOAg)_2{\cdot}2CH_3CN$ (**8**) (L^1 = 4-iodophenylethynide; L^2 = 3,4-dichlorophenylethynide; L^3 = 3-chlorophenylethynide; L^4 = 3-bromophenylethynide; L^5 = 2-chlorophenylethynide; L^6 = 2-fluorophenylethynide) have been synthesised and characterized by X-ray crystallography. All compounds contain the silver–halophenylethynide supramolecular synthon R_X–C≡C⊃Ag_n (n = 4, 5). In particular, the three-dimensional supramolecular structures in **1** and **2** are stabilized by strong Ag···I interactions, while that in **3** is consolidated by both Ag···Cl and van der Waals type F···Cl interactions. In isomorphous compounds **4** and **5**, the presence of respective F···Cl or F···Br contact contributes to the stability of the network. The silver aggregates in **6**, **7** and **8** are stabilized by Ag···Cl or Ag···F interactions between the *ortho*-halo substituent and the Ag_n basket.

© 2009 Elsevier Ltd. All rights reserved.

1. Introduction

The silver(I) cation, like other easily-polarizable metal cations, tends to associate with 'soft' non-metals such as sulfur, selenium, tellurium and iodine. Accordingly, intermolecular interactions of the type Ag···X (X = F, Cl, Br, I) have been used in the design and assembly of supramolecular structures [1]. Besides using halogen ions in their bare forms [2], several reports have demonstrated the feasibility of using X-aryl moieties to incorporate silver···halogen interactions into coordination networks. The Ag···I-aryl interaction (with Ag···I distances in the range of 2.719–3.357 Å) commonly occurs [1], while Ag···Br-aryl and Ag···Cl-aryl are less studied [3], and Ag···F-aryl is rarely reported.

In recent years, we have carried out a systematic investigation on the construction of silver–organic coordination networks based on silver–ethynide supramolecular synthons, which comprise silver aggregates stabilized by argentophilicity and silver–ethynide interactions of the σ, π and mixed (σ, π) types [4]. Among the compounds studied thus far, two examples exhibit significant silver···halogen interaction involving the F^- and $PF_2O_2^-$ ions [5]. Therefore, it is of interest to us to investigate the role played by the silver···halogen interactions in coordination network assembly based on the silver–ethynide supramolecular synthon [4b,6]. In this paper, we report the synthesis and structure characterization of eight new silver(I) halophenylethynide complexes: $AgL^1{\cdot}2AgCF_3COO$ (**1**), $AgL^1{\cdot}3AgNO_3$ (**2**), $2AgL^2{\cdot}5AgCF_3COO{\cdot}2CH_3CN{\cdot}H_2O$ (**3**), $4AgL^3{\cdot}6AgCF_3COO{\cdot}5CH_3CN$ (**4**), $4AgL^4{\cdot}6AgCF_3COO{\cdot}5CH_3CN$ (**5**), $2AgL^5{\cdot}4AgCF_3COO{\cdot}NC(CH_2)_4CN$ (**6**), $2AgL^5{\cdot}4AgCF_3COO{\cdot}2CH_3CN$ (**7**) and $AgL^6{\cdot}2CF_2(CF_2COOAg)_2{\cdot}2CH_3CN$ (**8**) (L^1 = 4-iodophenylethynide; L^2 = 3,4-dichlorophenylethynide; L^3 = 3-chlorophenylethynide; L^4 = 3-bromophenylethynide; L^5 = 2-chlorophenylethynide; L^6 = 2-fluorophenylethynide), which are stabilized by both silver(I)–ethynide and silver(I)···halogen interactions. In addition, C—H···X (X = Br, Cl) hydrogen bonds exist in **4** and **5**, respectively, and multiple halogen···halogen van der Waals interactions contribute to network stabilization in **3**, **4**, **5** and **6**.

2. Experimental

2.1. General

All chemicals are used as received from Aldrich® with no further purification. Degassing and desiccation are not performed for solvents of analytical reagent grade.

2.1.1. Synthesis of polymeric silver(I) halophenylethynides

$[AgL^1]_n$. (4-Iodophenylethynyl)trimethylsilane (1.00 g, 3.33 mmol) was dissolved in a mixed solvent of 20 mL acetonitrile, 2 mL triethylamine and 40 mL methanol, to which was subsequently added 10 mL acetonitrile solution containing dissolved silver nitrate (0.623 g, 3.66 mmol). A white precipitate formed immediately. After stirring for 10 h, the crude polymeric product was filtered off and washed with 20 mL acetonitrile, 10 mL diethyl

* Corresponding author. Tel.: +852 2609 6279; fax: +852 2603 5057.
E-mail address: tcwmak@cuhk.edu.hk (T.C.W. Mak).

0277-5387/$ - see front matter © 2009 Elsevier Ltd. All rights reserved.
doi:10.1016/j.poly.2009.05.004

ether and 10 mL distilled water trice, and then stored under −10 °C in wet form. Yield: 72% (based on TMS-C≡CPhI-4). IR: ν = 2034 cm^{-1} (w, $\nu_{C\equiv C}$).

[AgL^2]$_n$. 3,4-Dichlorophenylacetylene (1.00 g, 5.85 mmol) was dissolved in a mixture of 2 mL triethylamine and 60 mL acetonitrile, to which a 10 mL acetonitrile solution of silver nitrate (1.00 g, 5.88 mmol) was subsequently added. After stirring for 10 h, the crude polymeric salt was filtered off and washed with 20 mL acetonitrile and 10 mL distilled water trice, and then stored under −10 °C in wet form. Yield: 80%, IR: ν = 2026 cm^{-1} (w, $\nu_{C\equiv C}$). Similar procedures were conducted in obtaining the following four crude polymeric silver salts.

[AgL^3]$_n$. This material was prepared employing 3-chlorophenylacetylene. Yield: 80%, IR: ν = 2010 cm^{-1} (w, $\nu_{C\equiv C}$).

[AgL^4]$_n$. This material was prepared employing 3-bromophenylacetylene. Yield: 80%, IR: ν = 2010 cm^{-1} (w, $\nu_{C\equiv C}$).

[AgL^5]$_n$. This material was prepared employing 2-chlorophenylacetylene. Yield: 60%, IR: ν = 2025 cm^{-1} (w, $\nu_{C\equiv C}$).

[AgL^6]$_n$. This material was prepared employing 2-fluorophenylacetylene. Yield: 56%, IR: ν = 2054 cm^{-1} (w, $\nu_{C\equiv C}$).

2.1.2. Synthesis of silver(I) halophenylethynide complexes

*2.1.2.1. AgL^1·2AgCF$_3$COO (**1**).* AgBF$_4$ (0.384 g, 2 mmol) and AgCF$_3$COO (0.220 g, 1 mmol) were dissolved in 1 mL distilled water, and subsequently [AgL^1]$_n$ (~0.050 g) was added. The mixture was stirred vigorously for 1 h. During that time, 0.1 mL acetonitrile was introduced. The undissolved solid was then filtered off, and the filtrate stored under 25 °C in the dark. Crystallization happened two weeks later. Elemental Analysis (calculated): C: 18.78% (18.56%), H: 0.51% (0.52%). IR: ν = 2032 cm^{-1} (w, $\nu_{C\equiv C}$).

*2.1.2.2. AgL^1·3AgNO$_3$ (**2**).* AgNO$_3$ (0.600 g, 3.5 mmol) was dissolved in a mixture of 1 mL distilled water and 0.2 mL acetonitrile, and subsequently [AgL^1]$_n$ (~0.050 g) was added. The mixture was stirred for 1 h. The undissolved solid was then filtered off, and the filtrate was stored under 25 °C in the dark. Crystallization happened two weeks later. Elemental Analysis (calculated): C: 11.16% (11.38%), H: 0.50% (0.48%). IR: ν = 2022 cm^{-1} (w, $\nu_{C\equiv C}$).

*2.1.2.3. 2AgL^2·5AgCF$_3$COO·2CH$_3$CN·H$_2$O (**3**).* AgBF$_4$ (0.384 g, 2 mmol) and AgCF$_3$COO (0.220 g, 1 mmol) were dissolved in 1 mL distilled water, and subsequently [AgL^2]$_n$ (~0.050 g) was added. The mixture was stirred vigorously for 1 h. During that time, 0.1 mL acetonitrile was introduced. The undissolved solid was then filtered off, and the filtrate stored under 25 °C in the dark. Small plate-like crystals were obtained two months later. Elemental analysis (calculated): C: 20.30% (20.45%), H: 1.06% (0.92%), IR: ν = 2048 cm^{-1} (w, $\nu_{C\equiv C}$).

*2.1.2.4. 4AgL^3·6AgCF$_3$COO·5CH$_3$CN (**4**).* AgBF$_4$ (0.384 g, 2 mmol) and AgCF$_3$COO (0.220 g, 1 mmol) were dissolved in 1 mL distilled water, and subsequently [AgL^3]$_n$ (~0.050 g) was added. The mixture was stirred vigorously for 1 h. During that time, 0.4 mL acetonitrile was introduced. The undissolved solid was then filtered off, and the filtrate stored under 25 °C in the dark. Plate-like crystals were obtained in one week. Elemental analysis (calculated): C: 25.75% (25.90%), H: 1.40% (1.25%). IR: ν = 2065, 2000 cm^{-1} (w, $\nu_{C\equiv C}$).

*2.1.2.5. 4AgL^4·6AgCF$_3$COO·5CH$_3$CN (**5**).* AgBF$_4$ (0.384 g, 2 mmol) and AgCF$_3$COO (0.220 g, 1 mmol) were dissolved in 1 mL distilled water, and subsequently [AgL^4]$_n$ (~0.050 g) was added. The mixture was stirred vigorously for 1 h. During that time, 0.4 mL acetonitrile was introduced. The undissolved solid was then filtered off, and the filtrate stored under 25 °C in the dark. Needle-like crystals were obtained in one week. Elemental analysis (calculated): C: 23.85% (24.18%), H: 1.28% (1.16%). IR: ν = 2048, 2012 cm^{-1} (w, $\nu_{C\equiv C}$).

*2.1.2.6. 2AgL^5·4AgCF$_3$COO·NC(CH$_2$)$_4$CN (**6**).* AgBF$_4$ (0.384 g, 2 mmol) and AgCF$_3$COO (0.220 g, 1 mmol) were dissolved in the mixture of 1 mL distilled water, 0.5 mL acetonitrile and 0.1 mL adiponitrile, to which [AgL^5]$_n$ (~0.050 g) was added subsequently. The mixture was stirred for 4 h. The undissolved solid was then filtered off. Colorless block-like crystals were formed one week later. Elemental analysis (calculated): C: 24.21% (24.37%), H: 1.20% (1.09%). IR: ν = 2041 cm^{-1} (w, $\nu_{C\equiv C}$).

*2.1.2.7. 2AgL^5·4AgCF$_3$COO·2CH$_3$CN (**7**).* AgBF$_4$ (0.384 g, 2 mmol) and AgCF$_3$COO (0.220 g, 1 mmol) were dissolved in 1 mL distilled water, and subsequently [AgL^5]$_n$ (~0.050 g) was added. The mixture was stirred vigorously for 1 h. During that time, 0.4 mL acetonitrile was introduced. The undissolved solid was then filtered off, and the filtrate stored under 25 °C in the dark. Plate-like crystals were obtained in one week. Elemental analysis (calculated): C: 23.19% (23.15%), H: 1.10% (0.97%). IR: ν = 2058 cm^{-1} ($\nu_{C\equiv C}$).

*2.1.2.8. AgL^6·2Ag$_2$C$_3$F$_6$(COO)$_2$·2CH$_3$CN (**8**).* AgBF$_4$ (0.384 g, 2 mmol), hexafluoroglutaric acid (0.120 g, 0.5 mmol) and Ag$_2$O (0.116 g, 0.5 mmol) were dissolved in a mixture of 1 mL distilled water and 0.2 mL acetonitrile, to which [AgL^6]$_n$ (~0.050 g) was added subsequently. The mixture was stirred for 4 h and filtered afterwards. Colorless needle-like crystals were formed after two weeks. Elemental analysis (calculated): C: 21.81% (21.72%), H: 1.00% (0.83%). IR: ν = 2057 cm^{-1} (w, $\nu_{C\equiv C}$).

2.2. X-ray crystallography

Selected crystals were used for data collection on a BrukerAXS Kappa APEX2 CCD diffractometer at 293 K using frames of oscillation range 0.5° (Phi scan and Omega scan) with 2° < θ < 28° (compound **1**, **2**, **3**, **6**, **7**, **8**) or on a BrukerAXS SMART 1000 CCD diffractometer at 293 K using frames of oscillation range 0.3° (Omega scan) with 2° < θ < 28° (compound **4**, **5**). Empirical absorption corrections based on multi-scan method were applied using the SADABS program [7]. The structures were solved by the direct method and refined by full-matrix least squares based on F^2 using the programs in SHELXTL package [8]. The crystal data and details of refinement are summarized in Table 1.

3. Results and discussion

*3.1. AgL^1·2AgCF$_3$COO (**1**)*

As shown in Fig. 1, compound **1** features a centrosymmetric Ag$_6$ aggregate derived from two inversion-related Ag$_4$ baskets sharing one silver edge (Ag3···Ag3a). An ethynide group (C1≡C2) is attached to each Ag$_4$ basket in the μ_4–η^2, η^2, η^1, η^1 ligation mode. The distances between silver atoms range from 2.815(1) to 3.238(1) Å, suggesting the existence of significant argentophilic interaction. Such silver baskets and ethynide ligation mode are consistent with those in the previously established R–C≡C⊃Ag$_n$ (n = 4, 5) supramolecular synthon [4b,6].

The connection of Ag$_6$ aggregates by bridging trifluoroacetate ligands across crystallographic inversion centers gives rise to a two-dimensional coordination network, as shown in Figs. 1 and 2. The carboxyl group containing oxygen atoms (O3, O4) adopts the μ_4–O,O,O',O' ligation mode generates a centrosymmetric (AgCF$_3$COO)$_2$ unit (Fig. 2). The distance between two silver atoms (Ag1···Ag1a) within this unit is 2.993(1) Å, which lies within the argentophilic distance range; under such linkage, the silver

Table 1
Crystallographic data of compound **1**–**8**.

Compound	**1**	**2**	**3**	**4**	**5**	**6**	**7**	**8**
Formula	$C_{12}H_4O_4F_6IAg_3$	$C_8H_4N_3O_9Ag_4I$	$C_{30}H_{14}N_2O_{11}Ag_7Cl_4F_{15}$	$C_{54}H_{31}N_5O_{12}F_{18}Ag_{10}Cl_4$	$C_{54}H_{31}N_5O_{12}F_{18}Ag_{10}Br_4$	$C_{30}H_{16}N_2O_8Ag_6Cl_2F_{12}$	$C_{28}H_{14}N_2O_8Ag_6Cl_2F_{12}$	$C_{22}H_{10}N_2O_8Ag_5F_{13}$
Fw	776.66	844.52	1760.32	2504.34	2682.18	1478.57	1452.53	1216.67
Crystal system	Triclinic	Monoclinic	Monoclinic	Triclinic	Triclinic	Triclinic	Triclinic	Triclinic
Space group	*P* 1	*Cc*	*Cc*	*P* 1	*P* 1	*P* 1	*P* 1	*P* 1
a (Å)	8.3284(5)	8.9094(4)	23.416(1)	14.695(5)	14.846(5)	11.9499(4)	12.008(6)	9.2084(2)
b (Å)	10.0353(6)	25.562(1)	7.2186(4)	15.336(6)	15.362(5)	13.8333(4)	13.150(7)	13.3717(6)
c (Å)	11.0673(7)	7.1395(3)	27.567(2)	17.685(7)	17.715(5)	13.9590(4)	13.706(7)	13.9829(4)
α (°)	84.762(1)	90.00	90.00	73.350(5)	73.298(5)	114.503(1)	67.21(1)	113.748(1)
β (°)	74.189(1)	112.045(1)	102.212(2)	70.084(5)	70.934(5)	94.962(1)	81.68(1)	104.932(1)
γ (°)	71.732(1)	90.00	90.00	83.571(5)	84.054(5)	107.901(1)	80.18(1)	95.177(1)
V (Å^3)	845.11(9)	1507.1(1)	4554.3(4)	3590(2)	3657(2)	1936.1(1)	1959(2)	1485.7(1)
Z	2	4	4	2	2	2	2	2
*D*c (mg/m^3)	3.052	3.722	2.567	2.317	2.436	2.536	2.463	2.720
Total reflection	28,642	26,840	49,585	24,230	20,845	70,980	79,851	23,152
Reflection [$I > 2\sigma(I)$]	2882	2675	7438	9689	7085	6457	5645	5423
Parameters	252	215	712	931	873	575	557	441
R_{int}	0.0271	0.0261	0.0397	0.0365	0.0536	0.0231	0.0426	0.0193
R_1 (obsd)	0.0271	0.0181	0.0336	0.0485	0.0689	0.0220	0.0380	0.0216
wR_2 (all)	0.0619	0.0431	0.0770	0.1334	0.1870	0.0481	0.0951	0.0538
S (GooF)	1.053	1.110	1.039	1.022	1.007	1.089	1.016	1.086
ρ_{max} (eÅ^{-3})	1.285	0.926	1.164	1.635	1.511	0.990	1.141	1.212
$-\rho_{min}$ (eÅ^{-3})	1.335	1.216	1.295	1.387	1.092	0.885	1.115	1.202

aggregates are extended into an infinite silver chain along the *a* direction. Furthermore, the Ag_6 aggregates in parallel silver chains are also cross-linked by the other independent trifluoroacetate ligand (containing O1, O2) acting in the μ_3–*O,O,O′* mode to form a web-like layer in the *ab* plane, as shown in Figs. 1 and 2. It is notable that bridging between silver chains is assisted by silver···fluoro close contact. The bridged Ag2···F9 distance is 3.088(1) Å, being slightly shorter than the sum of van der Waals radii of F and Ag on the Bondi scale [9]. This kinds of close contact between silver and fluorine rarely occurs, though an example of this interaction was reported in our previous work on the crystal structure of $Ag_2C_4{\cdot}2AgF{\cdot}10AgC_2F_5CO_2{\cdot}CH_3CN{\cdot}12H_2O$ [5].

As shown in Fig. 3, the iodophenyl ethynide ligands are arrayed between the above-mentioned web-like layers, alternatively running parallel or anti-parallel with respect to the *c* axis. Their ethynide terminals are inserted into corresponding silver baskets, while

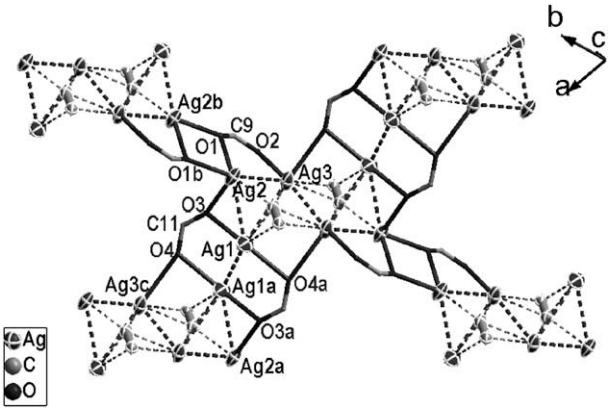


Fig. 2. Two-dimensional coordination network lying in the *ab* plane of complex **1**. CF_3 moieties of trifluoroacetate ions are omitted for clarity. Symmetry code: a 2 − *x*, −*y*, 1 − *z*; b 1 − *x*, 1 − *y*, 1 − *z*; c 1 + *x*, *y*, *z*.

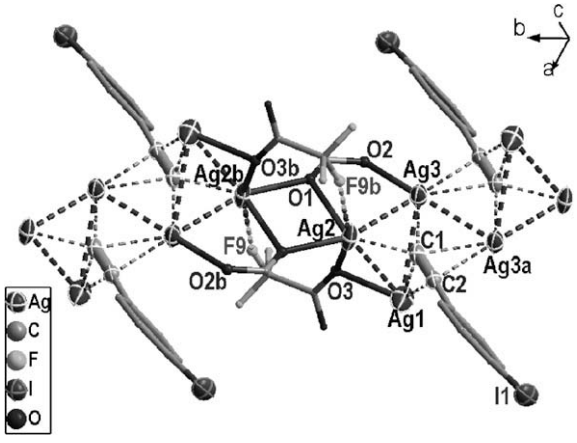


Fig. 1. Two Ag_6 aggregates in complex **1**, which are linked by carboxyl groups and Ag···F close contacts. For clarity, some CF_3 moieties of trifluoroacetate anions and all hydrogen atoms are omitted. Selected bond lengths [Å]: C1≡C2 1.222(6), C1···Ag1 2.341(5), C1···Ag2 2.164(5), C1···Ag3 2.253(4), C1···Ag3a 2.523(5), C2···Ag1 2.842(5), C2···Ag3a 2.673(5), Ag1···Ag2 3.026(1), Ag1···Ag3 3.238(1), Ag2···Ag3 2.781(1), Ag3···Ag3a 2.815(1). Symmetry code: a 1 − *x*, −*y*, 1−*z*; b 1 − *x*, 1 − *y*, 1 − *z*.

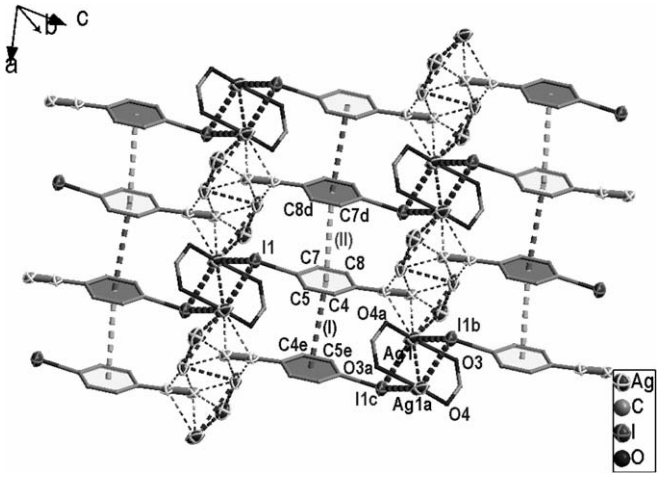


Fig. 3. Packing diagram of complex **1** in the *ac* plane. Trifluoroacetate anions are omitted for clarity, except for one bridging carboxyl moiety. Symmetry code: a 2 − *x*, −*y*, 1 − *z*; b *x*, *y*, 1 + *z*; c 2 − *x*, −*y*, −*z*; d 1 − *x*, −*y*, −*z*; e 2 − *x*, −*y*, −*z*.

each iodophenyl group is coordinated to a pair of silver atoms of the $(AgCF_3COO)_2$ structural unit by adopting the μ_2–*I* mode. The distance between silver and iodine atoms are 2.906(1) Å (Ag1···I1c) and 3.394(1) Å (Ag1···I1b), indicating the presence of strong silver···iodine interactions. The interlaced phenyl rings are stacked via two types of edge-to-edge π···π interaction of intermediate strength [6b]: C4–C5···C5e–C4e 3.670(1) Å and C7–C8···C8d–C7d 3.563(1) Å. The corresponding center-to-center distances of adjacent phenyl rings are 4.149(1) Å (**I**) and 4.199(1) Å (**II**). Thus the iodophenyl ethynide ligands connect the web-like layers altogether to generate a 3D network.

3.2. $AgL^1{\cdot}3AgNO_3$ (**2**)

In the non-centrosymmetric structural unit (Fig. 4) of compound **2**, the ethynide group (C1≡C2) inserts into a stand-alone Ag_4 basket in the μ_4–$\eta^2, \eta^2, \eta^1, \eta^1$ ligation mode, being similar to that in complex **1**. The distances between the silver atoms range from 2.909(1) to 3.021(1) Å. Three of the four silver atoms are coordinated by nitrate ions. There is one intramolecular C—H···O hydrogen bond between C8 and O9, in which the C···O distance is 3.177(6) Å and ∠OHC is 165°.

As shown in Fig. 4, adjacent structural units in compound **2** are linked by nitrate ions (upper limit of Ag—O bonding distance taken as 2.61 Å) [10] and silver···iodo interactions in the μ_2–*I* mode: each unit is connected to twelve neighboring ones (see Supplementary Material) to yield a three-dimensional network directly. The Ag···I distances are 3.211(1) Å for Ag1···I1 and 2.814(1) Å for Ag4···I1, respectively. With reference to the van der Waals radii of silver (1.72 Å) and iodine (1.95 Å) on the Bondi scale [9], the two contacts are ranked as strong silver···iodo interactions.

Along the *b* direction, the contents in the *ac* plane are arranged in the infinite sequence: silver baskets, nitrate ions, silver baskets, organic ligands, ... As shown in Fig. 5, the phenyl rings are interlaced by 60° and stacked alternately, forming face-to-face π···π interaction (centroid-to-centroid distance 3.595(1) Å) along the *c* direction. Alternatively, adjacent layers containing the π stacks are linked via silver···iodo interaction and bridged by nitrate anions attached to silver baskets: each iodine atom interacts with two vertices belonging to silver baskets in adjacent layers, and the linkages of nitrate anions occur mainly between silver baskets that are aligned head-to-head. In this manner, a three-dimensional network built by nitrate linkages and silver···iodo interactions is stabilized by inter-layer π···π interaction.

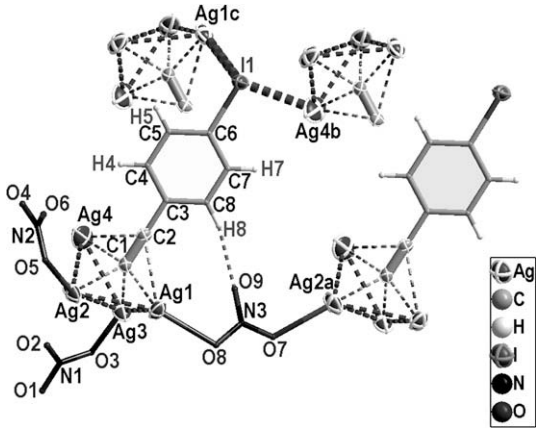


Fig. 4. Coordination geometry in **2** (50% thermo ellipsoids for Ag atoms), and the bridging of adjacent units. Selected bond lengths [Å]: C1≡C2 1.225(7), C1···Ag1 2.308(6), C1···Ag2 2.234(5), C1···Ag3 2.191(6), C1···Ag4 2.304(6), C2···Ag1 2.873(6), C2···Ag4 2.683(6), Ag1···Ag2 3.054(1), Ag1···Ag3 3.012(1), Ag2···Ag3 2.947(1), Ag2···Ag4 3.011(1), Ag3···Ag4 2.909(1), O9···C8 3.177(5). Symmetry code: a 1 + *x*, *y*, 1 + *z*; b 1 + *x*, 1 − *y*, 0.5 + *z*; c *x*, 1 − *y*, 0.5 + *z* .

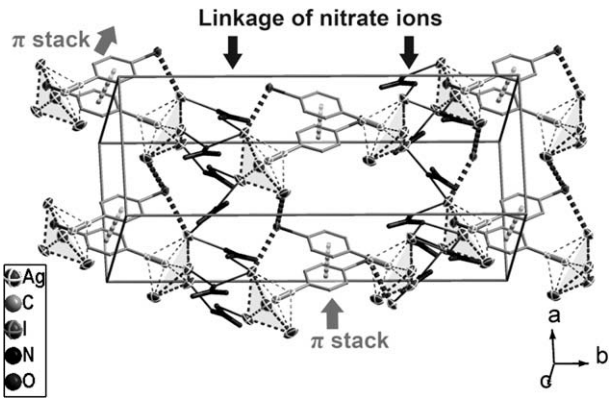


Fig. 5. Unit-cell content of complex **2**. Hydrogen atoms are omitted for clarity. Only those nitrate anions that bridge the silver baskets are included.

3.3. $2AgL^2{\cdot}5AgCF_3COO{\cdot}2CH_3CN{\cdot}H_2O$ (**3**)

In the structural unit of compound **3**, two parallelly aligned 3,4-dichlorophenylethynide ligands are inserted into separate Ag_5 baskets by adopting the μ_5–$\eta^2, \eta^2, \eta^2, \eta^1, \eta^1$ and μ_4–$\eta^2, \eta^2, \eta^2, \eta^1$ ligation modes. The silver baskets share one edge to give an Ag_8 aggregate, and such aggregates are anchored and stabilized by trifluoroacetate anions (Fig. 6). The Ag_8 aggregates are further connected together by sharing type Ag5···Ag6 edges of length 3.201(1) Å to form a silver chain. Two types of face-to-face π···π interactions occur between neighboring phenyl rings to form a zigzag stack alongside the extended silver chain. The distances between the ring centroids are 3.999(1) and 3.899(1) Å (average inter-planar distance: 3.63 and 3.71 Å), respectively.

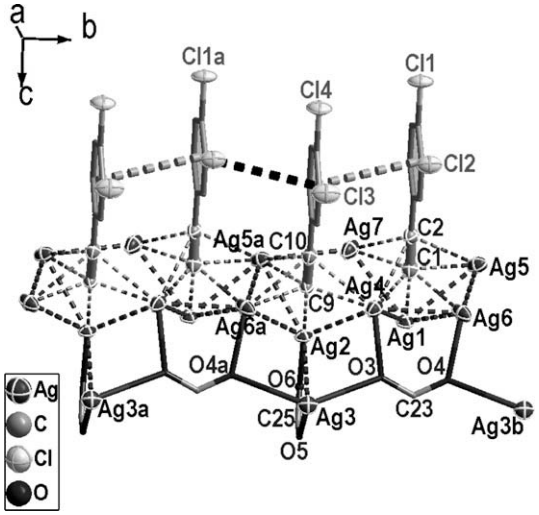


Fig. 6. Metal-ligand bonding in **3**. All hydrogen atoms, acetonitrile molecules, a water molecule, and CF_3 moieties of trifluoroacetate anions are omitted for clarity. Selected bond lengths [Å]: C1≡C2 1.191(11), C9≡C10 1.216(10). C1···Ag1 2.089(7), C1···Ag4 2.524(8), C1···Ag5 2.567(7), C1···Ag6 2.662(8), C1···Ag7 2.413(7), C2···Ag4 2.984(8), C2···Ag5 2.989(7), C2···Ag7 2.677(7), C9···Ag2 2.070(7), C9···Ag4 2.387(7), C9···Ag5a 2.476(7), C9···Ag6a 2.362(7), C10···Ag4 2.780(7), C10···Ag5a 2.959(7), C10···Ag6a 2.732(7), Ag1···Ag4 3.136(1), Ag1···Ag5 3.020(1), Ag1···Ag6 3.179(1), Ag1···Ag7 3.009(1), Ag2···Ag3 3.080(1), Ag2···Ag5a 2.951(1), Ag2···Ag6a 3.065(1), Ag4···Ag2 2.954(1), Ag4···Ag6 2.920(1), Ag5···Ag6 3.201(1), Ag7···Ag5a 3.097(1). Symmetry code: a *x*, *y* − 1, *z*; b *x*, *y* + 1, *z*.

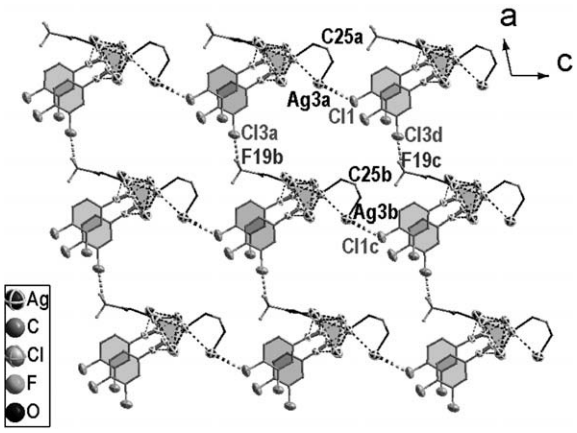


Fig. 7. Packing diagram of **3** viewed along *b* direction. The trifluoroacetate anions containing F19 are displayed, as well as the carboxyl groups of the anions containing C25. Other anions, hydrogen atoms and acetonitrile molecules are omitted for clarity. Symmetry code: a $x, -y, z-0.5$; b $x-0.5, 0.5-y, z-0.5$; c $x-0.5, 0.5+y, z$; d $x, 1+y, z$.

As shown in Fig. 6, independent atom Ag3 alone lies outside the silver basket and is anchored by type μ_4–*O*,*O*′,*O*′ (O3–O4) and μ_3–*O*,*O*′ (O5–O6) trifluoroacetate groups with further stabilization by argentophilic interaction (Ag3···Ag2 3.080(1) Å). Weak inter-chain silver···chloro interaction between Ag3 and Cl1 (Ag3···Cl1 3.287(2) Å) occurs in the *c* direction to generate a supramolecular layer, and inter-layer F···Cl contact in the *a* direction is of the van der Waals type [9,11] (F19···Cl3 3.23(1) Å). (Fig. 7).

3.4. $4AgL^3{\cdot}6AgC_2F_5COO{\cdot}5CH_3CN$ (**4**) and $4AgL^4{\cdot}6AgC_2F_5COO{\cdot}5CH_3CN$ (**5**)

Compound **4** and **5** are nearly isomorphous with the same kind of centrosymmetric structural unit. In compound **4** (Fig. 8), four parallel-related ethynides are inserted into respective Ag_5 baskets by adopting μ_5–$\eta^2,\eta^2,\eta^2,\eta^1,\eta^1$ (C9≡C10 and C17≡C18), μ_5–$\eta^2,\eta^2,\eta^1,\eta^1,\eta^1$ (C25≡C26) μ_5–$\eta^2,\eta^1,\eta^1,\eta^1,\eta^1$ (C1≡C2) ligation modes. The only difference in compound **5** is that C17≡C18 adopts the μ_5–$\eta^2,\eta^2,\eta^1,\eta^1,\eta^1$ mode. By sharing edges, the Ag_5 baskets are further united to form a columnar fragment. Four phenyl rings in each fragment are aligned on the same side of the silver column and stacked via weak face-to-face π···π interactions. Each fragment and its inversion-related neighbors share three Ag···Ag edges to generate an infinite column (Fig. 8).

In both **4** and **5**, C—H···X (X = Br, Cl) hydrogen bonds and weak halogen···halogen interactions are observed between the silver

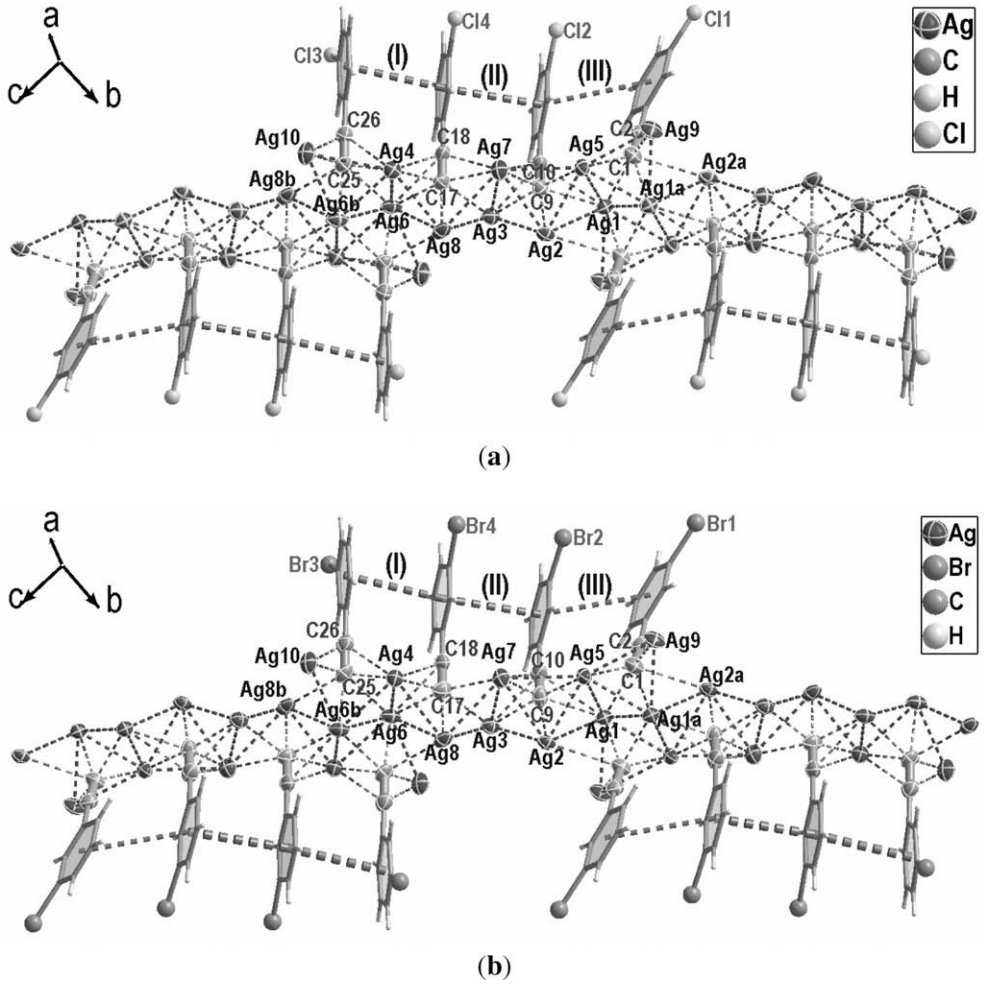


Fig. 8. Extension of silver chain in **4** (**a**) and **5** (**b**). Acetonitrile molecules and trifluoroacetate anions and a minor disordered part of Cl5/Br5 with C55 to C60 (of both) are omitted for clarity. Selected bond lengths [Å], **4**: C1≡C2 1.203(8), C9≡C10 1.211(9), C17≡C18 1.193(9), C25≡C26 1.200(9), C···Ag: 2.101(7) (C17···Ag8) to 3.022(8) (C18···Ag7), Ag···Ag: 2.882(1) (Ag6···Ag6b) to 3.277(1) (Ag4···Ag10)). **5**: C1≡C2 1.224(16), C9≡C10 1.203(16), C17≡C18 1.205(16), C25≡C26 1.200(15), C···Ag: 2.131(11) (C17···Ag8) to 3.012(13) (C25···Ag8b), Ag···Ag: 2.883(2) (Ag6···Ag6b) to 3.262(2) (Ag3···Ag7). Symmetry code **4**: a $1-x, 2-y, -z$; b $1-x, 1-y, 1-z$. **5**: a $1-x, 2-y, 1-z$; b $1-x, 1-y, 2-z$. Ring centroid-to-centroid distance in the sequence (**I**), (**II**), (**III**): **4**, 3.844(1), 3.810(1), 4.276(1) Å; **5**: 3.860(1), 3.860(1), 4.219(1), respectively.

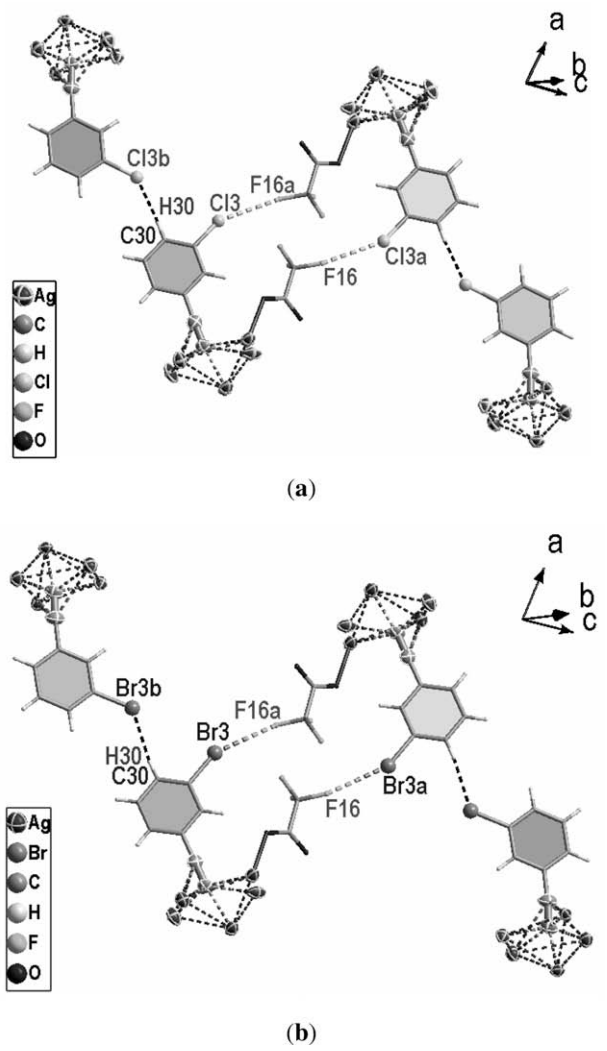


Fig. 9. Weak halogen···halogen interactions and C—H···X (X = Cl, Br) type hydrogen bonds in the crystal structure of **4** (**a**) and **5** (**b**). Symmetry code **4**: a 2 − *x*, 1 − *y*, 1 − *z*; b 2 − *x*, 1 − *y*, −*z*; **5**: a 2 − *x*, 1 − *y*, 2 − *z*; b 2 − *x*, 1 − *y*, 1 − *z*.

columns, leading to a three-dimensional supramolecular architecture [11–13] (Fig. 9). Hydrogen bonds occur between the halogen-substituted phenyl rings: *d*(Cl2b···C30) = 3.380(8) Å, ∠CHCl = 126° for **4**, *d*(Br2b···C30) = 3.456(9) Å, CHBr = 132° for **5**, while halogen···halogen interactions are observed between the Cl or Br atom at the *meta* position of the phenylethynide moiety and a fluorine atom of the CF_3COO^- anion: *d*(Cl3···F16) = 3.195(9) Å for **4** and *d*(Br3···F16) = 3.19(1) Å for **5**. Although the inter-halogen contacts are close to the sums of their van der Waals radii, their presence and attractive nature contribute to the stability of the network. It is noted that in compound **3**, van der Waals type Cl···F interaction also occurs between the *meta* chlorine atom and the fluorine atom of a CF_3COO^- anion.

3.5. $2AgL^5 \cdot 4AgCF_3COO \cdot NC(CH_2)_4CN$ (**6**) and $2AgL^5 \cdot 4AgCF_3COO \cdot 2CH_3CN$ (**7**)

In the structural units of these two complexes, parallelly-related ethynide ligands are inserted into Ag_5 baskets by adopting the μ_5–$\eta^2, \eta^2, \eta^1, \eta^1, \eta^1$(C1≡C2), μ_5–$\eta^2, \eta^1, \eta^1, \eta^1, \eta^1$(C9≡C10) (in **6**) and the μ_5–$\eta^2, \eta^2, \eta^2, \eta^2, \eta^1$(C1≡C2), μ_5–$\eta^2, \eta^2, \eta^1, \eta^1, \eta^1$(C9≡C10) (in **7**) ligation modes, with π···π interactions occurring between the phenyl rings. The centroid-to-centroid distances are 3.928(1) Å (**6**, average inter-planar distance 3.58 Å) and 3.941(2) Å (**7**, average inter-planar distance 3.54 Å) (Figs. 10 and 11). Both silver···chloro interaction and chloro···fluoro interaction are observed in complex **6** (Ag6···Cl1 3.191(4) Å, Ag7···Cl1 3.006(5) Å, Ag1···Cl2 3.404(1) Å, Cl2···F12 3.165(4) Å; Ag7 and Ag6 together represent a disordered silver atom with site occupancy ratio Ag6:Ag7 = 13:12.). The distance between Cl1 and Ag6/Ag7 is significantly smaller than the sum of their van der Waals radii by 0.3–0.5 Å [9], indicated a strong silver···halogen interaction. On the other hand, both silver···chloro and chloro···fluoro short contacts occur at Cl2, which has never been observed in our previous works. In **7**, only silver···chloro interaction is observed: Cl2···Ag6 3.280(3) Å, indicating a moderately-strong silver···halogen interaction.

In complex **6**, two adjacent inversion-related structural units are held by argentophilic interactions (Ag3···Ag3b and Ag5···Ag5a) to form a silver column in the *a* direction (Fig. 12a), and such columns are further expanded to a two-dimensional supramolecular structure via the linkage of adiponitrile molecules, as shown in Fig. 13a. In **7**, a silver column parallel to *a* axis is similarly formed (sharing edges Ag1···Ag1b and Ag3···Ag3a) (Fig. 12b), which is expanded into a three-dimensional supramolecular structure via the formation of two hydrogen bonds: C5–H5···F18 (C5···F18: 3.274(9) Å, ∠CHF = 170°) and C28–H20···O7 (C28···O7: 3.236(12) Å, ∠CHO = 162°) [13], as shown in Fig. 13b.

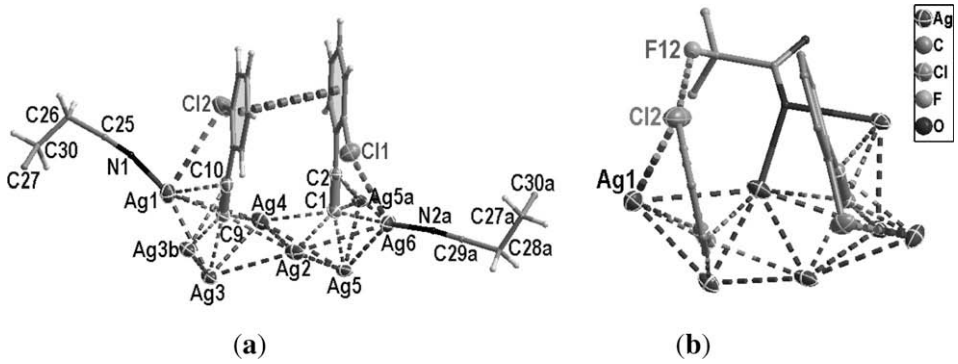


Fig. 10. (**a**) Coordination geometry of complex **6** (thermal ellipsoid 50%). All trifluoroacetate ions, hydrogen labels and disordered groups are omitted for clarity. Selected bond lengths [Å]: C1≡C2 1.217(5), C9≡C10 1.224(4), C1···Ag2 2.270(3), C1···Ag4 2.740(3), C1···Ag5 2.193(4), C1···Ag6 2.249(6), C1···Ag5a 2.626(3), C2···Ag6 2.602(6), C2···Ag5a 2.916(3), C9···Ag1 2.236(5), C9···Ag2 2.748(5), C9···Ag3 2.211(3), C9···Ag4 2.285(4), C9···Ag3b 2.532(4), C10···Ag1 2.687(4), C10···Ag3b 2.772(4), Cl1···Ag6 3.191(4), Cl2···Ag1 3.404(1), Ag1···Ag3 3.093(1), Ag1···Ag4 3.299(1), Ag2···Ag3 3.190(1), Ag2···Ag4 2.919(1), Ag2···Ag5 2.810(1), Ag3···Ag3b 2.832(1), Ag3···Ag4 2.780(1), Ag4···Ag5 3.234(1), Ag5···Ag6 3.078(3), Ag5···Ag5a 2.808(1). Symmetry code: a 1 + *x*, *y*, 1 + *z*; b − *x*, 1 − *y*, 1 − *z*. (**b**) Ag···Cl···F interaction. Cl2···F12: 3.165(4) Å.

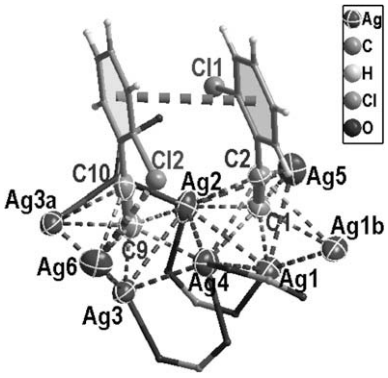


Fig. 11. Coordination geometry of complex **7** (thermal ellipsoid 50%). All CF_3 moieties of trifluoroacetate ions, acetonitrile molecules and hydrogen labels are omitted for clarity. Selected bond lengths [Å]: C1≡C2 1.219(6), C9≡C10 1.226(9), C1···Ag1 2.167(5), C1···Ag2 2.320(5), C1···Ag4 2.580(7), C1···Ag5 2.318(6), C1···Ag1b 2.608(5), C2···Ag2 2.982(5), C2···Ag4 2.937(7), C2···Ag5 2.850(7), C2···Ag1b 2.959(5), C9···Ag2 2.778(7), C9···Ag3 2.180(6), C9···Ag4 2.397(6), C9···Ag6 2.297(8), C9···Ag3a 2.599(6), C10···Ag6 2.618(8), C10···Ag3a 2.983(5), Cl2···Ag6 3.280(3), Ag1···Ag2 2.908(1), Ag1···Ag4 3.123(2), Ag1···Ag5 2.988(2), Ag1···Ag1b 2.862(1), Ag2···Ag3 3.160(1), Ag2···Ag4 3.011(2), Ag2···Ag5 3.236(2), Ag3···Ag4 2.804(1), Ag3···Ag6 3.134(2), Ag3···Ag3a 2.818(1). Symmetry code: a $1-x, 1-y, 1-z$; b $2-x, 1-y, 1-z$.

3.6. $AgL^6{\cdot}2CF_2(CF_2COOAg)_2{\cdot}2CH_3CN$ (**8**)

In compound **8**, the 2-fluorophenylethynide ligand is connected to a butterfly-shaped Ag_5 basket by adopting the μ_4–$\eta^2, \eta^2, \eta^1, \eta^1$ ligation mode (Fig. 14). The lone Ag5 atom is coordinated linearly by two acetonitrile ligands and a carboxylate oxygen atom: Ag···O (2.622(2) Å). One of the two independent hexafluoroglutarate dianions adopts a bent conformation to anchor on the Ag_5 basket, while the other one is fully extended. The distance between F13 and Ag2 is 3.106(3) Å, being approximately equal to the sum of their van der Waals radii [9].

By sharing one edge (Ag1···Ag1a), two inversion-related Ag_5 baskets form an Ag_8 aggregate. A halogen···π interaction (Fig. 15) is observed between F3 and the centroid of the phenyl ring belonging to an inversion-related unit (F3···centroid 3.292(2) Å; closest F···C contact F3a···C7 3.351(4) Å) [14] The centrosymmetric Ag_8 aggregates are further linked by bent hexafluoroglutarate dianions to form a silver–organic chain along the *a* axis, in which each carboxyl group adopts the μ_3–*O,O,O′*, mode. Notably, short F···Ag contacts are also observed between fluorine and silver atoms of adjacent Ag_8 aggregates: Ag3···F1c 3.044(2) Å, Ag4···F5c 2.915(2) Å (Fig. 15), being significantly shorter than the sum of their van der Waals radii, 3.19 Å [9]. On the other hand, along the *b* direction, the Ag_8 aggregates are linked by unbent hexafluoroglutaric dianions to yield a two-dimensional metal–organic network.

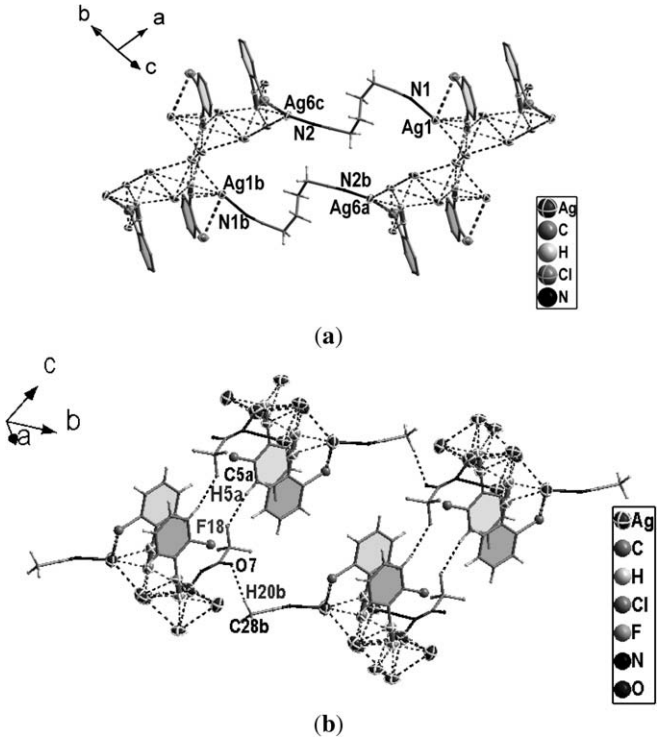


Fig. 13. (**a**) The two-dimensional coordination network of **6**. Symmetry code: a $-x, 1-y, 1-z$; b $1-x, 1-y, -z$; c $x-1, y, z-1$. (**b**) The 3D structure of **7** constructed by hydrogen bonds. Symmetry code: a $1-x, 1-y, 2-z$; b $x, 1+y, z$.

In this two-dimensional framework, the hexafluoroglutaric dianions form a loop structure, and the void space in the middle of it is filled by two linear $Ag(CH_3CN)_2$ moieties (N—Ag—N = 169°) oriented parallel to the *c* axis. The silver atom Ag5 of such a moiety is connected to the surrounding dianions via two weak Ag···O coordination interactions (Ag5···O5 2.622(2) Å, Ag5···O8 2.884(2) Å) and a C—H···F type hydrogen bond (C10···F8 3.296(5) Å, ∠CHF = 155°) A close contact of 3.002(2) Å is also observed between the ligand-unsupported Ag5 atom and F11a in the perfluoro arm of the surrounding dianion. Although this moiety does not serve as a bonding-linkage unit, it fills the ligand-inaccessible void space to stabilize the overall framework structure (Fig. 16).

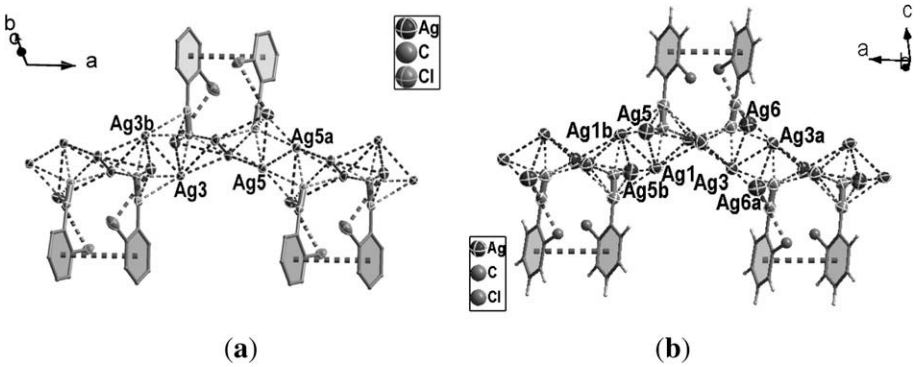


Fig. 12. (**a**) Formation of silver column in complex **6**. Symmetry code: a $1-x, 1-y, 1-z$; b $-x, 1-y, 1-z$. (**b**) Formation of silver column in **7**. Symmetry code: a $1-x, 1-y, 1-z$; b $2-x, 1-y, 1-z$. Hydrogen atoms, trifluoroacetate ions and acetonitrile/adiponitrile molecules are omitted for clarity.

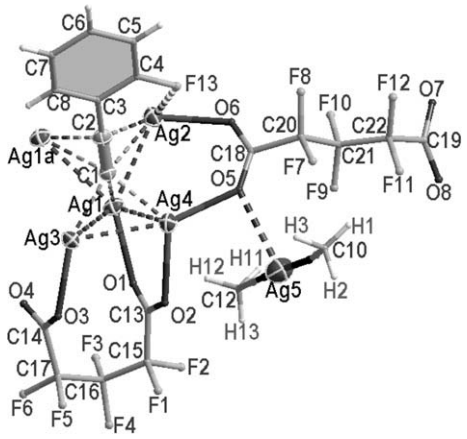


Fig. 14. Coordination geometry and atom labeling of **8**. Labels of hydrogen atoms are omitted. Selected bond lengths [Å]: C1≡C2 1.223(3), C1···Ag1 2.297(3), C1···Ag2 2.513(3), C1···Ag3 2.257(2), C1···Ag4 2.301(3), C1···Ag1a 2.554(3), C2···Ag2 2.609(3), C2···Ag1a 2.671(3), Ag1···Ag2 2.915(1), Ag1···Ag3 2.901(1), Ag1···Ag4 2.829(1), Ag1···Ag1a 3.012(1), Ag3···Ag4 2.876(1), Ag2···F13 3.106(3), O5···Ag5 2.622(2). Symmetry code: a $-x$, $1-y$, $1-z$.

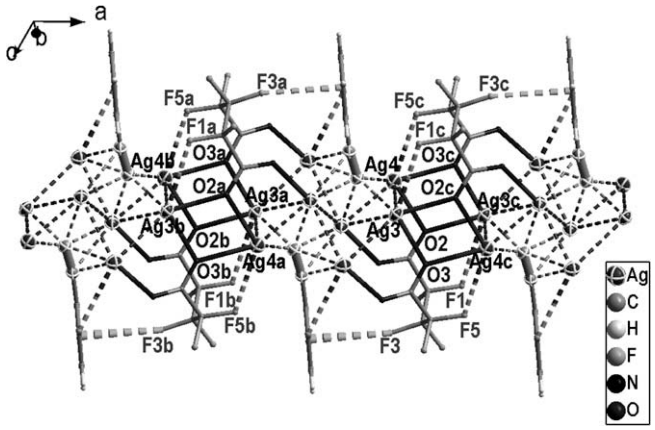


Fig. 15. The bridging linkage of Ag_8 clusters in **8** along the *a* direction. Acetonitrile molecules, Ag5 and the unbent hexafluoroglutarate anion are omitted for clarity. Symmetry code: *a* $-x$, $1-y$, $1-z$; b $x-1$, y, z; c $1-x$, $1-y$, $1-z$.

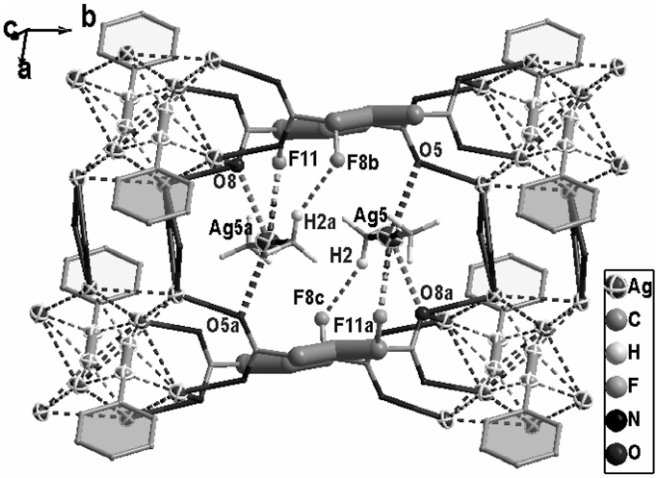


Fig. 16. Packing diagram of complex **8**. Symmetry code: a $1-x$, $-y$, $1-z$; b $-x$, $-y$, $1-z$; c $1+x$, y, z.

4. Conclusion

We have synthesised eight silver(I) halophenyl ethynide complexes bearing the supramolecular synthon R_X–C≡C⊃Ag_n (n = 4, 5; R_X = halophenyl). Strong silver···iodo interactions in two of the structures play an important role in constructing high-dimensional coordination networks, while in the other six complexes, silver···chloro interactions and chloro···fluoro, bromo···fluoro interactions are observed. The silver···iodo contacts in crystals are significantly shorter than those of silver···chloro and silver···fluoro, indicating that the silver···iodo interaction has greater strength, since the van der Waals radius of iodine is larger than those of the other two (I: 198 pm, Cl: 175 pm, F: 147 pm).

It is notable that, in compound **1** and **2**, the ligation mode of ethynide ligands toward Ag_n baskets is μ_4– rather than μ_5–, though the latter mode is commonly observed in our previous studies [4b,6]. Moreover, the respective ratios of ancillary ligands to the ethynide ligand are also smaller than expected. This is probably due to the significant strength of the silver···iodine interaction, the μ_2–*I* ligation mode, and the rigidity of the iodophenyl ligand which together account for little accessible void space for the accommodation of ancillary ligands. A better understanding of the role of silver···halogen interactions on stabilization of coordination networks needs to be further investigated.

Within the limited number of complexes reported here, all halogen atoms at the *para* position of the phenyl ring are observed to form silver···halogen interactions, while van der Waals type halogen (Cl, Br)···fluoro interactions are observed on all substituents at the *meta* position. This is an interesting phenomenon unnoticed in the past. On the other hand, *ortho* chloro atoms in **6** and **7** form moderate to strong silver···chloro interactions due to their relatively close location to the silver baskets; for the same reason, they are not involved in the generation of higher-dimensional structures.

The silver···fluoro close contacts observed in **8** are different from the silver···chloro(*ortho*) interactions in **6** and **7**: the strong electron-withdrawing fluoro substituent on the phenyl ring facilitates the formation of charge-induced F···π interaction. On the other hand, though the silver···fluoro interaction that involves contacts significantly shorter than the sum of respective van der Waals radii is not well-recognized due to too few reports in the literature, the occurrence of unusually large number of such contacts in one structure indicated its potentially significant role in the stabilization of coordination networks.

The present report demonstrates the feasibility of using halogen-substituted phenylethynide synthons R_X–C≡C⊃Ag_n (n = 4, 5) in the construction of silver(I) coordination and supramolecular networks. Variation on the type and the position of halogen substituents on the phenyl ring leads to network structures of different dimensionality due to the presence of subtle weak interactions in supramolecular organization. Further systematic investigation employing multi-substituted halophenylethynide ligands is required in order to shed additional light on the role of weak supramolecular interactions involving halogen atoms in the stabilization of coordination networks.

Acknowledgment

This work is supported by the Hong Kong Research Grants Council (GRF CUHK 402408) and the Wei Lun Foundation of The Chinese University of Hong Kong.

Appendix A. Supplementary data

CCDC 723285, 723286, 723287, 723288, 723289, 723290, 723291 and 723292 contain the supplementary crystallographic

data for this paper. These data can be obtained free of charge via http://www.ccdc.cam.ac.uk/conts/retrieving.html, or from the Cambridge Crystallographic Data Centre, 12 Union Road, Cambridge CB2 1EZ, UK; fax: (+44) 1223-336-033; or e-mail: deposit@ccdc.cam.ac.uk. Supplementary data associated with this article can be found, in the online version, at doi:10.1016/j.poly.2009.05.004.

References

[1] (a) M.R. Colsman, T.D. Newbound, L.J. Marshall, M.D. Noirot, M.M. Miller, G.P. Wulfsberg, J.S. Frye, O.P. Anderson, S.H. Strauss, J. Am. Chem. Soc. 112 (1990) 2349;
(b) D.M. Van Seggen, O.P. Anderson, S.H. Strauss, Inorg. Chem. 8 (1992) 2987;
(c) J. Powell, M. Horvath, A. Lough, J. Chem. Soc., Dalton Trans. (1996) 1669;
(d) J. Powell, M.J. Horvath, A. Lough, A. Phillips, J. Brunet, J. Chem. Soc., Dalton Trans. (1998) 637;
(e) I. Ino, L.-P. Wu, M. Munakata, M. Maekawa, Y. Suenaga, T. Kuroda-Sowa, Y. Kitamori, Inorg. Chem. 39 (2000) 2146;
(f) T. Petkova, M. Mitkovaa, Mir. Vlcek, S. Vassilev, J. Non-Cryst. Solids 326 (2003) 125;
(g) S.K. Chandran, R. Thakuria, A. Nangia, Cryst. Eng. Commun. 10 (2008) 1891.

[2] (a) D. Perreault, M. Drouin, A. Machel, V.M. Miskowski, W.P. Schaefer, P.D. Harvey, Inorg. Chem. 31 (1992) 695;
(b) Y.-S. Jiang, H.-G. Yao, S.-H. Ji, M. Ji, Y.-L. An, Inorg. Chem. 47 (2008) 3922.

[3] (a) Z.-G. Han, Y.-L. Zhao, J. Peng, H.-Y. Ma, Q. Liu, E.-B. Wang, N.-H. Hu, H.-Q. Jia, Eur. J. Inorg. Chem. (2005) 264;
(b) D.R. Whitcomb, M. Rajeswaran, Polyhedron 25 (2006) 2033;
(c) L.R. Falvello, J. Forniés, E. Lalinde, B. Menjón, M.A. García-Monforte, M.T. Moreno, M. Tomás, Chem. Commun. (2007) 3838.

[4] (a) T.C.W. Mak, X.-L. Zhao, Q.-M. Wang, G.-C. Guo, Coord. Chem. Rev. 251 (2007) 2311;
(b) L. Zhao, T.C.W. Mak, Chem. Asian. J. 2 (2007) 456.

[5] L. Zhao, M. Du, T.C.W. Mak, Chem. Asian. J. 2 (2007) 1240.

[6] (a) L. Zhao, T.C.W. Mak, J. Am. Chem. Soc. 127 (2005) 14966;
(b) L. Zhao, W.-Y. Wong, T.C.W. Mak, Chem. Eur. J. 12 (2006) 4865;
(c) L. Zhao, X.-L. Zhao, T.C.W. Mak, Chem. Eur. J. 13 (2007) 5927;
(d) L. Zhao, T.C.W. Mak, Organometallics 26 (2007) 4439;
(e) S.-Q. Zang, L. Zhao, T.C.W. Mak, Organometallics 27 (2008) 2396;
(f) L. Zhao, X.-D. Chen, T.C.W. Mak, Organometallics 27 (2008) 2483;
(g) S.-Q. Zang, T.C.W. Mak, Inorg. Chem. 47 (2008) 7094;
(h) L. Zhao, C.-Q. Wan, J. Han, X.-D. Chen, T.C.W. Mak, Chem. Eur. J. 14 (2008) 10437.

[7] G.M. Sheldrick, SADABS: Program for Empirical Absorption Correction of Area Detector Data, University of Göttingen, Göttingen, Germany, 1996.

[8] G.M. Sheldrick, SHELXTL 5.10 for Windows NT: Structure Determination Software Programs, Bruker Analytical X-ray Systems, Inc., Madison, WI, 1997.

[9] A. Bondi, J. Phys. Chem. 68 (1964) 441.

[10] (a) T. Zhang, J. Kong, Y. Hu, X. Meng, H. Yin, D. Hu, C. Ji, Inorg. Chem. 47 (2008) 3144;
(b) Y.-B. Dong, Q. Zhang, J.-P. Ma, R.-Q. Huang, D.Z. Shen, D.Z. Chen, Inorg. Chem. 44 (2005) 6591.

[11] (a) I. Shevchenko, V. Andrushko, E. Lork, G.-V. Roschenthaler, Eur. J. Inorg. Chem. (2007) 259;
(b) S. Arndt, R.R. Schrock, P. Muller, Organometallics 26 (2007) 1279;
(c) G. Luthe, D.C. Swenson, L.W. Robertson, Acta. Crystallogr. B63 (2007) 319;
(d) F. Wu, A.K. Dash, R.F. Jordan, J. Am. Chem. Soc. 126 (2004) 15360;
(e) J.F. Tannaci, M. Noji, J. McBee, T.D. Tilley, J. Org. Chem. 72 (2007) 5667;
(f) P. Metrangolo, F. Meyer, T. Pilati, G. Resnati, G. Terraneo, Angew. Chem. Int. Ed. 47 (2008) 6114.

[12] (a) E.A. Medlycott, K.A. Udachin, G.S. Hanan, Dalton Trans. (2007) 430;
(b) P.G. Hayes, W.E. Piers, M. Parvez, Chem. Eur. J. 13 (2007) 2632;
(c) C.B. Aakeroy, N. Schultheiss, J. Desper, C. Moore, Cryst. Eng. Commun. 9 (2007) 421;
(d) N. Feeder, R.J. Less, J.M. Rawson, P. Oliete, F. Palacio, Chem. Commun. (2000) 2449.

[13] (a) W. Mikenda, J. Mol. Struct. 147 (1986) 1;
(b) G.R. Desiraju, Science 278 (1997) 404;
(c) G.R. Desiraju, Chem. Commun. (1997) 1475;
(d) F. Grepioni, G. Cojazzi, S.M. Draper, N. Scully, D. Braga, Organometallics 17 (1998) 296;
(e) V.R. Thalladi, H.-C. Weiss, D. Bläser, R. Boese, A. Nangia, G.R. Desiraju, J. Am. Chem. Soc. 120 (1998) 8702;
(f) K. Reichenbächer, H.I. Süss, J. Hulliger, Chem. Soc. Rev. 34 (2005) 22.

[14] (a) B.L. Schottel, L.R. Hanton, M.D. Spicer, Chem. Commun. (2005) 46;
(b) C.A. Black, L.R. Hanton, M.D. Spicer, Inorg. Chem. 46 (2007) 3669;
(c) C.A. Black, L.R. Hanton, M.D. Spicer, Chem. Commun. (2007) 3171.

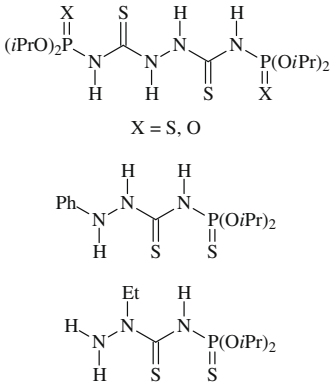
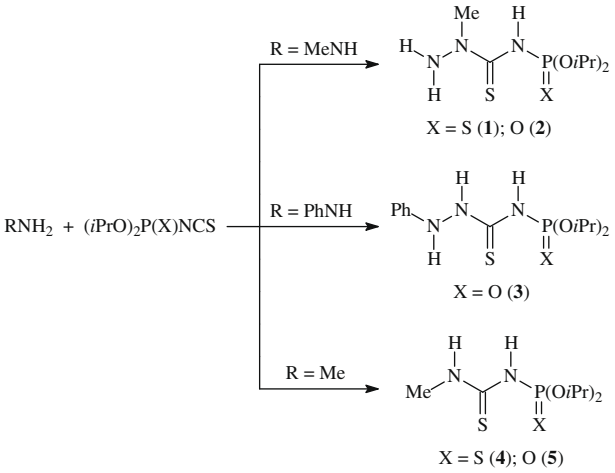


Chart 1.



Scheme 1.

PNH), 4.41–4.93 (m, 2H, OCH), 5.63 (br. s, PNH) ppm. ^{31}P NMR ($CDCl_3$): δ = 58.6 (t, $^3J_{POCH}$ = $^2J_{PNH}$ = 10.1 Hz, 3P), 64.2 (d. t, $^3J_{POCH}$ = 10.1 Hz, $^2J_{PNH}$ = 29.2 Hz, 1P) ppm. ^{31}P NMR (acetone-d_6): δ = 65.9 (br. s, 1P), 67.0 (t, $^3J_{POCH}$ = $^2J_{PNH}$ = 10.8 Hz, 1P) ppm. *Anal.* Calc. for $C_8H_{20}N_3O_2PS_2$ (285.36): C, 33.67; H, 7.06; N, 14.73. Found: C, 33.59; H, 7.15; N, 14.65%.

2: Yield: 1.09 g (81%). Viscous oil. ^{1}H NMR ($CDCl_3$): δ = 1.20–1.76 (m, 15H, CH_3, *i*Pr + Me), 3.24 (s, NH_2), 3.31 (s, NH_2), 3.35 (s, NH_2), 3.64 (s, NH_2), 4.10–5.07 (m, 2H, OCH), 6.73 (br. s, PNH), 8.87 (br. s, PNH), 10.60 (br. s, PNH) ppm. ^{1}H NMR (acetone-d_6): δ = 1.22–1.42 (m, 12H, CH_3, *i*Pr), 1.61 (br. s, 3H, Me), 3.19 (s, NH_2), 3.27 (s, NH_2), 4.40–4.90 (m, 2H, OCH), 7.56 (br. s, PNH) ppm. ^{31}P NMR ($CDCl_3$): δ = −7.4 (t, $^3J_{POCH}$ = $^2J_{PNH}$ = 7.5 Hz, 1.4P), −4.6 (br. s, 1.8P), 4.5 (t, $^3J_{POCH}$ = $^2J_{PNH}$ = 7.9 Hz, 1P) ppm. ^{31}P NMR (acetone-d_6): δ = −7.7 (t, $^3J_{POCH}$ = $^2J_{PNH}$ = 7.1 Hz, 3.5P), 3.9 (t, $^3J_{POCH}$ = $^2J_{PNH}$ = 8.2 Hz, 1P) ppm. *Anal.* Calc. for $C_8H_{20}N_3O_3PS$ (269.30): C, 35.68; H, 7.49; N, 15.60. Found: C, 35.79; H, 7.38; N, 15.64%.

3: Yield: 1.41 g (85%). Viscous oil. ^{1}H NMR ($CDCl_3$): δ = 1.39 (d, $^3J_{H,H}$ = 6.0 Hz, 6H, CH_3, *i*Pr), 1.42 (d, $^3J_{H,H}$ = 6.2 Hz, 6H, CH_3, *i*Pr), 4.80 (d. sept, $^3J_{POCH}$ = 13.9 Hz, $^3J_{H,H}$ = 6.9 Hz, 2H, OCH), 6.49 (s, 1H, PNH), 6.79–7.12 (m, 4H, Ph), 7.22–7.35 (m, overlapping with the solvent signal, Ph), 8.18 (br. s, 1H, PhNH), 10.50 (br. s, 1H, CNHN) ppm. ^{1}H NMR (acetone-d_6): δ = 1.33 (d, $^3J_{H,H}$ = 6.3 Hz, 6H, CH_3, *i*Pr), 1.39, 1.40 (d, $^3J_{H,H}$ = 6.1 Hz, 6H, CH_3, *i*Pr), 4.78 (d. sept, $^3J_{POCH}$ = 7.2 Hz, $^3J_{H,H}$ = 6.2 Hz, 2H, OCH), 6.79–7.00 (m, 3H, Ph), 7.15–7.33 (m, 2H, Ph), 7.36 (br. s, 1H, PNH), 7.63 (br. s, 1H, PhNH), 9.28 (br. s, 1H, CNHN) ppm. ^{31}P NMR ($CDCl_3$): δ = −6.0 (q, $^3J_{POCH}$ = 6.3 Hz, $^2J_{PNH}$ = 7.5 Hz, 1.3P), −5.1 (br. s, 1P) ppm. ^{31}P NMR (acetone-d_6): δ = −5.4 (t, $^3J_{POCH}$ = $^2J_{PNH}$ = 6.0 Hz, 1P), −4.6 (t, $^3J_{POCH}$ = $^2J_{PNH}$ = 7.8 Hz, 1P) ppm. *Anal.* Calc. for $C_{13}H_{22}N_3O_3PS$ (331.37): C, 47.12; H, 6.69; N, 12.68. Found: C, 47.00; H, 6.74; N, 12.57%.

4: Yield: 1.27 g (94%). M.p. 149 °C. ^{1}H NMR ($CDCl_3$): δ = 1.35 (t, $^3J_{H,H}$ = 6.2 Hz, 12H, CH_3, *i*Pr), 3.16 (d, $^3J_{H,H}$ = 4.5 Hz, 3H, CH_3, Me), 4.80 (d. sept, $^3J_{POCH}$ = 10.4 Hz, $^3J_{H,H}$ = 6.2 Hz, 2H, OCH), 7.10 (br. s, 1H, PNH), 7.96 (br. s, 1H, MeNH) ppm. ^{31}P NMR ($CDCl_3$): δ = 57.5 (t, $^3J_{POCH}$ = $^2J_{PNH}$ = 6.3 Hz) ppm. *Anal.* Calc. for $C_8H_{19}N_2O_2PS_2$ (270.34): C, 35.54; H, 7.08; N, 10.36. Found: C, 35.61; H, 7.04; N, 10.40%.

5: Yield: 1.03 g (81%). M.p. 84 °C. ^{1}H NMR ($CDCl_3$): δ = 1.34 (t, $^3J_{H,H}$ = 6.0 Hz, 6H, CH_3, *i*Pr), 1.36 (t, $^3J_{H,H}$ = 6.0 Hz, 6H, CH_3, *i*Pr), 3.13 (d, $^3J_{H,H}$ = 4.7 Hz, 3H, CH_3, Me), 4.67 (d. sept, $^3J_{POCH}$ = 7.3 Hz, $^3J_{H,H}$ = 6.1 Hz, 2H, OCH), 7.25 (br. s, overlapping with the solvent signal, PNH), 9.00 (br. s, 1H, MeNH) ppm. ^{31}P NMR ($CDCl_3$): δ = −6.7 (q, $^3J_{POCH}$ = 6.2 Hz, $^2J_{PNH}$ = 7.5 Hz) ppm. *Anal.* Calc. for $C_8H_{19}N_2O_3PS$ (254.28): C, 37.79; H, 7.53; N, 11.02. Found: C, 37.63; H, 7.59; N, 10.93%.

A solution of **1** (2 mmol, 0.57 g) in anhydrous acetone (10 mL) was left for two days. Afterwards X-ray suitable crystals of **6** were formed.

6: Yield: 0.64 g (98%). M.p. 128 °C. ^{1}H NMR ($CDCl_3$): δ = 1.31 (d, $^3J_{H,H}$ = 6.2 Hz, 6H, CH_3, *i*Pr), 1.32 (d, $^3J_{H,H}$ = 6.2 Hz, 6H, CH_3, *i*Pr), 1.63 (s, 6H, CH_3, $S(CH_3)_2CN$), 3.25 (s, 3H, CH_3, CH_3N), 4.37 (br. s, 1H, NH), 4.76 (d. sept, $^3J_{POCH}$ = 10.9 Hz, $^3J_{H,H}$ = 6.2 Hz, 2H, OCH) ppm. ^{31}P NMR ($CDCl_3$): δ = 67.3 (t, $^3J_{POCH}$ = 10.8 Hz) ppm. *Anal.* Calc. for $C_{11}H_{25}N_3O_2PS_2$ (326.43): C, 40.47; H, 7.72; N, 12.87. Found: C, 40.62; H, 7.66; N, 12.79%.

2.2. Physical measurements

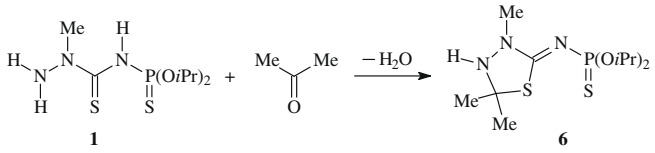
NMR spectra in were obtained on a Bruker Avance 300 MHz spectrometer at 25 °C. ^{1}H and ^{31}P NMR spectra were recorded at 299.948 and 121.420 MHz, respectively. Chemical shifts are reported with reference to $SiMe_4$ (^{1}H) and H_3PO_4 (^{31}P). Elemental analyses were performed on a CHNS HEKAtech EuroEA 3000 analyzer.

2.3. Crystal structure determination and refinement

The X-ray data for **4** was collected on a STOE IPDS-II diffractometer with graphite-monochromatized Mo Kα radiation generated by fine-focus X-ray tube operated at 50 kV and 40 mA. The images were indexed, integrated and scaled using the X-Area data reduction package [12]. Data were corrected for absorption using the PLATON program [13]. The structures were solved by direct methods using the SHELXS-97 program [14] and refined first isotropically and then anisotropically using SHELXL-97 [14]. Hydrogen atoms were revealed from $\Delta\rho$ maps and those bonded to C were refined using appropriate riding models. H atoms bonded to N were freely refined.

3. Results and discussion

Compounds **1–5** were synthesized by the treatment of methylhydrazine, phenylhydrazine or methylamine with the isothiocyanates $(iPrO)_2P(S)NCS$ or $(iPrO)_2P(O)NCS$ (Scheme 1). Recrystallization of **1** from an acetone solution gave the substituted 1,3,4-thiadiazolidine **6** after two days (Scheme 2). It should be noted that the recrystallization of **2** or the ethyl analog NH_2–N(Et)–C(S)–NH–P(S)(O*i*Pr)$_2$ (**7**) do not lead to the formation of the corresponding heterocycle, even when the compounds are heated in acetone solution under reflux for two days. Their compositions were proven by the microanalysis data.

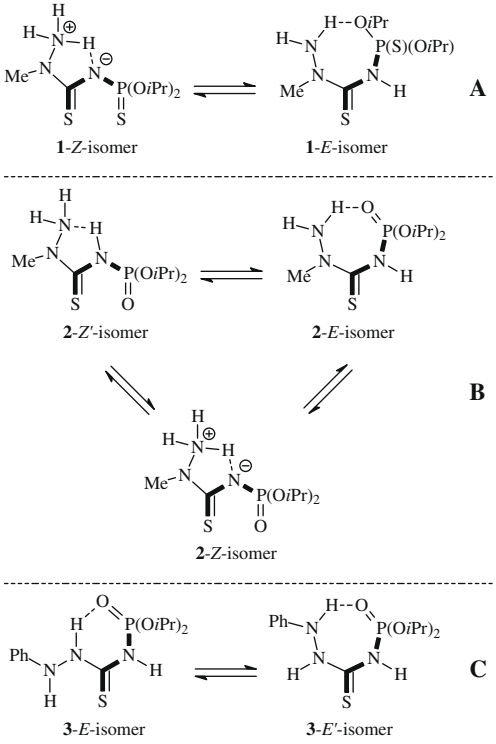


Scheme 2.

Condensation of isocyanates with phenylsubstituted hydrazines are reported to yield 1-substituted semicarbazides [10,15]. The reaction between monoalkylhydrazines and isocyanates give 2-substituted alkyl semicarbazides [10,16] due to the greater nucleophilic character of the secondary amine groups.

The ^{31}P NMR spectra of **1** in $CDCl_3$ and acetone-d_6 contain two signals at 58.6, 64.2 ($CDCl_3$) and 65.9, 67.0 (acetone-d_6) ppm. The integral intensity ratio changes from 3.0:1 to 1.0:1.0 for the high- and low-field signals, respectively. When the crystalline material is dissolved, two lines can be observed in the ^{31}P NMR spectra, indicating that the equilibrium reaction shown in Scheme 3, **A** is slow on the NMR timescale. We suppose that in a solution of **1** both *Z*- and *E*-forms are present, as was previously observed for **7** [10], which are both stabilized by intramolecular hydrogen bonds (Scheme 3 **A**). The high-field signals are in the same region as was observed in the ^{31}P NMR spectra of the thiourea analog **4** (δ = 57.5 ppm). Surprisingly, the low-field signals are in the area characteristic for the deprotonated form of *N*-thiophosphorylated thioureas [7,8]. This fact means that the **1**-*Z*-isomer is in a zwitterionic form (Scheme 3 **A**).

The ^{31}P NMR spectra of **2** contain three signals at −7.4, −4.6 and 4.5 ppm in $CDCl_3$, and two signals at −7.7 and 3.9 ppm in acetone-d_6. The relative integral intensities are 1.4:1.8:1 and 3.5:1.0, respectively. The high-field signals are in the same region as was observed in the ^{31}P NMR spectra of the thiourea analog **5** (δ = −6.7 ppm). Thus, the high-field signal corresponds to the **2**-*E*-isomer, while the signal at −4.6 ppm in $CDCl_3$ solution indicates the occurrence of the **2**-*Z*′-isomer (Scheme 3 **B**). The low-field signals are in the area characteristic for deprotonated *N*-phosphorylthioureas [7,8]. This fact testifies that the *Z*-isomer is partially in the zwitterion (**2**-*Z*′-isomer) form in $CDCl_3$, but is completely in this form in acetone-d_6 solution (Scheme 3 **B**).



Scheme 3.

There are two signals in the ^{31}P NMR spectra of **3** both in $CDCl_3$ and acetone-d_6 solutions. The signals are at −6.0 to −4.6 ppm with integral intensities ratio close to 1:1. The signals have practically the same chemical shift, as was observed for the *N*-phosphorylthiourea Ph–NH–C(S)–NH–P(O)(O*i*Pr)$_2$ [17]. This, along with a non-significant difference in the values for the high- and low-field signals, testifies about the one *E*-isomer form, but with different hydrogen bond formations (Scheme 3 **C**).

The substituted 1,3,4-thiadiazolidine **6** shows one signal at 67.3 ppm in the ^{31}P NMR spectrum. The signal is in the area characteristic for deprotonated *N*-thiophosphorylthioureas [7,8].

The ^{1}H NMR spectra of **1–6** contain all the characteristic signals (see Section 2).

Crystals of **5** were obtained by recrystallization from a dichloromethane–*n*-hexane solution (Table 1). The molecular conformation is shown in Fig. 1, and geometric parameters are given in Table 2. Compound **5** crystallizes in the space group $P2_1/c$. The parameters of the C=S, C–N, P–N and P=O bonds observed for **5** (Table 2) are in the typical range for *N*-phosphorylated thiourea derivatives [7,8,18]. The S(1)–C(1)–N(1)–P(1) backbone in the crystal phase has an *E*-conformation. The crystal structure of **5** is stabilized by an intramolecular hydrogen bond of the type N(2)–H(2)···O(3)=P(1). Molecules of **5** in the crystal structure form polymeric chains due to N(1)–H(1)···O(3)#1=P(1)#1 H-bonds (Table 4).

Crystals of **6** were obtained by recrystallization of **1** from an acetone solution (Table 1). The molecular conformation is shown in Fig. 2, and geometric parameters are given in Table 3. Compound **6** crystallizes in the space group *P*−1. There are intermolecular hydrogen bonds of the type N(3)–H(3)···S(1)#1–P(1)#1 in the crystal (Table 4), which are formed between the sulfur atoms of the P=S groups and the hydrogen atoms of the NH fragment of two molecules. As a result of the intermolecular interactions, a

Table 1
Crystal data, data collection and refinement details for **5** and **6**.[a]

	5	**6**
Empirical formula	$C_8H_{19}N_2O_3PS$	$C_{11}H_{24}N_3O_2PS_2$
Formula weight	254.28	325.42
Crystal system	monoclinic	triclinic
Space group	$P2_1/c$	*P*−1
a (Å)	13.533(2)	7.6154(8)
b (Å)	10.2203(10)	10.0015(11)
c (Å)	9.9053(13)	11.8127(14)
α (°)	90	104.069(9)
β (°)	97.543(11)	105.373(9)
γ (°)	90	97.287(9)
V (Å^3)	1358.2(3)	823.72(16)
Z	4	2
D_{calc} (Mg m^{-3})	1.244	1.312
Absorption correction, μ (mm^{-1})	0.348	0.422
F(0 0 0)	544	348
Crystal size (mm)	0.38 × 0.35 × 0.35	0.41 × 0.37 × 0.33
Recording range, θ_{max} (°)	3.38–25.61	3.56–25.60
Number of recorded reflections	2526	7207
Number of recorded independent reflections	2526 [R_{int} = 0.0895]	3064 [R_{int} = 0.0467]
Final *R* indices [$I > 2\sigma(I)$]	R_1 = 0.1009, wR_2 = 0.2644	R_1 = 0.0352, wR_2 = 0.0926
R indices (all data)	R_1 = 0.1338, wR_2 = 0.3208	R_1 = 0.0434, wR_2 = 0.0953
S	1.133	1.025

[a] Measurements at 173(2) K using Mo Kα with λ = 0.71073 (Å).

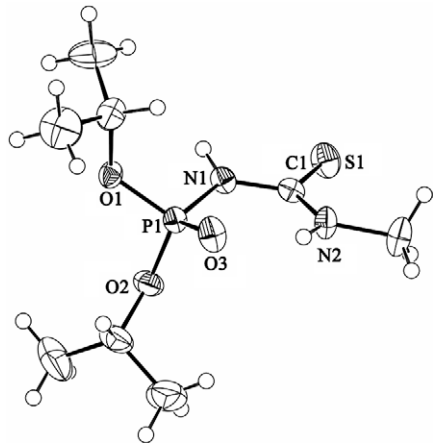


Fig. 1. Thermal ellipsoid representation of **5**. Ellipsoids are drawn at the 50% probability level.

Table 2
Selected bond lengths (Å), and bond angles (°) for 5.

Bond lengths			
P(1)–O(1)	1.559(4)	S(1)–C(1)	1.665(6)
P(1)–O(2)	1.553(4)	N(1)–C(1)	1.382(7)
P(1)–O(3)	1.465(4)	N(2)–C(1)	1.319(8)
P(1)–N(1)	1.659(5)		
Bond angles			
O(3)–P(1)–O(2)	115.3(3)	O(1)–P(1)–N(1)	105.2(2)
O(3)–P(1)–O(1)	116.1(2)	C(1)–N(1)–P(1)	127.6(4)
O(2)–P(1)–O(1)	103.3(2)	N(2)–C(1)–N(1)	116.5(5)
O(3)–P(1)–N(1)	111.5(2)	N(2)–C(1)–S(1)	123.7(5)
O(2)–P(1)–N(1)	104.2(2)	N(1)–C(1)–S(1)	119.8(4)
Torsion angles			
O(3)–P(1)–N(1)–C(1)	37.0(6)	C(2)–N(2)–C(1)–S(1)	0.0(9)
O(2)–P(1)–N(1)–C(1)	−88.0(5)	P(1)–N(1)–C(1)–N(2)	−17.5(7)
O(1)–P(1)–N(1)–C(1)	163.7(4)	P(1)–N(1)–C(1)–S(1)	164.0(3)
C(2)–N(2)–C(1)–N(1)	−178.4(5)		

Table 3
Selected bond lengths (Å), and bond angles (°) for 6.

Bond lengths			
P(1)–O(1)	1.5813(14)	S(2)–C(3)	1.8587(19)
P(1)–O(2)	1.5849(13)	N(1)–C(1)	1.304(2)
P(1)–N(1)	1.6276(15)	N(2)–C(1)	1.341(2)
P(1)–S(1)	1.9326(7)	N(2)–N(3)	1.422(2)
S(2)–C(1)	1.7620(19)	N(3)–C(3)	1.455(3)
Bond angles			
O(1)–P(1)–O(2)	106.04(7)	C(1)–N(1)–P(1)	123.63(14)
O(1)–P(1)–N(1)	108.71(8)	C(1)–N(2)–N(3)	117.08(16)
O(2)–P(1)–N(1)	98.25(8)	N(2)–N(3)–C(3)	106.65(14)
O(1)–P(1)–S(1)	108.96(6)	N(1)–C(1)–N(2)	120.19(17)
O(2)–P(1)–S(1)	114.79(6)	N(1)–C(1)–S(2)	129.34(14)
N(1)–P(1)–S(1)	119.04(6)	N(2)–C(1)–S(2)	110.46(13)
C(1)–S(2)–C(3)	89.06(9)	N(3)–C(3)–S(2)	104.79(13)
Torsion angles			
O(1)–P(1)–N(1)–C(1)	−84.56(17)	N(3)–N(2)–C(1)–N(1)	174.81(17)
O(2)–P(1)–N(1)–C(1)	165.32(16)	N(3)–N(2)–C(1)–S(2)	−6.4(2)
S(1)–P(1)–N(1)–C(1)	40.91(18)	C(3)–S(2)–C(1)–N(1)	165.47(19)
C(1)–N(2)–N(3)–C(3)	28.8(2)	C(3)–S(2)–C(1)–N(2)	−13.18(15)
P(1)–N(1)–C(1)–N(2)	164.61(14)	N(2)–N(3)–C(3)–S(2)	−35.32(17)
P(1)–N(1)–C(1)–S(2)	−13.9(3)	C(1)–S(2)–C(3)–N(3)	28.08(14)

centrosymmetric dimer is formed. The N(1)–C(1)[S(2)]–N(2)[(C2)]–N(3) moiety in **6** is significantly flattened. The S(1)–P(1)–N(1)–C(1)–S(2) backbone is in a *cis*-disposition with the

Table 4
Hydrogen bond lengths (Å) and angles (°) for **5** and **6**.

	D–H···A	*d*(D–H)	*d*(H···A)	*d*(D···A)	∠(DHA)
5[a]	N(1)–H(1)···O(3)#1	0.88	2.00	2.802(6)	150.6
	N(2)–H(2)···O(3)	0.88	2.04	2.800(7)	143(7)
6[b]	N(3)–H(3)···S(1)#1	0.83(3)	2.96(3)	3.6949(19)	148(2)

[a] Symmetry transformations used to generate equivalent atoms: #1 *x*, $-y+3/2$, $z+½$.
[b] Symmetry transformations used to generate equivalent atoms: #1 $-x+2$, $-y+1$, $-z+1$.

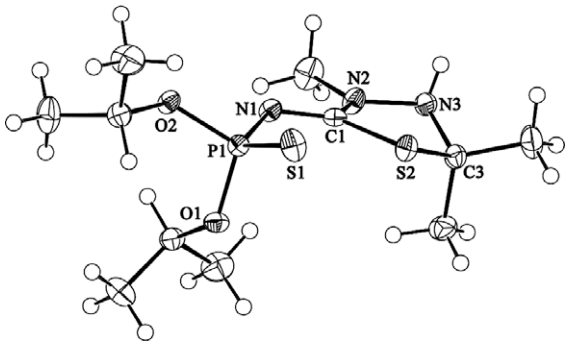


Fig. 2. Thermal ellipsoid representation of **6**. Ellipsoids are drawn at the 50% probability level.

E-isomer of the C(1)–S(2) and P(1)–N(1) fragments. The phosphorus atom is in a distorted-tetrahedral environment. The five-membered heterocycle is in a half-chair conformation with a maximal deviation of the N(3) [0.1909(19)°] and C(3) [−0.222(2)°] atoms from the least-square plane.

4. Conclusions

In summary, we have demonstrated the syntheses of new *N*-(thio)phosphorylated thiosemicarbazides and thioureas by the addition of (thio)phosphorylisothiocyanate to the corresponding hydrazine or amine.

An *E*-arrangement of the C=S and P–N bonds in the SCNP backbones was found for the thiosemicarbazide **3** and thioureas **4** and **5**. The thiosemicarbazides **1** and **2** are presence as a mixture of *E*- and *Z*-conformation isomers, stabilized by H-bonds in $CDCl_3$ and acetone-d_6 solutions. It was also established that the *Z*-isomers are partially or completely in the zwitterionic form.

Recrystallization of **1** from acetone solution gave the substituted 1,3,4-thiadiazolidine **5** after two days. Nothing similar was observed for **2** and the ethyl analog **7**.

Single crystal X-ray diffraction studies showed that the thiourea **5** forms both intra- and intermolecular hydrogen bonds, which in turn lead to polymeric chain formation. According to the X-ray data, the substituted heterocycle **6** forms intermolecular hydrogen bonds. As a result of the intermolecular interactions, a centrosymmetric dimer is formed.

5. Supplementary data

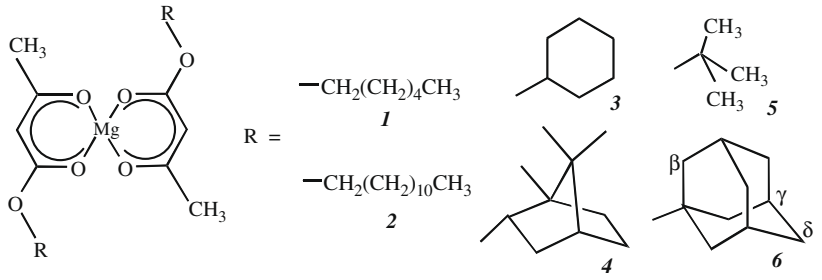
CCDC 720583 and 720584 contains the supplementary crystallographic data for 5 and 6. These data can be obtained free of charge via http://www.ccdc.cam.ac.uk/conts/retrieving.html, or from the Cambridge Crystallographic Data Centre, 12 Union Road, Cambridge CB2 1EZ, UK; fax: (+44) 1223-336-033; or e-mail: deposit@ccdc.cam.ac.uk.

Acknowledgments

This work was supported by the Russian Science Support Foundation. MGB and DAS thank DAAD for the scholarships (Forschungsstipendien 2008/2009).

References

[1] Data from CCNSC, Conformation Defined According to Cancer Chemotherapy Rept. 25 (1962) 1.
[2] L.A. Cates, J. Med. Chem. 10 (1967) 924.
[3] L.A. Cates, J. Med. Chem. 11 (1968) 1075.
[4] L.A. Cates, T.L. Lemke, J. Pharm. Sci. 63 (1974) 1736.
[5] M.J.M. Campbell, Coord. Chem. Rev. 15 (1975) 279.
[6] I.H. Hall, K.G. Rajendran, D.X. West, A.E. Liberta, Anti-Cancer Drug 4 (1993) 241.
[7] F.D. Sokolov, V.V. Brusko, N.G. Zabirov, R.A. Cherkasov, Curr. Org. Chem. 10 (2006) 27.
[8] F.D. Sokolov, V.V. Brusko, D.A. Safin, R.A. Cherkasov, N.G. Zabirov, Coordination diversity of *N*-phosphorylated amides and ureas towards VIIIB group cations, in: Bence Varga, Levente Kis (Eds.), Transition Metal Chemistry: New Research, 2008, p. 101.
[9] F.D. Sokolov, D.A. Safin, M. Bolte, E.R. Shakirova, M.G. Babashkina, Polyhedron 27 (2008) 3141.
[10] D.A. Safin, M. Bolte, E.R. Shakirova, M.G. Babashkina, Polyhedron 28 (2009) 501.
[11] D.A. Safin, M.G. Babashkina, M. Bolte, A. Klein, Polyhedron 28 (2009) 1403.
[12] Stoe & Cie, X-AREA. Area-Detector Control and Integration Software, Stoe & Cie, Darmstadt, Germany, 2001.
[13] A.L. Spek, J. Appl. Cryst. A36 (2003) 7.
[14] G.M. Sheldrick, Acta Crystallogr. Sect. A 64 (2008) 112.
[15] C. Pacilly, Rec. Trav. Chim. 55 (1936) 101.
[16] I.D. Morton, E. Hoggarth, in: E.H. Rodd (Ed.), Chemistry of Carbon Compounds, 1952, p. 919.
[17] F.D. Sokolov, D.A. Safin, N.G. Zabirov, P.V. Zotov, R.A. Cherkasov, Russ. J. Gen. Chem. 75 (2005) 1919.
[18] F.D. Sokolov, D.A. Safin, M.G. Babashkina, N.G. Zabirov, V.V. Brusko, N.A. Mironov, D.B. Krivolapov, I.A. Litvinov, R.A. Cherkasov, B.N. Solomonov, Polyhedron 26 (2007) 1550.



Scheme 1.

be stored for a long time (over a month) over molecular sieves without losing its fitness as a solvent for the syntheses described below.

2.2. Synthesis of the complexes

Bis(ethyl acetoacetato)magnesium(II) ($(EtAcac)_2Mg$) was synthesized by the procedure described in [10], mp 253–254 °C (lit. 250–252 °C).

Magnesium β-ketoesterates of higher alcohols were synthesized by two methods.

Method 1: To a solution of the proligand (30 mmol) and anhydrous triethylamine (30 mmol, 3.03 g) in dry DMF (200 ml) was added dropwise a solution of anhydrous magnesium chloride (15 mmol, 1.43 g) in dry DMF (70 ml) with vigorous stirring under an argon atmosphere. On termination of the addition, the reaction mixture was stirred for another 3 h. The starting substances were fed and the reaction was carried out in complete isolation from atmospheric moisture. DMF-soluble magnesium complexes were isolated as follows. On the termination of stirring, the precipitate $(C_2H_5)_3N{\cdot}HCl$ was filtered off, and the solvent was evaporated under 25 hPa vacuum. The solid residue was dried under 12 Pa vacuum at 60 °C to remove the remnants of the solvent; the pure complexes were isolated by crystallization. DMF-insoluble magnesium complexes (derivatives of *tert*-butyl, cyclohexyl and 1-adamantyl acetoacetate) precipitated as a result of the reaction in the form of a voluminous white precipitate. The precipitate was filtered off and washed twice with distilled water by vigorous stirring for 3 h to remove $(C_2H_5)_3N{\cdot}HCl$. The end product was dried under 12 Pa vacuum at 60 °C for 2 h and then purified by crystallization or washed with a hot solvent.

Method 2 (ligand-exchange route): The synthesis was carried out by gradual and continuous distilling of acetylacetone at 13 hPa and 60 °C off a solution of bis(acetylacetonato)magnesium(II) (3 mmol, 670 mg) in 100 ml of dimethylacetamide containing the higher β-ketoester (6 mmol). The course of the process was monitored and its exchange mechanism verified by means of a qualitative reaction of $FeCl_3$ with acetylacetone contained in the distillate. On the termination of the process, the oily residue was held under 12 Pa vacuum at 60 °C for 2 h to remove the traces of the solvent, then treated with hexane (or ethanol in the case of cyclohexyl acetoacetate), and the end product precipitate formed in this case was filtered off, then purified by crystallization.

2.2.1. Bis(hexyl acetoacetato)magnesium(II)

Complex **1** was prepared by method 1 using hexyl acetoacetate (30 mmol, 5.58 g), and was purified by crystallization from hexane at 5 °C. Yield: 4.7 g, 81%. *Anal.* Calc. for $C_{20}H_{34}O_6Mg$ (MW 394.79): C, 60.85; H, 8.68. Found: C, 60.81; H, 9.01%. Mp 152–154 °C. IR (KBr, cm^{-1}): 2863, 2931, 2959, 1659 (shoulder), 1637, 1565, 1526, 1471, 1429, 1386, 1365, 1289, 1263, 1182, 1080, 1016, 986, 956, 918, 778, 731, 599, 573, 510, 437.

Complex **1** was also prepared by method 2 using hexyl acetoacetate (6 mmol, 1.12 g), and was purified by crystallization from hexane at 5 °C. Yield: 861 mg, 73%. The compound was identified by its melting point and by comparing IR spectra of samples prepared by methods 1 and 2.

2.2.2. Bis(dodecyl acetoacetato)magnesium(II)

Complex **2** was prepared by method 1 using dodecyl acetoacetate (30 mmol, 8.11 g), and was purified by crystallization from hexane at 5 °C. Yield: 7.12 g, 85%. *Anal.* Calc. for $C_{32}H_{58}O_6Mg$ (MW 563.11): C, 68.26; H, 10.38. Found: C, 68.15; H, 10.75%. Mp 122–124 °C. IR (KBr, cm^{-1}): 2854, 2925, 2956, 1656 (shoulder), 1634, 1566, 1521, 1473, 1418, 1397, 1374, 1294, 1262, 1181, 1083, 1016, 962, 913, 774, 738, 711, 595, 519, 433.

Complex **2** was also prepared by method 2 using dodecyl acetoacetate (6 mmol, 1.62 g), and was purified by crystallization from hexane at 5 °C. Yield: 1.26 g, 75%. The compound was identified by its melting point and by comparing IR spectra of samples prepared by methods 1 and 2.

2.2.3. Bis(cyclohexyl acetoacetato)magnesium(II)

Complex **3** was prepared by method 1 using cyclohexyl acetoacetate (30 mmol, 5.52 g). Yield: 5.45 g, 93%. *Anal.* Calc. for $C_{20}H_{30}O_6Mg$ (MW 390.76): C, 61.48; H, 7.74. Found: C, 61.89; H, 7.90%. Mp 302–305 °C (decomposition). IR (KBr, cm^{-1}): 2939, 2856, 1656 (shoulder), 1632, 1548, 1458, 1424, 1370, 1320, 1276, 1181, 1132, 1067, 1028, 998, 964, 914, 880, 850, 829, 775, 736, 608, 563, 538, 488, 459, 419.

Complex **3** was also prepared by method 2 using cyclohexyl acetoacetate (6 mmol, 1.1 g). Yield: 875 mg, 75%. The compound was identified by its melting point and by comparing IR spectra of samples prepared by methods 1 and 2.

2.2.4. Bis(bornyl acetoacetato)magnesium(II)

Complex **4** was prepared by method 1 using bornyl acetoacetate (30 mmol, 7.15 g), and was crystallized from toluene at 5 °C. Yield: 5.9 g, 79%. *Anal.* Calc. for $C_{28}H_{42}O_6Mg$ (MW 498.94): C, 67.41; H, 8.48. Found: C, 67.58; H, 8.54%. Mp 289–291 °C (decomposition). IR (KBr, cm^{-1}): 2939, 2856, 1656 (shoulder), 1632, 1548, 1458, 1424, 1370, 1320, 1276, 1181, 1132, 1067, 1028, 998, 964, 914, 880, 850, 829, 775, 736, 608, 563, 538, 488, 459, 419.

Complex **4** was also prepared by method 2 using bornyl acetoacetate (6 mmol, 1.43 g), and was purified by crystallization from toluene at 5 °C. Yield: 1.05 g, 70%. The compound was identified by its melting point and by comparing IR spectra of samples prepared by methods 1 and 2.

2.2.5. Bis(tert-butyl acetoacetato)magnesium(II)

Complex **5** was prepared by method 1 using *tert*-butyl acetoacetate (30 mmol, 4.74 g), and was purified by repeated washing with hot toluene. Yield: 4.52 g, 89%. *Anal.* Calc. for $C_{16}H_{26}O_6Mg$ (MW 338.68): C, 56.74; H, 7.74. Found: C, 57.05; H, 7.94%. Mp

276–278 °C (decomposition). IR (KBr, cm^{-1}): 2932, 2981, 3010, 1656 (shoulder), 1634, 1543, 1481, 1466, 1456, 1428, 1396, 1373, 1296, 1283, 1260, 1196, 1166, 1071, 1039, 1001, 964, 837, 779, 738, 592, 568, 470, 433.

2.2.6. Bis(1-adamantyl acetoacetato)magnesium(II)

Complex **6** was prepared by method 1 using 1-adamantyl acetoacetate (30 mmol, 7.1 g), and was crystallized from toluene at 5 °C. Yield: 6.4 g, 87%. *Anal.* Calc. for $C_{28}H_{38}O_6Mg$ (MW 494.91): C, 67.95; H, 7.74. Found: C, 67.82; H, 8.18%. Mp 305–306 °C. IR (KBr, cm^{-1}): 2854, 2910, 1659 (shoulder), 1633, 1548, 1458, 1424, 1365, 1348, 1323, 1280, 1258, 1186, 1114, 1080, 1054, 1037, 999, 965, 914, 875, 803, 782, 756, 739, 718, 684, 620, 591, 532, 450, 424.

2.3. Physical measurements

The IR spectra were recorded in KBr pellets in the range 4000–400 cm^{-1} on a SPECORD M 80 spectrophotometer equipped with an IBM-compatible operating computing system. The elemental analysis was carried out on a CARLO ERBA 1106 analyzer.

The ^1H NMR spectra were recorded on a VARIAN VXR-300 spectrometer in $CDCl_3$ and DMSO-d6 solutions with an internal TMS standard. The ^{13}C NMR spectra were recorded on a BRUKER AVANCE 400 spectrometer in $CDCl_3$, DMSO-d6 and C_7D_8 (toluene-d8) solutions with an internal TMS standard.

2.4. X-ray crystallography

Suitable colorless single crystals of complex **6** were formed by crystallization from toluene. The single crystal X-ray diffraction data collection for the complex was performed on a BRUKER SMART APEX II diffractometer, using graphite-monochromated Mo Kα radiation ($\lambda = 0.71073$ Å) at 100 K. Reflection intensities were integrated using SAINT software and corrected for absorption by a numerical method using SADABS [11]. The structure was solved by direct methods and refined by full-matrix least squares on F^2 using the SHELXTL software package [12]. All non-hydrogen atoms were refined anisotropically. During the structure refinement, the atoms of the disordered toluene solvent molecule near the threefold axis, which is perpendicular to the aromatic ring plane, were observed but could not be modelled satisfactorily. The SQUEEZE routine in PLATON [13] was used to modify the structure factors in the HKL file, which correspond to the disordered toluene molecule. Two molecules of toluene correspond to one molecule of complex in the unit cell. All hydrogen atoms were positioned geometrically and refined using a riding model with $U_{iso}(H) = 1.5U_{eq}(C)$ for CH_3 and $U_{iso}(H) = 1.2U_{eq}(C)$ for CH and CH_2 groups. A summary of the crystal data, data collection parameters and convergence results are compiled in Table 1.

Table 1
Crystal data and structure refinement for $(AdAcac)_2Mg$.

Empirical formula	$C_{84}H_{114}Mg_3O_{18} * 0.5C_6H_5CH_3$
Formula weight	1534.68
Crystal system	trigonal
a (Å)	11.1684(6)
b (Å)	11.1684(6)
c (Å)	20.3179(16)
α (°)	90
β (°)	90
γ (°)	120
V (Å^3)	2194.8(2)
Z, calculated density (Mg/m^3)	1.123
Space group	$P\bar{3}$
Absorption coefficient (mm^{-1})	0.096
$F(0\,0\,0)$	798
Crystal size (mm)	0.46 × 0.38 × 0.20
θ Range for data collection (°)	1.00–26.25
Limiting indices	$-13 \leqslant h \leqslant 13$, $-13 \leqslant k \leqslant 13$, $-25 \leqslant l \leqslant 25$
Reflections collected/unique	17 943/2957 ($R_{int} = 0.1053$)
Completeness to $\theta = 26.25$ (%)	99.4
Absorption correction	multi-scan
Refinement method	full-matrix least-squares on F^2
Goodness-of-fit (GOF) on F^2	1.035
Final R indices [$I > 2\sigma(I)$]	$R_1 = 0.0735$, $wR_2 = 0.1886$
R indices (all data)	$R_1 = 0.1083$, $wR_2 = 0.2019$
Largest difference in peak and hole (e Å^{-3})	0.810 and −0.577

3. Results and discussion

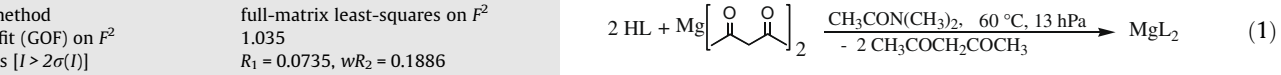
3.1. Synthesis

For magnesium β-diketonates, synthesis methods based on the reaction of metallic magnesium with dicarbonyl proligand HL in a water–ethanol solution (or toluene) and on exchange reactions between a magnesium salt and NaL or HL in an aqueous-alcoholic medium were proposed [14]. Magnesium complexes are always isolated from water-containing solutions as $MgL_2{\cdot}2H_2O$ hydrate. Since β-dicarbonyl compounds of magnesium are very prone to add water molecules and other Lewis bases, to obtain pure MgL_2 products is a non-trivial problem [1]. This concerns equally other magnesium complexes, such as carboxylates [15]. Anhydrous volatile complexes of magnesium with β-diketones are purified by sublimation. Among the unconventional methods, the solid-phase synthesis of magnesium β-diketonates is noteworthy [16]; sublimation is also employed in this case to purify the products.

At the same time, the use of procedures, developed for β-diketonates, for the synthesis of bis-chelates of magnesium with β-ketoesters involves a big problem, namely the possibility of transesterification or hydrolysis of the proligand in the course of the reaction. These side processes are noticeably catalyzed by alkalis. For this reason, the exchange reaction with magnesium methylate in absolute methanol is unsuitable, which is confirmed by the results given by Baker et al. [17] for a NMR spectroscopic study of the H^+-D^+ equilibrium between the magnesium complex $(CH_3O)_2MgL'$ (HL′ = methyl acetoacetate) and deuterated methanol in the presence of magnesium methylate.

Zaugg et al. described the preparation of a complex of magnesium with ethyl acetoacetate by the interaction of magnesium oxide (fresh calcined) with the proligand in benzene with azeotropic removal of water [10]. Our attempts to reproduce this procedure for β-ketoesters of higher alcohols have failed. This fact may be accounted for as proceeding from spatial concepts. Probably, the presence of bulky substituents hinders the simultaneous access of two proligand molecules to the magnesium oxide molecule.

The literature reports a method for the preparation of higher metal β-diketonates from acetylacetone derivatives by an exchange reaction (the reaction was carried out under hard conditions: 160 °C, in a CO_2 stream) [18]. The idea of this method was utilized by us for the synthesis of magnesium β-ketoesterates under mild conditions with continuous, slow removal of acetylacetone together with the solvent under vacuum. A disadvantage of the method is partial resinification of the reaction mass, which complicates the purification of products and makes it unsuitable in the case of β-ketoesters of tertiary alcohols.



(1)

It turned out in practice that an alternative method, which involves the interaction between anhydrous magnesium chloride in an aprotic solvent and β-ketoesters in the presence of triethyl-

Table 2
^{1}H NMR assignments of the Mg (II) complexes (δ in ppm).

Compound (solvent)	Protons position				
	–CH– (chelate cycle)	–OCH– or –OCH_2– (ester group)	–CCH_3	–CH_2– (hydrocarbon fragment of ester group)	–CH_3
$(EtAcac)_2Mg$ (DMSO-d6)	4.48	3.93, 3.91, 3.89, 3.86	1.68	-	1.13, 1.11, 1.09
$(HexAcac)_2Mg$(DMSO-d6)	4.41	3.84 m	1.68	1.48 m, 1.25	0.88, 0.86, 0.84
$(HexAcac)_2Mg$ ($CDCl_3$)	4.75 (4.65 m)[a]	4.14 m (4.20 m)[a]	1.78 m	1.96–1.85 m,1.67 m, 1.49 m, 1.27 m	0.89, 0.87, 0.85
$(DAcac)_2Mg$ (DMSO-d6)	4.46	3.82 m	1,67	1.47 m, 1.24	0.87, 0.85, 0.83
$(DAcac)_2Mg$ ($CDCl_3$)	4.78 (4.66 m)[a]	4.02 m (4.13 m)[a]	1.77	1.96–1.85 m, 1.68 m, 1.59 m, 1.49 m, 1.25	0.9, 0.88, 0.86
$(ChAcac)_2Mg$ (DMSO-d6)	4.44	4.49 m	1.67	1.77 m, 1.48 m, 1.23 m	-
$(ChAcac)_2Mg$ ($CDCl_3$)	4.78 (4.73 m)[a]	4.65 m	1.78	1.95–1.82 m, 1.60–1.15 m	-
$(BrlAcac)_2Mg$ (DMSO-d6)	4.50	4.73 d	1.67	2.20 m, 1.86 m, 1.74 m, 1.58 m, 1.25–1.05 m, 0.88 m	0.84, 0.82, 0.74
$(BrlAcac)_2Mg$ ($CDCl_3$)	4.83 (4.76 m)[a]	4.69 d, (4.97 d)[a]	1.81	2.36 m, 1.96 m, 1.69 m, 1.57 m, 1.31–1.09 m, 1.03 m, 0.97 m	0.91, 0.88, 0.84
$(tBuAcac)_2Mg$ (DMSO-d6)	4.38	-	1.65	-	1.34 m
$(tBuAcac)_2Mg$ ($CDCl_3$)	4.67	-	1.73	-	1.43 m
$(AdAcac)_2Mg$ (DMSO-d6)	4.37	-	1.63	2.01 $(-CH)_\gamma$, $(-CH_2)_\beta$, 1.58 $(-CH_2)_\delta$	
$(AdAcac)_2Mg$ ($CDCl_3$)	4.66 (4.69)[a]	-	1.72 m	2.11 m $(-CH)_\gamma$, $(-CH_2)_\beta$, 1.61 m $(-CH_2)_\delta$	

[a] Signals due to the presence of oligomer.

amine under the conditions of complete isolation from atmospheric moisture, is most suitable. The experimental technique which is employed in the syntheses of organolithium compounds is well suited for this method [19].

$$2\,HL + MgCl_2 \xrightarrow[DMF]{+\,2\,(C_2H_5)_3N} MgL_2 + 2\,(C_2H_5)_3N{\cdot}HCl \qquad (2)$$

The coordination compounds obtained are stable against atmospheric moisture; they are also stable against water when being washed free from amine hydrochloride. The preparation of identical compounds by two alternative synthesis methods is one of the proofs of their chemical structure.

3.2. Infrared spectra

When interpreting the IR spectra, special attention was paid to the range 1750–1450 cm^{-1}, where disappearance of absorption bands of parent β-ketoesters ($\nu_{(c=o)}$, 1750–1720 cm^{-1}) was observed, and absorption bands of stretches of the C–O and C–C bonds conjugated in the chelate ring (1640–1400 cm^{-1}) appeared. In the low frequency region, absorption bands appeared, which may be assigned to M–O bond stretches, mixed with chelate ring deformation vibrations (600–550 cm^{-1}) and C–CH_3 deformation vibrations [20]. IR spectra corroborate the absence of coordinated water in the molecules of the magnesium complexes synthesized.

3.3. ^{1}H and ^{13}C NMR spectra

Anhydrous alkaline-earth β-diketonates, such as magnesium β-diketonates, are known to be coordinatively unsaturated compounds, which gives rise to the formation of strong intermolecular bridge bonds and oligomerization of these complexes [21]. For alkaline-earth complexes, the presence of oligomeric forms both in solution and in the gas phase, as well as for derivatives containing branched alkyl substituents (dipivaloylmethane) has been established [22,23]. In comparison with β-diketonates, in complexes of magnesium with β-ketoesters formation of extra intermolecular bonds through the ester group oxygen atom may be assumed, due to which they may be still more associated. On the other hand, the complexes under investigation contain bulky alkyl groups, the steric effects of which must affect the degree of oligomerization [1]. The presence of oligomeric forms of the complexes in solutions can be indicated by the splitting of signals in ^{1}H NMR spectra [24].

Signals in the ^{1}H NMR spectra of the complexes under investigation were assigned by comparing them with the spectrum of the simplest analog, bis(ethyl acetoacetato)magnesium(II), and

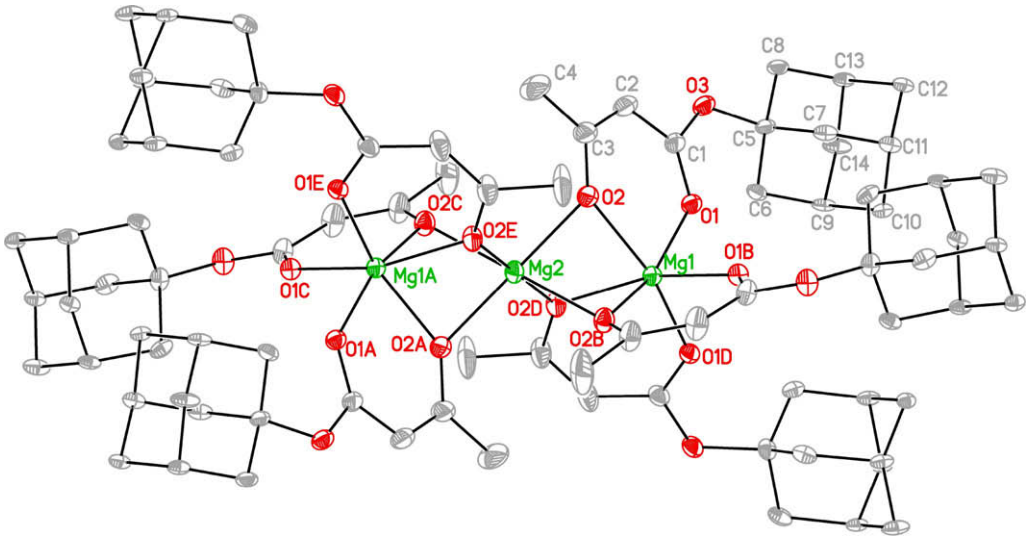


Fig. 1. Molecular structure of $(AdAcac)_2Mg$ (**6**). Hydrogen atoms are omitted for clarity.

taking into account the integral intensities of the peaks. In the spectrum of $(EtAcac)_2Mg$ there are a classical triplet (1.11 ppm, $J = 7$ Hz) and a classical quartet (3.90 ppm, $J = 7$ Hz) of ethoxy group protons, as well as singlets of the methyl group and methine proton in a strong and a weak field respectively.

The ^1H NMR spectra of the magnesium β-ketoesterates synthesized are complex in character. In a strong field, they are a sequence of overlapping multiplets, which is due to the peculiarities of the stereochemical structure of the hydrocarbon skeleton of the ester group. At the same time, the non-equivalence of multiplet splitting in the resonance region of the chelate ring methine proton (weak-field region) in the spectra of the same compound in solvents with different donor properties indicates that the compounds under investigation exist in solutions as a monomer–oligomer equilibrium. Chemical shifts of the main signals of the ^1H NMR spectra are listed in Table 2.

To obtain additional information, which allows one to determine the structure of the synthesized magnesium complexes in solution, we made use of ^{13}C NMR spectroscopy. Spectra of complex **1** in DMSO, $CDCl_3$ and C_7D_8 have been taken. As could be expected for a monomer, there are 10 individual ^{13}C $\{^1H\}$ resonance signals: 186.71 (OCO), 171.72 ($OCCH_3$), 82.53 (CH chelate ring), 61.80 (OCH_2), 31.35 ($OCCH_3$), 29.23, 27.86, 25.44, 22.41 (CH_2), 14.23 ppm (CH_3) in the spectrum of a solution of complex **1** in DMSO. The spectra of solutions of complex **1** in $CDCl_3$ and C_7D_8 are a superposition of peaks due to the presence of the monomer and oligomer.

3.4. Structure of bis(1-adamantyl acetoacetato)magnesium(II)

The molecular structure of **6**, along with the atom labelling scheme, is shown in Fig. 1. Selected bond lengths and angles are summarized in Table 3. Complex **6** crystallizes in the trigonal system with one molecule per unit cell. The asymmetric unit contains 1/6 of the compound. The whole molecule is generated by the inversion centre and the threefold axis. All Mg atoms occupy special positions on the threefold axis. Compound **6** is centrosymmetrical; Mg2 occupies a position on the inversion centre. The distance between neighboring magnesium atoms is 2.8779(18) Å. The Mg1 and Mg1A atoms are coordinated by ligand molecules with the formation of planar β-dicarbonylic metallocycles and form a distorted octahedral coordination environment (Fig. 1) with bond lengths and angles (Table 3) which are in good agreement with the related structure of $(EtAcac)_2Mg$ [25]. The mean deviation from the metallocycle plane (Mg1–O1–C1–C2–C3–O2) is 0.0111 Å; the torsion angles between the planes are 73.7°. The C1–O1 and C2–C3 lengths (Table 3) characterize the presence of double bonds between the corresponding atoms, which is characteristic of β-dicarbonyl complexes. The Mg2 coordination polyhedron is formed by bridging oxygen atoms (O2, O2A, O2B, O2C, O2D, O2E), which create a slightly distorted octahedron with a Mg2–O2 length of 2.079(2) Å and angles: O2–Mg2–O2C = 101.74(9)°, O2–Mg2–O2B = 78.26(9)°, O2–Mg2–O2A = 180.00 ° (Fig. 1).

Table 3
Selected bond lengths and bond angles for $(AdAcac)_2Mg$.

Bond Lengths (Å)		Angles (°)	
Mg1–O1 N	2.029(2)	O1–Mg1–O1A	92.00(10)
Mg1–O2 N	2.101(2)	O1–Mg1–O2B	107.32(9)
Mg2–O2 N	2.080(2)	O1–Mg1–O2A	85.22(8)
Mg1–Mg2	2.8799(17)	O1–Mg1–O2	160.55(9)
C1–O1	1.247(4)	O2–Mg1–O2A	77.30(11)
C3–O2	1.305(5)	O2C–Mg2–O2	180.00(9)
C1–C2	1.417(5)	O2D–Mg2–O2	101.76(9)
C2–C3A	1.344(6)	O2B–Mg2–O2	78.24(9)
		Mg2–O2–Mg1	87.08(9)
		Mg1–Mg2–Mg1A	180.0

4. Conclusions

The reaction of anhydrous magnesium salt with proligand in aprotic solvent in the presence of triethylamine under conditions of complete isolation from atmospheric moisture is most suitable for the preparation of anhydrous complexes of magnesium with β-ketoesters of higher alcohols. This method is apparently universal and can be used for the synthesis of anhydrous β-ketoesterates of other metals.

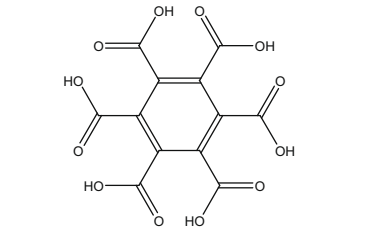
Taking into account that bis(1-adamantyl acetoacetato)magnesium(II) is a trimer in the crystalline state, it may be assumed with a high degree of probability that the other magnesium β-ketoesterates, which contain less bulky substituents, also have a trimeric structure. The compounds can exist in solutions as monomers or as a monomer–oligomer mixture, depending on the electron-donating properties of the solvent. The solubility of the synthesized complexes in a number of organic solvents, including non-polar ones, can be utilized to develop efficient drug formulations using Solid Lipid Nanoparticles (SLN) technologies.

Supplementary data

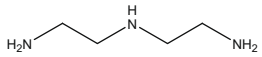
CCDC 686206 contains the supplementary crystallographic data for **6**. These data can be obtained free of charge via http://www.ccdc.cam.ac.uk/conts/retrieving.html, or from the Cambridge Crystallographic Data Centre, 12 Union Road, Cambridge CB2 1EZ, UK; fax: (+44) 1223-336-033; or e-mail: deposit@ccdc.cam.ac.uk.

References

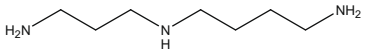
[1] D.J. Otway, W.S. Rees Jr., Coord. Chem. Rev. 210 (2000) 279.
[2] F. Benvenuti, C. Carlini, F. Marchetti, M. Marchionna, A.M. Raspolli Galletti, G. Sbrana, J. Organomet. Chem. 622 (2001) 286.
[3] Y. Suzuki, H. Komatsu, T. Ikeda, N. Saito, S. Araki, D. Citterio, D. Hisamoto, Y. Kitamura, T. Kubota, J. Nakagawa, K. Oka, K. Suzuki, Anal. Chem. 74 (6) (2002) 1423.
[4] D.W. Hutchinson, Antiviral Res. 5 (1985) 193.
[5] K.M. Fromm, E.D. Gueneau, Polyhedron 23 (2004) 1479.
[6] M. Sechi, A. Bacchi, M. Carcelli, C. Compari, E. Duce, E. Fisicaro, D. Rogolino, P. Gates, M. Derudas, L.Q. Al-Mawsawi, N. Neamati, J. Med. Chem. 49 (2006) 4248.
[7] E. Tramontanoa, F. Espositoa, R. Badasa, R. Di Santob, R. Costib, P. La Collaa, Antiviral Res. 65 (2005) 117.
[8] E.I. Bagrii, Adamantanes: Production, Properties, Application, Nauka, Moscow, 1989. p. 263.
[9] L.I. Koval, V.I. Dzyuba, O.L. Ilnitska, V.I. Pekhnyo, Tetrahedron Lett. 49 (2008) 1645.
[10] H.E. Zaugg, D.A. Dunningon, R.J. Michaels, L.R. Swett, T.S. Wang, A.H. Sommers, R.W. DeNet, J. Org. Chem. 26 (1961) 644.
[11] Bruker, SADABS, SAINT, SHELXTL and SMART, Bruker AXS Inc., Madison, Wisconsin, USA, 2003.
[12] G.M. Sheldrick, Acta Crystallogr. A64 (2008) 112.
[13] A.L. Spek, J. Appl. Cryst. 36 (2003) 7.
[14] G.S. Hammod, D.C. Nonhebel, Chin-Hua S. Wu, Inorg. Chem. 2 (1963) 73.
[15] E.N. Coker, T.J. Boyle, M.A. Rodriguez, T.M. Alam, Polyhedron 23 (2004) 1739.
[16] A.A. Petrova, A.V. Dudin, V.D. Makhaev, I.G. Zaitseva, N.P. Kuz'mina, Russ. J. Inorg. Chem. 50 (10) (2005) 1541.
[17] S.R. Baker, Michael L.F. Cadman, L. Crombie, David A.V. Edwards, J. Mistry, J. Chem. Soc., Perkin Trans. 1 (1996) 2705.
[18] L. Wolf, E. Butter, H. Weiner, Z. Anorg. Allg. Chem. 306 B (1960) 87.
[19] B.J. Wakefield, Organolithium Methods, Academic Press, London, 1988. Russian Ed., Mir, Moscow, 1991, p. 184.
[20] K. Nakamoto, Infrared and Raman Spectra of Inorganic and Coordination Compounds, fourth ed., Wiley, New York, 1986. Russian Ed., Mir, Moscow, 1991, p. 536.
[21] N.P. Kuz'mina, S.V. Eliseeva, N.V. Chugarov, L.I. Martynenko, Yo-Sep Min, Dae-Sig Kim, Russ. J. Coord. Chem. 28 (9) (2002) 603.
[22] A. Recca, F. Bottino, P. Finocchiaro, J. Inorg. Nucl. Chem. 40 (1978) 1997.
[23] G.V. Girichev, N.I. Giricheva, N.V. Belova, N.P. Kuz'mina, Russ. J. Coord. Chem. 25 (12) (1999) 833.
[24] S.V. Eliseeva, N.V. Chugarov, N.P. Kuz'mina, R.V. Nechiporuk, S.A. Ivanov, L.I. Martynenko, Russ. J. Inorg. Chem. 48 (7) (2003) 1014.
[25] G. Petrov, A. Alexiev, O. Angelova, J. Macicek, J. Coord. Chem. 25 (1992) 101.



mellitic acid (mlt)



diethylenetriamine (dien)



spermidine (spd)

Chart 1.

weighing; diethylenetriamine (Aldrich) was transformed into the corresponding hydrochloride and was used in this form. The purities of mlt, dien and spd, checked by potentiometric titrations with standard solutions of NaOH, were always higher than 99.5%. Sodium hydroxide and hydrochloric acid solutions were prepared by diluting concentrated Fluka ampoules and were standardised against potassium biphthalate and sodium carbonate, respectively. All the solutions were prepared by using ultrapure water (conductivity < 0.1 μS cm^{-1}) and grade A glassware.

2.2. Potentiometric measurements

Potentiometric titrations were carried out (at 25.0 ± 0.1 °C) using an apparatus consisting of a Metrohm Model 713 potentiometer, equipped with a combined glass electrode (Ross type 8102, from Orion) and a Metrohm Model 765 motorized burette. Estimated accuracy was ±0.2 mV and ±0.003 mL for e.m.f. and titrant volume readings, respectively. The apparatus was connected to a PC, and automatic titrations were performed using a suitable computer program to control titrant delivery, data acquisition and to check for e.m.f. stability. All titrations were carried out under magnetic stirring and presaturated N_2 was bubbled through the purified solution in order to exclude O_2 and CO_2 inside. A volume of 25 mL of the solution containing mlt at $C_L = 0.001$, 0.002 mol L^{-1} and the amine hydrochloride at $C_A = 0.001$ mol L^{-1} was titrated with standard NaOH up to 80–90% neutralization. Separate titrations of HCl at the same ionic strength as the sample under study, were carried out to determine standard electrode potential E^0 and to obtain pH $-\log [H^+]$ readings. The reliability of the calibration in the alkaline range was checked by calculating pK_w values.

2.3. Calorimetric measurements

The measurements were carried out using a Tronac model 450 Isoperibolic Titration calorimeter, coupled with a Keithley 196 system Dmm digital multimeter. A volume of 50 mL of solution, containing amine hydrochloride at $C_A = 0.001$, 0.002 mol L^{-1} and at $t = 25.000 \pm 0.001$ °C was titrated with a Na_6mlt standard solution. The titrant was delivered by a 2.5 mL capacity Hamilton syringe, model 1002TLL. A computer program was used for the acquisition of calorimetric data. Accuracy was checked by titrating a THAM (Tris-(hydroxymethyl)amino-methane) buffer with HCl. The heat of dilution was measured before each experiment. The accuracy of calorimetric apparatus was $Q \pm 0.008$ J and $v \pm 0.001$ cm^3.

2.4. Diffractometric measurements

Colourless crystals with an average radius of 0.2 mm were obtained by slow evaporation from water solutions. Data were collected on a a four-circles P4 Siemens diffractometer [Mo Kα ($\lambda = 0.71073$ Å)]. Cell parameters were obtained by the least-square refinement of centred angles referred to about 35 reflections in the $3.03 \leqslant 2\theta \leqslant 14.16°$ range. All reflections were collected at a fixed rate with the ω-scan technique up to $2\theta = 50°$. No decay was detected monitoring three standard reflections every 197 collected data. When necessary, Lorenz polarization and profile fitting corrections were achieved [18]. Data collections and reductions were accomplished by P3/V (Release 4.21/V. Siemens Analytical X-Ray Instruments Inc., Madison, Wisconsin, USA).

2.5. Calculations

All the parameters relative to alkalimetric purity determination were refined using the nonlinear least squares computer program ESAB2M. Formation constants were calculated using the nonlinear least squares computer programs STACO and BSTAC. Speciation profiles were obtained using the computer program ES4EC. Details of calculation methods and programs have already been reported [19].

Formation constants were extrapolated to zero ionic strength as already reported [20]. Both BSTAC and STACO computer programs can deal with potentiometric data obtained in variable ionic strength conditions. The dependence on ionic strength of formation constants was taken into account using the Debye–Hückel type equation:

$$\log \beta = \log^T \beta - z^* 0.51 \sqrt{I}/(1 + 1.5\sqrt{I}) + CI \quad (1)$$

where

$$C = (0.025 \pm 0.015) z^*, \quad \text{at } I \leq 0.15$$

$$z^* = \Sigma z^2_{\text{reactants}} - \Sigma z^2_{\text{products}}$$

(β = stoichiometric formation constant; ${}^T\beta$ = formation constant at infinite dilution; z = component charge).

Calorimetric titration data were analysed by the computer program ES5CM [21]. Concentrations and thermodynamic parameters are given in the molar scale. Errors are given as standard devia-

Table 1
Protonation[a] thermodynamic parameters of mlt, dien and spd at $t = 25$ °C and $I = 0$ mol L^{-1}.

Ligand	r	logβ	ΔH^{0}[b]
mlt	1	7.85[c]	13.0[d]
	2	14.30	10.6
	3	19.39	8.2
	4	22.86	5.6
	5	25.00	3.4
	6	25.92	1.0
dien	1	9.82[e]	−48.0[f]
	2	18.59	−98.5
	3	22.34	−131.8
spd	1	10.80[g]	−56.5[h]
	2	20.38	−109.5
	3	28.20	−158.0

[a] Reaction: X + rH = XH_r, with X = ligand (charges omitted for simplicity).
[b] Expressed in kJ mol^{-1}.
[c] Ref. [13].
[d] Ref. [24].
[e] Ref. [22].
[f] Ref. [25].
[g] Ref. [23].
[h] Ref. [9].

Table 2
Crystal data and structure refinement for I and II.

Identification code	I	II
Empirical formula	$C_{16}H_{27}N_3O_{16}$	$C_{19}H_{29}N_3O_{14}$
Formula weight	517.41	523.45
T (K)	293(2)	293(2)
Wavelength (Å)	0.71073	0.71073
Crystal system	orthorhombic	monoclinic
Space group	$P2(1)2(1)2(1)$	$P2(1)/c$
Unit cell dimensions		
a (Å)	9.5063(19)	9.7590(17)
b (Å)	14.261(3)	16.015(4)
c (Å)	16.211(3)	15.672(3)
β (°)	90	90.65
Volume (Å^3)	2197.8(8)	2449.2(9)
Z	4	4
Density (calculated) (Mg/m^3)	1.564	1.420
Absorption coefficient (mm^{-1})	0.142	0.123
F(0 0 0)	1088	1104
Crystal size (mm^3)	0.36 × 0.28 × 0.22	0.24 × 0.19 × 0.10
θ Range for data collection (°)	1.90–25.05	2.60–25.05
Index ranges	$-1 \leqslant h \leqslant 11$, $-1 \leqslant k \leqslant 16$, $-1 \leqslant l \leqslant 19$	$0 \leqslant h \leqslant 11$, $0 \leqslant k \leqslant 19$, $-18 \leqslant l \leqslant 18$
Reflections collected	2835	4632
Independent reflections	2226 [R_{int} = 0.0199]	4331 [R_{int} = 0.0163]
Completeness to 2θ	50	50
Absorption correction	none	none
Refinement method on 0.9878 and 0.9712 F^2	full-matrix least-squares	full-matrix least-squares
Data/restraints/parameters	2226/12/341	4331/0/332
Final R indices [$I > 2\sigma(I)$]	R_1 = 0.0328, wR_2 = 0.0655	R_1 = 0.0398, wR_2 = 0.0990
R indices (all data)	R_1 = 0.0538, wR_2 = 0.0727	R_1 = 0.0589, $wR2$ = 0.1031
Extinction coefficient	0.0096(7)	0.0021(5)
Largest difference in peak and hole (e Å^{-3})	0.168 and −0.173	0.290 and −0.231

tions. Protonation thermodynamic parameters of mlt, dien and spd used in the calculations are shown in Table 1 at I = 0 mol L^{-1} and t = 25 °C [9,13,22–25]. The interactions of amines with Cl$^-$ [23,25] and mellitate with Na$^+$ [13] were taken into account in the calculations.

Structures were solved by the new SIR2004 [26] and the refinement was managed by SHELXL97 [27]. In both structures a water molecule too disordered by dynamic or statistical motions was treated with the squeeze exclusion from the used reflection data. Published material was organized with the whole WINGX package [28] along with PARST97 [29]. Crystal data and structure refinement for I (dien–mlt) and II (spd–mlt) were reported in Table 2.

Table 3
Overall thermodynamic formation parameters of the triamine(A)-mellitate(L) species at I = 0, 0.15 mol L^{-1} and t = 25 °C.

Amine	Species	log$\beta^0 \pm s$[a]	logβ[b]	$-\Delta G^0$ [b]	$\Delta H^0 \pm s$[a,c]	TΔS^0[c]
dien	ALH_2	24.91 ± 0.04	22.83	142.2	−135 ± 3	7
	ALH_3	32.10 ± 0.03	29.26	183.2	−122 ± 1	61
	ALH_4	37.68 ± 0.06	34.28	215.1	−134 ± 3	81
	ALH_5	42.37 ± 0.04	38.59	241.8	−140.1 ± 0.8	102
	A_2LH_6	59.96 ± 0.07	56.03	342.3	−258 ± 3	84
spd	ALH_2	28.43 ± 0.05	26.32	162.3		
	ALH_3	38.31 ± 0.04	35.47	218.7	−149.5 ± 0.2	69
	ALH_4	43.10 ± 0.06	39.70	246.0		
	ALH_5	48.72 ± 0.05	44.94	278.1		
	ALH_6	52.49 ± 0.08	48.54	299.6		

[a] s = Standard deviation.
[b] At I = 0.15 mol L^{-1} in NaCl.
[c] Expressed in kJ mol^{-1}.

3. Results and discussion

3.1. Formation and stability of triamine–mellitate species and predictive relationships

Formation constants of dien–mlt and spd–mlt species were obtained by performing on the potentiometric data several trials with different sets of complex species. The speciation models selected, for both sytems, are those which very well fit experimental data. Tables 3 and 4 show thermodynamic formation parameters at t = 25 °C and I = 0, 0.15 mol L^{-1} in NaCl, according to the following reactions (charges omitted):

$$pA + L + rH = A_pLH_r \quad (2)$$

$$pH_iA + H_jL = A_pLH_r \quad pi + j = r \quad (3)$$

where A = amine and L = mellitate anion.

It was found for both systems the formation of species with p = 1 and r = 2…5. In addition, were also found the following species: A_2LH_6, for A = dien; ALH_6, for A = spd. As can be seen the stability of these species is quite high and increases with the charge of both polyammonium cation and polycarboxylic anion, reaching a maximum value when the amine is completely protonated and the ligand completely deprotonated. This trend was also observed in the preceding works on species formed by several polyamines and inorganic, carboxylic and nucleotidic ligands [9,10]. The comparison between the formation constant values of dien–mlt species with those of spd–mlt species having the same stoichiometry, shows high differences: $\Delta\log\beta$ (difference between logβ^0 of

Table 4
Thermodynamic formation parameters of triamine(A)-mellitate(L) species at I = 0, 0.15 mol L^{-1} and t = 25 °C.

Amine	Reaction	logK^0	log$K$[a]	logK^0/ζ[b]	logK/ζ[a,b]	$-\Delta G^{0c}$	ΔH^{0c}	TΔS^{0c}
dien	$H_2A^{2+} + L^{6-} = ALH_2^{4-}$	6.4	4.1	0.53	0.34	36.4	−36.5	0
	$H_2A^{2+} + HL^{5-} = ALH_3^{3-}$	5.7	3.8	0.57	0.38	32.6	−36.5	−4
	$H_2A^{2+} + H_2L^{4-} = ALH_4^{2-}$	4.8	3.3	0.60	0.41	27.6	−46.1	−18
	$H_3A^{3+} + H_2L^{4-} = ALH_5^{-}$	5.9	3.6	0.49	0.30	33.5	−18.9	15
	$2H_3A^{3+} + L^{6-} = A_2LH_6^0$	15.6	10.4	0.43	0.29	88.8	5.6	94
	$H_2A^{2+} + H_3A^{3+} + HL^{5-} = A_2LH_6^0$	11.4	7.7	0.46	0.26	64.9	−40.7	24
				0.51 ± 0.08	0.33 ± 0.06			
spd	$H_2A^{2+} + L^{6-} = ALH_2^{4-}$	8.0	5.7	0.67	0.47	45.7		
	$H_3A^{3+} + L^{6-} = ALH_3^{3-}$	10.1	6.6	0.56	0.37	57.7	8.5	66
	$H_3A^{3+} + HL^{5-} = ALH_4^{2-}$	7.1	4.2	0.47	0.28	40.5		
	$H_3A^{3+} + H_2L^{4-} = ALH_5^{-}$	6.2	3.9	0.52	0.32	35.4		
	$H_3A^{3+} + H_3L^{3-} = ALH_6^0$	4.9	3.2	0.54	0.36	28.0		
				0.55 ± 0.08	0.36 ± 0.07			
			total	0.53 ± 0.02	0.345 ± 0.02			

[a] At I = 0.15 mol L^{-1} in NaCl.
[b] ζ = Charge product = $z_{cation}|z_{anion}|$.
[c] Expressed in kJ mol^{-1}.

spd–mlt species with $\log\beta^0$ of dien–mlt species) for ALH_2, ALH_3, ALH_4, ALH_5 species, are 3.52, 6.21, 5.42, 6.35, respectively. Since the most probable reactions, referring to the same A_pLH_r species, are different for species containing dien respect to those containing spd, to give a more reliable picture of the stability it is better to compare log*K* values showed in Table 4. When the charges involved in the formation reaction are the same, these differences are not high. Moreover, there is a very good linear trend of log*K* versus ζ (charge products = z_{cation} $|z_{anion}|$): $\log K^0/\zeta = 0.51 \pm 0.08$, 0.55 ± 0.08, for dien and spd systems, respectively and $\log K^0/\zeta = 0.53 \pm 0.02$ considering dien and spd systems altogether; $\log K/\zeta$ (at $I = 0.1$ in NaCl) = 0.33 ± 0.06, 0.36 ± 0.07, for dien and spd systems, respectively and $\log K/\zeta = 0.345 \pm 0.02$ considering dien and spd systems altogether (see Table 4). By using the crude approximation $n = \zeta/2$, where n is the number of possible salt bridges, we obtain a mean formation free energy:

$$-\Delta G^0 = 6.1 \pm 0.3 \text{ kJ mol}^{-1}$$

which is consistent with $-\Delta G^0 = 6.3$ kJ mol^{-1} for species formed by several amines with several carboxylic ligands, as reported in our preceding work [10]. As pointed up in preceding works [6,30], the influence of the structure on the stability, such us the length of the methylene chain in the diamines and in general the distance between aminogroups, is a less important factor respect to that constituted by the charges in the formation reaction. Nevertheless the charges distance in the cation molecule is a factor to take in consideration for the prediction of the stability of these types of complexes. In fact the predictive power of equations containing the ζ term was generally increased by the introduction of a term which accounts for the distance of aminogroups. As an example the $R_{C/N}$ parameter, *i.e* the ratio of the number of C atoms with respect N atoms, is 1.33 for dien and 2.33 for spd [30,31]. It was found that the distance between the charges in the protonated amine is an unfavourable factor for the stability for species containing pyrophosphate or ATP. The species containing mlt show an opposite trend: when the charges involved in the formation reaction are the same, the species spd–mlt are more stable than those of dien.

3.2. ΔH and $T\Delta S$ contributions

Enthalpic and entropic formation parameters of the dien–mlt and spd–mlt species, according to the reactions 2 and 3, are shown in Tables 3 and 4, respectively. The formation of these species is generally exothermic, except for the reactions: $2H_3A^{3+} + L^{6-} = A_2LH_6^0$, with A = dien and $H_3A^{3+} + L^{6-} = ALH_3^{3-}$, with A = spd. This is in line with the results of Ref. [10], where, for the reaction of fully protonated amines with unprotonated carboxylate ligands ($j = 0$, in Eq. (3)), ΔH^0 values were always positive. $T\Delta S^0$ values are also a fairly linear function of charges involved in the formation reaction: for example $T\Delta S^0/\zeta = 0.4 \pm 1.6$ kJ mol^{-1} for dien system. Table 5 reports formation enthalpy and entropy values of the species formed by spd with citrate (cit), 1,2,3-tricarballylate (tca), 1,2,3,4-butanetetracarboxylate (btc) [9] and mlt, referring to the reaction of completely protonated amine with unprotonated carboxylate ligand, confirming the strict dependence of them on the ligand charge.

Table 5
Comparison of thermodynamic formation parameters[a] of spd-carboxylate species at $I = 0$ mol L^{-1} and $t = 25$ °C.

Ligand	z_a[b]	ΔH^{0}[c]	$T\Delta S^{0}$[c]	Ref.
cit	3	−0.9	23	[9]
tca	3	3.5	26	[9]
btc	4	3.9	35	[9]
mlt	6	8.5	64	this work

[a] According to the reaction $H_3spd^{3+} + L^{z-} = ALH_3^{(3-z)-}$.
[b] z_a = Anion charge.
[c] Expressed in kJ mol^{-1}.

3.3. Relevance of triamine–mellitate species

Speciation diagrams of the dien–mlt and spd–mlt systems clearly show the differences between them. Primarily, the formation percentages of spd–mlt species are higher than those containing dien and secondarily, the ALH_3 species formed by spd is absolutely predominant in a wide pH range (pH 6–9).

In the dien–mlt system, at $C_A = C_L = 1$ mmol L^{-1}, without background salt and $t = 25$ °C (Fig. 1a): in the acidic pH range 3–5, the ALH_5 species prevails, with a maximum formation percentage of 50.8 at pH 3.8; the ALH_4 and A_2LH_6 species achieve the formation percentages of 35.5 at pH 5.1 and 12.8 at pH 4.8, respectively. In the pH range 7–8, of interest for many natural waters, the main species are ALH_2 and ALH_3: at pH 7, $\%ALH_2 = 36.3$, $\%ALH_3 = 53.9$; at pH 8, $\%ALH_2 = 85.1$, $\%ALH_3 = 4.3$. At higher pH values the formation percentages of ALH_2 further increase (90.6, at pH 8.6). In the spd–mlt system (Fig. 1b), in the same conditions discussed for dien–mlt system, in the acidic pH range 2–5, ALH_6 and ALH_5 species achieve high formation percentages: the former, 69%, at pH 2.9; the latter, 73.4%, at pH 4.5; ALH_4 represents a minor species, with a maximum formation percentage of 15.5, at pH 5.2. In the pH range 7–8, there is almost only the ALH_3 species, with formation percentages from 99.1 to 98.7. At pH 9.5, ALH_3 species prevails with a formation percentage of 71.8 and ALH_2 achieves 27.9%.

3.4. Sequestering ability of mellitate towards amines and dependence on ionic strength, temperature and pH

The sequestering power of a ligand towards a metal or a cation such as a protonated amine can be expressed by the function $\sum(\%)$

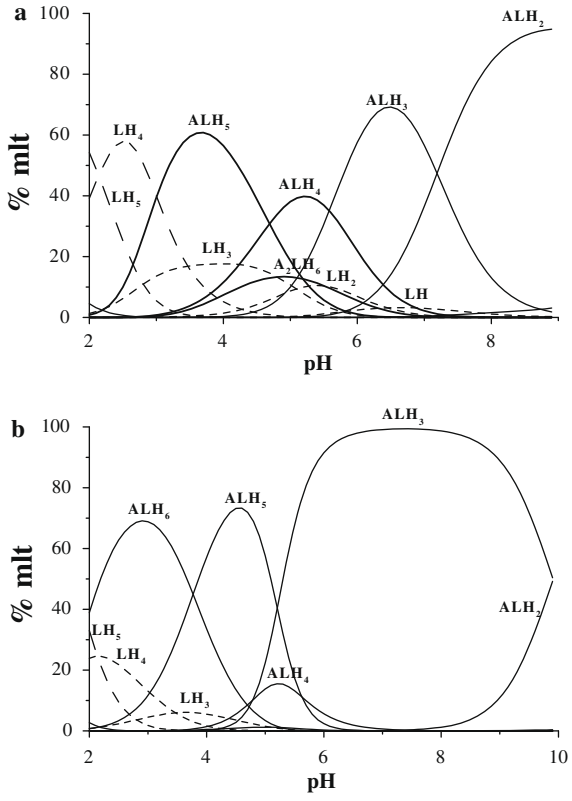


Fig. 1. Speciation diagrams of amine (A)-mlt (L) vs. pH at $C_A = C_L = 1$ mmol L^{-1}, without background salt and $t = 25$ °C. Indexes refer to reaction (2). Ligand protonated species are shown by dashed lines. (a): A = dien; (b): A = spd.

versus pL, where $\sum(\%)$ is the total percentage of amine protonated complexed and $pL = -\log [L]_{tot}$. Since this function is a typically sigmoidal curve (or a dose response curve), which rapidly increases over a relatively small change in concentration, we can use the Boltzmann type equation (with asymptotes of 100 for $pL \to -\infty$ and 0 for $pL \to +\infty$):

$$\Sigma(\%) = 100 \times \left[\frac{1}{1 + e^{(pL - pL_{50})/S}} - 1\right] \quad (4)$$

where pL_{50} is an empirical parameter, which defines the ligand concentration necessary to sequester 50% of cation and S is a measure of the slope in flex of the function ($\sum\%$) versus pL. The pL_{50} parameter is very useful because gives a representation of the binding ability of a ligand (L) towards a specific cation in the investigated conditions [24].

Fig. 2 reports the dependence on ionic strength of the sequestering power of mlt towards spd, showing the decreasing of the sequestering ability with the increasing of the ionic strength. Moreover, pL_{50} values, at C_{spd} = trace and t = 25 °C, are: (at pH 6), 7.67, 6.26, 5.76, 5.93 at I = 0, 0.05, 0.15, 0.1 mol L^{-1}, respectively; (at pH 7.4), 9.31, 7.22, 6.75, 6.51, at I = 0, 0.05, 0.15, 0.1 mol L^{-1}, respectively, with S = 0.434 in all cases. These results indicate a clear dependence of pL_{50} on I, as showed in Fig. 3. This dependence is very well described by a second order polynomial equation. For example, for spd–mlt species, we have:

$$\text{at pH 6} \quad pL_{50} = 7.67 - 8.13\, I^{1/2} + 8.3\, I \quad \sigma = 0.004$$

$$\text{at pH 7.4} \quad pL_{50} = 9.31 - 12.2\, I^{1/2} + 12.8\, I \quad \sigma = 0.011$$

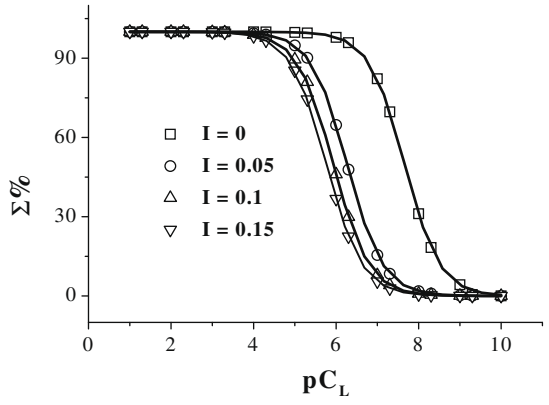


Fig. 2. Sequestration diagram for spd–mlt species at several ionic strengths (expressed in mol L^{-1}), at C_A = trace and t = 25 °C.

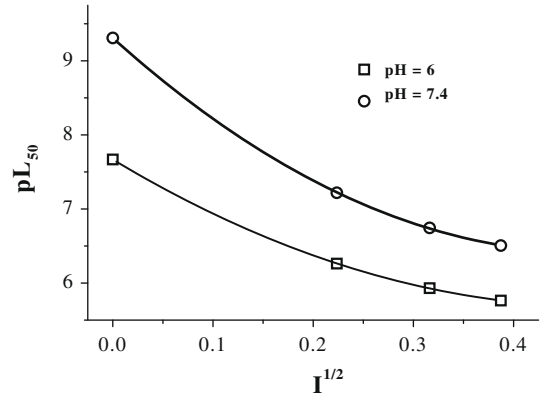


Fig. 3. pL_{50} vs. I (expressed in mol L^{-1}) for spd–mlt species at C_A = trace and t = 25 °C.

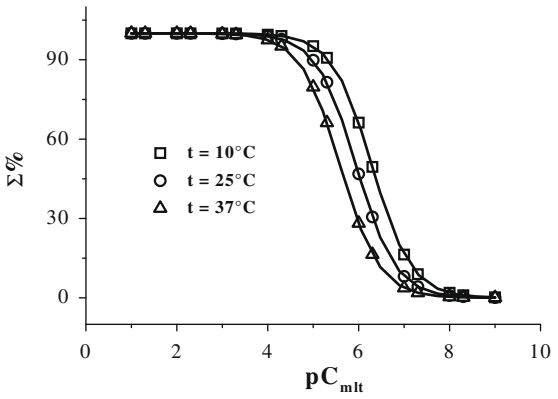


Fig. 4. Sequestration diagram for dien–mlt at C_A = trace, pH 7.4, I = 0 mol L^{-1} and at several temperatures.

For dien–mlt species there is a decrease of pL_{50} with the increasing of the ionic strength, too. For example, at C_{dien} = trace, t = 25 °C and pH 6, pL_{50} values are 5.25, 3.78 at I = 0, 0.15 mol L^{-1}, respectively; at pH 7.4, pL_{50} values are 5.95, 4.02 at I = 0, 0.15 mol L^{-1}, respectively. At the same pH value, the binding ability of mlt is significantly higher towards spd than towards dien. At pH 6, $pL_{50\ (spd)} - pL_{50\ (dien)}$ = 2.42, 1.99, at I = 0, 0.15 mol L^{-1}, respectively, at pH 7.4, $pL_{50\ (spd)} - pL_{50\ (dien)}$ = 3.36, 2.49, at I = 0,

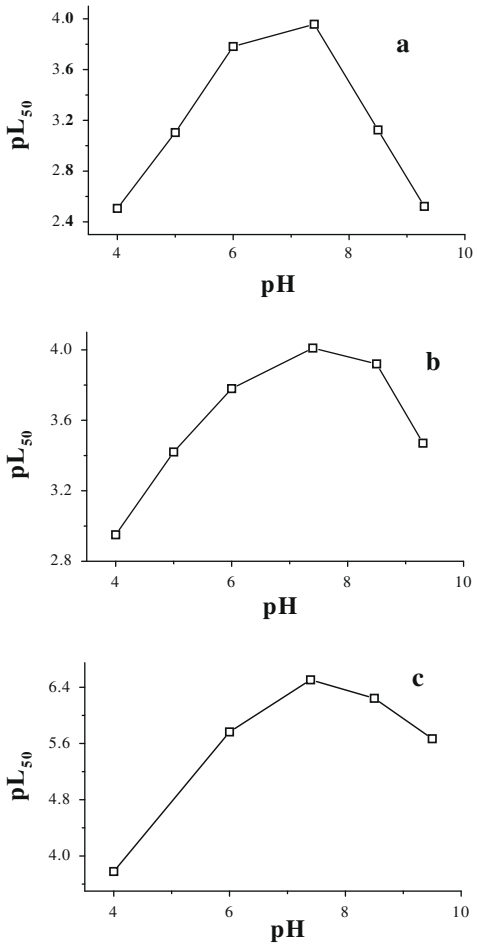


Fig. 5. pL_{50} vs. pH for amine(A)-mlt species at C_A = trace, I = 0.15 mol L^{-1} in NaCl and t = 25 °C. (a): en; (b): dien; (c): spd.

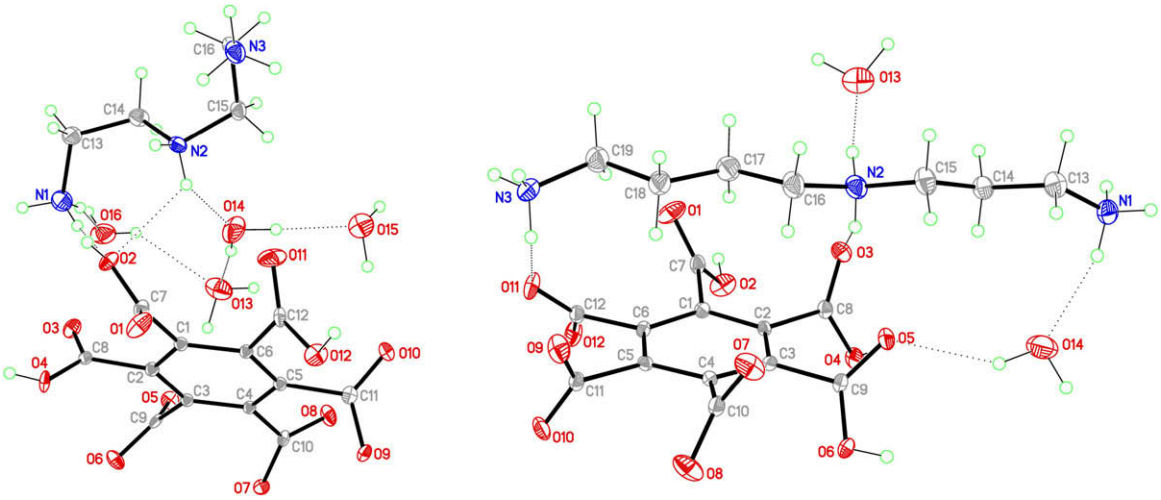


Fig. 6. Molecular representation of the asymmetric units for I and II. All non-hydrogen atoms are drawn with thermal ellipsoids at 30% of probability level.

0.15 mol L^{-1}, respectively. The sequestering ability of mlt towards a diamine, such as ethylenediamine, in the same pH and ionic strength conditions, further decreases. Sequestering ability of mlt towards amines is also influenced by the temperature, with a decreasing with the increasing of the temperature, as showed in Fig. 4. A linear type equation of pL_{50} versus t, well fits our data, for example for dien–mlt species we have:

at pH 6 $\quad pL_{50} = 6.56 - 0.026t \quad \sigma = 0.034$

at pH 7.4 $\quad pL_{50} = 5.79 - 0.022t \quad \sigma = 0.018$

Fig. 5a–c reports pL_{50} versus pH, at $I = 0.15$ mol L^{-1} in NaCl and $t = 25$ °C for en (data from Ref. [8]), dien and spd, showing that, with the increasing of pH, pL_{50} firstly increases, secondarily achieves a maximum value and finally decreases. If we ipotize that the dependence of pL_{50} on pH can be described by a Gaussian equation, the pH values which correspond to the pL_{50} maximum value are 6.77, 7.29, 7.69, for en, dien and spd, respectively.

3.5. Crystal structure

Several mellitate cocrystals with ammonium organic cations have been lately studied because of the great number of hydrogen bonds connected with the straightforward crystal engineering applications, biological and biomimetic behaviours, self assembly properties. Solid state structures, extended also to different protonation degrees of the potentially six chelated anions, often evidence the possibility to separate positive and negative supramolecular layers directed by noncovalent interactions [32,33]. However, few structures recorded in the crystallographic data-base concern mellitate anions with aliphatic ammonium species [34].

The asymmetric unit of I is occupied by one H_3dien^{3+} cation, one H_3L^{3-} anion, and four water molecules (Fig. 6). As already shown the O–H···O intermolecular hydrogen interactions between anionic units allow the formation of puckered supramolecular layers. The cationic units are obviously located between these anionic layers. Because of the short spacer between cationic centres (N atoms), every NH donor group bridges at least two close O acceptor atoms of the H_3L^{3-} units, whereas NH groups of same diethylentriammonium unit are, on their turn, bridged by central O acceptors. These interactions keep H_3L^{3-} units around a central trication in a pattern representable with the complex $R_1^2(7)R_2^1(5)R_2^3(6)R_2^1(5)R_2^1(7)R_2^2(9)$ graph-set [35]. Water molecules further enhance the hydrogen bonding network which holds the 3D solid state structure.

Asymmetric unit of II is occupied by one H_3spd^{3+} cation, one H_3L^{3-} anion and three water molecules (Fig. 6). Again hydrogen interactions among planar mlt species determines the formation of puckered supramolecular anionic layers able to embed water molecules and cations. Every ammonium ion is tightly coupled with a mlt unit because of the simultaneous presence of two N–H···O interactions involving N atoms on the opposite side of the longer N–H spacer and O acceptors on the opposite side of the mlt aromatic unit (graph-set $R_2^2(16)$). The spd moiety is almost planar and lays just 3.6 Å over the mlt aromatic plane, this allows also non-polar interactions (C–H···π) reinforcing the 1:1 molecular recognition. The other N–H···O interactions dock other spd–mlt units of the superior supramolecular layer, whereas other interactions involving also water molecules reinforce the overall hydrogen bonding network responsible for the crystal packing. Selected geometrical parameters, hydrogen bond lengths and angles are collected in Tables S1–S3 in the Supplementary data.

3.6. Comparisons

It is possible to compare the stability constants of dien– and spd–mlt species with those of the same amines with several carboxylate ligands published in preceding papers [6,9]. For example, considering the formation reaction $H_2dien^{2+} + L^{z-}$, with L = malonate ($z- = 2$), 1,2,3-tricarballylate ($z- = 3$), 1,2,3,4-butanetetracarboxylate ($z- = 4$), mlt ($z- = 6$) log$K$ = 2.1, 3.1, 4.2, 6.4, respectively. Moreover, for the formation reaction $H_3dien^{3+} + H_2L^{(z-2)-}$, with L = tca, btc, mlt, log$K$ = 2.5, 3.5, 5.9, respectively. In the case of spd: for the formation reaction $H_2spd^{2+} + L^{z-}$, with L = malate (mala, $z- = 2$), tca, btc, mlt, logK = 1.7, 2.4, 3.5, 8.0, respectively: for the formation reaction $H_3spd^{3+} + H_2L^{(z-2)-}$, with L = tca, btc, mlt, log$K$ = 1.1, 2.7, 6.2, respectively. All these examples, regarding the same amine, show that the stability regularly increases with the increasing of the ligand charge.

Table 6
Comparison between the formation stability constants of some alkaline earth metal–mellitate and triamine-mellitate species, at $I = 0$ mol L^{-1} and $t = 25$ °C.

Reaction	$B^{2+} = H_2dien^{2+}$ [a]	$B^{2+} = H_2spd^{2+}$ [a]	$B^{2+} = Mg^{2+}$ [b]	$B^{2+} = Ca^{2+}$ [b]
	logK			
$L^{6-} + B^{2+}$	6.4	8.0	6.39	7.50
$HL^{5-} + B^{2+}$	5.7		5.28	5.84

[a] This work.
[b] Ref. [13].

Another useful comparison can be made with the stability of alkaline earth metals-mellitate species. For example, the stability difference, regarding the formation reaction between unprotonated mellitate with H_2dien^{2+} and Mg^{2+}, is 0.01, as reported in Table 6. As can be seen, when reagent charges are the same, despite the nature of the cations is totally different, the stability is quite similar, confirming the determining role of the charges on the stability.

4. Final remarks

It was found, in solution for both the systems, the formation of several species having quite high stabilities, increasing with the charge of both polyammonium cation and polycarboxylic anion. There is a very good linear trend of log$K$ versus ζ (charge products = z_{cation} $|z_{anion|}$). By using the crude approximation $n = \zeta/2$, where n is the number of possible salt bridges, we obtain a mean energy value, $-\Delta G^0 = 6.1 \pm 0.3$ kJ mol^{-1}, which is consistent with results reported in our preceding work [10]. $T\Delta S^0$ values are also a fairly linear function of charges involved in the formation reaction: for example for dien system, $T\Delta S^0/\zeta = 0.4 \pm 1.6$ kJ mol^{-1}.

Speciation diagrams of the dien–mlt and spd–mlt systems show that the formation percentages of spd–mlt species are higher than those containing dien and that the ALH_3 species formed by spd is absolutely predominant in a wide pH range (pH 6–9).

The pL_{50} parameter, which gives a measure of the binding ability of mlt towards the triaminic cation, shows a clear dependence on ionic strength, temperature and pH. The sequestering ability of mlt towards each triamine: decreases with the increasing of the ionic strength, with a trend very well described by a second order polynomial equation; decreases with the increasing of the temperature, with a trend well described by a linear type equation; increases, with the increasing of pH, achieves a maximum value and finally decreases.

Diffractometric studies in the solid state fully support the formation of dien–mlt and spd–mlt complex species. The crystal structures is shown in Fig. 6: the asymmetric unit of I occupied by H_3dien^{3+} cation, H_3L^{3-} anion and four water molecules; the asymmetric unit of II occupied by H_3spd^{3+} cation, H_3L^{3-} anion and three water molecules. Moreover hydrogen bonding network, responsible for the crystal packing is strengthened by other interactions involving water molecules.

Acknowledgements

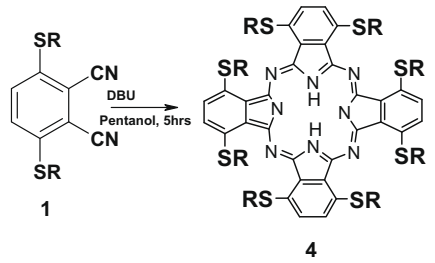
This work was supported by a grant from the University of Messina (PRA).

Appendix A. Supplementary data

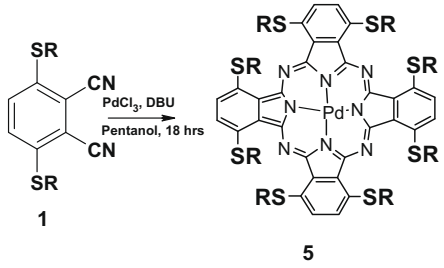
CCDC 728110 and 728111 contain the supplementary crystallographic data for the structures I and II. These data can be obtained free of charge via http://www.ccdc.cam.ac.uk/conts/retrieving.html, or from the Cambridge Crystallographic Data Centre, 12 Union Road, Cambridge CB2 1EZ, UK; fax: (+44) 1223-336-033; or e-mail: deposit@ccdc.cam.ac.uk. Supplementary data associated with this article can be found, in the online version, at doi:10.1016/j.poly.2009.05.019.

References

[1] H.J. Schneider, A. Yatsimirski, Principles and Methods in Supramolecular Chemistry, J.W. Sons, 2000.
[2] P.A. Gale, R. Quesada, Coord. Chem. Rev. 250 (2006) 3219.
[3] E. Garcìa-Espana, P. Diaz, J.M. Llinares, A. Bianchi, Coord. Chem. Rev. 250 (2006) 2952.
[4] A. Bianchi, M. Micheloni, P. Paoletti, Coord. Chem. Rev. 110 (1991) 17.
[5] A. Bencini, A. Bianchi, M.I. Burguete, P. Dapporto, A. Doménech, E. Garcìa-Espana, S.V. Luis, P. Paoli, J.A. Ramirez, J. Chem. Soc., Perkin Trans. 2 (1994) 569.
[6] A. De Robertis, C. De Stefano, O. Giuffrè, S. Sammartano, J. Chem. Soc., Faraday Trans. 92 (1996) 4219.
[7] A. De Robertis, C. De Stefano, A. Gianguzza, S. Sammartano, Talanta 48 (1999) 119.
[8] A. De Robertis, C. De Stefano, C. Foti, O. Giuffrè, S. Sammartano, J. Chem. Res. (S) (1996) 60.
[9] A. De Robertis, C. De Stefano, C. Foti, O. Giuffrè, S. Sammartano, Talanta 54 (2001) 1135.
[10] C. De Stefano, O. Giuffrè, S. Sammartano, J. Chem. Soc., Faraday Trans. 94 (1998) 2395.
[11] G.G. Choudhry, Toxicol. Environ. Chem. 4 (1981) 209.
[12] M. Schnitzer, in: Soil Organic Matter, Elsevier, Amsterdam, 1978. Chapter 1.
[13] A. De Robertis, C. De Stefano, C. Foti, Ann. Chim. (Rome) 86 (1996) 155.
[14] F. Crea, A. De Robertis, C. De Stefano, S. Sammartano, J. Solution Chem. 36 (2007) 479.
[15] Z.M. Wang, L.J. Van de Burgt, G.R. Choppin, Inorg. Chim. Acta 293 (1999) 167.
[16] G.R. Choppin, B.E. Stout, M. Pagès, J. Alloys Compd. 271–273 (1998) 774.
[17] D.E. Giammar, D.A. Dzombak, J. Solution Chem. 27 (1998) 89.
[18] R. Diamond, Acta Crystallogr., Sect. A 25 (1969) 43.
[19] C. De Stefano, S. Sammartano, P. Mineo, C. Rigano, in: Marine Chemistry – An Environmental Analytical Chemistry Approach, Kluwer Academic Publishers, Amsterdam, 1997, p. 71.
[20] P.G. Daniele, C. Foti, A. Gianguzza, E. Prenesti, S. Sammartano, Coord. Chem. Rev. 252 (2008) 1093.
[21] A. De Robertis, C. De Stefano, C. Rigano, Thermochim. Acta 138 (1986) 141.
[22] C. De Stefano, O. Giuffrè, S. Sammartano, J. Chem. Eng. Data 50 (2005) 1917.
[23] A. De Robertis, C. Foti, O. Giuffrè, S. Sammartano, J. Chem. Eng. Data 46 (2001) 1425.
[24] C. De Stefano, A. Gianguzza, O. Giuffrè, A. Pettignano, S. Sammartano, Appl. Organomet. Chem. 22 (2008) 1.
[25] C. Bretti, F. Crea, O. Giuffrè, S. Sammartano, J. Solution Chem. 37 (2008) 183.
[26] A. Altomare, M.C. Burla, M. Camalli, G.L. Cascarano, C. Giacovazzo, A. Guagliardi, A.G.G. Moliterni, G. Polidori, R. Spagna, J. Appl. Crystallogr. 32 (1999) 115.
[27] G.M. Sheldrick, SHELXL97. Program for Crystal Structure Refinement, University of Göttingen, Germany, 1997.
[28] L.J. Farrugia, J. Appl. Crystallogr. 32 (1999) 837.
[29] M. Nardelli, J. Appl. Crystallogr. 28 (1995) 659.
[30] C. De Stefano, C. Foti, A. Gianguzza, O. Giuffrè, S. Sammartano, J. Chem. Soc., Faraday Trans. 92 (1996) 1511.
[31] C. De Stefano, C. Foti, O. Giuffrè, S. Sammartano, Talanta 43 (1996) 707.
[32] I. Karle, R.D. Gilardi, C.C. Rao, K.M. Muraleedharan, S. Ranganathan, J. Chem. Crystallogr. 33 (2003) 727.
[33] L.K. Karle, Y.B.R.D. Rajesh, S. Ranganathan, J. Chem. Crystallogr. 35 (2005) 835.
[34] N. Kobayashi, T. Naito, T. Inabe, CrystEngComm 6 (2004) 189.
[35] J. Bernstein, R.E. Davis, L. Shimoni, N.-L. Chang, Angew. Chem., Int. Ed. Engl. 34 (1995) 1555.



Scheme 1. Synthesis of metal-free 1,4,8,11,15,18,22,25,-octapentylthiophthalocyanine (4).



Scheme 2. Synthesis of palladium 1,4,8,11,15,18,22,25,-octapentylthiophthalocyanine (5).

2. Experimental

2.1. Materials and equipment

1-Pentanol, dimethylformamide (DMF), pentanethiol, dimethylsulfoxide (DMSO) 1.8-diazabicyclo[5, 4, 0] undec-7-ene (DBU), cerium chloride, potassium carbonates, dichloromethane (DCM), 1-chloronaphthalene (CNP) and palladium (II) chloride were purchased from Sigma–Aldrich. Methanol, ethanol and chloroform were purchased from Merck. Chromatography was performed on silica gel 60 (0.04–0.063 mm). 1,2-Dichloro-4,5-dicyanobenzene (**2**) [25,26], 3,6-bis(pentathio)-4,5-dicyanobenzene (**1**) and 1,2-bis(pentylthiol)-4,5-dicyanobenzene (**3**) [24,27], were synthesised as reported in literature. The synthesis of palladium-2,3,9,10,16,17,23,24,-octakis(pentylthio)phthalocyanine (**7**) has been reported before [24]. UV–Vis spectra were recorded on a Cary 500 UV/Vis/NIR spectrophotometer, ^{1}H NMR spectra were recorded using a Bruker EMX 400 MHz NMR spectrometer. IR spectra (KBr pellets) were recorded on a Perkin–Elmer spectrum 2000 FTIR.

2.2. Binding and kinetic studies

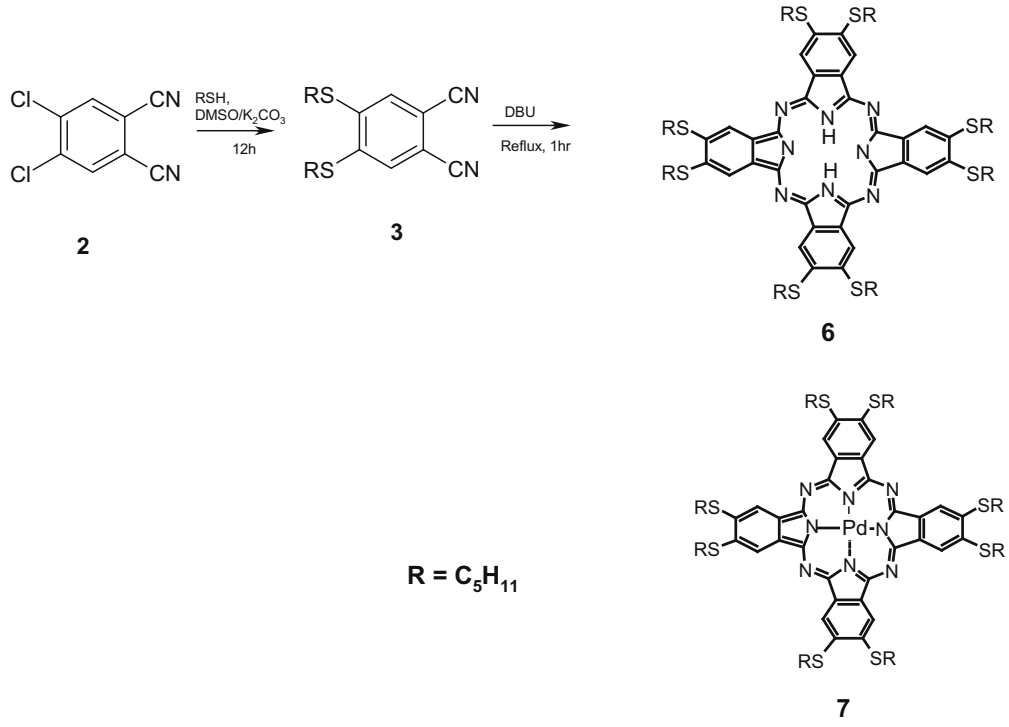
For all binding studies, $PdCl_2$ was dissolved in ethanol and the H_2Pc or PdPc complexes in DCM. In order to minimize dilution effects, very small volumes (μl) of the $PdCl_2$ stock solution were added to 2 mL of the Pc solution, and changes were monitored spectroscopically. For kinetic studies, varying concentrations of $PdCl_2$ (0–1×10^{-2} M) in ethanol were added to a fixed concentration (5×10^{-6} M) of the H_2Pc or PdPc derivatives, and the absorbance changes accompanying each addition monitored with time.

For equilibrium studies, the steady increase in absorbance of the Q band of the Pc product formed with increase in Pd (II) ion concentration was noted and used in the determination of the binding constants as well as number of bound Pd (II) ions, according to Eq. (1):

$$\mathrm{Log}[(A_{eq} - A_o)/(A_\infty - A_{eq})] = \log K + n \log[\mathrm{Pd}] \quad (1)$$

where A_{eq} is the equilibrium absorbance of the Pd-bound Pc (product); A_o, the initial absorbance before the addition of $PdCl_2$, and A_∞, the maximum attainable absorbance of the product. K is the binding constant, and n is the number of bound Pd(II) ions.

The complexes formed by the interaction between Pd(II) and unmetallated complexes **4** and **6** could be isolated by evaporating the solvents (ethanol/DCM) and recrystalyzing in ethanol. Elemental analyses for the complex between Pd and **4**:



Scheme 3. Synthesis of metal-free 2,3,9,10,16,17,23,24,-octapentylthiophthalocyanine (6) and the structure of 7 reported before [24].

Anal. Calc. for $C_{72}H_{98}N_8S_8(PdCl_2)_4$): C, 41.81; H, 4.80; N, 5.48. Found: C, 40.90; H, 4.92; N, 5.57%.

Elemental analyses for complex between Pd and **6**:

Anal. Calc. for $C_{72}H_{98}N_8S_8(PdCl_2)$: C, 52.79; H, 5.86; N, 7.04. Found: C, 52.07; H, 5.94; N, 6.93%.

2.3. Synthesis

2.3.1. Metal-free 1,4,8,11,15,18,22,25,-octakis(pentylthio)phthalocyanine (4), Scheme 1

In refluxing pentanol (10 ml), 3,6-bis(pentathio)-4,5-dicyanobenzene **(1)** (0.5 g, 1.5 mmol) and DBU (1.70 g, 11.17 mmol) were added. The solution was heated to reflux for 5 h. The solution was then allowed to cool and the solvent removed under reduced pressure, followed by titration with cold methanol to precipitate the product. The black precipitate was dissolved in DCM and passed through a silica column, DCM was used as the eluting solvent to afford **4**. Yield: 0.18 g (37%), UV/Vis [(CNP, λ_{max}/nm, (log ε)] 813 (5.05), 719 (3.5). *Anal.* Calc. for $C_{72}H_{98}N_8S_8$: C, 64.80; H, 6.87 N, 8.01, S, 20.32. Found: C, 64.87; H, 7.47, N, 7.71, S, 20.44%. ^{1}H NMR (400 mHz); δ ppm; ($CDCl_3$), 8.00 (8H, s, H_{arom}), 3.32–3.35 (16H, t, Ar–SCH_2–), 2.15–2.00 (16H, m, Ar–SCH_2–CH_2–), 1.65–1.2 (32H, m, $H_{aliphatic}$), 1.00–0.80 (24H, t, CH_3); [IR (KBr pellets) ν_{max}/cm^{-1}]; 1320, 1278, 1217, 1186, 1142, 1077, 939, 808, 736, 668 (C–S–C), 577, 499, 418; 3057 (N–H), 2953 (C–H), 2922 (C–H), 2358, 2336, 1865, 1791, 1730, 1652(C=N), 1556, 1538,1505, 1456.

2.3.2. Palladium-1,4,8,11,15,18,22,25,-octakis(pentylthio)phthalocyanine (5), Scheme 2

In refluxing pentanol (10 ml), 3,6-bis(pentathio)-4,5-dicyanobenzene **(1)** (0.5 g, 1.5 mmol), $PdCl_2$ (0.12 g, 0.75 mmol) and DBU (1.70 g, 11.17 mmol) were added. Reflux was continued for a further 18 h. Reaction was then cooled down and the solvent removed under reduced pressure, followed by titration with cold methanol to precipitate the product. The black precipitate was dissolved in DCM and passed through a silica column, DCM was used as the eluting solvent to afford **5**. Yield: 0.12 g (40%), UV/Vis [CNP, λ_{max}/nm, (log ε)] 750 (4.5), 679 (4.11). *Anal.* Calc. $C_{72}H_{96}N_8PdS_8$: C, 60.20; H, 6.74; N, 7.80. Found: C, 59.63; H, 6.87; N, 7.51%. ^{1}H NMR (400 MHz, $CDCl_3$) δ ppm: 8.71 (8H, s, Ar–H), 4.10 (16H, s, S–CH_2), 1.52–1.21 (48H, m, –$(CH_2)_3$), 1.21–0.92 (24H, m, –CH_3);[IR (KBr pellets) ν_{max}: 2929, 2859, 1732, 1650(C=N), 1572, 1466, 1338, 1293, 1236, 1163, 941, 799, 750, 650(C–S–C).

2.3.3. Metal-free 2,3,9,10,16,17,23,24,-octakis(pentylthio)phthalocyanine (6)

Compound **3** (0.5 g, 0.95 mmol) was heated in pentanol (5 ml) in the presence of DBU (1.66 ml, 1 mmol) with stirring and heated under reflux for 1 h in a nitrogen atmosphere. After cooling, the dark green product was precipitated with methanol, filtered and then purified using silica gel packed column chromatography with DCM as eluent. Yield: 0.37 g (74%), UV/Vis [(CNP, λ_{max}/nm, (log ε)] 737 (5.12), 710 (5.04), 673 (4.51), 640 (4.40), 457 (4.43). *Anal.* Calc. for $C_{72}H_{98}N_8S_8$: C, 64.80; H, 6.87 N,8.01, S, 20.32. Found: C, 65.93; H, 7.75, N, 6.16, S,19.91%. ^{1}H NMR (400 mHz); δ ppm ($CDCl_3$) 8.37 (8H, s, H_{arom}), 3.44–3.40 (16H, s, Ar–SCH_2–), 2.14–2.09 (16H, q, Ar–SCH_2–CH_2–), 1.82–1.78 (16H, q, $H_{aliphatic}$), 1.66–1.60 (16H, q, $H_{aliphatic}$), 1.31–1.22 (24H, t, CH_3–); [IR (KBr pellets) ν_{max}/cm^{-1}]; 3449 (N–H), 2957, 2926, 2858 (C–H), 1648(C=N), 1592, 1507, 1461, 1400, 1325, 1325, 1073, 1026, 935, 868, 749, 681 (C–S–C).

3. Results

3.1. Synthesis and characterization

The syntheses of complexes **4**–**6** were achieved by treating the corresponding phthalonitriles (**1** or **3**) with palladium chloride in 1-pentanol for complex **5**, Scheme 2 or with DBU only for unmetalated complexes **4** and **6**, Schemes 1 and 3, respectively. Column chromatography with silica gel was employed to obtain the pure products. The MPc derivatives were characterized by UV–Vis, IR and NMR spectroscopies, and elemental analyses. The analyses were consistent with the predicted structures. The sharp peak for the C≡N vibrations in the IR spectra of phthalonitriles **1** or **3** at ~2200 cm^{-1} disappeared after conversion into phthalocyanines

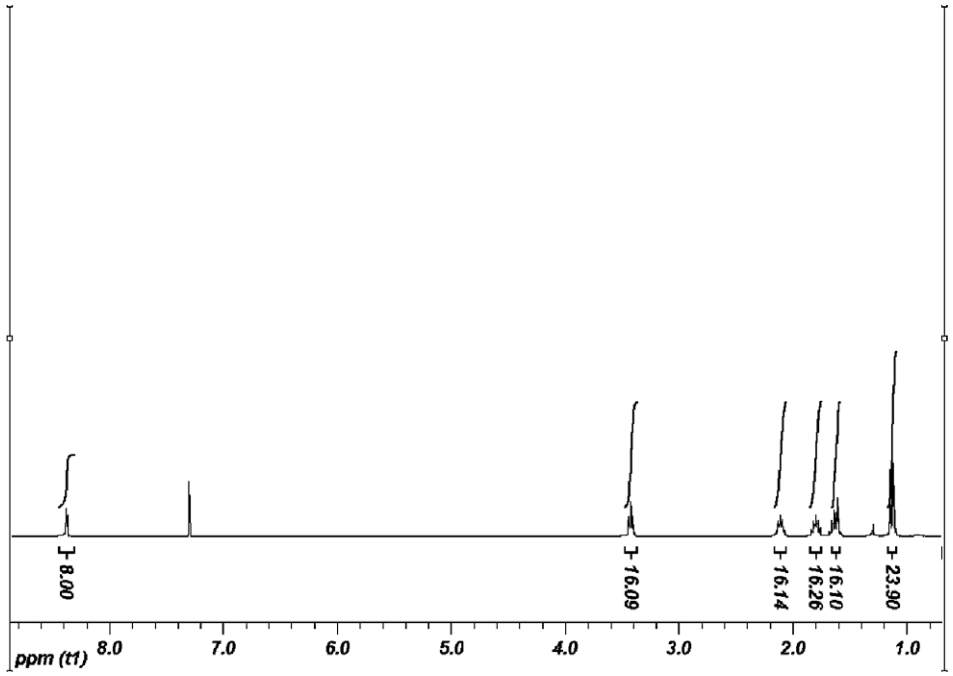


Fig. 1. ^{1}H NMR spectrum of **6** in $CDCl_3$.

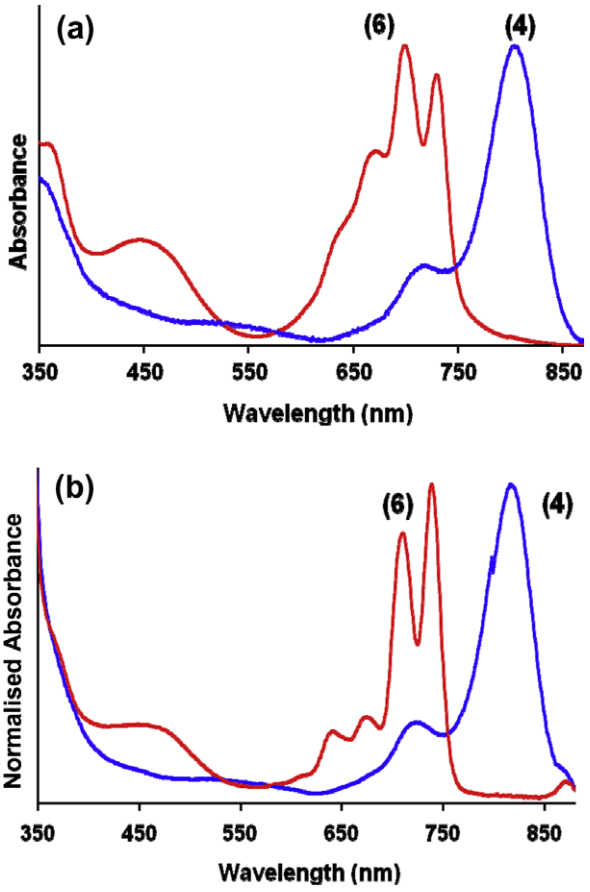


Fig. 2. Electronic absorption spectra of **4** and **6** in (a) DCM and (b) CNP. Concentration $\sim 1 \times 10^{-5}$ M.

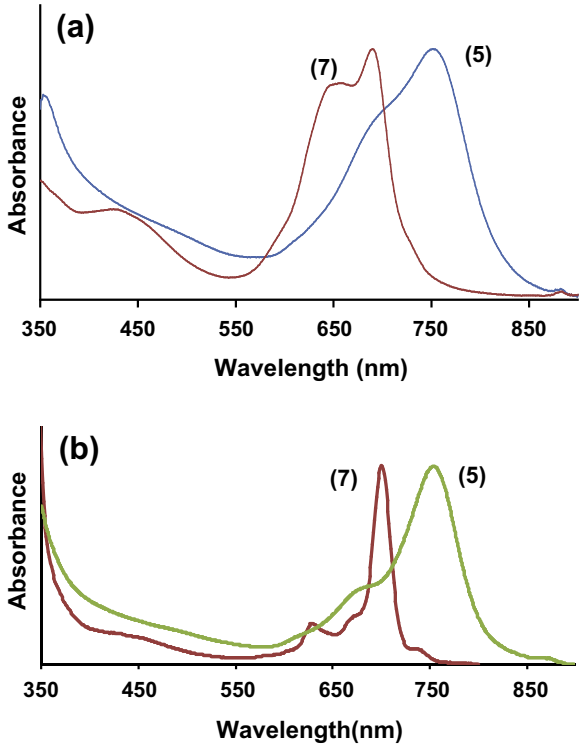


Fig. 3. Electronic absorption spectra of **5** and **7** in (a) DCM (b) CNP. Concentration $\sim 1 \times 10^{-5}$ M.

and there was appearance of a C≡N band at 1652, 1650 and 1645 cm^{-1} for **4**, **5** and **6,** respectively. The phthalocyanines showed vibrations due to C–S–C group between 650 and 688 cm^{-1}.

The ^{1}H NMR spectra of MPc derivatives in $CDCl_3$ showed all the substituent and Pc ring protons in their respective regions, Fig. 1. A singlet, assigned to Pc aromatic ring protons, appeared in the range 8.00–8.71 (integrating for 8 protons) in the ^{1}H NMR spectra of **4–6**. The S–CH_2 protons were observed between 3.32 and 4.10, integrating for a total of 16 protons for each complex (**4–6**). The rest of the aliphatic protons were observed between 1.2 and 2.15 intergrading for 48 protons for each complex (**4–6**). The methyl protons occurred between 0.8 and 1.31 intergrading for 24 protons. The cavity protons of the unmetalatted phthalocyanines [**4** and **6**] were not observed due to aggregation of the molecules in $CDCl_3$.

Pcs exhibit limited solubility in most solvents but substitution at the peripheral (β) and non-peripheral (α) positions allows for improved solubility [28]. Non-peripheral substitution in Pcs has been reported to result in higher solubility in comparison with peripheral substitution [29]. Fig. 2a shows the ground state electronic absorption spectra of **4** and **6** in DCM, while the spectra of **5** and **7** in the same solvent are shown in Fig 3a. It can be observed from these figures that the spectra of the non-peripherally substituted complexes: **4** and **5**, are significantly red-shifted relative to those of their peripherally substituted counterparts, as expected. The red shifting for non-peripherally substituted derivatives is attributed to greater electron density enhancement caused by substitution at the non-peripheral substitution compared with that at the peripheral position. The Q band for **4** is observed at 801 nm in DCM. For **6**, the components of the split Q band are observed at 698

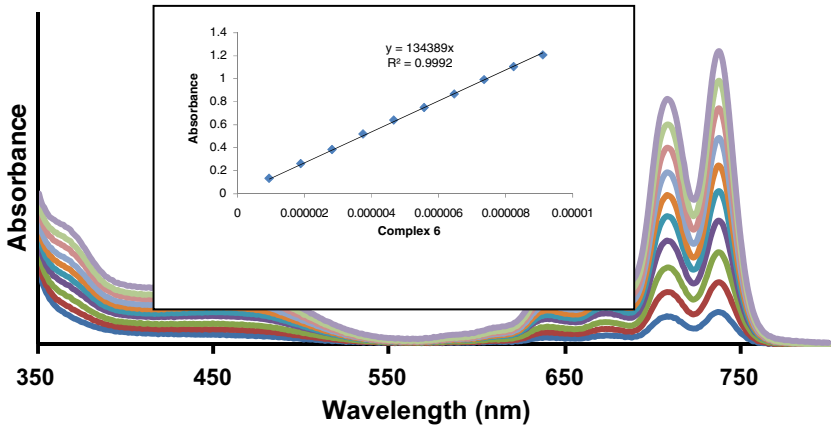


Fig. 4. (a)Absorption spectra of compound **6** in CNP at different concentrations. Inset: Beer–Lambert Plot.

and 730 nm in DCM. The spectrum of **4** does not show the typical split Q band expected for unmetalated phthalocyanines; it is known that the resolution of the split of the Q band decreases with increasing wavelength [30], hence for **4**, the large red shift must have resulted in an unsplit Q band. The Q bands for the metallated derivatives **5** and **7** are observed at 747 and 693 nm, respectively in DCM (Fig. 3a). The spectra for all complexes are broad in DCM, suggesting aggregation in this solvent. DCM is a non-coordinating solvent; hence it lacks the capacity to prevent π–π stacking of the PdPc units. Figs. 2b and 3b, respectively show the ground state absorption spectra of **4** and **6,** and **5** and **7** in CNP. The spectra in CNP are narrower than those in DCM for both the metallated (**5**,**7**) and unmetalated (**4**,**6**) derivatives, which is ascribed to the lower tendencies of the complexes to aggregate in CNP. However, complex **5** still shows broad spectrum in CNP. Aggregation in Pcs is usually depicted by broadening and/or splitting of Q band, indicating the presence of additional electronic levels of aggregates. Beer–Lambert law was obeyed for the complexes in CNP, even for concentrations less than 1×10^{-5} mol dm^{-3} (Fig. 4a). However in DCM, Beer–Lambert law was obeyed only at lower concentrations (>1×10^{-6} mol dm^{-3}), confirming the presence of aggregates. The Q band maxima of the Pcs are red shifted in CNP compared to DCM. In CNP, the Q band for **4** was at 813 nm compared to 801 nm in DCM, while the split Q band of **6** appeared at 707 and 736 nm in CNP compared to 693 and 731 nm in DCM. The Q band for **5** appears at 750 nm while that of **7** appears at 699 nm in CNP. Aromatic solvents have been known to result in red shift of the Q band in phthalocyanine complexes [31], hence the observed red shift in CNP. The observed spectral red-shifts in CNP relative to those in DCM could also be interpreted in terms of the higher refractive index of CNP [31].

3.2. Pd(II) binding to Pcs

3.2.1. Metal-free 1,4,8,11,15,18,22,25,-octapentylthiophthalocyanine (4)

It is possible that binding of Pd(II) to complex **4** and **6** will occur at the thio groups or at the central core of the Pc skeleton. On

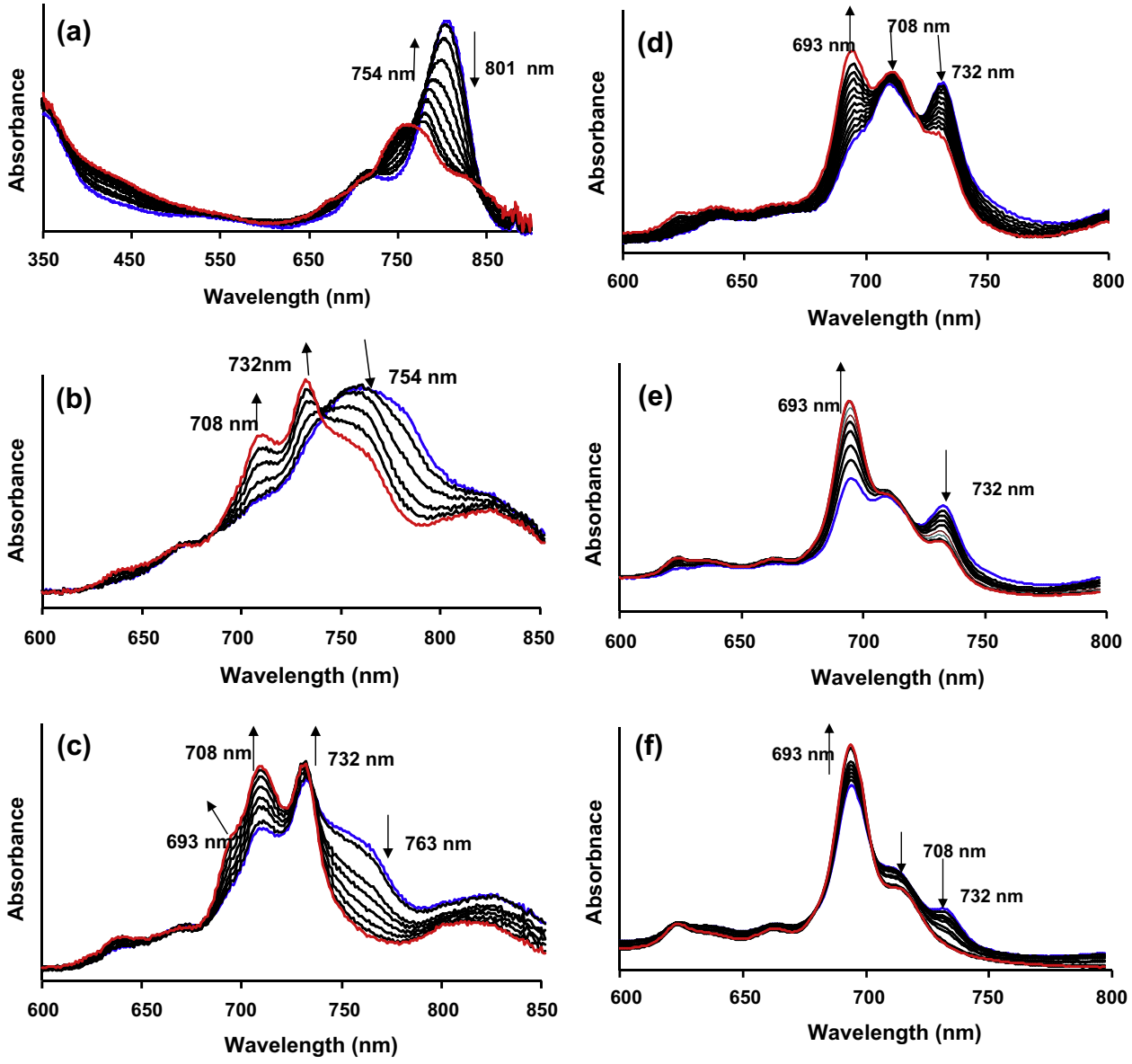


Fig. 5. UV–Vis spectral changes observed on addition of $PdCl_2$ in ethanol to complex **4** (concentration = 5×10^{-6} M) in DCM. Concentration of $PdCl_2$ (a) 6.5×10^{-4}–3.05×10^{-3} M (b) $3.05\ 10^{-3}$–7.20×10^{-3} M (c) 7.20×10^{-3}–1.0×10^{-2} M (d) 1.0×10^{-2}–1.18×10^{-2} M (e) 1.18×10^{-2}–1.32×10^{-2} M (f) 1.32×10^{-2}–1.5×10^{-2} M. The first spectrum in (b) is the same as the last spectrum in (a), the first spectrum in (c) is the same as the last spectrum in (b), and so on.

addition of Pd(II) to a solution of **4**, spectral changes shown in Fig. 5 were observed. The first part shown in Fig. 5a consists of a decrease in the Q band intensity (at 801 nm in DCM) accompanied by broadening and the shift of the band to high energy (754 nm). These spectral changes are consistent with formation of aggregates observed on metal binding in thio substituted MPc complexes [21]. The lack of clear isosbestic points, suggests that there may be more than two species in solution. Higher aggregates could also be present in solution. Further addition of Pd(II) resulted in spectral changes shown in Fig. 5b, which consist of the decrease in the broad peak at 754 nm and the formation of a split peak with maxima at 708 and 732 nm. The observed split in Q band suggests that a PdPc complex has not formed yet and the complex is still H_2Pc with Pd(II) ions coordinated to the pentylthio groups or the PdPc complex has formed with unsymmetrical substitution of Pd ions on the ring. Further addition of $PdCl_2$ resulted in the formation of a new band at 693 nm and the gradual disappearance of the split Q band (Fig. 5c and d). Elemental analysis confirmed to binding of four Pd(II) ions at this stage, see Section 2 for the data. The ^1H NMR spectra of the complex isolated at this stage showed a change in chemical shift of the protons relative to what obtained in the original ligand (**4**), the most conspicuous shift being the macrocyle protons indicating a change in electron distribution [15,18,20]. The singlet peak shifted downfield from 8.00 to 8.30 ppm which indicated higher resonance of the ring protons due to desheilding effect that resulted from reduced mesomeric effect of the sulfur lone pairs of electrons on the ring when part of those lone pairs were used in coordination with Pd ions. The IR spectrum of this complex also showed a dramatic change compared with that of 4. The bands between 1000 and 600 cm^{-1} showed conspicuous split, especially at 939, 808, and 736 cm^{-1}.

A gradual disappearance of the split Q band and the appearance of a new single Q band that was blue shifted compared to the original split Q band were observed on further addition of Pd(II) ions, Fig. 5e. The final spectrum in Fig. 5f is typical of a metallated phthalocyanine complex [32], and suggests the formation of a symmetrically substituted PdPc complex. No further spectral changes were observed on addition of more Pd ions.

The equilibrium studies for the binding of Pd(II) ions to complex **4**, were carried out for using Eq. (1). A plot $\log[(A_{eq}-A_o)/(A_\infty-A_{eq})]$ versus $\log[Pd^{II}]$ (Fig. 6), gave an equilibrium constant of $K = 1.2 \times 10^9$ dm^3 mol^{-1} and n of 5, thus showing that five Pd(II) ions are coordinated to the to the Pc at the end of the reaction.

When a large excess of $PdCl_2$ was added to **4**, spectral changes shown in Fig. 7 were observed, these consisted of direct formation of the final spectrum in Fig. 5f. These changes occurred with time allowing for the calculation of rate constants assuming first order kinetics since Pd(II) is in excess. The rate constants were obtained by first plotting absorbance versus time for each concentration of Pd(II) (ranging from 1.5×10^{-3} to 5.0×10^{-3}) to obtain initial rates, the latter were then plotted against [Pd(II)] (Fig. 7 inset) to get the rate constant from the slope using least square analysis. The value of the rate constant was 1.38×10^{-5} dm^3 mol^{-1} s^{-1}. When low concentrations ($<1 \times 10^{-4}$ M) of Pd(II) ions were employed for complex **4**, changes with time observed in Fig. 7 were not observed probably due to the slow nature of the spectral changes.

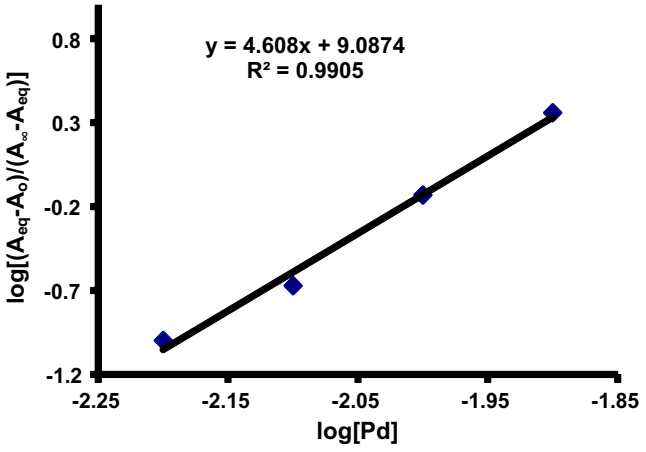


Fig. 6. Plot of $\log[(A_{eq}-A_o)/(A_\infty-A_{eq})]$ versus $\log[Pd^{II}]$ for complex **4** in DCM.

3.2.2. Metal-free 2,3,9,10,16,17,23, 24,-octapentylthiophthalocyanine (6)

The spectra generated on the addition of Pd(II) ions to complex **6** are shown in Fig. 8. For **6**, The Q band is split since this complex is blue shifted compared to **4**. Non-peripherally substituted MPc complexes show more red shifting compared to peripherally substituted. The absorption spectrum of the Pc before the addition of Pd(II) ions is shown in Fig. 8a(i). With the addition of Pd(II) ions the intensity of the peaks at 693 and 731 nm decreased and a new single peak appeared at 714 nm (Fig. 8a(ii)). This spectrum resembles that of MPc suggesting the insertion of the metal into

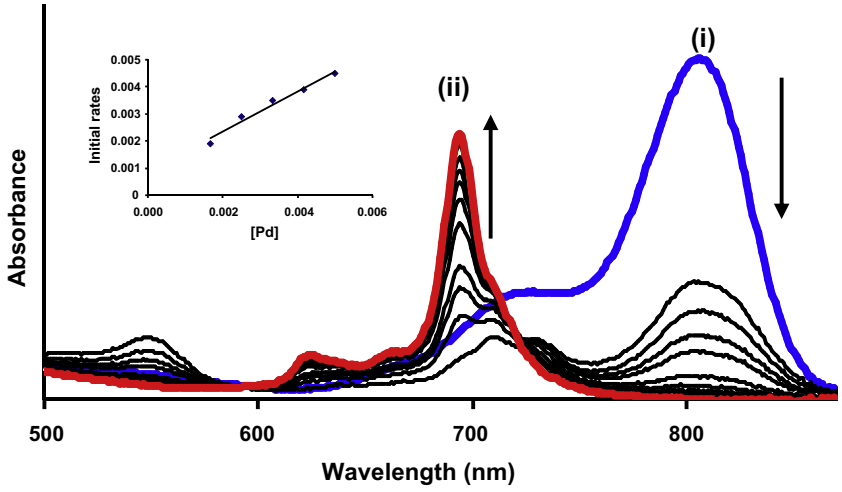


Fig. 7. UV–Vis spectral changes observed on addition of excess $PdCl_2$ in ethanol (concentration = 3×10^{-3} M) to a solution of complex **4** (1×10^{-5} M) in DCM. (i) before and (ii) after addition of $PdCl_2$. Inset: Plot of initial rates versus the concentration Pd.

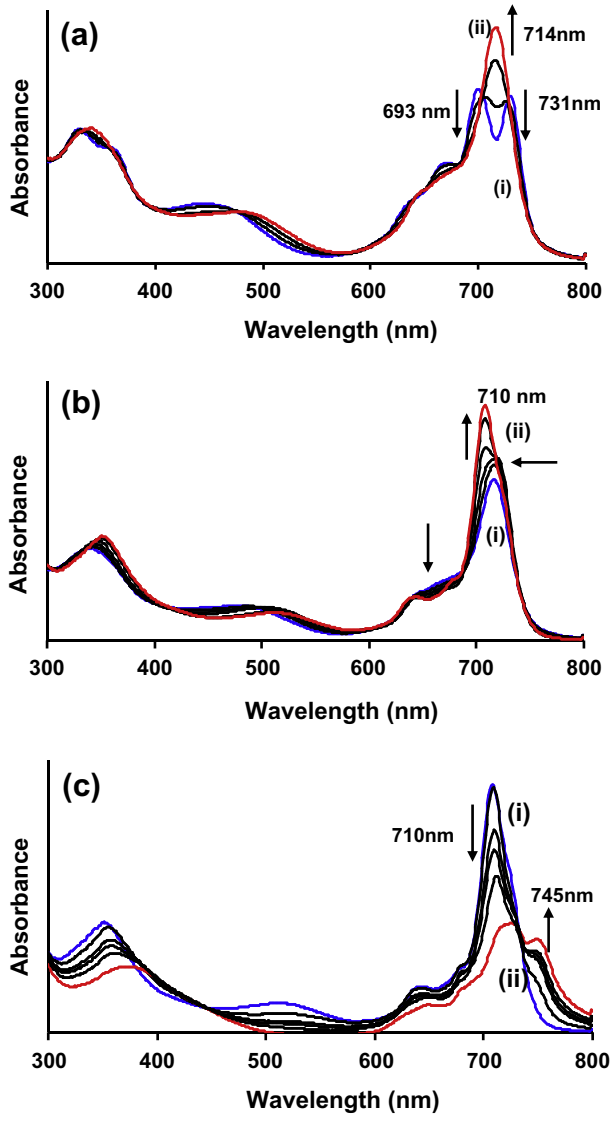


Fig. 8. UV–Vis spectral changes observed on addition of $PdCl_2$ in ethanol to complex **6** (concentration = 5×10^{-6} M) in DCM. Concentration of $PdCl_2$ (a) 4.00×10^{-4}–4.61×10^{-4} M, (b) 4.61×10^{-4}–5.06×10^{-4} M, (c) 5.06×10^{-4}–5.5×10^{-4} M. The first spectrum in (b) is the same as the last spectrum in (a), the first spectrum in (c) is the same as the last spectrum in (b).

the center of the Pc ring. The spectral changes could not be due to symmetric substitution of the Pd ions on the ring since a split Q band would still be observed. The ^{1}H NMR spectra of the complex formed here also show change in chemical shift of some of the peaks due to change in electronic distribution of the complex on coordination with Pd ions. The aromatic and S–CH_2 protons did not show significant shift while the aliphatic and methyl protons were observed as mutiplets and triplets at 1.24–1.19 ppm and 1.08–0.91 ppm integrating to 48 and 24 protons respectively. Elemental analysis of the complex at this stage confirmed the coordination of one Pd(II) ion, most probably into the center of the ring hence no splitting in the Q band. The same type of spliting that was observed in the IR spectrum of **4** was also noticed in the spectrum of **6** at 935, 868 and 749 cm^{-1}.

Further addition of Pd(II) ions resulted in increase in the intensity accompanied by blue-shifting of the peak at 714 nm (Fig. 8b) to 710 nm. The blue shifting is as a result of the binding of Pd(II) ions to the peripheral sulfur, which engages the lone pair of electrons on sulfur and therefore cancels their mesomeric contribution

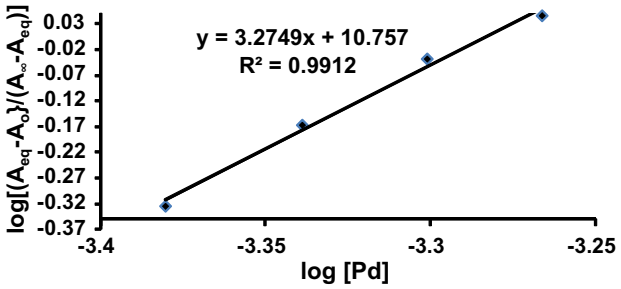
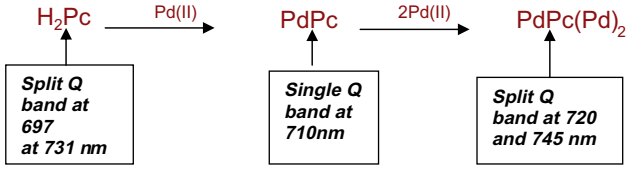


Fig. 9. Plot of $\log[(A_{eq}-A_o)/(A_\infty-A_{eq})]$ versus $\log[Pd^{II}]$ for complex **6** in DCM.



Scheme 4. Possible processes involved in Pd(II) coordination to 6.

to the ring electron density. As the addition of Pd(II) ions continued the broad peak around 710 nm started disappearing and a split band emerged at 720 and 745 nm as shown in Fig. 8c. This spectroscopic response might be due to unsymmetric substitution of Pd(II) ions. As was the case with complex **4**, no further spectral changes were observed on addition of more Pd ions. The number of Pd(II) ions bound to the Pc and equilibrium constant was determined for complex **6** using Eq. (1) and Fig. 9.

A plot $\log[(A_{eq}-A_o)/(A_\infty-A_{eq})]$ versus $\log[Pd^{II}]$ (Fig. 9), gave an equilibrium constant of $K = 5.7 \times 10^{10}$ dm^3 mol^{-1} and n of 3 for complex **6**, thus showing that three Pd(II) ions are coordinated to the to the Pc at the end of the reaction. Probably the two at the periphery coordinated to adjacent sulfur instead of opposite ones giving rise to the loss of symmetry. The possible processes occurring during the addition of Pd ion to solutions of complex **6** are shown by Scheme 4.The nature of Pd(II) binding differ between complexes **4** and **6** in that in **4**, five Pd ions are coordinated, while for complex **6** three Pd ions are coordinated. The differences in the binding abilities of the two compounds (**4** and **6**) could be due to accessibility of binding sites. Also the modes of coordination of Pd(II) ions may be different for peripherally (**6**) and non-peripherally (**4**) substituted complexes since in the latter there is a possibility of coordination between pentylthio groups on adjacent benzene groups.

3.2.3. Palladium octapentylthiophthalocyanine complexes *5* and *7*

Both **4** and **5** are non-peripherally substituted, however **5** has a central Pd(II) ion unlike **4** which is unmetalated. The same applies to **6** and **7**, which are both peripherally substituted, but the latter has a central Pd(II) ion and the former is unmetalated.

Fig. 10a(i) shows the spectra of **5** before and after addition of Pd(II) ions. On addition of Pd(II) ions, reduction in intensity coupled with blue shifting from 750 to 718 nm of the Q band was observed (Fig. 10a(ii)). Effect of further addition of Pd(II) ions is depicted in Fig. 10(b), and consists of continued blue-shifting of the Q band from 718 to 695 nm and there is narrowing of the Q band and its increase in its intensity. The continuous shift towards the blue is consistent with the engagement of S lone pairs in the substituents, thereby reducing the ring electron density and consequently causing the blue shift. The Q band maximum at 695 nm is

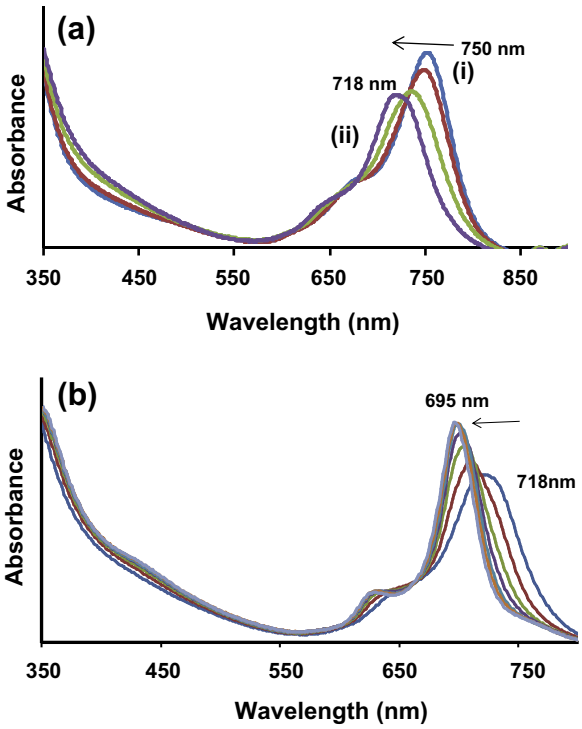
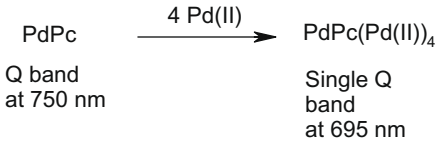


Fig. 10. UV–Vis spectral changes observed on addition of $PdCl_2$ in ethanol to complex **5** (concentration = 5×10^{-6} M) in 1-chloronaphthalene. Concentration of $PdCl_2$ (a) 9.00×10^{-5}–4.00×10^{-4} M (b) 4.00×10^{-4}–1.5×10^{-3} M. The first spectrum in (b) is the same as the last spectrum in (a).



Scheme 5. Possible processes involved in Pd(II) coordination to complex **5**.

similar to the final spectrum obtained for **4** following addition of Pd(II) ions (Q band at 693 nm), suggesting that the final complexes are the same.

The possible processes occurring during the addition of Pd(II) ion to solutions of complex **5** are shown by Scheme 5.

A plot $\log[(A_{eq}-A_o)/(A_\infty-A_{eq})]$ versus $\log[Pd^{II}]$ for **5** (Fig. 11), gave an equilibrium constant of $K = 1.66 \times 10^{13}$ dm^3 mol^{-1} and n of 4, thus showing that 4 Pd(II) ions are coordinated to the to the Pc at the end of the reaction, with the equilibrium favouring the

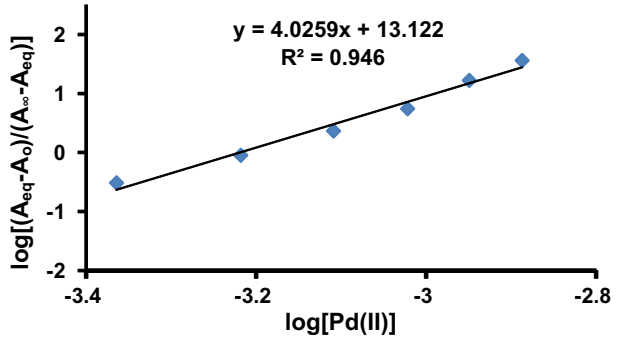


Fig. 11. Plot of $\log[(A_{eq}-A_o)/(A_\infty-A_{eq})]$ versus $\log[Pd^{II}]$ for complex **5** in CNP.

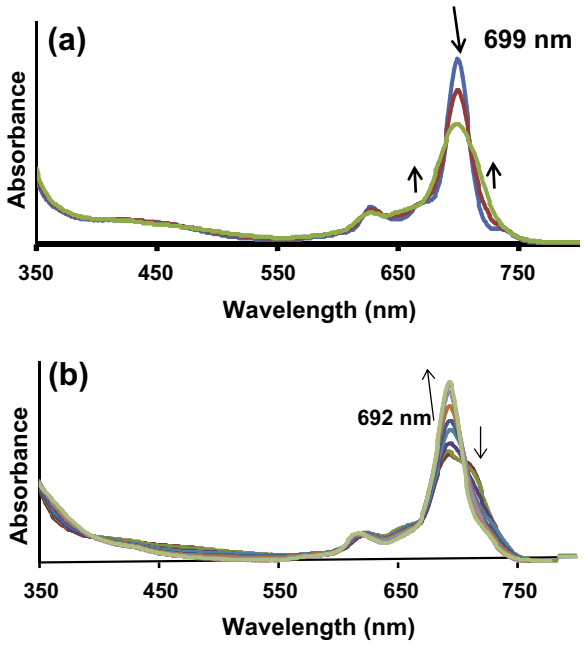


Fig. 12. UV–Vis spectral changes observed on addition of $PdCl_2$ in ethanol to complex **7** (concentration = 8×10^{-6} M) in 1-chloronaphthalene. Concentration of $PdCl_2$ (a) 3.00×10^{-5}–2.50×10^{-4} M (b) 2.50×10^{-4}–1.5×10^{-3} M. The first spectrum in (b) is the same as the last spectrum in (a).

formation of the complex with four Pd(II) ions coordinated all at the ring in a symmetrical fashion since the Q band of the final spectrum is not split.

For complex **7** which is peripherally substituted, Fig. 12a and 12b show that on titration with Pd(II) ions, the final spectrum shows a split Q band, suggesting unsymmetrical substitution by the Pd(II) ions as was the case with **6**, which is also peripherally substituted. Thus the point of substitution (peripheral or non-peripheral) determines the nature of binding (symmetrical or non-symmetrical) of Pd(II) ions to the MPc complexes.

4. Conclusions

Octasubstituted pentylthio derivatised phthalocyanines have been employed for the binding of Pd(II) binding. Each of the complexes gave a distinct spectroscopic response. Only three Pd ions could be bound to **6**, while for **4** five Pd ions could be bound. The final spectra for Pd(II) binding to **4** is similar to the spectra for coordination of Pd(II) to the corresponding **5** showing that similar complexes are formed. For complexes **6** and **7**, the final spectrum is split. The observed results show that the molecular architecture and symmetry play vital roles in the binding process and the nature of the final product.

Acknowledgements

This work was supported by the Department of Science and Technology (DST) and National Research Foundation (NRF) of South Africa through DST/NRF South African Research Chairs Initiative for Professor of Medicinal Chemistry and Nanotechnology and Rhodes University. TO thanks Africa Laser Center for funding.

References

[1] J.D. Spikes, J. Photochem. Photobiol. B 6 (1990) 259.
[2] I. Rosenthal, Photochem. Photobiol. 53 (1991) 859.
[3] D. Dini, M. Barthel, M. Hanack, Eur. J. Org. Chem. (2001) 3759.

[4] G. Guillaud, J. Simon, J.P. Germain, Coord. Chem. Rev. 180 (1998) 1433.
[5] C. Piechocki, J. Simon, A. Skoulious, D. Guillon, P.J. Weber, J. Am. Chem. Soc. 104 (1982) 5245.
[6] A. Grund, A. Kaltbeitzel, A. Mathy, R. Schwarz, C. Bubeck, P. Vernmehren, H. Hanack, J. Phys. Chem. 96 (1992) 7450.
[7] M. Ochner, J. Photochem. Photobiol. B: Biol. (1997) 39.
[8] D. Wohrle, V. Schmidt, J. Chem. Soc., Dalton Trans. (1988) 549.
[9] M. Hanack, M. Lang, Adv. Matter 6 (1994) 819.
[10] M. Durmus, T. Nyokong, Photochem. Photobiol. Sci. 6 (2007) 659.
[11] W. Freyer, D. Leupold, J. Photochem. Photobiol. A: Chem. 105 (1997) 153.
[12] W. Freyer, H. Stiel, M. Hild, K. Teuchner, D. Leupold, Photochem. Photobiol. 66 (1997) 596.
[13] M. Hu, Y. Xu, Z. Xiong, Chem. Lett. 33 (2004) 1092.
[14] R.J.C. Brown, A.R. Kucernak, N.J. Long, C. Mongay-Batalla, New J. Chem. 28 (2004) 676.
[15] B.B. Koleva, T. Kolev, M. Lamshöft, M. Spiteller, Trans. Met. Chem. 33 (2008) 911.
[16] B.B. Koleva, T. Kolev, S. Zareva, M. Spiteller, J. Coord. Chem. 61 (2008) 3534.
[17] B.B. Ivanova, H. Mayer-Figge, J. Coord. Chem. 58 (2005) 653.
[18] B.B. Ivanova, M.G. Arnaudov, H. Mayer-Figge, Polyhedron 24 (2005) 1624.
[19] B.B. Ivanova, Turkish J. Chem. 31 (2007) 97.
[20] B.B. Koleva, Ts. Kolev, S.Y. Zareva, M. Spiteller, J. Mol. Struct. 831 (2007) 165.
[21] N.Y. Meryem, M. Kandaz, A. Koca, B. Salih, J. Porphyrins Phthalocyanines 10 (2006) 1022.
[22] M. Kandaz, H.S. Cetin, A. Koca, A.R. Ozkaya, Dyes Pigments 74 (2007) 298.
[23] A. Bilgin, A. Mendi, U. Yildiz, Polymer 47 (2006) 8462.
[24] T.B. Ogunbayo, A. Ogunsipe, T. Nyokong, Dyes Pigments 82 (2009) 422.
[25] J.G. Young, W. Onyebuagu, J. Org. Chem. 55 (1990) 2155.
[26] D. Wöhrle, M. Eskes, K. Shigehara, A. Yamada, Synthesis (1993) 194.
[27] G. Mbambisa, P. Tau, E. Antunes, T. Nyokong, Polyhedron 26 (2007) 5355.
[28] A. Beck, K.M. Mangold, M. Hanack, Chem. Ber. 124 (1991) 2315.
[29] J.V. Bakboord, M.J. Cook, E. Hamuryudan, J. Porphyrins Phthalocyanines 4 (2000) 510.
[30] N. Kobayashi, H. Ogata, N. Nonaka, E.A. Lukyanets, Chem. Eur. J. 20 (2003) 5123.
[31] A. Ogunsipe, D. Maree, T. Nyokong, J. Mol. Struct. 650 (2003) 131.
[32] M.J. Stillman, T. Nyokong, in: C.C. Leznoff, A.B.P. Lever (Eds.), Phthalocyanines: Properties and Applications, vol. 1 VCH, New York, 1989 (Chapter 3).

(Merk, p.a.), chromium(III) nitrate nonahydrate (Aldrich 99%) and sulfuric acid (Cicarelli, p.a.), oxygen (99.99%). Aqueous solutions were prepared in milliQ deionised water (HPLC quality).

In experiments performed at pH 1–3, the pH of the solutions was achieved by addition of $HClO_4$ solution. In experiments at pH 7.0–7.5 the buffer used was 4-(2-hydroxyethyl-1-pyperazineetanesulfonic acid (Hepes). Concentration of stock solutions of $HClO_4$ was determined using standards analytical methods.

Caution: Cr^{VI} are human carcinogens, and Cr^{V} complexes are mutagenic and potential carcinogens [10]. Contact with skin and inhalation must be avoided. Acrylonitrile is a carcinogen and must be handled in a well-ventilated fume hood [11].

2.2. Methods

2.2.1. Spectrophotometric measurements

Spectrophotometric measurements were performed by monitoring absorbance changes using a Jasco-V-550 spectrophotometer with a fully thermostated cell compartment (±0.2 °C). Disappearance of Cr^{VI} in reactions with digal and trigal was followed spectrophotometrically at 350 nm under pseudo-first-order conditions, using at least a 50-fold molar excess of substrate over Cr^{VI}. Reactant solutions were previously thermo stated and transferred into a 1.0 cm path length cell immediately after mixing. Experiments were performed at 33 °C unless otherwise stated and mixtures of sodium perchlorate and perchloric acid were used to maintain a constant ionic strength (I) 1.0 M. The disappearance of Cr^{VI} was followed until at least 80% conversion. In the kinetic measurements, the initial concentration of Cr^{VI} was kept at 6.0×10^{-4} M and the digal/trigal concentration was varied from 0.03 to 0.09 M, [$HClO_4$] was kept constant at 0.2 M. Multiple measurements showed the reproducibility of the method. Rate constant (k_6, k_5) were deduced from multiple determinations and were within ±10% error for each other. The first-order dependence of the rate upon [Cr^{VI}] was verified in a set of experiments where the $[Cr^{VI}]_0$ was varied between 0.3 and 0.6 mM but temperature, $[digal]_0$ or $[trigal]_0$, [H^+] and I were kept constant.

The presence of superoxoCr^{III}, CrO_2^{2+}, in mixtures of digal or trigal/Cr^{VI} was investigated by periodic scanning UV–Vis spectrophotometry in the 220–500 nm region of O_2-saturated solutions, 1.26 mM, containing 0.1 M digal or trigal, [$HClO_4$] = 0.2 M, [Cr^{VI}] = 0.047 mM, I = 1.0 M at 25 °C. Periodic scanning of the reaction mixture showed that the Cr^{VI} band at 350 nm decreased in intensity, while new peaks at 290 and 247 nm, characteristic of CrO_2^{2+} grew in.

2.2.2. Chromium determination in polygal/Cr^{VI} supernatant mixtures

Perchloric acid used in the reaction mixture of polygal/Cr^{VI} protonates the carboxylate groups of polygal, producing its aggregation in particles of different sizes, which depends on the experimental conditions. In all experiences, polygal was generated by direct reaction of sodium polygalacturonate solutions with perchloric acid. Different mass of sodium polygalacturonate (25–1200 mg) were dissolved in 31.0 mL of distilled water at 60 °C, with constant stirring. 1.10 mL of $HClO_4$ 3.83 M was added to a heterogeneous mixture, which was then incubated for 10 min. Finally, 2.0 mL Cr^{VI} 0.30 M was added. The final composition of the mixture was [$HClO_4$] = 0.12 M, [Cr^{VI}] = 0.0176 M, [polygal] = 0.73–35.2 g/L. Reaction mixture was kept in close recipients thermostitazed at 60 °C. After 24 h of stirring, 2.0 mL aliquot of the suspension were centrifuged during 30 min at 5000 rpm. About 200–300 μL of the clear supernatant were taken and dried in a porcelain cap and calcinated until total elimination of organic material. The yellow solid [12] was taken up to a final volume of 5.0 mL with H_2SO_4 0.10 N and measurements of the absorbance at 350 nm allowed calculation of the [Cr^{VI}].

2.2.3. EPR measurements

The EPR spectra were obtained on a Bruker EMX0 spectrometer operating at X-band frequencies (~9–10 GHz). Microwave generation was means with a Bruker 04 ER and measured with a Bruker EMX 048T frequency meter. Spectra were recorded as first derivatives of the microwave absorption in 1024 point at 20 ± 1 °C using 10 mW microwave power, 100 kHz modulation frequency, and 0.29–2.00 G modulation amplitude. g-Values were determined by reference to (dpph) (g_{iso} = 2.0036) as an external standard. In EPR measurements, scanning speed and scans number were fixed in order to reduce the time used in each measurement. This was done to avoid fluctuations in the EPR signal during the sample scanning. Power values used in the EPR experiments did not overcome 10 mW in order to avoid signal saturation.

Long-lived oxo-Cr^{V}-oligouronic and polygal complexes were generated by reaction of $K_2Cr_2O_7$ with an aqueous solution containing GSH at 25 °C. In the experiments [Cr^{VI}] = [GSH]. Final concentration in mixtures polygal/GSH/Cr^{VI}, where [Cr^{VI}] = [GSH] = 0.012–0.014 M; [polygal] = 19.2–23.0 g/L.

All the EPR spectra were simulated using the PEST WINSIM [13] program assuming 100% Lorentzian line shapes. The spectral parameters for each Cr^{V} species were similar in all simulations, with a maximum deviation of ±0.0001 in the g_{iso} values. Values for a_{iso} (^{1}H) were included in the simulations only when were greater than the line width of the oxo-Cr^{V} species.

2.2.4. Polymerization test

The presence of free radicals in the reactions of digal and trigal with Cr^{VI} was tested by acrylonitrile polymerization test. About 0.2 mL of acrylonitrile was added to a solution of Cr^{VI} (0.0027 mmol) and digal/trigal (0.07 mmol) in $HClO_4$ 0.20 M (0.5 mL). After a few minutes at 33 °C, a white precipitate appeared. 0.5 mL of acrylonitrile was added to a reaction mixture containing 53.1 g/L of polygal and 8.0 mM of Cr^{VI}, in 2.0 mL of $HClO_4$ 0.01 M. The mixture was left 2.0 h at 60 °C. After this time, the white precipitate could be seen. ^{13}C NMR of a D_6-DMSO solution of the white solid and FT-IR of the solid showed the pattern characteristic of polyacrilonitrile. Blank experiments with either Cr^{VI} or polygal gave no detectable white precipitates. Control experiments (without Cr^{VI} or reductant present) did not show the formation of a precipitate. The possible reaction of Cr^{V} or Cr^{IV} with acrylonitrile was tested with Na[Cr^{V}O(ehba)$_2$] [14] and [Cr^{IV}O(ehba)$_2$] [15] (ehba = 2-ethyl-2-hydroxybutanoic acid). No precipitation occurred on mixing the Cr^{V} or Cr^{IV} complexes with acrylonitrile under the same conditions as those used in the Cr^{VI} + digal/trigal/polygal reactions.

2.2.5. Effect of external reducing agent (Na_2SO_3) in polygal/Cr^{VI} mixture

Reaction mixture of polygal and perchloric acid were 35.2 mg/L and 0.12 M, respectively. About 0.9 mmol of Na_2SO_3 and 2.0 mL of Cr^{VI} solution 0.3 M were added to 34.1 mL of the reaction mixture.

2.2.6. HCO_2H and CO_2 determination in polygal/Cr^{VI} mixtures

Supernatant of polygal/Cr^{VI} reaction mixture was employed to analyse oxidation products. Carbon dioxide was measured in 35.0 g/L polygal and Cr^{VI} 2.90 mmol/L mixture, in $HClO_4$ 0.12 M. The reaction mixture was continuously stirred and flushed with pure nitrogen at 60 °C. Gaseous products were passed trough three flasks containing NaOH solution. Once the reaction finished, NaOH solutions were titrated with standard HCl in order to determine the carbon dioxide generated. Supernatant was filtered employing a 0.2 μm of porous diameter membrane and analysed by HPLC, showing the presence of formic acid with retention time (R_t) 13.20 min. An aminex HPX-87H column at 25 °C and 0.6 mL/min flow, detection at 220 nm, was used for this experiment. Co

chromatography of polygal reaction mixture with a formic acid solution of known concentration afforded an increment in the 13.20 min peak, confirming identity of detected product. Additionally supernatant polygal/Cr^{VI} reaction mixture was taken to pH 2 with KOH 0.5 M, filtrated to eliminate $KClO_4$ and then distilled. To 5.0 mL of the distillate, 1.0 mL of $HgCl_2$ (2.0%) was added at 80 °C and a white precipitate of Hg_2Cl_2 was observed, which indicate the presence of a reducing compound [16]. Peak area versus [HCO_2H] calibration curves were obtained by HPLC and used for formic acid quantification.

3. Results and discussion

3.1. Digal, trigal or polygal/Cr^{VI} reaction intermediates

Time-dependent UV/Vis spectra of digal/Cr^{VI} and trigal/Cr^{VI} reaction mixtures showed absorbance decrease at 350 nm and 420–470 nm, while absorbance at 570 nm increased, without an isosbestic point, Fig. 1.

The lack of an isosbestic point indicated that there were two or more competing reactions at any time and that, intermediate chromium species coming from Cr^{VI} to Cr^{III} reduction, were present in appreciable concentrations. At the end of reaction, two d–d-bands ascribed to Cr^{III} were observed at λ_{max} 411 nm (ε = 17.5 M^{-1} cm^{-1}) and λ_{max} 570 nm (ε = 15.2 M^{-1} cm^{-1}), corresponding to $^4A_{2g} \rightarrow {}^4T_{1g}$ and $^4A_{2g} \rightarrow {}^4T_{2g}$ transitions of $[Cr(OH_2)_6]^{3+}$ ion [17]. Therefore, it was confirmed that Cr^{III} aqua ion was the only inorganic product under our experimental conditions.

3.1.1. Oxo-Cr^V species characterization by EPR spectroscopy

Presence of oxo-Cr^V-di or trigal species can be identified with great sensitivity by EPR spectroscopy, where strong and narrow isotropic signals were observed at room temperature in X-band spectra. Assignment of the structures of the oxo-Cr^V species in solutions have, therefore, been made on the basis of the isotropic EPR parameters g_{iso}, A_{iso} and $^1Ha_{iso}$.

3.1.1.1. Digal chromium(V) complexes. Multiplicity of EPR signals of digal/Cr^{VI} reaction mixture at pH 1–3 could not be resolved because the shf coupling constants were lower than the line width. Spectra were simulated with three singlets in order to obtain information from the average g_{iso} values of oxo-Cr^V species in the reaction mixture. At pH 7.0, EPR signals showed lower line width, and $^1Ha_{iso}$ values were obtained. Table 1 shows the results obtained from the experimental spectra simulation (Fig. 2).

The ^{53}Cr A_{iso} value belonging to oxo-Cr^V/digal species was 17.3×10^{-4} cm^{-1}, characteristic of oxo-Cr^V pentacoordinate species [18–21]. This result was in agreement with previous works where it was found that five-coordinated oxo-Cr^V species have higher g_{iso} and lower ^{53}Cr A_{iso} values than the corresponding six-coordinated species [21–23]. Taking into account spectral parameters, we were able to assign the g_{iso} 1.9780/1.9784 to a bischelate, where digal bounds an oxo-Cr^V through the carboxylate group and the oxygen of pyranosic ring Fig. 3a. Considering that digal acid is under the pyranosic form in water [24], coordination through the fragment of β-hydroxiacids was discarded because it implies formation of a six member chelate ring, which it is not a favourable situation [21]. g_{iso} = 1.9788 value belongs to a bischelate pentacoordinate oxo-Cr^V species, bound to carboxylate group and three alcoxy group [21], [$Cr^VO(O^{6(6')}$, O^{ring}-digal)/$O^{1'(3)}$,$O^{2'(4)}$-digal) (Fig. 3b).

At pH 7.0 the digal/Cr^{VI} reaction mixture afforded oxo-Cr^V complexes coordinated to a diolate group where the triplets were assigned to species [Cr^VO(*cis*-$O^{1'(3)}$,$O^{2'(4)}$-digalacturonate)$_2$] and mixed species [Cr^VO(*cis*-$O^{1'}$,$O^{2'}$-digalacturonate)(*cis*-O^3,O^4-digalacturonate)]$^-$ (Fig. 4).

3.1.1.2. Trigal chromium(V) complexes. Table 2 shows the results obtained after simulation of the EPR signals at different pH value (Fig. 5).

At pH 2.0 the mayor species (73.8%) presents a g_{iso} 1.9786 value. This signal was assigned to a bischelate of oxo-Cr^V pentacoordinate, where the metal is being bound by two molecules of trigal, through carboxylate groups and a ring oxygen [$Cr^VO(O^{CO2}$, O^{ring}-trigal)$_2$]$^-$. The other species with g_{iso} 1.9790/3 in a minor proportion was ascribed to [Cr^V $O(O^{CO2}$, O^{ring}-trigal)(*cis*-O–O-trigal)]$^-$ complex. At pH 3.0, the EPR spectrum shows that the species [Cr^V $O(O^{CO2}$, O^{ring}-trigal)$_2$]$^-$(g_{iso} 1.9786) and [$Cr^VO(O^{CO2}$, O^{ring}-trigal)(*cis*-O,O-trigal]$^-$(g_{iso}1.9792) were preponderant. A triplet signal at g_{iso} 1.9796 was assigned to [Cr^VO(*cis*-O,O-trigal)$_2$]$^-$ species. At pH 4.0, the proportion of species [Cr^VO(*cis*-O,O-trigal)$_2$]$^-$ (g_{iso} 1.9796 and 1.9800) were 39% of the $[Cr^V]_T$ in the reaction mixture, meanwhile at pH 7.0 the species of oxo-Cr^V-*cis*-diolate afforded the 100% of the $[Cr^V]_T$ in the solution. So, oxo-Cr^V species distribution with pH follows the same tendency observed in others uronic acids and polyhidroxocarboylic compounds [25].

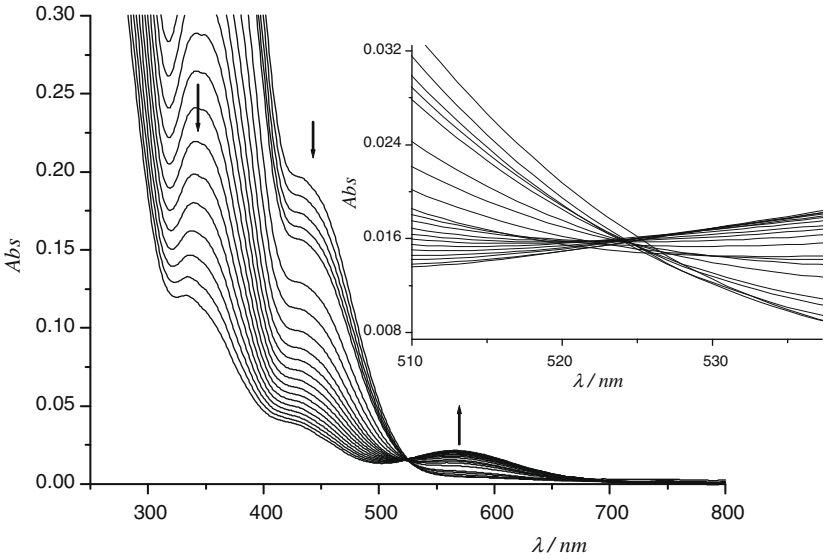


Fig. 1. Time evolution of the UV/Vis spectra from a mixture of trigal (0.04 M) and Cr^{VI} (1.35 mM) over a period of 2.0 h; [$HClO_4$] = 0.20 M; T = 33 °C and I = 1.0 M.

Table 1
EPR spectral parameters for Cr^{V} intermediates in the digal/Cr^{VI} reactions. [Cr^{VI}] = [GSH] = 0.97 mM; [digal] = 0.19 M; [digal] = 0.28 M; I = 1.0 M; T = 20 °C; mod. amp. = 0.40 G; $\nu \approx$ 9.76–9.38 GHz; s = singlet; t = triplet.

pH	g_{iso}	Multiplicity	$^{1}Ha_{iso}$ (10^{4} cm^{-1})	%
1	1.9788/1.9784/1.9780	s		64.3/26.7/9.0
2	1.9788/1.9784/1.9780	s		72.2/20.9/6.9
3	1.9788/1.9784/1.9780	s		71.0/20.3/87
7*	1.9800/1.9798/1.9796	t/t/t	0.84/0.51/0.82	17.0/22.8/60.2

* [Cr^{VI}] = [GSH] = 5.59 mM.

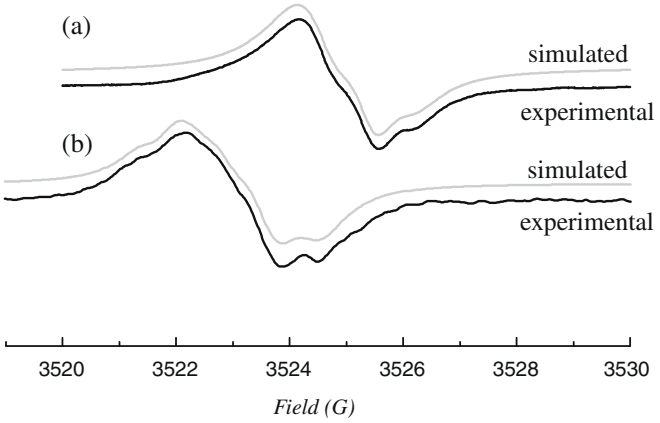


Fig. 2. Experimental and simulated X-band EPR spectra of mixtures digal/Cr^{VI}: (a) pH 3; [Cr^{VI}] = [GHS] = 1.22 mM; [digal] = 0.19 M; (b) pH 7; [Cr^{VI}] = [GSH] = 5.59 mM; [digal] = 0.28 M. T = 20 °C; $\nu \approx$ 9.76 GHz; I = 1.0 M; mod. amp. = 0.40–0.29 G.

3.1.1.3. Polygal chromium(V) complexes. EPR spectra of polygal with Cr^{VI} reaction mixture showed more complex and less resolved signals than in the former system. In general, the signals were very wide at every concentration of protons studied, which indicated the contribution of several Cr^{V} isomers. In a polygal/Cr^{VI} reaction mixture at pH 2–3, after 20 h of reaction, EPR spectra were composed by three signals (Fig. 6), g_{iso} values presented in Table 3.

The signal with average g_{iso} = 1.9783/5 belongs to species where the oxo-Cr^{V} was coordinated to two alcoxo groups and two carboxylate groups, meanwhile the signal with average g_{iso} = 1.9752/7 belongs to [$Cr^{V}O(O^{CO2}$,O-polygal)$(H_2O)_2]^{+}$ specie. Unlike the results observed in the olygomers, there was approximately a 20% of species in this pH range, where the oxo-Cr^{V} group is being coordinated with four alcoholate groups (g_{iso} 1.982–1.981) at the beginning of the reaction. As it is observed on Fig. 7, the proportion of species with average g_{iso} = 1.9783/5 increases with time, meanwhile the others decreases, at 50 h the species oxo-Cr^{V}-$(O_2CR)_2$ are clearly predominant.

The numerous chelating sites and the flexibility of the polymer chain, allowed the formation of several oxo-Cr^{V} species, coordinated with α-hydroxycarboxylate and diolates at acidic pH. Anyway, the predominant species with g_{iso} 1.9783 during reaction time, indicated that the coordination mode of $Cr^{V}O(O^{CO2}$, O^{ring}-polygal$)_2]^{-}$ was the most suitable from the thermodynamic point of view at acidic pH. Reaction mixture of polygal/Cr^{VI}/GSH at pH 7.0, showed an average g_{iso} = 1.9796. Fig. 8 shows time evolution of a reaction mixture of GSH/Cr^{VI} in presence of polygal.

In this figure, it is possible to notice that Cr^{V} produced by redox reaction between Cr^{VI} and GSH was coordinated faster by GSH than by the polymer. The specie Cr^{V}–GSH (g_{iso} 1.9857) exchanged GSH for polygal, affording g_{iso} = 1.9796, which belongs to species of oxo-Cr^{V} coordinated to four alcoholate groups. Therefore, at pH 7.0, average g_{iso} value indicates that coordination between Cr^{V} and polygal took place mainly through the alcoholate groups of the ligand.

3.2. Intermediacy of Cr^{II}

It is known that Cr^{IV} oxidizes alcohols as a two-electron oxidant to yield Cr^{II} and the oxidized organic product. The fact that Cr^{II} is

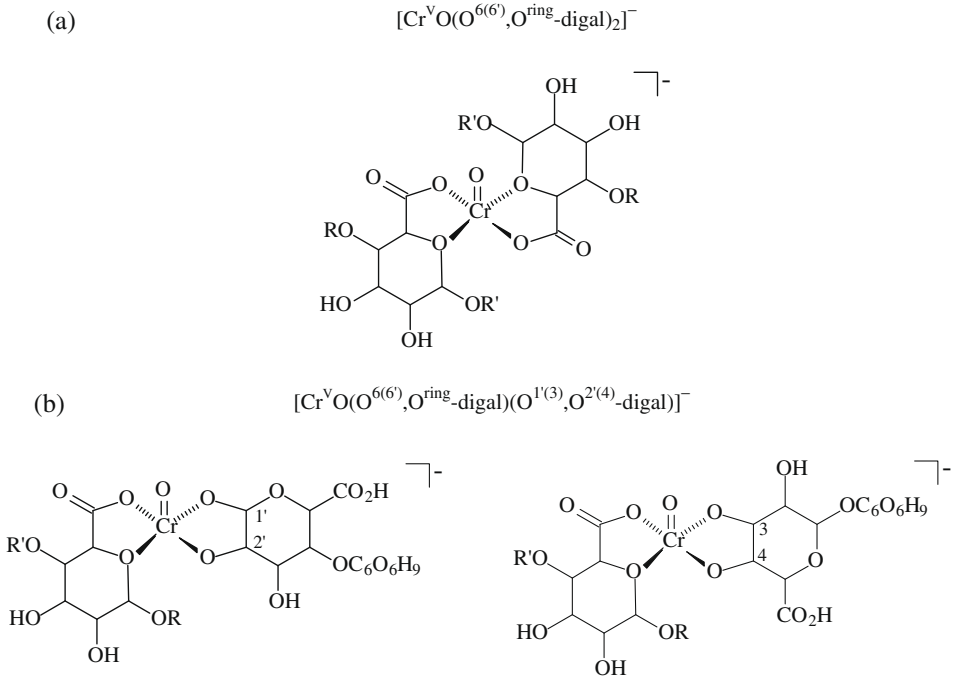


Fig. 3. Structures of Cr^{V} complexes with digal at pH 1–3. R = H and R′ = $C_6O_6H_9$ (coordination through the reducing residue) or R = $C_6O_6H_9$ y R′ = H (coordination through the non reducing residue).

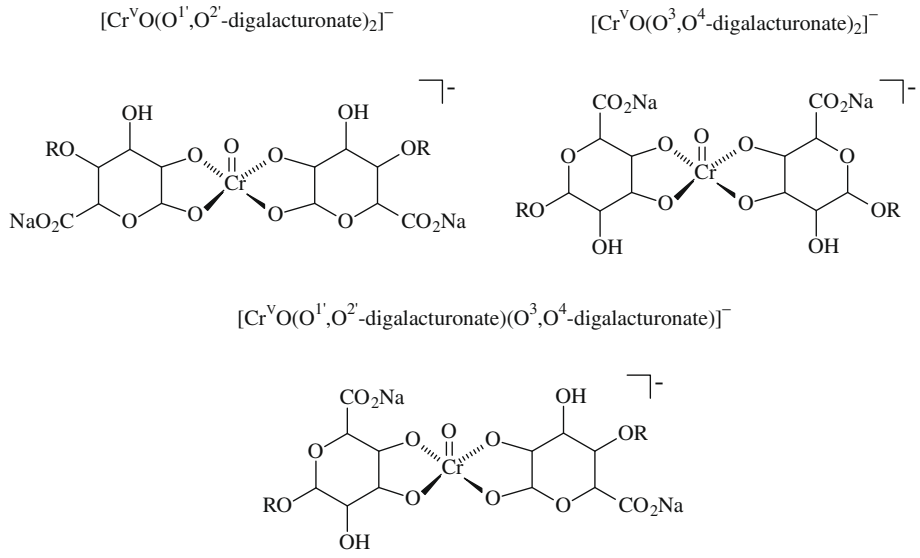


Fig. 4. Structures of Cr^{V} complexes with digal at pH 7.

involved in the oxidation mechanism of several alcohols by Cr^{IV} and Cr^{VI} in $HClO_4$ was demonstrated by conversion to CrO_2^{2+} upon reaction with molecular oxygen [26–30]. At high $[O_2]$ and low $[Cr^{VI}]$ the reaction of Cr^{II} with O_2 can compete successfully with the reaction of Cr^{II} with Cr^{VI} and the autocatalytic consumption of CrO_2^{2+} by Cr^{II}. If Cr^{II} is intermediate specie in the redox reaction, CrO_2^{2+} should be detected. The interdemiacy of Cr^{II} in the reaction of digal or trigal with Cr^{VI}, was monitored by the formation of CrO_2^{2+}, using low $[Cr^{VI}]$ and high $[O_2]$. A periodic scanning of O_2-saturated solution (1.26 mM) of a Cr^{VI} + digal or trigal reaction mixture in 0.20 M $HClO_4$ showed two absorption bands at 290 and 247 nm, characteristic of CrO_2^{2+} (Fig. 9).

Inset Fig. 9 shows CrO_2^{2+} absorption at 247 nm versus time. CrO_2^{2+} absorbance at 247 nm was calculated in the following way:

Table 2
EPR spectral parameters for Cr^{V} intermediates in the trigal/Cr^{VI} reactions. $[Cr^{VI}]$ = [GSH] = 1.22 mM; [trigal] = 0.19 M; I = 1.0 M; T = 20 °C; mod. amp. = 0.29 G; $\nu \approx 9.76$ GHz; t = triplet; s = singlet.

pH	g_{iso}	Multiplicity	$^{1}Ha_{iso}$ (10^4 cm^{-1})	%
2	1.9786	s		73.8
	1.9790	s		25.0
	1.9793	s		1.20
3	1.9786	s		68.2
	1.9792	s		29.0
	1.9796	t	0.78	2.70
4	1.9786	s		61.1
	1.9796	t	0.73	31.6
	1.9800	t	0.67	7.40
7	1.9800	t	1.02	25.7
	1.9796	t	0.94	74.3

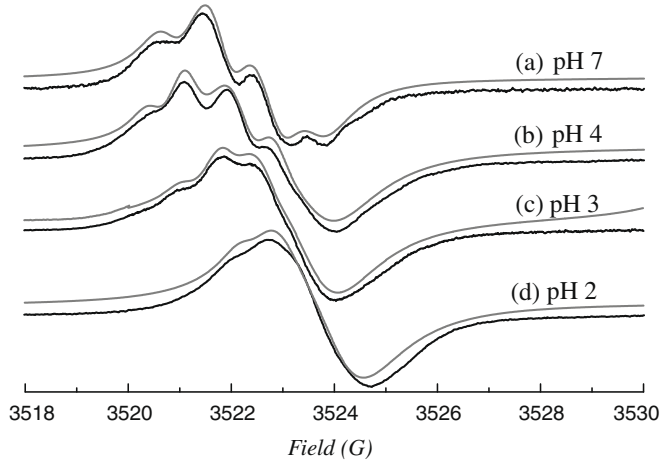


Fig. 5. Experimental and simulated X-band EPR spectra of mixtures trigal/Cr^{VI}; .$[Cr^{VI}]$ = [GHS] = 1.22 mM; [trigal] = 0.19 M; I = 1.0 M; T = 20 °C; mod. amp. = 0.29 G; $\nu \approx 9.76$ GHz; $^{*}[Cr^{VI}]$ = [GSH] = 1.22 mM.

Inset Fig. 9 shows CrO_2^{2+} absorption at 247 nm versus time. CrO_2^{2+} absorbance at 247 nm was calculated in the following way:

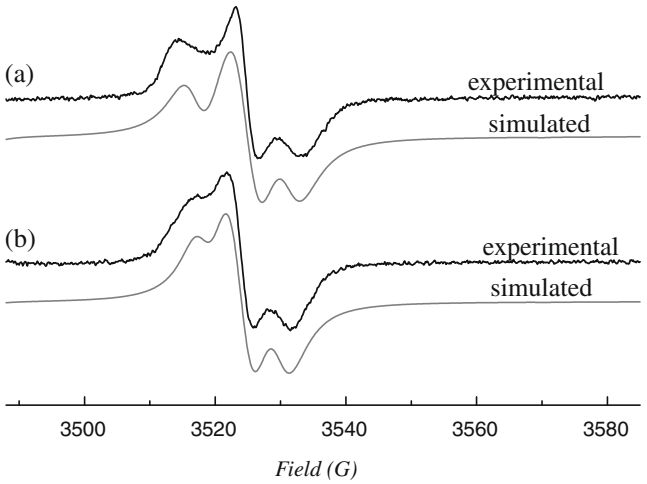


Fig. 6. Experimental and simulated X-band EPR spectra of mixtures polygal/Cr^{VI}; [polygal] = 19.2 g/L; [GHS] = $[Cr^{VI}]$ = 0.012 M; $\nu \approx 9.76$ GHz; T = 20 °C; mod. amp = 2.0 G; t = 20 h. (a) pH 2; (b) pH 3.

Table 3
EPR spectral parameters for Cr^{V} intermediates in the polygal/Cr^{VI} reactions [polygal] = 30.0 g/L; $[Cr^{VI}]$ = 0.975 mM; t = 20.0 h; $\nu \approx 9.76$ GHz; T = 20 °C; mod. amp. = 2.0 G.

	g_{iso}	%		g_{iso}	%
pH 2	1.9783	47.5	pH 3	1.9785	39.1
	1.9752	32.0		1.9757	38.0
	1.9820	20.5		1.9811	22.9

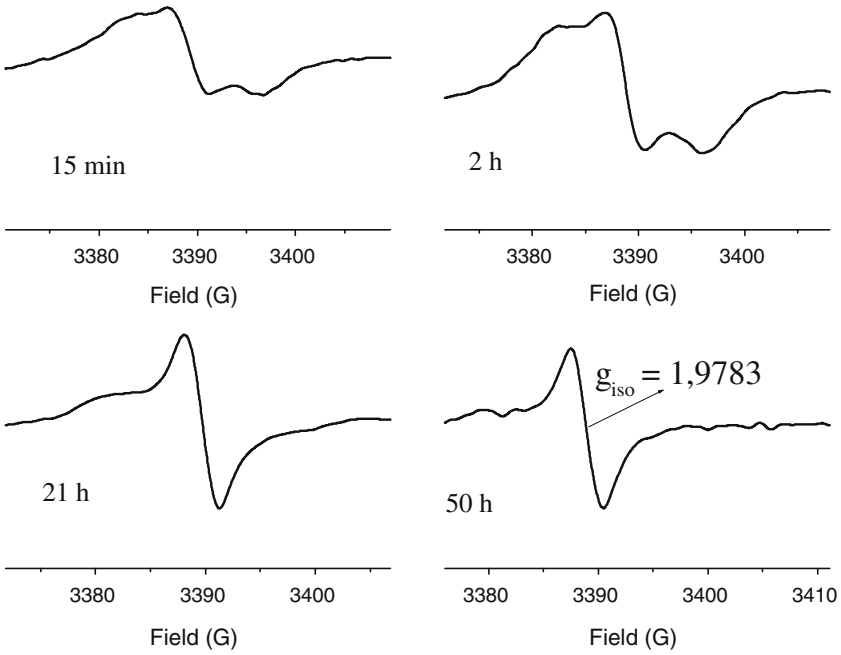


Fig. 7. EPR espectra time evolution of oxo-Cr^{V}-polygal species at acidic pH.

$$Abs^{247}(CrO_2^{2+}) = Abs^{247} - Abs^{350} \times (\varepsilon 1)^{-1} \times (\varepsilon 2)$$

where $\varepsilon 1$ and $\varepsilon 2$ represent the molar absorption coefficient of Cr^{VI} at 350 and 247 nm, respectively. In the experimental condition used $\varepsilon 1 = 1550\ M^{-1}\ cm^{-1}$ and $\varepsilon 2 = 1900\ M^{-1}\ cm^{-1}$. Keeping in mind that the molar absorption coefficient of CrO_2^{2+} at 247 nm is 7000 $M^{-1}\ cm^{-1}$ [27], the maximum concentration of CrO_2^{2+} (t_{max} = 12.1 - min) was 37%.

These spectroscopic results showed that Cr^{II} was produced in the redox reaction and this fact was taken as evidence that Cr^{IV} was implied in the redox mechanism of digal or trigal oxidation by Cr^{VI} in acidic media. The yielding of CrO_2^{2+} is expected to approach 100% if the reaction takes place exclusively through the $Cr^{VI} \rightarrow Cr^{IV} \rightarrow Cr^{II}$ pathway [27]. In these reactions $[CrO_2^{2+}]_{max}$ reached a value of 37% suggesting that one half of the $HCrO_4^-$ was reacting through a pathway that involved Cr^{II} .This behaviour was observed in another related systems [31]. Under the present kinetic measurements conditions, Cr^{IV} reacted with digal or trigal much faster than Cr^{VI}. High reactivity of Cr^{IV} against alcohols and aldehydes [27], neutral carbohydrates, aldonic, uronic, aldaric acids [32] and polysaccharides [33] has been experimentally demonstrated. This implies that Cr^{V} was the only chromium intermediate that accumulates in the reaction mixtures as can be seen by EPR.

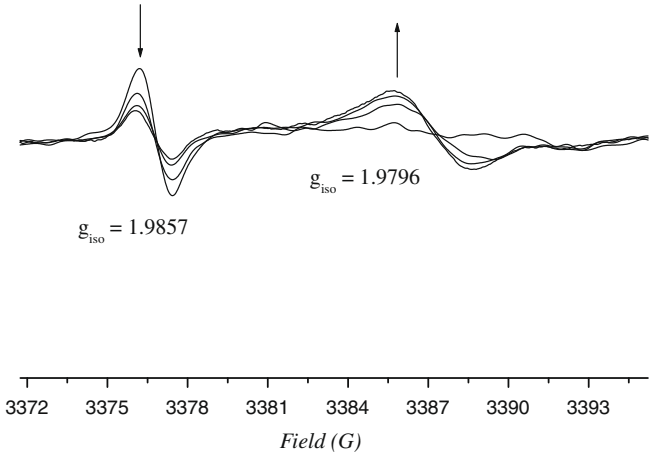


Fig. 8. EPR espectra time evolution of polygal/Cr^{VI}/GSH mixtures at pH 7.

3.3. Rate studies

Absorbance curves versus time at 350 nm of the digal or trigal/Cr^{VI} mixtures showed a monotonic decrease which cannot be described by a single exponential decay. These kinetics profiles were adequately described by the set of consecutive first-order reactions of Scheme 1. It is known that Cr^{V} species absorb strongly at 350 nm and may superimpose Cr^{VI} absorbance yielding the wrong interpretation of spectrophotometric absorbance decay values, especially when the Cr^{VI} and Cr^{V} decay rates are of the same order [34]. So, considering the Cr^{V} absorption superimposition, the absorbance at 350 nm, at any time during the redox reaction, is given by:

$$Abs^{350} = \varepsilon^{VI}[Cr^{VI}] + \varepsilon^{V}[Cr^{V}] \quad (1)$$

Combining Eq. (1) with rate expressions [35] derived from Scheme 1 yields

$$Abs^{350} = Abs_0 e^{-2k6t} + k_6 \varepsilon^{V}[Cr^{VI}]_0 (e^{-k5t} - e^{-2k6t})/(2k_6 - k_5) \quad (2)$$

In Eq. (2), ε^{V} refers to the molar absorptivity of Cr^{V}-digal or Cr^{V}-trigal at 350 nm (ε^{V} 1800 $M^{-1}\ cm^{-1}$). Parameters k_6 and k_5 refer to the rate of disappearance of Cr^{VI} and Cr^{V}, respectively, and were evaluated from a non-linear iterative computer fit of Eq. (2). It must be noted that in Eq. (2), k_6 appears in the numerator of the pre-exponential term and $2k_6$ appears in the denominator and in the exponential terms because, according to the proposed reaction scheme, only half of the Cr^{VI} reaches Cr^{III} through a Cr^{V} intermediate. At $HClO_4$ 0.2 M, in the 0.03–0.09 M digal or trigal range, the calculated values of k_6 and k_5 were very close ($k_6/k_5 \approx 2.50$–$1.95/1$). This fact implied that the slow redox steps involved the reduction of Cr^{VI} and Cr^{V}. The simulation of the kinetic profiles employing k_6 and k_5 values obtained from Eq. (2), showed that the maximal $[Cr^{V}]$ represented 33.3% of the total Cr in $HClO_4$ 0.2 M and trigal 0.09 M (Fig. 10).

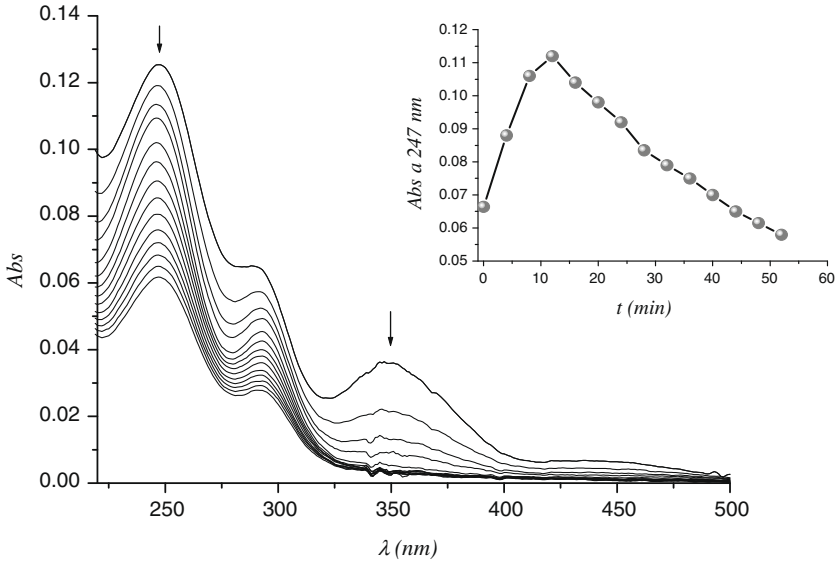


Fig. 9. CrO_2^{2+} formation of (λ_{max} 290, 247 nm) from the reaction between 0.10 M trigal, 1.26 mM O_2, 0,20 M $HClO_4$ and 0.047 mM Cr^{VI}, at 25 °C and I = 1,0 M. Spectra recorded every 4 min. Inset shows CrO_2^{2+} absorption at 247 nm vs. time.

$$2\,Cr^{VI} \longrightarrow Cr^{V} + Cr^{III} \longrightarrow Cr^{III}$$

Scheme 1.

These results were consistent with the fact that absorbance at 350 nm reflects changes in [Cr^{VI}] and [Cr^{V}]. The calculated kinetics parameters, k_6 and k_5, for various [trigal] and [digal] at fixed [$HClO_4$] are summarized in Table 4.

In 0.1 M $HClO_4$, the Cr^{V} EPR signal of a 155:1 digal:Cr^{VI} mixture grows and decays at 20 °C (Fig. 11).

The rate constants for the formation and disappearance of the intermediate Cr^{V} were calculated from the variation of the intensity of the EPR signal versus time, and the k_6 and k_5 values were obtained using Eq. (3) derived from Scheme 1 for the total Cr^{V} in the mixture at any time.

$$h = A\,k_6(\exp(-2k_6t) - \exp(-k_5t))/(k_5 - 2k_6) \quad (3)$$

where A depends on the spectrometer settings (gain, power, modulation, etc.).

In the range of substrate employed in this work, plots of k_6 and k_5 versus [trigal] and [digal] gave good straight lines from which values of k_{6h} and k_{5h} were determined (Fig. 12).

For 0.2 M $HClO_4$ the rate laws for the Cr^{VI} and Cr^{V} disappearance are then given by

$$-d[Cr^{VI}]/dt = 2k_{6h}[S][Cr^{VI}] \text{ and } -d[Cr^{V}]/dt = k_{5h}[S][Cr^{VI}]$$

where $k_{6h} = 0.027(3)\ M^{-2}\ s^{-1}$; $k_{5h} = 0.013(1)\ M^{-2}\ s^{-1}$ and S = digal

where $k_{6h} = 0.024(2)\ M^{-2}\ s^{-1}$; $k_{5h} = 0.010(1)\ M^{-2}\ s^{-1}$ and S = trigal

The fact that CrO_2^{2+} was detected in the redox reaction of digal and trigal with Cr^{VI}, coupled with the observation of Cr^{V} species and the successful trapping of organic radicals using acrylonitrile

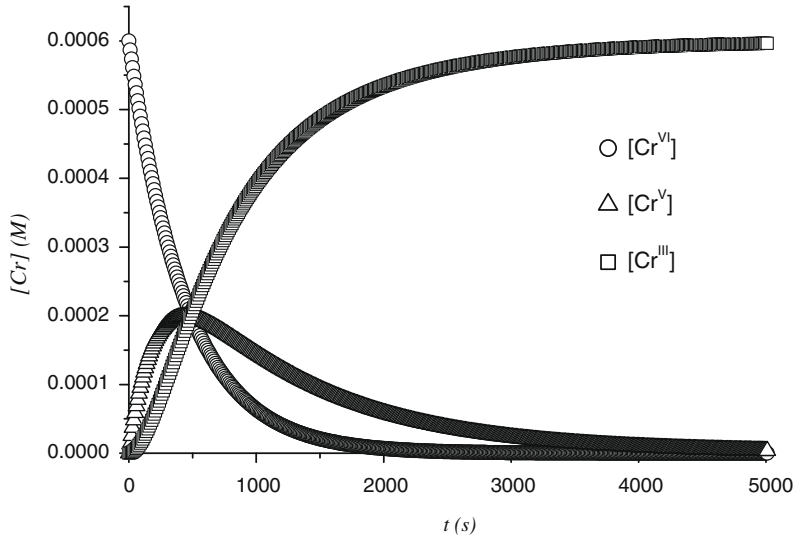


Fig. 10. Simulated kinetics profiles for Cr species. [Cr] calculated using k_6 = 0.00224 s^{-1}, k_5 = 0.00093 s^{-1}; [trigal] = 0.09 M; [$HClO_4$] = 0.20 M; T = 33 °C; I = 1.0 M; $[Cr]_T$ = 0.6 mM.

Table 4
Observed pseudo-first-order rate constants (k_6 and k_5) for different concentrations of digal–trigal at [$HClO_4$] 0.20 M.

[Digal or trigal] (M)	0.03	0.048	0.06	0.09
	$10^3\ k_6/s^{-1}$			
Digal	0.86(9)	1.3(1)	1.6(2)	2.4(2)
Trigal	0.69(7)	1.2(1)	1.4(1)	2.2(2)
	$10^3\ k_5/s^{-1}$			
Digal	0.36(4)	0.61(6)	0.81(8)	1.2(1)
Trigal	0.28(3)	0.52(5)	0.61(6)	0.93(9)

T = 33 °C; $[Cr^{VI}]_0$ = 0.6 mM; I = 1.0 M.

indicated that reaction occured through both one and two electron pathways involving Cr^{IV} and Cr^{V} intermediates species. However, under conditions employed in the kinetics measurements, Cr^{IV} reacted with digal and trigal faster than Cr^{VI} and does not accumulate in the reaction mixture. Therefore, Cr^{IV} should be involved in fast steps of the reaction pathway. In Scheme 2, a mechanism is proposed which combines $Cr^{VI} \rightarrow Cr^{IV} \rightarrow Cr^{II}$ and $Cr^{VI} \rightarrow Cr^{IV} \rightarrow Cr^{III}$ pathways, and takes into account: (a) kinetics results, (b) the polymerization test of acrylonitrile, (c) detection of oxo-Cr^{V} intermediates by EPR (d) observation of CrO_2^{2+}.

In the [$HClO_4$] under study, Cr^{VI} may exist as $HCrO_4^-$ [36], and this species is proposed as the reactive form of Cr^{VI}, in agreement with the first-order dependence of the reaction rate on [Cr^{VI}]. It is known that the chromic oxidation of alcohols, glycols and dicarboxylic acids are preceded by the formation of a chromate ester [36,37], so we proposed that the first step of the mechanism in Scheme 2 involves the formation of sustrate-Cr^{VI} mono-chelate (Eq. (4)), this chromate ester should be formed rapidly prior to the redox steps. The formation of the chromate ester is followed by the slow redox step where the C–C bond cleavage is proposed to occur through an acid catalyzed two-electron redox process to yield Cr^{IV}, HCO_2H and oxidized substrate (Eq. (5)).

The formation of Cr^{IV} was consistent with the observation of CrO_2^{2+}, the product of the reaction of Cr^{II} with O_2, which is taken as evidence of the Cr^{IV} formation [27,28]. After the slow redox step,

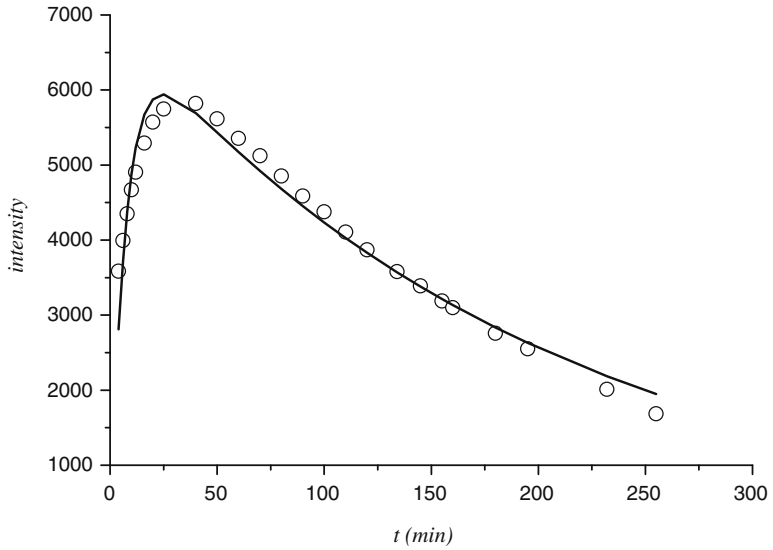


Fig. 11. Intensity of Cr^{V} EPR signals vs. time. [Cr^{VI}] = 0.97 mM, [digal] = 0.15 M [$HClO_4$] = 0.1 M, I = 1.0 M; T = 20 °C; mod. amp. = 2.0 G.

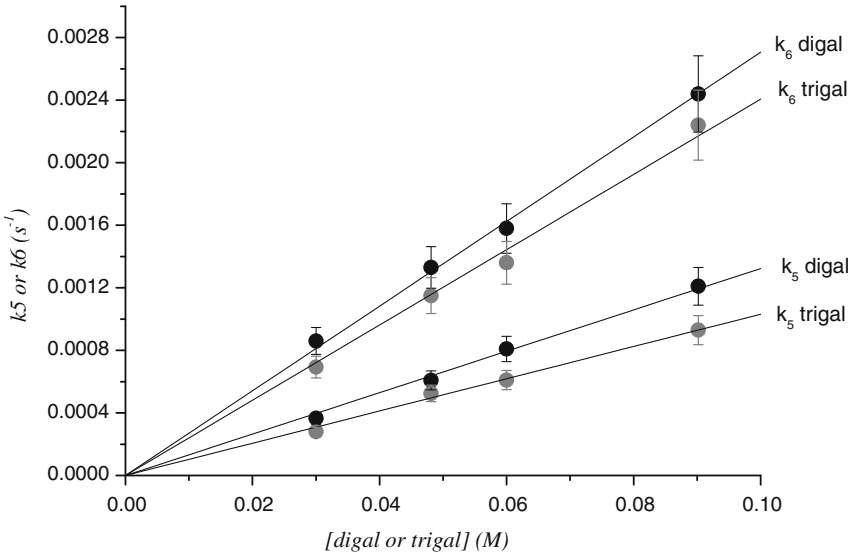
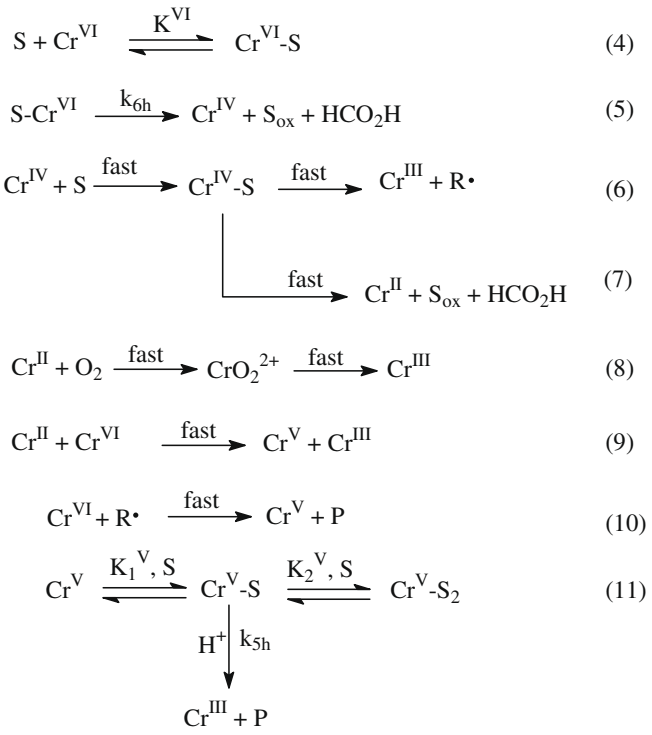


Fig. 12. Effect of [digal or trigal] on k_6 and k_5 at 33 °C; I = 1.0 M at [$HClO_4$] 0.2 M.



Scheme 2.

Cr^{IV} is predicted to react with excess substrate to yield Cr^{III} and radical or Cr^{II} and oxidize substrate through two alternative fast steps (Eqs. (6) and (7)). The first parallel step was supported by the observed polymerization of acrylonitrile when it was added to the reaction mixture, while the second one, by the formation of CrO_2^{2+}. Cr^{V} was produced by fast reaction of Cr^{II} with Cr^{VI} Eq. (9). Under the conditions used in the kinetic experiments, Eq. (8) can be neglected. The kinetic data indicate that Cr^{V} formed in the fast steps can further oxidize digal and trigal through an acid catalyzed step to yield Cr^{III} and the oxidized substrate as the final redox products. In Scheme 2, it is proposed that Cr^{V} reacts with digal or trigal to form an oxo-Cr^{V}-digal/trigal monochelate that yields the redox products through an acid catalyzed step ((11)). This proposal is in agreement with the EPR spectra at $[HClO_4]$ 0.20 M.

3.4. Cr^{VI} reduction and Cr^{III} retention by polygal

The redox reaction between Cr^{VI} and polygal and the tendency of the polysaccharide matrix in retaining Cr^{III} coming from redox reaction was studied. Under strong acidic media, polygal was fully protonated producing insoluble aggregates which consist in polymer chains joined by hydrogen bonds between the carboxyl and hydroxyl groups [38]. At pH 7.00, the polymer was soluble, due to the presence of deprotonated carboxylate groups. Speed of aggregation depends on the experimental conditions (acidity, temperature, shaking, etc.) and was standardized in order to obtain particles of uniform size. Reaction mixture of polygal/Cr^{VI} was performed keeping $[Cr^{VI}]$, $[HClO_4]$ and temperature constant. The amount of polygal was varied between 25 and 1200 mg. Absorbance measurements at 350 nm versus time performed on mixtures polygal/Cr^{VI} showed the disappearance of Cr^{VI}. At the same time, absorbance values at 570 nm did not show the corresponding increment of Cr^{III} because it was capturated on the solid matrix of the polymer as a cyan-coloured solid. The polygal efficiency in Cr^{III} retention – coming from the reduction of Cr^{VI} – was defined in Eq. (12) as *%E*.

$$\%E = 100 \times \left([Cr^{VI}]_0 - [Cr]_{final}\right)/[Cr^{VI}]_0 \quad (12)$$

Fig. 13 and Table 5 show the obtained results varying the mass of polygal.

As we can see, employing 990 mg of polygal, *%E* is almost 90%. Increasing the amount of polygal from 990 to 1200 mg does not produce a significative increment on the *%E* value. The chromium analysis on the solid, confirm the results of the supernatant. For the experience with 1200 mg of polygal, analysis of the solid afforded 23 mg Cr per solid g, which represents 88.5% of the initial $[Cr^{VI}]_0$ coincident with the value showed in Table 5, considering the experimental error. The efficiency of polygal for eliminating Cr was higher, as demonstrated in the determination of *%E* at different times even though the speed of redox process was low. Considering an amount of 780 mg polygal, in the experimental conditions of Table 5, the *%E* was 39.0 and 74.0 for 3.0 and 10 h, respectively. In order to check if the speed of reduction of $[Cr^{VI}]$ by polygal was the limiting process of the reaction, the same

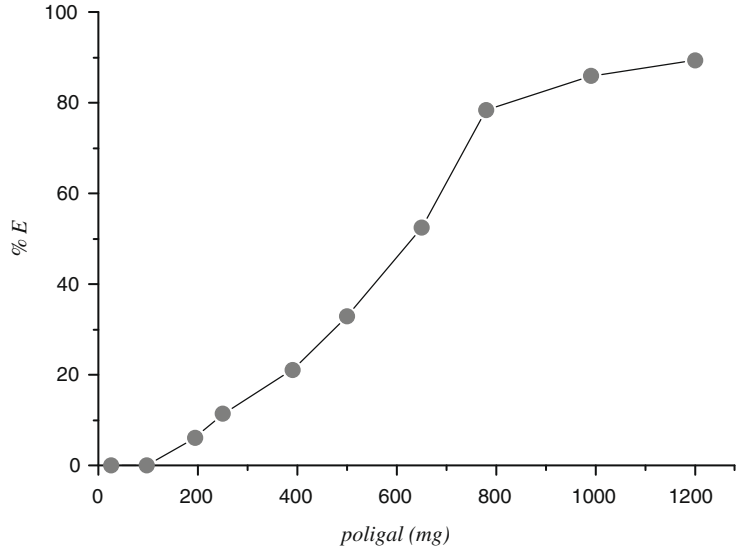


Fig. 13. Effect of [polygal] on *%E* at 60 °C; *I* = 1,0 M, *t* = 24 h at $[HClO_4]$ 0.12 M.

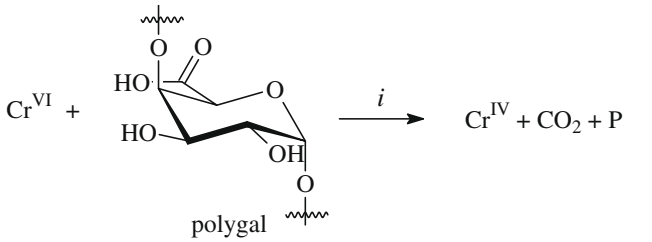
Table 5
Effect of [polygal] on %*E* at 60 °C; I = 1.0 M, t = 24 h at [$HClO_4$] 0.12 M.

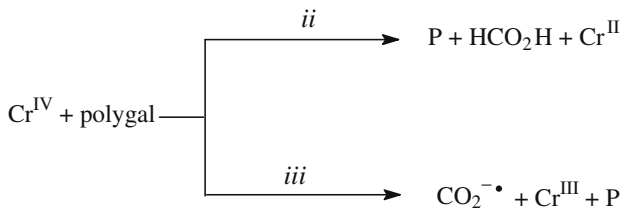
Polygal (mg)	$[Cr]_f$ (mM)	%*E*
1200	1.86	89.4
990	2.46	87.0
780	3.80	78.4
650	7.64	56.6
500	11.79	33.0
390	13.45	23.6
250	15.35	12.8
195	16.30	7.4
97.5	17.6	0
25	17.6	0

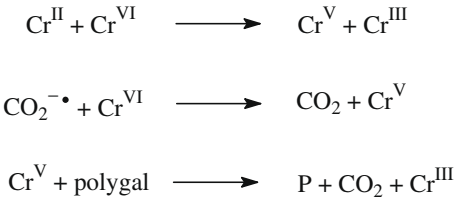
reaction mixture added with 0.9 mmol Na_2SO_3 was prepared. The reduction of Cr^{VI} to Cr^{III} was almost instantaneous and the %*E* value reached 90%, practically the same value obtained after 24 h without the addition of Na_2SO_3. This result confirms that Cr^{VI} reduction was the limiting step in the chromium elimination by polygal.

3.5. Polygal/Cr^{VI} reactions mixture: oxidation product

The oxidation of polygal with Cr^{VI} afforded two products: HCO_2H (determined by HPLC) and CO_2 determined by titration in alkaline medium. The quantification of these products afforded 0.3 mol HCO_2H and 1.1 mol CO_2 per mol Cr^{VI}. According to the experimental conditions employed, the formic acid could react with Cr^{VI} affording CO_2. The last reaction is slower than Cr^{VI}-polygal reaction [39] and the concentration of HCO_2H was lower than the carboxylate groups in polygal. Consequently, the transformation of formic acid in CO_2 by oxidation with Cr^{VI} was discarded. In the proposed mechanism (Scheme 3), if the consecutive steps (ii) and (iii) occur in the same proportion then, the stoichiometry of the global reaction could be written as the following reaction (Eq. (13)).







Scheme 3.

$$Cr^{VI} + 1.5\ \text{polygal} \rightarrow Cr^{III} + 1.5\ P + 1.25\ CO_2 + 0.25\ HCOOH \quad (13)$$

According to this stoichiometry, 1.25 mol of CO_2 and 0.25 mol of HCOOH per mol of Cr^{VI} should be produced, which is in agreement with the experimental results. The absence of signals belonging to monomers or oligomers of low molecular weight in the HPLC chromatograms of the supernatant reaction mixture, discarded the participation of the glucosidic linkage α (1–4) in the redox reaction with Cr.

Scheme 3 adjusts the reaction mechanism for oxidation of oxygenated compounds with Cr^{VI}, in agreement with sequences combination: $Cr^{VI} \rightarrow Cr^{IV} \rightarrow Cr^{II}$ and $Cr^{VI} \rightarrow Cr^{IV} \rightarrow Cr^{III}$.

4. Conclusions

The results presented in this report showed that digal, trigal and polygal were able to reduce Cr^{VI} to Cr^{III}. The redox reaction took place through the combination of $Cr^{VI} \rightarrow Cr^{IV} \rightarrow Cr^{II}$ and $Cr^{VI} \rightarrow Cr^{IV} \rightarrow Cr^{III}$ pathways related with Cr^{V} and radical species in digal–trigal/Cr^{VI} mixtures.

Besides, in this report the results evidence that polygal was able to reduce Cr^{VI} to Cr^{III} and trap efficiently the last form of chromium, so it turns out to be an interesting model for the study of biomaterials which possess a high proportion of this polymer in its composition. Since polygal is better as a Cr^{III} chelating agent than as a reducing agent of Cr^{VI}; the elimination of chromium from contaminated waste water could be more efficient employing biomaterial containing polygal. The results obtained are particularly important because the majority of the chromium remediation methods employed so far are meant for the reduction Cr^{VI} to Cr^{III}; without considering the free Cr^{III} in solution. Due to the fact that Cr^{III} could be oxidized biologically [40] or chemically under extreme environmental conditions [41], new methods of elimination of chromate from water should consider the elimination of chromium in both oxidation states [9].

EPR measurements show that species where Cr^{V} bounds to a ligand through the α-alcoxocarboxylate groups (or 2-O^{ring} carboxylate) predominate in acidic medium, meanwhile at pH 7.0 the species $[Cr^{V}O(\textit{cis}\text{-diolate})_2]^-$ predominate, as can be seen on aldonic acids, others uronic acids and polyhidroxocarboylic compounds [18,20,25].

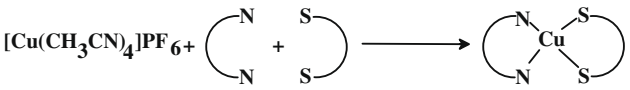
Acknowledgements

We thank the National Research Council of Argentina (CONICET); the National University of Rosario (UNR); the ALFA Program (CROCON Network ProjetALR/B7-30.11/94-7.0064.9); Secyt (Argentina) – OMFB (Hungary) bilateral agreement (project HU / A98-EVI/07); Secyt (Argentina)-Conicyt (Chile) bilateral Agreement (projet HC-PA/01-E04).

References

[1] B. Ridley, M. ÓNeill, D. Mohnen, Phytochemistry 57 (2001) 929.
[2] S. Angyal, Chem. Soc. Rev. 10 (1980) 415.
[3] S. Deiana, L. Erre, G. Micera, P. Piu, Inorg. Chim. Acta 46 (1980) 249.
[4] G. Micera, S. Deiana, Inorg. Chim. Acta 56 (1981) 109.
[5] A. Nguyen, I. Mulyani, A. Levina, P. Lay, Inorg. Chem. 46 (2008) 4299.
[6] S. Rengaraj, K. Yeon, S. Moon, J. Hazard. Mater. B87 (2001) 273.
[7] V. Konovalova, G. Dmytrenko, R. Nigmatullin, M. Bryk, P. Gvozdyak, Enzime Microb. Technol. 33 (2003) 899.
[8] S. Bailey, T. Olin, R. Bricka, D. Adrian, Water Res. 33 (1999) 2469.
[9] S. Bellú, S. García, Juan C. González, Ana M. Atria, Luis F. Sala, S. Signorella, Separation Sci. Technol. 43 (2008) 3200.
[10] International Agency for Research on Cancer (IARC), IARC Monogr. Eval. Carcinog. Risk Chem. Hum. 2 (Suppl. 7) (1987) 165.
[11] R. Feldam, Occupational and Environmental Neurotoxicology, Lippincott-Raven Publishers, Philadelphia, PA, 1999. p. 337.

[12] S.B. Asif, D. Dollimore, Thermochím. Acta 77 (1984) 395.
[13] WinSIM EPR calculations for MS-Windows, version 0.96: National Institute of Environmental Health Sciences, 1995.
[14] M. Krumpolc, J. Rocek, Inorg. Synth. 20 (1980) 63.
[15] M.C. Ghosh, E.S. Gould, Inorg. Chem. 30 (1991) 491.
[16] F. Feil, Spot Test in inorganic analysis, Elsevier, London, 1982. p. 341.
[17] A.B.P. Lever, in: Inorganic Electronic Spectroscopy, second ed., Elsevier, Amsterdam, 1984, p. 419.
[18] R. Codd, C.T. Dillon, A. Levina, P.A. Lay, Coord. Chem. Rev. 216/217 (2001) 537.
[19] M. Rizzotto, A. Levina, M. Santoro, S. García, M. Frascaroli, S. Signorella, L. Sala, P.A. Lay, J. Chem. Soc., Dalton Trans. (2002) 3206.
[20] S. Signorella, J. González, L. Sala, J. Argentine Chem. Soc. 90 (2002) 1.
[21] G. Barr-David, M. Charara, R. Codd, R. Farrell, J. Irwin, P. Lay, R. Bramley, S. Brumby, J.-Y. Ji, G. Hanson, J. Chem. Soc., Faraday Trans. 91 (1995) 1207.
[22] R. Bramley, J.-Y. Ji, R.J. Judd, P.A. Lay, Inorg. Chem. 29 (1990) 3089.
[23] R.P. Farrell, R.J. Judd, P.A. Lay, R. Bramley, J.-Y. Ji, Inorg. Chem. 28 (1989) 3401.
[24] C. Gouvión, K. Mazeau, A. Heyraud, F. Taravel, I. Tvaroska, Carbohydr. Res. 261 (1994) 187.
[25] J.C. González, V. Daier, S. García, B.A. Goodman, L.F. Sala, S. Signorella, Dalton Trans. 15 (2004) 2288.
[26] S. Scott, A. Bakac, J. Espenson, J. Am. Chem. Soc. 113 (1991) 7787.
[27] S. Scott, A. Bakac, J. Espenson, J. Am. Chem. Soc. 114 (1992) 4205.
[28] A. Al-Ajlouni, A. Bakac, J.H. Espenson, Inorg. Chem. 33 (1994) 1011.
[29] J. Pérez Benito, C. Arias, D. Lamrhari, New J. Chem. 18 (1994) 663.
[30] J. Pérez Benito, C. Arias, Can. J. Chem. 71 (1993) 649.
[31] J. González, S. García, N. Mamana, L.F. Sala, S. Signorella, Inorg. Chem. Commun. 9 (2006) 437.
[32] F. Mangiameli, J.C. González, S. García, S. Bellú, S. Signorella, L.F. Sala, unpublished results.
[33] S. Bellú, J. González, S. García, S. Signorella, L.F. Sala, J. Phys. Org. Chem. 21 (2008) 1059.
[34] G.P. Haight, G.M. Jursich, M.T. Kelso, P.J. Merrill, Inorg. Chem. 24 (1985) 2740.
[35] R.G. Wilkins, The Study of Kinetics and Mechanism of Reactions of Transition Metal Complexes, Allyn & Bacon, Boston, 1974. p. 20.
[36] M. Mitewa, P. Bontchev, Coord. Chem. Rev. 61 (1985) 241.
[37] J.K. Beattie, G.P. Haight, in: J.O. Edwards (Ed.), Inorganic Reaction Mechanisms. Part II, Wiley, New York, 1972.
[38] M. Alonso-Mougán, F. Fraga, F. Meijide, E. Rodriguez-Nuñez, J. Vázques-Tato, Carbohydrate Polymers 51 (2003) 37.
[39] C. Arias, J.F. Pérez-Benito, Collect. Czech. Chem. Commun. 57 (1992) 1821.
[40] A. Nguyen, I. Mulyani, A. Levina, P.A. Lay, Inorg. Chem. 47 (2008) 4299.
[41] A.D. Apte, S. Verma, V. Tare, P. bose, Journal of Hazardous Materials B121 (2005) 215.



Scheme 1. Synthesis of mixed-ligand complexes.

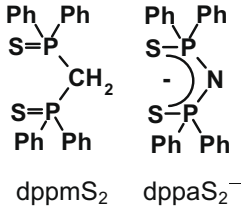


Fig. 1. Phosphinesulfide ligands.

2.2. X-ray measurements

X-ray crystallographic measurements were made on a Rigaku Saturn 70 CCD area detector with graphite-monochromated Mo Kα radiation. The crystal-to-detector distance was 54.90 mm. The data were collected at a temperature of −150 ± 1 °C to a maximum 2θ value of 57.5°. 1800 oscillation images were collected and the data were processed by using the CrystalClear software [11]. Absorption corrections were made by the numerical method for complex **1** and **2**, and by the spherical method for complex **3**. The intensity of the diffraction for complex **3** was weaker than that of the others, so complex **3** gave relatively high refinement residuals**.** The structure was solved by direct methods (SIR-92 [12]) and was refined by full matrix least squares procedures (SHELX-97 [13]). The non-hydrogen atoms are refined anisotropically and the positions of all hydrogen atoms were fixed at calculated positions. All calculations were performed by using the CrystalStructure crystallographic software package [14].

2.3. Synthesis of mixed-ligand Cu(1) complexes

2.3.1. [Cu(dmp)(dppmS$_2$)]PF$_6$ (*1*)

dmp (0.11 g, 0.50 mmol) and dppmS2 (0.22 g, 0.50 mmol) were dissolved in 10 ml of acetone. [Cu(CH$_3$CN)$_4$]PF$_6$ (0.19 g, 0.50 mmol) was then gradually added to the solution. After the solution was stirred for 2 h at room temperature, addition of diethylether (20 ml) to the solution gave orange crystals, which are collected by filtration. Yield 0.33 g (76%). *Anal.* Calc. for [Cu($C_{14}H_{12}N_2$)-($C_{25}H_{22}P_2S_2$)]PF6: C, 54.13; H, 3.96; N, 3.24. Found: C, 54.26; H, 4.14; N, 2.75%. ^{31}P NMR (acetone-d_6, 25 °C): δ 35.0.

2.3.2. [Cu(dmp)(dppaS$_2^-$)] (*2*)

dmp (0.11 g, 0.5 mmol) and K(dppaS$_2^-$) (0.24 g, 0.5 mmol) were dissolved in 10 ml of acetone. [Cu(CH$_3$CN)$_4$]PF$_6$ (0.19 g, 0.5 mmol) was then gradually added to the solution. The solution was stirred for 2 h at room temperature and an orange powder was obtained. Recrystallization of the powder from acetone/diethylether gave orange crystals. Yield 0.31 g (85%). *Anal.* Calc. for [Cu($C_{14}H_{12}N_2$)-($C_{24}H_{20}NP_2S_2$)]: C, 63.36; H, 4.48; N, 5.83. Found: C, 63.18; H, 4.21; N, 5.69%. ^{31}P NMR (acetone-d_6, 25 °C): δ 31.8.

2.3.3. [Cu(dpp)(dppaS$_2^-$)] (*3*)

This complex was prepared by a similar method used for the preparation of complex **3**; use of dpp (0.17 g, 0.5 mmol) instead of dmp gave purple crystals. Yield 0.29 g (71%). *Anal.* Calc. for [Cu($C_{24}H_{16}N_2$)($C_{24}H_{20}NP_2S_2$)]: C, 68.27; H, 4.30; N, 4.98. Found: C, 67.84; H, 4.09; N, 5.01%. ^{31}P NMR (acetone-d_6, 25 °C): δ 31.2.

3. Result and discussion

3.1. Synthesis and crystal structures

Treatment of [Cu(CH$_3$CN)$_4$]PF$_6$ with equimolar amount of dmp and dppmS$_2$ in acetone gave the mixed-ligand complex **1**. Attempt to prepare a similar complex to complex **1** by using dppaS$_2$ instead of dppmS$_2$ gave complex **2** containing dppaS$_2^-$ in which a proton on an amine moiety is eliminated from dppaS$_2$. Use of KdppaS$_2$ and dmp also led complex **2** readily. Treatment of KdppaS$_2$ and [Cu(CH$_3$CN)$_4$]$^+$ with dpp instead of dmp gave complex **3**.

The single crystals with X-ray quality of **1–3** were obtained by gradual addition of diethylether into the reaction solution. Structural data are summarized in Table 1. The structure of complex cation **1** is shown in Fig. 2. It was found that the complex has the tetrahedral structure in which each copper center is coordinated by dmp and dppmS$_2$ chelate ligands. Selected bond lengths, bond angles and torsion angles of **1** are shown in Table 2. The S–P bond lengths of **1** in dppmS$_2$ are 1.9670(7) and 1.9784(7) Å. Since it has been reported that P–S single-bond distance is 2.14 Å and P=S double-bond distance ranges from 1.916 to 1.959 Å, the P–S bond length in **1** shows the bonds almost have double-bond character [15]. The bond angle of S–Cu–S is 108.10(2)°, which is similar to that in the ideal tetrahedral structure. The chelate ring made of Cu-dppmS$_2$ moiety is like a twist boat, as deduced from the torsion angles within the chelate ring ranging from 14.6(2)° to 75.38(12)°.

Table 1
Crystallographic data for complex **1**, **2** and **3**.

Complex name	Complex **1**·acetone	Complex **2** (2 molecules)	Complex **3**
Formula	$H_{40}CuF_6N_2P_3S_2C_{42}O$	$C_{76}H_{64}Cu_2N_6P_4S_4$	$C_{48}H_{36}CuN_3P_2S_2$
Crystal size (mm)	0.25 × 0.25 × 0.20	0.40 × 0.20 × 0.10	0.20 × 0.16 × 0.12
Lattice type	triclinic	monoclinic	monoclinic
space group	$P\bar{1}$ (#2)	$P2_1/c$ (#14)	$P2_1/c$ (#14)
a (Å)	10.996(2)	10.649(6)	10.111(4)
b (Å)	11.249(2)	19.599(10)	21.340(8)
c (Å)	17.783(3)	32.222(17)	17.981(7)
α (°)	98.444(3)	90	90
β (°)	92.604(2)	92.990(3)	95.231(2)
γ (°)	107.468(3)	90	90
V (Å ^{3})	2066.1(7)	6716.1(60)	3863.8(25)
Z	2	4	4
D_{calcd} (g cm^{-3})	1.484	1.425	1.452
μ (Mo Kα) (cm^{-1})	8.09	9.03	7.97
R_1	0.033	0.052	0.079
wR_2	0.080	0.099	0.219

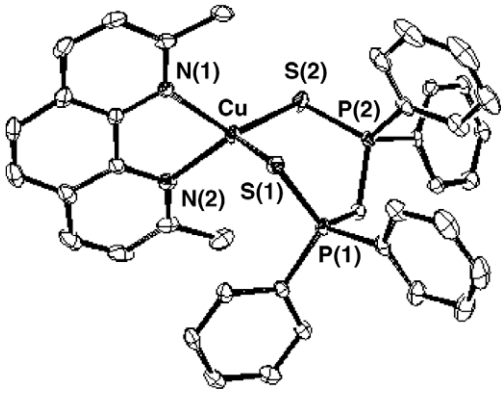


Fig. 2. X-ray structure of complex cation **1**.

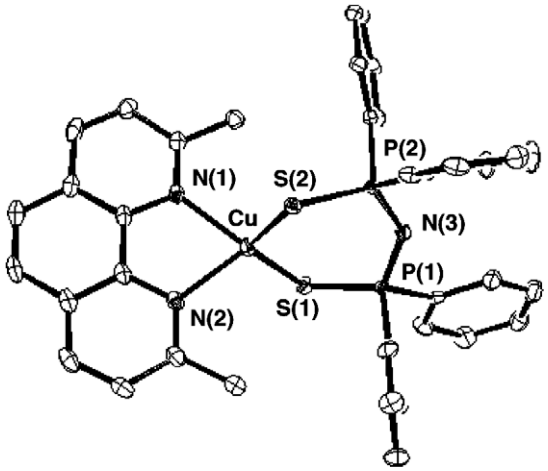


Fig. 3. X-ray structure of complex of **2**. The figure shows one of the two independent molecules in the unit cell.

Table 2
Selected bond distances (Å), bond angles (°) and torsion angles (°) in complex **1**.

Cu(1)–S(1)	2.2771(6)
Cu(1)–S(2)	2.3333(6)
Cu(1)–N(1)	2.1060(16)
Cu(1)–N(2)	2.0578(18)
S(1)–P(1)	1.9784(7)
S(2)–P(2)	1.9670(7)
S(2)–Cu(1)–S(1)	108.10(2)
Cu(1)–S(1)–P(1)	103.91(3)
Cu(1)–S(2)–P(2)	100.09(3)
N(2)–Cu(1)–N(1)	80.91(6)
Cu(1)–S(1)–P(1)–C(39)	−40.47(8)
Cu(1)–S(2)–P(2)–C(39)	−41.55(7)
S(1)–Cu(1)–S(2)–P(2)	63.78(2)
S(2)–Cu(1)–S(1)–P(1)	−23.74(3)
S(1)–P(1)–C(39)–P(2)	75.38(12)
S(2)–P(2)–C(39)–P(1)	−22.75(14)

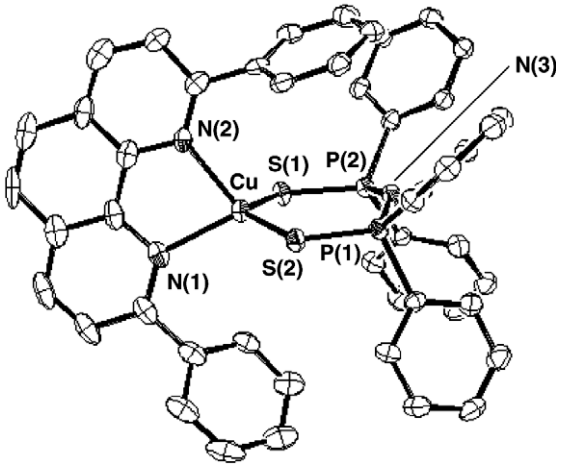


Fig. 4. X-ray structure of complex of **3**.

The structures of complex **2** and **3** containing $dppaS_2^-$ are described in Figs. 3 and 4. The selected bond lengths, bond angles and torsion angles of **2** and **3** are summarized in Tables 3 and 4, respectively. Complex **2** showed two independent molecules in the unit cell. The coordination geometry in one of the molecules is almost similar to each other. There are little differences between the structures of two independent molecules; the maximum of deviation for the corresponding bond angles is no more than 3.0°. In the $dppaS_2^-$ complexes, the S–P bond lengths range from 2.0043(8) to 2.0145(8) Å, which are slightly longer than those of **1**. The elongation should reflect the decrease of the P–S bond order, as shown in other reported transition metal complexes containing $dppaS_2^-$ ligand [10]. The bond angle of S–Cu–S in **2** is 117.77(2)° and 119.01(2)°, which is larger than that of **1**. It suggests that the chelate ring of $dppaS_2^-$ is somewhat more planar than that of $dppmS_2$. In addition, torsion angles within the chelate in **2** (11.28(4)–44.25(10)°) is smaller than those in **1** and the mean deviations from the least-squares planes which consists of six atoms in Cu-$dppaS_2$ chelate ring of two independent complexes of **2** are 0.238 and 0.256 Å, whereas that of **1** is 0.439 Å. They also show the planarity of the chelates in **2.** It should be caused by the negative charge on the imino nitrogen of the anionic ligand, $dppaS_2^-$, which promotes delocalization of π-electron within the S–P–N–P–S chelate. The coordination environment of **3** is similar to that of **2**. However, the torsion angles within the chelate ring of $dppaS_2^-$ are much smaller than those in **2**, and the mean deviation from the least-squares plane in Cu-$dppaS_2$ chelate ring of **3** is the smallest of the three complexes (0.120 Å). So they suggest that **3** has a more planar chelate ring of $dppaS_2^-$. It may be due to the repulsion from bulky phenyl rings of dpp, which forces the chelate ring of the $dppaS_2^-$ to be more planar.

3.2. Spectroscopic properties

NMR spectra have been measured to study the structures of the mixed-ligand complexes in solution. In the ^{31}P NMR spectra of **1**, a signal assigned as $dppmS_2$ was observed as a distinct singlet at δ 35.0, which is slightly shifted compared with the free ligand (δ 35.3), and no signals assigned to free ligand were observed. In addition, the phosphorus signal of **1** was shifted to higher field than that of $[Cu(dppmS_2)_2]PF_6$, which shows a singlet signal at δ 35.3. It suggests that the complexes keep mixed-ligand coordination even in solution. The spectra of **2** and **3** also show only a singlet signal of $dppaS_2^-$ moiety.

The absorption spectra of **1–3** in acetone are shown in Fig. 5. The absorption maximum of complex **1** is 457 nm with moderate intensity. ($\varepsilon = 3.1 \times 10^3\ mol^{-1}\ dm^3\ cm^{-1}$) It has been reported that mixed-ligand copper(I) complexes containing phenanthroline derivatives and diphosphines show absorption maxima ranging from 400 to 360 nm which have been assigned to MLCT transitions [2–4]. The band maximum of **1** are shifted to lower energy compared with the [Cu(diimine)(diphosphine)] complexes, but the

Table 3
Selected bond distances (Å), bond angles (°) and torsion angles (°) in complex **2**.

Cu(1)–S(1)	2.2761(7)
Cu(1)–S(2)	2.2957(7)
Cu(1)–N(1)	2.126(2)
Cu(1)–N(2)	2.124(2)
S(1)–P(1)	2.0130(8)
S(2)–P(2)	2.0043(8)
S(1)–Cu(1)–S(2)	117.77(2)
Cu(1)–S(1)–P(1)	100.92(3)
Cu(1)–S(2)–P(2)	102.06(3)
N(1)–Cu(1)–N(2)	79.18(8)
Cu(1)–S(1)–P(1)–N(3)	44.25(10)
Cu(1)–S(2)–P(2)–N(3)	40.71(10)
S(1)–Cu(1)–S(2)–P(2)	−24.10(4)
S(2)–Cu(1)–S(1)–P(1)	−11.28(4)
S(1)–P(1)–N(3)–P(2)	−40.4(2)
S(2)–P(2)–N(3)–P(1)	−13.9(2)
Cu(2)–S(3)–P(3)–N(6)	−39.21(10)
Cu(2)–S(4)–P(4)–N(6)	−39.51(10)
S(3)–Cu(2)–S(4)–P(4)	23.85(4)
S(4)–Cu(2)–S(3)–P(3)	9.10(4)
S(3)–P(3)–N(6)–P(4)	35.2(2)
S(4)–P(4)–N(6)–P(3)	15.5(2)
Cu(2)–S(3)	2.2768(7)
Cu(2)–S(4)	2.2909(7)
Cu(2)–N(4)	2.128(2)
Cu(2)–N(5)	2.118(2)
S(3)–P(3)	2.0145(8)
S(4)–P(4)	2.0068(8)
S(3)–Cu(2)–S(4)	119.01(2)
Cu(2)–S(3)–P(3)	101.62(3)
Cu(2)–S(4)–P(4)	101.26(3)
N(4)–Cu(2)–N(5)	79.60(8)

Table 4
Selected bond distances (Å), bond angles (°) and torsion angles (°) in complex **3**.

Cu(1)–S(1)	2.2470(11)
Cu(1)–S(2)	2.3048(11)
Cu(1)–N(1)	2.106(3)
Cu(1)–N(2)	2.154(3)
S(1)–P(1)	2.0065(15)
S(2)–P(2)	2.0021(14)
S(1)–Cu(1)–S(2)	121.14(4)
Cu(1)–S(1)–P(1)	104.00(5)
Cu(1)–S(2)–P(2)	104.88(5)
N(1)–Cu(1)–N(2)	79.57(13)
Cu(1)–S(1)–P(1)–N(3)	11.25(16)
Cu(1)–S(2)–P(2)–N(3)	−0.14(17)
S(2)–Cu(1)–S(1)–P(1)	9.91(7)
S(1)–Cu(1)–S(2)–P(2)	−14.88(7)
S(1)–P(1)–N(3)–P(2)	−39.8(4)
S(2)–P(2)–N(3)–P(1)	32.1(4)

band is reasonably assigned to MLCT involving the π^* orbitals of the dmp ligand, because the coordination of the sulfide having weaker σ-donor character leads to a decrease of energy levels of $d\sigma^*$ orbitals interactions in the complex and a decrease of the CT excitation energy [16]. However, there is another shoulder band in the lower energy region (500–550 nm) for complex **1**. The two bands may arise from two MLCT transitions to different π^* orbitals of the phen ligand as shown in $[Ru(bpy)(CN)_4]^{2-}$ which contains two quite distinct MLCT absorptions associated with the bpy ligand [17]. A second possibility is that the second absorption band might be assigned to a LLCT (ligand-to-ligand charge transfer) from the electron-rich S-donor ligand to the electron-poor phen ligands.

The absorption maximum of complex **2** is 427 nm. The absorption band is also assigned to MLCT transition involving the π^* orbital of dmp, whereas the maximum is shifted to higher energy

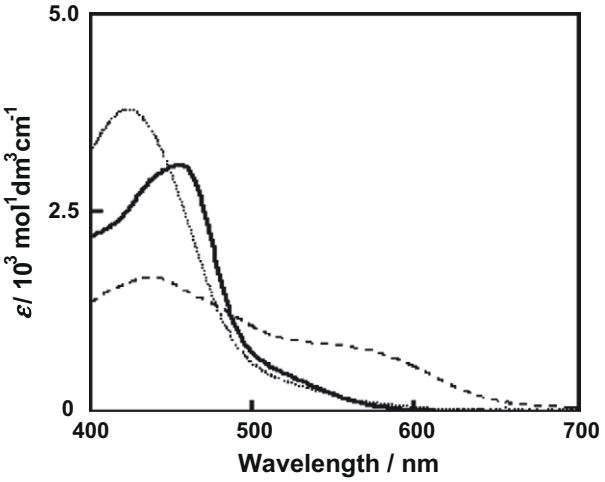


Fig. 5. Absorption spectra of complex cation **1** (solid line), **2** (dotted line) and **3** (dashed line) in acetone at room temperature.

than that of complex **1** which should reflect the stronger ligand field of $dppaS_2^-$. The shoulder band in lower energy region may be assigned to the second MLCT or LLCT as discussed for complex **1**. Complex **3** has an absorption maximum at 578 nm, which is shifted to lower energy due to extended π conjugated system of dpp compared with dmp. In order to confirm this hypothesis, the redox processes have been studied by cyclic voltammetry. Unfortunately, the redox potential in the cathodic region is too negative to estimate the potential for a diimine/diimine$^-$ redox couple. However, shoulder cathodic current in complex **3** was observed at −1.85 V versus SCE, which are clearly less negative than that of complex **1** and **2**. It may suggest that the red shift observed for dpp complex is reflected in a less negative ligand-based reduction process.

Both **1** and **2** show photoluminescence in the solid state as shown in Fig. 6. The emission maxima for **1** and **2** are 592 and 661 nm, respectively. The emissive excited states are assigned to MLCT transitions involving of the π^* orbital of dmp, as deduced from the luminescent behavior of $[Cu(dmp)2]^+$ and other mixed-ligand complexes. The Stokes shift observed for **2** (240 nm) is considerably large, whereas that of **1** is ca. 140 nm. It has been shown that a relatively large Stokes shift observed in Cu(I) com-

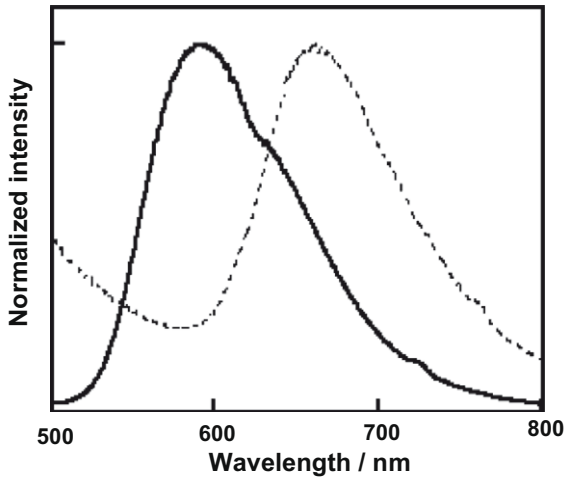


Fig. 6. Solid-state emission spectra of **1** (solid line) and **2** (dotted line) at room temperature.

plexes results from flattening distortion which occurs in the MLCT excited state [1a]. It suggests that the extent of distortion on excitation may become larger in **2** than **1**, which has relatively higher planarity of phosphinesulfide chelate than **1** as shown by X-ray analysis.

For both **1** and **2**, no emission is observed in solution. It contrasts with the fact that $[Cu(dmp)(dppe)]^+$ and $[Cu(dmp)(dppp)]^+$ emit in solution [2,4b]. It may be caused by the fact that coordination sphere around the copper atom of the diphosphine sulfide complexes is less crowded than the diphosphine complexes. The less crowded structure allows (1) the metal center to facilitate tetragonal flattening distortion of the excited luminophore and (2) the solvent molecules to attack the metal center in the excited states. These quenching mechanism [1a] should effectively affect the photophysical properties in solution.

4. Conclusions

Mixed-ligand Cu(I) complexes containing diimine and chelating phosphinesulfide ligands were synthesized. The isolated complexes, which have pseudo tetrahedral structure, were relatively stable in air. Two complexes of dmp show emission in the solid state, and their bands are assigned to MLCT.

5. Supplementary data

CCDC 715718, 715719 and 715720 contain the supplementary crystallographic data for **1**, **2** and **3**, respectively. These data can be obtained free of charge via http://www.ccdc.cam.ac.uk/conts/retrieving.html, or from the Cambridge Crystallographic Data Centre, 12 Union Road, Cambridge CB2 1EZ, UK; fax: (+44) 1223-336-033; or e-mail: deposit@ccdc.cam.ac.uk.

References

[1] (a) D.R. McMillin, K.M. McNett, Chem. Rev. 98 (1998) 1201;
(b) N. Armaroli, Chem. Soc. Rev. 30 (2001) 113;
(c) D.V. Scaltrito, D.W. Thompson, J.A. O'Callaghan, G.J. Meyer, Coord. Chem. Rev. 208 (2000) 243;
(d) S.B. Harkins, J.C. Peters, J. Am. Chem. Soc. 15 (2005) 2030.
[2] (a) S.-M. Kuang, D.G. Cuttell, D.R. McMillin, P.E. Fanwick, R.A. Walton, Inorg. Chem. 41 (2002) 3313;
(b) D.G. Cuttell, S.-M. Kuang, P.E. Fanwick, D.R. McMillin, R.A. Walton, J. Am. Chem. Soc. 124 (2002) 6.
[3] (a) N. Armaroli, G. Accorsi, M. Holler, O. Moudam, J.-F. Nierengarten, Z. Zhou, R.T. Wegh, R. Welter, Adv. Mater. 18 (2006) 1313;
(b) N. Armaroli, G. Accorsi, G. Bergamini, P. Ceroni, M. Holler, O. Moudam, C. Duhayon, B.D. Nicot, J.-F. Nierengarten, Inorg. Chim. Acta 360 (2007) 1032;
(c) A. Barbieri, G. Accorsi, N. Armaroli, Chem. Commun. (2008) 2185.
[4] (a) T. Tsukuda, A. Nakamura, T. Arai, T. Tsubomura, Bull. Chem. Soc. Jpn. 79 (2006) 288;
(b) K. Saito, T. Arai, T. Tsukuda, T. Tsubomura, Dalton Trans. 37 (2006) 4444;
(c) K. Saito, T. Tsukuda, T. Tsubomura, Bull. Chem. Soc. Jpn. 79 (2006) 437.
[5] T.S. Lobana, Prog. Inorg. Chem. 37 (1989) 495.
[6] T.S. Lobana, R. Mahajan, Transition Met. Chem. 26 (2001) 440.
[7] (a) R.K. Reigle, D.J. Casadonte Jr., Simon G. Bott, J. Chem. Cryst. 24 (1994) 753;
(b) R.K. Reigle, D.J. Casadonte Jr., Simon G. Bott, J. Chem. Cryst. 24 (1994) 769.
[8] G.J. Kubas, Inorg. Synth. 19 (1979) 90.
[9] C.O. Dietrich-Buchecker, Tetrahedron Lett. 23 (1982) 5291.
[10] I. Haidac, I. Silaghi-Dumitrescu, Coord. Chem. Rev. 74 (1986) 127.
[11] CrystalClear, Area Detector Processing Software, Rigaku and Molecular Structure Corp., 2000.
[12] SIR-92: A. Altomare, M.C. Burla, M. Camalli, M. Cascarano, C. Giacovazzo, A. Guagliardi, G.J. Polidori, Appl. Crystallogr. 27 (1994) 435.
[13] G.M. Sheldrick, SHELXL-97, Program for Crystal Determination and Refinement, University of Göttingen, Germany, 1997.
[14] CrystalStructure, ver.3.80: Single Crystal Structure Analysis Software, Molecular Structure Corporation.
[15] T.S. Lobana, Prog. Inorg. Chem. 37 (1989) 495 (and references herein).
[16] S. Sakaki, H. Mizutani, Y. Kase, Inorg. Chem. 31 (1992) 4575.
[17] M. Kovács, A. Horváth, Inorg. Chim. Acta 335 (2002) 69.

[Hg(quin)$_2$(OH$_2$)], aquabis(quinoline-2-carboxylato-κ^2*N*,*O*)mercury(II) (**1**), [(quinH$_2$)(HgCl$_3$)]·2quinH·H$_2$O, quinolinium-2-carboxylic acid trichloromercurate(II) bis(quinolinium-2-carboxylate) monohydrate (**2**), [Hg(quin)$_2$(EtOH)]·H$_2$O, bis(ethanol-κ*O*)bis-(quinoline-2-carboxylato-κ^2*N*,*O*)mercury-(II) monohydrate (**3**), [HgCl(quin)(quinH)], chloro(quinoline-2-carboxylato-κ^2*N*,*O*)(quinoline-2-carboxylic acid-κ^2*N*,*O*)mercury(II) (**4**) (Scheme 1).

2. Experimental

2.1. Materials and methods

All starting materials were of reagent grade and were used as received without further purification. Elemental analyses of C, H and N were carried out by Analytical Services Laboratories of the Institute Ruđer Bošković. The mercury content in the complexes was determined by complexometric titration, with diethyl dithiocarbamate, in the solution obtained after decomposition of the specimen in *aqua regia* [9]. IR spectra were obtained from KBr pellets in the range 4000–450 cm^{-1} with a Perkin–Elmer Spectrum RX I spectrometer. One- and two-dimensional homo- and heteronuclear ^{1}H, ^{13}C NMR spectra were recorded with a Bruker AV 600 spectrometer, operating at 600.133 MHz for the ^{1}H nucleus and 150.917 MHz for the ^{13}C nucleus. Samples were measured from DMSO-d$_6$ solutions at 25 °C (298 K) in 5 mm NMR tubes. Chemical shifts, in ppm, are referred to TMS. FID resolution in ^{1}H and ^{13}C NMR spectra was 0.29 and 0.54 Hz per point, respectively. The following measurement techniques were used: standard ^{1}H and ^{13}C gated proton decoupling, APT, COSY, HMQC and HMBC. The 2D NMR spectra were measured in a pulsed field gradient mode (z-gradient).

2.2. Preparative procedures and analytical data

2.2.1. [Hg(quin)$_2$(OH$_2$)] (**1**)

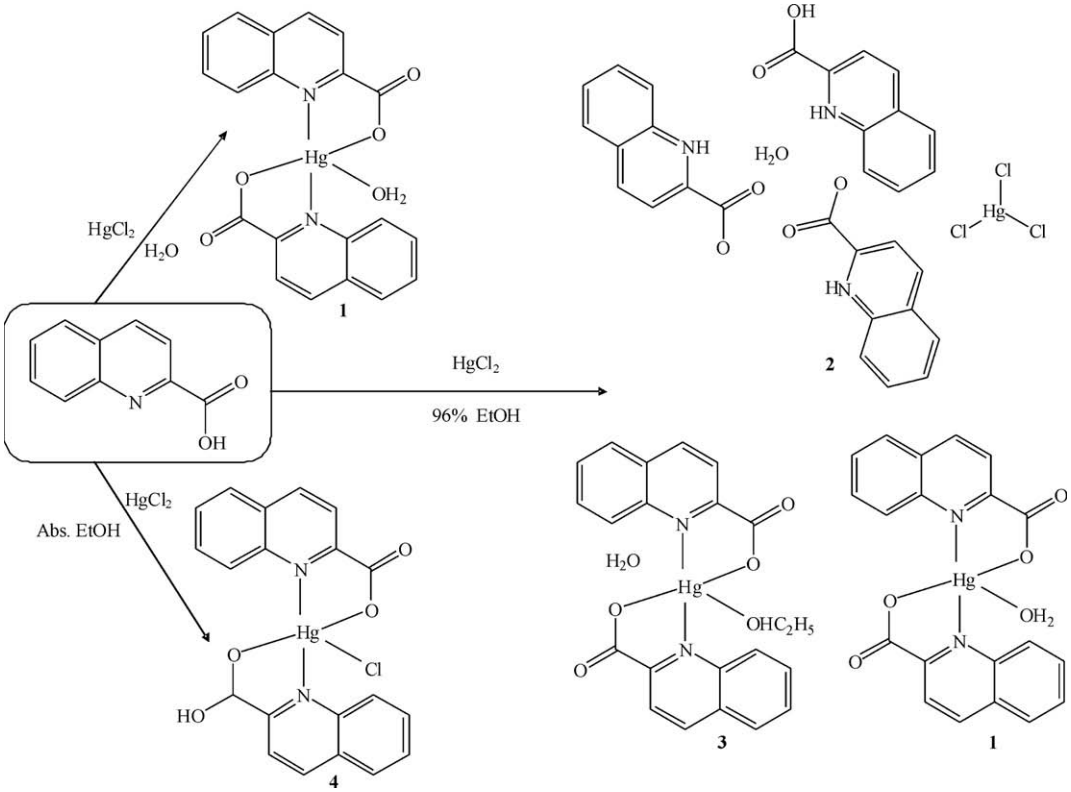
A solution of quinH (0.32 g, 1.85 mmol) in 40 mL H$_2$O was added dropwise to a solution of HgCl$_2$ (0.25 g, 0.92 mmol) in 10 mL H$_2$O. The colorless crystals were filtered off, washed with a small amount of water and dried in air. Yield: 0.48 g (92%). ^{1}H NMR (DMSO-d$_6$, ppm): δ_H 7.80 (t, J_{HH} = 7.51 Hz, H-6), 7.96 (t, J_{HH} = 7.25 Hz, H-7), 8.17 (d, J_{HH} = 8.03 Hz, H-5), 8.27 (bs, H-4), 8.29 (bs, H-8), 8.69 (d, J_{HH} = 7.45 Hz, H-3), 13.10 (bs, COO*H*). ^{13}C NMR (DMSO-d$_6$, ppm): δ_C 120.79 (d, J_{CH} = 168.12 Hz, C-4), 128.04 (d, J_{CH} = 163.93 Hz, C-5), 128.58 (d, J_{CH} = 163.27 Hz, C-6), 128.88 (s, C-2), 129.37 (d, J_{CH} = 161.83 Hz, C-8), 130.72 (d, J_{CH} = 163.19 Hz, C-7), 138.05 (d, J_{CH} = 166.98 Hz, C-3), 146.22 (s, C-10), 148.70 (s, C-9), 166.09 (s, *C*OOH). *Anal.* Calc. for C$_{20}$H$_{14}$N$_2$O$_5$Hg: C, 42.64; H, 2.51; N, 4.98; Hg, 35.63. Found: C, 42.98; H, 2.75; N, 4.80; Hg, 35.12%.

2.2.2. Mixture of [Hg(quin)$_2$(OH$_2$)] (**1**), [(quinH$_2$)(HgCl$_3$)]·2quinH·H$_2$O (**2**) and [Hg(quin)$_2$(EtOH)]·H$_2$O (**3**)

A solution of quinH (0.32 g, 1.85 mmol) in 30 mL aqueous EtOH was added dropwise to an aqueous ethanol solution of HgCl$_2$ (0.25 g, 0.92 mmol) in 10 mL. The clear solution was allowed to stand for one week. The obtained colorless crystals of various shapes were filtered off, washed with a small amount of ethanol and dried in air. Yield: 0.35 g.

2.2.3. [HgCl(quin)(quinH)] (**4**)

A solution of quinH (0.32 g, 1.85 mmol) in 30 mL abs. EtOH was added dropwise to a solution of HgCl$_2$ (0.25 g, 0.92 mmol) in 10 mL abs. EtOH. The clear solution was allowed to stand for one week. The colorless crystals were filtered off, washed with a small



Scheme 1. Preparation of compounds **1**–**4**.

amount of absolute ethanol and dried in air. Yield: 0.08 g (15%). ^{1}H NMR (DMSO-d_6, ppm): δ_H 7.77 (t, J_{HH} = 7.52 Hz, H-6), 7.92 (t, J_{HH} = 7.17 Hz, H-7), 8.13 (d, J_{HH} = 8.01 Hz, H-5), 8.19 (bs, H-4), 8.20 (bs, H-8), 8.61 (bs, H-3), 13.36 (bs, CO*OH*). ^{13}C NMR (DMSO-d_6, ppm): δ_C 120.82 (d, J_{CH} = 167.96 Hz, C-4), 128.07 (d, J_{CH} = 163.89 Hz, C-5), 128.61 (d, J_{CH} = 163.79 Hz, C-6), 128.92 (s, C-2), 129.34 (d, J_{CH} = 165.57 Hz, C-8), 130.78 (d, J_{CH} = 165.58 Hz, C-7), 148.78 (s, C-9), 166.02 (s, *C*OOH). *Anal.* Calc. for $C_{20}H_{13}N_2O_4ClHg$: C, 41.64; H, 2.25; N, 4.82; Hg, 34.50. Found: C, 41.33; H, 2.37; N, 4.65; Hg, 34.25%.

After isolation of [HgCl(quin)(quinH)] 0.20 g of a mixture of $[Hg(quin)_2(OH_2)]$ (**1**), $[(quinH_2)(HgCl_3)]\cdot 2quinH\cdot H_2O$ (**2**) and $[Hg(quin)_2(EtOH)]\cdot H_2O$ (**3**) was also obtained.

2.3. X-ray crystallography

Selected crystallographic and refinement data for structures **1**–**4** obtained by the single crystal X-ray diffraction method are reported in Table 1. Data collection for structures **1** and **3** were carried out on an Oxford Diffraction Xcalibur four-circle kappa geometry diffractometer with Sapphire 2 CCD detector, while for compounds **2** and **4** the intensity data were collected on the same diffractometer but with a Sapphire 3 CCD detector by applying the CRYSALIS Software system, Version 171.26 [10a]. The unit cell parameters were calculated and refined from the full data set, the Lorentz-polarization effect was corrected and the intensity data reduced by the CRYSALIS RED application of the CRYSALIS Software system, CRYSALIS Software system, Version 1.171.31.8 [10a] for data sets **2** and **4**, while data for **1** and **3** were reprocessed with CRYSALIS RED, Version 1.171.33.27 [10b]. The diffraction data were corrected for absorption effects by the multi-scanning method. **1** is a superstructure along the *b*-axis as can be nicely seen from a simulated precession photograph of the [*h k* 0] zone, showing strong reflections in every third row along $b*$. Structure of **3** decomposed during data collection so the data set is not complete; however 80% of the data were enough for a well refined structure. All attempts to get another crystal of good diffraction quality failed.

All structures were solved by direct methods and refined on F^2 by weighted full-matrix least-squares. Programs SHELXS97 and SHELXL97 [11] integrated in the WINGX Software system [12] were used to solve and refine all four structures. All non-hydrogen atoms, with exception of the disordered H_2O molecule in **3** (O2A and O2B with occupancies of 0.750(8) and 0.250(8), respectively) were refined anisotropically. H-atoms belonging to the bound and crystallization water molecules in **1** and **2**, respectively, and that of the ethanol molecule in **3** were found in the difference-Fourier map and were refined with restrained distances. Other H-atoms (except those on the disordered H_2O molecule of crystallization in **3**, which were not found nor could be modeled reliably) were placed in geometrically idealized positions [Csp^2–H 0.93 Å with U_{iso}(H) = 1.2 U_{eq}(C); O–H 0.82 Å with U_{iso}(H) = 1.5 U_{eq}(O)] and were constrained to ride on their parent atoms by using the appropriate SHELXL97 HFIX instructions. In **4** the hydrogen atom H2 on quin/quinH is both statistically and structurally disordered (by the presence of a twofold axis along the Hg–Cl bond). However small electron-density was found in a difference-Fourier map and this H-atom was given an occupancy factor of 0.5. The molecular geometry calculations and drawings were performed by ORTEP-3 [13], PLATON [14] and MERCURY [15].

Table 1
General and crystal data and summary of intensity data collection and structure refinement for compounds **1**–**4**.

Compound	**1**	**2**	**3**	**4**
Formula	$[Hg(quin)_2(OH_2)]$	$[(quinH_2)(HgCl_3)]\cdot 2quinH\cdot H_2O$	$[Hg(quin)_2(EtOH)]\cdot H_2O$	[HgCl(quin)(quinH)]
Brutto formula	$C_{20}H_{14}HgN_2O_5$	$C_{30}H_{24}Cl_3HgN_3O_7$	$C_{22}H_{20}HgN_2O_6$	$C_{20}H_{13}ClHgN_2O_4$
M_r	562.92	845.46	608.99	581.36
Crystal system, color and habit	monoclinic, colorless, prism	triclinic, colorless, prism	triclinic, colorless, prism	monoclinic, colorless, irregular prism
Space group	$P\,2_1/c$ (No. 14)	$P\bar{1}$ (No. 2)	$P\bar{1}$ (No. 2)	$C\,2/c$ (No.15)
Crystal dimensions (mm)	0.19 × 0.35 × 0.53	0.18 × 0.28 × 0.36	0.18 × 0.21 × 0.38	0.22 × 0.37 × 0.39
T (K)	296	296	296	296
Unit cell parameters				
a (Å)	16.2188(3)	7.3732(5)	7.8225(6)	15.2393(2)
b (Å)	22.9339(4)	11.5581(7)	11.5502(6)	13.8913(2)
c (Å)	15.6202(3)	17.6907(12)	14.2130(6)	8.69100(10)
α (°)	90.0	79.665(5)	72.201(4)	90.0
β (°)	114.304(2)	86.308(5)	80.057(5)	105.3228(15)
γ (°)	90.0	81.587(5)	70.709(6)	90.0
V (Å^3)	5295.17(19)	1466.06(17)	1150.37(12)	1774.43(4)
Z	12	2	2	4
D_c (g cm^{-3})	2.118	1.915	1.758	2.176
μ (mm^{-1})	8.757	5.577	6.728	8.856
F(0 0 0)	3216	824	588	1104
θ Range for data collection (°)	4–30	4–30	4–30	4–30
h,k,l Range	−22 to 22; −32 to 32; −21 to 21	−10 to 10, −16 to 16, −24 to 24	−10 to 6; −16 to15; −19 to 16	−21 to 21; −19 to 19; −12 to 12
Scan type	ω and φ	ω	ω	ω
Number of measured reflections	185376	46925	8360	19556
Number of independent reflections (R_{int})	15400 (0.062)	8527 (0.049)	5837 (0.022)	2593 (0.033)
Number of refined parameters	775	421	282	132
Number of observed reflections, $I \geqslant 2\sigma(I)$	10262	4530	4392	1930
g_1, g_2 in w	0.0421, 0	0.0300, 0	0.0506, 0	0.0278, 0.000
R, wR [$I \geqslant 2\sigma(I)$]	0.0326, 0.0683	0.0330, 0.0764	0.0359, 0.0819	0.0195, 0.0466
R, wR (all data)	0.0650, 0.0757	0.0768, 0.0655	0.0507, 0.0847	0.0304, 0.0513
Goodness of fit (GoF) on F^2, S	0.95	1.05	0.95	1.07
Maximum, minimum electron-density (e Å^{-3})	1.80, −1.43	1.60, −1.19	1.34, −0.95	0.39, −1.30
Maximum Δ/σ	0.003	0.001	<0.001	0.001

The general and crystallographic data for compounds **1**–**4** are listed in Table 1. The main geometrical features for structures **1**–**4** are given in Tables 2–5, respectively. Hydrogen bond geometry is given in Table 6 for compounds **1**–**4**.

3. Results and discussion

3.1. General aspects of preparation

In aqueous media mercury(II) chloride reacts with 2-quinaldic acid giving pure aquabis(quinoline-2-carboxylato-κ^2-*N,O*)mercury, $[Hg(quin)_2(OH_2)]$ (**1**) in an almost quantitative yield. If the reaction is performed in aqueous alcohol, a mixture of $[Hg(quin)_2(OH_2)]$ (**1**), $[(quinH_2)(HgCl_3)]\cdot 2quinH\cdot H_2O$ (**2**) and $[Hg(quin)_2(EtOH)]\cdot H_2O$ (**3**) is obtained. All attempts to separate these complexes failed due to their very similar solubility in common solvents. When the reaction is carried out in absolute alcohol a small amount of [HgCl(quin)(quinH)] (**4**) is obtained (cca 15% by mass). By concentration of the filtrate, again the mixture of **1**–**3** is obtained and single crystals of each compound could be separated by hand.

3.2. Structural studies

3.2.1. Structure of $[Hg(quin)_2(OH_2)]$ (**1**)

The asymmetric unit in the superstructure of **1** consists of three structurally slightly different molecules of $[Hg(quin)_2(OH_2)]$, Fig. 1a. The mercury atom is coordinated by two nitrogen and two oxygen atoms from two *N,O*-coordinating quinaldate ligands. The fifth coordination site is occupied by an oxygen atom from a water molecule. The N–Hg–N angle is in the range 167.57(11)–170.36(11)° (Table 2) and shows tendency towards linear coordination, which is in agreement with the distances Hg–N that are the shortest and range from 2.190(3) to 2.241(3) Å. The Hg–O distances are longer (2.310(4)–2.437(3) Å) and the coordination can therefore be described as deformed 2 + 3 trigonal-bipyramidal. This is confirmed by the index of the degree of trigonality, τ of 0.67 (calculated for the first molecule only as a difference between two largest angles divided by 60). This index is zero for a perfectly square-pyramidal and a unity for perfectly trigonal-bipyramidal geometry [16].

In all three molecules the Hg–O(OH_2) distance is longer than Hg–O(quin). Such bound water molecules are not uncommon in mercury compounds. The distance Hg–OH_2 can be even longer than in **1** such as in the structure of aquabromo(6-carboxypyridine-2-carboxylato-*O,N,O′*)mercury(II) [3] where it amounts to 2.634(5) Å. In that compound the mercury atom is also five-coordinated. Shorter Hg–OH_2 bonds are found in some organomercury compounds where

Table 3
Selected interatomic distances (Å) and valence angles (°) for compound **2**.

Selected bond distances (Å)	
Hg1–Cl1	2.3737(10)
Hg1–Cl2	2.4265(10)
Hg1–Cl3	2.4583(11)
Hg1···Cl2[a]	2.9949(11)
Hg1···Cl3[b]	3.2076(11)
O1–C11	1.232(4)
O2–C11	1.255(4)
O3–C21	1.243(5)
O4–C21	1.235(4)
O5–C31	1.204(4)
O6–C31	1.290(4)
Selected bond angles (°)	
Cl1–Hg1–Cl3	116.05(4)
Cl1–Hg1–Cl2[a]	91.78(4)
Cl2–Hg1–Cl3	110.93(4)
Cl2–Hg1–Cl2[a]	83.88(3)
Cl2[a]–Hg1–Cl3	97.80(3)
Cl1–Hg1–Cl2	132.97(4)

$a = 1 - x, 2 - y, 1 - z$.
$b = 2 - x, 2 - y, 1 - z$.

Table 4
Selected interatomic distances (Å) and valence angles (°) for compound **3**.

Selected bond distances (Å)			
Hg–N11	2.252(4)	O11–C11	1.266(6)
Hg–N21	2.263(4)	O12–C11	1.240(7)
Hg–O11	2.393(4)	O21–C21	1.254(7)
Hg–O21	2.313(5)	O22–C21	1.218(8)
Hg–O1	2.524(6)	O1–C1	1.407(10)
Hg···O11[a]	2.785(4)		
Selected bond angles (°)			
N11–Hg–N21	177.86(14)	O1–Hg–N11	89.16(17)
O11–Hg–N11	72.00(14)	O1–Hg–N21	90.98(18)
O11–Hg–N21	105.87(14)	O11–Hg–O21	168.19(15)
O21–Hg–N11	108.46(15)	O1–Hg–O11	90.05(16)
O21–Hg–N21	73.60(15)	O1–Hg–O21	101.74(18)

$a = 1 - x, 2 - y, 2 - z$.

Table 2
Selected interatomic distances (Å) and valence angles (°) for compound **1**.

Selected bond distances (Å)					
Hg1–N1	2.195(3)	Hg2–N3	2.241(3)	Hg3–N6	2.230(3)
Hg1–N2	2.190(3)	Hg2–N4	2.222(3)	Hg3–N5	2.199(3)
Hg1–O11	2.387(3)	Hg2–O31	2.310(4)	Hg3–O51	2.381(3)
Hg1–O21	2.362(3)	Hg2–O41	2.361(3)	Hg3–O61	2.316(3)
Hg1–O1	2.423(3)	Hg2–O2	2.374(3)	Hg3–O3	2.437(3)
O11–C11	1.238(6)	O31–C31	1.263(6)	O51–C51	1.245(6)
O12–C11	1.233(6)	O32–C31	1.235(6)	O52–C51	1.250(5)
O21–C21	1.257(6)	O41–C41	1.253(6)	O61–C61	1.259(6)
O22–C21	1.231(5)	O42–C41	1.236(5)	O62–C61	1.232(5)
Selected bond angles (°)					
N1–Hg1–N2	167.57(11)	N3–Hg2–N4	170.36(11)	N5–Hg3–N6	170.36(11)
O11–Hg1–N1	73.89(11)	O31–Hg2–-N3	73.87(12)	O51–Hg3–N5	74.01(13)
O21–Hg1–N1	106.45(12)	O41–Hg2–N3	97.81(11)	O61–Hg3–N5	114.18(12)
O1–Hg1–N1	84.00(11)	O2–Hg2–N3	101.91(12)	O3–Hg3–N5	95.75(11)
O1–Hg1–N2	106.90(11)	O2–Hg2–N4	85.85(11)	O3–Hg3–N6	85.47(11)
O11–Hg1–N2	95.84(11)	O31–Hg2–N4	108.78(12)	O51–Hg3–N6	96.81(11)
O21–Hg1–N2	73.67(11)	O41–Hg2–N4	73.58(11)	O61–Hg3–N6	73.96(12)
O11–Hg1–O21	126.19(11)	O31–Hg2–O41	134.05(13)	O51–Hg3–O61	131.02(13)
O1–Hg1–O11	113.58(11)	O2–Hg2–O31	111.81(13)	O3–Hg3–O51	115.63(11)
O1–Hg1–O21	120.01(10)	O2–Hg2–O41	114.12(12)	O3–Hg3–O61	111.48(12)

Table 5
Selected interatomic distances (Å) and valence and torsion angles (°) for compound **4.**

Selected bond distances (Å)	
Hg1–Cl1	2.3610(10)
Hg1–N1	2.2871(19)
Hg1–O1	2.4911(17)
C1–O1	1.232(3)
C1–O2	1.277(3)
Selected bond angles (°)	
Cl1–Hg1–O1	119.52(4)
Cl1–Hg1–N1	118.49(5)
O1–Hg1–N1	69.93(6)
O1–Hg1–O1^a	120.96(5)
O1–Hg1–N1^a	82.71(6)
N1–Hg1–N1^a	123.02(7)

$a = -x, y, 1/2 - z$.

Table 6
Hydrogen bond geometry (Å, °) for compounds **1–4**.

D–H···A	D–H	H···A	D···A	⟨D–H···A	Symmetry code
1					
O1–H11···O62	0.86(4)	1.83(5)	2.662(5)	162(5)	
O1–H12···O52	0.84(3)	1.87(3)	2.695(4)	167(5)	$x, 3/2-y, 1/2+z$
O2–H21···O42	0.86(4)	1.85(3)	2.685(4)	164(6)	$x, 3/2-y, -1/2+z$
O2–H22···O22	0.87(5)	1.79(5)	2.651(5)	175(7)	$1-x, 2-y, 1-z$
O3–H31···O32	0.86(3)	1.85(4)	2.651(5)	161(4)	$1-x, 1-y, 1-z$
O3–H32···O12	0.88(2)	1.78(2)	2.640(4)	165(4)	$x, 3/2-y, 1/2+z$
2					
N1–H11N···O1	0.89(3)	2.37(3)	2.688(4)	102(3)	
N1–H11N···O7	0.89(3)	1.90(4)	2.759(5)	165(4)	
N2–H12N···O1	0.95(4)	1.94(4)	2.870(4)	163(3)	
N3–H13N···O3	0.86(3)	1.92(4)	2.735(4)	159(3)	$-1+x, y, z$
O6–H16O···O2	0.94(5)	1.56(5)	2.503(4)	177(6)	$1-x, 2-y, -z$
O7–H17O···O4	0.93(6)	1.92(6)	2.801(5)	159(5)	$-1+x, y, z$
O7–H27O···O4	0.69(4)	2.10(4)	2.765(5)	161(5)	$2-x,1-y,-z$
3					
O1–H1···O12	0.86(6)	1.83(7)	2.661(7)	162(7)	$1-x, -y, -z$
O2A···O22			2.707(8)		$1+x, y, z$
4					
O2–H2···O2	0.70(5)	1.77(5)	2.443(3)	161(5)	$-x, y, 3/2-z$

the coordination of mercury is linear, *e.g.* in the structure of mercurated acetic acid it is 2.17(3) Å [17], or in a tetramercurated methane derivative, bis(aquamercurio)-bis-(sulfatomercurio)methane where it is 2.131(11) Å [18]. The C–O distances in the carboxylic groups are in the range 1.231(5)–1.263(6) Å.

All hydrogen atoms on the bound water molecules act as hydrogen bond donors and the carboxylic group oxygen atoms as acceptors. Four hydrogen bonds of the type O–H···O connect each molecule with four different neighboring ones into two-dimensional layers parallel to (1 0 0), Fig. 1b, Table 6. The layers are connected by π···π interactions. The shortest centroid (Cg) to centroid distances are: Cg3–Cg3 ($-x, -y, -z$) distance is 3.543(6) Å, slippage 1.055 Å (Cg3 is the centroid of the ring N1, C12–C15, C20); Cg4–Cg4 ($1-x, -y, -z$) is 3.564(6) Å, slippage 0.760 Å (Cg4 is the centroid of the ring N2, C22–C25, C3).

3.2.2. Structure of $[(quinH_2)(HgCl_3)]\cdot 2quinH\cdot H_2O$ (**2**)

The asymmetric unit of compound **2** (Fig. 2a) consists of a formally isolated trichloromercurate(II) anion, $[HgCl_3]^-$, two zwitterionic quinolinium-2-carboxylate molecules, quinH, a quinolinium-2-carboxylic cation, $[quinH_2]^+$, and one water molecule of crystallization. In the presence of large cations such as $[quinH_2]^+$ the major structural isomer adopted by $[HgCl_3]^-$ is a dimeric edge-shared bitetrahedron $[Hg_2Cl_6]^{2-}$ [19–26]. In some structures additional two Hg···Cl interactions connect the $[HgCl_3]^-$ anions into endless chains. In **2** each Hg atom is surrounded by five Cl^- ions forming a deformed trigonal-bipyramid with one short, two slightly longer bonds, and two long mercury to chlorine contacts [Hg1–Cl1 2.374(1) Å, Hg1–Cl2 2.427(1) Å, Hg1–Cl3 2.458(1), Hg1···Cl2^a ($a = 1-x, 2-y, 1-z$) 2.995(1), Hg1···Cl3^b ($b = 2-x, 2-y, 1-z$) 3.2076(11) Å] (Table 3). The two long contacts connect the $[HgCl_3]^-$ anions into endless chains along [1 0 0]. The Hg1–Cl1 bond distance value belongs to the covalent bond characteristic for trigonal mercury and chlorine (sum of the covalent radii of trigonal mercury and chlorine atoms is 2.38 Å), while Hg1–Cl2 and Hg1–Cl3 covalent bonds are more similar to mercury to chlorine covalent bonds characteristic for tetrahedral mercury (2.47 Å) [27–30]. The two long contacts are shorter than the van der Waals' radii sum for mercury and chlorine (3.23–3.60 Å) [27–31], but longer than mercury to chlorine covalent bond. According to Ref. [19–26] Hg–Cl distances of 2.3–2.6 Å are clearly formal covalent bonds, while Hg···Cl contacts up to 3.35 Å, and even longer, are considered to be interactions. Regarding such geometrical parameters, obviously, there is no clear definition about the border between a formal mercury to chlorine bond and a long contact which results in a structural variety for chloromercurate(II) systems. Polymeric chains of the $[HgCl_3]^-$ anions are found in

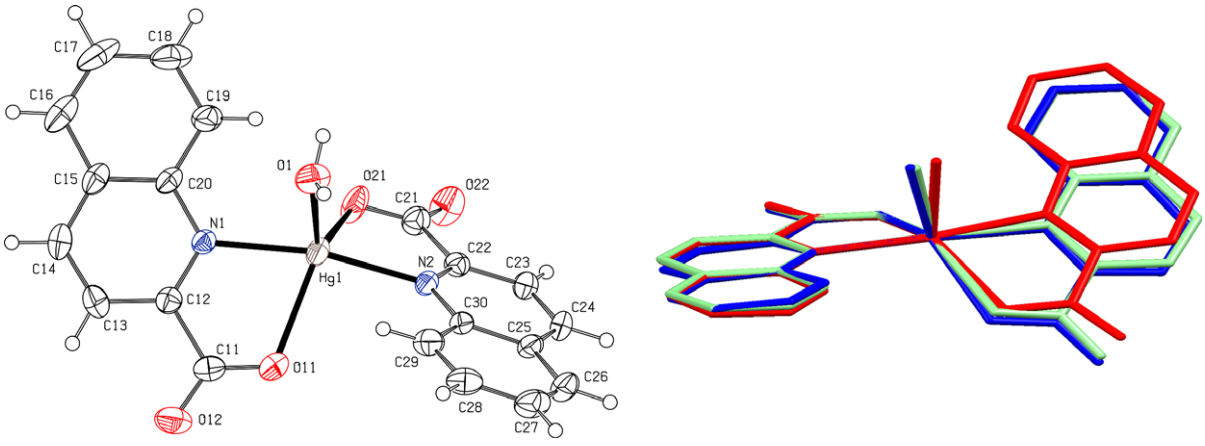


Fig. 1a. (a) ORTEP drawing of $[Hg(quin)_2(OH_2)]$, aquabis(quinoline-2-carboxylato-κ^2N,O)mercury(II), **1**, with the atomic numbering scheme. The thermal ellipsoids are drawn at the 40% probability level at 296 K. Only one of the three independent molecules in the asymmetric unit is shown. Other molecules have an analogous numbering scheme (Hg2, O2, N3, O31, O32, C31–40, N4, O41, O42, C41–50; Hg3, O3, N5, O51, O52, C51–C60, N6, O61, O62, C61–C70; Supplementary material, Fig. S1). (b) Diagram of the overlapping of three independent molecules.

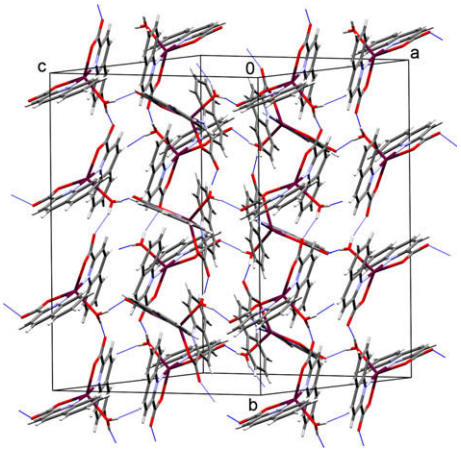


Fig. 1b. Packing of **1** in the unit cell. Hydrogen bonds are shown by blue dashed lines. Mercury is shown in purple color. (For interpretation of the references to color in this figure legend, the reader is referred to the web version of this article.)

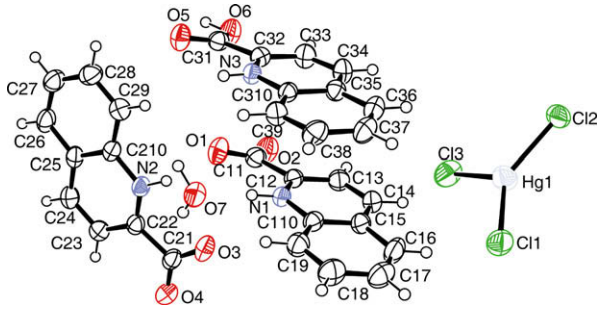
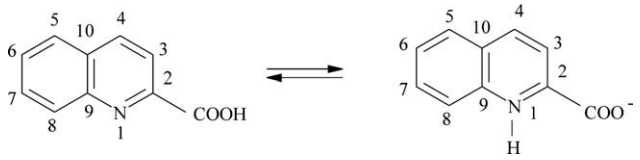


Fig. 2a. ORTEP drawing of the asymmetric unit of $[(quinH_2)(HgCl_3)]\cdot 2quinH\cdot H_2O$, quinolinium-2-carboxylic acid trichloromercurate(II) bis(quinolinium-2-carboxylate) monohydrate, **2**, with the atomic numbering scheme. The thermal ellipsoids are drawn at the 50% probability level at 296 K.

structures of triethylammonium catena(bis-μ_2-chloro)-chloromercury) (refcode: DORSIM) [32], catena(tetraethylammonium trichloro-mercury(II)) (refcode: EAMCHG [33], catena-(bis(chloro-(*N*,*N*,*N*′,*N*′-tetrakis(*N*-methylcarbamoylmethyl)ethane-1,2-diamine)-mercury(II)) tetrakis(μ_2-chloro)-dichloro-di-mercury(II)sesquihydrate) (refcode: NIMFOF) [34]. All these structures comprise 3 + 2 mercury coordination geometry revealing three formally coavlent mercury to chlorine bonds and two longer contacts which complete a trigonal-bipyramidal configuration. The longest Hg···Cl distances in these three mercury polymers amount 3.050(3) Å, 3.054(3) Å and 3.154(5) Å in the structure with refcodes NIMFOF, EAMCHG and DORSIM, respectively. The deformed 3 + 2 mercury coordination in **2** is confirmed by the bond angle range from 83.88(3)° for Cl2–Hg1–Cl2^a ($a = 1-x, 2-y, 1-z$) to 132.97(4)° for the Cl1–Hg1–Cl2 angle (Table 3).

Existence of two ligand molecules in the zwitterionic form *i.e.*, as quinolinium-2-carboxylate molecules, is revealed on the basis of the –COO fragment geometry (Table 3, Scheme 2). The C–O bond values for the carboxylate group are in the range 1.232(4) Å (for the O1–C11 bond) to 1.255(4) Å (for the O2–C11 bond). A similar bond range in the –COO fragment is found in the structure of the ligand itself [35] and in the structure of (benzoato-κ^2-*O*,*O*)(quinoline-2-carboxylato-κ^2-*N*,*O*(quinoline-2-carboxylic acid-κ^2-*N*,*O*)copper(II) [35], which contains the neutral ligand coordinated to the copper(II) ion.

The zwitterionic C–O bonds amount 1.263(2) Å and 1.248(2) Å in the ligand itself [35]. The quinolinium-2-carboxylic cation in **2**



Scheme 2. Tautomeric forms of quinoline-2-carboxylic acid and enumeration of the atoms.

contains a carboxylic –COOH group with the C–O dimensions 1.204(4) Å (for keto O5–C31 bond) and 1.290(4) Å (for the O6–C31 bond). The corresponding C–O bond distances in the ligand are 1.314(2) Å and 1.221(2) Å [35], while in the copper complex the corresponding bond distance values are 1.187(3) Å and 1.306(3) Å [36].

There are no hydrogen bonds between cations and anions, only cations and neutral zwitterions are interlaced by hydrogen bonds of the N–H···O and O–H···O type (Table 6; Fig. 2b). There are four hydrogen bonds of the N–H···O type; one being intramolecular (N1–H11N···O1 in one of the zwitterions), while the other three are formed by all three NH groups with the carboxylate O1 and O3 atoms and the water oxygen atom O7. The N···O distances are in the range 2.688(4)–2.870(4) Å. There are also three O–H···O hydrogen bonds, two of them formed by a water molecule acting as a double proton donor, and one by the –COOH carboxylic group [O···O range varies from 2.503(4) Å for the O6–H16O···O2 bond to 2.801(5) Å for the O7–H17O···O4 bond].

3.2.3. Structure of $[Hg(quin)_2(EtOH)]\cdot H_2O$ (**3**)

The structure of **3** consists of molecules of $[Hg(quin)_2(EtOH)]$ and H_2O molecules of crystallization, Fig. 3a. The mercury atom is coordinated by two quinaldate ligands at similar Hg–O distances as in **1** (2.313(5)–2.393(4) Å, Table 4), whereas the Hg–N distances are slightly longer (2.252(4) and 2.263(4) Å). At the fifth coordination site there is an oxygen atom from the ethanol molecule at the distance of 2.524(6) Å. These atoms form a square-pyramidal coordination which is not usual for Hg so dimers are often formed as is the case in **3**. There is a Hg···O contact of 2.785(4) Å with the carboxylate oxygen atom O11 from the neighboring centrosymmetrically related molecule ($-x, -y, -z$) connecting them into dimers and forming a 5 + 1 octahedral coordination around the mercury

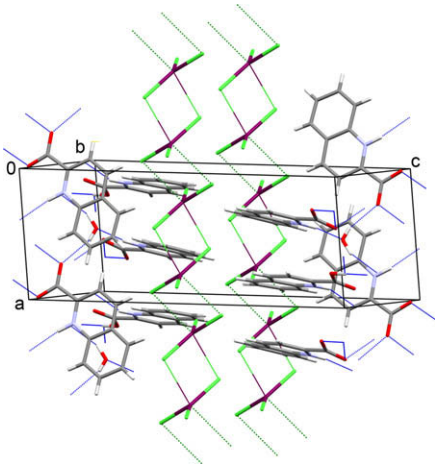


Fig. 2b. Packing of **2** in the unit cell. Hydrogen bonds are shown by blue dashed lines. Mercury is shown in purple color. Contacts Hg1···Cl2 are drawn by thin purple and green lines, Hg1···Cl3 contacts are drawn by dashed green lines. (For interpretation of the references to color in this figure legend, the reader is referred to the web version of this article.)

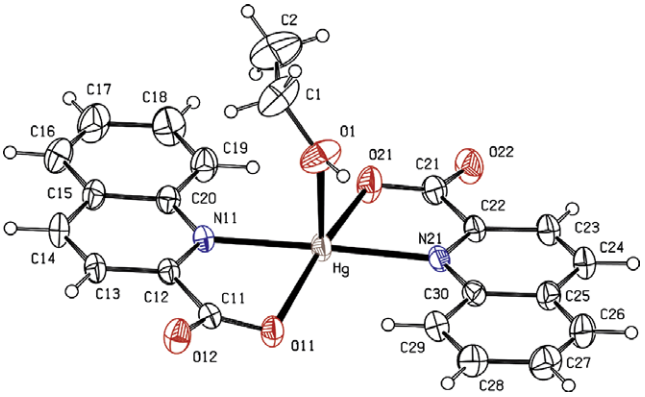


Fig. 3a. ORTEP drawing of $[Hg(quin)_2(EtOH)]\cdot H_2O$, bis(ethanol-κ*O*)bis(quinoline-2-carboxylato-κ^2N,O)mercury-(II) monohydrate, **3**, with the atomic numbering scheme. The thermal ellipsoids are drawn at the 50% probability level at 296 K.

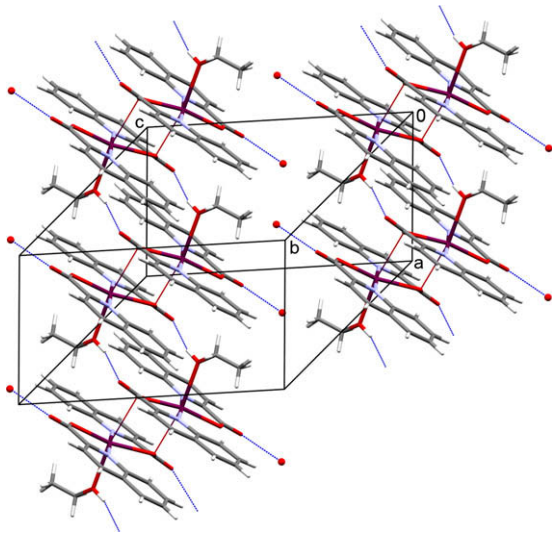


Fig. 3b. Packing of **3** in the unit cell. Hydrogen bonds are shown by blue dashed lines, and the Hg···O contacts by thin purple and red lines. Mercury is shown in purple color. The solvent H_2O molecule is shown as a small red ball. (For interpretation of the references to color in this figure legend, the reader is referred to the web version of this article.)

atom, Fig. 3b. Within the dimers there are also π···π interactions between the rings. The closest distance between the centroid of the ring defined by atoms N11, C12–15, C20 and the centroid of the centrosymmetrical pair (−*x*, −*y*, −*z*) of the ring defined by C25–C30 is 3.560(6) Å (slippage 0.681 Å). The carboxylic C–O bond lengths are in the range 1.218(8)–1.266(6) Å. As expected, the longer C–O distances include oxygen atoms that are bound to the mercury atom.

The dimeric molecules are connected by short hydrogen bonds between the hydrogen atom from the ethanol hydroxyl group and an oxygen from the carboxylic group (O1–H1···O12(1 − *x*, −*y*, −*z*) 2.661(7) Å, Table 6) into chains along [1 0 0]. The chains are connected by van der Waals and π···π interactions with neighboring chains. The shortest centroid (N21, C22–C24, C30) to centroid (the same ring related by −*x*, 1 − *y*, −*z*) distance is 3.661(6) Å, slippage 1.101 Å. Hydrogen atoms on the disordered H_2O molecules were not found, however, from the distance O2A···O22 (1 + *x*, *y*, *z*) of 2.707(8) Å, a hydrogen bond is expected.

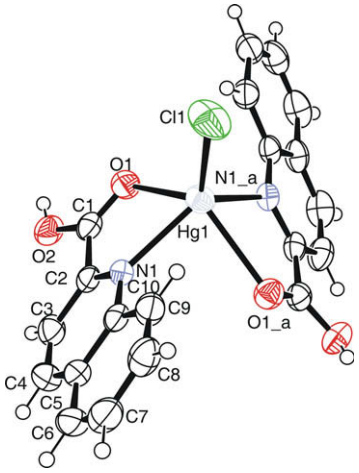


Fig. 4a. ORTEP drawing of [HgCl(quin)(quinH)], chloro(quinoline-2-carboxylato-κ^2N,O)(quinoline-2-carboxylic acid-κ^2N,O)mercury(II), **4**, with the atomic numbering scheme. The thermal ellipsoids are drawn at the 50% probability level at 296 K.

3.2.4. [HgCl(quin)(quinH)] (**4**)

Compound **4** (Fig. 4a) has twofold symmetry with the axis along the Hg1–Cl1 bond. The formula and the symmetry necessarily implicate both statistical and structural hydrogen atom disorder between the two ligands, $[quin]^-$ and quinH, maintaining complex neutrality.

Mercury is coordinated *via* the Cl1 atom (Hg1–Cl 2.361(1) Å) and *via N,O*-donor atoms of the bidentate quinaldate ion, $[quin]^-$, and one neutral quinaldic acid, quinH, [Hg1–O1 2.491(2) and Hg1–N1 2.287(2) Å] in a very irregular square-pyramidal coordination (Table 5). The coordination sphere is better described as 4 + 1 than 3 + 2 geometry according to the bond distance values and the bond angles range around the mercury atom [69.93(6)–123.02(7)°]. The τ value of 0.03 (see Ch. 3.2.1) reveals that the mercury coordination is in agreement with the square-pyramidal model. The geometry of this complex is similar to iodo(picolinato-κ^2N,O)(picolinic acid-κ^2N,O)mercury(II) recently reported by us [5], which contains a particularly short Hg–I bond distance comparable with the distance in the yellow form of HgI_2 [37] (2.615(6) and 2.620(6) Å). The mercury to chlorine bond distance in **4** is slightly shorter than the sum (2.39 Å) of the covalent radii for trigonal Hg (1.39 Å) and for chlorine (0.99 Å), and significantly longer than the radii sum for linear Hg and chlorine (2.29 Å) [27–30]. In the structure of $HgCl_2$ itself the mercury coordination can be described as 2 + 4 octahedral with the shortest Hg–Cl bond distance of 2.274(10) Å [38]. The Hg1–N1 bond distance of 2.287(2) Å is comparable with those found in **3** and in the iodo(picolinato-κ^2N,O)(picolinic acid-κ^2N,O)mercury(II) complex (2.298(3) Å) [5]. In relation to the Hg–N bond distances in the complexes which do not contain an Hg–Cl bond *i.e.*, complexes **1** and **3**, the value for the Hg1–N1 bond distance is longer in **4** (2.287(2) Å). The Hg1–O1 distance of 2.491(2) Å is also longer than in **1** or **3** and is comparable with 2.481(2) Å for the mercury to oxygen distance found in the iodo(picolinato-κ^2N,O)(picolinic acid-κ^2N,O)mercury(II) complex [5]. The covalent radii sum for trigonally coordinated Hg with N or O amounts to 2.09 Å and 2.05 Å, respectively.

The mercury to oxygen contacts are longer to some extent then the mercury to nitrogen contacts. These considerations are supported by the bond angles range being between 123.02(7)° for the N1–Hg1–N1^a ($a = -x, y, 0.5 - z$) angle and 69.93(6)° for the O1–Hg1–N1 angle. A similar situation is not found in the iodo(picolinato-κ^2N,O)(picolinic acid-κ^2N,O)mercury(II) complex [5] *i.e.*, the largest angle is N2′–Hg1–I1 of 125.11(6)°, while angle N2′–Hg1–N2 amounts to 109.78(13)°. The reason for that is a par-

ticular tendency of mercury to form strong covalent bonds with iodine atoms. The bite angle values are comparable in both complex **4** and the iodo(picolinato-κ^2N,O)(picolinic acid-κ^2N,O)mercury(II) complex and reflect the stereochemical rigidity of quinaldic and picolinic acid.

The 3 + 2 mercury coordination is found in the polymeric μ-bromo-μ-pyridine-3-carboxylato-$\kappa^3O,O':N$–mercury(II) complex [39] where mercury is coordinated by two Br atoms, two carboxylate atoms (Hg–O 2.353(6) Å and 2.478(7) Å) and an N atom (2.265(5) Å). It is obvious that the strongest bonds are to the N and halogen atom as is found in complex **4** and the iodo complex as well.

Geometry of the COO fragment in both ligands, $[quin]^-$ and quinH, is averaged between the carboxylic acid and carboxylate ion geometry (C1–O1 and C1–O2 bonds amount to 1.232(3) Å and 1.277(3) Å, respectively) (Scheme 2) supporting the hydrogen atom disorder. Similar values are found in iodo(picolinato-κ^2N,O)(picolinic acid-κ^2N,O)mercury(II) [5], 1.233(4) Å and 1.271(4) Å, while in the bromo derivative [39] these values are slightly affected by participation of carboxylate oxygen atoms in the coordination of Hg (1.226(11) Å and 1.259(10) Å). In the structure of the ligand itself, quinoline-2-carboxylic acid quinolinium-2-carboxylate [35], two tautomeric forms occur in the crystal: the neutral molecule and the zwitterion. In the neutral molecule of quinoline-2-carboxylic acid the C–O bond distances are 1.314(2) Å and 1.221(2) Å, while in the zwitterion they are 1.263(2) Å and 1.248(2) Å.

The intermolecular hydrogen bond O2–H2···O2 ($-x$, y, $3/2 - z$) of 2.443(3) Å connects molecules of the complex into infinite chains along the [1 0 1] direction (Fig. 4b).

3.3. Spectroscopy

3.3.1. IR spectra

The IR spectral data of quinH and its mercury(II) complexes **1** and **4** were analyzed. Their assignments were based on the literature data regarding other metal complexes with quinH [40–42]. In the solid state quinH exists in both neutral (C_9H_6NCOOH) and zwitterionic ($C_9H_6NH^+COO^-$) tautomeric forms [35].

In the IR spectrum of quinH absorption bands which support such structure were observed. The medium intensity band due to the C=O stretching vibration is observed at 1700 cm^{-1}. The antisymmetric (ν_{as}) and symmetric (ν_s) modes of the COO^- group were observed at 1650, 1618 cm^{-1} and 1380, 1317 cm^{-1}, respectively.

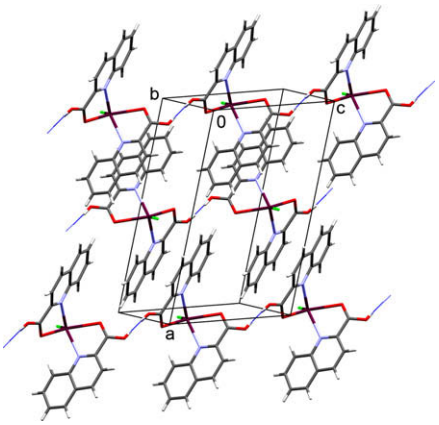


Fig. 4b. Packing of **4** in the unit cell (only one half of the unit cell is shown $b \leqslant 0.5$). Hydrogen bonds are shown by blue dashed lines. Mercury is shown in purple color. (For interpretation of the references to color in this figure legend, the reader is referred to the web version of this article.)

In the spectrum of **1** there is no band due to C=O stretching in the vicinity of 1700 cm^{-1}. Absorption bands at 1662, 1619 cm^{-1} were assigned as ν_{as} and the band at 1374 cm^{-1} as ν_s of COO^-.

In the IR spectra of **4** bands which indicate the existence of a coordinated quinaldate anion as well as a neutral quinaldic acid molecule were observed. The C=O stretching is found at 1699 cm^{-1}. Medium strong absorption bands at 1662 and 1623 cm^{-1} are assigned as ν_{as}. The corresponding symmetric stretch absorption of COO^- is observed at 1374 cm^{-1}.

Broad absorption bands in the 3100–1800 cm^{-1} region of the IR spectrum of quinH indicate the existence of N–H···O and O–H···O types of hydrogen bonds. In the IR spectra of complexes **1** and **2**, broadness, disappearing and lower intensity of bands in this region were observed, which implies different hydrogen bonding pattern in the mercury(II) complexes.

3.3.2. ^1H and ^{13}C NMR spectra

The NMR spectra of quinH, **1** and **4** are in agreement with their structures. The ^1H and ^{13}C NMR spectra revealed existence of monomercurated species in a DMSO-d_6 solution. The assignments of protons are supported by COSY spectra and the carbon atoms are confirmed by HMQC and HMBC measurements. The C-3 and C-10 signals in **4** are not observed because of the relaxation effects of nitrogen and mercury atoms.

The effects of mercury on both ^1H and ^{13}C chemical shifts are small and insufficient to clarify the conformation of the complexes in the solutions.

4. Conclusion

In this work we report the synthesis, IR, ^1H and ^{13}C NMR spectroscopy, and crystal and molecular structures determined by X-ray single crystal diffraction of several mercury(II) complexes with quinaldic acid: [Hg(quin)$_2$(OH$_2$)], aquabis(quinoline-2-carboxylato-κ^2N,O)mercury(II) (**1**), [(quinH$_2$)(HgCl$_3$)]·2quinH·H$_2$O, quinolinium-2-carboxylic acid trichloromercurate(II) bis(quinolinium-2-carboxylate) monohydrate (**2**), [Hg(quin)$_2$(EtOH)]·H$_2$O, bis(ethanol-κO)bis(quinoline-2-carboxylato-κ^2N,O)mercury-(II) monohydrate (**3**), [HgCl(quin)(quinH)], chloro(quinoline-2-carboxylato-κ^2N,O)(quinoline-2-carboxylic acid-κ^2N,O)mercury(II) (**4**).

The ligand, quinaldic acid is coordinated to Hg^{2+} ion as an *N,O*-chelating quinaldate ion, $quin^-$, in structures **1**, **3** and **4**. Different coordination polyhedra are obtained: in **1** a deformed 2 + 3 trigonal-bipyramidal with the fifth coordination site occupied by a water molecule, in **3** the fifth square-pyramidal coordination site is occupied by an ethanol molecule and in **4,** which resembles the 4 + 1 irregular square-pyramidal coordination, there is a chlorine atom attached to mercury at the fifth coordination site. In the structure of **3** centrosymmetrical dimers are formed by Hg···O contacts and a 5 + 1 effective mercury coordination is established. The structure of compound **2** is completely different, containing a trichloromercurate(II) anion, $[HgCl_3]^-$, two zwitterionic quinolinium-2-carboxylate molecules, quinH, a quinolinium-2-carboxylic cation, $[quinH_2]^+$, and one water molecule of crystallization. The$[HgCl_3]^-$ moieties are interconnected by two long Hg···Cl contacts into endless chains of $[HgCl_3]_n^{n-}$ anions revealing the 3 + 2 mercury coordination sphere.

The coordination spheres of mercury in compounds **1**–**4** are established on the basis of bond distances and angle values taking into account the criteria for characteristic and effective coordination spheres such as covalent and van der Waals' radii of Hg and donor atoms (N, O, Cl).

The crystal structures are characterized by O–H···O and N–H···O intermolecular hydrogen bonds (in **1** there is also one O–H···O intramolecular hydrogen bond and in **2** there are three N–H···O

intramolecular hydrogen bonds). These bonds form various crystal packing motifs: two-dimensional layers parallel to (1 0 0) in **1**, a 3D network in **2**, chains along [1 0 0] in **3** and infinite chains along the [1 0 1] direction in **4**.

Supplementary data

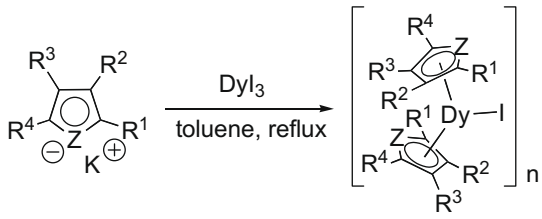
CCDC 719374, 719375, 719376, 719377 contain the supplementary crystallographic data for **1**–**4**. These data can be obtained free of charge *via* http://www.ccdc.cam.ac.uk/conts/retrieving.html, or from the Cambridge Crystallographic Data Centre, 12 Union Road, Cambridge CB2 1EZ, UK; fax: (+44) 1223-336-033; or e-mail: deposit@ccdc.cam.ac.uk. Structure factor tables are available from the authors. The Supplementary data also contains a Figure of **1** with the numbering scheme of all three independent molecules (Fig. S1) and a simulated precession photograph of the [*h k* 0] zone of **1** (Fig. S2).

Acknowledgements

The authors gratefully acknowledged the financial support of the Ministry of Science, Education and Sport of the Republic of Croatia, Zagreb (Grant Nos. 119-1193079-1332, 119-1193079-1084 and 098-0982929-2917).

References

[1] W. Kaim, B. Schwederski, Bioinorganic Chemisty: Inorganic Elements in the Chemistry of Life, J. Wiley and Sons, Chichester, 1996.
[2] M.J. Stillman, F.C. Shaw, K.T. Suzuki (Eds.), Metallothioneins: Synthesis, Structure and Properties of Metallothioneins, Phytochelatins, and Metal-Thiolate Complexes, VCH verlagsgessellschaft mbH, Weinheim, 1992.
[3] D. Matković-Čalogović, J. Popović, Z. Popović, I. Picek, Ž. Soldin, Acta Crystallogr. C58 (2002) m39.
[4] Z. Popović, G. Pavlović, D. Matković-Čalogović, Ž. Soldin, Acta Crystallogr. C59 (2003) m165.
[5] Z. Popović, G. Pavlović, Ž. Soldin, Acta Crystallogr. C62 (2006) m272.
[6] Z. Popović, D. Matković-Čalogović, J. Popović, I. Vicković, M. Vinković, D. Vikić-Topić, Polyhedron 26 (2007) 1045.
[7] Ž. Soldin, Ph.D. Thesis, University of Zagreb, Zagreb, 2006 (in Croatian; Abstract in English).
[8] P. Zhou, D. O'Hagan, U. Mocek, Z. Zeng, L.-D. Yuen, C.J. Unkefer, J.M. Beale, G.H. Floss, J. Am. Chem. Soc. 111 (1989) 51.
[9] P. Gouverneur, W. Hoedeman, Anal. Chim. Acta 30 (1964) 519.
[10] (a) CRYSALIS Software system, Version 1.171.31.8, Xcalibur CCD System, Oxford Diffraction Ltd., Abingdon, UK, 2007;
(b) CRYSALIS Software system, Version 1.171.33.27, Xcalibur CCD System, Oxford Diffraction Ltd., Abingdon, UK, 2008.
[11] G.M. Sheldrick, Acta Crystallogr. A64 (2008) 112.
[12] L.J. Farrugia, J. Appl. Crystallogr. 32 (1999) 837.
[13] L.J. Farrugia, J. Appl. Crystallogr. 30 (1997) 565.
[14] L. Spek, J. Appl. Crystallogr. 36 (2003) 7.
[15] C.F. Macrae, I.J. Bruno, J.A. Chisholm, P.R. Edgington, P. McCabe, E. Pidcock, L. Rodriguez-Monge, R. Taylor, J. van de Streek, P.A. Wood, J. Appl. Crystallogr. 41 (2008) 466.
[16] A.W. Addison, T.N. Rao, J. Reedijk, J. van Rijn, G.C. Verschoor, J. Chem. Soc., Dalton Trans. (1984) 1349.
[17] D. Grdenić, M. Sikirica, D. Matković-Čalogović, J. Organomet. Chem. 306 (1986) 1.
[18] D. Grdenić, B. Korpar-Čolig, D. Matković-Čalogović, J. Organomet. Chem. 522 (1996) 297.
[19] D.A. House, W.T. Robinson, V. McKee, Coord. Chem. Rev. 135/136 (1994) 533.
[20] A. Linden, B.D. James, J. Liesegang, N. Gonis, Acta Crystallogr. B55 (1999) 396.
[21] P.L. Goggin, P. King, D.M. McEwan, G.E. Taylor, P. Woodward, J. Chem. Soc., Dalton Trans. (1982) 875.
[22] F. Zouari, A.B. Salah, Acta Crystallogr. C51 (1995) 1563.
[23] P.S. Chaari, A.B. Salah, T. Jouini, A. Daoud, Acta Crystallogr. C45 (1989) 1495.
[24] D.C. Bebout, D.E. Ehmann, J.C. Trinidad, K.K. Crahan, M.E. Kastner, D.A. Parrish, Inorg. Chem. 36 (1997) 4257.
[25] A.B. Salah, A. Daoud, G. Constant, J. Jaud, J. Galy, Acta Crystallogr. C39 (1983) 63.
[26] H. Wen, S.E. Miller, D.A. House, V. McKee, W.T. Robinson, Inorg. Chim. Acta 193 (1992) 77.
[27] L. Pauling, General Chemistry, 3d ed., W.P. Freeman and Co., San Francisco, 1970.
[28] D. Grdenić, Quart. Rev. 19 (1965) 303.
[29] A. Bondi, J. Phys. Chem. 68 (1964) 441.
[30] (a) D. Matković-Čalogović, Ph.D. Thesis, University of Zagreb, Zagreb, 1994 (in Croatian; Abstract in English);
(b) D. Milić, Ž. Soldin, G. Giester, Z. Popović, D. Matković-Čalogović, Croat. Chem. Acta, in press.
[31] S.C. Nyburg, C.H. Faerman, Acta Crystallogr., Sect. B 41 (1985) 274.
[32] P.M. Boorman, C.L. Merrit, W.A.S. Nandana, J.F. Richardson, J. Chem. Soc., Dalton Trans. 186 (1986) 1251.
[33] M. Sandstrom, D.H. Liem, Acta Chem. Scand. A 32 (1978) 509.
[34] K. Krot, A.L. Llamas-Saiz, N. Vembu, K.B. Nolan, Z. Anorg. Allg. Chem. 633 (2007) 1900.
[35] D. Dobrzynska, L.B. Jerzykiewicz, J. Chem. Crystallogr. 34 (1) (2004) 51.
[36] N.D. Martins, M.R. Silva, J.A. Silva, A.M. Beja, A.J.F.N. Sobral, Acta Crystallogr. E64 (2008) m829.
[37] G.A. Jeffrey, M. Vlasse, Inorg. Chem. 6 (1967) 396.
[38] V. Subramanian, K. Seff, Acta Crystallogr. B36 (1980) 2132.
[39] Z. Popović, G. Pavlović, D. Matković-Čalogović, Ž. Soldin, Acta Crystallogr. C59 (2003) m165.
[40] M.A.S. Goher, F.A. Mautner, Polyhedron 12 (1993) 1863.
[41] W. Li, M.M. Olmstead, D. Miggins, R.H. Fish, Inorg. Chem. 35 (1996) 51.
[42] M.A.S. Goher, A.K. Hafez, T.C.W. Mak, Polyhedron 20 (2001) 2583.



1a: $R^1=R^2=R^4=tBu$, $R^3=H$, Z=CH, n=1
1b: $R^1=R^2=R^4=SiMe_3$, $R^3=H$, Z=CH, n=1
1c: $R^1=R^4=tBu$, $R^2=R^3=Me$, Z=P, n=1
1d: $R^1=R^4=SiMe_3$, $R^2=R^3=Me$, Z=P, n=2

Scheme 1. Synthesis of unsolvated organodysprosium(III) complexes.

Cp‴ (1,2,4-tris-trimethylsilyl-cyclopentadienyl), Dtp (1,4-bis-*t*-butyl-2,3-dimethylphospholyl) and Dsp (1,4-bis-trimethylsilyl-2,3-dimethylphospholyl). The reason for this selection is that stable divalent complexes of thulium(II) have been obtained with these ligands [2f–i,k].

The reaction works quite well and good yields have been obtained in all cases, thus establishing the generality of the method.

We had previously found that, despite its high paramagnetism, **1a** displayed a usable NMR spectrum in which three peaks could be assigned to the three inequivalent *t*Bu groups. Likewise, we found that **1b–d** also had interpretable NMR spectra. In **1b**, unlike in **1a**, two substituents on the ring ($SiMe_3$ groups) are equivalent. This might be due to free rotation of the substituted cyclopentadienyl around the centroid–Dy axis. In **1c** and **1d**, only peaks corresponding to the bulky *t*Bu or $SiMe_3$ on the phospholyl ring could be detected; presumably the phospholyl ring methyls are too close to the paramagnetic Dy center to be detected: note that the ring protons on **1a** and **1b** were not detected either.

2.2. Crystal structures of complexes *1b–d*

Complexes **1b–d** could be further characterised by their X-ray crystal structures and Figs. 1–3 represent ORTEP plots of these complexes; the X-ray data of all compounds are summarised in Table 1.

These structures confirm the η^5-bonding mode of the cyclopentadienyl and phospholyl ligands around dysprosium.

First of all, it is interesting to note that whilst the phospholyl complex possessing the Dsp ligand **1d** is a solid-state dimer, complex **1c** with the closely related Dtp ligand is a monomer. Thus, a subtle modification on the ligand substituents (from *t*-butyl in **1c** to trimethylsilyl in **1d**) can have a strong influence on the structure of the complexes. This change reflects the smaller steric bulk of the relatively flexible trimethylsilyl group, which is able to bend away from the cyclopentadienyl plane, more so than the more rigid *t*-butyl group.

Compounds **1b** and **1c** belong to the class of 7-coordinated unsolvated bis(π-complexed) halides; there are relatively few such compounds described in the literature that are structurally characterised [2i–k,8]. The structural features of **1b** and **1c** can be assessed by comparison with that of the previously described **1a** (Table 1); dimer **1d** (with the Dsp ligand) is different since it is 8-coordinated.

The four parameters in Table 2 were chosen because they can be used as indicators of the influence of the ligand. The metal–centred bond lengths and angles as defined above are expected to increase with the steric bulk of the ligand. The most precise indicator is the length of the Dy–I bond, which clearly points to the highest steric bulk of the Cp^{ttt} ligand. This confirms the earlier findings in

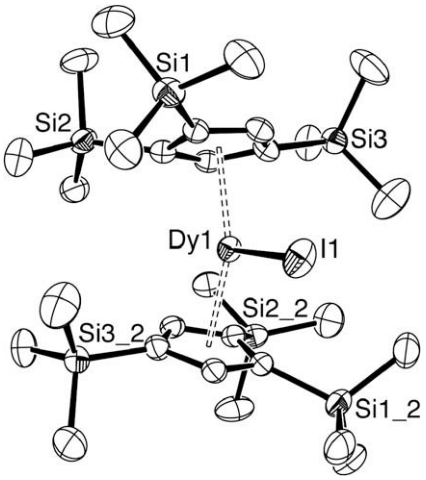


Fig. 1. An ORTEP plot of one molecule of **1b** (hydrogen atoms omitted). There are two other independent molecules in the unit cell (not represented).

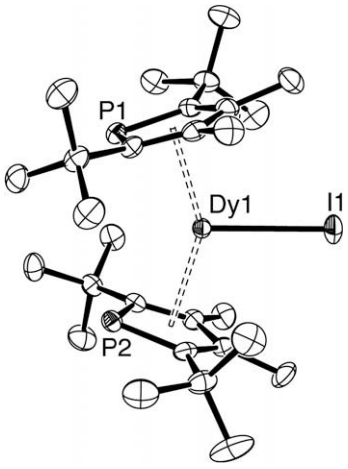


Fig. 2. An ORTEP plot of one molecule of **1c** (hydrogen atoms omitted).

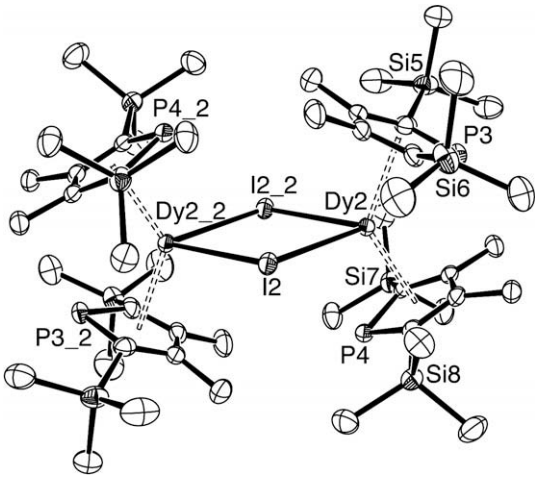


Fig. 3. An ORTEP plot of the dimeric structure of **1d** (hydrogen atoms omitted). There is one other independent dimer in the unit cell (not represented).

thulium chemistry [2f–i,k]. It is more difficult to compare the Dtp and the Cp‴ ligands from the dihedral and Ct–Dy–Ct angles. The Dy–C bond lengths have a high variability and a bias may exist

Table 1
A Summary of X-ray data for compounds **1b**, **1c**, **1d** and **4**.

Compound	**1b**	**1c**	**1d**	**4**
Molecular formula	$C_{28}H_{58}DyISi_6$	$C_{28}H_{48}DyIP_2$	$C_{48}H_{96}Dy_2I_2P_4Si_8$	$C_{59}H_{90}BrDyKO_7,C_7H_8$
Molecular weight	852.68	736.00	1600.65	1284.85
Crystal habit	colourless block	pale yellow block	yellow block	needle
Crystal diameter (mm)	0.24 × 0.20 × 0.18	0.22 × 0.20 × 0.20	0.12 × 0.10 × 0.10	0.20 × 0.08 × 0.06
Crystal system	monoclinic	monoclinic	triclinic	monoclinic
Space group	*C*2/*c* (no. 15)	$P2_1/c$ (no. 14)	$P\bar{1}$ (no. 2)	$P2_1/c$ (no. 14)
a (Å)	41.095(2)	10.8260(10)	11.7130(10)	12.633(1)
b (Å)	18.3960(10)	17.0250(10)	11.7720(10)	30.385(1)
c (Å)	32.965(2)	16.4470(10)	26.9880(10)	18.870(1)
α (°)	90	90	78.9660(10)	90
β (°)	125.6950(10)	91.8290(10)	79.8550(10)	116.352(1)
γ (°)	90	90	70.6780(10)	90
V (Å^3)	20239.2(19)	3029.8(4)	3421.1(4)	6490.6(7)
Z	20	4	2	4
d (g cm^{-3})	1.399	1.614	1.554	1.315
F[0 0 0]	8580	1460	1588	2680
μ (cm^{-1})	2.801	3.604	3.332	1.879
Maximum θ	27.48	30.03	30.03	23.25
Reflections measured	42 689	13 982	32 162	30 127
Unique data	23 151	8824	19 986	9247
R_{int}	0.0312	0.0182	0.0241	0.1036
Reflections used	17 056	7458	15 182	4598
wR_2	0.1030	0.0747	0.0637	0.1617
R_1	0.0377	0.0278	0.0315	0.0615
Goodness-of-fit (GOF)	1.035	1.060	1.005	0.898

Table 2
A comparison of the main structural features of compounds **1a–c**.

Cpd	Ligand	Dy–I[a]	Dy–C(av.)[b]	Ct–Dy–Ct[c]	Dihedral[d]	Reference
1a	Cp^{ttt}	2.9619(5)	2.68(3)	148	147	[2j]
1b	Cp$''$	2.917(9)[e]	2.63(3)	142	140	this work
1c	Dtp	2.9235(2)	2.74(3)	147	145	this work

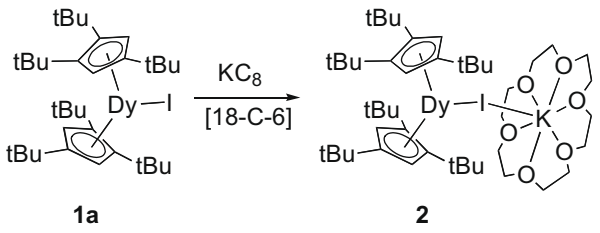
[a] Dy–I distance (Å).
[b] Dy–C average distance (Å).
[c] Metal–centred angle between the ligand rings centroids (°).
[d] Dihedral angle between the ligand rings mean planes (°).
[e] Average on the three independent molecules of the unit cell.

because of the heterocyclic nature of Dtp. However, it is clear that the Dsp ligand is the smallest from the dimeric solid-state nature of **1d**. Thus, a tentative classification of the ligands according to decreasing steric bulk would be Cp^{ttt} > Dtp > Cp$''$ > Dsp.

2.3. Attempted reduction of compounds *1b–d*

We found earlier that compound **1a** could be successfully reduced into **2** by reaction of KC_8 in the presence of crown ether (Scheme 2).

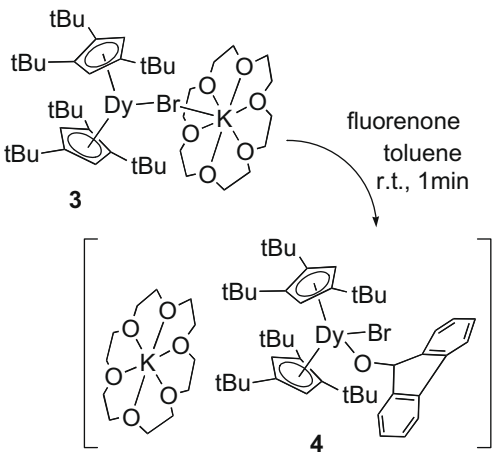
In order to try to find new dysprosium(II) compounds, we decided to subject compounds **1b–d** to the same reaction conditions. With compounds **1c** and **1d**, no apparent reduction occurred, whilst with **1b**, degradation quickly happened. With KC_8 in the absence of crown ether, no reaction took place with **1a**, **1c** and **1d**, whereas with **1b**, a red colour initially appeared and several new peaks were observed in the proton spectrum, which might be indicative of the transient presence of Dy^{II} species; however the colour gradually turned to light orange and no defined compound could be isolated. Therefore it seems that the stability of any Dy^{II} species is extremely sensitive to the ligand environment.



Scheme 2. Reduction of **1a** into an organodysprosium(II) complex.

2.4. A new organodysprosium(II) oxidation product

Since we have not been able to widen the scope of organodysprosium(II) complexes, in order to get more insight into the chemistry of these species, we decided to attempt to oxidise **2** with an aromatic ketone, a reaction which is known to occur with Sm^{II} and Yb^{II} precursors [9]. When fluorenone was added to a solution of **2**, a dark red colour developed but we were unable to isolate a solid complex. However, when the bridging halide in the organodysprosium(II) complex was changed from iodide to bromide and the reaction was performed with precursor **3**, an oxidation product (**4**) was isolated (Scheme 3).



Scheme 3. Oxidation of **3** into the organodysprosium(III) zwitterionic complex **4**.

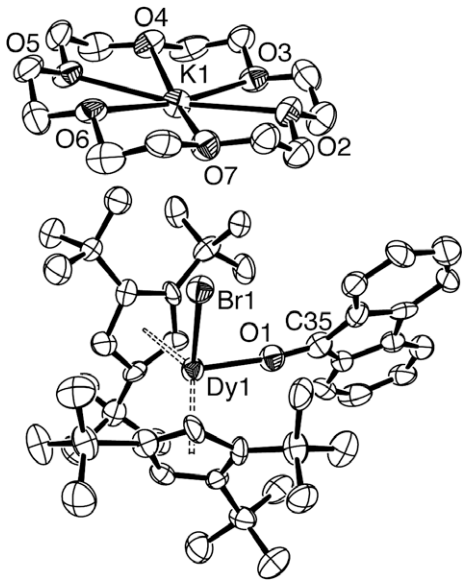


Fig. 4. An ORTEP plot of the charge-separated ionic complex **4** (hydrogen atoms omitted).

Compound **4** was characterised by X-ray crystallography (Fig. 4).

This figure clearly shows that **4** is a charge-separated ionic complex, where the potassium atom encapsulated by the crown ether is no longer bonded to the bromide (K1–Br1 distance = 4.6 Å). **4** is not a simple adduct of **3** with fluorenone, since this molecule has been reduced to the radical anion by electron transfer from dysprosium, as definitively proven by the length of the C35–O1 bond distance (1.32(1) Å), which points to a single bond; in fluorenone, this bond length is 1.22 Å [10]. Thus, the oxidation state of dysprosium in **4** is +III.

3. Conclusion

We have synthesized three new unsolvated organodysprosium(III) complexes with very bulky phospholyl and cyclopentadienyl ligands, one of which is interestingly a solid-state dimer, and attempted to reduce them in organodysprosium(II) species. The success of this reduction seems to be extremely sensitive to the ligand environment and reaction conditions. We have also been able to oxidise an organodysprosium(II) complex into a new, unprecedented charge-separated ionic organodysprosium(III) ketyl complex. We are still trying to discover more organodysprosium(II) complexes by finding new stabilising ligand environments.

4. Experimental

4.1. General data

All reactions were performed under high purity argon with purified dry and deoxygenated solvents, because of the exceedingly air-sensitive nature of all organolanthanide complexes synthesised in this study. The following compounds: sodium 1,2,4-tris-trimethylsilylcyclopentadienide (NaCp‴) [6], potassium 1,4-bis-*t*-butyl-2,3-dimethylphospholide (KDtp) [2g], potassium 1,4-bis-trimethylsilyl-2,3-dimethylphospholide (KDsp) [7] and complexes **1a** and **2** [2j] were prepared as previously described. All other reagents were commercial and used as received from the suppliers. NMR data were obtained at 300 MHz on a Bruker Avance 300 instrument, IR spectra were measured on a Perkin–Elmer Paragon 1000 spectrometer, and elemental analyses were obtained from the "Centre de Microanalyse de l'Université de Bourgogne", Dijon, France. Despite several attempts with highly purified complexes, it was only possible to get meaningful analyses for **1c**.

4.2. Syntheses

*General procedure (GP) for the preparation of complexes **1b–d**:* In the glovebox a mixture of DyI_3 (1.0 eq) and K(L) or Na(L) (2.2 eq) was prepared in a Schlenk tube fitted with a J. Young valve. Toluene (20 mL) was condensed onto this mixture at −78 °C and the suspension was allowed to warm to room temperature. Under stirring the reaction was heated to reflux for 48 h. After that time the yellow solution was cooled to room temperature and centrifuged. The solvent was evaporated and the crude product was recrystallised from pentane at −30 °C.

4.2.1. Synthesis of [Cp‴$_2$DyI] (**1b**)

From the reaction of DyI_3 (0.20 g, 0.37 mmol) and NaCp‴ (0.26 g, 0.85 mmol) according to the GP, **1b** was obtained as yellow powder in 66% yield (0.21 g, 0.24 mmol). ^{1}H NMR (C_6D_{12}): δ −70.1 (br s, 36H, $w_{1/2} \approx 1.5$ kHz, Si(CH_3)$_3$), −224 (br s, 18H, $w_{1/2} \approx 0.6$ kHz, Si(CH_3)$_3$). T_{subl} 210 °C/10^{-3} mbar. IR (NaCl, Nujol, cm^{-1}) 2952(vs), 2925(vs), 2868(sh), 2856(vs), 1459(m), 1452(sh), 1428(m), 1375(m), 1243(m), 1140(m), 1000(w), 940(w), 854(sh), 822(vs), 748(m), 680(w), 647(w), 637(w), 625(w). Crystals suitable for X-ray analysis were grown by from sublimation.

4.2.2. Synthesis of [Dtp$_2$DyI] (**1c**)

From the reaction of DyI_3 (0.20 g, 0.37 mmol) and K(Dtp) (0.20 g, 0.77 mmol) according to the GP, **1c** was obtained as yellow powder in 75% yield (0.21 g, 0.28 mmol) ^{1}H NMR (C_6D_{12}): δ −241 (br s, $w_{1/2} \approx 2.5$ kHz, C(CH_3)$_3$). Mp dec. > 140 °C. IR (NaCl, Nujol, cm^{-1}) 2959(vs), 2924(vs), 2860(vs), 1463(vs), 1381(s), 1362(s), 1246(w), 1201(w), 1136(w), 1023(w), 728(w), 614(w). *Anal.* Calc. for $C_{28}H_{48}DyIP_2$ = 736.03: C, 45.7; H, 6.6. Found: C, 46.2; H, 6.8%. Crystals suitable for X-ray analysis were grown in pentane at −30 °C.

4.2.3. Synthesis of [{Dsp$_2$DyI}$_2$] (**1d**)

From the reaction of DyI_3 (0.20 g, 0.37 mmol) and K(Dsp) (0.23 g, 0.77 mmol) according to the GP, **1d** was obtained as yellow powder in 70% yield (0.21 g, 0.26 mmol). ^{1}H NMR (C_6D_{12}): δ −214 (br s, $w_{1/2} \approx 1.5$ kHz, Si(CH_3)$_3$). T_{subl} 220 °C/10^{-3} mbar. IR (NaCl, Nujol, cm^{-1}) 2953(vs), 2923(vs), 2869(sh), 2856(vs), 1462(vs), 1380(s), 1248(m), 1138(w), 918(w), 830(m), 748(w), 680(w), 641(w). Crystals suitable for X-ray analysis were grown by sublimation.

4.2.4. Reaction of [K(18-crown-6)][(Cp^{ttt})$_2$DyBr] (**3**) with fluorenone

Addition of fluorenone (10 mg, 59 μmol) to a solution of **3** (60 mg, 59 μmol) in toluene (4 mL) led to an immediate colour change from dark red to brown. After 24 h [K(18-crown-6)][(Cp^{ttt})$_2$DyBr(fluorenone ketyl)] (**4**) precipitated from the solution in 82% yield (58 mg, 48 μmol). Crystals suitable for X-ray analysis were grown from toluene at room temperature.

4.3. X-ray experimental data

Crystals for X-ray analysis were obtained as described above. The crystals were handled in the dry box and mounted on a fiberglass needle using Paratone-N oil. Data collection were performed at 150 K on a Nonius KappaCCD diffractometer, using graphite-monochromated Mo Kα radiation (λ = 0.71069 Å). All pertinent tables are given in the supplementary material.

Supplementary data

CCDC 711601, 711602, 711603 and 711604 contain the supplementary crystallographic data for **1b**, **1c**, **1d** and **4**, respectively. These data can be obtained free of charge via http://www.ccdc.cam.ac.uk/conts/retrieving.html, or from the Cambridge Crystallographic Data Centre, 12 Union Road, Cambridge CB2 1EZ, UK; fax: (+44) 1223-336-033; or e-mail: deposit@ccdc.cam.ac.uk.

Acknowledgements

This work was supported by Ecole Polytechnique and CNRS.

References

[1] (a) W.J. Evans, Coord. Chem. Rev. 206–207 (2000) 263;
(b) W.J. Evans, Polyhedron 6 (1987) 803.
[2] (a) M.N. Bochkarev, I.L. Fedushkin, A.A. Fagin, T.V. Petrovskaya, J.W. Ziller, R.N.R. Broomhill-Dillard, W.J. Evans, Angew. Chem., Int. Ed. 36 (1997) 133;
(b) M.C. Cassani, D.J. Duncalf, M.F. Lappert, J. Am. Chem. Soc. 120 (1998) 12958;
(c) W.J. Evans, N.T. Allen, J.W. Ziller, J. Am. Chem. Soc. 122 (2000) 11749;
(d) M.N. Bochkarev, I.L. Fedushkin, S. Dechert, A.A. Fagin, H. Schumann, Angew. Chem., Int. Ed. 40 (2001) 3176;
(e) W.J. Evans, N.T. Allen, J.W. Ziller, Angew. Chem., Int. Ed. 41 (2002) 359;
(f) F. Nief, D. Turcitu, L. Ricard, Chem. Commun. (2002) 1646;
(g) D. Turcitu, F. Nief, L. Ricard, Chem.-Eur. J. 9 (2003) 4916;
(h) F. Nief, B.T. de Borms, L. Ricard, D. Carmichael, Eur. J. Inorg. Chem. (2005) 637;
(i) F. Jaroschik, F. Nief, L. Ricard, Chem. Commun. (2006) 426;
(j) F. Jaroschik, F. Nief, X.-F. Le Goff, L. Ricard, Organometallics 26 (2007) 1123;
(k) F. Jaroschik, F. Nief, X.-F. Le Goff, L. Ricard, Organometallics 26 (2007) 3552;
(l) P.B. Hitchcock, M.F. Lappert, L. Maron, A.V. Protchenko, Angew. Chem., Int. Ed. 47 (2008) 1;
(m) J. Cheng, J. Takats, M.J. Ferguson, R. McDonald, J. Am. Chem. Soc. 130 (2008) 1544;
(n) F. Jaroschik, A. Momin, F. Nief, X.-F. Le Goff, G.B. Deacon, P.C. Junk, Angew. Chem., Int. Ed. 48 (2009) 1117.
[3] L.R. Morss, Chem. Rev. 6 (1976) 827.
[4] (a) W.J. Evans, C.A. Seibel, J.W. Ziller, J. Am. Chem. Soc. 120 (1998) 6745;
(b) P.B. Hitchcock, M.F. Lappert, S. Tian, Organometallics 19 (2000) 3420;
(c) W.J. Evans, N.T. Allen, J.W. Ziller, J. Am. Chem. Soc. 123 (2001) 7927;
(d) I.L. Fedushkin, F. Girgsdies, H. Schumann, M.N. Bochkarev, Eur. J. Inorg. Chem. (2001) 2405.
[5] G. Meyer, Angew. Chem., Int. Ed. 47 (2008) 4962.
[6] M.A. Edelmann, P.B. Hitchcock, J. Hu, M.F. Lappert, New J. Chem. 19 (1995) 481.
[7] M. Visseaux, F. Nief, L. Ricard, J. Organomet. Chem. 647 (2002) 139.
[8] (a) O. Schmitt, G. Wolmershauser, H. Sitzmann, Eur. J. Inorg .Chem. (2003) 3105;
(b) L. Maron, E.L. Werkema, L. Perrin, O. Eisenstein, R.A. Andersen, J. Am. Chem. Soc. 127 (2005) 279;
(c) M.D. Walter, D. Bentz, F. Weber, O. Schmitt, G. Wolmershäuser, H. Sitzmann, New J. Chem. (2007) 305.
[9] (a) Z. Hou, T. Yoshimura, Y. Wakatsuki, J. Am. Chem. Soc. 116 (1994) 11169;
(b) Z. Hou, T. Miyano, H. Yamazaki, Y. Wakatsuki, J. Am. Chem. Soc. 117 (1995) 4421;
(c) T. Yoshimura, Z. Hou, Y. Wakatsuki, Organometallics 14 (1995) 5382;
(d) Z. Hou, A. Fujita, H. Yamazaki, Y. Wakatsuki, J. Am. Chem. Soc. 118 (1996) 2503;
(e) Z. Hou, A. Fujita, H. Yamazaki, Y. Wakatsuki, J. Am. Chem. Soc. 118 (1996) 7843;
(f) Z. Hou, A. Fujita, Y. Zhang, T. Miyano, H. Yamazaki, Y. Wakatsuki, J. Am. Chem. Soc. 120 (1998) 754;
(g) Z. Hou, T. Koizumi, M. Nishiura, Y. Wakatsuki, Organometallics 20 (2001) 3323;
(h) O. Tardif, Z. Hou, M. Nishiura, T. Koizumi, Y. Wakatsuki, Organometallics 20 (2001) 4565.
[10] H.R. Luss, D.L. Smith, Acta Crystallogr., Sect. B 28 (1972) 884.

2. Experimental

2.1. Materials and methods

Lead acetate trihydrate, $HSCH_2CH_2NMe_2{\cdot}HCl$, hexadecylamine (HDA) and other materials were obtained from SD Fine Chemicals and Fluka and were used without further purification. Bis(methylaminoethyl)diselenide [^{1}H NMR($CDCl_3$) δ: 2.26 (s, NMe_2); 2.63 (t, 7.1 Hz, $SeCH_2$); 3.05 (t, 7.1 Hz, NH_2)] was prepared by the reaction of Na_2Se_2 with $Me_2NCH_2CH_2Cl$ in DMF as described in the literature [33]. Diselenodipropionic acid, prepared by the reaction between Na_2Se_2 and $BrCH_2CH_2COOH$ in water, on esterification with methanol in the presence of sulfuric acid gave diselenodimethylpropionate and was purified by vacuum distillation (145 °C/3 mm) [^{1}H NMR ($CDCl_3$) δ: 2.81 (t, 7.2 Hz, $SeCH_2$); 3.09 (t, 7.1 Hz $SeCH_2CH_2$); 3.69 (s, COOMe)] [34]. Solvents were dried and distilled before use under a nitrogen atmosphere. HPLC grade toluene was used for optical studies. Melting points were determined in capillary tubes and are uncorrected.

Elemental analyses were carried out by the Radio Chemistry Division, B.A.R.C. IR spectra were recorded on a Bomem MB-102 FT IR spectrometer. ^{1}H NMR spectra were recorded on a Bruker Avance-200 NMR spectrometer operating at 200 MHz. Chemical shifts is relative to internal chloroform peak (δ 7.26 ppm). UV–Vis absorption spectra were recorded on a Chemito Spectrascan UV 2600 double beam spectrophotometer. Fluorescence spectra were recorded using a Hitachi F-4010 spectrofluorometer.

Thermogravimetric analyses (TGA) were carried out on a Nitzsch STA PC-Luxx TG-DTA instrument, which was calibrated with $CaC_2O_4{\cdot}H_2O$. TG curves were recorded at a heating rate of 5 °C min^{-1} under a flow of nitrogen. X-ray powder diffraction data were collected on a Philips X-ray diffractometer (Model PW 1729) using Cu Kα radiation. EDAX measurements were carried out on a JEOL JSM-T330A instrument. A JEOL-2000FX transmission electron microscope operating at accelerating voltages up to 200 kV was used for TEM studies. The samples for TEM were prepared by placing a drop of nanoparticles dispersed in acetone on a carbon coated copper grid.

2.2. Synthesis of complexes

2.2.1. $[Pb(SCH_2CH_2NMe_2)_2]$ (**1**)

To a methanolic solution of $HSCH_2CH_2NMe_2{\cdot}HCl$ (402 mg, 2.84 mmol) was added NaOMe (12.5 ml of 0.1 N, 5.87 mmol) in methanol and stirred for 5 min. To this a methanolic solution of $Pb(OAc)_2{\cdot}3H_2O$ (531 mg, 1.40 mmol) was added with stirring at room temperature under a nitrogen atmosphere. The whole was stirred for 3 h and colorless solution was dried *in vacuo* and the residue was washed with cold hexane (2×5 cm^3). The product was extracted with dichloromethane (3×10 cm^3) and filtered through a filtration assembly and the filtrate was evaporated under vacuum to give a white powder in 69% yield (401 mg), mp 130 °C. *Anal.* Calc. for $C_8H_{20}N_2PbS_2$: C, 23.1; H, 4.9; N, 6.7; S, 15.4. Found: C, 22.9; H, 4.7; N, 6.5; S, 15.2%. ^{1}H NMR (in $CDCl_3$) δ: 2.43 (s, 12H, NMe_2); 3.18 (t, 7 Hz, 4H, SCH_2); 3.74 (t, 7 Hz, 4H, NCH_2).

2.2.2. $[Pb(SeCH_2CH_2NMe_2)_2]$ (**2**)

A methanolic solution (20 cm^3) of $Pb(OAc)_2{\cdot}3H_2O$ (453 mg, 1.19 mmol) was added with stirring to a freshly prepared methanolic solution of $NaSeCH_2CH_2NMe_2$ (prepared from $(Me_2NCH_2CH_2Se)_2$ (364 mg, 1.20 mmol) and $NaBH_4$ (98 mg, 2.58 mmol)) under an argon atmosphere at room temperature. After 3 h, dark green solution was dried *in vacuo* and oily residue was washed with cold hexane (2×5 cm^3) and dried again *in vacuo*. The residue was extracted with CH_2Cl_2 (3×10 cm^3), filtered through a G3 filtration unit. The filtrate was evaporated under reduced pressure to give a light green solid, which was recrystallized from dichloromethane–hexane mixture (480 mg, 79%). Ageing of this complex was evident as it tended to become insoluble in organic solvents after keeping for few days, although microanalysis was unaltered. *Anal.* Calc. for $C_8H_{20}N_2PbSe_2$: C, 18.9; H, 4.0; N, 5.5. Found: C, 18.5; H, 3.9; N, 5.4%. UV–Vis λ_{max} ($CHCl_3$): 340 nm. ^{1}H NMR (in $CDCl_3$) δ: 2.43 (s, 12H, NMe_2); 3.34 (br, 4H, $SeCH_2$); 3.53 (br, 4H, NCH_2).

2.2.3. $[Pb(SeCH_2CH_2COOMe)_2]$ (**3**)

Prepared similar to **2** from $Pb(OAc)_2{\cdot}3H_2O$ (214 mg, 0.56 mmol) and $NaSeCH_2CH_2COOMe$ (prepared from $(MeCOOCH_2CH_2Se)_2$ (190 mg, 0.57 mmol) and $NaBH_4$ (48 mg, 1.27 mmol)) as a pale yellow crystalline solid in 90% yield (275 mg), mp 95 °C, melts with decomposition. *Anal.* Calc. for $C_8H_{14}O_4PbSe_2$: C, 17.8; H, 2.6. Found: C, 17.4; H, 2.1%. IR (Nujol) cm^{-1} 1654 and $1720_{(\nu C=O)}$. UV–Vis λ_{max} ($CHCl_3$): 360 nm. ^{1}H NMR (in $CDCl_3$) δ: 2.88 (m, 4H, $SeCH_2$); 3.08, 3.86 (each t, 7 Hz, 4H, $SeCH_2-$); 3.70 (s, 6H, COOMe).

2.3. Preparation of PbE nanoparticles

2.3.1. Thermolysis in HDA

In a three necked flask fitted with a thermometer, HDA (1.5 g) was degassed at 100 °C under an argon atmosphere for 1 h with continuous stirring. To this, a solution of **2** (130 mg, 0.26 mmol) in dichloromethane (3 cm^3) was injected rapidly. The temperature dropped to 80 °C and raised again slowly to maintain at 120 °C. The hot solution at the end of 25 min was cooled to 70 °C and methanol was added to precipitate brownish-black powder of PbSe, which was given a thorough washing with methanol followed by centrifuging and drying under vacuum.

2.3.2. Furnace pyrolysis

In a small quartz boat, **2** (100 mg, 0.2 mmol) was pyrolysed at 250 °C in a furnace under an argon atmosphere for 30 min where upon a black powder formed. After cooling the furnace to room temperature the black powder was collected. Similarly **1** and **3** were pyrolysed.

2.4. X-ray crystallography

Colorless single crystals of $[Pb(ECH_2CH_2NMe_2)_2]$ (E = S or Se) were obtained from hexane solution of the freshly prepared samples. X-ray data were collected on a Rigaku AFC 7S diffractometer at 298(2) K using graphite monochromated Mo Kα (0.71073 Å) radiation employing the $\omega - 2\theta$ scan technique. The unit cell parameters were determined from 25 reflections measured by random search routine. The intensity data were corrected for Lorentz, polarization and absorption effects [35]. The structures were solved using the SHELXS97 [36] and refined using the SHELXL97 [37] computer programs. The non-hydrogen atoms were refined anisotropically. Crystallographic data and refinement details are given in Table 1.

3. Results and discussion

3.1. Synthesis and spectroscopy

Reactions of $Pb(OAc)_2{\cdot}3H_2O$ with sodium salts of β-functionalized ethylchalcogenolate ligands gave homoleptic chalcogenolate complexes of composition, $[Pb(ER)_2]$ (ER = $SCH_2CH_2NMe_2$ (**1**), $SeCH_2CH_2NMe_2$ (**2**), $SeCH_2CH_2COOMe$ (**3**)) (Eq. (1)). Freshly prepared **1–3** are soluble in dichloromethane, chloroform and methanol, but solubility decreases with aging and finally leading to a poorly soluble product.

Table 1
Crystallographic and structural refinement data for $[Pb(ECH_2CH_2NMe_2)_2]$ (E = S or Se).

Chemical formula	$C_8H_{20}N_2PbS_2$	$C_8H_{20}N_2PbSe_2$
Formula weight	415.57	509.37
Crystal system	orthorhombic	orthorhombic
Space group	$P2_12_12_1$	$P2_12_12_1$
Unit cell dimensions		
a (Å)	11.083(4)	10.5065(4)
b (Å)	11.595(3)	11.2900(14)
c (Å)	10.496(4)	11.745(14)
V (Å^3)	1348.8(8)	1393.1(4)
Z	4	4
Number of reflections collected/unique	2554/1958	2654/2039
Number of data/restraints/parameters	1958/0/119	2039/2/115
Final R_1, ωR_2 indices	0.0546, 0.1406	0.0588, 0.1200
R_1, ωR_2 (all data)	0.1107, 0.1658	0.1708, 0.1561

The IR spectrum of **3** showed absorption at 1720 cm^{-1} attributed to free carbonyl group which is slightly shifted to lower wave-number relative to diselenide (1734 cm^{-1}) [34]. Absorption spectra of **2** and **3** in chloroform displayed a peak at 340 and 360 nm, respectively. These absorptions occur at lower energy than the corresponding diselenides and may be attributed to the transition in the selenolate group and metal–ligand charge transfer (MLCT) transitions. The ^{1}H NMR spectra of **1**–**3** showed singlets due to methyl protons whereas XCH_2 (X = N or CO) and ECH_2 resonances appeared either triplets or broad signal.

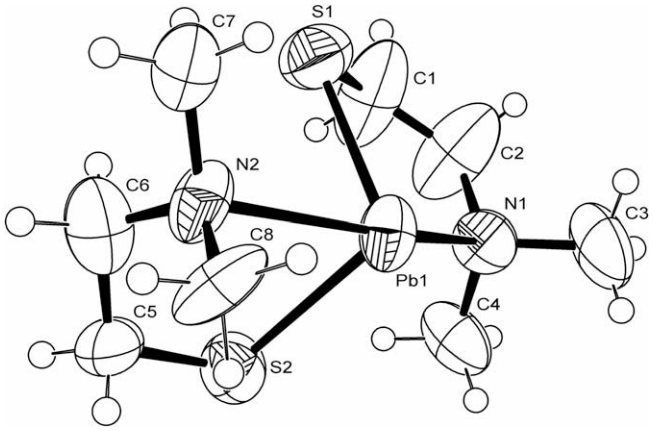
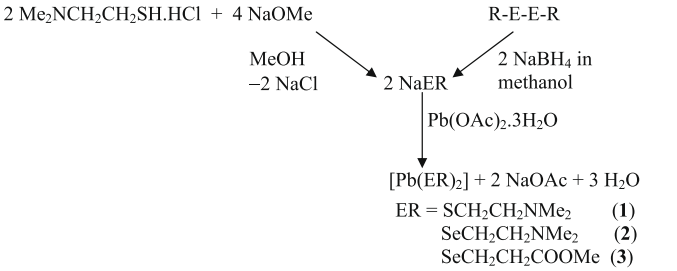


Fig. 1. Molecular structure of $[Pb(SCH_2CH_2NMe_2)_2]$, ORTEP drawn with 50% probability.



(1)

3.2. Structures of **1** and **2**

The molecular structures of $[Pb(ECH_2CH_2NMe_2)_2]$ (E = S or Se) have been established unambiguously by X-ray crystallography (Figs. 1 and 2), and selected bond lengths and angles are given in Table 2. Unlike bis(dithiolato)lead(II) complexes which are associated through secondary Pb···S interactions in the solid state [4–6], these complexes are discrete molecules and are isomorphous. The lead ion is coordinated to two non-planar five-membered chelating $Me_2NCH_2CH_2E$ ligands. The overall geometry around lead is distorted trigonal bipyramidal with nitrogen atoms occupying the axial positions. Two chalcogen atoms and stereochemically active lone pair of electrons occupy the equatorial positions. The repulsion of the lone pair of electrons is manifested in deviation of N(1)–Pb(1)–N(2) (158.0°) and E(1)–Pb(1)–E(2) (95.9(2)° for S and 97.03(11)° for Se) angles from idealized values of 180° and 120°, respectively. Significant difference between the two structures is observed in the torsion angles in one of the chelate rings (N(1)–C(2)–C(1)–E(1); 41(8)° (E = S) and 50(4)° (E = Se)). The two Pb–S and Pb–Se distances are essentially similar and are in the range reported in the literature [30,38]. One of the Pb–N distances is slightly longer than the other.

Although the structure of **3** resembles to that of $[Pb(SCH_2CH_2NH_2)_2]$ reported earlier [11], the latter exhibits a chain structure formed through NH···S hydrogen bridges. The absence of NH···S hydrogen bonding in **1**, results in contraction of the S–Pb–S angle (95.9(2)°) while the N–Pb–N angle (158.0(6)°) has opened up from the corresponding angles, (99.2(1)° and 149.3(3)°, respectively) in $[Pb(SCH_2CH_2NH_2)_2]$ [11]. The Pb–N bond is slightly elongated (av. 2.626 Å) in **1** as compared to the corresponding cysteamin derivative (2.593(9)°) indicating weaker coordination of tertiary nitrogen atom in **1**.

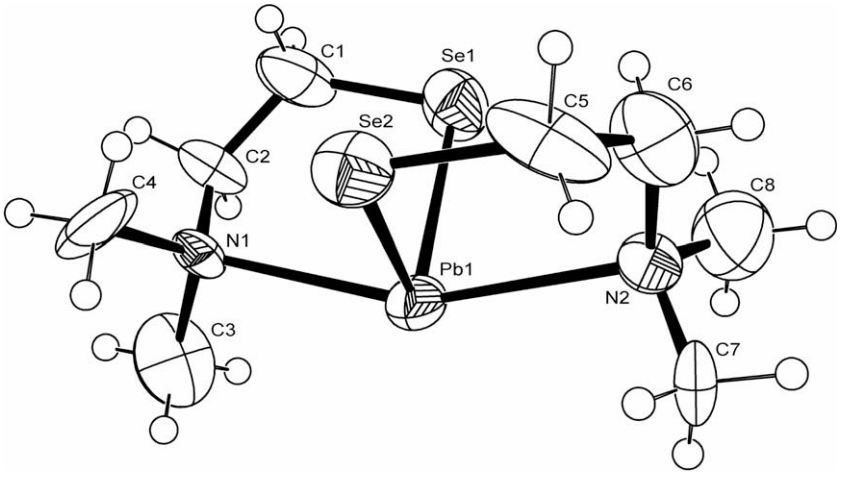


Fig. 2. Molecular structure of $[Pb(SeCH_2CH_2NMe_2)_2]$, ORTEP drawn with 50% probability.

Lead(II) complexes show different degree of distortion in the coordination sphere of lead depending on the steric requirements of the lone pair of electrons. Thus structures can vary between those where the lone pair has no steric influence (holodirected) or exert steric demands (hemidirected) [39,40]. In both the structures (**1** and **3**), the lone pair has pronounced influence (hemidirected) on overall geometry of the molecules, as a consequence there is a void which is manifested on Pb–S (shorter) and Pb–N (longer) bond distances. In fact the two distances (Pb–S and Pb–N) are comparable (av. 2.62 Å) despite significant difference in the ionic radii of sulfur and nitrogen.

3.3. Thermal studies

TG curve of **2** (Supplementary data) showed that the complex underwent a single step decomposition at 190 °C to lead selenide as inferred from the TG weight loss (% weight loss found (calcd.): 46.2 (43.8)). Pyrolysis of these complexes were carried out under different conditions. Pyrolysis at 200–250 °C in a furnace under a flowing argon atmosphere for 1 h afforded a black residue of cubic PbE (E = S or Se) as revealed by their XRD patterns (Fig. 3) [41,42]. The EDAX analysis (Found (calcd.): Pb, 74.3 (72.4); Se, 25.7 (27.6)%) for the residue obtained from **2** further confirmed the formation of PbSe. The average size estimated from Scherrer equation [43] for these particles is 50 (from **1**) and 34 nm (from **2** and **3**). PbS nanoparticles prepared using $[Pb(S_2CNR_2)_2]$ (R = Et or Bu^i) in TOPO at >150 °C have size >60 nm [12], while $[Pb(S_2CNBu^i{}_2)_2]$ gave a mixture of cubic and smaller spherical particles.

Decomposition of **2** in HDA yielded cubic phase of PbSe nanoparticles (supplementary data) with an average diameter of 13 nm estimated using Scherrer equation. The TEM picture (Fig. 4) showed that they were spherical in nature with an average size of 15 nm. A slight difference in the particle size estimated from the XRD pattern and TEM is because in XRD line width does not directly determine the particle size [44]. SAED pattern confirmed the cubic phase of these particles as determined by XRD. It has been reported earlier that the shape and size of PbSe markedly depend (10–120 nm) on the concentration of acetic acid when these particles were prepared by hot injection route using lead–oleate [23]. The PbSe nanoparticles synthesized by the reaction of lead carbox-

Table 2
Selected bond lengths (Å) and angles (°) for $[Pb(ECH_2CH_2NMe_2)_2]$ (E = S or Se).

	E = S	E = Se
Pb(1)–E(1)	2.621(6)	2.750(3)
Pb(1)–N(1)	2.611(17)	2.620(18)
E(1)–C(1)	2.71(3)	1.87(3)
C(1)–C(2)	1.35 (3)	1.436(18)
C(2)–N(1)	1.42(3)	1.38(3)
Pb(1)–E(2)	2.616(5)	2.727(3)
Pb(1)–N(2)	2.642(15)	2.642(19)
E(2)–C(5)	1.81(2)	1.93(3)
C(5)–C(6)	1.53(3)	1.477(18)
C(6)–N(2)	1.44(3)	1.45(4)
E(1)–Pb(1)–N(1)	76.7(5)	78.4(5)
E(1)–Pb(1)–N(2)	87.3(5)	87.4(7)
E(1)–Pb(1)–E(2)	95.9(2)	97.03(11)
Pb(1)–E(1)–C(1)	97.7(8)	93.2(7)
Pb(1)–N(1)–C(2)	109.6(14)	109.5(16)
E(2)–Pb(1)–N(2)	77.0(5)	77.2(6)
E(2)–Pb(1)–N(1)	89.7(5)	89.0(5)
N(1)–Pb(1)–N(2)	158.0(6)	158.9(6)
Pb(1)–E(2)–C(3)	99.8(8)	95.2(8)
Pb(1)–N(2)–C(6)	105.9(12)	109.3(17)
C(1)–C(2)–N(1)	118(3)	122(3)
N(2)–C(6)–C(5)	112(2)	111(3)
C(6)–C(5)–E(2)	119(2)	122(2)
C(2)–C(1)–(1)	129(3)	122(2)
N(1)–C(2)–C(1)–E(1)	41(8)	50(4)
N(2)–C(6)–C(5)–E(2)	59(3)	59(4)

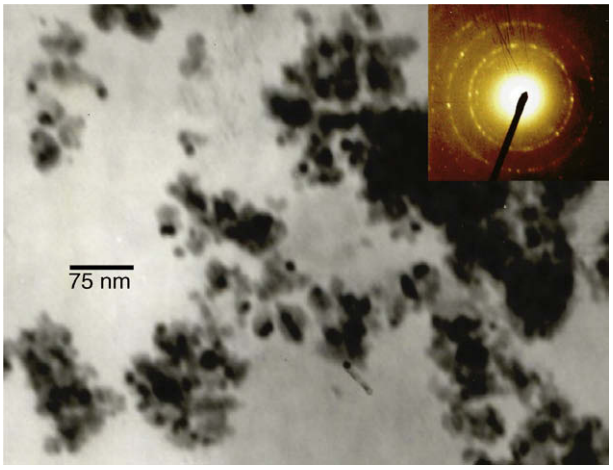


Fig. 4. TEM picture of PbSe nanoparticles obtained by pyrolysis $[Pb(SeCH_2CH_2NMe_2)_2]$ in HDA at 120 °C (inset shows corresponding SAED pattern).

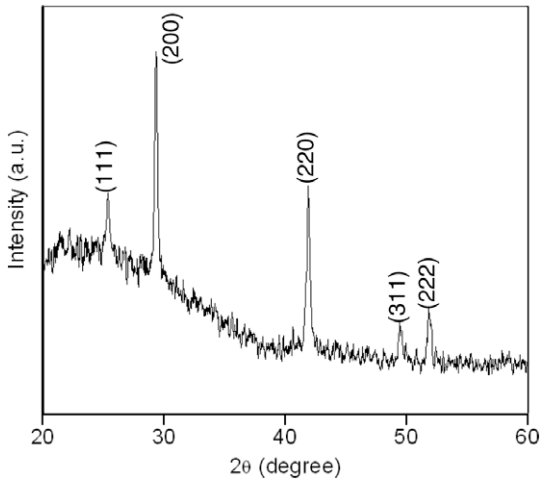


Fig. 3. XRD pattern of PbSe nanoparticles obtained by the pyrolysis of $[Pb(SeCH_2CH_2COOMe)_2]$ in a furnace at 200 °C for 1 h.

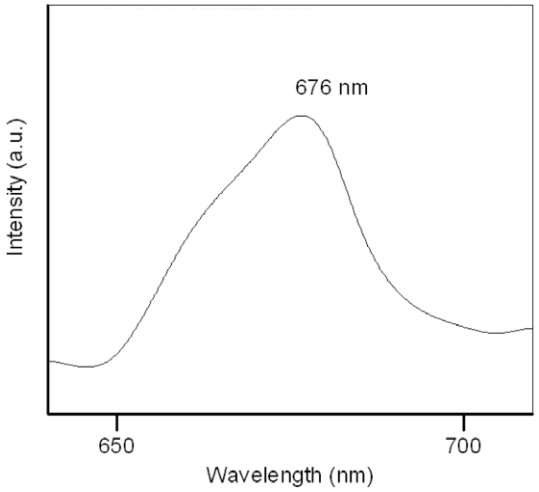


Fig. 5. Excitation profile of PbSe nanoparticles obtained by the pyrolysis of $[Pb(SeCH_2CH_2NMe_2)_2]$ in HDA at 120 °C.

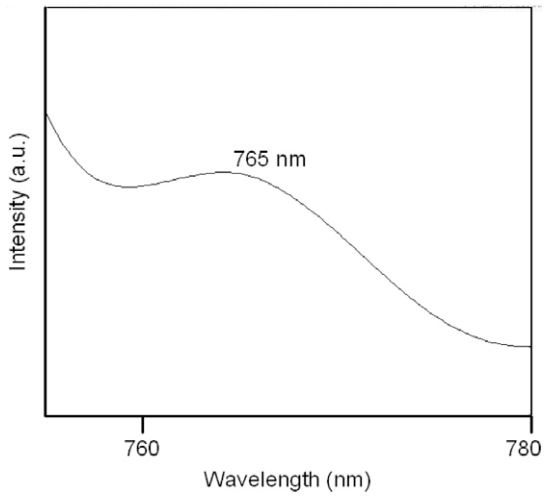


Fig. 6. Emission profile of PbSe nanoparticles obtained by the pyrolysis of $[Pb(SeCH_2CH_2NMe_2)_2]$ in HDA at 120 °C.

ylate and SeO_2 in the presence of TOP (trioctyl phosphine) yield cubic shaped PbSe nanoparticles of 15.6 nm as measured by TEM [45]. Recently, O'Brien et al. [12] have prepared cubic shaped lead selenide nanocrystals using $Pb(Se_2CNMeHex^n)_2$.

3.4. Optical properties

The absorption spectrum of PbSe nanoparticles obtained by pyrolysis of **2** in HDA showed very broad exciton peak 732 nm, which is blue shifted with respect to the bulk PbSe (λ_{max} 4745 nm) [28] showing the quantum confinement of the particles. The spectrum showed a small amount of tailing which may be due to the formation of some bulk PbSe. The excitation profile of PbSe nanoparticles (Fig. 5) displayed a peak at 676 whereas emission profile (Fig. 6) showed a broad peak at 765 nm corresponding to the band edge emission.

4. Conclusion

The complexes $[Pb(ER_2)_2]$ (ER = $SCH_2CH_2NMe_2$, $SeCH_2CH_2NMe_2$, $SeCH_2CH_2COOMe$) have been synthesized and the former two have been structurally characterized. They adopt a distorted trigonal bipyramidal configuration around lead. These complexes have been demonstrated for their use as molecular precursors for the synthesis of PbE nanoparticles at moderately low temperatures.

Acknowledgements

We thank Drs. T. Mukherjee and D. Das for encouragement of this work. The authors are grateful to Dr. S.K. Gupta and his group for SEM and EDAX measurements and Dr. V.K. Manchanda and his group for providing microanalysis of these complexes.

Appendix A. Supplementary data

CCDC 698265 and 698266 contain the supplementary crystallographic data for **1** and **2**. These data can be obtained free of charge via http://www.ccdc.cam.ac.uk/conts/retrieving.html, or from the Cambridge Crystallographic Data Centre, 12 Union Road, Cambridge CB2 1EZ, UK; fax: (+44) 1223 336 033; or e-mail: deposit@ccdc.cam.ac.uk. Supplementary data associated with this article can be found, in the online version, at doi:10.1016/j.poly.2009.05.054.

References

[1] P. Borgstrom, L.M. Ellis, E.E. Reid, J. Am. Chem. Soc. 51 (1929) 3649.
[2] (a) R.A. Shaw, H. Woods, J. Chem. Soc. A (1971) 1569;
(b) I.G. Dance, Polyhedron 5 (1986) 1037.
[3] J. Parr, in: G.F.R. Perkin, Comprehensive Coordination Chemistry-II, vol. 3 (J.A. McCleverty, T.J. Meyer (Eds.)), Elesevier Ltd., Oxford, 2004, p. 545 (Chapter 3.7).
[4] E.R.T. Tieknik, I. Haiduc, Prog. Inorg. Chem. 54 (2005) 127.
[5] P.J. Heard, Prog. Inorg. Chem. 53 (2005) 1.
[6] I. Haiduc, D.B. Sowerby, S.F. Lu, Polyhedron 14 (1995) 3389.
[7] E.W. Abel, J. Chem. Soc. (1960) 4406.
[8] G.G. Hoffmann, Z. Naturforsch. Teil B 40 (1985) 335.
[9] A. Singhal, V.K. Jain, J. Organomet. Chem. 494 (1995) 75.
[10] S. Acharya, U.K. Gautam, T. Sasaki, Y. Bando, Y. Golan, K. Ariga, J. Am. Chem. Soc. 130 (2008) 4594.
[11] H. Fleischer, D. Schollmeyer, Inorg. Chem. 43 (2004) 5529.
[12] D. Fan, M. Afzal, M.A. Mallik, C.Q. Nguyen, P. O'Brien, P.J. Thomas, Coord. Chem. Rev. 251 (2007) 1878.
[13] (a) V. Garcia-Montalvo, R. Cea-Olivares, G. Espinosa-Perez, Polyhedron 15 (1996) 829;
(b) J.S. Casas, A. Casteineiras, I. Haiduc, A. Sanchez, J. Sordo, E.M. Vazquez-Lopez, Polyhedron 13 (1994) 2873.
[14] V. Garcia-Montalvo, J. Novosad, P. Kilian, J.D. Woollins, A.M.Z. Slawin, P.G. Garcia, M. Lopez-Cardoso, G. Espinosa-Perez, R. Cea-Olivares, J. Chem. Soc., Dalton Trans. (1997) 1025.
[15] R. Ellinson, M. Beard, J. Johnson, P. Yu, O. Micic, A. Nozik, A. Shabaev, A. Efros, Nano Lett. 5 (2005) 865.
[16] S.A. McDonald, G. Konstantatos, S. Zhang, P.W. Cyr, E.J.D. Klen, L. Levina, E.H. Sargent, Nat. Mater. 4 (2005) 138.
[17] E.H. Sargent, Adv. Mater. 17 (2005) 515.
[18] M.T. Harrison, S.V. Kershaw, M.G. Burt, A.L. Rogach, A. Komowski, A. Eychmüller, H. Weller, Pure Appl. Chem. 73 (2000) 295.
[19] W.G. Lu, J.Y. Fang, K.L. Stokes, J. Lin, J. Am. Chem. Soc. 126 (2004) 11798.
[20] J.R. Sootsman, R.J. Pcionek, H. Kong, C. Uher, M.G. Kanatzidis, Chem. Mater. 18 (2006) 4993.
[21] K.F. Hsu, S. Loo, F. Guo, W. Chen, J.S. Dyck, C. Uher, T. Hogan, E.K. Polychroniadis, M.G. Kanatzidis, Science 303 (2004) 818.
[22] T. Mokari, M. Zhang, P. Yang, J. Am. Chem. Soc. 129 (2007) 9864.
[23] A.J. Houtepen, R. Koole, D. Vanmaekelbergh, J. Meeldijik, S.G. Hickey, J. Am. Chem. Soc. 128 (2006) 6792.
[24] J.S. Steckel, B.K.H. Yen, D.C. Oertel, M.G. Bawendi, J. Am. Chem. Soc. 128 (2006) 13032.
[25] C.R. Li, C.Z. Yao, X.H. Lu, F.L. Zheng, Z.P. Feng, X.L. Yu, C.Y. Su, Y.X. Tong, Chem. Mater. 20 (2008) 3306.
[26] K.A. Abel, J. Shan, J.C. Boyer, F. Harris, F.C.J.M. van Veggel, Chem. Mater. 20 (2008) 3794.
[27] M. Law, J.M. Luther, Q. Song, B.K. Hughes, C.L. Perkins, A.J. Nozik, J. Am. Chem. Soc. 130 (2008) 5974.
[28] T. Trindade, P. O'Brien, N.L. Pickett, Chem. Mater. 13 (2001) 3843.
[29] J. Sun, W.E. Buhro, Angew. Chem. Int., Ed. Engl. 47 (2008) 3215.
[30] T. Trindade, P. O'Brien, X. Zhang, M. Motevalli, J. Mater. Chem. 7 (1997) 1011.
[31] S. Dey, V.K. Jain, S. Chaudhury, A. Knoedler, W. Kaim, Polyhedron 22 (2003) 489.
[32] G. Kedarnath, S. Dey, V.K. Jain, G.K. Dey, B. Varghese, Polyhedron 25 (2006) 2383.
[33] S. Dey, V.K. Jain, S. Chaudhury, A. Knoedler, F. Lissner, W. Kaim, J. Chem. Soc., Dalton Trans. (2001) 723.
[34] L.B. Kumbhare, V.K. Jain, P.P. Phadnis, M. Nethaji, J. Organomet. Chem. 692 (2007) 1546.
[35] T. Higashi, ABSCOR-Empirical Absorption Correction based on Fourier Series Approximation, Rigaku Corporation, 3-9-12 Matsubara, Akishima, Japan, 1995.
[36] G.M. Sheldrick, SHELXS-97, Structure Solution Package, Universität Göttingen, Göttingen, Germany, 1997.
[37] G.M. Sheldrick, SHELXS-97, Structure Refinement Package, Universität Göttingen, Göttingen, Germany, 1997.
[38] C.W. Liu, T.S. Lobana, J.L. Xiao, H.Y. Liu, B.J. Liaw, C.M. Hung, Z. Lin, Organometallics 24 (2005) 4072.
[39] L. Shimoni, J.P. Glusker, C.P. Bock, Inorg. Chem. 37 (1998) 1853.
[40] R.D. Hancock, J.P. Reibenpies, H. Maumela, Inorg. Chem. 43 (2004) 2981.
[41] JCPDS File No. 78-1901.
[42] JCPDS File No. 78-1903.
[43] B.D. Cullity, in: Elements of X-ray diffraction, Addison Wesley Inc., London, 1978.
[44] H. Weller, Angew. Chem., Int. Ed. Engl. 32 (1993) 41.
[45] O. Chen, Y. Chen, Y. Yang, J. Lynch, H. Wu, J. Zhuang, Y.C. Cao, Angew. Chem., Int. Ed. Engl. 47 (2008) 8638.

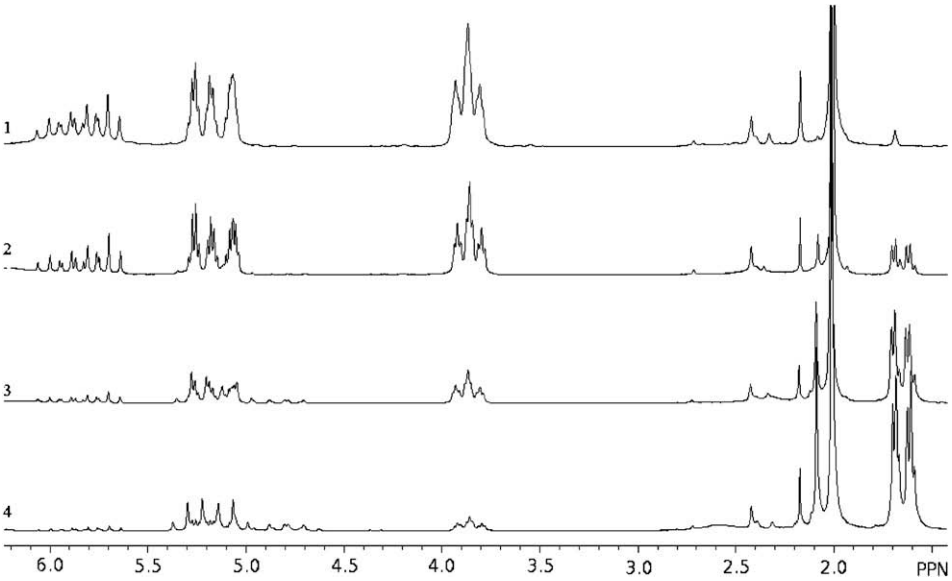
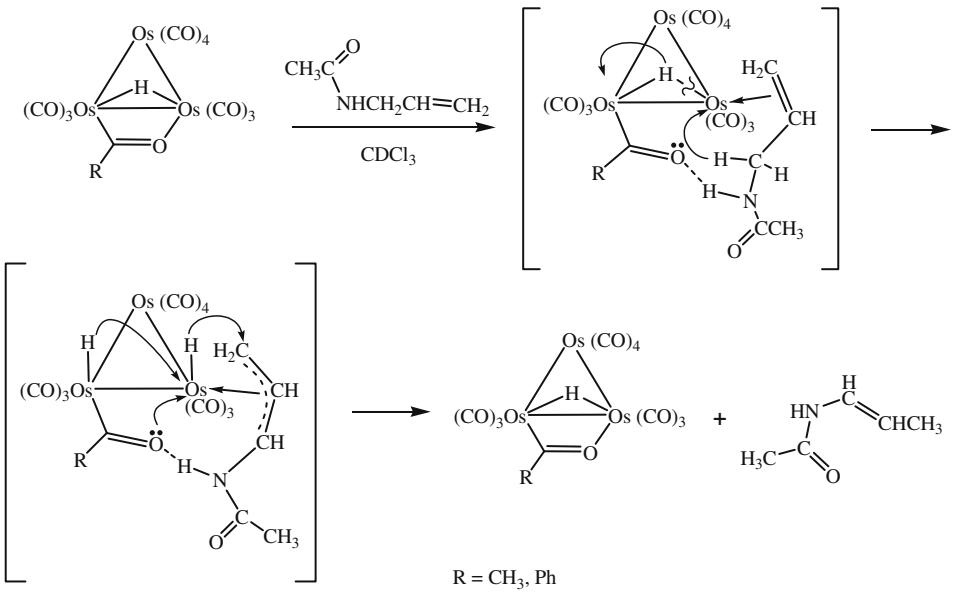


Fig. 1. The time dependence of ^{1}H NMR spectrum of the **2** and N-allylacetamide reaction mixture. The interval between spectra recording is 2 week.



Scheme 1.

whereas the insertion of the electron donating NEt_2 group into the phenyl ring enhances the cluster stability but lowers its catalytic activity.

An increase in the reaction temperature to 55 °C also did not promote the isomerization of N-allylacetamide catalyzed by clusters **1–3**. Therefore microwave irradiation was used to accelerate the N-allylacetamide isomerization in the presence of **1, 2**, and (μ-H)Os_3(μ-O=CNHCHMeCOOEt)$(CO)_{10}$ (**3**) clusters. It is known that the effect of microwave irradiation on solutions causes not only rapid heating of solutions. It also activates diffusion and mass transfer processes, changes the solvent ordering strength and the structure of a solvate shell of dissolved molecules, thus overall accelerating the chemical processes [13,14]. The irradiation of cluster complexes and N-allylacetamide solutions in $CDCl_3$ was performed in NMR tubes. To prevent sample heating over 45 °C a single irradiation time was no more than 30 s, after which the solution was cooled to ~18 °C. In total, the exposure time for each reaction mixture did not exceed 30 min. The course of the reaction was monitored by NMR spectroscopy. As a result, the following facts are revealed:

- Irradiation of N-allylacetamide solutions with **1** or **3** leads to a decrease in reaction times by 5–8%.
- Irradiation accelerates the isomerization rate of N-allylacetamide in the presence of **2** by more than 3000-fold.

Two test experiments were performed. In the first one, the solution of N-allylacetamide and cluster **2** was irradiated for 4 min, as described above, and then heated at 45 °C for 4 h. The 4 min microwave irradiation resulted in 50% isomerization of N-allylacetamide, whereas no changes were observed after 4 h heating. In the second test experiment, the similar solution was heated at 45 °C, but no visible changes were observed in the ^{1}H NMR spectra after 4 h.

Undoubtedly, the use of a conventional microwave oven without temperature control and stirring may sometimes cause local overheating of the solution. However, the reaction mixture overheating due to microwave irradiation cannot account for a 3000-fold acceleration of the allylic rearrangement. According to the literature, 50 ml of $CHCl_3$ is heated up to ~50 °C by the 1 min microwave irradiation (2450 MHz, 600 W) [15]. Since we have used an open system, strong overheating of the reaction mixture during 20–30 s irradiation is unlikely, and the local overheating cannot affect the reaction so drastically. Furthermore, such a dramatic effect was observed only for the reaction with $(\mu\text{-H})Os_3(\mu\text{-O=CPh})(CO)_{10}$, while the effect of microwave irradiation on the allylic rearrangement was minimum for $(\mu\text{-H})Os_3(\mu\text{-O=CMe})(CO)_{10}$ and $(\mu\text{-H})Os_3(\mu\text{-O=CNHCHMeCOOEt})(CO)_{10}$ complexes.

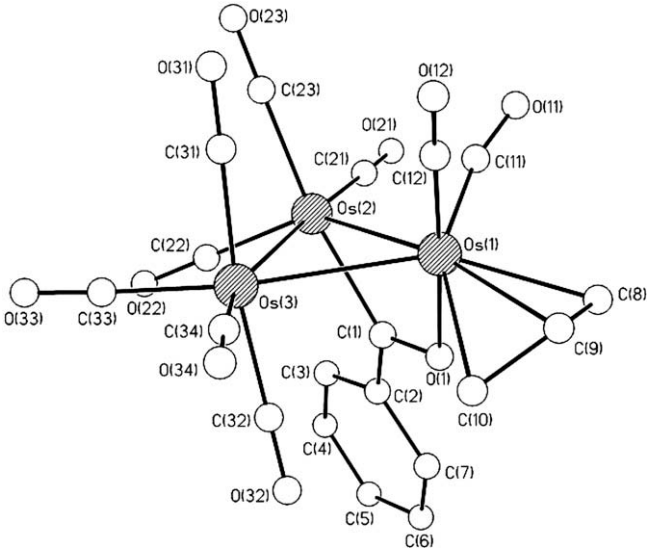


Fig. 2. Molecular structure of $Os_3\{(\mu,\eta^2\text{-O=CC}_6H_5)(\eta^3\text{-}C_3H_5)\}(CO)_9$ [18]. Selected distances (Å) and bond angles (°): Os(1)–Os(2) = 2.843(1), Os(2)–Os(3) = 2.836(1), Os(1)–Os(3) = 2.840(1), Os(1)–C(8) = 2.248(1), Os(1)–C(9) = 2.247(2), Os(1)–C(10) = 2.273(2), Os(1)–O(1) = 2.138(2), Os(2)–C(1) = 1.916(1); Os(2)–Os(3)–C(1) = 89.37(3), Os(2)–Os(1)–O(1) = 89.3(2), C(8)–C(9)–C(10) = 121.3(9).

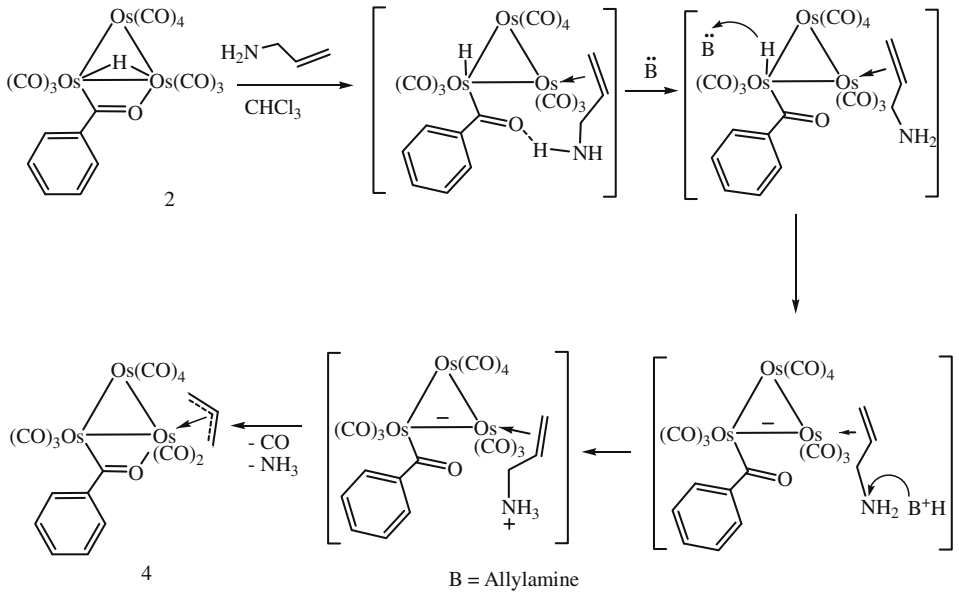
Unfortunately, we cannot at present unambiguously interpret the results obtained.

If the formation of NH···O=C hydrogen bond followed by Os–O bond dissociation is the key step of the N-allylacetamide isomerization (as described above), then the isomerization of allylamine, which has not yet been described, shall proceed under similar conditions. We have studied the isomerization of allylamine in the presence of $(\mu\text{-H})Os_3(\mu\text{-O=CPh})(CO)_{10}$ (**2**) in $CDCl_3$ and dioxane. The course of the reactions was controlled by TLC and ^1H NMR spectra of the reaction mixtures. No apparent solvent effect was observed. After chromatography of the reaction mixture, two yellow compounds were isolated and characterized.

One of these compounds was starting complex **2** (~30%). In the CO stretching region, the IR spectrum of the second product was similar to that of $Os_3(CO)_9$ with chelate-bridging ligands [16]. No NH bands were detected in the IR spectrum. The ^1H NMR spectrum confirmed the presence of the Ph group and the $\eta^3\text{-}C_3H_5$ ligand coordinated to the metal atom [17].

The single crystal of this complex was obtained and its X-ray diffraction analysis (Fig. 2) was reported in preliminary communication [18]. The η^3-allyl ligand is located in the position close to that of equatorial CO in **2**; C(8) and C(9) atoms are equidistant within the error limit, while C(10) is more remote. The bridging O(1)–C(1)–Ph ligand is located almost axially relative to the Os_3 triangle; the Os_3/Os(1)O(1)C(1)Os(2) interplanar angle is 103.40°.

Therefore, instead of the expected allylamine isomerization, the C–N bond breaks at room temperature with the coordination of the allyl fragment formed to the osmium atom in $Os_3(CO)_9(\mu,\eta^2\text{-O=C-Ph})(\eta^3\text{-}C_3H_5)$ (**4**) cluster. Transition metal complexes with the η^3-allyl ligand are mainly formed in their reactions with allyl halogenides and allylic alcohols [19,20]. Few examples of C–N bond cleavage under mild conditions and the formation of π-complexes can be mentioned. Platinum η^3-allyl complexes were synthesized at room temperature starting from allylamine and cationic Pt(II) complexes [21]. The ruthenium η^3-allyl complex was obtained by moderate heating of $[(C_5Me_5)RuCl_2]_n$ and allylamine solution in CH_2Cl_2 [22]. A similar complex was obtained by boiling the THF solution of allylamine and $[RuClH(CO)(PPh_3)]$ [23]. In most of these publications, the authors propose that C–N bond cleavage is caused by hydrogen atom transfer from the metal atom to the nitrogen of the coordinated allylamine. We also suggest that in our reaction,



Scheme 2.

the key step of C–N bond cleavage is the transfer of the terminal hydrogen atom as H^+ from the osmium atom to the nitrogen atom of allylamine (Scheme 2). The acidity of the terminal hydrogen atom in triosmium clusters and its abstraction with amines are known [24–26]. The proposed mechanism is shown below.

The reaction of allylamine with **2** was also studied at 65 °C. Cluster complex **3** forms along with an oily product, as in the reaction at room temperature. Although the composition and structure of this oily product has not been determined exactly, IR, ^1H, $C^{13}\{^1H\}$ NMR and mass spectral data indicate that it is a mixture of oligomers containing not more than 10 allylamine fragments.

3. Conclusions

The results obtained allow us to suppose that cluster complexes with the hemilabile bridging –C=O group are promising as catalysts for various processes. The capability of the substrate to form a hydrogen bond with the oxygen atom of the bridging ligand followed by Os–O bond cleavage and the formation of a vacant coordination site is likely to be a necessary condition of the catalytic activity of these clusters. In this case, the Os–O bond strength and hence the catalytic activity of the clusters strongly depend on the organic radical bonded by the bridging –C=O group.

4. Experimental

Deuterated solvents were used without further purification. Other solvents were distilled before the use. $Os_3(CO)_{10}(NCMe)_2$ [27], (μ-H)Os_3(μ-O=CR)$(CO)_{10}$ (R = Me (**1**); Ph (**2**)) [28], (μ-H)Os_3(μ-O=CNHCH$_2$CH=CH$_2$)$(CO)_{10}$ [29], (μ-H)Os_3(μ-O=CNHCHMeCOOEt)$(CO)_{10}$ [30] cluster complexes were prepared using the methods described in the literature. Analytical and preparative chromatography was performed on Silufole™ plates as well as on glass plates coated by the Silica gel 60 PF_{254}. IR spectra were obtained using a Scimitar FTS 2000 spectrofotometer. ^1H and ^{13}C NMR spectra were recorded on Bruker MSL-300 at 300 MHz (^1H) and Bruker DPX-250 at 250.1 MHz (^1H) or 62.3 MHz (^{13}C) spectrometers in $CDCl_3$ or in a $CDCl_3/CCl_4$ mixture (internal standard – TMS). The numeration of hydrogen atoms for signal assignment in ^1H NMR of $Os_3(CO)_9(\mu,\eta^2\text{-O=C-Ph})(\eta^3\text{-}C_3H_5)$ complex (**3**) corresponds to the numeration for carbon atoms given in Fig. 2. The mass spectra were measured on an Aligent 1100 HPLS-MS spectrometer using the electrospray ionization technique. A conventional microwave oven (2450 Hz, 600 W) was used to irradiate the samples. Elemental analyses were performed using a EURO EA 3000 C H N elemental analyzer or by manual burning, OsO_4 being caught by a low temperature trap.

4.1. Isomerization of N-allylacetamide

4.1.1. At room temperature

All reactions were performed in NMR tubes at room temperature. The clusters (μ-H)$Os_3(CO)_{10}(\mu,\eta^2\text{-O=C-Me})$ (**1**) (30 mg, 3.4×10^{-2} mmol), (μ-H)$Os_3(CO)_{10}(\mu,\eta^2\text{-O=CPh})$ (**2**) (30 mg, 3.1×10^{-2} mmol), and (μ-H)Os_3(μ-O=CNHCHMeCOOEt)$(CO)_{10}$ (**3**) (30 mg, 2.9×10^{-2} mmol) were dissolved in 0.5 ml of $CDCl_3$. Twenty six milligrams (0.29 mmol) of N-allylacetamide was added to each of the obtained solutions. The reactions courses were monitored by disappearance of starting N-allylacetamide signals (–CH_2–N) and arising of the N-(prop-1-enyl)acetamide signals (=CH–CH_3) in ^1H NMR spectra (Fig. 1).

4.1.2. At microwave irradiation

Reactions were performed in NMR tubes. The clusters **2** (30 mg, 3.1×10^{-2} mmol), **1** (30 mg, 3.3×10^{-2} mmol), and (μ-H)$Os_3(CO)_{10}(\mu,\eta^2\text{-O=}CC_6H_4NEt_2)$ (30 mg, 2.5×10^{-2} mmol) were dissolved in 0.5 ml of $CDCl_3$. N-allylacetamide (30 mg, 0.3 mmol) was added to each solution. The samples were irradiated for 8–30 min, the single irradiation time being no more 30 s with following cooling to ~18 °C. The reaction monitoring was as outlined above. The 50% conversion of N-allylacetamide is reached for 8 min in the presence of cluster **2**. No visible changes of NMR spectra were observed at microwave irradiation of N-allylacetamide solutions in the case **1** and **3** clusters.

4.2. Reaction of allylamine with [(μ-H)$Os_3(CO)_{10}(,\eta^2$-O=CPh)]

4.2.1. At room temperature in $CDCl_3$

To the solution of (μ-H)$Os_3(CO)_{10}(\mu,\eta^2\text{-O=CPh})$ (**2**) cluster (30 mg, 3.1×10^{-2} mmol) in 0.5 ml $CDCl_3$ 40 mg (0.7 mmol) freshly distilled over NaOH allylamine was added. The solution has been kept at room temperature for two months. The reaction course was monitored by disappearance of the allylamine signals and arising of coordinated allyl ligand signals in new complex **4** in ^1H NMR spectra of the reaction mixture. When reaction finished the solution was evaporated to dryness in vacuum and the residue was chromatographed on TLC plates using petroleum ether as eluent. Two yellow fractions were isolated with R_f 0.85 (starting (μ-H)$Os_3(CO)_{10}$(μ-O=CPh) (**2**); 8.5 mg, 28.6%) and R_f 0.65 ($Os_3(CO)_9(\mu,\eta^2\text{-O=CPh})(\eta^3\text{-Allyl})$ (**4**); 9.7 мг., 32.4%).

4.2.1.1. Cluster 4. IR (hexane, ν_{CO}/cm^{-1}): 2098 w, 2055 s, 2023 m, 2013 s, 1999 m, 1994 m, 1976 w. ^1H NMR ($CDCl_3$, 250 MHz): δ 7.68 (d, 2H, H^3, H^7); 7.57 (dd, 1H, H^5); 7.36 (dd, 2H, H^4, H^6); 5.36 (m, 1H, H^9); 5.23 (dd, $^3J_{HH}$ = 7 Hz, $^2J_{HH}$ = 3 Hz, 1H, $H^{8\beta,10\beta}$); 4.88 (dd, $^3J_{HH}$ = 7 Hz, $^2J_{HH}$ = 3 Hz, 1H, $H^{8\beta,10\beta}$); 2.59 (dd, $^3J_{HH}$ = 12 Hz, $^2J_{HH}$ = 3 Hz 1H, $H^{8\alpha,10\alpha}$); 1.72 (dd, $^3J_{HH}$ = 12 Hz, $^2J_{HH}$ = 3 Hz 1H, $H^{8\alpha,10\alpha}$) ppm. *Anal.* Calc. for $C_{19}H_{10}O_{10}Os_3$: C, 23.54; H, 1.03; Os, 58.71. Found: C, 23.82; H, 1.16; Os, 58.35%.

4.2.2. At room temperature in d_8-dioxane

To the solution of (μ-H)$Os_3(CO)_{10}(\mu,\eta^2\text{-O=CPh})$ (**2**) cluster (30 mg, 3.1×10^{-2} mmol) in 0.5 ml d_8-dioxane 42 mg (0.7 mmol) freshly distilled over NaOH allylamine was added. The solution has been kept at room temperature for nine weeks. The reaction course was controlled as described above. When reaction finished the solution was evaporated to dryness in vacuum and residue was chromatographed on TLC plates using petroleum ether as eluent. Two yellow fractions were isolated with R_f 0.85 (starting (μ-H)$Os_3(CO)_{10}$(μ-O=CPh) (**2**); 7.8 mg, 26.2%) and R_f 0.65 ($Os_3(CO)_9(\mu,\eta^2\text{-O=CPh})(\eta^3\text{-Allyl})$ (**4**); 8.6 мг., 28.7%.

4.2.3. At 65 °C in $CDCl_3$

The solution of (μ-H)$Os_3(CO)_{10}(\mu,\eta^2\text{-O=CPh})$ (**2**) (36 mg, 3.8×10^{-2} mmol) and allylamine (140 mg, 2.46 mmol) in 4 ml $CHCl_3$ in sealed glass ampoule was heated at 65 °C for 50 h. The color was turned from light yellow to orange and an oily product on the solution surface was formed. When reaction was finished, the oil was removed and the solution was evaporated in vacuum to dryness. Chromatography on TLC plates of the residue (eluent – petroleum ether) gave two main yellow fraction with R_f 0.85 (unreacted **2**, 19 mg, 52.5%) and 0.65 (**4**, 7 mg, 18%).

4.2.3.1. The oily product. IR (thin film, ν/cm^{-1}): 3420 vs, 2965 vs, 2036 m, 1956 m, 1610 s, 1509 s, 1459 s, 1150 w, 994 w, 945 w, 882 w, 755 w, 578 w. ^1H NMR (methanol-d_4, 250 MHz): δ 8.5 (br. 3H, $NR_{4-x}H_x^+$), 5.97 (m, 1H, CH=CH_2), 5.42 (m, 2H, CH_2=CH), 3.57 (m, 2H, CH_2–N), 3.03 (br. m, 6H), 2.6 (br. m, 1.7H), 2.15 (br. m, 4.8H), 1.9–0.85 (br. m, 14H) ppm. $^{13}C\{^1H\}$ NMR (methanol-d_4, 63 MHz : δ 130 (–CH=CH_2), 121 (CH_2=CH–), 43 (br.) (–CH_2–N–),

41 (br.), 36 (br.), 32 (br.), 28 (br.), 15 (br.), 18 (br.) ppm. MS (ESI+): *m*/*z* 505 (25%), 448 (25%), 391 (35%); 334 (60%); 277 (100%); 220 (85%); 163 (30%).

4.3. The synthesis of (μ-H)$Os_3(CO)_{10}$(,η^2-O=C-$C_6H_4NEt_2$) (**5**) cluster

The solution of $Os_3(CO)_{10}(NCMe)_2$ (130 mg, 0.139 mmol) and 4-(diethylamino)benzaldehyde (56 mg, 0.316 mmol) in 7 ml dioxane was heated at 80 °C for 30 min. After that the reaction mixture was evaporated at reduced pressure and the solid residue was chromatographed on glass plates coated with silicagel using petroleum ether as eluent. The extraction of the main yellow fraction with R_f 0.65 gave (μ-H)$Os_3(CO)_{10}$(μ,η^2-O=$CC_6H_4NEt_2$) (**5**) (88 mg, 62%). IR (hexane, ν_{CO}/cm^{-1}): 2106 w, 2066 s, 2055 s, 2023 s, 2015 s, 2008 w, 1993 w, 1977 w. ^{1}H NMR ($CDCl_3$, 250 MHz): δ 7.63 (m, 2H), 6.55 (m, 2H) (aromatic H); 3.43 (q, 4H, $-NCH_2-$); 1.23 (t, 6H, Me); -13.73 (s, 1H, μ-H). *Anal* Calc. for $C_{22}H_{15}NO_{12}Os_3$: C, 25.02; H, 1.43; Os, 54.04. Found: C, 25.20; H, 1.50; Os, 53.82%.

References

[1] C.S. Slone, D.A. Weinberger, C.A. Mirkin, The transition metal coordination chemistry of hemilabile ligands, in: K.D. Karlin (Ed.), Prog. Inorg. Chem., vol. 48, 1999, p. 233.
[2] P. Braunstein, F. Naud, Angew. Chem., Int. Ed. 40 (2001) 681.
[3] A. Bader, E. Lidner, Coord. Chem. Rev. 108 (1991) 27.
[4] R.D. Adams, F.A. Cotton (Eds.), Catalysis by Di- and Polynuclear Metal Cluster Complexes, Wiley-VCH, New York, 1998.
[5] J.A. Cabeza, Eur. J. Inorg. Chem. (2002) 1559.
[6] S.P. Tunik, Russ. Chem. Bull. 53 (2004) 2657.
[7] A.J. Arse, A.J. Deeming, J. Chem. Soc., Chem. Commun. (1980) 1102.
[8] K.A. Azam, A.J. Deeming, I.R. Rothwell, J. Chem. Soc., Dalton Trans. (1981) 91.
[9] V.A. Maksakov, V.A. Ershova, Russ. Chem. Bull. 35 (1986) 234.
[10] M.C. Henvenston, T.J. Lynch, Organometallics 6 (1987) 208.
[11] V.A. Maksakov, V.A. Ershova, V.P. Kirin, A.V. Golovin, J. Organomet. Chem. 532 (1997) 11.
[12] V.A. Maksakov, V.P. Kirin, S.V. Tkachev, A.V. Golovin, Russ. Chem. Bull. 48 (1999) 2158.
[13] H.M. Kingston, S.J. Haswell (Eds.), Microwave Enhanced Chemistry: Fundamentals, Sample Preparation and Applications, Amer. Chem. Soc., Washington, DC, 1997.
[14] A.G. Wittaker, D.M.P. Mingos, J. Microwave Power Electromagnetic Energy 29 (1994) 196.
[15] D.M.P. Mingos, D.P. Baghurst, Chem. Soc. Rev. (1991) 1.
[16] V.A. Maksakov, V.P. Kirin, A.V. Golovin, Russ. Chem. Bull. 44 (1995) 1941.
[17] L.A. Fedorov, Russ. Chem. Rev. 39 (1970) 655.
[18] V.A. Maksakov, N.V. Pervuhina, N.V. Podberezskaya, M.Yu. Afonin, V.A. Potemkin, V.P. Kirin, J. Struct. Chem. 49 (2008) 926.
[19] R.H. Crabtree, The Organometallic Chemistry of the Transition Metals, John Wiley & Sons Inc., Hoboken, New Jersey, 2005. P. 133.
[20] C. Eishenbroich, A. Salzer, Organometallics, VCH Verlagsgesellschaft mbH, Weinheim, 1989.
[21] (a) H. Kurosava, R. Okawara, J. Organomet. Chem. 81 (1974) C31; (b) H. Kurosava, Inorg. Chem. 15 (1976) 120.
[22] H. Nagashima, K. Mukal, Yu. Shiota, Ken-Ichi Ara, K. Itoh, H. Suzuki, N. Oshima, Y. Moro-oka, Organometallics 4 (1985) 1314.
[23] K. Hiraki, T. Matsunaga, Organometallics 13 (1994) 1878.
[24] S.P. Gubin, V.A. Maksakov, L.K. Kedrova, E.D. Korniets, Dokl. Akad. Nauk SSSR 271 (1983) 354 (in Russian).
[25] H.W. Walker, R.G. Pearson, P.C. Ford, J. Am. Chem. Soc. 105 (1983) 1179.
[26] R.T. Weberg, J.R. Norton, J. Am. Chem. Soc. 112 (1990) 1105.
[27] M. Tachikawa, J.R. Schapley, J. Organomet. Chem. 124 (1977) C 19.
[28] B.F.G. Jonson, J. Lewis, T.I. Odiaka, P.R. Raithby, J. Organomet. Chem. 216 (1981) C56.
[29] V.A. Maksakov, V.P. Kirin, S.N. Konchenko, N.M. Bravaya, A.D. Pomogaylo, A.V. Virovets, A.V. Podberezskaya, S.V. Tkachev, Russ. Chem. Bull. 42 (1993) 1293.
[30] V.A. Maksakov, N.V. Podberezskaya, E.V. Golubovskaya, V.P. Kirin, S.P. Babailov, S.P. Gubin, Rus. J. Inorg. Chem. 41(1996) 59–65.

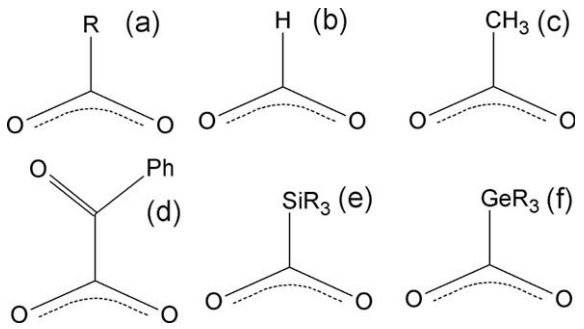
(SP → TBP), the Cu···Cu separation increases, thus the Cu···Cu distance parameter reflects the coordination sphere arrangement and only through that suggests the magnitude of the AFM interaction [2,4–6]. The main key factor crucial for the magnitude of the AFM interaction of this type of complexes is, however, the electronic structure of the carboxylate group carbon atom (O_2C). A larger orbital $2p_x$ population (the *x*-axis is along the R–C bond in O_2CR) of the carbon atom in the symmetric HOMO orbital gives a larger $|2J|$ value [6–11]. Thus, the characteristic magnitude of the AFM interaction for the methanoate dicopper *paddle-wheel* $[Cu_2(\mu\text{-}O_2CR)_4L_2]$ complexes is reported to be 390–560 cm^{-1} [1–3,6,12–16]. Such a magnitude is exceeded only by complexes having benzoyl formate $-2J \sim 650\ cm^{-1}$ [9,17], carboxysilanes and carboxygermanes $-2J \sim 1000$–$1200\ cm^{-1}$ [3,10] as the 'R' group in O_2CR (Scheme 1d–f). On the other hand, the vast majority of the carboxylates show significantly weaker AFM interaction (*e.g.* acetates $-2J \sim 300\ cm^{-1}$) [2,6,7,18]. The axial ligand L in $[Cu_2(\mu\text{-}O_2CR)_4L_2]$ is suggested not to take a stronger role for the AFM interaction, though certain effects are noticed [6]. The application of a 2-methylpyridine (2-mpy) molecule next to the carboxylate anion may serve as an additional ligand at the terminal position (one coordination site) of the mononuclear, binuclear or polynuclear coordination compound enabling additional stabilization due to its π-system and steric hindrance. Therefore, methanoate and 2-mpy as ligands could show interesting structural possibilities giving significant insight into the coordination moiety construction. Many examples are found in the literature confirming the key role for the AFM interaction magnitude of the dicopper *paddle-wheel* building blocks. Nevertheless, the binuclear methanoate central core $[Cu_2(\mu\text{-}O_2CR)_4]$ environment has not been so clearly described, despite a number of different types of coordination compounds with $[Cu_2(\mu\text{-}O_2CH)_4]$ building blocks that have been reported [2,3,16,19–24].

Herein, several methanoato complexes, *e.g.* mononuclear $[Cu(O_2CH)_2(2\text{-mpy})_2]$ (**1**), binuclear $[Cu_2(\mu\text{-}O_2CR)_4(2\text{-mpy})_2]$ (**2**) and two hybrids of mononuclear and binuclear building blocks in polymeric $\{[Cu(\mu\text{-}O_2CH)_2(2\text{-mpy})_2][Cu_2(\mu\text{-}O_2CH)_4]\}_n$ (**3**) and $\{Na_2[Cu(\mu\text{-}O_2CH)_2(O_2CH)_2][Cu_2(\mu\text{-}O_2CH)_4]\}_n$ (**4**) are presented and described.

2. Experimental

2.1. Physical measurements

C,H,N analyses were performed with a Perkin–Elmer 2400 CHN Elemental Analyzer. Metal analysis was carried out electrogravimetrically with Pt electrodes. Vibrational spectra were recorded by KBr pellets on a Perkin–Elmer FT-IR 1720x spectrometer. Electronic spectra were recorded as nujol mulls with a Perkin–Elmer Lambda 19 UV/Vis/NIR spectrometer. X-band powder EPR spectra for **4** were recorded at various temperatures on a Bruker Elexsys E500 electron spin resonance spectrometer. The room temperature magnetic susceptibility data of the powdered samples were obtained with a Sherwood Scientific MSB-1 balance using $Hg[Co(NCS)_4]$ as a calibrant. The instrument uses the Evans's method. The effective magnetic moments (per one copper atom) were calculated using the equation $\mu_{eff}/\mu_B = 2.828(\chi_M T)^{1/2}$. The magnetic susceptibility for **4** was additionally measured with a Quantum Design SQUID MPMS-XL-5 magnetometer, equipped with a 5 T magnet. These data were investigated in the temperature interval 2–300 K in a magnetic field strength of $H = 1000$ Oe and were corrected for the experimentally determined contribution of the sample holder. Corrections for the temperature dependant paramagnetism and the diamagnetic response of the compounds, due to the closed atomic shells as estimated from the Pascal's constants, were applied [25].



Scheme 1. Several carboxylate O_2CR ligands differing in the 'R' group covalently bonded to the carboxylate O_2C carbon atom.

2.2. X-ray crystallography

The single crystal data for **1** and **3** were collected on a Nonius Kappa CCD diffractometer with graphite monochromated Mo Kα radiation. They were processed using the DENZO-SMN program [26]. Both structures were solved by direct methods using SIR97 [27]. The positions of all the other hydrogen atoms in **1** and **3** were obtained from the difference Fourier map. Full-matrix least-squares refinement on *F* magnitudes was employed with anisotropic displacement factors for all non-hydrogen atoms using XTAL3.6 [28]. The parameters of the hydrogen atoms were not refined. The numbers of total measured and unique reflections are 20,070 and 2660 for **1**, while 9942 and 2741 for **3**, respectively. 2495 and 2553 reflections with 190 and 160 parameters were used for the refinement for **1** and **3**, respectively.

Figs. 1–3 were drawn using PLATON [29]. Details of the crystal data, data collection and refinement parameters are listed in Table 1. The selected bond lengths and angles are presented in Table 2.

2.3. Materials

β-$[Cu(\mu\text{-}O_2CH)_2]_n$ was isolated from methanoic acid (20 mL) and caustic copper(II) carbonate $Cu_2(OH)_2CO_3$ (2.0 g, 9.0 mmol) at room temperature. $Cu_2(OH)_2CO_3$ was prepared from the starting solutions of $CuSO_4{\cdot}5H_2O$ (15.2 g, 60 mmol) in 160 mL of water and $Na_2CO_3{\cdot}10H_2O$ (21.6 g, 75 mmol) in 240 mL of water at 65 °C. All reagents were obtained commercially and were used without further purification.

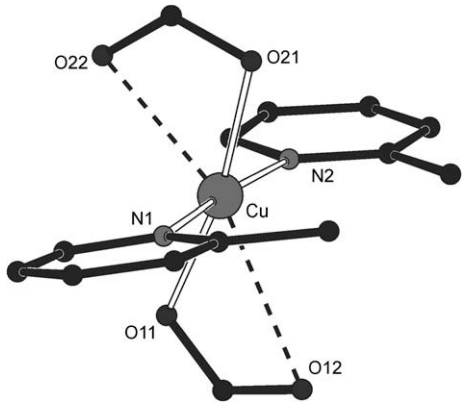


Fig. 1. The mononuclear complex **1** shows a *trans* orientation of the methanoate and 2-mpy ligands, the methyl 2-mpy groups are however *cis*. The dashed lines connecting the semi-coordinated O22 and O12 atoms with the central copper(II) ion clearly reflect the strong distortion from the theoretical elongated octahedral coordination sphere. Hydrogen atoms are omitted for clarity.

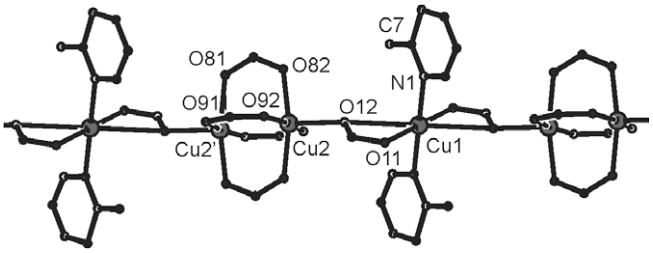


Fig. 2. Polymeric molecular structure of **3** composed of the mononuclear octahedral and the binuclear *paddle-wheel* units. H atoms are omitted for clarity.

2.4. Synthesis

Bis(methanoato-κ^2*O*,*O*′)-bis[(2-methylpyridine-κ*N*)copper(II)] **1**: 0.44 g (2.0 mmol) of $Cu_2(OH)_2CO_3$ in 1.0 mL of HCOOH was slowly added to 10 mL of 2-mpy and left at 40 °C for 5 min. The resulting mixture was then filtered and the filtrate was left at 6 °C for one day, giving violet crystals of **1**. Due to an instability of **1** in air, only single crystal XRD analysis was performed for this compound. The single crystals were preserved by the liquid nitrogen when removed from the mother-liquid for the XRD data collection. If the homogeneous violet product of **1** was filtered at room temperature, dried in air and then left in a desiccator above KOH for one day, the binuclear complex **2** is the final product. This was proven by IR and powder XRD analysis. Average yield for **2** by this procedure is 30%.

Tetrakis(μ-methanoato-κ*O*:κ*O*′)bis[(2-methylpyridine-κ*N*)copper(II)] **2**: The following synthesis procedure is different, as already described [1]. β-[μ-$Cu(O_2CH)_2]_n$ (0.46 g, 3.0 mmol) was slowly added to a liquid mixture of ethanol 20 mL and 2-mpy (6.7 mL) with heating and stirring. After boiling, the saturated solution was filtered off and left at 6 °C for one day. Light green crystals of **2** were filtered off, dried in air for 20 min and in a desiccator above KOH for a day. Average yield 40%. *Anal.* Calc. for $C_{16}H_{18}Cu_2N_2O_8$: C, 38.9; H, 3.68; N, 5.68; Cu, 25.8. Found: C, 39.0; H, 3.74; N, 5.67; Cu, 25.7%. IR ν_{max} 1644 $\nu_{as}(O_2C)$, 1606, 1574, 1490, 1456, 1379, 1356 $\nu_s(O_2C)$, 1305 cm^{-1}. UV–Vis λ_{max} 270, 380, 750 nm. Magnetic susceptibility: μ_{eff} = 1.14 μ_B.

Catena-poly[tetrakis(μ-methanoato-1κ*O*:2κ*O*′)bis(μ-methanoato-2κ*O*:3κ^2*O*,*O*′;1′κ*O*:3κ^2*O*,*O*′)bis(2-methylpyridine-3κ*N*)tricopper(II)] **3**: $Cu_2(OH)_2CO_3$ (0.66 g, 3.0 mmol) was added to a solution of ethanol (70 mL) and methanoic acid (0.90 mL). Subsequently, 2-mpy (0.85 mL, 8.6 mmol) was added dropwise. After 1 h reflux, the resulting mixture was filtered off and the solution was left at 6 °C for one day. Blue-violet crystals of **3** were filtered off, dried in air for 20 min and in a desiccator above KOH for one day. Average yield 75%. The product was recrystallized from ethanol. *Anal.* Calc. for $C_{18}H_{20}Cu_3N_2O_{12}$: C, 33.4; H, 3.12; N, 4.33; Cu, 29.5. Found: C, 33.7; H, 3.15; N, 4.14; Cu, 29.4%. IR ν_{max} 1655 $\nu_{as}(O_2C)$, 1615, 1580, 1565, 1491, 1463 1376, 1351 $\nu_s(O_2C)$, 1305 cm^{-1}. UV–Vis λ_{max} 280, 360, 715 nm. Magnetic susceptibility: μ_{eff} = 1.42 μ_B.

Catena-poly[disodium bis(μ-methanoato-1κ*O*:2κ*O*′)-bis(μ$_3$-methanoato-1κ*O*:2κ*O*′:3κ*O*′;1′κ*O*′:2′κ*O*:3κ*O*′)bis(μ-methanoato-2κ*O*:3κ*O*′;1′κ*O*:3κ*O*′)bis(2-methylpyridine-3κ*N*)tricuprate(II)] **4**: Com-

Table 1
Relevant crystal data and data collection with the refinement summary for **1** and **3**.

Compound	**1**	**3**
Chemical formula	$C_{14}H_{16}CuN_2O_4$	$C_{18}H_{20}Cu_3N_2O_{12}$
Formula weight	339.84	647.01
Crystal system	triclinic	triclinic
Space group	$P\bar{1}$ (No. 2)	$P\bar{1}$ (No. 2)
a (Å)	7.1845(3)	7.3744(2)
b (Å)	7.7474(4)	8.4911(3)
c (Å)	14.5439(8)	10.8364(4)
α (°)	99.227(2)	88.1732(13)
β (°)	99.697(2)	80.1801(14)
γ (°)	108.451(2)	65.2284(18)
Z	2	1
V (Å^3)	736.92(7)	606.48(4)
D_{calc} (g cm^{-3})	1.532	1.771
Crystal colour, shape	blue plate	violet plate
Crystal size (mm)	0.50 × 0.20 × 0.10	0.23 × 0.14 × 0.06
λ(Mo Kα) (Å)	0.71073	0.71073
T (K)	150	293
θ_{max} (°)	25.31	27.35
h/*k*/*l*	−8,8/−9,9/−17,17	−9,9/−10,10/−13,13
Measured reflections	20 070	9942
Independent reflections (R_{int})	2660 (0.038)	2741 (0.028)
Observed reflections (F^2) > 2.0 σ(F^2)	2250	2310
Contributed reflections	2495	2553
Parameters	190	160
R, R_w	0.036, 0.036	0.048, 0.040
$\Delta\rho_{max}/\Delta\rho_{min}$ (e Å^{-3})	0.561, −0.739	0.93, −1.12

$R = \sum(||F_o| - |F_c||)/\sum|F_o|$; $R_w = \sum(w(|F_o| - |F_c|))/\sum(w|F_o|)$.

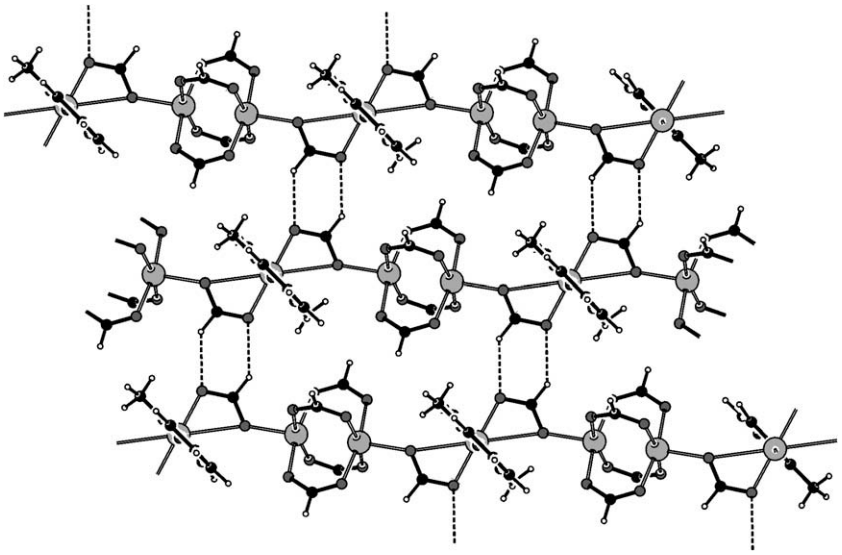


Fig. 3. The inter-chain C–H···O contacts (H···O seen as dotted lines) *via* the intra-chain bridging methanoates in the polymeric molecular structure of **3**.

Table 2
Selected bond lengths (Å), angles (°) and C–H···O contacts (Å, °) for **1** and **3**.

1					
Cu–N1	2.001(3)	Cu–N2	2.012(4)	Cu–O11	1.945(3)
Cu–O12	2.825(3)	Cu–O21	1.992(3)	Cu–O22	2.472(3)
N1–Cu–N2	174.92(12)	N1–Cu–O11	90.63(15)	N1–Cu–O12	84.37(11)
N1–Cu–O21	90.23(15)	N1–Cu–O22	92.28(11)	N2–Cu–O11	90.55(15)
N2–Cu–O12	92.49(11)	N2–Cu–O21	89.55(15)	N2–Cu–O22	91.92(11)
O11–Cu–O12	51.88(11)	O11–Cu–O21	169.04(10)	O11–Cu–O22	110.70(11)
O12–Cu–O21	139.05(11)	O12–Cu–O22	162.06(12)	O21–Cu–O22	58.34(12)
C8···O21	3.219(6)	C8–H81···O21	132		
C6···O22^{i}	3.286(6)	C6–H6···O22^{i}	131		
3					
Cu1–N1	1.978(2)	Cu1–O11	1.9707(17)	Cu1–O12	2.662(2)
N1–Cu1–O11	89.55(9)	N1–Cu1–O11^{ii}	90.45(9)	N1–Cu1–O12	86.22(9)
N1–Cu1–O12^{ii}	93.78(9)	O11–Cu1–O12	54.11(7)	O11–Cu1–O12^{ii}	125.89(7)
Cu2···Cu2^{i}	2.6364(5)	Cu2–O81	1.978(2)	Cu2–O82	1.983(2)
Cu2–O91	1.977(3)	Cu2–O92	1.963(3)	Cu2–O12	2.1234(18)
O12–Cu2–O81	93.86(8)	O12–Cu2–O82	98.12(8)	O12–Cu2–O91	95.95(9)
O12–Cu2–O92	95.86(9)	O81–Cu2–O82	168.02(10)	O81–Cu2–O91	89.25(13)
O81–Cu2–O92	89.47(12)	O82–Cu2–O91	89.12(14)	O82–Cu2–O92	89.71(13)
O91–Cu2–O92	168.18(10)	Cu1–O12–Cu2	160.10(10)	Cu12–O12–Cu2^{i}	176.38(5)
C7···O12	3.279(5)	C7–H72···O12^{ii}	153		
C1···O11	3.305(3)	C1–H1···O11^{iii}	133		

$^{i}1-x, 2-y, 1-z$, $^{ii}2-x, 2-y, -z$, $^{iii}1-x, 2-y, -z$.

plex **4** was synthesized as described previously [20]. *Anal.* Calc. for $C_{16}H_{18}Cu_2N_2O_{14}$: C, 16.1; H, 1.35; Cu, 31.9. Found: C, 15.8; H, 1.22; Cu, 32.3%. IR ν_{max} 1638, 1608, 1582 $\nu_{as}(O_2C)$, 1388, 1369, 1350, 1343, 1324, $\nu_s(O_2C)$ cm^{-1}. UV–Vis λ_{max} 260, 370(sh), 710 nm. Magnetic susceptibility: μ_{eff} = 1.43 μ_B.

3. Results and discussion

3.1. Description of the crystal structures

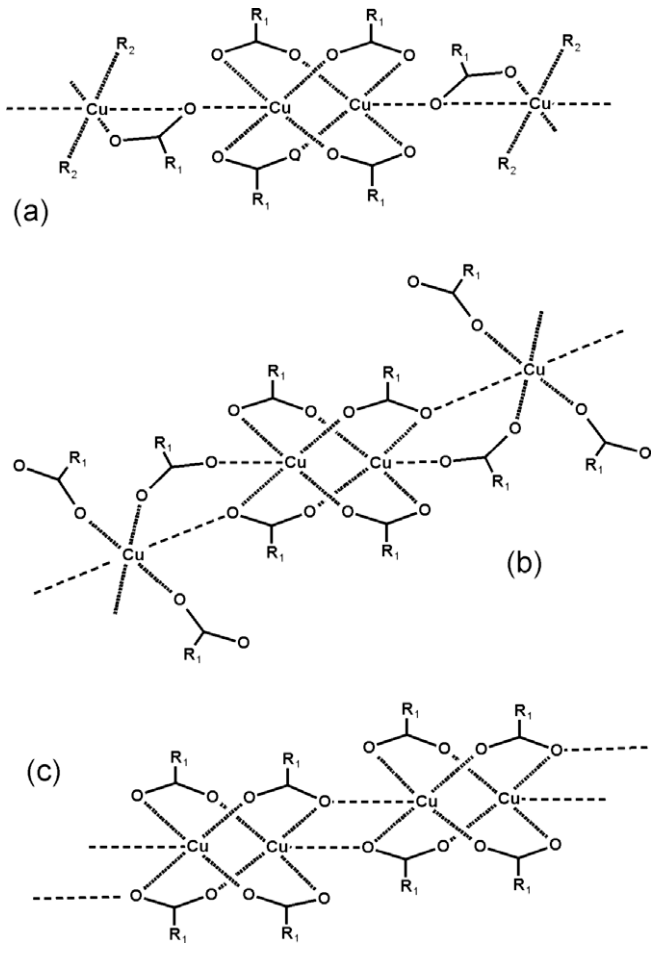
Mononuclear complex $[Cu(O_2CH)_2(2\text{-mpy})_2]$ (**1**) is composed of two methanoate anions and two 2-methylpyridine (2-mpy) molecules in a *trans* orientation (Fig. 1). The coordination sphere is highly unsymmetrical with two 2-mpy nitrogen atoms (Cu–N1 2.001(3), Cu–N2 2.012(4) Å) and two methanoate oxygen atoms (Cu–O11 1.945(3), Cu–O21 1.992(3) Å) in the basal square around the central copper(II) ion (Table 2). The semi-coordinated methanoate oxygen atoms (Cu–O22 2.472(3), Cu–O12 2.825(3) Å) are more distant, thus forming an elongated *z*-axis. This axis is strongly distorted, seen as an inclination of the Cu–O22 and Cu–O12 lines away from the normal vector of the basal plane (N1/N2/O11/O21) by 26.27(6)° (O22) and 43.94(6)° (O12), respectively. Therefore, the coordination sphere in **1** can be described either as a highly distorted octahedron, or as a distorted square-pyramid or even as a square-plane, putting the semi-coordinated O12 and O22 inside or outside the coordination sphere. The ligands are *trans* oriented, the 2-mpy methyl groups are, however, *cis*. Since no stronger H-bonds or π-stacking ($c_g\cdots c_g$ < 4.0 Å) are present to stabilize this heavily distorted molecular structure, compound **1** clearly reflects its instability outside the mother-liquid (see Section 2). It seems that numerous weak C–H···O contacts (Table 2) and π-stackings may maintain a solid compound in the mother-liquid, where these interactions are possible mostly due to 2-mpy acting as a solvent and as a ligand. A similar distorted coordination polyhedron (4+1+1) around copper(II) ion has also been observed in the crystal structure of $[Cu(O_2CCHCl_2)_2(2\text{-mpy})_2]$ [30].

The compound $[Cu_2(\mu\text{-}O_2CH)_4(2\text{-mpy})_2]$ (**2**) is much more stable than **1** (**2** is also the final product of the decomposition of **1** outside the mother-liquid (see the Section 2). A reason for such stability is found in a formation of the regular *paddle-wheel* type of binuclear complex with four methanoate bridges and 2-mpy as axial ligands, as previously described [3]. The stability of the compound is additionally strengthened by stronger π-stacking than in **1**, giving $c_g\cdots c_g$ 3.584(2), 3.819(2) Å. Several related methanoate *paddle-wheel* complexes have been described [12,13,15,21–24,31,32].

A combination of mononuclear and binuclear building blocks is found in the polymeric chain type of structure of $\{[Cu(\mu\text{-}O_2CH)_2(2\text{-mpy})_2][Cu_2(\mu\text{-}O_2CH)_4]\}_n$ (**3**) (Fig. 2). Some preliminary details of **3** have already been presented [19]. The mononuclear unit in **3** is formed by two chelate methanoate anions and two 2-mpy molecules in a *trans* orientation, similar as in **1**. However, the mononuclear methanoates in **3** are symmetrically assembled and the methyl groups of 2-mpy are *trans* to each other as well. The elongated octahedral coordination sphere is formed by two 2-mpy nitrogen atoms (Cu1–N1 1.978(2) Å) and two methanoate oxygen atoms (Cu1–O11 1.971(2) Å) in the basal plane, while two semi-coordinated methanoate oxygen atoms (Cu1–O12 2.662(2) Å) form the elongated O12–Cu–O12′ Jahn–Teller axis. The distortion of the octahedral coordination is less severe than in **1**, as this moiety in **3** is centrosymmetric and the Jahn–Teller or *z*-axis is 36.12(6)° inclined from the normal vector of the octahedral basal square-plane (N1/N1′/O11/O11′) compared to 26.27(6)° and 43.94(6)° found in **1**. The binuclear building blocks in **3** are of the *paddle-wheel* $[Cu_2(\mu\text{-}O_2CH)_4]$ type, as in the central core structure of **2** (Fig. 2). The axial positions in **3** are, however, without 2-mpy ligands as seen in **2**, but with the methanoate oxygen atoms (O12) that are in the semi-coordinated positions of the mononuclear building blocks as well (Cu_{mono}–O12 2.662(2), Cu_{bi}–O12 2.123(2) Å). Additional stabilization of the chain type structure in **3** is by weak inter-chain π-stacking ($c_g\cdots c_g$ 4.001(4) Å) and C–H···O contacts (Table 2). The methanoate O12–C1–O11 bridges of the chain in **3** also serve as inter-chain double C–H···O contacts (C1···O11^{iii} 3.305(3) Å, C1–H1···O11^{iii} 133°; $^{iii}1-x, 2-y, -z$) in $R_2^2(6)$ supramolecular synthons [33], as presented in Fig. 3. Similar supramolecular synthons between two methanoate groups, as found in **3** between the mononuclear units, have been observed in only two other copper(II) complexes, but there between the binuclear *paddle-wheel* methanoates $[Cu_2(\mu\text{-}O_2CH)_4(2\text{-mpy})_2]$ (**2**), and $[Cu_2(\mu\text{-}O_2CH)_4(3\text{-mpy})_2]$ [3]; and some for the other binuclear

methanoate complexes, e.g. with rhodium and molybdenum [34,35].

A similar binuclear-mononuclear chain type of a structure as in the molecular **3**, is found in the ionic compound $\{Na_2[Cu(\mu\text{-}O_2CH)_2(O_2CH)_2][Cu_2(\mu\text{-}O_2CH)_4]\}_n$ (**4**) (Scheme 2). Its synthesis and crystal structure determination were reported previously [20], however the other basic characterization, accompanied with a comparison to the other related methanoate complexes, is presented herein. As in **3**, the binuclear building blocks in **4** are of the *paddle-wheel* central core type, while the mononuclear units differ. The ligands in the mononuclear building blocks in **4** are solely methanoates, namely four oxygen atoms of four anions (two terminal and two bridging) completing the basal square of the elongated octahedral coordination sphere (Cu–O 1.937(6), 1.987(6) Å), while the semi-coordinated (Jahn–Teller) positions are occupied by oxygen atoms of another two methanoates. The last two oxygen atoms (semi-coordinated in the mononuclear unit) are also a part of the binuclear $[Cu_2(\mu\text{-}O_2CH)_4]$ units (Cu_{mono}–O 2.492(5), Cu_{bi}–O 1.965(5) Å). The axial position of the binuclear *paddle-wheel* building blocks in **4** is, however, occupied by an oxygen methanoate anion, where this last methanoate ligand is a triatomic bridge to the equatorial position of the mononuclear building block Cu_{bi}(axial)–O–C–O–Cu_{mono}(equatorial), and not a bridge and a chelate as in **3**. Only one methanoate ligand enables the mononuclear–binuclear bridge in **3**, while two methanoates are involved in each bridge in **4** (Scheme 2). If we assume a neutral charge for the binuclear $[Cu_2(\mu\text{-}O_2CH)_4]$, four methanoates remain per one mononuclear copper(II) cation in **4**, thus this polymeric coordination moiety as a whole is anionic, with two sodium counter cations. On the other hand, two methanoates and two 2-mpy ligands per one mononuclear copper(II) cation in **3** give a final neutral polymeric molecular complex. The sodium counter ions in **4** are surrounded by seven methanoate oxygen atoms (Na···O 2.319(9)–2.699(9) Å) [20]. Some non-methanoate examples of related alternate mononuclear–binuclear chain type of complexes are reported in the literature [36–40]. Only four complexes among them show similar coordination polymers as **3**, of the general formula $\{[Cu(\mu\text{-}O_2CR)_2(L)_2][Cu_2(\mu\text{-}O_2CR)_4]\}_n$, but they are not identical. The bridging carboxylate group between the monomeric and dimeric units in the crystal structures of the 3,3-dimethylbutyrato complex (L = 2,6-dimethylpyridine) [40] and 3,5-dinitrobenzoato complex (L = methanol) [39] are not chelating in the monomeric units. On the other hand, the benzoate complex (L = 3,5-dimethylpyrazole) [37] and the acetate complex (L = 1,4-bis[2-(5-phenyloxazoly)]benzene) [36] have similar coordination modes, though the carboxylate groups in the monomeric unit of the benzoate complex [37] are in a *cis* position and the acetate complex [36] is two-dimensional because the second ligand L forms a bridge too.



Scheme 2. The bridging mode in certain chain types of polymeric complexes. The building blocks are mononuclear and binuclear, as in **3** (a: R_1 = H, R_2 = 2-mpy) and **4** (b: R_1 = H), or solely binuclear, as seen for $[Cu_2(\mu\text{-}O_2CR)_4]_n$ (c).

3.2. Magnetic and spectroscopic analysis

The room temperature magnetic susceptibility data (Evans) give μ_{eff} = 1.14 μ_B for **2**, that is significantly lower compared to the vast majority of the dicopper *paddle-wheel* complexes $[Cu_2(\mu\text{-}O_2CR)_4]$ ($\mu_{eff} \sim$ 1.4–1.5 μ_B), but in agreement with the values for the previously presented methanoates of this type [1,41]. The room temperature measurements for the polymeric **3** and **4** give μ_{eff} = 1.42 and 1.43 μ_B, respectively (no susceptibility measurements were done for the unstable mononuclear **1**). Due to similar room temperature values of μ_{eff}/μ_B for **3** and **4**, but different for **2**, the temperature dependant magnetic susceptibility measurements (SQUID) were performed for **4** (**2** and **3** have already been already reported) [3,19]. The molar magnetic susceptibility as $\chi_M \cdot T$ versus T of **4** gradually decreases upon lowering temperature from 300 K to 100 K (Fig. 4). The curve then becomes parallel with the x-axis (100–25 K) at about 0.43 $cm^3\ K\ mol^{-1}$, and then again turns down (25–2 K). The 300–100 K step is characteristic for a strong antiferromagnetic (AFM) interaction due to the binuclear units with spin S = 1 at higher temperature, turning to the S = 0 ground state at lower temperatures. Therefore $\chi_M \cdot T$ of the binuclear units in **4** is 0 below 100 K. The constant $\chi_M \cdot T$ value (0.43 $cm^3\ K\ mol^{-1}$) in the region 100–25 K is typical for the paramagnetic S = ½ species, attributed to the mononuclear building blocks within the chain

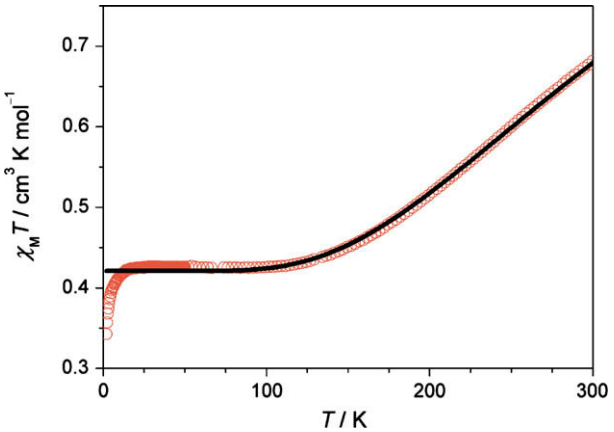


Fig. 4. Graph $\chi_M \cdot T$ *vs.* T with experimental (○) and calculated (solid line) curves for compound **4**. Parameters are: $2J = -477\ cm^{-1}$, g = 2.12.

in **4**. The final decrease of the $\chi_M \cdot T$ value below 25 K is possibly due to a weak AFM interaction between adjacent copper(II) species from mononuclear and/or binuclear units. Only the $\chi_M \cdot T(T)$ data for $T > 50$ K were fitted with Eq. (1):

$$\chi_M = \frac{2Ng^2\beta^2}{kT(3+e^{-2J/kT})} + \frac{Ng^2\beta^2}{4kT}, \quad (1)$$

where the first term was derived by Bleaney and Bowers and describes the behaviour of two copper(II) ions per molecule in the binuclear units, while the second term accounts for the mononuclear units of paramagnetic copper(II) ions [25]. The results of the calculations are $2J = -477\ cm^{-1}$ and $g = 2.12$. An almost identical shape of the $\chi_M \cdot T$ versus T graph was shown previously for complex **3** [19]. Herein the presented data for **3** ($2J = -444\ cm^{-1}$, $g = 2.12$) were obtained by a recalculation and they reveal slightly different values as reported originally. A literature survey of the AFM interaction magnitude for the methanoate *paddle-wheel* complexes show $-2J = 390–560\ cm^{-1}$ [1–3,6,12–16]. Thus, a similar room temperature μ_{eff} values (1.42, 1.43 μ_B) for the structurally related **3** and **4** are in agreement with the almost identical $\chi_M \cdot T(T)$ shape of the curve. Therefore, the higher μ_{eff}/μ_B value for the polymeric **3** and **4** than for the isolated binuclear complex **2** (1.14 μ_B) is attributed to an average μ_{eff} value of the binuclear moiety (two Cu(II) ~ 1.1 μ_B each) and the mononuclear unit (Cu(II) ~ 1.9 μ_B). A similar susceptibility analysis as for the room temperature data (Evans) was performed on the temperature dependent data (SQUID) of the polymeric **3** and **4**. Since it is reasonable to consider that only mononuclear building blocks participate in the paramagnetic signal in the graph $\chi_M \cdot T$ *versus* T (Fig. 4) in the region 25–100 K for **4**, the same constant value of $\chi_M \cdot T$ to the total susceptibility also at higher temperatures may be assumed. In this case we can subtract the mononuclear contribution of the product $(\chi_M \cdot T)_{mono}$ 0.40 and 0.43 $cm^3\ K\ mol^{-1}$ for **3** and **4**, respectively, (at room temperature) from the total measured $(\chi_M \cdot T)_{total}$ (0.65 $cm^3\ K\ mol^{-1}$ and 0.68 $cm^3\ K\ mol^{-1}$ for **3** and **4**, respectively). This difference $(\chi_M \cdot T)_{total} - (\chi_M \cdot T)_{mono} = (\chi_M \cdot T)_{bi}$ is thus 0.25 $cm^3\ K\ mol^{-1}$ for **3** and **4,** corresponding to $\mu_{eff} = 1.41\ \mu_B$ per dimer or 1.01 μ_B per each Cu(II). The last value (1.01 μ_B) is smaller than the 'Evans' room temperature μ_{eff}/μ_B of the isolated methanoate binuclear complex **2** ($\mu_{eff} = 1.14\ \mu_B$). This discrepancy can be explained by more accurate temperature dependant measurements and fitting, where temperature independent paramagnetism is additionally included.

The room temperature X-band EPR spectrum of solid **4** reveals a very broad signal at 300 mT. By decreasing the temperature below 200 K, signals of the elongated axial anisotropic symmetry are noticed giving $g_{\perp(x,y)} = 2.080(5)$ and $g_z = 2.304(5)$ (Fig. 5, 172 K). A further decrease of the temperature shows additional splitting of $g_\perp$, giving at 102 K $g_x = 2.042(5)$ and $g_y = 2.075(5)$, and a shift of g_z to 2.349(5), suggesting rhombic symmetry. These results are in good agreement with the susceptibility data (see Fig. 4). On the other hand, the axial symmetry signals are reported for the structurally related **3** already at room temperature [19], suggesting differences between **3** and **4** not seen from the susceptibility data. Interestingly, the typical spin $S = 1$ signals for the dicopper(II) *paddle-wheel* complexes were noticed for the isolated binuclear complex **2** [17], but not for the polymeric **3** and **4**, the last two also having the *paddle-wheel* building blocks. The axial symmetry signals found for **3** and **4** may well be assigned to spin $S = ½$ of the mononuclear building blocks. Namely, both complexes show a distorted elongated axial symmetry within the copper(II) mononuclear coordination sphere. The spin $S = 1$ signals expected for the binuclear *paddle-wheel* units are probably of a very low intensity, due to a very strong AFM interaction, the methanoate bridges playing the key role. An extreme broadening of the EPR signals in the spectra measured at room temperature is described also for the chain complexes formed only of $[Cu_2(\mu\text{-}O_2CR)_4]$ binuclear *paddle-wheel* building blocks (Scheme 2c) [18,42–45]. In the EPR spectra of these complexes recorded at lower temperatures, the $S = 1$ signals appear and usually also $S = ½$ signals of mononuclear impurities, whose intensity increase relatively to the $S = 1$ signals by decreasing the temperature. Eventually only the $S = ½$ signals remain, since the $S = 1$ state turns to $S = 0$ as the ground state of the complex with the AFM interaction. At least for these $[Cu_2(\mu\text{-}O_2CR)_4]_n$ complexes, the high temperature broadening of the signals is not related to the $S = ½$ species or an extremely strong AFM interaction. On comparison to the chain complexes formed solely of binuclear building blocks, one structural detail should be stressed as differing in the two polymeric complexes **3** and **4**. The magnetic interaction of the binuclear *paddle-wheel* complexes $[Cu_2(\mu\text{-}O_2CH)_4]_n$ takes place via the carboxylate intra-binuclear bridges, *e.g.* the equatorial oxygen atoms of the square-pyramidal coordination sphere. Therefore, the central copper ion d orbital $\{d_{x^2-y^2}\}^1$ is magnetic, while the axially oriented $\{d_{z^2}\}^2$ is not. One of the binuclear equatorial oxygen atoms in **4** is on the other side, also in the axial position of the mononuclear building block, towards which the non-magnetic $\{d_{z^2}\}^2$ orbital of the mononuclear copper(II) is oriented. No such bridges are found for **3** (Scheme 2). For $[Cu_2(\mu\text{-}O_2CR)_4]_n$, the high temperature broadening with lower temperature narrowing of the $S = 1$ EPR signals was explained by the $S = 1$ spin disturbing the adjacent $S = 1$ spin species [42–44]. In our case, in **4** the mononuclear $S = ½$ and the binuclear $S = 1$ species may disturb each other at high temperature, while the disturbance reason is not present at lower temperatures. Since the mononuclear $S = ½$ species are of the same number as the binuclear $S = 1$ species in a chain (not as an impurity), accompanied by the strong AFM interaction within the binuclear units, the $S = ½$ EPR signals are seen for **4** only at temperatures below 200 K. Differences in the EPR spectra of **3** and **4** are therefore probably related to their different bridging modes.

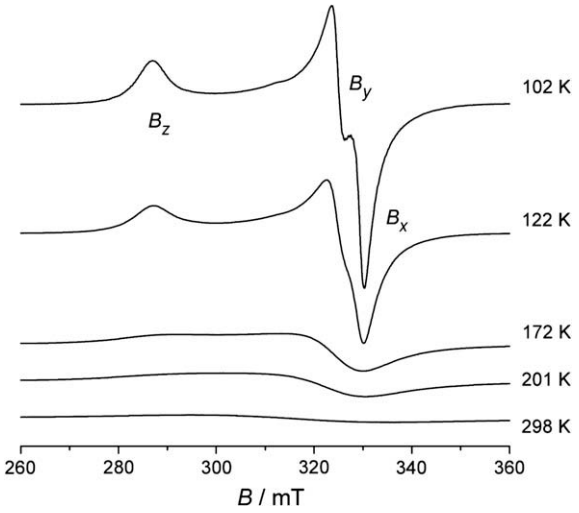


Fig. 5. X-band EPR spectra of complex **4**. The low intensity isotropic-like broad signal at room temperature gradually transforms by decreasing the temperature into three rhombic symmetry signals.

4. Conclusions

Several methanoate complexes, namely $[Cu(O_2CH)_2(2\text{-mpy})_2]$ (**1**) (2-mpy = 2-methylpyridine), $[Cu_2(\mu\text{-}O_2CH)_4(2\text{-mpy})_2]$ (**2**), $\{[Cu(\mu\text{-}O_2CH)_2(2\text{-mpy})_2][Cu_2(\mu\text{-}O_2CH)_4]\}_n$ (**3**) and $\{Na_2[Cu(\mu\text{-}O_2CH)_2(O_2CH)_2][Cu_2(\mu\text{-}O_2CH)_4]\}_n$ (**4**) have been synthesized and analyzed with an emphasis on their structural and magnetic properties. The mononuclear complex **1** shows *trans* oriented ligands

with asymmetric and a highly distorted octahedral coordination sphere. The compound is very unstable, most probably due to the unexpected *cis* orientation of the methyl groups of the 2-mpy ligands, non-symmetric chelate methanoates and stabilization only by weak C–H···O contacts. Compound **1** easily decomposes outside the mother-liquid, giving the binuclear *paddle-wheel* compound **2**. The other three herein described complexes **2**–**4** are much more stable. Isolated binuclear *paddle-wheel* molecules are found for **2**, while alternating mononuclear and binuclear building blocks are present in the chain type of structures in **3** and **4**. Magnetic susceptibility analysis shows a strong antiferromagnetic interaction for complexes **2**–**4**, with $-2J = 440–490\ cm^{-1}$, suggesting clearly the main role of the methanoate intra-binuclear bridges for the magnitude of this interaction. The inter-binuclear connections as C–H···O and π-stacking in the 'isolated' binuclear **2**, or even different types of mononuclear building blocks coordinative connecting the *paddle-wheel* species in the polymeric **3** and **4**, seem not to have a significant role in the AFM interaction. On the other hand, the EPR spectra suggest that the spin $S = ½$ species (mononuclear moiety) give higher intensity signals than the $S = 1$ species (binuclear *paddle-wheel*), especially due to a strong AFM interaction, giving a less populated $S = 1$ state even at room temperature. The involvement of the binuclear equatorial carboxylate oxygen atom simultaneously with the axial position of the mononuclear coordination sphere in **4** may be the reason for the broad EPR signal at room temperature, hiding the expected $S = ½$ spin symmetry signals of the mononuclear copper(II) unit.

5. Supplementary data

CCDC 718843 and 718842 contain the supplementary crystallographic data for **1** and **2**. These data can be obtained free of charge via http://www.ccdc.cam.ac.uk/conts/retrieving.html, or from the Cambridge Crystallographic Data Centre, 12 Union Road, Cambridge CB2 1EZ, UK; fax: (+44) 1223-336-033; or e-mail: deposit@ccdc.cam.ac.uk.

Acknowledgements

We thank Martina Maleković for her help during characterization of compound **4**. The financial support of MVZT P1-0175-103 and X-2000, Republic of Slovenia, is gratefully acknowledged.

References

[1] R.L. Martin, H. Waterman, J. Chem. Soc. (1959) 2960.
[2] D.M.L. Goodgame, N.J. Hill, D.F. Marsham, A.C. Skapski, M.L. Smart, P.G.H. Troughton, J. Chem. Soc., Chem. Commun. (1969) 629.
[3] M. Yamanaka, H. Uekusa, S. Ohba, Y. Saito, S. Iwata, M. Kato, T. Tokii, Y. Muto, O.W. Steward, Acta Crystallogr. B 47 (1991) 344.
[4] H. Uekusa, S. Ohba, T. Tokii, Y. Muto, M. Kato, S. Husebye, O.W. Steward, S.C. Chang, J.P. Rose, J.F. Pletcher, I. Suzuki, Acta Crystallogr. B 48 (1992) 650.
[5] Y. Muto, H. Horie, T. Tokii, M. Nakashima, M. Koikawa, O.W. Steward, S. Ohba, H. Uekusa, S. Husebye, I. Suzuki, M. Kato, Bull. Chem. Soc. Jpn. 70 (1997) 1573.
[6] A. Rodriguez-Fortea, P. Alemany, S. Alvarez, E. Ruiz, Chem. Eur. J. 7 (2001) 627.
[7] S. Ohba, M. Kato, T. Tokii, Y. Muto, O.W. Steward, Mol. Cryst. Liq. Cryst. 232 (1993) 695.
[8] P.M. Kuznesof, F.B.T. Pessini, R.E. Bruns, J. Am. Chem. Soc. 94 (1972) 9087.
[9] A. Harada, M. Tsuchimoto, S. Ohba, K. Iwasawa, T. Tokii, Acta Crystallogr. B 53 (1997) 654.
[10] O.W. Steward, R.C. McAfee, S.C. Chang, S.R. Piskor, W.J. Schreiber, C.F. Jury, C.E. Taylor, J.F. Pletcher, C.S. Chen, Inorg. Chem. 25 (1986) 771.
[11] P.J. Hay, J.C. Thibeault, R. Hoffmann, J. Am. Chem. Soc. 97 (1975) 4884.
[12] M. Barquin, M.J.G. Garmendia, L. Larrinaga, E. Pinilla, M.R. Torres, Inorg. Chim. Acta 359 (2006) 2424.
[13] F. Sapina, M. Burgos, E. Escriva, J.V. Folgado, D. Beltran, P. Gomez-Romero, Inorg. Chim. Acta 216 (1994) 185.
[14] H. Uekusa, S. Ohba, Y. Saito, M. Kato, O.W. Steward, T. Tokii, Y. Muto, Acta Crystallogr. C 46 (1990) 1805.
[15] R. Cejudo, G. Alzuet, J. Borras, M. Liu-Gonzalez, F. Sanz-Ruiz, Polyhedron 21 (2002) 1057.
[16] B. Kozlevčar, I. Kovšca, Z. Jagličić, A. Pevec, N. Kitanovski, P. Strauch, P. Šegedin, Croat. Chem. Acta, in press.
[17] Y. Muto, M. Nakashima, T. Tokii, I. Suzuki, S. Ohba, O.W. Steward, M. Kato, Bull. Chem. Soc. Jpn. 75 (2002) 511.
[18] M. Kato, Y. Muto, Coord. Chem. Rev. 92 (1988) 45.
[19] Z. Jagličić, P. Šegedin, J. Zlatič, A. Zorko, J. Pirnat, Z. Trontelj, J. Magn. Magn. Mater. 310 (2007) 1444.
[20] A. Golobič, M. Maleković, P. Šegedin, Acta Crystallogr. C 62 (2006) M102.
[21] D.B.W. Yawney, R.J. Doedens, Inorg. Chem. 9 (1970) 1626.
[22] M. Barquin, M.J.G. Garmendia, L. Larrinaga, E. Pinilla, M.R. Torres, Z. Anorg. Allg. Chem. 631 (2005) 2210.
[23] L.M. Zhu, Z. Kristallogr. NCS 220 (2005) 579.
[24] M.A. Bernard, M.M. Borel, F. Busnot, A. Leclaire, Rev. Chim. Miner. 16 (1979) 124.
[25] O. Kahn, Molecular Magnetism, VCH, New York, 1993.
[26] Z. Otwinowski, W. Minor, in: C.W. Carter Jr., R.M. Sweet (Eds.), Methods in Enzymology, Macromolecular Crystallography Part A, vol. 276, Academic Press, New York, 1997, pp. 307–326.
[27] A. Altomare, M.C. Burla, M. Camalli, G. Cascarano, C. Giacovazzo, A. Guagliardi, A.G.G. Moliterni, G. Polidori, R. Spagna, J. Appl. Crystallogr. 32 (1999) 115.
[28] S.R. Hall, D.J. du Boulay, R. Olthof-Hazekamp (Eds.), The XTAL3.6 System, University of Western Australia, Lamb, Perth, Australia, 1999.
[29] A.L. Spek, J. Appl. Crystallogr. 36 (2003) 7.
[30] G. Davey, F.S. Stephens, J. Chem. Soc. A (1971) 2577.
[31] H. Uekusa, S. Ohba, Y. Saito, M. Kato, T. Tokii, Y. Muto, Acta Crystallogr. C 45 (1989) 377.
[32] M. Bukowska-Strzyzewska, Rocz. Chem. 40 (1966) 567.
[33] J. Bernstein, R.E. Davis, L. Shimoni, N.L. Chang, Angew. Chem., Int. Ed. 34 (1995) 1555.
[34] F.P. Pruchnik, A. Jutarska, Z. Ciunik, M. Pruchnik, Inorg. Chim. Acta 350 (2003) 609.
[35] G.A. Robbins, D.S. Martin, Inorg. Chem. 23 (1984) 2086.
[36] S.M. Chen, C.Z. Lu, C.K. Xia, X.J. Xu, Q.G. Zhai, Cryst. Growth Des. 5 (2005) 1485.
[37] K. Deka, R.J. Sarma, J.B. Baruah, Inorg. Chem. Commun. 9 (2006) 931.
[38] J. Valo, M. Nasakkala, Acta Chem. Scand. 48 (1994) 20.
[39] T. Hokelek, Y. Mert, C. Unaleroglu, Acta Crystallogr. C 54 (1998) 310.
[40] Y. Kani, M. Tsuchimoto, S. Ohba, H. Matsushima, T. Tokii, Acta Crystallogr. C 56 (2000) 923.
[41] M. Kato, H.B. Jonassen, J.C. Fanning, Chem. Rev. 64 (1964) 99.
[42] B. Kozlevčar, I. Leban, M. Petrič, S. Petriček, O. Roubeau, J. Reedijk, P. Šegedin, Inorg. Chim. Acta 357 (2004) 4220.
[43] V.V. Gavrilov, Y.V. Yablokov, L.N. Milkova, A.V. Ablov, Phys. Status Solidi B 45 (1971) 603.
[44] J. Mrozinski, E. Heyduk, J. Coord. Chem. 13 (1984) 291.
[45] F.P.W. Agterberg, H. Kluit, W.L. Driessen, H. Oevering, W. Buijs, M.T. Lakin, A.L. Spek, J. Reedijk, Inorg. Chem. 36 (1997) 4321.

cis-[Ru(H-dcbpy$^-$)$_2$(Cl)(NO)] (H_2-dcbpy = 4,4′-dicarboxy-2,2′-bipyridine) and Na_4[Tb(TsPc)(acac)] (TsPc = tetrasulfonated phthalocyanines; acac = acetylacetone) are reported, and this system is suggested as an alternative for improving PDT.

2. Experimental

2.1. Apparatus

The ultraviolet–visible (UV–Vis) spectra were recorded on a Hitachi U-3501. Infrared spectra were registered on a Protegé 460 series FTIR spectrometer, using solid samples pressed in KBr pellets. Cyclic voltammetry was performed with an AUTOLAB® Model PGSTAT 30 potentiostat/galvanostat, by employing a conventional three-electrode cell arrangement with a glassy carbon disk working electrode, a platinum wire auxiliary electrode, and an Ag/AgCl reference electrode. The pH measurements were accomplished by means of a DM-20 pH meter from Digimed. The photochemical experiments were carried out using an Osram 150 W/l system equipped with a Xenon Lamp, in an 8500 model with selective filter λ_{max}/550 nm (transmit > 90% above 550 nm). Luminescent measurements were performed using a FLUOROLOG 3 ISA/Jobin-Yvon spectrofluorimeter equipped with an R928P Hamamatsu photomultiplier and Xenon Lamp 450 W/ozone free. A Corning filter (transmit > 90% in the 250–400 nm range; with no transmission in the visible range) was used in the light beam entrance. Excitation and emission slits were 8 and 4 nm, respectively. The singlet oxygen yield values were determined in an apparatus consisting of a Nd-YAG laser (Continuum, Santa Clara, CA) with excitation (8 nm half life) provided by the third harmonic at 355 nm. The luminescent decay kinetics was detected by employing a germanium detector operating at liquid nitrogen temperature. A silicon filter was used to avoid any fluorescent signal interfering with the singlet oxygen measurements. Pheophorbide-a in deuterated ethanol was used as reference [16]. NO release was measured with an ISO–NOP NO meter from Word Precision Instruments.

2.2. cis-[Ru(H-dcbpy$^-$)$_2$(Cl)(NO)] synthesis

The *cis*-[Ru(H-dcbpy$^-$)$_2$(Cl)(NO)] complex was prepared using *cis*-[Ru(dcbpyH$_2$)$_2$Cl$_2$]·2H$_2$O as the starting reagent. *cis*-[Ru(H_2-dcbpy)$_2$Cl$_2$]·2H$_2$O was obtained according to the procedure previously employed to synthesize *cis*-[Ru(bpy)$_2$Cl$_2$]·2H$_2$O [17]. *cis*-[Ru(H_2-dcbpy)$_2$Cl$_2$]·2H$_2$O (0.100 g, 0.14 mmol) was dissolved in distilled H_2O, and this solution was degassed for 30 min for oxygen removal. Gaseous NO was then generated by reaction between nitric acid solution (50%V/V) and metallic copper. The produced gaseous mixture was passed through a concentrated NaOH solution, to eliminate NO_2^- traces. The nitric oxide was then bubbled through the *cis*-[Ru(H_2-dcbpy)$_2$Cl$_2$]·2H$_2$O complex solution for 40 min, and the reaction mixture was stirred for another 6 h. This operation was repeated for three times, and a precipitate was formed during this procedure. The resulting brown precipitate was collected by filtration, washed with diethyl ether, and stored under vacuum in the dark. A typical yield for *cis*-[Ru(H-dcbpy$^-$)$_2$(Cl)(NO)] (53.6%) was obtained. (*Anal.* Calc. for $C_{24}H_{16}N_5O_9ClRu$: C, 43.96; H, 2.14; N, 10.68. Found: C, 42.77; H, 2.26; N, 10.32%).

2.3. Na$_4$[Tb(TsPc)(acac)] synthesis

The Na_4[Tb(TsPc)(acac)] complex was synthesized using terbium acetylacetonate, Tb(acac)$_3$, as the starting reactant. The latter complex was prepared as described in the literature [18]. Then, the sodium salt of phthalocyanine-tetrasulfonate (0.100 g, 0.10 mmol), Na_4(TsPc), was dissolved in dimethylsulfoxide (DMSO, 0.5 mL), under stirring. The reaction was carried out under argon flux for 4 h, by refluxing stoichiometric amounts of (TsPc)$^{4-}$ and Tb(acac)$_3$ in the presence of 1,8-diazabicyclo[5.4.0]undec-7-ene (DBU, 30 μL). It seems that the role of DBU in this reaction is the formation of the phthalocyanine dianion (TsPc)$^{6-}$, which reacts with terbium acetylacetonate. Propanone (80.0 mL) was added after the reflux, and the mixture was frozen overnight. The obtained green precipitate was filtered and washed with propanone and diethyl ether, and dried under vacuum. Na_4[Tb(TsPc)(acac)] (47%). *m/z* 358.9602 (Tb^{3+} fragment).

2.4. Cell culture and MTT assay

The B16F10 murine melanoma was purchased from the ATCC (Rockville, MD) and grown in RPMI-1640 medium supplemented with 10% fetal bovine serum. To determine cell growth *in vitro*, B16F10 cells were plated at an amount of 10 000 cells/well on a 96-well plate. Cells were grown in MEM + 10% FBS + nonessential amino acids. Cell numbers were determined at 24 h intervals, by replacing the culture medium with 0.1 mL of an MTT solution in serum-free DMEM without phenol red [0.5 mg of MTT (Sigma, St. Louis, MO) per mL]. Cells were incubated at 37 °C for 2 h, and then 200 μL of solubilizing solution (80% isopropanol, 20% DMSO, and 4% Tween 20) were added to each well. After mixing, absorbance was determined at 562 nm with a plate reader.

3. Results and discussion

The nitrosyl ruthenium complex was ascribed as *cis*-[Ru(H-dcbpy$^-$)$_2$(Cl)(NO)] mainly on the basis of elemental analysis with one deprotonated bipyridine type ligand. Addition of 0.1 M aqueous HCl or HPF_6 resulted in precipitation, which we tentatively ascribed as *cis*-[Ru(H-dcbpy)$_2$(Cl)(NO)]Cl$_2$ or *cis*-[Ru(H-dcbpy)$_2$-(Cl)(NO)](PF$_6$)$_2$. The electronic absorption data (Fig. 1) of *cis*-[Ru(H-dcbpy$^-$)$_2$(Cl)(NO)] displays a band at 305 nm (λ_{max}0.1 mol L^{-1} HCl; log ε 4.13) and a shoulder at 323 nm (log ε 3.97). The highest energy band is attributed to intraligand transitions involving NO and the H_2-dcbpy ligands, while the shoulder at 323 nm is due to the metal ligand charge transfer band (MLCT) with contributions from the $d\pi(Ru^{II}) \rightarrow \pi^*(NO)$ and $d\pi(Ru^{II}) \rightarrow \pi^*$(H-dcbpy$^-$) transitions [10]. In pH ⩾ 9.0 the UV–Vis spectrum of an aqueous solution containing *cis*-[Ru(H-dcbpy$^-$)$_2$(Cl)(NO)] shows band in the 450 nm region (NaOH), which is characteristic of bonded nitrite obtained by electrophilic attack of the hydroxide ion [7,10,12–13]. The

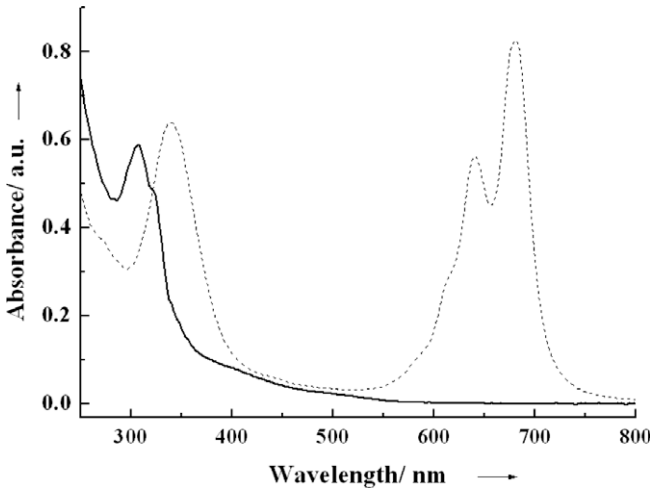


Fig. 1. Absorption spectrum in the UV–vis region: (—) *cis*-[Ru(H-dcbpy$^-$)$_2$(Cl)(NO)], 5.2×10^{-5} mol L^{-1}, in HCl 0.1 mol L^{-1}; (- - - -) Na_4[Tb(TsPc)(acac)], 1.2×10^{-5} mol L^{-1}, in aqueous solution.

nitrosyl ruthenium complex was also characterized by FTIR. The spectrum displays the typical NO frequency stretching at 1932 cm^{-1} (Ru–NO^+), as previously described for similar systems [10,12]. The cyclic voltammogram of the *cis*-[Ru(H-dcbpy$^-$)$_2$(Cl)(NO)] complex was performed in aqueous solution using KCl (0.1 mol L^{-1}) as the supporting electrolyte (Supplementary data: Fig. 1). A reversible cathodic wave can be seen at 0.10 V (versus Ag/AgCl), attributed to the redox process of the nitrosyl group ($NO^{+/0}$), and there is an irreversible wave at −0.50 V (versus Ag/AgCl), due to the $NO^{0/-}$ redox process. The electronic spectrum of Na_4[Tb(TsPc)(acac)] (Fig. 1) in aqueous solution displays absorption bands at 342 nm (λ_{max} in H_2O; log ε 4.54), 642 (log ε 4.49) and 682 (log ε 4.64), typical of phthalocyanine. These bands are designated as *B* band or Soret in the case of $\lambda_{max}(H_2O)$/nm 342, and *Q* bands for $\lambda_{max}(H_2O)$/nm 642 and 682 [19,20].

The fluorescence measurements in aqueous solution indicate that the emission of the nitrosyl ruthenium complex is silent when it is excited at 376 nm, although [Tb(TsPc)(acac)]$^{4-}$ presents an emission band at 691 nm (λ_{em} in H_2O; Fig. 2). The fluorescence intensity of the phthalocyanine chromophore is lower than that of the rare earth phthalocyanine compound, and the emission of the Tb^{3+} ion is observed only when the excitation is performed at 356 nm (λ_{ex} in H_2O), using a filter which transmits above λ_{max} = 550 nm (Supplementary data: Fig. 2) [21].

The photolysis of an aqueous solution containing equimolar amounts of *cis*-[Ru(H-dcbpy$^-$)$_2$(Cl)(NO)] and Na_4[Tb(TsPc)(acac)] in phosphate buffer solution (pH 5.0) is fascinating. NO release, accounted for by NO-sensor measurement, is observed during light irradiation at $\lambda_{max} \geqslant 550$ nm (Fig. 3). A similar experiment was performed with *cis*-[Ru(H-dcbpy$^-$)$_2$(Cl)(NO)] (Fig. 3) in the presence of an equimolar amount of Na_4(TsPc), but no signal was detected using NO-sensor.

NO release from *cis*-[Ru(H-dcbpy$^-$)$_2$(Cl)(NO)] in the presence of [Tb(TsPc)(acac)]$^{4-}$ during photolysis at $\lambda_{max} \geqslant 550$ nm was quantitatively analyzed under argon atmosphere. The experiment was conducted until a maximum of 30 min, to avoid chemical filter interference. The measured NO concentration using NO-sensor after 30 min was 1.21 ± 0.14 μmol L^{-1}, which corresponds to 4% of the starting *cis*-[Ru(H-dcbpy$^-$)$_2$(Cl)(NO)] concentration. The amount of NO release seems to be dependent on oxygen concentration, once the NO concentration measured in aerated condition was 1.51 ± 0.11 μmol L^{-1}, which suggests an effect of oxygen on the photochemical pathway of *cis*-[Ru(H-dcbpy$^-$)$_2$(Cl)(NO)] when it is photolysed in the presence of [Tb(TsPc)(acac)]$^{4-}$. The most probable photochemical pathway for NO release from the aerated

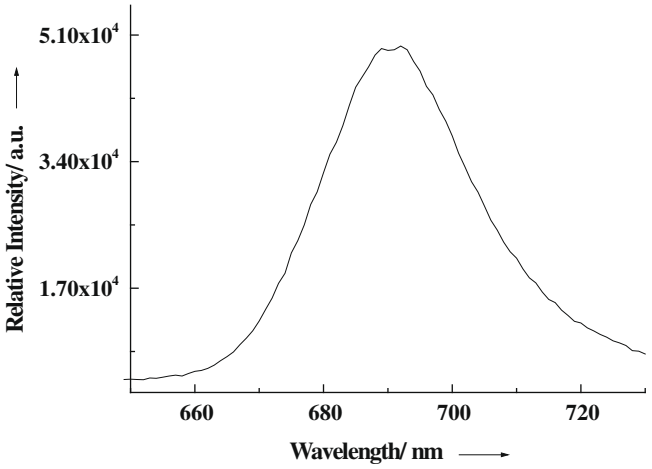


Fig. 2. Na_4[Tb(TsPc)(acac)] emission spectrum (λ_{ex}= 376 nm in H_2O) in aqueous solution. [complex] = 2.4 × 10^{-5} mol L^{-1}.

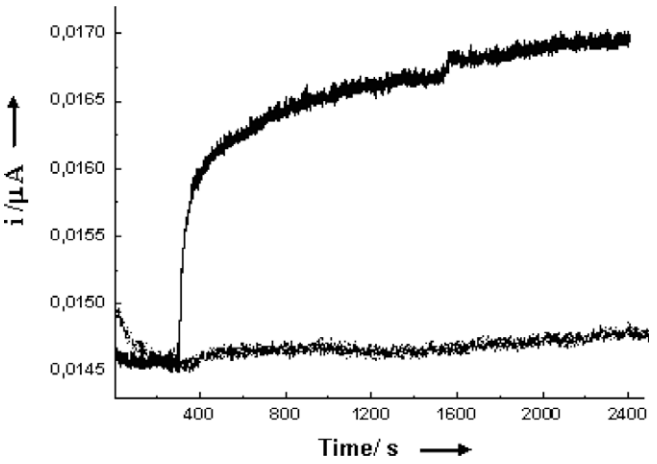
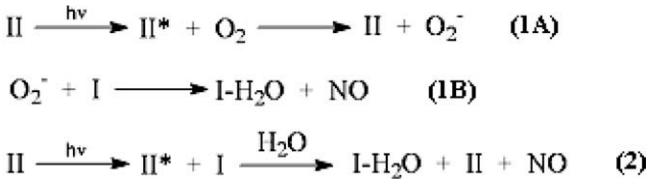


Fig. 3. Chronoamperograms of NO release by photolysis ($\lambda_{max} \geqslant 550$ nm): (**A**) *cis*-[Ru(H-dcbpy$^-$)$_2$(Cl)(NO)] complex and (**B**) the mixture of nitrosyl ruthenium and the terbium phthalocyanine complexes. [nitrosyl complex] = [terbium phthalocyanine complex] = 3.0 × 10^{-5} mol L^{-1}, in phosphate buffer solution (pH 5.0).

aqueous solution mixture containing *cis*-[Ru(H-dcbpy$^-$)$_2$(Cl)(NO)] and [Tb(TsPc)(acac)]$^{4-}$ involves a photoinduced electron transfer that is most likely a chemical reduction of *cis*-[Ru(H-dcbpy$^-$)$_2$(Cl)(NO)] (Scheme 1) by former superoxide. The assumption for superoxide formation (Scheme 1- Eq. 1A and 1B) is based on the qualitative assay using ferrocytochrome-C, a well-known superoxide scavenger [22]. Knowing that the superoxide reduction potential is −0.31 V versus Ag/AgCl, we can suppose that there is a favorable driving force for the reduction of *cis*-[Ru(H-dcbpy$^-$)$_2$- (Cl)(NO)] [23]. The second possible explanation for the photoinduced NO release comes from intermolecular photoinduced electron transfer (Scheme 1 Eq (2)), an assumption that is based mainly on the results from luminescence spectroscopy.

Changes in the fluorescence spectrum of [Tb(TsPc)(acac)]$^{4-}$ in phosphate buffer solution pH 5.0 (λ_{exc} = 376 nm) upon addition of *cis*-[Ru(H-dcbpy$^-$)$_2$(Cl)(NO)] can be observed. Differences in the shape and position of the fluorescence bands when only free [Tb(TsPc)(acac)]$^{4-}$ is present in the medium and when it is in the presence of the nitrosyl ruthenium complex are small, but the fluorescence intensity is diminished by 20% for an equimolar amount of *cis*-[Ru(H-dcbpy$^-$)$_2$(Cl)(NO)]. This quenching efficiency might be caused by hydrogen bonding interaction. From the Stern–Volmer analysis of I_0/I versus [*Q*] plots, it can be seen that the interaction [Tb(TsPc)(acac)]$^{4-}$–*cis*-[Ru(H-dcbpy$^-$)$_2$(Cl)(NO)] obeys a Stern–Volmer type analysis, forming a 1:1 stoichiometric association in aqueous solution. Fig. 4 depicts the Stern–Volmer plots based on the relation $I_0/I = 1 + K_D[Q]$, where $K_D = 9.0 \times 10^3$ is the interaction constant for a 1:1 stoichiometry [24], which we have tentatively ascribed to hydrogen bonding interaction taking place as represented in Fig. 5.

Phthalocyanines are known to generate singlet oxygen ($^1O_2$) upon photoirradiation, which was also observed for the terbium phthalocyanine tetrasulfonate compound when it was irradiated at λ_{max} = 691 nm [3]. The measured singlet oxygen quantum yield



Scheme 1. Photochemistry intermolecular electron transfer mechanism; **I** is *cis*-[Ru(H-dcbpy$^-$)$_2$(Cl)(NO)] and **II**, the sensitizer Na_4[Tb(TsPc)(acac)] complex.

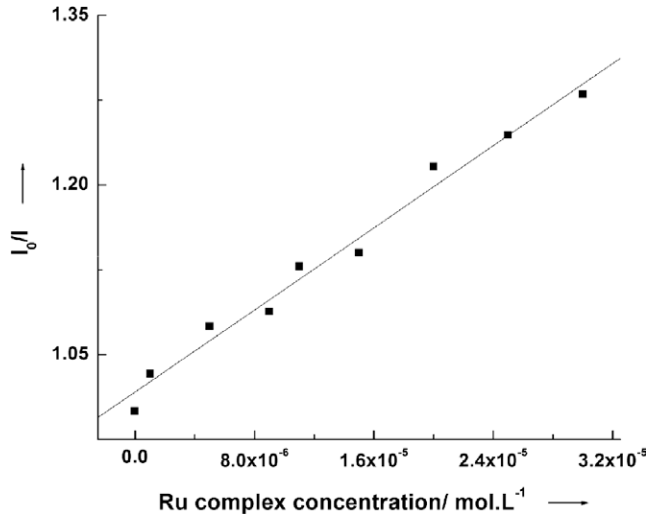


Fig. 4. Stern–Volmer plot for quenching of the fluorescence of ([Tb(TsPc)(acac)]$^{4-}$ (1.4×10^{-6} mol L^{-1}) in the presence of *cis*-[Ru(H-dcbpy$^-$)$_2$(Cl)(NO)], monitored at λ_{em} = 691 nm (λ_{ex} = 376 nm).

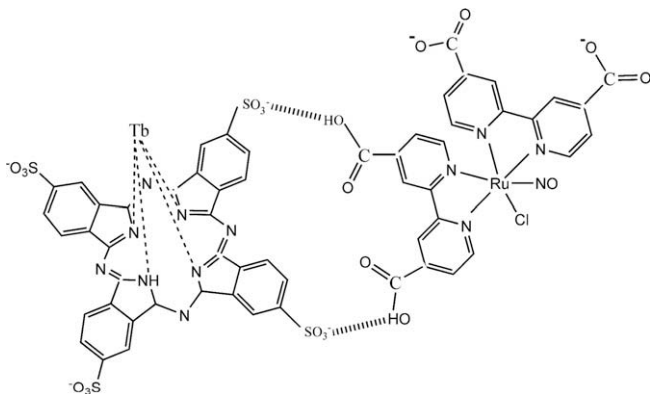


Fig. 5. Schematic diagram assumed for the self-assembled structure.

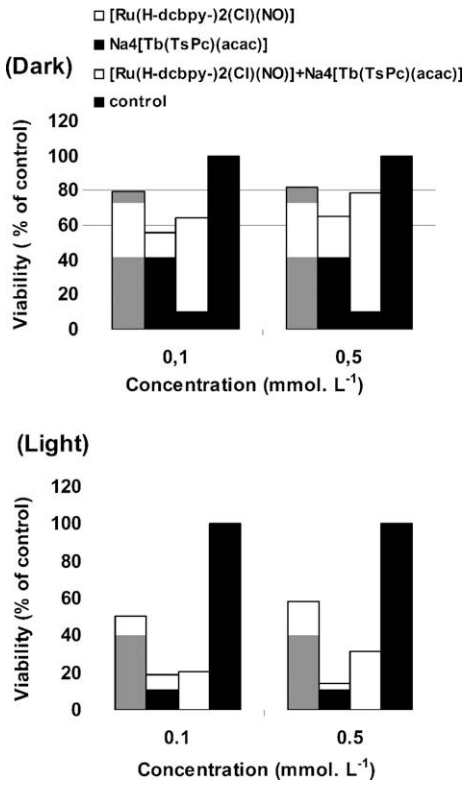


Fig. 6. Cell viability of the B16F10 cell line after treatment with *cis*-[Ru(H-dcbpy$^-$)$_2$(Cl)(NO)] and [Tb(TsPc)(acac)]$^{4-}$, as measured via the MTT assay. Results are represented as a percentage of the relative absorbance with respect to the control cells (100%, in black).

was 0.41, a value that can be taken as promising for a photosensitizer to be applied in the photodynamic therapy (PDT) of cancer [3–5]. To investigate whether [Tb(TsPc)(acac)]$^{4-}$–*cis*-[Ru(H-dcbpy$^-$)$_2$(Cl)(NO)], a NO release and $^1O_2$ producing agent, inhibits its cell viability, we have performed experiments using B16F10 cells. Fig. 6 depicts the cell viability experiment showing the cytotoxic effects of *cis*-[Ru(H-dcbpy$^-$)$_2$(Cl)(NO)] in the presence of an equal amount of [Tb(TsPc)(acac)]$^{4-}$ under visible light irradiation in B16F10 cells, which was performed using 100–500 μmol L^{-1} of each complex. The solution containing [Tb(TsPc)(acac)]$^{4-}$–*cis*-[Ru(H-dcbpy$^-$)$_2$(Cl)(NO)] strongly inhibits the cell viability in a light irradiation-dependent manner. The best result was achieved when the concentration of 100 μmol L^{-1} was used, which reduced cell viability to 20% of the control. The hypothesis for the cancer cell activity (não seria melhor mudar esta palavra pois o cancer é destruído) obtained by using [Tb(TsPc)(acac)]$^{4-}$–*cis*-[Ru(H-dcbpy$^-$)$_2$(Cl)(NO)] mainly involves $^1O_2$ formation, a well-known anticancer agent. The concomitant production of NO in this system could also improve its anticancer capacity due to the corroborative effect of NO, once it can induce apoptosis in a variety of cell types [7–10]. Apparently, as the concentration of *cis*-[Ru(H-dcbpy$^-$)$_2$- (Cl)(NO)] increases in the solution containing [Tb(TsPc)(acac)]$^{4-}$, cell activity decreases. Maybe NO is consumed by $^1O_2$ in a typical oxidation process, which could explain the cell viability decrease when a mixture of rare earth and nitrosyl ruthenium complexes was used as sensitizer [25]. On the other hand, the NO release agent itself decreases cell viability, which could be an indication that at low oxygen concentration the system could improve anticancer activity.

4. Conclusion

Our results document the effect of the concomitant formation of NO and $^1O_2$ on a cancer cell line. The amount of species employed in the cell viability experiments is around 1% of IC_{50}.

Acknowledgements

The authors thank CNPq, CAPES and FAPESP for financial support.

Appendix A. Supplementary data

Supplementary data associated with this article can be found, in the online version, at doi:10.1016/j.poly.2009.05.051.

References

[1] M.J. Rose, M.M. Olmstead, P.K. Mascharak, J. Am. Chem. Soc. 129 (2007) 5342.
[2] A.K. Patra, P.K. Mascharak, Inorg. Chem. 42 (2003) 7363.
[3] M.C. DeRosa, R.J. Crutchley, Coord. Chem. Rev. 233 (2002) 351.
[4] A. Sholto, B. Ehrenberg, Photochem. Photobiol. Sci. 7 (2008) 344.
[5] K. Lang, J. Mosinger, D.M. Wagnerová, Coord. Chem. Rev. 248 (2004) 321.
[6] Q. Chen, Z. Huang, H. Chen, H. Shapiro, J. Beckers, F.W. Hetzel, Photochem. Photobiol. 76 (2002) 197.
[7] M.G. Sauaia, R.G. de Lima, A.C. Tedesco, R.S. da Silva, Inorg. Chem. 44 (2005) 9946.
[8] S. Mocellin, V. Bronte, D. Nitti, Med. Res. Rev. 27 (2007) 317.

[9] S. Sortino, S. Petralia, G. Compagnini, S. Conoci, G. Condorelli, Angew. Chem. 114 (2002) 1994.
[10] M.G. Sauaia, R.S. da Silva, Transition Met. Chem. 28 (2002) 254.
[11] V. Togniolo, R.S. da Silva, A.C. Tedesco, Inorg. Chim. Acta 316 (2001) 7.
[12] M.G. Sauaia, F.S. Oliveira, A.C. Tedesco, R.S. da Silva, Inorg. Chim. Acta 355 (2003) 191.
[13] M.G. Sauaia, R.G. de Lima, A.C. Tedesco, R.S. da Silva, J. Am. Chem. Soc. 125 (2003) 14718.
[14] F.D. Oliveira, V. Togniolo, T.T. Pupo, A.C. Tedesco, R.S. da Silva, Inorg. Chem. Commun. 7 (2004) 160.
[15] R.S. da Silva, M.S.P. Marchesi, C. Khin, C.N. Lunardi, L.M. Bendhack, P.C. Ford, J. Phys. Chem. B 111 (2007) 6962.
[16] A. Bautista-Sanches, A. Kasselouri, M.-C. Desroches, J. Blais, P. Maillard, D.M. Oliveira, A.C. Tedesco, P. Prognon, J. Delaire, J. Photochem. Photobiol. B 81 (2005) 154.
[17] M.G. Sauaia, F.D.S. Oliveira, R.G. de Lima, A.D.L. Cacciari, E. Tfouni, R.S. da Silva, Inorg. Chem. Commun. 8 (2005) 347.
[18] V.E. Pushkarev, M.O. Breusova, E.V. Shulishov, Yu.V. Tomilov, Russ. Chem. Bull., Int. Ed. 54 (2005) 2087.
[19] C. Clarisse, M.T. Riou, Inorg. Chim. Acta 130 (1987) 139.
[20] K. Yoshino, S.B. Lee, T. Sonoda, H. Kawagishi, R. Hidayat, K. Nakayama, M. Ozaki, K. Ban, K. Nishizawa, K. Ohta, H. Shirai, J. Appl. Phys. 88 (2000) 7137.
[21] S.A. Cicillini, P.S. Calefi, C.R. Neri, E.J. Nassar, O.A. Serra, J. Non-Cryst. Sol. 247 (1999) 114.
[22] M. Kelm, R. Dahmann, D. Wink, M. Feelisch, J. Biol. Chem. 272 (1997) 9922.
[23] J.P. Hoare, in: A.J. Bard, R. Parsons (Eds.), Standard Potentials in Aqueous Solution, M. Dekker Inc., New York, 1985, p. 61.
[24] F.G. Prendergast, J. Lu, P.J. Callahan, J. Biol. Chem. 258 (1983) 4075.
[25] D.D. Thomas, M.G. Espey, M.P. Vitek, K.M. Miranda, D.A. Wink, Proc. Natl. Acad. Sci. USA 99 (20) (2002) 12691.

phenyl[iminodiacetate-O,O′,N]borane **1** and carry out a substitution nucleophilic reaction with benzyl bromide **a**, 3-methylbenzyl bromide **b**, 4-methylbenzyl bromide **c**, phenacyl bromide **d**, 2-bromo-4′-chloroacetophenone **e** and 2-bromo-4′-phenylacetophenone **f**, under reflux of acetonitrile/benzene (80/20) or acetonitrile to obtain (N → B) phenyl[N-alkyliminodiacetate-O,O′,N]boranes **2**–**7**, (Fig. 1). Effectively, the yields are between 40% and 80%. ^{1}H, ^{13}C and ^{11}B NMR and their high resolution mass spectra (HRMS) data of the compounds **2**–**7** are giving in the experimental part. Their ^{1}H NMR spectra clearly show the AB coupling patterns for the diastereotopic CH_2COO protons, which indicates the presence of the intramolecular N → B coordination bond. The $\delta(^{11}B)$ values confirm the tetrahedral environment of the boron nucleus, since they lie in the range reported previously for analogous boron heterocycles [9–11,13–16,19]. All compounds exhibit the expected ^{13}C NMR spectra. Suitable crystals of **2**, **4** and **5** were obtained for X-ray analysis and an ORTEP view and crystallographic numbering of **2**, **4** and **5** are giving in Figs. 2–4, respectively. Selected bond distance and torsion angles are listed in Tables 1–3. In general the bond distances are within the values characteristic of analogous compounds [17,19]. Compounds **2** and **4** crystallized with two independent molecules **2A**, **2B** and **4A**, **4B**, respectively and **5** exhibits only one. The conformations of the two five member ring in all molecules are different and not planar, as indicated by the torsion angles values (Tables 1–3). This can be due in part to the following intermolecular interactions: $O_{9A}\cdots H_{5A}$ 2.288,

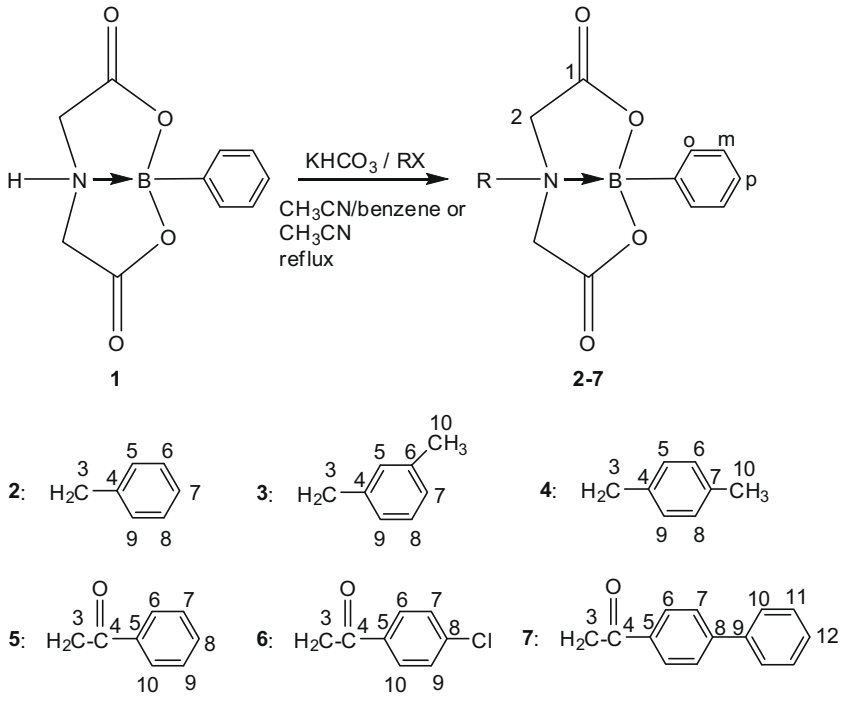


Fig. 1. Synthesis of boron heterocycles **2**–**7**.

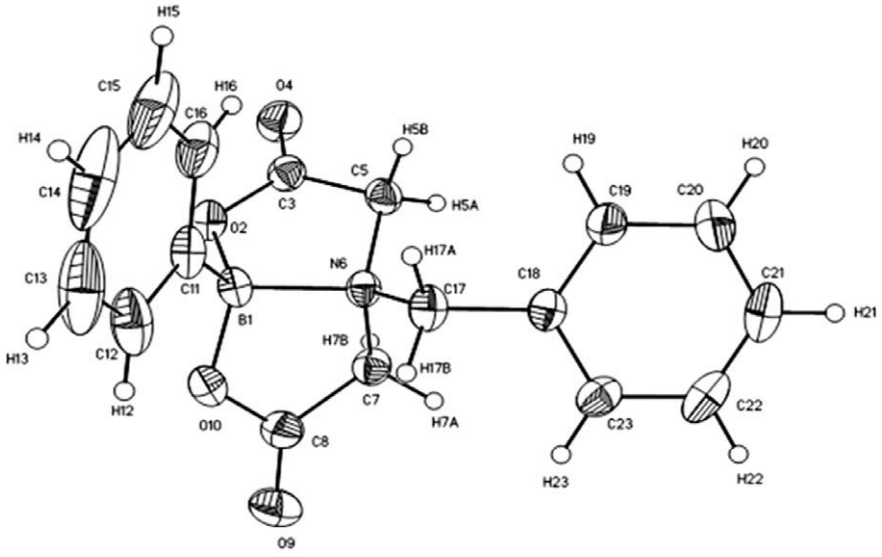


Fig. 2. Molecular structure of $C_{17}H_{16}BNO_4$ and crystallographic numbering scheme of molecule **2A**.

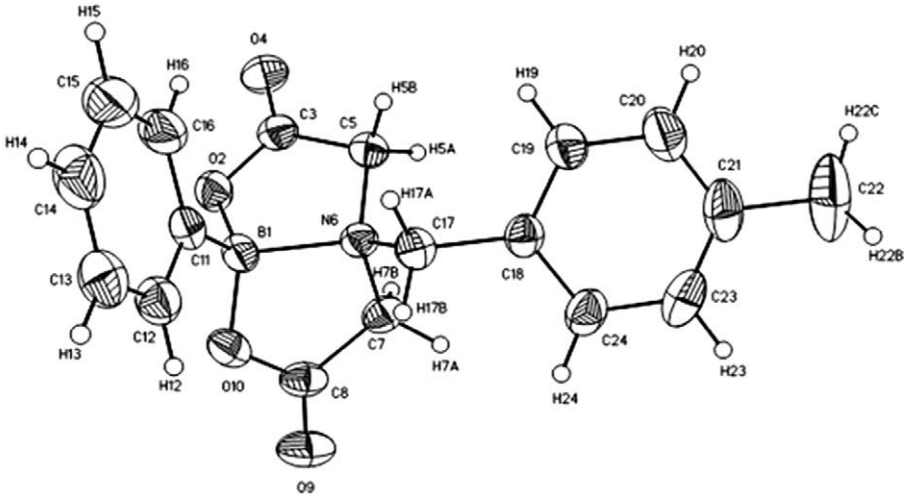


Fig. 3. Molecular structure of $C_{18}H_{18}BNO_4$ and crystallographic numbering scheme of molecule **4A**.

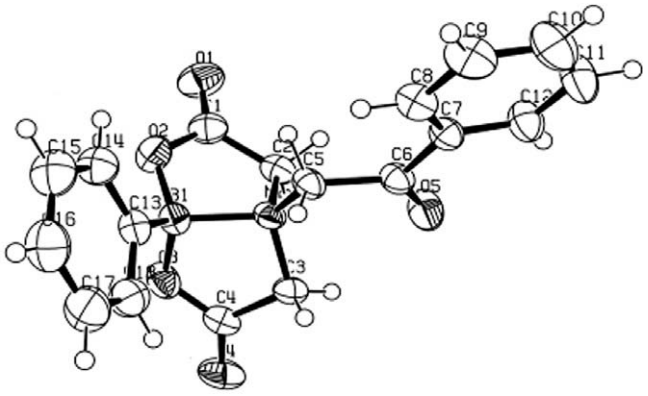


Fig. 4. Molecular structure of $C_{18}H_{16}BNO_5$ and crystallographic numbering scheme of molecule **5**.

$O_9\ldots H_{5A2}$ 2.522 and $O_{10}\ldots H_{16A}$ 2.544 Å for **2**, $O_4\ldots H_{5A1}$ 2.371, $O_{4A}\ldots H_{17D}$ 2.377, $O_9\ldots H_{17B}$ 2.450 and $O_{9A}\ldots H_{7B}$ 2.458 Å for **4** and $O_2\ldots H_{14}$ 2.5646, $O_5\ldots H_{3B}$ 2.4824, $O_5\ldots H_{2B}$ 2.5818 and $O_5\ldots H_{12}$ 2.4867 Å for **5**, which are significantly shorter than the sum of the van der Waals radii of oxygen and hydrogen (2.70 Å) [22]. On the another hand, the Ph–B and N–R groups are bent away from the N → B bond, as indicated by the bond angle values C_{11}–B_1–N_6 of 117.11 (13)° and C_{17}–N_6–B_1 of 112.90 (12)° for **2A**, C_{11a}–B_{1a}–N_{6a} of 115.42 (15)° and C_{17a}–N_{6a}–B_{1a} of 112.51 (13)° for **2B**, C_{11}–B_1–N_6 of 115.89 (19)° and C_{17}–N_6–B_1 of 114.29 (16)° for **4A**, C_{11a}–B_{1a}–N_{6a} of 115.9 (2)° and C_{17a}–N_{6a}–B_{1a} of 115.42 (17)° for **4B**, C_{13}–B_1–N_1 of 117.58 (14)° and C_5–N_1–B_1 of 113.39 (12)° for **5**. The molecular structures of the compounds **2**, **4** and **5** establish the bicyclic structures showing a N → B of bond length of 1.666 (2) Å for **2A**, 1.675 (2) Å for **2B**, 1.675 (3) Å for **4A**, 1.663 (3) Å for **4B** and 1.679 (2) Å for **5**, the values being comparable to the N → B bond length in analogous compounds [17,19].

Table 1
Bond distances selected (Å) and torsion angles (°) for $C_{17}H_{16}BNO_4$ (**2**).

Molecule **2A**		Molecule **2B**	
Bond distances (Å)			
O2–B1	1.486 (2)	O2a–B1a	1.484 (2)
O10–B1	1.460 (2)	O10a–B1a	1.467 (2)
N6–B1	1.666 (2)	N6a–B1a	1.675 (2)
O2–C3	1.332 (2)	O2a–C3a	1.322 (3)
O10–C8	1.326 (2)	O10a–C8a	1.329 (2)
O4–C3	1.201 (2)	O4a–C3a	1.201 (2)
O9–C8	1.202 (2)	O9a–C8a	1.203 (2)
C3–C5	1.510(2)	C3a–C5a	1.508 (3)
C7–C8	1.506 (2)	C7a–C8a	1.494 (3)
N6–C5	1.486 (2)	N6a–C5a	1.484 (2)
N6–C7	1.494 (2)	N6a–C7a	1.582 (3)
B1–C11	1.587 (3)	B1a–C11a	1.587 (3)
N6–C17	1.511 (3)	N6a–Cl7a	1.516 (3)
Torsion angles (°)			
N6–B1–O2–C3	−15.75(0.17)	N6a–B1a–O2a–C3a	−12.17 (0.20)
C5–C3–O2–B1	−0.61 (0.20)	C5a–C3a–O2a–B1a	−2.00 (0.23)
O2–C3–C5–N6	19.08 (0.18)	O2a–C3a–C5a–N6a	17.43 (0.21)
C3–C5–N6–B1	−27.09 (0.16)	C3a–C5a–N6a–B1a	−23.20 (0.18)
O2–B1–N6–C5	26.02 (0.15)	O2a–B1a–N6a–C5a	21.42 (0.21)
N6–B1–O10–C8	−15.15 (0.19)	N6a–B1a–O10a–C8a	−16.11 (0.19)
C7–C8–O10–B1	−1.14 (0.22)	C7a–C8a–O10a–B1a	8.16 (0.22)
N6–C7–C8–O10	19.15 (0.20)	N6a–C7a–C8a–O10a	4.95 (0.21)
C8–C7–N6–B1	−25.98 (0.16)	C8a–C7a–N6a–B1a	−13.63 (0.17)
O10–B1–N6–C7	24.97 (0.15)	O10a–B1a–N6a–C7a	17.45 (0.16)
C11–B1–N6–C17	28.72 (0.20)	C11a–B1a–N6a–C17a	21.45(0.21)

Table 2
Bond distances selected (Å) and torsion angles (°) for $C_{18}H_{18}BN0_4$ (**4**).

Molecule **4A**		Molecule **4B**	
Bond distances (Å)			
O2–B1	1.489 (3)	O2a–B1	1.466 (3)
O10–B1	1.454 (3)	O10a–B1a	1.482 (3)
N6–B1	1.675 (3)	N6a–B1a	1.663 (3)
O2–C3	1.319 (3)	O2a–C4a	1.311 (3)
C3–C5	1.508 (3)	C4a–C5a	1.488 (4)
N6–C5	1.484 (3)	N6a–C5a	1.495 (3)
N6–C7	1.498 (3)	N6a–C7a	1.484 (3)
C7–C8	1.503 (3)	C7a–C8a	1.506 (4)
O10–C8	1.320 (3)	O10a–C8a	1.315 (3)
O4–C3	1.202 (2)	O4a–C4a	1.205 (3)
O9–C8	1.196 (3)	O9b–C8b	1.206 (3)
Torsion angles (°)			
N6–B1–O2–C3	−20.70 (0.23)	N6a–B1a–O2a–C4a	−18.81 (0.26)
C5–C3–O2–B1	9.01 (0.26)	B1a–O2a–C4a–C5a	9.91 (0.30)
O2–C3–C5–N6	9.17 (0.25)	O2a–C4a–C5a–N6a	5.11 (0.29)
C3–C5–N6–B1	−20.56 (0.21)	C4a–C5a–N6a–B1a	−15.32 (0.23)
O2–B1–N6–C5	24.28 (0.20)	O2a–B1a–N6a–C5a	19.87 (0.22)
N6–B1–O10–C8	−17.32 (0.24)	N6a–B1a–O10a–C8a	−10.87 (0.25)
C7–C8–O10–B1	5.86 (0.28)	C7a–C8a–O10a–B1a	−6.30 (0.29)
N6–C7–C8–O10	10.18 (0.26)	N6a–C7a–C8a–O10a	22.48 (0.26)
C8–C7–N6–B1	−18.91 (0.21)	C8a–C7a–N6a–B1a	−26.91 (0.23)
O10–B1–N6–C7	21.50 (0.20)	O10a–B1a–N6a–C7a	22.81 (0.21)
C11–B1–N6–C17	25.76 (0.26)	C11a–B1a–N6a–C17a	21.96 (0.28)
C12–C11–B1–N6	−98.92 (0.27)	C12a–C11a–B1a–N6a	−79.95 (0.30)

Table 3
Bond distances selected (Å) and torsion angles (°) for $C_{18}H_{16}BNO_5$ (**5**).

Bond distances (Å)			
O2–B1	1.461 (2)	C1–C2	1.509 (3)
O3–B1	1.485 (2)	C3–C4	1.509 (2)
N1–B1	1.679 (2)	N1–C2	1.500 (2)
O2–C1	1.331 (2)	N1–C3	1.492 (2)
O3–C4	1.313 (2)	B1–C13	1.582 (2)
O1–C1	1.200 (2)	N1–C5	1.492 (2)
O4–C4	1.207 (2)	O5–C6	1.218 (2)
Torsion angles (°)			
B1–O2–C1–C2	−3.09 (0.21)	B1–N1–C3–C4	24.94 (0.16)
O2–C1–C2–N1	−14.41 (0.20)	C3–N1–B1–O3	−26.94 (0.15)
B1–N1–C2–C1	22.61 (0.16)	C4–O3–B1–N1	20.27 (0.18)
C2–N1–B1–O2	−23.81 (0.15)	C5–N1–B1–C13	−29.22 (0.20)
C1–O2–B1–N1	17.04 (0.18)	C14–C13–B1–O2	−15.04 (0.25)
B1–O3–C4–C3	−5.63 (0.21)	C18–C13–B1–O3	34.17 (0.25)
N1–C3–C4–O3	−14.22 (0.19)	C5–C6–C7–C8	8.57 (0.24)

3. Conclusion

The new method for the synthesis of six (N → B) phenyl[N-alkyliminodiacetate-O,O′,N]boranes improved the yields, evade to use bases and avoid the use of anhydrous reaction conditions. Therefore, the identification of all compounds by NMR, their high resolution mass spectra (HRMS) data are reported, as well as the crystal structure of compounds **2**, **4** and **5** gives evidence of the N-alkylation of **1** and establish the bicyclic structures due to N → B coordination bond.

4. Experimental

4.1. General procedure and measurements

The reagents were purchased from Aldrich Co. (N → B) phenyl [iminodiacetate-O,O′,N]borane (**1**) was prepared as described previously [14]. ^{1}H, ^{13}C and ^{11}B NMR spectra were recorded on a Jeol GLX-270, Jeol Eclipse-400 and Bruker Avance and 300-DPX spectrometers, DMSO-d_6 was used as solvent. The high resolution mass spectra (HRMS) were taken on Agilent Technologies, model LC/MSD-TOF spectrometer, coupled to HPLC 1100 with ESI as ionization source. Melting points were taken in open capillary tubes on a Gallenkamp MFB-595 apparatus and are uncorrected.

4.2. Preparation of compounds **2**–**7**

The procedure outlined below is general for the preparation of compounds **2**–**7**.

4.2.1. Synthesis of (N → B) phenyl [N-benzyliminodiacetate-O,O′,N]borane (**2**)

A suspension of 0.80 g (3.65 mmol) of (N → B) phenyl[iminodiacetate-O,O′,N]borane **1**, 0.62 g (3.6 mmol) of benzyl bromide **a**, 0.62 g (3.65 mmol) and 1.11 g (10.95 mmol) of $KHCO_3$ in 100 ml of a mixture of acetonitrile/benzene (80/20) was placed into a 250 ml flask equipped with a magnetic stirrer and a Dean–Stark trap. The suspension was refluxed for 8 h. After being cooled to room temperature, the solution was filtered and Na_2SO_4 anhydrous was added to the solution, which was filtered and the solvent was evaporated under vacuum. The solid obtained was crystallized from dichloromethane/hexane to yield 0.68 g (61%) of compound **2** as a white crystals, mp 227 °C. ^{1}H NMR δ(DMSO-d_6, J = Hz): CH_2CO 4.40 (H_A, d, J = 16.5), 3.90 (H_B, d, J = 16.5), CH_2N 3.80 (s), H aromatics 7.40–7.60 (m). ^{13}C NMR: $C_1$169.10, C_2 57.90, R group C_3 60.80, C_4 132.80, $C_{5,9}$ 128.90, $C_{6,8}$ 129.50, C_7 127.60, B-Phenyl C_o 131.60, C_m128.80, C_p130.60. ^{11}B NMR: +12.50. HRMS: $C_{17}H_{17}BNO_4$ $[M^+ + 1]^+$ Calc. 310.1245, found 310.1249, error 1.2415.

4.2.2. Synthesis of (N → B) phenyl[N-(3-methyl)benzyliminodiacetate-O,O′,N]borane (**3**)

Prepared from 1.0 g (4.56 mmol) of compound **1**, 0.84 (4.56 mmol) of 3-methylbenzyl bromide **b** and 1.39 g (13.7 mmol) of $KHCO_3$ in 120 ml of acetonitrile. The residue was crystallized from a mixture of dichloromethane/ether, 0.59 g (40%) of compound **4** were obtained as white solid, mp 251 °C ^{1}H NMR δ(DMSO-d_6, J = Hz), CH_2CO 4.05 (H_A, d, J = 16.57), 3.45 (H_B, d, J = 16.57), CH_2N 3.55 (s), CH_3 2.34 (s), H aromatics 7.0–7.24 (m), 7.40–7.62 (m). ^{13}C NMR: C_1 167.9, C_2 57.8, R group C_3 61.9, C_4 141.1, C_5 130.5, C_6 132.6, C_7 125.7, C_8 128.5, C_9 129.9, C_{10} 21.6, B-Phenyl C_o 135.7, C_m128.1, C_p130.9. ^{11}B NMR: +11.38. HRMS: $C_{18}H_{19}BNO_4$ $[M^+ + 1]^+$ Calc. 324.1401, found 324.1400, error −0.5091.

4.2.3. Synthesis of (N → B) phenyl[N-(4-methyl)benzyliminodiacetate-O,O′,N]borane (**4**)

Prepared from 1.0 g (4.56 mmol) of compound **1**, 0.62 (4.56 mmol) of 4-methylbenzylbromide **c** and 1.39 g (13.7 mmol) of $KHCO_3$ in 120 ml of acetonitrile. The residue was crystallized from a mixture of dichloromethane/ether, 1.10 g (75%) of compound **5** were obtained as white crystals, mp 187–189 °C. ^{1}H NMR δ(DMSO-d_6, J = Hz), CH_2CO 4.05 (H_A, d, J = 16.5), 3.47 (H_B, d, J = 16.5), CH_2N 3.65 (s), CH_3 2.36 (s), H aromatics 7.42–7.61 (m), 7.21($H_{5,9}$, d, J = 7.9), 7.09 ($H_{6,8}$ d, J = 7.9), ^{13}C NMR: C_1 167.5, C_2 58.1, R group C_3 60.9, C_4 139.9, $C_{5,9}$ 129.1, $C_{6,8}$ 127.4, C_7 128.8, C_{10} 20.9, B-Phenyl C_o 132.9, C_m 127.6, C_p128.7. ^{11}B NMR: +11.78. HRMS: $C_{18}H_{19}BNO_4$ $[M^+ + 1]^+$ Calc. 324.1401, found 324.1400, error −0.5091.

4.2.4. Synthesis of N → B) phenyl [N-phenacyliminodiacetate-O,O′,N]borane (**5**)

Among of 1.0 g (4.56 mmol) of compound **1**, 0.9 g (4.56 mmol) of phenacyl bromide **d** and 1.39 g (13.7 mmol) of $KHCO_3$ in 100 ml of a mixture of acetonitrile/benzene (80/20). The residue was dissolved from a mixture of dichloromethane/acetonitrile and precipitate with ether to produce 1.04 g (67.5%) of compound **6** were obtained as white crystals. mp 254–255 °C. ^{1}H NMR δ(DMSO-d_6, J = Hz): CH_2CO 4.60 (H_A, d, J = 17.38), 4.34 (H_B, d, J = 17.38), CH_2N 4.53 (s), H aromatics 7.40–7.60 (m), 7.54 ($H_{7,9}$, t, J = 7.0), 7.63 (H_8, t, J = 7.0). ^{13}C NMR: C_1 170.37, C_2 61.31, R group C_3 65.51, C_4 193.10, C_5 134.81, $C_{6,10}$ 129.38, $C_{7,9}$ 127.98, C_8 134.65. B-Phenyl C_o 133.13, C_m128.29, C_p129.66. ^{11}B NMR: +11.61. HRMS: $C_{18}H_{17}BNO_5$ $[M^+ + 1]^+$ Calc. 338.1194, found 338.1188, error −1.8620.

4.2.5. Synthesis of N → B) phenyl[N-(4-chloro) phenacyliminodiacetate-O,O′,N]borane (**6**)

Among of 1.0 g (4.56 mmol) of compound **1**, 1.06 g (4.56 mmol) of 2-bromo-4′-chloroacetophenone **e** and 1.39 g (13.7 mmol) of $KHCO_3$ in 100 ml of a mixture of acetonitrile/benzene (80/20). The residue was dissolved from a mixture of dichloromethane/acetonitrile and precipitate with ether to produce 1.19 g (73.5%) of compound **7** were obtained as white crystals, mp 226–227 °C. ^{1}H NMR δ(DMSO-d_6, J = Hz): CH_2CO 4.59 (H_A, d, J = 17.4), 4.33 (H_B, d, J = 17.4), CH_2N 4.51 (s), H aromatics 7.39–7.46 (m), 7.56 ($H_{6,10}$, d, J = 8.7), 7.54 ($H_{7,9}$, d, J = 8.7). ^{13}C NMR: C_1 170.59, C_2 61.57, R group C_3 65.60, C_4 192.60, C_5 139.79, $C_{6,10}$ 130.17, $C_{7,9}$ 129.86, C_8 133.88, B-Phenyl C_o133.88, C_m128.61, C_p129.98. ^{11}B NMR: +12.38. HRMS: $C_{18}H_{16}BNO_5Cl$ $[M^+ + 1]^+$ Calc. 372.0804, found 372.0808, error 0.9210.

*4.2.6. Synthesis of N → B) phenyl[N-(4-phenyl)phenacylimino diacetate-O,O',N]borane (**7**)*

Among of 1.0 g (4.56 mmol) of compound **1**, 1.25 g (4.56 mmol) of 2-bromo-4'-phenylacetophenone **f** and 1.39 g (13.7 mmol) of $KHCO_3$ in 100 ml of a mixture of acetonitrile/benzene (80/20). The residue was dissolved from a mixture of dichloromethane/acetonitrile and precipitate with ether to produce 1.52 g (80.8%) of compound **7** were obtained as yellow crystals, mp 248–249 °C. ^{1}H NMR δ(DMSO-d_6, J = Hz): CH_2CO 4.62 (H_A, d, J = 17.5), 4.36 (H_B, d, J = 17.5), CH_2N 4.56 (s), H aromatics 7.41–7.49 (m), 7.62 (H_6, d, J = 7.2), 7.81 (H_7 d, J = 7.2), 7.72 (H_{10}, d), 7.49 ($H_{11,12}$ 7.49 m) ^{13}C NMR: $C_1$170.68, C_2 61.67, R group C_3 65.84, C_4 192.94, C_5 146.15, C_6 127.76, C_7 128.03, C_8 139.29, C_9 129.51, C_{10} 127.85, C_{11} 129.98, C_{12} 133.91. B-Phenyl C_o133.46, C_m128.61, C_p129.51. ^{11}B NMR: +12.92. HRMS: $C_{24}H_{21}BNO_5$ $[M^+ + 1]^+$ Calc. 414.1507, found 414.1509, error 0.4110.

*4.3. Crystal structure determination of compounds **2**, **4** and **5***

Diffraction data from compound **2** were collected on an Enraf-Nonius CCD diffractometer at 293 K. Compound **2** with two independent molecules, $C_{17}H_{16}BN\,O_4$ (MW 309.12) crystallized in the space group $P\,2_1/n$, monoclinic; from dichloromethane/hexane as white colourless block, size 0.3 × 0.2 × 0.1 mm^3 with a = 10.934 (2), b = 16.927 (4), c = 17.100 (3) Å, V = 3111.0 Å (1)^3, α = 90.00°, β = 100.58 (10)°, γ = 90.00°, ρ = 1.320 mg/m^3, Z = 8, μ = 0.093 mm^{-1}, F(0 0 0) = 1296. Data collection: a total of 12763 reflections were measured, 6988 were independent and of these 4544 were considered observed [$F_o > 4.0\sigma(F_o)$]. Solution and refinement: direct methods, all non hydrogen atoms were refined anisotropically, R = 0.0499, Rw = 0.1174, $w = 1/\sigma^2$, GOF = 1.017, largest residual electron density peak/hole in the final difference map: 0.185/−0.281 eÅ^{-3}.

Compound **4** with two independent molecules, $C_{18}H_{18}BNO_4$ (MW 323.14) crystallized in the space group $P\,2_1/c$, monoclinic; from dichloromethane/ether as white colourless block, size 0.3 × 0.2 × 0.1 mm^3 with a = 11.2761 (4), b = 20.2614 (11), c = 15.2577 (6) Å, V = 3485.9 (3) Å^3, α = 90.00°, β = 89.953 (1)°, γ = 90.00°, ρ = 1.231 mg/m^3, Z = 8, μ = 0.086 mm^{-1}, F(0 0 0) = 1360. Data collection: a total of 19902 reflections were measured, 7054 were independent and of these 3803 were considered observed [$F_o > 4.0\sigma(F_o)$]. Solution and refinement: direct methods, all non hydrogen atoms were refined anisotropically, R = 0.0602, Rw = 0.1432, $w = 1/\sigma^2$, GOF = 1.040, largest residual electron density peak/hole in the final difference map: 0.296/−0.342 eÅ^{-3}.

Compound **5**, $C_{18}H_{16}BNO_5$ (MW 337.13) crystallized in the space group $P\,2_1/c$, monoclinic; from dichloromethane/ether as white colourless block size 0.3 × 0.3 × 0.2 mm^3 with a = 7.14030 (10), b = 18.7329 (5), c = 12.3949 (3) Å, V = 1645.10 (6) Å^3, α = 90.00°, β = 97.130 (1)°, γ = 90.00°, ρ = 1.361 mg/m^3, Z = 4, μ = 0.099 mm^{-1}, F(0 0 0) = 704. Data collection: a total of 6705 reflections were measured, 3719 were independent and of these 2324 were considered observed [$F_o > 4.0\sigma(F_o)$]. Solution and refinement: direct methods, all non hydrogen atoms were refined anisotropically, R = 0.0430, Rw = 0.1497, $w = 1/\sigma^2$, GOF = 0.716, largest residual electron density peak/hole in the final difference map: 0.188/−0.168 eÅ^{-3}.

Data reduction and molecular graphics were performed by WINGX program set [23]. All calculations were carried out with SHELX-S-97 and SHELX-L-97 [24]. Atomic scattering factors were taken from the International Tables for X-ray crystallography [25].

Supplementary data

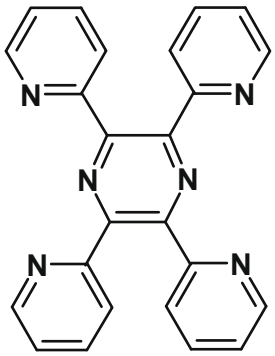
CCDC 714540, 714541 and 714542 contains the supplementary crystallographic data for compounds **2**, **4** and **5**, respectively. These data can be obtained free of charge via http://www.ccdc.cam.ac.uk/conts/retrieving.html, or from the Cambridge Crystallographic Data Centre, 12 Union Road, Cambridge CB2 1EZ, UK; fax: (+44) 1223-336-033; or e-mail: deposit@ccdc.cam.ac.uk.

Acknowledgments

The authors thank the "Consejo Nacional de Ciencia y Tecnología" (Conacyt-México) for financial support and for scholarship to R.M. Flores Ancona and M. López Martínez. We also acknowledge the help to Ing. Marco Antonio Leyva for X-ray crystallography.

References

[1] G.J. Baum, J. Organomet. Chem. 22 (1970) 269.
[2] S.H. Tung, K.M. Chang, S.L. Tah, S.L. Liu, S.L. Chang, Chem. Abstr. 66 (1967) 37990m.
[3] R. Csuk, H. Hönig, H. Weidmann, H.K. Zimmerman, Arch. Pharm. 317 (1984) 336.
[4] M.C. Miller III, A. Sood, B.F. Spielvogel, I.H. Hall, Anticancer Res. 17 (1997) 3299.
[5] S. Karthikeyan, A. Sood, J. Tomas, B.F. Spielvogel, I.H. Hall, Amino Acids 8 (1995) 323.
[6] C.A. Perks, A.J. Mill, G. Constantine, K.G. Harrison, J.A. Gibson, Br. J. Radiol. 61 (1988) 1115.
[7] H. Nemoto, J. Cai, N. Asao, J. Med. Chem. 38 (1995) 1673.
[8] J.P. Pignol, J.C. Abbe, O. Lefebvre, A. Stampfler, G. Methlin, J.C.R. Sahel, Acad. Sci. III 317 (1994) 543.
[9] T. Mancilla, S.L. Gálvez, Main Group Met. Chem. 15 (1992) 9.
[10] T. Mancilla, Ma.L. Alarcón, L. Carrillo, Heteroatom Chem. 15 (1994) 455.
[11] T. Mancilla, L. Carrillo, Ma.P. Reducindo, Polyhedron 15 (1996) 3777.
[12] G. Shtacher, W. Taub, J. Med. Chem. 9 (1966) 197.
[13] T. Mancilla, L. Carrillo, L.S. Zamudio Rivera, C. Camacho Camacho, D. de Vos, R. Kiss, F. Darro, B. Mahieu, E.R.T. Tiekink, H. Rahier, M. Gielen, M. Kemmer, M. Biesemans, R. Willem, Appl. Organomet. Chem. 15 (2001) 593.
[14] T. Mancilla, R. Contreras, B. Wrackmeyer, J. Organomet. Chem. 307 (1986) 1.
[15] T. Mancilla, R. Contreras, J. Organomet. Chem. 321 (1987) 191.
[16] N. Farfán, T. Mancilla, D. Castillo, G. Uribe, L. Carrillo, P. Joseph-Nathan, R. Contreras, J. Organomet. Chem. 381 (1990) 1.
[17] T. Mancilla, H. Höpfl, G. Bravo, L. Carrillo, Main Group Met. Chem. 20 (1997) 31.
[18] H.I. Beltrán, L.S. Zamudio Rivera, T. Mancilla, R. Santillán, N. Farfán, J. Oganomet. Chem. 657 (2002) 194.
[19] T. Mancilla, L.S. Zamudio Rivera, H.I. Beltrán, R. Santillán, N. Farfán, Arkivoc Part (IV) (2005) 366.
[20] T. Mancilla, M.A. Calixto-Romo, L. Amaya-Delgado, Polyhedron 26 (2007) 1023.
[21] T. Mancilla Percino, M. López Martínez, J.L. León, NPC 3 (2008) 329.
[22] A. Bondi, J. Phys. Chem. 68 (1964) 441.
[23] L.J. Farrugia, Department of Chemistry, University of Glasgow, UK, 2000.
[24] G.M. Sheldrick, SHELX-97, Program for Crystal Structure Solution, University of Göttingen, Germany, 1993.
[25] D.T. Cromer, I.T. Waber, International Tables for X-ray crystallography, vol. 4, Kynoch Press, England, 1974.



2,3,5,6-tetrakis(2-pyridyl)pyrazine

(tppz)

Scheme 1.

JASCO 7580 spectrophotometer. ^{1}H NMR spectra were recorded on a Bruker DRX-500 MHz, Avance spectrometer at ambient temperature in DMSO-d_6. Cyclic voltammograms were recorded by using a SAMA Research Analyzer M-500. Three electrodes were utilized in this system, a glassy carbon disk working electrode (ϕ 5 mm), a platinum wire auxiliary electrode and a Ag/AgCl reference electrode. The platinum disk working electrode was manually cleaned with 1-μm diamond polish prior to each scan. The supporting electrolyte, tetrabutylammonium hexafluorophosphate (TBAH), was twice recrystallized from ethanol–water (1/1) and vacuum-dried at 110 °C overnight. DMSO was distilled over CaH_2 and degassed under vacuum prior to use in the cyclic voltammetry. The solutions were deoxygenated by bubbling with Ar for 15 min. The procedure was performed at room temperature and the Ar atmosphere was maintained over the solution during measurements. Ferrocene (E^o = 0.665 V versus NHE, ΔE_p = 60 mV) was used as an internal reference [43]. The range of potential studied was between +1 and −2.2 V.

Emission spectra were taken on a CARY ECLIPS spectrophotometer. The spectra were measured in DMSO solution at room temperature. Solutions were taken in a 1 cm path length fused silica cell. Absolute emission quantum yields (Φ) were determined by comparison of the integrated emission intensity with that of Rhodamine B under identical conditions. Rhodamine B solutions absorb in plastics and should be kept in glass. *Caution:* Rhodamine B is suspected to be carcinogenic.

2.2. Synthesis of [{$CdCl_2$}$_2$(μ-tppz)].ethylene glycol

In a glass test tube, a solution of $CdCl_2{\cdot}H_2O$ (0.04 g, 0.2 mmol) in 5 mL 1:1 (V/V) ethanol/acetone was carefully layered on top of a solution of tppz (0.0388 g, 0.1 mmol) in 5 mL chloroform using ethylene glycol (3 mL) as an interlayer. After 5 days at room temperature, colorless single-crystals suitable for X-ray crystallography appeared at the boundary, in a yield of 22%. *Anal.* Calc. for $C_{26}H_{22}Cd_2Cl_4N_6O_2$: C, 38.21; H, 2.71; N, 10.28. Found: C, 38.55; H, 2.76; N, 10.39%. ^{1}H NMR (δ ppm, 500 MHz, DMSO-d_6, 298 K): 8.57 (d, 4H), 8.09 (d, 4H), 7.84 (dd, 4H), 7.59 (dd, 4H).

2.3. Synthesis of [Rh(tppz)(bpy)Cl][PF_6]$_2$.acetylacetone

A solution of tppz (0.37 g, 0.95 mmol) in 20 mL ethanol was slowly added to a solution of $RhCl_3{\cdot}xH_2O$ (0.25 g, 0.95 mmol) in 25 mL ethanol. The mixture was heated at reflux temperature for 5 h while being stirred vigorously. Upon cooling, a fine brown–green powder product was precipitated and filtered out. The product was washed with cold ethanol followed by diethyl ether and air dried. The yield of [Rh(tppz)Cl_3] was 0.493 g (86.8%). A mixture of [Rh(tppz)Cl_3] (0.298 g, 0.5 mmol) and 2,2′-bipyridine (0.078 g, 0.5 mmol) in 90 mL 2:1 (V/V) ethanol/water was heated at reflux temperature for 1 h. To the solution was then added $AgNO_3$ (0.17 g, 1 mmol) and the resulting solution was stirred at reflux temperature for 1 h. The solution was cooled to −5 °C overnight and filtered through Celite to remove the fine white AgCl precipitate. The filtrate was evaporated to dryness on the rotary evaporator. The brown powdery residue was dissolved in 20 mL water and precipitated from solution as a hexafluorophosphate salt by the addition of NH_4PF_6 (0.326 g, 2 mmol). The PF_6^- counter ion increased the solubility of the complex in polar organic solvents and resulted in easier purification. The product, [Rh(tppz)(bpy)Cl][PF_6]$_2$ was collected by suction filtration, washed with cold water and diethyl ether, and air dried. The crude product

Table 1
Crystallographic data and structure refinement summary for [Rh(tppz)(bpy)Cl][PF_6]$_2$.acetylacetone and [{$CdCl_2$}$_2$(μ-tppz)].ethylene glycol.

Complex	[Rh(tppz)(bpy)Cl][PF_6]$_2$.acetylacetone	[{$CdCl_2$}$_2$(μ-tppz)].ethylene glycol
Chemical formula	$C_{39}H_{32}ClF_{12}N_8O_2P_2Rh$	$C_{26}H_{22}Cd_2Cl_4N_6O_2$
Formula weight	1073.03	817.10
Temperature (K)	120(2)	120(2)
Crystal system	monoclinic	monoclinic
Space group	$P2_1/c$	$C2/c$
a (Å)	14.5083(9)	20.701(4)
b (Å)	17.3663(10)	12.196(2)
c (Å)	17.3145(10)	13.787(2)
β (°)	107.1130(10)	125.088(7)
V (Å^3)	4169.3(4)	2848.4(8)
Z	4	4
Calculated density (Mg/m^3)	1.709	1.905
Crystal size (mm)	0.11 × 0.08 × 0.03	0.24 × 0.21 × 0.18
F(0 0 0)	2152	1600
θ ranges (°)	1.47–25.99	2.06–28.99
Absorption correction	semi-empirical from equivalents	semi-empirical from equivalents
Reflections collected	36393	15097
Independent reflections (R_{int})	8200 [$R_{(int)}$ = 0.0611]	3741 [$R_{(int)}$ = 0.0287]
Data/restraints/parameters	8200/0/586	3741/0/181
Goodness-of-fit (GOF) on F^2	1.063	1.069
Final R indices	R_1 = 0.0478, wR_2 = 0.1076	R_1 = 0.0278, wR_2 = 0.0690
R indices (all data)	R_1 = 0.0729, wR_2 = 0.1271	R_1 = 0.0308, wR_2 = 0.0710
Range of h, k, l	−17/17, −21/21, −21/21	−28/28, −16/16, −18/18

was purified by column chromatography (alumina, grade IV, weakly acidic, 150 mesh with column dimensions: height 50 cm and diameter 3 cm). Elution with 3:1 acetonitrile/toluene gave a yellow–green band, which was collected, evaporated to dryness, and then recrystallized by slow evaporation of a 1:1 acetonitrile/acetylacetone solution of the complex. After 4 days at room temperature, yellow–green single-crystals suitable for X-ray crystallography were formed in a yield of 63%. *Anal.* Calc. for $C_{39}H_{32}ClF_{12}N_8O_2P_2Rh$: C, 43.65; H, 3.00; N, 10.44. Found: C, 43.94; H, 2.97; N, 10.60%. ^{1}H NMR (δ ppm, 500 MHz, DMSO-d_6, 298 K): 10.11 (d, 1H), 9.80 (d, 1H), 9.69 (1H, d), 9.56 (d, 1H), 8.78 (dd, 1H), 8.64 (d, 2H), 8.33 (dd, 1H), 8.16 (dd, 1H), 8.21 (d, 2H), 8.07 (d, 2H), 7.94 (dd, 2H), 7.83 (dd, 2H), 7.56 (dd, 1H), 7.45 (d, 2H), 7.30 (m, 4H).

2.4. X-ray crystallography

The colorless crystals of [{$CdCl_2$}$_2$(μ-tppz)].ethylene glycol were grown at the boundary of a Cd(II) solution in acetone/ethanol (1:1 V/V) and a tppz solution in $CHCl_3$ in the presence of ethylene glycol as an interlayer solvent. The yellow–green crystals of [Rh(tppz)(bpy)Cl][PF_6]$_2$.acetylacetone were grown by the slow evaporation of a 1:1 acetonitrile/acetylacetone solution of the complex. Single-crystal X-ray diffraction measurements of the complexes were carried out on a Bruker Apex II, using graphite-monochromated Mo Kα radiation (λ = 0.71073 Å) at 120(2) K. Unit cell parameters were determined by the least-squares calculations with θ angles ranging from 2.06° to 28.99° for [{$CdCl_2$}$_2$(μ-tppz)].ethylene glycol and 1.47° to 25.99° for [Rh(tppz)(bpy)Cl][PF_6]$_2$.acetylacetone.

The structures were solved by direct method and refined by full-matrix least-squares against F^2 in anisotropic (for non-hydrogen atoms) approximation. All hydrogen atoms were located from the difference Fourier syntheses and placed in geometrically calculated positions. All hydrogen atom positions were refined in an isotropic approximation in the riding model with the U_{iso}(H) parameters equal to 1.5 U_{eq}(Ci) for methyl groups and 1.2 U_{eq}(Ci) for other carbon atoms, where U(Ci) are the equivalent thermal parameters of the atoms to which corresponding H atoms are bonded. All calculations were performed on an IBM PC/AT using the SHELXTL version 5.1 software [44], giving a final R_1 = 0.0278, WR_2 = 0.0690 (for 3392 reflections with $I > 2\sigma(I)$) for [{$CdCl_2$}$_2$(μ-tppz)].ethylene glycol and R_1 = 0.0478, WR_2 = 0.1076 (for 6030 reflections with $I > 2\sigma(I)$) for [Rh(tppz)(bpy)Cl][PF_6]$_2$ acetyl acetone. The largest diffraction peak and hole on the final difference-Fourier map were 1.238 and −0.622 e Å^{-3} for [{$CdCl_2$}$_2$(μ-tppz)]. ethylene glycol and 1.719 and −0.479 e Å^{-3} for [Rh(tppz)(bpy)Cl][PF_6]$_2$.acetylacetone. Further details of the structural analyses are given in Table 1.

Table 2
Selected bond lengths (Å) and angles (°) for [Rh(tppz)(bpy)Cl][PF_6]$_2$.acetylacetone.

Bond lengths (Å)	
Rh(1)–N(4)	1.952(3)
Rh(1)–N(3)	2.033(3)
Rh(1)–N(2)	2.034(3)
Rh(1)–N(5)	2.033(3)
Rh(1)–N(1)	2.048(3)
Rh(1)–Cl(1)	2.3258(10)
Bond angles (°)	
N(4)–Rh(1)–N(3)	81.10(13)
N(4)–Rh(1)–N(2)	98.53(13)
N(3)–Rh(1)–N(2)	89.48(13)
N(4)–Rh(1)–N(5)	80.79(13)
N(3)–Rh(1)–N(5)	161.87(14)
N(2)–Rh(1)–(5)	92.45(13)
N(4)–Rh(1)–N(1)	178.66(13)
N(3)–Rh(1)–N(1)	99.07(13)
N(2)–Rh(1)–N(1)	80.14(13)
N(5)–Rh(1)–N(1)	99.02(13)
N(4)–Rh(1)–Cl(1)	86.32(10)
N(3)–Rh(1)–Cl(1)	89.15(10)
N(2)–Rh(1)–Cl(1)	174.68(10)
N(5)–Rh(1)–Cl(1)	90.45(10)
N(1)–Rh(1)–Cl(1)	95.01(9)

3. Results and discussion

The selected bond lengths and angles of complexes [Rh(tppz)(bpy)Cl][PF_6]$_2$ and [{$CdCl_2$}$_2$(μ-tppz)] are listed in Tables 2 and 3, respectively.

There are three general classes of structures that arise from the tridentate-coordination mode of the tppz ligand, including the [M(tppz)], [M(tppz)$_2$], and [M$_2$(μ-tppz)] structures. The simplest of these are the [M(tppz)] structures that involve coordination of one mono-tridentate tppz to a single metal, leaving the other side free [45]. This binding mode is observed for the mononuclear Rh(III) complex [Rh(tppz)(bpy)Cl][PF_6]$_2$. Fig. 1 shows the coordination geometry of the ligands about the Rh(III) ion. A distorted octahedral coordination at Rh(III) is defined by the N donor atoms of a tppz ligand bound in a κ-N(3),N(4),N(5) mode with the N(3) and N(5) atoms *trans* to each other, the N donor atoms of a bpy ligand and one Cl^- anion. The N(2) atom of the bpy ligand is *trans* to Cl^-.

The pyridyl rings of the uncoordinated tppz molecule are planar within experimental errors, but the tppz ligand as a whole is far from being planar due to the steric effects between the hydrogen atoms on the 3-pyridyl positions. Low energy conformations of tppz are predicted to have each pyridyl ring twisted from coplanarity with the pyrazine by roughly 50° [8,45,46]. For the tppz ligand, the dihedral angle between the mean planes of the two coordinated pyridyl rings is 3.97° whereas that between the two uncoordinated pyridyl rings is 48.92°. It deserves to be noted that the free N(6) and N(8) pyridyl nitrogen atoms are up and down from the pyrazine ring. It seems that the weak hydrogen bonds involving N(6)···H(12A) (2.523 Å) and N(8)···H(23A) (2.535 Å) occur in the structure of [Rh(tppz)(bpy)Cl][PF_6]$_2$. The pyridyl rings of bpy ligand are nearly coplanar, with a dihedral angle between the mean planes of 2.68°.

Table 3
Selected bond lengths (Å) and angles (°) for [{$CdCl_2$}$_2$(μ-tppz)].ethylene glycol.

Bond lengths (Å)	
Cd(1)–N(1)	2.3274(19)
Cd(1)–N(15)	2.3591(19)
Cd(1)–N(8)	2.4346(18)
Cd(1)–Cl(2)	2.4492(8)
Cd(1)–Cl(1)	2.5161(7)
Cd(1)–Cl(2)#1	3.0431(8)
Cl(2)–Cd(1)#1	3.0431(8)
Bond angles (°)	
N(1)–Cd(1)–N(15)	134.85(7)
N(1)–Cd(1)–N(8)	68.59(6)
N(15)–Cd(1)–N(8)	67.49(6)
N(1)–Cd(1)–Cl(2)	114.44(5)
N(15)–Cd(1)–Cl(2)	107.93(5)
N(8)–Cd(1)–Cl(2)	147.01(5)
N(1)–Cd(1)–Cl(1)	94.72(5)
N(15)–Cd(1)–Cl(1)	91.30(5)
N(8)–Cd(1)–Cl(1)	110.90(5)
Cl(2)–Cd(1)–Cl(1)	101.72(3)
N(1)–Cd(1)–Cl(2)#1	80.98(5)
N(15)–Cd(1)–Cl(2)#1	92.56(5)
N(8)–Cd(1)–Cl(2)#1	68.67(5)
Cl(2)–Cd(1)–Cl(2)#1	79.20(3)
Cl(1)–Cd(1)–Cl(2)#1	175.55(2)
Cd(1)–Cl(2)–Cd(1)#1	99.54(3)

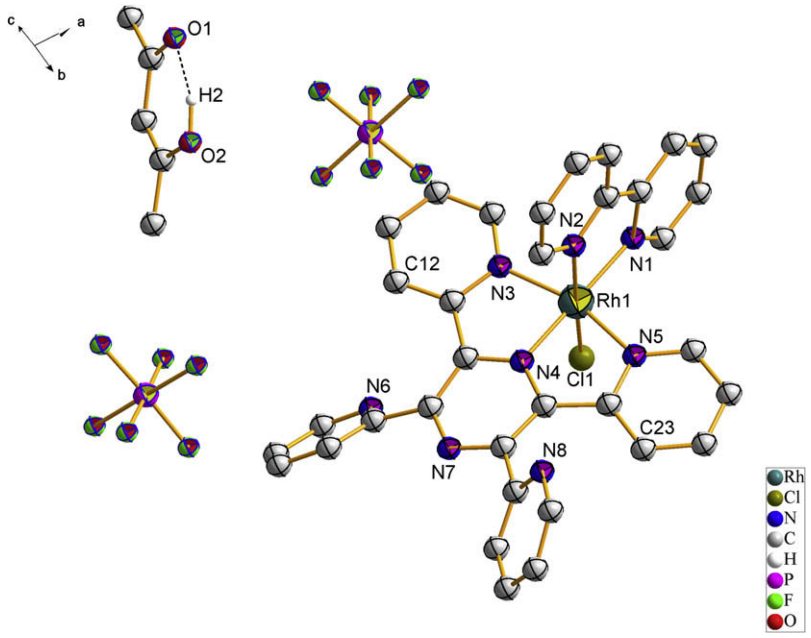


Fig. 1. View of the coordination environment of Rh(III) in [Rh(tppz)(bpy)Cl][PF_6]$_2$.acetylacetone.

The bite angles are defined as N–Rh–N angles involving the nitrogen atoms of a tppz or bpy ligand. The ideal bite angles for a tridentate ligand in an octahedral environment would be 90° and 180°. The Rh–tppz bite angles are less than the ideal angles at 81.10°, 80.79° and 161.87°. The ideal bite angle for bpy in an octahedral coordination geometry is 90°. The Rh–bpy bite angle (N(2)–Rh(1)–N(1) = 80.14°) is less than 90°.

The shortness of the Rh–N(pyrazine) bond compared with the Rh–N(pyridine) bonds (Table 2) is suggested to be due to the stronger π-accepting properties of the pyrazine ring. Crystallography revealed one acetylacetone molecule (enol form) per complex [Rh(tppz)(bpy)Cl][PF_6]$_2$ in the crystal structure. This solvent of crystallization has an intramolecular hydrogen bond between the O atom of the carbonyl group and the enolic H atom (O(2)–H(2)···O(1), d(H···O) = 1.65 Å). In the keto–enol tautomerism, the enol form is usually unstable, does not survive long, and changes into the keto form. This is because the oxygen is more electronegative than carbon and thus forms stronger multiple bonds. Hence, a carbon–oxygen (carbonyl) double bond is more than twice as strong as a carbon–oxygen single bond, but a carbon–carbon double bond is weaker than two carbon–carbon single bonds. 1,3-Diketones, such as acetylacetone, are particularly prone to form stable enols or enolates because of conjugation of the enol or enolate with the other carbonyl group and the stability gained in forming a six-membered ring (hydrogen bonded in the case of the enol or containing the counter ion in the case of the enolate).

The Rh^{III}–Cl bond length of 2.3258(10) Å is larger than the Rh–N distances. The Rh^{III}–Cl distance compares well with the reported

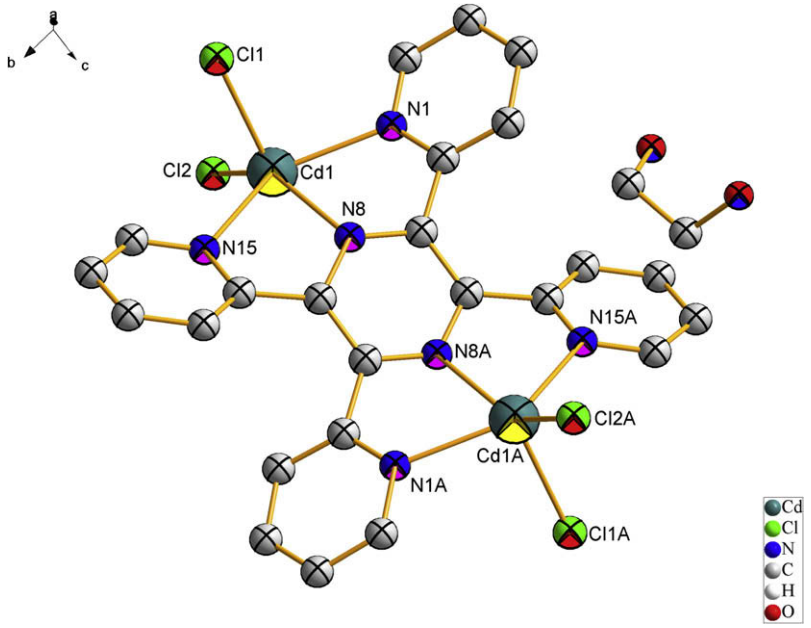


Fig. 2. The structure of one of the independent complex molecules, [{$CdCl_2$}$_2$(μ-tppz)].ethylene glycol. H atoms have been omitted.

Rh^{III}–Cl distances [47–49]. The Rh^{III}–Cl bond length is shorter than the average Ru^{II}–Cl bond length that was derived from the *cis,cis*-[{Ru(DMSO)Cl_2}$_2$(μ-tppz)]·2Me_2CO·2H_2O structure [42]. The shorter Rh^{III}–Cl distance indicates significant σ bonding in this bond. A π donation from the Cl^- ligand to Rh(III) is not possible because of its d^6 (t_{2g}^6) electron configuration. Fig. 1 also shows two PF_6^- counter ions. The P–F bond lengths range from 1.578 (4) to 1.604(3) Å, with an average of 1.596(8) Å. The lattice structure is further stabilized by a network of weak hydrogen bonds between the H atoms of the acetylacetone or pyridyl rings of the tppz ligand and the F atoms of the PF_6^- anions, with C–H···F distances of 2.409–3.950 Å.

The literature reveals many crystal structures of the [M_2(μ-tppz)] binding mode [14,29,31,32,34,38,39,41,42,50]. The major significance of these complexes is that they can serve as precursors for mixed valence complexes. The binding mode [M_2(μ-tppz)] is observed for the dinuclear Cd(II) complex [{$CdCl_2$}$_2$(μ-tppz)] (Fig. 2). The Cd(II) compound is a neutral and centrosymmetric dinuclear complex in which the tppz ligand functions in a

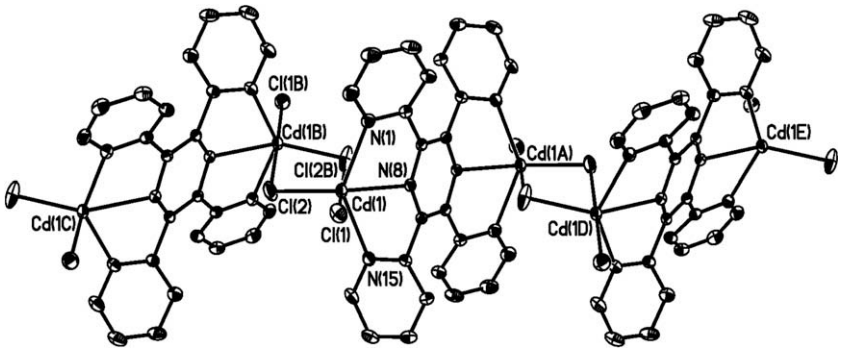


Fig. 3. The infinite chain of [{$CdCl_2$}$_2$(μ-tppz)] is formed by additional coordination Cd(1)–Cl(2)$_{-x+1,y,-z+1/2}$ 3.0431(8) Å.

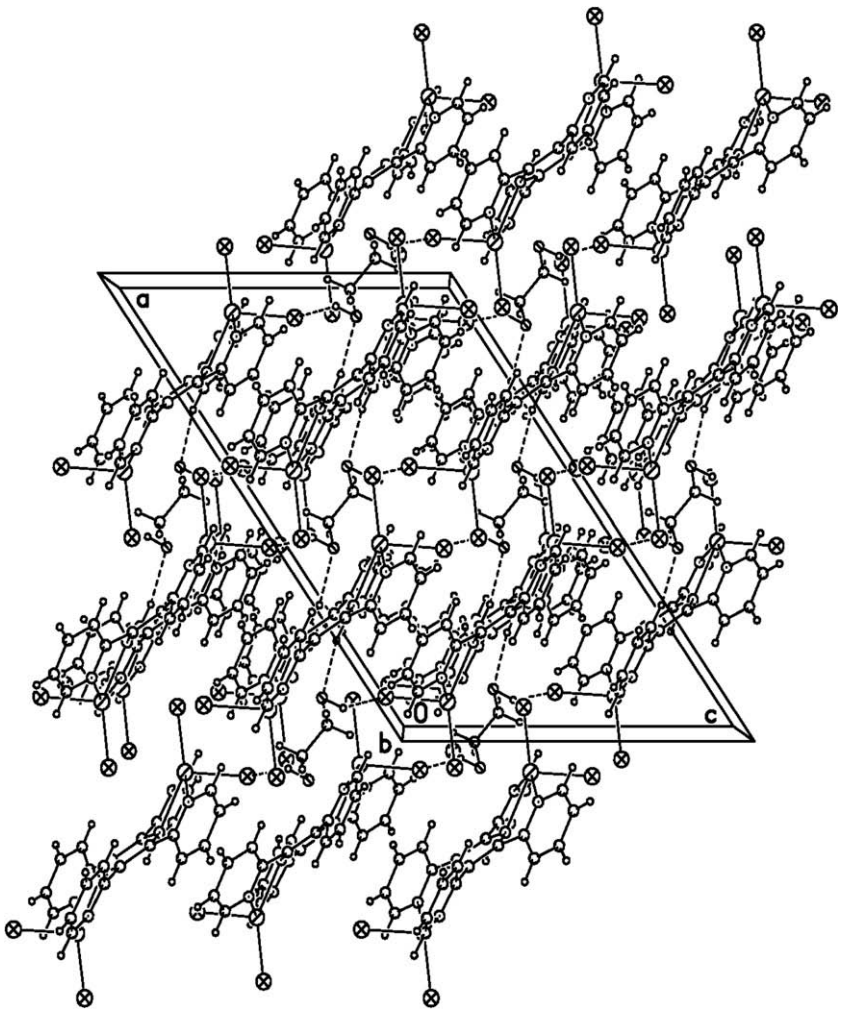


Fig. 4. Fragment of crystal packing (projection along the *b* crystal axis) of [{$CdCl_2$}$_2$(μ-tppz)].ethylene glycol. In the crystal, hydrogen bonds between the complex and ethylene glycol solvate molecules are presented: O(1S)–H(1S)...Cl(1)$_{-x+1/2,y-1/2,-z+1/2}$.

bis-tridentate bridging manner to link two Cd(II) ions that are separated by 7.286 Å. Each Cd(II) center is five-coordinated by three N donor atoms of tppz in one plane and two Cl^- ions normal to this plane; the Cl–Cd(II)–Cl angle is 101.72(3)°. The molecular structures of five-coordinate transition metal complexes show an extensive range from regular trigonal bipyramidal (RTBP) to regular square-based pyramidal (RSBP). The structure index parameter, $\tau = (\beta - \alpha/60)$, was evaluated by the two large angles ($\alpha < \beta$) in the five-coordinated geometry, where $\tau = 1.0$ for a RTBP geometry and $\tau = 0.0$ for a RSBP [51]. The coordination geometry around Cd(II) is slightly distorted from regular square-based pyramidal, as ascertained by the observed τ value of 0.20. One Cl^- and three nitrogen atoms of the tppz ligand constitute the basal plane of the square pyramid, and the remaining Cl^- occupies the apical position (Fig. 2). The Cd^{II}–N(pyrazine) distance is very slightly longer than the Cd^{II}–N(pyridyl) distances. The π-accepting property of tppz is saturated by two Cd(II) metal centers, leading to the longer distance. The Cd^{II}–Cl distances of 2.4492(8) and 2.5161(7) Å compare well with the reported Cd^{II}–Cl distances [52,53]. However, if one accepts weak intermolecular Cd···Cl ($1-x$, y, $1/2-z$) interactions of 3.0431(8) Å, the coordination geometry can be described as being based on an octahedron (Fig. 3). The Cd···Cl weak coordination leads to the formation of a 1D chain in the solid state (Fig. 3). The Cd(1)···Cd(1B) distance through the two bridging chloride ligands is 4.211 Å. The two Cd(II) ions are, respectively, below and above the plane of the pyrazine moiety of the bridging tppz ligand. This conformation probably minimizes steric strain while at the same time maximizes the bonding interaction of the tppz ligand with the Cd(II) ions. The dihedral angle between the mean planes of the two coordinated pyridyl rings is 44.83°. The dihedral angles between the pyrazine ring and each of the pyridyl rings are 36.19° (C(2)–C(6)/N(1)) and 34.42° (C(10)–C(14)/N(15)). Unlike the bidentate complexes of tppz, the two pyridine rings of most tridentate tppz complexes do not bow out of the pyrazine ring plane. Instead, the pyrazine ring twists to push one pyridine ring up and the other ring down. The two pyridine rings then rotate in the opposite direction to bring their lone pairs close to the metal ion [45]. Fig. 4 shows the fragment of crystal packing (projection along the *b* crystal axis) of [{$CdCl_2$}$_2$(μ-tppz)].ethylene glycol. In the crystal, hydrogen bonds between the complex and ethylene glycol solvate molecules are presented (O(1S)–H(1S)···Cl(1)).

Data for the infrared spectra for tppz, and the mono and bimetallic complexes were obtained as solids in KBr. Predominant vibrations for the free tppz ligand are associated with ν(C=C), ν(C=N) and ring stretching. The reported separation between ν(C=C) and ν(C=N) is close to 20 cm^{-1} for polypyridyl ligands [54,55], and thus the observed vibrational absorption bands for tppz at 1592 and 1567 cm^{-1} may be due to either different ν(C=N) on the pyrazine and pyridine rings or ν(C=C) and ν(C=N) with coincidental equivalence of the different rings [55]. An intense band at 1393 cm^{-1} is assigned to ring stretching of both the pyrazine and pyridine rings of tppz. The FT-IR spectrum of [Rh(tppz)(bpy)Cl][PF_6]$_2$ shows a absorption pattern in the 4000–400 cm^{-1} region similar to the bpy and tppz ligands. A strong band at 1617 cm^{-1} is assigned to ν(C=O) of the acetylacetone. The strong absorption band at 841 cm^{-1} is assigned to ν(P–F) and demonstrates the existence of PF_6^- as a counter ion [54].

The FT-IR bands of [{$CdCl_2$}$_2$(μ-tppz)] were assigned by a comparison with the free tppz values. This complex shows moderately sharp absorptions at 1595, 1572 and 1395 cm^{-1}, which are assigned to the stretching of the coordinated tppz ligand.

The results obtained from the ^{1}H NMR spectra support the structures obtained from the X-ray analysis and suggest that the structures of the complexes [Rh(tppz)(bpy)Cl][PF_6]$_2$ and [{$CdCl_2$}$_2$(μ-tppz)] are retained in DMSO-d_6 solution. The NMR assignment for the mixed ligand complex [Rh(tppz)(bpy)Cl][PF_6]$_2$ is aided by integration values and comparison to the known systems bpy, tppz, [Ru(L)(tppz)Cl]ClO_4 (L = 2,2′-dipyridylamine) [7], [Ru(tppz)(4,4′-(CH_3)bpy)Cl]PF_6 [56], [Ru(dpk)(tppz)Cl][ClO_4] (dpk = 2,2′-dipyridylketone) [57] and [Ru(tpy)(tppz)][PF_6]$_2$ (tpy = 2,2′:6′,2″-terpyridine) [8]. Metal-free tppz shows four well-resolved ^{1}H NMR signals (8.05, 7.80, 7.23 and 8.38 ppm) at room temperature [8,58]. In the ^{1}H NMR spectrum of [Rh(tppz)(bpy)Cl][PF_6]$_2$ in DMSO-d_6, the bpy protons are non-equivalent as one ring is *trans* to Cl and one ring is *trans* to the pyrazine nitrogen of tppz. Therefore, the protons on each ring of bpy are non-equivalent and integrate with relative value (1). The non-equivalency for the tppz protons arises from the coordination of one end of the ligand to Rh(III), with the subsequent upfield shift of the resonances produced by an increase in electronic density due to π-backbonding. The resonances of the uncoordinated tppz rings shift downfield, as observed for similar complexes [7,8,56,57].

All the pyridine rings of [{$CdCl_2$}$_2$(μ-tppz)] are magnetically equivalent, and only 4 signals attributable to coordinated tppz can be observed in the ^{1}H NMR spectrum. This means that both the cadmium atoms have the same coordination environment.

The electronic absorption spectroscopy of [Rh(tppz)(bpy)Cl][PF_6]$_2$ was found to be quite complicated due to the many possible transitions. It is possible to have tppz $\pi \rightarrow \pi^*$ and $n \rightarrow \pi^*$ transitions as well as ligand field (LF) ($t_{2g}^6 \rightarrow e_g$), MLCT (Rh → tppz and/or Rh → bpy) and LMCT (Cl → Rh) transitions. The electronic absorption spectroscopy of $4d^6$ and $5d^6$ complexes with polypyridyl ligands is characterized by intense ligand $\pi \rightarrow \pi^*$ and $n \rightarrow \pi^*$ transitions in the ultraviolet region and metal (dπ) → ligand (π^*)

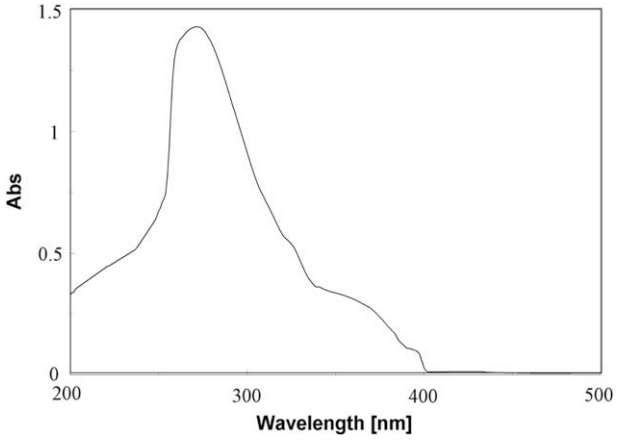


Fig. 5. Absorption spectrum of [Rh(tppz)(bpy)Cl][PF_6]$_2$ in DMSO.

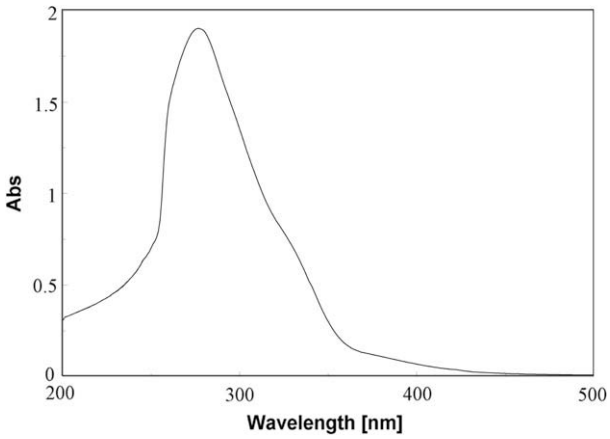


Fig. 6. Absorption spectrum of [{$CdCl_2$}$_2$(μ-tppz)] in DMSO.

charge transfer (MLCT) transitions in the visible region [7,20,55,59–61]. In general only the first spin-allowed LF band of Rh(III) complexes may be observed, the second band frequently being obscured by the CT absorption [59]. The electronic spectrum of $[Rh(tppz)(bpy)Cl][PF_6]_2$ was taken in DMSO (Fig. 5). The intense absorption bands at 272 and 322 nm most likely arise from the spin-allowed ligand-centered (LC) ($\pi \rightarrow \pi^*$) transitions. The absorption band (shoulder) at about 355 nm is assigned as the $d\pi(Rh) \rightarrow \pi^*(tppz)$ charge transfer transition (MLCT) on the basis of the assignments of mononuclear tppz complexes of Ir(III), Rh(III), Ru(II) and Os(II) [7,28,55,59–62], while the weak shoulder at about 398 nm is most likely a LF transition.

The absorption spectrum of $[\{CdCl_2\}_2(\mu\text{-tppz})]$ in DMSO (Fig. 6) displayed a band at 277 nm. This intense band is assigned to a LC ($\pi \rightarrow \pi^*$) transition.

A representative cyclic voltammogram of $[\{CdCl_2\}_2(\mu\text{-tppz})]$ at a glassy carbon electrode is given in Fig. 7. The voltammetric response of this complex shows an irreversible wave at −1.175 V which can be attributed to cadmium reduction process, since cadmium(II) nitrate shows a peak at −0.67 V. Upon formation of a tppz bridged dinuclear complex, the bridging tppz becomes easier to reduce due to stabilization of the π^* orbital induced by the coordination of the second electron deficient metal center. For example, in $[Ru(tpy)(tppz)]^{2+}$ (tpy = 2,2′:6′,2″-terpyridine), two reduction couples of tppz ($tppz^{0/-}$ and $tppz^{-/2-}$) were observed at −0.97 and 1.60 V, while in $[(tpy)Ru(\mu\text{-tppz})Ru(tpy)]^{4+}$, two reduction couples of tppz were recorded at −0.35 and −0.84 V [20,58,63]. In a neutral complex $[\{CdCl_2\}_2(\mu\text{-tppz})]$, the $tppz^{0/-}$ and $tppz^{-/2-}$ couples were observed at −1.58 and −1.88 V, respectively.

The cyclic voltammogram of $[Rh(tppz)(bpy)Cl][PF_6]_2$ is shown in Fig. 8. The electrochemical behavior of $[Rh(tppz)(bpy)Cl][PF_6]_2$ is characterized by metal based and ligand based reductions. The first irreversible two-electron reduction (−0.71 V) is assigned as Rh(III/I), the second and third reductions (−1.11 and −1.67 V) are assigned as $tppz^{0/-}$ and $tppz^{-/2-}$, and the fourth reduction (−1.96 V) is assigned as $bpy^{0/-}$. The $tppz^{0/-}$ and $tppz^{-/2-}$ couples occur prior to the $bpy^{0/-}$ reduction due to the larger π system of tppz ligand as a result of the

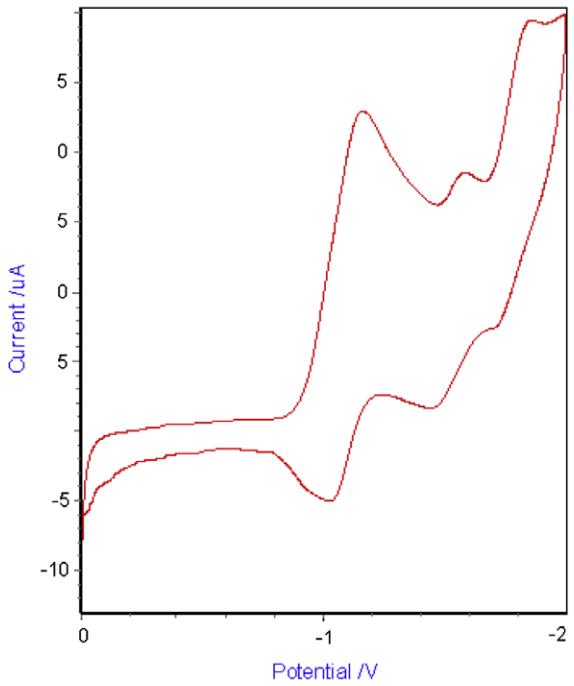


Fig. 7. Cyclic voltammogram of $[\{CdCl_2\}_2(\mu\text{-tppz})]$ in DMSO at a scan rate of 100 mVs^{-1}; 0.1 M TBAH as the supporting electrolyte.

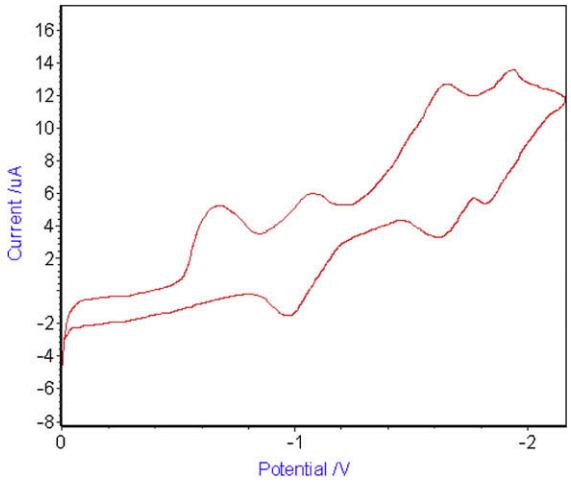


Fig. 8. Cyclic voltammogram of $[Rh(tppz)(bpy)Cl][PF_6]_2$ in DMSO at scan rate of 100 mVs^{-1}; 0.1 M TBAH as the supporting electrolyte.

two extra pyridyl rings on tppz as well as the extra electron accepting character of the pyrazine ring. Tppz has a substantially lower energy π^* orbital than bpy. The two-electron reduction of Rh(III) therefore results in accumulation of an electron on the metal center and destabilizes the complex. This can rationalize the "electron-transfer chemical-reaction (EC)" process, in which the chemical reaction involves loss of a chloride ion, which proceeds and leads to the irreversible process at the first reduction wave. In *cis*-$[Rh(bpy)_2X_2]^+$ (X = Cl^-, Br^-, and I^-), the irreversible Rh(III/I) couple was observed at a negative potential [64]. The electrochemistry reported for the $[Rh^{III}(SacSac)_3]$ (SacSac = dithioacetylacetone) complex indicates a structural instability associated with reduction of this species, consistent with the expectation for addition of the electron into a d_σ-type (d^*) orbital [65,66].

The photoluminescence properties of both complexes were studied at room temperature in DMSO solution. Because of the low solubility of the complexes, we have been forced to study the spectral and emission measurements in DMSO solution. Since tppz itself hardly fluoresces, the fluorescence of the tppz complexes may result from the change in the lowest excited state from the n,π^* triplet to the π,π^* singlet, which becomes lower in energy than the n,π^* triplet due to the complexation with the metal ion as a strong Lewis acid [23,67,68]. In the absence of metal ions, the

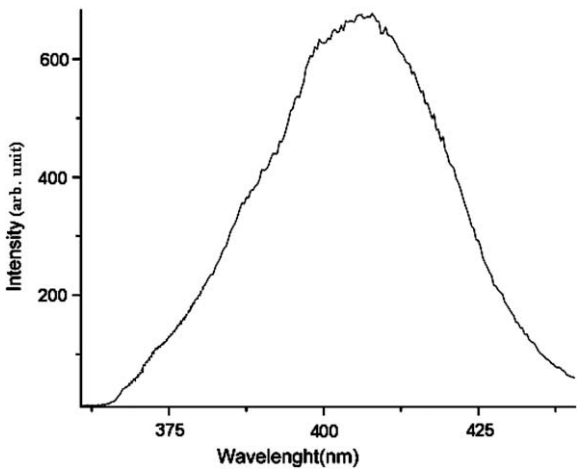


Fig. 9. Emission spectrum of $[\{CdCl_2\}_2(\mu\text{-tppz})]$ in DMSO at room temperature (λ_{exc} = 277 nm).

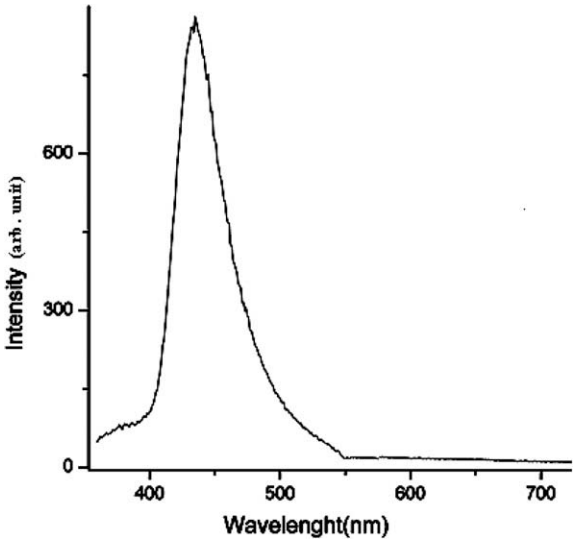


Fig. 10. Emission spectrum of $[Rh(tppz)(bpy)Cl][PF_6]_2$ in DMSO at room temperature (λ_{exc} = 322 nm).

fluorescence of the ligand is probably quenched by the occurrence of a photoinduced electron transfer (PET) process due to the presence of lone pairs of electrons of the donor atoms in the ligand. PET is an electron transfer which occurs when certain photoactive materials interact with light. The fluorescent emission of $[\{CdCl_2\}_2(\mu\text{-tppz})]$ at the excitation wavelength of 277 nm is shown in Fig. 9. Although $CdCl_2$ is not luminescent, interestingly many cadmium coordination complexes containing polypyridyl ligands show an intense fluorescence band upon excitation at the ligand's absorption band in solution as well as in the solid state. No emissions originating from metal-centered and MLCT or LMCT excited states are expected for the Cd(II) complexes, since the Cd(II) ion is difficult to oxidize or reduce due to its d^{10} configuration [52,69–73]. Thus, the emission observed at 406 nm (Φ = 0.29) in $[\{CdCl_2\}_2(\mu\text{-tppz})]$ is tentatively assigned to the $^1(\pi-\pi^*)$ intraligand fluorescence.

The emission spectrum of a deoxygenated solution of $[Rh(tppz)(bpy)Cl][PF_6]_2$ at the excitation wavelength of 322 nm is shown in Fig. 10. The maximum emission peak of this complex is located at 435 nm ($\Phi = 8 \times 10^{-3}$). Since electrochemical data indicated that the reduction orbital of the metal center is d^*, instead of π^* in nature, participating luminescence, the following emission in $[Rh(tppz)(bpy)Cl][PF_6]_2$ can thus be ruled out: metal-to-ligand charge transfer (MLCT), sigma-bond-to-ligand charge transfer (SBLCT), halide-to-ligand charge transfer (XLCT), ligand-to-ligand charge transfer (LLCT) or ligand-centered (LC) emission [74]. This conclusion in turn supports the πd^* emission assignment at room temperature. For the complexes *cis*-$[Rh(bpy)(DPA)Cl_2]$ and *cis*-$[Rh(phen)(DPA)Cl_2]$ (DPA = the deprotonated form of 2,2′-dipyridylamine), only a one-electron reduction process occurs at the metal with elimination of a Cl^- anion. Based on the luminescence and electrochemical data, the emission of these complexes was assigned as πd^* [74]. Some pseudo-octahedral Rh(III) complexes which contain the *ortho*-metallated phenylpyridine anion as a ligand are phosphorescent at room temperature [75].

4. Conclusion

In this study, two tppz complexes, $[Rh(tppz)(bpy)Cl][PF_6]_2$.acetylacetone and $[\{CdCl_2\}_2(\mu\text{-tppz})]$.ethylene glycol, have been synthesized and characterized.

Luminescent polynuclear d^{10} metal complexes such as Cd(II) are of great interest because of their potential application in chemical optical sensors, photosensitization and electroluminescent devices. It is interesting that the dinuclear complex $[\{CdCl_2\}_2(\mu\text{-tppz})]$ has a very strong emission band centered at 406 nm upon excitation at 277 nm. Metal ions can enhance or quench the fluorescence emission of polypyridyl ligands. Quenching of fluorescence of a ligand by transition metal ions during complexation is a rather common phenomenon which is explained by processes such as magnetic perturbation, redox activity and electronic energy transfer. Enhancement of fluorescence through complexation is, however, of much interest as it opens up the opportunity for photochemical applications of these complexes [52]. The fluorescent intensity of the dinuclear Cd(II) complex is significantly stronger than that of free tppz, probably due to the conformational rigidity enhancement of the coordinated tppz, thereby reducing the non-radiative decay of the intraligand $^1(\pi-\pi^*)$ excited state. Thus, $[\{CdCl_2\}_2(\mu\text{-tppz})]$ may be used as an advanced material for light emitting diode devices and may be an excellent candidate for solvent-resistance fluorescent material because it is almost insoluble in most common solvents such as methanol, ethanol, acetone, $CHCl_3$, CH_2Cl_2 and water.

Rhodium (III) complexes have played a central role in the understanding of the electrochemical, photochemical and photophysical processes of d^6 complexes. The mononuclear Rh(III) complex, $[Rh(tppz)(bpy)Cl][PF_6]_2$, shows only an irreversible two-electron reduction process at the metal center with elimination of chloride. At room temperature, this complex shows a blue emission, assigned as πd^* phosphorescence. The electrochemical data also provide evidence in support of the assigned πd^* emission of the complex. In summary, $[Rh(tppz)(bpy)Cl][PF_6]_2$ is an example for the rational design of a transition metal complex which under ambient conditions exhibits a phosphorescence at relatively short wavelength.

5. Supplementary material

CCDC 716058 and 716059 contains the supplementary crystallographic data for $[\{CdCl_2\}_2(\mu\text{-tppz})]$.ethylene glycol and $[Rh(tppz)(bpy)Cl]$ $[PF_6]_2$.acetylacetone. These data can be obtained free of charge via http://www.ccdc.cam.ac.uk/conts/retrieving.html, or from the Cambridge Crystallographic Data Centre, 12 Union Road, Cambridge CB2 1EZ, UK; fax: (+44) 1223-336-033; or e-mail: deposit@ccdc.cam.ac.uk.

Acknowledgements

We are grateful to the Isfahan University of Technology (IUT) and Shahid Bahonar University for financial support. We thank Professor Per Lincoln (Chalmers University of Technology, Göteborg, Sweden) who provided us with the photoluminescence study facilities.

References

[1] V.C. Gibson, C. Redshaw, G.A. Solan, Chem. Rev. 107 (2007) 1745.
[2] V. Balzani, A. Juris, M. Venturi, S. Campagna, S. Serroni, Chem. Rev. 96 (1996) 759.
[3] G.R. Newkome, E. He, C.N. Moorefield, Chem. Rev. 99 (1999) 1689.
[4] J.P. Danks, N.R. Champness, M. Schröder, Coord. Chem. Rev. 174 (1998) 417.
[5] W.A. Alves, P.A. Fiorito, S.I. Córdoba de Torresi, R.M. Torresi, Biosen. Bioelectron. 22 (2006) 298.
[6] G.-Y. Hsu, C.-W. Chen, S.-C. Cheng, S.-H. Lin, H.-H. Wei, C.-J. Lee, Polyhedron 24 (2005) 487.
[7] N. Chanda, B. Sarkar, J. Fiedler, W. Kaim, G.K. Lahiri, J. Chem. Soc., Dalton Trans. (2003) 3550.
[8] S. Zhao, S.M. Arachchige, C. Slebodnick, K.J. Brewer, Inorg. Chem. 47 (2008) 6144.
[9] M. Bortoluzzi, E.D. Faveri, S. Daniele, B. Pitteri, Eur. J. Inorg. Chem. (2006) 3393.

[10] M. Trivedi, D.S. Pandey, N.P. Rath, Inorg. Chim. Acta 362 (2009) 284.
[11] E.C. Constable, A.M.W.C. Thompson, J. Chem. Soc., Dalton Trans. (1995) 1615.
[12] M. Koley, B. Sarkar, S. Ghumaan, E. Bulak, J. Fiedler, W. Kaim, G.K. Lahiri, Inorg. Chem. 46 (2007) 3736.
[13] H.A. Goodwin, F. Lions, J. Am. Chem. Soc. 81 (1959) 6415.
[14] H. Hadadzadeh, A.R. Rezvani, G.P.A. Yap, R.J. Crutchley, Inorg. Chim. Acta 358 (2005) 1289.
[15] S.W. Jones, L.M. Vrana, K.J. Brewer, J. Organomet. Chem. 554 (1998) 29.
[16] M. Graf, H. Stoeckli-Evans, A. Escuer, R. Vicente, Inorg. Chim. Acta 257 (1997) 89.
[17] J. Carranza, C. Brennan, J. Sletten, J.M. Clemente-Juan, F. Lioret, M. Julve, Inorg. Chem. 42 (2003) 8716.
[18] E. Burkholder, S. Wright, V. Golub, C.J. O'Connor, J. Zubieta, Inorg. Chem. 42 (2003) 7460.
[19] E. Burkholder, V. Golub, C.J. ÒConnor, J. Zubieta, Inorg. Chem. 42 (2003) 6729.
[20] C.R. Arana, H.D. Abruña, Inorg. Chem. 32 (1993) 194.
[21] E. Burkholder, V. Golub, C.J. ÒConnor, J. Zubieta, Inorg. Chem. 43 (2004) 7014.
[22] M. Maskus, H.D. Abruña, Langmuir 12 (1996) 4455.
[23] J. Yuasa, S. Fukuzumi, J. Am. Chem. Soc. 130 (2008) 566.
[24] S. Flores-Torres, G.R. Hutchison, L.J. Soltzberg, H.D. Abruña, J. Am. Chem. Soc. 128 (2006) 1513.
[25] S. Fantacci, F. De Angelis, J. Wang, S. Bernhard, A. Selloni, J. Am. Chem. Soc. 126 (2004) 9715.
[26] S. Rubino, P. Portanova, A. Girasolo, G. Galvaruso, S. Orecchio, G.C. Stocco, Eur. J. Med. Chem. 44 (2009) 1041.
[27] W.A. Alves, V. Pfaffen, P.I. Ortiz, S.I. Córdoba de Torresi, R.M. Torresi, J. Braz. Chem. Soc. 19 (2008) 651.
[28] M. Maekawa, T. Minematsu, H. Konaka, K. Sugimoto, T. Kuroda-Sowa, Y. Suenaga, M. Munakata, Inorg. Chim. Acta 357 (2004) 3456.
[29] M.S. Sadjadi, A. Ebadi, K. Zare, V. Amani, H.R. Khavasi, Acta Crystallogr., Sect. E 64 (2008) m1050.
[30] X. Chen, F.J. Femia, J.W. Babich, J.A. Zubieta, Inorg. Chim. Acta 315 (2001) 66.
[31] M.F. Ahmet, B. Coutinho, J.R. Dilworth, J.R. Miller, S.J. Parrott, Y. Zheng, Polyhedron 15 (1996) 2041.
[32] C.M. Hartshorn, N. Daire, V. Tondreau, B. Loeb, T.J. Meyer, P.S. White, Inorg. Chem. 38 (1999) 3200.
[33] W.M. Teles, N.L. Speziali, C.A.L. Filgueiras, Polyhedron 19 (2000) 739.
[34] D. Hargrman, P. Hagrman, J. Zubieta, Inorg. Chim. Acta 300 (2000) 212.
[35] Y. Yamada, Y. Miyashita, K. Fujisawa, K. Okamoto, Bull. Chem. Soc. Jpn. 73 (2000) 1843.
[36] C. Metcalfe, S. Spey, H. Adams, J.A. Thomas, J. Chem. Soc., Dalton Trans. (2002) 4732.
[37] P. Lainé, A. Gourdon, J.-P. Launay, Inorg. Chem. 34 (1995) 5156.
[38] N. Chanda, R.H. Laye, S. Chakraborty, R.L. Paul, J.C. Jeffery, M.D. Ward, G.K. Lahiri, J. Chem. Soc., Dalton Trans. (2002) 3496.
[39] M. Graf, H. Stoeckli-Evans, Acta Crystallogr., Sect. C 50 (1994) 1461.
[40] J.K. Bera, C.S. Campos-Fernández, C. Rodolphe, K.R. Dunbar, Chem. Commun. (2002) 2536.
[41] E.C. Constable, A.J. Edwards, D. Phillips, P.R. Raithby, Supramol. Chem. 5 (1995) 93.
[42] H. Hadadzadeh, G.P.A. Yap, R.J. Crutchley, Acta Crystallogr., Sect. E 62 (2006) m2002.
[43] T. Gennett, D.F. Milner, M.J. Weaver, J. Phys. Chem. 89 (1985) 2787.
[44] G.M. Scheldrick, SHELXS V. 5.1, Structure Determination Software Suite, Bruker AXS, Madison, Wisconsin, USA, 1998.
[45] C.W. Padgett, W.T. Pennington, T.W. Hanks, Cryst. Growth Des. 5 (2005) 737.
[46] L.M. Toma, D. Armentano, G. De Munno, J. Sletten, F. Lloret, M. Julve, Polyhedron 26 (2007) 5263.
[47] G. Malaisé, J.-B. Sortais, L. Barloy, M. Pfeffer, N. Kyritsakas, Polyhedron 25 (2006) 3349.
[48] C. Pettinari, R. Pettinari, M. Fianchini, F. Marchetti, B.W. Skelton, A.H. White, Inorg. Chem. 44 (2005) 7933.
[49] P.G. Gueorguieva, G.G. Stanley, F.R. Fronczek, Acta Crystallogr., Sect. E 60 (2004) m1043.
[50] M. Graf, B. Greaves, H. Stoeckli-Evans, Inorg. Chim. Acta 204 (1993) 239.
[51] A.W. Addison, T.N. Rao, J. Reedijk, J. VanRijn, G.C. Verschoor, J. Chem. Soc., Dalton Trans. (1984) 1349.
[52] S. Basak, S. Sen, C. Marschner, J. Baumgartner, S.R. Batten, D.R. Turner, S. Mitra, Polyhedron 27 (2008) 1193.
[53] J.M. Li, Acta Crystallogr., Sect. E 63 (2007) m2241.
[54] K. Nakamato, Infrared and Raman Spectra of Inorganic and Coordination Compounds. Part II: Application in Coordination, Organometallic and Bioinorganic Chemistry, 5th ed., Wiley-Interscience, New York, 1997.
[55] R.R. Ruminski, C. Letner, Inorg. Chim. Acta 162 (1989) 175.
[56] V. Tondreau, A.M. Leiva, B. Loeb, D. Boys, L.K. Stultz, T.J. Meyer, Polyhedron 15 (1996) 2035.
[57] S. Ghumaan, B. Sarkar, N. Chanda, M. Sieger, J. Fiedler, W. Kaim, G.K. Lahiri, Inorg. Chem. 45 (2006) 7955.
[58] R. Thummel, S. Chirayil, Inorg. Chim. Acta 154 (1988) 77.
[59] A.B.P. Lever, Inorganic Electronic Spectroscopy, 2nd ed., Elsevier, Amsterdam, 1984.
[60] H. Hadadzadeh, A.R. Rezvani, F. Belanger-Gariepy, J. Mol. Struct. 740 (2005) 165.
[61] R.R. Ruminski, K.D.K. Zimmer, K.A. Rita, M.A. Knobbe, C. Dean, Inorg. Chim. Acta 362 (2009) 1772.
[62] G. Mansouri, A.R. Rezvani, H. Hadadzadeh, H.R. Khavasi, H. Saravani, J. Organomet. Chem. 692 (2007) 3810.
[63] L.M. Volger, K.J. Brewer, Inorg. Chem. 35 (1996) 818.
[64] D. Amarante, C. Cherian, C. Emmel, H.-Y. Chen, S. Dayal, M. Koshy, E.G. Megehee, Inorg. Chim. Acta 358 (2005) 2231.
[65] A.M. Bond, G.A. Heath, R.L. Martin, J. Electrochem. Soc. 117 (1970) 1362.
[66] J.T. Merrill, M.K. DeArmond, J. Am. Chem. Soc. 101 (1979) 2045.
[67] F.D. Lewis, G.D. Reddy, J.E. Elbert, B.E. Tillberg, J.A. Meltzer, M. Kojima, J. Org. Chem. 56 (1991) 5311.
[68] S. Fukuzumi, N. Satoh, T. Okamoto, K. Yasui, T. Suenobu, Y. Seko, M. Fujitsuka, O. Ito, J. Am. Chem. Soc. 123 (2001) 7756.
[69] D. Das, B.G. Chand, J. Dinda, C. Sinha, Polyhedron 26 (2007) 555.
[70] M.K. Paira, J. Dinda, T.-H. Lu, A.R. Paital, C. Sinha, Polyhedron 26 (2007) 4131.
[71] H. Chowdhury, R. Ghosh, Sk.H. Rahaman, B.K. Ghosh, Polyhedron 26 (2007) 5023.
[72] R.-X. Yuan, R.-G. Xiong, Y.-L. Xie, X.-Z. You, S.-M. Peng, G.-H. Lee, Inorg. Chem. Commun. 4 (2001) 384.
[73] Y. Gong, R. Wang, D. Yuan, W. Su, Y. Huang, C. Yue, F. Jiang, M. Hong, Polyhedron 26 (2007) 5309.
[74] M.C. Tseng, F.K. Li, J.H. Huang, W.L. Su, S.P. Wang, W.L. Huang, Inorg. Chim. Acta 359 (2006) 401.
[75] H. Kunkely, A. Volger, Chem. Phys. Lett. 319 (2000) 486.

different physiological conditions. Moreover, one of the earlier reports described a mononuclear Cu(II) complex showing lower chemical nuclease activity than its dinuclear analogue [20] and opened the scope of studying the structure function relationship based upon the nuclearity of the metal complexes. All these data acted as a motivation to carry out DNA binding and cleavage studies of **1** and **2** as well as the free pro-ligand. Both **1** and **2** showed moderate DNA binding property, with binding constants of the order of $10^4\ M^{-1}$, as was obtained from UV–Vis DNA titration data of the respective complexes. To investigate the mode of the binding interaction of these two complexes with the DNA double strands, circular dichroic (CD) spectra of DNA in absence and presence of both complex solutions were performed. These analyses indicated intercalation as the probable mode of interaction, without any significant change in the right handed helicity of the DNA strands, although viscosity measurements of DNA solutions in absence and presence of solutions of **1** and **2** proved conclusively that both **1** and **2** interact with the same via non-classical mode, probably by producing kinks or bends in the DNA structure. The plasmid DNA, pUC19, cleavage ability of **1**, **2** and the free pro-ligand in the presence or absence of H_2O_2 or scavengers like sodium azide and DMSO were also carried out. Of the two complexes studied, the dinuclear one was seen to have stronger chemical nuclease activity than the mononuclear one and in both the cases the complexes were more potent chemical nucleases than the free ligand. The scavengers of hydroxyl and superoxide radicals were seen to reduce the extent of cleavage to a considerable extent for **1** where as for **2** they had no effect. Thus the oxidative cleavage mechanism for **1** was surely dependent on both singlet oxygen and diffusible hydroxyl radicals, i.e. reactive oxygen species (ROS), but for **2** the cleavage must have taken place by some other mechanism.

Hydrazones and molecules having hydrazide residues in their structures are capable of showing antifungal and antibacterial activities, and thus we explored the Cu(II)-hydrazone complexes and the free pro-ligand from this point of view as well. Complex **2** showed antimicrobial activity towards both Gram positive and Gram negative bacteria where as the free pro-ligand and **1** showed no activity.

Thus in this paper, we report, along with the crystal structures of the two Cu(II)-hydrazone complexes, the binding and cleavage properties of the complexes with CT-DNA and super coiled (SC) pUC19 DNA, respectively, as well as their antimicrobial activity.

2. Experimental

2.1. Materials

Benzhydrazide, pyridine-2-carboxaldehyde, Cu(II) perchlorate hexahydrate and sodium azide (Fluka) were used as received without further purification. All the solvents were of reagent grade. The CT-DNA and plasmid supercoiled (SC) pUC19 DNA were purchased from Bangalore GeNei; the Tris buffer, sodium chloride and hydrochloric acid (AR) were from Merck. Tris(hydroxymethyl)-aminomethane–HCl (Tris–HCl) buffer was prepared using deionized and sonicated triple-distilled water.

2.2. Physical measurements

Elemental analyses were carried out using a Perkin–Elmer 2400 II elemental analyzer. The infrared spectra were recorded on a Perkin–Elmer RX I FT-IR spectrophotometer with a KBr disc. The electronic spectra were recorded, in acetonitrile or in 5 mM Tris–50 mM NaCl buffer (pH ~7.5), on a Perkin–Elmer Lambda 40 (UV–Vis) spectrophotometer. Electrochemical studies were carried out with a VersaStat- PotentioStat II cyclic voltammeter using saturated calomel electrode (SCE) as the reference electrode in a three-electrode system. The CD spectra were recorded on a Jasco J-720 spectropolarimeter, in the same buffer medium, at room temperature, with $1/r = 1/3$, where $r = [1]/[DNA]$. The final spectrum was an average of five cycles and the spectra for the buffer had been subtracted automatically.

The fluorescence study, for the DNA–ethidium bromide assay, was done using a Hitachi 4010 FluoroMax spectrofluorimeter. A solution of CT-DNA [50 μM] was incubated with ethidium bromide [EthBr] at 27 °C for half an hour. The fluorescence spectrum of this solution was then recorded, subtracting the reading for the buffer only. Subsequent addition of the complexes, **1** and **2** were done with $[complex]_{Tot}/[DNA]_{Tot}$ up to 1.5.

Viscosity measurements were conducted on an Ubbelodhe viscometer, immersed in a thermostated water bath maintained at 298 K. The relative viscosities of the samples were determined using the equation $\eta = (t - t_0)/t_0$, where t_0 is the flow time for buffer alone and t is the flow time of either only DNA solution or DNA solution + different concentrations of complexes **1** and **2**.

The pro-ligand HPBH, **1** and **2** were studied for their antimicrobial activity against Gram negative bacteria *Escherichia coli* MTCC 739, Gram positive bacteria *Staphylococcus aureus* MTCC 96, and yeast *Saccharomyces cerevisiae* MTCC 170. The antimicrobial tests were carried out in Luria-Bertani medium (1% Bacto-Tryptone, 1% NaCl, 0.5% Yeast extract, pH 7.0) for bacteria and YPD medium (1% Yeast extract, 2% Peptone, 2% Dextrose, pH 5.0) for yeast. 1.8% agar was used for preparing the plates.

The minimum inhibitory concentration (MIC), the lowest concentration of the compound which inhibits microbial growth, was determined by broth dilution and cup agar diffusion assay. The compounds were tested in the 1–1000 μg/ml range. The inoculum was obtained by O/N broth cultures. The growth was measured by determining OD_{600} after 24 h incubation at 37 °C for bacteria and 48 h at 30 °C for yeast. For the cup assay, the zone of inhibition around the cup (if any) was checked.

The CT-DNA was dissolved in Tris buffer and its purity was checked from the absorbance ratio A260/A280. For all the solutions this ratio was in the range 1.8–1.9. Therefore no further deproteinization of the solutions was performed. The concentration of CT-DNA was determined from the absorption intensity at 260 nm with a known ε value of $6600\ M^{-1}\ cm^{-1}$ [21].

The cleavage of Supercoiled (SC) pUC19 DNA (Bangalore Genie) by **2** was investigated by agarose gel electrophoresis. Briefly, the reaction was carried out by mixing plasmid DNA (0.50 μg) and different concentrations of **1** and **2** (10–30 μM), with and without hydroxyl radical/singlet oxygen scavengers (5.6 μL DMSO, 4 mM NaN_3, respectively), in Tris–HCl (50 mM) buffer containing 18 mM NaCl, (pH 7.2) to yield a final volume of 15 μL. The samples were then incubated for 1 h at 37 °C, followed by the addition of loading buffer containing bromophenol blue (0.25%), xylene cyanole (0.25%) and glycerol (30%). The reaction products were subjected to electrophoresis on 1% agarose gel in 1X TBE buffer (45 mM Tris, 45 mM H_3BO_3, 1 mM EDTA) containing 2 μL/100 ml of ethidium bromide (10 mg/ml) at 80 V for 2 h. The resolved bands were visualized under UV light and photographed. The extent of cleavage of the SC DNA was quantified by measuring the intensities of the bands using the Gel Documentation System (Bio Rad). The intensity of the band relative to the plasmid supercoiled form has been multiplied by 1.43 to take account of its reduced affinity for ethidium bromide [22].

It is worth mentioning here that to ascertain the nuclearity and probable structure of **2** after dissolution in aqueous buffer medium, we performed IR and UV–Vis analysis on the residue obtained after evaporation of the aqueous solution of the same. These spectra matched with that of the solid crystalline product of the complex.

This indicated the retention of structure for **2** after dissolution in water.

2.3. Preparation of the ligand and complexes

2.3.1. Synthesis of ligand HPBH

The pro-ligand was synthesized by condensing benzhydrazide with pyridine-2-carboxaldehyde following a method reported elsewhere [23]. The resulting light yellow solution was used without further purification.

Caution! Perchlorate salts are potentially explosive and should be prepared in small quantity and handled with much care.

2.3.2. Synthesis of [{Cu (PBH)$_2$] (**1**)

To a methanolic solution (20 ml) of copper perchlorate hexahydrate (0.370 g, 1 mmol), a solution of the hydrazone pro-ligand (**HPBH)** (1 mmol) was added and the mixture was stirred at room temperature for 30 min. The final solution was kept in a refrigerator, yielding dark green square crystals suitable for X-ray diffraction after 1 day. The crystals were isolated by filtration and were air-dried. Yield: 67%

Anal. Calc. for $C_{26}H_{20}CuN_6O_2$: C, 60.99; H, 3.94; N, 16.41. Found: C, 60.95; H, 3.91; N, 16.40%.

2.3.3. Synthesis of [{Cu (PBH) ($\mu_{1,1}$-NNN)}$_2$] (**2**)

The isolation of single crystals of **2** afforded a great challenge and so the whole reaction was carried out at −4 °C in a salt-ice mixture. The crystals of **1** (1 mmol) were dissolved in 1:1 methanol–acetonitrile mixture by stirring and to it was added 1 mmol of sodium azide (0.065 g) solution dissolved in minimum quantity of ice cold water. The reaction mixture was not stirred any further after this addition and was refrigerated immediately. Single crystals suitable for X-ray diffraction were isolated after few hours. Yield: 73%.

Anal. Calc. for $C_{26}H_{20}Cu_2N_{12}O_2$: C, 47.34; H, 3.06; N, 25.48. Found: C, 47.31; H, 3.01; N, 25.44%.

2.4. X-ray data collection and structure refinement

Data collection for **1** was made using a Bruker SMART CCD area detector diffractometer equipped with a Mo Kα radiation (λ = 0.71073 Å) source in the φ and ω scan modes at 296 K whereas for **2**, a Rigaku rotating anode single-crystal X-ray diffractometer at the University of St. Andrews was used and data were initially collected at 93 K. Crystallographic data for complexes **1** and **2** are provided in Table 1.

Table 1
Crystallographic and refinement data for complexes **1** and **2**.

Complex	**1**	**2**
Chemical formula	$C_{26}H_{20}CuN_6O_2$	$C_{26}H_{20}Cu_2N_{12}O_2$
Formula weight	512.02	659.62
Crystal system	monoclinic	monoclinic
Space group	*P*21/*n* (No. 14)	*P*21/n (No. 14)
Z	4	4
a (Å)	9.8183(3)	13.926(3)
b (Å)	23.7794(7)	10.6293(17)
c (Å)	10.2419(3)	18.175(3)
α (°)	90	90
β (°)	105.507(3)	100.554(4)
γ (°)	90	90
V (Å^3)	2304.17(12)	2644.8(8)
Temperature (K)	296	93
Density (Mg/m^3)	1.476	1.657
Absorption coefficient (mm^{-1})	0.985	1.659
F(0 0 0)	1052	1336
Crystal size (mm)	0.41 × 0.23 × 0.17	0.20 × 0.20 × 0.20
θ range for data collection (°)	4.64–29.15	2.0–25.3
Reflections collected	17691	16839
Independent reflections (R_{int})	5568 (0.0348)	4797 (0.107)
Goodness-of-fit, F^2	0.919	0.95
R indices (all data)	R_1 = 0.0890, wR_2 = 0.0933	R_1 = 0.0687, wR_2 = 0.1441
Largest difference in peak and hole (e Å^{-3})	0.321 and −0.439	0.64 and −0.73

3. Results and discussion

3.1. Infrared spectra

The IR spectra of the complexes in the region 4000–400 cm^{-1} were analyzed in comparison with that of the free ligand. The data gave evidence for the coordination of the ligand PBH$^-$ to the metal ion via two nitrogen atoms and one oxygen atom. The infrared spectra of both **1** and **2** displayed IR absorption bands at 1610 and 1615 cm^{-1} respectively which could be assigned to the C=N stretching frequencies of the coordinated ligand **PBH**$^-$, whereas for the free ligand the same band was observed at 1663 cm^{-1}. The shifts of this band on complexation towards lower wavenumbers indicated coordination of the azomethine nitrogen to the metal centre [21]. In the spectrum of **2** a strong bifurcated band at 2169 and 2234 cm^{-1} indicated the presence of a bridging azide group [24]. The ligand coordination to the metal centre was substantiated by two bands at 407 cm^{-1} for **1**, and at 426 cm^{-1} for **2** which can be attributable to ν_{Cu-N}.

3.2. Electronic spectra

The electronic spectra of **1** and **2** in acetonitrile solution showed a strong absorption band around 280 nm. This band is clearly charge-transfer in origin. The band around 387 nm for the free pro-ligand was assigned to the n–π^* transition of the azomethine group. In the spectra of the complexes, the bands for the azomethine chromophore giving rise to the n–π^* transition were shifted to lower frequencies, indicating that the imine nitrogen atom was involved in coordination to the metal ion [25]. The visible spectrum of **1** displayed a single broad band at 590 nm. This spectral feature is consistent with the tetragonally distorted six-coordinate geometry of the Cu(II) complexes. As the axial bonds in tetragonally distorted complexes are far longer than the four basal bonds, the t_{2g} to e_g transition splits into two components. The longer axial bonds lead to the stabilization of d_{z2}, d_{xz} and d_{yz} orbitals and as a consequence a series of transitions ($d_{x2-y2} \leftarrow d_{z2}$, $d_{x2-y2} \leftarrow d_{xz}$ and $d_{x2-y2} \leftarrow d_{yz}$) are expected, which in most cases are observed as blue shifted broad bands [26]. The appearance of such a broad band in the blue shifted region indicate a tetragonally distorted geometry around the Cu(II) centre of **1**. The visible band for **2** was observed at 673 nm, which could be attributed to a distorted square pyramidal geometry around Cu(II). In general typical Cu(II) complexes of SP or distorted SP geometries exhibit a band in the range 550–660 nm, whereas the corresponding TBP complexes usually show a maximum at $\lambda > 800$ nm with a higher energy shoulder [27–29]. This indicates that the solution spectra of **2** is adequately explained by a *d*–*d* transition for the Cu(II) ion in a distorted SP geometry where the absorption band observed in the visible region results from a $^2E \rightarrow {}^2B_1$ transition.

3.3. Crystal Structure of [{Cu(PBH)$_2$](**1**)

An ORTEP diagram of **1** is presented in Fig. 1 with its atom numbering scheme, and bond dimensions are listed in Table 2. Complex **1** is a simple Cu(II) hydrazone monomer where two mono-negative hydrazone ligands PBH$^-$ coordinate the central metal ion in a *mer* arrangement, and the coordination sphere is occupied by a N_4O_2 donor set from the two ligand units. A similar structure with Mn(II)

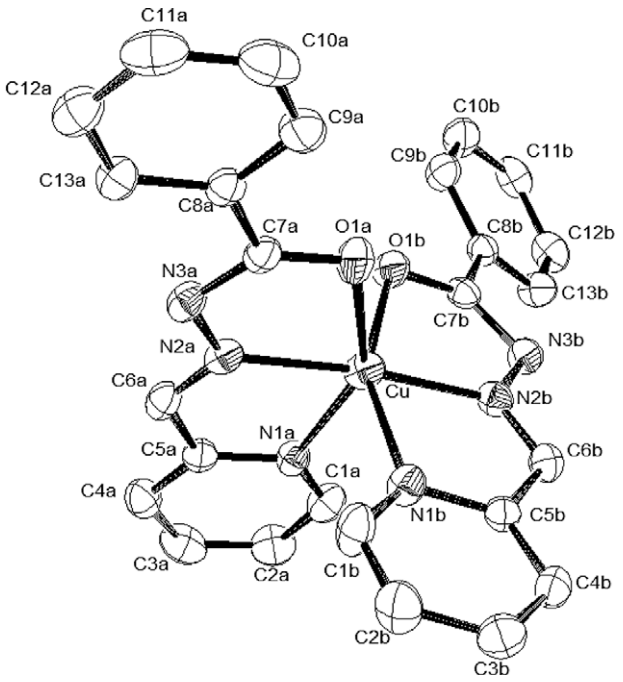


Fig. 1. ORTEP diagram of **1** showing the atom-numbering scheme, ellipsoids are drawn at the 30% probability level. H atoms are not shown for clarity.

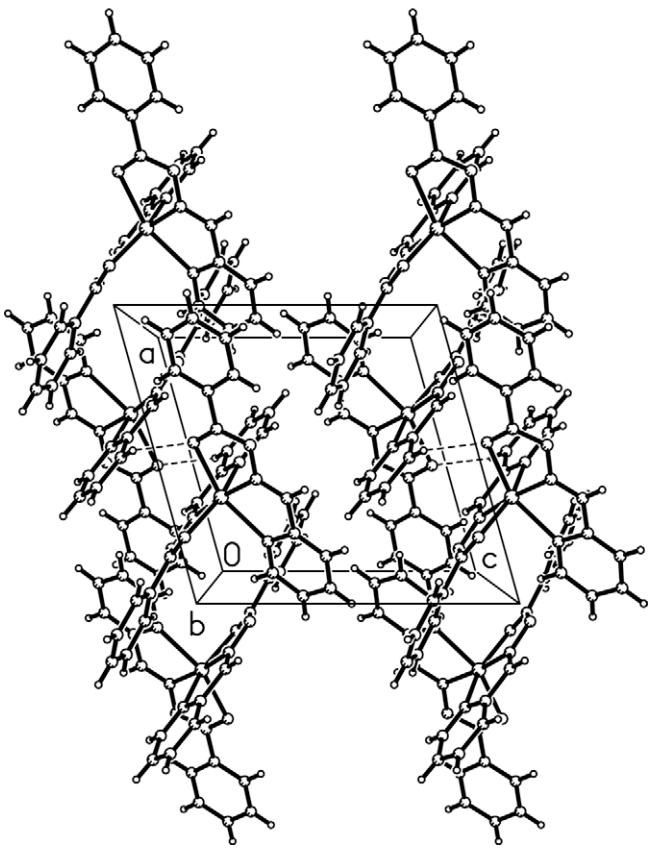


Fig. 2. Packing diagram of **1**.

Table 2
Bond lengths (Å) and bond angels (°) in **1**.

Bond lengths (Å)	
O1b–Cu	2.1055(14)
N1b–Cu	2.1366(17)
N2b–Cu	1.9427(17)
O1a–Cu	2.3024(17)
N1a–Cu	2.2861(18)
N2a–Cu	1.9735(18)
Bond angels (°)	
N1a–Cu–O1a	150.13(6)
N2b–Cu–N2a	172.45(8)
O1b–Cu–O1a	97.21(6)
O1b–Cu–N2b	76.97(6)
O1a–Cu–N2a	73.46(7)

Table 3
Hydrogen bonds for **1** [Å and °].

D–H···A	d(D–H)	d(H···A)	d(D···A)	<(DHA)
C(4b)–H(b)···O(1a)#1	0.93	2.37	3.172(3)	143.8

Symmetry transformations used to generate equivalent atoms: #1 $-x, -y, -z+1$.

with the same ligand has been reported by us previously [7]. The axial positions of the distorted octahedron are occupied by N1a and O1a of one hydrazone ligand unit and these two bonds are, as usual, much longer than the four basal bonds. The axial *trans* base angle [150.13°(6)] shows considerable deviation from its ideal value. One of the basal planes is occupied by the remaining nitrogen atom (N2a) of the ligand which spans the axial position, and the remaining basal positions are occupied by other nitrogen and oxygen donors (N1b, N2b, O1b) from the other hydrazone ligand unit.

The monomeric units form H-bonded dimeric structures (Fig. 2, Table 3) where the H atom residing upon C4b is linked to O1a of a neighboring mononuclear unit.

3.4. Crystal Structure of [{Cu(PBH)($\mu_{1,1}$-NNN)}$_2$] (**2**)

An ORTEP diagram of **2** with the atom numbering scheme is given in Fig. 3. Bond dimensions about the copper atoms are listed in Table 4. The structural study reveals that **2** is a non-centrosymmetric dimer in which the copper centers are five-coordinate, bonded to three coordinating atoms [N_2O] from the PBH^- ligand and the nitrogen atoms from two bridging azide ligands. Recently our group reported a very similar structure where cyanate served as a bridge between the two metal centers, though it was centrosymmetric [8]. The small Cu–Cu separation (3.211 Å) is achieved through the *end-on* bridging mode of the azide ligand. The azide ligands span the axial positions of one Cu(II) center and the basal position of the other, and thus coordinate in a base apical fashion. The average axial Cu–N_{azide} bond length is 2.423 Å where as the average basal Cu–N_{azide} bond length is 1.964 Å which gives Δd = 0.459 Å for the Cu–N_{azide} bonds. The average bridge angle is found to be 93.52°. The geometry of the Cu(II) centres is distorted square pyramidal with τ = 0.262, [$\tau = |\beta - \alpha|/60°$, where β and α are the two largest angles around the central atom; τ = 0 and 1 for the perfect square pyramidal and trigonal bipyramidal geometries, respectively] [30].

3.5. DNA binding study

3.5.1. Electrochemical studies

The electrochemical studies of **1** and **2** alone and CT-DNA added to the solutions of **1** and **2** were performed in Tris buffer medium. For **1** alone, there was an irreversible reduction–oxidation band (Fig. 4a), the reduction band in the Tris buffer medium was

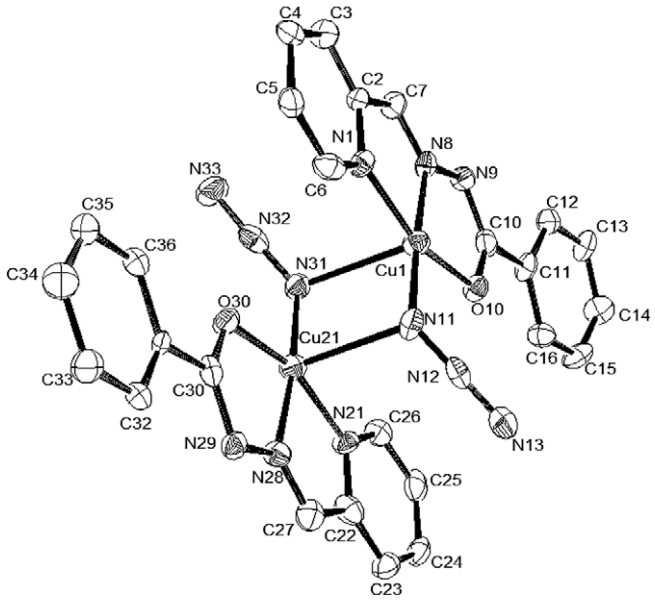


Fig. 3. ORTEP diagram of **2** showing the atom numbering scheme, ellipsoids are drawn at the 30% probability level. H atoms are not shown for clarity.

Table 4
Bond lengths (Å) and bond angels (°) in **2**.

Bond lengths (Å)	
Cu1–O10	1.978(4)
Cu1–N1	2.007(6)
Cu1–N8	1.929(6)
Cu1–N11	1.958(6)
Cu1–N31	2.460(5)
Cu21–O30	1.965(4)
Cu21–N11	2.386(5)
Cu21–N21	2.022(6)
Cu21–N28	1.935(6)
Cu21–N31	1.970(6)
Bond angels (°)	
O10–Cu1–N1	106.2(2)
O10–Cu1–N8	79.8(2)
O10–Cu1–N11	101.0(2)
O10–Cu1–N31	98.93(18)
N1–Cu1–N31	87.6(2)
N8–Cu1–N11	175.9(2)
N8–Cu1–N31	98.3(2)
O30–Cu21–N11	97.64(18)
O30–Cu21–N21	160.1(2)
O30–Cu21–N28	79.3(2)
O30–Cu21–N31	100.0(2)
N11–Cu21–N21	89.5(2)
N21–Cu21–N31	98.9(2)
N28–Cu21–N31	173.5(2)
Cu1–N31–Cu21	92.2(2)

observed at −181.50 mV whereas the oxidation band was observed at 66 mV. Upon addition of DNA solution the reduction band shifted to a more positive value of −122.50 mV, whereas the oxidation band shifted towards a more negative value of 54.25 mV.

For **2** in the same buffer medium, one irreversible reduction band at 134.50 mV was observed (Fig. 4b). The same reduction band was obtained at 118.75 mV by adding CT-DNA to the metal complex solution. The shift of the reduction band to a more negative value upon addition of CT-DNA to **2** implies lower reducibility of the species present in that solution.

The results of the CV clearly indicate that **1** and **2** interact with DNA strands via two different mechanisms.

3.5.2. Electronic absorption titration, CD spectral analyses and ethidium bromide assay

Before adding CT-DNA to **1** and **2**, their behavior in a buffer solution at room temperature was monitored by UV–Vis spectroscopy for 24 h. Liberation of the ligand [PHB^- and N_3^-] was not observed under these conditions. This suggests that the complexes are stable under the conditions studied.

The UV–Vis titrations of **1** and **2** with CT-DNA were done in Tris buffer medium in the wave length range of 800–200 nm. For **1**, a distinct band appeared at 486 nm (Fig. 5a), which was obviously charge transfer in origin. This band upon addition of successive amounts of CT-DNA (0–50 μM) showed significant hypochromism along with a small blue shift of the band to 476 nm. For **2**, in the UV region a band at 358 nm (Fig. 5b) was observed. Upon addition of successive amounts of DNA (0–50 μM) to the solution of **2** this band showed considerable hyperchromism without any significant band shift.

As was reported previously [22], a significant change in band intensity upon addition of DNA to metal complexes imply interaction of the same with the DNA base pairs, so in this case also we can conclude that the complexes interact with the DNA double strands. The apparent binding constants of **1** and **2** with CT-DNA were calculated from the absorption titration data using the following equation [31–35],

$$1/\Delta A = 1/\Delta A_{max} + 1/K_{app}\Delta A_{max} \times 1/(C_D - C_O) \quad (1)$$

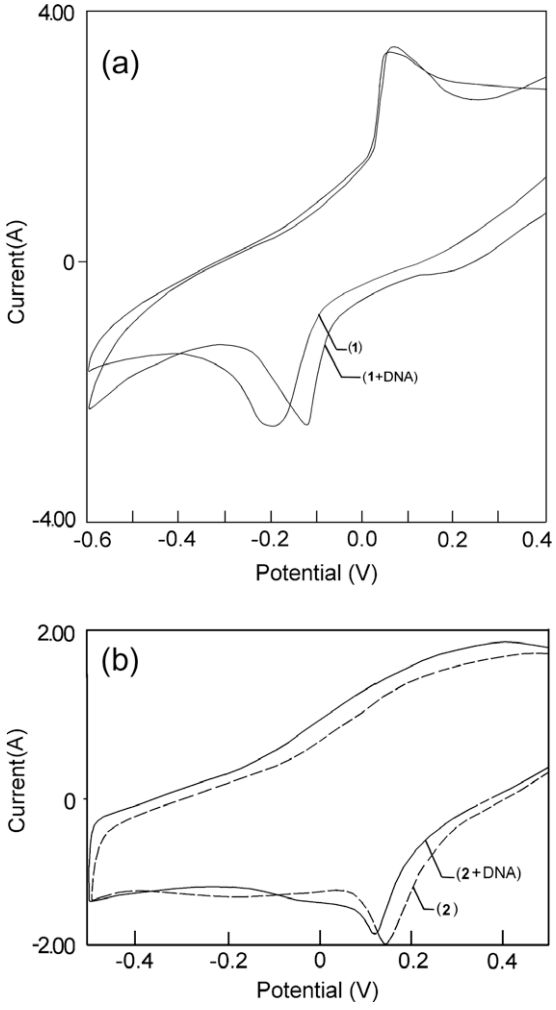


Fig. 4. Cyclic voltammograms showing changes in peak position of (a) **1** and (b) **2** upon addition of CT-DNA.

where C_D and C_O are the concentrations of CT-DNA and the complexes at various stages of the titration, respectively, and ΔA is the change in absorbance upon adding DNA to the complex solution. A plot of $1/\Delta A$ versus $1/(C_D - C_O)$ gave $1/\Delta A_{max}$ from its intercept and $1/K_{app}\ \Delta A_{max}$ from its slope. The K_{app} value obtained for **1** was $2.048 \times 10\ M^{-1}$ (±0.006) and for **2** with CT-DNA $1.644 \times 10^4\ M^{-1}$ (±0.008). The hypochromism and higher binding constant value for **1** with DNA may indicate it has a stronger interaction with DNA [13].

The CD spectral analysis is very useful when it comes to the investigation of morphological changes in DNA double strands due to the interaction with small molecules. The band at 275 nm, due to base stacking, and at 246 nm, due to right handed helicity of the strands, are very sensitive towards the interaction with such small molecules. Any change in the base stacking pattern or the helicity of the strands is manifested by either a change in the band position, the intensity, or both. A simple electrostatic interaction or groove binding has nearly no or a very insignificant effect on the band at 275 nm, whereas the same band undergoes considerable change in intensity due to intercalation by small molecules [36,37]. In this case the CD spectra of CT-DNA in the presence of both **1** and **2** showed a considerable increase in the intensity of the band at 275 nm, whereas the band at 248 nm did not show any significant change (Fig. 6). The intensity increase of the band at 275 nm was less pronounced for **1** than for **2**. This indicates that both **1** and **2** might interact with the DNA double strands by the intercalative mode between the base pairs of DNA strands without any significant change in the right handed helicity of the DNA.

EthBr is a well known DNA intercalator with a very high DNA binding constant [$K_{EthBr} \sim 10^7\ mole^{-1}$] [38]. On its own, it has no emission band at 618 nm when excited at 510 nm, but when it intercalates with DNA a strong fluorescence emission is observed at 618 nm when excited at 510 nm [38]. If the complexes under test could intercalate with the DNA base pairs more strongly than EthBr, then successive addition of **1** and **2** will show a progressive decrease in the intensity of this emission [38]. When solutions of **1** and **2** were added to a solution containing DNA and EthBr in a 50:1 mmolar ratio, even in large excess, there was no change in the fluorescence intensity of the original solution. Even when $[complex]_{Tot.}/[DNA]_{Tot.}$ was 1.5, the intensity of the fluorescence band due to intercalation of EthBr with DNA did not show any reduction. So the probe for the binding mode of the complexes with DNA involving EthBr assay did not yield any specific result.

3.5.3. Viscosity measurement

With the addition of some small molecules (like ethidium bromide), the viscosity of a DNA solution may increase with an increase in the concentration of the former additive. This is because of the fact that the small molecules intercalate between the DNA base pairs and lengthen it, and thus raise the viscosity of the solution containing DNA. On the other hand a molecule which binds to the grooves of DNA does not alter the viscosity of the DNA on addition to the DNA solution [e.g. Hoechst 33258]. Lastly, if the viscosity of DNA solution decreases with the addition of an additive, then it indicates non-classical interactions like the formation of bend or kinks in the double helical structure [39,40]. In the present case, the relative viscosities of the DNA solutions decreased progressively with progressive increase in the concentrations of both **1** and **2**. The initial drop of relative viscosity upon addition of the Cu(II) complexes for **1** was more pronounced than for **2**. For **2** the viscosity of DNA decreased steadily with the rise in concentration of **2**, whereas the same for **1** remained nearly unaltered for quite a large concentration interval after the initial drop, after which the viscosity of DNA solution showed a marked decrease upon addition of further aliquots of **1**. In Fig. 7 η/η_o is plotted against [Complex]/[DNA], where η is the relative viscosity of a solution of DNA solution containing a definite concentration of either **1** or **2** and η_o is the relative viscosity of DNA solution only. This proved that **1** and **2** interact with DNA double strands via a non-classical interaction mode.

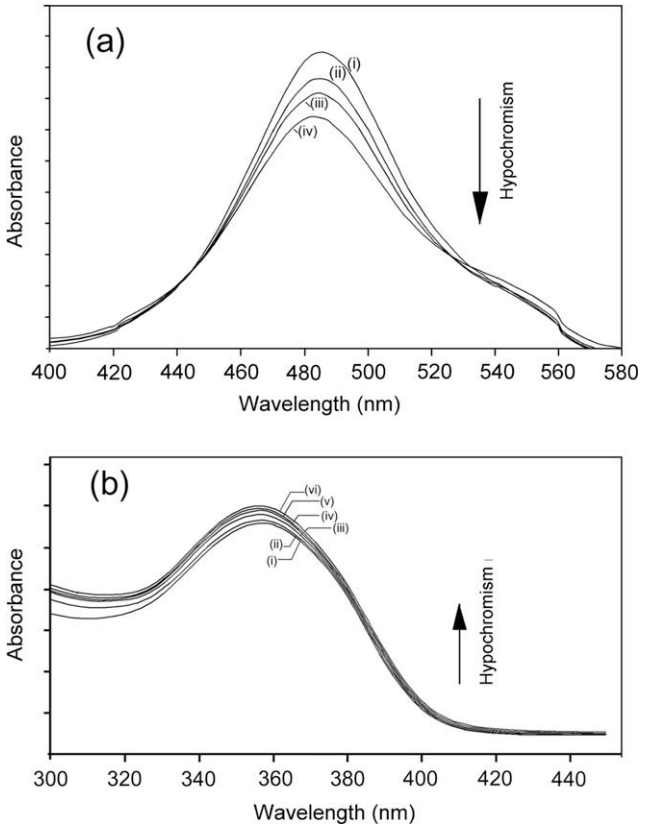


Fig. 5. Changes in the absorption spectra of (a) **1** and (b) **2** on titration with increasing CT-DNA concentration (0–50 μM).

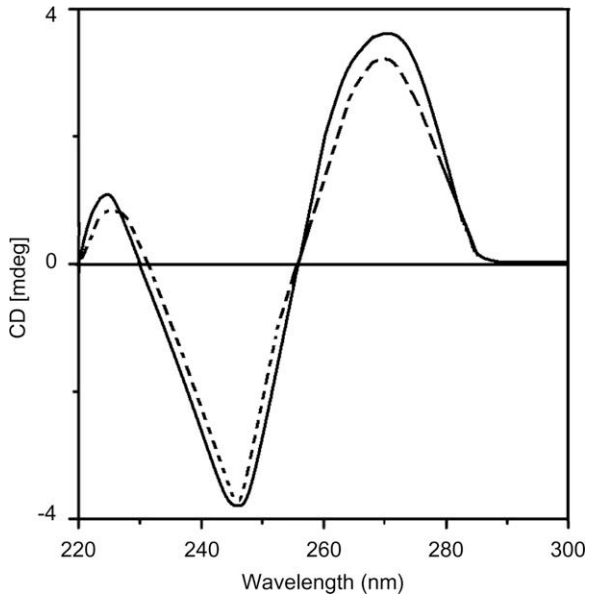


Fig. 6. CD spectra of CT-DNA (dashed line) and CT-DNA + **2** (solid line) in 5 mM Tris–50 mM NaCl buffer (pH ~7.5).

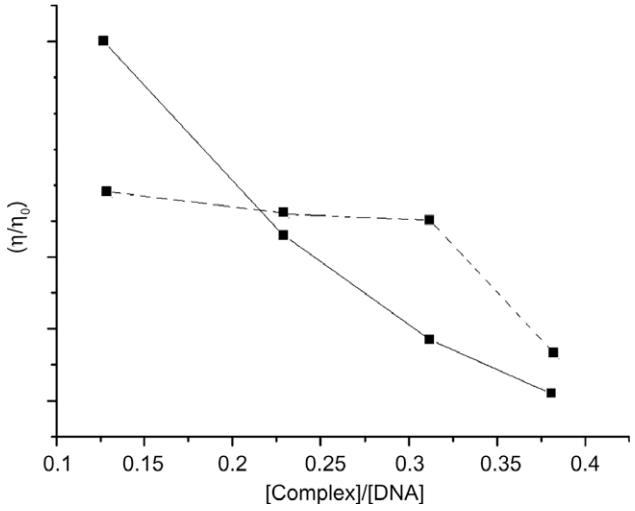


Fig. 7. The plot showing the effect of increasing concentrations of **1** and **2** on the viscosity of DNA. The dotted line shows the variation of viscosity of DNA with increasing concentration of **1** whereas the solid line shows the same effect for **2**.

3.6. DNA cleavage study

The effect of both **1** and **2** on SC plasmid DNA pUC19 in the presence of H_2O_2 and other additives have been investigated by agarose gel electrophoresis. In a typical reaction mixture 0.5 μg of the SC DNA was mixed with different concentrations of the complexes and H_2O_2 in a total volume of 15 μL and these solutions were incubated at 37 °C for 1 h. The electrophoresis was carried out at 100 V for 2 h and the bands were stained with ethidium bromide and visualized under UV light. The different bands were compared with the un-cleaved SC DNA control [the composition of various lanes for both the gels are depicted as footnotes to Figs. 8a and 9a).

For **1** and **2**, in the presence of H_2O_2, with a variation of the concentration from 10 to 30 μM, the cleavage of the super coiled form increased (Figs. 8 and 9, lane 3–7), yielding the nicked circular form for **1** and both the nicked circular form and the linear form for **2** in a regular dose dependent manner. At the highest dose of the complexes [30μM] in the presence of H_2O_2, **2** showed a nearly four times greater ability to cleave pUC19 than **1** (Figs. 8b and 9b, lane 7), and thus is a far better choice as a chemical nuclease. Both were seen to be nearly completely inactive to cleave DNA in the absence of H_2O_2, as is evident from lane 8 of Figs. 8 and 9. The effect of the ligand alone on pUC19 is insignificant in comparison to both the complexes. This proves the cooperative increase of nuclease activity of **1** and **2** after complexation of the ligand with Cu(II).

The hydroxyl radical quencher DMSO and the singlet oxygen quencher sodium azide have different effects towards the cleavage activities by **1** and **2**. For **1**, both of these two quenchers are seen to have an effect reducing the cleavage of the super coiled form of the DNA (Fig. 8a lane 10 and 11). This indicates that the cleavage activity of **1** is produced by the generation of reactive oxygen species (ROS) in solution in the presence of H_2O_2. For **2**, these two quenchers have no effect on the cleavage activity of the plasmid super coiled DNA (Fig. 9a lane 11 and 12), and thus it could be concluded that the oxidative DNA cleavage for **2** takes place via a mechanism which does not involve diffusible hydroxyl radicals or singlet oxygen.

3.7. Antimicrobial study

The antimicrobial activity of **2** against *Staphylococcus aureus* and *Escherichia coli* showed MIC values ranging from 50 to 100 μg/ml. The activity against yeast was not significant (EC_{50} > 400 μg/ml) (Table 5). **1** and the free ligand show no significant activity against the same strains of microbes. The trend in antimicrobial activity can be correlated to the respective compound's DNA cleavage activity. **2** being the most potent chemical nuclease among **1**, **2** and the free ligand LH, showed maximum antibacterial activity.

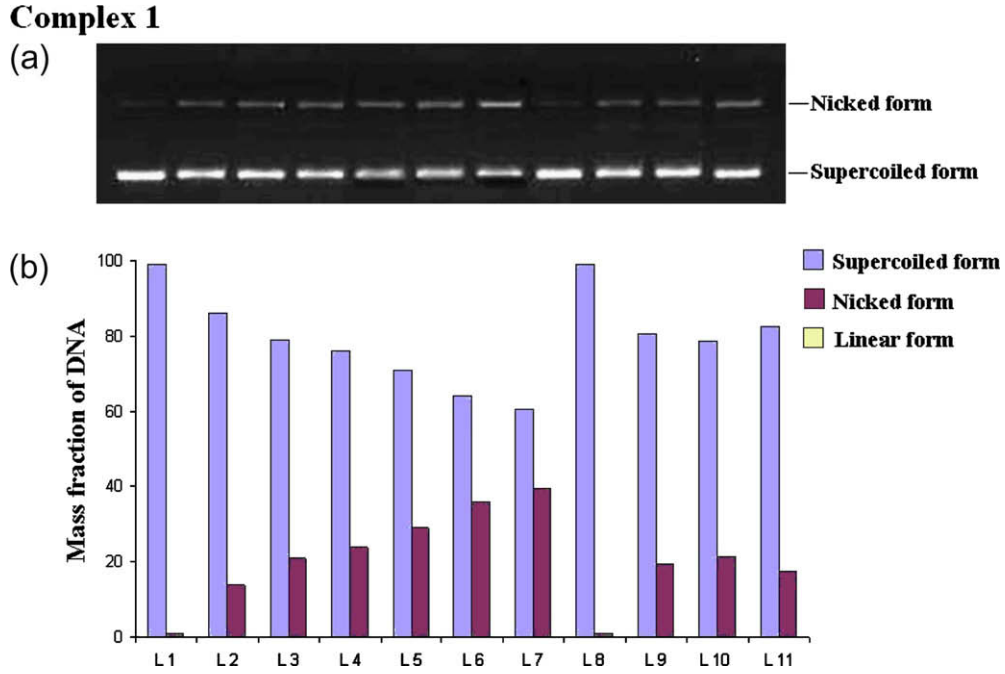


Fig. 8. Agarose gel electrophoresis diagrams and corresponding histograms showing cleavage of SC pUC19 DNA(0.5 μg) by **1** in a dose and time dependent manner in Tris–HCl/NaCl (50 mM, pH 7.2), Lane1: DNA control, 2: DNA + H_2O_2 (60 μM), 3: DNA + H_2O_2 + **1** (10 μM), 4: DNA + H_2O_2 + **1** (15 μM), 5: DNA + H_2O_2 + **1** (20 μM), 6: DNA + H_2O_2 + **1** (25 μM), 7: DNA + H_2O_2 + **1** (30 μM), 8: DNA + **1** (20 μM), 9: DNA + H_2O_2 + LH(20 μM), 10: DNA + H_2O_2 + **1** (20 μM) + DMSO (μL), 11: DNA + H_2O_2 + **1** (20 μM) + NaN_3 (4 mM).

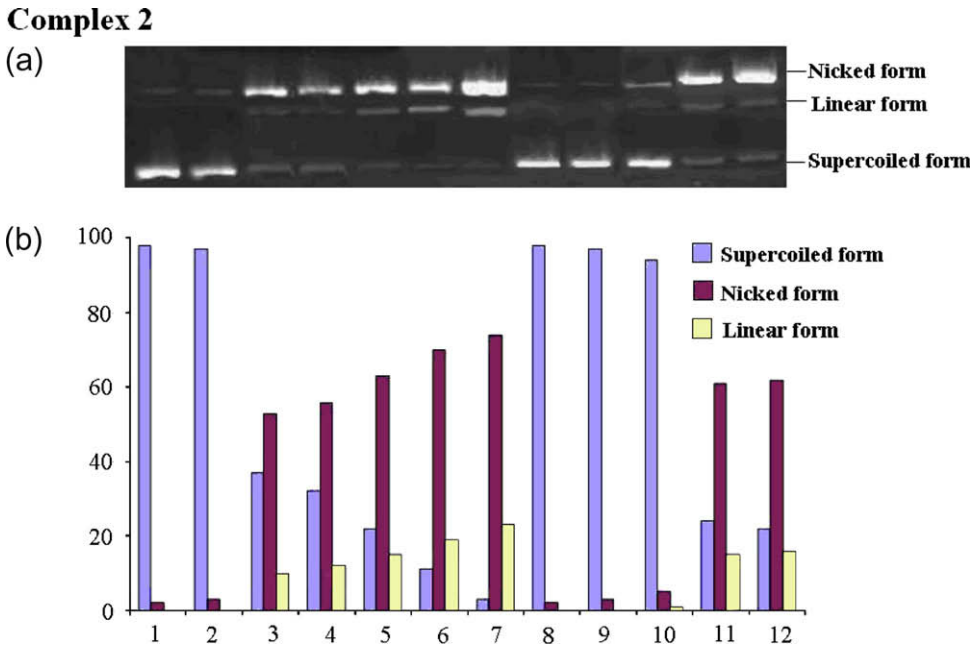


Fig. 9. Agarose gel electrophoresis diagrams and corresponding histograms showing cleavage of SC pUC19 DNA(0.5 μg) by **2** in a dose and time dependent manner in Tris–HCl/NaCl (50 mM, pH 7.2), Lane1: DNA control, 2: DNA + H_2O_2 (60 μM), 3: DNA + H_2O_2 + **2** (10 μM), 4: DNA + H_2O_2 + **2** (15 μM), 5: DNA + H_2O_2 + **2** (20 μM), 6: DNA + H_2O_2 + **2** (25 μM), 7: DNA + H_2O_2 + **2** (30 μM), 8: DNA + **2** (20 μM), 9: DNA + H_2O_2 + Cu(II) (20 μM), 10: DNA + H_2O_2 + LH(20 μM), 11: DNA + H_2O_2 + **2** (20 μM) + DMSO (μL), 12: DNA + H_2O_2 + **2** (20 μM) + NaN_3 (4 mM).

Table 5
MIC values of **2** against different microorganisms.

Microorganisms	MIC (μg/ml)
Escherichia coli MTCC 739	50–100
Staphylococcus aureus MTCC 96	50–100
Saccharomyces cerevisiae MTCC 170	EC_{50} > 400

This fact is again supported by the point that **2** showed more activity against recombination deficient bacterial strain *E. Coli* $DH_{5\alpha}$, indicating that **2** might have DNA damaging activity.

4. Discussion

In the free pro-ligand fragment, HPBH, both the aromatic rings can rotate freely and thus may not favour their interaction with DNA base pairs, whereas for both the complexes at least the pyridyl rings get fixed due to their coordination to the metal centres [Supplementary Fig. S1]. Thus the complexes can now easily interact and even intercalate within the DNA base pairs. This could be one of the reasons why the ligand did not show any binding ability with DNA double strands whereas both the complexes did. The reason why complex **2** showed higher nuclease activity than **1** could be attributed to the presence of coordinatively unsaturated Cu(II) centers in **2** in comparison to **1**. The reason why complex **2** showed higher antimicrobial activity than both **1** and the free ligand HPBH could be attributed to the higher nuclease activity of **2** in comparison to both **1** and the free ligand.

5. Conclusion

By choosing proper experimental conditions, we have been able to synthesize an azido bridged dinuclear hydrazone Cu(II) complex, **2**, from its mononuclear precursor **1**. From the structural description it is clear that the pyridyl N and the enolato O in **2** have shorter bond distances with the Cu(II) ions than in **1**. More over the axial bond in **2** is much longer than all the bond lengths in **1**. Both complexes showed moderate binding ability with CT-DNA, though with respect to their chemical nuclease activity or antimicrobial activity **2** was found to be a far better choice than **1**. This difference in activity in going from the mononuclear to the dinuclear complex could be attributed to the presence of coordinatively unsaturated Cu(II) centers in **2** in comparison to **1**. Antimicrobial studies using **2** against Gram positive, Gram negative bacteria and yeast showed a good degree of inhibition of bacterial growth. Complex **2** has DNA binding and cleavage properties as is mentioned and is more active towards a recombination deficient bacterial strain, indicating the cell inhibitory effect has its origin in it's greater nuclease activity.

Acknowledgements

We acknowledge DRDO New Delhi and AICTE New Delhi, India for funding this research work. We sincerely acknowledge CSIR (Indian Institute of Chemical Biology), Department of Biotechnology, Jadavpur University, India for funding to support the biological work.

Appendix A. Supplementary data

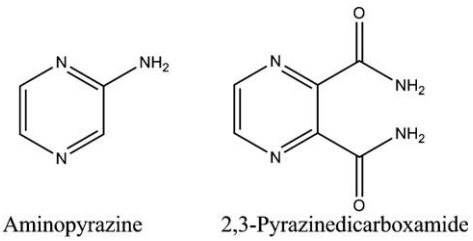
Supplementary data CCDC 659430 and CCDC 671864 contain the supplementary crystallographic data for **1** and **2** respectively. These data can be obtained free of charge via www.ccdc.cam.ac.uk or from the Cambridge Crystallographic Data Center, 12 Union Road, Cambridge CB2 1EZ, UK; fax: (+44) 1223-336-033 or email: deposit@ccdc.cam.ac.uk.

Supplementary data associated with this article can be found, in the online version, at doi:10.1016/j.poly.2009.05.071.

References

[1] S. Pal, J. Pushparaju, N. Rajaiah Sangeetha, S. Pal, Transition Met. Chem. 25 (2000) 529.

[2] S. Naskar, S. Biswas, D. Mishra, B. Adhikary, L.R. Falvello, T. Soler, C.H. Schwalbe, S.K. Chattopadhyay, Inorg. Chim. Acta 357 (2004) 4257.
[3] S. Pal, S. Pal, J. Chem. Soc., Dalton Trans. (2002) 2102.
[4] D.G. Paschalidis, I.A. Tossidis, M. Gdaniec, Polyhedron 19 (2000) 2629.
[5] R. Dinda, P. Sengupta, S. Ghosh, T.C.W. Mak, Inorg. Chem. 41 (2002) 1684.
[6] N.R. Sangeetha, S. Pal, Polyhedron 19 (2000) 1593.
[7] S. Banerjee, A. Ray, S. Sen, S. Mitra, D.L. Hughes, R.J. Butcher, S.R. Batten, D.R. Turner, Inorg. Chim. Acta 361 (2008) 2692.
[8] S. Banerjee, S. Sen, S. Basak, S. Mitra, D.L. Hughes, C. Desplanches, Inorg. Chim. Acta 361 (2008) 2707.
[9] S. Sen, P. Talukder, G. Rosair, S. Mitra, Struct. Chem. 16 (2005) 605.
[10] S. Sen, S. Mitra, D.L. Hughes, G. Rosair, C. Desplanches, Polyhedron 26 (2007) 1740.
[11] S. Banerjee, S. Sen, S. Mitra, C. Rizzoli, G.M. Rosair, Dalton Trans. (2008) 1783.
[12] L. Li, K.D. Karlin, S.E. Rokita, J. Am. Chem. Soc. 127 (2005) 520.
[13] J.-H. Li, J.-T. Wang, P. Hu, L.-Y. Zhang, Z.-N. Chen, Z.-W. Mao, L.-N. Ji, Polyhedron 27 (2008) 1898.
[14] D. Kong, J. Reibenspies, J. Mao, A. Clearfield, A.E. Martell, Inorg. Chim. Acta 342 (2003) 1568.
[15] L.M. Rossi, A. Neves, R. Hörner, H. Terenzi, B. Szpoganicz, J. Sugai, Inorg. Chim. Acta 337 (2002) 366.
[16] K.J. Humphreys, K.D. Karlin, S.E. Rokita, J. Am. Chem. Soc. 124 (2002) 6009.
[17] G.N. De Iuliis, G.A. Lawrance, S. Fieuw-Makaroff, Inorg. Chem. Commun. 3 (2000) 307.
[18] L. Zhu, O. dos Santos, C.W. Koo, M. Rybstein, L. Pape, J.W. Canary, Inorg. Chem. 42 (2003) 7912.
[19] S.-P. Tang, L. Hou, Z.-W. Mao, L.-N. Ji, Polyhedron 28 (2009) 586.
[20] K.J. Humphreys, A.E.J.K.D. Karlin, S.E. Rokita, J. Biol. Inorg. Chem. 7 (2002) 835.
[21] M.E. Reichmann, S.A. Rice, C.A. Thomas, P. Doty, J. Am. Chem. Soc. 76 (1954) 3047.
[22] J. Bermadou, G. Pratviel, F. Bennis, M. Girardet, B. Meunier, Biochemistry 28 (1989) 7268.
[23] T.E. Khalil, L. Labib, M.F. Iskander, L.S. Refaat, Polyhedron 13 (1994) 2569.
[24] R.T. Conley, Infrared Spectroscopy, Allyn & Bacon, Boston, 1966.
[25] K. Nakamoto, Infrared and Raman Spectra of Inorganic and Coordination Compounds, Part: B, fifth ed., Wiley, New York, 1997. pp. 23.
[26] H. Köhler, A. Kolbe, G. Lux, Z. Anorg. Allg. Chem. 428 (1977) 103.
[27] A.B.P. Lever, Inorganic Electronic Spectroscopy, second ed., Elsevier, Amsterdam, 1984.
[28] P. Dapporto, M. Formica, V. Fusi, L. Giothi, M. Micheloni, P. Paoli, R. Pontellini, P. Rossi, Inorg. Chem. 40 (2001) 6186.
[29] T. Gajda, A. Jancsó, S. Mikkola, H. Lönnberg, H. Sirges, J. Chem. Soc., Dalton Trans. (2002) 1757.
[30] A.W. Addison, T.N. Rao, J. Reedijk, J. van Rijn, G.C. Verschoor, J. Chem. Soc., Dalton Trans. (1984) 1349.
[31] V. Rajendiran, R. Karthik, M. Palaniandavar, H. Stoeckli-Evans, V.S. Periasamy, M.A. Akbarsha, B.S. Srinag, H. Krishnamurthy, Inorg. Chem. 46 (2007) 8208.
[32] S. Roy, R. Banerjee, M. Sarkar, J. Inorg. Biochem. 100 (2006) 1320.
[33] J.M. Kelly, M.J. Murphy, D.J. McConnell, C. OhUigin, Nucleic Acids Res. 13 (1985) 67.
[34] V.A. Bloomfield, D.M. Crothers, I. Tinico Jr., In Physical Chemistry of Nucleic Acids, Harper and Row, New York, 1974. pp. 187.
[35] S. Das, D. Dasgupta, J. Inorg. Biochem. 99 (2005) 707.
[36] P.U. Maheswari, M. Palaniandavar, J. Inorg. Biochem. 98 (2004) 219.
[37] N.A. Kasyanenko, A.V. Zanina, O.V. Nazarova, E.F. Panarin, Langmuir 15 (1999) 7912.
[38] X. Sheng, X. Guo, X.-M. Lu, G.-Y. Lu, Y. Shao, Bioconj. Chem. 19 (2008) 490.
[39] S. Satyanarayana, J.C. Darbrowiak, J.B. Chaires, Biochemistry 31 (1992) 9319.
[40] J.M. Veal, R.L. Rill, Biochemistry 30 (1991) 1132.



Scheme 1. Structure of aminopyrazine, (ampyz) and 2,3-pyrazinedicaroxamide, (pyzdic).

2,3-pyrazine dicarboxamide were purchased from Sigma Aldrich Company.

2.2. Synthesis of the complexes

2.2.1. Synthesis of $[Ag_2(amPyz)(NO_3)_2]_n$, **1**

To an aqueous solution (20 cm^3) of $AgNO_3$ (0.34 g, 2.0 mmol), 0.095 g (1 mmol) of aminopyrazine in 15 cm^3 ethanol was added dropwise under continuous stirring. A brown precipitate was formed, filtered off, and the clear filtrate was left undisturbed for a week. Very tiny brown crystals suitable for X-ray measurements were formed, collected by filtration and dried in air with a yield of 80% with respect to the ligand. *Anal.* Calc.: C, 11.05; H, 1.16; N, 16.18; Ag, 49.57. Found: C, 11.12; H, 1.10; N, 16.23; Ag, 49.20%. FT-IR, KBr (cm^{-1}) (v, very; s, strong; m, medium; w, weak; br, broad; sh, shoulder): 3331 s, br, 3153 s, br, 1646 vs, 1585 vs, 1533 s, 1481 sh, 1207 m, 1041 m, 1004 m, 822 s, 607 s, 427 m, 409 m, 388 s, 367 m, 343 m, 294 m, 270 s.

2.2.2. Synthesis of $\{[Ag(2,3\text{-}pyzdica)](NO_3)\}_n$, **2**

To an aqueous solution (20 cm^3) of $AgNO_3$ (0.34 g, 2.0 mmol), 0.34 g (2 mmol) of 2,3-pyrazinedicarboxamide in 15 cm^3 ethanol was added dropwise under continuous stirring. The clear mixture was left undisturbed for a week. Colourless needles suitable for X-ray measurements were formed, collected by filtration and dried in air with a yield of 60% with respect to the ligand. *Anal.* Calc.: C, 21.45; H, 1.80; N, 20.85; Ag, 32.11. Found: C, 22.15; H, 1.20; N, 21.34; Ag, 32.19% (the sample was not so pure). FT-IR, KBr (cm^{-1}) (v, very; s, strong; m, medium; w, weak; br, broad; sh, shoulder): 3430 vs, 3308 vs, 3198 vs, 1695 s, 1672 s, 1611 s, 1560 s, 1533 m, 1381 vs, br, 1191 m, 1102 s, 1060 m, 878 m, 823 m, 739 s, 700 s, 648 s, 343 m, 294 w, 270 s.

2.3. X-ray crystallography

Crystallographic measurements were made on a Siemens Smart CCD diffractometer with graphite monochromated Mo Kα radiation. The structures were solved by direct methods and subsequently refined by full-matrix least-squares, including anisotropic thermal parameters for all non-hydrogen atoms. Hydrogen atoms were refined isotropically with use of geometrical restraints. The calculations were carried out with the SHELXTL program package [20]. The rocking curve width for complex **1** is 1.6° (rocking curve measures how much the molecules are ordered in the crystal structure. A narrow curve around 0.5° is an indication for good crystals).

2.4. Network analysis

The topology of the nets were established by computing the vertex symbol (extended Schläfli or long symbol) [21] with OLEX [22,23] and comparing both the symbol and the experimental net with the ideal net. The cumulative coordination sum up to the 10th sphere was calculated with the nearest neighbour function in CRYSTALMAKER 8.1.5 [24]. Abbreviations for 3D-nets have been taken from O'Keeffe and Yaghi, Reticular Chemistry Structure Resource [25], where crystallographic coordinates and other useful details for 3D-nets can be obtained.

2.5. Corrosion test

2.5.1. Preparation of the metal specimen

Commercial mild steel with chemical composition of: C, 0.37; Si, 0.23; Mn, 1.21; P, 0.021; S, 0.017; Cu, 0.016; Ni, 0.02; Cr, 0.02 and V, 0.003 wt% was employed as working electrodes. Before measurement, the specimens were ground on a series of emery papers down to 1200 grit.

2.5.2. Electrolyte

The solutions were prepared using distilled water and A.R. nitric acid. The complexes were dissolved separately in distilled water by warming and stirring for 5 min. A stock solution of 0.03 M of complex **1** and 0.01 M of complex **2** were prepared from which different concentrations were then prepared. These solutions were tested in the presence of 0.1 M HNO_3 acid at room temperature.

2.5.3. Electrochemical measurements

A three-electrode cell assembly consisting of working electrode (the mild steel to be tested with cross section area is 0.95 cm^2), counter electrode (a platinum mesh of negligible impedance) and reference electrode (saturated calomel electrode) was used for electrochemical measurements. The temperature of the electrolyte was maintained at 27 °C.

Potentiodynamic measurements have been achieved by connecting the electrochemical cell to a Wenking MP87 Potentiostate instrument. Plotting potential versus current the polarization curves (Tafel curves) were obtained. The corresponding anodic and cathodic Tafel slopes (β_a and β_c) were calculated as the slopes of these curves after corrosion potential (E_{corr}) by ±50 mV (since at the beginning of the experiment all the metals show the same corrosion behavior) using a computer least square analysis. The corrosion currents (I_{corr}) were determined as the points at which the extrapolates of both anodic and cathodic slopes cross. The sweep rate used in this study was 30 mV/min. The percentage reduction in the corrosion current (% I_{corr}) was calculated from the following relationship:

$$\%\ I_{corr} = 100 \times \left[1 - \frac{I_{corr}}{(I_{corr})_0}\right]$$

where $(I_{corr})_0$ and I_{corr} are the corrosion current for the mild steel in the absence and the presence of certain concentration of the inhibitors, respectively.

3. Results and discussion

3.1. Synthesis and IR spectral analysis

The newly synthesized complexes for this study were simply obtained through direct reaction between aqueous solutions of the metal salt ($AgNO_3$) and ethanolic solutions of different organic ligands which afforded crystalline complexes suitable for X-ray diffraction measurements. The IR spectrum of **1** shows a number of bands which can be assigned to the functional groups of the ligands as well as the coordination of the ligand to the silver ion. The two strong broad bands at 3331 and 3153 cm^{-1} are assigned to (ν_{as} NH_2) and (ν_s NH_2) vibration frequencies of aminopyrazine, respectively. The nitrate group vibration frequencies appear as a strong band at 1533 cm^{-1} and as a weak shoulder at 1481 cm^{-1} which confirm the bridging coordination of the nitrate group to

the silver (I) ions ($\mu_{O,O'}$-NO_3) [17]. In complex **2** the (ν_{as} NH_2) and (ν_s NH_2) of 2,3-pyrazinedicarboxamide appear as very strong sharp bands at 3430, 3308 and 3198 cm^{-1}. The two very strong bands found at 1695 and 1672 cm^{-1} were assigned to the vibration frequencies of the two amide carbonyl groups, (ν C=O). The nitrate vibration frequencies appear as very strong broad band, (ν_s NO_3) at 1381 and strong sharp band, (ν_{as} NO_3) at 1533 cm^{-1} [26].

3.2. Structure description

Pyrazine and its derivatives have a remarkable ability to form monomeric as well as 1D, 2D and 3D polymeric structures when reacted with silver(I) salts. This structural diversity of silver(I) pyrazino complexes is often dependent on the counter ions and the solvents used [11].

The crystal data and structure refinement for complexes **1** and **2** are found in Table 1, and the atom numbering scheme are shown in Figs. 1 and 4, respectively.

3.2.1. Structure of $[Ag_2(ampyz)(NO_3)_2]_n$, *1*

The molecules in the crystal structure are disordered and the crystals are twinned with a β angle close to 90° simulating an orthorhombic system. The twinning law is described (in SHELXL terminology) by TWIN 1 0 0 0 −1 0 0 0 −1 matrix with 0.991(3)/0.009(3) volume ratio. Silver(I) is coordinated to two NO_3 groups each through one of their O-atoms, and one aminopyrazine ligand *via* one N-atom, in a distorted trigonal planar coordination geometry, the silver(I) ion being 0.162 Å out of the plane defined by O1/N1/O3^i. Both the NH_2 group and the H2 atom connected to atoms C2 have 0.5 occupancy. The Ag–N bond distance (see Table 2) is slightly shorter than those reported for similar tri-coordinated silver(I) pyrazine complexes $[Ag_2(pyz)_3](BF_4)_2$, $[Ag_2(2,3\text{-}Me_2\text{-}pyz)_3](SbF_6)_2$ and $\{[Ag_2(pyrazine)_3](CF_3SO_3)_2{\cdot}2H_2O\}_n$ where Ag–N bond distances ranges from 2.244 to 2.500 Å [11]. Also the Ag–O bond distances are shorter than those found for [Ag(2,5-dimethylpyrazine)$(NO_3)]_n$ and $[Ag_4(3\text{-aminopyridine})_3(NO_3)_4]_n$ ranging from 2.44 to 2.58 Å [27]. The bridging $\mu_{O,O'}$-NO_3 groups connect silver(I) ions forming rather flat helices running along the *b*-axis. The $\mu_{N,N'}$-aminopyrazine ligand as bridging ligand further connects these chains to form a (6,3)-2D sheet structure, with three-connected Ag^+ nodes linked by nitrate ions or pyrazine (see Fig. 2).

Strong intermolecular hydrogen bonds of the type N–H···O and also weaker C–H···O (see Table 3) extend this structure to three-dimensions. The nitrate oxygen not coordinating to silver bind to the pyrazine amine functionality, and the amine protons bind to two different nitrates in adjacent sheets, thus extending the dimensionality in the *c*-direction to give a 3D network structure. In this way also the nitrates become three-connected nodes, linking two silver ions and connected also another nitrate through the NO···H–N–H···ON hydrogen bond link.

The topology of the resulting 3D-net needs to be checked carefully to avoid possible confusion with other networks [28]. It is clear from visual inspection that the net in **1** is part of the (10,3) family (thus the connectivity at each node is three and the shortest circuit between nodes is 10), described by Wells [29] and discussed in detail by others [30–32]. Node assignment and a schematic

Table 1
Crystal data and structure refinement for complexes **1** and **2**.

	1	**2**
Empirical formula	$C_4H_5Ag_2N_5O_6$	$C_6H_6AgN_5O_5$
Formula weight	434.86	336.03
T (K)	173(2)	173(2)
Wavelength (Å)	0.71073	0.71073
Crystal system	monoclinic	monoclinic
Space group	$P2_1/c$	$P2_1/c$
Unit cell dimensions		
a (Å)	3.4018(4)	7.3142(7)
b (Å)	8.5614(10)	18.7038(19)
c (Å)	16.6870(19)	7.6787(8)
α (°)	90	90
β (°)	90.169(2)	115.918(2)
γ (°)	90	90
Volume (Å^3)	485.99(10)	944.82(16)
Z	2	4
Colour	colourless opaque	colourless
Habit	curved conical needle	needle
Size of crystal (mm)	0.30 × 0.06 × 0.06	0.78 × 0.21 × 0.16
Density (calculated) (Mg m^3)	2.972	2.362
Absorption coefficient (mm^{-1})	4.059	2.156
Reflections collected	5188	14 526
Independent reflections	846 [R_{int} = 0.0386]	2752 [R_{int} = 0.0458]
Observed reflections [$I > 2\theta(I)$]	682	2297
θ Range for data collection (°)	1.22–25.06	2.18–30.00
Absorption correction	multiscan	multiscan
Refinement method	full-matrix least-squares on F^2	full-matrix least-squares on F^2
Data/restraints/parameters	846/0/83	2752/0/154
Goodness-of-fit (GOF) on F^2	0.974	1.001
Final *R* indices [$I > 2\theta(I)$]	R_1 = 0.0298, wR_2 = 0.0790	R_1 = 0.0467, wR_2 = 0.1202
R indices (all data)	R_1 = 0.0454, wR_2 = 0.0875	R_1 = 0.0578, wR_2 = 0.1273

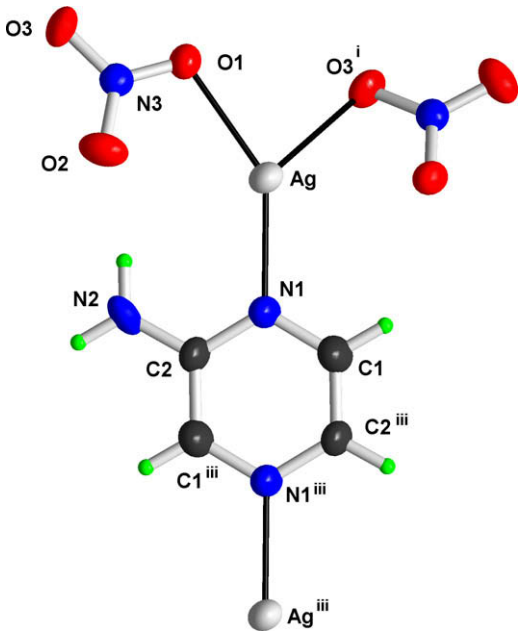


Fig. 1. Numbering scheme with atomic displacement ellipsoids drawn at 50% probability level for $[Ag_2(ampyz)(NO_3)_2]_n$, **1**.

Table 2
Bond lengths [Å] and angles [°] for $[Ag_2(ampyz)(NO_3)_2]_n$, **1**.

Ag–N1	2.207(5)
Ag–O1	2.328(4)
Ag–O3^i	2.499(5)
N1–Ag–O1	143.69(18)
N1–Ag–O3^i	127.98(18)
O1–Ag–O3^i	86.61(16)

Symmetry transformations used to generate equivalent atoms: (i): $-x,y-1/2,-z+½$.

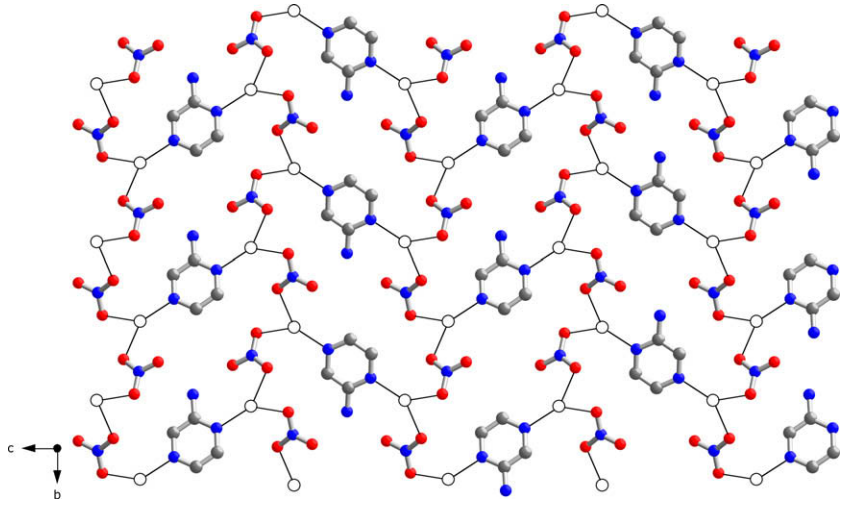


Fig. 2. A perspective view of $[Ag_2(ampyz)(NO_3)_2]_n$, **1** on the *b*,*c*-plane showing the (6,3)-2D network structure, Ag(I) atoms are drawn as hollow circles and H atoms are omitted for clarity.

Table 3
Hydrogen bonds for $[Ag_2(ampyz)(NO_3)_2]_n$, **1** [Å and °]. Note the half occupancy for atoms in the NH_2 group.

D–H···A	*d*(D–H)	*d*(H···A)	*d*(D···A)	∠(DHA)
N2–H2A···O2^{iv}	0.88	2.07	2.860(13)	149.6
N2–H2B···O2	0.88	2.08	2.871(14)	148.7
C1–H1···O3^{v}	0.95	2.55	3.403(9)	149.3
C1–H1···O1^{i}	0.95	2.53	3.286(9)	136.1

Symmetry transformations used to generate equivalent atoms: (i): $-x,y-1/2,-z+1/2$ (iv): $-x+1,-y+1,-z+1$ (v): $x-1,y-1,z$.

drawing of one of the 10-gons are depicted in Fig. 3a. As can be seen in Fig. 3b the net contains helices with alternating chirality in the rows defined by the projection on the *a*,*c*-plane. This is characteristic of the (10,3)-d or 10^3-**utp** net whose most symmetric form is shown in Fig. 3c for comparison. To further support this assignment the vertex symbol was calculated, and found to be $10_2{\cdot}10_4{\cdot}10_4$, in agreement with a **utp**-net. However, vertex symbols are sometimes not unique, and it so happens that another, more common, (10,3)-net has the same symbol, namely the **ths**-net, also known as the (10,3)-b net. In such cases the coordination sequence needs to be calculated, that is we sum all neighbours starting from a central node and usually going up to the 10th coordination sphere. This cumulated value, often referred to as the C10 or TD10 value [25], was calculated to 622 for structure **1** in agreement with the **utp** assignment and clearly different from the C10 value of 608 for the **ths**-net.

However, the network structure of **1** is complicated by the 50% disorder of the amine group, which means that this link will be absent in 25% of the network. In theory one could therefore construct a much more complicated network where some 10-gons have been replaced by 16-gons. However, the network analysis should be a tool in understanding the chemistry and such a complicated exercise would add nothing to our overall perception of the structure. In fact, one could argue that in the absence of the amine, there will be a very weak C–H···O hydrogen bond interaction. Moreover, considering the entire network with three different links from each of the two nodes, the overall effect will be that only 5% of the links in the net are missing, thus the **utp** description is nevertheless adequate. In Fig. 3d, a projection in the *b*,*c*-plane is shown of both the network and all atoms in the structure. In this plot the 50% disorder has been dealt with by removing every second amine group in a regular fashion.

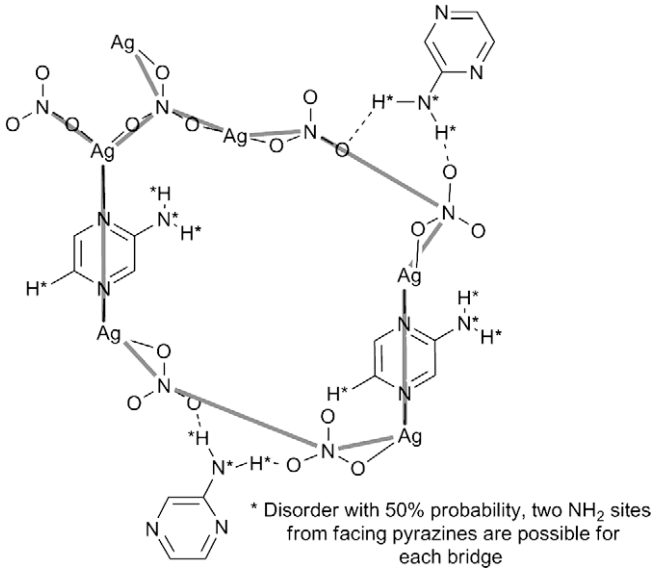


Fig. 3a. Schematic drawing of $[Ag_2(ampyz)(NO_3)_2]_n$, **1** showing one of the (10,3) rings (the nitrates and the silver ions are three-connected nodes).

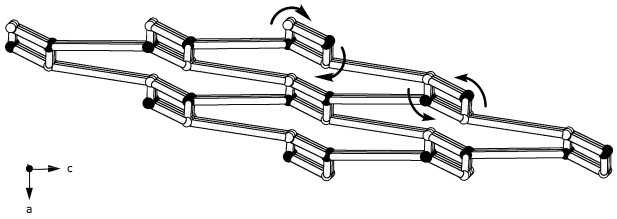


Fig. 3b. A perspective view of $[Ag_2(ampyz)(NO_3)_2]_n$, **1** on the *a*,*c*-plane showing helices superimposed on the entire structure.

3.2.2. Structure of {[Ag(2,3-pyzdic)](NO$_3$)}$_n$, ***2***

The silver(I) ion is linearly coordinated to two 2,3-pyrazinedicarboxamide each *via* the bridging $\mu_{N,N'}$-pyrazine ring thus forming 1D chains, Fig. 5a. The Ag–N bond distances (Table 4) are longer than the normal range reported for similar linear silver(I) pyrazine complexes; $[Ag(pyz)](BF_4)$ and $[Ag_2(C_{20}H_{28}N_2)_2(NO_3)_2{\cdot}1.5MeOH{\cdot}H_2O]_n$ (2.187(3)–2.260(5) Å) and the bond angles are also smaller than

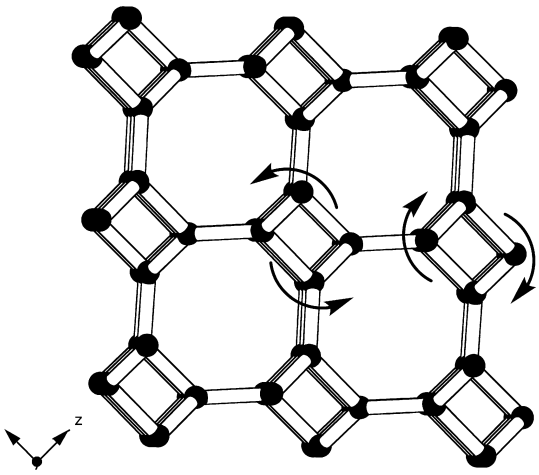


Fig. 3c. Ideal 10^3-**utp** net.

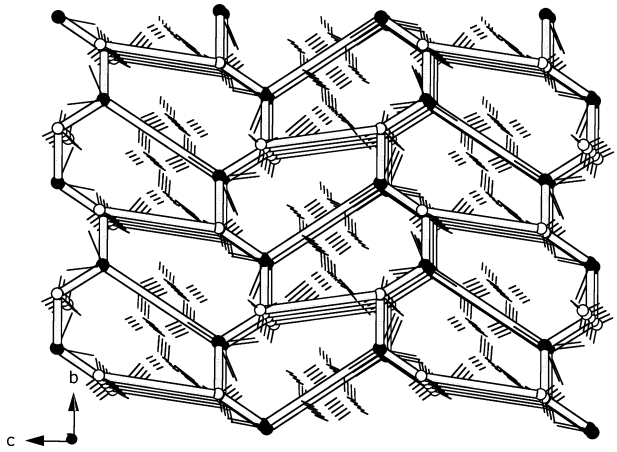


Fig. 3d. A perspective view of $[Ag_2(ampyz)(NO_3)_2]_n$, **1** on the *b*,*c*-plane showing all atoms and network in the structure.

reported for these compounds (173.6(2) and 173.80(14)°) [11]. These longer bond distances and smaller angle are attributed to strong interamolecular hydrogen bonding, N8–H8B···O7^{iv} between the two carboxamido groups of each two adjacent ligand moieties. Strong interactions are also found between the silver(I) ion and both the nitrate oxygen atom and the carboxamido group oxygen atom of the above chain ligand. These interactions in addition to strong intermolecular N–H···O hydrogen bonding (Table 5) are responsible for the extension of the structure to form a 3D network, Fig. 5b. In contrary with complex **1**, however, this network does not reveal any easily recognizable 3D-net. While a network analysis is, in principle, always possible, this structure needs to be described by at least three different nodes, and in addition the possibility of Ag–O bonds complicates the matter further. We thus conclude that such an analysis will not lead to a better understanding of the structure and refrain from pursuing this point further.

3.3. Corrosion test

The potentiodynamic polarization curves (Tafel curves) for mild steel in 0.1 M nitric acid, using different concentrations of $[Ag_2(ampyz)(NO_3)_2]_n$, **1** and $\{[Ag(pyzdic)](NO_3)\}_n$, **2**, at room temperature are presented in Fig. 6a and b, respectively. Corrosion currents were determined by the intersection of the cathodic and anodic Tafel lines and open-circuit potential. The electrochemical parameters for the used inhibitors obtained from their polarization curves are summarized in Table 6. Fig. 7 shows the corrosion inhibition efficiencies (represented as the surface coverage θ) as a function of inhibitor concentrations. An increase in the surface coverage and corrosion inhibitory effect is observed with increasing concentration.

3.3.1. Corrosion inhibition

Tafel lines of approximately equal slopes [16] indicate that both complexes have both cathodic and anodic inhibitory effects in 0.1 M HNO_3 media [33]. E_{corr} are shifted to more anodic values as the concentrations of both inhibitors were increased. This means that the inhibitor molecules were adsorbed on the metal surface and behaved as mixed type inhibitors with dominant anodic inhibitory action [34,35]. Corrosion current, I_{corr} decreases with increasing inhibitors concentrations [36,37]. A concentration of 10^{-4} M of complex **1**, $[Ag_2(ampyz)(NO_3)_2]_n$, gives 37% inhibition efficiency, while the same concentration, 10^{-4} M of complex **2**, $\{[Ag(pyzdic)](NO_3)\}_n$, gives only 10% inhibition efficiency. This increased activity of complex **1** at low concentrations can be explained on the basis of structure activity relationship. The *O*,*O*′-bridging nitrates present in the

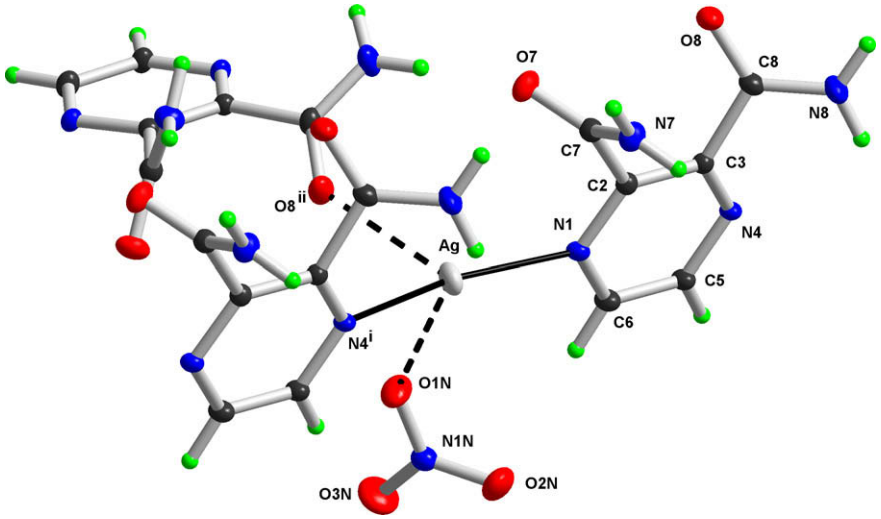


Fig. 4. Numbering scheme with atomic displacement ellipsoids drawn at 50% probability level for $\{[Ag(2,3\text{-pyzdic})](NO_3)\}_n$, **2**. The close Ag–O contacts are shown as broken lines. For symmetry codes see Table 4.

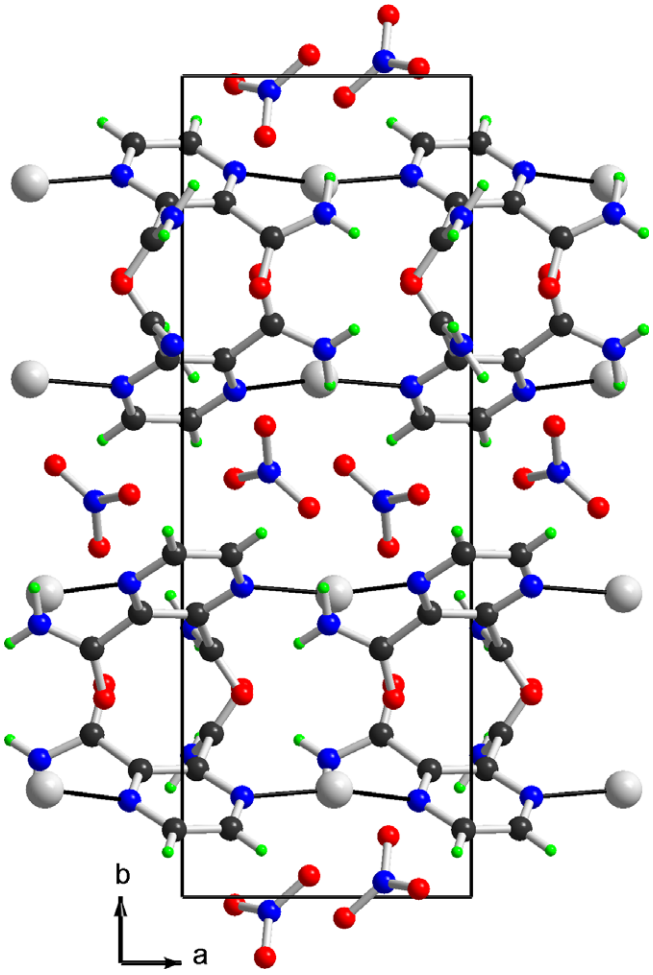


Fig. 5a. Projection of the content of the unit cell along the *c*-axis of {[Ag(2,3-pyzdic)](NO$_3$)}$_n$, **2**. 1D chains are built up in the *a*-direction.

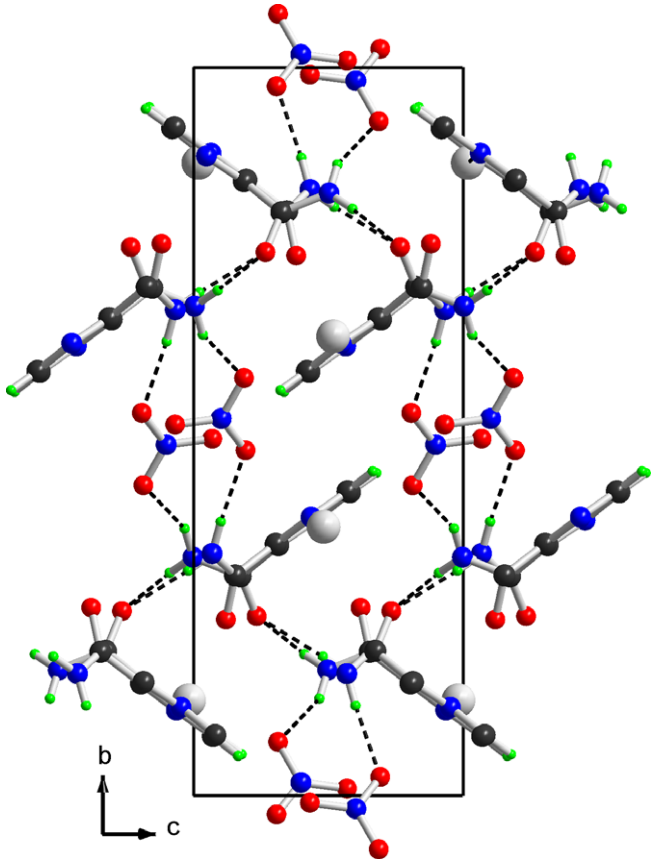


Fig. 5b. Projection of the content of the unit cell along the *a*-axis of {[Ag(2,3-pyzdic)](NO$_3$)}$_n$, **2**. An extensive hydrogen bonding pattern is built up in the *b*,*c*-plane, thus supporting the 3D crystal structure.

structure of complex **1** are oxidizing passivating inhibitors which cause a large anodic shift of the corrosion potential due to the formation of different oxides [38]. The nonporous chromium oxide then protects the mild steel surface from further corrosion at higher inhibitor concentrations (see Fig. 6a), and a cathodic shift of the corrosion current is recognized. Complex **2** has non-coordinated nitrate groups, which can be solvated easily, so their effects are minimized in low concentrations. Also the presence of lone pairs of electrons on both pyrazine nitrogen atoms and on the amino group nitrogen atom enhances the adsorption of both inhibitors to the mild steel surface. Maximum corrosion inhibition efficiencies are 68% for 2×10^{-3} M of complex **1** and 50% for 10^{-3} M of complex **2**. These results are comparable to those reported for 4-aminopiperidine and piperazine free ligands in perchloric acid medium, which were 63.54% and 62.03%, respectively [39].

3.3.2. Adsorption isotherms

Different equations have been developed to model surface adsorption, and in this present investigation two of these were used.

The Langmuir adsorption isotherm is described by

$$\left[\frac{\theta}{(1-\theta)}\right] = KC \qquad (1)$$

in which K is the equilibrium constant of the adsorption reaction, C is the inhibitor concentration in bulk of the solution and θ can be obtained from Eq. (2) as:

Table 4
Bond lengths [Å] and angles [°] for {[Ag(2,3-pyzdic)](NO$_3$)}$_n$, **2**.

Ag–N1	2.242(4)
Ag–N4^{i}	2.330(4)
Ag–O8^{ii}	2.506(3)
Ag–O1N	2.535(4)
O8–Ag^{iv}	2.506(3)
N1–Ag–N4^{i}	162.99(13)
N1–Ag–O8^{ii}	120.78(12)
N4^{i}–Ag–O8^{ii}	74.49(12)
N1–Ag–O1N	98.77(13)
N4^{i}–Ag–O1N	88.65(13)
O8^{ii}–Ag–O1N	88.05(12)

Symmetry transformations used to generate equivalent atoms: (i): $x-1,y,z$ (ii): $x-1,-y+3/2,z-1/2$ (iv): $x+1,-y+3/2,z+1/2$.

Table 5
Hydrogen bonds for {[Ag(2,3-pyzdic)](NO$_3$)}$_n$, **2** [Å and °].

D–H···A	*d*(D–H)	*d*(H···A)	*d*(D···A)	∠(DHA)
N(7)–H(7A)···O(7)^{v}	0.88	2.28	3.142(5)	167.7
N(7)–H(7B)···O(1N)^{vi}	0.88	2.01	2.831(5)	155.6
N(8)–H(8A)···O(7)^{iv}	0.88	2.08	2.944(5)	166.3
N(8)–H(8B)···O(2N)^{vii}	0.88	2.06	2.935(6)	175.2
C(5)–H(5)···O(1N)^{iii}	0.95	2.49	3.190(6)	130.9
C(5)–H(5)···O(3N)^{viii}	0.95	2.34	3.034(6)	129.6
C(6)–H(6)···O(2N)	0.95	2.44	3.329(6)	155.9

Symmetry transformations used to generate equivalent atoms: (iii): $x+1,y,z$ (iv): $x+1,-y+3/2,z+1/2$ (v): $x,-y+3/2,z+1/2$ (vi): $x+1,y,z+1$ (vii): $-x+2,-y+1,-z+1$ (viii): $-x+1,-y+1,-z$.

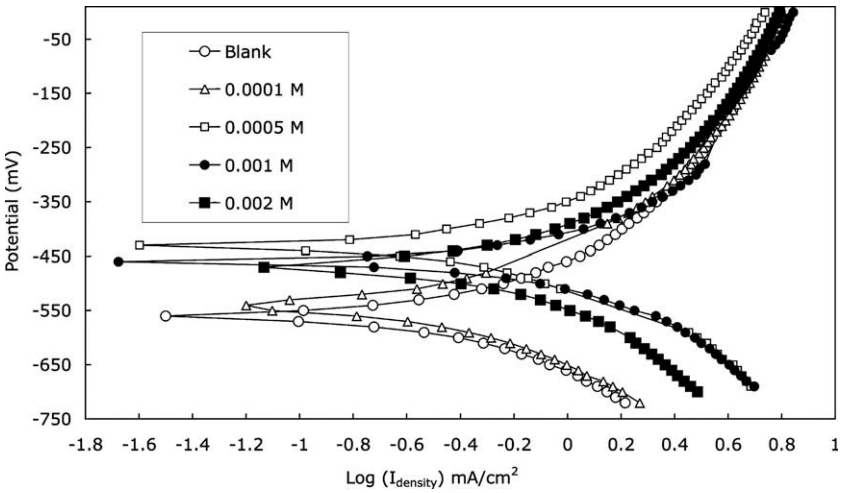


Fig. 6a. Potentiodynamic polarization curves for mild steel in 0.1 M HNO_3 in the presence of different concentrations of $[Ag_2(ampyz)(NO_3)_2]_n$, complex **1**.

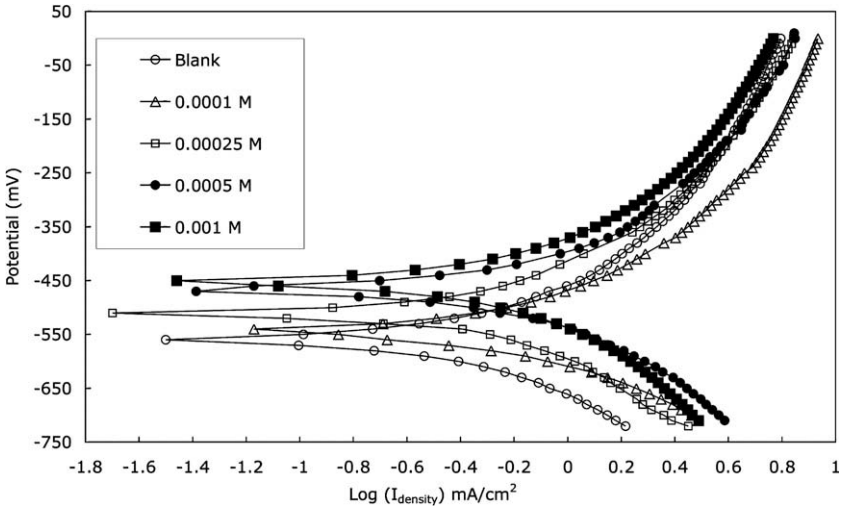


Fig. 6b. Potentiodynamic polarization curves for mild steel in 0.1 M HNO_3 in the presence of different concentrations of $\{[Ag(pyzdic)](NO_3)\}_n$, complex **2**.

Table 6
Electrochemical parameters obtained from potentiodynamic polarization curves for mild steel in 0.1 M HNO_3 in the presence of different concentrations of $[Ag_2(ampyz)(NO_3)_2]_n$, inhibitor **1** and $\{[Ag(pyzdic)](NO_3)\}_n$, inhibitor **2**.

Inhibitor	Concentration (M)	E_{corr} (mV)	I_{corr} (mA/cm^2)	B_a (mV/decade)	$-B_c$ (mV/decade)	% IE
Complex **1**	Blank	−550	0.70	78	78	
	1×10^{-4} M	−540	0.44	53	49	37
	5 × 10−4 M	−430	0.30	27	27	57
	1×10^{-3} M	−460	0.25	17	14	64
	2×10^{-3} M	−470	0.22	17	17	68
Complex **2**	Blank	−560	0.70	78	78	
	1×10^{-4} M	−540	0.63	51	42	10
	2.5×10^{-4} M	−510	0.47	49	47	32
	5×10^{-4} M	−460	0.44	34	34	37
	1×10^{-3} M	−450	0.35	32	32	50

$$\theta = \frac{1 - R_{inh}}{R_0} \quad (2)$$

In this expression (R_{inh}) and (R_0) are the corrosion rates in the presence and absence of the inhibitor, respectively. Only complex **2** (Fig. 8a) fits to the Langmuir equation with equilibrium constant of adsorption, $K = 898$.

The kinetic-thermodynamic model is somewhat more elaborate, as can be seen in the below equation:

$$\log\left[\frac{\theta}{(1-\theta)}\right] = \log K' + y \log C \quad (3)$$

Here, K' is a constant related to the binding constant K, by the following relationship, in Eq. (4), where y is the number of inhibitor molecules occupying one active site and $1/y$ represents the number of active sites of the surface occupied by one molecule of the inhibitor.

$$K = K'^{1/y} \quad (4)$$

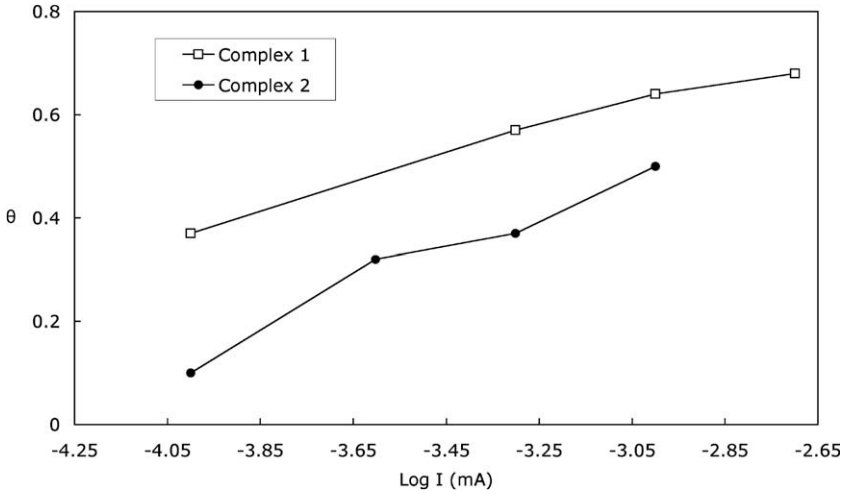


Fig. 7. Plot of inhibition efficiency against inhibitor concentrations.

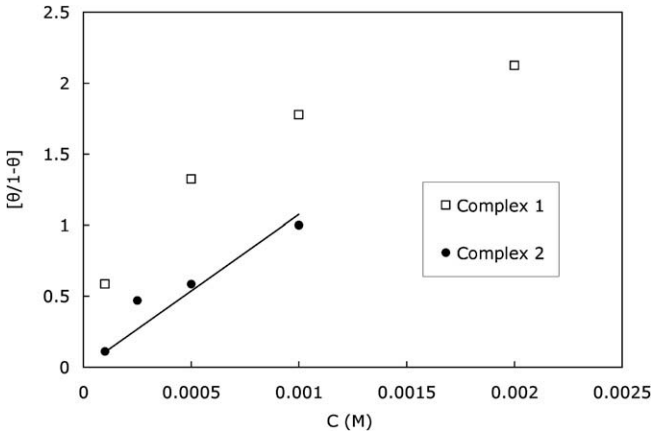


Fig. 8a. Langmuir adsorption isotherms, where only complex **2** fits to Langmuir equation with equilibrium constant of adsorption, $K = 898$.

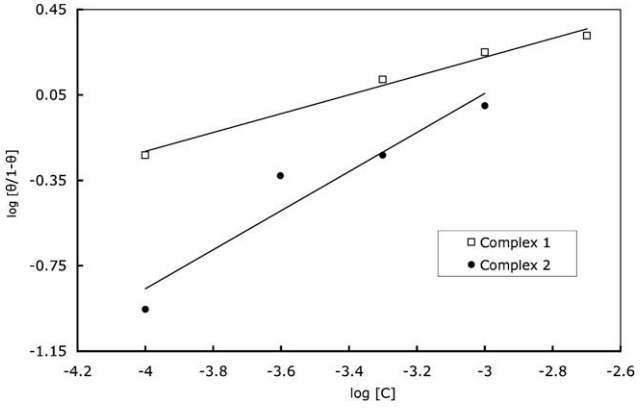


Fig. 8b. Both complexes **1** and **2** fit the kinetic-thermodynamic model, with binding constants $K = 3263$ and 1147, respectively.

Both complexes **1** and **2** (Fig. 8b) fit to the kinetic-thermodynamic model. For complex **1**: $y = 0.44$ and $1/y = 2.27$. This means that more than one layer of the inhibitor are adsorbed on the surface of the steel. The binding constant, $K = 3263$ indicates a strong interaction between the inhibitor molecules and the surface. In case of complex **2**, $y = 0.92$, $1/y = 1.09$ and the binding constant $K = 1147$, which indicates that multilayer inhibitor molecules are also formed on the surface of the mild steel, but with weaker binding interaction than complex **1**. This value of binding constant for inhibitor **2** agrees with the value of equilibrium constant of adsorption for the same inhibitor calculated from Langmuir adsorption isotherm. The high negative values of Gibb's free energies for complexes **1** and **2** are $-20\,009$ and $-17\,402$ kJ K^{-1} mol^{-1}, respectively; indicate that both complexes are chemically adsorbed on the surface of the mild steel used.

4. Conclusion

The results obtained in the present study allow us to draw the following conclusions: (i) The inhibition efficiency measured through electrochemical tests can reach about 68% for inhibitor **1** at concentration of 2×10^{-3} M at 27 °C and about 50% for inhibitor **2** at concentration of 1×10^{-3} M. (ii) The electrochemical results obtained from potentiodynamic polarization indicate that the inhibitor molecules were adsorbed on the metal surface and behaved as mixed type corrosion inhibitors with dominant anodic inhibitory action for mild steel in nitric acid medium. (iii) The free energy changes indicate chemisorption mechanisms for both complexes on the surface of the mild steel used.

5. Supplementary data

CCDC 712117 and 712118 contain the supplementary crystallographic data for compounds **1** and **2**, respectively. These data can be obtained free of charge via http://www.ccdc.cam.ac.uk/conts/retrieving.html, or from the Cambridge Crystallographic Data Centre, 12 Union Road, Cambridge CB2 1EZ, UK; fax: (+44) 1223-336-033; or e-mail: deposit@ccdc.cam.ac.uk.

Acknowledgments

This work was supported by the Swedish Research Council and the Swedish International Development Agency through the SIDA-Swedish Research Links program (348-2004-5473).

References

[1] G.H. Koch, M.P.H. Brongers, N.G. Thompson, Y.P. Virmani, J.H. Payer, Corrosion Costs and Preventive Strategies in the United States, Publication No. FHWA-RD-01-156, US Federal Highway Administration, 2002.
[2] S. Rangelov, V. Mircheva, Corros. Sci. 38 (1996) 301.
[3] B.I. Ita, O.E. Offiong, Mater. Chem. Phys. 48 (1997) 164.
[4] S.A. Al-thabaiti, F.M. Al-Nowaiser, Pigm. Resin Technol. 33 (2004) 15.

[5] K.F. Khaled, K. Babic-Samardzija, N. Hackerman, Corros. Sci. 48 (2006) 3014.
[6] H. Ashassi-Sorkhabi, T.A. Aliyev, S. Nasiri, R. Zareipoor, Electrochim. Acta 52 (2007) 5238.
[7] Sha Cheng, Sh. Chen, T. Liu, X. Chang, Y. Yin, Electrochim. Acta 52 (2007) 5932.
[8] P. Narmada, M.V. Rao, G. Venkatachari, B.V. Appa Rao, Anti-Corros. Methods Mater. 53 (2006) 310.
[9] K.D. Demadis, E. Mavredaki, A. Stathoulopoulou, E. Neofotistou, C. Mantzaridis, Desalination 213 (2007) 38.
[10] H. Amar, J. Benzakour, A. Derja, D. Villemin, B. Moreau, T. Braisaz, A. Tounsi, Corros. Sci. 50 (2008) 124.
[11] P.J. Steel, C.M. Fitchett, Coord. Chem. Rev. 252 (2008) 990.
[12] S.I. Mostafa, S.A. Abd El-Maksoud, Monatsh. Chem. 129 (1998) 455.
[13] M.S. Morad, A.M. Kamal El-Dean, Corros. Sci. 48 (2006) 3398.
[14] H. Ashassi-Sorkhabi, B. Shaabani, D. Seifzadeh, Electrochim. Acta 50 (2005) 3446.
[15] M. Abdallah, E.A. Helal, A.S. Fouda, Corros. Sci. 48 (2006) 1639.
[16] F. Bensajjay, S. Alehyen, M. El Achori, S. Kertit, Anti-Corros. Methods Mater. 50 (2003) 402.
[17] M.A.M. Abu-Youssef, R. Dey, Y. Gohar, A.A. Massoud, L. Öhrström, V. Langer, Inorg. Chem. 46 (2007) 5893.
[18] M.A.S. Goher, F.A. Mautner, M.A.M. Abu-Youssef, A.K. Hafez, A.M.A. Badr, J. Chem. Soc., Dalton Trans. (2002) 3309.
[19] M.A.S. Goher, F.A. Mautner, A.K. Hafez, M.A.M. Abu-Youssef, C. Gspan, A.M.A. Badr, Polyhedron 22 (2003) 975.
[20] G.M. Sheldrick, Acta Crystallogr., Sect. A 64 (2008) 112.
[21] M. O'Keeffe, M. Eddaoudi, H.L. Li, T. Reineke, O.M. Yaghi, J. Solid State Chem. 152 (2000) 3.
[22] O.V. Dolomanov, OLEX, http://www.ccp14.ac.uk/ccp/web-mirrors/lcells/index.htm.
[23] O.V. Dolomanov, A.J. Blake, N.R. Champness, M. Schroder, J. Appl. Crystallogr. 36 (2003) 1283.
[24] CRYSTALMAKER, CrystalMaker Software Ltd., 2008.
[25] Reticular Chemistry Structure Resource, Arizona State University, Tempe, 2009, http://rcsr.anu.edu.au.
[26] K. Nakamoto, Infrared and Raman Spectra of Inorganic and Coordination Compounds, fourth ed., John Wiley, NY, 1978.
[27] M.A.M. Abu-Youssef, V. Langer, L. Öhrström, Dalton Trans. (2006) 2542.
[28] (a) L. Öhrström, K. Larsson, S. Borg, S.T. Norberg, Chem. Eur. J. 7 (2001) 4805. The net in this reference is mistakenly assigned as **ths** but is in fact of the **utp** type;
(b) C.A. Black, L.R. Hanton, Cryst. Growth Des. 7 (2007) 1868.
[29] A.F. Wells, Three-Dimensional Nets and Polyhedra, John Wiley and Sons, New York, 1977.
[30] E. Koch, W. Fischer, Z. Kristallogr. 210 (1995) 407.
[31] L. Öhrström, K. Larsson, Dalton Trans. 3 (2004) 347.
[32] L. Öhrström, K. Larsson, Molecule-Based Materials: The Structural Network Approach, Elsevier, Amsterdam, 2005.
[33] A. Dadgarnezhad, I. Sheikhshoaie, F. Baghaei, Anti-Corros. Methods Mater. 51 (2004) 266.
[34] G. Bereket, A. Pinarbasi, C. Ogretir, Anti-Corros. Methods Mater. 51 (2004) 282.
[35] Qun-Jie Xu, Guo-Ding Zhou, Hui-Feng Wang, Wen-Bin Cai, Anti-Corros. Methods Mater. 53 (2006) 207.
[36] L. Elkadi, B. Mernari, M. Traisnel, F. Bentiss, M. Lagrenee, Corros. Sci. 42 (2000) 703.
[37] E.M. Sherif, Su-Moon Park, Corros. Sci. 48 (2006) 4065.
[38] P.R. Roberge, Handbook of Corrosion Engineering, McGraw-Hill, New York, 1999.
[39] K. Babic-Samaradzija, K.F. Khaled, N. Hackerman, Anti-Corros. Methods Mater. 52 (2005) 11.

tetrakis-acetonitrilecopper(I) hexafluorophosphate [20] were synthesised according to established procedures. Dry KBr for FTIR was supplied in small sachets by Thermo Fisher. All other reagents were obtained commercially as ACS grade and used without further purification. IR spectra were recorded on a Bruker TENSOR 27 spectrometer. Single crystal X-ray diffraction data were collected on a Bruker CCD-1000 diffractometer with Mo Kα radiation. Thermal data (TGA) were measured on a Perkin Elmer TGA 7, CHN analyses were performed using a Perkin Elmer 2400 CHNS Analyzer, and analyses for Mo and Cu were obtained using ICP-OES at the Forschungzentrum Jülich (Jülich, Germany) ZCH elemental analysis service.

2.2. Preparation of $[Cu(CH_3CN)_4]_2[Mo_8O_{26}Cu_2(CH_3CN)_4]$ (**1**) and $[Cu(CH_3CN)_4]_4[Mo_8O_{26}]\cdot 2CH_3CN$ (**2**) and their decomposition to $Cu_4[Mo_8O_{26}]\cdot 0.6CH_3CN\cdot 16H_2O$ (**3**)

tetrakis-Acetonitrilecopper(I) hexafluorophosphate (0.428 g, 1.14 mmol) was added to a solution of tetrabutylammonium dimolybdate (0.40 g, 0.51 mmol) in acetonitrile (20 mL), resulting in instantaneous production of a yellow–brown precipitate. After reflux for 3 days under an inert atmosphere the resulting suspension was hot filtered to give a pale green solution. Crystallisation by diffusion of diethyl ether into the acetonitrile solution produced red–orange crystals of β-octamolybdate **1**, and colourless crystals of **2**. Note: higher rates of ether diffusion favour crystallisation of **1**. Both **1** and **2** decompose upon exposure to air, rapidly forming a hygroscopic brown material with the stoichiometry $Cu_4[Mo_8O_{26}]\cdot 0.6CH_3CN\cdot 16H_2O$ (**3**) (0.024 g, 0.014 mmol, 11%). While **1** and **2** could not be recovered quickly enough to record individual yields, FTIR spectra were obtained by very rapidly transferring crystals to KBr. FTIR of **1** (KBr disc): cm^{-1} 3500 (s), 2976 (w), 2927 (w), 2363 (vw), 2254 (vw), 1616 (m), 1404 (w), 1365 (w), 1046 (w), 950 (vs), 915 (vs), 848 (s), 715 (s), 666 (s), 560 (w). FTIR of **2** (KBr disc): cm^{-1} 3474 (m), 2967 (w), 2926 (w), 2363 (vw), 2254 (vw), 2135 (w), 2099 (vw), 1655 (m), 1613 (m), 1405 (w), 1365 (w), 950 (vs), 910 (vs), 846 (s), 712 (s), 672 (s), 560 (w). FTIR of **3** (KBr disc): cm^{-1} 3442 (s), 2926 (w), 1619 (m), 10 310 (w), 942 (s), 907 (s), 707 (s). Elemental *Anal.* Calc. for $C_{1.2}CuH_{33.8}Mo_8N_{0.6}O_{42}$ (**3**): C, 0.82; H, 1.94; N, 0.48; Cu, 14.52; Mo, 43.84. Found: C, 0.83; H, 1.75; N, 0.42; Cu, 14.70; Mo, 43.60%. Thermogravimetric analysis of **3** is consistent with this formula, indicating a mass loss of *ca.* 18% by 250 °C.

2.3. Synthesis of $Cu_4[Mo_8O_{26}]\cdot 0.6CH_3CN\cdot 16H_2O$ (**3**) via $[Cu(CH_3CN)_4]_4[Mo_8O_{26}]\cdot 2CH_3CN$ (**2**)

tetrakis-Acetonitrilecopper(I) hexafluorophosphate (0.070 g, 0.19 mmol) was added to a solution of tetrabutylammonium octamolybdate (0.050 g, 0.023 mmol) in acetonitrile (5 mL), producing a yellow solution. After stirring for 7 h, the now slightly cloudy solution was filtered before vapour diffusion of diethyl ether produced colourless crystals of **2**. These rapidly decomposed upon removal from the mother liquor, producing **3** (0.031 g, 95%).

2.4. Single crystal structure determination

Suitable single crystals of **1** and **2** were mounted on the end of a thin glass fibre under ambient conditions using Fomblin oil, and X-ray diffraction intensity data were measured at 193 K on a Bruker CCD-1000 diffractometer [λ(Mo Kα) = 0.7107 Å, graphite monochromator]. For each compound, initial cell constants were obtained from three 30 frame series of ω scans at different starting angles, while final cell constants were calculated from a set of strong reflections from the actual data collection. These datasets were corrected for Lorentz and polarization effects and the absorption correction was based on fitting a function to the empirical transmission surface as sampled by multiple equivalent measurements [21] using SADABS software [22]. Structure solution and refinement was carried out using the SHELXTL program suite [22]. Compound **1** crystallized in the space group $P\bar{1}$ and **2** in *P2(1)/n*. Both structures were solved by a combination of direct methods and difference Fourier syntheses and refined against F^2 by the full-matrix least-squares technique. Hydrogen atoms were placed in the structure factor calculation at idealized positions and were allowed to ride on the neighboring atoms with relative isotropic displacement coefficients. Crystal data, data collection parameters and refinement statistics for **1** and **2** are listed in Table 1.

Table 1
Crystallographic data for compounds **1** and **2**.

	1	**2**
Chemical formula	$[Cu(CH_3CN)_4]_2[Mo_8O_{26}Cu_2(CH_3CN)_4]$	$[Cu(CH_3CN)_4]_4[Mo_8O_{26}]\cdot 2CH_3CN$
Formula weight	1930.33	2176.65
Crystal system	triclinic	monoclinic
Space group	$P\bar{1}$	$P2(1)/n$
a (Å)	11.158(2)	12.387(3)
b (Å)	11.699(2)	13.064(3)
c (Å)	12.173(2)	22.378(6)
α (°)	62.991(2)	90
β (°)	74.332(2)	103.044(5)
γ (°)	80.637(3)	90
V (Å^3)	1361.6(3)	3527.7(16)
Z	1	2
T (K)	193(2)	193(2)
ρ_{calc} (g cm^{-3})	2.354	2.049
μ (mm^{-1})	3.386	2.629
Reflections collected	12 427	31 082
Unique reflections (R_{int})	6299(0.0311)	8448(0.1068)
Completeness to θ = 25.00°	99.6%	100%
Data/restraints/parameters	6299/0/340	8448/0/424
Goodness-of-fit (GOF) on F^2	1.031	0.998
Residuals*: R_1; wR_2	0.0316; 0.0785	0.0464; 0.1257

* $R_1 = \sum||F_o|-|F_c||/\sum|F_o|$. $wR_2 = \{\sum[w(F_o^2 - F_c^2)^2]/\sum[w(F_o^2)^2]\}^{1/2}$.

3. Results and discussion

3.1. Synthesis of $[Cu(CH_3CN)_4]_2[Mo_8O_{26}Cu_2(CH_3CN)_4]$ (**1**) and $[Cu(CH_3CN)_4]_4[Mo_8O_{26}]\cdot 2CH_3CN$ (**2**); decomposition to $Cu_4[Mo_8O_{26}]\cdot 0.6CH_3CN\cdot 16H_2O$ (**3**)

The red β-octamolybdate $[Cu(CH_3CN)_4]_2[Mo_8O_{26}Cu_2(CH_3CN)_4]$ (**1**, Fig. 1) and colourless α-octamolybdate $[Cu(CH_3CN)_4]_4[Mo_8O_{26}]\cdot 2CH_3CN$ (**2**, Fig. 3), have both been characterized by high quality crystal structures, and are formed in the same reaction between tetrabutylammonium dimolybdate and *tetrakis*-acetonitrile copper(I) hexafluorophosphate in refluxing acetonitrile. Upon removal from the mother liquor, both materials rapidly decompose (e.g. within seconds) forming insoluble, hygroscopic dark brown materials with identical FTIR spectra – thus preventing their characterization by elemental analysis or thermal techniques. FTIR spectra of **1** and **2** (see Supplementary data), which appear very similar, were obtained before complete decomposition by pipetting crystals on to a filter paper and rapidly transferring them to dry KBr. In addition to FTIR, the dark brown material has been characterized by full elemental analysis (Mo, Cu, C, H and N) and TGA to reveal the composition $Cu_4[Mo_8O_{26}]\cdot 0.6CH_3CN\cdot 16\ H_2O$ (**3**). This indicates that **3** is formed by rapid expulsion of acetonitrile from the structure with an accompanying uptake of atmospheric water, while its insolubility suggests formation of a Cu(I) linked $\{Mo_8\}$ coordination polymer.

Octamolybdates such as **1** and **2** are typically synthesized by acidifying aqueous solutions of sodium molybdate [8], and

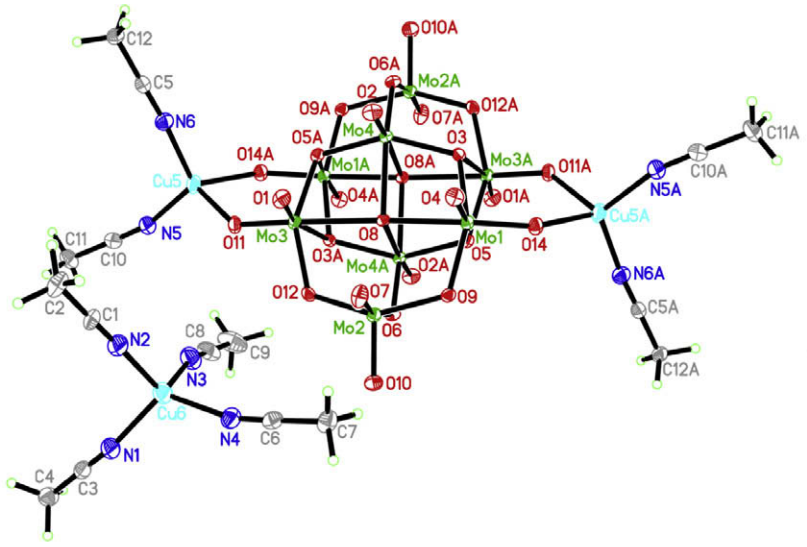


Fig. 1. ORTEP representation of the $[Cu(CH_3CN)_4]^+$ cation and $[Mo_8O_{26}Cu_2(CH_3CN)_4]^{2-}$ cluster anion in **1**. Thermal ellipsoids are drawn at the 30% probability level. C atoms are grey; N, blue; O, red; Mo, green; Cu, cyan; H atoms are white spheres of arbitrary radius. (For interpretation of the references to colour in this figure legend, the reader is referred to the web version of this article.)

although we have previously observed rearrangement of hexamolybdate anions to such species upon treatment with Ag(I) [17–19], to our knowledge they have not previously been synthesized by self-assembly of small molybdate building blocks in organic media. One unusual alkoxo-substituted $\{Mo_8\}$ cluster, constructed from two weakly bridged, readily dissociated corner sharing $\{Mo_4\}$ units has previously been assembled from $(NBu_4)_2[Mo_2O_7]$ in methanol [23]. However, this is a fundamentally different type of isopolyanion to the more highly condensed α- and β-octamolybdates reported here.

The ability of our conditions to induce condensation of molybdate polyhedra may be a consequence of the Lewis acidity of Cu(I), with coordination of terminal Mo=O groups to Cu(I) activating them as leaving groups in an analogous fashion to protonation in aqueous systems. It is also worth noting that interconversion of α- and β-octamolybdates has previously been observed [24], suggesting that **1** and **2** form via a common reaction pathway. Mixtures of **1** and **2** are also obtained by refluxing α-$\{Mo_8\}$ (as $(NBu_4)_4[Mo_8O_{26}]$) and $[Cu(CH_3CN_4](PF_6)$ in acetonitrile, while compound **2** could be prepared exclusively by simple, room temperature cation metathesis of $(NBu_4)_4[Mo_8O_{26}]$ with $[Cu(CH_3CN_4]$ (PF_6), leading to a high yield (95%) of isolated **3**. This implies that the uncoordinated octamolybdate cluster **2** forms first and then, given sufficient thermal energy, displaces acetonitrile ligands from $[Cu(CH_3CN)_4]^+$ to form **1**. As such, **1** can be seen as an intermediate step in the conversion of **2** to the almost acetonitrile free Cu(I) octamolybdate **3**.

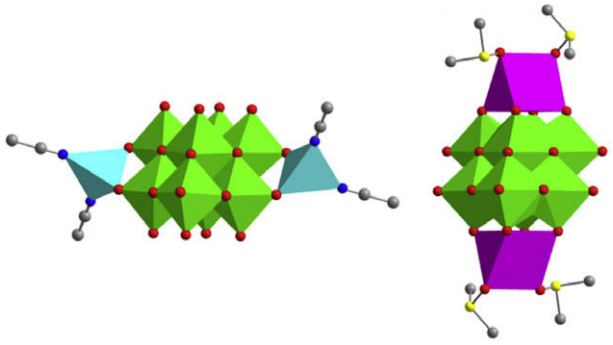


Fig. 2. Polyhedral representation comparing the derivatised β-octamolybdate anions $[Mo_8O_{26}Cu_2(CH_3CN)_4]^{2-}$ (**1**, this work) and $[Ag_2Mo_8O_{26}(dmso)_4]^{2-}$ (Ref. [17]). Colour scheme is as Fig. 1, with Ag purple, S yellow and H omitted. (For interpretation of the references to colour in this figure legend, the reader is referred to the web version of this article.)

3.2. X-ray structural characterization

Good quality X-ray structural data were obtained for both **1** and **2**. The cluster anion in compound **1**, which crystallises in the space group $P\bar{1}$, is a β-octamolybdate cluster composed of two oxygen

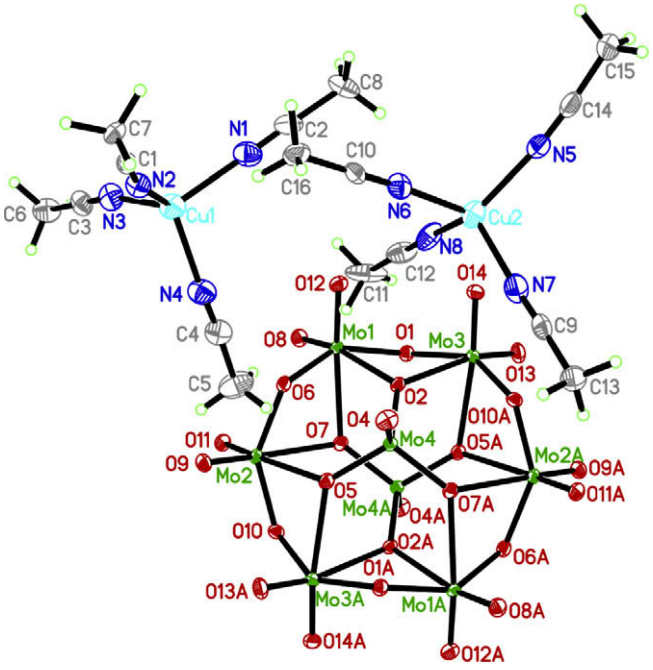


Fig. 3. ORTEP representation of the $[Mo_8O_{26}]^{4-}$ cluster anion and two crystallographically independent $[Cu(CH_3CN)_4]^+$ cations in **2**. The acetonitrile solvent molecule has been omitted for clarity. Colour scheme as for Fig. 1.

centred $\{Mo_4O_{13}\}$ units (Fig. 1) with $\{Cu(CH_3CN)_2\}$ units bound to terminal oxo positions on opposite sides of the cluster.

The cluster anion in **1** is comparable to our previously isolated $[Ag–Mo_8O_{26}–Ag]^{2-}$ synthon, $[Ag_2Mo_8O_{26}(dmso)_4]^{2-}$ [17], with terminal ligation provided by CH_3CN rather than DMSO. However, the geometries and locations of the transition metal heteroatoms in these structures are different (Fig. 2). Each Ag(I) in $[Ag_2Mo_8O_{26}(dmso)_4]^{2-}$ has a trigonal prismatic geometry and binds to four terminal Mo=O groups on the "top" or "bottom" of the cluster, while the preference of Cu(I) for tetrahedral coordination means that in **1** the two Cu(I) atoms each coordinate to two terminal oxo positions on the "sides" of the cluster. In this way, the β-octamolybdate cluster in **1** is comparable to a number of transition metal derivatised β-octamolybdates. However, these clusters typically feature completely oxidized transition metals with terminal coordination sites occupied by more strongly binding amine ligands such as example di-2-picolylamine [25] or 1,10-phenanothroline [26]. As such, **1** can be seen as an isolated, reactive intermediate cluster or "synthon" – with its propensity to form networks indicated by the rapid formation of the presumed coordination polymer $Cu_4[Mo_8O_{26}]\cdot 0.6CH_3CN\cdot 16H_2O$ (**3**) upon removal from acetonitrile saturated environments.

In **1**, the β-$\{Mo_8\}$ cluster is formed by two $\{Mo_4O_{13}\}$ units which are connected off centre to each other with the central μ5-oxo position (O8) of each $\{Mo_4O_{13}\}$ unit positioned directly above/below one of the surrounding Mo atoms (Mo4) of the other tetramolybdate subunit, Mo–O distances are displayed in Table 2. A further six bridging oxo ligands complete the link between the equatorial coordination sites of each $\{Mo_4O_{13}\}$ unit and the axial coordination sites of its partner. The two symmetry related Cu(I) atoms each coordinate to two terminal oxo sites, with a slight lengthening of the Mo–O distances indicating a corresponding weakening of the Mo–O double bond character (Table 2). While bond valence sum calculations [27] suggest roughly equal probabilities for a fully oxidized molybdate cluster coordinated to Cu(I), or a mixed valence cluster coordinated to Cu(II), the *pseudo*-tetrahedral Cu coordination environment provides a clear indicator that copper is in the +1 oxidation state. Slight distortion from idealized tetrahedral geometry is indicated by the tight O–Cu–O angle (87.9(2)°) resulting from coordination to the molybdate oxygen sites, while the terminal acetonitrile ligands coordinate with Cu–N distances that are slightly shorter than those observed in the accompanying $[Cu(CH_3CN)_4]^+$ cation (Table 1). Nonetheless, these ligands appear to be highly labile, as indicated by expulsion of acetonitrile in the ambient atmosphere leading to formation of **3**. The extended structure of **1** is constructed from layers of molybdate clusters running parallel to the crystallographic *ab* plane, separated by layers of $[Cu(CH_3CN)_4]^+$ cations; note that the numerous short contacts between the acetonitrile ligands and molybdate oxygens (C···O distances ranging from *ca.* 2.94 to 3.18 Å) may be responsible for the distortion observed in the $[Cu(CH_3CN)_4]^+$ cation (two large N–Cu–N angles of 119.9(2) and 117.4(2)°).

Table 3
Coordination bond lengths (Å) and selected angles (°) in $[Cu(CH_3CN)_4]_4[Mo_8O_{26}]\cdot 2CH_3CN$ (**2**).

	Mo centres		Cu centres	
Mo=O	Mo1–O8	1.704(5)	Cu1–N1	2.002(9)
	Mo1–O8	1.699(5)	Cu1–N2	1.985(8)
	Mo2–O9	1.704(5)	Cu1–N3	2.012(9)
	Mo2–O11	1.701(5)	Cu1–N4	2.021(9)
	Mo3–O13	1.701(5)	Cu2–N5	1.974(8)
	Mo3–O14	1.706(5)	Cu2–N6	2.006(8)
	Mo4–O4	1.707(5)	Cu2–N7	1.979(9)
μ_2 Mo–O	Mo1–O1	1.908(5)	Cu2–N8	1.988(9)
	Mo1–O6	1.916(5)	N2–Cu1–N1	103.9(3)
	Mo2–O6	1.915(5)	N2–Cu1–N3	113.2(3)
	Mo2–O10	1.906(5)	N1–Cu1–N3	116.0(3)
	Mo3–O1	1.912(5)	N2–Cu1–N4	120.2(3)
	Mo3–O10a	1.920(5)	N1–Cu1–N4	104.4(3)
			N3–Cu1–N4	99.5(3)
μ_3 Mo–O	Mo1–O2	2.400(4)	N5–Cu2–N7	104.5(3)
	Mo1–O7	2.411(5)	N5–Cu2–N8	120.4(3)
	Mo2–O5	2.394(5)	N7–Cu2–N8	113.6(3)
			N5–Cu2–N6	108.9(3)
	Mo2–O7	2.412(5)	N7–Cu2–N6	108.4(3)
	Mo3–O2	2.419(5)	N8–Cu2–N6	100.6(3)
	Mo3–O5a	2.421(5)		
	Mo4–O2	1.782(5)		
	Mo4–O5	1.784(5)		
	Mo4–O7a	1.782(5)		

Table 2
Coordination bond lengths (Å) and selected angles (°) in $[Cu(CH_3CN)_4]_2[Mo_8O_{26}Cu_2(CH_3CN)_4]$ (**1**).

Mo centres				Cu centres	
Mo=O	Mo1–O4	1.696(3)	Cluster anion	Cu5–N5	1.944(4)
	Mo2–O7	1.702(3)		Cu5–N6	1.947(4)
	Mo2–O10	1.695(3)		Cu5–O11	2.086(3)
	Mo3–O1	1.700(3)		Cu5–O14a	2.065(3)
	Mo4–O2	1.685(3)		N5–Cu5–N6	114.67(17)
Mo=O–Cu	Mo1–O14	1.726(3)		N5–Cu5–O14a	114.68(15)
	Mo3–O11	1.726(3)		N6–Cu5–O14a	112.83(15)
μ_2 Mo–O	Mo1–O9	1.884(3)		N5–Cu5–O11	113.70(15)
	Mo2–O9	1.923(3)		N6–Cu5–O11	110.22(15)
	Mo2–O12	1.996(3)		O14a–Cu5–O11	87.84(11)
	Mo2–O6	2.273(3)			
	Mo3–O12	1.888(3)			
	Mo4–O6a	1.748(3)			
μ_3 Mo–O	Mo1–O3	1.996(3)	Cation	Cu6–N1	1.987(4)
	Mo1–O5	2.375(3)		Cu6–N2	1.987(4)
	Mo3–O3a	2.364(3)		Cu6–N3	1.993(5)
	Mo3–O5a	1.994(3)		Cu6–N4	1.994(4)
	Mo4–O3	1.931(3)		N1–Cu6–N3	102.30(19)
	Mo4–O5a	1.942(3)		N1–Cu6–N4	119.86(18)
μ_5 Mo–O	Mo1–O8	2.252(3)		N2–Cu6–N1	106.00(17)
	Mo2–O8	2.564(3)		N2–Cu6–N3	117.4(2)
	Mo3–O8	2.267(2)		N2–Cu6–N4	106.80(17)
	Mo4–O8	2.161(3)		N3–Cu6–N4	105.14(18)
	Mo4–O8a	2.430(2)			

Compound **2** crystallises in $P2(1)/n$ and is simply an α-$[Mo_8O_{26}]^{4-}$ cluster anion accompanied by $[Cu(CH_3CN)_4]^+$ cations. The α-octamolybdate cluster anion in **2** can be viewed as an $\{Mo_6O_{18}\}$ belt capped by two $\{MoO_4\}$ tetrahedra (Fig. 3); selected bond lengths and angles are shown in Table 3. There are two crystallographically independent $[Cu(CH_3CN)_4]^+$ positions present with Cu–N distances ranging from 1.975(9) to 2.021(9) Å. More significant distortion is observed in the N–Cu–N bond angles of these *pseudo*-tetrahedral cations, which range from *ca.* 100 to 120°. Such distortion is to be expected from the combination of such coordinatively flexible d^{10} metal cations with large molybdate anions capable of exerting substantial crystal packing forces. In the extended structure, alternating layers of octamolybdate clusters and cations/solvent propagate parallel to a plane described by the crystallographic *b* axis and a line intersecting *c* at 31.68°.

4. Conclusions

$[Cu(CH_3CN)_4](PF_6)$ is capable of inducing aggregation of $[Mo_2O_7]^{2-}$ to form larger molybdate species, presumably as a consequence of the Lewis acidity of Cu(I), and also provides a source of Cu(I) that can coordinate to the resulting polyoxoanions. This is shown by the isolation of a novel $\{Cu(CH_3CN)_2\}$ derivatised β-octamolybdate cluster anion, in which the preference of Cu(I) for tetrahedral coordination results in it occupying a different coordination site on the cluster anion to the previously described $\{Ag(DMSO)_2\}$ analogue. As such, $[Cu(CH_3CN)_4](PF_6)$ is an interesting reagent for use in non-aqueous POM chemistry. In this study, the isolation of cluster anions belonging to known structural types suggests the absence of templation effects from the $[Cu(CH_3CN)_4]^+$ cation, in contrast to our previous work with several organic cations. This may be because the high lability of the Cu(I)–N coordination bond compared to covalent bonds, coupled with the absence of hydrogen bonding groups that can interact strongly with molybdate anions, limits the ability of this $[Cu(CH_3CN_4]^+$ to template molybdates. In future studies, we aim to use organic co-cations to help stabilise compound **1**, and exploit its reactivity as a building block for reaction with organic ligands and coordination clusters.

Acknowledgements

We thank Dr. Arkady Ellern of Iowa State University for providing access to, and training J.F. to use, a single crystal X-ray diffractometer. Ames Laboratory is operated for the US Department of Energy by Iowa State University under Contract No. DEACD2 07CH11358.

Appendix A. Supplementary data

CCDC 726620 and 726621 contain the supplementary crystallographic data for **1** and **2**. These data can be obtained free of charge via http://www.ccdc.cam.ac.uk/conts/retrieving.html, or from the Cambridge Crystallographic Data Centre, 12 Union Road, Cambridge CB2 1EZ, UK; fax: (+44) 1223-336-033; or e-mail: deposit@ccdc.cam.ac.uk. Supplementary data associated with this article can be found, in the online version, at doi:10.1016/j.poly.2009.05.058.

References

[1] D.-L. Long, E. Burkholder, L. Cronin, Chem. Soc. Rev. 36 (2007) 105.
[2] (a) H. Liu, C.J. Gómez-García, J. Peng, J. Sha, Y. Li, Y. Yan, Dalton Trans. (2008) 6211;
(b) M.D. Ritorto, T.M. Anderson, W.A. Neiwert, C.L. Hill, Inorg. Chem. 43 (2004) 44.
[3] A. Proust, R. Thouvenout, P. Gouzerh, Chem. Commun. (2008) 1837.
[4] P. Mialane, A. Dolbecq, F. Sécheresse, Chem. Commun. (2006) 3477.
[5] A. Müller, E. Krickemeyer, S.K. Das, P. Kögerler, S. Sarkar, H. Bögge, M. Schmidtmann, S. Sarkar, Angew. Chem., Int. Ed. 39 (2000) 1612.
[7] E. Coronado, C. Giménez-Saiz, C.J. Gómez-García, Coord. Chem. Rev. 249 (2005) 1776.
[8] W.G. Klemperer, Inorg. Synth. 27 (1990) 74.
[9] S. Takara, S. Ogo, Y. Watanabe, K. Nishikawa, I. Kinoshita, K. Isobe, Angew. Chem., Int. Ed. 38 (1999) 3051.
[10] T.M. Che, V.W. Day, L.C. Francesconi, M.F. Fredrich, W.G. Klemperer, W. Shum, Inorg. Chem. 24 (1985) 4055.
[11] R. Villanneau, R. Delmont, A. Proust, P. Gouzerh, Chem. Eur. J. 6 (2000) 1184.
[12] A. Proust, R. Thouvenot, S.-G. Roh, J.-K. Yoo, P. Gouzerh, Inorg. Chem. 34 (1995) 4106.
[13] B. Hasenknopf, R. Delmont, P. Herson, P. Gouzerh, Eur. J. Inorg. Chem. (2002) 1081.
[14] H. Kang, J. Zubieta, J. Chem. Soc., Chem. Commun. (1988) 1192.
[15] D.-L. Long, P. Kögerler, L.J. Farrugia, L. Cronin, Angew. Chem., Int. Ed. 42 (2003) 4180.
[16] D.-L. Long, P. Kögerler, A.D.C. Parenty, J. Fielden, L. Cronin, Angew. Chem., Int. Ed. 45 (2006) 4798.
[17] H. Abbas, A.L. Pickering, D.-L. Long, P. Kögerler, L. Cronin, Chem. Eur. J. 11 (2005) 1071.
[18] H. Abbas, C. Streb, A.L. Pickering, A.R. Neil, D.-L. Long, L. Cronin, Cryst. Growth Des. 8 (2008) 635.
[19] E.F. Wilson, H. Abbas, B.J. Duncombe, C. Streb, D.-L. Long, L. Cronin, J. Am. Chem. Soc. 130 (2008) 13876.
[20] G.J. Kubas, Inorg. Synth. 19 (1979) 90.
[21] R.H. Blessing, Acta Crystallogr., Sect. A 51 (1995) 33.
[22] G. Sheldrick, SHELXTL (v 5.1) Program Library, Bruker Analytical X-Ray Systems, Madison, WI, 1997.
[23] L. Ma, S. Liu, J. Zubieta, Chem. Commun. (1989) 440.
[24] X. Wang, X.-X. Xu, Q.-Y. Wang, Y.-L. Zhai, Polyhedron 11 (1992) 1423.
[25] R.S. Rarig Jr., J. Zubieta, J. Solid State Chem. 167 (2002) 370.
[26] R.-Z. Wang, J.-Q. Xu, G.-Y. Yang, W.-M. Bu, Y.-H. Xing, D. -Mei Li, S.-Q. Liu, L. Ye, Y.-G. Fan, Polyhedron 18 (1999) 2971.
[27] Bond valence sum calculations were performed using VaList, release 2008, A.S. Wills, program available from www.ccp14.ac.uk.

reported relative to TMS. Infrared spectra were obtained with a Digilab FTS 3100 Excalibur HE spectrophotometer with solid samples prepared as KBr disks. Microanalyses were obtained on a Carlo Erba EA 1108 elemental analyser.

2.3. Synthesis of [Re(dhp)(PPh_3)$_2$]I (**1**)

To a suspension of 0.100 g (115 μmol) of *cis*-[$ReO_2I(PPh_3)_2$] in 25 cm^3 of ethanol was added 0.078 g (242 μmol) of H_2dhp. After the mixture was heated under reflux for 2 h, it was cooled to room temperature and a brown precipitate was removed by filtration. Recrystallization from dichloromethane/ethanol gave brown crystals, which were suitable for X-ray diffraction study. Yield = 46% (0.063 g). *Anal.* Calc. for $C_{55}H_{43}N_3O_2P_2IRe$. 0.59 CH_2Cl_2: C, 55.50; H, 4.71; N, 3.49. Found: C, 55.31; H, 4.71; N, 3.22%. IR (cm^{-1}): ν(Re–N) 512 m, 527 m, ν(Re–O) 446 m, ν(C=N) 1596s. ^{1}H NMR(ppm): 7.68–7.56 (m, 32H), 7.52 (d, 2H), 7.31 (t, 1H), 7.15 (t, 2H), 6.97 (d, 2H), 6.82 (t, 2H).

2.4. Synthesis of [Re(dhp)(PPh_3)$_2$](ReO_4) (**1a**)

H_2dhp (0.066 g, 209 μmol) was added to a solution of *trans*-[$ReOBr_3(PPh_3)_2$] (0.100 g, 103 μmol) in 20 cm^3 methanol, and the mixture was heated under reflux for 90 min. After cooling to room temperature, a brown precipitate was collected by filtration. The mother liquor was left to evaporate slowly at room temperature, and after two days brown crystals, suitable for X-ray diffraction study, were collected. They were washed with ethanol and diethyl ether. Yield = 42% (0.055 g). *Anal.* Calc. for $C_{55}H_{43}N_3O_6P_2Re_2$: C, 51.76; H, 3.40; N, 3.29. Found: C, 51.43; H, 3.61; N, 3.52%. IR (cm^{-1}): ν(Re–N) 501 m, 529 m, ν(Re–O) 453 m, ν(C=N) 1601s, ν(Re^{VII}=O) 898vs.

2.5. Synthesis of fac-[Re(CO)$_3$(H_2dhp)Br] (**2**)

H_2dhp (0.079 g, 250 μmol) was dissolved in 10 cm^3 of toluene, and added to 0.100 g (246 μmol) of [$Re(CO)_5Br$] in 10 cm^3 of toluene. The mixture was heated under reflux for 2 h under nitrogen, and then cooled to room temperature. An orange precipitate was removed by filtration, and it was washed with ethanol and diethyl ether. Orange crystals, suitable for X-ray diffraction study, were obtained from the slow evaporation of the mother liquor at room temperature. Total yield = 69% (0.113 g). *Anal.* Calc. for $C_{22}H_{15}N_3O_5BrRe$: C, 39.59; H, 2.27; N, 6.30. Found: C, 39.16; H, 2.24; N, 6.58%. IR (cm^{-1}): ν(C≡O)$_{fac}$ 2026s, 1907s, ν(Re–N(1)) 473 m, ν(Re–N(2)) 438 m; ν(C=N) 1635s, 1598s. ^{1}H NMR (ppm): 10.48 (s, 1H), 10.39 (s, 1H), 9.43 (d, 1H), 9.38 (t, 1H), 8.59 (d, 1H), 8.18–8.46 (m, 4H), 8.12 (t, 1H), 6.86–7.32 (m, 5H).

2.6. X-ray crystallography

Intensity data collection was performed at 200 K on a Nonius Kappa CCD detector system using the ω scan technique with Mo Kα radiation. Intensities were corrected for Lorentz and polarization effects. The structures were solved by direct methods and were refined by full-matrix least-squares procedures using the SHELXL-97 package [21]. Crystal and structure refinement data for **1, 1a** and **2** are given in Table 1. Non-hydrogen atoms were refined with anisotropic displacement parameters; hydrogen atoms were idealized and fixed. Selected bond lengths and angles are given in Table 2.

3. Results and discussion

3.1. [Re(dhp)(PPh_3)$_2$]I (**1**)

The compound was synthesized by the reaction of *cis*-[$ReO_2I(PPh_3)_2$] with two molar equivalents of H_2dhp in refluxing ethanol under nitrogen. The surprising aspect of this reaction is the reduction of the *cis*-dioxorhenium(V) center to rhenium(III) in the product **1**. The fact that the reaction yield is low (less than 50%) would seem to indicate that **1** may be the product of a disproportionation reaction, with perrhenate also being produced in the process, according to the equation.

Table 1
Crystallographic data for complexes **1** and **2**.

	1	**1a**	**2**
Formula	$C_{55}H_{43}N_3O_2P_2IRe.0.59CH_2Cl_2$	$C_{55}H_{43}N_3O_6P_2Re_2$	$C_{22}H_{15}N_3O_5BrRe$
Formula weight	1203.1	1276.3	667.48
Crystal system	orthorhombic	triclinic	monoclinic
Space group	*Pnma*	*P*1	$P2_1/c$
a (Å)	20.6023(4)	11.1742(5)	13.2243(7)
b (Å)	14.1721(3)	12.4223(5)	10.7117(7)
c (Å)	17.0332(3)	18.7651(9)	16.8929(9)
α (°)		75.549(4)	
β (°)		78.399(4)	
γ (°)		68.988(4)	111.810(3)
V (Å^3)	4973.3(2)	2336.6(2)	2221.7(2)
Z	4	2	4
D_{calc} (g cm^{-3})	1.606	1.814	1.996
μ (mm^{-1})	3.237	5.301	7.307
Absorption correction	multiscan	numerical	none
F(0 0 0)	2370	1244	1272
Crystal size (mm)	0.02 × 0.14 × 0.20	0.19 × 0.13 × 0.06	0.04 × 0.04 × 0.05
θ Range (°)	3.2–27.5	3.7–26.3	3.2–26.0
Index ranges	$-26 \leqslant h \leqslant 26$	$-13 \leqslant h \leqslant 13$	$-16 \leqslant h \leqslant 16$
	$-18 \leqslant k < 18$;	$-13 \leqslant k < 15$	$-13 \leqslant k < 13$
	$-19 \leqslant \ell \leqslant 22$	$-23 \leqslant \ell \leqslant 19$	$-20 \leqslant \ell \leqslant 20$
Reflections/unique	65 883/5938	17 717/9400	14 813/4340
Observed data [$I > 2s(I)$]	4236	5858	2871
Parameters	347	613	289
Goodness-of-fit (GOF)on F^2	1.04	0.88	0.96
Final *R* indices: *R*	0.0304	0.0339	0.0355
wR_2	0.0687	0.0639	0.0588
Largest differences in peak and hole (e/Å^{-3})	2.05/−1.18	2.26/−1.55	1.44/−0.73

Table 2
Selected bond lengths (Å) and angles (°) for **1**, **1a** and **2**.

	1	1a		1	1a
Re–P(1)	2.464(1)	2.490(2)	Re–P(1a)	2.464(1)	2.464(2)
Re–O(1)	2.087(3)	2.087(4)	Re–O(2)	2.060(3)	2.058(4)
Re–N(1)	2.105(4)	2.117(5)	Re–N(3)	2.111(4)	2.116(5)
Re–N(2)	2.080(3)	2.064(4)	N(1)–C(2)	1.426(7)	1.410(8)
N(1)–C(7)	1.311(6)	1.296(8)	N(3)–C(13)	1.312(6)	1.296(8)
P(1)–Re–P(1a)	172.81(3)	173.30(5)	O(1)–Re–N(1)	73.6(1)	73.9(2)
P(1)–Re–O(1)	87.87(2)	90.0(1)	N(1)–Re–N(2)	71.2(1)	71.0(2)
P(1)–Re–O(2)	86.56(2)	84.7(1)	N(3)–Re–N(2)	70.9(1)	71.5(2)
P(1)–Re–N(1)	92.18(2)	88.6(1)	O(2)–Re–N(3)	73.9(1)	74.5(2)
P(1)–Re–N(2)	93.41(2)	97.0(1)	C(7)–N(1)–C(2)	119.5(4)	121.5(5)
P(1)–Re–N(3)	90.04(2)	92.5(1)	C(13)–N(3)–C(14)	120.3(4)	122.2(5)

2

Re–C(1)	1.898(6)	Re–N(1)	2.167(5)
Re–C(2)	1.905(7)	Re–N(2)	2.241(4)
Re–C(3)	1.904(6)	Re–Br	2.6076(7)
N(1)–C(10)	1.284(9)	N(3)–C(16)	1.261(8)
C(1)–Re–Br	178.4(2)	C(1)–Re–C(2)	90.6(3)
C(2)–Re–N(2)	168.8(2)	C(1)–Re–C(3)	92.1(3)
C(3)–Re–N(1)	173.7(2)	C(1)–Re–N(1)	93.8(2)
N(1)–Re–N(2)	74.7(2)	C(1)–Re–N(2)	94.1(2)
C(4)–N(1)–C(10)	118.4(5)	C(15)–C(16)–N(3)	118.9(6)

$$2[ReO_2I(PPh_3)_2] + H_2dhp \rightarrow [Re(dhp)(PPh_3)_2]I + H[ReO_4] + HI$$

In order to test this assumption, we have also reacted *trans*-[ReOBr$_3$(PPh$_3$)$_2$] with a twofold molar excess of H$_2$dhp in methanol. The compound [Re(dhp)(PPh$_3$)$_2$](ReO$_4$) (**1a**) was isolated as the only product. Both **1** and **1a** are 1:1 electrolytes in DMF, and are only soluble in acetonitrile, DMSO and DMF.

The single peaks in the infrared spectrum of **1** at 446 and 1596 cm^{-1} are assigned to ν(Re–O) and ν(C=N), respectively, which illustrate the identical structural environment of the two hydroxyphenyliminomethyl fractions of the chelate dhp in the complex. The ^{1}H NMR spectrum consists of poorly-resolved broad peaks, showing paramagnetic shifts and line broadening of the signals.

The molecular structure of the complex cation of **1** is illustrated in Fig. 1. The rhenium(III) is placed on a mirror plane at the center of a distorted pentagonal–bipyramid (interestingly, the rhenium in **1a** does not lie on any symmetry element, which is due to a twist in the Re–O(1)–N(1)–Re chelate ring). The basal plane is defined by the phenolate oxygens O(1) and O(2), the imino nitrogens N(1) and N(3), and the pyridinic nitrogen N(2). The two phosphorus atoms are in *trans* axial positions.

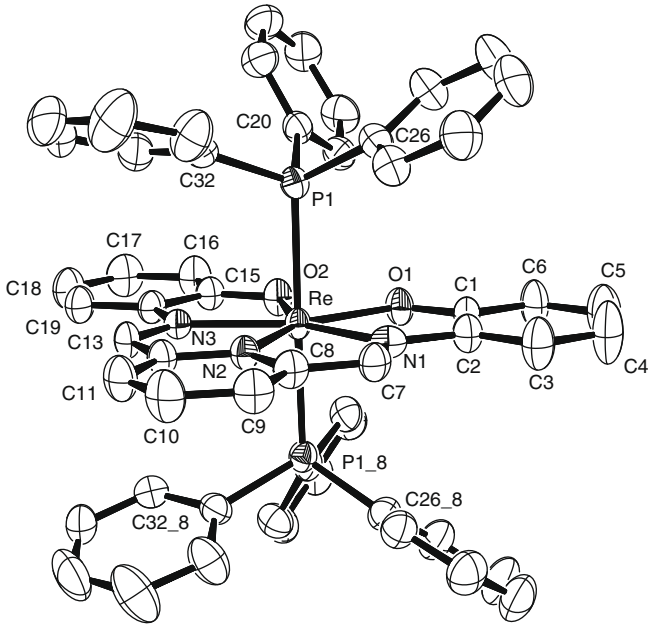


Fig. 1. Structure of the complex cation of compound **1**. The iodide, hydrogens and dichloromethane solvent of crystallization have been omitted for clarity.

Selected bond distances and angles are given in Table 2. Distortion from an ideal rhenium-centered pentagonal bipyramid in **1** mainly results in a nonlinear P(1)–Re–P(1a) axis of 172.81(3)°, with the angles P(1)–Re–O(1) = 87.87(2)°, P(1)–Re–O(2) = 86.56(2)°, P(1)–Re–N(1) = 92.18(2)°, P(1)–Re–N(2) = 93.41(2)° and P(1)–Re–N(3) = 90.04(2)°. Dhp acts as a dianionic pentadentate chelate, with the bite angles O(1)–Re–N(1) = 73.6(1)°, O(2)–Re–N(3) = 73.9(1)°, N(1)–Re–N(2) = 71.2(1)° and N(3)–Re–N(2) = 70.9(1)°. The corresponding Re–N(1) and Re–N(3) bond lengths are 2.105(4) and 2.111(4) Å, respectively, and the average Re–O bond length equals 2.073(3) Å. The observed range for rhenium(V)–imino nitrogen bond lengths is 2.03(1)–2.15(1) Å [22,23], and for Re^V–O (phenolate) the observed range is 2.015(2)–2.097(5) Å [24]. The intraligand distances are all within the expected ranges, with the N(1)–C(7) [1.311(6) Å] and N(3)–C(13) [1.312(6) Å] showing unequivocally that dhp is coordinated in the diimine, rather than the diamine, form.

The bond parameters of **1a** are similar to those in **1** and do not warrant any discussion (see Table 2).

Amongst the numerous examples of seven-coordinate rhenium(III) complexes in the literature are the compounds [Re(terpy)$_2$X]Y$_2$ (X = OH, Cl, NCS; Y = PF$_6$, SCN), which were obtained by the reaction of 2,2′:6′,6″-terpyridine (terpy) with [ReO$_2$(py)$_4$]$^+$ [25]. This reduction/substitution route of the oxorhenium(V) moiety was also observed in the synthesis of the seven-coordinate complex [Re^{III}(PPh$_3$)(mdt)] from the reaction of Hmdt (5-methoxy-5,6-diphenyl-4,5-dihydro-2H-[1,2,4]triazine-3-thione) with *trans*-[ReOCl$_3$(PPh$_3$)$_2$] or [ReO$_2$I(PPh$_3$)$_2$] [26]. The same technique has been used to prepare the five-coordinate rhenium(III) complex [Re(PPh$_3$)$_2$(mbm)$_3$] from *trans*-[ReOCl$_3$(PPh$_3$)$_2$] and *p*-methoxybenzyl mercaptan (Hmbm) [27]. However, the most convenient method for the preparation of rhenium(III) complexes is by ligand substitution reactions of [ReX$_3$(MeCN)(PPh$_3$)$_2$] [28–30].

3.2. *fac*-[Re(CO)$_3$(H$_2$dhp)Br] (**2**)

The rhenium(I) complex **2** was prepared by the reaction of [Re(CO)$_5$Br] with an equimolar quantity of H$_2$dhp in refluxing toluene.

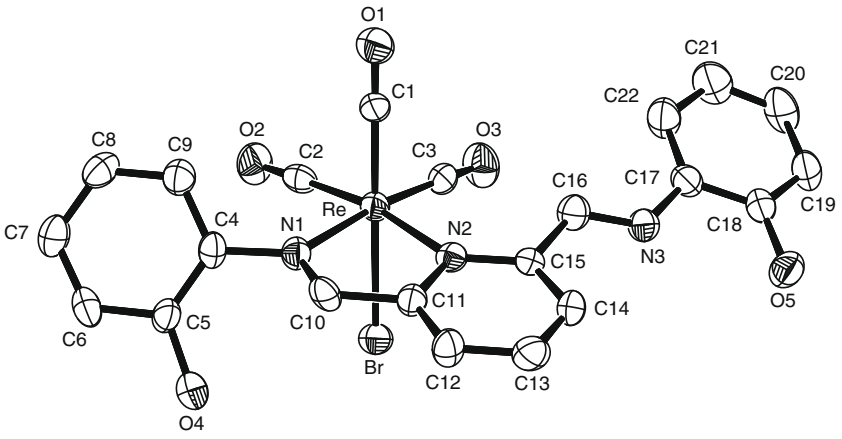


Fig. 2. ORTEP drawing of **2**, with thermal ellipsoids shown at 40% probability.

The infrared spectrum exhibits a sharp, strong band at 2026 cm^{-1} and a broad, intense absorption at 1907 cm^{-1}, attributed to ν(C≡O) of the *fac*-$[Re(CO)_3]^+$ unit. Two medium intensity peaks at 438 and 473 cm^{-1} are assigned to ν(Re–N(1)) and ν(Re–N(2)), respectively. The ^1H NMR spectrum is complex and integrates for 13 protons in the aromatic region, with two singlets at 10.48 and 10.39 ppm, assigned to the methine protons H(10) and H(16), respectively.

A perspective view of the asymmetric unit of **2** is shown in Fig. 2. The X-ray results show that the complex contains the chemically robust *fac*-$[Re(CO)_3]^+$ core in a distorted octahedral geometry. The metal is coordinated to three carbonyl donors in a *facial* orientation, to the neutral imino nitrogen N(1), the pyridinic nitrogen N(2) and a bromide. The imino nitrogen N(3) and the two phenolic oxygens O(4) and O(5) are uncoordinated. The Re–CO bond lengths [average of 1.902(7) Å] fall in the range observed [1.900(2)–1.928(2)] Å for similar complexes [31,32]. The Re–N(1) bond [2.167(5) Å] is significantly shorter than the Re–N(2) [2.241(4) Å] one, and they are typical to other similar bonds [33–35]. The distortion from octahedral ideality is mainly the result of the *trans* angles, which fall in the range 168.8(2)–178.4(2)° (Table 2). These distortions are mainly the result of the constraints imposed by the bidentate coordination of H_2dhp, with a bite angle of 74.7(2)°. As a result, the bromide distorts the two nitrogen atoms less [average Br–Re–N angle is 84.8(1)°] then the two carbonyl carbons [average Br–Re–C angle is 89.8(2)°].

The H_2dhp intraligand bonding distances show the effect of the coordination on the imine group, with the N(1)–C(10) bond [1.284(9) Å] markedly longer than the free N(3)–C(16) bond [1.261(8) Å]. Also, the N(1)–C(10) bond length is shorter than the corresponding bonds in **1** [average 1.312(6) Å], illustrating the higher Lewis acidity of the rhenium(III) centre. The C(4)–C(9) and C(17)–C(22) phenolic rings make dihedral angles of 50.78° and 21.27° with the pyridyl ring, and 36.65° with each other.

It has been shown before that the *fac*-$[Re(CO)_3]^+$ core has a low affinity for anionic oxygen donor atoms [36]. However, neutral tridentate ligands of the N_3-donor atom type like bis(imidazol-2-ylmethyl)amine and bis(quinoline-2-ylmethyl)amine (L^3) have been used to give cationic species of the type *fac*-$[Re(CO)_3L^3]Br$ [37]. Bidentate nitrogen-donor ligands like *N,N′*-dimethylpiperazine and bis(diethylamino)methane (L) have been reacted with $[Re(CO)_5X]$ (X = Cl, Br) to produce the complexes $[Re(CO)_3(L)X]$ [38]. Complexes of the type $[Re^I(CO)_3(L)_2Cl]$, with different monodentate pyridine derivatives L, have been prepared by using $[Re(CO)_5Cl]$ as starting material [39].

4. Conclusion

The reaction of the potentially pentadentate Schiff base ligand 2,6-bis(2-hydroxyphenyliminomethyl)pyridine (H_2dhp) with *cis*-$[ReO_2I(PPh_3)_2]$ or *trans*-$[ReOBr_3(PPh_3)_2]$ leads to the disproportionation of rhenium(V), to form the seven-coordinate rhenium(III) cation $[Re(dhp)(PPh_3)_2]^+$ and perrhenate. However, in its reaction with $[Re(CO)_5Br]$, H_2dhp acts as a bidentate chelate in the product *fac*-$[Re(CO)_3(H_2dhp)Br]$.

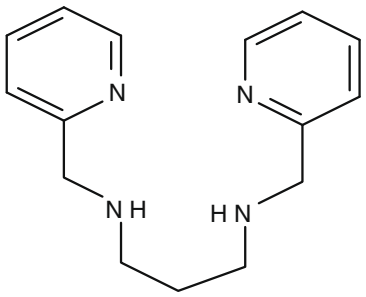
5. Supplementary data

CCDC 721475, 721476 and 721477 contain the supplementary crystallographic data for **1, 1a** and **2**. These data can be obtained free of charge via http://www.ccdc.cam.ac.uk/conts/retrieving.html, or from the Cambridge Crystallographic Data Centre, 12 Union Road, Cambridge CB2 1EZ, UK; fax: (+44) 1223-336-033; or e-mail: deposit@ccdc.cam.ac.uk.

References

[1] A.R. Middleton, A.F. Masters, G. Wilkinson, J. Chem. Soc. (1979) 542.
[2] S. Goyal, K. Lal, J. Indian Chem. Soc. 66 (1989) 477.
[3] F. Fulop, J. Matttinen, K. Pihlaja, Tetrahedron 46 (1990) 6545.
[4] Z. Li, Y. Li, L. Lei, C. Che, X. Zhou, Inorg. Chem. Commun. 8 (2005) 307.
[5] A.D. Garnovski, A.L. Nivorozhkin, V.I. Minkin, Coord. Chem. Rev. 126 (1993) 1.
[6] P.J. Blower, Transition Met. Chem. 23 (1998) 109.
[7] N. Hoshino, Coord. Chem. Rev. 174 (1998) 77.
[8] L. Canali, D.C. Sherrington, Chem. Soc. Rev. 28 (1999) 85.
[9] X. Lin, D.M.J. Doble, A.J. Blake, C. Harrison, C. Wilson, M. Schröder, J. Am. Chem. Soc. 125 (2003) 9476.
[10] S. Uhlenbrock, R. Wegner, B. Krebs, J. Chem. Soc., Dalton Trans. (1996) 3731.
[11] J.R. Dilworth, S.J. Parrott, Chem. Soc. Rev. 27 (1998) 43.
[12] J.C. Reubi, J. Nucl. Med. 36 (1995) 1825.
[13] F. Tisato, M. Porchia, C. Bolzati, F. Refosco, A. Vittadini, Coord. Chem. Rev. 250 (2006) 2034.
[14] C. Bolzati, M. Porchia, G. Bandoli, A. Boschi, E. Malago, L. Uccelli, Inorg. Chim. Acta 315 (2001) 205.
[15] J.Y. Kim, Y.J. Ji, H.-J. Ha, H.K. Chae, Bull. Korean Chem. Soc. 24 (2003) 504.
[16] A. Sachse, N.C. Mösch-Zanetti, G. Lyashenko, J.W. Wielandt, K. Most, J. Magull, F. Dall'Antonia, A. Pal, R. Herbst-Irmer, Inorg. Chem. 46 (2007) 7129.
[17] B.S. Furniss, A.J. Hannaford, P.W.G. Smith, A.R. Tatchell, Vogel's Textbook of Practical Organic Chemistry, fifth ed., Longman Scientific and Technical, England, 1989.
[18] G.F. Ciani, G. D'Alfonso, P. Romiti, A. Sironi, M. Freni, Inorg. Chim. Acta 72 (1983) 29.
[19] N.P. Johnson, C.J.L. Lock, G. Wilkinson, Inorg. Synth. 9 (1967) 145.
[20] X.-X. Sun, C.-M. Qi, S.-L. Ma, H.-B. Huang, W. Zhu, Y.-C. Liu, Inorg. Chem. Commun. 9 (2006) 911.
[21] G.M. Sheldrick, SHELXL-97, Programs for Structure Solution and Refinement, University of Göttingen, Germany, 1997.
[22] H.J. Banberg, F.S. McQuillan, T.A. Hamor, C.J. Jones, J.A. McCleverty, Inorg. Chim. Acta 170 (1990) 23.

[23] G. Gilli, M. Sacerdoti, V. Bertolasi, R. Rossi, Acta Crystallogr. B28 (1982) 100.
[24] X. Chen, F.J. Femia, J.W. Babich, J. Zubieta, Inorg. Chim. Acta 308 (2000) 80.
[25] J. Rall, F. Weingart, D.M. Ho, M.J. Heeg, F. Tisato, E. Deutsch, Inorg. Chem. 33 (1994) 3442.
[26] E. Lopez-Torres, U. Abram, Inorg. Chem. 47 (2008) 2890.
[27] M.S. Papadopoulos, P. Bouziotis, I.C. Pirmettis, C.P. Raptopoulou, A. Terzis, E. Chiotellis, Inorg. Chim. Acta 290 (1999) 247.
[28] T. Maina, A. Pecorale, A. Dolmella, G. Bandoli, U. Mazzi, J. Chem. Soc., Dalton Trans. (1994) 2437.
[29] P. Ghosh, A. Pramanik, N. Bag, A. Chakravorty, J. Chem. Soc., Dalton Trans. (1992) 1883.
[30] B. Machura, J. Mrozinski, R. Kruszynski, J. Kusz, Polyhedron 27 (2008) 3013.
[31] I. Booysen, T.I.A. Gerber, E. Hosten, P. Mayer, J. Iran Chem. Soc. 5 (2008) 689.
[32] L. Maria, C. Moura, A. Paulo, I.C. Santos, J. Organomet. Chem. 691 (2006) 4773.
[33] C. Meliān, C. Kremer, L. Suescun, A. Mombrü, R. Mariezcurrena, E. Kremer, Inorg. Chim. Acta 306 (2000) 70.
[34] T.I.A. Gerber, P. Mayer, Z.R. Tshentu, J. Coord. Chem. 58 (2005) 1271.
[35] T.I.A. Gerber, D. Luzipo, P. Mayer, J. Coord. Chem. 57 (2004) 1419.
[36] P. Mayer, T.I.A. Gerber, B. Buyambo, A. Abrahams, Polyhedron 28 (2009) 1174.
[37] L. Wei, S.R. Banerjee, M.K. Levadala, J. Babich, J. Zubieta, Inorg. Chim. Acta 357 (2004) 1499.
[38] N.S. Fleur, J.C. Hili, A. Mayr, Inorg. Chim. Acta 362 (2009) 1571.
[39] J.R. Farrell, C. Becker, D.P. Lavoie, J.L. Shaw, C.J. Ziegler, J. Organomet. Chem. 689 (2004) 1122.



Scheme 1. N,N′-bis(2-pyridylmethyl)-1,3-propanediamine (also called: 1,7-bis-(2′-pyridyl)-2,6-diazaheptane), abbreviated as pypn.

obtained on a Bruker-EMX*plus* electron spin resonance spectrometer (field calibrated with DPPH (g = 2.0036).

2.2. Synthesis of the ligand

The ligand pypn was synthesised according to the literature [13] and was isolated as the tetrahydrochloride salt (pypn·4HCl). The purity of the ligand was verified by spectroscopic techniques (NMR, IR) and elemental analysis.

2.3. Synthesis of complexes *1*, *2* and *3*

A mixture of sodium acetate trihydrate (0.54 g, 4 mmol) and ligand hydrochloride pypn•4HCl (0.40 g, 1 mmol) in absolute ethanol (30 mL) was stirred while boiling (10 min, water bath), then cooled and the sodium chloride which precipitated was filtered off. Then 1 mmol of metal perchlorate hexahydrate (for compounds **1** and **3**), iron(III) nitrate trihydrate (for compound **2**) in absolute ethanol (20 mL) was added dropwise to the filtrate and the solution was stirred for 10 min at room temperature. The solution was filtered to remove any undissolved material and was left concentrated in the open air. After few days crystals suitable for X-ray were formed and they were collected, washed with the mother liquid and dried at room temperature. Compound **1**: purple, plate crystals; yield: 0.39 g (75%). *Anal.* Calc. for $C_{30}H_{42}Cl_4Cu_2N_8O_{17}$: C, 34.1; H, 4.0; N, 10.6; Cu, 12.0. Found: C, 33.9; H, 4.2; N, 10.7; Cu, 11.9%. Compound **2**: red block crystals; yield: 0.22 g, (50%). *Anal.* Calc. for $C_{15}H_{18}Cl_2FeN_5$: C, 40.5; H, 4.5; N, 15.7; Fe, 12.6. Found: C, 40.8; H, 4.2; N, 15.5; Fe, 12.3%. Compound **3**: colorless needle-shaped crystals; yield: 0.25 g, (55%). *Anal.* Calc. for $C_{15}H_{20}Cl_2N_4O_4Zn$: C, 39.5; H, 4.4; N, 12.3; Fe, 14.3. Found: C, 39.8; H, 4.2; N, 12.1; Zn, 14.1%.

2.4. Synthesis of complexes *4*, *5* and *6*

These complexes were obtained by a similar method described above, but in this case by adding 2 mmol of ammonium thiocyanate, or sodium azide dissolved in 5 mL of ethanol, or 5 mL of water, respectively. Compound **4**: red needle-shaped crystals; yield: 0.35 g, (65%). *Anal.* Calc. for $C_{17}H_{20}ClCoN_6O_4S_2$: C, 38.5; H, 3.8; N, 15.8; Co, 11.1. Found: C, 38.7; H, 3.5; N, 15.7; Co, 11.4%. Compound **5**: red needle-shaped crystals; yield: 0.40 g, (80%). *Anal.* Calc. for $C_{15}H_{20}ClCoN_{10}O_4$: C, 36.1; H, 4.0; N, 28.1; Co, 11.8. Found: C, 36.2; H, 3.9; N, 28.0; Co, 11.6%. Compound **6**: colorless needle crystals; yield: 0.26 g, (50%). *Anal.* Calc. for $C_{17}H_{20}N_6S_2Zn$: C, 46.6; H, 4.6; N, 19.2; Zn, 14.9. Found: C, 46.3; H, 4.8; N, 18.9; Zn, 14.7%. *Note:* Azide and perchlorate compounds are potential explosive. They must be handled with care and used in small quantities.

2.5. X-ray crystallography

For compounds **1, 2** and **6**: A suitable crystal was selected from the mother liquid and mounted to a glass fiber using the oil-drop method; data were collected on a Nonius KappaCCD diffractometer (graphite-monochromated Mo Kα radiation). The intensity data were corrected for Lorentz and polarization effects, for absorption and extinction. The structure was solved by direct methods. The programs COLLECT [14], SHELXS-97[15], SHELXL-97 [15] were used for

Table 1
Crystallographic data.

Compound	**1**	**2**	**3**	**4**	**5**	**6**
Formula	$C_{30}H_{42}Cl_4Cu_2N_8O_{17}$	$C_{15}H_{18}Cl_2FeN_5$	$C_{15}H_{20}Cl_2N_4O_4Zn$	$C_{17}H_{20}ClCoN_6O_4S_2$	$C_{15}H_{20}ClCoN_{10}O_4$	$C_{17}H_{20}N_6S_2Zn$
Molecular weight	1049.57	443.09	456.64	530.91	498.79	437.92
Crystal system	orthorhombic	monoclinic	monoclinic	triclinic	triclinic	monoclinic
Space group	Pnma (No.62)	P21/c (No.14)	P21/c (No.14)	P-1 (No.2)	P-1 (No.2)	P21/c (No.14)
a (Å)	13.714(2)	11.848(2)	12.3766(3)	8.3356(3)	8.6521(9)	15.8669(17)
b (Å)	26.283(5)	12.474(2)	7.4973(2)	9.1440(3)	10.8312(8)	8.0206(8)
c (Å)	11.167(2)	12.301(2)	21.1657(5)	16.0893(5)	11.8637(10)	15.5456(15)
α (°)	90	90	90	82.231(2)	75.867(5)	90
β (°)	90	94.56(3)	102.753(1)	76.904(2)	76.152(8)	99.821(5)
γ (°)	90	90	90	66.672(1)	69.478(9)	90
V (Å3)	4025.1(12)	1812.2(5)	1915.54(8)	1095.38(6)	995.13(15)	1949.4(3)
Z	4	4	4	2	2	4
$D_{calc.}$ (g cm^{-3})	1.732	1.624	1.583	1.610	1.665	1.492
F(0 0 0)	2136	908	936	544	512	904
μ (cm^{-1})	1.406	1.153	1.589	1.133	1.045	1.488
Crystal size (mm)	0.02 × 0.10 × 0.20	0.27 × 0.24 × 0.20	0.06 × 0.08 × 0.40	0.06 × 0.12 × 0.25	0.12 × 0.04 × 0.02	0.01 × 0.04 × 0.22
Colour, shape	purple, plate	red, block	colorless, needle	red, needle	red, needle	colorless, plate
Temperature (K)	173(2)	173(20)	293(2)	293(2)	173(2)	293(2)
θ_{min}, θ_{max} (°)	2.8, 26.0	2.82, 27.58	1.7, 30.0	1.3, 30.1	2.04, 25.50	1.3, 25.0
Total reflections	50 607	30 180	48 611	26 482	14 744	13 212
Total unique reflections	3962 (R_{int} = 0.103)	4170(R_{int} = 0.0338)	5619 (R_{int} = 0.031)	6374 (R_{int} = 0.031)	3701 (R_{int} = 0.0533)	3450 (R_{int} = 0.089)
Number of refined data, parameters	3962, 302	4170, 235	5619, 235	6374, 298	3701, 307	3450, 235
R [a], $wR2$ [b]	0.0868, 0.2144	0.0325, 0.0906	0.0394, 0.1388	0.0480, 0.1465	0.0492, 0.1334	0.0808, 0.2228
S[c]	1.09	1.053	1.05	1.03	1.078	1.09
Min. and max. resd. dens. (e/Å^3)	−0.71, 1.02	−0.323, 0.873	−0.74, 1.07	−0.46, 0.70	−0.575, 1.211	−0.84, 1.17

[a] $R_1 = \Sigma||F_o| - |F_c||/\Sigma|F_o|$.
[b] $wR_2 = [\Sigma[w(F_o^2 - F_c^2)^2]/\Sigma[w(F_o^2)^2]]^{1/2}$.
[c] Goodness-of-fit $S = [\Sigma w(F_o^2 - F_c^2)^2/(n-p)]^{1/2}$, where n is the number of reflections and p the number of parameters.

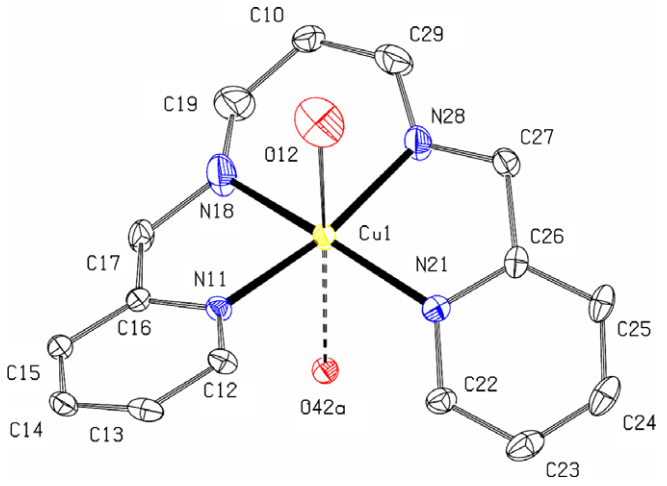


Fig. 1. Atomic displacement plot (30% probability level) of the the molecular structure of **1**. Hydrogen atoms and the water molecule are omitted for clarity. Only one of the oxygen atoms connected to the Cu-atom is shown, due to the severe disordering of the perchlorate anions.

data reduction, structure solution and structure refinement, respectively. Refinement of F^2 was done against all reflections. All non-hydrogen atoms were refined anisotropically. All H atoms were introduced in calculated positions and refined with fixed geometry with respect to their carrier atoms. Details of compound **1**: the disordered perchlorate anions were refined as rigid groups. The H atoms were geometrically fixed and allowed to ride on the attached atoms. H atoms of the disordered water molecules were not located. Details of compound **5**: the disordered perchlorate anion was refined as a rigid group in two positions with population parameters 0.7 and 0.3.

For compounds **3, 4 and 6**: the crystal data were collected on a Siemens SMART three-circle CCD diffractometer using monochromatic Mo Kα radiation (λ = 0.71073 Å). The structure was solved by the direct method and refined by full matrix least squares, based on F^2 using the SHELX-TL software package [16]. An empirical absorption correction based on symmetric equivalent reflections was applied using the SADABS program [17,18]. All the hydrogen positions were initially located in the difference map and for the final refinement the hydrogen atoms were placed geometrically and held in the riding mode. The last cycles of the refinement included atomic positions for all the atoms, anisotropic thermal parameters for all non-hydrogen atoms and isotropic thermal parameters for all the hydrogen atoms.

Crystallographic data are presented in a summary Table 1.

3. Results and discussion

3.1. Crystal and molecular structure of $[Cu(pypn)(ClO_4)_2](H_2O)_{1/2}$ (1)

The structure of **1** consists of a $[Cu(pypn)]^{2+}$ cation, two disordered semi-coordinating ClO_4^- anions and a disordered water molecule. The structure is depicted in part in Fig. 1 together with the numbering scheme. Selected bond distances and angles are listed in Table 2. The Cu-atom has a distorted elongated octahedral coordination with the basal plane comprised of four nitrogens from the chelating pypn ligand (Cu–N distances vary from 2.000(6) to 2.019(8) Å) and with trans-equatorial angles of 168.3(3) (N11–Cu–N28) and 164.7(4)° (N18–Cu–N21). The conformation around the Cu ions can be described as $m_s m_a$ [19]. The apical positions are occupied by two oxygen atoms of the two different disordered perchlorate anions (Cu–O distances vary from 2.49(2) to 2.61(1) Å). The lattice structure is stabilized by a weak hydrogen bonding between the oxygen of the perchlorate anion and the N18 hydrogen atom (N18···O 3.36(2) Å). Details of the hydrogen bonds are given in Table 3.

Table 2
Selected bond lengths (Å) and angles (°) for the several compounds.

Compound ***1***			
Cu(1)–N(21)	2.000(6)	Cu(1)–N(11)	2.013(6)
Cu(1)–N(28)	2.012(7)	Cu(1)–N(18)	2.019(8)
Cu(1)–O22*	2.58(1)	Cu(1)–O(12)*	2.61(1)
Cu(1)–O43*	2.49(2)	Cu(1)–O(33)*	2.51(2)
N(11)–Cu(1)–N(28)	168.3(3)	N(21)–Cu(1)–N(18)	164.7(4)
Compound ***2***			
Fe(1)–N(21)	2.145(2)	Fe(1)–N(18)	2.146(2)
Fe(1)–N(28)	2.154(2)	Fe(1)–N(11)	2.175(2)
Fe(1)–Cl(2)	2.2598(7)	Fe(1)–Cl(1)	2.2754(7)
N(21)–Fe(1)–N(18)	165.69(7)	N(11)–Fe(1)–Cl(2)	169.05(5)
N(28)–Fe(1)–Cl(1)	169.98(5)		
Compound ***3***			
Zn–Cl1	2.2813(7)	Zn–N1	2.087(2)
Zn–N2	2.138(2)	Zn–N3	2.111(3)
Zn–N4	2.176(2)		
Cl1–Zn–N1	107.71(6)	Cl1–Zn–N2	96.37(7)
Cl1–Zn–N3	122.08(7)	Cl1–Zn–N4	94.72(6)
N1–Zn–N3	130.19(9)	N2–Zn–N4	168.59(9)
Compound ***4***			
Co–N1	1.912(3)	Co–N2	1.899(3)
Co–N3	1.952(2)	Co–N4	1.957(3)
Co–N5	1.936(2)	Co–N6	1.957(3)
N1–Co–N5	175.71(12)	N2–Co–N4	179.04(11)
N3–Co–N6	175.79(12)		
Compound ***5***			
Co(1)–N(4)	1.933(3)	Co(1)–N(21)	1.943(3)
Co(1)–N(11)	1.960(3)	Co(1)–N(1)	1.962(3)
Co(1)–N(18)	1.964(3)	Co(1)–N(28)	1.966(3)
N(4)–Co(1)–N(11)	175.13(15)	N(21)–Co(1)–N(18)	179.11(14)
N(1)–Co(1)–N(28)	179.70(15)		
Compound ***6***			
Zn1–N1	2.229(11)	Zn1–N2	2.055(8)
Zn1–N3	2.161(6)	Zn1–N4	2.169(7)
Zn1–N5	2.187(8)	Zn1–N6	2.179(6)
N1–Zn1–N3	170.1(3)	N2–Zn1–N5	169.8(3)
N4–Zn1–N6	167.9(3)		

* Disordered atoms.

3.2. Crystal and molecular structure of $[Fe(pypn)Cl_2](NO_3)$ (2)

The structure of **2** is depicted in Fig. 2, together with the numbering scheme. Selected bond distances and angles are listed in Table 2.

The Fe(III) ion has an octahedral geometry comprised of four nitrogens from the chelating pypn ligand in a non-planar orientation with the $m_s f$ [19] conformation (Fe–N distances vary from 2.145(2) to 2.175(2) Å) and two *cis*-oriented chloride anions (Fe–Cl distances 2.2598(7) and 2.2754(7) Å). The angles are 165.69(7), 169.05(5) and 169.98(5)° (for N21–Fe–N18, N11–Fe–Cl2, N28–Fe–Cl1, respectively). The lattice structure is stabilised by a medium strong hydrogen bond between the N18 hydrogen atom to a neighboring chloride anion (N···Cl distance 3.288(2) Å) and between the N28 hydrogen atom to the oxygen atoms of the nitrate anion (N···O distances 2.919(2) and 3.183(3) Å) (see Fig. 3 for details). Details of the hydrogen bond geometries are given in Table 3. The bond distances and angles of this structure are comparable to a related type of structure, $[Fe(pypn)Cl_2](ClO_4)$, in the literature [12], which gives also the same type of hydrogen bonds.

3.3. Crystal and molecular structure of $[Zn(pypn)Cl](ClO_4)$ (3)

A plot showing the numbering scheme of compound **3** is presented in Fig. 4, and selected bond distances and angles are given

Table 3
Hydrogen bonding parameters details of the 6 compounds.

Compound 1				
D–H···A	D–H (Å)	H···A (Å)	D···A (Å)	D–H···A (°)
N(18)–H(18A)···O(24)*	0.93	2.49	3.36(2)	155
*Compound **2***				
D–H···A	D–H (Å)	H···A (Å)	D···A (Å)	D–H···A (°)
N(18)–H(18A)···Cl(1) [1−*x*, −*y*, 1−*z*]	0.93	2.47	3.288(2)	147
N(28)–H(28A)···O(1)	0.93	2.08	2.919(2)	150**
N(28)–H(28A)···O(3)	0.93	2.41	3.183(3)	140**
*Compound **3***				
D–H···A	D–H (Å)	H···A (Å)	D···A (Å)	D–H···A (°)
N(2)–(H2)···(Cl)1 [1−x, 2−y, 1−z]	0.91	2.46	3.327(2)	159
N(3)–(H3)···(O3) [1−*x*, 2−*y*, 1−*z*]	0.91	2.17	3.041(5)	160
*Compound **4***				
D–H···A	D–H (Å)	H···A (Å)	D···A (Å)	D–H···A (°)
N(4)–H(4N)···O(2) [−1 + *x*, *y*, *z*]	0.91	2.21	3.093(6)	162
N(6)–H(6N)···O(1)	0.91	2.27	2.994(5)	137
*Compound **5***				
D–H···A	D–H (Å)	H···A (Å)	D···A (Å)	D–H···A (°)
N(18)–H(18A)···N(1) [−*x*, −*y*, 1−*z*]	0.93	2.16	3.067(5)	165**
N(18)–H(18A)···N(2) [−*x*, −*y*, 1−*z*]	0.93	2.54	3.321(5)	142**
N(28)–H(28A)···O(13)* [−*x*, 1−*y*, 1−*z*]	0.93	2.29	3.043(6)	138
*Compound **6***				
D–H···A	D–H (Å)	H···A (Å)	D···A (Å)	D–H···A (°)
N(4)–H(4′)···S(2) [1−*x*, −1/2 + *y*, 1/2−*z*]	0.91	2.66	3.524(8)	159

* Disordered atom.
** Bifurcated H-bonds.

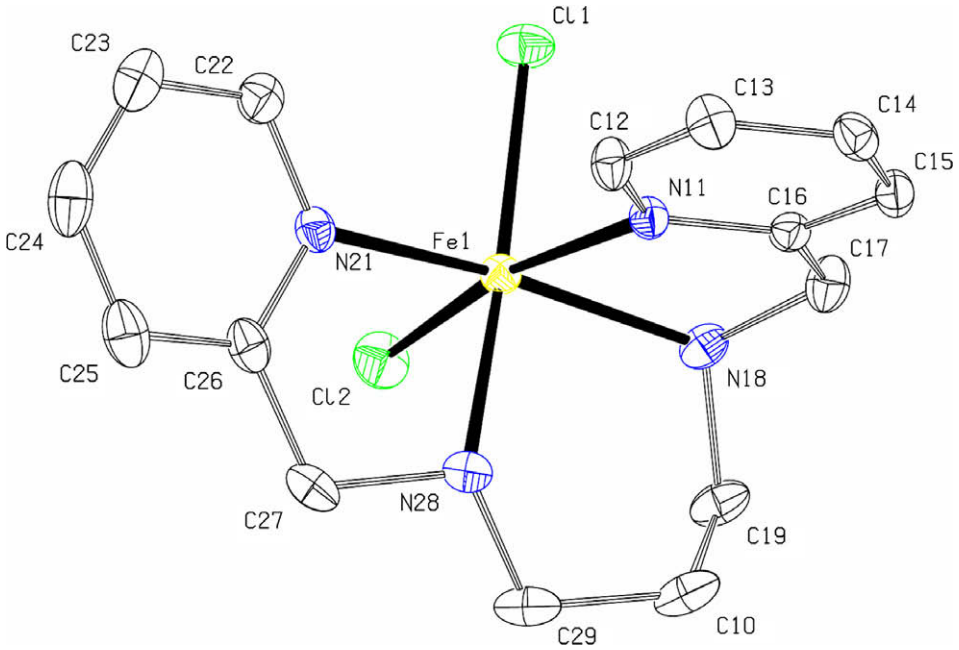


Fig. 2. Atomic displacement plot (30% probability level) of the cationic part of the molecular structure of **2**. Hydrogen atoms and nitrates have been omitted for clarity.

in Table 2. The Zn(II) ion is five coordinated with four nitrogen atoms of a chelating pypn ligand (Cu–N distances from 2.087(2) to 2.176(2) Å). The fifth position is occupied by chloride ion with a Cu–Cl distance of 2.2813(7) Å. The basal angles are 168.59(9) and 130.19(9)° (for N2–Zn–N4 and N1–ZnN3).

The distortion of the Zn coordination polyhedron from trigonal bipyramidal can be best described by the structural parameter τ (τ describes the relative amount of trigonality; $\tau = 0$ corresponds to for square pyramidal geometry and $\tau = 1$ to trigonal bipyramidal) [20]. For the title compound, $\tau = 0.64$, indicating that the coordination geometry can be described as a significantly distorted trigonal bipyramid.

The lattice structure is stabilised by hydrogen bonding of which one H bond is from the N2 hydrogen atom to a neighboring chloride ion (N···Cl distance 3.327(2) Å). The other H bond is from the N3 hydrogen atom to the oxygen atom of a perchlorate anion (N···O distance 3.041(5) Å) (see Fig. 5). Details of the hydrogen bonds are given in Table 3.

3.4. Crystal and molecular structure of $[Co(pypn)(NCS)_2](ClO_4)$ **(4)**

The structure of **4** consists of a $[Co(pypn)(NCS)_2]^+$ cation, in which the starting Co^{2+} has been oxidized to Co^{3+} and one disordered non-coordinating ClO_4^- anion. The structure is depicted in

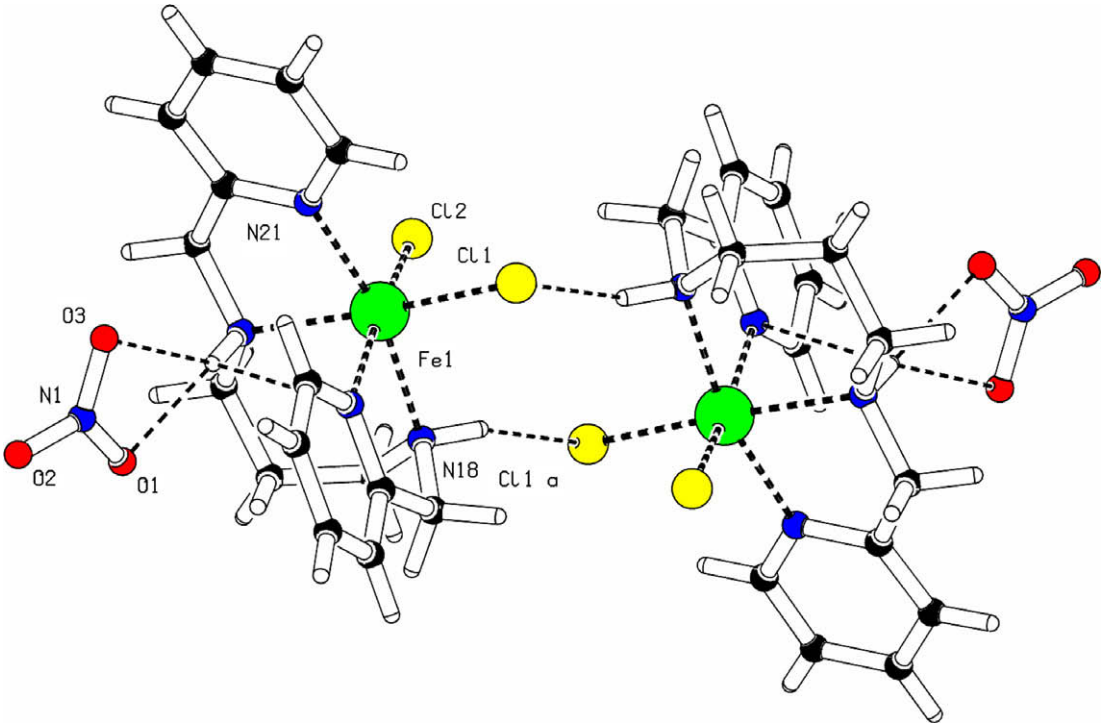


Fig. 3. The hydrogen bond system of **2**, showing a dimerisation with both Cl and NO_3 displayed.

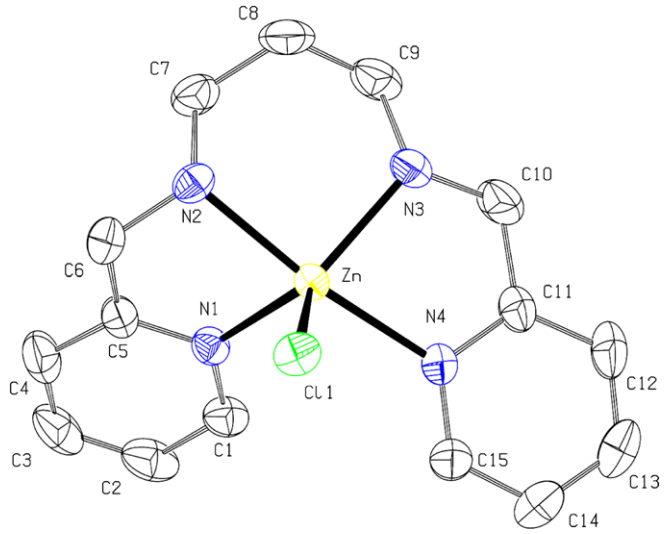


Fig. 4. Atomic displacement plot (30% probability level) of the cationic part of the molecular structure of **3**. The non-coordinating perchlorate anion and the hydrogen atoms are omitted for clarity.

Fig. 6 together with the numbering scheme. Selected bond distances and angles are listed in Table 2.

The Co(III) ion has an octahedral geometry comprised of four nitrogens from the chelating pypn ligand displaying the *m,f* [19] conformation (Co–N distances vary from 1.936(2) to 1.957(3) Å) and two *cis*-oriented nitrogen atoms of two thiocyanate anions (Co–N distances 1.912(3) and 1.899(3) Å). The angles are almost linear, 175.71(12), 175.79(12) and 179.04(11)° (for N1–Co–N5), N3–Co–N6, N2–Co–N4, respectively). The lattice structure is stabilised by a medium to strong hydrogen bonding (for definitions: see Refs. [21,22]) between the N4 and N6 hydrogen atoms to the oxygen atoms of the perchlorate anions (N···O distances from 2.994(5) to 3.257(15) Å). Details of the hydrogen bonds are given in Table 3.

3.5. Crystal and molecular structure of $[Co(pypn)(N_3)_2](ClO_4)$ (5)

The structure of **5** consists of a $[Co(pypn)(N_3)_2]^+$ cation, in which the starting Co^{2+} has been oxidized to Co^{3+} and one disordered non-coordinating ClO_4^- anion. The structure is depicted in Fig. 7 together with the numbering scheme. Selected bond distances and angles are listed in Table 2.

The Co(III) ion has an octahedral geometry comprised of four nitrogens from the chelating pypn ligand with the *m,f* [19] conformation (Co–N distances vary from 1.943(3) to 1.966(3) Å) and two nitrogen atoms of two azide anions (Cu–N distances 1.933(3) and 1.962(3) Å). The angles are almost linear, 175.13(15), 179.11(14) and 179.70(15)° (for N4–Co–N11), N21–Co–N18, N1–Co–N28, respectively). The lattice structure is stabilized by a medium strong hydrogen bonding between the N18 hydrogen atom and the nitrogen atoms of neighboring azide anions (N18···N_{azide} 3.067(5) and 3.321(5) Å) and between the N28 hydrogen atom to the oxygen atoms of neighboring perchlorate anions (N28···O_{ClO4} 3.043(6) and 3.438(6) Å). Details of the hydrogen bonds are given in Table 3.

3.6. Crystal and molecular structure of $[Zn(pypn)(NCS)_2]$ (6)

The structure of **6** is depicted in Fig. 8 together with the used numbering scheme. Selected bond distances and angles are listed in Table 2.

The Zn atom has an octahedral geometry comprised of four nitrogens from the chelating pypn ligand with the *m,f* [19] conformation (Zn–N distances vary from 2.161(6) to 2.187(8) Å) and two nitrogen atoms of two thiocyanato anions (Zn–N distances 2.055(8) and 2.229(11) Å). The ligand is folded in such a way that the NCS anions are in a cis position. The angles are 167.9(3), 169.8(3) and 170.1(3)° (for N4–Zn–N6), N2–Zn–N5, N1–Zn–N3, respectively). The lattice structure is stabilised by a medium strong hydrogen bond between the N4 hydrogen atom to the sulfur atom of one of the thiocyanato anion (N···S distance 3.524(8) Å),

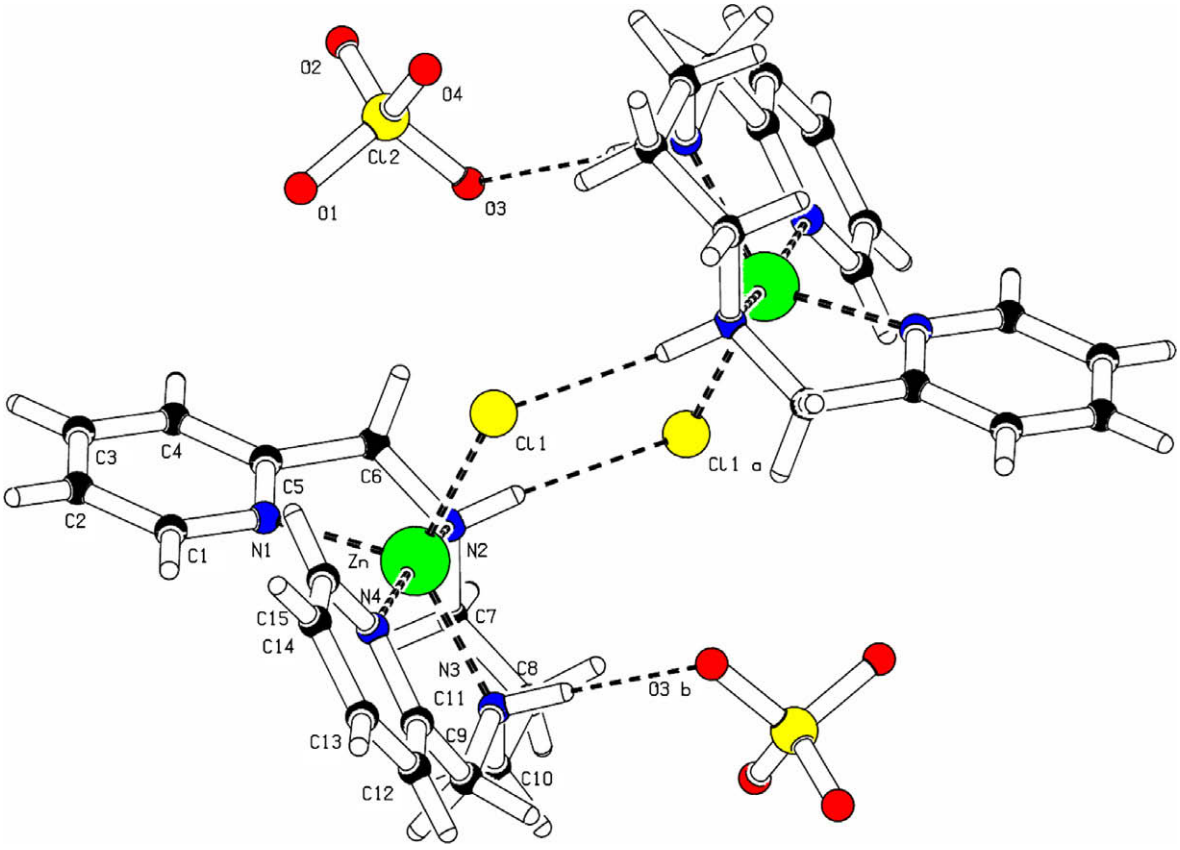


Fig. 5. The hydrogen bond system of **3**, showing a latticed dimerisation of 2 units.

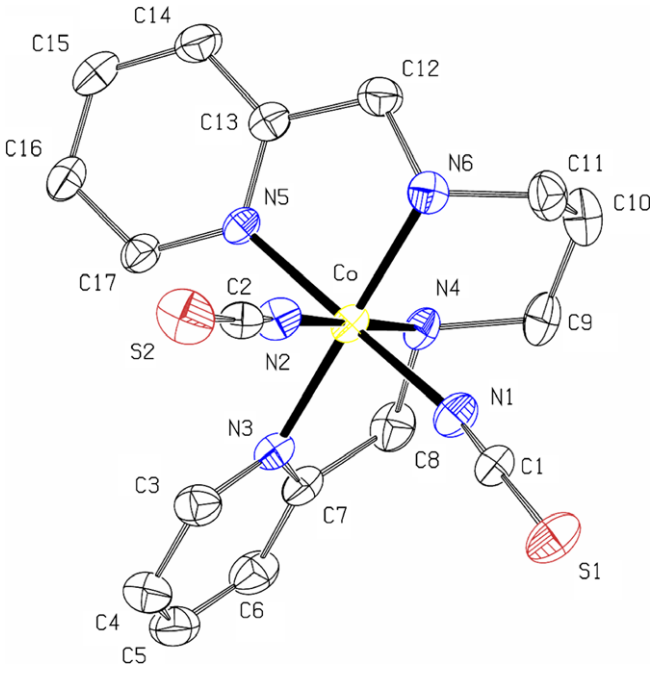


Fig. 6. Atomic displacement plot (30% probability level) of the cationic part in the molecular structure of **4**. Hydrogen atoms and non-coordinating anions are omitted for clarity.

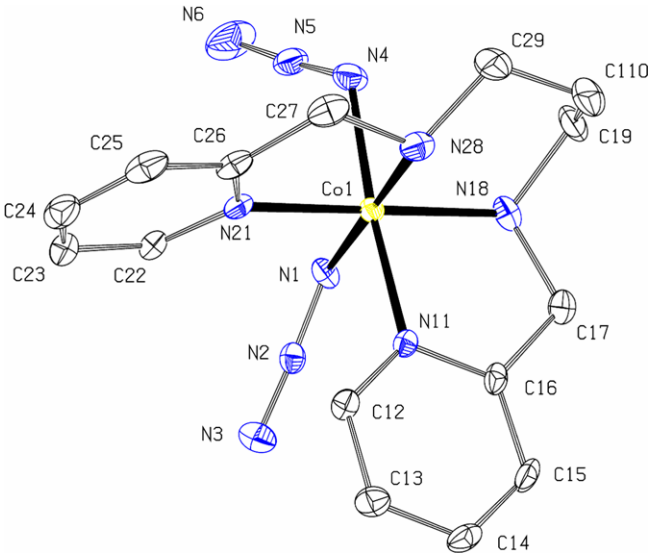


Fig. 7. Atomic displacement plot (30% probability level) of the cationic part in the molecular structure of **5**. Hydrogen atoms and non-coordinating anions are omitted for clarity.

forming in this way a type of dinuclear unit (Fig. 9). Details of the hydrogen bonds are given in Table 3.

3.7. Spectroscopy, IR, ligand field and EPR

The most relevant IR and the ligand field parameters are given in Table 4. In the IR spectra the most characteristic bands are from the NH vibrations, the pyridyl ring vibrations and the anions. The

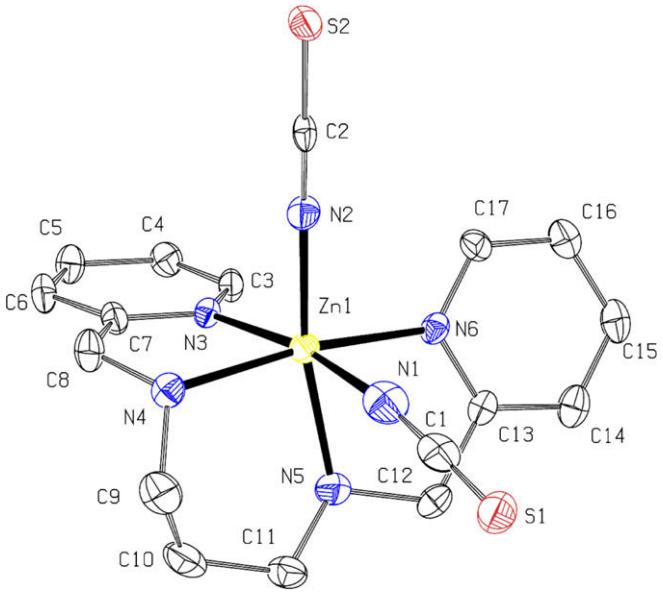


Fig. 8. Atomic displacement plot (30% probability level) of the molecular structure of **6**. Hydrogen atoms have been omitted for clarity.

NH vibrations are found between 3140 and 3255 cm^{-1}, as single bands (compounds **1, 3** and **6**), or as split broad bands (compounds **2, 4** and **5**), which arise from the molecular symmetry or from solid-state effects [1]. The pyridyl ring vibrations are found between 1604–1613 and 1572–1575 cm^{-1}, while these vibrations are observed at 1590 and 1570 cm^{-1} in the free ligand [1]. The bands of the anions are given in Table 4 and are according to the literature [23].

The ligand field transitions measured as a solid with the diffuse reflectance technique are observed for compound **1** (Cu^{2+} compound) as a broad band with a maximum at 17.2 $\times$ 10^3 cm^{-1} and for compounds **4** and **5** (Co^{3+} compounds) as two bands at 17.9 and 10.4 $\times$ 10^3 cm^{-1} and at 18.9 and 12.5 $\times$ 10^3 cm^{-1}, for compounds **4** and **5**, respectively. These are normal ligand field transitions for (distorted) octahedral Cu^{2+} and Co^{3+} geometries [24]. For compound **2** a very broad band with a maximum at around 18.0 ± 0.5 $\times$ 10^3 cm^{-1} is observed, which is attributed to a charge-transfer band of the Fe^{3+} ion.

The EPR spectra of compound **1** was recorded as a polycrystalline powder at RT and 77 K and shows a $S = 1/2$ spectrum with a $g_{\perp}$ of 2.06 and an unresolved $g_{//}$ of 2.18, which are values are consistent with a d_{x2-y2} based geometry [24].

4. Concluding remarks

In the present study 6 different transition metal (Fe^{3+}, Co^{3+}, Cu^{2+}, Zn^{2+}) compounds with the tetradentate ligand (N,N′-bis(2-Pyridylmethyl)-1,3-propanediamine, have been synthesised and fully characterized by IR, LF and X-ray structure analysis. Depending on the metal cation and the anion, different types of structures and a large variety of interesting H-bonding patterns were observed, including the formation of lattice dimers. Compounds **2** and **3** appeared to contain coordinated Cl^- ions, which originated from the remaining HCl in the used ligand. Compounds **4, 5** and **6** have quite strongly coordinated anions, i.e. N_3^- and NCS^-. The ligand folding around the metal ions is in all cases $m_s f$ [19] except for compound **1**, where it is $m_s m_a$. The overall charge of the compounds is compensated by perchlorate, or nitrate ions.

Our present ligand is related with (N,N′-bis(2-Pyridylmethyl)-1,2-ethanediamine) (abbreviated as pyen), which contains one CH_2 group less than pypn. In the CSD (Cambridge Structural Database), to the best of our knowledge, no crystal structures of that ligand containing the thiocyanate anion are present; with the azide anion only one Ni^{2+} compound has been published [25]. Related to

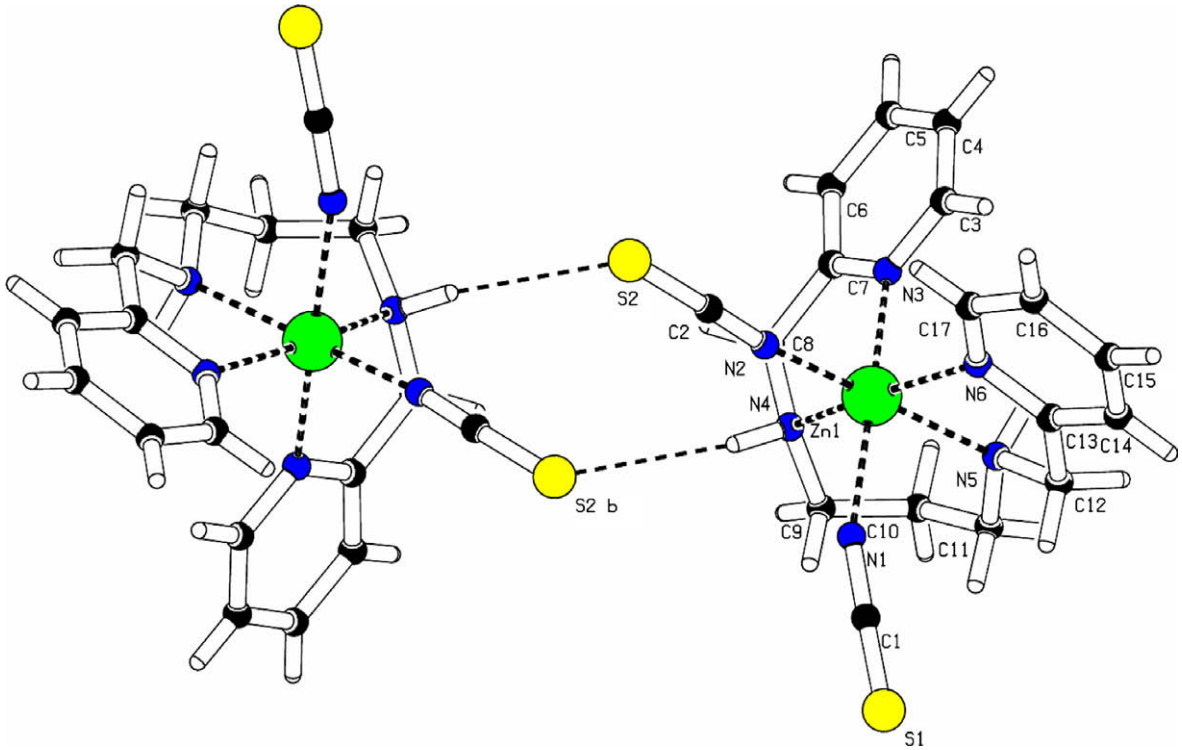


Fig. 9. The hydrogen bond system of **6**, showing a dimerization in the lattice through NH···S bonds.

Table 4
Diffuse reflectance and IR details of the compounds.

	Compound	Colour	Diffuse reflectance Max (10^3 cm^{-1})		Infrared		
					NH	Pyridyl ring	Anion
1.	$[Cu(pypn)(ClO_4)_2](H_2O)_{1/2}$	purple	17.2		3255	1613 1573	1056(br)
2.	$[Fe(pypn)Cl_2](NO_3)$	brown-red	18.0 ± 0.5		3215 3124	1607 1575	1290
3.	$[Zn(pypn)Cl](ClO_4)$	colorless			3235	1606 1572	1083
4.	$[Co(pypn)(NCS)_2](ClO_4)$	red	12.5	18.9	3232 3182	1609 1570	2076(CN) 1057(ClO_4)
5.	$[Co(pypn)(N_3)_2](ClO_4)$	red	10.4	17.9	3198 3140	1610 1575	2024(N_3) 1058(ClO_4)
6.	$[Zn(pypn)(NCS)_2]$	colorless			3252	1604 1573	2075(CN)

compound **1** is the compound $[Cu(pyen)(ClO_4)_2]$ [26]. In that case however the perchlorate anion is bridging between two Cu ions, contrary to compound **1**. For comparison with compound **2** with pyen, the crystal structure of $[Fe(pyen)Cl_2](ClO_4)$ is known [27], which has the same ligand conformation as compound **2**. Only the hydrogen bond is quite different, as the perchlorate ions are bridging between two ions, and not the chloride as in **2**.

Supplementary data

Crystallographic data (excluding structure factors) for the structure reported in this paper have been deposited with the Cambridge Crystallographic Data Centre as supplementary publication no. CCDC-723651, 723652, 723653, 723654, 723655, 723756, for compounds **1, 2, 3, 4, 5** and **6**, respectively. Copies of available material can be obtained, free of charge, on application to the Director, CCDC, 12 Union Road, Cambridge CB2 1EZ, UK, (fax: +44-(0)1223-336033 or Email: deposit@ccdc.cam.ac.uk.

Acknowledgments

The work described in the present paper has been supported by the Leiden University Study group WFMO (Werkgroep Fundamenteel MaterialenOnderzoek). Financial support and coordination by the FP6 Network of Excellence "MAGMANet " (Contract number 515767) is kindly acknowledged.

References

[1] J.G. Gibson, E.D. McKenzie, J. Chem. Soc. A (1971) 1666.
[2] J. Glerup, P.A. Goodson, D.J. Hodgson, M.H. Lynn, K. Michelsen, Inorg. Chem. 31 (1992) 4785.
[3] D.J. Hodgson, K. Michelsen, E. Pedersen, D.K. Towle, J. Chem. Soc., Chem. Commun. (1988) 426.
[4] D.J. Hodgson, K. Michelsen, E. Pedersen, D.K. Towle, Inorg. Chem. 30 (1991) 815.
[5] E.Q. Gao, J.K. Tang, D.Z. Liao, Z.H. Jiang, S.P. Yan, G.L. Wang, Inorg. Chem. 40 (2001) 3134.
[6] N.A. Bailey, E.D. McKenzie, J. Chem. Soc., Dalton Trans. (1972) 1566.
[7] N. Arulsamy, P.A. Goodson, D.J. Hodgson, J. Glerup, K. Michelsen, Inorg. Chim. Acta 216 (1994) 21.
[8] H.R. Fischer, D.J. Hodgson, K. Michelsen, E. Pedersen, Inorg. Chim. Acta 88 (1984) 143.
[9] P.A. Goodson, J. Glerup, D.J. Hodgson, K. Michelsen, H. Weihe, Inorg. Chem. 30 (1991) 4909.
[10] N. Shaikh, S. Goswami, A. Panja, H.L. Sun, F. Pan, S. Gao, P. Banerjee, Inorg. Chem. 44 (2005) 9714.
[11] E.D. McKenzie, F.S. Stephens, Inorg. Chim. Acta 42 (1980) 1.
[12] N.W. Alcock, E.V. Rybak-Akimova, D.H. Busch, Acta Crystallogr., Sect. C 53 (1997) 1385.
[13] K. Michelsen, Acta Chem. Scand. A 31 (1977) 429.
[14] Nonius, COLLECT, Nonius BV, Delft, The Netherlands, 2002.
[15] G.M. Sheldrick, Acta. Crystallogr. A 64 (2008) 112.
[16] G.M. Sheldrick, SHELXTL NT v 5.10, Bruker AXS, Inc. Madison, Wis. 53719, USA 1999.
[17] R.H. Blessing, Acta Crystallogr. A 51 (1995) 33.
[18] G.M. Sheldrick, SADABS v2.03: Area-Detector Absorption Correction, University of Göttingen, Germany, 1999.
[19] R.M. Hartshorn, D.A. House, J. Chem. Soc., Dalton Trans. (1998) 2577.
[20] A.W. Addison, T.N. Rao, J. Reedijk, J. van Rijn, G.C. Verschoor, J. Chem. Soc., Dalton Trans. (1984) 1349.
[21] G.A. Jeffrey, H. Maluszynska, J. Mitra, Int. J. Biol. Macromol. 7 (1985) 336.
[22] M.R. Sundberg, Rev. Inorg. Chem. 20 (2000) 195.
[23] K. Nakamoto, Infrared and Raman Spectra of Inorganic and Coordination Compounds, Wiley, New York, 1978. pp. 221–291.
[24] B.J. Hathaway, Comprehensive Coordination Chemistry, vol. 5, Pergamon Press, Oxford, 1987 (Chapter 53).
[25] E.Q. Gao, D.Z. Liao, Z.H. Jiang, S.P. Yan, S.F. Zhang, Acta Chim. Sinica 59 (2001) 1294.
[26] E.V. Rybak-Akimova, A.Y. Nazarenko, L. Chen, P.W. Krieger, A.M. Herrera, V.V. Tarasov, P.D. Robinson, Inorg. Chim. Acta 324 (2001) 1.
[27] N. Arulsamy, D.J. Hodgson, J. Glerup, Inorg. Chim. Acta 209 (1993) 61.

reactivity of $[ReCl_3(MeCN)(PPh_3)_2]$ towards the dpk ligand. The $[ReCl_3(MeCN)(PPh_3)_2]$ complex has proven to be useful precursor in the synthesis of Re(III) compounds [16–18]. The $[ReCl_3(MeCN)(PPh_3)_2]$ also easily reacts with di-2-pyridylketone to give $[ReCl_3(dpk\text{-}N,O)(PPh_3)]$ (**1**) with rarer N,O-coordination of dpk ligand. The solid $[ReCl_3(dpk\text{-}N,O)(PPh_3)]$ can be handled in air without significant degradation, but rapid isomerisation with oxidation of coordinated PPh_3 occurs in organic solvents at room temperature in the presence of atmospheric oxygen. In fact, the starting purple solution of $[ReCl_3(dpk\text{-}N,O)(PPh_3)]$ in chloroform turns to dark red and crystals of $[ReCl_3(dpk\text{-}N,N')(OPPh_3)]$ (**2**) with N,N-coordination of dpk ligand are deposited.

N,N′,O coordination mode of monoanionic form of $(2\text{-py})_2CO$ has been confirmed in the $[ReOBr_3(dpk\text{-}OH)]\cdot 2(dpkH^+Br^-)$ (**3**), isolated from the reaction of $[ReOBr_3(PPh_3)_2]$ with excess of di-2-pyridylketone in acetone in air.

The structures of all the complexes $[ReCl_3(dpk\text{-}N,O)(PPh_3)]$ (**1**), $[ReCl_3(dpk\text{-}N,N')(OPPh_3)]$ (**2**) and $[ReOBr_3(dpk\text{-}OH)]\cdot 2(dpkH^+Br^-)$ (**3**) have been proven by X-ray diffraction. The complexes $[ReCl_3(dpk\text{-}N,N')(OPPh_3)]$ and $[ReOBr_3(dpk\text{-}OH)]$, which are stable in solution, have been also studied by UV–vis spectroscopy. The electronic spectra of $[ReCl_3(dpk\text{-}N,N')(OPPh_3)]$ and $[ReOBr_3(dpk\text{-}OH)]$ have been discussed in detail using the density functional theory (DFT) and time-dependent DFT (TDDFT) calculations.

Currently the density functional theory (DFT) is commonly used to examine the electronic structure of transition metal complexes. It meets with the requirements of being accurate, easy to use and fast enough to allow the study of relatively large molecules of transition metal complexes [19]. Recent studies have also supported the TDDFT method to be applicable for open- and closed-shell of 5d-metal complexes giving good assignment of experimental spectra [20–22].

2. Experimental

2.1. General procedure

The reagents used to the synthesis were commercially available and were used without further purification. The $[Re(MeCN)Cl_3(PPh_3)_2]$ [16] and $[ReOBr_3(PPh_3)_2]$ [23] complexes were prepared according to the literature methods.

IR spectra were recorded on a Nicolet Magna 560 spectrophotometer in the spectral range 4000–400 cm^{-1} with the samples in the form of KBr pellets. Electronic spectra were measured on a spectrophotometer Lab Alliance UV–vis 8500 in the range 1000–180 nm in acetonitrile solution. Elemental analyses (CHN) were performed on a Perkin–Elmer CHN-2400 analyzer.

2.2. Preparation of $[ReCl_3(dpk\text{-}N,O)(PPh_3)]$ (**1**)

$[Re(MeCN)Cl_3(PPh_3)_2]$ (0.5 g, 0.58 mmol) and di-2-pyridylketone (0.11 g, 0.60 mmol) in CH_2Cl_2 (80 cm^3) were heated under argon atmosphere for 5 h. The starting material gradually dissolved and the color of the reaction solution became blue-purple. The volume of the reaction solution was condensed to 10 cm^3 and allowed to cool to room temperature. Dark pink microcrystalline precipitate was formed and filtered off.

IR (KBr; ν/cm^{-1}): 1646(s) $\nu_{C=O}$; 1608(w), 1590(m), 1572(m) and 1538(w) ν_{CN} and $\nu_{C=C}$.

Anal. Calc. for $C_{29}H_{23}Cl_3N_2OPRe$: C, 47.13; H, 3.14; N, 3.79. Found: C, 47.61; H, 3.42; N, 3.62%.

2.3. Preparation of $[ReCl_3(dpk\text{-}N,N')(OPPh_3)]$ (**2**)

A solution of $[ReCl_3(dpk\text{-}N,O)(PPh_3)]$ in chloroform was stood for several days in air and dark red crystals were deposited.

IR (KBr; ν/cm^{-1}): 1649(vs) $\nu_{C=O}$; 1609(m), 1591(m), 1575(m) and 1542(w) ν_{CN} and $\nu_{C=C}$; 1135(vs) and 1119(vs) $\nu_{Re=O}$.

Anal. Calc. for $C_{29}H_{23}Cl_3N_2O_2PRe$: C, 46.13; H, 3.07; N, 3.71. Found: C, 46.79; H, 3.30; N, 3.45%.

2.4. Preparation of $[ReOBr_3(dpk\text{-}OH)]\cdot 2(dpkH^+Br^-)$ (**3**)

A mixture of $[ReOBr_3(PPh_3)_2]$ (0.50 g, 0.52 mmol), di-2-pyridylketone (0.28 g, 1.52 mmol) and acetone (100 ml) was stirred at room temperature for 12 h. Half of the solvent was removed and diethyl ether (50 ml) was added to precipitate the product as green solid, which was filtered off and dried. Yield 85%. Crystals suitable for X-ray investigation were obtained by recrystallization from acetonitrile.

IR (KBr; ν/cm^{-1}): 1683(vs) $\nu_{C=O}$; 1599(s), 1579(s) and 1520(s) ν_{CN} and $\nu_{C=C}$; 958(s) $\nu_{Re=O}$.

Anal. Calc. for $C_{33}H_{27}Br_4N_6O_5Re$: C, 36.25; H, 2.49; N, 7.69. Found: C, 36.89; H, 2.37; N, 7.39%.

2.5. Crystal structures determination and refinement

The X-ray intensity data of **1**, **2** and **3** were collected on a KM-4-CCD automatic diffractometer equipped with CCD detector and graphite monochromated Mo Kα radiation (λ = 0.71073 Å). Details concerning crystal data and refinement are given in Table 1. Lorentz, polarization and absorption correction [24] were applied. The structures were solved by the Patterson method and subsequently completed by the difference Fourier recycling. All the non-hydrogen atoms were refined anisotropically using full-matrix, least-squares technique. The hydrogen atoms were treated as "riding" on their adjacent atoms and assigned isotropic temperature factors equal 1.2 times the value of equivalent temperature factor of the aromatic parent atoms and equal 1.5 times the value of equivalent temperature factor of the oxygen atom (OH). SHELXS97 [25], SHELXL97 [26] and SHELXTL [27] programs were used for all the calculations. Atomic scattering factors were those incorporated in the computer programs.

2.6. Computational details

The ground states geometries of $[ReCl_3(dpk\text{-}N,N')(OPPh_3)]$ and $[ReOBr_3(dpk\text{-}OH)]$ were optimized without any symmetry restrictions with the DFT method using the hybrid B3LYP functional of GAUSSIAN-03 [28–30].

The calculations were performed using ECP basis set LANL2DZ [31] with an additional *d* and *f* function with the exponent α = 0.3811 and α = 2.033 [32] for rhenium and the standard 6-31G basis set for other atoms. For chloride, bromide, oxygen, nitrogen and phosphorous atoms, diffuse and polarization functions were added [33–38]. Vibrational frequencies of $[ReCl_3(dpk\text{-}N,N')(OPPh_3)]$ and $[ReOBr_3(dpk\text{-}OH)]$ were calculated to ensure that optimized geometries represented minima.

The electronic spectra of $[ReCl_3(dpk\text{-}N,N')(OPPh_3)]$ and $[ReOBr_3(dpk\text{-}OH)]$ were calculated with the TDDFT method, and the solvent effect (acetonitrile) was simulated using the polarizable continuum model with the integral equation formalism (IEF-PCM) [39–42].

Natural bond orbital (NBO) calculations for $[ReOBr_3(dpk\text{-}OH)]$ were performed with the NBO code [43] included in GAUSSIAN-03.

2.7. Magnetic measurement

Magnetization measurements of polycrystalline samples were carried out with a Quantum Design SQUID magnetometer (MPMSXL-5-type) at a magnetic field of 0.5 T over the temperature range 1.8–300 K. Magnetization measurements versus magnetic field (0–5 T) were made at 2 K.

Table 1
Crystal data and structure refinement for **1**, **2** and **3** complexes.

	1	**2**	**3**
Empirical formula	$C_{29}H_{23}Cl_3N_2OPRe$	$C_{29}H_{23}Cl_3N_2O_2PRe$	$C_{33}H_{27}Br_4N_6O_5Re$
Formula weight	739.01	755.01	1093.45
Temperature (K)	293(2)	293(2)	120(1)
Wavelength (Å)	0.71073	0.71073	0.71073
Crystal system	monoclinic	orthorhombic	triclinic
Space group	$P2_1/n$	$P2_12_12_1$	$P\bar{1}$
Unit cell dimensions (Å, °)	a = 11.621(2) b = 12.505(3) c = 18.938(4) β = 90.12(3)	a = 9.9643(3) b = 13.9694(5) c = 19.7787(6)	a = 8.98070(10) b = 13.0557(2) c = 16.2930(2) α = 69.0060(10) β = 81.8530(10) γ = 79.3880(10)
Volume (Å^3)	2752.1(10)	2753.10(15)	1747.05(4)
Z	4	4	2
D_{calc} (mg/m^3)	1.784	1.822	2.079
Absorption coefficient (mm^{-1})	4.791	4.794	8.102
F(0 0 0)	1440	1472	1044
Crystal size (mm)	0.05 × 0.08 × 0.19	0.04 × 0.18 × 0.20	0.183 × 0.181 × 0.176
θ Range for data collection (°)	3.22–25.00	2.90–25.00	1.76–25.05
Index ranges	$-13 \leqslant h \leqslant 13$ $-10 \leqslant k \leqslant 14$ $-22 \leqslant l \leqslant 22$	$-9 \leqslant h \leqslant 11$ $-15 \leqslant k \leqslant 16$ $-23 \leqslant l \leqslant 23$	$-10 \leqslant h \leqslant 10$ $-15 \leqslant k \leqslant 15$ $-19 \leqslant l \leqslant 19$
Reflections collected	15 206	17 510	17 564
Independent reflections	4710 (R_{int} = 0.0471)	4852 (R_{int} = 0.0556)	6200 (R_{int} = 0.0272)
Completeness to 2θ (%)	98.6	99.8	99.9
Maximum and minimum transmission	0.792 and 0.641	0.822 and 0.405	0.259 and 0.241
Data/restraints/parameters	4710/0/334	4852/0/343	6200/0/443
Goodness-of-fit (GOF) on F^2	0.857	1.083	1.050
Final R indices [$I > 2\sigma(I)$]	R_1 = 0.0294, wR_2 = 0.0506	R_1 = 0.0260, wR_2 = 0.0722	R_1 = 0.0217, wR_2 = 0.0533
R indices (all data)	R_1 = 0.0681, wR_2 = 0.0554	R_1 = 0.0303, wR_2 = 0.0731	R_1 = 0.0264, wR_2 = 0.0550
Largest difference in peak and hole (e Å^{-3})	1.210 and −0.739	0.927 and −0.985	0.593 and −1.432

Corrections are based on subtracting the sample – holder signal and contribution χ_D estimated from the Pascal constants [44] and equal – 376 × 10^{-6} for complex Re(III). The effective magnetic moment was calculated from the equation, $\mu_{eff} = 2.83(\chi_M^{corr} \times T)^{1/2}$ B.M.

3. Results and discussion

3.1. Preparation and infrared data

The [$ReCl_3$(dpk-N,O)(PPh_3)] (**1**) complex was prepared in good yield by ligand exchange reaction starting from [$ReCl_3$(MeCN)-(PPh_3)] and di-2-pyridylketone (dpk):

[$ReCl_3$(MeCN)(PPh_3)$_2$] + dpk → [$ReCl_3$(dpk-N,O)(PPh_3)] + PPh_3 + MeCN

The solid [$ReCl_3$(dpk-N,O)(PPh_3)] can be handled in air without significant degradation, but rapid isomerisation with oxidation of coordinated PPh_3 occurs in organic solvents at room temperature in the presence of atmospheric oxygen. The [$ReCl_3$(dpk-N,N′)-($OPPh_3$)] (**2**) compound has been isolated during crystallization of [$ReCl_3$(dpk-N,O)(PPh_3)] from chloroform in air.

The [$ReOBr_3$(dpk-OH)]·2(dpkH$^+$Br$^-$) (**3**) compound has been obtained in the reaction of [$ReOBr_3$(PPh_3)$_2$] with excess of di-2-pyridylketone in acetone in a system open to the atmosphere. In this case the carbonyl oxygen atom of the di-2-pyridylketone is subject to nucleophilic attack by water and *gem*-diol form of dpk is formed.

The elemental analyses of the **1**, **2** and **3** complexes are in good agreement with their formulation. The selected frequencies observed in the IR spectra of **1**, **2** and **3** complexes are given in Section 2.

A band due to the ν(C=O) vibration of dpk appears at 1646, 1649 and 1683 cm^{-1} for **1**, **2** and **3**, respectively. In the case of **3** this band is consequence of ν(C=O) vibration of the protonated ligand present in the outer coordination sphere. The characteristic bands corresponding to the ν(CN), ν(C=C) modes of dpk and dpk-OH are observed in the range 1610–1500 cm^{-1}. The strong ν(Re=O) stretching band of **3** is found at 958 cm^{-1}. The medium intensity band at 3045 cm^{-1} assignable to ν(OH) vibrations confirms the monoanionic *gem*-diol form of *dpk* in the coordination sphere of **3**. The strong bands at 1135 and 1119 cm^{-1} in the IR spectrum of **2** confirm the presence of the coordinated $OPPh_3$ molecule [45].

3.2. Crystal structures

The crystallographic data of the **1**, **2** and **3** complexes are summarized in Table 1. The short intra- and intermolecular contacts [46,47] detected in the **1**, **2** and **3** are gathered in Table 2. The perspective drawings of **1**, **2** and **3** are presented in Figs. 1–3, and the selected bond distances and angles of **1**, **2** and **3** are collected in Tables 3–5, respectively.

The overall structure of **1** can be considered as a distorted octahedral with the largest deviation from the expected 90° bond angles coming from the bite angle di-2-pyridylketone coordinated in N,O-mode. It equals to 76.08(14)°, and it is similar to that reported for the related [Ru(Cp)(dpk-N,O)] (78.38(7)°) [13]. The bite angles O–M–N in the structures with α-iminoketo chelate ligands bounded to transition metals depend mainly on the size of the metal center, the smallest values (down to 67°) were found for Ag^I complexes and the largest angles (up to 85°) were observed for compounds with Cu^{II} [48].

The electron rich central ion of **1** shows larger affinity towards the less basic but strongly π accepting carbonyl oxo atom, and the Re–O(1) is slightly shorter than the Re–N(1) bond (Table 3). The pyridyl rings of dpk ligand are planar in the range of experimental error and they are inclined at 5.9(3)°.

The chloride ions of **1** are arranged in a *facial* fashion, typical of the [ReX_3(L–L)(PPh_3)] compounds with bipy-like ligands [49]. In the [ReX_3(L–L)(PPh_3)] complexes with two excellent π acceptor ligands coordinated to π-donor rhenium(III) center the back-bonding

Table 2
Hydrogen bonds for **1**, **2** and **3** complexes.

D	A	H···A	D···A	D—H···A
1				
C(8)	Cl(2)	2.69	3.444(5)	138.2
C(8)	O(1)	2.59	3.150(6)	119.5
C(18)	Cl(2)	2.73	3.539(6)	146.2
C(26)	N(2)	2.29	2.899(7)	122.3
C(29)	Cl(1)	2.69	3.286(7)	123.0
2				
C(9)	Cl(2)#1	2.68	3.506(8)	148.5
C(15)	Cl(3)#2	2.73	3.474(7)	137.6
C(27)	O(1)#3	2.48	2.886(8)	106.7
C(18)	Cl(2)	2.77	3.683(7)	166.8
3				
O(3)	Br(99)	2.36	3.175(2)	171.5
N(22)	Br(98)	2.39	3.153(3)	148.6
N(22)	O(21)	2.25	2.620(4)	106.0
N(42)	N(41)	2.08	2.685(4)	126.5
C(28)	N(21)	2.30	2.919(5)	123.3
N(42)	Br(99)#4	2.68	3.377(3)	138.8
C(11)	Br(2)#5	2.90	3.787(4)	159.4
C(29)	Br(98)#6	2.91	3.715(4)	145.7
C(51)	O(2)#4	2.46	3.316(4)	153.7

#1: 0.5 + *x*, 1.5 − *y*, 1 − *z*; #2: 0.5 − *x*, 2 − *y*, −0.5 + *z*; #3: −0.5 + *x*, 2.5 − *y*, 1 − *z*; #4: 1 − *x*, 1 − *y*, 1 − *z*; #5: 2 − *x*, −*y*, −*z*; and #6: 3 −1 + *x*, *y*, *z*.

effect is maximized in the *facial* disposition, which ensures minimum competition between the two ligands for identical metal orbitals.

The *fac* geometry of chloride ions are also confirmed in complex **2**. However, in this case *facial* arrangement seems to be sustained by steric advantages. Phosphine oxides are purely donor in character, and lack acceptor properties favor the meridional configuration of chloride ligands in the complexes $[ReX_3(L–L)(OPPh_3)]$ with approximately planar L–L ligands. The di-2-pyridylketone is coordinated to the Re(III) center of **2** in a nonplanar N,N-mode, and nonplanarity seems to be responsible for *fac* Chloride arrangement in **2**. Upon coordination of di-2-pyridylketone to the rhenium *via* two nitrogen atoms, a six-membered cycle is formed, and the formed ring shows a *boat* conformation with the rhenium and the carbonyl group off the plane defined by the two nitrogen and two carbon atoms. The planar in the range of experimental error pyridyl rings are inclined at 51.3(2)°. By forming a six-membered chelate ring dpk allows Re(III) center to achieve a geometry that is closer to octahedral than is possible for α-iminoketo which form five-membered chelate.

The asymmetric unit of **3** contains one complex molecule [$ReOBr_3$(dpk-OH)], two bromide anions and two 2-pyridyl-2-pyrydiniumketone cations. In complex molecule of **3** monoanionic gem-diol form $(2\text{-py})_2C(OH)O^-$ coordinates to the Re(V) center through the deprotonated hydroxy group and two pyridyl nitrogen atoms. The coordination sphere of [$ReOBr_3$(dpk-OH)] is completed by two bromide and terminal oxo ligands, and the geometry about Re(V) can be described as a very distorted octahedral.

The oxygen atom of dpk-OH is coordinated in *trans* position to the terminal oxo ligand. The high concentration of electronic density along the Re–O axis strongly influences the positions of the adjacent halogen atoms, which are pushed away. The planar in the range of experimental error pyridyl rings of the diol are inclined at 72.72(10)°. Aromatic rings of cations are inclined at distinctly smaller angles: 24.8(2)° and 22.4(2)°. The pyridine ring is in *trans* arrangement to the pyrydinium ring in one of cations and *cis* in second one.

The Re–N bond lengths of **1** and **2** are similar to those found for the rhenium(III) polypyridyl compounds ($[ReCl_2(bipy)_2]PF_6$ – 2.094(5) and 2.096(5) Å [50] and in the $[ReL(terpy)_2]^{2+}$ (L = Cl, OH, NCS) complexes – about 2.10 Å [51]) and significantly shorter than comparable distances of **3**, where metal-to-ligand π-back bonding is not possible.

The Re–Cl(3) distance of **1** is affected by *trans* influence of triphenylphospine and is longer than the Re—Cl(1) and Re—Cl(2) bond lengths located in *trans* positions to the dpk ligand.

The Re–O_t bond length of **3** falls in the range 1.639–1.76 Å, which is typical of mononuclear complexes of rhenium(V) having $[ReO]^{3+}$ core, and indicates the presence of a triple bond Re≡O [52]. The interatomic distance between the rhenium atom and the oxygen atom of dpk-OH ligand is somewhat shorter in comparison with an ideal single Re–O bond length (ca. 2.04 Å) [53], and indicates small delocalization in the O(2)–Re(1)–O(1) moiety. In keeping with that, the O(1)–Re(1)–O(2) angle is equal 157.10(11), notably less than 180°.

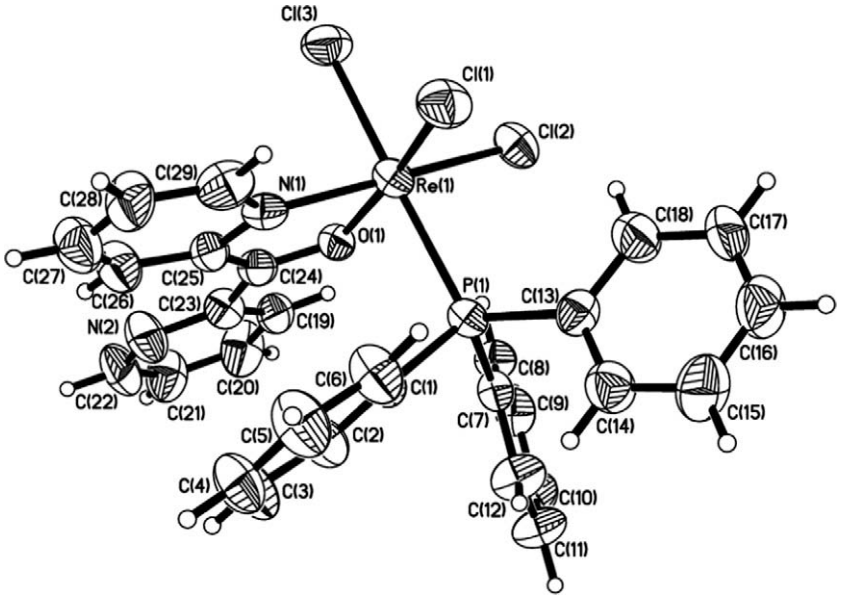


Fig. 1. The molecular structure of **1**.

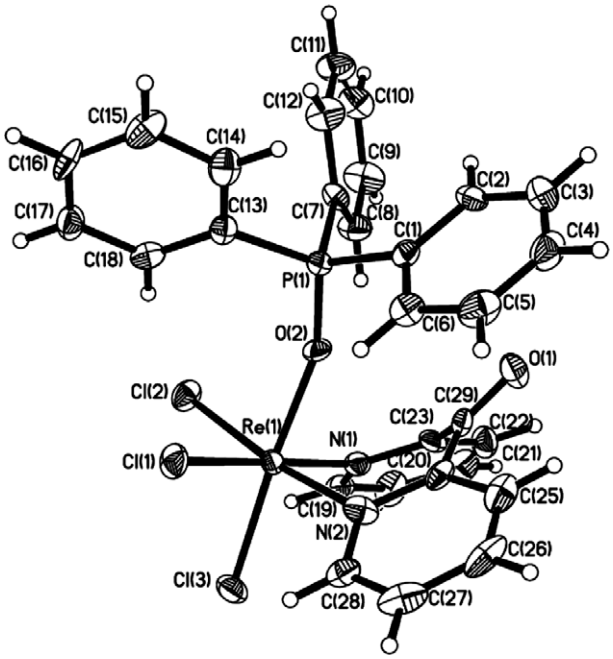


Fig. 2. The molecular structure of **2**.

In all the compounds the molecules (and ions in **3**) are connected via intermolecular interaction to the three-dimensional nets, however, in compounds **1** and **2** the intermolecular bonds are weak due to absence of strong hydrogen bond donors. In **3** the medium strength hydrogen bonds link molecules and ions to the $[ReOBr_3(dpk\text{-}OH)]\cdots Br^-\cdots Hdpk^+$ trimers and $Br^-\cdots Hdpk^+$ dimers and these clusters are connected via weak C–H···A hydrogen bonds to the three-dimensional net.

3.3. Magnetic properties

The magnetic properties of **2** under the form molar magnetic susceptibility (χ_M) and $\chi_M T = f(T)$ are shown in Fig. 4.

The complex **2** shows in the whole temperature range lowering of the magnetic moment from 2.59 B.M. at 300 K up to 0.91 B.M. at 1.8 K.

This behavior is characteristic of mononuclear Re(III) complexes ($^3T_{1g}$ ground state) with d^4 low-spin octahedral [54–62] and arise from the large spin–orbit coupling ($\zeta = 2500\ cm^{-1}$ [63]),which gives diamagnetic ground state. It seems that in room temperature, in accordance Boltzmann's distribution, it is populated higher magnetic state, which is depopulated with temperature lowering and decreasing of the magnetic moment is observed.

The variation of the magnetization *M* versus the magnetic field *H* for complex **2** at 2 K is shown in Fig. 5.

The magnetization versus magnetic field curve for complex very slowly increases and indicates value of the magnetization 0.36 B.M at 5 T, confirms that the ground state of the complex is diamagnetic.

Table 3
The experimental bond lengths (Å) and angles (°) for **1**.

Bond lengths	Experimental	Bond angles	Experimental
Re(1)–O(1)	1.997(3)	O(1)–Re(1)–N(1)	76.08(14)
Re(1)–N(1)	2.091(4)	N(1)–Re(1)–Cl(1)	93.88(12)
Re(1)–Cl(1)	2.3314(15)	N(1)–Re(1)–Cl(2)	168.94(12)
Re(1)–Cl(2)	2.3524(15)	N(1)–Re(1)–Cl(3)	86.62(12)
Re(1)–Cl(3)	2.3979(15)	O(1)–Re(1)–Cl(1)	169.79(10)
Re(1)–P(1)	2.4469(15)	O(1)–Re(1)–Cl(2)	93.77(10)
		O(1)–Re(1)–Cl(3)	89.52(10)
		Cl(1)–Re(1)–Cl(2)	96.38(5)
		Cl(3)–Re(1)–Cl(2)	88.95(6)
		Cl(3)–Re(1)–Cl(1)	91.74(6)
		O(1)–Re(1)–P(1)	90.43(10)
		N(1)–Re(1)–P(1)	95.04(12)
		Cl(1)–Re(1)–P(1)	88.61(5)
		Cl(2)–Re(1)–P(1)	89.33(5)
		Cl(3)–Re(1)–P(1)	178.28(5)

3.4. Geometry optimization

The geometries of $[ReCl_3(dpk\text{-}N,N')(OPPh_3)]$ and $[ReOBr_3(dpk\text{-}OH)]$ complexes were optimized by the DFT method with the B3LYP functional. The geometry of $[ReCl_3(dpk\text{-}N,N')(OPPh_3)]$ was optimized in triplet and singlet states, and geometry of $[ReOBr_3(dpk\text{-}OH)]$ – in singlet state. For complex $[ReCl_3(dpk\text{-}N,N')(OPPh_3)]$ the energy of the triplet state is of 22.12 kcal/mol smaller in comparison with the singlet state. It is in good agreement with the magnetic measurements. The effective magnetic moment of $[ReCl_3(dpk\text{-}N,N')(OPPh_3)]$ is equal to 2.59 B.M. at 300 K and decreases with temperature lowering (to 0.91 B.M. at 1.8 K). This behavior is characteristic of mononuclear octahedral Re(III) complex with d^4 low-spin ($^3T_{1g}$ ground state). The optimized geometric parameters of $[ReCl_3(dpk\text{-}N,N')(OPPh_3)]$ (triplet state)

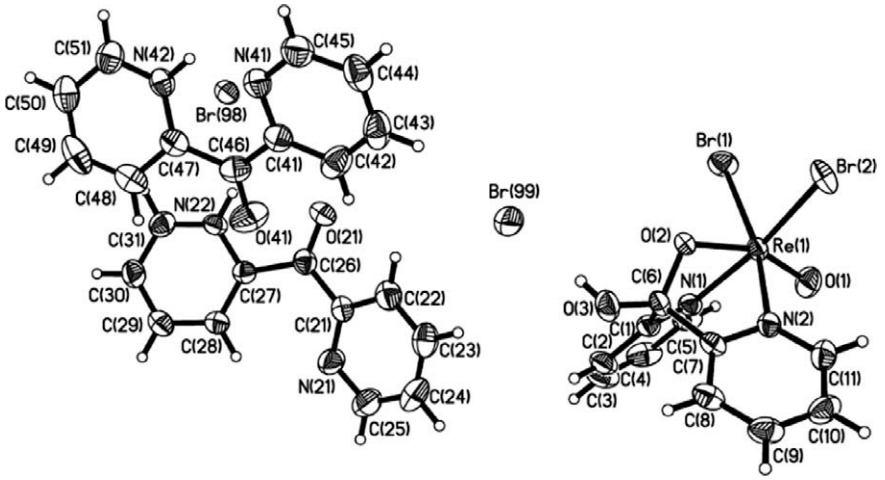


Fig. 3. The molecular structure of **3**.

Table 4
The experimental and optimized bond lengths (Å) and angles (°) for **2**.

Bond lengths	Experimental	Optimized	Bond angles	Experimental	Optimized
Re(1)–O(2)	2.061(4)	2.080	N(2)–Re(1)–N(1)	87.3(2)	86.93
Re(1)–N(2)	2.055(5)	2.082	O(2)–Re(1)–N(1)	87.8(2)	87.57
Re(1)–N(1)	2.079(6)	2.080	N(1)–Re(1)–Cl(1)	175.85(15)	174.95
Re(1)–Cl(1)	2.3831(15)	2.442	N(1)–Re(1)–Cl(2)	90.55(15)	89.97
Re(1)–Cl(2)	2.3792(17)	2.441	N(1)–Re(1)–Cl(3)	89.35(17)	90.78
Re(1)–Cl(3)	2.3315(17)	2.383	N(2)–Re(1)–Cl(1)	88.69(17)	90.07
O(2)–P(1)	1.513(5)	1.537	N(2)–Re(1)–Cl(2)	172.67(17)	176.02
			N(2)–Re(1)–Cl(3)	92.18(17)	90.23
			O(2)–Re(1)–Cl(1)	90.82(13)	89.45
			O(2)–Re(1)–Cl(2)	87.78(13)	89.73
			O(2)–Re(1)–Cl(3)	176.17(13)	176.48
			Cl(2)–Re(1)–Cl(1)	93.30(6)	92.84
			Cl(3)–Re(1)–Cl(1)	91.86(6)	93.30
			Cl(3)–Re(1)–Cl(2)	94.80(6)	92.33
			N(2)–Re(1)–O(2)	85.1(2)	87.57
			P(1)–O(2)–Re(1)	158.8(3)	150.54

Table 5
The experimental and optimized bond lengths (Å) and angles (°) for **3**.

Bond lengths	Experimental	Optimized	Bond angles	Experimental	Optimized
Re(1)–O(1)	1.681(2)	1.680	O(1)–Re(1)–O(2)	157.10(11)	154.81
Re(1)–O(2)	1.961(2)	2.022	O(1)–Re(1)–N(1)	88.21(11)	88.66
Re(1)–N(1)	2.144(3)	2.196	O(2)–Re(1)–N(1)	74.38(9)	72.99
Re(1)–N(2)	2.151(3)	2.197	O(1)–Re(1)–N(2)	89.88(11)	88.72
Re(1)–Br(1)	2.4858(4)	2.536	O(2)–Re(1)–N(2)	74.16(9)	72.98
Re(1)–Br(2)	2.4796(4)	2.536	N(1)–Re(1)–N(2)	85.02(10)	85.14
			O(1)–Re(1)–Br(2)	103.30(9)	103.37
			O(2)–Re(1)–Br(2)	93.65(6)	94.11
			N(1)–Re(1)–Br(2)	168.02(7)	167.08
			N(2)–Re(1)–Br(2)	91.62(7)	90.35
			O(1)–Re(1)–Br(1)	102.69(8)	103.39
			O(2)–Re(1)–Br(1)	92.47(6)	94.04
			N(1)–Re(1)–Br(1)	90.71(7)	90.35
			N(2)–Re(1)–Br(1)	166.61(7)	167.00
			Br(2)–Re(1)–Br(1)	89.967(13)	91.41

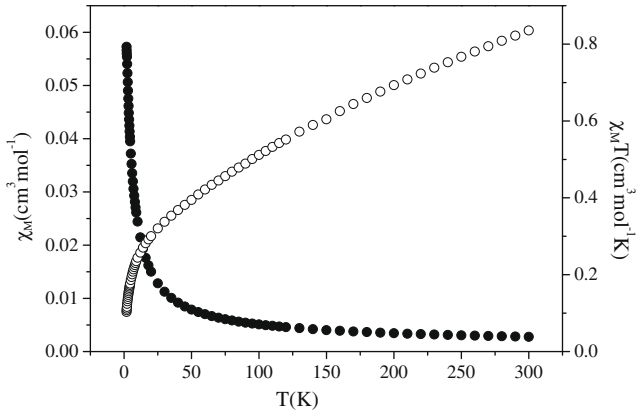


Fig. 4. Experimental magnetic plotted as χ_M (●) and $\chi_M T$ (○) versus T for complex **2**.

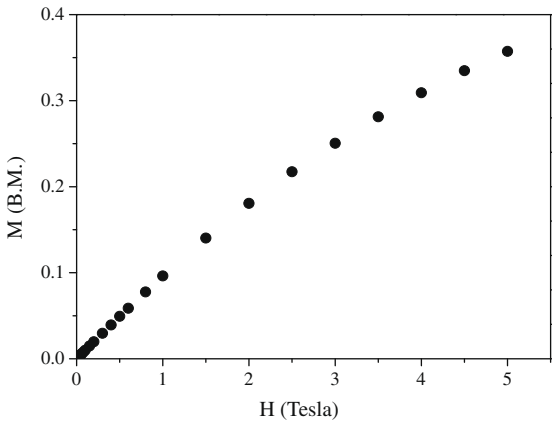


Fig. 5. Field dependence of the magnetization for complex **2**.

and [$ReOBr_3$(dpk-OH)] (singlet state) are gathered in Tables 4 and 5, respectively. Generally, the predicted bond lengths and angles are in agreement with the values based upon the X-ray crystal structure data, and the general trends observed in the experimental data are well reproduced in the calculations.

3.5. Molecular orbitals

The energies and characters of several highest occupied and lowest unoccupied molecular orbitals of [$ReCl_3$(dpk-N,N′)($OPPh_3$)] and [$ReOBr_3$(dpk-OH)] are presented in Tables 6 and 7, respectively. The selected contours of frontier orbitals of [$ReCl_3$(dpk-N,N′)($OPPh_3$)] and [$ReOBr_3$(dpk-OH)] are presented in Figs. 6 and 7, respectively.

Among the highest occupied MOs of [$ReCl_3$(dpk-N,N′)($OPPh_3$)] the largest numbers constitute π orbitals of the phenyl rings with a contribution from Cl atoms. The rhenium d_{xz}, d_{yz} and d_{xy} orbitals make main contributions into the HOMO−2, HOMO−1 and HOMO with α spin and HOMO, LUMO and LUMO+1 with β spin. In all these molecular orbitals, the rhenium d_{xz}, d_{yz} and d_{xy} orbitals bear

Table 6
The energy and character of the selected molecular orbitals with α and β spins for [$ReCl_3$(dpk-N,N′)($OPPh_3$)].

	MOs with α spin		MOs with β spin	
	E (eV)	Character	*E* (eV)	Character
HOMO−5	−7.256	π(Ph)	−7.366	π(Ph)
HOMO−4	−7.113	π(Ph)	−7.282	π(Ph)
HOMO−3	−7.062	π(Ph)	−7.248	π(Ph)
HOMO−2	−6.388	d_{xz}(Re), π(Cl), $\pi(O_{OPPh_3})$	−7.106	π(Ph)
HOMO−1	−6.230	d_{yz}(Re), π(Cl), $\pi(O_{OPPh_3})$	−7.045	π(Ph), π(Cl)
HOMO	−5.853	d_{yz}(Re), π(Cl), π(dpk)	−5.081	d_{xy}, π(dpk), π(Cl)
LUMO	−2.856	π^*(dpk), d_{xy}	−2.997	d_{xz}(Re), π^*(dpk)
LUMO +1	−1.667	π^*(dpk)	−2.978	d_{yz}(Re), π^*(dpk)
LUMO+2	−1.438	$\pi^*(OPPh_3)$, π^*(dpk), d_z^2	−2.734	π^*(dpk), d_{yz}
LUMO+3	−1.308	π^*(dpk), d_z^2, $\pi^*(OPPh_3)$	−1.552	π^*(dpk), d_{xz}
LUMO+4	−1.194	$\pi^*(OPPh_3)$	−1.355	π^*(dpk), $\pi^*(OPPh_3)$
LUMO+5	−0.876	$\pi^*(OPPh_3)$	−1.236	π^*(dpk), $\pi^*(OPPh_3)$
LUMO+6	−0.792	π^*(dpk), d_z^2	−1.178	$\pi^*(OPPh_3)$
LUMO+7	−0.735	d_z^2	−0.862	$\pi^*(OPPh_3)$

Table 7
The energy and character of the selected molecular orbitals for [$ReOBr_3$(dpk-OH)].

	E (eV)	Character
HOMO−5	−8.123	π(dpk-OH), π(Br), $\pi(O_t)$
HOMO−4	−7.932	π(Br), $\pi(O_t)$
HOMO−3	−7.648	π(dpk-OH), π(Br), $\pi(O_t)$
HOMO−2	−7.550	π(Br), π(dpk-OH)
HOMO−1	−7.291	π(Br)
HOMO	−6.264	d_{yz}(Re), π(Br)
LUMO	−3.066	d_{yz}, π(O)
LUMO+1	−2.860	d_{yz}, π(O)
LUMO+2	−1.903	π^*(dpk-OH), d_{yz}
LUMO+3	−1.532	π^*(dpk-OH), $d_{x^2-y^2}$
LUMO+4	−1.378	$d_{x^2-y^2}$
LUMO+5	−1.349	π^*(dpk-OH)
LUMO+6	−0.673	π^*(dpk-OH)
LUMO+7	−0.270	d_z^2

antibonding character towards the p_π orbitals of the chloride ions and oxygen donor. The d_z^2 rhenium orbital has a significant contribution in the LUMO+7 with α spin and the LUMO+11 with β spin, whereas the LUMO+10 with α spin and the LUMO+13 with β have predominantly $d_{x^2-y^2}$ character. Among the lowest unoccupied MOs of[$ReCl_3$(dpk-N,N′)($OPPh_3$)], the largest numbers constitute π orbitals of the dpk ligand. The π phenyl ring orbitals of the triphenylphosphine oxide ligand participate in the higher unoccupied orbitals.

The HOMO of [$ReOBr_3$(dpk-OH)] is mainly localized on the d_{xy} rhenium orbital and p_π chloride orbitals. The LUMO and LUMO+1 are also to a large extent formed by rhenium dπ atomic orbital (d_{xz} and d_{yz} orbitals) with some contribution of p_π oxygen orbitals. The LUMO+4 is of $d_{x^2-y^2}$ character, and d_z^2 rhenium orbital contributes to the LUMO+7.

3.6. NBO analysis

The nature of rhenium–terminal oxygen interaction in [$ReOBr_3$(dpk-OH)] has been studied by NBO analysis. The occupancy and composition of the calculated Re–O_t natural bond orbitals (NBOs) are given in Table 8. Each natural bond orbital (NBO) σ_{AB} can be written in terms of two directed valence hybrids (NHOs) h_A and h_B on atoms A and B:

$$(1)\sigma_{AB} = c_A h_A + c_B h_B,$$

where c_A and c_B are polarization coefficients. Each valence bonding NBO must in turn be paired with a corresponding valence *anti*-bonding NBO:

$$(2)\sigma^*_{AB} = c_B h_A - c_A h_B$$

to complete the span of the valence space. The Lewis-type (donor) NBOs are thereby complemented by the non-Lewis-type (acceptor) NBOs that are formally empty in an idealized Lewis picture. The interactions between 'filled' Lewis-type NBOs and 'empty' non-Le-

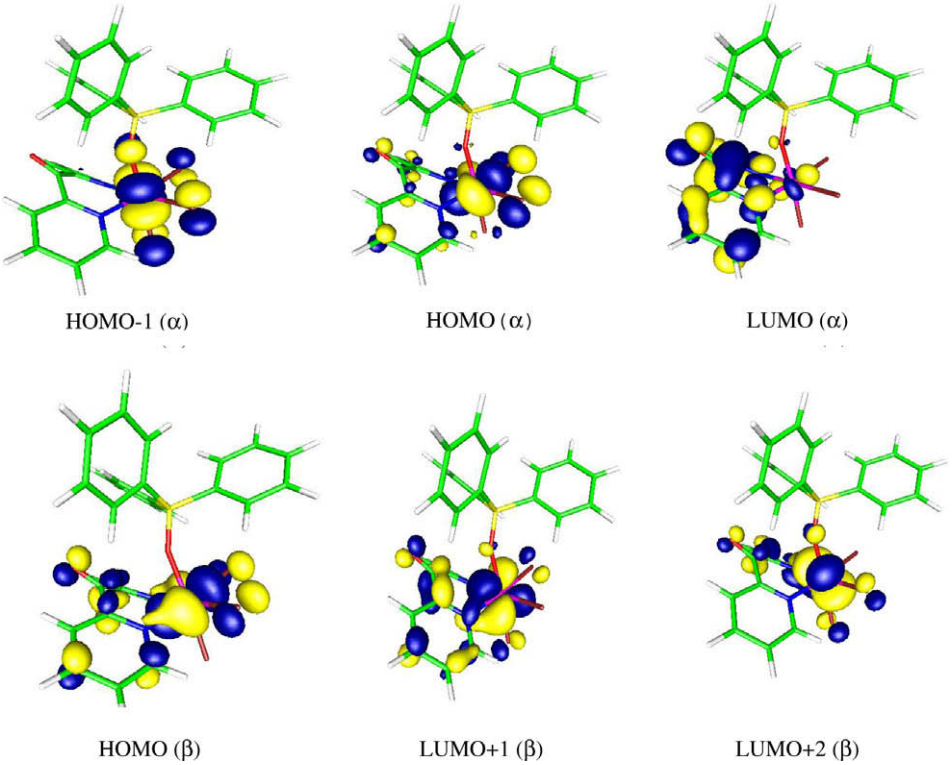


Fig. 6. The selected HOMO and LUMO orbitals with α and β spin for [$ReCl_3$(dpk-N,N′)($OPPh_3$)].

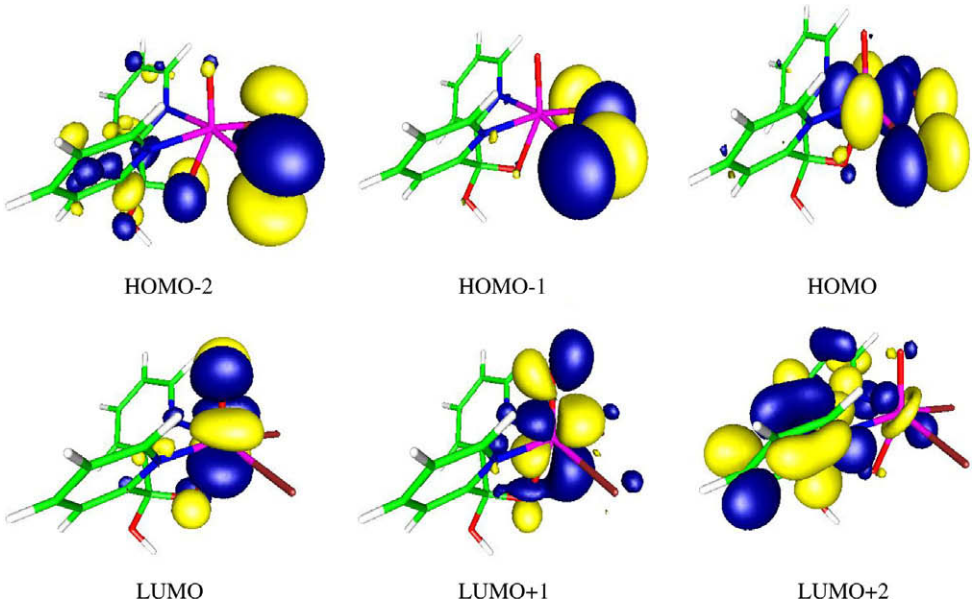


Fig. 7. The selected HOMO and LUMO orbitals for [$ReOBr_3$(dpk-OH)].

Table 8
The occupancy of the calculated natural bond orbitals (NBOs) between the rhenium and the oxo ligand for [$ReOBr_3$(dpk-OH)].

BD	Occupancy	Composition of NBO	BD*	Occupancy
Re–O_t	1.994	$0.566(d)_{Re} + 0.825(p)_O$	$0.825(d)_{Re} - 0.566(p)_O$	0.255
Re–O_t	1.984	$0.566(d)_{Re} + 0.824(p)_O$	$0.824(d)_{Re} - 0.566(p)_O$	0.307

*Denotes antibond NBO.
BD: denotes two-center bond.

wis NBOs lead to loss of occupancy from the localized NBOs of the idealized Lewis structure into the empty non-Lewis orbitals, and they are referred to as 'delocalization' corrections to the zeroth-order natural Lewis structure [43].

The detected natural Re–O_t bond orbitals of **3** are π orbitals – the p_x and p_y oxygen orbitals and d_{xz} and d_{yz} rhenium orbitals are involved in their formation. Not detected σ_{Re-O_t} bond has character of predominant Coulomb-type interactions between the central ion and ligands [64]. The terminal oxo ligand of **1** has two lone pair orbitals, and electron density from one of them is strongly delocalized into non-Lewis rhenium orbital. Accordingly, NBO analysis confirms a triple bond between the rhenium and the terminal oxygen ligand.

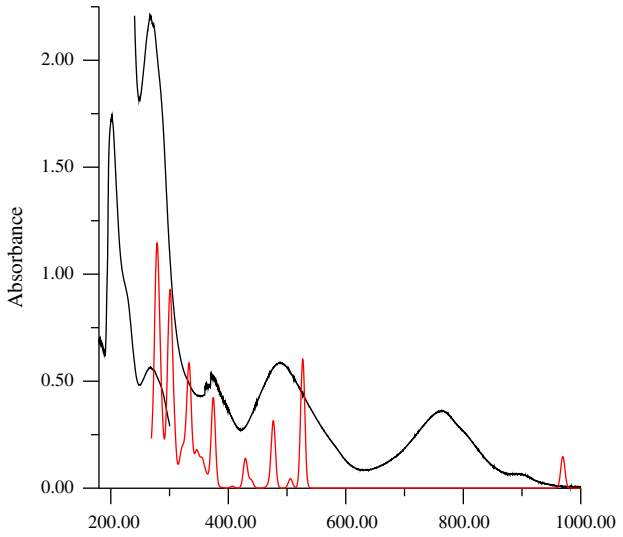


Fig. 8. The experimental (black) and calculated (red) electronic absorption spectra of the solution of **2** in acetonitrile. (For interpretation of the references to color in this figure legend, the reader is referred to the web version of this article.)

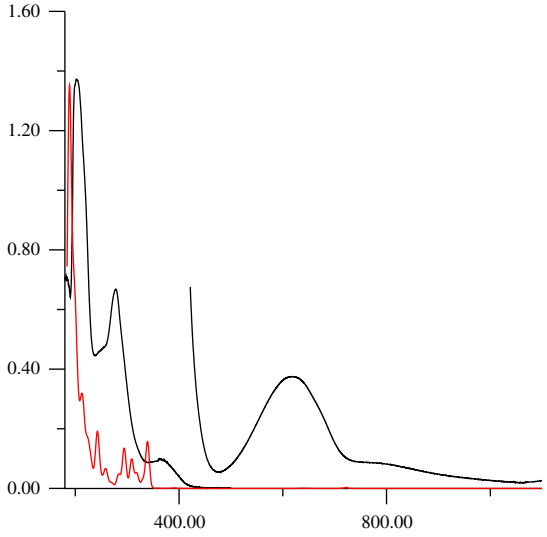


Fig. 9. The experimental (black) and calculated (red) electronic absorption spectra of the solution of **3** in acetonitrile. (For interpretation of the references to color in this figure legend, the reader is referred to the web version of this article.)

3.7. Electronic spectra

The experimental and calculated electronic spectra of [$ReCl_3$(dpk-N,N′)($OPPh_3$)] and [$ReOBr_3$(dpk-OH)] are presented in Figs. 8 and 9, respectively. Each calculated transition is represented by a gaussian function $y = ce^{-bx^2}$ with the height (c) equal to the oscillator strength and b equal to 0.04 nm^{-2}.

Tables 9 and 10 present the most important electronic transitions calculated with the TDDFT method assigned to the observed absorption bands of [$ReCl_3$(dpk-N,N′)($OPPh_3$)] and [$ReOBr_3$(dpk-OH)]. For the high energy part of the spectrum, only transitions with oscillator strengths larger than 0.020 are listed in Tables 9 and 10. The assignment of the calculated orbital excitations to the experimental bands was based on an overview of the contour plots and relative energy to the orbitals HOMO and LUMO involved in the electronic transitions. As seen in Figs. 8 and 9, TDDFT/PCM calculations well reproduce the absorption spectra of [$ReCl_3$(dpk-N,N′)($OPPh_3$)] and [$ReOBr_3$(dpk-OH)] in terms of the energy of the experimental bands and calculated transitions.

3.8. [$ReCl_3$(dpk-N,N′)($OPPh_3$)]

The low-energy absorption band at 761.0 nm originates from the transition between HOMO and LUMO+2 with β spins. As can be seen from the Fig. 6, the β HOMO is delocalized on central ion, chloride ions and dpk ligand, whereas the β LUMO+2 are formed of d_{Re} orbitals and π^*-bonding orbitals of dpk ligand. Accordingly, the transition can be seen as a delocalized MLLCT (*Metal–Ligand-to-Ligand CT*) transition. The same character can be assigned to the experimental absorptions at 487.1, 372.7 and 266.9 nm.

The investigated complex is of large size; the numbers of basis functions are equal to 646. The calculated electron transitions (100) do not comprise all the experimental absorption bands; the

Table 9
The energy and molar absorption coefficients of experimental absorption bands and the electronic transitions calculated with the TDDFT method for [$ReCl_3$(dpk-N,N′)($OPPh_3$)].

The most important orbital excitations	Character	λ (nm)	E (eV)	f	Experimental Λ [nm] (E [eV]) ε
H(β) → L+2(β)	d/π(Cl)/π(dpk) → π*(dpk)/d	969.6	1.28	0.0184	897.2 (1.38) 200
					761.0 (1.63) 1050
H(α) → L(α)	d/π(Cl)/π(dpk) → π*(dpk)/d	526.7	2.35	0.0753	487.1 (2.55) 1750
H(β) → L+3(β)	d/π(Cl)/π(dpk) → π*(dpk)/d	476.6	2.60	0.0394	
H(α) → L+1(α)	d/π(Cl)/π(dpk) → π*(dpk)	374.4	3.31	0.0525	372.7 (3.33) 1580
H−8(β) → L+1(β)	π(Cl)/π(dpk) → d/π*(dpk)	333.7	3.72	0.0339	266.9 (4.65) 42 700
H−1(α) → L+1(α)	d/π(Cl)/π(O_{OPPh_3}) → π*(dpk)	331.6	3.74	0.0241	
H−1(α) → L+3(α)	d/π(Cl)/π(O_{OPPh_3}) → π*(dpk)/π*($OPPh_3$)/d	300.9	4.12	0.0511	
H−12(β) → L+1(β)	π(dpk)/π(Cl)/π(O_{OPPh_3}) → d/π*(dpk)				
H−12(α) → L(α)	π(Cl)/π(dpk) → π*(dpk)/d	286.0	4.34	0.0229	
H−10(β) → L+2(β)	π(Cl)/π(dpk)/π(O_{OPPh_3}) → π*(dpk)/d				
H−14(α) → L(α)	π(dpk)/π(Cl)/π(O_{OPPh_3}) → π*(dpk)/d	277.8	4.46	0.0301	
H(β) → L+15(β)	d/π(dpk)/π(Cl) → π*(dpk)	269.4	4.60	0.0205	
H−13(β) → L+2(β)	π(dpk)/π(Cl) → π*(dpk)/d				202.0 (6.14) 131 600

ε – molar absorption coefficient [$dm^3\ mol^{-1}\ cm^{-1}$]; f – oscillator strength; H – highest occupied molecular orbital; and L – lowest unoccupied molecular orbital.

Table 10
The energy and molar absorption coefficients of experimental absorption bands and the electronic transitions calculated with the TDDFT method for [$ReOBr_3$(dpk-OH)].

The most important orbital excitations	Character	λ (nm)	E (eV)	f	Experimental Λ [nm] (E [eV]) ε
H → L	d/π(Br) → d	721.7	1.72	0.0014	794.1 (1.56) 50
H → L+1	d/π(Br) → d	640.0	1.94	0.0003	623.6 (1.99) 230
H → L+2	d/π(Br) → π*(dpk-OH)/d	339.2	3.66	0.0781	367.4 (3.37) 7300
H−2 → L	π(Br)/π(dpk-OH) → d				
H−2 → L+1	π(Br)/π(dpk-OH) → d	330.3	3.75	0.0127	
H−4 → L	π(Br)/π(O_t) → d	318.5	3.89	0.0248	
H → L+3	d/π(Br) → π*(dpk-OH)/d	308.3	4.02	0.0430	278.1 (4.46) 82 000
H−4 → L	π(Br)/π(O_t) → d	296.6	4.18	0.0147	
H → L+5	d/π(Br) → π*(dpk-OH)	293.8	4.22	0.0531	
H−3 → L+2	π(Br)/π(dpk-OH)/π(O_t) → π*(dpk-OH)/d	243.0	5.10	0.0707	
H−4 → L+2	π(Br)/π(O_t) → π*(dpk-OH)/d	229.5	5.40	0.0229	204.0 (6.08) 105 300
H−3 → L+5	π(Br)/π(dpk-OH)/π(O) → π*(dpk-OH)	216.4	5.73	0.0283	
H−7 → L+2	π(Br)/π(dpk-OH)/π(O) → π*(dpk-OH)/d	214.0	5.79	0.0507	
H−5 → L+3	π(dpk-OH)/π(O)/π(Br) → π*(dpk-OH)/d	209.8	5.91	0.0376	
H−1 → L+7	π(Br) → d	202.4	6.13	0.1187	
H−8 → L+2	π (dpk-OH) → π*(dpk-OH)/d	198.1	6.26	0.1226	
H−10 → L+3	π(Br)/π(dpk-OH)/π(O_t) → π*(dpk-OH)/d	197.6	6.27	0.0552	
H−2 → L+6	π(Br)/π(dpk-OH) → π*(dpk-OH)				
H−7 → L+5	π(Br)/π(dpk-OH)/π(O_t) → π*(dpk-OH)	195.1	6.35	0.0625	
H−10 → L+2	π(Br)/π(dpk-OH)/π(O) → π*(dpk-OH)/d	192.6	6.44	0.0258	
H−16 → L+1	π(O_t)/π(dpk-OH) → d	189.5	6.54	0.0625	
H−9 → L+4	π(Br)/π(dph-OH)/π(O_t) → d	189.2	6.55	0.3537	
H−10 → L+3	π(Br)/π(dpk-OH)/π(O_t) → π*(dpk-OH)/d	187.7	6.60	0.0656	
H−3 → L+7	π(Br)/π(dpk-OH)/π(O_t) → d	186.3	6.66	0.0440	
H−11 → L+2	π(Br)/π(dpk-OH) → π*(dpk-OH)/d	185.5	6.68	0.0322	
H−4 → +6	π(Br)/π(O_t) → π*(dpk-OH)	185.4	6.69	0.0234	
H−13 → L+2	π(Br)/π(dpk-OH) → π*(dpk-OH)/d	184.7	6.71	0.0281	
H−8 → L+5	π(dpk-OH) → π*(dpk-OH)	184.4	6.72	0.0559	

ε – molar absorption coefficient [$dm^3\ mol^{-1}\ cm^{-1}$]; f – oscillator strength; H – highest occupied molecular orbital; and L – lowest unoccupied molecular orbital.

UV–vis spectrum was calculated to ~270 nm. Thus the shortest wavelength experimental band of **2** is not assigned to the calculated transitions; some intraligand and interligand transitions are expected to be found at higher energies in the calculations for **2**.

3.9. [$ReOBr_3$(dpk-OH)]

The two longest wavelength experimental bands of **3** originate in the HOMO−LUMO and HOMO−LUMO+1 transitions, respectively. As can be seen from the Fig. 7, the LUMO and LUMO+1 orbitals are mainly formed from rhenium *d* atomic orbitals, the HOMO orbital is delocalized among rhenium ion and bromide orbitals. Accordingly, the transitions assigned to the experimental bands at 794.1 and 623.6 nm can be seen as mixed bromide → Re (*Ligand-Metal Charge Transfer*; *LMCT*) and d → d (*Ligand Field; LF*) transitions.

The experimental absorption band at 367.4 nm can be assigned to *Ligand-Metal Charge Transfer* transitions occurring from the bromide, oxo, and dpk-OH ligands to *d* rhenium orbitals.

The absorption bands at 278.1 and 204.0 nm result mainly from *Ligand-Ligand Charge Transfer* and interligand (*IL*) transitions, but participation of *Ligand-Metal Charge Transfer* into this band is also confirmed by the calculations.

Supplementary data

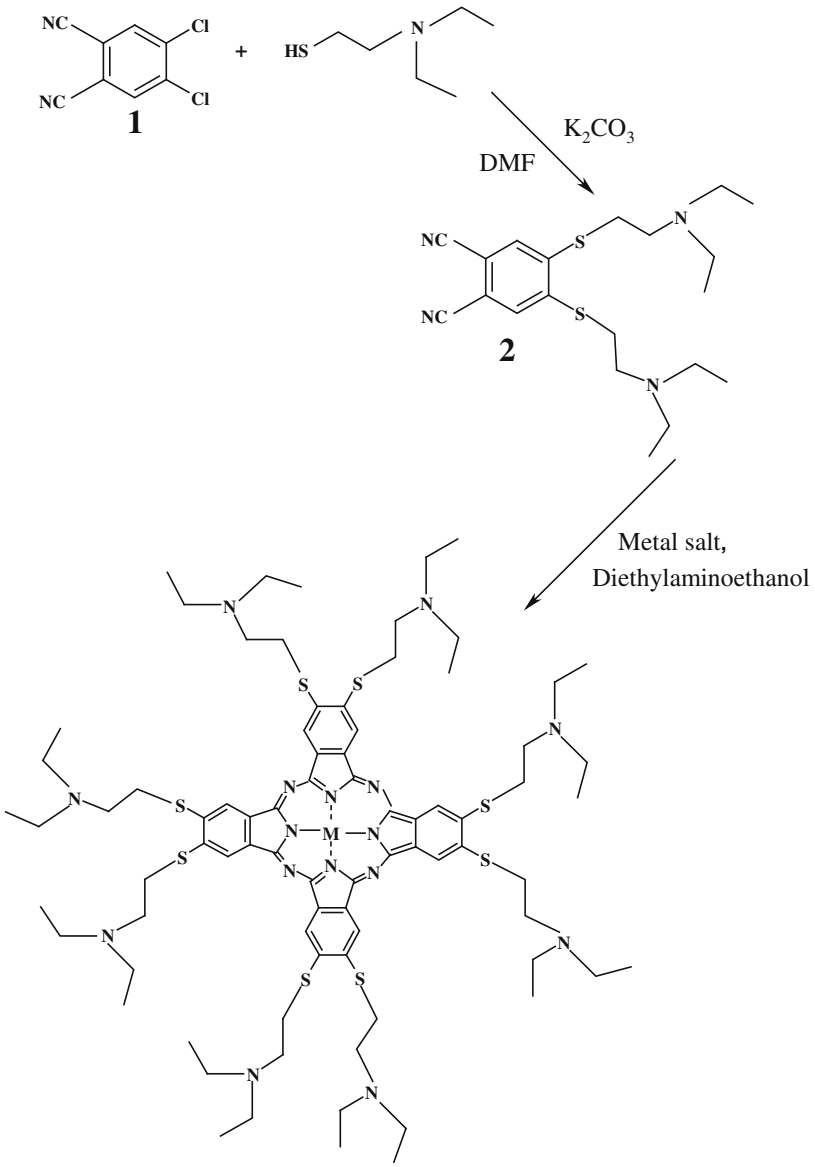
CCDC 731661, 731662 and 731663 contain the supplementary crystallographic data for $C_{29}H_{23}Cl_3N_2OPRe$, $C_{29}H_{23}Cl_3N_2O_2PRe$ and $C_{33}H_{27}Br_4N_6O_5Re$. These data can be obtained free of charge via http://www.ccdc.cam.ac.uk/conts/retrieving.html, or from the Cambridge Crystallographic Data Center, 12 Union Road, Cambridge CB2 1EZ, UK; fax: (+44) 1223-336-033; or e-mail: deposit@ccdc.cam.ac.uk.

Acknowledgements

The GAUSSIAN-03 calculations were carried out in the Wrocław Center for Networking and Supercomputing, WCSS, Wrocław, Poland, http://www.wcss.wroc.pl, under calculational Grant No. 51/96.

References

[1] U. Abram, in: J.A. McCleverty, T.J. Meyer (Eds.), Comprehensive Coordination Chemistry, second ed., vol. 5, Elsevier, p. 271 (Chapter 5.3).
[2] J.R. Dilworth, S.J. Parrott, Chem. Soc. Rev. 27 (1998) 43.
[3] P. Blower, Dalton Trans. (2006) 1705.
[4] R.L. Richards, Coord. Chem. Rev. 154 (1996) 83.
[5] M.D. Fryzuk, S.A. Johnson, Coord. Chem. Rev. 200–202 (2000) 379.
[6] A.J.L. Pombeiro, M.F.C. Guedes da Silva, R.A. Michelin, Coord. Chem. Rev. 218 (2001) 43.
[7] F.E. Kühn, A. Scherbaum, W.A. Herrmann, J. Organomet. Chem. 689 (2004) 4149.
[8] G.S. Owens, J. Arias, M.M. Abu-Omar, Catal. Today 55 (2000) 317.
[9] A.M. Kirillov, M. Haukka, M.V. Kirillova, A.J.L. Pombeiro, Adv. Synth. Catal. 347 (2005) 1435.
[10] A. Deloffre, S. Halut, L. Salles, J.-M. Brégeault, J.R. Gregorio, B. Denise, H. Rudler, J. Chem. Soc., Dalton Trans. (1999) 2897.
[11] K.N. Crowder, S.J. Garcia, R.L. Burr, J.M. North, M.H. Wilson, B.L. Conley, P.E. Fanwick, P.S. White, K.D. Sienerth, R.M. Granger, Inorg. Chem. 43 (2004) 72.
[12] M. Toyama, M. Nakahara, N. Nagao, Bull. Chem. Soc. Jpn. 80 (2007) 937.
[13] C. Godard, S.B. Duckett, S. Parsons, R.N. Perutz, Chem. Commun. (2003) 2332.
[14] J. Grewe, A. Hagenbach, B. Stromburg, R. Alberto, E. Vazquez-Lopez, U. Abram, Z. Anorg. Allg. Chem. 629 (2003) 303.
[15] G. Bandoli, A. Dolmella, T.I.A. Gerber, J.G.H. du Preez, H.J. Kemp, Inorg. Chim. Acta 217 (1994) 141.
[16] G. Rouschias, G. Wilkinson, J. Chem. Soc. A (1967) 993.
[17] P. Ghosh, A. Pramanik, N. Bag, A. Chakravorty, J. Chem. Soc., Dalton Trans. (1992) 1883.
[18] B. Machura, M. Jaworska, R. Kruszynski, Polyhedron 23 (2004) 1819.
[19] H. Chermette, Coord. Chem. Rev. 178–180 (1998) 699.
[20] M.C. Aragoni, M. Arca, T. Cassano, C. Denotti, F.A. Devillanova, F. Isaia, V. Lippolis, D. Natali, L. Niti, M. Sampietro, R. Tommasi, G. Verani, Inorg. Chem. Commun. 5 (2002) 869.
[21] P. Romaniello, F. Lelj, Chem. Phys. Lett. 372 (2003) 51.
[22] P. Norman, P. Cronstrand, J. Ericsson, Chem. Phys. 285 (2002) 207.
[23] G. Rouschias, G. Wilkinson, J. Chem. Soc. A (1966) 465.
[24] (a) CrysAlis RED, Oxford Diffraction Ltd., Version 1.171.29.2.;
(b) STOE & Cie, X-RED, Version 1.18, STOE & Cie GmbH, Darmstadt, Germany, 1999.
[25] G.M. Sheldrick, Acta Cryst. A 46 (1990) 467.
[26] G.M. Sheldrick, SHELXL97, Program for the Refinement of Crystal Structures, University of Göttingen, Germany, 1997.
[27] G.M. Sheldrick, SHELXTL: Release 4.1 for Siemens Crystallographic Research Systems, 1990.
[28] M.J. Frisch, G.W. Trucks, H.B. Schlegel, G.E. Scuseria, M.A. Robb, J.R. Cheeseman, J.A. Montgomery, Jr., T. Vreven, K.N. Kudin, J.C. Burant, J.M. Millam, S.S. Iyengar, J. Tomasi, V. Barone, B. Mennucci, M. Cossi, G. Scalmani, N. Rega, G.A. Petersson, H. Nakatsuji, M. Hada, M. Ehara, K. Toyota, R. Fukuda, J. Hasegawa, M. Ishida, T. Nakajima, Y. Honda, O. Kitao, H. Nakai, M. Klene, X. Li, J.E. Knox, H.P. Hratchian, J.B. Cross, V. Bakken, C. Adamo, J. Jaramillo, R. Gomperts, R.E. Stratmann, O. Yazyev, A.J. Austin, R. Cammi, C. Pomelli, J.W. Ochterski, P.Y. Ayala, K. Morokuma, G.A. Voth, P. Salvador, J.J. Dannenberg, V.G. Zakrzewski, S. Dapprich, A.D. Daniels, M.C. Strain, O. Farkas, D.K. Malick, A.D. Rabuck, K. Raghavachari, J.B. Foresman, J.V. Ortiz, Q. Cui, A.G. Baboul, S. Clifford, J. Cioslowski, B.B. Stefanov, G. Liu, A. Liashenko, P. Piskorz, I. Komaromi, R.L. Martin, D.J. Fox, T. Keith, M.A. Al-Laham, C.Y. Peng, A. Nanayakkara, M. Challacombe, P.M.W. Gill, B. Johnson, W. Chen, M.W. Wong, C. Gonzalez, J.A. Pople, GAUSSIAN-03, Revision D.01, Gaussian, Inc., Wallingford, CT, 2004.
[29] A.D. Becke, J. Chem. Phys. 98 (1993) 5648.
[30] C. Lee, W. Yang, R.G. Parr, Phys. Rev. B 37 (1988) 785.
[31] P.J. Hay, W.R. Wadt, J. Chem. Phys. 82 (1985) 299.
[32] K. Eichkorn, F. Weigend, O. Treutler, R. Ahlrichs, Theor. Chem. Acc. 97 (1997) 119.
[33] W.J. Hehre, R. Ditchfield, J.A. Pople, J. Chem. Phys. 56 (1972) 2257.
[34] P.C. Hariharan, J.A. Pople, Theor. Chim. Acta 28 (1973) 213.
[35] M.M. Francl, W.J. Petro, W.J. Hehre, J.S. Binkley, M.S. Gordon, D.J. DeFrees, J.A. Pople, J. Chem. Phys. 77 (1982) 3654.
[36] T. Clark, J. Chandrasekhar, P.V.R. Schleyer, J. Comp. Chem. 4 (1983) 294.
[37] R. Krishnam, J.S. Binkley, R. Seeger, J.A. Pople, J. Chem. Phys. 72 (1980) 650.
[38] P.M.W. Gill, B.G. Johnson, J.A. Pople, M.J. Frisch, Chem. Phys. Lett. 197 (1992) 499.
[39] M.T. Cances, B. Mennucci, J. Tomasi, J. Chem. Phys. 107 (1997) 3032.
[40] M. Cossi, V. Barone, B. Mennucci, J. Tomasi, Chem. Phys. Lett. 286 (1998) 253.
[41] B. Mennucci, J. Tomasi, J. Chem. Phys. 106 (1997) 5151.
[42] M. Cossi, G. Scalmani, N. Rega, V. Barone, J. Chem. Phys. 117 (2002) 43.
[43] E.D. Glendening, A.E. Reed, J.E. Carpenter, F. Weinhold, NBO (Version 3.1). E. Reed, L.A. Curtiss, F. Weinhold, Chem. Rev. 88 (1988) 899.
[44] E. König, Magnetic Properties of Coordination and Organometallic Transition Metal Compounds, Springer, Berlin, 1966.
[45] K. Nakamoto, Infrared and Raman Spectra of Inorganic and Coordination Compounds, fourth ed., Wiley-Interscience, New York, 1986.
[46] G.A. Jeffrey, W. Saenger, Hydrogen Bonding in Biological Structures, Springer-Verlag, 1994.
[47] G.R. Desiraju, T. Steiner, The Weak Hydrogen Bond in Structural Chemistry and Biology, Oxford University Press, 1999.
[48] W. Kaim, B. Schwederski, O. Heilmann, F.M. Hornung, Coord. Chem. Rev. 182 (1999) 323.
[49] F.H. Allen, Acta Crystallogr. B 58 (2002) 380.
[50] L.E. Helberg, S.D. Orth, M. Sabat, W.D. Harman, Inorg. Chem. 35 (1996) 5584.
[51] J. Rall, F. Weingart, D.M. Ho, M.J. Heeg, F. Tisato, E. Deutsch, Inorg. Chem. 33 (1994) 3442.
[52] J.M. Mayer, Inorg. Chem. 27 (1988) 3899.
[53] S.R. Fletcher, A.C. Skapski, J. Chem. Soc., Dalton (1972) 1073.
[54] J.E. Fergusson, Coord. Chem. Rev. 1 (1966) 459.
[55] B.N. Figgis, J. Lewis, Prog. Inorg. Chem. 6 (1964) 37.
[56] B.N. Figgis, Introduction to Ligand Field, Wiley-Interscience, New York, 1966. p. 248.
[57] J. Chatt, G.J. Leigh, D.M.P. Mingos, E.W. Randall, D. Shaw, J. Chem. Soc., Chem. Commun. (1968) 419.
[58] H.P. Gunz, G.J. Leigh, J. Chem. Soc. (1971) 2229.
[59] B. Coutinho, J.R. Dilworth, P. Jobanputra, R.M. Thompson, S. Schmidt, J. Strähle, C.M. Archer, J. Chem. Soc., Dalton Trans. (1995) 1663.
[60] M. Hirsch-Kuchma, T. Nicholson, A. Davison, W.M. Davis, A.G. Jones, Inorg. Chem. 36 (1997) 3237.
[61] C.A. McConnachie, E.I. Stiefel, Inorg. Chem. 36 (1997) 6144.
[62] C. Pearson, A.L. Beauchamp, Can. J. Chem. 75 (1997) 220.
[63] A. Earnshaw, B.N. Figgis, J. Lewis, R.D. Peacock, J. Chem. Soc. (1961) 3132.
[64] M.L. Kuznetsov, A.J.L. Pombeiro, J. Chem. Soc., Dalton Trans. (2003) 738.



Scheme 1. Synthetic pathway for octakis-(2-diethylaminoethanethiol)-phthalocyanine. **M** = MnAc (**3**), Ni (**4**), Fe (**5**) and Co (**6**) [4].

The synthesis of cobalt octakis-(2-diethylaminoethanethiol)-phthalocyanine (**6**) has been reported before [4].

2.2. Electrochemical studies

All electrochemical experiments were performed using Autolab potentiostat PGSTAT 302 (Eco Chemie, Utrecht, The Netherlands) driven by the general purpose Electrochemical System data processing software (GPES, software version 4.9). Square wave voltammetric analysis was carried out at a frequency of 10 Hz, amplitude; 50 mV and step potential; 5 mV. A conventional three-electrode system was used. The working electrode was a bare glassy carbon electrode (GCE), Ag|AgCl wire and platinum wire were used as the pseudo reference and auxiliary electrodes respectively. The potential response of the Ag|AgCl pseudo-reference electrode was less than the Ag|AgCl (3 M KCl) by 0.015 ± 0.003 V. Prior to use, the working electrode surface was polished with alumina on a Buehler felt pad and rinsed with excess millipore water. All electrochemical experiments were performed in freshly distilled dry DMF or DCM containing $TBABF_4$ as supporting electrolyte.

Spectroelectrochemical data were obtained using a home-made optically transparent thin-layer electrochemical (OTTLE) cell which was connected to a Bioanalytical Systems (BAS) CV 27 voltammograph.

2.3. Equipment

UV/Vis spectra were recorded on Cary 500 UV/Vis/NIR spectrophotometer. IR (KBr disks) was recorded on Bruker Vertex 70-Ram II spectrophotometer. Elemental analysis was performed using Vario Elementar Microcube EL111. ^{1}H nuclear magnetic resonance (^{1}H NMR, 400 MHz) was obtained in $CDCl_3$ using Bruker EMX 400 NMR spectrometer.

2.4. Synthesis

2.4.1. 1,2-Bis-(diethylaminoethanethiol)-4, 5-dicyanobenzene (*2*)

1,2-Dichloro-4,5-dicyanobenzene (**1**) was synthesised according to reported procedures [17]. 1,2-Bis-(2-diethylaminoethanethiol)-4,5-dicyanobenzene (**2**) was also synthesised according to literature procedure [4], with slight modification as follows:

compound **1** (2.32 g, 11.75 mmol) was dissolved in anhydrous DMF (100 ml) under nitrogen and 2-diethylaminoethanethiol hydrochloride (6 g, 35.34 mmol) was added. After stirring for 10 min, finely ground anhydrous K_2CO_3 (19.5 g, 141.36 mmol) was added in portions over 2 h with stirring. The reaction mixture was stirred at room temperature for 48 h under nitrogen. Then the solution was poured into ice water (600 g). The precipitate was filtered off, washed with water, until the filtrate was neutral. The product was then dried in air. Yield: 3.61 g (80%). IR (KBr) υ_{max}/cm^{-1}: 3075, 2970–2812, 2229, 1562, 1459, 1382, 1343, 1275, 1200, 1113, 1066, 991, 733, 529. ^1H NMR ($CDCl_3$) δ = 7.54 (s, 2H,Ar–H), 3.12–3.08 (t, 4H, SCH_2), 2.80–2.77 (t, 4H, NCH_2), 2.61–2.55 (qnt, 8H, CH_2C), 1.05–1.01 (t, 12H, CH_3) ppm.

*2.4.2. Manganese(III)acetate (**3**), nickel (**4**) and iron (**5**) octakis-(2-diethylaminoethanethiol)-phthalocyanine*

Manganese(III)acetate (**3**), nickel (**4**) and iron (**5**) octakis-(2-diethylaminoethanethiol)-phthalocyanine were synthesised according to the procedure recently reported [3,4] with some modifications. A mixture of compound **2** (0.6 g, 1.54 mmol), manganese acetate (0.066 g, 0.38 mmol) or nickel(II) chloride (0.049 g, 0.38 mmol) or iron(II) chloride (0.049 g, 0.38 mmol) and 2-(dimethylaminoethanol) (1.2 ml) was refluxed for 12 h under nitrogen. After cooling to room temperature, the mixture was treated with excess MeOH: H_2O (1:1 ml) in order to precipitate the products. The products were filtered and dried in air. The products were then purified using column chromatography with neutral alumina as column material and DCM/methanol (20:1) as eluent.

*2.4.2.1. Complex **3**.* Yield: 0.54 g (86.72%) (*Anal.* Calc. for $C_{80}H_{120}N_{16}S_8MnOAc{\cdot}CH_2Cl_2$: C, 58.51; H, 7.34; N, 13.16. Found: C, 57.11; H, 6.72; N, 12.63%); UV–Vis (THF): λ_{max} (nm) (log ε): 353(4.6), 423(4.5), 465(4.5), 503(4.4), 676(4.3), 750(5.0); IR (KBr) υ_{max}/cm^{-1}; 2966–2805 (CH_2), 1413, 1377, 1327, 1070, 781, 744, 705, 606.

*2.4.2.2. Complex **4**.* Yield: 0.15 g (24.03%) (*Anal.* Calc. for $C_{80}H_{120}N_{16}S_8Ni{\cdot}CH_2Cl_2$: C, 56.97; H, 7.15; N, 13.13. Found: C, 56.35; H, 6.93; N, 13.17%); UV–Vis (THF): λ_{max} (nm) (log ε): 425(4.4), 695(4.8); IR (KBr) υ_{max}/cm^{-1} 2970–2802 (CH_2), 1410, 1367, 1307, 1080, 786, 754, 725, 686.

*2.4.2.3. Complex **5**.* Yield: 0.28 g (44.94%) (*Anal.* Calc. for $C_{80}H_{120}N_{16}S_8Fe{\cdot}2CH_2Cl_2$: C, 55.07; H, 6.93; N, 12.52. Found: C, 54.71; H, 6.71; N, 12.34%); UV–Vis (DMF): λ_{max} (nm) (log ε): 360(4.4), 451(3.9), 621(3.7), 657(3.9), 686(4.1), 746(3.8); IR (KBr) υ_{max}/cm^{-1} 2972–2805 (CH_2), 1412, 1357, 1317, 1080, 789, 758, 735, 688.

3. Results and discussion

3.1. Synthesis and characterization

3.1.1. Synthesis

Scheme 1 shows the synthetic route involved in the formation of complexes **3**, **4** and **5**. The phthalonitrile, compound **2**, was obtained via a based-catalyzed (K_2CO_3) nucleophilic aromatic substitution reaction, with the 2-diethylaminoethanethiol acting as the nucleophile. Cyclotetramerization of compound **2** to form the corresponding MPc occurred in the presence of the desired metal salt; $Mn(CH_3COO)_2$, $NiCl_2$ and $FeCl_2$ for complexes **3**, **4** and **5**, respectively. Purification of these complexes was achieved by column chromatography on alumina. Complex **3** was soluble in solvents such as THF, DCM and DMF while complex **4** dissolved in THF and DCM. Complex **5** was soluble in DMF and DCM but insoluble in THF.

These complexes were characterized by IR and UV–Vis spectroscopies as well as elemental analysis. The results obtained were consistent with the predicted structures shown in Scheme 1. The formation of complexes **3**, **4** and **5** was confirmed by the disappearance of the sharp C≡N vibration at 2229 cm^{-1} of **2**.

3.1.2. Spectroscopic characterization

All the complexes exhibited spectral properties characteristic of metallophthalocyanine (MPc). Complex **3** showed characteristic Q-band absorption, in THF, at 750 nm, Fig. 1. The absorption in the 450 nm region is usually associated with charge transfer in MnPc [10]. Complex **4** showed considerable aggregation in THF, with the peak at 694 nm attributed to the monomer while that at 633 nm is due to the aggregate, Fig. 1. Extensive aggregation of NiPc derivatives has been observed before [18]. Fig. 1 shows that the Q-band due to complex **3** is appreciably red-shifted compared to complex **4**. This observation is characteristic of MnPc complexes [10].

Fig. 2a shows the effect of increasing concentration (3.3×10^{-6}–8.8×10^{-6} M) on the spectra of complex **3**. Inset in Fig. 2a is a linear plot of absorbance, due to the Q-band (750 nm), against concentration of complex **3**. There was no evidence of aggregation in Fig. 2a and Beer's law was obeyed for concentrations less than 1×10^{-5}. Fig. 2b shows the effect of changing concentration (1.7×10^{-6}–1.02×10^{-5}M) on the spectra of complex **4**. The intensities of both the monomeric (694 nm) and dimeric peaks (633 nm) decreased with decreasing concentration. The Q-band due to the aggregate became less pronounced, compared to that due to the monomer, as concentration decreased, thus confirming the aggregated nature of the complex. Inset in Fig. 2b is the plot of absorbance, due to the Q-band at 694 nm, versus concentration. Even though the plot is almost linear at these concentrations, the UV–Vis spectra do give evidence of aggregation.

Complex **5** (not soluble in THF) exhibited spectra (Fig. 2c) characteristic of stacked monomer in FePc complexes, which is normally observed at about 630 nm in DMF [19]. The UV/visible spectral analysis of FePc complexes has been a subject of extensive research due to the complexity and the wide variety of species that may be formed in solution. For example, perchlorinated iron(II) phthalocyanine dissolved in DMF is known [20] to react with oxygen, resulting in oxidation and formation of a μ-oxo species, $Pc^{-2}Fe^{III}–O–Fe^{III}Pc^{-2}$, which changes back to the original monomeric species upon reduction. In the present study, Fig. 2c, the spectra were obtained in freshly prepared DMF solutions which had been de-aerated, suggesting that the peak near 630 nm is

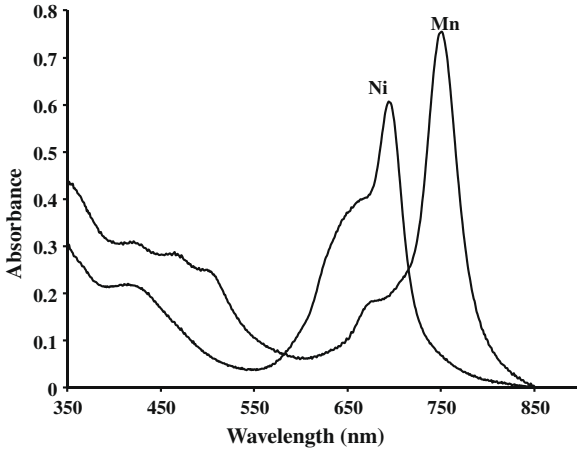


Fig. 1. UV–Vis spectra of 6.7×10^{-6} M of complex **3** (Mn) and complex **4** (Ni) in THF.

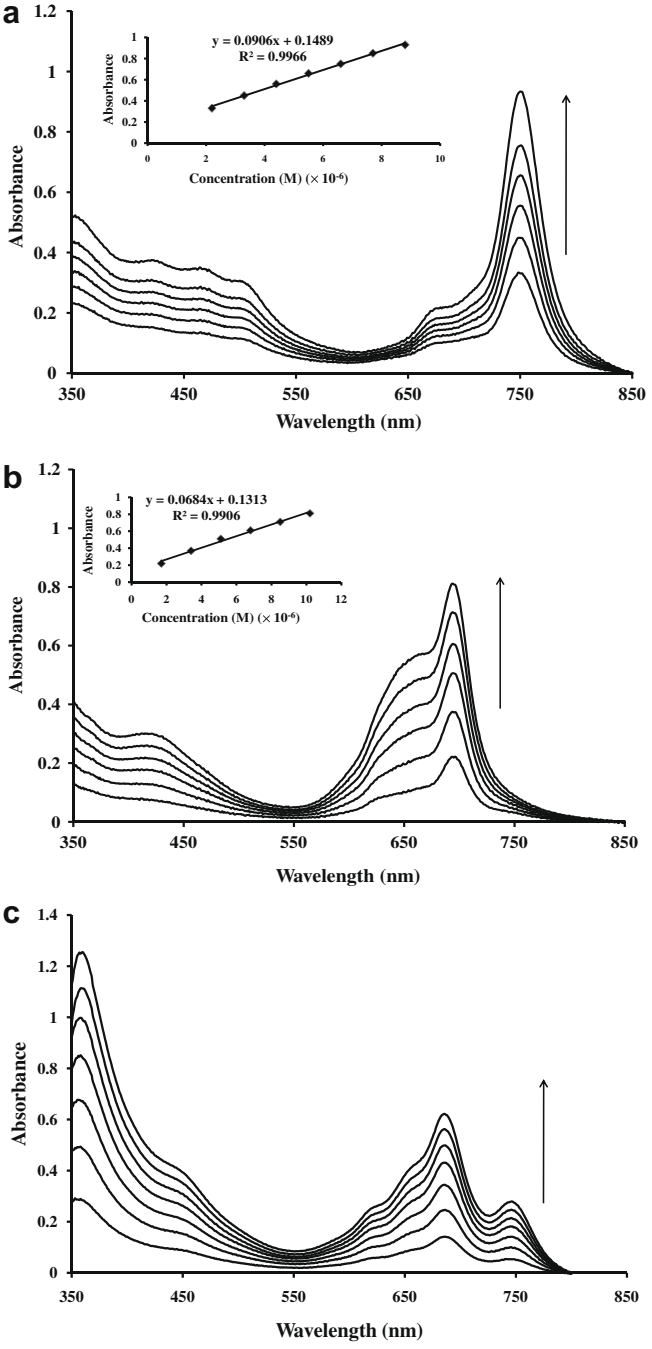


Fig. 2. Effect of changing concentration on the UV–Vis spectra of (a) complex **3** (3.3–8.8 × 10^{-6} M) in THF; (b) complex **4** (1.7 × 10^{-6}–1.02 × 10^{-5} M) in THF and (c) complex **5** (7.42 × 10^{-6}–5.2 × 10^{-5} M) in DMF.

not related to the μ-oxo species, but only to the presence of monomeric species as well as cofacially aggregated one. On dilution (5.2 × 10^{-5} M–7.42 × 10^{-6}), the peak near 630 nm decreased faster than the main peak at 686 nm. Aggregation (the presence of the band near 630 nm) was evident, even at concentration as low as 7.42 × 10^{-6} M, Fig. 2c. The split in the main Q-band suggests the presence of $Fe^{III}Pc$ species [10].

3.1.3. Voltammetric and spectroelectrochemical characterization

Voltammetric properties of complexes **3**, **4**, **5** and **6** are reported in this work. The peak potentials for the complexes are summarized in Table 1. In the current work, clearly defined reversible ring reductions were observed for all the complexes, but the reduction products get easily adsorbed on the electrode and the complexes degrade fast upon oxidation, especially the FePc derivative.

3.1.3.1. Complex **3**. Fig. 3 shows the cyclic and square wave (inset) voltammetry profiles of ~1 × 10^{-3} M of complex **3** in freshly distilled dimethyl formamide (DMF) containing 0.1 M $TBABF_4$ as supporting electrolyte. Three distinct processes, labeled **I**, **II** and **III**, can be identified. Redox couples **II** ($E_{1/2}$ = −0.12 V) and **III** ($E_{1/2}$ = −0.82 V) versus Ag|AgCl, have both anodic and cathodic components but with larger peak separation, ΔE (120 mV), than the expected 60 mV, thus suggesting slow electron transfer. These processes were quasi-reversible since ΔE value for ferrocene, at the same scan rate (100 mV versus Ag|AgCl), was 91 mV versus Ag|AgCl. The cathodic to anodic peak current ratio were near unity for both processes. Plots of peak current (I_p) versus square root of scan rate ($v^{1/2}$) (not shown) were linear for both processes, thus suggesting diffusion control. Redox couple **II** is assigned to $Mn^{III}Pc^{-2}/Mn^{II}Pc^{-2}$ while couple **III** is assigned to $Mn^{II}Pc^{-2}/Mn^{II}Pc^{-3}$ in comparison with literature [21], Table 1. Process **I** is irreversible (E_p = +0.78 V versus Ag|AgCl), it is assigned to ring oxidation, $Mn^{III}Pc^{-1}/Mn^{III}Pc^{-2}$ in comparison with literature, Table 1, [21]. The lack of reversibility of the oxidation processes is typical of thio substituted MPc complexes [14]. The redox processes and the number of electron transferred in each case were confirmed using spectroelectrochemical studies.

Spectroelectrochemical studies were carried out using optically transparent thin-layer electrode (OTTLE) cell. Fig. 4a shows the spectral changes observed on the application of potential of couple **II** (−0.12 V versus Ag|AgCl). The initial spectrum showed very pronounced peak at 653 nm with the main Q-band at 757 nm. The slight shift in the Q-band from 750 nm (Fig. 1) to 757 nm (Fig. 4a) is due to differences in solvents and the presence of electrolyte. The peak at 653 nm is characteristic of MnPc μ-oxo complexes [22]. This species is observed in DMF (Fig. 4a) but was not observed in THF (Fig. 1). The peak at 757 nm is due to $Mn^{III}Pc$ species. There is no $Mn^{II}Pc$ species before reduction. We used DMF for electrochemistry of complex **3** for comparative purposes with the other complexes under discussion in this work.

The presence of the μ-oxo MnPc species was confirmed by monitoring the spectral transformations of complex **3** in DMF solution when not de-aerated and when de-aerated with dry N_2 gas. This was evident by the decrease of the peak at 653 nm on bubbling nitrogen. However attempts to exclude oxygen completely during spectroelectrochemical studies were unsuccessful. The cyclic and square wave voltammograms reported above (Fig. 3) were reported under an atmosphere of nitrogen hence are due to mainly the $Mn^{III}Pc$ species.

Upon reduction at potentials of processes **II**, there was a blue shift in the Q-band from 757 to 705 nm and the color of the complex changed from purple to green, a gradual disappearance of the charge transfer bands in the 500 nm region was also noticed, with an isobestic point at 736 nm. The isobestic point observed was not so clear, which suggests the presence of more than two species, thus confirming the presence of the μ-oxo complex with the starting $Mn^{III}Pc^{-2}$ species and the electro-generated species, $Mn^{II}Pc^{-2}$. The formation of the latter was accompanied by the formation of more μ-oxo MnPc species. The persistence of μ-oxo MnPc species has been observed for some MnPc complexes [23].

A shift in the position of the Q-band without a decrease in intensity is typical of metal-based electro reduction process, and a blue shift in the Q-band is usually associated with the reduction of $Mn^{III}Pc^{-2}$ to $Mn^{II}Pc^{-2}$ [10]. These spectra changes thus confirmed that redox couple **II** in Fig. 3 is due to the reduction of $Mn^{III}Pc^{-2}$ to $Mn^{II}Pc^{-2}$ (n was calculated to be approximately 1 using the Eq. (1),

Table 1
Electrochemical data of thiol substituted MnPc, FePc, NiPc and CoPc. Half-wave ($E_{1/2}$) and peak (E_p) potentials in V versus Ag|AgCl. Values were recorded in DMF containing $TBABF_4$ unless otherwise stated.

Complex	$M^{II}Pc^{-4}/M^{II}Pc^{-3}$	$M^{I}Pc^{-3}/M^{I}Pc^{-2}$	$M^{II}Pc^{-3}/M^{II}Pc^{-2}$	$M^{II}Pc^{-2}/M^{I}Pc^{-2}$	$M^{III}Pc^{-2}/M^{II}Pc^{-2}$	$M^{II}Pc^{-1}/M^{II}Pc^{-2}$	$M^{III}Pc^{-1}/M^{III}Pc^{-2}$	Ref[c]
MnPc derivatives								
3			−0.82		−0.12		+0.78	TW
MnTMPyPc[a]					−0.057		+1.34	5
MnODMPc[a]			−1.24		−0.46		+ 0.75	12
MnTBMPc[a]			−0.98		−0.26		+0.83	28
4[a]	−0.69		−0.02			+0.92		
FePc derivatives								
5		−0.96		−0.35	+0.26		+0.87	
FeOBMPc[b]		−0.70		−0.26	+0.25		+0.60	29
FeTBMPc		−0.78		−0.37	+0.36		+0.70	26
FeTDMPc[a]		−0.84		−0.53	+0.62		+1.01	26
CoPc derivatives								
6		−1.40		−0.32	+0.80			
CoOBMPc[b]		−0.58		−0.096	+0.72		+1.16	29
CoTBMPc		−1.41		−0.38	+ 0.42		+0.89	26
CoTDMPc[a]				−0.46	+0.44		+0.66	26

TDMPc = tetra dodecylmercapto phthalocyanine, ODMPc = octa dodecylmercapto phthalocyanine TBMPc = tetra benzylmercapto phthalocyanine, TMPyPc = tetra mercaptopyridine phthalocyanine.
[a] Values recorded in DCM, using $TBABF_4$.
[b] Electrolyte = tetrabutylammonium perchlorate.
[c] TW = this work.

$$Q = nFVC \quad (1)$$

where n, F, V and C are the number of electrons transferred, Faraday's constant, volume and concentration of the electroactive species, respectively.

Increase in intensity of the band at 653 nm confirmed the presence of the μ-oxo complex, as earlier discussed, together with the electro-generated $Mn^{II}Pc^{-2}$ species. This observation has been reported before [5,22,23]. It was suggested that a form of equilibrium, as shown below, exists between MnPc species in DMF and in the presence of oxygen.

$$PcMn^{II} + O_2 \rightleftarrows PcMn^{III}(O_2) \quad (2)$$

$$PcMn^{III}(O_2) + PcMn^{II} \rightleftarrows PcMn^{III}{-}O_2{-}Mn^{III}Pc \quad (3)$$

$$PcMn^{III}{-}O_2{-}Mn^{III}Pc \rightleftarrows 2PcMn^{IV}O \quad (4)$$

$$2PcMn^{IV}O + 2PcMn^{II} \rightleftarrows 2PcMn^{III}{-}O{-}Mn^{III}Pc \quad (5)$$

$$4PcMn^{II} + O_2 \rightarrow 2PcMn^{III}{-}O{-}Mn^{III}Pc \text{ (Net equation)} \quad (6)$$

Further reduction of complex **3**, at the potentials of couple **III**, resulted in the spectral changes shown in Fig. 4b. A decrease in intensity of the new Q-band (705 nm) and emergence of new bands, with decreased intensities, at 543 and 590 nm are characteristic of ring-based redox process [24]. This observation confirmed that process **III** is a ring-based reduction, thus justifying the assignment of the couple to $Mn^{II}Pc^{-2}/Mn^{II}Pc^{-3}$ redox process. This supports the claim that first reduction in $Mn^{II}Pc^{-2}$ occur at the ring [25], although, other authors have reported metal reduction to the $Mn^{I}Pc^{-2}$ species [5,10]. Ring versus metal reduction in

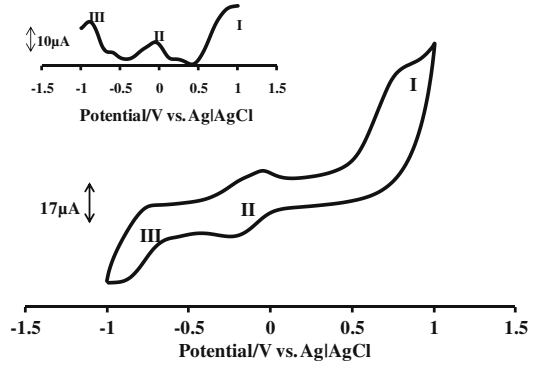


Fig. 3. Cyclic and square wave (inset) voltammograms of 10^{-3} M of complex **3** in freshly distilled DMF containing 0.1 M $TBABF_4$. Scan rate: 100 mVs^{-1}.

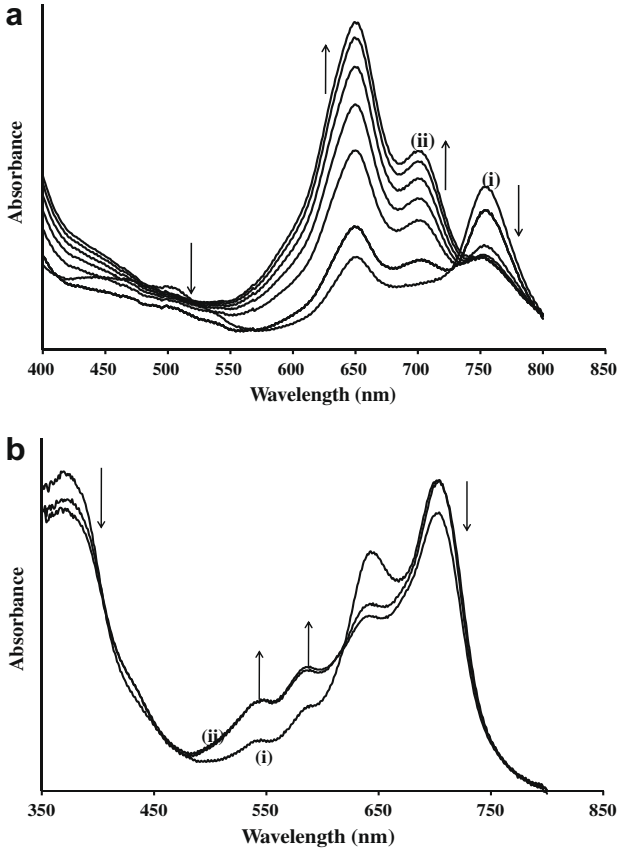


Fig. 4. UV–Vis spectral changes observed for complex **3** during controlled potential electrolysis at (a) −0.12 V (process **II**) and (b) −0.82 V (process **III**). (i) Spectra before electrolysis and (ii) spectra after electrolysis. The first spectrum in (b) is the same as the last spectrum in (b). Electrolyte = DMF containing 0.1 M $TBABF_4$.

$Mn^{II}Pc$ complexes is highly dependent on the nature of substituents [5]. A decrease in intensity was also observed for the band (653 nm) associated with the μ-oxo complex.

Application of potential of process **I** resulted in the formation of a new less intense band at 509 nm, typical of ring oxidation in MPc [24], complicated by redox processes based on the ring substituents. Process **I** is thus assigned to ring oxidation, $Mn^{III}Pc^{-1}$/$Mn^{III}Pc^{-2}$.

*3.1.3.2. Complex **4**.* Fig. 5 shows the cyclic and square wave (inset) voltammograms of 10^{-3} M complex **4** in a mixture of freshly distilled DCM and DMF (2:1) containing 0.1 M $TBABF_4$ as supporting electrolyte. This mixture was used because of the difficulty of obtaining a clearly defined cyclic voltammogram of the complex in DCM and the insoluble nature of the complex in DMF alone. Three processes can be observed: processes **I** (E_p = +0.92 V), **II** ($E_{1/2}$ = −0.02 V) and **III** ($E_{1/2}$ = −0.69 V). All redox processes are assigned to the ring since only ring reduction or oxidation has been documented for NiPc complexes in solution [10]. The first reduction process is observed at less negative potentials than has been reported [18] for NiPc complexes, probably due to the presence of sulfur and nitrogen in the ring substituents which will make the ring easier to oxidize. Couple **II** and **III** were reversible, while process **I** was irreversible. Due to the aggregated nature of the complex, it was not possible to do reliable spectroelectrochemical studies, however only ring-based redox processes occur for NiPc derivatives.

*3.1.3.3. Complex **5**.* The cyclic and square wave (inset) voltammetry profiles of ~1 × 10^{-3} M of complex **5**, in freshly distilled DMF containing 0.1 M $TBABF_4$ as supporting electrolyte, are shown in Fig. 6. Wider potential window (−1.3–+1.3 V versus Ag|AgCl) was used compared to that used for complexes **3** and **4** (−1–+1 V versus Ag|AgCl), because ring-based processes were not observed for complex **5** within the latter potential window. Even though the UV–Vis spectra showed complex behavior, the cyclic voltammetry peaks were well resolved in Fig. 6. The cyclic voltammetry will be dominated by $Fe^{II}Pc$ derivatives since the spectrum of the complex showed this species to be dominant. Four distinct processes were observed. Process **I** (E_p = +0.87 V versus Ag|AgCl) was assigned to ring oxidation, $Fe^{III}Pc^{-1}/Fe^{III}Pc^{-2}$. This process is irreversible as was the case for complexes **3** and **4**. Process **II** ($E_{1/2}$ = +0.26 V versus Ag|AgCl) was assigned to metal oxidation, $Fe^{III}Pc^{-2}/Fe^{II}Pc^{-2}$, in comparison with other alkyl or aryl thio substituted FePc complexes [26], Table 1. Process **II**, with a weak cathodic component compared to the anodic component, was quasi-reversible. Process

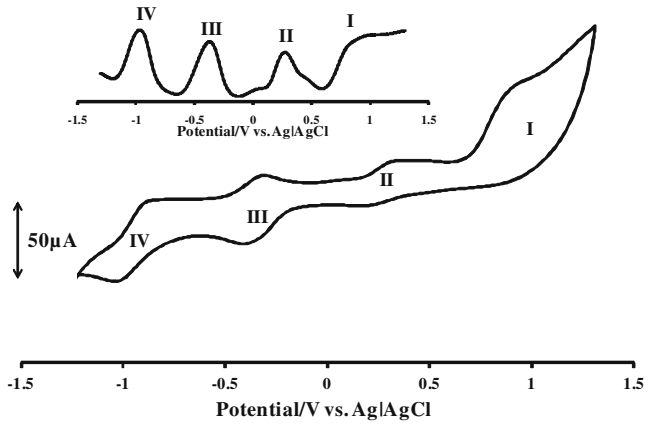


Fig. 6. Cyclic and square wave (inset) voltammograms of 10^{-3} M of complex **5** in freshly distilled DMF containing 0.1 M $TBABF_4$. Scan rate: 100 mVs^{-1}.

III ($E_{1/2}$ = −0.35 V versus Ag|AgCl) was assigned to metal reduction, $Fe^{II}Pc^{-2}/Fe^{I}Pc^{-2}$. This process was reversible, with peak separation, ΔE, of 60 mV versus Ag|AgCl, and cathodic to anodic current ratio of near unity. Process **IV** ($E_{1/2}$ = −0.96 V versus Ag|AgCl) was assigned to ring reduction, $Fe^{I}Pc^{-2}/Fe^{I}Pc^{-3}$.This process was quasi-reversible, with cathodic to anodic current ratio of near unity and peak separation, ΔE, of 120 mV versus Ag|AgCl compared to 91 mV for ferrocene at the same scan rate, 100 mV versus Ag|AgCl.

Due to the presence of more than one species in solution, spectroelectrochemical studies were not successful in the assignment of the cyclic voltammetry peaks. However, the assignments were based on the well known electrochemistry of FePc complexes in comparison with FePc complexes substituted with alkylthio groups, Table 1.

*3.1.3.4. Complex **6**.* The synthesis of the cobalt analogue of complexes **3**, **4** and **5** has been reported before [4], but it's electrochemical and spectroelectrochemical properties were not reported, hence they are reported in the current work, for the purpose of comparison with that of the new complexes. Fig. 7 shows both the cyclic and square wave (inset) voltammograms of ~1 × 10^{-3}M of complex **6** in freshly distilled DMF containing 0.1 M $TBABF_4$. A wider potential range (−2.0–+1.0 V) was used, compared to the other complexes, in order to observe the ring reduction processes. In coordinating solvents such as DMF, Co^{III}/Co^{II} couple occurs before the ring oxidation in CoPc complexes [27], thus process I (at 0.8 V) may be assigned to this process,

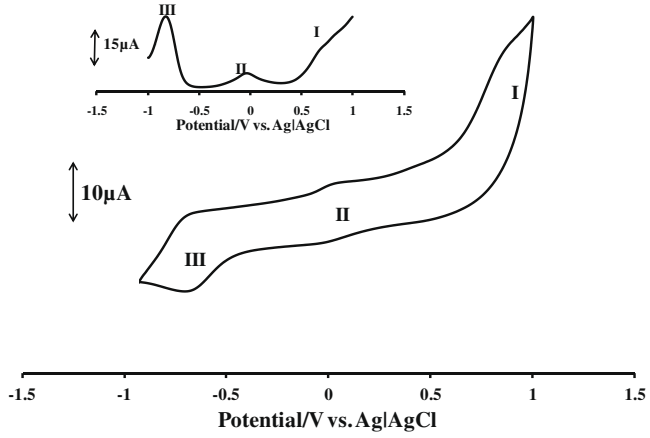


Fig. 5. Cyclic and square wave (inset) voltammograms of 10^{-3} M of complex **4** in distilled mixture of DCM and DMF containing 0.1 M $TBABF_4$. Scan rate: 100 mVs^{-1}.

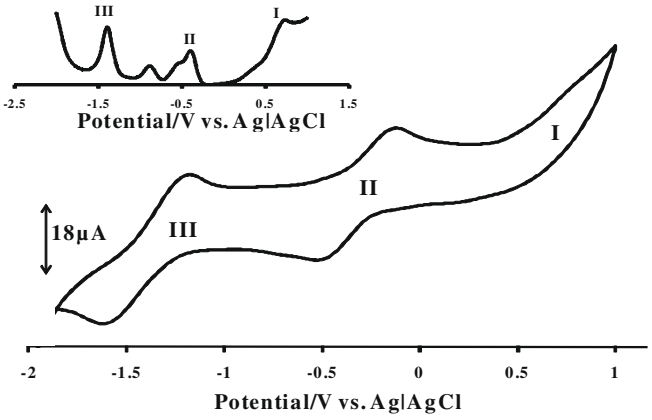


Fig. 7. Cyclic and square wave (inset) voltammograms of 10^{-3} M of complex **6** in freshly distilled DMF containing 0.1 M $TBABF_4$. Scan rate: 100 mVs^{-1}.

but complicated by contribution from the oxidation of ring substituent as was the case for the rest of the complexes. The process occurs at more positive potential values compared to CoPc complexes in general, but is within the range of some arylthio substituted CoPc derivatives [28,29], Table 1.

Processes **II** ($E_{1/2}$ = −0.32 V versus Ag|AgCl) and **III** ($E_{1/2}$ = −1.4 V versus Ag|AgCl) were quasi-reversible. Process **II** is in the potential range for $Co^{II}Pc^{2-}/Co^{I}Pc^{2-}$ species, while process **III** is typical of $Co^{I}Pc^{2-}/Co^{I}Pc^{3-}$ [27], Table 1. The more sensitive square wave voltammogram showed the presence of another process (−0.9 V). This was not observed on the cyclic voltammogram. The origin of the peak is not clear at the moment.

Spectroelectrochemical studies were used to confirm some of the assigned processes. The spectral changes in Fig. 8a were observed on the application of the potential of process **II**. The starting spectrum (curve i) shows considerable aggregation as a result of the high concentration used for the OTTLE cell. The peaks at 692 and 655 nm are associated with monomer and dimer respectively. A red-shift in the position of the Q-band, from 692 to 726 nm, was observed on the application of the potential of process **II**. There was an emergence of a new peak at 492 nm with increased intensity. New intense peak between 400 to 500 nm are characteristic of $Co^{I}Pc$ species [10]. The shift in Q-band without decrease in intensity is characteristic of metal-based reduction in MPc complexes. Thus spectral changes shown in Fig. 8a confirmed that couple **II** was as a result of the reduction of $Co^{II}Pc$ to $Co^{I}Pc$ (the number of moles of electrons transferred, n, was calculated to be approximately 1, using Eq. (1)). Also, distinct isobestic points at 580 and 710 nm showed that the process is a clear reduction involving two species. Application of the potential of process **III** resulted in the spectral changes shown in Fig. 8b. The starting spectrum (curve i), which is the last spectrum in Fig. 8a, has peaks at 726, 663, 492 and 604 nm. The peaks at 726 and 663 nm decrease in intensity without change in positions, while that at 492 nm shifted to 496 nm. The decrease in the intensity of Q-band is typical of ring-based process in MPcs. Bands in the 500 to 600 nm region are characteristic of ring-based reduction and the formation of a Pc^{3-} species [24]. Hence, reduction at potential of couple **III** resulted in the formation of $Co^{I}Pc^{3-}$ species.

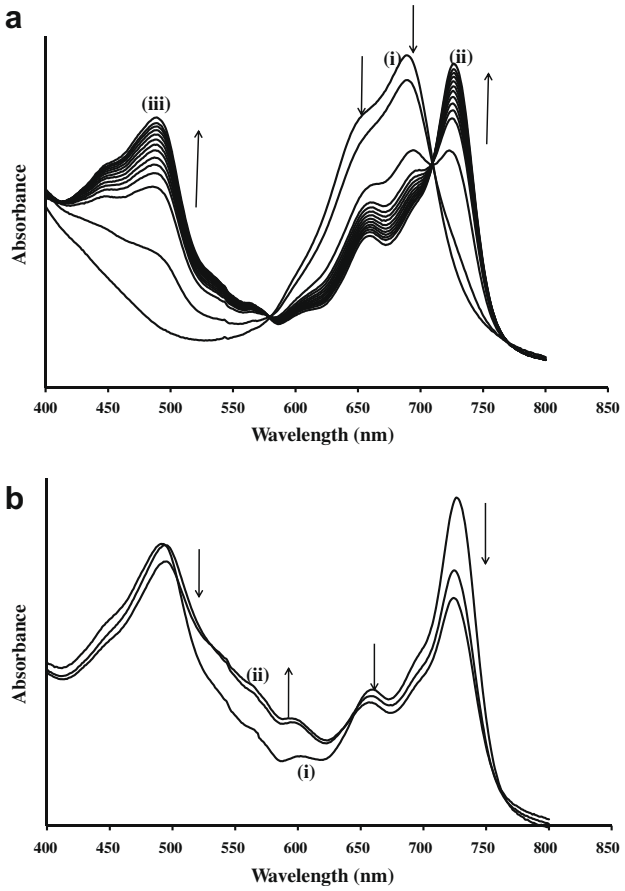


Fig. 8. UV–Vis spectral changes observed for complex **6** during controlled potential electrolysis at (**a**) −0.32 V (process **II**), (**b**) −1.40 V (process **III**). (i) Spectrum before electrolysis and (ii) spectrum after electrolysis. Electrolyte = DMF containing 0.1 M $TBABF_4$. The final spectrum in (**a**) is the starting spectrum in (**b**).

4. Conclusions

The syntheses, spectroscopic and electrochemical properties of the new complexes: manganese (**3**), nickel (**4**) and iron (**5**) octakis-(2-diethylaminoethanethiol) phthalocyanines are reported. The observed spectroscopic and electrochemical properties of the complexes were distinctly defined by the nature of the central metals. During spectroelectrochemical studies, the UV–Vis spectra of complex **3** in DMF showed bands characteristic of μ-oxo complex in MnPc complexes and that associated with the monomeric species. Well defined redox processes, assigned to $Mn^{III}Pc^{-2}/M^{II}Pc^{-2}$ and $Mn^{II}Pc^{-2}/M^{II}Pc^{-3}$ species, were observed and confirmed using spectroelectrochemical studies. Complex **4** showed aggregation behavior, characteristic of NiPc complexes, in THF. Complex **5** showed spectral property characteristic of stacked monomer in FePc. Solution electrochemistry of complex **5** showed four distinct redox processes, assigned to $Fe^{III}Pc^{-2}/Fe^{II}Pc^{-2}$, $Fe^{III}Pc^{-1}/Fe^{III}Pc^{-2}$, $Fe^{II}Pc^{-2}/Fe^{I}Pc^{-2}$ and $Fe^{I}Pc^{-2}/Fe^{I}Pc^{-3}$. Solution electrochemistry of the cobalt derivative (6) showed redox processes characteristic of $Co^{II}Pc^{-2}/Co^{I}Pc^{-2}$ and $Co^{I}Pc^{-2}/Co^{I}Pc^{-3}$ species.

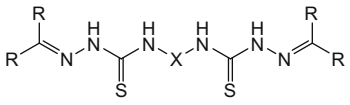
Acknowledgements

This work was supported by the Department of Science and Technology (DST) and National Research Foundation (NRF) of South Africa through DST/NRF South African Research Chairs Initiative for Professor of Medicinal Chemistry and Nanotechnology and Rhodes University.

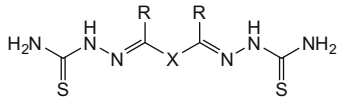
References

[1] C.C. Leznoff, A.B.P. Lever, Phthalocyanines Properties and Applications, vols. 1–4, Weinheim, VCH, 1989–1996.
[2] N.B. Mckeown, in: Phthalocyanine Materials, Cambridge University Press, 1998.
[3] M. Idowu, T. Nyokong, Polyhedron 28 (2009) 416.
[4] Z.A. Bayur, Dyes Pigm. 65 (2005) 235.
[5] N. Sehlotho, M. Durmuş, V. Ahsen, T. Nyokong, Inorg. Chem. Commun. 11 (2008) 479.
[6] J. Zhu, F. Gu, J. Zhag, Mater. Lett. 61 (2007) 1296.
[7] W. Posiuk-Bronikoswska, M. Krajewska, I. Pfis-Kabulska, Polyhedron 18 (1998) 561.
[8] S. Knecht, K. DÜrr, G. Schmid, L.R. Subramanian, M. Hanack, J. Porphyr. Phthalocyan. 3 (1999) 292.
[9] D.K. Rittenberg, L. Baarrs-Hibbe, A. Böhm, J.S. Miller, J. Mater. Chem. 10 (2000) 241.
[10] M.J. Stillman, T. Nyokong, in: C.C. Leznoff, A.B.P. Lever (Eds.), Phthalocyanines: Properties and Applications, vol. 1, VCH, New York, 1989 (Chapter 3).
[11] P. Tau, T. Nyokong, Dalton Trans. (2006) 4482.
[12] G. Mbambisa, P. Tau, E. Antunes, T. Nyokong, Polyhedron 26 (2007) 5355.
[13] G. Mbambisa, T. Nyokong, Polyhedron 27 (2008) 2799.
[14] A.R. Ozkaya, A.G. Gurek, A. Gul, O. Bekaroglu, Polyhedron 16 (1997) 1877.
[15] K. Takahashi, M. Kawashima, Y. Tomita, M. Itoh, Inorg. Chim. Acta 232 (1995) 69.
[16] P. Tau, T. Nyokong, Electrochim. Acta 52 (2007) 4547.
[17] N.B. McKeown, in: K.M. Kadish, K.M. Smith, R. Guilard(Eds.), Porphyrin Handbook, Phthalocyanine Properties and Materials, vol. 15, 2003, Academic Press, New York (Chapter 98).

[18] J. Obirai, N. Pereira Rodrigues, F. Bedioui, T. Nyokong, J. Porphyr. Phthalocyan. 7 (2003) 508.
[19] A. Hadasch, A. Sorokin, A. Rabion, B. Meunier, New J. Chem. 22 (1998) 45.
[20] N. Grootboom, T. Nyokong, J. Mol. Cat. A: Chem. 179 (2002) 113.
[21] B. Agboola, K. Ozoemena, P. Westbroek, T. Nyokong, Electrochim. Acta 52 (2007) 2520.
[22] J. Janczak, R. Kubiak, M. Śledź, H. Borrmann, Y. Grin, Polyhedron 22 (2003) 2689.
[23] J. Obirai, T. Nyokong, Electrochim. Acta 50 (2005) 3296.
[24] M.J. Stillman, in: C.C. Leznoff, A.B.P. Lever (Eds.), Phthalocyanines: Properties and Applications, vol. 3, VCH Publishers, New York, 1993 (Chapter 5).
[25] C.C. Leznoff, L.S. Black, A. Heibert, P.W. Causey, D. Christendat, A.B.P. Lever, Inorg. Chim. Acta 359 (2006) 2690.
[26] B.O. Agboola, K.I. Ozoemena, T. Nyokong, Electrochim. Acta 51 (2006) 4379.
[27] A.B.P. Lever, E.R. Milaeva, G. Speier, in: C.C. Leznoff, A.B.P. Lever (Eds.), Phthalocyanines: Properties and Applications, vol. 3, VCH Publishers, New York, 1993, p. 1.
[28] B. Agboola, K. Ozoemena, T. Nyokong, Electrochim. Acta 51 (2006) 4379.
[29] F. Matemadomboa, M.D. Maree, K.I. Ozoemena, P. Westbroek, J. Porphyr. Phthalocyan. 9 (2005) 484.



dithiosemicarbazone



bis(thiosemicarbazone)

Fig. 1. Example of a dithiosemicarbazone and a bis(thiosemicarbazone) (X = aliphatic or aromatic spacer).

Palladium dichloride was received as a donation from Anglo Platinum. Ethane-1,2-dithiosemicarbazide [26], benzene-1,4-dithiosemicarbazide [23], and $Pd(PPh_3)_2Cl_2$ [27] were prepared following reported literature procedures. Solvents were freshly distilled and dried over the appropriate drying agents.

2.2. Instrumentation

Nuclear magnetic resonance (NMR) spectra were recorded on either a Varian Mercury XR300 MHz spectrometer (^{1}H at 300.08 MHz, ^{13}C at 75.46 MHz, ^{31}P at 121.47 MHz) or a Varian Unity XR400 MHz spectrometer (^{1}H at 399.95 MHz, ^{13}C at 100.58 MHz, ^{31}P at 161.90 MHz). ^{1}H and $^{13}C\{^1H\}$ NMR chemical shifts are reported using tetramethylsilane (TMS) as the internal standard and $^{31}P\{^1H\}$ spectra were measured relative to H_3PO_4 as the external standard. Infrared (IR) spectra were determined using a Perkin–Elmer Spectrum One FT-IR spectrometer and were recorded using KBr pellets. Elemental analyses (C, H and N) were recorded on a Thermo Flash 1112 Series CHNS-O Analyser. Mass spectrometry was carried out at the University of Stellenbosch on a Waters API Quattro Micro triple quadrupole mass spectrometer. Data were recorded using Electrospray Ionisation (ESI) mass spectrometry in the negative or positive modes. Melting points are corrected and were determined on a Reichert Thermovar hot stage microscope.

2.3. Synthesis of ethylene- (**1**–**3**) and phenylene-bridged (**4**–**6**) dithiosemicarbazone ligands

General procedure: Either ethane-1,2-dithiosemicarbazide or benzene-1,4-dithiosemicarbazide (1 equiv.) was dissolved in *N,N*-dimethylformamide (20 mL) at 120 °C. Upon complete dissolution, the appropriate salicylaldehyde (2 equiv.), dissolved in DMF (5 mL), was then added dropwise to the solution. The mixture was stirred at 120 °C for 5 h. Cold water was added to induce precipitation of the product in all cases. The resulting precipitate was collected by filtration and washed with cold water. The products were dried in the oven at 110 °C.

Compound **1** was prepared from ethane-1,2-dithiosemicarbazide (0.205 g, 0.985 mmol) and salicylaldehyde (0.210 mL, 1.97 mmol). Compound **1** was isolated as a light yellow powder. Yield 0.307 g (74.7%). M.p. 223–227 °C. *Anal.* Calc. for $C_{18}H_{20}N_6S_2O_2$: C, 51.90; H, 4.84; N, 20.17; S, 15.40. Found: C, 51.58; H, 5.11; N, 20.30; S, 16.06%. ν_{max}/cm^{-1} 1618 (C=N). ^{1}H NMR (400 MHz, DMSO-d_6, 25 °C): δ = 3.83 (4H, s, CH_2), 6.77 (2H, t, J = 7.72, Ar), 6.85 (2H, d, J = 8.17, Ar), 7.19 (2H, t, J = 7.53, Ar), 7.96 (2H, d, J = 7.73, Ar), 8.39 (2H, s, CH=N), 8.57 (2H, s, $NHCH_2$), 9.86 (2H, s, OH), 11.47 (2H, s, C=NNH) ppm. $^{13}C\{^1H\}$ NMR (75 MHz, DMSO-d_6, 25 °C): δ = 43.32, 115.85, 118.99, 120.22, 126.61, 130.78, 139.64, 156.22, 177.23 ppm. MS ESI: m/z 415 (100%, $[M-H]^+$).

Compound **2** was prepared from ethane-1,2-dithiosemicarbazide (0.205 g, 0.986 mmol) and 2-hydroxy-3-methoxy-benzaldehyde (0.300 g, 1.97 mmol). The product was isolated as a pale yellow powder. Yield 0.441 g (93.7%). M.p. 245–249 °C. *Anal.* Calc. for $C_{20}H_{24}N_6S_2O_4$: C, 50.40; H, 5.08; N, 17.63; S, 13.46. Found: C, 49.99; H, 5.34; N, 17.36; S, 12.92%. ν_{max}/cm^{-1} 1671 (CN). ^{1}H NMR (400 MHz, DMSO-d_6, 25 °C): δ = 3.80 (6H, s, OMe), 3.83 (4H, s, CH_2), 6.73 (2H, t, J = 7.98, Ar), 6.94 (2H, d, J = 7.03, Ar), 7.58 (2H, d, J = 7.86, Ar), 8.41 (2H, s, CH=N), 8.56 (2H, s, $NHCH_2$), 9.12 (2H, s, OH), 11.5 (2H, s, CH=NNH) ppm. $^{13}C\{^1H\}$ NMR (75 MHz, DMSO-d_6, 25 °C): δ = 43.32, 55.79, 112.84, 118.14, 118.74, 120.68, 139.44, 145.8, 147.78, 177.23 ppm. MS ESI: m/z 475 (100%, $[M-H]^+$).

Compound **3** was prepared from ethane-1,2-dithiosemicarbazide (0.204 g, 0.979 mmol) and 3-*tert*-butyl-salicylaldehyde (0.340 mL 1.96 mmol). Compound **3** was isolated as a pale yellow powder. Yield 0.365 g (73.9%). M.p. 226–230 °C. *Anal.* Calc. for $C_{24}H_{36}N_6S_2O_2$: C, 57.11; H, 7.19; N, 16.65; S, 12.71. Found: C, 57.55; H, 6.88; N, 16.44; S, 12.80%. ν_{max}/cm^{-1} 1599 (C=N). ^{1}H NMR (400 MHz, DMSO-d_6, 25 °C): δ = 1.39 (18H, s, ^{t}Bu), 3.84 (4H, s, CH_2), 6.84 (2H, t, J = 7.67, Ar), 7.24 (4H, m, Ar), 8.29 (2H, s, CH=N), 8.60 (2H, s, $NHCH_2$), 9.96 (2H, s, OH), 11.41 (2H, s, CH=N–NH) ppm. $^{13}C\{^1H\}$ NMR (100 MHz, DMSO-d_6, 25 °C): δ = 30.06, 35.15, 44.33, 119.52, 120.02, 129.14, 129.99, 137.49, 147.66, 156.00, 177.88 ppm. MS ESI: m/z 529 (100%, $[M+Na]^+$).

Compound **4** was synthesized from benzene-1,4-dithiosemicarbazide (0.205 g, 0.800 mmol) and salicylaldehyde (0.171 mL, 1.60 mmol). The precipitate was isolated as a pale yellow powder. Yield 0.323 g (86.9%). M.p. 233–241 °C. *Anal.* Calc. for $C_{22}H_{20}N_6S_2O_2$: C, 56.88; H, 4.34; N, 18.09; S, 13.80. Found: C, 56.32; H, 4.36; N, 17.63; S, 13.41%. ν_{max}/cm^{-1} 1622 (C=N). ^{1}H NMR (300 MHz, DMSO-d_6, 25 °C): δ = 6.85 (4H, m, Ar), 7.23 (2H, t, J = 8.46, Ar), 7.55 (4H, s, Ph), 8.02 (2H, d, J = 7.78, Ar), 8.49 (2H, s, CH=N), 9.89 (2H, s, OH), 9.93 (2H, s, S=CNHPh), 11.64 (2H, s, CH=NNH) ppm. $^{13}C\{^1H\}$ NMR (75 MHz, DMSO-d_6, 25 °C): δ = 116.03, 119.16, 120.15, 124.88, 127.15, 131.16, 136.02, 140.45, 156.47, 175.72 ppm. MS ESI: m/z 465 (100%, $[M+H]^+$).

Compound **5** was prepared using benzene-1,4-dithiosemicarbazide (0.206 g, 0.800 mmol) and 2-hydroxy-3-methoxy-benzaldehyde (0.245 g, 1.60 mmol). Compound **5** was isolated as a pale yellow powder. Yield 0.273 g (65.1%). M.p. 233–236 °C. *Anal.* Calc. for $C_{24}H_{24}N_6S_2O_4$: C, 54.95; H, 4.61; N, 16.02; S, 12.22. Found: C, 54.10; H, 4.65; N, 16.84; S, 12.94%. ν_{max}/cm^{-1} 1659 (CN). ^{1}H NMR (300 MHz, DMSO-d_6, 25 °C): δ = 3.83 (6H, s, OMe), 6.81 (2H, t, J = 7.96, Ar), 6.99 (2H, d, J = 8.06, Ar), 7.48–7.66 (2H, m, Ar), 7.57 (4H, s, Ph), 8.52 (2H, s, CH=N), 9.82 (2H, m, OH), 9.93 (2H, m, S=CNHPh), 11.66 (2H, s, CH=NNH) ppm. $^{13}C\{^1H\}$ NMR (75 MHz, DMSO-d_6, 25 °C): δ = 55.89, 113.16, 118.58, 118.86, 120.58, 124.99, 135.99, 140.18, 146.15, 147.88, 175.70 ppm. MS ESI: m/z 525 (10%, $[M+H]^+$); 391 (100%, $[M-C_8H_6O_2]^+$).

Compound **6** was prepared using benzene-1,4-dithiosemicarbazide (0.153 g, 0.596 mmol) and 3-*tert*-butyl-salicylaldehyde (0.204 mL, 1.19 mmol) in a DMF/EtOH solution. Compound **6** was isolated as a pale yellow powder. Yield 0.098 g (28.5%). M.p. 288–292 °C. *Anal.* Calc. for $C_{30}H_{36}N_6S_2O_2$: C, 62.47; H, 6.29; N, 14.57; S, 11.12. Found: C, 62.19; H, 6.57; N, 14.55; S, 11.05%. ν_{max}/cm^{-1} 1667 (CN). ^{1}H NMR (300 MHz, DMSO-d_6; 25 °C): δ = 1.33 (18H, m, ^{t}Bu), 6.95 (2H, m, Ar), 7.75–7.21 (8H, m, Ar/Ph), 8.39 (2H, s, CH=N), 10.07 (4H, m, OH/NHPh), 11.58 (2H, m, CH=NNH) ppm. $^{13}C\{^1H\}$ NMR (75 MHz, DMSO-d_6; 25 °C): δ = 29.17, 34.42, 118.75, 119.24, 121.09, 125.10, 128.50, 129.43, 136.857, 147.47, 155.42, 176.40 ppm. MS ESI: m/z 577 (100%, $[M+H]^+$).

2.4. Synthesis of binuclear palladium complexes (**7**–**12**)

2.4.1. General procedure

A heated solution (50 °C) of either ethane-1,2-dithiosemicarbazone or benzene-1,4-dithiosemicarbazone (1 equiv.) in ethanol (50 mL) was stirred under nitrogen. To the mixture was added, 1 equiv. of triethylamine. Upon dissolution of the dithiosemicarbazone, $Pd(PPh_3)_2Cl_2$ (2 equiv.) was added resulting in an orange reaction mixture. The reaction mixture was refluxed for 6 h and then cooled to room temperature. The resulting orange precipitate was filtered, washed with ethanol and dried *in vacuo*.

2.4.2. Compound **7**

Compound **1** (0.103 g, 0.247 mmol), triethylamine (0.035 mL) and $Pd(PPh_3)_2Cl_2$ (0.347 g, 0.494 mmol) were refluxed in ethanol. The product was obtained as a light orange powder. Yield 0.213 g (74.9%). M.p. 274–283 °C (with decomposition). *Anal.* Calc. for $C_{54}H_{46}N_6S_2P_2O_2Pd_2$: C, 56.40; H, 4.03; N, 7.31; S, 5.58. Found: C, 56.08; H, 4.04; N, 7.02; S, 5.09%. ν_{max}/cm^{-1} 1599 (C=N). ^1H NMR (300 MHz, DMSO-d_6, 25 °C): δ = 3.36 (4H, s, CH_2), 6.55 (4H, m, Ar), 6.98 (2H, s, N*H*CH_2), 7.18 (2H, t, J = 8.78, Ar), 7.38 (2H, d, J = 7.80, Ar), 7.39–7.68 (30H, m, PPh_3), 8.33 (2H, d, J = 13.98, CH=N) ppm. $^{13}C\{^1H\}$ NMR (75 MHz, DMSO-d_6, 25 °C): δ = 44.99, 114.31, 117.77, 119.81, 128.38–134.02, 148.82, 161.47, 169.16 ppm. ^{31}P NMR (120 MHz, DMSO-d_6, 25 °C): δ = 25.58 (2P, s, PPh_3) ppm. MS ESI: m/z 1151 (100%, $[M+H]^+$).

2.4.3. Compound **8**

Compound **2** (0.119 g, 0.249 mmol), triethylamine (0.035 mL) and $Pd(PPh_3)_2Cl_2$ (0.350 g, 0.498 mmol) were refluxed in ethanol. The product was isolated as an orange powder. Yield 0.286 g (94.9%). M.p. 264–271 °C (with decomposition). *Anal.* Calc. for $C_{56}H_{50}N_6S_2P_2O_4Pd_2$: C, 55.58; H, 4.17; N, 6.90; S, 5.30. Found: C, 56.00; H, 4.49; N, 6.36; S, 5.30%. ν_{max}/cm^{-1} 1598 (C=N). ^1H NMR (300 MHz, DMSO-d_6, 25 °C): δ = (OMe signal suppressed by H_2O), 3.59 (4H, s, CH_2), 5.72 (2H, s, N*H*CH_2), 6.52 (2H, t, J = 7.41, Ar), 6.86 (2H, m, Ar), 7.10 (2H, d, J = 7.41, Ar), 7.20–7.88 (30H, m, PPh_3), 8.27 (2H, d, J = 14.01, CH=N) ppm. $^{13}C\{^1H\}$ NMR (75 MHz, DMSO-d_6, 25 °C): δ = 44.97, 55.87, 113.52, 114.24, 117.42, 125.85, 128.13–134.14, 149.04, 150.68 152.87, 168.83 ppm. ^{31}P NMR (120 MHz, DMSO-d_6, 25 °C): δ = 19.61 (2P, s, PPh_3) ppm. MS ESI: m/z 1210 (20%, $[M+H]^+$); 279 (100%, $[M-C_8H_6N_2SO_2Pd(PPh_3)_2]^+$).

2.4.4. Compound **9**

Compound **3** (0.122 g, 0.243 mmol), triethylamine (0.034 mL) and $Pd(PPh_3)_2Cl_2$ (0.341 g, 0.485 mmol) were refluxed in ethanol. This yielded the product **9** as an orange powder. Yield 0.221 g (72.1%). M.p. 258–262 °C (with decomposition). *Anal.* Calc. for $C_{62}H_{62}N_6S_2P_2O_2Pd_2$: C, 59.00; H, 4.95; N, 6.66; S, 5.08. Found: C, 60.21; H, 5.32; N, 5.89; S, 4.94%. ν_{max}/cm^{-1} 1593 (C=N). ^1H NMR (300 MHz, $CDCl_3$, 25 °C): δ = 0.75 (18H, s, ^{t}Bu), 3.38 (2H, s, CH_2), 5.08 (2H, s, N*H*CH_2), 6.56 (2H, t, J = 7.57, Ar), 7.19–7.79 (34H, m, PPh_3, Ar), 8.28 (2H, d, J = 14.19, CH=N) ppm. $^{13}C\{^1H\}$ NMR (75 MHz, DMSO-d_6, 25 °C): δ = 30.08, 34.95, 45.91, 114.39, 118.88, 128–135, 139.92, 151.07, 161.95 ppm. ^{31}P NMR (120 MHz, $CDCl_3$, 25 °C): δ = 24.35 (2P, s, PPh_3) ppm. MS ESI: m/z 1263 (50%, $[M+H]^+$); 675 (100%, $[M-C_{11}H_{13}N_2SOPdPPh_3]^+$).

2.4.5. Compound **10**

Compound **4** (0.100 g, 0.210 mmol), triethylamine (0.031 mL) and $Pd(PPh_3)_2Cl_2$ (0.312 g, 0.430 mmol) were refluxed in dry ethanol. Compound **10** was isolated as an orange powder. Yield 0.239 g (95.1%). M.p.: does not melt below 300 °C. *Anal.* Calc. for $C_{58}H_{46}N_6S_2P_2O_2Pd_2$: C, 58.15; H, 3.87; N, 7.02; S, 5.35. Found: C, 57.45; H, 3.83; N, 6.96; S, 5.50%. ν_{max}/cm^{-1} 1598 (CN). ^1H NMR (300 MHz, DMSO-d_6, 25 °C): δ = 6.60 (4H, m, Ar), 7.21 (4H, m, Ar), 7.57–7.71 (34H, m, PPh_3, Ph), 8.63 (2H, d, J = 13.78, CH=N), 9.26 (2H, s, N*H*Ph) ppm. ^{31}P NMR (120 MHz, DMSO-d_6, 25 °C): δ = 25.61 (2P, s, PPh_3) ppm.

2.4.6. Compound **11**

Compound **5** 0.113 g, 0.210 mmol), triethylamine (0.030 mL) and $Pd(PPh_3)_2Cl_2$ (0.301 g, 0.430 mmol) were refluxed in ethanol. A dark orange powder (**11**) was isolated. Yield 0.241 g (91.3%). M.p.: does not melt below 300 °C. *Anal.* Calc. for $C_{60}H_{50}N_6S_2P_2O_4Pd_2$: C, 57.28; H, 4.01; N, 6.68; S, 5.10. Found: C, 57.62; H, 3.84; N, 6.84; S, 5.21%. ν_{max}/cm^{-1} 1589 (C=N). ^1H NMR (300 MHz, DMSO-d_6, 25 °C): δ = 3.63 (6H, s, OMe), 6.56 (2H, t, J = 7.81, Ar), 6.91 (2H, d, J = 7.70, Ar), 7.16 (2H, d, J = 8.24, Ar), 7.76–7.49 (34H, m, PPh_3, Ar), 8.61 (2H, d, J = 13.85, CH=N), 9.23 (2H, s, N*H*Ph) ppm. ^{31}P NMR (120 MHz, DMSO-d_6, 25 °C): δ = 19.73 (2P, s, PPh_3) ppm.

2.4.7. Compound **12**

Compound **6** (0.126 g, 0.219 mmol), triethylamine (0.031 mL) and $Pd(PPh_3)_2Cl_2$ (0.307 g, 0.438 mmol) were refluxed in ethanol. A dark orange powder was isolated. Yield 0.227 g (79.12%). M.p.: does not melt below 300 °C. *Anal.* Calc. for $C_{66}H_{62}N_6S_2P_2O_2Pd_2$: C, 60.50; H, 4.77; N, 6.42; S, 4.89. Found: C, 60.45; H, 4.91; N, 6.88; S, 4.95%. ν_{max}/cm^{-1} 1593 (C=N). ^1H NMR (300 MHz, DMSO-d_6, 25 °C): δ = 0.69 (18H, s, ^{t}Bu), 6.53 (2H, t, J = 7.56, Ar), 7.08–7.86 (38H, m, Ar/Ph), 8.59 (2H, d, J = 14.05, CH=N), 9.12 (2H, s, N*H*Ph) ppm. $^{13}C\{^1H\}$ NMR (100 MHz, $CDCl_3$-*d*, 25 C): δ = 29.4, 34.8, 114.1, 118.1, 119.4, 128.4–134.8, 140.3, 153.2, 162.4, 164.8 ppm. ^{31}P NMR (120 MHz, DMSO-d_6, 25 °C): δ = 25.67 (2P, s, PPh_3) ppm. MS ESI: m/z 1311 (10%, $[M+H]^+$).

2.5. X-ray crystallography

Crystals suitable for X-ray diffraction study for **7**·2 DMSO and **11**·4 DMSO were grown from concentrated DMSO solutions of complexes **7** and **11**, respectively. An orange crystal of **7**·2 DMSO was mounted on a Stoe Image Plate Diffraction system equipped with a ϕ circle goniometer, using Mo Kα graphite monochromated radiation (λ = 0.71073 Å) with ϕ range 0–200°, increment of 1.2°, $D_{max} - D_{min}$ = 12.45–0.81 Å. Whereas a yellow crystal of **11**·4 DMSO was mounted on a Nonius Kappa-CCD diffractometer using graphite monochromated Mo Kα radiation (λ = 0.71073 Å), equipped with an Oxford Cryostream cooling system. Data were evaluated using the Bruker Nonius "Collect" program and was scaled and reduced using DENZO-SMN software. Both structures were solved by direct methods using the program SHELXS-97 [28]. The refinement and all further calculations were carried out using SHELXL-97 (see Table 1) [29]. The hydrogen atoms were included in calculated positions and treated as riding atoms using the SHELXL default parameters. All non-H atoms were refined anisotropically, using weighted full-matrix least-square on F^2. Figs. 2 and 3 were drawn with ORTEP [30]. Packing diagram (Fig. 4) was produced using the program PovRay [31] and the graphic interface X-seed [32].

2.6. Cytotoxic assay

The dithiosemicarbazone ligands were evaluated for their *in vitro* anticancer activity against three oesophageal cancer cell lines, WHCO1, WHCO5 and WHCO6, derived from biopsies of primary oesophageal squamous cell carcinomas [33] and kindly provided by Professor Rob Veale (University of Witwatersrand, South Africa). IC_{50} determinations were carried out using the MTT assay. Briefly, 3000 cells were seeded per well in 96-well plates. Cells were incubated at 37 °C under 5% CO_2 (24 h), after which aqueous DMSO solu-

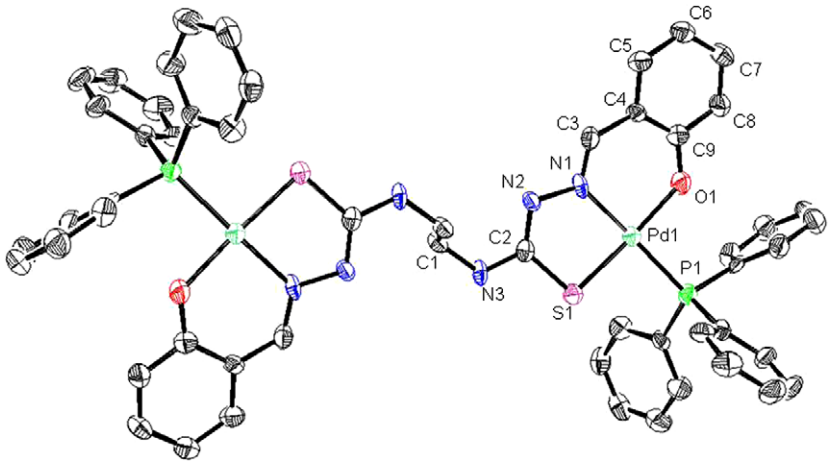


Fig. 2. Molecular structure of complex **7** showing ellipsoids at the 50% probability level with hydrogen atoms and solvent molecules omitted for clarity.

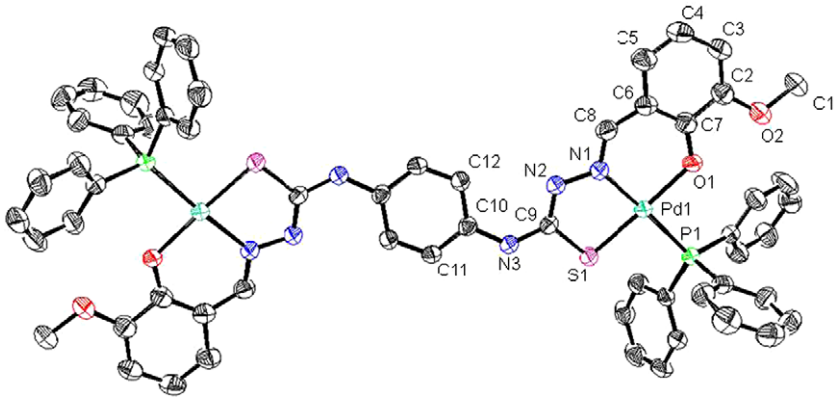


Fig. 3. Molecular structure of complex **11** showing ellipsoids at the 50% probability level with hydrogen atoms and solvent molecules omitted for clarity.

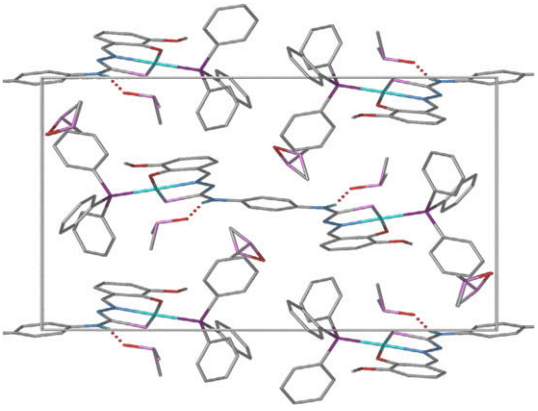


Fig. 4. Crystal packing arrangement of compound **11**·4 DMSO.

tions of each compound (10 μL, with a constant final concentration of DMSO = 0.2%) were plated at various concentrations. After 48 h incubation, observations were made, and MTT (10 μL) solution added to each well. After a further 4 h incubation, solubilization solution (100 μL) was added to each well, and plates were incubated overnight. Plates were read at 595 nm on a BioTek microplate reader.

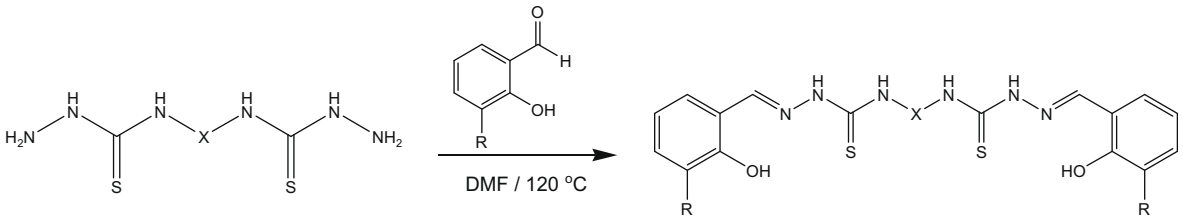
3. Results and discussion

3.1. Synthesis and characterization of dithiosemicarbazone ligands (*1*–*6*)

A series of ethylene- and phenylene-bridged salicylaldimine dithiosemicarbazones were synthesized using a procedure similar to that previously reported by Scovill [26] and Dilworth et al. [23]. Our initial attempts at preparing dithiosemicarbazones via amination reactions of the appropriate aryl thiosemicarbazide with either ethylenediamine or phenylenediamine proved to be unsuccessful, despite refluxing for extended periods or using microwave-assisted techniques.

Two different routes were followed to prepare the bridged dithiosemicarbazone ligands. The synthesis of the ethylene-bridged dithiosemicarbazone ligands via the known reaction of hydrazine with a diacid precursor produced ethane-1,2-dithiosemicarbazide [26]. Benzene-1,4-dithiosemicarbazide was obtained using a simple one-step procedure via the reaction of hydrazine with phenylene diisothiocyanate as the starting precursor [23]. Subsequent Schiff-base condensation of either ethane-1,2-dithiosemicarbazide or benzene-1,4-dithiosemicarbazide with salicylaldehyde, 2-hydroxy-3-methoxy benzaldehyde or 3-*tert*-butyl salicylaldehyde afforded the ethylene-bridged (**1–3**) and phenylene-bridged (**4–6**) dithiosemicarbazones (Scheme 1).

The ethylene- and phenylene-linked dithiosemicarbazone ligands (**1–6**) were isolated by precipitation in water, as pale yellow



X = C_2H_4 (**1-3**) ; C_6H_4 (**4-6**)
R = H (**1**, **4**) ; OMe (**2**, **5**) ; ^{t}Bu (**3**, **6**)

Scheme 1. Synthetic route to dithiosemicarbazones **1–6**.

powders in varying yields (65–94%) and the proposed structures are supported by analytical and spectroscopic data.

The structures of dithiosemicarbazone ligands **1–6** were confirmed by ^{1}H, ^{13}C, COSY and HSQC NMR spectroscopy. The ^{1}H NMR spectra of the products show a singlet in the range δ 8.3–8.5 ppm, assigned to the imine protons. A characteristic singlet is observed for the ethylene (**1–3**) and phenylene protons (**4–6**) at about δ 3.83 ppm and δ 7.55 ppm respectively, due to the symmetrical nature of the dithiosemicarbazone compounds. Generally, the phenylene-bridged thiosemicarbazone ligands (**4–6**) show similar trends in the NMR spectra to those of the ethylene-bridged ligands (**1–3**). ^{13}C{^{1}H} NMR spectral assignments were made with the aid of 2D Heteronuclear Single Quantum Coherence (HSQC) spectroscopy. Peaks assigned to the carbons of the aromatic groups are observed in the region of δ 115–156 ppm. A peak assigned to the imine carbon is observed around δ 140 ppm.

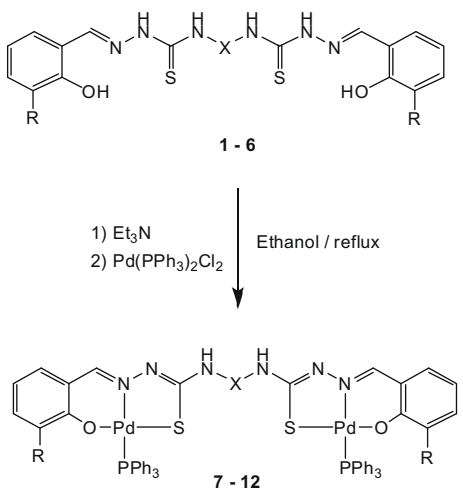
Further information on the integrity of the ligands was gleaned from infrared spectroscopic techniques. The IR spectra of the Schiff base dithiosemicarbazone ligands showed a strong absorption band for the imine functionality at around 1622–1598 cm^{-1}. The absorption band at 850–820 cm^{-1} in the free ligand may be assigned to the thioamide vibration $\nu_{(C=S)}$, indicating that the ligands exist in the thione form.

The ESI mass spectra for compounds **1–2**, **4–6** recorded in the negative mode generally showed a 100% relative intensity peak (base peak) due to the $[M-H]^+$ ion. For compound **3**, however, a base peak at m/z 527 is observed in the ESI spectrum, attributed to the presence of a sodium adduct, $[M+Na]^+$.

3.2. Binuclear dithiosemicarbazone salicylaldiminato palladium(II) complexes (*7–12*)

For polydentate ligands such as compounds **1–6**, various bonding modes are possible depending on the ligand to metal ratio. In an attempt to prepare binuclear palladium dithiosemicarbazones, the palladium(II) complexes (**7–12**) were selectively prepared by reacting the corresponding dithiosemicarbazone ligands (**1–6**) with $Pd(PPh_3)_2Cl_2$ in a 1:2 stoichiometric ratio (ligand:metal), giving rise to binuclear palladium complexes (Scheme 2). The synthesis of the complexes was performed using methodologies similar to those reported previously by Halder et al. [34].

The palladium complexes (**7–12**) are isolated as orange powders in high yields (75–95%). They are air-stable as solids and in solution. The ethylene-bridged palladium(II) complexes (**7–9**) are readily soluble in polar solvents such as DMSO, chlorinated solvents (CH_2Cl_2), and are sparingly soluble in alcoholic solvents. The phenylene-bridged palladium(II) complexes (**10, 11**), however, are found to be far less soluble than their ethylene-bridged counterparts. Surprisingly, complex **12** shows greater solubility than the analogous phenylene-bridged palladium complexes. The bimetallic complexes (**7–12**) have been characterized by elemental analyses, ^{1}H, ^{13}C, ^{31}P NMR and IR spectroscopies, and ESI-MS.



X = C_2H_4 (**1-3**, **7-9**); C_6H_4 (**4-6**, **10-12**);
R = H (**1**, **4**, **7**, **10**); OMe (**2**, **5**, **8**, **11**); ^{t}Bu (**3**, **6**, **9**, **12**)

Scheme 2. General synthetic pathway to complexes **7–12**.

3.2.1. NMR spectroscopy

The ethylene- and phenylene-bridged palladium complexes display in the ^{1}H NMR spectra the expected singlet for the ethylene and phenylene protons at around δ 3.38 ppm and δ 7.47–7.71 ppm, respectively, due to the symmetrical nature of the compounds. Evidence for the formation of palladium complexes is seen by the notable shift of the signal for the imine proton, suggesting coordination of palladium to the imine nitrogen. Splitting of the imine signal into a doublet in the region at around δ 8.33 ppm is observed and is attributed to coupling of the imine proton to the nucleus of the phosphorus atom ($^4J_{P-H}$ = 13.98 Hz). The disappearance of the signal for the hydroxyl proton, together with the observed shift of the imine proton observed in the ^{1}H NMR spectrum, provides good evidence of coordination of palladium, resulting in a six-membered ring with N,O donor atoms. In addition to this, the disappearance of the signal assigned to the hydrazinic proton adjacent to the imine group, confirms the formation of a second imine bond upon coordination of palladium, suggesting that the sulfur atom coordinates in the thiolate form rather than the thione form, thus forming a five-membered chelate ring (N, S donor atoms). The phenylene-bridged complexes (**10, 11**) were difficult to characterize using NMR spectroscopic techniques due to their low solubility in most deuterated solvents, including DMSO-d_6. The ^{1}H NMR spectrum of compound **10**, specifically, was not well-resolved, but a trend similar to that of the ethylene-bridged complex **7** was discernible and assignments made on that basis.

All the expected peaks are observed in the $^{13}C\{^1H\}$ NMR spectra for compounds **7–12**. It was not possible to obtain ^{13}C NMR spectral data for the phenylene-bridged complexes (**10, 11**), even at elevated temperatures, due to the poor solubility of these complexes. A sharp singlet is observed in the $^{31}P\{^1H\}$ NMR spectra for each palladium-PPh_3 complex in the region around δ 25.6 ppm.

3.2.2. Infrared spectroscopy

Infrared spectroscopy is a useful diagnostic tool to confirm coordination of palladium. The IR spectra of the palladium complexes **7–12** show a band of medium to strong intensity within 1599–1589 cm^{-1}, attributed to the C=N–N=C fragment of the coordinated dithiosemicarbazone ligand. The shift of the imine absorption band (ν_{C-N}) in the free ligand (1600–1671 cm^{-1}) to lower wavenumbers in the metal complexes, is indicative of the coordination of palladium to the imine nitrogen. The IR spectra of the [Pd(L)(PPh_3)] (L = dithiosemicarbazone) complexes (**7**–**12**) generally show many vibrations of different intensities in the 1600–400 cm^{-1} region and are qualitatively very similar. Three diagnostic bands for the PPh_3 ligands near 533, 694 and 743 cm^{-1} are observed for all the complexes. The characteristic bands due to the $\nu_{(P-C)}$ vibration are also observed in the region 1098–1095 cm^{-1}, indicative of the presence of coordinated PPh_3 in the complexes [35–37]. Bands involving the C=S functional group are often difficult to assign. Coordination by sulfur induces changes in position and intensity of the bands and the proximity of the phenyl ring bands (triphenylphosphine ligand) makes it difficult to clearly assign the vibration modes. The disappearance of the C=S band observed in the free ligand, correlates with the loss of double-bond character upon deprotonation of the NH group. This supports the lengthening of the C–S bond which we observe in representative molecular structures. For thiosemicarbazones bonding in the thiolate form, the C=S band generally shifts to lower energy in the region 820–790 cm^{-1}. However, no definite assignment of each individual band to a specific vibration could be made.

3.2.3. Mass spectrometry

ESI-mass spectrometry further confirmed the integrity of the binuclear complexes. The ESI spectrum of compound **7** displays a base peak for the complex in its protonated form $[M+H]^+$ at *m*/*z* 1151. The spectrum of compound **8** reveals a peak at *m*/*z* 1210 for the $[M+H]^+$ ion of 20% intensity. A base peak at *m*/*z* 279, accounts for the fragment, $[M-C_8H_6N_2SO_2Pd(PPh_3)_2]^+$. The spectrum of compound **9** displays a peak of 50% intensity for the protonated complex at *m*/*z* 1263. In addition to this, a base peak at *m*/*z* 675, corresponds to the fragment, $[M-C_{11}H_{13}N_2SOPdPPh_3]^+$. The poor solubility of complexes **10** and **11** precluded an accurate determination by ESI-mass spectrometry.

3.3. Solid-state structures of complexes 7 and 11

To further confirm the mode of coordination of these palladium dithiosemicarbazone complexes, molecular structures of one member of each group (ethylene- and phenylene-bridged) have been determined using single-crystal X-ray crystallography. Single crystals of compounds **7** and **11** were obtained from concentrated dimethyl sulfoxide solutions. Figs. 2 and 3 show the molecular structures of **7** and **11**, respectively, while Table 2 gives selected bond lengths and angles.

The crystal structures show that the dithiosemicarbazone ligands coordinate to each palladium center *via* the phenolic oxygen, imine nitrogen and sulfur atoms in a square-planar geometry, as the spectroscopic data suggests. These two structures confirm that the fourth coordination site is occupied by a triphenylphosphine ligand. Both complexes show that the dithiosemicarbazone ligands (**1** and **5**) are coordinated to palladium in the expected tridentate (O–N–S) fashion on either side of the dithiosemicarbazone. The structures show the formation of six- and five-membered chelate rings upon coordination, thus imposing distortion around the square-planar metal centers. Indeed, the structures display O(1)–Pd(1)–N(1) and N(1)–Pd(1)–S(1) bite angles of 93.1(2)° and 84.55(17)° in **7** and of 92.15(12)° and 84.03(10)° in **11**. In both, a triphenylphosphine ligand is found trans to the nitrogen atom with Pd–P distances of 2.273(2) and 2.284(1) Å, respectively and with O(1)–Pd(1)–P(1) and S(1)–Pd(1)–P(1) bite angles of 88.53(14) and 93.91(7)° in **7** and of 91.28(8) and 92.44(4)° in **11**. These parameters are comparable to those in other trans P–N, S–O square-planar palladium complexes [16]. In addition to this, it can be seen that coordination of the dithiosemicarbazone sulfur atoms occur *via* the thiolate form, rather than the thione form (Figs. 2 and 3) due to the formation of a second imine bond

Table 1
Crystallographic data and structure refinement parameters for complexes **7**·2 DMSO and **11**·4 DMSO

	7·2 DMSO	**11**·4 DMSO
Chemical formula	$C_{58}H_{56}N_6O_4P_2Pd_2S_4$	$C_{68}H_{74}N_6O_8P_2Pd_2S_6$
Formula weight	1304.07	1570.43
Crystal system	monoclinic	monoclinic
Space group	*C* 2/*c*	*P* 2_1/*n*
Crystal colour and shape	orange rod	yellow needle
Crystal size	0.12 × 0.07 × 0.06	0.24 × 0.11 × 0.11
a (Å)	30.436(3)	10.4372(3)
b (Å)	10.0175(9)	14.8288(4)
c (Å)	18.732(2)	22.7294(5)
α (°)	90	90
β (°)	100.57(1)	100.526(1)
γ (°)	90	90
V (Å^3)	5614.3(9)	3458.7(2)
Z	4	2
T (K)	173(2)	173(2)
D_c (g cm^{-3})	1.543	1.508
μ (mm^{-1})	0.899	0.806
Scan range (°)	4.28 < 2θ < 52.42	3.30 < 2θ < 50.84
Unique reflections	5553	6344
Reflections used [$I > 2\sigma(I)$]	1533	5063
R_{int}	0.1920	0.0685
Final *R* indices [$I > 2\sigma(I)$][a]	0.0336, wR_2 0.0488	0.0444, wR_2 0.1096
R indices (all data)	0.1786, wR_2 0.0734	0.0611, wR_2 0.1194
Goodness-of-fit (GOF)	0.478	1.051
Maximum, minimum $\Delta\rho$ (e Å^{-3})	0.524, −1.125	1.073, −0.906

[a] Structures were refined on F_o^2: $wR_2 = [\sum[w(F_o^2 - F_c^2)^2]/\sum w(F_o^2)^2]^{1/2}$, where $w^{-1} = [\sum(F_o^2) + (aP)^2 + bP]$ and $P = [\max(F_o^2, 0) + 2F_c^2]/3$

Table 2
Selected bond lengths (Å) and angles (°) for complexes **7** and **11**.

	7		**11**
Pd(1)–P(1)	2.273(2)	Pd(1)–P(1)	2.284(1)
Pd(1)–S(1)	2.238(2)	Pd(1)–S(1)	2.244(1)
Pd(1)–N(1)	2.028(5)	Pd(1)–N(1)	2.018(3)
Pd(1)–O(1)	2.019(4)	Pd(1)–O(1)	2.062(3)
N(1)–C(3)	1.284(8)	N(1)–C(8)	1.296(5)
N(1)–N(2)	1.403(7)	N(1)–N(2)	1.405(4)
N(2)–C(2)	1.311(7)	N(2)–C(9)	1.300(5)
N(3)–C(2)	1.354(7)	N(3)–C(9)	1.352(5)
N(3)–C(1)	1.455(8)	N(3)–C(10)	1.413(5)
S(1)–C(2)	1.781(6)	S(1)–C(9)	1.769(4)
P(1)–Pd(1)–S(1)	93.91(7)	P(1)–Pd(1)–S(1)	92.44(4)
P(1)–Pd(1)–O(1)	88.53(14)	P(1)–Pd(1)–O(1)	91.28(8)
P(1)–Pd(1)–N(1)	177.82(17)	P(1)–Pd(1)–N(1)	175.64(10)
S(1)–Pd(1)–N(1)	84.55(17)	S(1)–Pd(1)–N(1)	84.03(10)
S(1)–Pd(1)–O(1)	176.59(14)	S(1)–Pd(1)–O(1)	175.68(8)
N(1)–Pd(1)–O(1)	93.1(2)	N(1)–Pd(1)–O(1)	92.15(12)
C(1)–N(3)–C(2)	120.9(6)	C(8)–N(1)–N(2)	114.1(3)
C(3)–N(1)–N(2)	115.8(5)	N(1)–N(2)–C(9)	113.4(3)
N(1)–N(2)–C(2)	113.3(5)	N(2)–C(9)–N(3)	121.8(3)
N(2)–C(2)–N(3)	121.4(6)	C(9)–N(3)–C(10)	129.4(3)

Table 3
IC_{50} values (μM) of dithiosemicarbazone ligands (**1**–**3**, **5**, **6**) in various oesophageal cancer cells.

Compound	IC_{50} values in μM (95% CI)		
	WHCO1	WHCO5	WHCO6
1	8.62 (7.06–10.54)	5.63 (4.72–6.72)	10.36 (9.34–11.49)
2	2.53 (1.78–3.58)	5.88 (5.57–6.21)	3.56 (2.92–4.36)
3	6.38 (5.42–7.52)	3.26 (2.39–4.45)	11.70 (10.62–12.89)
5	2.67 (2.08–3.43)	1.64 (1.14–2.35)	12.37 (9.59–15.94)
6	1.28 (0.97–1.69)	1.24 (0.93–1.66)	30.97 (12.81–74.91)

between C(2) and N(2) in **7** and between C(9) and N(2) in **11**: Values of 1.311(7) and 1.300(5) Å being found for these bonds. This further supports that these C–N bonds tend towards double-bond character upon coordination. Comparison of these distances to the C(2)–N(3) and C(9)–N(3) bond lengths, shows that the latter are slightly longer (1.354(7) and 1.352(5) Å) and therefore tend towards single-bond character. The C–S bond lengths are also found to be consistent with coordination of sulfur in the thiolate form, with values of 1.781(6) and 1.769(4) Å, respectively. A previous study by Halder et al. [34] based on similar monomeric complexes, reported C–S values of approximately 1.75 Å. In simple systems it would be expected that a single C–S bond length would be approximately 1.82 Å and a double C=S bond would exhibit a length of 1.56 Å. The length obtained in this study, therefore appears to be close to the nature of a single C–S bond.

Further analysis of compound **11** reveals that the packing arrangement displays four solvent molecules (DMSO) of crystallisation per complex. This can be seen in the crystal lattice (Fig. 4). Closer inspection of the packing arrangement of compound **11** reveals hydrogen bonding of two oxygen atoms of two of the DMSO molecules to the secondary amine groups on either side of the complex. This bonding is depicted by N(3)–H(3)N···O(1X) on the right-hand side of the molecule. The same phenomenon is observed on the adjacent end of the complex. In **7**, in which two symmetry related molecules of DMSO crystallized per complex, the oxygen atom of the solvent interacts with two adjacent hydrogen atoms of the dithiosemicarbazone phenyl groups. The H···O distances are 2.686 and 2.691 Å and the C–H···O angles 122.9° and 124.4°, respectively.

The information obtained herein therefore allowed us to further confirm the integrity of these molecules, in addition to their spectral properties. We were therefore able to rationalize the modes of coordination upon complexation of the metals.

3.4. Preliminary biological evaluation

The dithiosemicarbazone ligands were evaluated for their *in vitro* anticancer activity against three oesophageal cancer cell lines (WHCO1, WHCO5, WHCO6). All the dithiosemicarbazone ligands, with the exception of ligand **4**, were cytotoxic in the cell lines evaluated, showing IC_{50} values in the range 1.2–35 μM. The fact that ligand **4** did not show any biological activity is ascribed to the poor solubility of the ligand. The IC_{50} values calculated from the dose-survival curves obtained after 48 h drug treatment from the MTT assay, are shown in Table 3. Unfortunately, the cytotoxicity of the palladium complexes could not be determined due to the poor solubility of these complexes. Detailed studies are currently underway to prepare more soluble palladium(II) salicylaldiminato dithiosemicarbazone complexes.

4. Conclusions

In summary, we have shown that palladium(II) complexes of salicylaldimine dithiosemicarbazones containing ethylene or phenylene spacers may be prepared by the reaction of the new salicylaldehyde-derived dithiosemicarbazone ligands (**1–6**) with $Pd(PPh_3)_2Cl_2$. This involved the preparation of ethylene- and phenylene-bridged dithiosemicarbazides, that were condensed with the appropriate salicylaldehydes, and thereafter metallated to give rise to the new binuclear palladium complexes (**7–12**). For each binuclear complex, it was found that in their solid-state structures, both palladium centers coordinate in a tridentate (O–N–S) manner. The expected square-planar geometry of the metal was also observed. Preliminary *in vitro* antitumour activity of the dithiosemicarbazone ligands showed a moderate to good cytotoxicity for the indicated cell lines. Biological activity of the palladium(II) complexes of the dithiosemicarbazones could not be determined due to poor solubility. Further investigations are underway to increase the solubility of the palladium complexes and to explore their anticancer activity.

Supplementary data

CCDC 723512 and 719351 contain the supplementary crystallographic data for **7**·2 DMSO and **11**·4 DMSO. These data can be obtained free of charge via http://www.ccdc.cam.ac.uk/conts/retrieving.html, or from the Cambridge Crystallographic Data Centre, 12 Union Road, Cambridge CB2 1EZ, UK; fax: (+44) 1223-336-033; or e-mail: deposit@ccdc.cam.ac.uk.

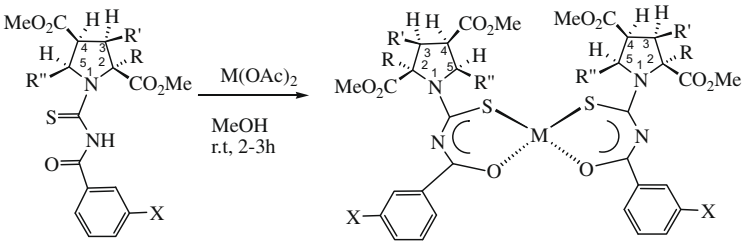
Acknowledgements

We gratefully thank the University of Cape Town, the National Research Foundation (NRF) of South Africa, Anglo Platinum Corporation and Johnson Matthey for financial support.

References

[1] M. Akbar Ali, S.E. Livingstone, Coord. Chem. Rev. 13 (1974) 115.
[2] M.J.M. Campbell, Coord. Chem. Rev. 15 (1975) 279.
[3] D.X. West, S. Padhye, P.B. Sonawane, Struct. Bond. 76 (1991) 4.
[4] D.X. West, A.E. Liberta, S. Padhye, R.C. Chilkate, P.B. Sonawane, A.S. Kumbhar, R.G. Yerande, Coord. Chem. Rev. 123 (1993) 49.
[5] D.J. Drain, C.L. Goodacre, D.E. Seymour, J. Pharm. Pharmacol. 1 (1949) 784.
[6] A. Lewis, R.G. Shepherd, in: A. Burger (Ed.), Medicinal Chemistry, Wiley, New York, 1970, p. 431.
[7] D.C. Greenbaum, Z. Mackey, E. Hansell, P. Doyle, J. Gut, C.R. Caffrey, J. Lehrman, P.J. Rosenthal, J.H. MsKerrow, K. Chibale, J. Med. Chem. 47 (2004) 3212.
[8] C. Biot, B. Pradines, M. Sergeant, J. Gut, P.J. Rosenthal, K. Chibale, Bioorg. Med. Chem. Lett. 17 (2007) 6434.
[9] P. Malatesta, G.P. Accinelli, G. Quaglia, Ann. Chim. 49 (1959) 397.
[10] E.W. Ainscough, A.M. Brodie, W.A. Denny, G.J. Finlay, J.D. Ranford, J. Inorg. Biochem. 70 (1998) 175.
[11] H. Beraldo, D. Gambino, Mini Rev. Med. Chem. 4 (2004) 31.
[12] D.S. Kalisnowski, D.R. Richardson, Pharmacol. Rev. 75 (2005) 547.
[13] D.S. Kalinowski, D.R. Richardson, Chem. Res. Toxicol. 20 (2007) 715.
[14] M.A. Ali, S.E. Livingstone, Coord. Chem. Rev. 13 (1974) 101.
[15] S. Padhye, Coord. Chem. Rev. 63 (1985) 127.
[16] J.S. Casas, M.S. Garcia-Tasende, J. Sordo, Coord. Chem. Rev. 209 (2000) 197.
[17] A.G. Quiroga, C.N. Ranninger, Coord. Chem. Rev. 248 (2004) 119.
[18] S.N. Pandeya, J.R. Dimmock, Pharmazie 48 (1993) 659. and refs. therein.
[19] J.K. Swearingen, D.X. West, Transition Met. Chem. 25 (2000) 241.
[20] D.M. Wiles, B.A. Gingras, T. Suprunchuk, Can. J. Chem. 45 (1967) 1735.
[21] O.P. Pandey, S.K. Sengupta, M.K. Mishra, C.M. Tripathi, Bioinorg. Chem. Appl. 1 (2003) 35.
[22] B.A. Gingras, T. Suprunchuk, O. Bernardini, C.H. Bayley, Can. J. Chem. 41 (1963) 1629.
[23] M. Christlieb, H.S.R. Struthers, P.D. Bonnitcha, A.R. Cowley, J.R. Dilworth, Dalton Trans. (2007) 5043.
[24] S. Tripathi, S.K. Sengupta, O.P. Pandey, Russ. J. Coord. Chem. 33 (2007) 704.
[25] D.X. West, S.B. Padhye, P.B. Sonawane, Struct. Bond. 76 (1991) 1. and refs. therein.
[26] J.P. Scovill, Phosphorous, Sulfur Silicon Relat. Elem. 60 (1991) 15.
[27] W.A. Hermann, S. Slazer, Synth. Meth. Organomet. Inorg. Chem. 1 (1996) 160.
[28] G.M. Sheldrick, Acta Crystallogr. A 46 (1990) 467.
[29] G.M. Sheldrick, SHELXL-97, University of Göttingen, Göttingen, Germany, 1999.
[30] L.J. Farrugia, J. Appl. Crystallogr. 30 (1997) 565.

[31] I.J. Bruno, J.C. Cole, P.R. Edgington, M. Kessler, C.F. Macrae, P. McCabe, J. Pearson, R. Taylor, Acta Crystallogr. B 58 (2002) 389.
[32] L.J. Barbour, J. Supramol. Chem. 1 (2001) 189.
[33] R.B. Veale, A.L. Thornley, S. Afr. J. Sci. 85 (1989) 375.
[34] S. Halder, S.-M. Peng, G.-H. Lee, T. Chatterjee, A. Mukherjee, S. Dutta, U. Sanyal, S. Bhattacharya, New J. Chem. 32 (2008) 105.
[35] T.S. Lobana, Rekha, G. Bawa, R.J. Butcher, A. Castineiras, F. Bermejo, P.V. Bharatam, Inorg. Chem. 45 (2006) 1535.
[36] T.S. Lobana, G. Bawa, R.J. Butcher, B.-J. Liaw, C.W. Liu, Polyhedron 25 (2006) 2897.
[37] T.S. Lobana, S. Khanna, R.J. Butcher, A.D. Hunter, M. Zeller, Polyhedron 25 (2006) 2755.



(1)

a. R = $PhCH_2$, R' = H, R'' = Ph, X = H
b. R = $CH_3(CH\text{-})CH_2CH_3$, R' = H, R'' = Ph, X = H
c. R = H, R' = H, R'' = Ph, X = H
d. R = Ph, R' = H, R'' = Ph, X = H
e. R = H , R' = CO_2Me, R'' = Naphtyl, X = H
f. R = Ph, R' = H, R'' = Ph, X = Cl
g. R = $PhCH_2$, R' = H, R'' =4-methoxyphenyl, X = H

(2) R = $PhCH_2$, R' = H, R'' = Ph, X = H
a. M = Ni(II), 86%
b. M = Pd(II), 82%
c. M = Cu(II), 90%

(3) R = $CH_3(CH\text{-})CH_2CH_3$, R' = H, R'' = Ph, X = H
a. M = Ni(II), 78%
b. M = Pd(II), 72%
c. M = Cu(II), 90%

(4) R = H, R' = H, R'' = Ph, X = H
a. M = Ni(II), 86%
b. M = Pd(II), 72%
c. M = Cu(II), 88%

(5) R = Ph, R' = H, R'' = Ph, X = H
a. M = Ni(II), 86 %
b. M = Pd(II), 82%
c. M = Cu(II), 92%

(6) R = H , R' = CO_2Me, R'' = Naphtyl, X = H
M = Ni(II), 76%

(7) R = Ph, R' = H, R'' = Ph, X = Cl
M = Ni(II), 89%

(8) R = $PhCH_2$, R' = H, R'' = 4-methoxyphenyl, X = H
M = Ni(II), 87%

Scheme 1.

2.1. NMR and FT-IR spectra

In the ^{1}H NMR spectra ($CDCl_3$) of ligands (**1a**–**g**), the NH protons appear at 8.60–7.85 ppm as broad singlets. This signal is absent in the ^{1}HNMR spectra of the corresponding nickel, palladium and copper complexes as a consequence of the deprotonation that occurs upon coordination. Similarly in the IR spectra, all ligands (**1a**–**g**) show NH stretching vibrations in the range 3375–3260 cm^{-1} but these signals are absent in the spectra of the corresponding metal complexes. In the ^{13}C NMR spectra, the carbon atom of the thiocarbonyl group appears at 177.5–189.9 ppm for (**1a**–**g**) and this shifts to 173.4–174.5 ppm in the respective metal complexes as a consequence of complex formation.

The IR bands at 1731–1752 cm^{-1} and 1237–1285 cm^{-1} in the spectra of the metal complexes are assigned to the ester ν(C=O) and ν(C–O), respectively. All the compounds show ν(C=O) amide vibration band in the 1681–1640 cm^{-1} range owing to conjugation with the aromatic ring [21,25,26]. These appear at almost the same wavenumber in their metal complexes indicating that the ester carbonyl group is not involved in coordination. The thionyl ν(C–S) vibration bands appears at 1210–1187 cm^{-1} for the ligands and shifts to lower values, 1209–1169 cm^{-1}, in their corresponding metal complexes as a result of the coordination the sulfur atom [19,24,27] to the metal. In all the metal complexes a strong peak appears in the 1358–1419 cm^{-1} range corresponding to the coordinated oxygen of the delocalised amide coordinated to the metal cations [6–8].

2.2. Crystal structures of *2a* and *8*

A view of crystal structure of compound **2a**, $[C_{29}H_{27}N_2O_5S]_2Ni$, and **8** $[C_{30}H_{29}N_2O_6S]_2Ni$ are depicted in Figs. 1 and 3, and selected atomic distances and bond angles are listed in Table 2. The structure of **2a**, red prisms, and **8**, pale violet plates, solved in the triclinic space group $P\bar{1}$ and the asymmetric unit contains one molecule of the complex and in the case of **2a** contains dichloromethane (occupancy 0.4) both in general positions (Table 1). Many hydrogen atoms could be located in the Fourier difference map but, in the final stages of refinement, all were placed geometrically and refined using a riding model. C–H distances: CH_3, 0.98 Å; CH_2, 0.99 Å; CH, 1.00 Å; aromatic, 0.95 Å. The square planar Ni(II) ion is coordinated by two thiocarbonyl S atoms and two carbonyl O atoms.

The ligands of compound **2a** are coordinated in a relatively undistorted manner and the angles between O(7b)–Ni(1)–S(8a) and O(7a)–Ni(1)–S(8b) are 174.84(6)° and 174.48(5)°, respectively. The bond lengths for Ni(1)–O(7a) = 1.8602(15) Å, Ni(1)–O(7b) = 1.8670(15) Å, Ni(1)–S(8a) = 2.1201(6) Å and Ni(1)–S(8b) = 2.1495(6) Å are well within the range expected [4,6,23]. The bond lengths of carbonyl moieties O(7a)–C(7a) = 1.272(2) Å, O(7b)–C(7b) = 1.270(3) Å and thiocarbonyl moieties S(8a)–C(8a) = 1.724(2) Å and S(8b)–C(8b) Å = 1.727(2) Å are longer than the average C=O and C=S [8,23,51]. The C–N bonds for N(7a)–C(8a) = 1.339(3) Å, N(7a)–C(7a) = 1.333(3) Å and N(7b)–C(7b) = 1.333(3) Å, N(7b)–C(8b) = 1.345(3) Å in the complex ring are shorter than the average C–N single bonds but within the range of C=N double bond distances [8,23,28]. The crystal structure of the ligand **1a** has been derived from the crystal structure of **2a** (Fig. 2).

The ligands of compound **8** are coordinated in a relatively undistorted manner and the angles between O(5a)–Ni(1)–S(1b) and O(5b)–Ni(1)–S(1a) are 176.25(6)° and 175.16(6)°, respectively. The bond lengths for Ni(1)–O(5b) = 1.8725(14) Å, Ni(1)–O(5a)) = 1.8965(15) Å, Ni(1)–S(1b) = 2.1543(6) Å and Ni(1)–O(5a) = 2.1794(6) Å, are well within the range expected [4,6,23]. The bond lengths of carbonyl moieties C(4a)–O(5a) = 1.276(2) Å, C(4b)–O(5b) = 1.282(2) Å and thiocarbonyl moieties S(1a)–C(2a) = 1.748(2) Å and S(1b)–C(2b) = 1.748(2) Å are longer than the average C=O and C=S [8,23,51]. The C–N bonds for C(2a)–N(3a) = 1.349(3) Å, N(3a)–C(4a) = 1.348(3) Å and N(3b)–C(4b) = 1.345(3) Å, C(2b)–N(3b) = 1.354(3) Å in the complex ring are shorter than the average C–N single bonds but within the range of C=N double bond distances [23,28]. These bond angles and atomic distances for **2a** and **8** are similar to those observed for related compounds [4,6,23,28].

Inspection of the crystallographic data of **2a** and **8** show them to be *meso* compounds and there is no evidence of either inter- or intramolecular π–π stacking.

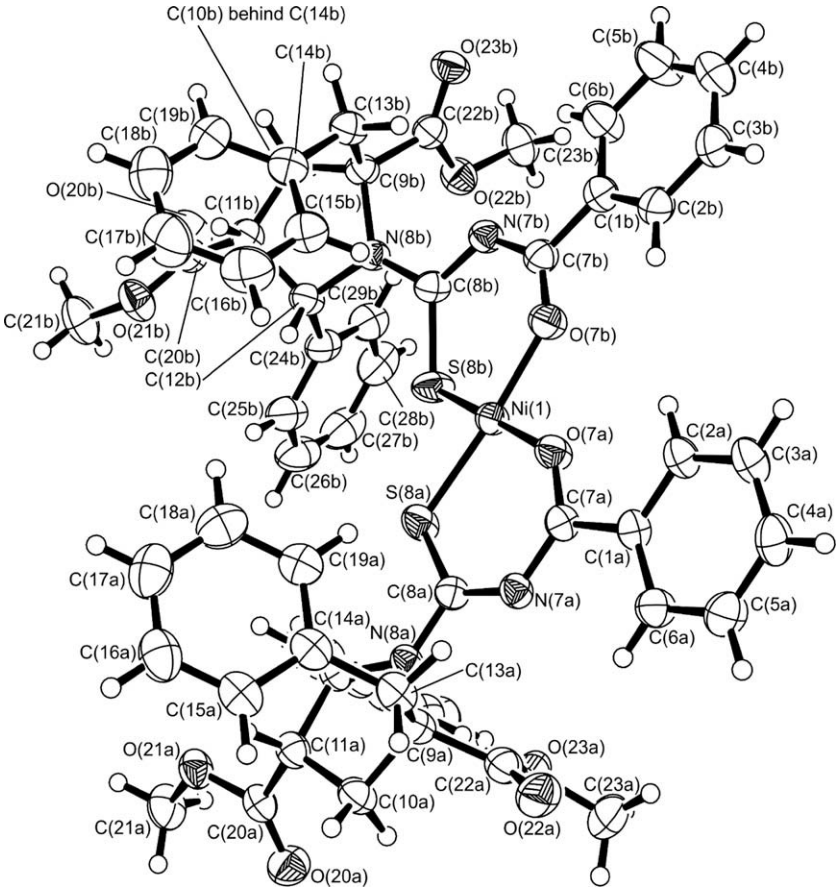


Fig. 1. Crystal structure of compound **2a**.

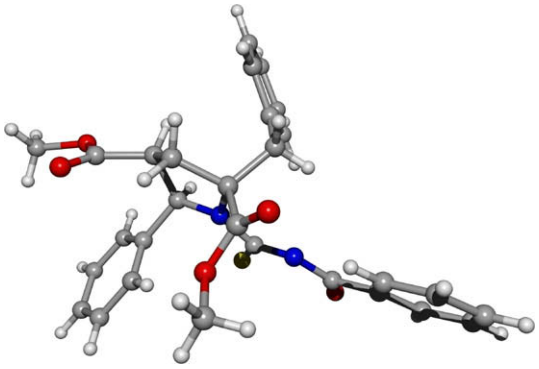


Fig. 2. Crystal structure of ligand **1a**.

3. Antifungal activity against yeast *Saccharomyces cerevisae* and fungus *Penicillium* digitatum

Antifungal susceptibility testing was performed by modification of literature methods [6–8,52–57]. The yeast cell inoculum was prepared from the stock culture of *S. cerevisae* grown in Tryptic Soy Broth (TSB) at room temperature (25 °C) for 24 h. The yeast concentration was adjusted according to Mcfarland 0.5 turbidity tubes ($\sim 10^5$ cells per ml) using sterilized TSB. Stock solutions of chemical derivatives were prepared in DMSO at 1000 μg/ml. A modified macrodilution test was applied for antimicrobial activity. One millilitre TSB was added to each of ten sterilized tubes. One millilitre of chemical derivative solution was added to the first tube and 2-fold dilutions of the stock solution were prepared (1/2–1/1024) of yeast cell (McFarland 0.5; 20 μl) was added to each tube except the last control tube. Only 2 ml of yeast cell was added in to control tube without chemical and used as control for growing. All tubes were incubated at 25 °C for 24 h. After the incubation, the minimal inhibitor concentrations (MIC) concentrations were noted by controlling the growth inhibition. For confirmation and determination the minimal fungicidal concentrations (MFC), subcultivations were done from four dilutions (two dilutions from preinhibition, two dilutions from postinhibition) by inoculation of 20 μl samples from the tubes to Sabaroud Dextrose Agar (SDA). All agar plates were incubated at 25 °C for 24 h. The same procedures were performed for filamentous fungus *Penicillium* spp. except the incubation time was 4 days at 25 °C.

The benzoylaminocarbothioyl pyrrolidines (**1a**–**e**) and metal complexes (**2a**, **3c**, **4a** and **6**), were tested against the yeast *S. cerevisae and* the fungus *P. digitatum.* Activities (Table 3) were disappointingly low. Sensitivity of the compounds tested was found to be different between both microorganisms. In general, filamentous fungal growth inhibition was higher than yeast growth inhibition for the ligand and nickel complexes. The ligands (**1b** and **d**) and metal complexes (**3c** and **4a**) were found to be most active when tested against *P. digitatum* giving MIC values of 31.25 μg/ml. No detectable correlation was found between ligands and their metal complexes. However, some correlation as seen between the ligand (**1b**) and its metal complex (**3c**) and similarly between the ligand (**1e**) and its metal complex (**6**). The metal complex (**3c**), MIC value of 62.5 was twice as active as the ligand (**1b**), MIC value of 125 μg/ml and an identical trend was found for metal complex (**6**) and ligand (**1e**) against *S. cerevisae*. A similar trend of the metal complex displaying greater activity than the ligand is seen for

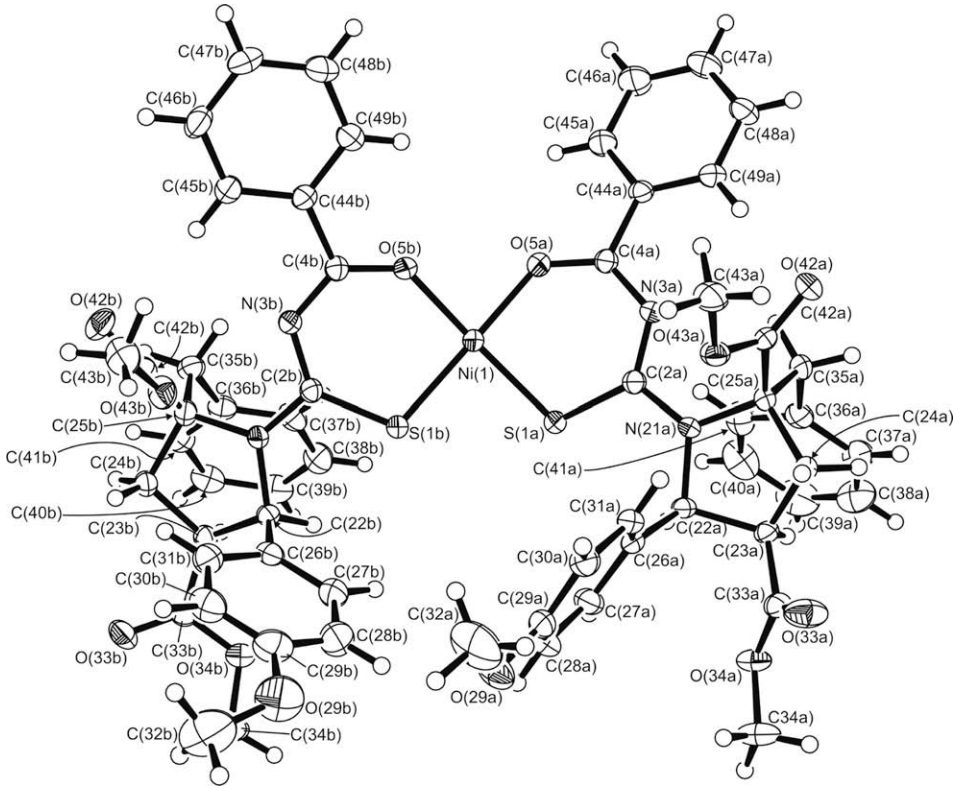


Fig. 3. Crystal structure of compound **8**.

Table 1
Summary of crystallographic data and structural parameters of compounds **2a** and **8**.

Compound	**2a**	**8**
Formula	$C_{58.40}H_{54.80}Cl_{0.80}N_4NiO_{10}S_2$	$C_{60}H_{58}N_4NiO_{12}S_2$
M	1123.86	1149.93
Crystal size (mm)	0.31 × 0.22 × 0.13	0.35 × 0.10 × 0.03
Crystal colour and shape	Red prisms	Pale violet plate
Crystal system	Triclinic	Triclinic
Space group	$P\bar{1}$	$P\bar{1}$
a (Å)	11.79480(10)	13.5938(13)
b (Å)	15.1474(2)	15.4514(17)
c (Å)	17.1359(3)	15.5251(18)
α (°)	88.2470(5)	82.199(6)
β (°)	83.5150(5)	82.425(5)
γ (°)	74.2140(9)	66.923(5)
Z	2	2
D_{calc} (Mg.M^{-3})	1.275	1.29
F (0 0 0)	1173.6	1204
μ (mm^{-1})	0.498	0.461
Diffractometer	Nonius-Kappa CCD	Nonius-Kappa CCD
Data collection range	$2.19 \leqslant \theta \leqslant 26°$	$2.19 \leqslant \theta \leqslant 28.75°$
Number of unique reflections	55945	64608
Number of observations	9691 [$I > 2\sigma(I)$]	9657 [$I > 2\sigma(I)$]
T (K)	150(2)	150
R_1	0.0535	0.0889
Rw	0.1233	0.1099
Goodness-of-fit (GOF)	1.021	1.001
$\Delta\rho$ max, min (e Å^{-3})	1.042–0.411	0.576–0.565

metal complex (**4a**) and ligand (**1e**) against the fungus *P. digitatum* (Table 3).

In summary, technically simple metal catalysed imine-azomethine ylides-1,3-dipolar cycloaddition cascades [40] provide access to novel highly functionalized aroylaminocarbothioyl pyrrolidines and their metal complexes. The antifungal effect of these against pathogenic fungi and yeast was found to be disappointing low.

4. Experimental

4.1. General technical data

IR spectra were recorded on a Shimadzu 435 spectrophotometer, using KBr pellets or on a Varian Scimitar Series 1000 FT-IR spectrophotometer, using horizontal ATR. Nuclear magnetic resonance spectra and decoupling experiments were determined at 400 MHz on a Varian instrument, at 500 MHz on a Bruker AM500 and at 300 MHz on a Bruker Ultrashield TM spectrometer as specified. Chemical shifts are given in parts per million (δ) downfield from tetramethylsilane as internal standard. Spectra were determined in deuteriochloroform except where otherwise stated. The following abbreviations are used; s = singlet, d = doublet, t = triplet, q = quartet, m = multiplet, br = broad and brs = broad singlet. Flash column chromatography was performed using silica gel 60 (230–400 mesh). Kieselgel columns were packed with silica gel GF254 (Merck 7730). Petroleum ether refers the fraction with b.p. 40–60 °C unless otherwise specified. Melting points were determined on a digital electrothermal model 9200 or Stuart SMP3 hot stage apparatus and are uncorrected. Microanalyses were obtained using a Carlo-Erba Model 1106 instrument or Varian Liberty Series II ICP-AES Axial CHNS-932(LECO). Magnetic susceptibilities were determined on a Sherwood scientific magnetic susceptibility balance (Model K1) at 20 °C using $Hg[Co(SCN)_4]$ as a calibrant; diamagnetic corrections were calculated from Pascal's constants [58]. Mass spectra were recorded at 70 eV on a VG Autospec or Agilent LC/MSD mass spectrometer for the ligands. Accurate molecular masses were recorded on a Bruker micrOTOF instrument employing electrospray ionisation techniques. The X-ray crystal structure data were collected on a Stadi 4-circle diffractometer. All solvents were purified according to procedures given in the literature [59]. The ligands (**1a**–**e**) were prepared as reported previously [50,51] and the ligands (**1f** and **g**) were prepared as indicated below.

Table 2
Selected bond angles (°) and interatomic distances (Å) with s.u.s. in parentheses for compound **2a** and **8**.

Bond angles (°) for ***2a***			
O(7a)–Ni(1)–O(7b)	85.98(6)	O(7a)–Ni(1)–S(8a)	95.33(5)
O(7b)–Ni(1)–S(8a)	174.84(6)	O(7a)–Ni(1)–S(8b)	174.48(5)
O(7b)–Ni(1)–S(8b)	94.55(5)	S(8a)–Ni(1)–S(8b)	84.63(2)
C(8a)–S(8a)–Ni(1)	108.90(7)	C(8b)–S(8b)–Ni(1)	104.99(7)
Bond angles (°) for ***8***			
O(5b)–Ni(1)–O(5a)	84.86(6)	O(5b)–Ni(1)–S(1b)	95.12(5)
O(5a)–Ni(1)–S(1b)	176.25(6)	O(5b)–Ni(1)–S(1a)	175.16(6)
O(5a)–Ni(1)–S(1a)	93.77(5)	S(1b)–Ni(1)–S(1a)	86.55(2)
C(2a)–S(1a)–Ni(1)	104.86(7)	C(2b)–S(1b)–Ni(1)	108.47(8)
Atomic distances (Å) for ***2a***			
Ni(1)–O(7a)	1.8602(15)	Ni(1)–O(7b)	1.8670(15)
Ni(1)–S(8a)	2.1201(6)	Ni(1)–S(8b)	2.1495(6)
S(8a)–C(8a)	1.724(2)	S(8b)–C(8b)	1.727(2)
O(7a)–C(7a)	1.272(2)	O(7b)–C(7b)	1.270(3)
N(7b)–C(7b)	1.333(3)	N(7b)–C(8b)	1.345(3)
N(7a)–C(7a)	1.333(3)	N(7a)–C(8a)	1.339(3)
Atomic distances (Å) for ***8***			
Ni(1)–O(5b)	1.8725(14)	Ni(1)–O(5a)	1.8965(15)
Ni(1)–S(1b)	2.1543(6)	Ni(1)–O(5a)	2.1794(6)
S(1a)–C(2a)	1.748(2)	S(1b)–C(2b)	1.748(2)
C(4a)–O(5a)	1.276(2)	C(4b)–O(5b)	1.282(2)
N(3b)–C(4b)	1.345(3)	C(2b)–N(3b)	1.354(3)
N(3a)–C(4a)	1.348(3)	C(2a)–N(3a)	1.349(3)

Table 3
Antifungal activity of some benzoylaminocarbothioyl pyrrolidines and metal complexes.

Compound	*S. cerevisae*[a]		*P. digitatum*[b]	
	MIC (μg/ml)	MFC (μg/ml)	MIC (μg/ml)	MFC (μg/ml)
1a	62.5	125	62.5	125
1b	125	250	31.25	62.5
1c	62.5	125	62.5	125
1d	125	250	31.25	62.5
1e	125	250	62.5	125
2a	62.5	125	62.5	125
3c	62.5	125	31.25	62.5
4a	125	250	31.25	62.5
6	62.5	125	62.5	125

MIC: minimal inhibition concentrations, MFC: minimal fungicidal concentrations.
[a] Activity of each compound after 24 h at 25 °C.
[b] Activity of each compound after 4 days at 25 °C.

4.2. General procedure for the synthesis of aroylaminocarbo-N-thioyl pyrrolidines (**1f**, **g**)

To a stirred solution of aroylisothiocyanate (1.22 mmol) in freshly distilled, dry, degassed acetonitrile (20 mL) was added a stirred solution of pyrrolidine cycloadduct (1.22 mmol) in acetonitrile (10 mL) over 15 min and the mixture stirred at ambient temperature under a nitrogen atmosphere for 5–6 h. The solvent was evaporated under reduced pressure (bath temperature not higher than 30 °C) and the residue purified by column chromatography eluting with 1:2 v/v ether–petroleum ether afforded the product.

4.2.1. 1-(3-Chlorobenzoylaminocarbothioyl)-2,5-diphenyl-pyrrolidine-2,4-dicarboxylicacid dimethyl ester (**1f**)

After a reaction time of 5 h and work up the product (88%) crystalised from ether as a pale yellow prisms, as a 1:3 rotamer mixture, m.p. 110–112 °C. (*Anal.* Calc. $C_{28}H_{25}ClN_2O_5S$ requires: C, 62.60; H, 4.70; N, 5.20; S, 5.95. Found: C, 62.75; H, 4.80; N, 5.55; S, 5.65%.) *vmax* (KBr): 3260, 3063, 2950, 1740, 1676, 1598, 1496, 1433, 1402, 1229 and 1203 cm^{-1}. δ_H(300 MHz): 7.87(brs, 1H, NH), 7.77–7.06(m, 14H, Ar–H), 5.88(d, 1H, 5-H, minor rotamer), 5.81(d, 1H, 5-H, major rotamer), 3.92(s, 3H, OCH_3, major rotamer), 3.74(s, 3H, OCH_3, minor rotamer), 3.40(m, 1H, 4-H), 3.34(s, 3H, OCH_3, minor ratomer), 3.26(s, 3H, OCH_3, major rotamer), 2.57–2.47(m, 2H, 3-H). δ_C(75 MHz): 187.21 and 179.16 (C=S, rotamers), 171.50 and 170.72 (C=O, rotamers), 170.15 and 169.13 (C=O, rotamers), 168.74 and 163.41 (C=O, rotamers). *m/z* (%) (ES): 537.2 (MH^+, 100), 539.2 (MH^+, 35).

4.2.2. 1-Benzoylaminocarbothioyl-2-benzyl-5-(4-methoxyphenyl)-pyrrolidine-2,4-dicarboxylic acid dimethyl ester (**1g**)

After a reaction time of 6 h and work up the product (91%) crystalised from ether as pale yellow prisms as a 1:3 rotamer mixture, m.p. 161–163 °C. (*Anal.* Calc. $C_{30}H_{30}N_2O_6S$ requires: C, 65.90; H, 5.55; N, 5.15; S, 5.85. Found: C, 66.10; H, 5.70; N, 5.25; S, 5.55%.) *vmax* (KBr): 3279, 3034, 2950, 1736, 1681, 1612, 1516, 1454, 1405, 1233, 1187 cm^{-1}. δ_H(300 MHz): 8.15 (brs, 1H, NH), 7.59–6.78(m, 14H, Ar-H), 5.23(d, 1H, 5-H, minor rotamer), 5.09(d, 1H, 5-H, major rotamer), 4.68(d, 1H, 4-H, major rotamer), 4.21(d, 1H, 4-H, minor ratomer), 3.94(s, 3H, OCH_3), 3.81(s, 3H, OCH_3, major rotamer), 3.77(s, 3H, OCH_3, minor rotamer), 3.51–3.01(m, 2H, –CH_2Ph), 3.17(s, 3H, OCH_3, minor ratomer), 3.12(s, 3H, OCH_3, major rotamer), 2.41–2.17(m, 2H, 3-H). δ_C(75 MHz): 186.43 and 177.58 (C=S, rotamers), 173.47 and 172.18 (C=O, rotamers), 172.02 and 169.85(C=O, rotamers), 169.39 and 163.96(C=O, rotamers). *m/z* (%) (ES): 547.1 (MH^+, 100).

4.3. General procedure for complex formation

The Ni(II), Pd(II) and Cu(II) complexes of (**1a**–**g**) were prepared by modification of a literature method [4,5,20]. A solution of ligand (1.0 mmol) in methanol was mixed with a solution of metal acetate (0.5 mmol) in methanol and the reaction mixture stirred at ambient temperature for 2–3 h. during which time the product precipitated. The product was filtered off and crystallized from dichloromethane–methanol.

4.3.1. Ni complex of 1-benzoylaminocarbothioyl-2-benzyl-5-phenyl-pyrrolidine-2,4-dicarboxylic acid dimethyl ester (**2a**)

After a reaction time of 2 h and work up the product (86%) as crystallised from dichloromethane–methanol as red prisms, m.p. 198–200 °C. (*Anal.* Calc. $C_{58}H_{54}N_4O_{10}S_2Ni$ requires: C, 63.75; H, 5.10; N, 5.10. Found: C, 63.70; H, 5.00; N, 5.00%.) *vmax* (KBr): 3028, 2949, 1742, 1600, 1502, 1409, 1367, 1251, 1202, 1025 and 703 cm^{-1}. δ_H(500 MHz): 8.06 (m, 4H, Ar-H), 7.58–6.99(m, 26H, ArH), 5.0 and 4.94(2 × d, 2H, 5-H), 4.23 and 4.20(2 × d, 2H, CH_2Ph), 3.78 and 3.74(2 × s, 6H, OMe), 3.35(m, 2H, CH_2Ph), 3.10 and 3.09(2 × s, 6H, OMe), 2.91(m, 2H, 3-H), 2.24–2.17(m, 4H, 4-H and 3′-H). δ_C(125 MHz): 174.00 and 173.59 (C=S), 173.30 and 173.27 (C=O), 173.15 and 173.05 (C=O), 169.67 (2C=O).

4.3.2. Pd complex of 1-benzoylaminocarbothioyl-2-benzyl-5-phenyl-pyrrolidine-2,4-dicarboxylic acid dimethyl ester (2b)

After a reaction time of 2 h and work up the product (82%) crystallised from dichloromethane–methanol as a yellow prisms, m.p. 272–274 °C. ν_{max} (KBr): 3060, 2949, 1743, 1598, 1497, 1402, 1367, 1245, 1173, 1024 and 699 cm^{-1}. δ_H(400 MHz): 8.17–8.15(m, 4H, Ar-H), 7.52–7.14(m, 26H, ArH), 5.10 and 5.04(2 × d, 2H, 5-H), 4.32 and 4.25(2 × d, 2H, CH_2Ph), 3.82 and 3.76(2 × s, 6H, OMe), 3.45 and 3.37(2 × d, 2H, CH_2Ph), 3.13 and 3.11(2 × s, 6H, OMe), 2.98(m, 2H, 3-H), 2.32–2.24(m, 4H, 4-H and 3′-H). δ_C(100 MHz): 173.40 (2C=S), 172.89 and 172.48 (C=O), 172.09 and 171.97 (C=O), 169.80 (2C=O).

4.3.3. Cu complex of 1-benzoylaminocarbothioyl-2-benzyl-5-phenyl-pyrrolidine-2,4-dicarboxylic acid dimethyl ester (**2c**)

After a reaction time of 2 h and work up the product (90%) crystallised from dichloromethane–methanol as green prism, m.p.

257–259 °C (decomp.). (*Anal.* Calc. for $C_{58}H_{54}N_4O_{10}S_2Cu$ requires: C, 63.60; H, 4.95; N, 5.10; S, 5.85. Found: C, 63.15; H, 4.85; N, 4.95; S, 5.45%.) *vmax* (ATR): 3060, 2946, 1733, 1597, 1494, 1451, 1400, 1363, 1252, 1204, 1022, 699 cm^{-1}. Gouy Balance μ_{eff} [B.M.], Found: 1.92, requires: 1.73.

4.3.4. Ni complex of 1-benzoylaminocarbothioyl-2-sec-butyl-5-phenyl-pyrrolidine-2,4-dicarboxylic acid dimethyl ester (**3a**)

After a reaction time of 2 h and work up the product (78%) crystallised from dichloromethane–methanol as a red prisms, m.p. 285–287 °C. (Anal. Calc. for $C_{52}H_{58}N_4O_{10}S_2Ni$ requires: C, 61.10; H, 5.70; N, 5.50; S, 6.30. Found: C, 60.95; H, 5.50; N, 5.40; S, 5.85%.) *vmax* (KBr): 3000, 2965, 1741, 1506, 1409, 1364, 1245, 1204, 1025 and 720 cm^{-1}. δ_H(400 MHz): 7.92(m, 2H, ArH), 7.41–7.15(m, 18H, Ar-H), 5.41(m, 2H, 5-H), 3.60(m, 2H, 4-H), 360 and 3.58(2 × s, 6H, OMe), 3.20(brs, 6H, OMe), 2.94(m, 2H, 3-H), 2.75(m, 2H, 3′-H), 2.37(m, 2H, CH), 1.92–0.80(m, 16H, $CH_3CHCH_2CH_3$). δ_C(100 MHz): 174.10 (C=S), 173.68 (C=S), 173.58 (C=O), 173.29 (2C=O), 169.93 (C=O), 169.87 (2C=O). *m/z* (%) (ES+): 1021.3(MH^+). HRMS (ES+) found MH^+ 1021.3021, $C_{52}H_{59}N_4O_{10}S_2Ni$ requires MH^+ 1021.3065.

4.3.5. Pd complex of 1-benzoylaminocarbothioyl-2-sec-butyl-5-phenyl-pyrrolidine-2,4-dicarboxylic acid dimethyl ester (**3b**)

After a reaction time of 2 h and work up the product (72%) crystallised from dichloromethane–methanol as a yellow prism, m.p. 231–233 °C (decomp.). ν_{max} (ATR): 3059, 2963, 1736, 1586, 1497, 1389, 1364, 1258, 1171, 1021, 697 cm^{-1}. δ_H(500 MHz): 8.08(m, 6H, ArH), 7.83–7.17(m, 14H, Ar-H), 5.51 and 5.47(2 × d, 2H, 5-H), 3.72 and 3.71(2 × s, 6H, OMe), 3.67(m, 2H, 4-H), 3.31 and 3.30(2 × s, 6H, OMe), 3.01(m, 2H, 3-H), 2.84(m, 2H, 3′-H), 2.48(m, 2H, CH), 1.29–0.82(m, 16H, $CH_3CHCH_2CH_3$). δ_C(125 MHz): 173.46 (C=S), 173.36 (C=S), 172.59 and 172.53 (C=O) 171.86 and 171.84 (C=O), 169.69 (C=O) and169.62 (C=O). *m/z* (%) (ES+): 1069.3(MH^+). HRMS (ES+) found 1069.2702, $C_{52}H_{59}N_4O_{10}S_2Pd$ requires MH^+ 1069.2714.

4.3.6. Cu complex of 1-benzoylaminocarbothioyl-2-sec-butyl-5-phenyl-pyrrolidine-2,4-dicarboxylic acid dimethyl ester (**3c**)

After a reaction time of 2 h and work up the product (90%) separated from dichloromethane–methanol as a green amorphous, m.p. 194–196 °C. (*Anal.* Calc. for $C_{52}H_{58}N_4O_{10}S_2Cu$ requires: C, 60.85; H, 5.70; N, 5.45; S, 6.25. Found: C, 60.50; H, 5.55; N, 5.45; S, 5.70%.) *vmax* (KBr): 3000, 2967, 1740, 1507, 1406, 1362, 1243, 1202, 1025 and 703 cm^{-1}. *m/z* (%) (ES+): 1026.3(MH^+). HRMS (ES+) found 1026.2963, $C_{52}H_{59}N_4O_{10}S_2Cu$ requires MH^+ 1026.2926. Gouy Balance μ_{eff} [B.M.], Found: 1.92, requires: 1.73.

4.3.7. Ni complex of 1-benzoylaminocarbothioyl-5-phenyl-pyrrolidine-2,4-dicarboxylic acid dimethyl ester (**4a**)

After a reaction time of 2 h and work up the product (86%) crystallised from dichloromethane–methanol as red prisms, m.p. 287–289 °C. (Anal. Calc. for $C_{44}H_{42}N_4O_{10}S_2Ni$ requires: C, 58.10; H, 4.65; N, 6.15; S, 7.05. Found: C, 57.85; H, 4.55; N, 6.15; S, 6.70%.) *vmax* (ATR): 3061, 2947, 1752, 1586, 1497, 1409, 1362, 1275, 1169, 1031, 713 cm^{-1}. δ_H(400 MHz): 8.01–7.22(m, 20H, ArH), 5.80 and 5.45(2 × m, 2xH, 5-H), 4.78(m, 2H, 2-H), 3.78 and 3.75(2 × s, 6H, OMe), 3.55–3.40(m, 2H, 3-H), 3.48 and 3.46(2 × s, 6H, OMe), 2.62–2.44(m, 4H, 4-H and 3′-H). δ_C(100 MHz): 174.47 and 174.42 (C=S), 173.80 and 173.62 (C=O), 171.82 and 171.72 (C=O) 169.23 (2C=O).

4.3.8. Pd complex of 1-benzoylaminocarbothioyl-5-phenyl-pyrrolidine-2,4-dicarboxylic acid dimethyl ester (**4b**)

After a reaction time of 2 h and work up the product (72%) crystallised from dichloromethane–methanol as pale yellow prisms, m.p. 252–254 °C. (*Anal.* Calc. for $C_{44}H_{42}N_4O_{10}S_2Pd$ requires: C, 55.20; H, 4.40; N, 5.85; S, 6.70. Found: C, 54.95; H, 4.40; N, 5.95; S, 6.30%.) *vmax* (ATR): 3038, 2943, 1749, 1588, 1499, 1427, 1405, 1363, 1265, 1171, 1025, 713 cm^{-1}. δ_H(400 MHz): 8.14–7.24(m, 20H, ArH), 5.65(m, 2H, 5-H), 4.84(m, 2H, 2-H), 3.74 and 3.72(2 × s, 6H, OMe), 3.53–3.35(2 × m, 2H, 3-H), 3.42(s, 6H, OMe), 2.65–2.40(m, 4H, 4-H and 3′-H).

4.3.9. Cu complex of 1-benzoylaminocarbothioyl-5-phenyl-pyrrolidine-2,4-dicarboxylic acid dimethyl ester (**4c**)

After a reaction time of 2 h and work up the product (88%) crystallised from dichloromethane–methanol as green prisms, m.p. 211–213 °C (decomp.). ν_{max} (ATR): 3052, 2945, 1743, 1585, 1510, 1404, 1358, 1238, 1169, 1021, 712 cm^{-1}. *m/z* (%) (ES+): 914.2(MH^+) and 936.2 (MNa^+). HRMS (ES+) found 914.1711, $C_{44}H_{43}N_4O_{10}S_2Cu$ requires MH^+ 914.1725. Gouy Balance μ_{eff} [B.M.], Found: 1.95, requires: 1.73.

4.3.10. Ni complex of 1-benzoylaminocarbothioyl-2,5-diphenyl-pyrrolidine-2,4-dicarboxylic acid dimethyl ester (**5a**)

After a reaction time of 2 h and work up the product (86%) crystallised from dichloromethane–methanol as red prisms, m.p. 198–200 °C. (*Anal.* Calc. for $C_{56}H_{50}N_4O_{10}S_2Ni$ requires: C, 63.25; H, 4.90; N, 5.25. Found: C, 63.00; H, 4.60; N, 5.20%.) *vmax* (ATR): 3062, 2947, 1742, 1584, 1497, 1397, 1361, 1242, 1179, 1021 and 716 cm^{-1}. δ_H(500 MHz): 7.59–7.13(m, 30H, ArH), 5.63–5.59(m, 2H, 5-H), 3.65 and 3.63(2 × s, 6H, OMe), 3.30 and 3.25(2 × s, 6H, OMe), 3.28–3.12(m, 4H, 3-H and 4-H), 2.33(m, 2H, 3′-H). δ_C(125 MHz): 174.31 and 173.94 (C=S), 173.50(2C =O), 171.26 and 171.20 (C=O), 169.18 (2C=O).

4.3.11. Pd complex of 1-benzoylaminocarbothioyl-2,5-diphenyl-pyrrolidine-2,4-dicarboxylic acid dimethyl ester (**5b**)

After a reaction time of 2 h and work up the product (82%) crystallised from dichloromethane–methanol as yellow amorphous. m.p. 272–274 °C. *vmax* (ATR): 3060, 2949, 1739, 1586, 1495, 1360, 1242, 1224, 1170, 1023, 698 cm^{-1}. δ_H(500 MHz): 7.65–7.53(m, 8H, ArH), 7.42–7.11(m, 22H, ArH), 5.70 and 5.68(2 × d, 2H, 5-H), 3.61 and 3.59(2 × s, 6H, OMe), 3.32 and 3.31(2 × s, 6H, OMe), 3.30–3.25(m, 4H, 3-H and 4-H), 2.45–2.37(m, 2H, 3′-H). δ_C(125 MHz): 172.62 and 172.27 (C=S), 172.11 and 171.93 (C=O), 171.17 and 171.11 (C=O), 169.11 (2C=O). *m/z* (%) (ES+): 1109.2(MH^+). HRMS (ES+) found 1109.2076, $C_{56}H_{51}N_4O_{10}S_2Pd$ requires MH^+ 1109.2091.

4.3.12. Cu complex of 1-benzoylaminocarbothioyl-2,5-diphenyl-pyrrolidine-2,4-dicarboxylic acid dimethyl ester (**5c**)

After a reaction time of 2 h and work up the product (92%) crystallised from dichloromethane–methanol as green prisms, m.p. 248–250 °C. (*Anal.* Calc. for $C_{56}H_{50}N_4O_{10}S_2Cu$ requires: C, 63.05; H, 4.70; N, 5.25; S, 5.50. Found: C, 62.85; H, 4.60; N, 5.30; S, 5.70%.) *vmax* (ATR): 3058, 2948, 1740, 1585, 1494, 1397, 1360, 1241, 1174, 1022, 697 cm^{-1}. Gouy Balance μ_{eff} [B.M.], Found: 1.88, requires: 1.73.

4.3.13. Ni complex of 1-benzoylaminocarbothioyl-5-(naphthalen-3-yl)-pyrrolidine-2,3,4-tricarboxylic acid trimethyl (**6a**)

After a reaction time of 2 h and work up the product (76%) crystallised from dichloromethane–methanol as red prisms, m.p. 213–215 °C. ν_{max} (KBr):3056, 2950, 1743, 1502, 1419, 1360, 1237, 1170, 1054 and 712 cm^{-1}. δ_H(400 MHz): 8.20–7.10(m, 24H, ArH), 5.70–5.60(m, 2H, 5-H), 3.70(s, 6H, OMe), 3.65(m, 2H, 2-H), 3.25(brs, 12H, OMe), 3.18(m, 2H, 4-H), 2.38(m, 2H, 3-H). δ_C(100 MHz): 174.56 and 174.14 (C=S), 173.78 and 173.72 (C=O), 171.47 and 171.39 (C=O) 169.29 and 169.27(2C =O) *m/z* (%) (ES+):

1125.2(MH^+). HRMS (ES+) found 1125.2191, $C_{56}H_{51}N_4O_{10}S_2Ni$ requires MH^+ 1125.2393.

*4.3.14. Cu complex of 1-benzoylaminocarbothioyl-5-(naphthalen-3-yl)-pyrrolidine-2,3,4-tricarboxylic acid trimethyl (**6b**)*

After a reaction time of 2 h and work up the product (92%) crystallised from dichloromethane–methanol as green prisms, m.p. 248–250 °C. ν_{max} (ATR): 3055, 2948, 1736, 1598, 1497, 1402, 1358, 1283, 1204, 1166, 1052, 710 cm^{-1}. Gouy Balance μ_{eff} [B.M.], Found: 1.88, requires: 1.73. *m/z* (%) (ES+): 1130.2(MH^+), 1153.2 (MNa^+). HRMS (ES+) found 1130.2134, $C_{56}H_{51}N_4O_{10}S_2Cu$ requires MH^+ 1130.2163.

*4.3.15. Ni complex of 1-benzoylaminocarbothioyl-2,5-diphenyl-pyrrolidine-2,4-dicarboxylic acid dimethyl ester (**7**)*

After a reaction time of 3 h and work up the product (89%) crystallised from dichloromethane–methanol as red prisms in yield, m.p. 295–297 °C. (*Anal.* Calc. for $C_{56}H_{48}$ $Cl_2N_4O_{10}S_2Ni$ requires: C, 59.50; H, 4.25; N, 4.95. Found: C, 59.05; H, 4.35; N, 4.65%.) *vmax* (ATR): 3065, 2988, 1740, 1512, 1394, 1243, 1198, 1028, 746 and 703 cm^{-1}. δ_H(500 MHz): 7.70–7.50(m, 6H, ArH), 7.40–7.07(m, 22H, ArH), 5.58(m, 2H, 5-H), 3.68 and 3.66(2 × s, 6H, OMe), 3.30 and 3.29(2 × s, 6H, OMe), 3.32–3.22(m, 4H, 3-H and 4-H), 2.40(m, 2H, 3′-H). δ_C(125 MHz): 174.57 and 174.24 (C=S), 171.95 (2C=O) 171.23 and 171.16 (C=O) 169.06 (2C=O) *m/z* (%) (ES+): 1129.1(MH^+), 1131.1(MH^+). HRMS (ES+) found 1129.1615, $C_{56}H_{49}Cl_2N_4O_{10}S_2Ni$ requires MH^+ 1129.1663.

*4.3.16. Ni complex of 1-benzoylaminocarbothioyl-2-benzyl-5-(4-methoxyphenyl)-pyrrolidine-2,4-dicarboxylic acid dimethyl ester (**8**)*

After a reaction time of 3 h and work up the product (87%) crystallised from dichloromethane–methanol as pale violet plate, m.p. 255–257 °C. (*Anal.* Calc. for $C_{60}H_{58}N_4NiO_{12}S_2{\cdot}0.5H_2O$ requires: C, 62.25; H, 5.10; N, 4.85; S, 5.30. Found: C, 62.00; H, 5.10; N, 4.90; S, 5.20%.) *vmax* (ATR): 3062, 2949, 1731, 1610, 1508, 1402, 1245, 1201, 1025, 749 and 704 cm^{-1}. δ_H(300 MHz) ($CDCl_3$): 8.08(m, 4H, Ar-H), 7.52–7.19(m, 20H, Ar-H), 6.86 and 6.75(2 × d, 4H, Ar-H), 5.01 and 4.95(2 × d, 2H, 5-H), 4.24(m, 2H, CH_2Ph), 3.85, 3.80, 3.79 and 3.77(4 × s, 12H, OMe), 3.40–3.33(m, 2H, 4-H), 3.17 and 3.15(2 × s, 6H, OMe), 2.97(m, 2H, CH_2Ph), 2.31–2.13(m, 4H, 3-H and 3′-H). δ_C($CDCl_3$): 173.88 and 173.42 (C=S), 173.35 (2C=O), 173.03 (C=O), 172.94 (C=O) and 169.82 (2C=O). *m/z* (%) (ES+): 1149.3(MH^+). HRMS (ES+) found 1149.2919, $C_{60}H_{59}N_4O_{12}S_2Ni$ requires MH^+ 1149.2866.

Supplementary data

CCDC 721640 and 721641 contain the supplementary crystallographic data for **2a** and **8**. These data can be obtained free of charge via http://www.ccdc.cam.ac.uk/conts/retrieving.html, or from the Cambridge Crystallographic Data Centre, 12 Union Road, Cambridge CB2 1EZ, UK; fax: (+44) 1223-336-033; or e-mail: deposit@ccdc.cam.ac.uk.

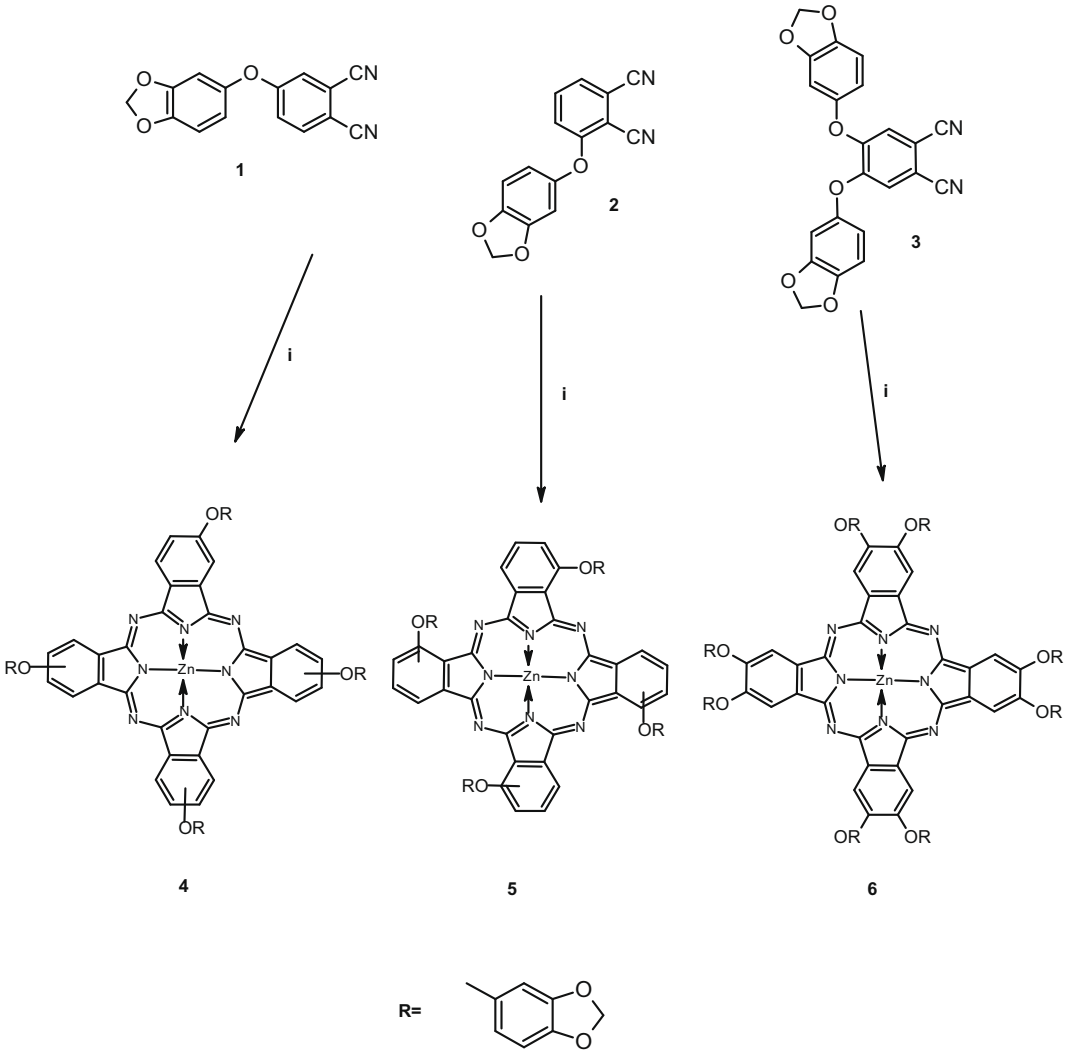
Acknowledgements

We thank Mersin University for a project Grant BAB-ECZ F (HAD) 2004-2. The support of The University Leeds and Ege University are gratefully acknowledged.

References

[1] W.H. Pearson, in: A. Rahman (Ed.), Studies in Natural Product Chemistry, vol. 1, Elsevier, 1988. pp. 323–358.
[2] F. Sternfeld, A.R. Guiblin, R.A. Jelley, V.G. Matassa, A.J. Reeve, P.A. Hunt, M.S. Beer, A. Heald, J.A. Stanton, B. Sohal, A.P. Watt, L.J. Street, J. Med. Chem. 42 (1999) 677.
[3] P. Gupta, P. Butler, N.B. Shepperson, A. McHarg, Eur. J. Pharmacol. 398 (2000) 73.
[4] E. Rodríguez-Fernández, J.L. Manzano, J.J. Benito, R. Hermosa, E. Monte, J.J. Criado, J. Inorg. Biochem. 99 (2005) 1558.
[5] J.J. Criado, E. Rodríguez-Fernández, E. García, M.R. Hermosa, E. Monte, J. Inorg. Biochem. 69 (1998) 113.
[6] R. Del Campo, J.J. Criado, E. García, M.R. Hermosa, A. Jiménez-Sánchez, J.L. Manzano, E. Monte, E. Rodríguez-Fernández, F. Sanz, J. Inorg. Biochem. 89 (2002) 74.
[7] E. Rodríguez-Fernández, E. García, M.R. Hermosa, A. Jiménez-Sánchez, M.M. Sánchez, E. Monte, J.J. Criado, J. Inorg. Biochem. 75 (1999) 181.
[8] R. Del Campo, J.J. Criado, R. Gheorghe, F.J. González, M.R. Hermosa, F. Sanz, J.L. Manzano, E. Monte, E. Rodríguez-Fernández, J. Inorg. Biochem. 98 (2004) 1307.
[9] C. Sacht, M.S. Datt, S. Otto, A. Roodt, J. Chem. Soc., Dalton Trans. 5 (2000) 727.
[10] C. Sacht, M.S. Datt, Polyhedron 19 (2000) 1347.
[11] N. Rasanu, L. Barbes, Rev. Chim. 53 (2002) 758.
[12] Z.H. Khalil, A.A. Abdel-Hafez, A.S. Yanni, A.M. Moharam, Bull. Chem. Soc. Jpn. 61 (1988) 4143.
[13] R.C. Tweit, R.D. Muir, S. Mizuba, J. Med. Chem. 12 (1969) 343.
[14] B. Latli, M. Hrapchak, V. Gorys, C.A. Busacca, C. Senanayake, J. Label, Compd. Radiopharm. 48 (2005) 447.
[15] D.L. Wyles, K.A. Kaihara, R.T. Schooley, Antimicrob. Agents Chemother. 52 (2008) 1862.
[16] A. Ranise, F. Bondavalli, O. Bruno, S. Schenone, C. Losasso, M. Costantino, M.L. Cenicola, D. Donnoli, E. Marmo, Farmaco 46 (1991) 317.
[17] A. Ranise, A. Spallarossa, O. Bruno, S. Schenone, P. Fossa, G. Menozzi, F. Bondavalli, L. Mosti, A. Capuano, F. Mazzeo, G. Falcone, W. Filippelli, IL Farmaco 58 (2003) 765.
[18] P. Mühl, K. Gloe, F. Dietze, E. Hoyer, L. Beyer, Z. Chem. 26 (1986) 81.
[19] L. Beyer, E. Hoyer, J. Liebscher, H. Hartman, Z. Chem. 21 (1981) 81.
[20] L. Beyer, E. Hoyer, E. Hennig, H. Kirmse, H. Hartman, J. Liebscher, J. Prakt. Chem. (Leipzig) 317 (1975) 829.
[21] F. Lessmann, L. Beyer, R. Richter, R. Meusinger, Z. Naturforsch., (B) 53 (1998) 981.
[22] K.R. Koch, Coord. Chem. Rev. 216–217 (2001) 473.
[23] K.R. Koch, O. Hallale, S.A. Bourne, J. Miller, J. Bacsa, J. Mol. Struct. 561 (2001) 185.
[24] A. Irving, K.R. Koch, M. Matoetoe, Inorg. Chim. Acta 206 (1993) 193.
[25] A. Mohamadou, I. Dechamps-Olivier, J.-P. Barbier, Polyhedron 13 (1994) 1363.
[26] E. Guillon, A. Mohamadou, I. Dechamps-Olivier, J.-P. Barbier, Polyhedron 15 (1996) 947.
[27] W. Hernandez, E. Spodine, L. Beyer, U. Schröder, R. Richter, J. Ferreira, M. Pavani, Bioinorg. Chem. Appl. 3 (2005) 299.
[28] X. Shen, X. Shi, B. Kang, Y. Tong, Y. Liu, L. Gu, Q. Liu, Y. Huang, Polyhedron 18 (1999) 33.
[29] M. Dominguez, E. Antico, L. Beyer, A. Aguirre, S. Garcia-Granda, V. Salvado, Polyhedron 21 (2002) 1429.
[30] K.H. König, M. Schuster, B. Steinbrech, G. Schneeweis, R. Schlodder, Fresenius Z. Anal. Chem. 321 (1985) 457.
[31] P. Vest, M. Schuster, K.H. König, Fresenius Z. Anal. Chem. 335 (1989) 759.
[32] P. Vest, M. Schuster, K.H. König, Fresenius Z. Anal. Chem. 339 (1991) 142.
[33] P. Vest, M. Schuster, K.H. König, Fresenius Z. Anal. Chem. 341 (1991) 566.
[34] M. Iwakuma, S. Nakamura, Y. Baba, Solvent Extr. Res. Dev., Jpn. 11 (2004) 103.
[35] M. Schuster, E. Unterreitmeier, Fresenius Z. Anal. Chem. 346 (1993) 630.
[36] M. Schuster, M. Sandor, Fresenius Z. Anal. Chem. 356 (1996) 326.
[37] E. Unterreitmeier, M. Schuster, Anal. Chim. Acta 309 (1995) 339.
[38] M. Schuster, M. Schwarzer, Fresenius Anal. Chim. Acta 328 (1996) 1.
[39] K.H. König, M. Schuster, G. Schneeweiss, B. Steinbrech, Fresenius Z. Anal. Chem. 319 (1984) 66.
[40] R. Grigg, Chem. Soc. Rev. 16 (1987) 89.
[41] H.A. Dondas, R. Grigg, unpublished results.
[42] H.A. Dondas, R. Grigg, C. Kilner, Tetrahedron 59 (2003) 8481.
[43] A.D. Barr, R. Grigg, N.H.Q. Gunarate, J. Kemp, P. Mc Meekin, V. Sridharan, Tetrahedron 44 (1988) 557.
[44] H.A. Dondas, R. Grigg, M. Thornton-Pett, Tetrahedron 52 (1996) 13455.
[45] H.A. Dondas, Y. Durust, R. Grigg, M.J. Slater, M.A.B. Sarker, Tetrahedron 61 (2005) 10667.
[46] H.A. Dondas, C.W.G. Fiswick, R. Grigg, C. Kilner, Tetrahedron 60 (2004) 3473.
[47] R. Grigg, M. Thornton-Pett, J. Xu, L.H. Xu, Tetrahedron 55 (1999) 13841.
[48] H.A. Dondas, R. Grigg, W.S. MacLachlan, D.T. MacPerson, J. Markandu, V. Sridharan, S. Suganthan, Tetrahedron Lett. 41 (2000) 967.
[49] H.A. Dondas, J. Duraisingham, R. Grigg, W.S. MacLaclan, D.T. MacPherson, M. Thornton-Pett, V. Sridharan, S. Suganthan, Tetrahedron 56 (2000) 4063.
[50] H.A. Dondas, O. Altınbaş, Heterocycl. Commun. 10 (2004) 167.
[51] H.A. Dondas, Y. Nural, N. Duran, C. Kilner, Turk. J. Chem. 30 (2006) 573.
[52] National Committee for Clinical Laboratory Standards, Reference method for broth dilution antifungal susceptibility testing of yeasts, Approved standard NCCLS document M27-A, National Committee for Clinical Laboratory Standards, Wayne, PA, 2002.
[53] C.J. Alexopoulos, C.W. Mims, Introductory Mycology, 3rd ed., Wiley, NY, 1979.
[54] M.A. Ghannoum, L.A. Rice, Clin. Microbiol. Rev. 12 (1999) 501.

[55] F.G. Burlesson, T.M. Chambers, D.L. Wedbrauk, Virology. A Laboratory Manual, Academic Press, New York, 1992.
[56] E. Borenfreund, J.A. Puerner, J. Tissue Culture Met. 9 (1984) 7.
[57] E. Borenfreund, J.A. Puerner, Toxicol. Lett. 24 (1985) 119.
[58] A. Earnshaw, Introduction to Magnetochemistry, Academic Press, London, 1968. p. 4.
[59] D.D. Perrin, W.L.F. Armarego, D.R. Perrin, Purification of Laboratory Chemicals, 2nd ed., Pergamon Press, New York, 1980.



Scheme 1. Synthetic route of three phthalonitriles (**1**, **2** and **3**), and their zinc phthalocyanines derivatives (i) anhydrous $Zn(Ac)_2$, 1-pentanol, 15 h, argon atm.

diazabicyclo[5.4.0] undec-7-ene (DBU), potassium carbonate, and zinc acetate were purchased from Aldrich.

FT-IR spectra (KBr pellets) were recorded on a Perkin–Elmer spectrum 2000 FT-IR spectrometer. UV–Vis spectra were recorded on a Cary 500 UV–Vis/NIR spectrophotometer. ^1H and ^{13}C NMR spectra were obtained in $CDCl_3$ using a Bruker EMX 400 NMR spectrometer. Elemental analyses were done on Vario Elementar EL III. Fluorescence spectra were recorded on the Varian Eclipse spectrofluoremeter. Triplet absorption and decay kinetics were recorded on a laser flash photolysis system, the excitation pulses were produced by a Nd: YAG laser (Quanta-Ray, 1.5 J/90 ns) pumping a dye laser (Lambda Physic FL 3002, Pyridin 1 in methanol). The analyzing beam source was from a Thermo Oriel xenon arc lamp, and a photomultiplier tube was used as detector. Signals were recorded with a two-channel digital real-time oscilloscope (Tektronix TDS 360); the kinetic curves were averaged over 256 laser pulses. Photo-irradiations were done using a General Electric Quartz line lamp (300 W). A 600 nm glass cut off filter (Schott) and a water filter were used to filter off ultraviolet and infrared radiations, respectively. An interference filter (Intor, 670 nm with a band width of 20 nm) was additionally placed in the light path before the sample. Light intensities were measured with a POWER MAX 5100 (Molelectron detector incorporated) power meter. Mass spectras were obtained using a ABI Voyager DE-STR Maldi TOF instrument at University of Stellenbosch.

2.2. Synthesis

2.2.1. 4-[3,4-(Methylendioxy)-phenoxy]-phthalonitrile (*1*)

The 4-nitrophthalonitrile (4.40 g, 25.35 mmol) was dissolved in DMF (35 ml) under argon and 3,4-(methylendioxy)-phenol (3.50 g, 25.35 mmol) was added. After stirring for 30 min at room temperature, finely ground anhydrous potassium carbonate (8.65 g, 63.40 mmol) was added in portions during 4 h with efficient stirring. The reaction mixture was stirred under argon atmosphere at room temperature for 24 h. Then the mixture was poured into 400 ml ice water, and the precipitate was filtered off, washed with water and methanol and then dried. The crude product was recrystallized from methanol. Finally the pure product was dried in vacuum. Thin layer chromatography with silica gel was employed to confirm the absence of the starting phthalonitrile.

Yield: 4.50 g (67%). IR spectrum (cm^{-1}): 3084 (Ar–CH), 2226 (C≡N), 1599 (C=C), 1564, 1486, 1417, 1306, 1249, 1096 (C–O–C), 1037, 966, 778, 664. ^1H NMR ($CDCl_3$): δ = 7.75 (d, J = 8.41 Hz, 1H, Ar–H), 7.32 (2H, broad s, Ar–H), 6.89 (d, J = 8.16 Hz, 1H, Ar–H), 6.59 (2H, s, Ar–H), 6.08 (2H, s, CH_2). ^{13}C NMR ($CDCl_3$): δ = 162.69 (Ar–CO), 149.55 (Ar–CO), 148.19 (Ar–CO), 146.31 (Ar–CH), 135.75 (Ar–C), 121.46 (Ar–CH), 118.46 (Ar–CH), 115.76 (Ar–CN), 113.74 (Ar–CH), 109.30 (Ar–CH), 109.21 (Ar–CH), 102.54 (O–CH). *Anal.* Calc. for $C_{15}H_8N_2O_3$: C, 68.18; H, 3.05; N, 10.06. Found: C, 68.23; H, 3.01; N, 10.01%.

*2.2.2. 3-[3,4-(Methylendioxy)-phenoxy]-phthalonitrile (**2**)*

The synthesis of **2** was similar to that of **1**, except 3-nitrophthalonitrile (1.25 g, 7.25 mmol) instead of 4-nitrophthalonitrile was employed. The amounts of the other reagents were: 3,4-(methylendioxy)-phenol, 1.00 g (7.25 mmol) and anhydrous potassium carbonate, 2.50 g (18.12 mmol).

Yield: 1.34 g (70%). IR spectrum (cm^{-1}): 3087, 3073 (Ar–CH), 2228 (C≡N), 1576 (C=C), 1438, 1389, 1243, 1097 (C–O–C), 1034, 990, 866, 799, 719. ^1H NMR ($CDCl_3$): δ = 7.58 (d, J = 8.42 Hz, 1H, Ar–H), 7.47 (d, J = 7.53 Hz, 1H, Ar–H), 7.13 (d, J = 8.46 Hz, 1H, Ar–H), 6.87 (d, J = 8.33 Hz, 1H, Ar–H), 6.65 (2H, s, Ar–H), 6.07 (2H, s, CH_2). ($CDCl_3$): δ = 161.83 (Ar–CO), 150.03 (Ar–CO), 148.45 (Ar–CO), 146.30 (Ar–CH), 134.71 (Ar–C), 120.37 (Ar–CH), 117.72 (Ar–CH), 115.49 (Ar–CN), 113.01 (Ar–CH), 109.15 (Ar–CH), 106.16 (Ar–CH), 102.50 (O–CH). *Anal.* Calc. for $C_{15}H_8N_2O_3$: C, 68.18; H, 3.05; N, 10.06. Found: C, 68.15; H, 3.08; N, 10.11%.

*2.2.3. 4,5-[3,4-(Methylendioxy)-phenoxy-phthalonitrile (**3**)*

The synthesis of **3** was similar to that of **1**, except 4,5-dichlorophthalonitrile (0.71 g, 3.62 mmol) instead of 4-nitrophthalonitrile was employed. The amounts of the other reagents were: 3,4-(methylendioxy)-phenol, 1.02 g (7.25 mmol) and anhydrous potassium carbonate, 2.50 g (18.12 mmol).

Yield: 1.00 g (69%). IR spectrum (cm^{-1}): 3084, 3050 (Ar–CH), 2230 (C≡N), 1599 (C=C), 1486, 1444, 1249, 1096 (C–O–C), 1037, 966, 884, 778, 664. ^1H NMR ($CDCl_3$): δ = 7.16 (2H, s, Ar–H), 6.88 (d, J = 8.35 Hz, 2H, Ar–H), 6.65 (d, J = 2.38 Hz, 2H, s, Ar–H), 6.59 (dd, J = 8.36, 2.42 Hz, 2H, Ar–H), 6.08 (4H, s, CH_2). ^{13}C NMR ($CDCl_3$): δ = 152.72 (Ar–CO), 149.50 (Ar–CO), 148.37 (Ar–CO), 135.46 (Ar–C), 121.40 (Ar–CH), 115.55 (Ar–CN), 113.23 (Ar–CH), 110.52 (Ar–CH), 109.21 (Ar–CH), 102.91 (O–CH). *Anal.* Calc. for $C_{22}H_{12}N_2O_6$: C, 66.00; H, 3.02; N, 7.00. Found: C, 65.94; H, 2.99; N, 7.05%.

*2.2.4. (4)-Tetra[3,4-(methylendioxy)-phenoxy]phthalocyaninato zinc(II) (**4**)*

Compound **1** (0.50 g, 1.89 mmol), anhydrous zinc acetate (0.41 g, 1.89 mmol) and 3 ml of dry 1-pentanol were placed in a standard Schlenk tube in the presence of 1,8-diazabicyclo[5.4.0] undec-7-ene (DBU) (0.45 ml, 0.29 mmol) under a nitrogen atmosphere and held at reflux temperature for 15 h. After cooling to room temperature, the reaction mixture was precipitated by adding it drop-wise into *n*-hexane. The crude product was precipitated, collected by filtration and washed with hot hexane, ethanol and methanol. The crude green product was further purified by chromatography over a silica gel column using THF, $CHCl_3$ and a mixture of THF and CH_2Cl_2 (1:15 by volume), as eluents, respectively.

Yield: 0.25 g (47%). UV–Vis (DMSO): λ_{max} nm (log ε) 358 (4.95), 613 (4.74), 680 (5.43), (toluene): λ_{max} nm (log ε) 351 (4.84), 612 (4.70), 680 (5.40), (DCM): λ_{max} nm (log ε) 357 (4.97), 612 (4.72), 681 (5.45). IR spectrum (cm^{-1}): 3073 (Ar–CH), 2945, 2892 (CH), 1608 (C=C), 1482, 1396, 1335, 1218, 1093 (C–O–C), 952, 815, 745, 731 (Pc skeletal). ^1H NMR ($CDCl_3$): δ = 8.11–6.43 (24H, m, Ar–H), 5.99 (8H, s, CH_2). *Anal.* Calc. for $C_{60}H_{32}N_8O_{12}Zn$: C, 64.21; H, 2.87; N, 9.98. Found: C, 64.35; H, 3.03; N, 9.73%. MS (ES^+), (m/z): Calc. 1122.4. Found: 1123.6 [M^+].

*2.2.5. (3)-Tetra[3,4-(methylendioxy)-phenoxy]phthalocyaninato zinc(II) (**5**)*

The synthesis and purification of **5** was as outlined for **4**, except compound **2** (0.50 g, 1.89 mmol) instead of complex **1** was employed. The amounts of the other reagents were anhydrous zinc acetate (0.41 g, 1.89 mmol), dry 1-pentanol (3 ml) and DBU (0.45 ml, 0.29 mmol).

Yield: 0.20 g (38%). UV–Vis (DMSO): λ_{max} nm (log ε) 365 (4.75), 626 (4.72), 697 (5.40), (Toluene): λ_{max} nm (log ε) 352 (4.82), 626 (4.83), 696 (5.53), (DCM): λ_{max} nm (log ε) 358 (4.70), 627 (4.61), 694 (5.39). IR spectrum (cm^{-1}): 3077 (Ar–CH), 2955, 2885 (–CH), 1607 (C=C), 1477, 1395, 1333, 1236, 1090 (C–O–C), 1038, 968, 928, 878, 815, 744 (Pc skeletal). ^1H NMR ($CDCl_3$): δ = 8.43–6.49 (24H, m, Ar–H), 5.98 (8H, s, CH_2). *Anal.* Calc. for $C_{60}H_{32}N_8O_{12}Zn$: C, 64.21; H, 2.87; N, 9.98. Found: C, 64.15; H, 3.01; N, 9.77%. MS (ES^+), (m/z): Calc. 1122.4. Found: 1123.6 [M^+].

*2.2.6. 2,3-Octakis-[3,4-(methylendioxy)-phenol]phthalocyaninato zinc(II) (**6**)*

The synthesis and purification of **6** was as outlined for **4**, except compound **3** (0.50 g, 1.25 mmol) instead of complex **1** was employed. The amounts of the other reagents were anhydrous zinc acetate (0.27 g, 1.25 mmol), dry 1-pentanol (3 ml) and DBU (0.45 ml, 0.29 mmol).

Yield: 0.13 g (25%). UV–Vis (DMSO): λ_{max} nm (log ε) 359 (5.01), 629 (4.78), 679 (5.24), (Toluene): λ_{max} nm (log ε) 363 (4.63), 614 (4.49), 680 (5.11), (DCM): λ_{max} nm (log ε) 359 (4.99), 612 (4.74), 680 (5.350). IR spectrum (cm^{-1}): 3074 (Ar–CH), 2957, 2890 (–CH), 1605 (C=C), 1482, 1391, 1334, 1237, 1097 (C–O–C), 1038, 993, 930, 865, 814, 744 (Pc skeletal). ^1H NMR ($CDCl_3$): δ = 7.16–6.39 (32H, m, Ar–H), 5.56 (16H, s, CH_2). *Anal.* Calc. for $C_{88}H_8N_8O_{24}Zn$: C, 63.41; H, 2.90; N, 6.72. Found: C, 63.01; H, 3.12; N, 6.97%. MS (ES^+), (m/z): Calc. 1666.7; Found: 1667.6 [M^+].

2.3. Photophysical studies

2.3.1. Fluorescence quantum yields

Fluorescence quantum yields (Φ_F) were determined by the comparative method) [24,25], (Eq. (1)):

$$\Phi_F = \Phi_{F(Std)} \frac{F \cdot A_{Std} \cdot n^2}{F_{Std} \cdot A \cdot n_{Std}^2} \quad (1)$$

where F and F_{Std} are the areas under the fluorescence curves of **4**–**6** and the standard, respectively. A and A_{Std} are the respective absorbances of the sample and standard at the excitation wavelengths (which was ~0.05 in all solvents used), and n and n_{Std} are the refractive indices of solvents used for the sample and standard, respectively. ZnPc in DMSO (Φ_F = 0.20) [26], was employed as the standard.

2.3.2. Triplet quantum yields and lifetimes

The solutions for triplet quantum yields and lifetimes were introduced into a 1.0 mm pathlength UV–Vis spectrophotometric cell, deaerated using nitrogen and irradiated at the Q-band maxima. Triplet state quantum yields (Φ_T) of **4**–**6** were determined by the triplet absorption method [27], using zinc phthalocyanine (ZnPc) as a standard; Eq. (2):

$$\Phi_T = \Phi_T^{Std} \cdot \frac{\Delta A_T \cdot \varepsilon_T^{Std}}{\Delta A_T^{Std} \cdot \varepsilon_T} \quad (2)$$

where ΔA_T and ΔA_T^{Std} are the changes in the triplet state absorbances of **4**–**6** and the standard, respectively. ε_T and ε_T^{Std} are the triplet state molar exctinction coefficients for **4**–**6** and the standard, respectively. Φ_T^{Std} is the triplet quantum yield for the standard, ZnPc (Φ_T = 0.65 in DMSO [28] and 0.65 in toluene [29]). ε_T and ε_T^{Std} were determined from the molar extinction coefficients of their respective ground singlet state (ε_s and ε_S^{Std}) and the changes in absorbances of the ground singlet states (ΔA_S and ΔA_S^{Std}), according to Eq. (3):

$$\varepsilon_T = \varepsilon_S \cdot \frac{\Delta A_T}{\Delta A_S} \quad (3)$$

Quantum yields of internal conversion (Φ_{IC}) were obtained from Eq. (4), which assumes that only three processes (fluorescence, intersystem crossing and internal conversion), jointly deactivate the excited singlet state of the **4**–**6** molecules.

$$\Phi_{IC} = 1 - (\Phi_F + \Phi_T) \quad (4)$$

2.4. Photochemical studies

2.4.1. Singlet oxygen quantum yields

Quantum yields of singlet oxygen photogeneration were determined as previously explained in detail [30–32] in air (no oxygen bubbled) using the relative method with ZnPc as reference and DPBF as chemical quencher for singlet oxygen, using Eq. (5):

$$\Phi_{\Delta} = \Phi_{\Delta}^{\mathrm{Std}} \cdot \frac{R_{\mathrm{DPBF}} I_{\mathrm{abs}}^{\mathrm{Std}}}{R_{\mathrm{DPBF}}^{\mathrm{Std}} I_{\mathrm{abs}}} \tag{5}$$

where $\Phi_{\Delta}^{\mathrm{Std}}$ is the singlet oxygen quantum yield for the standard, ZnPc (Φ_{Δ} = 0.67 in DMSO [33] and 0.58 in toluene [32]). R_{DPBF} and $R_{\mathrm{DPBF}}^{\mathrm{Std}}$ are the DPBF photobleaching rates in the presence of **4–6** and the standard, respectively. I_{abs} and $I_{\mathrm{abs}}^{\mathrm{Std}}$ are the rates of light absorption by **4–6** and the standard, respectively. To avoid chain reactions induced by DPBF in the presence of singlet oxygen [34], the concentration of DPBF was $\sim 3 \times 10^{-5}$ mol l^{-1}. Solutions of sensitizer (absorbance = 0.2 at the irradiation wavelength) containing DPBF were prepared in the dark and irradiated in the Q-band region using the setup described above. DPBF degradation at 417 nm was monitored. The light intensity for singlet oxygen studies was 2×10^{15} photons s^{-1} cm^{-2}. The error in the determination of Φ_{Δ} was ~10% (determined from several Φ_{Δ} values).

2.4.2. Photodegradation quantum yields

For determination of photodegradation quantum yields, the usual Eq. (6) was employed [30–32]:

$$\Phi_{\mathrm{Pd}} = \frac{(C_0 - C_t) V N_A}{I_{\mathrm{abs}} S t} \tag{6}$$

where C_0 and C_t in mol dm^{-3} are the concentrations of **4–6** before and after irradiation, respectively; V is the reaction volume; S is the irradiated cell area (2.0 cm^2); t is the irradiation time; N_A is the Avogadro's number and I_{abs} is the overlap integral of the radiation source intensity and the absorption of **4–6** (the action spectrum) in the region of the interference filter transmittance. The light intensity for photodegradation studies was 5×10^{16} photons s^{-1} cm^{-2}.

3. Results and discussion

3.1. Syntheses and characterization

The synthetic routes to novel phthalocyanines (**4–6**) are shown in Scheme 1. These complexes were prepared by the template cyclotetramerization of 4-[3,4-(methylendioxy)-phenoxy]-phthalonitrile (**1**), 3-[3,4-(methylendioxy)-phenol]-phthalonitrile (**2**), 4,5-[3,4-(methylendioxy)-phenol]-phthalonitrile (**3**) and anhydrous $Zn(OAc)_2$ in the presence of 1-pentanol at reflux temperature under argon atmosphere and in the presence of 1,8-diazabicyclo[5.4.0] undec-7-ene (DBU) as a strong base. All of these new zinc phthalocyanines were purified by column chromatography and were obtained in a moderate yield (47% for **4**, 38% for **5**, and 25% for **6**) and were also characterized by elemental analysis together with the spectral data (^{1}H NMR, FT-IR, mass and UV–Vis spectra).

The characterization data of the new compounds are consistent with the assigned formula. The tetra-substituted complexes (**4** and **5**) were isolated as a mixture of isomers, as expected. The presence of isomers might be verified by the slight broadening encountered in the UV–Vis absorption bands and broadening in the ^{1}H NMR spectra as compared with the spectra of octa-substituted phthalocyanines which are composed of a single isomer [35–38]. No attempt was made to separate the isomers of **4** and **5**.

The characteristic vibrations corresponding to CN and ethers groups (C–O–C) at 2226, 2228 and 2230 cm^{-1} and 1096, 1097, 1096 cm^{-1} were observed for **1**, **2** and **3** in the FT-IR spectra, respectively. Aromatic C–H peaks occurred above 3050 cm^{-1} for all the phthalonitriles. The ^{1}H NMR spectrum of the compounds **1**, **2** and **3** showed signals with δ ranging from 7.75 to 6.59, belonging to aromatic protons and 6.07 and 6.08 ppm belonging to aliphatic H integrating for a total of 8 protons for **1** and **2**, and 12 protons for **3** as expected. ^{13}C NMR spectral data were in good agreement with the proposed structure. The characteristic signals related to aromatic carbon atoms and dicyano carbon atoms about δ = 135 and 115 ppm, respectively for **1–3** supported the structures.

After conversion into zinc phthalocyanine derivations, the characteristic CN stretch at ~2230 cm^{-1} of phthalonitriles **1**, **2** and **3** disappeared in the FT-IR spectra, indicative of metallophthalocyanine formation. The characteristic vibrations corresponding to ether groups (C–O–C) were observed at 1093 (for **4**), 1090 cm^{-1} (for **5**) and 1097 cm^{-1} (for **6**) and aromatic C–H peaks were above 3000 cm^{-1} for the complexes.

The compounds were found to be pure by ^{1}H NMR with both the substituents and ring protons observed in their respective regions. The ^{1}H NMR spectra of tetra-substituted phthalocyanine derivatives (**4** and **5**) and octa-substituted derivative (**6**) were almost identical with that of the starting compounds **1**, **2** and **3** except for broadening and small shift. Complexes **4** and **5** showed complex patterns due to the mixed isomer character of these compounds. In the ^{1}H NMR spectrum of **4** and **5** the aromatic and Pc protons appear between 6.43 and 8.11 ppm (for **4**, integrating for 24H), 6.49 and 8.43 ppm (for **5**, integrating for 24H), and 6.39 and 7.16 ppm (for **6**, integrating for 32H). For all complexes aliphatic protons, were observed at about at 6 ppm, integrating for a total of 8 protons for **4** and **5** and 16 protons for complex **6**. In the mass spectrum of Zn phthalocyanines (**4–6**), the presence of molecular ion peaks at m/z 1123.6 $[M]^+$, 1123.6 $[M]^+$ and 1667.6 $[M]^+$, respectively, confirmed the proposed structures. Elemental analysis results also were consistent with the proposed structures of all compounds **1–6**.

3.2. Ground state electronic absorption spectra

The UV–Vis spectra of the phthalocyanine complexes exhibit characteristic Q- and B-bands. Two principle π–π^* transitions are seen for phthalocyanines: a Q-band (~700 nm, a π–π^* transition from the highest occupied molecular orbital (HOMO) to the lowest unoccupied molecular orbital (LUMO) of the complexes) and a B-band (~300–350 nm, a deeper π–π^* transition from the HOMO's (a_{1u} and a_{2u}) to the LUMO (e_g)) [39,40]. The Q-band absorptions in the UV–Vis absorption spectra of the phthalocyanines (**4**, **5** and **6**) were observed as a single high intensity band due to a π–π^* transition at 681, 697 and 680 nm in DMSO, 681, 694 and 680 nm in DCM and 677, 693 and 679 nm in toluene, respectively, Table 1 and Fig. 1.

In DMSO, toluene and DCM, the Q-band positions of **5** are red-shifted relative to those of **4** and **6**, with the greatest red-shifting being observed in DMSO. Non-peripheral substitution greatly influences the energy levels of molecular orbitals and hence the absorption spectrum, whereas peripheral substitution has a smaller effect on the Q-band position. In **5**, the (methylendioxy)-phenoxy substituents are closer to the ring, hence they bring about greater destabilization of the a_{1u} orbital (HOMO), and result in larger bathochromic shifts.

The consequence of the substitution with four [3,4-(methylendioxy)-phenoxy] is clearly observed by the high solubility of the Pcs **4**, **5** and **6** in organic solvents such as DCM, $CHCl_3$, THF, DMF, DMSO, toluene and acetone. Aggregation behavior of Pc is depicted

Table 1
Spectral parameters of **4**, **5** and **6** in DMSO and toluene.

Compound	Solvent	Q-band, λ_{max} (nm)	(log ε)	Excitation, λ_{Ex} (nm)	Emission, λ_{Em} (nm)	Stokes shift, Δ_{Stokes} (nm)
4	DMSO	681	5.43	682	693	12
	toluene	677	5.40	679	689	12
5	DMSO	697	5.40	699	712	15
	toluene	693	5.53	695	705	10
6	DMSO	680	5.24	682	692	12
	toluene	679	5.11	681	689	10

as a coplanar association of rings progressing from monomer to dimer and higher order complexes and it is dependent on concentration, nature of solvent and substituents, metal ions and temperature [41]. In this study, the aggregation behavior of the Pcs derivatives (**4**, **5** and **6**) were investigated in DMSO, DCM and toluene at different concentrations. As the concentration was increased, the intensity of absorption of the Q-band also increased and there was no new bands due to the aggregated species [42], Fig. 2. Complexes **4**, **5** and **6** did not show aggregation in these solvents. Though complex **6** did not show aggregation in toluene, chloroform, THF and DCM, it showed broad band around 627 nm because of aggregation just in DMSO (Fig 1). DMSO is known to prevent aggregation since it is strong coordinating solvent. However, it has been observed [43] before that aggregation occurs in DMSO and in less coordinating solvents for some MPc derivatives. Except for **6** in DMSO, Lambert–Beer law was obeyed for these compounds in the concentrations ranging from 2.0×10^{-6} to 1.0×10^{-5} mol dm^{-3} as given an example for **5** in toluene in Fig. 2.

3.3. Fluorescence spectra, and quantum yields

Fig. 3 shows the absorption, fluorescence excitation and emission spectra of **4**, **5** and **6** in DMSO. The excitation spectra were similar to absorption spectra and both were mirror images of the fluorescent spectra for **4** and **5**. For complex **6** the emission spectrum shows little less broadening when compared to excitation and absorption spectra, confirming that the aggregates do not fluoresce. The proximity of the wavelength of each component of the Q-band absorption to the Q-band maxima of the excitation spectra for both complexes suggest that the nuclear configurations of the ground and excited states are similar and not affected by excitation [44]. Fluorescence emission peaks were observed at: 693 nm for **4**, 712 nm for **5**, 692 nm for **6** in DMSO (Table 1). The Stokes' shifts range from 10 to 15 nm, which is usual for ZnPc derivatives [45].

The fluorescence quantum yield (Φ_F) values are different for **4**, **5** and **6** in DMSO, but the values are similar for the three complexes in toluene, with **4** showing larger values in both solvents, Table 2. Φ_F values in the two solvents demonstrate that fluorescence is influenced by the environment of the fluorescing molecule, e.g., solvent parameters. Solvent effects on Φ_F are usually interpreted in terms of the Förster–Hoffman equation [46] (Eq. (7)), which predicts a direct dependence of Φ_F on solvent viscosity.

$$\log \Phi_F = C + x \log \eta \quad (7)$$

The values of Φ_F in the two solvents are in conformity with the Förster–Hoffman equation for the complexes. The viscosities of DMSO and toluene are 1.99 and 0.59 cP, respectively.

Peripherally tetra-substituted complex (**4**) shows the largest (Φ_F) value in DMSO compared to the other complexes. The octa-substituted complex (**6**) shows lowest Φ_F value in DMSO. The very low Φ_F value for **6** in DMSO can be explained by the aggregation tendencies of the molecules in this solvent. Aggregation reduces the likelihood of radiative deactivation (fluorescence) through dissipation of energy by the aggregates. Complex **6** showed larger quantum yield for internal conversion (Φ_{IC}, Table 2) in DMSO when compared to complexes **4** and **5**, most likely due to aggregation.

3.4. Triplet quantum, yields and lifetimes

Triplet quantum yield (Φ_T) represents the fraction of absorbing molecules that undergo intersystem crossing to the metastable triplet excited state. Therefore, factors which induce spin–orbit coupling will certainly populate the triplet excited state. Transient spectrum for complex **4** in DMSO as shown in Fig. 4, and shows a maximum at 490 nm, hence triplet lifetimes and yields were determined at this wavelength. Fig. 5 displays the triplet decay curves of the complexes (using complex **6** in toluene as an example). The triplet life time for **4** (210 μs), **5** (210 μs) and **6** (190 μs) in DMSO and of 150 (**4**), 140 (**5**) and 180 μs (**6**) in toluene are lower than for unsubstituted ZnPc (350 μs) in DMSO and (330 μs) in toluene [47] respectively. This suggests that the [3,4-(methylendioxy)-phenoxy] substituents quench the triplet state. The τ_T values are higher in DMSO for all complexes. The reason for the large difference in value (going from DMSO to toluene) is not clear, but could partly be ascribed to the higher viscosity of DMSO (1.99 cP) than toluene (0.58 cP). In high viscocity solvents, translational and rotational motions are reduced, thereby reducing the likelihood of non-radiative deactivation of the excited singlet state via internal conversion.

The triplet quantum yields (Φ_T) for substituted complexes (**4**, **5** and **6**) in toluene are high compared to ZnPc standard in toluene (Φ_T = 0.65 for ZnPc). The high values of Φ_T in toluene suggest efficient intersystem crossing (ISC) in the presence of the substituents for substituted complexes (**4**, **5** and **6**). Complex **6** showed low Φ_T value in DMSO due to the aggregation in this solvent.

3.5. Photochemical properties

3.5.1. Singlet oxygen quantum yields

Singlet oxygen quantum yield Φ_Δ is a measure of singlet oxygen generation and the Φ_Δ values were obtained using Eq. (5). Singlet oxygen quantum yields were studied in DMSO and toluene using a chemical method (1,3-diphenylisobenzofuran, DPBF). Fig. 6 shows spectral changes observed during photolysis of complex **4** in toluene in the presence of DPBF. The disappearance of DPBF was monitored using UV–Vis spectroscopy. There were no changes in the Q-band intensities during the Φ_Δ determinations, confirming that complexes are not degraded during singlet oxygen studies [48]. The Φ_Δ values of three complexes were higher in toluene than in DMSO, corresponding to high Φ_T values in this solvent. The Φ_Δ values for **4**, **5** and **6** (0.80, 0.74 and 0.65 in toluene and 0.48, 0.43 and 0.22 in DMSO, respectively) are lower when compared to unsubtituted ZnPc in DMSO (0.67 [33]) and higher in toluene (0.58 [32]). Complex **6** has the lowest the value of Φ_Δ in DMSO (0.22) due to aggregation.

The magnitude of the S_Δ (=Φ_Δ/Φ_T) represents the efficiency of quenching of the triplet excited state by singlet oxygen. Compound

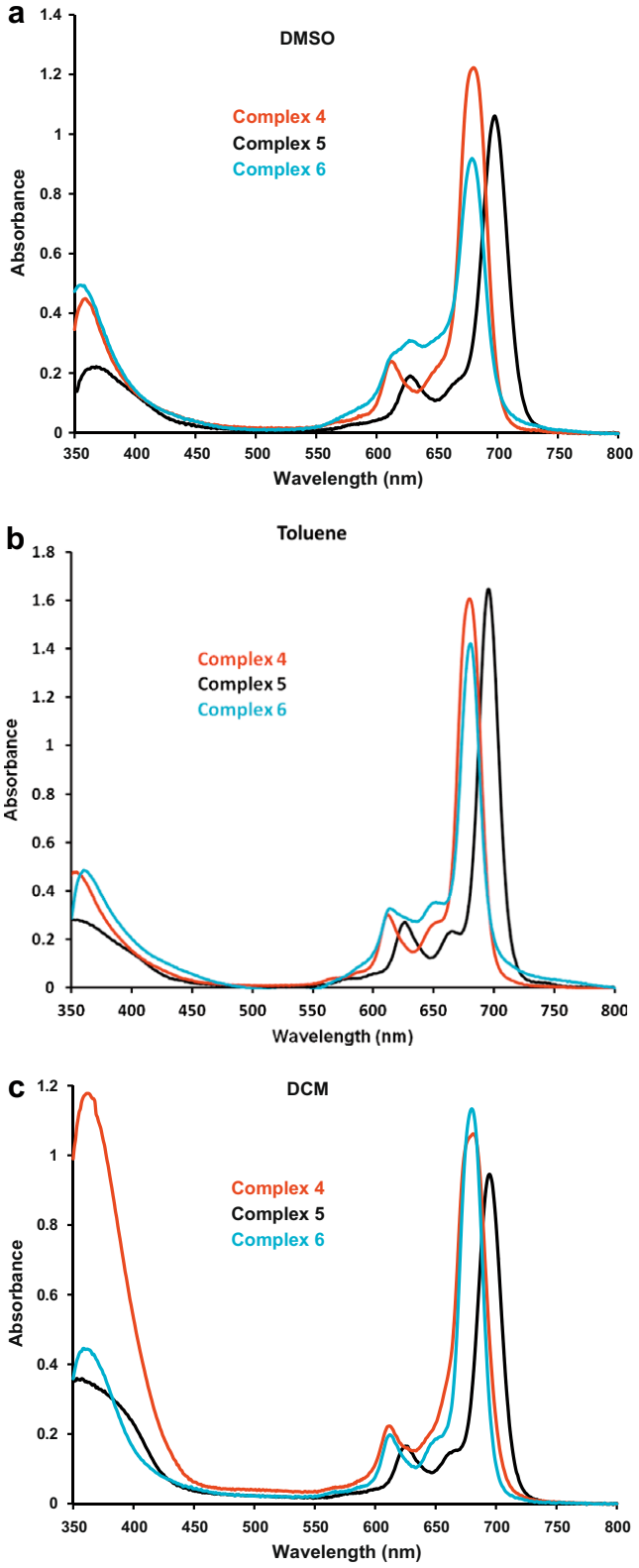


Fig. 1. UV–Vis absorption spectra of **4**, **5** and **6** in DMSO (a), concentration = 4×10^{-6} mol dm^{-3}; toluene (b), concentration = 4×10^{-6} mol dm^{-3} for **4** and **5**, 10×10^{-6} mol dm^{-3} for **6**; DCM (c), concentration = 4×10^{-6} mol dm^{-3}.

4, **5** and **6** displayed S_Δ of near unity in toluene and DMSO. However, complex **6** showed very low value in DMSO due to aggregation.

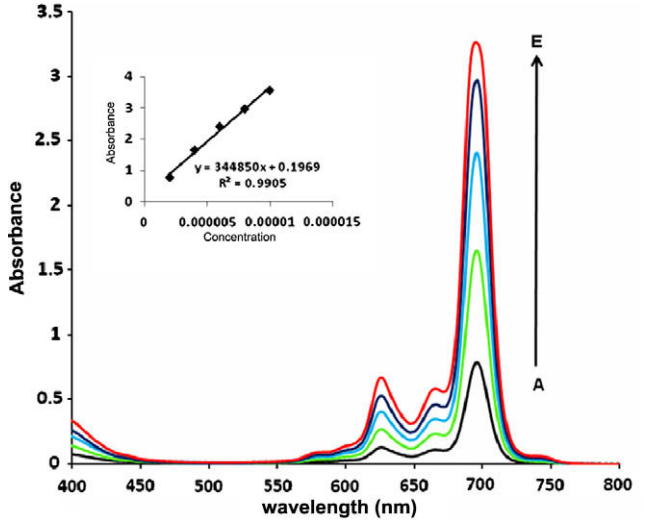


Fig. 2. Absorption spectra of **5** in toluene at different concentration: (A) 2×10^{-6}, (B) 4×10^{-6}, (C) 6×10^{-6}, (D) 8×10^{-6}, (E) 10×10^{-6} mol dm^{-3}.

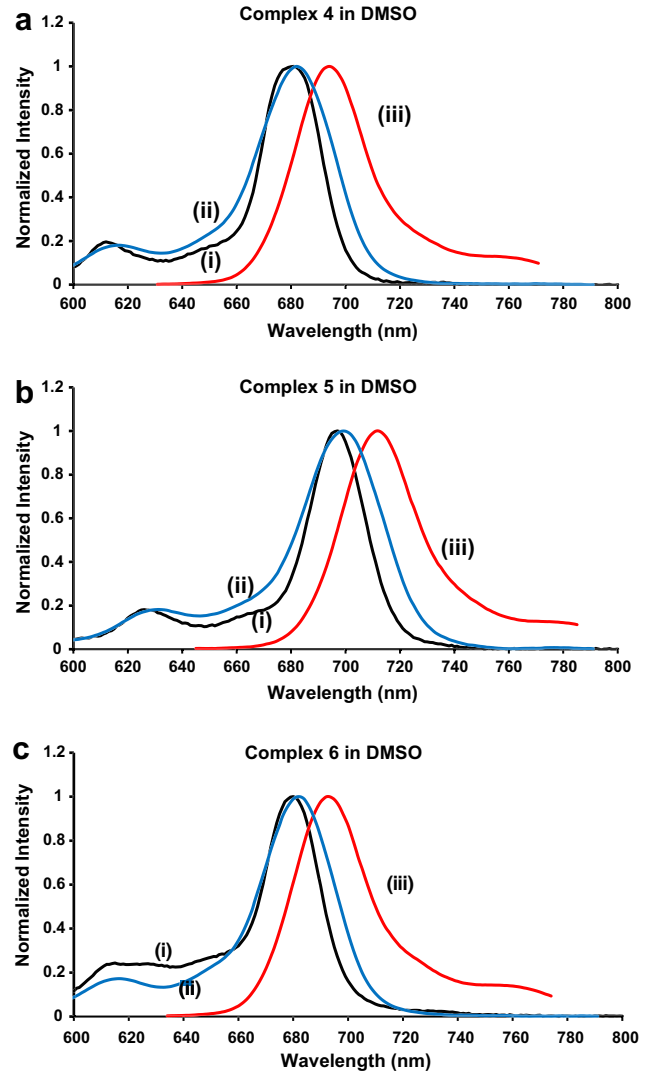


Fig. 3. Absorption (i), excitation (ii) and emission (iii) spectra of the compounds **4** (a), **5** (b), and **6** (c) in DMSO. Excitation wavelength = 682 nm for (**4**) 699 nm for (**5**) and 682 nm for (**6**) in DMSO.

Table 2
Photophysical and photochemical properties of **4**, **5** and **6** in DMSO and toluene.

Compound	Solvent	Φ_F	τ_T	Φ_T	Φ_{IC}	Φ_d (10^6)	Φ_Δ	S_Δ
4	DMSO	0.18	210	0.66	0.16	1.20	0.48	0.80
	toluene	0.06	150	0.85	0.09	0.83	0.80	0.94
5	DMSO	0.13	210	0.59	0.28	2.00	0.43	0.73
	toluene	0.05	140	0.79	0.16	0.72	0.74	0.89
6	DMSO	0.10	190	0.55	0.35	8.53	0.22	0.26
	toluene	0.05	180	0.73	0.22	0.98	0.65	0.78

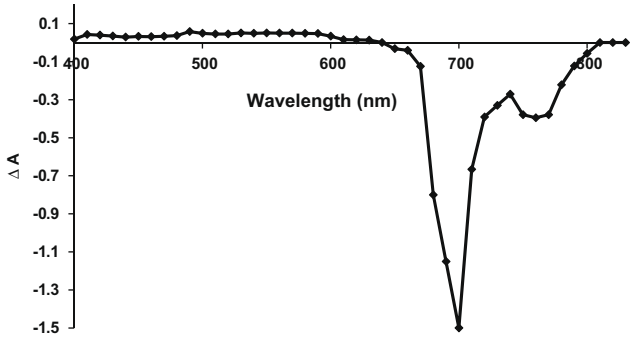


Fig. 4. Transient difference spectrum of complex **4** in DMSO.

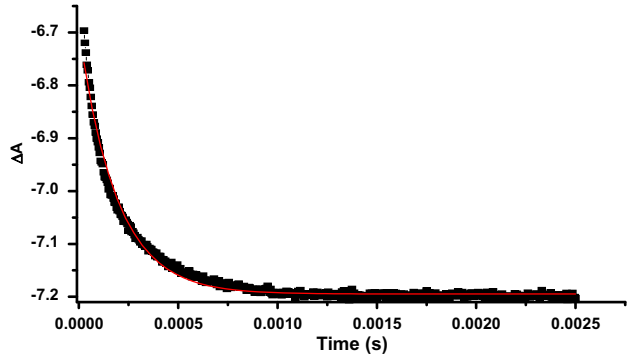


Fig. 5. Mono-exponential triplet decay profile for complex **6** in toluene.

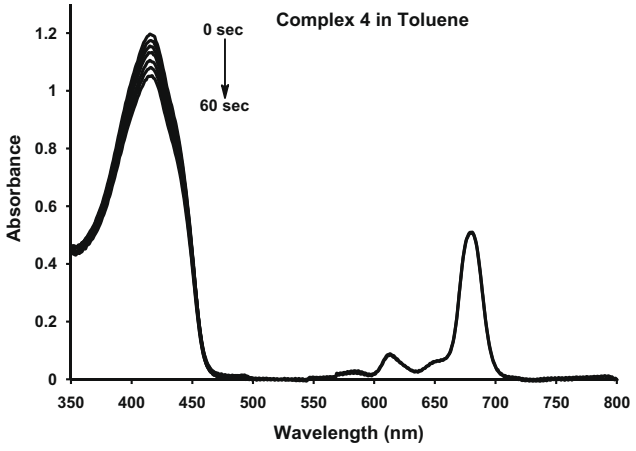


Fig. 6. A typical spectrum for the determination of singlet oxygen quantum yield. This figure was for complex **4** in toluene at a concentration 4×10^{-6} mol dm^{-3}.

3.5.2. Photodegradation quantum yields

Photodegradation is a process where a phthalocyanine is degraded under light irradiation. It can be used to determinate MPcs stability and this is especially important for those molecules intented for use as photocatalysts. The photobleaching stabilities of complexes **4**, **5** and **6** were determined in DMSO and toluene by monitoring the decrease in the intensity of the Q-band under irradiation with increasing time. The photodegradation quantum yield (Φ_d) values for the complexes are listed in Table 2 and are of the order of 10^{-6}. These values show that the molecules are of high stability in two solvents used. Stable ZnPc molecules show values as low as 10^{-6} and for unstable molecules, values of the order 10^{-3} have been reported [49]. Photobleaching quantum yields for the complexes were smaller in toluene than in DMSO, indicating that they are more stable in toluene than in DMSO. This could be due to the high singlet oxygen quantum yields in toluene. Since photobleaching is initiated by singlet oxygen attack. The order of stability among the substituted complexes was **4** > **5** > **6** in DMSO and **5** > **4** > **6** in toluene.

4. Conclusion

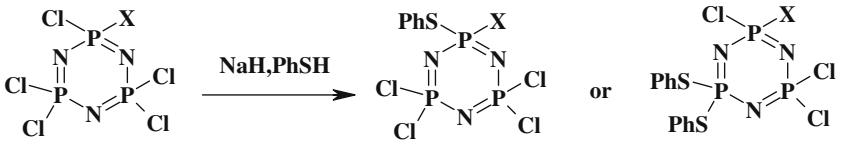
In this study, the syntheses, spectral and photophysicochemical properties of soluble peripheral and non-peripheral tetrakis- and octakis [3,4-(methylendioxy)-phenoxy]-substituted zinc phthalocyanines (**4**, **5** and **6**), respectively are discussed. The complexes have good solubility and are mainly monomeric in solution. The introduction of [3,4-(methylendioxy)-phenoxy on the ring results in high triplet quantum yields (ranging from 0.55 to 0.85 in DMSO and toluene). All complexes showed similar and typical fluorescence quantum yields for MPcs in DMSO. Complex **6** has a low triplet quantum yield (0.65) and singlet quantum yield values (0.22) in DMSO due to aggregation. Triplet lifetimes are higher in DMSO than in toluene for substituted complexes (**4**, **5** and **6**). The tetra-substituted complexes (**4** and **5**) have good singlet oxygen quantum yields especially complex **4** which has the highest value in both solvents. The Pcs reported in this study can be applied as efficient candidates for solution studies requiring monomeric form of this material. The singlet oxygen quantum yields, which give indication of the potential of the complexes as photosensitizers in applications where singlet oxygen is required (Type II mechanism) ranged from 0.22 to 0.80. Thus, these complexes show potential as Type II photosensitizers and can be used in photodynamic therapy.

Acknowledgements

This work was supported by the Department of Science and Technology (DST) and National Research Foundation (NRF), South Africa through DST/NRF South African Research Chairs Initiative for Professor of Medicinal Chemistry and Nanotechnology as well as Rhodes University.

References

[1] C.C. Leznoff, A.B.P. Lever (Eds.), Phthalocyanines Properties and Applications, vols. 1–4, VCH, New York, 1989–1996.
[2] J. Jiang, K. Kasuga, D.P. Arnold, in: H.S. Nalwa (Ed.), Supramolecular Photosensitive and Electroactive Materials, Academic Press, San Diego, CA, 2001, pp. 188–189.
[3] M. Calvete, G.Y. Yang, M. Hanack, Synth. Met. 141 (2004) 231.
[4] M. Kandaz, S.L.J. Michel, B.M. Hoffman, J Porphyr. Phthalocya. 7 (2003) 700.
[5] P. Tau, T. Nyokong, Polyhedron 25 (2006) 1802.
[6] J.J. Simon, H.J. Andre, Molecular Semiconductors, Springer, Berlin, 1985.
[7] H. Ali, J.E. van Lier, Chem. Rev. 99 (1999) 2379.
[8] N.B. McKeown, Phthalocyanine Materials, Cambridge University Press, Cambridge, 1998.
[9] (a) K. Katrin, A. Nihal, C. Tracy, B. David, M. Hasan, Cancer Res. 60 (2000) 5984; (b) D. Phillips, Pure Appl. Chem. 67 (1995) 117; (c) R. Bonnett, Chem. Soc. Rev. 24 (1995) 19.
[10] S.B. Brown, T.G. Truscott, Chem. Br. 29 (1993) 955.
[11] I. Rosental, E. Ben-Hur, in: C.C. Leznoff, A.B.P. Lever (Eds.), Phthalocyanines Properties and Applications, vol. 1, VCH, NewYork, 1989 (Chapter 6).
[12] I. Seotsanyana-Mokhosi, T. Kresfelder, H. Abrahamse, T. Nyokong, J. Photochem. Photobiol. B: Biol. 83 (2006) 55.
[13] I. Rozental, Photochem. Photobiol. 53 (1991) 859.
[14] P. Zimcik, M. Miletin, J. Ponec, M. Kostka, Z. Fiedler, J. Photochem. Photobiol. A: Chem. 55 (2003) 127.
[15] S.V. Kudrevich, A. Hasrat, J.E. van Lier, J. Chem. Soc., PerkinTrans. 1 (1994) 2767.
[16] C.M. Allen, W.M. Sharman, J.E. van Lier, J. Porphyr. Phthalocya. 5 (2001) 161.
[17] E.A. Lukyanets, J. Porphyr. Phthalocya. 3 (1999) 424.
[18] A. Segalla, C.D. Borsarelli, S.E. Braslavsky, J.D. Spikes, G. Roncucci, D. Dei, G. Chiti, G. Jori, E. Reddi, Photochem. Photobiol. Sci. 1 (2002) 641.
[19] J.D. Huang, W.P. Fong, E.Y.M. Chan, M.T.M. Choi, W.K. Chan, M.C. Chan, D.K.P. Ng, Tetrahedron Lett. 44 (2003) 8029.
[20] W. Liu, T.J. Jensen, F.R. Fronczek, R.P. Hammer, K.M. Smith, M.G.H. Vicente, J. Med. Chem. 48 (2005) 1033.
[21] B. Ertem, A. Bilgin, Y. Gök, H. Kantekin, Dye Pigment 77 (2008) 537.
[22] A. Bilgin, B. Ertem, Y. Gök, Eur. J. Inorg. Chem. (2007) 1703.
[23] A. Bilgin, Y. Gök, Supramol. Chem. 18 (2006) 491.
[24] S. Fery-Forgues, D. Lavabre, J. Chem. Ed. 76 (1999) 1260.
[25] J. Fu, X.Y. Li, D.K.P. Ng, C. Wu, Langmuir 18 (2002) 3843.
[26] A. Ogunsipe, J.Y. Chen, T. Nyokong, New J. Chem. 7 (2004) 822.
[27] P. Kubát, J. Mosinger, J. Photochem. Photobiol. A: Chem. 96 (1996) 93.
[28] T.H. Tran-Thi, C. Desforge, C.C. Thiec, J. Phys. Chem. 93 (1989) 1226.
[29] S.M. Bishop, A. Beeby, A.W. Parker, M.S.C. Foley, D. Phillips, J. Photochem. Photobiol. A: Chem. 90 (1995) 39.
[30] P. Tau, A.O. Ogunsipe, S. Maree, M.D. Maree, T. Nyokong, J. Porphyr. Phthalocya. 7 (2003) 439.
[31] I. Seotsanyana-Mokhosi, N. Kutnetsova, T. Nyokong, J. Photochem. Photobiol. A: Chem. 140 (2001) 215.
[32] A. Ogunsipe, D. Maree, T. Nyokong, J. Mol. Struct. 650 (2003) 131.
[33] N. Kuznetsova, N. Gretsova, E. Kalmykova, E. Makarova, S. Dashkevich, V. Negrimovskii, O. Kaliya, E. Luk'yanets, Russ. J. Gen. Chem. 70 (2000) 133.
[34] W. Spiller, H. Kliesch, D. Wöhrle, S. Hackbarth, B. Roder, G. Schnurpfeil, J. Porphyr. Phthalocya. 2 (1998) 145.
[35] M. Kandaz, I. Yılmaz, Ö. Bekaroglu, Polyhedron 19 (2000) 115.
[36] M.N. Yarasir, M. Kandaz, A. Koca, B. Salih, Polyhedron 26 (2007) 1139.
[37] S. Wei, D. Huang, L. Li, Q. Meng, Dye Pigment 56 (2003) 1.
[38] M.N. Yarasir, M. Kandaz, A. Koca, B. Salih, J. Porphyr. Phthalocya. 10 (2006) 1022.
[39] M. Özer, A. Altındal, A.R. Özkaya, M. Bulut, B. Salih, Ö. Bekaroglu, Polyhedron 25 (2006) 3593.
[40] M. Kandaz, M.N. Yarasır, A. Koca, Ö. Bekaroglu, Polyhedron 21 (2002) 255.
[41] H. Enkelkamp, R.J.M. Nolte, J. Porphyr. Phthalocya. 4 (2000) 454.
[42] H.S. Nalwa, J.S. Shirk, in: C.C. Leznoff, A.B.P. Lever (Eds.), Phthalocyanines: Properties and Applications, vol. 4, VCH Publishers, New York, 1996, pp. 179–181.
[43] P. Tau, T. Nyokong, Dalton Trans. (2006) 4482.
[44] M. Durmuş, T. Nyokong, Inorg. Chem. Commun. 10 (2007) 332.
[45] M.O. Senge, M.W. Renner, W.W. Kalisch, J. Fajer, J. Chem. Soc., Dalton Trans. (2000) 381.
[46] T. Förster, G. Hoffmann, Z. Phys. Chem. 75 (1971) 63.
[47] T. Nyokong, Coord. Chem. Rev. 251 (2007) 1707.
[48] M. Durmuş, T. Nyokong, Spectrochim. Acta A 69 (2008) 1170.
[49] S. Maree, T. Nyokong, J. Porphyr. Phthalocya. 5 (2001) 782.



X		X		X	
(2)	$NHPr^i$	(3)	$NHPr^i$	(9)	$N(Me)_2$
(4)	NHPh	(5)	NHPh	(11)	$N(CH_2Ph)_2$
(6)	$NHBu^t$	(7)	$NHBu^t$	(13)	$N(C_4H_8)$
(8)	$N(Me)_2$				
(10)	$N(CH_2Ph)_2$				
(12)	$N(C_4H_8)$				

Scheme 1.

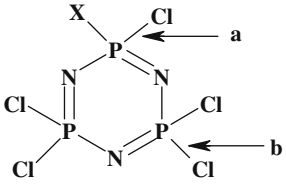
2. Result and discussion

*2.1. Syntheses and characterisations of cyclotriphosphazatrienes **3**, **5**, **7**, **9**, **11**, and **13***

It is investigated firstly the reactions of primary amino-substituted cyclotriphosphazenes **(2**, **4**, **6)** with thiophenol in the presence of NaH in THF at room temperature for 24 h and obtained novel cyclotriphosphazene derivatives **(3**, **5**, **7)** in this work. The chloro atom in P–Cl bond (designated as *a* in Fig. 1) has replaced with a thiolate group probably by a proton abstraction-chloride ion elimination reaction mechanism at these reactions according to ^{31}P NMR (Scheme 2). A dissociative route, the conjugate base mechanism, S_N1 (CB), shown in Scheme 2, is believed to be operative in the formation of geminal isomers [1]. In this process, a base abstracts a proton from the mono primary aminophosphazene. This is followed by loss of chloride ion leading to a coordinatively unsaturated transition state. Attack by thiophenol on the phosphoranimine leads to the observed geminally substituted product [1,22].

Furthermore, an understanding of why the reaction of cyclotriphosphazenes with thiophenol resulted in substitution at the P–Cl bond (*a* in Fig. 1) rather than geminal substitution at PCl_2 group is provided from the crystal structures of **1**, **2, 6** [23–25]. Table 1 shows that the P–Cl bond in the PNHCl group is longer than the PCl_2 bonds owing to the electron-releasing capacity of the –NHR group. Therefore, P–Cl bond (*a*) is more reactive to nucleophilic substitution with thiophenol than those of the PCl_2 groups [1,18a,20].

Secondly, it is investigated the reactions of secondary amino-substituted cyclotriphosphazenes **(8**, **10**, **12)** with thiophenol at the same conditions of **2**, **4**, **6** and obtained new cyclotriphosphazene derivatives **(9**,**11**, **13)** in present work. It is shown that electron-releasing groups have a greater effect on the lengthening of PNCl bonds (e.g. P–Cl: 2.041 Å for **10** in Table 1). However, steric effects are shown to dominant in the reaction of thiophenol with **10**. For sterically crowded amines (dibenzylamine, dimethylamine) and strongly electron donating amine (pyrrolidine), the pathway lead to nongeminal product [1]. The thiophenol substitution of untouched PCl_2 group may be performed via an S_N2 mechanism (Scheme 3). This pathway is similar in the reactions of secondary

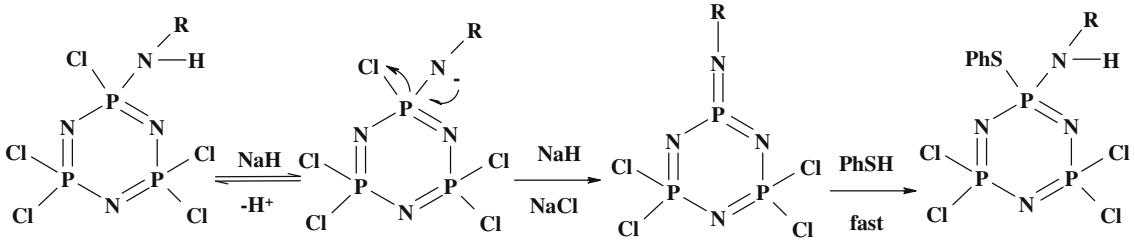


X	
(1)	Cl
(2)	$NHPr^i$
(6)	$NHBu^t$
(10)	$N[(CH_2)Ph_2]$

Fig. 1. Designation of P–Cl bond lengths for **1**, **2**, **6** and **10**.

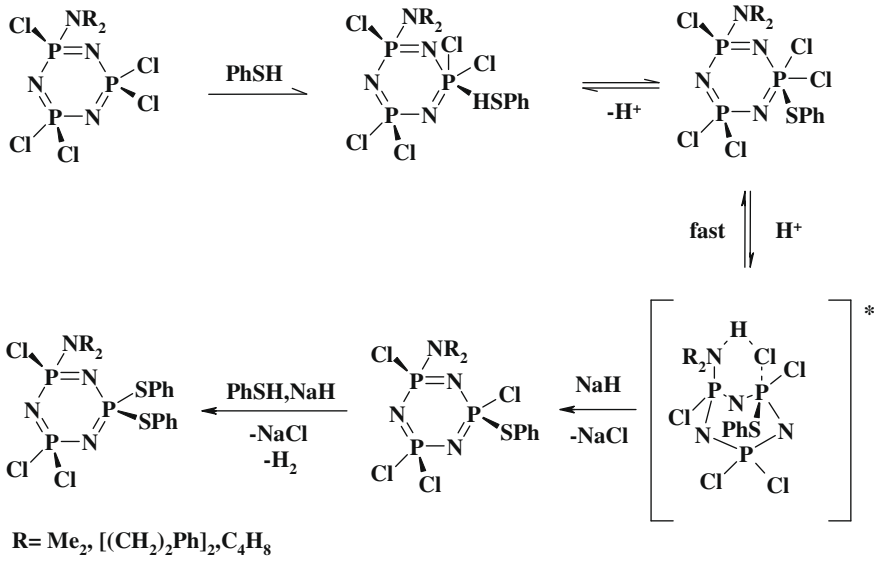
Table 1
P–Cl bond lengths for structures of **1**, **2**, **6**, and **10**.

Compound	a (Å)	b (Å)	Reference
1		1.984 (2)	[23]
2	2.010 (4)	1.983 (4)	[24]
6	2.017 (1)	1.991 (1)	[25]
10	2.041 (2)	1.998 (3)	[19b]



R= Pr^i, Bu^t, Ph

Scheme 2.



Scheme 3.

Table 2
$^{31}P\{^{1}H\}$ NMR parameters of **2–13**.

Compound	$\delta(^{31}P$ NMR) (ppm)						$^{2}J_{(PP)}$ (Hz)				
	PCl_2	$P(SPh)_2$	P(NHR)Cl	P(NR)Cl	P(NHR)SPh	R	1,2	1,3	1,4	2,4	1,5
	1	2	3	4	5						
2[a]	22.2		17.4			Pr^i		47.6			
3[b]	21.0				29.1	Pr^i					21.9
4[c]	22.4		12.8			Ph		49.4			
5[b]	21.4				24.3	Ph					26.0
6[c]	21.2		13.5			Bu^t		47.6			
7[d]	20.4				26.0	Bu^t					21.7
8[d]	22.1			23.9		$(Me)_2$			47.9		
9[e]	21.5	47.4		25.9		$(Me)_2$			43.4		
10[a]	21.7			20.8		$(CH_2Ph)_2$			36.8		
11[f]	20.6	47.6		22.3		$(CH_2Ph)_2$			47.5	5.6	
12[a]	21.9		19.9			C_4H_8		45.7			
13[f,*]	26.0	51.6		26.8		C_4H_8			42.4	3.0	

[a] A_2B spin system.
[b] AX_2 spin system.
[c] A_2X spin system.
[d] AB_2 spin system.
[e] AMX spin system.
[f] AXX′ spin system.
[*] In Toluene-d_8 solvent.

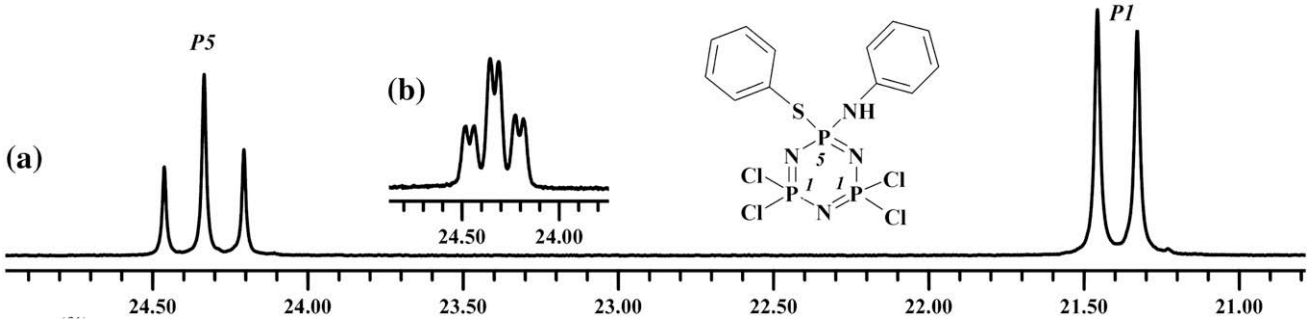


Fig. 2. (a) $^{31}P\{^{1}H\}$ NMR spectrum of **5**, and (b) expanded proton coupled ^{31}P NMR signals of >P(NHPh)(SPh) group, respectively.

amines with $N_3P_3Cl_6$ [19]. The nucleophilic attack of thiophenol seems to proceed via the S_N1 type [1,15]. These pathways are seen that the respective sulfur bases, like sodium thiophenol and dimercaptoethylene, prefer geminal substitution of two chlorine atoms at non macrocyclic phosphorus atom (in PCl_2 group) of cyclotriphosphazene containing 16-membered crown ether ring [26].

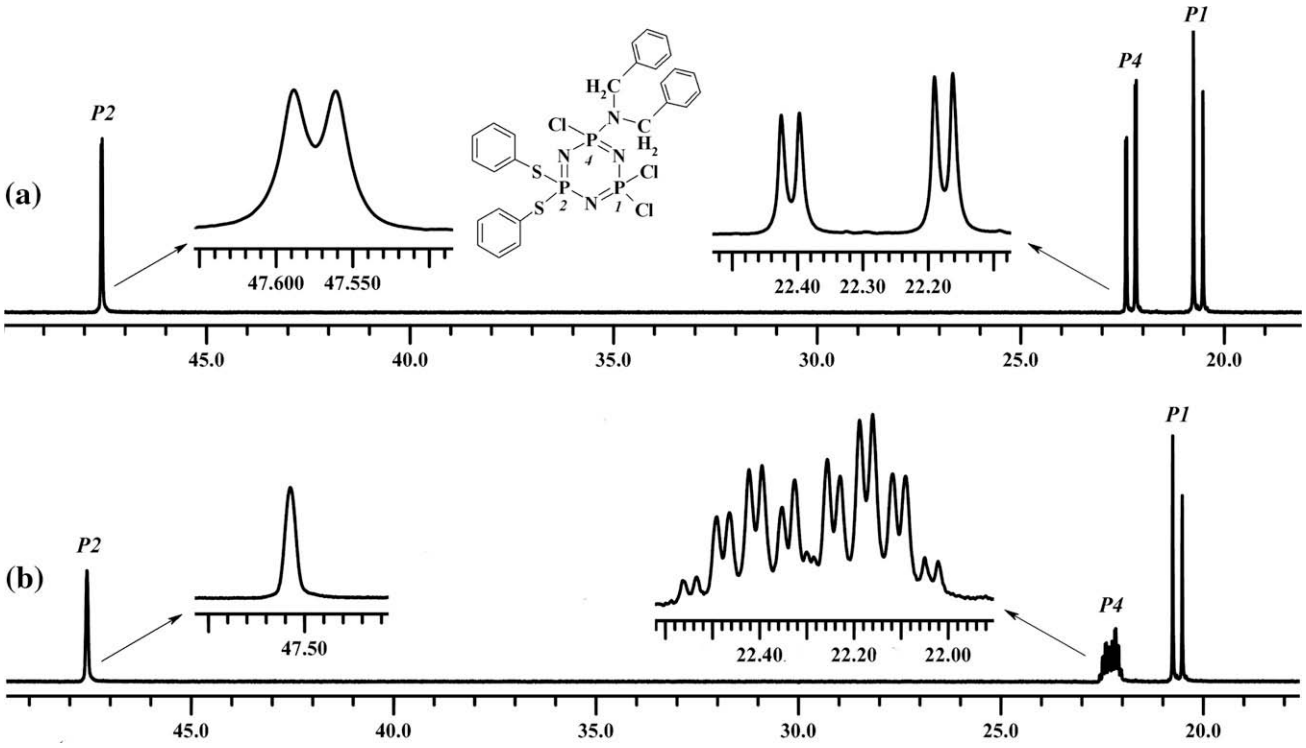


Fig. 3. (a) ^{31}P $\{^{1}H\}$, and (b) proton coupled ^{31}P NMR spectra of **11**, respectively.

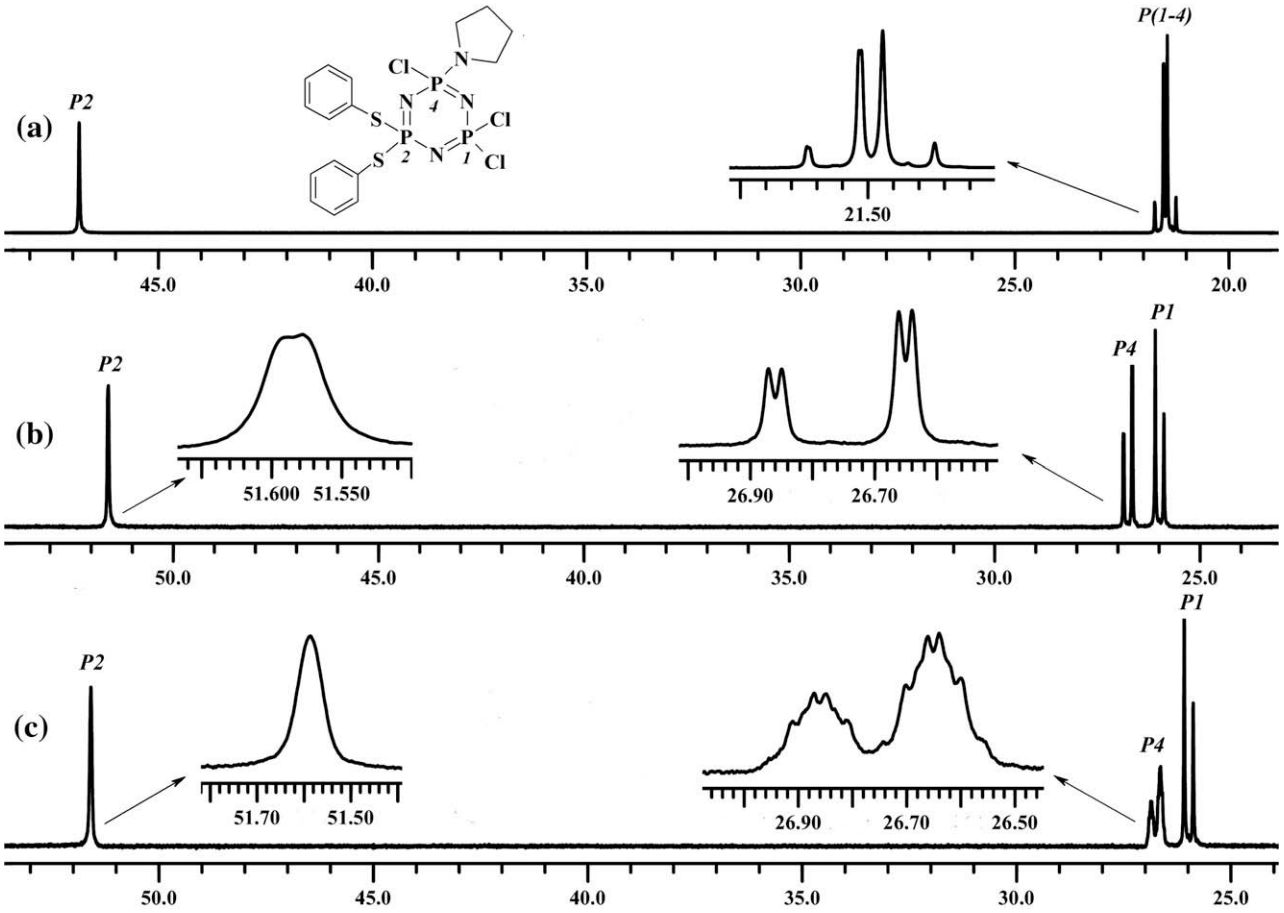


Fig. 4. (a) ^{31}P $\{^{1}H\}$ NMR spectrum of **13** in $CDCl_3$, (b) ^{31}P $\{^{1}H\}$NMR spectrum of **13** in toluene-d_8, and (c) proton coupled ^{31}P NMR signals of **13** in toluene-d_8, respectively.

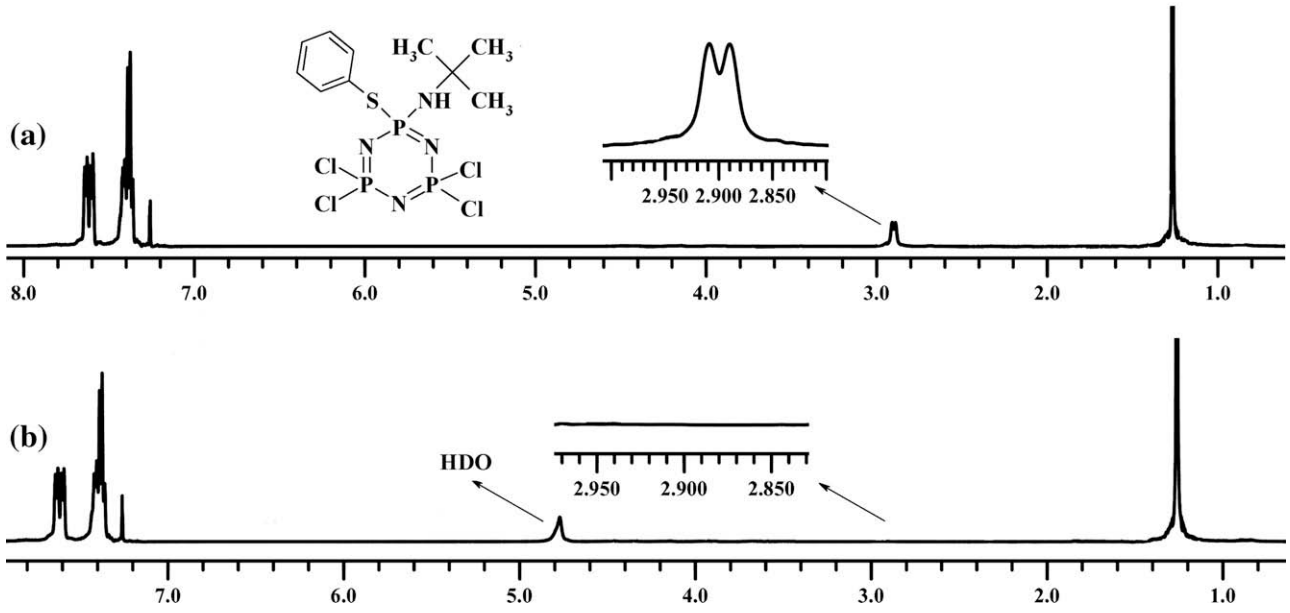


Fig. 5. (a) ^{1}H NMR spectrum of **7** in $CDCl_3$, and (b) the ^{1}H NMR spectrum of **7** after treatment with D_2O, respectively.

Table 3
Crystallographic data for **5** and **13**.

	5	**13**
Empirical formula	$C_{12}H_{11}Cl_4N_4P_3S$	$C_{16}H_{18}Cl_3N_4P_3S_2$
Formula weight	478.02	529.72
Crystal system	monoclinic	monoclinic
Space group	$P2_1/n$	$P2_1/n$
a (Å)	10.2628(2)	8.7534(2)
b (Å)	9.9822(2)	24.9491(4)
c (Å)	18.7566(3)	10.4801(3)
α (°)	90.00	90.00
β (°)	104.635(2)	106.188(2)
γ (°)	90.00	90.00
V (Å^3)	1859.18(6)	2198.00(9)
Z	4	4
μ (cm^{-1}) (Mo Kα)	1.011	0.837
ρ (calc.) (g cm^{-1})	1.708	1.601
Number of reflections collected	15737	35846
Number of reflections total	4596	5519
Number of reflections unique	4151	5130
R_{int} (merging R value)	0.0202	0.0227
$2\theta_{max}$ (°)	56.84	56.88
T_{min}/T_{max}	0.659/0.705	0.6699/0.8504
Number of parameters	221	253
R [$F^2 > 2\sigma(F^2)$]	0.0233	0.0255
wR	0.0586	0.0606

Table 4
The selected bond lengths (Å) and angles (°) for **5** and **13**.

	5	**13**
P1–N1	1.6037(12)	1.6136(12)
P1–N3	1.6012(12)	1.5921(12)
P2–N1	1.5761(12)	1.5739(12)
P2–N2	1.5860(13)	1.5690(13)
P3–N2	1.5832(13)	1.5934(13)
P3–N3	1.5647(12)	1.5854(12)
N1–P1–N3	116.39(16)	115.80(6)
N1–P2–N2	119.45(7)	120.08(7)
N2–P3–N3	119.43(7)	119.17(7)
P1–N1–P2	118.15(7)	121.86(8)
P2–N2–P3	118.79(8)	119.19(8)
P1–N3–P3	121.66(8)	122.18(8)

The structures of **3**, **5**, **7**, **9**, **11**, **13** are defined by MS, elemental analysis, ^{1}H and ^{31}P NMR spectroscopies. All the results are consistent with the proposed structures as shown in Scheme 1. The ^{31}P{^{1}H} NMR data for **2–13** are given Table 2.

The ^{31}P{^{1}H} NMR spectra of **3**, **5**, **7** show that the two different phosphorus nuclei are non-equivalent (analysed as AX_2 or AB_2, as appropriate) with characteristic chemical shifts for the >PCl_2 of 20.4–21.0 ppm and >P–(NHR)SPh of 24.3–29.1 ppm moieties in these compounds (Table 2). ^{31}P NMR spectra of **9**, **11**, **13** analysed as AMX or AXX′ spin systems due to three different phosphorus environment within the molecules. It is investigated in detail the ^{31}P NMR spectra of some compounds (e.g. **5**, **11**, **13**) in this work.

The ^{31}P {^{1}H} NMR spectrum (AX_2 spin system) of **5** consisting of one triplet of >P(NHPh)(SPh)(δ = 24.3 ppm) and one doublet of >PCl_2 (δ = 21.4 ppm) groups is shown in Fig. 2a. The expanded proton coupled ^{31}P NMR signals as doublets of triplet of >P(NHPh)(SPh) group are seen at ca. 24.0–24.5 ppm in Fig. 2b, and this signals are emerged from coupling by other phosphorus atoms and proton of NH group.

The ^{31}P {^{1}H} NMR spectrum (AXX′ spin system) of **11** consisting of one doublet of >P[$(CH_2)_2Ph_2$] at ca. 22.3 ppm, one doublet of >PCl_2 at ca. 20.6 ppm and >$P(SPh)_2$ at ca. 47.6 is shown in Fig. 3a. The proton coupled ^{31}P NMR signals as multiplet of >P[$(CH_2)_2Ph_2$] are observed at ca. 22.3 ppm which are coupling from other phosphorus atoms and CH_2 groups, the signals of >PCl_2 (δ = 20.6 ppm) and >$P(SPh)_2$ (δ = 47.6 ppm) groups remain unchanged in Fig. 3b.

The ^{31}P {^{1}H} NMR spectrum (AXX′ spin system) of **13** is shown in $CDCl_3$ in Fig. 4a. The chemical shifts(δ) and $^{2}J_{(PP)}$(Hz) of signals of >PCl_2 and >P(NR)Cl groups could not be analysed using this solvent. Therefore, ^{31}P{^{1}H} NMR spectrum is taken in toluene-d_8 (Fig. 4b). The doublet of >P[(NC_4H_8)Cl] group at ca. 26.8 ppm, one doublet of >PCl_2 at ca. 26.0 ppm, one doublet of >$P(SPh)_2$ at ca. 51.6 ppm, and multiplet of >P[(NC_4H_8)Cl] at ca. 26.5–26.9 ppm are presented in Fig. 4b and c, respectively.

^{1}H NMR spectrum (δ = 1.2 ppm (s, 9H, CH_3), δ = 2.9 ppm (d, H, NH), δ = 7.60–7.62 ppm (*m*-, *p*-, 3H, Ar–CH), δ = 7.4 ppm (*o*-, 2H, Ar–CH) of compound **7** is shown in Fig. 5a as an example of the proton spectroscopy. The ^{1}H NMR spectrum of **7** has been treated with D_2O to eliminate the N–H coupling (Fig. 5b).

Table 5
Hydrogen-bond geometries (Å, °) for **5** and **13**.

	D–H···A	D–H	H···A	D···A	D–H···A
5	C12–H12···N3	0.93	2.36	3.071(2)	133
	C4–H4···Cg3^{i}	0.93	2.89	3.698(2)	147
13	C9–H9···N2^{ii}	0.93	2.57	3.443(2)	156
	C4–H4···Cg4^{iii}	0.93	2.73	3.638(2)	165

Symmetry codes: (i) $x-½, ½-y, z-½$, (ii) $x+½, ½-y, z+½$, (iii) $x-1, y, z-1$, where Cg3 and Cg4 are centroids of rings (C7–C12) in compounds **5** and **13**.

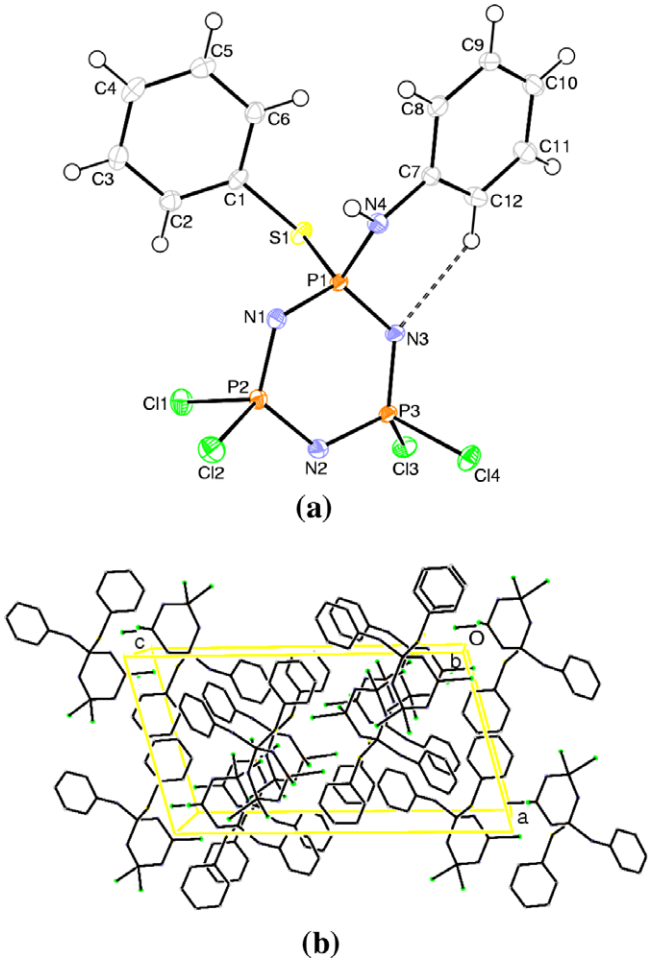


Fig. 6. (a) An ORTEP-3 [28] drawing of **5** with the atom-numbering scheme. Displacement ellipsoids are drawn at the 50% probability level, hydrogen bond is shown as dashed line, (b) a partial packing diagram of **5**, respectively.

2.2. X-ray crystallographic characterisation of *5* and *13*

The x-ray structural determinations of compounds **5** and **13** confirm the assignments of their structures from spectroscopic data. Crystallographic data are listed in Table 3. Selected bond lengths and angles are given in Table 4, and hydrogen bonds data are given in Table 5, respectively. The molecular structures and the packing diagrams of **5** and **13** along with the atom-numbering schemes are depicted in Figs. 6a and 7a, respectively. The phosphazene rings of **5** and **13** are not planar and are in flattened-boat forms [$\varphi_2 = -165.8(1)°$, $\theta_2 = 125.2(1)°$ and $\varphi_2 = -163.3(4)°$, $\theta_2 = 83.7(4)°$] having total puckering amplitudes Q_T of 0.706(1) (for **5**) and 0.149(1) (for **13**) [27].

In **5**, the six-membered aromatic rings (C1–C6) and (C7–C12) are oriented at a dihedral angle of 27.09(4)°. Intramolecular C–H···N hydrogen bond (Table 5) results in the formation of a six-membered ring (P1/N3/N4/C7/C12/H12) having twisted conformation. In the crystal structure, the molecules are elongated along the c axis and stacked along the b axis (Fig. 6b). There exists a C–H···π interaction (Table 5).

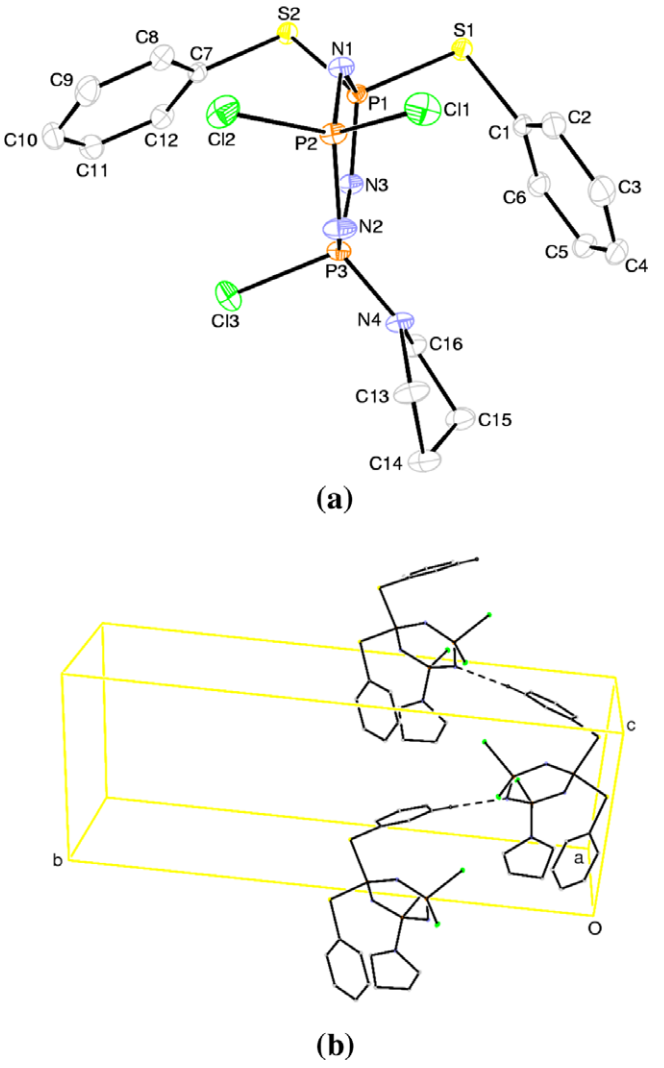


Fig. 7. (a) An ORTEP-3 [28] drawing of **13** with the atom-numbering scheme. Displacement ellipsoids are drawn at the 50% probability level, (b) a partial packing diagram of **13**, hydrogen bonds are shown as dashed lines, respectively.

In **13**, the six-membered aromatic rings (C1–C6) and (C7–C12) are oriented at a dihedral angle of 85.66(5)°, while the five-membered ring (N4/C13–C16) adopts envelope conformation with atom C15 displaced by 0.613(2) Å from the plane of the other ring atoms. In the crystal structure, intermolecular C–H···N hydrogen bonds (Table 5) link the molecules into chains along the *c* axis (Fig. 7b), in which they may be effective in the stabilisation of the structure. There also exists a C–H···π interaction (Table 5). In the phosphazene rings, the P–N bond lengths are in the ranges 1.5647(12)–1.6037(12) Å (for **5**) and 1.5690(13)–1.6136(12) Å (for **13**). The phosphazene rings P–N bonds generally show double-bond character (Table 4).

3. Conclusion

In this paper, six novel cyclotriphosphazatrienes **(3**, **5**, **7**, **9**, **11**, **13)** are synthesised and characterised. Mechanisms of **3**, **5**, **7** can be formed via a proton abstraction-chloride elimination and **9**, **11**, **13** may be constituted both the S_N2 and S_N1 reaction, respec-

tively with respect to our results and previous works e.g. [1,14,18,26]. These compounds can be also a promising candidate as a building block for optical materials [14b]. This original work is potentially very useful addition to the literature and may guide to some high-polymer works.

4. Experimental

4.1. General remarks

Hexachlorocyclotriphosphazene (a gift from the Shin Nisso Kako Co. Ltd.) was purified by fractional crystallisation from *n*-hexane. The following chemicals were obtained from Merck; THF (⩾99.0%), *n*-hexane (>96%), NaH (60% dispersion in mineral oil), dichloromethane (⩾99.0%), dimethylamine (40% aqueous solution), tert-butylamine (>99%), thiophenol (>98.0%), dibenzylamine (>95%), aniline (>95%), diethylether (>99.5%), petroleum ether (40–60 °C), acetonitrile (99%), C_4H_8NH (⩾99.0%), triethylamine (>98.0%), Na_2SO_4 (⩾99.0%). All solvents used in this work were purified by conventional methods. THF was distilled over a sodium–potassium alloy under an atmosphere of dry argon. Solvents ($CDCl_3$ and toluene-d_8) for NMR spectroscopy are obtained from Merck.

Elemental analyses were obtained using a Carlo Erba 1106 Instrument. Mass spectra were obtained by Bruker MicrOTOF LC/MS spectrometer using electrospray ionisation (ESI); ^{35}Cl values were used for calculated masses. Analytical Thin Layer Chromatography (TLC) was performed on silica gel (Merck, Kieselgel 60, 0.25 mm thickness) with F_{254} indicator. Column chromatography is performed on silica gel (Merck, Kieselgel 60, 70–230 mesh; for 3 g crude mixture, 100 g silica gel was used in a column of 3 cm in diameter and 60 cm in length). ^1H and ^{31}P NMR spectra were recorded in $CDCl_3$ solutions on a Varian INOVA 500 MHz spectrometer using TMS as an internal reference for ^1H NMR and 85% H_3PO_4 as an external reference for ^{31}P.

4.2. X-ray crystallography

Colourless crystals of **5** and **13** were re-crystallised from dichloromethane–petroleum ether (1:1) and dichloromethane-*n*-hexane (1:1) at room temperature, respectively. Crystallographic data were recorded on a Bruker Kappa APEXII CCD area-detector diffractometer using Mo Kα radiation (λ = 0.71073 Å) at T = 100(2) K. Absorption corrections by multi-scan have been applied [29]. Structures were solved by direct methods and refined by full-matrix least squares against F^2 using all data [30]. All non-H atoms were refined anisotropically. In compound **5**, only the H atom of NH group was located in a difference synthesis and refined isotropically [N–H = 0.861(15) Å, U_{iso}(H) = 0.026(5) Å^2]. The remaining H atom positions were calculated geometrically at distances of 0.93 Å (CH) and 0.97 Å (CH_2) from the parent C atoms; a riding model was used during the refinement process and the U_{iso}(H) values are constrained to be $1.2U_{eq}$(carrier atom).

4.3. Synthesis and reactions

2-Isopropilamino-2,4,4,6,6-pentachlorocyclotriphosphazatriene **(2)** was prepared as described by Das et al. [31]. Compound **6** was prepared as described by Bartlett et al. [25]. Compounds **4**, **8**, **10** and **12** were prepared as in the literatures [32–35], respectively.

4.3.1. Synthesis of compound *3*

A solution of NaH (60% oil suspension, 0.02 g, 1.35 mmol) in 10 mL dry THF was added dropwise to a stirred solution of thiophenol (0.15 g, 1.35 mmol) in 5 mL dry THF under atmosphere of argon in a 100 mL three-necked round bottomed flask. Then, **2** (0.35 g, 1.35 mmol) in 20 mL dry THF was added. The reaction mixture was stirred under an atmosphere of argon at room temperature for 24 h. Sodium chloride was filtered off and the solvent removed under reduced pressure at 30 °C. The crude product was subjected to column chromatography using *n*-hexane–CH_2Cl_2 (3:2) as eluent. 2-isopropilamino-2-thiophenoxy-4,4,6,6-tetrachlorocyclotriphosphazatriene **(3)** was isolated as an oil (Rf: 0.57, 0.15 g, 20%). *Anal.* Calc. for $C_9H_{13}Cl_4N_4P_3S$: C, 24.35; H, 2.95; N, 12.62; M, 444. Found: C, 24.34; H, 2.94; N, 12.60; ($M+Na^+$), 467%. ^1H NMR, δ = 1.21 ppm (d, 6H, CH_3), δ = 3.65 ppm (m, H, CH), δ = 2.93 ppm (H, NH), δ = 7.6 ppm (*m*-, *p*-, 3H, Ar–CH), δ = 7.4 ppm (*o*-, 2H, Ar–CH).

4.3.2. Synthesis of compound *5*

A solution of NaH (60% oil suspension, 0.1 g, 2.5 mmol) in 10 mL dry THF was added dropwise to a stirred solution of thiophenol (0.27 g, 2.5 mmol) in 5 mL dry THF under an atmosphere of argon in a 100 mL three-necked round bottomed flask. Then, **4** (1 g, 2.5 mmol) in 10 mL dry THF was added. The reaction mixture was stirred under an atmosphere of argon at room temperature for 24 h. Sodium chloride was filtered off and the solvent removed under reduced pressure at 30 °C. The crude product was subjected to column chromatography using *n*-hexane–CH_2Cl_2 (1:1) as eluent. 2-anilino-2-thiophenoxy-4,4,6,6-tetrachlorocyclotriphosphazatriene **(5)** was isolated as a white powder and re-crystallised from dichloromethane–petroleum ether (1:1) (m.p.:132 °C, Rf: 0.49, 0.33 g, 28%). *Anal.* Calc. for $C_{12}H_{11}Cl_4N_4P_3S$: C, 30.15; H, 2.32; N, 11.72; M, 475. Found: C, 30.16; H, 2.33; N, 11.74; (MH^+): 476%. ^1H NMR, δ = 2.93 ppm (H, NH), δ = 7.10–7.75 ppm (*m*-, *p*-, 3H, NH–Ar–CH), δ = 6.99 ppm (*o*-, 2H, NHAr–CH), δ = 7.63–7.66 ppm (*m*-, *p*-, 3H, S–Ar–CH), δ = 7.54 ppm (*o*-, 2H, S–Ar–CH).

4.3.3. Synthesis of compound *7*

A solution of NaH (60% oil suspension, 0.014 g, 0.98 mmol) in 10 mL dry THF was added dropwise to a stirred solution of thiophenol (0.108 g, 0.98 mmol) in 10 mL dry THF under an atmosphere of argon in a 100 mL three-necked round bottomed flask. Then, **6** (0.5 g, 0.98 mmol) in 10 mL dry THF was added. The reaction mixture was stirred under an atmosphere of argon at room temperature for 24 h. Sodium chloride was filtered off and the solvent removed under reduced pressure at 30 °C. The crude product was subjected to column chromatography using *n*-hexane–THF (7:1) as eluent. 2-tert-butylamino-2-thiophenoxy-4,4,6,6-tetrachlorocyclotriphosphazatriene **(7)** was isolated as an oil (Rf: 0.65, 0.018 g, 4%). *Anal.* Calc. for $C_{10}H_{15}Cl_4N_4P_3S$: C, 26.22; H, 3.30; N, 12.23; M, 456. Found: C, 26.21; H, 3.28; N, 12.22; (MH^+), 457%.

4.3.4. Synthesis of compound *9*

A solution of NaH (60% oil suspension, 0.56 g, 1.4 mmol) in 10 mL dry THF was added dropwise to a stirred solution of thiophenol (0.15 g, 1.4 mmol) in 5 mL dry THF under an atmosphere of argon in a 100 mL three-necked round bottomed flask. Then, **8** (0.5 g, 1.4 mmol) in 10 mL dry THF was added. The reaction mixture was stirred under an atmosphere of argon at room temperature for 24 h. Sodium chloride was filtered off and the solvent removed under reduced pressure at 30 °C. The crude product was subjected to column chromatography using *n*-hexane–CH_2Cl_2 (1:1) as eluent. 2-dimethylamino-4,4-thiophenoxy-2,6,6-trichlorocyclotriphosphazatriene **(9)** was isolated as an oil (Rf: 0.49, 0.33 g, 28%). *Anal.* Calc. for $C_{14}H_{16}Cl_3N_4P_3S_2$: C, 33.38; H, 3.20; N, 11.12; M, 503. Found: C, 33.40; H, 3.21; N, 11.13; ($M+Na^+$), 527%. ^1H NMR, δ = 5.5 ppm (s, 6H, CH_3), δ = 7.42–7.93 ppm (10H, Ar–CH).

4.3.5. Synthesis of compound *11*

A solution of NaH (60% oil suspension, 0.02 g, 1.3 mmol) in 10 mL dry THF was added dropwise to a stirred solution of

thiophenol (0.143 g, 1.3 mmol) in 5 mL dry THF under an atmosphere of argon in a 100 mL three-necked round bottomed flask. Then, **10** (0.5 g, 1.3 mmol) in 10 mL dry THF was added. The reaction mixture was stirred under an atmosphere of argon at room temperature for 24 h. Sodium chloride was filtered off and the solvent removed under reduced pressure at 30 °C. The crude product was subjected to column chromatography using *n*-hexane–THF (6:1) as eluent. 2-dibenzylamino-4,4-thiophenoxy-2,6,6-trichlorocyclotriphosphazatriene **(11)** was isolated as an oil (Rf: 0.80, 0.1 g, 20%). *Anal.* Calc. for $C_{26}H_{24}Cl_3N_4P_3S_2$: C, 47.61; H, 3.69; N, 8.54; M, 656. Found: C, 47.62; H, 3.70; N, 8.55; ($M+Na^+$), 679%. ^1H NMR, δ = 4.2 ppm (d, 4H, CH_2), δ = 7.34–7.49 ppm (*m*-, *p*-, 6H, N–CH_2Ar–CH), δ = 7.68 ppm (*o*-, 4H, NCH_2Ar–CH), δ = 7.61–7.93 ppm (*m*-, *p*-, 6H, S–Ar–CH), δ = 7.42 ppm (*o*-, 4H, S–Ar–CH).

*4.3.6. Synthesis of compound **13***

A solution of NaH (60% oil suspension, 0.15 g, 1.9 mmol) in 10 mL dry THF was added dropwise to a stirred solution of thiophenol (0.2 g, 1.9 mmol) in 5 mL dry THF under argon pressure in a 100 mL three-necked round bottomed flask. Then, **12** (0.72 g, 1.9 mmol) in 10 mL dry THF was added. The reaction mixture was stirred under an atmosphere of argon at room temperature for 24 h. Sodium chloride was filtered off and the solvent removed under reduced pressure at 30 °C. The crude product was subjected to column chromatography using *n*-hexane–THF (8:1) as eluent. 2-pyrrolidino-4,4-thiophenoxy-2,6,6-trichlorocyclotriphosphazatriene **(13)** was isolated as a white powder and re-crystallised from dichloromethane-*n*-hexane (1:1) (m.p.: 88 °C, Rf: 0.45, 0.33 g, 28%). *Anal.* Calc. for $C_{16}H_{18}Cl_3N_4P_3S_2$: C, 36.28; H, 3.42; N, 10.58; M, 528. Found: C, 36.26; H, 3.41; N, 10.56; (MH^+), 529%. ^1H NMR, δ = 2.64 ppm (4H, CH_2), δ = 2.77–3.15 ppm (4H, NCH_2), δ = 7.42–7.93 ppm (10H, Ar–CH).

Supplementary data

CCDC 731622 and 731623 contain the supplementary crystallographic data for **5** and **13**. These data can be obtained free of charge http://www.ccdc.cam.ac.uk/conts/retrieving.html, or from the Cambridge Crystallographic Data Centre, 12 Union Road, Cambridge CB2 1EZ, UK; fax: (+44) 1223-336-033, or e-mail: deposit@ccdc.cam.ac.uk.

Acknowledgement

We would like to thank the Gebze Institute of Technology Research Fund for partial support (Project No: BAP 2008-A3). We also thank Anadolu University and Medicinal Plants and Medicine Research Center of Anadolu University Eskişehir, for allowing us to use the X-Ray facility.

References

[1] C.W. Allen, Chem. Rev. 91 (1991) 119.
[2] V. Chandrasekhar, Inorganic and Organometallic Polymers, Springer-Verlag, Heidelberg, Germany, 2005.
[3] J.E. Mark, H.R. Allcock, R. West, Inorganic Polymers, second ed., Oxford University Press, New York, 2005.
[4] T. Sedaghat, A. Tarassoli, A. Mojaddami, J. Coord. Chem. 62 (5) (2009) 840.
[5] A. Tarassoli, T. Sedaghat, H.-R. Goudarzi, Cent. Eur. J. Chem. 7 (1) (2006) 130.
[6] E. Çil, M. Arslan, Inorg. Chim. Acta 362 (2009) 1421.
[7] P. Sozzani, A. Comotti, S. Bracco, Angew. Chem., Int. Ed. 43 (2004) 2792.
[8] K. Inoue, Prog. Polym. Sci. 25 (2000) 453.
[9] G. Gahungu, J. Zhang, B. Zhang, T. Ndikumana, J. Phys. Chem. A 113 (1) (2009) 246.
[10] O. Rolland, C.-O. Turrin, G. Bacquet, R. Poupot, M. Poupot, A.-M. Caminade, J.-P. Majoral, Tetrahedron Lett. 50 (18) (2009) 2078.
[11] L. Wang, Y. Ye, S.B. Zhong, Y.F. Zhao, Chin. Chem. Lett. 20 (2009) 58.
[12] H.R. Allcock, Chemistry and Applications of Polyphosphazenes, Wiley-Interscience, Hoboken, NJ, 2003.
[13] B. Thomas, G. Grossmann, Z. Anorg. Allg. Chem. 448 (1979) 100.
[14] (a) A.P. Carroll, R.A. Shaw, J. Chem. Soc. (A) (1966) 914;
(b) T. Fushimi, H.R. Allcock, Dalton Trans. (2009) 2477.
[15] O.-S. Jung, S.H. Park, Y.-A. Lee, Y. Cho, K.M. Kim, S. Lee, H.K. Chae, Y.S. Sohn, Inorg. Chem. 35 (23) (1996) 6899.
[16] G.A. Carriedo, F.J. Garćıa Alonso, S. Ĺopez Vizcáıno, C.D. Valenzuela, N. Yutronic, Phosphorus, Sulfur, and Silicon 178 (2003) 1549.
[17] S. Begeç, S. Alataş, Phosphorus, Sulfur, and Silicon 181 (2006) 2387.
[18] (a) S.J. Coles, D.B. Davies, M.B. Hursthouse, H. Ibişoğlu, A. Kılıç, R.A. Shaw, Acta Cryst. E63 (2007) o375;
(b) A. Vij, S.J. Geib, R.L. Kirchmeier, J.M. Shreeve, Inorg. Chem. 35 (10) (1996) 2915.
[19] (a) H.R. Allcock, Chem. Rev. 72 (4) (1972) 315;
(b) S. S.Beşli, S.J. Coles, D.B. Davies, M.B. Hursthouse, A. Kılıç, T.A. Mayer, R.A. Shaw, A. Uslu, Acta Cryst. B58 (2002) 545.
[20] G.A. Carriedo, J. Jimenez, P. Gómez-Elipe, F.J. García Alonso, Macromol. Rapid. Commun. 22 (2001) 444.
[21] S.S. Krishnamurty, R.A. Shaw, M. Woods, Curr. Sci. 45 (12) (1976) 433.
[22] S. Ganapathiappan, S.S. Krishnamurthy, J. Chem. Soc., Dalton Trans. (1987) 585.
[23] G.J. Bullen, J. Chem. Soc. (A) (1971) 1450.
[24] G.J. Bullen, J. Cryst. Spectrosc. Res. 12 (1) (1982) 11.
[25] S.W. Bartlett, S.J. Coles, D.B. Davies, M.B. Hursthouse, H. İbişoğlu, A. Kılıç, R.A. Shaw, İ. Ün, Acta Cryst. B62 (2006) 321.
[26] R. Kruszynski, M. Siwy, I. Porwolik-Czomperlik, A. Trzesowska, Inorg. Chim. Acta 359 (2006) 649.
[27] D. Cremer, J.A. Pople, J. Am. Chem. Soc. 97 (6) (1975) 1354.
[28] L.J. Farrugia, J. Appl. Cryst. 30 (1997) 565.
[29] Bruker (2005), SADABS, Bruker AXS Inc. Madison, Wisconsin, USA.
[30] G.M. Sheldrick, SHELXS97 and SHELXL97, University of Göttingen, Germany, 1997.
[31] S.K. Das, R. Keat, R.A. Shaw, B.C. Smith, J. Chem. Soc. (A) (1966) 1677.
[32] V.B. Desai, R.A. Shaw, B.C. Smith, J. Chem. Soc. (A) (1970) 2023.
[33] R. Keat, R.A. Shaw, J. Chem. Soc. (1965) 2215.
[34] M. Hasan, R.A. Shaw, M. Woods, J. Chem. Soc., Dalton Trans. (1975) 2202.
[35] A.A. Korepecheva, N.M. Kashnikova, Zhurnal Obshchei Khimii 35 (11) (1965) 1988.

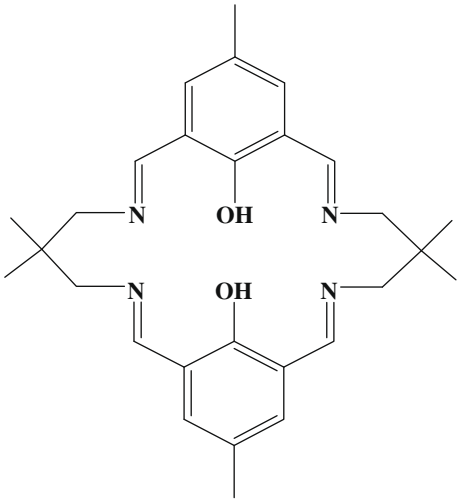


Chart 1. Chemical structure of H_2L.

a Perkin–Elmer LS-50B spectrofluorometer was utilized to study emission spectra.

2.2. Syntheses

2.2.1. $[H_4L](ClO_4)_2$ (**1**)

The diprotonated perchlorate salt, $[H_4L](ClO_4)_2$, of the macrocyclic Schiff base ligand H_2L has been synthesized by the condensation of 4-methyl-2,6-diformylphenol with 2,2′-dimethyl-1,3-diaminopropane following the procedure of Nag et al. to prepare the related other macrocyclic ligand [2]. To a boiling methanol solution (30 mL) containing 2,6-diformyl-4-methylphenol (0.33 g, 2 mmol), $NaClO_4$ (1 g, 8 mmol) and acetic acid (0.25 ml, 4 mmol) was added a methanol solution of 2,2′-dimethyl-1,3-propanediamine (0.208 g, 2 mmol). The solution was removed from the source of heating and kept at room temperature overnight. The product separated as orange crystals that were collected by filtration and washed with methanol and diethyl ether. Yield 0.60 g (90%). *Anal.* Calc. for $C_{28}H_{38}N_4O_{10}Cl_2$: C, 50.83; H, 5.74; N, 8.47. Found: C, 50.75; H, 5.63; N, 8.51%. Selected IR data on KBr (cm^{-1}): ν(C=N), 1655s; ν(perchlorate), 1145s, 1117s, 626 m. ^1H NMR (300 MHz, CD_3CN) δ values (ppm): 13.92 (s, 4H, N–H···O); 8.47, 8.43 (dd, 4H, CH=N); 7.36 (s, 4H, 4-ArH); 3.89, 3.87 (dd, 8H, α-CH_2); 2.17–1.93 (m, 6H, H_3C–Ar); 1.37 (s, 12H, H_3C–amine).

2.2.2. $[Pb^{II}_2L(NO_3)_2]$ (**2**)

This dinuclear complex of Pb(II) was synthesized according to the procedure reported by Nag et al. for the synthesis of related other Pb^{II}_2 complexes [16]. To a boiling methanol solution (100 ml) of 2,6-diformyl-4-methylphenol (1.64 g, 10 mmol) was added a DMF solution (15 ml) of $Pb(NO_3)_2$ (1.61 g, 5 mmol) and $Pb(OAc)_2$ (1.9 g, 5 mmol). After one hour reflux, a methanol solution (20 ml) of 2,2′-dimethyl-1,3-propanediamine (1.040 g, 10 mmol) was added to the boiling solution. Reflux was continued for another 4 h to get yellow crystalline compound which was collected by filtration and washed with methanol. Yield 3.89 g (78%). *Anal.* Calc. for $C_{28}H_{34}N_6O_8Pb_2$: C, 33.73; H, 3.44; N, 8.43. Found: C, 33.85; H, 3.55; N, 8.51%. Selected IR data on KBr (cm^{-1}): ν(C=N), 1633s; ν(nitrate), 1384s, 1305s, 995w.

2.2.3. $[Zn^{II}L(NO_3)(H_2O)](ClO_4)$ (**3**)

To a stirred methanolic suspension (20 ml) of **2** (1 g, 1 mmol) a methanol solution (10 ml) of $ZnCl_2$ (0.273 g, 2 mmol) was added dropwise. With the addition of $ZnCl_2$ solution, the suspension slowly converted into solution. After two hours stirring, a white precipitate of $PbCl_2$ was separated and removed by filtration. To the filtrate, $NaClO_4$ (0,5 g, 4 mmol) in methanol was added slowly and solution was kept for slow evaporation. After two days later a yellowish crystalline compound containing diffractable single crystals was collected. Yield 0.585 g (76%). *Anal.* Calc. for $C_{28}H_{36}N_5O_{10}ClZn_2$: C, 43.74; H, 4.72; N, 9.10. Found: C, 43.95; H, 4.63; N, 9.25%. Selected IR data on KBr (cm^{-1}): ν(water), 3382br; ν(C=N), 1637s; ν(nitrate), 1438s, 1300s, 1006 m; ν(perchlorate), 1095s, 623 m. ^1H NMR (300 MHz, CD_3CN) δ values (ppm): 8.26 (s, 4H, CH=N); 7.39 (s, 4H, 4-ArH); 3.80 (s, 8H, α-CH_2); 2.29 (s, 6H, H_3C–Ar); 1.02 (s, 12H, H_3C–amine).

2.2.4. $[Zn^{II}_2L(H_2O)_2](ClO_4)_2.(H_2O)_2$ (**4**)

An acetonitrile solution (10 ml) of zinc(II) acetate dihydrate (0.440 g, 2 mmol) was added to a CH_3CN solution (10 ml) of **1** (0.661 g, 1 mmol) with stirring. After two hours stirring, the volume of the yellow solution obtained was reduced to 10 ml. From the concentrated solution a yellow compound was separated out which was collected in suction and washed with ether. Recrystallization from acetonitrile–ethanol (1:1) yielded yellow crystalline compound. Yield 0.731 g (85%). *Anal.* Calc. for $C_{28}H_{42}N_4O_{14}Cl_2Zn_2$: C, 39.09; H, 4.92; N, 6.51. Found: C, 39.35; H, 4.81; N, 6.42%. Selected IR data on KBr (cm^{-1}): ν(water), 3417br; ν(C=N), 1639s; ν(perchlorate), 1092s, 625 m. ^1H NMR (300 MHz, CD_3CN) δ values (ppm): 8.29 (s, 4H, CH=N); 7.44 (s, 4H, 4-ArH); 3.82 (s, 8H, α-CH_2); 2.31 (s, 6H, H_3C–Ar); 1.03 (s, 12H, H_3C–amine).

2.3. Crystal structure determination of **1** and **3**

The crystallographic data of these two compounds (**1** and **3**) are summarized in Table 1. Diffraction data for both **1** and **3** were collected on a Nonius APEX-II diffractometer at 293 K with data collection and reduction using the Nonius program suite DENZO-SMN

Table 1
Crystallographic data for **1** and **3**.

	1	**3**
Empirical formula	$C_{28}H_{38}Cl_2N_4O_{10}$	$C_{28}H_{36}N_5O_{10}ClZn_2$
Formula weight	661.52	768.81
Crystal system	orthorhombic	orthorhombic
Space group	*Fdd*2	$P2_12_12$
a (Å)	21.850(4)	14.9133(10)
b (Å)	33.290(5)	16.8533(12)
c (Å)	8.8199(15)	12.6589(8)
V (Å^3)	6415.4(17)	3181.7(4)
Z	8	4
D_{calc}, g cm^{-3})	1.370	1.605
λ (Mo Kα), Å	0.71073	0.71073
μ (mm^{-1})	0.263	1.655
T (K)	293(2)	293(2)
F(0 0 0)	2784	1584
2θ Range for data collection (°)	4.46–57.82	4.22–63.04
Index ranges	$-17 \leqslant h \leqslant 27$ $-44 \leqslant k \leqslant 32$ $-11 \leqslant l \leqslant 11$	$-21 \leqslant h \leqslant 19$ $-24 \leqslant k \leqslant 20$ $-11 \leqslant l \leqslant 18$
Number of measured reflections	9293	39030
Number of independent reflections	3178	10432
R_{int}	0.0261	0.0292
Number of refined parameters	251	486
Number of observed reflections, $I \geqslant 2\sigma(I)$	2552	8159
Goodness-of-fit (GOF) on F^2, *S*	1.103	1.030
R_1[a], wR_2[b] [$I \geqslant 2\sigma(I)$]	0.0519, 0.1286	0.0481, 0.1181
R_1[a], wR_2[b] [all data]	0.0699, 0.1437	0.0684, 0.1305
Maximum, minimum electron density (eÅ^{-3})	0.303, −0.243	1.375, −1.035

[a] $R_1 = [\Sigma||F_o|-|F_c||/\Sigma|F_o|]$.
[b] $wR_2 = [\Sigma w(F_o^2-F_c^2)^2/\Sigma w(F_o^2)^2]^{1/2}$.

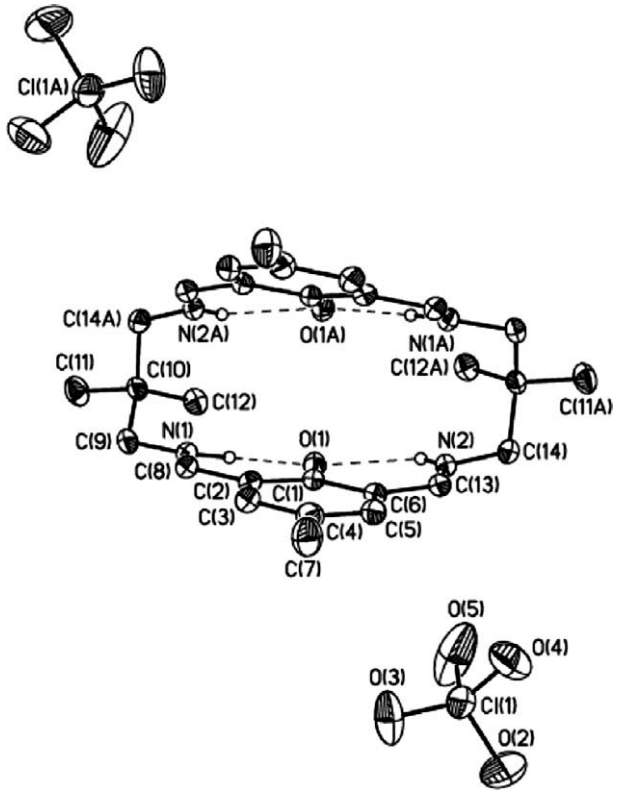


Fig. 1. ORTEP representation (30% thermal ellipsoids) of the macrocyclic ligand (**1**) with atom-labeling schemes. All the hydrogen atoms except those involved in intramolecular hydrogen bonding are omitted for clarity. Symmetry code A: $-x-0.5$, $0.5-y$, z.

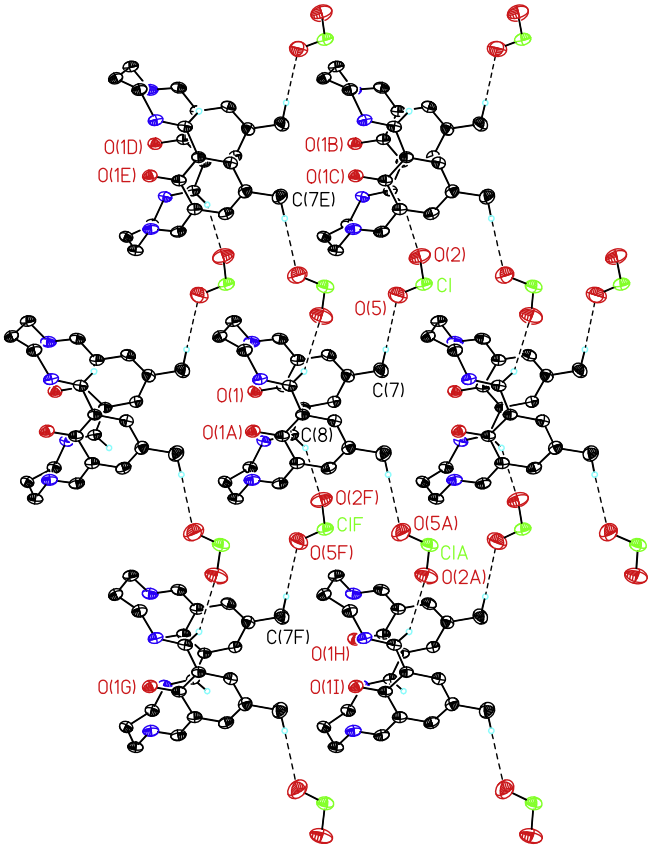


Fig. 2. Two-dimensional chain created by perchlorate oxygen (O(2) and O(5)) in *ac*-plane in compound **1**. View down the *b*-axis. Symmetry codes: A, $-0.5-x$, $0.5-y$, z; B, $0.5+x$, y, $0.5+z$; C, $-x$, $0.5-y$, $0.5+z$; D, $0.5+x$, y, $-0.5+z$; E, $-x$, $0.5-y$, $-0.5+z$; F, $-0.5+x$, y, $-0.5+z$; G, $1-x$, $0.5-y$, $-0.5+z$; H, $-0.5+x$, y, $0.5+z$; I, $-1-x$, $0.5-y$, $0.5+z$; J, $0.25+x$, $0.25-y$, $1.25+z$; K, $-0.25-x$, $-0.25+y$, $1.25+z$.

Table 2
Selected bond lengths (Å) and angles (°) for $[H_4L](ClO_4)_2$ (**1**). Symmetry as in the figure.

N(1)–C(8)	1.280(5)
N(2)–C(13)	1.268(6)
N(1)–C(9)	1.476(4)
N(2)–C(14)	1.469(5)
O(1)–C(1)	1.281(4)
N(1)···O(1)	2.573
N(1)–H(1)	0.97(3)
O(1)···H(1)	1.773
N(2)···O(1)	2.636
N(2)–H(2)	0.66(4)
O(2)···H(2)	2.163
N(1)–C(8)–C(2)	122.0(3)
N(2)–C(13)–C(6)	125.0(4)
C(8)–N(1)–C(9)	125.1(3)
C(13)–N(2)–C(14)	125.4(4)
N(1)–C(9)–C(10)	113.8(3)
N(2)–C(14)–C(10A)	114.6(3)
N(1)–H(1)···O(1)	138.0
N(2)–H(2)···O(1)	129.7

package [40,41]. All data for the compound **1** and **3** were corrected for Lorentz, polarisation, background and absorption effects. For both the compounds, crystal structures were determined by Direct methods and subsequent Fourier and difference Fourier syntheses, followed by full-matrix least-squares refinements on F^2 using SHELXL-97 [42]. Only water and methyl hydrogen atoms of **3** were refined using restraints. All other hydrogen atoms of **3** and all hydrogen atoms of **1** were refined freely. Using anisotropic treatment of the non-hydrogen atoms and isotropic treatment of the hydrogen atoms of these two compounds, the final refinements converged at the R_1 values ($I > 2\sigma(I)$) 0.0519 and 0.0481 for **1** and **3**, respectively.

3. Results and discussion

3.1. Syntheses and characterization

The template condensation of 2,6-diformyl-4-methylphenol and 2,2′-dimethyl-1,3-diaminopropane in the presence of lead(II) nitrate and lead(II) acetate results in the formation of the dinuclear Pb(II) complex $[Pb^{II}_2L(NO_3)_2]$ (**2**). When complex **2** is treated with $ZnCl_2$, metal substitution reaction takes place and the dinuclear zinc(II) complex $[Zn^{II}_2L(NO_3)(H_2O)](ClO_4)$ (**3**) is formed in good yield and in single crystalline form, suitable for single crystal analysis. On the other hand, the condensation of 2,6-diformyl-4-methylphenol and 2,2′-dimethyl-1,3-diaminopropane in presence of acetic acid and sodium perchlorate produces the diprotonated free macrocyclic salt $[H_4L](ClO_4)_2$ (**1**). The treatment of **1** with zinc(II) acetate in acetonitrile, deprotonation of $[H_4L]^{2+}$ and incorporation of the metal ion in the ligand compartment takes place resulting in the formation of the dinuclear zinc(II) complex (**4**). Although microcrystals of **4** can be isolated from acetonitrile–ethanol, it has not been possible to prepare diffraction quality crystals of this compound. Similarly, it has not been possible to get diffraction quality crystals of the dinuclear Pb(II) complex **2**. Attempts to prepare single crystals of **2** and **4** in several ways were not successful.

The IR spectrum (in the range of 500–1800 cm^{-1}) of **2**–**4** is compared. The IR spectrum of **1** exhibits one strong signal at 1655 cm^{-1}

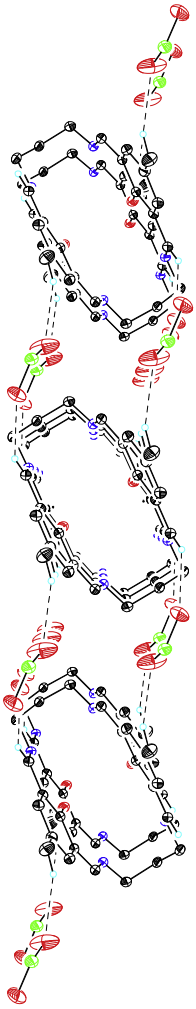


Fig. 3. Perspective view of the above 2-D along the *c*-axis.

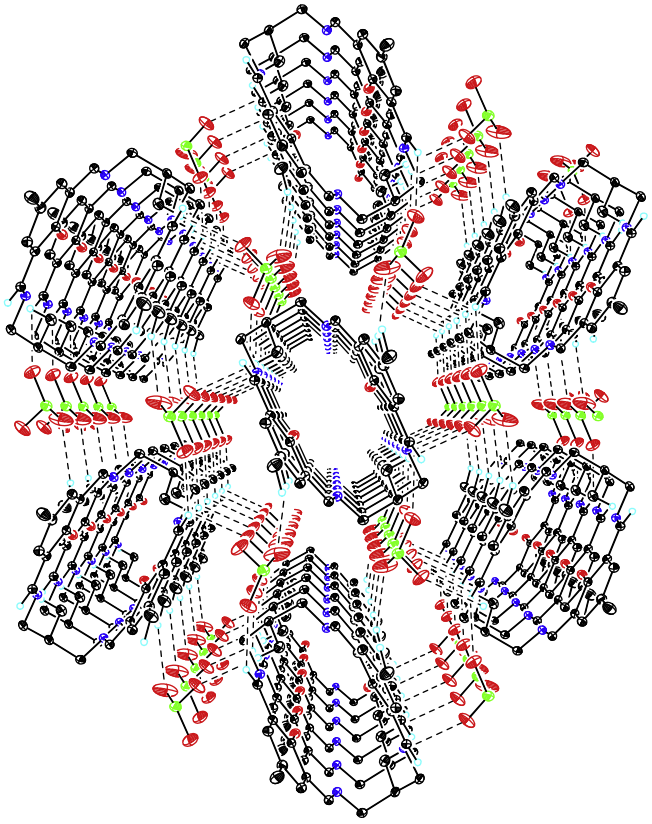


Fig. 4. View down the *c*-axis of three-dimensional supramolecular structure in **1**.

Table 3
Geometries (distances in (Å) and angles in (°)) of the hydrogen bonds in $[H_4L](ClO_4)_2$ (**1**) and $[Zn^{II}_2L(NO_3)(H_2O)](ClO_4)$ (**3**). Symmetry codes as in the figures.

Compound	D–H···A	D···A	H···A	D–H···A
1	C(7)–H(7A)···O(5)	3.426	2.516	158.26
	C(8)–H(8B)···O(2)	3.228	2.446	141.26
	C(12J)–H(12CJ)···O(3)	3.445	2.524	160.84
3	O(6)–H(6A)···O(7)	2.732	1.869	148.04
	O(6)–H(6B)···O(3E)	3.054	2.184	148.58
	O(6)–H(6B)···O(5E)	2.770	1.922	144.52
	C(27)–H(27A)···O(8)	3.498	2.552	164.92
	C(28)–H(28)···O(10B)	3.138	2.451	132.58

due to $\nu_{C=N}$ vibration. In comparison, the characteristics C=N stretching for metal complexes **2**, **3** and **4** is observed as a single strong signal at slightly lower energy (1633, 1637 and 1639 cm^{-1}, respectively). The strong absorption due to ionic perchlorate of **1** is observed at 1117 cm^{-1} [43]. The lower energy signal of ionic perchlorate of **1** appears as a medium intensity band at 626 cm^{-1} [44]. The appearance of a strong intensity band (1095 cm^{-1} for **3** and 1092 cm^{-1} for **4**) and one medium intensity band (623 cm^{-1} for **3** and 625 cm^{-1} for **4**) are indicative of the presence of ionic perchlorate(s) in **3** and **4** [43,44]. Although the region of nitrate vibration is crowded by several absorptions due to the macrocyclic ligand, two strong intensity bands (1384 and 1305 cm^{-1} for **2**; 1384 and 1300 cm^{-1} for **3**) and one medium intensity band (994 cm^{-1} for **2** and 1006 cm^{-1} for **3**) may be assigned to the absorption due to nitrates. The observation of these three bands indicates unidentate nitrates in both the complexes **2** and **3** [43]. It may be noted that single X-ray structure of **3** confirms the unidentate coordinating mode of nitrate in this complex.

3.2. Description of the structure of $[H_4L](ClO_4)_2$ (**1**)

The crystal structure of $[H_4L](ClO_4)_2$ (**1**) is shown in Fig. 1, while the selected bond lengths and angles including the geometries of the hydrogen bonds are listed in Table 2. The compound has a centrosymmetric structure with the center of inversion at the geometric center of the cation $[H_4L]^{2+}$. The conformation of $[H_4L]^{2+}$ is reminiscent of calixarenes [45] and of related Schiff-base macrocycles [2], with the phenyl ring folded downwards to leave the N and O donor atoms on an exposed face. The azomethine linkages are evident from the N(1)–C(8) and N(2)–C(13) bond lengths (1.280(5) and 1.268(6) Å, respectively), N(1)–C(8)–C(2) and N(2)-C(13)–C(6) angles (122.0(3) and 125.0(4)°, respectively), and the C(9)–N(1)–C(8)–C(2) and C(14)–N(2)–C(13)–C(6) torsion angles (177.64 and 174.35°, respectively). These bond length involving the phenyl carbon and the phenoxo oxygen, C(1)–O(1), is 1.281(4) Å. The values of these structural parameters are in the range as observed in the previously reported related macrocyclic cations [2,5].

The macrocyclic cation in **1** is stabilized by four intramolecular hydrogen bonds involving the phenolic oxygens and the imino nitrogen (Fig. 1). Between two possibilities regarding the type of the hydrogen bonds, N–H···O and O–H···N, the former is the reasonable choice because the range of N···H distances (0.66(4) and 0.97(3) Å) is much smaller than the O···H distances (1.773 and 2.163 Å). The donor···acceptor contacts of the four N–H···O inter-

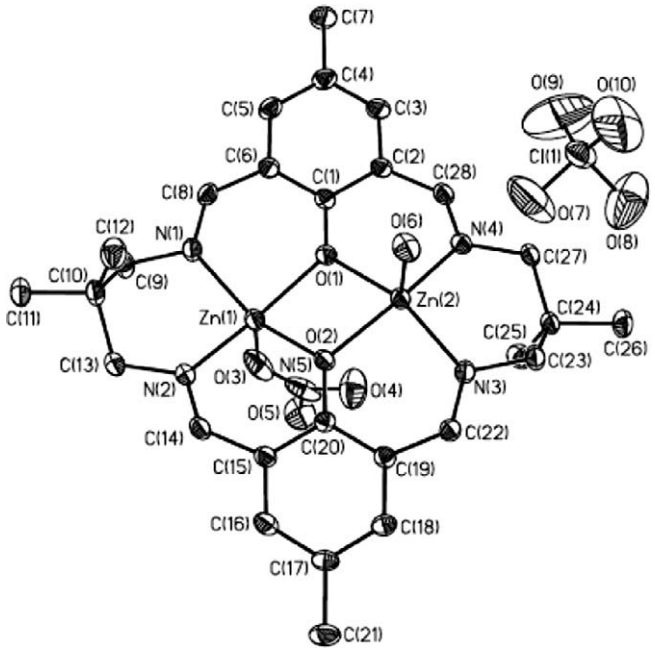


Fig. 5. ORTEP representation (30% thermal ellipsoids) of **3** with atom-labeling schemes. Hydrogen atoms are omitted for clarity.

Table 4
Selected bond lengths (Å) and angles (°) for $[Zn^{II}_2L(NO_3)(H_2O)](ClO_4)$ (**3**).

Zn(1)–O(1)	2.047(2)
Zn(1)–O(2)	2.055(2)
Zn(1)–N(1)	2.061(3)
Zn(1)–N(2)	2.067(3)
Zn(1)–O(3)	2.049(4)
Zn(2)–O(1)	2.039(2)
Zn(2)–O(2)	2.049(2)
Zn(2)–N(3)	2.036(3)
Zn(2)–N(4)	2.059(3)
Zn(2)–O(6)	2.049(3)
Zn(1)···Zn(2)	3.186
O(1)–Zn(1)–N(2)	153.24(13)
O(2)–Zn(1)–N(1)	152.34(13)
O(3)–Zn(1)–O(1)	105.26(13)
O(3)–Zn(1)–N(1)	99.87(15)
O(3)–Zn(1)–N(2)	100.47(14)
O(3)–Zn(1)–O(2)	106.74(15)
O(1)–Zn(1)–N(1)	88.68(11)
O(1)–Zn(1)–O(2)	77.31(9)
N(1)–Zn(1)–N(2)	94.12(12)
N(2)–Zn(1)–O(2)	88.44(11)
O(1)–Zn(2)–N(3)	155.37(12)
O(2)–Zn(2)–N(4)	158.63(11)
O(6)–Zn(2)–O(1)	102.02(13)
O(6)–Zn(2)–N(4)	98.54(12)
O(6)–Zn(2)–N(3)	101.07(14)
O(6)–Zn(2)–O(2)	100.42(12)
O(1)–Zn(2)–N(4)	88.89(11)
O(1)–Zn(2)–O(2)	77.60(10)
N(4)–Zn(2)–N(3)	96.09(12)
N(3)–Zn(2)–O(2)	89.89(11)
Zn(1)–O(1)–Zn(2)	102.47(11)
Zn(1)–O(2)–Zn(2)	101.85(10)

actions lie in the range 2.573–2.636 Å, while the N–H···O angles vary between 129.7° and 138°, which indicate that the intramolecular hydrogen bonds are quite strong. Similarly strong hydrogen bonds are also observed in the previously reported compounds. It may be mentioned that four six-membered rings are formed due to the four N–H···O hydrogen bonds in **1** and in analogous salts resulting in extra stabilization. The dihedral angle (20°) between the two symmetry related phenyl rings in $[H_4L]^{2+}$ is larger than the range of the dihedral angles (0–14°) observed in previously reported analogous systems, indicating that the macrocyclic moiety in **1** is most twisted [2–5].

Weak C–H···O hydrogen bonds involving three perchlorate oxygen atoms (O(2), O(3) and O(4)) and three C–H moieties (C(7)–H(7A)···O(5), C(8)–H(8B)···O(2) and C(12J)–H(12CJ)···O(3)) (Fig. S1) result in the formation of three-dimensional self-assembly in $[H_4L](ClO_4)_2$ (**1**). As shown in Fig. 2, a two-dimensional network (in *ac*-plane) is generated due to two hydrogen bonds, C(7)–H(7A)···O(5) and C(8)–H(8B)···O(2). A perspective view along the *c*-axis of the 2-D sheet is shown in Fig. 3. These two-dimensional sheets are further interlinked by C(12J)–H(12CJ)···O(3) interactions to generate overall three-dimensional topology in **1** (Fig. 4). The geometries of these weak interactions are listed in Table 3.

3.3. Description of the structure of $[Zn^{II}_2L(NO_3)(H_2O)](ClO_4)$ (**3**)

The crystal structure of this compound is shown in Fig. 5, while the selected bond lengths and angles are listed in Table 4. The structure shows that compound $[Zn^{II}_2L(NO_3)(H_2O)](ClO_4)$ (**3**) is a diphenoxo-bridged dinuclear zinc(II) complex consisting of $[Zn^{II}_2L(NO_3)(H_2O)]^+$ cation and one perchlorate anion. Each zinc(II) ion is five coordinated, bonded to two imine nitrogen atoms and two endogenous bridging phenolate oxygen atoms in the basal plane, with nitrate oxygen (O(3)) and water oxygen (O(6)) satisfying the apical position of Zn(1) and Zn(2) centers, respectively, and the apical oxygens for the two zinc(II) ions coordinate in a *trans* arrangement. The Addison distortion index [46] (τ = 0.015 and 0.05 for Zn(1) and Zn(2), respectively) for the two zinc(II) centers is close to 0 indicating that the coordination geometry of the both the metal ions is slightly distorted square pyramidal. Deviation of the NO basal donor sets from the N_2O_2 mean planes lie in the ranges −0.009 to +0.010 Å for Zn(1) and −0.031 to +0.031 Å for Zn(2). The metal centers, Zn(1) and Zn(2), are displaced towards the axial coordinated oxygen by 0.459 and 0.371 Å, respectively, from the corresponding least-squares N_2O_2 planes. The dihedral angle (5.4°) between the two basal N_2O_2 planes and the average deviation (0.058 Å) from the nitrogen and oxygen atoms from the least-squares N(1)N(2)N(3)N(4)O(1)O(2) planes may apparently indicate that the bridging moiety is almost planar. However, Zn(1) and Zn(2) are displaced from the least-squares N(1)N(2)N(3)N(4)O(1)O(2) plane towards the opposite directions by 0.441 and 0.387 Å, respectively, which indicate the deviation of the bridging core from planarity. All the five bond lengths (2.047(2)–2.067(3) Å for Zn(1); 2.036(3)–2.059(3) Å for Zn(2)) for the coordination environment of both the metal ions are very close. However, the distortion of the coordination environment can be evidenced from the significant deviation, in comparison to the ideal values, of the *transoid* angles (152.34(13)° and 153.24(13)° for Zn(1); 155.37(12)° and 158.63(11)° for Zn(2)) in the basal plane and the *cisoid* angles (77.31(9)–106.74(15)° for Zn(1); 77.60(10)–102.47(11)° for Zn(2)). It may be mentioned that the displacement of the metal ions from the basal plane is the reason of the smaller values of the *transoid* angles and the wide range of the *cisoid* angles resulting in the distortion of the coordination environment. In this compound the planarity of the macrocyclic ligand is evident from the 0.9° dihedral angle between the two phenyl rings. The two metal centers are separated to each other by 3.186 Å. The two bridge angles, Zn(1)–O(1)–Zn(2) and Zn(1)–O(2)–Zn(2) are 102.47(11) and 101.85(10)°, respectively.

Five hydrogen bonds, three O–H···O type and two C–H···O type, link the individual component in $[Zn^{II}_2L(NO_3)(H_2O)](ClO_4)$ (**3**) into a two-dimensional network (Fig. 6). One hydrogen (H(6B)) of the coordinated water $H_2O(6)$ forms bifurcated hydrogen bonds with two nitrate oxygen (O(3E) and O(5E)) of the nitrate ion of a

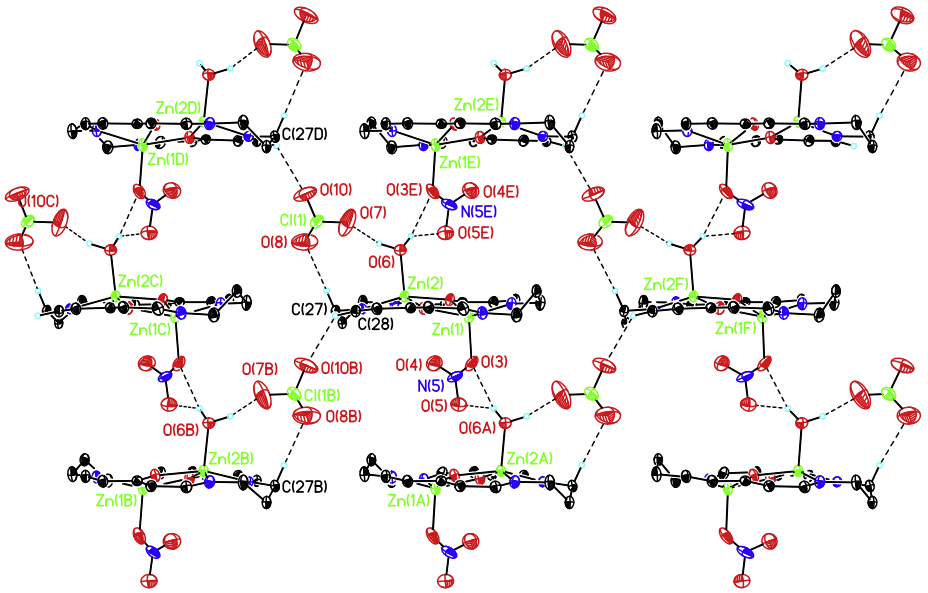


Fig. 6. View down the *b*-axis of the two-dimensional sheet of the compound **3**. Symmetry code; A, $x-0.5, 0.5-y, 0.5-z$; B, $x-0.5, 0.5-y, -z$; C, $x, y, z-1$; D, $0.5+x, 0.5-y, -z$; E, $0.5+x, 0.5-y, -z$; F, $x, y, 1+z$.

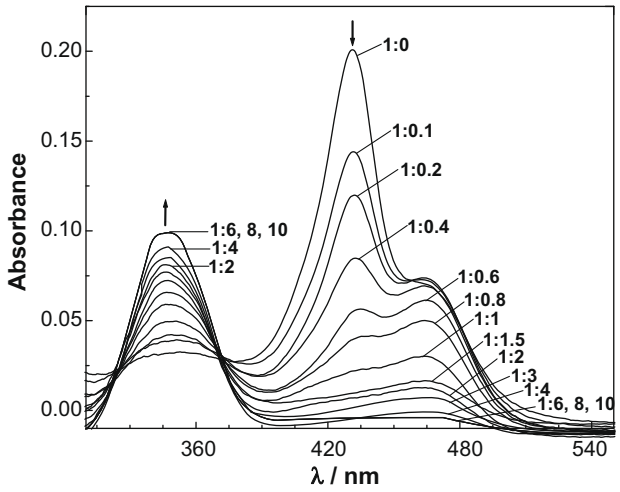


Fig. 7. Spectrophotometric titration of the macrocycle $[H_4L](ClO_4)_2$ (0.5×10^{-5}) with triethylamine (0.5×10^{-5}) in acetonitrile. Equivalent ratio of the macrocycle and triethylamine has been indicated in the figure.

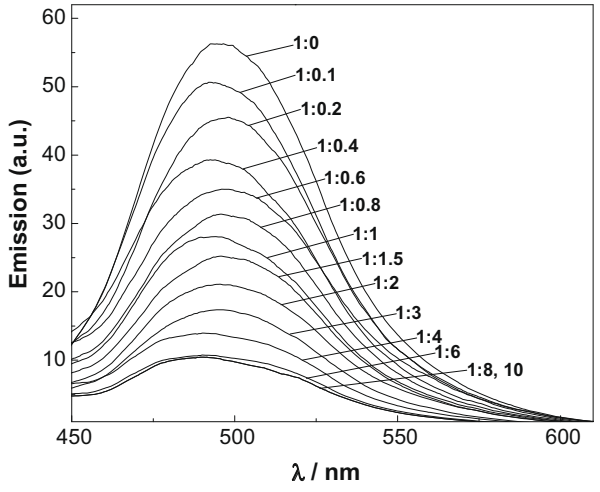


Fig. 8. Changes in emission intensity of the macrocycle $[H_4L](ClO_4)_2$ (0.5×10^{-5}) in acetonitrile upon addition of triethylamine (0.5×10^{-5}). $\lambda_{ex} = 431$ nm.

neighbouring molecule. Another hydrogen atom (H(6A)) of $H_2O(6)$ acts as a single donor to a perchlorate oxygen O(7) of another neighbouring molecule. As shown in Fig. 6, the two-dimensional topology may be considered to generate as a result of these three O–H···O bonds. However, two more hydrogen bonds (C(27)–H(27A)···O(8) and C(28)–H(28)···O(10B); Fig. 6) also participate in developing the 2-D self-assembly.

3.4. Absorption and emission spectroscopy

The UV–Vis spectrum (Fig. 7) of $[H_4L](ClO_4)_2$ in acetonitrile in the wave length range 300–900 nm shows one band at 430 nm, one shoulder at 465 nm and a weak and broad envelop at 350 nm, all of which arise due to internal $\pi \rightarrow \pi^*$ transitions. $[H_4L](ClO_4)_2$ exhibits fluorescence behavior on irradiation at 430 nm and the peak of the luminescence spectrum lies at 495 nm (Fig. 8).

Both spectrophotometric and spectrofluorimetric titrations have been carried out to understand the effect of a base such as triethylamine on $[H_4L](ClO_4)_2$. The absorption and emission profiles are represented in Figs. 7 and 8, respectively. The intensity of the band at 430 nm and the shoulder at 465 nm is continuously diminished, while the broad envelop at 350 nm becomes more intense as the saturation of the spectral profiles takes place at $[H_4L](ClO_4)_2$:Et_3N ratio of 1:6. All the absorption curves pass through an isosbestic point at 372 nm which indicates that the deprotonation process takes place smoothly. Again, as shown in Fig. 8, the fluorescence intensity gradually decreases with the increasing amount of base added and the saturation in this case also takes place at 1:6 ratio, indicating that the spectrophotometric and spectrofluorimetric titrations are consistent to each other. It may be mentioned that similar spectral changes are observed for a number of similar compounds reported by Nag et al. However, in contrast to 1:6 ratio in the case of $[H_4L](ClO_4)_2$, the saturation reaches in the reported related compounds when 25 times base is added [2].

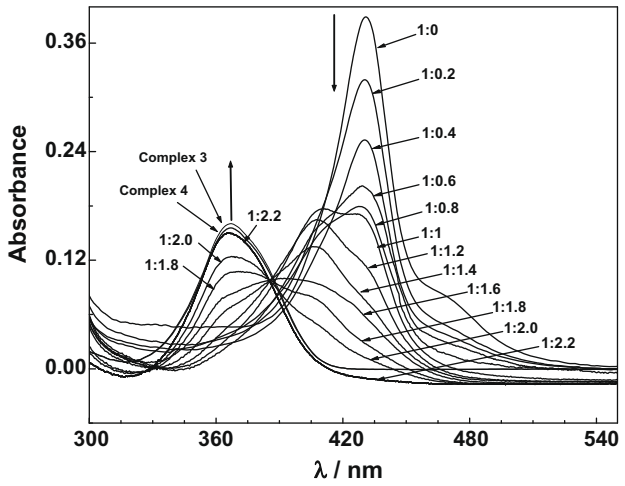


Fig. 9. Spectrophotometric titration of the macrocycle $[H_4L](ClO_4)_2$ (1×10^{-5}) with various numbers of equivalents of $Zn(OAc)_2{\cdot}2H_2O$ in acetonitrile.

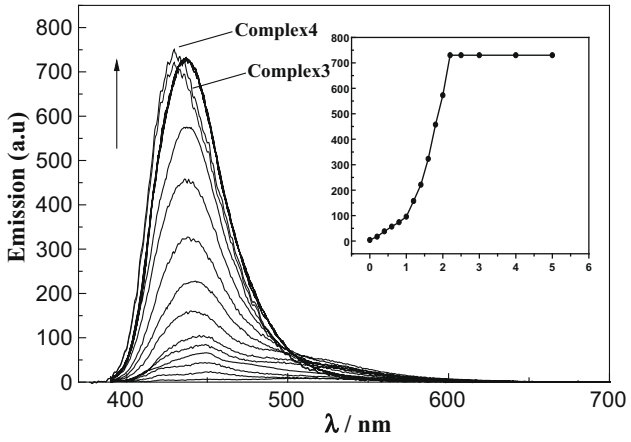


Fig. 10. Spectrofluorimetric titration of the macrocycle $[H_4L](ClO_4)_2$ (1×10^{-5}) with various numbers of equivalents of $Zn(OAc)_2{\cdot}2H_2O$ in acetonitrile. The arrow indicates the increasing concentration of $Zn(OAc)_2{\cdot}2H_2O$ added. The inset shows the variation of emission intensity with number of equivalents of $Zn(OAc)_2{\cdot}2H_2O$ added. λ_{ex} = 367.5 nm.

Absorption spectra of both of **3** and **4** show only one band at 367 nm with almost identical extinction coefficient (Fig. 9). Again, with 367 nm as the excitation wavelength, both of the complexes exhibit fluorescence with almost equal intensity and the emission peak is observed at 435 nm (Fig. 10).

To understand the reaction equilibria for the reaction of the macrocycle and zinc(II) ion, both the spectrophotometric and spectrofluorimetric titrations of $[H_4L](ClO_4)_2$ with $Zn(OAc)_2{\cdot}2H_2O$ have been carried out in acetonitrile. In these titrations (Figs. 9 and 10), ligand–metal ratio has been increased gradually until no further spectral change is taking place.

During the interval of addition of 0–1 equivalent of metal acetate, a new band at 410 nm is generated with the gradual loss intensity of the ligand band at 430 nm and the shoulder at 465 nm. On further addition of zinc acetate, the intensity of the band at 410 nm is diminished, while another new band at 367 nm is gradually generated. Saturation of this spectrophotometric titration takes place at 1:2.2 ligand–metal ratio. As compared in Fig. 9, the saturated spectrum is almost identical with the spectra of both the dinuclear complexes $[Zn^{II}_2L(NO_3)(H_2O)](ClO_4)$ (**3**) and $[Zn^{II}_2L(H_2O)_2](ClO_4)_2.(H_2O)_2$ (**4**). The generation of the two bands at 410 and 367 nm at the two stages of the spectrophotometric titration indicates that the complex formation takes place in stepwise manner (Eqs. (1) and (2)). However, while during the interval of addition of 1–2.2 equivalent of the metal ion, the absorption curves pass through an isosbestic point at 385 nm, the spectral profiles in the initial stages are not defined by an isosbestic point.

$$[H_4L]^{2+} + Zn(OAc)_2 \overset{K_1}{\rightleftharpoons} [Zn(H_2L)]^{2+} + 2HOAc \quad (1)$$

$$[Zn(H_2L)]^{2+} + Zn(OAc)_2 \overset{K_2}{\rightleftharpoons} [ZnL]^{2+} + 2HOAc \quad (2)$$

Inspite of the stepwise formation of the complex species, as already mentioned, it has not been possible to isolate the mononuclear zinc(II) complex. Evidently, two equilibrium constants are overlapped. It may be mentioned at this point that although both the mononuclear and dinuclear zinc(II) complexes can be isolated in some cases of the related ligands, attempts to synthesize the mononuclear complexes have been failed in some other cases due to more overlapping of the two equilibrium constants [37].

The spectrofluorometric titration is shown in Fig. 9. On exciting at 367 nm ($\lambda_{max.}$ of the dinuclear zinc(II) complexes), the emission intensity gradually increases with the addition of zinc(II) to $[H_4L]^{2+}$. The shapes of the luminescence profiles are indicative of the overlapping of the two steps of the complex formation.

4. Conclusions

A little investigated tetraiminodiphenolate ligand obtained on condensation of 2,6-diformyl-4-methylphenol and 2,2′-dimethyl-1,3-diaminopropane is addressed in the present study. In this investigation, this ligand is synthesized in its free diprotonated form. Template synthesis of a dinuclear lead(II) complex $[Pb^{II}_2L(NO_3)_2]$ (**2**), synthesis of a dinuclear zinc(II) complex $[Zn^{II}_2L(NO_3)(H_2O)](ClO_4)$ (**3**) through metal substitution reaction and synthesis of another dinuclear zinc(II) complex $[Zn^{II}_2L(H_2O)_2](ClO_4)_2.(H_2O)_2$ (**4**), structures of **1** and **3**, spectrophotometric and spectrofluorometric titrations of **1** with triethylamine as well as with zinc(II) acetate are described in the present study. The free ligand **1**, complexes **2**–**4** and their structural and spectroscopic studies are additions in the important family of Robson type macrocycles. The significant aspect of the present study is the zinc-induced fluorescence enhancement of an organic fluorophore $[H_4L](ClO_4)_2$ (**1**). These types of studies are important to develop zinc fluorophore and metal ion sensor.

Acknowledgment

Financial support from the Department of Science and Technology, the Government of India (SR/S1/IC-12/2008), Council for Scientific and Industrial Research (Fellowship to S. Hazra and S. Majumder) is gratefully acknowledged.

Appendix A. Supplementary data

CCDC 731565 and 731566 contain the supplementary crystallographic data for this paper. These data can be obtained free of charge via http://www.ccdc.cam.ac.uk/conts/retrieving.html, or from the Cambridge Crystallographic Data Centre, 12 Union Road, Cambridge CB2 1EZ, UK; fax: (+44) 1223-336-033; or e-mail: deposit@ccdc.cam.ac.uk.

Supplementary data associated with this article can be found, in the online version, at doi:10.1016/j.poly.2009.06.039.

References

[1] N.H. Pilkington, R. Robson, Aust. J. Chem. 23 (1970) 2225.
[2] B. Dutta, P. Bag, B. Adhikary, U. Flörke, K. Nag, J. Org. Chem. 69 (2004) 5419.
[3] N.A. Bailey, D.E. Fenton, P.B. Roberts, A.M. Walford, J. Chem. Soc., Dalton Trans. (1987) 1865.

[4] A.J. Atkins, D. Black, A.J. Blake, A. Marin-Becerra, S. Parsons, L. Ruiz-Ramirez, M. Schröder, J. Chem. Soc., Chem. Commun. (1996) 457.
[5] A. Aguiari, E. Bullita, U. Casellato, P. Guerriero, S. Tamburini, P.A. Vigato, Inorg. Chim. Acta 202 (1992) 157.
[6] J. Hodačová, M. Budšnský, Org. Lett. 9 (2007) 5641.
[7] R.R. Nazmutdinov, N.V. Roznyatovskaya, D.V. Glukhov, I. Manyurov, V.M. Mazin, G.A. Tsirlina, M. Probst, Inorg. Chem. 47 (2008) 6659.
[8] C.L. Spiro, S.L. Lambert, T.J. Smith, E.N. Duesler, R.R. Gagne, D.N. Hendrickson, Inorg. Chem. 20 (1981) 1229.
[9] R.C. Long, D.N. Hendrickson, J. Am. Chem. Soc. 105 (1983) 1513.
[10] S.K. Mandal, K. Nag, J. Chem. Soc., Dalton Trans. (1983) 2429.
[11] S.K. Mandal, K. Nag, J. Chem. Soc., Dalton Trans. (1984) 2141.
[12] S. Mandal, B. Adhikary, K. Nag, J. Chem. Soc., Dalton Trans. (1986) 1175.
[13] P. Lacroix, O. Kahn, F. Theobald, J. Leory, C. Wakselman, Inorg. Chim. Acta 142 (1988) 129.
[14] B. Bosnich, Inorg. Chem. 38 (1999) 2557.
[15] A.W. Addision, Inorg. Nucl. Chem. Lett. 12 (1976) 899.
[16] S.K. Mandal, L.K. Thompson, K. Nag, J.-P. Charland, E.J. Gabe, Inorg. Chem. 26 (1987) 1391.
[17] S.K. Mandal, L.K. Thompson, K. Nag, J.-P. Charland, E.J. Gabe, Can. J. Chem. 65 (1987) 2815.
[18] S.K. Mandal, L.K. Thompson, M.J. Newlands, E.J. Gabe, K. Nag, Inorg. Chem. 29 (1990) 1324.
[19] P. Zanello, S. Tamburini, P.A. Vigato, G.A. Mazzocchin, Coord. Chem. Rev. 77 (1987) 165.
[20] K. Brychcy, K. Dragger, K.-J. Jens, M. Tilset, U. Behrens, Chem. Ber. 127 (1994) 465.
[21] K. Brychcy, K.-J. Jens, M. Tilset, U. Behrens, Chem. Ber. 127 (1994) 991.
[22] K. Brychcy, K. Dragger, K.-J. Jens, M. Tilset, U. Behrens, Chem. Ber. 127 (1994) 1817.
[23] A.J. Atkins, A.J. Blake, M. Schröder, J. Chem. Soc., Chem. Commun. (1993) 353.
[24] D. Black, A.J. Blake, R.L. Finn, L.F. Lindoy, A. Nezhdali, G. Rougnaghi, P.A. Tasker, M. Schröder, Chem. Commun. (2002) 340.
[25] B.F. Hoskins, R. Robson, G.A. Williams, Inorg. Chim. Acta 16 (1976) 121.
[26] Y. Tian, J. Tang, G. Frenzen, J.-Y. Sun, J. Org. Chem. 64 (1999) 1442.
[27] J.J. Fraústo da Silva, R.J.P. Williams, The Biological Chemistry of the Elements, Clarendon Press, Oxford, 1991.
[28] J.M. Berg, Y. Shi, Science 271 (1996) 1081.
[29] W.N. Lipscomb, N. Sträter, Chem. Rev. 96 (1996) 2375.
[30] D.E. Wilcox, Chem. Rev. 96 (1996) 2435.
[31] H. Steinhagen, G. Helmchem, Angew. Chem., Int. Ed. Engl. 35 (1996) 2339.
[32] C.G. Dealwis, L. Chen, C. Brennan, W. Mandecki, C. AbadZaptero, Protein Eng. 8 (1995) 865.
[33] Y. Zhang, J.Y. Liang, H. Huang, H. Ke, W.N. Lipscomb, Biochemistry 32 (1993) 7844.
[34] S.K. Burley, P.R. David, A. Taylor, W.N. Lipscomb, Proc. Natl. Acad. Sci. USA 87 (1990) 6878.
[35] S.L. Roderick, B.W. Mathews, Biochemistry 32 (1993) 3907.
[36] P. Jiang, Z. Guo, Coord. Chem. Rev. 248 (2004) 205.
[37] B. Dutta, P. Bag, U. Flörke, K. Nag, Inorg. Chem. 44 (2005) 147.
[38] J.C. Byen, W.H. Lee, C.H. Han, Inorg. Chem. Commun. 9 (2006) 563.
[39] J.C. Byen, C.H. Han, K.J. Kim, Inorg. Chem. Commun. 9 (2006) 171.
[40] Z. Otwinowski, W. Minor, Methods Enzymol. 276 (1997) 307.
[41] V.N. Sonar, M. Venkatraj, S. Parkin, P.A. Crooks, Acta Crystallogr., Sect. C 63 (2007) o493.
[42] G.M. Sheldrick, SHELXL-97, Crystal Structure Refinement Program, University of Göttingen, 1997.
[43] K. Nakamoto, Infrared and Raman Spectra of Inorganic and Coordination Compounds (Part B: Applications in Coordination, Organometallic, and Bioinorganic Chemistry), 5th ed., John Wiley & Sons, Inc., New York, 1997. pp. 82–83.
[44] M. Nayak, R. Koner, H.-H. Lin, U. Flörke, H.-H. Wei, S. Mohanta, Inorg. Chem. 45 (2006) 10764.
[45] C.D. Gutsche, Calixarenes, Royal Society of Chemistry, Cambridge, UK, 1989.
[46] W. Addison, T.N. Rao, J. Reedijk, J.V. Rijn, G.C. Verschoor, J. Chem. Soc., Dalton Trans. (1984) 1549.

investigate the chemistry of Ca with the other isomeric nitrobenzoic acids to understand the role of the nitro substituent in the structural chemistry of calcium-nitrobenzoates. The disposition of the $-NO_2$ substituent, ortho to the –COOH group in 2-nitrobenzoic acid (2-nbaH), results in the formation of a coordination polymer, with the carboxylate moiety of 2-nba (2-nitrobenzoate) functioning as a bridging ligand.

2. Experimental

2.1. Materials and methods

All the chemicals used in this study were of reagent grade and were used as received. The starting materials and reaction products are air stable and hence were prepared under normal laboratory conditions. Infrared (IR) spectra were recorded on a Shimadzu (IR prestige -21) FT-IR spectrometer in the range 4000–400 cm^{-1}. Samples for IR spectra were diluted with solid KBr and the signals referenced to polystyrene bands. UV–Vis diffuse-reflectance spectra were obtained using a Shimadzu UV-2450 double beam spectrophotometer. $BaSO_4$ powder was used as a reference (100% reflectance). Absorption data were calculated from the reflectance data using the Kubelka–Munk function $(a/S = (1-R)^2/2R$ where a is the absorption coefficient, R the reflectance and S the scattering coefficient). TG-DSC measurements were performed in Al_2O_3 crucibles on a STA-409PC simultaneous thermal analyzer from Netzsch in flowing air. A heating rate of 10 K min^{-1} was employed for all measurements. Acidification of **1** and **2** with a slight excess of dilute HCl resulted in the quantitative formation of the free carboxylic acid (2-nbaH), which was extracted with ether. Evaporation of the ether, followed by drying and weighing, afforded the 2-nbaH content as described earlier [50]. Pyrolysis of **1** and **2** at 800 °C resulted in the quantitative formation of CaO. Isothermal weight loss studies were performed in an electric furnace fitted with a temperature controller. Metal analysis was performed as described earlier [49,51].

2.2. Preparation of $[Ca(H_2O)_2(2\text{-}nba)_2]$, **1**

A mixture of calcium carbonate (1.0 g, 10 mmol) and 2-nitrobenzoic acid (2-nbaH) (3.34 g, 20 mmol) was taken in water (50 ml) and heated on a steam bath. The insoluble $CaCO_3$ slowly started dissolving, accompanied by brisk effervescence. The heating of the reaction mixture was stopped when there was no more evolution of CO_2. At this stage, the reaction mixture was almost clear. The hot pale yellow solution was filtered and left undisturbed for 9–10 days. The colorless crystalline blocks that separated were filtered, washed thoroughly with ether and dried. Yield: 3.42 g (84%). The crystals obtained in this method were suitable for X-ray studies. **1** can also be prepared starting from $CaCl_2$ as the Ca source. The sodium salt of 2-nba was first generated *in situ* by reacting 2-nbaH (1.67 g, 10 mmol) with $NaHCO_3$ (0.84 g, 10 mmol) in water. Into this, an aqueous solution of $CaCl_2$ (0.555 g, 5 mmol) was added and the reaction mixture was filtered and left aside for crystallization. The crystals that separated after a few days were isolated in 71% yield. The IR spectrum and the DSC thermogram of the product obtained by this method were identical to that of the product obtained using $CaCO_3$ as the Ca source.

Anal. Calc. for $C_{14}H_{12}CaN_2O_{10}$ (408.34): C, 41.18; H, 2.96; N 6.86; Ca, 9.82; 2-nbaH, 81.86; CaO, 13.73. Found: C, 41.10; H, 2.98; N, 6.58; Ca, 9.80; 2-nbaH, 80.35; CaO, 13.70%.

IR (in cm^{-1}): 3649, 3591, 3350, 3078, 2864, 2425, 2000, 1967, 1859, 1626, 1568, 1526, 1485, 1423, 1350, 1306, 1265, 1144, 1076, 968, 870, 851, 795, 789, 746, 702, 650, 430.

UV–Vis (in nm): 250, 350.

DSC (°C): 144 (Endo), 322 (Exo), 354 (Exo), 544 (Exo); residual mass 14.3%.

2.3. Preparation of anhydrous bis(2-nitrobenzoato)calcium(II) **2**

A powdered sample of **1** (0.325 g) was heated at 150 °C for 15 min. This resulted in the formation of the anhydrous compound **2**. The observed mass loss of 8.80% is in agreement with the expected value (8.81%) for the loss of two moles of water.

Anal. Calc. for $C_{14}H_8CaN_2O_8$ (372.34): C, 45.17; H, 2.17; N 7.52; Ca, 10.76; 2-nbaH, 89.78; CaO, 15.06. Found: C, 44.53; H, 2.1; N, 7.40; Ca, 10.5; 2-nbaH, 88.15; CaO, 14.80%.

IR (in cm^{-1}): 3074, 2866, 1585, 1566, 1524, 1517, 1485, 1415, 1350, 1308, 1265, 1153, 1078, 961, 864, 847, 785, 737, 700, 648, 432.

DSC (°C): 322 (Exo), 354 (Exo), 544 (Exo); residual mass 14.3%.

2.4. Rehydration studies

The anhydrous compound **2** was prepared from **1** as mentioned above. Equilibration of a powdered sample of **2** over water vapor resulted in the formation of the starting material 1 in near quantitative yield in about a day. The IR spectrum and the DSC thermogram of the rehydrated compound are identical to that of **1**.

2.5. X-ray crystallography

Intensity data for 1 were collected on a Bruker (SMART APEX) CCD diffractometer using graphite-monochromated Mo Kα radiation. The data integration and reduction were carried out using SAINT-PLUS [52] software. An empirical absorption correction was applied to the collected reflections with SADABS [52]. The structure was solved with direct methods using SHELXS-97 [53] and refinement was done against F^2 using SHELXL-97 [53]. All non-hydrogen atoms were refined anisotropically. Aromatic hydrogens were introduced in calculated positions and included in the refinement riding on their respective parent atoms. The hydrogen atoms of the coordinated water molecules were located in the difference map but were not stable on subsequent refinements and hence were fixed at calculated positions by using the DFIX command and later refined isotropically using a riding model. The technical details of data acquisition and selected crystal refinement results for **1** are summarized in Table 1.

3. Results and discussion

3.1. Synthesis and spectroscopy

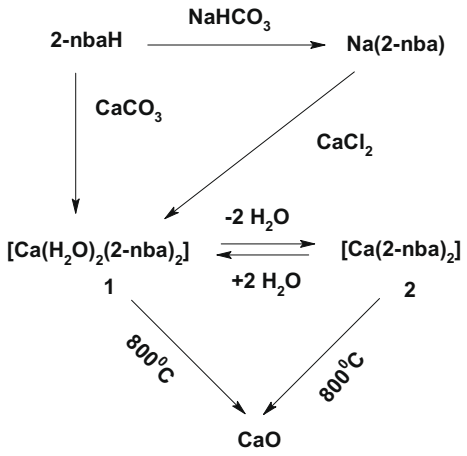
During the course of our studies on metal-carboxylates [50,54], we have shown that crystalline hydrates of metal-nitrobenzoates can be conveniently prepared in good yields under ambient conditions by an aqueous reaction of an alkali-metal carbonate with 4-nbaH or by the reaction of the *in situ* generated sodium salt of 4-nbaH with a metal halide. The generality of these reactions for the synthesis of hydrated metal-carboxylates can be evidenced by the synthesis of 4-nba compounds of alkaline-earths [49,50,55–57] as well as transition metals [58–60], the synthesis of a polymeric Ba compound [61] containing 2-nba as well as the Ca compound described herein. In the present work, the direct reaction of $CaCO_3$ with 2-nbaH in water resulted in the formation of a crystalline hydrate **1** containing Ca:2-nba:H_2O in a 1:2:2 mole ratio. Compound **1** could also be prepared by reacting an aqueous solution of $CaCl_2$ with *in situ* generated sodium salt of 2-nbaH. The composition of **1** was arrived at based on elemental analysis, 2-nbaH content

Table 1
Technical details of data acquisition and selected refinement results for **1**.

Empirical formula	$C_{14}H_{12}CaN_2O_{10}$
Formula weight	408.34
T (K)	293(2)
λ (Å)	0.71073
Crystal system	triclinic
Space group	$P\bar{1}$
Unit cell dimensions	
a (Å)	7.7477(10)
b (Å)	10.1953(13)
c (Å)	11.2808(15)
α, (°)	80.851(2)
β (°)	82.233(2)
γ (°)	89.333(2)
V (Å^3)	871.6(2)
Z, D_{calc} (Mg/m^3)	2, 1.556
Absorption coefficient (mm^{-1})	0.418
F (0 0 0)	420
Crystal size (mm^3)	0.38 × 0.32 × 0.20
θ range for data collection (°)	1.85–25.93
Index ranges	$-9 \leqslant h \leqslant 9$, $-11 \leqslant k \leqslant 12$, $-13 \leqslant l \leqslant 13$
Reflections collected/unique	6780/3753 (R_{int} = 0.0204)
Completeness to θ = 25.93°	98.4%
Refinement method	full-matrix least-squares on F^2
Data/restraints/parameters	3353/4/260
Goodness-of-fit (GOF) on F^2	1.077
Final R indices [$I > 2\sigma(I)$]	R_1 = 0.0395, wR_2 = 0.0863
R indices (all data)	R_1 = 0.0461, wR_2 = 0.0896
Extinction coefficient	0.0040(2)
Largest difference peak and hole (e Å^{-3})	0.215 and −0.202

obtained by acidification and CaO formed on pyrolysis and weight loss studies. Compound **1** can be dehydrated to the anhydrous bis(2-nitrobenzoato)calcium(II) **2** by heating at 150 °C (Scheme 1). The temperature for the dehydration reaction was chosen based on the thermal property (*vide infra*) of **1**. Equilibration of the anhydrous compound **2** in an atmosphere of water vapor resulted in the regeneration of compound **1**. This was confirmed by a comparison of the IR spectrum and the TG-DSC thermogram of the rehydrated product with that of **1**. Both **1** and **2** are decomposed to CaO by heating in a furnace at 800 °C.

The diffuse reflectance spectrum of compound **1**, which absorbs strongly at around 350 nm, is very similar to that of the free acid (Supplementary Fig. 1) and this can be assigned to the intramolecular charge transfer transition of the aromatic 2-nitrobenzoate. In addition **1** also exhibits a signal at around 250 nm, unlike the free acid, and the diffused reflectance spectrum of the anhydrous compound **2** is very similar to that of **1**. The IR spectra of **1** and **2** exhibit



Scheme 1. Synthesis of **1** and **2**.

several sharp bands in the mid-infrared region, clearly indicating the presence of the organic moiety. The strong signals at 3649 and 3591 cm^{-1} in **1** indicate the presence of water and can be assigned to the O–H stretching vibration. The IR spectrum of **2** is devoid of bands above 3074 cm^{-1}, which is indicative of the anhydrous nature of **2**. Below 3074 cm^{-1}, the IR spectrum is very similar to that of **1**. Although the IR spectra **1** and **2** exhibit absorptions due to the vibrations of the carboxylate and nitro groups, no definite conclusions can be drawn on the exact nature of the binding of the 2-nba ligand based only on infrared data.

3.2. Thermal studies

Compound **1** exhibits an endothermic event in its TG-DSC thermogram (Fig. 1) at 144 °C, accompanied by a mass loss of 8.5%. This value is in good agreement with that expected (8.83%) for the loss of two molecules of water. Above this temperature, the thermogram shows only exothermic processes with signals at 322, 354 and 544 °C. The first two closely related exotherms can be attributed to the decomposition of 2-nitrobenzoate. In view of the absence of mass spectral data of the emitted fragments, we do not wish to comment on the exact nature of the decomposition processes at these high temperatures. However it should be noted that the observed residual mass of 14.3% is in good agreement for the formation of CaO. The formation of the oxide phase can also be evidenced by the featureless infrared spectrum of the residue as well as its powder pattern. The residue on exposure to atmosphere shows an increase in weight corresponding to the formation of calcium carbonate. The results of the isothermal weight loss studies at 150 °C and at 800 °C in a furnace add more credence to the TG-DSC data. The TG-DSC thermogram of the anhydrous compound **2** is devoid of the first endothermic signal observed for the dehydration of **1**. A comparison of the TG-DSC thermograms of **1** and **2** (Fig. 1) shows the identical nature of the TG-DSC curve of **2** to that of **1** above 150 °C. The observed residual mass of 13.7% can be accounted for by the formation of CaO.

3.3. Description of the crystal structure of *1*

Compound **1** crystallizes in the centrosymmetric triclinic space group $P\bar{1}$ with all atoms situated in general positions. The central metal is eight coordinated and is bonded to two oxygen atoms of

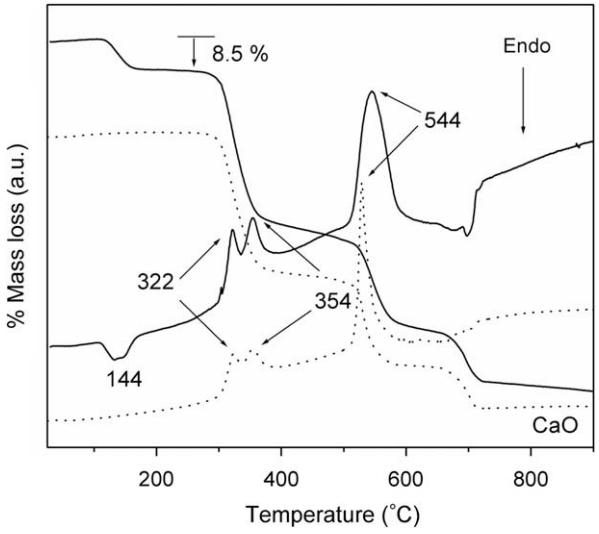


Fig. 1. TG-DSC thermograms of $[Ca(2\text{-nba})_2(H_2O)_2]_n$ **1** (solid line) and $[Ca(2\text{-nba})_2]_n$ **2** (dotted lines). (Heating rate 5 K min^{-1}; air atmosphere.)

two terminal aqua ligands and six oxygen atoms from four symmetry related 2-nba anions, resulting in a distorted triangular dodecahedral $\{CaO_8\}$ coordination polyhedron (Fig. 2). The geometric parameters of the 2-nba ligand are in the normal range and are in agreement with reported values [61]. The observed Ca–O bond distances vary between 2.3442(13) and 2.6539(15) Å (Table 2), while the O–Ca–O angles range from 77.32(6)° to 153.76(6)°. These values are comparable with those reported for other Ca(II)-carboxylates [7–12]. The Ca(II) center is linked to the O9 and O10 atoms of the water molecules by bonds of lengths 2.3918(18) and 2.4121(17) Å, respectively.

The structure of compound **1** is a one-dimensional (1-D) polymer and hence it is formulated as $[Ca(2\text{-nba})_2(H_2O)_2]_n$. Each formula unit of **1** contains Ca(II) coordinated to two aqua ligands and two unique 2-nitrobenzoate ligands, both of which function as bridging ligands. The first unique μ_2–η^2:η^1 2-nba ligand (O1, O2) binds to Ca(II) in a bidentate fashion with Ca1–O1 and Ca1–O2 distances of 2.4548(15) and 2.6313(15) Å, respectively. The O2 oxygen is further linked to a symmetry related Ca(II) center at a distance of 2.3498(14) Å, resulting in a Ca···Ca separation of 3.9865(8) Å. A pair of such μ_2–η^2:η^1 2-nba ligands are linked to two Ca(II) ions resulting in the formation of a tricyclic dicalcium-dicarboxylate unit (Fig. 3) which constitutes the basic building block of the coordination polymer. This tricyclic unit differs from the well-known eight membered cyclic dimetal-dicarboxylate unit in several dinuclear carboxylates where $(-COO)^-$ functions as a μ_2–η^1:η^1 bidentate bridging ligand. The second independent 2-nba ligand (O5, O6) binds to two symmetry related Ca(II) ions in an identical fashion resulting in a tricyclic dicalcium-dicarboxylate unit with a Ca···Ca separation of 3.9967(9) Å (Supplementary Fig. 2). The Ca–O bond lengths formed by this ligand are different. With this ligand, a Ca(II) ion is linked to the O5 and O6 oxygen atoms in a bidentate manner (Ca1–O5 2.4213(14); Ca1–O6 2.3442(13) Å) and the O6 atom is further linked to a second Ca(II) ion at 2.6539(15) Å. In the crystal structure of **1** alternating pairs of the two crystallographically independent μ_2–η^2:η^1 2-nba ligands link pairs of $\{Ca(H_2O)_2\}^{2+}$ units into a 1-D polymeric chain extending along the *a*-axis (Fig. 4). As a result, alternating Ca···Ca separations of 3.9865(8) and 3.9967(9) Å are observed in the infinite chain (Fig. 4). These values are in very good agreement with the Ca···Ca separations of 3.8585(7) and 3.8432(3) Å reported for the coordination polymers $[Ca(L^1)(4\text{-nba})_2]_n$ (L^1 = N-methylimidazole)

Table 2
Selected bond distances (Å) for $[Ca(2\text{-nba})_2(H_2O)_2]_n$ **1**.

Ca(1)–O(6)	2.3442(13)	Ca(1)–O(5)	2.4213(14)
Ca(1)–O(2)^{ii}	2.3498(14)	Ca(1)–O(1)	2.4548(15)
Ca(1)–O(9)	2.3918(18)	Ca(1)–O(2)	2.6313(15)
Ca(1)–O(10)	2.4121(17)	Ca(1)–O(6)^{i}	2.6539(15)
Ca(1)–Ca(1)^{ii}	3.9865(8)	Ca(1)–Ca(1)^{i}	3.9967(9)
O(6)–Ca(1)–O(2)^{ii}	148.82(5)	O(5)–Ca(1)–O(1)	88.01(5)
O(6)–Ca(1)–O(9)	77.32(6)	O(6)–Ca(1)–O(2)	128.87(5)
O(2)^{ii}–Ca(1)–O(9)	82.91(6)	O(2)^{ii}–Ca(1)–O(2)	73.82(5)
O(6)–Ca(1)–O(10)	84.37(5)	O(9)–Ca(1)–O(2)	153.76(6)
O(2)^{ii}–Ca(1)–O(10)	77.70(6)	O(10)–Ca(1)–O(2)	82.04(5)
O(9)–Ca(1)–O(10)	104.97(7)	O(5)–Ca(1)–O(2)	75.15(5)
O(6)–Ca(1)–O(5)	124.91(5)	O(1)–Ca(1)–O(2)	50.88(4)
O(2)^{ii}–Ca(1)–O(5)	77.78(5)	O(6)–Ca(1)–O(6)^{i}	73.97(5)
O(9)–Ca(1)–O(5)	88.40(6)	O(2)^{ii}–Ca(1)–O(6)^{i}	124.74(5)
O(10)–Ca(1)–O(5)	150.25(5)	O(9)–Ca(1)–O(6)^{i}	77.23(6)
O(6)–Ca(1)–O(1)	80.89(5)	O(10)–Ca(1)–O(6)^{i}	157.29(5)
O(2)^{ii}–Ca(1)–O(1)	124.69(5)	O(5)–Ca(1)–O(6)^{i}	50.95(4)
O(9)–Ca(1)–O(1)	150.53(5)	O(1)–Ca(1)–O(6)^{i}	77.85(5)
O(10)–Ca(1)–O(1)	92.27(6)	O(2)–Ca(1)–O(6)^{i}	106.15(5)

Symmetry transformations are used to generate equivalent atoms: (i) $-x+1$, $-y+2$, $-z$; (ii) $-x+2$, $-y+2$, $-z$.

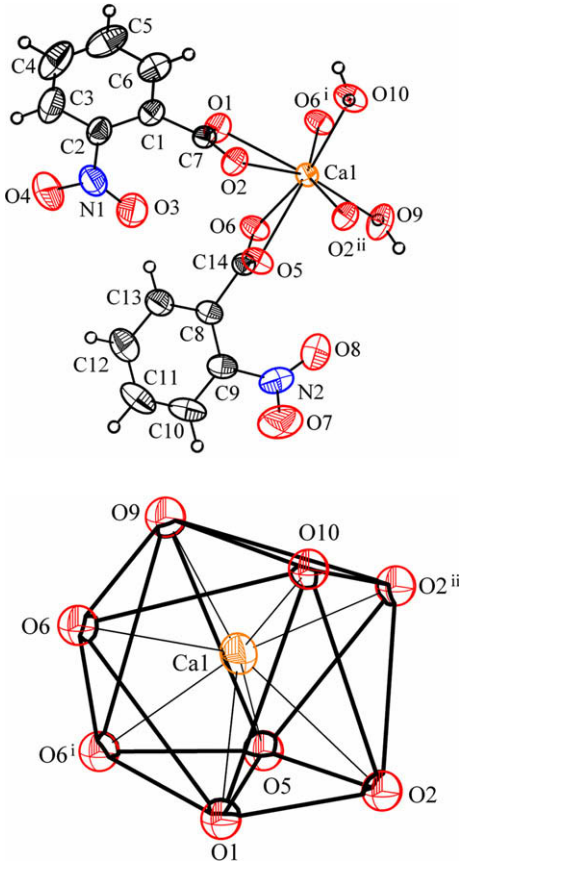


Fig. 2. A view of the coordination sphere of Ca(II) in $[Ca(2\text{-nba})_2(H_2O)_2]_n$ **1**, showing the atom-labeling scheme. Displacement ellipsoids are drawn at the 50% probability level excepting for the H atoms, which are shown as circles of arbitrary radius (top). The coordination polyhedron around Ca(II) in 1 (bottom). Symmetry code: (i) $-x+1$, $-y+2$, $-z$; (ii) $-x+2$, $-y+2$, $-z$. Color code: C, black; N, blue; O, red; Ca, orange. (For interpretation of the references to color in this figure legend, the reader is referred to the web version of this article.)

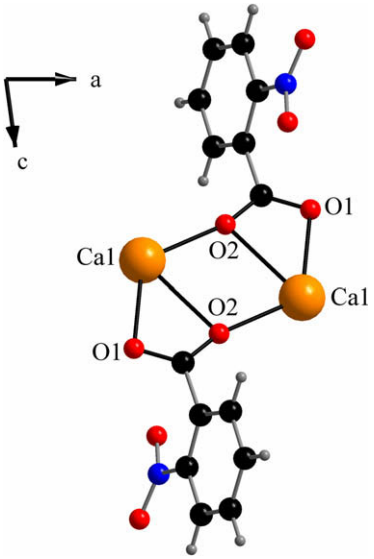


Fig. 3. A view along *b* showing the tricyclic dicalcium-bis(2-nitrobenzoate) unit formed by a pair of μ_2–η^2:η^1 2-nba ligands between two Ca(II) ions. Color code: C, black; H, medium gray; N, blue; O, red; Ca, orange. (For interpretation of the references to color in this figure legend, the reader is referred to the web version of this article.)

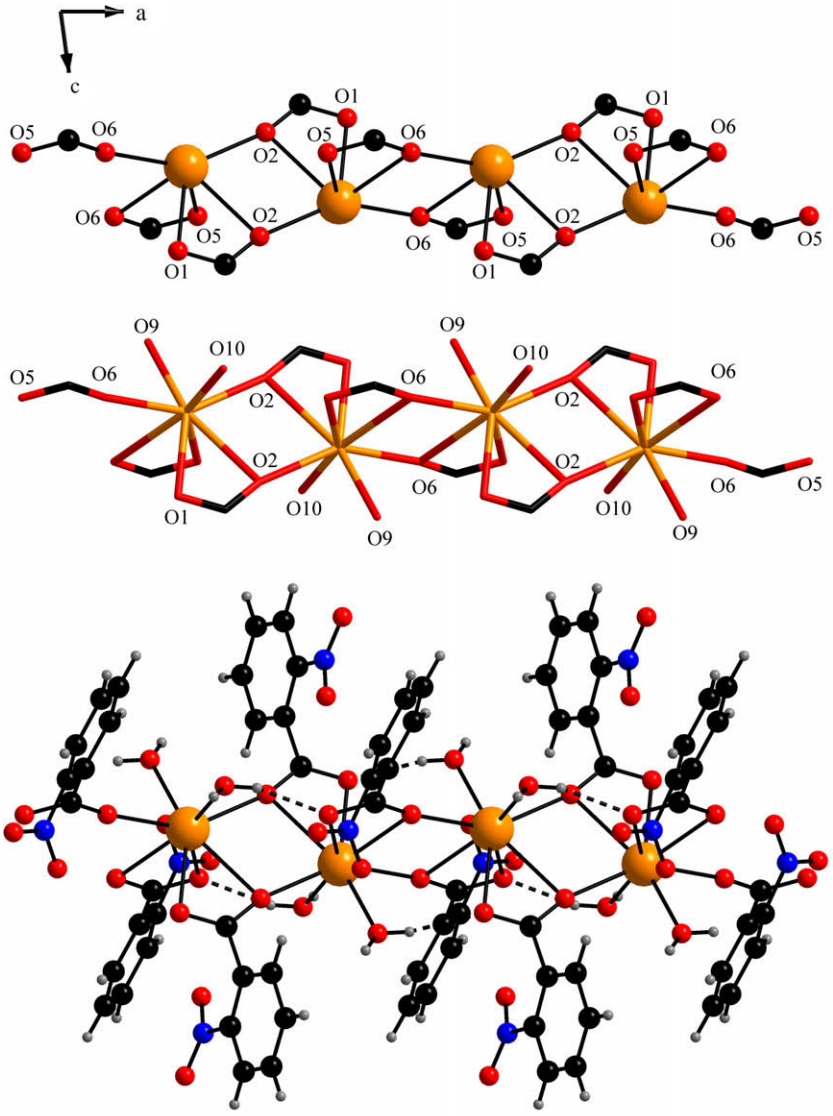


Fig. 4. A portion of the 1-D polymeric chain in **1** showing the linking of tricyclic dicalcium-bis(2-nitrobenzoate) units into an infinite chain extending along the *a*-axis. For clarity the coordinated water molecules and aromatic ring are not shown (top). A wireframe model of the polymeric chain wherein the oxygen atoms O9 and O10 of water are included (middle). The aromatic rings and the H atoms of water are included in the polymeric chain to show the intrachain O–H···O bonds in broken lines. Color code: C, black; H, medium gray; N, blue; O, red; Ca, orange. (For interpretation of the references to color in this figure legend, the reader is referred to the web version of this article.)

[47] and $[Ca(L^2)(H_2O)(4\text{-nba})_2]_n$ (L^2 is 2-methylimidazole), respectively [48].

A scrutiny of the crystal structure of **1** reveals that each eight coordinated Ca(II) complex in the polymeric chain is H-bonded to six neighboring complexes with the aid of two varieties of H-bonding interactions comprising of three O–H···O hydrogen bonds and three C–H···O interactions (Supplementary Fig. 3). All these O···H contacts are shorter than the sum of their van der Waals radii and their geometric parameters are listed in Table 3. The O9–H9···O1^{i} and O10–H10B···O5^{ii} (for symmetry code see Table 3) interactions between the coordinated water molecules and the carboxylate oxygen atoms O1 and O5 occur within the 1-D polymeric chain (Fig. 4) and thus are intrachain interactions. The oxygen atoms of the nitro group function as H-acceptors and this behavior has been observed in several nitrobenzoates [47–49,55–61]. The nitro oxygen atoms O4 and O7 in one polymeric chain are hydrogen bonded to the H11 and H10A atoms in an adjacent chain via C11–H11···O4^{v} and O10–H10A···O7^{iii}, and these can be termed as interchain interactions. Likewise the H-bonding between O9 (water) and O1 (carboxylate) with the H atoms of the aromatic ring serve to link parallel chains (Supplementary Fig. 3).

Table 3
Hydrogen-bonding geometry (Å, °) for $[Ca(2\text{-nba})_2(H_2O)_2]_n$ **1**.

D–H···A	d(D–H)	d(H···A)	D(D···A)	<DHA
Intrachain interactions				
O9–H9···O1^{i}	0.817	1.965	2.769	168
O10–H10B···O5^{ii}	0.832	1.953	2.754	161
Interchain interactions				
O10–H10A···O7^{iii}	0.823	2.257	2.999	150
C3–H3···O9^{iv}	0.930	2.623	3.548	173
C11–H11···O4^{v}	0.929	2.523	3.404	158
C10–H10···O1^{vi}	0.929	2.539	3.464	174

Symmetry code: (i) $-x+1, -y+2, -z$; (ii) $-x+2, -y+2, -z$; (iii) $x, y+1, z$; (iv) $x, y, 1+z$; (v) $1-x, 1-y, 1-z$; (vi) $x, -1+y, z$.

A comparison of the structure of the recently reported polymeric barium compound of 2-nba, namely $[Ba(H_2O)_3(2\text{-nba})_2]_n$ [61], with that of compound 1 reveals certain similarities and

Table 4
Metal coordination number, number of coordinated waters and binding mode of carboxylate groups in some Ca(II) coordination polymers.

Number	Compound	C.N.	D	Bridging $(RCOO)^-$ present	Space group	Ref.
1	$[Ca(N\text{-}MeIm)(4\text{-}nba)_2]_n$	6	1-D	yes	$P\bar{1}$	[47]
2	$[Ca(Phen)(Sa)_2]_n$	6	1-D	yes	*P*nab	[19]
3	$[Ca_{1.5}(DEF)(\mu\text{-}BDC)_{1.5}]_n$	6,7	1-D	yes	*I*2/a	[15]
4	$[[Ca(NH_2\text{-}NHCO_2)_2]\cdot H_2O]_n$	8	1-D	yes	$P\bar{1}$	[20]
5	$[Ca(2\text{-}MeIm)(H_2O)(4\text{-}nba)_2]_n$	7	1-D	yes	$P2_1/n$	[48]
6	$[Ca(gly)_2(H_2O)]_n$	8	1-D	yes	$P\bar{1}$	[7]
7	$[Ca(H_2O)(dnSa)]_n$	7	1-D	yes	$P2_1/c$	[21]
8	$[Ca(H_2O)(DMF)(benz)_2]_n$	8	1-D	yes	$P2_1/n$	[22]
9	$[Ca(val)_2(H_2O)]_n$	8	1-D	yes	$C2/c$	[7]
10	$[Ca(H_2O)_2(4\text{-}aba)_2]_n$	8	1-D	yes	$P2_12_12_1$	[8]
11	$[Ca(2\text{-}nba)_2(H_2O)_2]_n$	8	1-D	yes	$P\bar{1}$	this work
12	$[Ca_2(H_2O)_2(OAc)_3(NO_3)]_n$	8	1-D	yes	*P*nma	[23]
13	$[Ca(H_2O)_2(3\text{-}aba)_2]_n$	8	1-D	yes	*P*bcn	[11]
14	$[Ca(H_2O)_2(4\text{-}CNbenz)_2]_n$	8	1-D	yes	$P2/n$	[24]
15	$[[Ca(H_2O)_2(Nic)_2]\cdot(H_2O)_3]_n$	7	1-D	yes	$C2/c$	[25]
16	$[Ca(H_2O)_2(2\text{-}OPA)_2]_n$	8	1-D	yes	$Pna2_1$	[26]
17	$[Ca(C_4H_4O_5)_2\cdot 2H_2O]_n$	8	1-D	yes	$C2/c$	[43]
18	$[Ca(leu)_2(H_2O)_3]_n$	8	1-D	yes	$P\bar{1}$	[7]
19	$[Ca(H_2O)_3(bpdc)]_n$	8	1-D	yes	*I*ma2	[46]
20	$[Ca(H_2O)_3(2\text{-}aba)_2]_n$	7	1-D	yes	*P*bcn	[9]
21	$[[Ca(H_2O)_3(4\text{-}fba)](4\text{-}fba)]_n$	8	1-D	yes	$P2_1/c$	[27]
22	$[[Ca(H_2O)_3(benz)_2]_n$	8	1-D	yes	$P2_1/c$	[28]
23	$[Ca(H_2O)_2(C_8H_5O_3)_2]_n$	8	1-D	yes	$C2/c$	[29]
24	$[[Ca(H_2O)_2(Py\text{-}Thr)_2]\cdot(H_2O)_2]_n$	8	1-D	yes	$C2$	[30]
25	$[Ca(H_2O)_3(C_9H_{11}N_6O_5)_2]_n$	10	1-D	yes	$C2/c$	[31]
26	$[Ca(H_2O)_3(1,4\text{-}bdc)]_n$	8	1-D	yes	$P2_1/c$	[32,33]
27	$[[Ca(H_2O)_2(1,3\text{-}bdc)]_{2.5}\cdot 4\ H_2O]_n$	8	1-D	yes	$C2/c$	[34]
28	$[[Ca_5(1,3\text{-}bdc)_5(H_2O)_9]\cdot 8H_2O]_n$	8	1-D	yes	$C2/c$	[35]
29	$[[Ca(H_2O)]_2(L)(\mu\text{-}H_2O)]_n$	8	1-D	yes	$P\bar{1}$	[36]
30	$[Ca(\mu\text{-}DMF)(\mu\text{-}NDC)]_n$	8	3-D	yes	*P*nma	[15]
31	$[Ca(\mu\text{-}DEF)(\mu\text{-}TPDC)]_n$	8	3-D	yes	*P*nma	[15]
32	$[Ca(\mu\text{-}DMF)(\mu\text{-}DADC)]_n$	8	3-D	yes	*P*nma	[15]
33	$[Ca(HBTC)\cdot 2H_2O]_n$	8	2-D	yes	*P*1	[16]
34	$[Ca(H_2O)(tda)]_n$	8	2-D	yes	$P\bar{1}$	[41]
35	$[Ca_3(H_2O)_8(BTA)_2]_n\cdot 3H_2O$	7,8	2-D	yes	$P\bar{1}$	[42]
36	$[Ca(H_2O)(O_2C)_2C_6H_3CO_2H)]_n$	8	2-D	yes	$P\bar{1}$	[37]
37	$[[Ca(H_2O)_2(DTBB)]0.5C_2H_5OH]_n$	8	2-D	yes	$C2/c$	[10]
38	$[Ca(H_2O)(Hpdc)]_n$	7	3-D	yes	$P2_1/c$	[38]
39	$[Ca_2(A_3Br)]_n\cdot 5H_2O$	6	3-D	yes	*P*nma	[39]
40	$[Ca(H_2O)(C_{10}H_8O_6)]_n$	8	3-D	yes	$P2_1/c$	[40]
41	$[Ca(H_2O)_3(5\text{-}OH\text{-}BDC)]_n\cdot H_2O$	8	2-D	yes	$P2_1/c$	[44]
42	$[Ca(C_3H_3O_4)_2]_n$	8	3-D	yes	$P2_1/c$	[45]
43	$[Ca(H_2O)(bpdc)]_n$	7	3-D	yes	$P2_1$	[46]
44	$[Ca_2(H_2O)_2(NDC)]_n$	7	3-D	yes	$P2_1/c$	[46]
45	$[[Ca(H_2O)_4(Hpdc)]\cdot H_2O]_n$	8	1-D	yes	$P2_1/c$	[38]
46	$[[Ca(H_2O)_4(Hpdc)]\cdot 2H_2O]_n$	7	1-D	no	$P2_1/n$	[38]
47	$[[Ca(H_2O)_4(AIP)_2](H_2O)]_n$	8	1-D	no	*R*-3	[12]
48	$[Ca(H_2O)_4(\eta^1\text{-}4\text{-}nba)(\eta^2\text{-}4\text{-}nba)]$	7	0-D	no	$P2_1/c$	[49]

Abbreviations used: C.N. = coordination number; D = dimensionality of polymer; N-MeIm = N-methylimidazole; 4-nba = 4-nitrobenzoate; Phen = 1,10-phenanthroline; Sa = salicylato; BDC – benzene-1,4-dicarboxylate, DEF = N,N-diethylformamide; 2-MeIm = 2-methylimidazole; gly = glycinate; dnSa = 3,5 dinitrosalicylato; DMF = N,N-dimethylformamide; benz = benzoate; val = rac-valinate; 4-aba = 4-aminobenzoate; 2-nba = 2-nitrobenzoate; OAc = acetate; 3-aba = 3-aminobenzoate; 4-CNbenz = 4-cyanobenzoate; Nic = nicotinate; OPA = 2-oxo-1,2-dihydropyridine-1-acetate; $C_4H_4O_5$ = malate; leu = rac-leucinate; bpdc = 4,4′-biphenyldicarboxylic acid; 2-aba = 2-aminobenzoate; 4-fba = 4-fluorobenzoate; $C_8H_5O_3$ = 2-formylbenzoate;PY-Thr = N-(6-amino-3,4-dihydro-3-methyl-5-nitroso-4-oxopyrimidin-2-yl) thronato; $C_9H_{11}N_6O_5$ = bis[N-(6-amino-3,4-dihydro-3-methyl-5-nitroso-4-oxopyrimidine-2-yl) glycylglycinate; 1,4-bdc = 1,4-benzenedicarboxylate; 1,3-bdc = 1,3-benzenedicarboxylate; L = 4-(2-nitrophenyl)-3,6-dioxaoctane dioate; NDC – naphthalene 2,6-dicarboxylate; TPDC – 4,5,9,10-tetrahydropyrene-2,7-dicarboxylate; DADC – 5,10-dihydroanthracene-2,7-dicarboxylate; H_3BTC = benzene-1,3,5-tricarboxylic acid; tda = $S(CH_2COO)_2^{2-}$; BTA = 1,3,5-benzenetriacetate; $(O_2C)_2C_6H_3CO_2H$ = trimellitate; DTBB = 2,2′-dithiobis(benzoate); Hpdc = 3,5-pyrazoledicarboxylate; A_3Br = 1,3-biscarboxyethylimidazolium bromide; $C_{10}H_8O_6$ = benzene 1,4-dioxylacetate; 5-OH-BDC = 5-hydroxy isophthalate; $C_3H_3O_4$ = malonate; AIP = 5-aminoisopthalate.

several differences. Both compounds contain alkaline-earth:2-nba in a 1:2 ratio and are 1-D polymers based on dinuclear units. The alkalnei-earth metals in both compounds are linked to four different carboxylate ligands. However the compounds are differently hydrated and Ba adopts a 9 coordination. Of the two crystallographically independent 2-nba ligands in the Ba compound, one ligand binds in a μ_2–η^2:η^1 manner, as observed in the Ca compound, while the other 2-nba ligand functions as a monoatomic bridge between two adjacent Ba ions in the chain with one of the nitro oxygen atoms bonded to one Ba, resulting in a denticity of three for this second 2-nba ligand. This binding mode of the carboxylate moiety in $[Ba(H_2O)_3(2\text{-}nba)_2]_n$ can be designated as μ_2–η^1:η^1. In the 1-D polymeric chain alternating pairs of bivalent metals are bridged by a pair of 2-nba ligands.

In order to understand the role of the nitro group in the structural chemistry of Ca-nitrobenzoates, a comparison of the structural features of the title Ca compound **1** with the related monomeric Ca compound [49] of 4-nba namely $[Ca(H_2O)_4(\eta^1\text{-}4\text{-}nba)(\eta^2\text{-}4\text{-}nba)]$ is made. In the 4-nba compound, containing the nitro group para to the carboxylate functionality, the heptacoordinated Ca(II) is linked to two crystallographically independent 4-nba ligands which coordinate in a monodentate (η^1) and bidentate

(η^2) manner, respectively. In our original report [49] on the structural aspects of [Ca(H_2O)$_4$(η^1-4-nba)(η^2-4-nba)] only the O–H···O interactions were described, and the weak C–H···O interactions were not mentioned. A reinvestigation of the structure data reveals that one nitro oxygen atom on each unique 4-nba is involved in a C–H···O interaction at distances of 2.61 and 2.45 Å, accompanied by CHO angles of 158–166°, respectively. Hence the –NO_2 group in the 4-nba and 2-nba compounds of Ca, which are differently disposed with respect to the carboxylate in the benzene ring, are very similar in terms of their secondary interactions. However there is a noticeable difference between 1 and [Ca(H_2O)$_4$(η^1-4-nba)(η^2-4-nba)] in terms of the number of coordinated waters, which can account for the observed structural variation in these two compounds.

3.4. Comparative study of Ca(II) coordination polymers

In the 4-nba compound [Ca(H_2O)$_4$(η^1-4-nba)(η^2-4-nba)], each Ca(II) ion is linked to four oxygen atoms from water, and the monodentate and bidentate coordination of 4-nba results in hepta-coordination around Ca. In contrast, the tridenticity of the two crystallographically independent bridging 2-nba ligands in **1** leads to an eight coordination around Ca in the diaqua compound [Ca(2-nba)$_2$(H_2O)$_2$]$_n$ **1**, a feature observed in several calcium-carboxylates [19]. The attainment of a higher coordination number appears to be a key feature in Ca structural chemistry. It is noted that when there are a lesser number of coordinated water molecules in a calcium-carboxylate, the carboxylate ligand prefers to adopt a bridging mode of ligation. The importance of the number of coordinated waters can be evidenced by a comparative study of calcium-carboxylates, several of which are listed in Table 4.

Polymeric Ca-carboxylates of varying dimensionalities, derived from different carboxylic acids, are listed in Table 4. The coordination number of Ca(II) varies from 6 to 10, with eight coordination being observed in the majority of the compounds. It is interesting to note that in all the coordination polymers, excepting the three Ca compounds (entry numbers 45–47) derived from the dicarboxylic acids Hpdc (3,5-pyrazoledicarboxylate) and AIP (5-aminoisophthalate), the number of coordinated water molecules is three or less and in all such compounds the carboxylate ligand exhibits a bridging coordination mode leading to a polymeric chain. In the helical chain compound [[Ca(H_2O)$_4$(AIP)$_2$](H_2O)]$_n$, which has four water molecules, the entire AIP ligand acts as a bridge between two symmetry related Ca(II) ions, with each carboxylate showing a bidentate coordination to one Ca(II). In this case, octacoordination around Ca can be achieved without a bridging carboxylate mode of binding. Likewise in [[Ca(H_2O)$_4$(Hpdc)]·2H_2O]$_n$, the Hpdc ligand functions as a bridge between two Ca(II) ions with each carboxylate group binding in a monodentate fashion to one Ca. Additionally one of the pyrazole N atoms is also ligated in one of the ligands. It is to be noted that both AIP and Hpdc are ditopic ligands as they contain two carboxylate groups anchored onto a ring, and the ditopicity is responsible for the polymeric structure, without making use of a bridging carboxylate mode in these compounds. It is interesting to note that in the 1-D polymer [[Ca(H_2O)$_4$(Hpdc)].H_2O]$_n$, synthesized at a more acidic pH, a bridging carboxylate ligation is observed even though the Ca is coordinated to four water molecules. In this case pyrazole N ligation is not observed. From Table 4 it is very clear that when the number of coordinated water molecules is three or less, a bridging carboxylate binding mode is always observed. In Ca(II) compounds derived from mono carboxylic acids like 4-nbaH, for example [Ca(H_2O)$_4$(η^1-4-nba)(η^2-4-nba)] (entry number 48 in Table 4) seven coordination around Ca is observed due to the mono and chelating binding modes of the crystallographically independent 4-nba ligands, and this compound exhibits a zero-dimensional structure. When the number of water ligands in this compound is reduced by heating, the 4-nba adopts a bridging binding mode leading to a polymeric structure, as reported by us recently [47,48]. Another noteworthy feature is the tendency for the majority of the compounds to crystallize in centrosymmetric space groups.

4. Conclusions

In the present work we have described the synthesis, spectral and thermal properties and structural characterization of a new Ca(II) coordination polymer based on a tricyclic dicalcium-dicarboxylate building block. A comparative study of several Ca polymers shows that when the number of coordinated water molecules is three or less, in a Ca-carboxylate, the carboxylate ligand adopts a bridging mode of ligation.

Acknowledgement

B.R.S. thanks Prof. Samar K. Das School of Chemistry, University of Hyderabad, for the X-ray intensity data of **1** and the University Grants Commission, (UGC) New Delhi for financial support under the Special Assistance Program (DRS-II).

Appendix A. Supplementary data

CCDC 690437 contains the supplementary crystallographic data for compound 1. These data can be obtained free of charge via http://www.ccdc.cam.ac.uk/conts/retrieving.html, or from the Cambridge Crystallographic Data Centre, 12 Union Road, Cambridge CB2 1EZ, UK; fax: (+44) 1223-336-033; or e-mail: deposit@ccdc.cam.ac.uk.

Supplementary data associated with this article can be found, in the online version, at doi:10.1016/j.poly.2009.06.085.

References

[1] H. Einspahr, C.E. Bugg, Acta Crystallogr., B 36 (1980) 264.
[2] A.K. Katz, J.P. Glusker, S.A. Beebe, C.W. Bock, J. Am. Chem. Soc. 118 (1996) 5752.
[3] X. Shao, B.A. Davletov, R.B. Sutton, T.C. Sudhof, J. Rizo, Science 273 (1996) 248.
[4] K.M. Fromm, E.D. Gueneau, Polyhedron 23 (2004) 1479.
[5] R.C. Mehrotra, R. Bohra, Metal Carboxylates, Academic Press, London, 1983.
[6] F.A. Cotton, G. Wilkinson, C.A. Murillo, M. Bochmann, Advanced Inorganic Chemistry, 6th ed., John Wiley and Sons, Inc., Chichester, 1999.
[7] S. Fox, I. Büsching, W. Barklage, H. Strasdeit, Inorg. Chem. 46 (2007) 818.
[8] R. Murugavel, V.V. Karambelkar, G. Anantharaman, Indian J. Chem. 39A (2000) 843.
[9] R. Murugavel, V.V. Karambelkar, G. Anantharaman, M.G. Walawalkar, Inorg. Chem. 39 (2000) 1381.
[10] R. Murugavel, K. Baheti, G. Anantharaman, Inorg. Chem. 40 (2001) 6870.
[11] R. Murugavel, S. Banerjee, Inorg. Chem. Commun. 6 (2003) 810.
[12] R. Murugavel, P. Kumar, M.G. Walawalkar, R. Mathialagan, Inorg. Chem. 46 (2007) 6828.
[13] M. Dinca, J.R. Long, J. Am. Chem. Soc. 127 (2005) 9376.
[14] J.A. Rood, B.C. Noll, K.W. Henderson, Inorg. Chem. 45 (2006) 5521.
[15] C.A. Williams, A.J. Blake, C. Wilson, P. Hubberstey, M. Schroder, Cryst. Growth Des. 8 (2008) 911.
[16] M.J. Platers, R.A. Howie, A.J. Roberts, Chem. Commun. (1997) 893.
[17] K.M. Fromm, Coord. Chem. Rev. 252 (2008) 856. and references therein.
[18] H. Einspahr, C.E. Bugg, Acta Crystallogr., B 37 (1981) 1044.
[19] R. Murugavel, R. Korah, Inorg. Chem. 46 (2007) 11048.
[20] A. Brainbanti, A.M. Lanfredi, M.A. Pellinghelli, A. Tiripicchio, Chem. Commun. (1970) 377.
[21] W.-D. Song, X.-X. Guo, C.-H. Zhang, Acta Crystallogr., E 63 (2007) m399.
[22] S. Yano, M. Numata, M. Kato, S. Motoo, T. Nishimura, Acta Crystallogr., E 57 (2001) m488.
[23] B.G. Cooksey, L.T. Gibson, A.R. Kennedy, D. Littlejohn, L. Stewart, N.H. Tennent, Acta Crystallogr., C 55 (1999) m324.
[24] R.-X. Yuan, R.-G. Xiong, Z.-F. Chen, X.-Z. You, S.-M. Peng, G.-H. Lee, Inorg. Chem. Commun. 4 (2001) 430.
[25] B.L. Cole, E.M. Holt, Inorg. Chim. Acta 108 (1985) 159.
[26] J.-G. Zhao, S. Gao, Z.-Y. Zhang, L.-H. Huo, H. Zhao, Acta Crystallogr., E 62 (2006) m278.
[27] A. Karipides, C. McKinney, K. Peiffer, Acta Crystallogr., C 44 (1988) 46.

[28] I. Senkovska, U. Thewalt, Acta Crystallogr., C 61 (2005) m448.
[29] M. Odabaşoğlu, O. Büyükgüngör, Acta Crystallogr., E 63 (2007) m712.
[30] M.L.G. Salido, P.A. Mascaros, R.L. Garzon, M.D.G. Valero, J.N. Low, J.F. Gallagher, C. Glidewell, Acta Crystallogr., B 60 (2004) 46.
[31] J.N. Low, P. Arranz, J. Cobo, M.A. Fontecha, M.L. Godino, R. Lopez, D. Cannon, A. Quesada, C. Glidewell, Acta Crystallogr., C 57 (2001) 680.
[32] R.H. Groeneman, J.L. Atwood, Cryst. Eng. 2 (1999) 241.
[33] S.H. Dale, M.R.J. Elsegood, Acta Crystallogr., E 59 (2003) m586.
[34] L.-C. Yu, Z.-F. Chen, H. Liang, C.-S. Zhou, Y. Li, J. Mol. Struct. 750 (2005) 35.
[35] S.H. Dale, M.R.J. Elsegood, Acta Crystallogr., C 59 (2003) m540.
[36] A. Bacchi, M. Carcelli, C. Pelizzi, G. Pelizzi, P. Pelagatti, D. Rogolino, M. Tegoni, C. Viappiani, Inorg. Chem. 42 (2003) 5871.
[37] C. Volkringer, T. Loiseau, G. Férey, J.H. Warren, D.S. Wragg, R.E. Morris, Solid State Sci. 9 (2007) 455.
[38] L. Pan, T. Frydel, M.B. Sander, X. Huang, J. Li, Inorg. Chem. 40 (2001) 1271.
[39] Z. Fei, T.J. Geldbach, R. Scopelliti, P.J. Dyson, Inorg. Chem. 45 (2006) 6331.
[40] Y. Yang, G. Jiang, Y.-Z. Li, J. Bai, Y. Pan, X.-Z. You, Inorg. Chim. Acta 359 (2006) 3257.
[41] A. Grirrane, A. Pastor, E. Álvarez, R. Moyano, A. Galindo, Inorg. Chem. Commun. 10 (2007) 1125.
[42] H.-F. Zhu, Z.-H. Zhang, W.-Y. Sun, T. Okamura, N. Ueyama, Cryst. Growth Des. 5 (2005) 177.
[43] T. Jini, K.V. Saban, G. Varghese, S. Naveen, M.A. Shridhar, J.S. Prasad, J. Alloys Compd. 433 (2007) 211.
[44] Q. Shuai, S. Chen, S. Gao, Inorg. Chim. Acta 360 (2007) 1381.
[45] K. Aliouane, N. Rahahlia, A. Guehria-Laidoudi, S. Dahaoui, C. Lecomte, Acta Crystallogr., E 63 (2007) m1834.
[46] C. Volkringer, J. Marrot, G. Ferey, T. Loiseau, Cryst. Growth Des. 8 (2008) 685.
[47] B.R. Srinivasan, S.Y. Shetgaonkar, J.V. Sawant, P. Raghavaiah, Polyhedron 27 (2008) 3299.
[48] B.R. Srinivasan, S.Y. Shetgaonkar, C. Nather, W. Bensch, Polyhedron 28 (2009) 534.
[49] B.R. Srinivasan, J.V. Sawant, P. Raghavaiah, Indian J. Chem. 45A (2006) 2392.
[50] B.R. Srinivasan, S.C. Sawant, Thermochim. Acta 402 (2003) 45.
[51] B.R. Srinivasan, J.V. Sawant, P. Raghavaiah, J. Chem. Sci. 119 (2007) 11.
[52] Bruker SMART V5.630, SAINT-PLUS V6.45 and SADABS Bruker–Nonius Analytical X-ray Systems Inc., Madison, Wisconsin, USA, 2003.
[53] G.M. Sheldrick, Acta Crystallogr. 64A (2008) 112.
[54] B.R. Srinivasan, S.C. Sawant, S.N. Dhuri, Indian J. Chem. 41A (2002) 290.
[55] B.R. Srinivasan, P. Raghavaiah, J.V. Sawant, Acta Crystallogr. 63E (2007) m2251.
[56] B.R. Srinivasan, J.V. Sawant, C. Näther, W. Bensch, J. Chem. Sci. 119 (2007) 243.
[57] B.R. Srinivasan, J.V. Sawant, S.C. Sawant, P. Raghavaiah, J. Chem. Sci. 119 (2007) 593.
[58] B.R. Srinivasan, S.C. Sawant, S.K. Das, Indian J. Chem. 43A (2004) 1066.
[59] B.R. Srinivasan, G.K. Rane, J. Chem. Sci. 120 (2009) 145.
[60] B.R. Srinivasan, J.V. Sawant, P. Raghavaiah, Indian J. Chem. 48A (2009) 181.
[61] B.R. Srinivasan, S.Y. Shetgaonkar, P. Raghavaiah, J. Chem. Sci. 120 (2008) 249.

FTIR transmission spectra were taken on Perkin Elmer Spectrum BX model Infrared Spectrophotometer from 4000 to 400 cm^{-1}.

Scanning Electron Microscopy (SEM) analysis was performed on a FEI XL40 Sirion FEG Digital Scanning Microscope. Samples were coated with gold at 10 mA for 2 min prior to SEM analysis.

Magnetic measurements were carried out with the Quantum Design Model 6000 Vibrating Sample Magnetometer (VSM) and parameters like specific saturation magnetization (Ms), coercive force (Hc) and remanence (Mr) were evaluated.

2.2. Procedure

In an appropriate ratio, analytical grade of cobalt nitrate ($Co(NO_3)_2{\cdot}6H_2O$), zinc nitrate ($Zn(NO_3)_2{\cdot}6H_2O$), ferric nitrate ($Fe(NO_3)_3{\cdot}9H_2O$) and constant amount of urea (1 g) were mixed to obtain precursor solutions. The crucibles containing the precursor solution was introduce into a microwave oven one by one. Initially, the solution boils and undergoes dehydration followed by decomposition with the evolution of large amount of gases (N_2O and CO_2). After the solution reaches to the point of spontaneous combustion, it begins to burn and releases lots of heat, vaporizes all the solution instantly and becomes solid burning at high temperature. The entire combustion process takes only 5 min to produce ferrite powders in a microwave oven.

3. Results and discussion

3.1. XRD analysis

The X-ray diffraction patterns (Fig. 1) of the prepared samples, $Co_xZn_{1-x}Fe_2O_4$ ($x = 0.2, 0.4, 0.8$) exhibited the 11 reflection planes (1 1 1), (2 2 0), (3 1 1), (2 2 2), (4 0 0), (4 2 2), (5 1 1), (4 4 0), (6 2 0), (5 3 3) and (6 2 2) that indicate the presence of the spinel cubic structure [26]. All XRD peaks are correspondent with the JCPDS card no. 89-1012 ($ZnFe_2O_4$) and 22-1086 ($CoFe_2O_4$).

The reaction can be described as follows:

$$(1-x)Zn(NO_3)_2(s) + xCo(NO_3)_2(s) + 2Fe(NO_3)_3(s) + 7CO(NH_2)_2(s) + 13O_2(g) \rightarrow Co_xZn_{(1-x)}Fe_2O_4(s) + 11N_2O(g) + 14H_2O(g) + 14CO_2(g)$$

To determine the crystallite size distribution of the samples, the diffraction profiles (11 reflection planes) were fitted according to the Eq. (1) in Wejrzanowski et al. [27] which allows the estimation of average crystallite size and its standard deviation from XRD profile fitting. The calculated average crystallite sizes, D, and their standard deviations, σ, were presented in Table 1.

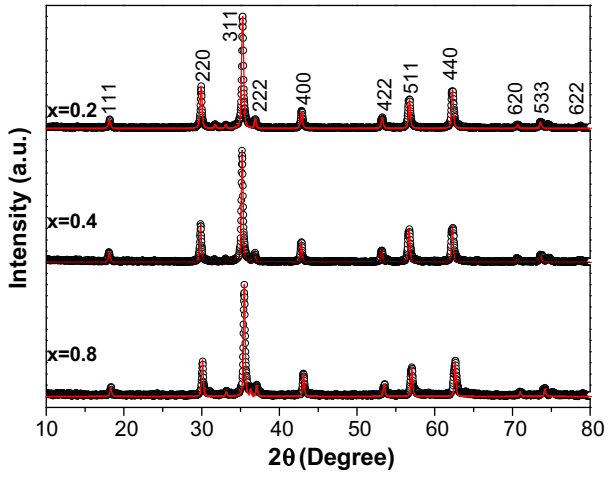


Fig. 1. XRD powder patterns of $Co_xZn_{1-x}Fe_2O_4$ ($x = 0.2, 0.4, 0.8$) nanoparticles.

The lattice constant for each peak of each sample was calculated by using the formula:

$a = d\,(h^2 + k^2 + l^2)^{1/2}$, where h, k, and l are miller indices of the crystal planes. To determine the exact lattice parameter for each composition (sample), Nelson–Riley method was used. The Nelson–Riley function $F(\theta)$ is given as $F(\theta) = 1/2[(\cos^2\theta/\sin\theta) + \cos^2\theta/\theta]$. The values of lattice constant a_o of all the peaks for a sample was plotted against $F(\theta)$ (not given). Then using a least square fit method exact lattice constant a_o was determined (Table 1). The point where the least square fit straight line cut the y-axis (where $F(\theta) = 0$) is the actual lattice parameter of the composition.

It was observed that the lattice constant for each composition decreases with increasing Co substitution and follows Vegard's law (Table 1). This probably due to variation of ionic sizes of the Zn^{2+} and Co^{2+} cations since ionic size of Co^{2+} (0.72 Å) is lower than that of Zn^{2+} (0.82 Å) [28,29]. A similar behavior was also observed by Hossain et al. [30]. Because the lattice constants (a_o) were found to be within the range of the lattice constants of $ZnFe_2O_4$ and $CoFe_2O_4$.

3.2. FTIR analysis

FTIR spectrum of as-made ferrite nanocrystals is presented in Fig. 2. Two main broad metal-oxygen bands are seen in the FTIR spectra of all spinels, and ferrites in particular. The highest one, ν_1, is generally observed in the range 600–500 cm^{-1}, and it corresponds to intrinsic stretching vibrations of the metal at the tetrahedral site (T_d), $M_{tetra} \leftrightarrow O$, whereas the ν_2 lowest band is usually observed in the range 430–385 cm^{-1}, is assigned to octahedral-metal stretching (O_h), $M_{octa} \leftrightarrow O$ [3–9,31–34]. In the FTIR spectrum of the products, we also observed the band at 600 cm^{-1} is assigned as ν_1 ($M_{tetra} \leftrightarrow O$). Due to the limitation of our FTIR instrument near 400 cm^{-1}, ν_2 (430–385 cm^{-1}), and below 400 cm^{-1}, ν_3 (328 cm^{-1}) and ν_4 (below 300 cm^{-1}) were not detected clearly. The absorption bands observed at ~3450 and ~1630 cm^{-1} prove the presence of adsorbed water on the surface of the ferrite nanocrystals. The small absorption band at around 1380 and 1720 cm^{-1} in the as-prepared material may be assigned to the unreacted metallic salts and carbonyl (from urea), respectively. In the $Co_xZn_{1-x}Fe_2O_4$ nanocrystals, Zinc ion occupies the tetrahedral (T_d) site while cobalt and iron have two valences, therefore partially occupy both the tetrahedral and octahedral sites [35]. Consequently, the ν_1 band, observed at 561 cm^{-1} for $ZnFe_2O_4$ can be assigned to tetrahedral Zn^{2+} stretching and the ν_2 band, observed at 425 cm^{-1}, involves the Fe^{3+} vibration at the octahedral site. In the $Co_xZn_{1-x}Fe_2O_4$ sample, when Zn^{2+} are replaced by smaller Co^{2+} ions with lower atomic weight, the ν_1 vibration shifts to higher wavenumber.

3.3. SEM analysis

The scanning electron micrographs of $Co_xZn_{1-x}Fe_2O_4$ nanocrystals (Fig. 3) shows that the sample has a large grain structure. Heating has resulted in sintering of the well-faceted grains to form solid bodies. It is a very porous network of sintered bodies. The scanning

Table 1
Calculated crystallite sizes (nm) with standard deviations of $Co_xZn_{1-x}Fe_2O_4$ ($x = 0.2$, 0.4, 0.6) nanoparticles from XRD and their lattice constants (a_o).

Nanoparticles	D (nm)	Sigma	Lattice constant (Å)
$Co_{0.2}Zn_{0.8}Fe_2O_4$	39.1	9.8	8.426(±1)
$Co_{0.4}Zn_{0.6}Fe_2O_4$	35.1	11.2	8.412(±3)
$Co_{0.8}Zn_{0.2}Fe_2O_4$	37.5	12	8.396(±2)

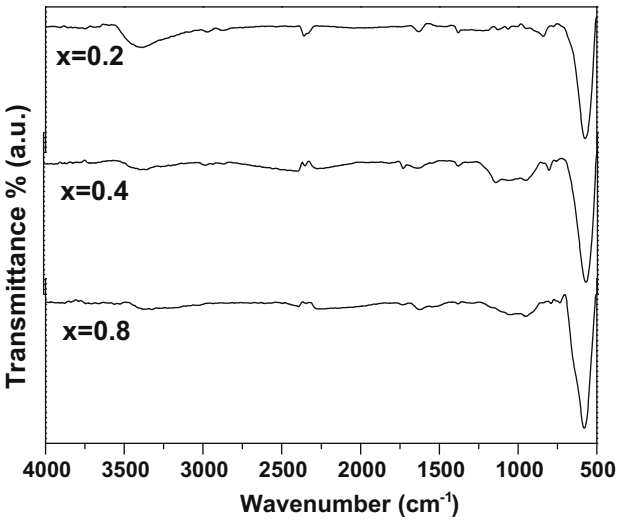


Fig. 2. FTIR spectrum of $Co_xZn_{1-x}Fe_2O_4$ ($x = 0.2, 0.4, 0.8$) nanoparticles.

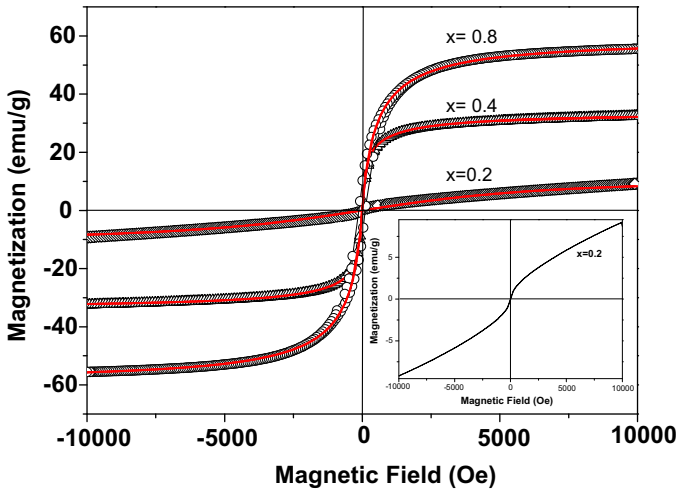


Fig. 4. Magnetic hysteresis loops of $Co_xZn_{1-x}Fe_2O_4$ nanoparticles at room temperature The solid lines represents the best fits for the Langevin function (The inset shows the M–H curve of $Co_xZn_{1-x}Fe_2O_4$ ($x = 0.2$) nanoparticles).

electron micrograph reveals a porous network, more like a foam. The surface of the powders shows pores formed by the escaping gases during the combustion reaction. These particles exhibit a network with voids and pores typical of combustion – synthesized powders [3,8,36]. The porous powders are highly friable, which facilitate easy grinding to obtain finer particles [37].

3.4. VSM analysis

All magnetic measurements have been carried out by using Quantum Design Vibrating Sample Magnetometer (QD-VSM). The samples were cooled either in the presence of an external magnetic field (Field cooling case-FC) or in zero field (Zero field cooling case-ZFC) and, the magnetic hysteresis curves were recorded by sweeping the external field between ±10 kOe at different temperatures.

We have taken $Co_xZn_{1-x}Fe_2O_4$ ($x = 0.2, 0.4, 0.8$) as a basic system for the following reasons. This sample is a mixture of $CoFe_2O_4$ with long range ferrimagnetic transition temperature at 790 K and $ZnFe_2O_4$ with antiferromagnetic Neel temperature at 9 K. It has been reported that $CoFe_2O_4$ has the highest anisotropy constant K_1 among the ferrite spinels due to the presence of Co^{2+} ions on B sites. $CoFe_2O_4$ is a good candidate for magnetic recording media and magnetic fluids whereas, $ZnFe_2O_4$ is used as a catalyst [38–40].

Fig. 4 represents the room temperature magnetic hysteresis of the $Co_xZn_{1-x}Fe_2O_4$ nanocrystals over the field range −10 kOe to 10 kOe. The value of magnetization sharply increases with the external magnetic field strength at low field region. However, it can not reach a saturation state yet in the presence of a relatively strong magnetic field of even 10 kOe. Similar reports about room temperature magnetization have been coated by others [41,42].

For all samples, a typical superparamagnetic 'S'-like shape of hysteresis curves (without open loops- coercive fields are zero) were observed at room temperature. Those 'S'-like shape loops can be divided into two parts: linear parts and curvature parts. While the M–H curve shows no hysteresis and no saturation for $x = 0.2$ and $x = 0.4$ samples, it shows a small hysteretic behavior with a coercivity of 117 Oe for $x = 0.8$ sample. The saturation magnetization of the samples were found (obtained by extrapolating M vs. 1/H plot to 1/H = 0) for $x = 0.2$, 0.4, 0.8 compositions as 11.5 emu/g, 34.1 emu/g and 59.0 emu/g, respectively.

The increase in the saturation magnetization and the coercivity of the nanocrystals by increasing the Co content can be attributed to the magnetic character and the anisotropic nature of cobalt. Since more Co ions replace with Zn ions by increasing the "x", the saturation magnetization and the coercivity increases and the sample with $x = 0.8$, $Co_{0.8}Zn_{0.2}Fe_2O_4$, shows ferromagnetic behavior at room temperature.

At room temperature, the absence of saturation, remanent magnetization and coercivity in M–H curves indicates the superparamagnetic nature of the particles ($x = 0.0$ and $x = 0.4$), $ZnFe_2O_4$ and $Co_{0.4}Zn_{0.6}Fe_2O_4$, which relax back their spins by rotation on removal of applied magnetic field so as to give a zero net magnetic moment [4,43–47]. The absence of coercivity at room temperature could also be attributed to the presence of more Zn concentration in the otherwise ferromagnetic cobalt ferrite phase, for the presented composition [48,49].

Fig. 5 shows M–H loops at 10 K for $Co_xZn_{1-x}Fe_2O_4$ samples with different Co content. $Co_xZn_{1-x}Fe_2O_4$ nanocrystals show a considerable saturation magnetization, the coercivity and remanence at lowest temperature and they increase with the increase of Co content. The samples does not show saturation even at 10 kOe. The saturation magnetization is found to increase from 64.32 emu/g for the $x = 0.2$ to 106 emu/g for the $x = 0.8$ at the temperature of 10 K.

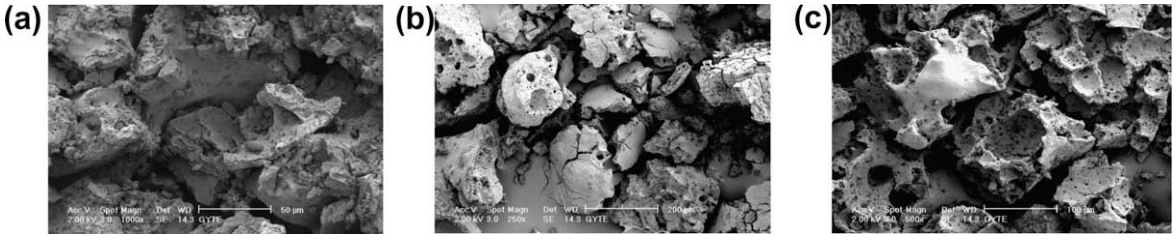


Fig. 3. SEM micrographs of $Ni_xCo_{1-x}Fe_2O_4$ nanoparticles; (a) $x = 0.2$, (b) $x = 0.4$, (c) $x = 0.8$.

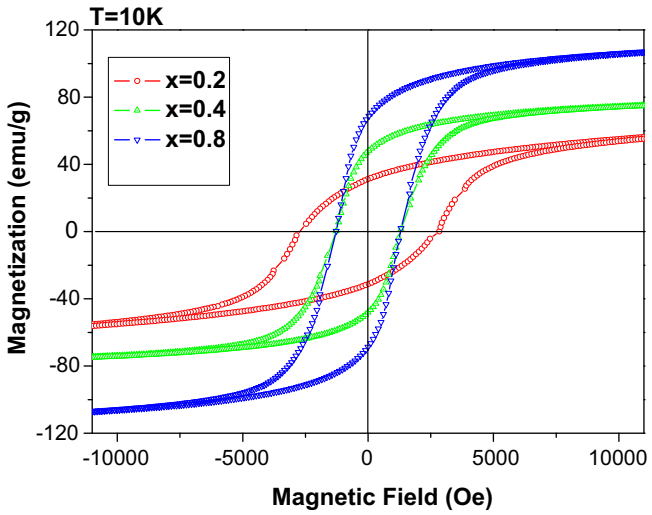


Fig. 5. Magnetic hysteresis loops of $Co_xZn_{1-x}Fe_2O_4$ nanoparticles at 10 K.

The wide hysteresis loop for $x = 0.2$ at 10 K with a coercive field (H_c) of 2.8 kOe and remanent magnetization (M_r) of 32 emu/g confirm the presence of large ferromagnetic order at low temperatures. The large values of coercive field (H_c) and irreversibility field (H_{irr}) below the blocking temperature is associated with the increase of effective anisotropy field (K_{eff}), where $K_{eff} = 4\pi M_s H_{irr}$. This can be attributed to the random freezing of clusters in locally canted states, for which the random anisotropy energy will act as pinning potential. The decrease of remanent magnetization (M_r) and saturation magnetization (M_s) suggest the decrease of strongly interacted magnetic state towards a paramagnetic state [42,44,50].

For $x = 0.4$ and $x = 0.8$ remanent magnetizations of 46 emu/g and 67 emu/g, a coercivity of 1280 Oe and 1282 Oe, the saturation magnetization of 78.6 emu/g and 106 emu/g are observed at 10 K.

The changes in magnetic properties such as M_s, H_c, and M_r are due to the influence of the cationic stoichiometry and their occupancy in the specific sites. The magnetic order in the cubic system of ferromagnetic spinels is due to super-exchange interaction mechanism occurring between the metal ions in the tetrahedral A-sites and octahedral B-sites. The substitution of Zn^{2+} ion (with zero magnetic moment), which has a preferential A site occupancy results in the reduction of super-exchange interaction between A and B sites. Hence, it is possible to vary the magnetic properties by varying the degree of Zn substitution [29]. Additionally, the changes can also be attributed to the formation of dead layer on the surface, existence of random canting of particle surface spins, non-saturation effects due to random distribution of particle size, deviation from the normal cation distribution, presence of adsorbed water, etc. [8,42,51–54].

Zero field cooled (ZFC) and field cooled (FC) temperature dependent magnetizations performed on a VSM device for $Co_xZn_{1-x}Fe_2O_4$ nanocrystals are presented in Fig. 6. In ZFC measurements, the samples are cooled from room temperature to 5 K without applying an external magnetic field. After reaching 5 K, a 100 Oe magnetic field is applied (FC) and the magnetization is recorded as the temperature is increased. As seen in Fig. 6a, for $x = 0.2$ the ZFC case upon increasing the measurement temperature, the magnetization of $Co_{0.2}Zn_{0.8}Fe_2O_4$ nanoparticle increases and reaches a maximum value of 8.5 emu/g at the blocking temperature (127 K), T_B. Above the blocking temperature, the magnetization

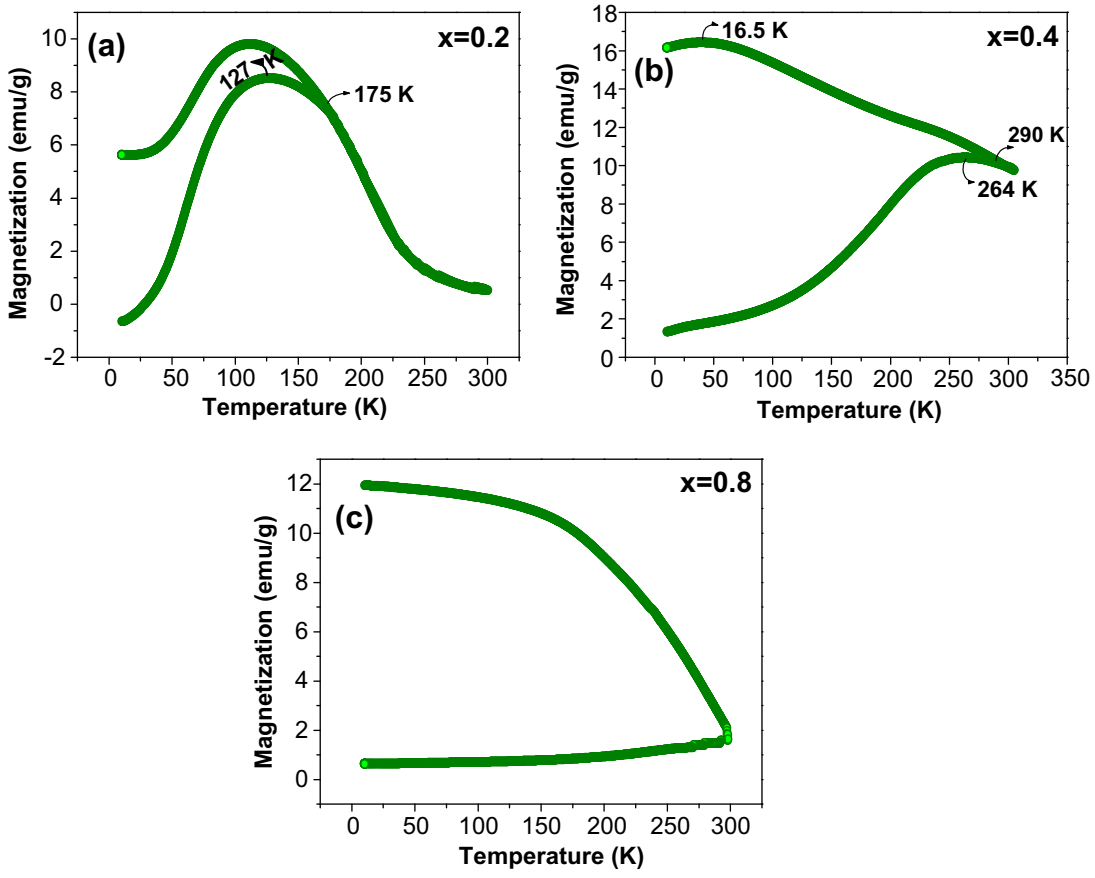


Fig. 6. M–T curve of $Co_xZn_{1-x}Fe_2O_4$ nanoparticles with applied field of 100 Oe.

starts to decrease and displays a typical paramagnetic behavior. FC magnetization curve of $Co_{0.2}Zn_{0.8}Fe_2O_4$ nanocrystals follows the same path as ZFC curve, but it unstucks from ZFC curve at 175 K. The separation between the ZFC and the FC curves gives an indication that there is a non-equilibrium magnetization and represents the irreversibility temperature, T_{irr} [55]. And the FC magnetization curve reaches to a maximum magnetization of 9.8 emu/g at 110 K then starts to decrease by decreasing temperature.

Fig. 6b displays the M–T curves of the $Co_{0.4}Zn_{0.6}Fe_2O_4$ nanoparticle at the applied magnetic field of 100 Oe. In the case of the FC curve, the magnetization increases to a value of 16.5 emu/g down to 50 K, which is due to the decrease of the interactions among the particles with decreasing applied field [56]. Below this temperature, it slightly decreases.

For the ZFC curve, the magnetization slowly increases down to 270 K. At around 264 K it exhibits typical features of an assembly of magnetic particles with a distribution of blocking temperatures and the particles indicate the spin-glass behavior [57]. This is compatible with the heat capacity results obtained by Hamdeh et al. [58]. In detail, the magnetization increases slowly with the rise of the temperature up to 100 K. While the temperature exceeds 100 K, as a result of the uncompensated spins in the two sublattices, magnetization increases rapidly with the rise of the temperature, and reaches a peak at about 264 K. At this temperature, the relaxation time of spins are equal to the measurement time of VSM, the magnetization decreases, indicating the spins become disordered, namely superparamagnetic.

The magnetic properties of $Co_{0.8}Zn_{0.2}Fe_2O_4$ nanocrystals have been studied by measuring the magnetization as a function of temperature; ZFC and FC (with field of 200 Oe) M–T curves are shown in Fig. 6c. While the ZFC curve slightly increasing with the temperature, FC curve slightly decreases up to 150 K and rapidly above 150 K. Both curves do not come together up to room temperature. This means that the blocking temperature of the sample is higher than the room temperature.

4. Conclusion

Using nitrates of nickel, cobalt, and iron in combination with urea, fine cobalt doped zinc ferrite powders have been successfully synthesized by microwave-induced combustion method. XRD and FT-IR analysis confirm the composition and structure as spinel ferrite. Average crystallite sizes obtained by XRD line-profile fitting were between 35 and 39 nm. The novel combustion method provides a rapid and reproducible route for the preparation of crystalline spinel ferrite. The scanning electron micrograph revealed that products were porous network powders with a substantial surface area. Magnetization measurements have revealed that the samples having less Co content shows superparamagnetic behavior at room temperature. Temperature dependent magnetization measurements presented the spin-glass like nature of the samples. The blocking temperature of the sample has also increased by increasing the cobalt content, which indicates that the samples show a magnetic phase transition from superparamagnetic to ferromagnetic phase.

Acknowledgements

This work is supported by Fatih University under BAP Grant Nos. P50010701 and P50020803-2.

References

[1] R.D.K. Misra, A. Kale, R.S. Srivatsava, O. Senkov, Mater. Sci. Technol. 19 (2003) 826.
[2] Y. Qu, H. Yang, N. Yang, Y. Fan, H. Zhu, G. Zou, Mater. Lett. 60 (2006) 3548.
[3] A. Baykal, N. Kasapoğlu, Y. Köseoğlu, A.C. Basaran, H. Kavas, M.S. Toprak, Cent. Eur. J. Chem. 6 (1) (2008) 125.
[4] Y. Köseoğlu, A. Baykal, M.S. Toprak, F. Gözüak, A.C. Basaran, B. Aktas, J. Alloy Compd. 462 (2008) 209.
[5] A. Baykal, N. Kasapoğlu, Y. Köseoğlu, M.S. Toprak, H. Bayrakdar, J. Alloys Compd. 464 (2008) 514.
[6] N. Kasapoglu, B. Birsoz, A. Baykal, Y. Köseoğlu, M.S. Toprak, Cent. Eur. J. Chem. 5 (2) (2007) 570.
[7] A.K.M. Akther Hossain, H. Tabata, T. Kawai, J. Magn. Magn. Mater. 320 (2008) 1157.
[8] N. Kasapoğlu, A. Baykal, Y. Köseoğlu, M.S. Toprak, Scripta Materialia 57 (2007) 441.
[9] R. Arulmurugan, B. Jeyadevan, G. Vaidyanathan, S. Sendhilnathan, J. Magn. Magn. Mater. 288 (2005) 470.
[10] M.A. Ahmed, M.K. El-Nimr, A. Tawfik, A.M. Abbo El-Ata, J. Mater. Sci. Lett. 7 (1988) 639.
[11] B.K. Kuanr, G.P. Srivatava, J. Appl. Phys. 75 (1994) 6115.
[12] T.A.S. Ferreira, J.C. Waerenborgh, M.H.R.M. Mendonça, M.R. Nunes, F.M. Costa, Sol. Stat. Sci. 5 (2003) 383.
[13] X. He, G. Song, J. Zhu; Mater. Lett. 59 (2005) 1941.
[14] P.S.A. Kumar, J.J. Shrotri, C.E. Deshpande, J. Appl. Phys. 81 (8) (1997) 4788.
[15] S. Singhal, J. Singh, S.K. Barthwal, K. Chandra, J. Sol. Stat. Chem. 178 (2005) 3183.
[16] Z. Yue, J. Zhou, L. Li, H. Zhang, Z. Gui, J. Magn. Magn. Mater. 208 (2000) 55.
[17] T. Mimani, K.C. Patil, Mater. Phys. Mech. 4 (2001) 134.
[18] A.C.F.M. Costa, E. Tortella, M.R. Morelli, R.H.G.A. Kiminami, J. Magn. Magn. Mater. 256 (2003) 174.
[19] Y.P. Fu, K.Y. Pan, C.H. Lin, Mater. Lett. 57 (2002) 291.
[20] N. Kasapoglu, Synthesis, Characterization and ESR Studies of Magnetic Spinel Compounds, Master Thesis, Fatih University, Istanbul, 2008.
[21] C.C. Hwang, T.Y. Wu, J. Wan, J.S. Tsai, Mater. Sci. Eng. B 111 (2004) 49.
[22] K.J. Rao, B. Vaidhyanathan, M. Ganguli, P.A. Ramakrishnan, Chem. Mater. 11 (1999) 882.
[23] M. Sertkol, Synthesis and Magnetic Characterization of Microwave Absorbing Materials, Master Thesis, Fatih University, Istanbul, 2008.
[24] O. Carp, L. Patron, A. Reler, Mater. Chem. Phys. 101 (1) (2007) 142.
[25] P. Pigram, Microwaves: Theory and Application in Materials Processing, II 1993, vol. 36, American Ceramic Society, Cincinnati, Westerville, 1993, p. 123. Ceram. Trans..
[26] A.M. El Sayed, Ceram. Int. 28 (2002) 363.
[27] T. Wejrzanowski, R. Pielaszek, A. Opalinska, H. Matysiak, W. Łojkowski, K.J. Kurzydłowski, Appl. Surf. Sci. 253 (2006) 204.
[28] R.D. Shannon, Acta Crystallogr. A 32 (1976) 751.
[29] G. Vaidyanathan, S. Sendhilnathan, Physica B 403 (2008) 2157.
[30] A.K.M. Akther Hossain, M. Seki, T. Kawai, H. Tabata, J. Appl. Phys. 96 (2004) 1273.
[31] S.A. Patil, V.C. Mahajan, A.K. Ghatage, S.D. Lotke, Mater. Chem. Phys. 57 (1998) 86.
[32] B.K. Labde, C. Madan Sable, N.R. Shamkuwar, Mater. Lett. 57 (2003) 1651.
[33] S.S. Bellad, R.B. Pujar, B.K. Chougule, Indian J. Pure Appl. Phys. 36 (1998) 598.
[34] G.M. Bhongale, D.K. Kulkarni, V.B. Sapre, Bull. Mater. Sci. 15 (1992) 121.
[35] A. Tawfik, I.M. Hamada, O.M. Hemeda, JMMM 250 (2002) 77.
[36] O.A. Lopez, J. McKittrick, L.E. Shea, J. Lumin. 71 (1997) 1.
[37] Y. Zhang, G.C. Stangle, J. Mater. Res. 9 (1994) 1997.
[38] J.L. Dorman, M. Nogues, J. Phys.: Condens. Matter 2 (1990) 1223.
[39] D. Fiorani, S. Vitticoli, Solid State Commun. 29 (1979) 239.
[40] K.P. Belov, A.N. Goryaga, A.N. Lymzin, Sov. Phys. Solid State 30 (1988) 715.
[41] H. Xue, Z. Li, X. Wang, X. Fu, Mater. Lett. 61 (2007) 347.
[42] F. Li, H. Wang, L. Wang, J. Wang, J. Magn. Magn. Mater. 309 (2007) 295.
[43] V. Kumar, A. Rana, M.S. Yadav, R.P. Pant, J. Magn. Magn. Mater. 320 (2008) 1729.
[44] F. Gözüak, Y. Köseoğlu, A. Baykal, H. Kavas, J. Magn. Magn. Mater. 321 (2009) 2170.
[45] R.N. Bhowmik, R. Ranganathan, J. Magn. Magn. Mater. 248 (2002) 101.
[46] D. Fiorani, S. Vitiocoli, J.L. Dorman, J.L. Tholence, A.P. Murani, Phys. Rev. B 30 (1984) 2776.
[47] D. Fiorani, S. Viticoli, J. Magn. Magn. Mater. 49 (1985) 83.
[48] M.S. Tomar, S.P. Singh, O. Perales-Perez, R.P. Guzman, E. Calderon, C. Rinaldi-Ramos, Microelectron. J. 36 (3–6) (2005) 475.
[49] F. Gözuak, Synthesis and Magnetic Characterization of $Co_xZn_{1-x}Fe_2O_4$ Nanocrystalline, Master Thesis, Fatih University, Istanbul, 2008.
[50] S. Mukherjee, R. Ranganath an, S.B. Roy, Solid State Commun. 98 (1996) 321.
[51] D.H. Han, J.P. Wang, H.L. Lou, J. Magn. Magn. Mater. 136 (1994) 176.
[52] G.M. Kale, T. Asokan, Appl. Phys. Lett. 62 (19) (1993) 2324.
[53] Y. Köseoğlu, H. Kavas, B. Aktaş, Phys. Stat. Sol. (a) 203 (2006) 1595.
[54] Y. Köseoğlu, H. Kavas, J. Nanosci, Nanotechnology 8 (2008) 584.

[55] Nathani, R.D.K. Misra, Mater. Sci. Eng. B 113 (2004) 228.
[56] M.R. Anantharaman, S. Jagatheesan, K.A. Malini, S. Sindhu, A. Narayanasamy, C.N. Chinnasamy, J.P. Jacops, S. Reijne, H. Seshan, R.H.H. Brongersma, J. Magn. Magn. Mater. 189 (1998) 83.
[57] M. Sertkol, Y. Köseoğlu, A. Baykal, H. Kavas, A.C. Başaran, J. Magn. Magn. Mater. 321 (2009) 157.
[58] H.H. Hamdeh, J.C. Ho, S.A. Oliver, R.J. Willey, J. Kramer, Y.Y. Chen, S.H. Lin, Y.D. Yao, M. Daturi, G. Busca, IEEE Trans. Magn. 31 (1995) 3808.

green crystals that formed during the reaction were filtered and washed with small portions of water and ethanol. Yield: 17%.

Anal. Calc. for $C_{16}H_{10}N_2NiO_4$: C, 54.44; H, 2.86; N, 7.94; Ni, 16.62. Found: C, 53.32; H, 3.09; N, 7.68; Ni, 15.95%.

IR (KBr, vw – very weak, w – weak, s – strong, vs – very strong, cm^{-1}): 3446w, 3123vw, 3066w, 3015vw, 2961vw, 2920vw, 2854vw, 1599s, 1553vs, 1536s, 1459w, 1424s, 1413s, 1372s, 1347w, 1198w, 1144w, 1109vw, 1087vw, 1043vw, 903vw, 862s, 855w, 801w, 785vw, 727s, 698s, 681w, 659w, 644vw, 590vw, 565vw, 428vw.

2.3. Physical methods

Elemental analyses were performed on a Perkin–Elmer CHN 2400 Elemental Analyzer (CHN) and AAS (Varian Spectra AA 240 FS) instrument (Ni) after mineralization of the sample in aqua regia. The IR spectra were recorded on a Nicolet-Avatar 330 FT-IR spectrometer using the KBr pellets technique (concentration 2:200). Thermal stability was checked on a Netzsch Sta 409 PC/PG instrument.

2.4. X-ray structure analysis

X-ray experiments for **1** were carried out on an imaging plate area detector system [18] equipped with graphite-monochromatized Mo Kα radiation (λ = 0.71073 Å) at 193(2) K. Rotation method data acquisition using ω scans was used. Accurate cell parameters and an orientation matrix were determined by the least-squares fit of 7998 reflections. The structure was solved by direct methods using the SHELXS97 program [19]. All non-hydrogen atoms were refined anisotropically using the SHELXL-97 program [19]. Hydrogen atoms were put in calculated positions and refined using the "riding" model with tied isotropic thermal parameters. Crystal data and structure refinement parameters are gathered in Table 1, while selected geometric parameters are summarized in Table 2. The figures were drawn using the DIAMOND program [20].

2.5. Magnetic and thermodynamic measurements

Magnetic susceptibility measurements of a powdered sample with a mass of 122.1 mg have been performed in a commercial Quantum Design SQUID magnetometer. The specific heat of a powdered sample pressed into a thin pellet with a mass of 4.2 mg was experimentally studied in a commercial, Quantum Design PPMS device. Both susceptibility and specific heat data were corrected for the contribution of the sample holder, which was determined in separate runs.

Table 1
Crystal data and structure refinement for **1**.

Empirical formula	$C_{16}H_{10}NiN_2O_4$
Formula weight	352.96
Crystal system	monoclinic
Space group	*P*2/*c*
Unit cell dimensions	
a (Å)	12.2190(7)
b (Å)	9.9998(4)
c (Å)	22.6733(13)
β (°)	96.949(6)
Z	4
V (Å^3)	2750.0(4)
$D_{calc.}$ (g cm^{-3})	1.705
T (K)	193(2)
μ (mm^{-1})	1.434
Index ranges	$-14 \leqslant h \leqslant 14$
	$-11 \leqslant k \leqslant 11$
	$-26 \leqslant l \leqslant 26$
θ Range for data collection	2.64–25.00
Reflection collected	19332
Independent reflections (R_{int})	4802(0.0341)
Data/restrains/parameters	4802/0/415
Goodness-of-fit on F^2	0.809
Final *R* indices [$I > 2\sigma(I)$]	R_1 = 0.0243, wR_2 = 0.0458
R indices (all data)	R_1 = 0.0431, wR_2 = 0.0483
Largest peak and hole (e Å^{-3})	0.26(6) and −0.38(6)

Table 2
Selected geometric parameters for **1**.

Ni1–O1	2.0496(19)
Ni1–O4	2.0210(16)
Ni1–O5	2.1099(17)
Ni1–O6	2.1380(16)
Ni1–N1	2.079(2)
Ni1–N2	2.064(2)
Ni2–O2	2.0440(17)
Ni2–O3	2.026(2)
Ni2–O7	2.1469(17)
Ni2–O8	2.1331(16)
Ni2–N3	2.0921(19)
Ni2–N4	2.090(2)
O5–C5	1.265(3)
O6–C5	1.263(3)
O7–C8	1.266(3)
O8–C8	1.261(3)
C5–C6	1.481(3)
C6–C7	1.323(3)
C7–C8	1.485(3)
N2–Ni1–N1	80.61(8)
O5–Ni1–O6	62.44(6)
N3–Ni2–N4	79.63(8)
O7–Ni2–O8	62.00(6)

3. Results and discussion

3.1. Synthesis

Previously, several fumarato complexes of Ni(II) with various N-donor ligands were prepared using solution techniques. As examples we can mention two structurally characterized complexes containing the *phen* ligand, ionic [Ni(*phen*)$_3$]*fum*·2H$_2$*fum*·4H$_2$O and dinuclear [Ni$_2$(*phen*)$_4$(*fum*)(H$_2$O)$_2$]*fum*·16H$_2$O [21,22]. On the other hand, hydrothermal conditions have been used for the preparation of some carboxylato complexes of Co(II), e.g. {Co$_2$(*suc*)$_2$(*phen*)$_2$}$_n$ (*suc* = succinato anion) [23]. The use of solvothermal conditions in the case of the Ni-*phen*-*fum* system led, in our case, to the formation of single crystals of the title compound **1**. It is interesting to note that single crystals were formed only in the case of a Ni:*phen* ratio of 1:2, however, this preparation method was reproducible. Other Ni:*phen* ratios after solvothermal treatment led to the formation of green solutions, which upon standing did not yield single crystals but only badly defined solid residues. Our attempts to prepare the title compound using simple solution techniques were unsuccessful. The formed crystals of **1** were characterized by chemical analyses, which gave satisfactory agreement with the assumed composition (see Section 2). The formed crystals are thermally rather stable, as checked by TG measurements; no mass loss was observed up to 350 °C.

3.2. IR spectroscopy

The IR spectrum of **1** is displayed in Fig. 1. In the spectrum two absorption bands positioned at 3066 and 3017 cm^{-1} can easily be identified; these bands, according to the literature data [24], can be attributed to the ν(C$_{ar}$–H) stretching vibrations of the *phen* ligand. In the spectrum of solid *phen* the corresponding bands were found at 3056 and 3025 cm^{-1}. Several very strong absorption bands (see Section 2) are observed in the IR spectrum between 1600 and

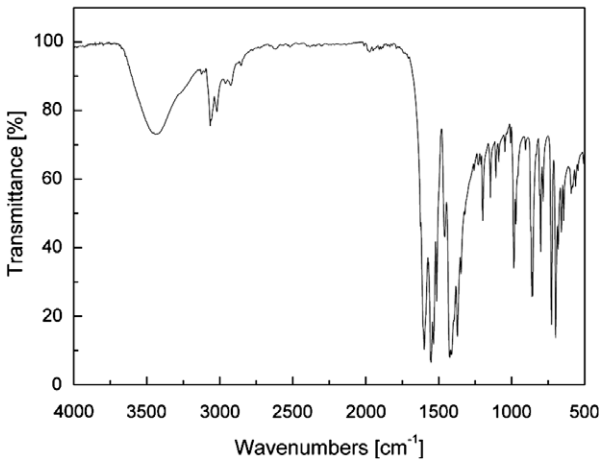


Fig. 1. FT-IR spectrum of **1**.

1340 cm^{-1}; the absorption bands at 1599 and 1553 cm^{-1} can be attributed to the asymmetric vibrations of the carboxylate groups, ν_{as}(OCO), and the absorption bands positioned at 1424, 1413 and 1372 cm^{-1} can be attributed to the symmetric vibration of the carboxylate group, ν_s(OCO). The corresponding absorption bands in Mn(*fum*) were observed at 1575 and 1387 cm^{-1} [25]. Moreover, in this region a medium to strong very sharp absorption band can be observed at 1514 cm^{-1}; we suggest that this band arises from the ν(ring) vibration of the *phen* ligand. In the spectrum of solid *phen* the corresponding absorption band is present at 1503 cm^{-1}.

3.3. Crystal and molecular structure

Crystal structure of **1** exhibits 2D character and is built of $\{Ni_2(fum)_2\}_n$ layers which are perpendicular to the [0 1 0] direction (Fig. 2). A similar 2D crystal structure is formed by a Co(II) central atom and an another dicarboxylato anion, succinato anion(2−) (*suc*), resulting in $\{Co_2(suc)_2(phen)_2\}_n$ [23].

Both crystallographically independent Ni(II) atoms, Ni1 and Ni2, are hexa-coordinated in the form of deformed octahedra *cis*-$NiO_2O_2N_2$; two coordination sites are occupied by one chelate bonded *phen* ligand and four by *fum* ligands (Fig. 3). It is interesting to note that both *cis*-$NiO_2O_2N_2$ octahedra are chiral but the structure is not optically active as the structure is centrosymmetric. Such a type of Ni(II) atom coordination by a combination of aromatic amine (*phen* or *bipy*) and carboxylate groups is, to our knowledge, unique, and has not been observed to date. A somewhat similar type of coordination was found in the polymeric $[Ni(H_2O)(phen)(ter)]_n$ (*ter* = terephatlato) complex in which hexacoordinated Ni(II) atoms contain in the coordination sphere one chelate bonded *phen* ligand, one chelate bonded *ter* ligand, one monodentate *ter* ligand and an aqua ligand [26].

There are two crystallographically different *fum* ligands which also differ by their coordination modes. The first type of *fum* ligand coordinates to four Ni(II) atoms (μ_4-ligand) and the coordination fashion of both carboxylato groups is of the *syn-anti* type. As a consequence a dimeric arrangement of Ni atoms is formed (Fig. 2). The distance between the nickel atoms within the $\{Ni_2\}$ dimer is 4.4905(9) Å. A similar pairing of Ni(II) atoms, but with a substantially shorter Ni···Ni distance (2.9772(13) Å) due to the *syn–syn* type of coordination of the carboxylato groups was observed in $[(F_3CCOO)_2(tmsa)_2Ni]$ (*tmsa* = η^3-2-trimethylsilylallyl) [27]. A somewhat longer distance between the Ni(II) atoms (3.058 Å) was found in dinuclear $[(MeOH)(L)Ni(\mu_2\text{-}CCl_3CO_2)Ni(L)(CCl_3CO_2)]$ where L is a phenolate like anion $\{(O^-)(C_6H_4CH{=}NCH_2\text{-}CH_2N(CH_3)_3)\}$ [28]. The second type of *fum* ligand in **1** coordinates as a bis(chelate) ligand, bridging two Ni(II) atoms and leading to a 1D arrangement of Ni atoms in the [0 0 1] direction (Figs. 2 and 3).

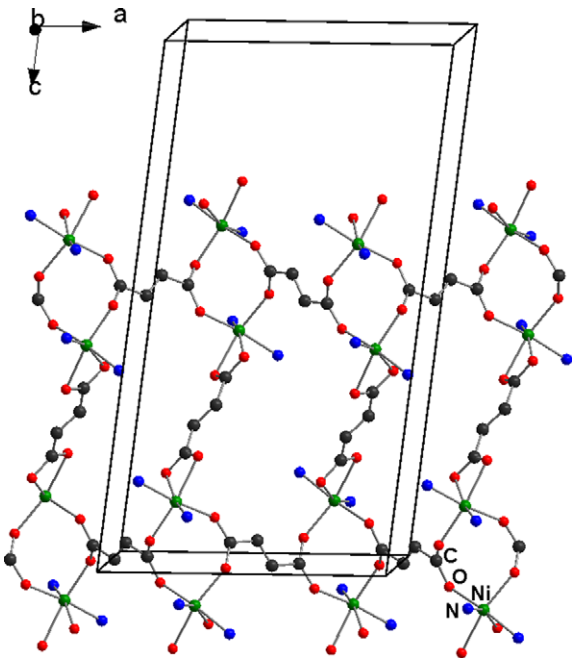


Fig. 2. View of the 2D crystal structure of **1**. The hydrogen atoms as well as the carbon atoms of the *phen* ligand are omitted for the sake of clarity.

As a consequence of the chelate bonding of the carboxylato groups, the O–Ni–O angles within the nickel central atoms coordination spheres (62.44(6)° for O5–Ni1–O6 and 62.00(6)° for O7–Ni2a–O8) are very deformed (Table 2). Similar values of O–Ni–O angles (61.1(2) and 61.2(2)°) for the same type of four-membered metallocycle were observed in $[Ni_2(py)_6(fum)_2]\cdot 2py$ (*py* = pyridine), which exhibits a 1D crystal structure [16]. The Ni–O distances in **1** vary from 2.0210(16) to 2.1469(17) Å; the Ni–O bonds to oxygen atoms from the chelate bonded carboxylate group (mean value is 2.1469(17) Å) are longer than the Ni–O ones formed by oxygen atoms from *syn-anti* bridging carboxylate group (mean value is 2.0210(16) Å). Similar differences in Ni–O distances were observed in $[Ni_2(py)_6(fum)_2]\cdot 2py$ in which the mean Ni–O bond lengths are 2.165 and 2.015 Å for the chelate bonded carboxylate and the *syn–syn* type bridging carboxylate group, respectively [16]. The Ni–N distances in the title compound **1** are almost the same (Table 2); slightly shorter values (range from 2.064(2) to 2.0921(19) Å) were observed in $[Ni_2(phen)_2(adip)_2(H_2O)_2]$ (*adip* = adipato) [29]. The geometric parameters within the respective N- and O-donor ligands (*fum*, *phen*) in **1** exhibit their usual values [16,26].

The aromatic ring of the *phen* ligands from neighbouring layers interact via π–π interactions (Fig. 4). The distances between aromatic rings, defined as distances between the centroid of one aromatic ring and the nearest carbon atom in the second one, vary between 3.296 and 3.530 Å; these values are as expected [30]. These interactions contribute to the packing forces of the crystal structure.

3.4. Magnetic and thermodynamic properties

The crystal structure of **1** contains two sets of crystallographically non-equivalent Ni(II) positions (Fig. 3). The geometry of the corresponding local octahedra mildly differ in bond lengths and angles (Table 2) and the determination of the character of distortion which gives rise to magnetic anisotropy is non-trivial. Following the approach developed in Ref. [31] for heteroleptic Ni(II)

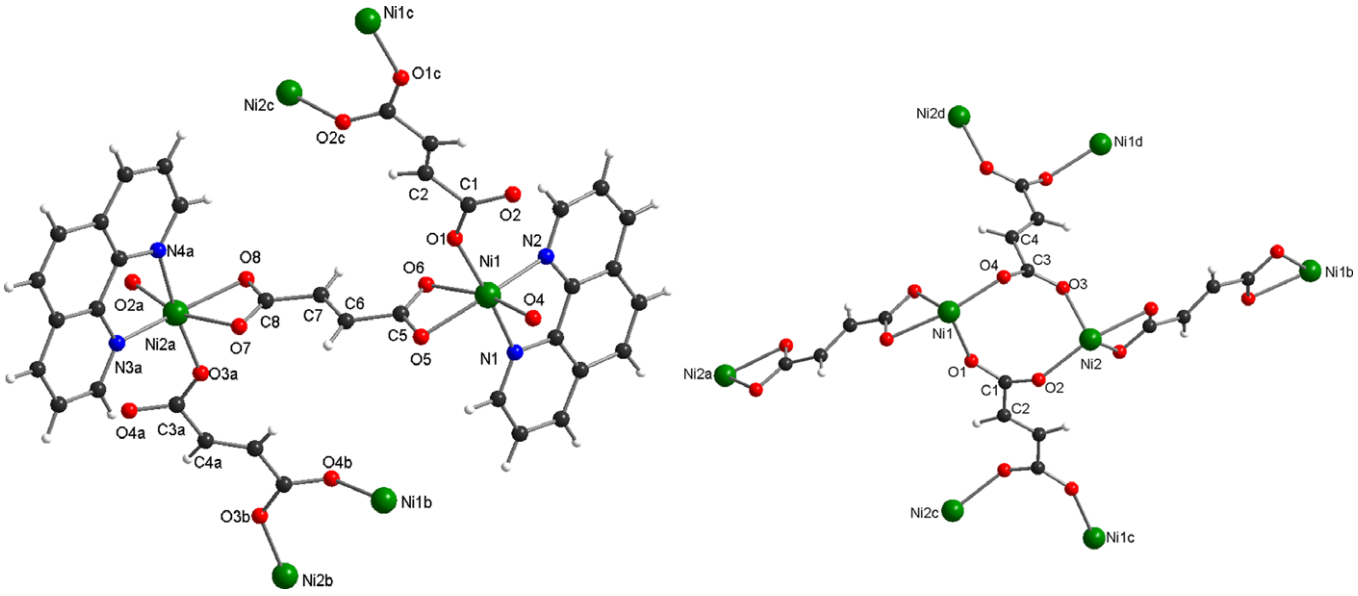


Fig. 3. Partial views of the crystal structure of **1** displaying the bis(chelate) type bridging ability of the *fum* ligand (symmetry codes: (a): x, $1-y$, $-0.5+z$; (b): $1-x$, y, $0.5-z$; (c): $2-x$, $1-y$, $1-z$) (left), and μ_4-bridging *fum* ligand along with formation of nickel dimers (symmetry codes: (a): x, $1-y$, $-0.5+z$; (b): x,$1-y$, $0.5+z$; (c): $2-x$, $1-y$, $1-z$; (d): $1-x$, $1-y$, $1-z$) (right). The *phen* ligands coordinated to the Ni atoms are partially omitted for the sake of clarity. Thermal ellipsoids are drawn at the 50% probability level.

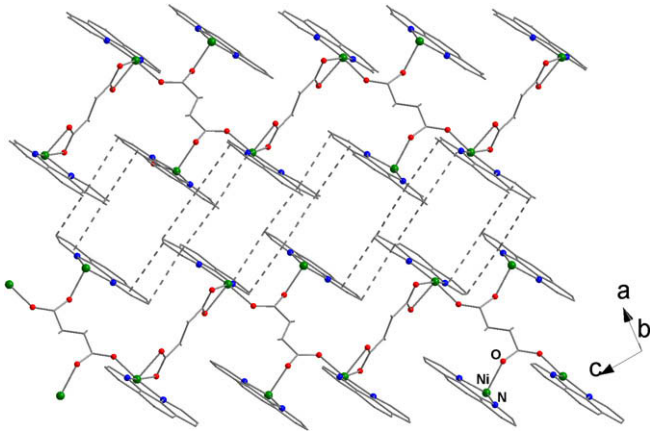


Fig. 4. View on the π–π interactions between the *phen* ligands from the neighbouring layers.

complexes, the effective axial distortion D_{str} was calculated using the bond lengths within the chromophore. The calculations for each octahedron yielded $D_{str}(1) = -4.65$ pm and $D_{str}(2) = -4.86$ pm and according to the semi empirical relation between structural distortion and magnetic anisotropy D derived in Ref. [31], such distortion should induce easy-axis magnetic anisotropy $D/k_B = -7 \pm 3$ K. Significant rhombic distortion of the octahedra implies the presence of a rather strong rhombic anisotropy characterized by a parameter E in the spin Hamiltonian $H = DS_z^2 + E(S_x^2 - S_y^2)$. Thus, in the first approximation, both sets of octahedral surroundings can be treated as a suppressed octahedron with a significant rhombic distortion.

Concerning the magnetic correlations between Ni(II) ions, magnetic orbitals d_{z^2} and $d_{x^2-y^2}$ support the formation of exchange pathways potentially along all three directions. The most significant exchange coupling J_1 can be expected between the Ni1 and Ni2 ions within the pairs, mediated by a double *syn-anti* type carboxylate exchange bridge –O–C–O–. Much weaker couplings J_2 and J_3 can be expected along the c and a axes mediated by *fum* ligands. Consequently, a [Ni(*phen*)(*fum*)] magnetic subsystem might represent a 2D array of magnetic dimers (J_1 interaction within the dimer) coupled via J_2 and J_3 interactions within a structural layer identical to the *ac* plane.

The magnetic susceptibility was experimentally studied in a field of 10 mT and in the temperature range from 2 to 300 K. A rather significant difference between the data obtained in field cooling (FC) and zero field cooling (ZFC) regimes appears below 10 K and might indicate a magnetic anisotropy effect or the presence of a phase transition. In the quantitative analysis, only the data above 10 K were taken into account. The data were corrected for the contribution of core diamagnetism which was estimated using Pascal constants, $\chi^{cor} = -153.10^{-6}$ emu/mol. In this region, the susceptibility is characterized by a typical monotonic decrease (Fig. 5) and the effective magnetic moment reaches a value of 3.4 μ_B at room temperature, which is close to the value expected for a $S = 1$ system. The temperature dependence of the effective magnetic moment is characterized by a sharp peak below 10 K, which may be ascribed to the aforementioned FC–ZFC differences (Fig. 6). The temperature dependence of the inverse susceptibility shows above 100 K a slight deviation from linearity, probably resulting from an inaccurate estimation of the diamagnetic contribution, which becomes crucial at high temperatures. To avoid the inaccuracy, the temperature range from 15 to 100 K was chosen for fitting the data by the Curie-Weiss law (Fig. 6). The fitting procedure provided an estimation of the g-factor and the Curie temperature Θ, $g = 2.2 \pm 0.1$ and $\Theta = -1.5 \pm 0.5$ K, respectively. The obtained value for the g-factor is typical for Ni(II) compounds while a non-zero value of the Curie temperature indicates the combined influence of magnetic (single-ion) anisotropy and magnetic correlations between Ni(II) ions. To estimate the importance of individual mechanisms, the susceptibility data were compared with the theoretical predictions for an $S = 1$ paramagnet with single-ion anisotropy $D/k_B = -7$ K, as derived from structural analysis (Fig. 5). The logarithmic scale enables the detection of deviations between the data and theory which appear below 10 K. A satisfactory agreement observed at higher temperatures may indicate suppression of magnetic correlations by thermal fluctuations and, correspondingly, the dominant influence of single-ion anisotropy.

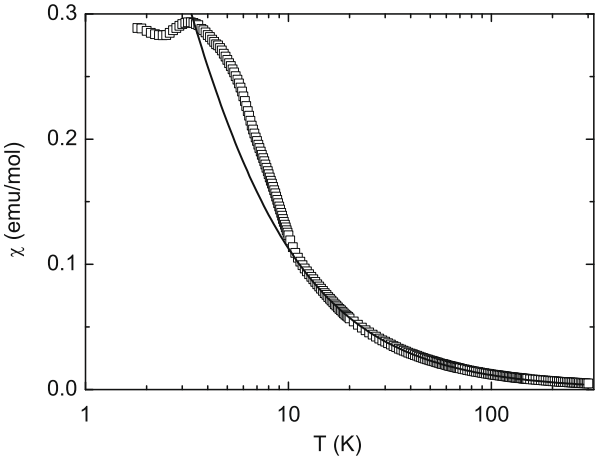


Fig. 5. Temperature dependence of the magnetic susceptibility of a powdered sample of **1** obtained in the ZFC regime. The solid line represents the theoretical prediction for a $S = 1$ paramagnet with single-ion anisotropy $D/k_B = -7$ K and $g = 2.15$.

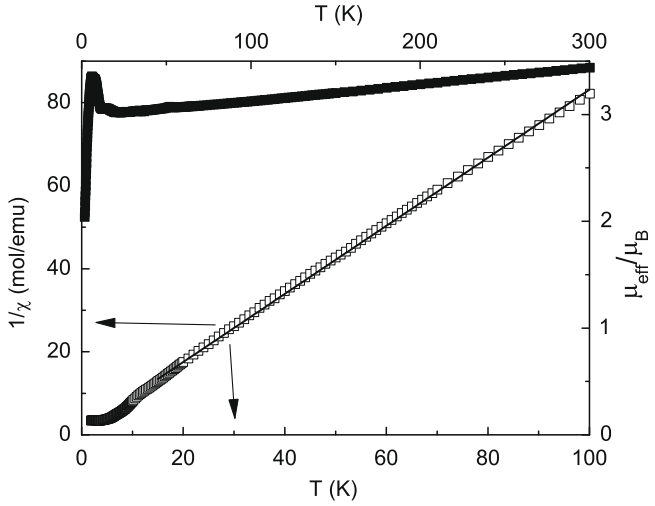


Fig. 6. Temperature dependence of the effective magnetic moment of a powdered sample of **1** derived from ZFC susceptibility data (full squares). Temperature dependence of inverse ZFC susceptibility (empty squares). The solid line represents the fit by the Curie Weiss law.

Since the monotonic behaviour of susceptibility data above 10 K allows uncritical application of other models, such analysis cannot provide reliable results and in a further step the specific heat was studied to refine the physical model of magnetic subsystem.

The specific heat was experimentally studied in a zero magnetic field in the temperature range from 2 K to 30 K. The behaviour of the data is dominated by a round anomaly at 4.2 K and a monotonic increase is observed at higher temperatures (Fig. 7). No phase transition is observed down to 2 K. Since **1** represents a magnetic insulator, the total specific heat, C_{tot}, is determined by the contribution of lattice vibrations, C_{latt}, and the magnetic subsystem, C_{mag}. The individual contributions were determined in the temperature interval from 12 to 26 K by a fitting procedure using a high temperature approximation for the magnetic specific heat, $C_{mag} = a/T^2$ and a low temperature approximation for the lattice specific heat [32], $C_{latt} = bT^3 + cT^5 + dT^7$. Corresponding coefficients have been found, $a = 293$ JK/mol, $b = 0.0041$ J/K^4 mol), $c = -8.1 \times 10^{-6}$ J/K^6 mol), $d = 6.1 \times 10^{-9}$J/K^8 mol) and the magnetic specific heat was obtained by subtracting the lattice contribution from the total specific heat (Fig. 8).

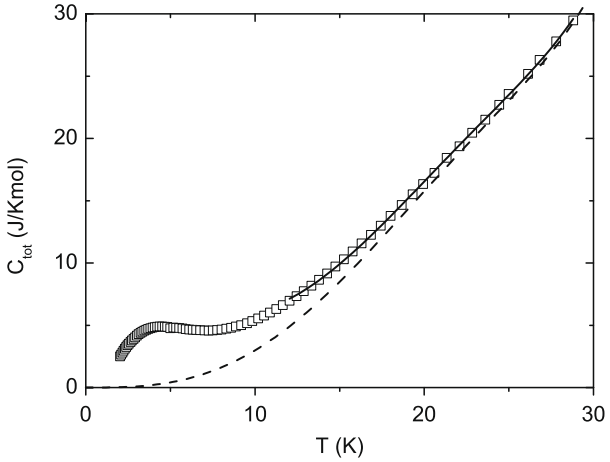


Fig. 7. Temperature dependence of the total specific heat of a powdered sample of **1** in a zero magnetic field (empty squares). The dashed line represents the lattice contribution, $C_{latt} = bT^3 + cT^5 + dT^7$.

Like the magnetic susceptibility, the present magnetic specific heat data were compared with the theoretical prediction for the $S = 1$ paramagnet with single ion anisotropy $D/k_B = -7$ K (Fig. 8). It is evident, that the model is far from reality (at least with respect to the specific heat maximum height) and it is necessary to include other mechanisms. As was mentioned above, the crystal structure analysis indicates a rather strong rhombic distortion of a local octahedron, thus the experimental data were compared with the model of the $S = 1$ paramagnet with single ion anisotropy and rhombic anisotropy. The best agreement was found for the parameters $E/D = 0.27$, $D/k_B = -13.5$ K and $E/k_B = -3.6$ K (Fig. 8). Rather large values of the parameters indicate the need to incorporate other mechanism to obtain more realistic estimates. Assuming the aforementioned interaction J_1 is much stronger than the others, a model of an antiferromagnetic dimer with single ion anisotropy [33] was applied (Fig. 8). A comparison of the dimer model with selected parameters $D/J = 1$, $D/k_B = J/k_B = -6$ K indicates that the introduction of exchange coupling leads to a more realistic estimate of the single ion anisotropy parameter. Thus, for refining all the D, J, E parameters, a more sophisticated analysis is required to incorporate all mechanisms at the same time. For the sake of comparison it is interesting to note that in the above mentioned nickel dinuclear

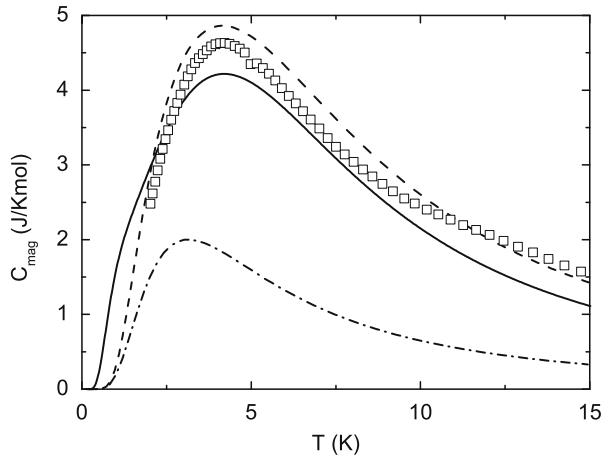


Fig. 8. Temperature dependence of the magnetic specific heat of **1** (open square). The dashed-dotted line represents the theoretical prediction for an $S = 1$ paramagnet with $D/k_B = -7$ K, the dashed line corresponds to the $S = 1$ paramagnet with $E/D = 0.27$, $D/k_B = -13.4$ K and $E/k_B = -3.6$ K. The solid line represents a theoretical prediction for the $S = 1$ dimer with $D/J = 1$, $D/k_B = J/k_B = -6$ K.

[(MeOH)(L)Ni(μ_2-CCl_3CO_2)Ni(L)(CCl_3CO_2)] complex with a substantially shorter Ni···Ni distance of 3.058 Å, a higher value of the antiferromagnetic intra-dimer interaction $J_1/k_B = -17.2$ K was found [28].

4. Conclusions

Based on the presented experimental data and discussion it can be concluded that under solvothermal conditions a new low-dimensional Ni(II) complex [Ni(*phen*)(*fum*)] (**1**) has been prepared and characterised. Its crystal structure is 2D and is based on hexa-coordinated Ni(II) atoms linked by bridging *fum* ligands; the *phen* molecules act as blocking ligands. Within the formed layers, pairs of nickel atoms linked by two *syn-anti* fashioned carboxylate bridges can be distinguished. The layers are held by π−π interactions. The results of susceptibility and heat capacity studies down to 2 K allow the conclusion that **1** can be approximated by a system of $S = 1$ dimers with single ion and rhombic anisotropy, comparable to intra-dimer exchange coupling. Further experiments are necessary at lower temperatures to refine the magnetic model.

5. Supplementary data

CCDC 721837 contains the supplementary crystallographic data for [Ni(*fum*)(*phen*)]. These data can be obtained free of charge via http://www.ccdc.cam.ac.uk/conts/retrieving.html, or from the Cambridge Crystallographic Data Centre, 12 Union Road, Cambridge CB2 1EZ, UK; fax: (+44) 1223-336-033; or e-mail: deposit@ccdc.cam.ac.uk.

Acknowledgements

The authors thank prof. W. Massa (Philipps-Universität Marburg, Germany) for kind permission to use the diffractometer. This work was supported by the Slovak grant agency APVV under contracts Nos. APVV-VVCE-0058-07 and APVV-0006-07, and by grant agency VEGA (grants 1/0078/09, 1/0089/09) and RNP ESF HFM-8. The support from P.J. Šafárik University (VVGS 37/09-10) is acknowledged.

References

[1] E. Dagotto, Phys. World (1996) 22.
[2] U. Schollwöck, J. Richter, D.J.J. Farnel, R.F. Bishop, Quantum Magnetism, Springer-Verlag, Berlin, 2004.
[3] D. Gatteschi, R. Sessoli, J. Villain, Molecular Nanomagnets, Oxford University Press Inc., New York, 2006.
[4] R.G. Wilett, Z. Wang, S. Molnar, K. Brewer, C.P. Landee, M.M. Turnbull, W. Zhang, Mol. Cryst. Liq. Cryst. 233 (1993) 277.
[5] F.A.A. Paz, J. Klinowski, Pure Appl. Chem. 79 (2007) 1097.
[6] D.B. Leznoff, B.Y. Xue, R.J. Batchelor, F.W.B. Einstein, B.O. Patrick, Inorg. Chem. 40 (2001) 6026.
[7] Y. Rodríguez-Martín, M. Hernández-Molina, F.S. Delgado, J. Pasán, C. Ruiz-Pérez, J. Sanchiz, F. Lloret, M. Julve, Cryst. Eng. Commun. 4 (2002) 440.
[8] X.J. Zhao, Z.H. Zhang, Y. Wang, M. Du, Inorg. Chim. Acta 360 (2007) 1921.
[9] J. Hanko, M. Orendáč, J. Kuchár, Z. Žák, J. Černák, A. Orendáčová, A. Feher, Solid State Commun. 142 (2007) 128.
[10] A. Vlček, M. Orendáč, A. Orendáčová, M. Kajňaková, T. Papageorgiou, J. Chomič, J. Černák, W. Massa, A. Feher, Solid State Sci. 9 (2007) 116.
[11] J. Paharová, J. Černák, R. Boča, Z. Žák, Inorg. Chim. Acta 346 (2003) 25.
[12] J. Černák, J. Lipkowski, E. Čižmár, A. Orendáčová, M. Orendáč, A. Feher, M.W. Meisel, Solid State Sci. 5 (2003) 579.
[13] C. Ruiz-Pérez, J. Sanchiz, M.H. Molina, F. Lloret, M. Julve, Inorg. Chim. Acta 298 (2000) 202.
[14] F.S. Delgado, M. Hernandez-Molina, J. Sanchiz, C. Ruiz-Perez, Y. Rodriguez-Martin, T. Lopez, F. Lloret, M. Julve, Cryst. Eng. Commun. 6 (2004) 106.
[15] Y.H. Xue, J.G. Liu, D.J. Xu, J. Coord. Chem. 58 (2005) 1071.
[16] W. Mori, S. Takamizawa, C.N. Kato, T. Ohmura, T. Sato, Micropor. Mesopor. Mater. 73 (2004) 31.
[17] H.Z. Xie, Y.Q. Zheng, Q.S. Wu, Z. Kristallogr. New Cryst. Struct. 218 (2003) 111.
[18] Stoe & Cie, X-AREA. Stoe & Cie, Darmstadt, Germany, 2007.
[19] G.M. Sheldrick, Acta Crystallogr., Sect. A 64 (2007) 112.
[20] K. Brandenburg, DIAMOND. Crystal Impact (version 3.1f) GbR, Bonn, Germany, 2008.
[21] J.L. Lin, Y.Q. Zheng, Z. Kristallogr. New Cryst. Struct. 219 (2004) 230.
[22] J.F. Ma, J. Yang, J.F. Liu, Acta Crystallogr., Sect. E 59 (2003) m900.
[23] X. Xy, Y. Ma, Y. Lu, E. Wang, J. Coord. Chem. 60 (2007) 1005.
[24] M. Horák, D. Papoušek, Infračervená spektra a struktura molekul, Academia Praha, 1976.
[25] M. Devereux, M. McCann, V. Leon, M. Geraghty, V. McKee, J. Wikaira, Polyhedron 19 (2000) 1205.
[26] Y.B. Go, X. Wang, E.V. Anokhina, A.J. Jacobson, Inorg. Chem. 43 (2004) 5360.
[27] W. Massa, N. Faza, H.-C. Kang, C. Focke, W. Heitz, Acta Polym. 48 (1997) 432.
[28] S.K. Dey, M. Salah El Fallah, J. Ribas, T. Matsushita, V. Gramlich, S. Mitra, Inorg. Chim. Acta 357 (2004) 1517.
[29] Y.Q. Zheng, W.H. Liu, J.L. Lin, L.Y. Gu, Z. Anorg. Allg. Chem. 628 (2002) 829.
[30] J.W. Steed, J.L. Atwood, Supramolecular Chemistry, John Wiley and Sons, Chichester, England, 2000.
[31] R. Ivaniková, R. Boča, L. Dlháň, H. Fuess, A. Mašlejová, V. Mrázová, I. Svoboda, J. Titiš, Polyhedron 25 (2006) 3261.
[32] D.R. Huffman, M.H. Norwood, Phys. Rev. 117 (1960) 709.
[33] J. Strečka, M. Jaščur, M. Hagiwara, Y. Narumi, J. Kuchár, S. Kimura, K. Kindo, J. Phys. Chem. Sol. 66 (2005) 1828.

this system. The purpose of this study is, on one hand, to obtain additional experimental data on the magnetic anisotropy in this molecular antiferromagnet, and on the other hand, to summarize all experimental data obtained through various physical techniques on this material by us to look into the origin of the uncompensated magnetization below T_N in $\{N(n\text{-}C_5H_{11})_4[Mn^{II}Fe^{III}(ox)_3]\}_\infty$. In this paper we concentrate mainly on the results of these studies obtained at low temperatures.

2. Experimental

The polycrystalline material of $\{N(n\text{-}C_5H_{11})_4[Mn^{II}Fe^{III}(C_2O_4)_3]\}_\infty$ (Mn–Fe in short) was synthesised according to Ref. [3] and its X-ray diffraction pattern was consistent with the literature data [11]. AC susceptibility data were collected for a polycrystalline sample of ≈100 mg by means of a 7225 Lake Shore instrument. Both real (χ') and imaginary (χ'') components of $\chi_{AC} = \chi' - i\chi''$ were registered as a function of increasing temperature. The frequency f of the driving field was changed in the range 40–4000 Hz, the dependence of the output signal on the amplitude H_{AC} of the driving field was tested for H_{AC} = 1–15 Oe. Isothermal magnetization curves at T = 4.2, 10, 20, 30, 40, 48, 64 and 92 K and isofield temperature dependences of magnetization in the ZFC and FC modes were measured with the DC option of the same set-up using the extraction method.

Magnetization measurements were carried out with a SQUID MPMS XL magnetometer at 5 K with 10 mg of a powder sample, whereas the heat capacity measurements were done with a PPMS 6000 calorimeter. For heat capacity measurements, the polycrystalline material was pressed into a pellet and a small part (mass 1.4377 mg) was used for the heat capacity measurements. Heat capacities were measured in the 2–50 K range. The temperature jump adopted for the relaxation was 1% of the absolute temperature for all measurements. Mössbauer spectra were recorded using a conventional constant-acceleration spectrometer with a liquid helium bath cryostat and a superconducting magnet to produce a magnetic field parallel to the γ-ray propagation. The hyperfine parameters were obtained by least squares fitting to Lorentzian lines using the Recoil (1.03a) Mössbauer software analysis program.

3. Results and discussion

3.1. Magnetic measurements

AC magnetic susceptibility data of $\{N(n\text{-}C_5H_{11})_4[Mn^{II}Fe^{III}(ox)_3]\}_\infty$, measured with various amplitudes H_{AC} of the driving field, are given in Fig. 1a. The χ' value, which at T = 4.2 K is ~0.35 emu/mol, increases slowly with increasing temperature. The Néel temperature T_N is marked with a weak narrow spike at 28.8 K. The χ'' component, equal to about 1% of χ', points to the presence of the uncompensated moment in the system. The χ'' peak is located also at 28.8 K. As expected for an antiferromagnet, there is no susceptibility dependence on H_{AC}. Above T_N the χ' component does not decrease but shows a wide hump at around 54 K. Fig. 1b presents the temperature dependence of χ' for f = 40, 625 and 4000 Hz. It appears that with higher frequencies the peak at T_N becomes invisible; at the present stage it is difficult to say whether for higher f the low temperature side of the hump gets enhanced and shifts to lower temperatures or a peak at T_N which gets wider (see Fig. 1b insert). In spite of the poor accuracy of the data, conditioned by the low magnetic response of the sample, we can state that there is no frequency dependence of χ' detected for T < 20 K. Also no effect of frequency is seen at the high-temperature side of the bump for T above ≈ 120 K. The overall χ' vs. T dependence with the weak peak at T_N and a hump above T_N is typical for two-dimensional Heisenberg antiferromagnets, showing strong short-range correlations above the transition temperature. The temperature T_{max} of the susceptibility hump maximum is a measure of the intraplanar exchange coupling J. Using the relation $\frac{k_B T_{max}}{abs(J)S(S+1)} \approx 2$ (Ref. [10], p. 64) one gets $J/k_B \approx -3.1$ K, close to the value obtained from the heat capacity data (see below) [14]. The χ_{AC} vs. T dependence observed by us is similar to that reported for a novel layered magnet $[Fe(C_2O_4)(CH_3OH)]_n$ which exhibits magnetic ordering at $T_N \approx 23$ K [17]. The crystal structure of the latter does not possess a honeycomb lattice and spin canting originates from the non-centered structural features of the compound. The χ_{AC} of $[Fe(C_2O_4)(CH_3OH)]_n$ is ca. 3 times stronger, yet did not show dependence on frequency as checked for 10, 100 and 1000 Hz ([13], ESI).

In order to learn more about the low- and high-temperature behavior of the $\{N(n\text{-}C_5H_{11})_4[Mn^{II}Fe^{III}(ox)_3]\}_\infty$ compound,

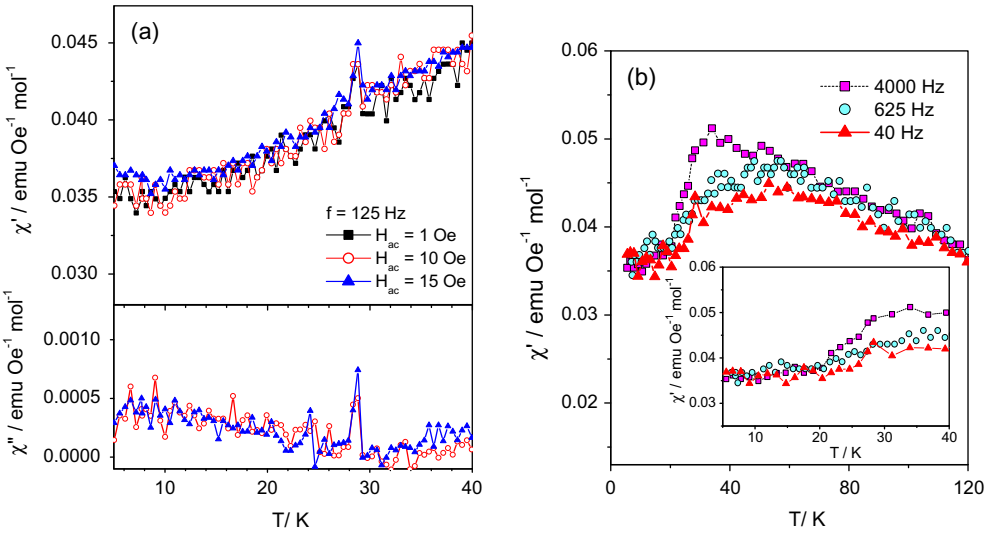


Fig. 1. (a) AC magnetic susceptibility (χ' and χ'') at frequency f = 125 Hz measured with varied amplitudes of the oscillating field; (b) temperature dependence of χ' for f = 40, 625 and 4000 Hz, insert: same data in a smaller temperature range.

magnetization curves at $T = 4.2$, 10, 20, 30, 40, 48, 64 and 92 K, and isofield temperature dependences of magnetization in the ZFC and FC modes have been measured by means of the Lake Shore instrument. The obtained results are in accordance with the adequate $M(H)$ data recorded with the SQUID magnetometer and reported in [13]. Fig. 2a shows the magnetization curve at $T = 4.2$ K and the corresponding susceptibility $\chi_{DC} = M/H$ for increasing and decreasing magnetic field. At the highest field the magnetization is 2635 emu/mol (0.47 μ_B), which is less than 5% of the expected saturation value. The irreversible χ_{DC} vs. H dependence is the result of the weak ferromagnetic moment coming from small canting of the antiferromagnetically coupled moments. The $M(H)$ dependence is not linear, but weakly concave and may be fitted to a Boltzmann sigmoidal function $y + \frac{A_1 - A_2}{1 + e^{x - x_0}/dx} + A_2$, where A_1 and A_2 are left and right horizontal asymptotes and x_0 refers to the curve inflection point. The fitted $A_2 - A_1$ value equals 49700 emu/mol (8.9 μ_B), close to the expected saturation value of 10 μ_B, while x_0 is equal to 219 kOe. The last value should be understood as the critical field for the reorientation of the spin axis from the direction of the easy axis to that perpendicular to it, i.e. the spin flop transition. Spin flop occurs in "metamagnetic-like" antiferromagnets showing an anisotropy, where the anisotropy energy H_A is smaller than the exchange energy H_E [18,19]. The poorly pronounced sigmoidal shape of the $M(H)$ curve in Fig. 2a suggests that in our system $H_A << H_E$. Fig. 2b gives χ_{DC} in fields of 5, 10, 15, 20, 30, 40, 50 and 56 kOe, obtained from the $M(H)$ curves taken at various temperatures, together with $M_{ZFC}(T)$ and $M_{FC}(T)$ in 20 kOe. The insert gives the difference in χ_{DC} when determined at 56 kOe and at 5 kOe,

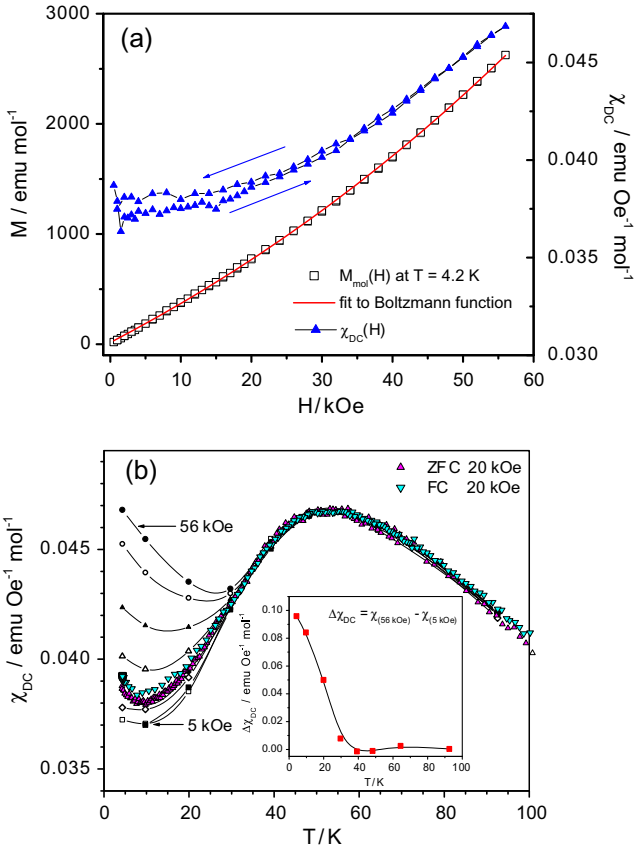


Fig. 2. (a) $M(H)$ magnetization curve at $T = 4.2$ K fitted to Boltzmann sigmoidal function (left scale) and DC susceptibility obtained from $M(H)$ (right scale); the increasing and decreasing field is marked with arrows; (b) black empty and solid symbols – χ_{DC} in the fields of 5, 10, 15, 20, 30, 40, 50 and 56 kOe obtained from the $M(H)$ curves; up- and down-triangles $M_{ZFC}(T)$ and $M_{FC}(T)$ in 20 kOe; insert: $\Delta\chi_{DC} = \chi_{(56\ kOe)} - \chi_{(5\ kOe)}$.

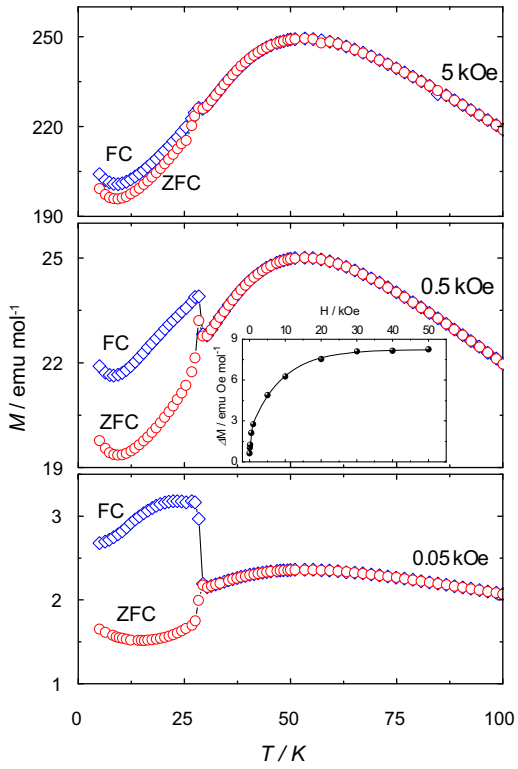


Fig. 3. Temperature variation of magnetization for $\{N(n\text{-}C_5H_{11})_4[Mn^{II}Fe^{III}(ox)_3]\}_\infty$ in ZFC and FC protocols under different applied magnetic fields. Insert shows the variation of the estimated ΔM values with applied magnetic field, where the solid curve is a fit to Eq. (1).

$\Delta\chi_{DC} = \chi_{(56\ kOe)} - \chi_{(5\ kOe)}$, as a function of temperature. $\Delta\chi_{DC}$ is positive because of the sigmoidal shape of the $M(H)$ curves, while the sigmoidal character originates from the anisotropy of the system. Therefore, the $\Delta\chi_{DC}$ vs. T curve shown in the insert in Fig. 2b reflects the decrease of anisotropy with temperature. $\Delta\chi_{DC}$ becomes zero at $T \geqslant T_N$, and so obviously does the weak ferromagnetic moment. The vanishing of $\Delta\chi_{DC}$ coincides with the bifurcation point of the ZFC-FC $M(T)$ curves (see Fig. 3 below). One should also note that the M(H) curves measured at temperatures above T_N up to $T = 92$ K showed strong short-range antiferromagnetic correlations. One can estimate that the spin system becomes uncorrelated only for $T > 150$ K.

In Fig. 3 we show some selected plots of temperature dependence of M of Mn–Fe under ZFC and FC measurement protocols in the 5–100 K range studied in a SQUID magnetometer under various magnetic fields (H) ranging between 0.01 and 50 kOe in FC and ZFC modes. The differences in the magnetization values ($\Delta M = M_{FC} - M_{ZFC}$), which is a measure of anisotropy, have been estimated for the 5 K values of M under each applied magnetic field. The insert of Fig. 3 shows the variation of ΔM values with applied magnetic field. The ΔM values are found to fit with the following relation:

$$\Delta M = \Delta M_{H=0} + A_1(1 - e^{-H/t_1}) + A_2(1 - e^{-H/t_2}) \quad (1)$$

This is a reflection of two different types of responses of the spins to the applied magnetic field, indicating the existence of at least two magnetically different spin sites or magnetic sub-lattices.

3.2. Heat capacity studies

The observed calorimetric results for Mn–Fe in the 2–50 K temperature range under 0 and 90 kOe magnetic fields, evaluated in

terms of molar heat capacity under constant pressure C_p, are shown in Fig. 4. Apparently the $C_p(T)$ plots show no thermal anomaly around T_N, expected from magnetic studies, as well as any significant magnetic field dependence. The excess heat capacity due to magnetic phase transition (C_{mag}) have been estimated by considering the lattice heat capacities as the following polynomial function of temperature,

$$C_p = C_p(\text{lattice}) + C_{mag}(\text{short -range order}) = \sum_{i=3}^{n} a_i T^i + bT^{-2} \quad (2)$$

and then subtracting those from the observed C_p values. The observed C_p data were well fitted to Eq. (2) in the 32–50 K range for $n = 5$ with parameters $a_3 = 8.579 \times 10^{-3}$ J K^{-4}, $a_4 = -2.297 \times 10^{-4}$ J K^{-5} mol^{-1}, $a_5 = 1.754 \times 10^{-6}$ J K^{-6} mol^{-1} for $H = 0$ and 90 kOe, whereas $b = 2.175 \times 10^4$ J K mol^{-1} and 2.013×10^4 J K mol^{-1} for $H = 0$ and 90 kOe, respectively. Estimated C_{mag} values thus calculated from the observed C_p values for both magnetic field conditions are shown in Fig. 5. A heat capacity anomaly due to magnetic phase transition can now easily be seen in this plot at 27.1 K for $H = 0$ and at 28.2 K for $H = 90$ kOe. The fact that the magnetic phase transition temperature shifts to higher temperature with increasing H seems to indicate that the observed magnetic phase transition is ferromagnetic. In general, however, ferromagnets and ferrimagnets show the tendency that the heat capacity peak due to magnetic phase transition shifts to higher temperature and simultaneously broadens with increasing H. Therefore, such a slight shift and non-broadening of the magnetic phase transition by applying the strong magnetic field of 90 kOe rather suggests that this magnetic phase transition is antiferromagnetic.

A remarkable feature of the plots in Fig. 4 is the existence of a dominant short-range order manifested by the large tail of the magnetic heat capacity. A heat capacity anomaly above the magnetic transition temperature due to the short-range ordering in the present case can be well represented by a $S = 5/2$ 2D antiferromagnetic Heisenberg model for a honeycomb lattice with $J/k_B = -3.29$ K [14]. The solid curve in Fig. 5 indicates the theoretical heat capacity following such a model. Although the present complex has a 2D magnetic structure of the Heisenberg type, the occurrence of the magnetic phase transition does not conflict with the existence of dominant 2D interactions. When a 3D interaction, even though weak, exists at low temperatures, dimensional crossover between 2D and 3D may happen and bring about a phase transition. In fact, the heat capacities in the spin wave excitation region are well-reproduced with $C_{SW} \propto T^{d/n}$ (d: dimensionality, n: exponent of dispersion relation), where the exponent is approximated by $d/n \approx 3$, implying that the ordered state at low temperatures is actually a 3D antiferromagnet [14] [at $T < T_N$: for $H = 0$: $C_{mag} = 1.314 \times 10^{-2} T^{2.819} \approx 1.057 \times 10^{-2} T^{3/1}$; for $H = 90$ kOe: $C_{mag} = 1.755 \times 10^{-2} T^{2.669} = 1.165 \times 10^{-2} T^{3/1}$]. The magnetic entropy gain is obtainable by integration of C_{mag} with respect to ln$T$: $\Delta S = \int C_{mag} d\ln T$. The estimated entropy gain for the magnetic phase transition is 33.22 J K^{-1} mol^{-1} and 31.99 J K^{-1} mol^{-1} for $H = 0$ and 90 kOe, respectively, which are slightly higher than the expected magnetic entropy [$R\ln\{(2S + 1) \times (2S + 1)\} = 29.80$ J K^{-1} mol^{-1} for $S = 5/2$]. Application of spin wave theory [14] for C_{mag} values at $T/T_N < 0.5$ led to an interlayer exchange interaction $J'/k_B = \pm 0.014$ K, but was unable to predict the nature of the interlayer interaction in the present material. The dashed curve shows the heat capacity in accordance with the spin wave theory for 3D antiferromagnets.

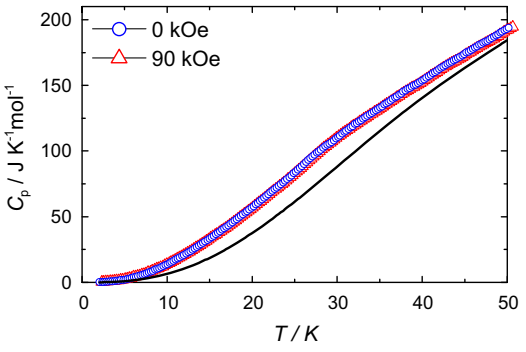


Fig. 4. Temperature variation of molar heat capacity C_p of $\{N(nC_5H_{11})_4[Mn^{II}Fe^{III}(ox)_3]\}_\infty$ in the 2–50 K range under two applied magnetic field conditions. The solid curve indicates the lattice heat capacity.

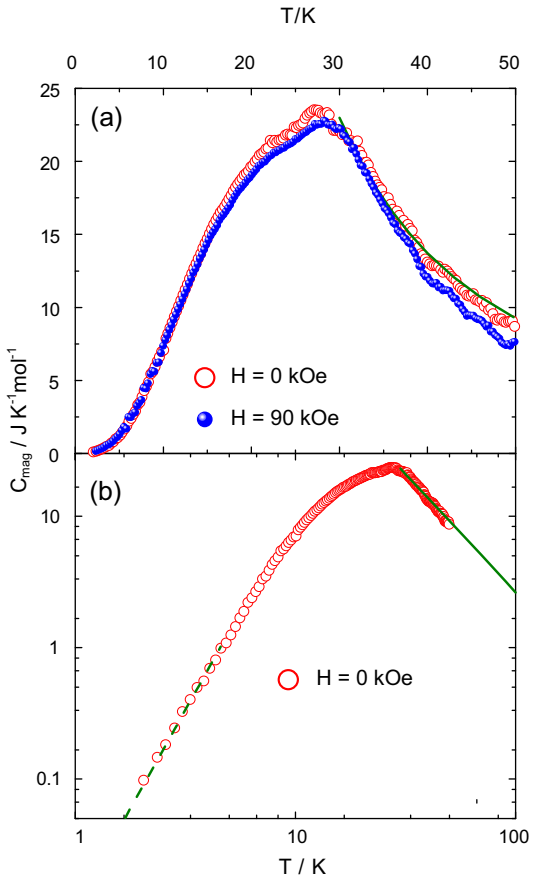


Fig. 5. (a) Temperature variation of magnetic heat capacity of $\{N(n\text{-}C_5H_{11})_4[Mn^{II}Fe^{III}(ox)_3]\}_\infty$ under zero and 90 kOe magnetic fields; (b) Temperature variation of the magnetic heat capacity of $\{N(n\text{-}C_5H_{11})_4[Mn^{II}Fe^{III}(ox)_3]\}_\infty$ under a zero magnetic field in logarithmic scale. The solid curve indicates the theoretical heat capacity for an $S = 5/2$ two-dimensional antiferromagnetic Heisenberg model of a honeycomb lattice with $J/k_B = -3.29$ K. The dashed curve shows the heat capacity in accordance with the spin wave theory for three-dimensional antiferromagnets.

3.3. Mössbauer study

The Mössbauer spectra of Mn–Fe obtained at 4.2 K under zero and 50 kOe magnetic fields are shown in Fig. 6. At 4.2 K, well below T_N, the zero-field spectrum appears as sextets. These sextets indicate the presence of long range magnetic order in the complex at this temperature. The spectra could be fitted to two sextets, say Fe_A^{III} (light gray) and Fe_B^{III} (gray). At 4.2 K and under zero magnetic field, the estimated values of the isomer shift δ (with respect to α-iron), quadrupole splitting ΔE_Q, hyperfine field H_n and areal intensity for Fe_A^{III} are 0.46, 0.30 mm s^{-1}, 500 kOe and 75%, respectively, whereas those for Fe_B^{III} ions are 0.47,

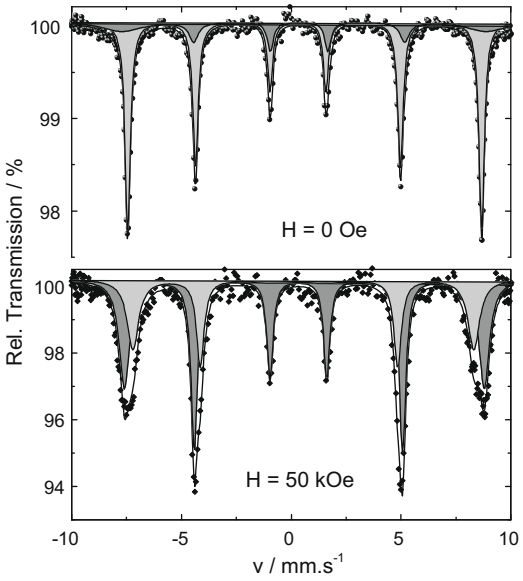


Fig. 6. Mössbauer spectra of $\{N(n\text{-}C_5H_{11})_4[Mn^{II}Fe^{III}(ox)_3]\}_\infty$ at 4.2 K under zero and 50 kOe magnetic field.

0.22 mm s^{-1}, 515 kOe and 25%, respectively. The estimated isomer shift, quadrupole splitting and hyperfine field values are in general agreement with those observed for high spin Fe^{III} ions in this type of molecular system [15] under zero applied magnetic field. Under zero applied magnetic field the areal intensity ratio of $Fe^{III}{}_A$- and $Fe^{III}{}_B$-sextets is 3:1, which on application of an external magnetic field of 50 kOe becomes 36:64 ≈ 3:5. It is understood that the present compound has two Fe^{III} spin sites and the responses of these spin sites towards the external magnetic field are of dissimilar nature, which has been observed in the *M* vs. *T* plots. From Fig. 6, it is also clear that there is significant variation of the intensity among the border-line sextets under application of a magnetic field, which are the usual signatures of a canted spin structure [16].

The H_n values determined at 4.2 K under 50 kOe magnetic field for $Fe^{III}{}_A$- and $Fe^{III}{}_B$-sextets are 508 and 481 kOe, respectively, which are quite a lot lower than the saturation value of the hyperfine field expected for high spin Fe^{III} under zero applied magnetic field (550 kOe). The magnetic interaction between the high spin Mn^{II} and Fe^{III} in the present compound is already established to be antiferromagnetic [2,11]. Under the applied magnetic field of 50 kOe, the Mössbauer spectrum of a single crystal having two Fe^{III} ions coupled antiferromagnetically, may exhibit two sextets, giving rise to H_n values close to (550 ± 50) kOe for the high spin Fe^{III} ions parallel and antiparallel to the applied magnetic field direction, respectively [16]. Thus, the presently observed Mössbauer spectra under 50 kOe magnetic field and the H_n values (508 and 481 kOe), certainly indicate that $Fe^{III}{}_A$- and $Fe^{III}{}_B$-spins are antiparallel to the applied magnetic field direction, but are mutually parallel to each other. Presuming a single type of Mn^{II} site in the present compound and considering the intralayer antiferromagnetic interaction between two neighboring Mn^{II} and Fe^{III} sites [2], it may be conjectured that the Mn–Fe compound has two sub-lattices as (Mn^{II}–ox–$Fe^{III}{}_A$–ox–Mn^{II}–ox–$Fe^{III}{}_A$–...) and (Mn^{II}–ox–$Fe^{III}{}_B$–ox–Mn^{II}–ox–$Fe^{III}{}_B$–...). As the $Fe^{III}{}_A$ and $Fe^{III}{}_B$-spins are parallelly aligned with each other between the adjacent layers, they should be interlayer nearest neighbors. This will make [Mn^{II} and $Fe^{III}{}_A$] and [Mn^{II} and $Fe^{III}{}_B$] interlayer nearest neighbors, giving rise to an interlayer ferromagnetic interaction in accordance with the polarized neutron diffraction study of the related $\{P(C_6D_5)_4[Mn^{II}Fe^{III}(ox)_3]\}_n$ compound [20] and as evidenced by heat capacity and Mössbauer studies of this material.

The estimated magnetic hyperfine field is a powerful parameter of the magnetic properties of the atoms and their immediate environment [21]. The hyperfine field H_n at any spin site may be correlated with the net atomic magnetic moment as proportional to the sum of the magnetic moment of that site and the contribution due to magnetic interactions with the nearest neighbors. This can be written as $H^{\beta}_{n_\alpha} = a\mu^{\beta}_{\alpha} + b\mu' f(z,\theta)$, where μ' = contribution due to magnetic interactions with the nearest neighbors; α = ionic site Mn or Fe; β = spin site of Fe; μ = magnetic moment of metal atoms; z = number of nearest neighbors; θ = spin canting angle; *a*, *b* = proportionality constants. Thus, the $H_{n^{\beta}_{\alpha}}$ value for any particular spin site will reflect the change in its magnetic environment, as μ' is a function of the number of nearest neighbors and their respective spin canting angle with the spin at the site under consideration. The presence of local spin configurations with a different magnetic environment leading to a varying amount of μ' may lead to the hyperfine field distribution in the lattice. Now, from the description of the magnetic lattice structure of the present compound, and the analogy between the hyperfine field and atomic magnetic moments of the different Mn^{II} and Fe^{III} sites, it is evident that the hyperfine field distribution in the (Mn^{II}–ox–$Fe^{III}{}_A$–ox–Mn^{II}–ox–$Fe^{III}{}_A$–...) and (Mn^{II}–ox–$Fe^{III}{}_B$–ox–Mn^{II}–ox–$Fe^{III}{}_B$–...) layers will create a frustration in the magnetic interactions between different Mn^{II} and Fe^{III} spin pairs. Moreover, in these compounds, the metal centers show alternating chirality. The net effect due to frustration on the near-neighbor magnetic interactions will be more prominent in the intralayer than in the interlayer interactions as the intralayer magnetic interaction will dominate the overall magnetic property of this compound. This situation can easily be held responsible for resulting into various competing magnetic interactions leading to net uncompensated magnetization seen in the present compound at temperatures below the transition temperature.

4. Discussion and conclusions

Magnetic measurements, both AC and DC, of antiferromagnetic $\{N(n\text{-}C_5H_{11})_4[Mn^{II}Fe^{III}(C_2O_4)_3]\}_\infty$ under different measuring protocols have revealed the existence of a substantial uncompensated magnetic moment in this compound at temperatures below T_N of 27 K. It has also been found that the antiferromagnetic short-range coupling through the oxalate bridges of iron and manganese moments influences the magnetization of the system well above T_N and the spins become uncorrelated only for $T > 150$ K.

The estimated magnetic entropy from heat capacity studies established the high spin species of Mn and Fe ions. Application of a magnetic field shifts the transition temperature towards higher temperatures. The present magnetic system is an $S = 5/2$ 2-D Heisenberg antiferromagnet system with the intralayer exchange parameter $J/k_B = -3.29$ K. Application of spin wave theory to the magnetic heat capacity below $0.5T_N$ revealed the existence of a very weak interlayer exchange interaction, but could not assign its nature.

Mössbauer spectroscopy complemented the results obtained from heat capacity studies and highlighted the nature of the interlayer interaction. The Mössbauer study resolved the co-existence of different Fe^{III} spin sites in the lattice at low temperatures and has portrayed the interlayer ferromagnetic arrangement of different Fe^{III} spins. The honeycomb layered structure of the compound contains non-equivalent magnetic sub-lattices, (Mn^{II}–ox–$Fe^{III}{}_A$–...) and (Mn^{II}–ox–$Fe^{III}{}_B$–...), with different responses of the $Fe^{III}{}_A$ and $Fe^{III}{}_B$ spin sites towards the external magnetic field. It is concluded

that the different behavior of the Fe^{III} spin sites might be responsible for the uncompensated magnetization in this compound observed below the Néel temperature.

The reason for two non-equivalent Fe^{III}_A and Fe^{III}_B spin sites within the iron sub-lattice of $\{N(n\text{-}C_5H_{11})_4[Mn^{II}Fe^{III}(ox)_3]\}_\infty$ is not straightforward to explain. It is known that in the $A[M(II)M'(III)(ox)_3]$ structure, where bimetallic layers are separated by the organic cation A, the different metal centers show alternating chirality. As recently discussed by Fishman et al. [22], the mutual alignment of the chiral axes, collinear in two-dimensional (2D) and non-collinear in three-dimensional (3D) oxalates, gives rise to the quite different magnetic properties, in spite of the almost identical exchange coupling and local crystal-field environment in both systems. The spin–orbit coupling with the non-collinear orbital moments causes the spins to cant in 3D compounds. In our case the $S = 5/2$ Mn(II) and Fe(III) $3d^5$ multiplets are orbital singlets, but a possible small difference in the g-factors for the Mn^{II} and Fe^{III} ions has been mentioned in [11] along with a relatively large zero-field splitting for Mn^{II}. Additionally, the $N(n\text{-}C_5H_{11})_4$ cation may play a role in breaking the local symmetry of the Fe^{III} spin sites, like in the case of $N(n\text{-}C_4H_9)_4[Fe^{II}Fe^{III}(ox)_3]$, discussed in [23]. The presence of two Fe^{III} sites with subtly different behavior is also consistent with the lower symmetry group of $\{N(n\text{-}C_5H_{11})_4[Mn^{II}Fe^{III}(ox)_3]\}_\infty$ as compared to other $\{A[Mn^{II}Fe^{III}(C_2O_4)_3]\}_\infty$ compounds [11]. Therefore, in spite of the same electronic ground states of Mn^{II} and Fe^{III}, the system under study is not a simple layered antiferromagnet and the net effect of anisotropy and frustration on the near-neighbor magnetic interactions will be more prominent in the intralayer than in the interlayer interactions, as the former dominates the overall magnetic properties of the system under study. This situation can easily be held responsible for resulting into various competing magnetic interactions leading to net uncompensated magnetization seen in the present compound at temperatures below the transition temperature.

Acknowledgements

For this work a Grant-in-Aid for JSPS Fellow, a Grant-in-Aid for Scientific Research on Priority Areas "Metal-Assembled Complexes" from the Ministry of Education, Culture, Sports and Science, Japan, and also financial support from the Deutsche Forschungsgemeinschaft (Priority Program 1137 "Molecular Magnetism"), the Fonds der Chemischen Industrie and the Materialwissenschaftliches Forschungszentrum of the University of Mainz are gratefully acknowledged.

References

[1] H. Tamaki, Z.J. Zhong, N. Matsumoto, S. Kida, M. Koikawa, N. Achiwa, Y. Hashimoto, H. Ōkawa, J. Am. Chem. Soc. 114 (1992) 6974.
[2] H. Ōkawa, N. Matsumoto, H. Tamaki, S. Kida, M. Ohba, Mol. Cryst. Liq. Cryst. 233 (1993) 257.
[3] R. Pellaux, W.H. Schmalle, R. Huber, P. Fischer, T. Hauss, B. Ouladdiaf, S. Decurtins, Inorg. Chem. 36 (1997) 2301.
[4] M. Pilkington, S. Decurtins, in: J.S. Miller, M. Drillon (Eds.), Chapter in From Molecules to Materials II, Wiley-VCH, Weinheim, 2001.
[5] E. Coronado, J.R.G. Mascaros, M.C. Gimenez-Lopez, M. Almeida, J.C. Waerenborgh, Polyhedron 26 (2007) 1838.
[6] J.S. Miller, M. Drillon (Eds.), From Molecules to Materials IV, Wiley-VCH, Weinheim, 2003.
[7] K.R. Dunbar (Ed.), Proceedings of the 7th International Conference on Molecule-Based Magnets, Polyhedron 20 (2001).
[8] O. Kahn (Ed.), Proceedings of the 6th International Conference on Molecule-Based Magnets, Mol. Cryst. Liq. Cryst. 334/335 (1999).
[9] E. Coronado, P. Delhaes, D. Gatteschi, J.S. Miller (Eds.), Molecular Magnetism, NATO ASI Series, Kluwer Academic Publishers, 1996.
[10] L.J. de Jongh, A.R. Miedema, Adv. Phys. 23 (1974) 1.
[11] C. Mathonière, C.J. Nuttall, S.G. Carling, P. Day, Inorg. Chem. 35 (1996) 1201.
[12] S.G. Carling, C. Mathonière, P. Day, K.M.A. Malik, S.J. Coles, M.B. Hursthouse, J. Chem. Soc., Dalton Trans. (1996) 1839.
[13] A. Bhattacharjee, P. Gütlich, J. Magn. Magn. Mater. 268 (2004) 380.
[14] A. Bhattacharjee, Y. Miyazaki, M. Sorai, J. Magn. Magn. Mater. 280 (2004) 1.
[15] A. Bhattacharjee, P. Gütlich, J. Phys.: Condens. Matter 19 (2007) 356201.
[16] N.S. Ovanesyan, G.V. Shilov, N.A. Sanina, A.A. Pyalling, L.O. Atovmyan, L. Bottyan, Mol. Cryst. Liq. Cryst. 335 (1999) 91.
[17] Bin Zhang, Yan Zhang, Junchao Li, Daoben Zhu, J. Chem. Soc., Dalton Trans. (2008) 5037.
[18] R.L. Carlin, Magnetochemistry, Springer Verlag, Berlin, 1986.
[19] X.-Y. Wang, L. Wang, Z.-M. Wang, G. Su, S. Gao, Chem. Mater. 17 (2005) 6369.
[20] C.J. Nuttall, P. Day, Inorg. Chem. 37 (1998) 3885.
[21] C.E. Johnson, J. Phys. D: Appl. Phys. 29 (1996) 2266.
[22] R.S. Fishman, S. Okamoto, F.A. Reboredo, Phys. Rev. Lett. 101 (2008) 116402.
[23] R.S. Fishman, M. Clemente-Leon, E. Coronado, Inorg. Chem. 48 (2009) 3039.

able for the analysis of biomolecules, for instance, phospholipids [15,16] and proteins/peptides [9].

This study was undertaken to investigate the MALDI-TOF mass spectrometric behaviour of Pt(II) and Pd(II) complexes under the typical experimental conditions (i.e. the addition of trifluoroacetic acid and/or high salt content) applied for MALDI-TOF MS analysis. The obtained results demonstrate differences in the MALDI-TOF mass spectra of Pt(II) and Pd(II) complexes in dependence on the combination of the metal complex and matrix and, additionally, point to the optimal conditions for MALDI-TOF mass spectrometric analysis of Pt(II) and Pd(II) complexes.

2. Materials and methods

2.1. Chemicals

Platinum(II) and palladium(II) complexes: [$PtCl_2$(*en*)] (ethylenediamine Pt(II) chloride;), [$PtCl_2$(*dach*)] (diaminocyclohexane Pt(II) chloride), and [PdCl(*dien*)]Cl (diethylenetriamine Pd(II) chloride) were synthesised as described in the literature [17,18]. Chemical analysis, UV–Vis and ^{1}H NMR spectral data of these complexes were in good agreement with those obtained in previous preparations. Trifluoroacetic acid solution, matrices for MALDI-TOF MS – 2,3-DHB and α-CHCA were also purchased from Sigma Aldrich Chemie Gmbh (München, Germany) and they were applied without further purification.

2.2. Preparation of samples for MALDI-TOF mass spectrometry

Pt(II) complexes were resuspended in distilled water and kept refrigerated (+4 °C) prior to applying onto the sample plate. The following concentrations of the suspensions were prepared: 0.08 and 0.1 M for [$PtCl_2$(*en*)] and [$PtCl_2$(*dach*)], respectively. The water solution of [PdCl(*dien*)]Cl was of 0.02 M concentration. Matrices – 2,5-DHB and α-CHCA were prepared fresh prior to use. The following solutions of the matrices were used: 0.5 M 2,5-DHB in methanol and 5 mM α-CHCA in acetonitrile/water (1:1, v/v). For some experiments, solutions of NaCl or KCl (final concentration 0.4%) were added to the matrix solutions.

The suspensions of the complexes were vigorously vortexed prior to applying onto the MALDI-TOF sample plate made of stainless steel; the same volume of the matrix solution (1.2 μL) was subsequently applied onto the sample plate. The matrix/analyte mixture was then left to co-crystallise at room temperature. This approach was shown to yield co-crystals with the best homogeneity.

2.3. MALDI-TOF mass spectrometry

MALDI-TOF mass spectra were acquired on a Bruker Daltonics workstation (Bruker Daltonik GmbH, Germany) with a 50 Hz pulsed nitrogen laser emitting at λ = 337 nm. The extraction voltage was 20 kV and all spectra were recorded under delayed extraction conditions and in the reflector mode, thus improving mass accuracy and resolution. Spectra were acquired without low mass gate and each spectrum represents an average of at least 100 single laser shots.

3. Results and discussion

3.1. MALDI-TOF mass spectrometry of Pt(II) complexes

The MALDI-TOF mass spectra of Pt(II) and Pd(II) complexes were acquired with 2,5-DHB or with CHCA as matrices. The positive ion mode MALDI-TOF mass spectra of [Pt(*en*)Cl_2] are shown in Fig. 1: the spectra given in (a) and (b) are acquired with DHB, whereas CHCA was used for the spectra presented in (c) and (d). TFA was added to the matrix solutions applied for the spectra given in (b) and (d). All peaks arising from Pt-complexes are listed in Table 1 and their *m*/*z* ratios are also indicated in the figure.

It should be pointed out that the individual peaks arising from Pt-complexes are complicated due to a great number of naturally occurring isotopes of Pt, which has six isotopes. Therefore, a great number of combinations with isotopes of other atoms composing the complex are possible. In certain cases, as it will be demonstrated further in the text, the overlapping with the peaks arising from polymerisation products of the matrix itself additionally complicates the spectra. An inset in Fig. 1a is given to illustrate the complexity of individual peaks that arise from Pt-complexes. However, this characteristic pattern of the MALDI-TOF mass spectra of Pt(II) and Pd(II) complexes can make the monitoring of their interaction with biomolecules much easier.

[Pt(*en*)Cl_2] yields two peaks with the DHB matrix (Fig. 1a): at *m*/*z* = 409.2 and at *m*/*z* = 446.2. These peaks are generated by the addition of one ligand (*ethylenediamine*) to the complex, followed by cationisation with sodium (at *m*/*z* = 409.2), and by the addition of two ligands (*en*) and further ionisation with proton (*m*/*z* = 446.2). This behaviour is different from the spectra obtained with other matrices, such as flavonoids [14]. When flavonoids were used as matrices for MALDI-TOF MS of Pt(II) and Pd(II) complexes, undetectable loss of ligands and no fragmentation of complexes were noticed. On the other hand, under conditions more suitable for a MS analysis of biomolecules, certain peaks recognised as peaks arising from Pt(II) or Pd(II) can be explained only by the addition of ligands previously eliminated from Pt-complexes. This is not necessarily surprising, since higher laser intensities are required for the spectra acquisition with DHB or CHCA, in comparison to flavonoids, and with higher laser intensity the elimination of ligands occurs to a higher extent. In addition, this might explain why it is also possible to detect other unusual peaks arising from the complexes in MALDI-TOF mass spectra when "traditional" matrices, such as DHB and CHCA, are used.

In the next experiments we added a small amount of TFA to the matrix solution, since this approach had been shown to increase the signal-to-noise ratio in the analysis of biomolecules [9,19]. We wanted to test whether the peak pattern arising from Pt(II) complexes would change in the presence of this proton source and whether the TFA addition would result in increased fragmentation of the complexes.

Upon addition of TFA (Fig. 1b) the spectra of [Pt(*en*)Cl_2] looks much simpler than the spectra recorded without TFA. In this case, the number of peaks decreased and the signals arising from the analyte were more intense. In the spectra of [Pt(*en*)Cl_2], there are almost no peaks arising from the DHB matrix. Only the peaks at *m*/*z* = 409.2 and at *m*/*z* = 446.2 generated by adding the ligand, *ethylenediamine*, to the Pt(II) complex and further cationisation, are detectable in the spectra of this Pt(II) complex acquired with DHB containing small amounts of TFA.

The spectra of the same complex acquired with CHCA are much more complicated (Fig. 1c). Apart from the already described peak at *m*/*z* = 446.2 (*cf.* Table 1), there are peaks generated by the addition of matrix molecule and the further incorporation of a proton (the peak at *m*/*z* = 478.3), as well as the peak corresponding to the product of hydrolysis (i.e. replacement of one Cl^- ion with the OH^-) of the complex (peak at *m*/*z* = 330.6, *cf.* Table 1 for peak assignment). The hydrolysis of the complexes is favoured by the low concentration of chloride ions in the solution. Since distilled water has been used for the suspension of the complexes, it is possible to detect the products of hydrolysis. On the other hand, these hydrolysis products were not detectable in the spectra acquired with DHB. This has to be

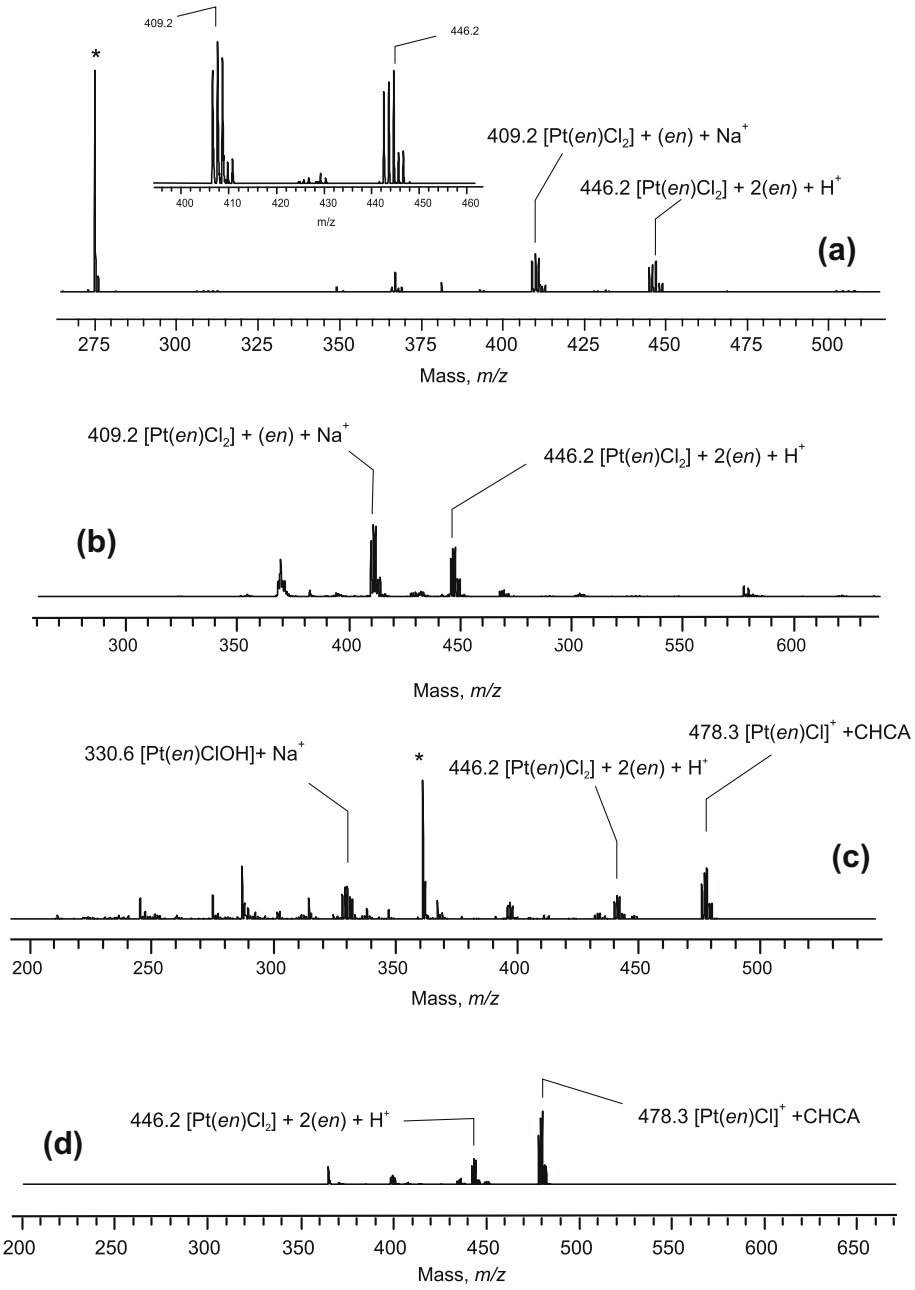


Fig. 1. Positive ion MALDI-TOF mass spectra of [Pt(*en*)Cl_2] acquired with DHB (a and b) and with CHCA (c and d) matrices. In the spectra given in (b) and (d) TFA was added to the matrix solution (0.1% final concentration). The identity of peaks and their position (*m*/*z* ratios) are indicated in the figure. Peaks arising from matrix are labelled with an asterisk.

related to the nature of the matrix itself: since higher laser intensities are required for DHB compared to CHCA, it is possible that this peak is beyond the detection limit for the applied experimental conditions.

In a similar manner to the spectra acquired with DHB containing TFA, the spectra of [Pt(*en*)Cl_2] acquired with CHCA containing small amounts of TFA (Fig. 1d) are simpler compared to the spectra without TFA. There are two peaks: at *m*/*z* = 446.2 and at *m*/*z* = 478.3 that arise from the complex, whereas the peaks arising from the applied matrix were of much low intensity in the presence of TFA. The former peak was detected also in the spectra recorded with DHB, whereas the latter, at a higher *m*/*z* ratio, is related to the CHCA matrix since it has been generated by eliminating Cl^- from the Pt(II) complex investigated and subsequent addition of CHCA to the generated cation (*cf.* Table 1). Interestingly, under these conditions, the formation of clusters with two ligands is favoured when the spectra are recorded with CHCA matrices, and these ions seem to be more stable than those obtained with the DHB matrix.

Positive ion mode MALDI-TOF mass spectrum of [Pt(*dach*)Cl_2] shows a somewhat different spectral pattern. MALDI-TOF mass spectra of this complex acquired with DHB matrix are presented in Fig. 2a and b, whereas CHCA was used as matrix for the spectra given in 2c and d. Small amounts of TFA were added to the spectra given in Fig. 2b and d.

Two peaks that correspond to the sodium (*m*/*z* = 403.2) and to the potassium (*m*/*z* = 419.2) adducts of the molecule dominate the spectrum recorded with the DHB matrix (Fig. 2a). There are also some additional peaks that arise from the ion generated by adding one ligand, *dach* (peak at *m*/*z* = 498.4) to the molecule and

Table 1
Peaks detected in the positive ion MALDI-TOF mass spectra of Pt(II) and Pd(II) complexes. CHCA indicated neutral form of this matrix.

Peak position (m/z)	Peak assignment
209.1	$[Pd(dien)Cl]^+ - HCl$
245.1	$[Pd(dien)Cl]^+$
306.3	n.d.
313.8	$[Pd(dien)Cl]^+ - HCl + (dien)$
318.3	$[Pd(dien)Cl]Cl + K^+$
330.6	$[Pt(en)ClOH] + Na^+$
362.2	n.d.
364.2	$[Pd(dien)Cl]^+ - HCl + DHB$
403.2	$[Pt(dach)Cl_2] + Na^+$
409.2	$[Pt(en)Cl_2] + (en) + Na^+$
419.2	$[Pt(dach)Cl_2] + K^+$
446.2	$[Pt(en)Cl_2] + 2(en) + H^+$
452.4	n.d.
460.9	n.d.
478.3	$[Pt(en)Cl]^+ + CHCA$
498.4	$[Pt(dach)Cl_2] + (dach) + Na^+$
534.2	$[Pt(dach)Cl]^+ + CHCA$
724.2	$[Pt(dach)Cl]^+ + [Pt(dach)Cl_2]$

cationising with sodium. There are also some peaks (*cf.* Table 1) which could not be identified, but which most probably contain Pt (judging according to the peak pattern).

When the TFA was added to the matrix solution, a more pronounced loss of ligand occurs and the clusters between the Pt(II) complex and the ligand become detectable (Fig. 2b). This can be observed as a peak at $m/z = 498.4$. The peak at $m/z = 419.2$ arises from the potassium adduct of the complex, whereas the identity of the peak at 452.4 is so far unknown. It might be a result of adding already fragmented ligand (*dach*) to the complex, but this assumption has to wait for its final confirmation.

In the spectra of the same complex, recorded with the CHCA matrix (Fig. 2c), the distribution of peaks is similar to the spectrum recorded with the assistance of the DHB matrix. There is also an additional peak at $m/z = 534.2$ generated from the complex by eliminating a Cl^- ion and adding neutral CHCA.

The spectra of $[Pt(dach)Cl_2]$ acquired with CHCA in the presence of TFA (Fig. 2d) are simple, since they contain only one peak corresponding to the potassium adduct of the complex. Other adducts are not detectable under these experimental conditions.

In summary to this part of the work, we may say that the addition of TFA to the matrices that can be used for the analysis of Pt(II) complexes, but also for the analysis of biomolecules, does not lead to the increased fragmentation of complexes, but results in increased signal intensity corresponding to the complex. Although there are some unidentified peaks in these spectra, it is clear that they arise from Pt.

3.2. MALDI-TOF mass spectrometry of [Pd(dien)Cl]Cl

In the next part of our work, we analysed the spectra of the cationic complex, $[Pd(dien)Cl]^+Cl^-$. The positive ion mode MALDI-TOF mass spectra of the complex acquired with DHB and CHCA matrices are given in Fig. 3: in (a) and (c) the spectra with DHB are given and in (b) and (d) the spectra recorded with CHCA are presented. TFA was added to the matrices used for the spectra given in (c) and (d).

In accordance with the spectra acquired with flavonoids, [14] two peaks at $m/z = 209.1$ and at $m/z = 245.1$ are generated by the loss of Cl^- ion and subsequent elimination of HCl, whereas the loss of the easy-leaving Cl^- ion leaves the complex detectable at $m/z = 245.1$. In addition to these peaks there are two peaks in the spectra of Pd(II) complex acquired with the assistance of DHB: the peak at $m/z = 318.3$, corresponding to the addition of potassium to the complex, and the peak at $m/z = 364.2$ generated by adding DHB molecule to the fragment generated by the loss of Cl^- ion and elimination of HCl (*cf.* Table 1 for peak identity).

When the spectra of [Pd(*dien*)Cl]Cl were recorded with the CHCA matrix (Fig. 3b), only two peaks were detectable: at $m/z = 245.1$ and at $m/z = 209.1$. Neither matrix adducts nor peaks corresponding to the addition of any cation to the complex could be detected. The reason for this might be the lower content of inorganic ions in CHCA, and the complex's weaker tendency to generate clusters with the matrix when CHCA was used for the analysis. One can easily observe differences in the intensity of individual peaks that correspond to the complex in the spectra acquired with the two matrices, while the intensity of the peaks at $m/z = 209.1$ and at $m/z = 245.1$ is rather low with DHB (Fig. 3a), the intensity of their counterparts in the spectra acquired with CHCA (Fig. 3b) is higher. Since higher laser intensities must be applied for the spectra acquisition with DHB, in comparison to CHCA, it is possible that these clusters at higher m/z are generated only at higher laser intensities, which has already been observed for other molecules analysed with the DHB matrix [16].

After adding TFA to the matrix solution, Pd(II) complex was barely detectable, as only one peak could be observed. This peak was, according to the above described peaks, most probably overlapping with the matrix peak (peak at $m/z = 361.2$), preventing its reliable identification. These results are in contrast to those obtained with flavonoids. Namely, when the spectra were acquired with flavonoids, the Pd(II) complex was stable even after the addition of TFA.

3.3. MALDI-TOF mass spectrometry of Pt(II) and Pd(II) complexes in the presence of high salt content

A higher salt content is characteristic for samples of biological origin. This fact might affect the choice of the method to be used for the analysis of some important biological processes and elucidation of the interactions of e.g. drugs with biomolecules. Most commonly, MS methods are sensitive to salt content. On the other hand, MALDI-TOF MS, which is still primarily used for the analysis of biomolecules, appears to tolerate somewhat higher content of salts and, up to a certain concentration, there is no need to remove salts from the solution prior to analysis. To test the possibility for the application of MALDI-TOF MS for monitoring the interactions between metallo-drugs and biomolecules under more physiologically relevant conditions (i.e. in the presence of physiological solutions and a high content of inorganic ions), we analysed Pt(II) and Pd(II) complexes with DHB and CHCA in the presence of 0.4% NaCl or KCl.

The spectra of $[Pt(en)Cl_2]$ and $[Pt(dach)Cl_2]$ acquired with DHB and 0.4% NaCl are given in Fig. 4a and b, respectively. Interestingly, signals were suppressed when the same spectra were recorded with the assistance of CHCA (data not shown). This might also be related to better ionisation properties of CHCA, in comparison to DHB: a higher content of salt demanded a higher laser intensity, which in turn most probably resulted in the saturation of the detector with inorganic salts.

In the spectra of $[Pt(en)Cl_2]$, two peaks are detectable: at $m/z = 409.2$ and at $m/z = 446.2$. They are also detectable in the spectra of the same complex acquired under somewhat different conditions and their identity is given in Table 1. Although expected, no higher adducts with sodium could be detected, but the quality of the spectra was better compared to the same spectra recorded without the addition of salt.

The spectra of $[Pt(dach)Cl_2]$ in the presence of NaCl (Fig. 4b) have the same pattern as the spectra recorded in the absence of salt. There are three peaks: at $m/z = 403.2$, 419.2 and 460.9 arising from the complex (*cf.* Table 1 for peak identity), whereas the peak

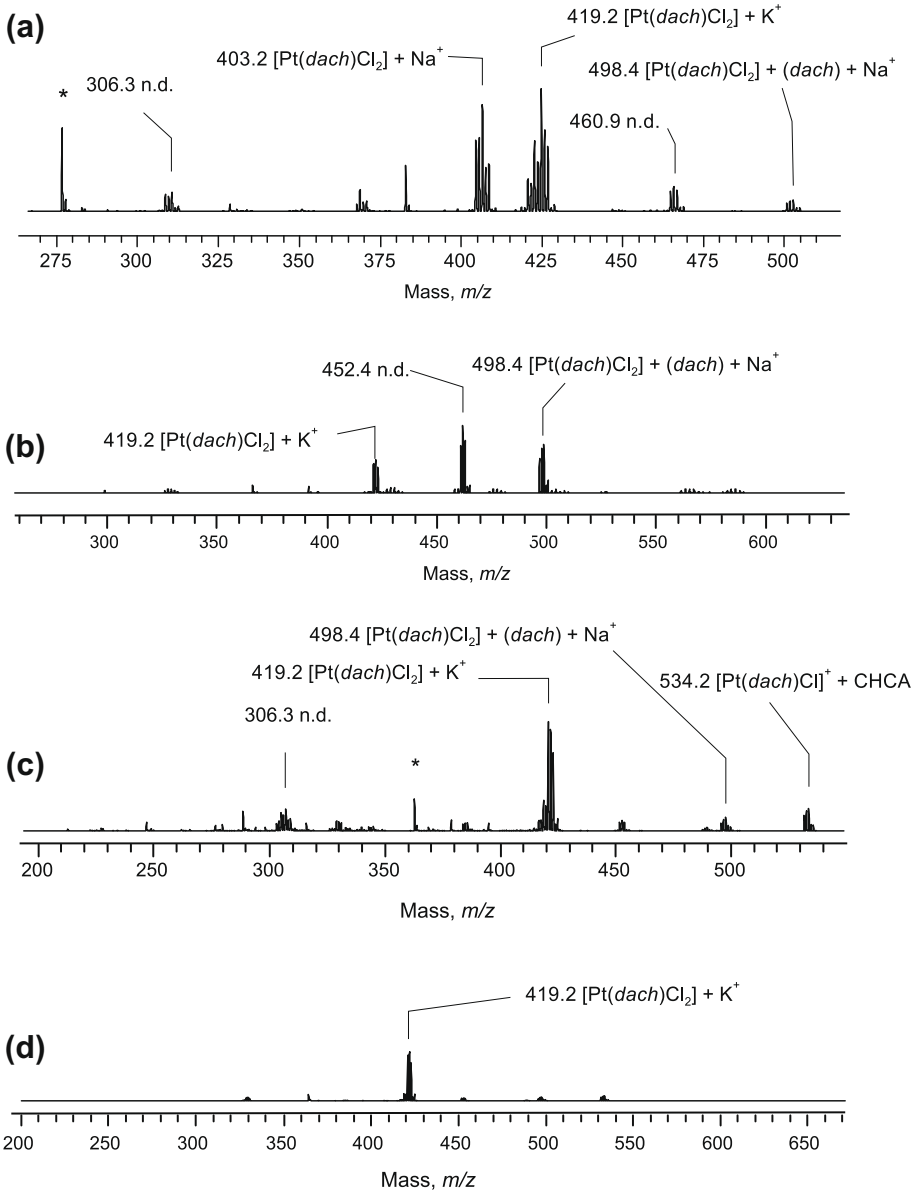


Fig. 2. Positive ion MALDI-TOF mass spectra of [Pt(*dach*)Cl_2] acquired with DHB (a and b) and with CHCA (c and d) matrices. In the spectra given in (b) and (d) TFA was added to the matrix solution (0.1% final concentration). The identity of peaks and their position (*m*/*z* ratios) are indicated in the figure. Peaks arising from matrix are labelled with an asterisk; n.d. is "not determined".

at *m*/*z* = 724.2 most probably represents the cluster generated from the complex and the same complex that has previously lost Cl^-. Obviously, a higher content of sodium could not suppress the peak arising from the potassium adduct of [Pt(*dach*)Cl_2] (peak at *m*/*z* = 419.2). However, the quality of the spectra was much worse in the presence of higher sodium content.

The presence of a higher potassium content (also 0.4%) in the solution of matrix resulted in a different spectra pattern, but also in a reduced number of detectable peaks in the spectra of Pt(II) complexes. The spectra of [Pt(*en*)Cl_2] are given in Fig. 5a and c, whereas the positive ion mode MALDI-TOF mass spectra of [Pt(*dach*)Cl_2] are presented in Fig. 5b and d. The spectra presented in 5a and b are acquired with DHB as matrix, whereas for the spectra in 5c and d CHCA was used. Both matrix solutions contained 0.4% KCl and 0.1% TFA.

The peak at *m*/*z* = 362.2 was detectable in the spectra of [Pt(*en*)Cl_2] acquired with both matrices and in the presence of high K^+ ion content (Fig. 5a and c). The identity of this peak could not be determined, but it seems that it is overlapping with the signal arising from the matrix. In the spectrum 5a, there is an additional peak at *m*/*z* = 446.2 that can be assigned to the Pt-complex to which two ligands were added and which was further ionised by proton.

The positive ion MALDI-TOF mass spectra of [Pt(*dach*)Cl_2] in the presence of KCl are much simpler compared to the above described spectra of [Pt(*en*)Cl_2]. Only one peak at *m*/*z* = 419.2 was detectable. This peak corresponds to the potassium adduct of [Pt(*dach*)Cl_2] (*cf.* Table 1), whereas other peaks are suppressed. This difference observed in the spectra pattern between these complexes can be attributed to the different nature of the ligand coordinatively bound to Pt and the differences in their affinity towards different inorganic ions, as observed for other molecules.

In Fig. 6a and b, the spectra of [Pd(*dien*)Cl]Cl acquired with DHB and with CHCA matrices, respectively, containing 0.4% of KCl are shown. Obviously, in this case, the presence of high potassium content led to barely detectable signals. Although, according to the peak pattern, certain peaks could be attributed to species that con-

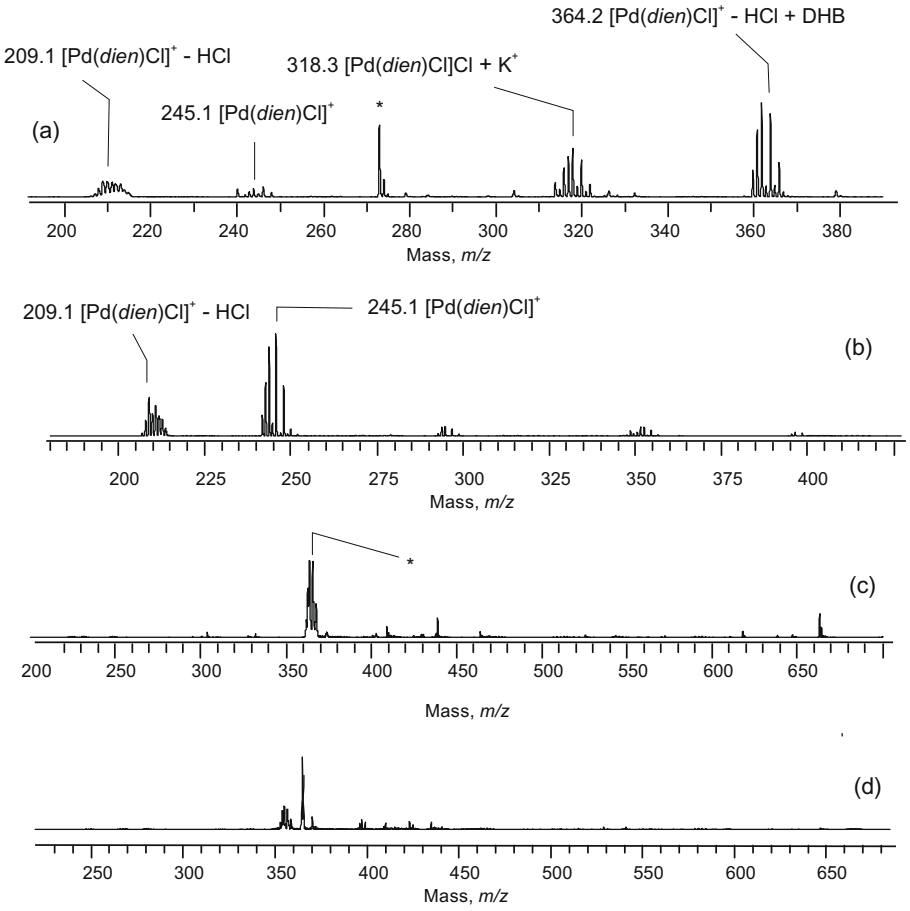


Fig. 3. Positive ion MALDI-TOF mass spectra of [Pd(*dien*)Cl]Cl acquired with DHB (a and c) and with CHCA (b and d). For the spectra presented in (c) and (d) 0.1%, TFA was added to the matrix solution. The identity of peaks and their position (*m*/*z* ratios) are indicated in the figure. Peaks arising from matrix are labelled with an asterisk.

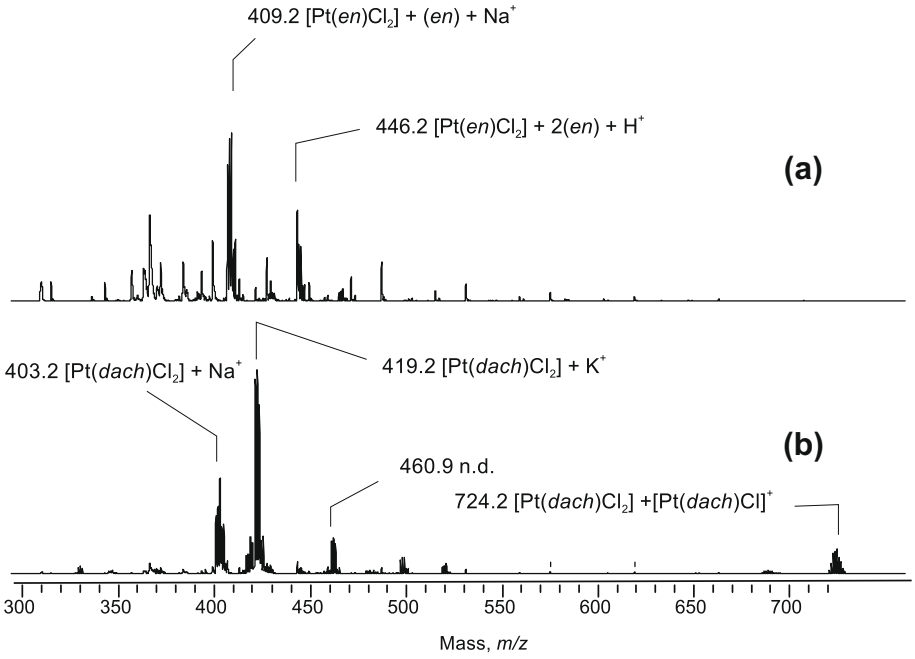


Fig. 4. Positive ion mode MALDI-TOF mass spectra of [Pt(*en*)Cl_2] (a) and [Pt(*dach*)Cl_2] (b) acquired with the DHB matrix in the presence of 0.4% NaCl. The identity of peaks and their position (*m*/*z* ratios) are indicated in the figure.

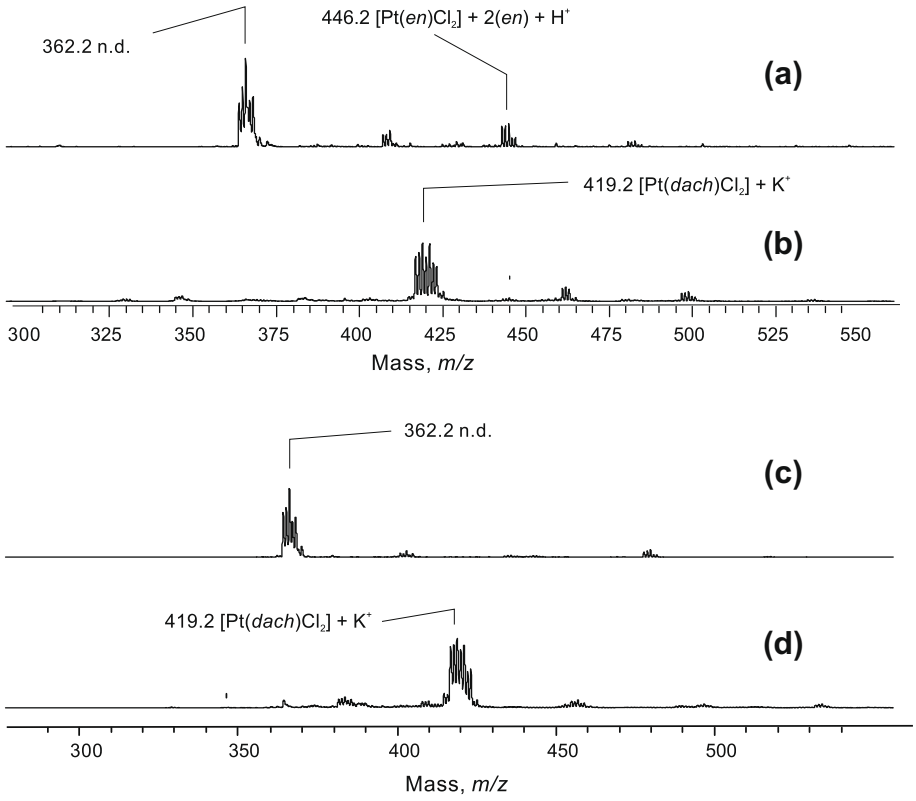


Fig. 5. Positive ion mode MALDI-TOF mass spectra of [Pt(*en*)Cl_2] (a and c) and [Pt(*dach*)Cl_2] (b and d) acquired in the presence of 0.4% KCl and 0.1% TFA. The spectra in (a) and (b) were acquired with DHB, whereas for the spectra given in (c) and (d) CHCA was used as a matrix. The identity of peaks and their position (*m*/*z* ratios) are indicated in the figure.

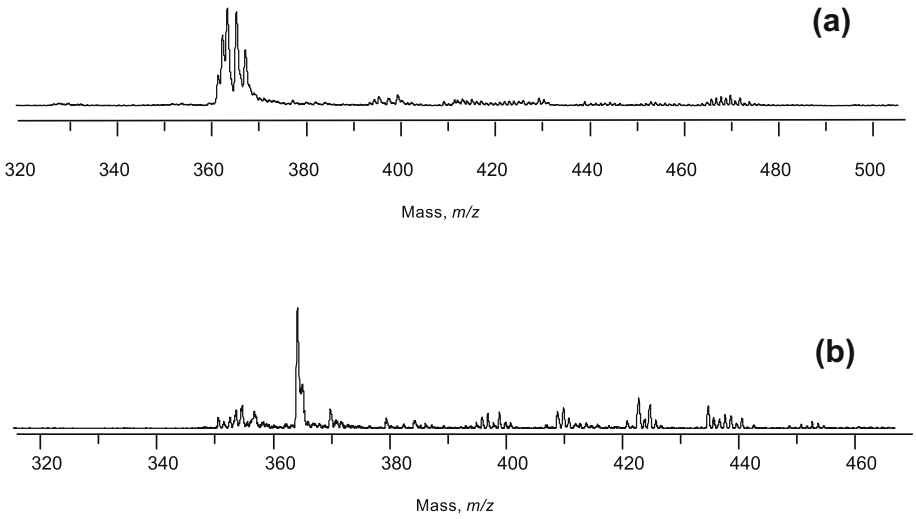


Fig. 6. Positive ion mode MALDI-TOF mass spectra of [Pd(*dien*)Cl]Cl acquired with the DHB (a) and CHCA (b) matrices. In both spectra, a high content of KCl (0.4% in the matrix solution) was present.

tain Pd, their intensity is by far too low for any reliable peak identification.

4. Summary

The analysis of the MALDI-TOF mass spectra of transition metals (Pt(II), Pd(II)) and their complexes acquired with the DHB and CHCA matrices, with the addition of TFA and with a high inorganic salt content, demonstrated differences in their behaviour depending on the metal/ligand combination and on the matrix used for the analysis. While Pt(II) complexes could be easily and reliably analysed with the DHB matrix, it seems that CHCA is better suitable for MALDI-TOF MS of Pd(II) complex used in this study. On the other hand, the spectra obtained under experimental conditions usually applied in the MALDI-TOF mass spectrometric analysis of biomolecules (which might contain a higher content of inorganic salts in the sample) and with the addition of small

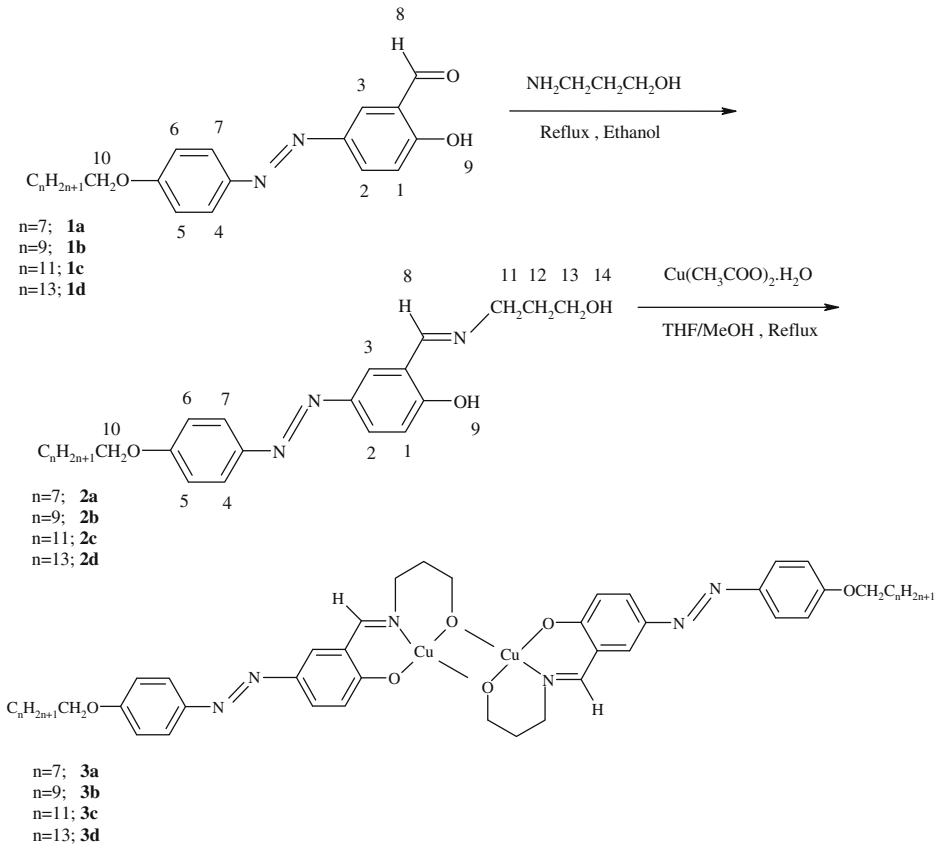
amounts of TFA have to be subjected to careful analysis. It is possible that certain complexes, such as cationic Pd(II) complex, do not tolerate acidic conditions for the analysis and the absence of the corresponding peak might be misinterpreted.

Acknowledgments

This work was supported by the Serbian Ministry of Sciences and Technological Development of the Republic of Serbia, Grant No. 142051b. The assistance of colleagues from the Institute of Medical Physics and Biophysics, University of Leipzig, Germany is also greatly acknowledged.

References

[1] M. Galanski, V. Arion, M. Jakupec, B. Keppler, Curr. Pharm. Des. 9 (2003) 2078.
[2] B.A.J. Jansen, J. Brouwer, J. Reedijk, J. Inorg. Biochem. 89 (2002) 197.
[3] J. Turkson, S. Zhang, L.B. Mora, A. Burns, S. Sebti, R. Jove, J. Biol. Chem. 280 (2005) 32979.
[4] P. Heffeter, U. Jungwirth, M. Jakupec, C. Hartinger, M. Galanski, L. Elbling, M. Micksche, B. Keppler, W. Berger, Drug Resist. Update 11 (2008) 1.
[5] M. Jakupec, M. Galanski, B. Keppler, Rev. Physiol. Biochem. Pharmacol. 146 (2003) 1.
[6] D. Petrović, B. Stojimirović, B. Petrović, Z.M. Bugarčić, Ž.D. Bugarčić, Bioorg. Med. Chem 15 (2007) 4203.
[7] D. Vasić, J. Savić, Z. Bugarcić, D. Krstić, N. Tomić, M. Colović, M. Petković, V. Vasić, Z Naturforsch. C 64 (2009) 103.
[8] L. Xu, S. Shi, J. Li, S. Liao, K. Zheng, L. Ji , Dalton Trans. (2008) 291.
[9] F. Hillenkamp, J. Peter-Katalinic (Eds.), Maldi Ms, Wiley-VCH Verlag GmbH & Co. KGaA, Weinheim, 2007.
[10] S. Mwelase, J. Bariyanga, J. Mol. Struct. 608 (2002) 235.
[11] E. Royo, H. Brintzinger, J. Organomet. Chem. 663 (2002) 213.
[12] A. Mazzaglia, L. Scolaro, D. Garozzo, P. Malvagna, R. Romeo, J. Organomet. Chem. 690 (2005) 1978.
[13] J. Bariyanga, J. Bioact. Compat. Polym. 17 (2002) 37.
[14] M. Petković, A. Vujačić, J. Schiller, Z. Bugarčić, J. Savić, V. Vasić, Rapid Commun. Mass Spectrom. 23 (2009) 1467.
[15] J. Schiller, R. Süß, B. Fuchs, M. Müller, M. Petković, O. Zschörnig, H. Waschipky, Eur. Biophys. J. 36 (2007) 517.
[16] M. Petković, J. Schiller, M. Müller, R. Süß, K. Arnold, J. Arnhold, Z. Naturforsch. – Sect. B: J. Chem. Sci. 64 (2009) 331.
[17] L.P. Battaglia, A.B. Corradi, C.G. Palmieri, M. Nardelli, M.E.V. Tani, Acta Crystallogr., Sect. B 29 (1973) 762.
[18] G. Mahal, R. Van Eldik, Inorg. Chim. Acta 127 (1987) 203.
[19] M. Petković, J. Schiller, J. Müller, M. Müller, K. Arnold, J. Arnhold, Analyst 126 (2001) 1042.



Scheme 1. Synthetic route to the dicopper complexes.

then the crude 4-^{n}alkoxynitrobenzene homologous were purified by recrystallization from ethanol. The 4-^{n}alkoxyaniline homologous prepared by reducing the corresponding 4-^{n}alkoxynitrobenzenes as described in the literature [29].

2.2. Physical measurements

Elemental (C, H and N) analyzes were carried out on a Perkin–Elmer automatic equipment model 240B. Electron impact (70 eV) mass spectra were recorded on a Finnegan-mat GC–MS–DS spectrometer model 8430. Infrared spectra were taken with a FT-IR Bruker, vector 22 spectrometer using KBr pellets in the 400–4000 cm^{-1} range. The DSC thermograms of the compounds were obtained on a Mettler–Toledo DSC 822e module, which was calibrated with indium metal (T = 156.6 ± 0.3, ΔH = 28.45 ± 0.6 J g^{-1}). Samples of 2–5 mg in the solid form were placed in aluminum pans (40 μl) with a pierced lid, and heated or cooled at a scan rate of 10 °C min^{-1} under a nitrogen flow. TGA thermograms were carried out on a Mettler–Toledo TGA 851e at a heating rate of 10 °C min^{-1} under a nitrogen atmosphere. The optical observations were made with a Zeiss polarizing microscope equipped with a Linkam THMSG 600 heating and cooling stage and Linkam THMS 93 programmable temperature-controller. ^{1}H NMR spectra were obtained in deuterated chloroform as the solvent on a Bruker FT-NMR AC-400 (400 MHz) spectrometer. All chemical shifts are reported in δ(ppm) relative to tetramethylsilane as an internal standard.

2.3. Materials

All homologous materials were prepared similarly as described in the literature [30].

2.3.1. 5-(4-Octyloxyphenylazo)salicylaldehyde (**1a**)

Yellow, yield 80%, mp 126 °C. MS m/z (relative intensity): 355.4 (M+1, 15), 354.3 (M, 40). *Anal.* Calc. for $C_{21}H_{26}N_2O_3$: C, 71.16; H, 7.39; N, 7.90. Found: C, 70.8; H, 7.1; N, 7.5%. ^{1}H NMR (400 MHz, $CDCl_3$) δ: 11.27 (s, H-8), 10.02 (s, H-9), 8.18 (d, J 3.2 Hz, H-3), 8.14 (dd, J 3.1, 8.4 Hz, H-2), 7.91 (dd, J 3.1, 8.2 Hz, H-4, H-7), 7.10 (d, J 8.7 Hz, H-1), 7.01 (dd, J 3.6, 8.3 Hz, H-5,H-6), 4.05 (t, J 7.1 Hz, H-10), 1.81–1.00 (15H, alkyl chain). IR (KBr, cm^{-1}) ν: 3416 (O–H), 3069 (C–H, aromatic), 2921, 2959 (C–H, aliphatic), 1661 (C=O), 1600 (C=C, aromatic), 1500 (N=N), 1245 (C–O, ether), 1150 (C–O, phenolic).

2.3.2. 5-(4-Decyloxyphenylazo)salicylaldehyde (**1b**)

Yellow, yield 80%, mp 124 °C. MS m/z (relative intensity): 383.4 (M+1, 15), 382.3 (M, 40). *Anal.* Calc. for $C_{23}H_{30}N_2O_3$: C, 72.19; H, 7.84; N, 7.32. Found: C, 71.8; H, 7.5; N, 7.0%. ^{1}H NMR (400 MHz, $CDCl_3$) δ: 11.27 (s, H-8), 10.02 (s, H-9), 8.18 (d, J 3.2 Hz, H-3), 8.14 (dd, J 3.1, 8.4 Hz, H-2), 7.91 (dd, J 3.1, 8.2 Hz, H-4, H-7), 7.10 (d, J 8.7 Hz, H-1), 7.01 (dd, J 3.6, 8.3 Hz, H-5,H-6), 4.05 (t, J 7.1 Hz, H-10), 1.81–1.00 (19H, alkyl chain). IR (KBr, cm^{-1}) ν: 3417 (O–H), 3065 (C–H, aromatic), 2923, 2957 (C–H, aliphatic), 1661 (C=O), 1599 (C=C, aromatic), 1501 (N=N), 1245 (C–O, ether), 1149 (C–O, phenolic).

2.3.3. 5-(4-Dodecyloxyphenylazo)salicylaldehyde (**1c**)

Yellow, yield 80%, mp 123 °C. MS m/z (relative intensity): 411.6 (M+1,14), 410.6 (M, 45). *Anal.* Calc. for $C_{25}H_{34}N_2O_3$: C, 73.15; H, 8.35; N, 6.83. Found: C, 72.8; H, 8.2; N, 6.5%. ^{1}H NMR (400 MHz, $CDCl_3$) δ: 11.26 (s, H-9), 10.02 (s, H-8), 8.15 (d, J 2.8 Hz, H-3), 8.13 (dd, J 2.9, 8.2 Hz, H-2), 7.89 (dd, J 3.0, 7.9 Hz, H-4, H-7), 7.11 (d, J 8.1 Hz, H-1), 7.01 (dd, J 3.2, 7.9 Hz, H-5, H-6), 4.04 (t, J

6.7 Hz, H-10), 1.84-0.87 (23H, alkyl chain). IR (KBr, cm^{-1}) *v*: 3416 (O–H), 3065 (C–H, aromatic), 2921, 2851 (C–H, aliphatic), 1661 (C=O), 1600 (C=C, aromatic), 1500 (N=N), 1245 (C–O, ether), 1148 (C–O, phenolic).

*2.3.4. 5-(4-Tetradecyloxyphenylazo)salicylaldehyde (**1d**)*

Yellow, yield 76%, mp 122 °C. MS *m*/*z* (relative intensity): 439.6 (M+1, 13), 438.6 (M, 42). *Anal.* Calc. for $C_{27}H_{38}N_2O_3$: C, 73.97; H, 8.68; N, 6.39. Found: C, 73.6; H, 8.3; N, 6.0. ^{1}H NMR (400 MHz, $CDCl_3$) δ: 11.26 (s, H-9), 10.02 (s, H-8), 8.15 (d, *J* 2.8 Hz, H-3), 8.13 (dd, *J* 2.9, 8.2 Hz, H-2), 7.89 (dd, *J* 3.0, 7.9 Hz, H-4, H-7), 7.11 (d, *J* 8.1 Hz, H-1), 7.01 (dd, *J* 3.2, 7.9 Hz, H-5, H-6), 4.03 (t, *J* 6.7 Hz, H-10), 1.83–0.88 (27H, alkyl chain). IR (KBr, cm^{-1}) *v*: 3418 (O–H), 3065 (C–H, aromatic), 2919, 2850 (C–H, aliphatic), 1660 (C=O), 1600 (C=C, aromatic), 1500 (N=N), 1244 (C–O, ether), 1149 (C–O, phenolic).

2.4. Syntheses of the ligands

All the homologous materials were prepared in similar manners. Thus, 0.02 mol of 3-amino-1-propanol and 0.02 mol of the related 5-(4-^{n}dodecyloxyphenylazo)salicylaldehyde were dissolved in 100 ml absolute ethanol with a few drops of glacial acetic acid as a catalyst. The solution was refluxed for 1 h and then left at room temperature. After cooling, the ligands were obtained as yellow micro crystals. The micro crystals were filtered off, washed with 15 ml of cold absolute ethanol and then recrystallized several times in ethanol–chloroform (1:3, v/v).

*2.4.1. 5-(4-Octyloxyphenylazo)salicylaldimine-N-(3-hydroxypropyl) (**2a**)*

Yellow, yield 80%, mp 107.4 °C. MS *m*/*z* (relative intensity): 412.4 (M+1, 13), 411.3 (M, 42). *Anal.* Calc. for $C_{24}H_{33}N_3O_3$: C, 70.07; H, 8.03; N, 10.22. Found: C, 69.7; H, 7.8; N, 9.9%. ^{1}H NMR (400 MHz, $CDCl_3$) δ: 14.21 (s, H-9), 10.12 (s,H-14), 8.45 (s, H-8), 7.93 (dd, *J* 8.2, 2.8, Hz, H-2), 7.83–7.89 (H-3, H-4, H-7),7.03 (d, *J* 8.3 Hz, H-1), 6.97 (d, *J* 8.3 Hz, H-5, H-6), 4.03 (t, J 6.8 Hz, H-10), 3.75–3.81 (4H, H-11, H-13), 1.99 (p, *J* 4.2 Hz, H-12), 0.86–1.84 (15H, alkyl chain). IR (KBr, cm^{-1}) *v*: 3390 (O–H, alcoholic), 3220 (OH, phenolic), 3069 (C–H, aromatic), 2921, 2851 (C–H, aliphatic), 1640 (C=N), 1601 (C=C, aromatic), 1503 (N=N), 1254 (C–O, ether), 1149 (C–O, phenolic).

*2.4.2. 5-(4-Decyloxyphenylazo)salicylaldimine-N-(3-hydroxypropyl) (**2b**)*

Yellow, yield 90%, mp 112.2 °C. MS *m*/*z* (relative intensity): 440.4 (M+1, 12), 439.3 (M, 60). *Anal.* Calc. for $C_{26}H_{37}N_3O_3$: C, 71.07; H, 8.43; N, 9.57%. Found: C, 70.7; H, 8.1; N, 9.2%. ^{1}H NMR (400 MHz, $CDCl_3$) δ: 14.22 (s, H-9), 10.14 (s, H-14), 8.45 (s, H-8), 7.93 (dd, *J* 2.8, 8.2 Hz, H-2), 7.82–7.89 (H-3, H-4, H-7), 7.03 (d, *J* 8.3 Hz, H-1), 6.97 (d, *J* 8.3 Hz, H-5, H-6), 4.04 (t, *J* 6.8 Hz, H-10), 3.76–3.83 (4H, H-11, H-13), 1.99 (p, J 4.2 Hz, H-12), 0.86–1.85 (19H, alkyl chain). IR (KBr, cm^{-1}) *v*: 3415 (O–H, alcoholic), 3223 (OH, phenolic), 3065 (C–H, aromatic), 2919, 2851 (C–H, aliphatic), 1638 (C=N), 1603 (C=C, aromatic), 1502 (N=N), 1254 (C–O, ether), 1152 (C–O, phenolic).

*2.4.3. 5-(4-Dodecloxyphenylazo)salicylaldimine-N-(3-hydroxypropyl) (**2c**)*

Yellow, yield 75%, mp 116.6 °C. MS *m*/*z* (relative intensity): 468.4 (M+1, 12), 467.3 (M, 60). *Anal.* Calc. for $C_{28}H_{41}N_3O_3$: C, 71.95; H, 8.78; N, 8.99. Found: C, 71.6; H, 8.4; N, 8.6%. ^{1}H NMR (400 MHz, $CDCl_3$) δ: 14.20 (s, H-9), 10.12 (s, H-14), 8.45 (s, H-8), 7.93 (dd, J 2.6, 8.3 Hz, H-2), 7.83–7.90 (H-3, H-4, H-7), 7.03 (d, *J* 8.2 Hz, H-1), 6.97 (d, *J* 8.4 Hz, H-5, H-6), 4.04 (t, *J* 6.9 Hz, H-10), 3.76–3.83 (4H, H-11, H-13), 1.99 (p, *J* 4.1 Hz, H-12), 0.86–1.85 (23H, alkyl chain). IR (KBr, cm^{-1}) *v*: 3413 (O–H, alcoholic), 3224 (OH, phenolic), 3068 (C–H, aromatic), 2918, 2852 (C–H, aliphatic), 1638 (C=N), 1603 (C=C, aromatic), 1502 (N=N), 1252 (C–O, ether), 1147 (C–O, phenolic).

*2.4.4. 5-(4-Tetradecyloxyphenylazo)salicylaldimine-N-(3-hydroxypropyl) (**2d**)*

Yellow, yield 82%, mp 110.5 °C. MS *m*/*z* (relative intensity): 496.5 (M+1, 12), 495.4 (M, 60). *Anal.* Calc. for $C_{30}H_{45}N_3O_3$: C, 72.73; H, 9.09; N, 8.48. Found: C, 71.4; H, 8.7; N, 8.7%. ^{1}HNMR (400 MHz, $CDCl_3$) δ: 14.20 (s, H-9), 10.12 (s,H-14), 8.45 (s, H-8), 7.93 (dd, *J* 2.8, 8.2 Hz, H-2), 7.82–7.89 (H-3, H-4, H-7), 7.03 (d, *J* 8.3 Hz, H-1), 6.97 (d, *J* 8.3 Hz, H-5, H-6), 4.04 (t, *J* 6.8 Hz, H-10), 3.76–3.83 (4H, H-11, H-13), 1.99 (p, *J* 4.2 Hz, H-12), 0.85–1.85 (27H, alkyl chain). IR (KBr cm^{-1}) *v*: 3417 (O–H, alcoholic), 3223 (OH, phenolic), 3069 (C–H, aromatic), 2955, 2918, 2849 (C–H, aliphatic), 1638 (C=N), 1604 (C=C, aromatic), 1503 (N=N), 1251 (C–O, ether) 1152 (C–O, phenolic).

2.5. Syntheses of the copper complexes

The copper complexes were prepared in similar manners with slight modifications, using the method described elsewhere [31]. Thus, an alcoholic solution containing 10 mmol of 3-amino-1-propanol was added to a solution of 5-alkoxyphenylazosalicylaldehyde (10 mmol) in 50 ml of boiling methanol. Then 10 mmol sodium acetate in 10 ml water was added to the above reaction system. Finally 50 ml boiling methanol solution containing 10 mmol $Cu(CH_3COO)_2{\cdot}H_2O$ was added. The reaction mixture was kept boiling for 30 min. The crystals precipitated from the solution and recrystallization was performed from the methanol/THF (2:1 v/v) solution. The copper complexes were obtained as dark green crystals. The micro crystals were filtered off, washed with absolute ethanol and then recrystallized from methanol/THF (2:1 v/v).

*2.5.1. Complex **3a***

Brown, yield 85%. *Anal.* Calc. for $C_{48}H_{62}N_6O_6Cu_2$: C, 60.95; H, 6.56; N, 10.16. Found: C, 60.6; H, 6.2; N, 9.8%. IR (KBr, cm^{-1}) *v*: 3417 (O–H, alcoholic), 3223 (OH, phenolic), 3069 (C–H, aromatic), 2955, 2918, 2849 (C–H, aliphatic), 1638 (C=N), 1604 (C=C, aromatic), 1503 (N=N), 1251 (C–O, ether), 1152 (C–O, phenolic).

*2.5.2. Complex **3b***

Brown, yield 80%. *Anal.* Calc. for $C_{52}H_{70}N_6O_6Cu$: C, 63.34; H, 6.99; N, 8.39. Found: C, 63.0; H, 6.7; N, 8.3%. IR (KBr, cm^{-1}) *v*: 3417 (O–H, alcoholic), 3223 (OH, phenolic), 3069 (C–H, aromatic), 2955, 2918, 2849 (C–H, aliphatic), 1638 (C=N), 1604 (C=C, aromatic), 1503 (N=N), 1251 (C–O, ether), 1152 (C–O, phenolic).

*2.5.3. Complex **3c***

Brown, yield 75%. *Anal.* Calc. for $C_{56}H_{78}N_6O_6Cu$: C, 63.57; H, 7.38; N, 7.95. Found: C, 63.3; H, 7.0; N, 7.6%. IR (KBr, cm^{-1}) *v*: 3417 (O–H, alcoholic), 3223 (OH, phenolic), 3069 (C–H, aromatic), 2955, 2918, 2849 (C–H, aliphatic), 1638 (C=N), 1604 (C=C, aromatic), 1503(N=N), 1251 (C–O, ether) 1152 (C–O, phenolic).

*2.5.4. Complex **3d***

Brown, yield 75%. *Anal.* Calc. for $C_{60}H_{86}N_6O_6Cu$: C, 64.68; H, 7.73; N, 7.55. Found: C, 64.3; H, 7.4; N, 7.2%. IR (KBr cm^{-1}) *v*: 3417 (O–H, alcoholic), 3223 (OH, phenolic), 3069 (C–H, aromatic), 2955, 2918, 2849 (C–H, aliphatic), 1638 (C=N), 1604 (C=C, aromatic), 1503 (N=N), 1251 (C–O, ether), 1152 (C–O, phenolic).

3. Results and discussion

3.1. Synthesis

The Schiff base ligands were synthesised in a four-step process, in which the hydroxyl group in 4-nitrophenol is first replaced by an alkoxy chain, followed by reduction of the nitro group to an amine. In the third step, salicylaldehyde is coupled with the diazonium chloride obtained from the 4-alkoxyaniline. As a final step, the Schiff base ligands were obtained by the reaction of 5-(4-^{n}alkoxyphenylazo)salicylaldehyde with 3-amino-1-propanol (Scheme 1) by refluxing in absolute ethanol, using a few drops of acetic acid as a catalyst. The 5-(4-^{n}alkoxyphenylazo)salicylaldehyde homologous (**1a–d**) and the Schiff base ligands (**2a–2c)** were purified by repeated crystallization from ethanol to give a single spot on thin layer chromatography and characterized by IR, ^{1}H NMR, mass spectroscopy and elemental analyzes. The dicopper complexes were characterized by C, H, N elemental analyzes and IR spectroscopy. Physical and characterization data for the ligands and the complexes are given in the Section 2.

A comparison of the IR spectra of the metal complexes with those of the free ligands shows that the stretching frequency of the C=N bond is shifted to lower wavenumbers (ca. 15 cm^{-1}) after coordination. This shift is due to reduction of the double-bond character of the C=N bond as a result of coordination of the nitrogen to the metal center, and is in agreement with the results obtained for other similar complexes described previously [10,19,20]. On the other hand, the disappearance of the OH bands of the free ligands in the spectra of the metal complexes indicates that the OH groups have been deprotonated and coordinate to the metal ion as –O. Based on these observations and elemental analyzes results, we concluded that the Schiff base ligands are coordinated to the metal center as tridentate (NOO) ligands in a 1:1 ratio (see scheme 1).

3.2. Mesomorphism

The mesomorphic properties of the 5-(4-^{n}alkoxyphenylazo)salicylaldehyde homologous (**1a–d**), the Schiff ligands (**2a–d**) and related dicopper complexes (**3a–d**) have been studied by polarizing optical microscopy observations using a heating- cooling stage and the phase transition temperatures and enthalpies were obtained by differential scanning calorimetry (DSC).

All the 5-(4-^{n}alkoxyphenylazo)salicylaldehyde homologous (**1a–d**) and the Schiff base ligands (**2a–d**) were not mesomorphic. The absence of liquid crystalline behavior in the free ligands can be attributed to the strong intermolecular hydrogen bonding brought about by the presence of the two hydroxyl groups (phenolic and alcoholic OH) in the ligand molecular structure.

All the dicopper complexes (**3a–d**) exhibit liquid crystalline character as revealed by polarizing optical microscopy. Phase transition temperatures along with the corresponding enthalpy values for the Schiff base ligands (**2a–d**) and the dicopper complexes (**3a–d**) are summarized in Table 1. Fig. 1 shows the DSC curves of the dicopper complexes in the heating process. A complete set of DSC curves for **3a** in the heating and cooling processes is illustrated as a representative example.

The thermal behaviors of the complexes are similar as it is apparent from the DSC curves. Compounds **3a** and **3d** show one solid–solid transition at 176.1 and 173.8 °C with ΔH values of 1.7 and 4.7 kJ mol^{-1}, respectively. Compound **3b** exhibits two solid–solid transitions at 69.8 and 154.5 °C with ΔH values of 6.8 and 3.7 kJ mol^{-1}, respectively. The dicopper complexes (**3a–3d**) display endothermic transitions at 225.9, 205.8, 195.4 and 192.5 °C with ΔH values of 51.4, 54.4, 40.5 and 43.6 kJ mol^{-1}, respectively. Such a high value of the enthalpy of fusion is in agreement with the presence of a crystal phase to a mesophase transition. However, the melting temperatures of the dicopper compounds decrease slightly by increasing the alkyl chain length. The texture of the mesophase was investigated by polarizing optical microscopy (POM). For all the complexes, a viscous mesophase organized as a focal conic texture after the melting process, which indicates the formation of an SmA mesophase. Continued heating of the complexes **3a–3d** mesophases causes a considerable amount of decomposition at 278.9, 281.1, 282.0 and 282.2 °C respectively which has been detected by exothermic peaks in the DSC trace, TGA thermograms and optical observations. A microscopic picture from the SmA mesophase for complex **3b** is illustrated in Fig. 2 as a representative example. To understand the thermal decomposition process, the dicopper compounds were examined by thermo gravimetric analysis (TGA). The TGA thermograms of the dicopper compounds at a heating rate of 10 °C/min show that decomposition begins at around 280 °C, as is seen optically, which is near the temperature of clearing to the isotropic liquid. All the dicopper compounds have similar TGA thermograms. Fig. 3 gives the TGA thermogram of **3a** as a representative example. Thermodynamic data for the Schiff base ligands and dicopper complexes are tabulated in Table 1.

Table 1
Transition temperatures, enthalpy changes, mesophase type and temperature range of the mesophase for the dicopper complexes.

Compound	Transition [a]	T[b]/°C	ΔH[b]/kJ mol^{-1}	Temperature range, ΔT (°C)
2a	Cr–I	107.4	85.9	
2b	Cr–I	112.2	91.3	
2c	Cr–I	116.6	87.5	
2d	Cr–I	110.5	91.7	
3a	Cr_1–Cr_2	176.1	1.7	53.0
	Cr_2–SmA	225.9	51.4	
	S_A–I(dec.)[c]	278.9		
3b	Cr_1–Cr_2	69.8	6.8	75.3
	Cr_2–Cr_3	154.5	3.7	
	Cr_3–SmA	205.8	54.4	
	S_A–I(dec.)[c]	281.1		
3c	Cr–SmA	195.4	40.5	86.5
	S_A–I(dec.)[c]	282.0		
3d	Cr_1–Cr_2	173.8	4.7	88.7
	Cr_2–SmA	192.5	43.6	
	S_A–I(dec.)[c]	281.2		

[a] Cr:Crystal, SmA: Smectic A, I: Isotropic liquid.
[b] Data obtained from first DSC cycle.
[c] Decomposition occurred immediately at clearing point.

These complexes represent a further example of a mesomorphic complex derived from a non-mesogenic ligand. Based on our knowledge, only a few dicopper compounds based on salicylaldimine ligands have been reported as liquid crystalline materials. Similar mesomorphic properties were previously reported by Lai et al. for dicopper complexes with a similar coordination environment based on salicylaldimine Schiff bases ligands, but without a 4-alkoxyphenyazo linkage [31]. In the case of the dicopper complexes reported in Ref. [31], the temperature range of the mesophase was narrow (from 18.6 to 25.1 °C) and varied slightly with alkyl chain length, but the complexes reported in this research work have fairly wide temperature range of mesophase. From Table 1, it can be seen clearly that the mesophase of complexes **3a–3d** is stable in for temperature ranges (ΔT) of 53.0, 75.3, 86.5 and 88.7 °C, respectively. This fact may be related to the presence of the alkoxyphenylazo moiety in the structure of the complexes. The mesophase range increases with increasing alkyl chain length, and is in agreement with results obtained from other complexes, described previously by our research group [26,27].Furthermore, Lai et al. [32] reported a new type of dicopper(II) complex derived

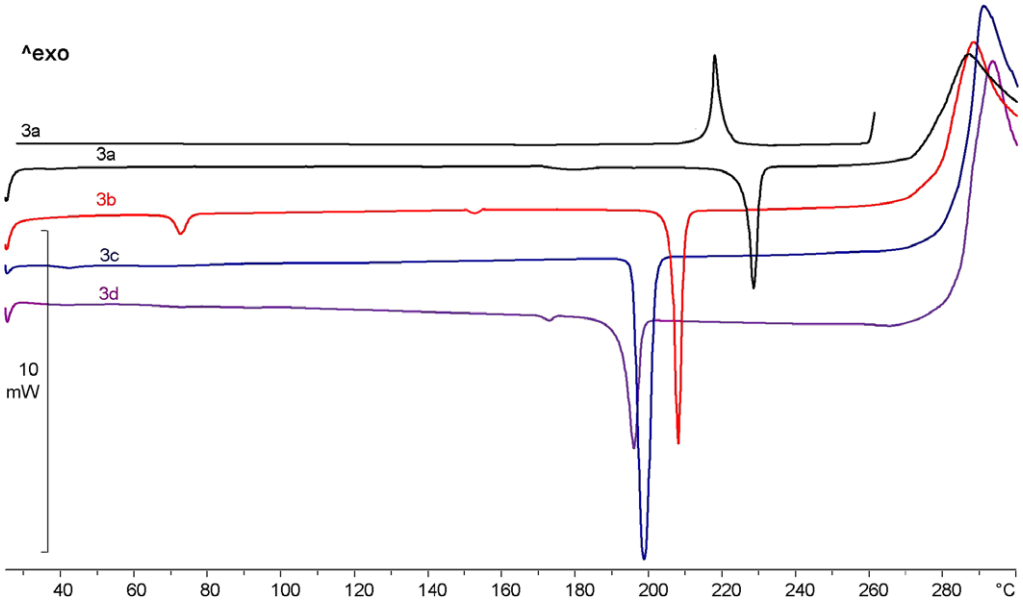


Fig. 1. DSC thermograms of the dicopper complexes.

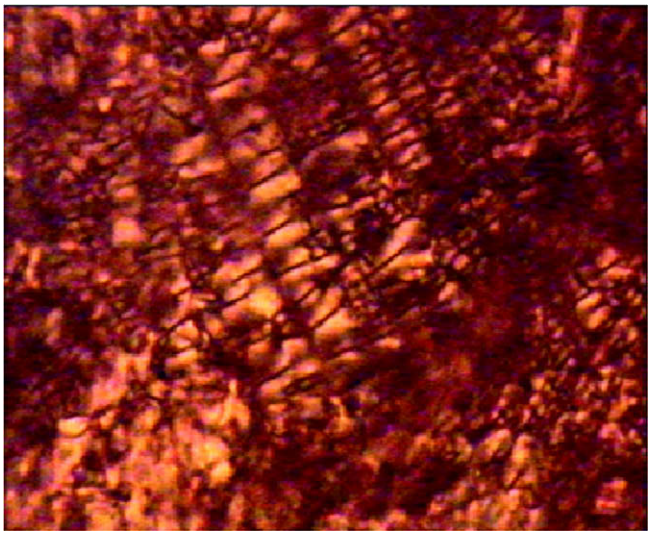


Fig. 2. Optical texture observed for the copper complex **3b** through crossed polarizers at 212 °C.

from μ-exogenous 3,4,5-trialkoxybenzoate- or acetate-bridged *N*,*N*′-(propane-2-ol)-bis(4-alkoxysalicylal-dimines), prepared by the condensation of 2-hydroxy-4-alkoxybenzaldehydes with 1,3-diaminopropane-2-ol. The formation of mesomorphic phases was found to be dependent upon the bridging groups used, acetate-bridged compounds formed a smectic A (SmA) phase and benzoate-bridged compounds formed a hexagonal columnar (Col_h) phase. The temperature range of mesophases was very narrow (from 5.8 to 12.9 °C) and varied slightly with alkyl chain length.

The induction and formation of mesophases are mainly controlled and/or determined by attractive interactions between neighboring molecules. These weak interactions are of various types, for example dipole–dipole, dispersion, hydrogen bonding, charge transfer and dative coordination. Transition metal ions can induce mesomorphism in non-mesogenic ligands. The coordination geometry of the metal center in this type of material greatly influences the molecular packing in the formation of the mesophase. While in classic organic structures, the intention is, frequently, to increase intermolecular contacts to induce mesomorphism, in coordination compounds the objective is to avoid intermolecular contacts and strong dipolar interactions that are sufficiently strong to cause three-dimensional order. Hence, it

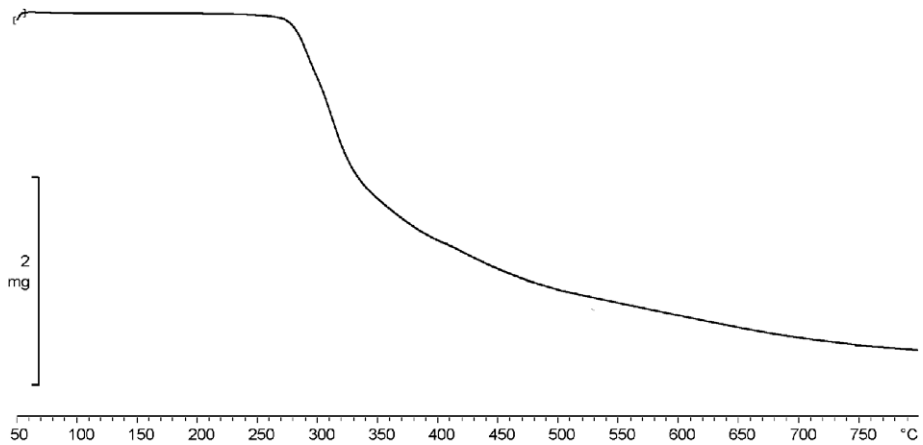


Fig. 3. TGA thermogram of **3a**.

is fundamentally important to achieve a delicate balance in the magnitude of molecular interactions by tuning the molecular geometries in order to optimize the liquid crystalline behavior. The addition of a long aliphatic chain to the rigid nucleus furnishes both the anisotropy and irregular packing needed to promote mesomorphism [33,34].

4. Conclusion

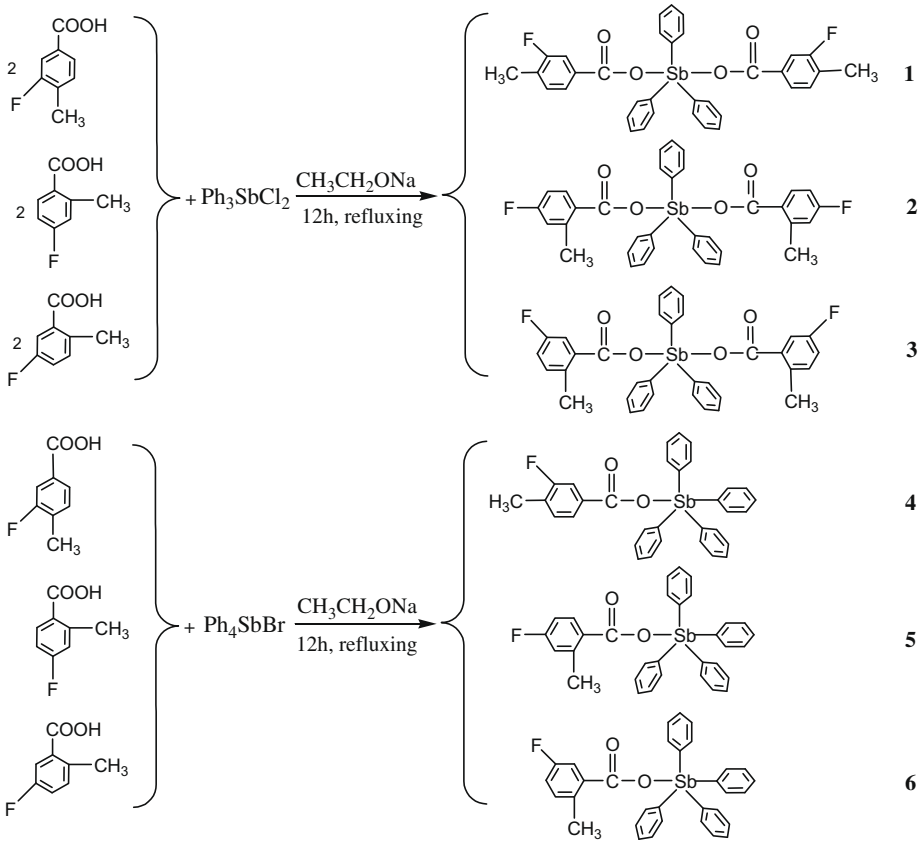
In this work we have prepared dicopper complex homologous derived from tridentate 5-(4-^{n}alkoxyphenylazo)salicylaldimine-N-(3-hydroxypropyl) ligands. While the Schiff base ligands do not show any liquid crystalline character, the dicopper complexes have mesomorphic properties and form a smectic A mesophase as confirmed by their typical texture. For all the dicopper complexes, the mesophase was decomposed immediately at the clearing point. The mesophases have a wide temperature range which increased with increasing alkyl chain length.

Acknowledgement

The authors sincerely appreciate the financial support from the Azarbaijan University of Tarbiat Moallem research vice chancellor and of the faculty of basic science.

References

[1] A.M. Giroud, Coord. Chem. Rev. 180 (1998) 1485.
[2] R. Gimenez, D.P. Lydon, J.L. Serrano, Curr. Opin. Solid State Mater. Sci. 6 (2002) 527.
[3] U. Pietrasik, J. Szydłowska, A. Krówczyński, Chem. Mater. 16 (2004) 1485.
[4] K. Binnemans, Chem. Rev. 105 (2005) 4148.
[5] I.S. Shashikala, D.W. Bruce, Dalton Trans. (2008) 1128.
[6] A.A. Knyazev, Y.G. Galyametdinov, B. Goderis, K. Driesen, K. Goossens, C. Görller-Walrand, K. Binnemans, T. Cardinaels, Eur. J. Inorg. Chem. (2008) 756.
[7] I.V. Ovchinnikov, T.A. Ivanova, V.E. Petrashen, Yu.G. Galyametdinov, G.I. Ivanova, Appl. Mag. Reson. 29 (2005) 325.
[8] J.H. Lee, S.M. Choi, B.D. Pate, M.H. Chisholm, Y.S. Han, J. Mater. Chem. 16 (2006) 2785.
[9] J.H. Lee, H.S. Kim, B.D. Pate, S.M. Choi, J. Appl. Cryst. 40 (Supplement) (2007) s68.
[10] N.E. Domracheva, I.V. Ovchinnikov, A.N. Turanov, V.N. Konstantinov, J. Mag. Mag. Mater. 269 (2004) 385.
[11] L. Laesker, T. Fischer, S.R. Marder, W.E. Torruellas, M. Blanchard-Desce, V. Ricci, G.I. Stegeman, S. Gilmour, J.L. Bredas, J. Li, G.U. Bublitz, S.G. Boxer, Science 276 (1997) 1233.
[12] W.M. Gibson, P.J. Shannon, S.T. San, B.J. Swetlin, Nature 351 (1991) 49.
[13] I. Aiello, M. Ghedini, M. La Deda, D. Pucci, O. Francescangeli, Eur. J. Inorg. Chem. (1999) 1367.
[14] J.L. Serrano, T. Sierra, Chem. – A Eur. J. 6 (2000) 759.
[15] S. Suárez, D. Imbert, F. Gumy, C. Piguet, Jean-C.G. Bünzli, Chem. Mater. 16 (2004) 3257.
[16] N. Marquestaut, A. Martin, D. Talaga, L. Servant, S. Ravaine, S. Reculusa, D.M. Bassani, E. Gillies, F. Lagugné-Labarthet, Langmuir 24 (2008) 11313.
[17] M. Mathews, N. Tamaoki, J. Am. Chem. Soc. 130 (2008) 11409.
[18] C.J. Barrett, J. Mamiya, K.G. Yager, T. Ikeda, Soft Matter 3 (2007) 1249.
[19] S. Xiao, X. Lu, Q. Lu, B. Su, Macromolecules 41 (2008) 3884.
[20] D. Rais, Y. Zakrevskyy, J. Stumpe, S. Nešpůrek, Z. Sedláková, Opt. Mater. 30 (2008) 1335.
[21] E. Wolarz, E. Chrzumnicka, T. Fischer, J. Stumpe, Dyes Pigm. 75 (2007) 753.
[22] A.A. Khandar, Z. Rezvani, Polyhedron 18 (1998) 129.
[23] K. Nejati, Z. Rezvani, New J. Chem. 27 (2003) 1665.
[24] Z. Rezvani, L. Rahimi Ahar, K. Nejati, S.M. Seyedahmadian, Acta Chim. Slov. 51 (2004) 675.
[25] Z. Rezvani, A.R. Abbasi, K. Nejati, S.M. Seyedahmadian, Polyhedron 24 (2005) 1461.
[26] Z. Rezvani, B. Divband, A.R. Abbasi, K. Nejati, Polyhedron 25 (2006) 1915.
[27] Z. Rezvani, K. Nejati, M. Seyedahmadian1, B. Divband, Mol. Cryst. Liq. Cryst. 493 (2008) 71.
[28] R.V. Deun, K. Binnemans, J. Alloys Compd. 303–304 (2000) 146.
[29] E.C. Horning, Organic Syntheses, Collective, vol. III, John Wiley and Sons, New York, 1955, p. 130.
[30] A.A. Khandar, Z. Rezvani, K. Nejati, A.I. Yanovsky, J.M. Martinez, Acta Chim. Slov. 49 (2002) 733.
[31] Y.F. Leu, C.K. Lai, J. Chin. Chem. Soc. 44 (1997) 89.
[32] S.M. Ku, C.Y. Wu, C.K. Lai, J. Chem. Soc., Dalton Trans. (2000) 3491.
[33] C.K. Lai, R. Lin, M.Y. Lu, K.C. Kao, J. Chem. Soc., Dalton Trans. (1998) 1857.
[34] C.K. Lai, Y.S. Pang, C.H. Tsai, J. Mater. Chem. 8 (1998) 2605.



Scheme 1. The reaction procedure.

2.2. Syntheses of complexes **1–6**

2.2.1. Synthesis of [3-F-4-(CH_3)C_6H_3COO]$_2$SbPh$_3$ (**1**)

The reaction was carried out under nitrogen atmosphere. 3-Fluoro-4-methyl-benzoic acid (0.077 g, 0.5 mmol) and sodium ethoxide (0.6 mmol) were added to a stirred solution of methanol (30 ml) in a Schlenk flask and stirred for 0.5 h. Triphenylantimony dichloride (0.106 g, 0.25 mmol) was then added to the reactor and the reaction mixture was stirred for 12 h at room temperature. The resulting clear solution was evaporated under vacuum. The product was crystallized from a mixed of dichloromethane/ether (1:1) to yield colourless blocks of crystals, yield: 82%, m.p. 210–212 °C. *Anal.* Calc. for $C_{34}H_{27}F_2O_4Sb$ (Mw = 659.31): C, 61.93; H, 4.13; F, 5.76. Found: C, 61.77; H, 4.24; F, 5.87%. IR (KBr) ν(cm^{-1}): 3066 (m, Ar–H), 1638 (s, C=O), 561 (s, Sb–C), 458 (s, Sb–O). ^{1}H NMR (400 MHz, $CDCl_3$, 25 °C) δ: 8.10 (m, 6H, Sb–PhH: H-3, H-5), 7.41–7.69 (m, 13H, Sb–PhH: H-2, H-4, H-6 and PhH: H-2, H-6), 7.14 (t, J = 7.6 Hz, 2H, PhH: H-5), 2.27 (s, 6H, CH_3). ^{13}C NMR (100 MHz, $CDCl_3$, 25 °C) δ: 169.16 (COO), 135.47, 129.80, 128.66, 128.41 (Sb–PhC), 160.81, 135.31, 131.14, 129.25, 125.08, 116.57 (PhC), 15.10 (CH_3–Ph). ^{19}F NMR (376 MHz, $CDCl_3$, 25 °C) δ: −118.08.

2.2.2. Synthesis of [4-F-2-(CH_3)C_6H_3COO]$_2$SbPh$_3$ (**2**)

Complex **2** was prepared in the same way as **1**. The colourless solid was recrystallized from a mixed of dichloromethane/ether (1:1) to give colourless powder, yield: 77%, m.p. 200–202 °C. *Anal.* Calc. for $C_{34}H_{27}F_2O_4Sb$ (Mw = 659.31): C, 61.93; H, 4.13; F, 5.76. Found: C, 61.80; H, 4.22; F, 5.89%. IR (KBr) ν(cm^{-1}): 3066 (m, Ar–H), 1635 (s, C=O), 560 (s, Sb–C), 473 (s, Sb–O). ^{1}H NMR (400 MHz, $CDCl_3$, 25 °C) δ: 8.10 (m, 6H, Sb–PhH: H-3, H-5), 7.31–7.57 (m, 13H, Sb–PhH: H-2, H-4, H-6 and PhH: H-5, H-6), 6.81 (t, J = 8.0 Hz, 2H, PhH: H-3), 2.26 (s, 6H, CH_3). ^{13}C NMR (100 MHz, $CDCl_3$, 25 °C) δ: 170.14 (COO), 136.94, 129.72, 128.68, 128.51 (Sb–PhC), 170.50, 139.69, 130.47, 126.09, 116.41, 112.03 (PhC), 20.69 (CH_3–Ph). ^{19}F NMR (376 MHz, $CDCl_3$, 25 °C) δ: −113.16.

2.2.3. Synthesis of [5-F-2-(CH_3)C_6H_3COO]$_2$SbPh$_3$ (**3**)

Complex **3** was prepared in the same way as **1**. The colourless solid was recrystallized from a mixed of dichloromethane/ether (1:1) to give colourless crystals, yield: 80%, m.p. 183–185 °C. *Anal.* Calc. for $C_{34}H_{27}F_2O_4Sb$ (Mw = 659.31): C, 61.93; H, 4.13; F, 5.76. Found: C, 61.73; H, 4.26; F, 5.89%. IR (KBr) ν(cm^{-1}): 3061 (m, Ar–H), 1632 (s, C=O), 557 (s, Sb–C), 449 (s, Sb–O). ^{1}H NMR (400 MHz, $CDCl_3$, 25 °C) δ: 8.10 (m, 6H, Sb–PhH: H-3, H-5), 7.50 (m, 9H, Sb–PhH: H-2, H-4, H-6), 7.40 (d, J = 9.2 Hz, 2H, PhH: H-6), 6.94–7.05 (m, 4H, PhH: H-3, H-4), 2.29 (s, 6H, CH_3). ^{13}C NMR (100 MHz, $CDCl_3$, 25 °C) δ: 171.10 (COO), 138.59, 132.45, 131.16, 129.37 (Sb–PhC), 159.24, 134.83, 132.52, 129.37, 117.79, 116.81 (PhC), 20.65 (CH_3–Ph). ^{19}F NMR (376 MHz, $CDCl_3$, 25 °C) δ: −118.24.

2.2.4. Synthesis of [3-F-4-(CH_3)C_6H_3COO]SbPh$_4$ (**4**)

The reaction was carried out under nitrogen atmosphere. 3-Fluoro-4-methyl-benzoic acid (0.0385 g, 0.25 mmol) and sodium ethoxide (0.3 mmol) were added to a stirred solution of methanol (30 ml) in a Schlenk flask and stirred for 0.5 h. Tetraphenylantimony bromide (0.128 g, 0.25 mmol) was then added to the reactor and the reaction mixture was stirred for 12 h at room temperature. The colourless solid was recrystallized from a mixed of dichloromethane/petroleum ether (1:1) to give colourless crystals, yield: 76%, m.p. 156–158 °C. *Anal.* Calc. for $C_{32}H_{26}FO_2Sb$ (Mw = 583.28): C, 65.89; H, 4.49; F, 14.48. Found: C, 65.83; H, 4.51; F, 14.50%. IR (KBr) ν(cm^{-1}): 3066 (m, Ar–H), 1631 (s, C=O), 562 (s, Sb–C), 458 (s, Sb–O). ^{1}H NMR (400 MHz, $CDCl_3$, 25 °C) δ: 7.70 (m, 8H,

Sb–PhH: H-3, H-5), 7.47–7.50 (m, 14H, Sb–PhH: H-2, H-4, H-6 and PhH: H-2, H-6), 7.04 (t, J = 7.6 Hz, 1H, PhH: H-5), 2.22 (s, 3H, CH_3). ^{13}C NMR (100 MHz, $CDCl_3$, 25 °C) δ: 168.57 (COO), 137.71, 130.29, 127.25, 127.07 (Sb–PhC), 161.89, 135.17, 130.38, 128.96, 124.71, 115.61 (PhC), 14.60 (CH_3–Ph). ^{19}F NMR (376 MHz, $CDCl_3$, 25 °C) δ: −119.10.

2.2.5. Synthesis of [4-F-2-(CH_3)C_6H_3COO]$SbPh_4$ (**5**)

Complex **5** was prepared in the same way as **4**. The colourless solid was recrystallized from a mixed of dichloromethane/petroleum ether (1:1) to give colourless crystals, yield: 74%, m.p. 132–134 °C. *Anal.* Calc. for $C_{32}H_{26}FO_2Sb$ (Mw = 583.28): C, 65.89; H, 4.49; F, 14.48. Found: C, 65.81; H, 4.53; F, 14.57%. IR (KBr) ν(cm^{-1}): 3063 (m, Ar–H), 1627 (s, C=O), 560 (s, Sb–C), 461 (s, Sb–O). ^{1}H NMR (400 MHz, $CDCl_3$, 25 °C) δ: 7.68 (m, 8H, Sb–PhH: H-3, H-5), 7.25–7.51 (m, 14H, Sb–PhH: H-2, H-4, H-6 and PhH: H-5, H-6), 6.72 (t, J = 2.8 Hz, 1H, PhH: H-3), 2.18 (s, 3H, CH_3). ^{13}C NMR (100 MHz, $CDCl_3$, 25 °C) δ: 170.37 (COO), 135.23, 130.09, 128.79, 128.15 (Sb–PhC), 171.35, 140.47, 131.66, 126.30, 116.09, 111.56 (PhC), 21.09 (CH_3–Ph). ^{19}F NMR (376 MHz, $CDCl_3$, 25 °C) δ: −113.46.

2.2.6. Synthesis of [5-F-2-(CH_3)C_6H_3COO]$SbPh_4$ (**6**)

Complex **6** was prepared in the same way as **4**. The colourless solid was recrystallized from a mixed of dichloromethane/petroleum ether (1:1) to give colourless crystals, yield: 80%, m.p. 151–153 °C. *Anal.* Calc. for $C_{32}H_{26}FO_2Sb$ (Mw = 583.28): C, 65.89; H, 4.49; F, 14.48. Found: C, 65.81; H, 4.53; F, 14.51. IR (KBr) ν(cm^{-1}): 3066 (m, Ar–H), 1630 (s, C=O), 569 (s, Sb–C), 426 (s, Sb–O). ^{1}H NMR (400 MHz, $CDCl_3$, 25 °C) δ: 7.66 (m, 8H, Sb–PhH: H-3, H-5), 7.41 (m, 12H, Sb–PhH: H-2, H-4, H-6), 7.16 (d, J = 2.8 Hz, 1H, PhH: H-6), 6.80–6.84 (m, 2H, PhH: H-3, H-4), 2.18 (s, 3H, CH_3). ^{13}C NMR (100 MHz, $CDCl_3$, 25 °C) δ: 170.41 (COO), 136.39, 129.35, 128.91, 128.52 (Sb–PhC), 158.24, 135.47, 131.56, 129.04, 121.92, 113.81 (PhC), 22.88 (CH_3–Ph). ^{19}F NMR (376 MHz, $CDCl_3$, 25 °C) δ: −119.38.

2.3. X-ray crystallography

Single crystals suitable for X-ray analysis were mounted on a fiber. All measurements were made on a Bruker Smart-1000 CCD diffractometer with graphite monochromated Mo Kα (λ = 0.71073 Å) radiation at 298(2) K using the ω and φ scans technique. The structures were solved by the direct method and different Fourier syntheses using the SHELXL-97 program, and refined by full-matrix least squares on F^2. All non-hydrogen atoms were refined anisotropically. Hydrogen atoms were placed at calculated positions with methyl C–H distances of 0.96 Å and aromatic C–H distances of 0.93 Å and riding on carrier atoms. Crystallographic data and experimental details of the structure determinations are listed in Table 1.

3. Results and discussion

3.1. IR spectra

The infrared spectroscopic data provide further support for the molecular constitution of the complexes. In the IR spectra of ligands, the stretching vibration bands of O–H appear at 3300–3500 cm^{-1}, which disappear from the spectra of the complexes

Table 1
Crystal data and structure refinement details for complexes **1**, **3**, **4**, **5** and **6**.

Complex	**1**	**3**	**4**	**5**	**6**
Empirical formula	$C_{34}H_{27}F_2O_4Sb$	$C_{34}H_{27}F_2O_4Sb$	$C_{32}H_{26}FO_2Sb$	$C_{32}H_{26}FO_2Sb$	$C_{32}H_{26}FO_2Sb$
Formula weight	659.31	659.31	583.28	583.28	583.28
Crystal system	triclinic	monoclinic	triclinic	triclinic	monoclinic
Space group	$P\bar{1}$	$C2/c$	$P\bar{1}$	$P\bar{1}$	$P2(1)/n$
a (Å)	8.7364(13)	16.257(2)	10.0501(10)	9.9660(10)	10.1796(13
b (Å)	11.5048(16)	9.6767(14)	10.2039(11)	10.5161(11)	13.2777(16)
c (Å)	15.9795(18)	18.920(2)	14.7540(15)	13.7839(15)	19.701(2)
α (°)	108.446(2)	90	86.695(2)	87.472(2)	90
β (°)	98.7600(10)	91.6800(10)	81.0900(10)	76.5690(10)	94.527(2)
γ (°)	100.406(2)	90	65.7030(10)	70.1440(10)	90
V (Å^3)	1460.3(3)	2975.1(7)	1362.3(2)	1320.6(2)	2654.5(6)
Z	2	4	2	2	4
Calculated density	1.499	1.472	1.422	1.467	1.459
Absorption coefficient	0.994	0.976	1.045	1.078	1.073
F(0 0 0)	664	1328	588	588	1176
Crystal size (mm)	0.35 × 0.19 × 0.17	0.40 × 0.35 × 0.17	0.49 × 0.45 × 0.44	0.29 × 0.19 × 0.07	0.40 × 0.35 × 0.23
θ Range for data collection	1.38–25.00	2.15–25.01	1.40–25.01	2.06–25.01	1.85–25.02
Limiting indices	$-10 \leqslant h \leqslant 10$, $-10 \leqslant k \leqslant 13$, $-18 \leqslant l \leqslant 18$	$-19 \leqslant h \leqslant 14$, $-11 \leqslant k \leqslant 11$, $-22 \leqslant l \leqslant 22$	$-11 \leqslant h \leqslant 11$, $-11 \leqslant k \leqslant 12$, $-17 \leqslant l \leqslant 15$	$-11 \leqslant h \leqslant 11$, $-9 \leqslant k \leqslant 12$, $-15 \leqslant l \leqslant 16$	$-12 \leqslant h \leqslant 11$, $-15 \leqslant k \leqslant 11$, $-22 \leqslant l \leqslant 23$
Reflections collected/ unique	7648/5054 [R_{int} = 0.0259]	7234/2627 [R_{int} = 0.0348]	7018/4686 [R_{int} = 0.0182]	6698/4530 [R_{int} = 0.0321]	13 556/4670 [R_{int} = 0.0273]
Completeness to θ = 25.01 (%)	98.1	99.8	97.8	97.3	99.9
Maximum and minimum transmission	0.8491 and 0.7222	0.8516 and 0.6961	0.6562 and 0.6284	0.9283 and 0.7450	0.7904 and 0.6735
Data/restraints/ parameters	5054/0/382	2627/0/188	4686/0/336	4530/0/325	4670/0/326
Goodness-of-fit (GOF) on F^2	1.001	1.001	1.009	1.007	1.001
Final R indices [$I > 2\sigma(I)$]	R_1 = 0.0470, wR_2 = 0.1139	R_1 = 0.0297, wR_2 = 0.0645	R_1 = 0.0275, wR_2 = 0.0740	R_1 = 0.0575, wR_2 = 0.1362	R_1 = 0.0265, wR_2 = 0.0581
R indices (all data)	R_1 = 0.0722, wR_2 = 0.1334	R_1 = 0.0388, wR_2 = 0.0703	R_1 = 0.0327, wR_2 = 0.0799	R_1 = 0.0874, wR_2 = 0.1571	R_1 = 0.0425, wR_2 = 0.0690
Largest difference in peak and hole	0.968 and −1.207	0.464 and −0.470	0.440 and −0.740	1.451 and −1.460	0.526 and −0.335

Table 2
Selected bond lengths (Å) and bond angles (°) of complexes **1**, **3**, **4**, **5** and **6**.

Complex ***1***			
Sb(1)–C(23)	2.102(5)	Sb(1)–C(17)	2.107(5)
Sb(1)–C(29)	2.112(5)	Sb(1)–O(1)	2.122(3)
Sb(1)–O(3)	2.127(3)		
C(23)–Sb(1)–C(17)	106.7(2)	C(23)–Sb(1)–C(29)	143.6(2)
C(17)–Sb(1)–C(29)	109.8(2)	C(23)–Sb(1)–O(1)	91.1(2)
C(17)–Sb(1)–O(1)	87.4(2)	C(29)–Sb(1)–O(1)	90.5(2)
C(23)–Sb(1)–O(3)	91.7(2)	C(17)–Sb(1)–O(3)	87.3(2)
C(29)–Sb(1)–O(3)	90.0(2)	O(1)–Sb(1)–O(3)	174.5(1)
Complex ***3***			
Sb(1)–C(9)	2.120(3)	Sb(1)–C(9)a	2.120(3)
Sb(1)–C(15)	2.128(4)	Sb(1)–O(1)	2.136(2)
Sb(1)–O(1)a	2.136(2)		
C(9)–Sb(1)–C(9)a	151.4(2)	C(9)–Sb(1)–C(15)	104.3(9)
C(9)a–Sb(1)–C(15)	104.3(9)	C(9)–Sb(1)–O(1)	91.4(1)
C(9)a–Sb(1)–O(1)	89.6(1)	C(15)–Sb(1)–O(1)	87.9(6)
C(9)–Sb(1)–O(1)a	89.6(1)	C(9)a–Sb(1)–O(1)a	91.4(1)
C(15)–Sb(1)–O(1)a	87.9(6)	O(1)–Sb(1)–O(1)a	175.8(1)
Complex ***4***			
Sb(1)–C(27)	2.116(3)	Sb(1)–C(15)	2.117(3)
Sb(1)–C(21)	2.127(3)	Sb(1)–C(9)	2.173(3)
Sb(1)–O(1)	2.275(2)		
C(27)–Sb(1)–C(15)	129.4(1)	C(27)–Sb(1)–C(21)	114.7(1)
C(15)–Sb(1)–C(21)	113.1(1)	C(27)–Sb(1)–C(9)	94.3(1)
C(15)–Sb(1)–C(9)	94.7(1)	C(21)–Sb(1)–C(9)	98.3(1)
C(27)–Sb(1)–O(1)	85.0(1)	C(15)–Sb(1)–O(1)	84.4(1)
C(21)–Sb(1)–O(1)	83.8(1)	C(9)–Sb(1)–O(1)	178.0(8)
Complex ***5***			
Sb(1)–C(27)	2.106(8)	Sb(1)–C(15)	2.128(9)
Sb(1)–C(21)	2.154(8)	Sb(1)–C(9)	2.179(7)
Sb(1)–O(1)	2.261(5)		
C(27)–Sb(1)–C(15)	110.8(3)	C(27)–Sb(1)–C(21)	109.8(3)
C(15)–Sb(1)–C(21)	137.4(3)	C(27)–Sb(1)–C(9)	99.4(3)
C(15)–Sb(1)–C(9)	93.0(3)	C(21)–Sb(1)–C(9)	92.8(3)
C(27)–Sb(1)–O(1)	85.3(2)	C(15)–Sb(1)–O(1)	85.5(2)
C(21)–Sb(1)–O(1)	85.3(3)	C(9)–Sb(1)–O(1)	175.3(2)
Complex ***6***			
Sb(1)–C(15)	2.121(3)	Sb(1)–C(21)	2.121(3)
Sb(1)–C(27)	2.126(3)	Sb(1)–C(9)	2.176(3)
Sb(1)–O(1)	2.255(2)		
C(15)–Sb(1)–C(21)	115.9(1)	C(15)–Sb(1)–C(27)	131.3(1)
C(21)–Sb(1)–C(27)	108.7(1)	C(15)–Sb(1)–C(9)	96.7(1)
C(21)–Sb(1)–C(9)	97.6(1)	C(27)–Sb(1)–C(9)	96.0(1)
C(15)–Sb(1)–O(1)	85.5(1)	C(21)–Sb(1)–O(1)	84.0(1)
C(27)–Sb(1)–O(1)	80.4(1)	C(9)–Sb(1)–O(1)	176.4(1)

Symmetry code: (a) $-x, y, -z+3/2$.

1–**6**. The disappearance of ν(OH) indicates that deprotonation and subsequent coordination of the carboxylate group with antimony metal have occurred as expected. In addition, the frequencies of Sb–C deformations appear between 550 and 570 cm^{-1}, which are consistent with the literature [22]. The formation of Sb–O bond is further supported by the appearance to a weak to medium intensity band in the region 420–460 cm^{-1} and is assigned to νSb–O [23].

The IR stretching vibration frequencies of carbonyl groups in organoantimony carboxylates are very important for determining their structure: When there are interactions between the antimony atom and the carbonyl oxygen atoms of the carboxylate groups, the asymmetric absorption vibration frequencies [ν_{masy} (CO_2)] of carboxylate groups decrease, while the symmetric absorption vibration frequencies [ν_{msym} (CO_2)] increase [24]. Therefore, their differences [$\Delta\nu$ (CO_2)] decrease [25,26]. In the IR spectra of the complexes, the carboxylate bands are observed in the characteristic regions: ν_{masy} (CO_2) between 1606 and 1650 cm^{-1} and ν_{msym} (CO_2) between 1318 and 1384 cm^{-1}. On the basis of the difference in $\Delta\nu$ (CO_2), we can assume that there has been weak interaction or no interaction between the antimony atom and the carbonyl oxygen atoms of the carboxylate groups.

3.2. NMR spectra

In the ^{1}H NMR spectra of the free ligands, the single resonance of the –COOH group is observed at δ 10.85 ppm and is absent in the spectra of the complexes, thus indicating the deprotonation of the –COOH group and confirming that the carboxylate ligand coordinate to the antimony atom. The signals for CH_3 protons in the complexes appeared at δ 2.18–2.30 ppm as singlet. And the aryl protons of the complexes appeared at δ 6.72–8.10 ppm as multiplet and do not allow any clear interpretation. They shift downfields 0.1–0.4 ppm as compared with free ligands, as the electron density reduced when they coordinated with Sb atom.

The ^{13}C NMR spectra of all complexes show a significant downfield shift of all carbon resonances compared with the free ligand because of an electron density transfer from the ligand to the metal. In complexes **1**–**6**, ^{13}C signals for CH_3 appeared at δ 14.60–22.88 ppm. The ^{13}C signals due to aryl group were assigned which appeared at δ 111.56–171.35 ppm. And the signals for carbonyl appeared at δ 168.57–171.10 ppm.

In complexes **1** and **4**, 2 and **5**, 3 and **6**, the ^{19}F signals appeared at δ −118.08 to −119.10 ppm, −113.16 to −113.46 ppm, −118.24 to −119.38 ppm, respectively. The F signal appeared as singlet in all these derivatives. The F_3 signals appeared at higher field as compared to the F_4 chemical shift, indicating that the electron density

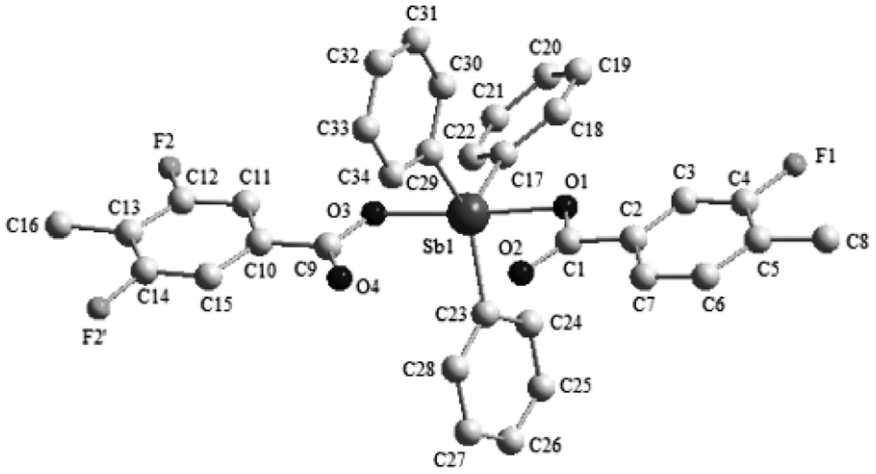


Fig. 1. The molecular structure of complex **1**.

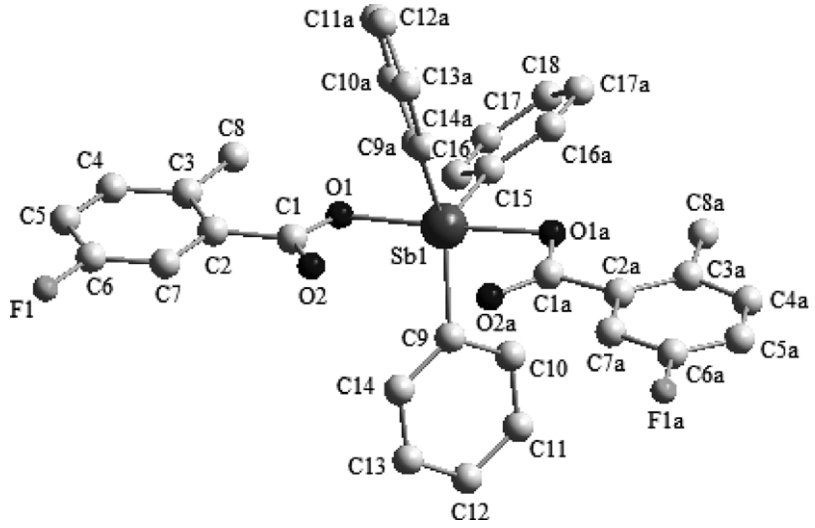


Fig. 2. The molecular structure of complex **3**.

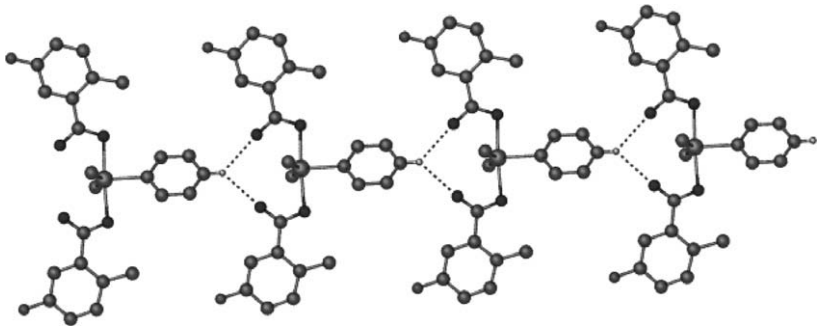


Fig. 3. The supramolecular structure of complex **3**, showing a 1D extended chain structure linked by intermolecular C–H···O contacts, for clarity, the carbon atoms which contact to the central Sb atoms stand for the phenyl groups.

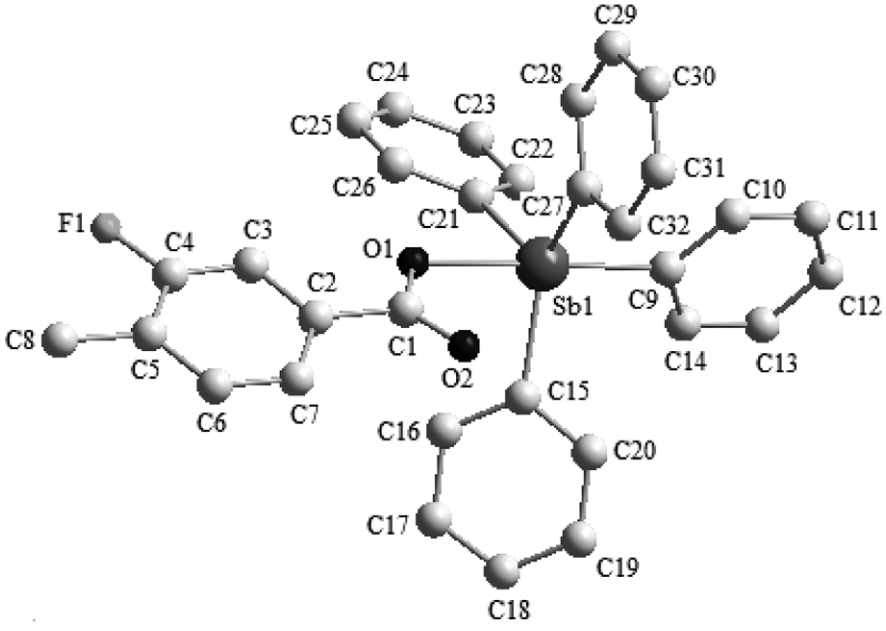


Fig. 4. The molecular structure of complex **4**.

has been withdrawn due to the carboxylate group coordinated with the antimony atom. This observation is in accordance to previous studies that the carbon atoms of perfluorinated benzene ring feel high electron density due to diminished inductive effect of

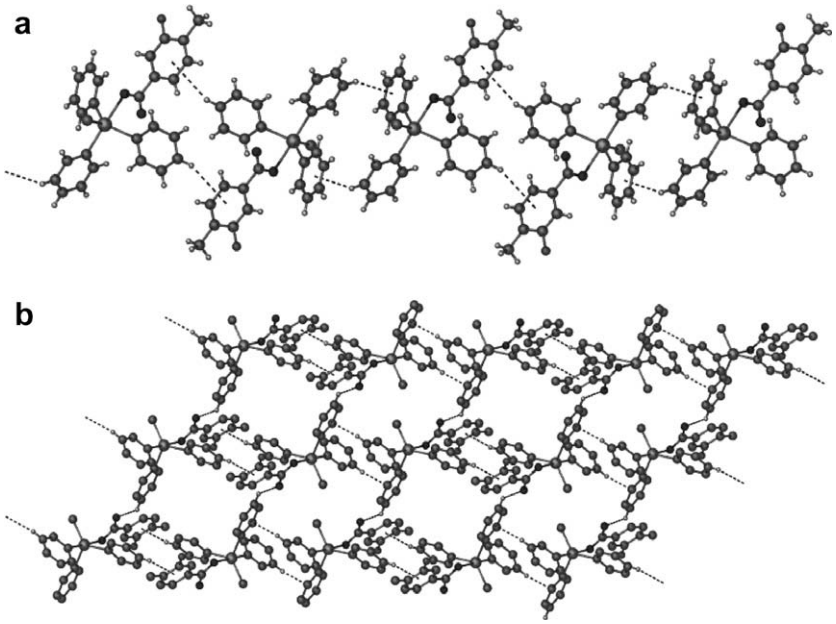


Fig. 5. The supramolecular structure of complex **4**, (a) showing C–H···π stacking interactions and (b) showing 2D framework via C–H···pi stacking interactions and C–H···O hydrogen bonds, for clarity, the carbon atoms which contact to the central Sb atoms stand for the phenyl groups.

fluorine atom and donation of electron density from the unshared p electron of fluorine to the π system of the ring [27,28].

3.3. Crystal structure of [3-F-4-(CH_3)C_6H_3COO]$_2$$SbPh_3$ (**1**)

Selected bond distances and angles of complex **1** are given in Table 2 and the molecular structure is shown in Fig. 1.

As is shown in Fig. 1, the central antimony atom is five-coordinated with a slightly distorted trigonal bipyramidal geometry. Around the central Sb(1) atom, C(17), C(23) and C(29) occupy the equatorial plane, while O(1) and O(3) lie in axial sites. The sum of the equatorial angles is 360.07° [C(23)–Sb(1)–C(17) 106.7(2)°, C(23)–Sb(1)–C(29) 143.6(2)°, C(17)–Sb(1)–C(29) 109.8(2)°] and the corresponding axial–Sb–axial angle is 174.5(1)°, which suggests that it has slightly deviated from an ideal trigonal bipyramidal geometry. The Sb–O bond lengths in organoantimony compounds are extremely variable, ranging from 1.935 Å in triphenylstibine oxide [29] to 2.506 Å in tetraphenylstibonium benzenesulphonate hydrate [30]. The Sb–O distances [Sb(1)–O(1) 2.122(3) Å and Sb(1)–O(3) 2.127(3) Å] in complex **1** lie within this range. The Sb–C bond distances [Sb(1)–C(17) 2.107(5) Å, Sb(1)–C(23) 2.102(5) Å, Sb(1)–C(29) 2.112(5) Å] fall in the normal range for Sb–C(phenyl) bonds (2.10–2.13 Å).

3.4. Crystal structure of [5-F-2-(CH_3)C_6H_3COO]$_2$$SbPh_3$ (**3**)

Selected bond distances and angles of complex **3** are given in Table 2. The molecular structure and 1D extended chain structure are shown in Figs. 2 and 3, respectively.

As is shown in Fig. 2, the structure consists of discrete monomeric units with both carboxylate bound to the antimony atom through oxygen [Sb(1)–O(1) 2.136(2) Å]. The coordination environment around the antimony can be described as slightly distorted trigonal bipyramidal with equatorial Sb–C bonds and axial oxygen atoms [O(1)–Sb(1)–O(1)a angles of 175.8(1)°]. The SbC_3 unit is planar (the sum of the C–Sb–C angle is 359.99°) and C–Sb–O angles lie in the range of 87.9(6)–91.4(1)°. The average Sb–O bond of 2.136(2) Å is approximately equal to the sum of the covalent radii of Sb and O (2.07 Å), while the average Sb–C bond of 2.122 Å is slightly shorter than the sum of the covalent radii of Sb and C (2.18 Å) [31], as expected for the axial and equatorial positions of a trigonal bipyramid.

In the crystal structure, which is shown in Fig. 3, molecules are connected by intermolecular C–H···O hydrogen-bonding interactions forming a 1D extended chain structure. It can be seen that each discrete molecule link with other monomers through two intermolecular C(18)–H(18)···O(2) hydrogen bonds and a 8-membered heart-shaped ring is formed by the two such hydrogen bonds. The H(18)···O(2), C(18)···O(2) distance and the C(18)–H(18)···O(2) angle are 2.52 Å, 3.246 Å, 135.1°, respectively.

3.5. Crystal structure of [3-F-4-(CH_3)C_6H_3COO]$SbPh_4$ (**4**)

Selected bond distances and angles of complex **4** are given in Table 2. The molecular structure and 2D network structure are depicted in Figs. 4 and 5, respectively.

As is shown in Fig. 4, there are four planar phenyl rings and one carboxylate ligand in the inner coordination sphere of complex **4**.

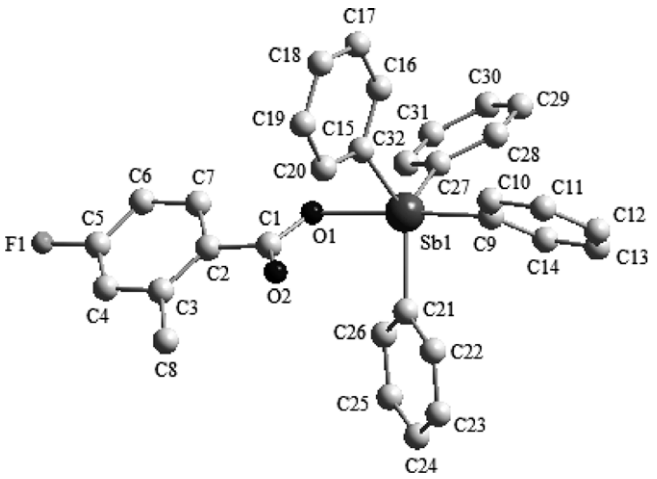


Fig. 6. The molecular structure of complex **5**.

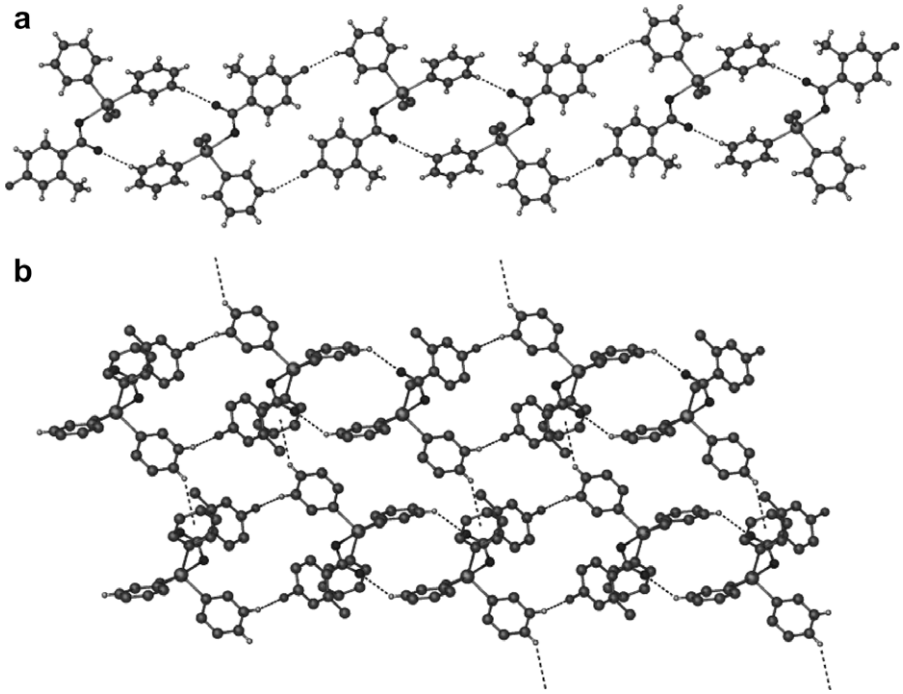


Fig. 7. The supramolecular structure of complex **5**, (a) showing C–H···O and C–H···F hydrogen bonds and (b) showing 2D framework via C–H···π stacking interactions and C–H···O, C–H···F hydrogen bonds, for clarity, the carbon atoms which contact to the central Sb atoms stand for the phenyl groups.

These exhibit a distorted trigonal bipyramidal neighbouring environment of the antimony atom (with the coordination number equal to 5). Three phenyl rings forming the short chemical bonds Sb(1)–C(15), Sb(1)–C(21), Sb(1)–C(27) (2.117(3), 2.127(3), 2.116(3) Å) are in the equatorial plane of the discussed trigonal bipyramid, while the fourth, less strongly bound, phenyl ring: Sb(1)–C(9) 2.173(3) Å and the carboxylate group: Sb(1)–O(1) 2.275(2) Å define two axial positions. The C(9)–Sb(1)–O(1) angle is equal to 178.0(8)° that is close to the corresponding value in the ideal trigonal bipyramid (TBP) – 180°.

The salient feature of the supramolecular structure of complex **4** is dominated by intramolecular C–H···O hydrogen-bonding interactions and C–H···π stacking interactions. The intermolecular edge-to-face C–H···π stacking interactions has been identified between the C(11), C(18) and the phenyl ring, showing in Fig. 5a. C(11)–H(11)···Cg(1) [Cg(1) center of the C(21) to C(26), C(11)···Cg(1) = 3.533 Å, H(11)···Cg(1) = 2.716 Å, C(11)–H(11)···Cg(1) = 147.18°] and C(18)–H(18)···Cg(2) [(Cg(2) center of the C(2) to C(7), C(18)···Cg(2) = 4.410 Å, H(18)···Cg(2) = 3.534 Å, C(18)–H(18)···Cg(2) = 157.93°] and C(24)–H(24)···O(2) [C(24)···O(2) = 3.309(5) Å, H(24)···O(2) = 2.55 Å, C(24)–H(24)···O(2) = 138.5°)] forming a 2D network structure (Fig. 5b). Interestingly, as shown in Fig. 5, the 14-membered cycle and 20-membered macrocycle are formed by the two intermolecular C–H···π stacking interactions between discrete molecules. To our knowledge, this similar structure has not been reported so far.

3.6. Crystal structure of [4-F-2-(CH_3)C_6H_3COO]$SbPh_4$ (**5**)

Selected bond distances and angles of complex **5** are given in Table 2. The molecular structure and 2D network structure are depicted in Figs. 6 and 7, respectively.

The molecular structure of complex **5** is illustrated in Fig. 6. The coordination about the antimony atom is only slightly distorted from a regular trigonal bipyramidal geometry. The angle C(9)–Sb(1)–O(1) 175.3(2)° is close to a linear arrangement. The sum of the angles subtended at the antimony atom in the trigonal plane is 358.0°, so that the atoms Sb(1), C(15), C(21), and C(27) are almost in the same plane. The Sb–C distances [2.106(8)–2.179(7) Å] are equal within experimental error and close to the single-bond value for trigonal bipyramidal antimony [32]. And the Sb–O distance in complex **5** [2.261(5) Å] lies within the range from 1.935 to 2.506 Å [29,30], showing that the oxygen atom is strongly bound to the central Sb atom.

It is worthwhile to note that the supramolecular structure of the complex **5** is linked into a 2D network structure through intramolecular C–H···O, C–H···F hydrogen-bonding interactions and C–H···π stacking interactions. The intermolecular edge-to-face C–H···π stacking interactions have been identified between the C(30) and the phenyl ring, showing in Fig. 7b. As shown in Fig. 7a, 1D infinite chain structure is linked by intermolecular C–H···O and C–H···F hydrogen-bonding interactions. It is noteworthy that complex **5** contains two types of macrocycles: one is 16-membered macrocycle which is formed by two intermolecular C–H···O [C(11)···O(2) = 3.212 Å, H(11)···O(2) = 2.59 Å, C(11)–H(11)···O(2) =

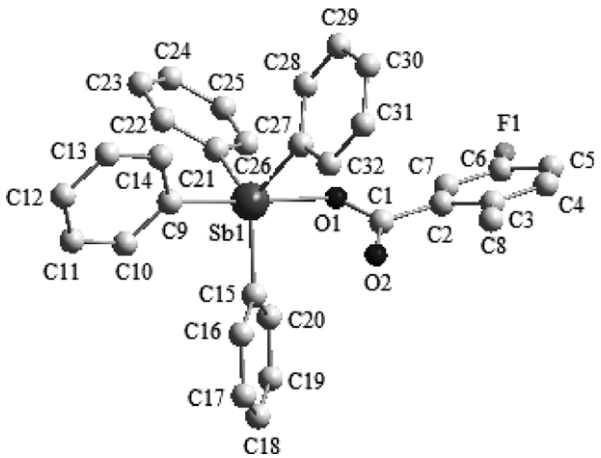


Fig. 8. The molecular structure of complex **6**.

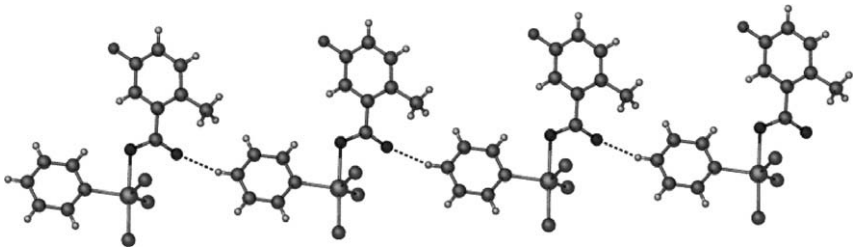


Fig. 9. The supramolecular structure of complex **6**, showing a 1D extended chain structure linked by intermolecular C–H···O contacts, for clarity, the carbon atoms which contact to the central Sb atoms stand for the phenyl groups.

125.0°)] hydrogen bonds between two discrete molecules, the other is 24-membered macrocycle which is formed by two intermolecular C–H···F [C(31)···F(1) = 3.245 Å, H(31)···F(1) = 2.40 Å, C(31)–H(31)···F(1) = 151.7°)] hydrogen bonds between two discrete molecules. Furthermore, as shown in Fig. 7b, C(30)–H(30)···Cg(1) [Cg(1) center of the C(21) to C(26), C(30)···Cg(1) = 4.012 Å, H(15)···Cg(1) = 3.202 Å, C(15)–H(15)···Cg(1) = 146.59°] forming a head-to-tail 2D network.

3.7. Crystal structure of [5-F-2-(CH_3)C_6H_3COO]$SbPh_4$ (**6**)

Selected bond distances and angles of complex **6** are given in Table 2. The molecular structure and 1D extended chain structure are depicted in Figs. 8 and 9, respectively.

In the crystal structure of complex **6**, which is shown in Fig. 8, the coordination geometry around the antimony center is best described as a distorted trigonal bipyramid, in which one carboxylate group and one phenyl ring occupy the apical sites. The C(9)–Sb(1)–O(1) angle is 176.4(1)°. In the equatorial plane of the structure, the C(15)–Sb(1)–C(21), C(21)–Sb(1)–C(27) and C(27)–Sb(1)–C(15) angles are 115.9(1)°, 108.7(1)° and 131.3(1)°, respectively, which are close to the normal 120°. The Sb(1)–C(15), Sb(1)–C(21), Sb(1)–C(27) bond distances [2.120(3), 2.122(3), 2.126(3) Å] are similar to the corresponding distances in $[SbPh_3(O_2CCF_3)]_2O$ [2.100(6)–2.112(6) Å] [33]. The Sb–O distance [2.2556(19) Å] does not lie within the range from 1.935 to 2.506 Å, but shorter than the sum (3.6 Å) of the van der Waals radii of antimony and oxygen atoms (2.2 and 1.4 Å, respectively) [34], showing that the oxygen atom is weakly bound to the central Sb atom.

In Fig. 9 the supramolecular structure exhibits a zigzag 1D infinite chain structure via intermolecular C–H···O hydrogen-bonding interactions. It can be seen that each discrete molecule link with other monomers through one intermolecular C(24)–H(24)···O(2) hydrogen bonds. The H(24)···O(2), C(24)···O(2) distance and the C(24)–H(24)···O(2) angle are 2.34 Å, 3.209 Å, 154.7°, respectively.

4. Conclusions

The molecular structures of six new organoantimony(V) complexes have been reported. Although the various isomers of fluoromethylbenzoate ligands have the same coordination capacity function as a rigid bridging carboxylate binding the antimony atoms through oxygen atoms, and antimony atoms are in a trigonal bipyramidal environment, different intermolecular interactions which lead to aggregation and assembly of these complexes into 1D or 2D supramolecular frameworks are observed in the solid state.

Supplementary data

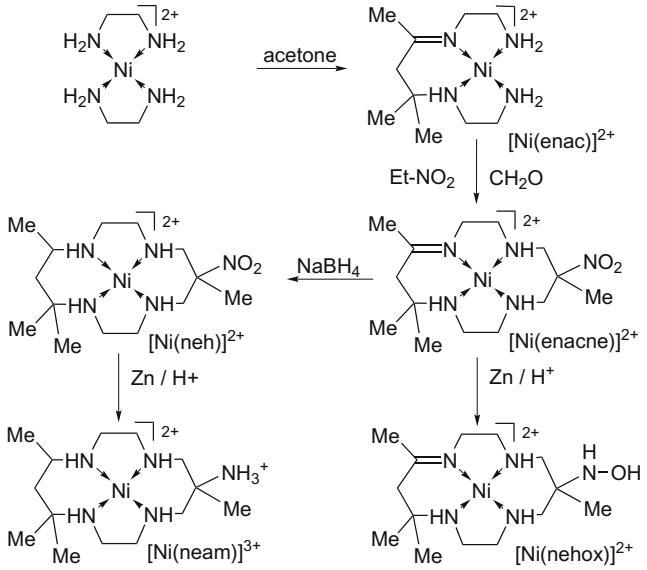
CCDC 713406, 713405, 715112, 720255 and 715111 contain the supplementary crystallographic data for complexes **1**, **3**, **4**, 5 and **6**. These data can be obtained free of charge via http://www.ccdc.cam.ac.uk/conts/retrieving.html, or from the Cambridge Crystallographic Data Centre, 12 Union Road, Cambridge CB2 1EZ, UK; fax: (+44) 1223-336-033; or e-mail: deposit@ccdc.cam.ac.uk.

Acknowledgments

We acknowledge the financial support of the Natural Science Foundation of China (No. 20771053) and Shangdong Province Science Foundation (No. 2005ZX09).

References

[1] I. Haiduc, D.B. Sowerby, S.-F. Lu, Polyhedron 14 (1995) 3389.
[2] M.A. Said, K.C. Kumara Swamy, D.M. Poojary, A. Clearfield, M. Veith, V. Huch, Inorg. Chem. 35 (1996) 3235.
[3] H.J. Breunig, T. Krüger, E. Lork, Angew. Chem., Int. Ed. Engl. 36 (1996) 615.
[4] H. Mahalakshmi, V.K. Jain, E.R.T. Tiekink, Main Group Met. Chem. 23 (2000) 519.
[5] K.V. Domasevitch, N.N. Gerasimchuk, A. Mokhir, Inorg. Chem. 39 (2000) 1227.
[6] C. Silvestru, L. Silaghi-Dumitrescu, I. Haiduc, M.J. Begley, M. Nunn, D.B. Sowerby, J. Chem. Soc., Dalton Trans. (1986) 1031.
[7] C. Silvestru, M. Curtui, I. Haiduc, M.J. Begley, D.B. Sowerby, J. Organomet. Chem. 426 (1992) 49.
[8] C. Silvestru, I. Haiduc, E. Tiekink, D. de Vos, M. Biesemans, R. Willem, M. Gielen, Appl. Organomet. Chem. 9 (1995) 597.
[9] C. Silvestru, C. Socaciu, A. Baba, I. Haiduc, Anticancer Res. 10 (1990) 803.
[10] V.K. Jain, R. Bohra, R.C. Mehrotra, Struct. Bonding (Berlin) 52 (1982) 147.
[11] M.N. Gibbons, D.B. Sowerby, Phosphorus, Sulfur Silicon 93 (1994) 305.
[12] C. Silvestru, A. Silvestru, I. Haiduc, D.B. Sowerby, K.H. Ebert, H.J. Breunig, Polyhedron 16 (1997) 2643.
[13] S.S. Garje, V.K. Jain, Main Group Met. Chem. 22 (1999) 45.
[14] A.I. Poddel'sky, N.V. Somov, Y.A. Kurskii, V.K. Cherkasov, G.A. Abakumov, J. Organomet. Chem. 693 (2008) 3451.
[15] K.R. Chaudhari, V.K. Jain, V.S. Sagoria, E.R.T. Tiekink, J. Organomet. Chem. 692 (2007) 4928.
[16] H.D. Yin, L. Quan, L.W. Li, Inorg. Chem. Commun. 11 (2008) 1121.
[17] G.B. Deacon, R.J. Phillips, Coord. Chem. Rev. 33 (1980) 227.
[18] Y.Q. Ma, J.S. Li, Z.A. Xuan, R.C. Liu, J. Organomet. Chem. 620 (2001) 235.
[19] K. Hartke, H.M. Wolff, Chem. Ber. 113 (1980) 1394.
[20] P.L. Millington, D.B. Sowerby, J. Chem. Soc., Dalton Trans. (1992) 1199.
[21] H. Preut, M. Domagala, F. Huber, Acta Crystallogr., Sect. C 43 (1987) 416.
[22] A. Gupta, R.K. Sharma, R. Bohra, V.K. Jain, J.E. Drake, M.B. Hursthouse, M.E. Light, J. Organomet. Chem. 645 (2002) 118.
[23] S.S. Garje, V.K. Jain, Main Group Met. Chem. 18 (1995) 387.
[24] L. Yu, Y.Q. Ma, R.C. Liu, G.C. Wang, J.S. Li, G.H. Du, J.J. Hu, Polyhedron 23 (2004) 823.
[25] J.S. Li, Y.Q. Ma, R.C. Liu, J. Li, Appl. Organomet. Chem. 15 (2001) 227.
[26] J.S. Li, Y.Q. Ma, J.R. Cui, R.Q. Wang, Appl. Organomet. Chem. 15 (2001) 639.
[27] A.K. Saxena, A. Ranjan, K. Misra, P.S. Venkataramani, Indian J. Chem. 37 (1998) 736.
[28] S.K. Shukla, A. Ranjan, A.K. Saxena, Polyhedron 25 (2006) 1415.
[29] G. Ferguson, C. Glidewell, B. Kaitner, D. Lloyd, S. Metcalfe, Acta Crystallogr., Sect. C 43 (1987) 824.
[30] R. Ruether, F. Huber, H. Preut, J. Organomet. Chem. 295 (1985) 21.
[31] A. Gupta, R.K. Sharma, R. Bohra, V.K. Jain, J.E. Drake, M.B. Hursthouse, M.E. Light, Polyhedron 21 (2002) 2387.
[32] C.L. Ma, Q.F. Zhang, J.F. Sun, R.F. Zhang, J. Organomet. Chem. 691 (2006) 2567.
[33] M.N. Gibbons, D. Bryan Sowerby, J. Organomet. Chem. 555 (1998) 271.
[34] R.C. Liu, Y.Q. Ma, L. Yu, J.S. Li, J.R. Cui, R.Q. Wang, Appl. Organomet. Chem. 17 (2003) 662.



Scheme 1. Showing preparations of $[Ni(enac)]^{2+}$, $[Ni(enacne)]^{2+}$, $[Ni(neh)]^{2+}$, $[Ni(nehox)]^{2+}$ and $[Ni(neamH)]^{3+}$.

been reported for compounds of Co(III) [26] and Ni(II) [27] which have ligands with hydroxylamino-nitrogen atoms coordinated.

The nitro function of the cyclic tetraamine cation $[Ni(neh)]^{2+}$ is reduced by zinc/acid under similar conditions to form the 13-amine-substituted cyclic amine cation (13-amine-5,5,7,13-tetramethyl-1,4,8,11-tetraazacyclotetradecane-κ^4)nickel(II), $[Ni(neam)]^{2+}$. This was isolated from acid solution as the tetrachlorozincate chloride salt, with the 13-amino-substituent protonated, $[NineamH)][ZnCl_4]Cl{\cdot}2.25H_2O$, for which the structure is reported.

Structures have been determined for the related compounds $[Ni(enacne)][ZnCl_4]$* [9], $[Cu(enacnp)(OH_2)](ClO_4)_2$* [10], $[Cu(enacne)(NCS)]ClO_4$* [28] and $[Cu(enacnp)][Ni(CN_4)]{\cdot}H_2O$* [11] and β-$[Ni(neh)](ClO_4)_2{\cdot}H_2O$*, β-$[Ni(neh)](ClO_4)_2$, α-$[Ni(neh)](ClO_4)_2$, β-$[Ni(neh)]_2[ZnCl_4][ZnCl_3(OH_2)]_2{\cdot}H_2O$*, *catena-trans*-β-$[Ni(neh)(\mu\text{-}C_2O_4)]_n{\cdot}3nH_2O$* and β-$[Cu(nph)Cl]ClO_4$* (where enacnp and nph are the 13-ethyl homologues and α indicates the 1*R*,4*R*,8*R*,11*R* nitrogen configuration (V) and β the 1*R*,4*R*,8*S*,11*S* configuration (III) [12]. The structures marked * have disorder arising from co-crystallisation of enantiomers, manifest as superimposed 5,7,7-trimethyl and 5,5,7-trimethyl configurations (or 5,7,7-trimethyl–5-ene and 5,5,7-trimethyl-7-ene configurations), which results in disorder in the location of the axial component of the gem-dimethyl function, with the axially oriented methyl group is distributed over partially occupied sites on ring atoms C5 and C7.

The preparation of 6-amino-1,4,8,11-tetraazacyclotetradecane (L) has been reported and its coordination properties with nickel(II) described [29]. The structure of $[Ni(L)](ClO_4)_2$ shows nickel(II) in square-pyramidal coordination, with the four N–H groups of the cyclic tetraamine all oriented to the same side of the N_4 plane (configuration I of the nitrogen centres) with the amino-substituent group coordinated axially on the opposite side. The amines 6-amino-6-methyl-1,4,8,11-tetraazacyclotetradecane [17–21] and 6-amino-6-methyl-13-hydroxyl-1,4,8,11-tetraazacyclotetradecane [22] have been prepared by zinc/acid reduction of the nitro function of the 6-nitro substituted copper(II) compounds and structures reported for copper(II), cobalt(III) and chromium(III) compounds. The M(III) compounds commonly have the amine substituent coordinated.

2. Results

2.1. The preparation and structure of (13-hydroxylamino-5,5,7,13-tetramethyl-1,4,8,11-tetraazacyclotetradec-4-ene-κ^4)nickel(II) tetrachlorozincate(II), [Ni(nehox)][$ZnCl_4$]

The cation $[Ni(enacne)]^{2+}$ is readily reduced by zinc in dilute acid to form $[Ni(nehox)]^{2+}$, isolated as the orange coloured singlet ground state tetrachlorozincate salt. The structure of [Ni(nehox)][$ZnCl_4$] has been determined by X-ray diffractometry, see Section 4.2 for details.

The asymmetric unit of [Ni(nehox)][$ZnCl_4$] contains one square-planar (13-hydroxylamino-5,7,7,13-tetramethyl-1,4,8,11-tetraazacyclotetradec-4-ene)nickel(II) cation (see Fig. 1) and one tetrahedral tetrachlorozincate anion. The dimensions about the nickel(II) ion are normal for singlet ground state square-planar nickel(II), see Table 1. The hydroxylamino group is axially oriented on the chair conformation six-membered chelate ring, with the N–OH group oriented away from the nickel(II) ion, in projection lying approximately midway between C14 and C13.

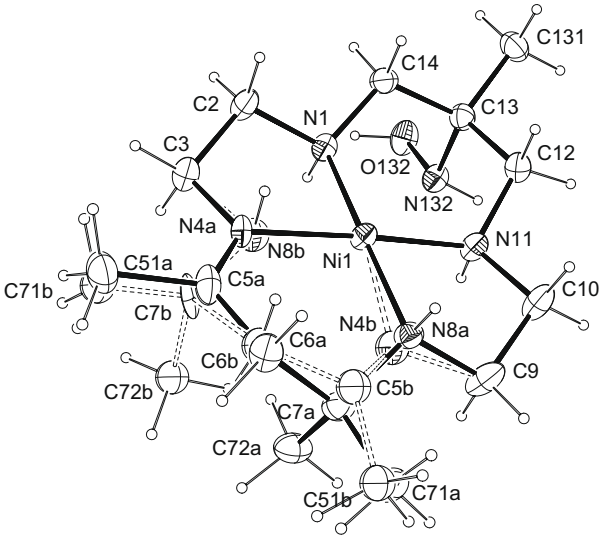


Fig. 1. The cation of [Ni(nehox)][$ZnCl_4$], drawn [31] with displacement ellipsoids at the 50% confidence level. Hydrogen atoms are shown as circles of arbitrary radii. Bonds to the minor disorder components are shown as dashed lines.

Table 1
Selected dimensions (Å/°) for [Ni(nehox)][$ZnCl_4$].

Atoms	Distance/angle	Atoms	Distance/angle
Ni1–N1	1.936(1)	N4A–C5A	1.501(3)
Ni1–N4A	1.937(2)	N4B–C5B	1.501(3)
Ni1–N4B	1.937(3)	C7A–N8A	1.263(3)
Ni1–N8A	1.917(2)	C7B–N8B	1.263(4)
Ni1–N8B	1.95(1)	O132–N132	1.449(2)
Ni1–Cl4[a]	2.9058(4)	C13–N132	1.479(2)
Ni1–Cl2	3.7118(4)		
N1–Ni1–N4A	85.45(7)	N4B–Ni1–N8B	89.9(6)
N1–Ni1–N4B	173.3(8)	N4B–Ni1–N11	87.4(6)
N1–Ni1–N8A	174.9(2)	N8A–Ni1–N11	86.5(1)
N1–Ni1–N8B	89.3(3)	N8B–Ni1–N11	169.0(3)
N1–Ni1–N11	92.10(5)	C12–C13–C14 1	111.00(1)
N4A–Ni1–N4B	94.8(6)	C13–N132–O132	110.4(1)
N4A–Ni1–N8A	95.8(1)	N132–O132–H132	109.5
N4A–Ni1–N11	176.83(8)	Ni1–Cl2–Zn1	120.98(1)
Cl2–Ni1–Cl4[a]	151.25(1)	Ni1–Cl4[a]–Zn1[a]	117.96(1)

Symmetry operation $A = x + ½, -y + ½, z + ½$.
[a] Zn1–Cl: 2.2478(4)–2.3082(4) Å; Cl–Zn1–Cl: 103.90(2)–113.17(2)°.

The cation shows disorder arising from co-crystallisation of enantiomers of the chiral centre at C13 (chiral because of the different substitutions at C5 and C7). This leads to disorder in location of the axial component of the gem-dimethyl group, with partial occupancy of sites axial with respect to C5 and C7. The disorder components have the N4···N8 trimethyl substituted amine-imine chelate ring reversed, with atoms labelled N4A–C5A(C51A)–C6A–C7A(C71A, C72A)–N8A for the major component and N4B–C5B(C51B)–C6B–C7B(C71B, C72B)–N8B for the minor component. All the atoms of the two disorder components were resolved and refined with common s.o.f. of 0.766(3) for the 1*S*,8*R*,11*R*,13*S*-configuration and 0.234(3) for the 1*R*,8*S*,11S,13*R*-configuration. Two sites were resolved for nitrogen atoms N4 and N8, with N–C distances and associated bond angles corresponding with the imine character of the N4–C5 and N4A–C5A bonds and the amine character of the C7–N8 and C7A–N8A bonds, see Table 1. The r.m.s. displacements from the best N_4 donor atom plane N1,N4A,N8A,N11 are ±0.024(2) Å with Ni1 0.060(2) Å from the plane and for the plane N1,N4B,N8B,N11 are ±0.038(7) Å with Ni1 0.145(6) Å from the plane. Displacements of other atoms from the planes defined by Ni,N4A,N8A,N11 and N1,N4B,N8B,N11 are listed in Table S1 of the Supplementary data.

The cation has approximate mirror symmetry through C13, N131, C131, Ni1 and C6/C6A, as is usual for square-planar cyclam-like azamacrocycle compounds, with N1–H1 and N11–H11 oriented to the same side of the NiN_4 'plane' as the hydroxylamine group and the partial occupancy axial methyl groups C72A and C72B, with the partial occupancy N4A–H4A and N4B–H4B groups oriented to the other side of the coordination 'plane'.

The $[Ni(nehox)]^{2+}$ cations and $[ZnCl_4]^{2-}$ anions are linked into chains, with N–H···Cl and O–H···Cl hydrogen bonds (see Table S2 of the Supplementary data) and with weak approximately axial interactions, Ni···Cl4 ($-x+½, -y+½, -z-½$) = 2.9058(4) Å, on the less crowded side of the NiN_4 'plane' and Ni···Cl2 = 3.7118(4) Å) on the other side.

2.2. The preparation and structure of (5,5,7,13-tetramethyl-13-azonium-1,4,8,11-tetraazacyclotetradecane)nickel(II) chloride tetrachlorozincate 2.25 hydrate, [Ni(neamH)][ZnCl$_4$]Cl·2.25H$_2$O

The cation $[Ni(neh)]^{2+}$ is readily reduced by zinc in dilute acid to form (13-azonium-5,5,7,13-1,4,8,11-tetraazacyclotetradecane) nickel(II), $[Ni(neam)]^{2+}$, isolated from acid solution as the orange coloured singlet ground state tetrachlorozincate chloride salt with the 13-amino-substituent protonated, [Ni(neamH)][$ZnCl_4$]Cl·2.25H_2O, for which the structure has been determined by X-ray diffractometry, see Section 4.2 for details.

The asymmetric unit contains two (tetraazamacrocycle)nickel(II) cations (cation 1 with ring atoms N1–C14 and cation 2 with ring atoms N21–C34, two tetrachlorozincate anions, (anion 1 with Zn1 and Cl1–Cl4 and anion 2 with Zn2 and Cl5–Cl8) and two independent chloride anions (Cl9 and Cl0), see Fig. 2 and Table 2 for dimensions.

The triply charged cations have 13-azonium-5,5,7,13-tetramethyl-1,4,8,11-tetraazacyclotetradecane macrocycles in square-planar coordination to singlet ground state nickel(II). The N_4 donor atom groups are tetrahedrally twisted, (r.m.s. displacements from best N_4 planes N1,N4,N8,N11 and N21,N24,N28,N31 are ±0.068(1) Å and ±0.031(1) Å, respectively, with Ni1 and Ni2 displaced from these planes by 0.031(1) Å and 0.013(1) Å, respectively). See Fig. 3 for a representation of the cation 1. Both macrocycles have the 1*R*,4*R*,8*S*,11*S* configuration III of the coordinated nitrogen centres which is usual for planar coordination of cyclam-like macrocycles, with the six-membered chelate rings in chair and the five-membered chelate rings in gauche conformations (see Table S3 of Supplementary data for displacements of atoms from NiN_2 chelate planes). The 13-azonium substituents of both cations are axially oriented, on the same side of the N_4 plane as the axial methyl substituent. The closest axial interactions for the nickel(II) ions are with tetrachlorozincate(II) chloride ions

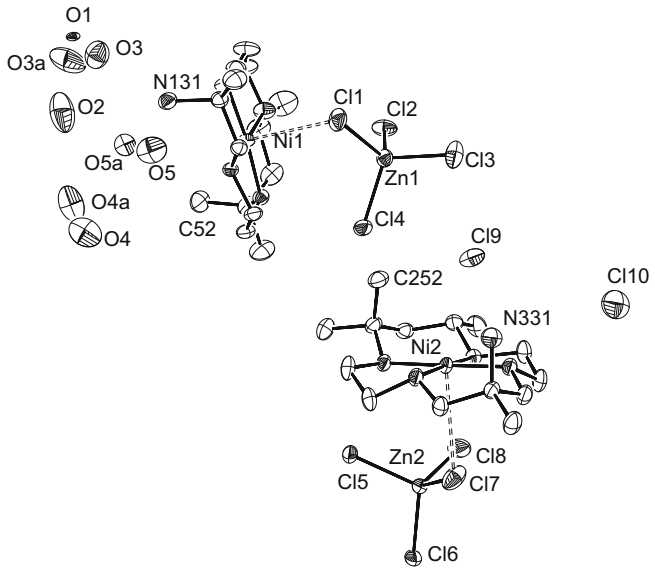


Fig. 2. The asymmetric unit of [Ni(neamH)][ZnCl4]Cl·2.25H_2O, drawn as for Fig. 1. Hydrogen atoms and minor disorder components are omitted for clarity.

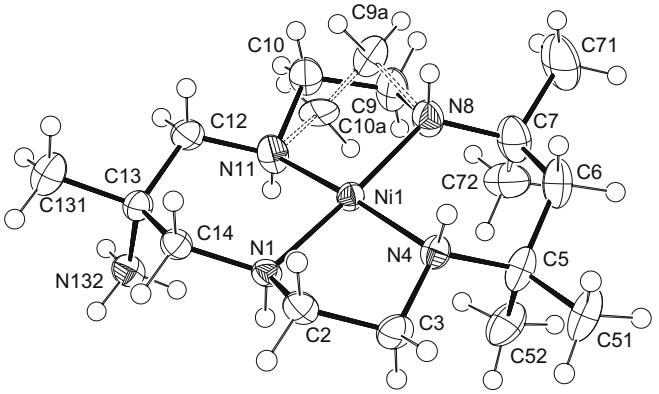


Fig. 3. The cation including Ni1 of [Ni(neamH)][$ZnCl_4$]Cl·2.25H_2O, drawn as for Fig. 1. Bonds to the minor disorder components C9a, C10a and C72 are shown as dashed lines. The cation including Ni2 is similar, but without the disorder of C9 and C10.

Table 2
Selected dimensions (Å, °) for [Ni(neamH)][$ZnCl_4$]Cl·2.25H_2O.

Atoms, cation 1	Dimension	Atoms, cation 2	Dimension
Ni1–N1	1.923(2)	Ni2–N21	1.926(2)
Ni1–N4	1.943(2)	Ni2–N24	1.944(2)
Ni1–N8	1.932(2)	Ni2–N28	1.943(2)
Ni1–N11	1.924(2)	Ni2–N31	1.936(2)
Ni1–Cl1	3.060(1)	Ni2–Cl7	3.234(1)
Ni1–Cl10^A	3.561(1)	Ni2–Cl9	3.442(1)
N1–Ni1–N4	87.1(1)	N21–Ni2–N24	85.8(1)
N1–Ni1–N8	177.1(1)	N21–Ni2–N28	177.1(1)
N1–Ni1–N11	91.8(1)	N21–Ni2–N31	94.6(1)
N4–Ni1–N8	94.2(1)	N24–Ni2–N28	93.0(1)
N4–Ni1–N11	174.5(1)	N24–Ni2–N31	178.8(1)
N8–Ni1–N11	87.1(1)	N28–Ni2–N31	86.6(1)

Symmetry operation $A = x-1, y+1, z$.

{Ni1···Cl2 = 3.059 Å and Ni2···Cl7 = 3.234 Å}, both on the side of the N_4 planes remote from the axial substituents. There are longer 'off axis" interactions with free chloride ions on the other side, with Ni1···Cl10 = 3.561 and Ni2···Cl9 = 3.442 Å.

The cations show disorder arising from co-crystallisation of enantiomers, similar to that shown by the previous compound. This is manifest as disorder in the location of the axial component of the gem-dimethyl group, with significant electron density in the axial substitution sites near C5 and C7, modelled as partial occupancy methyl groups. For the cation 1 the methyl group in the axial site near C5, $(C52)H_3$ has s.o.f. = 0.87(1) and that in the site near C7, $(C272)H_3$ has s.o.f. = 0.13(1) and for the cation 2 the methyl group $(C252)H_3$ has s.o.f. = 0.72(1) and the group $(C252)H_3$ has s.o.f. = 0.28(1). The major component for both cations has the configuration, 1*R*,4*R*,7*S*,8*S*,11*S*,13*R*.

The cation 1 also has disorder of one of the five-membered chelate rings, modelled with alternative gauche conformations {s.o.f. for sites $(C9)H_2$ and $(C10)H_2$ = 0.78(2) and s.o.f. for $(C9A)H_2$ and $(C10A)H_2$ = 0.22(2)}. The conformation usually observed for planar cyclam complexes, with approximate mirror symmetry through C6, Ni1 and C13, would have sites C9 and C10 occupied. The similarity of the s.o.f. for $(C52)H_3$ (0.87(1) and $(C9)H_2$ (0.78(2) suggests that these site occupancies are probably correlated.

Several residual electron density peaks were assigned as oxygen of water molecules. Refinement of the s.o.f. indicated that site O1, which lies on a centre of symmetry has s.o.f. = 0.5 whilst site O2 has s.o.f. = 1, within the uncertainties, so the s.o.f. of these atoms were fixed at these values for final refinement. Six other isolated sites occurred as pairs which had s.o.f. which were complementary within the uncertainties, and were assigned as water molecules O3, O4 and O5 with disordered sites. Sites O3 (s.o.f = 0.78(1) and O3A have separation 1.81(2) Å; O4 (s.o.f. = 0.72(1) and O4A, have separation 0.94(2) Å and O5 (s.o.f. = 0.80(1) and O5A have separation 0.69(3) Å. The C72 site is 2.76(1) Å from the O4A site and 3.67(1) Å from the O4B site, whilst the C272 site is 2.39(1) Å from the O3A site and 3.93(1) Å from the O3B site. Steric repulsion arising from occupancy of the C72 site would give preference to the more remote O4A site, and that of the C272 site to the more remote O3A site. The O5 sites are close to the O4 sites and presumably linked to them by hydrogen bonding so that occupation of the O4B site would give preference to the closer O5B site {O4B···O5B = 2.264 Å}.

The asymmetric unit thus has 4.5 water molecules for 2 cations (assuming that the half-occupancy water molecule on the inversion centre is not an artifact), making the compound a 2.25 hydrate. Not all the water hydrogen atoms were located.

Hydrogen bonds link the cations, anions and water molecules. The azonium ions are each hydrogen bonded to the water molecule including O2 ($-x, -y, -z$) and a free chloride ion. Hydrogen bonds are listed in Table S4 of the Supplementary data.

3. Discussion

The reduction of the nitro-function of $[Ni(enacne)]^{2+}$ to form the hydroxylamino function by zinc/acid is somewhat surprising, as the nitro-functions of a variety of related cations are reduced to amine functions by zinc/acid [1,3–6,13–22]. The related di-nitro-substituted cation 6,13-dimethyl-6,13-dinitro-1,4,8,11-tetraazacyclotetradecane)nickel(II) [1,30], which is reduced by catalytic hydrogenation to form the 6,13-diamine cation [30], is also readily reduced to the diamine-substituted cyclic tetramine by zinc/acid.

The hydroxylamine function is relatively uncommon and few structures of compounds with the function have been reported, see the Supplementary data for a listing of structures reported in the Cambridge Crystallographic Data Base.

The hydroxylamine group for $[Ni(nehox)][ZnCl_4]$ is not coordinated and attempts to prepare compounds with the group coordinated were unsuccessful, although similarly structurally situated amino groups readily coordinate to nickel(II) [30].

The nitro group of the nitro-substituted cyclic tetraamine cation $[Ni(neh)]^{2+}$ is reduced by zinc/acid to form the amine-substituted tetraamine cation $[Ni(neam)^{2+}$, isolated as $[Ni(neamH)][ZnCl_4]Cl{\cdot}2.25H_2O$. The non-protonated cation $[Ni(neam)]^{2+}$ was formed in solution by adding 3 mol proportions of $NaHCO_3$ and filtering off the $ZnCO_3$. The solution was yellow, indicating that the primary amino group was not coordinated. Attempts to isolate this cation as a crystalline product were unsuccessful. This behaviour is in contrast to that reported for 6-amino-1,4,8,11-tetraazacyclotetradecane (L) [29]. This amine reacted with $[Ni(H_2O)_6](ClO_4)_2$ in water at pH 8.5 and the isolated salt $[Ni(L)](ClO_4)_2$ had a cation with the amine substituent group coordinated axially, with the nitrogen configuration I (1*R*,4*S*,8*R*,11*S*) with all four N–H groups on the same side of the N_4 plane. In acid this formed a metastable square-planar cation with the amine group protonated, which slowly isomerized to the stable configuration III cation with a configuration and conformation analogous to $[Ni(neamH)]^{3+}$. This process was reversed in base. The related amine-substituted cyclic amines 6-amine-6-methyl- [13–21] and 6-amine-6-methyl-13-hydroxy-1,4,8,11-tetraazacyclotetradecane [22] form compounds with the amine substituent coordinated, though no compounds of nickel(II) have been described.

Both the $[Ni(nehox)]^{2+}$ and $[Ni(neamH)]^{3+}$ structures reported show disorder arising from reversal of the trimethyl-substituted 1,3-amine-imine or 1,3-diamine chelate ring, as also observed for a number of related compounds (above). The main structural difference between the disorder components is in the location of the axial methyl substituent, and this apparently has only a small effect on the packing of the cell components, with the s.o.f. ratio of the components typically about 0.7:0.3. For $[Ni(nehox)]^{2+}$, as for $[Ni(enacne]^{2+}$, the reversed 1,3-amine-imine chelate ring of the disorder components would have conformational asymmetries arising from the differences between the trigonal imine and tetrahedral amine donor groups, which would extend to the linking chelate rings. For most of the compounds showing this disorder only the axial methyl substituents of the disorder components were resolved, but for $[Ni(nehox)][ZnCl_4]$ all the atoms of the disorder components of the 1,3-amine-imine chelate ring were resolved. For the $[Ni(neamH)]^{3+}$ cation, as for $[Ni(neh)]^{2+}$, the reversed1,3-diamine chelate ring components would have smaller differences in conformation, so the disorder components were not resolved for $[Ni(neamH)][ZnCl_4]Cl{\cdot}2.25H_2O$ (though some atoms were resolved for $[Ni(neh)(\mu\text{-}C_2O_4)]_n{\cdot}3nH_2O$ [12]). For one cation present for $[Ni(neamH)][ZnCl_4]Cl{\cdot}2.25H_2O$ the disorder extends to an adjacent chelate ring and apparently also determines the location of water molecules.

The nitro-methyl substituted C13 atom of $[Ni(enacne)]^{2+}$ is a chiral centre, and reductions of the nitro-function to hydroxylamino or amine functions generate no new chirality. Reduction of the C7–N8 imine function of $[Ni(enacne)]^{2+}$ generates a new chiral centre at C7, and in principle a pair of diastereoisomerides (discounting the labile chiral coordinated secondary amine centres). Only one reduction product, $[Ni(neh)]^{2+}$, was isolated, in high yield [12], and the chirality of this is retained when the nitro-function of $[Ni(neh)]^{2+}$is reduced to form $[Ni(neam)]^{2+}$.

4. Experimental

The compounds $[Ni(enacne)](ClO_4)_2$ [11] and $[Ni(neh)](ClO_4)_2$ [12] were prepared as previously reported.

4.1. Synthesis

4.1.1. (13-Hydroxylamino-5,7,7,13-tetramethyl-1,4,8,11-tetraazacyclotetradec-4-ene)nickel(II) tetrachlorozincate, [Ni(nehox)][ZnCl$_4$]

(5,7,7,13-tetramethyl-13-nitro-1,4,8,11-tetraazacyclotetradec-4-ene)nickel(II) perchlorate (2 g) was dissolved in 1 mol dm^{-1} hydrochloric acid (50 cm^3). Mercuric chloride (5 mg) was added, followed by zinc wool (2 g). The mixture was stirred for 1 d, then filtered and rotary-evaporated. The orange product sometimes crystallised, though crystallisation was usually slow unless the solution was seeded with the product. More usually the solution evaporated to leave an orange gum. This was heated with methanol, when the orange coloured *product* crystallised. This was filtered off and recrystallised by evaporation from water. *Anal. calc.* for $C_{14}H_{32}Cl_4N_5NiOZn$: C, 30.4; H, 6.0; N, 12.7. Found: C, 30.5; H, 5.6; N, 12.6%. IR spectrum (band maxima/cm^{-1}) ν(OH), 3384, ν(NH), 3243, 3204, 3153; ν(C=N), 1647.

4.1.2. (13-Azonium-5,5,7,13-tetramethyl-1,4,8,11-tetraazacyclotetradecane)nickel(II) tetrachlorozincate chloride 2.25 hydrate, [Ni(neamH)][ZnCl$_4$]Cl·2.25H$_2$O

This orange compound was prepared by reducing (5,5,7,13-tetramethyl-13-nitro-1,4,8,11-tetraazacyclotetradecane)nickel(II) perchlorate, as for the previous compound. The orange *product* was recrystallised by evaporation from water. Nucleation was generally very slow unless the solution was seeded. *Anal. Calc.* for $C_{14}H_{38.5}Cl_5N_5NiO_{2.25}Zn$: C, 27.4; H, 6.3; N, 11.4 Found: C, 27.4; H, 6.2; N, 11.3%. IR spectrum (band maxima/cm^{-1}) ν(OH), 3370s, ν(NH), 3243, 3189, 3209, 3165; 3155; δ(HOH), 1646w.

Table 3
Crystallography.

Compound	[Ni(nehox)][ZnCl$_4$]	[Ni(neam)][ZnCl$_4$]Cl·2.25H$_2$O
Empirical formula	[C$_{14}$H$_{31}$N$_5$NiO][ZnCl$_4$]	[C$_{14}$H$_{34}$N$_5$Ni][ZnCl$_4$]Cl·2.25H$_2$O
Formula weight	551.33	614.36
T (K)	120(2)	106(2)
Crystal system	monoclinic	triclinic
Space group	$P21/n$ (Hall -P 2yn)	$p\bar{1}$, (Hall -P 1)
a, b, c/Å	9.0809(2), 8.7915(3), 3.5380(2)	10.915(1), 15.829(2), 16.375(2)
α (°)	90	88.522(1)
β (°)	108.202(1)	77.223(2)
γ (°)	90	70.656(1)
V (Å)$^{(3)}$	2194.58(7)	2599.8(4)
Cell determination (reflections, θ_{min}, θ_{max} (°))	7478, 2.6, 30.01	9757, 2.14, 32.48
Z	4	4
ρ_{calc}/g/cm^3	1.443	1.564
μ/mm^{-1}	2.452	2.180
F(000)	1136	1269
Crystallisation	crystal grown from water	crystal grown from water
Crystal, size/mm	orange plate, 0.48 × 0.25 × 0.08	orange plate, 0.36 × 0.14 × 0.10
θ Range for data collection	1.92, 30.0	2.6, 35.0
T_{max}, T_{min}	0.822, 0.550	0.804, 0.589
Index ranges	$-12 \leqslant h \leqslant 12$; $-26 \leqslant k \leqslant 26$; $-19 \leqslant l \leqslant 19$	$-8 \leqslant h \leqslant 14$; $-19 \leqslant k \leqslant 20$; $-16 \leqslant l \leqslant 21$
Reflections collected	29938, [R_{int} 0.0260]	28191, [R_{int} 0.0256]
Independent reflections	6406	17535
Reflections [$I > 2\sigma$ (I)]	5635	12882
Data/restraints/parameters	6401/1/277	11853/5/604
Goodness-of-fit on F^2	1.013	1.032
Final R indexes [$I>2\sigma$ (I)]	R_1 = 0.023, wR_2 = 0539	R_1 = 0.033, wR_2 = 0.081
Final R indexes [all data]	R_1 = 0.028, wR_2 = 0.056	R_1 = 0.045, wR_2 = 0.068

4.2. Crystallography

Diffraction data was collected by using a Bruker CCD diffractometer with Mo Kα radiation (0.71073 Å) from a fine-focus sealed tube with graphite monochromator, using phi and omega scans, and absorption corrections applied [32,33]. The structure was solved by direct methods and full-matrix refined [34], with anisotropic parameters for all non-H atoms. The components of the disordered chelate ring were located from difference maps and refined as separate parts with common s.o.f. Hydrogen atoms are in calculated positions (except for H132 which was located from difference syntheses) and refined using a riding model. See Table 3 for details. SADI restraints were applied to N4A–C5A, N4B–C5B and C7A–N8A, C7b–N8B for [Ni(nehox)][ZnCl$_4$].

Appendix A. Supplementary data

CCDC 711582 and 711583 contain the supplementary crystallographic data for [Ni(nehox)][ZnCl$_4$] and [Ni(neamH)][ZnCl$_4$]Cl·2.25H$_2$O. These data can be obtained free of charge via http://www.ccdc.cam.ac.uk/conts/retrieving.html, or from the Cambridge Crystallographic Data Centre, 12 Union Road, Cambridge CB2 1EZ, UK; fax: (+44) 1223-336-033; or e-mail: deposit@ccdc.cam.ac.uk.

Supplementary data associated with this article can be found, in the online version, at doi:10.1016/j.poly.2009.06.084.

References

[1] P. Comba, N.F. Curtis, G.A. Lawrance, A.M. Sargeson, B.W. Skelton, A.H. White, Inorg. Chem. 25 (1986) 4260.
[2] P.V. Bernhardt, G.A. Lawrance, Coord. Chem. Rev. 104 (1990) 297.
[3] P. Comba, N.F. Curtis, G.A. Lawrance, M.A. O'Leary, B.W. Skelton, A.H. White, J. Chem. Soc., Dalton Trans. (1988) 2145.
[4] P. Comba, N.F. Curtis, G.A. Lawrance, M.A. O'Leary, B.W. Skelton, A.H. White, J. Chem. Soc., Dalton Trans. (1988) 497.
[5] G.A. Lawrance, M. Rossignoli, B.W. Skelton, A.H. White, Aust. J. Chem. 40 (1987) 1441.
[6] G.A. Lawrance, M. Maeder, M.A. O'Leary, F.H. Woon, Polyhedron 9 (1990) 2227.
[7] N.F. Curtis, J. Chem. Soc., Dalton Trans. (1972) 1357.
[8] N.F. Curtis, H.K.J. Powell, H. Puschmann, C.E.F. Rickard, J.M. Waters, Inorg. Chim. Acta 355 (2003) 25.
[9] N.F. Curtis, K. Flood, W.T. Robinson, Polyhedron 25 (2006) 1313.
[10] N.F. Curtis, H. Puschmann, Polyhedron 25 (2006) 1204.
[11] N.F. Curtis, H. Puschmann, Acta Crystallogr., Sect. C 60 (2004) m410.
[12] N.F. Curtis, K. Flood, W.T. Robinson, J.M. Waters, Polyhedron 28 (2009) 2103.
[13] P.G. Lye, G.A. Lawrance, M. Maeder, J. Chem. Soc., Dalton Trans. (2001) 2376.
[14] R.W. Hay, E. Kiss, C. Loechel, T. Clifford, Polyhedron 17 (1998) 2167.
[15] Y. Baran, A. Bayada, G.A. Lawrance, P.G. Lye, M. Maeder, E.N. Wilkes, Trans. Metal Chem. (Dordrecht) 28 (2003) 460.
[16] P.V. Bernhardt, F. Bozoglian, B.P. Macpherson, M. Martinez, J. Chem. Soc., Dalton Trans. (2004) 2582.
[17] P.V. Bernhardt, N.L. Creevey, J. Chem. Soc., Dalton Trans. (2004) 914.
[18] P.V. Bernhardt, B.P. Macpherson, M. Martinez, J. Chem. Soc., Dalton Trans. (2002) 1435.
[19] P.V. Bernhardt, F. Bozoglian, M. Font-Bardia, M. Martinez, A.P. Meacham, B. Sienra, X. Solans, Eur. J. Inorg. Chem. (2007) 5270.
[20] P.V. Bernhardt, B.P. Macpherson, Acta Crystallogr., Sect. C. 59 (2003) m533.
[21] G.A. Lawrance, M. Martinez, B.W. Skelton, A.H. White, J. Chem. Soc., Dalton Trans. (1992) 823.
[22] J.M. Harrowfield, Y. Kim, G.A. Koutsantonis, Y.H. Lee, P. Thuery, Inorg. Chem. 43 (2004) 1689.
[23] K.S. Hagen, P.A. Lay, A.M. Sargeson, Inorg. Chem. 27 (1988) 3424.
[24] R.J. Balahura, G. Ferguson, B.L. Ruhl, R.G. Wilkins, Inorg. Chem. 22 (1983) 3990.
[25] R. Reichenbach-Klinke, M. Zabel, B. Koenig, J. Chem. Soc., Dalton Trans. (2003) 141.
[26] S.V. Fokin, G.V. Romanenko, V.I. Ovcharenko, Mendeleev Commun. (2001) 127.
[27] S.A. D'yachenko, Y.A. Simonov, A.I. Stetsenko, A.A. Dvorkin, T.I. Malinovskii, L.B. Volodarskii, Proc. Nat. Acad. Sci. USSR 244 (1979) 636.
[28] N.F. Curtis, K. Flood, W.T. Robinson, Unpublished observations.

[29] E. Kimura, M. Haruta, T. Koike, M. Shionoya, K. Takenouchi, Y. Iitaka, Inorg. Chem. 32 (1993) 2779.
[30] N.F. Curtis, G.J. Gainsford, A. Siriwardena, D.C. Weatherburn, Aust. J. Chem. 46 (1993) 755.
[31] L.J. Farrugia, J. Appl. Cryst. 30 (1997) 565.
[32] Bruker SMART (Version 5.054), SADABS (Version 2.03) and SAINT (Version 6.02A), Bruker AXS Inc., Madison, Wisconsin, USA, 1997.
[33] R.H. Blessing, Acta Crystallogr., Sect. A 51 (1995) 33.
[34] G.M. Sheldrick, SHELXTL (Version 5.10). Programs for the Solution and Refinement of Crystal structures, 1997.

mathematical representation of a color on CIE1931 (Commission Internationale de l'Eclairage) *xyz* or L-a-b color space under potential application.

2. Experimental

2.1. Materials and instrumentations

All reagents were obtained from Sigma Aldrich and were used without purification. 4′-(6-Hydroxyhexylthio)-1,2-dicyanobenzene and 3′-(6-hydroxy hexylthio)-1,2-dicyanobenzene were prepared according to literature procedures [15,16]. FTIR (KBr) were recorded on a Shimatzu IR-prestige-2 spectrophotometer. Elemental analysis (C, H, N and S) was performed at the instrumental Analysis Laboratory of Marmara University. Routine UV–Vis spectra were recorded on an Agillent Model 8453 diode array spectrophotometer. Matrix-assisted laser desorption/ionisation time-of-flight (MALDI-TOF) mass spectra (MS) were measured using a Bruker Autoflex III mass spectrometer equipped with a nitrogen UV-Laser operating at 337 nm. The cyclic voltammetry (CV) and differential pulse voltammetry (DPV) measurements were carried out with a Gamry Reference 600 potentiostat/galvanostat. UV–vis absorption spectra and chromaticity diagrams were measured by an OceanOptics QE65000 diode array spectrophotometer.

2.2. Synthesis

2.2.1. 1(4),8(11),15(18),22(25)-(6-Hydroxyhexylthio)-phthalocyaninato manganese (III) chloride (**2**) and 2(3),9(10),16(17),23(24)-tetrakis – {β-6-hydroxyhexylthio}-phthalocyaninato manganese (III) chloride (**3**)

A mixture of 3′-(6-hydroxyhexylthio)-1,2-dicyanobenzene (**1**) or 4′-(6-hydroxyhexylthio)-1,2-di cyanobenzene (**1′**) (∼0.15 g, 0.58 mmol), and anhydrous $MnCl_2$ (∼0.02 g, 0.170 mmol) in *n*-hexanol (∼1.00 mL) was heated to reflux in a sealed tube under N_2 atmosphere for 6 h. The color of the mixture turned brown during the course of time. The brown product was cooled to room temperature after additional heating for about 3 h. Then the mixture was diluted with petroleum ether. The crude product was washed several times, first with cold *i*-PrOH, and then with cold CH_3CN successively to remove impurities. Finally, the product was further purified by silica gel chromatography (with chloroform ($CHCl_3$) and then with $CHCl_3$/MeOH (20:1 v/v) and sephadex with tetrahydrofuran (THF)/$CHCl_3$). The final product is soluble in MeOH, THF, dimethylformamide (DMF), dimethylsulfoxide (DMSO) and insoluble in diethylether.

Yield of **2**: 0.030 g (13.58 %). *Anal.* Calc. for $C_{56}H_{64}N_8O_4S_4Mn$ (1095 g/mol): C, 61.37; H, 5.84; N, 10.23; S, 11.69. Found: C, 60.88; H, 5.92; N, 9.88; S, 11.33%. IR (KBr) ν/cm^{-1}: 3325 (OH), 3017, 2929, 2856, 1714 (H–O···H, weak), 1594, 1568, 1450 (w), 1394 (st), 1313, 1238, 1192, 1155, 1107, 1055, 883, 880, 730. ^{1}H NMR ([D6]-DMSO) δ: 7.75–7.15 (br, m, 12H, phenyl H5, phenyl H3, phenyl H6), 4.20 (s, br, 4H, –CH_2–*OH*, D_2O exchangable), 3.58 (t, br 8H, –*CH*$_2$OH), 2.98 (br, *CH*$_2$–S–), 1.65–1.32 (m, br, 32H, 4 × $CH_2CH_2CH_2CH_2$). UV–Vis (THF), λ_{max}/nm: 769, 691, 510, 354, 289; MS (Maldi-TOF, dihydroxybenzoic acid (DHBA as matrix): *m*/*z* (%): 1095 $[M+H]^+$.

Yield of **3**: 0.04 g (15.83 %). *Anal.* Calc. for $C_{56}H_{64}N_8O_4S_4Mn$ (1095 g/mol): C, 61.37; H, 5.84; N, 10.23; S, 11.69. Found: C, 61.04; H, 6.11; N, 9.95; S, 11.22%. FTIR (KBr) ν/cm^{-1}: 3370, 3248 (–OH), 3082 (Ar–H), 2927, 2854 (Aliph-H), 1725 (H–O···H, weak), 1645, 1585, 1544, 1400, 1390, 1205, 1123, 1067, 1037, 895, 827, 740. ^{1}H NMR ([D6]-DMSO) δ: 7.88–7.45 (broad, m, 12H, phenyl H5, phenyl H3, phenyl H6), 4.24 (s, 4H br, –CH_2–*OH*, D_2O exchangable), 3.60 (t, br 8H, –*CH*$_2$OH), 3.02 (br, *CH*$_2$–S–), 1.65–1.35 (m, br, 32H, 4 × $CH_2CH_2CH_2CH_2$). UV–Vis (THF), λ_{max}/nm: 747, 667, 502, 367, 291; MS (Maldi-TOF, dihydroxybenzoic acid (DHBA as matrix): *m*/*z* (%): 1095 $[M+H]^+$.

2.3. Electrode preparation

For electrocoating measurements, the CV technique was employed with a glassy carbon electrode (GCE) as the working electrode with a surface area of 0.071 cm^2. A Pt wire as the counter electrode and a saturated calomel electrode (SCE) as the reference electrode were employed. Electrochemical grade tetrabutylamonium perchlorate (TBAP) in spectroscopic grade dimethyl sulfoxide (DMSO) (0.10 mol dm^{-3}) was employed as the supporting electrolyte. 50 successive CV cycles between the potential windows of TBAP/DMSO electrolyte system were employed to follow coating of **2** and **3** on the working electrode. Coating of the complexes on the working electrode was followed by a increase of the present peaks or by formation of new peaks whose currents increased with the repetitive CV cycles. The modified electrodes were abbreviated as GCE/**2** and GCE/**3**.

2.4. Electrochemical measurements

The CV and DPV measurements were carried out utilizing a three-electrode configuration at 25 °C. The working electrode was a Pt disc with a surface area of 0.071 cm^2. A Pt wire served as the counter electrode. A saturated calomel electrode (SCE) was employed as the reference electrode and separated from the bulk of the solution by a double bridge. Electrochemical grade TBAP in extra pure DMSO was employed as the supporting electrolyte at a concentration of 0.10 mol dm^{-3}.

2.5. In situ spectroelectrochemical and in situ electrocolorimetric measurements

In situ spectroelectrochemical measurements were carried out by utilizing a three-electrode configuration of thin-layer quartz thin-layer spectroelectrochemical cell at 25 °C. The working electrode was Pt tulle. A Pt wire counter electrode separated by a glass bridge and a SCE reference electrode separated from the bulk of the solution by a double bridge were used. *In situ* electrocolorimetric measurements, under potentiostatic control, were obtained using an OceanOptics QE65000 diode array spectrophotometer in the color measurement mode by utilizing a three-electrode configuration of a thin-layer quartz spectroelectrochemical cell. The standard illuminant A with a 2-degree observer at constant temperature in a light booth designed to exclude external light was used. Prior to each set of measurements, background color coordinates (*x*,*y* and *z* values) were taken at open-circuit, using the electrolyte solution without the complexes under study. During the measurements, readings were taken as a function of time under kinetic control, however only the color coordinates at the beginning and end of each redox processes were reported.

2.6. Electrocatalytic measurements

Electrocatalytic measurements were performed by using CV, chronoamperometry (CA) and chronocoulometry (CC) techniques in aqueous solution. The working electrodes were modified GCE/**2**, GCE/**3** and bare GCE electrodes. A spiral Pt wire as the counter electrode and SCE as the reference electrode were used. Aqueous phosphate buffer solution containing 0.1 mol dm^{-3} NaCl as an electrolyte in triple distilled water was employed as the supporting electrolyte. The pH was adjusted by addition of 0.2 mol dm^{-3} NaOH or conjugated acid solutions.

3. Results and discussions

3.1. Synthesis and characterization

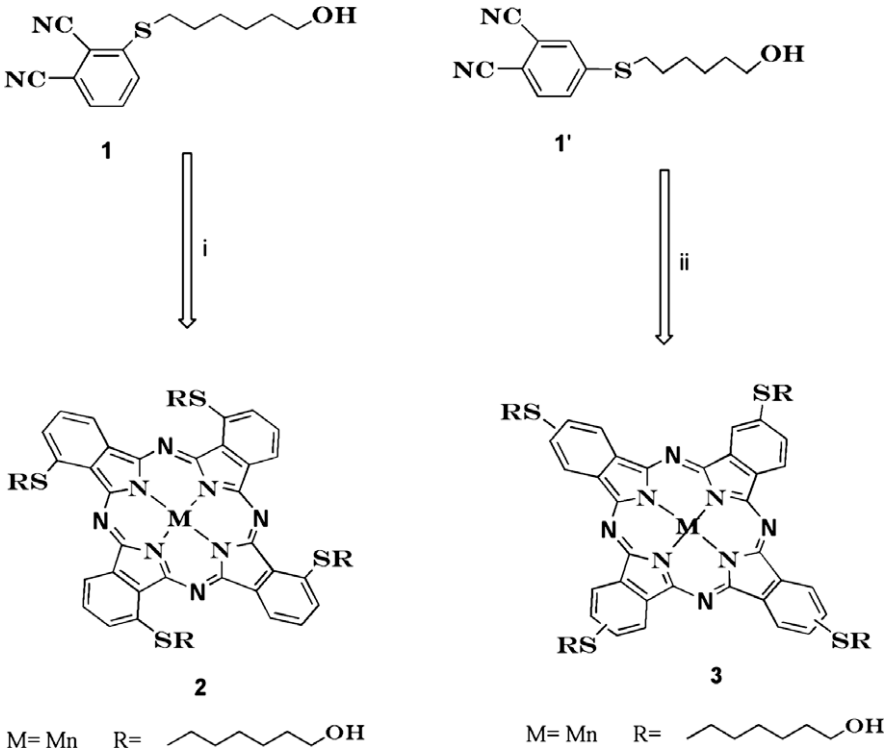
3′-(6-Hydroxyhexylthio)-phthalonitrile and 4′-(6-hydroxyhexylthio)-phthalonitrile can be obtained by nucleophilic aromatic substitution reactions of 6-mercapto-1-hexanol on 3- or 4-nitrophthalonitrile [15,16]. Manganese phthalocyanines, {Mn[Pc(α-S(CH$_2$)$_6$-OH)$_4$]Cl} (**2**) and {Mn[Pc(β-S(CH$_2$)$_6$OH)$_4$]Cl} (**3**) were accomplished by heating a pulverized mixture of 3′- or 4′-(6-hydroxyhexylthio)-phthalonitrile with anhydrous $MnCl_2$ salts at ca. 170 °C under N_2 atmosphere in the presence of 1,8-diazabicyclo [5.4.0] undec–7-ene (DBU) (Scheme 1). Synthesis and purification of MnPcs are, generally, more difficult than those of other MPcs due to the three forms of MnPcs: Mn(II)Pc, Mn(III)PcX (where X is an axial ligand coordinated on the metal center such as Cl^-, OAc^- or OH^-), and μ-oxo manganese(III) phthalocyanines (Mn(III)Pc–O–PcMn(III)) [20]. In all cases, a mixture of four possible structural isomers are obtained. The presence of the isomers could be verified by a slight broadening encountered in the UV–Vis absorption spectrum as compared with those of octa-substituted phthalocyanines composed of a single isomer [16,21,22].

The structures of the phthalocyanines (**2** and **3**) were verified by FTIR, elemental analysis, UV–vis and MALDI-TOF-MS spectroscopic methods. UV–Vis spectra of the MnPcs exhibit characteristic Q- and B-bands, at ca. 700–800 nm (Q-band) attributed to the π–π^* transition from the highest occupied molecular orbital (HOMO) to the lowest unoccupied molecular orbital (LUMO) of the Pc^{2-} ring, and the other in the UV region at ca. 340–370 nm (B-band) arising from deeper π–π^* transitions [23]. Both **2** and **3**, gave a single Q-band with high intensity at 769 and 747 nm due to a π–π^* transition, as expected as a result of their D_{4h} symmetry, with shoulders at the slightly higher energy side of the Q-band (691 and 667 nm) in addition to B-bands in UV region. The broad bands between 450 and 550 nm may be due to charge transfer from the electron-rich ring to the electron-poor metal center [21,25]. The B-bands are very clear due to the unsuperimposition of the B1 and B2 bands in the 340–370 nm region [21].

Fig. 1 shows the change of the UV–vis spectra of **2** upon titration with water. The Q band of **2** shifted to longer wavelength in water (789 nm) due to the higher polarization effect of water exchanged with the Cl^- counter anion. Quantitative analysis of the titration indicates 1:1 coordination of water exchanged with the Cl^- anion on the axial position of the Mn(III) center of the MnPc. Fig. 1 also shows that the complexes do not aggregate in THF and water, although it is known that phthalocyanine molecules tend to aggregate especially in polar media [20]. The non-aggregating behaviors of complexes **2** and **3** may due to the existence of polar peripheral functional end groups and the axial ligand, Cl^-, which reduce the π–π^* interaction between two macrocycle units [20]. A MALDI-MS spectrum (2,5-dihydroxybenzoic acid (DHB)) of **2** is given in Fig. 2 [16,21]. The protonated molecular ion peak was observed at 1095 Da with the other isotopic peaks.

3.2. Voltammetric and spectroelectrochemical characterization

The CV and DPVs (Figs. 3 and 4) of **2** and **3** were obtained in a deaerated DMSO/TBAP electrolyte system on a Pt working electrode. Table 1 lists the assignments of the redox couples and estimated electrochemical parameters, including the half-wave peak potentials ($E_{1/2}$), ratio of anodic to cathodic peak currents ($I_{p,a}/I_{p,c}$), peak to peak potential separations (ΔE_p) and difference between the first oxidation and reduction processes ($\Delta E_{1/2}$). As shown in Fig. 3, within the potential window of the DMSO/TBAP electrolyte system, three reduction processes (labeled $\mathbf{R_1}$–$\mathbf{R_3}$) and one oxidation process (labeled $\mathbf{O_1}$) are recorded for the complexes. Both complexes have redox processes approximately at the same potentials, indicating a similar effect of the substituents at the α and β positions to the electronic nature of the Pc ring. Couples $\mathbf{R_1}$ and $\mathbf{R_2}$ are well resolved and reversible with anodic to cathodic



Scheme 1. Synthetic route of 1(4),8(11),15(18),22(25)-tetrakis(6-hydroxyhexylthio)-manganese (III) phthalocyanine (**2**) and 2(3),9(10),16(17),23(24)-tetrakis(6-hydroxyhexylthio)-manganese (III) phthalocyanine (**3**) i and ii: anhydrous $MnCl_2$, quinoline, dbu.

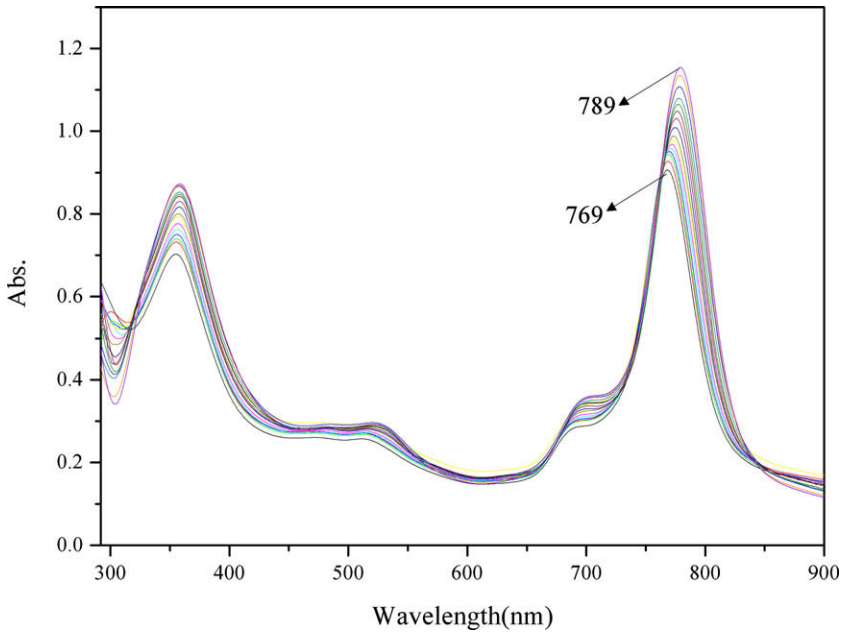


Fig. 1. UV–Vis spectra of **2** in THF/MeOH (1:1v/v) during titration with H_2O.

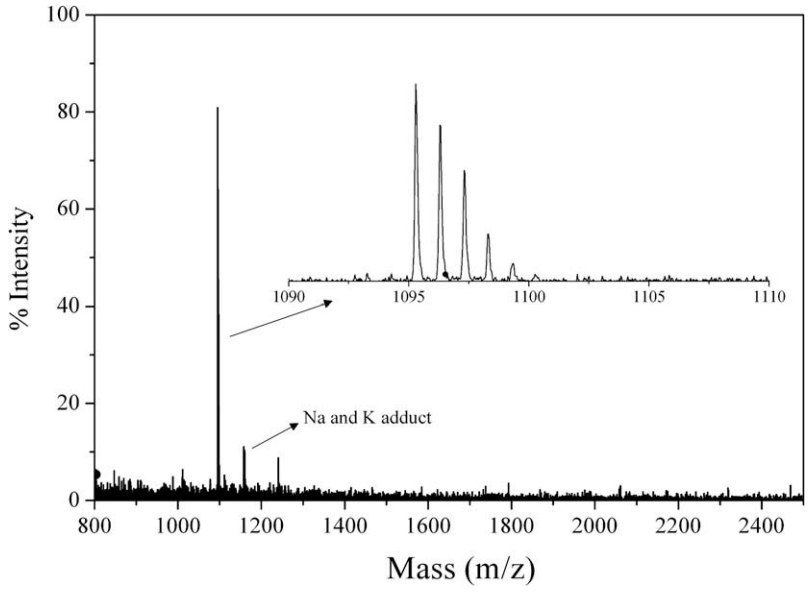


Fig. 2. The positive ion and reflectron mode MALDI-MS spectrum of **2** without metal ion was obtained in 2,5-dihydroxybenzoic acid MALDI matrix using nitrogen laser accumulating 50 laser shots. Inset spectrum shows the expanded molecular mass region of the complex.

peak separations (ΔE) ranging from 60 to 130 mV with increasing scan rates from 10 to 500 mVs^{-1} (ΔE_ps of 60–110 mV were obtained for a ferrocene reference). Unity of the $I_{p,a}/I_{p,c}$ ratio at all scan rates and linear variation of the peak currents with the square root of the scan rates indicated the purely diffusion controlled mass transfer of the complexes. Reversibility of the redox processes shows that axial ligand Cl^- may present as being bonded to the metal center after the redox processes or the axial ligand exchange reactions are very fast. Therefore, these chemical reactions did not disrupt the reversibility of the processes.

In comparison with the MnPcs in the literature [20–26], the first two reduction processes are assigned to metal-based processes, $Mn^{III}Pc^{-2}/Mn^{II}Pc^{-2}$ and $Mn^{II}Pc^{-2}/Mn^{I}Pc^{-2}$, and the third one is assigned to a ligand-based process, $Mn^{I}Pc^{-2}/Mn^{I}Pc^{-3}$. The oxidation process of the complexes is also a metal-based process, $Mn^{III}Pc^{-2}/Mn^{IV}Pc^{-2}$. *In situ* spectroelectrochemical experiments were employed to confirm the identities of these redox processes. In situ UV–Vis spectral changes and a chromaticity diagram of **2** are given in Fig. 5. Fig. 5A shows the *in situ* UV–Vis spectral changes observed upon controlled potential reduction of **2** at −0.40 V, corresponding to couple $\mathbf{R_1}$. The band at 517 nm and red shifted Q band at 781 nm are characteristic of $Mn^{III}Pc^{-2}$ species. Upon reduction, the Q band at 781 nm shifts to 716 nm, and new bands are formed at 582 and 918 nm. The formation of $Mn^{II}Pc^{-2}$ is characterized by shifting of the Q band to shorter wavelength values (~70 nm) and the formation of new bands at the charge transfer region [20–25]. Clear isosbestic points at 350, 396, 456, 537, 739 and 872 nm in the spectra are recorded. These spectral changes

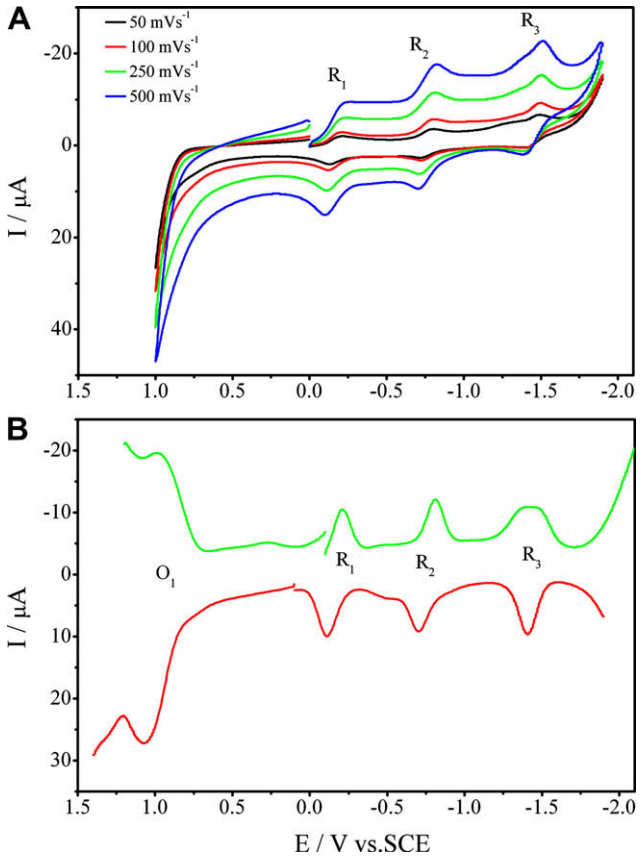


Fig. 3. CV (A) and DPV (B) of **2** at various scan rates on Pt in DMSO/TBAP.

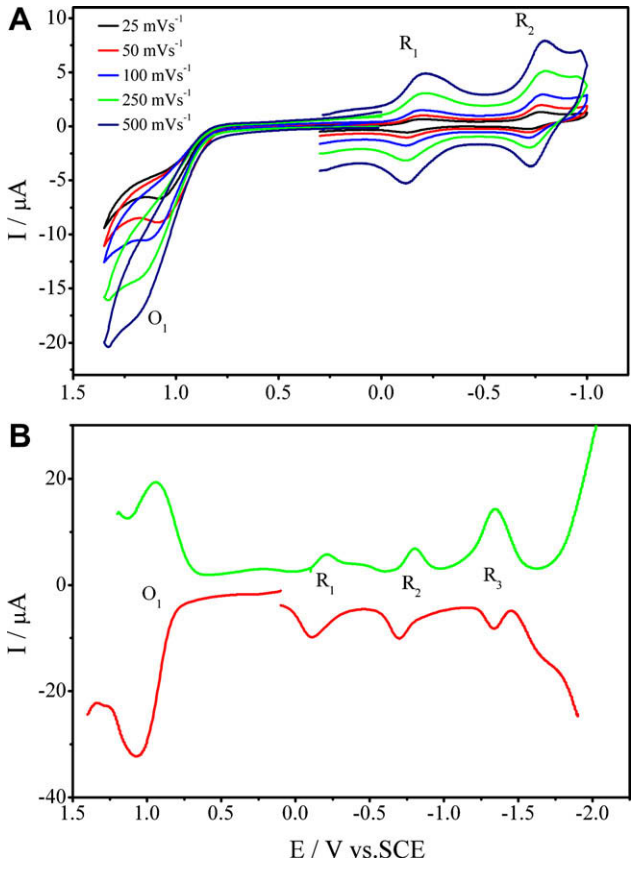


Fig. 4. CV (A) and DPV (B) of **3** at various scan rates on Pt in DMSO/TBAP.

suggest that the $\mathbf{R_1}$ couple observed at −0.16 V is a metal-based reduction process, $Mn^{III}Pc^{-2}/Mn^{II}Pc^{-2}$. Color changes of the complex in solution during the redox processes were recorded by *in situ* electrocolorimetric measurements. Fig. 5D gives the chromaticity diagrams of **2** recorded simultaneously during the spectroelectrochemical measurements. Without any potential application, the solution of **2** is light brown ($x = 0.372$ and $y = 0.352$) (point □ in Fig. 5D). As the potential is stepped from 0 to −0.40 V, the color of neutral **2**, $Mn^{III}Pc^{-2}$, starts to changes and the light green color ($x = 0.325$ and $y = 0.349$) (point ○ in Fig. 5D) of the monoanionic form of **2**, $Mn^{II}Pc^{-2}$, was obtained at the end of the first reduction.

The reduction of the $Mn^{II}Pc^{-2}$ species has been a subject of some controversy, with some reports proposing ring-reduction to the $Mn^{II}Pc^{-3}$ species and others suggesting metal reduction to the $Mn^{I}Pc^{-2}$ species [20]. Fig. 5B shows further spectral changes observed during the $\mathbf{R_2}$ process. The spectral changes are typical of a metal-based reduction with the formation of a broad band at 533 nm, because the band at 533 nm characterizes $Mn^{I}Pc^{-2}$ species [26]. At the same time while the Q band decreases in intensity, a new band is observed at 873 nm instead of the band at 918 nm. Clear isosbestic points at 385, 466, 667, 827 and 904 nm in the spectra are recorded. Similarly the color of the dianionic species, $Mn^{I}Pc^{-2}$ was recorded as light purple ($x = 0.311$ and $y = 0.246$) with in situ colorimetric measurements (point △ in Fig. 5D). The ring-reduction process, upon further reduction of the $Mn^{I}Pc^{-2}$ species, is represented in inset of Fig. 5B. Formation of a new broad band at 570 nm and a decrease of the Q band in intensity are characteristics of the process, $Mn^{I}Pc^{-2}/Mn^{I}Pc^{-3}$. During this process, the band at 533 nm, characterizing $Mn^{I}Pc$ species, is still present. The color of the $Mn^{I}Pc^{-3}$ species was recorded as light blue ($x = 0.275$ and $y = 0.226$) (point ◇ in Fig. 5D). The original spectra (in Fig. 5A) could be regenerated (to >90%) by application of a positive potential (0.50 V), after the formation of the $Mn^{I}Pc^{-3}$ species. To confirm origin of the oxidation process, $\mathbf{O_1}$, *in situ* UV–Vis changes were recorded under controlled potential application at 1.20 V (Fig. 5C). During this process, the Q band increases in intensity with a red shift from 781 to 788 nm, while the bands at 441 and 500 nm increases in intensity. These spectral changes are characteristics of a metal-based oxidation process in MnPcs, thus the couple of $\mathbf{O_1}$ is easily assigned to the $Mn^{III}Pc^{-2}/Mn^{IV}Pc^{-2}$ redox process [20–26]. Similarly the color of the monocationic species, $Mn^{IV}Pc^{-2}$ was recorded as light red ($x = 0.402$ and $y = 0.293$) with *in situ* colorimetric measurements (point ☆ in Fig. 5D).

To determine formation of μ-oxo MnPc species and its effects on the spectral changes, *in situ* UV–Vis changes were also recorded without purging with N_2 gas. Fig. 6 represents the *in situ* UV–Vis spectral changes with (Fig. 6A and B; case 1) and without (Fig. 6C and D; case 2) dissolved O_2 during controlled potential reduction processes. When we compare the spectral changes in Fig. 6A with those in Fig. 6C, it is shown that while complex **2** gives two new bands at 582 and 917 nm in case 1, these bands are not recorded in case 2 under controlled potential application at −0.40 V. The charge transfer band of the neutral $Mn^{III}Pc^{2-}$ species recorded at 514 nm disappears in case 2 while it is not changed in case 1. There are also considerable spectral change differences between case 1 and case 2 during the second reduction process. While the spectral changes indicate a metal-based reduction in case 1 (Fig. 6B), it is a ligand-based reduction in case 2 (Fig. 6D), because in case 2, the new band at 590 nm and the decrease of the Q band at 716 nm without shift are characteristics of a ligand-based reduction. However, two new bands at 533 and 873 nm are recorded in case 1 during the second reduction process, which are characteristics of a metal-based reduction process. All of these

Table 1
Voltammetric data of the complexes with the related metallophthalocyanines for comparison.

Complex		Ring oxidation	Mn^{IV}/Mn^{III}	Mn^{III}/M^{II}	Mn^{II}/Mn^{I}	Ring reductions		[d]$\Delta E_{1/2}$	Ref
2	[a]$E_{1/2}$ (V vs. SCE) in DMSO		1.03[e]	−0.16	−0.76	−1.45		1.19	
	[b]ΔE_p (mV)			75	73	76			tw
	[c]$I_{p,a}/I_{p,c}$			1.00	0.88	0.89			
3	[a]$E_{1/2}$ (V vs. SCE) in DMSO		1.00[e]	−0.16	−0.75	−1.34[e]		116	
	[b]ΔE_p (mV)			63	58				tw
	[c]$I_{p,a}/I_{p,c}$			1.00	0.85				
MnPc	$E_{1/2}$ (V vs. Ag/AgCl) in DMF	0.56		−0.31		−1.06			[6]
MnPc	$E_{1/2}$ (V vs. Ag/AgCl) in DMF	0.75	0.58	−0.31		−0.98			[6]
MnPc	$E_{1/2}$ (V vs. Fc/Fc^+) in THF	0.55	0.23	−0.90					[19]
MnPc	$E_{1/2}$ (V vs. Fc/Fc^+) in THF	0.55	0.23	−0.36		−1.69	−2.17		[19]
MnPc	$E_{1/2}$ (V vs. Fc/Fc^+) in THF			−1.09		−1.37			[19]
MnPc	$E_{1/2}$ (V vs. Ag/AgCl) in DCM	0.75	0.47	−0.46		−1.24			[17]
MnPc	$E_{1/2}$ (V vs. Ag/AgCl) in DMF			−0.06		−0.68	−1.19		[25]
MnPc	$E_{1/2}$ (V vs. SCE) in DMSO			−0.08	−0.76				[36]
MnPc	$E_{1/2}$ (V vs. SCE) in DMSO/Cl			−0.12	−0.77				[36]
MnPc	$E_{1/2}$ (V vs. SCE) in DMF	0.87		−0.14	−0.69	−1.46			[36]

tw: This work.
[a] $E_{1/2} = (E_{pa} + E_{pc})/2$ at 0.100 Vs^{-1}.
[b] $\Delta E_p = E_{pa} + E_{pc}$ at 0.100 Vs^{-1}.
[c] $I_{p,a}/I_{p,c}$ for reduction, $I_{p,c}/I_{p,a}$ for oxidation processes at 0.100 Vs^{-1} scan rate;
[d] $\Delta E_{1/2} = \Delta E_{1/2}$ (first oxidation)$-\Delta E_{1/2}$ (first reduction).
[e] Recorded by DPV.

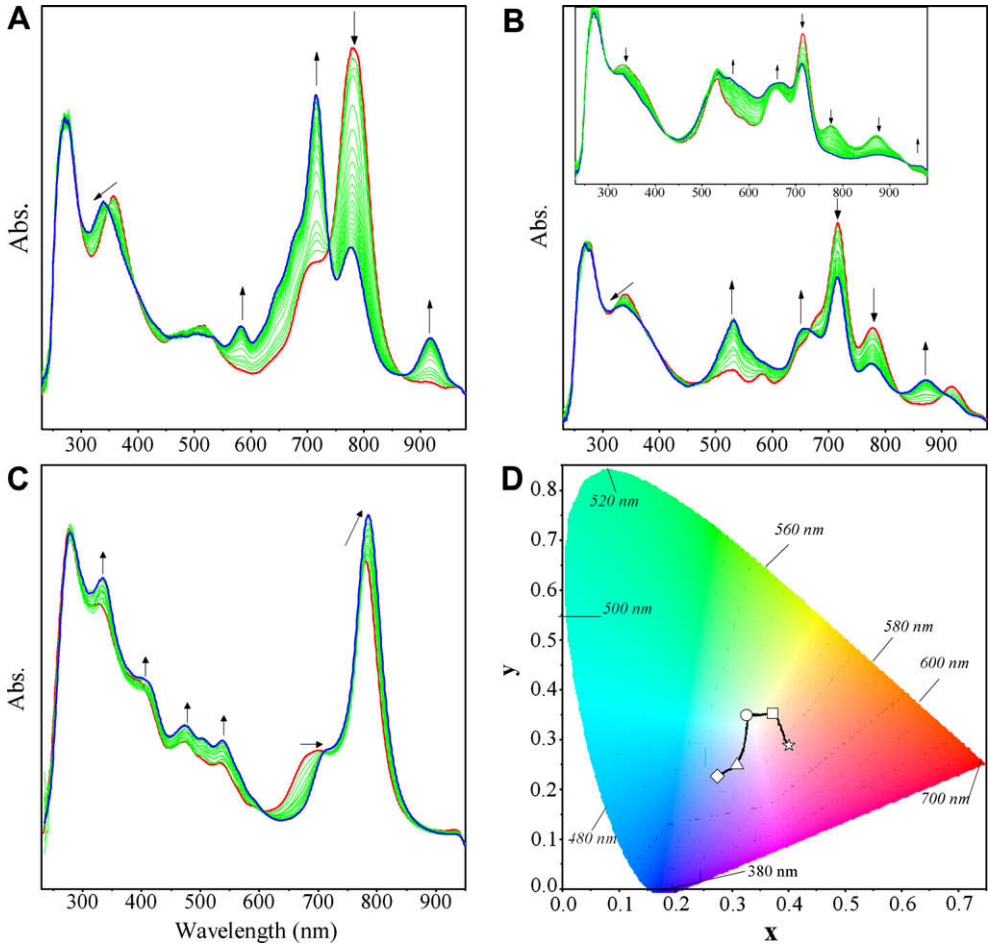


Fig. 5. *In situ* UV–Vis spectral changes of **2**. (A) $E_{app} = -0.40$ V. (B) $E_{app} = -1.00$ V (Inset: $E_{app} = -1.70$ V). (C) $E_{app} = 1.20$ V. (D) Chromaticity diagram of **2** (each symbol represents the color of electro-generated species; □: neutral **2**, $Mn^{III}Pc^{-2}$, ○: $Mn^{II}Pc^{-2}$, △: $Mn^{I}Pc^{-2}$, ◇: $Mn^{I}Pc^{-3}$, ☆: $Mn^{IV}Pc^{-2}$.

spectral changes indicate the reaction of $Mn^{III}Pc^{2-}$ species with O_2 dissolved in the solution and the formation of μ-oxo MnPc species. Formation of μ-oxo MnPc species was also stated by Nyokong et al. [26]. She stated that during the reduction processes of MnPc, new bands were recorded indicating the presence of μ-oxo MnPc species in solution.

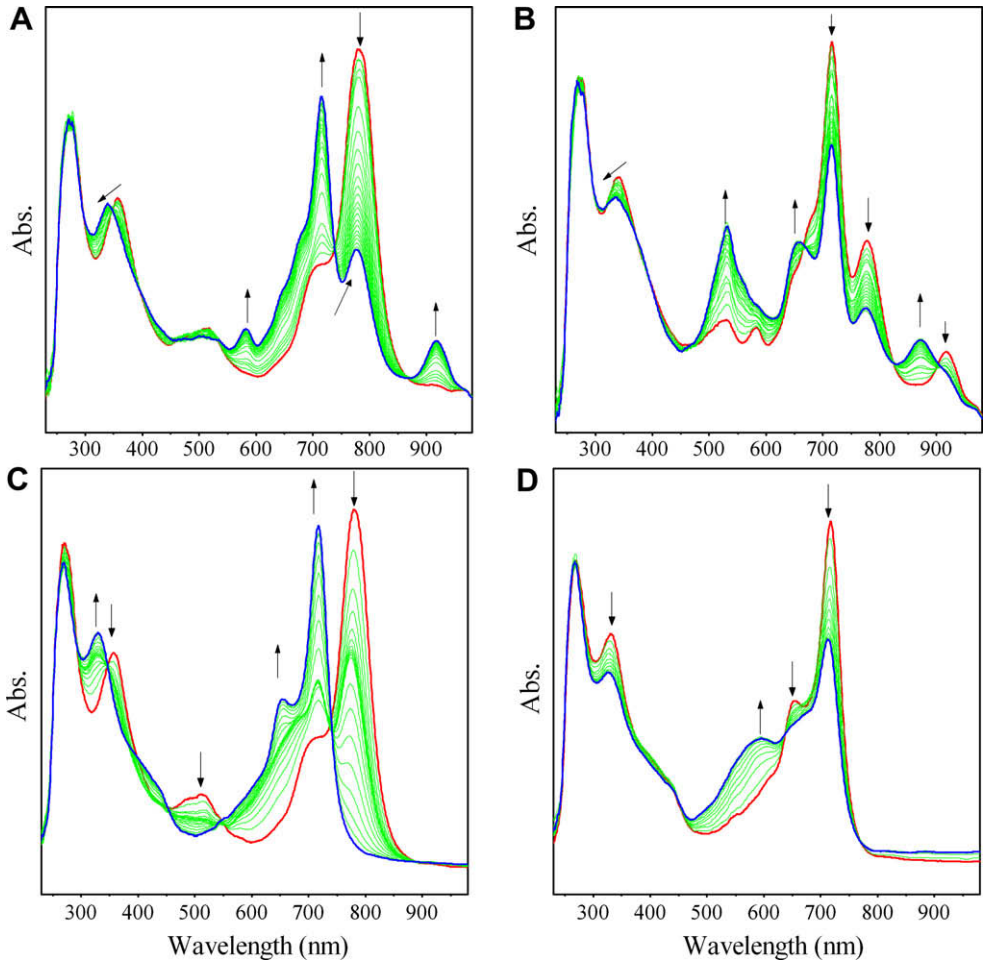


Fig. 6. *In situ* UV–Vis spectral changes of **2**. (A) E_{app} = −0.40 V without O_2 (case 1, purged with N_2 gently). (B) E_{app} = −1.00 V without O_2 (case 1, purged with N_2 gently). (C) E_{app} = −0.40 V with O_2 (case 2, not purged with N_2). (B) E_{app} = −1.00 V with O_2 (case 2, not purged with N_2).

Complex **3** has very similar electrocolorimetric and spectroelectrochemical responses with **2**. *In situ* UV–Vis spectral changes and a chromaticity diagram of **3** are given in Fig. 7. During reduction under a controlled potential at −0.40 V, corresponding to the couple $\mathbf{R_1}$, the Q band at 750 nm shifts to 698 nm and new bands are formed at 587, 647 and 902 nm (Fig. 7A). The formation of $Mn^{II}Pc^{-2}$ is characterized by the shift of the Q band to shorter wavelength values and formation of new bands at the charge transfer region. Differently, a band at 647 nm is also recorded, while this was not the case with the complex **2**. This may be the result of the μ-oxo MnPc species due to the reaction of the reduced species with oxygen, which may have entered the cell during the reduction process. It was stated in the literature that a band at around 640 nm indicates the existence of μ-oxo MnPc species [26]. Clear isosbestic points at 320, 404, 542, 716 and 846 nm in the spectra are recorded. These spectral changes suggest the formation of $Mn^{II}Pc^{-2}$. Thus, couple $\mathbf{R_1}$ observed at −0.16 V is assigned to $Mn^{III}Pc^{-2}/Mn^{II}Pc^{-2}$. Fig. 7D gives the chromaticity diagrams of complex **3** recorded simultaneously during the spectroelectrochemical measurements. Without any potential application, the solution of **3** is light brown (x = 0.375 and y = 0.374) (point □ in Fig. 7D). As the potential is stepped from 0 to −0.40 V, the light green color (x = 0.320 and y = 0.360) (point ○ in Fig. 7D) of the monoanionic form of **3**, $Mn^{II}Pc^{-2}$, was obtained at the end of the first reduction. Fig. 7B shows further spectral changes observed during further reduction processes. The spectral changes during the second reduction process are typical of a metal-based reduction, with the formation of split bands at 533 and 563 nm. At the same time, while the Q band decreases in intensity, the band at 902 nm shifts to 863 nm. Clear isosbestic points at 397, 488, 624, and 798 nm in the spectra are recorded. The color of the dianionic species, $Mn^{I}Pc^{-2}$, was recorded as light purple (x = 0.301 and y = 0.288) with *in situ* colorimetric measurement (point △ in Fig. 7D). The ring-reduction process upon further reduction of the $Mn^{I}Pc^{-2}$ species is represented in the inset of Fig. 7B. The formation of a new broad band in the charge transfer region, leaving the bands at 533 and 563 nm without change, and a decrease of the Q band in intensity are characteristics of the process, $Mn^{I}Pc^{-2}/Mn^{I}Pc^{-3}$. The color of the $Mn^{I}Pc^{-3}$ species was recorded as light blue (x = 0.301 and y = 0.259) (point ♢ in Fig. 5D). During the controlled potential application at 1.20 V, The Q band increases in intensity with a red shift from 750 to 758 nm, while the bands at 535 and 563 nm increase in intensity. These spectral changes are characteristics of a metal-based oxidation process in MnPc complexes, thus the couple of $\mathbf{O_1}$ is easily assigned to the $Mn^{III}Pc^{-2}/Mn^{IV}Pc^{-2}$ redox process. Similarly, the color of the monocationic species, $Mn^{IV}Pc^{-2}$ was recorded as light red (x = 0.404 and y = 0.266) with *in situ* colorimetric measurements (point ☆ in Fig. 7D).

3.3. Electrocatalytic measurements

Solution electrochemistry shows that the MnPc complexes have multi electron metal-based reduction couples having diffusion

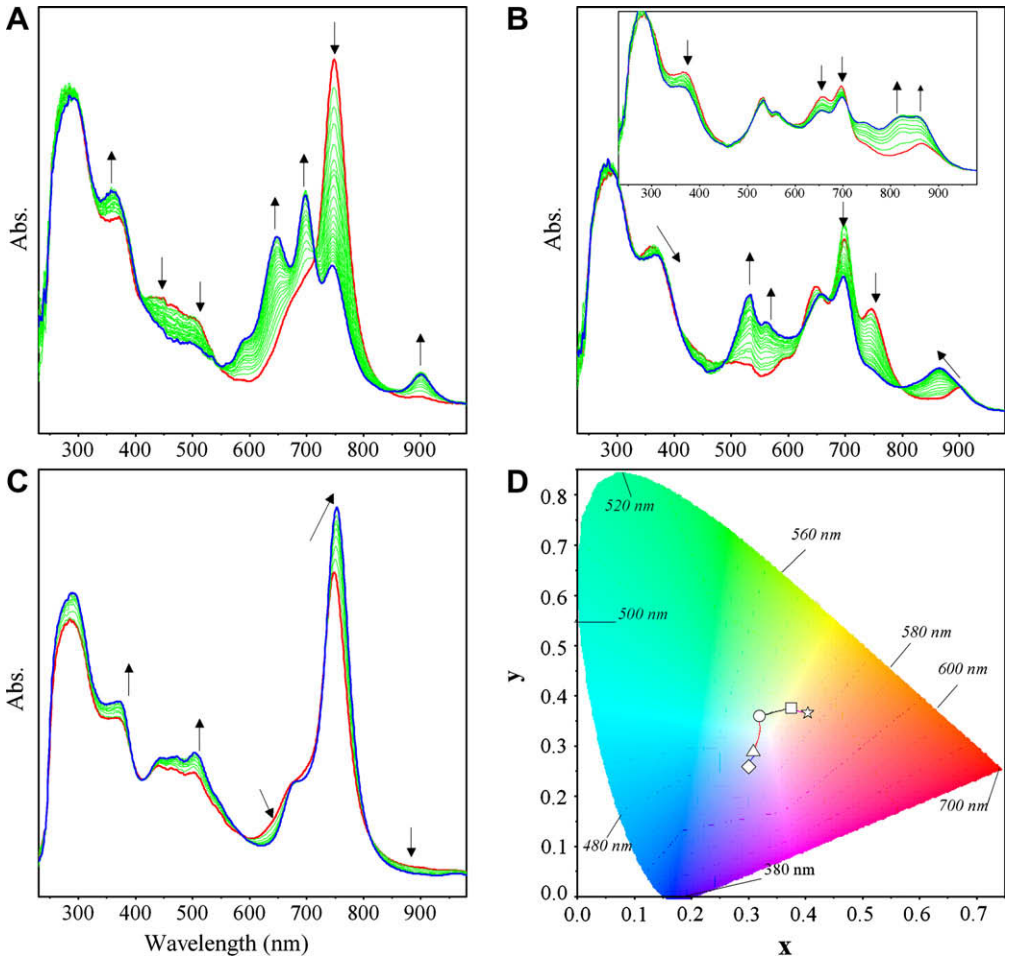


Fig. 7. *In situ* UV–Vis spectral changes of **3**. (A) $E_{app} = -0.40$ V. (B) $E_{app} = -1.00$ V (Inset: $E_{app} = -1.70$ V). (C) $E_{app} = 1.10$ V. (D) Chromaticity diagram of **3** (each symbol represents the color of electro-generated species; □: neutral **3**, $Mn^{III}Pc^{-2}$, ○: $Mn^{II}Pc^{-2}$, △: $Mn^{I}Pc^{-2}$, ◇: $Mn^{I}Pc^{-3}$, ☆: $Mn^{IV}Pc^{-2}$.

controlled reversible and/or *quasi*-reversible characters between 0.0 and −1.50 V versus SCE. These distinctive properties of the complexes indicate their possible electrocatalystic application. Therefore, electrocatalytic activities of the complexes were investigated for hydrogen evolution reaction in aqueous solution. The complexes were potentiostatically coated on a GCE for electrocatalytic applications. Electrocoating of the complexes was studied using CV performed in the TBAP/DMSO electrolyte system on a GCE working electrode. Repetitive scanning (50 scans) between the negative and positive potential windows of the electrolyte systems shows the appearance and gradual increase of new redox waves and the changing of the properties of the existence waves. During the repetitive scanning, while the redox waves of **2**, recorded at −0.22, −0.82, −1.46, and 0.45 V, disappeared gradually, new enhanced waves were recorded at −0.52, −0.68, −1.66 and −1.87 V (Fig. 8). These CV responses are easily attributed to the polymerization of **2** on the working electrode [20,27,28].

The electrocatalytic activities of the complexes for the hydrogen evolution reaction (*her*) in aqueous solution were studied using CV and CA performed in the presence of 0.1 mol dm^{-3} NaCl in phosphate buffer aqueous solution at different pHs with manganese phthalocyanine modified working electrodes (GCE/**2** and GCE/**3**). We compared the proton reduction potentials (from CV graphs) and charges passed during the proton reduction at constant reduction potentials (from CA and CC graphs). Electrocatalytic measurements show that both complexes catalyze the *her* reaction in a similar manner and degree. While the complexes are almost inactive at acidic and neutral media, their activities increase in basic media. As shown in Fig. 9, while the proton reduction reaction starts at −1.65 V on a bare GCE electrode (CV, CA and CC are represented with label "*i*") at pH 10.20, it starts at −1.50 V on modified electrodes, having higher hydrogen discharge currents (CV, CA and CC are represented with label "*ii* and *iii*"). During the CA and CC measurements (Fig. 9B), higher currents and charges recorded on the modified electrodes with respect to the bare GCE electrode support the catalytic activity of the complexes. The aim of the electrocatalytic reactions for hydrogen production is to reduce the reduction potential by decreasing the over potential of the working electrode and to gain a higher current at the same potential [29–31]. Therefore, accomplishing the proton reduction on modified electrodes at approximately 0.160 V lesser potential with a higher current than those on the bare electrode displays the catalytic activity of the MnPcs for the *her*.

The redox reaction of the MnPc derivatives is a very significant factor to their electrocatalytic activities towards the *her*. Due to the high hydrogen discharge currents, the redox waves of the complexes are invisible in Fig. 9A. Thus, expanded forms of the CV recorded on GCE/**2** with different switching potentials are given as an inset in Fig. 9A. Two cathodic waves are recorded on the GCE/**2** electrode at ca. −0.30 V corresponding to $Mn^{III}Pc^{2-}/Mn^{II}Pc^{2-}$ and at ca. −0.90 V corresponding to $Mn^{II}Pc^{2-}/Mn^{I}Pc^{2-}$ processes (CV "c"). These waves were then followed by a very sharp increase in current due to the *her*. Disappearance of the anodic couples of the peaks during the reverse scan indicates the regeneration of

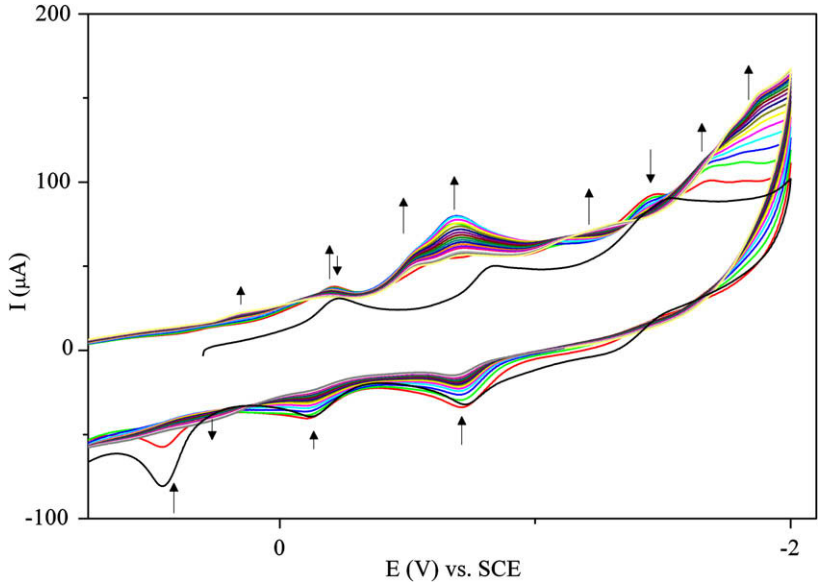


Fig. 8. Potentiodynamic coating of **2** at 0.100 Vs^{-1} scan rate on a GCE in the TBAP/DMSO electrolyte system.

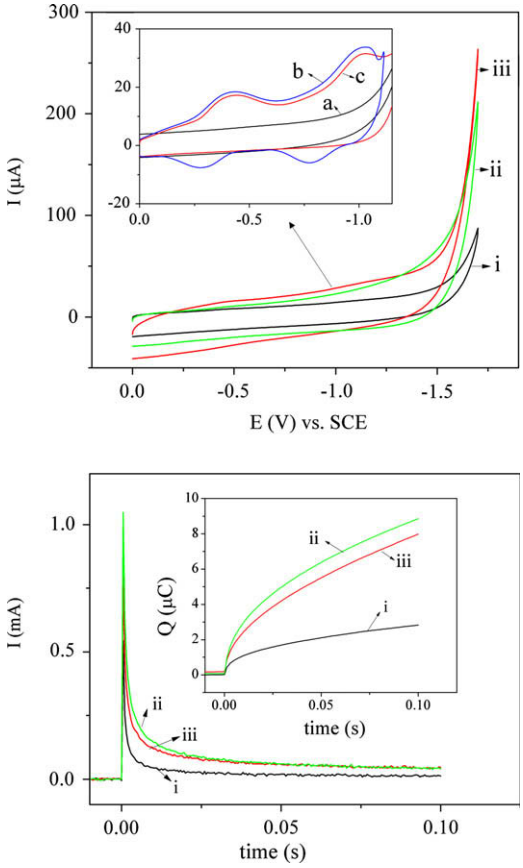


Fig. 9. (A) Comparative CV responses of bare GCE and modified electrodes (GCE/**2** and GCE/**3**) in aqueous phosphate buffer solution containing 0.10 mol dm^{-3} NaCl as the supporting electrolyte. pH 10.20. Scan rate: 0.100 Vs^{-1}(i: GCE bare electrode, ii: GCE/**2**, iii: GCE/**3**). (Inset shows enlarged CV graph recorded with a: GCE**,** b: GCE/**2** when the potential was switched before H^+ reduction, **c**: GCE/**2** when the potential was switched after H^+ reduction). (B) CA and CC (inset) responses recorded at pH 10.20 with i: GCE bare electrode, ii: GCE/**2**, and iii: GCE/**3**).

the original species after the *her*. When the potential was reversed before the *her*, the anodic couples of these peaks are still present (CV "b"). These results clearly affirm the electrocatalytic contribution of the complexes to the *her*. According to the literature on transition metal complexes which catalyzed H_2 production, stable or transient hydride complexes can be generated via either a chemical route (C mechanism) or an electrochemical route (E mechanism) [32–35]. For example, Savèant and coworkers demonstrated that hydrogen evolution by iron porphyrins begins with reduction of the catalyst followed by its protonation to a transient $Fe^{II}H$ species. H_2 production proceeds subsequently through proton/hydride coupling [32]. Kaneko and coworkers reported that porphyrin and phthalocyanine derivatives could catalyze proton reduction to generate hydrogen. They proposed that there exist at least two steps for hydrogen evolution; one-step is reduction of the complex, and the second one is the proton reduction by the protonated-reduced complex [35]. In summary, it is well documented in the literature that first, second and/or third reduced transition metal complexes may catalyze the proton reduction process depending on the substituent environment of the complex. In this study, increasing of the activity of the complexes in basic media shows that the second reduced MnPc species may catalyze the proton reduction process depending on the pH of the media.

4. Conclusion

α- and β-substituted tetrakis{6-hydroxy-hexylthiol)-phthalocyaninato manganese (III) chloride complexes have been prepared and characterized by elemental analysis, FTIR, MS and UV–Vis spectral data. A Q-band maximum in the near-IR region of the electronic spectra was due to the Mn (III) metal center of the complexes. UV–Vis spectral changes of $\{Mn[Pc(\alpha\text{-}S(CH_2)_6OH)_4]Cl\}$ upon titration with water show exchange of the axial chloride ion with water. The voltammetric and spectroelectrochemical studies of the complexes show that the complexes exhibit three reversible one-electron reduction processes, assigned to $Mn^{III}Pc^{2-}/Mn^{II}Pc^{2-}$, $Mn^{II}Pc^{2-}/Mn^{I}Pc^{2-}$ and $Mn^{I}Pc^{2-}/Mn^{I}Pc^{3-}$ and an oxidation assigned to $Mn^{III}Pc^{2-}/Mn^{IV}Pc^{2-}$, respectively. These solution properties of the complexes are in harmony with similar MnPcs with small potential shifts due to the different substituents. Orientation of the 6-hydroxyhexylthiol substituents at α and β does not affect the solution properties of the complexes. Measurement of the xyz coordinates allows quantification of the color of each electro-generated anionic and cationic redox species which is very important in deciding their possible electrochromic application. Presence of O_2

in the reaction medium during the reduction of the complexes causes the formation of μ-oxo MnPc species, which affect the spectral changes and redox states of the species. Decreasing of the over potential and increasing the hydrogen discharge current indicate electrocatalytic activity of the complexes coated on GCE potentiostatically.

Acknowledgement

We thank the Research Funds of Sakarya University and TUBİTAK (Project nos: MAG-106M286 and 108T094).

References

[1] N. He, Y. Chen, J. Doyle, Y. Liu, W.J. Blau, Dyes Pigments 76 (2008) 569.
[2] C. Piechocki, J. Simon, A. Skoulios, D. Guillon, P. Weber, J. Am. Chem. Soc. 104 (1982) 5245.
[3] E. Ben-Hur, W.S. Chan, Phthalocyanines in Photobiology and Their Medical Applications, in: K.M. Kadish, K.M. Smith, R. Guilard (Eds.), The Porphyrin Handbook, vol. 19, Academic Press, Boston, MA, 2003, pp. 1–35.
[4] J. Simon, P. Bassoul (Eds.), Design of Molecular Materials: Supramol. Eng, John Wiley and Sons, Chichester, 2000, pp. 197–291.
[5] D. Dini, M.J.F. Calvete, M. Hanack, R.G.S. Pong, S.R. Flom, J.S. Shirk, J. Phys. Chem. B 110 (2006) 12230.
[6] N. Nombona, P. Tau, N. Sehlotho, T. Nyokong, Electrochim. Acta 53 (2008) 3139.
[7] A. Sanmatias, D. Benito, J.A. Bastos, J. Navarro-Laboulais, J.J. Garciıa-Jaren, F. Vicente, Int. J. Inorg. Mater. 1 (1999) 361.
[8] P. Tau, T. Nyokong, J. Mol. Catal. A-Chem. 273 (2007) 149.
[9] Ö.A. Osmanbaş, A. Koca, M. Kandaz, F. Karaca, Int. J. Hydrogen Energy 33 (2008) 3281.
[10] J. Spadavecchia, G. Ciccarella, R. Rella, Sens. Actuators B Chem. 106 (2005) 212.
[11] B. Adhikari, S. Majumdar, Prog. Polym. Sci. 29 (2004) 699.
[12] M. Kandaz, S.L.J. Michel, B.M. Hoffman, J. Porphyr. Phthalocya. 7 (2003) 700.
[13] J. Janczak, R. Kubiak, M. Sledz, H. Borrmann, Y. Grin, Polyhedron 22 (2003) 2689.
[14] S.J. Lange, J.W. Sibert, A.G.M. Barrett, B.M. Hoffman, Tetrahedron 56 (2000) 7371.
[15] M.N. Yarasir, M. Kandaz, B.F. Şenkal, A. Koca, B. Salih, Dyes Pigments 77 (2008) 7.
[16] M.N. Yarasir, M. Kandaz, A. Koca, B. Salih, Polyhedron 26 (2007) 1139.
[17] N. Nombona, T. Nyokong, Dyes Pigments 80 (2009) 130.
[18] G.W. Rayner-Canham, A.B.P. Lever, Inorg. Nucl. Chem. Lett. 9 (1973) 513.
[19] C.C. Leznoff, L.S. Black, A. Hiebert, P.W. Causey, D. Christendat, A.B.P. Lever, Inorg. Chim. Acta 359 (2006) 2690.
[20] M.J. Stillman In C.C. Leznoff, A.B.P. Lever (Eds.), Phthalocyanines: Properties and Applications, vol. 3, VCH, New York, 1993.
[21] I. Yilmaz, New J. Chem. 32 (2008) 37.
[22] C.L. Lin, C. Lee, K. Ho, J. Electroanal. Chem. 524 (2002) 81.
[23] M. Gouterman, in: D. Dolphin (Ed.), The Porphyrins, vol. 3, Academic Press, New York, 1978, pp. 1–65.
[24] R.J. Mortimer, A.L. Dyer, J.R. Reynolds, Displays 27 (2006) 2.
[25] J. Obirai, T. Nyokong, Electrochim. Acta 50 (2005) 3296.
[26] N. Sehlotho, M. Durmuş, V. Ahsen, T. Nyokong, Inorg. Chem. Commun. 11 (2008) 479.
[27] C. Miry, D. Le Brun, J.M. Kerbaol, M. L'Her, J. Electroanal. Chem. 494 (2000) 53.
[28] O. El Mouahid, A. Rakotondrainibe, P. Crouigneau, C.A.L. Léger, J. Electroanal. Chem. 455 (1998) 209.
[29] F. Taguchi, T. Abe, M. Kaneko, J. Mol. Catal. A-Chem. 140 (1999) 41.
[30] F. Zhao, J. Zhang, T. Abe, D. Wöhrle, M. Kaneko, J. Mol. Catal. A-Chem. 145 (1999) 245.
[31] A. Koca, M.K. Şener, M.B. Koçak, A. Gül, Int. J. Hydrogen Energy 31 (2006) 2211.
[32] I. Bhugun, D. Lexa, J.M. Saveant, J. Am. Chem. Soc. 118 (1996) 3982.
[33] J.F. Capon, F. Gloaguen, P. Schollhammer, J. Talarmin, Coord. Chem. Rev. 249 (2005) 1664.
[34] O. Pantani, E.A. Mallart, A. Aukauloo, P. Millet, Electrochem. Commun. 9 (2007) 54.
[35] T. Abe, F. Taguchi, S. Tokita, M. Kaneko, J. Mol. Catal. A-Chem. 126 (1997) 89.
[36] A.B.P. Lever, P.C. Minor, J.P. Wilshire, Inorg. Chem. 20 (1981) 2550.

powder was recrystallised in ethanol. Yield for the complex 90%, m.p. 249–251 °C. Elemental analysis, *Anal.* Calc. for $C_{16}H_{18}O_8Cu$: C, 47.82; H, 4.51. Found: C, 47.35; H, 4.78%.

2.1.2. Synthesis of (**1**) and (**2**)

Trans-bisaquabis(*o*-vanillinato)copper(II) (1 mmol, 0.4 g), dissolved in methanol (100 ml), was added dropwise with stirring at 50 °C to a suspension of 1,8-diamino-3,6-dioxaoctane (1 mmol, 0.15 g) or (R)-(−)-2-amino-1-butanol (2 mmol, 0.09 g) in methanol. The reaction mixture was then cooled to room temperature. The dark green crystals formed were filtered and washed with 10 ml of acetone. Yield: 68%, m.p. 184 °C for (**1**) and yield: 77%; m.p. 163 °C for (**2**).

Table 1
Crystal data and structure refinement parameters of (**1**) and (**2**).

	(**1**)	(**2**)
Formula	$C_{22}H_{26}N_2O_6Cu$	$C_{24}H_{32}N_2O_6Cu$
Molecular weight	477.99	508.07
T (K)	293(2)	293(2)
λ (Å)	0.71073	0.71073
Crystal system	trigonal	triclinic
Symmetry space group name H–M	$R\bar{3}$	$P\bar{1}$
Symmetry int tables number	148	1
Unit cell dimensions		
a (Å)	30.105(3)	8.054(7)
b (Å)	30.105(3)	8.684(7)
c (Å)	12.3204(11)	10.258(8)
α (°)	90.00	79.452(6)
β (°)	90.00	70.454(6)
γ (°)	120.00	65.427(6)
V (Å^3)	9669.9(16)	613.97(9)
Z	18	1
Calculated density (Mg m^{-3})	1.477	1.374
μ (mm^{-1})	1.058	0.930
F (0 0 0)	4482	267
Crystal size (mm)	0.260 × 0.190 × 0.140	
θ Range	1.35–26.07	2.6–29.5
Index ranges	$-36 \leqslant h \leqslant 36$	$-11 \leqslant h \leqslant 11$
	$-21 \leqslant k \leqslant 36$	$-11 \leqslant k \leqslant 11$
	$-13 \leqslant l \leqslant 15$	$-814 \leqslant l \leqslant 13$
Independent reflections	4147	13962
Reflections observed (>2σ)	1883	12888
Goodness-of-fit (GOF) on F^2	0.810	0.94
R, R_w [$I > 2\sigma(I)$]	0.0402, 0.0749	0.037, 0.086
R_{int} indices (all data)	0.0738	0.036, 0.085

Elemental analysis (%): *Anal.* Calc. for $C_{22}H_{26}N_2O_6Cu$ (**1**): C, 55.28; H, 5.48; N, 5.86. Found: C, 55.67; H, 5.34; N, 5.41%. *Anal.* Calc. for $C_{24}H_{32}N_2O_6Cu$ (**2**): C, 56.74; H, 6.35; N, 5.51. Found C, 56.67; H, 6.04; N, 5.28%.

2.2. Materials and measurements

Elemental analyses were performed by standard methods at TÜBİTAK (The Turkish Scientific Research Centre). The UV–Vis spectra were obtained for the methanol solution of the title complexes with a Unicam UV2 spectrometer in the range 900–200 nm. The IR spectra were recorded on a Jasco 430 FT/IR spectrophotometer using KBr pellets and operating at 4000–200 cm^{-1}. Magnetic susceptibility measurements at room temperature were performed using a Sherwood Scientific MXI model Gouy magnetic balance. A TG8110 thermal analyzer was used to record simultaneous TG and DTA curves in static air atmosphere at a heating rate of 10 K min^{-1} in the temperature range 20–1000 °C using platinum crucibles. Highly sintered α-Al_2O_3 was used as a reference and the DTG sensitivity was 0.05 mg s^{-1}.

2.3. Crystallographic analyses

For (**1**) and (**2**), all H atoms were refined using a riding model for C–H bonds with d(C–H) = 0.93–0.97 Å. The U_{iso} values for these H atoms were assigned to $1.2U_{eq}$(C) [$1.5U_{eq}$(methyl C)]. A summary of the crystallographic data, experimental details and refinement results for (**1**) and (**2**) are given in Table 1.

Data collection: Stoe X-AREA [24]; cell refinement: Stoe X-AREA [24]; data reduction: Stoe X-RED [24]; program used to solve structures: SHELXS-97 [25]; program used to refine structures: SHELXL97 [25]; molecular graphics: ORTEP-3 for Windows [26]; software used to prepare material for publication: WINGX [27].

3. Results and discussion

3.1. UV–Vis spectra and magnetic properties

The electronic spectrum was measured at room temperature in methanol (10^{-4} M) for the dark green complex bis(*o*-vanillinato)-triethylenglycoldiiminecopper(II) (**1**), and it exhibited two absorption bands. The bands at 370 nm (ε = 9101 L mol^{-1} cm^{-1}) and 472 nm (ε = 1556 L mol^{-1} cm^{-1}) have been assigned to $\pi \rightarrow \pi^*$

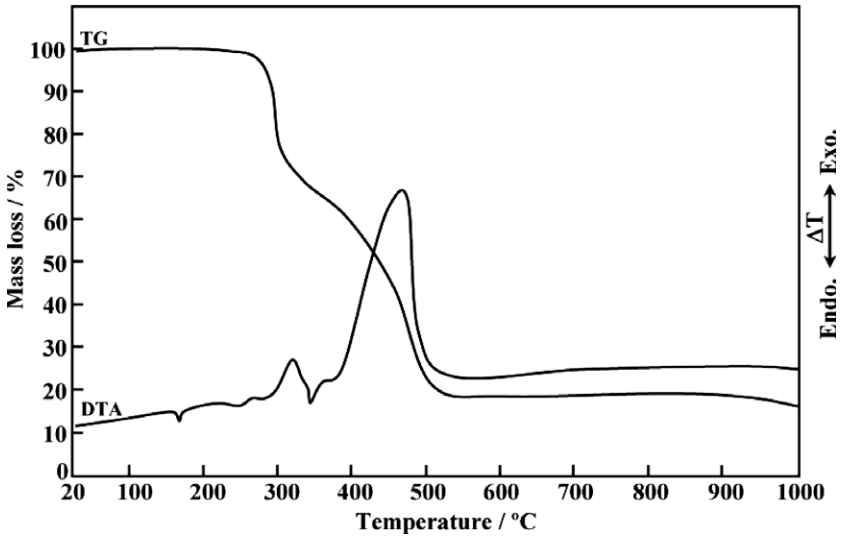


Fig. 1. TG and DTA curves of (**1**).

and $n \rightarrow \pi^*$ transitions of the bis(*o*-vanillinato)-triethylenglycoldiimine ligand, respectively. d–d transitions were not observed in the spectrum. This band may be remain under the $n \rightarrow \pi^*$ transition.

The electronic spectrum was measured at room temperature in methanol (10^{-3} M) for the dark green complex (**2**), and it exhibited a broad d–d absorption transition centered at 646 nm (ε = 115.15 L mol^{-1} cm^{-1}). This value was assigned to the $b_{2g} \rightarrow b_{1g}$ transition, thereby suggesting a square planar geometry around the Cu(II) center.

The complexes exhibit experimental magnetic moment values of 1.89 BM for (**1**) and 1.82 BM for (**2**), which correspond to one unpaired electron.

3.2. IR spectra

The IR spectrum of (**1**) displays a strong absorption at 1636 cm^{-1} which is assigned to a C=N stretching mode in the Schiff base. A band observed at 1450 cm^{-1} is due to υ(C–O) of the phenolic group of the title complex. The coordination of the azomethine nitrogen and phenolic oxygen to Cu(II) is observed at 513 cm^{-1} and 420 cm^{-1}, respectively. Similar M–O and M–N stretching bands are reported in the previous work on N-(*o*-vanillinidene)-*p*-anisidine and N,N′-bis(*o*-vanillinidene)-ethylenediamine complexes [28].

The IR spectrum of (**2**) displays a strong absorption bands at 3515 cm^{-1} and 2950 cm^{-1} which are attributed to the stretching bands of the free hydroxyl and methylene groups of (R)-(−)-2-amino-1-butanol, respectively. The strong absorption band at 1616 cm^{-1} is assigned to a C=N stretching mode in the Schiff base and a band at 1444 cm^{-1} due to υ(C–O) of the phenolic group is observed.

3.3. Thermal analyses

The thermal analysis curves of the studied complexes are shown in Figs. 1 and 2. The complexes decompose in a similar

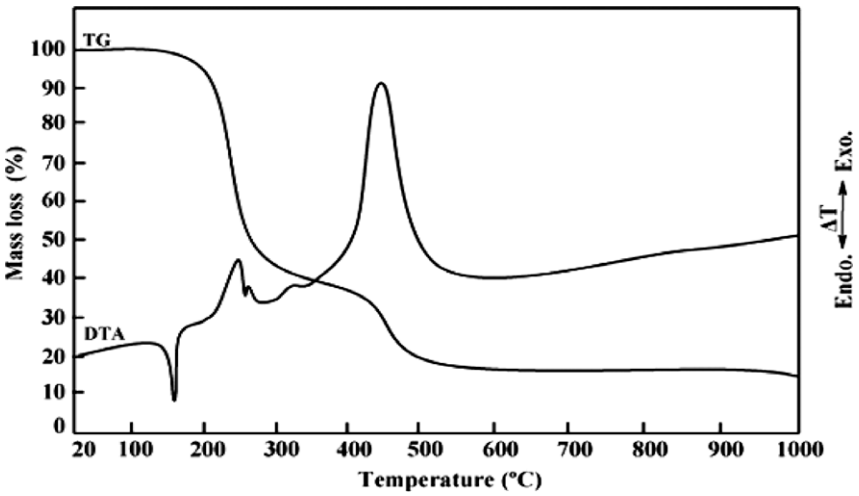


Fig. 2. TG and DTA curves of (**2**).

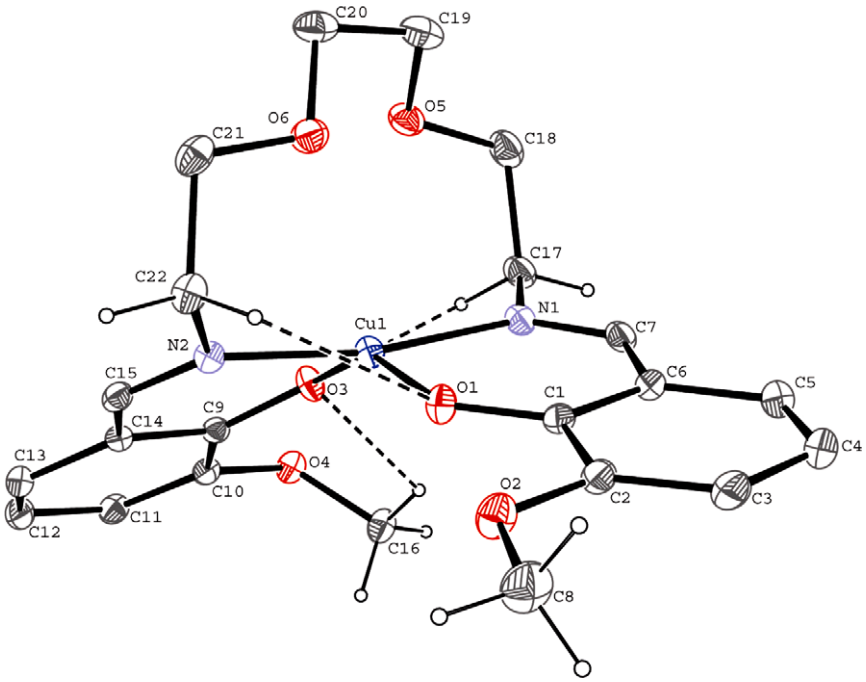


Fig. 3. Molecular structure and atom-labeling scheme of (**1**).

manner. Complex (**1**) melts at 184 °C and is thermally stable up to 245 °C. Complex (**2**) is thermally stable up to 146 °C and begins to decompose with melting (endothermic $DTA_{max.}$: 163 °C). Thermal decomposition of complexes proceeds in two exothermic stages. The first mass loss stage of these complexes was observed in the range 290–550 °C for (**1**) and 146–550 °C for (**2**). This first stage of each complex is related to the partial decomposition of the Schiff base ligands. The second stage of decomposition is associated with a strong exothermic oxidation process (DTA curves: 476 and 444 °C for the complexes (**1**) and (**2**), respectively). During this stage, the remaining organic part is abruptly burnt in these complexes. The total weight losses are 82.61% for (**1**) and 83.98% for (**2**), suggesting that the final decomposition product is CuO (calcd. 83.35%). The final decomposition products were identified by IR spectroscopy and also confirmed by mass loss calculations. On the basis of the first decomposition temperature, the thermal stability of the complexes follows the order: (**1**) (245 °C) > (**2**) (146 °C) in static air atmosphere.

3.4. Crystal structures

3.4.1. Bis(o-vanillinato)-triethylenglycoldiiminecopper(II) (1)

The molecular structure and packing diagrams of (**1**) are illustrated in Figs. 3 and 4, respectively, and selected bond distances and angles are listed in Table 2. Tetra-coordinated Schiff base metal complexes may form *trans* or *cis* planar or tetrahedral structures. A strictly planar or slightly distorted coordination is characteristic for transition metal complexes of copper(II) with a CuN_2O_2 coordination sphere [28]. In (**1**), bis(*o*-vanillinato)-triethylenglycoldiiminecopper(II), the *o*-vanillinato ligands moieties of the molecule are in a *trans* configuration and the Cu atom is coordinated by two imine N atoms and two phenol O atoms from the Schiff base ligand in a slightly distorted square planar coordination (Fig. 3). The N1–Cu1–O1, N1–Cu1–O3, N2–Cu1–O1 and N2–Cu1–O3 bond angles are 92.41(13)°, 90.78(12)°, 90.27(11)° and 91.29(11)°, respectively. The Cu–N distances [1.953(3) and 1.965(3) Å] are longer than the Cu–O distances [1.891(2) and

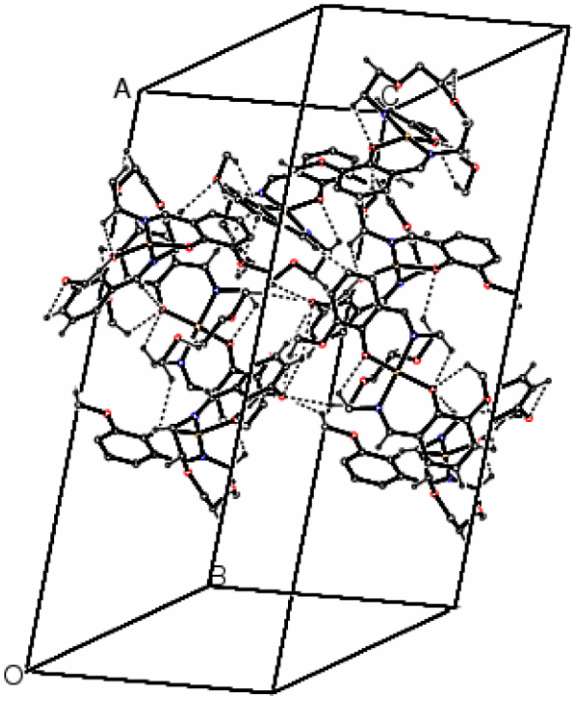


Fig. 4. An ORTEP ([27]) view of the packing diagram of (**1**).

Table 2
Crystal data and structure refinement parameters of (**1**) and (**2**).

Selected atoms			
*Complex (**1**)*			
N(1)–Cu(1)	1.965(3)	O(1)–Cu(1)	1.912(2)
N(2)–Cu(1)	1.953(3)	O(3)–Cu(1)	1.891(2)
N(1)–Cu(1)–O(1)	92.41(13)	N(2)–Cu(1)–O(3)	91.29(11)
N(2)–Cu(1)–O(1)	90.27(11)	N(1)–Cu(1)–O(3)	90.78(12)
O(1)–Cu(1)–O(3)	151.41(11)	N(1)–Cu(1)–N(2)	170.37(12)
*Complex (**2**)*			
N(1)–Cu(1)	1.953(2)	O(3)–Cu(1)	1.907(19)
N(2)–Cu(1)	1.955(3)	O(4)–Cu(1)	1.903(19)
N(1)–Cu(1)–N(2)	157.37	N(2)–Cu(1)–O(4)	92.82
N(2)–Cu(1)–O(1)	93.83	N(1)–Cu(1)–O(4)	93.69
O(1)–Cu(1)–N(1)	94.36	O(1)–Cu(1)–O(4)	141.83

Table 3
Hydrogen-bonding interactions in the complexes.

D–H···A	d(D–H) (Å)	d(H···A) (Å)	d(D···A) (Å)	<(DHA) (°)
*Complex **1***				
C16–H16A···O3	0.96	2.35	2.900 (4)	116.1
C17–H17A···O3	0.97	2.30	2.907 (4)	119.9
C22–H22A···O1	0.97	2.41	2.975 (5)	116.7
C8–H8B···O4^{i}	0.96	2.69	3.492 (5)	141.2
C11–H11···O4^{ii}	0.93	2.94	3.607 (4)	129.5
C12–H12···O2^{iii}	0.93	2.79	3.515 (5)	135.8
C15–H15···O3^{iv}	0.93	2.96	3.884 (4)	173.3
C18–H18A···O1^{v}	0.97	2.69	3.463 (5)	136.9
C19–H19A···O5^{vi}	0.97	2.74	3.637 (5)	154.2
C21–H21B···O4^{vii}	0.97	2.64	3.598 (5)	169.9
*Complex **2***				
O3–H3O···O4	0.92(7)	2.16(7)	2.884(4)	135.6
O3–H3O···O5	0.92(7)	2.21(7)	3.012(4)	149.4
O6–H6O···O1	0.98(4)	1.97(4)	2.800(3)	144.3
O6–H6O···O2	0.98(4)	2.33(4)	3.091(4)	134.3
C7–H7···O6^{viii}	0.93	2.76	3.610(4)	152.7
C5–H5···O6^{viii}	0.93	2.61	3.494(4)	159.3
C23–H23···O2^{ix}	0.93	2.77	3.568(4)	145.0
C27–H2···O3^{ix}	0.93	2.49	3.408(5)	169.8

Symmetry codes: (i) *x*, *y*, *z* − 1; (ii) 2 3 − *x*,1 3 − *y*,7 3 − *z*; (iii) 1 3 − *y*, *x* − *y* − 1 3,2 3 + *z*; (iv) 1 3 − *y*, *x* − *y* − 1 3, *z* − 1 3; (v) 1 3 + *x* − *y*, *x* − 1 3,5 3 − *z*; (vi) 1 − *x*, − *y*, 2 − *z*; (vii) 2 3 − *x* + *y*,1 3 − *x*, *z* − 2 3. (viii) *x*, +*y*, +*z* + 1; (ix) *x* − 1, +*y* + 1, +*z*.

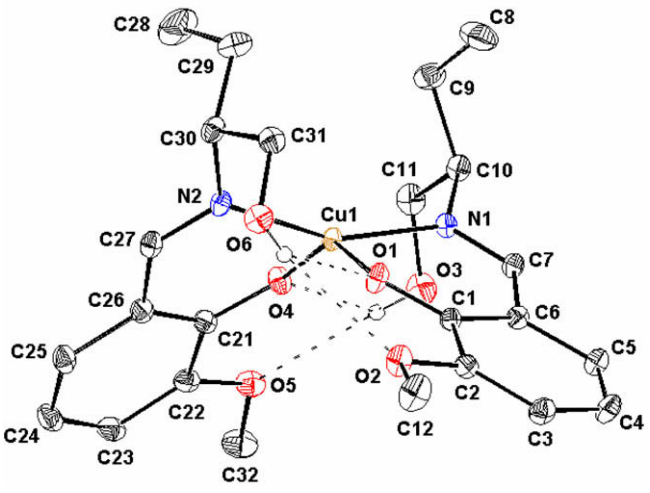


Fig. 5. Molecular structure and atom-labeling scheme of (**2**).

1.912(2) Å]. The bond lengths and angles around the Cu(II) ion in the title complex are in good agreement with the values found in similar copper complexes [22,23,28].

Complex (**1**) contains rings A (Cu1/N1/C7/C6/C1/O1), B (C1/C2/C3/C4/C5/C6), C (Cu1/N2/C15/C14/C9/O3) and D (C9/C10/C11/C12/C13/C14), and the dihedral angles between A/B, A/C, A/D, B/C, B/D and C/D are 2.19(12)°, 34.76(9)°, 41.84(11)°, 36.93(12)°, 43.97(14)° and 7.69(11)°, respectively. In our previous work, the *o*-vanillinato ligands were in a *cis* configuration and the dihedral angles were 3.45(11)°, 6.53(10)°, 6.47(11)°, 3.20(11)°, 4.21(12)°, 2.91(13)° and 20.47° (10)°, respectively, in the *cis*-aquabis(*o*-vanillinato)copper(II) compound [28].

The title compound does not display classical hydrogen bonds, π–π or π-ring interactions, but there are three intra- and seven inter-molecular C–H···O hydrogen bonds (Table 3, Fig. 4). These C–H···O interactions employ most of the available topological features to stabilize the crystal structure.

3.4.2. Bis[(R)-(−)-hydroxymethylpropylimine o-vanillinato]copper(II) (**2**)

The molecular structure and packing diagrams of (**2**) are illustrated in Figs. 5 and 6, respectively. A summary of the crystallographic data, experimental details, and refinement results for (**2**) are given in Table 1. The crystal structure determination of (**2**) reveals that the local coordination geometry around the Cu(II) center is tetrahedrally distorted square planar. In the *trans*-[CuN_2O_2] coordination, the bond angels of N(1)–Cu(1)–N(2), O(4)–Cu(1)–O(3), O(4)–Cu(1)–N(1) and O(4)–Cu(1)–N(2) are 157.35(11)°, 141.83(10)°, 93.66(8)° and 92.85(8)°, respectively. Selected bond distances are listed in Table 2. The Cu(1)–O(3) and Cu(1)–O(4) distances of 1.9074(19) and 1.9032(19) Å, respectively, are similar to the corresponding values in bis(*o*-vanillinato)-triethylenglycoldiiminecopper(II) [Cu–O = 1.912(2) and 1.891(2) Å]. The Cu(1)–N(1) and Cu(1)–N(2) bond distances of 1.953(2) and 1.955(3) Å, respectively are also similar to the corresponding values of similar complexes (1.949(7)–1.962(7) Å) [2]. The Schiff base acts as a bidentate ligand and chelates to Cu(II) through the O atom and N atom. The bond angles are 94.35(8)° for O(3)–Cu(1)–N(1) and 92.85(8)° for O(4)–Cu(1)–N(2), which are reasonable near the ideal angle of 90° in a regular square planar. The dihedral angels between the Cg1 and Cg2 (Cg1 = C1/C2/C3/C4/C5/C6, Cg2 = C21/C22/C23/C24/C25/C26), Cg1 and the Cu1/N1/C7/C10 plane, Cg2 and the Cu1/N2/C27/C30 plane are 79.15(9)°, 15.36(9)°, 22.65(1)°, respectively.

Complex **(2)** has four classical intramolecular-hydrogen bonds, four intermolecular-hydrogen C–H···O bonds and four C–H···π interactions (Table 3, Fig. 6). Both hydrogen-bonding and C–H···π

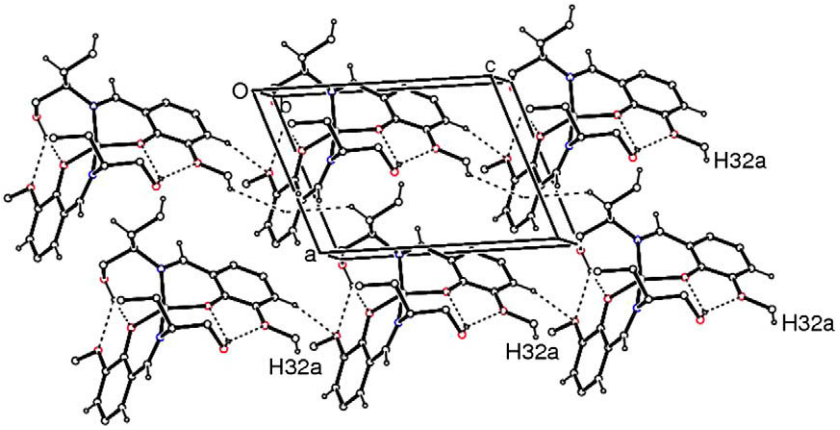


Fig. 6. An ORTEP ([27]) view of the packing diagram of (**2**) along the *c*-axis [hydrogen-bonding and π–π stacking (dashed lines). H atoms not involved in hydrogen-bonding have been omitted].

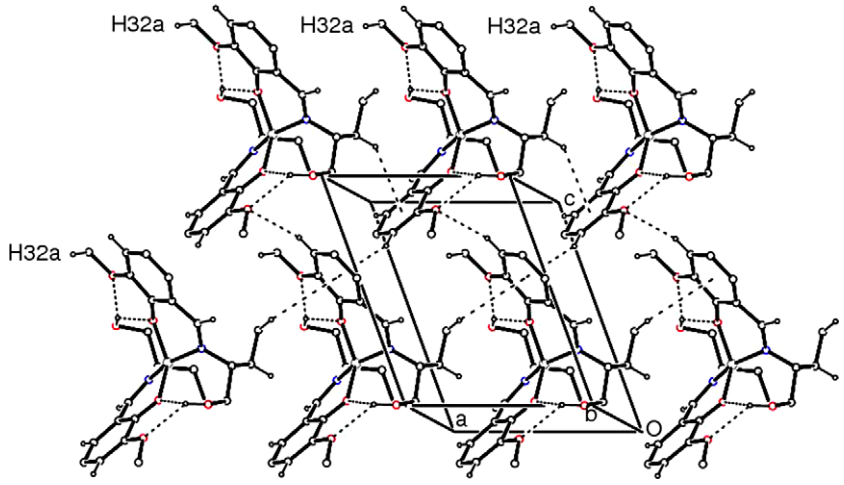


Fig. 7. An ORTEP ([27]) view of the packing diagram of (**2**) along the *a*-axis [hydrogen-bonding and π–π stacking (dashed lines). H atoms not involved in hydrogen-bonding have been omitted].

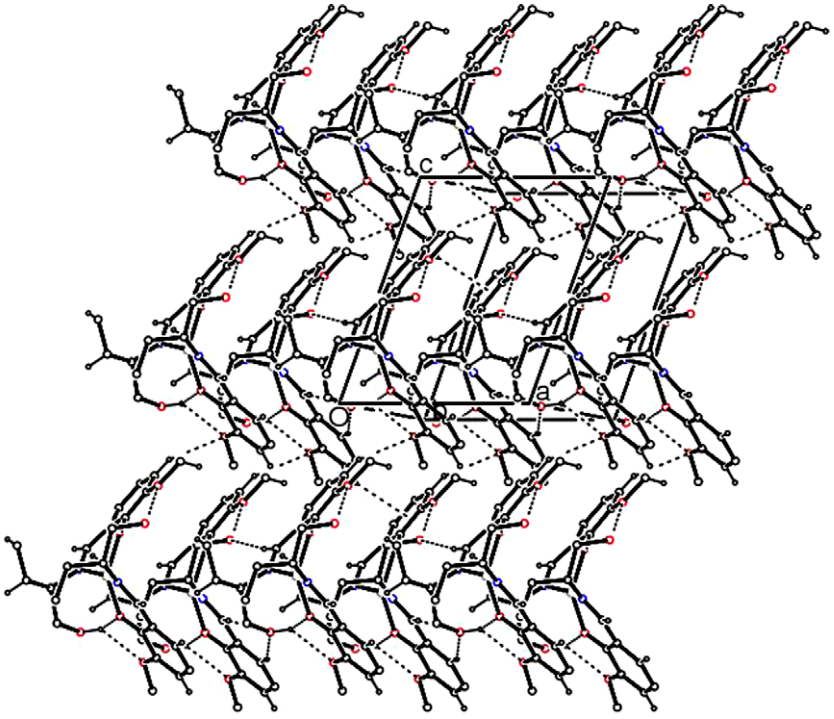


Fig. 8. An ORTEP ([27]) view of the packing diagram of (**2**) [hydrogen-bonding and π–π stacking (dashed lines). H atoms not involved in hydrogen-bonding have been omitted].

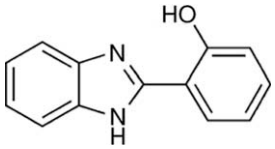
interactions combine to stabilize the extended structure (Figs. 7 and 8). The C3–H3···Cg2$^{(viii)}$ [(viii): $1+x$, y, $-1+z$; 145.70°], C28–H28···Cg2$^{(viii)}$ [132.50°], C29–H29···Cg1$^{(ix)}$ [(ix): $-1+x$, y, z; 133.26°] C32–H32···Cg1$^{(ix)}$ [124.65°] are 2.6816(4), 3.3316(5), 3.2024(4), 2.7181(4) Å, respectively.

Supplementary data

CCDC 719334 and 719335 contain the supplementary crystallographic data for this paper. These data can be obtained free of charge via http://www.ccdc.cam.ac.uk/conts/retrieving.html, or from the Cambridge Crystallographic Data Centre, 12 Union Road, Cambridge CB2 1EZ, UK; fax: (+44) 1223-336-033; or e-mail: deposit@ccdc.cam.ac.uk.

References

[1] Z. Guoliang, F. Yunlong, W. Yihang, J. Rare Earth 24 (2006) 268.
[2] A.A. Khandar, K. Nejati, Polyhedron 19 (2000) 607.
[3] A. Nabei, T. Kuroda-Sowa, T. Okubo, M. Maekawa, M. Munakata, Inorg. Chim. Acta 361 (2008) 3489.
[4] L.C. Nathan, J.E. Koehne, J.M. Gilmore, K.A. Hannibal, W.E. Dewhirst, T.D. Mai, Polyhedron 22 (2003) 887.
[5] W.-Y. Bi, X.-Q. Lü, W.-L. Chai, J.-R. Song, W.-Y. Wong, W.-K. Wong, R.A. Jones, J. Mol. Struct. 891 (2008) 450.
[6] R.C. Maurya, P. Patel, S. Rajput, Synth. React. Inorg. Met.-Org. Chem. 33 (2003) 817.
[7] N.S. Enikolopyan, K.A. Bogdanova, K.A. Askarov, Russ. Chem. Rev. 52 (1983) 13.
[8] H. Zhang, S. Xiang, J. Xiao, C. Li, J. Mol. Catal. A: Chem. 238 (2005) 175.
[9] T. Katsuki, Chem. Soc. Rev. 33 (2004) 437.
[10] P.J. McCarthy, R.J. Hovey, K. Veno, A.E. Martell, J. Am. Chem. Soc. 77 (1955) 5820.
[11] J.K. Barton, Science 233 (1986) 727.
[12] C.J. Burrows, J.G. Muller, Chem. Rev. 98 (1998) 1109.
[13] K.E. Erkkila, D.T. Odom, J.K. Barton, Chem. Rev. 99 (1999) 2777.
[14] S. Delaney, M. Pascaly, P.K. Bhattacharya, K. Han, J.K. Barton, Inorg. Chem. 41 (2002) 1966.
[15] A.J. Crowe, P.J. Smith, G. Atassi, Chem. Biol. Interact. 32 (1980) 171.
[16] M. Wang, L.F. Wang, Y.Z. Li, Trans. Met. Chem. 26 (2001) 307.
[17] S.D. Dhumwad, K.B. Gudasi, T.R. Go-dar, Indian J. Chem. 33A (1994) 320.
[18] K.H. Reddy, P.S. Reddy, P.R. Bab, Trans. Met. Chem. 25 (2000) 154.
[19] H. Singh, S.L.D. Yadav, S.B.S. Mishra, J. Inorg. Nucl. Chem. 43 (1981) 1701.
[20] N.K. Singh, S.B. Singh, Indian J. Chem. 40A (2001) 1070.
[21] V. Mishra, S.N. Pandeya, S. Anathan, Acta Pharm. Turc. 42 (2000) 139.
[22] L.C. Nathan, C.A. Traina, Polyhedron 22 (2003) 3213.
[23] L.Z. Zhang, P.-Y. Bu, L.-J. Wang, P. Cheng, Acta Crystallogr., C 57 (2001) 1166.
[24] Stoe and Cie, X-AREA (Version 1.18) and X-RED32 (Version 1.04), Stoe and Cie, Darmstadt, Germany, 2002.
[25] G.M. Sheldrick, SHELXS97 and SHELXL97. University of Gottingen, Germany, 1997.
[26] L.J. Farrugia, J. Appl. Crystallogr. 30 (1997) 565.
[27] L.J. Farrugia, WINGX – A Windows Program for Crystal Structure Analysis, University of Glasgow, Scotland, 1999.
[28] M. Odabaşoğlu, F. Arslan, H. Ölmez, O. Büyükgüngör, Dyes Pigments 75 (2007) 507.



Scheme 1. Structure of Hhpb ligand.

As an extension of this work, we decided to examine the reactivity of $[ReOX_3(EPh_3)_2]$ (X = Cl, Br; E = As, P) towards 2-(2-hydroxyphenyl)-1H-benzimidazole (Hhpb, Scheme 1).

Imidazole and its derivatives are an important class of heterocycle with N-donor atoms, which can be excellent organic ligands to generate various complexes upon ligation. Recently some new cobalt(II), copper(II) and zinc(II) coordination compounds with 2-(benzimidazol-2-yl)phenolato ligand have been synthesized and characterized [16–20]. As far as rhenium compounds are concerned, only one complex with the relative ligand 2-(1-methyl-1H-benzimidazol-2-yl)phenolato has been obtained so far [21].

Here, we present the synthesis, structural and spectroscopic characterization of *trans*-$[ReOCl_2(hpb)(PPh_3)]$ (**1a**), *cis*-$[ReOCl_2(hpb)(PPh_3)]$ (**1b**), *trans*-$[ReOBr_2(hpb)(PPh_3)]$ (**2a**), *cis*-$[ReOBr_2(hpb)(PPh_3)]$ (**2b**), *cis*-$[ReOCl_2(hpb)(AsPh_3)]$ (**3**), *cis*-$[ReOBr_2(hpb)(AsPh_3)]$ (**4**) and $[ReO(OMe)(hpb)_2]\cdot MeCN$ (**5**) complexes. The experimental studies have been accompanied computationally by the density functional theory (DFT) and time-dependent DFT calculations. Currently density functional theory (DFT) is commonly used to examine the electronic structure of transition metal complexes. It meets with the requirements of being accurate, easy to use and fast enough to allow the study of relatively large molecules of transition metal complexes [22,23].

2. Experimental

2.1. General procedure

All the reagents used to the synthesis were commercially available and were used without further purification. The $[ReOX_3(PPh_3)_2]$ and $[ReOX_3(AsPh_3)_2]$ complexes were prepared according to the literature methods [24].

IR spectra were recorded on a Nicolet Magna 560 spectrophotometer in the spectral range 4000–400 cm^{-1} with the samples

Table 1
Crystal data and structure refinement for **1a**, **1b**, **2a**, **3**, **4** and **5**.

	1a	**1b**	**2a**	**3**	**4**	**5**
Empirical formula	$C_{31}H_{24}Cl_2N_2O_2PRe$	$C_{31}H_{24}Cl_2N_2O_2PRe$	$C_{31}H_{24}Br_2N_2O_2PRe$	$C_{31}H_{24}AsCl_2N_2O_2Re$	$C_{31}H_{24}AsBr_2N_2O_2Re$	$C_{29}H_{24}N_5O_4Re$
Formula weight	744.59	744.59	833.51	788.54	877.46	692.73
T [K]	293.0(2)	293.0(2)	293.0(2)	293.0(2)	293.0(2)	293.0(2)
Wavelength [Å]	0.71073	0.71073	0.71073	0.71073	0.71073	0.71073
Crystal system	orthorhombic	triclinic	orthorhombic	triclinic	triclinic	monoclinic
Space group	*Pbca*	$P\bar{1}$	*Pbca*	$P\bar{1}$	$P\bar{1}$	$P2_1/n$
Unit cell dimensions						
a [Å]	8.9609(7)	13.7024(6)	9.0389(3)	13.8479(10)	13.847(2)	12.1795(4)
b [Å]	18.2096(11)	13.7427(6)	18.4507(8)	14.2676(12)	13.915(2)	17.4605(7)
c [Å]	33.690(2)	17.4581(8)	34.4156(12)	17.3595(13)	17.664(3)	12.5971(5)
α [°]	90	107.618(4)	90	108.233(7)	104.409(14)	90.0
β [°]	90	104.623(4)	90	102.945(6)	107.367(14)	99.764(3)
γ [°]	99.764(3)	94.458(8)	90	96.284(6)	95.505(13)	90.0
V [Å^3]	5497.3(5)	2989.2(2)	5739.6(4)	3114.5(4)	3092.4(9)	2640.10(17)
Z	8	4	8	4	4	4
Density (calculated) [Mg/m^3]	1.799	1.655	1.929	1.682	1.885	1.743
Absorption coefficient [mm^{-1}]	4.707	4.328	7.106	5.157	7.605	4.648
F(0 0 0)	2912	1456	3200	1528	1672	1360
Crystal size [mm]	0.04 × 0.08 × 0.2	0.048 × 0.10 × 0.18	0.05 × 0.07 × 0.24	0.10 × 0.10 × 0.14	0.09 × 0.2 × 0.24	0.10 × 0.20 × 0.30
θ Range for data collection [°]	2.81–25.00	2.98–25.00	2.77– 25.00	2.99–25.00	3.08–25.00	2.85–25.00
Index ranges	$-6 \leqslant h \leqslant 10$, $-20 \leqslant k \leqslant 21$, $-40 \leqslant l \leqslant 39$	$-16 \leqslant h \leqslant 16$, $-16 \leqslant k \leqslant 10$, $-20 \leqslant l \leqslant 20$	$-9 \leqslant h \leqslant 10$, $-21 \leqslant k \leqslant 21$, $-40 \leqslant l \leqslant 39$	$-16 \leqslant h \leqslant 14$, $-16 \leqslant k \leqslant 16$, $-16 \leqslant l \leqslant 20$	$-13 \leqslant h \leqslant 16$, $-16 \leqslant k \leqslant 16$, $-21 \leqslant l \leqslant 17$	$-14 \leqslant h \leqslant 14$, $-17 \leqslant k \leqslant 20$, $-14 \leqslant l \leqslant 14$
Reflections collected	31 349	19 004	34 199	17 712	11 553	16 122
Independent reflections	4832 (R_{int} = 0.0745)	10 243 (R_{int} = 0.0238)	5054 (R_{int} = 0.0543)	10 981 (R_{int} = 0.0952)	10 921 (R_{int} = 0.0306)	4626 (R_{int} = 0.0181)
Completeness to 2θ = 25° [%]	99.7	97.3	99.8	99.9	99.9	99.4
Minimum and maximum transmission	0.598 and 0.814	0.598 and 0.814	0.558 and 0.697	0.548 and 0.601	0.179 and 0.500	0.338 and 0.632
Data/restraints/parameters	4832/0/352	10 243/0/703	5054/0/352	10 981/0/703	10 921/0/703	4626/0/354
Goodness-of-fit (GOF) on F^2	1.040	0.949	0.989	1.063	0.957	1.048
Final R indices [$I > 2\sigma(I)$]	R_1 = 0.0395, wR_2 = 0.0641	R_1 = 0.0229, wR_2 = 0.0372	R_1 = 0.0227, wR_2 = 0.0566	R_1 = 0.0507, wR_2 = 0.1439	R_1 = 0.0440, wR_2 = 0.1029	R_1 = 0.0163, wR_2 = 0.0412
R indices (all data)	R_1 = 0.0641, wR_2 = 0.0807	R_1 = 0.0409, wR_2 = 0.0386	R_1 = 0.0479, wR_2 = 0.0664	R_1 = 0.0893, wR_2 = 0.1870	R_1 = 0.0880, wR_2 = 0.1199	R_1 = 0.0227, wR_2 = 0.0427
Largest difference in peak and hole [e Å^{-3}]	1.622 and −1.115	0.832 and −0.446	0.927 and −0.794	3.205 and −4.424	1.877 and −1.447	0.543 and −0.409

in the form of KBr pellets. Electronic spectra were measured on a spectrophotometer Lab Alliance UV–VIS 8500 in the range 1100–180 nm. Elemental analyses (C, H, N) were performed on a Perkin–Elmer CHN-2400 analyzer. ^{1}H NMR spectrum was obtained in $CDCl_3$ using Bruker Avance 400 spectrometer.

2.2. Preparation of [$ReOCl_2$(hpb)(PPh_3)] (**1a** and **1b**)

[$ReOCl_3(PPh_3)_2$] (0.50 g, 0.6 mmol) was added to 2-(2-hydroxyphenyl)-1H-benzimidazole (0.13 g, 0.62 mmol) in acetonitrile (50 ml) and the reaction mixture was refluxed for 2 h. The resulting solution was reduced in volume to ~10 ml and allowed to cool to room temperature. A green crystalline precipitate of [$ReOCl_2$(hpb)(PPh_3)] was filtered off and dried in the air. Yield 80%.

Single crystals of *trans*-[$ReOCl_2$(hpb)(PPh_3)] (**1a**) and *cis*-[$ReOCl_2$(hpb)(PPh_3)] (**1b**) were obtained by recrystallization from acetonitrile, and they were collected in 10% and 70% yield, respectively. Crystals of **1a** and **1b** were separated using microscope.

Anal. Calc. for $C_{31}H_{24}PCl_2N_2O_2Re$: C, 50.00; H, 3.25; N, 3.76. Found: C, 50.45; H, 3.45; N, 3.59%.

IR of **1a** (KBr; ν/cm^{-1}): 3249 (m) ν_{NH}, 1620 (w), 1603 (m), 1568 (w) and 1535 (m) ν_{CN} and $\nu_{C=C}$; 962 (s) $\nu_{Re=O}$.

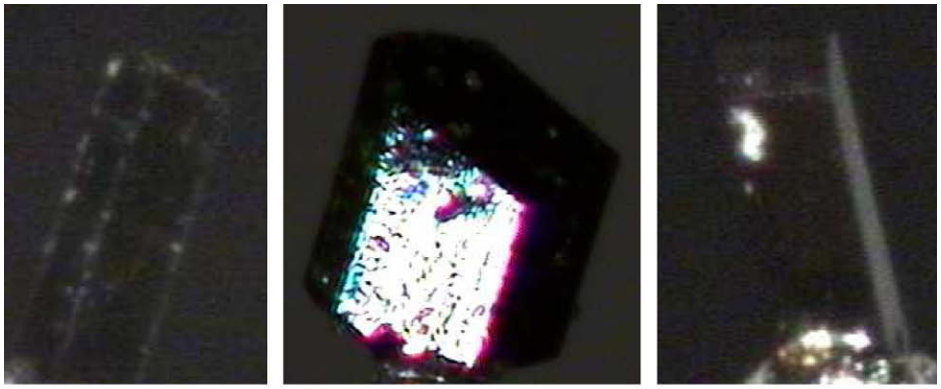
IR of **1b** (KBr; ν/cm^{-1}): 3211 (m) ν_{NH}, 1622 (w), 1602 (m), 1571 (w) and 1536 (w) ν_{CN} and $\nu_{C=C}$; 968(s) $\nu_{Re=O}$.

^{1}H NMR of **1a** (400 MHz; DMSO) δ = 14.03 (1H, N–H), 8.11 (d, 1H,), 7.89 (d, 1H). 7.88–7.74 (m, 5H), 7.68 (d, 1H), 7.64–7.52 (m, 10H), 7.51 (t, 1H), 7.43 (t, 1H), 7.18–7.10 (m, 2H), 5.76 (d, 1H).

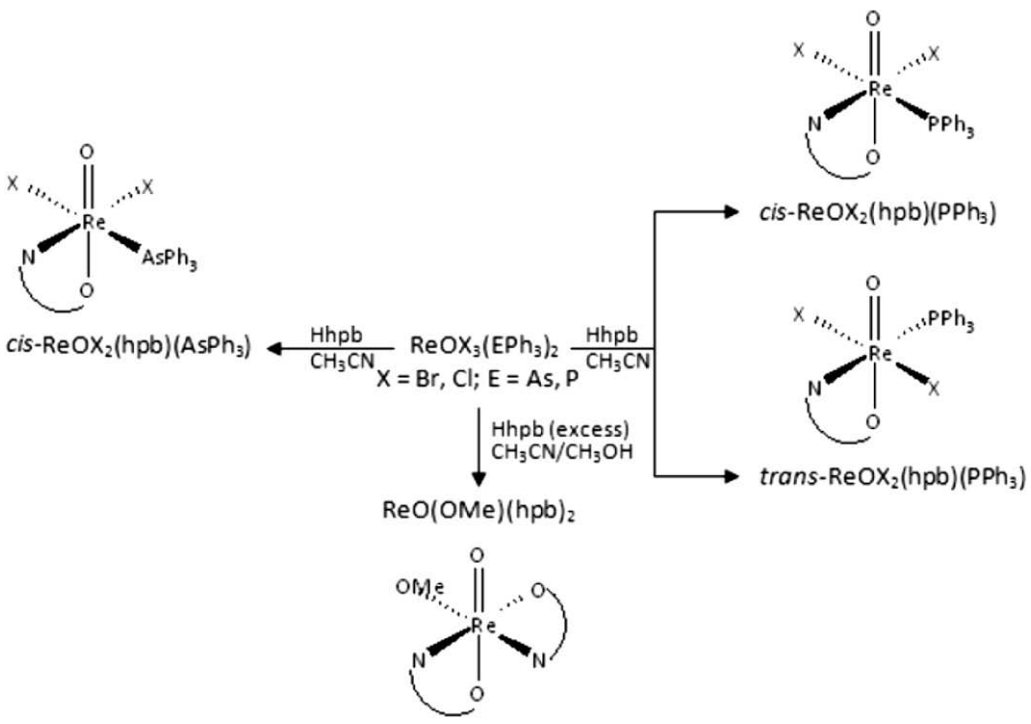
^{1}H NMR of **1b** (400 MHz; DMSO) δ = 13.58 (1H, N–H), 7.72 (d, 1H,), 7.66–7.52 (m, 5H), 7.48–7.38 (m, 4H), 7.31–7.19 (m, 10H), 7.03 (d, 1H), 6.96 (t, 1H), 6.80 (d, 1H).

UV–Vis of **1a** (CH_3CN; λ_{max} [nm] (ε; [dm^3 mol^{-1} cm^{-1}])): 635.8 (50), 397.7 (3400), 302.2 (21 500), 225.1 (46 180) and 201.3 (10 8300).

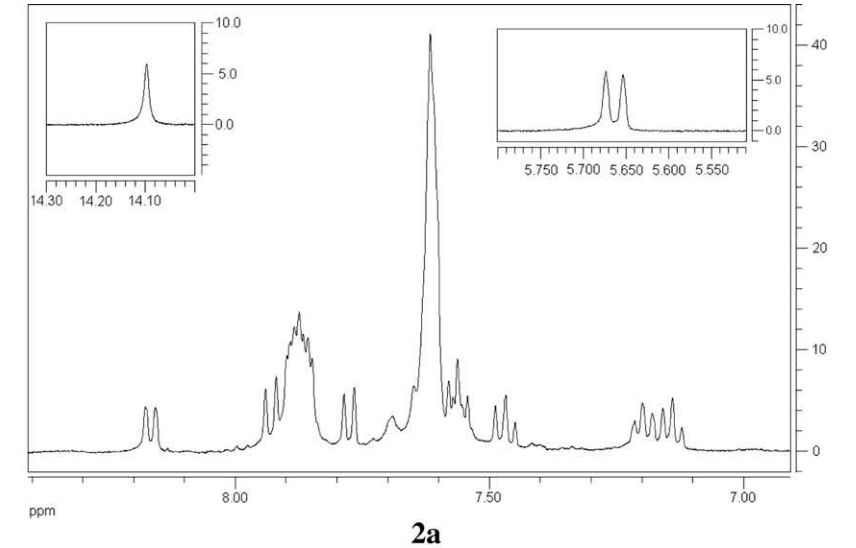
UV–Vis of **1b** (CH_3CN; λ_{max} [nm] (ε; [dm^3 mol^{-1} cm^{-1}])): 651.1 (25), 408.0 (1000), 309.2 (9950), 230.5 (22 650), 207.5 (46 430).



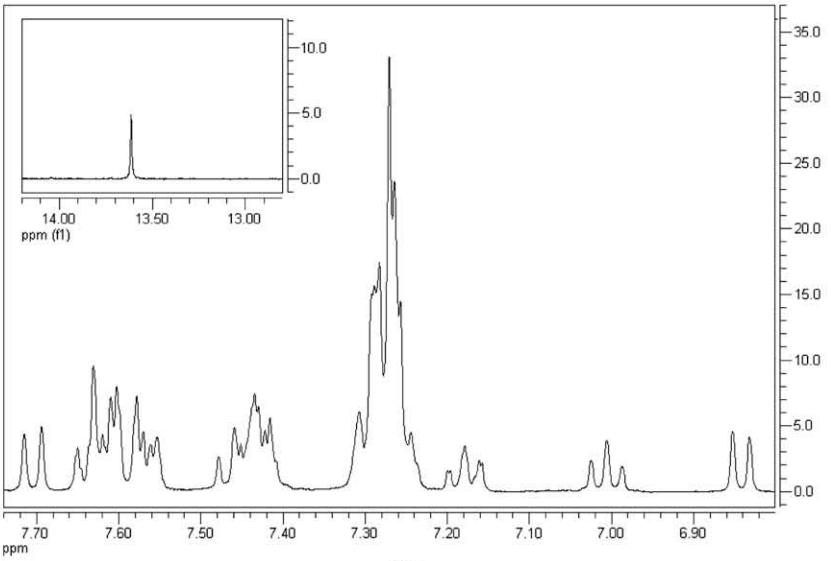
1a 1b 2a



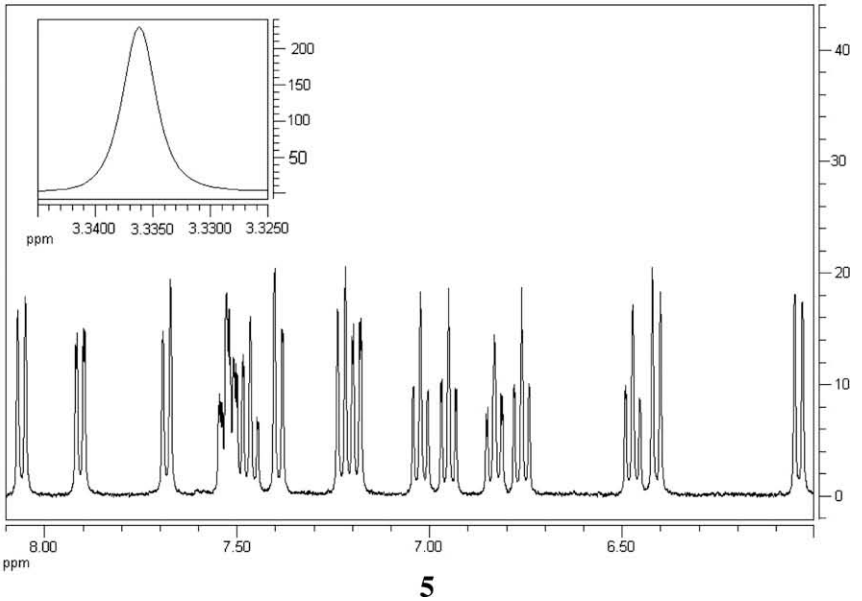
Scheme 2.



2a



2b



5

Fig. 1. ^{1}H NMR spectra of **2a**, **2b** and **5**.

Table 2
Short intra- and intermolecular contacts detected in **1a**, **1b**, **2a**, **3, 4** and **5** complexes.

D–H···A	D–H	H···A	D···A	D–H···A
1a				
N2 H2N Cl2_$1	0.86	2.41	3.247(5)	163.2
C8 H8 O1	0.93	2.46	3.259(8)	144.7
C15 H15 Cl2_$2	0.93	2.80	3.496(7)	132.6
C27 H27 O1	0.93	2.51	3.094(8)	121.0
1b				
N2 H2 Cl3	0.86	2.40	3.228(3)	162.1
N4 H4 Cl2_$3	0.86	2.47	3.299(3)	162.8
C8 H8 O1	0.93	2.54	2.940(4)	106.3
C17 H17 O2_$4	0.93	2.54	3.384(4)	150.3
C18 H18 O2	0.93	2.45	3.197(4)	137.6
C27 H27 O1	0.93	2.27	2.883(5)	122.6
C43 H43 Cl4	0.93	2.75	3.612(4)	153.8
C49 H49 O3	0.93	2.57	3.130(4)	118.9
C58 H58 O3	0.93	2.27	2.893(4)	123.8
2a				
N2 H2A Br1_$5	0.86	2.55	3.393(5)	166.1
C2 H2 O1	0.93	2.49	3.294(7)	145.0
C15 H15 Br1_$6	0.93	2.91	3.634(6)	136.1
C27 H27 O1	0.93	2.50	3.073(7)	120.4
3				
N2 H2N Cl3	0.86	2.41	3.239(11)	160.7
N4 H4N Cl2_$3	0.86	2.42	3.274(10)	170.5
C5 H5 Cl1_$4	0.93	2.80	3.581(12)	142.3
C6 H6 O2	0.93	2.59	3.340(17)	137.9
C27 H27 O1	0.93	2.32	2.918(18)	121.3
C46 H46 O4_$7	0.93	2.59	3.500(14)	165.6
C54 H54 Cl2_$3	0.93	2.83	3.747(13)	169.2
C61 H61 O3	0.93	2.36	2.936(15)	119.8
4				
N2 H2 Br3	0.86	2.53	3.357(11)	160.6
N4 H4 Br2_$8	0.86	2.70	3.541(10)	165.8
C8 H8 O2	0.93	2.58	3.337(15)	138.6
C9 H9 O2_$9	0.93	2.59	3.445(16)	153.4
C27 H27 O1	0.93	2.39	2.978(18)	121.5
C54 H54 N4	0.93	2.60	2.91(2)	100.2
C58 H58 O3	0.93	2.40	2.972(17)	120.0
5				
N2 H2 N99	0.86	2.10	2.937(4)	165.9
N4 H4 O2_$10	0.86	1.87	2.692(3)	158.9
C2 H2A O1	0.93	2.59	3.140(4)	118.4
C22 H22 N4	0.93	2.53	2.858(3)	100.8
C27 H27C O4	0.96	2.36	2.785(4)	106.3
C98 H98A O3_$11	0.96	2.36	3.282(4)	160.7

Symmetry transformations used to generate equivalent atoms: #1: 1/2 + *x*,*y*,1/2−*z*; #2: 1/2−*x*,1/2 + *y*,*z*; #3: 1−*x*,1−*y*,1−*z*; #4 1−*x*,2−*y*,1−*z*; #5: −1/2 + *x*,*y*,1/2−*z*; #6 3/2−*x*,−1/2 + *y*,*z*; #7: −*x*,−*y*,−*z*; #8: 2−*x*,1−*y*,1−*z*; #9: 3−*x*,1−*y*,1−*z*; #10: 1/2 + *x*,3/2−*y*,1/2 + *z*; #11: 1/2−*x*,−1/2 + *y*,3/2−*z*.

2.3. Preparation of [$ReOBr_2$(hpb)(PPh_3)] (**2a** and **2b**)

A procedure similar to that for **1** was used with [$ReOBr_3(PPh_3)_2$] (0.50 g, 0.52 mmol) and Hhpb (0.11 g, 0.52 mmol). Crystalline green precipitate of *trans*-[$ReOBr_2$(hpb)(PPh_3)] (**2a**) and *cis*-[$ReOBr_2$(hpb)(PPh_3)] (**2b**) were collected in 15% yield and 65%, respectively.

Anal. Calc. for $C_{31}H_{24}Br_2N_2O_2PRe$: C, 44.67; H, 2.90; N, 3.36. Found: C, 44.35; H, 2.79; N, 3.49%.

IR of **2a** (KBr; ν/cm^{-1}): 3254 (m) ν_{NH}, 1619 (w), 1602 (m), 1567 (m) and 1532 (m) ν_{CN} and $\nu_{C=C}$; 962 (s) $\nu_{Re=O}$.

IR of **2b** (KBr; ν/cm^{-1}): 3251 (m) ν_{NH}, 1618 (w), 1601 (m), 1570 (m) and 1533 (m) ν_{CN} and $\nu_{C=C}$; 963 (s) $\nu_{Re=O}$.

^{1}H NMR of **2a** (400 MHz; DMSO) δ = 14.10 (1H, N–H), 8.16 (d, 1H,), 7.93 (d, 1H), 7.91–7.83 (m, 5H), 7.77 (d, 1H), 7.67–7.59 (m, 10H), 7.56 (t, 1H), 7.47 (t, 1H), 7.22–7.12 (m, 2H), 5.66 (d, 1H).

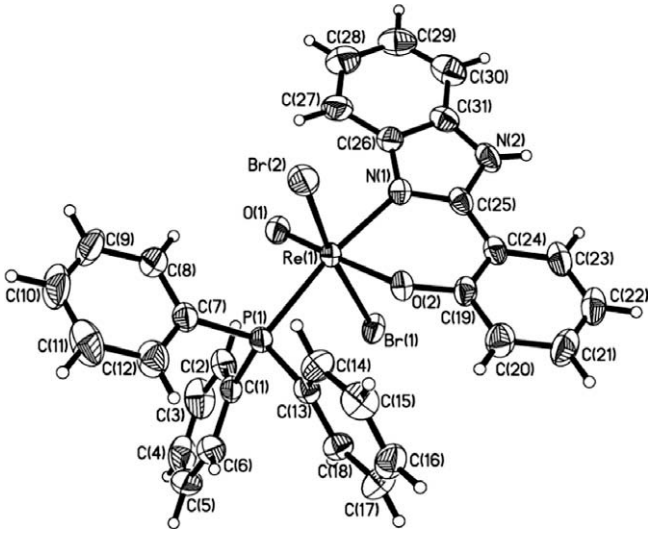


Fig. 2. The molecular structure of **2a**. Displacement ellipsoids are drawn at 50% probability.

^{1}H NMR of **2b** (400 MHz; DMSO) δ = 13.61 (1H, N–H), 7.71 (d, 1H,), 7.66–7.55 (m, 5H), 7.48–7.40 (m, 4H), 7.32–7.23 (m, 10H), 7.17 (t, 1H), 7.00 (t, 1H), 6.84 (d, 1H).

UV–Vis of **2a** (CH_3CN; λ_{max} [nm] (ε; [$dm^3\ mol^{-1}\ cm^{-1}$])): 649.8 (20), 407.6 (2250), 308.5 (16 950), 232.9 (32 950) and 209.3 (71 500).

UV–Vis of **2b** (CH_3CN; λ_{max} [nm] (ε; [$dm^3\ mol^{-1}\ cm^{-1}$])): 647.3 (290), 415.5 (3280), 310.0 (27 465), 224.4 (77 450) and 201.2 (16 5250).

2.4. Preparation of [$ReOCl_2$(hpb)($AsPh_3$)] (**3**)

A procedure similar to that for **1** was used with [$ReOCl_3(AsPh_3)_2$] (0.5 g, 0.54 mmol) and Hhpb (0.12 g, 0.57 mmol). Green crystals of *cis*-[$ReOCl_2$(hpb)($AsPh_3$)] were collected in 75% yield.

Anal. Calc. for $C_{31}H_{24}Cl_2N_2O_2AsRe$: C, 47.22; H, 3.07; N, 3.55. Found: C, 47.82; H, 3.01; N, 3.34%.

IR (KBr; ν/cm^{-1}): 3274 (m) ν_{NH}, 1620 (w), 1601 (m), 1570 (m) and 1536 (m) ν_{CN} and $\nu_{C=C}$; 964 (s) $\nu_{Re=O}$.

^{1}H NMR (400 MHz; DMSO) δ = 14.01 (1H, N–H), 8.18 (dd, 1H), 7.91–7.76 (m, 17H), 7.61 (d, 1H), 7.59–7.54 (m, 2H), 7.29 (d, 1H), 7.14 (t, 1H).

UV–Vis (CH_3CN; λ_{max} [nm] (ε; [$dm^3\ mol^{-1}\ cm^{-1}$])): 665.9 (40), 400.7 (1280), 300.0 (16 650), 243.3 (28 700), 198.1 (76 950).

2.5. Preparation of [$ReOBr_2$(hpb)($AsPh_3$)] (**4**)

A procedure similar to that for **1** was used with [$ReOBr_3(AsPh_3)_2$] (0.50 g, 0.47 mmol) and Hhpb (0.15 g, 0.47 mmol). Crystalline green precipitate of **4** was collected in 80% yield.

Anal. Calc. for $C_{31}H_{24}Br_2N_2O_2AsRe$: C, 42.43; H, 2.76; N, 3.19. Found: C, 42.89; H, 2.93; N, 3.35%.

IR (KBr; ν/cm^{-1}): 3254 (m) ν_{NH}, 1622 (w), 1598 (m), 1569 (m) and 1541 (m) ν_{CN} and $\nu_{C=C}$; 963 (s) $\nu_{Re=O}$.

^{1}H NMR (400 MHz; DMSO) δ = 14.10 (1H, N–H), 8.13 (dd, 1H), 7.91–7.77 (m, 17H), 7.61 (d, 1H), 7.58–7.56 (m, 2H), 7.27 (d, 1H), 7.16 (t, 1H).

UV–Vis (CH_3CN; λ_{max} [nm] (ε; [$dm^3\ mol^{-1}\ cm^{-1}$])): 665.9 (55), 398.8 (1350), 306.6 (21 000), 245.2 (28 500), 202.1 (85 000).

Table 3
The selected experimental and optimized bond lengths [Å] and angles [°] for **2a**.

Bond lengths	Experimental	Optimized	Bond angles	Experimental	Optimized
Re(1)–O(1)	1.691(4)	1.68441	O(1)–Re(1)–O(2)	172.22(17)	173.906
Re(1)–O(2)	1.935(4)	1.97921	O(1)–Re(1)–N(1)	94.08(18)	96.441
Re(1)–N(1)	2.146(4)	2.15168	O(2)–Re(1)–N(1)	80.98(16)	81.045
Re(1)–Br(1)	2.5800(6)	2.65593	O(1)–Re(1)–Br(1)	91.08(13)	91.524
Re(1)–Br(2)	2.5166(6)	2.61150	O(2)–Re(1)–Br(1)	82.67(11)	98.641
Re(1)–P(1)	2.4543(14)	2.52962	N(1)–Re(1)–Br(1)	86.67(12)	86.988
			O(1)–Re(1)–Br(2)	98.83(13)	98.641
			O(2)–Re(1)–Br(2)	87.23(11)	86.822
			N(1)–Re(1)–Br(2)	90.00(12)	87.324
			Br(1)–Re(1)–Br(2)	169.74(2)	168.849
			O(1)–Re(1)–P(1)	93.32(13)	92.996
			O(2)–Re(1)–P(1)	91.29(11)	89.535
			N(1)–Re(1)–P(1)	171.80(13)	170.559
			Br(1)–Re(1)–P(1)	89.68(4)	92.495
			Br(2)–Re(1)–P(1)	92.34(4)	91.544

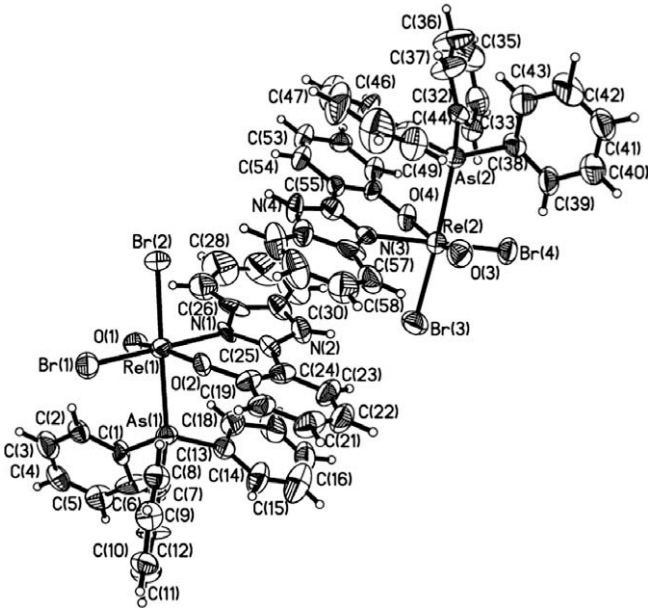


Fig. 3. The molecular structure of **4**. Displacement ellipsoids are drawn at 50% probability.

2.6. Preparation of [ReO(OMe)(hpb)$_2$]·MeCN (**5**)

[$ReOBr_3(AsPh_3)_2$] (0.50 g, 0.47 mmol) was added to 2-(2-hydroxyphenyl)-1H-benzimidazole (0.23 g, 1.10 mmol) in a mixture of acetonitrile (50 ml) and methanol (50 ml), and the reaction mixture was refluxed for 6 h. The resulting solution was allowed to cool to room temperature and reduced in volume to ~10 ml. A blue crystalline precipitate of [ReO(OMe)(hpb)$_2$]·MeCN was filtered off and dried in the air. Yield 75%.

Anal. Calc. for $C_{29}H_{24}N_5O_4Re$: C, 50.28; H, 3.49; N, 10.11. Found: C, 50.97; H, 3.63; N, 10.47%

IR (KBr; ν/cm^{-1}): 3228 (m) ν_{NH}, 1624 (m), 1603 (s), 1564 (s) and 1541 (s) ν_{CN} and $\nu_{C=C}$; 955 (s) $\nu_{Re=O}$.

^{1}H NMR (400 MHz; CD_3OD) δ = 8.06 (d, 1H), 7.91 (dd, 1H), 7.68 (d, 1H), 7.55–7.45 (m, 3H), 7.39 (dd, 1H), 7.22 (d, 1H), 7.19 (dd, 1H,), 7.02 (dt, 1H), 6.95 (dt, 1H), 6.83 (dt, 1H), 6.76 (dt, 1H), 6.47 (dt, 1H), 6.41 (d, 1H), 6.04 (d, 1H), 3.34 (s, 3H).

2.7. Crystal structures determination and refinement

The X-ray intensity data of **1a**, **1b**, **2a**, **3, 4** and **5** were collected on a KM-4-CCD automatic diffractometer equipped with CCD detector and graphite monochromated Mo Kα radiation (λ = 0.71073 Å) at room temperature. Details concerning crystal data and refinement are given in Table 1. Lorentz, polarization and empirical absorption correction using spherical harmonics implemented in SCALE3 ABSPACK scaling algorithm [25] were applied. The structures were solved by the Patterson method and subsequently completed by the difference Fourier recycling. All the non-hydrogen atoms were refined anisotropically using full-matrix, least-squares technique. The hydrogen atoms were treated as "riding" on their parent carbon atoms and assigned isotropic temperature factors equal 1.2 (non-methyl) and 1.5 (methyl) times the value of equivalent temperature factor of the parent atom. The methyl groups were allowed to rotate about their local threefold axis. SHELXS97 [26], SHELXL97 [27] and SHELXTL [28] programs were used for all the calculations. Atomic scattering factors were those incorporated in the computer programs.

2.8. Computational details

The gas phase ground state geometries of **2a**, **4** and **5** were optimized without any symmetry restrictions with the DFT method using the hybrid B3LYP functional of GAUSSIAN-03 [29–31]. The calculations were performed using ECP LANL2DZ basis set [32] with an additional *d* and *f* function with the exponent α = 0.3811 and 2.033 [33] for rhenium and the standard 6-31G basis set for other atoms. For bromine, oxygen, nitrogen and phosphorous atoms, diffuse and polarization functions were added [34–39]. All vibrations in the calculated vibrational spectra of **2a**, **4** and **5** were real thus the geometries correspond to true energy minimum.

The electronic spectra of **2a**, **4** and **5** were calculated with the TDDFT method [40], and the solvent effect (acetonitrile for **2a** and **4**, and methanol for **5**) was simulated using the polarizable continuum model with the integral equation formalism (IEF-PCM) [41–44].

Natural bond orbital (NBO) calculations were performed with the NBO code [45] included in GAUSSIAN03.

3. Results and discussion

3.1. Preparation and infrared data

The [$ReOX_2$(hpb)(EPh_3)] (X = Cl, Br; E = As, P) complexes were prepared in good yield by ligand exchange reactions starting from [$ReOX_3(EPh_3)_2$] complexes and 2-(2-hydroxyphenyl)-1H-benzimidazole (Hhpb) in acetonitrile:

$$[ReOX_3(EPh_3)_2] + Hhpb \rightarrow [ReOX_2(hpb)(EPh_3)] + HX + EPh_3$$
$$X = Cl,\ Br;\ E = As,\ P$$

Table 4
The selected experimental and optimized bond lengths [Å] and angles [°] for **4**.

Bond lengths	Experimental	Optimized	Bond angles	Experimental	Optimized
Re(1)–O(1)	1.684(8)	1.68102	O(1)–Re(1)–O(2)	167.2(3)	164.184
Re(1)–O(2)	1.945(7)	1.99998	O(1)–Re(1)–N(1)	90.5(4)	90.666
Re(1)–N(1)	2.133(10)	2.17123	O(2)–Re(1)–N(1)	82.2(4)	80.877
Re(1)–Br(1)	2.5144(16)	2.57904	O(1)–Re(1)–Br(1)	98.7(3)	99.292
Re(1)–Br(2)	2.5315(14)	2.57472	O(2)–Re(1)–Br(1)	89.2(2)	90.093
Re(1)–As(1)	2.5618(13)	2.66761	N(1)–Re(1)–Br(1)	170.6(3)	169.611
			O(1)–Re(1)–Br(2)	98.0(3)	101.563
			O(2)–Re(1)–Br(2)	92.1(2)	91.174
			N(1)–Re(1)–Br(2)	86.6(3)	85.716
			Br(1)–Re(1)–Br(2)	89.86(5)	89.368
			O(1)–Re(1)–As(1)	84.1(3)	83.804
			O(2)–Re(1)–As(1)	85.8(2)	83.562
			N(1)–Re(1)–As(1)	93.2(3)	94.468
			Br(1)–Re(1)–As(1)	90.06(5)	89.577
			Br(2)–Re(1)–As(1)	177.89(5)	174.630
Re(2)–O(3)	1.672(9)		O(3)–Re(2)–O(4)	166.6(4)	
Re(2)–O(4)	1.941(8)		O(3)–Re(2)–N(3)	92.3(4)	
Re(2)–N(3)	2.162(10)		O(4)–Re(2)–N(3)	81.4(4)	
Re(2)–Br(4)	2.5140(15)		O(3)–Re(2)–Br(4)	98.0(3)	
Re(2)–Br(3)	2.5339(16)		O(4)–Re(2)–Br(4)	88.8(2)	
Re(2)–As(2)	2.5689(14)		N(3)–Re(2)–Br(4)	169.6(3)	
			O(3)–Re(2)–Br(3)	100.8(3)	
			O(4)–Re(2)–Br(3)	90.9(3)	
			N(3)–Re(2)–Br(3)	88.6(2)	
			Br(4)–Re(2)–Br(3)	87.95(5)	
			O(3)–Re(2)–As(2)	82.4(3)	
			O(4)–Re(2)–As(2)	85.7(3)	
			N(3)–Re(2)–As(2)	89.4(2)	
			Br(4)–Re(2)–As(2)	93.46(5)	
			Br(3)–Re(2)–As(2)	176.32(5)	

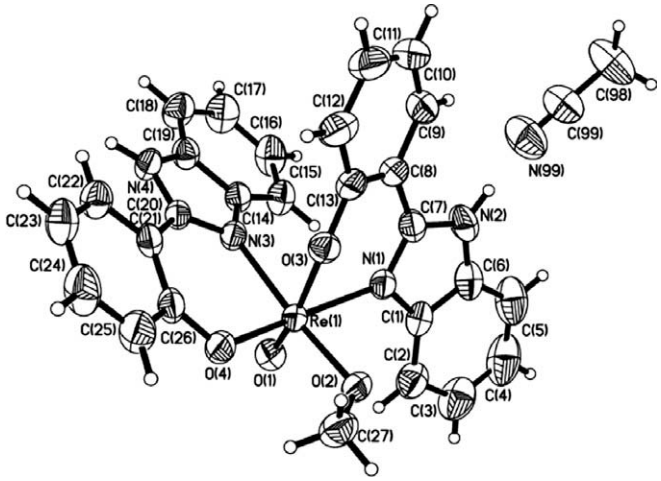


Fig. 4. The molecular structure of **5**. Displacement ellipsoids are drawn at 50% probability.

The starting arsine oxocompounds react with Hhpb to give only *cis*-[$ReOX_2(hpb)(AsPh_3)$] (**3** and **4**), whereas the reactions of [$ReOX_3(PPh_3)_2$] with 2-(2-hydroxyphenyl)-1H-benzimidazole lead to a mixture of *cis* and *trans* stereoisomers of [$ReOX_2(hpb)(PPh_3)$] (**1a**, **1b**, **2a** and **2b**). The majority of the known [$ReOX_2$(O–N)(PPh_3)] structures has halide ligands in *cis* arrangement. The *trans-Cl,Cl* conformation is far more rarely in this type of complex, and it has been previously confirmed for [$ReCl_2(APO)(PPh_3)$] and [$ReOCl_2(DPO)(PPh_3)$] (APOH = 4-anilino-3-penten-2-one; DPOH = 4-[2,6-dimethylanilino]-3-penten-2-one) [46]. It is interesting to note that mixture of *cis* and *trans* stereoisomers were also isolated from the analogous reactions of [$ReOX_3(PPh_3)_2$] with 2-(2′-hydroxyphenyl)-2-benzothiazole, whereas reactions of [$ReOX_3(EPh_3)_2$] (E = P, As) with related 2-(2′-hydroxyphenyl)-2-benzoxazoline have resulted in the isolation only [$ReOX_2$(N–O)(EPh_3)] with *cis*-halide arrangement [9–14]. It confirms that even small changes of the electronic properties in the ligand have significant impact on the reactivity towards [$ReOX_3(EPh_3)_2$].

The disubstituted [$ReO(OMe)(hpb)_2$]·MeCN chelate (**5**) has been isolated from the reaction of [$ReOX_3(EPh_3)_2$] with ligand excess in a mixture of acetonitrile and methanol (Scheme 2).

All the isolated complexes are air stable and slightly soluble in acetonitrile, dichloromethane, chloroform, sparingly soluble in benzene and toluene. The solubility of the *cis* stereoisomers in acetonitrile is better than the *trans* ones, thus the stereoisomers of [$ReOX_2(hpb)(PPh_3)$] can be separated by fractional crystallization. Furthermore, due to the difference in crystal shape of [$ReOX_2(hpb)(PPh_3)$] stereoisomers, they can be easily separated by hand (using microscope).

The IR spectroscopic measurements outlined in the Section 2 are not distinctive for molecular structure determination. The IR spectra of the *cis* and *trans* stereoisomers are very similar in terms of the position, intensity and shape of the bands in the whole region 4000–400 cm^{-1}. The strong ν(Re=O) stretching bands of both *cis* and *trans* stereoisomers of [$ReOX_2(hpb)(EPh_3)$] are found in the narrow range 960–970 cm^{-1}, similar to those observed for the other [$ReOX_2$(O–N)(EPh_3)] chelates [9–14]. Relatively high wavenumbers of the ν(Re=O) absorption bands suggest that the Re–hydroxy bond *trans* to the oxo ligand does not compete effectively for the Re_d orbitals and indicate the presence of very stable {O≡Re–O} structural moiety in the examined structures. Characteristic bands corresponding to the ν(CN), ν(C=C) modes of the hpb^- ligand appear in the range 1650–1500 cm^{-1}, and strong band in the range 3300–3200 cm^{-1} confirms the presence N–H group in the coordinated hpb^- ligand of the examined complexes.

^{1}H NMR spectra (summarized in Section 2 and presented in Fig. 1) make it possible to distinguish between *cis and trans* sterei-

Table 5
The selected experimental and optimized bond lengths [Å] and angles [°] for **5**.

Bond lengths	Experimental	Optimized	Bond angles	Experimental	Optimized
Re(1)–O(1)	1.682(2)	1.693	O(1)–Re(1)–O(2)	104.43(9)	104.62
Re(1)–O(2)	1.9917(17)	1.938	O(1)–Re(1)–O(3)	165.15(8)	162.13
Re(1)–O(3)	2.0224(18)	2.074	O(1)–Re(1)–O(4)	102.39(9)	104.04
Re(1)–O(4)	1.9822(18)	2.007	O(2)–Re(1)–O(3)	88.08(7)	91.35
Re(1)–N(1)	2.111(2)	2.133	O(4)–Re(1)–O(2)	87.21(8)	89.27
Re(1)–N(3)	2.131(2)	2.194	O(4)–Re(1)–O(3)	85.93(8)	83.77
			O(1)–Re(1)–N(1)	91.78(9)	92.85
			O(1)–Re(1)–N(3)	87.75(9)	85.23
			O(2)–Re(1)–N(1)	84.14(8)	81.76
			O(2)–Re(1)–N(3)	167.73(8)	170.09
			O(3)–Re(1)–N(1)	81.42(8)	81.41
			O(3)–Re(1)–N(3)	80.08(8)	79.05
			O(4)–Re(1)–N(1)	164.89(9)	162.45
			O(4)–Re(1)–N(3)	88.71(8)	87.29
			N(1)–Re(1)–N(3)	97.18(8)	99.02

Table 6
The selected experimental bond lengths [Å] and angles [°] for **1a**, **1b** and **3**.

Bond lengths	**1a** E = P; X = Cl	**1b** E = P; X = Cl	**3** E = As; X = Cl	Bond angles	**1a**	**1b**	**3**
Re(1)–O(1)	1.694(4)	1.688(2)	1.685(7)	O(1)–Re(1)–O(2)	171.97(19)	167.36(10)	165.6(3)
Re(1)–O(2)	1.940(4)	1.953(2)	1.948(7)	O(1)–Re(1)–N(1)	94.5(2)	90.21(11)	89.4(4)
Re(1)–N(1)	2.146(5)	2.120(3)	2.099(10)	O(2)–Re(1)–N(1)	81.10(19)	81.38(10)	81.4(4)
Re(1)–X(1)	2.3715(17)	2.3701(9)	2.375(3)	O(1)–Re(1)–X(1)	99.06(15)	98.78(8)	99.6(3)
Re(1)–X(2)	2.4348(16)	2.4070(10)	2.406(3)	O(2)–Re(1)–X(1)	87.79(13)	90.37(7)	90.4(3)
Re(1)–E(1)	2.4528(17)	2.4619(9)	2.5606(12)	N(1)–Re(1)–X(1)	90.85(15)	170.17(8)	170.4(3)
				O(1)–Re(1)–X(2)	90.36(15)	98.07(8)	98.2(3)
				O(2)–Re(1)–X(2)	82.65(13)	90.75(7)	92.1(2)
				N(1)–Re(1)–X(2)	86.16(15)	85.88(8)	86.1(3)
				X(1)–Re(1)–X(2)	170.32(6)	88.92(3)	89.39(10)
				O(1)–Re(1)–E(1)	93.28(15)	85.17(8)	85.7(3)
				O(2)–Re(1)–E(1)	90.63(13)	86.10(7)	84.3(2)
				N(1)–Re(1)–E(1)	171.09(15)	94.48(8)	95.1(3)
				X(1)–Re(1)–E(1)	92.14(6)	90.25(3)	88.75(8)
				X(2)–Re(1)–E(1)	89.52(6)	176.74(3)	175.94(7)
Re(2)–O(3)		1.680(2)	1.698(8)	O(3)–Re(2)–O(4)		168.03(11)	165.9(4)
Re(2)–O(4)		1.943(2)	1.941(7)	O(3)–Re(2)–N(3)		91.26(11)	90.2(4)
Re(2)–N(3)		2.134(3)	2.133(9)	O(4)–Re(2)–N(3)		81.80(10)	82.3(3)
Re(2)–X(4)		2.3647(9)	2.372(3)	O(3)–Re(2)–X(4)		99.45(8)	99.6(3)
Re(2)–X(3)		2.4035(10)	2.393(3)	O(4)–Re(2)–X(4)		88.21(7)	88.6(2)
Re(2)–E(2)		2.4670(10)	2.5646(13)	N(3)–Re(2)–X(4)		168.75(8)	169.8(2)
				O(3)–Re(2)–X(3)		100.16(9)	100.6(3)
				O(4)–Re(2)–X(3)		89.28(7)	91.0(2)
				N(3)–Re(2)–X(3)		87.18(8)	87.3(3)
				X(4)–Re(2)–X(3)		87.53(3)	88.33(11)
				O(3)–Re(2)–E(2)		83.86(9)	83.7(3)
				O(4)–Re(2)–E(2)		86.42(7)	84.5(2)
				N(3)–Re(2)–E(2)		90.23(8)	90.5(3)
				X(4)–Re(2)–E(2)		94.33(3)	93.07(8)
				X(3)–Re(2)–E(2)		175.26(4)	175.19(8)

Table 7
Atomic charges from the Natural Population Analysis (NPA) for **2a**, **4** and **5**.

Atom	**2a**	**4**	**5**
Re(1)	0.176	0.151	1.155
O(1)	−0.334	−0.342	−0.423
O(2)	−0.599	−0.610	−0.642
O(3)			−0.649
O(4)			−0.630
Br(1)	−0.271	−0.194	
Br(2)	−0.225	−0.179	
N(1)	−0.472	−0.470	−0.482
N(3)			−0.495
P(1)/As(1)	1.516	1.523	

somers of $[ReOX_2(hpb)(PPh_3)]$ chelates. However, molecular configuration can not be predicted on this basis.

3.2. Crystal structures

A definite proof for the structures of $[ReOX_2(hpb)(EPh_3)]$ and $[ReO(OMe)(hpb)_2]\cdot MeCN$ is provided by the X-ray diffraction results. The crystallographic data of **1a**, **1b**, **2a**, **3, 4** and **5** are summarized in Table 1. The *cis*-halide complexes $[ReOX_2(hpb)(EPh_3)]$ (**1b**, **3** and **4**) are isostructural and crystallise in the triclinic $P\bar{1}$ space group with two crystallographically independent molecules of $[ReOX_2(hpb)(EPh_3)]$ in the asymmetric unit. Because these molecules are connected by center of pseudo-symmetry the asymmetric unit contains one pair of enantiomers of two pairs occupying unit cell. Due to small gap between lengths of *a* and *b* unit cell edges, and small changes of unit cell dimensions (originating from differences in compounds composition), the *a* and *b* axes are interchanged in compound **4** in comparison to compounds **1b** and **3** (the unit cell edge of compound **4** corresponding

to *a* axis of compounds **1b** and **3** is not shortest unit cell edge). The *trans* stereoisomers (**1a** and **2a)** are also isostructural but consist of discrete and well-separated [$ReOX_2(O–N)(EPh_3)$] monomers and crystallise in the orthorhombic Pbca space group. The disubstituted chelate crystallises as acetonitrile solvate in the monoclinic $P2_1/n$ space group. The short intra- and intermolecular contacts [47,48] detected in the **1a**, **1b**, **2a**, **3, 4** and **5** are gathered in Table 2. In general hydrogen bonding schemes in isostructural compounds are similar and small observed changes originate mainly from minor differences in packing. The medium strength N–H···X hydogen bonds of **1b**, **3** and **4** create cyclic tetramer described by $N_2R_2^2(24)$ motif. In **1a** and **2a** medium strength N–H···X hydrogen bonds forms zig-zag chain along crystallographic *a* axis and it is described by $N_1C(6)$ graph. In **5** the N–H···O hydrogen bonds links complex molecules to $N_1C(6)$ chain extending along crystallographic [1 0 1] direction. Additionally, in all the structures exist short C–H···O, C–H···N and C–H···X intermolecular interactions, which can be considered as weak or very weak hydrogen bonds. In the structures of **1b**, **3** and **4** exists solvent accessible voids (SOVs), however close inspection of residual electron density show no obvious maxima in SOVs regions, thus it can be supposed that SOVs contains no solvent and they existence originate from crystal packing.

The perspective drawing of *trans*-[$ReOBr_2(hpb)(PPh_3)$] (**2a)** is presented in Fig. 2, and the selected bond distances and angles of **2a** are collected in Table 3. Fig. 3 presents the molecular structure of *cis*-[$ReOBr_2(hpb)(AsPh_3)$] (**4**), and selected bond distances and angles of **4** are gathered in Table 4. The molecular structure of the disubstituted [$ReO(OMe)(hpb)_2$]·MeCN chelate (**5**) is shown in Fig. 4, and Table 5 presents its selected bond distances and

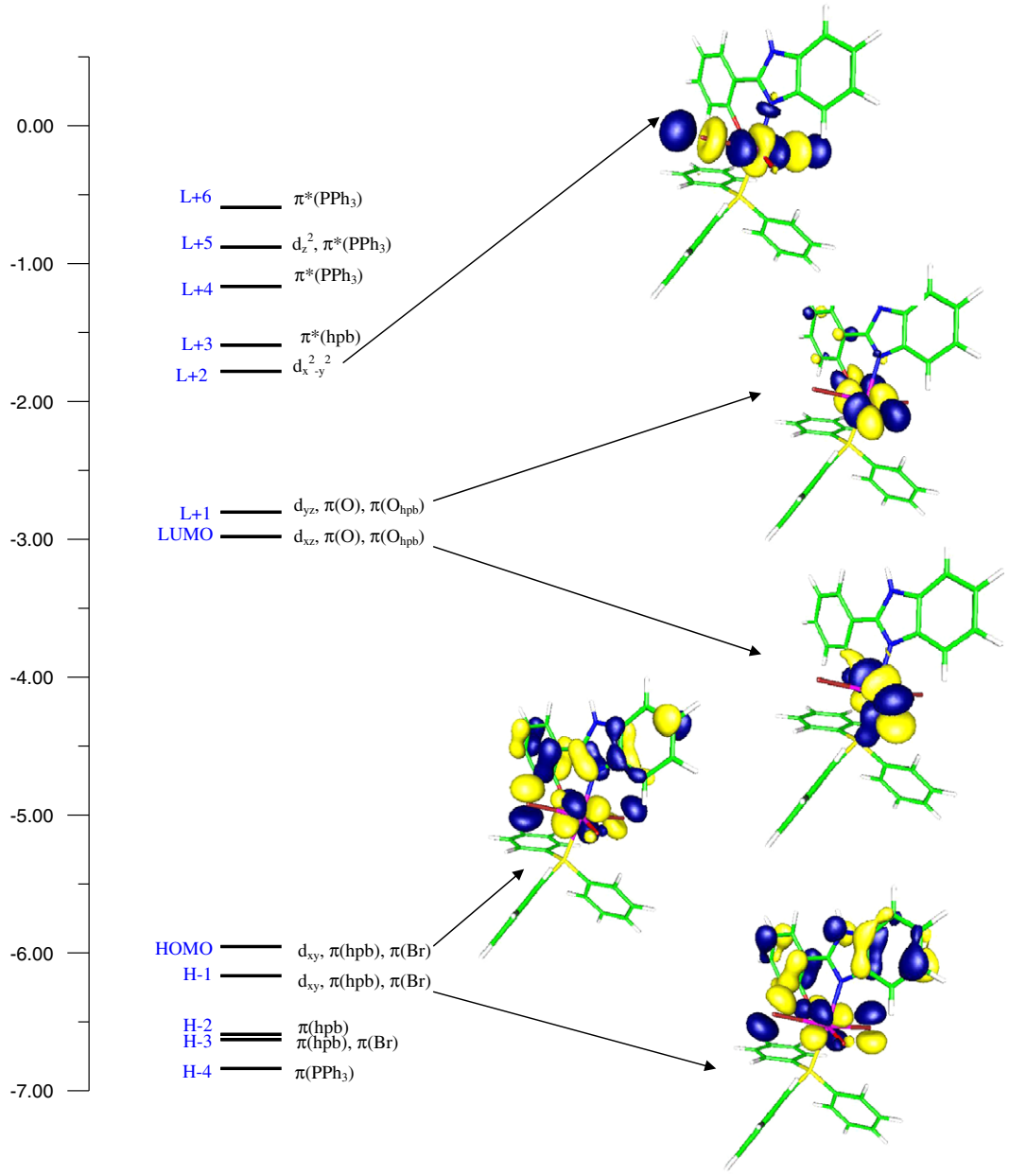


Fig. 5. The energy (eV), character and some contours of the unoccupied molecular orbitals of **2a**. Positive values of the orbital contour are represented in blue (0.04 au) and negative values in yellow (−0.04 au). (For interpretation of the references to colour in this figure legend, the reader is referred to the web version of this article.)

angles. The selected bond distances and angles of the other complexes are gathered in Table 6.

3.3. $[ReOX_2(hpb)(EPh_3)]$ complexes

All the complexes $[ReOX_2(hpb)(EPh_3)]$ show octahedral geometry about the central rhenium atom defined by the terminal oxo-group, two halide ions, the phosphorus or arsine atom of EPh_3 molecule, and the bidentate N,O donors of the hpb^- ligand. The halide ions of **1b**, **3** and **4** are arranged in *cis* geometry, whereas the halide ligands of **1a** and **2a** occupy *trans* positions to each other. In all the complexes triphenylphosphine or triphenylarsine molecule with their π-acidity adopts *cis* position with respect to the linear O≡Re–O unit. Consequently, the O≡Re–O core with multiply bonded oxo ligand is stabilized to some extent due to accessible π-donation from rhenium to triphenylphosphine or triphenylarsine molecule. The multiple bonding ligand (terminal oxo) and narrow bite angle of the chelating ligand contribute to clear distortions of the pseudooctahedral environment of Re center in both *cis*- and *trans*-halide complexes.

In complexes **1a** and **2a**, the rhenium atom is displaced, respectively 0.1795(16) and0.1862(13) Å from the plane formed by the two halogen, one nitrogen and one phosphorous (or arsine) atoms (plane A), 0.0516(17) and 0.0617(13) Å from the plane formed by the two oxygen and two halogen atoms (plane B), 0.0920(20) and 0.0793(18) Å from the plane formed by two oxygen, one phosphorous and one nitrogen atoms (plane C). Least squares plane A is inclined at 87.40(8)°, 87.26(7)°, to plane B and at 89.37(9)°, 89.45(7)°, to plane C; planes B and C are inclined at 89.51(8)°, 89.84(18)°, respectively as above.

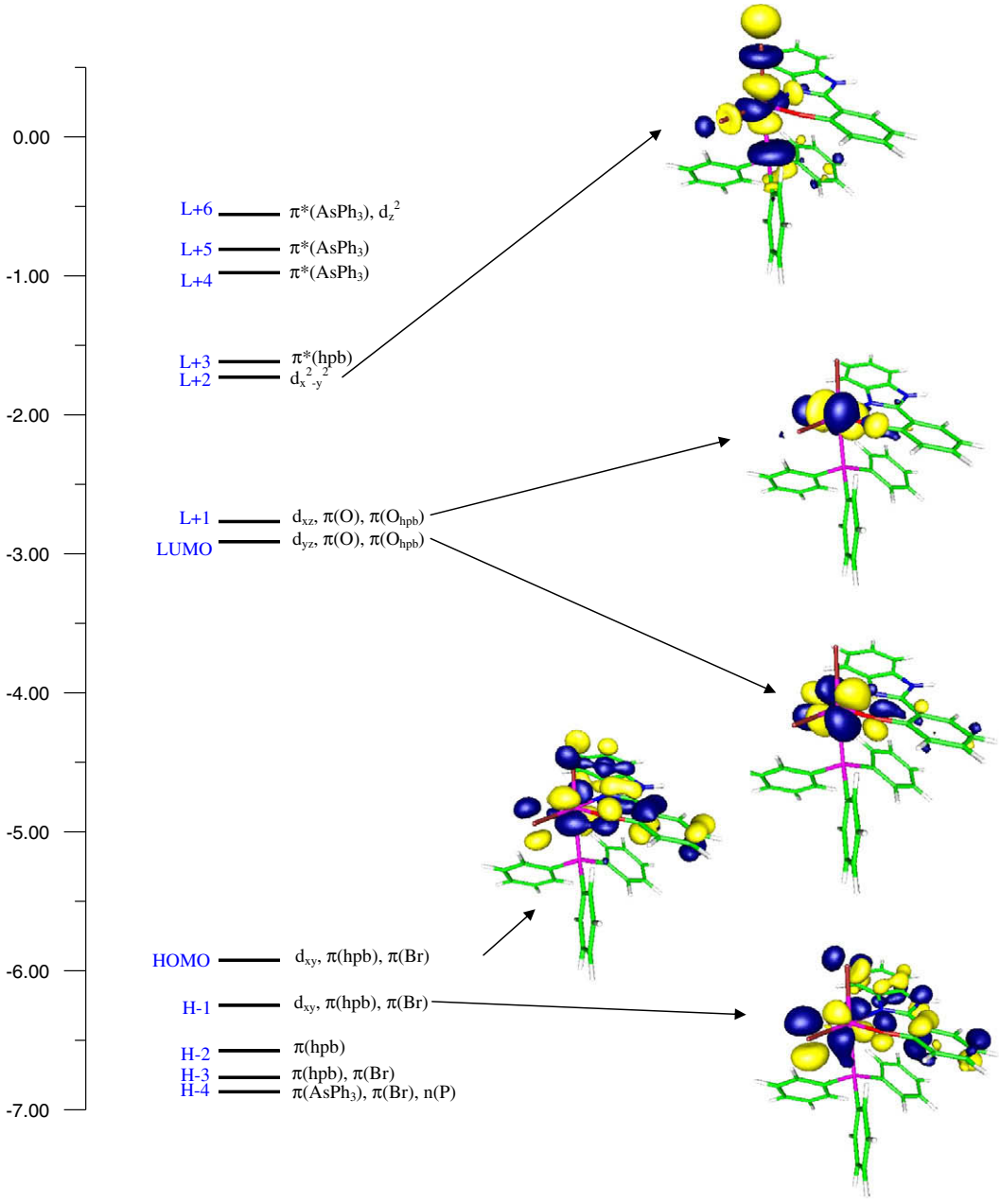


Fig. 6. The energy (eV), character and some contours of the uno ccupied molecular orbitals of **4**. Positive values of the orbital contour are represented in blue (0.04 au) and negative values in yellow (−0.04 au). (For interpretation of the references to colour in this figure legend, the reader is referred to the web version of this article.)

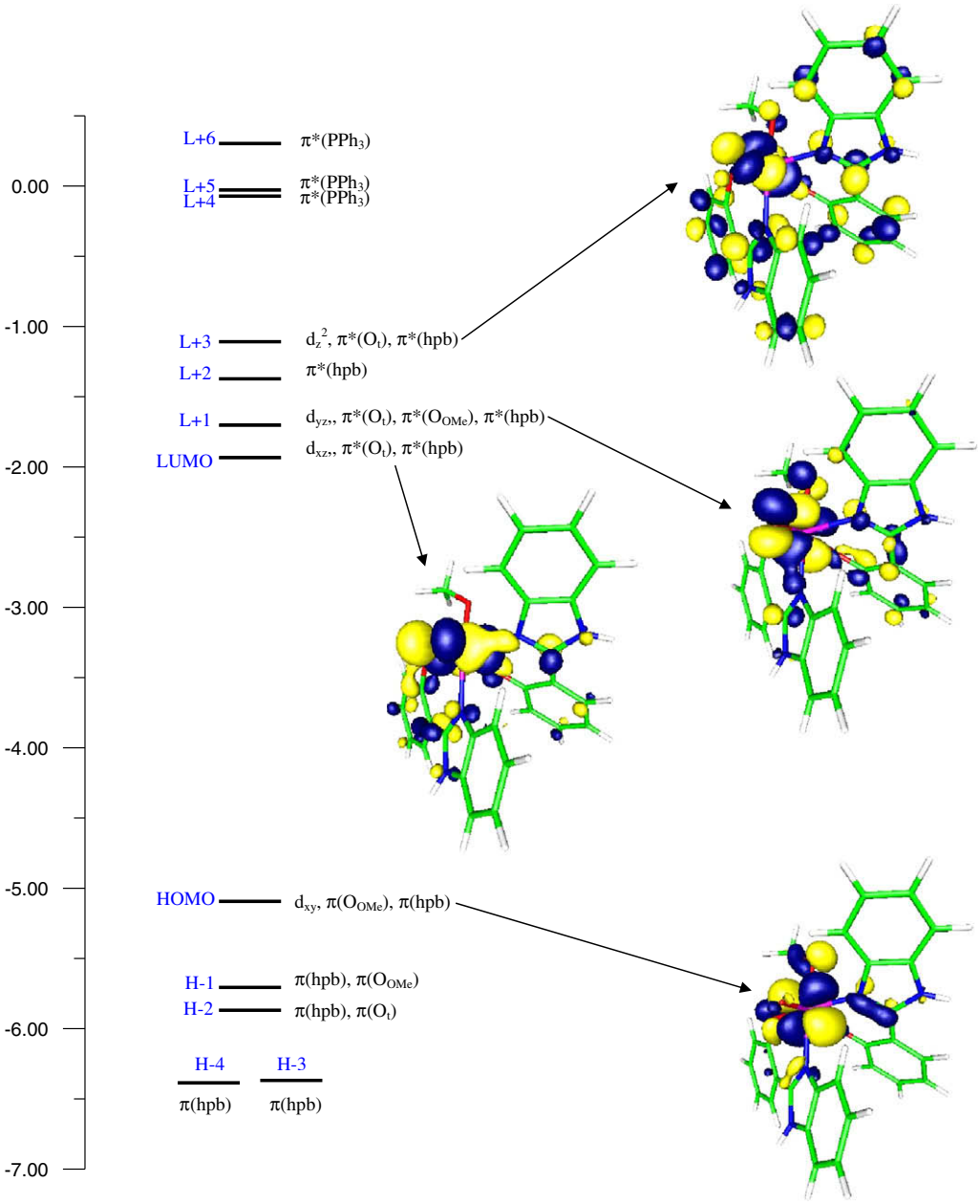


Fig. 7. The energy (eV), character and some contours of the unoccupied molecular orbitals of **5**. Positive values of the orbital contour are represented in blue (0.04 au) and negative values in yellow (−0.04 au). (For interpretation of the references to colour in this figure legend, the reader is referred to the web version of this article.)

Table 8
The occupancy and composition of the calculated natural bond orbitals (NBOs) between the rhenium and the oxo ligand for **2a, 4** and **5**.

BD	Occupancy	Composition of NBO	BD*	Occupancy
2a				
Re–O_t	1.987	$0.554(d)_{Re} + 0.833(p)_O$	$0.833(d)_{Re} - 0.554(p)_O$	0.255
Re–O_t	1.987	$0.578(d)_{Re} + 0.816(p)_O$	$0.816(d)_{Re} - 0.578(p)_O$	0.175
4				
Re–O_t	1.990	$0.566(d)_{Re} + 0.824(p)_O$	$0.8242(d)_{Re} - 0.566(p)_O$	0.207
Re–O_t	1.986	$0.569(d)_{Re} + 0.823(p)_O$	$0.823(d)_{Re} - 0.569(p)_O$	0.254
5				
Re–O_t	1.991	$0.548(d)_{Re} + 0.836(sp^{6.43})_O$	$0.836(d)_{Re} - 0.548(sp^{6.43})_O$	0.257
Re–O_t	1.990	$0.557(d)_{Re} + 0.831(p)_O$	$0.831(d)_{Re} - 0.557(p)_O$	0.272

BD denotes 2-center bond.
* Denotes anti-bond NBO.

Table 9
Stabilization energies associated with delocalisation from the lone pair orbitals of the terminal oxo ligand for **2a**, **4** and **5**.

Donor orbital	Occupancy of donor orbital	Acceptor orbital	ΔE_{ij} [kcal/mol]
2a			
$(sp^{0.98})_{O(t)}$	1.914	$(sp^{0.22}d^{1.29})_{Re}$	18.90
$(sp^{1.08})_{O(t)}$	1.575	$(sp^{0.22}d^{1.29})_{Re}$	243.81
4			
$(sp^{0.86})_{O(t)}$	1.909	$(sp^{0.33}d^{1.55})_{Re}$	14.59
$(sp^{1.60})_{O(t)}$	1.580	$(sp^{0.33}d^{1.55})_{Re}$	207.15
5			
$(sp^{0.70})_{O(t)}$	1.914	$(sp^{0.50}d)_{Re}$	13.55
$(sp^{2.61})_{O(t)}$	1.576	$(sp^{0.50}d)_{Re}$	207.96
		$(d)_{Re}$	12.31

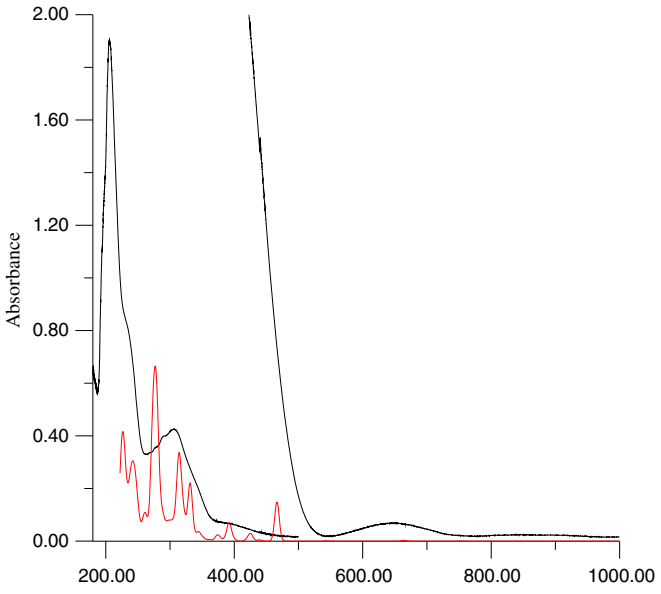


Fig. 8. The experimental (black) and calculated (red) electronic absorption spectra of **2a**. (For interpretation of the references to colour in this figure legend, the reader is referred to the web version of this article.)

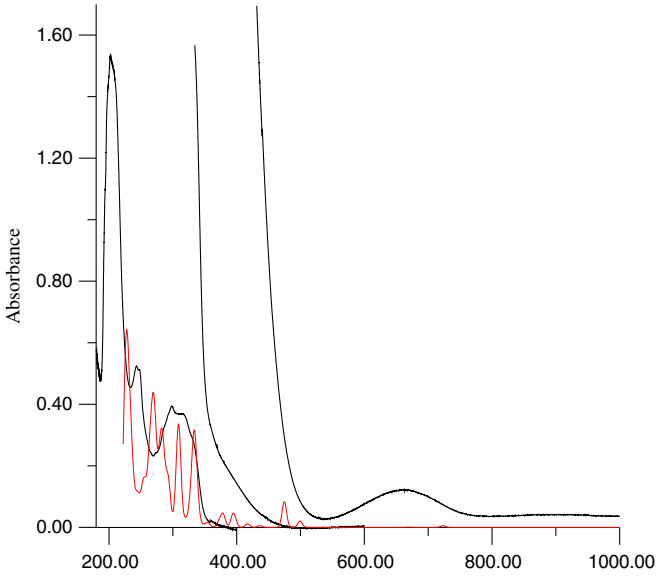


Fig. 9. The experimental (black) and calculated (red) electronic absorption spectra of **4**. (For interpretation of the references to colour in this figure legend, the reader is referred to the web version of this article.)

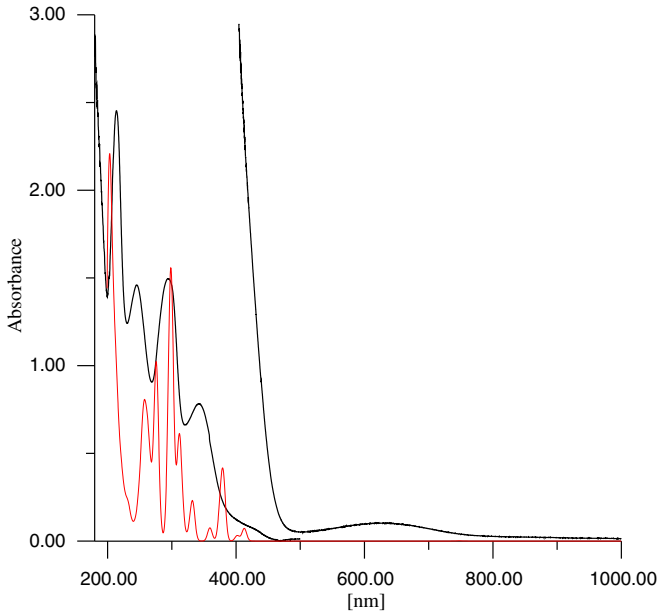


Fig. 10. The experimental (black) and calculated (red) electronic absorption spectra of **5**. (For interpretation of the references to colour in this figure legend, the reader is referred to the web version of this article.)

In complexes **1b**, **3** and **4** the Re(1) atom is displaced respectively 0.1166(9), 0.124(3), 0.112(3) Å from the plane formed by the two halogen, one nitrogen and one phosphorous (or arsine) atoms (plane A), 0.0648(8), 0.062(3), 0.063(3) Å from the plane formed by the two oxygen, one halogen and phosphorous (or arsine) atoms (plane B) and 0.0255(11), 0.044(4), 0.050(4) Å from the plane formed by two oxygen, one nitrogen and one halogen atoms (plane C). Least squares plane A is inclined at 89.83(4)°, 89.77(17)°, 89.54(15)° to plane B and at 88.44(5)°, 88.17(20)°, 88.32(15),° to plane C; planes B and C are inclined at 88.76(5)°, 89.11(18)°, 89.0(3)°, respectively as above.

No extraordinary features in terms of bond lengths and angles can be noticed between *cis*- and *trans*-halide $[ReOX_2(hpb)(PPh_3)]$ complexes. The Re–O_t (O_t = terminal oxygen) bond lengths fall in the range 1.639–1.76°Å, typical of mononuclear complexes of rhenium(V) having $[ReO]^{3+}$ core, and indicate the presence of a triple bond Re≡O [49].

The interatomic distances between the rhenium atom and the oxygen atom of hpb^- ligand are somewhat shorter than an ideal single Re–O bond length (*ca.* 2.04 Å) [50], indicating only small delocalization in the O(2)–Re(1)–O(1) moiety.

For *cis*-halide $[ReOX_2(hbt)(PPh_3)]$ complexes the Re–X distances *trans* to the phosphorus or arsine atom of EPh_3 molecule are slightly longer than the Re–X bonds *trans* to the nitrogen atom of the hpb^- ligand. It indicates *structural trans* effect of the EPh_3 ligands. A similar trend was observed in the other $[ReOCl_2(O–N)(PPh_3)]$ chelates [9–15].

3.4. [ReO(OMe)(hpb)$_2$]·MeCN complex

The geometry of $[ReO(OMe)(hpb)_2]$ compound also reveals typical features of quasi-octahedral oxorhenium(V)complexes with oxygenated bidentate ligands. For complex $[ReO(OMe)(hpb)_2]$ the rhenium atom is displaced 0.2252(10) Å from the equatorial plane formed by the two nitrogen and two oxygen atoms (plane A) and 0.0437(9) and 0.0325(8) Å from the axial planes formed, respectively by O(1), O(2), O(3) and N(3) atoms (plane B) and O(1), O(3), O(4) and N(1) atoms (plane C). Least squares plane A is in-

clined at 88.91(5)° to the plane B and at 88.40(5)° to the plane C. The planes B and C are inclined at 87.18(5)°. Clear distortions of the pseudooctahedral environment of Re center in [ReO(OMe)(hpb)$_2$] is induced by the multiple bonding ligand (terminal oxo ligand –O$_t$) and narrow bite angle of the chelating ligands.

Similar to the [ReOX$_2$(hpb)(PPh$_3$)] complexes, the Re–O$_t$ bond length of [ReO(OMe)(hpb)$_2$] falls in the range typical of a triple bond Re≡O [47]. The interatomic distance between the rhenium atom and the oxygen atom of hpb$^-$ in *trans* position to the terminal oxo ion is somewhat longer than the corresponding Re–O bond in the equatorial plane (in *trans* position to the nitrogen atom). This structural *trans* influence of O$_t$ ligand is common in mononuclear six-coordinate oxoRe(V) complexes with an monoanionic oxygen *trans* to the oxo-group [51].

3.5. Geometry optimisations, charge distributions, electronic structures and NBO analyses

The geometries of **2a**, **4** and **5** were optimized in singlet states by the DFT method with the B3LYP functional. The optimized geometric parameters of **2a**, **4** and **5** are gathered in Tables 3–5, respectively. In general, the predicted bond lengths and angles are in agreement with the values based upon the X-ray crystal structure data, and the general trends observed in the experimental data are well reproduced in the calculations. The largest differences are found for the Re–Br and Re–E (E = P, As) bond distances. It may come from the basis sets which are approximated to a certain extent or may indicate the influence of the crystal packing on the values of the experimental bond lengths. The theoretical calculations do not consider the effects of chemical environment.

Table 7 presents the atomic charges from the Natural Population Analysis (NPA) for **2a**, **4** and **5**. The calculated charges on the rhenium atoms in **2a** and **4** are almost the same, whereas the calculated charge on the Re atom in complex **5** is considerably larger in comparison with the monosubstituted compounds. However, all the values are lower than the formal charge +5 as a result of significant charge donation from the donor atoms of the ligands. For all the complexes considerable differences in values of charges are observed for the terminal oxo ligand and the oxygen atom of hpb$^-$ ligand – less negative are the terminal oxo ligands, which indicate the higher electron density delocalization from the terminal ligands towards the rhenium centers and correspond to differences in the Re–O$_t$ and Re–O$_{hpb}$ bonds lengths. As far as the charge on the terminal oxo ligand is concerned, some difference between the monosubstituted and disubstituted complexes is visible. The higher charge donation from the terminal oxo ligand is observed for **2a** than **4**. For *cis* and *trans* isomers are also observed some differences in values of charges on the bromide ions. The higher charge donation from the bromide ions is noticed for the *cis*-[ReOBr$_2$(hpb)(PPh$_3$)] complex.

The **2a**, **4** and **5** are closed-shell structures. Their partial molecular orbital diagrams with the several highest occupied and lowest unoccupied molecular orbital contours are presented in Figs. 5–7, respectively.

Two highest occupied MOs of **2a**, are of d$_{xy}$ type with some contributions from p$_\pi$ bromide and hpb$^-$ orbitals. The LUMO and LUMO+1 are predominately localized on the rhenium atom (d$_{xz}$ and d$_{yz}$ orbitals) with some contribution of p$_\pi$ oxygen orbitals. The LUMO+2 is of d$_{x^2-y^2}$ character, and d$_z^2$ rhenium orbital contributes mainly to the LUMO+15. The value of the energy separation

Table 10
The energy and molar absorption coefficients of experimental absorption bands and the electronic transitions calculated with the TDDFT method for **2a**.

The most important orbital excitations	Character	λ [nm]	E [eV]	f	Experimental λ [nm] (E [eV])ε
H → L	d/π(hpb)/π(Br) → d	752.5	1.65	0.0002	649.8 (1.91) 20
H → L+1	d/π(hpb)/π(Br) → d	663.9	1.87	0.0015	
H−1 → L	d/π(hpb)/π(Br) → d	543.5	2.28	0.0003	
H−1 → L+1	d/π(hpb)/π(Br) → d	466.4	2.66	0.0742	407.6.9 (3.04) 2250
H−3 → L	π(hpb)/π(Br) → d	425.7	2.91	0.0123	
H−2 → L+1	π(hpb) → d	391.5	3.17	0.0282	
H−7 → L	π(PPh$_3$)/π(Br) → d	373.2	3.22	0.0090	
H−9 → L+1	π(Br)/π(PPh$_3$)/π(O$_t$) → d	343.1	3.61	0.0124	308.5 (4.02) 16 950
H → L+3	d/π(hpb)/π(Br) → π*(hpb)	331.2	3.74	0.0960	
H−12 → L	π(Br)/π(PPh$_3$) → d	321.9	3.85	0.0330	
H−14 → L	π(Br)/π(hpb) → d	316.4	3.92	0.0405	
H−1 → L+3	d/π(hpb)/π(Br) → π*(hpb)	313.4	3.96	0.1300	
H−15 → L	π(Br) → d	306.0	4.05	0.0221	
H−13 → L+1	π(hpb)/π(Br) → d	288.3	4.30	0.0270	
H−16 → L	dπ(O$_t$)/π(Br)/n(P)/π(hpb) → d	280.0	4.43	0.1223	
H−4 → L+2	π(PPh$_3$) → d	278.1	4.46	0.0399	
H → L+5	d/π(hpb)/π(Br) → π*(PPh$_3$)/d	278.0	4.46	0.0381	
H−2 → L+3	π(hpb) → π*(hpb)	277.4	4.47	0.0521	
H−3 → L+3	π(hpb)/π(Br) → π*(hpb)	273.8	4.53	0.1403	
H−7 → L+2	π(PPh$_3$)/π(Br) → d	272.0	4.56	0.0567	
H−5 → L+3	π(Br)/π(PPh$_3$)/n(P) → π*(hpb)	260.9	4.75	0.0269	
H−3 → L+4	π(hpb)/π(Br) → π*(PPh$_3$)	249.8	4.96	0.0208	232.9 (5.32) 32 950
H−4 → L+4	π(PPh$_3$) → π*(PPh$_3$)	245.7	5.05	0.0334	209.3 (5.92) 71 500
H−5 → L+4	π(Br)/π(PPh$_3$)/n(P) → π*(PPh$_3$)	241.0	5.14	0.0283	
H−4 → L+4	π(PPh$_3$) → π*(PPh$_3$)				
H−7 → L+4	π(PPh$_3$)/π(Br) → π*(PPh$_3$)	238.8	5.19	0.0356	
H−9 → L+4	π(Br)/π(PPh$_3$)/π(O$_t$) → π*(PPh$_3$)	228.5	5.43	0.0257	
H−13 → L+3	π(hpb)/π(Br) → π*(hpb)	227.2	5.46	0.0352	
H → L+10	d/π(hpb)/π(Br) → π*(PPh$_3$)				
H−18 → L	π(PPh$_3$) → d	226.0	5.49	0.0229	
H−18 → L	π(PPh$_3$) → d	226.9	5.49	0.0290	
H−16 → L+2	π(O)/π(Br)/n(P) → d				
H−2 → L+6	π(hpb) → π*(PPh$_3$)	222.7	5.57	0.0460	

between the highest occupied molecular orbital (HOMO) and the lowest unoccupied molecular orbital (LUMO) equals to 2.98 eV.

The qualitative molecular orbitals scheme of **2a** is almost the same as for **4**. HOMO and HOMO−1 of **2a** and **4** are of d_{xy} type with some contributions from p_π bromide and hpb^- orbitals. The LUMO and LUMO+1 are predominately localized on the rhenium atom (d_{xz} and d_{yz} orbitals) with significant contribution of p_π oxygen orbitals. The LUMO+2 is of $d_{x^2-y^2}$ character, and d_z^2 rhenium orbital contributes to the higher unoccupied MO. The HOMO−LUMO gap of **4** is equal to 3.01 eV, and is almost the same as for **2a**.

The HOMO−LUMO gap of **5** is equal to 3.16 eV. The HOMO of **5** is comprised of rhenium d_{xy} and π orbitals of $O_{(OMe)}$ and hpb^-. The LUMO and LUMO+1 are predominately localized on the rhenium atom (d_{xz} and d_{yz} orbitals) with significant contribution of the p_π oxygen orbitals. However, in comparison with corresponding orbitals of **2a** and **4** they are more delocalized, with higher contribution of the π-anti-bonding orbitals of hpb^- ligands. The $d_{x^2-y^2}$ character, and d_z^2 rhenium orbital contributes to the higher unoccupied MO.

The nature of rhenium–terminal oxygen (O_t) interaction in **2a**, **4** and **5** has been studied by NBO analysis. The occupancy and composition of the calculated Re–O_t natural bond orbitals (NBOs) are given in Table 8.

Each natural bond orbital (NBO) σ_{AB} can be written in terms of two directed valence hybrids (NHOs) h_A and h_B on atoms A and B:

$$\sigma_{AB} = c_A h_A + c_B h_B$$

where c_A and c_B are polarization coefficients. Each valence bonding NBO must in turn be paired with a corresponding valence *anti*-bonding NBO:

$$\sigma^*_{AB} = c_B h_A - c_A h_B$$

to complete the span of the valence space. The Lewis-type (donor) NBOs are thereby complemented by the non-Lewis-type (acceptor) NBOs that are formally empty in an idealized Lewis picture. The interactions between 'filled' Lewis-type NBOs and 'empty' non-Lewis NBOs lead to loss of occupancy from the localized NBOs of the idealized Lewis structure into the empty non-Lewis orbitals, and they are referred to as 'delocalization' corrections to the zeroth-order natural Lewis structure [52].

Similar to the previously described [$ReOX_2(O–N)(PPh_3)$] and [$ReOX(O–N)_2$] chelates [9–14], two strongly polarized to the oxygen atom natural Re–O_t bond orbitals were detected for **2a**, **4** and **5**. For each complex the both detected natural Re–O_t bond

Table 11
The energy and molar absorption coefficients of experimental absorption bands and the electronic transitions calculated with the TDDFT method for **4**.

The most important orbital excitations	Character	λ [nm]	*E* [eV]	*f*	Experimental Λ [nm] (*E* [eV])ε
H → L	d/π(hpb)/π(Br) → d	723.4	1.71	0.0030	665.9 (1.86) 55
H → L+1	d/π(hpb)/π(Br) → d	668.6	1.85	0.0004	
H−1 → L	d/π(hpb)/π(Br) → d	499.2	2.48	0.0112	
H−1 → L+1	d/π(hpb)/π(Br) → d				
H−1 → L	d/π(hpb)/π(Br) → d	474.6	2.61	0.0462	398.8 (3.11) 1350
H−1 → L+1	d/π(hpb)/π(Br) → d				
H−4 → L	π($AsPh_3$)/n(As)/π(Br) → d	394.1	3.15	0.0200	
H−2 → L+1	π(hpb) → d				
H−3 → L+1	π(hpb)/π(Br) → d	377.8	3.28	0.0204	
H−8 → L	π($AsPh_3$) → d	336.1	3.69	0.0281	306.6 (4.04) 21 000
H−1 → L+2	π(hpb)/π(Br) → d				
H → L+3	d/π(hpb)/π(Br) → π*(hpb)	333.0	3.72	0.1100	
H−11 → L	π(Br)/π(O_t) → d	329.4	3.76	0.0249	
H−10 → L+1	π($AsPh_3$) → d	311.1	3.99	0.0286	
H−1 → L+3	d/π(hpb)/π(Br) → π*(hpb)	308.8	4.02	0.1392	
H−14 → L	π(Br)/π(hpb)/n(As) → d	307.4	4.03	0.0225	
H−2 → L+2	π(hpb) → d	292.5	4.24	0.0799	
H−3 → L+2	π(hpb)/π(Br) → d	285.8	4.34	0.0238	
H−4 → L+2	π($AsPh_3$)/n(As)/π(Br) → d				
H−14 → L+1	π(Br)/π(hpb)/n(As) → d	284.3	4.36	0.0623	
H−13 → L+1	π(hpb) → d				
H−3 → L+2	π(hpb)/π(Br) → d	283.6	4.37	0.0362	
H → L+4	d/π(hpb)/π(Br) → π*($AsPh_3$)				
H−2 → L+3	π(hpb) → π*(hpb)	279.6	4.43	0.0943	245.2 (5.06) 28 500
H−15 → L+1	π(Br)/π(O_t)/π(hpb) → d	272.6	4.55	0.0638	
H−4 → L+2	π($AsPh_3$)/n(As)/π(Br) → d	270.3	4.59	0.0867	
H−3 → L+3	π(hpb)/π(Br) → π*(hpb)	268.4	4.62	0.0822	
H−1 → L+4	d/π(hpb)/π(Br) → π*($AsPh_3$)	264.8	4.68	0.0238	
H−6 → L+2	π($AsPh_3$) → d	264.6	4.69	0.0245	
H−1 → L+4	d/π(hpb)/π(Br) → π*($AsPh_3$)	262.7	4.72	0.0288	
H−7 → L+2	π($AsPh_3$)/π(Br) → d	261.1	4.75	0.0218	
H−16 → L+1	π(Br)/π(O_t)/π(hpb) → d	254.5	4.87	0.0203	
H → L+7	d/π(hpb)/π(Br) → π*($AsPh_3$)	253.6	4.89	0.0250	
H−19 → L+1	σ(Br) → d	234.7	5.28	0.0298	202.1 (6.13) 85 000
H−3 → L+4	π(hpb)/π(Br) → π*($AsPh_3$)	232.4	5.33	0.0553	
H−5 → L+4	π($AsPh_3$)/π(Br) → π*($AsPh_3$)	228.7	5.42	0.0377	
H−14 → L+2	π(Br)/π(hpb)/n(As) → d	228.3	5.43	0.0392	
H−13 → L+3	π(hpb) → π*(hpb)	227.5	5.45	0.0735	
H → L+12	d/π(hpb)/π(Br) → π*(hpb)				
H−3 → L+5	π(hpb)/π(Br) → π*($AsPh_3$)	226.8	5.47	0.0384	
H−2 → L+6	π(hpb) → π*($AsPh_3$)/d	226.2	5.48	0.0301	
H−4 → L+5	π($AsPh_3$)/n(As)/π(Br) → π*($AsPh_3$)	225.3	5.50	0.0591	
H−1 → L+9	d/π(hpb)/π(Br) → π*($AsPh_3$)/π*(hpb)				

orbitals are similar in energy and they are composed of the p oxygen and d rhenium orbitals. The terminal oxo ligand of **2a**, **4** and **5** has two lone pair orbitals, and electron density from one of them is strongly delocalized into non-Lewis rhenium orbital (see Table 9). It can be assumed that the detected natural Re–O_t bond orbitals are of π character and not detected σ_{Re-Ot} bond has ionic character, similar as Re–N bond orbital in $[ReCl_4(MeCN)_2]$ [53].

Accordingly, NBO analysis confirms a triple bond between the rhenium and the terminal oxygen ligand in **2a**, **4** and **5**.

3.6. Electronic spectra

The experimental and calculated electronic spectra of **2a**, **4** and **5** are presented in Figs. 8–10, respectively. The positions of absorption bands for the other $[ReOX_2(hbo)(EPh_3)]$ complexes are given in the experimental part. Each calculated transition for **2a**, **4** and **5** complexes is represented by a gaussian function $y = ce^{-bx^2}$ with the height (c) equal to the oscillator strength and b equal to 0.04 nm^{-2}.

Tables 10–12 present the most important electronic transitions calculated with the TDDFT method assigned to the observed absorption bands of **2a**, **4** and **5**, respectively. For the high energy part of the spectrum, only transitions with oscillator strengths larger than 0.020 are listed in Tables 10–12. The assignment of the calculated orbital excitations to the experimental bands was based on an overview of the contour plots and relative energy to the occupied and unoccupied orbitals involved in the electronic transitions.

3.7. Electronic spectrum of *2a*

The longest wavelength experimental band of **2a** at 649.8 nm originates in the HOMO → LUMO, HOMO−1 → LUMO and HOMO → LUMO+1 transitions. As can be seen from Fig. 4, the LUMO orbital is mainly formed from rhenium d atomic orbital, the HOMO−1 and HOMO orbitals are delocalized among rhenium ion, bromide and hpb^- ligands. Accordingly, the transitions assigned to the longest wavelength experimental band can be seen as mixed bromide/hpb → Re (*Ligand–Metal Charge Transfer*; *LMCT*) and d → d (*Ligand Field; LF*) transitions.

The experimental absorption band at 407.6 nm can be assigned to *Ligand–Metal Charge Transfer* transitions occurring from the bromide, triphenylphosphine and hpb^- ligands to d rhenium orbitals.

The absorption bands at 308.5 and 209.3 nm result mainly from *Ligand–Ligand Charge Transfer* and interligand (*IL*) transitions. However, some contribution of the *Ligand–Metal Charge Transfer* from

Table 12
The energy and molar absorption coefficients of experimental absorption bands and the electronic transitions calculated with the TDDFT method for **5**.

The most important orbital excitations	Character	λ [nm]	E [eV]	f	Experimental Λ [nm] (E [eV])ε
H → L	d/π(hpb)/π(OMe) → d/π*(hpb)	747.6	1.66	0.0004	639.6 (1.94) 65
H → L+1	d/π(hpb)/π(OMe) → d/π*(hpb)	413.2	3.00	0.0180	413.0 (3.00) 22 400
H−1 → L	π(hpb)/π(OMe) → d/π*(hpb)	411.6	3.01	0.0065	
H → L+3	d/π(hpb)/π(OMe) → d/π*(hpb)	401.8	3.09	0.0104	
H−2 → L	π(hpb)/π(O_t) → d/π*(hpb)	380.0	3.26	0.1121	342.7 (3.62) 61 000
H−1 → L+1	π(hpb)/π(OMe) → d/π*(hpb)	375.4	3.30	0.0525	
H−2 → L+1	π(hpb)/π(O_t) → d/π*(hpb)	359.2	3.45	0.0251	
H−1 → L+2	π(hpb)/π(OMe) → π*(hpb)	332.5	3.72	0.0656	
H−5 → L	π(hpb) → d/π*(hpb)	317.3	3.91	0.0252	294.0 (4.21) 116 000
H−5 → L	π(hpb) → d/π*(hpb)	313.9	3.95	0.0287	
H−2 → L+2	π(hpb)/π(O_t) → π*(hpb)	311.4	3.98	0.1677	
H−7 → L	π(OMe)/π(O_t) → d/π*(hbt)	302.9	4.09	0.0400	
H−4 → L+1	π(hpb) → d/π*(hpb)	299.3	4.14	0.3330	
H−7 → L	π(OMe)/π(O_t) → d/π*(hbt)				
H−2 → L+3	π(hpb)/π(O_t) → d/π*(hpb)	297.4	4.17	0.0861	
H−5 → L+1	π(hpb) → d/π*(hpb)	295.5	4.20	0.1301	
H−3 → L+2	π(hpb) → π*(hpb)	276.0	4.49	0.1979	
H−4 → L+2	π(hpb) → π*(hpb)	275.3	4.50	0.1323	
H−5 → L+2	π(hpb) → π*(hpb)	269.0	4.61	0.0440	245.2 (5.06) 113 000
H−11 → L	π(hpb)/π(OMe)/π(O_t) → d/π*(hpb)	264.2	4.69	0.0350	
H−4 → L+3	π(hpb) → d/π*(hpb)	261.5	4.74	0.0818	
H → L+8	d/π(hpb)/π(OMe) → π*(hpb)				
H−5 → L+3	π(hpb) → d/π*(hpb)	256.4	4.84	0.0965	
H−9 → L	π(hpb) → d/π*(hpb)	255.1	4.86	0.0358	
H−10 → L+1	π(hpb)/π(OMe) → d/π*(hpb)				
H → L+9	d/π(hpb)/π(OMe) → π*(hpb)	253.9	4.88	0.0519	
H−9 → L	π(hpb) → d/π*(hpb)	249.9	4.96	0.0334	
H−11 → L+2	π(hpb)/π(OMe)/π(O_t) → π*(hpb)	218.8	5.66	0.0319	213.7 (5.80) 190 000
H−2 → L+9	π(hpb)/π(O_t) → π*(hpb)	213.6	5.80	0.0312	
H−3 → L+4	π(hpb) → π*(hpb)	213.5	5.81	0.0511	
H−9 → L+3	π(hpb) → d/π*(hpb)	210.9	5.88	0.0673	
H−2 → L+9	π(hpb)/π(O_t) → π*(hpb)				
H−13 → L	π(hpb) → d/π*(hpb)	207.2	5.98	0.0354	
H−5 → L+5	π(hpb) → π*(hpb)				
H−5 → L+5	π(hpb) → π*(hpb)	206.6	6.00	0.0599	
H−5 → L+5	π(hpb) → π*(hpb)	206.1	6.01	0.0931	
H−1 → L+14	π(hpb)/π(OMe) → d	203.4	6.10	0.1271	
H−1 → L+14	π(hpb)/π(OMe)→d	202.3	6.13	0.0969	
H−4 → L+6	π(hpb) → π*(hpb)				
H−1 → L+14	π(hpb)/π(OMe) → d	201.7	6.15	0.1700	
H−14 → L+1	π(hpb)/π(O_t) → d/π*(hpb)				
H−13 → L+1	π(hpb) → d/π*(hpb)	200.3	6.19	0.1536	
H−4 → L+8	π(hpb) → d/π*(hpb)	199.2	6.23	0.0307	

the bromide, triphenylphosphine and hpb$^-$ orbitals to the d rhenium orbitals in these bands is also confirmed by the calculations.

3.8. Electronic spectrum of **4**

As can be seen from Figs. 8 and 9, the UV/Vis spectra of the *cis* and *trans* stereoisomers are very similar in terms of the position, intensity and shape of the bands, as well as character of the assigned transitions (see Tables 10 and 11). The longest wavelength experimental band of **2** at 665.9 nm can be seen as mixed bromide/hpb → Re (*Ligand–Metal Charge Transfer*; *LMCT*) and d → d (*Ligand Field; LF*) transitions. The experimental absorption band at 398.8 nm is attributed to *Ligand–Metal Charge Transfer* transitions occurring from the bromide, triphenylarsine and hpb$^-$ ligands to *d* rhenium orbitals.

The absorption bands at 306.6, 245.2 and 202.1 nm result mainly from *Ligand–Ligand Charge Transfer* and interligand (*IL*) transitions. However, some contribution of the *Ligand–Metal Charge Transfer* from the bromide, triphenylphosphine and hpb$^-$ orbitals to the d rhenium orbitals in these bands is also confirmed by the calculations.

3.9. Electronic spectrum of **5**

The longest wavelength experimental band of **5** at 639.9 originates in the HOMO → LUMO transition. The HOMO and LUMO orbitals are delocalized among rhenium ion, bromide, oxo and hpb ligands, so a delocalized *MLLCT* (metal–ligand-to-ligand CT) description can be used. However, considering that HOMO and LUMO comprise mainly rhenium 5d atomic orbitals (Fig. 5), the HOMO → LUMO may be also ascribed as transition of d → d character.

The experimental bands at 413.0 and 342.7 nm can be assigned to *Ligand–Metal Charge Transfer* transitions occurring from the bromide, oxo and hpb$^-$ ligands to d rhenium orbitals.

The experimental bands below 300 nm result mainly from *Ligand–Ligand Charge Transfer* and interligand (*IL*) transitions.

Supplementary data

CCDC 734586, 734587, 734588, 734589, 734590 and 734591 contain the supplementary crystallographic data for this paper. These data can be obtained free of charge via http://www.ccdc.cam.ac.uk/conts/retrieving.html, or from the Cambridge Crystallographic Data Centre, 12 Union Road, Cambridge CB2 1EZ, UK; fax: (+44) 1223-336-033; or e-mail: deposit@ccdc.cam.ac.uk.

Acknowledgements

The GAUSSIAN-03 calculations were carried out in the Wrocław Centre for Networking and Supercomputing, WCSS, Wrocław, Poland, http://www.wcss.wroc.pl, under calculational Grant No. 51/96.

References

[1] C.C. Romão, F.E. Kühn, W.A. Hermann, Chem. Rev. 97 (1997) 3197.
[2] A.A. Shteinman, Russ. Chem. Bull., Int. Ed. 50 (2001) 1795.
[3] F.E. Kühn, A. Scherbaum, W.A. Herrmann, J. Organomet. Chem. 689 (2004) 4149.
[4] G.S. Owens, J. Arias, M.M. Abu-Omar, Catal. Today 55 (2000) 317.
[5] A.M. Kirillov, M. Haukka, M.V. Kirillova, A.J.L. Pombeiro, Adv. Synth. Catal. 347 (2005) 1435.
[6] A. Deloffre, S. Halut, L. Salles, J.-M. Brégeault, J.R. Gregorio, B. Denise, H. Rudler, J. Chem. Soc., Dalton Trans. (1999) 2897.
[7] J.R. Dilworth, S.J. Parrott, Chem. Soc. Rev. 27 (1998) 43.
[8] P. Blower, Dalton Trans. (2006) 1705.
[9] B. Machura, S. Michalik, R. Kruszynski, J. Kusz, Polyhedron 26 (2007) 2837.
[10] B. Machura, R. Kruszynski, Polyhedron 26 (2007) 2957.
[11] B. Machura, R. Kruszynski, Polyhedron 26 (2007) 3686.
[12] B. Machura, J. Kusz, Polyhedron 27 (2008) 187.
[13] B. Machura, R. Kruszynski, J. Kusz, Polyhedron 27 (2008) 1679.
[14] B. Machura, R. Kruszynski, J. Kusz, Polyhedron 26 (2007) 3455.
[15] B. Machura, J. Kusz, Polyhedron 27 (2008) 923.
[16] Y.-P. Tong, S.-L. Zheng, X.-M. Chen, Eur. J. Inorg. Chem. (2005) 3734.
[17] Y.-P. Tong, Acta Crystallogr., Sect. E: Struct. Rep. Online 61 (2005) m1771.
[18] H.-Y. Bu, Y.-J. Liu, Q.-F. Liu, J.-F. Jia, Acta Crystallogr., Sect. E: Struct. Rep. Online 61 (2005) m1986.
[19] Y. Xi, J. Li, F. Zhang, Acta Crystallogr., Sect. E: Struct. Rep. Online 61 (2005) m1953.
[20] P. Tong, Acta Crystallogr., Sect. E: Struct. Rep. Online 61 (2005) m1595.
[21] R. Czerwieniec, A. Kapturkiewicz, R. Anulewicz-Ostrowska, J. Nowacki, J. Chem. Soc. Dalton Trans. (2002) 3434.
[22] J. Gancheff, C. Kremer, E. Kremer, O.N. Ventura, J. Mol. Struct. (Theochem) 580 (2002) 107.
[23] M.L. Kuznestov, E.A. Klestova-Nadeeva, A.I. Dement'ev, J. Mol. Struct. (Theochem) 671 (2004) 229.
[24] G. Rouschias, G. Wilkinson, J. Chem. Soc. A (1966) 465.
[25] CRYSALIS RED, Oxford Diffraction Ltd., Version 1.171.29.2. G.M. Sheldrick, Acta Crystallogr., Sect. A 46 (1990) 467.
[26] G.M. Sheldrick, Acta Crystallogr., Sect. A 46 (1990) 467.
[27] G.M. Sheldrick, SHELXL97. Program for the Refinement of Crystal Structures, University of Gttingen, Germany, 1997.
[28] G.M. Sheldrick, SHELXTL: Release 4.1 for Siemens Crystallographic Research Systems, 1990.
[29] M.J. Frisch, G.W. Trucks, H.B. Schlegel, G.E. Scuseria, M.A. Robb, J.R. Cheeseman, J.A. Montgomery, Jr., T. Vreven, K.N. Kudin, J.C. Burant, J.M. Millam, S.S. Iyengar, J. Tomasi, V. Barone, B. Mennucci, M. Cossi, G. Scalmani, N. Rega, G.A. Petersson, H. Nakatsuji, M. Hada, M. Ehara, K. Toyota, R. Fukuda, J. Hasegawa, M. Ishida, T. Nakajima, Y. Honda, O. Kitao, H. Nakai, M. Klene, X. Li, J.E. Knox, H.P. Hratchian, J.B. Cross, V. Bakken, C. Adamo, J. Jaramillo, R. Gomperts, R.E. Stratmann, O. Yazyev, A.J. Austin, R. Cammi, C. Pomelli, J.W. Ochterski, P.Y. Ayala, K. Morokuma, G.A. Voth, P. Salvador, J.J. Dannenberg, V.G. Zakrzewski, S. Dapprich, A.D. Daniels, M.C. Strain, O. Farkas, D.K. Malick, A.D. Rabuck, K. Raghavachari, J.B. Foresman, J.V. Ortiz, Q. Cui, A.G. Baboul, S. Clifford, J. Cioslowski, B.B. Stefanov, G. Liu, A. Liashenko, P. Piskorz, I. Komaromi, R.L. Martin, D.J. Fox, T. Keith, M.A. Al-Laham, C.Y. Peng, A. Nanayakkara, M. Challacombe, P.M.W. Gill, B. Johnson, W. Chen, M.W. Wong, C. Gonzalez, J.A. Pople, GAUSSIAN 03, Revision D.01, Gaussian Inc., Wallingford CT, 2004.
[30] A.D. Becke, J. Chem. Phys. 98 (1993) 5648.
[31] C. Lee, W. Yang, R.G. Parr, Phys. Rev. B 37 (1988) 785.
[32] P.J. Hay, W.R. Wadt, J. Chem. Phys. 82 (1985) 299.
[33] K. Eichkorn, F. Weigend, O. Treutler, R. Ahlrichs, Theor. Chem. Acc. 97 (1997) 119.
[34] W.J. Hehre, R. Ditchfield, J.A. Pople, J. Chem. Phys. 56 (1972) 2257.
[35] P.C. Hariharan, J.A. Pople, Theor. Chim. Acta 28 (1973) 213.
[36] M.M. Francl, W.J. Petro, W.J. Hehre, J.S. Binkley, M.S. Gordon, D.J. DeFrees, J.A. Pople, J. Chem. Phys. 77 (1982) 3654.
[37] T. Clark, J. Chandrasekhar, P.v.R. Schleyer, J. Comp. Chem. 4 (1983) 294.
[38] R. Krishnam, J.S. Binkley, R. Seeger, J.A. Pople, J. Chem. Phys. 72 (1980) 650.
[39] P.M.W. Gill, B.G. Johnson, J.A. Pople, M.J. Frisch, Chem. Phys. Lett. 197 (1992) 499.
[40] M.E. Casida, in: J.M. Seminario (Ed.), Recent Developments and Applications in Modern Density Functional Theory, Theoretical and Computational Chemistry, vol. 4, Elsevier, Amsterdam, 1996.
[41] M.T. Cances, B. Mennucci, J. Tomasi, J. Chem. Phys. 107 (1997) 3032.
[42] M. Cossi, V. Barone, B. Mennucci, J. Tomasi, Chem. Phys. Lett. 286 (1998) 253.
[43] B. Mennucci, J. Tomasi, J. Chem. Phys. 106 (1997) 5151.
[44] M. Cossi, G. Scalmani, N. Rega, V. Barone, J. Chem. Phys. 117 (2002) 43.
[45] E.D. Glendening, A.E. Reed, J.E. Carpenter, F. Weinhold, NBO Version 3.1.
[46] A. Sachse, N.C. Mösch-Zanetti, G. Lyashenko, J.W. Wielandt, K. Most, J. Magull, F. Dall'Antonia, A. Pal, R. Herbst-Irmer, Inorg. Chem. 46 (2007) 7126.
[47] G.A. Jeffrey, W. Saenger, Hydrogen Bonding in Biological Structures, Springer-Verlag, 1994.
[48] G.R. Desiraju, T. Steiner, The Weak Hydrogen Bond in Structural Chemistry and Biology, Oxford University Press, 1999.
[49] J.M. Mayer, Inorg. Chem. 27 (1988) 3899.
[50] S.R. Flechter, A.C. Skapski, J. Chem. Soc., Dalton Trans (1972) 1073.
[51] F.H. Allen, Acta Crystallogr., Sect. B 58 (2002) 380.
[52] E. Reed, L.A. Curtiss, F. Weinhold, Chem. Rev. 88 (1988) 899.
[53] M.L. Kuznestov, A.J.L. Pombeiro, J. Chem. Soc., Dalton Trans. (2003) 738.

2.2. Synthesis of the complex $\{[Fe^{II}(phen)_3]_2[Fe^{III}ox_5]\}\cdot 11H_2O$ (**1**)

Complex **1**, as red plates, can be prepared (yield about 75%) by slow evaporation of aqueous solutions (30 mL) containing iron(III) chloride (0.5 mmol), oxalic acid (1 mmol), and the phenantroline ligand (1.0 mmol) previously solubilized in the minimum amount of ethanol. The crystals were filtered off and dried on filter paper at air. *Anal.* Calc. for $C_{82}H_{70}Fe_4N_{12}O_{31}$ (**1**): C, 50.99; H, 3.63; N, 8.65. Found: C, 50.92; H; 3.68; N, 8.71%. Water content was confirmed by thermogravimetric analysis (TGA).

2.3. Crystallographic data collection and structure determinations

X-ray diffraction data were collected using a Bruker–Nonius X8APEX CCD area detector diffractometer. Graphite-monochromated Mo Kα radiation (α = 0.71073 Å) was used. The theta range for data collection is 1.63–32.09°, the index ranges are $-18 \leqslant h \leqslant 18$, $-19 \leqslant k \leqslant 19$, $-20 \leqslant l \leqslant 19$.

The data were processed through the SAINT [11] reduction and SADABS [12] absorption software. The structures were solved by direct methods and subsequently completed by Fourier recycling using the SHELXTL software package. [13] Non-hydrogen atoms were refined anisotropically, with the exception of the O(6w) atom. This latter has been located on the Δ*F* map, with an occupancy factor of 0.5, and shows a very large thermal motion. The hydrogen atoms of the O(6w) water molecule were not defined, while those of the other water molecules were located on the Δ*F* map and refined with restrains. The short O(6 W)···O(5Wb) contact [2.392(8) Å, (b) $-x+1, -y+2, -z$] is most likely a consequence of the high thermal disorder of O(6w).

The final formulation of the compound is in agreement with the residual electron density and elemental analysis.

3. Results and discussion

The structure of compound **1** consists of centrosymmetric dinuclear $[Fe_2(ox)_5]^{4-}$ anions, mononuclear $[Fe(phen)_3]^{2+}$ cations (Fig. 1) and crystallization water molecules linked together by means of electrostatic interactions and hydrogen bonds. The resulting structure is similar to that found in the parent compound of formula $[Fe(bpm)_3]_2[Fe_2(ox)_5]\cdot 8H_2O$ (**2**) that we have previously reported [10].

The anionic unit contains two Fe(III) atoms, four terminal and one bridging oxalato ligands. Each iron(III) ion has a distorted octahedral environment. The iron-bridging-oxalato bond lengths are significantly longer than those involving the terminal oxalato ligands, as already observed in complex **2**. The bridging oxalato is planar because of the inversion center located at the midpoint of the C–C bond. The $[Fe(phen)_3]^{2+}$ cation consists of iron(II) ion coordinated to three phenantroline molecules in a distorted octahedral geometry.

The average Fe(1)–N bond length is in the range of the observed bond lengths for low-spin tris-chelated iron(II) complexes [14]. The iron(III) and iron(II) bond length are reported in Table 2. The phenantroline ligands are planar, as expected.

Non-covalent interactions are expected to occur in compounds containing π systems. In the case of compound **1**, the tris-chelated cations are connected by π–π interactions in such a way as to form a supramolecular bi-dimensional motif. All the three phen ligands are involved in these stacking interactions, the mean distance between the phenantroline planes being 3.48(1) Å. A similar supramolecular arrangement is not found in compound **2**, where only two of the bpm molecules of the $[Fe(bpm)_3]^{2+}$ cation are involved in stacking interactions, leading to a chain motif along the *b* crystallographic axis. The anionic dimers in **1** alternate with the cations

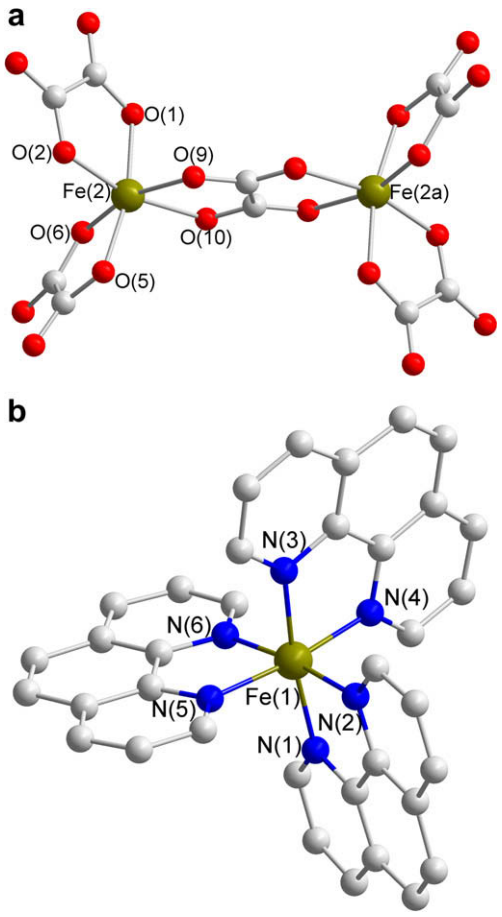


Fig. 1. A view of the anionic dimeric unit (a) and the monomeric cation (b) with the atomic labeling scheme. Hydrogen atoms have been omitted for clarity.

Table 1
Crystal data and structure refinement for compounds **1**.

Empirical formula	$C_{41}H_{35}Fe_2N_6O_{15.5}$
Formula weight	971.45
Temperature (K)	273(2)
Wavelength (Å)	0.71073
Crystal system	triclinic
Space group	$P\bar{1}$
Unit cell dimensions	
a (Å)	13.3131(5)
b (Å)	13.5155(5)
c (Å)	13.8183(7)
α (°)	60.792(1)
β (°)	72.293(2)
γ (°)	72.971(1)
Volume (Å^3)	2036.0(2)
Z	2
D_{calc} (Mg/m^3)	1.585
Absorption coefficient (mm^{-1})	0.795
F(0 0 0)	998
Crystal size (mm)	0.30 × 0.22 × 0.15
θ Range for data collection	1.63–25.00°
Reflections collected	34 151
Independent reflections [R_{int}]	7150 [0.0323]
Completeness to θ = 25.00°	99.9%
Data/restraints/parameters	7150/15/608
Goodness-of-fit (GOF) on F^2	1.086
Final *R* indices [$I > 2\sigma(I)$]	[a] $R_1 = 0.0383$, [b,c] $wR_2 = 0.0996$
R indices (all data)	[a] $R_1 = 0.0505$, [b,c] $wR_2 = 0.1062$
Largest difference in peak and hole (e Å^{-3})	0.534 and −0.606

[a] $R_1 = \sum(|F_o| - |F_c|)/\sum|F_o|$.
[b] $wR_2 = \{\sum[w(F_o^2 - F_c^2)^2]/\sum[w(F_o^2)^2]\}^{1/2}$.
[c] $w = 1/[\sigma^2(F_o^2) + (aP)^2 + bP]$ with $P = [F_o^2 + 2F_c^2]/3$, $a = 0.0612$ and $b = 0.24$.

Table 2
Selected bond lengths (Å) and angles (°) of compound **1**.

Fe(1)–N(4)	1.976(2)	Fe(2)–O(2)	1.958(2)
Fe(1)–N(6)	1.977(2)	Fe(2)–O(5)	1.969(2)
Fe(1)–N(1)	1.979(2)	Fe(2)–O(6)	1.986(2)
Fe(1)–N(3)	1.982(2)	Fe(2)–O(1)	2.009(2)
Fe(1)–N(5)	1.985(2)	Fe(2)–O(9)	2.055(2)
Fe(1)–N(2)	1.988(2)	Fe(2)–O(10)	2.086(2)
N(4)–Fe(1)–N(6)	93.19(7)	O(2)–Fe(2)–O(5)	89.6(1)
N(4)–Fe(1)–N(1)	92.86(8)	O(2)–Fe(2)–O(6)	102.99(9)
N(6)–Fe(1)–N(1)	93.41(8)	O(5)–Fe(2)–O(6)	81.6(1)
N(4)–Fe(1)–N(3)	82.68(8)	O(2)–Fe(2)–O(1)	80.44(9)
N(6)–Fe(1)–N(3)	92.97(8)	O(5)–Fe(2)–O(1)	167.1(1)
N(1)–Fe(1)–N(3)	172.41(8)	O(6)–Fe(2)–O(1)	92.4(1)
N(4)–Fe(1)–N(5)	173.35(8)	O(2)–Fe(2)–O(9)	93.44(9)
N(6)–Fe(1)–N(5)	82.54(8)	O(5)–Fe(2)–O(9)	93.2(1)
N(1)–Fe(1)–N(5)	92.48(8)	O(6)–Fe(2)–O(9)	162.69(9)
N(3)–Fe(1)–N(5)	92.42(8)	O(1)–Fe(2)–O(9)	95.7(1)
N(4)–Fe(1)–N(2)	92.5487)	O(2)–Fe(2)–O(10)	164.8(1)
N(6)–Fe(1)–N(2)	173.15(8)	O(5)–Fe(2)–O(10)	104.1(1)
N(1)–Fe(1)–N(2)	82.54(8)	O(6)–Fe(2)–O(10)	85.83(9)
N(3)–Fe(1)–N(2)	91.48(8)	O(1)–Fe(2)–O(10)	86.9(1)
N(5)–Fe(1)–N(2)	92.09(8)	O(9)–Fe(2)–O(10)	79.39(8)

within the supramolecular planes. Water molecules are located among the anionic dimers, filling the gaps between these planes.

The most interesting feature of the solid state structure of **1** is the formation of decanuclear water clusters (Fig. 2) self-assembled by means of hydrogen bonding interactions between water molecules. The classification of the decamer in the Infantes and Motherwell nomenclature is not obvious to us [2a]. Each decanuclear water cluster consists of a cyclic hexanuclear water cluster hydrogen bonded to an unclosed trinucler cluster and an additional water molecule. The $(H_2O)_{10}$ clusters display extensive multiple interactions with the dimeric units, by means of hydrogen bonds with the terminal oxalate ligands. These multiple interactions play a key role in the structural stabilization and formation of an extended 3D supramolecular assembly, wherein extended tapes of hexameric water clusters interconnected with dodecameric hybrid water–$O_{oxalate}$ clusters can be recognized (Figs. 3 and 4) when the equally strong H-bonding interactions of water molecules with the inorganic host are included.

The geometrical parameters of the decameric water clusters and their interactions with the bimetallic host are collected in Table 3.

Symmetry-generated water molecules [O(1 W)···O(2Wd)···O(3Wa)···O(1Wb)···O(2Wc)···O(3We), where (a) $-x, -y+1, -z+1$; (b) $-x, -y+1, -z+2$; (c) $-x+1, y, z+1$; (d) $-x+1, -y+1, -z+1$; (e) $x, y, z+1$] are interconnected to assemble the $(H_2O)_6$ cluster with a slightly puckered conformation (mean deviation from the ideal plane of 0.14(1) Å). Cyclic planar water hexamer is the basic structural motif found in ice II structure under high pressure [15] and a computational simulation determinated that it is a predominant structural unit [16] in liquid water, too. A quasi-planar hexamer was also detected within a helium droplet [17]. The planar water hexamers can be regarded as the simplest supramolecular analogues of benzene.

Each water molecules within the hexanuclear cluster act at once as donor and acceptor of two hydrogen bonds. Within the hexameric water clusters the average O···O contact is of ca. 2.816(3) Å, comparable to that observed in other discrete $(H_2O)_6$ clusters [7–9,18] which are trapped by various metal–organic matrixes. This distance in regular ice, in liquid water, and in the vapor phase is, respectively, 2.74, 2.85, and 2.98 Å [19]. The average O···O distances reported for the Ice II phase are 2.77–2.84 [20]. The nonbonding O···Ô···O angles (Table 1) in **1** span a wide range [108.9(3)–132.1(3)°] deviating considerably from an ideal benzene-like structure.

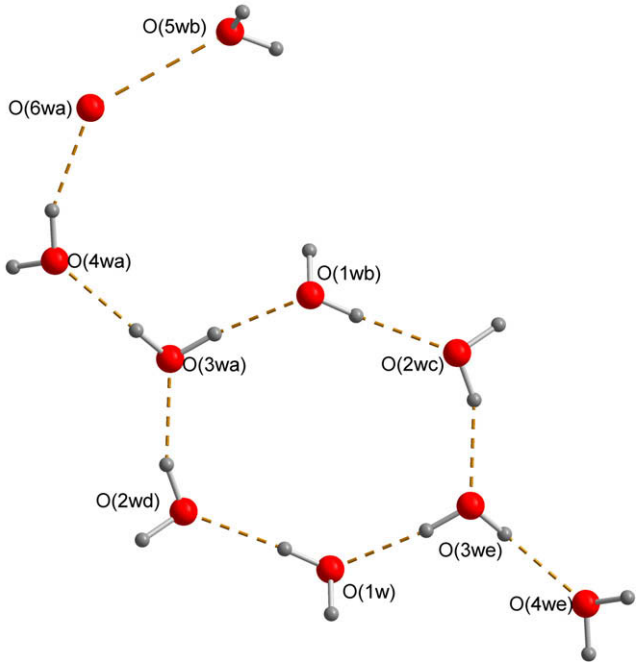


Fig. 2. A view of the decanuclear water cluster showing the atomic labeling scheme. (Symmetry transformations used to generate equivalent atoms: (a) $-x, -y+1, -z+1$; (b) $-x, -y+1, -z+2$; (c) $-x+1, y, z+1$; (d) $-x+1, -y+1, -z+1$; (e) $x, y, z+1$.)

The unclosed trinuclear cluster is defined by the O(4wa), O(5wb) and O(6wa) set of atoms, hydrogen bonded *via* O(4wa) to the O(3wa) water molecule of the exanuclear cluster, the mean O···O distance being 2.859(6) Å.

The decanuclear clusters are connected to the anionic dimers, by means of hydrogen bonding interactions with the oxygen atoms of the oxalate ligands [O(1wb)···O(3b), O(2wd)···O(6), O(4wa)···O(7f), O(4wa)···O(8f), O(5wb)···O(3b), O(5wb)···O(4b) and O(5wb)···O(7 g), where (f) $-x, -y+2, -z+1$; (g) $x-1, y, z+1$], the mean O···O distance being 2.988(4) Å, generating a 3D supramolecular network as showed in Fig. 3b. The atomic labeling scheme is reported in Fig. 4a. Taking into account these water–oxalate interactions, the total H-bond pattern can be alternatively described as extended tapes of fused water hexamers and hybrid dodecameric water–$O_{oxalate}$ clusters (Fig. 4b). This latter accommodate in its cavity a dangling water molecule [O(6wa)] which interact by means of hydrogen bonds with two water molecules of the cluster [O(6wa)···O(4wa), O(6wa)···O(5wb) and O(6wa)···O(5wh), where (h) $x-1, y+1, z$]. Other hybrid water clusters containing water molecules hydrogen bonded with other solvents, counterions, or small molecules have been reported [21].

For comparing compound **1** with the previously reported compound **2**, we performed a careful analysis of the crystal structure that reveals the presence of isolated hexameric water clusters with a chair-like conformation in compound **2**.

Within the hexameric water clusters the average O···O contact is of ca. 2.925(3) Å, and the nonbonding O···Ô···O angles span a wide range [70.3(2)–125.3(2)°]. These values are essentially in agreements with those reported for other water cluster with a chair conformation [7]. The presence of a longer interaction [O(14)···O(13b) 3.136(2) Å, (b) $1-x, -y, -z$], if compared with the other O···O contacts within the cluster, and of a small nonbonding O···Ô···O angle [O(11)···Ô(13b)···O(14) 70.3(2)°] let suppose a very strained hexamerix water cluster conformation, that tends towards the limit of two isolated trimers.

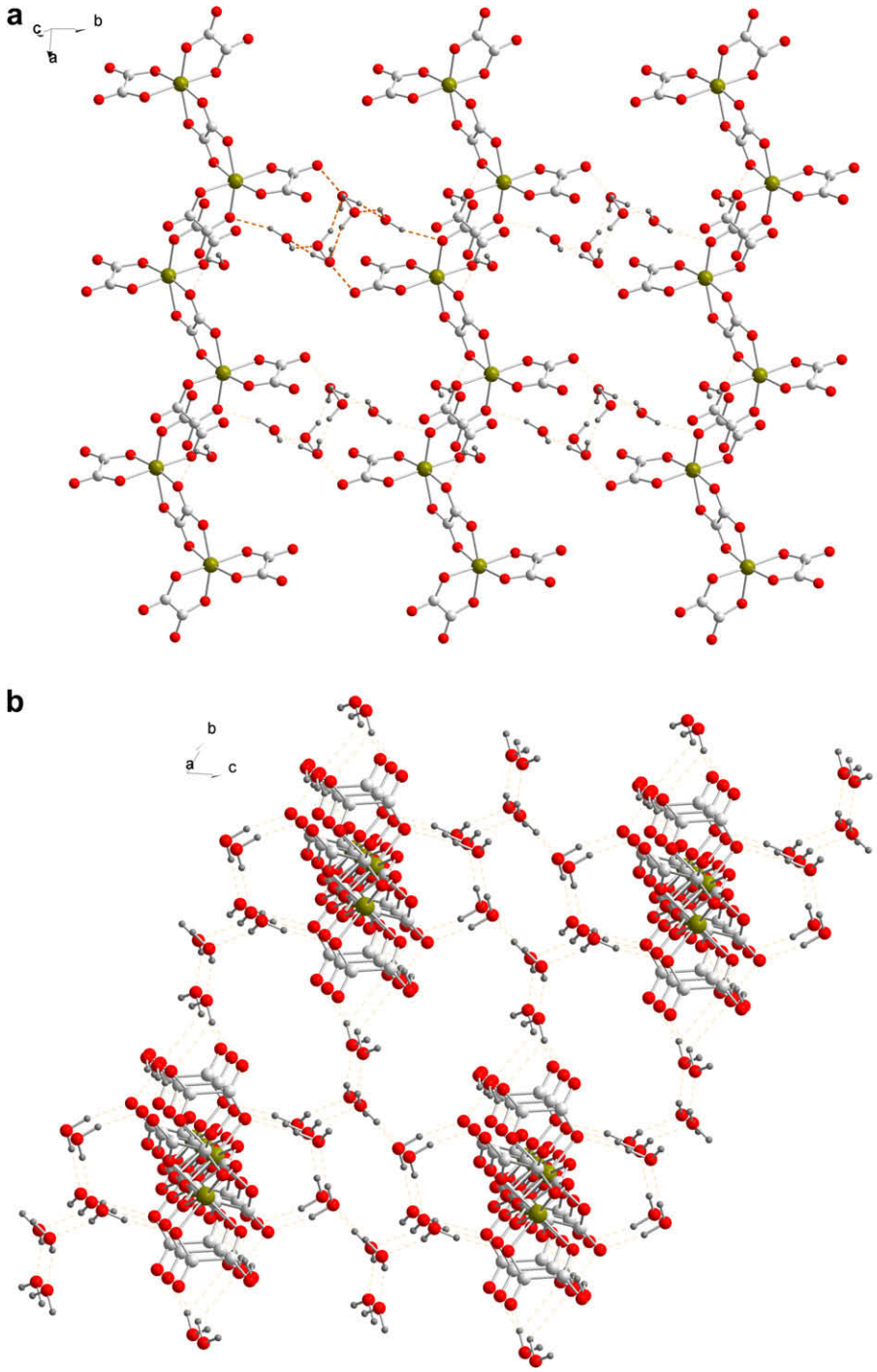


Fig. 3. A view of the 2D (a) and 3D (b) supramolecular motif in compounds **2** and **1**, respectively. The O(6w) water molecule has been omitted for clarity in this picture.

In this case the clusters are directly hydrogen bonded to the oxygen atoms of the oxalate ligands of two dimeric units [O(11)···O(5) 2.879 Å, O(13)···O(4a) 2.942(2) Å, (a) $3-x$, $1-y$, $-z$]. The anionic dimers are also involved in H-bonding interactions with additional water molecules [O(12)···O(8) 2.879(2) Å, O(12)···O(9b) 3.049(2) Å, (b) $1-x$, $-y$, $-z$], these latter interactions producing a supramolecular chain motif along the *a* crystallographic axes. The atomic labeling scheme is shown in Fig. 5. The sum of both interactions leads to a supramolecular bi-dimensional motif in the *xy* plane (see Fig. 6a). The $[Fe(bpm)_3]^{2+}$ cations are sandwiched between these planes. On the contrary in compound **1** the resulting supramolecular structure provided by the H-bonding interactions is trhee-dimensional and cations and anions nearly lie within a same plane.

We want to conclude this work with some considerations on the different nuclearity of water aggregates in compounds **1** and **2** and the changed conformation of the water hexamer moiety in both compounds.

The $[Fe(phen)_3]^{2+}$ cations result to be more effective in the construction of extended water clusters, if compared with the $[Fe(bpm)_3]^{2+}$ cation, since acting like a bulkier spacer it's able to create larger voids between the anions which are filled by a major

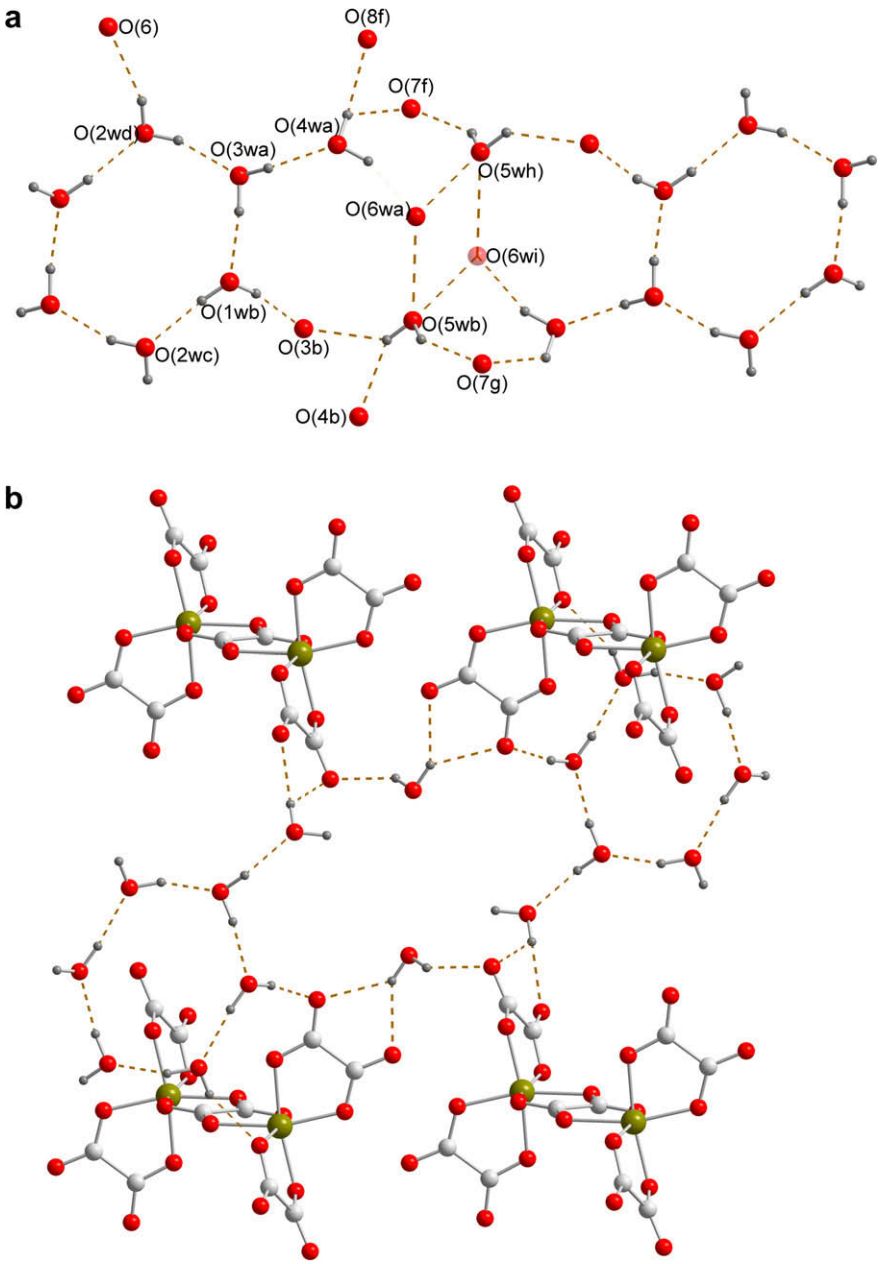


Fig. 4. A view of the interaction of the decanuclear water clusters with the oxalate dimers showing the atomic labeling scheme (a). The two equivalent positions of the O(6w) water molecule are showed in the picture. Fragment of the crystal packing diagram showing the hexameric water clusters interconnected with the dodecameric hybrid water···$O_{oxalate}$ cluster . The O(6w) water molecule has been omitted for clarity. (b) Symmetry transformations used to generate equivalent atoms: (f) $-x$, $-y+2$, $-z+1$; (g) $x-1$, y, $z+1$; (h) $x-1$, $y+1$, z; (i) $x-1$, $y+1$, $z+1$.

number of water molecules. These hipotesys are also supported by the comparison of both structures with those of the other dinuclear penta-oxalate compounds reported in the crystallographic database. To the best of our knowledge, only the compound of formula $\{(NH_2CH_2CH_2)_2[Zn_2ox_5]\}\cdot 8H_2O$ containing the piperazinium cation show the presence of a tetranuclear water cluster [22]. The smaller or linear-shaped cations of the other compounds [23] seems not allowing the formation of similar water clusters.

Both compounds shows the presence of cyclic hexanuclear motifs with different conformations. As stated before, theoretical calculations for the hexameric conformation have revealed the existence of several almost isoenergetic conformations, suggesting that the conformation that will be detected for a cluster strongly depends on its chemical environment. On this subject it has been recently reported that a gradual tuning of the chemical environment is a general strategy to promote the inclusion of relatively large water clusters in certain crystalline salts and to control their size and shape [3].

In our case, the occurrence of hydrogen bonding interactions with the anionic dimers and the presence of two bulky and globular-shaped cations are responsible of the formation of the hexameric water clusters in both compounds. The conformation of such water molecules arrays, on the contrary, seems be most likely affected by the size of the templating cation and the resulting supramolecular arrangement. While the $[Fe(phen)_3]^{2+}$ cation stabilize an higher nuclearity clusters and the almost planar form of the hexameric cluster in **1,** the $[Fe(bpm)_3]^{2+}$ cation support the chair conformation. The Fe···Fe distances between the two $[Fe_2(ox)_5]^{4-}$

Table 3
Hydrogen bonds for compound **1** (Å and °).

D–H···A	*d*(D–H)	*d*(H···A)	*d*(D···A)	<(DHA)
O(1 W)–H(1WB)···O(2 Wd)	0.94(1)	1.97(2)	2.855(3)	157(3)
O(2W)–H(2WB)···O(3 Wl)	0.95(1)	1.90(2)	2.773(3)	153(3)
O(3W)–H(3WA)···O(1 Wm)	0.95(1)	1.87(1)	2.819(3)	172(3)
O(1W)–H(1WA)···O(3)	0.95(1)	1.85(1)	2.777(4)	166(3)
O(3 W)–H(3WB)···O(4 W)	0.867(2)	1.942(3)	2.809(4)	178.6(2)
O(4 W)–H(4WA)···O(7n)	0.95(1)	2.57(3)	3.195(5)	124(3)
O(5 W)–H(5 WB)···O(3)	0.95(1)	2.21(3)	3.003(5)	141(4)
O(5W)–H(5WA)···O(7d)	0.96(1)	2.07(3)	2.908(5)	146(4)
O(2 W)–H(2WA)···O(6d)	0.95(1)	2.20(2)	3.075(3)	152(3)
O(4 W)–H(4WA)···O(8n)	0.95(1)	2.05(2)	2.957(4)	159(4)
O(5 W)–H(5WB)···O(4)	0.95(1)	2.21(3)	3.003(5)	141(4)
O(4 W)–H(4WB)···O(6 W)	0.95(1)	1.98(2)	2.864(9)	153(4)

Symmetry transformations used to generate equivalent atoms: (d) $-x+1, -y+1, -z+1$, (l) $x+1, y, z$, (m) $x, y, z-1$, (n) $x, y-1, z$.

anions supporting the hexameric cluster increases from 11.51(1) Å in **2** to 12.86(1) Å in **1** (Fig. 6), as a result of the altered supramolecular arrangements caused by the presence of a different cations, namely $[Fe(phen)_3]^{2+}$ in **1**. The passage from the chair conformation to a quasi-planar one seems to represent the attempt of the water molecules to fit into a larger void and optimize the hydrogen bonding interactions with the anionic dimers.

4. Conclusions

In summary, we reported on the self-assembly of an extended 3D array comprising interconnected water hexamers and hybrid water–$O_{oxalate}$ clusters, originated in the compound of formula $[Fe^{II}(phen)_3]_2[Fe^{III}ox_5]\cdot 11H_2O$ (**1**). A comparative study was possible between the supramolecular structure of **1** and that found in the parent compound formula $[Fe(bpm)_3]_2[Fe_2(ox)_5]\cdot 8H_2O$ (**2**). The presence of different cations seem to influence the water cluster nuclearity, that increase from hexa- (**2**) to decanuclear (**1**), and the hexanuclear cluster conformation, passing from a chair (**2**) to a quasi-planar form (**1**). They are also responsible of the two different supramolecular organizations, namely the bi- and three-dimensional ones. We want finally to remark that the comparative studies on water clusters in crystalline materials are not banal, since they are in general hindered by the serendipitous nature of their occurrence and the unpredictability of their structures.

Supplementary data

CCCDC 710269 contains the supplementary crystallographic data for compounds **1**. These data can be obtained free of charge via http://www.ccdc.cam.ac.uk/conts/retrieving.html, or from the Cambridge Crystallographic Data Centre, 12 Union Road, Cambridge CB2 1EZ, UK; fax: (+44) 1223-336-033; or e-mail: deposit@ccdc.cam.ac.uk.

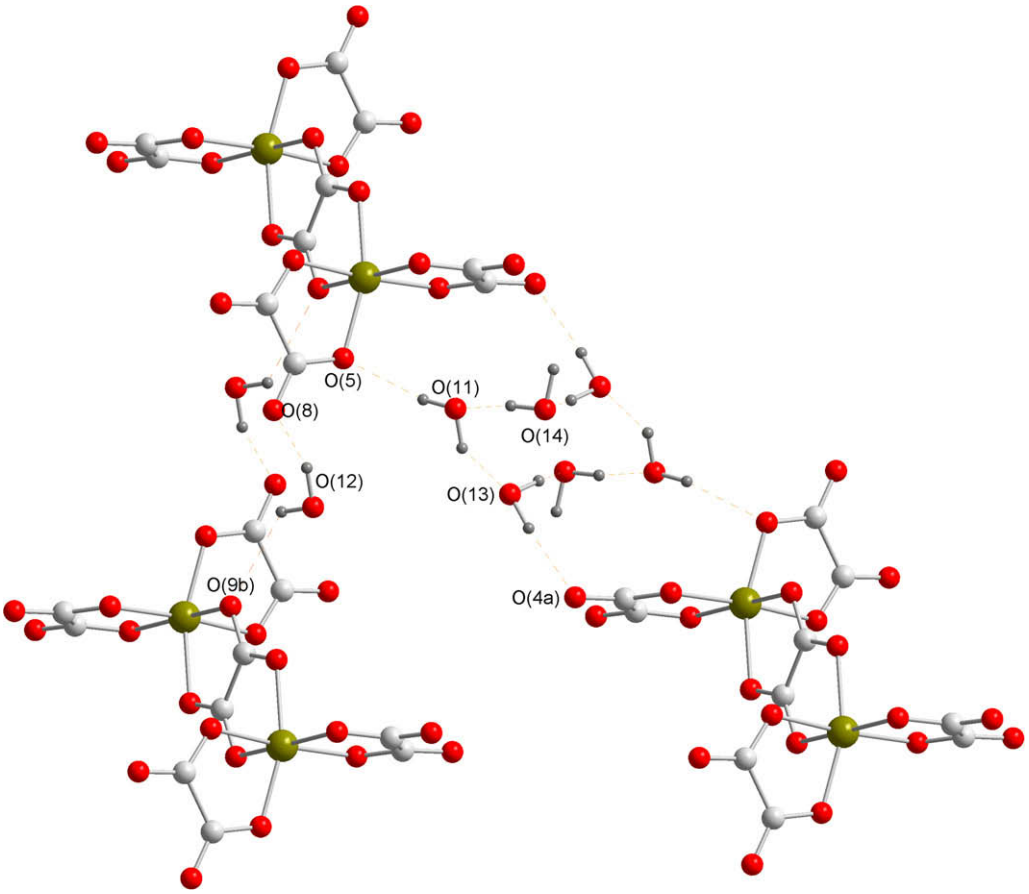


Fig. 5. Fragment of the supramolecular motif found in compound **2** showing the atomic labeling scheme.

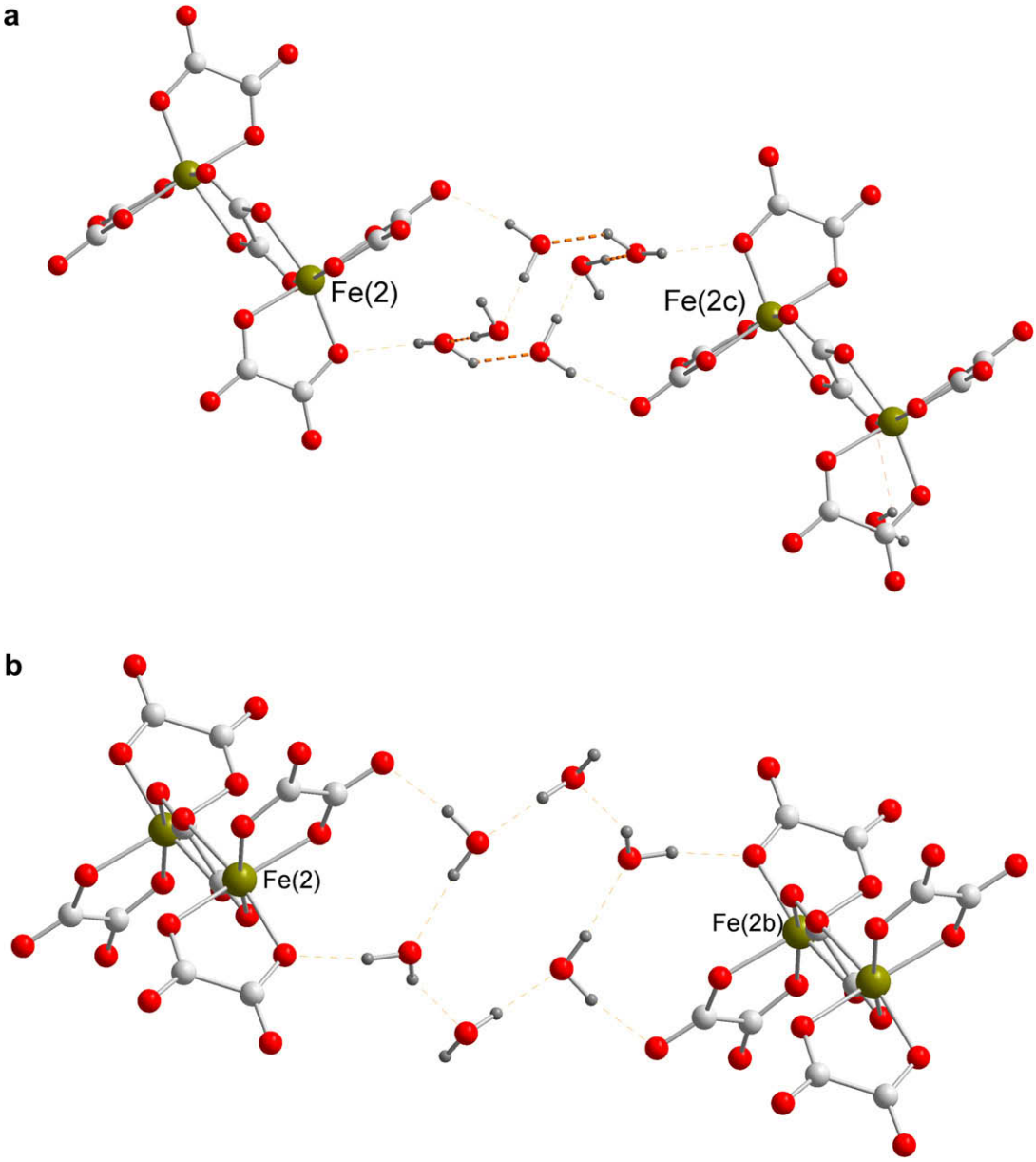


Fig. 6. A view of the two anionic dimers supporting the hexameric water clusters in compounds **2** and **1** respectively. The shorter Fe···Fe distances are 11.508(8) and 12.836(1) Å [Fe(2)···Fe(2c), where (c) $1-x$, $1-y$, $-z$ (**2**) or Fe(2)···Fe(2b), where (b) $-x$, $-y+1$, $-z+2$; (**1**)] in compounds **2** and **1**, respectively.

Acknowledgment

Financial support received from the Ministero dell'Istruzione, dell'Università e della Ricerca Scientifica (MiUR) through the Centro di Eccellenza CEMIF.CAL (CLAB01TYEF) is gratefully acknowledged.

References

[1] (a) S.D. Colson, T.H. Dunning Jr., Science 43 (1994) 265;
(b) K. Liu, J.D. Krujan, R.J. Saykally, Science 271 (1996) 929;
(c) R. Ludwig, Angew. Chem., Int. Ed. 40 (2000) 1808;
(d) J.M. Ugalde, I. Alkorta, J. Elguero, Angew. Chem., Int. Ed. 39 (2000) 717;
(e) R. Ludwig, Angew. Chem., Int. Ed. 40 (2001) 1808;
(f) M. Matsumoto, S.Saito, I. Ohmine, Nature 416 (2002) 409.
[2] (a) L. Infantes, S. Motherwell, CrystEngComm 4 (2002) 454;
(b) S.K. Ghosh, P.K. Bharadwaj, Inorg. Chem. 42 (2003) 8250;
(c) L. Infantes, J. Chisholm, S. Motherwell, CrystEngComm 5 (2003) 480;
(d) M. Mascal, L. Infantes, J. Chisholm, Angew. Chem., Int. Ed. 45 (2006) 32;
(e) P.S. Lakshminarayanan, E. Suresh, P. Ghosh, Angew. Chem., Int. Ed. 45 (2006) 3807;
(f) J. Wang, L.L. Zheng, C.J. Li, Y.Z. Zheng, M.L. Tong, Cryst. Growth Des. 6 (2006) 357;
(g) J. Yang, J.-F. Ma, Y.-Y. Liu, J.-C. Ma, H.-Q. Jia, N.-H. Hu, Eur. J. Inorg. Chem. (2006) 1208;
(h) Y.Y. Karabach, A.M. Kirillov, M.F.C.G. da Silva, M.N. Kopylovich, A.J.L. Pombeiro, Cryst. Growth Des. 6 (2006) 2200;
(i) S. Upreti, A. Datta, A. Ramanan, Cryst. Growth Des. 7 (2007) 966;
(j) X.F. Shi, W.Q. Zhang, Cryst. Growth Des. 7 (2007) 595;
(k) S.O. Kang, D. Powell, V.W. Day, K. Bowman-James, Cryst. Growth Des. 7 (2007) 606;
(l) T. Yuge, N. Tohnai, T. Fukuda, I. Hisaki, M. Miyata, Chem. Eur. J. 13 (2007) 4163.
[3] B.C.R. Sansam, K.M. Anderson, J.W. Steed, Cryst. Growth Des. 7 (2007) 2649.
[4] (a) K. Liu, J.D. Cruzan, R.J. Saykally, Science 271 (1996) 929;
(b) F.N. Keutsch, R.J. Saykally, Proc. Natl. Acad. Sci. USA 98 (2001) 10533;
(c) R.E. Dehl, C.A. Hoeve, J. Chem. Phys. 50 (1969) 3245;
(d) C. Migchelsen, H.J.C. Berendsen, A. Rupprecht, J. Mol. Biol. 37 (1968) 235;
(e) F. Steckel, S. Szapiro, Trans. Faraday Soc. 59 (1963) 331;
(f) S.D. Colson, T.H. Dunning, Science 265 (1994) 43;
(g) K. Liu, J.D. Cruzan, R.J. Saykally, Science 271 (1996) 929;
(h) L.J. Barbour, G.W. Orr, J.L. Atwood, Chem. Commun. (2000) 859.
[5] (a) J.K. Gregory, D.C. Clary, K. Liu, M.G. Brown, R.J. Saykally, Science 275 (1997) 814;
(b) R. Custelcean, C. Afloroaei, M. Vlassa, M. Polverejan, Angew. Chem., Int. Ed. 39 (2000) 3094.

[6] (a) J. Kim, K.S. Kim, J. Chem. Phys. 109 (1998) 5886;
(b) C.J. Tsai, K.D. Jordan, Chem. Phys. Lett. 213 (1993) 181;
(c) K. Kim, K.D. Jordan, T.S. Zwier, J. Am. Chem. Soc. 116 (1994) 11568.
[7] (a) R. Custecean, C. Afloroaei, M. Vlassa, M. Polverejan, Angew. Chem., Int. Ed. 39 (2000) 3094;
(b) C. Foces-Foses, F.H. Cano, M. Martinez-Ripoli, R. Faure, C. Roussel, R.M. Claramunt, C. Lopez, D. Sanz, J. Elguero, Tetrahedron: Asymmetry 1 (1990) 65;
(c) B.-H. Ye, B.-B. Ding, Y.-Q. Weng, X.-M. Chen, Inorg. Chem. 43 (2004) 6866;
(d) S.K. Ghosh, P.K. Bharadwaj, Inorg. Chem. 42 (2003) 8250.
[8] (a) K.M. Park, R. Kuroda, T. Iwamoto, Angew. Chem., Int. Ed. Engl. 32 (1993) 884;
(b) S.K. Ghosh, P.K. Bharadwaj, Inorg. Chem. 43 (2004) 5180;
(c) Y.-P. Ren, L.-S. Long, B.-W. Mao, Y.-Z. Yuan, R.-B. Huang, L.-S. Zheng, Angew. Chem., Int. Ed. 42 (2003) 532.
[9] (a) K.M. Park, R. Kuroda, T. Iwamoto, Angew. Chem., Int. Ed. Engl. 32 (1993) 884;
(b) J.N. Moorthy, R. Natarajan, P. Venugopalan, Angew. Chem., Int. Ed. 41 (2002) 3417;
(c) S.tK. Ghosh, P.K. Bharadwaj, Eur. J. Inorg. Chem. (2005) 4880;
(d) G. De Munno, R. Ruiz, F. Lloret, J. Faus, R. Sessoli, M. Julve, Inorg. Chem. 34 (1995) 408.
[10] D. Armentano, G. De Munno, J. Faus, F. Lloret, M. Julve, Inorg. Chem. 40 (2001) 655.
[11] SAINT – Ver. 6.45 Copyright (c) Bruker Analytical X-ray Systems, 2003, Inc, Madison, Wisconsin, USA.
[12] G.M. Sheldrick, SADABS Program for Absorption Correction, Version 2.10, Analytical X-ray Systems, 2003, Madison, Wisconsin, USA.
[13] SHELXTL, Bruker Analytical X-ray Instruments, Madison, WI, 1998.
[14] (a) S. Decurtins, H.W. Schmalle, P. Schneuwly, H.R. Oswald, Inorg. Chem. 32 (1993) 1888;
M.E. Garcya Posse, M.A. Juri, P.J. Aymoning, O.E. Piro, H.A. Negri, Inorg. Chem. 23 (1984) 948;
(b) L. Johansson, M. Molund, A. Oskarsson, Inorg. Chim. Acta 31 (1978) 117;
(c) T. Fujiwara, E. Iwamoto, Y. Yamamoto, Inorg. Chem. 23 (1984) 115;
(d) C.K. Cho, A. Secco, Acta Crystallogr., Sect. C 48 (1992) 165;
(e) L.L. Koh, Y. Xu, A.K. Hsieh, Acta Crystallogr., Sect. C 50 (1994) 884.
[15] B. Kamb, Acta Crystallogr., Sect. 17 (1964) 1437.
[16] A. Rahaman, F.H. Stillinger, J. Am. Chem. Soc. 95 (1973) 7943.
[17] K. Nauta, R.E. Miller, Science 287 (2000) 293.
[18] (a) L. Infantes, S. Motherwell, CrystEngComm 4 (2002) 454;
(b) L. Infantes, J. Chisholm, S. Motherwell, CrystEngComm 5 (2003) 480;
(c) S.K. Ghosh, P.K. Bharadwaj, Inorg. Chem. 42 (2003) 8250;
(d) U. Mukhopadhyay, I. Bernal, Cryst. Growth Des. 5 (2005) 1687;
(e) M. Mascal, L. Infantes, J. Chisholm, Angew. Chem., Int. Ed. 45 (2006) 32;
(f) W.H. Zhu, Z.M. Wang, S. Gao, Dalton Trans. (2006) 765;
(g) J. Wang, L.L. Zheng, C.J. Li, Y.Z. Zheng, M.L. Tong, Cryst. Growth Des. 6 (2006) 357;
(h) J. Yang, J.-F. Ma, Y.-Y. Liu, J.-C. Ma, H.-Q. Jia, N.-H. Hu, Eur. J. Inorg. Chem. (2006) 1208;
(i) X.-Y. Song, L.-C. Li, D.-Z. Liao, Z.-H. Jiang, Shi-P. Yan, Cryst. Growth Des. 7 (2007) 1220.
[19] D. Eisenberg, W. Kauzmann, The Structure and Properties of Water, Oxford University Press, Oxford, 1969.
[20] G.A. Jeffrey, An Introduction to Hydrogen Bonding, Oxford University Press, Oxford, 1997.
[21] (a) K. Raghuraman, K.K. Katti, L.J. Barbour, N. Pillarsetty, C.L. Barnes, K.V. Katti, J. Am. Chem. Soc. 125 (2003) 6955;
(b) P.S. Lakshminarayanan, D.K. Kumar, P. Ghosh, Inorg. Chem. 44 (2005) 7540;
(c) I. Ravikumar, P.S. Lakshminarayanan, E. Suresh, P. Ghosh, Cryst. Growth Des. 6 (2006) 2630;
(d) M.N. Kopylovich, E.A. Tronova, M. Haukka, A.M. Kirillov, V. Yu. Kukushkin, J.J.R. Fraústo da Silva, A.J.L. Pombeiro, Eur. J. Inorg. Chem. (2007) 4621;
(e) M.C. Das, P.K. Bharadwaj, Eur. J. Inorg. Chem. (2007) 1229.
[22] R. Vaidhyanathan, S. Nathrajan, C.N.R. Rao, Dalton Trans. (2001) 699.
[23] (a) E. Coronado, J.R. Galan-Mascaros, C.J. Gomez-Garcia, Dalton Trans. (2000) 205;
(b) D. Armentano, G. De Munno, F. Lloret, M. Julve, Cryst. Eng. Comm. 7 (2005) 57;
(c) S. Rashid, S.S. Turner, P. Day, M.E. Light, M.B. Hursthouse, Inorg. Chem. 39 (2000) 2426;
(d) V.M. Masters, C.A. Sharrad, P.V. Bernhardt, L.R. Gahan, B. Moubaraki, K.S. Murray, Dalton Trans. (1998) 413;
(e) P. Roman, C. Guzman-Miralles, A. Luque, J.I. Beitia, J. Cano, F. Lloret, M. Julve, S. Alvarez, Inorg. Chem. 35 (1996) 3741.

observed X-ray powder diffraction pattern with a calculated pattern generated from the single crystal X-Ray analysis results.

X-ray powder diffraction data were collected on a Philips APD 1700 instrument. Infrared spectra were measured on KBr pellets with a Scimitar FTS 2000c spectrometer in the range 4000–400 cm^{-1}. Elemental analyses: Vario EL of Elementar Analysensysteme GmbH; NMR: Bruker CXP-300.

2.2. General procedure for the syntheses of compounds 1–3

Seventy milligram of the appropriate Re_4 cluster compound, namely $[Re_4Se_4(TeBr_2)_4Br_8]$ for compound **1**, $[Re_4Te_4(TeBr_2)_4Br_8]$ for compound **2** and $[Re_4Te_4(TeCl_2)_4Cl_8]$ for compound **3**, and an excess of PMe_2Ph (0.06 ml) were dissolved in 10 mL of CH_2Cl_2 and stirred at room temperature for 24 h. The resulting dark brown solutions were filtered and diethyl ether was layered. After 1 week, the black crystalline products obtained were decanted and washed with small amounts of diethyl ether and acetone. Yields: 38 mg (65%) (**1**), 43 mg (74%) (**2**), 45 mg (67%) (**3**). Single crystals for X-Ray study were separated from obtained crystalline products.

$[Re_4Se_4(PMe_2Ph)_4Br_8]\cdot 1.5CH_2Cl_2$ (**1**): *Anal.* Calc. for $C_{33.5}H_{47}Br_8Cl_3P_4Re_4Se_4$ (**1**) 2379.86: C, 16.9; H, 1.99. Found: C, 17.2; H, 2.10%. ^{31}P NMR (CD_2Cl_2): δ −41.1, −41.8, −42.9, −44.1. IR (cm^{-1}): ν(P–C(C_6H_5)) 1098, ν(P–C(CH_3)) 704.

$[Re_4Te_4(PMe_2Ph)_4Br_8]\cdot CH_2Cl_2$ (**2**): *Anal.* Calc. for $C_{33}H_{46}Br_8Cl_2P_4Re_4Te_4$ (**2**) 2531.96: C, 15.7; H, 1.83. Found: C, 15.8; H, 2.21%. ^{31}P NMR (CD_2Cl_2): δ −50.5, −51.0. IR (cm^{-1}): ν(P–C(C_6H_5)) 1100, ν(P–C(CH_3)) 708.

$[Re_4Te_4(PMe_2Ph)_4Cl_8]\cdot CH_2Cl_2$ (**3**): *Anal.* Calc. for $C_{33}H_{46}Cl_{10}P_4Re_4Te_4$ (**3**) 2176.28: C, 18.2; H, 2.13. Found: C, 18.3; H, 2.21%. ^{31}P NMR (CD_2Cl_2): δ −33.0, −34.3, −35.5, −36.4. ν(P–C(C_6H_5)) 1097, ν(P–C(CH_3)) 704.

2.3. X-ray crystal structure analysis

The single crystals of **1**–**3** were selected directly from the reaction mixtures and attached to glass fibers using epoxy resin. At room temperature, the crystals lost their crystallinity within several minutes after their removal from the mother liquor. Thus, X-ray experiments were carried at low temperature. Single-crystal X-ray diffraction data were collected with the use of graphite monochromatized Mo Kα radiation (λ = 0.71073 Å) at 100 K on a Bruker Nonius X8Apex diffractometer equipped with a 4 K CCD area detector. The φ-scan technique was employed to measure intensities. Decomposition of the crystals did not occur during data collection. Corrections were applied for Lorentz and polarization effects and for absorption [26]. The structures were solved by direct methods by employing difference Fourier syntheses and refined anisotropically by full-matrix least-squares techniques on F^2 using the SHELXL-97 RELEASE 97-2 software package [27]. All nonhydrogen atoms were refined anisotropically. The positions of hydrogen atoms of PMe_2Ph ligands and solvate CH_2Cl_2 molecules were calculated corresponding to their geometrical conditions and refined using the rigid model. Crystallographic data as well as details of data collection and refinement for complexes **1**–**3** are given in Table 1.

3. Result and discussion

3.1. Synthesis

Three new molecular tetrahedral rhenium cluster complexes, namely, $[Re_4Se_4(PMe_2Ph)_4Br_8]\cdot 1.5CH_2Cl_2$ (**1**), $[Re_4Te_4(PMe_2Ph)_4Br_8]\cdot CH_2Cl_2$ (**2**), and $[Re_4Te_4(PMe_2Ph)_4Cl_8]\cdot CH_2Cl_2$ (**3**) have been prepared by the reactions of corresponding chalcohalides $[Re_4Q_4(TeX_2)_4X_8]$ (X = Br, Q = Se (for **1**), Te (for **2**); X = Cl, Q = Te (for **3**)) with dimethylphenylphosphine in CH_2Cl_2, stirring for 24 h at room temperature. The products were isolated as black crystalline precipitates by layering of diethyl ether on the resulting CH_2Cl_2 solutions. The compounds lose easily their crystallinity under contact with air at room temperature. However, they are highly soluble in CH_2Cl_2 and can be recrystallized using the same technique.

During the reactions, the $\{Re_4Q_4\}$ cluster core remains as an unalterable unit, while the four outer sphere neutral TeX_2 ligands can be easily replaced by the neutral PMe_2Ph ligands, forming the appropriated compounds. The analogous substitution was observed in the reaction of $[Re_4Te_4(TeCl_2)_4Cl_8]$ with DMF, which resulted in the molecular complex $[Re_4Te_4(DMF)_4Cl_8]$ [19]. In the

Table 1
Crystal Data and Structure Refinement for compounds **1-3.**

	1	2	3a	3b
Empirical formula	$C_{33.5}H_{47}Br_8Cl_3P_4Re_4Se_4$	$C_{33}H_{46}Br_8Cl_2P_4Re_4Te_4$	$C_{33}H_{46}Cl_{10}P_4Re_4Te_4$	$C_{33}H_{46}Cl_{10}P_4Re_4Te_4$
Fw	2379.86	2531.96	2176.28	2176.28
Crystal size, mm	0.12 × 0.08 × 0.08	0.15 × 0.12 × 0.04	0.12 × 0.10 × 0.03	0.18 × 0.12 × 0.06
Crystal system	monoclinic	monoclinic	monoclinic	triclinic
Space group	$P2_1/n$	$P2_1/c$	$P2_1/c$	$P\bar{1}$
a (Å)	13.9630(5)	16.9538(5)	16.8131(3)	11.3116(5)
b (Å)	22.0653(10)	13.0571(3)	12.9700(3)	16.6255(7)
c (Å)	19.2027(7)	24.8898(6)	24.5628(6)	16.7453(9)
α (°)				104.391(2)
β (°)	110.561(2)	107.1690(10)	107.5810(10)	107.4760(10)
γ (°)				104.758(2)
V/Å^3	5539.4(4)	5264.3(2)	5106.1(2)	2718.4(2)
Z	4	4	4	2
ρ_{calc}, Mg/m^3	2.854	3.195	2.831	2.659
μ (mm^{-1})	17.397	17.662	12.367	11.615
Index ranges	$-17 \leqslant h \leqslant 13$	$-21 \leqslant h \leqslant 21$	$-13 \leqslant h \leqslant 21$	$-12 \leqslant h \leqslant 14$
	$-26 \leqslant k \leqslant 26$	$-15 \leqslant k \leqslant 16$	$-16 \leqslant k \leqslant 16$	$-20 \leqslant k \leqslant 16$
	$-17 \leqslant l \leqslant 23$	$-31 \leqslant l \leqslant 22$	$-30 \leqslant l \leqslant 29$	$-20 \leqslant l \leqslant 20$
Maximum and minimum transmission	0.3366 and 0.2293	0.5385 and 0.1770	0.7080 and 0.3184	0.5425 and 0.2289
Reflections collected/unique, R_{int}	37292/10369, 0.0615	35946/10761, 0.0524	35353/10431, 0.0352	19878/10829, 0.0510
Data/restraints/parameters	10369/20/532	10761/18/504	10431/20/484	10829/82/522
Final R indices [$I > 2\sigma(I)$]	R_1 = 0.0382	R_1 = 0.0330	R_1 = 0.0290	R_1 = 0.0556
	wR_2 = 0.0834	wR_2 = 0.0622	wR_2 = 0.0640	wR_2 = 0.1230
R indices (all data)	R_1 = 0.0670	R_1 = 0.0613	R_1 = 0.0442	R_1 = 0.0918
	wR_2 = 0.0906	wR_2 = 0.0673	wR_2 = 0.0676	wR_2 = 0.1336

case of compounds **1** and **3**, a set of signals in the ^{31}P NMR spectra indicate to the formation of either isomeric cluster complexes with a different arrangement of the terminal ligands or complexes containing different number of the PMe_2Ph ligands in solution. Whereas the data of chemical analyses are in a good agreement with the reported formulas, the first assumption is more plausible. Therefore, we have studied a number of crystals for these two samples. For compound **1,** all the crystals checked had similar unit cell parameters. However, in the case of compound **3** we were able to find and characterize single crystals with two different unit cell parameters, revealing two isomers of the cluster compound $[Re_4Te_4(PMe_2Ph)_4Cl_8]$. Most likely, compound **1** also forms isomers, but our efforts to confirm this assumption by X-ray diffraction were unsuccessful.

3.2. Crystal structures

All three compounds obtained were characterized by single-crystal X-ray diffraction analysis. Their structures are based on a $\{Re_4Q_4\}^{8+}$ (Q = Se in **1** or Te in **2** and **3**) cluster core in which the Re_4 tetrahedron is coordinated by four μ_3-Q atoms (Figs. 1 and 2). The Re–Re and Re–Q interatomic distances in compounds **1**–**3** are assembled in Table 2, and do not appreciably differ from those in the starting materials and other related compounds. Each Re atom is ligated by two halide atoms (bromide in **1** and **2** or chloride in **3a** and **3b**) as well as one dimethylphenylphosphine ligand, resulting in neutral charged cluster units. It is worth noting that the molecular cluster complexes $[Re_4Q_4(PMe_2Ph)_4X_8]$ **1**–**3** also contain CH_2Cl_2 as solvate molecules.

Compounds **1** and **2** represent one isomeric type; while for compound **3** two isomers (**3a** and **3b**) were isolated. The isomerism in this system is due to the different orientation of outer ligands around the cluster core. When the $\{Re_4Q_4\}$ cluster core is considered as a cube and the coordination number of Re atoms being equal to 6 (including outer and μ_3-ligands), these two isomeric forms could be represented by Scheme 1. Isomeric form A corresponds to the compounds **1**, **2** and **3a**, while isomeric form B describes the compound **3b**. As can be seen in Scheme 1, ligand arrangements in $\{ReQ_3(PMe_2Ph)Cl_2\}$ units numbered 1, 2, and 3 are identical in both isomeric forms, while those in the units numbered 4 are different in A and B isomeric forms.

The hetero-nuclear cluster compound $[Re_3CoS_4Cl_6(PMe_2Ph)_4]$ [28] described recently exists also in two isomeric forms, deriving from the different orientation of terminal ligands Cl^- and dimethylphenylphosphine connected with Re atoms. The coordination environment of Co atom is not taken into account, because it has only one terminal ligand. Analogically to Re_4

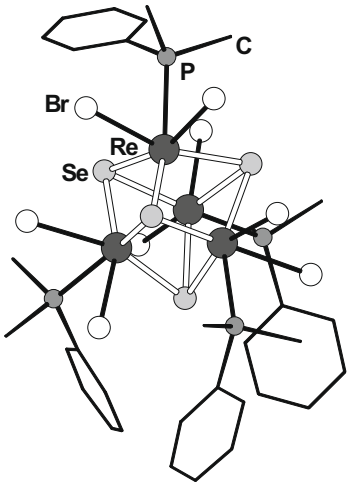


Fig. 1. Molecular structure of compound **1**.

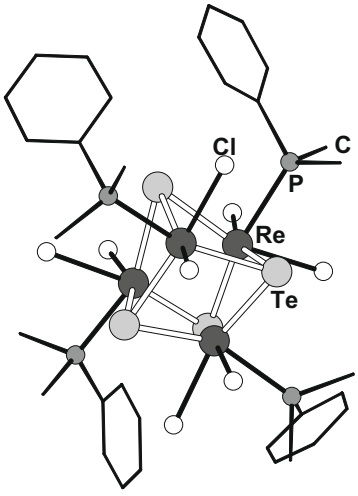
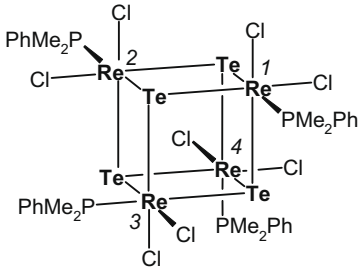


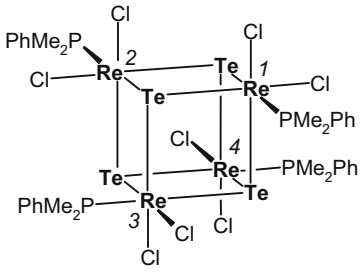
Fig. 2. Molecular structure of compound **3b**.

Table 2
Selected interatomic distances in the compounds **1**-**3**.

	1	2	3a	3b
Re–Re	2.8282(6)–2.8748(6)	2.9117(5)–2.9413(5)	2.8891(4)–2.9205(4)	2.8932(8)–2.9180(8)
Re–Q	2.452(1)–2.463(1)	2.5983(6)–2.6218(7)	2.5983(5)–2.6220(5)	2.595(1)–2.620(1)
Re–X	2.575(1)–2.600(1)	2.6102(9)–2.6392(9)	2.456(2)–2.487(2)	2.458(4)–2.478(4)
Re–P	2.572(3)–2.589(3)	2.575(2)–2.585(2)	2.556(2)–2.564(2)	2.532(4)–2.558(4)



Isomeric form A



Isomeric form B

Scheme 1.

cluster compounds, the Re_3Co cluster forms isomers at which two of three Re atoms have a similar coordination environment, while the coordination environment of the third Re atom is different in both isomers. Moreover, the three dimethylphenylphosphine ligands connected with Re1, Re3, Re4 atoms to occur in the isomeric forms A and B of **3a** and **3b** are oriented in the same way as it was found in the corresponding $[Re_3CoS_4Cl_6(PMe_2Ph)_4]$ isomers, respectively.

It can also be stated that the above mentioned complex $[Re_4Te_4(DMF)_4Cl_8]$ and the starting materials possess the same symmetrical orientation of DMF or TeX_2 ligands, respectively, as the compound **3b** (isomeric form B). This means that during the reaction the ligand arrangement around the Re atoms in the complexes have to be changed. Thus, it can be concluded that we do not have a simple ligand exchange reaction between TeX_2 and PMe_2Ph. Rather, most likely, a reaction occurs at which an intermediate product that contains Re atoms with four terminal ligands (2X, TeX_2 and PMe_2Ph) releases TeX_2 fragments. Thus, taking into account both of the above mentioned assumptions, the observed isomeric structures are formed in accordance with the recently reported heterometallic cluster compound $[Re_3CoS_4Cl_6(PMe_2Ph)_4]$ [28]. Derived from that, it can be concluded that the isomeric form A of Re_4 and Re_3Co cluster compounds is the thermodynamically controlled product.

Supplementary data

CCDC 721592, 721593, 721592 and 721595 contains the supplementary crystallographic data for **1**, **2**, **3a** and **3b**. These data can be obtained free of charge via http://www.ccdc.cam.ac.uk/conts/retrieving.html, or from the Cambridge Crystallographic Data Centre, 12 Union Road, Cambridge CB2 1EZ, UK; fax: (+44) 1223-336-033; or e-mail: deposit@ccdc.cam.ac.uk.

Acknowledgements

This research was supported by the grant RFBR 08-03-90413 and by the Bundesministerium für Bildung und Forschung (WTZ-Projekt RUS 07/005). We are indebted to Dr. D.Y. Naumov and A.I. Smolentsev, Nikolaev Institute of Inorganic Chemistry of SB RAS, for collection of X-ray intensities through the use of the Bruker Nonius X8Apex diffractometer.

References

[1] J.C.P. Gabriel, K. Boubekeur, S. Uriel, P. Batail, Chem. Rev. 101 (2001) 2037.
[2] H.D. Selby, B.K. Roland, Z.P. Zheng, Acc. Chem. Res. 36 (2003) 933.
[3] H.D. Selby, B.K. Roland, J.R. Cole, Z.P. Zheng, Macromol. Symp. 209 (2004) 23.
[4] H.D. Selby, Z.P. Zheng, Comments Inorg. Chem. 26 (2005) 75.
[5] V.E. Fedorov, Y.V. Mironov, N.G. Naumov, M.N. Sokolov, V.P. Fedin, Russ. Chem. Rev. 76 (2007) 529.
[6] J.T. Rhule, C.L. Hill, D.A. Judd, R.F. Schinazi, Chem. Rev. 98 (1998) 327.
[7] B. Hasenknopf, Front. Biosci. 10 (2005) 275.
[8] C.E. Müller, J. Iqbal, Y. Baqi, H. Zimmermann, A. Röllich, H. Stephan, Bioorg. Med. Chem. Lett. 16 (2006) 5943.
[9] Z.P. Zheng, J.R. Long, R.H. Holm, J. Am. Chem. Soc. 119 (1997) 2163.
[10] Z.P. Zheng, R.H. Holm, Inorg. Chem. 36 (1997) 5173.
[11] T. Yoshimura, K. Umakoshi, Y. Sasaki, A.G. Sykes, Inorg. Chem. 38 (1999) 5557.
[12] Y.V. Mironov, M.A. Shestopalov, K.A. Brylev, S.S. Yarovoi, G.V. Romanenko, V.E. Fedorov, H. Spies, H.J. Pietzsch, H. Stephan, G. Geipel, G. Bernhard, W. Kraus, Eur. J. Inorg. Chem. (2005) 657.
[13] M.A. Shestopalov, Y.V. Mironov, K.A. Brylev, S.G. Kozlova, V.E. Fedorov, H. Spies, H.J. Pietzsch, H. Stephan, G. Geipel, G. Bernhard, J. Am. Chem. Soc. 129 (2007) 3714.
[14] Y.V. Mironov, T.E. Albrecht-Schmitt, J.A. Ibers, Inorg. Chem. 36 (1997) 944.
[15] E.S. Lang, U. Abram, J. Stahle, Zeitschrift Anorg. Allg. Chem. 622 (1996) 251.
[16] Y.V. Mironov, T.E. Albrecht-Schmitt, J.A. Ibers, Zeitschrift Cryst. New Cryst. Struct. 212 (1997) 308.
[17] Y.V. Mironov, Eur. J. Inorg. Chem. (1999) 997.
[18] Y.V. Mironov, Polyhedron 19 (2000) 437.
[19] Y.V. Mironov, T.E. Albrecht-Schmitt, D.M. Smith, J.A. Ibers, Zeitschrift Cryst. New Cryst. Struct. 216 (2001) 517.
[20] Y.V. Mironov, A.V. Virovets, W.S. Sheldrick, V.E. Fedorov, Polyhedron 20 (2001) 969.
[21] Y.V. Mironov, M.A. Pell, T.E. Albrecht-Schmitt, J.A. Ibers, Inorg. Chem. 40 (2001) 5472.
[22] Y.V. Mironov, S.S. Yarovoi, D.Y. Naumov, N.V. Kuratieva, S.G. Kozlova, A. Simon, V.E. Fedorov, Eur. J. Inorg. Chem. (2005) 2476.
[23] O.A. Efremova, Y.V. Mironov, V.E. Fedorov, Eur. J. Inorg. Chem. (2006) 2533.
[24] O.A. Efremova, Y.V. Mironov, H.J. Pietzsch, H. Stephan, C. Perrin, V.E. Fedorov, J. Clust. Sci. 20 (2009) 77.
[25] N.I. Kolbin, K.V. Ovchinnikov, Zh. Neorg. Khim. 13 (1968) 2306.
[26] SADABS, Version 2.11; Bruker Advanced X-ray Solutions, Bruker AXS Inc., Madison, WI, USA, 2004.
[27] G.M. Sheldrick, SHELXTL DOS/Windows/NT Version 5.10, Bruker Analytical X-ray Instruments, Inc., Madison, WI, 1997.
[28] N. Sakai, T. Saito, Polyhedron 23 (2004) 2611.

2. Experimental

2.1. Materials and methods

Tetrahydroisoquinoline, piperidine, carbon disulfide, sodium hydroxide, cadmium chloride, hexadecylamine (HDA) (98%) and tri-octylphosphine (TOP) (90%) were purchased from Aldrich and were used as purchased. Toluene (BDH, 99%), methanol (BDH, 99.8%) and dichloromethane (BDH, >99%) were used as solvents without further purification.

2.2. Physical measurements

The C, H, N, S elemental analysis was carried out with Leco-CHNS 932 analyzer. Roughly 2.0 mg of sample was introduced into Ag capsule and was placed in a furnace, which was maintained at 800 °C. The products of combustion in the CHNS analysis (CO_2, H_2O and SO_x gases) were carried through the system by the He carrier. Adjustments for blank, calibration and weights were applied to the final integrated signal and the results were displayed as weight percentage of carbon, hydrogen, nitrogen and sulfur.

FT-IR spectra of various powder samples of ligands and complexes were recorded on a Bruker Tensor 27 spectrometer with a 4 cm^{-1} resolution and 32 scans in the mid IR (200–4000 cm^{-1}) region. PL and UV–Vis absorption spectra were measured at room temperature with a Perkin Elmer LS 55 luminescence spectrometer and a Varian Cary 50 Conc UV–Vis spectrophotometer, respectively. Photoluminescence spectra were recorded by placing the sample in a quartz cuvette of 1 cm path length. The excitation wavelength for PL measurement was 400 nm. The samples were analyzed at a scan speed of 500 nm min^{-1} within a scan range of 200–800 nm. UV–Vis spectra were recorded by placing the samples in a quartz cuvette of 1 cm path length at an absorption range of 200–800 nm with the scan rate of 600 nm min^{-1}. Toluene was used as a solvent (as reference in UV) in the measurements. Powder XRD patterns were recorded for all the samples in order to verify the formation and structure of materials. The dry samples were ground with the help of a mortar and pestle and the fine powder of nanoparticles was packed on the surface of a sample holder. The diffraction patterns were recorded in the high angle 2θ range of 10–80° using a Bruker AXS D8 Advance X-ray diffractometer, equipped with nickel filtered Co Kα radiation (λ = 1.5418 Å) at 40 kV, 40 mA and at room temperature. The scan speed and step size were 0.05° min^{-1} and 0.00657, respectively. For the transmission electron microscopy (TEM and HRTEM) measurements, samples were prepared by placing a drop of dilute solution of nanoparticles on Formvar-coated grids (150 mesh). The samples were allowed to dry completely at room temperature and viewed using a JEOL 1010 TEM and JEOL 2100 HRTEM. Viewing was done at an accelerating voltage of 100 kV (TEM) and 200 kV (HRTEM), and the images were captured digitally using a Megaview III camera; stored and measured using Soft Imaging Systems iTEM software.

2.3. Preparation of ligands

A standard solution of NaOH 4 M (25.0 mL) was cooled in an ice bath and the corresponding secondary amine, piperidine or tetrahydroisoquinoline (25.0 mL) was added. To this suspended mixture in ice, CS_2 (7.0 mL) was added dropwise while stirring. The solution was allowed to stand for 1 h and the solidified mixture was dried in air. The solid was re-crystallised using 100.0 mL of dichloromethane and methanol (50:50 – v:v) mixture and was maintained at ice cold conditions overnight. The resultant precipitate was filtered and washed with excess dichloromethane.

$C_{10}H_{10}NS_2Na$: CHNS analysis: Calc.: C, 51.93; H, 4.36; N, 6.06; S, 27.72. Found: C, 51.58; H, 4.07; N, 5.85; S, 27.47%; Percentage yield: 54%; melting point: 137.8–138.2 °C. Significant IR bands: $\nu_{(C-N)}$: 1473 cm^{-1}; $\nu_{(C-S)}$: 949 cm^{-1}.

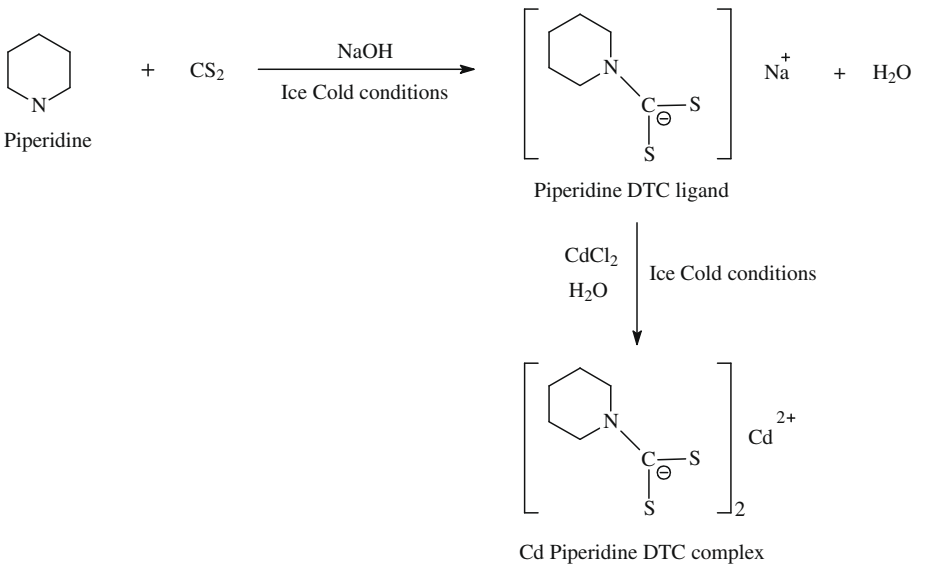
$C_6H_{10}NS_2Na$: CHNS analysis: Calc.: C, 39.32; H, 5.50; N, 7.64; S, 34.99. Found: C, 38.47; H, 5.98; N, 7.43; S, 34.51. Percentage yield: 58%; melting point: 133.2–135.4 °C. Significant IR bands: $\nu_{(C-N)}$: 1435 cm^{-1}; $\nu_{(C-S)}$: 958 cm^{-1}.

2.4. Preparation of complexes

2.4.1. Synthesis of [Cd ($S_2CNC_5H_{10}$)$_2$] (**I**)

A $CdCl_2$ solution, 10.0 mmol (25.0 mL) was added dropwise to the 25.0 mL solution of piperidine DTC ligand (5.0 mmol) at ice cold temperature (Scheme 1). The reaction was stirred for 1 h and the white precipitate formed was filtered, washed with distilled water and vacuum dried.

CHNS analysis: Calc.: C, 33.29; H, 4.66; N, 6.47; S, 29.62. Found: C 34.29; H, 4.56; N, 6.18; S, 29.47%. Percentage yield: 46%, melting



Scheme 1. Reaction scheme for the synthesis of Cd piperidine DTC complex.

point: 258–269 °C. Significant IR bands: $\nu_{(C-N)}$: 1482 cm^{-1}; $\nu_{(C-S)}$: 976 cm^{-1}; $\nu_{(Cd-S)}$: 227 cm^{1}.

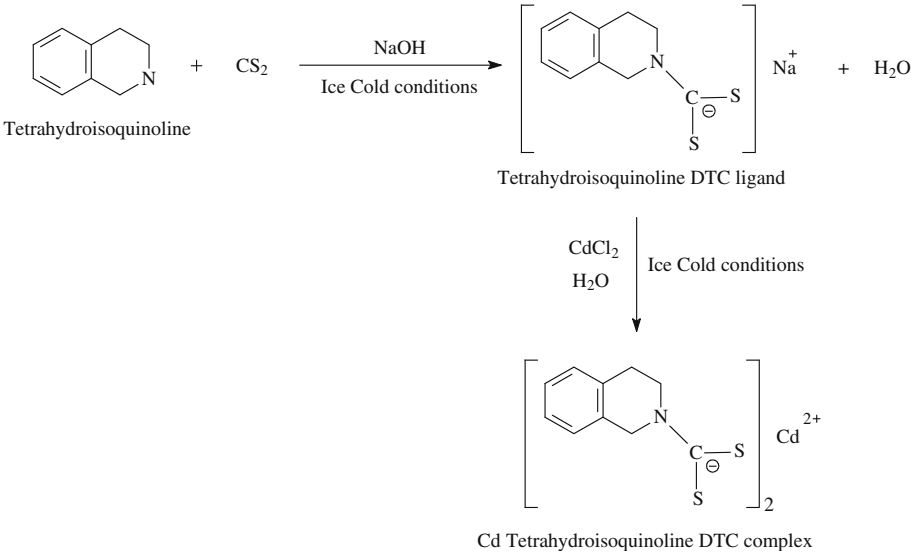
2.4.2. Synthesis of [Cd ($S_2CNC_9H_{10})_2$] (**II**)

A $CdCl_2$ solution, 10.0 mmol (25.0 mL) was added dropwise to the 25.0 mL solution of tetrahydroisoquinoline (5.0 mmol) DTC ligand at ice cold temperature (Scheme 2). The mixture was then stirred for 1 h and the pale yellow precipitate was filtered. The product was washed with distilled water and vacuum dried.

CHNS analysis: Calc.: C, 45.41; H, 3.81; N, 5.30; S, 24.24. Found: C, 45.09; H, 3.662; N, 5.05; S, 24.18%. Percentage yield: 39%, melting point: 269.3–270.1 °C. Significant IR bands: $\nu_{(C-N)}$: 1438 cm^{-1}, $\nu_{(C-S)}$: 965 cm^{-1}, $\nu_{(Cd-S)}$: 262 cm^{-1}.

2.5. Synthesis of HDA capped CdS nanoparticles

Cadmium sulfide nanoparticles were prepared from the single source precursors **I** and **II**. The thermolysis was carried out by varying the amount of the capping agent hexadecylamine (HDA) at a constant temperature (140 or 180 °C). In each thermolysis reaction 0.5 g of the complex was used, with 3.0 and 6.0 g of HDA. The complexes were dissolved in tri-octylphosphine (TOP) and injected into a three-necked flask containing hot HDA at 140 °C. The solution



Scheme 2. Reaction scheme for the synthesis of Cd tetrahydroisoquinoline DTC complex.

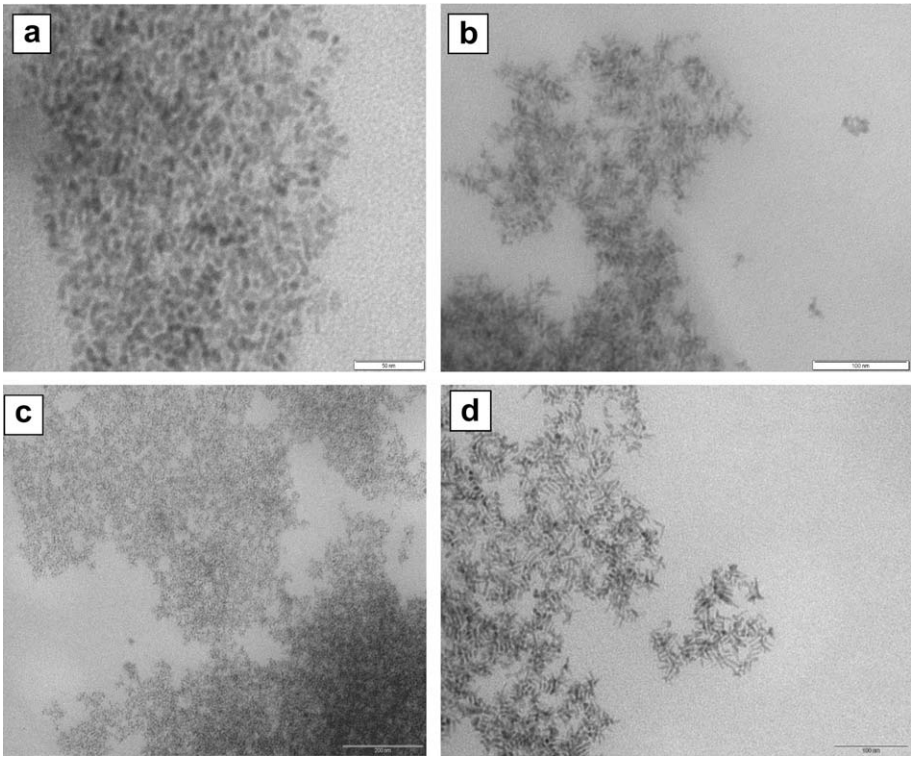


Fig. 1. TEM images of CdS nanoparticles prepared with 0.5 g of complex **I** with (a) 3.0 g, (b) 6.0 g of HDA and complex **II** with (c) 3.0 g, (d) 6.0 g of HDA at 140 °C (1 h).

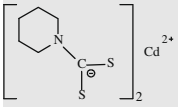
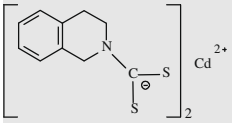
turned bright yellow instantaneously after injection. The reaction was allowed to proceed for 1 h. Excess methanol was added to the cooled solution to flocculate the particles. The resultant precipitate (CdS nanoparticles) was separated by centrifugation. The yellow CdS nanoparticles were then dispersed in toluene for optical studies. The procedure was repeated at 180 °C to study the effect of temperature.

3. Results and discussion

The final morphology of nanoparticles in any solution is governed by the preferred growth regime of the reaction. The reaction can proceed in either a kinetic or a thermodynamic growth regime [2,15]. Parameters such as monomer concentration, reaction temperature, and capping group influence the type of growth regime. The thermodynamic growth regime is favored by high temperatures and low monomer concentration yielding stable isotropic particles. In contrast non-equilibrium kinetic conditions are favoured by low reaction temperatures and high monomer concentration yielding selective anisotropic particles (i.e. rods, tetrapods) [2,15,16].

Fig. 1 shows the TEM images for CdS nanoparticles synthesized from complexes **I** and **II** at different concentrations (3.0 and 6.0 g HDA) at 140 °C. The results of the TEM studies are summarized in Table 1. At the highest concentration (0.5 precursor in 3.0 g HDA) the CdS nanoparticles synthesized from **I** were predominantly oblate in shape with an average diameter size of 7.9 ± 0.9 nm. At a lower concentration under similar reaction conditions the shape of the particles changes to rods. For complex **II** at both concentrations the particles are rod shaped with bipods and tripods also present at the lower concentration.

Table 1
CdS nanocrystals synthesized with 0.5 g of complexes **I** and **II** with 3.0 and 6.0 g of HDA at 140 and 180 °C (reactions 1, 2, 4, 5, 7, 8, 10, and 11).

Cd complex	Mass of HDA (g)	Reaction temp. (°C)	Particle shape	Particle size (nm)
	3.0	140	oblate	diameter = 7.9 ± 0.9
	6.0	140	rods	length = 14.1 ± 2.1
				breadth = 4.1 ± 0.65
	3.0	180	dots	19.71 ± 3.24
	6.0	180	rods	length = 19.35 ± 2.98
			bipods tripods	breadth = 5.80 ± 0.78
	3.0	140	rods	length = 9.99 ± 1.38
				breadth = 5.31 ± 0.9
	6.0	140	rods	length = 18.18 ± 2.10
			bipods tripods	breadth = 4.82 ± 0.77
	3.0	180	dots	diameter = 20.61 ± 4.72
	6.0	180	rods	length = 20.91 ± 2.96
			bipods tripods	breadth = 6.13 ± 1.02

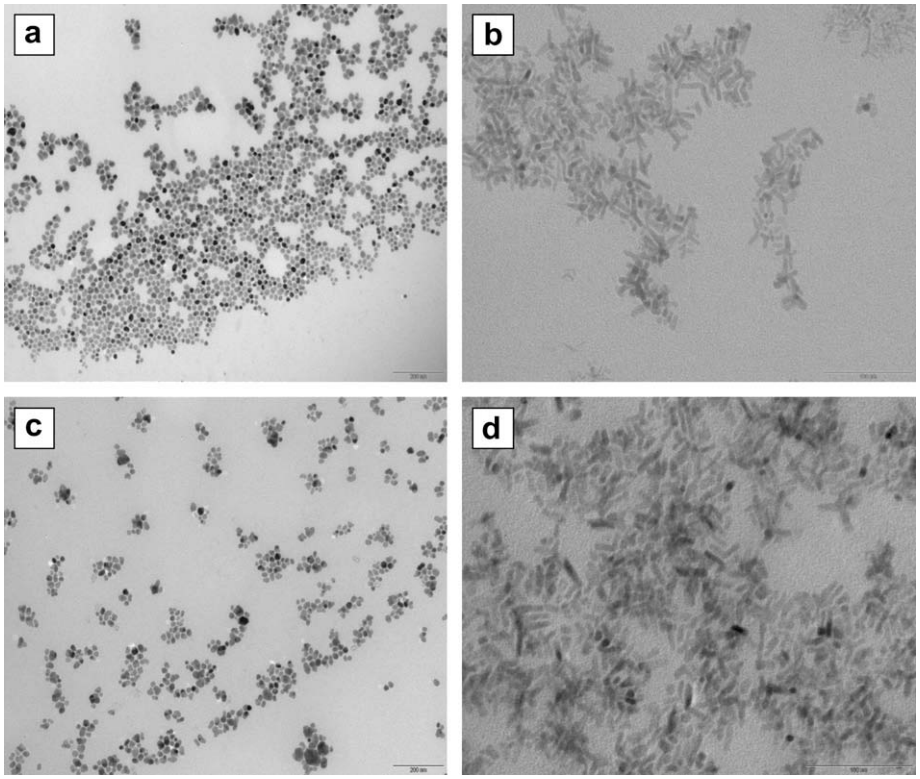


Fig. 2. TEM images of CdS nanoparticles prepared with 0.5 g of complex **I** with (a) 3.0 g, (b) 6.0 g of HDA and complex **II** with (c) 3.0 g, (d) 6.0 g of HDA at 180 °C.

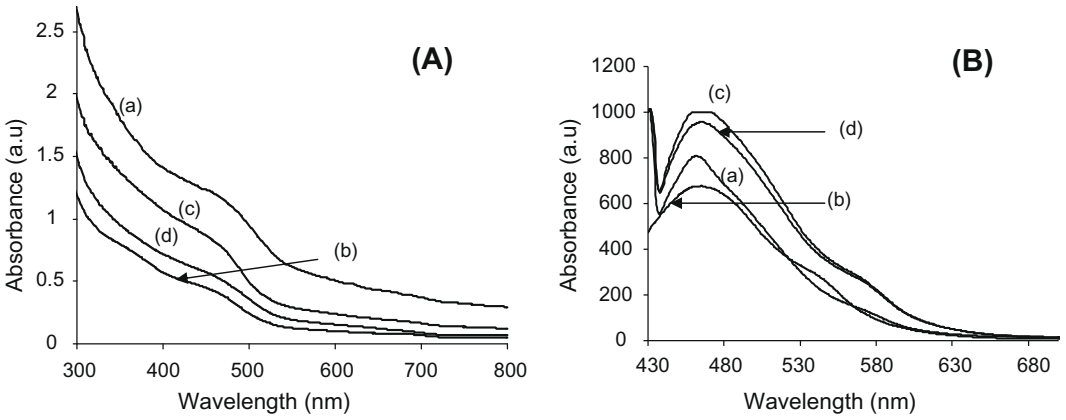


Fig. 3. Optical absorption (A) and corresponding photoluminescence (B) spectra of CdS nanoparticles synthesized with 0.5 g of complex **I** and (a) 3.0 g, (b) 6.0 g of HDA; and with 0.5 g of complex **II** and (c) 3.0 g, (d) 6.0 g of HDA at 180 °C.

When the temperature is increased to 180 °C similar trends are observed for the particles synthesized from both complexes at varying concentrations. For complex **I**, at high concentration, very well defined close to spherical particles (dots) with an average diameter of 19.71 ± 3.24, are observed (Fig. 2a). A reduction of the precursor concentration results in an evolution of shape, with rods, bipods and tripods observed (Fig. 2b). For complex **II** a similar trend is observed (Fig. 2c and d), with shape transformation from isotropic to anisotropic shaped particles clearly evident. The evolution of shape from close to spherical particles to distinct rod shaped particles with decrease in concentration of the precursor is in contrast to previous reports [2,15,16]. Nair and Scholes [17] reported that anisotropic particle growth could be due to oriented attachment. Recently it has been reported that low reaction temperatures can slow down the rate of decomposition of the single source precursor [18]. At this condition nanorods are produced through a mechanism of self assembly. We can conclude from our results that other factors such as the nature of precursor in addition to temperature and concentration can also influence the mechanism of formation of the final particle morphology.

The absorption spectra for the CdS nanoparticles synthesized at 180 °C from both complexes at the two concentrations are shown in Fig. 3A. The absorption band edges (ca. 500 nm) [Fig. 3(A) a and c] for the particles synthesized at higher concentrations for both complexes are distinctly sharper and more pronounced than the band edges [Fig. 3(A) b and d] of the particles synthesized at lower concentrations. The broadening of the band edges at the lower concentrations is an indication of a broader size distribution or the presence of larger elongated particles. This observation is confirmed by the TEM measurements which show the presence of rod shaped particles at lower concentrations (Fig. 2d). The photoluminescence (PL) spectra (Fig. 3B) of all the samples show broad emission peaks with an absorption maximum at 465 nm. The broad emission peaks are indicative of particles with large size distributions and/or the presence of anisotropic particles. A secondary emission shoulder is observed at 575 nm for all samples except for complex I at high concentration. This secondary peak maybe attributed to emission from a subset of larger particles and/or aggregation of particles. Emission due to recombination of charge carriers from surface defects could also account for the emission shoulder [19].

The powder X-ray diffraction patterns for the CdS nanoparticles prepared from complexes **I** and **II** (6.0 g HDA, 180 °C) are shown in Fig. 4. The presence of the (1 1 0), (1 0 3) and (1 1 2) planes in the diffraction patterns is characteristic of the hexagonal phase of CdS. The observed narrow peaks at (1 0 0), (0 0 2) and (1 0 1) show that the nanoparticles are elongated towards the *c*-axis which is the characteristic of rod shaped particles.

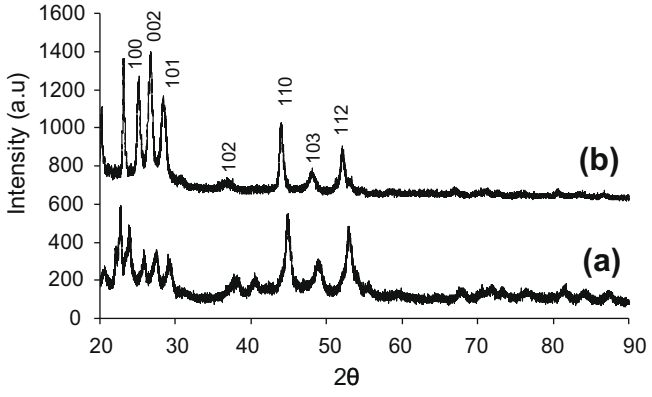


Fig. 4. XRD patterns of CdS nanocrystals synthesized with 0.5 g of complexes **I** and **II** with 6.0 g of HDA at 180 °C.

4. Conclusions

Heterocyclic cadmium dithiocarbamate complexes were successfully used as single source precursors in the synthesis of CdS nanoparticles. At high temperature, 180 °C, and high concentrations very distinct, close to spherical particles were observed. An evolution of rods and bipods and tripods shape was observed with the decrease in concentration of the precursor. The optical measurements also support the presence of anisotropic particles at lower precursor concentrations. The XRD patterns confirm the hexagonal phase of CdS. The inherent nature of the precursor has an influence on the shape of the particles.

Acknowledgement

The work was supported by the NRF/DST Chair of Nanotechnology, University of Zululand.

References

[1] Y. Li, X. Li, C. Yang, Y. Li, J. Mater. Chem. 13 (2003) 2641.
[2] Z. Peng, X. Peng, J. Am. Chem. Soc. 124 (2002) 3343.
[3] N. Revaprasadu, S.N. Mlondo, Pure Appl. Chem. 78 (2006) 1691.
[4] M.A. Malik, P. O'Brien, N. Revaprasadu, Phosphorus, Sulfur Silicon Relat. Elem. 180 (2005) 689.
[5] N.L. Pickett, P. O'Brien, Chem. Rec. 1 (2001) 467.
[6] M.A. Malik, N. Revaprasadu, P. O'Brien, Chem. Mater. 13 (2001) 913.

[7] M. Chunggaze, M.A. Malik, P. O'Brien, J. Mater. Chem. 9 (1999) 2433.
[8] P.S. Nair, T. Radhakrishnan, N. Revaprasadu, G.A. Kolawole, P. O'Brien, J. Mater. Chem. 12 (2002) 2722.
[9] J.C. Bruce, N. Revaprasadu, K.R. Koch, New J. Chem. 31 (2007) 1647.
[10] N. Moloto, N. Revaprasadu, M.J. Moloto, P. O'Brien, M. Helliwell, Polyhedron 26 (2007) 3947.
[11] S.N. Mlondo, N. Revaprasadu, P. Christian, P. O'Brien, Polyhedron 28 (2009) 2097.
[12] B.S. Garg, R.K. Garg, M.J. Reddy, Indian J. Chem. 32A (1993) 697.
[13] L. Qu, X. Peng, J. Am. Chem. Soc. 124 (2002) 2049.
[14] D.V. Talapin, A.L. Rogach, A. Kornowski, M. Haase, H. Weller, Nano Lett. 1 (2001) 207.
[15] X.G. Peng, L. Manna, W.D. Yang, J. Wickham, E. Scher, A. Kandavich, A.P. Alivisatos, Nature 404 (2000) 59.
[16] J.T. Hu, L.S. Li, W.D. Yang, L. Manna, A.P. Alivisatos, Science 292 (2001) 2060.
[17] P.S. Nair, G.D. Scholes, J. Mater. Chem. 16 (2006) 467.
[18] S.G. Thoma, A. Sanchez, P.P. Provecio, B.L. Abrams, J.P. Wilcoxon, J. Am. Chem. Soc. 127 (2005) 7611.
[19] N. Chestnoy, T.D. Harris, R. Hull, L.E. Brus, J. Phys. Chem. 90 (1986) 3393.

L2 = oxalate anion, L3 = glutarate anion and L4 = 1,4-naphthalenedicarboxylate anion). Our study shows that the structures of dicarboxylate anions play important role in the formation of these silver(I) complexes.

2. Experimental

2.1. Materials and Instrumentation

All reagents and solvents in the syntheses were of reagent grade, and they were used without further purification. Infrared spectra were recorded on a Nicolet AVATAT FT-IR360 spectrometer as KBr pellets in the frequency range 4000–400 cm^{-1}. The elemental analyses (C, H, N contents) were determined on a CE instruments EA 1110 analyzer. Photoluminescence measurements were performed on a Hitachi F-4500 fluorescence spectrophotometer with solid powder on a 1 cm quartz round plate.

2.2. Synthesis of complex $[Ag_2(L1)_2(L2)]\cdot 2H_2O$ (**1**)

A mixture of $AgNO_3$ (170 mg, 1 mmol), 2-aminopyrimidine (94 mg, 1 mmol) and oxalate (90 mg, 1 mmol) were stirred in CH_3OH–H_2O mixed solvent (10 mL, v/v: 1/1). Then aqueous NH_3 solution (25%) was dropped into the mixture to give a clear solution. The resultant solution was allowed slowly to evaporate in darkness at room temperature for several days to give colorless crystals of **1** (Yield, 50%). They were washed with a small volume of cold CH_3OH and diethyl ether. *Anal.* Calc. for $Ag_2C_{10}H_{14}N_6O_6$: C, 22.66; H, 2.66; N, 15.85. Found: C, 22.61; H, 2.71; N, 15.76%. IR (KBr): $\nu(cm^{-1})$ = 3398 (m), 3296 (m), 2962 (m), 2925 (m), 1625 (s), 1600 (s), 1569 (s), 1478 (s), 1351 (m), 1313 (m), 1223 (m), 788 (m), 660 (w), 520 (w), 462 (m).

2.3. Synthesis of complex $[Ag_2(L1)_2(L3)]\cdot H_2O$ (**2**)

The synthesis of **2** was similar to that of **1**, but with glutarate (132 mg, 1 mmol) in place of oxalate. Colorless crystals of **2** were obtained in 62% yield. *Anal.* Calc. for $Ag_2C_{13}H_{17}N_6O_5$: C, 28.23; H, 3.09; N, 15.19. Found: C, 28.31; H, 3.14; N, 15.25%. IR (KBr): $\nu(cm^{-1})$ = 3400 (m), 3300 (m), 2958 (m), 2924 (m), 1630 (s), 1567 (s), 1472 (s), 1396 (m), 1349 (m), 1219 (m), 1185 (m), 1056(w), 790 (m), 660 (w), 517 (w), 462 (m).

2.4. Synthesis of complex $[Ag_2(L1)_2(L4)]\cdot 2H_2O$ (**3**)

The synthesis of **3** was similar to that of **1**, but with 1,4-naphthalenedicarboxylate (216 mg, 1 mmol) in place of oxalate. Colorless crystals of **3** were obtained in 55% yield. *Anal.* Calc. for $Ag_2C_{20}H_{20}N_6O_6$: C, 36.61; H, 3.07; N, 12.81. Found: C, 36.70; H, 3.12; N, 12.88%. IR (KBr): $\nu(cm^{-1})$ = 3393 (m), 3301 (m), 1626 (s), 1570 (s), 1479 (s), 1410(m), 1364 (m), 1223 (m), 789 (m), 660 (w), 512 (w), 468 (m).

2.5. X-ray crystallography

Single crystals of the complexes **1–3** with appropriate dimensions were mounted on a glass fiber and used for data collection. Data was collected on a Bruker-AXS CCD diffractometer equipped with a graphite-monochromated Mo Kα radiation source (λ = 0.71073 Å) for **1–3**. All absorption corrections were performed with the SADABS program [46]. All the structures were solved by direct methods using SHELXS-97 [47] and refined by full-matrix least-squares techniques using SHELXL-97 [48]. All the non-hydrogen atoms were treated anisotropically. The positions of hydrogen atoms were generated geometrically. The crystallographic details of **1–3** are summarized in Table 1. Selected bond lengths and bond angles of **1–3** are displayed in Table 2. The hydrogen bond geometries are shown in Table S1 (in the Supplementary data).

3. Results and discussion

3.1. Syntheses and IR spectra

The syntheses of complexes **1–3** are carried out in the darkness to avoid photodecomposition and summarized in Scheme S1, in the Supplementary data. The formation of the products is not significantly affected by changes of the reaction mole ratio of organic ligands to metal ions, and the resultant crystals are insoluble in water and common organic solvents. The infrared

Table 1
Crystallographic data for complexes **1–3**.

Complexes	**1**	**2**	**3**
Formula	$Ag_2C_{10}H_{14}N_6O_6$	$Ag_2C_{13}H_{17}N_6O_5$	$Ag_2C_{20}H_{20}N_6O_6$
M_r	530.02	553.06	656.16
Crystal system	monoclinic	monoclinic	orthorhombic
Space group	*C*2/*c*	*C*2/*c*	*Pnna*
a (Å)	15.0954(4)	8.3565(9)	12.4033(5)
b (Å)	6.4357(2)	9.8212(9)	17.4377(8)
c (Å)	14.9699(5)	20.530(2)	10.0645(4)
α (°)	90	90	90
β (°)	95.793(3)	95.071(5)	90
γ (°)	90	90	90
Z	4	4	4
V (Å^3)	1446.91(8)	1678.3(3)	2176.8(2)
D_c (g cm^{-3})	2.433	2.189	2.002
μ (mm^{-1})	2.752	2.374	1.851
F(0 0 0)	1032	1084	1296
Number of unique reflections	1235	1627	1871
Number of observed reflections [$I > 2\sigma(I)$]	1176	1270	1524
Parameters	117	123	155
Goodness-of-fit (GOF)	0.985	0.934	1.076
Final *R* indices [$I > 2\sigma(I)$][a,b]	R_1 = 0.0223, wR_2 = 0.0579	R_1 = 0.0470, wR_2 = 0.1130	R_1 = 0.0379, wR_2 = 0.0938
R indices (all data)	R_1 = 0.0240, wR_2 = 0.0592	R_1 = 0.0617, wR_2 = 0.1262	R_1 = 0.0482, wR_2 = 0.0978
Largest difference peak and hole (e Å^{-3})	0.700 and −0.719	1.371 and −1.318	0.635 and −0.505

[a] $R_1 = \sum||F_o|-|F_c||/\sum|F_o|$.
[b] $wR_2 = [\sum w(F_o^2 - F_c^2)^2/\sum w(F_o^2)^2]^{0.5}$.

Table 2
Selected bond distances (Å) and angles (°) for **1**–**3**.

Complex ***1***					
Ag(1)–N(1)	2.313(2)	Ag(1)––N(3)^{ii}	2.540(3)	Ag(1)^{iii}–N(2)	2.312(2)
Ag(1)–O(2)	2.630(4)				
N(2)^{i}–Ag(1)–N(1)	123.33(9)	N(2)^{i}–Ag(1)–N(3)^{ii}	104.81(8)		
N(1)–Ag(1)–N(3)^{ii}	100.47(8)				
Complex ***2***					
Ag(1)–N(2)	2.219(5)	Ag(1)–O(2)	2.290(5)	Ag(1)–N(1)^{i}	2.317(5)
Ag(1)–Ag(1)^{ii}	3.241(1)	Ag(1)–Ag(1)^{iii}	3.269(1)	Ag(2)–O(2)	2.485(5)
Ag(2)–O(3)	2.674(5)				
N(2)–Ag(1)–O(2)	135.2(2)	N(2)–Ag(1)–N(1)^{i}	127.8(2)		
O(2)–Ag(1)–N(1)^{i}	95.2(2)	N(2)–Ag(1)–Ag(1)^{ii}	99.1(1)		
O(2)–Ag(1)–Ag(1)^{ii}	76.2(1)	N(1)^{i}–Ag(1)–Ag(1)^{ii}	77.6(1)		
N(2)–Ag(1)–Ag(1)^{iii}	72.1(1)	O(2)–Ag(1)–Ag(1)^{iii}	119.4(1)		
Ag(1)^{ii}–Ag(1)–Ag(1)^{iii}	164.18(3)				
Complex ***3***					
Ag(1)–N(3)	2.322(4)	Ag(1)–O(1)	2.406(3)	Ag(2)–N(1)	2.180(4)
Ag(2)–O(1)^{iii}	2.579(3)				
N(3)–Ag(1)–N(3)^{i}	105.0(2)	N(3)–Ag(1)–O(1)^{i}	104.9(1)		
N(3)–Ag(1)–O(1)	132.9(1)	N(1)^{ii}–Ag(2)–N(1)	148.6(2)		
O(1)^{i}–Ag(1)–O(1)	79.3(2)	N(1)–Ag(2)–O(1)^{iii}	102.0(1)		
N(1)–Ag(2)–O(1)^{iv}	103.2(1)	O(1)^{iii}–Ag(2)–O(1)^{iv}	73.1(2)		
Ag(1)–O(1)–Ag(2)^{iii}	103.8(1)				

Symmetry transformations used to generate equivalent atoms: (i), $x, y+1, z$, (ii), $-x+1/2, y+1/2, -z+1/2$, (iii), $x, y-1, z$, for **1**; (i), $x-1/2, y+1/2, z$, (ii), $-x-1/2, -y+1/2, -z$, (iii), $-x-1, -y, -z$, for **2**; (i), $-x-1/2, -y+1, z$, (ii), $-x+1/2, -y+1, z$, (iii), $-x, -y+1, -z+2$, (iv), $x+1/2, y, -z+2$, for **3**.

spectra and elemental analyses of **1**–**3** are fully consistent with their formations. Their IR spectra exhibit the absorptions in the range of ~3296 to ~3400 cm^{-1}, corresponding to the N–H stretching vibrations of the amide group. Strong characteristic bands of carboxylic groups are observed in the range of ~1630 to ~1560 cm^{-1} for the asymmetric vibrations and ~1480 to ~1350 cm^{-1} for symmetric vibrations, respectively. The absence of the characteristic bands at around ~1700 cm^{-1} attributed to

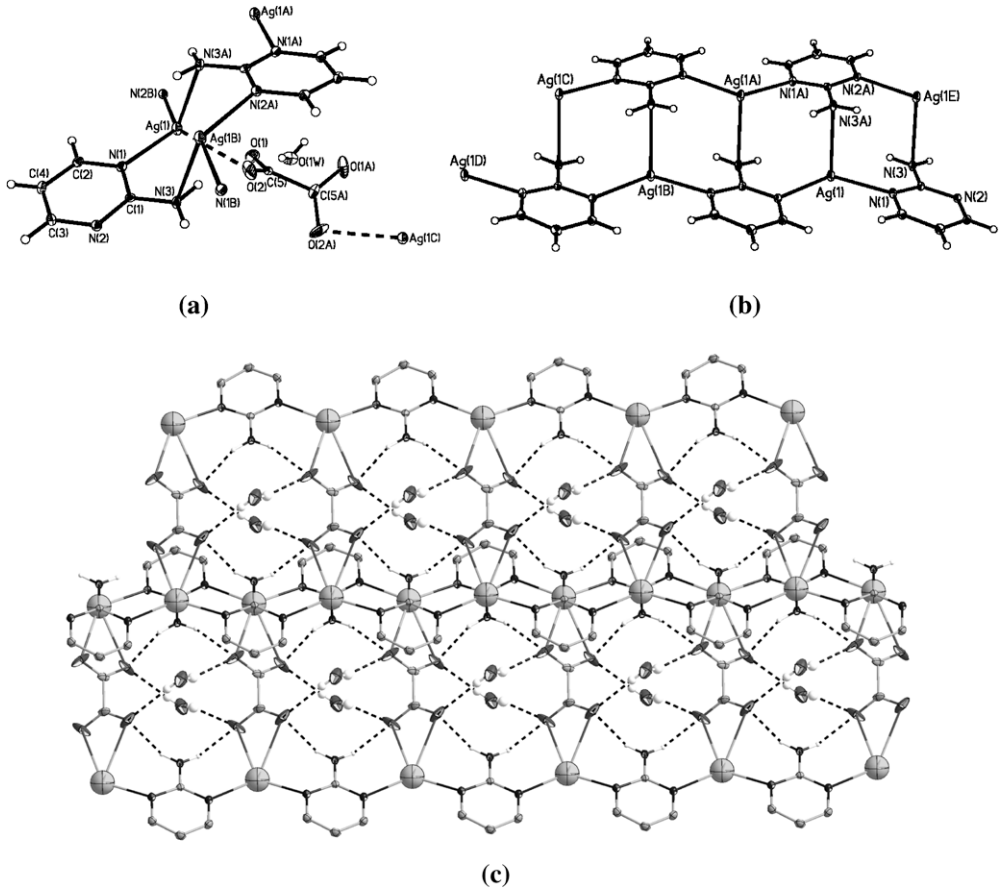


Fig. 1. (a) ORTEP drawing of **1** showing the coordination environment around Ag(I) centers at 40% probability level. (b) A view of the 1-D ladder formed by silver centers and L1 ligands in **1** along the *c* axis. (c) A view of the 2-D pleated molecular sheets in **1** along the *c* axis. Hydrogen atoms in pyrimidyl groups were omitted for clarity. The dashed lines correspond to the hydrogen bonds. Ag stressed in bigger ball.

the protonated carboxylic groups, indicating that the complete deprotonation of all carboxylate groups in **1**-**3** upon reaction with Ag ions [49].

3.2. Crystal structure of $[Ag_2(L1)_2(L2)]\cdot 2H_2O$ (**1**)

The present X-ray crystal structure analysis suggests that complex **1** crystallizes in the monoclinic space group $C2/c$. The C_2 axis lies in the midpoint of C–C single bond of L2 anion, hence, each asymmetric unit contains one Ag(I) ion, one L1 ligand, a half L2 anion and one uncoordinated water. As shown in Fig. 1a, each four-coordinate Ag, which adopts a distorted tetrahedral geometry, is coordinated by two bridging L1 nitrogen atoms, one amino nitrogen atom and one deprotonated oxalic acid oxygen atom. The largest N(2)–Ag(1)–O(2) angle opened up to 132.69(8)° from the ideal tetrahedral angle while the remaining angles are in the range from 104.81(8) to 123.33(9)°. It is noteworthy that the Ag–N distances to amino nitrogen atoms [Ag(1)–N(3A) = 2.540(3) Å] are significantly longer than those to the pyrimidyl nitrogen atoms [Ag(1)–N(1) = 2.313(2) and Ag(1)–N(2B) = 2.312(2) Å]. This difference may partially be due to the electronic effect between amino nitrogen and pyrimidyl nitrogen atoms. Interestingly, As far as we know, most of aminopyrimidine derivatives often adopt *N*-monodentate and *N*,*N*′-bidentate coordination modes with silver atoms *via* pyrimidyl nitrogen atoms, and the only example with tridentate fashion was ever reported by Wang [40]. Here, L1 ligands are coordinated to the Ag(I) metal centers by taking this rare *N*,*N*′,*N*″-tridentate modes to form 1-D ladder structures (Fig. 1b), which were interlinked by L2 anions [Ag(1)–O(2) = 2.630(4) Å] to generate 2-D pleated molecular sheets (Fig. 1c). Each L2 anion is coordinated to the metal centers in a bidentate μ_1-O, μ_1-O′-bonding mode.

In addition, as shown in Fig. 1c, in each molecular sheet, the Ag(I) ions, L1 ligands and L2 anions are interlinked to form chair-like eight-membered binuclear ring and 18-membered metallocycles in each molecular sheet. Two kinds of intermolecular hydrogen bonds are observed in the 18-membered metallocycles, including N–H···O hydrogen bonds where the amino group of L1 ligands serve as donors while the uncoordinated oxygen atoms on the L2 anions act as acceptors [N(3)–H(3C)···O(1)^{i}, 2.843(4) Å, ∠N–H···O, 141.7°; symmetry code: (i), x, $y-1$, z], and O–H···O hydrogen bonds where oxygen atoms of L2 anions serve as acceptors while hydrogen atoms of uncoordinated water act as donors [O(1W)–H(1WB)···O(2)^{ii}, 2.957(6) Å, ∠O–H···O, 157.0°; symmetry code: (ii), $-x+1$, $y+1$, $-z+1/2$].

3.3. Crystal structure of $[Ag_2(L1)_2(L3)]\cdot H_2O$ (**2**)

When oxalate is replaced by more flexible glutarate and reacted with $AgNO_3$ and L1 ligand under the similar synthetic conditions, a fascinating 3-D structure of **2** is produced. The molecular ORTEP drawing of **2** together with the atom-numbering scheme is depicted in Fig. 2a. X-ray crystal structure determination displays that **2** consists of molecular bilayers with T-shaped blocks as the fundamental building units, in which each central Ag(I) cation adopts a T-shaped coordination configuration with two pyrimidyl nitrogen donors [Ag(1)–N(1A) = 2.317(5) and Ag(1)–N(2) = 2.219(5) Å] of L1 ligand in the horizontal direction. The coordination sphere is completed by one oxygen donor [Ag(1)–O(2) = 2.290(5) Å] of one deprotonated glutarate (L3) in the axial

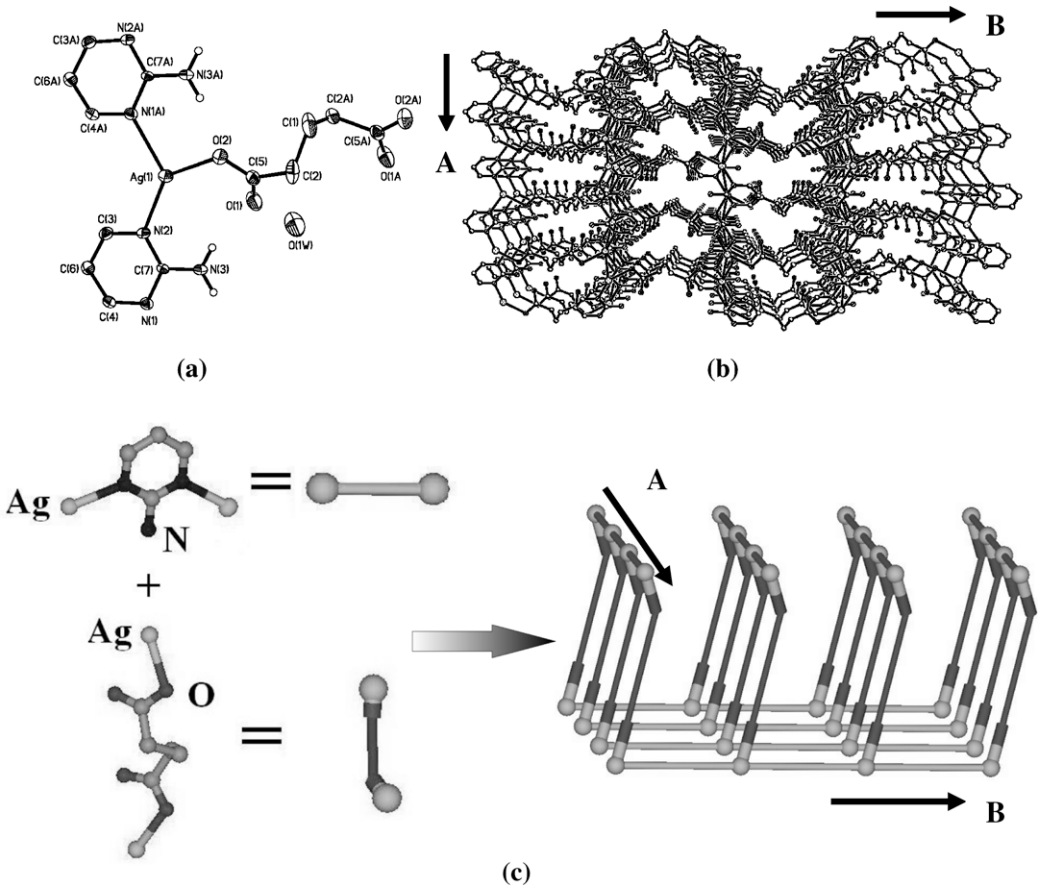


Fig. 2. (a) ORTEP drawing of **2** showing the coordination environment around Ag(I) centers at 40% probability level. (b) Packing diagram of **2** showing microporous tongue-and-groove structure along the *c* axis. All hydrogen atoms and solvent molecules have been omitted for clarity. (c) Schematic representation of molecular bilayer motif of **2**.

direction, forming a new type of T-shaped unit. Fig. 2b shows that **2** contains molecular bilayer motifs, and Fig. 2c gives the schematic representation of corresponding bilayer motif. Each L1 as a bidentate ligand links Ag(I) centers to form infinite 1-D chains in the *ab* plane, and intramolecular N–H···O hydrogen bonds occur in the 1-D chains where oxygen atoms of L3 anions serve as acceptors while the uncoordinated amino groups of L1 ligands act as donors [H···O, 2.02–2.06 Å, N···O, 2.863(6)–2.897(7) Å, ∠N–H···O, 163.7–167.5°]. Interestingly, two kinds of extended modes are observed for these 1-D chains (herein designated as A and B). When viewed from above the *ab* plane, Fig. 2b shows that two related $[Ag(L1)]_{\infty}$ chains are interlaced. The complete deprotonated L3 anions, acting as pillars, interlink the upper and lower chains to generate bilayer galleries. The width of the galleries is determined by the length of L1 ligand (6.448 Å), and their height is fixed by the length of L3 anion (9.847 Å).

To the best of our knowledge, most of the reported silver(I) metal–organic frameworks containing such bilayer motifs have focused on the structures based on single ligand 4,4′-bipy or other mixed ligands with 4,4′-bipy bridges. However, there are no such a distinctive tongue-and-groove structure of 3-D frameworks of coordination polymers with aminopyrimidine bridges reported in the literature. Furthermore, a remarkable feature of the structure of **2** is that the bilayer is sustained by the long L3 anion and short L1 ligand and displays an unusual entanglement (see Fig. S1, in the Supplementary data). Its structure belongs to a kind of 2-D to 3-D parallel interpenetration of "thick" layers: the 2-D layers interpenetrate each other in quintuple mode and the 5-fold interpenetrating results in Ag···Ag interactions. The separations between silvers are alternatively 3.269 and 3.241 Å, which are slightly shorter than the summed van der Waal radius of two silver atoms (3.44 Å) [50,51], indicating the existence of weak Ag···Ag interactions. In the molecular bilayer, the lattice water molecule is enclathrated in the cavity of the bilayer and it forms a hydrogen bond with the O1 atom of L3 anion [$O(1w)\cdots O(1)^{i}$ = 2.809(7) Å, symmetry code: (i), $-x-1/2$, $y+1/2$, $-z-1/2$].

Obvious changes are observed from the structures and dimensions (2-D(**1**) to 3-D(**2**)) of **1** and **2**. The striking structural difference between **1** and **2** is simply caused by different $-CH_2-$ spacers in the dicarboxylate anions, *i.e.*, L3 anion with longer spacers than L2 anion shows more flexible in nature, which allows the anion to bend and rotate freely when coordinating to metal centers.

3.4. Crystal structure of $[Ag_2(L1)_2(L4)]\cdot 2H_2O$ (**3**)

When using rigid aromatic 1,4-naphthalenedicarboxylate instead of oxalate to react with $AgNO_3$ and L1 under the similar synthetic conditions, complex **3** with a different structural type from others has been obtained. Single crystal X-ray analysis reveals that complex **3** crystallizes in the orthorhombic space group *Pnna*. The asymmetric unit consists of two Ag(I) ions, two L1 ligands, one L4 anion, and two uncoordinated water molecules. The charge neutrality is achieved by the fully deprotonated carboxylate groups

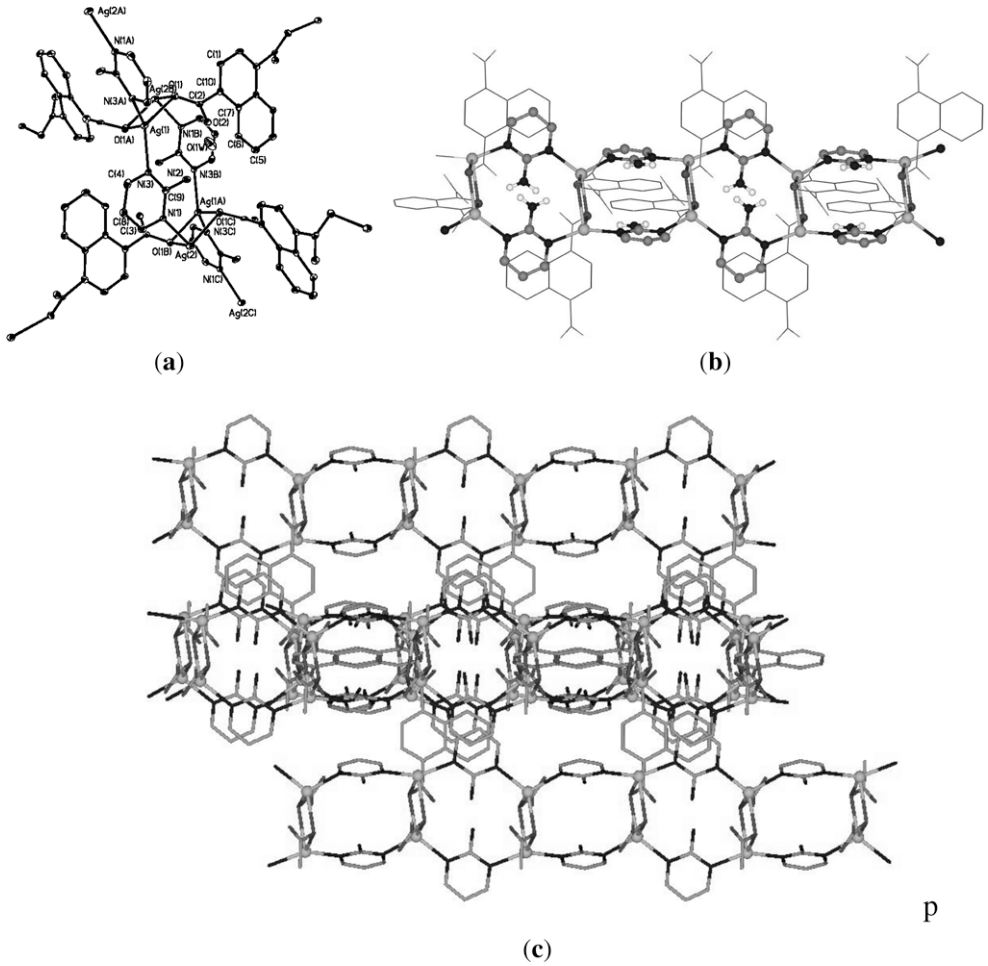


Fig. 3. (a) ORTEP drawing of **3** showing the coordination environment around Ag(I) centers at 40% probability level. (b) A packing diagram showing the 1-D ladder structure in **3**. (c) The 3-D supramolecular structure of **3**. All hydrogen atoms and solvent molecules have been omitted for clarity.

of 1,4-naphthalenedicarboxylate. As shown in Fig. 3a, two independent Ag(I) ions have similar coordination environments, and each central Ag(I) ion is coordinated by two nitrogen atoms [Ag(1)–N(3) = 2.322(4), Ag(1)–N(3A) = 2.322(4) Å; Ag(2)–N(1) = 2.180(4), Ag(2)–N(1A) = 2.180(4) Å] from two L1 ligands and two oxygen atoms [Ag(1)–O(1) = 2.406(3), Ag(1)–O(1A) = 2.406(3) Å; Ag(2)–O(1B) = 2.579(3), Ag(2)–O(1C) = 2.579(3) Å] from different L4 anions in a tetrahedral geometry. All the Ag–N and Ag–O bond distances are within the normal range [35,52,53]. Two such asymmetric units are connected to form a centrosymmetrically tetranuclear 12-membered metallocycle $[Ag_4(L1)_2(L4)_2]$. There is a quadrangle core in the discrete tetranuclear unit. The interatomic distances of Ag–Ag are 6.287 Å on the long sides of the quadrangle and 3.925 Å on the short sides of the quadrangle, excluding any direct metal–metal interaction. The 12-membered rings are interconnected each other through L1 ligands to generate 1-D double polymeric chains (Fig. 3b). Each L1 ligand has similar *N*,*N*′-bidentate coordination mode. Moreover, acting as bridging linkers through corresponding μ^2-carboxylates, L4 anions connect a pair of adjacent Ag(I) atoms to yield 3-D supramolecular networks (Fig. 3c). It is noteworthy that L4 anions hold the same coordination mode with different naphthyl orientation. In addition, lattice water molecules occupy the residual space and are hydrogen bonded to the carboxylate groups from L4 anions [O(1w)···O(2) = 2.941(6) and O(1w)···O(2)^{i} = 2.944(5) Å, symmetry code: (i) x, $-y + 3/2$, $-z + 5/2$].

4. Conclusions

With the principal aim of obtaining new high-dimensional coordination polymers with interesting photoluminescence, we try to introduce dicarboxylates into previous silver/aminopyrimidine system, and get three new silver(I) coordination polymers spanning from 2-D to 3-D frameworks. The analysis of the crystallographic data of **1–3** clearly shows that the structures of dicarboxylate anions are the key factors in directing self-assembly such diverse structures of these silver(I) complexes.

Acknowledgments

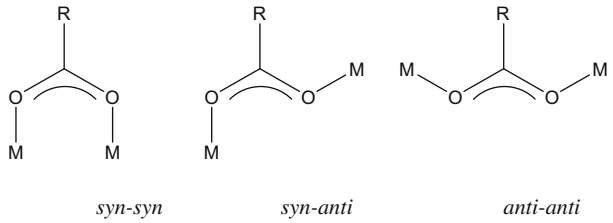
This work was financially supported by the National Natural Science Foundation of China (No. 20721001) and 973 Project (Grant 2007CB815301) from MSTC.

Appendix A. Supplementary data

CCDC 714483, 714484 and 714485 contain the supplementary crystallographic data for **1**, **2** and **3**. These data can be obtained free of charge via http://www.ccdc.cam.ac.uk/conts/retrieving.html, or from the Cambridge Crystallographic Data Centre, 12 Union Road, Cambridge CB2 1EZ, UK; fax: (+44) 1223-336-033; or e-mail: deposit@ccdc.cam.ac.uk. Supplementary data associated with this article can be found, in the online version, at doi:10.1016/j.poly.2009.07.013.

References

[1] S.R. Batten, R. Robson, Angew. Chem., Int. Ed. 37 (1998) 1460.
[2] P.J. Hagrman, D. Hagrman, J. Zubieta, Angew. Chem., Int. Ed. 38 (1999) 2638.
[3] X.M. Zhang, M.L. Tong, X.M. Chen, Angew. Chem., Int. Ed. 41 (2002) 1029.
[4] S. Subramanian, M. Zaworotko, Coord. Chem. Rev. 127 (1994) 357.
[5] S. Leininger, B. Olenyuk, P.J. Stang, Chem. Rev. 100 (2000) 853.
[6] M. Eddaoudi, D.B. Moler, H. Li, B. Chen, T.M. Reineke, M. O'Keeffe, O.M. Yaghi, Acc. Chem. Res. 34 (2001) 319.
[7] B. Moulton, M.J. Zaworotko, Chem. Rev. 101 (2001) 1629.
[8] S.L. James, Chem. Soc. Rev. 32 (2003) 276.
[9] R.H. Wang, M.C. Hong, J.H. Luo, R. Cao, J.B. Weng, Chem. Commun. (2003) 1018.
[10] D. Braga, Chem. Commun. (2003) 2751.
[11] M. Munakata, L.P. Wu, T. Kuroda-Sowa, M. Mackawa, K. Moriwaki, S. Kitagawa, Inorg. Chem. 36 (1997) 5416.
[12] Y. Suenaga, S.G. Yan, L.P. Wu, I. Ion, T. Kuroda-Sowa, M. Maekawa, M. Munakata, J. Chem. Soc., Dalton Trans. (1998) 1121.
[13] L. Carlucci, G. Ciani, P. Macchi, D.M. Proserpio, A. Sironi, Chem. Commun. (1997) 631.
[14] K.A. Hirsch, S.R. Wilson, J.S. Moore, Inorg. Chem. 36 (1997) 2960.
[15] S.Y. Yang, L.S. Long, Y.B. Jiang, R.B. Huang, L.S. Zheng, Chem. Mater. 14 (2002) 3229.
[16] A. Michaelides, S. Skoulika, V. Kiritsis, A. Aubry, Chem. Commun. (1995) 1415.
[17] J.H. Yang, S.L. Zheng, X.L. Yu, X.M. Chen, Cryst. Growth Des. 4 (2004) 834.
[18] K. Xia, C.Z. Lu, X.Y. Wu, Q.Z. Zhang, J.J. Zhang, D.M. Wu, Polyhedron 26 (2007) 941.
[19] S.L. Zheng, M.L. Tong, H.L. Zhu, X.M. Chen, New J. Chem. 25 (2001) 1425.
[20] R.L. Sang, L. Xu, Eur. J. Inorg. Chem. (2006) 1260.
[21] M.L. Tong, Y.M. Wu, J. Ru, X.M. Chen, H.C. Chang, S. Kitagawa, Inorg. Chem. 41 (2002) 4846.
[22] F. Pointillart, P. Herson, K. Boubekeur, C. Train, Inorg. Chim. Acta 361 (2008) 373.
[23] B.H. Ye, M.L. Tong, X.M. Chen, Coord. Chem. Rev. 249 (2005) 545.
[24] J. Yang, Q. Yue, J.D. Li, J.J. Cao, G.H. Li, J.S. Chen, Inorg. Chem. 45 (2006) 2857.
[25] J. Yao, W. Huang, B. Li, S. Gou, Y. Xu, Inorg. Chem. Commun. 5 (2002) 711.
[26] S. Dalai, P.S. Mukherjee, G. Rogez, T. Mallah, M.G.B. Drew, N.R. Chaudhuri, Eur. J. Inorg. Chem. 31 (2002) 3292.
[27] X.J. Zheng, L.P. Jin, S. Gao, S.Z. Lu, Inorg. Chem. Commun. 8 (2005) 72.
[28] X.J. Zheng, L.P. Jin, S. Gao, S.Z. Lu, New J. Chem. 29 (2005) 798.
[29] X.L. Wang, C. Qin, E.B. Wang, Y.G. Li, N. Hao, C.W. Hu, L. Xu, Inorg. Chem. 43 (2004) 1850.
[30] W. Chen, J.Y. Wang, C. Chen, Q. Yue, H.M. Yuan, J.S. Chen, S.N. Wang, Inorg. Chem. 42 (2003) 944.
[31] F.S. Delgado, J. Sanchiz, C.R. Pérez, F. Lloret, M. Julve, CrystEngComm 5 (2003) 280.
[32] J.A.R. Navarro, E. Barea, M.A. Galindo, J.M. Salas, M.A. Romero, M. Quirós, N. Masciocchi, S. Galli, A. Sironi, B. Lippert, J. Solid State Chem. 178 (2005) 2436.
[33] W. Saenger, Principles of Nucleic Acid Structure, Springer, New York, 1984.
[34] K. Aoki, M. Inaba, S. Teratani, H. Yamazaki, Y. Miyashita, Inorg. Chem. 33 (1994) 3018.
[35] G. Smith, B.A. Cloutt, D.E. Lynch, K.A. Byriel, C.H.L. Kennard, Inorg. Chem. 37 (1998) 3236.
[36] C.V.K. Sharma, S.T. Griffin, R.D. Rogers, Chem. Commun. (1998) 215.
[37] H. Cai, H.M. Hu, W.Z. Chen, H.G. Zhu, X.Z. You, Chem. Lett. (1999) 221.
[38] D.R. Armstrong, F. Benevelli, A.D. Bond, N. Feeder, E.A. Harron, A.D. Hopkins, M. Mcpartlin, D. Moncrieff, D. Saez, E.A. Quadrelli, A.D. Woods, D.S. Wright, Inorg. Chem. 41 (2002) 1492.
[39] C.K. Terajima, H. Miyasaka, T. Ishii, K. Sugiura, M. Yamashita, Inorg. Chim. Acta 332 (2002) 210.
[40] Y.H. Wang, K.L. Chu, H.C. Chen, C.W. Yeh, Z.K. Chan, M.C. Suen, J.D. Chen, J.C. Wang, CrystEngComm 8 (2006) 84.
[41] Y.N. Chi, K.L. Huang, F.Y. Cui, Y.Q. Xu, C.W. Hu, Inorg. Chem. 45 (2006) 10605.
[42] H.P. Wu, C. Janiak, G. Rheinwald, H. Lang, J. Chem. Soc., Dalton Trans. (1999) 183.
[43] C. Janiak, L. Uehlin, H.-P. Wu, P. Klufers, H. Piotrowski, T.G. Scharmann, J. Chem. Soc., Dalton Trans. (1999) 3121.
[44] G.G. Luo, R.B. Huang, J.H. Chen, L.R. Lin, L.S. Zheng, Polyhedron 27 (2008) 2791.
[45] G.G. Luo, R.B. Huang, N. Zhang, L.R. Lin, L.S. Zheng, Polyhedron 27 (2008) 3231.
[46] R.H. Blessing, Acta Crystallogr., Sect. A 51 (1995) 33.
[47] G.M. Sheldrick, SHELXS 97: Program for Crystal Structure Solution, University of Göttingen, Göttingen, Germany, 1997.
[48] G.M. Sheldrick, SHELXL 97: Program for Crystal Structure refinement, University of Göttingen, Göttingen, Germany, 1997.
[49] L.J. Bellamy, The Infrared Spectra of Complex Molecules, Wiley, New York, 1958.
[50] A. Bondi, J. Phys. Chem. 68 (1964) 441.
[51] M. Jansen, Angew. Chem., Int. Ed. 26 (1987) 1098.
[52] R.P. Feazell, C.E. Carson, K. Klausmeyer, Inorg. Chem. 45 (2006) 2635.
[53] W.H. Bi, R. Cao, D.F. Sun, D.Q. Yuan, X. Li, M.C. Hong, Inorg. Chem. Commun. 6 (2003) 1426.



Scheme 1.

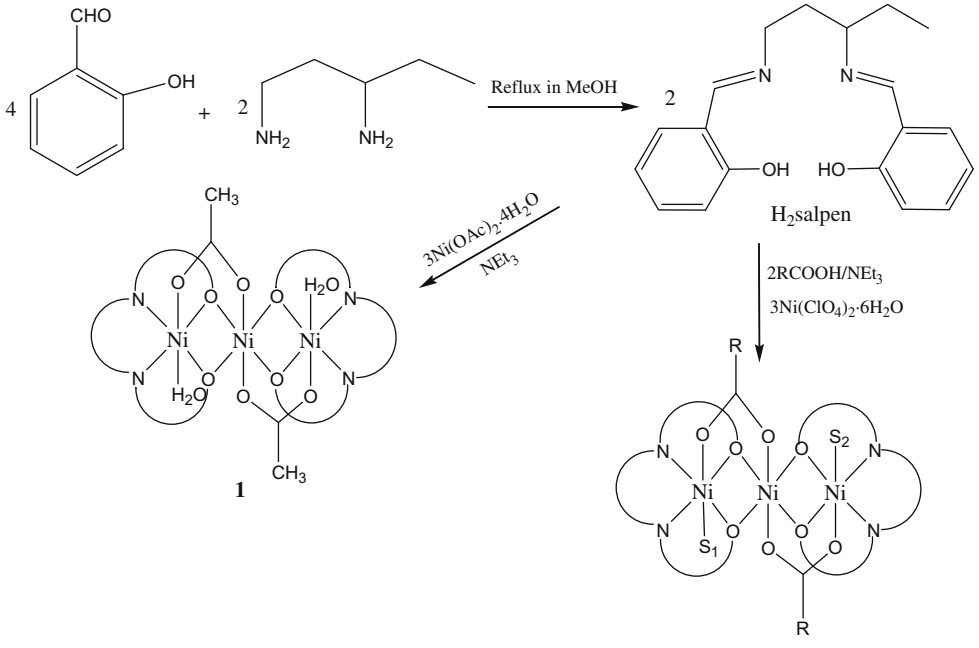
bridges yielded quite a few linear trinuclear complexes with hexacoordinated Ni(II) centres [20–23]. However, the potential for utilizing the bridging properties of carboxylate groups other than acetate has not been investigated apart from one example with formate [24]. One benzoate bridged trinuclear Ni(II) compound is also reported [25] but this is with the reduced di-Schiff base ligand. It is also to be noted that although several papers have reported the synthesis and X-ray structural analyses of such kind of linear trinuclear complexes [20–25], detailed magnetic characterizations are seldom forthcoming.

We, therefore, intend to investigate the variation in the structure and magnetic properties by systematically varying the carboxylate bridge. For this purpose, we have taken acetate, benzoate, phenylacetate and cinnamate ion along with the di-Schiff base H_2salpen (*N*,*N*′-bis(salicylidene)-1,3-pentanediamine) and have produced successfully the linear trinuclear Ni(II) complexes ($[Ni_3(salpen)_2(OAc)_2(H_2O)_2]\cdot 4H_2O$ (**1**), $[Ni_3(salpen)_2(OBz)_2]$ (**2**), $[Ni_3(salpen)_2(OPh)_2(EtOH)]$ (**3**) and $[Ni_3(salpen)_2(OCn)_2(CH_3CN)_2]$ (**4**), where OAc = acetate, CH_3COO^-; OBz = benzoate, $PhCOO^-$; OPh = phenyl acetate, $PhCH_2COO^-$; OCn = cinnamate, PhCH CHCOO$^-$) (Scheme 2). The structure of the complexes reveal for the first time that the coordination geometry around Ni(II) can be tuned i.e. it may be hexacoordinated or pentacoordinated depending upon the bridging carboxylate group. Variable-temperature magnetic measurements show antiferromagnetic couplings within the trinuclear units of Ni(II) in all four compounds. The variations in the structures and geometry around Ni(II) in the present complexes afford better insight into the key structural parameters that control the strength and sign of the magnetic interactions as well as zero-field splitting (ZFS) parameters *D*, both factors which are extremely important in the rational design of new complexes which contain the desired properties of a molecular based magnet.

Moreover, the morphology of complexes **1**–**4** has been examined by scanning electron microscopy (SEM) experiments. Among these complexes, the compound with phenylacetate, $[Ni_3(salpen)_2(OPh)_2(EtOH)]$ (**3**) shows a very interesting dye absorption property by forming vesicles and fused vesicles depending upon the concentration of the solution. Its structure and solution state property has been reported by us recently [26]. The SEM experiments have also been performed for the rest of the complexes. They show porous architecture when samples are prepared from CH_2Cl_2 and show microcrystalline nature when samples are prepared from CH_2Cl_2/EtOH solvent mixture. Observation of such morphology of the solids obtained from the different solvent systems proved to be immensely helpful in choosing the appropriate solvent for growing X-ray quality single crystals.

2. Experimental

Salicylaldehyde, 1,3-pentanediamine, N-methyl-1,3-propanediamine, $Ni(OAc)_2\cdot 4H_2O$ (OAc = acetate), benzoic acid (HOBz), phenyl acetic acid (HOPh) and cinnamic acid (HOCn) were purchased from commercial sources and used as received. All other solvents were of reagent grade and were used without further purification.



In **2**, $S_1 = S_2$ = none, R = Ph
In **3**, S_1 = none, $S_2 = CH_3CH_2OH$, $R = PhCH_2$
In **4**, $S_1 = S_2 = CH_3CN$, R = PhCH=CH

Scheme 2.

2.1. Synthesis of the Schiff base ligands N,N′-bis(salicylidene)-1,3-pentanediamine (H_2salpen)

The tetradentate Schiff base ligand was prepared by the condensation of salicylaldehyde (1.05 cm^3, 10 mmol) and 1,3-pentanediamine (0.596 cm^3, 5 mmol) in methanol (10 cm^3) as reported earlier [27].

2.2. Synthesis of $[Ni_3(salpen)_2(OAc)_2(H_2O)_2]\cdot 4H_2O$ (**1**)

A suspension of $Ni(OAc)_2\cdot 4H_2O$ (1.86 g, 7.5 mmol), in methanol (10 cm^3) was added to a methanolic solution (10 cm^3) of the ligand (Hsalpen) (5 mmol) and stirred for ca. 10 min. Triethylamine (1.4 cm^3, 10 mmol) was added dropwise with constant stirring. A green precipitate separated out within an hour. The green solid was then filtered and washed with diethyl ether and then redissolved in CH_2Cl_2. Layering of the green solution with ethanol gave well formed X-ray diffraction quality green single crystals of **1**.

Complex **1**: (Yield: 1.96 g; 80%). *Anal.* Calc. for $C_{44}H_{62}N_4Ni_3O_{14}$: C, 53.98; H, 5.34; N, 5.71. Found: C, 53.48; H, 5.29; N, 5.75%. IR (KBr pellet, cm^{-1}): 1627 ν(C=N), 1584 ν_{as}(C=O), 1415 ν_s(C=O), λ_{max}/nm (ε_{max}/dm^3 mol^{-1} cm^{-1}) (CH_2Cl_2), 826, 617 (663).

2.3. Synthesis of $[Ni_3(salpen)_2(OBz)_2]$ (**2**) and $[Ni_3(salpen)_2(OCn)_2(CH_3CN)_2]$ (**4**)

A 10 cm^3 methanolic solution of the ligand H_2salpen (5 mmol) was added to a methanolic solution of $Ni(ClO_4)_2\cdot 6H_2O$ (2.74 g, 7.5 mmol). Methanolic solutions of either benzoic acid, PhCOOH (for **2**) (0.61 g, 5 mmol) or cinnamic acid, PhCH=CHCOOH (for **4**) (0.74 g, 5 mmol) were then added to (10 cm^3) of this solution. Triethylamine (2.2 cm^3, 15 mmol) was added drop wise to each of the solution with constant stirring. In both cases green precipitate appeared immediately. The green solids (for **2** and **4**) were then filtered and washed with diethyl ether and then redissolved in CH_2Cl_2. Layering of the green solution of **2** and **4** with ethanol and acetonitrile, respectively, gave well formed X-ray diffraction quality green single crystals.

Complex **2**: (Yield: 1.76 g; 82%). *Anal.* Calc. for $C_{52}H_{50}N_4Ni_3O_8$: C, 60.34; H, 4.87; N, 5.41. Found: C, 60.12; H, 4.79; N, 5.56%. IR (KBr pellet, cm^{-1}): 1617 ν(C=N), 1558 ν_{as}(C=O), 1401 ν_s(C=O), λ_{max}/nm (ε_{max}/dm^3 mol^{-1} cm^{-1}) (CH_2Cl_2), 833, 621 (568).

Complex **4**: (Yield: 1.76 g; 78%). *Anal.* Calc. for $C_{54}H_{61}N_6Ni_3O_8$: C, 59.06; H, 5.60; N, 7.65. Found: C, 59.12; H, 5.19; N, 7.36%. IR (KBr pellet, cm^{-1}): 1631 ν(C=N), 1559 ν_{as}(C=O), 1395 ν_s(C=O), λ_{max}/nm (ε_{max}/dm^3 mol^{-1} cm^{-1}) (CH_2Cl_2), 830, 617 (590).

2.4. Physical measurements

Elemental analyses (C, H and N) were performed using a Perkin–Elmer 240C elemental analyzer. IR spectra in KBr (4500–500 cm^{-1}) were recorded using a Perkin–Elmer RXI FT-IR spectrophotometer. The electronic absorption spectra (1200–350 nm) of the complexes were recorded in CH_2Cl_2 with a Hitachi U-3501 spectrophotometer, SEM (Scanning Electron Microscopy) experiments were performed using VEGA II LSU electron microscope. Magnetic measurements were carried out in the "Unitat de Mesures Magnètiques (Universitat de Barcelona)" on polycrystalline samples (20 mg) with a Quantum Design SQUID MPMS-XL magnetometer working in the 2–300 K range. The magnetic field was 5000 G. The field-dependent magnetization was measured in the applied magnetic field range 0–5 T at 2 K. The diamagnetic corrections were evaluated from Pascal's constants.

2.5. Crystal data collection and refinement

Crystal data for the three crystals are given in Table 1. Intensity data were measured via the Oxford X-Calibur CCD System using Mo Kα radiation. The crystals were positioned at 50 mm from the CCD. 321 frames were measured with a counting time of 10 s. Data analyses were carried out with the CRYSALIS program [28]. The structures were solved using direct methods with the SHELXS97 program [29]. The non-hydrogen atoms were refined with anisotropic thermal parameters. The hydrogen atoms bonded to carbon were included in geometric positions and given thermal parameters equivalent to 1.2 times those of the atom to which they were attached. The hydrogen atoms of the water molecules in **1** could not be located. Empirical absorption corrections were carried out using the ABSPACK program [30]. The structures were refined on F^2 using SHELXL97 [29] to give R_1 0.1028, 0.0838 and 0.0900; wR_2 0.2432, 0.1611 and 0.1441 for 7867, 2893 and 5776 independent reflections with $I > 2\sigma(I)$ for **1**, **2** and **4**, respectively.

3. Results and discussion

3.1. Synthesis of the complexes and electronic microscopic study in search of crystallinity

We have synthesized four trinuclear Ni(II) complexes with a tetradentate di-Schiff base ligand (H_2salpen). Complexes **1**, **2** and **4** have been synthesized varying only the bridging carboxylate moiety. For **1**, a methanol solution of nickel acetate and H_2salpen (*N*,*N*′-bis(salicylidene)-1,3-pentanediamine) were reacted in 3:2 molar ratio. Complexes **2** and **4** were synthesized in similar ways – by addition a methanol solution of $Ni(ClO_4)_2\cdot 6H_2O$, to a methanol solution containing, benzoic acid (for **2**), or cinnamic acid (for **4**) and the Schiff base ligand H_2salpen followed by triethylamine. In all the four complexes, we have utilized the bridging properties of the phenoxo as well as carboxylate groups to obtain the trinuclear complexes by maintaining the metal:ligand ratio 3:2. The formation of the complexes **1**, **2** and **4** and their crystallization deserve some comments. Literature data shows that the di-Schiff base, salpn (the 2:1 condensate of salicyldehyde and 1,3-propanediamine) and its derivative yielded quite a few such linear trinuclear complexes [5–7] but interestingly none is reported with the well-studied analogue salen (the 2:1 condensate of salicyldehyde and 1,2-ethanediamine); the only trinuclear complex reported with salen is not linear [31]. The difference in crystal field stabiliza-

Table 1
Crystal data and structure refinement of complexes **1**, **2** and **4**.

Complex	**1**	**2**	**4**
Formula	$C_{44}H_{62}N_4Ni_3O_{14}$	$C_{52}H_{50}N_4Ni_3O_8$	$C_{54}H_{61}N_6Ni_3O_8$
M	1471.51	1035.08	1128.22
Crystal system	monoclinic	monoclinic	rhombohedral
Space group	$P2_1/n$	$P2_1/c$	$R\bar{3}$
Cell dimensions			
a (Å)	13.2534(11)	13.133(2)	32.1589(10)
b (Å)	14.5401(9)	10.7870(7)	32.1589(10)
c (Å)	35.9266(15)	17.4112(14)	15.4937(5)
α (°)	(90)	(90)	(90)
β (°)	96.612(6)	109.50(1)	(90)
γ (°)	(90)	(90)	(120)
U (Å^3)	6877.2(8)	2325.0(4)	13876.8(8)
Z	4	4	9
D_c (g cm^{-3})	1.421	1.479	1.215
μ (Mo Kα) (mm^{-1})	1.281	1.263	5292
$R_{(int)}$	0.060	0.096	0.057
No. of unique data	18939	6722	8927
No. of data with $I > 2\sigma(I)$	7867	2893	5776
R_1, wR_2	0.1028, 0.2769	0.0838, 0.1940	0.0900, 0.2334

tion energies of the Schiff base ligands seems to play an important role in the formation of these complexes. The greater steric hindrance due to the bulkier trimethylene group in salpn compared to the dimethylene group in salen between the N atoms causes a weaker ligand field for the Schiff bases derived from 1,3-propanediamine and its derivative and consequently facilitates the formation of a linear trinuclear structure, bridged either by acetate and phenoxo- by increasing the coordination number of Ni(II) beyond four. Hence, we choose the di-Schiff base H_2salpen for the synthesis of such linear trinuclear Ni(II) complexes. The presence of the ethyl group in the diamine chelate ring of the ligand provides an advantage over its 1,3-propanediamine analogue by making the complexes more soluble in organic solvents e.g. dichloromethane. However, slow evaporation of the solvent or slow diffusion of diethylether or *n*-hexane which are common practice to obtain single crystals proved to be unsuccessful for these compounds. As the compounds were sparingly soluble in many other common organic solvents (methanol, ethanol, acetonitrile), we decided to investigate the microcrystalline nature of the product which was obtained initially just after the addition of the solvents to the dichloromethane solution with the help of scanning electron microscopy (SEM). We found that the solid obtained by simple evaporation of the dichloromethane solution does not show any crystalline nature and the compound remains as a porous amorphous material as evidenced by SEM experiments (Fig. 1, and Figs. S1 and S2 for compounds **1**, **2** and **4**, respectively). The crystalline nature of the product was also not visible when diethylether or *n*-hexane was added to separate the solid compound from dichloromethane solution. On the other hand, addition of methanol, ethanol and acetonitrile to the dichloromethane solution produced a good microcrystalline product and among them the best formed crystallite is formed by ethanol (for **1** and **2**) and acetonotrile (for **4**). Therefore we chose the slow diffusion of ethanol (for **1** and **2**) or acetonitrile (for **4**) to the dichloromethane solution of the respective compounds to obtain the X-ray quality single crystals. During these studies we observed the formation of vesicles and dye absorption properties of compound **3** in dichloromethane solution, which has been reported recently [26].

3.2. IR and UV–Vis spectra of complexes

In the IR spectra of complex **1**, the appearance of a broad band near 3400 cm^{-1} indicates the presence of water molecule. The attributions of the IR spectra in the 1300–1650 cm^{-1} region are difficult due to the appearance of several absorption bands from both, the Schiff base and the carboxylate ligands. However, by comparing the IR spectra of the Ni(II) complexes of the same ligand but with other anion (NO_3^-, and halides), the moderately strong and sharp band at 1627, 1617 and 1631 cm^{-1}, respectively for **1**, **2** and **4** are assigned to the azomethine ν(C=N) group. The strong bands at 1584, 1558 and 1559 cm^{-1} are likely to be due to the antisymmetric stretching mode of the carboxylate group and the bands

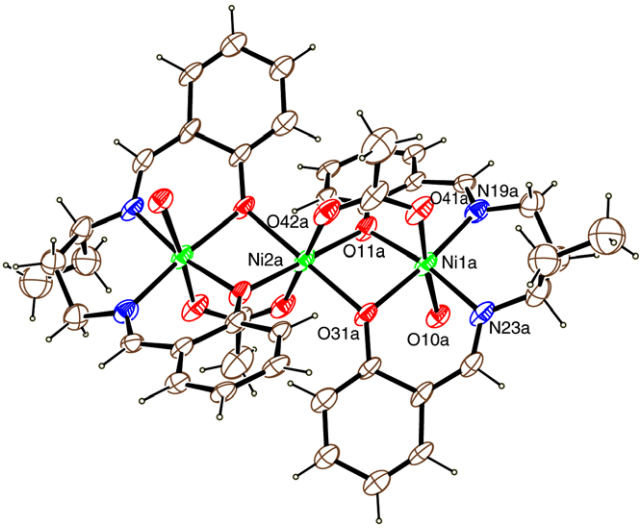


Fig. 2. ORTEP-3 view of the asymmetric unit of **1-A** with ellipsoids at 30% probability (the hydrogen atoms on the coordinated water molecules O(10) could not be located, solvent water molecules are omitted for clarity).

at 1415, 1401 and 1395 cm^{-1} for the symmetric stretching modes for the carboxylates [32,33].

The electronic absorption spectra of complexes **1**, **2** and **4** were studied in CH_2Cl_2 solutions. The absorption spectra of all these complexes show a broad band at ca. 830 nm, well separated from the second transition at ca 617 nm, as is usual for octahedral and pentacoordinated Ni(II) complexes [34–36]. The higher energy d–d bands are obscured by strong charge-transfer transitions.

3.3. Description of the structure of $[Ni_3(salpen)_2(OAc)_2(H_2O)_2]\cdot 4H_2O$ (**1**), $[Ni_3(salpen)_2(OBz)_2]$ (**2**) and $[Ni_3(salpen)_2(OCn)_2(CH_3CN)_2]$ (**4**)

Complexes **1**, **2** and **4** consist of similar trinuclear structures showing three nickel atoms in an approximately linear disposition. The ethyl group introduces a chiral atom, C3 on 1,3-pentanediamine. For the synthesis of the complexes we used racemic (D,L) source of diamine. The X-ray analysis shows that all three structures crystallize in centrosymmetric space groups, therefore contain both enantiomers i.e. there is no spontaneous resolution at the crystal level. The crystal structure of **1** contains two trinuclear units with similar structures – A, containing a crystallographic centre of symmetry and B in a general position. In addition there are four solvent water molecules, two of which were refined with 50% occupancy. A labeled diagram of the centrosymmetric trinuclear molecule **1-A** of complex **1** is shown in Fig. 2 while the trinuclear molecule **1-B** in a general position is shown in Fig. S3. Complexes **2** and **4** comprise of discrete centrosymmetric trinuclear units of the neutral compound $[Ni_3(salpen)_2(OBz)_2]$ and

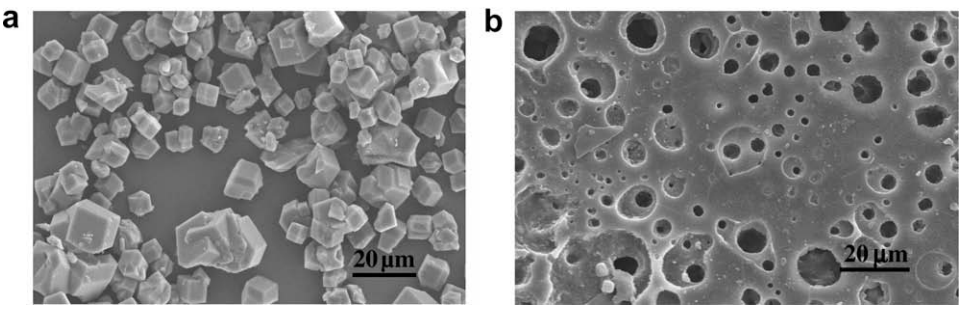


Fig. 1. SEM images of complex **1**; (a) crystalline state (obtained from CH_2Cl_2/CH_3CH_2OH, 1:1 v/v) and (b) amorphous state (obtained from CH_2Cl_2).

$[Ni_3(salpen)_2(OCn)_2(CH_3CN)_2]$ and are shown in Figs. 3 and 4, respectively. The selected bond lengths and angles of the complexes are summarized in Table 2. For all three complexes, the two tetradentate ligands are bound to the two terminal nickel atoms and also bridged through their two phenoxo-oxygen atoms to the central nickel atom. There are two carboxylates, RCO_2^- where R = CH_3, C_6H_5 and $C_6H_5CH{=}CH$ in **1**, **2** and **4**, respectively, bridging from the central nickel atom to the two outer nickel atoms.

In all three complexes the central nickel atom, Ni(2) has a coordination number of six being bonded to the four oxygen atoms of the two outer Ni(salpen) moieties, at distances ranging 2.046(5)–2.088(4) Å in both molecules of **1** and 2.063(4)–2.064(4) Å in **2** and 2.056(3)–2.066(4) Å in **4**, that form the square plane of the Ni(II) while the trans axial positions are occupied by the bridging oxygen atom O(42) of the carboxylates; acetate in **1-A** and **1-B**, benzoate in **2** and cinnamate in **3** at distances of 2.098(8) Å in **1-A**, 2.011(4) and 2.037(4) Å in **1-B**, 2.051(4) Å in **2** and 2.049(4) Å in **4**.

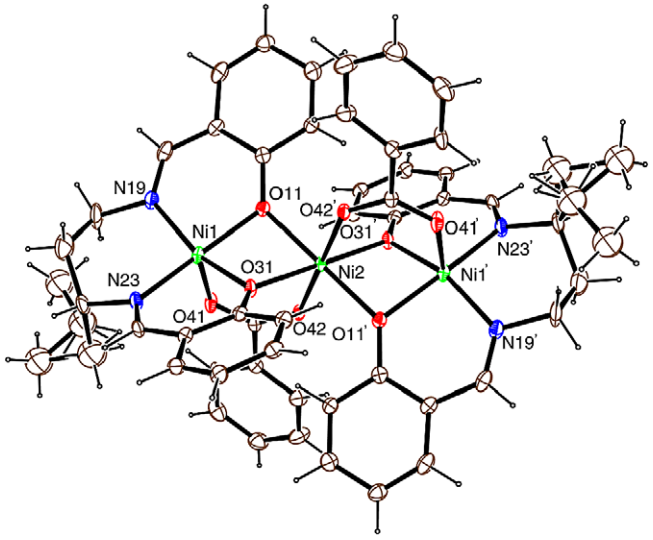


Fig. 3. ORTEP-3 view of the asymmetric unit of **2** with ellipsoids at 30% probability.

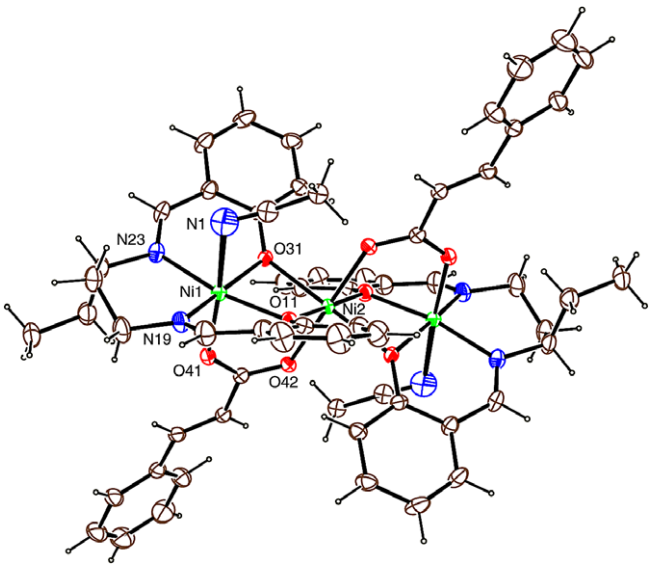


Fig. 4. ORTEP-3 view of the asymmetric unit of **4** with ellipsoids at 30% probability.

The bond distances involving the central nickel atom, Ni(2) are longer than those to the terminal nickel atoms, Ni(1) in all three complexes. The two outer nickel atoms in **1**, **2** and **4** are bonded to four atoms from ligand salpen making up the equatorial plane, with two oxygen atoms O(11), O(31) and two imine nitrogen atoms N(19) and N(23) with Ni(1)–O distances of 1.994(5), 2.015(6) Å in **1-A**, and in the range of 1.960(5)–2.018(4) Å in **1-B** and Ni–N distances of 2.017(8), 2.047(7) Å in **1-A**, and in the range of 2.004(6)–2.105(19) Å in **1-B**. Ni(1)–O and Ni(1)–N distances are,1.995(4), 2.000(4) and 1.995(4), 2.029(5) Å in **2** and 2.005(3), 2.007(3) and 2.004(5)–2.032(4) Å in **4**. In both molecules of **1**, the outer nickel atoms Ni(1) have six-coordinate distorted octahedral environments being bonded to the oxygen atom of the solvent water molecule Ni(1)–O(10) at 2.260(6) Å in **1-A** and 2.344(5), 2.247(5) Å in **1-B**. In **2**, the terminal nickel atoms are five-coordinate while in **4**, there is significant electron density in the other axial position trans to O(41) which is refined as an acetonitrile solvent molecule with 50% occupancy but this identification is not definitive. In all the three complexes, the dimensions involving the other five atoms in the coordination sphere are similar although in **1** and **4**, the Ni(1)–O(41) bond trans to the respective solvent molecules (water for **1** and CH_3CN for **4**) is somewhat lengthened being 2.049(7) Å in **1-A**, 2.050(5), 2.098(8) Å in **1-B**, and 2.027(4) Å in **4** compared to 1.999(4) Å in **2** where there is no trans atom. Among the three complexes the coordination sphere in **2** is mostly distorted from octahedral with a maximum deviation of 22° of the ideal 90° or 180°. The coordination spheres in **1** are least distorted from octahedral with all angles within 8° of the ideal 90° or 180° while complex **4** shows intermediate deviation. Moreover in **1**, the dimensions in **1-B** symmetry are similar although atoms at one end have high thermal motion as is apparent in Fig. S5 and as a result standard deviations are high. The mean deviation of four donor atoms from their respective mean plane are 0.0265 Å in **1-A**, 0.021 and 0.013 Å in **1-B**, 0.08 Å in **2** and 0.017 Å in **4** while the metal atom Ni(1) is deviated by 0.059 Å in **1-A**, 0.101 and 0.120 Å in **1-B**, 0.262 Å in 2 and 0.164 Å in **4** in the direction of the axial O(41). The nickel atoms are separated at the average Ni···Ni distances 3.013 Å in **1-A**, 3.030 and 2.975 Å in **1-B**, 3.027 Å in **2** and 3.010 Å in **4**.

A comparison of the structure of the complexes shows an interesting variation in the geometry of the terminal nickel atoms. In compound **1** where the bridging carboxylate is an acetate group, the water molecule coordinates to one of the axial positions of both the terminal Ni(II) atoms. However, this water molecule is loosely bound as is evident from the comparatively long bond distance Ni(1)–O(10) 2.260(6) Å in **1-A** and 2.344(5) and 2.247(5) Å in **1-B**. In complex **2** where the benzoate ion bridges the nickel atom, no solvent molecule coordinates to the axial position of the terminal Ni(II) leaving the metals in pentacoordinated square pyramidal geometry. The greater steric demand of the bulkier phenyl group of the benzoate ion seems to prevent any solvent molecule from being coordinated. In complex **4**, the phenyl group of the bridging cinnamate is not in close proximity to the terminal Ni(II) and therefore allows a solvent acetonitrile molecule to coordinate in its axial position. It can be noted that a water molecule which is smaller in size than ethanol or acetonitrile could have been coordinated to the terminal Ni(II) to complete a six-coordinate co-ordination sphere in complexes **2–4**, but the hydrophobic nature of the aromatic ring seems to exclude that possibility. In this context it is worth mentioning that in all the reported trinuclear complexes of tetradentate di-Schiff base ligand, the bridging carboxylate is acetate except in one compound where it is formate and in all of them the terminal Ni(II) atoms are hexacoordinated being bonded by a solvent molecule. Thus by introducing a phenyl ring in the bridging carboxylate with varying distances the geometry of the terminal Ni(II) atom could be monitored.

Table 2
Dimensions (distance, Å, angles, °) in the metal coordination spheres.

Complex	**1-A**	**1-B**		**2**	**4**
	a	b	c		
*(a) Dimensions involving the outer nickel atoms in the trinuclear units. **1-A**, **2** and **4** contain crystallographic centres of symmetry. **1-B** is in a general position*					
Ni(1)–O(11)	1.994(5)	2.018(4)	1.960(5)	2.000(4)	2.007(3)
Ni(1)–N(19)	2.017(8)	2.004(6)	2.072 (15)	1.995(5)	2.004(5)
Ni(1)–N(23)	2.047(7)	2.022(5)	2.105(19)	2.029(5)	2.032(4)
Ni(1)–O(31)	2.015(6)	1.992(4)	1.998(6)	1.995(4)	2.005(3)
Ni(1)–O(41)	2.049(7)	2.050(5)	2.098(8)	1.999(4)	2.027(3)
Ni(1)–O(42)					
Ni(1)–N(1)					2.199(4)
Ni(1)–O(10)	2.260(6)	2.344(5)	2.248(5)		
O(11)–Ni(1)–O(10)	89.8(2)	82.0(2)	86.9(2)		
O(31)–Ni(1)–O(10)	89.2(2)	79.8(2)	89.9(2)		
N(19)–Ni(1)–O(10)	89.1(3)	92.4(2)	85.6(4)		
N(23)–Ni(1)–O(10)	85.3(3)	91.7(2)	86.7(4)		
O(41)–Ni(1)–O(10)	175.7(3)	167.4(2)	175.6(4)		
O(31)–Ni(1)–N(19)	172.2(3)	171.2(2)	170.4(4)	158.6(2)	167.90(17)
O(31)–Ni(1)–O(41)	95.0(3)	90.7(2)	94.0(3)	100.0(2)	93.26(14)
N(19)–Ni(1)–O(41)	86.9(3)	96.4(2)	90.3(4)	99.9(2)	96.57(17)
O(31)–Ni(1)–O(11)	82.3(2)	86.3(2)	79.7(2)	79.9(2)	82.60(13)
N(19)–Ni(1)–O(11)	90.1(3)	88.6(2)	91.6(4)	90.5(2)	89.93(16)
O(41)–Ni(1)–O(11)	91.7(3)	89.3(2)	91.6(3)	95.4(2)	92.50(14)
O(31)–Ni(1)–N(23)	89.0(3)	90.6(2)	91.5(6)	89.9(2)	90.31(15)
N(19)–Ni(1)–N(23)	98.5(3)	93.7(2)	96.6(6)	96.1(2)	95.77(18)
O(41)–Ni(1)–N(23)	93.8(3)	96.6(2)	95.4(5)	94.9(2)	95.30(16)
O(11)–Ni(1)–N(23)	170.1(3)	173.3(2)	169.1(6)	166.6(2)	90.31(15)
O(11)–Ni(1)–O(42)					
O(31)–Ni(1)–O(42)					
N(19)–Ni(1)–O(42)					
N(23)–Ni(1)–O(42)					
O(41)–Ni(1) –O(42)					

Complex	**1-A**	**2**	**4**
*(b) The coordination sphere of the central nickel atom in the centrosymmetric trinuclear units in **1-A**, **2** and **4***			
Ni(2)–O(42)	2.098(8)	2.051(4)	2.048(3)
Ni(2)–O(31)	2.068(5)	2.062(4)	2.058(3)
Ni(2)–O(11)	2.048(5)	2.062(4)	2.065(3)
Ni(2)–O(32)			
O(42)–Ni(2)–O(31)	88.2(3)	89.6(2)	90.01(13)
O(42)–Ni(2)–O(11)	90.0(3)	89.5(2)	90.77(13)
O(31)–Ni(2)–O(11)	79.8(2)	76.9(2)	79.92(13)
O(32)–Ni(2)–O(11)			
O(32)–Ni(2)–O(42)			

*(c) The coordination sphere of the central nickel atom in the trinuclear unit of **1-B***			
Ni(2)–O(42c)	2.011(4)	O(42b)–Ni(2)–O(11b)	87.8(2)
Ni(2)–O(42b)	2.037(4)	O(42b)–Ni(2)–O(31b)	87.4(2)
Ni(2)–O(11b)	2.088(4)	O(42b)–Ni(2)–O(11c)	93.9(2)
Ni(2)–O(31b)	2.044(4)	O(42b)–Ni(2)–O(31c)	95.4(2)
Ni(2)–O(11c)	2.046(5)	O(11b)–Ni(2)–O(31b)	83.2(2)
Ni(2)–O(31c)	2.058(4)	O(11b)–Ni(2)–O(11c)	176.9(2)
O(42c)–Ni(2)–O(42b)	171.0(2)	O(11b)–Ni(2)–O(31c)	100.8(2)
O(42c)–Ni(2)–O(11b)	85.3(2)	O(31b)–Ni(2)–O(11c)	99.6(2)
O(42c)–Ni(2)–O(31b)	86.1(2)	O(31b)–Ni(2)–O(31c)	175.2(2)
O(42c)–Ni(2)– O(11c)	93.4(2)	O(11c)–Ni(2)–O(31c)	76.4(2)
O(42c)–Ni(2)– O(31c)	91.5(2)		

The centrosymmetric trinuclear complex **1-A** forms a two-dimensional porous architecture through intermolecular hydrogen bonds with water molecules (Fig. S4). Complexes **2** and **4** have no significant hydrogen bonding interactions.

3.4. Magnetic properties

Temperature-dependence molar susceptibility measurements of powdered samples of **1–4** were carried out in an applied field of 5000 G in the temperature range of 2–300 K. The magnetic properties of complexes **1–4** under the form of $\chi_M T$ versus T plots are shown, together with χ_M versus T plot (χ_M is the molar susceptibility per Ni_3 unit), in Figs. 5 and Figs. S5–S7, respectively**.** The $\chi_M T$ value at 300 K is 3.86 $cm^3\ mol^{-1}\ K$ (for **1**), 3.45 $cm^3\ mol^{-1}\ K$ (for **2**), 4.03 $cm^3\ mol^{-1}\ K$ (for **3**) and 3.63 $cm^3\ mol^{-1}\ K$ (for **4**) which are closely the spin-only value of 3.00 $cm^3\ mol^{-1}\ K$ ($g = 2.00$), for a non-interacting Ni_3 unit. On lowering the temperature, the $\chi_M T$ values for complexes **1**, **2**, **3** and **4**, decrease slowly until 60–70 K, then decrease dramatically to 0.49, 0.26, 0.45 and 0.44 $cm^3\ mol^{-1}\ K$ at 2 K for **1–4**, respectively. The profile of the curves suggests weak antiferromagnetic coupling between the Ni(II) ions and an active D parameter at low temperatures.

According to the structural data, for complex **1** there are two crystallographically independent trinuclear units, **1-A** with a crystallographic centre of symmetry and **1-B** in a general position but with a similar geometry with all nickel atoms six-coordinate. For complex **2**, the trinuclear entity also centrosymmetric with the central Ni(II) ion hexa-coordinate while the terminal Ni(II) ions

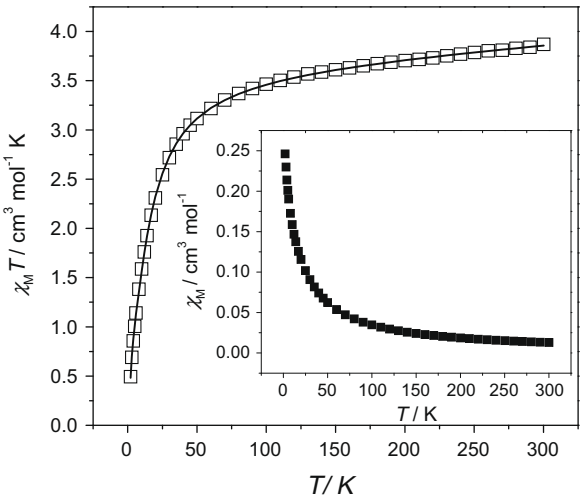


Fig. 5. Thermal dependence of $\chi_M T$ at 5000 G for **1**. The solid line represents the best-fit curve. Inset: thermal dependence of χ_M at 5000 G for **1**.

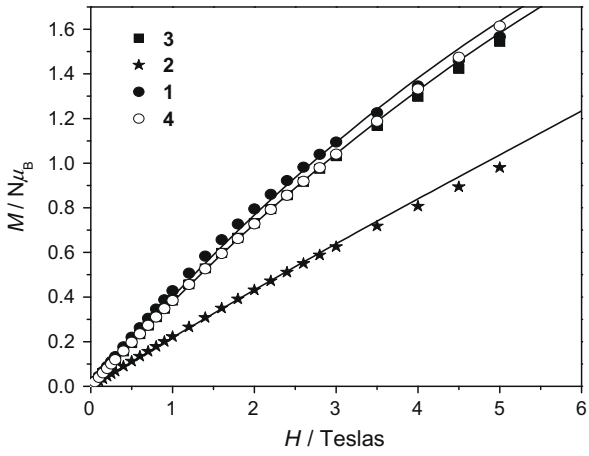


Fig. 6. Magnetization versus H at 2 K for **1–4.** The solid line represents the best-fit curve.

are five-coordinate. For complex **3**, the trinuclear unit contains no imposed symmetry, with the central and one of the terminal Ni(II) ion hexa-coordinate and the other terminal Ni(II) ion is five-coordinate. For complex **4**, the trinuclear unit is centrosymmetric and all the Ni(II) ions are hexa-coordinate. Taking into account these features, the magnetic interactions, between the Ni(II) ions for complexes **1**, **2**, **3** and **4**, could be evaluated.

The experimental data of complexes **1–4** can be fitted using the following Hamiltonian equation:

$$H = -2J(S_1S_2 + S_2S_3) + \sum_{i=1-3}(g_{Ni}\beta S_i \cdot H_i + S_i \cdot D_i \cdot S_i)$$

according to which the single-ion anisotropy D is assumed to be the same for the three Ni(II) ions $D_1 = D_2 = D_3 = D$ while only one exchange constant, J. The reason for using single-ion anisotropy in the Hamiltonian formalism is the drastic decrease of the susceptibility data at low temperatures. The best-fits with the above equation to the magnetic data were found with $J = -3.2(1)$ cm^{-1}, $g = 2.25$ and $D = +9.1(2)$ cm^{-1} for **1**, $J = -4.6(1)$ cm^{-1}, $g = 2.10$, $D = +14.2(2)$ cm^{-1} for **2**, $J = -3.2(1)$ cm^{-1}, $g = 2.20$, $D = +9.8(2)$ cm^{-1} for **3**, and $J = -2.8(1)$ cm^{-1}, $g = 2.10$ and $D = +8.6(1)$ cm^{-1} for **4** (Table 3). The magnetization measurements at 2 K corroborate the effect of the D parameter, i.e. the reduced magnetization ($M/N\beta$ at 5 T are only consistent with 1.6 electrons for **1**, 0.98 electrons for **2**, 1.5 electrons for **3** and 1.6 electrons for **4**, instead of six electrons which should be the theoretical value for three isolated Ni(II) ions with $g = 2.00$ (Fig. 6)**.** The same model is used for the simulation of the magnetization data using the parameters obtained from the fit of the susceptibility data, the results are shown in Fig. 6 as solid lines and reproduces the behaviour of the magnetization versus field quite well. Both data sets confirm the large values of the single-ion anisotropy of the Ni(II) ions.

The magnetic susceptibilities and magnetization data treatment of compounds **1–4** were made using the MAGPACK program [37] employed with a nonlinear least-squares curve-fitting program, DSTEPIT [38].

4. Discussion

Considering the absence of magnetic interaction between the terminal Ni(II) ions in the trinuclear compounds, the Ni···Ni interactions between the spin $S = 1$ are transmitted, between each pair of Ni(II) ions, through two oxo groups of the tetradentate ligand and one carboxylate in bis-monodentate *syn–syn* mode in **1–4.** Magneto-structural correlations for a series of octahedral and square pyramidal dinuclear Ni(II) complexes with the oxo group of phenoxy-ligand, acting as a bridge in dinickel(II) complexes, show a linear relationship between the J values and the Ni–O–Ni bridge angle [39] and inversion from antiferromagnetic to ferromagnetic coupling is anticipated at a bridge angle of 97°. The effect of the acetate bridge in *syn–syn* configuration is weak antiferromagnetic [40]. The values of the calculated average J parameters, for complexes **1–4**, seem to be logical, taking into account the symmetry and geometry of the Ni(II) ions. The Ni–O–Ni angles in complexes **1–4** are in the range of 92–97°. These values are very near the crossover point between ferromagnetic and antiferromagnetic behaviour, therefore, the type of interaction mediated by this pathway may not be anticipated, and will be weak in any case. The additional exchange pathway occurs *via* a carboxylate ligand in a *syn–syn* configuration that facilitates moderate antiferromagnetic couplings. The latter will, thus, dominate the exchange in the **1–4** system, which will consequently be of antiferromagnetic nature.

The data, compiled for mononuclear hexacoordinate Ni(II) compounds, show that the D parameters adopt values between −22 and +12 cm^{-1} [41]. The D parameter has been evaluated only for a few Ni(II) compounds with chain structures and they show moderate D values between −7 and 7 cm^{-1}[42–45]. Among the 30 similar trinuclear Ni(II) complexes which are reported to date, D parameter has been calculated from the magnetic data of only one complex [46] The difficulties for calculating the D values lies in the strong correlations between the intermolecular coupling with the zero-field splitting parameter at low temperature and such calculations usually led to unrealistic values. Hence evalua-

Table 3
Comparison of magnetic data along with bond angles within the bridges for complexes **1–4**.

Complex		J (cm^{-1})	g	Ni–O–Ni (°)
1	$D = +9.1(2)$ cm^{-1}	−3.2(1)	2.25	96.4(2), 95.2(2)[a] 98.3(2), 92.8(2)[b] 94.8(2), 96.7(2)[c]
2	$D = +14.2(2)$ cm^{-1}	−4.6(1)	2.10	96.3(2), 96.5(2)
3	$D = +9.8(2)$ cm^{-1}	−3.2(1)	2.20	95.2(4), 96.7(4)
4	$D = +8.6(1)$ cm^{-1}	−2.8(1)	2.10	95.3(1), 95.6(1)

[a] Centrosymmetric part of complex **1**.
[b,c] Non-centrosymmetric part of complex **1**.

tion of realistic D value from magnetic data is a difficult task for this kind of systems. For complexes **1–4**, we have succeeded in calculating D values which are well related to the geometry around the Ni(II) ion as indicated by some systematic investigations of the zero-field splitting correlated with the degree of distortion in the coordination polyhedra in octahedral Ni(II) mononuclear complexes which appeared recently [47–50]. Pentacoordinated mononuclear Ni(II) complexes show higher anisotropy than hexacoordinate ones, and this feature implies high D values (around 15 cm^{-1}) as is found in the few examples studied in the literature [51].

The values of D for complexes **1–4** are in the high range of those already reported in the literature. The highest D value of +14.2(2) and +9.8(2) cm^{-1} for complexes **2** and **3**, respectively, agree with the pentacoordinated geometry of the two terminal nickel(II) ions in **2** and one terminal nickel(II) ion in **3**.

5. Conclusions

We have succeeded in synthesizing trinuclear Ni(II) complexes with the monocarboxylate anions: acetate, benzoate, phenylavetate and cinnamate as bridging ligands. The systematic variation of the carboxylate ligand nicely illustrates how a slight change in the steric properties of the bridging carboxylate can influence the coordination geometry of the terminal nickel atom in such complexes. The variable-temperature magnetic measurements reveal the antiferromagnetic couplings within the trinuclear Ni(II) units in all four complexes **1**–**4** containing tetradentate ligand (H_2salpen). The tuning of pentacoordination and hexacoordination in the terminal Ni(II) allow us to calculate the D parameters in the polynuclear Ni(II) compounds with different degree of distortion in the coordination polyhedra. Expectedly, the compounds (**2** and **3**) containing pentacoordinated terminal Ni(II) possess high D values. Growing suitable single crystals for X-ray diffraction is one of the most challenging parts of research in chemical, physical or biological sciences and in most cases "trial-and-error" methods are applied to select the proper solvent systems to obtain the crystal. We have shown here that observation of the morphology of the initially separated solid by an SEM study can help one to move quickly in the right direction for choosing the proper solvents for successful crystallization.

Acknowledgments

We thank CSIR, Government of India [Senior Research Fellowship to P.M., Sanction No. 09/028 (0663)/2006-EMR-I] and EPSRC and the University of Reading for funds for the the X-Calibur system. We also thank Spanish Government (Grant CTQ2006-03949) for their financial support.

Appendix A. Supplementary data

CCDC 723299, 723300 and 723301 contain the supplementary crystallographic data for **1**, **2** and **4**. These data can be obtained free of charge via http://www.ccdc.cam.ac.uk/conts/retrieving.html, or from the Cambridge Crystallographic Data Centre, 12 Union Road, Cambridge CB2 1EZ, UK; fax: (+44) 1223-336-033; or e-mail: deposit@ccdc.cam.ac.uk. Supplementary data associated with this article can be found, in the online version, at doi:10.1016/j.poly.2009.07.014.

References

[1] J.-M. Lehn, Supramolecular Chemistry: Concepts and Perspectives, VCH, Weinheim, 1995. p. 139.
[2] D. Philp, J.F. Stoddart, Angew. Chem. 108 (1996) 1242.
[3] V.L. Pecoraro, A.J. Stemmler, B.R. Gibney, J.J. Bodwin, H. Wang, J. Kampf, A. Barwinsky, Prog. Inorg. Chem. 45 (1997) 83.
[4] R.W. Saalfrank, B. Demleitner, Perspect. Supramol. Chem. 5 (1999) 1.
[5] E. Uller, B. Demleitner, I. Bernt, R.W. Saalfrank, Struct. Bond. 96 (2000) 149.
[6] D.L. Caulder, K.N. Raymond, Acc. Chem. Res. 32 (1999) 975.
[7] D. Gatteschi, R. Sessoli, A. Cornia, J. Chem. Soc., Chem. Commun. (2000) 725.
[8] D. Gatteschi, A. Caneschi, L. Pardi, R. Sessoli, Science 265 (1994) 1054.
[9] S. Kokot, C.M. Harris, E. Sinn, Aust. J. Chem. 25 (1972) 45.
[10] A.M. Greenaway, C.J. O'Connor, J.W. Overman, E. Sinn, Inorg. Chem. 20 (1981) 1508.
[11] R.J. Butcher, J.W. Overman, E. Sinn, J. Am. Chem. Soc. 102 (1980) 3276.
[12] J. Pasan, J. Sanchiz, C. Ruiz-Perez, F. Lloret, M. Julve, Eur. J. Inorg. Chem. (2004) 4081. and references therein.
[13] C. Ruiz-Perez, J. Sanchiz, M.H. Molina, F. Lloret, M. Julve, Inorg. Chem. 39 (2000) 1363.
[14] F.S. Delgado, J. Sanchiz, C. Ruiz-Pérez, F. Lloret, M. Julve, Inorg. Chem. 42 (2003) 5938.
[15] Z.L. Huang, M. Drillon, N. Masciocchi, A. Sironi, J.T. Zao, P. Rabu, P. Panissod, Chem. Mater. 12 (2000) 2805. and references therein.
[16] L. Pan, B.S. Finkel, X. Huang, J. Li, Chem. Commun. (2001) 105.
[17] J. Pasan, J. Sanchiz, C. Ruiz-Perez, F. Lloret, M. Julve, Inorg. Chem. 44 (2005) 7794.
[18] R. Baldoma, M. Monfort, J. Ribas, X. Solans, M.A. Maestro, Inorg. Chem. 45 (2006) 8144.
[19] A.K. Ghosh, D. Ghoshal, E. Zangrando, J. Ribas, N.R. Chaudhuri, Inorg. Chem. 46 (2007) 3057.
[20] A. Elmali, Y. Elerman, I. Svoboda, H. Fuess, K. Griesar, W. Haase, Z. Naturforsch., B: Chem. Sci. 51 (1996) 665.
[21] J. Reglinski, S. Morris, D.E. Stevenson, Polyhedron 21 (2002) 2167.
[22] D. Ulku, F. Ercan, O. Atakol, F.N. Dincer, Acta Crystallogr., Sect. C 53 (1997) 1056.
[23] O. Atakol, C. Arici, M.N. Tahir, R. Kurtaran, D. Ulku, Anal. Sci. 15 (1999) 933.
[24] C. Arici, D. Yuzer, O. Atakol, H. Fuess, I. Svoboda, Acta Crystallogr., Sect. E: Struct. Rep. Online 61 (2005) m91.
[25] A. Akay, C. Arici, O. Atakol, H. Fuess, I. Svoboda, J. Coord. Chem. 59 (2006) 933.
[26] P. Mukherjee, M.G.B. Drew, A. Ghosh, Inorg. Chem. 48 (2009) 2364.
[27] P. Mukherjee, C. Biswas, M.G.B. Drew, A. Ghosh, Polyhedron 26 (2007) 3121.
[28] CRYSALIS, v1, Oxford Diffraction Ltd., Oxford, UK, 2005.
[29] G.M. Sheldrick, SHELXL-97, University of Göttingen, Göttingen, Germany, 1997.
[30] ABSPACK, Oxford Diffraction Ltd., Oxford, UK, 2005.
[31] L. Carbonaro, M. Isola, P.L. Pegna, L. Senatore, F. Marchetti, Inorg. Chem. 38 (1999) 5519.
[32] J.P. Costes, F. Dahan, J.P. Laurent, Inorg. Chem. 24 (1985) 1018.
[33] B. Sarkar, M.G.B. Drew, M. Estrader, C. Diaz, A. Ghosh, Polyhedron 27 (2008) 2625. and references therein.
[34] M. Dey, C.P. Rao, P.K. Saarenketo, K. Rissanen, Inorg. Chem. Commun. 5 (2002) 924.
[35] S. Koizumi, M. Nihei, H. Oshio, Chem. Lett. 32 (2003) 812.
[36] S. Banerjee, M.G.B. Drew, C.-Z. Lu, J. Tercero, C. Diaz, A. Ghosh, Eur. J. Inorg. Chem. (2005) 2376. and references cited therein.
[37] J.J. Borrás-Almenar, J.M. Clemente-Juan, E. Coronado, B.S. Tsukerblat, J. Comput. Chem. 9 (2001) 985.
[38] Program 66, Quantum Chemistry Program Exchange, Indiana University, Bloomington, IN, 1965.
[39] K.K. Nanda, L.K. Thompson, J.N. Bridson, K. Nag, J. Chem. Soc., Chem. Commun. (1994) 1337.
[40] A. Rodriguez-Fortea, P. Alemany, S. Alvarez, E. Ruiz, Chem. Eur. J. 7 (2001) 627.
[41] R. Boca, Coord. Chem. Rev. 248 (2004) 757.
[42] B.J. Kennedy, K.S. Murray, J. Chem. Soc., Dalton Trans. (1987) 825.
[43] M. Orendác, A. Orendácová, J. Cernák, A. Feher, P.J.C. Signore, M.W. Meisel, S. Merah, M. Verdaguer, Phys. Rev. B 52 (1995) 3435.
[44] J. Cernák, K.A. Abboud, J. Chomic, M.W. Meisel, M. Orendác, A. Oredácová, A. Feher, Inorg. Chim. Acta 311 (2000) 126.
[45] B. Zurowska, J. Mrozinski, M. Julve, F. Lloret, A. Maslejova, W.S. Dobrowolska, Inorg. Chem. 41 (2002) 1771.
[46] A.K. Sharma, F. Lloret, R. Mukherjee, Inorg. Chem. 46 (2007) 5128.
[47] O. Atakol, R. Boca, I. Ercan, F. Ercan, H. Fuess, W. Haase, R. Herchel, Chem. Phys. Lett. 423 (2006) 192.
[48] A. Maslejová, R. Ivanikova, I. Svoboda, B. Papánková, L. Dlhán, D. Miklos, H. Fuees, R. Boca, Polyhedron 25 (2006) 1823.
[49] P. Baran, M. Boca, R. Boca, A. Krutosiková, J. Miklovic, J. Pelikán, J. Titis, Polyhedron 24 (2005) 1510.
[50] R. Ivaniková, R. Boca, L. Dlhán, H. Fuees, A. Maslejová, V. Mrázová, I. Svoboda, J. Titis, Polyhedron 25 (2006) 3261.
[51] R. Vicente, A. Escuer, X. Solans, M. Font-Bardía, Inorg. Chim. Acta 248 (1966) 59.

Table 1
Crystal data and structure refinement for complexes **1**–**6**.

	1	2	3	4	5	6
Formula	$C_{24}H_{16}N_2O_4Fe$	$C_{24}H_{16}N_2O_4Co$	$C_{34}H_{36}O_{20}Co_4$	$C_{48}H_{36}N_4O_{10}Ni_2$	$C_{72}H_{52}N_4O_8Ni_2$	$C_{48}H_{36}N_4O_{10}Cd_2$
Formula weight	452.24	455.32	1000.35	946.23	1218.60	526.80
Space group	$P2_1/n$	$P2_1/n$	$P2_1/c$	$C2$	$P\bar{1}$	$P2_1/n$
a (Å)	9.6873(19)	10.024	12.859(3)	22.539(5)	9.861(2)	11.627(2)
b (Å)	9.5946(19)	9.6125(19)	20.382(4)	11.299(2)	15.816(3)	11.017(2)
c (Å)	20.379(4)	20.617(4)	15.551(3)	18.823(4)	18.870(4)	16.753(3)
α (°)	90	90	90	90	79.96(3)	90
β (°)	91.94(3)	90.45(3)	108.84(3)	119.84(3)	82.73(3)	98.17(3)
γ (°)	90	90	90	90	81.31(3)	90
Volume (Å^3)	1893.0(7)	1986.5(7)	3857.5(13)	4158.3(15)	2849.2(10)	2124.2(7)
Z	4	4	4	4	2	2
ρ (g/cm^3)	1.587	1.522	1.722	1.511	1.420	1.647
[a]R_1	0.0558	0.0550	0.0482	0.0379	0.0494	0.0264
[b]wR_2	0.1437	0.1646	0.1414	0.0892	0.1481	0.0885

[a] $R_1 = \sum||F_o| - |F_c||/\sum|F_o|$.
[b] $wR_2 = \sum[w(F_o^2 - F_c^2)^2]/\sum[w(F_o^2)^2]^{1/2}$.

Table 2
Selected bond lengths (Å) for complexes **1** to **6**.

1			
Fe(1)–O(4)	2.094(3)	Fe(1)–O(2)	2.120(2)
Fe(1)–O(1)#1	2.114(3)	Fe(1)–O(3)#2	2.129(2)
Fe(1)–N(1)	2.257(3)	Fe(1)–N(2)	2.262(3)
2			
Co(1)–O(2)	2.084(3)	Co(1)–O(4)	2.091(3)
Co(1)–O(1)	2.091(3)	Co(1)–O(3)	2.094(3)
Co(1)–N(2)	2.180(3)	Co(1)–N(1)	2.189(3)
3			
Co(1)–O(9)#1	2.012(3)	Co(1)–O(15)	2.103(3)
Co(1)–O(8)	2.071(3)	Co(1)–O(2)#2	2.191(3)
Co(1)–O(14)	2.102(3)	Co(1)–O(5)#1	2.214(3)
Co(1)–O(8)	2.071(3)	Co(1)–O(2)#2	2.191(3)
Co(1)–O(14)	2.102(3)	Co(1)–O(5)#1	2.214(3)
Co(2)–O(15)	1.949(3)	Co(2)–O(7)	2.088(3)
Co(2)–O(11)	1.973(3)	Co(2)–O(4)	2.263(3)
Co(2)–O(1)#2	1.971(3)	Co(3)–O(15)	2.017(3)
Co(3)–O(3)	2.028(3)	Co(3)–O(16)	2.099(4)
Co(3)–O(6)#1	2.094(3)	Co(3)–O(14)	2.127(3)
Co(3)–O(17)	2.102(4)	Co(4)–O(10)	2.009(3)
Co(4)–O(10)#1	2.009(3)	Co(4)–O(8)#1	2.303(3)
Co(4)–O(5)#1	2.148(3)	Co(4)–O(8)	2.303(3)
Co(4)–O(5)	2.148(3)	Co(5)–O(12)	2.054(3)
Co(5)–O(12)#2	2.054(3)	Co(5)–O(1)	2.131(3)
Co(5)–O(4)	2.132(3)	Co(5)–O(1)#2	2.131(3)
Co(5)–O(4)#2	2.132(3)		
4			
Ni(1)–O(1)	2.051(2)	Ni(1)–O(7)	2.069(2)
Ni(1)–N(2)#1	2.092(3)	Ni(1)–O(3)	2.115(2)
Ni(1)–N(1)	2.118(3)	Ni(1)–O(5)	2.152(2)
Ni(2)–O(9)	2.040(3)	Ni(2)–O(9)#2	2.040(3)
Ni(2)–O(6)#2	2.076(2)	Ni(2)–O(6)	2.076(2)
Ni(2)–N(4)#1	2.090(4)	Ni(3)–O(4)	2.032(2)
Ni(3)–O(4)#3	2.032(2)	Ni(3)–O(10)#3	2.083(3)
Ni(3)–N(5)	2.096(4)	Ni(3)–O(10)	2.083(3)
Ni(3)–N(6)#4	2.132(4)		
5			
Ni(1)–N(4)#1	2.066(3)	Ni(1)–O(1)	2.063(3)
Ni(1)–O(2)	2.070(3)	Ni(1)–O(4)	2.087(2)
Ni(1)–N(2)	2.082(3)	Ni(1)–O(3)	2.078(2)
Ni(2)–N(1)	2.072(3)	Ni(2)–O(8)	2.081(3)
Ni(2)–O(5)	2.077(2)	Ni(2)–N(3)	2.081(3)
Ni(2)–O(7)	2.076(2)	Ni(2)–O(6)#2	2.082(3)
6			
Cd(1)–O(2)	2.1924(18)	Cd(1)–N(1)	2.365(2)
Cd(1)–O(3)	2.253(2)	Cd(1)–O(5)	2.383(2)
Cd(1)–N(2)	2.320(2)	Cd(1)–O(4)	2.583(2)

Symmetry transformations used to generate equivalent atoms for complex **1**: #1 $-x$, $-y+1$, $-z$; #2 $-x$, $-y$, $-z$. Symmetry transformations used to generate equivalent atoms for complex **3**: #1 $-x$, $-y+1$, $-z$; #2 $-x+1$, $-y+1$, $-z+1$. Symmetry transformations used to generate equivalent atoms for complex **4**: #1: x, $y-1$, z; #2: $-x+1$, y, $-z+1$; #3: $-x$, y, $-z$; #4: x, $y+1$, z. Symmetry transformations used to generate equivalent atoms for complex **5**: #1 x, $y+1$, $z-1$; #2 $-x+1$, $-y+1$, $-z+1$.

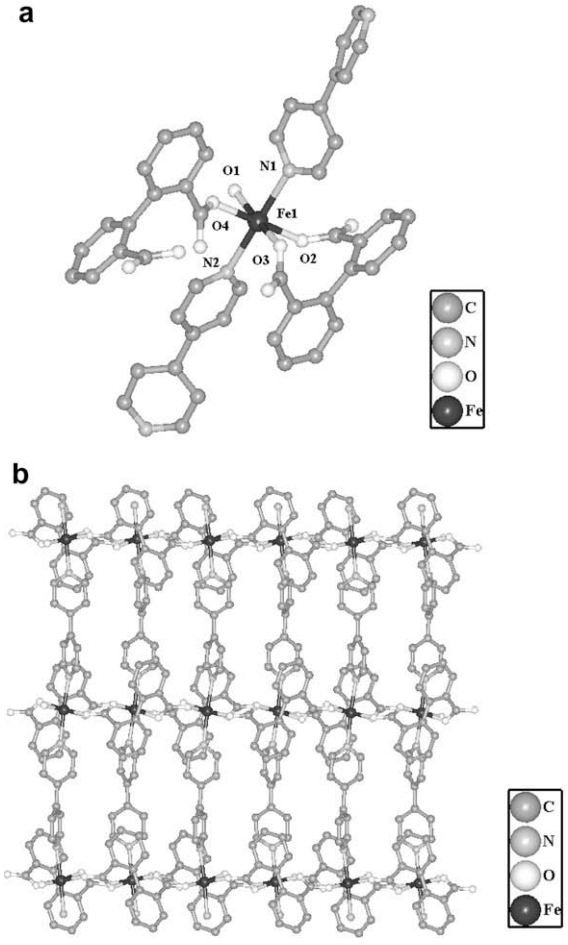


Fig. 1. (a) The fundamental unit of complex **1**. (b) The two-dimensional layer structure of complex **1**.

were performed on a Perkin–Elmer TGA7 instrument in flowing N_2 with a heating rate of 10 °C min^{-1}. Variable temperature magnetic susceptibility was measured at 1000 Oe from 1.99 to 300 K (SQUID Quantum Design).

2.2. Synthesis of the complexes

2.2.1. Synthesis of *1*

A mixture of $FeCl_2{\cdot}4H_2O$ (0.080 g, 0.40 mmol), dpa (0.192 g, 0.80 mmol), 4,4′-bipy (0.125 g, 0.80 mmol) and 8 ml H_2O was stir-

red for 30 min, and then the pH value was adjusted to 5 with 1 M NaOH. After stirring for another 30 min, the mixture was transferred to a 23 ml Teflon-lined stainless steel bomb and kept at 170 °C under autogenously pressure for 4 days. The reaction system was cooled to room temperature over 24 h. A large amount of green block crystals of **1** were obtained. Yield: 63% (based on Fe). *Anal.* Calc. for $C_{24}H_{16}N_2O_4Fe$: C, 63.74; H, 3.57; N, 6.19. Found: C, 63.69; H, 3.41; N, 6.33%. IR (cm^{-1}): 1582 (m), 1556 (w), 1520 (s), 1451 (w), 1378 (s), 1269 (w), 1068 (w), 1008 (w), 965 (m), 849 (w), 748 (m), 721 (m), 624 (w), 556 (m).

2.2.2. Synthesis of *2* and *3*

Complexes **2** and **3** were prepared from a mixture of $Co(OAc)_2{\cdot}4H_2O$ (0.099 g, 0.40 mmol), dpa (0.192 g, 0.80 mmol) and 4,4′-bipy (0.125 g, 0.80 mmol) in 8 ml H_2O. The mixture was stirred for 25 min, and the pH value was then adjusted to 5 with 1 M NaOH. After this, the mixture was transferred to a 23 mL Teflon-lined stainless steel bomb and it was kept at 165 °C under autogenously pressure for 4 days. Red crystals of **2** and purple crystals of **3** were obtained. For complex **2**: Yield: 41% (based on Co). *Anal.* Calc. for $C_{24}H_{16}N_2O_4Co$: C, 63.25; H, 3.54; N, 6.15. Found: C, 63.36; H, 3.68; N, 6.27%. IR (cm^{-1}): 3441 (w), 1586 (m), 1558 (w), 1527 (s), 1371 (s), 1129 (m), 1076 (w), 1014 (w), 958 (m), 761 (m), 717 (m), 642 (w). For complex **3**: Yield: 18% (based on Co). *Anal.* Calc. for $C_{34}H_{36}O_{20}Co_4$: C, 40.79; H, 3.63. Found: C, 40.66; H, 3.49%. IR (cm^{-1}): 3315 (s), 3210(s), 1616 (w), 1583 (s), 1561 (w), 1420 (s), 1402 (w), 1366 (w), 1225 (w), 1193 (w), 1134 (w), 1067 (w), 983 (w), 922 (w), 858 (m), 751 (w), 644 (w).

2.2.3. Synthesis of *4* and *5*

Complexes **4** and **5** were prepared from a mixture of $Ni(OAc)_2{\cdot}4H_2O$ (0.099 g, 0.40 mmol), dpa (0.192 g, 0.80 mmol) and 4,4′-bipy (0.125 g, 0.80 mmol) in 8 ml H_2O. The mixture was stirred for 20 min and the pH value was then adjusted to 5 with 1 M NaOH. After this, the mixture was transferred to a 23 mL Teflon-lined stainless steel bomb, and it was kept at 180 °C under autogenously pressure for 5 days. After cooling the reaction system to room temperature over 24 h, green needle crystals of **4** and green block crystals of **5** were obtained. For complex **4**: Yield: 41% (based on Ni). *Anal.* Calc. for $C_{48}H_{36}N_4O_{10}Ni_2$: C, 60.87; H, 3.84; N, 5.92. Found: C, 60.68; H, 3.92; N, 6.01%. IR (cm^{-1}): 3312 (s), 3056 (s), 1604 (w), 1576 (s), 1532 (s), 1435 (w), 1380 (s), 1241 (w), 1125 (w), 1101 (m), 1041 (w), 1012 (m), 971 (w), 951 (w), 884 (w), 846 (w), 835 (w), 791 (m), 673 (w), 652 (w), 623 (w). For complex **5**: Yield: 22% (based on Ni). *Anal.* Calc. for $C_{72}H_{52}N_4O_8Ni_2$: C, 70.90; H, 4.30; N, 4.63. Found: C, 70.98; H, 4.47; N, 4.76%. IR (cm^{-1}): 1581 (w), 1543 (s), 1399 (s), 1276 (w),

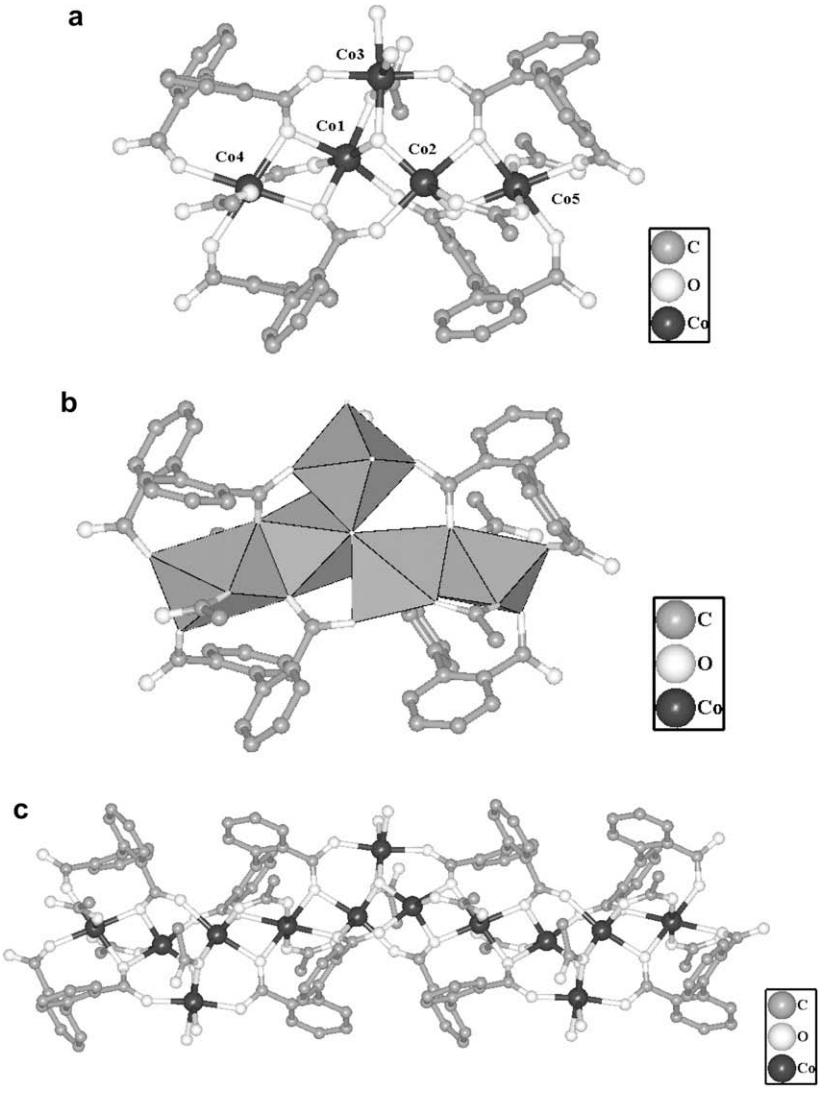


Fig. 2. (a) The fundamental unit of complex **3**. (b) The one-dimensional chain-like structure of complex **3**.

1248 (w), 1170 (w), 1064 (w), 1003 (w), 991 (w), 853 (m), 759 (w), 702 (w).

2.2.4. Synthesis of **6**

Complex **6** was prepared from a mixture of $Cd(OAc)_2{\cdot}2H_2O$ (0.107 g, 0.40 mmol), dpa (0.192 g, 0.80 mmol) and 2,2′-bipy (0.125 g, 0.80 mmol) in 8 ml H_2O. The mixture was stirred for 15 min and sealed in a 23 mL Teflon-lined stainless steel bomb. The bomb was kept at 170 °C under autogenously pressure for 5 days. The reaction system was then cooled to room temperature over 24 h, and yellow block crystals of **6** were obtained. Yield: 71% (based on Cd). *Anal.* Calc. for $C_{48}H_{36}N_4O_{10}Cd_2$: C, 54.67; H, 3.44; N, 5.32. Found: C, 54.81; H, 3.51; N, 5.27%. IR (cm^{-1}): 3243 (s), 3105 (s), 1548 (s), 1479(s), 1351 (s), 1266 (w), 1212 (w), 1186 (m), 965 (w), 832 (m), 779 (m), 736 (m), 708 (w), 682 (w), 559 (w).

2.3. X-ray crystallography study

Crystallographic data for **1** to **6** were all collected at 298 K with a Bruker AXS SMART APEX II CCD diffractometer. The structures were solved by the direct method and refined by the full-matrix least-squares method on F^2 using the SHELXTL 97 crystallographic software package [34,35]. Carbon-bound hydrogen atoms were placed in calculated positions, with C–H = 0.93 Å, and treated as riding atoms in the final cycles of refinement. Oxygen-bound hydrogen atoms were located in the difference Fourier maps, refined with isotropic temperature factors and kept in that position. Further details of the X-ray structural analysis are given in Table 1. Selected bond lengths are listed in Table 2.

3. Result and discussion

3.1. Structural description

3.1.1. $[Fe(dpa)(4,4'\text{-bipy})]_n$ (**1**) and $[Co(dpa)(4,4'\text{-bipy})]_n$ (**2**)

Complex **1** is composed of a two-dimensional layer of Fe(dpa)(4,4′-bipy). The asymmetric unit of complex **1** consists of one crystallographic independent Fe atom, as shown in Fig. 1a. Fe(1) adopts a distorted octahedral coordination mode and connects with four oxygen atoms from three dpa ligands and two

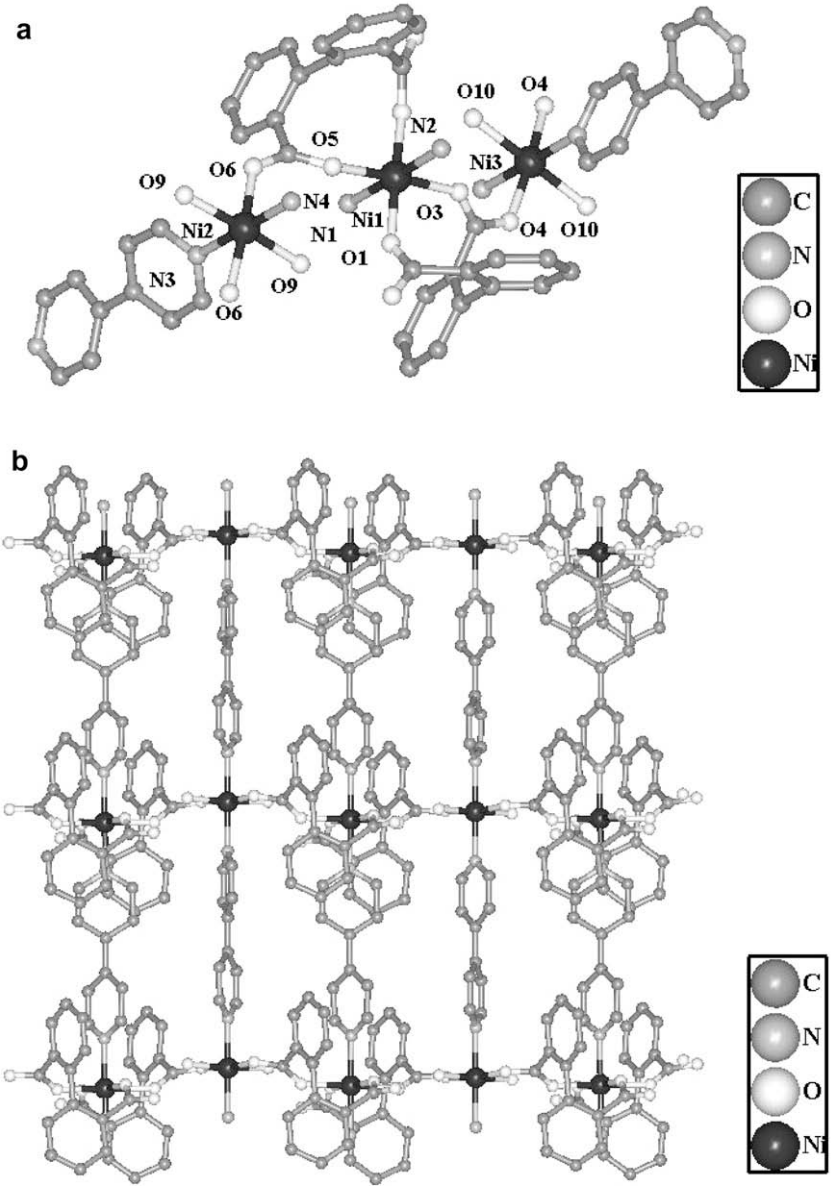


Fig. 3. (a) The fundamental unit of complex **4**. (b) The two-dimensional layer structure of complex **4**.

nitrogen atoms from two 4,4′-bipy ligands. The Fe–O distances range from 2.094–2.129 Å, the O–Fe–O bond angles are in the range 87.09 to 176.58°, and the average Fe–N bond distance is 2.260 Å. In this complex, the dpa ligand adopts only one kind of coordination mode, two carboxylate groups of the dpa ligand are deprotonated and both adopt bridging coordination modes as shown in Fig. S1. The carboxylate oxygen atoms of the dpa ligands connect the adjacent Fe atoms and form a one-dimensional chain-like structure. Furthermore, the 4,4′-bipy ligands link such neighboring chains and form a two-dimensional layer structure, as shown in Fig. 1b.

When $FeCl_2{\cdot}4H_2O$ is replaced by $Co(OAc)_2{\cdot}4H_2O$, complex **2** is successfully synthesized. The crystal structure of complex **2** is isomorphic to complex **1**, with little difference.

3.1.2. $\{[Co_4(dpa)_2(CH_3COO)_3(OH)(H_2O)_2]\cdot 3H_2O\}_n$ (**3**)

To our interest, during the synthesis of complex **2**, we obtained complex **3** accidentally. The single crystallographic analysis reveals that complex **3** shows a one-dimensional chain-like structure. There exist five crystallographic independent Co atoms in the fundamental unit, as shown in Fig. 2a. Co1 connects with six oxygen atoms, three from dpa ligands, two from OAc^- ligands, and one from an OH^- group. The Co–O bond distances range from 2.012 to 2.214 Å and the O–Co–O bond angles are in the range 79.00 to 171.05°. This results in distorted octahedral coordination geometry. Similar to Co1, Co3, Co4, and Co5 also adopt the same coordination manners, but with different bond lengths and bond angles. Different to the above four Co atoms, Co2 adopts a square pyramidal coordination mode and connects with five oxygen atoms. The two carboxylate groups in the dpa ligand both adopt bridging coordination modes, as shown in Fig. S2, the OAc^- ligand adopts two kinds of coordination modes, as shown in Fig. S3, and with such connection modes, five crystallographic independent Co atoms are connected together and form an interesting pentanuclear Co building unit. To our knowledge, such a kind of building unit has seldom been synthesized in previous works. Adjacent pentanuclear Co clusters are further connected by dpa ligands and OAc^- to form a one-dimensional chain-like structure, as shown in Fig. 2b.

3.1.3. $[Ni_2(dpa)_2(4,4'\text{-bipy})_2(H_2O)]_n$ (**4**)

Single crystal X-ray diffraction analysis reveals that complex **4** is also a two-dimensional covalent network, derived from $Ni_2(dpa)_2(4,4'\text{-bipy})_2(H_2O)$. There exist three crystallographic independent Ni atoms in the fundamental unit, as shown in Fig. 3a. Ni(1) adopts an octahedral coordination mode and connects with four oxygen atoms from two different dpa ligands and two nitrogen atoms from two different 4,4′-bipy ligands. The Ni(1)–O bond distances are in the range 2.051–2.152 Å, and the O–Ni–O bond angles range from 78.28 to 176.33°. The average Ni–N bond distance is 2.105 Å. Ni(2) also adopts an octahedral coordination mode and connects with two oxygen atoms from dpa ligands, two nitrogen atoms from 4,4′-bipy ligands and the other two coordination sites are occupied by two water molecules. The Ni–O distances are in the range 2.040–2.076 Å, and the bond angles range from 88.42 to 175.18°. The average Ni–N distance is 2.099 Å. Ni(3) adopts the same coordination mode as Ni(2), but with different bond lengths and angles. In this complex, two carboxylate groups in dpa ligand adopt two kinds of coordination modes. One is bridging, and the other is monodentate, as shown in Fig. S4. The adjacent Ni

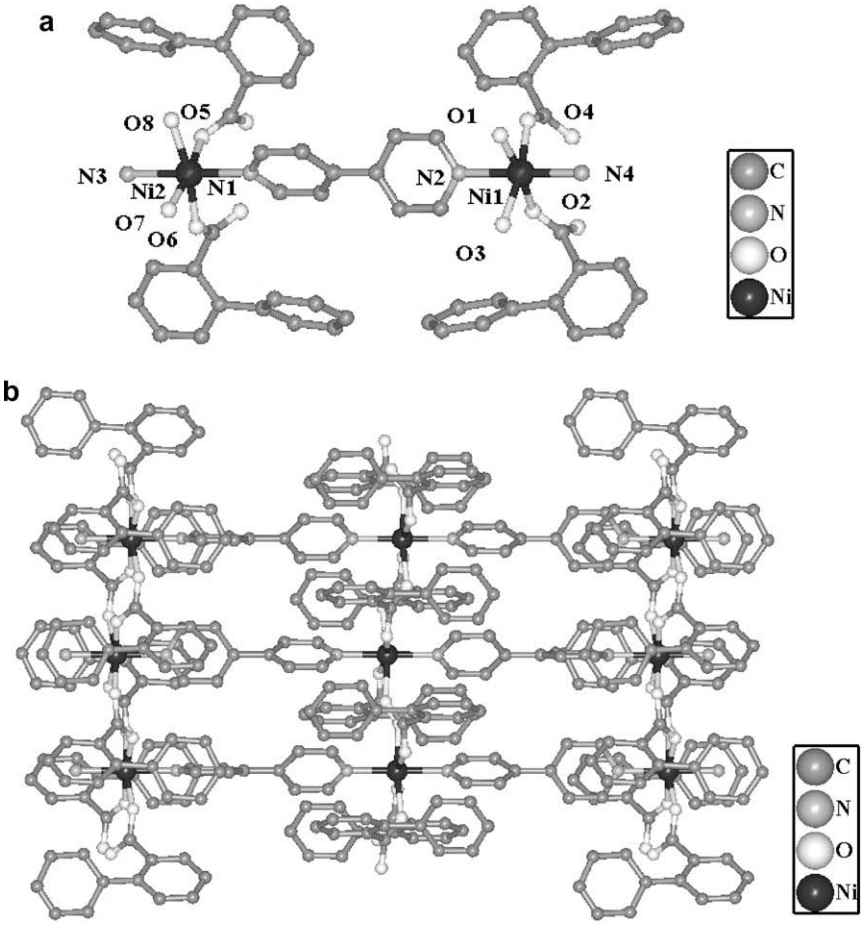


Fig. 4. (a) The fundamental unit of complex **5**. (b) The two-dimensional layer structure of complex **5**.

atoms are linked by dpa ligands to form a one-dimensional chain-like structure. The 4,4′-bipy ligands link neighboring chains and form a two-dimensional layer structure, as shown in Fig. 3b.

To our interest, complex **4** crystallizes in a chiral space group. Although some complexes with helical structures have been synthesized from dpa ligands, to date homochiral complexes have never been synthesized from the dpa ligand.

3.1.4. $[Ni_2(2\text{-bpa})_4(4,4'\text{-bipy})_2]_n$ (**5**)

During the synthesis of complex **4**, we obtained complex **5**. Like complex **4**, complex **5** is also a two-dimensional layer network. There exist two crystallographic independent Ni atoms in this complex, as shown in Fig. 4a. Ni(1) adopts an octahedral coordination mode, connected with four oxygen atoms from four different carboxylate groups and two nitrogen atoms from different 4,4′-bipy ligands. The Ni(1)–O bond distances range from 2.063 to 2.086 Å and the O–Ni–O bond angles are in the range 88.35–172.67°. Ni(2) adopts the same coordination mode, but with different bond angles and bond lengths. The carboxylate group adopts a bridging coordination mode, as shown in Fig. S5, and connects the above two kinds of Ni atoms to form a one-dimensional chain-like structure. Such chains are further connected by 4,4′-bipy ligands and form a two-dimensional layer structure, as shown in Fig. 4b.

It is surprising that one of the two carboxylate groups of the dpa ligand decomposes during the reaction process and the dpa ligand turns into 1,1′-biphenyl-2-carboxylate acid (2-bpa). To our knowledge, this phenomenon has been reported in previous studies [36].

3.1.5. $[Cd_2(dpa)_2(2,2'\text{-bipy})_2(H_2O)_2]_n$ (**6**)

Single crystal X-ray diffraction study reveals that there exists only one crystallographic independent Cd atom in complex **6**, which adopts an octahedral coordination mode. It connects with

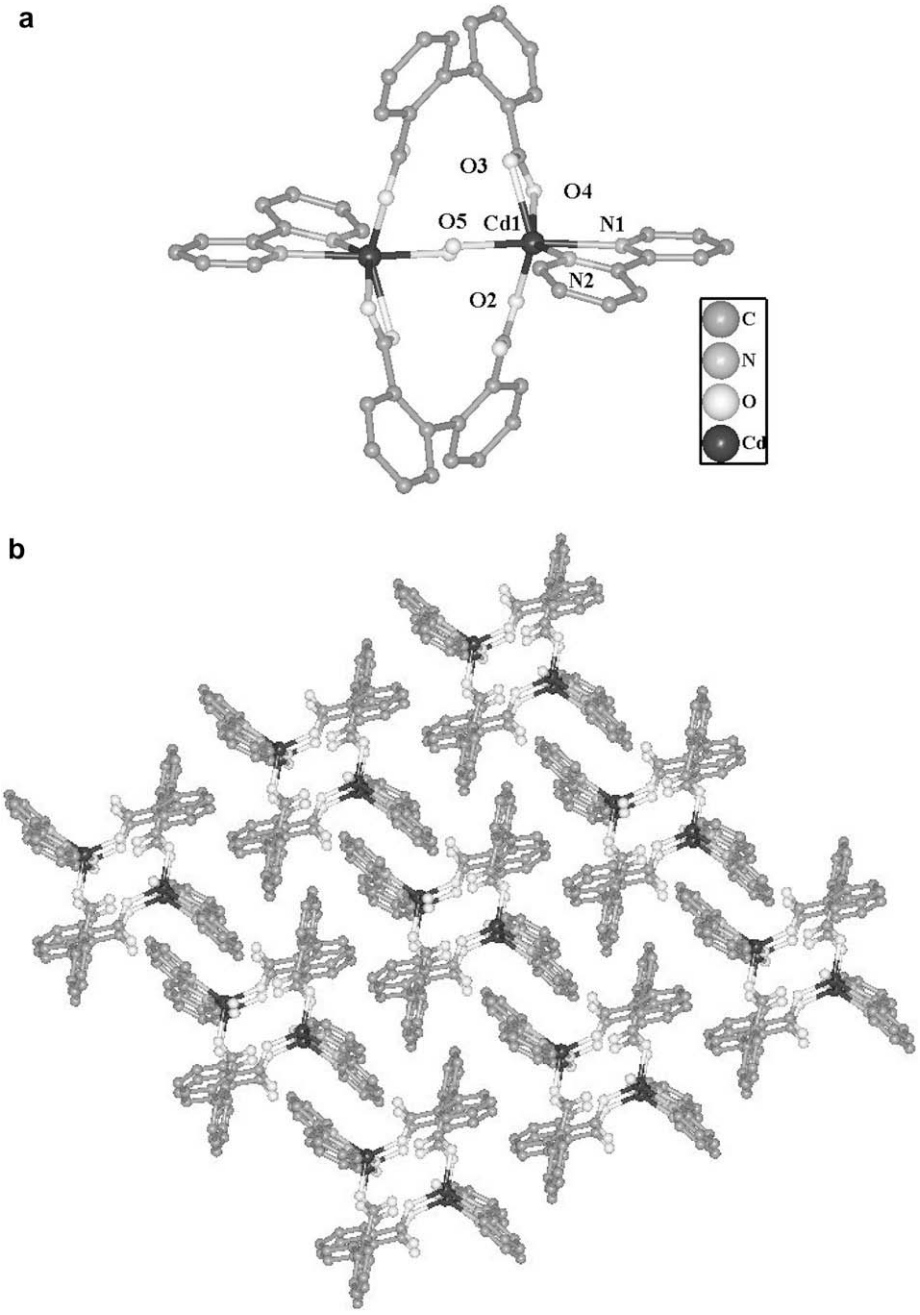


Fig. 5. (a) The fundamental unit of complex **6**. (b) The three-dimensional supramolecular network of complex **6**.

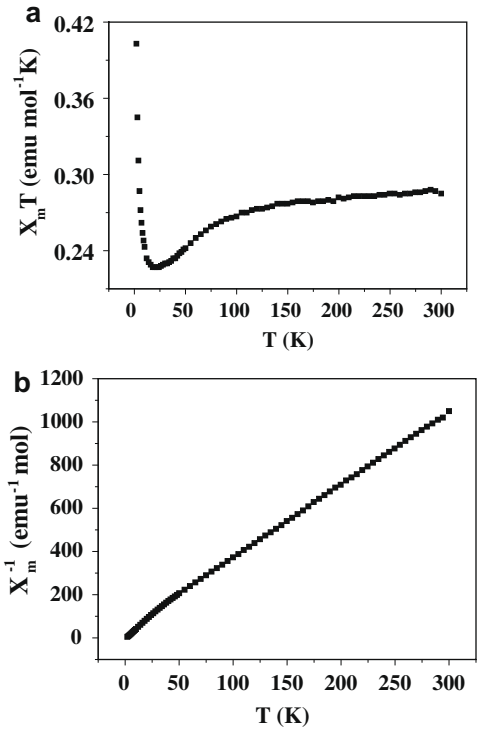


Fig. 6. Thermal variation of $\chi_m T$, $1/\chi_m T$ for complex **2**.

three oxygen atoms from two dpa ligands, two nitrogen atoms from 2,2′-bipy ligands, and the other coordination mode is occupied by a water molecule, as shown in Fig. 5a. The Cd(1)–O bond distances range from 2.192 to 2.583 Å and the O–Cd–O bond angles are in the range 53.38–123.79°. The carboxylate groups in the dpa ligand adopt two kinds of coordination modes, one is chelating and the other is monochelating, as shown in Fig. S6. Based on these two modes, an 18-membered ring is formed. Furthermore, the rings are extended to form an interesting three-dimensional supramolecular network through π–π interactions between the phenyl rings from the dpa ligands and 2,2′-bipy ligands. The distances of the adjacent phenyl rings range from 3.50 to 3.57 Å, as shown in Fig. 5b.

3.2. Thermal properties

The thermal stability properties have been determined on single crystalline samples in a nitrogen atmosphere by thermo gravimetric analysis (TGA). For complex **1**, the TG curve shows that chemical decomposition starts at 369 °C and ends at 458 °C, with a weight loss of 87.69% (Calculated: 87.74%), which is equivalent to the loss of the dpa and 4,4′-bipy ligands. For complex **3**, the TG curve exhibits two weight losses: the first (10.56%), from 90 to 170 °C, represents the loss of water molecules (Calculated: 10.70%), the second (65.82%), from 360 to 481 °C, represents the loss of organic ligands (Calculated: 65.68%). For complex **4**, a weight loss of 1.82% is observed from 167 to 198 °C, equivalent to the loss of coordinated water molecules (Calculated: 1.90%). The second weight loss of 83.60%, from 408 to 506 °C, corresponds to the loss of the dpa and 4,4′-bipy ligands (Calculated: 83.70%). For complex **5**, the weight loss of 90.38%, from 391 to 474 °C, corresponds to the loss of organic ligands (Calculated: 90.27%). For complex **6**, the first weight loss (3.51%), from 134 to 166 °C, corresponds to the loss of water (Calculated: 3.42%); the second (75.29%), from 376 to 457 °C, represents the loss of organic ligands (Calculated: 75.17%).

3.3. Magnetic properties

For complex **2**, the magnetic susceptibility data was studied in the temperature range 1.99 to 300 K, as shown in Fig. 6. The inverse susceptibility plot as a function of temperature is linear in the temperature range 50 to 300 K, closely following the Curie–Weiss law with $C = 0.2904$ emu K mol^{-1} and $\Theta = -6.30$ K. This suggests typical antiferromagnetic interactions in above 50 K. The $\chi_m T$ versus T plot shows a value of 0.28 emu mol^{-1} K at 300 K, and continuously decreases on cooling to a value of 0.22 emu mol^{-1} K at 15 K. However, an abruptly increase at around 13 K was observed and $\chi_m T$ reaches 0.40 emu mol^{-1} K at 1.99 K. This indicates the occurrence of ferromagnetic behavior [37].

4. Conclusions

In this work, a series of coordination polymers generated from mixed-ligand systems of dpa and isomeric bipyridine mixed ligands have been successfully synthesized under hydrothermal conditions. It is anticipated that more coordination polymers containing the flexible dpa ligand with interesting structures as well as physical properties will be synthesized.

Acknowledgements

We gratefully acknowledge financial support from the Education Ministry of China and the Postdoctoral Station Foundation of North East University.

Appendix A. Supplementary data

CCDC 731111, 65084, 650802, 65085, 650806 and 650810 contain the supplementary crystallographic data for complexes **1**–**6**. These data can be obtained free of charge via http://www.ccdc.cam.ac.uk/conts/retrieving.html, or from the Cambridge Crystallographic Data Centre, 12 Union Road, Cambridge CB2 1EZ, UK; fax: (+44) 1223-336-033; or e-mail: deposit@ccdc.cam.ac.uk. Supplementary data associated with this article can be found, in the online version, at doi:10.1016/j.poly.2009.07.043.

References

[1] M. O'Keeffe, Chem. Soc. Rev. 38 (2009) 1215.
[2] L.J. Murray, M. Dincă, J.R. Long, Chem. Soc. Rev. 38 (2009) 1294.
[3] T. Uemura, N. Yanaia, S. Kitagawa, Chem. Soc. Rev. 38 (2009) 1228.
[4] T. Düren, Y.S. Baeb, R.Q. Snurrb, Chem. Soc. Rev. 38 (2009) 1237.
[5] L.-Q. Ma, C. Abney, W.-B. Lin, Chem. Soc. Rev. 38 (2009) 1248.
[6] J.-R. Li, R.J. Kuppler, H.-C. Zhou, Chem. Soc. Rev. 38 (2009) 1477.
[7] M.D. Allendorf, C.A. Bauer, R.K. Bhakta, R.J.T. Houk, Chem. Soc. Rev. 38 (2009) 1330.
[8] D.J. Tranchemontagne, J.L. Mendoza-Cortés, M. O'Keeffe, O.M. Yaghi, Chem. Soc. Rev. 38 (2009) 1248.
[9] X.-L. Wang, Y.-Q. Chen, G.-C. Liu, H.-Y. Lin, W.-Y. Zhang, J.-X. Zhang, J. Organomet. Chem. 694 (2009) 2263.
[10] S.-L. Li, Y.-Q. Lan, J.-F. Ma, J. Yang, G.-H. Wei, L.-P. Zhang, Z.-M. Su, Cryst. Growth Des. 8 (2008) 675.
[11] F. Luo, Y.-T. Yang, Y.-X. Che, J.-M. Zheng, CrystEngComm 10 (2008) 981.
[12] W.M. Teles, R.A. Farani, M.I. Yoshida, A.J. Bortoluzzi, M. Hörner, L.F.C. Oliveira, F.C. Machado, Polyhedron 26 (2007) 1469.
[13] L. Carlucci, G. Ciani, S. Maggini, D.M. Proserpio, Cryst. Growth Des. 8 (2008) 165.
[14] C.W. Yeh, J.D. Chen, J.C. Wang, Polyhedron 27 (2008) 3611.
[15] J.-D. Lin, Z.-H. Li, J.-R. Li, S.-W. Du, Polyhedron 26 (2007) 107.
[16] H.-Y. Lin, X.-L. Wang, H.-L. Hu, B.-K. Chen, G.-C. Liu, Solid State Sci. 11 (2009) 643.
[17] J.Y. Lu, V. Schauss, Inorg. Chem. Commun. 6 (2003) 1332.
[18] J.M. Rueff, S. Pillet, N. Claiser, G. Bonaventure, M. Souhassou, P. Rabu, Eur. J. Inorg. Chem. (2002) 895.
[19] J.M. Rueff, S. Pillet, G. Bonaventure, M. Souhassou, P. Rabu, Eur. J. Inorg. Chem. (2003) 4173.
[20] D.C. Pascal, B. Richard, F. Hemler, J. Chem. Soc., Dalton Trans. (2006) 586.
[21] R.-H. Wang, Y.-Q. Gong, L. Han, D.-Q. Yuan, B.-Y. Lou, B.-L. Wu, M.-C. Hong, J. Mol. Struct. 784 (2006) 1.

[22] R.-H. Wang, M.-C. Hong, J.-H. Luo, R. Cao, J.-B. Weng, Chem. Commun. (2003) 1018.
[23] R.-H. Wang, Y.-F. Zhou, Y.-Q. Sun, D.-Q. Yuan, L. Han, B.-Y. Lou, B.-L. Wu, M.-C. Hong, Crystal. Growth Des. 5 (2005) 251.
[24] Y.-B. Wang, X.-J. Zheng, W.-J. Zhuang, L.-P. Jin, Eur. J. Inorg. Chem. (2003) 1355.
[25] R.-H. Wang, M.-C. Hong, J. -H Luo, R. Cao, J.-B. Weng, Eur. J. Inorg. Chem. (2002) 2082.
[26] X.-L. Wang, C. Qin, Y.-Q. Lan, K.-Z. Shao, Z.-M. Su, E.-B. Wang, Chem. Commun. (2009) 410.
[27] X.-L. Wang, Y.-F. Bi, G.-C. Liu, H.-Y. Lin, T.-L. Hu, X.-H. Bu, CrystEngComm 10 (2008) 349.
[28] X.-L. Wang, B.-K. Chen, H.-Y. Lin, H.-L. Hu, J. Li, Transition Met. Chem. 34 (2009) 307.
[29] F.-Y. Lian, R.-H. Wang, L. Han, F.-L. Jiang, M.-C. Hong, Z. Anorg. Allg. Chem. 631 (2005) 2485.
[30] R.-H. Wang, L. Han, Y.-Q. Sun, Y.-Q. Gong, D.-Q. Yuan, M.-C. Hong, J. Mol. Struct. 694 (2004) 79.
[31] R.-H. Wang, F.-L. Jiang, L. Han, Y.-Q. Gong, Y.-F. Zhou, M.-C. Hong, J. Mol. Struct. 699 (2004) 79.
[32] Q. Miao, M.-L. Hu, F. Chen, Acta Crystallogr. E60 (2004) m1314.
[33] P.-X. Yin, J. Zhang, J.-K. Cheng, Z.-J. Li, Y.-G. Yao, Inorg. Chem. Commun. (2006) 541.
[34] G.M. Sheldrick, SHELXS 97, Program for the Solution of Crystal Structure, University of Göttingen, Germany, 1990.
[35] G.M. Sheldrick, SHELXL 97, Program for the Refinement of Crystal Structure, University of Göttingen, Germany, 1997.
[36] J.B. Sperry, D.L. Wright, J. Chem. Res. 35 (2006) 605.
[37] M.-B. Zhang, Y.-M. Chen, S.-T. Zheng, G.-Y. Yang, Eur. J. Inorg. Chem. (2006) 1423.

2.2. Characterization

XRD patterns were recorded by a Rigaku D-max C III, X-ray diffractometer using Ni-filtered Cu Kα radiation. Elemental analyses were obtained from Carlo ERBA Model EA 1108 analyzer. Scanning electron microscopy (SEM) images were obtained on Philips XL-30ESEM equipped with an energy dispersive X-ray spectroscope. Transmission electron microscopy (TEM) images were obtained on a Philips EM208 transmission electron microscope with an accelerating voltage of 100 kV. X-ray photoelectron spectroscopy (XPS) of the as-prepared products was measured on an ESCA-3000 electron spectrometer with non-monochromatized Mg Kα X-ray radiation as the excitation source. Room temperature photoluminescence (PL) was studied on an F-4500 fluorescence spectrophotometer. Fourier transform infrared (FT-IR) spectra were recorded on Shimadzu Varian 4300 spectrophotometer in KBr pellets. The electronic spectra of the complexes were taken on a Shimadzu UV–Vis scanning spectrometer (Model 2101 PC).

2.3. Synthesis of ZrO_2 nanoparticles

The current synthetic procedure is a modified version of the method developed by the Hyeon group for the synthesis of various nanoparticles of metals and oxides, which employs the thermal decomposition of metal–surfactant complexes in hot surfactant solution [26]. A stock solution of $[Zr(HAP)_3]$–surfactant complex, prepared by reacting 0.6 g of bis-aqua, tris-2-hydroxyacetophenato zirconium (IV) nitrate, $[Zr(HAP)_3(H_2O)_2](NO_3)$, with 5 ml of oleylamine at 150 °C, was slowly injected into 5 g of triphenylphosphine (TPP) under vigorous stirring at 250 °C. The mixture was heated at 250 °C and the resulting solution was stirred at this temperature for 90 min. The initial white color of the solution slowly turned yellow, indicating that nanoparticles were generated. The reaction mixture was then cooled to room temperature and the white nanoparticles were retrieved by adding 30 ml of ethanol, followed by centrifugation. The final products were washed with ethanol at least three times to remove impurities, if any, and dried at 100 °C. The retrieved powder form of the nanoparticles could be easily redispersed in non-polar organic solvents such as hexane or toluene (Scheme 1).

3. Results and discussion

3.1. Thermogravimetric analysis of the $[Zr(HAP)_3(H_2O)_2](NO_3)$ precursor

The TGA curve for the decomposition of $[Zr(HAP)_3(H_2O)_2](NO_3)$ was recorded in air atmosphere and is shown in Fig. 1. As shown in Fig. 1, a total of two weight losses were observed. A weight loss of 9% occurred between 100 and 180 °C, and this weight loss is indicative of the loss of one coordinated H_2O molecule. The TG curve of the complex shows a gradual loss of weight of about 70% around 460 °C to give a residual mass consisting of about 30%, close to that expected for a complete conversion to ZrO_2. The weight loss from 250 to 460 °C is linked with burning of 2-hydroxyacetophenato (exothermic) to acetone, CO_2 and H_2O [27]. There was no organic residue left after 450 °C, as confirmed by the FT-IR spectrum of the residual mass.

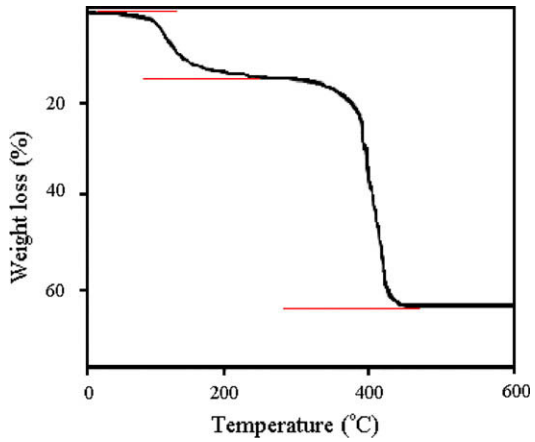


Fig. 1. TG curve of the $[Zr(HAP)_3(H_2O)_2](NO_3)$ precursor in air.

3.2. XRD analysis of the products

The XRD diffraction pattern of the ZrO_2 was recorded for the identification of the product (Fig. 2). From the XRD data, the crystallite size (D_c) of the as-prepared ZrO_2 particles was calculated to be 40 nm using the Debey–Scherrer equation [28],

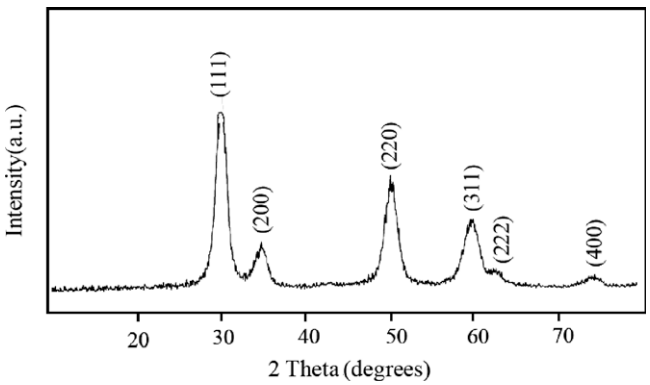
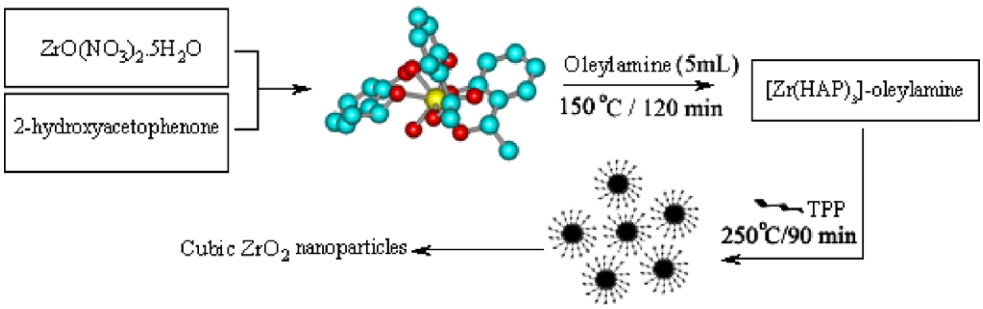


Fig. 2. XRD patterns of ZrO_2 nanoparticles.



Scheme 1. Synthetic procedure for ZrO_2 nanoparticles.

$$D_c = \frac{K\lambda}{\beta \cos\theta}$$

where β is the breadth of the observed diffraction line at its half-intensity maximum, K is the so-called shape factor, which usually takes a value of about 0.9, and λ is the wavelength of X-ray source used in the XRD. All of the reflections of the XRD pattern in Fig. 2 can be indexed to the standard pattern of the pure cubic phase of ZrO_2, which is in good agreement with the reported data (JCPDS No. 27–0997). This revealed that the ZrO_2 sample produced a single-phase cubic structure. Three observed peaks with 2θ values of 30.46°, 50.45° and 60.37° correspond to the (1 1 1), (2 2 0) and (3 1 1) diffraction peaks of crystalline zirconia, respectively. Zirconia nanocrystallite with an average size of 35 nm was estimated by using the Debye–Scherrer formula.

3.3. TEM studies

The TEM image of the sample is shown in Fig. 3, from which it can be seen that the ZrO_2 is composed of some agglomerated particles with an average size of about 30–40 nm. The TEM image shows quasi-spherical nanoparticles. The size of the nanoparticles obtained from the XRD diffraction patterns are in close agreement with the TEM studies, which show sizes of 30–40 nm (Fig. 3).

3.4. Photoluminescence study

Fluorescence spectra were measured with several excitation wavelengths between 230 and 290 nm. While the fluorescence intensity changes to some extent with the excitation wavelength, the fluorescence band position and the band shape remained about the same for excitation wavelengths below 290 nm. This indicates that the fluorescence involves the same initial and final states even when the excitation wavelength is varied between 230 and 290 nm. This result can be explained by fast relaxation from the final state reached by photo-excitation to those states from which the fluorescence originates. Fig. 4 shows one representative fluorescence spectrum with an excitation wavelength of 265 nm. The spectrum features a broad fluorescence band centered at 371 nm [29,30]. The broad band and the substantial red shift of the band maximum compared to the band gap (5.6 eV) of the bulk material [31,32] strongly indicate that the fluorescence involves extrinsic states. Because the particle size distribution is very narrow, the broad fluorescence band seems to be mostly caused by the small particle size leading to an inhomogeneous broadening from a distribution of surface or defect states [33].

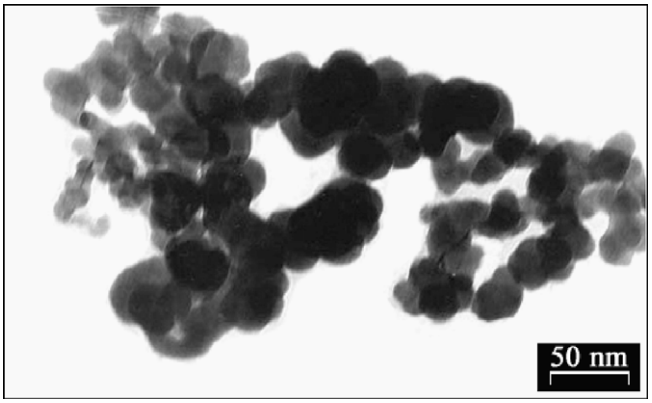


Fig. 3. TEM image of ZrO_2 nanoparticles.

3.5. FT-IR spectra of the products

The FT-IR spectra for the free TPP, oleylamine, $[Zr(HAP)_3(H_2O)_2](NO_3)$ and the as-prepared ZrO_2 nanoparticles are shown in Fig. 5a–d. As shown in Fig. 5a and b, peaks corresponding to P–Ph stretching at 1710 cm^{-1}, rocking and bending mode of the methylene group $\omega(CH_2)$ at 1270 cm^{-1}, the bending mode of the phenyl group $\gamma(=CH)$ at 742 $cm^{-1}$and ν (benzene ring) at 697 cm^{-1}can be seen. The only difference among these characteristic peaks is either the peak intensity or a slight shift in the peak position. For example, the peak position of the longitudinal modes of oleylamine and TPP shifts to lower wavenumbers after TPP and oleylamine are adsorbed on the surface of the ZrO_2 nanocrystals. In the case of $[Zr(HAP)_3(H_2O)_2](NO_3)$ (see Fig. 5c), the presence of bands at 1526 cm^{-1} and 1590 cm^{-1} are due to metal bonded C–O and bands at 1451 cm^{-1} and 1382 cm^{-1} are due to the C–C bond of the 2-hydroxyacetophenone group [34,35]. In free 2-hydroxyacetophenone two C–O bonds give a band pattern at 1600 cm^{-1} and 1500 cm^{-1} whereas two C–C bonds give a band pattern at 1450 cm^{-1} and 1260 cm^{-1}. The lowering of the absorption frequency of these two bonds indicates chelation of the 2-hydroxyacetophenone group to the metal center. A very broad peak at 3440–3100 cm^{-1} is assigned to a water molecule present in the complex. Absorption peaks at 500–650 cm^{-1} are due to a M–O bond. However, there are no absorption bands around this range in 2-hydroxyacetophenone. Therefore, the added 2-hydroxyacetophenone was thought to be fully chelated to the zirconium ion, and no free 2-hydroxyacetophenone exists in the solution. It is well known that FT-IR spectra are very useful for the determination of the crystal phase for ZrO_2 [36]. The extended spectrum in the 400–4000 cm^{-1} region signified a structure with the surface of the sample having chemisorbed H_2O molecules. The spectra of ZrO_2, (Fig. 5d), shows two very weak stretch vibrations at 2925 and 2865 cm^{-1}, attributed to the C–H stretching models of the car-

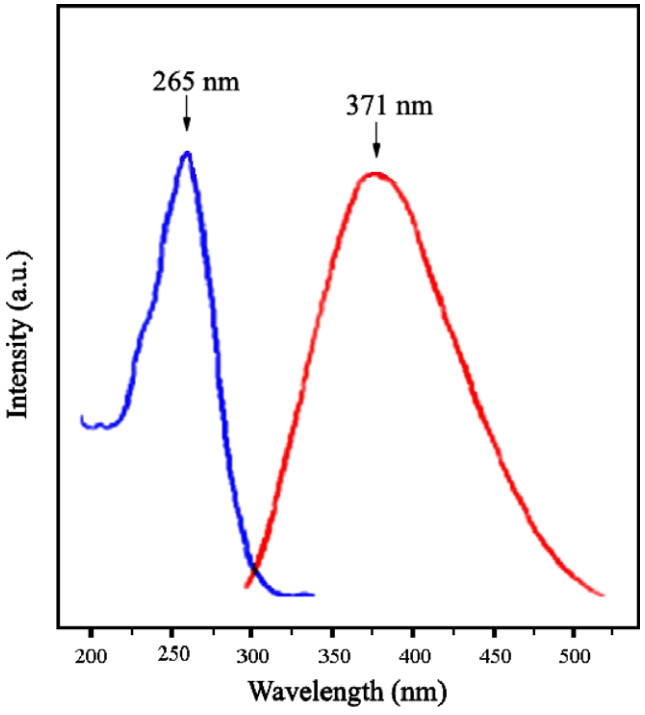


Fig. 4. Photoluminescence spectra of ZrO_2 nanocrystals (excited at 265 nm (blue color), the excitation spectrum of the emission recorded at 371 nm (red color)). (For interpretation of the references to color in this figure legend, the reader is referred to the web version of this article.)

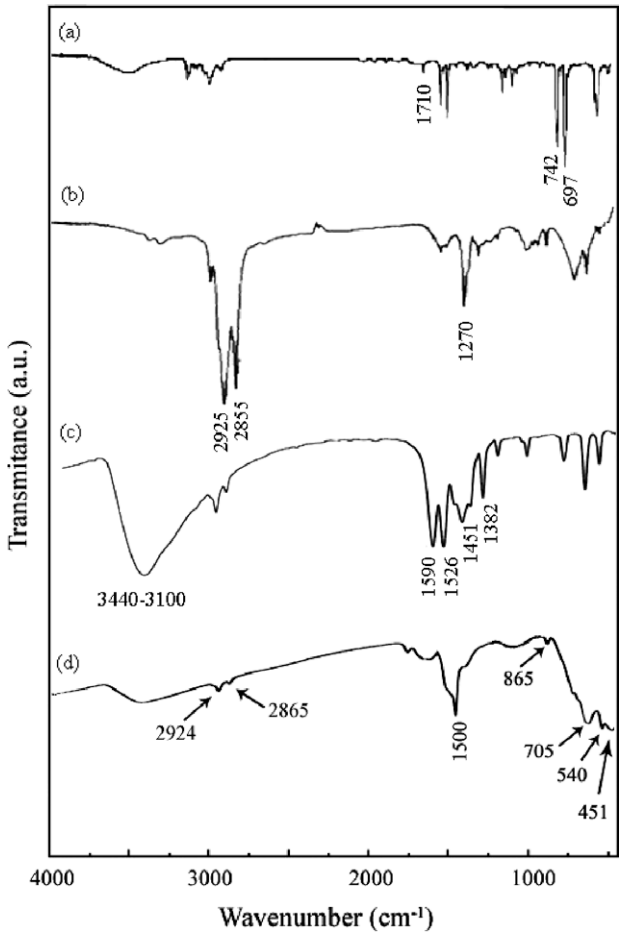


Fig. 5. IR spectra for (a) TPP, (b) oleylamine, (c) $[Zr(HAP)_3(H_2O)_2](NO_3)$ and (d) ZrO_2 nanoparticles.

bon chain of oleylamine that were adsorbed on the surface of the ZrO_2 nanocrystals. The spectrum in Fig. 5d showed broad bands at 451, 540 and 705 cm^{-1} related to the c-ZrO_2 phase (Fig. 5) [37]. The trend is consistent with the fact that for cubic ZrO_2 only one fundamental mode is IR active and the active modes increase markedly upon lowering the symmetry of the structure by going from cubic to tetragonal and then to monoclinic ZrO_2. Two bands of c-ZrO_2 nanocrystallites were obtained at 865 and 1500 cm^{-1}. By comparing the infrared spectra of the nanoparticles with free surfactants we can see that the organic molecules have indeed become a small part of the nanoparticles.

3.6. X-ray photoelectron spectroscopy (XPS) analysis

The chemical state of the zirconia nanoparticles was analyzed by XPS measurements. In an X-ray photoelectron spectroscopy (XPS) experiment, the samples are exposed to monochromic X-radiation and the properties of the inner-shell electrons are probed. Fig. 6 displays the XPS spectra of the Zr 3d and O 1s core levels. The peaks located at 181.3 and 183.8 eV are attributed to the spin–orbit splitting of the Zr 3d components, Zr $3d_{5/2}$, Zr $3d_{3/2}$. The binding energy of O 1s in zirconia is located at 530.1 eV. The peak positions and their relative intensities are basically consistent with those of a standard cubic structure of zirconia [31]. It is noted in Fig. 6 that the peaks of Zr 3d and O 1s shift to higher binding energies with increasing particle diameter. The result is in good agreement with the results obtained by XRD.

3.7. Synthesis of ZrO_2 under different condition

In addition, the ZrO_2 nanoparticles have been prepared under different conditions (Table 1). By controlling the quality of the nanoparticles, ZrO_2 with various sizes can be formed. $[Zr(HAP)_3(H_2O)_2](NO_3)$ calcined at 600 °C for 4 h (sample 1) resulted in ZrO_2 spherical shapes with sizes of 40–50 nm (Fig. 7), 0.6 g of $[Zr(HAP)_3(H_2O)_2](NO_3)$ and 5 ml of oleylamine mixed and heated

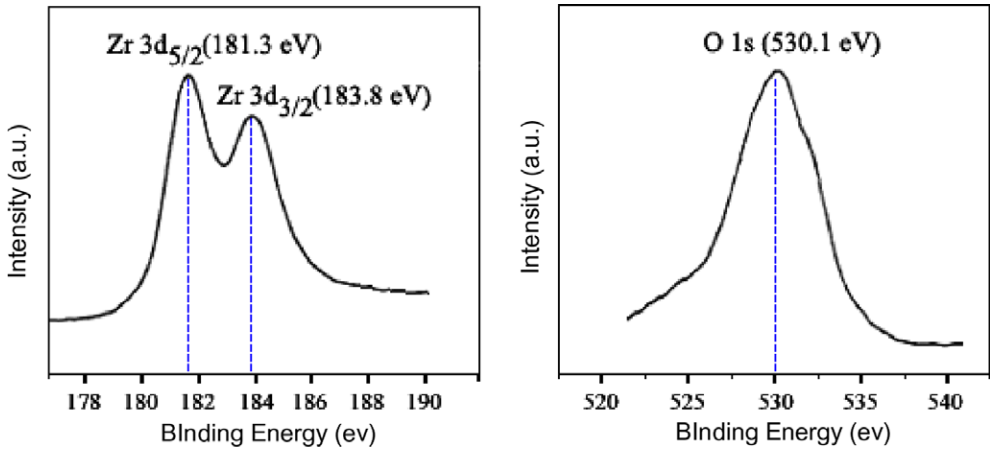


Fig. 6. XPS spectra of ZrO_2 nanoparticles, Zr 3d and O 1s.

Table 1
Preparation of ZrO_2 under different conditions.

Sample	Capping agent	Temperature (°C)	Time	Particles size
1		600	4 h	40–50 nm
2	oleylamine	250	90 min	30 nm (according to XRD)
3	TPP	250	90 min	no product
4	oleylamine + TPP	250	90 min	30–40 nm

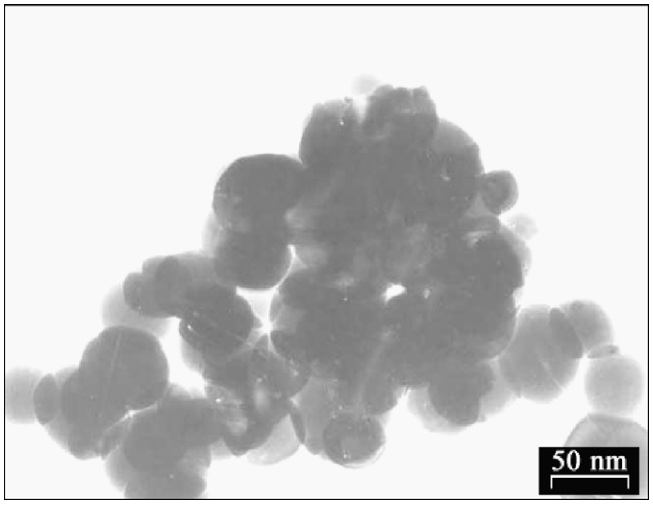


Fig. 7. TEM image of ZrO_2 nanoparticles ((sample 1); $[Zr(HAP)_3(H_2O)_2](NO_3)$ was calcined at 600 °C for 4 h).

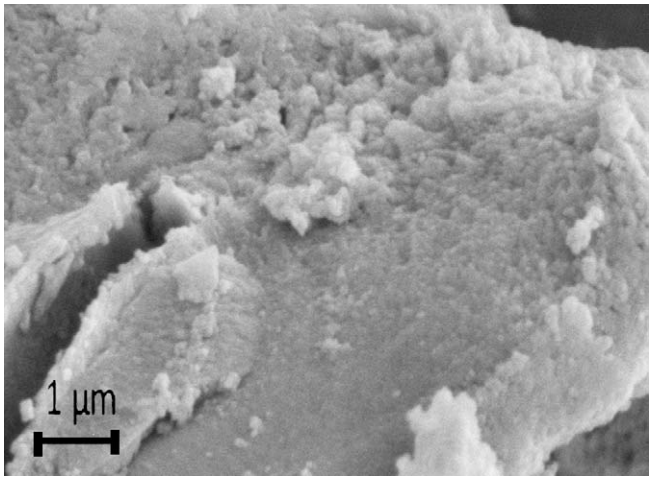


Fig. 8. SEM image of the ZrO_2 nanoparticles (sample 2).

to 245 °C for 90 min led to ZrO_2 nanoparticles with a quasi-spherical shape and an average size of about 30 nm, but the products are agglomerated (sample 2) (Fig. 8). Also 0.6 g $[Zr(HAP)_3(H_2O)_2](NO_3)$ and 5 g of TPP (sample 3) were heated together at 250 °C for 90 min, but after washing with ethanol no precipitation was obtained. To prepare ZrO_2 spherical nanocrystals (sample 4), the procedure mentioned in Section 2, including $C_{18}H_{37}N$ and TPP, was carried out. Considering the different conditions employed to prepare these samples, it is obvious that using both $C_{18}H_{37}N$ and TPP as capping agents are preferred in ZrO_2 nanoparticle synthesis.

In summary, pure zirconium oxide nanoparticles arrays were successfully prepared by the thermolysis method. We have used SEM, TEM, XRD, XPS, FT-IR and PL techniques to characterize the structure of the zirconia nanoparticles. XRD analysis indicated that the nanoparticles closely resembled cubic zirconia nanoparticles. ZrO_2 was also prepared by heat-treatment of bis-aqua, tris-2-hydroxyacetophenato zirconium (IV) nitrate, $[Zr(HAP)_3(H_2O)_2](NO_3)$. The morphology and particle size of the obtained products were compared with each other. Considering the different conditions employed in the synthesis of nanoparticles, it is obvious that using both oleylamine and triphenylphosphine as capping agents are preferred for the synthesis of small size, pure ZrO_2 nanoparticles.

4. Conclusion

ZrO_2 nanoparticles powders were prepared via thermolysis of a new precursor, $[Zr(HAP)_3(H_2O)_2](NO_3)$. ZrO_2 nanoparticles were synthesized under different conditions. The TEM image shows that the size of the quasi-spherical nanoparticles synthesized in the presence of oleylamine and TPP are about 30–40 nm. According to the XRD pattern, to prepare cubic ZrO_2 nanospherical particles, oleylamine and TPP must be used together. Thermolysis is a simple method to prepare ZrO_2 nanoparticles and is one that can be used for large-scale syntheses.

Acknowledgment

Authors are grateful to the Council of the University of Kashan for providing financial support to undertake this work.

References

[1] V. Grover, R. Shukla, A.K. Tyagi, Scripta Mater. 57 (2007) 699.
[2] W. Li, H. Huang, H. Li, W. Zhang, H. Liu, Langmuir 24 (2008) 8358.
[3] G.-Y. Guo, Y.-L. Chen, J. Solid State Chem. 178 (2005) 1675.
[4] J. Liang, X. Jiang, G. Liu, Z. Deng, J. Zhuang, F. Li, Y. Li, Mater. Res. Bull. 38 (2003) 161.
[5] V.A. Sadykov, V.I. Zaikovskii, D.A. Zyuzin, E.M. Moroz, E.B. Burgina, A.V. Ishchenko, Mater. Res. Soc. Symp. Proc. E 878 (2005) 481.
[6] D. Vollath, K.E. Sickafus, Nanostruct. Mater. 1 (1992) 427.
[7] V.V. Srdic, M. Winterer, J. Eur. Ceram. Soc. 26 (2006) 3145.
[8] C. Stocker, A. Baiker, J. Non-Cryst. Solids 223 (1998) 165.
[9] I.I. Stefanc, S. Music, G. Stefanic, A. Gajovic, J. Mol. Struct. (1999) 480.
[10] J.A. Wang, M.A. Valenzuela, J. Salmones, A. Vazquez, A. Garcia-Ruiz, X. Bokhimi, Catal. Today 68 (2001) 21.
[11] N.L. Wu, T.F. Wu, J. Am. Ceram. Soc. 83 (2000) 3225.
[12] P.E. Meskin, V.K. Ivanov, A.E. Barantchikov, B.R. Churagulov, Y.D. Tretyakov, Ultrason. Sonochem. 13 (2006) 47.
[13] R. Nitsche, M. Rodewald, G. Skandan, H. Fuess, H. Hahn, Nanostruct. Mater. B 7 (1996) 535.
[14] R.D. Purohit, S. Saha, A.K. Tyagi, Mater. Sci. Eng. B 130 (2006) 57.
[15] H.Y. Lee, W. Riehemann, B.L. Mordike, J. Eur. Ceram. Soc. 10 (1992) 245.
[16] F. Davar, Z. Fereshteh, M. Salavati-Niasari, J. Alloys Compd. 476 (2009) 797.
[17] M. Salavati-Niasari, Z. Fereshteh, F. Davar, Polyhedron 28 (2008) 126.
[18] M. Salavati-Niasari, F. Davar, Mater. Lett. 63 (2009) 441.
[19] M. Salavati-Niasari, F. Davar, M. Mazaheri, Mater. Lett. 62 (2008) 1890.
[20] M. Salavati-Niasari, F. Davar, N. Mir, Polyhedron 27 (2008) 3514.
[21] G.I. Spijksma, H.J.M. Bouwmeester, D.H.A. Blanka, V.G. Kessler, Chem. Commun. (2004) 1874.
[22] C. Hagfeldt, V. Kessler, I. Persson, J. Chem. Soc., Dalton. Trans. (2004) 2142.
[23] G.I. Spijksma, H.J.M. Bouwmeester, D.H.A. Blank, A. Fischer, M. Henry, V.G. Kessler, Inorg. Chem. 45 (2006) 4938.
[24] M. Putknen, L. Niinisto, J. Mater. Chem. 11 (2001) 3141.
[25] M. Hussain, M. Mazhar, M.K. Rauf, M. Ebihara, T. Hussain, Bull. Korean Chem. Soc. 29 (2008) 92.
[26] T. Hyeon, S.S. Lee, J. Park, Y. Chung, H.B. Na, J. Am. Chem. Soc. 123 (2001) 12794.
[27] J.V. Hoene, R.G. Charles, W.M. Hickam, J. Phys. Chem. 62 (1958) 1098.
[28] B.D. Cullity, S.R. Stock, Elements of X-ray Diffraction, Prentice Hall, Englewood Cliffs, 2001.
[29] J. Yang, Z.W. Quan, D.Y. Kong, X.M. Liu, J. Lin, J. Cryst. Growth Des. 7 (2007) 730.
[30] M.N. Tahir, L. Gorgishvili, J. Li, T. Gorelik, U. Kolb, L. Nasdala, W. Tremel, Solid State Sci. 9 (2007) 1105.
[31] J. Joo, T. Yu, Y.W. Kim, H.M. Park, F. Wu, J.Z. Zhang, T. Hyeon, J. Am. Chem. Soc. 125 (2003) 6553.
[32] N. Zhao, D. Pan, W. Nie, X. Ji, J. Am. Chem. Soc. 128 (2006) 10118.
[33] A. Feinberg, C.H. Perry, J. Phys. Chem. Solids 42 (1981) 513.
[34] K. Nakamoto, Infrared Spectra of Inorganic and Coordination Compounds, 4th Ed., Chemical Industry Press, Beijing, 1991.
[35] D.-Y. Kim, C.-H. Lee, S.J. Park, J. Mater. Res. 11 (1996) 2583.
[36] S.F. Wang, F. Gu, M.K. Lü, Z.s. Yang, G.J. Zhou, H.P. Zhang, Y.Y. Zhou, S.M. Wang, Opt. Mater. 28 (2006) 1222.
[37] M.M. Rashad, H.M. Baioumy, J. Mater. Process. Technol. 195 (2008) 178.

2. Experimental

2.1. Materials and physical measurements

All chemicals and solvents were purchased from commercial sources and were used without further purification. Elemental analyses for C, H, N and S were carried by an Elementar Vario El III. IR spectra of the complexes were determined as KBr discs using a Perkin Elmer 100 FT-IR spectrometer within the 4000–400 cm^{-1} frequency range. Magnetic susceptibility measurements were performed using a Sherwood Scientific MXI model Gouy magnetic balance at room temperature. The UV–Vis spectra were obtained for aqueous solutions of the complexes (10^{-3} M) with a Shimadzu UV-3150 spectrometer in the range 900–190 nm. Thermal analyses were performed with a Diamond TG/DTA thermal analyzer in static air atmosphere from 30 to 550 °C at heating rate of 10 °C/min using platinum crucibles.

2.2. Preparation of the complexes

2.2.1. $\{[Cu_2(\mu\text{-}tdc)_2(ampy)]\cdot 2DMF\}_n$

A solution of $Cu(CH_3COO)_2\cdot H_2O$ (0.23 g, 1.15 mmol) in water (10 mL) was added slowly to a solution of DMF containing ampy (0.13 g, 1.15 mmol) and thiophene-2,5-dicarboxylic acid (0.2 g, 1.16 mmol). The mixture solution was stirred for about 4 h at 55 °C and then cooled to room temperature. Several days later navy blue crystals were formed and collected. *Anal.* Calc. for $C_{30}H_{34}Cu_2N_6O_{10}S_2$: C, 43.42; H, 4.13; N, 10.13; S, 7.73. Found: C, 43.38; H, 4.11; N, 10.21; S, 7.68%.

2.2.2. $[Cu(H_2O)_2(en)_2](tdc)$

A solution of $Cu(CH_3COO)_2\cdot H_2O$ (0.58 g, 2.90 mmol) in water (10 mL) was added to a solution of thiophene-2,5-dicarboxylic acid (0.5 g, 2.90 mmol) in water (20 mL). After 10 min, a blue precipitate was formed and the mixture was stirred for about 4 h at 50 °C. After that, an aqueous solution of an ethylenediamine (0.35 g, 5.8 mmol) aqueous solution was added. A clear solution was observed, stirred for 4 h at 60 °C and then cooled to room temperature. Several days later, glossy dark blue crystals were formed and collected. *Anal.* Calc. for $C_{10}H_{22}CuN_4O_6S$: C, 30.80; H, 5.69; N, 14.37; S, 8.22. Found: C, 30.72; H, 5.58; N, 14.33; S, 8.19%.

2.2.3. $[Cu(H_2O)_2(4\text{-}meim)_4](tdc)\cdot 4H_2O$

The same synthetic method was applied for the second and third complexes, but using 4-methylimidazole (0.95 g, 0.012 mol) in place of ethylenediamine. Again glossy dark blue crystals were formed and collected. *Anal.* Calc. For $C_{22}H_{38}CuN_8O_{10}S$: C, 39.43; H, 5.72; N, 16.72; S, 4.78. Found: C, 39.38; H, 5.64; N, 16.74; S, 4.67%.

2.3. Crystallographic analyzes

Diffraction experiments were carried out at 293 (2) K on a Stoe IPDS diffractometer. The structures were solved by direct methods and refined using the programs SHELXS97 and SHELXL97 [22]. All non-hydrogen atoms were refined anisotropically by full-matrix least-squares methods [22]. The hydrogen atoms were placed in geometrically idealized positions and refined as riding atoms. Data collection: X-AREA, cell refinement: X-AREA, data reduction: X-RED [23]; program(s) used for molecular graphics: ORTEP-3 for Windows [24]; software used to prepare material for publication: WINGX [25].

3. Results and discussion

3.1. Synthesis

The aim of this work was to study the effects of diverse N-ligands containing two nitrogen atoms as a co-ligand on the coordination mode of tdc in mixed-ligand complexes. The reaction of aqueous solutions of different N-donor ligands yielded compounds of the formulas $\{[Cu_2(\mu\text{-}tdc)_2(ampy)_2]\cdot 2DMF\}_n$ (**1**), *trans*-$[Cu(H_2O)_2(en)_2](tdc)$ (**2**) and *trans*-$[Cu(H_2O)_2(4\text{-}meim)_4](tdc)\cdot 4H_2O$ (**3**). The composition of the complexes was determined by IR and thermal analysis in detail. In addition, their structures were determined by the single crystal X-ray diffraction technique.

3.2. UV–Vis spectra and magnetic properties

The electronic spectra of aqueous solutions of the complexes display broad absorption bands at 683 (ε = 25 L mol^{-1} cm^{-1}), 564 (ε = 52 L mol^{-1} cm^{-1}) and 352 (ε = 17 L mol^{-1} cm^{-1}), respectively, which are assigned to the $E_g \rightarrow T_{2g}$ transition. The strong absorption bands below 300 nm are due to intraligand transitions.

The magnetic behaviors of the three Cu(II) complexes have been investigated at room temperature. The complexes exhibit a magnetic moment value of 1.86 for **1**, 1.65 for **2** and 1.55 for **3**, which corresponds to one unpaired electron.

3.3. IR spectra

The IR spectrum of thiophene-2,5-dicarboxylic acid exhibits broad absorption bands in the region 2850–2500 cm^{-1}, characteristic of associated acids, and at 1662, 1415 and 930 cm^{-1}.

In the IR spectra of complexes **1**, **2** and **3**, an insignificant shift in the frequency of vibrations of the thiophene ring is revealed. Bands characteristic of H_2tdc are retained. In the IR spectrum of **1**, characteristic bands of carboxylic groups occur at 1531 cm^{-1} for asymmetric stretching and at 1448 cm^{-1} for the symmetric stretching. These values are shown in Table 1. The comparatively low Δ value (83 cm^{-1}, $\Delta = \nu_{as}COO^- - \nu_sCOO^-$) possibly indicates [26] that tdc is bidentate in **1**. The NH_2 stretching bands of the ampy ligand occur at 3158 cm^{-1}.

For complex **2**, intense bands appear at 1560 cm^{-1} for asymmetric stretching and 1350 cm^{-1} for symmetric stretching. The corresponding absorption bands for **3** are observed nearly at the same frequencies, being at 1559 and 1352 cm^{-1}. The comparatively low Δ values (210 and 207 cm^{-1}, respectively) possibly indicate [26] that tdc is in an ionic form in **2** and **3**. The NH_2 stretching band of ethylenediamine for **2** was at 3294 cm^{-1} and for complex **3** the NH stretching band of 4-methylimidazole was at 3159 cm^{-1}. A broad feature is observed in the 3450 cm^{-1} region and is attributed to the stretching modes of the coordinated water molecules for **2** and **3**. These bands are also significantly different due to the existence of various hydrogen bonds in **2** and **3**.

Table 1
IR data of **1**, **2** and **3**.

Complex	νOH	νNH/NH_2	νCH/CH_2	νC=O/C=N	$\nu_{as}COO^-$	ν_sCOO^-	νCu–O	νCu–N
1	3437	3158–3254	2930–2852	/1674	1531	1448	561	458
2	3401	3158–3294	2952–2889		1560	1350	540	461
3	3437	3159	2925–2868	/1607	1559	1352	530	461

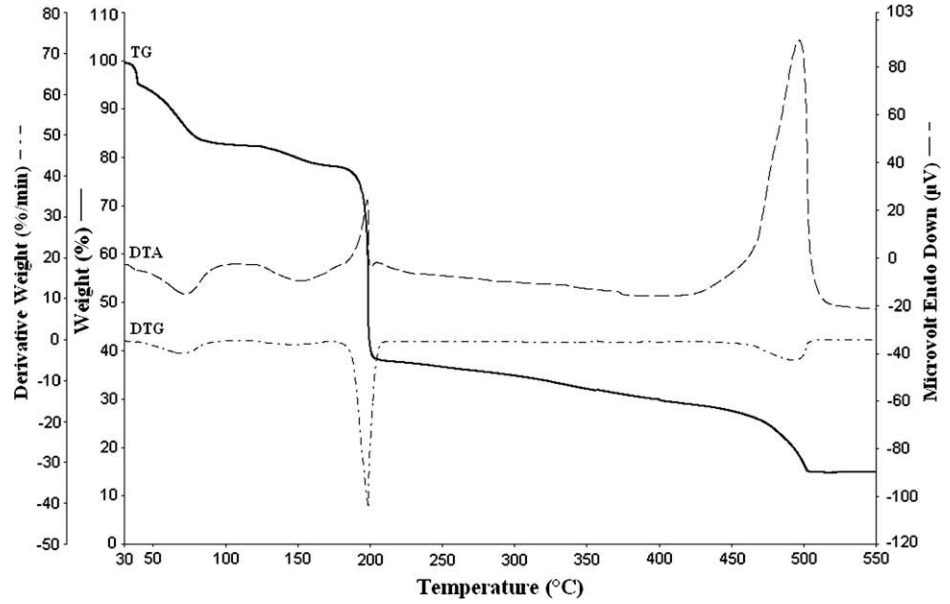


Fig. 1. TG, DTG and DTA curves of **1**.

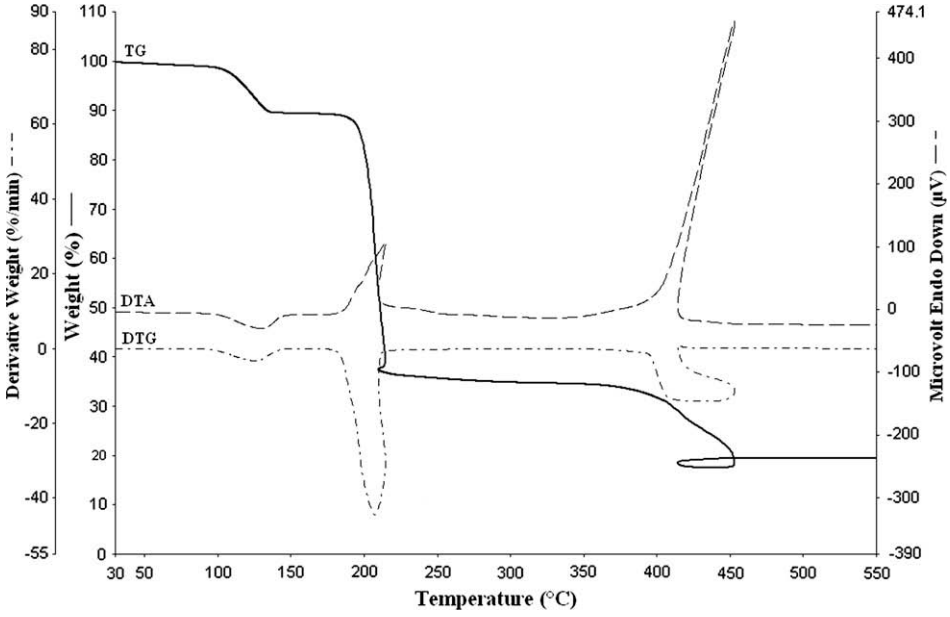


Fig. 2. TG, DTG and DTA curves of **2**.

3.4. Thermal analyzes

Thermal analyzes (TG/DTG and DTA) were carried out to examine the thermal stabilities and to make sure about the proposed formulas and structures of the Cu(II) complexes. Thermograms are shown in Figs. 1–3, respectively for complexes **1**–**3**.

For the complex **1**, the TG shows a three component weight loss. The first step occurs at a maximum temperature of 68 °C. The weight loss of two DMF molecules was 15.20%, with a calculated value is 17.6%. The second step, occurring between 150 and 216 °C, corresponds to the loss of two ampy ligands and two CO_2 molecules, representing a weight loss of 36.70%, with a calculated value of 42.00%. The third step occurring between 216 and 525 °C corresponds to the loss of $-C_4H_4S$, representing a weight loss of 19.80%, with a calculated value of 22.94%. The final thermal product obtained at 550 °C was CuO.

The thermal decomposition of the complex **2** occurs in three steps. The first step falls in the range 25–148 °C, and is assigned to the loss of two water molecules with a weight loss of 10.56% and a calculated value of 9.24%. The second step occurring between 148 and 218 °C corresponds to the loss of the two en ligands and two CO_2 molecules, representing a weight loss of 52.9% with a calculated value of 53.38%. The third step occurs at 218–502 °C, corresponding to the loss of C_4H_4S (organic moiety) and representing a weight loss of 21.00% with a calculated value of 17%. The final thermal product obtained at 550 °C was CuO.

The thermal decomposition of the complex **3** proceeds approximately with main three degradation steps. The first stage occurs at a maximum temperature of 86 °C. The weight loss associated with this stage is 15.10%, which is very close to the theoretical value of 16.13% corresponding to the loss of six water molecules, as is described in Table 2. The second step, occurring at 114–252 °C,

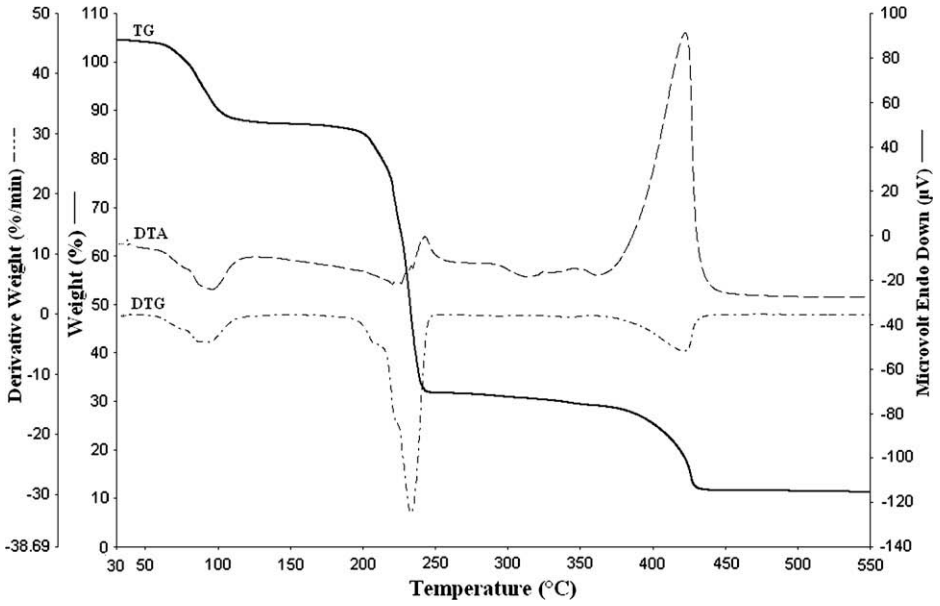


Fig. 3. TG, DTG and DTA curves of **3**.

Table 2
Thermoanalytical results (TG, DTG and DTA) of the complexes.

Complex	Steps	Temperature range (°C)	DTG peak (°C)	TG weight loss (%)		Decomposition product
				Calc.	Found	
1	1st	40–150	68	17.6	15.2	–2DMF
	2nd	150–216	199	36.7	42.0	$-C_{14}H_{16}O_4N_4$
	3rd	216–525	493	19.80	22.94	$-C_4H_4S$
				19.2	14.84	–CuO (residue)
2	1st	25–148	128	9.24	10.6	$-2H_2O$
	2nd	148–218	207	53.38	52.9	$-C_4H_8N_2O_4$
	3rd	218–502	430	21.0	17.0	$-C_4H_4S$
				20.4	19.5	–CuO (residue)
3	1st	56–114	86	16.13	15.10	$-6H_2O$
	2nd	114–252	230	48.97	50.08	$-C_{16}H_{24}N_8$
	3rd	252–470	438	23.0	21.4	$-C_6H_3O_3S$
				11.87	11.23	–CuO (residue)

Table 3
Crystal data and structure refinement parameters for **1**-**3**.

	1	**2**	**3**
Empirical formula	$C_{30}H_{34}Cu_2N_6O_{10}S_2$	$C_{10}H_{22}CuN_4O_6S$	$C_{22}H_{38}CuN_8O_{10}S$
Formula weight	829.83	389.92	670.20
Temperature (K)		293 (2)	
Wavelength (Å)		0.71073 Mo Kα	
Crystal system	orthorhombic	monoclinic	monoclinic
Space group	$Pna2_1$	$P21/m$	$P21/c$
a (Å)	15.0602 (3)	6.1386 (4)	9.4968 (3)
b (Å)	14.0418 (4)	21.8416 (11)	19.1494 (6)
c (Å)	17.3003 (3)	7.1004 (5)	17.3902 (5)
β (°)	90	114.845 (5)	98.634 (2)
V (Å^3)	3658.53 (14)	863.89 (9)	3126.71 (17)
Z	4	2	4
Absorption coefficient (mm^{-1})	1.34	1.42	0.83
D_{calc} (Mg m^{-3})	1.507	1.499	1.424
Crystal size (mm)	0.56 × 0.48 × 0.37	0.74 × 0.62 × 0.41	0.62 × 0.38 × 0.07
θ Range for data collection (°)	1.18–27.29	1.87–27.30	1.18–27.30
Measured reflections	36750	13385	35230
Independent reflections	7575	1878	6639
Absorption correction	integration		
Final R indices [$I>2\sigma(I)$]	R_{int} = 0.057	R_{int} = 0.035	R_{int} = 0.038
$R[F^2 > 2\sigma(F^2)]$	0.036	0.024	0.038
$wR(F^2)$	0.089	0.068	0.097
Goodness-of-fit on F^2	0.96	1.14	1.05
Largest difference in peak and hole (e Å^{-3})	0.27 and −0.21	0.32 and −0.30	0.55 and −0.53

Table 4
Comparison of the bond distances and angles (Å, °) in the complexes.*

Selected atoms			
Complex **1**			
N1–Cu1	1.982 (4)	O1–Cu1	1.963 (3)
N2–Cu1	1.980 (3)	O3–Cu2	1.972 (3)
N3–Cu2	1.981 (3)	O5–Cu2	1.942 (3)
N4–Cu2	1.988 (3)	O7–Cu1	1.956 (3)
O7–Cu1–O1	91.97 (13)	O5–Cu2–O3	92.20 (12)
O7–Cu1–N2	171.73 (13)	O5–Cu2–N3	174.04 (13)
O1–Cu1–N2	93.91 (13)	O3–Cu2–N3	92.97 (14)
O7–Cu1–N1	92.42 (16)	O5–Cu2–N4	93.22 (12)
O1–Cu1–N1	175.61 (16)	O3–Cu2–N4	172.54 (13)
N2–Cu1–N1	81.72 (16)	N3–Cu2–N4	81.91 (15)
Complex **2**			
N1–Cu1	2.012 (13)	Cu1–O1	2.556(13)
N2–Cu1	2.020 (13)		
$N1^{i}$–Cu1–N2	95.53 (5)	N1–Cu1–N2	84.47 (5)
Complex **3**			
N1–Cu1	1.991 (2)	N5–Cu1	1.984 (2)
N3–Cu1	2.015 (2)	N7–Cu1	2.010 (2)
N5–Cu1–N1	177.52 (8)	N5–Cu1–N3	89.97 (7)
N5–Cu1–N7	90.12 (7)	N1–Cu1–N3	89.48 (7)
N1–Cu1–N7	90.61 (7)	N7–Cu1–N3	175.86 (8)

* Symmetry code: (i) $-x+1, -y+1, -z+1$ for 2.

corresponds to the loss of 4-meim and represents a weight loss of 50.08%, with a calculated value of 48.97%. The third step occurring at 252–470 °C corresponds to the loss of tdc, representing a weight loss of 21.4%, with a calculated value of 23%. The final thermal product obtained at 550 °C was CuO.

In the present investigation the general thermal behavior of the complexes in terms of stability ranges and peak temperatures are shown in Table 2.

3.5. Structure of the complexes

3.5.1. $\{[Cu_2(\mu\text{-tdc})_2(ampy)_2]?2DMF\}_n$ (**1**)

The relevant crystal data and experimental conditions, along with the final parameters, are summarized in Table 3. Selected bond lengths and angles are given in Table 4. The crystal structure with the atom labeling for the structure of **1** is shown in Fig. 4. An X-ray analysis reveals that complex **1** exhibits a one-dimensional zig-zag polymeric chain. Each Cu(II) ion is coordinated by two N atoms of ampy and four O atoms from two carboxylate groups of tdc ligands, acting in a bis(bidentate) fashion in a distorted octahedral geometry (Fig. 4.). The Cu1–N bond lengths (1.982 (4) and 1.980 (3) Å) are similar to those of $[Cu(ampy)_2(CF_3SO_3)_2]$ [27], but shorter than those of $[Cu(sac)_2(ampy)_2]$ [28]. The Cu1–O1/O7 [average length = 1.960 Å] and Cu2–O3/O5 bond distances [average length = 1.957 Å] are in agreement with those observed in $[Cu(tdc)(phen)(H_2O)]_n$ (Cu–O 1.932(2) and 1.971(2) [14]). The axial Cu1–O2 (2.596 Å) and Cu2–O4 (2.578 Å) bond distances are longer than those in the related complex $\{[Cd(tdc)(H_2O)_3]\cdot 4H_2O\}_n$ Cd–O = 2.365(3) and 2.454(3) Å [16] and the equatorial bond distances due to the Jahn–Teller effect. The tdc ligand behaves as a bis(bidentate) ligand bridging two adjacent Cu(II) atoms through four oxygen atoms from both carboxylate groups. The C7–O2, C12–O4, C19–O6 and C24–O7 bond distances of the carboxylate groups are significantly shorter (1.230(5), 1.249(5), 1.228(4) and 1.226(5) Å, respectively) than the C7–O1, C12–O3, C19–O5 and C24–O7 distances of 1.273(5), 1.260(5), 1.280(4) and 1.289(5) Å, respectively, which are considered to be due to the weaker coordination with an ionic bond contribution. The dihedral angles formed between the carboxylate plane and the aromatic ring in the tdc anion is 7.55 Å for O5–C19–O6. The intra-chain Cu···Cu distance is 9.767(3) Å, which is comparable to the intra-helix Cd···Cd distance (10.577 Å) [18]. Between adjacent chains, the shortest Cu···Cu distance is 4.767 Å.

The crystal packing in **1** displays strong hydrogen bond interactions. The strong N–H···O hydrogen bonds between the nitrogen atoms of the amine group of the ampy ligand (N2 and N4) and the oxygen atoms of carboxylate groups (O4, O6 and O8) (O4···N2 = 2.887(5), O6···N2 = 2.951(4) and O8···N4 = 2.905(4) Å) and an oxygen atom of a DMF molecule (O10) (O10···N4 = 3.003(9) Å) were found within the chains (Table 5). These intermolecular interactions give rise to a three-dimensional framework.

3.5.2. Trans-$[Cu(H_2O)_2(en)_2](tdc)$ (**2**)

X-ray analysis indicates that the asymmetric unit of **2** contains a $[Cu(H_2O)_2(en)_2]^{2+}$ cation and a tdc^{2-} anion (Fig. 5.). Each Cu(II) ion in **2** is coordinated by four nitrogen atoms of two chelating en ligands and two oxygen atoms of the trans aqua ligands, and thus adopts a distorted octahedral N_4O_2 environment. The basal plane is defined by N1, $N1^{i}$, N2 and $N2^{i}$ from the two en ligands, the apical position is occupied by O1 and $O1^{i}$ of the aqua ligands. The Cu1–N1 and Cu1–N2 distances are 2.012(1) and 2.020(1) Å, respectively, while the Cu(1)–O1 bond distance of 2.556(1) Å is strongly elongated due to Jahn–Teller distortion. Similar geometrical parameters for the coordination sphere have been reported for other diaquabis(ethylenediamine) copper(II) salts [29,30].

The tdc dianion acts as a fully deprotonated counterion. The dihedral angle between the thiophen plane and the carboxylate group is 8.06°. The O–C bond lengths (1.251(2) and 1.252(2) Å) in

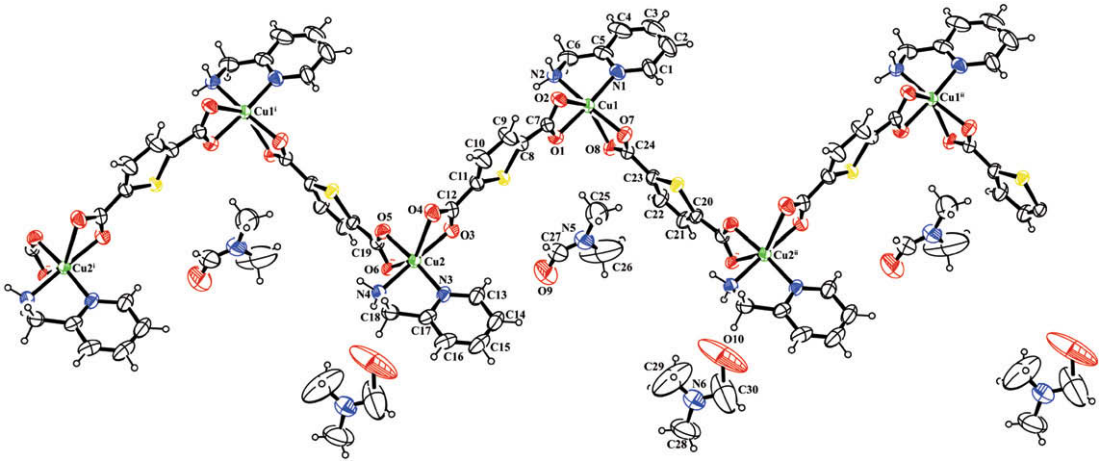


Fig. 4. A fragment of the one-dimensional zig-zag chain of **1**.

Table 5
Hydrogen bonding interactions in the complexes.

D–H···A	*d*(D–H), Å	*d*(H···A), Å	*d*(D···A), Å	⟨(DHA), °
Complex **1**				
N2–H2A···O4^{i}	0.90	2.00	2.887 (5)	167
N2–H2B···O6^{ii}	0.90	2.17	2.951 (4)	145
N4–H4A···O8^{iii}	0.90	2.02	2.905 (4)	169
N4–H4B···O10^{iv}	0.90	2.29	3.003 (9)	137
Symmetry codes: (i) $x-1/2, -y+1/2, z$; (ii) $-x+1/2, y+1/2, z+1/2$; (iii) $x+1/2, -y+1/2, z$; (iv) $x, y-1, z$				
Complex **2**				
N1–H1C···O2^{ii}	0.90	2.16	3.024 (2)	162
N1–H1D···O1 W^{iii}	0.90	2.17	3.048 (2)	165
N2–H2C···O3^{iv}	0.90	2.08	2.953 (2)	162
N2–H2D···O2	0.90	2.23	3.025 (2)	147
O1 W–HW11···O2^{iv}	0.85 (2)	1.94 (2)	2.777 (2)	167 (2)
O1W–HW12···O3^{v}	0.80 (2)	1.99 (2)	2.779 (2)	171 (2)
Symmetry codes: (ii) $x, y, z+1$; (iii) $-x, -y+1, -z+1$; (iv) $x-1, y, z$; (v) $-x+1, -y+1, -z$				
Complex **3**				
N2–H2···O4^{i}	0.86	1.99	2.848 (3)	174
N4–H4···O7^{ii}	0.86	2.02	2.842 (3)	160
N6–H6···O10^{iii}	0.86	2.03	2.882 (3)	169
N8–H8···O8	0.86	1.96	2.809 (3)	171
O1–H1A···O6^{iv}	0.85	2.282	3.131 (3)	173 (4)
O1–H1B···O3^{v}	0.86	2.004	2.858 (3)	174 (4)
O2–H2A···O3	0.83	2.018	2.839 (2)	169 (4)
O2–H2B···O6^{ii}	0.85	1.935	2.780 (3)	175 (3)
O7–H7A···O3	0.83	2.095	2.921 (3)	178 (4)
O7–H7B···O10^{ii}	0.81	2.12 (3)	2.876 (3)	154 (4)
O8–H8D···O6	0.82	2.07 (3)	2.853 (3)	157 (5)
O8–H8E···O9	0.83	1.960	2.783 (3)	175 (5)
O9–H9A···O5^{vi}	0.84	2.03 (2)	2.863 (3)	172 (4)
O9–H9B···O4^{vii}	0.82	2.03 (2)	2.820 (3)	162 (4)
O10–H10A···O5	0.82	1.89 (2)	2.705 (3)	170 (6)
O10–H10B···O7^{vii}	0.77	2.15 (3)	2.876 (3)	156 (5)

Symmetry codes: (i) $x-1, -y+3/2, z-1/2$; (ii) $-x+1, y+1/2, -z+3/2$; (iii) $-x+2, y+1/2, -z+3/2$; (iv) $-x+1, -y+1, -z+1$; (v) $x, -y+3/2, z-1/2$; (vi) $x-1, y, z$; (vii) $-x+1, y-1/2, -z+3/2$.

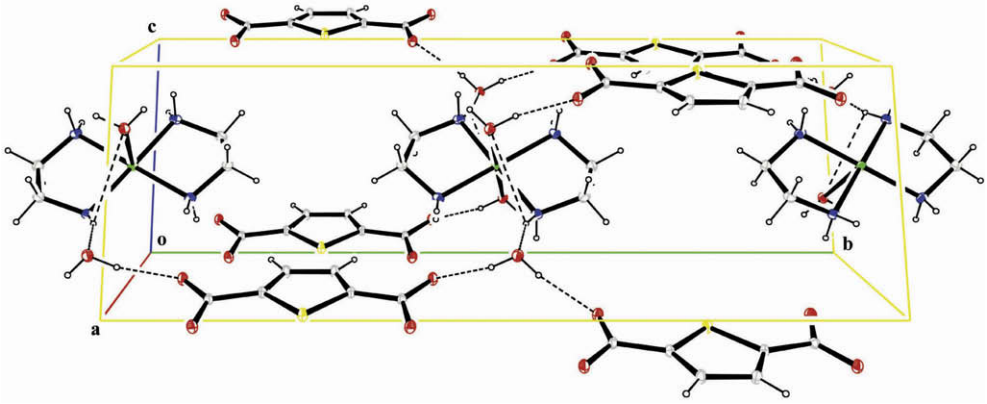


Fig. 5. Packing diagram of a unit cell of **2**.

the tdc anion are in agreement with related structures [31]. The crystal packing is mainly stabilized by intra and inter-molecular hydrogen bonding between the oxygen atoms of the tdc anion and aqua ligand and nitrogen atoms of the en ligands [N2···O2 = 3.025(2), N···O (average) = 3.008 and O···O (average) = 2.778(2) Å] (Fig. 5.).

3.5.3. Trans-[Cu(H$_2$O)$_2$(4-meim)$_4$](tdc)·4H$_2$O (**3**)

The molecular structure of **3** is illustrated in Fig. 6. Table 4 lists selected bond distances and angles. The molecule consists of a complex cation, $[Cu(H_2O)_2(4\text{-meim})_4]^{2+}$, one tdc ion and four lattice water molecules. In the complex cation, the Cu(II) is coordinated by four 4-meim ligands and two water molecules. The coordination geometry around the Cu(II) centre is a distorted octahedral. Both 4-meim ligands are essentially planar and are almost perpendicular to each other. The angle between the corresponding planes is 90.12(7)°, 90.61(7)°, 89.97(7)° and 89.48(7)°. The Cu-N distances range from 1.984(2) to 2.015(2) Å, while the average distance of the Cu–O bonds is 2.623 (2) Å due to the Jahn–Teller effect. Bond angles and distances are similar to the previously observed values for Cu(II) complexes containing 4-meim ligands [32–34].

The crystal structure is stabilized through strong intra- and inter-molecular hydrogen bonding and weak C–H···π interactions (Fig. 6.). Details of hydrogen bonding geometries are given in Table 5. These interactions give rise to a three-dimensional framework.

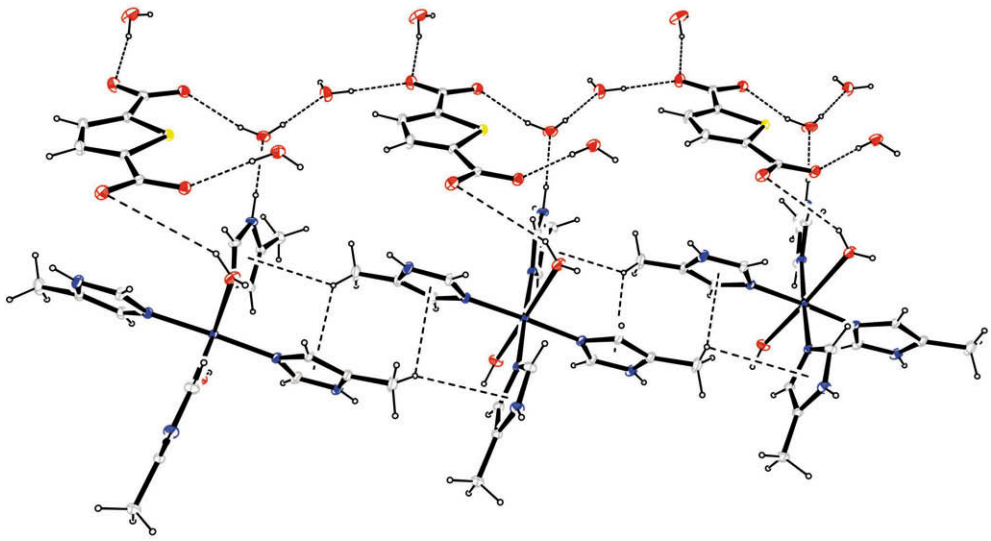


Fig. 6. The C–H···π and π···π interactions of **3**.

4. Conclusion

In summary, we have synthesized and structurally characterized three 3D Cu(II) complexes which are derived from 2,5-thiophenedicarboxylate with dissimilar ligands. One of the complexes has a 1-D zigzag polymeric structure and tdc behaves as a bidentate ligand. In the other complexes, the tdc dianion acts as a counter ion. In all these complexes the Cu(II) atom has a distorted octahedral coordination geometry. Three-dimensional frameworks are constructed though hydrogen bonding and/or C–H···π interactions in all the synthesized complexes.

Supplementary data

CCDC 716509, 716508 and 716507 contain the supplementary crystallographic data for **1**, **2** and **3**. These data can be obtained free of charge via http://www.ccdc.cam.ac.uk/conts/retrieving.html, or from the Cambridge Crystallographic Data Centre, 12 Union Road, Cambridge CB2 1EZ, UK; fax: (+44) 1223 336 033; or e-mail: deposit@ccdc.cam.ac.uk

Acknowledgement

This work was supported by the Eskişehir Osmangazi University by Project No. 200819042.

References

[1] O.M. Yaghi, H. Li, T.L. Groy, J. Am. Chem. Soc. 118 (1996) 9096.
[2] R.H. Groeneman, L.R. MacGillivray, J.L. Atwood, Chem. Commun. (1998) 2735.
[3] S.S.-Y. Chui, S.M.-F. Lo, J.P.H. Charmant, A.G. Orpen, L.D. Williams, Science 283 (1999) 1148.
[4] K.X. Xu, Handbook of Fine Organic Chemical Engineering Raw Material and Intermediate, Chemical Industry, Beijing, 1986.
[5] J.C. MacDonald, P.C. Dorrestein, M.M. Pilley, M.M. Foote, J.L. Lundburg, R.W. Henning, A.J. Schultz, J.L. Manson, J. Am. Chem. Soc. 122 (2000) 11692.
[6] M. Devereux, M.M. Cann, V. Leon, V.M. Kee, R.J. Ball, Polyhedron 21 (2002) 1063.
[7] R. Burriel, C.J. O'Conner, R.L. Carlin, Inorg. Chem. 24 (1985) 3706.
[8] S. Konar, S.C. Manna, E. Zangrando, N.R. Chaudhuri, Inorg. Chim. Acta 357 (2004) 1593.
[9] X.H. Li, Q. Shi, M.L. Hu, H.P. Xiao, Inorg. Chem. Commun. 7 (2004) 912.
[10] C.J. O'Connor, E. Sinn, Inorg. Chem. 20 (1981) 545.
[11] M. Wenkin, M. Devillers, B. Tinant, J.P. Declercq, Inorg. Chim. Acta 258 (1997) 113.
[12] R. Prajapati, L. Mishra, K. Kimura, P. Raghavaiah, Polyhedron 28 (2009) 600.
[13] S. Kitagawa, R. Kitaura, S. Noro, Angew. Chem., Int. Ed. 43 (2004) 2334.
[14] B.L. Chen, K.F. Mok, S.C. Ng, Y.L. Feng, S.X. Liu, Polyhedron 17 (1998) 4237.
[15] B.L. Chen, K.F. Mok, S.C. Ng, M.G.B. Drew, Polyhedron 18 (1999) 1211.
[16] H.P. Xiao, Acta Crystallogr., Sect. E 61 (2005) m2592.
[17] X.Z. Sun, Y.F. Sun, B.H. Ye, X.M. Chen, Inorg. Chem. Commun. 6 (2003) 1412.
[18] Z.P. Deng, S. Gao, L.H. Huo, H. Zhao, Acta Crystallogr. Sect. E 62 (2006) m87.
[19] X.Z. Sun, Z.L. Huang, H.Z. Wang, B.H. Ye, X.M. Chen, Z. Anorg. Allg. Chem. 631 (2005) 919.
[20] Z. Chen, Y. Zuo, X.H. Li, H. Wang, B. Zhao, W. Shi, P. Cheng, J. Mol. Struct. 888 (2008) 360.
[21] J.G. Wang, C.C. Huang, X.H. Huang, D.S. Liu, Cryst. Growth Des. 8 (2008) 795.
[22] G.M. Sheldrick, SHELXS-97 and SHELXL-97. Program for Refinement of Crystal Structures, University of Göttingen, Germany, 1997.
[23] Cie Stoe, X-AREA (Version 1.18) and X-RED32 (Version 1.04), Stoe&Cie, Darmstadt, Germany, 2002. 2001.
[24] L.J. Farrugia, J. Appl. Crystallogr. 30 (1997) 565.
[25] L.J. Farrugia, J. Appl. Crystallogr. 32 (1999) 837.
[26] K. Nakamoto, Infrared and Raman Spectra of Inorganic and Coordination Compounds, fifth ed., Wiley Interscience, New York, 1997. p. 59.
[27] M.E. Quiroz-Castro, G.A. van Albada, I. Mutikainen, U. Turpeinen, J. Reedijk, Inorg. Chim. Acta 297 (2000) 129.
[28] V.T. Yılmaz, S. Caglar, W.T.A. Harrison, J. Coord. Chem. 58 (2005) 549.
[29] L.A. Kovbasyuk, I.O. Fritsky, V.N. Kokozay, T.S. Iskenderov, Polyhedron 16 (1997) 1723.
[30] P.J. Baesjou, W.L. Driessen, J. Reedijk, A.L. Spek, Inorg. Chim. Acta 306 (2000) 237.
[31] S.M. Wu, M. Li, J.F. Xiang, L.J. Yuan, J.T. Sun, Acta Crystallogr. Sect. E62 (2006) o2951.
[32] C. Nather, M. Wriedt, I. Jeβ, Acta Crystallogr. Sect. E58 (2002) m63.
[33] C.Y. Wu, C.C. Su, Polyhedron 16 (1997) 2465.
[34] S.G. Baca, S.T. Malinovskii, P. Franz, C. Ambrus, H.S. Evans, N. Gerbeleu, S. Decurtins, J. Solid State Chem. 177 (2004) 2841.

Given this, it is perhaps unfortunate that many reports of 3d/4f systems only describe a small number of aggregates, rather than presenting a systematic study of a range of what might be termed "lanthanologues".

The present work describes the synthesis, structures, magnetochemistry and ^{57}Fe Mössbauer spectroscopy of a series of isostructural tetranuclear complexes $[Fe_3Ln(\mu_3\text{-}O)_2(CCl_3COO)_8(H_2O)(THF)_3]\cdot THF$ (Ln = Ce^{III} (**1**), Pr^{III} (**2**), Nd^{III} (**3**)) and $[Fe_3Ln(\mu_3\text{-}O)_2(CCl_3COO)_8(H_2O)(THF)_3]\cdot THF\cdot C_7H_{16}$ (Ln = Sm^{III} (**4**), Eu^{III} (**5**), Gd^{III} (**6**), Tb^{III} (**7**), Dy^{III} (**8**), Ho^{III} (**9**), Lu^{III} (**10**) and Y^{III} (**11**)). All compounds were prepared by the reaction between $[Fe_2BaO(CCl_3COO)_6(THF)_6]$ [14] and the corresponding Ln^{III} nitrate salt. We have previously reported the crystal structure of the europium compound **5** [12]. Its cell determination in the present paper is given for comparison only.

2. Experimental

2.1. General

All chemicals and solvents used for synthesis were purchased from Aldrich and were of reagent grade and used without further purification. The precursor trichloroacetate $[Fe_2BaO(CCl_3COO)_6(THF)_6]$ was prepared as described elsewhere [14].

2.2. Preparations

2.2.1. $[Fe_3LnO_2(CCl_3COO)_8H_2O(THF)_3]THF$

All compounds were synthesised by the reaction between $[Fe_2BaO(CCl_3COO)_6(THF)_6]$ (1.50 g, 0.90 mmol) and $Ln(NO_3)_3\cdot 6H_2O$ (0.23–0.28 g, 0.60 mmol) in acetone (30 ml) at 50 °C with stirring for 30 min. After filtration, the solution was evaporated and the solid product was dissolved in THF (30 ml) followed by addition of heptane (6 ml). A brown, microcrystalline material precipitated from this solution after 7 days and was isolated by filtration, washed with benzene and air dried. Yield: 54–66%, except 42% for the Y^{III} complex. Compound **1**: Yield 750 mg (63%). Elemental *Anal.* Calc. for $C_{32}H_{34}Cl_{24}CeFe_3O_{23}$: C, 19.76; H, 1.76. Found: C, 19.94; H, 1.92%. IR (KBr, cm^{-1}): 3450 (w), 2958 (w), 1706 (m), 1680 (vs), 1628 (w), 1371 (vs), 1023 (w), 968 (w), 918 (w), 850 (s), 836 (s), 742 (s), 686 (vs), 543 (w), 512 (w), 457 (w). Compounds **1**–**11** give rise to very similar infrared spectra over the range 4000–400 cm^{-1} as Ln–O bond vibrations are not found in this range. The IR spectrum of the Fe_3Ce compound, together with a list of main peaks, is available in the Supporting Information. The luminescence spectra for compounds **3**–**5**, measured both in the solid state and in aqueous solutions, together with analysis of the influence of Fe^{3+} on the luminescence intensities of the lanthanides ions have already been reported [15].

Compound **2**: Yield 690 mg (60%). Elemental *Anal.* Calc. for $C_{32}H_{34}Cl_{24}Fe_3O_{23}Pr$: C, 19.75; H, 1.76. Found: C, 19.65; H, 2.00%. Compound **3**: Yield 695 mg (60%). Elemental *Anal.* Calc. for $C_{32}H_{34}Cl_{24}Fe_3NdO_{23}$: C, 19.75; H, 1.76. Found: C, 19.77; H, 2.01%. Compound **4**: Yield 810 mg (66%). Elemental *Anal.* Calc. for $C_{39}H_{50}Cl_{24}Fe_3O_{23}Sm$: C, 22.78; H, 2.45. Found: C, 22.94; H, 2.35%. Compound **5**: Yield 780 mg (66%). Elemental *Anal.* Calc. for $C_{39}H_{50}Cl_{24}EuFe_3O_{23}$: C, 22.77; H, 2.45. Found: C, 22.91; H, 2.47%. Compound **6**: Yield 720 mg (57%). Elemental *Anal.* Calc. for $C_{39}H_{50}Cl_{24}Fe_3GdO_{23}$: C, 22.71; H, 2.44. Found: C, 22.88; H, 2.48%. Compound **7**: Yield 720 mg (57%). Elemental *Anal.* Calc. for $C_{39}H_{50}Cl_{24}Fe_3O_{23}Tb$: C, 22.69; H, 2.44. Found: C, 22.54; H, 2.66%. Compound **8**: Yield 810 mg (66%). Elemental *Anal.* Calc. for $C_{39}H_{50}Cl_{24}Fe_3DyO_{23}$: C, 22.65; H, 2.44. Found: C, 22.79; H, 2.39%. Compound **9**: Yield 750 mg (60%). Elemental *Anal.* Calc. for $C_{39}H_{50}Cl_{24}Fe_3HoO_{23}$: C, 22.62; H, 2.43. Found: C, 22.78; H, 2.32%. Compound **10**: Yield 690 mg (54%). Elemental *Anal.* Calc. for $C_{39}H_{50}Cl_{24}Fe_3LuO_{23}$: C, 22.52; H, 2.42. Found: C, 22.77; H, 2.62%. Compound **11**: Yield 510 mg (42%). Elemental *Anal.* Calc. for $C_{39}H_{50}Cl_{24}Fe_3O_{23}Y$: C, 23.49; H, 2.52. Found: C, 23.14; H, 2.22%.

2.3. Physical measurements

The FTIR spectra were measured using KBr discs on a Perkin–Elmer Spectrum One Spectrometer. Elemental analyses for C and H were carried out at the Institute for Inorganic Chemistry at the University of Karlsruhe. The ^{57}Fe Mössbauer spectra were acquired using a conventional spectrometer in the constant-acceleration mode equipped with a ^{57}Co source (3.7 GBq) in a rhodium matrix. Isomer shifts are given relative to α-Fe at room temperature. The sample was cooled inside an Oxford Instruments Mössbauer-Spectromag 4000 Cryostat, in which the sample temperature can be varied between 3.0 and 300 K. The spectra were fitted using the NORMOS Mössbauer Fitting Program. The magnetic susceptibility measurements were carried out on polycrystalline samples using a Quantum Design SQUID magnetometer MPMS-XL, with the ac option using an exciting field of 4 Oe, or in the magnetization measurement mode with an applied field of 1000 Oe. They coincided in all instances. The T = 1.8 K magnetization measurements were performed up to a field of 9 T using a Quantum Design PPMS magnetometer. Data were corrected for the sample holder and the diamagnetic contribution estimated from Pascal's constants.

2.4. Crystal structure determination

Crystals suitable for crystallography were grown from THF:heptane (5:1) mixture. Data were measured on a Bruker SMART Apex CCD diffractometer using graphite-monochromated Mo $K\alpha$ radiation and corrected for absorption using SADABS [16]. Structure solution by direct methods and full-matrix least-squares refinement against F^2 (all data) was carried out using SHELXTL [17]. All ordered non-H atoms were refined anisotropically. Trichloroacetate and THF ligands are often found to show disorder, and the structures here were no exception. A combination of geometrical (SAME and SADI in SHELXTL) and similarity (DELU, SIMU) restraints were often necessary for successful refinement, particularly when threefold disorder of trichloroacetates was involved. Crystallographic data and details of structure refinements are summarized in Table 1 for complexes **1**–**4**, **8** and **9**. The geometries of the $\{Fe_3Ln(\mu_3\text{-}O)_2\}$ cores are summarized in Table S2. The unit cells of **6**, **7**, **10** and **11** (for which the ligand disorder precluded satisfactory refinement) are compared with those of **8** and **9** in Table 2.

3. Results and discussion

3.1. Synthesis

All eleven tetranuclear trichloroacetates have been obtained by the reaction of the iron–barium μ_3-oxotrinuclear compound $[Fe_2BaO(CCl_3COO)_6(THF)_6]$ [14] with the corresponding Ln^{III} nitrates in acetone. After removal of barium nitrate and evaporation of acetone, crystals were obtained in a reproducible manner from a THF:heptane (5:1) mixture in good yield (54–66%, except for the Y^{III} complex, which was obtained in 42% yield). The complexes are brown crystalline substances insoluble in water but readily soluble in a variety of polar organic solvents, and can be recrystallized from THF–heptane mixture without change of composition. They are stable to storage in air under ambient conditions. We used $[Fe_2BaO(CCl_3COO)_6(THF)_6]$ and lanthanide nitrates because Ba^{II} has an ionic radius only a little larger than those of the lanthanides, and $Ba(NO_3)_2$ has a low solubility in the usual organic solvents, so that

Table 1
Crystallographic data and structure refinement for complexes **1–4, 8** and **9**.

	1	**2**	**3**	**4**	**8**	**9**
Formula	$C_{32}H_{34}Cl_{24}CeFe_3O_{23}$	$C_{32}H_{34}Cl_{24}Fe_3O_{23}Pr$	$C_{32}H_{34}Cl_{24}Fe_3NdO_{23}$	$C_{39}H_{50}Cl_{24}Fe_3O_{23}Sm$	$C_{39}H_{50}Cl_{24}DyFe_3O_{23}$	$C_{39}H_{50}Cl_{24}Fe_3HoO_{23}$
Mr [g mol^{-1}]	1945.06	1945.85	1949.18	2055.49	2067.64	2070.07
Crystal size [mm]	0.26 × 0.18 × 0.16	0.44 × 0.41 × 0.34	0.39 × 0.35 × 0.31	0.28 × 0.19 × 0.11	0.39 × 0.32 × 0.27	0.26 × 0.21 × 0.08
Crystal system	orthorhombic	orthorhombic	orthorhombic	triclinic	monoclinic	monoclinic
Space group	$P2_12_12_1$	$P2_12_12_1$	$P2_12_12_1$	$P1$	$P2_1$	$P2_1$
T [K]	200	100	120	100	100	200
a [Å]	14.4625(4)	14.2095(7)	14.1657(6)	13.3844(5)	12.9734(4)	13.1150(8)
b [Å]	18.8843(5)	18.5873(8)	18.6058(8)	14.4633(5)	14.2658(5)	14.5574(9)
c [Å]	25.7590(7)	25.634(1)	25.657(1)	22.2930(8)	19.8576(7)	19.9921(13)
α [°]	90	90	90	99.686(1)	90	90
β [°]	90	90	90	100.155(1)	93.896(1)	93.990(1)
γ [°]	90	90	90	115.265(1)	90	90
V [Å^3]	7035.1(3)	6770.5(5)	6762.4(5)	3695.1(2)	3666.7(2)	3807.6(4)
Z	4	4	4	2	2	2
F(0 0 0)	3816	3820	3824	2032	2040	2042
D_{calc} [Mg m^{-3}]	1.836	1.909	1.915	1.847	1.873	1.806
μ (Mo $K\alpha$) (mm^{-1})	2.216	2.350	2.400	2.293	2.529	2.493
Reflections collected	28 533	28 926	26 943	18 455	25 700	19 275
Unique reflections	14 825	14 134	14 656	15 440	15 914	14 903
R_{int}	0.0647	0.0287	0.0487	0.0180	0.0174	0.0306
Reflections with $I > 2\sigma(I)$	11 894	12 237	13 319	14 615	13 493	11 278
Parameters/restraints	805/5	808/27	772/2	1643/55	1081/326	928/20
R_1 [$I>2\sigma(I)$]	0.0667	0.0363	0.0611	0.0385	0.0468	0.0507
wR_2 (all data)	0.1687	0.0715	0.1496	0.0991	0.1248	0.1250
S (all data)	0.991	1.004	1.047	1.037	1.016	0.995
Largest residuals [e Å^{-3}]	+1.73/−2.86	+0.95/−0.60	+3.02/−3.26	+1.66/−0.88	+1.44/−1.17	+1.50/−0.81

Table 2
Unit cell parameters (space group $P2_1$, $Z = 2$) for **5–11**.

	a [Å]	b [Å]	c [Å]	β [°]	V [Å^3]	T [K]
5 (Ln = Eu)	12.9971(10)	14.3607(12)	19.9431(16)	93.849(2)	3713.9(5)	100
6 (Ln = Gd)	13.0627(10)	14.5251(11)	19.8763(15)	93.718(1)	3763.3(5)	200
7 (Ln = Tb)	12.986(3)	14.452(3)	20.040(4)	93.76(3)	3752.9(14)	293
8 (Ln = Dy)	12.9734(4)	14.2658(5)	19.8576(7)	93.896(1)	3666.7(2)	100
9 (Ln = Ho)	13.1150(8)	14.5574(9)	19.9921(13)	93.990(1)	3807.6(4)	200
10 (Ln = Lu)	12.9535(7)	14.2947(7)	19.7716(10)	93.773(1)	3653.1(3)	100
11 (Ln = Y)	13.0515(10)	14.5745(11)	20.0068(16)	93.882(1)	3796.9(5)	200

exchange of barium by lanthanides should be favorable. Several solvents were investigated, but the heterometallic clusters were obtained only using acetone as solvent. Although $BaSO_4$ is also insoluble in organic solvents, reactions of lanthanide sulfates in presence of small quantity of water (due to the insolubility of $Ln_2(SO_4)_3$ in acetone) only gave rise to a homometallic tetranuclear Fe_4 compound. Probably, the presence of water redirects the reaction to homometallic product. The original intention was to use $[Fe_2BaO(CCl_3COO)_6(THF)_6]$ to obtain isostructural compounds with a $\{Fe_2LnO\}$ core. However, it appears that during the synthesis a rearrangement of the presumed initial $\{Fe_2LnO\}$ cluster takes place, leading to the isolated tetranuclear $\{Fe_3LnO_2\}$ products. Attempts to obtain the same products using either simple iron salts or trinuclear clusters such as $[Fe_3O(CCl_3COO)_6(L)_3]^+A^-$ as starting material were unsuccessful.

3.2. Structural analysis

The complexes are generally isostructural, and only small changes in Ln–O bond lengths, resulting from the lanthanide contraction, are observed. The structure of the Pr^{III} analogue **2** will be described as an example; the bond lengths and angles for the six complexes which were fully crystallographically characterized are compared in Table S2.

The $[Fe_3Pr(\mu_3\text{-}O)_2(CCl_3COO)_8(H_2O)(THF)_3]$ molecule in **2** (Fig. 1) is of the well-known tetranuclear "butterfly" type, with two $Fe_2Pr(\mu_3\text{-}O)$ triangles sharing the Pr(1)···Fe(2) edge. The two triangles are close to coplanar, with the two (μ_3-O) ligands O(1) and O(2) lying respectively 0.132(3) and 0.011(3) Å out of the plane of their respective Fe_2Pr triangles. The $Fe_2Pr(\mu_3\text{-}O)$ triangles are markedly non-equilateral. The two Fe(2)–O–Ln(1) angles are in the range 99–101°, while the remaining angles are much larger, 124–134°. Three of the four outer M···M edges are bridged by two trichloroacetate ligands; Fe(2)···Fe(3) is bridged by just one trichloroacetate, as is Pr(1)···Fe(2). All trichloroacetate ligands have the same *syn, syn*-μ:η^1:η^1-bridging mode which is common in lanthanide [18] and iron [14] trichloroacetates; the latter bridge has the effect of making the two triangles non-coplanar, the dihedral angle between the two Fe_2Pr triangles is 147.32(2)°. Three THF ligands coordinate to Fe(1), Fe(3) and Pr(1), and the coordination sphere of Fe(3) is completed by an aqua ligand. This latter, O(22), forms two hydrogen bonds, one intramolecular to the carboxylate oxygen O(16), and one to the lattice THF molecule, O(31).

All three Fe centers have distorted octahedral coordination geometries. That of Fe(2) consists of the two (μ_3-O) ligands mutually *cis*, and four chloroacetate oxygens. Those of Fe(1) and Fe(3) consist of a (μ_3-O) ligand and a THF oxygen *trans* to each other, and either four chloroacetate oxygens Fe(1) or three chloroacetate oxygens and an aqua oxygen Fe(3) forming an equatorial plane. Thus the coordination environment of Fe(2) is significantly different from the other two. The environment of Pr(1) is eight-coordinate, with a rather irregular coordination polyhedron that may best be described as a distorted bicapped trigonal prism. The Ce^{III} used in the synthesis of **1** could oxidize to Ce^{IV} during the reaction,

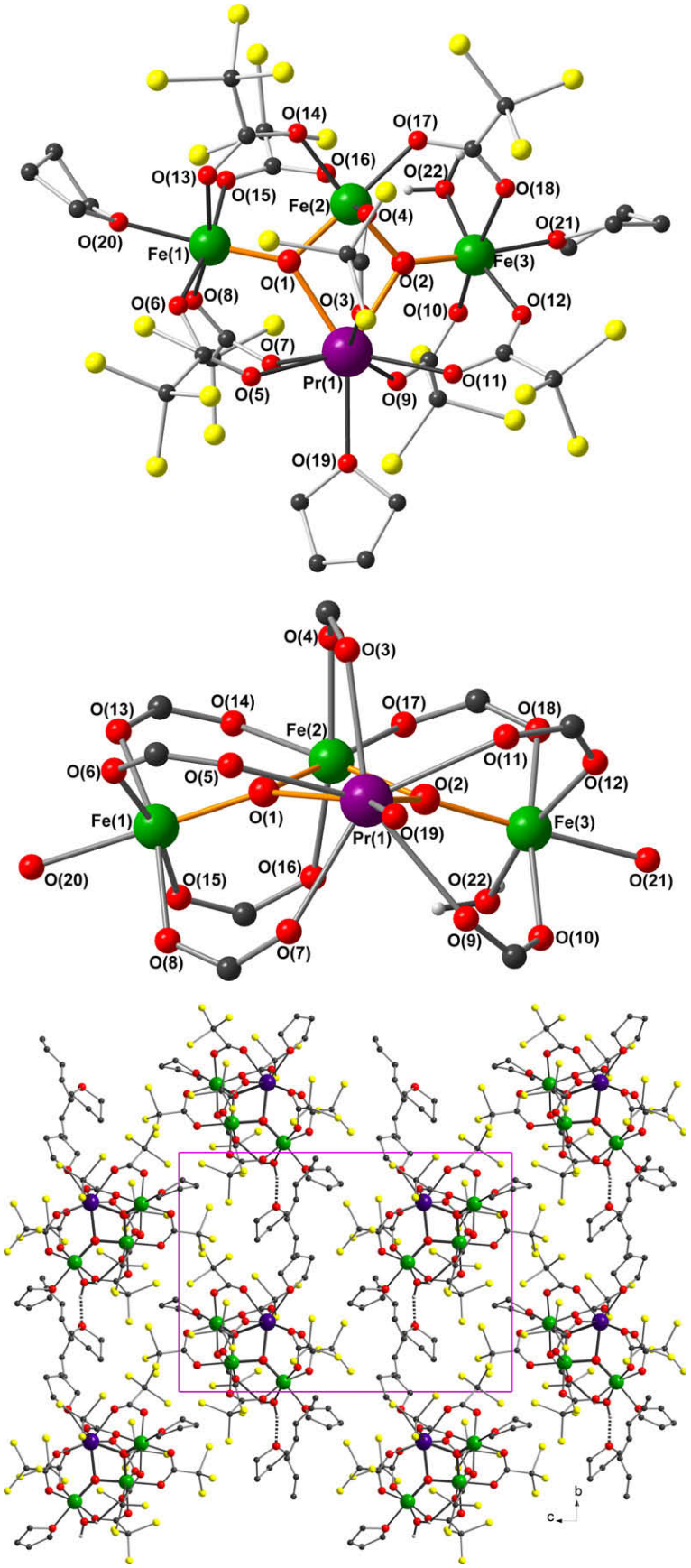


Fig. 1. Molecular structure of complex **2** (organic H-atoms and minor disorder components omitted for clarity) (top); core of complex **2** showing just bridging groups and coordinated oxygens of terminal ligands (middle); packing diagram for 8 viewed along the *a*-axis, with H-bonds to lattice THF molecules shown dotted (bottom).

and there is also the possibility of intramolecular electron transfer from Ce^{III} onto one of the Fe^{III} centers, although the latter possibility is less likely since the Fe–O bond lengths in **1** are in line with the other compounds in the series. The oxidation state of Ce(1) in **1** was checked by Bond Valence Sum Analysis [19], and the calculated value was 2.81.

Although the tetranuclear complex molecules in **1**–**11** are essentially isostructural, they crystallize in three different structural types, which appear to depend on the ionic radius of the lanthanide. Complexes **1**–**3** crystallise in the orthorhombic space group $P2_12_12_1$ with $Z = 4$. The asymmetric unit contains one tetranuclear complex and one lattice THF molecule. The Fe_3Sm complex **4** crystallizes, unusually for a molecular metallo–organic complex, in the acentric triclinic space group $P1$. The metal centers correspond closely to the more usual $P\bar{1}$, but refinement in this space group resulted in severe and mostly unresolvable disorder of the ligands and unacceptably high R-factors ($R_1 = 0.1343$). Refinement in $P1$, on the other hand, gave mostly ordered ligands and $R_1 = 0.0385$, and it is considered that intermolecular ligand–ligand interactions are such as to result in ordering of the trichloroacetate groups to give the acentric structure. In contrast to the orthorhombic structure type of **1**–**3**, complex **4** crystallizes with one molecule of THF and one of n-heptane in the crystal lattice. Compounds **5**–**11** crystallize isomorphously in the monoclinic space group $P2_1$ with $Z = 2$; as for the structure of **4**, the asymmetric unit also contains one THF and one heptane molecule. The structures of **8** and **9**, although showing some ligand disorder, could be refined without particular problems, but for **6**, **10** and **11** the disorder was such that even with application of extensive restraints the structures could not be refined satisfactorily. The unit cells of the six compounds are compared in Table 2. It may be that within the series **5**–**11**, the molecules of **8** and **9** are an ideal size for this crystal packing, whereas those at either end of the series, for which the lanthanide ionic radius is either larger or smaller, the slight differences in molecular size are sufficient for the packing to be less efficient, leading to the extensive ligand disorder. In none of the structures reported here were there any unusually short intermolecular contacts, apart from the hydrogen bond from the aqua ligand to the lattice THF molecule already mentioned.

3.3. Magnetic properties

The magnetic behavior of all the compounds was investigated in the temperature range 1.8–300 K and the obtained data are presented as χT vs T plots shown in Fig. 2. The Fe_3Lu (**10**) and Fe_3Y (**11**) compounds, with their diamagnetic Lu(III) and Y(III) metal ions, show similar behavior to compounds **1**–**5**, with χT in the range of 4–5.5 $cm^3\ K\ mol^{-1}$ at 300 K, and showing only a very slow decrease as the temperature is reduced, with a final sharper decrease at very low temperatures. By contrast, compounds **6**–**9** show much higher values of χT at 300 K, with a slow decrease as T decreases, followed by a faster decrease below *ca.* 50 K. This effect is related to the antiferromagnetic coupling between the Fe_3 trinuclear unit and the magnetic Ln^{III} cations. As seen in Table 3, the χT products at room temperature for the Y and Lu compounds are very close to those expected for an asymmetric Fe_3 unit with strong antiferromagnetic coupling ($J/k_B \approx -50$ K) between each of the outer, or "wingtip" Fe(1) and Fe(3) and the central Fe(2), and negligible coupling between Fe(1) and Fe(3). This result suggests that the Fe_3 unit has a robust $S = 5/2$ ground state, with two spins parallel (Fe(1) and Fe(3)) and one antiparallel (Fe(2)). In Fig. 4, left panel, the χT data at 300 K (taken from Table 3) are shown as squares, together with calculated values (the sum of the Fe_3 contribution and the Ln contribution, calculated as $\chi_{Ln}T = \mu^2_{eff,Ln}/8$, where $\mu_{eff,Ln}$ is taken from external Tables [20]) shown as the solid line; the value for the Fe_3Lu is shown with a dotted line as a reference point. The calculated values are followed reasonably well by the experimental results, indicating that the Ln metals are weakly coupled to the Fe_3 core.

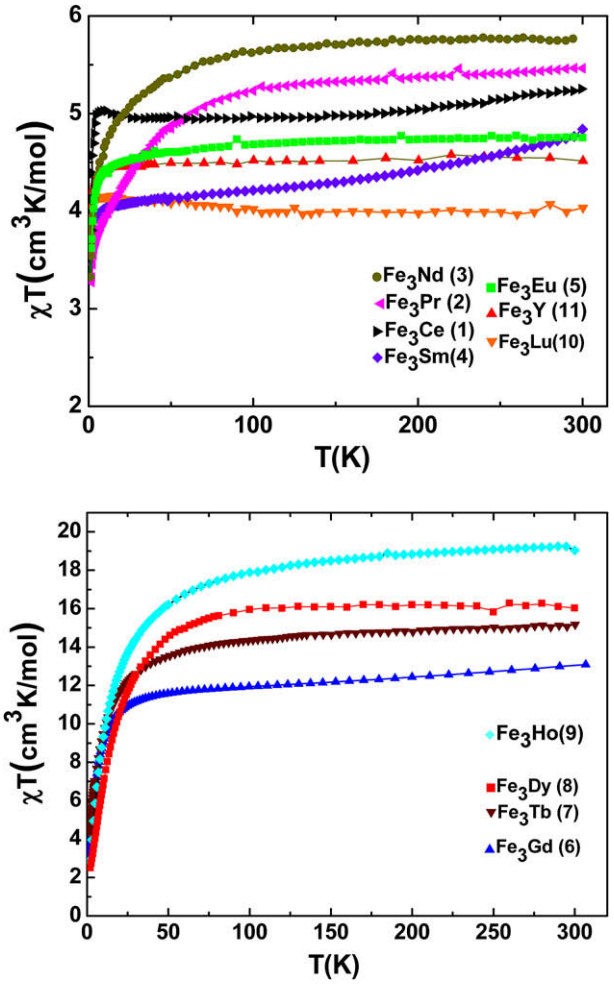


Fig. 2. Temperature-dependence of the χT product (χ being the magnetic susceptibility defined as M/H) for **1–5, 10, 11** (top) and **6–9** (bottom). Lines are guides to the eyes.

Table 3
Magnetic parameters extracted from the data.

Compounds	Curie constant expected for Ln in cm^3 K/mol [21]	Curie constant expected for [Fe_3Ln] in cm^3 K/mol	χT measured at 300 K in cm^3 K/mol	Experimental Curie constant in cm^3 K/mol	θ (K)
Fe_3Ce (**1**)	0.8	13.925	5.30(5)	5.00(5)	−0.29(1)
Fe_3Pr (**2**)	1.6	14.725	5.27(5)	5.57(6)	−7.0(1)
Fe_3Nd (**3**)	1.64	14.765	5.76(6)	5.82(6)	−2.74(3)
Fe_3Sm (**4**)	0.09	13.215	4.57(5)	4.28(4)	−1.07(1)
Fe_3Eu (**5**)	0	13.125	4.78(5)	4.77(5)	−1.23(1)
Fe_3Gd (**6**)	7.875	21.0	13.1(1)	12.2(1)	−3.74(4)
Fe_3Tb (**7**)	11.815	24.94	15.2(2)	15.5(1)	−7.44(7)
Fe_3Dy (**8**)	14.17	27.295	16.0(2)	16.2(1)	−0.59(1)
Fe_3Ho (**9**)	14.075	27.2	19.2(1)	19.9(2)	−11.5(2)
Fe_3Lu (**10**)	0	13.125	4.00(4)	4.03(4)	−0.15(1)
Fe_3Y (**11**)	0	13.125	4.51(4)	4.54(4)	−0.27(1)

The experimental data fit well to the Curie–Weiss law $\chi = C/(T - \theta)$, where $C = C_{Fe_3} + C_{Ln}$. The fit parameters C and θ for the [Fe_3Ln] samples are given in Table 3. C_{Fe_3} are taken as those of the Ln = Y and Lu entries in column 5. The Weiss constant θ pro-

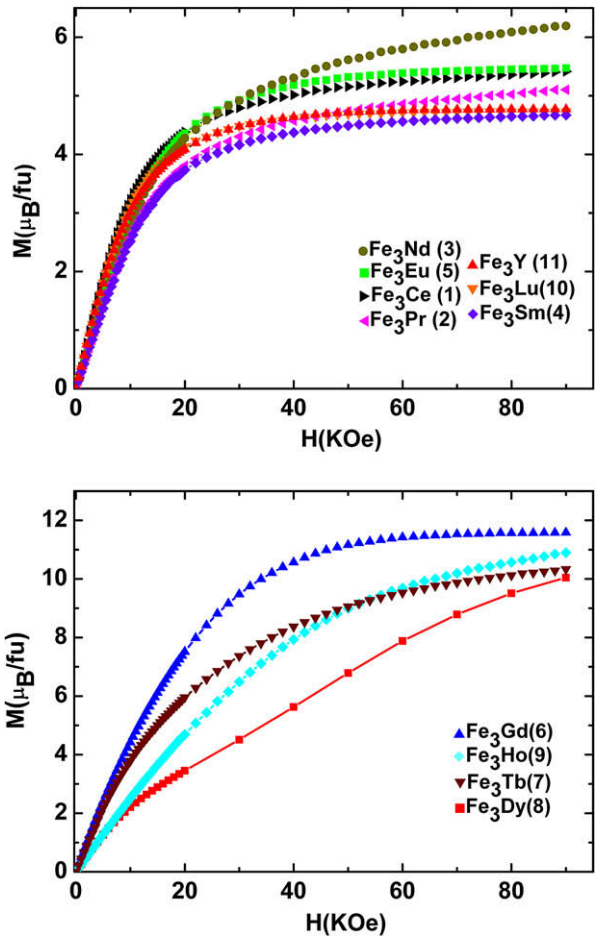


Fig. 3. Field dependence of the magnetization for compounds **1**–**5, 10, 11** (top) and **6**–**9** (bottom) at 1.8 K. Lines are guides to the eyes.

vides a measure of the intercomplex interactions, probably of dipolar character. They are weak as may be expected for well separated complexes.

The field dependences of the magnetization measured at 1.8 K for the complexes are shown in Fig. 3. As may be expected, the complexes containing diamagnetic (Lu^{III} **10**, Y^{III} **11**) or isotropic (Gd^{III} **6**) lanthanides show clear saturation above *ca.* 60 kOe. The saturation values for **10** and **11** are *ca.* 4.7 μ_B, in good agreement with the expected value for three strongly antiferromagnetically-coupled Fe^{III} centers with an overall $S = 5/2$ ground state. The magnetization for **6** saturates at *ca.* 11.8 μ_B at 90 kOe, close to the sum of the values for $S = 7/2$ Gd^{III} and an $S = 5/2$ Fe_3 unit. Moreover, fitting of the curve using Brillouin functions has shown that the Gd–Fe_3 interactions were negligible at 1.8 K [22].

In Fig. 4, right panel, the measured M values at $H = 90$ kOe (squares) are compared to the expected values (the sum of the Ln^{III} free ion value and the $S = 5/2$ Fe_3 contribution, shown as the solid line). Except for **6** with Ln = Gd^{III}, the experimental values are lower than the respective calculated values due to the effects of Ln^{III} crystal field splitting, spin–orbit coupling or exchange with the Fe_3 entity. For the complexes containing anisotropic lanthanide cations, there is a clear distinction between the lighter and heavier lanthanides. Compounds **1**–**5** ($4f^1$–$4f^6$) show either near or complete saturation behavior. By contrast, compounds **7**–**9** ($4f^8$–$4f^{10}$) show no saturation of their magnetization as expected in the presence of low lying excited states and/or magnetic anisotropy. The Fe_3Eu compound **5** has a magnetization of 6.2 μ_B at 9 kOe without complete saturation. Since Eu^{III} should have an $S = 0$ ground state, this higher value compared to those for the Fe_3Lu and Fe_3Y complexes (both *ca* 4.7 μ_B) must result from the incompletely quenched orbital moment of the Eu^{III} ground state.

In order to assess whether these molecules exhibit a slow relaxation of their magnetisation, ac magnetic susceptibility measurements were performed. The measurements were carried out over the 1.8–30 K range under 3.5 G ac field oscillating in 1–1420 Hz range. As an example, complex **7** showed a weak signal with a low ratio χ''/χ' frequency-dependent out-of-phase signal (Fig. 5), which could be the tail of a maximum lying at a temperature below 1.8 K. The fact that the out-of-phase component of the ac susceptibility signal is rather small, is not unprecedented as many molecules exhibiting claimed SMM behavior have a similarly weak χ''/χ' ratio [23]. The analysis of the magnetic properties of the compounds **1**–**11** with fitting of the data (magnetization and χT for Fe_3Y, Fe_3Lu and Fe_3Gd) will be presented in more detail elsewhere [22].

3.4. Mössbauer spectra

The Mössbauer spectra of complexes **1**–**4** were investigated by ^{57}Fe Mössbauer spectroscopy at 300 and 15 K. As already discussed, all complexes have a butterfly structure in which the three Fe^{III} centers all have FeO_6 coordination environments. However, these environments are made up of different combinations of types of oxygens, either oxo ligands or oxygens from carboxylate, aquo or

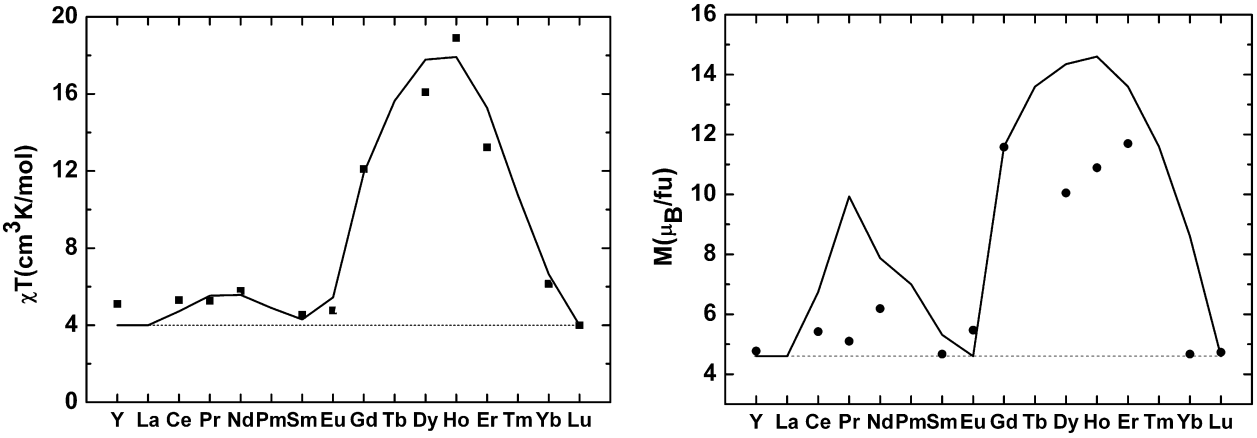


Fig. 4. (Left) Comparison between the experimental χT values at $T = 300$ K (■) and the calculated values (—). Sample (**10**) is given as a reference (- - -). (Right) Comparison between the magnetization experimental values (at $H = 90$ kOe) at 1.8 K (•) and the calculated free ion saturation values (—). Sample (**10**) is given as a reference (- - -).

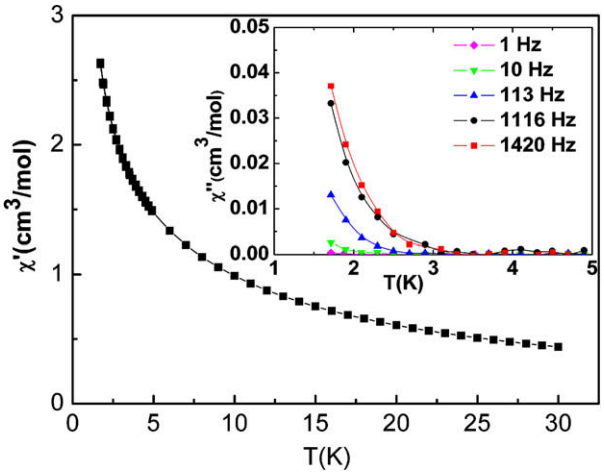


Fig. 5. Plots of the in-phase (χ') and the out-of-phase (χ'') ac susceptibility data for **7** under a zero static magnetic field and with different oscillating frequencies.

Table 4
Mössbauer spectroscopic parameters[a] of complexes **1–4.**

Complex	T [K]	Pattern	δ_{Fe}, [mm/s]	ΔE_q, [mm/s]	Γ [mm/s]	Area [%]
1	295	doublet 1	0.34	1.24	0.34	66.7
		doublet 2	0.26	1.05	0.35	33.3
	15	doublet 1	0.48	1.71	0.67	66.7
		doublet 2	0.49	0.88	0.53	33.3
2	295	doublet 1	0.36	1.25	0.38	66.7
		doublet 2	0.25	1.04	0.36	33.3
	15	doublet 1	0.48	1.60	1.19	66.7
		doublet 2	0.51	1.13	0.91	33.3
3	295	doublet 1	0.36	1.26	0.39	66.7
		doublet 2	0.21	0.97	0.40	33.3
	15	doublet 1	0.48	1.60	0.51	66.7
		doublet 2	0.47	1.05	0.41	33.3
4	295	doublet 1	0.35	1.23	0.39	66.7
		doublet 2	0.21	0.96	0.40	33.3
	15	doublet 1	0.49	1.53	0.57	66.7
		doublet 2	0.49	0.95	0.49	33.3

[a] The average errors for all listed parameters = ±0.02 mm/s. The relative areas were constrained to the values given.

THF ligands, as follows: Fe(1): $(\mu_3\text{-O})(O_{carb})_4(O_{THF})$; Fe(2): $(\mu_3\text{-O})_2(O_{carb})_4$, Fe(3): $(\mu_3\text{-O})(O_{carb})_3(O_{aq})(O_{THF})$. The ^{57}Fe Mössbauer spectra of the complexes **1**–**4** (Fig. 6), both at room temperature and 15 K, each consist of two asymmetrical and rather broad peaks, which were fitted with two doublets, with relative areas in a 2:1 ratio, in each case. The Mössbauer parameters (Table 4) of the two doublets, with isomer shift (δ_{Fe}) and quadrupole splitting (ΔE_q) ranging between 0.22 and 0.52 mm s^{-1} and between 0.94 and 1.72 mm s^{-1} respectively, indicate that all the Fe^{III} ions are in a high-spin state ($S = 5/2$) and that the electronic structures and related interactions around two of the distinct Fe^{III} centers, probably Fe(1) and Fe(3), are similar although probably not identical.

According to ΔE_q values at 15 K, the symmetry of the electronic environment around the Fe(2) nucleus is higher than around the other two iron nuclei, Fe(1) and Fe(3). An increase in the isomer shift at cryogenic temperatures is the result of the second-order Doppler effect [24]. The nature of lanthanide ion in the complex has little effect on the electronic interaction of the Fe^{III} ions, and

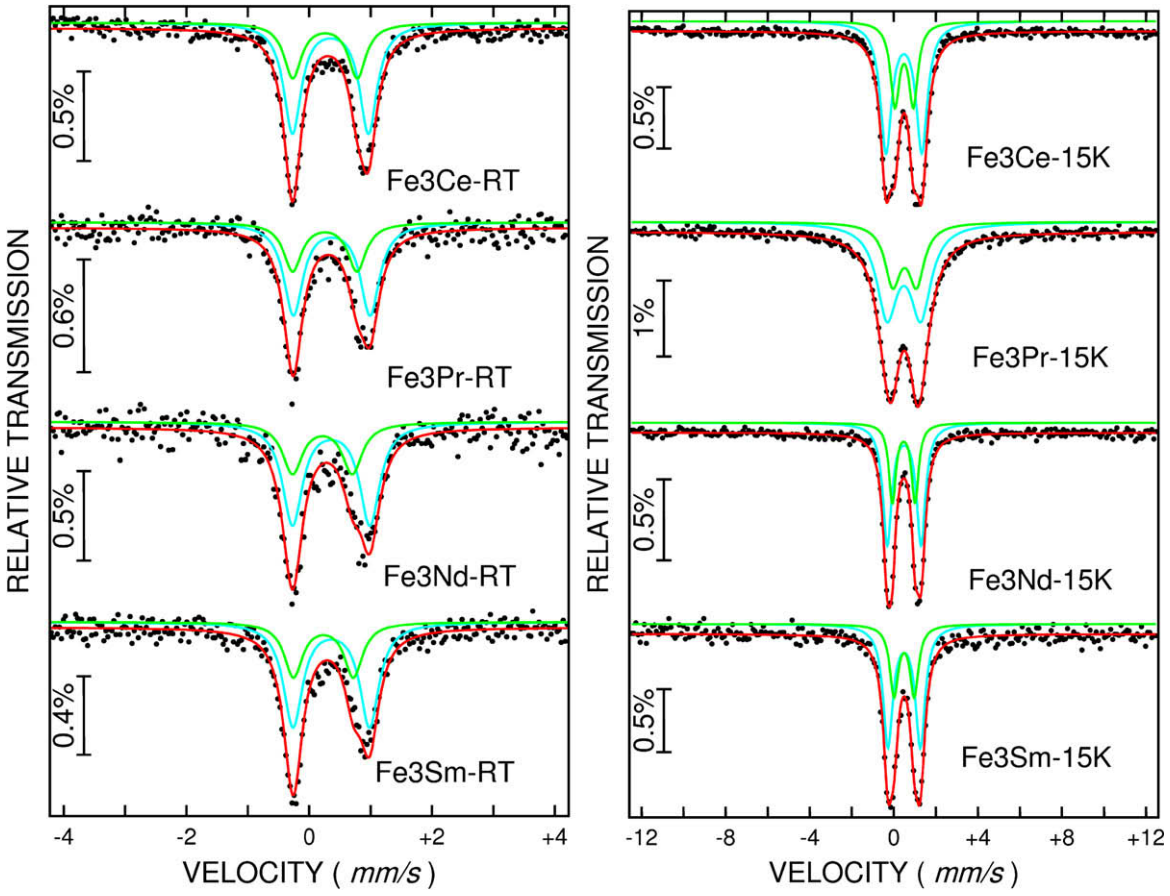


Fig. 6. The ^{57}Fe Mössbauer spectra of complexes **1**–**4** at 295 (left) and 15 K (right); the solid line is the least-squares fit.

Table 5
Parameters of the Mössbauer spectra function of applied field and temperature for **7** (B – field at nucleus; δ_{Fe} – isomer shift; quadrupole splitting ΔE_q or ε – its projection in the presence of field; Γ – line-width; the relative areas were fixed during the fitting).

Field [T]	T [K]	Pattern	B [T]	δ_{Fe}, [mm/s]	ΔE_q or (ε), [mm/s]	Γ [mm/s]	Area [%]
6.5	3	Sextet 1	42.2	0.52	0.25	0.79	33.3
		Sextet 2	39.8	0.53	0.27	0.72	33.3
		Sextet 3	45.6	0.54	−0.06	0.93	33.3
0.0	3	Sextet 1	46.7	0.57	0.49	0.64	33.3
		Sextet 2	45.8	0.54	0.89	0.91	33.3
		Sextet 3	39.9	0.55	−0.28	0.57	33.3
0.0	77	Doublet 1	0	0.50	1.34	0.58	66.7
		Doublet 2	0	0.51	0.98	0.42	33.3
0.0	150	Doublet 1	0	0.49	1.31	0.53	66.7
		Doublet 2	0	0.47	0.92	0.48	33.3
0.0	300	Doublet 1	0	0.43	1.30	0.42	66.7
		Doublet 2	0	0.39	0.88	0.34	33.3

Errors: ±0.02 mm/s and ±0.1 T.

the Mössbauer spectra for compound **1** support the conclusion that the Ce is in the +3 oxidation state, since the values from the spectrum of **1** are in line with those for the other complexes.

The Mössbauer spectra down to 15 K do not show evidence for any magnetic ordering around the iron nuclei for the compounds studied. As discussed above, ac susceptibility measurements showed no evidence for slow relaxation of magnetisation for the complexes involving the lighter lanthanides, but the measurements on complex **7** did indicate such slow relaxation. Therefore, Mössbauer measurements at lower temperatures than 15 K were carried out for compound **7**. The spectra measured at 3 K could be fitted with three sextets (resulting from antiferromagnetically-coupled high-spin Fe^{III}, according to the isomer shift values) with the area ratio 1:1:1. But at this temperature, the electron spins are not completely blocked or frozen on the Mössbauer time scale (*ca.* 10^{-7} s), being still in a rather slow relaxation regime as derived from the line-width values of the sextets (Table 5). In other words, we see evidence of blocking of the magnetization below 3 K for compound **7**.

Under an applied field of 6.5 T, one sextet showed an increased splitting while the other two showed smaller splittings, relative to the 3 K spectrum without applied field, as can be seen from the values in Table 5. The "in field" data suggest that one sub-lattice, in this case that of Fe(2), is antiferromagnetically-coupled to the other two belonging to Fe(1) and Fe(3). The doublets seen in the spectra measured at 77, 150 and 300 K showed a decrease of the quadrupole interactions with increasing temperature. The more pronounced asymmetric shape of the peaks in the Mössbauer spectra at higher temperatures, is the result of a smaller degree of overlap between the doublets, caused by a reduced interaction (see Table 5) for the inner doublet, assigned to Fe(2), derived from a careful evaluation of the data [22] dealing with electronic mechanisms.

The compounds with Ln^{III} ions located in the first half of the lanthanide series showed no spin blocking at very low temperatures, but a much stronger temperature-dependence of the quadrupole interaction was observed, as clearly seen in the spectra shown in Fig. 6. Their quadrupole splittings are larger than that observed (Fig. 7) for compound **7**, with its higher number of 4f electrons.

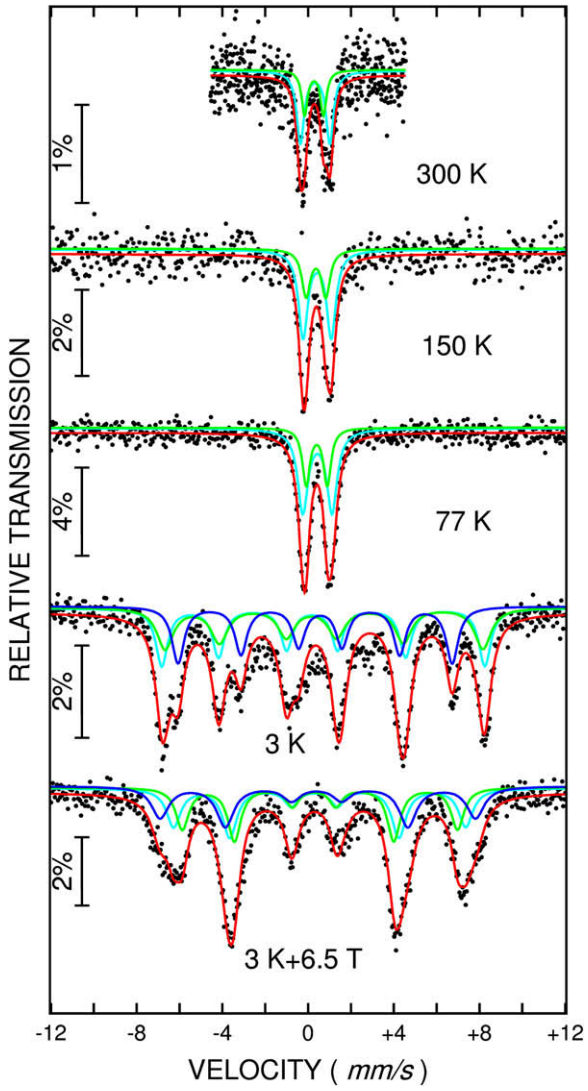


Fig. 7. The ^{57}Fe Mössbauer spectra for **7** at 300, 150, 77 and 3 K in zero-applied magnetic field and at 3 K in applied magnetic field of 6.5 T. See Table 5 for the fitting parameters.

4. Conclusions

A series of new heterotetranuclear trichloroacetate complexes $[Fe^{III}_3Ln^{III}(\mu_3\text{-}O)_2(CCl_3COO)_8(H_2O)(THF)_3]$ (Ln = Ce, Pr, Nd, Sm, Eu, Gd, Tb, Dy, Ho, Lu, Y) has been prepared and structurally characterized. Magnetochemical and Mössbauer studies were interpreted in terms of the tetranuclear structure of the compounds. The complexes exhibit strong intramolecular antiferromagnetic exchange between the Fe^{III} metal ions. The temperature-dependence of the χT products showed two different patterns, with one type of behavior for complexes containing lighter or diamagnetic lanthanides, and another for the complexes containing the heavier lanthanides Gd^{III}–Ho^{III}. The Mössbauer investigation showed that all the Fe^{III} centers are high-spin ($S = 5/2$), and also showed the existence of two different type of Fe sites, with distinct interactions, in the molecule, which were assigned to the two "wingtip" Fe(1) and Fe(3) and to the central Fe(2). At low temperatures, evidence for magnetic blocking, i.e. slow relaxation of the spins, was observed in the Mössbauer spectra for compound **7**, confirming the results of ac magnetic susceptibility measurements.

Acknowledgements

This work was supported by the INTAS No. 05-1000008-7834, bilateral Grant ASM-BMBF (09.820.05.09GF), and partially supported by MAGMANet, contracts 114/ 2006 "CORINT" and 235/ 2007 "IDEI", MEC MAT08/1077, the Conseil Régional d'Aquitaine, the Université of Bordeaux, and the CNRS.

Appendix A. Supplementary data

CCDC 721159, 721160, 721161, 721162, 721163 and 721164 contain the supplementary crystallographic data for complexes **1–4**, **8** and **9**. These data can be obtained free of charge via http://www.ccdc.cam.ac.uk/conts/retrieving.html, or from the Cambridge Crystallographic Data Centre, 12 Union Road, Cambridge CB2 1EZ, UK; fax: (+44) 1223-336-033; or e-mail: deposit@ccdc.cam.ac.uk.

Supplementary data associated with this article can be found, in the online version, at doi:10.1016/j.poly.2009.06.025.

References

[1] (a) D. Gatteschi, R. Sessoli, A. Cornia, Chem. Commun. (2000) 725;
(b) G. Christou, D. Gatteschi, D.N. Hendrickson, R. Sessoli, MRS Bull. 25 (2000) 66.
[2] D. Gatteschi, R. Sessoli, Angew. Chem., Int. Ed. 42 (2003) 268.
[3] W. Wernsdorfer, N. Aliaga-Alcalde, D.N. Hendrickson, G. Christou, Nature 416 (2006) 406.
[4] (a) A. Bencini, C. Benelli, A. Caneschi, R.L. Carlin, A. Dei, D. Gatteschi, J. Am. Chem. Soc. 107 (1985) 8128;
(b) M. Andruh, I. Ramade, E. Codjovi, O. Guillou, O. Kahn, J.C. Trombe, J. Am. Chem. Soc. 115 (1993) 1822;
(c) C. Aronica, G. Pilet, G. Chastanet, W. Wernsdorfer, J.-F. Jacquot, D. Luneau, Angew. Chem., Int. Ed. 45 (2006) 4659.
[5] (a) M.L. Kahn, C. Mathonière, O. Kahn, Inorg. Chem. 38 (1999) 3692;
(b) J.-P. Sutter, M.L. Kahn, O. Kahn, Adv. Mater. 11 (1999) 863;
(c) M.L. Kahn, J.-P. Sutter, S. Golhen, P. Guionneau, L. Ouahab, O. Kahn, D. Chasseau, J. Am. Chem. Soc. 122 (2000) 3413;
(d) M.L. Kahn, P. Lecante, M. Verelst, C. Mathonière, O. Kahn, Chem. Mater. 12 (2000) 3073;
(e) M.L. Kahn, R. Ballou, P. Porcher, O. Kahn, J.-P. Sutter, Chem. Eur. J. 8 (2002) 525.
[6] V. Chandrasekhar, B.M. Pandian, R. Azhakar, J.J. Vittal, R. Clérac, Inorg. Chem. 46 (2007) 5140.
[7] (a) C. Benelli, M. Murrie, S. Parsons, R. Winpenny, J. Chem. Soc., Dalton Trans. (1999) 4125;
(b) C. Zaleski, E. Depperman, J. Kampf, M. Kirk, V. Pecoraro, Angew. Chem., Int. Ed. 43 (2004) 3912;
(c) A. Mishra, W. Wernsdorfer, K. Abboud, G. Christou, J. Am. Chem. Soc. 126 (2004) 15648;
(d) A. Mishra, W. Wernsdorfer, S. Parson, G. Christou, E. Brechin, Chem. Commun. (2005) 2086;
(e) V. Mereacre, A.M. Ako, R. Clérac, W. Wernsdorfer, G. Filoti, J. Bartolomé, C.E. Anson, A.K. Powell, J. Am. Chem. Soc. 129 (2007) 9248;
(f) V. Mereacre, A.M. Ako, R. Clérac, W. Wernsdorfer, I.J. Hewitt, C.E. Anson, A.K. Powell, Chem. Eur. J. 14 (2008) 3577.
[8] (a) E. Brechin, S. Harris, S. Parsons, R. Winpenny, J. Chem. Soc., Dalton Trans. (1997) 1665;
(b) J.-P. Costes, F. Dahan, A. Dupuis, J.-P. Laurent, Inorg. Chem. 36 (1997) 4284;
(c) T. Shiga, N. Ito, A. Hidaka, H. Okawa, S. Kitagawa, M. Ohba, Inorg. Chem. 46 (2007) 3492;
(d) A.M. Madalan, N. Avarvari, M. Fourmiguè, R. Clérac, L.F. Chibotaru, S. Clima, M. Andruh, Inorg. Chem. 47 (2007) 940.
[9] J.-P. Costes, A. Dupuis, J.-P. Laurent, Eur. J. Inorg. Chem. (1998) 1543.
[10] J.-P. Costes, F. Dahan, F. Dumestre, J.M. Clemente-Juan, J. Garcia-Tojal, J.-P. Tuchagues, Dalton Trans. (2003) 464.
[11] A. Figureuerola, C. Diaz, J. Ribas, V. Tangoulis, J. Granell, F. Lloret, J. Mahia, M. Maestro, Inorg. Chem. 42 (2003) 641.
[12] (a) S.G. Shova, C.I. Turta, Yu. Simonov, M. Gdaniec, D.N. Prodius, V.M. Mereacre, Acta Cryst. A60 (2004) 271;
(b) C.I. Turta, D.N. Prodius, V.M. Mereacre, S.G. Shova, M. Gdaniec, Yu.A. Simonov, V. Kuncser, G. Filoti, A. Caneschi, L. Sorace, Inorg. Chem. Commun. 7 (2004) 576.
[13] (a) M. Murugesu, A. Mishra, W. Wernsdorfer, K. Abboud, G. Christou, Polyhedron 26 (2006) 613;
(b) A.M. Ako, V. Mereacre, R. Clérac, I.J. Hewitt, Y. Lan, C.E. Anson, A.K. Powell, Dalton Trans. (2007) 5245.
[14] D.N. Prodius, C.I. Turta, V.M. Mereacre, S.G. Shova, Yu.A. Simonov, J. Lipkowski, A. Caneschi, Polyhedron 25 (2006) 2175.
[15] V.P. Antonovich, S.B. Meshkova, K.I. Turta, D.N. Prodius, V.M. Mereacre, A.V. Kiriyak, Ukrainian J. Chem. 71 (2005) 23. rus.
[16] G.M. Sheldrick, SADABS (the Siemens Area Detector Absorption Correction), University of Göttingen, 1996.
[17] G.M. Sheldrick, SHELXTL 6.12, Bruker AXS Inc., 6300 Enterprise Lane, Madison, WI 53719-1173, USA, 2003.
[18] P.C. Junk, C.J. Kepert, L. Wei-Min, B.W. Skelton, A.H. White, Aust. J. Chem. 52 (1999) 459.
[19] P.L. Roulhac, G.J. Palenik, Inorg. Chem. 42 (2003) 118.
[20] www.radiochemistry.org/periodictable/1a_series/L8.html.
[21] C. Benelli, D. Gatteschi, Chem. Rev. 102 (2002) 2369.
[22] J. Bartolomé, G. Filoti, V. Kuncser, G. Schinteie, V. Mereacre, C.E. Anson, A.K. Powell, R. Clérac, D. Prodius, C. Turta, Phys. Rev. B., in press.
[23] (a) C. Dendrinou-Samara, M. Alexiou, C.M. Zaleski, J.W. Kampf, M.L. Kirk, D.P. Kessissoglou, V.L. Pecoraro, Angew. Chem., Int. Ed. 42 (2003) 3763;
(b) H.J. Choi, J.J. Sokol, J.R. Long, Inorg. Chem. 43 (2004) 1606;
(c) P. King, W. Wernsdorfer, K.A. Abboud, G. Christou, Inorg. Chem. 43 (2004) 7315;
(d) M. Murugesu, J. Raftery, W. Wernsdorfer, G. Christou, E.K. Brechin, Inorg. Chem. 43 (2004) 4203;
(e) E.M. Rumberger, S.J. Shah, C.C. Beedle, L.N. Zakharov, A.L. Rheingold, D.N. Hendrickson, Inorg. Chem. 44 (2005) 2742;
(f) Y. Li, W. Wernsdorfer, R. Clérac, I.J. Hewitt, C.E. Anson, A.K. Powell, Inorg. Chem. 45 (2006) 2376.
[24] (a) R.V. Pound, G.A. Rebka, Phys. Rev. Lett. 4 (1960) 274;
(b) B.D. Josephson, Phys. Rev. Lett. 4 (1960) 341.

Shimadzu-470 spectrometer. UV–Vis spectra were obtained on a Shimadzu 2100 spectrometer using a 1 cm path length cell. The melting point is uncorrected and was obtained by a Kofler Heizbank Rechart type 7841 melting point apparatus. Elemental analysis was performed using a Heraeus CHN–O Rapid analyzer.

2.2. X-ray data collection and structure refinement

The X-ray diffraction measurements were made on a STOE IPDS-II diffractometer with graphite monochromated Mo Kα radiation. For [Pt(5,5′-dmbipy)Cl_4] (**1**) and [Pt(6-mbipy)Cl_4] (**2**), yellow prismatic crystals with dimensions of $0.21 \times 0.18 \times 0.11$ and $0.27 \times 0.23 \times 0.21$ mm, respectively, were mounted on a glass fiber and used for data collection. Cell constants and an orientation matrix for data collection were obtained by least-squares refinement of the diffraction data from 3963 for **1** and 3691 for **2** unique reflections. Data were collected at a temperature of 298(2) and 120(2) K to a maximum 2θ value of 58.36° for **1** and 53.26° for **2** and in a series of ω scans in 1° oscillations and integrated using the Stoe X-AREA [27] software package. The numerical absorption coefficient, μ, for the Mo Kα radiation are 10.217 mm^{-1} for **1** and 10.909 mm^{-1} for **2**. A numerical absorption correction was applied using X-RED and X-SHAPE [28] software. The data were corrected for Lorentz and Polarizing effects. The structures were solved by direct methods [29] and subsequent difference Fourier map and then refined on F^2 by a full-matrix least-squares procedure using anisotropic displacement parameters [29]. All of the hydrogen atoms were located in a difference Fourier map and then after refined isotropically. Subsequent refinement then converged with R factors and parameter errors significantly better than for all attempts to model the solvent disorder. All refinements were performed using the X-STEP32 crystallographic software package [30]. A summary of the crystal data, experimental details and refinement results is given in Table 1.

Table 1
Crystallographic and structure refinement data for complexes **1** and **2**.

	Complex **1**	Complex **2**
Formula	$C_{12}H_{12}Cl_4N_2Pt$	$C_{11}H_{10}Cl_4N_2Pt$
Formula weight	521.12	507.09
T (K)	298(2)	120(2)
Wavelength λ (Å)	0.71073	0.71073
Crystal system	triclinic	monoclinic
Space group	$P\bar{1}$	$P2_1/n$
Crystal size (mm^3)	$0.17 \times 0.18 \times 0.21$	$0.21 \times 0.23 \times 0.27$
a (Å)	9.0203(9)	8.2986(6)
b (Å)	9.8501(10)	11.7988(7)
c (Å)	9.9969(10)	14.5511(10)
α (°)	87.374(8)	90
β (°)	70.796(8)	104.118(6)
γ (°)	65.015(7)	90
V ($Å^3$)	755.80(15)	1381.72(16)
Z	2	4
Density (calc.) (g cm^{-1})	2.290	2.438
θ Ranges for data collection	2.17–29.17	2.25–29.13
F(0 0 0)	488	944
Absorption coefficient (mm^{-1})	9.975	10.909
Index ranges	$-12 \leqslant h \leqslant 11$ $-13 \leqslant k \leqslant 13$ $-13 \leqslant l \leqslant 13$	$-11 \leqslant h \leqslant 11$ $-16 \leqslant k \leqslant 13$ $-19 \leqslant l \leqslant 15$
Data collected	8730	9631
Unique data (R_{int})	4048, (0.0759)	3691, (0.0589)
Parameters, restrains	173, 0	163, 0
Final R_1, wR_2 (observed data)[a]	0.0498, 0.1434	0.0445, 0.1208
Final R_1, wR_2 (all data)[a]	0.0532, 0.1455	0.0450, 0.1212
Goodness of fit (GOF) on F^2 (S)	1.165	1.243
Largest difference in peak and hole (e $Å^{-3}$)	3.277, −2.788	3.053, −3.788

[a] $R_1 = \sum||F_o|-|F_c||/\sum|F_o|$, $wR_2 = [\sum(w(F_o^2 - F_c^2)^2)/\sum w(F_o^2)^2]^{1/2}$.

2.3. Synthesis of [Pt(5,5′-dmbipy)Cl_4] (**1**)

5,5′-Dimethyl-2,2′-bipyridine (0.15 g, 0.79 mmol) in 5 ml methanol was added to a solution of $H_2PtCl_6{\cdot}6H_2O$ (0.41 g, 0.79 mmol) in methanol (10 ml) and the resulting yellow solution was stirred at 40–45 °C for 15 min. Suitable crystals for X-ray diffraction measurement were obtained by methanol diffusion to a yellow solution of **1** in DMSO over one week (yield 0.32 g, 77.7%, decompose <298 °C). ^{1}H NMR (DMSO-d_6): 2.61 (s, 3 H), 8.42 (d, 1 H), 8.81 (d, 1 H), 9.26 (satellite, 1 H, $^4J_{HPt}$ = 26 Hz) ppm.

^{13}C NMR (DMSO-d_6): 19.1, 126.2, 141.1, 144.6, 147.1, 152.4 ppm. ^{195}Pt NMR (DMSO-d_6): 1724.6(s) ppm. UV–Vis (DMSO) λ (cm^{-1}): 3.8×10^4, 3.1×10^4, 2.97×10^4. IR (KBr, cm^{-1}): 3106w, 3042m (νCH), 1482s, 1473s, 1454w, 1393m, 1374m, 1338w, 1320m, 1311s, 1292w, 1247m, 1229s, 1153m, 1137w, 1076w, 1056m, 1035w, 994w, 919w, 857m, 839s, 712m, 667w, 519m, 509m, 429m, 387m, 348s (νPt–Cl), 280m (νPt–N). *Anal.* Calc.: C, 27.64; H, 2.30; N, 5.37. Found: C, 27.51; H, 2.26; N, 5.26%.

Table 2
Selected bond distances (Å) and bond angles (°) for complexes **1** and **2**.

1			
Pt1–Cl1	2.302(3)	Cl2–Pt1–Cl3	91.03(10)
Pt1–Cl2	2.312(3)	Cl2–Pt1–Cl4	176.29(9)
Pt1–Cl3	2.299(2)	Cl2–Pt1–N1	89.3(2)
Pt1–Cl4	2.320(3)	Cl2–Pt1–N2	86.4(2)
Pt1–N1	2.018(8)	Cl3–Pt1–Cl4	91.89(10)
Pt1–N2	2.026(7)	Cl3–Pt1–N1	95.3(2)
Cl1–Pt1–Cl2	91.37(12)	Cl3–Pt1–N2	175.4(2)
Cl1–Pt1–Cl3	88.36(10)	Cl4–Pt1–N1	88.1(2)
Cl1–Pt1–Cl4	90.99(11)	Cl4–Pt1–N2	90.5(2)
Cl1–Pt1–N1	176.3(2)	N1–Pt1–N2	80.9(3)
Cl1–Pt1–N2	95.5(3)		
2			
Pt1–Cl1	2.2988(15)	Cl2–Pt1–Cl3	178.86(5)
Pt1–Cl2	2.3105(15)	Cl2–Pt1–Cl4	89.59(6)
Pt1–Cl3	2.3226(15)	Cl2–Pt1–N1	91.33(16)
Pt1–Cl4	2.3023(15)	Cl2–Pt1–N2	91.45(15)
Pt1–N1	2.076(5)	Cl3–Pt1–Cl4	89.68(4)
Pt1–N2	2.037(5)	Cl3–Pt1–N1	90.81(6)
Cl1–Pt1–Cl2	92.79(6)	Cl3–Pt1–N2	87.746(15)
Cl1–Pt1–Cl3	88.30(6)	Cl4–Pt1–N1	173.49(16)
Cl1–Pt1–Cl4	86.74(6)	Cl4–Pt1–N2	93.65(16)
Cl1–Pt1–N1	99.65(16)	N1–Pt1–N2	79.9(2)
Cl1–Pt1–N2	175.75(15)		

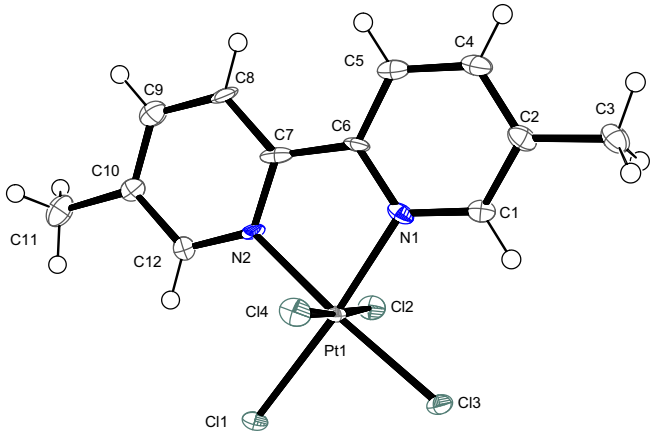


Fig. 1. ORTEP view of the title compound **1** with the atom numbering scheme. Displacement ellipsoids for non-H atoms are drawn at the 50% probability level.

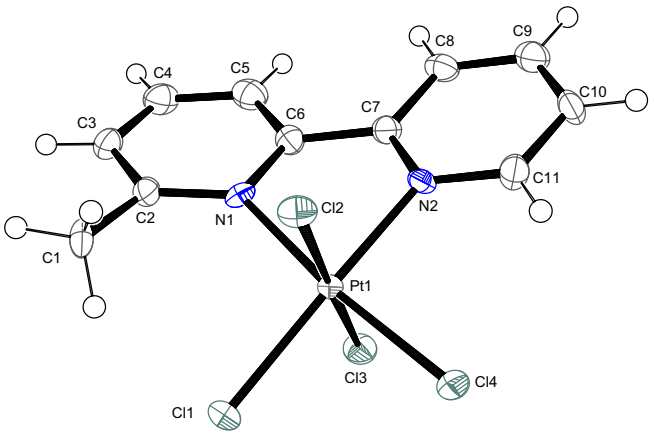


Fig. 2. ORTEP view of the title compound **2** with the atom numbering scheme. Displacement ellipsoids for non-H atoms are drawn at the 50% probability level.

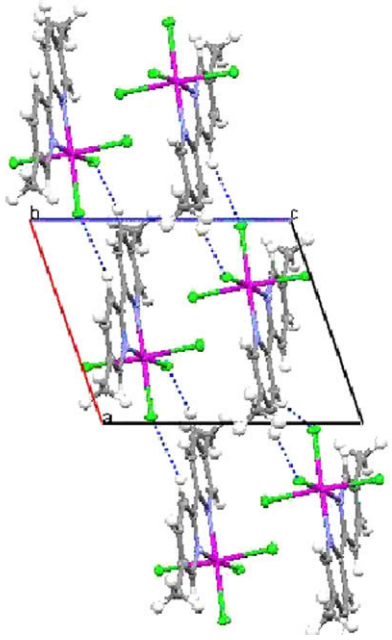


Fig. 3. A view of the intermolecular hydrogen bonding interactions of the title compound **1** viewed down the *b*-axis.

2.4. Synthesis of [Pt(6-mbipy)Cl$_4$] (**2**)

6-Methyl-2,2′-bipyridine (0.14 g, 0.79 mmol, 0.13 ml) in 5 ml methanol was added to a solution of $H_2PtCl_6{\cdot}6H_2O$ (0.41 g, 0.79 mmol) in methanol (10 ml) and the resulting yellow solution was stirred at 313–318 K for 15 min. Suitable crystals for X-ray diffraction measurement were obtained by methanol diffusion to the yellow solution in DMSO over one week (yield 0.31 g, 77.4%, M.p 285–286 °C). ^{1}H NMR (DMSO-d$_6$): 3.29 (s, 3 H), 7.86 (d, 1 H), 8.07 (s, 1 H), 8.41 (t, 1 H), 8.55 (t, 1 H), 8.75 (d, 1 H), 8.84 (d, 1 H), 9.48 (d, 1 H, $^4J_{HPt}$ = 26 Hz) ppm. ^{13}C NMR (DMSO-d$_6$): 26.5(s), 124.5(t), 126.7(t), 129.3(t), 132.8(t), 143.1(s), 144.3(s), 148.1(s), 156.1(s), 156.5(s), 165.7(s) ppm. ^{195}Pt NMR (DMSO-d$_6$): 2012.9(s) ppm. UV–Vis (DMSO) λ (cm^{-1}): 3.78×10^4 and 3.11×10^4. IR (KBr, cm^{-1}): 3082m, 2919w, 2844w (νCH), 1599m, 1565m,1493m, 1456s,1379w, 1329w, 1292m, 1269w, 1235m, 1174m, 1128w, 1092m, 1040w, 1016m, 894w, 805m, 778s, 723w, 660w, 584w, 345s (νPt–Cl), 254m (νPt–N). *Anal.* Calc.: C, 26.03; H, 1.97; N, 5.52. Found: C, 25.87; H, 1.89; N, 5.42%.

3. Results and discussion

Compounds **1** and **2** were obtained from the reaction of 1 equivalent of $H_2PtCl_6{\cdot}6H_2O$ with 1 equivalent of the appropriate bipyridine ligand in a methanol solution around 40 °C over 15 min. The products were isolated in about 77% yield. These compounds were recrystallized in a DMSO/methanol solution to obtain suitable crystals for X-ray studies. Table 1 shows details of the data collection and refinement of the X-ray crystal structure determinations for **1** and **2**. Selected bond lengths and bond angles are presented in Table 2. The ORTEP view with the numbering schemes for compounds **1** and **2** are shown in Figs. 1 and 2, respectively. In the title complexes, the Pt(IV) atom has a distorted octahedral coordination by two N atoms from two 3-methylpyridine and four terminal Cl atoms in **1** and by two N atoms from one 2-methylpyridine and one pyridine, and four terminal Cl atoms in **2**. The Pt–Cl bonds are in the range 2.299–2.323 Å in complexes **1** and **2**. In both complexes, the shorter Pt–Cl bond lengths are for the bond *trans* to the N and reveal the significance of *trans* effects. The Pt–N bond distances are between 2.018 and 2.037 Å in **1** and **2**, with the exception of one Pt–N bond, equal to 2.076 Å in **2**, that is adjacent to the 2-methyl pyridine. This bond is a little larger due to steric hindrance of the methyl group. The Pt–Cl and Pt–N bond lengths are in good agreement with the corresponding values in [PtCl$_4$(bpym)]·MeOH [15], [PtCl$_4$(bipy)] [16], [PtCl$_4${pz(py)$_2$}] [18]

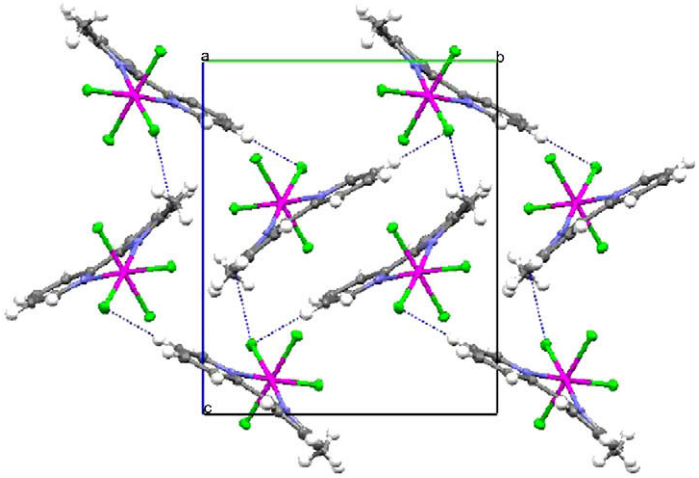


Fig. 4. A view of the intermolecular hydrogen bonding interactions of the title compound **2** viewed down the *a*-axis.

Table 3
Hydrogen bond geometries of complex **1** in the crystal packing (Å, °).

D–H···A	D–H	H···A	D···A	D–H···A
C1–H1···Cl3	0.93	2.63	3.240(17)	124
C5–H5···Cl3^{i}	0.93	2.68	3.569(18)	161
C9–H9···Cl1^{i}	0.93	2.81	3.502(18)	132
C12–H12···Cl1	0.93	2.63	3.239(18)	123

Symmetry codes: (i) 1 + *x*, *y*, *z*.

Table 4
Hydrogen bond geometries of complex **2** in the crystal packing (Å, °).

D–H···A	D–H	H···A	D···A	D–H···A
C1–H1B···Cl1	0.96	2.36	3.143(8)	139
C5–H5···Cl2^{i}	0.93	2.77	3.543(9)	142
C10–H10···Cl4^{ii}	0.93	2.68	3.611(7)	176
C11–H11···Cl4	0.93	2.65	3.197(8)	119

Symmetry codes: (i) 1 + *x*, *y*, *z*; (ii) 3/2−*x*, −1/2 + *y*, 1/2−*z*.

and [$PtCl_4$(4,4′-dmbipy)] [19]. The pyridine ring is slightly distorted from planarity with a maximum deviation of 0.119(6) Å for atom N1 in **1** and 0.207(5) Å for atom C3 in **2**. The mean planes of rings A (Pt1/N1/N2/C6/C7), B (N1/C1/C2/C4/C5/C6) and C (N2/C7/C8/C9/C10/C12) in **1** make the following dihedral angles with each other: A/B = 4.39(10), A/C = 4.54(9) and B/C = 7.78(13)°. In **2**, the mean planes of rings A (Pt1/N1/N2/C6/C7), B (N1/C2/C3/C4/C5/C6) and C (N2/C7/C8/C9/C10/C11) make the following dihedral angles with each other: A/B = 14.87(13), A/C = 9.48(13) and B/C = 16.75(14)°. It appears that deviation from planarity is larger in **2** than **1** due to steric hindrance of the methyl groups in **2** and also due to unsymmetrical substitution in the pyridine rings in compound **2**. The packing diagrams for compounds **1** and **2** are shown in Figs. 3 and 4, respectively. In these compounds, there are some weak intermolecular C–H···Cl hydrogen contacts (Tables 3 and 4) that seem to be effective in the stabilization of the crystal structures. The highest peaks and deepest holes for compounds **1** and **2** are around the Pt atoms (a distance of 0.85 and 0.82 Å for highest peaks and 0.78 and 0.73 Å for deepest holes for **1** and **2**, respectively).

NMR spectroscopy reveals that the structures of compound **1** and **2** are held in solution. In compound **1**, the ^{1}H NMR spectrum shows three signals at around 8–9 ppm for aromatic protons and a signal at 2.61 ppm for the methyl protons. H_2 and H_3 are split and show a doublet pattern as expected. Only H_1, which is close to the platinum centre, shows a 1:4:1 satellite pattern due to coupling with the ^{195}Pt atom, trace A of Fig. 5. In the ^{13}C NMR spectrum, five distinct signals are seen for the aromatic carbon around 126–153 ppm. Both ^{1}H and ^{13}C spectra confirm the symmetry of the compounds seen in the solid state by X-ray diffraction. However in compound **2** the ^{13}C signals are increased to 10 in 124–166 ppm region due to chemically different carbons in the aromatic region. The ^{1}H NMR signals show that only H_1 is seen with satellites of the platinum nucleus. Other protons are split by neighboring hydrogen atoms as expected. Full assignments of the protons are shown in Fig. 5. The ^{195}Pt NMR spectrum shows a signal for **1** at 1724.6 ppm and one for **2** at 2012.9 ppm, relative to the Na_2PtCl_4 reference to an external sample of Na_2PtCl_4 at −1642 ppm relative to H_2PtCl_6 at 0 ppm. Similar positions are reported for Pt^{IV} bearing chloride and nitrogen ligands [14]. The ^{195}Pt signals are relatively broad due to coordination of the quadruple nitrogen nucleus, especially in compound **2**.

The vibrational bands present around 3000 cm^{-1} in complexes **1** and **2** are assigned as ν(C–H). The bands observed in the range 1600–1400 cm^{-1} are assigned to ν(C=N) and ν(C=C) vibrations. The medium to strong vibrations in the region 960–550 cm^{-1} are assigned to the deformation vibrations of δ(C=C=N) and δ(C=C=C) in the pyridine rings [31,32]. Far infrared spectra of complexes **1** and **2** were recorded between 500 and 250 cm^{-1}. Pt–N stretching

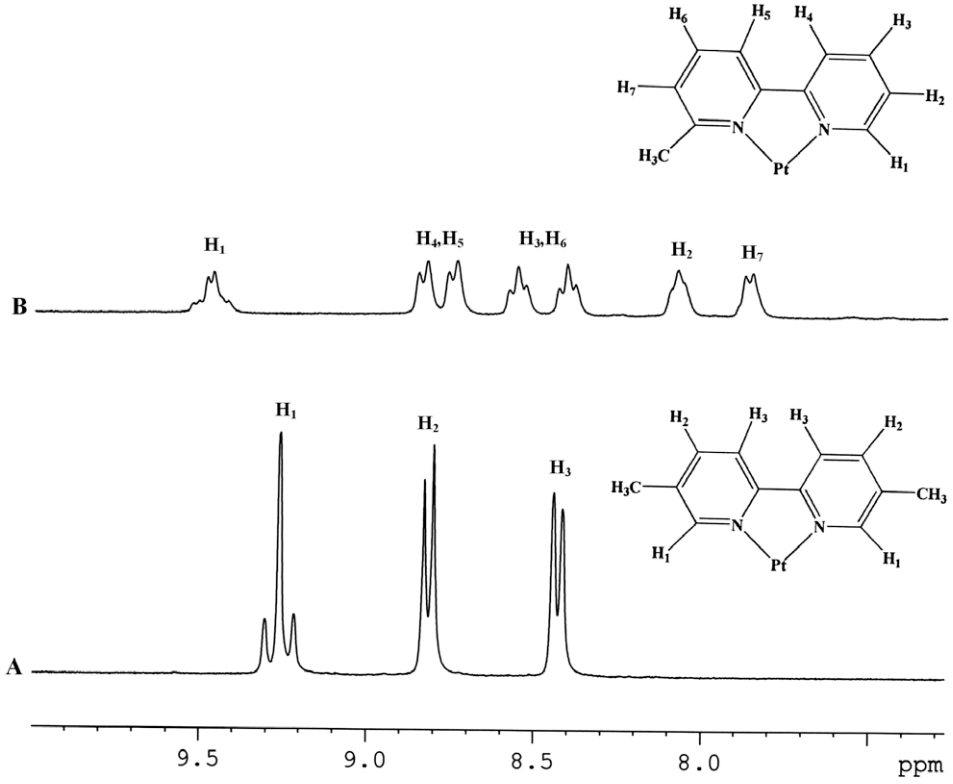


Fig. 5. Aromatic region of ^{1}H NMR spectra of compounds **1** and **2** in DMSO-d_6.

vibrations for complexes **1** and **2** are seen at 280 and 254 cm^{-1}, respectively. Pt–Cl frequencies appear at 348 and 345 cm^{-1}, as expected [12,21,33,34].

Supplementary data

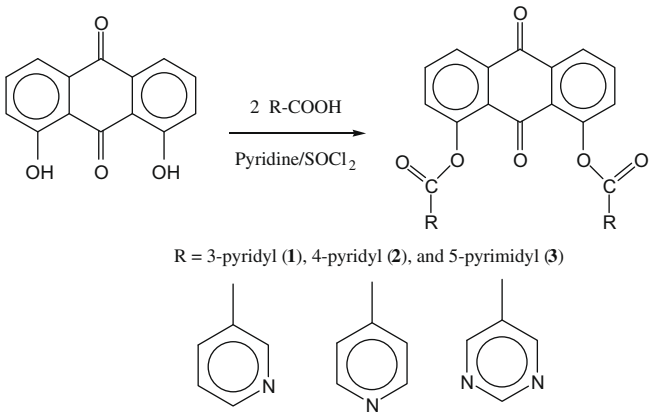
CCDC 699392 and 699393 contain the supplementary crystallographic data for **1** and **2**, respectively. These data can be obtained free of charge via http://www.ccdc.cam.ac.uk/conts/retrieving.html, or from the Cambridge Crystallographic Data Centre, 12 Union Road, Cambridge CB2 1EZ, UK; fax: (+44) 1223-336-033; or e-mail: deposit@ccdc.cam.ac.uk.

Acknowledgment

We would like to thank the Graduate Study Councils of Shahid Beheshti University for financial support (Project 600/2441).

References

[1] B. Rosenberg, L. VanCamp, J.E. Trosko, V.H. Mansour, Nature 222 (1969) 385.
[2] L.H. Einhorn, J. Donohue, Ann. Intern. Med. 87 (1977) 293.
[3] R.F. Ozols, R.C. Young, Semin. Oncol. 11 (1984) 251.
[4] M.S. Soloway, J. Urol. 120 (1978) 716.
[5] E. Pantoja, A. Gallipoli, S.V. Zutphen, D.M. Tooke, A.L. Spek, C.N. Ranninger, J. Reedijk, Inorg. Chim. Acta 359 (2006) 4335.
[6] S. Shamsuddin, C.C. Santillan, J.L. Stark, K.H. Whitmire, Z.H. Siddik, A.R. Khokhar, J. Inorg. Biochem. 71 (1998) 29.
[7] E.J. Lee, M.J. Jun, Y.S. Sohn, Bull. Korean Chem. Soc. 20 (1999) 1295.
[8] Y.E. Kwon, K.J. Whang, Y.J. Park, K.H. Kim, Bioorg. Med. Chem. 11 (2003) 1669.
[9] M. Marković, N. Knežvić, M. Momčilović, S.G. Šipka, L. Harhaji, V. Trajković, M.M. Stojković, T. Sabo, D. Miljković, Eur. J. Pharmacol. 517 (2005) 28.
[10] M.S. Ali, S.R.A. Khan, H. Ojima, I.Y. Guzman, K.H. Whitmire, Z.H. Siddik, A.R. Khokhar, J. Inorg. Biochem. 99 (2005) 795.
[11] G.N. Kaludjerović, D. Miljković, M. Momcilović, V.M. Djinović, M.M. Stojković, T.J. Sabo, V. Trajković, Int. J. Cancer 116 (2005) 47.
[12] J.S. Casas, A. Castineiras, Y. Parajo, A. Sanchez, A.S. Gonzalez, J. Sordo, Polyhedron 24 (2005) 1196.
[13] J.M. Pérez, L.R. Kelland, E.I. Montero, F.E. Boxall, M.A. Fuertes, C. Alonso, C.N. Ranninger, Mol. Pharmacol. 63 (2003) 933.
[14] M.J. Arendse, G.K. Anderson, R.N. Majola, N.P. Rath, Inorg. Chim. Acta 340 (2002) 65.
[15] A. Gaballa, C. Wagner, H. Schmidt, D. Steinborn, Z. Anorg. Allg. Chem. 629 (2003) 703.
[16] T.W. Hambley, Acta Crystallogr., Sect. C 42 (1986) 49.
[17] J. Hafizovic, U. Olsbye, K.P. Lillerud, Acta Crystallogr., Sect. E 62 (2006) m414.
[18] P. Delir Kheirollahi Nezhad, F. Azadbakht, V. Amani, H.R. Khavasi, Acta Crystallogr., Sect. E 64 (2008) m575.
[19] K.N. Crowder, S.J. Garcia, R.L. Burr, J.M. North, M.H. Wilson, B.L. Conley, P.E. Fanwick, P.S. White, K.D. Sienerth, R.M. Granger, Inorg. Chem. 43 (2004) 72.
[20] L. Hojjat Kashani, M. Yousefi, V. Amani, H.R. Khavasi, Acta Crystallogr., Sect. E 64 (2008) m905.
[21] H. Junicke, K. Schenzel, F.W. Heinemann, K. Pelz, H. Bogel, D. Steinborn, Z. Anorg. Allg. Chem. 623 (1997) 603.
[22] A.V. Khripun, S.I. Selivanov, V.Y. Kukushkin, M. Haukka, Inorg. Chim. Acta 359 (2006) 320.
[23] H. Witkowski, E. Freisinger, B. Lippert, Chem. Commun. (1997) 1315.
[24] J.K. Jaworska, M. Kubiak, T. Glowiak, Acta Crystallogr., Sect. C 44 (1988) 437.
[25] J.K. Jaworska, M. Kubiak, T. Glowiak, B.J. Trzebiatowska, Acta Crystallogr., Sect. C 46 (1990) 2046.
[26] M. Yousefi, S. Teimouri, V. Amani, H.R. Khavasi, Acta Crystallogr., Sect. E 63 (2007) m2869.
[27] Stoe & Cie, X-AREA, Version 1.30: Program for the Acquisition and Analysis of Data; Stoe & Cie GmbH: Darmatadt, Germany, 2005.
[28] (a) Stoe & Cie, X-RED, Version 1.28b: Program for Data Reduction and Absorption Correction; Stoe & Cie GmbH: Darmatadt, Germany, 2005.;
(b) Stoe & Cie, X-SHAPE, Version 2.05: Program for Crystal Optimization for Numerical Absorption Correction; Stoe & Cie GmbH: Darmatadt, Germany, 2004.
[29] G.M. Sheldrick, Acta Crystallogr., Sect. A 64 (2008) 112.
[30] Stoe & Cie, X-STEP32, Version 1.07b: Crystallographic Package; Stoe & Cie GmbH: Darmstadt, Germany, 2000.
[31] V. Amani, N. Safari, H.R. Khavasi, Polyhedron 26 (2007) 4257.
[32] V. Amani, N. Safari, H.R. Khavasi, P. Mirzaei, Polyhedron 26 (2007) 4908.
[33] C. Bruhn, H.-H. Drews, B. Meynhardt, W. Preetz, Z. Anorg. Allg. Chem. 621 (1995) 373.
[34] C. Bruhn, H.-H. Drews, W. Preetz, Z. Anorg. Allg. Chem. 622 (1996) 1623.



Scheme 1.

2.0 mL of 0.022 M (0.044 mmol) $[Ag(CH_3CN)_4](BF_4)$ were combined, filtered and diffused with diethyl ether to yield yellow crystals. Elemental analyses calculated for $[Ag_2(C_{26}H_{14}N_2O_6)_2](BF_4)_2$: C, 48.41; H, 2.19; N, 4.34. Found: C, 49.52; H, 2.39; N, 4.36%.

*[Ag(1,8-bis(nicotinyloxy)anthracene-9,10-dione)$_2$](PF$_6$) (**5**)*: 0.020 g (0.044 mmol) of **1** in ~15 mL of hot acetonitrile and 4.0 mL of 0.022 M (0.088 mmol) $[Ag(CH_3CN)_4](PF_6)$ were combined, filtered and diffused with diethyl ether to yield yellow crystals. Elemental analyses calculated for $[Ag(C_{26}H_{14}N_2O_6)_2](PF_6)$: C, 54.14; H, 2.45; N, 4.86. Found: C, 54.13; H, 2.59; N, 4.94%.

*[Ag$_2$(1,8-bis(isonicotinyloxy)anthracene-9,10-dione)$_2$(CH$_3$CN)$_2$]-(PF$_6$)$_2$ (**6**)*: 0.020 g (0.044 mmol) of **2** in ~15 mL of hot acetonitrile and 2.0 mL of 0.022 M (0.044 mmol) $[Ag(CH_3CN)_4]$-(PF_6) were combined, filtered and diffused with diethyl ether to yield yellow crystals. Elemental analyses calculated for $[Ag_2(C_{26}H_{14}N_2O_6)_2$-$(CH_3CN)](PF_6)_2$: C, 44.80; H, 2.16; N, 4.83. Found: C, 44.32; H, 2.14; N, 4.93%.

*[Cu$_2$(1,8-bis(isonicotinyloxy)anthracene-9,10-dione)$_2$(CH$_3$CN)$_2$]- (BF$_4$)$_2$ (**7**)*: 0.020 g (0.044 mmol) of **2** in ~15 mL of hot acetonitrile and 2.0 mL of 0.022 M (0.044 mmol) $[Cu(CH_3CN)_4]$-(BF_4) were combined, filtered and diffused with diethyl ether to yield yellow crystals. Elemental analyses calculated for $[Cu_2(C_{26}H_{14}N_2O_6)_2](BF_4)_2$: C, 51.98; H, 2.35; N, 4.66. Found: C, 52.11; H, 2.45; N, 4.66%.

Catena-$[Ag_2$(1,8-bis(isonicotinyloxy)anthracene-9,10-dione$)_3]$-$(BF_4)_2$ (**8**): 0.020 g (0.044 mmol) of **2** in ~15 mL of hot acetonitrile and 3.0 mL of 0.022 M (0.066 mmol) $[Ag(CH_3CN)_4](BF_4)$ were combined, filtered and diffused with diethyl ether to yield yellow crystals. Elemental analyses calculated for $[Ag_2(C_{26}H_{14}N_2O_6)_3]$-$(BF_4)_2$: C, 53.40; H, 2.46; N, 4.95%. Found: C, 53.82; H, 2.43; N, 4.82%.

*Catena-[Ag(1,8-bis(pyrimidyl-5-carboxyloxy)anthracene-9,10-dione)(CH$_3$CN)](PF$_6$) (**9**)*: 0.020 g (0.044 mmol) of **3** in ~15 mL of hot acetonitrile and 2.0 mL of 0.022 M (0.044 mmol) $[Ag(CH_3CN)_4]$-(PF_6) were combined, filtered and diffused with diethyl ether to yield yellow crystals. Elemental analyses calculated for $[Ag(C_{24}H_{12}$-$N_4O_6)](PF_6)$: C, 40.87; H, 1.72; N, 7.94. Found: C, 39.92; H, 2.22; N, 7.76%.

Table 1
Crystallographic and refinement data for 1,8-*bis*(pyrimidyl-5-carboxyloxy)anthraquinone (**3**); $[Ag_2$(1,8-*bis*(nicotinyloxy)anthracene-9,10-dione$)_2](BF_4)_2{\cdot}2CH_3CN$ (**4**); $[Ag$(1,8-*bis*(nicotinyloxy)anthracene-9,10-dione$)_2](PF_6)$ (**5**); $[Ag_2$(1,8-*bis*(isonicotinyloxy)anthracene-9,10-dione$)_2(CH_3CN)_2](PF_6)_2$ (**6**); $[Cu_2$(1,8-*bis*(isonicotinyloxy)anthracene-9,10-dione$)_2(CH_3CN)_2](BF_4)_2$ (**7**); Crystallographic and refinement data for *cat*-$[Ag_2$(1,8-*bis*(nicotinyloxy)anthracene-9,10-dione$)_3](BF_4)_2{\cdot}0.5CH_3CN$ (**8**); *cat*-[Ag(1,8-*bis*(pyrimidyl-5-carboxyloxy)anthracene-9,10-dione)$(CH_3CN)](PF_6)$ (**9**).

	3	**4**	**5**	**6**	**7**	**8**	**9**
Empirical formula	$C_{24}H_{12}N_4O_6$	$C_{56}H_{34}N_6O_{12}B_2F_8Ag_2$	$C_{52}H_{28}N_4O_{12}PF_6Ag$	$C_{56}H_{34}N_6O_{12}P_2F_{12}Ag_2$	$C_{56}H_{34}N_6O_{12}B_2F_8Cu_2$	$C_{316}H_{168}N_{26}O_{72}B_8F_{32}Ag_8$	$C_{26}H_{15}N_5O_6F_6PAg$
Formula weight	452.38	1372.25	1153.62	1488.58	1283.59	7038.21	746.27
System	Bruker APEXII	Smart APEXII	Bruker APEXII	Bruker APEXII	Smart APEXII	Bruker APEXII	Bruker APEXII
Temperature (K)	121(2)	100(2)	119(2)	116(2)	125(2)	100(2)	119(2)
Crystal system	monoclinic	triclinic	monoclinic	triclinic	triclinic	Orthorhombic	Monoclinic
Space group	*P* 21/c	$P\bar{1}$	C2/m	$P\bar{1}$	$P\bar{1}$	Pnna	Cc
a (Å)	12.9728(5)	8.336(2)	13.3076(5)	8.6488(2)	9.0413(6)	9.5874(5)	9.7350(3)
b (Å)	13.8064(5)	10.181(2)	15.2552(6)	10.4536(3)	9.4572(6)	16.2485(8)	31.714(1)
c (Å)	11.9530(4)	17.232(4)	12.5226(3)	16.3250(4)	16.4198(11)	44.488(2)	8.4939(3)
α (°)		81.723(2)		82.204(1)	88.856(1)		
β (°)	114.432(2)	82.897(2)	117.7960	83.179(1)	82.281(1)		96.812(2)
γ (°)		68.858(2)		71.263(1)	73.670(1)		
Volume (Å^3)	1949.2(1)	1345.7(5)	2248.9(1)	1380.37(6)	1334.9(2)	6930.4(6)	2603.9(2)
Z	4	1	2	1	1	1	4
Density (calc) g.cm^{-3}	1.542	1.693	1.704	1.791	1.597	1.689	1.904
Absorbption coefficient (mm^{-1})	0.114	0.826	0.584	0.879	0.896	0.669	0.934
F(0 0 0)	464	1368	1160	1480	1298	7078	740
θ range	2.3/25.0	2.3/25.0	1.8/25.0	1.3/25.0	2.4/25.0	2.5/25.0	2.3/25.0
Index ranges	*h*(−15,15), *k*(−16,16), *l*(−14,14)	*h*(−9,9), *k*(−12,12), *l*(−20,20)	*h*(−15,15), *k*(−18,18), *l*(−14,14)	*h*(−10,10), *k*(−12,12), *l*(−19,19)	*h*(−10,10), *k*(−11,11), *l*(−19,19)	*h*(−11,11), *k*(−19,19), *l*(−52,52)	*h*(−11,11), *k*(−37,37), *l*(−10,10)
Reflections collected	37911	12656	21659	26579	13244	64451	24980
Independent reflections	3612	4715	2055	4868	4726	6129	4560
Observed reflections	2795	4182	1962	4429	3153	5153	4310
Maximum/Minimum transmission	0.972/0.940	0.922/0.790	0.912/0.783	0.844/0.779	0.932/0.800	0.912/0.800	0.912/0.736
Data/restraints/ parameter	3612/0/307	4715/0/389	2055/0/249	4868/2/424	4726/0/389	6129/9/572	4560/6/428
Goodness-of-fit	1.088	1.034	1.105	1.199	1.008	1.018	1.153
Final *R* indices[$I > 2\sigma(I)$]	0.0373	0.0402	0.0261	0.0252	0.0452	0.0553	0.0343
R indices (all data)	0.1146	0.1022	0.0645	0.0727	0.0860	0.1407	0.0791
Peak/hole	0.25/−0.32	1.324/−0.880	0.63/−0.51	0.39/−0.38	0.58/−0.51	0.25/-0.32	0.35/-0.66
CCDC #	724518	724519	724520	724521	724522	724523	724524

Crystallographic data were collected at low temperature using Mo Kα radiation on Bruker CCD APEXII diffractometers. Cell constants were determined after integration from typically more than 6,000 reflections [12]. Structures were solved by direct methods using SIR97 [13] and refined using SHELXL-97 [14]. Data reduction and refinement were completed using the WINGX suite of crystallographic software [15]. All hydrogen atoms were placed in ideal positions and refined as riding atoms with relative isotropic displacement parameters. Table 1 lists additional crystallographic and refinement information.

Compound **5** has a spherically disordered hexafluorophosphate anion in ~50:50 relative occupancies. Compound **6** has a hexafluorophosphate anion with similar disorder in a ~90:10 relative ratio with the smaller occupancy refined isotropically. One of the nicotinyl ligands is disordered in Compound **8** in a 50:50 ratio. There is also an acetonitrile solvate group that is present in 50% occupancy when the disordered nicotinyl does not occupy that position. In addition both tetrafluoroborate anions were modeled as rotationally disordered in ~50:50 ratios and left isotropic. Compound **9** has the entire anthraquinone moiety disordered over two positions in a ~50:50 ratio, and both components were refined isotropically.

3. Results

A new disubstituted anthraquinone ligand that contains pyrimidine groups, compound **3**, was synthesized in the same manner as that reported for the dinicotinyl (**1**) and diisonicotinyl (**2**) anthraquinone ligands (Scheme 1) [9,10]. The structure of the dipyrimidine adduct has also been determined (Table 1), which confirms the structure of the compound and a thermal ellipsoid diagram has been placed in supporting information only (Fig. S1).

Reaction of ligands **1–3** with $[M(CH_3CN)_4]X$ (M = Ag(I),Cu(I) and X = BF_4^-, PF_6^-) produce a variety of different chelating and bridging motifs and a variety of different coordination geometries. Reaction of one equivalent of the nicotinyl-containing ligand, **1**, with one equivalent of $[Ag(CH_3CN)_4](BF_4)$ results in the formation of a new dimer where the nicotinyl groups bridge two silver atoms, $[Ag_2(\mathbf{1})_2](BF_4)_2.2CH_3CN$ (**4**) (Fig. 1). This is a different binding mode than that previously observed where **1** has been shown to chelate a metal center [9]. In this complex, the Ag···Ag distance is greater than 5.1 Å, indicating no metal–metal bond is formed, and the acetonitrile solvate present in the crystal also has large interatomic Ag–$NCCH_3$ distances, producing a near linear two-coordinate silver(I) coordination geometry. Reaction of two equivalents of **1** with one equivalent of $[Ag(CH_3CN)_4](PF_6)$ however, produces an entirely

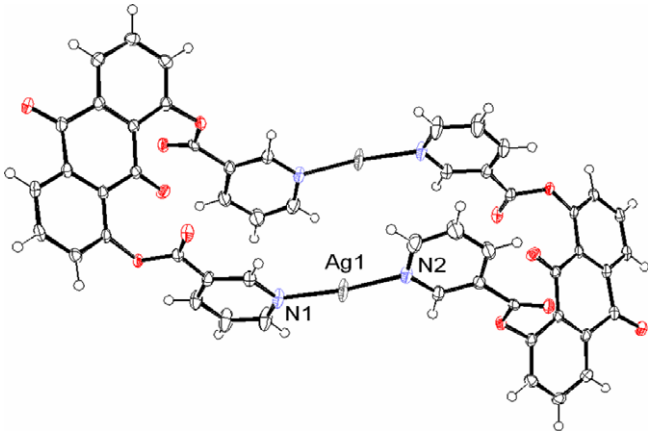


Fig. 1. Thermal ellipsoid diagram (50%) of $[Ag_2(1,8\text{-}bis(\text{nicotinyloxy})\text{anthracene-9,10-dione})_2](BF_4)_2{\cdot}2CH_3CN$ (**4**). The non-coordinating acetonitrile and tetrafluoroborate anions have been omitted for clarity. Ag1–N1 = 2.158(3), Ag1–N2 = 2.153(3), Ag–N3 (CH_3CN, not shown) = 2.86 and 3.73, Ag1–Ag1 = 5.168(5) Å.

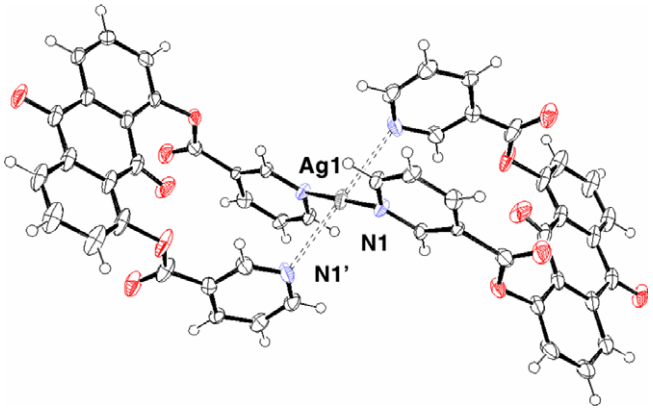


Fig. 2. Thermal ellipsoid diagram (50%) of $[Ag(1,8\text{-}bis(\text{nicotinyloxy})\text{anthracene-9,10-dione})_2](PF_6)$ (**5**). The hexafluorophosphate anion has been omitted for clarity. Ag1–N1 = 2.226(5), Ag1–N1′ = 2.763(6) Å.

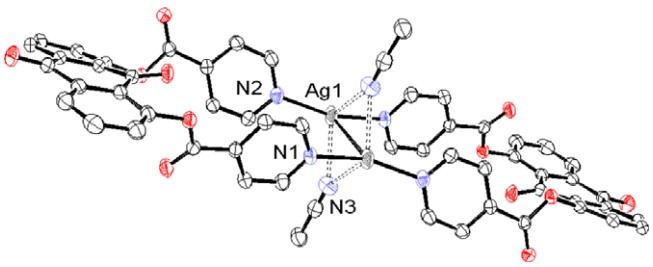


Fig. 3. Thermal ellipsoid diagram (50%) of $[Ag_2(1,8\text{-}bis(\text{isonicotinyloxy})\text{anthracene-9,10-dione})_2(CH_3CN)_2](PF_6)_2$ (**6**). The hexafluorophosphate anions and hydrogen atoms have been omitted for clarity. Ag1–N1 = 2.179(2), Ag1–N2 = 2.163(2), Ag1–N3 = 2.555(3), Ag1′–N3 = 2.817(3), Ag–Ag = 3.266(4) Å.

different complex, $[Ag(\mathbf{1})_2](PF_6)$ (**5**), where the nicotinyl groups are now found chelating the silver(I) center (Fig. 2). The chelating ability of **1** has previously been demonstrated [9]. In complex **5**, two short and two long Ag–N bonds are observed as related by symmetry, adopting a pseudo linear Ag(I) geometry, but more accurately described as square planar in geometry when including the longer Ag–N bonds.

Reaction of one equivalent of the isonicotinyl-anthraquinone ligand **2** with both Ag(I) and Cu(I) produce similar structures where the anthraquinone ligands bridge two metal centers: $[Ag_2(\mathbf{2})_2(CH_3CN)_2](PF_6)$ – Fig. 3 and $([Cu_2(\mathbf{2})_2(CH_3CN)_2](BF_4)$ – Fig. 4. One acetonitrile from the crystallization solvent is found bridging the metal atoms on each face of the dimer. In complex **6**, the Ag–N bond distances for the acetonitrile are significantly longer than the Ag–pyridyl bond distances and are unequal in length, Ag1–N3 = 2.555(3), Ag1′–N3 = 2.817(3). For the copper adduct, **7**, the acetonitrile group is localized on only one Cu(I) atom almost equal to the pyridyl Cu–N bonds, rather than bridging two metal atoms as is the case with **6**; Cu1–N3 = 2.050(4), Cu1'–N3 = 3.40 Å. We have been unable to isolate other caged structures by the addition of excess amounts of **2**, ie. $[Ag_2(\mathbf{2})_4]^{2+}$.

We have also isolated a catenated structure of ligand **1** when reacted with Ag(I), *catena*-$[Ag_2(\mathbf{1})_3](BF_4)_2.0.5CH_3CN$ (**8**, Fig. 5). Combining ligand **1** and Ag(I) in a 3:2 ratio, a unique ladder structure results. Here two anthraquinone ligands bridge two silver atoms to yield the sides of the ladder, where the pyridyl groups on each anthraquinone ligand face in opposite directions. The rungs of the ladder are formed by the third anthraquinone ligand that bridges the silver atoms on each side. The pyridyl groups in this third ligand are also pointed in opposite directions. The silver centers are distinctly trigonal planar in geometry with a Ag···Ag internuclear distance, representing the distance between sides of the

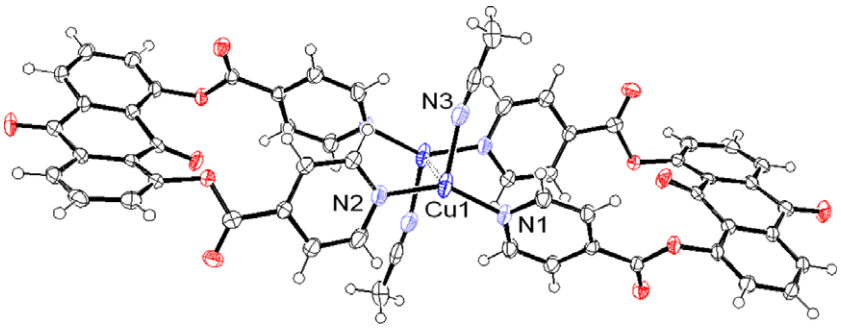


Fig. 4. Thermal ellipsoid diagram (50%) of $[Cu_2(1,8\text{-}bis(isonicotinyloxy)anthracene\text{-}9,10\text{-}dione)_2(CH_3CN)_2](BF_4)_2$ (**7**). The tetrafluoroborate anions have been omitted for clarity. Cu1–N1 = 1.946(3), Cu1–N2 = 1.949(3), Cu1–N3 = 2.050(4), Cu1′–N3 = 3.40, Cu–Cu = 3.141(5) Å.

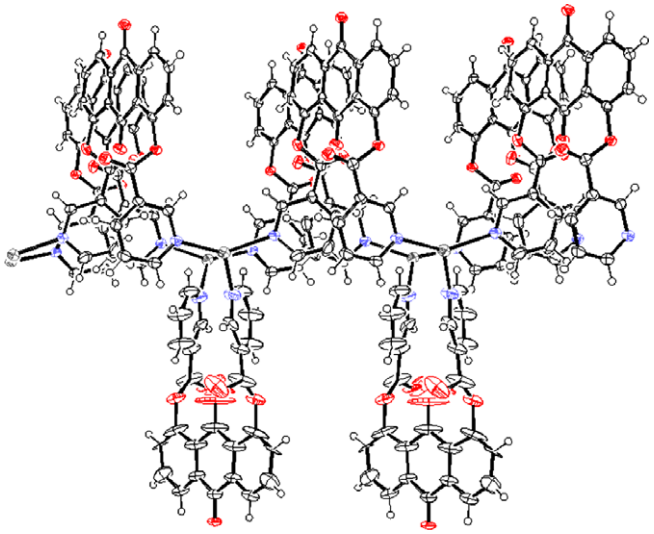


Fig. 5. Thermal ellipsoid diagram (50%) of the *catenate* structure of $[Ag_2(1,8\text{-}bis(nicotinyloxy)anthracene\text{-}9,10\text{-}dione)_3](BF_4)_2.0.5CH_3CN$ (**8**). The solvates and tetrafluoroborate anions have been omitted for clarity. Ag1–N1 = 2.284(5), Ag1–N2 = 2.222(9), Ag1–N3 = 2.212(5), Ag1···g1′ = 6.50 Å. A figure of the metal coordination environment is provided in the supporting information.

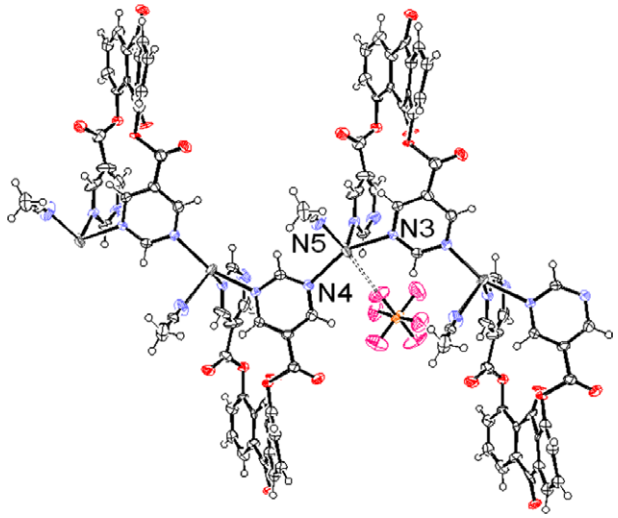


Fig. 6. Thermal ellipsoid diagram (50%) of the *catenate* structure of $[Ag(1,8\text{-}bis(pyrimidine\text{-}5\text{-}carboxyloxy)anthracene\text{-}9,10\text{-}dione)\text{-}(CH_3CN)](PF_6)$ (**9**). Ag1–N1 = 2.284(5), Ag1–N3 = 2.222(9), Ag1–N4 = 2.212(5), Ag1–N5 = 2.222(x), Ag1···F4 = 2.812 Å. A figure of the metal coordination environment is provided in the supporting information.

ladder, equal to 6.51 Å. Within the crystal, layers of anthraquinone units between separate one-dimension chains form infinite pi-stacks (not shown).

The multidentate pyrimidine-containing ligand, **3**, has been reacted with one equivalent of Ag(I) to yield another catenated, one-dimensional coordination polymer of composition *catena*-$[Ag(\mathbf{3})(CH_3CN)](PF_6)$ (**9**, Fig. 6). Two pyrimidines on the same anthraquinone scaffold act together as a chelating ligand, similar to that observed previously for **1**, and at the same time as a μ^2 ligand, one of the pyrimidine groups bridging two silver atoms. An additional acetonitrile complexes to the silver metal center and a semi-short metal–anion interaction (Ag1–F4 = 2.82 Å) yields a trigonal bipyrimidal coordination geometry. At this time, we have been unable to synthesize additional complexes containing higher ligand **3** to M(I) ratios.

4. Discussion

The most notable observation is that the coordination of dinicotinyl and diisonicotinyl anthraquinone ligands have been expanded to include bridging motifs, and these have been observed for both Ag(I) and Cu(I). As opposed to previous work [10], where coordination of water competes with dimer formation, the judicious choice of acetonitrile-solvated starting complexes that promote low coordination number and linear coordination geometries has produced new bridged, dimeric products. The nicotinyl-anthraquinone (**1**) complexes, in fact, show three widely different binding motifs: chelating as in **5** (Fig. 3), bridging-*syn* as in **6** (Fig. 2), and bridging-*anti* as in **8** (Fig. 6) that results in an unusual ladder structure. Pyrimidine-5-carboxylate has been previously investigated for formation of solid network structures coordinated to first row transition metals [16]; however only monomeric complexes were formed that did not involve coordination of both pyrimidine nitrogens. The introduction of ligand **3** and complexation with Ag(I) ion shows that coordination of both pyrimidine nitrogens is possible under the right conditions (Fig. 6), producing a linear one-dimensional coordination polymer in this case.

For the bridging isonicotinic complexes (Figs. 3 and 4), the Ag–Ag bond distance in **6** equals 3.27 Å and the Cu–Cu bond distance in **7** equals 3.14 Å. A recent revisit of covalent radii from data retrieved from the *Cambridge Structural Database* shows the covalent radius for Cu and Ag equal 1.32(4) and 1.45(5) Å, respectively [17]. Doubling these values and taking into consideration the uncertainties, ballpark figures for homonuclear metal–metal bond distances may be estimated, i.e. 2.56–2.72 Å for Cu–Cu and 2.80–3.00 Å for Ag–Ag. Although there is controversy regarding what exactly constitutes a metal–metal bond, the small difference between the largest CSD metal–metal covalent bond distance and the experimental bond distance observed in **6** shows a credibly strong argentophillic interaction between the two silver metal

atoms, and a bond has been drawn between Ag atoms in Fig. 3. The fact that the isonicotinic groups are also "bowed in" provides some support for the presence of a metal–metal interaction. The silver–silver bond distance in compound **6** also matches other silver–silver internuclear distances found in the literature [18]. The nicotinyl dimer, **4** (Fig. 1), on the other hand, has a Ag–Ag internuclear distance of 5.12 Å, no metal–metal bond, and an internuclear distance that ideally matches the distance between the 1,8-positions of substitution on the anthraquinone backbone of 5.04 Å. Although the difference between the CSD value and the Cu–Cu bond distance determined for in **7** is larger, the "bowing in" effect of the isonicotinic ligands again infers a metal–metal interaction, although presumably weaker. Additionally, the coordination of the acetonitrile ligands correlates with the metal–metal bond order. The acetonitrile ligands in complex **6** are attached by longer Ag–N bonds and are shared between the silver atoms. Complex **7**, with a weaker metal–metal interaction, has short and non-bridging Cu–acetonitrile bonds. The Cu–Cu internuclear distance here is longer than previously found in other Cu(I) dimer complexes [19].

Finally, coordination geometries for these silver complexes vary greatly. With the exception of compound **9**, most complexes exhibit coordination numbers of three or less, which likely limits the formation of caged complexes with higher coordination numbers, i.e. $[Ag_2(\mathbf{2})_4]^{2+}$, and unfortunately does little to limit coordination to exclusively linear geometries desired for the controlled synthesis of building blocks in supramolecular applications.

Acknowledgments

The authors thank NSF-EPSCOR (EPS-0554609) and the South Dakota Governor's 2010 Initiative for financial support and the purchase of a Bruker SMART APEX II CCD diffractometer. The elemental analyzer was provided by funding from NSF-URC (CHE-0532242). S.P. was supported by NSF-REU (CHE-0532242), and A.G.S is also grateful for a grant from the ACS-PRF-UFS program and additional support from the Truman and Beverley Schwartz Fund, University of South Dakota, College of Arts and Science.

Appendix A. Supplementary data

Supplementary data associated with this article can be found in the online version, at doi:10.1016/j.poly.2009.06.024.

References

[1] (a) L.T. Ellis, D.F. Perkins, P. Turner, T.W. Hambley, Dalton Trans. (2003) 2728;
(b) E. Boseggia, M. Gatos, L. Lucatello, F. Mancin, S. Moro, M. Palumbo, C. Sissi, P. Tecilla, U. Tonellato, G. Zagotto, J. Am. Chem. Soc. 126 (2004) 4543.
[2] (a) I.R. Butler, A.G. Callabero, G.A. Kelly, J.R. Amey, T. Kraemer, D.A. Thomas, M.E. Light, T. Gelbrich, S.J. Coles, Tetrahedron Lett. 45 (2004) 467;
(b) E.M. McGale, B.H. Robinson, J. Simpson, Organometallics 22 (2003) 931;
(c) M. Murata, M. Yamada, T. Fujita, K. Kojima, M. Kurihara, K. Kubo, Y. Kobayashi, H. Nishihara, J. Am. Chem. Soc. 123 (2001) 12903.
[3] (a) H.M. Ali, S. Nadiah, A. Halim, S. Koushik, S.W. Ng, Acta Crystallogr., Sect. E 61 (2005) ml431;
(b) H.M. Ali, S. Nadiah, A. Halim, S. Koushik, N.H. Lajis, W.J. Basirun, S.W. Ng, Acta Crystallogr., Sect. E 61 (2005) m691;
(c) T. Moriuchi, T. Watanabe, I. Ikeda, A. Ogawa, T. Hirao, Eur. J. Inorg. Chem. (2001) 277.
[4] M.J. Maroney, R.O. Day, T. Psyris, L.M. Fleury, J.P. Whitehead, Inorg. Chem. 28 (1989) 173.
[5] (a) M. Kadarkaraisamy, A.G. Sykes, Polyhedron 26 (2007) 1323;
(b) M. Kadarkaraisamy, A.G. Sykes, Inorg. Chem. 45 (2006) 779;
(c) Z. Liu, A.G. Sykes, J. Chem. Crystallogr. 36 (2006) 875;
(d) M. Kadarkaraisamy, E. Dufek, D. Lone Elk, A.G. Sykes, Tetrahedron 61 (2005) 479;
(e) B. Kampmann, Y. Lian, K. Klinkel, P.A. Vecchi, H.L. Quiring, C.C. Soh, A.G. Sykes, J. Org. Chem. 67 (2002) 3878;
(f) V.G. Young Jr., A.G. Sykes, Inorg. Chem. 37 (1998) 376;
(g) V.G. Young Jr., H.L. Quiring, A.G. Sykes, J. Am. Chem. Soc. 119 (1997) 12477.
[6] M. Kadarkaraisamy, G. Caple, A.R. Gorden, A.G. Sykes, Inorg. Chem. 47 (2008) 11644.
[7] W. Nakanishi, S. Hayashi, N. Itoh, J. Org. Chem. 69 (2004) 1676.
[8] K.A. Opperman, S.L. Mecklenburg, T.J. Meyer, Inorg. Chem. 33 (1994) 5295.
[9] M. Kadarkaraisamy, D. Mukherjee, C.C. Soh, A.G. Sykes, Polyhedron 26 (2007) 4085.
[10] D. Engelhart, M. Kadarkaraisamy, A.G. Sykes, J. Coord. Chem. 61 (2008) 3887.
[11] G.J. Kubas, in: D.F. Shriver(Ed.), Inorganic Synthesis, vol. XIX, Plenum, NY, 1979, P. 90.
[12] SAINT V6.1, Bruker Analytical X-ray Systems, Madison, WI, 1999.
[13] A. Altomare, M.C. Burla, M. Camalli, G.L. Cascarano, C. Giacovazzo, A. Guagliardi, A.G.G. Moliterni, G. Polidori, R. Spagna, J. Appl. Crystallogr. 32 (1999) 115.
[14] G.M. Sheldrick, Acta Crystallogr., Sect. A 64 (2008) 112.
[15] L.J. Farrugia, J. Appl. Crystallogr. 32 (1999) 837.
[16] C.B. Aakeroy, J. Desper, B. Levin, J. Valdes-Martinez, Inorg. Chim. Acta 359 (2006) 1255.
[17] B. Cordero, V. Gomez, A.E. Platero-Prats, M. Reves, J. Echeverra, E. Cremandes, F. Barragan, S. Alvarez, Dalton Trans. (2008) 2832.
[18] (a) R.H. Laye, Inorg. Chim. Acta 360 (2007) 439;
(b) N.L.S. Yue, M.C. Jennings, R.J. Puddephatt, Eur. J. Inorg. Chem. (2007) 1690;
(c) H. Wu, X.W. Dong, J.F. Ma, Acta Crystallogr., Sect. E 62 (2006) m1227;
(d) E. Bosch, C.C. Barnes, J. Coord. Chem. 58 (2005) 1021;
(e) F.F. Li, J.F. Ma, S.Y. Song, J. Yang, Y.Y. Liu, Z.M. Su, Inorg. Chem. 44 (2005) 9374;
(f) S. Abuskhuna, J. Brody, M. McCann, M. Devereaux, K. Kavanagh, J.B. Fontecha, V. McKee, Polyhedron 23 (2004) 1249;
(g) C.H. Chen, J. Cai, X.L. Feng, X.M. Chen, Polyhedron 21 (2002) 689.
[19] (a) J.P. Coyle, W.H. Monillas, G.P. Yap, S.T. Barry, Inorg. Chem. 47 (2008) 683;
(b) D. Walther, L. Boltcher, J. Blumhoff, S. Schebesta, H. Gorls, K. Schmuck, S. Rau, M. Rudolph, Eur. J. Inorg. Chem. (2006) 2385;
(c) L.C. Song, W.X. Zhang, Q.M. Hu, L.Q. Zhao, Trans. Met. Chem. 29 (2004) 603;
(d) R. Kempe, H. Noss, H. Fuhrmann, Chem. Eur. J. 7 (2001) 1630;
(e) L.R. Falvello, E.P. Urriolabeitia, U. Mukhopadhyay, D. Ray, Acta Crystallogr., Sect. C 55 (1999) 170;
(f) M. Maekawa, M. Munakata, S. Kitagawa, T. Kuroda-Sowa, Y. Suenaga, M. Yamamoto, Inorg. Chim. Acta 271 (1998) 129;
(g) S. Freitag, W. Kolodziejski, F. Paver, D. Stalke, J. Chem. Soc., Dalton Trans. (1993) 3479;
(h) R. Schmid, J. Strahle, Z. Anorg. Allg. Chem. 575 (1989) 187.

spheres. Since, a higher solution pH (pH > 9) is required to produce Hap particles, $Ca(OH)_2$ is suitable for the reaction instead of $CaCl_2$. Therefore, the authors have investigated in the present study the formation of Hap particles by using a $Ca(OH)_2$–tpp mixed solution instead of the $CaCl_2$–tpp one employed in the previous study [21]. The formation of transparent balloon-like hollow sphere was also attempted.

2. Experimental

2.1. Materials

Following the method reported by the authors in the previous paper [21], we produced calcium phosphate particles by aging a solution of $Ca(OH)_2$ [1.0×10^{-3}–1.0×10^{-2} mol/dm^3] and Natpp [1.0×10^{-3}–$.0 \times 10^{-1}$ mol/dm^3] in a 20-cm^3 Teflon-lined screw-capped Pyrex test tube. In this study, $Ca(OH)_2$ was used instead of $CaCl_2$. To facilitate the aging, the test tubes were allowed to stand for 18 h at various temperatures (100–150 °C) in an air turbulent oven. The standard aging temperature examined was 100 °C. The resulting particles were thoroughly washed by filtration with deionized and distilled water and finally dried in an air-oven at 70 °C for 18 h. The solution pH, before and after aging, was monitored at room temperature. Guaranteed reagent grade chemicals from Wako Pure Chemical Co. Inc. (Osaka, Japan) were used without further purification.

2.2. Characterization

The resulting particles were characterized by transmission electron microscope (TEM), thermogravimetry and differential thermal analysis (TG-DTA), Fourier transform infrared spectrophotometry embedded in KBr pellets (0.2 wt.%) (FTIR), powder X-ray diffraction measurement (XRD) and adsorption experiments of N_2 [8–13]. The adsorption isotherms of N_2 were measured at liquid N_2 temperature with an ordinary house built automatic volumetric flow method using a Baratron diaphragm-type manometer with a mass flow meter attached. The degree of confidence on the specific surface area measured by this apparatus was within 2%. Prior to these N_2 adsorption measurements, the samples were evacuated at 100 °C for 2 h. The chemical composition of the precipitated particles (concentration of calcium and phosphorus) was determined by dissolving a few milligrams in concentrated nitric acid. The solutions were diluted and the calcium and phosphorus concentrations were determined by inductively coupled plasma atomic emission spectroscopy (ICP-AES).

3. Results and discussion

3.1. Particle morphology and crystal form

Fig. 1 displays (a) the solution pH and (b) the morphology of the particles precipitated after aging the solution for 18 h at 100 °C. The grey circles suggest the solution produced precipitates before aging. The solution pH of 9.69–13.27 was dropped 0.4–5.2 units by the reaction. It has reported that the hydrolysis of tpp ions is expressed as the following two reactions (1) and (2) [22]

$$P_3O_{10}^{5-} + 2H_2O \rightarrow 3PO_4^{3-} + 4H^+ \quad (1)$$

$$2P_3O_{10}^{5-} + H_2O \rightarrow 3P_2O_7^{4-} + 2H^+ \quad (2)$$

Reaction (1) shows that the tpp ions are completely hydrolyzed to orthophosphate ions, though the tpp ions are not completely hydrolyzed and still remain as pp ions in reaction (2). Since the solutions are almost neutral to alkaline after the reaction (7.43 < pH < 12.89), the protonated states of the orthophosphate (HPO_4^{2-}) and pyrophosphate ($HP_2O_7^{3-}$) ions were ignored in reactions (1) and (2). Both the reactions generate protons in any event. Therefore, the pH drop watched in this experiment proves that the tpp ions are hydrolyzed. Figs. 2 and 3 show the TEM pictures and XRD patterns of the typical particle precipitates at the points A–G in Fig. 1. The assayed results and properties of these particles are listed in Table 1. Clearly, calcium pyrophosphates (α-$CaNa_2P_2O_7{\cdot}4H_2O$; JCPDS 97-002-0572) with small aggregates are produced at a higher concentration of tpp ions (sample A). On the other hand, amorphous and spherical or small spherical aggregated particles are produced at other concentration domains (samples B and D). It should be emphasized that Hap particles with lower (sample C) and higher crystallinity (samples E–G) are precipitated in the present study. Especially, highly crystallized Hap particles are formed in the lower concentration region of tpp (samples E–G) where the precipitates are produced before aging the solution (grey circles). Sample A contains pp ions, suggesting that the hydrolysis reaction of tpp ions was incomplete and is following reaction (1). The Ca/P molar ratio of the sample A is 1.38, suggesting that the composition of sample A can be described as α-$CaNa_2(P_2O_7)_{0.36}(OH)_{2.56}{\cdot}2.5H_2O$ by assuming that a part of the $P_2O_7^{4-}$ ions are exchanged to OH^- ions (see in Table 1). The Ca/P molar ratios of amorphous samples B and D are 0.93 and 1.08,

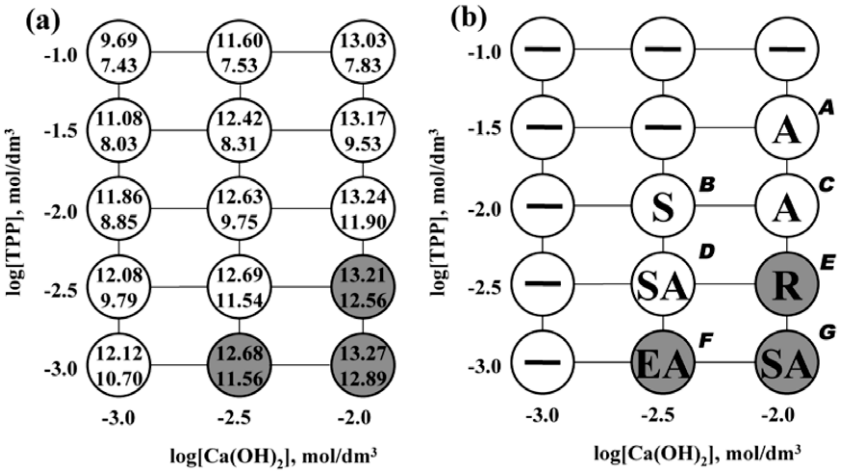


Fig. 1. (a) The pH and states of mixed solutions of $Ca(OH)_2$ and Natpp for aging at 100 °C. Upper and lower numbers are solution pH before and after aging, respectively. Grey circles indicate the solution produced precipitates before aging. (b) Particle shape of precipitates after aging. R: rod-like, S: spheres, A: aggregates, E: ellipsoidal. Bar in the circle indicates no precipitate after aging.

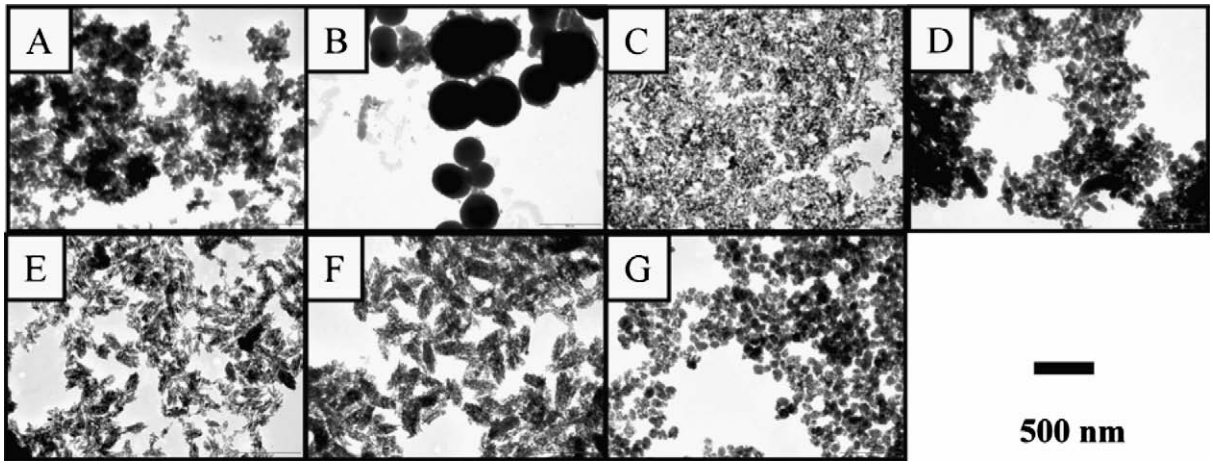


Fig. 2. TEM pictures of typical samples A–G in Fig. 1.

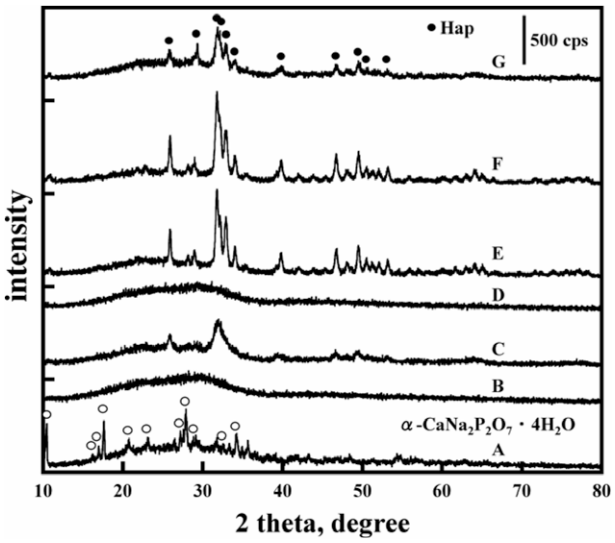


Fig. 3. XRD patterns of samples A–G in Fig. 1.

respectively. The Ca/P molar ratios of the low crystallized Hap Sample C is 1.26, though the highly crystallized samples E and F are 1.63 and 1.62, respectively. These latter values are slightly lower than the stoichiometric one of Hap (1.67), indicating that these particles are calcium-deficient. From these Ca/P molar ratios, the chemical compositions of these particles can be calculated as $Ca_{9.78}(HPO_4)_{0.22}(PO_4)_{5.78}(OH)_{1.78}\cdot 0.22H_2O$ and $Ca_{9.72}(HPO_4)_{0.28}(PO_4)_{5.72}(OH)_{1.72}\cdot 0.28H_2O$ (Table 1). Here, we assumed that the weight loss from 25 to 500 °C, shown in Fig. 4, is due to elimination of water of crystallization. Unfortunately, sample G could not be dissolved in nitric acid solution, thus the Ca/P molar ratio and chemical composition could not be determined. The crystal phase of the samples formed after heated the samples in an oven at 800 °C for 2 h is also listed in Table 1. Sample A, α-$CaNa_2P_2O_7\cdot 4H_2O$, was crystallized to α-$CaNa_2P_2O_7$ by dehydration, though samples B–D were crystallized to β-$Ca_2P_2O_7$ or α- and β-$Ca_3(PO_4)_2$.

The crystallization of sample A to α-$CaNa_2P_2O_7$ was further confirmed by TG-DTA measurement, as is shown in Fig. 4. A small exothermic peak can be recognized at 570 °C in the DTA curves on sample A. In addition, a large endothermic peak appears at ca. 25–140 °C together with a large weight loss (ca. 8 wt.) in the TG curves. This endothermic peak and weight loss are due to dehydration of water molecules that remained in the poorly ordered amorphous particles and water of crystallization. On samples B and D, a similar exothermic peak can be seen at 540 and 650 °C, respectively. These peaks can be also naturally identified as crystallization to β-$Ca_2P_2O_7$.

3.2. Formation mechanism of Hap particles

To disclose the formation mechanism of Hap, a time resolved TEM experiment was done on the formation of sample E. As has been described before, this system produced small precipitates before aging (0 h). The time resolved TEM pictures are displayed in Fig. 5 together with their Ca/P molar ratios. The XRD patterns of these precipitates are also shown in Fig. 6. Clearly, very small amorphous particles precipitated before aging are grown to ellipsoidal particles with aging the solution at 100 °C. After aging for 6 h, highly crystallized Hap particles are formed. This result strongly indicates that the crystallization of the Hap particles takes place on the surface of tiny amorphous particles precipitated before aging. These tiny particles would play the role as nuclei for Hap crystallization. The domain for producing samples E–G is located in the lower tpp concentration. The lower tpp concentration is adequate for fully hydrolyze tpp to produce orthophosphate ions together with the high pH values in this domain after the reaction (11.56–12.89).

3.3. Effects of forced hydrolysis temperature

In the previous paper [21], the authors attempted to raise the aging temperature from 100 to 150 °C in order to increase the degree of hydrolysis of tpp ions under the conditions for producing monodisperse spherical particles. The authors incidentally found that an aging temperature of 125 °C supplies transparent balloon-like hollow spheres. Therefore, we investigated again in the present study, using the $Ca(OH)_2$–tpp system, whether or not balloon-like hollow spheres could be attained under the conditions for producing spherical particles (sample B). Fig. 7 shows the TEM pictures of sample B formed at various aging temperatures together with their Ca/P molar ratios. Clearly, solid spherical particles are produced up to 120 °C. However, hollow spheres can be seen at 125 °C and finally transparent balloon-like hollow spheres can be recognized at 127 °C. The wall thickness of the balloon-like hollow spheres is approximately 10 nm (measured from TEM micrographs). Small needle-like particles are produced together with balloon-like ones at 127 °C. However, above 130 °C, no balloon-like hollow spheres are recognized, but small rod-like ones are mainly detected. The XRD patterns of those particles are shown in Fig. 8.

Table 1
Results and properties of samples A–G.

	Ca/P molar ratio	XRD (as precipitated)	Chemical composition	After heating at 800 °C for 2 h	Specific surface area (m^2/g)[a]
A	1.38	α-$CaNa_2P_2O_7{\cdot}4H_2O$	α-$CaNa_2(P_2O_7)_{0.36}(OH)_{2.56}{\cdot}2.5H_2O$	α-$CaNa_2P_2O_7$	18
B	0.93	amorphous	amorphous	β-$Ca_2P_2O_7$	2
C	1.26	low crystallized Hap	–	α-$Ca_3(PO_4)_2$, β-$Ca_3(PO_4)_2$	168
D	1.08	amorphous	amorphous	β-$Ca_2P_2O_7$	66
E	1.63	Hap	$Ca_{9.78}(HPO_4)_{0.22}(PO_4)_{5.78}(OH)_{1.78}{\cdot}0.22H_2O$	Hap	65
F	1.62	Hap	$Ca_{9.72}(HPO_4)_{0.28}(PO_4)_{5.72}(OH)_{1.72}{\cdot}0.28H_2O$	Hap	86
G	–	Hap		Hap	122

[a] Preheated at 100 °C.

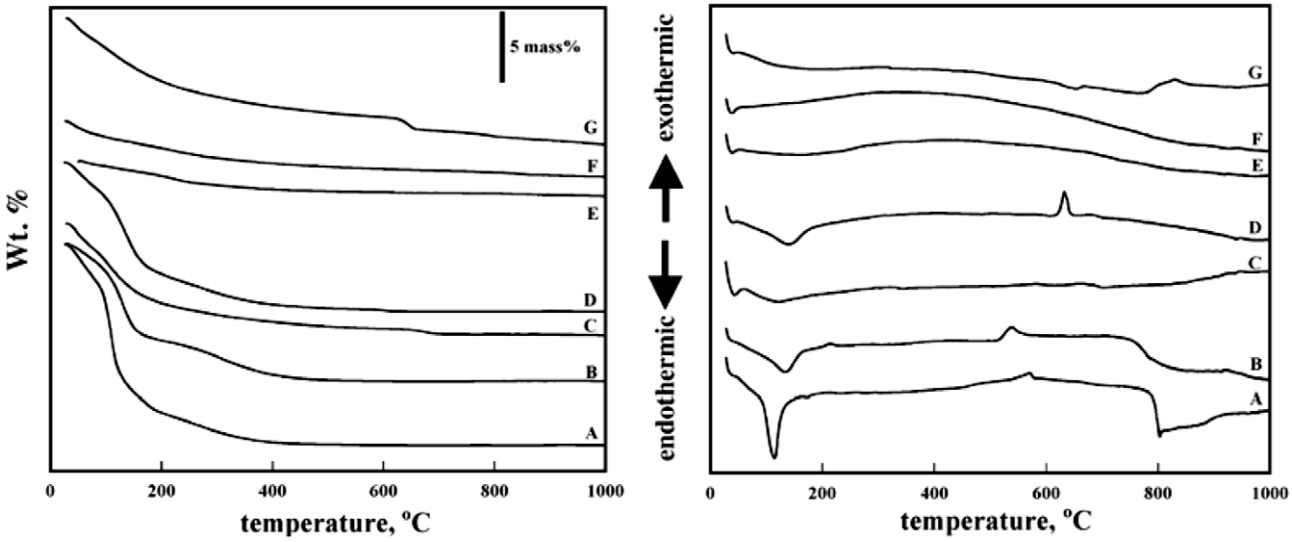


Fig. 4. TG and DTA curves of samples A–G in Fig. 1.

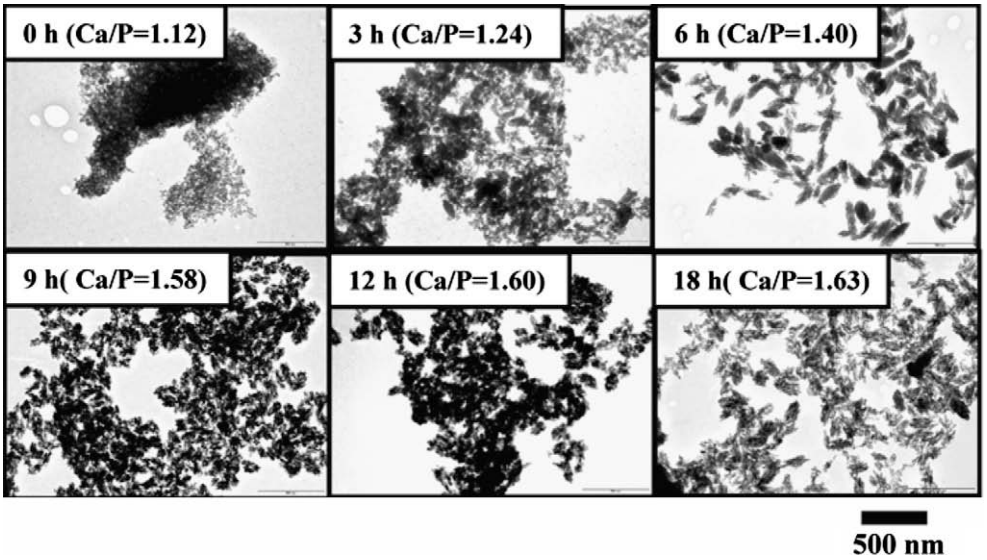


Fig. 5. Time resolved TEM pictures of precipitates for producing Hap particles at 100 °C (sample E in Fig. 1).

The spherical particles and/or balloon-like hollow spheres are amorphous, but the characteristic peaks of Hap (JCPDS 9-432) appear for the samples produced above 127 °C though their crystallinity is low, with a small *S*/*N* ratio. The Ca/P molar ratios of the amorphous particles are 0.89–0.91, though these values increased to 1.30–1.50 by raising the aging temperature. Even though the XRD patterns suggest a Hap crystal form, the Ca/P molar ratios of these particles are less than the expected stoichiometric value of 1.67. This fact indicates that the Hap particles are Ca-deficient with a low crystallinity. The formation of the Hap crystal form of the particles is also identified by FTIR measurement (data not shown). These results indicate that the transparent balloon-like hollow spheres can be produced not only by the $CaCl_2$–tpp system, but also by the $Ca(OH)_2$–tpp one. The specific surface area (abbreviated

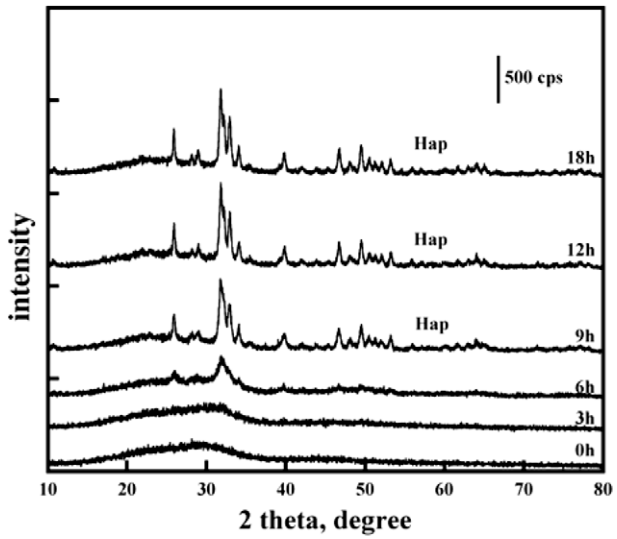


Fig. 6. Time resolved XRD patterns of precipitates for producing Hap particles at 100 °C as shown in Fig. 5.

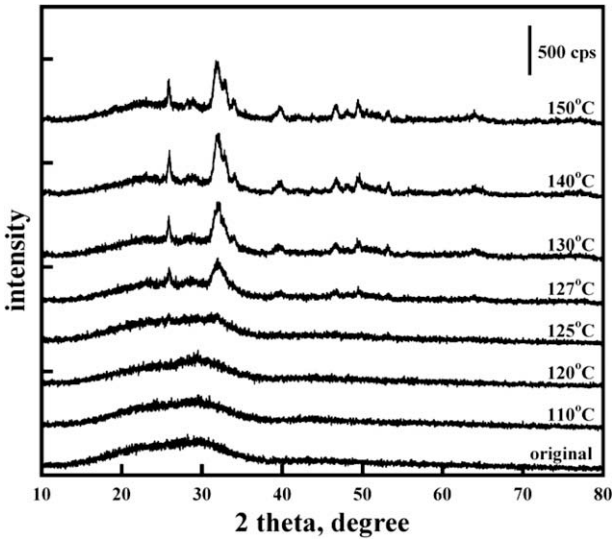


Fig. 8. XRD patterns of precipitates as shown in Fig. 7.

as S_n) of the hollow-like particles produced at 127 °C measured by the N_2 adsorption measurement was about 56 m^2/g, coinciding with a calculated S_n value of ca. 63 m^2/g in the hollow spheres with an outer diameter (φ_1) of 790 nm and an inside diameter (φ_2) of 770 nm (the theoretical density ρ of Hap is 3.16 g/cm^3, $S_n = \frac{6(\phi_1^2+\phi_2^2)}{(\phi_1^3+\phi_2^3)\rho}$) [23]. The coincidence of the S_n value strongly supports the fact the balloon-like particles have a hollow structure.

In Fig. 7, we successfully prepared calcium phosphate particles with a fairly uniform and transparent balloon-like structure. Recently, various efforts have been made to prepare inorganic hollow spheres by using different templates, including polyelectrolyte nano-particles [24], emulsion droplets [25,26], polymer micelles [27], or simply a sacrificial metastable precursor phase [28]. Recently, a double hydrophilic block copolymer (DHBC) and mixed solvents of surfactants and DHBC have also been used as templates for preparing $CaCO_3$ hollow spheres by Cölfen [29]. They explained that the hollow spheres develop from spheres by a dissolution process staring at the center of the sphere. Qi et al. reported the synthesis of micrometer sized calcite hollow spheres by the cooperative effect of DHBC-surfactant complex micelles as the templates [30]. Furthermore, many methods have already been reported on the synthesis of calcium phosphate particles, including microemulsion templating [31], ultrasonic spray pyrolysis [32], emulsion templating [33], block copolymer templating [34], polyelectrolyte mediated crystallization [35] and high temperature ceramic methods [36]. However, the sizes of the hollow particles reported in these literature articles were large and they possess a poor quality surface with a porous shell. Even though they produce nano-particles [33,34], the preparation methods include complicated procedures such as calcinations for removing the templates. Comparing to these particles, the present work is a simple single pot method and the balloon-like hollow spheres produced in this experiment have a unique structure, *i.e.*, fairly uniform, transparent and a smooth surface. Therefore, it is worthwhile to elucidate the formation mechanism of this unique structure. Thus, a detailed time-dependent experiment was conducted at 127 °C to track the formation of the balloon-like particles in the next section.

Fig. 9 illustrates time resolved TEM pictures of precipitates for producing the balloon-like particles at 127 °C in Fig. 7. When the hydrolysis reaction was conducted for 10 h, many solid spherical particles ca. 500–800 nm in diameter were produced. The reaction was further continued to 12.5 h, however, some of the spherical solid spheres changed into transparent balloon-like hollow spheres.

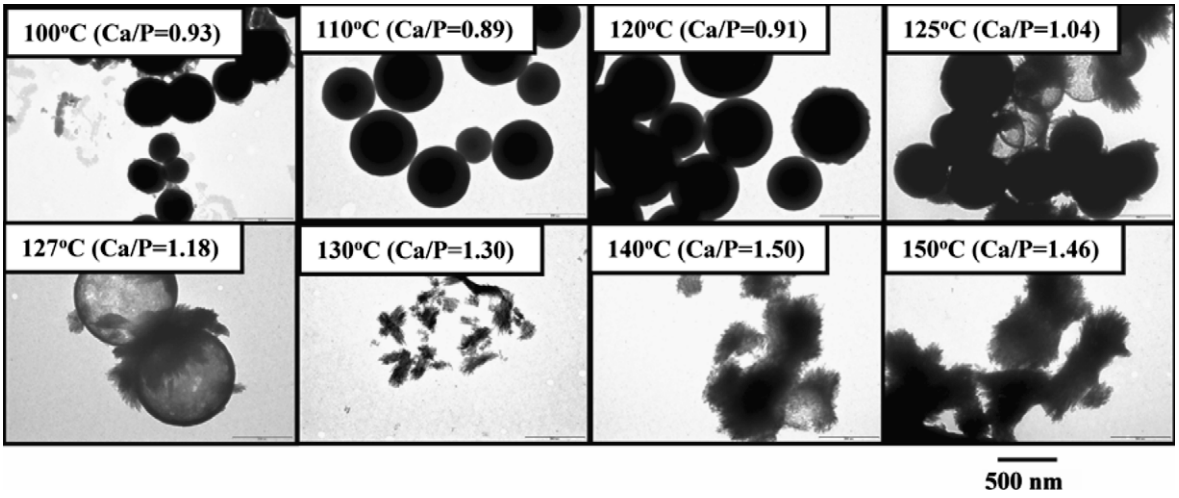


Fig. 7. TEM pictures of precipitates for producing spherical solid particles at various aging temperatures.

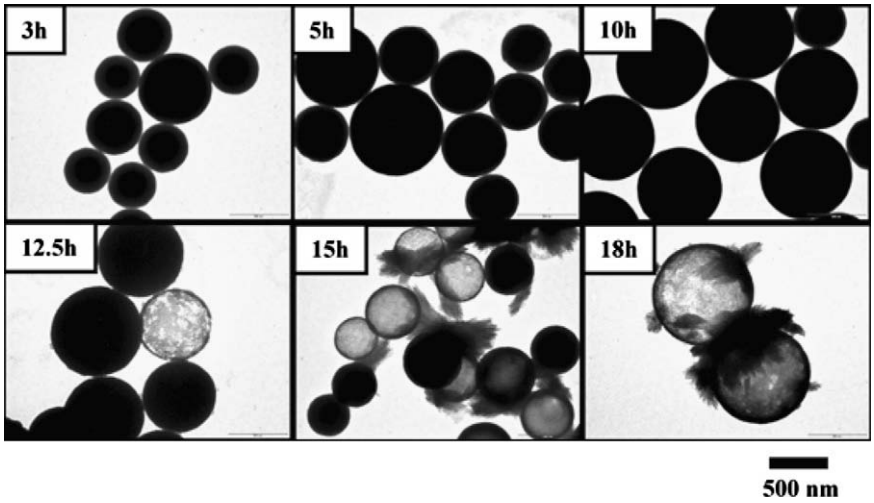


Fig. 9. Time resolved TEM pictures of precipitates for producing balloon-like particles at 127 °C in Fig. 7.

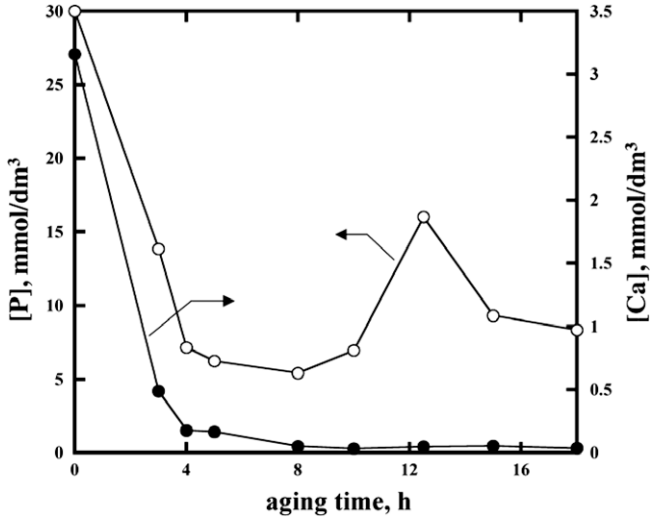


Fig. 10. Changes of concentrations of phosphate and calcium ions in the aging solution for producing balloon-like particles at 127 °C.

After aging for 15 h, many transparent balloon-like hollow spheres can be seen together with rod- or needle-like small particles. To follow this structural change of the solid spherical particles, we further investigated the change of concentrations of phosphate ([P]) and calcium ([Ca]) ions by ICP-AES measurement. The result is displayed in Fig. 10. Clearly, the [Ca] value decreases steeply until 8 h, but the [P] one reduces by 80%. Since the reduction of [P] was only 20% in the previous study using $CaCl_2$, this promotion of [P] reduction in the present study could be due to the $Ca(OH)_2$ used as a starting material. $Ca(OH)_2$ raised the solution pH and increased the hydrolysis of tpp. Another finding in Fig. 10 is the [P] value is at a maximum at an aging time of 12.5 h. This increase of [P] strongly supports that the inside of the solid spherical particles is dissolved as well, as was discussed in our previous paper [21]. However, this value decreases quickly again on further aging. This decrease is probably due to the production of small rod-like calcium phosphate particles (probably Hap), as can be seen in the TEM pictures produced after 15–18 h in Fig. 9. Since tpp and pp ions have a very strong adsorption ability to the Hap surface, as the authors already revealed before [37], the unhydrolyzed tpp and also the pp ions of the hydrolysis product of tpp ions would be adsorbed on the solid spherical particles initially produced. The adsorption of tpp and pp ions may protect the dissolution of the particles' shell and turns out the balloon-like structure. The explanation of this formation mechanism will be the subject of further work. Hollow spheres of calcium phosphate hold potential as drug delivery vehicles, for example, and have biocompatibility advantages over other materials.

4. Conclusions

The preparation procedure employed in this work precipitated large spherical and/or small aggregated spherical particles with an extremely fast rate of reaction under 100 °C. The large spherical particles were amorphous but the small aggregated ones were α-$CaNa_2P_2O_7{\cdot}4H_2O$, and the former ones crystallized to β-$Ca_2P_2O_7$ after being calcined above 600 °C.

Calcium hydroxyapatite with rod-like and ellipsoidal or spherical aggregates was successfully produced using polyphosphates as a source of orthophosphate ions.

The aging temperature drastically varied the particle shape under conditions for producing uniform amorphous spherical particles. Fully transparent balloon-like hollow spheres were produced with mere trace amounts of small rod-like particles after aging the solution above 127 °C.

TEM observation and ICP-AES measurements revealed that the particles with unique structures such as the balloon-like hollow spheres were produced by dissolving the interior of solid spherical particles after reinforced their shell by the adsorption of unhydrolyzed ttp and/or pp ions hydrolyzed from tpp ones.

References

[1] E. Susa, J. Polym. Sci. Part C: Polym. Chem. (1963) 399.
[2] T. Klein, A.A. Driessen, K. de Groot, A. van der Hoff, J. Biomed. Mater. Res. Part A 17 (1983) 769.
[3] E. Katsanis, E. Matijevic, Colloids Surf. 5 (1982) 43.
[4] R.B. Wilhelmy, R.C. Patel, E. Matijevic, Inorg. Chem. 24 (1985) 3290.
[5] T. Ishikawa, E. Matijevic, J. Colloid Interface Sci. 123 (1988) 122.
[6] R.B. Wilhelmy, E. Matijevic, Colloids Surf. 22 (1987) 111.
[7] I.I. Springsteen, E. Matijevic, Colloids Polym. Sci. 267 (1989) 1007.
[8] K. Kandori, M. Toshioka, H. Nakashima, T. Ishikawa, Langmuir 9 (1993) 1031.
[9] K. Kandori, H. Nakashima, T. Ishikawa, J. Colloid Interface Sci. 160 (1993) 499.
[10] K. Kandori, T. Imazato, A. Yasukawa, T. Ishikawa, Colloid Polym. Sci. 274 (1996) 290.
[11] K. Kandori, N. Ikeguchi, A. Yasukawa, T. Ishikawa, J. Colloid Interface Sci. 181 (1996) 425.
[12] K. Kandori, N. Ikeguchi, A. Yasukawa, T. Ishikawa, J. Colloid Interface Sci. 202 (1998) 369.

[13] K. Kandori, T. Kuwae, T. Ishikawa, J. Colloid Interface Sci. 300 (2006) 225.
[14] T. Kawasaki, S. Takahashi, K. Ikeda, Eur. J. Biochem. 152 (1985) 361.
[15] T. Kawasaki, M. Niikura, S. Takahashi, K. Kobayashi, Biochem. Int. 13 (1986) 969.
[16] T. Kawasaki, K. Ikeda, S. Takahashi, Y. Kuboki, Eur. J. Biochem. 155 (1986) 249.
[17] A. Tiselius, S. Hjertén, Ö. Levin, Arch. Biochem. Biophys. 65 (1956) 132.
[18] J.D. McGilvery, J.P. Crowther, Can. J. Chem. 32 (1954) 174.
[19] R.P. Mitra, B.R. Thukral, Chem. Sect. A: Inorg. Bioinorg. Phys. Theor. Anal. Chem. 8 (1970) 350.
[20] Y. Miyazaki, G. Kura, H. Tsuzuki, H. Sakashita, J. Chem. Soc., Faraday Trans. 92 (1996) 3587.
[21] K. Kandori, K. Tada, M. Fukusumi, Y. Morisada, Bull. Chem. Soc. Jpn. 81 (2008) 1567.
[22] R.K. Osterheld, in: H. Barman (Ed.), Topics in Phosphorus Chemistry, vol. 7, John Wiley and Sons Inc., 1972. p. 103.
[23] T. He, D. Chen, X. Jias, Y. Xu, Y. Gu, Langmuir 20 (2004) 8404.
[24] F. Caruso, Chem. Eur. J. 6 (2000) 413.
[25] S. Schacht, Q. Huo, I.G. Viogt-Martin, S.G. Stucky, F. Schüth, Science 273 (1996) 768.
[26] Y.R. Ma, L.M. Qi, J.M. Ma, H.M. Cheng, Langmuir 19 (2003) 4040.
[27] T. Liu, Y. Xie, B. Chu, Langmuir 16 (2000) 9015.
[28] S.H. Yu, H. Cölfen, M. Antonietti, J. Phys. Chem. B 107 (2003) 7396.
[29] H. Cölfen, Macromol. Rapid Commun. 22 (2001) 219.
[30] L.M. Qi, J. Li, J. Ma, Adv. Mater. 14 (2002) 300.
[31] C.E. Fowler, M. Li, S. Mann, H.C. Margolis, J. Mater. Chem. 15 (2005) 3317.
[32] T. Ohno, M. Aizawa, Key Eng. Mater. 309–311 (2006) 235.
[33] H.T. Schmidt, M. Kroczynski, Y. Chen, R. Josephs, A.E. Ostafin, J. Microencapsulation 23 (2006) 769.
[34] W. Tjandra, P. Rani, R. Yao, K.C. Tam, Nanotechnology 17 (2006) 5988.
[35] A. Bigi, E. Boanini, D. Welsh, S. Mann, Angew Chem., Int. Ed. Engl. 41 (2004) 2163.
[36] Q. Wang, W. Huang, D. Wang, B.W. Darvell, D.E. Day, M.N. Rahaman, J. Mater. Sci. Mater. Med. 17 (2006) 641.
[37] K. Kandori, S. Oda, S. Tsuyama, J. Phys. Chem. B 112 (2008) 2542.

2. Experimental

2.1. Materials

$Mn_2(CO)_{10}$ (Alfa), $RuCl_3{\cdot}xH_2O$ (Aldrich), 2,2′-bipyridine (Merck), 4,4′-bipyridine (Fluka), $AgCF_3SO_3$ (Alfa), and NH_4PF_6 (Alfa) were used as received. All solvents used for the synthesis were of reagent grade and for spectral measurements spectral grade was used.

2.2. Physical measurements

UV–Vis spectra were recorded on Analtikjena Specord S100 spectrophotometer and emission spectra were measured in JASCO FP6300 spectrofluorimeter. All the samples used for emission were purged with dry nitrogen gas for about 20 min. IR spectra were measured using JASCO FT-IR spectrophotometer. The samples were recorded in the form of KBr pellets. All the mass spectra were recorded using a Quattro LC triple-quadrupole mass spectrometer (Micromass, Manchester, UK) interfaced to an (Electro Spray ionization) ESI source; data acquisition was done under the control of Masslynx software (version 3.2). The ESI capillary voltage was maintained between 4.0 and 4.2 kV and the cone voltage kept at 25 V. Nitrogen was used as desolvation and nebulization gas. The source and desolvation temperatures were 100 °C.

2.3. Electrochemistry

The redox potentials of the complexes were determined by cyclic voltammetric and differential pulse voltammetric techniques using EG & G Princeton Applied Research Potentiostat/Galvanostat Model 273 A. Measurements were performed by purging the solution in acetonitrile (spectroscopic grade) by dry nitrogen gas for 30 min. The supporting electrolyte was 0.1 M TBAP, Pt was the working electrode, and Ag/AgCl was the reference electrode.

2.4. Lifetime and transient measurements

The excited state lifetime measurements for all the complexes were made, after degassing the solutions with argon for 30 min, and the details are given in previous reports [32]. Transient absorption measurements were made with laser flash photolysis technique as described elsewhere [32].

2.5. Syntheses

The complexes **bRu** [33], **bRuRub** [33], **pRub** [34], **pRuRup** [34] and [$Mn(CO)_3(NN)(CF_3SO_3)$] [35] were synthesized by reported procedures.

2.6. [$Mn(CO)_3(bpy)(4,4'\text{-bpy})](PF_6$) (bMn)

To a degassed solution of [$Mn(CO)_3(bpy)(CF_3SO_3)$] (0.2 g, 0.45 mmol) in CH_3CN (25 mL), 4,4′-bipyridine (0.7 g, 4.5 mmol) was added. It was constantly protected from light and stirred for 45 min at RT. The completion of the reaction was monitored by TLC. The solvent was evaporated under reduced pressure. The residue was dissolved in minimum of acetone and excess ether was added. The product precipitated was filtered and dried. This was repeated for 2–3 times to remove the excess 4,4′-bipyridine. Finally the product was metathesized to PF_6^- salt by dissolving in minimum amount of acetone and adding an aqueous solution of NH_4PF_6. The yellow precipitate formed was washed with water and ether, dried *in vacuo* for overnight. Yield = 74%. IR (KBr, cm^{-1}): 2041, 1949; ESI-MS (*m/z*): 451.

2.7. [$(CO)_3(bpy)Mn(4,4'\text{-bpy})Mn(bpy)(CO)_3](PF_6)_2$ (bMnMnb)

$Mn(CO)_3(bpy)(CF_3SO_3)$ (0.2 g, 0.45 mmol) was dissolved in degassed CH_3CN and protected from light. 4,4′-Bipyridine (0.036 g, 0.23 mmol) was added and the solution was stirred for 18 h at RT. The solvent was evaporated under reduced pressure and the contents were dried. The product was purified by column chromatography by using pet.ether/CH_2Cl_2. The column was constantly protected from light. Finally, the product was metathesized to PF_6^- salt by dissolving in minimum amount of acetone and adding an aqueous solution of NH_4PF_6. The yellow precipitate formed was washed with water and ether, dried *in vacuo* for overnight. Yield 72%. IR (KBr, cm^{-1}): 2043, 1933; ESI-MS (*m/z*): 839.

2.8. [$Mn(CO)_3(phen)(4,4'\text{-bpy})](PF_6$) (pMn)

$Mn(CO)_3(phen)(CF_3SO_3)$ (0.2 g, 0.43 mmol) was dissolved in degassed CH_3CN (25 mL), and 4,4′-bipyridine (0.67 g, 4.3 mmol) was added. It was stirred under dark for 45 min at RT. The completion of the reaction was monitored by TLC. At the end of the reaction the solvent was evaporated under reduced pressure. The residue was dissolved in minimum of acetone and excess ether was added. The product precipitated was filtered and dried. This was repeated for 2–3 times to remove the excess 4,4′-bipyridine. Finally, the product was metathesized to PF_6^- salt by dissolving in minimum amount of acetone and adding an aqueous solution of NH_4PF_6. The yellow precipitate formed was washed with water and ether, dried *in vacuo* for overnight. Yield = 77%. IR (KBr, cm^{-1}): 2041, 1941; ESI-MS (*m/z*): 474.

2.9. [$(CO)_3(phen)Mn(4,4'\text{-bpy})\ Mn(phen)(CO)_3](PF_6)_2$ (pMnMnp)

$Mn(CO)_3(phen)(CF_3SO_3)$ (0.2 g, 0.43 mmol) was dissolved in degassed CH_3CN and protected from light. 4,4′-bipyridine (0.034 g, 0.22 mmol) was added and the solution was stirred for 20 h at RT. The solvent was evaporated under reduced pressure and the contents were dried. The product was purified by column chromatography by using pet.ether/CH_2Cl_2. Finally, the product was metathesized to PF_6^- salt by dissolving in minimum amount of acetone and adding an aqueous solution of NH_4PF_6. The yellow precipitate formed was washed with water and ether, dried *in vacuo* for overnight. Yield = 76%. IR (KBr, cm^{-1}): 2043, 1933; ESI-MS (*m/z*): 939.

2.10. [$(CO)_3(bpy)Mn(4,4'\text{-bpy})Ru(bpy)_2Cl](PF_6)_2$ (bMnRub)

The complex **bRu** (0.186 g, 0.25 mmol) was dissolved in degassed EtOH and protected from light. To this solution was added $Mn(CO)_3(bpy)(CF_3SO_3)$ (0.11 g, 0.25 mmol) and stirred for 8 h under nitrogen at RT and constantly protected from light. The solvent was evaporated under reduced pressure and the contents were dried. The complex was purified by column chromatography by packing the column with alumina and eluting with pet. ether/ethanol mixture. During the purification, the column was protected from light. A yellow band of unreacted Mn(I) complex eluted first. Upon increasing the composition of ethanol a brown band of the product got eluted. The product was dried under reduced pressure and metathesized to PF_6^- salt by dissolving in minimum amount of acetone and adding an aqueous solution of NH_4PF_6. The precipitate formed was washed with water and ether, dried *in vacuo* for overnight. Yield: 72% IR (KBr, cm^{-1}): 2038, 1935; ESI-MS (*m/z*): 1045.

2.11. [$(CO)_3(phen)Mn(4,4'\text{-bpy})Ru(phen)_2Cl](PF_6)_2$ (pMnRup)

To a degassed solution of **pRu** (0.140 g, 0.175 mmol) in EtOH was added $Mn(CO)_3(phen)(CF_3SO_3)$ (0.082 g, 0.175 mmol). The contents were stirred for 10 h under nitrogen at RT and constantly

protected from light. The solvent was evaporated under reduced pressure and the contents were dried. The complex was purified by column chromatography by using alumina as the solid support and eluting with pet. ether/ethanol mixture. The column was protected from light during the purification. A yellow band of unreacted Mn(I) complex eluted first. Upon increasing the composition of ethanol a brown band of the product got eluted. The product was dried under reduced pressure and metathesized to PF_6 salt by dissolving in minimum amount of acetone and adding an aqueous solution of NH_4PF_6. The precipitate formed was washed with water and ether, dried *in vacuo* for overnight. Yield: 70%. IR (KBr, cm^{-1}): 2038, 1934; ESI-MS (*m/z*): 1116.

3. Results and discussion

3.1. Synthesis

The manganese(I) and ruthenium(II) complexes used in the present work are shown in Chart 1. The ruthenium(II) complexes **bRu**, **pRu**, **bRuRub** and **pRuRup** were prepared by literature procedures [33,34]. The Mn(I) carbonyl complexes were prepared by treating the precursor complex $[Mn(CO)_3(NN)(CF_3SO_3)]$ [35] with the ligand 4,4′-bpy. The reactions were carried out under inert atmosphere and protected from light. The Mn–Ru heterobimetallic complexes were prepared by complex as metal/complex as ligand strategy [36]. The Mn(I) precursor complex was treated with the corresponding Ru(II) monometallic complex. The complexes were characterized by ESI-MS, IR, cyclic voltammetry, absorption and emission spectral techniques.

3.2. ESI-MS

The Mn(I) monometallic and bimetallic complexes were characterized by ESI-MS spectral technique. These complexes show a peak corresponding to the loss of PF_6^- ion. The *m/z* values corresponding to the loss of a PF_6^- ion for the complexes **bMn**, **pMn**, **bMnMnb**, **pMnMnp** and **bMnRub** are 451, 474, 891, 939 and 1045 respectively. The other peaks are assigned to loss of 4,4′-bipyridine, followed by a carbonyl moiety and then two carbonyl groups. This trend is followed in all the complexes. The ESI-MS spectra of the complexes **bMn**, **bMnMnb** and **bMnRub** are given in Figs. S1–S3.

Table 1
IR spectral and Electrochemical data[a] of monometallic and bimetallic complexes containing 2,2′-bipyridine.

Complex	$E_{1/2}$ (V) $Ru^{3+/2+}$	E_P (V) $Mn^{2+/+}$	$E_{1/2}$ (V)		ν(CO) cm^{-1}
			$bpy^{0/-}$	4,4′-$bpy^{0/-}$	
bRu	0.75		−1.59	−0.96	
bRuRub	0.89	1.9	−1.61	−0.97	2041, 1949
bMn	1.01	1.71	−1.6	−0.93	2043, 1933
bMnMnb		1.57	−1.6	−0.88	2038, 1935
bMnRub			−1.49	−0.9	

[a] Ag/AgCl reference electrode; 0.1 M TBAP supporting electrolyte.

3.3. IR spectra

The IR spectra for all the complexes were recorded in KBr pellets. The presence of two strong ν(CO) stretching frequencies indicate the *fac.* configuration for these complexes. When the halide (X = Br^-) is replaced with 4,4′-bipyridine, the carbonyl stretching frequency is increased. This is due to the decrease in electron density at the metal center (Mn^I) when 4,4′-bipyridine is coordinated to Mn^I, because 4,4′-bpy is a strong π-accepting ligand. The IR spectral data are collected in Tables 1 and 2.

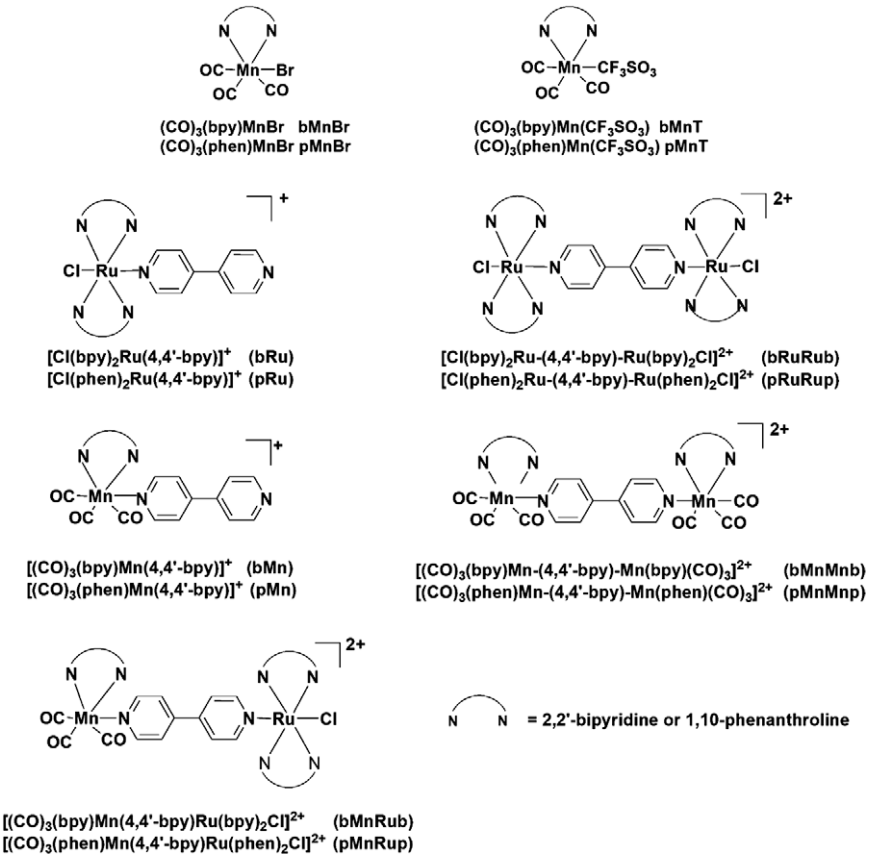


Chart 1. Structure of complexes.

Table 2
IR spectral and Electrochemical data[a] of monometallic and bimetallic complexes containing 1,10-phenanthroline.

Complex	$E_{1/2}$ (V) $Ru^{3+/2+}$	E_P (V) $Mn^{2+/+}$	$E_{1/2}$ (V)		ν(CO) cm^{-1}
			phen$^{0/-}$	4,4′-bpy$^{0/-}$	
pRu	0.81		−1.61	−0.97	
pRuRup	0.85	1.53	−1.63	−0.99	2041, 1941
pMn	1.01	1.54	−1.49	−1.03	2043, 1933
pMnMnp		1.53	−1.6	−1.09	2038, 1934
pMnRup			−1.49	−1.06	

[a] Ag/AgCl reference electrode; 0.1 M TBAP supporting electrolyte.

In the case of Ru–Mn heterobimetallic complexes the ν(CO) stretching frequency is slightly decreased compared to monometallic and homobimetallic Mn^{I} complexes. This indicates the attachment of $Mn(CO)_3$ unit into the Ru^{II} complex and the decrease in the ν(CO) stretching frequency is due to electron donation from Ru^{II} unit.

3.4. Electrochemistry

The electrochemical properties of all the complexes were studied in CH_3CN using Ag/AgCl as the reference electrode. The manganese complexes show poor reversibility on applying the potential. In the anodic scan, the complexes **bMn** and **bMnMnb** undergo oxidation at the manganese site ($Mn^{I/II}$). In the cathodic scan, the complexes undergo reduction occurring at the ligands. The reduction at less negative potential can be attributed to the reduction of bridging ligand (4,4′-bpy$^{0/-}$) and the one at large potential is due to ancillary ligand (bpy$^{0/-}$) [37]. The electrochemical data of all the complexes are given in Tables 1 and 2. The DPV of **bMn** is shown in Fig. S4. For the manganese complexes with phenanthroline ligands **pMn** and **pMnMnp**, oxidation occurs at *ca* 1.54 V. In the negative region reduction occurs at −1.09 and −1.60 V due to the bridging ligand and phen ligand. The ruthenium complexes **bRu** and **bRuRub** show oxidation with the $E_{1/2}$ value of 0.75 and 0.89 V, respectively due to $Ru^{II/III}$ [34]. In the cathodic region reduction occurs at considerably lower potential (−0.99 V) which can be assigned to the reduction of bridging ligand and other two reductions at large negative potentials can be assigned to the reduction of ancillary bipyridine ligands. Similar assignments can be made for ruthenium complexes with phenanthroline ligand [34]. The anodic part of the cyclic voltammogram of **pRuRup** is shown in Fig. S5.

The Mn–Ru heterobimetallic complexes **bMnRub** and **pMnRup** show two oxidation peaks. The differential pulse voltammogram of **pMnRup** is shown in Fig. 1.

From the comparison of ruthenium(II) monometallic and homobimetallic complexes, the peak at 1.01 V is assigned to $Ru^{II/III}$. Another peak at +1.54 V is due to $Mn^{I/II}$ oxidation and this is assigned based on the observed redox potentials for Mn^{I} monometallic and bimetallic complexes. The attachment of Mn^{I} unit into Ru^{II} monometallic complexes **bRu** and **pRu** can be seen in the shift in the oxidation potential values. In the heterobimetallic complexes the oxidation potential of the ruthenium(II) unit is shifted towards more positive value, indicating it is difficult to get oxidized upon coordination of $Mn(CO)_3$ unit, and the oxidation potential of the manganese(I) unit is shifted towards less positive value due to electron donation from Ru(II) unit. This result is in agreement with what we observe in IR spectra.

3.5. Absorption spectra

The absorption spectra for all the complexes were recorded in CH_3CN at room temperature. The absorption spectra of complexes **bMnBr**, **bMnT**, **pMnBr** and **pMnT** are shown in Figs. S6 and 2. From the absorption spectra it is evident that on replacing Br^- with $CF_3SO_3^-$, a blue shift to a tune of 53 nm is observed because of poor π-accepting ligand [35]. The absorption spectral data of the complexes with 2,2′-bipyridine ancillary ligand are given in Table 3.

The manganese complexes with 2,2′-bpy ancillary ligands **bMn** and **bMnMnb**, have a peak at 290 nm due to ligand centered $\pi \rightarrow \pi^*$ transition. These complexes show a broad absorption in the region 320–400 nm because of ^{1}MLCT transition arising out of transfer of an electron from Mn(dπ) → (π*) [35]. The absorption spectrum of **bMnMnb** is shown in Fig. S7. Similarly manganese complexes with 1,10-phenanthroline ligand **pMn** and **pMnMnp** have $\pi \rightarrow \pi^*$ transition at 265 nm and a broad absorption in the region 320–400 nm due to ^{1}MLCT transition. The absorption spectrum of **pMnMnp** is shown in Fig. 3. The absorption spectral data of the complexes with phenanthroline ancillary ligand are given in Table 4.

Ruthenium(II) complexes **bRu** and **bRuRub** display ligand centered transition at 290 nm and MLCT transitions in the region 325–375 nm and 470–500 nm with maximum absorption occurring at 487 and 489 nm, respectively. The absorption spectrum of the complex **bRuRub** is shown in Fig. S7. For the known complexes the absorption spectral data observed here are very similar to the reported values [33,34]. Similarly the ruthenium(II) complex with phenanthroline ancillary ligand **pRuRup** show intense transitions in the UV region due to ligand centered $\pi \rightarrow \pi^*$ transition and low energy ^{1}MLCT transition in the region 450–475 nm (Fig. 3). In the case of Mn^{I}–Ru^{II} heterobimetallic complexes **bMnRub** and **pMnRup** intense peaks in the UV region at 290 and 264 nm are assigned to ligand centered $\pi \rightarrow \pi^*$ transition. In the visible region ^{1}MLCT transition is seen at 447 and 448 nm, respectively, for the complexes **bMnRub** and **pMnRup**. When we compare the absorption spectrum of the complex **bMnRub** with that of monometallic and homobimetallic ruthenium(II) complexes **bRu** and **bRuRub**, a blue shift to a tune of 40 and 42 nm, respectively is observed. Similarly for the complex **pMnRup** a blue shift to a magnitude of 15 nm is observed when compared to **pRuRup**. The blue shift can be attributed to the attachment of strong π-accepting $Mn(CO)_3$ core. This observation is supported by IR and cyclic voltammetry results. This kind of blue shift is seen in related ruthenium(II) and osmium(II) complexes when more π-accepting ligands like triphenyl phosphine and carbonyl are attached [38].

3.6. Emission spectra

The emission spectra of all the complexes were recorded in CH_3CN at room temperature and spectral data are collected in

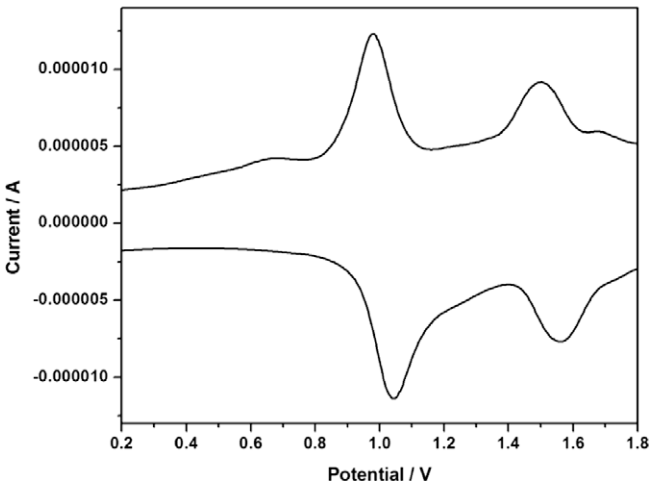


Fig. 1. Differential Pulse Voltammogram of **pMnRup** in CH_3CN.

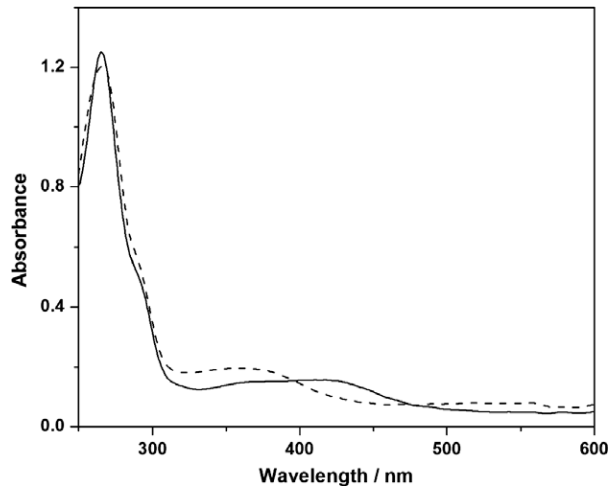


Fig. 2. Absorption spectra of complexes **pMnBr** (solid line) and **pMnT** (dotted line) in CH_3CN at RT.

Table 3
Photophysical properties of monometallic and bimetallic complexes with 2,2′-bipyridine ligand in CH_3CN at 298 K.

Complex	$\lambda_{\xi\alpha\mu}$	$\lambda_{\xi\alpha\mu,\mu\varepsilon}$	τ (ns)	$\varphi_{\mu\varepsilon}$	$k_{r\ 10}{}^{4}$	$k_{nr\ 10}{}^{6}$
$Ru(bpy)_3{}^{2+}$	290, 452	615	1100	0.064	5.8	0.85
bRu	292, 377, 487	722	28	0.0015	1.5	36
bRuRub	291, 354, 489	726	28	0.0023	7.8	35
bMn	290, 354	a	a	a	2.3	8.3
bMnMnb	290, 354	a	a	a		
bMnRub	290, 447	614	120	0.0027		

a = No detectable emission.

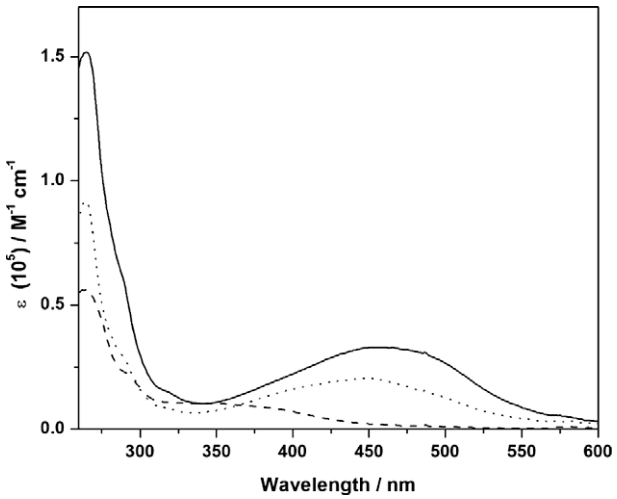


Fig. 3. Absorption spectra of complexes **pRuRup** (—), **pMnMnp** (——) and **pMnRup** (. . .) in CH_3CN at RT.

Tables 3 and 4. The manganese complexes **bMn**, **pMn**, **bMnMnb** and **pMnMnp** have no detectable emission. The ruthenium(II) complexes **bRu** and **bRuRub** display emission at 722 and 726 nm, respectively, from ^{3}MLCT state upon excitation at 489 nm and the emission maximum is independent of excitation wavelength. The emission spectrum of **bRuRub** is shown in Fig. S8. Similarly ruthenium complexes with phenanthroline ligand **pRu** and **pRuRup** emit from ^{3}MLCT state at 680 and 684 nm, respectively, upon excitation at the wavelength corresponding to ^{1}MLCT absorption. The emission spectrum of **pRuRup** is shown in Fig. 4.

Table 4
Photophysical properties of monometallic and bimetallic complexes with 1,10-phenanthroline ligand in CH_3CN at 298 K.

Complex	$\lambda_{\xi\alpha\mu}$	$\lambda_{\xi\alpha\mu,\mu\varepsilon}$	τ (ns)	$\varphi_{\mu\varepsilon}$	$k_{r\ 10}{}^{4}$	$k_{nr\ 10}{}^{6}$
$Ru(phen)_3{}^{2+}$	266, 442	604	460	0.028	6.08	2.1
pRu	265, 451	680	33	0.0035	10.6	30.1
pRuRup	264, 463	684	72	0.004	5.55	13.8
pMn	265, 351	a	a	a		
pMnMnp	265, 352	a	a	a		
pMnRup	264, 448	599	249	0.012	4.8	4

a = No detectable emission.

The emission spectrum of the heterobimetallic complex **bMnRub** is shown in Fig. S8. The complex displays emission at 613 nm from ^{3}MLCT state and it has the same emission maximum irrespective of excitation wavelength. On comparing the emission maximum of heterobimetallic complex **bMnRub** with the corresponding monometallic and homobimetallic complexes **bRu** and **bRuRub**, a blue shift to a tune of 109 and 113 nm, respectively, has been observed. Also the emission intensity of the heterobimetallic complex is increased compared to the ruthenium(II) homobimetallic complex **bRuRub**. The emission spectrum of **pMnRup** is shown in Fig. 4 and it displays emission maximum at 599 nm, which is independent of excitation wavelength. A blue shift to a magnitude of 81 and 85 nm is observed compared to **pRu** and **pRuRup**, respectively. As seen in **bMnRub**, the emission intensity of **pMnRup** is also increased compared to **pRuRup**. These results are in line with what we observe in absorption spectra, in which also a blue shift occurs in heterobimetallic complexes. Hence emission spectra also confirm the attachment of more π-accepting $Mn(CO)_3$ core into ruthenium(II) monometallic complex leading to increased energy gap between ground state and excited state. The increase in the emission intensity of heterobimetallic Mn–Ru complexes can be explained by energy gap law [6], which states that the non-radiative decay rate increases exponentially with decrease in the energy gap between ground and excited states. Hence in Mn–Ru heterobimetallic complexes, the increase in energy difference between ground and excited state decreases the rate of non-radiative decay. When we look into the absorption spectra of manganese(I) complexes, the ^{1}MLCT transition appears in the high energy region compared to ruthenium(II) complexes. So in the manganese(I)–ruthenium(II) heterobimetallic complexes, the emission intensity of ruthenium is not quenched. Since Mn(I) complexes have no detectable emission, the intrinsic non-radiative

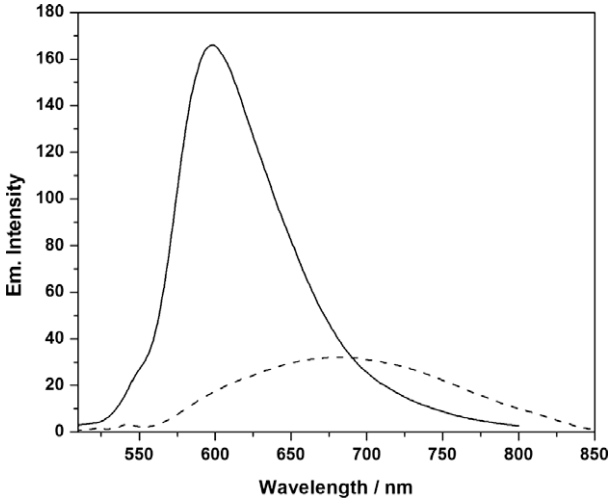


Fig. 4. Emission spectra of **pRuRup** and **pMnRup** in CH_3CN at RT.

decay may compete with energy transfer from *Mn(I) to Ru(II). Since there is no luminescence quenching of Ru(II), electron transfer from or to Mn(I) can be excluded. The uncorrected excitation spectrum of **pMnRup**, shown in Fig. 5, was recorded by using the emission wavelength of 599 nm, which is the emission maximum of this complex. The excitation spectrum of **pMnRup** is similar to the absorption spectrum, which shows that the complex is stable under irradiation of UV–Vis light.

3.7. Excited state lifetime and quantum yield

The excited state lifetime and quantum yield of all the complexes **bRu**, **bRuRub, pRu** and **pRuRup** are given in Tables 3 and 4. The ruthenium(II) complexes **bRu** and **bRuRub** have excited state lifetime of 28 ns each. The lifetime decreased substantially for complex **bRu** when compared to $[Ru(bpy)_3]^{2+}$ which has an excited state lifetime of 1100 ns in CH_3CN [6]. These values indicate that the lowest excited level is bridge localized ^{3}MLCT state and this interpretation is supported by the observation of long wavelength emission at 722 nm for **bRu**. Similarly the lifetime of complexes **pRu** and **pRuRup** decreased tremendously compared to $[Ru(phen)_3]^{2+}$ which has an excited state lifetime of 460 ns and quantum yield of 0.028 [7]. The decrease in the lifetime and quantum yield values of **bRu**, **bRuRub**, **pRu**, and **pRuRup** can be explained in terms of energy gap law [6]. Since the energy gap between ground and excited state is less for these complexes, it facilitates faster non-radiative relaxation which leads to low excited state lifetime. Also, thermal deactivation through ligand-field state is possible, since Cl^- is a weak field ligand it may keep the ligand-field state close to ^{3}MLCT state. Interestingly the lifetime and quantum yield of heterobimetallic complexes **bMnRub** and **pMnRup** are enhanced when compared to ruthenium(II) monometallic and homobimetallic complexes (Tables 3 and 4). The increase in lifetime of heterobimetallic complexes can also be explained by energy gap law [6]. The attachment of electron withdrawing $Mn(CO)_3$ unit in heterobimetallic complex increases the energy gap between the ground and excited state of ruthenium(II), and decreases the non-radiative decay (*vide supra*).

3.8. Transient spectra

The transient absorption spectra of the complexes were recorded in acetonitrile solution at room temperature following excitation at 355 nm. The transient spectrum of ruthenium(II) complex **bRuRub**, (Fig. S9), shows a bleach around 490 nm due to the decay of the ground state ^{1}MLCT absorption. The transient spectrum of parent complex $[Ru(bpy)_3]^{2+}$ shows bleaching around 450 nm due to the decay of ground state ^{1}MLCT absorption and formation in the region 370–390 nm due to bpy$^{\cdot}$ radical anion absorption. Similar decay around 490 nm observed for **bRu** and **bRuRub** indicates the decay of ground state ^{1}MLCT, and a broad absorption seen at 590 nm is due to 4,4′-bipyridine radical absorption [37] which indicates that ^{1}MLCT state is bridge localized. This happens because the π^* level of 4,4′-bpy is lower than that of 2,2′-bpy. The transient absorption spectrum of manganese(I)–ruthenium(II) heterobimetallic complex, **bMnRub**, recorded at various time intervals, is shown in Fig. 6.

The transient absorption spectrum shows bleach in the region 400–470 nm with maximum at 450 nm and absorption at 370 nm. The bleach is due to disappearance of ^{1}MLCT state of ruthenium(II) [10] and the absorption is due to the formation of 4,4′-bpy$^{\cdot}$ radical anion. The transient absorption spectrum of **pMnRup** is shown in Fig. S10. The bleach observed around 450 nm for **pMnRup** is due to the decay of ground state ^{1}MLCT of ruthenium(II). When we look into the results of transient spectra of rhenium(I)–ruthenium(II) heterobimetallic complexes [39], obtained by placing Re(I) instead of Mn(I), similar bleach is observed in the region 450–490 nm, due to decay of ^{1}MLCT state of ruthenium(II). In the transient absorption spectra of heterobimetallic complexes, the bleach observed at the time scale is very short (Figs. 6 and S10) compared to ruthenium(II) complex. Hence in **bMnRub** and **pMnRup** the bleach, observed due to the disappearance of ruthenium(II), may be partly due to energy transfer from *Mn(I) to Ru(II). After the formation of excited MLCT state, in the absence of detectable emission, there are two ways for its deactivation. Either the MLCT state of the Mn(I) component may come directly to the ground state via non-radiative decay or it may undergo energy transfer process. When we look into the absorption spectra shown in Fig. 3 and Fig. S7, at 355 nm, which is the wavelength used for excitation, Mn(I) and Ru(II) have almost similar absorption. So it is not possible to selectively generate ^{1}MLCT state of Mn(I), though Ru(II) ^{1}MLCT state is also formed. Although the intrinsic non-radiative decay of *Mn(I) will be fast, a small portion of the energy may be transferred to Ru(II) since the ^{1}MLCT state of Mn(I) is lying higher than that of Ru(II). However at this stage we are not able to provide a clear evidence to prove the energy transfer. The occurrence of non-radiative energy transfer process is a well established phenomenon in recent years [40]. Since Mn(I) complexes are non-luminescent, it is not possible to follow the

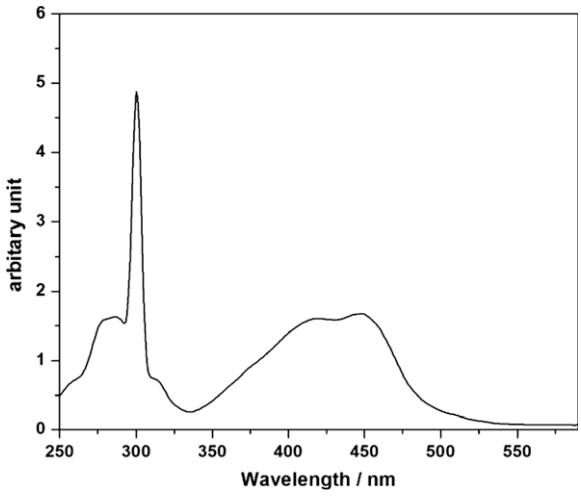


Fig. 5. Excitation spectrum of **pMnRup** in CH_3CN.

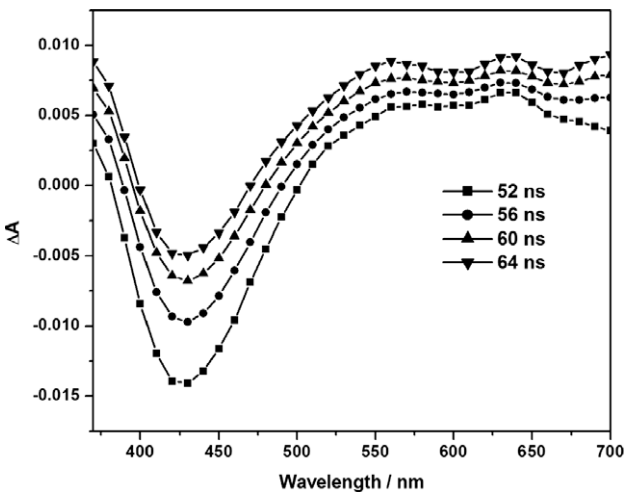


Fig. 6. Transient absorption spectra of **bMnRub** recorded at various time intervals in degassed CH_3CN upon excitation at 355 nm at RT.

emission intensity of Mn(I) complexes. However the time resolved infrared (TRIR) spectroscopy, which measures the change in the stretching vibration frequency of IR active groups (here CO stretching frequency can be followed) when the excited state is formed, can be used. Also this technique can operate on very short time scales (picoseconds) so that the processes that are so fast can be detected. In order to get the rate of intramolecular process, TRIR studies will be carried out.

4. Conclusions

In this work, six new complexes, (two monometallic manganese(I) complexes, two homobimetallic manganese(I) complexes and two heterobimetallic manganese(I)–ruthenium(II) complexes) were synthesized and characterized by various spectral techniques. Upon attaching $Mn(CO)_3$ unit, the absorption and emission maxima are blue-shifted in heterobimetallic complexes compared to ruthenium(II) monometallic and homobimetallic complexes. Also the heterobimetallic complexes show enhanced lifetime and quantum yield compared to ruthenium(II) monometallic and homobimetallic complexes. In order to corroborate intramolecular energy transfer, TRIR studies will be attempted.

Acknowledgement

M.V. and S.R. thank Department of Science and Technology (DST), New Delhi, India for sanctioning a project to carry out this research work.

Appendix A. Supplementary data

Supplementary data associated with this article can be found, in the online version, at doi:10.1016/j.poly.2009.06.021.

References

[1] V. Balzani, A. Credi, M. Venturi, ChemSusChem 1 (2008) 26.
[2] F. Barigelletti, L. Flamigni, Chem. Soc. Rev. 29 (2000) 1.
[3] L. Sun, L. Hammarström, B. Åkermark, S. Styring, Chem. Soc. Rev. (2001) 36.
[4] V. Balzani, A. Juris, Coord. Chem. Rev. 211 (2001) 97.
[5] V. Balzani, P. Bergamini, F. Marchioni, P. Ceroni, Coord. Chem. Rev. 250 (2006) 1245.
[6] K. Kalyanasundaram, Photochemistry of Polypyridine and Porphyrin Complexes, Academic Press, London, 1992.
[7] A. Juris, V. Balzani, F. Barigelletti, S. Campagna, P. Belser, A. von Zelewsky, Coord. Chem. Rev. 84 (1988) 85.
[8] D.M. Guldi, M. Maggini, E. Menna, G. Scorrano, P. Ceroni, M. Marcaccio, F. Paolucci, S. Roffia, Chem. Eur. J. 7 (2001) 1597.
[9] H.A. Meylemans, C.-F. Lei, N.H. Damrauer, Inorg. Chem. 47 (2008) 4060.
[10] M. Falkenström, O. Johansson, L. Hammarström, Inorg. Chim. Acta 360 (2007) 741.
[11] E.M. Sproviero, J.A. Gascon, J.P. McEvoy, G.W. Brudvig, V.S. Batista, J. Am. Chem. Soc. 130 (2008) 6728.
[12] D. Burdinski, K. Wieghardt, S. Steenken, J. Am. Chem. Soc. 121 (1999) 10781.
[13] R.T.F. Jukes, V. Adamo, F. Hartl, P. Belser, L. De Cola, Coord. Chem. Rev. 249 (2005) 1327.
[14] L. De Cola, P. Belser, Coord. Chem. Rev. 177 (1998) 301.
[15] A. Juris, L. Prodi, A. Harriman, R. Ziessel, M. Hissler, A. El-ghayoury, F. Wu, E. Riesgo, R.P. Thummel, Inorg. Chem. 39 (2000) 3590.
[16] T.L. Easun, W.Z. Alsindi, M. Towrie, K.L. Ronayne, X.-Z. Sun, M.D. Ward, M.W. George, Inorg. Chem. 47 (2008) 5071.
[17] V. Balzani, A. Juris, M. Venturi, S. Campagna, S. Serroni, Chem. Rev. 96 (1996) 759.
[18] A. Harriman, R. Ziessel, Chem. Commun. (1996) 1707.
[19] R. Ziessel, M. Hissler, A. El-ghayoury, A. Harriman, Coord. Chem. Rev. 178–180 (1998) 1251.
[20] J. Leveque, B. Elias, C. Moucheron, A. Kirsch-De Mesmaeker, Inorg. Chem. 44 (2005) 393.
[21] X.-Y. Wang, A.D. Guerzo, S. Baitalik, G. Simon, G.B. Shaw, L.X. Chen, R. Schmehl, Photosynth. Res. 87 (2006) 83.
[22] A.C. Benniston, A. Harriman, P. Li, C.A. Sams, J. Phys. Chem. A 109 (2005) 2302.
[23] M. Razavet, V. Artero, C. Cavazza, Y. Oudart, C. Lebrun, J.C. Fontecilla-Camps, M. Fontecave, Chem. Commun. (2007) 2805.
[24] D.J. Butcher, A. Zybin, M.A. Bolshov, K. Niemax, Anal. Chem. 71 (1999) 5379.
[25] A. Rosa, G. Ricciardi, E.J. Baerends, D.J. Stufkens, Inorg. Chem. 37 (1998) 6244.
[26] G.J. Stor, D.J. Stufkens, P. Vernooijs, E.J. Baerends, J. Fraanje, K. Goubitz, Inorg. Chem. 34 (1995) 1588.
[27] J. Connolly, G.W. Goodban, G. Reid, A.M.Z. Slawin, J. Chem. Soc., Dalton Trans. (1998) 2225.
[28] J. Connolly, M.K. Davies, G. Reid, J. Chem. Soc., Dalton Trans. (1998) 3833.
[29] W. Levason, S.D. Orchard, G. Reid, Organometallics 18 (1999) 1275.
[30] M.L. Man, K.C. Lam, W.N. Sit, S. Man Ng, Z. Zhou, Z. Lin, C.P. Lau, Chem. Eur. J. 12 (2006) 1004.
[31] S. Sun, C.A. Dullaghan, G.B. Carpenter, A.L. Rieger, P.H. Rieger, D.A. Sweigart, Angew. Chem., Int. Ed. Engl. 34 (1995) 2540.
[32] P. Thanasekaran, T. Rajendran, S. Rajagopal, C. Srinivasan, R. Ramaraj, P. Ramamurthy, B. Venkatachalapathy, J. Phys. Chem. A 101 (1997) 8195.
[33] M.J. Powers, T.J. Meyer, J. Am. Chem. Soc. 102 (1980) 1289.
[34] N.I. Veletsky, I.A. Dementiev, A.Y. Ershov, A.B. Nikol'skii, J. Photochem. Photobiol. A: Chem. 89 (1995) 99.
[35] R.M. Carlos, I.A. Carlos, B.S. Lima Neto, M.G. Neumann, Inorg. Chim. Acta 299 (2000) 231.
[36] S. Serroni, S. Campagna, F. Puntoriero, C. Di Pietro, N.D. McClenaghan, F. Loiseau, Chem. Soc. Rev. 30 (2001) 367.
[37] G. Tapolsky, R. Duesing, T.J. Meyer, Inorg. Chem. 29 (1990) 2285.
[38] D. Xu, J.Z. Zhang, B. Hong, J. Phys. Chem. A 105 (2001) 7979.
[39] M. Velayudham, S. Rajagopal, unpublished results.
[40] K. Aslan, I. Gryczynski, J. Malicka, E. Matveeva, J.R. Lakowicz, C.D. Geddes, Curr. Opin. Biotechnol. 16 (2005) 55.

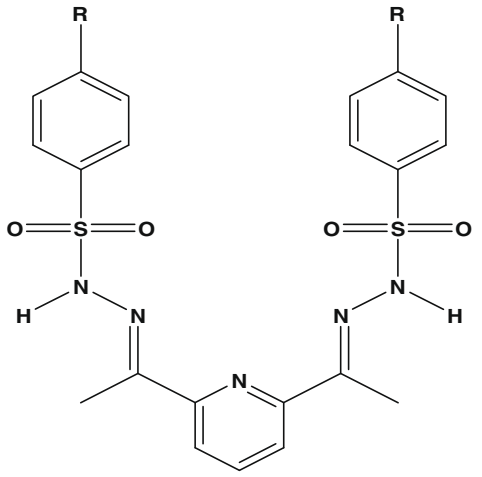


Fig. 1. Chemical diagram of the Schiff bases [R = H (L^1), CH_3 (L^2) and OCH_3 (L^3)].

2.2. Preparation of the Schiff bases

2.2.1. General method for the preparation of the Schiff bases

L^1 was obtained by adding benzenesulfonohydrazine (0.516 g, 0.20 mmol) dropwise into an acidified ethanolic solution of 2,6-diacetylpyridine (0.245 g, 0.10 mmol). The mixture was refluxed for about 3 h. On cooling to room temperature, the resulting white precipitate was filtered off, washed with cold ethanol and dried over silica gel. L^2 and L^3 were obtained following the same procedure as for L^1, by adding the relevant benzenesulfonohydrazine compounds, 4-methylbenzenesulfonohydrazine and 4-methoxybenzenesulfonohydrazine, respectively.

2.2.2. L^1

Yield: 84%. Melting point: 210 °C. *Anal.* Calc. for $C_{21}H_{21}N_5O_4S_2$: C, 53.49; H, 4.49; N, 14.85. Found: C, 53.55; H, 5.29; N, 14.89%. IR [ν_{max} (cm^{-1}) (KBr)]: ν_{N-H} 3194; $\nu_{C=N}$ 1618; $\nu_{as}(SO_2)$ 1327; $\nu_s(SO_2)$ 1167. δ_H: (DMSO-d_6): 2.27 (6H, s, C–CH_3); 10.91 (s, NH); 7.95 (2H, d, pyH); 7.82–7.61 (Ar), δ_C: (DMSO-d_6): 12.62 (C–CH_3); 120.10, 137.45, 153.47 (py-C); 127.59, 129.25, 133.24, 138.97 (phenyl-C); 153.42 (C=N). UV–Vis [λ_{max} (nm) (DMSO)]: 280 ($\pi \rightarrow \pi^*$); 300 ($n \rightarrow \pi^*$).

2.2.3. L^2

Yield: 87%. Melting point: 210–220 °C. *Anal.* Calc. for $C_{23}H_{25}N_5O_4S_2$: C, 55.08; H, 5.04; N, 13.97. Found: C, 54.96; H, 5.34; N, 14.38%. IR [ν_{max} (cm^{-1}) (KBr)]: ν_{N-H} 3194; $\nu_{C=N}$ 1595; $\nu_{as}(SO_2)$ 1341; $\nu_s(SO_2)$ 1162. δ_H: (DMSO-d_6): 2.22 (6H, s, C–CH_3); 2.32 (6H, s, Ar-CH_3); 10.77 (s, NH); 7.38 (2H, d, pyH); 7.79–7.72 (Ar), δ_C: (DMSO-d_6): 13.01 (C–CH_3); 21.53 (Ar-CH_3); 120.47, 137.87, 153.89 (py-C); 128.07, 130.10, 136.57, 144.06 (phenyl-C); 153.61 (C=N). UV–Vis [λ_{max} (nm) (DMSO)]: 290 ($\pi \rightarrow \pi^*$); 315 ($n \rightarrow \pi^*$).

2.2.4. L^3

Yield: 79%. Melting point: 220–225 °C. *Anal.* Calc. for $C_{23}H_{25}N_5O_6S_2$: C, 51.78; H, 4.73; N, 13.97. Found: C, 51.66; H, 4.90; N, 13.92%. IR [ν_{max} (cm^{-1}) (KBr)]: ν_{N-H} 3214; $\nu_{C=N}$ 1596; $\nu_{as}(SO_2)$ 1330; $\nu_s(SO_2)$ 1159. δ_H: (DMSO-d_6): 2.22 (6H, s, C–CH_3); 3.37 (6H, s, Ar-OCH_3); 10.69 (s, NH); 7.11 (2H, d, pyH); 7.87–7.75 (Ar), δ_C: (DMSO-d_6): 13.00 (C–CH_3); 56.18 (Ar-OCH_3); 129.96, 137.85, 153.94 (py-C); 114.89, 130.90, 131.01, 163.20 (phenyl-C); 153.49 (C=N). UV–Vis [λ_{max} (nm) (DMSO)]: 250 ($\pi \rightarrow \pi^*$); 303 ($n \rightarrow \pi^*$).

2.3. Preparation of the copper(II) complexes

2.3.1. General method for the preparation of the copper(II) complexes

Each Schiff base (0.30 mmol) was dissolved in ethanol (50 mL) and three drops of triethylamine were added, followed by an ethanolic solution containing a stoichiometric amount of hydrated copper(II) acetate. The mixture was refluxed for 5 h. The resultant dark brown solids were filtered and dried over silica gel.

The most suitable solvents used for all the complexes were dimethylsulfoxide and pyridine, and the crystals of [CuL^3·py]·py for single crystal X-ray diffraction analysis were successfully recrystallized from the latter solvent.

2.3.2. [$CuL^1 \cdot H_2O$]

Yield: 63%. Melting point: 225–228 °C. *Anal.* Calc. for $C_{21}H_{21}N_5O_5S_2Cu$: C, 45.75; H, 3.84; N, 12.71. Found: C, 45.69; H, 3.49; N, 12.40%. IR [ν_{max} (cm^{-1}) (KBr)]: ν_{OH} 3449; $\nu_{C=N}$ 1597; $\nu_{as}(SO_2)$ 1334; $\nu_s(SO_2)$ 1162; $\nu_{dis}(SO_2)$ 1080; UV–Vis [λ_{max} (nm) (DMSO)]: 270 ($\pi \rightarrow \pi^*$); 335 ($n \rightarrow \pi^*$), 440 (LMCT), 765(d–d transition). μ_{eff} = 1.84 BM.

2.3.3. [$CuL^2 \cdot H_2O$]

Yield: 67%. Melting point: 227–230 °C. *Anal.* Calc. for $C_{23}H_{25}N_5O_5S_2Cu$: C, 47.54; H, 4.36; N, 12.09. Found: C, 47.34; H, 4.39; N, 12.16%. IR [ν_{max} (cm^{-1}) (KBr)]: ν_{OH} 3488, $\nu_{C=N}$ 1593; $\nu_{as}(SO_2)$ 1316; $\nu_s(SO_2)$ 1151; $\nu_{dis}(SO_2)$ 1077; UV–Vis [λ_{max} (nm) (DMSO)]: 265 ($\pi \rightarrow \pi^*$); 330 ($n \rightarrow \pi^*$), 412 (LMCT), 770(d–d transition). μ_{eff} = 1.87 BM.

2.3.4. [$CuL^3 \cdot H_2O$]

Yield: 65%. Melting point: 231–234 °C. *Anal.* Calc. for $C_{23}H_{25}N_5O_5S_2Cu$: C, 45.19; H, 4.38; N, 11.46. Found: C, 45.47; H, 4.38; N, 11.31%. IR [ν_{max} (cm^{-1}) (KBr)]: ν_{OH} 3448, $\nu_{C=N}$ 1592; $\nu_{as}(SO_2)$ 1332; $\nu_s(SO_2)$ 1162; $\nu_{dis}(SO_2)$ 1081; UV–Vis [λ_{max} (nm) (DMSO)]: 240 ($\pi \rightarrow \pi^*$); 330 ($n \rightarrow \pi^*$), 410 (LMCT), 770(d–d transition). μ_{eff} = 1.94 BM.

2.4. X-ray structure analyses

A single crystal of [CuL^3·py]·py suitable for X-ray diffraction was mounted on a glass fibre using perfluoropolyether oil and cooled rapidly to 100 K in a stream of cold N_2. Diffraction data were measured using a Bruker APEX II CCD area-detector diffractometer (graphite-monochromated Mo Kα radiation, λ = 0.71073 Å). The orientation matrix, unit cell refinement and data reduction were all handled by the APEX II software (SAINT integration, SADABS absorption correction) [8]. The structure was solved using direct methods and vectors in the program SHELXS-97 [9] and was refined by the full matrix least-squares method on F^2 with SHELXL-97 [9]. All the non-hydrogen atoms were refined anisotropically and all the hydrogen atoms were placed at calculated positions and refined isotropically. Drawings of the molecules were produced with XSEED [10].

2.5. Antimicrobial activity

2.5.1. Microorganisms

Bacteria strains: Methicillin-resistant *S. aureus:* MRSA 0701-4, MRSA 1, MRSA 0307-28, MRSA 0302-4, MRSA 0704-3 and MDR-*Salmonella typhi* TP MDR 160/99 were isolated from the Labour Ward, Hospital Kuala Kubu, Selangor, Malaysia. MDR-*Escherichia coli* EC 187 and MDR-*Pseudomonas aeruginosa* PA 339 were obtained from the Institute of Medical Research, Kuala Lumpur, Malaysia. MDR-*Acinetobacter baumannii* AC/01601-10 was supplied by the University of Malaya Medical Center, Kuala Lumpur, Malaysia.

2.5.2. Antibacterial screening

The antibacterial activity of the Schiff bases and their copper(II) complexes was determined by the disc diffusion method [11]. Muller-Hinton agar was employed as the bacteria growth medium. A suspension of tested microorganism (10^8 CFU/mL) was spread on the solid media plates. Filter paper discs (6 mm in diameter) were soaked with 10 μl of the solutions and placed on the inoculated plates. After keeping the plates at 2 °C for 2 h, they were incubated at 37 °C for 24 h for bacteria. The tested compounds were prepared in dimethyl sulfoxide with a concentration of 10 mg mL^{-1}. The inhibition zones were measured in millimeters and the assays were performed in duplicate.

2.5.3. Determination of minimum inhibitory concentration (MIC)

The minimal inhibitory concentration of each of the tested compounds was defined as the lowest concentration exhibiting no visible growth compared with the drug-free control wells. Muller-Hinton Broth was employed as the bacteria growth medium. Serial concentrations of each of the tested compounds in the range 0.156–10.0 mg/mL were prepared for the determination of MICs and inoculated with different strain Methicillin-resistant *S. aureus* bacteria. After incubation at 37 °C for 24 h, the first well without turbidity was determined as the minimal inhibitory concentration.

3. Results and discussion

3.1. General characterizations

3.1.1. Infrared spectra

The IR spectra of the copper(II) complexes show strong typical absorptions in the region 1592–1597 cm^{-1} related to the C=N stretching vibration of the Schiff base imino group. The strong band at 1595–1618 cm^{-1} attributed to the C=N stretching vibration in the ligands is shifted to lower energy in the complexes, indicating coordination of the azomethine nitrogen [12]. The IR spectra of the complexes also do not contain the ν(N–H) absorption band of the free ligand, suggesting the proton on the imine nitrogen atom of the ligand is lost upon complexation [13]. In the complexes, the remaining band of $\nu_s(SO_2)$ at 1151–1162 cm^{-1} and the weaker intensity of $\nu_{as}(SO_2)$ at 1316–1334 cm^{-1} together with the appearance of a new band at 1077–1081 cm^{-1}, assigned to the bending SO_2 group, suggest the distortion of one of the SO_2 groups from its structure [3]. The broad band in the region 3448–3488 cm^{-1} and two weaker bands in the regions 803–809 and 597–600 cm^{-1} are assigned to the coordinated water molecule, and are due to ν(–OH) rocking and wagging mode vibrations [5,14].

3.1.2. Absorption spectra and magnetic studies

An intense band centered at 303–315 nm is attributable to $n \rightarrow \pi^*$ transitions associated with the azomethine chromophore [15]. There is another intense band in the high-energy region (250–290 nm) of the spectra of the free ligands which is related to $\pi \rightarrow \pi^*$ transitions of aromatic rings [16]. These transitions are also found in the spectra of the complexes, but they undergo hypsochromic or bathochromic shifts, confirming the coordination of the ligands to the metallic ions [17,18]. In the spectra of the copper(II) complexes, the intense and broad bands in the 410–440 nm region are attributable to the $O \rightarrow Cu^{II}$ (LMCT) transition, which further supports coordination of the ligands to the copper(II) ion via one of the oxygen atoms. The absorption bands in the range 765–770 nm in the spectra of the copper(II) complexes correspond to d–d transitions, and this is consistent with a square pyramidal geometry of the copper(II) complexes [19]. The magnetic moment of the copper(II) complexes (1.84–1.94 BM) is normal for a $3d^9$ metal ion in a magnetically dilute environment [20] and in the range approximately similar to other square pyramidal copper(II) complexes [19,21].

3.2. Crystal and molecular structure of [CuL^3·py]·py

The structure of the complex [CuL^3·(py)]·py is depicted in Fig. 2. Crystal data and structure refinement details are compiled in Table 1. Some bond lengths and bond angles are listed in Table 2. The

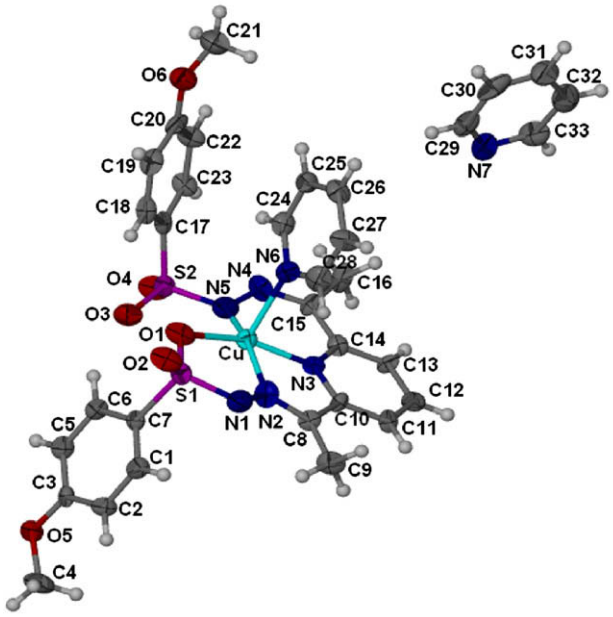


Fig. 2. The molecular structure of [CuL^3·(py)]·py showing the atom labelling scheme (50% probability ellipsoids).

Table 1
Crystal data and structure refinement for complex [CuL^3·(py)]·py.

Empirical formula	$C_{33}H_{33}CuN_7O_6S_2$
Formula weight (g/mol)	751.32
Crystal system	triclinic
Space group	$P\bar{1}$
Unit cell dimensions	
a (Å)	10.820(2)
b (Å)	13.047(2)
c (Å)	13.888(2)
α (°)	95.680(8)
β (°)	111.541(8)
γ (°)	109.194(8)
V (Å^3)	1667.5(4)
Z	2
Density (calculated) (g cm^{-3})	1.496
Absorption coefficient (mm^{-1})	0.837
F(0 0 0)	778
Crystal size (mm^3)	0.23 × 0.11 × 0.03
Crystal description	black, block
θ Range for data collection (°)	2.11–25.00
Index ranges	$-13 \leqslant h \leqslant 15$, $-18 \leqslant k \leqslant 18$, $-19 \leqslant l \leqslant 19$
Reflections collected/unique (%)	11 619/8409 [R_{int} = 0.1027]
Completeness to θ = 25.00	97.2
Maximum and minimum transmission	0.9753 and 0.8308
Refinement method	full-matrix least-squares on F^2
Data/restraints/parameters	5714/0/446
Goodness-of-fit (GOF) F^2	0.930
Final R indices [$I > 2\sigma(I)$]	R_1 = 0.0846, wR_2 = 0.1707
R indices (all data)	R_1 = 0.1910, wR_2 = 0.2047
Largest difference in peak and hole (e Å^{-3})	1.046 and −1.104

Table 2
Selected bond lengths (Å) and angles (°) for complex $[CuL^3{\cdot}(py)]{\cdot}py$

Bond lengths	
S(1)–O(1)	1.450(5)
S(1)–O(2)	1.433(6)
S(2)–O(3)	1.466(6)
S(1)–O(4)	1.418(5)
S(1)–N(2)	1.623(7)
S(2)–N(5)	1.662(7)
N(4)–C(15)	1.289(9)
N(2)–C(8)	1.280(9)
Cu–O(1)	2.138(6)
Cu–N(5)	1.912(7)
Cu–N(3)	1.971(6)
Cu–N(2)	2.012(7)
Cu–N(6)	2.253(6)
Bond angles	
N(2)–Cu–O(1)	79.7(2)
N(2)–Cu–N(3)	79.5(3)
N(3)–Cu–N(5)	91.4(3)
N(5)–Cu–O(1)	108.0(3)
O(1)–Cu–N(6)	91.4(2)
N(2)–Cu–N(6)	100.8(3)
N(3)–Cu–N(6)	93.9(2)
N(5)–Cu–N(6)	97.4(3)
N(5)–Cu–N(2)	160.2(3)
N(3)–Cu–O(1)	159.1(2)

$[CuL^3{\cdot}(py)]{\cdot}py$ complex crystallizes in the triclinic space group $P\bar{1}$, and the copper ion has a penta-coordinate environment.

The structure shows that the complex is a monomer in which the copper(II) ion has a five-coordinate geometry with the Schiff base being asymmetrically coordinated to it as a binegatively charged tetradentate chelating agent containing three N atoms and one oxygen atom in an almost planar arrangement around the copper ion. The other chain in the ligand includes only the deprotonated hydrazine N atom with the rest of the chain remaining pendant. A nitrogen atom of the pyridine molecule occupies the fifth apical site.

While coordinating with the copper(II) ion, deprotonation of the ligands generates a negative charge on the sulfonyl oxygen atom on one of the five-membered chelate rings N(2)–N(1)–S(1)–O(1). This is delocalized over the O(1)–S(1)–N(2) group [O(1)–S(1) 1.452(5) Å and S(1)–N(2) 1.623(7) Å]. The corresponding O(1)–S(1) and S(1)–N(2) bonds of the free ligands of related compounds are 1.423(4)–1.436(4) Å and 1.626(2)–1.645(2) Å, respectively [22,23].

The index τ is used to define the five coordination shape in terms of the two largest bond angles (α and β) around the central atom as [$\tau = (\beta-\alpha)/60$]. If $\tau = 0$, the coordination is an ideal square pyramid and if $\tau = 1$, the coordination is an ideal trigonal bipyramid [24]. The geometrical parameter τ has a value of 0.01, indicating the coordinated $(L^3)^{2-}$ ligand presents a geometry much closer to square pyramidal ($\tau = 0$). The distortion is also shown by the angles between the pyridine nitrogen atom at the apical position, the metal atom and donor set of the basal plane, which is larger than 90° [91.5(2)–100.7(3)°]. In the equatorial plane, the ideal square pyramidal geometry is distorted by the steric requirements imposed by the chelate rings, N(2)–Cu–N(3), 79.5(3)° and O(1)–Cu–N(5), 108.0(3)°, as compared to the ideal value of 90°.

The distance of $Cu–N_{pyridine}$ [1.971(6) Å] is significantly longer than $Cu–N_{amine}$ [1.912(7) Å] in a similar study on the square pyramidal structure of $[Cu(Hdapsox)H_2O]^+$ [21].

3.3. Biological activity

The ligands and their copper(II) complexes were investigated for antibacterial activity against gram-positive and gram-negative bacteria. None of the Schiff bases showed antibacterial activity against all the gram-positive and gram-negative bacteria. However, significant inhibition was displayed by all the copper(II) complexes against all strains of gram-positive bacteria, Methicillin-resistant *S. aureus* (Table 3). The MIC values of the copper(II) complexes that showed positive results in the screening process were determined as a quantitative measurement of antibacterial activity (Table 4). The results revealed that $[CuL^1{\cdot}H_2O]$ is most effective against *S. aureus* MRSA 1 with a MIC value of 1250 μg/mL, while $[CuL^2{\cdot}H_2O]$ proved to be the best against *S. aureus* MRSA 0701-4 and *S. aureus* MRSA 1 with a MIC value of 2500 μg/mL. $[CuL^3{\cdot}H_2O]$ was found to be most effective against *S. aureus* MRSA 0307-28, *S. aureus* MRSA 0302-4 and *S. aureus MRSA 0704-3* (2500 μg/mL). Also, $[CuL^1{\cdot}H_2O]$ is effective against *S. aureus* MRSA 0701-4, *S. aureus* MRSA 0307-28, *S. aureus* MRSA 0302-4 and *S. aureus* MRSA 0704-3 (2500 μg/mL). From a comparative study of the results in Tables 3 and 4, it was concluded that the antibacterial activities of the ligands are enhanced when they are chelated with copper(II) ions and the activity of the copper(II) complexes decreases when there are substituents in the ligands.

It is important to note that previous studies on other compounds have shown that the antibacterial activity of copper(II) complexes is generally better than their parent ligands [25]. There is also a report on the antibacterial activities for copper(II) complexes of valine-Schiff bases which have shown good inhibition against clinically isolated gram-positive Methicillin-resistant *S. aureus*. Chelation of

Table 3
Zone of inhibition of the Schiff bases and their copper(II) complexes.

Microorganisms	Source	Diameter of inhibition zone (mm)						
		L^1	$[CuL^1{\cdot}H_2O]$	L^2	$[CuL^2{\cdot}H_2O]$	L^3	$[CuL^3{\cdot}H_2O]$	Standard
Gram-positive								
Staphylococcus aureus	MRSA 0701-4		18		18		16	10[a]
Staphylococcus aureus	MRSA 1		16		13		14	11[a]
Staphylococcus aureus	MRSA 0307-28		17		13		13	10[a]
Staphylococcus aureus	MRSA 0302-4		18		14		14	10[a]
Staphylococcus aureus	MRSA 0704-3		18		14		14	11[a]
Gram-negative								
Escherichia coli	EC187							13[b]
Pseudomonas aeruginosa	PA 339							19[c]
Acinetobacter baumannii	AC/01601-10							11[d]
Salmonella typhi	TP MDR 160/99							14[e]

[a] Amikacin.
[b] Ceftazimide.
[c] Gentamicin.
[d] Imipenem.
[e] Ampicillin/sulbactan.

Table 4
MIC results of the copper(II) complexes.

Microorganisms	Source	MIC (μg/mL)		
		$[CuL^1 \cdot H_2O]$	$[CuL^2 \cdot H_2O]$	$[CuL^3 \cdot H_2O]$
Staphylococcus aureus	MRSA 0701-4	2500	2500	5000
Staphylococcus aureus	MRSA 1	1250	2500	5000
Staphylococcus aureus	MRSA 0307-28	2500	5000	2500
Staphylococcus aureus	MRSA 0302-4	2500	5000	2500
Staphylococcus aureus	MRSA 0704-3	2500	5000	2500

the copper(II) ion to a heterocyclic ligand containing a nitrogen atom such as pyridine is believed to increase the activity of the compounds against the microorganism [4]. It may be suggested that these copper complexes deactivate various cellular enzymes, which play role in various metabolic pathways of gram-positive bacteria, Methicillin-resistant *S. aureus* [26]. It has also been proposed that the ultimate action of the toxicant, i.e. the copper complex, is the denaturation of one or more proteins of the cell, which as a result, impairs normal cellular processes [25].

Generally, it was observed that the gram-negative bacteria were resistant to all the synthesized compounds. The extra outer layer on the cell wall of the gram-negative bacteria acts as a barrier and needs high penetration of the compounds to reach the cell [27]. The bacteria cell may also change the structure of its cell membrane and prevent the compound from entering the cell [28]. However, it is not yet possible to correlate the bioactivity of these compounds to any of their structural features due to the limited data. To the best of our knowledge, there is no report on the antibacterial activity of 2,6-diacetylpyridine bis(benzenesulfonohydrazide) Schiff bases and their copper(II) complexes and our present findings show that it is worth exploring more in this area in the future.

4. Conclusion

The 2,6-diacetylpyridine bis(benzenesulfonohydrazide) Schiff bases behave as binegatively charged tetradentate O, N, N, N chelates with copper(II), forming five-coordinate copper(II) complexes with a water molecule apically coordinated to the copper(II) ion. The crystal structure of $[CuL^3 \cdot (py)] \cdot py$ shows that the Cu(II) cation has a penta-coordinate and near square pyramidal geometry within the asymmetric unit, with a pyridine molecule replacing the water molecule at the apical position. Antibacterial tests for all the compounds reveal that the antibacterial activity of the Schiff bases against Methicillin-resistant *S. aureus* (MRSA) is enhanced when they are chelated with a copper(II) ion.

Supplementary data

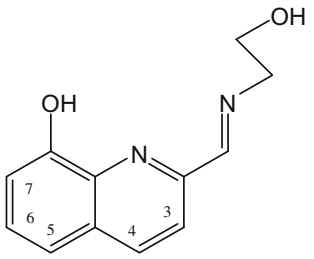
CCDC 730751 contains the supplementary crystallographic data for $[CuL3 \cdot (py)] \cdot py$. These data can be obtained free of charge via http://www.ccdc.cam.ac.uk/conts/retrieving.html, or from the Cambridge Crystallographic Data Centre, 12 Union Road, Cambridge CB2 1EZ, UK; fax: (+44) 1223-336-033; or e-mail: deposit@ccdc.cam.ac.uk.

Acknowledgements

The authors would like to thank the Department of Chemistry and the Institute of Biological Science, Faculty of Science, University of Malaya for the provision of laboratory facilities. The financial support of PJP FS 350/2008A by the Ministry of Higher Education (MOHE) and PPP PS 224/2008B by University of Malaya is also highly appreciated.

References

[1] L. Larabi, Y. Harek, A. Reguig, M.M. Mostafa, J. Serb. Chem. Soc. 68 (2003) 85.
[2] T.H. Rakha, A.A. El-Asmy, M.M. Mostafa, Transition Met. Chem. 12 (1987) 125.
[3] T.H. Rakha, M.M. Bekheit, K.M. Ibrahim, Transition Met. Chem. 14 (1989) 371.
[4] J. Lv, T. Liu, S. Cai, X. Wang, L. Liu, Y. Wang, J. Inorg. Biochem. 100 (2006) 1888.
[5] G.B. Bagihalli, P.G. Avaji, S.A. Patil, P.S. Badami, Eur. J. Med. Chem. 43 (2008) 2639.
[6] A. Masunari, L.C. Tavares, Bioorg. Med. Chem. 15 (2007) 4229.
[7] M. Burd, H. Humphres, G. Glyn, E. Mitchell, P. McDonald, H. Johnsonm, B. McDonnell, D. Doyle, A. Rossney, J. Hosp. Infect. 53 (2003) 297.
[8] Bruker APEX2 and SAINT, Bruker AXS Inc., Madison, Wisconsin, USA, 2007.
[9] G.M. Sheldrick, Acta Crystallogr., Sect. A 64 (2008) 112.
[10] L.J. Barbour, J. Supramol. Chem. 1 (2001) 189.
[11] G.V. Doern, P.R. Murray, E.J. Baron, M.A. Pfaller, F.C. Tenover, R. Yolken, Susceptibility Tests of Fastidious Bacteria. Manual of Clinical Microbiology, sixth ed., American Society for Microbiology, Washington, DC, 1995. p. 1342.
[12] I. Procter, B. Hathaway, P. Nicholls, J. Chem. Soc. A 7 (1968) 1678.
[13] S. Patil, U. Kantak, D. Sen, Inorg. Chim. Acta 63 (1982) 261.
[14] S. Chandra, A.K. Sharma, Spectrochim. Acta, Part A 72 (2009) 851.
[15] S.D. Bella, I. Fragala, I. Ledoux, M.A. Diaz-Garcia, T.J. Marks, J. Am. Chem. Soc. 119 (1997) 9550.
[16] A. Bottcher, T. Takeuchi, K.I. Hardcastle, T.J. Meade, H.B. Gray, Inorg. Chem. 36 (1997) 2498.
[17] Z.-L. Lu, W. Xiao, B.-S. Kang, C.-Y. Su, J. Liu, J. Mol. Struct. 523 (2000) 133.
[18] I.I. Seifullina, N.V. Shmatkova, A.V. Mazepa, Russ. J. Coord. Chem. 28 (2002) 15.
[19] M.A. Ali, A.H. Mirza, A.L. Tan, F.H. Bujang, M.H.S.A. Hamid, P.V. Bernhardt, Polyhedron 25 (2006) 3245.
[20] M.A. Ali, H.J.H.A. Bakar, A.H. Mirza, S.J. Smith, L.R. Gahan, P.V. Bernhardt, Polyhedron 27 (2008) 71.
[21] I. Ivanovic-Burmazovic, A. Bacchi, G. Pelizzi, V.M. Leovac, K. Andjelkovic, Polyhedron 18 (1999) 119.
[22] H.M. Ali, J. Yusnita, S.W. Ng, Acta Crystallogr., Sect. E 63 (2007) o2733B.
[23] B.T. Gowda, S. Foro, K.S. Babitha, H. Fuess, Acta Crystallogr., Sect. E 64 (2008) o1691.
[24] A.W. Addison, T.N. Roa, J. Reedijk, J. Vanrijn, G.C. Verchoor, J. Chem. Soc., Dalton Trans. (1984) 1349.
[25] L.T. Yildrima, R. Kurtaran, H. Namli, A.D. Azaz, O. Atakol, Polyhedron 26 (2007) 4187.
[26] N. Dharmaraj, P. Viswanathamurthi, K. Natarajan, Transition Met. Chem. 26 (2001) 105.
[27] R. Nair, A. Shah, S. Baluja, S. Chanda, J. Serb. Chem. Soc. 71 (2006) 733.
[28] G.L. Patrick, An Introduction to Medicinal Chemistry, third ed., Oxford University Press, New York, 2005. p. 433.



Scheme 1. Chemical structure of the 8-hydroxyquinoline derivative, 2-[(2-hydroxyethylimino)methyl]quinolin-8-ol (H_2L).

collected at 100 K on a Bruker CCD SMART1000 diffractometer, using graphite-monochromated Mo Kα radiation ($\lambda = 0.71073$ Å) from a fine focus sealed tube. Data were processed and corrected for Lorentz, polarisation and absorption effects. The structure was solved by standard direct methods, and refined by full matrix least squares on F^2 using the SHELX-97 program package [10]. Non-hydrogen atoms were anisotropically refined, while H atoms of HL^- were found in the Fourier maps, and then isotropically treated. Methyl H atoms of the acetate groups were included in the structure factor calculation in geometrically idealised positions, with thermal parameters depending of the parent atom, although their orientations were also refined.

2.3. Ligand synthesis

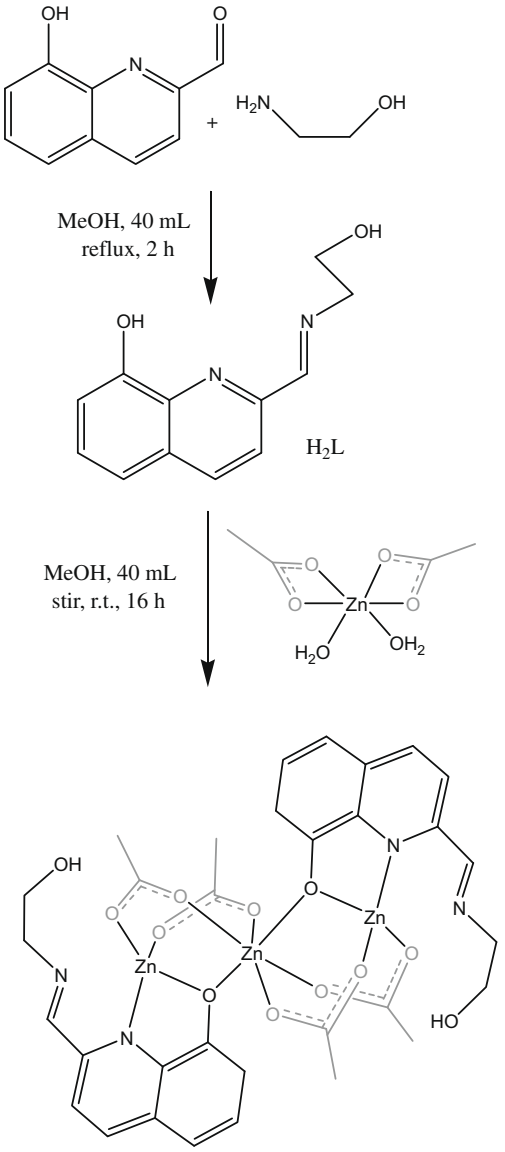
2-((2-Hydroxyethylimino)methyl)quinolin-8-ol (H_2L in Scheme 2) was obtained by refluxing a methanol solution (40 mL) containing 8-hydroxyquinoline-2-carboxaldehyde (0.352 g, 2 mmol) and 2-aminoethanol (0.12 mL, 2 mmol) for about 2 h. Vacuum concentration of the resulting yellow solution yielded a yellow solid that was filtered, washed with diethyl ether, and recrystallised in MeOH.

2.3.1. H_2L

Yellow powder (0.359 g, 83%). Anal. Calc. for $C_{12}H_{12}N_2O_2$ (M, 216.2 g.mol^{-1}) requires: C, 66.6; H, 5.6; N, 13.0. Found: C, 66.2; H, 5.4; N, 12.7%. *m/z* (ESI$^+$-TOF, methanol): 217.1 (100%) M^+; FTIR (KBr, cm^{-1}): ν(O_{phen}–H) 3379(b,s), ν(C=N) 1599(vs); ^{1}H NMR (300 MHz, $CDCl_3$, ppm) 8.57 (s, 1H, *H*CN), 8.55 (d, 1H, H3), 8.32 (d, 1H, H4), 8.16 (d, 1H, H5), 8.12 (t, 1H, H6), 8.07 (d, 1H, H7), 4.01 (t, 2H, H_2CO), 3.91 (t, 2H, H_2CN).

Table 1
Crystal and refinement data for $Zn_3(HL)_2(AcO)_4$.

	$Zn_3(HL)_2(AcO)_4$
Formula	$C_{32}H_{34}N_4O_{12}Zn_3$
M_r	862.74
Crystal system	monoclinic
Space group (No. 14)	$P2_1/n$
Unit cell	
a (Å)	7.680(1)
b (Å)	10.353(2)
c (Å)	20.773(4)
β (°)	90.973(3)
V (Å^3)	1651.6(5)
Z	2
D_c (Mg/m^3)	1.735
μ (mm^{-1})	2.233
F (0 0 0)	880
Intervalo de θ (%)	1.96 (Å) 27.10° (99.9)
Reflection collected/independent reflections	15389/3643
R_{int}	0.0515
Data/restraints/parameters	3643/0/278
R_1, wR_2 [$I > 2\sigma(I)$]	0.0267, 0.0676
R_1, wR_2 (all data)	0.0338, 0.0703
Residuals (e A^{-3})	0.448, −0.510



Scheme 2. Synthetic route used to obtain H_2L and $Zn_3(HL)_2(OAc)_4$.

2.4. Complex synthesis

$Zn_3(HL)_2(OAc)_4$ was obtained when 8-hydroxyquinoline-2-carboxaldehyde (0.176 g, 1 mmol) and 2-aminoethanol (0.06 mL, 1 mmol) were firstly refluxed in methanol (*ca.* 40 mL), and $Zn(OAc)_2{\cdot}2H_2O$ (0.329 g, 1.5 mmol) subsequently added to the resulting solution, which was stirred for about 16 h at room temperature. The same result was also obtained when using a 4:2 molar ratio. Vacuum concentration of the resulting solution yielded a solid that was filtered, washed with diethyl ether, and then dried in vacuum.

Single crystals suitable for X-ray diffraction studies were obtained from the mother liquor by simple evaporation at room temperature. Likewise, recrystallisation in acetone of the crude solid isolated from the mentioned reaction also resulted in the same. The same result was obtained by *r*.

2.4.1. $Zn_3(HL)_2(OAc)_4$

Orangish powder (0.240 g, 56%); Anal. Calc. for $C_{32}H_{34}N_4O_{12}Zn_3$ (M, 862, 8 g mol^{-1}) requires: C, 44.6; H, 4.0; N, 6.5. Found: C, 44.3; H, 4.0; N, 6.4%. FTIR (KBr, cm^{-1}): ν(C=N) 1620(vs), ν_a(COO)

1575(vs), ν_s(COO) 1405(s); ^{1}H NMR (500 MHz, Cl_3CD, ppm) 8.58 (s, 2H, *H*CN), 8.42(d, 2H, *H*C3), 7.65 (d, 2H, *H*C4), 7.30 (d, 2H, *H*C5), 7.12 (t, 2H, *H*C6), 7.02 (d, 2H, *H*C7), 4.08 (m, 4H, H_2C–OH), 4.05 (m, 4H, H_2C–N), 2.07 (s, 12H, H_3C); ^{1}H NMR (500 MHz, DMSO-d_6, ppm) 8.68 (2H, *H*CN), 8.59 (2H, *H*C3), 7.93 (2H, *H*C4), 7.45 (2H, *H*C5), 7.04 (2H, *H*C6), 6.82 (2H, *H*C7), 4.71 (2H, *H*O–CH_2), 3.79 (8H, H_2C–H_2C–N), 1.81 (12H, H_3C).

3. Results and discussion

3.1. Ligand characterisation

Although $Zn_3(HL)_2(OAc)_4$ has been prepared from a methanol solution of the non isolated H_2L, this was additionally isolated as a solid, with the aim of showing some characterisation data that proved its previous formation. Elemental analysis, IR, mass and ^{1}H NMR spectroscopies evidence the identity of the ligand.

The IR spectrum of H_2L exhibits an intense band assignable to ν(C=N) that clearly indicates the aldehyde–amine condensation. The observation of a high intensity peak attributable to the molecular ion M^+ at 217.1 *m/z* in the ESI$^+$-TOF spectrum of free H_2L supports this previous statement. The presence of the expected signals for azomethine, aromatic and methylene protons [5,6b] in the spectrum of H_2L evidence the formation of the Schiff base ligand.

3.2. Molecular structure of $Zn_3(HL)_2(OAc)_4$

The asymmetric unit of $Zn_3(HL)_2(OAc)_4$ only contains a half molecule of the complex, since the other half is generated by means of an inversion around the centre located on the origin of the cell unit, and on which the central atom of the complex (Zn2) is located. This symmetry operation ($-x$, $-y$, $-z$) is indicated in the labelling scheme of Fig. 1 by $^{\#1}$, on the atoms generated by this inversion. The symmetry of the linear trinuclear complex is also shown by the coplanarity of each pair of equivalent ligands around the metal centres. Some significant bond distances and angles have been listed in Table 2.

Observation of the Zn–N bond distances shows that Zn1–N2 is sensibly longer than Zn1–N1. Since the first one exceeds the sum of the covalent radii of Zn and N atoms (1.330 and 0.700 Å, respectively) in more than 0.4 Å, the interactions between the imine N atoms and the two terminal zinc ions have been considered as secondary rather than proper coordination interactions. This is also supported by the slight differences observed for angles and bond distances affecting the azomethine group, when they are compared with those reported for some free Schiff base ligands [11]. For that reason, the terminal metal ions, Zn1 and Zn1$^{\#1}$, display O_3N coordinative environments can be considered in a distorted tetrahedral fashion. Each one involves the bidentate *O,N* site of the monodeprotonated hydroxyquinoline residue present in HL^-, and one of the O atoms of each pair of μ_2–η^1:η^1 bridging acetate ligands that connect both Zn1 and Zn1$^{\#1}$ with Zn2. The distortion of these tetrahedral coordination polyhedrons is intimately related with the secondary Zn–N_{imine} interaction mentioned.

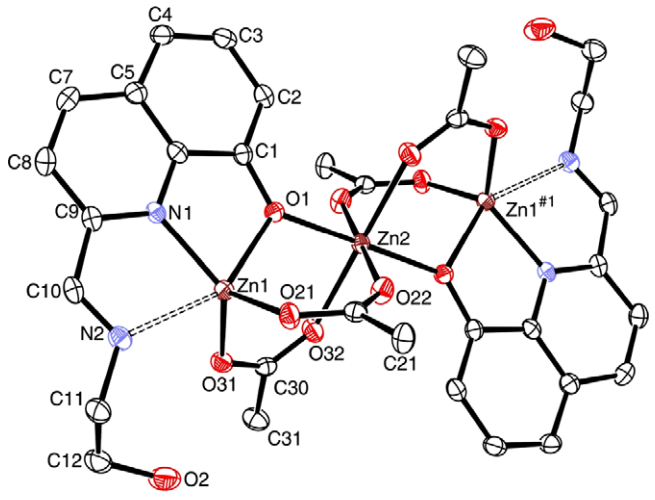


Fig. 1. An ORTEP view of the molecular structure of $Zn_3(HL)_2(OAc)_4$. Ellipsoids are drawn at 50% probability. Secondary interactions are represented as dotted lines. Hydrogen atoms were omitted for clarity.

Table 2
Selected geometric parameters for $Zn_3(HL)_2(OAc)_4$.

Atoms	Distance (Å)	Atoms	Distance (Å)
Zn1–O21	1.9354(15)	Zn2–O1	2.0160(14)
Zn1–O31	1.9655(15)	Zn2–O22	2.1343(15)
Zn1–N1	2.0188(17)	Zn2–O32	2.1348(15)
Zn1–O1	2.1019(14)		
Zn1···N2	2.4173(17)	Zn2···Zn1	3.397(2)
Atoms	**Angle (°)**	**Atoms**	**Angle (°)**
O21Zn1–N1	125.06(7)	O1–Zn2–O22	88.05(6)
O21–Zn1–O1	101.80(6)	O1–Zn2–O22$^{\#1}$	91.95(6)
O21–Zn1–N2	97.62(6)	O1–Zn2–O32	87.89(6)
O31–Zn1–N1	124.49(7)	O1–Zn2–O32$^{\#1}$	92.11(6)
O31–Zn1–N2	90.14(6)	O22–Zn2–O32	89.14(6)
O1–Zn1–N1	78.15(6)	O22–Zn2–O32$^{\#1}$	90.86(6)
N1–Zn1–N2	72.90(6)		

$^{\#1}$Atoms generated by the symmetry operation $-x$, $-y$, $-z$.

Respect to the central zinc(II) ion, this is in an O_6 coordinative environment that comprises four oxygen atoms (one from each bridging acetate group) and two phenoxo bridges (one from each Schiff base ligand) with a quasi-octahedral disposition. This could be understood as the four O atoms of the acetate bridges forming the equatorial plane, while the two capping phenoxo bridges show a *trans*-configuration, with a slight elongation.

Comparison of $Zn_3(HL)_2(OAc)_4$ with other linear trinuclear zinc complexes bridged by carboxylate (and phenolate) oxygen atoms, allows observing some trends in the formation of this type of trinuclear assembly. Thus, their central Zn^{II} ion displays quasi-octahedral O_6 coordination polyhedra related with the carboxylate (and phenolate) groups. Likewise, on one hand, the obtaining of bis(carboxylate) complexes of the type $Zn_3(L)_2(carboxylate)_2$ has been reported with several dianionic tetradentate ligands containing phenolate groups [12]. On the other hand, examples of linear trinuclear zinc complexes containing endogenous ligands with a lower denticity are much less common. In this latter case, either neutral monodentate ligands as quinoline, or bidentate ligands as bipy or phen, yielded *hexakis*(carboxylate) complexes of the type $Zn_3(L)_2(carboxylate)_6$ [13]. To the best of our knowledge, one complex of the type $Zn_3(L)_2(carboxylate)_4$ has been reported for a monoanionic tridentate Schiff base [14], which in that case shows a real coordination through the imine N atom. Therefore, the coordinative behaviour of HL^- in $Zn_3(HL)_2(OAc)_4$ means a novelty. Regarding to the values of Zn–O and Zn···Zn distances; they do not seem to merit further comment, since they appear in normal ranges.

Apart from the clear intramolecular interactions between the two hydroxyl groups of the 2-aminoethanol residues and one of the O atoms of the acetate ligands (O2–H2···O31, Fig. 1), no intermolecular hydrogen bonds were detected. In view of this, the significant π–π interactions, with inter-planar distances of about 3.3 Å (Fig. 2) appear to play a crucial role in the crystal packing scheme. This is facilitated by the extended planarity resulting of the conjugation of the imine groups with the 8-hydroxyquinoline residues, being both π systems coplanar in the molecule. Likewise,

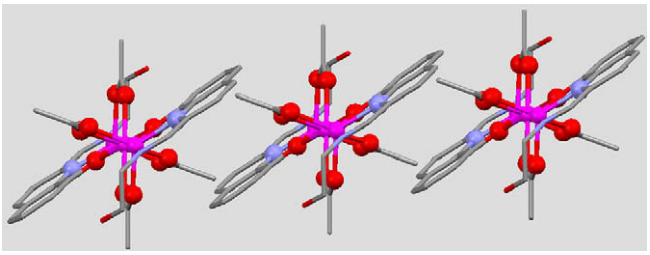


Fig. 2. Balls and sticks diagram showing the π–π stacking of neighbouring $Zn_3(HL)_2(OAc)_4$ molecules, and the coplanarity of the ligands (grey: C; red: O; blue: N, and fuchsia: Zn). (For interpretation of the references to colour in this figure legend, the reader is referred to the web version of this article.)

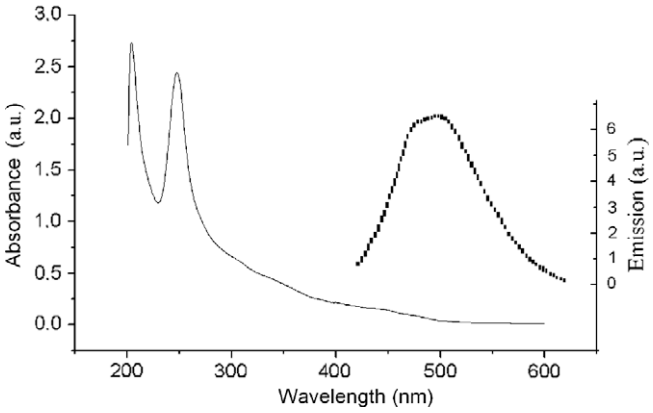


Fig. 3. UV–Vis absorption (left) and emission (right) spectra of H_2L in MeOH solution (10^{-3} M).

significant C–H···O interactions between methyl and carboxylic groups of neighbouring acetate ligands contribute to the crystal packing.

3.3. Physicochemical characterisation of the compounds

The presence of two intense absorption bands at 202 and 248 nm (Fig. 3), and which are also present in the spectrum of 8-hydroxyquinoline-2-carboxaldehyde, is a characteristic spectral feature of free H_2L.

The photoluminescence spectrum of H_2L (Fig. 3) displays a low intensity band at about 500 nm, by excitation of the solution at 398 nm. The formation of the Schiff base ligand results in a red-shift of the fluorescence wavelength, when this is compared with that of 8-hydroxyquinoline-2-carboxaldehyde (see below). This fact may be related to the increase of the conjugation that provides the imine bond to the ligand arm [15].

The IR spectrum of $Zn_3(HL)_2(OAc)_4$ exhibits two intense bands assignable to $\nu_a(COO)$ and $\nu_s(COO)$ that support the presence of coordinated acetate groups. The Δ value $[\nu_a(COO) - \nu_s(COO)]$ of about 170 cm^{-1}, which is close to those reported for other acetate bridged zinc complexes [16], indicates a bidentate bridging behaviour of the acetate ligand.

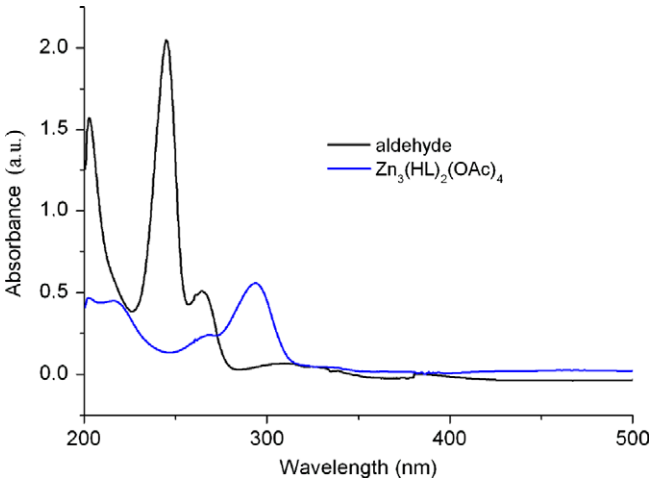


Fig. 4. UV–Vis absorption spectra (in MeOH, 10^{-5} M) of 8-hydroxyquinoline-2-carboxaldehyde and $Zn_3(HL)_2(OAc)_4$.

$Zn_3(HL)_2(OAc)_4$ presents a signal near to 1.8 ppm in its ^1H NMR spectrum, in agreement with the coordination of the acetate ligand to the metal centres. The presence of a signal near to 8.7 ppm, which is attributable to the azomethine proton *H*CN, indicates the coordination of the Schiff base ligand.

3.4. Photophysical study of $Zn_3(HL)_2(OAc)_4$

The UV–Vis absorption spectra, and the photoluminescence spectra of $Zn_3(HL)_2(OAc)_4$, as well of 8-hydroxyquinoline-2-carboxaldehyde were measured at room temperature in dilute methanol solutions. Table 3 summarises the main data obtained from these studies.

The absorption bands of $Zn_3(HL)_2(OAc)_4$ (in the range 200–350 nm) may be attributed to n–π^* and π–π^* intraligand transitions, involving the π-system of the quinoline residue, in addition to MLCT transitions [17–22]. The pronounced changes in the absorption spectrum of the aldehyde as result of the formation of the Schiff base ligand H_2L and its metal complexation are shown in Fig. 4. The presence of two new intense absorption bands at 216 and 294 nm, which have been related to the metal–ligand interaction, is a characteristic spectral feature of $Zn_3(HL)_2(OAc)_4$.

The photoluminescence emission maxima of the aldehyde and the zinc complex, which emit at the same wavelength (402 nm) are shown in Fig. 5. The quantum yield of $Zn_3(HL)_2(OAc)_4$ ($\Phi_F = 0.07$) is slightly higher than that of 8-hydroxyquinoline-2-carboxaldehyde ($\Phi_F = 0.06$). Since d^{10} metal ions are unable to participate in low energy charge transfer, or in metal-centred transitions, the excited states resulting from $Zn_3(HL)_2(OAc)_4$ is typically ligand-centred in nature [23]. Hence, the emission is believed to arise from an excited state centred on the ligand.

Emission from a predominantly ligand-based excited state should give a large Stokes shift between the MLCT absorption and the emission band [24]. $Zn_3(HL)_2(OAc)_4$ exhibits not very large Stokes shift (70 nm), while the 8-hydroxyquinoline-2-carboxaldehyde shows a larger shift (92 nm). This seems to indicate that the emission observed for $Zn_3(HL)_2(OAc)_4$ could be predominately caused by a ligand-based excited state, rather than by a MLCT state.

Table 3
Photophysical data for 8-hydroxyquinoline-2-carboxaldehyde and $Zn_3(HL)_2(OAc)_4$.

Compound	Absorption (λ_{max}/nm) (ε/mmol^{-1} cm^2)	Excitation (λ_{exc}/nm)	Emission (λ_{max}/nm)
Aldehyde	203(157200), 245(204900), 265(50900), 310(6500)	310	402
$Zn_3(HL)_2(AcO)_4$	202(46700), 216(45000), 268(24000), 294(55800), 332(4600), 472(2400)	332	402

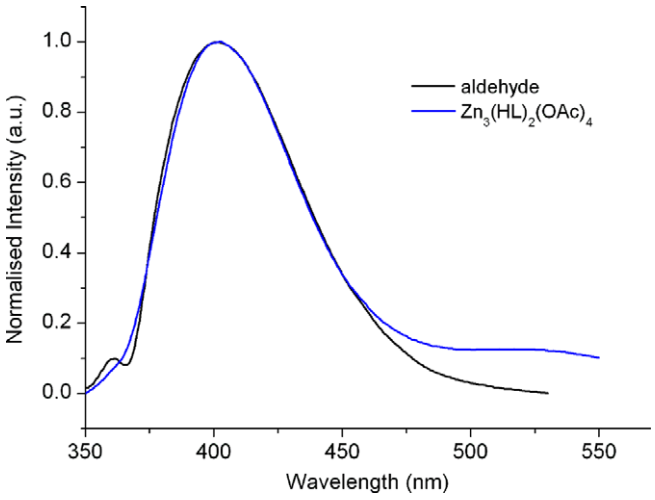


Fig. 5. Emission spectra (in MeOH, 10^{-4} M) of 8-hydroxyquinoline-2-carboxaldehyde (λ_{exc} = 310 nm) and $Zn_3(HL)_2(OAc)_4$ (λ_{exc} = 332 nm).

4. Conclusions

H_2L offers an *N,O* chelating site related to the 8-hydroxyquinoline residue, to which the conjugated imine *N* atom can join to act as a planar tridentate unit. Even in very mild reaction conditions, the acidity of the phenoxyl H atom leads to H_2L to act as monoanionic. Its interaction with zinc(II) acetate leads to the obtaining of $Zn_3(HL)_2(OAc)_4$ using both 3:2 and 4:2 $Zn(AcO)_2$:H_2L molar ratios.

The presence of the uncoordinated hydroxyl groups corresponding to the 2-aminoethanol residues allows the formation of hydrogen bonds that participate in the packing scheme of $Zn_3(HL)_2(OAc)_4$, via intra- or intermolecular interactions. The conjugation of the imine group with the 8-hydroxyquinoline residue facilitates an extended planarity that is responsible for some significant π–π interactions in the crystal packing.

The quantum yield of $Zn_3(HL)_2(OAc)_4$ (Φ_F = 0.07) is slightly higher than that of 8-hydroxyquinoline-2-carboxaldehyde (Φ_F = 0.06). The fluorescent emission of $Zn_3(HL)_2(OAc)_4$ is predominately caused by a ligand-based state rather than a MLCT state.

Supplementary data

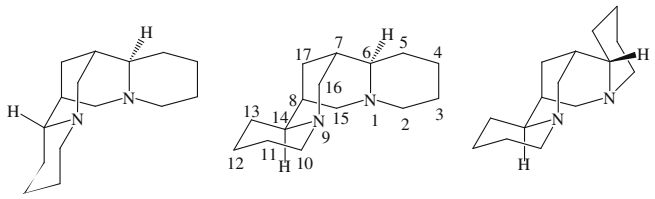
CCDC 710289 contains the supplementary crystallographic data for this paper. These data can be obtained free of charge via http://www.ccdc.cam.ac.uk/conts/retrieving.html, or from the Cambridge Crystallographic Data Centre, 12 Union Road, Cambridge CB2 1EZ, UK; fax: (+44) 1223-336-033; or e-mail: deposit@ccdc.cam.ac.uk.

Acknowledgements

Financial support by the Xunta de Galicia (PGIDIT06PXIB209043PR) is gratefully acknowledged.

References

[1] C.W. Tang, S.A. Van Slyke, Appl. Phys. Lett. 51 (1987) 913.
[2] C.H. Chen, J.-M. Shi, Coord. Chem. Rev. 171 (1998) 161.
[3] M. Albrecht, O. Blau, K. Witt, E. Wegelius, M. Nissinen, K. Rissanen, R. Fröhlich, Synthesis (1999) 1819.
[4] (a) M. Albrecht, K. Witt, E. Wegelius, K. Rissanen, Tetrahedron 56 (2000) 591;
(b) M. Albrecht, K. Witt, R. Fröhlich, O. Kataeva, Tetrahedron 58 (2002) 561.
[5] (a) E.G. Petkova, R.D. Lampeka, M.V. Gorichko, K.V. Domasevitch, Polyhedron 20 (2001) 747;
(b) R. Mladenova, M. Ignatova, N. Manalova, T. Petrova, I. Rashkov, Eur. Polym. J. 38 (2002) 989.
[6] (a) A. Petitjean, N. Kyritsakas, J.-M. Lehn, Chem. Commun. (2004) 1168;
(b) A. Petitjean, N. Kyritsakas, J.-M. Lehn, Chem. Eur. J. 11 (2005) 6818.
[7] (a) M. Albretch, M. Fiege, O. Osetska, Coord. Chem. Rev. 252 (2008) 812;
(b) M. Albrecht, O. Blau, R. Fröhlich, Chem. Eur. J. 5 (1999) 48.
[8] M. Albrecht, K. Witt, P. Weis, E. Wegelius, R. Fröhlich, Inorg. Chim. Acta 341 (2002) 25.
[9] B. Valeur, Molecular Fluorescence: Principles and Applications, Wiley-VCH, Weinheim, 2002.
[10] G.M. Sheldrick, SHELX-97 (SHELXS 97 and SHELXL 97), Programs for Crystal Structure Analyses, University of Göttingen, Germany, 1998.
[11] (a) J. Mahía, M. Maestro, M. Vázquez, M.R. Bermejo, J. Sanmartín, M. Maneiro, Acta Crystallogr., C 55 (1999) 1545;
(b) J. Mahía, M. Maestro, M. Vázquez, M.R. Bermejo, A.M. González, M. Maneiro, Acta Crystallogr., C 56 (2000) 347;
(c) J. Mahía, M. Maestro, M. Vázquez, M.R. Bermejo, A.M. González, M. Maneiro, Acta Crystallogr., C 56 (2000) 492;
(d) M. Vázquez, M.R. Bermejo, J. Sanmartín, A.M. García-Deibe, C. Lodeiro, J. Mahía, J. Chem. Soc., Dalton Trans. (2002) 870;
(e) M.R. Bermejo, J. Sanmartín, A.M. García-Deibe, M. Fondo, F. Novio, D. Navarro, Inorg. Chim. Acta 347 (2003) 53;
(f) J. Sanmartín, A.M. García-Deibe, M. Fondo, F. Novio, N. Ocampo, M.R. Bermejo, Inorg. Chim. Acta 359 (2006) 31.
[12] (a) See for example: D. Ülku, L. Tatar, O. Atakol, M. Aksu, Acta Crystallogr., C 57 (2001) 273;
(b) Z.-L. Youa, H.-L. Zhua, W.-S. Liu, Z. Anorg. Allg. Chem. 630 (2004) 1617;
(c) T. Yu, K. Zhang, Y. Zhao, C. Yang, H. Zhang, D. Fan, W. Dong, Inorg. Chem. Commun. 10 (2007) 401;
(d) T. Yu, K. Zhang, Y. Zhao, C. Yang, H. Zhang, L. Qian, D. Fan, W. Dong, L. Chen, Y. Qiu, Inorg. Chim. Acta 361 (2008) 233;
(e) J. Reglinski, S. Morris, D.E. Stevenson, Polyhedron 21 (2002) 2175.
[13] (a) W. Clegg, I.R. Little, B.P. Straughan, J. Chem. Soc., Dalton Trans. (1986) 1283;
(b) W. Clegg, I.R. Little, B.P. Straughan, J. Chem. Soc., Chem. Commun. (1985) 73;
(c) X.-W. Wang, F.-P. Chen, L. Chen, J.-Z. Chen, W.-J. Jiang, T.-J. Cai, Q. Deng, J. Mol. Struct. 842 (2007) 75.
[14] P. de Hoog, L. Durán Pachón, P. Gamez, M. Lutz, A.L. Spek, J. Reedijk, Dalton Trans. (2004) 2614.
[15] J.-P. Wei, H.-P. Zeng, D.-F. Xu, J. Liu, Chin. J. Chem. 26 (2008) 1299.
[16] (a) S. Pal, J.W. Gohdes, W.C.A. Wilish, W.H. Armstrong, Inorg. Chem. 31 (1992) 713;
(b) K. Wieghardt, U. Bossek, L. Zsolnai, G. Huttner, G. Blondin, J.J. Girerd, F. Babonneau, J. Chem. Soc., Chem. Commun. (1987) 651.
[17] H. Huang, C. Zhong, Y. Zhou, Eur. Polym. J. 44 (2008) 2944.
[18] J.M. Ouyang, Z.-M. Zhang, X.-L. Zhang, Q.-J. Chao, C.-J. Ye, H.-W. Di, Thin Solid Films 363 (2000) 130.
[19] Z.H.A. El-Wahab, J. Coord. Chem. 61 (2008) 3284.
[20] Q. Mei, B. Tong, L. Liang, M. Lu, J. Photochem. Photobiol. A: Chem. 191 (2007) 216.
[21] Q. Mei, N. Du, M. Lu, Eur. Polym. J. 43 (2007) 2380.
[22] Y.-L. Sui, B. Yan, J. Photochem. Photobiol. A: Chem. 182 (2006) 1.
[23] (a) C.L. Dollberg, C. Turro, Inorg. Chem. 40 (2001) 2484;
(b) D.M. Roundhill, in: J.P. Fackler (Ed.), Photochemistry and Photophysics of Metal Complexes, Modern Inorganic Chemistry Series, Plenum Press, New York, 1994, p. 56.
[24] (a) S. Lamansky, P. Djurovich, D. Murphy, F. Abdel-Razzaq, J.-E. Lee, C. Adachi, P.E. Burrows, S.R. Forrest, M.E. Thompson, J. Am. Chem. Soc. 123 (2001) 4304;
(b) C. Yi, C.-J. Yang, J. Liu, M. Xu, J.-H. Wang, Q.-Y. Cao, X.-C. Gao, Inorg. Chim. Acta 360 (2007) 3493.



Scheme 1. Three diastereomers of (−)-sparteine.

2. Experimental

2.1. Materials and preparation

All reagents and solvents were obtained commercially either from Fisher Scientific Co. or Aldrich Chemical Co. and were used without further purification, except where noted. Anhydrous ethanol was distilled from calcium hydride and stored under argon. (−)-Sparteine (Sp; $C_{15}H_{26}N_2$) was purchased from Sigma Chemical Company. The (−)-α-isosparteine (α-Sp; α-$C_{15}H_{26}N_2$) was derived from commercially available (−)-sparteine by a method in the literature [25].

2.1.1. Cu(Sp)(NCS)$_2$ (**1**) and Cu(Sp)(N$_3$)$_2$ (**2**)

The precursor copper(II) complex, [Cu(Sp)$(NO_3)_2$], was prepared by mixing an ethanol-triethylorthoformate (5:1 v/v) solution of copper(II) nitrate hemipentahydrate (3.00 g, 12.42 mmol) with a stoichiometric amount of (−)-sparteine at room temperature for 2 h. The resulting blue precipitate was filtered off, washed with triethylorthoformate, and then dried in a vacuum. Complex **1**, [Cu(Sp)$(NCS)_2$], was prepared from the substitution reaction of [Cu(Sp)$(NO_3)_2$] (1.00 g, 2.37 mmol) with a stoichiometric amount of NaNCS in 50 ml ethanol-triethylorthoformate (5:1 v/v) solution. The reddish brown precipitate was filtered off, washed with cold absolute ethanol, and then dried in a vacuum. The yield of the product was 78.5%. Dark reddish brown single crystals were obtained by recrystallization at about 278 K from a dichloromethane–triethylorthoformate (5:1 v/v) solution under carbon tetrachloride vapor. *Anal.* Calc. for $CuC_{17}H_{26}N_4S_2$: C, 49.31; H, 6.33; N, 13.53. Found: C, 49.08; H, 6.35; N, 13.63%. IR (in cm^{-1}, KBr): 2934 (s, ν_s(C–H)), 2856 (s, ν_s(C–H)), 2077 (vs, ν_a(NCS)), 2058 (vs, ν_a(NCS)), 1467 (m, ν_a(C–H)), 1434 (s, ν_a(C–H)), 1304 (s, ν_s(NCS)), 1292 (m, ν_s(NCS)), 432 (w, ν(Cu–N_{Sp})). Complex **2**, [Cu(Sp)$(N_3)_2$], was prepared from the substitution reaction of [Cu(Sp)$(NO_3)_2$] (1.00 g, 2.37 mmol) with a stoichiometric amount of NaN_3 in 50 ml ethanol-triethylorthoformate (5:1 v/v) solution as reported [21]. The yield of the dark yellowish brown precipitate obtained was 85.3%. *Anal.* Calc. for $CuC_{15}H_{26}N_8$: C, 47.17; H, 6.86; N, 29.34. Found: C, 47.83; H, 6.91; N, 29.59%. IR (in cm^{-1}, KBr): 2929 (s, ν_s(C–H)), 2861 (s, ν_s(C–H)), 2048 (vs, $\nu_a(N_3)$), 2058 (vs, $\nu_a(N_3)$), 1466 (m, ν_a(C–H)), 1447 (s, ν_a(C–H)), 1283 (s, $\nu_s(N_3)$), 468 (w, ν(Cu–N_{Sp})).

2.1.2. Cu(α-Sp)(NCS)$_2$ (**3**) and Cu(α-Sp)(N$_3$)$_2$ (**4**)

The precursor copper(II) complex, [Cu(α-Sp)$(NO_3)_2$], was prepared in a glove box by mixing an ethanol-triethylorthoformate (5:1 v/v) solution of copper(II) nitrate hemipentahydrate (1.20 g, 5.16 mmol) with a stoichiometric amount of (−)-α-isosparteine. The resulting blue precipitate was filtered off, washed with triethylorthoformate, and then dried in a vacuum. Complex **3**, [Cu(α-Sp)$(NCS)_2$], was prepared from the substitution reaction of [Cu(α-Sp)$(NO_3)_2$] (1.00 g, 2.37 mmol) with a stoichiometric amount of NaNCS in 60 ml ethanol-triethylorthoformate (5:1 v/v) solution. The reddish brown precipitate was filtered off, washed with cold absolute ethanol, and then dried in a vacuum. The yield of the product was 79.6%. Dark reddish brown single crystals were obtained by recrystallization at about 278 K from a dichloromethane–triethylorthoformate (5:1 v/v) solution under carbon tetrachloride vapor. *Anal.* Calc. for $CuC_{17}H_{26}N_4S_2$: C, 49.31; H, 6.33; N, 13.53. Found: C, 49.01; H, 6.42; N, 13.39%. Complex **4**, [Cu(α-Sp)$(N_3)_2$], was prepared from the substitution reaction of [Cu(α-Sp)$(NO_3)_2$] (1.00 g, 2.37 mmol) with a stoichiometric amount of NaN_3 in 50 ml ethanol-triethylorthoformate (5:1 v/v) solution as reported [22]. The yield of the dark yellowish brown precipitate obtained was 77.4%. *Anal.* Calc. for $CuC_{15}H_{26}N_8$: C, 47.17; H, 6.86; N, 29.34. Found: C, 47.47; H, 6.89; N, 29.67%.

2.2. Physical measurements

Elemental analyses were carried out using a Profile HV-3 Elemental Analyzer System (Germany) at the Korean Basic Science Institute (Busan Branch). Infrared spectra were obtained using standard KBr pellet techniques with a Mattson Polaris FT-IR spectrometer. The resolution was 4 cm^{-1}. X-band (9.44 GHz) ESR spectra were acquired at room temperature and 77 K using a Bruker Instruments ESP-300S ESR spectrometer at the Korean Basic Science Institute (Seoul Branch).

2.3. X-ray crystal structure determination

Crystals of complexes **1** and **3** for X-ray analysis were obtained by slow evaporation from dichloromethane–triethylorthoformate solutions. The dark reddish brown crystals of **1** and **3** were mounted and aligned on a CAD-4 diffractometer [26]. Accurate cell parameters were refined from setting angles of 40 reflections with $4.87^\circ \leqslant \theta \leqslant 12.54^\circ$ for **1** and 51 reflections with $5.20^\circ \leqslant \theta \leqslant 11.99^\circ$ for **3**. 2508 independent reflections for **1** in an asymmetric unit in range $-11 \leqslant h \leqslant 1$, $-1 \leqslant k \leqslant 17$, $-11 \leqslant l \leqslant 11$ and 2717 independent reflections for **3** in an asymmetric unit in range $-1 \leqslant h \leqslant 10$, $-15 \leqslant k \leqslant 1$, $-1 \leqslant l \leqslant 20$ were collected using graphite-monochromated Mo Kα radiation and the $2\theta/\omega$ scan mode.

All non-H atoms were found by direct methods and their parameters were refined successfully with a full matrix least-squares procedure. The function minimized during least-squares refinement was $\omega^{-1} = [\sigma^2(F_o)^2 + (0.0467P)^2 + 1.7583P]$ for **1** and $\omega^{-1} = [\sigma^2(F_o)^2 + (0.0237P)^2]$ for **3**. H atoms were geometrically positioned and fixed. Empirical absorption corrections by using psi-scan for crystals **1** and **3** were applied to the intensity data (T_{max} and T_{min} are 0.9814 and 0.8493 for **1**, and 0.2699 and 0.2370 for **3**, respectively). Data collection and cell refinement: Bruker XSCANS [27]. Data reduction: SHELXTL [28]. Program used to solve and refine the structures: SHELXS97 and SHELXL97 [29]. Molecular graphics: ORTEP-3 for windows [30].

3. Results and discussion

3.1. Characterization of the compounds

Among the three diastereomers of sparteine, (−)-sparteine was commercially available and (−)-α-isosparteine was derived from (−)-sparteine according to the literature method [25]. The copper(II) sparteine pseudohalide complexes, Cu(Sp)$(NCS)_2$ **1**, Cu(Sp)$(N_3)_2$ **2**, Cu(α-Sp)$(NCS)_2$ **3** and Cu(α-Sp)$(N_3)_2$ **4**, were prepared from the substitution reaction of copper(II) sparteine dinitrate complexes with stoichiometric amounts of the corresponding sodium salts (NaNCS and NaN_3) in ethanol solution. Characterization of these complexes and the precursor complexes, Cu(Sp)$(NO_3)_2$ and Cu(α-Sp)$(NO_3)_2$, was conducted by IR spectros-

copy and elemental analyses (see Section 2). Single crystals of the complexes **1** and **3** were obtained by recrystallization at 278 K from dichloromethane solutions. Although complexes **2** and **4** have already been reported [21,22], these complexes were also prepared in order to compare them with the other CuN_4 type complexes.

3.2. X-ray crystal structure

The pseudo-tetrahedral geometry around the Cu^{II} center of the copper(II) sparteine complexes in the ultimate molecular structure is due to the steric requirements imposed by the bulky sparteine ligand and the influence of the anionic ligand. In order to evaluate the extent of the distortion imposed by the conformation of the sparteine diastereomers and/or by the different anionic ligands, we determined the crystal structures of complexes **1** and **3**. Crystallographic data and structural refinements are summarized in Table 1 and selected bond distances and bond angles are listed in Table 2.

As shown in Figs. 1 and 2, both complexes **1** and **3** contain a copper(II) atom ligated by sparteine (Sp or α-Sp) with two isothiocyanate ligands in the remaining coordination sites, forming a distorted CuN_4 chromophore. The conformation of the coordinated (−)-sparteine in **1** consists of one terminal ring folded down over the copper(II) atom (endo) and the other terminal ring folded back away from the copper(II) atom (exo), whereas that of the coordinated (−)-α-isosparteine in **3** consists of both two terminal rings folded down over the copper(II) atom (endo). These conformations of the sparteine ligands are identical to those of the free ligands, Sp and α-Sp, as already shown in the crystal structures of **2** and **4** [21,22].

The dihedral angles between N_{Sp}–Cu–N_{Sp} and N_{NCS}–Cu–N_{NCS} in **1** and **3** are 58.2(6)° and 52.2(9)°, respectively, which are comparable with those between N_{Sp}–Cu–N_{Sp} and N_{N3}–Cu–N_{N3} [55.3(2)° and 50.2°, respectively] in **2** and **4** [21,22]. These values of the dihedral angles indicate that the steric effect of Sp is larger than that of α-Sp and the dihedral angle of the copper(II) complex with the NCS ligand is larger than that with the N_3 ligand. Therefore, the dihedral angle can be estimated by the steric effect of the sparteine diastereomers together with the crystal field stabilization effect caused by the influence of the anionic ligands (NCS^- and N_3^-) bound terminally to the copper(II) center.

The 'tilt' of the bidentate sparteine ligand with respect to the N_{NCS}–Cu–N_{NCS} plane is another parameter to evaluate the extent of the distortion of the tetrahedron. In **1**, the mid-point of the N1···N9 line does not lie exactly in the N3–Cu–N4 plane, but is tilted towards atom N9 by 0.045 Å (3.2% of half of the N1···N9 distance). Similarly, the mid-point of the N3···N4 line also does not lie exactly in the N1–Cu–N9 plane, but is tilted towards atom N3 by 0.132 Å (8.9% of half of the N3···N4 distance). In the case of **3**, the mid-points are tilted towards atom N9 by 0.086 Å (6.1%) and atom N3 by 0.046 Å (3.2%). On the other hand, in **1** and **3**, the N1–Cu–N3 and N9–Cu–N4 angles differ by only 0.5° and 0.9°, whereas the N1–Cu–N4 and N9–Cu–N3 angles differ by 2.8° and 2.9°, respectively (see Table 2). Therefore, the distortion towards

Table 1
Crystallographic data for the complexes **1** and **3**.

	$Cu(C_{15}H_{26}N_2)(NCS)_2$, **1**	$Cu(\alpha\text{-}C_{15}H_{26}N_2)(NCS)_2$, **3**
Chemical formula	$CuC_{17}H_{26}N_4S_2$	$CuC_{17}H_{26}N_4S_2$
Formula weight (FW) (amu)	414.08	414.08
Crystal description	brown plate	brown irregular
Crystal size (mm)	0.38 × 0.22 × 0.08	0.34 × 0.32 × 0.26
Crystal system	monoclinic	orthorhombic
Space group	$P2_1$	$P2_12_12_1$
T (K)	293(2)	293(2)
Radiation (Mo Kα) (λ/Å)	0.71073	0.71073
a (Å)	8.6426(12)	8.853(2)
b (Å)	13.180(2)	13.138(3)
c (Å)	8.7032(10)	16.687(3)
β (°)	103.098(10)	90.000
V (Å^3)	965.6(2)	1940.8(7)
Z	2	4
$D_{calcd.}$ (Mg m^{-3})	1.424	1.417
μ (mm^{-1})	1.353	1.347
F (0 0 0)	434	868
Intensity variation (%)	1.0	1.0
Absorption correction	empirical T_{max} = 0.981, T_{min} = 0.849	empirical T_{max} = 0.270, T_{min} = 0.237
Independent reflections	2057	2534
Observed reflections	1069	676
Final R	0.0762	0.0642
ωR	0.1328	0.0907
Threshold expression	$I \geqslant 2\sigma(I)$	$I \geqslant 2\sigma(I)$
Parameters	218	218
$(\Delta/\sigma)_{max}$	1.000	1.000
Goodness-of-fit (GOF)	1.058	0.927
Flack parameter	−0.02(6)	−0.06(6)

Table 2
Selected bond distances (Å) and bond angles (°) for the complexes **1** and **3**.

Complex ***1***			
Cu–N1	1.998(12)	N3–C18	1.130(19)
Cu–N9	1.996(10)	C18–S1	1.629(18)
Cu–N3	1.933(16)	N4–C19	1.15(2)
Cu–N4	1.931(14)	C19–S2	1.61(2)
N1–Cu–N9	90.6(5)	N3–Cu–N4	100.3(6)
N1–Cu–N3	99.6(6)	Cu–N3–C18	158.6(16)
N1–Cu–N4	136.2(7)	Cu–N4–C19	154.3(17)
N9–Cu–N3	139.0(6)	N3–C18–S1	179(2)
N9–Cu–N4	99.1(5)	N4–C19–S2	176.2(18)
Complex ***3***			
Cu–N1	2.051(13)	N3–C18	1.14(2)
Cu–N9	2.003(13)	C18–S1	1.628(19)
Cu–N3	1.921(15)	N4–C19	1.099(18)
Cu–N4	1.924(14)	C19–S2	1.662(17)
N1–Cu–N9	89.3(6)	N3–Cu–N4	98.3(6)
N1–Cu–N3	97.6(7)	Cu–N3–C18	152.8(18)
N1–Cu–N4	140.7(6)	Cu–N4–C19	163.4(18)
N9–Cu–N3	143.6(7)	N3–C18–S1	173(2)
N9–Cu–N4	98.5(7)	N4–C18–S2	178(2)

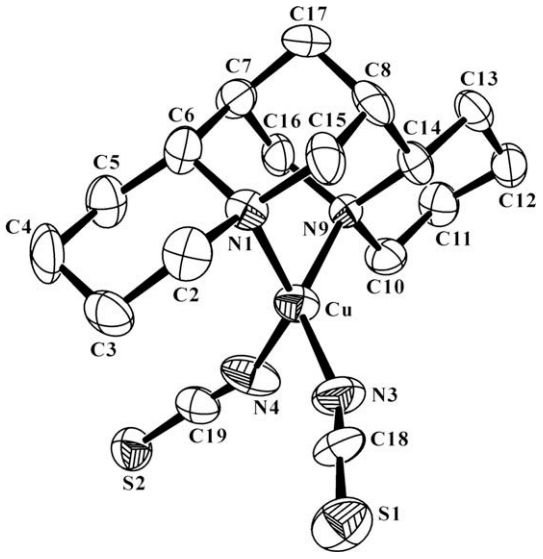


Fig. 1. ORTEP-3 diagram of complex **1** showing the atom numbering scheme and 30% probability ellipsoids. H atoms have been omitted for clarity.

The 'tilt' of the bidentate sparteine ligand with respect to the N_{NCS}–Cu–N_{NCS} plane is another parameter to evaluate the extent of the distortion of the tetrahedron. In **1**, the mid-point of the N1···N9 line does not lie exactly in the N3–Cu–N4 plane, but is tilted towards atom N9 by 0.045 Å (3.2% of half of the N1···N9 distance). Similarly, the mid-point of the N3···N4 line also does not lie exactly in the N1–Cu–N9 plane, but is tilted towards atom N3 by 0.132 Å (8.9% of half of the N3···N4 distance). In the case of **3**, the mid-points are tilted towards atom N9 by 0.086 Å (6.1%) and atom N3 by 0.046 Å (3.2%). On the other hand, in **1** and **3**, the N1–Cu–N3 and N9–Cu–N4 angles differ by only 0.5° and 0.9°, whereas the N1–Cu–N4 and N9–Cu–N3 angles differ by 2.8° and 2.9°, respectively (see Table 2). Therefore, the distortion towards

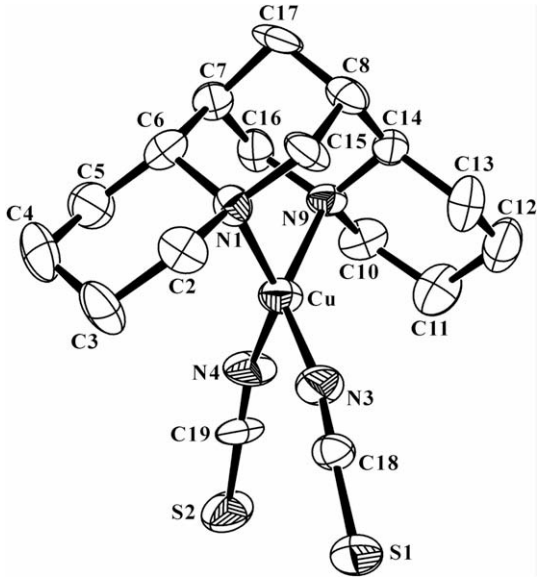


Fig. 2. ORTEP-3 diagram of complex **3** showing the atom numbering scheme and 30% probability ellipsoids. H atoms have been omitted for clarity.

a tetrahedron for both **1** and **3** is quite symmetrically twisted and similar to that for both **2** and **4** [21,22]. The Cu–N_{Sp} distances in **1** are slightly smaller than those in **3**, whereas the Cu–N_{NCS} distances in **1** are similar to those in **3** (see Table 2). This result is in a good agreement with that obtained from copper(II) diazide complexes with Sp and α-Sp, **2** and **4** [21,22].

3.3. Electron spin resonance spectra

X-band electron spin resonance (ESR) spectra of the complexes **1–4** have been recorded in CH_2Cl_2/DMF (1:1 v/v) at 77 K and the electron spin Hamiltonian parameters are summarized in Table 3. As shown in Fig. 3, all ESR spectra exhibit axial symmetry with $g_{||} > g_{\perp} > 2.0023$, indicating that the geometry around the copper(II) center of complexes **1–4** is tetrahedrally distorted and the copper(II) center has a $d_{x^2-y^2}$ ground state. The ESR spectra of **1–4**, which have a $Cu^{II}N_4$ chromophore, showed a relatively small $A_{||}$ value in the range 130–141 $\times 10^{-4}$ cm^{-1}. It is well known that the parallel hyperfine coupling $A_{||}$ value for $CuCl_4^{2-}$ decreases by over 100×10^{-4} cm^{-1} upon distortion from D_{4h} to D_{2d}-distorted tetrahedral [7] and the $A_{||}$ value for square–planar copper(II) complexes having a $Cu^{II}N_4$ chromophore is always greater than 140×10^{-4} cm^{-1} [31,32]. Therefore, the low $A_{||}$ values displayed by complexes **1–4** are caused by the reduction of the site symmetry from D_{4h} to D_{2d} and the ESR spectral results indicate that the coordination geometry and covalency of the metal–ligand binding interaction co-determine the $A_{||}$ values.

A plot of the dihedral angle between the N_{Sp}–Cu–N_{Sp} and N_L–Cu–N_L (L = NCS^- and N_3^-) planes versus the parallel hyperfine coupling $A_{||}$ value for **1–4** is shown in Fig. 4. A good correlation between the dihedral angle in the X-ray structure and the $A_{||}$ value in the ESR spectra was observed. As the dihedral angle between N_{Sp}–Cu–N_{Sp} and N_L–Cu–N_L increases, the parallel hyperfine coupling $A_{||}$ value decreases because of the lower coupling between the electron spin and the orbital. The results of X-ray crystallography and ESR spectroscopy are in a good agreement with the assumption that the degree of distortion from planarity to tetrahedron will reduce the $A_{||}$ value of four-coordinate copper(II) complexes if the set of donor atoms are maintained.

Table 3
Spin Hamiltonian parameters for the complexes **1–4** in CH_2Cl_2/DMF (1:1 v/v) at 77 K.

Compound	$g_{||}$	$g_{\perp}$	$A_{||}$ ($\times 10^4$ cm^{-1})
Cu(Sp)$(NCS)_2$ **1**	2.255	2.042	130.3
Cu(Sp)$(N_3)_2$ **2**	2.230	2.027	135.1
Cu(α-Sp)$(NCS)_2$ **3**	2.283	2.061	139.2
Cu(α-Sp)$(N_3)_2$ **4**	2.267	2.075	141.3

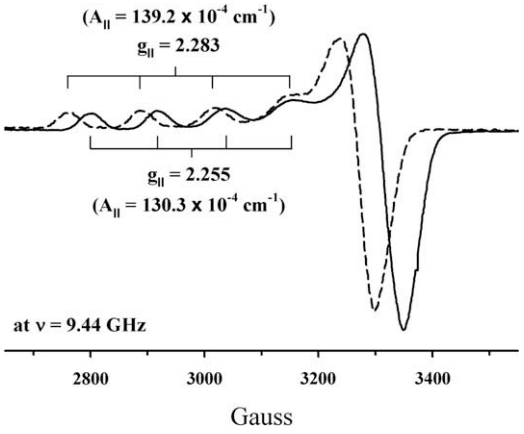


Fig. 3. X-band ESR spectra of the complexes **1** (solid line) and **3** (dashed line) in CH_2Cl_2/DMF (1:1 v/v) at 77 K.

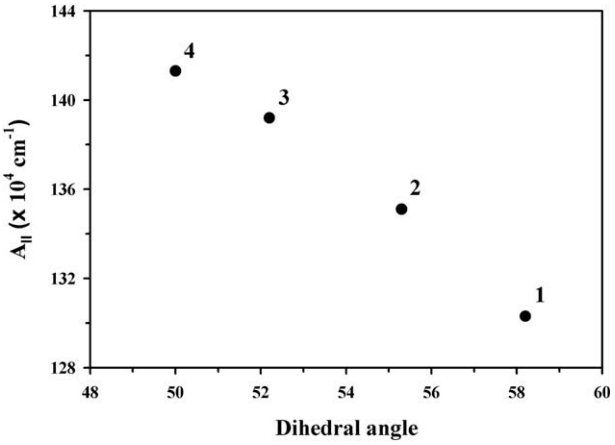


Fig. 4. Plot of the dihedral angle between the N_{Sp}–Cu–N_{Sp} and N_L–Cu–N_L (L = NCS^- and N_3^-) planes vs. the parallel hyperfine coupling $A_{||}$ value for complexes **1–4**.

4. Conclusion

The crystal structures of copper(II) isothiocyanate complexes with two sparteine epimers, Sp and α-Sp, were determined and compared with copper(II) azide complexes previously reported [21,22]. The dihedral angle between the N_{Sp}–Cu–N_{Sp} and N_L–Cu–N_L (L = NCS^- and N_3^-) planes increased in the order **1** > **2** > **3** > **4**. As a result, the ESR parallel hyperfine coupling $A_{||}$ value decreased in the order **1** < **2** < **3** < **4** because the electron spin and orbital coupling reduced according to the increase of the degree of distortion from planar to tetrahedral. These results indicate that the steric effect imposed by Sp and NCS^- ligands is larger than that imposed by α-Sp and N_3^- ligands.

Supplementary data

CCDC 726870 and 726871 contain the supplementary crystallographic data for **1** and **3**, respectively. These data can be obtained

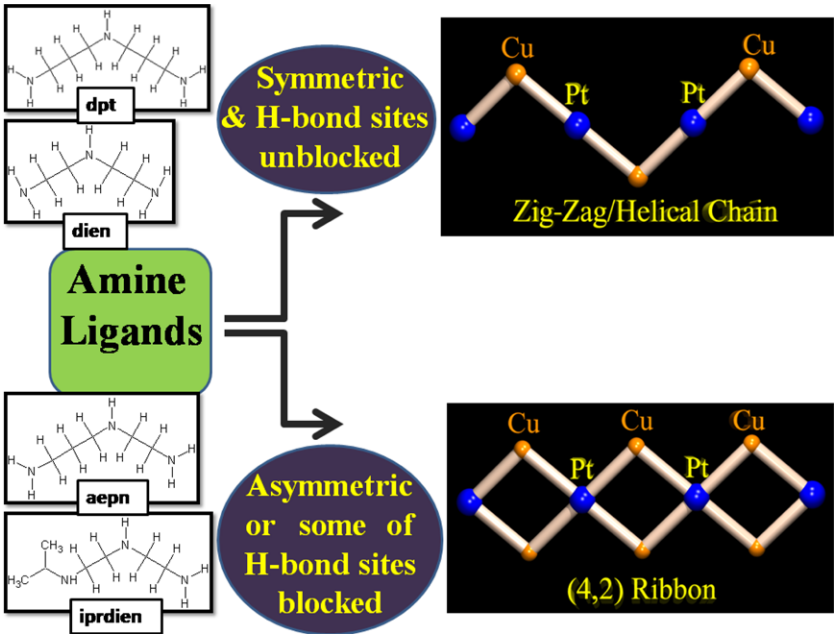
free of charge via http://www.ccdc.cam.ac.uk/conts/retrieving.html, or from the Cambridge Crystallographic Data Centre, 12 Union Road, Cambridge CB2 1EZ, UK; fax: (+44) 1223-336-033; or e-mail: deposit@ccdc.cam.ac.uk.

Acknowledgement

This work was supported by Korean Research Foundation Grant funded by the Korean Government (MOEHRD) (Grant No. R05–2004-000–10851-0).

References

[1] W.H. Armstrong, in: L. Que Jr. (Ed.), Metalloprotein Crystallography in Metal Cluster in Proteins, American Chemical Society, Washington, DC, 1988.
[2] E.I. Solomon, M.D. Lowery, L.B. Lacriox, D.E. Root, Methods Enzymol. 226 (1993) 1.
[3] G.E. Norris, B.F. Anderson, E.N. Baker, J. Am. Chem. Soc. 108 (1986) 2784.
[4] M.M. Whittaker, W.R. Duncan, J.W. Whittaker, Inorg. Chem. 35 (1996) 382.
[5] K. Pierloot, J.O.A. De Kerpel, U. Rydo, B.O. Roos, J. Am. Chem. Soc. 119 (1997) 218.
[6] J.M. Guss, P.R. Harrowell, M. Murata, V.A. Norris, H.C. Freeman, J. Mol. Biol. 192 (1986) 361.
[7] E.I. Solomon, M.J. Baldwin, M.D. Lowery, Chem. Rev. 92 (1992) 521.
[8] Y.-J. Kim, S.-O. Kim, Y.-I. Kim, S.-N. Choi, Inorg. Chem. 40 (2001) 4481.
[9] W.A. Cady, E. Boschmann, R.S. Choi, J.F. Heidelman, S.L. Smith, Inorg. Chem. 16 (1977) 1958.
[10] P. Beak, A. Basu, D.J. Gallagher, Y.S. Park, S. Thayumanavan, Acc. Chem. Res. 29 (1996) 552.
[11] R.A. Kretchmer, J. Org. Chem. 37 (1972) 2744.
[12] S.F. Mason, R.D. Peacock, J. Chem. Soc., Dalton Trans. (1973) 226.
[13] L.S. Childers, K. Folting, L.L. Merritt Jr., W.E. Streib, Acta Crystallogr. B31 (1975) 924.
[14] S.-N. Choi, M.-A. Kwon, Y. Kim, R.D. Bereman, P. Singh, B. Knight, K. Seff, J. Coord. Chem. 34 (1995) 241.
[15] S. Lopez, I. Muravyov, S.R. Pulley, S.W. Keller, Acta Crystallogr. C54 (1998) 355.
[16] Y.-M. Lee, G. Chung, M.-A. Kwon, S.-N. Choi, Acta Crystallogr. C56 (2000) 67.
[17] Y.-M. Lee, M.-A. Kwon, S.K. Kang, J.H. Jeong, S.-N. Choi, Inorg. Chem. Commun. 6 (2003) 197.
[18] S.K. Kang, Y.-M. Lee, Y.-I. Kim, Y. Kim, K. Seff, S.-N. Choi, Inorg. Chim. Acta 357 (2004) 2602.
[19] B. Jasiewicz, W.Ł. Boczoń, A. Kowalczyk, J. Coord. Chem. 60 (2007) 2441.
[20] B. Jasiewicz, B. Warżajtis, U. Rychlewska, T. Toliński, J. Mol. Struct. 921 (2009) 314.
[21] Y.-K. Kim, B.-J. Kim, S.K. Kang, S.-N. Choi, Y.-M. Lee, Acta Crystallogr. C59 (2003) m64.
[22] B.-J. Kim, Y.-M. Lee, E.H. Kim, S.K. Kang, S.-N. Choi, Acta Crystallogr. C58 (2002) m361.
[23] Y.-M. Lee, S.-N. Choi, I.-H. Suh, R.D. Bereman, Acta Crystallogr. C54 (1998) 1582.
[24] B.N. Figgis, in: Introduction to Ligand Fields, John Wiley and Sons Inc., New York, USA, 1966.
[25] N.J. Leonard, R.E. Beyler, J. Am. Chem. Soc. 72 (1950) 1316.
[26] Enraf-Nonius, CAD-4 Software: Version 5.0, Delft, The Netherlands, 1989.
[27] Siemens, XSCANS: Version 2.2, Siemens Analytical X-ray Instruments Inc., Madison, Wisconsin, USA, 1996.
[28] Bruker, SHELXTL: Version 5.1, Bruker AXS Inc., Madison, Wisconsin, USA, 1997.
[29] G.M. Sheldrick, SHELX97 – Program for the Refinement of Crystal Structures, University of Göttingen, Germany, 1997.
[30] L.J. Farrugia, J. Appl. Cryst. 30 (1997) 565.
[31] T. Vannegard, in: H.M. Swartz, J.R. Bolton, D.C. Borg (Eds.), Biological Applications of Electron Spin Resonance, Wiley Interscience Press, New York, 1972, p. 411.
[32] S.-N. Choi, R.D. Bereman, J.R. Wasson, J. Inorg. Nucl. Chem. 37 (1975) 2087.



Scheme 1.

2. Experimental

2.1. Materials

High purity (98%) *N*-(2-aminoethyl)-1,3-propanediamine (aepn), diethylenetriamine (dien), 3,3′-imino bispropylamine (dpt), N′-isopropyldiethylenetriamine (iprdien) and potassium tetracyanoplatinate(II) were purchased from the Aldrich Chemical Co. Inc. and were used as received. All others chemicals were of AR grade.

2.2. Physical measurements

Elemental analyses (carbon, hydrogen and nitrogen) were performed using a Perkin–Elmer 240C elemental analyzer. IR spectra were measured from KBr pellets on a Nicolet 520 FTIR spectrometer. The magnetic measurements were carried out on polycrystalline samples using a Quantum Design MPMS SQUID magnetometer working in the temperature region 300–2 K. Diamagnetic corrections were estimated from Pascal's table [47].

2.3. Synthesis

2.3.1. $[\{Cu_2(aepn)_2Pt(CN)_42H_2O\}\cdot 2(H_2O)\cdot\{Pt(CN)_4\}]_n$ (**1**)

N-(2-aminoethyl)-1,3-propanediamine (aepn) (2 mmol, 0.234 g) was added dropwise to an aqueous solution (10 cm^3) of $Cu(ClO_4)_2\cdot 6H_2O$ (2 mmol, 0.741 g) with constant stirring for a few minutes. To the resulting deep blue solution, an aqueous solution (10 cm^3) of $K_2[Pt(CN)_4]\cdot 2H_2O$ (2 mmol, 0.754 g) was added slowly and the reaction mixture was stirred for 1 h and then filtered and the filtrate was kept in a $CaCl_2$ desiccator. Shiny deep blue single crystals suitable for X-ray analysis were obtained after a few days. Yield 65%. *Anal.* Calc. for $C_{18}H_{38}Cu_2N_{14}O_4Pt_2$ (**1**): C, 20.95; H, 3.71; N, 19.00. Found: C, 20.75; H, 3.64; N, 19.16%. IR spectra (KBr disk; cm^{-1}) 3300–3500 [ν(O–H)]; 3200–3400 [ν(N–H)]; 2141 [ν(C–N)].

2.3.2. $[\{Cu(dpt)Pt(CN)_4\}]_n$ (**2**)

Complex **2** was synthesized by the same procedure adopted for **1** using 3,3′-imino bispropylamine (dpt), (2 mmol, 0.262 g) instead of aepn. Yield 70%. *Anal.* Calc. for $C_{10}H_{17}CuN_7Pt$ (**2**): C, 24.29; H, 3.44; N, 19.84. Found: C, 24.25; H, 3.41; N, 19.82%. IR (KBr disk; cm^{-1}) 3200–3400 [ν(N–H)]; 2138 [ν(C–N)].

2.3.3. $[\{Cu(dien)Pt(CN)_4\}]_n$ (**3**)

Complex **3** was synthesized by the same procedure adopted for **1** using diethylenetriamine (dien) (2 mmol, 0.206 g) instead of aepn. Yield 70%. *Anal.* Calc. for $C_8H_{13}CuN_7Pt$ (**3**): C, 20.61; H, 2.79; N, 21.04. Found: C, 20.59; H, 2.76; N, 21.01%. IR (KBr disk; cm^{-1}) 3200–3400 [ν(N–H)]; 2155 [ν(C–N)].

2.3.4. $[\{Cu_2(iprdien)_2Pt(CN)_4\}\cdot 2(ClO_4)\cdot 2(H_2O)]_n$ (**4**)

Complex **4** was synthesized by the same procedure adopted for **1** using N′-isopropyldiethylenetriamine (iprdien) (2 mmol, 0.284 g) instead of aepn. Yield 70%. *Anal.* Calc. for $C_{18}H_{32}Cu_2N_{10}PtCl_2O_8$ (**4**) C, 23.65; H, 3.82; N, 15.14. Found: C, 23.75; H, 3.52; N, 15.39%. IR (KBr disk; cm^{-1}) 3200–3400 [ν(N–H)]; 2190, 2181, 2140 [ν(C–N)].

2.4. Crystallographic data collection and refinement

Diffraction data collection of all four complexes was carried out on a Bruker SMART diffractometer, equipped with a graphite monochromator and Mo Kα radiation (λ = 0.71073 Å). The data integration and reduction were processed with SAINT [48] software. An empirical absorption correction was applied to the collected reflections with SADABS [49] using XPREP [50]. The structures were solved by the Patterson method. Metal atoms in all four complexes were located from the *E*-maps. Other non-hydrogen atoms were located in successive difference Fourier syntheses and refined with anisotropic thermal parameters on F^2. The water hydrogen atoms in **1** were located from the difference Fourier map and refined isotropically but the positions of the hydrogen atoms attached to the carbon atoms were calculated geometrically with a fixed thermal parameter 1.2 times that of their parent atoms. Water hydrogen atoms in **4** could not be located from the difference Fourier map. Crystallographic data and experimental details for the structural analyses are listed in Table 1. Large residual electron densities in **1** and **3** are within 1 Å of the heavy metals (Pt) and are due to a series truncation error having no chemical significance. All calcula-

Table 1
Crystal data and structure refinement of complexes **1**–**4**.

	1	2	3	4
Empirical formula	$C_{18}H_{38}Cu_2N_{14}Pt_2O_4$	$C_{10}H_{17}CuN_7Pt$	$C_8H_{13}CuN_7Pt$	$C_{18}H_{38}Cu_2N_{10}PtCl_2O_9$
Formula weight	1031.85	493.94	465.88	933.67
Crystal system	triclinic	monoclinic	triclinic	monoclinic
Space group	$P\bar{1}$	$P2_1/n$	$P\bar{1}$	$P2_1/c$
a (Å)	7.5269(15)	11.573(4)	6.7921(10)	28.566(3)
b (Å)	7.8994(16)	10.288(3)	8.2103(12)	15.0584(17)
c (Å)	14.296(3)	13.789(4)	12.0987(18)	16.3217(19)
α (°)	91.808(3)	90	82.804(2)	90
β (°)	98.747(3)	109.601(5)	80.561(2)	103.881(2)
γ (°)	109.151(2)	90	79.422(2)	90
V (Å^3)	790.6(3)	1546.6(8)	651.08(17)	6815.9(13)
Z	1	4	2	8
ρ_{calc} (g cm^{-1})	2.167	2.121	2.376	1.816
μ (mm^{-1})	10.194	10.407	12.354	5.544
Unique data	3467	3785	3063	17 024
Data $I > 2\sigma(I)$	2989	3155	2737	11 034
Goodness-of-fit (GOF) (F^2)	1.11	1.01	1.05	0.98
R	0.0490	0.0310	0.0474	0.0404
wR_2[a]	0.1476	0.0672	0.1307	0.0841

[a] $R_1 = \sum||F_o|-|F_c||/\sum|F_o|$, $wR_2 = [\sum w(F_o^2 - F_c^2)^2/\sum w(F_o^2)^2]^{1/2}$.

tions were carried out using SHELX97 [51], PLATON [52], ORTEP-32 [53] and the WINGX system, Ver 1.64.05 [54].

2.5. Crystal structure descriptions

2.5.1. Crystal structure description of complex *1*

The X-ray crystal structure determination of complex **1** reveals that the Cu(II) centers are bridged by tetracyanoplatinate anions to form a cationic 1D coordination polymer having a (4,2) ribbon-like topology (Scheme 1), with the formula $[Cu_2(aepn)_2Pt(CN)_4 2H_2O]_n^{-}$. The ORTEP diagram showing the (4,2) ribbon of the complex has been depicted in Fig. 1. The polymeric ribbons run along the crystallographic *b*-axis. Charge neutrality of the complex has been satisfied through the incorporation of free tetracyanoplatinate units. These also play vital role in the determination of the supramolecular architecture of the complex by acting as a strong hydrogen bond acceptor. In the formation of the cationic (4,2) ribbon, all CN groups of a $Pt(CN)_4^{2-}$ unit take part in bridging four Cu(II) centers. The coordination bond lengths and angles are given in Table S1. The octahedral environment comprises of three N atoms (N1, N2, N3) of aepn and a cyanide N atom (N4), which form the equatorial plane, and the apical positions are occupied by a N atom (N5) of another cyanide ligand and an O atom (O2w) of a water molecule. The Cu–N(amine) bond distances are in the range 2.009(7)–2.044(8) Å, and match well with this type of Cu(II) complex and are almost comparable to the basal Cu–N4(cyano) bond length of 2.026(8) Å. On the other hand, the apical Cu–N5 distance is 2.288(9) Å. In the bridging $[Pt(CN)_4]^{2-}$ anions, the Pt–C bond distances are 1.983(9) and 2.020(10) Å. In the free $Pt(CN)_4^{2-}$ anions, the Pt–C bond distances are 1.985(9) and 2.009(11) Å.

The assembly created through the hydrogen bonding interaction (Table 2) between the CN groups of free $[Pt(CN)_4]^{2-}$ and the coordinated water/amine is shown in Fig. 2. Each free $[Pt(CN)_4]^{2-}$ interacts with four adjacent Cu(II) centers from each (4,2) ribbon. This leads to a 3D hydrogen bonded supramolecular assembly with

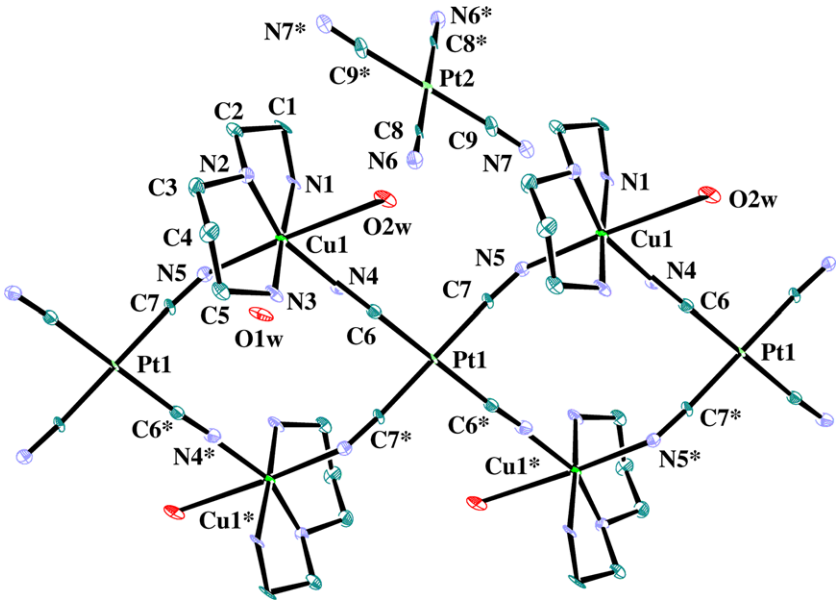


Fig. 1. The ORTEP diagram with 30% ellipsoidal probability of complex **1**, showing the (4,2) ribbon.

Table 2
Hydrogen bonding interactions (Å, °) of complexes **1**, **2**, **3** and **4**.

	D–H···A	*d*(D–H) Å	*d*(H···A) Å	*d*(D···A) Å	∠DHA (°)	Symmetry
1	N1–H1NA···N6	0.90	2.26	3.043(11)	146.0	*x*,1 + *y*,*z*
	N1–H1NB···N7	0.90	2.33	3.116(12)	146.0	
	N2–H2···N7	0.91	2.53	3.439(13)	172.0	−1 + *x*,*y*,*z*
	N3–H3NA···O1W	0.90	2.11	2.990(10)	167.0	1−*x*, 1−*y*, 1−*z*
	N3–H3NB···O1W	0.90	2.27	3.143(13)	165.0	−1 + *x*,1 + *y*,*z*
	O1W–H1W1···N3	0.86	2.16	2.979(11)	160.0	1−*x*,1−*y*,1−*z*
	O1W–H2W1···N3	0.86	2.50	3.136(13)	131.0	1 + *x*,−1 + *y*,*z*
	O2W–H1W2···N7	0.86	2.00	2.819(12)	160.0	−1 + *x*,*y*,*z*
	O2W–H2W2···N6	0.86	2.06	2.917(12)	175.0	*x*,1 + *y*,*z*
2	N2–H2A···N5	0.90	2.17	3.039(7)	161.0	1/2 + *x*,1/2−*y*,1/2 + *z*
	N3–H3···N7	0.91	2.07	2.984(8)	177.0	3/2−*x*,−1/2 + *y*,1/2−*z*
	N4–H4A···N7	0.90	2.50	3.182(8)	133.0	1−*x*,−*y*,−*z*
3	N5–H5D···N3	0.90	2.49	3.334(8)	157.0	1 + *x*,*y*,*z*
	N5–H5C···N3	0.90	2.20	3.074(9)	164.0	−*x*,2−*y*,1−*z*
	N6–H6···N2	0.91	2.51	3.297(8)	145.0	1−*x*,2−*y*,2−*z*
	N7–H7C···N2	0.90	2.15	3.004(8)	157.0	*x*,−1 + *y*, *z*
4	N4–H4N···O4	0.91	2.24	3.131(6)	164.0	2−*x*,1−*y*,1−*z*
	N5–H5N···O11	0.91	2.54	3.412(7)	162.0	
	N8–H8N···O4	0.91	2.49	3.316(6)	151.0	*x*,3/2−*y*,−1/2 + *z*
	N9–H9N···O9	0.91	2.30	3.194(7)	168.0	2−*x*,−1/2 + *y*,1/2−*z*
	N14–H14N···O1W	0.91	2.35	3.194(9)	154.0	1−*x*,1/2 + *y*,1/2−*z*
	N19–H19N···O16	0.91	2.33	3.228(8)	170.0	*x*,3/2−*y*,−1/2 + *z*
	N20–H20N···O1W	0.91	2.25	3.101(9)	156.0	
	N3–H31N···O1	0.90	2.34	3.198(6)	160.0	2−*x*,−1/2 + *y*,1/2−*z*
	N10–H101···O2	0.90	2.53	3.086(6)	120.0	2−*x*,1/2 + *y*,1/2−*z*
	N10–H101···O2	0.90	2.28	3.048(6)	144.0	*x*,3/2−*y*,−1/2 + *z*
	N13–H132···O15	0.90	2.60	3.385(13)	146.0	
	N18–H181···O14	0.90	2.58	3.045(9)	113.0	
	N18–H181···O15	0.90	2.47	3.335(11)	161.0	
	N18–H182···O7	0.90	2.31	3.156(10)	156.0	
	C4–H4A···O5	0.97	2.49	3.337(12)	146.0	2−*x*,1−*y*,1−*z*
	C6–H6A···O1	0.97	2.46	3.390(7)	162.0	2−*x*,1−*y*,1−*z*
	C15–H15···N7	0.98	2.61	3.248(7)	123.0	
	C17–H17A···N6	0.96	2.51	3.424(7)	158.0	2−*x*,−1/2 + *y*,1/2−*z*
	C34–H34···N16	0.98	2.54	3.135(6)	119.0	1−*x*,−1/2 + *y*,1/2−*z*
	C36–H36A···N17	0.96	2.61	3.543(7)	163.0	

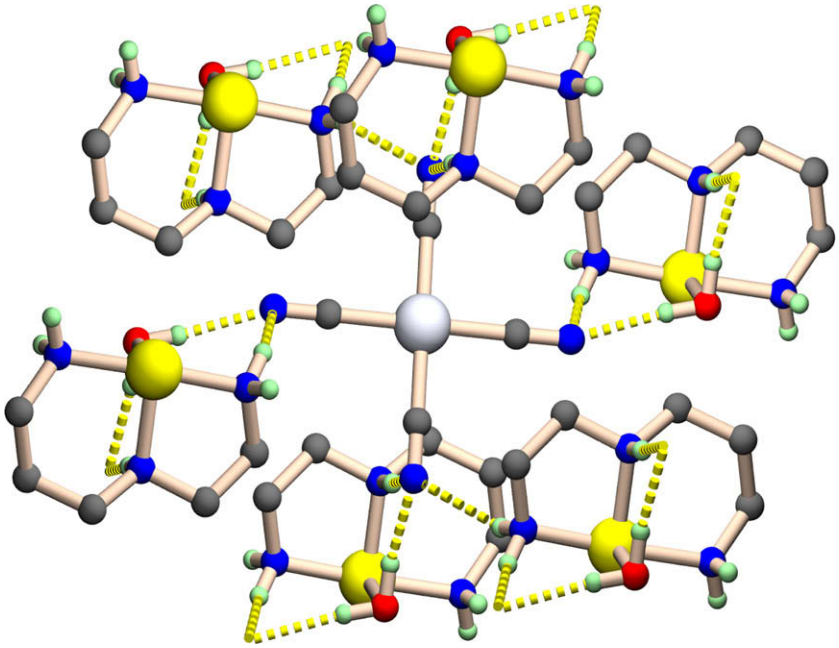


Fig. 2. The hydrogen bonding arrangement around free $[Pt(CN)_4]^{2-}$ units.

two types of channels along the *b*-axis, where lattice water molecules reside inside a wider rectangular channel (7.2 × 4.3 Å) (Fig. 3). The $R_2^4(16)$ hydrogen bonded motif between free $[Pt(CN)_4]^{2-}$ units and coordinated water molecules lead to the generation of narrower channels (Fig. 3). Within the rectangular channels lattice water molecules stay nearly in the middle and establish

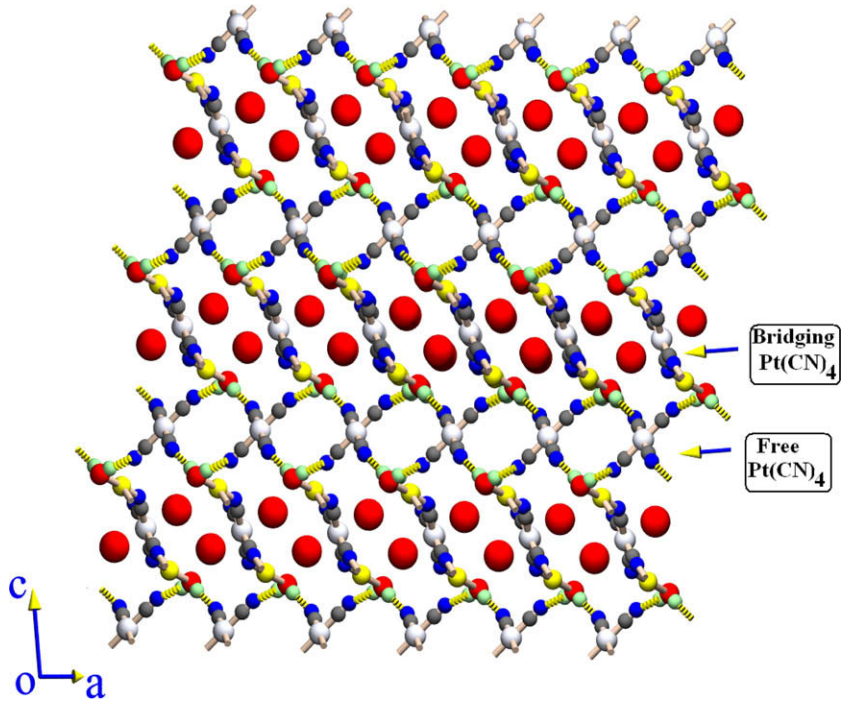


Fig. 3. The supramolecular assembly in complex **1** viewed along the *b*-axis.

contact with the channel wall through the formation of hydrogen bonds with one of the amine terminals (N3) of the chelated triamine. It is of note that the plane of the free $[Pt(CN)_4]^{2-}$ units makes an angle of ~59.4° with the corresponding plane of $[Pt(CN)_4]^{2-}$ units in the ribbon and optimally positions itself to maximize hydrogen bonding interactions.

2.5.2. Crystal structure description of complex ***2***

X-ray crystal structure analysis reveals a neutral helical polymeric chain (formula $[Cu(dpt)Pt(CN)_4]_n$) to be the basic unit of the complex. The ORTEP diagram of the polymeric chain has been depicted in Fig. 4. The coordination bond lengths and angles of the complex are given in Table S2. Three N atoms of the triamine (N2, N3, N4) and one cyanide nitrogen (N1) of a $[Pt(CN)_4]^{2-}$ unit form the basal plane of distorted square pyramidal Cu(II) coordination environment ($\tau = 0.13$). The apical position is occupied by the N6* (* = 1/2−*x*,−1/2 + *y*,1/2−*z*) cyanide nitrogen from an adjacent symmetry related $[Pt(CN)_4]^{2-}$ unit. The Cu atom is located 0.267(1) Å towards the apical N6* above the mean plane formed by basal N1, N2, N3 and N4 atoms, which reflects the degree of distortion of the metal coordination environment. The Cu–N(amine) bond distances in the present complex fall in the range 2.013(6)–2.023(4) Å, and are typical of Cu(II) complexes. The apical Cu–N6* distance is 2.200(5) Å. In the bridging $[Pt(CN)_4]^{2-}$ anions, the Pt–C bond distances are 1.982(5) and 1.992(6) Å. Two nitrogen atoms of $[Pt(CN)_4]^{2-}$, which are *cis* to each other, bridge two Cu(II) centers, one forms the apex of one Cu(II) square pyramid but the other one, together with three amine nitrogens, constitute the

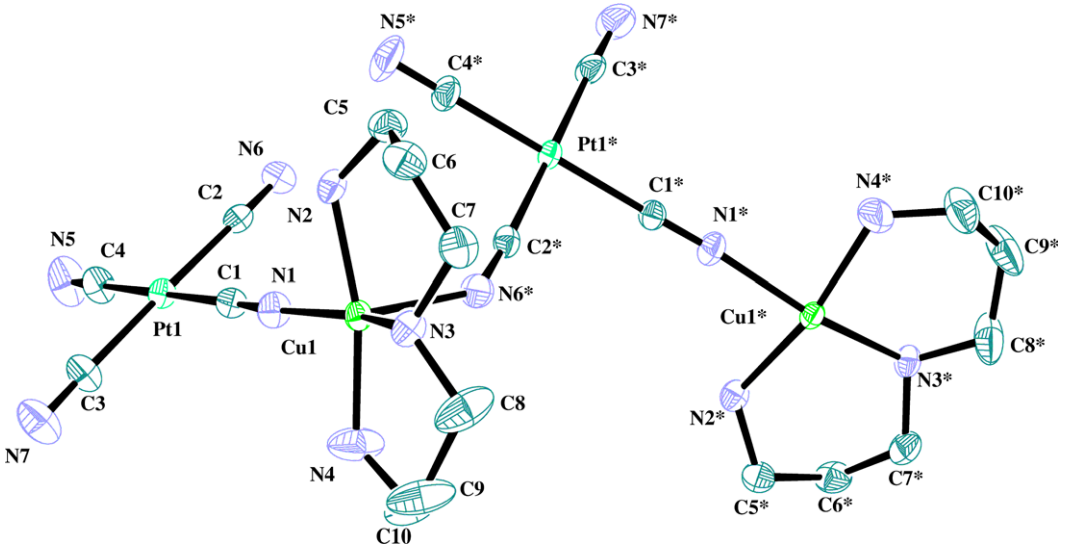


Fig. 4. The ORTEP diagram with 30% ellipsoidal probability of complex **2**.

basal plane of the adjacent Cu(II) square pyramid. This axial to basal bridging by $[Pt(CN)_4]^{2-}$ enforces the rotation of successive Cu(II) square pyramids. The polymeric assembly thus results in a helical 1D chain along the crystallographic *b*-axis (2_1) (Fig. 5). The screw pitch of the helix is equal to the length of the *b*-axis, which is 10.29 Å.

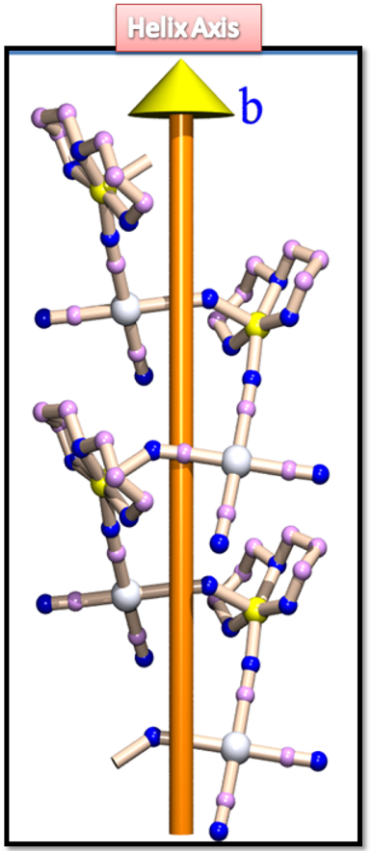


Fig. 5. Helical 1D chain along the crystallographic *b*-axis in complex **2**.

A view of the crystal packing of these helical chains down the helix axis (*b*) is portrayed in Fig. 6. The cross-section of the helix is a parallelogram with Cu(II) square pyramids and square–planar $[Pt(CN)_4]^{2-}$ units occupying diagonally opposite corners of the parallelogram. It is interesting to note that the free CN^- terminals of the $[Pt(CN)_4]^{2-}$ units and amine terminals of the chelated triamine at the Cu(II) centers are all directed away from the central region of the helix and facilitate the maximum number of hydrogen bonding contacts with the adjacent helices. In the hydrogen bonding contacts, the NH terminals of the chelated triamine act as a donor and the free CN^- terminals act as an acceptor. One of the free CN^- groups takes part in bifurcated hydrogen bonding (N3–H3···N7 and N4–H4A···N7) to establish contact with two nearby helices (Table 2).

Interestingly, the N3–H3···N7 interactions leads to a supramolecular sheet in the *ab* plane (Fig. 7), whereas N4–H4A···N7 interactions generates a sheet in the $(1\,0\,\bar{1})$ plane (Fig. 8). Through the other free CN^- terminal, a single N2–H2A···N5 contact is established with another adjacent helix in the $(1\,0\,\bar{1})$ plane (Fig. 9). Considering the existence of four free CN^- terminals at the two diagonally opposite corners of the helix, a total of six hydrogen bonding contacts are established from any helix to six other helices surrounding it. So from a packing viewpoint, hexagonal packing that has maximum packing efficiency is achieved. The maximum packing efficiency is the result of the maximization of the hydrogen bonding using all the available amine donors.

2.5.3. Crystal structure description of complex 3

The ORTEP drawing of the polymeric chain of this complex is shown in Fig. 10. The coordination bond lengths and angles of the complex are given in Table S3. Three N atoms of the triamine (N5, N6, N7) and one cyanide nitrogen (N4) of a $[Pt(CN)_4]^{2-}$ unit form the basal plane of the distorted square pyramidal ($\tau = 0.21$) coordination environment at the Cu(II) centers. The apical position of the square pyramid is occupied by the N1 cyanide nitrogen from an adjacent symmetry related $[Pt(CN)_4]^{2-}$ unit. The Cu atom resides 0.242(1) Å towards the apical N1 above the mean plane formed by the basal N4, N5, N6 and N7 atoms, which reflects the degree of distortion of the metal coordination environment. The Cu–N(amine) bond

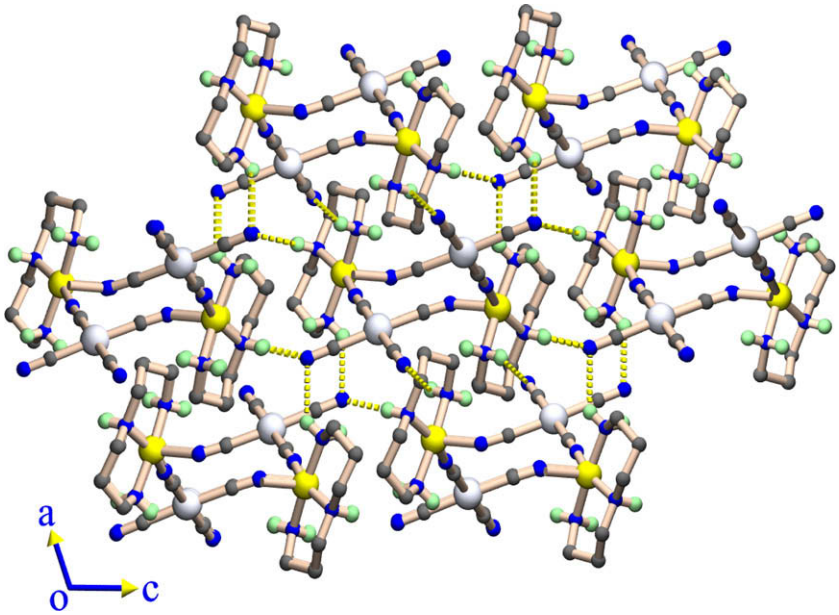


Fig. 6. Crystal packing of the helical chains down the *b*-axis for complex **2**.

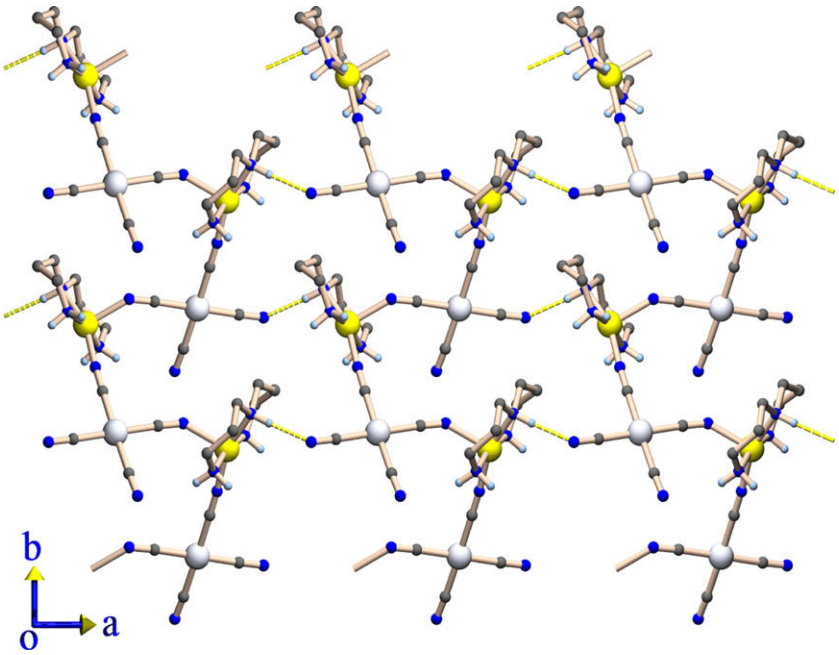


Fig. 7. Arrangement of helices in the *ab* plane through N3–H3···N7 hydrogen bonding in complex **2**.

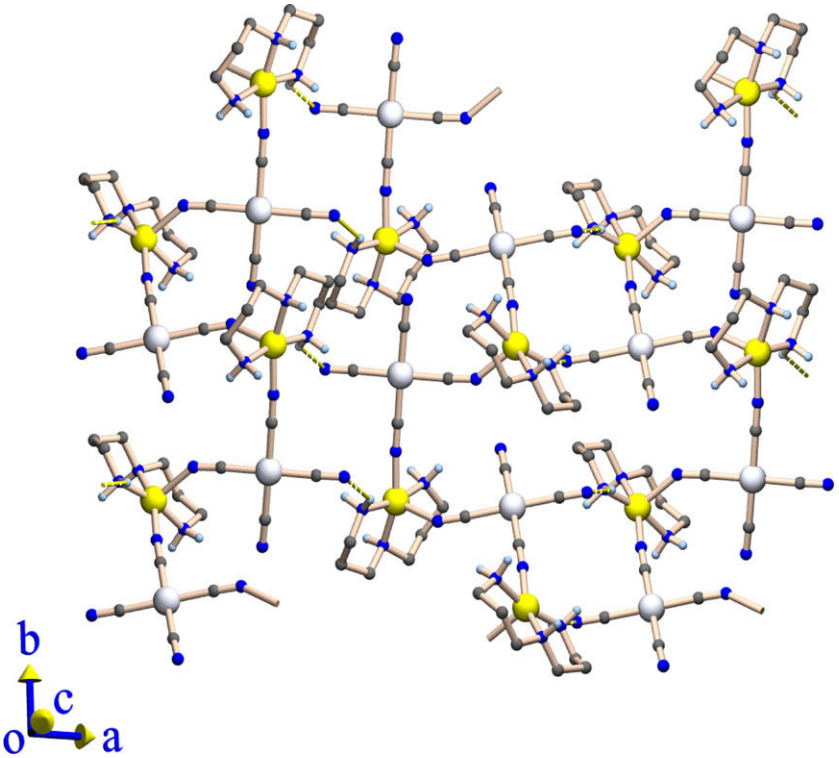


Fig. 8. Arrangement of helices in the $(10\bar{1})$ plane through N4–H4A···N7 hydrogen bonding in complex **2**.

distances in the basal plane vary in the range 1.985(5)–2.025(5) Å, as is usually found in this type of Cu(II) complex. On the other hand, the apical Cu–N5 distance is 2.160(5) Å. In the bridging $[Pt(CN)_4]^{2-}$ anions, the Pt1–C1 bond distance is 1.987(6) Å and Pt2–C4 is 1.995(6) Å.

In contrast to complex **2**, in the present case the *trans* binding mode of the $[Pt(CN)_4]^{2-}$ units enforces a zig-zag arrangement of Cu and Pt centers leading to 1D polymeric chains. Successive apical to apical and basal to basal bridging of Cu(II) square pyramids by $[Pt(CN)_4]^{2-}$ enforces rotation of successive Cu and Pt centers by ~90° and renders a saw-tooth nature of the polymeric chain. Successive Cu(II) and Pt(II) centers are separated by 10.179 and 7.725 Å, respectively.

A 3D supramolecular hydrogen bonded assembly of these zig-zag chains can be easily understood in terms of the formation of two 2D supramolecular sheets. The free ends (N2 and N3) of

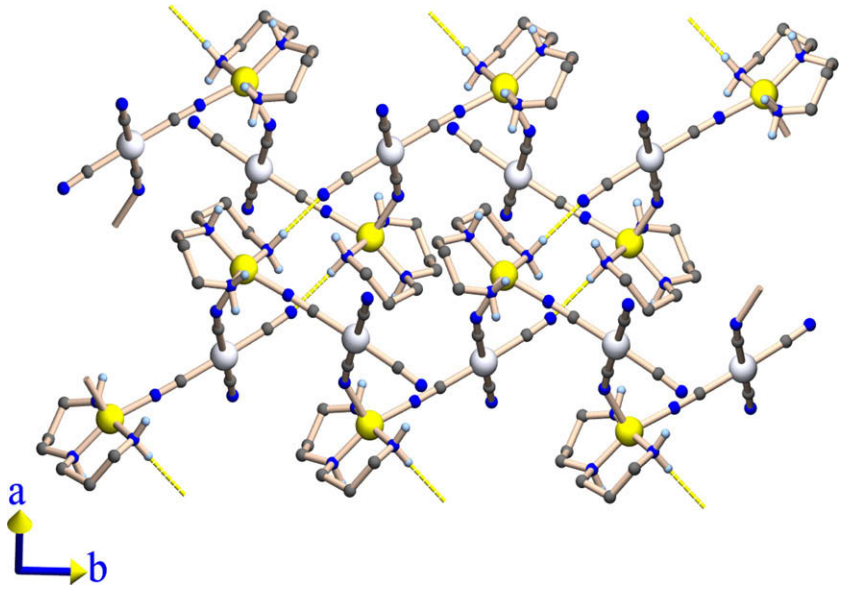


Fig. 9. Arrangement of helices in the $(10\bar{1})$ plane through N2–H2A···N5 hydrogen bonding in complex **2**.

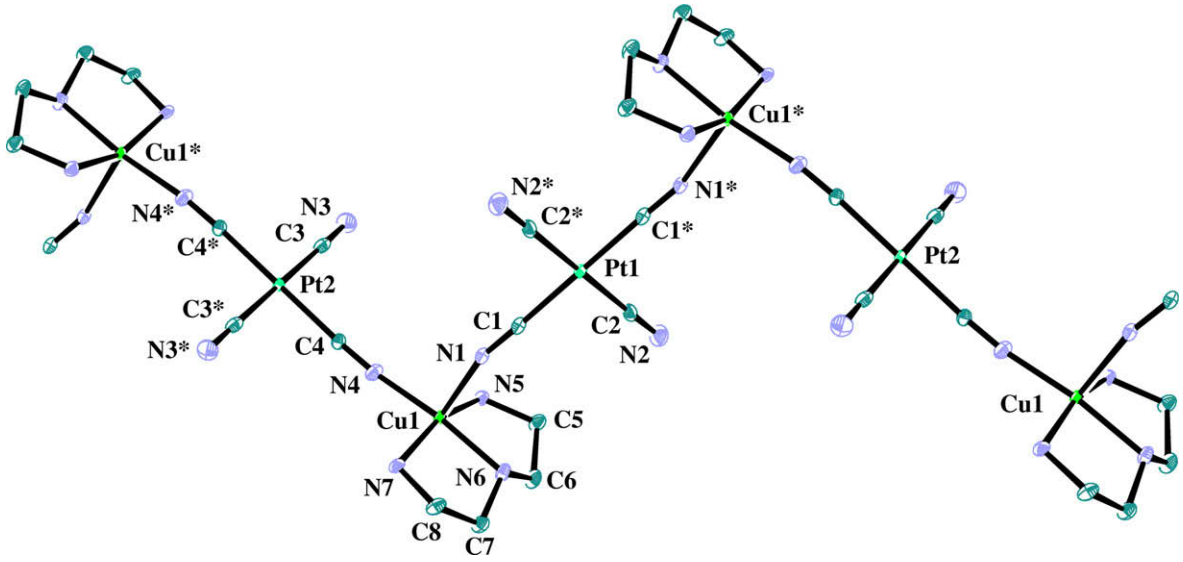


Fig. 10. ORTEP diagram (30% ellipsoidal probability) with the atomic labelling scheme of complex **3**.

$[Pt(CN)_4]^{2-}$ assemble the chains in the bc plane through hydrogen bonding (N7–H7C···N2 and N5–H5C···N3) interactions and in the $(10\bar{1})$ planes through (N6–H6···N2 and N5–H5D···N3) interactions (Fig. 11 and Table 2). Thus arrangement of the sheets to form a 3D supramolecular assembly is through two bifurcated hydrogen bonding interactions of N2 and N3 (Fig. 12). In so doing, the free ends of $[Pt(CN)_4]^{2-}$ prefer a trans mode coordination so that it can exhaust all the amine donors for maximal hydrogen bonding interactions.

*2.5.4. Crystal structure description of complex **4***

An ORTEP drawing showing the (4,2) ribbon of complex **4** is given in Fig. 13. The coordination bond lengths and angles of the complex are given in Table S4. The structure consists of two independent polymeric chains with a (4,2) ribbon-like topology (Fig. 13). These chains are inclined with respect to each other by approximately 46°. In one of the chains (type A), Pt1 through its four CN terminals (N1, N2, N6, N7) bridges successive Cu1 and Cu2 centers whereas in the other chain (type B), Pt2 through its four CN terminals (N11, N12, N16, N17) doubly bridges successive Cu3 and Cu4 centers. Like the previous complexes, the triamine nitrogen atoms and one of the bridging CN nitrogen atoms form the basal plane of the square pyramid ($\tau = 0.18$) and its apical position is occupied by one of the cyanide nitrogen atoms. In the basal plane the Cu–N(amine) bond distances fall in the range 1.941(4)–2.079(5) Å, as is usually found in this type of Cu(II) complex. On the other hand, the apical Cu–N1 distances vary in the range 2.220(3)–2.197(4) Å. The Cu1, Cu2, Cu3 and Cu4 atoms are located 0.311(1), 0.328(1), 0.239(1) and 0.333(1) Å, respectively towards their individual apical N6* ($* = 2-x,-1/2+y,1/2-z$), N1*, N12 and N17 atoms above the mean planes. In the bridging $[Pt(CN)_4]^{2-}$ anions, the Pt–C bond distances vary in the range 1.949(5)–1.987(5) Å.

Two types of (4,2) ribbons are arranged in a herringbone pattern (Fig. 14). Two perchlorate counter-ions play the charge-balancing role and maintain overall neutrality of the complex (Fig. 15 and Table 2). The perchlorates act as hydrogen bonded bridges between successive (4,2) ribbons by acting as acceptors for the amine

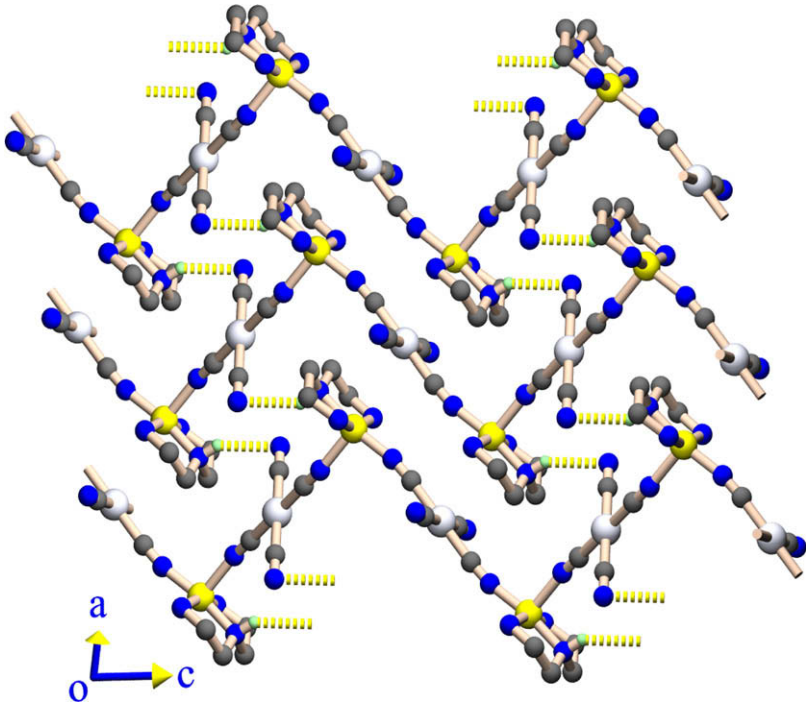


Fig. 11. 2D supramolecular hydrogen bonded sheet of complex **3**.

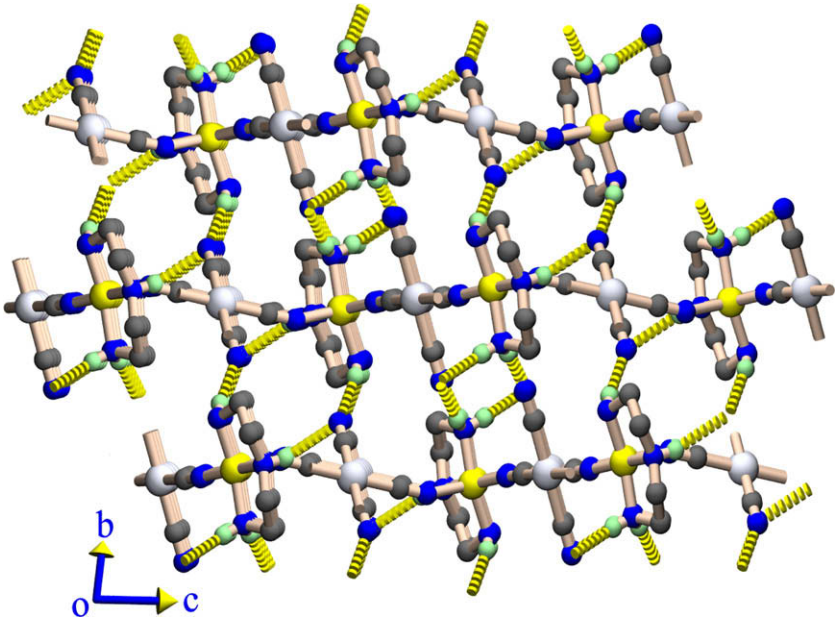


Fig. 12. 3D packing of layers in complex **3**.

hydrogens (Table 2). Lattice water molecules also form hydrogen bonds with the amine groups. It is to be noted that unlike the previous complexes, no hydrogen bonding acceptors from $[Pt(CN)_4]^{2-}$ units are available, instead perchlorate anions take part in the hydrogen bonding.

2.6. Comparative discussion of the structural features

From the above structural discussion, it is interesting to note that we have diverse structural topologies for the same synthetic procedure of $Cu(ClO_4)_2{\cdot}6H_2O$ with aepn/dpt/dien/iprdien. In complex **1**, the Cu(II) centers are chelated by an asymmetric triamine with two carbon atoms and three carbon atoms respectively on either side of the central nitrogen atom. The Cu(II) coordination environment in this case is an octahedral one with a coordinated water molecule forming the apex of the octahedron with a Jahn–Teller elongated $Cu–O_w$ bond. This water molecule plays a vital role in the supramolecular assembly of the complex by acting as a strong hydrogen bond donor.

A closer look into the structure of complex **1** reveals that all the amine terminals of the chelated triamine also act as hydrogen bond donors. To utilize all the hydrogen bonding sites, interestingly free

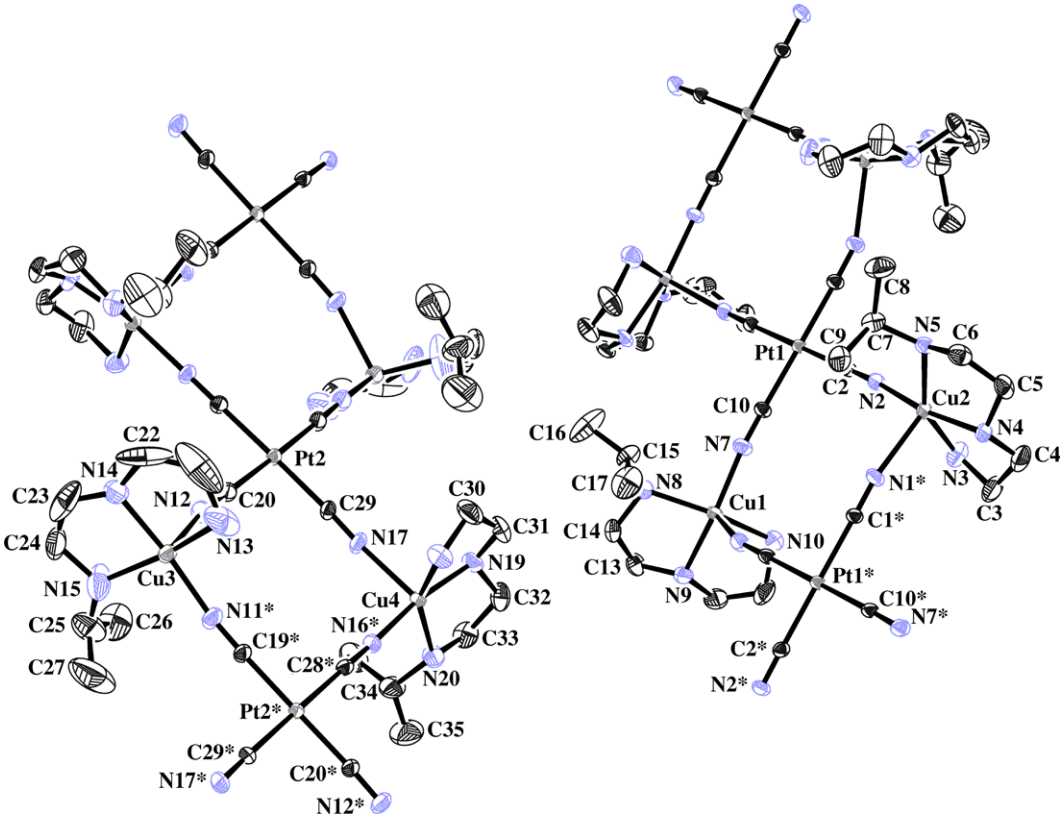


Fig. 13. The ORTEP diagram with 30% ellipsoidal probability of complex **4**.

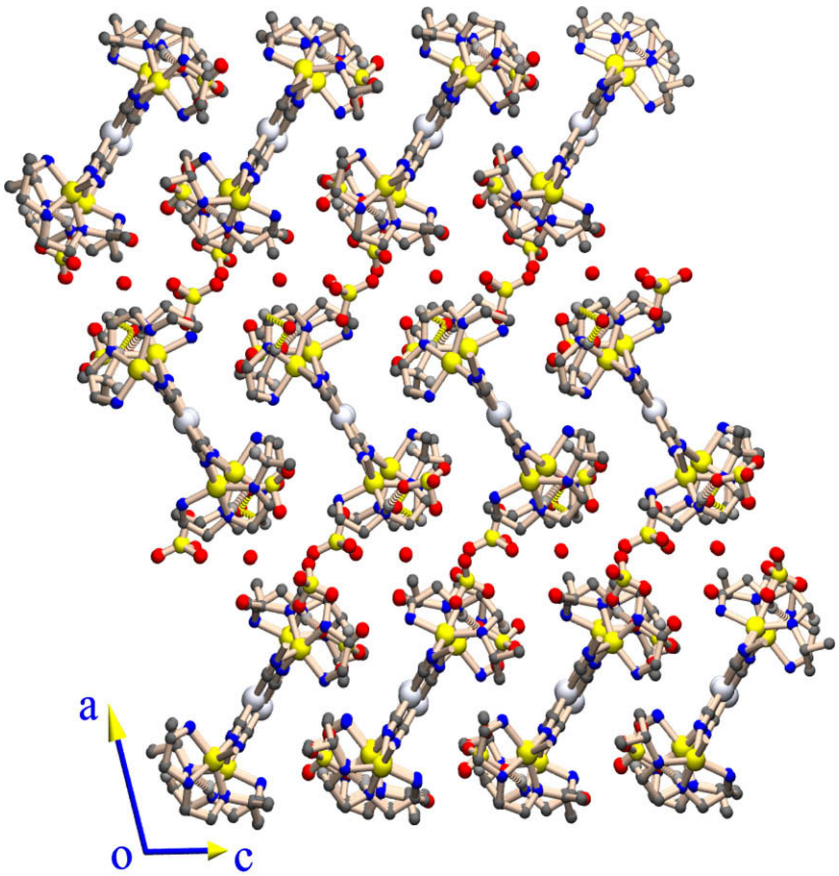


Fig. 14. Herringbone packing of (4,2) ribbons in complex **4**.

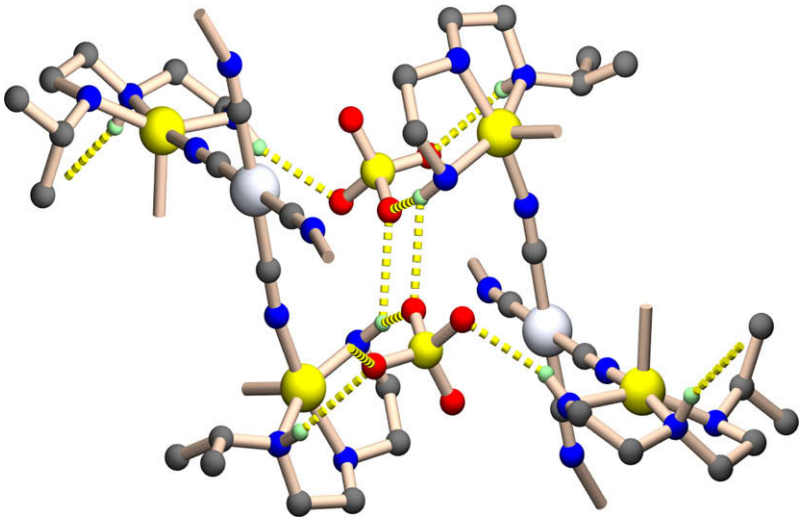


Fig. 15. Hydrogen bonding arrangement of perchlorate anions with the amine groups in complex **4**.

$[Pt(CN)_4]^{2-}$ units take part in the complexation instead of the perchlorate counter-ions, though they are available in solution as a possible charge-balancing and hydrogen bonding agent. This should be due to the preference of strong hydrogen bond donors (coordinated water) for strong hydrogen bond acceptors {$[Pt(CN)_4]^{2-}$ units in this case} instead of perchlorate counter-ions which are relatively weak hydrogen bond acceptors. In the supramolecular network of the complex all the amine sites are maximally utilized in hydrogen bonding. Lattice water molecules participate in hydrogen bonding to stabilize the structure.

In complex **2**, a symmetric triamine with three carbon atoms on both side of the central nitrogen of the triamine chelates the Cu(II) centers. $[Pt(CN)_4]^{2-}$ units in this case bridge in a cis mode and establish apical to basal contacts between successive Cu(II) square pyramidal coordination units, leading to a helical 1D neutral polymeric chain.

In complex **3**, a symmetric triamine has also been used but it forms a smaller chelate ring around the Cu(II) centers with two carbon atoms on either side of the middle nitrogen. In this case $[Pt(CN)_4]^{2-}$ units bridge in a trans mode and establish successive apical to apical and basal to basal contacts between successive Cu(II) square pyramidal coordination units, leading to a symmetric zig-zag 1D neutral polymeric chain.

A careful look into the supramolecular assembly in these two complexes (**2** and **3**) reveals that in both cases all three amine terminals of the triamines have been used to establish hydrogen bonding contacts with the free CN terminals of the bridging $[Pt(CN)_4]^{2-}$ units. In the case of complex **3**, due to the small size of the chelate ring both intra-chain and inter-chain hydrogen bonding has become possible, leading to the establishment of maximum number of hydrogen bonding contacts. On the other hand in the case of complex **2**, the larger chelate ring size due to the presence of six carbon atoms on the triamine would have prohibited intra-chain hydrogen bonding if the assembly of the chains was in a similar trans bridging mode as that of complex **3**, and so to maximize the utilization of all the amine terminals for hydrogen bonding the *cis* mode bridging into helical turning of the chains is preferred so that hydrogen bonding contacts with the maximum number of adjacent chains could be established.

In summary, the supramolecular structures of the complexes reveal the following features: (a) Asymmetric ligand; complex **1** possesses four donor sites. $[Pt(CN)_4]^{2-}$ plays a dual role, a linker forming a (4,2) ribbon and a free anion forming a supramolecular network. (b) Symmetric ligand; complex **2** possesses three donor sites. $[Pt(CN)_4]^{2-}$ prefers only two coordinations. (c) Symmetric ligand; complex **3** possesses the same number of donor sites. $[Pt(CN)_4]^{2-}$ prefers only two coordinations, keeping two ends free. (d) Thus decrease in the number of donor sites increases the possibility of coordination and vice versa. (e) The chain length determines a *cis* or *trans* mode.

These observations have led us to carry out further experimentation by blocking one of the possible hydrogen bonding sites of the triamine with a substitution made on that site and with this we make the ligand asymmetric. So a triamine with one of the amine terminals bearing a bulky isopropyl group is used in case of complex **4**. A bi-bridged (4,2) ribbon-like polymeric chain appeared. A perchlorate counter-ion balances the charge. In this case the unavailability of the amine terminals for supramolecular assembly is the driving force behind the appearance of bi-bridged chains so that all the nitrogen atoms of $[Pt(CN)_4]^{2-}$ prefer coordinative bonding to the Cu(II) center. Due to the lack of strong donors, the weak ClO_4^- acceptor appears to play a role in the structure. From complexes **1** and **4**, we observe again the old rule that strong donors prefer strong acceptors while weak donors prefer weak acceptors.

The observations motivated us to propose an empirical rule: (a) if the maximum hydrogen bonding sites are available for symmetric amine ligands through the use of all the amine terminals, one gets a singly bridged chain, (b) if hydrogen bonding sites are blocked for asymmetric amine ligands, one gets a doubly bridged (4,2) ribbon.

2.7. Magnetic properties of the complexes

The magnetic properties of complexes **1–4** as $\chi_M T$ versus T plots (χ_M is the molar magnetic susceptibility for one or two Cu(II) ions) are shown in Fig. 16 [for **1**] and Figs. S1–S3 [for **2**–**4**]. As expected, the magnetic overlap is negligibly small through the diamagnetic $[Pt(CN)_4]^{2-}$ pathway. Table S5 gives the main important crystallographic data from a magnetic point of view, together to the best-fit J and g values. In all cases, the short–short magnetic pathway for distorted square pyramidal Cu (II) ions has only been considered for doing the fit. For this reason compounds **1**, **2**, **3** and **4** were fit as dinuclear applying the typical Bleaney–Bower formula. Starting from room temperature, the $\chi_M T$ values are practically constant to 50 K, below this temperature to 2 K, they quickly decrease. This feature is characteristic of a very weak antiferromagnetic interaction.

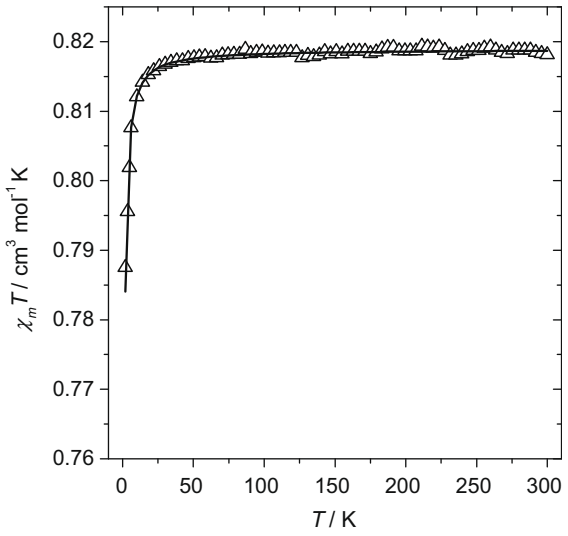


Fig. 16. Plot of $\chi_M T$ vs. T in the temperature range 2–300 K for complex **1**. Solid line represents the curve obtained with the best-fit parameters.

The calculated J and g values are given in Table S5. The small (almost negligible) J values for the four complexes can be interpreted as a consequence of the almost nil overlap between the Cu(II) ions through the long diamagnetic $[Pt(CN)_4]^{2-}$ bridge. These very small J values hamper any attempt to draw magneto-structural correlations, because in all cases intermolecular interactions have not been taken into account in the formulae used. These interactions can have the same order of magnitude of the main J values. Looking at the literature, we note several Cu(II) systems with diamagnetic $[M(CN)_4]^{2-}$ bridging ligands (M = Ni, Pd, Pt), but without magnetic studies [55–57]. However, the limited number of studies [58–60] with 1D zig-zag chains or bridging Cu–Pt complexes showed antiferromagnetic interactions of a similar order of magnitude as the present bridged structures (**1–4**).

The number of analogous complexes with magnetic studies is scarce [61,62] but the results are similar to those previously reported for the $[Ni(CN)_4]^{2-}$ analogue derivatives [35]. Considering the small values of J in both series (Cu–Pt and Ni–Pt) it is impossible to draw any conclusion, because together to the intra-chain coupling there are inter-chain magnetic pathways that, due to the diamagnetic character of the cyanide bridge, can be of a similar order. The conclusion is thus that these diamagnetic ligands do not allow a strong (or medium) transmission of magnetic coupling, as expected.

3. Conclusion

Four coordination complexes of $[Pt(CN)_4]^{2-}$ bridged Cu(II) complexes have been synthesized and crystallographically characterized. The 1D polymeric complexes have two types of topology, zig-zag/helical chains are obtained when $[Pt(CN)_4]^{2-}$ bridges in a bi-coordination mode, and on the other hand tetra-coordinated bridging by $[Pt(CN)_4]^{2-}$ lead to a (4,2) ribbon topology. A careful investigation of the packing of these complexes reveal that zig-zag/helical chains or (4,2) ribbons is the result of competition between hydrogen bonding and coordinative forces. A zig-zag/helical 1D chain appears when the chelating amine at the Cu(II) center is capable of forming the maximum number of hydrogen bonds, but when one or more amine sites are blocked or due to asymmetry steric hindrance prevents maximization of the hydrogen bonds in the usual way, (4,2) ribbons appear. These finding may act as a guiding principle for the designed construction of cyano bridged transition metal 1D polymers that should find important applications in the promising field of singe chain magnets.

Acknowledgements

R.S. acknowledges financial support from the Council of Scientific and Industrial Research (CSIR), New Delhi under the JRF program (09/096(0565)2008-EMR-I). G.M. acknowledges Jadavpur University for a research grant under the "Nano Science and Technology Program" with the University with Potential for Excellence Scheme of UGC (India).

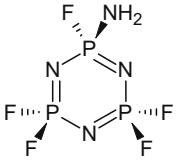
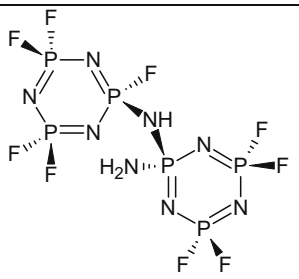
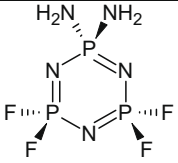
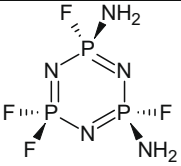
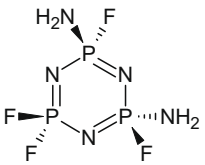
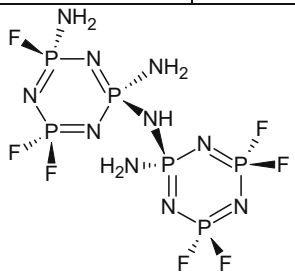
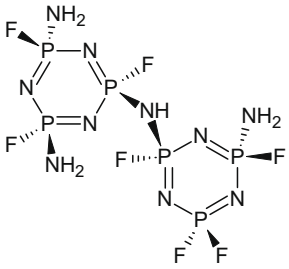
Appendix A. Supplementary data

CCDC 707703, 707704, 707705 and 707706 contain the supplementary crystallographic data for complexes **1**, **2**, **3** and **4**, respectively. These data can be obtained free of charge via http://www.ccdc.cam.ac.uk/conts/retrieving.html, or from the Cambridge Crystallographic Data Centre, 12 Union Road, Cambridge CB2 1EZ, UK; fax: (+44) 1223-336-033; or e-mail: deposit@ccdc.cam.ac.uk. Supplementary data associated with this article can be found, in the online version, at doi:10.1016/j.poly.2009.06.076.

References

[1] J.L. Atwood, W.J. Steed, Supramolecular Chemistry, VCH: Verlag Gmbh, Weinheim, Germany, 2000.
[2] G.R. Desiraju, C.V.K. Sharma, Perspectives in Supramolecular Chemistry, Wiley, Chichester, 1995.
[3] K. Uemura, K. Saito, S. Kitagawa, H. Kita, J. Am. Chem. Soc. 128 (2006) 16122.
[4] R. Matsuda, R. Kitaura, S. Kitagawa, Y. Kubota, T.C. Kobayashi, S. Horike, M. Takata, J. Am. Chem. Soc. 126 (2004) 14063.
[5] D. Ghoshal, A.K. Ghosh, J. Ribas, E. Zangrando, G. Mostafa, T.K. Maji, N. Ray Chaudhuri, Cryst. Growth Des. 5 (2005) 941.
[6] D. Ghoshal, A.K. Ghosh, J. Ribas, G. Mostafa, N. Ray Chaudhuri, CrystEngComm 7 (2005) 616.
[7] G.M. Davies, S.J.A. Pope, H. Adams, S. Faulkner, M.D. Ward, Inorg. Chem. 44 (2005) 4656.
[8] J.-M. Herrera, S.J.A. Pope, H. Adams, S. Faulkner, M.D. Ward, Inorg. Chem. 45 (2006) 3895.
[9] D.J. Darensbourg, A.L. Phelps, Inorg. Chim. Acta 357 (2004) 1603.
[10] R. Brahmi, C. Kappenstein, J. Cerńak, D. Duprez, A. Sadel, J. Phys. Chem. 96 (1999) 487.
[11] D. William, J. Kouvetakis, M. O'Keefe, Inorg. Chem. 37 (1998) 4617.
[12] M.P. Shores, L.G. Beauvais, J.R. Long, J. Am. Chem. Soc. 121 (1999) 775.
[13] M.P. Shores, L.G. Beauvais, J.R. Long, Inorg. Chem. 38 (1999) 1648.
[14] M.V. Bennett, L.G. Beauvais, M.P. Shores, J.R. Long, J. Am. Chem. Soc. 123 (2001) 8022.
[15] M. Kämper, M. Wagner, A. Weiss, Angew. Chem., Int. Ed. 91 (1979) 517.
[16] T. Niu, A.J. Jacobson, Inorg. Chem. 38 (1999) 5346.
[17] K.K. Klausmeyer, T.B. Rauchfuss, S.R. Wilson, Angew. Chem., Int. Ed. 37 (1998) 1694.
[18] A.M.A. Ibrahim, Polyhedron 18 (1999) 2111.
[19] L. Ouyang, P.M. Aguiar, R.J. Batchelor, S. Kroeker, D.B. Leznoff, Chem. Commun. 7 (2006) 744.
[20] L. Jiang, X.-L. Feng, T.-B. Lu, S. Gao, Inorg. Chem. 45 (2006) 5018.
[21] M. Atanasov, P. Comba, S. Förster, G. Linti, T. Malcherek, R. Miletich, A.I. Prikhodko, H. Wadepohl, Inorg. Chem. 45 (2006) 7722.
[22] R. Lescoüezec, L.M. Tomaa, J. Vaissermann, M. Verdaguer, F.S. Delgado, C. Ruiz-Pérez, F. Lloret, M. Julve, Coord. Chem. Rev. 249 (2005) 2691.
[23] S. Tanase, J. Reedijk, Coord. Chem. Rev. 250 (2006) 2501.
[24] H.J. Choi, J.J. Sokol, J.R. Long, Inorg. Chem. 43 (2004) 1606.
[25] Y.-Z. Zhang, S. Gao, Z.-M. Wang, G. Su, H.-L. Sun, F. Pan, Inorg. Chem. 44 (2005) 4534.
[26] Z.-H. Ni, H.-Z. Kou, Y.-H. Zhao, L. Zheng, R.-J. Wang, A.-L. Cui, O. Sato, Inorg. Chem. 44 (2005) 2050.
[27] Y.-Z. Zhang, S. Gao, H.-L. Sun, G. Su, Z.-M. Wang, S.-W. Zhang, Chem. Commun. (2004) 1906.
[28] J. Crnák, K.A. Abboud, Acta Crystallogr., Sect. C 58 (2002) m167.
[29] H.-Z. Kou, S. Gao, B.-Q. Ma, D.-Z. Liao, Chem. Commun. (2000) 713.
[30] S. Tanase, F. Tuna, P. Guionneau, T. Maris, G. Rombaut, C. Mathonière, M. Andruh, O. Kahn, J.-P. Sutter, Inorg. Chem. 42 (2003) 1625.
[31] W. Dong, L.-N. Zhu, H.-B. Song, D.-Z. Liao, Z.-H. Jiang, S.-P. Yan, P. Cheng, S. Gao, Inorg. Chem. 43 (2004) 2465.
[32] H.-Z. Kou, S. Gao, J. Zhang, G.-H. Wen, G. Su, R.K. Zheng, X.X. Zhang, J. Am. Chem. Soc. 123 (2001) 11809.
[33] J.J. Sokol, A.G. Hee, J.R. Long, J. Am. Chem. Soc. 124 (2002) 7656.
[34] E.J. Schelter, A.V. Prosvirin, K.R. Dunbar, J. Am. Chem. Soc. 126 (2004) 15004.

[35] D. Ghoshal, A.K. Ghosh, T.K. Maji, J. Ribas, G. Mostafa, E. Zangrando, N. Ray Chaudhuri, Inorg. Chim. Acta 359 (2006) 593.
[36] T.K. Maji, P.S. Mukherjee, G. Mostafa, E. Zangrando, N. Ray Chaudhuri, Chem. Commun. (2001) 1368.
[37] T. Akitsu, Y. Einaga, Acta Crystallogr., Sect. E 62 (2006) m862.
[38] J. Kuchár, J. Crnák, K.A. Abboud, Acta Crystallogr., Sect. C 60 (2004) m492.
[39] S.-Z. Zhan, D. Guo, X.-Y. Zhang, C.-X. Du, Y. Zhu, R.-N. Yang, Inorg. Chim. Acta 298 (2000) 57.
[40] J. Crnák, J. Skoršepa, K.A. Abboud, M.W. Meisel, M. Orendá, A. Orendáčová, A. Feher, Inorg. Chim. Acta 326 (2001) 3.
[41] M. Munakata, J.C. Zhong, I. Ino, T. Kuroda-Sowa, M. Maekawa, Y. Suenaga, N. Oij, Inorg. Chim. Acta 317 (2001) 268.
[42] L. Toma, R. Lescoüezec, J. Vaissermann, F.S. Delgado, C. Ruiz-Pérez, R. Carrasco, J. Cano, F. Lloret, M. Julve, Chem. Eur. J. 10 (2004) 6130.
[43] L. Toma, R. Lescoüezec, J. Vaissermann, P. Herson, V. Marvaud, F. Lloret, M. Julve, New J. Chem. 29 (2005) 210.
[44] S. Hayami, K. Hashiguchi, G. Juhász, M. Ohba, H. Ohkawa, Y. Maeda, K. Kato, K. Osaka, M. Takata, K. Inoue, Inorg. Chem. 43 (2004) 4124.
[45] M. Ferbinteanu, H. Miyasaka, W. Wernsdorfer, K. Nakata, K.-i. Sugiura, M. Yamashita, C. Coulon, R. Clérac, J. Am. Chem. Soc. 127 (2005) 3090.
[46] R. Clérac, H. Miyasaka, M. Yamashita, C. Coulon, J. Am. Chem. Soc. 124 (2002) 12837.
[47] O. Khan, Molecular Magnetism, VCH, Weinheim, Germany, 1993.
[48] SMART and SAINT, Bruker AXS Inc., Madison, WI, 1999.
[49] G.M. Sheldrick, SADABS, Empirical Absorption Correction Program, University of Göttingen, Germany, 1997.
[50] XPREP, Siemens Industrial Automation Inc., Madison, WI, 1995.
[51] G.M. Sheldrick, SHELX 97, Program for Crystal Structure Refinement, University of Gottingen, Germany, 1998.
[52] A.L. Spek, J. Appl. Crystallogr. 36 (2003) 7.
[53] L.J. Farrugia, J. Appl. Crystallogr. 30 (1997) 565.
[54] L.J. Farrugia, J. Appl. Crystallogr. 32 (1999) 837.
[55] J. Cernaka, K.A. Abboud, Acta Crystallogr., Sect. C 58 (2002) m167.
[56] N.F. Curtis, H. Puschmann, Acta Crystallogr., Sect. C 60 (2004) m410.
[57] L.R. Falvello, M. Tomás, Chem. Commun. (1999) 273.
[58] A. Karada?, A. Şenocak, I. Önal, Y. Yerli, E. Şahin, A. Cemil Başaran, Inorg. Chim. Acta 362 (7) (2009) 2299.
[59] I.P.-C. Liu, G.-H. Lee, S.-M. Peng, M. Bénard, M.-M. Rohmer, Inorg. Chem. 46 (23) (2007) 9602.
[60] T. Akitsu, Y. Einaga, Inorg. Chim. Acta 360 (2) (2007) 497.
[61] Z. Smekal, Z. Travnicek, J. Mrozinski, J. Marek, Inorg. Chem. Commun. 6 (2003) 1395.
[62] J. Cernak, J. Skorsepa, K.A. Abboud, M.W. Meisel, M. Orendac, A. Orendacova, A. Feher, Inorg. Chim. Acta 326 (2001) 3.

Product *	Derivative and compound number	Structural formula
1:1	 **1**	 **2** (bridged derivative)
1:2	 **3** (geminal)	 **4** (nongeminal cis-)  **5** (R,S nongeminal trans-)
	 **6**  **7** (some bridged derivatives)	

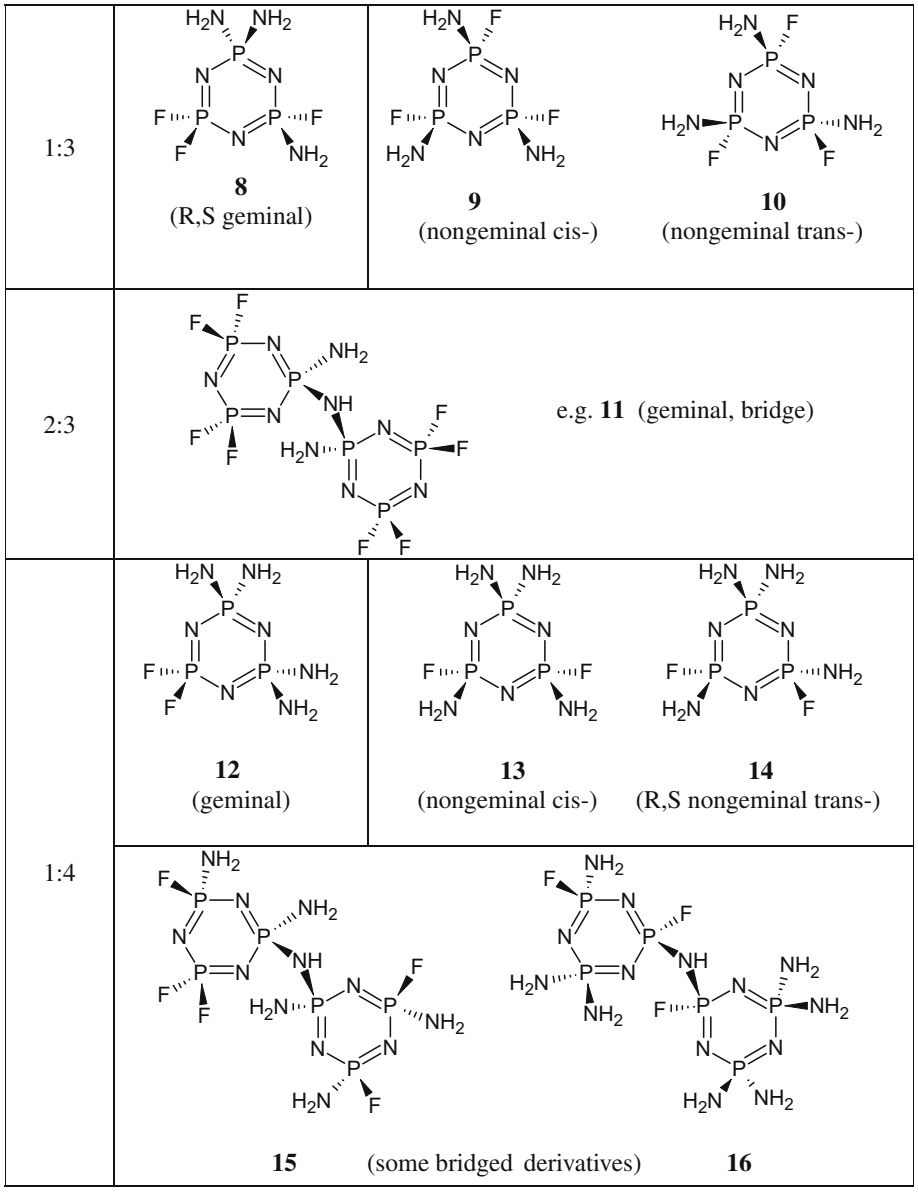
Scheme 1. Possible products in the reaction of $P_3N_3F_6$ with ammonia (1:8).

derivatives were isolated from a direct reaction of $P_3N_3F_6$ with various amines [30–33]. Geminal disubstituted $P_3N_3F_4(NMe_2)_2$ was described by Chivers et al. [32]. Nevertheless, the authors elucidated its formation from geminal $P_3N_3F_4Cl_2$ whose residues were found in the starting $P_3N_3F_6$. Fluorination of aminochlorophosphazenes by SbF_3 or KSO_2F [34–36] is the most common way used for the preparation of multiple-substituted aminoderivatives of hexafluoro-*cyclo*-triphosphazene.

It is known that the reaction of $P_3N_3Cl_6$ with gaseous ammonia in diethylether leads to the formation of disubstituted derivative $P_3N_3Cl_4(NH_2)_2$ [37–39]. Monosubstituted aminoderivative $P_3N_3Cl_5NH_2$ can be prepared by adding dry gaseous HCl to the solution of $P_3N_3Cl_4(NH_2)_2$ in acetonitrile [40] or in dioxane [41]. On the contrary, ammonolysis of $P_3N_3F_6$ carried out in diethylether at −25 °C yielded monosubstituted $P_3N_3F_5NH_2$ as the main product [42]. Geminal disubstituted derivative $P_3N_3F_4(NH_2)_2$ was prepared by fluorination of the corresponding chlorophosphazene $P_3N_3Cl_4(NH_2)_2$ by CsF in acetonitrile [43]. Structure of $P_3N_3F_4(NH_2)_2$ was determined by X-ray analysis [44], elemental analysis, melting point and mass spectrum can be found in [43].

Direct syntheses of higher-substituted amino fluorophosphazenes from $P_3N_3F_6$ and ammonia, have not been described yet. The only information available can be found in [45] where the behavior of $P_3N_3F_6$ and ammonia in various solvents at increasing molar ratio of starting compounds up to 1:24 was studied. The reaction mixtures, even after long reaction times, were found to be very complex and no effective way to separate individual reaction products was found. Mass spectrometry proved the presence of at most trisubstituted aminoderivatives of $P_3N_3F_6$ and dimer compounds while in the case of reaction between hexachloro-*cyclo*-triphosphazene with excess ammonia it was possible to prepare fully substituted aminoderivative [46,47].

Therefore our effort to elucidate the reaction system $P_3N_3F_6$ and ammonia was concentrated on finding such reaction conditions (molar ratio of starting compounds, solvent, reaction time) that would enable to prepare also higher-substituted aminoderivatives of $P_3N_3F_6$. Molar ratio of starting compounds of 1:8 was chosen for our studies. In this case at most tetrasubstituted aminoderivatives of $P_3N_3F_6$ can be expected (4 NH_3 molecules are used for substitution, 4 NH_3 molecules serve as acceptor of released HF). There are



* number of phosphazene rings : number of amino (imino, respectively) groups

Scheme 1. *(continued)*

many possibilities how to combine reaction products, some of them are summarized in Scheme 1.

Results of our investigations of the reaction system $P_3N_3F_6$/ammonia/solvent are summarized in this article.

2. Experimental

2.1. Reagents and general procedures

$P_3N_3F_6$ was prepared by fluorination of $P_3N_3Cl_6$ with NaF in acetonitrile [48]. The solvent was distilled off and a crude semi-solid product was obtained. Anhydrous $MgSO_4$ was added with the aim to remove last traces of water. Then, $P_3N_3F_6$, due to its volatility, was distilled off in vacuum from this mixture.

Liquid ammonia (Chemopetrol Litvínov a.s., CZ) was prepared by condensation from gaseous ammonia that was dried by passing it through a column filled with KOH (Lachema Brno, CZ) and metallic sodium wire (Ferak Berlin, BRD).

All operations were performed under dry gaseous nitrogen using conventional Schlenk techniques and vacuum lines.

Solvents – 1,1,2,2-tetrachlorethane, diethylether (Penta Chrudim, CZ), and acetonitrile (Lach-Ner s. r. o. Neratovice, CZ) were of reagent grade purity and dried by methods described in Perrin and Armarego [49].

2.2. Instrumentation

Elemental analysis was performed after mineralization of a sample with sodium peroxide in Parr bomb. The content of phosphorus was determined gravimetrically by precipitation with quinoline [50]. The content of fluorine was obtained from the difference between masses of the sample before and after fuming off SiF_4 (in the presence of sulfuric acid and silica sand). The content of nitrogen was determined by Kjeldahl method.

The IR spectra were recorded in nujol and Kel-F mulls using a FTIR Bruker 28 spectrometer (measuring range 4000–400 cm^{-1}, resolution 2 cm^{-1}). Measurements were performed in demountable KBr cell. Raman spectra of solid samples in original Raman capillaries were measured on Bruker IFS55 Equinox apparatus, with Raman adapter FRA106/S (laser λ = 1064 nm, W = 150–400 mW) equipped.

Table 1
The compounds and their content determined by GC (in %).[a]

Retention time (min)	M^+ (found/calculated)	Compound	Filtrate	**S1** 160 °C + 6 h	**S2** 65 °C + 6 h	**S3** 80°C + 6 h
5.8	246/245.965	$P_3N_3F_5NH_2$ (**1**)	1	0	0	0
9.4	243/242.962	*gem*$P_3N_3F_4(NH_2)_2$ (**3**)	20	20	0	0
10.5	243/242.962	new *cis* and *trans non-gem* $P_3N_3F_4(NH_2)_2$ (**4**, **5**)	20	5	10	5
10.9	243/242.962		20	5	10	5
12.3	472/471.896	new compound (**2**)	39	0	4	35

[a] The content of components is related to their content in filtrate.

The ^{31}P NMR spectra were measured using FT NMR spectrometer Bruker Avance DRX 500 (frequency 202.404 MHz). Spectra were referred to 85% H_3PO_4. The samples were filled in the Simax® tubes (external diameter 4 mm). These tubes were inserted into original cuvettes Wilmad® (external diameter 5 mm) filled by D_2O that was used as the deuterium lock.

Mass spectra (EI) were measured by a spectrometer Finnigan MAT Trio 1000, series II, connected to a gas chromatograph GC 8000 and column DB-5. Excitation energy was 70 eV and 1–2 μl of liquid samples were sprayed into the column. The temperature of the heating zone was 50–280 °C and the rate of temperature rise was 10 or 15 °C min^{-1}. Nitrogen was used as carrier gas (flow 1.8 cm^3 min^{-1}).

The melting points were determined using electric Boethius apparatus Nagema PHMK 05. The samples were sealed in a glass capillary.

The structures of the compounds were determined using a KUMA KM-4 CCD κ-axis diffractometer with a graphite monochromatized Mo Kα radiation (λ = 0.71069 Å). The structure was solved through direct methods. Non-hydrogen atoms were refined anisotropically while hydrogen atoms were inserted in calculated positions and isotropically refined assuming a "ride-on" model. SHELX-97 program package [51] was used for the structure determinations; the drawings were made by XP program of Bruker SHELXTL V5.1 program package [52].

2.3. Quantum chemical calculations

The quantum chemical calculations were carried out with the molecular ADF program, version 2007.01 [53–55].

In the ADF calculation of the two-dimensional conformational PES two dihedral angles were changed in steps of 20°, all other nuclear coordinates being optimized, and DZP basis set, middle frozen core, integration accuracy to 4 digits, and LDA (VWN) functional was used. Molecular geometries for the two local minima closest to the by X-ray diffraction determined conformers were optimized with QZ4P basis set, no frozen core, integration accuracy to 6 digits, and OPBE [56] functional that combines OPTX (exchange) [57] and PBEc (correlation) [58]. The calculations of the IR spectra were carried out at the same level with no scaling factor.

2.4. Synthesis of $P_3N_3F_5$–NH–$P_3N_3F_4NH_2$ (**2**)

Ammonolysis of $P_3N_3F_6$ with liquid ammonia was carried out at a molar ratio of 1:8. Amount 2.489 g (10 mmol) of $P_3N_3F_6$ was placed into 30 cm^3 of acetonitrile in a sealed Schlenk tube connected to a vacuum line and 1.32 g (80 mmol) of ammonia was added by condensation of gaseous ammonia. The mixture was kept at 20 °C for 24 h. Precipitated NH_4F was filtered off by a Schlenk frit (porosity S4).

The solvent was removed from the filtrate by means of vacuum distillation (oil pump). A white solid, crude **2,** was obtained and purified by vacuum sublimation (2 Pa, 80 °C, 6 h).

This sublimation product was recrystallized from 1,1,2,2-tetrachloroethane. The substance **2** was isolated in the form of two polymorphs **2A** or **2B**.

The yield of the compound **2** was 35%, as related to $P_3N_3F_6$. Its melting point was determined from microcrystalline material to be 186 °C. The crystals of **2** for X-ray diffraction were grown from 1,1,2,2-tetrachloroethane.

Elemental analysis of **2**: found/calc. (%): P – 38.13/39.37, F – 35.78/36.23, N – 23.51/23.75.

Mass spectrum of **2**: M^+ = 472 ($P_6N_6F_9N_2H_3^+$), 457 ($P_6N_6F_9NH_2^+$), 456 ($P_6N_6F_9NH^+$), 453 ($P_6N_6F_8N_2H_3^+$), 438 ($P_6N_6F_8NH_2^+$), 436 ($P_6N_6F_8N^+$), 433 ($P_6N_6F_7N_2H_2^+$), 423 ($P_6N_6F_8H^+$), 397 ($P_6N_6F_6N^+$), 353 ($P_5N_5F_6N^+$), 245 ($P_3N_3F_5NH^+$), 230 ($P_3N_3F_5^+$), 227 ($P_3N_3F_4NH_2^+$), 212 ($P_3N_3F_4H^+$), 211 ($P_3N_3F_4^+$), 209 ($P_3N_3F_3NH_2^+$), 197 ($P_3N_2F_4^+$), 166 ($P_2N_2F_4^+$), 152 ($P_2NF_4^+$), 148 ($P_2N_2F_3H^+$), 129 ($P_2N_2F_2H^+$), 128 ($P_2N_2F_2^+$), 114 ($P_2NF_2^+$), 107 (PF_4^+), 88 (PF_3^+), 69 (PF_2^+), 50 (PF^+), 46 (PNH^+).

Raman spectrum of **2A**: 211 vw, 259 vw, 289 w, 292 w, 297 w, 300 vw, 317 vw, 355 vw, 399 vw, 407 vw, 463 vw, 474 vw, 526 vw, 538 vw, 550 sh, 554 w, 600 vw, 736 vs, 782 vw, 948 vw, 1545 vw, 2712 vw, 3043 bvw, 3273 vw.

Raman spectrum of **2B**: 211 vw, 260 vw, 288 w, 293 w, 295 w, 302 vw, 317 vw, 335 vw, 368 vw, 445 vw, 463 vw, 474 vw, 526 vw, 537 w, 550 w, 555 vw, 601 vw, 737 vs, 792 vw, 854 vw, 945 vw, 1546 vw, 2714 vw, 2992 bvw, 3270 vw.

Infrared spectrum of **2A**: 409 vw, 430 vw, 445 w, 463 m, 446 s, 485 m, 505 s, 509 sh, 527 vw, 537 vw, 560 vw, 569 vw, 596 vw, 723 vw, 738 vw, 792 w, 809 s, 817 s, 826 vs, 842 vs, 861 sh, 888 m, 898 sh, 937 sh, 949 vs, 962 sh, 1009 m, 1040 m, 1180 vw, 1196 vw, 1252 sh, 1279 vs, 1371 m, 1544 vw, 1559 vw, 2714 vw, 3080 bvw, 3282 vw, 3302 vw, 3423 w, 3444 vw.

Infrared spectrum of **2B**: 411 vw, 432 vw, 445 s, 486 m, 506 s, 528 vw, 538 vw, 560 vw, 570 vw, 595 vw, 723 vw, 738 vw, 791 w, 816 s, 826 vs, 840 vs, 864 sh, 887 m, 935 sh, 947 vs, 962sh, 1002 vw, 1012 m, 1041 m, 1180 vw, 1200 vw, 1218 vw, 1235 vw, 1245 sh, 1269 vw, 1278 vs, 1372 m, 1543 vw, 1559 vw, 2714 vw, 3081 bvw, 3280 vw, 3297 vw, 3423 w, 3442 vw.

2.5. Identification of other reaction products

Mass spectrum of $P_3N_3F_5NH_2$ (**1**): M^+ = 246 ($P_3N_3F_5NH_2^+$), 230 ($P_3N_3F_5^+$), 227 ($P_3N_3F_4NH_2^+$), 216 ($P_3N_2F_5^+$), 212 ($P_3N_3F_4H^+$), 207 ($P_3N_3F_3NH^+$), 197 ($P_3N_2F_4^+$), 171 ($P_2NF_5^+$), 167 ($P_2N_2F_4H^+$), 152 ($P_2NF_4^+$), 133 ($P_2NF_3^+$), 129 ($P_2N_2F_2H^+$), 114 ($P_2NF_2^+$), 107 (PF_4^+), 104 ($PNF_3H_2^+$), 88 (PF_3^+), 84 (PNF_2H^+), 81 (P_2F^+), 69 (PF_2^+), 66 ($PNFH_2^+$), 50 (PF^+), 46 (PNH^+).

Mass spectrum of $P_3N_3F_4(NH_2)_2$ (**3, 4, 5**)[1]: M^+ = 243 ($P_3N_3F_4(NH_2)_2^+$), 227 ($P_3N_3F_4NH_2^+$), 224 ($P_3N_3F_3(NH_2)_2^+$), 212 ($P_3N_3F_4H^+$), 207 ($P_3N_3F_3NH^+$), 198 ($P_3N_2F_4H^+$), 197 ($P_3N_2F_4^+$), 194 ($P_3N_3F_3H_2^+$), 192 ($P_3N_3F_3^+$), 182 ($P_2N_3F_4H_2^+$), 178 ($P_3N_2F_3^+$), 168 ($P_2N_2F_4H_2^+$), 167 ($P_2N_2F_4H^+$), 166 ($P_2N_2F_4^+$), 164 ($P_3NF_3^+$), 152

[1] All mass spectra are identical, only intensities of fragments are rather different.

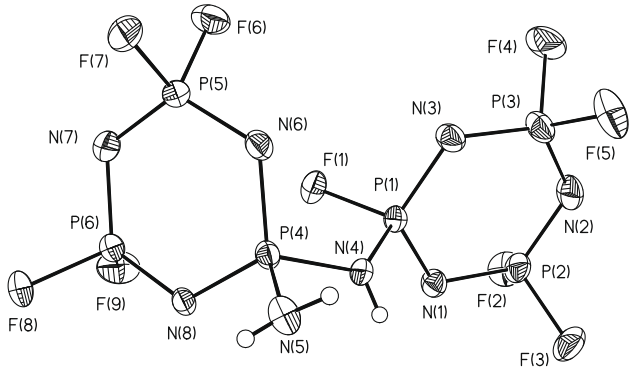


Fig. 1. The molecular structure of **2A**. Thermal ellipsoids are drawn with 50% probability.

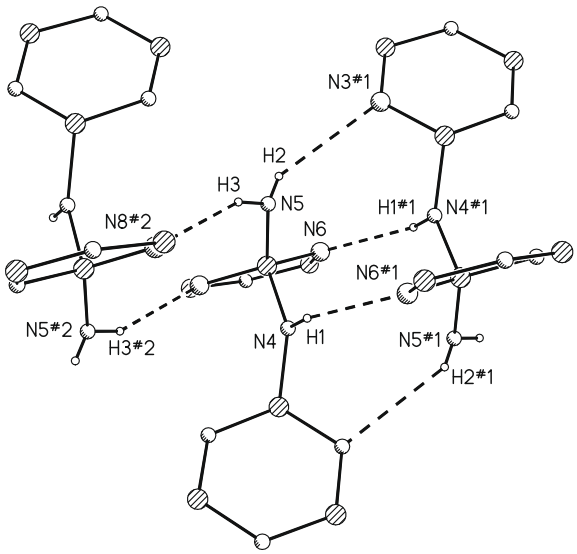


Fig. 2. A part of a column of molecules in the structure of **2A** showing hydrogen bonds. Fluorine atoms are omitted for clarity. Symmetry code: #1 $-x+1$, $-y$, $-z+1$; #2 $-x+2$, $-y$, $-z+1$.

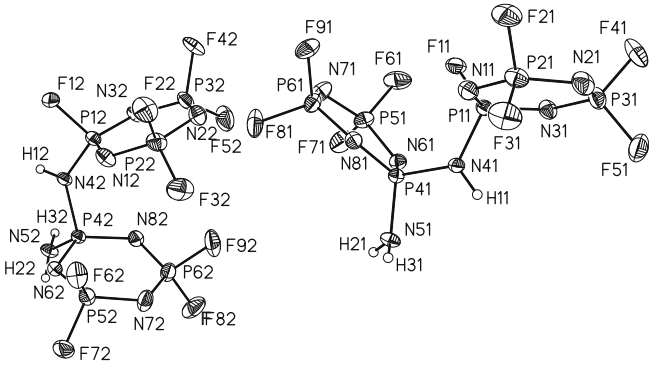


Fig. 3. Perspective view of molecules $\mathbf{2B_a}$ (left) and $\mathbf{2B_b}$ (right) of the structure of **2B**. Thermal ellipsoids are drawn with 30% probability.

($P_2NF_4^+$), 149 ($P_2N_2F_3H_2^+$), 148 ($P_2N_2F_3H^+$), 133 ($P_2NF_3^+$), 129 ($P_2N_2F_2H^+$), 128 ($P_2N_2F_2^+$), 114 ($P_2NF_2^+$), 107 (PF_4^+), 104 ($PNF_3H_2^+$), 95 (P_2NF^+), 88 (PF_3^+), 85 ($PNF_2H_2^+$), 84 (PNF_2H^+), 81 (P_2F^+), 69 (PF_2^+), 66 ($PNFH_2^+$), 50 (PF^+), 46 (PNH^+).

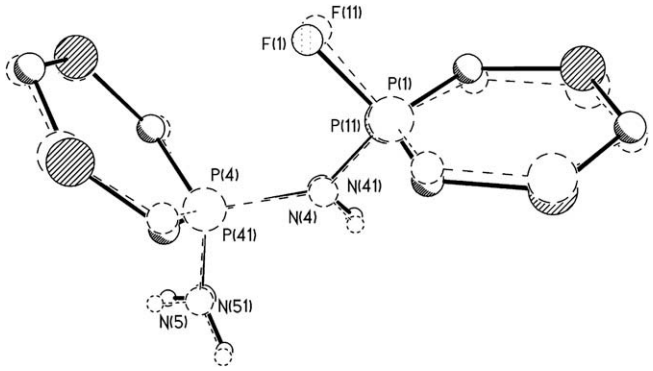


Fig. 4. The best fit of **2A** and $\mathbf{2B_a}$ molecules.

^{31}P NMR spectrum of **3**: $P(NH_2)_2$ triplet at $\delta = 19.7$ ppm and split PF_2 triplet at $\delta = 11.9$ ppm; *^{31}P NMR spectrum of* **4**, **5**: $PFNH_2$ dublet of broad signals at $\delta = 25.1$ ppm and split PF_2 triplet at $\delta = 10.6$ ppm.

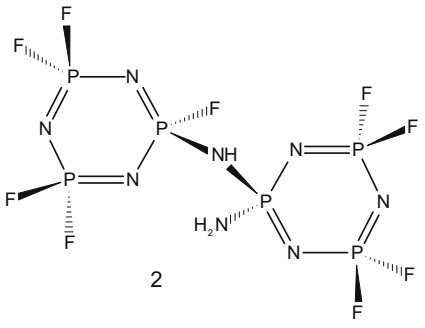
3. Results and discussion

Ammonolysis of $P_3N_3F_6$ was studied by simple mixing of the substrate ($P_3N_3F_6$) with liquid ammonia in a Schlenk tube in acetonitrile. The molar ratio of reactants was kept at 1:8, the reaction was carried out at 20 °C for 24 h. Solid NH_4F was formed in the course of the reaction and was filtered off. The solvent, together with volatile $P_3N_3F_5NH_2$ (**1**), were evaporated from the filtrate and **1** was identified by MS spectrometry. The residue in the form of a white powder was obtained. Its purification was carried out by vacuum sublimation at 2 Pa. Several fractions of a solid (**S1**, **S2**, **S3**) were isolated in the course of vacuum sublimation. Fraction **S1** was obtained at 60 °C after 6 h, fraction **S2** at 65 °C after another 6 h of sublimation. Thus more volatile products **3**, **4, 5** were removed from the crude product. The sublimation at 80 °C for additional 6 h led to the isolation of an unknown compound **2**.

The composition of the filtrate and sublimation fractions was studied by NMR spectrometry and GC/MS (see Table 1).

It follows from Table 1 that the first sublimation fraction **S1** contains mostly geminal $P_3N_3F_4(NH_2)_2$ (**3**), fraction **S2** has majority of nongeminal *cis* or *trans*-$P_3N_3F_4(NH_2)_2$ (**4**, **5**) that have not been described so far. The signals of **4**, **5** were identified in ^{31}P NMR spectrum of the sublimation fraction **S3** dissolved in acetonitrile. Diamines $P_3N_3F_4(NH_2)_2$, (**3, 4**, **5**) were also identified by GC/MS.

The third sublimation fraction **S3** contains mainly the substance **2**. Recrystalization of **2** from 1,1,2,2-tetrachloromethane yielded pure crystals suitable for X-ray analysis. X-ray diffraction experiments showed that the substance **2** is the hitherto not described dimeric phosphazene aminoderivative in which two phosphazene cycles are connected via a NH-bridge.



2

Two kinds of monoclinic crystals (polymorphs **2A**, **2B**) were obtained by crystallization of the sublimation fraction **S3** from 1,1,2,2-tetrachloroethane (see below).

If the ammonolysis of $P_3N_3F_6$ was performed in diethylether the NMR analysis of the reaction mixture showed that monoamine $P_3N_3F_5NH_2$ (**1**) was present as the main product in the reaction mixture (>95% yield). Other substitution products, geminal (**3**) and *cis* and *trans* nongeminal isomers $P_3N_3F_4(NH_2)_2$ (**4**, **5**), and new derivative (**2**) were present only in negligible amounts as indentified by GC/MS.

3.1. X-ray structure analysis of **2**

The crystals of polymorph **2A** are monoclinic, space group $P2_1/n$. The asymmetric unit contains one molecule of **2A** in a general position (Fig. 1). The angle between the best planes through both P–N rings is 123.7(1)° with P1–N4–P4 bridging angle 128.6(1)°. The P1–F1 bond of P1–N1–P2–N2–P3–N3 (ring **R1**) is fairly parallel to the P4–N6–N7–P6–N8 ring (ring **R2**) and thus F1 and N5 are mutually in *trans* position. Both P–N rings are slightly twisted and thus deviating from exact planarity. The largest deviations of N atoms from the planes defined by P atoms are 0.058(3) Å (**R1**, N3) and 0.121(2) Å (**R2**, N8).

There are three possible hydrogen bond systems involving all three hydrogen atoms which bind the molecules into parallel columns: N4(H1)···N8 (2.19 Å), N5(H2)···N1 (2.67 Å), and N5(H3)···N6 (2.34 Å) (Fig. 2 and Table 5 upper part).

The structure of polymorph **2B** is also monoclinic, space group *C2/c*. The asymmetric unit contains two molecules ($\mathbf{2B_a}$ and $\mathbf{2B_b}$) in general positions. However, contrary to the structure of **2A**, the molecules are two different conformers (Fig. 3).

3.1.1. $2B_a$ molecule

The molecule $\mathbf{2B_a}$ is the same conformer as that in the polymorph **2A** (Fig. 4).

Thus the angle between the best planes drawn through P11–N11–P21–N21–P31–N31 (ring **R11**) and P41–N61–P51–N71–P61–N81 (ring **R21**) is 132.5(1)° (123.7° in **1A**) with P11–N41–P41 bridging angle 129.4(1)° (128.6° in **2A**). Deviation of both rings from planarity is practically the same both in **2A** and $\mathbf{2B_a}$. The largest deviations of N atoms from the best planes defined by P atoms are 0.048(3) Å (**R11**, N21) and 0.148(3) Å (**R21**, N81).

3.1.2. $2B_b$ molecule

$\mathbf{2B_b}$ can be derived from $\mathbf{2B_a}$ (or **2A**) by rotating one P–N ring by approx. 180° around the P–N(H) bond. As a result, F11 and N51(H) are mutually in a *cis* position.

Thus the angle between the best planes drawn through P12–N12–P22–N22–P32–N32 (ring **R12**) and P42–N62–P52–N72–P62–N82 (ring **R22**) is 30.9(1)° and P12–N42–P42 bridging angle 124.2(2)° (128.6° in **1A**, 129.4° in $\mathbf{2B_a}$. The largest deviations of N atoms from the best planes defined by P atoms are 0.126(3) Å (**R12**, N12) and 0.133(3) Å (**R22**, N82).

The crystal structure of **2B** is built from alternating columns of molecules propagating along the axis *b*, each column being composed of the same conformer only (Fig. 5). Within each column the molecules are connected by hydrogen bonds (Table 5, lower part).

Crystal data and structure refinement for **2A** and **2B** are given in Table 2, selected bond lengths in Table 3 and selected bond angles in Table 4.

The comparison between bond parameters of **2A**, **2B** with analogical data, e.g. for compounds **1**, **3,** shows that bond P–N and P–F lengths are similar. However, P–N bonds in the P–N ring, which are in the vicinity of P1, P4, or P7, P10 atoms, respectively, are somewhat longer (1.601–1.617 Å) as compared to published data (1.582–1.597 Å) [44,59,60].

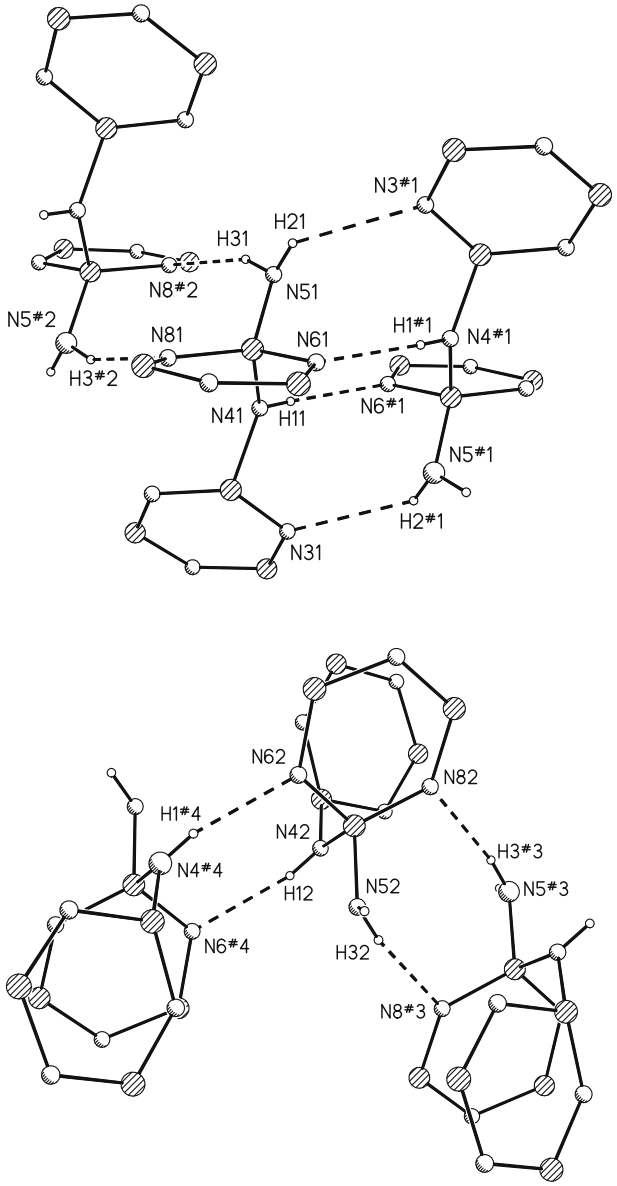


Fig. 5. Parts of $\mathbf{2B_a}$ (upper) and $\mathbf{2B_b}$ (lower) molecular columns showing hydrogen bonds in the structure of **2B**. Fluorine atoms are omitted for clarity. Symmetry code: #1 1 − *x* + 1/2, −*y* + 1/2, −*z* + 1; #2 −*x* + 1/2, −*y* + 3/2, −*z* + 1; #3 −*x*, −*y* + 1, −*z*, #4 −*x*, −*y* + 2, −*z*.

3.2. Quantum chemical calculations for **2**

The agreement between the metrical parameters from X-ray and from ADF calculation is very good except for the two sloppy torsions around P–N bonds in the P–NH–P bridge. Selected metrical parameters are shown in Table 6. The two-dimensional potential energy surface (PES) is in Fig. 6. It shows 8 minima with the torsion angles given in Table 7. The calculated minima for the gas phase molecules with the labels **a** and **b** in Fig. 6 and Table 7 differ in those dihedral angles by 6–12° from X-ray data. The conformational PES extends within 30 kJ/mol including apparent local maxima, in fact saddle points of second order. All the 8 local

Table 2
Crystal data and structure refinement for **2A** and **2B**.

Compound	**2A**	**2B**
Empirical formula	$P_6N_8F_9H_3$	$P_6N_8F_9H_3$
Formula weight	471.92	471.92
T (K)	120	120
Wavelength (Å)	0.71069	0.71069
Crystal system	monoclinic	monoclinic
Space group	$P2_1/n$	$C2/c$
Unit cell dimensions		
a (Å)	7.4732(15)	38.064(8)
b (Å)	21.965(4)	7.3852(15)
c (Å)	9.3845(19)	22.165(4)
α (°)	90	90
β (°)	107.76(3)	113.08(3)
γ (°)	90	90
V (Å^3)	1467.1(5)	5732(2)
Z	4	16
Calculated density (Mg m^{-3})	2.137	2.187
Absorption coefficient (mm^{-1})	0.840	0.860
F(0 0 0)	920	3680
Crystal size (mm)	0.25 × 0.10 × 0.04	0.40 × 0.20 × 0.20
θ range for data collection (°)	2.94–25.0	2.91–25
Limiting indices	$-7 \leqslant h \leqslant 8$; $-26 \leqslant k \leqslant 26$; $-11 \leqslant l \leqslant 11$	$-44 \leqslant h \leqslant 44$; $-8 \leqslant k \leqslant 6$; $-26 \leqslant l \leqslant 26$
Reflections collected/unique [R_{int}]	10 023/2574 [0.0434]	32 575/5038 [0.0392]
Completeness to 2θ = 25.00 (%)	99.7	99.8
Absorption correction	ψ-scan	ψ-scan
Maximum and minimum transmission	0.9672 and 0.8174	0.8468 and 0.7247
Refinement method	full-matrix least-squares on F^2	full-matrix least-squares on F^2
Data/restrains/parameters	2574/0/211	5038/0/421
Goodness-of-fit (GOF) on F^2	1.047	1.065
Final R indices [$I > 2\sigma(I)$]	R_1 = 0.0310, wR_2 = 0.0837	R_1 = 0.0410, wR_2 = 0.1004
R indices (all data)	R_1 = 0.0382, wR_2 = 0.0877	R_1 = 0.0474, wR_2 = 0.1040
Largest difference in peak and hole (e Å^{-3})	0.420/−0.427	0.547/−0.565

$wR_2 = \{\sum[w(F_o^2 - F_c^2)^2]/\sum[w(F_o^2)^2]\}^{1/2}$, $R_1 = \Sigma||F_o| - |F_c||/\Sigma|F_o|$, GOF $= S = \{\sum[w(F_o^2 - F_c^2)^2]/(n-p)\}^{1/2}$, where n is the number of refections and p is the total number of parameters refined.

Table 3
Selected bond lengths (Å) for **2A** and **2B**.

2A		**2B$_a$**		**2B$_b$**	
P(1)–F(1)	1.544(2)	P(11)–F(11)	1.549(2)	P(12)–F(12)	1.549(2)
P(1)–N(1)	1.579(2)	P(11)–N(11)	1.577(3)	P(12)–N(12)	1.574(3)
P(1)–N(3)	1.591(2)	P(11)–N(31)	1.578(3)	P(12)–N(32)	1.579(3)
P(1)–N(4)	1.642(2)	P(11)–N(41)	1.635(3)	P(12)–N(42)	1.641(3)
N(1)–P(2)	1.559(2)	N(11)–P(21)	1.556(3)	N(12)–P(22)	1.565(3)
P(2)–F(3)	1.523(2)	P(21)–F(31)	1.524(2)	P(22)–F(32)	1.521(2)
P(2)–F(2)	1.538(2)	P(21)–F(21)	1.532(2)	P(22)–F(22)	1.522(3)
P(2)–N(2)	1.568(3)	P(21)–N(21)	1.558(4)	P(22)–N(22)	1.562(4)
N(2)–P(3)	1.567(3)	N(21)–P(31)	1.557(4)	N(22)–P(32)	1.554(4)
P(3)–F(4)	1.525(2)	P(31)–F(41)	1.522(3)	P(32)–F(42)	1.531(2)
P(3)–F(5)	1.528(2)	P(31)–F(51)	1.524(2)	P(32)–F(52)	1.521(2)
P(3)–N(3)	1.576(2)	P(31)–N(31)	1.566(3)	P(32)–N(32)	1.563(3)
N(4)–P(4)	1.664(2)	N(41)–P(41)	1.665(3)	N(42)–P(42)	1.658(3)
P(4)–N(6)	1.618(3)	P(41)–N(61)	1.603(3)	P(42)–N(62)	1.600(3)
P(4)–N(8)	1.610(2)	P(41)–N(81)	1.602(3)	P(42)–N(82)	1.602(3)
P(4)–N(5)	1.608(2)	P(41)–N(51)	1.611(3)	P(42)–N(52)	1.617(3)
N(6)–P(5)	1.556(2)	N(61)–P(51)	1.561(2)	N(62)–P(52)	1.563(2)
P(5)–F(7)	1.530(2)	P(51)–F(71)	1.522(2)	P(52)–F(72)	1.525(2)
P(5)–F(6)	1.534(2)	P(51)–F(61)	1.522(3)	P(52)–F(62)	1.524(2)
P(5)–N(7)	1.568(3)	P(51)–N(71)	1.559(3)	P(52)–N(72)	1.563(3)
N(7)–P(6)	1.577(3)	N(71)–P(61)	1.558(3)	N(72)–P(62)	1.558(3)
P(6)–F(9)	1.527(2)	P(61)–F(91)	1.523(2)	P(62)–F(92)	1.525(3)
P(6)–F(8)	1.535(2)	P(61)–F(81)	1.528(2)	P(62)–F(82)	1.522(3)
P(6)–N(8)	1.560(2)	P(61)–N(81)	1.561(3)	P(62)–N(82)	1.562(3)

minima and the first order saddle points are thermally accessible. So, the molecule is stereochemically nonrigid which is connected not only to the P–NH–P bridge but also to the easy distortions of the P_3N_3 ring that is planar and comparably rigid, perhaps, only in $P_3N_3F_6$ [21,22]. The Fig. 6 suggests that all barriers to internal rotation around exocyclic P–N bonds in **2** are very low, less than 15 kJ/mol, in the gas phase. This is in the agreement with the special bonding pattern of the phosphazene rings (e.g. [22]) that leaves those bonds with no π-contribution.

The numerical labels of local minima correspond to the Table 7; **a** corresponds to **2B$_a$** (or **2A**, respectively), **b** corresponds to **2B$_b$**.

Energy is expressed in kJ/mol relative to the lowest local minimum labeled **e**; the step for isolines amounts to 2 kJ/mol; α is the torsion angle N(7)–P(4)–N(4)–P(1) in Fig. 1; β is the torsion angle P(4)–N(4)–P(1)–F(1) in Fig. 1.

3.3. IR and raman spectra of *2A*

The calculated IR spectra have been useful in the assigning experimental bands to a mode of vibrational motion in most cases. Fig. 7 compares calculated and experimental IR spectra of **2A**.

The bands near 3444, 3423, 3302, 3282 cm^{-1} in the experimental IR spectrum of **2A** are in agreement with ADF calculations and were assigned to valence vibrations ν of NH_2 and NH group. The broad band extending from 3150 cm^{-1} to 2850 cm^{-1} belongs to the system of hydrogen bridges. There are two types of H-bridges that are identical in both types of the molecules **2A** and **2B** (Figs. 2 and 5). The low intensity band at 2714 cm^{-1} can be probably assigned to the combination vibration (overtone) of NH group (2 × δ NH). The double band of low intensity at 1559 and 1544 cm^{-1} belongs unambiguously to the deformation vibration δ of NH_2 group (ADF calculations 1540 cm^{-1}). The group of absorption bands in the region from 1279 sh, 1252 vs, 1196 s to 1180 sh cm^{-1}, can by ascribed, with agreement with ADF calculations (1282 s, 1278 vs, 1247 m, 1217 w) to several types of vibrations: deformation vibration δ of NH group, valence vibrations ν of both phosphazene

Table 4
Selected angles (°) for **2A** and **2B**.

2A		**$2B_a$**		**$2B_b$**	
N(1)–P(1)–N(3)	117.1(1)	N(11)–P(11)–N(31)	117.3(2)	N(12)–P(12)–N(32)	116.6(2)
N(2)–P(2)–N(1)	119.3(1)	N(21)–P(21)–N(11)	119.5(2)	N(22)–P(22)–N(12)	118.8(2)
N(3)–P(3)–N(2)	119.7(1)	N(31)–P(31)–N(21)	119.1(2)	N(32)–P(32)–N(22)	119.8(2)
P(2)–N(1)–P(1)	122.3(2)	P(21)–N(11)–P(11)	121.6(2)	P(22)–N(12)–P(12)	121.7(2)
P(3)–N(2)–P(2)	120.3(2)	P(31)–N(21)–P(21)	120.8(2)	P(32)–N(22)–P(22)	120.4(2)
P(3)–N(3)–P(1)	121.1(2)	P(31)–N(31)–P(11)	121.5(2)	P(32)–N(32)–P(12)	121.2(2)
N(8)–P(4)–N(6)	114.0(1)	N(81)–P(41)–N(61)	114.3(2)	N(82)–P(42)–N(62)	113.7(2)
N(7)–P(5)–N(6)	119.8(1)	N(71)–P(51)–N(61)	119.2(2)	N(72)–P(52)–N(62)	119.2(2)
N(8)–P(6)–N(7)	119.9(1)	N(81)–P(61)–N(71)	119.7(2)	N(82)–P(62)–N(72)	119.6(2)
P(5)–N(6)–P(4)	123.1(2)	P(51)–N(61)–P(41)	123.1(2)	P(52)–N(62)–P(42)	123.2(2)
P(6)–N(7)–P(5)	119.6(2)	P(61)–N(71)–P(51)	120.2(2)	P(62)–N(72)–P(52)	119.8(2)
P(6)–N(8)–P(4)	122.9(2)	P(61)–N(81)–P(41)	122.3(2)	P(62)–N(82)–P(42)	123.1(2)
F–P–F[a]	98.0	F–P–F[a]	98.4	F–P–F[a]	98.5
F(1)–P(1)–N(4)	101.5(1)	F(11)–P(11)–N(41)	102.6(1)	F(12)–P(12)–N(42)	98.1(1)
N(5)–P(4)–N(4)	102.2(1)	N(51)–P(41)–N(41)	102.3(2)	N(52)–P(42)–N(42)	100.4(2)
P(1)–N(4)–P(4)	128.6(1)	P(11)–N(41)–P(41)	129.4(2)	P(12)–N(42)–P(42)	124.9(2)

[a] Average.

Table 5
Hydrogen bonds for **2A** and **2B** (Å and °).

D–H···A	**d(D–H)**	***d*(H···A)**	***d*(D···A)**	**<(DHA)**
		2A[a]		
N(4)–H(1)···N(6)#1	0.88	2.19	2.937(3)	142.8
N(5)–H(2)···N(3)#1	0.66	2.67	3.253(4)	147.2
N(5)–H(3)···N(8)#2	0.86	2.34	3.145(4)	155.7
		2B[b]		
N(41)–H(11)···N(61)#1	0.88	2.20	2.927(4)	139.1
N(51)–H(21)···N(31)#1	0.81	2.57	3.217(4)	137.9
N(51)–H(31)···N(81)#2	0.91	2.25	3.114(4)	158.3
N(52)–H(32)···N(82)#3	0.86	2.25	3.102(4)	171.3
N(42)–H(12)···N(62)#4	0.88	2.23	2.903(4)	132.8

[a] Symmetry transformations used to generate equivalent atoms:
#1 $-x+1, -y, -z+1$,
#2 $-x+2, -y, -z+1$.
[b] Symmetry transformations used to generate equivalent atoms:
#1 $-x+1/2, -y+1/2, -z+1$,
#2 $-x+1/2, -y+3/2, -z+1$,
#3 $-x, -y+1, -z$,
#4 $-x, -y+2, -z$.

cycles (denoted as "breathing" of the cycle), the coupled vibrations δ NH, and valence vibrations ν of phosphazene cycles.

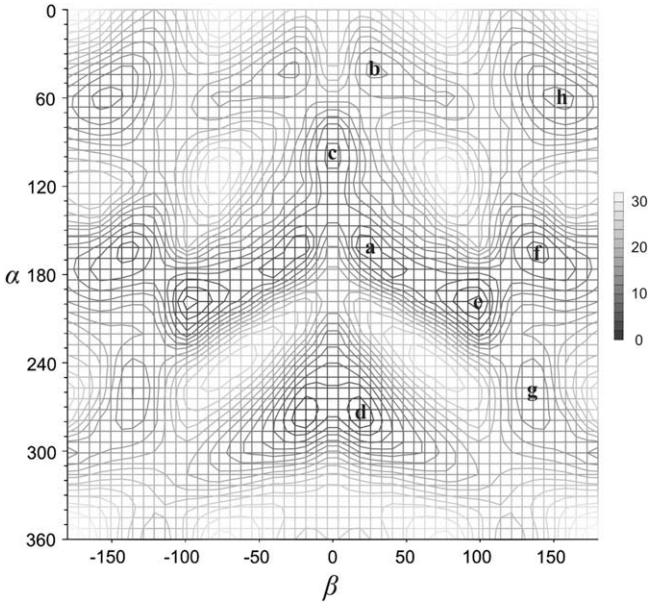


Fig. 6. Potential energy surface for the rotations around bonds P–N in the P–NH–P bridge in **2**. All other coordinates except for α and β were optimized.

Table 6
Selected metrical parameters of X-ray and ADF-calculation.

2A			**$2B_a$**			**$2B_b$**		
Torsion angles (°)	**X-ray**	**ADF**	**Torsion angles (°)**	**X-ray**	**ADF**	**Torsion angles (°)**	**X-ray**	**ADF**
N(7)–P(4)–N(4)–P(1)	20	25	N(71)–P(41)–N(41)–P(11)	18	25	N(72)–P(42)–N(42)–P(12)	18	24
P(4)–N(4)–P(1)–F(1)	28	43	P(41)–N(41)–P(11)–F(11)	29	43	P(42)–N(42)–P(12)–F(12)	157	164
N(5)–P(4)–N(4)–P(1)	163	158	N(51)–P(41)–N(41)–P(11)	165	158	N(52)–P(42)–N(42)–P(12)	165	156
P(4)–N(4)–P(1)–N(2)	153	140	P(41)–N(41)–P(11)–N(21)	153	140	P(42)–N(42)–P(12)–N(22)	23	15
Bond angles (°)	**X-ray**	**ADF**	**Bond angles (°)**	**X-ray**	**ADF**	**Bond angles (°)**	**X-ray**	**ADF**
F(1)–P(1)–N(4)	101.5	103.2	F(11)–P(11)–N(41)	102.6	103.2	F(12)–P(12)–N(42)	98.1	97.1
N(4)–P(4)–N(5)	102.2	99.5	N(41)–P(41)–N(51)	102.3	99.5	N(42)–P(42)–N(52)	100.4	99.6
P(1)–N(4)–P(4)	128.6	129.3	P(11)–N(41)–P(41)	129.4	129.3	P(12)–N(42)–P(42)	124.9	128.3
N(1)–P(1)–N(3)	117.1	119.8	N(11)–P(11)–N(31)	117.3	119.8	N(12)–P(12)–N(32)	116.6	118.9
N(6)–P(4)–N(8)	113.9	117.5	N(61)–P(41)–N(81)	114.3	117.5	N(62)–P(42)–N(82)	113.7	117.4
Bond lengths (Å)	**X-ray**	**ADF**	**Bond lengths (Å)**	**X-ray**	**ADF**	**Bond lengths (Å)**	**X-ray**	**ADF**
P(1)–N(1)	1.58	1.59	P(11)–N(11)	1.58	1.59	P(12)–N(12)	1.57	1.59
P(1)–N(3)	1.59	1.59	P(11)–N(31)	1.58	1.59	P(12)–N(32)	1.58	1.59
P(1)–N(4)	1.64	1.66	P(11)–N(41)	1.64	1.66	P(12)–N(42)	1.64	1.67
P(4)–N(4)	1.66	1.69	P(41)–N(41)	1.67	1.69	P(42)–N(42)	1.66	1.68
P(4)–N(5)	1.61	1.65	P(41)–N(51)	1.61	1.65	P(42)–N(52)	1.62	1.66
P(4)–N(6)	1.62	1.60	P(41)–N(61)	1.60	1.60	P(42)–N(62)	1.60	1.60
P(4)–N(8)	1.61	1.60	P(41)–N(81)	1.60	1.60	P(42)–N(82)	1.60	1.60

Table 7
Torsion angles α and β for the local energy minima on the two-dimensional conformational PES.

Conformer[a]	E (kJ) mol^{-1}[b]	α (°)[c]	β (°)[d]
a	1.7	24	164
b	12.5	23	40
c	0.9	18	82
d	1.1	20	280
e	0.0	102	204
f	3.8	147	167
g	11.3	140	260
h	7.8	152	54

[a] The numerical labels correspond to Fig. 6.
[b] Energy relative to the lowest local minimum ***e.***
[c] α is the torsion angle N(7)–P(4)–N(4)–P(1) in Fig. 1.
[d] β is the torsion angle P(4)–N(4)–P(1)–F(1) in Fig. 1.

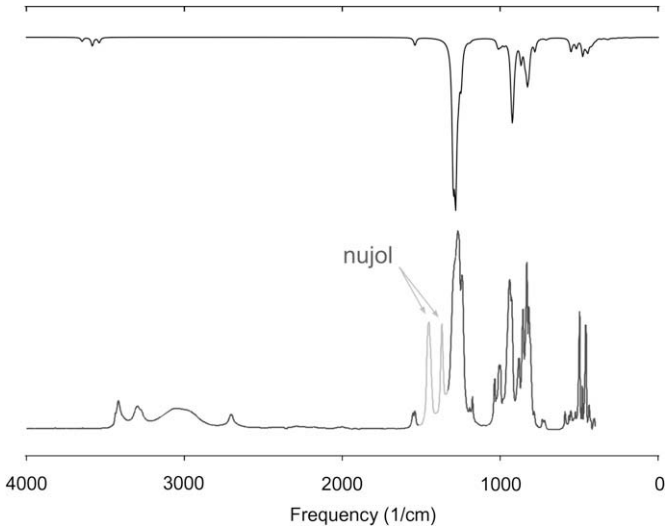


Fig. 7. The calculated (upper) and experimental (lower) IR spectra of **2A**.

Signals at 962, 949, and 937 cm^{-1} correspond to the valence vibrations of "endocyclic" P–N bonds.

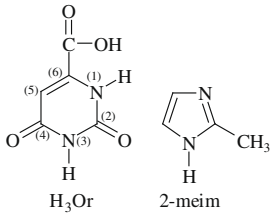
Dominating signals at 736 cm^{-1} **2A** and 737 cm^{-1} **2B,** respectively, in the Raman spectra in both polymorphs correspond to the valence vibration of the PF group.

Acknowledgements

This work was supported by the Ministry of Education, Youth, and Sports of the Czech Republic, Grant No. MSM0021622411. The authors express their gratitude to the Czech Grant Agency for the Grant No. 203/02/0436 and the Grant KAN101630651 of the Czech Academy of Sciences.

References

[1] I. Haiduc, The Chemistry of the Inorganic Ring Systems, vol. 2, Wiley-Interscience, London, 1970 (Chapter 5).
[2] S.S. Krishnamurthy, A.C. Sau, Adv. Inorg. Chem. Radiochem. 21 (1978) 41.
[3] C.W. Allen, in: I. Haiduc, D.B. Sowerby (Eds.), The Chemistry of Inorganic Homo- and Hetero- Cycles, vol. 2 Acadamic Press, London, 1987, p. 501.
[4] J.F. Labarre, Top. Curr. Sci. 102 (1982) 1.
[5] K. Brandt, Z. Jedlinami, Makromol. Chem. Suppl. 9 (1985) 109.
[6] D.E. Gong, H.M. Li, US Patent 5 105 001, 1992; Chem. Abstr., 117, 61662y (1992), assigned to Ethyl Corp.
[7] R.H.S. Wang, G. Irido, US Patent 4 080 361, 1978; Chem. Abstr., 89, 1111x (1978), assigned to Eastman Kodak.
[8] C.W. Allen, J. Fire Sci. 11 (1993) 320.
[9] J.K. Valaitis, G.S. Kymer, J. Appl. Polym. Sci. 23 (1979) 765.
[10] J.P. Critchley, G.J. Knight, M.M. Wright, Heat-Resistant Polymers, Plenum Press, New York, 1983.
[11] H.R. Allcock, in: M. Chasám, R. Langer (Eds.), Biodegradable Polymers as Drug Delivery Systems, Marcel Dekker, New York, 1990, p. 163.
[12] A.G. Scopelianos, in: S.W. Shalaby (Ed.), Biomedical Polymers, Hanser, Munich, 1994, p. 153.
[13] L.G. Payne, S.A. Jenkins, A. Andrianov, B.E. Roberts, in: M.F. Powell, M.J. Newman (Eds.), Vaccine Design: The Subunit and Adjuvant Approach, Plenum Press Div, New York, 1995, p. 473.
[14] L.G. Payne, S.A. Jenkins, A. Andrianov, R. Langer, B.E. Roberts, in: J. Mestecky et al. (Eds.), Advances in Mucose Immunology, Plenum Press, New York, 1995, p. 1475.
[15] G. Golemme, E. Drápli, J. Inorg. Organomet. Polym. 6 (1996) 341.
[16] M. Guglielmi, G. Brusatin, G. Facchin, M. Gleria, R. Jaeger, M. Musiani, J. Inorg. Organomet. Polym. 6 (221) (1996) 98.
[17] M. Guglielmi, G. Brusatin, G. Facchin, M. Gleria, Appl. Organomet. Chem. 13 (1999) 339.
[18] H.R. Allcock, in: J.D. MacKenzie, D.R. Ulrich (Eds.), Ultrastructure Processing of Advanced Ceramics, Wiley-Interscience, New York, 1988, p. 705.
[19] H.R. Allcock, M.F. Wolker, M. Parvez, Chem. Mater. 4 (1992) 296.
[20] M. Gleria, R. Bertani, R. Jaeger, S. Lora, J. Fluorine Chem. 125 (2004) 329.
[21] L. Kapička, D. Dastych, V. Richterová, M. Alberti, P. Kubáček, Magn. Reson. Chem. 43 (2005) 294.
[22] L. Kapička, P. Kubáček, P. Holub, J. Mol. Struct. (Theochem) 820 (1–3) (2007) 148.
[23] A.S. Freund, M. Calichman, C.W. Allen, Z. Anorg. Allg. Chem. 630 (2004) 2059.
[24] A.J. Elias, K. Muralidharan, Inorg. Chem. Commun. 6 (2003) 584.
[25] C.W. Allen, Chem. Rev. 91 (1991) 119.
[26] A. Vij, S.J. Geib, R.L. Kirchmeier, J.M. Shreeve, Inorg. Chem. 35 (1996) 2915.
[27] E. Lork, D. Boehler, R. Mens, Angew. Chem., Int. Ed. Engl. 34 (1995) 2696.
[28] H.R. Allcock, Phosphorus–Nitrogen Compounds. Cyclic, Linear, and High Polymeric Systéme, Academic Press, New York, USA, 1972 (Chapter 16), p. 343.
[29] H.R. Allcock, Phosphorus–Nitrogen Compounds, Cyclic, Linear, and High Polymeric Systems, Academic Press, New York and London, 1972. p. 183.
[30] O. Glemser, E. Niecke, H.W. Roesky, Chem. Commun. (1969) 282.
[31] T. Chivers, N.L. Paddock, J. Chem. Soc., Chem. Commun. (1969) 337.
[32] T. Chivers, R.T. Oakley, N.L. Paddock, J. Chem. Soc. (A) (1970) 2324.
[33] E. Niecke, H. Thamm, G. Flaskerud, Chem. Ber. 104 (1971) 3729.
[34] B. Green, D.B. Sowerby, J. Chem. Soc. A (1970) 987.
[35] B. Green, D.B. Sowerby, P. Clare, J. Chem. Soc. A (1971) 3487.
[36] B. Green, J. Chem. Soc., Dalton Trans. (1974) 1113.
[37] H.N. Stokes, Am. Chem. J. 17 (1895) 275.
[38] H. Moureu, A.M. Ficquelmont, Compt. Rend. 198 (1934) 1417.
[39] M. Becke-Göhring, K. John, Angew. Chem. 70 (1958) 657.
[40] M. Alberti, J. Břínek, J. Marek, J. Toužín, Z. Anorg. Allg. Chem. 623 (1997) 637.
[41] G.R. Feistel, T.J. Moeller, Inorg. Nucl. Chem. 29 (1967) 2731.
[42] H.W. Roesky, E. Niecke, Inorg. Nucl. Chem. Lett. 4 (1968) 463.
[43] H.D. Thamm, Ph.D. Thesis, Göttingen, 1972.
[44] S. Pohl, B. Krebs, Chem. Ber. 109 (1976) 2622.
[45] J. Vojáčková, Thesis, Masaryk University Brno, 1997.
[46] L.F. Audrieth, D.B. Sowerby, Chem. Ind. (1959) 748.
[47] D.B. Sowerby, Chem. Ber. 94 (1961) 2670.
[48] W. Dougill, J. Chem. Soc. (1963) 3211.
[49] W.L.F. Armarego, D.D. Perrin, Purification of Laboratory Chemicals, 4th ed., Elsevier, 1997.
[50] C.H. Perrin, J. Assoc. Off. Agri. Chem. 41 (1958) 758.
[51] G.M. Sheldrick, SHELX-97 Program Package, University of Goettingen, 1997.
[52] G.M. Sheldrick, SHELXTL V 5.1, Bruker AXS GmbH, 1997.
[53] G. te Velde, F.M. Bickelhaupt, S.J.A. van Gisbergen, C. Fonseca Guerra, E.J. Baerends, J.K. Snijders, T. Ziegler, J. Comput. Chem. 22 (2001) 931.
[54] C.F. Guerra, J.K. Snijders, G. te Velde, E.J. Baerends, Theor. Chem. Acc. 99 (1998) 391.
[55] Possibly: list of authors and contributors: E.J. Baerends, J. Autschbach, A. Bérces, F.M. Bickelhaupt, P.M. Boerrigter, L. Cavallo, D.P. Chong, L. Deng, R.M. Dickson, D.E. Ellis, M. van Faassen, L. Fan, T.H. Fischer, C. Fonseca Guerra, S.J.A. van Gisbergen, A.W. Götz, J.A. Groeneveld, O.V. Gritsenko, M. Grüning, F.E. Harris, P. van den Hoek, C.R. Jacob, H. Jacobsen, L. Jensen, G. van Kessel, F. Kootstra, M.V. Krykunov, E. van Lenthe, D.A. McCormack, A. Michalak, J. Neugebauer, V.P. Nicu, V.P. Osinga, S. Patchkovskii, P.H.T. Philipsen, D. Post, C.C. Pye, W. Ravenek, J.I. Rodriguez, P. Ros, P.R.T. Schipper, G. Schreckenbach, J.G. Snijders, M. Solà, M. Swart, D. Swerhone, G. Velde, P. Vernooijs, L. Versluis, L. Visscher, O. Visser, F. Wang, T.A. Wesolowski, E.M. van Wezenbeek, G. Wiesenekker, S.K. Wolff, T.K. Woo, A.L. Yakovlev, T. Ziegler, ADF2008.01, SCM, Theoretical Chemistry, Vrije Universteit, Amsterdam, The Netherlands, http://www.scm.com.
[56] M. Swart, A.W. Ehlers, K. Lammertsma, Mol. Phys. 102 (2004) 2467.
[57] N.C. Handy, A.J. Cohen, Mol. Phys. 99 (2001) 403.
[58] C. Adamo, V. Barone, J. Chem. Phys. 108 (1998) 664.
[59] S. Pohl, B. Krebs, Chem. Ber. 108 (1975) 2934.
[60] M. Calichman, A. Derecskei-Kovacs, C.W. Allen, Inorg. Chem. 46 (2007) 2011.



Scheme 1. Structures of the ligands: H_3Or = orotic acid; 2-meim = 2-methylimidazole.

activities and crystal structures of the orotate complexes of Co(II), Ni(II), Cu(II) and Zn(II) with 2-methylimidazole ligand (Scheme 1).

2. Experimental

2.1. Preparation of the complexes

A solution of orotic acid monohydrate (0.871 g, 5 mmol) in water (50 mL) was added dropwise with stirring at 80 °C to a solution of $Co(CH_3COO)_2{\cdot}4H_2O$ (1.25 g, 5 mmol) (**1**) or $Ni(CH_3COO)_2{\cdot}4H_2O$ (1.24 g, 5 mmol) (**2**) or $Cu(CH_3COO)_2{\cdot}H_2O$ (1.00 g, 5 mmol) (**3**) or $Zn(CH_3COO)_2{\cdot}2H_2O$ (1.09 g, 5 mmol) (**4**) in distilled water (25 mL). The solutions immediately became suspensions and were stirred for 4 h at 60 °C. Then 2-methylimidazole (1.65 g, 20 mmol) for all in water (10 mL) was added dropwise to these suspensions. The clear solutions that formed were stirred for 2 h at 60 °C and then cooled to room temperature. The reddish for (**1**), green for (**2**), light blue for (**3**), colorless for (**4**) crystals that formed were filtered and washed with 10 mL of water and dried in air.

2.2. Materials and measurements

All chemicals used were analytical reagents and were commercially purchased. IR spectra were obtained with a Perkin Elmer 100 FT-IR spectrometer using KBr pellets in the 4000–400 cm^{-1} range. The UV–Vis spectra were obtained for an aqueous solution of the complex (10^{-3} M) with a Shimadzu UV-3150 spectrometer in the range 900–190 nm. Magnetic susceptibility measurements at room temperature were performed using a Sherwood Scientific MXI model Gouy magnetic balance. A Perkin Elmer Diamond TG/DTA Thermal Analyzer was used to record simultaneous TG, DTG and DTA curves in static air atmosphere at a heating rate of 10 °C min^{-1} in the temperature range of 30–1000 °C for **1** and 30–700 °C for **2**–**4** using platinum crucibles.

2.3. Crystallographic analyses

Data collection was performed on a STOE IPDS II image plate detector using Mo Kα radiation (λ = 0.71073 Å). Data collections: Stoe X-AREA [46]. Cell refinement: Stoe X-AREA [46]. Data reduction: Stoe X-RED [46]. The structure was solved by direct-methods using SIR97 [47] and anisotropic displacement parameters were applied to non-hydrogen atoms in a full-matrix least-squares refinement based on F^2 using SHELXL-97 [48]. Molecular drawings were obtained using ORTEP-III [49].

2.4. Antimicrobial activity studies

Escherichia coli W3110, *Pseudomonas aeruginosa* ATCC 27853, *Staphylococcus aureus* ATCC 6535, *Bacillus cereus* ATCC 7064, *Candida albicans* ATCC 10231 and clinical isolate (Methicillin Resistant *S. aureus* (MRSA) – Orthopedy Exuda, *Pseudomonas aeruginosa* – urology–urine isolates, from Ondokuz Mayıs University, Faculty of Medicine) were used for the antimicrobial assays. Antimicrobial activity tests were carried out using the broth dilution method as described by the NCCSL standards [50]. All stock solutions of the orotic acid and the complexes were prepared in dimethylsulfoxide (DMSO, Merck) according to the needed concentrations for experiments.

For the broth dilution method, cultures were grown in 5 mL nutrient broth (Merck) at 37 °C for 18 h in an orbital shaker incubator shaking at 175 rpm. These cultures were used as starter cultures. Initial bacterial concentrations (approximately 5×10^5 cfu/mL) were estimated for the cultures at 600 nm by matching with 0.5 McFarland turbidity standards. Nutrient broth containing microorganisms were transferred 1 mL in test tubes and made twofold serial dilution in nutrient broth from 3000 to 23.4 μg/mL. The compounds were tested in twofold serial dilution; eventually the ranges were narrowed to define more exact values. Growth inhibition was determined by measuring MICs, defined as the lowest concentration in which microbial growth was prevented. As indicated by the lack of turbidity or colour change after 24 h of incubation at 37 °C, represents the mean of at least three determinations. The solvents were also tested for antimicrobial activity. Standard antibiotics (chloramphenicol, oflaxacin, rifampicin, cefuroxime, tetracycline, nystatin) were also tested by disc diffusion method for the cultures at an optical density at 600 nm by matching with 0.5 McFarland turbidity standards (approximately 10^6 cfu/mL). Test strains were spread on solid nutrient agar surfaces using a sterile glass rod. Standard antibiotic discs were placed on the agar surface and were incubated 37 °C for 24 h.

3. Results and discussion

The Co(II), Ni(II) and Cu(II) complexes exhibit magnetic moment values of 4.66, 2.54 and 1.26 BM which corresponds to three, two and one unpaired electrons, respectively, which are consistent with a weak field octahedral geometry as expected. The Zn(II) complex is diamagnetic. All the complexes comprise broad composite bands in the UV region, being due to $\pi \rightarrow \pi^*$ and $n \rightarrow \pi^*$ intraligand transitions of HOr and 2-meim ligands. The λ_{max} value of the absorption band in the spectrum of **1** is 499 nm. This value was assigned to the following d–d transitions, $^4T_{1g} \rightarrow {}^4T_{2g}$. The $^4T_1g \rightarrow {}^4A_{2g}$ and $^4T_{1g} \rightarrow {}^4T_{1g}(P)$ transitions were not observed which are shift to the UV and IR regions, respectively. The UV–Vis spectrum for **2** exhibits three d–d absorption transitions at 888, 638 and 390 nm which support the octahedral geometry. These values were assigned to $^3A_{2g} \rightarrow {}^3T_{2g}$, $^3A_{2g} \rightarrow {}^3T_{1g}$, $^3A_{2g} \rightarrow {}^3T_{1g}$ (P), respectively. The UV–Vis spectrum for **3** exhibits a broad d–d absorption transition centered at 707 nm. This value was assigned to a1 → b1 transition. The colourless Zn(II) complex does not show d–d bands as expected.

The strong and broad absorption bands of ν(OH) vibrations of H_2O in complexes are observed between 3402 and 3361 cm^{-1}. IR spectra of the complexes exhibit a medium intensity and broad band in the 3272–3178 cm^{-1} region which can be attributed to the N–H stretching vibration. The relatively weak two close bands at 2752–2964 cm^{-1} are due to the ν(CH) vibrations. The strong and broad bands appeared in the 1653–1623 and 1488–1382 cm^{-1} regions in all complexes are ascribed to the asymmetric and symmetric stretching vibrations of the coordinated carboxylate groups of the orotate ligand, respectively. Similar absorption values have already been reported earlier for Ni(II) and Co(II)-orotate complexes with imidazole and its derivatives [16,19,33,51] and the positions of these bands have been well described in recently reports [52]. Separation between asymmetric and symmetric stretching frequencies for complexes range from 167 to 141 cm^{-1} is in agreement with monodentate coordination mode for the

Table 1
IR data of the complexes.[a]

Assignment[a]	Co(II)[b]	1	2	3	4
ν(OH)	3544s	3402s, br	3361s, br	3400s	–
νNH_{meim}	3255m	3266m	3268m	3272m	3254sh
νNH_{HOr}	3207m	–	3199sh	3204w	3178br
νCH	3087–2971w	3092sh–2925m	3104sh–2930m	3120sh, 2925w	2930w
$\nu C{=}O_{acid} + \nu C_{(2)}{=}O$	1639s	1642s	1651s	1653s	1651s, br
$\nu C_{(6)}{=}O + \nu C{=}C$	1620s	1623s	1628s	1626s	1628s
$\nu C{=}N$	1483m	1486m	1488s	1485m	1484m
δNH	1427w; 1373m	1398m, 1382m	1399s, 1382m	1399vs	1392s
M–O; M–N	522w; 466w	595w, 481m	576m, 487m	593m	583m, 481m

[a] *Abbreviations*: sh, shoulder; w, weak; m, medium; s, strong; vs, very strong; br, broad.
[b] $[Co(HOr)(H_2O)(4\text{-meim})_3]$ [19].

carboxylate group. In IR spectra of the complexes, $\nu(OH_{acid})$ band at 2500 cm^{-1} in the orotic acid completely disappeared and a new carboxylate band ν(COO) appeared between 1488 and 1382 cm^{-1}, respectively, indicating that the carboxylate group participates in the coordination with the metal ions by deprotonation (Table 1).

3.1. Thermal analyses

3.1.1. $[Co(HOr)(H_2O)_2(2\text{-meim})_2]$ (**1**) and $[Zn(HOr)(H_2O)_2(2\text{-meim})]$ (**4**)

The thermal behaviour of **1** and **4** are quite similar and they show a three stage mass loss (Supplementary Figs. S1 and S2). The first stage between 37 and 199 °C for **1**, 33 and 212 °C for **4** corresponds to the endothermic elimination of two aqua ligands with an experimental mass loss of 9.06% and 11.19% (calc. mass loss 8.71% and 10.66%). The removal of 2-meim ligands occurs in the second stage between 199 and 391 °C for **1**, 212 and 373 °C for **4** with an experimental mass loss of 40.54% and 23.49% respectively (calc. mass loss 39.73% and 24.32%). In the last stage, a strong exothermic peak on the DTA curve (DTA_{max} = 423 and 529 °C, respectively) is associated with decomposition and burning of the orotate ligands. The overall experimental mass losses, 82.92% for **1** and 75.18% for **4**, are in agreement with this stoichiometry. The thermal decomposition products were identified as CoO or ZnO (calc. 81.85% and 75.88%).

3.1.2. $[Ni(HOr)(H_2O)_2(2\text{-meim})_2]$ (**2**)

The complex **2** shows three stages decomposition process (Supplementary Fig. S3). Although the complex is containing aqua ligands, it is stable up to 151 °C. In the first stage, complex **2** starts to lose aqua ligands between 151 and 225 °C with an experimental mass loss of 8.71% (calc. mass loss 9.73%). The second stage is related to the release of two imidazole ligands by giving endothermic effect (found = 41.11, calc. = 39.74%). This type of behaviour of methylimidazole ligands in the *mer*-$[Mn(\mu\text{-}HOr)(H_2O)(2\text{-meim})_2]_n$ [16] and $[Ni(HOr)(H_2O)(4\text{-meim})_3]$ [19] complexes have been reported earlier. In the last extremely exothermic stage between 398 and 474 °C orotate ligand is abruptly burnt (DTA = 454 °C). The total mass loss of all decomposition process is 82.82% (calc. 81.88%) suggest that NiO is the end product.

3.1.3. $[Cu(HOr)(H_2O)_2(2\text{-meim})]$ (**3**)

The complex **3** shows four stages decomposition process (Supplementary Fig. S4). In the first stage, the complex starts to lose one aqua ligand between 37 and 160 °C with an experimental mass loss of 5.65% (calc. 5.36%). The second stage is related to the release of other aqua ligand by giving endothermic effect (found = 6.22, calc. = 5.36 %). The third stage in the temperature range of 246–288 °C related to release of 2-meim ligand (found 23.42, calc. 24.45%, DTA_{max} = 267 °C). In the last extremely exothermic stage between 288 and 458 °C orotate ligand is abruptly burnt (DTA = 423 °C). The total mass loss of all decomposition process is 77.61% (calc. 76.29%) suggest that CuO is the end product.

3.2. Crystal structures

Details of crystal data, data collection, structure solution and refinement are given in Table 2. The molecular structures of **1** and **2** with the atom-numbering scheme are shown in Fig. 1. Selected bond lengths and angles together with the hydrogen bonding geometry are collected in Table 3. The structures of **1** and **2** consist of the *mer*-$[M(HOr)_2(H_2O)_2(2\text{-meim})_2]$ (M = Co(II) and Ni(II)) molecules. Both metal ions are coordinated bidentate orotate ligand thought oxygen atom of carboxylate group and nitrogen atom of pyrimidine ring, two aqua ligands and two 2-methylimidazole ligands. The basal plane of the distorted octahedral is formed by N1, O4, O5 and O6 atoms. The Co–O (average 2.108 (1) Å), Ni–O (average 2.071 (1) Å) and Co–N1 (2.138 (1) Å), Ni–N1 (2.087 (1) Å) bond distances are longer than previously reported values ($[Co(HOr)(H_2O)_4]\cdot 2.5H_2O$ [47], $[Co(HOr)(en)_2](H_2Or)\cdot 5H_2O$ [18] and *mer*-$[Ni(HOr)(H_2O)_2(ata)_2]$ [43]). However these bond distances are similar to the corresponding values found in reported $[Co(HOr)(H_2O)_3]_n$, $[Ni(HOr)(H_2O)_3]_n$ [23] and [Ni(HOr)(bipy)] [53]. Distorted octahedral geometry is completed with two nitrogen atoms by monodentate coordination of two 2-meim ligands (Co1–N3/N5 = 2.164(2)/2.158(2) and Ni1–N3/N5 = 2.127 (2)/2.123 (2) Å).

The crystal packing of **1** and **2** are stabilized through strong intra- and intermolecular hydrogen bonding interactions (Fig. 2a). Each HOr ligand is doubly hydrogen bonded forming DA:AD dimer between the O1, N2 of HOr and the O4 atom of carboxylate group and aqua ligand (O5) [N2···O4 = 2.896 (2) for **1**, 2.882 (2) for **2** and O5···O1 = 2.757 (2) for **1**, 2.736 (2) for **2**] with a pattern $R_2^2(8)$ in Etter's notation [54]. There are also $\pi\cdots\pi$ interaction between the symmetry related 2-meim rings [Cg*A* = N(3)–C(6)–C(7)–N(4)–C(8) and Cg*B* = N(5)–C(10)–C(11)–N(6)–C(12), Cg*A*–CgA^i = 3.8251 (i = $-x$, $-y$, $-z$) and Cg*B*–CgB^i = 3.9814 Å, i = $1-x$, $1-y$, $-z$) (Fig. 2b).

In pentacoordinated systems, the actual geometry of the complex can be described by a structural index parameter τ such that $\tau = \alpha - \beta/60°$, where α and β are the two largest angles ($\alpha > \beta$). Thus, the geometric parameter τ is applicable to pentacoordinated structures as an index of the degree of trigonality, within the structural continuum between trigonal bipyramidal (τ = 1) and square pyramidal (τ = 0). The complex **3** and **4** have τ values of 0.20 for **3** [$\tau = (169.81 - 158.00)/60 = 0.20$] and 0.60 for **4** [$\tau = (164.91 - 128.77)/60 = 0.60$], indicating a distorted square bipyramidal and trigonal bipyramidal geometries, respectively (Fig. 3). The M ion in $[M(HOr)(H_2O)_2(2\text{-meim})]$ (M = Cu(II) and Zn(II)) is coordinated by a bidentate HOr ligand, two coordinated water molecules and one 2-meim ligand [Cu1–N1 = 1.992(2), Cu1–O4 = 2.073(1), Zn1–O4 = 2.083 (2) and Zn1–N1 = 2.066 (2) Å]

Table 2
Crystallographic data and structure refinement parameters for the complexes.

Complexes	**1**	**2**	**3**	**4**
Empirical formula	$C_{13}H_{18}N_6O_6Co$	$C_{13}H_{18}N_6O_6Ni$	$C_9H_{12}N_4O_6Cu$	$C_9H_{12}N_4O_6Zn$
Formula weight	413.26	413.04	335.77	337.60
Crystal system	monoclinic	monoclinic	triclinic	triclinic
Space group	$P2_1/c$	$P2_1/c$	$P\bar{1}$	$P\bar{1}$
a (Å)	8.3165 (4)	8.2609 (5)	7.5760 (6)	7.1751 (5)
b (Å)	14.1580 (4)	14.1719 (6)	8.1422 (6)	8.2451 (6)
c (Å)	15.3992 (7)	15.3190 (9)	11.5213 (9)	11.9655 (8)
α (°)	90	90	69.657 (6)	73.759 (6)
β (°)	102.478 (4)	102.791 (5)	85.372 (6)	87.218 (6)
γ (°)	90	90	77.057 (6)	71.923 (5)
V (Å^3)	1770.35 (13)	1748.93 (17)	649.43 (9)	645.51 (8)
Z	4	4	2	2
μ (mm^{-1})	1.01	1.15	1.71	1.94
D_{calc} (Mg m^{-3})	1.551	1.569	1.717	1.737
Crystal size (mm)	0.35 × 0.30 × 0.23	0.58 × 0.49 × 0.41	0.46 × 0.33 × 0.25	0.37 × 0.28 × 0.14
θ Range (°)	1.98–26.5	1.98–26.5	1.89–26.5	2.71–26.5
Measured reflections	14 984	13 938	7124	6765
Independent reflections	3679	3633	2677	2668
R_{int}	0.025	0.041	0.046	0.047
$R[F^2 > 2\sigma(F^2)]$, $wR(F^2)$	0.028, 0.079	0.028, 0.080	0.030, 0.079	0.034, 0.091
Goodness-of-fit on F^2	1.04	1.07	1.09	1.05
$\Delta\rho_{max}$, $\Delta\rho_{min}$ (e Å^{-3})	0.27; −0.40	0.29; −0.30	0.57; −0.56	0.45; −0.62

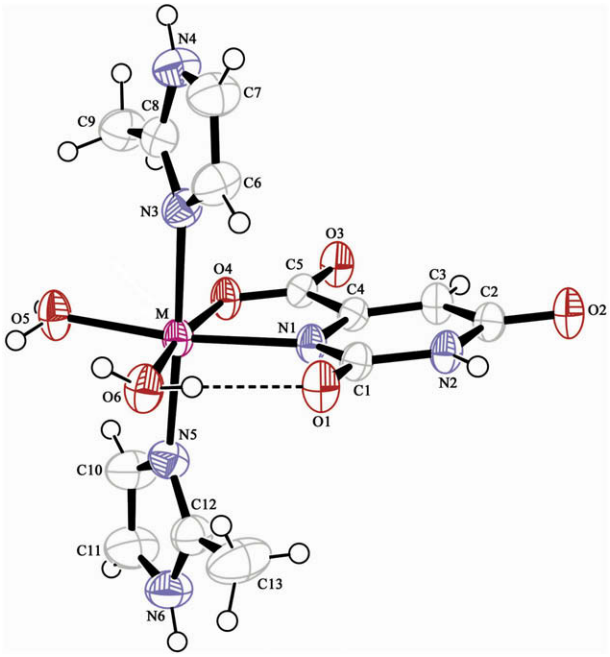


Fig. 1. Ortep III view of **1** and **2** with the atom-numbering scheme (M = Co1 and Ni1).

(Table 4). These distances are found to be similar to those of previously reported complexes [7,18,41,55]. The dihedral angle between the pyrimidine and imidazole rings is 67.65 Å for **3** and 66.79 for **4**. The C5–O4 bond distance (1.260 Å for **3** and 1.251 Å for **4**) is longer than C5–O3 bond distance (1.240 Å for **3** and 1.241 Å for **4**) in HOr ligand due to the coordination of M(II) ion.

The presence of aqua ligands and carboxyl or carbonyl groups make extensive hydrogen bonding interactions in complexes **3** and **4**, which are listed in Table 4. Each of the HOr ligand is doubly hydrogen bonded to corresponding ligands of a neighbouring HOr ligand, forming DA:AD dimer [N2···O2^{i} = 2.830 (**2**) for **3** and 2.897 (**3**) Å for **4**, N2–H2···O2^{i} = 172 for **3** and 170° for **4**, (i) $-x+2$, $-y$, $z+1$ for **3** and $x+2$, $-y$, $-z+1$ for **4**]. These arrangement gives rise

Table 3
Selected bond distances (Å), angles (°) and hydrogen bonding geometries (Å, °) for **1** and **2**.

Bond lengths (Å)			
Complex **1**		Complex **2**	
N1–Co1	2.138 (1)	N1–Ni1	2.0874 (13)
N3–Co1	2.164 (2)	N3–Ni1	2.1272 (15)
N5–Co1	2.158 (2)	N5–Ni1	2.1233 (15)
O4–Co1	2.104 (1)	O4–Ni1	2.062 (1)
Co1–O5	2.105 (1)	Ni1–O5	2.070 (1)
Co1–O6	2.114 (1)	Ni1–O6	2.081 (1)
Angles (°)			
O4–Co1–O5	92.42 (5)	O4–Ni1–O5	91.95 (5)
O4–Co1–O6	171.52 (5)	O4–Ni1–O6	173.61 (5)
O5–Co1–O6	95.83 (5)	O5–Ni1–O6	93.98 (5)
O4–Co1–N1	79.18 (5)	O4–Ni1–N1	80.55 (5)
O5–Co1–N1	170.23 (5)	O5–Ni1–N1	171.01 (5)
O6–Co1–N1	92.76 (5)	O6–Ni1–N1	93.74 (5)
O4–Co1–N5	87.98 (5)	O4–Ni1–N5	88.09 (5)
O5–Co1–N5	88.50 (6)	O5–Ni1–N5	88.86 (6)
O6–Co1–N5	90.28 (6)	O6–Ni1–N5	89.65 (6)
N1–Co1–N5	96.11 (6)	N1–Ni1–N5	95.79 (5)
O4–Co1–N3	90.88 (5)	O4–Ni1–N3	90.98 (5)
O5–Co1–N3	88.54 (6)	O5–Ni1–N3	88.24 (6)
O6–Co1–N3	91.28 (6)	O6–Ni1–N3	91.59 (6)
N1–Co1–N3	86.63 (5)	N1–Ni1–N3	86.95 (5)
N5–Co1–N3	176.78 (6)	N5–Ni1–N3	176.92 (5)
D–H···A	H···*A* (Å)	*D*···*A* (Å)	*D*–H···*A* (°)
*Complex **1***			
N2–H2···O4^{i}	2.04	2.8960 (18)	177
N6–H6C···O2^{ii}	2.10	2.906 (2)	156
N4–H4···O3^{iii}	2.03	2.843 (2)	157
O6–H6B···O1	1.939 (16)	2.7373 (19)	156 (2)
O5–H5B···O2^{iv}	1.858 (17)	2.6689 (18)	166 (2)
O5–H5A···O1^{v}	1.899 (16)	2.7572 (19)	175 (2)
O6–H6A···O3^{vi}	1.888 (17)	2.7065 (18)	169 (2)
*Complex **2***			
N2–H2···O4^{i}	2.02	2.8818 (19)	177
N6–H6C···O2^{ii}	2.09	2.900 (2)	156
N4–H4···O3^{iii}	2.02	2.830 (2)	156
O6–H6B···O1	1.938 (16)	2.7358 (18)	155 (2)
O5–H5B···O2^{iv}	1.851 (17)	2.6661 (18)	166 (2)
O5–H5A···O1^{v}	1.935 (16)	2.7730 (19)	176 (2)
O6–H6A···O3^{vi}	1.906 (18)	2.7150 (17)	165 (2)

Symmetry codes: (i) x, $-y+1/2$, $z+1/2$; (ii) $-x+1$, $y-1/2$, $-z+3/2$; (iii) $-x+1$, $-y+1$, $-z+1$; (iv) $x-1$, $-y+1/2$, $z-1/2$; (v) x, $-y+1/2$, $z-1/2$; (vi) $x-1$, y, z for **1** and **2**.

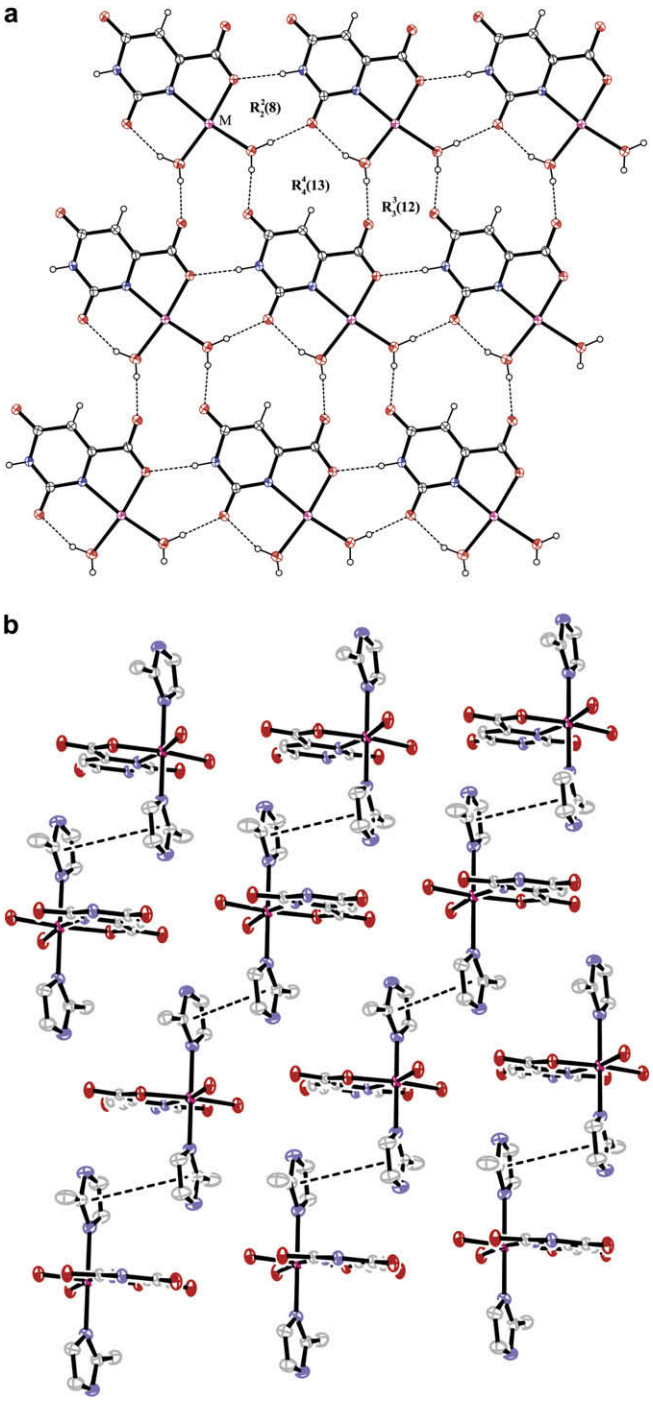


Fig. 2. Part of the crystal structure of **1** and **2**, showing the formation of hydrogen bonding [2-meim ligands are omitted] (a) and π···π interaction [H atoms are omitted] (b).

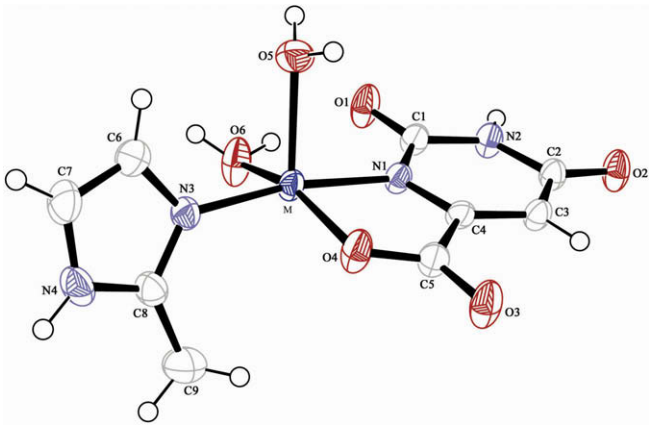


Fig. 3. Ortep III view of **3** and **4** with the atom-numbering scheme (M = Cu1 and Zn1).

Table 4
Selected bond distances (Å), angles (°) and hydrogen bonding geometries (Å, °) for **3** and **4**.

Bond lengths (Å)			
Complex **3**		Complex **4**	
N1–Cu1	1.992 (2)	N1–Zn1	2.066 (2)
N3–Cu1	1.961 (2)	N3–Zn1	2.008 (3)
O4–Cu1	1.973 (2)	O4–Zn1	2.083 (2)
Cu1–O6	1.994 (2)	Zn1–O5	1.988 (2)
Cu1–O5	2.204 (2)	Zn1–O6	2.071 (2)
Angles (°)			
N3–Cu1–O4	90.81 (7)	O5–Zn1–N3	112.7 (1)
N3–Cu1–N1	169.81 (7)	O5–Zn1–N1	128.8 (1)
O4–Cu1–N1	81.50 (6)	N3–Zn1–N1	117.97 (9)
N3–Cu1–O6	92.51 (7)	O5–Zn1–O6	88.22 (9)
O4–Cu1–O6	158.00 (9)	N3–Zn1–O6	97.98 (10)
N1–Cu1–O6	92.20 (7)	N1–Zn1–O6	91.96 (8)
N3–Cu1–O5	94.21 (7)	O5–Zn1–O4	87.61 (9)
O4–Cu1–O5	103.90 (7)	N3–Zn1–O4	97.01 (9)
N1–Cu1–O5	94.13 (7)	N1–Zn1–O4	79.44 (8)
O6–Cu1–O5	97.54 (8)	O6–Zn1–O4	164.91 (9)
D–H···A	H···*A* (Å)	*D*···*A* (Å)	*D*–H···*A* (°)
*Complex **3***			
N2–H2···O2^{i}	1.98	2.830 (2)	172
N4–H4···O3^{ii}	2.02	2.870 (3)	169
N4–H4···O4^{ii}	2.61	3.194 (2)	126
O5–H5A···O1^{iii}	1.961 (19)	2.798 (2)	171 (3)
O5–H5B···O2^{iv}	1.965 (18)	2.783 (2)	170 (4)
O6–H6A···O1	1.83 (2)	2.633 (3)	157 (3)
O6–H6B···O3^{v}	1.884 (19)	2.715 (2)	168 (4)
*Complex **4***			
N2–H2···O2^{i}	2.05	2.897 (3)	170
N4–H4···O3^{ii}	1.98	2.822 (3)	166
O6–H6B···O3^{iii}	1.86 (2)	2.680 (3)	179 (4)
O5–H5B···O1^{iv}	1.89 (2)	2.686 (3)	165 (5)
O5–H5A···O2^{v}	1.89 (2)	2.706 (3)	175 (5)
O6–H6A···O1	1.83 (2)	2.634 (3)	162 (4)

Symmetry codes: (i) $x, -y+1/2, z+1/2$; (ii) $-x+1, y-1/2, -z+3/2$; (iii) $-x+1, -y+1, -z+1$; (iv) $x-1, -y+1/2, z-1/2$; (v) $x, -y+1/2, z-1/2$; (vi) $x-1, y, z$ for **3** and (i) $-x+2, -y, -z+1$; (ii) $-x, -y+1, -z$; (iii) $-x+1, -y+1, -z+1$; (iv) $-x+1, -y, -z+1$; (v) $x, y+1, z$ for **4**.

to eight membered rings that can be described as $R_2^2(8)$ [54] (Fig. 4). These intermolecular hydrogen bonding interactions are very important in the construction of the crystal edifice of complexes **3** and **4**. Similar orotate complexes containing double hydrogen bonding interactions were reported [41–45]. In addition, the layers are interlinked together into a network by π···π interactions between both pyrimidine rings of orotate ligand [Cg*A* = N(1)–C(1)–N(2)–C(2)–C(3)–C(4)] (CgA···CgA^{i}) is 3.863 Å for **3** (i = $1-x$, $1-y$, z) and 4.011 Å for **4** (i = $1-x$, $-y$, $1-z$) and imidazole rings [Cg*B* = N(3)–C(6)–C(7)–N(4)–C(8)], the contact distance of two adjacent aromatic rings (CgB···CgB^{i}) is 3.763 for 3 ($-x$, $2-y$, $-z$) and 3.895 Å for **4** (i = $-x$, $2-y$, $-z$). All of these intermolecular interactions give three-dimensional framework results (Fig. 5).

3.3. Antimicrobial activities

The complexes were tested for their in vitro antimicrobial activities against two Gram-positive bacteria (*S. aureus* and *B. cereus*), two Gram-negative bacteria (*E. coli* and *P. aeruginosa*), one fungi *C. albicans* and two clinical isolate (MRSA and *P. aeruginosa*). For

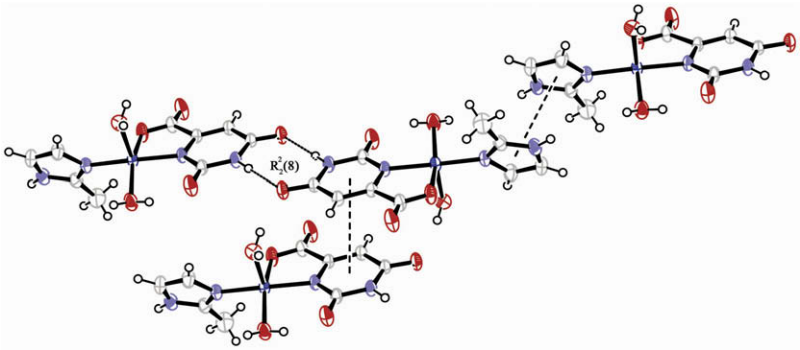


Fig. 4. The π···π and hydrogen bonding interactions of **3** and **4**.

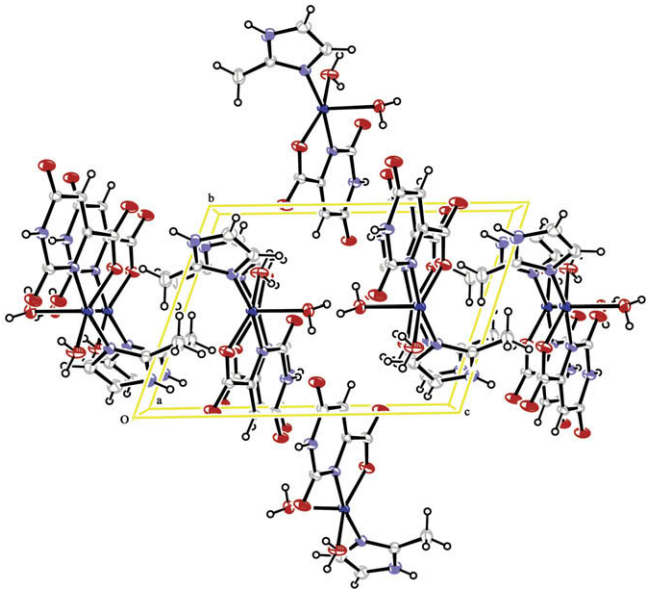


Fig. 5. Packing diagram of **3**.

comparison, the orotic acid and its metal complexes ([Co(HOr)-$(H_2O)_4]\cdot H_2O$ (**5**) [18], $[Ni(HOr)(H_2O)_4]\cdot H_2O$ (**6**) [7], [Cu(HOr)-$(H_2O)_4]\cdot H_2O$ (**7**) [22] and $[Zn(HOr)(H_2O)_4]\cdot H_2O$ (**8**) [7]) were tested for MIC values. The results are presented in Table 5 as minimum inhibitor concentration (MIC) values (μg/mL) which is the minimum concentration to inhibit the growth of bacteria or fungi.

While orotic acid showed activity at higher concentrations on *C. albicans* (2000 μg/mL) and *E. coli* (1375 μg/mL), MICs of other studied microorganism were approximately 1000 μg/mL exception *B. cereus* (750 μg/mL). The antimicrobial activities of **5** and **8** are higher than the orotic acid, **6** and **7** on the all tested microorganisms. While MIC values of **6** according to orotic acid was decreased at *E. coli* (from 1375 to 750 μg/mL), *S. aureus* (from 1000 to 750 μg/mL), *C. albicans* (from 2000 to 750 μg/mL), its activity was increased *P. aeruginosa* (from 1000 to 1500 μg/mL), *B. cereus* (from 750 to 1000 μg/mL), MRSA (from 1000 to 1800 μg/mL) clinical isolate *P. aeruginosa* (from 1000 to 1250 μg/mL). Compared to the orotic acid, the MICs of **7** did not approximately change effective dose on microorganism. Complex **8** had the highest activity on wild type microorganisms between complexes.

The MICs of new complex **1** for strains, gram (−) wild type *E. coli*, *P. aeruginosa*, and clinic isolate *P. aeruginosa* were 800, 700 and 1000 μg/mL respectively, while the growth of *S. aureus*, *B. cereus* and clinic strain MRSA were inhibited more effectively at 400, 400, 250 μg/mL. For **2**, the growth of all the strains with exception MRSA were inhibited at approximately concentration of 1100–1300 μg/mL of the complex, while the MICs for MRSA was 900 μg/mL. **3** had much the same MIC values for all the strains. As can clearly be seen from Table 5, the effective dose of **1**–**4** were, almost without exception, superior to that of metal orotic acid ligands **5**–**8** across all of the bacterial and the fungal strains studied, except for **4** at *S. aureus* and MRSA. As a result, antimicrobial activities were decreased with to be synthesized from **5**–**8** ligands to **1**–**4**. Complex **4** is more effective at both wild type and clinic strain *S. aureus* in comparison to **8** and orotic acids.

1, **4** and **5** have higher activity against Gram-positive than Gram-negative bacteria. In classifying the antibacterial activity as Gram-positive or Gram-negative, it would generally be expected that to be more active against Gram-positive than Gram-negative bacteria because of outer membrane [55]. The **8** has activity on both Gram-positive and Gram-negative bacteria at wild type. The

Table 5
Minimal inhibitory concentration (MIC) values of the complexes against wild type microorganisms (μg/mL) and clinical isolates.

Complexes	Wild type				Clinical isolate		Wild type
	Gram (−)		Gram (+)		Gram(+)	Gram (−)	Eucaryota
	E. coli	*P. aeruginosa*	*S. aureus*	*B. cereus*	Methicillin resistant *S. aureus*	*P. aeruginosa*	*C. albicans*
H_3Or	1375	1000	1000	750	1000	1000	2000
1	800	700	400	400	250	1000	1100
2	1200	1300	1100	1000	900	1100	1300
3	1800	1500	1800	1500	1500	1600	1800
4	800	1500	100	500	100	1300	1500
5	500	500	125	250	125	500	250
6	750	1500	750	1000	1800	1250	1000
7	1000	1000	1500	1000	1375	1250	1000
8	125	250	250	250	500	750	750

Table 6
Antimicrobial assays of same antibiotics against wild type and clinical isolates by disc diffusion method (diameter in mm).

Wild type strains	C (30 μg)	OFX (5 μg)	RD (2 μg)	CXM (30 μg)	TE (30 μg)	N (10 μg)
S. aureus	20	27	27	16	30	–
B. cereus	23	24	9	–	28	–
E. coli	28	30	9	23	27	–
P. aeruginosa	21	17	18	17	20	–
C. albicans	–	–	–	–	–	24
Clinic isolates						
MRSA	22	–	–	–	13	–
P. aeroginosa	–	21	–	–	18	–

C: chloramphenicol, OFX: oflaxacin, RD: rifampicin, CXM: cefuroxime, TE: tetracycline, N: nystatin.

presence of metal ions plays an important role at antimicrobial activity. We think that the disparity at antimicrobial activities between complexes on the microorganisms is change bond characteristics on target area of metal ions because of identical molecular structures of **1**–**8**. Orotic acid and metal complexes have been demonstrated to possess antibacterial and antifungal properties [43,56].

The results of our study indicate that clinic isolates are more resistant than wild type microorganism at standard antibiotics (Table 6). It is a well-known fact that hospital infections are quite important for the public healthy and quite resistant against standard antibiotics. Therefore, there is an urgent demand for new antibiotics and new classes of chemical formula that will efficiently inhibit the growth of pathogenic microorganism. In this study, as part of our efforts into the development of new metal based antimicrobial complexes, new complex **4** could be a new candidate for therapy of *S. aureus* infections and **5** could be candidate for therapy of candidal infection diseases.

Acknowledgment

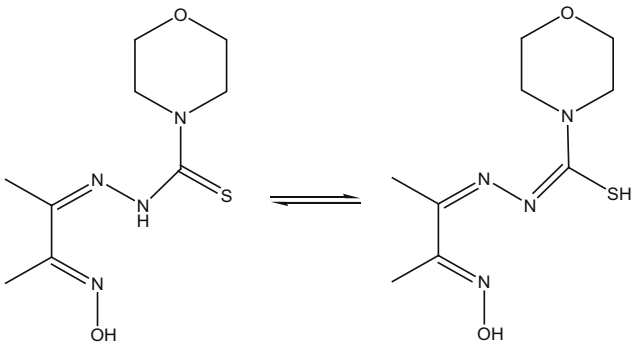
This work was supported by the Eskişehir Osmangazi University by Project No. 200819042.

Appendix A. Supplementary data

Supplementary data associated with this article can be found, in the online version, at doi:10.1016/j.poly.2009.06.052.

References

[1] C. Janiak, Dalton Trans. (2003) 278.
[2] C.N.R. Rao, S. Natarajan, R. Vaidhyanathan, Angew. Chem., Int. Ed. 43 (2004) 1466.
[3] L. Jiang, X. Feng, C. Su, X. Chen, T. Lu, Inorg. Chem. 46 (2007) 2637.
[4] S.L. James, D.M.P. Mingos, X. Xu, A.J.P. White, D.J. Williams, J. Chem. Soc., Dalton Trans. (1998) 1335.
[5] O.Z. Yeşilel, O. Büyükgüngör, Solid State Sci. 9 (2007) 485.
[6] D. Szeleny, J. Sos, Arzneim.– Forsch. 21 (1991) 777.
[7] M. Sabat, D. Zglinska, B. Jezowska-Trzebiatowska, Acta Crystallogr., Sect. B 36 (1980) 1187.
[8] A. Karipides, B. Thomas, Acta Crystallogr., Sect. C 42 (1986) 1705.
[9] T. Solin, K. Matsumoto, K. Fuwa, Bull. Chem. Soc. Jpn. 54 (1984) 3731.
[10] P. Castan, E. Colacio-Rodriguez, A.L. Beauchamp, S. Cros, S. Wimmer, J. Inorg. Biochem. 38 (1990) 225.
[11] J. Leberman, A. Kornberg, E.S. Simms, J. Biol. Chem. 215 (1955) 403.
[12] P. Castan, E. Colacio-Rodriguez, A.L. Beauchamp, S. Cros, S. Wimmer, J. Inorg. Chem. 38 (1990) 225.
[13] A.Q. Wu, F.K. Zheng, X. Liu, G.C. Guo, L.Z. Cai, Z.C. Dong, Y. Takano, J.S. Huang, Inorg. Chem. Commun. 9 (2006) 347.
[14] C.P. Raptopoulou, V. Tangoulis, V. Psycharis, Inorg. Chem. 39 (2000) 4452.
[15] O.Z. Yeşilel, G. Kaştaş, O. Büyükgüngör, Inorg. Chem. Commun. 10 (2007) 936.
[16] O.Z. Yeşilel, H. Erer, A. Mutlu, O. Büyükgüngör, Polyhedron 28 (2009) 150.
[17] M.J. Plater, M.R.J. Foreman, J.M.S. Skakle, R.A. Howie, Inorg. Chim. Acta 332 (2002) 135.
[18] H. Icbudak, H. Ölmez, O.Z. Yesilel, F. Arslan, P. Naumov, G. Jovanovski, A.R. Ibrahim, A. Usman, H.K. Fun, S. Chantrapromma, S.W. Ng, J. Mol. Struct. 657 (2003) 255.
[19] O.Z. Yeşilel, M.S. Soylu, H. Ölmez, O. Büyükgüngör, Polyhedron 25 (2006) 2985.
[20] O.Z. Yeşilel, H. Ölmez, C. Arıcı, Polyhedron 26 (2007) 3669.
[21] A. Karipides, B. Thomas, Acta Crystallogr., Sect. C 42 (1986) 1705.
[22] D. Michalska, K. Hernik, R. Wysokiński, B. Morzyk-Ociepa, A. Pietraszko, Polyhedron 26 (2007) 4303.
[23] D. Sun, R. Cao, Y. Liang, M. Hong, Y. Zhao, J. Weng, Aust. J. Chem. 55 (2002) 681.
[24] S. Bekiroglu, O. Kristiansson, J. Chem. Soc., Dalton Trans. (2002) 1330.
[25] D.A. Köse, B. Zümreoglu-Karan, O. Şahin, O. Büyükgüngör, J. Mol. Struct. 789 (2006) 147.
[26] D. Mentzafos, N. Katsaros, A. Terzis, Acta Crystallogr., Sect. C 43 (1987) 1905.
[27] X. Li, Q. Shi, D. Sun, W. Bi, R. Cao, Eur. J. Inorg. Chem. (2004) 2747.
[28] I. Mutikainen, Finn. Chem. Lett. (1985) 193.
[29] T.T.B. Ha, A.M. Larsonneur-Galibert, P. Castan, J. Jaud, J. Chem. Crystallogr. 29 (1999) 565.
[30] M.S. Soylu, O.Z. Yeşilel, B. Karabulut, O. Büyükgüngör, Polyhedron 28 (2009) 2487.
[31] O.Z. Yeşilel, F. Tezcan, H. Ölmez, H. Paşaoğlu, O. Büyükgüngör, Z. Anorg. Allg. Chem. 631 (2005) 2497.
[32] A. Bulut, H. İçbudak, O.Z. Yeşilel, H. Ölmez, O. Büyükgüngör, Acta Crystallogr., Sect. E 59 (2003) m736.
[33] O.Z. Yeşilel, H. Olmez, C. Arıcı, Acta Crystallogr., Sect. C 63 (2007) m240.
[34] O.Z. Yeşilel, H. Paşaoğlu, K. Akdağ, O. Büyükgüngör, Z. Anorg. Allg. Chem 633 (2007) 1731.
[35] O.Z. Yeşilel, H. Ölmez, I. Uçar, A. Bulut, C. Kazak, Z. Anorg. Allg. Chem. 631 (2005) 3100.
[36] O.Z. Yeşilel, K. Akdağ, H. Paşaoğlu, O. Büyükgüngör, Z. Naturforsch. 62b (2007) 818.
[37] I. Ucar, A. Bulut, O.Z. Yesilel, H. Ölmez, O. Büyükgüngör, Acta Crystallogr., Sect. C 60 (2004) m563.
[38] O.Z. Yeşilel, E. Şahin, Z. Anorg. Allg. Chem. 633 (2007) 1087.
[39] O.Z. Yeşilel, A. Mutlu, C. Öğretir, O. Büyükgüngör, J. Mol. Struct. 889 (2008) 421.
[40] H. Ölmez, H. İçbudak, O.Z. Yeşilel, C. Arıcı, D. Ülkü, Z. Kristollg. 219 (2004) 300.
[41] O.Z. Yeşilel, H. Paşaoğlu, K. Akdağ, O. Büyükgüngör, Polyhedron 26 (2007) 2761.
[42] O.Z. Yeşilel, H. Ölmez, H. Içbudak, O. Büyükgüngör, Z. Naturforsch. 60b (2005) 1138.
[43] O.Z. Yeşilel, N. Dege, C. Darcan, O. Büyükgüngör, Z. Naturforsch. 62b (2007) 1590.
[44] O.Z. Yeşilel, I. Uçar, A. Bulut, H. Ölmez, O. Büyükgüngör, Z. Naturforsch. 61b (2006) 147.
[45] O.Z. Yeşilel, H. Paşaoğlu, K. Akdağ, O. Büyükgüngör, Z. Anorg. Allg. Chem. 633 (2007) 1731.
[46] Stoe & Cie, X-AREA (Version 1.18), X-RED32 (Version 1.04), Stoe & Cie, Darmstadt, Germany, 2002.
[47] A. Altomare, M.C. Burla, M. Camalli, G.L. Cascarano, C. Giacovazzo, A. Guagliardi, A.G.G. Moliterni, G. Polidori, R. Spagna, J. Appl. Crystallogr. 32 (1999) 115.
[48] G.M. Sheldrick, SHELXS97, University of Göttingen, Germany, 1997.
[49] L.J. Farrugia, J. Appl. Crystallogr. 30 (1997) 565.
[50] Clinical and Laboratory Standards Institute, Methods for dilution antimicrobial susceptibility tests for bacteria that grow aerobically; approved standard, 7th ed. CLSI document M7–A7. Clinical Laboratory Standards Institute, Wayne, PA, 2006.
[51] O.Z. Yeşilel, H. Ölmez, H. İçbudak, J. Therm. Anal. Calorim. 89 (2007) 555.
[52] A. Hernanz, F. Billes, I. Bratu, R. Navarro, Biopolymers 57 (2000) 187.
[53] L. Xing, C. Rong, S.D. Fong, H.M. Chun, Chinese J. Struct. Chem. 21 (2002) 374.
[54] M.C. Etter, J.C. MacDonald, J. Bernstein, Acta Crystallogr., Sect. B 46 (1990) 256.
[55] A.R. Mc Cutcheon, S.M. Ellis, R.E.W. Hancock, G.H.N. Towers, J. Ethnopharmacol. 37 (1992) 213.
[56] P. Ruasmadiedo, J.C. Badagancedo, E.G. Fernandez, D.G. Dellano, C.G. Delos Reyes Gavilan, J. Food Protect. 59 (1996) 502.



Scheme 1. Thione–thiol tautomerism.

In course of this investigation, we further observed that the reaction of diacetylmonoxime with morpholine N-thiohydrazide in ethanol under reflux in absence of any metal ion for a longer period of time (16 h) afforded a zwitterionic nitrogen–sulfur heterocyclic compound, N-(3,4-dimethyl-1,2,5-thiadiazol-2-ium-2-yl)morpholine-4-carbothioate. This paper also records the results of this investigation (Scheme 2).

2. Experimental

2.1. Materials and physical measurements

The solvents and chemicals were purified and dried before use by standard procedures. Diacetylmonoxime (damnx) was purchased from Aldrich and used as received and morpholine N-thiohydrazide (mth) was prepared by literature method [36,37]. $[Zn(OAc)_2]\cdot 2H_2O$ was purchased from SRL Mumbai, India and used as received. The elemental analyses were carried out at the Regional Sophisticated Instrumentation Center, Central Drug Research Institute, Lucknow, India. The electronic spectrum was recorded on a Simadzu UV-1601 spectrophotometer and infrared spectral data were collected (KBr disc) on a Perkin–Elmer L120-000A spectrophotometer and NMR spectra were recoded at Indian Institute of Chemical Biology, Kolkata, India. The molar conductance was measured using an Elico CM-180 conductivity bridge in double distilled water (10^{-3} M).

2.2. Synthesis

2.2.1. Nitrogen–sulfur heterocyclic (dtmc) (**5**)

Diacetylmonoxime (0.5 g, 0.005 mol) was treated with an ethanolic solution (50 ml) of morpholine N-thiohydrazide (0.8 g, 0.005 mol) containing few drops of water under reflux for 16 h. The light yellow colored solution on slow evaporation gave a light yellow compound, which was filtered off, washed with cold chloroform and dried in *vacuo*. Finally the compound was re-crystallized from chloroform. Light-yellow crystals suitable for single crystal X-ray diffraction were obtained.

M.p 254 °C Yield, 0.58 g, (45%). ^{1}H NMR ($CDCl_3$, 300 MHz, δ ppm): CH_3(singlet) (2.51, 2.28 ppm), N–CH_2 (singlet) 3.17 ppm, O–CH_2 (singlet) 3.60 ppm. ^{13}C NMR ($CDCl_3$, 300 MHz, δ ppm) 152.82 (C_7), 147.90 (C_6), 47.57 (C_1), 66.82 (C_2), 15.48 (C_8), 12.40 (C_9), 179.11 (C_5). IR (KBr pellet) ν_{max} (cm^{-1}) 1589 (C_7=N_4), 1569 (C_6=N_3), 772 (C_5–S_1), 1035 (N_3–N_2). λ_{max}/nm(ε/M^{-1} cm^{-1}) ($CHCl_3$) 238 (5970), 260 (4555). *Anal.* Calc. for $C_9H_{14}N_4OS_2$: C, 41.84; H, 5.46; N, 21.69. Found C, 41.71; H, 5.42; N, 21.49%.

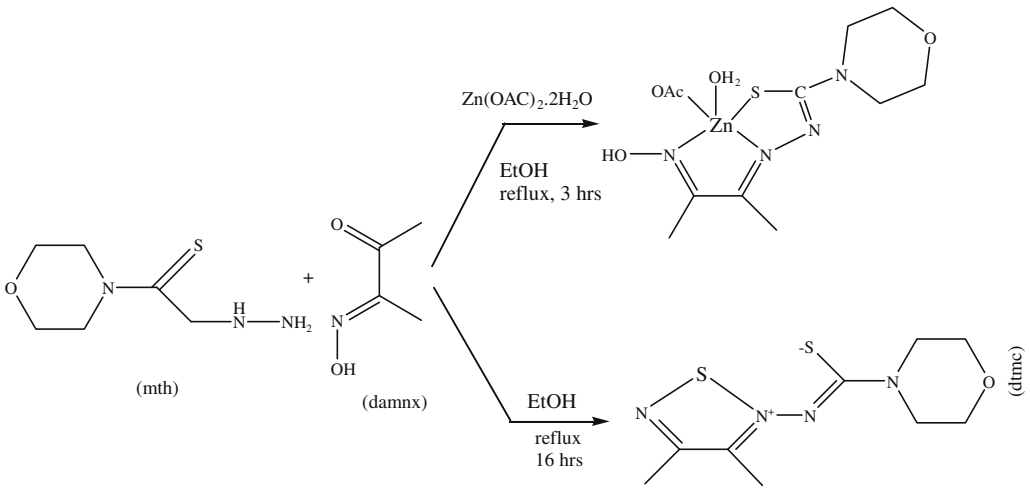
2.2.2. $[Zn(Hdammthiol)(OAc)(H_2O)]\cdot H_2O$

The mixture of diacetylmonoxime (0.5 g, 0.005 mol) and morpholine N-thiohydrazide (0.8 g, 0.005 mol) was heated under gentle reflux in the presence of $[Zn(OAc)_2]\cdot 2H_2O$ (1.095 g, 0.005 mol) in ethanol (50 ml) for 3 h. The yellow colored compound thus formed, was re-crystallized from chloroform. Crystals suitable for single crystal X-ray diffraction were obtained.

Yield 1.58 g (75%). M.p. 285 °C ^{1}H NMR ($CDCl_3$, 300 MHz, δ ppm) CH_3 [2.33 (singlet), 2.04 ppm(singlet)], N–CH_2 (singlet) 3.47 ppm, O–CH_2 (singlet) 3.89 ppm, OH_2 (co-ordinated) 7.27 ppm (singlet), OH_2 (lattice) 2.2 ppm (singlet). ^{13}C NMR ($CDCl_3$, 300 MHz, δ ppm) 151.47 (C_7), 147.73 (C_6), 47.5 (C_1), 66.46 (C_2), 15.03 (C_8), 11.99 (C_9), 180.53 (C_5). IR (KBr pellet) ν_{max} (cm^{-1}) 1608 (C_7=N_4), 1570 (C_6=N_3), 756 (C_5–S_1), 1027 (N_3–N_2), 948 (N_4–O_5) and 2990–3264 (O_5–H_3, oxime). λ_{max}/nm(ε/M^{-1} cm^{-1}) ($CHCl_3$) 242 (6490), 322 (5930), 392 (1280) and 480 (720) (shoulder). *Anal.* Calc. for $C_{11}H_{20}O_5N_4SZn$: C, 32.72; H, 5.49; N, 13.88; Zn, 16.20. Found: C, 32.31; H, 5.19; N, 14.46; Zn, 16.91%. Λ_M = 14.9 Ω^{-1} cm^2 mol^{-1}.

2.3. X-ray crystal structure and refinement

Single crystal X-ray diffraction measurement of the Zn-complex and the S–N heterocyclic compound was carried out on a Brüker-AXS APEX CCD diffractometer by ω-scan method with a graphite-monochromated Mo Kα radiation (k = 0.71073 Å) at 295(2) K. The structure was solved by direct methods with SHELXS97 [38]



Scheme 2. Synthetic pathway for the preparation of the compounds.

and refined by full matrix least-square procedure based on F^2 using SHELXL97 program [38]. Crystal data and structure refinement parameters are summarized in Table 1. The data-set was treated with SADABS absorption corrections based on redundant multi-scan data [38]. All hydrogen atoms were treated as idealized contributions. Structure factors are contained in the SHELXTL 6.12 program library [38]. Graphics were obtained with ORTEP 3 for Windows at the 50% probability level [39,40]. Additional figures were drawn with PLATON for Windows [41,42].

3. Results and discussion

The reaction of morpholine N-thiohydrazide with diacetylmonoxime under reflux (16 h) afforded a light yellow crystalline compound. Single crystal X-ray diffraction and other analytical data show that the product is a zwitterionic nitrogen–sulfur heterocyclic compound, N-(3,4-dimethyl-1,2,5-thiadiazole-2-ium-2-yl)morpholine-4-carbothioate (dtmc). Although *in situ* reaction of the above components in the presence of $[Zn(OAc)_2]\cdot 2H_2O$ in stoichiometric ratios in ethanol under gentle reflux yielded a light yellow compound, $[Zn(Hdammthiol)(OAc)(H_2O)]\cdot H_2O$, where Hdammthiol is the mono anion of the thiol form H_2dammthiol (Scheme 1). The schematic representation of the formation of nitrogen–sulfur heterocyclic compound is shown below in Scheme 3.

The probable mechanism for the formation of the zwitterionic nitrogen–sulfur heterocyclic compound is given in Scheme 3. The acid hydrolysis of morpholine N-thiohydrazide produces hydrazide and H_2S which protonates the morpholine N-thiohydrazide to form the imminium salt (**1a**). The Schiff base (**2**) (formed by the reaction of diacetylmonoxime and morpholine N-thiohydrazide) in presence of H_2S is converted to 3,4-dimethyl-1,2,5-thiadiazole (**3**) and morpholine-4-carbothioamide (**4**) [43,44]. The thiadiazole in turn reacts with the imminium salt (**1a**) to yield finally zwitterionic nitrogen–sulfur heterocyclic compound, N-(3,4-dimethyl-1,2,5-thiadiazol-2-ium-2-yl)morpholine-4-carbothioate(**5**)

3.1. Structure of the nitrogen–sulfur heterocyclic compound (*5*)

The perspective view of the nitrogen–sulfur heterocyclic compound together with atom-numbering scheme is shown in Fig. 1 and the geometric parameters are given in Table 2. The structure shows that the nitrogen–sulfur heterocyclic compound is in zwitterionic form. The bond lengths of N(2)–C(5) [1.336(2) Å] and N(3)–C(6) [1.337(2) Å] are little larger than N(4)-C(7) [1.319(2) Å] bond. This lengthening of N-C bond lengths may be due to delocalization of π-bonded electron. All other inter atomic distances are normal. The morpholine ring exists in a chair conformation.

The C(5)–S(1) bond distance of the heterocyclic compound is 1.7033 (19) Å. This bond distance is shorter than a C–S single bond (1.81 Å) but longer than a C–S double bond (1.62 Å), suggesting partial double bond character in the compound [46,47]. This lengthening of bond distance is possibly due to resonance stabilization.

The heterocyclic compound possesses a short non-bonded $S^-\cdots S$ contact with the distance of 2.738 Å. This contact may arise due to nucleophilic approaching of S^- in the N(3)–S(2)–N(4) plane along posterior extension of N(4) → S(2) or N(3) → S(2) bond, which is interpreted as an interaction of S^- with σ^* orbital of N(4) → S(2) or N(3) → S(2) bonds [45].

In the nitrogen–sulfur heterocyclic compound, the adjacent mononuclear units are locked by C(9)–H(9B)···O(1) hydrogen bonding along a axis by the formation of 1D supramolecular chain. The H(9B)···O(1)[a] ($a = 1 + x, y, z$) distance is 3.456(3) Å and C(9)–H(9B)···O(1) angle is 174°. This 1D chain is further extended to two dimensional supramolecular sheet by face-to-face π–π interactions along b axis. The Cg···Cg distance (Cg is the centroids of the interacting rings) is 4.260(3)[b] Å and the dihedral angle is 1° ($b = 1 - X, -1/2 + Y, 1/2 - Z$). The molecules are arranged in an offset manner to maximize such interactions and generate a 2D supramolecular sheet along *ab* plane (Fig. 2). The disposition of the adjacent sheets is shown in Fig. 3.

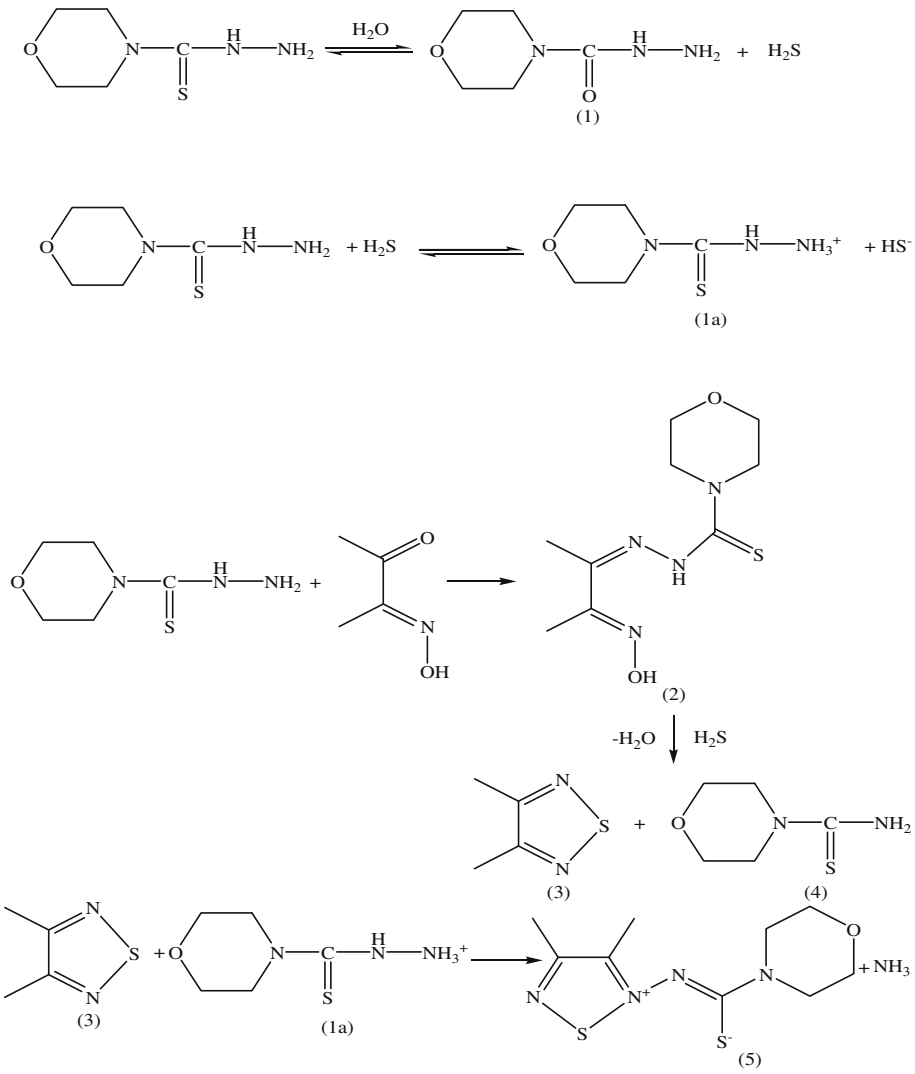
3.2. Structure of the zinc complex

Representations of the X-ray crystal structure of the $[Zn(Hdammthiol)(OAc)(H_2O)]\cdot H_2O$ complex is shown in Fig. 4 and a selection of bond lengths are given in Table 2. The metal ion is contained in geometrically similar distorted square pyramidal environment ($\tau = 0.05$) [48]. The distortion of the complex from idealized geometry is most likely caused by ligand constraints. The O(2)–Zn–N(3) (152.96(8)°) angle would remain approximately linear for both idealized sq pyr geometry, lying in the basal plane of the square pyramid.

The oxime nitrogen, azomethine nitrogen, deprotonated thiol sulfur of Hdammthiol and acetato oxygen defines the equatorial plane of the square pyramid while the axial position is occupied by oxygen (O4) of coordinated water molecule. The zinc ion is 0.3766 (8) Å off the basal plane towards the O(4). The two Zn–O distances of the $[Zn(Hdammthiol)(OAc)(H_2O)]\cdot H_2O$ which are

Table 1
Crystallographic data and structure refinement parameters for sulfur–nitrogen heterocyclic compound and zinc complex.

	(dtmc) (**5**)	$[Zn(Hdammthiol)(H_2O)(OAc)]\cdot H_2O$
Empirical formula	$C_9H_{14}N_4OS_2$	$C_{11}H_{22}N_4O_6SZn$
Formula weight	258.36	403.76
Crystal system	monoclinic	triclinic
Space group	$P2(1)/c$	$P\bar{1}$
a (Å)	12.457(7)	7.9322(13)
b (Å)	7.020(4)	10.3348(17)
c (Å)	14.358(8)	11.1953(19)
α (°)	90	91.579(3)
β (°)	114.315(7)	100.778(2)
γ (°)	90	105.568(2)
V (Å^3)	1144.3(11)	865.6(2)
Z	4	2
T (K)	120(2)	298(2)
μ (Mo Kα) (mm^{-1})	0.450	1.573
Data collected	6159	9752
Unique data (R_{int})	2528 (0.0242)	3891 (0.0169)
Final R indices ($I > 2\sigma(I)$)	0.0369	0.0315
Goodness-of-fit (GOF) (S)	1.014	1.004



Scheme 3. Schematic representation of the formation of dtmc (**5**).

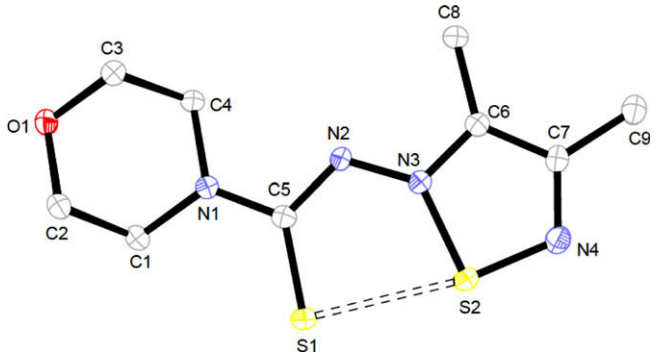


Fig. 1. ORTEP drawing of the nitrogen–sulfur heterocyclic compound with the $S^{-}\cdots S$ contact and the atom labeling scheme, and with 50% probability.

slightly different, are the shortest of the five coordinating bond lengths. Significantly shorter bond lengths show that axial ligation is stronger to the softer water O-donor than acetate-O. The deprotonation of the ligands results in extensive delocalisation of charge and as a consequence the C–S bond length (1.7459(18) Å) are much closer in length to a C–S single bond (1.82 Å), which has partial double bond character [46,47]. The Zn–N(3) (azomethine) distance [2.0985(16) Å] is slightly shorter than Zn–N(4) (oxime) distance [2.1901(16) Å]. This shortening of C=N distance may be due to intramolecular hydrogen bonding.

Table 2
Selected bond lengths (Å) and bond angles (°) of sulfur–nitrogen heterocyclic compound and the zinc complex.

Bond lengths		Bond angels	
*dtmc (**5**)*			
N(2)–C(5)	1.336(2)	C(5)–N(2)–N(3)	118.16(14)
N(3)–C(6)	1.337(2)	C(6)–N(3)–S(2)	109.69(12)
N(3)–S(2)	1.7615(16)	N(2)–N(3)–S(2)	131.67(12)
N(4)–C(7)	1.319(2)	C(7)–N(4)–S(2)	113.16(12)
N(4)–S(2)	1.6316(18)	N(4)–S(2)–N(3)	91.95(8)
S(1)–C(5)	1.7033(19)	N(1)–C(5)–S(1)	122.18(13)
[Zn(Hdammthiol)(H_2O)(OAc)]·H_2O			
Zn–O(2)	2.0034(15)	O(2)–Zn–O(4)	102.68(8)
Zn–O(4)	2.0265(16)	O(2)–Zn–N(3)	152.96(8)
Zn–N(3)	2.0985(16)	O(4)–Zn–N(3)	103.73(7)
Zn–N(4)	2.1901(16)	O(2)–Zn–N(4)	99.11(6)
Zn–S(1)	2.3678(6)	O(4)–Zn–N(4)	93.47(7)
S(1)–C(5)	1.7459(18)	N(3)–Zn–N(4)	73.60(6)
N(2)–C(5)	1.324(2)	O(2)–Zn–S(1)	96.48(4)
N(3)–C(6)	1.286(2)	O(4)–Zn–S(1)	108.14(5)
N(4)–C(7)	1.277(3)	N(3)–Zn–S(1)	80.77(4)
		N(4)–Zn–S(1)	149.79(5)

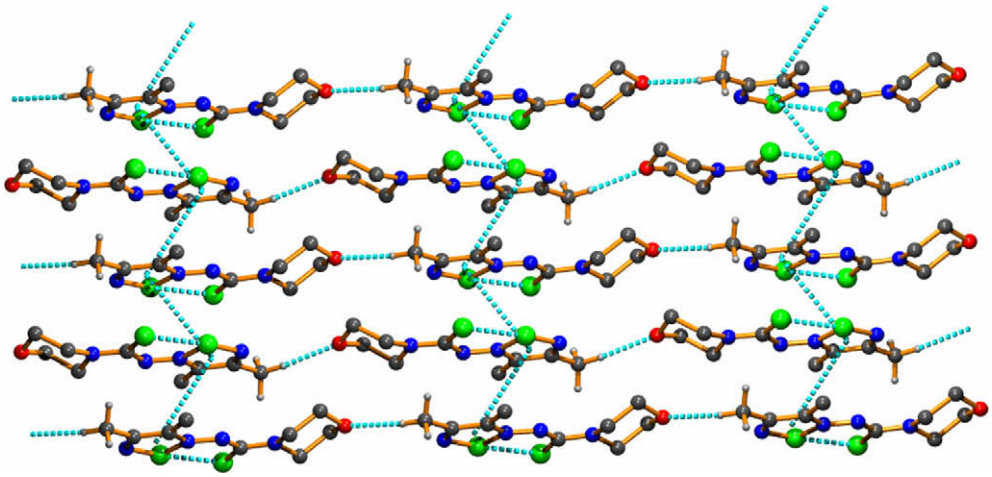


Fig. 2. Two dimensional supramolecular sheet of the heterocyclic compound (**5**) along the *ab* plane.

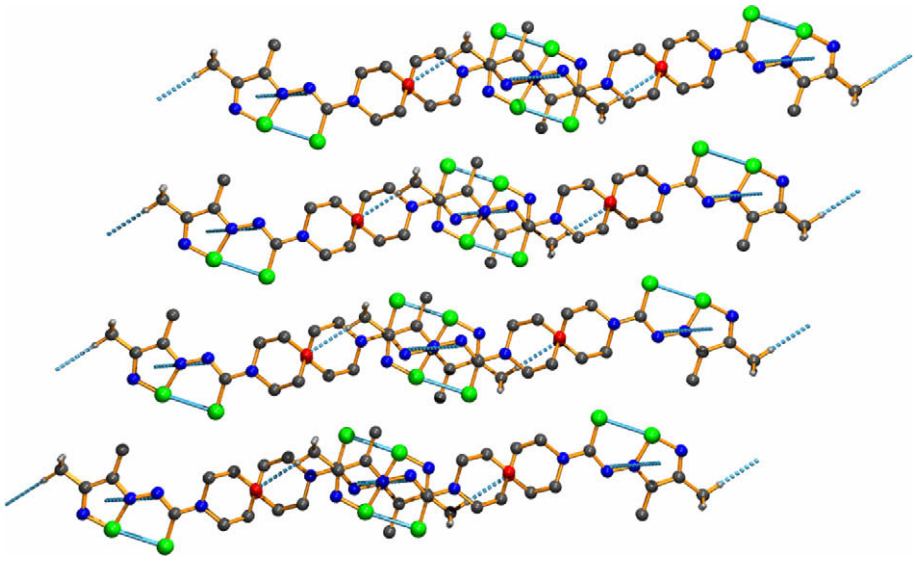


Fig. 3. A perspective view of the disposition of adjacent sheets of the nitrogen–sulfur heterocycle compound (**5**).

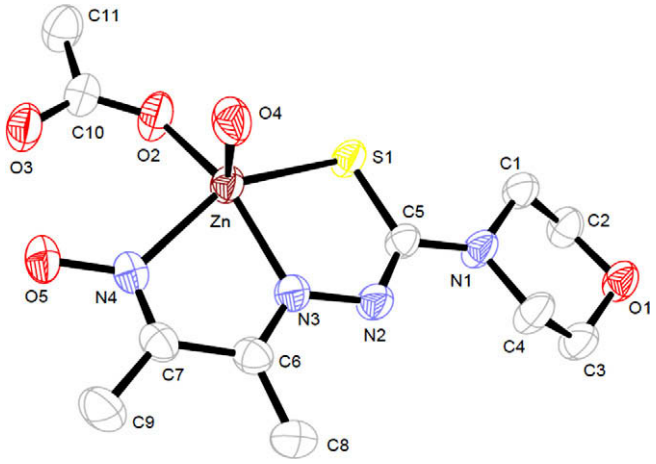


Fig. 4. Molecular drawing of [Zn(Hdammthiol)(OAc)(H_2O)] with atom labeling scheme and anisotropic displacement ellipsoid depicted at 50% probability.

Structure of zinc complex displays some interesting hydrogen bonding network. The two hydrogen atoms of coordinated water molecule form one dimensional hydrogen bonding network diagonally to *ab* plane (Fig. 5). The H(1) of coordinated water molecule is hydrogen bonded to morpholinic oxygen O(1) while H(2) is hydrogen bonded to acetate oxygen O(3). The H(2)···O(3)^{c} (1.87(3) Å, $c = 2 - x,\ 2 - y,\ 2 - z$) distance is slightly shorter than the H(1)···O(1)^{d} (2.18(3) Å, $d = 1 - x,\ 1 - y,\ 1 - z$) distance.

3.3. ^{1}H NMR, ^{13}C NMR and IR spectra

The following differences can be drawn from the comparison between the nitrogen–sulfur heterocyclic compound and the Zn-complex based on their spectroscopic characterization data: (a) the small differences in the carbon resonance in the ^{13}C NMR spectrum between the heterocycle and the zinc complex may be due to some conformational change of the morpholine ring [49], (b) the lowering in the δ values of C6 and C7 in the Zn-complex compared to that of heterocycle suggest the bonding to the Zn atom through N(4) and N(3) attached with C6 and C7, (c) the ν(C=S) of the thioketo form of the ligand (HL^{1}) generally absorbs at around 800 cm^{-1} in the infrared spectrum [50], which in the Zn-complex is absent, instead a new band around 756 cm^{-1} was observed, assignable to ν(C–S), suggesting thereby the coordination of Zn(II) ion through

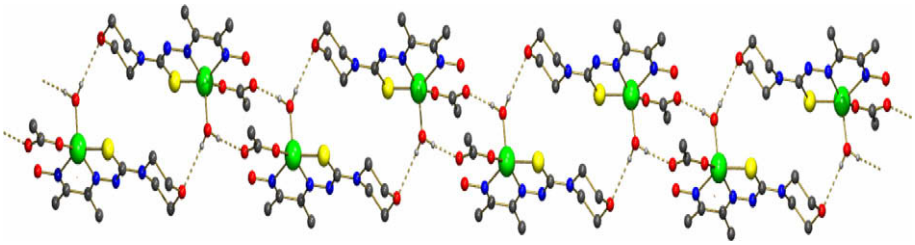


Fig. 5. 1D hydrogen bonding chain of [Zn(Hdammthiol)(OAc)(H_2O)] diagonal to the *ab* plane.

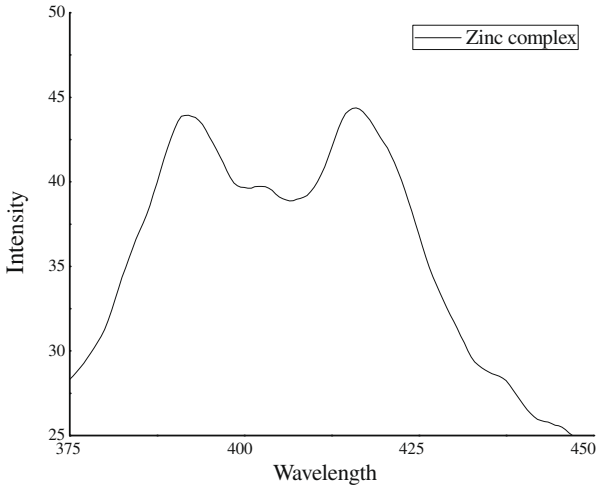


Fig. 6. Emission spectra of a 10^{-6}M solution of [Zn(Hdmmthiol)(H_2O)(OAc)]·H_2O in $CHCl_3$, λ_{ex} = 322 nm.

thiol sulfur *via* deprotonation [51]. The *ν*(C=S) band of heterocyclic compound is observed at 772 cm^{-1}.

The ^1H NMR spectra for the nitrogen–sulfur heterocyclic compound (**5**) does not show any chemical shift due to oxime –OH and –SH proton in $CDCl_3$. Two singlets one at *δ* 2.50 ppm and another at 2.28 ppm may tentatively be assigned to the two sets of methyl protons of (**5**) [52]. The chemical shifts of N–CH_2 (4H) and O–CH_2 (4H) of the morpholine ring are observed at *δ* 3.17 ppm (singlet) and *δ* 3.60 ppm (singlet), respectively [53].

The methyl protons of the Zn(II) complex are observed at *δ* = 2.33 ppm (singlet) and 2.04 ppm (singlet) [54] while for the methylene protons {N–CH_2 (4H) and O–CH_2 (4H)} of the morpholine ring at *δ* = 3.47 ppm (singlet) and 3.89 ppm (singlet), respectively [53]. The zinc complex also exhibits peaks at 7.27 ppm (broad singlet) and 2.2 ppm (singlet) for coordinated and lattice water, respectively [54,55].

The ^{13}C NMR spectrum of (**5**) shows seven signals due to the presence of nine carbon atoms. Two signals at 152.82 ppm and 147.90 ppm are due to carbon atom of –C=N–S and –C=N–N group of the five member ring. The signal at 179.11 ppm may be due to carbon atom of N=C–S^-. The other signals of the heterocyclic compound at 47.57, 66.82, 15.48 and 12.40 are due to C(1), C(2), C(8) and C(9), respectively [49,56].

The zinc(II) complex shows nine signals in ^{13}C NMR spectra. The extra two signals are due to the presence of acetate group in the complex. The signals at 151 ppm and 147.73 ppm are due to carbon atom of –C=N–O and –C=N–N groups. The signal at 180.53 ppm may be due carbon atom of N=C–S–Zn. The other signals of the zinc complex are at 47.5, 66.46, 15.03 and 11.99 are due to C(1), C(2), C(8) and C(9), respectively [49,56]. The small differences in the carbon resonances in the heterocyclic and the zinc complex may due to conformational change of morpholine ring [57].

3.4. Luminescence spectrum of zinc complex

In the electronic spectra of the zinc complex, recorded in chloroform solution, an absorption band in the range 320–392 nm was observed, which may be associated with a $\pi \rightarrow \pi^*$ transition originating mainly in the azomethine chromophore (imine $\pi \rightarrow \pi^*$ transition). Since Zn^{2+} ion has no unoccupied valence electron orbitals, therefore does not exhibit fluorescent characteristics. The zinc complex, [Zn(Hdammthiol)(OAc)(H_2O)]·H_2O shows two intense peaks at about 392 and 416 nm in the chloroform solution at room temperature when excited at 322 nm (Fig. 6) which may be interpreted as the intraligand fluorescence and (π–π^*) phosphorescence [58]. The ligand under influence of Zn^{2+} ion forms a rigid chelate ring (Fig. 4). When irradiated under an ultraviolet light, the ligand absorbs the light energy and transition occurs. So, the emission of complex in $CHCl_3$ at 298 K (λ_{max} = 322 nm) is dominated by the intraligand fluorescence of the thiohydrazone ligand.

4. Conclusion

Heterocycles containing sulfur and/or nitrogen atoms are useful as components of functional materials since heteroatoms in their rings are helpful to stabilize ions or ion-radical species, and extended π-conjugation decreases Coulombic repulsion. In addition, intermolecular interactions caused by heteroatom contacts can be expected to form novel molecular assemblies. Here in this paper we focused on reaction of diacetylmonoxime with morpholine N-thiohydrazide in absence and in presence of metal ion. The reaction of diacetylmonoxime with morpholine N-thiohydrazide under refluxing (16 h) condition in ethanol afforded zwitterionic nitrogen–sulfur heterocyclic compound, N-(3,4-dimethyl-1,2,5-thiadiazole-2-ium-2-yl)morpholine-4-carbothioate (dtmc) with non-bonded S···S interaction. This heterocyclic compound forms 2D supramolecular sheet *via* C–H···O and π···π interactions. A suitable mechanism has been proposed for the formation of heterocyclic compound. However, reaction of this two components in presence of [$Zn(OAc)_2$]·$2H_2O$ in ethanol yielded a zinc complex, [Zn(Hdammthiol)(H_2O)(OAc)]·H_2O. The 1D supramolecular chain diagonally to *ab* plane has been formed in this molecule also by O–H···O hydrogen bonding. The zinc complex shows both intraligand fluorescence and π–π^* phosphorescence in chloroform solution at room temperature.

Supplementary data

CCDC 721752 and 721753 contain the supplementary crystallographic data for nitrogen–sulfur heterocyclic compound (dtmc) and [Zn(Hdammthiol)(H_2O)(OAc)]·H_2O. These data can be obtained free of charge via http://www.ccdc.cam.ac.uk/conts/retrieving.html, or from the Cambridge Crystallographic Data Centre, 12

Union Road, Cambridge CB2 1EZ, UK; fax: (+44) 1223-336-033; or e-mail: deposit@ccdc.cam.ac.uk.

Acknowledgements

One of us (K.D.) is thankful to the U.G.C. (New Delhi) for Emeritus Fellowship and financial grant. We are also thankful to The Regional Sophisticated Instrumentation Center, Central Drug Research Institute, Lucknow for elemental analysis and Indian Institute of Chemical Biology, Kolkata for NMR data, respectively. We are indebted to the Department of Science and Technology, Govt. of India for donation of Spectrophotometers (UV–Vis and IR) in a Scheme of Funding for Improvement under Science and Technology. We are also thankful to Dr. K. Ghosh and Prof. S.C. Chattopadhyay, Department of Chemistry, University of Kalyani, India for useful discussions.

References

[1] X. Tai, X. Yin, Q. Chen, M. Tan, Molecule 8 (2003). and references cited therein.
[2] M. Liu, R.G. Xiong, X.Z. You, Y.J. Liu, K.K. Cheung, Polyhedron 15 (1996) 565.
[3] S.S. Djebbar, B.O. Benali, J.P. Deloume, Trans. Met. Chem. 23 (1998) 443.
[4] Y.J. Hamada, IEEE Trans. Electron Dev. 44 (1997) 1208.
[5] M. Ji, B. Benkmil, H. Vahren Kamp, Inorg. Chem. 44 (2005) 3518. and references cited therein.
[6] C.O.R. de Barhavin, N.A. Bailey, D.E. Fenton, Q.-Yu. He, J. Chem. Soc., Dalton Trans. (1997) 161. and references cited therein.
[7] A.L. Singer, D.A. Atwood, Inorg. Chim Acta 277 (1998) 157. and references cited therein.
[8] A. Abufarang, H. Vahren Kamp, Inorg. Chem. 34 (1995) 3279. and references cited therein.
[9] U. Brand, H. Vahren Kamp, Inorg. Chem. 34 (1995) 3285. and references cited therein.
[10] R. Klement, F. Stock, H. Elias, H. Paulus, P. Pelikan, M. Valko, M. Mazur, Polyhedron 18 (1999) 3041.
[11] K.D. Karlin, J. Zubbieta, Biological and Inorganic Copper Chemistry, Adenine Press, New York, 1983.
[12] B.L. Vallee, R.J.P. Williams, Proc. Natl. Acad. Sci. USA 59 (1968) 489.
[13] T.G. Spiro (Ed.), Zinc Enzymes, Wiley, New York, 1983.
[14] A. Galdes, B.L. Vallee, in: H. Sigel (Ed.), Zinc and its Role in Biology and Nutrition, Marcel Dekker, New York, 1983.
[15] J.J.R. Frausto da Silva, R.J.P. Williams, The Biological Chemistry of the Elements, Charendon Press, Oxford, 1991. p. 299.
[16] B.L. Vallee, D.S. Auld, Biochemistry 29 (1990) 5647.
[17] B.L. Vallee, D.S. Auld, Biochemistry 32 (1993) 6493.
[18] D.E. Fenton, H. Okawa, J. Chem. Soc., Dalton Trans. (1993) 1349.
[19] D.W. Christianson, Adv. Protein Chem. 42 (1991) 281.
[20] H. Sigel, R.B. Martin, Chem. Soc. Rev. 94 (1994) 83.
[21] J.P. Glusker, Adv. Protein Chem. 42 (1991) 1.
[22] S.J. Chiou, C.G. Riordan, A.L. Rheingold, Proc. Natl. Acad. Sci. USA 100 (2003) 3695.
[23] C.R. Warthen, B.S. Hammes, C.J. Carrano, J. Biol. Inorg. Chem. 6 (2001) 82.
[24] M.A. Boshra, A.S. Ferwanah, A.M. Awadallah, N.M. El-Halabi, Asian J. Chem. 14 (2002) 1235.
[25] A. Cansiz, M. Koparir, A. Demirdag, Molecules 9 (2004) 204.
[26] A.A.F. Wasfy, J. Chem. Res. 8 (2003) 457.
[27] P.S. Kumar, K.E.V. Nagoji, B.V.V. Ravikum, Asian J. Chem. 15 (2003) 515.
[28] W.L.E. Armarego, Adv. Heterocycl. Chem. 24 (1979) 1.
[29] D. Raffa, G. Diadone, B. Maggio, D. Schillaci, F. Plescia, Arch. Pharm. Pharm. Med. Chem. 332 (1999) 317.
[30] V. Alagarsamy, A. Thangathirupathy, S.C. Mandal, Indian Pharm. Sci. 68 (2006) 108.
[31] J.P. Mayer, G.S. Lewis, M.J. Curtis, J. Zhang, Tetrahedron Lett. 389 (1997) 8445.
[32] J.B. Jiang, D.P. Hessan, Dusak, D.L. Dexter, G.J. Kag, E. Hamel, J. Med. Chem. 33 (1990) 1721.
[33] F. Eienne, Zyl. Van, Forensic Sci. Int. 122 (2001) 142.
[34] A.W. Bauer, W.W.M. Sherris, J.C. Turck, Am. J. Clin. Pathol. 45 (1966) 493.
[35] M. Garcia-Valverde, T. Torroba, Molecule 10 (2005) 318. and references cited therein.
[36] D.J. Baner, P.W. Sadler, Brit. 1026401 (Cl. CO7c, d) April 20, 1966.
[37] D.J. Baner, P.W. Sadler, Chem. Abstr. 65 (1966) 2224e.
[38] G. Sheldrick, Bruker-AXS, 2001.
[39] L.J. Farrugia, ORTEP 3 for Windows, Version 1.076, University of Glasgow, 1997–2002.
[40] L.J. Farrugia, J. Appl. Cryst. 30 (1997) 565.
[41] A.L. Spek, J. Appl. Cryst. 36 (2003) 7.
[42] A.L. Spek, PLATON Version 1.14, 2008.
[43] V.G. Pesin, Russ. Chem. Rev. 39 (1970) 923.
[44] Heng-Shan Dong, Kun Wei, Qing-Lian Wang, Bin Quan, Synth. Commun. 31 (2001) 81.
[45] R.E. Rosenfield Jr., R. Parthasarathy, J.D. Duntiz, J. Am. Chem. Soc. 99 (1977) 4860.
[46] S. Biswas, S. Sarkar, I.M. Steele, S. Sarkar, G. Mostafa, B.B. Bhaumik, K. Dey, Polyhedron 26 (2007) 5061.
[47] S. Biswas, G. Mostafa, I.M. Steele, S. Sarkar, K. Dey, Polyhedron 28 (2009) 1010.
[48] A.W. Addison, T.N. Rao, J. Reedijk, J. van Rijn, G.C. Vershoor, J. Chem. Soc., Dalton Trans. (1984) 1349.
[49] R.M. Silverstein, F.X. Webster, Spectrometric Identification of Organic Compounds, 6th ed., John Wiley and Sons, Inc., New York, 1998. p. 233.
[50] G.C. Perey, D.A. Thoruton, Inorg. Nucl. Chem. Lett. 7 (1971) 599.
[51] K. Dey, D. Bandyopadhayay, Indian J. Chem. 31A (1992) 34.
[52] J.P. Naskar, S. Chowdhury, M.G.B. Drew, D. Datta, Cryst. Eng. Commun. 6 (2004) 556.
[53] E. Tas, M. Ulusoy, M. Guler, Synth. React. Inorg. Met.-Org. Chem. 34 (2004) 1211.
[54] C.L. Dollberg, C. Turro, Inorg. Chem. 40 (2001) 2484.
[55] P. Kofod, P. Harris, S. Larsen, Inorg. Chem. 36 (1970) 2258.
[56] A. Bilgin, Y. Gök, Synth. React. Inorg. Met.-Org. Chem. 31 (2001) 1717.
[57] M.M. Mostafa, K.M. Ibrahim, M.N.H. Mousa, Trans. Met. Chem. 9 (1984) 243.
[58] K.-Y. Ho, W.-Y. Yu, K.-K. Cheung, C.-M. Che, J. Chem. Soc., Dalton Trans. (1999) 1581.

and with cone and desolvation gas flows of 5–10 and 500 L/h, respectively (details and spectra Figs. S2–S12 in Supplementary material).

2.2. Preparation of the ligands

A mixture of cytosine (1 mmol) and *N,O*-bis(trimethylsilyl)acetamide (BSA) (3 mmol) was heated under reflux in dry acetonitrile (3.3 mL) for 1 h. The solution was cooled to 0 °C and sulfonyl chloride (1.2 mmol) was added. The reaction mixture was heated for 16 h at 80 °C, cooled and treated with a small amount of methanol. The resulting solid was filtered off and recrystallized.

2.2.1. 1-(p-Toluenesulfonyl)cytosine (**1**)

Synthesis of ligand **1** was performed according to the procedure reported by Kašnar-Šamprec et al. [7]. [^{1}H NMR (DMSO-d_6) δ/ppm: 8.14 (d, 1H, $J_{6,5}$ = 7.8 Hz, H-6), 7.95 (brd, 2H, NH_2), 7.87 (d, 2H, $J_{b,c}$ = 8.1 Hz, Ph-b), 7.46 (d, 2H, $J_{c,b}$ = 8.1 Hz, Ph-c), 5.98 (d, 1H, $J_{5,6}$ = 7.8 Hz, H-5), 2.42 (s, 3H, CH_3); ^{13}C NMR (DMSO-d_6) δ/ppm: 166.27 (s, C-4), 151.22 (s, C-2), 145.61 (s, Ph-d), 139.73 (d, C-6), 134.47 (s, Ph-a), 129.80 (d, Ph-c), 129.02 (d, Ph-b), 97.50 (d, C-5), 21.20 (q, CH_3)]. *Anal.* Calc. for $C_{11}H_{11}N_3O_3S$ (M_r = 265.30): C, 49.80; H, 4.18; N, 15.84. Found: C, 50.09; H, 4.02; N, 15.89%.

Additional data for 1-(*p*-toluenesulfonyl)cytosine (**1**): ^{1}H NMR (CD_3CN) δ/ppm: 8.13 (d, 1H, $J_{6,5}$ = 7.9 Hz, H-6), 7.92 (brd, 2H, $J_{b,c}$ = 8.4 Hz, Ph-b), 7.46 (d, 2H, $J_{c,b}$ = 8.0 Hz, Ph-c), 6.42 (brd 2H, NH_2), 5.98 (d, 1H, $J_{5,6}$ = 7.8 Hz, H-5), 2.49 (s, 3H, CH_3).

2.2.2. 1-Methanesulfonylcytosine (**6**)

1-Methanesulfonylcytosine (**6**) was prepared according to the literature method [8]. [^{1}H NMR (DMSO-d_6) δ/ppm: 8.21 (brs, 1H, NH), 8.05 (brs, 1H, NH), 7.87 (d, 1H, $J_{6,5}$ = 7.8 Hz, H-6), 5.96 (d, 1H, $J_{5,6}$ = 7.9 Hz, H-5), 3.63 (s, 3H, CH_3); ^{13}C NMR (DMSO-d_6) δ/ppm: 165.44 (s, C-4), 151.42 (s, C-2), 139.45 (d, C-6), 96.64 (d, C-5), 41.13 (q, CH_3)]. *Anal.* Calc. for $C_5H_7N_3O_3S$ (M_r = 189.20): C, 31.74; H, 3.73; N, 22.21. Found: C, 31.92; H, 4.01; N, 22.02%.

2.3. Preparation of the complexes

To a water or methanol solution of $MCl_2 \times nH_2O$ (1 equiv.), the 1-sulfonylcytosine ligand (2 equiv.) in methanol was added and the reaction mixture was left stirring. The solid product obtained by evaporation was filtered off, washed with methanol and dried.

2.3.1. Cu(1-TsC-N3)$_2$Cl$_2$ (**2**)

Starting materials: solutions of 1-(*p*-toluenesulfonyl)cytosine (**1**) (133 mg, 0.5 mmol) in methanol (23 mL), $CuCl_2 \times 2H_2O$ (43 mg, 0.25 mmol) in methanol (5 mL). The resulting dark green solution was left to slowly evaporate at room temperature in order to obtain high quality single crystals. After 7 days, two types of single crystals were present in the crystallization vessel – deep blue prisms (X-ray structure **2**) and turquoise plates [methanol solvate of **2**, X-ray structure **3** (**2** × $2CH_3OH$)]. After selection of single crystals suitable for X-ray diffraction experiments, the remaining crystals were filtered off and dried in vacuum to remove the methanol yielding 110 mg (66%) of the blue-green complex **2**: ^{1}H NMR (DMSO-d_6) δ/ppm: 8.25 (brs, 1H, H-6), 7.89 (brs, 2.5H, Ph-b + part of NH_2), 7.42 (brs, 3.5H, Ph-c + part of NH_2), 2.34 (brs, 3H, CH_3); ^{1}H NMR (CD_3CN) δ/ppm: 9.48 (brs, 1H), 8.71 (brs, 2H), 7.79 (brs, 2H), 2.59 (brs, 3H, CH_3); ^{13}C NMR (DMSO-d_6) δ/ppm: 143.22 (s, Ph-d), 132.13 (s, Ph-a), 127.58 (d, Ph-c), 126.75 (d, Ph-b), 19.27 (q, CH_3). *Anal.* Calc. for $C_{22}H_{22}Cl_2CuN_6O_6S_2 \times 2H_2O$ (M_r = 701.06): C, 37.69; H, 3.74; N, 11.99. Found: C, 37.29; H, 4.10; N, 11.74%. ESI-HRMS (*m*/*z*): $[M-TsC-Cl]^+$ ($C_{11}H_{11}N_3O_3SCuCl$): calc. 362.9506, found: 362.9494 (3.3 ppm); $[M-Cl]^+$ ($C_{22}H_{22}N_6O_6S_2CuCl$): calc. 628.0027, found: 627.9995 (5.1 ppm); $[M+TsC-Cl]^+$ ($C_{33}H_{33}N_9O_9S_3CuCl$): calc. 893.0548, found: 893.0547 (0.1 ppm).

2.3.2. Cd(1-TsC-N3)$_2$Cl$_2$ (**4**)

Starting materials: solutions of 1-(*p*-toluenesulfonyl)cytosine (**1**) (133 mg, 0.5 mmol) in methanol (23 mL), 2 M aqueous solution of $CdCl_2$ (0.125 mL, 0.25 mmol). The colorless solution was stirred overnight and was then left to evaporate at room temperature. After 4 days, colorless prisms were obtained. One transparent colorless crystal was picked for the X-ray diffraction study, and the remaining crystals were filtered off and dried in vacuum to give 131 mg (77%) of white powder **4**: ^{1}H NMR (DMSO-d_6) δ/ppm: 8.75 (brs, 1H, NH), 8.26 (brs, 1H, NH), 8.22 (d, 1H, $J_{6,5}$ = 8.0 Hz, H-6), 7.88 (d, 2H, $J_{b,c}$ = 8.3 Hz, Ph-b), 7.48 (d, 2H, $J_{c,b}$ = 8.1 Hz, Ph-c), 6.06 (d, 1H, $J_{5,6}$ = 8.0 Hz, H-5), 2.41 (s, 3H, CH_3); ^{1}H NMR (CD_3CN) δ/ppm: 8.19 (brd, 1H, H-6), 8.08 (brs, 1H, NH), 7.90 (brd, 2H, Ph-b), 7.43 (brd, 2H, Ph-c), 7.39 (brs, 1H, NH), 6.10 (brd, 1H, H-5), 2.45 (brs, 3H, CH_3); ^{13}C NMR (DMSO-d_6) δ/ppm: 163.35 (s, C-4), 148.38 (s, C-2), 146.02 (s, Ph-d), 140.38 (d, C-6), 133.29 (s, Ph-a), 129.71 (d, Ph-c), 129.01 (d, Ph-b), 97.13 (d, C-5), 21.17 (q, CH_3). ESI-HRMS (*m*/*z*): $[M-TsC-Cl]^+$ ($C_{11}H_{11}N_3O_3SCdCl$): calc. 413.9243, found: 413.9225 (4.3 ppm); $[M-Cl]^+$ ($C_{22}H_{22}N_6O_6S_2CdCl$): calc. 678.9764, found: 678.9730 (5.0 ppm); $[M+TsC-Cl]^+$ ($C_{33}H_{33}N_9O_9S_3CdCl$): calc. 944.0286, found: 944.0291 (0.5 ppm).

2.3.3. Co(1-TsC-N3)$_2$Cl$_2$ (**5**)

Starting materials: solutions of 1-(*p*-toluenesulfonyl)cytosine (**1**) (130 mg, 0.5 mmol) in methanol (40 mL), $CoCl_2 \times 6H_2O$ (60 mg, 0.25 mmol) in methanol (4 mL). The resulting dark violet solution was left to slowly evaporate at room temperature yielding 112 mg of blue powder **5**: ^{1}H NMR (DMSO-d_6) δ/ppm: 8.10 (d, 1H, $J_{6,5}$ = 8 Hz, H-6), 7.90 (brd, 2H, NH_2), 7.84 (d, 2H, $J_{b,c}$ = 8.4 Hz, Ph-b), 7.44 (d, 2H, $J_{c,b}$ = 8.4 Hz, Ph-c), 5.93 (d, 1H, $J_{5,6}$ = 7.9 Hz, H-5), 2.40 (s, 3H, CH_3); ^{1}H NMR (CD_3CN) δ/ppm: 8.05 (brd, 1H, H-6), 7.85 (brd, 2H, Ph-b), 7.40 (brd, 2H, Ph-c), 6.33 (brs, 2H, NH_2), 2.42 (brs, 3H, CH_3). ESI-HRMS (*m*/*z*): $[M-Cl]^+$ ($C_{22}H_{22}N_6O_6S_2CoCl$): calc. 624.0063, found: 624.0041 (3.5 ppm); $[M+TsC-Cl]^+$ ($C_{33}H_{33}N_9O_9S_3CoCl$): calc. 889.0584, found: 889.0582 (0.2 ppm).

2.3.4. Cu(1-MsC-N3)$_2$Cl$_2$ (**7**)

Starting materials: solutions of 1-methanesulfonylcytosine (**6**) (113 mg, 0.6 mmol) in methanol (40 mL), $CuCl_2 \times 2H_2O$ (51 mg, 0.3 mmol) in methanol (2 mL). The resulting turquoise solution was left to slowly evaporate at room temperature in order to obtain high quality single crystals. After 5 days, dark green prisms were obtained, one of which was picked for X-ray diffraction measurements, while the others were filtered off, yielding 137 mg (89%) of dark green powder **7**: ^{1}H NMR (DMSO-d_6) δ/ppm: 7.97 (brs, 2H, NH_2), 7.32 (brs, 1H, H-6), 3.67 (s, 3H, CH_3); ^{13}C NMR (DMSO-d_6) δ/ppm: 136.06 (d, C-6), 39.01 (q, CH_3). ESI-HRMS (*m*/*z*): $[M-Cl]^+$ ($C_{10}H_{14}N_6O_6S_2CuCl$): calc. 475.9401, found: 475.9388 (2.7 ppm).

2.3.5. Cd(1-MsC-N3)$_2$Cl$_2$ (**8**)

Starting materials: solutions of 1-methanesulfonylcytosine (**6**) (113 mg, 0.6 mmol) in methanol (40 mL), 2 M aqueous solution of $CdCl_2$ (0.15 mL, 0.3 mmol). After 1 h, a white precipitate was formed. It was filtered off and dried in vacuum to give 131 mg (77%) of snow-white powder **8**. The mother liquor was left to crystallize, but the colorless prisms formed after four days turned out to be single crystals of ligand **6**. Complex **8**: ^{1}H NMR (DMSO-d_6) δ/ppm: 7.92 (brs, 1H, NH), 7.89 (brs, 1H, NH), 7.84 (d, 1H, $J_{6,5}$ = 7.8 Hz, H-6), 5.90 (d, 1H, $J_{5,6}$ = 7.8 Hz, H-5), 3.62 (s, 3H, CH_3); ^{13}C NMR (DMSO-d_6) δ/ppm: 166.06 (s, C-4), 152.08 (s, C-2), 139.08 (d, C-6), 96.68 (d, C-5), 41.05 (q, CH_3). ESI-HRMS (*m*/*z*): $[M-Cl-HCl]^+$ ($C_{10}H_{13}N_6O_6S_2Cd$): calc. 490.9372, found: 490.9345

(5.5 ppm); $[M-Cl-HCl+TsC]^+$ ($C_{15}H_{20}N_9O_9S_3Cd$): calc. 679.9580, found: 679.9556 (3.5 ppm).

2.4. X-ray structural analysis

Crystal data, data collection and refinement parameters are summarized in Table 1. Data collections were performed on an Enraf Nonius CAD4 diffractometer using graphite monochromated Cu Kα radiation (λ = 1.54179 Å) (structures **2**, **3** and **4**) and on an Oxford Diffraction Xcalibur Nova R diffractometer with a microfocusing Cu tube (structures **6** and **7**). The X-ray structure of ligand **1** was reported in our previous paper [6]. Data reduction and cell refinement were carried out using the procedures incorporated into the WINGX package [9] for structures **2**, **3** and **4**, while, CRYSALIS software [10] was used for the structures **6** and **7**. Intensities were measured at room temperature. All structures were solved using direct methods with SIR2002 [11] and refined using full matrix least-squares refinement based on F^2, with SHELX97 [12]. Molecular illustrations were prepared with ORTEP-3 [13] and PLATON [14]. All non-hydrogen atoms in the structures were refined anisotropically and hydrogen atoms were included in their geometrically calculated positions (except for some hydrogen atoms included in hydrogen bonding), and refined according to the riding model.

3. Results and discussion

3.1. Synthesis

The organic ligands were synthesized by procedures described in the literature [7,8]. Condensation of silylated cytosine with *p*-toluenesulfonyl chloride (TsCl) or methanesulfonyl chloride (MsCl) gave the corresponding ligands 1-tosylcytosine, **1** (1-TsC), and 1-mesylcytosine, **6** (1-MsC). The mononuclear complexes described in this paper were prepared by the reaction of Cu(II), Cd(II) and Co(II) chlorides with the corresponding ligands in a 1:2 molar ratio of reactants in methanol and led to complexes of the $M(L)_2Cl_2$ type (Scheme 1).

Two forms of copper complexes with the 1-tosylcytosine ligand **1** were isolated in the process of crystal growth from a diluted methanolic solution: Cu(1-TsC-*N*3)$_2$Cl$_2$ (**2**) and its solvated pseudopolymorph Cu(1-TsC-*N*3)$_2$Cl$_2$ × 2CH$_3$OH (**3**), with suitable monocrystals for X-ray diffraction studies. Crystals suitable for X-ray crystallography were also obtained in the reaction of copper(II) chloride with 1-mesylcytosine **6**, yielding the complex Cu(1-MsC-*N*3)$_2$Cl$_2$ (**7**), and yielding the complex Cd(1-TsC-*N*3)$_2$Cl$_2$ (**4**) in the reaction of cadmium(II) chloride with 1-tosylcytosine **1**. On the other hand, the IR and NMR studies suggested the existence of the Co(II) complex with ligand **1** and the Cd(II) complex with ligand **2**, for which we assume them to be the N3 coordinated species Co(1-TsC-*N*3)$_2$Cl$_2$ (**5**) and Cd(1-MsC-*N*3)$_2$Cl$_2$ (**8**); their molecular formulas were confirmed by HRMS spectrometry.

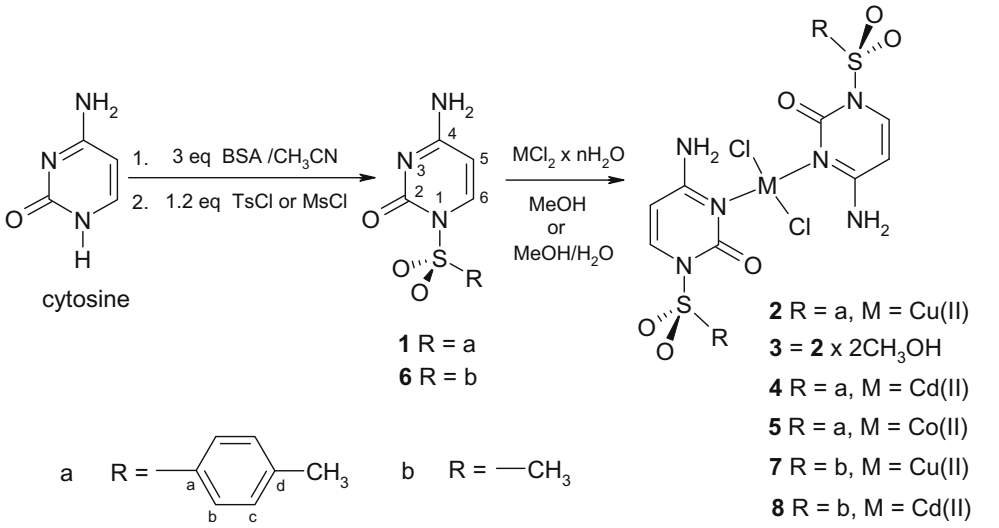
3.2. NMR Spectroscopy

In the ^{1}H NMR spectrum (measured in DMSO-d_6), complex Cd(1-TsC-*N*3)$_2$Cl$_2$ (**4**) displays a slight downfield shift of the signals for two sets of doublets in the aromatic region corresponding to the H-6 and H-5 protons (δ 8.22 and 6.06 ppm) and phenyl Ph-b and Ph-c protons (δ 7.88 and 7.48 ppm) relative to the free ligand **1**. The H-6 ($\Delta\delta$ 0.03 ppm), H-5 ($\Delta\delta$ 0.06 ppm) and NH ($\Delta\delta$ 0.28 and 0.16 ppm) signals in the Cd(1-MsC-*N*3)$_2$Cl$_2$ (**8**) complex are slightly shifted to higher frequencies compared to those of the free cytosine ligand **6**, which is in accord with coordination *via* N3. These very small changes are in agreement with other cytosine complexes [15].

NMR peak positions are particularly sensitive to the presence of paramagnetic species and "diamagnetic" ^{1}H NMR spectroscopy has not been applied extensively to Cu(II) and Co(II) coordination complexes because of their paramagnetism, which complicates the spectra acquisition and interpretation. On the other hand, almost all signals for complexes Cu(1-TsC-*N*3)$_2$Cl$_2$ (**2**), Co(1-TsC-*N*3)$_2$Cl$_2$ (**5**) and Cu(1-MsC-*N*3)$_2$Cl$_2$ (**7**) were registered in the "diamagnetic" (in the range δ = 0–14 ppm) part of the ^{1}H NMR spectra, showing broad resonances (doublets collapsed into broad singlets). The

Table 1
Crystallographic parameters for compounds **2**, **3**, **4**, **6**, and **7**.

Compound	**2**	**3**	**4**	**6**	**7**
Formula	$C_{22}H_{22}Cl_2CuN_6O_6S_2$	$C_{22}H_{22}Cl_2CuN_6O_6S_2 \times 2CH_3OH$	$C_{22}H_{22}Cl_2CdN_6O_6S_2$	$C_5H_7N_3O_3S$	$C_{10}H_{14}Cl_2CuN_6O_6S_2$
Formula weight (g mol^{-1})	665.02	727.08	713.88	189.2	512.8
Crystal color and habit	blue plate	turquoise plate	colorless prism	colorless prism	green prism
Crystal dimensions (mm)	0.25 × 0.11 × 0.09	0.25 × 0.15 × 0.10	0.25 × 0.18 × 0.15	0.20 × 0.18 × 0.15	0.12 × 0.10 × 0.10
Space group	*P*21/*c*	*P*21/*n*	*P*-1	$P2_1/n$	$P2_1/c$
a (Å)	11.909(2)	14.244(1)	8.7910(3)	5.1275(3)	22.1814(3)
b (Å)	13.247(2)	14.096(1)	13.0760(5)	24.675(1)	7.0616(1)
c (Å)	8.7883(8)	16.003(2)	13.3430(4)	6.3307(5)	12.4291(2)
α (°)	90.00	90.00	113.641(3)	90.00	90.00
β (°)	100.44(2)	104.75(1)	97.747(3)	106.32(1)	103.152(1)
γ (°)	90.00	90.00	97.840(3)	90.00	90.00
V (Å^3)	1363.5(3)	3107.3(5)	1361.25(9)	768.68(9)	1895.78(5)
Z	2	4	2	4	4
μ (Cu Kα) (mm^{-1})	4.803	4.317	10.105	3.567	6.680
Absorption correction	Ψ-scan	Ψ-scan	Ψ-scan	multi-scan	multi-scan
θ max (°)	76.59	76.18	76.39	75.88	76.24
hkl	0,15; −16,16; −11,10	−17,17; −17,0; −20,0	−10,11; −16,0; −15,16	−6,6; −29,30; −7,7	−27,26; −8,8; −15,15
Number of reflections collected	5856	6725	5958	4440	10 263
Number of reflections unique	2865	6493	5702	1593	3881
Number of reflections observed [$I > 2\sigma(I)$]	2474	4430	5106	1534	3357
R_{int}	0.0417	0.0357	0.0194	0.0162	0.0232
R_σ	0.0380	0.0453	0.0256	0.0135	0.0211
Parameters	187	404	384	126	262
R_1 [$I > 2\sigma(I)$]	0.0421	0.0649	0.0415	0.0356	0.0354
R_1, all	0.0491	0.1058	0.0479	0.0364	0.0410
wR_2	0.1134	0.1970	0.1168	0.1152	0.1023
Goodness-of-fit, *S*	1.095	1.067	1.025	1.081	1.081
ρ_{max}, ρ_{min} (e Å^{-3})	0.53, −0.77	0.88, −0.65	1.37, −1.77	0.27, −0.28	0.79, −0.55



Scheme 1.

signal of H-5, a proton of the cytosine moiety, which is not in the nearest neighborhood to the coordination center, disappeared from the range of "diamagnetic" spectra for complexes **2**, **5** and **7** (*Figs.* S13 and S14 Supplementary material).

The spectrum of complex Co(1-TsC-*N*3)$_2$Cl$_2$ (**5**) exhibits signals of the free ligand **1** in DMSO-d_6 solution (*Figs.* S13), indicating low stability of the complex in polar coordinative solvent. However, the ^{1}H NMR spectrum of **5** measured in CD_3CN shows the disappearance of the H-5 signal, as can be seen for the paramagnetic Cu(II) complex **2**; all other broad resonances are slightly shifted to higher field compared to the spectrum of the free ligand **1** (*Figs.* S14). Due to the lack of an X-ray structure for the Co(II) complex **5**, we can only suggest that the binding probably takes place at the N-3 atom of the cytosine moiety.

3.3. Infrared spectroscopy

The infrared spectra of the free ligands, 1-tosylcytosine **1** and 1-mesylcytosine **6**, together with their complexes with copper, cadmium and cobalt, are shown in Figs. 1 and 2, while the band assignments are given in Table 2. Direct evidence of complexation is the presence of absorption bands due to the metal–chlorine stretching vibration in the spectral region below 500 cm^{-1}. In the region corresponding to ν(NH) vibrations, the spectra of 1-tosylcytosine **1** and 1-mesylcytosine **6** undergo prominent changes due to complexation, both in the band positions and intensities.

3.4. The molecular and crystal structures of 1-tosylcytosine complexes *2*, *3* and *4*

The molecular structures of the Cu(II) complexes, pseudopolymorphs **2** and **3**, as well as of the Cd(II) complex **4** are given in Figs. 3–5, respectively. The geometries of the pyrimidine rings in complexes **2**, **3** and **4** are given in Table 3. As the Cu(II) ion in complex **2** lies on an inversion center, and consequently the molecule possesses C_i symmetry, the two cytosine rings have identical geometries. This is, however, not the case of complexes **3** and **4**. Moreover, in the cytosine ring 1 (cy1) of complex **3**, the values of bond lengths N3–C4 and C4–N4 suggest an increase of the single bond character of the former, and an increase of the double bond character of the latter, compared to complexes **2** and **4** as well as to the other cytosine ring (cy2) of the same complex (Table 3). They

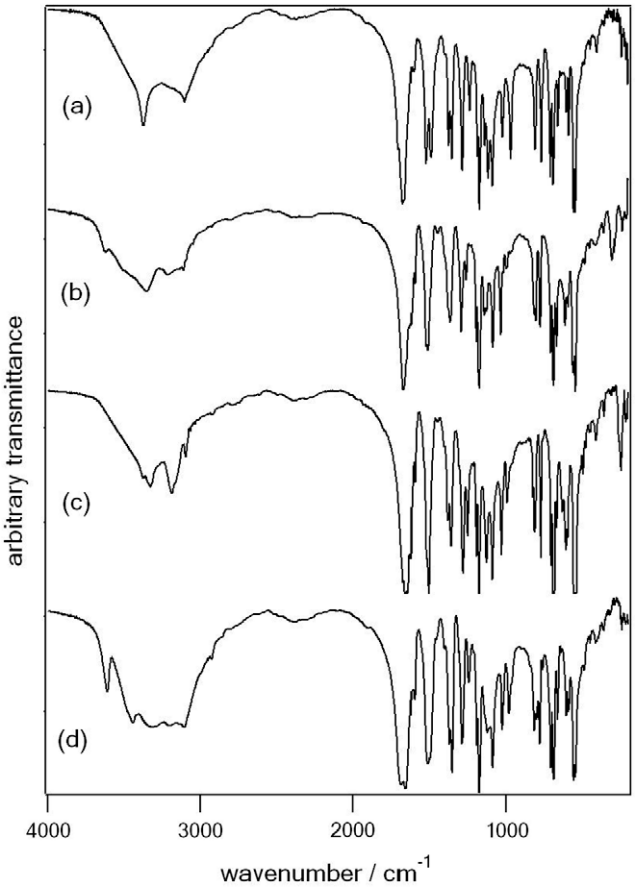


Fig. 1. Infrared spectra of (a) 1-tosylcytosine **1**, (b) Cu(1-TsC-*N*3)$_2$Cl$_2$ x 2CH$_3$OH (**3**), (c) Cd(1-TsC-*N*3)$_2$Cl$_2$ (**4**) and (d) Co(1-TsC-*N*3)$_2$Cl$_2$ (**5**).

are, in fact, in very good accord with the analogous average values extracted from the current version of *CSD* [16] for a set of 14 structures containing the iminooxo form of *N*-1-substituted cytosine [N3–C4, 1.359(5) Å; C4–N4, 1.300(4) Å]. This is due to charge delocalization over the bonds N3–C4 and C4–N4, caused by the copper coordination. Search of the same version of the *CSD* has revealed

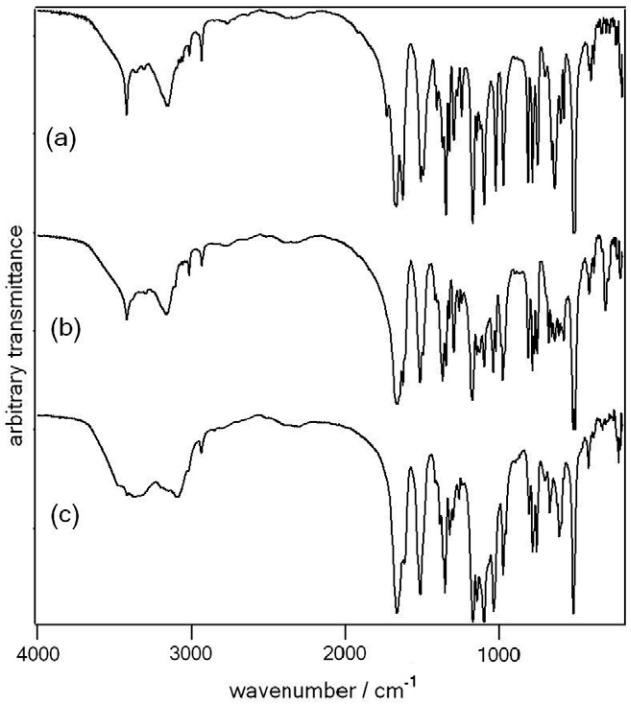


Fig. 2. Infrared spectra of (a) 1-mesylcytosine **6**, (b) Cu(1-MsC-*N*3)$_2$Cl$_2$ (**7**) and (c) Cd(1-MsC-*N*3)$_2$Cl$_2$ (**8**).

291 structures containing the preferred amino-oxo form of *N*-1-substituted cytosine. In this set, the average values for these bond lengths are: N3–C4, 1.346(1) Å, and C4–N4, 1.323(1) Å, which correspond to the analogous values in complexes **2** and **4**, and also, approximately, to the bond lengths revealed by the cytosine ring 2 (cy2) of complex **3**.

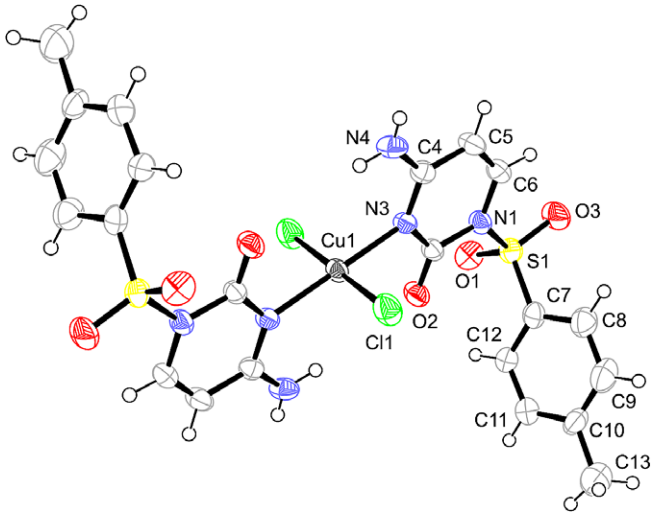


Fig. 3. ORTEP drawing of **2**. Thermal ellipsoids are scaled at the 50% probability level.

In both copper complexes **2** and **3**, the central ion forms a square-planar coordination sphere, almost ideal in the case of **2**, and considerably distorted in the case of **3** (Table 4). On the other hand, while the two coordinated pyrimidine rings are in a *trans*-arrangement with respect to the central Cu(II) ion [N3–Cu1–N3*i*, 180(11)°, see Table 4] and are virtually coplanar (head-to-tail oriented), they are mutually *cis*-oriented in complex **3** [N3–Cu1–N23, 90.88(14)°, see Table 4], and their corresponding *ls* planes

Table 2
Characteristic infrared bands (wavenumbers in cm^{-1}) in the 4000–200 cm^{-1} range and with tentative band assignments.

1	3	4	5	6	7	8	Assignation
	3621 w[a]						Adsorbed MeOH ν(OH)
			3608 m[b]				Adsorbed water ν(OH)
3372s	3355 s, b	3374 s	3441 s	3418 s	3418 s	3369 s, b	ν_{asym}(NH)
		3325 m	3311 s	3358 m	3381 sh		ν(NH)
				3306 m	3300 w	3318 w, b	ν(NH)
3186 w, sh	3217 m	3186 m	3200 m	3188 w, sh	3193 w, sh	3192 m	ν(NH)
3101 m	3109 m	3091 m	3100 m	3155 s	3162 s	3102 s	ν_{sym}(NH)
				3096 m	3110 m		ν(NH)
1702 m, sh				1729 m			δ(NH$_2$)
1673 vs	1667 vs	1671 vs	1684 vs	1677 vs	1663 vs	1663 vs	ν(C=O)
1662 vs	1647 m, sh	1656 vs	1655 vs	1668 vs	1650 s, sh	1648 s, sh	ν(C=C), ν(C=N), δ(NH$_2$)
1648 m, sh	1620 m, sh	1641 vs		1655 w, sh			ν(ring), ν(C=N), δ(NH)
1601 m	1596 m	1623 m, sh	1596 m	1626 s	1626 s	1629 vs	δ(NH)
		1595 m					δ(NH)
1523 s	1511 s	1506 s	1512 s	1509 s	1513 s	1511 s	ν(ring), ν(C–NH$_2$), δ(NH)
1490 s			1499 s	1493 s	1496 m		δ(NH), ν(C–N), ν(ring), δ(CH)
1377 m	1379 m, sh	1380 m	1371 s	1366 m	1365 s	1362 m	ν(SO$_2$)
1354 s	1367 m	1359 m	1353 s	1345 s	1344 s	1350 s	ν(SO$_2$)
1286 s	1293 s	1281 s	1287 s	1293 s	1294 s	1298 m	Cytosine breathing
1186 m	1194 m		1191 s		1180 m		ν_{ring}
1174 s	1173 s	1177 s	1175 vs	1171 s	1172 m	1171 m	ν_{ring}
1139 m	1142 m	1137 w, sh	1137 w, sh	1145 m	1145 m	1143 m	ρ(NH$_2$)
765 m	774 m	770 m	775 s		775 s	775 w, sh	γ(NH$_2$)
554 s	557 s	549 s	554 vs	520 s	523 s	520 s	τ(NH$_2$)
542 s	543 s	538 s	542 vs		509 s		τ(NH$_2$)
				387 m	387 m	389 m	δ(CO) or δ(CN)
	302 m	249 m	227 w		311 m	227 m	ν(MCl)

vs: very strong; s: strong; m: medium; w: weak: stretching; : deformation; γ: out-of-plane bending; τ: torsion.
M: Cu(II) (complexes **3** and **7**); Cd(II) (complexes **4** and **8**); Co(II) (complex **5**).

[a] Thermogravimetry of **3** shows a continuous mass loss of 6.45%. This, together with the IR band position, shows that methanol is only weakly adsorbed to the crystal of **3** (Figs. S1a).

[b] The thermogram of the complex **5** reveals a continuous mass loss of 2.66%, which corresponds to one water molecule per formula unit. This, together with the IR band position, indicates that water is only weakly adsorbed to the crystal of **5** (Figs. S1b).

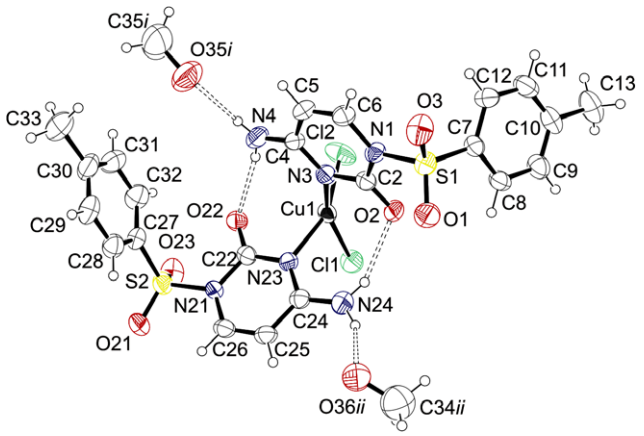


Fig. 4. ORTEP drawing of **3**. Thermal ellipsoids are scaled at the 40% probability level Hydrogen bonds are given by dashed lines.

form an angle of 72.5(2)°. The crystal structure of **2** is characterized by a complex three-dimensional hydrogen bonded molecular network where each complex molecule is connected to two others through amino-group protons forming hydrogen bonds towards O2*i* and O3*i* of the neighboring molecule (Table 5a and Fig. 6). The crystal packing is less complicated by far in the structure of complex **3**, where a single complex molecule is connected through intermolecular hydrogen bonds to only two neighboring solvent molecules, forming with them discrete hydrogen bonded units (Table 5a and Fig. 4). The refinement of the OH group hydrogens of both solvent molecules does not converge, and consequently they are not included in the model. They might however extend the hydrogen bonding network in this structure.

Table 4
Geometry of the coordination spheres in complexes **2**, **3**, **4**, and **7**.

	2	**3**	**4**	**7**
Bond (Å)				
M–N3	1.988(2)	2.033(4)	2.260(3)	2.0176(19)
M–N3*i* (N23)	1.988(2)	2.030(3)	2.278(3)	2.0333(19)
M–Cl1	2.2547(7)	2.2349(14)	2.4490(10)	2.2173(8)
M–Cl1*i* (Cl2)	2.2547(7)	2.2216(15)	2.4707(9)	2.2267(8)
Angle (°)				
N3–M–N3*i* (N23)	180.00(11)	90.88(14)	129.66(11)	91.21(8)
N3–M–Cl1	90.76(6)	157.87(11)	101.19(8)	91.12(6)
N3–M–Cl1*i* (Cl2)	89.24(6)	91.04(11)	108.37(8)	156.54(6)
N3*i* (N23)–M–Cl1	89.24(6)	90.23(10)	107.84(8)	161.08(7)
N3*i* (N23)–M–Cl1*i* (Cl2)	90.76(6)	156.70(11)	98.95(8)	88.29(6)
Cl1–M–Cl1*i* (Cl2)	180.00(3)	96.59(6)	110.33(4)	96.90(4)

Complex **4** is a neutral complex where the positive charge of the central Cd(II) ion is compensated by two chlorine anions, forming together with two endocyclic N3 atoms that belong to cytosine rings of the two ligand molecules a slightly distorted tetrahedral coordination sphere (Table 4 and Fig. 5). Its crystal structure is characterized by a complex hydrogen bonded three-dimensional molecular network. Two ligand molecules coordinated to the central Cd(II) ion form different hydrogen bonds *via* their amino groups, thus creating an asymmetric environment around the Cd(II) cation (Table 5a). While cytosine 1 of complex **4** forms one intramolecular H-bond *via* N4-H4A, and one intermolecular hydrogen bond with the chlorine from the neighboring molecule *via* N4-H4B, cytosine 2 forms, besides these two hydrogen bonds, an

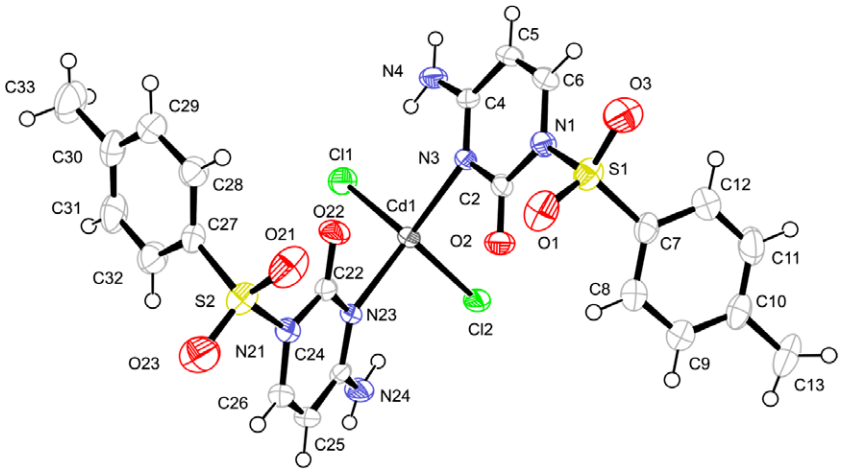


Fig. 5. ORTEP drawing of **4**. Thermal ellipsoids are scaled at the 50% probability level.

Table 3
Bond distances in the cytosine ring (Å).

Bond	**2**	**3** (cy1)	**3** (cy2)	**4** (cy1)	**4** (cy2)	**6**	**7** (cy1)	**7** (cy2)
N1–C2	1.409(3)	1.400(6)	1.410(6)	1.412(4)	1.403(5)	1.433(2)	1.394(3)	1.404(3)
C2–O2	1.222(3)	1.228(6)	1.223(6)	1.214(5)	1.224(5)	1.227(2)	1.237(3)	1.226(3)
C2–N3	1.360(3)	1.351(6)	1.349(6)	1.362(5)	1.360(5)	1.341(2)	1.344(3)	1.349(3)
N3–C4	1.339(3)	1.355(6)	1.328(6)	1.339(4)	1.338(4)	1.337(2)	1.345(3)	1.333(3)
C4–N4	1.320(4)	1.299(7)	1.310(7)	1.319(5)	1.320(5)	1.317(2)	1.310(4)	1.313(4)
C4–C5	1.428(4)	1.417(7)	1.440(7)	1.436(5)	1.435(5)	1.437(2)	1.426(4)	1.432(4)
C5–C6	1.333(4)	1.316(8)	1.323(8)	1.335(6)	1.329(6)	1.323(2)	1.318(4)	1.327(4)
C6–N1	1.383(3)	1.383(6)	1.375(7)	1.377(5)	1.378(5)	1.391(2)	1.388(3)	1.383(3)

Table 5a
Hydrogen bonds in 1-tosylcytosine complexes **2**, **3** and **4**.

D–H···A	*d* (D–H)/Å	*d* (H···A)/Å	*d* (D···A)/Å	∠ (D–H···A)/°	Symm. operation
Complex ***2*** *[Cu(1-TsC-N3)$_2$Cl$_2$]*					
N4–H4A···O3*i*	0.86(4)	2.49(4)	2.991(3)	118(3)	(*i*) −*x*, 1/2 + *y*, 1/2 − *z*
N4–H4B···O2*i*	0.72(4)	2.41(4)	3.086(3)	157(4)	(*i*) −*x*, 1/2 + *y*, 1/2 − *z*
Complex ***3*** *[Cu(1-TsC-N3)$_2$Cl$_2$ × 2CH$_3$OH]*					
N4–H4A···O35*i*	0.76(6)	2.21(6)	2.951(9)	166(6)	(*i*) 1 − *x*, −*y*, −*z*
N4–H4B···O22	0.80(6)	2.24(6)	2.986(7)	156(6)	
N24–H24A···O2	0.79(10)	2.30(10)	3.031(7)	153(9)	
N24–H24B···O36*ii*	0.81(7)	2.07(7)	2.847(9)	159(7)	(*ii*) 1 − *x*, −*y*, 1 − *z*
Complex ***4*** *[Cd(1-TsC-N3)$_2$Cl$_2$]*					
N4–H4A···Cl1	0.90(7)	2.36(7)	3.247(4)	168(5)	
N4–H4B···Cl2*i*	0.90(6)	2.44(6)	3.296(4)	158(5)	(*i*) −*x*,1 −*y*, −*z*
N24–H24A···Cl2	0.93(8)	2.61(8)	3.371(4)	139(6)	
N24–H24A···O21*ii*	0.93(8)	2.40(7)	3.141(5)	136(6)	(*ii*) −1 + *x*, *y*, *z*
N24–H24B···Cl2*iii*	0.79(7)	2.51(6)	3.273(4)	164(5)	(*iii*) −*x*, 2 − *y*, −*z*

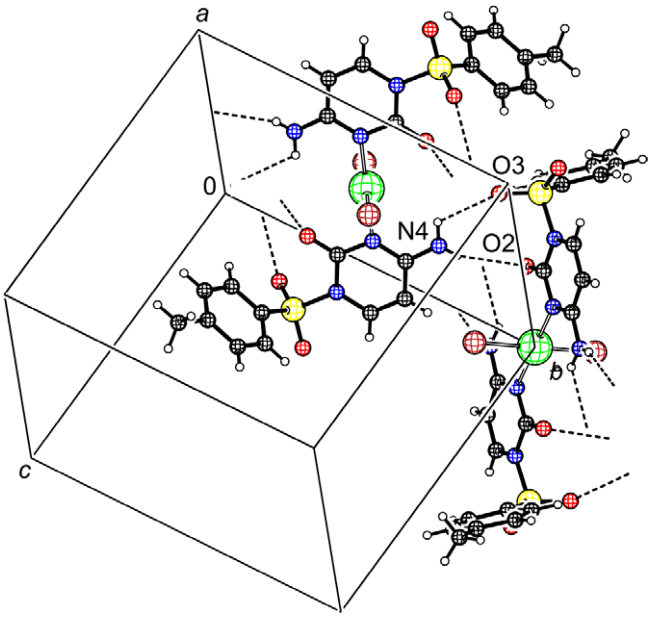


Fig. 6. Crystal packing of **2**.

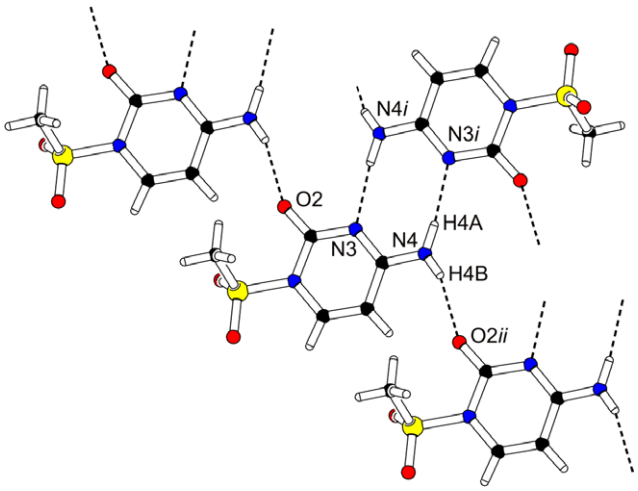


Fig. 7. Hydrogen bonding in **6**.

additional hydrogen bond N24–H24A···O21*ii*, thus creating a bifurcated hydrogen bond *via* the H24A proton.

*3.5. The molecular and crystal structures of 1-mesylcytosine **6** and its Cu(II) complex **7***

The hydrogen bonding pattern of ligand **6** is given in Fig. 7. The molecular structure of this ligand reveals no unexpected features. The geometry of the pyrimidine ring is typical of an N1-substituted cytosine in the preferred aminooxo form [6]. The hydrogen bonding pattern (Table 5b) reveals centrosymmetric dimers formed by the H-bond N4–H4A···N3*i*. These dimers are further connected into endless chains *via* the N4–H4B···O2*ii* hydrogen bond. The ORTEP drawing of complex **7** is given in Fig. 8 and its crystal packing is displayed in Fig. 9. In complex **7**, the Cu(II) ion resides in the center of a rather unusual, severely distorted coordination sphere that could be described as a transition state between a square planar and a tetrahedral arrangement, and strongly resembles the coordination sphere of Cu(II) in complex **3**. Relevant geometry parameters are given in Table 4. Both of these complexes lack molecular C_i symmetry, unlike complex **2** where the central Cu(II) ion lies on an inversion center and reveals a square-planar coordination sphere. Four ligand atoms (N3, N23, Cl1 and Cl2) reveal strong deviations from the *ls* plane calculated through them and the central Cu(II) ion, with the average absolute value of 0.38(2) Å. The angle between the planes defined by Cl1, Cu1 and Cl2 and by N3, Cu1 and N23 is 28.97(4)°. These values describe the coordination sphere of complex **7** as a severely distorted square plane, rather than as a severely distorted tetrahedron. Angles N3–Cu1–N23 and Cl1–Cu1–Cl2 [91.21(8)° and 96.26(4)°, see Table 4] further support this conclusion and, moreover, suggest a *cis*-arrangement. An obvious result is the angle of 73.56(6)° formed by the *ls* planes of two pyrimidine rings, which are, hence, close to a mutual perpendicular arrangement, similarly as in complex **3**, and unlike in complex **2**, where the two pyrimidine rings are coplanar and *trans* oriented with respect to the central Cu(II) ion (*vide supra*). The crystal structure of **7** is characterized by endless hydrogen bonded molecular chains along the crystallographic *b* axis (Fig. 9). These chains are formed by the N4–H4A···O2*i* hydrogen bond (Table 5b). Through its remaining hydrogen, H4B, N4 forms an intramolecular hydrogen bond, N4–H4B···O22, symmetrical (with respect to Cu(II)) with the hydrogen bond N24–H24B···O2 (Fig. 8). Hence, O2 acts as a double acceptor, taking part in one intramolecular and one intermolecular hydrogen bond. Nevertheless, two exocyclic nitrogen atoms from two cytosine rings, N4 and N24, reveal an asymmetrical hydrogen bonding pattern. N4 forms an intermolecular bond to O2*i* and an intramolecular one to O22 (*vide supra*), while N24 forms an intramolecular hydrogen bond to O2, and an

Table 5b
Hydrogen bonds in 1-mesylcytosine **6** and its Cu(II) complex **7**.

D–H···A	*d* (D–H)/Å	*d* (H···A)/Å	*d* (D···A)/Å	∠ (D–H···A)/°	Sym. operation
Ligand ***6*** *(MsC)*					
N4–H4A···N3*i*	0.90(2)	2.04(2)	2.938(2)	175(2)	(*i*) 1 − *x*, −*y*, 2 − *z*
N4–H4B···O2*ii*	0.80(2)	2.24(2)	3.011(2)	162(2)	(*ii*) *x* − 1, *y*, *z* − 1
Complex ***7*** *[Cu(1-MsC-N3)$_2$Cl$_2$]*					
N4–H4A···O2*i*	0.80(3)	2.27(4)	3.056(2)	167(1)	(*i*) *x*, −1 + *y*, *z*
N4–H4B···O22	0.76(2)	2.23(5)	2.950(3)	157(1)	
N24–H24A···Cl2*ii*	0.85(5)	2.33(8)	3.172(4)	171(1)	(*ii*) *x*, 5/2 − *y*, −1/2 + *z*
N24–H24B···O2	0.81(4)	2.23(7)	2.998(6)	159(1)	

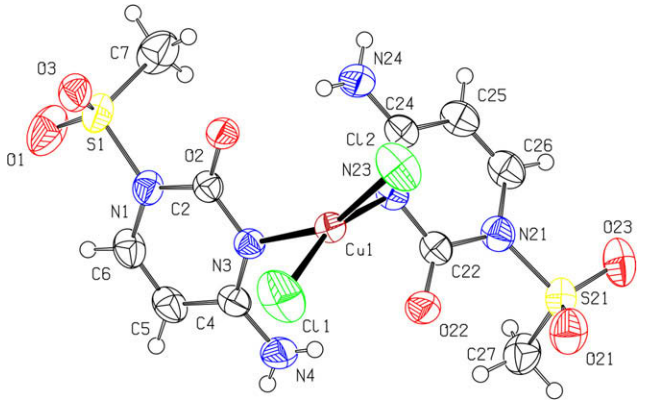


Fig. 8. ORTEP drawing of **7**. Thermal ellipsoids are scaled at the 50% probability level.

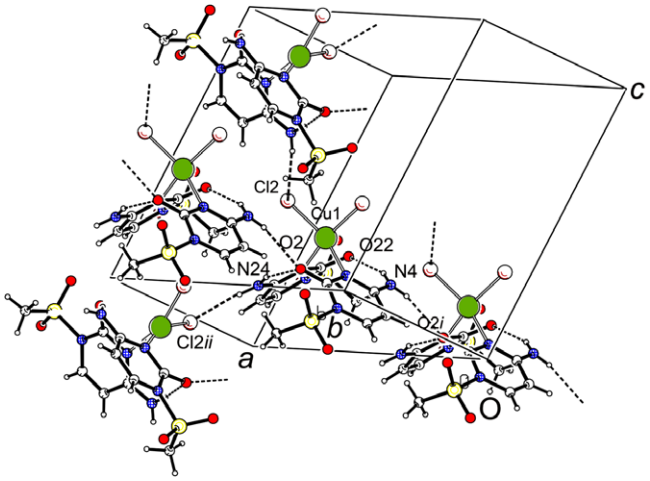


Fig. 9. Crystal packing of **7**.

intermolecular bond N24–H24a···Cl*ii* through which the above described molecular chains along the crystallographic *b* axis are interconnected, forming a two-dimensional molecular grid which propagates parallel to the *bc* plane. A narrow *zig-zag* channel separates two neighboring grids.

4. Conclusions

The mononuclear complexes of the type M(L$_2$)Cl$_2$ described in this paper were prepared by the reaction of Cu(II), Cd(II) and Co(II) chlorides with the 1-tosylcytosine **1** or 1-mesylcytosine **6** ligands. NMR and IR spectra show clear evidence of the complexation of ligands **1** and **6** with Cu(II) [complexes **3** and **7**], Cd(II) [complexes **4** and **8**] and Co(II) [complex **5**].

Two forms of copper complexes with 1-tosylcytosine ligand **1** were isolated in the process of crystal growth from a diluted methanolic solution: Cu(1-TsC-*N*3)$_2$Cl$_2$ (**2**) and its solvated pseudopolymorph Cu(1-TsC-*N*3)$_2$Cl$_2$ × 2CH$_3$OH (**3**). The X-ray structure of the complex **3** revealed charge delocalization inside the cytosine ring, prompted by metal coordination, which is the first step towards tautomerization. This, to the best of our knowledge, has not been observed previously with the copper complexes of *N*-1 substituted cytosine.

Acknowledgments

We appreciate the financial support of the Ministry of Science, Education and Sports of the Republic of Croatia through Grant Nos. 098-0982914-2935, 098-1191344-2943 and 098-0982904-2927. We also thank Renata Kobetić and Dubravka Gembarovski for HRMS, Ernest Sanders for TG measurements, and Krešimir Molčanov for X-ray data collection for compounds **6** and **7**.

Appendix A. Supplementary data

CCDC 729010, 729011, 729012, 729013 and 729014 contains the supplementary crystallographic data for **2**, **3**, **4**, **6** and **7**. These data can be obtained free of charge via http://www.ccdc.cam.ac.uk/conts/retrieving.html, or from the Cambridge Crystallographic Data Centre, 12 Union Road, Cambridge CB2 1EZ, UK; fax: (+44) 1223-336-033; or e-mail: deposit@ccdc.cam.ac.uk. Supplementary data associated with this article can be found, in the online version, at doi:10.1016/j.poly.2009.06.088.

References

[1] (a) M.A. Salam, K. Aoki, Inorg. Chim. Acta 311 (2000) 15;
(b) L. Jing, Z. Wenchao, H.K. Angela, L. Yi, Nucleic Acids Res. 28 (2000) 481;
(c) A.Y. Louie, T.J. Meade, Chem. Rev. 99 (1999) 2711;
(d) M. Sabat, A. Satyshur, M. Sundaralingam, J. Am. Chem. Soc. 105 (1983) 976.
[2] (a) J. Müller, R.K.O. Sigel, B. Lippert, J. Inorg. Biochem. 79 (2000) 261;
(b) J.C. Verheijen, G.A. van der Marel, J.H. van Boom, N. Metzler-Nolte, Bioconjugate Chem. 11 (2000) 741;
(c) S.J. Lippard, in: I. Bertini, H.B. Gray, S.J. Lippard, J.S. Valentine (Eds.), Bioorganic Chemistry, University Science Books, Mill Valley, CA, 1994, p. 505.
[3] (a) S. Sikova, S.J. Rowan, J. Chem. Soc. Rev. 34 (2005) 9;
(b) J.A.R. Navarro, B. Lippert, Coord. Chem. Rev. 22 (2001) 219;
(c) G. Mukherjee, T. Ghosh, J. Inorg. Biochem. 59 (1995) 827.
[4] V.A. Malkov, O.N. Voloshin, V.N. Soyfer, M.D. Frank-Kamenetskii, Nucleic Acids Res. 21 (1993) 585.
[5] (a) Lj. Glavaš-Obrovac, I. Karner, B. Žinić, K. Pavelić, Anticancer Res. 21 (2001) 1979;
(b) F. Supek, M. Kralj, M. Marjanović, L. Šuman, T. Šmuc, I. Krizmanić, B. Žinić, Invest. New Drugs 26 (2008) 97;
(c) A. Višnjevac, M. Žinić, M. Luić, D. Žiher, T. Kajfež Novak, B. Žinić, Tetrahedron 63 (2007) 86.
[6] A. Višnjevac, M. Luić, R. Kobetić, D. Gembarovski, B. Žinić, Polyhedron 28 (2009) 1057.
[7] J. Kašnar-Šamprec, Lj. Glavaš-Obrovac, M. Pavlak, I. Mihaljević, V. Mrljak, N. Štambuk, P. Konjevoda, B. Žinić, Croat. Chem. Acta 78 (2005) 261.
[8] B. Žinić, M. Žinić, I. Krizmanić, EP 0 877 022 B1 Synthesis of the sulfonylpyrimidine derivatives with anticancer activity, 2003.
[9] L.J. Faruggia, J. Appl. Cryst. 32 (1999) 837.

[10] CrysAlis CCD, Oxford Diffraction Ltd., Version 1.171.32.29 (release 10-06-2008 CrysAlis171 .NET).
[11] M.C. Burla, M. Camalli, B. Carrozzini, G.L. Cascarano, C. Giaccovazzo, G. Polidori, R. Spagna, SIR2002, Version 1.0, A Program for Automatic Solution and Refinement of Crystal Structures, University of Bari, Bari, Italy, 2002.
[12] G.M. Sheldrick, SHELX97: Program for the Refinement of Crystal Structures, Universität Göttingen, Germany, 1997.
[13] L.J. Farrugia, J. Appl. Crystallogr. 30 (1997) 565.
[14] (a) A.L. Spek, Acta Crystallogr., Sect. A 46 (1990) C34;
[b] A.L. Spek, PLATON, A Multipurpose Crystallographic Tool, Utrecht University, Utrecht, The Netherlands, 1998.
[15] (a) T. Pizzino, A. Fontana, F. Maggio, Monatsh. Chem. 121 (1990) 3;
(b) M. Concepcio Capllonch, A. Garcıa-Raso, A. Terron, M. Cristina Apella, E. Espinosa, E. Molins, J. Inorg. Biochem. 85 (2001) 173.
[16] F.H. Allen, Acta Crystallogr., Sect. B 58 (2002) 380.

NMR and ^{13}C NMR spectra were recorded on a Bruker 300 spectrometer instruments. Multiplities are given as s (singlet), d (dublet), t (triplet). FT-IR was recorded on SHIMADZU IR-PRESTIGE-2 Spectrophotometer. Elemental analysis (C, H and N) was performed at the instrumental Analysis Laboratory. Routine UV–Vis spectra were obtained in a quartz cuvette on an Agilelt 8453 UV–Vis spectrophotometer. Mass spectra were performed on a Bruker Autoflex III mass spectrometer. Spectra were recorded both in linear and reflectron modes with average of 50 and 100 shots for linear and reflectron modes. 2,5-Dihydroxy benzoic acid (DHB) MALDI matrix for **3** was prepared. MALDI samples were prepared by mixing complexes (2 mg/mL in acetonitrile) with the matrix solution (1:10 v/v) in a 0.5 mL eppendorf® micro tube. Finally 1 μL of this mixture was deposited on the sample plate, dried at room temperature and then analyzed. Fluorescence spectra were measured by a JASCO FP-777 W spectrophotometer (Japan Spectroscopic Co. Ltd.) at 25 °C; the slits for the excitation and emission monochrometers were 5 nm; and the spectral scan rate was 50.0 nm/min. The concentration of compound **3** was 5 μM and that of **2** was 20 μM since four derivative of benzofuran groups were bounded to one ZnPc core.

2.1. Synthesis

2.1.1. 6-(3,4-Dicyanophenylthio)-hexyl–2-chloroacetate (**1**)

About 1.0 g (3.84 mmol) of 4′-(1-hydroxyhexylthio)-1,2-dicyanobenzene (**1**) and ca. 0.32 mL (excess) of triethylamine were dissolved in 20 mL of THF at room temperature. The mixture was placed in an ice-bath. About 0.45 mL (4.2 mmol, excess 10%) of 2-chloroethylchloride was added dropwise to a stirred solution at −5 °C. The mixture was stirred at 0 °C for 3 h and at room temperature for 12 h and finally was heated for 1 h at 30 °C. The reaction mixture was poured into water and the resulting precipitates was filtered and washed with lots of water. It was dried under vacuum for 12 h at room temperature. It was chromatographed over silica gel column using a mixture of $CHCl_3$:MeOH 100/5 as eluent, giving yellow 6-(3,4-dicyanophenylthio)-hexyl-2-chloroacetate finally pure powder was dried in vacuum.

Yield: 1.04 g (80.47%) m.p.: 80 °C, *Anal.* Calc. for $C_{16}H_{17}ClN_2O_2S$ (336.5 g/mol): C, 57.05; H, 5.09; N, 8.32; S, 9.52. Found: C, 56.77; H, 5.11; N, 8.08; S, 9.36%. FT-IR (KBr thin film) ν/cm^{-1}: 3020 (w), 2956, 2928, (Aliph-CH_2), 2226 (CN, st), 1755, 1721 (–COOR, strong), 1476 (w), 1450, 1389, 1370, 1311, 1244 (Ar–S–CH_2), 1145 (st), 1048, 960, 873, 931, 879, 748, 699.; ^1H NMR ([D6]-DMSO) δ: 7.68 (dd, 1H, *ortho* to Ar–S–), 7.64 (s, isomer, 1H, *ortho* to CN and Ar–H), 7.60 (dd, 1H, *ortho* to CN and Ar–H, Phenyl H6), 4.35 (s, br, –COCH_2Cl Aliph., 4.10 (t, 2H, CH_2CH_2–OCO), 2.78 (t, 2H, –S–CH_2–CH_2–) 1.54–1.63 (multiplet, superimposed 4H, –O–CH_2CH_2–CH_2– and –S–CH_2–CH_2–CH_2), 1.27–1.31 (multiplet, 4H, –OCH_2 CH_2CH_2–CH_2– and –S–CH_2–CH_2–CH_2). ^{13}C NMR ([300 MHz, δ, D6]-DMSO): 167.2 (C=O), 143,2 (isomer, Ar–*C*–S), 132,6 (Bz), 132.1, 129.9, 116.8 112.7(Bz), 64.7 (CH_2OCO), 40.9(CO–CH_2Cl) 40.4 (DMSO), 36.8 (S–CH_2), 30.9 (SCH_2CH_2), 28.6 (OCH_2 CH_2), 28.2 ($SCH_2CH_2CH_2$), 25.4 ($CH_2CH_2CH_2CH_2O$) ppm. MS (ESI-MS): *m/z* (%): 370, 0 $[M]^+$.

2.1.2. 6-(3,4-Dicyanophenylthio)-hexyl–2-benzofuranate, BzF (**2**)

About 0.49 g (3.56 mmol) of K_2CO_3 in 50 mL of CH_3CN (Acetonitrile) was added to 0.38 mL (3.56 mmol) of salicylaldehyde. The mixture was stirred at room temperature for 1 h and heated at 40 °C for 1 h. About 1.00 g (2.96 mmol) of 6-(3,4-dicyanophenylthio)-hexyl-2-chloroacetate was added to this mixture at room temperature. The reaction was continued at room temperature for 1 h and refluxed for 6 h. The product formed was poured into water (100 mL). The precipitated product was filtered and washed with excess of water and was dried at 40 °C under vacuum. The product was crystallized from EtOH.

Yield: 1.04 g (86.96%) m.p.: 80 °C, *Anal.* Calc. for $C_{23}H_{20}N_2O_3S$ (404 g/mol): C, 68.32; H, 4.95; N, 6.93; S, 7.92. Found: C, 67.89; H, 4.90; N, 6.48; S, 7.46%. FT-IR (KBr thin film) ν/cm^{-1}: 3093 (w), 3057 (w), 2953, 2906, 2874 (Aliph-CH_2, st), 2231 (CN, st), 1732 (–COOR, strong), 1685, 1599 (w), 1489, 1460, 1396, 1354, 1280 (Ar–S–CH_2), 1195, 1145, 1165, 977, 933, 871, 833, 759(st), 640, 532.; ^1H NMR ([D6]-DMSO) δ: 7.96 (dd, 1H, *ortho* to Ar–S–), 7.72–7.58 (s, isomer, 1H, *ortho* to CN and dd, 1H, *ortho* to CN and Ar–H, Phenyl H6), 7.10–7.22 (multiplet, superimposed benzofuran 5 H), 4.15 (t, 2H, CH_2CH_2–OCO), 3.30 (DMSO, CH_3), 2.96 (t, 2H, –S–CH_2–), 2.52 (DMSO, H_2O), 1.70–1.62 (multiplet, superimposed 4H, –O–CH_2CH_2– and –S–CH_2–CH_2), 1.40–1.20 (multiplet, 4H, –$OCH_2CH_2CH_2$– and –S–CH_2–CH_2–CH_2). ^{13}C NMR ([300 MHz, δ, D6]-DMSO): 169.7 (C=O, ester), 160.7 (O–C–Ar–H (Bz), 147,4 (O–C2 (furan), 137.0 (Bz1, Ar–S), 134.4, 131.1, 130.9 (Bz1), 130.9 (Benzofuran C4), 128.3, 125.2, 122.2 (Bz, Benzofuran C4, C5, C6), 116.8 (Ar–C, *ortho* Ar–S), 116.4 (–CN), 115.8 (CN), 114.6 (Bz1, Ar–*C*–CN), 113.3 (Furan C3), 110.1 (Benzofuran C7), 65.3 (CH_2OCO), 40.99 (DMSO, CH_3), 39.31(S–CH_2), 30.99 (SCH_2CH_2), 28.5 (OCH_2CH_2), 28.3 (SCH_2CH_2), 25.3 ($CH_2CH_2CH_2O$) ppm. MS (Maldi-TOF): *m/z* (%): 405, 2 $[M+1]^+$.

2.1.3. 2,9,16,23-Tetrakis-{6-(-benzofuran-2-carboxylate)-hexylthio}-phthalocyaninato zinc (II) ZnPcBzF (**3**)

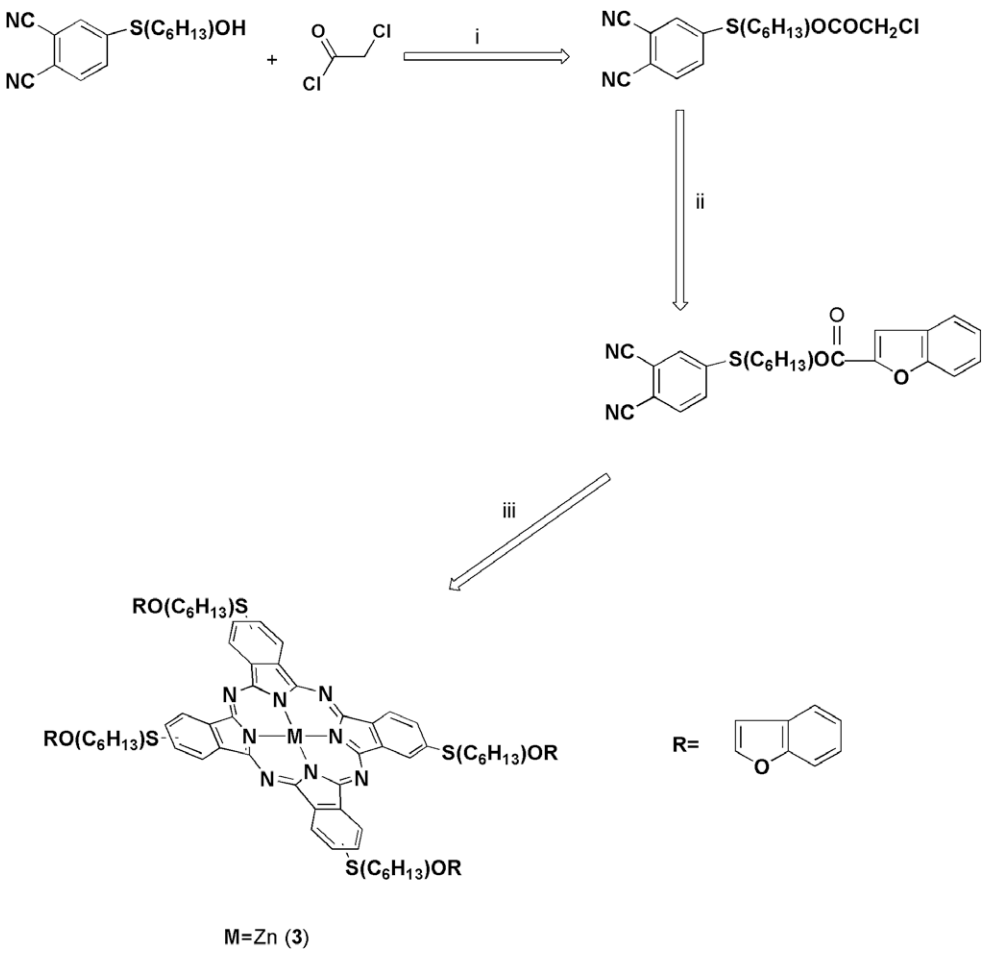
A mixture of **2** (0.150 g, 0.405 mmol), anhydrous Zn $(O_2CMe)_2$ (0.019 g, 0.107 mmol), DBU (one drop) and hexan-1-ol (∼0,2 mL) in a sealed tube was heated 6 h with efficient stirring at 150–160 °C under N_2 atmosphere. After cooling to room temperature, resulting solid was washed successively with MeOH, MeCN, and *i*-PrOH (2-propanol) and filtered to remove impurities until the filtrate was clear. The green–blue product was isolated by silica gel column chromatography with $CHCl_3$/MeOH (9,1 v/v) as eluent. Pure **3** was obtained as viscous green oil after column chromatography over sephadex (THF/$CHCl_3$, 1:2 v/v eluent) and then dried in vacuum. This product exhibited moderate solubility in $CHCl_3$ and excellent solubility in THF, DMF, DMSO and pyridine.

Yield: 0.036 g (23.0%). *Anal.* Calc. for $C_{92}H_{80}N_8O_{12}S_4Zn$ (1681 g/mol): C, 67.68; H, 4.76; N, 6.66; S, 7.61. Found: C, 67.14; H, 4.80; N, 6.45; S, 7.37%. FT-IR (KBr thin film) ν/cm^{-1}: 3085 (w), 3057 (w), 2954, 2906, 2874 (Aliph-CH_2, st), 2231 (CN, st), 1735 (–COOR, strong),1685 1595 (w), 1482, 1456, 1395, 1350, 1282 (Ar–S–CH_2), 1186, 1140, 986, 927, 852, 750, 544.; ^1H NMR ([D6]-DMSO) δ: 8.05–7.90 (dd, 4H, *ortho* to Ar–S–), 7.75–7.43 (m, 8H, *ortho* to CN and Ar–H, Phenyl H6), 7.35–6.96 (m, superimposed 20 H (Benzofuran)), 4.20 (t, 8H, CH_2CH_2–OCO), 3.35 (DMSO, CH_3), 2.98 (t, 8H, –S–CH_2–), 2.53 (DMSO, H_2O), 1.74–1.60 (multiplet, superimposed 16H, –O–CH_2CH_2– and –S–CH_2–CH_2), 1.43–1.20 (multiplet, 16H, –$OCH_2CH_2CH_2$– and –S–CH_2–CH_2–CH_2). ^{13}C NMR ([300 MHz, δ, D6]-DMSO): 170.2 (C=O, ester), 148,5 (O–C2 (furan), 136.8 (Bz1, Ar–S), 135.0, 132.4, 131.0 (Bz1), 130.2 (Benzofuran C4), 128.6, 124.5, 123.6 (Bz, Benzofuran C4, C5, C6), 116.2 (Ar–C, *ortho* Ar–S), 115.4 (–CN), 115.0 (CN), 114.7 (Bz1, Ar–*C*–CN), 114.0 (furan C3), 111.4 (Benzofuran C7), 64.6 (CH_2OCO), 40.9 (DMSO, CH_3), 38.2 (S–CH_2), 29.7 (SCH_2CH_2), 28.2 (OCH_2CH_2), 28.0 (SCH_2CH_2), 25.5 ($CH_2CH_2CH_2O$) ppm. UV–Vis (THF, λ_{max}/nm: 688 (Q), 662 (agg), 620, 355 (B); MS (Maldi-TOF): *m/z* (%): 1682, 4 $[M+1]^+$ and the peaks at 1683, 16584, 1685 and 1686 show the isotopic peak distributions of protonated molecular peak of the complex.

3. Results and discussion

Benzofuran attached zinc phthalocyanine, ZnPcBzF, (**3**), was synthesized by heating pulverized compound **2** with anhydrous

$Zn(O_2CMe)_2$ salt at ca. 150–160 °C under N_2 atmosphere in the presence of 1,8-diazabicyclo [5.4.0] undec-7-ene (DBU) as a strong base (Scheme 1). The yield of ZnPcBzF (**3**) was low (23.0%). Final product was obtained as pure sample after purifications via column chromatography over silica gel. Purification steps were tedious because of peripheral reactive end-group. The blue–green ZnPcBzF (**3**) was isolated as a mixture of isomers as expected. The structures of newly synthesized compounds were verified by FT-IR, ^{1}H NMR, UV–Vis and MALDI-TOF MS spectroscopic methods, as well as by elemental analysis. All the analytical and spectral data are consistent with the predicted structures. While the major strong –CN band appeared at 2231 in the IR spectrum of BzF (**2**) disappeared after conversion to ZnPcBzF (**3**), the strong COOR band in the compound ZnPcBzF (**3**), at around 1700 cm^{-1} came out with small shift. The aliphatic and aromatic peaks at above and below 3000 cm^{-1} and the rest of the spectra is closely similar to that of compound **2** and diagnosed easily. The ^{1}H NMR spectra of ZnPcBzF (**3**), was almost identical with starting compound **1** and BzF (**2**) except small shifts and broadening. The aromatic, aliphatic protons in the lower and higher field region of the ^{1}H NMR spectrum on the periphery and sixteen different aromatic carbon atoms between 110 and 170 ppm in addition to the aliphatic ones (30–65 ppm) in ^{13}C APT spectrum are the most instinctive indicator signals for (**1**), BzF (**2**) and ZnPcBzF (**3**). UV–Vis spectra of the ZnPcBzF (**3**), exhibit characteristic Q and B bands, one in the visible region at *ca*. 600–700 nm (Q-band) attributed to the π–π^* transition from HOMO (Highest occupied molecular orbital) to the LUMO (Lowest unoccupied molecular orbital) of the Pc^{2-} ring, and the other in the UV region at *ca*. 300–400 nm (B-band) arising from the deeper π–π^* transitions [21]. The Q-band absorptions in the UV–Vis absorption spectra of ZnPcBzF (**3**), was observed as a single band with high intensity due to a single π–π^* transition at 688, with shoulder at slightly higher energy side of the Q-band of ZnPcBzF (**3**). The absorption positions of spectrum are dependent on the ionic radii of the metal center and peripheral substitutions. The effect of S-substitution on the periphery for the ZnPcBzF (**3**) was a shift in these intense Q-bands to longer wavelengths as a result of the electron-donating thioether substituents when compared with those of unsubstituted and alkyl or O-substituted derivatives[19,20,22,23]. Maldi-MS spectroscopy has been extensively used to characterize metal-base phthalocyaninates. Therefore, the mass spectra of **1**, BzF (**2**) and ZnPcBzF (**3**), confirmed the proposed structures. The protonated mono isotopic molecular ion peaks were easily identified at *m/z*: 1682 $[M+H]^+$ for ZnPcBzF (**3**). Protonated molecular ion peak was observed at 1682 Da that was exactly overlapped with the mass of the lowest mass of the isotopic mass distribution of complex ZnPcBzF (**3**), calculated theoretically from the elemental composition of the zinc complex. Isotopic peaks resulted from isotopic distribution of the protonated molecular ion of the ZnPcBzF (**3**) was observed in between 1682 and 1690 Da with 1 Da increment in the high mass range. Following the protonated molecular ion peak, a peak group was observed at 38 Da mass higher than the protonated molecular ion peak group resulting almost same pattern. This peak is resulted from the potassium adduct of the neutral ZnPcBzF (**3**).



Scheme 1. Synthetic route of 2,9,16,23-tetrakis-{6-(-thiophene-2-carboxylate)-hexylthio}-metallophthalocyanine {Zn [Pc(S-$C_6H_{12}OH)_4]_2$}. (i) Choloroacetylchloride, TEA, THF, −5 °C, (ii) K_2CO_3, CH_3CN, salicylaldehyde, (iii) $Zn(O_2CMe)_2$, dbu, hexanol.

3.1. Peripheral silver ion binding

3.1.1. UV-measurement

Sulfur donor atoms on the periphery of the tetra or octa substituted phthalocyanines act as heavy metal ionophore and impart a preference for coordination with soft heavy metal ions with different size [3,17,18,23]. Soft-acid and soft-base coordination on peripheral side of ZnPcBzF (**3**) was carried out with Ag^+ ion as acceptor and readily monitored by UV–Vis spectroscopy. Addition of Ag^+ ion to the solution of ZnPcBzF (**3**) caused a gradual color change, from blue–green to intractable black–darkgreen, suggesting the complex formation of ZnPcBzF (**3**), with Ag^+ (Fig. 1). As seen from Fig. 1, binding of Ag^+ to the donor atoms of ZnPcBzF (**3**) resulted in pronounced effects in the Q and B bands, and in the n–π^* transitions. As shown in the Fig. 1, while addition of small increment of Ag^+ to ZnPcBzF (**3**) leads to gradual disappearance of monomeric species at which show absorption at 688, simultaneously enhancing the intensity of the oligomeric aggregated species around 642 nm (inset figure in Fig. 1). B-band of the ZnPcBzF (**3**) shifts to higher energy sides about 10 nm, such as from 362 to 352 nm together with change in intensity. These spectroscopic changes indicate the coordination of Ag^+ by the donor atoms of the phthalocyanines to form less soluble oligomeric aggregated species [3,18,23].

3.1.2. Fluorescence measurements

Excitation spectra of BzF (**2**) and ZnPcBzF (**3**) in THF were obtained upon titration with Ag^+ ion (Fig. 2). As seen from Fig. 2, BzF (**2**) displays three distinct peaks centered near 252 nm, 298 nm and 336 nm. When substituted on Pc ring, the peaks of benzofuran derivative at shorter and longer wavelengths regions are 9 nm red shifted. Both of the excitation intensities of BzF (**2**) and ZnPcBzF (**3**) were diminished by addition of silver ion and there was no spectral shift in maxima of the peaks. When excited at 345 nm of wavelength, BzF (**2**) and ZnPcBzF (**3**) exhibit maximum emission at 402 and 425 nm, respectively (Fig. 3). The maximum fluorescence emission of ZnPcBzF (**3**) gradually reduced and shifted to red region upon addition of Ag^+ ion. Silver ion titration also influenced the emission spectra of BzF (**2**) causing to quenching of fluorescence intensity but spectral shift in maximum was not observed (Fig. 3, inset). Two possibilities must be considered for the reason of the fluorescence quenching effect: The first is attributed to electron density variations on benzofuran moiety, caused by introducing positively charged ions. The second is that the decreased fluorescence is the result of benzofuran substituted Pc aggregations [24].

A bathochromic shift was observed from $\lambda = 425$ nm to $\lambda = 470$ nm along with a steady quenching of the fluorescence intensity on addition of silver ion (Fig. 4). Red shifts in spectra can be explained by a lowering of the LUMO energy level upon binding of benzofuran moiety to Pc core because formation of dimmer spicies

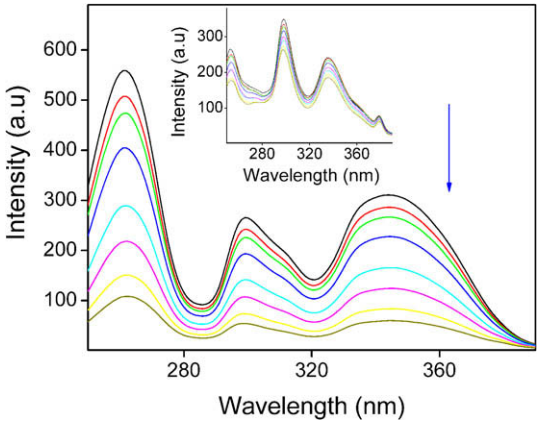


Fig. 2. Excitation spectra of 5 μM **3** in THF as function of Ag^+ ion titration. *Inset*: excitation spectra of 20 μM **2** upon titration with Ag^+ ion. Arrow shows the increase in Ag^+ ion concentration. ($\lambda_{em} = 425$ nm).

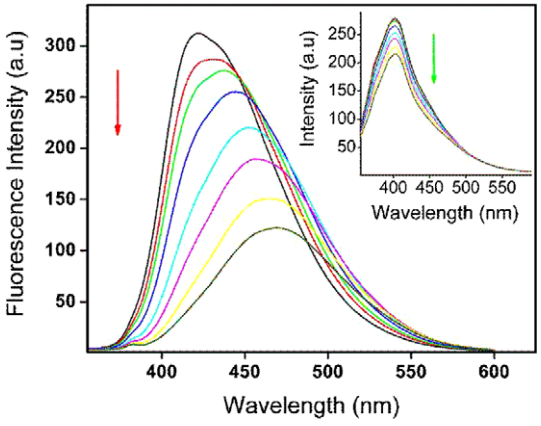


Fig. 3. Emission intensity responses of 5 μM **3** and 20 μM **2** (inset figure) in THF upon addition of 1.0, 2.5, 5.0, 7.5, 10, 25 and 50 μM Ag^+ ion. Arrow shows the increase in Ag^+ ion concentration. ($\lambda_{ex} = 345$ nm).

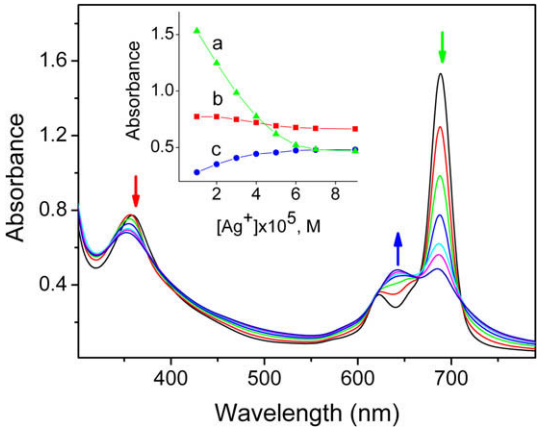


Fig. 1. UV–Visible spectra of 10 μM **3** in THF upon addition of 10, 20, 30, 40, 50, 60, 70, 90 μM Ag^+ ion. *Inset:* spectroscopic changes in Q-band (a), B-band (b) and non-bonding band (c) of **3** during Ag^+ ion titration.

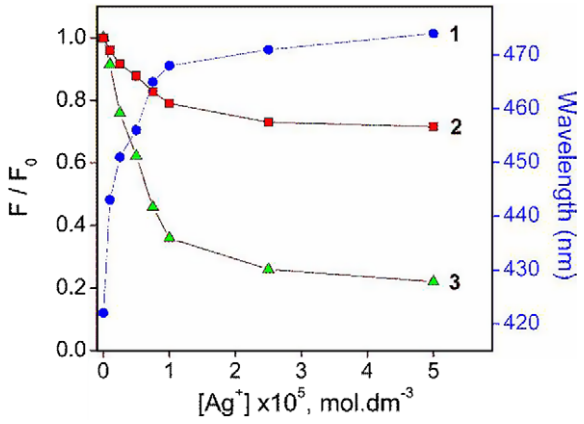


Fig. 4. Change in the maximum emission wavelength of **3** (1) and F/Fo values for **2** (2) and **3** (3) in THF with regard to Ag^+ concentration. ($\lambda_{ex} = 345$ nm).

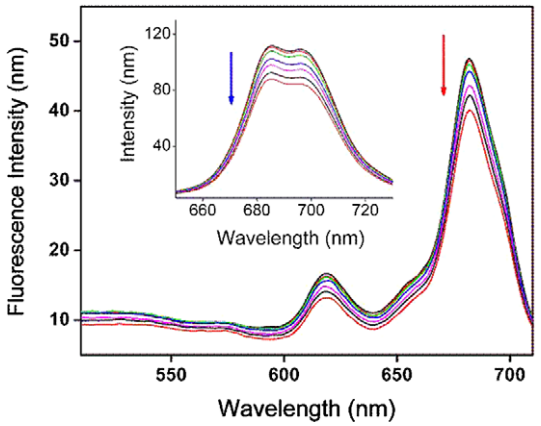


Fig. 5. Excitation spectra of **3** recorded for emission at 730 nm as a function of Ag^+ concentration. *Inset:* emission obtained for excitation at 616 nm. Arrow indicates decrease in intensity.

of ZnPcBzF (**3**) in solution effects π-electron conjugation on molecule causing to lowered LUMO energy level [25,26].

The variation of the electron density of the benzofuran backbone caused by Ag^+ ion plays a minor role both in the quenching of fluorescence and bathochromic effect on the emission spectra of ZnPcBzF (**3**). From the above analysis, it is reasonably deduced that the amplified fluorescence quenching effect of benzofuran moiety results mainly from the Ag^+-induced Pc core aggregation. These facts allow us to conclude that the emission band shift of BzF (**2**) on silver-cation addition is due to cation-π electron interactions [27]. The fluorescence intensity of BzF (**2**) is solely quenched without an accompanying band shift showing that the association between the sulfur atom on BzF (**2**) molecule and the silver-cation is rather weak (Fig. 4). This observation indicates that the electron transfer from the sulfur atom to the photoexcited Pc unit should be weakly depressed by the complexation of sulfur with silver ion.

Fig. 5 depicts the plots of excitation spectra belonging to Pc core [28] of ZnPcBzF (**3**) in long wavelength region with regard to titration with Ag^+ ion. As seen from Fig. 5, the excitation intensity of ZnPcBzF (**3**) was decreased by the addition of silver ion. When excited at wavelength of 616 nm, which is the isobestic point of Pc core, the fluorescence emission of ZnPcBzF (**3**) was also decreased with the increase in the silver ion concentration. This demonstrates that formation of the silver ion complex via sulfur atom on BzF (**2**) influences the fluorescence emission of Pc core. This effect is probably due to the intermolecular aggregation induced by silver ion, which brings Pc unit close each other and interacts with the π-electrons of the Pc core, causes to quenching of fluorescence emission.

4. Conclusion

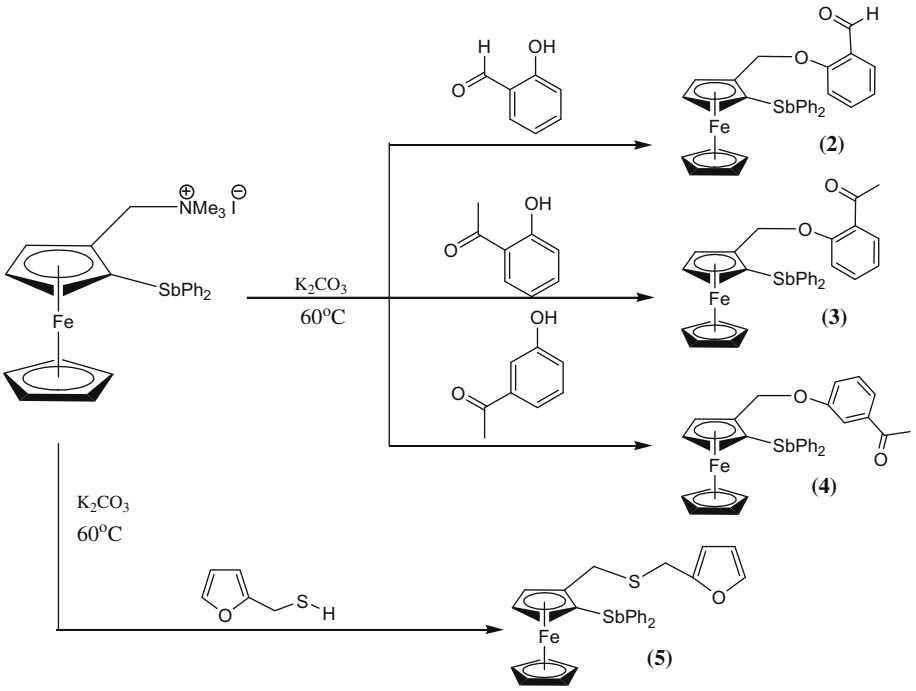
In conclusion, we described the complete synthesis and characterization of a new family of peripherally functionalized zinc phthalocyanine bearing benzofuran derivative which can be used as a new fluorescent chemosensor for Ag(I). Fluoroprobe bounded Pc; ZnPcBzF (**3**), exhibits distinct changes in both spectra of absorbance and fluorescence upon titration with Ag^+ ion where as derivative of benzofuran, BzF (**2**), does not exhibit a definite affinity for Ag^+ ion. Q-band absorption peak of ZnPcBzF (**3**) gradually disappeared and dimeric peak increased in response to treatment with Ag^+ in solution. Fluorescence emission intensities at shorter and longer wavelength regions were quenched but there was only spectral shift at shorter wavelength region which belongs to BzF (**2**). This indicates the complex formation between Ag^+ and ZnPcBzF (**3**), and also shows that Ag^+-induced Pc aggregation plays a major role in the amplified fluorescence quenching.

Acknowledgements

We thank the Research Funds of TUBİTAK (TBAG: Project No: 108T094) and ITU (BAP: Project No: 31472).

References

[1] C.C. Leznoff, A.B.P. Lever (Eds.), Phthalocyanines: Properties and Applications, VCH, Weinheim, 1989 (vol. 1), 1993 (vols. 2 and 3), 1996 (vol. 4).
[2] L. Valli, Adv. Colloid Interf. Sci. 116 (2005) 13.
[3] S.L.J. Michel, A.G.M. Barrett, B.M. Hoffman, Inorg. Chem. 42 (2003) 814.
[4] J.J. Simon, H.J. Andre, Molecular Semiconductors, Springer, Berlin, 1985.
[5] X. Li, L.E. Sinks, B. Rybtchinski, M.R. Wasielewski, J. Am. Chem. Soc. 126 (2004) 10810.
[6] M. Brumbach, D. Placencia, N.R. Armstrong, J. Phys. Chem. C 112 (2008) 3142.
[7] Z. Ou, J. Shen, K.M. Kadish, Inorg. Chem. 45 (2006) 9569.
[8] J.R. Siqueira Jr., L.H.S. Gasparotto, O.N. Oliveira Jr., V. Zucolotto, J. Phys. Chem. C 11 (2008) 9050.
[9] M. Kimura, T. Hamakawa, K. Hanabusa, H. Shirai, N. Kobayashi, Inorg. Chem. 40 (2001) 4775.
[10] Z. Zhao, K.I. Ozoemena, D.M. Maree, T. Nyokong, J. Chem. Soc., Dalton Trans. 7 (2005) 1241.
[11] A. Muranaka, K. Yoshida, T. Shoji, N. Moriichi, S. Masumoto, T. Kanda, Y. Ohtake, N. Kobayashi, Org. Lett. 12 (2006) 2447.
[12] O. Güney, Y. Yılmaz, Ö. Pekcan, Sens. Actuators B 85 (2002) 86.
[13] X.B. Zhang, C.C. Guo, Z.Z. Li, G.L. Shen, R.Q. Yu, Anal. Chem. 74 (2002) 821.
[14] R. Ostuni, M.C. Larciprete, G. Leahu, A. Belardini, C. Sibilia, M. Bertolotti, J. Appl. Phys. 101 (2007) 33116.
[15] A.P. De Silva, H.Q.N. Gunaratne, A.J.M. Huxley, C.P. Mc Coy, J.T. Rademacher, T.E. Rice, Chem. Rev. 97 (1997) 1515.
[16] A. Ehrlich, P.J. Skrdla, W.K. Jarrell, J.W. Sibert, N.R. Armstrong, S.S. Saavedra, A.G.M. Barrett, B.M. Hoffman, Inorg. Chem. 39 (2000) 3963.
[17] M.N. Yarasir, M. Kandaz, B.F. Senkal, A. Koca, Polyhedron 26 (2007) 5235.
[18] M.N. Yarasir, M. Kandaz, B.F. Senkal, A. Koca, B. Salih, Dyes Pigments 77 (2008) 7.
[19] J.G. Young, W. Onyebuagu, J. Org. Chem. 55 (7) (1990) 2155.
[20] M.N. Yarasir, M. Kandaz, A. Koca, B. Salih, Polyhedron 26 (2007) 1139.
[21] M. Gouterman, in: D. Dolphin (Ed.), The Porphyrins, vol. 3, Academic Press, New York, 1978, p. 1.
[22] M. Kandaz, I. Yılmaz, Ö. Bekaroğlu, Polyhedron 19 (2000) 115.
[23] S.J. Lange, J.W. Sibert, A.G.M. Barrett, B.M. Hoffman, Tetrahedron 56 (2000) 7371.
[24] B. Valeur, Molecular Fluorescence Principles and Applications, Wiley-VCH, Weinheim, Germany, 2002.
[25] M. Schmittel, H. Lin, Inorg. Chem. 46 (2007) 9139.
[26] J.I. Kim, I.S. Shin, H. Kim, J.K. Lee, J. Am. Chem. Soc. 127 (2005) 1614.
[27] J. Kang, M. Choi, J.Y. Kwon, E.Y. Lee, J. Yoon, J. Org. Chem. 67 (12) (2002) 4384.
[28] J.C. Swarts, M.D. Maree, J. Porphyrins Phthalocyanins 11 (8) (2007) 613.



Scheme 1.

The methylene protons of the $FcCH_2O$–/$FcCH_2S$– moiety are not magnetically equivalent. This phenomenon has been observed in the ^1H NMR spectra of complexes containing both monodentate and bidentate 1,2-disubstituted ferrocenyl ligands [19,20]. This is also a consequence of the asymmetry of the disubstituted Cp ring.

As expected a higher chemical shift for both aromatic and ferrocenyl protons adjacent to Sb–C bond, as a consequence of the dπ–pπ bond between the metal and the carbon atoms in comparison to those of similar ferrocenyl phosphines [21]. This higher chemical shift is also observed in ^{13}C NMR spectrum of these compounds with respect to phosphines.

The molecular structures of (**2**–**5**) have been confirmed by X-ray crystallography and are shown in Figs. 1–4. Crystal data for all structural analyses are given in Table 1. Selected bond lengths and angles for all compounds are listed in Table 2. All these compounds are monomeric in nature and no significant inter or intramolecular interactions were observed. All these compounds possess planar chirality. Single crystals of (**2**–**5**) were obtained by slow diffusion of hexane in dichloromethane solution. Few other ferrocenyl stibines have previously been characterized by X-ray diffraction. All compounds adopt a mononuclear distorted trigonal pyramid structure considering the lone pair of the antimony atom.

The average $Sb–C_{ferrocenyl}$ bond length found in these ferrocenylstibines is 2.126 Å, which is slightly shorter than that $Sb–C_{phenyl}$ bond length presented by other tertiary stibine, a similar observation was reported earlier also [22,8]. This shortening $Sb–C_{ferrocenyl}$ bond length is ascribed to the effect of bidentate and electron

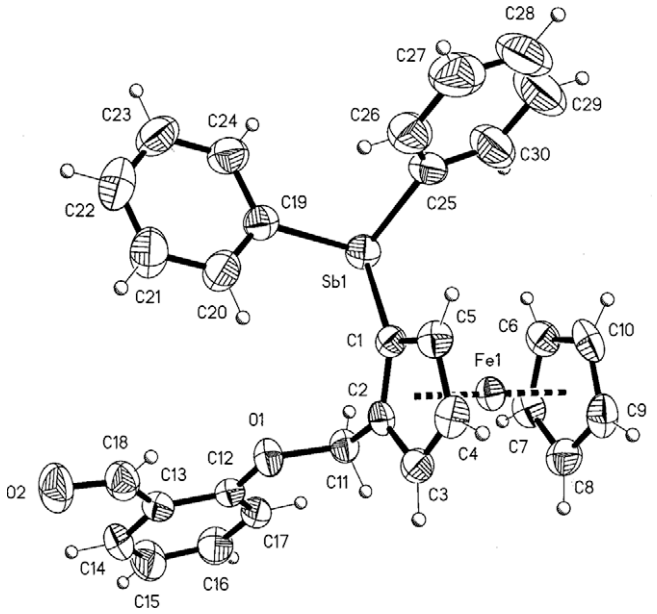


Fig. 1. ORTEP diagram of diphenyl [2-(2-hydroxy-benzaldehyde) methylferrocen-1-yl]stibine (**2**).

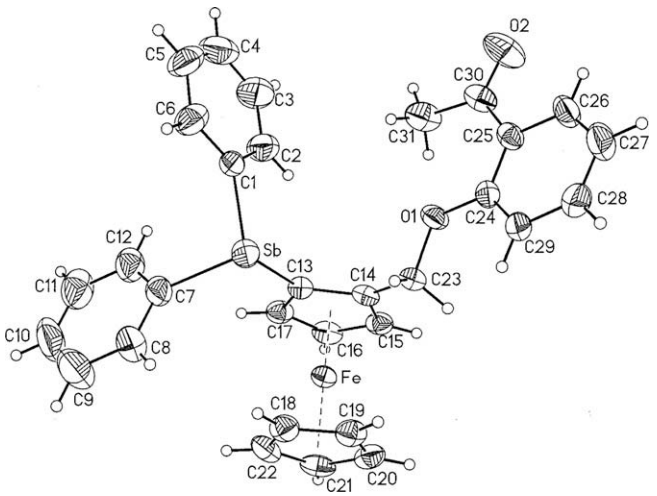


Fig. 2. ORTEP diagram of diphenyl [2-(2-acetyl-hydroxyphenyl) methylferrocen-1-yl]stibine (**3**). One o-acetylphenoxy fragment distorted is not drawn.

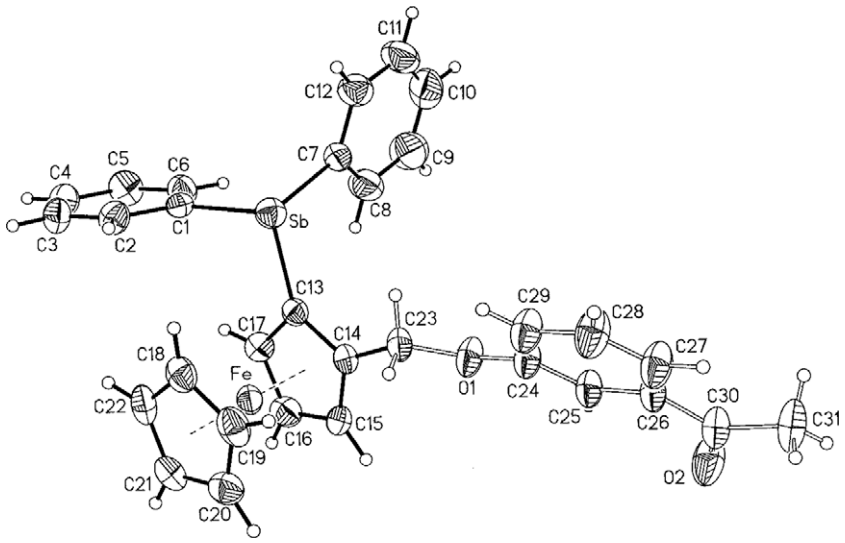


Fig. 3. ORTEP diagram of diphenyl [2-(3-acetyl-hydroxyphenyl) methylferrocen-1-yl]stibine (**4**). One *m*-acetylphenoxy fragment distorted is not drawn.

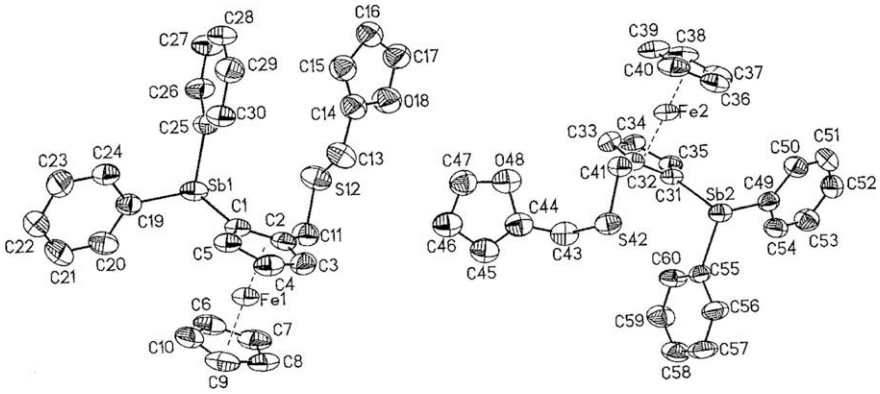


Fig. 4. ORTEP diagram of diphenyl [2-(furan-2-ylmethylthio) methylferrocen-1-yl]stibine (**5**).

Table 1
Crystallographic data for compounds **2**–**5**.

Compound	**2**	**3**	**4**	**5**
Empirical formula	$C_{30}H_{25}FeO_2Sb$	$C_{31}H_{27}FeO_2Sb$	$C_{31}H_{27}FeO_2Sb$	$C_{28}H_{25}FeOSSb$
Formula weight	595.10	609.13	609.13	587.14
Crystal color and shape	yellow plates	yellow prism	yellow prism	Red prism
Crystal system	monoclinic	monoclinic	triclinic	Triclinic
Space group	$P2_1/C$	$P2_1/C$	$P\bar{1}$	$P\bar{1}$
Crystal size mm	0.412 × 0.362 × 0.048	0.34 × 012 × 0.04	0.22 × 0.10 × 0.04	0.28 × 0.22 × 0.15
a (Å)	22.742(2)	22.9382(14)	7.4906(6)	10.6155(12)
b (Å)	8.630(1)	8.5981(5)	10.1133(8)	15.1319(18)
c (Å)	13.283(4)	13.9076(8)	17.5075(14)	16.827(2)
α (°)	90	90	93.048(2)	110.291(2)
β (°)	105.391(1)	107.8080(10)	97.913(2)	99.988(2)
γ (°)	90	90	94.106(2)	96.150(2)
V (Å^3)	2513.5(4)	2611.5(3)	1307.61(18)	2455.6(5)
Z	4	4	2	4
D_{calc} (g cm^{-3})	1.573	1.549	1.547	1.588
μ (mm^{-1})	1.677	1.616	1.613	1.794
2Θ (°)	1.86–25.38	1.86–25.00	1.18–25.00	1.56–25.34
Reflections collected	20 328	20 695	10 750	20 394
Independent reflections	4589	4599	4603	8946
R_{int}	0.0512	0.0567	0.0369	0.0228
R_1 [$I > 2\sigma(I)$]	0.0345	0.0417	0.0410	0.0450
Goodness-of-fit (GOF)	1.000	1.001	1.000	1.000
Maximum/minimum $\Delta\rho$ (e Å^{-3})	0.926/−0.322	0.641/−0.284	0.641/−0.301	0.933/−0.398

Table 2
Selected bond length (Å) and selected bond angles (°) for compounds **2**–**5**.

Compound **2**		Compound **3**		Compound **4**	
Sb–C1	2.127(3)	Sb–C1	2.141(4)	Sb–C1	2.146(4)
Sb–C19	2.146(3)	Sb–C7	2.148(4)	Sb–C7	2.156(4)
Sb–C25	2.149(4)	Sb–C13	2.119(4)	Sb–C13	2.132(4)
C2–C11	1.485(4)	C14–C23	1.491(5)	C14–C23	1.486(6)
C11–O1	1.447(3)	C23–O1	1.441(4)	C23–O1	1.402(7)
O1–C12	1.364(4)	O1–C24	O1–C24	O1–C24	1.374(9)
C18–O2	1.205(4)	C30–O2	1.212(5)	C30–O2	1.228(11)
C1–Sb–C19	96.51(12)	C13–Sb–C1	96.34(16)	C13–Sb–C1	93.71(16)
C1–Sb–C25	96.06(13)	C13–Sb–C7	96.23(16)	C13–Sb–C7	97.79(16)
C19–Sb–C25	95.09(14)	C1–Sb–C7	94.89(17)	C1–Sb–C7	98.75(16)
C12–O1–C11	118.4(2)	C24–O1–C23	118.4(3)	C24–O1–C23	122.5(6)
O2–C18–C13	123.7(4)	O2–C30–C25	118.8(4)	O2–C30–C26	121.4(9)
O1–C11–C2	108.4(2)	O1–C23–C14	108.5(3)	O1–C23–C14	116.3(4)
O1–C12–C17	124.2(3)	O1–C24–C25	117.3(4)	O1–C24–C29	123.9(8)

Compound **5**			
Sb1–C1	2.132(4)	Sb2–C31	2.122(4)
Sb1–C19	2.166(5)	Sb2–C49	2.155(4)
Sb1–C25	2.143(4)	Sb2–C55	2.152(4)
C2–C11	1.489(6)	C32–C41	1.495(5)
C11–S12	1.808(5)	C41–S42	1.817(4)
S12–C13	1.794(6)	S42–C43	1.805(5)
C13–C14	1.506(8)	C43–C44	1.511(10)
C1–Sb–C19	96.85(16)	C31–Sb2–C49	95.52(15)
C1–Sb–C25	96.11(16)	C31–Sb2–C55	96.26(15)
C19–Sb–C25	96.62(17)	C49–Sb2–C55	96.94(16)
C11–S12–C13	101.4(3)	C41–S42–C43	99.9(2)
C2–C11–S12	115.0(3)	C32–C41–S42	113.0(3)
C14–C13–S12	111.0(5)	C44–C43–S42	113.4(14)
C17–O18–C14	108.5(6)	C47–O48–C44	105.5(8)

donating. This may be due to the pπ–dπ bonding to a greater extent and thus shortening of Sb–$C_{ferrocenyl}$ bond length in all the compounds [12].

The unit cell of compound (**4**) contains two independent molecules per asymmetric unit. The *m*-acetylphenoxy portion is disordered and it was modeled in two major contributions. The average Sb–C bond length value is 2. 142 Å, with a Sb–$C_{ferrocenyl}$ bond length of 2.135 Å, which is slightly larger than those found in compounds (**2**) and (**3**).

The Sb–$C_{ferrocenyl}$ bond distances found in compounds (**2**–**5**) are slightly larger than Sb–$C_{ferrocenyl}$ bond lengths found in previously reported stibine (2.124 Å) [12,13], which may be due to the electron withdrawing capabilities of the organic moiety. In these stibines, similar bond distances and bond angles of the ferrocenyl –CH_2OR/–CH_2SR groups have been observed without any significant changes.

In compounds (**2**), (**3**), (**4**) and (**5**) geometry around antimony is pyramidal, showing average C–Sb–C angles of 95.91, 95.82, 96.74 and 96.37 respectively which are not very similar to the bond angles found in other tertiary stibines [23–25]. It is worthy to note that there is no evidence of Sb–O or Sb–S intramolecular interactions, which is probably caused by stereoelectronic factors in compounds (**2**–**5**). This type of interaction was found in similar compounds with CH_2NR_2 pendant arm.

3. General synthesis

All the solvents were distilled immediately prior to use. All the reactions were performed under an atmosphere of oxygen-free dry nitrogen. Melting points were obtained on a MEL-TEMP II Fisher and are uncorrected. FAB^+ mass spectra were recorded on a JEOL SX102 double-focusing mass spectrometer with reverse geometry using a 6-kV Xenon beam (10 am); nitrobenzyl alcohol was used as matrix for recording the mass spectra. ^1H and ^{13}C NMR spectra were recorded in $CDCl_3$ or CD_3OD on JEOL ECLIPSE 300 (^1H: 300.5311 MHz; ^{13}C: 75.5757) spectrometer.

3.1. Diphenyl [2-(2-hydroxy-benzaldehyde) methylferrocen-1-yl]stibine (*2*)

In a Schlenk tube, under N_2, 0.14 mL (1 mmol) of salicyladehyde were added to a mixture of 0.645 g (1 mmol) of *Rac*-diphenyl[(*N,N*-trimethylaminomethylferrocenyl)iodide]stibine (**1**) [12] and 1.38 g (10 mmol) of K_2CO_3 in acetonitrile. After stirring for 8 h at 80 °C the solvent was evaporated and the mixture was extracted with a water/chloroform mixture and dried with Na_2SO_4 anhydrous. Compound (**2**) was obtained as red crystals after recrystallization from a chloroform/hexane mixture. Yield : 75%, IR (ν cm^{-1}): 3041.46 (C–H aromatic), 11681.38 (C=O), 484.90 (Sb–C) ^1H NMR ($CDCl_3$, 300 MHz; δ: ppm): 4.55 (1H, s, C*H*, C_3H_5), 4.91,5.05 (2H, d^2, J = 10 Hz, CH_2), 7.25–7.36 (14H, m, Ph), 4.13 (5H, s, C_5H_5); 10.02 (1H, s, C*H*O), ^{13}C NMR ($CDCl_3$, 75 MHz; ppm): 75.45(C_{FC}–Sb), 138.16(C_{Ph}–Sb), 52.85 (CH_2), 189.6(CHO), 69.28(C_5H_5), MS-FAB^+ *m/z* (%): 595 (90%) $[M]^+$, 473 (100%) $[M-C_7H_5O_2]^+$, 275 (15%) $[M-C_{17}H_{17}FeO_2]^+$, 199 (18%) $[C_{11}H_{10}Fe]^+$.

3.2. Diphenyl [2-(2-acetyl-hydroxiphenyl) methylferrocen-1-yl]stibine (*3*)

By following the same procedure used for the preparation of (**2**), the red–orange product (**3**) was obtained after 8 h stirring from *Rac*-diphenyl[(*N,N*-trimethylaminomethyl ferrocenyl)iodide]stibine (**1**) (0.645 g, 1 mmol) and 1-(2-hydroxyphenyl)-ethanone (0.13 mL, 1 mmol). Yield: 80%, IR (ν cm^{-1}): 3060.33 (C–H aromatic), 1661.13 (C=O), 487.02 (Sb–C) ^1H NMR ($CDCl_3$, 300 MHz; δ: ppm): 4.55 (1H, s, C*H*, C_3H_5), 6.97–7.22 (14H, m, Ph), 4.09, 5.25 (2H, d^2, J = 8 Hz CH_2), 4.09 (5H, s, C_5H_5), 2.28 (3H, s, CH_3), ^{13}C NMR ($CDCl_3$, 75 MHz; ppm): 87.30(C_{FC}–Sb), 138.63(C_{Ph}–Sb),

31.02 (CH_3), 158(C=O), 69.25 (C_5H_5), MS-FAB$^+$ *m/z* (%):608 (34%) $[M]^+$, 473 (75%) $[M-C_8H_7O_2]^+$, 275 (46%) $[M-C_{19}H_{17}FeO_2]^+$, 199 (100%) $[C_{11}H_{10}Fe]^+$.

3.3. Diphenyl [2-(3-acetil-hydroxyphenyl) methylferrocen-1-yl]stibine (*4*)

By following the same procedure used for the preparation of (**2**), the red–orange product (**4**) was obtained after 8 h stirring from *Rac*-diphenyl [(*N*,*N*-trimethylaminomethylferrocenyl) iodide]stibine (**1**) (0.645 g, 1 mmol) and 1-(3-hydroxiphenyl)-etanone (0.12 mL, 1 mmol). Yield: 79%, IR (ν cm^{-1}): 3047.11 (C–H aromatic), 1683.25 (C=O), 484.90 (Sb–C), ^{1}H NMR ($CDCl_3$, 300 MHz; δ: ppm): 4.53 (1H, s, C_3H_5), 7.24–7.36 (14H, m, Ph), 4.84, 4.98 (2H, d^2, J = 7 Hz CH_2), 4.12 (5H, s, C_5H_5), 2.52 (3H, s, CH_3), ^{13}C NMR ($CDCl_3$, 75 MHz; ppm): 75.28 (C_{FC}–Sb), 139.38 (C_{Ph}–Sb), 30.41 (CH_2), 69.28 (C_5H_5), 198.17 (C=O), MS-FAB$^+$ *m/z* (%): 608 (100%) $[M]^+$, 473 (84%) $[M-C_8H_7O_2]^+$, 275 (33%) $[M-C_{19}H_{17}FeO_2]^+$, 199 (74%) $[C_{11}H_{10}Fe]^+$.

3.4. Diphenyl [2-(furan-2-ylmethylthio) methylferrocen-1-yl]stibine (*5*)

By following the same procedure used for the preparation of (**2**), the red–orange product (**5**) was obtained after 8 h stirring from *Rac*-diphenyl[(*N*,*N*-trimethylaminomethylferrocenyl) iodide]stibine (**1**) (0.645 g, 1 mmol) and 2-furyl-mercaptane (0.1 mL, 1 mmol). Yield: 74%, IR (ν cm^{-1}): 3476 (O–H), 3057 (C–H aromatic), 1063 (C–S), 452 (Sb–C) ^{1}H NMR ($CDCl_3$, 300 MHz; δ: ppm): 3.80 (1H, s, C_3H_5), 7.22–7.58 (10H, m, Ph), 4.25, 4.37 (2H, d^2, J = 10 Hz CH_2), 6.27 (2H, d, J = 15 Hz, C_4H_3O), 3.99 (5H, s, C_5H_5) 6.05 (1H, d, J = 15 Hz, C_4H_3O), ^{13}C NMR ($CDCl_3$, 75 MHz; ppm): 89.98 (C_{FC}–Sb), 32.6(CH_2), 136.9 (C_{Ph}–Sb), 69.37(C_5H_5) MS-FAB$^+$ *m/z* (%):586 (100%) $[M]^+$, 473 (84%) $[M-C_5H_5SO]^+$, 397 (7%) $[M-C_{10}H_{10}SO]^+$, 275 (10%) $[M-C_{17}H_{15}FeSO]^+$, 199 (74%) $[C_{11}H_{10}Fe]^+$.

4. X-ray crystallography

The X-ray intensity data were measured at 293°K on a Bruker SMART APEX CCD-based X-ray diffractometer by using monochromated Mo Kα radiation (λ = 0.71073 Å). The detector was placed at a distance of 4.837 cm from the crystals in all cases. Empirical absorption correction's and SHELXTL V 6.12 (Sheldrick, 2000) program were used for compounds **2** and **3**. For compounds **4** and **5** the absorption correction method was multi-scans and the program used was SADABS, Bruker (2004). SADABS and SAINT-PLUS. Bruker AXS Inc., Madison, Wisconsin, USA.

Supplementary data

CCDC 719548, 719549, 719550 and 719551 contain the supplementary crystallographic data for compounds **2**, **3**, **4** and **5**. These data can be obtained free of charge via http://www.ccdc.cam.ac.uk/conts/retrieving.html, or from the Cambridge Crystallographic Data Centre, 12 Union Road, Cambridge CB2 1EZ, UK; fax: (+44) 1223-336-033; or e-mail: deposit@ccdc.cam.ac.uk

Acknowledgement

Authors are grateful to DGAPA, UNAM for granting a project (IN 206809).

References

[1] F.A. Cotton, J. Organomet. Chem. 637 (2001) 18.
[2] O.B. Sutcliffe, M.R. Bryce, Tetrahedron: Asymmetry 14 (2003) 2297. and references quoted therein.
[3] A. Federman Neto, A.C. Pelegrino, V.A. Darin, Trends Organomet. Chem. 4 (2002) 147.
[4] S. Cabrera, O.G. Mancheno, R.G. Arrayas, I. Alonso, P. Mauleon, J.C. Carretero, Pure Appl. Chem. 78 (2006) 257.
[5] R. Gomez Arrayas, J. Adrio, J.C. Carretero, Angew. Chem., Int. Ed. Engl. 45 (2006) 7674.
[6] R.C.J. Atkinson, V.C. Gibson, N.J. Long, Chem. Soc. Rev. 33 (2004) 313.
[7] T.J. Colacot, Chem. Rev. 103 (2003) 3101.
[8] H.-U. Blaser, Adv. Synth. Catal. 344 (2002) 17. and references quoted therein.
[9] R.C. Atkinson, V.C. Gibson, N.J. Long, Chem. Soc. Rev. 33 (2004) 313.
[10] T.J. Colacot, Platinum Met. Rev. 45 (2001) 22.
[11] U. Siemeling, T.-C. Auch, Chem. Soc. Rev. 34 (2005) 584.
[12] P. Sharma, J.G. López, C. Ortega, N. Rosas, A. Cabrera, C. Álvarez, A. Toscano, E. Reyes, Inorg. Chem. Commun. 9 (2006) 82.
[13] J. Vázquez, P. Sharma, A. Cabrera, A. Toscano, S. Hernández, J. Pérez, R. Gutiérrez, J. Organomet. Chem. 692 (2007) 3486.
[14] P. Barbaro, C. Bianchini, G. Giambastiani, S.L. Parisel, Coord. Chem. Rev. 248 (2004) 2131.
[15] M. Lotz, K. Polborn, P. Knochel, Angew. Chem., Int. Ed. Engl. 41 (2002) 4708.
[16] F. Spindler, C. Malan, M. Lotz, M. Kesselgruber, U. Pittelkow, A. Rivas-Nass, O. Briel, H.U. Blaser, Tetrahedron: Asymmetry 15 (2004) 2299.
[17] T. Sturm, W. Weissensteiner, F. Spindler, Adv. Synth. Catal. 345 (2003) 160.
[18] A.M. Ortiz, P. Sharma, D. Pérez, N. Rosas, A. Cabrera, L. Velasco, A. Toscano, S. Hernández, J. Organomet. Chem. 694 (2009) 2037.
[19] M. Weinman, A. Gehrig, B. Schiemenz, G. Huttner, B. Nuber, G. Reiwald, H. Lang, J. Organomet. Chem. 563 (1998) 3147.
[20] Y. Takaguchi, A. Hosowaka, S. Yamada, J. Motoyoshishya, H. Aoyama, J. Chem. Soc., Perkin Trans. I (1998) 5299.
[21]] R. Malacea, L. Routaboul, E. Manoury, J.C. Daran, R. Poli, J. Organomet. Chem 693 (2008) 1469.
[22] H.-U. Blaser, W. Brieden, B. Pugin, F. Spindler, M. Studer, A. Togni, Top. Catal. 19 (2002) 3. and references quoted therein.
[23] P. Sharma, N. Rosas, A. Cabrera, A. Toscano, M.J. Silva, D. Pérez, L. Velasco, J. Pérez, R. Gutiérrez, J. Organomet. Chem. 690 (2005) 3286.
[24] J. Vela, P. Sharma, A. Cabrera, C. Álvarez, N. Rosas, S. Hernández, A. Toscano, J. Organomet. Chem. 634 (2001) 5.
[25] P. Sharma, A. Cabrera, N. Rosas, S. Hernández, R. Lelagadec, J. Valdés, J.L. Arias, Main Group Met. Chem. 21 (1998) 303.

(Θ_{zz}) or the sum of the Hammett constants σ_p and σ_m ($\sum\sigma_p$ and $\sum\sigma_m$) of the substituted Cp rings are explored.

2. Computational methods

All substituted Cp anions were optimized and characterized via frequency calculations at the RHF/6-311++G** level of theory for the purpose of determining the quadrupole moments, Θ_{zz}. The RHF/6-311G** level of theory was chosen because it gives excellent agreement between the calculated and experimental Θ_{zz} values of benzene (calculated: −8.76 DÅ [19,20]; experimental: −8.7 ± 0.5 DÅ [21]) and hexafluorobenzene (calculated: +10.06 DÅ [19,20]; experimental: +9.5 ± 0.5 DÅ [21]). We employed the 6-311++G** basis set for this work because a proper description of the electron density of anions requires diffuse functions. Of course, the molecular quadrupole moment is a 3 X 3 tensor and the calculations gave the diagonal quadrupole moment tensor components Θ_{ii} ($i = x, y$ or z) and the off-diagonal tensor components Θ_{ij} ($i = x, y$ or z; $j = x, y, z$; $i \neq j$). The Θ_{zz} values were determined from the equation $\Theta_{zz} = \Theta_{zz} - 0.5(\Theta_{xx} + \Theta_{yy})$. For the planar Cp rings the off-diagonal tensor components are all zero and the equation requires no approximations. For the Cp anions with substituents that extend above and below the plane of the ring the off-diagonal tensor components are non-zero, however, their magnitudes range from 0.1% to 10% of the value of the diagonal tensor components and therefore the equation is an excellent approximation of the Θ_{zz} value.

The Cp–Li and Cp–Na complexes were optimized, characterized and binding energies were calculated at the MP2(full)/6-311++G** level of theory, and the counterpoise method was subsequently employed to account for basis set superposition error (BSSE) [22]. This level of theory was chosen for binding energy calculations because the MP2(full)/6-311G** calculated Na^+-benzene binding energy gives excellent agreement with experiment; the calculated ΔH_{298} is −24.51 kcal/mol and the gas-phase experimental value is −22.13 ± 1.39 kcal/mol [23]. As was the case with the Θ_{zz} calculations, we incorporated diffuse functions to describe the anionic character of Cp. Metal charges were determined using the NBO method [24]. Hammett σ_m and σ_p constants were taken from standard references [25].

The Cp and Cp-cation geometries conformed to the highest level of symmetry, however, at the MP2(full)/6-311++G** level of theory the frequency calculation for certain Cp anions had one or more imaginary frequencies, indicating the optimized structure was not a minimum (details can be found in Supplementary material). These curious imaginary frequencies disappeared for methods other than MP2, and they were also absent when diffuse functions were omitted from the basis set. Similar results have been recently documented for aromatic compounds optimized at the MP2, MP3, CISD, and CCSD levels of theory, and explained as arising from a two-electron basis set incompleteness error (BSIE) where distortion from planarity improves the ability of the basis sets to recover σ–π electron correlation to which correlated wave functions such as MP2 are susceptible [26]. To account for the anionic nature of the Cp ring, all binding energies are reported at the MP2(full)/6-311++G** level of theory. For the Cp rings that were not minima at the MP2(full)/6-311++G** level of theory, the minimum character was assured by the absence of imaginary frequencies when the optimizations were done at the RHF/6-311++G** theoretical level. For the Cp-cation complexes that were not minima at the MP2(full)/6-311++G** level of theory, the minimum character was assured by the absence of imaginary frequencies when the optimizations were done at the MP2(full)/6-311G** theoretical level. All calculations were performed using the GAUSSIAN03 suite of programs [27].

3. Results and discussion

The quadrupole moments of the parent and substituted Cp anions, calculated at the RHF/6-311++G** level of theory, are shown in Table 1. The MP2(full)/6-311++G** Cp–Li and Cp–Na ring centroid-metal distances (dCp–Li, dCp–Na), binding energies ($E_{bind,Li}$, $E_{bind,Na}$), and the NBO calculated metal charges (q_{Li}, q_{Na}) are also collected in Table 1. The general structure of the complexes is shown in Fig. 1.

3.1. Effects of substitution on Cp-metal distance

The values calculated for the Cp–Li and Cp–Na ring centroid-metal distances are in agreement with results obtained by previous computational work [15]. The calculated distances of 1.72 Å for Cp–Li and 2.22 Å for Cp–Na are significantly shorter than the Cp–Li and Cp–Na distances found in the solid-state. The solid-state literature is rich with examples of Cp–Li and Cp–Na complexes with differently substituted Cp rings and/or different solvent conditions [6] and these complexes have ring centroid-metal distances about 0.2–0.3 Å longer than the calculated values presented here. For instance, the crystal structure of a Cp–Li complex where the Li^+ metal is solvated by TMEDA has a ring centroid-metal distance of 1.92 Å and a Cp–Na complex where the Na^+ metal is solvated by three pyridine molecules has a solid-state Cp–Na distance of 2.40 Å [6]. As has previously been discussed, the primary reason for the discrepancy between the calculated values and the solid-state values is due to solvent coordination in the latter [15]. As shown in Fig. 2, the correlation between Cp–Li bond distances and the Cp Θ_{zz} values for the entire set of 30 substituted Cp rings is bad ($R^2 = 0.24$). The greatest outlier from the line of best fit is the amide (–NHC-OCH_3) substituted Cp (**27**) with a Cp–Li distance of 1.83 Å. This is the only substituted Cp where the substituent chelates to the metal and the calculated structure is shown in Fig. 3. This essentially mimics what is observed in the solid-state; chelation of Li^+ either by solvent or other complexing agents results in a longer Cp–Li ring centroid-metal distance. Removing the chelating Cp (**27**) from the analysis substantially improves the correlation with the Cp Θ_{zz} values, however, the R^2 of 0.55 is still not very good (Fig. 2). Although none of the other substituents chelate to the Li^+, the other major deviations from the line of best fit generally belong to Cp rings with substitution patterns that are likely to cause steric interactions between the Cp substituents and the lithium cation. Thus, if we omit the Cp rings with substituents that contain three or more linearly bonded atoms (**15**, **16**, **21**, **22**, **24**, **25** and **27**), along with those containing four or more methyl groups (**17**, **18** and **20**) we see a marked improvement for the correlation between the Cp–Li distance and the Cp Θ_{zz} values ($R^2 = 0.93$, Fig. 2).

Extending this analysis to the correlation between the Cp–Li distance and the $\sum\sigma_p$ values of the Cp rings shows slightly different results (Fig. 2). For all Cp rings, the correlation is significantly better ($R^2 = 0.45$) than it was with the Θ_{zz} values, and when Cp (**27**) is omitted the correlation is decent ($R^2 = 0.74$). However, for the Cp rings with the 20 sterically least hindering substitution patterns the correlation with the Cp $\sum\sigma_p$ values is much worse ($R^2 = 0.68$) than it was for Θ_{zz} values (Fig. 2). We next looked at the correlation between the Cp–Li distance and the Cp $\sum\sigma_m$ values and found significant improvement. For all 30 substituted Cp rings the line of best fit has an R^2 value of 0.53, and when Cp (**27**) is omitted the correlation improves to near-unity ($R^2 = 0.95$, Fig. 2). Omitting the Cp rings with sterically hindering substitution patterns does not improve the correlation ($R^2 = 0.95$, Fig. 2). Thus, the $\sum\sigma_m$ values of the substituted Cp rings allow us to discuss trends in Cp–Li ring centroid-metal distances without discarding certain substituents or substitution patterns based on the somewhat arbitrary definitions of steric hindrance we introduced above.

Table 1
The RHF/6-311++G** calculated quadrupole moments, Θ_{zz} (DÅ), for the substituted the cyclopentadienyl anions (Cp), and the MP2(full)/6-311++G** calculated Cp-metal distances (d_{Cp-Li}, d_{Cp-Na} (Å)), binding energies ($E_{bind,Li}$, $E_{bind,Na}$ (kcal/mol)), and NBO metal charges (q_{Li}, q_{Na}) for the Cp–Li (normal font) and Cp–Na (italicized font) complexes.

Cp	Θ_{zz}	d_{Cp-Li} d_{Cp-Na}	$E_{bind,Li}$ $E_{bind,Na}$	q_{Li} q_{Na}	Cp	Θ_{zz}	d_{Cp-Li} d_{Cp-Na}	$E_{bind,Li}$ $E_{bind,Na}$	q_{Li} q_{Na}
1	−3.84	1.7248 *2.2236*	−166.3 *−134.1*	0.7545 *0.8836*	**16**	+4.91	1.7314 *2.2268*	−164.0 *−132.1*	0.7631 *0.8836*
2	+15.73	1.7859 *2.3082*	−134.9 *−108.4*	0.8488 *0.9466*	**17**	+7.47	1.7146 *2.2153*	−167.0 *−133.0*	0.8051 *0.9169*
3	+3.43	1.7514 *2.2573*	−153.4 *−123.5*	0.7965 *0.9133*	**18**	+5.40	1.7168 *2.2166*	−166.7 *−133.0*	0.7959 *0.9097*
4	−0.02	1.7358 *2.2405*	−158.5 *−127.8*	0.7769 *0.9005*	**19**	−0.99	1.7247 *2.2227*	−166.6 *−134.5*	0.7625 *0.8852*
5	+15.61	1.7813 *2.2791*	−131.5 *−107.1*	0.8905 *0.9297*	**20**	+9.41	1.7228 *2.2246*	−165.2 *−132.3*	0.8236 *0.9258*
6	+12.66	1.7721 *2.2684*	−136.2 *−110.5*	0.8734 *0.9336*	**21**	+6.34	1.7465 *2.2444*	−153.0 *−123.9*	0.7881 *0.9057*
7	+8.14	1.7610 *2.2611*	−142.9 *−115.7*	0.8508 *0.9306*	**22**	+4.39	1.7508 *2.2484*	−151.4 *−122.7*	0.7910 *0.9076*
8	+4.17	1.7502 *2.2490*	−149.9 *−121.2*	0.8236 *0.9215*	**23**	+0.65	1.7355 *2.2330*	−164.4 *−133.4*	0.7790 *0.8978*
9	+1.11	1.7389 *2.2356*	−157.4 *−127.1*	0.7932 *0.9073*	**24**	−0.87	1.7333 *2.2339*	−163.4 *−132.9*	0.7724 *0.9008*
10	+15.15	1.7890 *2.2889*	−129.7 *−106.1*	0.8851 *0.9146*	**25**	+4.43	1.7338 *2.2336*	−163.2 *−132.8*	0.7723 *0.9006*
11	+8.66	1.7675 *2.2675*	−140.8 *−114.3*	0.8520 *0.9270*	**26**	+0.90	1.7311 *2.2259*	−166.4 *−135.1*	0.7822 *0.8981*
12	+5.17	1.7544 *2.2544*	−148.1 *−119.9*	0.8255 *0.9212*	**27**	+1.91	1.8258 *2.3026*	−175.9 *−146.2*	0.7363 *0.8756*
13	+2.75	1.7407 *2.2380*	−156.2 *−126.1*	0.7949 *0.9081*	**28**	+9.08	1.7652 *2.2641*	−142.1 *−114.8*	0.8088 *0.9192*
14	+6.16	1.7406 *2.2387*	−157.9 *−128.2*	0.8144 *0.9152*	**29**	+6.65	1.7466 *2.2466*	−154.1 *−124.4*	0.7843 *0.9008*
15	+4.34	1.7313 *2.2261*	−164.2 *−133.0*	0.7826 *0.8985*	**30**	+3.23	1.7385 *2.2376*	−158.1 *−127.6*	0.7994 *0.9091*

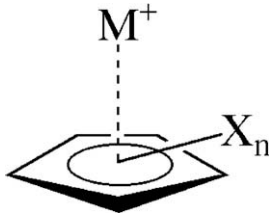


Fig. 1. General structure for the Cp-cation complexes.

Similar results are obtained for the Cp–Na complexes. The correlation between the Cp–Na ring centroid-metal distance and either the Θ_{zz} or $\sum\sigma_p$ values is poor to decent depending on whether all substituted rings are included in the analysis, Cp (**27**) with the metal chelating amide group is discarded, or the sterically hindering substitution patterns are discarded, and they can be found in Supplementary material. However, the correlation between the Cp–Na distance and the Cp $\sum\sigma_m$ values is excellent so long as Cp (**27**) is omitted (R^2 = 0.91, Fig. 4). Discarding the Cp rings with the sterically hindering substitution patterns doesn't improve the correlation. The $\sum\sigma_m$ graphs for all Cp–Na complexes and for

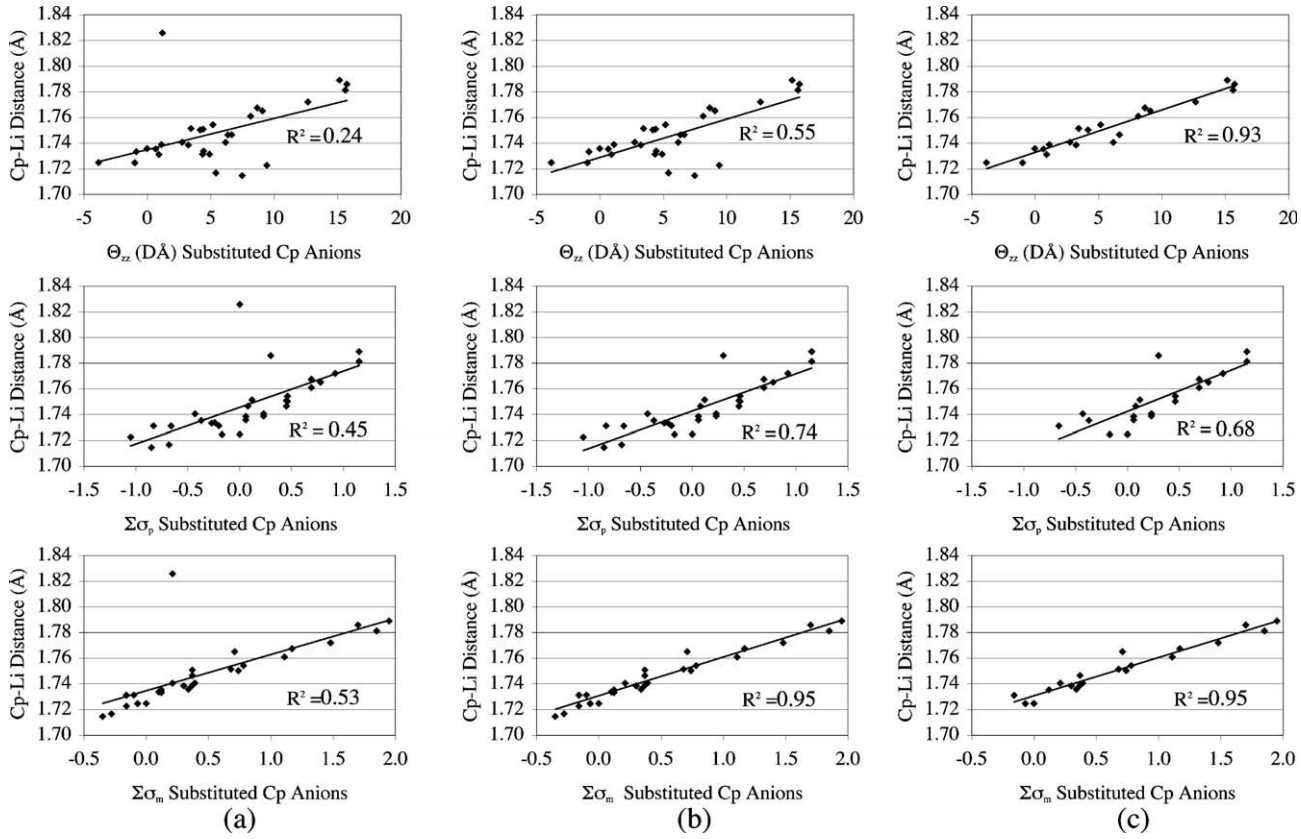


Fig. 2. Cp–Li distances plotted against Cp Θ_{zz}, $\sum\sigma_p$ and $\sum\sigma_m$ values for (a) all Cp rings; (b) all Cp rings except the metal coordinating amide-substituted Cp (**27**); (c) the 20 sterically least hindering groups.

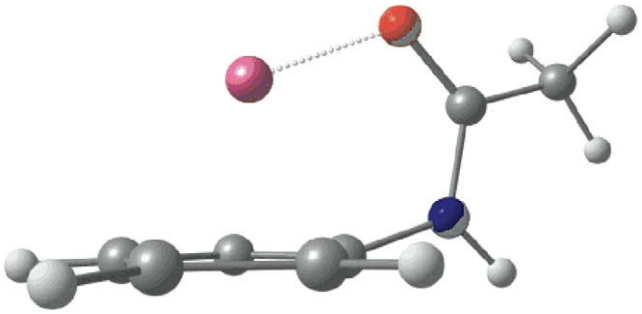


Fig. 3. Structure of Li^+ bound to methylamide substituted Cp anion (**27**). The amide oxygen chelates the lithium.

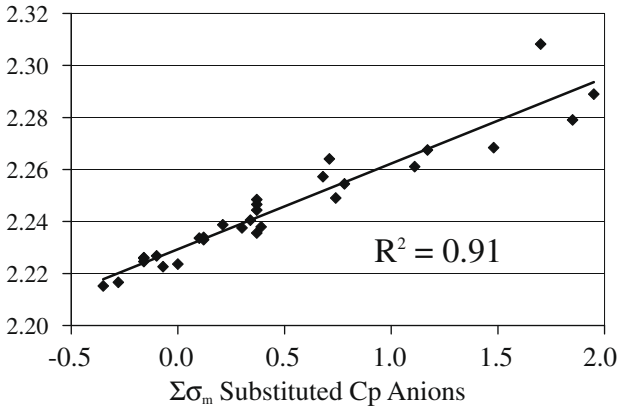


Fig. 4. Cp–Na distances plotted against Cp $\sum\sigma_m$ values for all Cp rings except the metal coordinating amide-substituted Cp (**27**).

the Cp–Na complexes without sterically hindering groups are in Supplementary material. It is worth noting at this point that the Hammett constants σ_p and σ_m were not developed for the purpose of predicting the properties of Cp-metal complexes. They were derived from the ionization of *para*- and *meta*-substituted benzoic acids, respectively, and have traditionally been employed to understand the reactivity of an atom or group directly attached to an aromatic [28]. More specifically, they are commonly used to probe how the reactivity of the atom or group attached to an aromatic ring changes upon *para*- or *meta*-substitution [28]. Recently, however, Hammett constants have been investigated for how well they correlate with arene–arene binding energies [29–31] and the work presented here extends their use along a similar vein.

The best predictor of Cp–Li and Cp–Na ring centroid-metal distances is the Cp $\sum\sigma_m$ value. The more inductively electron-donating the substituent (negative σ_m), the shorter the distance and, as shown in Figs. 2b and 4, the correlation is exceptional. This is by no means a surprising result. The more electron donating groups attached to the Cp ring, the more electron-rich the anion and thus the more the anionic ring is attracted to the cation. Of course this analysis is predicated on the binding force for the Cp–Li and Cp–Na complexes being electrostatic, and this has been illustrated in previous theoretical work [15]. The explanation for the correlation with the Cp $\sum\sigma_p$ values uses the exact same rationale, although the line of best fit has a significantly poorer R^2 value (Fig. 2). The correlation with the Cp Θ_{zz} values is also readily explained; the more electron-rich the substituted Cp, the more negative (or less

positive) the Θ_{zz} value and the shorter the ionic Cp-metal distance. Again, this explanation carries the caveat that the R^2 values are significantly decreased except when the smallest subset of Cp rings is included in the analysis for Cp–Li (Fig. 2).

The more interesting aspect of these results is that the Cp $\sum\sigma_m$ values correlates so well with the Cp-metal distances while the correlation with the Cp Θ_{zz} and $\sum\sigma_p$ values is relatively poor. The poor correlation with the Cp Θ_{zz} values is likely due to this property being a descriptor for the electron density of the entire molecule. Thus, when all Cp rings except the chelating Cp (**27**) are included in the correlation graph (Fig. 2b) there are many instances where the molecular electron density involves much more than just the π-density. It is in just these cases where the deviation from the line of best fit is greatest. For instance, in the graph correlating Cp–Li distances with Cp Θ_{zz} values in Fig. 2b the three greatest outliers with Θ_{zz} values of 5.40, 7.47 and 9.41 DÅ belong to the tetramethyl-, pentamethyl-, and hydroxytetramethyl-substituted Cp rings. Of course, these are among the group of Cp rings with sterically hindering substitution patterns that were omitted in the Fig. 2c graphs, and thus the significant improvement in the correlation between the Cp–Li distance and the Cp Θ_{zz} values. It is worth noting this result is highly fortuitous and the Θ_{zz} values of the Cp rings with sterically non-hindering substitution patterns do not correlate with the Cp–Na distances (graph shown in Supplementary material). The poor correlation with the $\sum\sigma_p$ values is more difficult to explain. The binding in Cp–Li and Cp–Na complexes is certainly a result of the attraction between the cation and the Cp π-electron density. For substituted benzenes the Hammett σ_p constant describes both the resonance and inductive effects of the substituent, whereas the σ_m constant describes only the inductive effects. Thus, it would seem most reasonable for the Cp $\sum\sigma_p$ values to correlate best with the Cp-metal distances. Yet, our results suggest the opposite and including the resonance contributions of the substituents to the Cp π-density is not only unnecessary, which would be surprising in itself, yet it decreases the correlation with the Cp-metal distances. Put another way, the substituent constant that provides the more complete description of the Cp π-density does a poorer job of predicting Cp–Li and Cp–Na distances. One explanation for why the Cp $\sum\sigma_m$ values better predict the Cp-metal distances may be that the interaction between the cation and the Cp substituents is important, and the inductive effects of the substituents captured in the σ_m values is a good descriptor of the electron density at the substituent. We have previously shown the importance of anion-substituent interactions in anion-π complexes of substituted benzenes [32] and Houk has shown the importance of substituent–substituent interactions in arene–arene interactions [29], and thus it is reasonable to suppose such interactions are important in complexes like Cp–Li and Cp–Na where a cationic Li^+ or Na^+ is interacting with the anionic π-cloud of a Cp ring. In Houk's work it was suggested substituent–substituent interactions would best be described by σ_m values, and thus it is not wholly unexpected to find the excellent correlation with the $\sum\sigma_m$ values. Still, the idea that the attraction between Cp and either Li^+ or Na^+ is guided by Cp substituent–metal interactions, and why this interaction is so well described by $\sum\sigma_m$ values (and not $\sum\sigma_p$ values) is not completely understood and current work in our group is exploring this issue.

3.2. Effects of substitution on Cp-metal binding energies

The calculated binding energies (E_{bind}) of Cp–Li and Cp–Na are −166.3 and −138.0 kcal/mol (Table 1) and these are very similar to those reported in previous computational studies [15]. Previous theoretical investigations have also shown the Cp–Li and Cp–Na binding energies are almost entirely electrostatic in nature [15] and the highly ionic Cp-metal bond weakens according to Coulomb's law with increasing Cp–M distance for M = Li^+, Na^+, K^+ [16,17]. The correlations between either the Cp–Li or Cp–Na E_{bind} values and the Cp Θ_{zz}, $\sum\sigma_p$ or $\sum\sigma_m$ values follows the same general trends shown for the Cp-metal distances (Fig. 2). For the Cp Θ_{zz} values the correlation with Cp–Li and Cp–Na binding energies is relatively poor until the Cp rings with sterically hindering substitution patterns are omitted. For the $\sum\sigma_p$ values the correlation is never above $R^2 = 0.80$. The correlation between the Cp $\sum\sigma_m$ values and either the Cp–Li and Cp–Na binding energies is excellent when Cp (**27**) with the metal chelating group is omitted, as shown in Fig. 5. Paring the Cp rings to those with sterically non-hindering substitution patterns does not improve the correlation. The other $\sum\sigma_m$ graphs, along with all Θ_{zz} and $\sum\sigma_p$ graphs are in Supplementary material. All discussion on Cp–Li and Cp–Na binding energies mirrors what was stated above for the Cp-metal distances. The same reasoning that was employed to explain the Cp-metal distance correlations with Cp Θ_{zz}, $\sum\sigma_p$ and $\sum\sigma_m$ values extends to Cp–Li and Cp–Na binding energies, and the same questions concerning why the Cp $\sum\sigma_m$ values correlate so well with the Cp-metal distances, while the $\sum\sigma_p$ values do not, remain for the binding energies.

3.3. Effects of substitution on the metal charge in Cp-metal complexes

Finally, we also investigated the correlation between the metal NBO charge in Cp–Li or Cp–Na complexes and the Cp Θ_{zz}, $\sum\sigma_p$ and $\sum\sigma_m$ values. Fig. 6 shows the graphs correlating the Cp–Li NBO lithium charges with the Θ_{zz} and $\sum\sigma_m$ values of the Cp anions for all substituted Cp rings (Fig. 6a), omitting Cp (**27**) with the amide-chelating group (Fig. 6b), and omitting the Cp rings with sterically hindering substitution patterns (Fig. 6c). The corresponding Cp–Na graphs are shown in Fig. 7. The $\sum\sigma_p$ graphs are not included because the correlations are so poor. The graphs can be

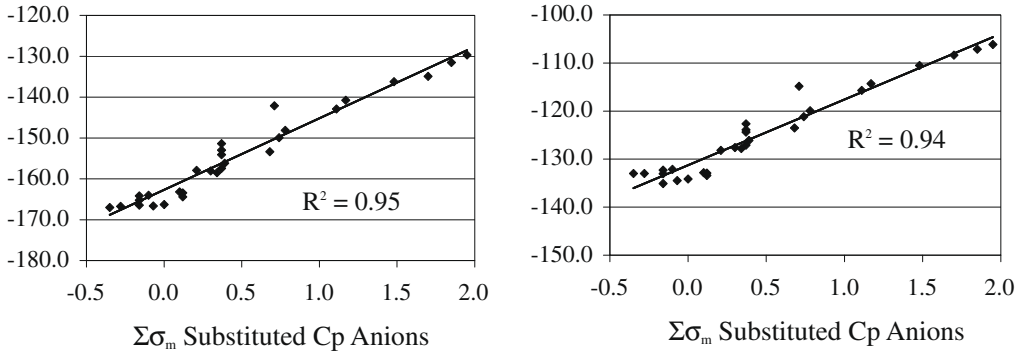


Fig. 5. Cp–Li (left graph) and Cp–Na binding energies plotted against Cp $\sum\sigma_m$ values for all Cp rings except the metal coordinating amide-substituted Cp (**27**).

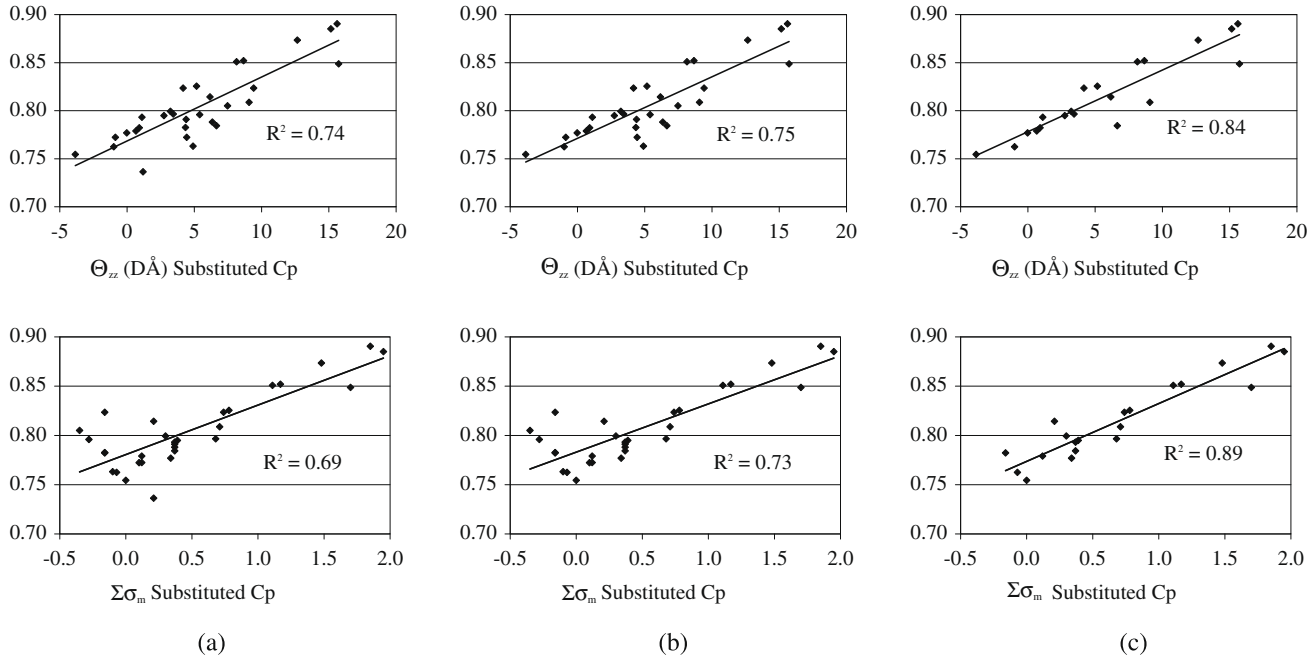


Fig. 6. Lithium NBO charge in Cp–Li complexes plotted against Cp Θ_{zz} and $\sum\sigma_m$ values for (a) all Cp rings; (b) all Cp rings except the metal coordinating amide-substituted Cp (**27**); (c) the 20 sterically least hindering groups.

found in Supplementary material. The relative performance of the Cp Θ_{zz}, $\sum\sigma_p$ and $\sum\sigma_m$ values in predicting the metal NBO charges does not mirror what was found for the Cp-metal distances and binding energies. The correlation between the metal NBO charge and either the Θ_{zz} or $\sum\sigma_m$ values for all substituted Cp rings is decent (Figs. 6a and 7a), compared to the Cp-metal distance and binding energy graphs. However, omission of Cp (**27**) does not improve the correlation as it did with the Cp-metal distance and binding energy graphs. Thus, whereas almost perfect correlation was found between the Cp-metal distances or binding energies and the Cp $\sum\sigma_m$ values, the correlation for the metal NBO charge is only decent for the Cp–Li complexes (Fig. 6b, Θ_{zz}: $R^2 = 0.75$; $\sum\sigma_m$: $R^2 = 0.73$) and it is worse for the Cp–Na complexes (Fig. 7b, Θ_{zz}: $R^2 = 0.61$; $\sum\sigma_m$: $R^2 = 0.48$). When only the Cp rings with sterically non-hindering substitution patterns are considered, the correlation between Cp–Li lithium charges is quite good with both the Cp Θ_{zz} ($R^2 = 0.84$) and $\sum\sigma_m$ ($R^2 = 0.89$) values (Fig. 6c), however, only decent correlation is found for the Cp–Na complexes (Fig. 7c, Θ_{zz}: $R^2 = 0.70$; $\sum\sigma_m$: $R^2 = 0.66$).

Explaining the correlation between the metal NBO charges in the Cp-metal complexes and the Cp Θ_{zz}, $\sum\sigma_p$ or $\sum\sigma_m$ values is also quite different than it was for the Cp-metal distances and binding

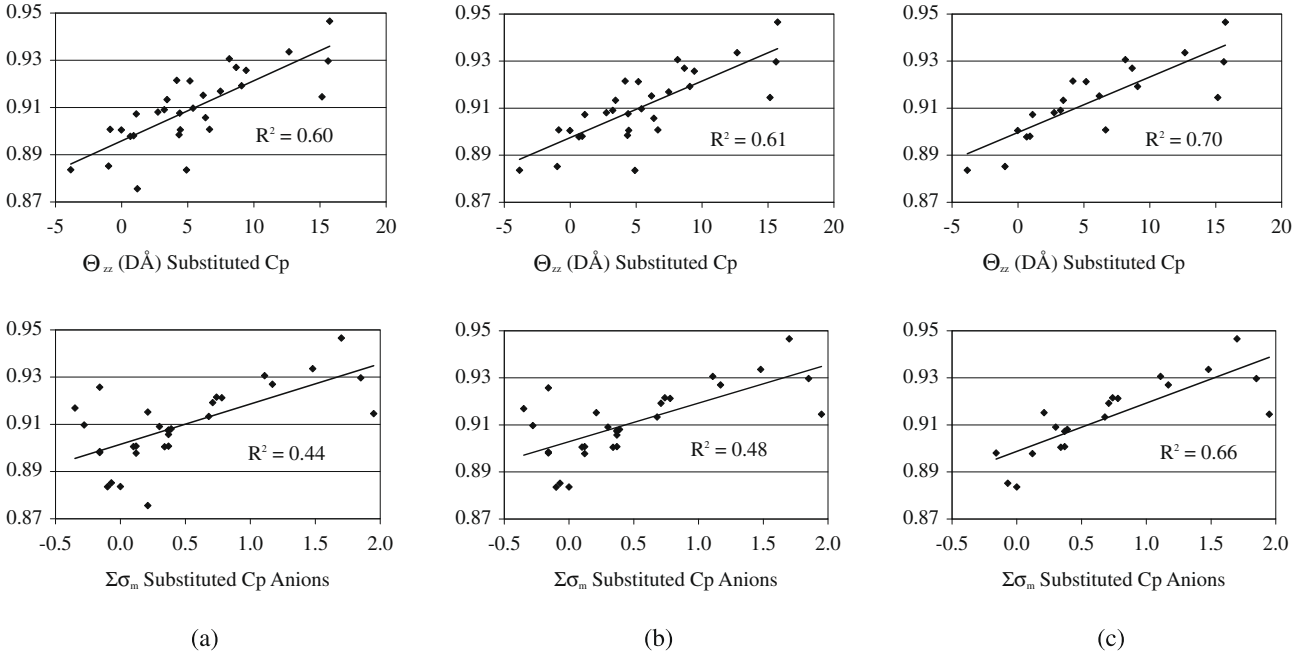


Fig. 7. Sodium NBO charge in Cp–Na complexes plotted against Cp Θ_{zz} and $\sum\sigma_m$ values for (a) all Cp rings; (b) all Cp rings except the metal coordinating amide-substituted Cp (**27**); (c) the 20 sterically least hindering groups.

energies, however, the exercise leads to some interesting insights. The one similarity is that the correlation with the Cp $\sum\sigma_m$ values is far better than with the $\sum\sigma_p$ values and thus including substituent resonance effects significantly decreases the ability to predict the metal charge. As is shown by the graphs in Supplementary material, the correlations with the $\sum\sigma_p$ values is very poor, to the point of precluding an explanation of the observed trend. The correlation between the metal NBO charge in the Cp-metal complexes and either the Cp Θ_{zz} or $\sum\sigma_m$ values seems counterintuitive. The more electron-rich the Cp ring, as dictated either by a less positive/negative Θ_{zz} value or a less positive/negative $\sum\sigma_m$ value, the less positive the Li^+ or Na^+. This is, of course, the opposite of what would be expected. Regardless of how much ionic or covalent character one assigns to the Cp-metal bond, increasing the electron density of the Cp π-cloud should give a more positive metal charge. Looking at how the charge on the substituted Cp atoms change upon Li^+ complexation (Table 2) provides an explanation for this curious trend. Upon Li^+ complexation for the parent (**1**) and perfluorinated (**2**) Cp rings, the charge on the ring carbon atoms remain largely unchanged and the H and F atoms become more positive by 0.048 and 0.044 charge units, respectively. When the perchloro- and perbromo-substituted Cp rings, **5** and **10**, are complexed with Li^+ the Cp carbon atoms become significantly more negative, by 0.069 and 0.073 charge units, and the Cl and Br atoms become substantially more positive, by 0.091 and 0.096 charge units. Thus, when the Cp ring is substituted with the large, polarizable Cl and Br substituents, Li^+ complexation causes electron density to be transferred from the halogens to the metal, which explains the increased positive charge at the halogen atoms (Table 2). However, this electron density does not stay at the metal, but instead it is transferred to the Cp ring carbon atoms, which explains the increased negative charge at the Cp carbon atoms (Table 2). The effect of electron density being transferred from the electron-withdrawing substituent to the metal cation and onto the Cp ring carbon (Fig. 8) is most likely to occur with large, polarizable groups, and this is what the changes in Cp atomic charges upon metal complexation show in Table 2. It so happens that the trend in inductive electron-withdrawing ability, using σ_m values as the measure, is the same as the trend for substituent polarizability. The bromine and chlorine atoms have the largest σ_m, and thus are classified as being the most inductively electron withdrawing, and they are also the most polarizable. This analysis offers a valuable insight. If electron density is flowing as shown in Fig. 8, and σ_m is a measure of substituent polarizability, then for the purpose of predicting the charge on the metal cation the sign of the σ_m value is irrelevant. For instance, for OH σ_m = +0.12 while for NH_2 σ_m = −0.16. By any definition an amino group is more polarizable than a hydroxyl group, the sign of the σ_m values simply inform us that the NH_2 is inductively electron donating while the OH group is inductively electron withdrawing. Thus, the correlations for $\sum\sigma_m$ in Figs. 6 and 7 are not quite right. Instead the important correlation would be between the metal NBO charges and the $\sum|\sigma_m|$ values since it is the absolute σ_m values that inform us about the relative polarizability and how well the substituents will donate electron density to the metal cation, as illustrated in Fig. 8. The graphs showing these correlations are given in Figs. 9 and 10 for Cp–Li and Cp–Na, respectively, and the improvements in the R^2 values are striking. For all substituted Cp rings the correlation between the Li^+ NBO charge in Cp–Li complexes and the $\sum|\sigma_m|$ values is R^2 = 0.87 (Fig. 9a) compared to 0.69 when the $\sum\sigma_m$ values are used (Fig. 6a). When the metal chelating Cp (**27**) is omitted the correlation with $\sum|\sigma_m|$ values is R^2 = 0.90 (Fig. 9b) compared to 0.73 for $\sum\sigma_m$ values (Fig. 6b). Only for the subset of twenty substituted Cp rings with sterically non-hindering substituent patterns are the R^2 values comparable: R^2 = 0.93 for $\sum|\sigma_m|$ values (Fig. 9c) and 0.89 for $\sum\sigma_m$ values (Fig. 6c). Of course, the more points are omitted, the more correlation one will generally find. That the correlation with the Cp $\sum|\sigma_m|$ values is very good for all points shows its value over the $\sum\sigma_m$ values for predicting Li^+ charges in Cp–Li complexes. Unfortunately, the charge on Na^+ in the Cp–Na complex does not have a very good correlation with the Cp $\sum|\sigma_m|$ values, as shown in Fig. 10. However, the correlation for all substituted Cp rings has an R^2 value of 0.59 and this is considerably better than the R^2 value of 0.44 with Cp $\sum\sigma_m$ values. Still, the fact that the metal charges in Cp–Li and Cp–Na significantly improve when Cp $\sum|\sigma_m|$ values are considered instead of $\sum\sigma_m$ values supports the view of electron density redistribution upon metal complexation shown in Fig. 8. Ultimately, the correlation trend when $\sum\sigma_m$ values are employed is a red herring because besides measuring inductive electron withdrawing ability, the Hammett σ_m constants also contain information about substituent polarizabilities. When considering the effect Cp substitution has on the metal charge in Cp-metal complexes it is the latter property of σ_m constants that is important. Of course, our explanation for the correlation between the metal charges and Cp $\sum|\sigma_m|$ values stems from the charge-transfer model proposed in Fig. 8, and this was derived from looking at the change in charge values Δq(C) and Δq(X) calculated using the NBO method. As further support for this model we also considered the Δq(C) and Δq(X) values calculated using the Mulliken method and the same relative trends were observed. The Mulliken charge data is given in Supplemental material.

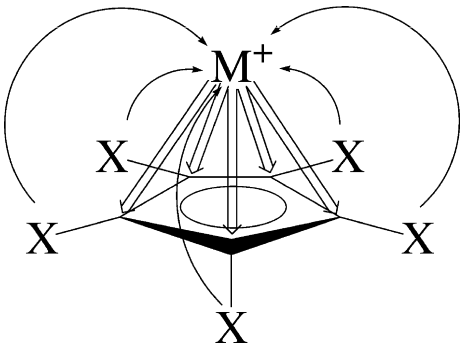


Fig. 8. Cp complexation of Li^+ or Na^+ causes electron density to flow from the polarizable X groups, to the metal, and ultimately to the Cp carbon atoms.

Table 2
The MP2(full)/6-311++G** calculated NBO Cp atomic charges (q(C) and q(X)) for the non-complexed and Li^+-complexed ring, and the change in atomic charge upon Li^+ complexation (Δq(C) and Δq(X)).

C_5X_5	Cp charges		Cp charges in lithium complex		Change in Cp charges	
X=	q(C)	q(X)	q(C)	q(X)	Δq(C)	Δq(X)
H (**1**)	−0.355	+0.156	−0.355	+0.204	+0.000	+0.048
F (**2**)	+0.214	−0.414	+0.200	−0.370	−0.014	+0.044
Cl (**5**)	−0.155	−0.045	−0.224	+0.046	−0.069	+0.091
Br (**10**)	−0.236	+0.036	−0.309	+0.132	−0.073	+0.096

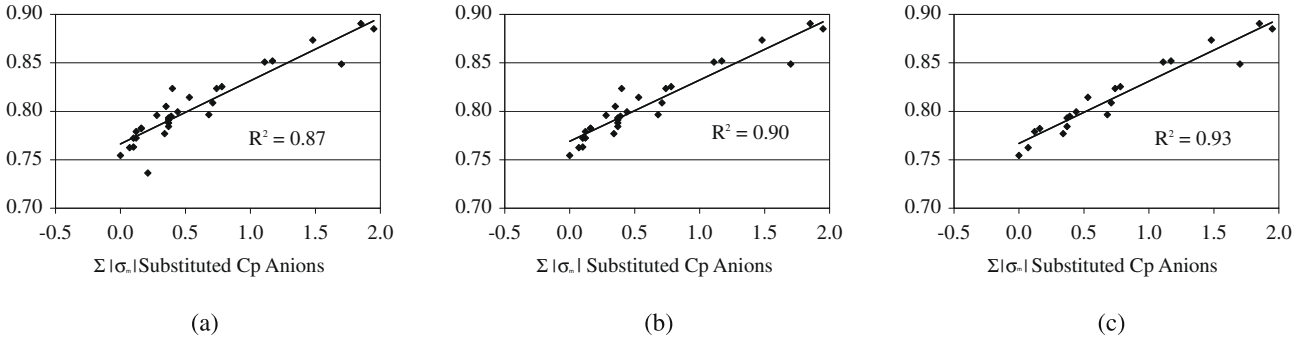


Fig. 9. Lithium NBO charge in Cp–Li complexes plotted against Cp Θ_{zz} and $\sum|\sigma_m|$ values for (a) all Cp rings; (b) all Cp rings except the metal coordinating amide-substituted Cp (**27**); (c) the 20 sterically least hindering groups.

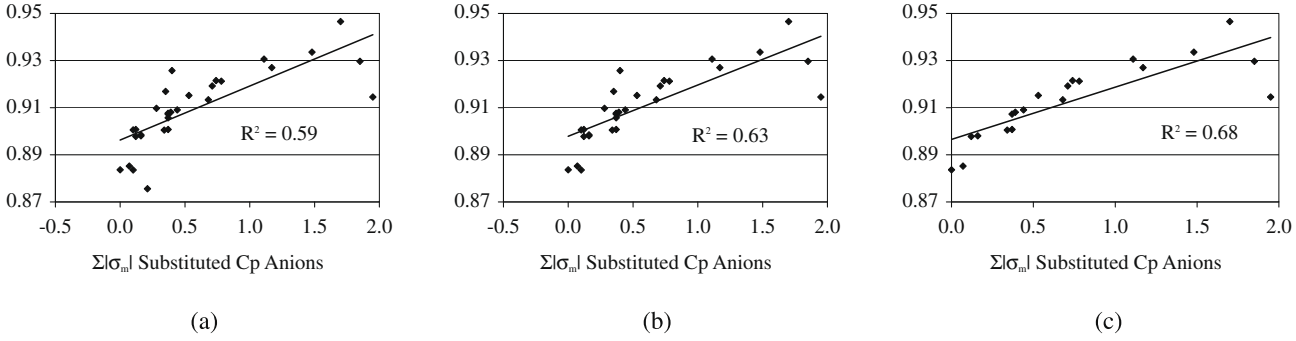


Fig. 10. Sodium NBO charge in Cp–Na complexes plotted against Cp Θ_{zz} and $\sum|\sigma_m|$ values for (a) all Cp rings; (b) all Cp rings except the metal coordinating amide-substituted Cp (**27**); (c) the 20 sterically least hindering groups.

4. Conclusion

Cp–Li and Cp–Na ring centroid-metal distances and binding energies correlate exceptionally well with the $\sum\sigma_m$ values of the substituted Cp rings so long as the substituents do not chelate with the metal. If only Cp rings with sterically non-hindering substitution patterns are considered, these values also correlate very well with the Θ_{zz} values of the Cp rings. Still, the prediction of the Cp-metal distance and binding energy for a complex between a substituted Cp and either Li^+ or Na^+ is best done using the $\sum\sigma_m$ value of the Cp. The Cp-metal bond will be shorter and the binding energy will be stronger when inductively electron-donating substituents are present on the Cp (negative $\sum\sigma_m$ values). Surprisingly, the correlation between Cp-metal distances and binding energies and the Cp $\sum\sigma_p$ values is significantly worse than for the $\sum\sigma_m$ values. Thus, including the resonance effects of the Cp substituents gives a poorer correlation and current work in our group is aimed at understanding this result. The metal charge in the Cp–Li and Cp–Na complexes correlates about equally with the Cp $\sum\sigma_m$ or Θ_{zz} values, and once again the correlation with the Cp $\sum\sigma_p$ values is poor. The correlation trend with either the Cp $\sum\sigma_m$ or Θ_{zz} values is not immediately intuitive. The more electron-rich the Cp (negative $\sum\sigma_m$ and Θ_{zz} values), the less positive the metal cation. Thus, the shorter and stronger the Cp-metal bond, the less positive the Li^+ or Na^+. Regardless of how much ionic or covalent character one assigns to the Cp-metal bond, this trend defies a simple explanation. The explanation we offer involves the Cp substituents donating electron density back to the metal, and the metal donating this electron density onto the Cp carbon atoms. The more polarizable the substituents, as defined by the $|\sigma_m|$ values, the more likely this electron flow. The fact that substituent $|\sigma_m|$ values contain information about the substituent polarizability is important to recognize. Instead of the confusing view that Cp rings with electron-withdrawing substituents (electron-poor Cp rings) have Cp-metal complexes with the most positive metals, we end up with the more consistent view that Cp rings with polarizable substituents have Cp-metal complexes with the most positive metals. The charge-transfer model we present here is related to recent work by Houk and co-worker [33] and Frontera et al. [34] where they illustrate the importance of through-space interactions in cation-substituted benzene complexes [33] and cation-substituted paracyclophane complexes [34].

Acknowledgements

This work was partially supported by the National Center for Supercomputing Application under CHE050039N and utilized the SGI Altix system.

Appendix A. Supplementary data

Supplementary data associated with this article can be found, in the online version, at doi:10.1016/j.poly.2009.06.074.

References

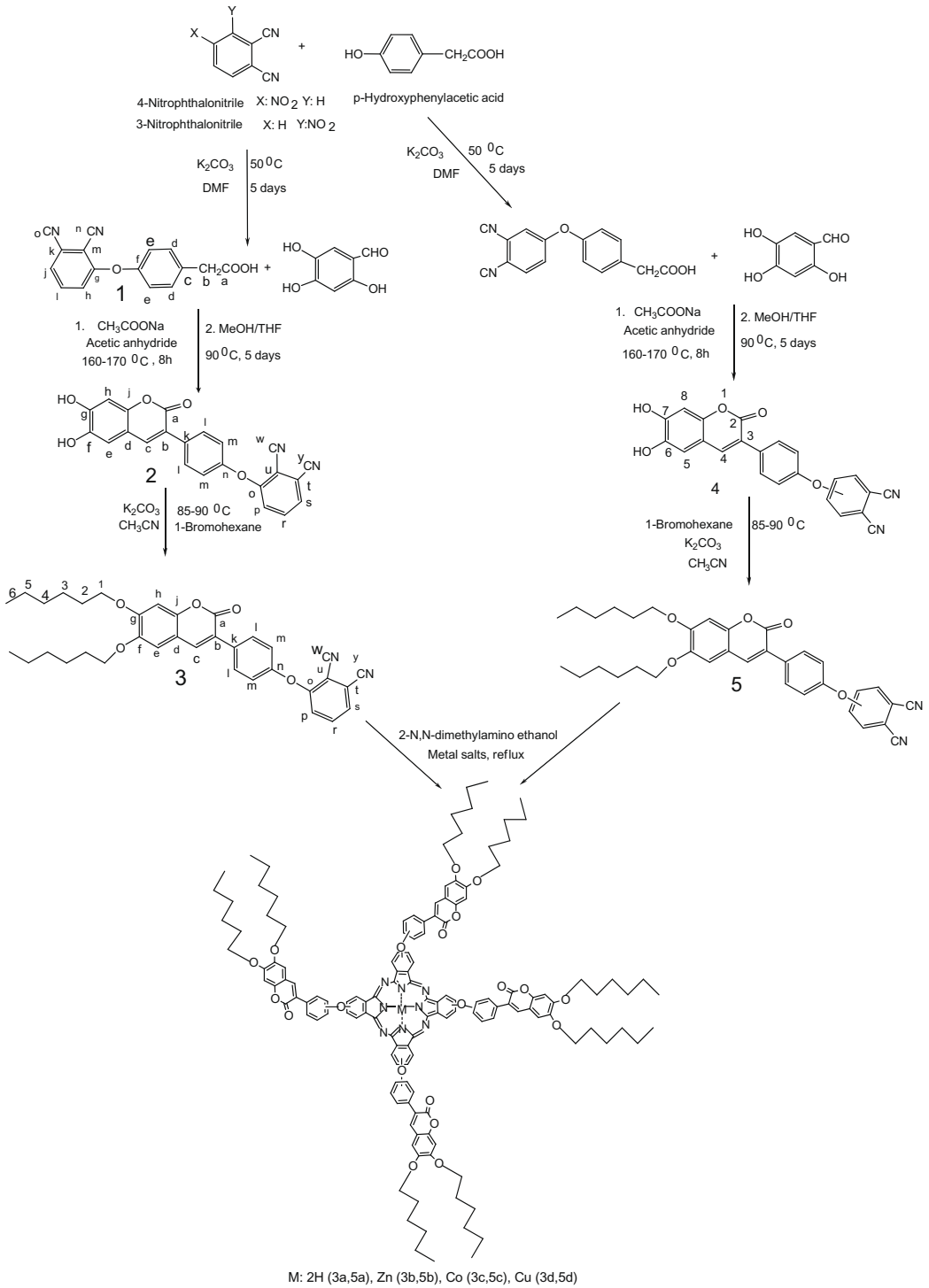
[1] G. Wilkinson, M. Rosenblum, M.C. Whiting, R.B. Woodward, J. Am. Chem. Soc. 74 (1952) 2125.
[2] E.O. Fischer, W.Z. Pfab, Naturforsch B7 (1952) 377.
[3] T. Kealy, P. Pauson, Nature 168 (1951) 1039.
[4] P.A. Deck, Coord. Chem. Rev. 250 (2006) 1032.
[5] T.P. Hanusa, Organometallics 21 (2002) 2559.
[6] P. Jutzi, N. Burford, Chem. Rev. 99 (1999) 969.
[7] L. Kaufmann, H. Vitze, M. Bolte, H.-W. Lerner, M. Wagner, Organometallics 26 (2007) 1771.
[8] M.J. Harvey, T.P. Hanusa, Organometallics 19 (2000) 1556.
[9] G. Fraenkel, X. Chen, A. Chow, J.C. Gallucci, H. Liu, J. Org. Chem. 70 (2005) 9131.
[10] H. Jiao, P.v.R. Schleyer, Y. Mo, m.A. McAllister, T.T. Tidwell, J. Am. Chem. Soc. 119 (1997) 7075.

[11] M. Buehl, N.J.R.V.E. Hommes, P.v.R. Schleyer, U. Fleischer, W. Ketzelnigg, J. Am. Chem. Soc. 113 (1991) 2459.
[12] C. Uffing, R. Koppe, H. Schnockel, Organometallics 17 (1998) 3512.
[13] C. Dohmeier, E. Baum, A. Ecker, R. Koppe, H. Schnockel, Organometallics 15 (1996) 4702.
[14] R. Blom, K. Faegri Jr., T. Midtgaard, J. Am. Chem. Soc. 113 (1991) 3230.
[15] V.M. Rayon, G. Frenking, Chem. Eur. J. 8 (2002) 4693.
[16] S. Harder, M.H. Prosenc, U. Rief, Organometallics 15 (1996) 118.
[17] C. Lambert, P.v.R. Schleyer, Angew. Chem., Int. Ed. Engl. 33 (1994) 1129.
[18] S. Harder, M. Lutz, S.J. Obert, Organometallics 18 (1999) 1808.
[19] D. Tran, S. Beg, A. Clements, M. Lewis, Chem. Phys. Lett. 425 (2006) 347.
[20] M. Lewis, Z. Wu, R. Glaser, Chapter 7 in anisotropic organic materials – approaches to polar order, in: R. Glaser, P. Kaszynski (Eds.), ACS Symposium Series, vol. 798, American Chemical Society, Washington, DC, 2001, pp. 97–111.
[21] M.R. Battaglia, A.D. Buckingham, J.H. Williams, Chem. Phys. Lett. 78 (1981) 421.
[22] S.F. Boys, F. Bernardi, Mol. Phys. 19 (1970) 553.
[23] J.C. Amicangelo, P.B. Armentrout, J. Phys. Chem. A 104 (2000) 11420.
[24] J.E. Carpenter, F. Weinhold, J. Mol. Struct. 169 (1988) 41.
[25] C. Hansch, A. Leo, R.W. Taft, Chem. Rev. 91 (1991) 165.
[26] D. Moran, A.C. Simmonett, F.E. Leach III, W.D. Allen, P.v.R. Schleyer, H.F. Schaefer, J. Am. Chem. Soc. 128 (2006) 9342.
[27] M.J. Frisch et al., GAUSSIAN 03, Revision C.02, GAUSSIAN, Inc., Wallingford, CT, 2004.
[28] P. Sykes, A Guidebook to Mechanism in Organic Chemistry, sixth ed., Pearson, England, 1986. p. 358.
[29] A.L. Ringer, C.D. Sherrill, J. Am. Chem. Soc. 131 (2009) 4574.
[30] S.E. Wheeler, K.N. Houk, J. Am. Chem. Soc. 130 (2008) 10854.
[31] S. Beg, K. Waggoner, Y. Ahmad, M. Watt, M. Lewis, Chem. Phys. Lett. 455 (2008) 98.
[32] A. Clements, M. Lewis, J. Phys. Chem. A 110 (2006) 12705.
[33] S.E. Wheeler, K.N. Houk, J. Am. Chem. Soc. 131 (2009) 3126.
[34] A. Frontera, D. Quinonero, C. Garau, A. Costa, P. Ballester, P.M. Deya, J. Phys. Chem. A 110 (2006) 5144.

metal cation on the spectroscopic and aggregation properties of Pcs in different solvents, tetrahydrofuran (THF) and dimethylformamide (DMF) are investigated.

2. Experimental

Routine IR-spectra were recorded on a Shimadzu Fourier Transform FTIR-8300 Infrared Spectrophotometer using KBr pellets, electronic spectra on a Shimadzu UV-1601 UV–Visible Spectrophotometer. ^{1}H and ^{13}C NMR spectra on a Varian Unity Inova 500 MHz NMR Spectrophotometer using TMS as internal reference. Elemental analysis was performed by the Instrumental Analysis Laboratory of TUBITAK Ankara Test and Analysis Laboratory. Mass spectra were performed on a Bruker Daltonic Autoflex III MALDI-TOF spectrometer at Marmara University. 2,5-Dihydroxybenzoic acid (DHB) (20 mg/mL in THF) matrix for compounds (**1**–**4**) was used. MALDI samples were prepared by mixing the complex [2 mg/mL in tetrahydrofuran (THF)] with the matrix solution (1:10 v/v) in a 0.5 mL Eppendorf micro tube. Finally, 1 μL of this



Scheme 1. The synthesis of coumarin (**2**–**5**) and phthalocyanines (**3a**–**3d** and **5a**–**5d**).

mixture was deposited on the sample plate, dried at room temperature and then analyzed. Fluorescence excitation and emission spectra were recorded on a HITACHI F-7000 Fluorescence spectrophotometer using 1 cm pathlength cuvettes at room temperatures.

4-Nitrophthalonitrile, 3-nitrophthalonitrile and *p*-(3,4-dicyanophenoxy)phenylacetic acid were synthesized according to the reported procedures [22–24]. All reagents and solvents were of reagent-grade quality obtained from commercial suppliers. All solvents were dried and purified. The solvents were stored over molecular sieves (4 Å). The homogeneity of the products was tested in each step by TLC (SiO_2).

2.1. General procedure for the synthesis of p-(2,3-dicyanophenoxy)phenylacetic acid (**1**)

4-Hydroxyphenylacetic acid (1.75 g, 11.56 mmol) and 3-nitrophthalonitrile (2.0 g, 11.56 mmol) were dissolved in dry DMF (20 ml) under nitrogen and anhydrous K_2CO_3 (3.19 g, 23.12 mmol) was added. After stirring for 5 days at 50–60 °C, the reaction mixture was treated with diluted HCl under ice cooling. The pure precipitate was filtered, washed with water to neutralize, and dried. Yield: 1.8 g (56%). m.p.: 178–183 °C. IR ν(cm^{-1}): 3510 (carboxylic acid OH), 3083–3062 (Ar–CH), 2970–2932 (aliphatic CH), 2230 (C≡N), 1705 (C=O), 1600–1548 (Ar C=C), 1250 (Ar–O–Ar), 1210, 1164, 1081, 945, 842, 810, 670 and 530. ^{1}H NMR (d-DMSO 500 MHz, δ ppm): 12.21 (s, 1H, COOH), 8.11 (d, 1H, Ar–H), 7.74 (d, 1H, Ar–H), 7.41 (d, 1H, Ar–H), 7.38 (dd, 2H, Ar–H), 7.21 (dd, 2H, Ar–H), 3.77 (s, 2H, CH_2). ^{13}C NMR (d-DMSO 500 MHz, δ ppm): 175,1 (acid C=O, C_a), 164.8 (Ar, C_g), 155.1 (Ar, C_f), 138.0 (Ar, C_l), 134.3 (Ar, $2C_d$), 133.2 (Ar, C_c), 124.3 (Ar, C_j), 123.4 (Ar, C_h), 122.6, (Ar, $2C_e$), 119.4 (Ar, C_k), 117.6 (C≡N, C_n), 117.0 (C≡N, C_o), 106.8 (Ar, C_m), 41.2 (CH_2, C_b). MS (MALDI-TOF): *m/z* 278 $[M]^+$. UV–Vis λ_{max} (nm) (log ε) (THF) (1.10^{-5} M): 310 (3.78).

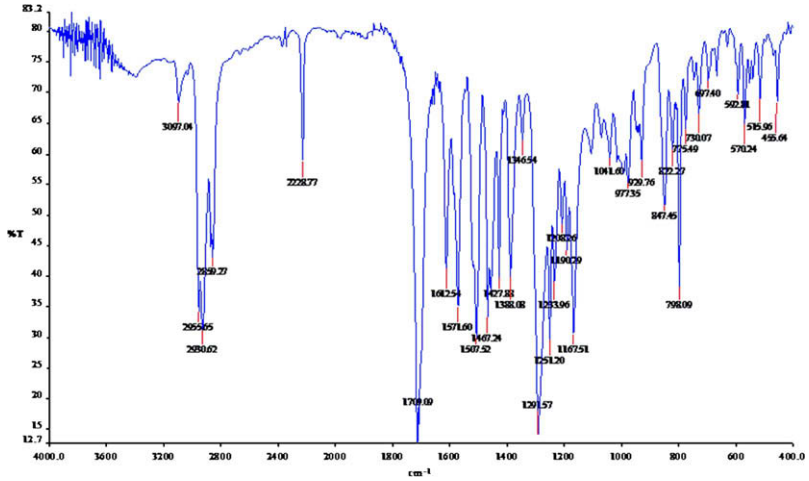
2.2. General procedure for the synthesis of 6,7-dihydroxy-3-[p-(2′,3′-dicyanophenoxy)phenyl]coumarin (**2**) and 6,7-dihydroxy-3-[p-(3′,4′-dicyanophenoxy)phenyl]coumarin (**4**)

A mixture of *p*-(2,3-dicyanophenoxy)phenylacetic acid (**1**) (1.8 g, 6.48 mmol) or *p*-(3,4-dicyanophenoxy)phenylacetic acid (2.0 g, 7.19 mmol), 2,4,5-trihydroxybenzaldehyde (1.10 g, 7.19 mmol)/(0.99 g, 6.48 mmol), sodium acetate (2.94 g, 35.90 mmol)/(2.65 g, 32.3 mmol) and anhydrous acetic anhydrite (15 ml) was heated and stirred at 160–170 °C in a sealed glass tube for 8 h under nitrogen. After cooling to room temperature, water was added and the mixture was stirred for overnight.

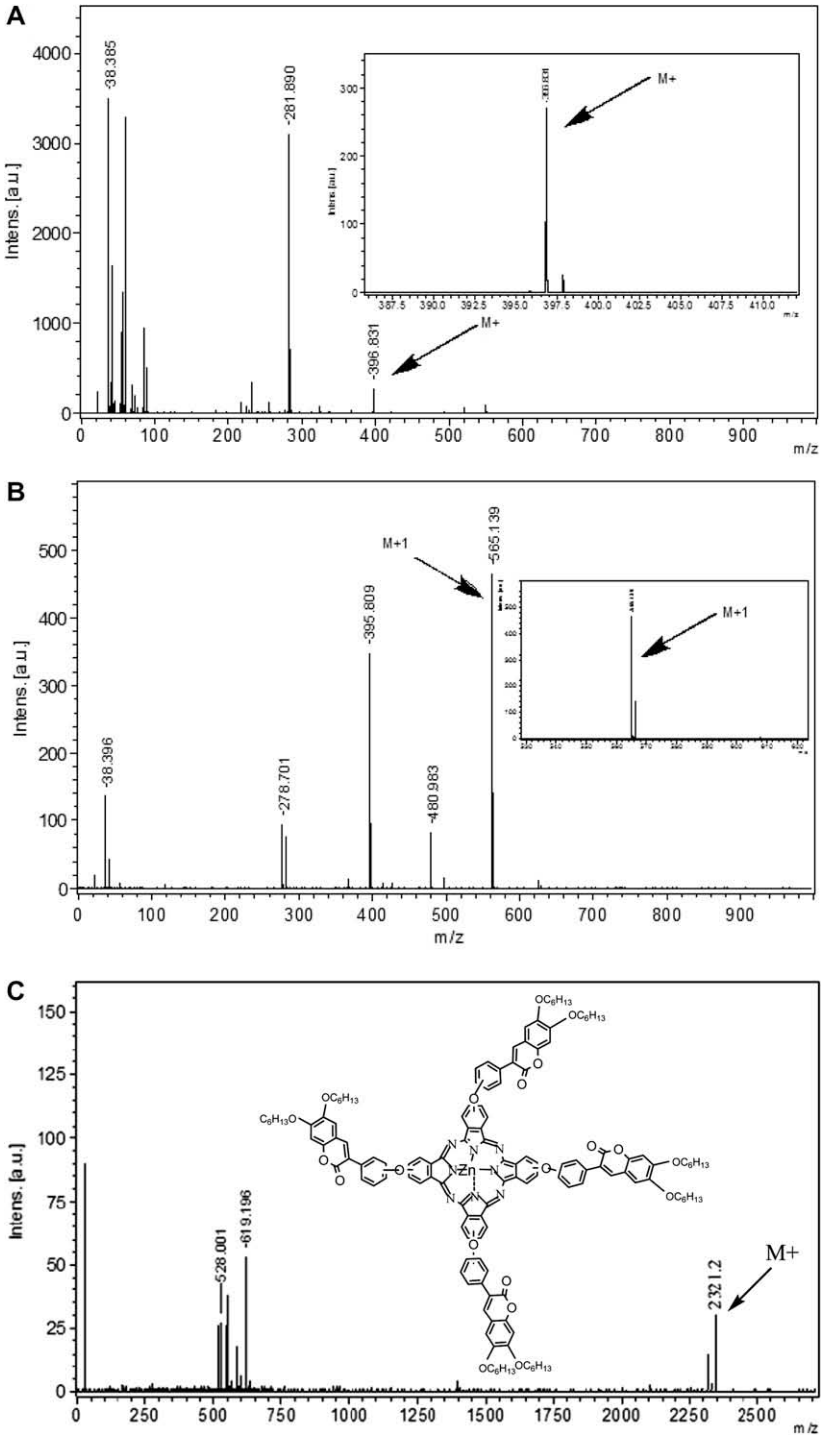
The resulting solid (6,7-diacetoxy-3-[*p*-(2′,3′-dicyanophenoxy)phenyl]coumarin)/(6,7-diacetoxy-3-[*p*-(3′,4′-dicyanophenoxy)-phenyl]coumarin) was filtered, washed with water and dried. The crude product was suspended in methanol. About 10% HCl was added to adjust pH to 3 and the ensuing mixture was heated and stirred at 60 °C for 5 days under nitrogen. The resulting solid (6,7-dihydroxy-3-[*p*-(2′,3′-dicyanophenoxy)phenyl]coumarin)/(6,7-dihydroxy-3-[*p*-(3′,4′-dicyanophenoxy)phenyl]coumarin) was filtered, washed with water and dried. The slightly brown products were purified by silica gel column chromatography using $CHCl_3$ as eluent.

The compound **2** is soluble in ethanol, methanol, tetrahydrofuran (THF), dimethylsulfoxide (DMSO) and dimethylformamide (DMF). Yield: 1.73 g (60%), m.p.: >300 °C. IR ν(cm^{-1}): 3461–3398 (OH), 3098 (Ar–H), 2923–2898 (alkyl–CH), 2240 (C≡N), 1707 (C=O lactone), 1632 (C=C), 1586–1492 (Ar C=C), 1244 (Ar–O–Ar). UV–Vis λ_{max} (nm) (log ε) (THF) ($1.01.10^{-5}$ M): 360 (4.30), 305 (4.13). ^{1}H NMR (500 MHz; DMSO): δ_H, ppm 9.28 (s, 1H, OH), 8.25 (s, 1H, OH), 8.08 (s, 1H, lactone 4-H), 7.87 (dd, *J* = 8 Hz, 1H, Ar–H), 7.60 (dd, *J* = 8 Hz, 1H, Ar–H), 7.54 (dd, *J* = 8 Hz, 1H, Ar–H), 7.42 (dd, *J* = 8 Hz, 2H, Ar–H), 7.04 (dd, *J* = 8 Hz, 2H, Ar–H), 6.76 (s, 1H, Ar–H), 6.66 (s, 1H, Ar–H). ^{13}C NMR (d-DMSO 500 MHz, δ ppm): 160.5 (lactone C=O, C_a), 160.3 (Ar, C_o), 156.2 (Ar, C_n), 149.9 (Ar, C_j), 145.4 (Ar, C_g), 142.7 (Ar, C_f), 141.1 (Ar, C_c), 133.4 (Ar, C_r), 128.8 (Ar, $2C_l$), 128.0 (Ar, C_k), 126.0 (Ar, C_s), 124.7 (Ar, C_b), 122.5 (Ar, C_p), 117.4 (Ar, $2C_m$), 116.2 (Ar, C_d), 115.5 (Ar, C_t), 115.8 (C≡N, C_y), 113.5 (C≡N, C_w), 113.9 (Ar, C_e), 103.8 (Ar, C_h), 103.5 (Ar, C_u). *Anal.* Calc. for $C_{23}H_{12}N_2O_5$: C, 69.69; H, 3.03; N, 7.07. Found: C, 69.56; H, 3.12; N, 6.48%. Fluorescence data: (EM) $1.01.10^{-5}$ M, λ_{em}: 458 nm and (EX) $1.01.10^{-6}$ M, λ_{ex}: 364 nm (20 slitt) (THF). MS (MALDI-TOF): *m/z* 396 $[M]^+$, 397 $[M+1]^+$.

The compound **4** is soluble in ethanol, methanol, THF, DMSO and DMF. Yield: 1.73 g (60%), m.p.: >300 °C. IR ν(cm^{-1}): 3400–3396 (OH), 3100 (Ar–H), 2950–2890 (alkyl–CH), 2200 (C≡N), 1703 (C=O lactone), 1600 (C=C), 1566–1488 (Ar C=C), 1245 (Ar–O–Ar). UV–Vis λ_{max} (nm) (log ε) (THF) ($1.01.10^{-5}$ M): 357 (4.25). ^{1}H NMR (500 MHz; DMSO): δ_H, ppm 9.31 (s, 1H, OH), 8.28 (s, 1H, OH), 8. 12 (d, *J* = 8 Hz, 1H, Ar–H), 8.08 (s, 1H, lactone 4-H), 7.82 (d, *J* = 3 Hz, 1H, Ar–H), 7.42 (dd, *J* = 8 Hz, 2H, Ar–H), 7.24 (dd, *J* = 8 Hz, 1H, Ar–H), 7.04 (dd, *J* = 8 Hz, 2H, Ar–H), 6.76 (s, 1H, Ar–H), 6.66 (s, 1H, Ar–H). ^{13}C NMR (d-DMSO 500 MHz, δ ppm): 162.0 (Ar, C_p), 160.5 (lactone C=O, C_a), 156.2 (Ar, C_n), 149.9 (Ar, C_j), 145.4 (Ar, C_g), 142.7 (Ar, C_f), 141.1 (Ar, C_c), 134.4 (Ar, C_s),



Scheme 2. The IR-spectra of **3**.



Scheme 3. The positive ion and linear mode MALDI-TOF spectrum of **2 (A)**, **5 (B)** and **5b (C)** (in the presence of 2,5-dihydroxybenzoic acid (DHB) (20 mg/mL in THF) as a matrix) were obtained using nitrogen laser accumulating 50 laser shots. Inset spectrum shows expanded molecular mass region of the complex.

128.8, (Ar, $2C_i$), 128.0 (Ar, C_k), 124.7 (Ar, C_b), 122.5 (Ar, C_r), 121.8 (Ar, C_o), 117.4 (Ar, $2C_m$), 116.2, (Ar, C_d) 115.5 (Ar, C_u), 115.8 (C≡N, C_y), 115.6 (C≡N, C_w), 113.9 (Ar, C_e), 108.9 (Ar, C_t), 103.8 (Ar, C_h). *Anal.* Calc. for $C_{23}H_{12}N_2O_5$: C, 69.69; H, 3.03; N, 7.07. Found: C, 68.21; H, 3.08; N, 7.14%. Fluorescence data: (EM) $1.01.10^{-5}$ M, λ_{em}: 440 nm and (EX) $1.01.10^{-6}$ M, λ_{ex}: 369 nm (5 slitt) (THF). MS (MALDI-TOF): *m/z* 396 $[M]^+$.

*2.3. General procedure for the synthesis of 6,7-dihexyloxy-3-[p-(2′,3′-dicyanophenoxy)phenyl]coumarin (**3**) and 6,7-dihexyloxy-3-[p-(3′,4′-dicyanophenoxy)phenyl]coumarin (**5**)*

6,7-Dihydroxy-3-[*p*-(2′,3′-dicyanophenoxy)phenyl]coumarin **2** (1.0 g, 2.5 mmol) or 6,7-dihydroxy-3-[*p*-(3′,4′-dicyanophenoxy)phenyl]coumarin **4** (1.0 g, 2.5 mmol) and 1-bromohexane

(0.83 g, 5 mmol) were dissolved in dry DMF (20 ml), anhydrous potassium carbonate (0.69 g, 5 mmol) and tetrabutylammonium bromide (0.02 g, excess) as catalyst were added. After heating (80 °C) and stirring for 5 days under nitrogen the reaction mixture was poured into iced water and acidified with aqueous HCl solution. The precipitate formed was filtered, washed with water and the crude product was dried. The products were purified on silica gel column chromatography with chloroform as eluent.

The compound **3** is soluble in THF, chloroform ($CHCl_3$), dichloromethane (CH_2Cl_2) DMF and DMSO. Yield: 1.50 g (97%), m.p.: 178–183 °C. IR $\nu(cm^{-1})$: 3097 (Ar–H), 2955–2830 (alkyl–CH), 2228 (C≡N), 1709 (C=O lactone), 1612 (C=C), 1571–1467 (Ar C=C), 1233 (Ar–O–Ar). UV–Vis λ_{max} (nm) (log ε) (THF) ($1.063.10^{-5}$ M): 360 (4.32), 323 (4.06). ^{1}H NMR (500 MHz, DMSO): δ_H, ppm 8.09 (s, 1H, lactone 4-H), 7.87 (dd, J = 8 Hz, 1H, Ar–H), 7.85 (dd, J = 8 Hz, 2H, Ar–H), 7.60 (dd, J = 8 Hz, 1H, Ar–H), 7.54 (dd, J = 8 Hz, 1H, Ar–H), 7.30 (dd, J = 8 Hz, 2H, Ar–H), 7.10 (s, 1H, Ar–H), 7.05 (s, 1H, Ar–H), 4.12 (t, J = 6 Hz, 2H, OCH_2), 4.06 (t, J = 6 Hz, 2H, OCH_2), 1.78 (m, 4H, $OCCH_2$), 1.45 (m, 4H, $OCCCH_2$), 1.32 (m, 8H, $OCCC(CH_2)_2$), 0.98 (t, J = 6 Hz, 3H, CH_3), 0.92 (t, J = 6 Hz, 3H, CH_3). ^{13}C NMR (d-DMSO 500 MHz, δ ppm): 160.5 (lactone C=O, C_a), 160.3 (Ar, C_o), 156.2 (Ar, C_n), 148.1 (Ar, C_j), 146.3 (Ar, C_g), 146.0 (Ar, C_f), 141.1 (Ar, C_c), 133.4 (Ar, C_r), 128.8, (Ar, $2C_i$), 128.0 (Ar, C_k), 126.0 (Ar, C_s), 124.7 (Ar, C_b), 122.5 (Ar, C_p), 117.4 (Ar, $2C_m$), 115.8 (C≡N, C_y), 115.5 (Ar, C_t), 114.4 (Ar, C_d), 113.5 (C≡N, C_w), 109.5 (Ar, C_e), 103.5 (Ar, C_u), 103.5 (Ar, C_h), 69.0 (alkyl, $2C_1$), 31.8 (alkyl, $2C_4$), 29.6 (alkyl, $2C_2$), 25.6 (alkyl, $2C_3$), 22.7 (alkyl, $2C_5$), 14.1 (alkyl, $2C_6$). *Anal.* Calc. for $C_{35}H_{36}N_2O_5$: C, 74.47; H, 6.38; N, 4.96. Found: C, 75.43; H, 6.64; N, 5.21%. Fluorescence data: (EM) $1.063.10^{-5}$ M, λ_{em}: 454 nm and (EX) $1.063.10^{-6}$ M, λ_{ex}: 364 nm (20 slitt) (THF). MS (MALDI-TOF): m/z 564 $[M]^+$, 566 $[M+2]^+$.

The compound **5** is soluble in THF, $CHCl_3$, CH_2Cl_2, DMF and DMSO. Yield: 1.45 g (96%), m.p.: 174–176 °C. IR $\nu(cm^{-1})$: 3074 (Ar–H), 2925–2890 (alkyl–CH), 2220 (C≡N), 1700 (C=O lactone), 1650 (C=C), 1560–1481 (Ar C=C), 1245 (Ar–O–Ar). UV–Vis λ_{max} (nm) (log ε) (THF) ($1.063.10^{-5}$ M):0354 (4.42). ^{1}H NMR (500 MHz, DMSO): δ_H, ppm 8.20 (d, J = 8 Hz, 1H, Ar–H), 8.12 (d, J = 3 Hz, 1H, Ar–H), 8.09 (s, 1H, lactone 4-H), 7.85 (dd, J = 8 Hz, 2H, Ar–H), 7.30 (dd, J = 8 Hz, 2H, Ar–H), 7.46 (dd, J = 8 Hz, 1H, Ar–H), 7.10 (s, 1H, Ar–H), 7.05 (s, 1H, Ar–H), 4.09 (t, J = 6 Hz, 2H, OCH_2), 4.01 (t, J = 6 Hz, 2H, OCH_2), 1.76 (m, 4H, $OCCH_2$), 1.43 (m, 4H, $OCCCH_2$), 1.29 (m, 8H, $OCCC(CH_2)_2$), 0.92 (t, J = 6 Hz, 3H, CH_3), 0.88 (t, J = 6 Hz, 3H, CH_3). ^{13}C NMR (d-DMSO 500 MHz, δ ppm): 162.0 (Ar, C_p), 160.5 (lactone C=O, C_a), 156.2 (Ar, C_n), 148.1 (Ar, C_j), 146.3 (Ar, C_g), 146.0 (Ar, C_f), 141.1 (Ar, C_c), 134.4 (Ar, C_s), 128.8, (Ar, $2C_i$), 128.0 (Ar, C_k), 124.7 (Ar, C_b), 122.5 (Ar, C_r), 121.8 (Ar, C_o), 117.4 (Ar, $2C_m$), 115.8 (C≡N,C_w), 115.6 (C≡N, C_y), 115.5 (Ar, C_u), 114.4 (Ar, C_d), 109.5 (Ar, C_e), 108.9 (Ar, C_t), 103.5 (Ar, C_h), 69.0 (Alkyl, $2C_1$), 31.8 (Alkyl, $2C_4$), 29.6 (Alkyl, $2C_2$), 25.6 (Alkyl, $2C_3$), 22.7 (Alkyl, $2C_5$), 14.1 (Alkyl, $2C_6$). *Anal.* Calc. for $C_{35}H_{36}N_2O_5$: C, 74.47; H, 6.38; N, 4.96. Found: C, 74.48; H, 6.51; N, 5.12%. Fluo-

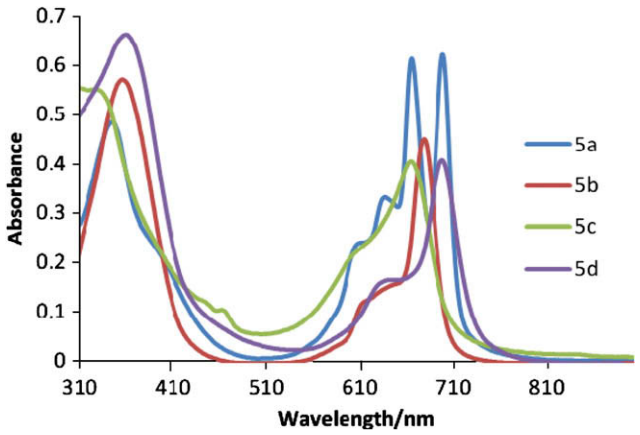
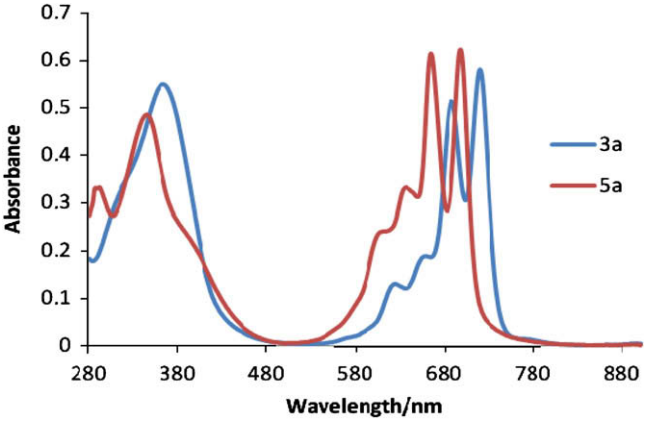


Fig. 2. UV–Vis spectra of **5a** ($1.328 \cdot 10^{-5}$ M) and **5b** ($1.290 \cdot 10^{-5}$ M) in THF, **5c** ($1.295 \cdot 10^{-5}$ M) and **5d** ($1.293 \cdot 10^{-5}$ M) in DMF.



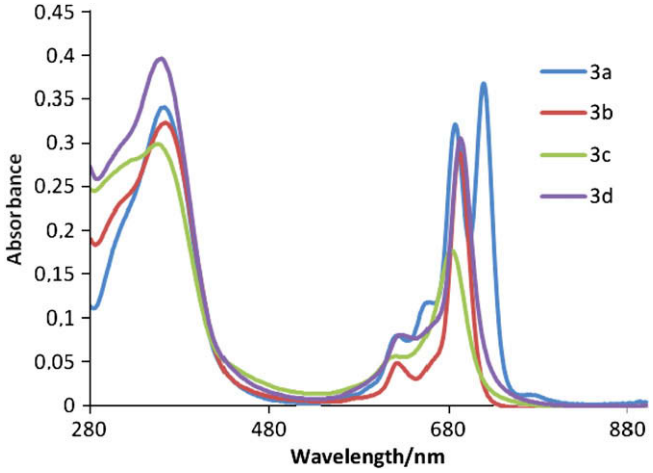


Fig. 1. UV–Vis spectra of **3a** ($1.328 \cdot 10^{-5}$ M) and **3d** ($1.295 \cdot 10^{-5}$ M) in THF, **3b** ($1.290 \cdot 10^{-5}$ M) and **3c** ($1.293 \cdot 10^{-5}$ M) in DMF.

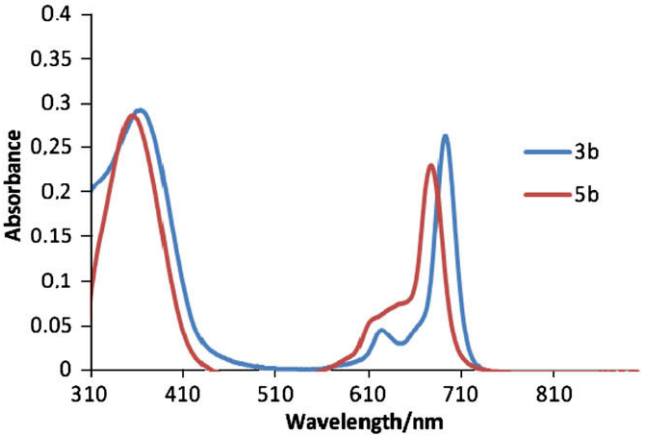


Fig. 3. UV–Vis spectra of **3a** ($1.328 \cdot 10^{-5}$ M) and **3b** ($1.290 \cdot 10^{-5}$ M) as compared with that of **5a** ($1.328 \cdot 10^{-5}$ M) and **5b** ($1.290 \cdot 10^{-5}$ M) in THF.

rescence data: (EM) $1.063.10^{-5}$ M, λ_{em}: 439 nm and (EX) $1.063.10^{-6}$ M, λ_{ex}: 368 nm (5 slitt) (THF), MS (MALDI-TOF): *m/z* 564 $[M]^+$, 565 $[M+1]^+$.

2.4. 2,9,16,23-Tetrakis[6,7-dihexyloxy-3-(3-oxyphenyl) coumarin]phthalocyanine (3a) and 2,9,16,23-tetrakis[6,7-dihexyloxy-3-(4-oxyphenyl)coumarin]phthalocyanine (**5a**)

A solution of **3** (0.1 g, 0.17 mmol) or **5** (0.1 g, 0.17 mmol) in dry 2-*N*,*N*-dimethylaminoethanol (DMAE) (2 ml) was refluxed with stirring for 48 h under N_2. After cooling to room temperature, methanol was added in order to precipitate the product. The green product was filtered and washed with water, methanol, ethanol, acetonitrile, ethyl acetate, acetone, acetic acid and diethyl ether.

The compound **3a** is soluble in THF, $CHCl_3$, DMF and DMSO. Yield: 0.07 g (70%), m.p.: >300 °C. IR $\nu(cm^{-1})$: 3250 (N–H), 3068–3049 (Ar–H), 2925–2890 (alkyl–CH), 1720 (C=O lactone), 1630 (C=C), 1504–1462 (Ar C=C), 1250 (Ar–O–Ar). UV–Vis λ_{max} (nm) (log ε) (THF) ($1.328.10^{-5}$ M): 354 (4.83), 685 (4.82), 717 (4.87). *Anal.* Calc. for $C_{140}H_{146}N_8O_{20}$: C, 74.40; H, 6.47; N, 4.96. Found: C, 73.97; H, 6.41; N, 4.18%. Fluorescence data: (EM) $1.328.10^{-5}$ M, λ_{em}: 721 nm and (EX) $0.265.10^{-6}$ M, λ_{ex}: 657 nm (20 slitt) (THF). MS (MALDI-TOF), (2,5-dihydroxybenzoic acid as matrix): *m/z* 2259 $[M+1]^+$.

The compound **5a** is soluble in THF, DMF and DMSO. Yield: 0.08 g (80%), m.p.: >300 °C. IR $\nu(cm^{-1})$: 3268 (N–H), 3070–3052 (Ar–H), 2930–2892 (alkyl–CH), 1722 (C=O lactone), 1635 (C=C), 1510–1462 (Ar C=C), 1248 (Ar–O–Ar). UV–Vis λ_{max} (nm) (log ε) (THF) ($1.328.10^{-5}$ M): 338 (4.75), 663 (4.83), 696 (4.82). *Anal.* Calc. for $C_{140}H_{146}N_8O_{20}$: C, 74.40; H, 6.47; N, 4.96. Found: C, 74.21; H, 6.30; N, 4.14%. Fluorescence data: (EM) $1.328.10^{-5}$ M, λ_{em}: 720 nm and (EX) $0.265.10^{-6}$ M, λ_{ex}: 660 nm (20 slitt) (THF). MS (MALDI-TOF), 2,5-dihydroxybenzoic acid as matrix): *m/z* 2258 $[M]^+$.

2.5. General procedure for the synthesis of 2,9,16,23-tetrakis dihexyloxy-3-(3-oxyphenyl)coumarin]phthalocyaninatozinc (**3b**), 2,9,16,23-tetrakis[6,7-dihexyloxy-3-(4-oxyphenyl) coumarin] phthalocyaninatozinc (**5b**), 2,9,16,23-tetrakis[6,7-dihexyloxy-3-(3-oxyphenyl)coumarin]phthalocyaninatocobalt (**3c**), 2,9,16,23-tetrakis[6,7-dihexyloxy-3-(4-oxyphenyl) coumarin] phthalocyaninatocobalt (**5c**), 2,9,16,23-tetrakis[6,7-dihexyloxy-3-(3-oxyphenyl)coumarin]phthalocyaninatocopper (**3d**) and 2,9,16,23-tetrakis[6,7-dihexyloxy-3-(4-oxyphenyl) coumarin] phthalocyaninatocopper (**5d**)

Compound **3** (0.1 g, 0.18 mmol) or **5** (0.1 g, 0.18 mmol), $Zn(AcO)_2{\cdot}2H_2O$ (0.0097 g, 0.045 mmol)/$Co(AcO)_2{\cdot}4H_2O$ (0.011 g, 0.045 mmol)/$Cu(AcO)_2{\cdot}4H_2O$ (0.0076 g, 0.045 mmol) and dry DMAE (2 ml) were refluxed with stirring under N_2 atmosphere for 24 h. After cooling to room temperature, they were treated with methanol, then the products were filtered off; washed with water, methanol, ethanol, acetonitrile, ethyl acetate, acetone, acetic acid and diethyl ether.

The compound **3b** is soluble in THF, DMF and DMSO. Yield: 0.054 g (53%), m.p.: >300 °C. IR $\nu(cm^{-1})$: 3114–3056 (Ar–H), 2932–2895 (alkyl–CH), 1724 (C=O lactone), 1633 (C=C), 1250 (Ar–O–Ar). UV–Vis λ_{max} (nm) (log ε) (THF) ($1.290.10^{-5}$ M): 356 (4.38), 690 (4.34). *Anal.* Calc. for $C_{140}H_{144}N_8O_{20}Zn$: C, 72.38; H, 6.20; N, 4.83. Found: C, 72.44; H, 6.24; N, 4.12%. Fluorescence data: (EM) $1.290.10^{-5}$ M, λ_{em}: 700 nm and (EX) $0.258.10^{-6}$ M, λ_{ex}: 655 nm (10 slitt) (THF). MS (MALDI-TOF), (2,5-dihydroxybenzoic acid as matrix): *m/z* 2322 $[M+1]^+$.

The compound **5b** is soluble in THF, DMF and DMSO. Yield: 0.041 g (43%), m.p.: 300 °C. IR $\nu(cm^{-1})$: 3082–3028 (Ar–H), 2925–2890 (alkyl–CH), 1720 (C=O lactone), 1630 (C=C), 1248 (Ar–O–Ar). UV–Vis λ_{max} (nm) (log ε) (THF) ($1.290.10^{-5}$ M): 350 (5.04), 671 (4.93). *Anal.* Calc. for $C_{140}H_{144}N_8O_{20}Zn$: C, 72.38; H, 6.20; N, 4.83. Found: C, 71.56; H, 6.04; N, 5.12%. Fluorescence data: (EM) $1.290.10^{-5}$ M, λ_{em}: 694 nm and (EX) $0.258.10^{-6}$ M, λ_{ex}: 681 nm (10 slitt) (THF). MS (MALDI-TOF), (2,5-dihydroxybenzoic acid as matrix): *m/z* 2321.2 $[M]^+$.

The compound **3c** is soluble in DMF and DMSO. Yield: 0.043 g (42%), m.p.: >300 °C. IR $\nu(cm^{-1})$: 3072–3033 (Ar–H), 2956–2898 (alkyl–CH), 1726 (C=O lactone), 1630 (C=C), 1251 (Ar–O–Ar). UV–Vis λ_{max} (nm) (log ε) (DMF) ($1.295.10^{-5}$ M): 346 (4.86), 680 (4.65). *Anal.* Calc. for $C_{140}H_{144}N_8O_{20}Co$: C, 72.57; H, 6.22; N, 4.84. Found: C, 72.54; H, 5.37; N, 5.04%. MS (MALDI-TOF), (2,5-dihydroxybenzoic acid as matrix): *m/z* 2318 $[M+2]^+$.

The compound **5c** is soluble in DMF and DMSO. Yield: 0.052 g (51%), m.p.: >300 °C. IR $\nu(cm^{-1})$: 3066–3028 (Ar–H), 2934–2896 (alkyl–CH), 1722 (C=O lactone), 1624 (C=C), 1250 (Ar–O–Ar). UV–Vis λ_{max} (nm) (log ε) (DMF) ($1.295.10^{-5}$ M): 319 (4.62), 653 (4.44). *Anal.* Calc. for $C_{140}H_{144}N_8O_{20}Co$: C, 72.57; H, 6.22; N, 4.84. Found: C, 72.42; H, 5.34; N, 4.82%. MS (MALDI-TOF), (2,5-dihydroxybenzoic acid as matrix): *m/z* 2316 $[M]^+$.

The compound **3d** is soluble in THF, DMF and DMSO. Yield: 0.041 g (43%), m.p.: >300 °C. IR $\nu(cm^{-1})$: 3112–3094 (Ar–H), 2985–2898 (alkyl–CH), 1726 (C=O lactone), 1620 (C=C), 1250 (Ar–O–Ar). UV–Vis λ_{max} (nm) (log ε) (THF) ($1.293.10^{-5}$ M): 351 (4.87), 690 (4.75). *Anal.* Calc. for $C_{140}H_{144}N_8O_{20}Cu$: C, 72.38; H, 6.20; N, 4.83. Found: C, 71.44; H, 6.38; N, 5.01%. MS (MALDI-TOF), (2,5-dihydroxybenzoic acid as matrix): *m/z* 2321 $[M+1]^+$.

The compound **5d** is soluble in DMF and DMSO. Yield: 0.056 g (55%), m.p.: >300 °C. IR $\nu(cm^{-1})$: 3059–3027 (Ar–H), 2925–2890 (alkyl–CH), 1721 (C=O lactone), 1615 (C=C), 1248 (Ar–O–Ar).

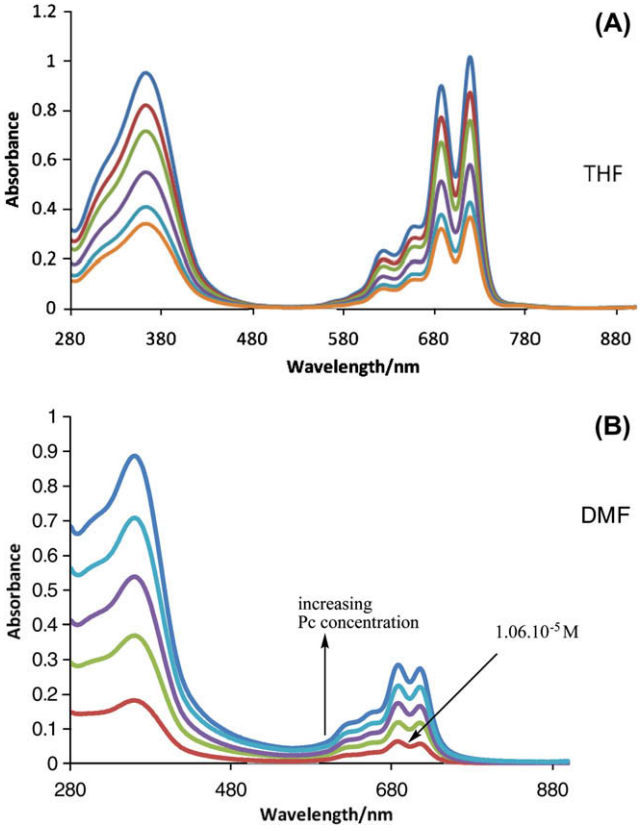


Fig. 4. The aggregation behaviour of the H_2Pc complex (**3a**) was monitored at several concentrations in THF (A) and DMF (B).

UV–Vis λ_{max} (nm) (log ε) (DMF) ($1.293.10^{-5}$ M): 351 (4.70), 694 (4.50). *Anal.* Calc. for $C_{140}H_{144}N_8O_{20}Cu$: C, 72.38; H, 6.20; N, 4.83. Found: C, 70.59; H, 6.24; N, 4.96%. MS (MALDI-TOF), (2,5-dihydroxybenzoic acid as matrix): *m/z* 2320 $[M]^+$.

3. Result and discussion

6,7-Dihydroxy-3-[*p*-(2′,3′-dicyanophenoxy)phenyl]coumarin (**2**) and 6,7-dihydroxy-3-[*p*-(3′,4′-dicyanophenoxy)phenyl]coumarin (**4**) were prepared according to the literature [24,25], which involve the condensation of 2,4,5-trihydroxybenzaldehyde with *p*-(2,3-dicyanophenoxy)phenylacetic acid (**1**) or *p*-(3,4-dicyanophenoxy)phenylacetic acid in the presence of sodium acetate and acetic anhydride at 160 °C. The formed diacetoxy derivatives (not isolated) of compounds **2** and **4** were then deacetylated in 10% HCl/CH_3OH solution. The crude products were purified by silica gel column chromatography using $CHCl_3$ as eluent. Compounds **2** and **4** were reacted with 1-bromohexane in the presence of K_2CO_3 in DMF to obtain 6,7-dihexyloxy-3-[*p*-(2′,3′-dicyanophenoxy)phenyl]coumarin (**3**) and 6,7-dihexyloxy-3-[*p*-(3′,4′-dicyanophenoxy)phenyl]coumarin (**5**). Cyclotetramerization of the phthalonitrile derivative **3** and **5** to the metal-free Pcs (**3a** and **5a**) were accomplished in DMAE at 145 °C in a sealed glass tube. The MPcs (**3b**–**3d** and **5b**–**5d**) were obtained from the reaction of dicyano derivatives **3**, **5** and the corresponding metal salts [$Zn(AcO)_2{\cdot}2H_2O$, $Co(AcO)_2{\cdot}4H_2O$ or $Cu(AcO)_2{\cdot}4H_2O$] in DMAE at reflux temperature (Scheme 1). The novel Pcs (**3a**–**3d** and **5a**–**5d**) were reasonably soluble in DMF, $CHCl_3$ and THF due to the long alkyl substituents; consequently easily purified with silica gel chromatography. The spectroscopic characterization of the newly synthesized intermediates and Pcs included elemental analysis, ^1H NMR, IR, fluorescence spectra, MALDI-TOF mass and UV–Vis spectral investigations. These results were in accordance with the proposed

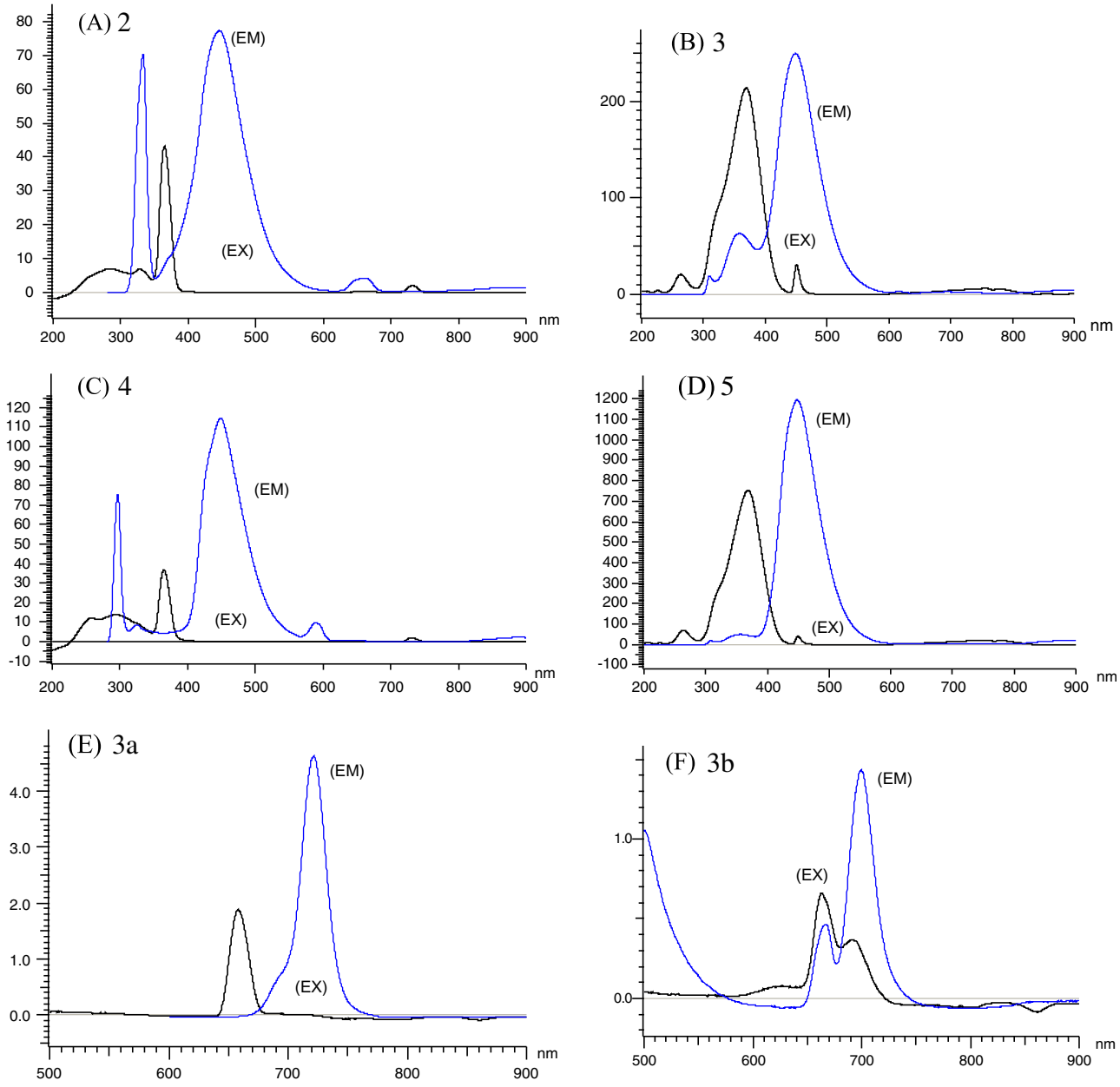


Fig. 5. Fluorescence emission and excitation spectra of **2**–**5** and **3a**, **3b** in THF. Excitation wavelength = 364 nm for **2 (A)**, 364 nm for **3 (B)**, 369 nm for **4 (C)**; 368 nm for **5 (D)**, 657 nm for **3a (E)** and 655 nm for **3b (F)**.

structures. The yields were satisfactory and depended upon the metal cation.

The IR-spectra of **2/4** exhibit the intense absorption band at 2240/2200 cm^{-1} corresponding to the C≡N stretching, and characteristic frequencies at 3461–3398/3400–3396 (–OH), 3098/3100 (Ar–H) and 1707/1703 (lactone C=O) cm^{-1}. The broad absorption band at 3461–3398/3400–3396 cm^{-1} corresponding to –OH stretching, disappeared after conversion to **3/5** (Scheme 2). The ^1H NMR spectra of **2/4** indicated the –OH protons at 9.28 and 9.31 ppm as singlets, the aromatic protons at 6.66–8.25/6.66–8.28 ppm as doublets and the proton of coumarin at position 4 at 8.08 ppm as a singlet. In the IR-spectra of **2/4**, alkyl groups ($–CH_2–$ and $–CH_3$) gave intense absorptions at 2923–2898/2950–2890 cm^{-1}. The C≡N band appeared at 2240/2220 cm^{-1} and the lactone –C=O group stretched around 1707/1703 cm^{-1}. In the ^1H NMR analysis of **3/5** in DMSO, the proton of coumarin at position 4 appeared at 8.09 ppm as a singlet, the aromatic protons at 7.05–8.09/7.05–8.20 ppm as doublets and the $–CCH_2C–$ protons in the long chains at the range of 1.32–1.78/1.29–1.76 ppm as multiplets. The CH_3 protons at the end of the chains were observed as two triplets at 0.98/0.92 ppm and 0.92/0.88 ppm. The triplets at 4.12/4.09 ppm and 4.06/4.01 ppm indicated the presence of two $–OCH_2–$ groups adjacent to an aromatic ring.

Cyclotetramerization of the dinitriles (**3** and **5**) to the Pcs (**3a–3d** and **5a–5d**) were confirmed by the disappearance of the sharp C≡N vibration at 2228/2220 cm^{-1}. The IR-spectra of metal-free (**3a**/**5a**) and metallo Pcs (**3b–3d** and **5b–5d**) are very similar, except ν(NH) vibrations of the inner Pc core in the metal-free molecule at 3250/3268 cm^{-1}. In addition to the elemental analysis results, mass spectra were definitive. The mass spectra of **2/4** and **3/5** confirmed the proposed structures. The mass spectral studies by the MALDI-TOF technique on the newly synthesized compounds identified at m/z: 396 $[M]^+$ for **2/4** and m/z: 564 $[M]^+$ for **3/5** (Scheme 3A and B). Values of the molecular ions show good agreement with the calculated values for metal-free Pc **3a/5a** (m/z 2258), ZnPc **3b/5b** (m/z 2321) (Scheme 3C), CoPc **3c/5c** (m/z 2316) and CuPc **3d/5d** (m/z 2320) in the presence of 2,5-dihydroxybenzoic acid (DHB) (20 mg/mL in THF) as a matrix.

The ground state electronic spectra of the compounds showed characteristic absorptions in the Q band region at 685/663 and 717/696 nm for **3a**/**5a**, 690/671 nm for **3b**/**5b**, 680/653 nm for **3c**/**5c** and 690/694 nm for **3d**/**5d** in THF and DMF (Figs. 1 and 2). The B band region was observed around 338–350 nm in THF and DMF. The 3-phenylcoumarins show high absorption in the near UV range around 340–346 nm [26]. After Pc formation, four 6,7-dihexyloxy-3-[*p*-(2′,3′-dicyanophenoxy)phenyl]coumarin (**3**) and 6,7-dihexyloxy-3-[*p*-(3′,4′-dicyanophenoxy)phenyl]coumarin (**5**) groups are present in each Pc molecule, so the B band absorption intensity can probably be multified as that of Pc core alone. The absorption of **3a–3d** and **5a–5d** can be carelessly named as only B band of Pc core around 350 nm; this covers also the absorption of coumarin units. There were also characteristic shoulders at slightly higher energy side of the Q band for each Pc. The spectra of **3b–3d** and **5b–5d** in THF/DMF showed monomeric behaviour evidenced by a narrow Q band, typical of metallo Pc complexes. The metal-free Pc complexes **3a/5a** gives a doublet Q band as a result of the D_{2h} symmetry. It was found that the Q bands of H_2Pc and ZnPc are red shifted 20 nm for **3a** and 5 nm for **3b** as compared with that of **5a** and **5b** in THF (Fig. 3).

Aggregation is usually depicted as a coplanar association and strongly dependent on the concentration and nature of the solvent. For Pcs, the aggregation behaviour in solution is a good indication of interaction between the aromatic macrocycles. Upon formation of higher order complexes, the coupling between the electronic states of individual monomeric Pc units causes significant spectral perturbations. Thus, aggregation is easily detected from optical absorption studies. The UV–Vis spectra of the Pc compound (**3a**) in THF are relatively narrow as compared with those in DMF. It is clear that while **3a** is in the form of monomeric species in THF, it is aggregated in DMF. THF seems to be able to disrupts π–π stacking by coordination to the metal center. Thus, the aggregation of the Pc compounds can be inhibited by using THF as the solvent. In the case of aggregation, any increase in concentration generally results in the broadening of the Q band absorption and insignificant peak around 620 nm Pc molecules, which accompanied by a blue shift of the Q band with some decrease in intensity [27]. For this reason, in this study, the aggregation behaviour of the Pc complex **3a** was monitored at several concentrations in THF and DMF (Fig. 4). Fig. 4 indicates the effect of increasing concentration on the UV–Vis spectra of $1.06 \cdot 10^{-6}$ mol dm^{-3} **3a** in DMF. At the beginning (for $1.06 \cdot 10^{-6}$ mol dm^{-3} **3a**), the intensities of two bands are approximately equal to each other. As the concentration of **3a** is increased, the band with the lower wavelength becomes higher in intensity as compared with the higher one. The changes in the Q band absorption with increasing concentration in the spectra of **3a** provide additional support for the presence of aggregation in DMF and the absence of aggregation in THF.

Fluorescence emission spectra for ligands (**2–5**) and Pcs (**3a** and **3b**) in THF were shown in Fig. 5. While the Pcs **3a** and **3b** showed similar fluorescence behaviour, the Pc **3c**/5c and **3d**/**5d** does not show fluorescence at excitation wavelength. The emission peaks for **2–5** and **3a**/**5a**, **3b**/**5b** were observed at 458, 454, 440, 439 nm and 721/720, 700/694 nm, respectively. The excitation spectra of the compounds are similar to that of absorption spectra, and are mirror images of the fluorescence spectra (Table 1).

Table 1
Absorption, excitation and emission spectral data for ligands and phthalocyanines **2–5**, **3a**, **3b** and **5a**, **5b** in THF.

Compound	Q band λ_{max} (nm)	log ε	Excitation λ_{Ex} (nm)	Emission λ_{Em} (nm)	Stokes shift Δ_{stokes} (nm)
2	360/305	4.30/4.13	364	458	98/153
3	360/323	4.32/4.06	364	454	94
4	357	4.25	369	440	71
5	354	4.42	368	439	85
3a	717/685	4.87/4.82	657	721	4/36
3b	690	4.34	655	700	10
5a	696/663	4.82/4.83	660	720	24/57
5b	671	4.93	681	694	23

Acknowledgement

We are thankful to the Scientific and Research Council of Turkey, TUBITAK (Project Nos: 107T347 and 108T623).

References

[1] K. Gunther, Inorg. Chem. 35 (1996) 7916.
[2] C.C. Leznoff, A.B.P. Lever, The Pthalocyanines Vol. 1: Properties, CRC Press, Boca Raton, Florida, 1983.
[3] E. Kol'tsov, T. Basova, P. Semyannikov, I. Igumenov, Mater. Chem. Phys. 86 (2004) 222.
[4] P. Yong, C. Wenxing, L. Sufang, Z. Yifeng, Dyes Pigm. 66 (2005) 115.
[5] P.F. Maria, D. Donata, F. Lia, R. Gabrio, Tetrahedron Lett. 41 (2000) 9143.
[6] B. Shuguang, L. Xianggao, S. Lei, C. Jianfeng, J. Mater. Sci. Technol. 22 (4) (2006) 533.
[7] D.W. Karolien, W. Philippe, T. Eduard, J. Electroanal. Chem. 567 (2004) 167.

[8] S. Ünlü, M.N. Yaraşır, M. Kandaz, A. Koca, B. Salih, Polyhedron 27 (13) (2008) 2805.
[9] M. Kandaz, I. Yılmaz, Ö. Bekaroglu, Polyhedron 19 (2000) 115.
[10] M. Durmus, T. Nyokong, Polyhedron 26 (2007) 2767.
[11] H. Çakıcı, A.A. Esenpınar, B. Bulut, Polyhedron 27 (18) (2008) 3625.
[12] K.P. Dennis, C. R. Chim. 6 (2003) 903.
[13] Y.E. Orlov, Russ. Chem. Rev. 46 (7) (1977) 671.
[14] Z.M. Nofal, M.I. El-Zahar, S.S. Abd El-Karim, Molecules 5 (2000) 99.
[15] M.A. Al-Haiza, M.S. Mostafa, M.Y. El-Kady, Sci. J. King Faisal Univ. (Basic App. Sci.) 6 (1) (2005) 1426.
[16] I. Kostova, Curr. Med. Chem. Anti-Cancer Agents 5 (2005) 29.
[17] B. Tyagi, M.K. Mishra, R.V. Jasra, J. Mol. Catal. A: Chem. 276 (2007) 47.
[18] F.F. Ye, J.R. Gao, W.J. Sheng, J.H. Jia, Dyes Pigm. 77 (2008) 556.
[19] A.J. Jagtap, V.S. Satam, R.N. Rajule, V.R. Kanetkar, Dyes Pigm. 82 (2009) 84.
[20] P. Feng, J. Zhu, Z. Cheng, Z. Zhang, X. Zhu, Polymer 48 (2007) 5859.
[21] R.F. Rodrigues, A.K. Tashima, R.M.S. Pereira, R.S. Mohamed, F.A. Cabral, J. Supercrit. Fluids 43 (2008) 375.
[22] J.G. Young, W. Onyebuagu, J. Org. Chem. 55 (1990) 2155.
[23] R.D. George, A.W. Snow, J. Heterocycl. Chem. 32 (1995) 495.
[24] M. Çamur, M. Bulut, Dyes Pigm. 77 (2008) 165.
[25] Ü. Çakır, M. Özer, M.A. İçen, H.İ. Uğraş, M. Bulut, Dyes Pigm. 60 (2004) 177.
[26] Ç. Erk, M. Bulut, J. Heterocycl. Chem. 38 (2001) 1291.
[27] N.J. Stillman, T. Nyokong, in: C.C. Leznoff, A.B.P. Lever (Eds.), Phthalocyanines Properties and Applications, vol. 1, VCH, Weinheim, 1989 (Chapter 3).

1-Ethyl-, 1-tert-butyl- and 1-(1-adamantyl)-5-thiotetrazoles were prepared by the reaction of commercial alkyl isothiocyanates with sodium azide in refluxing aqueous 2-propanol [16]. Potassium tetrachloroaurate and sodium borohydride were of analytical reagent grade and were used without further purification.

2.2. Characterization

2.2.1. Transmission electron microscopy (TEM)

The particle size and morphology of the NPs were examined on a JEOL JEM 1010 transmission electron microscope operating at 200 kV. Samples were prepared by drop-casting of a dilute solution of the NPs in toluene on 400-mesh carbon-coated copper grids and quickly removing of the excess of solution.

2.2.2. UV–Vis spectroscopy

UV–Vis absorption spectra of toluene solutions of the NPs were recorded on a Cary 500 Scan UV–Vis–NIR (Varian Ltd.) spectrophotometer over the range 300–900 nm. The liquid samples were placed in a quartz cell with a 1 mm path length.

2.2.3. X-ray diffraction

XRD patterns were recorded on a DRON-2 X-ray diffractometer using a focused monochromatic Co Kα source. The registered coverage was contained in the range $2\theta = 40-100^\circ$. Solutions of the NPs were placed on Si support and evaporated.

2.2.4. Fourier transform infrared (FTIR) spectroscopy

FTIR spectra were acquired on a Thermo Nicolet AVATAR-300 FTIR spectrometer over the range 400–4000 cm^{-1}. Solutions of the gold NPs or thiotetrazoles were placed on a NaCl plate and the spectra were collected after evaporation of solvent at room temperature.

2.2.5. Thermogravimetric analysis (TGA)

TGA was carried out on a NETZSCH STA429 thermoanalyzer in a nitrogen atmosphere over a temperature range 30–600 °C at a heating rate of 10 °C/min.

2.3. Synthesis of the gold nanoparticles

The current synthetic procedure is a modified version of the method developed by the Brust group based on reduction of the tetrachloroaurate anion with sodium borohydride in the presence of a phase transfer catalyst and a stabilizing agent in a two-phase system [5]. In a typical procedure, 10 ml of an aqueous solution of potassium tetrachloroaurate (0.04 M) was mixed with 30 ml of a toluene solution of Aliquat 336 (0.05 M). The mixture was vigorously stirred for 30 min until the gold solution was extracted into the organic layer almost completely. The top toluene layer was separated from the aqueous layer, and washed with water. 1-R-5-thiotetrazole (0.0025 mmol) was added to the toluene solution with stirring. A freshly prepared aqueous solution of sodium borohydride (12 ml, 0.2 M) was added slowly. Stirring of the resulting mixture was continued for 3 h at room temperature. The organic and aqueous phases were separated upon completion of the reaction. The toluene layer was concentrated with a rotary evaporator under reduced pressure. The obtained residue was washed with hexane (R = Et) or ethanol (R = t-Bu, 1-adamantyl). The final product could easily be redispersed in organic solvents, such as chloroform or toluene.

3. Results and discussion

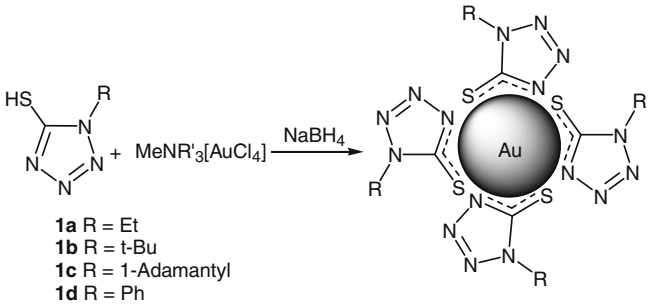
We found that reduction of the tetrachloroaurate anion with sodium borohydride in the presence of the phase transfer catalyst Aliquat 336 and 1-substututed 5-thiotetrazoles, **1**, in a water–toluene biphasic solution yielded spherical gold NPs with a relatively narrow size distribution (Scheme 1).

Fig. 1 shows TEM images of the obtained NPs. The sizes of the obtained NPs are strongly dependant on the hydrocarbon substituent R. The largest NPs (4.7 nm, $\sigma = 0.09$) were obtained using tetrazole **1a**, with relatively small ethyl substituent. The presence of bigger tert-butyl and 1-adamantyl substituents in the molecule of stabilizing agent, **1b** and **1c**, leads to the formation of smaller NPs with sizes 2.8 nm ($\sigma = 0.42$) and 3.2 nm ($\sigma = 0.36$), correspondingly. The influence of the substituent in the capping agent on the size of gold NPs obtained by two-phase reduction is not very clear. We can assume that tetrazoles **1b** and **1c** are stronger stabilizers of NPs in comparison with **1a** due to the bulky structure of the tert-butyl and 1-adamantyl substituents, while the linear ethyl substituent prevents growth and aggregation of NPs to a lesser extent. This dependence is consistent with one for alkanethiol capped gold NPs. In the latter case the increase of a methylene unit in the alkanethiol decreases the NP core size [17]. However, this dependence can be non-monotonic [18]. Fig. 2 shows the UV–Vis spectra of the as synthesized gold NPs. They displayed a broad peak around 510 nm, which is a peculiar characteristic of the gold surface plasmon band [19].

The NPs capped with thiotetrazoles **1a–c** are readily redispersed in non-polar solvents such as toluene and chloroform, showing no color changes and precipitation after 3 months storage under ambient conditions. An example photo of a toluene solution of gold NPs capped with tetrazole **1a** after 3 months storage at ambient conditions is presented in the inset of Fig. 2. It should be noted that 1-phenyl-5-thiotetrazole **1d** was also investigated as a capping agent in the synthesis of gold NPs. However, NPs capped with this ligand have tendency to coagulate and their solutions are stable for less than 1 week. Such behavior of NPs capped with **1d** was observed also during the synthesis of CdS NPs [12] and can be explained by π–π interactions between the phenyl rings of single NPs, leading to their agglomeration.

The XRD pattern of the gold NPs capped with thiotetrazole **1b** is shown in Fig. 3. Bragg's reflections for the above mentioned NPs are observed in the XRD pattern at 2θ values of 44.7, 52.1, 76.7 and 93.5°, representing the [1 1 1], [2 0 0], [2 2 0] and [3 1 1] planes of a face centered cubic lattice of gold (JCPDS File No. 4-0784). Gold NPs capped with tetrazoles **1a** and **1c** showed similar reflections.

Comparative analysis of the IR spectra of synthesized NPs and the corresponding free ligands confirmed the presence of thiotetrazoles at the surface of the NPs. As an example, the IR spectra of **1b** and gold NPs capped with this ligand are presented in Fig. 4. The IR spectra clearly indicate that the surface of the NPs is covered with 1-R-5-thiotetrazolate anions, SCN_4R^-, which form under



Scheme 1. Synthesis of gold NPs capped with thiotetrazoles.

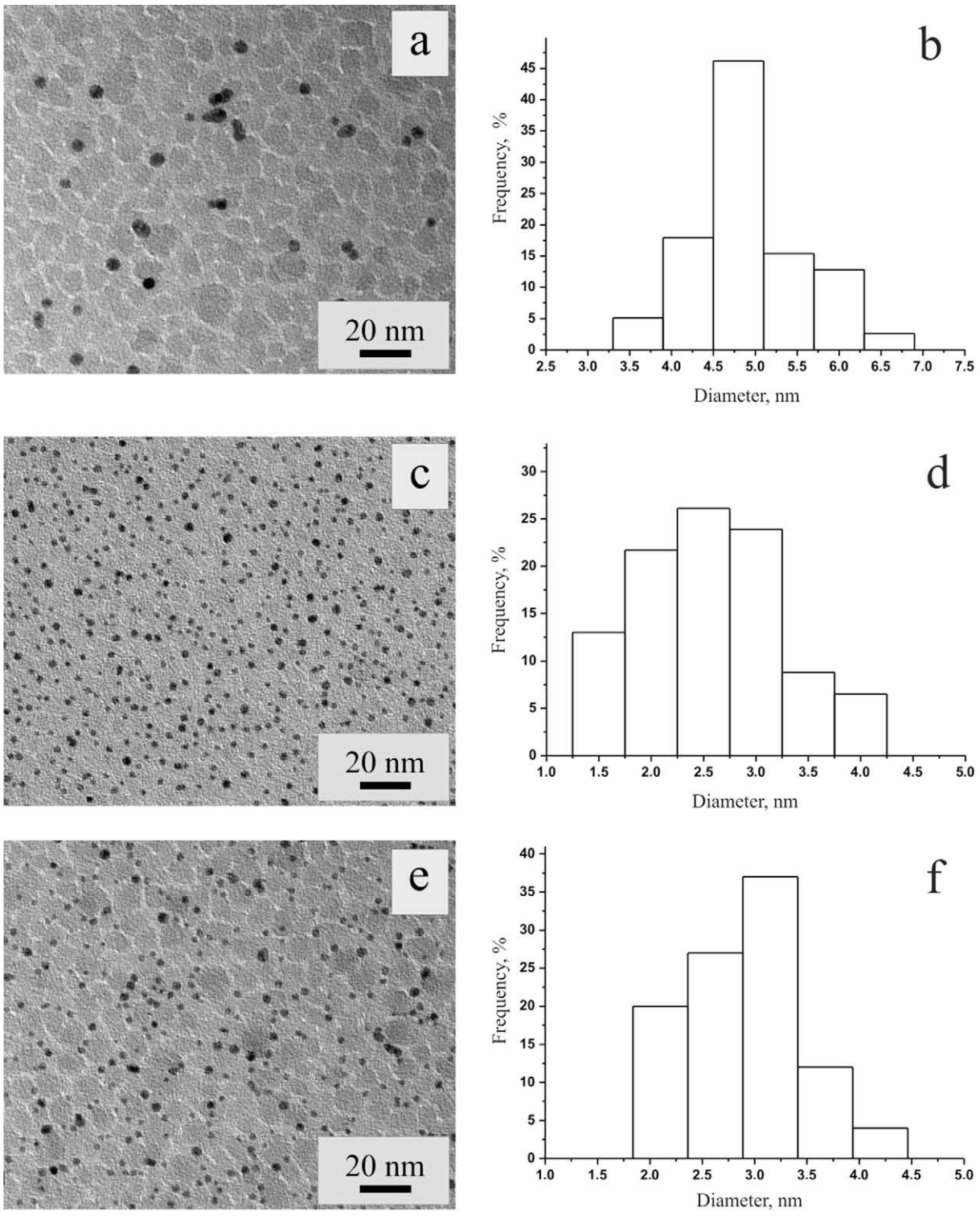


Fig. 1. TEM images and histograms of gold NPs capped with thiotetrazoles **1a** (a and b), **1b** (c and d), **1c** (e and f).

deprotonation of tetrazoles **1** and present a stable 6π-electron ring system. Disappearance of the duplet band of the S–H bond at 2540 and 2575 cm^{-1} and the appearance of a new duplet at 1733 and 1621 cm^{-1} in the spectra of NPs is typical for thiotetrazolate anions [20].

Fig. 5 shows TGA curves of thiotetrazole **1b** and the corresponding NPs. It indicates that thermolysis of the ligand bonded with NPs is characterized with a more fluent lost of weight and proceeds in a wider temperature range in comparison with the free ligand molecule. Since it is well-known [12] that thiotetrazolate salts are characterized with higher thermal stability in comparison with the corresponding thiotetrazoles, the observed differences in thermal behavior can be explained by the presence of the thiotetrazolate anion on NPs surface.

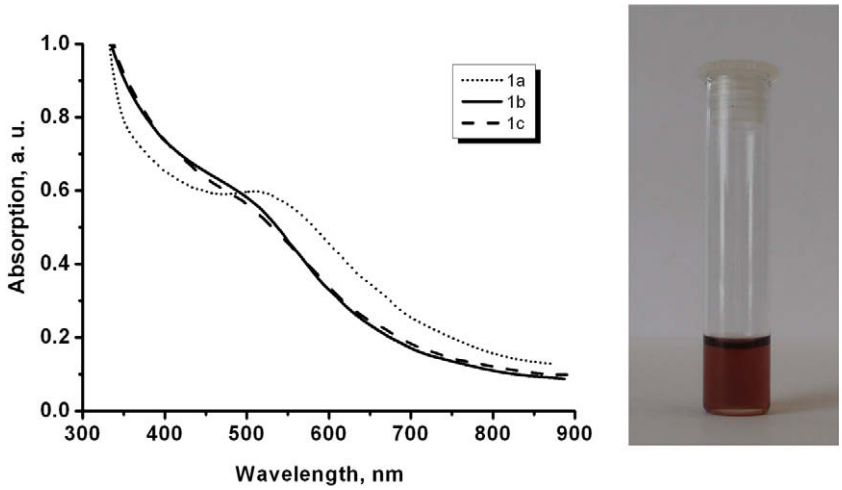


Fig. 2. UV–Vis spectra of gold NPs capped with tetrazoles **1** and a photograph of the solution of gold NPs capped with tetrazole **1a** after 3 months storage under ambient conditions.

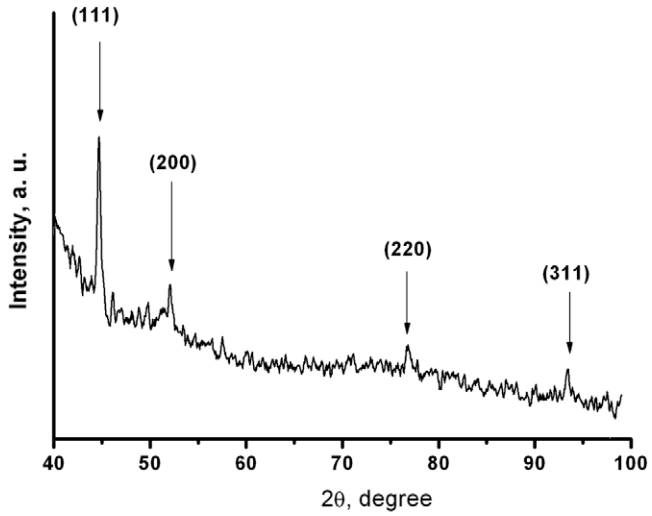


Fig. 3. X-ray power diffraction of gold NPs capped with **1b**.

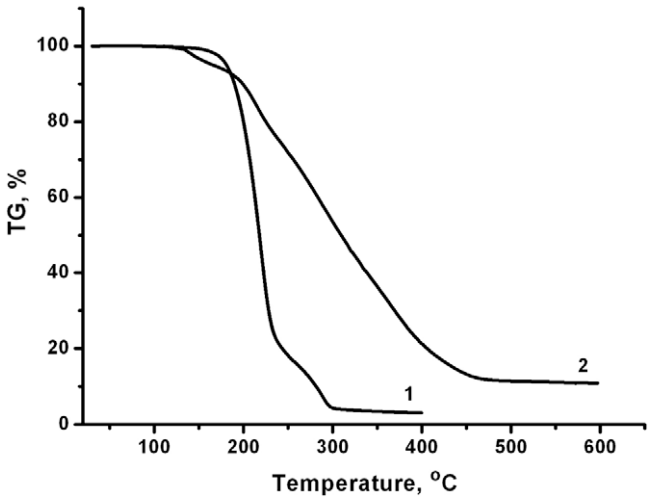


Fig. 5. TGA curves of pure tetrazole **1b** (1) and gold NPs, capped with **1b** (2).

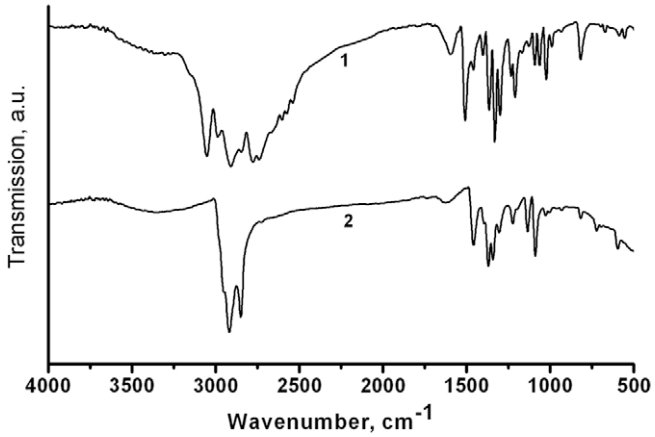
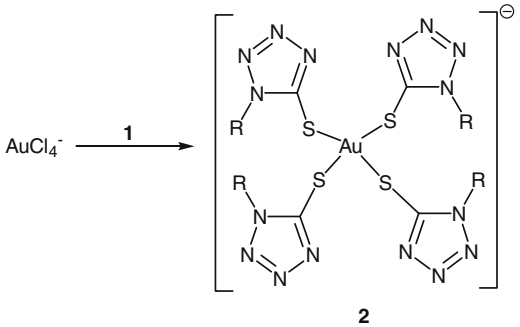


Fig. 4. FT-IR spectra of pure **1b** (1) and gold NPs capped with **1b** (2).

It should be noted that during addition of tetrazoles **1** to a toluene solution of the aurate salt, the color changes from yellow to orange or red-orange. Probably, this change is due to the formation of tetrakis(1-R-5-mercaptotetrazolato)-gold(III) complexes, **2**, which form by the replacement of the chloride ligands by thiotetrazolate in $AuCl_4^-$ [21]. According to X-ray analysis in such complexes, the tetrazole moiety is coordinated through sulfur atoms. However, in the formed NPs, binding of the thiotetrazolate anion with NPs can occur not only via sulfur atom, but also *via* nitrogen, and for the above mentioned ligands S-monodentate and N(4),S-bridging modes are favoured [14].



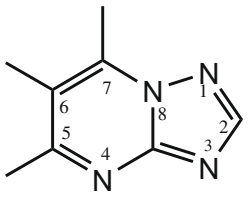
2

4. Conclusion

In summary, 1-R-5-thiotetrazoles were investigated as a novel ligands for stabilization of gold NPs. NPs capped with these easily available ligands were obtained by reduction of the tetrachloroaurate anion with sodium borohydride in the presence of the phase transfer catalyst Aliquat 336 and thiotetrazoles in a water – toluene two-phase system. These NPs are attractive for making efficient catalysts and electronic materials based on "naked" nanostructures.

References

[1] G. Schmid, B. Corain, Eur. J. Inorg. Chem. 17 (2003) 3081.
[2] R. Shenhar, V.M. Rotello, Acc. Chem. Res. 36 (2003) 549.
[3] (a) J.M. Clostranec, W.C.W. Chan, Adv. Mater. 45 (2006) 1953;
(b) X. Huang, I.H. El-Sayed, W. Qian, M.A. El-Sayed, J. Am. Chem. Soc. 128 (2006) 2115.
[4] M. Daniel, D. Astruc, Chem. Rev. 104 (2004) 293.
[5] M. Brust, C.J. Kiely, in: F. Caruso (Ed.), Colloids and Colloid Assemblies. Synthesis, Modificaion, Organization and Utilization of Colloid Particles, Wiley-VCH, Weinheim, 2004, pp. 96–119.
[6] (a) M. Aslam, L. Fu, M. Su, K. Vijayamohananb, V.P. Dravid, J. Mater. Chem. 14 (2004) 1795;
(b) X. Liu, N. Wu, B.H. Wunsch, R.J. Barsotti Jr., F. Stellacci, Small 2 (2006) 1046;
(c) O. Masala, R. Seshadri, Annu. Rev. Mater. Res. 34 (2004) 41;
(d) M. Hasan, D. Bethell, M. Brust, J. Am. Chem. Soc. 124 (2002) 1132;
X. Zhou, J.M. El Khoury, L. Qu, L. Dai, Q. Li, J. Colloid Interface Sci. 308 (2007) 381.
[7] E.W. Edwards, M. Chanana, D. Wang, H. Mohwald, Angew. Chem. Int. Ed. 47 (2008) 320;
E.W. Edwards, M. Chanana, D. Wang, J. Phys. Chem. C 112 (2008) 15207.
[8] M. Kanehara, E. Kodzuka, T. Teranishi, J. Am. Chem. Soc. 128 (2006) 13084.
[9] J. Kim, Y. Piao, T. Hyeon, Chem. Soc. Rev. 38 (2009) 372.
[10] X. Huang, I.H. El-Sayed, W. Qian, M.A. El-Sayed, J. Am. Chem. Soc. 128 (2006) 2115.
[11] D.V. Talapin, C.B. Murray, Science 310 (2005) 86;
D. Yu, C. Wang, P. Guyot-Sionnest, Science 300 (2003) 1277;
R.M. Rioux, H. Song, M. Grass, S. Habas, K. Niesz, J.D. Hoefelmeyer, P. Yang, G.A. Somorjai, Top. Catal. 39 (2006) 167.
[12] S.V. Voitekhovich, D.V. Talapin, C. Klinke, A. Kornowski, H. Weller, Chem. Mater. 20 (2008) 4545.
[13] (a) R.N. Butler, Tetrazoles, in: A.R. Katritzky, C.W. Rees, E.F.V. Scriven (Eds.), Comprehensive Heterocyclic Chemistry II, vol. 4, Pergamon, New York, USA, 1996, pp. 621–678;
(b) V.A. Ostrovskii, G.I. Koldobskii, R.E. Trifonov, Tetrazoles, in: A.R. Katritzky, C.A. Ramsden, E.F.V. Scriven, R.J.K. Taylor, V.V. Zhdankin (Eds.), Comprehensive Heterocyclic Chemistry III, vol. 6, Elsevier, Oxford, Tokyo, 2008, pp. 257–423.
[14] P.N. Gaponik, S.V. Voitekhovich, O.A. Ivashkevich, Russ. Chem. Rev. 75 (2006) 507.
[15] (a) S. A Vorobyova, N.S. Sobal, A.I. Lesnikovich, Colloid Surf. A: Physicochem. Eng. Aspects 176 (2000) 271;
(b) M.N. Nichick, S. A Vorobyova, A.I. Lesnikovich, A.V. Kukhta, E.E. Kolesnik, in: V.E. Borisenko, S.V. Gaponenko, V.S. Gurin (Eds.), Physics, Chemistry and Application of Nanostructures, Proceedings of the International Conference "Nanomeeting – 2007" Minsk, Belarus, World Scientific Publishing Co. Pvt. Ltd., Singapore, 2007, pp. 336–339.
[16] (a) E. Lieber, J. Ramachandran, Can. J. Chem. 37 (1959) 101;
(b) H. Quast, L. Bieber, Chem. Ber. 114 (1981) 3253.
[17] M.J. Schadt, W. Cheung, J. Luo, Ch.-J. Zhong, Chem. Mater. 18 (2006) 5147.
[18] B.L.V. Prasad, S.I. Stoeva, Ch.M. Sorensen, K.J. Klabunde, Langmuir 18 (2002) 7515.
[19] S. Link, Z.L. Wang, M.A. El-Sayed, J. Phys. Chem. B 103 (1999) 3529.
[20] (a) B. Pergolese, A. Bigotto, J. Mol. Struct. 655 (2003) 479;
(b) A. Gomez-Zavaglia, I.D. Reva, L. Frija, M.L. Cristiano, R. Fausto, J. Mol. Struct. 786 (2006) 182;
(c) B. Sagmuller, P. Freunscht, S. Schneider, J. Mol. Struct. 482–483 (1999) 231;
(d) X.R. Ye, X.Q. Xin, J.J. Zhu, Z.L. Xue, Appl. Surf. Sci. 35 (1998) 307.
[21] U. Abram, J. Mack, K. Ortner, M. Muller, J. Chem. Soc., Dalton Trans. (1998) 1011;
H. Noth, W. Beck, K. Burger, Eur. J. Inorg. Chem. (1998) 93.



Scheme 1. The ligand tmtp (5,6,7-trimethyl[1,2,4]triazolo[1,5-*a*]pyrimidine) and its IUPAC recommended ring-atom numbering system.

2.2. Synthesis of the ligand

The synthesis of the ligand tmtp was carried out by a known condensation procedure [2,22] at 160 °C, from a diketone and 3-amino-1,2,4-triazole schematically as summarized in Scheme 2, followed by recrystallization using ethanol. Observed yields were 60–70% depending on small variations in the conditions. Characterisation of the free ligand was done by elemental analysis, IR and NMR spectroscopy.

2.3. Synthesis of the coordination compounds

The coordination compounds were prepared by the following general recipes:

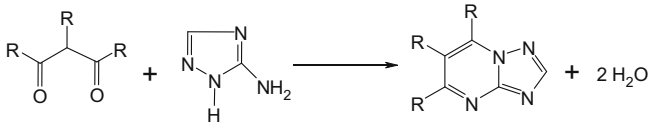
A solution of 1–2 mmol of the metal salt in 10–20 mL water was added to a warm aqueous solution of the ligand (1–5 mmol). Upon standing at room temperature crystals appeared, which were collected by filtration. In some cases, MeOH/water or pure MeOH were used as a solvent. To prepare the thiocyanate compounds a metathesis reaction was used, starting from the aqueous metal nitrate and ammonium thiocyanate (1:2). Yields were found to be between 30% and 60% depending on the metal and anion. Satisfactory elemental analysis was obtained for all compounds.

2.4. Physical and analytical methods

C, H, N determinations were performed on a PerkinElmer 2400 Series II analyzer. Ligand field spectra in the 300–2000 nm range were obtained on a PerkinElmer Lambda 900 spectrophotometer using the diffuse reflectance technique, using MgO as a reference. Infrared spectra of all compounds were recorded on a PerkinElmer Paragon 1000 FTIR spectrophotometer equipped with a Golden Gate ATR device, using the reflectance technique (4000–300 cm^{-1}, res. 4 cm^{-1}). (Far-)FTIR spectra were obtained on a Bruker IFS 113v infrared spectrophotometer as polyethylene mulls (600–100 cm^{-1}, Mylar 6 μ, res. 2 cm^{-1}). X-band powder EPR spectra were obtained on a Bruker EMX*plus* electron spin resonance spectrometer (field calibrated with DPPH (g = 2.0036)).

2.5. X-ray diffraction studies

For each coordination compound a suitable crystal was selected from the mother liquid and mounted to a glass fiber using the oil-drop method. Diffraction data were collected on a Nonius KappaCCD diffractometer (graphite-monochromated Mo Kα radiation).



Scheme 2. Synthesis scheme of substituted triazolopyrimidines; for tmtp: R = Me.

The structures were solved by direct methods. The programs COLLECT [23], SHELXS-97 [24], SHELXL-97 [25] were used for data reduction, structure solution and structure refinement, respectively. Refinement of F^2 was performed against all reflections. All non-hydrogen atoms were refined anisotropically. The water Hydrogen atoms of compounds **6**, **9** and **10** were picked from difference maps and refined isotropically. All other H-atoms were introduced in calculated positions and refined with fixed geometry with respect to their carrier atoms. Details of compound **5**: one of the two methanol molecules and the water molecule were found to be severely disordered. The methanol C7 and the water O9 were each refined with an occupancy factor of 0.5, while the methanol O8 atom was refined in three positions with site occupancy factors of 1/3. The H-atoms of these water and disordered methanol molecules could neither be determined, nor fixed.

Crystallographic data of the compounds are summarized in Table 1. Compound **11**, was found to be isomorphous with compounds **9** and **10**, as deduced from infrared and X-ray powder diffraction.

3. Results and discussion

3.1. General observations and spectral analyses

A variety of metal salts has been reacted in alcoholic or aqueous solution with the ligand, and a (micro)crystalline, reproducible product was formed, irrespective of the used metal to ligand ratio. The so-obtained products are listed in Table 2 with their composition and with some spectral characteristics. All compounds have been characterized by common physical methods, i.e. infrared, ligand field, and C, H, N analysis. The Cu compounds were also characterized by EPR, and the Zn compound also by NMR. In 10 cases an X-ray structure determination was carried out to obtain molecular structure details (*vide infra*). These compounds are numbered **1–10**.

3.2. Description of the X-ray structures

The compound $[CuCl_2(tmtp)_2]$ (**1**) crystallizes in the monoclinic space group $P2_1/c$. An ortep perspective view of **1** is shown in Fig. 1. Selected bond lengths and angles are given in Table 3. The Cu(II) ion is in a distorted tetrahedral environment formed by two tmtp ligands and two chlorides. Such tetrahedrally distorted geometries are not uncommon for Cu(II) with N donor ligands [26]; a packing diagram is given in Fig. S1. The degree of distortion of the Cu(II) ion can be expressed by the parameter τ_4 (τ_4 = 0.46 for Cu; τ_4 = 0 for a square planar geometry and τ_4 = 1 for a tetrahedral geometry) [27]. The Cu–N and Cu–Cl bond distances are in typical ranges for this type of $[CuN_2Cl_2]$ tetrahedron, see Table 3 [28,29].

The corresponding bromide $[CuBr_2(tmtp)_2]$ (**2**). crystallizes in the orthorhombic space group $Pca2_1$. The unit cells contains two slightly different chromophores, but both very similar to the chloride in Fig. 1. An ortep perspective view of **2** is shown in Fig. S2 and a packing figure in Fig. S3. Both Cu ions are in quite distorted tetrahedral environment (τ_4 = 0.54 for Cu; τ_4 = 0 for a square planar geometry and τ_4 = 1 for a tetrahedral geometry) [27], formed by two bromido ligands and to monodentate tmtp ligands. The Cu–N and Cu–Br bond distances are in typical ranges for this type of $[CuN_2Br_2]$ tetrahedron [28,29].

The compound $[ZnBr_2(tmtp)_2]$ **3** crystallizes in the monoclinic space group $P2_1/c$. An ortep perspective view of compound **3** is depicted in Fig. S4 and a packing diagram is given in Fig. S5. In this case the distortion from tetrahedral is much smaller, as commonly seen for Zn(II) d^{10} ions. The Zn(II) ions are in an almost perfect tetrahedral environment (τ_4 = 0.89 for Zn; τ_4 = 0 for a square planar

Table 1
Crystallographic data for compounds **1**–**10**.

Compound	(**1**)	(**2**)	(**3**)	(**4**)	(**5**)	(**6**)	(**7**)	(**8**)	(**9**)	(**10**)
Formula	$C_{16}H_{20}Cl_2CuN_8$	$C_{16}H_{20}Br_2CuN_8$	$C_{16}H_{20}Br_2N_8Zn$	$C_{16}H_{20}CuN_{10}O_6$	$C_{103}H_{144}Cu_6N_{48}O_{31.5}S_6$	$C_{18}H_{22}CuN_{10}OS_2$	$C_{18}H_{20}N_{10}S_2Zn$	$C_{18}H_{20}CdN_{10}S_2$	$C_{32}H_{44}B_2CoF_8N_{16}O_2$	$C_{32}H_{44}B_2F_8N_{16}O_2Zn$
Molecular weight	458.84	547.76	549.59	511.96	3132.7	522.12	505.93	552.96	917.38	923.82
Crystal system	monoclinic	orthorhombic	monoclinic	triclinic	trigonal	monoclinic	monoclinic	triclinic	triclinic	triclinic
Space group	$P2_1/c$ (No. 14)	$Pca2_1$ (No. 29)	$P2_1/c$ (No. 14)	$P\bar{1}$ (No. 2)	$R\bar{3}$ (No. 148)	$P2_1/n$ (No. 14)	$P2_1/c$ (No. 14)	$P\bar{1}$ (No. 2)	$P\bar{1}$ (No. 2)	$P\bar{1}$ (No. 2)
a (Å)	13.798(2)	16.563(3)	13.653(2)	7.023(1)	32.121(8)	8.238(1)	14.714(3)	10.530(2)	9.807(3)	9.8788(7)
b (Å)	15.193(1)	13.230(3)	15.211(1)	8.533(2)	32.121(8)	13.501(2)	9.941(2)	10.953(2)	10.6920(7)	10.7374(9)
c (Å)	9.2571(7)	18.811(3)	9.7587(7)	9.075(2)	11.175(2)	20.052(5)	15.915(3)	11.850(2)	11.191(2)	11.202(1)
α (°)	90	90	90	74.34(3)	90	90	90	66.44(3)	91.92(1)	91.676(9)
β (°)	96.90(1)	90	91.667(8)	71.00(3)	90	99.93(3)	104.95(3)	73.56(3)	113.14(2)	113.639(6)
γ (°)	90	90	90	81.04(3)	120	90	90	61.40(3)	112.61(1)	112.840(5)
V (Å^3)	1926.5(3)	4122(1)	2025.8(4)	493.8(2)	9985(4)	2196.8(7)	2249.1(8)	1092.8(4)	972.3(4)	978.8(2)
Z	4	8	4	1	3	4	4	2	1	1
D_{calc} (g cm^{-3})	1.582	1.765	1.802	1.722	1.563	1.579	1.494	1.681	1.567	1.567
F(000)	940	2168	1088	263	4860.5	1076	1040	556	473	476
μ (cm^{-1})	1.430	4.955	5.176	1.168	1.127	1.219	1.305	1.219	0.536	0.721
Crystal size (mm)	0.20 × 0.20 × 0.18	0.18 × 0.11 × 0.06	0.30 × 0.30 × 0.20	0.30 × 0.20 × 0.20	0.30 × 0.20 × 0.20	0.20 × 0.06 × 0.003	0.30 × 0.20 × 0.20	0.30 × 0.30 × 0.30	0.22 × 0.17 × 0.15	0.40 × 0.40 × 0.30
Colour, shape	green, block	brown, plate	colorless, block	blue, block	blue, block	brown, needle	colorless, block	colorless, block	orange, block	colorless, block
θ_{min}, θ_{max} (°)	2.59; 27.53	2.90; 26.50	2.00; 26.50	3.05; 27.61	2.66; 27.56	2.56; 25.05	3.00; 27.54	2.43; 27.55	2.59; 26.00	3.24; 25.50
Total reflections	33 837	53 536	30 945	7965	58 328	26 480	37 194	18 870	14 034	13 759
Total unique reflections	4416 (R_{int} = 0.0269)	8518 (R_{int} = 0.1007)	4194 (R_{int} = 0.0568)	2269 (R_{int} = 0.0165)	5093 (R_{int} = 0.0301)	3871 (R_{int} = 0.1344)	5127 (R_{int} = 0.0277)	5007 (R_{int} = 0.0177)	3808 (R_{int} = 0.0291)	3617 (R_{int} = 0.0162)
N No. of refined data, parameters	4416, 250	8518, 500	4194, 250	2269, 154	5093, 311	3871, 298	5127, 286	5007, 289	3808, 286	3617, 286
R_1[a], wR_2[b]	0.0247, 0.0678	0.0431, 0.1008	0.0351, 0.0736	0.0238, 0.0648	0.0321, 0.0930	0.0656, 0.1698	0.0266, 0.0825	0.0180, 0.0465	0.0366, 0.0917	0.0290, 0.0776
S[c]	1.053	1.053	1.098	1.064	1.048	1.021	0.993	1.119	1.036	1.041
Minimum and maximum residual density (e Å^{-3})	0.326; −0.366	0.776; −0.527	0.592; −0.540	0.348; −0.336	0.481; −0.470	0.469; −0.726	0.325; −0.379	0.304; −0.371	0.492; −0.408	0.521; −0.463

[a] $R_1 = \Sigma||F_o| - |F_c||/\Sigma|F_o|$.
[b] $wR_2 = [\sum[w(F_o^2 - F_c^2)^2]/\sum[w(F_o^2)^2]]^{1/2}$.
[c] Goodness-of-fit $S = [\sum w(F_o^2 - F_c^2)^2/(n-p)]^{1/2}$, where n is the number of reflections and p the number of parameters.

Table 2
Composition, colour and selected spectral data for the compounds **1** to **11**.

Compound	Colour	Diffuse reflectance (10^3 cm^{-1})	EPR (solid, RT)	IR (cm^{-1}); selection of non-ligand bands
1. $CuCl_2(tmtp)_2$	green	11.7 9.7 (br)	$g_\perp = 2.07$ $g_{\|\|} = 2.26$	309 (Cu–Cl) 284 (Cu–N)
2. $CuBr_2(tmtp)_2$	brown	11.6 9.1 (br) 18.5 (CT)	$g = 2.11$ (br)	246 (Cu–N) 160 (Cu–Br)
3. $ZnBr_2(tmtp)_2$	white	colorless	–	248 (Zn–N) 213/200 (Zn–Br)
4. $Cu(NO_3)_2(tmtp)_2$	blue	16.1 13.1 (sh)	$g_\perp = 2.08$ $g_{\|\|} = 2.24$	1270, 798 (NO_3)
5. $[Cu(SO_4)_2(tmtp)_2]_2(CH_3OH)_{2⅓}(H_2O)_{1/6}$	blue	13.0 9.7 (sh, br)	$g = 2.10$ (vbr)	3416 (OH, br) 1205, 1145, 1121, 994 (SO_4)
6. $[Cu(NCS)_2(tmtp)_2(H_2O)]$	red brown	12.5 9.1 (vbr.) 18.9 (CT)	$g_1 = 2.28$ $g_2 = 2.11$ $g_3 = 2.05$	3442 (OH, br) 2051 (C–N)
7. $Zn(NCS)_2(tmtp)_2$	white	colorless	–	2076 (C–N)
8. $[Cd(NCS)_2(tmtp)_2]_n$	white	colorless		2097 (C–N)
9. $[Co(H_2O)_2(tmtp)_4](BF_4)_2$,	orange	20.6 9.2		3471, 3331 (OH, br) 1050 (BF_4)
10. $[Zn(H_2O)_2(tmtp)_4](BF_4)_2$,	white	colorless		3470, 3332 (OH, br) 1049 (BF_4)
11. $[Ni(H_2O)_2(tmtp)_4](BF_4)_2$,	blue	27.0 16.4 9.9		3420(w), 3320 (OH) 1050 (BF_4)

sh = shoulder, (v)br = (very)broad, w = weak, CT = charge transfer band.

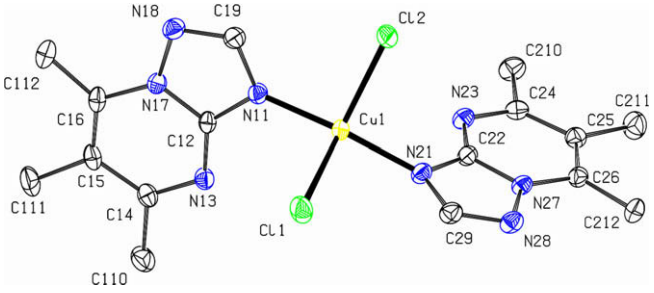


Fig. 1. ORTEP drawing (30% probability level) of [CuCl2(tmtp)2] (**1**). Hydrogen atoms are omitted for clarity.

geometry and $\tau_4 = 1$ for a tetrahedral geometry) [27], formed by two bromido ligands and to monodentate tmtp ligands. Selected bond lengths and angles are given in Table 3. The dihedral angles of the two largest angles from which τ_4 is calculated are 116.05(8) and 118.70(2)°. The Zn–N and Zn–Br bond distances are in typical ranges for this type of $[ZnN_2Br_2]$ tetrahedron [28,29].

The compound $[Cu(NO_3)_2(tmtp)_2]$ (**4**) crystallizes in the triclinic space group $P\bar{1}$. An ortep perspective view of **4** is shown in Fig. 2. Selected bond lengths and angles are given in Table 3. The geometry is distorted octahedral with chelating nitrates, having one long band (Cu–O3 = 2.529(2) Å) and one short bond (Cu–O1 = 1.964(1) Å) to the Cu(II) ion. The crystal packing is depicted in Fig. S6 and is uneventful.

The compound $[Cu(SO_4)_2(tmtp)_2]_2(CH_3OH)_{2⅓}(H_2O)_{1/6}$ (**5**) crystallizes in the trigonal space group $R\bar{3}$. An ortep perspective view of the dinuclear sulfate-bridged unit of **5** is presented in Fig. 3. Selected bond lengths and angles are given in Table 3. The compound has a quite unique bis(sulfato)-bridged dinuclear structure, where each Cu(II) ion is 5-coordinated in a geometry close to tetragonal pyramidal ($\tau_5 = 0.10$; $\tau_5 = 0$ for a square pyramidal geometry and $\tau_5 = 1$ for a trigonal bipyramidal geometry; [30]). The sulfate is chelating to one Cu, with Cu–O distances of 1.97–1.99 Å, and providing a third O atom to the other Cu(II) ion, with Cu–O = 2.216(2) Å. The chelating O–Cu–O angle is 71.6(1)°. The crystal lattice of **5** contains water and MeOH molecules (of which one MeOH molecule and the water molecule are disordered); hydrogen bonds exist between the MeOH molecule and the sulfate oxygen atom and between the water and the MeOH molecules. Details are given in Table S1. A packing diagram is depicted in Fig. S7.

Compound **6**, $[Cu(H_2O)(NCS)_2(tmtp)_2]$, crystallizes in the monoclinic space group $P2_1/c$ and has the Cu^{II} ion is in a coordination environment which is intermediate between trigonal bipyramidal and square-pyramidal ($\tau_5 = 0.49$; $\tau_5 = 0$ for a square pyramidal geometry and $\tau_5 = 1$ for a trigonal bipyramidal geometry; [30]), formed by two crystallographically equivalent thiocyanate anions (nitrogen atoms N1 and N1a) and one water molecule (oxygen atom O1) in the trigonal plane, and by two symmetry-related tmtp ligands (nitrogen atoms N11 and N11a) at the apical positions. Intramolecular hydrogen bonding between the coordinated water and the non-coordinating N23 (N···O = 2.77(1) Å is observed. The structure is depicted in Fig. 4, and the packing diagram is shown in Fig. S8.

The structure of $[Zn(NCS)_2(tmtp)_2]$, **7**, is uneventful; it crystallizes in the in the monoclinic space group $P2_1/c$ and resembles somewhat compound **3** with the bromide. The molecular structure is depicted in Fig. S9, with the packing diagram given in Fig. S10.

The compound $[Cd(NCS)_2(tmtp)_2]$, **8**, is quite different from that of **7**; it crystallizes in the in the triclinic space group $P\bar{1}$. The difference with Zn is ascribed to the much larger ionic radius of Cd(II), compared to Zn(II), allowing now an octahedral coordination. The octahedral geometry is reached by bridging (thiocyanato-N,S) ligands, as depicted in Fig. 5. A packing diagram is depicted in Fig. S11.

Changing the anion to the non-coordinating tetrafluoridoborate, it appeared possible to coordinate as much as four tmtp ligands to the metal; crystals for X-ray diffraction were obtained for Co and Zn, resulting in the compounds: $[Co(tmtp)_4(H_2O)_2](BF_4)_2$, **9**, and $[Zn(H_2O)_2(tmtp)_4](BF_4)_2$, **10**. They crystallize in the in the triclinic space group $P\bar{1}$. In addition a similar Ni(II) compound was obtained, found to be isomorphous as a powder. The structure of **9** is depicted in Fig. 6, and its packing is shown in Fig. S12. The Zn compound is isomorphous and its structure and packing is shown in figures S13 and S14. The octahedrally-based geometry is reached by two additional water ligands, which at the same time provide medium-strong hydrogen bonds to the lone pairs of the ligand N3 atoms (N···O = 2.75–2.85 Å).

Table 3
Selected bond lengths (Å) and angles (°) of compounds **1**–**10**.

Compound **1** [$CuCl_2(tmtp)_2$]			
Cu1–N11	1.968(1)	Cu1–N21	1.980(1)
Cu1–Cl1	2.2470(5)	Cu1–Cl2	2.2398(5)
Cl1–Cu1–Cl2	139.45(2)	N11–Cu1–N21	155.72(6)
Cl1–Cu1–N11	95.12(4)	Cl1–Cu1–N21	94.53(4)
Cl2–Cu1–N11	94.18(4)	Cl2–Cu1–N21	92.85(4)
Compound **2** [$CuBr_2(tmtp)_2$]			
Cu1–N11	1.998(5)	Cu1–N21	1.984(4)
Cu1–Br1	2.365(1)	Cu1–Br2	2.381(1)
Br1–Cu1–Br2	99.88(4)	N11–Cu1–N21	93.4(2)
Br1–Cu1–N11	96.1(1)	Br1–Cu1–N21	141.4(1)
Br2–Cu1–N11	142.2(1)	Br2–Cu1–N21	95.1(1)
Compound **3** [$ZnBr_2(tmtp)_2$]			
Zn1–N11	2.033(3)	Zn1–N21	2.016(3)
Zn1–Br1	2.3473(5)	Zn1–Br2	2.3749(5)
Br1–Zn1–Br2	118.70(2)	N11–Zn1–N21	108.3(1)
Br1–Zn1–N11	105.07(7)	Br1–Zn1–N21	116.05(8)
Br2–Zn1–N11	104.42(8)	Br2–Zn1–N21	103.41(8)
Compound **4** [$Cu(NO_3)_2(tmtp)_2$]			
Cu1–N1	2.022(1)	Cu1–O1	1.964(1)
Cu1–O3	2.529(2)		
O1–Cu1–N1	89.08(6)	O1–Cu1–N1a	90.93(6)
O1a–Cu1–N1a	89.07(6)		
a = −*x*, −*y*, −*z* + 2			
Compound **5** [$Cu(SO_4)_2(tmtp)_2]_2(CH_3OH)_{2\frac{1}{3}}(H_2O)_{1/6}$			
Cu1–N11	1.964(2)	Cu1–O1	1.997(2)
Cu1–O2	1.977(2)	Cu1–O3a	2.216(2)
Cu1–N21	1.981(2)		
N11–Cu1–O2	97.09(7)	N11–Cu1–O1	165.66(7)
N11–Cu1–N21	94.93(7)	N21–Cu1–O2	159.66(7)
O2–Cu1–O1	71.57(7)	N21–Cu1–O1	93.68(7)
O2–Cu1–O3a	102.96(6)	N11–Cu1–O3a	89.45(7)
a = −*x* + 2/3, −*y* + 1/3, −*z* − 2/3			
Compound **6** [$Cu(H_2O)(NCS)_2(tmtp)_2$]			
Cu1–N1	1.940(5)	Cu1–N11	2.119(5)
Cu1–N4	1.942(6)	Cu1–O1	2.177(6)
Cu1–N21	2.011(5)	O1…N23	2.770(6)
N1–Cu1–N4	91.3(2)	N21–Cu1–N11	94.4(2)
N1–Cu1–N21	91.0(2)	N1–Cu1–O1	139.1(2)
N4–Cu1–N21	168.3(3)	N4–Cu1–O1	81.5(2)
N1–Cu1–N11	129.1(2)	N21–Cu1–O1	89.3(2)
N4–Cu1–N11	93.1(2)	N11–Cu1–O1	91.6(2)
Compound **7** [$Zn(NCS)_2(tmtp)_2$]			
Zn1–N1	1.934(2)	Zn1–N4	1.942(2)
Zn1–N11	2.021(2)	Zn1–N21	2.007(2)
N1–Zn1–N4	115.29(7)	N1–Zn1–N21	114.75(7)
N4–Zn–N21	102.95(7)	N1–Zn1–N11	106.34(7)
N4–Zn1–N11	114.07(7)		
Compound **8** [$Cd(NCS)_2(tmtp)_2$]			
Cd1–N6	2.297(2)	Cd1–N11	2.380(2)
Cd1–S1	2.733(1)		
N6–Cd1–N11a	95.43(6)	N6–Cd1–N11	84.57(6)
N6–Cd1–S1	91.77(4)		
a = −*x* + 1, −*y* + 1, −*z* + 1			
Compound **9** [$Co(tmtp)_4(H_2O)_2](BF_4)_2$]			
Co1–O1	2.061(2)	Co1–N11	2.161(2)
Co1–N21	2.138(2)		
O1–Co1–N21	91.18(6)	O1–Co1–N21a	88.82(6)
O1–Co1–N11	88.33(6)	O1–Co1–N11a	91.67(6)
N11–Co1–N21a	91.27(6)		
a = −*x*, −*y*, −*z*			
Compound **10** [$Zn(tmtp)_4(H_2O)_2](BF_4)_2$]			
Zn1–O1	2.073(1)	Zn1–N11	2.149(1)
Zn1–N21	2.196(1)		
O1–Zn1–N21	87.83(5)	O1–Zn1–N21a	92.15(5)
O1–Zn1–N11	91.21(6)	O1–Zn1–N11a	88.79(5)
N11–Zn1–N21	89.74(5)		
a = −*x*, −*y*, −*z*			

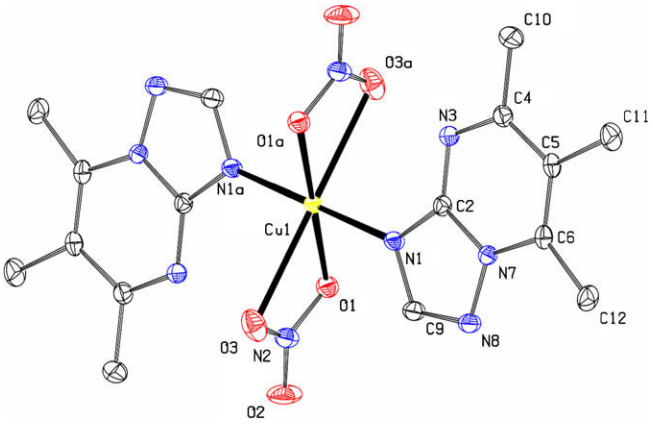


Fig. 2. ORTEP drawing (30% probability level) of [Cu(NO3)2(tmtp)2] (**4**). Hydrogen atoms are omitted for clarity.

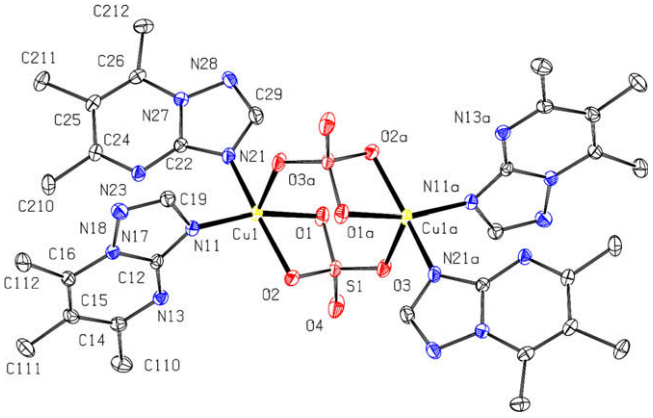


Fig. 3. ORTEP drawing (30% probability level) of $[Cu(SO_4)_2(tmtp)_2]_2(CH_3OH)_{2\frac{1}{3}}(H_2O)_{1/6}$ (**5**). Hydrogen atoms, lattice MeOH and water molecules are omitted for clarity.

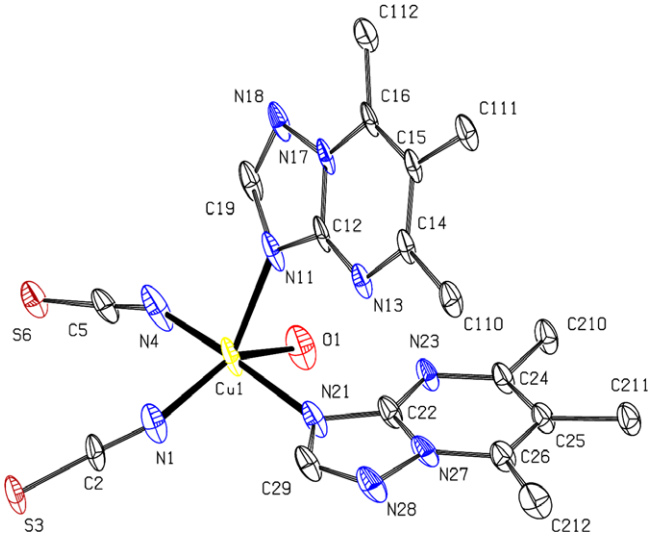


Fig. 4. ORTEP drawing (30% probability level) of [Cu(NCS)2(tmtp)2(H2O)] (**6**). Hydrogen atoms are omitted for clarity.

4. IR, Ligand field and EPR spectroscopy

In Table 2 selected infrared vibrations are presented. In all compounds vibrations of the ligand are easily recognized, and for the polyatomic anions also the anions are visible. The mid-IR spectra of compounds **1, 2** and **3** are identical. In the far-IR the Cu–N vibrations are observed at 284, 246 and 248 cm^{-1} for 1, 2 and 3, respec-

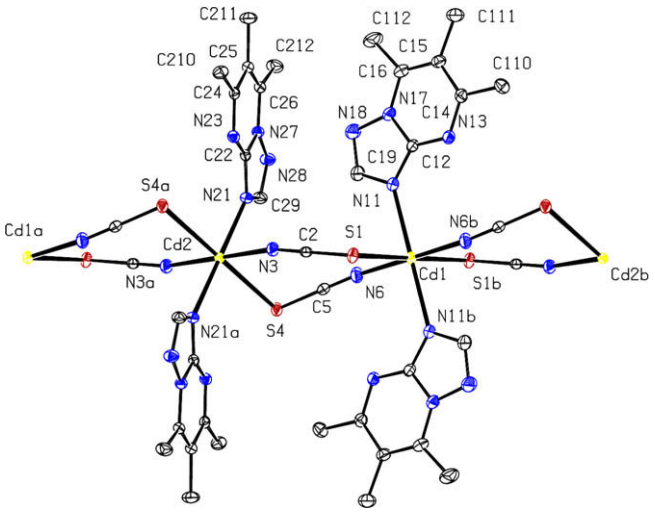


Fig. 5. ORTEP drawing (30% probability level) of a few units in the chain of [Cd(NCS)2(tmtp)2] (**8**). Hydrogen atoms are omitted for clarity.

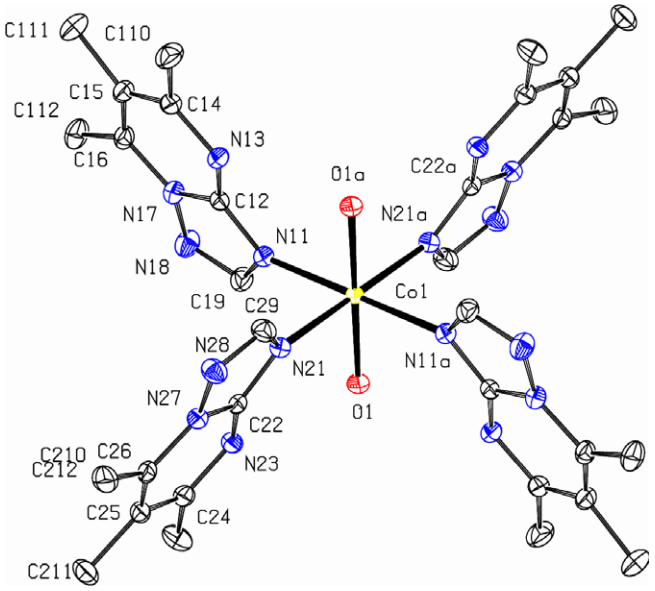


Fig. 6. ORTEP drawing (30% probability level) of a few units in the chain of [Co(tmtp)4(H2O)2](BF4)2 (**9**). Hydrogen atoms are omitted for clarity.

tively. The Cu–Cl vibration in 1 is observed at 309 cm^{-1}, while the Cu–Br vibration is observed at 160 cm^{-1}. For compound **3** the Zn–Br vibration is observed as a strong split band at 213–200 cm^{-1}. These vibrations are consistent with the literature [31–33]. For the other compounds the anion vibrations are listed, i.e. for compound **4** the nitrate vibrations at 1270 and 798 cm^{-1}, other nitrate vibrations which should be visible for bonded nitrate [34] are obscured by ligand vibrations. The NC vibrations of NCS compounds **6, 7** and **8** are observed at around 2051–2097 cm^{-1}. The highest vibration is from the bidentate coordinating NCS. The IR spectra of compounds **9, 10** and **11** are virtually identical, suggesting the same structure, the BF_4 vibrations of these three compounds are observed at around 1050 cm^{-1}. All these values are in agreement with the literature [34] for non-coordinated tetrafluoridoborate. The bridging sulfate anion in compound **5** gives four peaks at 1205, 1145, 1121 and 994 cm^{-1}, which is according to the literature for bridging sulfate [34].

Compounds containing water and/or MeOH show vibrations around 3400 cm^{-1} in compounds, i.e. for **5, 6, 9, 10** and **11** a broad band (sometimes a small splitting is observed) is observed, which are attributed to the OH vibration of methanol and/or water. For coordinated water the wagging en rocking vibrations can be observed in the 700–600 cm^{-1} and the M–O vibrations around 450 cm^{-1} [35]. Indeed for compounds **9**, **10** and **11** in compound **9** two very broad vibrations are observed at ca. 660, 600 and 450 cm^{-1}, for compound **10** at around 630 and 450 cm^{-1} and for compound **11** at around 680, 620 and 480 cm^{-1}, which is confirming the observations in the literature [35].

The powder EPR spectra of compounds **2** and **5** reveal at RT a broad isotropic band due to $S = ½$ (around $g = 2.10$); for compounds **1** and **4** an axial signal with $g_\perp$ of 2.07–2.08 and a $g_{||}$ of 2.24–2.26. These signals are in agreement with a $d_{x^2-y^2}$ configuration for the ground state [36]. For compound **6** a rhombic signal ($g_1 = 2.28$, $g_2 = 2.11$ and $g_3 = 2.05$) is observed, which is in consistence with the five coordinated geometry of the Cu(II) ion [36].The ligand field transitions measured as a solid with the diffuse reflectance technique for the Cu(II) compounds (**1, 2, 4, 5, 6**) are observed in general as broad bands with a maximum which vary from 16.1 to 11.6 $\times 10^3$ cm^{-1} with a shoulder, which vary from 13.1 to 9.1 $\times 10^3$ cm^{-1}. These bands are in agreement with common ligand field transitions for square-planar based geometries with a variety of distortions [36,37]. Also the ligand field transitions of the Co(II) compound (**9**) and the Ni(II) compound (**11**) are in agreement with the literature for octahedral Co(II) and Ni(II) [37,38].

5. Concluding remarks

The study described above on the coordination behavior of the ligand tmtp, an example of one of the several easily accessible triazolopyridimidine ligands, has shown that such ligands are versatile in their behavior. The resulting coordination compound display interesting structural and electronic properties, and in some cases interference with hydrogen bonding from solvent and to anions is seen. Fine-tuning of the formed structure appears possible by proper choice of counterions and solvents in the synthesis. Which compounds are formed as described above is difficult to determine a priori, and depends strongly on the used metal and the selected anion.

Acknowledgements

This work was performed in the framework of freshmen students research project "Leren Onderzoeken 1" (Learning Research 1) in the BSc programme "Molecular Science and Technology" a recently started concept in the joint programme of Delft University of Technology and Leiden University. The present student co-authors, *Huub Adriaanse, Sven Askes, Yorrick van Bree, Stefan van Oudheusden, Eelke van den Bos, Esref Günay,* have performed this project in a team of six freshmen students.

Appendix A. Supplementary data

CCDC 732869, 732870, 732871, 732872, 732873, 732874, 732875, 732876, 732877 and 732878 contain the supplementary crystallographic data for **1**, **2**, **3**, **4**, **5**, **6**, **7**, **8**, **9** and **10**. These data can be obtained free of charge via http://www.ccdc.cam.ac.uk/conts/retrieving.html, or from the Cambridge Crystallographic Data Centre, 12 Union Road, Cambridge CB2 1EZ, UK; fax: (+44) 1223-336-033; or e-mail: deposit@ccdc.cam.ac.uk.

Figures for the molecular structures of compounds **2**, **3, 7** and **9**; packing diagrams for all 10 compounds and detailed hydrogen bond information for all compounds are given as supplementary

material. Supplementary data associated with this article can be found, in the online version, at doi:10.1016/j.poly.2009.07.001.

References

[1] J.M. Salas, M.A. Romero, M.P. Sanchez, M. Quiros, Coord. Chem. Rev. 195 (1999) 1119.
[2] J.G. Haasnoot, Coord. Chem. Rev. 200 (2000) 131.
[3] M. Biagini Cingi, A.M. Manotti Lanfredi, A. Tiripicchio, J.P. Cornelissen, J.G. Haasnoot, J. Reedijk, Inorg. Chim. Acta 127 (1987) 183.
[4] M. Biagini Cingi, A.M. Manotti Lanfredi, A. Tiripicchio, J.G. Haasnoot, J. Reedijk, Acta Cryst. C42 (1986) 1509.
[5] M. Biagini Cingi, A.M. Manotti Lanfredi, A. Tiripicchio, J.G. Haasnoot, J. Reedijk, Inorg. Chim. Acta 86 (1984) 137.
[6] E.J. Dirks, J.G. Haasnoot, A.J. Kinneging, J. Reedijk, Inorg. Chem. 26 (1987) 1902.
[7] A.T.H. Lenstra, H.J.B. Slot, P.T. Beurskens, J.G. Haasnoot, J. Reedijk, Recl. Trav. Chim. Pays-Bas 108 (1989) 133.
[8] S.B. Sanni, H. Behm, P.T. Beurskens, J.P. Cornelissen, J.G. Haasnoot, A.T.H. Lenstra, J. Crystall. Spectr. Res. 17 (1987) 81.
[9] E. Szlyk, A. Wojtczak, M. Jaskolski, M. Gilski, J.G. Haasnoot, J. Reedijk, Inorg. Chim. Acta 260 (1997) 145.
[10] G.A. van Albada, R.A.G. de Graaff, J.G. Haasnoot, J. Schild, J. Reedijk, Acta Crystallogr. Sect. C–Cryst. Struct. Commun. 47 (1991) 946.
[11] A.H. Velders, A. Bergamo, E. Alessio, E. Zangrando, J.G. Haasnoot, C. Casarsa, M. Cocchietto, S. Zorzet, G. Sava, J. Med. Chem. 47 (2004) 1110.
[12] I. Lakomska, E. Szlyk, J. Sitkowski, L. Kozerski, J. Wietrzyk, M. Pelczynska, A. Nasulewicz, A. Opolski, J. Inorg. Biochem. 98 (2004) 167.
[13] I. Lakomska, A. Wojtczak, J. Sitkowski, L. Kozerski, E. Szlyk, Polyhedron 26 (2007) 803.
[14] M.A. Romero, J.M. Salas, M. Quiros, D.J. Williams, J. Molina, Trans. Met. Chem. 18 (1993) 595.
[15] J.M. Salas, C. Enrique, M.A. Romero, K. Takagi, K. Aoki, Y. Miyashita, I.H. Suh, Polyhedron 11 (1992) 2903.
[16] E. Szlyk, I. Lakomska, A. Surdykowski, T. Glowiak, L. Pazderski, J. Sitkowski, L. Kozerski, Inorg. Chim. Acta 333 (2002) 93.
[17] E. Szlyk, L. Pazderski, I. Lakomska, L. Kozerski, J. Sitkowski, Magn. Reson. Chem. 40 (2002) 529.
[18] A. Bencini, D. Gatteschi, C. Zanchini, J.G. Haasnoot, R. Prins, J. Reedijk, Inorg. Chem. 24 (1985) 2812–2815.
[19] S. Ferrer, J.G. Haasnoot, J. Reedijk, E. Muller, M. Biagini-Cingi, M. Lanfranchi, A.M. Manotti-Lanfredi, J. Ribas, Inorg. Chem. 39 (2000) 1859–1867.
[20] I. Riggio, G.A. van Albada, I. Mutikainen, U. Turpeinen, J. Reedijk, Acta Cryst. 56 (2000) E380–E381.
[21] J.M. Balkaran, S.C.P. van Bezouw, J. van Bruchem, J. Verasdonck, P.C. Verkerk, A.G. Volbeda, I. Mutikainen, U. Turpeinen, G.A. van Albada, P. Gamez, J.G. Haasnoot, J. Reedijk, Inorg. Chim. Acta 362 (2009) 861–868.
[22] C. Bülow, K. Haas, Chem. Ber. 42 (1909) 4638–4642.
[23] Nonius, in, COLLECT. Nonius BV, Delft, The Netherlands, 2002.
[24] G.M. Sheldrick, SHELXS-97. Program for Crystal Structure Solution, University of Göttingen, Germany, 1997.
[25] G.M. Sheldrick, SHELXL-97. Program for Crystal Structure Refinement, University of Göttingen, Germany, 1997.
[26] W.E. Estes, W.E. Hatfield, J.A.C. van Ooijen, J. Reedijk, J. Chem. Soc., Dalton Trans. 1980 (1980) 2121.
[27] L. Yang, D.R. Powell, R.P. Houser, Dalton Trans. (2007) 955–964.
[28] S.B. Sanni, J.M.M. Smits, P.T. Beurskens, J.G. Haasnoot, J. Schild, A.T.H. Lenstra, J. Crystallogr. Spectrosc. Res. 16 (1986) 823–832.
[29] O. Celik, S. Ide, M. Kurt, S. Yurdakul, Acta Crystallogr. E 60 (2004) M424–M425.
[30] A.W. Addison, T.N. Rao, J. Reedijk, J. van Rijn, G.C. Verschoor, J. Chem. Soc., Dalton Trans. (1984) 1349–1356.
[31] G.A. Bowmaker, J.D. Cotton, P.C. Healy, J.D. Kildea, S.B. Silong, B.W. Skelton, A.H. White, Inorg. Chem. 28 (1989) 1462–1466.
[32] J.R. Ferraro, Low Frequency Vibrations of Inorganic and Coordination Compounds, Plenum Press, New York, 1971.
[33] G. Ondrejovič, A. Kotočova, Chem. Pap.–Chem. Zvesti. 60 (2006) 10–21.
[34] K. Nakamoto, Infrared and Raman Spectra of Inorganic and Coordination Compounds, Wiley, New York, 1978.
[35] J. Dillen, A.T.H. Lenstra, J.G. Haasnoot, J. Reedijk, Polyhedron 2 (1983) 195–201.
[36] B.J. Hathaway, in: G. Wilkinson, R.D. Gillard, J.A. McCleverty (Eds.), Pergamon, Press Oxford, 1987.
[37] J. Reedijk, W.L. Driessen, W.L. Groeneveld, Recl. Trav. Chim. Pays-Bas 88 (1969) 1095–1104.
[38] J. Reedijk, P.W.N.M. van Leeuwen, W.L. Groeneveld, Recl. Trav. Chim. Pays-Bas 87 (1968) 129–143.

electronic (diffuse and absorbance) spectra, 5000–50 000 cm^{-1}, were collected using a Cary 500 Scan NIR–Vis–UV Spectrophotometer (Varian). The analysis of the spectra was based on a variable digital method and the deconvolution of the spectral contour into Gaussian components [23–28]. Thermal analysis: TGA and DTA were performed on Setsys TG-DTA 16 Setaram equipment at a heating rate 2 °C/min under N_2.

2.2. Synthesis of the complex

A solution of benzoylglycine (1.50 mmol, 0.269 g) and benzimidazole (3.76 mmol, 0.444 g) in 20 cm^3 of 1-propanol was added dropwise to a solution of $Cu(CH_3COO)_2{\cdot}2H_2O$ in 1-propanol (0.75 mmol, 0.150 g), 10 cm^3. The mixture was kept at room temperature. After several days, blue needle-like crystals were obtained (yield 71%). *Anal.* Calc. for $C_{140}H_{146}Cu_4N_{24}O_9$: C, 58.33; H, 5.10; N, 11.66. Found: C, 58.40; H, 4.80; N, 12.05%. IR spectrum, cm^{-1}: 3460(m), 3316(s), 3137(m), 3064(s), 2999(s), 2843(s), 1606(vs), 1542(vs), 1497(s), 1420(vs), 1297(vs) 1253(s), 1161(w), 1055(w), 1005(w), 977(w), 932(w), 859(m), 747(s), 695(m), 614(m), 559(m), 444(m), 426(m), 388(w), 339(w), 310(w), 294(w), 264(w), 239(w), 245(w), 204(vw), 182(w).

2.3. X-ray structure determination

Diffraction measurements were made on an Xcalibur PX kappa-geometry diffractometer with a CCD Onyx camera (graphite monochromatized Cu Kα radiation). Intensities were recorded at 100(2) K. Data collection and processing parameters are summarized in Table 1. The structure was solved by direct methods using SHELXS-97 [29]. The *n*-propanol molecule was found to be disordered and was refined in two positions with the occupancy factors fixed at 0.5. The C–C and C–O distances for both propanol molecules were restrained. Furthermore in the crystal, the water molecule was found; the occupancy factor was initially refined and finally fixed at 0.25. The hydrogen atoms were generated geometrically (except for those of the water molecule) and were allowed to ride on their carrier atoms. The Flack parameter refined to a value close to 0.45(5), indicating twinning by inversion.

Table 1
Crystal data and structure refinement for $[Cu(hipp)_2(bim)_2]{\cdot}PrOH{\cdot}0.25H_2O$.

Crystal shape	needle
Colour	blue
Size (mm)	0.36 × 0.02 × 0.02
Chemical formula	$C_{35}H_{36.5}CuN_6O_{7.25}$
Formula weight	720.74
Crystal system	orthorhombic
Space group	$Pna2_1$
Unit cell dimensions	
a (Å)	9.938(3)
b (Å)	16.3095
c (Å)	20.943
Cell volume (Å^3)	3394.4(18)
Z	4
D_{calc}, g cm^{-3}	1.409
$\lambda_{Cu\ K\alpha}$ (Å)	1.5418
Temperature (K)	100(2)
F(0 0 0)	1502
θ Range	3.43–75.27
Independent reflections	5946
Observed reflections	26342
Minimum/maximum transmission	0.786, 0.980
Number of refined parameters	478
$R[F^2 > 2\sigma(F^2)]$	0.055
$wR[F^2]$	0.099
Goodness-of-fit	1.012

2.4. Computational details

The optimized geometry of $[Cu(hipp)_2(bim)_2]$, harmonic frequencies, IR intensities and Raman scattering activities were calculated with the density functional theory DFT at the UB3LYP level [30,31]. The effective core potential (ECP) of Hay and Wadt and the concomitant LanL2DZ basis set has been used [32]. Since our model complex contains the Cu(II) ion, which is an open-shell system (d^9), we have performed unrestricted UB3LYP calculations. The details concerning the IR and Raman spectra will be published elsewhere. The disadvantage of unrestricted hybrid DFT functionals, incorporating the Hartree-Fock exchange, is that unrestricted wave functions are not eigenfunctions of the spin-squared operator $\hat{S}^2$ e.g. they are contaminated by states of higher spin multiplicity [33]. The final $\langle\hat{S}^2\rangle$ value was adjusted at the end of the complex geometry optimization to exactly 0.7500, which corresponds to a doublet ground state wave-function with no spin contamination, and confirm the validity of used method [34,35]. To obtain the natural charges, Natural Bond Orbital (NBO) analysis has been performed [36]. All calculations were carried out with the GAUSSIAN 03 package [37].

3. Results and discussion

3.1. Crystal structure

A perspective view of the molecule of the complex together with the atom numbering scheme is shown in Fig. 1, where the displacement ellipsoids are plotted with 50% probability. The solvent

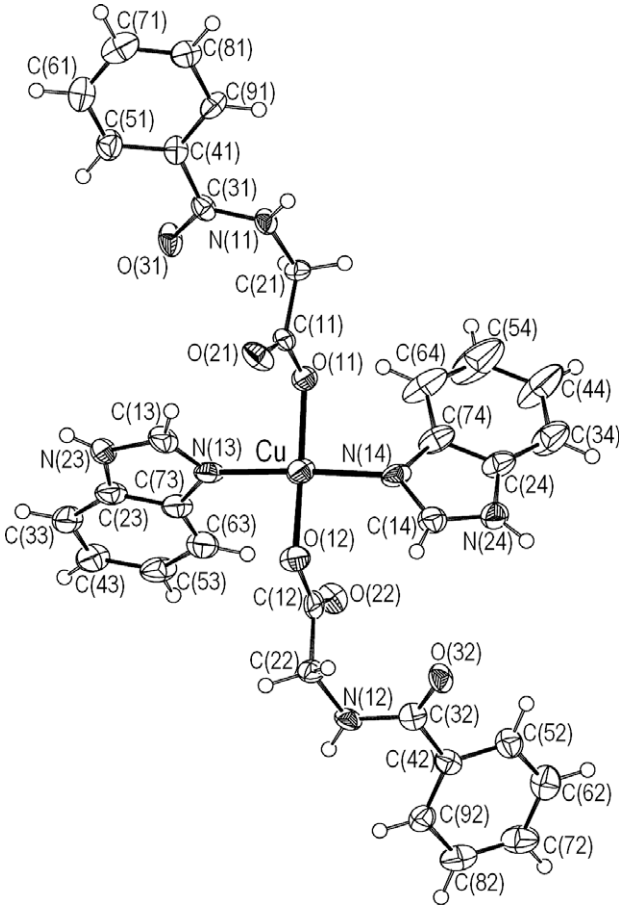


Fig. 1. The molecular structure of $[Cu(hipp)_2(bim)_2]$ with the atom numbering scheme, plotted with 50% probability of displacement ellipsoids.

Table 2
Selected bond lengths (Å) and angles (°) for **1** measured and calculated with the UB3LYP/LanL2DZ level.

	X-ray	calc		X-ray	calc
Cu–O(11)	1.932(4)	2.012	O(11)–Cu–O(12)	163.42(17)	168.3
Cu–O(12)	1.954(4)	1.980	O(11)–Cu–N(13)	92.06(18)	89.0
Cu–N(13)	1.966(4)	2.008	O(12)–Cu–N(13)	90.77(18)	93.1
Cu–N(14)	1.990(4)	2.008	O(11)–Cu–N(14)	90.02(17)	90.6
Cu–O(17)	2.679(16)		O(12)–Cu–N(14)	92.45(17)	89.6
			N(13)–Cu–N(14)	161.56(18)	168.2
O(11)–C(11)	1.302(6)	1.322	O(11)–Cu–O(17)	95.9(4)	
O(21)–C(11)	1.234(7)	1.267	O(12)–Cu–O(17)	67.7(4)	
O(31)–C(31)	1.227(6)	1.268	N(13)–Cu–O(17)	90.7(4)	
C(11)–C(21)	1.512(7)	1.542	N(14)–Cu–O(17)	107.3(4)	
C(21)–N(11)	1.452(6)	1.462			
N(11)–C(31)	1.338(6)	1.375			
C(31)–C(41)	1.527(7)	1.501			
O(12)–C(12)	1.288(6)	1.319			
O(22)–C(12)	1.233(7)	1.264			
O(32)–C(32)	1.222(6)	1.270			
C(12)–C(22)	1.538(8)	1.552			
C(22)–N(12)	1.459(6)	1.463			
N(12)–C(32)	1.348(6)	1.374			
C(32)–C(42)	1.495(7)	1.503			

molecules are omitted for clarity. Selected structural data for **1**, derived from the X-ray study and calculated by theoretical methods are listed in Table 2. The asymmetric unit of the crystal is built of a copper(II) ion, two hippurate ions, two benzimidazole molecules, one propanol molecule and one quarter of a water molecule. The TGA experiment has been performed to justify the results of the crystallographic study concerning the solvent molecules. During the thermal decomposition of the title complex, two endothermic events occur at 159 and 164 °C (Fig. S1. Suppl. Mat.). This observation confirms that molecules of different solvents are present in the crystal, however the partial overlap of the decomposition processes make the precise estimation of the weight loss impossible.

The coordination polyhedron of the copper ion can be described as tetrahedrally distorted square, the symmetry of the CuN_2O_2 moiety is very close to C_{2v}. The carboxylate *trans*-O(11)–Cu–O(12) and imidazole *trans*-N(13)–Cu–N(14) bond angles are 163.42(17)° and 161.56(18)°, respectively, showing a marked tetrahedral distortion from the square planar geometry [38–43]. The *cis*-N–Cu–O bond angles fall into the range from 90.0(2)° to 92.4(2)°. A degree of the tetrahedral distortion can be also expressed by the dihedral angle between two opposite CuNO planes [44–51]. The (Cu–N(13)–O(12))–(Cu–N(14)–O(11)) angle of 24.80° (24.41° between the second pair of planes) corresponds to a significant tetrahedral deformation of the $[CuN_2O_2]$ core.

The copper ion is four coordinated by two oxygen atoms from non-equivalent hippurate ions and by two nitrogen atoms from non-equivalent benzimidazole molecules. The copper-oxygen distances, (O(11) and O(12) equal to 1.932(4) and 1.954(4) Å, respectively), are shorter than those found in the $[Cu(hipp)_2(im)_2]$ complex (1.976(3) Å) [14] and in $[Cu(hipp)(phen)]ClO_4{\cdot}2H_2O$ (2.0195(16) Å) [17], whereas the Cu–N distances are very similar to the bond lengths observed for copper-benzimidazole nitrogen bonds [19,52]. The water molecule occupies statistically one quarter of the apical positions at a distance of 2.68(2) Å from the central Cu(II) ion. Moreover, two non-bonding contacts with uncoordinated carboxylate oxygens are observed (2.999 and 3.142 Å).

The molecules of the studied compound, connected by a system of intermolecular N–H···O hydrogen bonds (Table 3), form a 2D infinite network parallel to the *ab* plane of the unit cell (Fig. 2). Only one of the disordered propanol molecules is attached to the complex via hydrogen bonds (Table 3), although both are located within the layers. One set of propanol molecules acts as a donor in a weak hydrogen bond (O(16)–H(16)···O(12)), the distance of the oxygen atom O(15) from the second set of propanol molecules to the closest acceptor atom (O12) is considerably large (3.584 Å) and cannot be regarded as a hydrogen bond. The presence of the non-hydrogen bonded hydroxyl group is confirmed by the medium intensity sharp band found in the IR spectrum of the complex at 3460 cm^{-1} [53].

Table 3
Hydrogen-bond geometry for $[Cu(hipp)_2(bim)_2]{\cdot}PrOH{\cdot}0.25H_2O$ (Å, °).

D–H···*A*	*D*–H	H···*A*	*D*···*A*	*D*–H···*A*
N(11)–H(11)···(31)^{i}	0.88	2.02	2.858(5)	157
N(12)–H(12)···O(32)^{ii}	0.88	2.08	2.896(5)	153
N(23)–H(23)···O(21)^{iii}	0.88	1.84	2.710(6)	169
N(24)–H(24)···O(22)^{iv}	0.88	1.87	2.679(6)	152
O(16)–H(16)···O(12)	0.85	2.44	2.951(10)	119
C(13)–H(13)···O(21)	0.95	2.35	3.128(6)	139
C(14)–H(14)···O(12)	0.95	2.56	2.977(7)	107
C(63)–H(63)···O(22)	0.95	2.40	3.185(7)	140
C(64)–H(64)···O(11)	0.95	2.40	3.002(8)	121
C(91)–H(91)···O(31)^{i}	0.95	2.44	3.343(7)	158
C(25)–H(25A)···N(23)^{i}	0.99	2.49	3.48(3)	174

Symmetry codes: (i) 1/2 + *x*,1/2−*y*,*z*; (ii) −1/2 + *x*,3/2−*y*,*z*; (iii) −1/2 + *x*,1/2−*y*,*z*; (iv) 1/2 + *x*,3/2−*y*,*z*.

3.2. Theoretical study

The structure of $[Cu(hipp)_2(bim)_2]$ has been fully optimized at the UB3LYP/LanL2dz level [30,31]. The molecular parameters predicted for $[Cu(hipp)_2(bim)_2]$ are in good agreement with the X-ray diffraction results. The metal–ligand distances are equal to 1.980 and 2.012 Å for the Cu–O bonds and 2.008 Å for the copper-nitrogen bonds. A comparison of atomic distances and intramolecular angles is presented in Table 2. Some discrepancies between the theoretical and experimental bond lengths should be attributed to intermolecular hydrogen bonding in the crystal, since the theoretical study has been done for an isolated molecule.

Natural Bond Orbital (NBO) analysis has provided detailed insight into the nature of electronic conjugations between bonds in the molecule. According to the NBO results, the electronic configuration of Cu is $[core]4s^{0.30}3d^{9.34}4p^{0.01}$: 18 core electrons, 9.64 valence electrons (on 4s and 3d atomic orbitals) and 0.01 Rydberg electrons, mainly on the 4p orbital. This gives the total of 27.65 electrons, which is consistent with the calculated natural charge (+1.35) on the Cu atom in $[Cu(hipp)_2(Hbim)_2]$. Table 4 collects the calculated natural charges on the atoms. The largest negative charges are located on the carboxylate oxygen atoms O11 and O12 coordinated to copper (−0.824 and −0.844 e, respectively).

The NBO analysis can be used to estimate delocalization of electron density between occupied Lewis-type orbitals and formally unoccupied non-Lewis NBOs (antibonding or Rydberg), which corresponds to a stabilizing donor-acceptor interaction [36]. Second order perturbation theory allows to make conclusions about the strength of these interactions. According to the calculations, four bonds between the copper atom and the donor atoms of the organic ligands can be described as donation of electron density from lone pair orbitals of the oxygen and nitrogen atoms to unoccupied copper atom orbitals. The calculated values of the second-order interaction energy (E^2) between the donor–acceptor orbitals are equal to 11.51, 12.10, 17.79 and 17.75 kcal/mol for LP(2)O11 → LP*(6)Cu, LP(2)O12 → LP*(6)Cu, LP(1)N13 → LP*(6)Cu and LP(1)N14 → LP*(6)Cu, respectively. These values suggest similar strength metal-ligand bonds in complex **1**. The donations of electron density from the donor atoms of the organic ligands to the antibonding orbitals of copper can be described as ligand to metal coordination bonds.

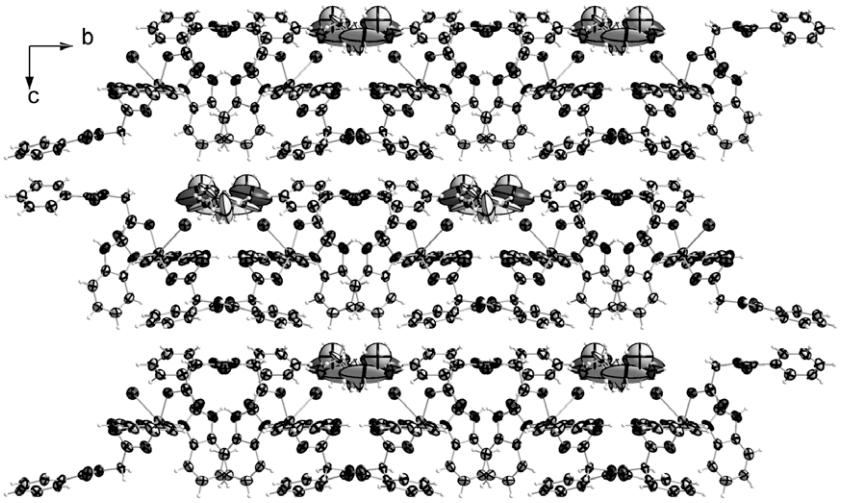


Fig. 2. 2D layers parallel to the *ab* plane of the crystal.

Table 4
Natural charge (e) on selected atoms of $[Cu(hipp)_2(Hbim)_2]$ calculated at the DFT/B3LYP/LanL2DZ level.

Atom	Charge	Atom	Charge
Cu1	1.346	N11	−0.652
O2	−0.824	O31	−0.703
O12	−0.844	C21	−0.305
N13	−0.655	C31	0.713
N14	−0.662	C41	−0.124
C11	0.803	C13	0.340
O21	−0.714	N23	−0.594

3.3. Spectroscopic and magnetic study

The EPR spectrum of polycrystalline complex **1** exhibits parallel components of copper hyperfine splitting, suggesting that the Cu(II) centers are efficiently isolated by the diamagnetic ligands (Fig. S2. Suppl. Mat.). It unambiguously indicated that the symmetry of the coordination polyhedron is axial, in agreement with the tetrahedrally distorted square geometry shown by the crystal structure studies. The spectrum observed for the similar complex $Cu(hipp)_2im_2$ was not resolved due to a hyperfine interaction and its form was much more complicated and g parameters debatable [14]. The simulation of the experimental EPR spectra of $Cu(hipp)_2(bim)_2$ gave the spin Hamiltonian parameters $g_{II} = 2.27$, $g_{\perp} \sim 2.07$ and $A_{II} = 190 \times 10^{-4}\ cm^{-1}$. These values are usually observed for complexes with two chelating ON ligands (Table S1) or for N4 coordination of four monodentate nitrogen donors coplanar with Cu(II) [54]. It is probable that the relatively small distance of one of copper–oxygen bond, with the length of 1.932 Å as compared to the distance of 1.976 Å for $Cu(hipp)_2(Im)_2$ [14], may be responsible for the stronger ligand field, leading to the observed spin Hamiltonian parameters. The splitting due to the copper hyperfine interaction was also previously observed for the polycrystalline sample of $[Cu(1\text{-benzyl-2-hydroxymethylimidazole})_4](NO_3)_2$ [54], with a Cu–Cu distance of 9.6 Å, close to the distance in **1**, which equals 9.437(4) Å.

The reflectance spectrum of **1** exhibits a characteristic broad asymmetric *d–d* band with a maximum at 16100 cm^{-1} and a poorly marked shoulder at *ca* 11500 cm^{-1} (Fig. 3S, Suppl. Mat.). The absorbance spectrum in propanol (Fig. 3) shows a slight blue shift in energy. The bands in the higher energy region over 25000 cm^{-1} are assigned as carboxylate-to-copper ligand-to-metal charge transfer bands (LMCT) and to $\pi \rightarrow \pi^*$ intraligands transitions.

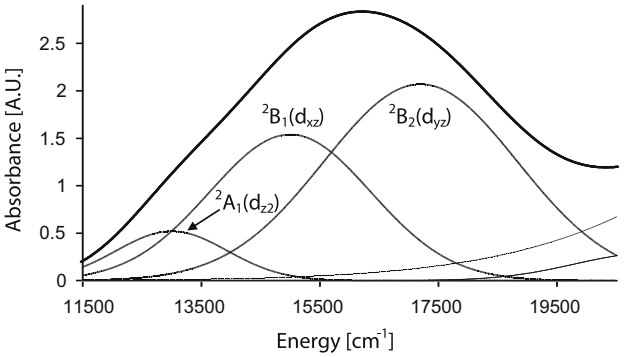


Fig. 3. The NIR–Vis–UV electronic absorption spectrum (in propanol) of $[Cu(hipp)_2(bim)_2]\cdot PrOH\cdot 0.25H_2O$ and Gaussian deconvolution.

For a tetrahedrally distorted square planar CuX_4 configuration, the unpaired electron occupies the $d_{x^2-y^2}$ orbital (a_1 representation of C_{2v} point group), whereas d_{xz} (b_1) and d_{yz} (b_2) are lowest in energy. Three electric dipole transitions, d_{z^2} (a_1) → $d_{x^2-y^2}$, d_{xz} (b_1) → $d_{x^2-y^2}$ and d_{yz} (b_2) → $d_{x^2-y^2}$, are spin-allowed while the d_{xy} (a_2) → $d_{x^2-y^2}$ transition is forbidden.

Analysis of polarized crystal spectra and angular overlap model calculations gave the orbital energy order: $d_{x^2-y^2} > d_{xy} > d_{z^2} > d_{yz} > d_{xz}$, according to [55,56]. Thus, the asymmetric absorption band in solution was considered as the envelope of three spin-allowed transitions. The individual transfers were distinguished from the absorption shape using Gaussian analysis, assuming a maximum of three components. The bands obtained from the curve fitting at 13000, 15000 and 17200 cm^{-1} (Fig. S4, Supplementary material) were assigned to the three spin-allowed transitions, $^2A_1(d_{x^2-y^2}) \rightarrow {}^2A_1(d_{z^2})$, $^2B_1(d_{xz})$ and $^2B_2(d_{yz})$, respectively.

The ligand field energy levels scheme derived from the NIR–Vis–UV spectra are consistent with EPR results. In C_{2v} rhombic symmetry, the *g*-values for the copper(II) ion with the $^2A_1(d_{x^2-y^2})$ ground level are given by [57,58]:

$$g_x - 2.0023 = -2k_x^2\lambda/E_{yz}, \quad (1)$$

$$g_y - 2.0023 = -2k_y^2\lambda/E_{xz}, \quad (2)$$

$$g_z - 2.0023 = -2k_z^2\lambda/E_{xy}, \quad (3)$$

where k_x, k_y, k_z are the orbital reduction coefficients, λ is the spin-orbit constant ($-830\ cm^{-1}$ for the copper(II) free ion), and $E_{yz} = E(^2A_1 \leftarrow {}^2B_2)$, $E_{xz} = E(^2A_1 \leftarrow {}^2B_1)$ and $E_{xy} = E(^2A_1 \leftarrow {}^2A_2$, spin-forbidden). With the above-quoted transition energies and $k_x \approx k_y \approx k_z \approx 0.72$ [59] the values of $g_x = 2.052$ and $g_y = 2.060$ are obtained. After inserting the experimental value of $g_z = 2.27$ into Eq. (3), the forbidden $^2A_1 \leftarrow {}^2A_2$ transition may be estimated. The value of $12860\ cm^{-1}$ situates the d_{xy} orbital below the d_z^2 orbital.

The magnetic susceptibility of **1** shows Curie-Weiss behavior in the entire temperature range, with a magnetic moment $\mu = 1.91\ \mu_B$ and Weiss constant $\theta = -0.1$ K, both values being characteristic of mononuclear Cu(II) compounds with extremely weak magnetic exchange interactions. The same conclusion may be inferred from the field dependence of the magnetization (Fig. S4. Suppl. Mat). The experimental data are perfectly simulated with the Brillouin function for $S = 1/2$. The best fit g value, equal to 2.126, is almost identical to the average EPR value $g_{av} = 2.13$ [$g_{av}^2 = (g_x^2 + g_y^2 + g_z^2)/3$].

Acknowledgements

The Poznań Supercomputer and Networking Center and the Wrocław Centre for Networking and Supercomputing are acknowledged for generous computer time. We thank Wrocław University of Technology for financial support of this research.

Appendix A. Supplementary data

CCDC 683977 contains the supplementary crystallographic data for the title compound. These data can be obtained free of charge via http://www.ccdc.cam.ac.uk/conts/retrieving.html, or from the Cambridge Crystallographic Data Centre, 12 Union Road, Cambridge CB2 1EZ, UK; fax: (+44) 1223-336-033; or e-mail: deposit@ccdc.cam.ac.uk. Supplementary data associated with this article can be found, in the online version, at doi:10.1016/j.poly.2009.07.028.

References

[1] J.J.R. Fraústo da Silva, R.J.P. Williams, The Biological Chemistry of Elements: The Inorganic Chemistry of Life, Oxford, Clarendon Press, 1991.
[2] L. Stryer, Biochemistry, W.H. Freeman and Company, New York, 1995.
[3] I. Šperlingová, L. Dabrowská, V. Stránský, J. Kučera, M. Tichý, Anal. Bioanal. Chem. 387 (2007) 2419.
[4] G. Battistuzzi, M. Borsari, L. Menabue, M. Saladini, M. Sola, Inorg. Chem. 35 (1996) 4239.
[5] J.N. Brown, L.M. Trefonas, Inorg. Chem. 12 (1973) 1730.
[6] D.J. Darensbourg, M.W. Holtcamp, E.M. Longridge, K.K. Klausmeyer, J.H. Reibenspies, Inorg. Chim. Acta 227 (1994) 223.
[7] S.A. Sadeek, M.S. Refat, S.M. Teleb, S.M. El-Megharbel, J. Mol. Struct. 737 (2005) 139.
[8] M.M. Morelock, M.L. Good, L.M. Trefonas, D. Karraker, L. Maleki, H.R. Eichelberger, R. Majeste, J. Dodge, J. Am. Chem. Soc. 101 (1979) 4858.
[9] M.M. Morelock, M.L. Good, L.M. Trefonas, R. Majeste, D. Karraker, Inorg. Chem. 21 (1982) 3044.
[10] H. Grewe, M.R. Udupa, B. Krebs, Inorg. Chim. Acta 63 (1982) 119.
[11] F. Huber, M. Domagala, H. Preut, Acta Crystallogr., Sect. C 44 (1988) 828.
[12] P.G. Jones, R. Schelbach, Chem. Commun. 19 (1988) 1338.
[13] E.D. Vieira, G. Fachin, M.H. Torre, A.J. Costa-Filho, J. Braz. Chem. Soc. 19 (2008) 1614.
[14] L. Antolini, L.P. Battaglia, A.B. Corradi, G. Marcotrigiano, L. Menabue, G.C. Pellacani, M. Saladini, Inorg. Chem. 21 (1982) 1391.
[15] D. Dobrzyńska, T. Lis, J. Woźniak, Acta Crystallogr., Sect. E 62 (2006) m1006.
[16] M.C. Capllonch, A. Garcia-Raso, A. Terron, M.C. Apella, E. Espinosa, E. Molins, J. Inorg. Biochem. 85 (2001)173.
[17] G.-Q. Gui, F.-P. Chen, H.-Y. Jin, X.-W. Wang, B. Hu, Acta Crystallogr., Sect. E 62 (2006) m2555.
[18] F.-P. Chen, X.-W. Wang, Y. Chen, J.-Z. Chen, Acta Crystallogr., Sect. E 62 (2006) m3044.
[19] B. Coyle, P. Kinsella, M. McCann, M. Devereux, R. O'Connor, M. Clynes, K. Kavanagh, Toxicol. In Vitro 18 (2004) 63.
[20] M. Devereux, D. O'Shea, M. O'Connor, H. Grehan, G. Connor, M. McCann, G. Rosair, F. Lyng, A. Kellett, M. Walsh, D. Egan, B. Thati, Poyhedron 26 (2007) 4073.
[21] J.P. Klinman, Chem. Rev. 96 (1996) 2541.
[22] E.I. Solomon, R.K. Szilagyi, S. DeBeer George, L. Basumallick, Chem. Rev. 104 (2004) 419.
[23] G. Bierman, H. Ziegler, Anal. Chem. 58 (1986) 536.
[24] J. Myrczek, Spectr. Lett. 23 (1990) 1027.
[25] A. Wojciechowska, Z. Staszak, W. Bronowska, A. Pietraszko, M. Cieślak-Golonka, Polyhedron 20 (2001) 2063.
[26] I.A. Slavić, Nucl. Instr. Meth. 134 (1976) 285.
[27] A. Bartecki, Z. Staszak, Comp. Enh. Spectr. 2 (1984) 129.
[28] Z.G. Szabo, K. Kamaras, S. Szebeni, I. Ruff, Spectrochim. Acta A34 (1978) 607.
[29] G.M. Sheldrick, Acta Crystallgr., Sect. A 64 (2008) 112.
[30] A.D. Becke, J. Chem. Phys. 104 (1996) 1040.
[31] C. Lee, W. Yang, R.G. Parr, Phys. Rev. B37 (1988) 785.
[32] P.J. Hay, W.R. Wadt, J. Chem. Phys. 82 (1985) 270, (and also 299).
[33] A.S. Menon, L. Radom, J. Phys. Chem. A112 (2008) 13225.
[34] P.M. Wojciechowski, W. Zierkiewicz, D. Michalska, P. Hobza, J. Chem. Phys. 118 (2003) 10900.
[35] D. Michalska, K. Hernik, R. Wysokiński, B. Morzyk-Ociepa, A. Pietraszko, Polyhedron 26 (2007) 4303.
[36] A.E. Reed, L.A. Curtiss, F. Weinhold, Chem. Rev. 88 (1988) 899.
[37] M.J. Frisch, G.W. Trucks, H.B. Schlegel, G.E. Scuseria, M.A. Robb, J.R. Cheeseman, J.A. Montgomery Jr., T. Vreven, K.N. Kudin, J.C. Burant, J.M. Millam, S.S. Iyengar, J. Tomasi, V. Barone, B. Mennucci, M. Cossi, G. Scalmani, N. Rega, G.A. Petersson, H. Nakatsuji, M. Hada, M. Ehara, K. Toyota, R. Fukuda, J. Hasegawa, M. Ishida, T. Nakajima, Y. Honda, O. Kitao, H. Nakai, M. Klene, X. Li, J.E. Knox, H.P. Hratchian, J.B. Cross, C. Adamo, J. Jaramillo, R. Gomperts, R.E. Stratmann, O. Yazyev, A.J. Austin, R. Cammi, C. Pomelli, J.W. Ochterski, P.Y. Ayala, K. Morokuma, G.A. Voth, P. Salvador, J.J. Dannenberg, V.G. Zakrzewski, S. Dapprich, A.D. Daniels, M.C. Strain, O. Farkas, D.K. Malick, A.D. Rabuck, K. Raghavachari, J.B. Foresman, J.V. Ortiz, Q. Cui, A.G. Baboul, S. Clifford, J. Cioslowski, B.B. Stefanov, G. Liu, A. Liashenko, P. Piskorz, I. Komaromi, R.L. Martin, D.J. Fox, T. Keith, M.A. Al-Laham, C.Y. Peng, A. Nanayakkara, M. Challacombe, P.M.W. Gill, B. Johnson, W. Chen, M.W. Wong, C. Gonzalez, J.A. Pople, Gaussian 03, Revision C.01, Gaussian, Inc., Wallingford CT, 2004.
[38] G.A. van Albada, W.J.J. Smeets, N. Veldman, A.L. Spek, J. Reedijk, Inorg. Chim. Acta 290 (1999) 105.
[39] T. Akitsu, S. Komorita, Y. Kushi, Inorg. Chim. Acta 315 (2001) 18.
[40] S. Youngme, C. Chailuecha, G.A. van Albada, Ch. Pakawatchai, N. Chaichit, J. Reedijk, Inorg. Chim. Acta 357 (2004) 2532.
[41] T. Akitsu, Y. Einaga, Polyhedron 24 (2005) 2933.
[42] S. Basak, S. Sen, S. Mitra, C. Marschner, W.S. Sheldrick, Struct. Chem. 19 (2008) 115.
[43] T. Akitsu, Polyhedron 26 (2007) 2527.
[44] L.P. Battaglia, A. Bonamartini Corradi, G. Marcotrigiano, L. Menabue, G.C. Pellacani, Inorg. Chem. 18 (1979) 148.
[45] U. Sakaguchi, A.W. Addison, J. Chem.Soc., Dalton Trans. (1979) 600.
[46] P. Comba, T.W. Hambley, M.A. Hitchman, H. Stratemeier, Inorg. Chem. 34 (1995) 3903.
[47] J.M. Fernández-G., Ma. del Rocío Patiño-Maya, R. Toscano, L. Velasco, M. Otero-López, M. Aquilar-Martínez, Polyhedron 16 (1997) 4371.
[48] M.H.M. Olsson, U. Ryde, B.O. Roos, K. Pierloot, J. Biol. Inorg. Chem. 3 (1998) 109.
[49] J. Casanova, G. Alzuet, S. Ferrer, J. Latorre, J.A. Ramirez, J. Borrás, Inorg. Chim. Acta 304 (2000) 170.
[50] L. Gutierrez, G. Alzuet, J. Borrás, M. Liu-González, F. Sanz, A. Castiñeiras, Polyhedron 20 (2001) 703.
[51] R.C. Chikate, A.R. Belapure, S.B. Padhye, D.X. West, Polyhedron 24 (2005) 889.
[52] L. Sieroń, M. Bukowska-Strzyżewska, Acta Crystallgr., Sect. C 55 (1999) 1230.
[53] N.P.G. Roeges, A Guide to the Complete Interpretation Of Infrared Spectra of Organic Compounds, John Wiley & Sons, Chichester, 1998.
[54] B. Barszcz, T. Głowiak, J. Jezierska, Polyhedron 18 (1999) 3713.
[55] T. Akitsu, S. Komorita, A. Urushiyama, Bull. Chem. Soc. Jpn. 74 (2001) 851.
[56] M.A. Atanasov, M.A. Hitchman, Inorg. Chem. 32 (1993) 3973.
[57] I. Bertini, D. Gatteschi, A. Scozzafava, Coord. Chem. Rev. 29 (1979) 67.
[58] M.A. Hitchman, Inorg. Chem. 24 (1985) 4762.
[59] B.N. Figgis, M.A. Hitchman, Ligand Field Theory and Its Applications, Wiley-VCH, New York, 2000.

Table 1
Crystal data and structure refinements for compounds **1**–**5**.

Compound	**1**	**2**	**3**	**4**	**5**
Formula	$C_{38}H_{32}N_4O_9Cd$	$C_{38}H_{30}N_4O_8Zn$	$C_{38}H_{30}N_4O_8Co$	$C_{38}H_{30}N_4O_8Ni$	$C_{38}H_{36}N_4O_{11}Cu_2$
Formula weight	801.08	736.03	729.59	729.37	851.79
Crystal system	triclinic	monoclinic	monoclinic	monoclinic	triclinic
Space group	$P\bar{1}$	$C2/c$	$C2/c$	$C2/c$	$P\bar{1}$
a (Å)	11.047(2)	20.535(4)	20.504(3)	20.380(2)	8.484(3)
b (Å)	11.936(2)	9.951(3)	9.936(2)	9.925(3)	9.914(2)
c (Å)	14.397(3)	16.532(4)	16.493(2)	16.389(3)	11.446(2)
α (°)	100.306(2)	90	90	90	110.651(3)
β (°)	108.342(2)	107.336(3)	106.931(4)	106.454(2)	93.259(2)
γ (°)	96.557(3)	90	90	90	90.615(3)
V (Å^3)	1743.0(6)	3224.8(2)	3214.4(9)	3179.3(1)	898.9(8)
Z	2	4	4	4	1
D_{calc}.(g cm^{-3})	1.526	1.516	1.508	1.524	1.570
μ (mm^{-1})	0.689	0.825	0.598	0.675	1.252
F (0 0 0)	816	1520	1508	1512	436
Reflections collected	8848	9625	7935	7883	4616
Independent reflections (R_{int})	6063 (0.0097)	3797 (0.0227)	2837 (0.0268]	2808 (0.0294)	3148 (0.0141)
Data/restraints/parameters	6063/0/477	3797/0/231	2837/0/231	2808/0/231	3148/0/261
Goodness-of-fit (GOF) on F^2	1.049	1.051	1.036	1.047	1.053
R_1[a] [$I > 2\sigma(I)$]	0.0272	0.0402	0.0392	0.0461	0.0369
wR_2[b] (all data)	0.0688	0.1124	0.1079	0.1282	0.0897

[a] $R_1 = \sum||F_o| - |F_c||/\sum|F_o|$.
[b] $wR_2 = |\sum w(|F_o|^2 - |F_c|^2)|/\sum|w(F_o{}^2)^2|^{1/2}$.

Table 2
Selected bond lengths (Å) and angles (°) for compounds **1**–**5**.[a]

*Compound **1***			
Cd(1)–O(1)#1	2.334(2)	Cd(1)–O(2)#1	2.4967(2)
Cd(1)–O(5)	2.514(2)	Cd(1)–O(6)	2.3846(2)
Cd(1)–N(1)	2.378(2)	Cd(1)–N(2)#2	2.354(2)
Cd(1)–N(3)#3	2.389(2)		
O(1)#1–Cd(1)–N(2)#2	92.10(8)	N(2)#2–Cd(1)–O(2)#1	89.04(7)
O(1)#1–Cd(1)–N(1)	90.51(8)	N(1)–Cd(1)–O(2)#1	81.53(8)
N(2)#2–Cd(1)–N(1)	166.17(7)	O(6)–Cd(1)–O(2)#1	89.88(6)
O(1)#1–Cd(1)–O(6)	143.78(6)	N(3)#3–Cd(1)–O(2)#1	136.06(6)
N(2)#2–Cd(1)–O(6)	84.16(7)	O(1)#1–Cd(1)–O(5)	162.75(6)
N(1)–Cd(1)–O(6)	85.72(7)	N(2)#2–Cd(1)–O(5)	86.15(7)
O(1)#1–Cd(1)–N(3)#3	82.32(7)	N(1)–Cd(1)–O(5)	95.28(8)
N(2)#2–Cd(1)–N(3)#3	97.78(7)	O(6)-Cd(1)–O(5)	53.14(6)
N(1)–Cd(1)–N(3)#3	96.03(8)	N(3)#3–Cd(1)–O(5)	80.93(6)
O(6)–Cd(1)–N(3)#3	133.90(6)	O(2)#1–Cd(1)–O(5)	142.99(6)
O(1)#1–Cd(1)–O(2)#1	53.98(6)		
*Compound **2***			
Zn(1)–O(1)	2.333(2)	Zn(1)–O(2)	2.053(6)
Zn(1)–N(1)#2	2.090(7)		
O(2)–Zn(1)–O(1)	59.69(6)	O(2)–Zn(1)–N(1)#2	99.56(7)
N(1)#3–Zn(1)–O(1)	89.34(7)	O(2)–Zn(1)–N(1)#3	101.73(7)
N(1)#2–Zn(1)–N(1)#3	93.85(1)	O(2)–Zn(1)–O(2)#1	148.63(1)
O(1)–Zn(1)–O(1)#1	94.94(1)	N(1)#2–Zn(1)–O(1)	159.19(6)
O(2)#1–Zn(1)–O(1)	98.00(7)		
*Compound **3***			
Co(1)–O(1)	2.239(2)	Co(1)–O(2)	2.0785(2)
Co(1)–N(1)#2	2.094(2)		
O(2)–Co(1)–O(1)	60.82(6)	O(2)–Co(1)–N(1)#2	98.60(7)
N(1)#3–Co(1)–O(1)	89.72(7)	O(2)–Co(1)–N(1)#3	99.86(7)
N(1)#2–Co(1)–N(1)#3	93.42(1)	O(2)–Co(1)–O(2)#1	152.95(1)
O(1)–Co(1)–O(1)#1	94.46(1)	N(1)#2–Co(1)–O(1)	159.40(6)
O(2)#1–Co(1)–O(1)	99.78(7)		
*Compound **4***			
Ni(1)–O(1)	2.160(2)	Ni(1)–O(2)	2.072(2)
Ni(1)–N(1)#2	2.052(2)		
O(2)–Ni(1)–O(1)	62.17(8)	O(2)–Ni(1)–N(1)#2	97.50(9)
N(1)#3–Ni(1)–O(1)	90.80(9)	O(2)–Ni(1)–N(1)#3	98.53(8)
N(1)#2–Ni(1)–N(1)#3	91.84(1)	O(2)–Ni(1)–O(2) #1	156.88(1)
O(1)–Ni(1)–O(1)#1	93.00(1)	N(1)#2–Ni(1)–O(1)	160.69(8)
O(2)#1–Ni(1)–O(1)	101.01(8)		
*Compound **5***			
Cu(1)–O(2)#2	2.097(2)	Cu(1)–N(1)	1.954(3)
Cu(1)–N(2)#1	1.946(2)		
N(2)#1–Cu(1)–O(2)#2	109.69(1)	N(2)#1–Cu(1)–N(1)	145.81(1)
N(1)–Cu(1)–O(2)#2	104.14(9)		

[a] Symmetry transformations used to generate equivalent atoms: for **1**: #1 $x+1, y, z$; #2 $x+1, y+1, z$; #3 $-x+1, -y+1, -z+1$; for **2**: #1 $-x, y, -z+1/2$; #2 $-x+1/2, y-1/2, -z+1/2$; #3 $x-1/2, y-1/2, z$; for **3**: #1 $-x+1, y, -z-1/2$; #2 $-x+3/2, y-1/2, -z-1/2$; #3 $x-1/2, y-1/2, z$; for **4**: #1 $-x, y, -z+1/2$; #2 $-x+1/2, y-1/2$, #3 $x-1/2, y-1/2, z$; $-z+1/2$; for **5**: #1 $x-1, y-1, z-1$; #2 $x-1, y-1, z$.

spectrofluorometer (Varian) equipped with a xenon lamp and quartz carrier at room temperature. Thermogravimetric (TG) analysis was performed on a Perkin–Elmer TG-7 analyzer heated from 40 to 700 °C under nitrogen.

2.2. Syntheses of the compounds

2.2.1. Synthesis of $[Cd(L3)_2]\cdot H_2O$ (**1**)

A mixture of $Cd(OOCCH_3)_2\cdot 2H_2O$ (0.30 mmol, 0.080 g), L3 (0.20 mmol, 0.036 g) and NaOH (0.60 mmol, 0.024 g) in H_2O (14 ml) was sealed in a 25 ml Teflon-lined stainless steel container, which was heated at 150 °C for 72 h and then cooled down to room temperature at a rate of 5 °C h^{-1}. Colorless crystals of **1** were collected and washed with distilled water and dried in air to give the product; yield, 35 mg (44% based on Cd(II) salts). Elemental *Anal.* Calc. for $C_{38}H_{32}N_4O_9Cd$ (801.08): C, 56.98; H, 4.03; N, 6.99. Found C, 56.96; H, 4.01; N, 6.97%. IR (KBr pellet, cm^{-1}): 3493 (w), 3072 (w), 1607 (m), 1557 (s), 1474 (w), 1435 (m), 1403 (m), 1371 (s), 1327 (m), 1154 (s), 1043 (m), 851 (w), 783 (s), 704 (m), 642 (w).

2.2.2. Synthesis of $[Zn(L3)_2]$ (**2**)

Similar procedures were performed to obtain colorless crystals of compound **2**, except that $Zn(OOCCH_3)_2\cdot 2H_2O$ (0.30 mmol, 0.066 g) was used instead of $Cd(OOCCH_3)_2\cdot 2H_2O$. Yield, 25 mg (38% based on Zn(II) salts). Elemental *Anal.* Calc. for $C_{38}H_{30}N_4O_8Zn$ (736.03): C, 62.01; H, 4.11; N, 7.61. Found C, 62.04; H, 4.12; N, 7.64%. IR (KBr pellet, cm^{-1}): 3432 (w), 3041 (w), 1605 (m), 1553 (s), 1474 (m), 1440 (m), 1410 (s), 1374 (s), 1319 (m), 1143 (s), 1053 (m), 782 (m), 706 (m), 649 (w).

2.2.3. Synthesis of $[Co(L3)_2]$ (**3**)

Similar procedures were performed to obtain purple crystals of compound **3**, except that $Co(OOCCH_3)_2\cdot 4H_2O$ (0.30 mmol, 0.075 g) was used instead of $Cd(OOCCH_3)_2\cdot 2H_2O$. Yield, 31 mg (41% based on Co(II) salts). Elemental *Anal.* Calc. for $C_{38}H_{30}N_4O_8Co$ (729.59): C, 62.56; H, 4.14; N, 7.68. Found C, 62.53; H, 4.14; N, 7.65%. IR (KBr pellet, cm^{-1}): 3432 (m), 3042 (w), 1609 (m), 1542 (s), 1474 (m), 1415 (s), 1376 (s), 1319 (m), 1293 (w), 1143 (s), 1052 (s), 781 (m), 706 (w).

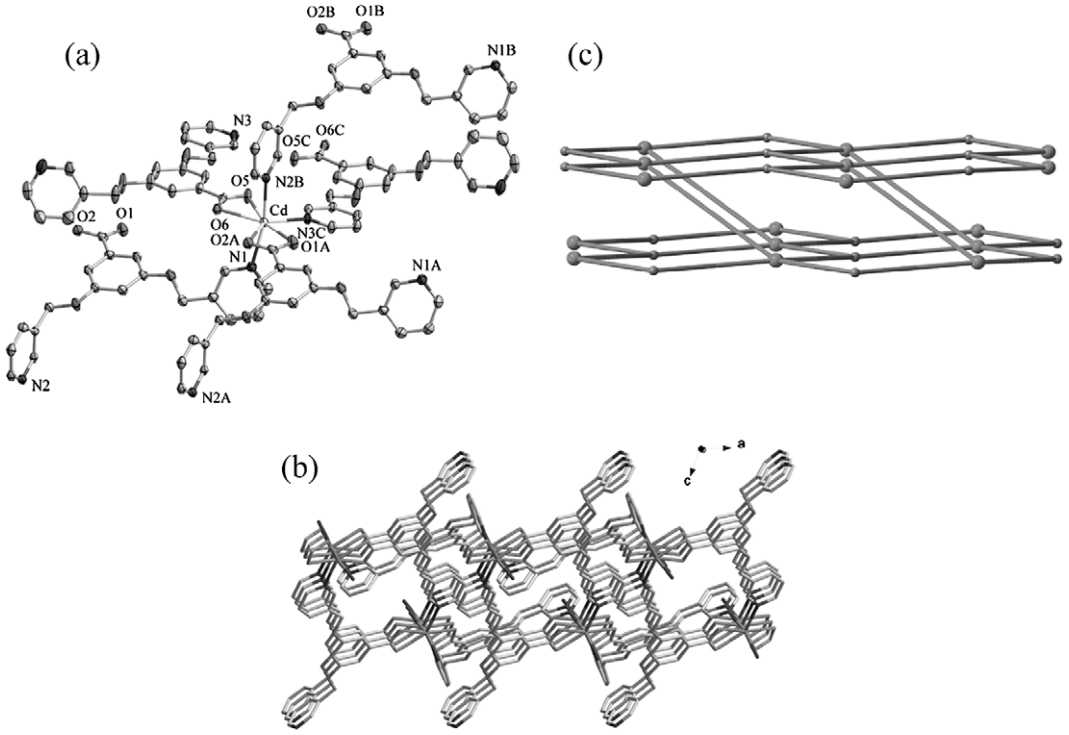
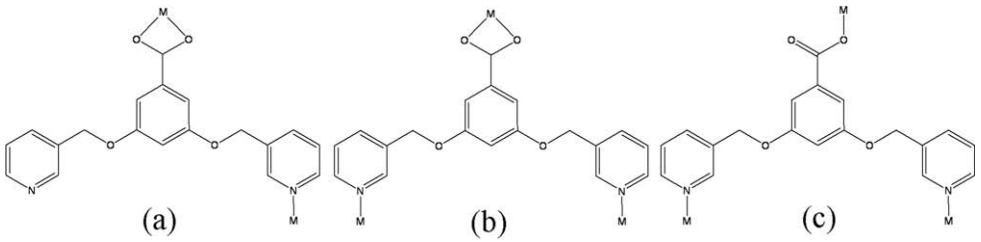


Fig. 1. (a) The coordination environment of Cd^{II} atom in compound **1**. All of the hydrogen atoms and lattice-water molecule were omitted for clarity. (b) View showing the bilayer structure formed by connecting the Cd^{II} atom with tri-connected L3 and bridged L3 from *b*-axis. (c) Schematic view of the 2D binodal (3,4)-connected network of **1** with $(6^3)(6^6)$ topology. (Symmetry transformations used to generate equivalent atoms: A, $1+x, y, z$; B, $1+x, 1+y, z$; C, $1-x, 1-y, 1-z$.)



Scheme 1. Coordination modes of the L3 ligand in compounds **1**–**5**.

*2.2.4. Synthesis of [Ni(L3)$_2$] (**4**)*

Similar procedures were performed to obtain green crystals of compound **4**, except that $NiCl_2{\cdot}6H_2O$ (0.30 mmol, 0.072 g) was used instead of $Cd(OOCCH_3)_2{\cdot}2H_2O$. Yield, 25 mg (35% based on Ni(II) salts). Elemental *Anal.* Calc. for $C_{38}H_{30}N_4O_8Ni$ (729.37): C, 62.58; H, 4.15; N, 7.68. Found C, 62.56; H, 4.16; N, 7.66%. IR (KBr pellet, cm^{-1}): 3432 (m), 3041 (w), 1610 (m), 1535 (s), 1475 (m), 1419 (s), 1376 (s), 1319 (m), 1292 (w), 1143 (s), 1051 (m), 783 (s), 705 (w).

*2.2.5. Synthesis of [Cu$_2$(L3)$_2$]·3H$_2$O (**5**)*

Similar procedures were performed to obtain brown crystals of compound **5**, except that CuI (0.30 mmol, 0.057 g) was used instead of $Cd(OOCCH_3)_2{\cdot}2H_2O$. Yield, 16 mg (28% based on Cu(I) salts). Elemental *Anal.* Calc. (%) for $C_{38}H_{36}N_4O_{11}Cu_2$ (851.79): C, 53.58; H, 4.26; N, 6.58. Found C, 53.55; H, 4.29; N, 6.57%. IR (KBr pellet, cm^{-1}): 3394 (s), 1603 (m), 1540 (s), 1371 (m), 1276 (s), 1115 (w), 1023 (m), 782 (m), 705 (w).

2.3. X-ray crystallography analysis

Data collection of compounds **1**–**5** were performed on a Bruker SMART APEX II CCD diffractometer with graphite-monochromated Mo Kα radiation (λ = 0.71073 Å) at room temperature. All absorption corrections were performed by using the SADABS program. The crystal structure was solved by direct methods and refined with full-matrix least-squares (SHELXTL-97) with atomic coordinates and anisotropic thermal parameters for all nonhydrogen atoms. The hydrogen atoms of aromatic rings were included in the structure factor calculation at idealized positions by using a riding model. The hydrogen atoms from water molecules were directly located from successive Fourier differences syntheses. In compound **5**, the hydrogen atoms of one lattice-water molecules have not been found from Fourier maps due to the high disorder of water molecules. The detailed crystallographic data and structure refinement parameters for compounds **1**–**5** are summarized in Table 1. Selected bond lengths and angles are given in Table 2.

3. Results and discussion

3.1. Description of the structures

*3.1.1. [Cd(L3)$_2$]·H$_2$O (**1**)*

The single-crystal X-ray diffraction analysis reveals that the structure of **1** contains one kind of Cd^{II} atom, two kinds of L3 ligands and one lattice-water molecule in an asymmetric unit. Each Cd^{II} atom is coordinated by four carboxylate oxygen atoms (Cd–O 2.334(2)–2.514(2) Å) of two L3 ligands and three nitrogen atoms (Cd–N 2.354(2)–2.389(2) Å) of three L3 ligands to furnish a pentag-

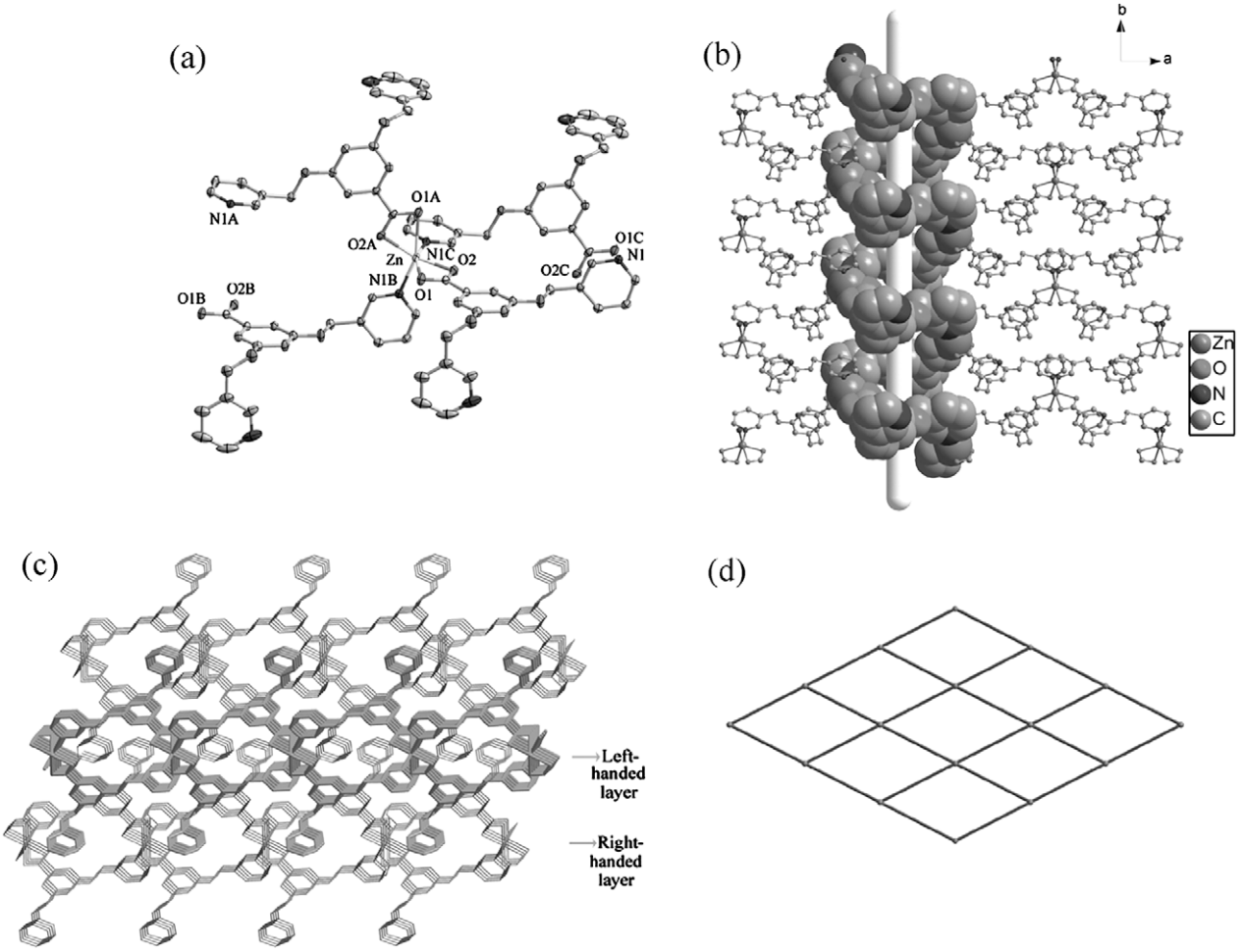


Fig. 2. (a) The coordination environment of Zn^{II} atom in compound **2**. All of the hydrogen atoms were omitted for clarity. (b) Left-handed layer formed by L3 ligands and Zn^{II} atoms in **2** along the *b*-axis. (c) The packing diagram of the 2D polymeric layers in **2**. (d) Schematic view of the uninodal (4,4)-connected net with ($4^4 \cdot 6^2$) Schläfli symbol. (Symmetry transformations used to generate equivalent atoms: A, $-x$, y, $0.5 - z$; B, $-0.5 + x$, $-0.5 + y$, z; C, $0.5 - x$, $-0.5 + y$, $0.5 - z$.)

onal bipyramidal coordination geometry (Fig. 1a). The Cd–O and Cd–N bond distances are all in the normal ranges [44–49].

The coordination modes of L3 ligand in this work are summarized in Scheme 1. In compound **1**, L3 ligands adopt two coordination modes: one bridges two Cd^{II} atoms through one carboxylate group and one pyridyl-N atom, containing an uncoordinated pyridyl-N atom; and the other connects three Cd^{II} atoms through one carboxylate group and two pyridyl-N atoms (Schemes 1a and 1b). As depicted in Fig. 1b, each tri-connected L3 ligand connects with three metal centers to form (6,3)-connected net, which is further linked by bridged L3 ligands to form the final 2D bilayer structure. If the two bridged L3 ligands between two Cd^{II} atoms can be considered as one linker, each Cd^{II} atom can be treated a 4-neccted node, the structure of **1** is a binodal (3,4)-connected network with $(6^3)(6^6)$ topology (Fig. 1c). Moreover, the lattice-water molecules form hydrogen-bonding interactions with carboxylate group and uncoordinated pyridyl-N atom of L3 ligands in the adjacent layers (dOw···O5*i* = 2.951 Å, *i*: $1-x$, $1-y$, $1-z$; dOw-N4*ii* = 2.884 Å, *ii*: x, y, $-1+z$) to extend the 2D layer into a 3D supramolecular net.

3.1.2. $[M(L3)_2]$ (M = Zn, **2**; Co, **3**; Ni, **4**)

Single-crystal X-ray diffraction analyses reveal that compounds **2**–**4** are isostructural, and crystallize in the monoclinic space group *C*2/*c*; thus, only the structure of **2** is representatively described in detail here. The crystal structure of **2** contains one kind of Zn^{II} atom and one kind of L3 ligand in an asymmetric unit. As shown in Fig. 2a, each Zn^{II} atom is coordinated by four carboxylate oxygen atoms (Zn–O 2.053(6)–2.333(2) Å) of two L3 ligands and two nitrogen atoms (Zn–N 2.090(7) Å) of two L3 ligands, showing a distorted octahedral coordination geometry. The Zn–O and Zn–N bond distances are all in the normal ranges [50–53]. It should be noteworthy that the adjacent Zn^{II} atoms are linked to each other through pyridyl-N atom and carboxylate group of L3 ligands (Scheme 1a) to form helical chains running along *b*-axis (Fig. 2b). The adjacent helical chains are also linked by L3 ligands to generate a 2D rhombic structure (9.95×20.54 Å^2) involving 44-membered rings. With in the layer, all Zn–L3 helical chains display the same chirality, while those in adjacent layers display opposite chirality (Fig. 2c). So the overall structure of **2** is a racemic structure. If L3 ligands are considered as linear linkers, Zn^{II} atoms are considered as 4-connected nodes, the structure of **2** can be symbolized as a uninodal (4,4)-connected net with $(4^4 \cdot 6^2)$ Schläfli symbol (Fig. 2d).

3.1.3. $[Cu_2(L3)_2]\cdot 3H_2O$ (**5**)

Single-crystal X-ray diffraction analysis reveals that compound **5** crystallizes in the triclinic space group $P\bar{1}$ and there are one crystallographic independent Cu^{I} atom, one L3 ligand and one and a half lattice-water molecules in an asymmetrical unit. As shown in Fig. 3a, the Cu^{I} atom is in a trigonal coordination geometry with one carboxylate oxygen atom (Cu–O 2.097(2) Å) of one L3 ligand and two nitrogen atoms (Cu–N 1.946(2)–1.954(3) Å) of two L3 ligands. The Cu–O and Cu–N bond distances are all in the normal ranges [54–57].

Different from that of compounds **1** and **2**, each L3 ligand acts as a tri-connector linking three Cu^{I} atoms in compound **5** (Scheme 1c), the carboxylate group connects one Cu^{I} atom through a mono-dentate oxygen atom, two pyridyl-N atoms bind to two Cu^{I} atoms, consequently resulting in the formation of a 2D layer. By treating the Cu^{I} atom as a single node and connecting the nodes according to the connectivity defined by the geometrical centers of the L3 ligand, a distorted 2D bimodal (6,3) network sustained by 3-connected nodes is then yielded, as illustrated in Fig. 3b. Two types of supramolecular interactions, $\pi\cdots\pi$ stacking interactions between phenyl rings of adjacent layer (3.490 Å) and hydrogen-bonding interactions between lattice-water molecules and uncoor-

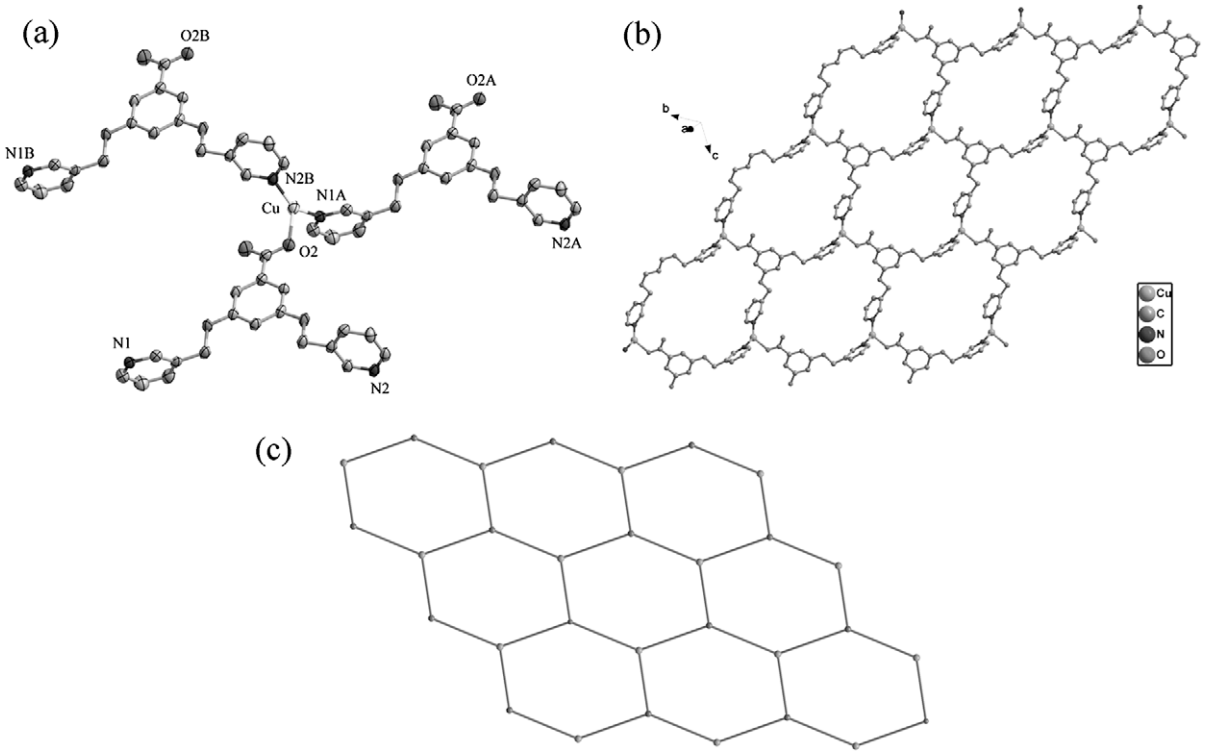


Fig. 3. (a) The coordination environment of Cu^{I} atom in compound **5**. All of the hydrogen atoms and lattice-water molecules were omitted for clarity. (b) 2D layer structure of **5**. (c) Topology of **5** showing the binodal (6,3)-net based on the Cu^{I} atoms and L3 ligands. (Symmetry transformations used to generate equivalent atoms: A, 1+x, 1+y, z; B, x, y, -1+z.)

dinated carboxylate oxygen atoms, contribute to the formation of the 3D supramolecular architecture.

As to the syntheses of compounds **1**–**5**, all the reaction conditions are the same except for the difference of metal ions. From the structural analyses of **1**–**5**, we can see that the increase in coordination number (from 3 to 7) of metal ions induces the progressive increase in complexity of the ultimate net (from (6,3)-net to bilayer (3,4)-net); in other words, the coordination number of metal ions plays a significant role in tuning the connectivity of a specific network [58,59]. On the other hand, flexible L3 ligand has the advantages in that its flexibility and conformational freedom allow it to conform to the coordination environment of transition-metal ions. This is further evidence that the selection of suitable metal ions and organic ligands is a major strategy to synthesize functional materials with useful properties.

3.2. Properties

3.2.1. Luminescent properties

Taking into account of the excellent luminescent properties of Cd(II) and Zn(II), the solid-state luminescent spectra of **1** and **2** have been studied at room temperature. As shown in Fig. 4, compound **1** shows the emission maxima at 453 nm (λ_{ex} = 340 nm), compound **2** shows the emission maxima at 464 nm (λ_{ex} = 349 nm). In order to understand the nature of the emission, we analyzed the photoluminescent property of L3 ligand and found that the strongest emission peak at 392 nm (λ_{ex} = 246 nm). The emission of the ligand may be assigned to $\pi^* \rightarrow n$ and $\pi^* \rightarrow \pi$ transitions of the intraligands. In comparison with the free ligand, the emission of compounds **1** and **2** may be attributed to ligand to metal charge transfer (LMCT) [60–63]. These observations indicate that these condensed polymeric compounds could be potentially used as photoactive materials, since they are thermally stable and insoluble in common polar and nonpolar solvents.

3.2.2. Thermal properties

To study the thermal stability of compounds **1**–**5**, thermogravimetric (TG) analyses were performed on polycrystalline samples under a nitrogen atmosphere with a heating rate of 10 °C min^{-1} (Fig. 5). The TG curve of **1** shows that the first weight loss of 2.46% between 46 and 120 °C corresponding to the loss of the lattice-water molecules (calcd. 2.25%). A total weight loss of 81.39% occurred in the temperature range of 240–560 °C, mainly corresponding to the removal of the L3 ligands (calcd. 81.72%), no weight loss were observed up to 700 °C indicating the complete deposition of the compound with the formation of CdO as the final product. The TG curves of **2**–**4** all show one main weight loss. No weight losses were observed for the compounds up to 280 °C; above 280 °C, significant weight losses occurred and ended at 610 °C, 660 °C, 560 °C, respectively, indicating the removal of the corresponding organic components. The remaining weight may correspond to the final products of ZnO in **2** (obsd. 11.23%, calcd. 11.06%), CoO in **3** (obsd. 11.46%, calcd. 10.27%) and NiO in **4** (obsd. 10.42%, calcd. 10.24%). The TG curve of **5** shows that the first weight loss of 6.08% between 70 °C and 130 °C, corresponding to the loss of the lattice-water molecules (calcd. 6.35%). The framework collapsed in the temperature range of 220–450 °C before the final formation of a metal oxide.

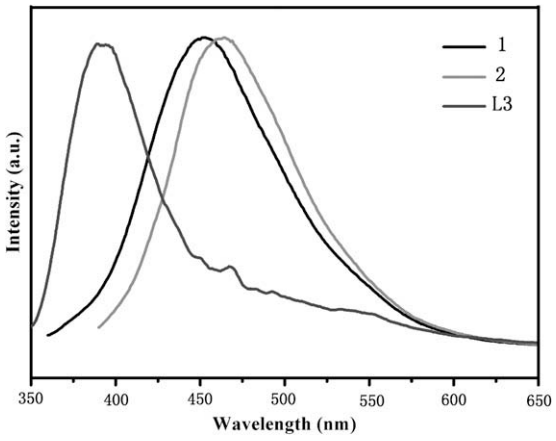


Fig. 4. Solid-state luminescent spectra of L3, **1** and **2** at room temperature.

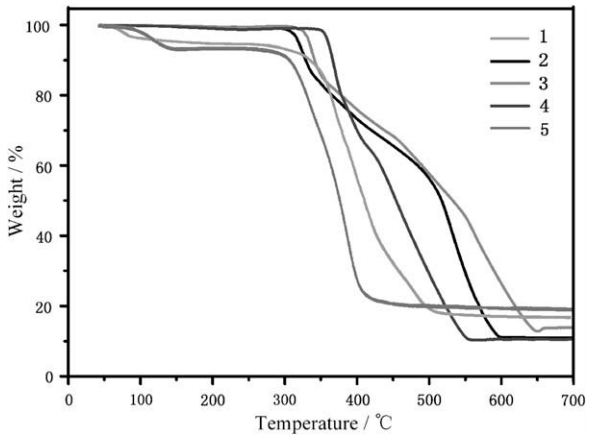


Fig. 5. TG curves of **1**–**5**.

4. Conclusion

In summary, we have synthesized five new coordination polymers based on 3,5-bis(pyridin-3-ylmethoxy)benzoic acid ligand under hydrothermal conditions. The successful syntheses of the five compounds indicate that it is promising to build up unusual architectures via combining transition metals and L3 ligands. Further work on the properties of this new flexible organic ligand and its metal compounds are still explored in our laboratory.

Supplementary data

CCDC 722283, 722284, 722285, 722286, and 722287 contain the supplementary crystallographic data for this paper. These data can be obtained free of charge via http://www.ccdc.cam.ac.uk/conts/retrieving.html, or from the Cambridge Crystallographic Data Centre, 12 Union Road, Cambridge CB2 1EZ, UK; fax: (+44) 1223-336-033; or e-mail: deposit@ccdc.cam.ac.uk.

Acknowledgements

The authors gratefully acknowledge the financial support from the National Natural Science Foundation of China (Project No. 20703008), Chang Jiang Scholars Program (2006), Program for Changjiang Scholars and Innovative Research Team in University (IRT0714), the Training Fund of NENU's Scientific Innovation Project (NENU-STC07017) and Science Foundation for Young Teachers of Northeast Normal University (20080502).

References

[1] S.R. Batten, R. Robson, Angew. Chem., Int. Ed. 37 (1998) 1460.
[2] P.J. Hagrman, D. Hagrman, J. Zubieta, Angew. Chem., Int. Ed. 38 (1999) 2639.

[3] M. O'Keeffe, M. Eddaoudi, H.L. Li, T. Reineke, O.M. Yaghi, J. Solid State Chem. 152 (2000) 3.
[4] O.M. Yaghi, M. O'Keeffe, N.W. Ockwig, H.K. Chae, M. Eddaoudi, J. Kim, Nature 423 (2003) 705.
[5] A.N. Khlobystov, A.J. Blake, N.R. Champness, D.A. Lemenovskii, A.G. Majouga, N.V. Zyk, M. Schröder, Coord. Chem. Rev. 222 (2001) 155.
[6] S.L. James, Chem. Soc. Rev. 32 (2003) 276.
[7] X.C. Huang, Y.Y. Lin, J.P. Zhang, X.M. Chen, Angew. Chem., Int. Ed. 45 (2006) 1557.
[8] M. Fujita, Y.J. Kwon, S. Washizu, K. Ogura, J. Am. Chem. Soc. 116 (1994) 1151.
[9] S. Kitagawa, R. Kitaura, S.I. Noro, Angew. Chem., Int. Ed. 43 (2004) 2334.
[10] N.L. Rosi, J. Eckert, M. Eddaoudi, D.T. Vodak, J. Kim, M. O'Keeffe, O.M. Yaghi, Science 300 (2003) 1127.
[11] M. Daniel, R. Daniel, V. Jaume, Chem. Soc. Rev. 36 (2007) 770.
[12] C.J. Kepert, T.J. Prior, M.J. Rosseinsky, J. Am. Chem. Soc. 123 (2001) 10001.
[13] M.J. Zaworotko, Nature 451 (2008) 410.
[14] Y.C. Liang, M.C. Hong, R. Cao, J.B. Weng, W.P. Su, Inorg. Chem. Commun. 4 (2001) 599.
[15] Y.H. He, Y.L. Feng, Y.Z. Lan, Y.H. Wen, Cryst. Growth Des. 8 (2008) 3586.
[16] Y.C. Liang, R. Cao, W.P. Su, M.C. Hong, W.J. Zhang, Angew. Chem., Int. Ed. 39 (2000) 3304.
[17] M.L. Tong, S. Kitagawa, H.C. Chang, M. Ohba, Chem. Commun. (2004) 418.
[18] Y.L. Wei, H.W. Hou, L.K. Li, Y.T. Fan, Y. Zhu, Cryst. Growth Des. 5 (2005) 1405.
[19] X.L. Wang, C. Qin, E.B. Wang, Y.G. Li, N. Hao, C.W. Hu, L. Xu, Inorg. Chem. 43 (2004) 1850.
[20] S.K. Ghosh, P.K. Bharadwaj, Inorg. Chem. 42 (2003) 8250.
[21] S.K. Ghosh, P.K. Bharadwaj, Inorg. Chem. 43 (2004) 2293.
[22] S.K. Ghosh, J. Ribas, P.K. Bharadwaj, Cryst. Eng. Commun. 6 (2004) 250.
[23] B. Zhao, P. Cheng, Y. Dai, C. Cheng, D.Z. Liao, S.P. Yan, Z.H. Jiang, G.L. Wang, Angew. Chem., Int. Ed. 42 (2003) 934.
[24] M.L. Tong, J. Wang, S. Hu, S.R. Batten, Inorg. Chem. Commun. 8 (2005) 48.
[25] X.L. Wang, C. Qin, E.B. Wang, Y.G. Li, C.W. Hu, L. Xu, Chem. Commun. (2004) 378.
[26] J.F. Eubank, R.D. Walsh, P. Poddar, H. Srikanth, R.W. Larsen, M. Eddaoudi, Cryst. Growth Des. 6 (2006) 1453.
[27] D. Min, S.S. Yoon, D.Y. Jung, C.Y. Lee, Y. Kim, W.S. Han, S.W. Lee, Inorg. Chim. Acta 324 (2001) 293.
[28] R. García-Zarracino, H. Höpfl, Angew. Chem., Int. Ed. 43 (2004) 1507.
[29] S.M. Humphrey, P.T. Wood, J. Am. Chem. Soc. 126 (2004) 13236.
[30] Y.L. Liu, V.C. Kravtsov, D.A. Beauchamp, J.F. Eubank, M. Eddaoudi, J. Am. Chem. Soc. 127 (2005) 7266.
[31] C. Qin, X.L. Wang, E.B. Wang, Z.M. Su, Inorg. Chem. 44 (2005) 7122.
[32] Y.L. Lu, J.Y. Wu, M.C. Chan, S.M. Huang, C.S. Lin, T.W. Chiu, Y.H. Liu, Y.S. Wen, C.H. Ueng, T.M. Chin, C.H. Hung, K.L. Lu, Inorg. Chem. 45 (2006) 2430.
[33] C.L. Ma, J.K. Li, R.F. Zhang, J. Coord. Chem. 59 (2006) 1891.
[34] D. Min, S.W. Lee, Inorg. Chem. Commun. 5 (2002) 978.
[35] D.W. Min, S.S. Yoon, J.H. Lee, M. Suh, S.W. Lee, Inorg. Chem. Commun. 4 (2001) 297.
[36] Y.H. Zhao, Z.M. Su, Y.M. Fu, K.Z. Shao, P. Li, Y. Wang, X.R. Hao, D.X. Zhu, S.D. Liu, Polyhedron 27 (2008) 583.
[37] S.L. Zheng, J.H. Yang, X.L. Yu, X.M. Chen, W.T. Wong, Inorg. Chem. 43 (2004) 830.
[38] M.C. Hong, Y.J. Zhao, W.P. Su, R. Cao, M. Fujita, Z.Y. Zhou, A.S.C. Chan, Angew. Chem., Int. Ed. 39 (2000) 2468.
[39] E.C. Yang, H.K. Zhao, B. Ding, X.G. Wang, X.J. Zhao, Cryst. Growth Des. 7 (2007) 2009.
[40] X.W. Wang, J.Z. Chen, J.H. Liu, Cryst. Growth Des. 7 (2007) 1227.
[41] L.Y. Zhang, J.P. Zhang, Y.Y. Lin, X.M. Chen, Cryst. Growth Des. 6 (2006) 1684.
[42] L. Han, M.C. Hong, R.H. Wang, J.H. Luo, Z.Z. Lin, D.Q. Yuan, Chem. Commun. (2003) 2580.
[43] K.O. Ashiry, Y.H. Zhao, K.Z. Shao, Z.M. Su, G.J. Xu, Polyhedron 28 (2009) 975.
[44] A.J. Carty, N.J. Taylor, Inorg. Chem. 16 (1977) 177.
[45] J.C. Dai, X.T. Wu, Z.Y. Fu, C.P. Cui, S.M. Hu, W.X. Du, L.M. Wu, H.H. Zhang, R.Q. Sun, Inorg. Chem. 41 (2002) 1391.
[46] X.J. Luan, X.H. Cai, Y.Y. Wang, D.S. Li, C.J. Wang, P. Liu, H.M. Hu, Q.Z. Shi, S.M. Peng, Chem. Eur. J. 12 (2006) 6281.
[47] F.A.A. Paz, J. Klinowski, Inorg. Chem. 43 (2004) 3948.
[48] R.Q. Zou, X.H. Bu, R.H. Zhang, Inorg. Chem. 43 (2004) 5382.
[49] Y.Q. Lan, S.L. Li, Y.M. Fu, Y.H. Xu, L. Li, Z.M. Su, Q. Fu, Dalton Trans. (2008) 6796.
[50] X.M. Zhang, M.L. Tong, M.L. Gong, X.M. Chen, Eur. J. Inorg. Chem. (2003) 138.
[51] A.D. Burrows, R.W. Harrington, M.F. Mahon, S.J. Teat, Eur. J. Inorg. Chem. (2003) 766.
[52] Y.Y. Liu, J.F. Ma, J. Yang, J.C. Ma, G.J. Ping, Cryst. Eng. Commun. 10 (2008) 565.
[53] K.Z. Shao, Y.H. Zhao, Y. Xing, Y.Q. Lan, X.L. Wang, Z.M. Su, Cryst. Growth Des. 8 (2008) 2986.
[54] K. Uemura, A. Maeda, H. Kita, Polyhedron 27 (2008) 2939.
[55] X.Q. Liang, H.P. Xiao, B.L. Liu, Y.Z. Li, J.L. Zuo, X.Z. You, Polyhedron 27 (2008) 2494.
[56] S.W. Liang, M.X. Li, M. Shao, X. He, J. Mol. Struct. 875 (2008) 17.
[57] G.F. Liu, W.H. Zhang, Y. Chen, D. Liu, J.P. Lang, Inorg. Chem. Commun. 10 (2007) 1049.
[58] B.F. Hoskins, R. Robson, J. Am. Chem. Soc. 111 (1989) 5962.
[59] B.F. Hoskins, R. Robson, J. Am. Chem. Soc. 112 (1990) 1546.
[60] Y.Y. Qin, J. Zhang, Z.J. Li, L. Zhang, X.Y. Cao, Y.G. Yao, Chem. Commun. (2008) 2532.
[61] Q.R. Fang, G.S. Zhu, M. Xue, J.Y. Sun, F.X. Sun, S.L. Qiu, Inorg. Chem. 45 (2006) 3582.
[62] S.L. Li, Y.Q. Lan, J.F. Ma, Y.M. Fu, J. Yang, G.J. Ping, J. Liu, Z.M. Su, Cryst. Growth Des. 8 (2008) 1610.
[63] J. Tao, M.L. Tong, J.X. Shi, X.M. Chen, S.W. Ng, Chem. Commun. (2000) 2043.

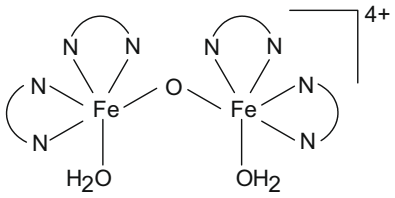


Fig. 1. Schematic drawing of $[Fe_2(\mu\text{-}O)(phen)_4(H_2O)_2]^{4+}$. $\widehat{NN}$ is 1,10-phenanthroline.

of pyruvic acid oxidation by higher valent metal oxidants are rather limited in the literature [40–46].

The title complex is not a powerful oxidant (E^0_{red} for $Fe^{III}{}_2/Fe^{III}Fe^{II}$ = −0.18 V *versus* NHE [33]). An estimated value for the one-electron oxidation potential for pyruvic acid is about −0.10 V *versus* NHE [40]. In spite of the unfavorable potentials, redox between these species occurs at a moderate rate. Thus, among the goals of this study is to examine the factors, including increased basicity of the μ-oxo bridge of the reduced **1**, that could reduce the activation barriers for the overall two electron redox leading to thermodynamically stable products.

2. Experimental

2.1. Materials

The complex salt $[Fe_2O(phen)_4(H_2O)_2](NO_3)_4{\cdot}5H_2O$, (**1**), was prepared from stoichiometric proportions of $Fe(NO_3)_3{\cdot}9H_2O$ and phen in water [21] and identified by elemental (CHN) analysis and optical spectroscopy [21]. The preparation, standardization and storage of pyruvic acid [44] and sodium nitrate [47] have been described previously. 1,10-Phenanthroline (G.R., E. Merck) and D_2O (Aldrich, 99.9 atom% D) were used as received. All other chemicals were of reagent grade. Chromium(II)-scrubbed nitrogen gas was used for deoxygenating the reacting solutions to study the effect of dissolved oxygen on the reaction rate. Freshly boiled doubly distilled water was used throughout. All the reported kinetic and equilibrium data are at (25.0 ± 0.1) °C and at I = 1.0 M maintained by $NaNO_3$ unless mentioned otherwise.

2.2. Physical measurements and kinetics

All absorbances and electronic spectra were recorded with a Shimadzu (1601 PC) spectrophotometer using 1.00 cm quartz cells in the electrically controlled thermostated (25.0 ± 0.1 °C) cell housing (CPS – 240 A). The kinetics was monitored *in situ* in the 'kinetic mode' of the instrument at 510 nm, the visible absorption maximum of the product iron species, $[Fe(phen)_3]^{2+}$ [48,49]. All kinetic runs included excess 1,10-phenanthroline concentration, C_{phen} (=$[Hphen^+]$ + [phen]), in the range of 3–10 mM. Solution pH values (2.58–5.50) were measured with an Orion pH-meter (model 710 A) electrode, the electrode calibration was described earlier [50,51]. For reactions in D_2O, pD was calculated as pD = $(pH)_{measured}$ + 0.40 [52,53] where $(pH)_{measured}$ is the pH-meter reading in D_2O. Total pyruvate concentration, T_R (= [Hpy] + $[Py^-]$), was at least 10 times that of the oxidant. The observed rate constants (first-order) were determined from the least squares fit of absorbance *versus* time data (*vide infra*).

2.3. Stoichiometry and reaction products

The stoichiometry was determined under kinetic conditions ($T_R > [Fe^{III}{}_2]$) by measuring the absorbance of the reduction product, $[Fe(phen)_3]^{2+}$ at 510 nm ($\varepsilon = 1.11 \times 10^4\ M^{-1}\ cm^{-1}$) [48,49] and by detecting CO_2 and acetic acid. The UV–Vis spectra of product solutions indicate quantitative formation (98 ± 3%) of $[Fe(phen)_3]^{2+}$ as the sole iron product. The generation of gaseous CO_2 as oxidation product of pyruvic acids was qualitatively detected by GC analysis as follows [54]. The gaseous product formed during the reaction was collected over a saturated sodium chloride solution and analysed by gas chromatography using a Chemito (India) GCHT 8610 equipped with TCD, a Porapack Q and molecular sieve 13X column. Splitless mode injection of 500 μL of sample was used. The oven temperature, injector and detector temperature were kept at 50 °C, 100 °C and 150 °C, respectively. The carrier hydrogen gas flow was adjusted to 30 mL min^{-1}. Formation of acetic acid from oxidation of pyruvic acid was ensured with the aid of $La(NO_3)_3/I_2$ test [55]. For this purpose, the red coloured $[Fe(phen)_3]^{2+}$ was precipitated from the product mixture as the perchlorate salt by addition of excess $NaClO_4$. $NaNO_3$, phen or $NaClO_4$ did not interfere in the detection of acetic acid as described.

2.4. Equilibrium measurements

The acid dissociation constant, K_a of pyruvic acid was measured using a Titrino Autotitrator (Metrohm, 736 GP) at (25.0 ± 0.1) °C by pH-metric titration of 15.0 mL of 1.0 mM solution of the acid with standard carbonate free NaOH at 1.0 M $NaNO_3$ solution both in H_2O and in 95% D_2O media.

3. Results and discussion

3.1. Stoichiometry and reaction products

Absorbance measurements at 510 nm established the quantitative (twice that of $[Fe^{III}{}_2]$) formation of ferroin, $[Fe(phen)_3]^{2+}$. The presence of acetic acid in the product solution was confirmed by the $La(NO_3)_3/I_2$ test [55]. These observations lead to the stoichiometric relation shown in Eq. (1):

$$\left[Fe^{III}_2(\mu-O)(phen)_4(H_2O)_4\right]^{4+} + CH_3COCO_2H + 2phen \rightarrow 2[Fe(phen)_3]^{2+} + CO_2 + CH_3CO_2H + 2H_2O \quad (1)$$

3.2. Equilibrium measurements

Results of at least 10 independent determinations of pK_a of pyruvic acid yielded values of 2.50 in H_2O and 2.75 in 95% D_2O, respectively, at 25.0 °C and at I = 1.0 M ($NaNO_3$). The associated experimental uncertainty is well within 0.1 pK_a units. These acidity values are in good agreement with literature values [40,45].

3.3. Kinetics

No immediate spectral change was observed on mixing pyruvic acid with **1** over the entire range of experimental pH and T_R. Because of slow self-decomposition of **1** in the presence of excess phen, parallel blanks were performed for each set of conditions and the absorbance (at 510 nm) *versus* time data were adjusted accordingly. After adjustment, plots of $\log_{10}(A_\mu - A_t)$ *versus* time proved to be linear through at least four half-lives ($r^2 \geqslant 0.98$) in both H_2O and in D_2O media and the *pseudo*-first-order rate constants, k_0, were evaluated from the slopes of these linear plots. Averages of k_0 values from at least three independent runs were taken and the average coefficient of variation (CV) for these measurements were well within 3%. Some representative k_0 values are displayed in Table 1.

Table 1
Some representative first-order rate constants for the oxidation of pyruvic acid by the dinuclear iron(III,III) complex[a], T = 25.0 °C, I = 1.0 M ($NaNO_3$).

pH	T_R (M)	C_{phen}, (mM)	10^5 k_0 (s^{-1})	CV in %[b]
2.58	0.02	3	46	2.5
3.05	0.02	3	62	2.6
3.45	0.02	3	53	2.8
3.93	0.02	3	38	2.8
4.42	0.02	3	15	2.7
4.96	0.02	3	4.2	2.9
5.5	0.02	3	0.9	2.6
4.49	0.005	3	3.2	2.8
4.52	0.01	3	5.9	2.5
4.52	0.04	3	24	2.6
4.94	0.02	3	6.5[c]	2.9
4.98	0.02	3	9.0[d]	2.7
3.95	0.02	3	38[e]	2.6
4.01	0.02	6	37	2.6
2.98	0.02	5	62[f]	2.9
4.53	0.01	3	4.6[g]	2.9
4.51	0.02	3	12[h]	2.8

[a] $[Fe^{III}{}_2]$ = 0.05 mM unless otherwise stated.
[b] CV was measured using the relation: CV = sd × 100/x, where sd = standard deviation of the measurements of k_0 and x = average k_0.
[c] At I = 0.50 M ($NaNO_3$).
[d] At I = 0.10 M ($NaNO_3$).
[e] 0.20 mM $[Fe(phen)_3]^{2+}$ added.
[f] $[Fe^{III}{}_2]$ = 0.025 mM.
[g] At I = 1.0 M (0.50 M ($NaNO_3$) + 0.50 M (NaCl)).
[h] At I = 1.0 M (0.50 M ($NaNO_3$) + 0.50 M (NaBr)).

The k_0 values remain unchanged when the reactions were carried out with varied complex concentration (0.025–0.1 mM), in presence of added phen (3.0–10.0 mM) and at different monitoring wavelengths in the region 440–530 nm. The presence of excess phen (pK_a of $Hphen^+$ = 5.12 and of H_2phen^{2+} = 1.9 [56]) and pyruvic acid (pK_a = 2.5) controls any pH drift during the reactions well within 0.05 units. Use of excess phen also ensured quantitative formation of the tris(phenanthroline) product $[Fe(phen)_3]^{3+}$ and $[Fe(phen)_3]^{2+}$ from any transient bis intermediate. The presence or absence of dissolved oxygen did not alter the observed rate significantly (within 5%).

The variation of k_0 with pH in the range 2.58 < pH < 5.50, is shown in Fig. 2. The rate increases at first as pyruvic acid is deprotonated above its pK_a. This substantiates a common observation that deprotonated reductants react faster than their protonated forms [33–37,57]. The reduction in rate beyond pH 3 can be attributed to the conversion of the fully protonated complex, **1** to the less reactive deprotonated **2** and **3** (pK_{a1} and pK_{a2} of **1** are 3.71 ± 0.05 and 5.28 ± 0.10, respectively under our conditions [33]) and this more than compensates for the higher reactivity of Py^-, which is already over 75% of T_R at pH 3. Deprotonated metal

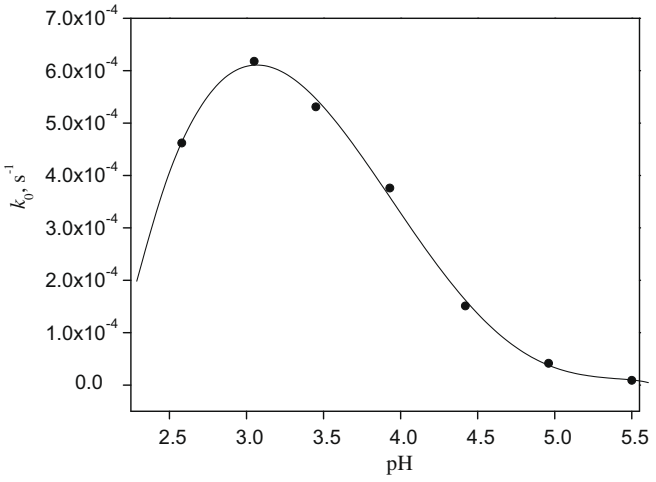


Fig. 2. Plot of k_0 (s^{-1}) *vs.* pH at $[Fe^{III}{}_2]$ = 0.05 mM, T_R = 0.02 M, C_{phen} = 3.0 mM, T = 25.0 °C, I = 1.0 M ($NaNO_3$). The solid line represents the fit of Eq. (9).

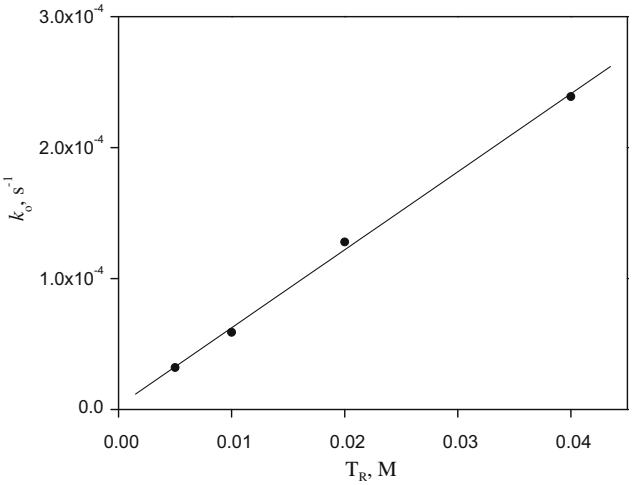


Fig. 3. Plot of k_0 (s^{-1}) *vs.* T_R at $[Fe^{III}{}_2]$ = 0.05 mM, pH 4.5, C_{phen} = 3.0 mM, T = 25.0 °C, I = 1.0 M ($NaNO_3$).

complexes are generally less reactive than their conjugate acids [33,35,37,38,45]. Ionic strength had a noticeable effect on the observed rate – the k_0 values increase at lower ionic strength. This is as expected for reaction between the positively charged metal complex and negatively charged pyruvate ion. [58,59]. The k_0 values were found to increase linearly with T_R at a particular acidity

$$[Fe^{III}{}_2(\mu\text{-}O)(phen)_4(H_2O)_2]^{4+} \underset{pK_{a1} = 3.71}{\overset{K_{a1}}{\rightleftharpoons}} [Fe^{III}{}_2(\mu\text{-}O)(phen)_4(H_2O)(OH)]^{3+} + H^+ \quad (2)$$
(**1**) (**2**)

$$[Fe^{III}{}_2(\mu\text{-}O)(phen)_4(H_2O)(OH)]^{3+} \underset{pK_{a2} = 5.28}{\overset{K_{a2}}{\rightleftharpoons}} [Fe^{III}{}_2(\mu\text{-}O)(phen)_4(OH)_2]^{2+} + H^+ \quad (3)$$
(**2**) (**3**)

$$HPy \overset{K_a}{\rightleftharpoons} H^+ + Py^- \qquad pK_a = 2.5 \quad (4)$$

$$\mathbf{1} + Py^- \xrightarrow{k_1} \text{Products} \quad (5)$$

$$\mathbf{2} + Py^- \xrightarrow{k_2} \text{Products} \quad (6)$$

$$\mathbf{3} + Py^- \xrightarrow{k_3} \text{Products} \quad (7)$$

Scheme 1.

(Fig. 3) suggesting the absence of stoichiometrically significant amounts of adduct formation between the Fe^{III}_2 dimer and Py^- (*vide infra*).

Scheme 1 (Eqs. (2)–(7)) defines a general sequence for the redox reaction where HPy has not been included owing to its low pK_a and (expected) non-reactivity.

Defining the rate as in Eq. (8), Scheme 1 leads to the relation given in Eq. (9):

$$\text{Rate} = -\mathrm{d}[Fe_2^{III,III}]/\mathrm{dt} = k_d[Fe_2^{III,III}] = +1/2\,\mathrm{d}[Fe(phen)_3]/\mathrm{dt} \quad (8)$$

$$k_d[H^+]^2/(T_R\alpha_1\alpha_2) = k_1[H^+]^2 + k_2K_{a1}[H^+] + k_3K_{a1}K_{a2} \quad (9)$$

where k_d is the derived *pseudo*-first-order rate constant, α_1 is the fraction of the total iron complex present as **1** and α_2 is the fraction of total pyruvic acid present as Py^-.

A fit of the observed first-order rate data to Eq. (9) indicates that the third term is negligible; *i.e.* the deprotonated complex, **3**, does not contribute to the reaction under our conditions. The excellent fit (solid line in Fig. 2) also justifies the assumption that HPy is not involved in the redox. Noting that the observed rate is twice that defined by Eq. (8), we may now reformulate the reaction in terms of the formation of the iron(II) product (Scheme 2).

Eq. (9) now reduces to Eq. (12), written in terms of the *pseudo*-first-order observed rate constant, k_0 and the two constants represented in Scheme 2.

$$k_0[H^+]/(T_R\alpha_1\alpha_2) = k_1'[H^+] + k_2'/K_{a1} \quad (12)$$

The best fit of the experimental k_0 values leads to k_1' and k_2' (in $M^{-1}\,s^{-1}$) of 4.7 (±0.2) × 10^{-2} and 3.5 (±0.1) × 10^{-4}, respectively. Since the rate of $[Fe(phen)_3]^{2+}$ formation is twice that of dimer disappearance, these values are twice those of the corresponding parameters of Eq. (9). They are listed in Table 2 for both H_2O and 95% D_2O solutions.

It is well-established that hydration of α-oxo acids and their anions form the respective gem diols [60–69], and the extent of hydration is higher for the free acid forms than their respective anions, the pyruvate anion being the least hydrated. However potential influences that could affect the rate like keto-enol tautomeric equilibria [70,71], dimerisation equilibria [72,73] and polymerization of pyruvate [74,75] are negligible at the low concentrations of pyruvic acid used in this study [60–71].

4. Mechanism

The observed order for the second order rate constants, $k_1 > k_2 \gg k_3$ clearly demonstrates the increased reactivity of protonated oxidants over their conjugate bases. This trend is common for reactions of the title complex, **1**, [31–38] as well as other metal ion complexes [76–80]. While there are examples of hydrated α-oxo-acids with higher reactivity than their (hydrated) conjugate bases [41,42,45,46], a greater reducing power of deprotonated reductants is a common phenomenon [33–37,57] including in pyruvate chemistry [45,81]. Although we were unable to work below the pK_a of pyruvic acid, our observation that pyruvate anion is the more reactive species is consistent with other studies [45,81].

Table 2
Second order rate constants[a] (in $M^{-1}\,s^{-1}$) for the oxidation of pyruvic acid by the dinuclear iron(III,III) complex at T = 25.0 °C, I = 1.0 M ($NaNO_3$), C_{phen} = 3.0 mM.

Reaction path	Rate constant (in H_2O)	Rate constant (in 95% D_2O)
k_1'	(4.7 ± 0.2) × 10^{-2}	(1.8 ± 0.1) × 10^{-2}
k_2'	(3.5 ± 0.1) × 10^{-4}	(1.7 ± 0.1) × 10^{-5}

[a] These values are for Fe(II) formation and are therefore equal to twice the rate constants for dimer disappearance as shown in Eq. (9).

An inner-sphere binding of pyruvic acid with trivalent [82,83] as well as with divalent [84,85] metal centers has been reported to occur with formation constants lying in the range 10^1–10^2. The absence of a more complex [Py^-] term leads to the conclusion that there is no significant pre-equilibrium between the reactants in our system. Hence, we estimate a maximum value for the pre-equilibrium constant (K_i) around 1 M^{-1} holding the inequality $K_i[Py^-] \ll 1$ with no obvious lower limit. Inner-sphere replacement of iron(III)-bound H_2O by Py^-, while weak at best still appears to be involved in the initial process leading to overall redox. The rate retardation in the presence of Cl^- (Table 1) is likely due to a competitive process where non-reducing chloride, present in heavy excess, competes with Py^- for adduct formation. It is well-documented that solutions of $[L_4Cl_2(\mu\text{-}O)Fe^{III}_2]^{4+}$ [85] rapidly aquate to generate $[L_4(H_2O)_2(\mu\text{-}O)Fe^{III}_2]^{4+}$ and also instantaneously produce $[L_4(SCN)_2(\mu\text{-}O)Fe^{III}_2]^{2+}$ upon addition of KSCN (L = 2,2′-bipyridine or phen) [86,87]. These observations clearly demonstrate the labile nature of the monodentate ligands, *viz.* Cl^- and H_2O bound to each d^5 high-spin Fe^{III} center. Although substitution at low-spin d^5 iron(III) is slow, d^5 high-spin species are labile to substitution [88]. Thus the formation of a weak oxidant–pyruvate complex by the substitution of labile H_2O molecules prior to electron transfer is a distinct possibility.

The much lower reactivity of the deprotonated complexes **2** and (apparently non-reactive) **3** seems justified for several reasons. Inner-sphere adduct formation, prior to electron transfer, is less favorable for **2** than that for **1** due to decreased number of water molecules present (one *versus* two). Not only should **1** form an adduct more easily, but it should also dominate kinetically since the iron centers in **1** are the most electron deficient due to the charge effects and back-donation from the π electrons of the hydroxide ligands in **2**. It has been noted that in most redox systems involving cationic complexes protonation of the oxidant increases the reactivity [31–38,76–80]. The presence of $Fe^{III} \leftarrow OH$ π-bonding also reduces lability, thus inhibiting metal–pyruvate interaction. Although π interactions cause an increase in water exchange rate for the high-spin d^5 Fe(III) center of $[Fe(H_2O)_5(OH)]^{2+}$ ($1.2 \times 10^5\ s^{-1}$) over $[Fe(H_2O)_6]^{3+}$ ($1.6 \times 10^2\ s^{-1}$) [88], this is a *trans*-effect and cannot apply to the first step of the present system since there are no labile ligands *trans* to the hydroxide. The absence of any labile water in **3** would further inhibit ligand replacement, thus adding credence to the postulation of an inner-sphere mechanism with pre-equilibrium adduct formation between the diiron(III,III) complex and pyruvate.

The overall two electron redox is expected to occur in steps where the initial one-electron transfer (Eq. (12)) is proposed to be the rate-determining step and the subsequent steps are kinetically silent.

$$1/2\ \mathbf{1} + 1/2\ Py^- \xrightarrow{k_1'} [Fe(phen)_3]^{2+} + \text{oxidation products} \quad (10)$$

$$1/2\ \mathbf{2} + 1/2\ Py^- \xrightarrow{k_2'} [Fe(phen)_3]^{2+} + \text{oxidation products} \quad (11)$$

Scheme 2.

$$Fe^{III}—O—Fe^{III} + Py^{-} \underset{slow}{\overset{k}{\rightarrow}} Fe^{III}—O—Fe^{II} + Py^{\cdot} \quad (13)$$

Generation of pyruvate radical during oxidation of pyruvic acid has been reported elsewhere [40,44,45].

The Fe^{III}–O–Fe^{III} linkage in the title oxidant is stable. The $\{Fe_2O\}^{4+}$ core unit gains stability from the super-exchange of the two high-spin d^5 metal centers linked by an oxo-bridge [89,90]. However, after redox, the $\{Fe_2O\}^{3+}$ product would be less strongly bound to the oxygen since antibonding electrons in both oxidation states are directed towards the formal bond axes. This would impart weaker Fe^{III}–O–Fe^{II} and Fe^{II}–O–Fe^{II} bonds, both of which should be rapidly broken by aquation or further (rapid) reaction with the pyruvate radical produced in (13). In fact, the oxo-bridge in the mixed-valent system is persistent only with a limited number of stabilizing ligands [2,91–93]. Thus, we propose that the Fe^{III}–O–Fe^{II} dimer formed in the rate-determining step instantaneously collapses either by aquation to Fe(II) and Fe(III) monomers or by further reduction to Fe(II) monomers. If formed, the iron(III) monomer, $[Fe(phen)_2(H_2O)_2]^{3+}$ is further reduced to iron(II) monomer with complexation by a third phen ligand either before or after reduction [94,95]. The pyruvate radical formed in the rate-determining step (Eq. (13)) could reduce Fe(III) monomers rapidly, or this reduction could involve Py^{-}. In separate experiments, we have verified that $[Fe(phen)_3]^{3+}$ is almost instantaneously reduced to ferroin by pyruvic acid, used in concentrations comparable to that in our study. $[Fe(phen)_2(H_2O)_2]^{3+}$ is expected to react even faster. Moreover, we observed that the reaction studied in 6% (*v*/*v*) acrylonitrile showed polymerization confirming the involvement of radicals in the reaction.

There are reports in the literature where the intermediate mixed valence $Fe^{III,II}{}_2$ form generated by one-electron reduction of $[(trispicMeen)ClFe^{III}OFe^{III}Cl(trispicMeen)]^{2+}$ (trispicMeen = N,N,N′-tris(2-pyridylmethyl)-N′-methylethane-1,2-diamine) and in $[(MeTACN)_2Fe_2(OH)(RCO_2)_2]^{2+}$ (TACN = 1,4,7-triazacyclononane) slowly (within one hour) disproportionate to a mixture of $Fe^{III}{}_2$ and $Fe^{II}{}_2$ forms [96,97]. Also, it was nicely demonstrated that the mixed-valent $Fe^{III,II}{}_2$ (semi-met) produced at the first phase of the overall three-phase reduction of the binuclear iron(III,III) active sites in the octameric metHr from *Themiste zostericola* by several one-equivalent cobalt(II) and chromium(II) reagents disproportionates to $Fe^{III,III}{}_2$ and $Fe^{II,II}{}_2$ within minutes by intramolecular electron transfer [98]. Although we did not observe any deviations from first-order behavior in our experiments, which had half-lives from about 20 min to several hours, we cannot rule out disproportionation of mixed-valent $Fe^{II}Fe^{III}$ intermediates which could be occurring without affecting the kinetic determinations.

The basicity of the oxo-bridge is expected to increase tremendously in the one-electron reduced iron dimer, $\{Fe^{II}–O–Fe^{III}\}^{3+}$, in comparison to the oxo-bridge in $\{Fe^{III}–O–Fe^{III}\}^{4+}$ as the one-unit positive charge reduction favors immediate uptake of a proton from the solvent. Such differences in basicities of the oxo-bridges in di- or multinuclear higher valent Mn complexes are well-established [99,100] and are key feature in redox steps of the Kok cycle in Photosystem II [101,102]. The possibility of protonation of the oxo-bridge in **1** is ruled out under our kinetic conditions as during its synthesis (*vide supra*), pH as low as ~1.9 is inherently maintained. We find that the available evidence on hemerythrin [103,104] argue against protonation of the oxo-bridge in the one-electron reduction of the diferric site in methemerytrin. Protonation of the oxo-bridge after one-electron reduction could reduce thermodynamic and/or kinetic barriers to further reduction [105]. Proton coupled electron transfer is the basic mechanism for the bioenergetic redox conversions in proteins [106–111]. Protonation of $\{Fe_2O\}^{3+}$ (Eq. (13)) thus remains an essential step in the overall reaction; reactions shown in Eqs. (14)–(16) are fast and kinetically silent

$$\{Fe^{II}—O—Fe^{III}\}^{3+} + H^{+} \rightleftharpoons \{Fe^{II}—\underset{H}{O}—Fe^{III}\}^{4+} \quad (14)$$

$$\{Fe^{II}—\underset{H}{O}—Fe^{III}\}^{4+} \overset{red}{\rightarrow} 2Fe^{II} \quad (15)$$

$$Fe^{II} \overset{phen}{\rightarrow} [Fe(phen)_3]^{2+} \quad (16)$$

In order to collect further information on the proposed mechanism involving the possible involvement of proton coupled electron transfer as described in steps (13) and (14), we performed several kinetic runs in aqueous media partially substituted with D_2O and found a detectable lowering in rate. All the calculations in D_2O media were done using $pK_{a1} = 3.92 \pm 0.10$, $pK_{a2} = 5.36 \pm 0.10$, for complex **1** measured in D_2O [33]. Variations in rate resulting from substitution of D_2O for solvent H_2O are expected to be slight for simple electron transfer reactions but substantial rate retardation is expected when such transfer is coupled with the movement of protons that are in equilibrium with solvent protons [77,112]. A plot of k_0 *versus* mole fraction of D_2O for these experiments is linear (Fig. 4, $r > 0.98$). The linearity of the plot is indicative of the transfer of a single proton in the rate-determining step of the redox process [113]. This relationship is mechanistically reminiscent of the results for the deoxygenation process of the oxygen binding to hemerythrin [114]. We are thus able to state that simultaneous electron/proton transfer is a thermodynamic driving force for the title redox. Additionally, exceptional stability of low-spin $[Fe(phen)_3]^{2+}$ formed as the sole iron product in presence of excess phen also encourages the reaction to completion.

The second order rate constants were also determined in 95% D_2O media and compared with those in H_2O (Table 2). The observed difference in kinetic isotope effect is seen to be prominent at higher pH (k_2 path is much more affected than k_1). The hydroxo ligand is much more basic than H_2O and makes the iron centers less electron accepting thus increasing the basicity of the oxo-bridges in the order **3** > **2** > **1**. A similar trend in isotope effect was also observed in the reduction of $[Mn^{IV}_2(\mu\text{-}O)_2(\mu\text{-}MeCO_2)(bipy)_2(H_2O)_2]^{3+}$ ($MeCO_2H$ = acetic acid, bipy = 2,2′-bipyridine) and its hydrolytic derivatives with hydroxylamine [47].

In conclusion, we find substantial differences in the reactivities of **1**, **2** and **3** towards pyruvate. There is no evidence for involvement of fully deprotonated complex, **3**, in the pH range studied.

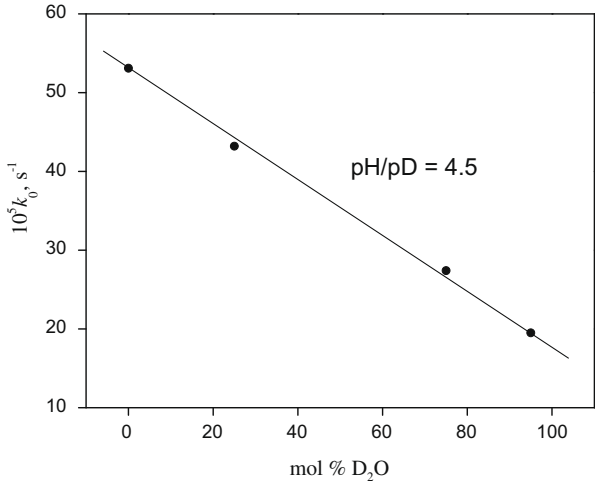


Fig. 4. Effect of mole% D_2O on k_0 (s^{-1}) at [complex] = 0.05 mM, T_R = 0.02 M, C_{phen} = 3.0 mM, T = 25.0 °C, I = 1.0 M ($NaNO_3$).

The kinetic isotope effect is particularly prominent in the k_2 path where the basicity of the oxo-bridge of the one-electron reduced dimer, *viz.* $[(phen)_2(H_2O)Fe^{III}OFe^{II}(phen)_2(OH)]^{2+}$ is higher than that of $[(phen)_2(H_2O)Fe^{III}OFe^{II}(phen)_2(H_2O)]^{3+}$. This clearly demonstrates that oxo-bridge protonation is important in the proposed mechanism.

Only acetic acid and CO_2 were found as oxidation products. Initial decarboxylation to acetaldehyde can be ruled out here because further oxidation would be expected to produce a mixture of formic and acetic acids [115,116]. Furthermore, separate experiments have shown that acetaldehyde reacts too slowly with the title diiron complex to account for the production of acetic acid.

Acknowledgement

Financial support of this work from the Council of Scientific and Industrial Research (CSIR, New Delhi; Grant Number: 01(2182)/07/EMR-II) is thankfully acknowledged.

References

[1] P.C. Wilkins, R.G. Wilkins, Coord. Chem. Rev. 79 (1987) 195.
[2] R.E. Stenkamp, Chem. Rev. 94 (1994) 715.
[3] E.Y. Tshuiva, S.J. Lippard, Chem. Rev. 104 (2004) 987.
[4] S.V. Kryatov, E.V. Rybak-Akimova, Chem. Rev. 105 (2005) 2175.
[5] T. Klabunde, B. Crebs, Struct. Bond. 89 (1997) 177.
[6] A. Jordan, P. Reichard, Annu. Rev. Biochem. 67 (1998) 71.
[7] L.W. Guddat, A.S. McAlpine, D. Hume, S. Hamilton, J. de Jersey, J.L. Martin, Structure 7 (1999) 757.
[8] M.P. Woodland, H. Dalton, J. Biol. Chem. 259 (1984) 53.
[9] A.C. Rosenzweig, C.A. Frederick, S.J. Lippard, P. Nordland, Nature 366 (1993) 537.
[10] M. Merkx, D.A. Kopp, M.H. Sazinsky, J.L. Blazyk, J. Miiler, S.J. Lippard, Angew. Chem., Int. Ed. 40 (2001) 4000.
[11] E.C. Theil, Annu. Rev. Biochem. 56 (1987) 289.
[12] P.D. Hempstead, A.J. Hudson, P.J. Artymiuk, S.C. Andrews, M.J. Banfield, J.R. Guest, P.M. Harrison, FEBS Lett. 350 (1994) 258.
[13] Z. Gdaniec, G.H. Sierzputowska, E.C. Theil, Biochemistry 38 (1999) 5676.
[14] J.D. Pikus, J.M. Studts, C. Achim, K.E. Kauffmann, E. Münck, R.J. Steffan, K. McClay, B.G. Fox, Biochemistry 35 (1996) 9106.
[15] J. Shanklin, E. Whittle, B.G. Fox, Biochemistry 33 (1994) 12787.
[16] F. Bonomi, D.M. Kurtz Jr., X. Cui, J. Bioinorg. Chem. 1 (1996) 67.
[17] F. de maré, D.M. Kurtz Jr., P. Nordland, Nat. Struct. Biol. 1 (1996) 453.
[18] S. Jin, D.M. Kurtz Jr., Z.-J. Liu, J. Rose, B.-C. Wang, J. Am. Chem. Soc. 124 (2002) 9845.
[19] D.M. Kurtz Jr., Chem. Rev. 90 (1990) 585.
[20] M. Costas, K. Chen, L. Que Jr., Coord. Chem. Rev. 200–202 (2000) 517.
[21] J.E. Plowman, T.M. Loehr, C.K. Schauer, O.P. Anderson, Inorg. Chem. 23 (1984) 3553.
[22] C. Duboc-Toia, S. Ménage, J.-M. Vincent, M.-T. Averbuch-Pouchot, M. Fontecave, Inorg. Chem. 36 (1997) 6148.
[23] A.G.J. Lightenbarg, P. Oosting, G. Royelfes, R.M. La Crois, M. Lutz, A.L. Spek, R. Hage, B.L. Feringa, Chem. Commun. (2001) 385.
[24] C. Stadler, J. Daub, J. Kohler, R.W. Saalfrank, V. Coropceanu, V. Schunemann, C. Ober, A.X. Trautwein, S.F. Parker, M. Poyraz, T. Inomata, R.D. Cannon, J. Chem. Soc., Dalton Trans. (2001) 3373.
[25] D. Lee, S.J. Lippard, J. Am. Chem. Soc. 123 (2001) 4611.
[26] F. Verge, C. Lebrun, M. Fontecave, S. Mënage, Inorg. Chem. 42 (2003) 499.
[27] R.F. Moreira, E.Y. Tshuva, S.J. Lippard, Inorg. Chem. 43 (2004) 4427.
[28] S.V. Kryatov, S. Taktak, I.V. Korendovych, E.V. Rybak-Akimova, J. Kaizer, S. Torelli, X. Shan, S. Mandal, V.L. MacMurdo, A. Payeras, L. Que Jr., Inorg. Chem. 44 (2005) 85.
[29] A. Ghosh, F.T. de Oliveira, T. Yano, T. Nishioka, E.S. Beach, I. Kinoshita, E. Münck, A.D. Ryabov, C.P. Horwitz, T.J. Collins, J. Am. Chem. Soc. 127 (2005) 2505.
[30] F. Lee, M. Wang, C. Ma, A. Gao, H. Chen, L. Sun, Dalton Trans. (2006) 2427.
[31] B. Chaudhuri, R. Banerjee, Can. J. Chem. 76 (1998) 350.
[32] B. Chaudhuri, R. Banerjee, J. Chem. Soc., Dalton Trans. (1998) 3451.
[33] J. Bhattacharyya, K. Dutta, S. Mukhopadhyay, Dalton Trans. (2004) 2910.
[34] J. Bhattacharyya, S. Mukhopadhyay, Helv. Chim. Acta 88 (2005) 2661.
[35] J. Bhattacharyya, S. Mukhopadhyay, Transition Met. Chem. 31 (2006) 256.
[36] R. Mukherjee, B.B. Dhar, R. Banerjee, S. Mukhopadhyay, J. Coord. Chem. 59 (2006) 1157.
[37] J. Bhattacharyya, S. Das, S. Mukhopadhyay, Dalton Trans. (2007) 1214.
[38] S. Das, J. Bhattacharyya, S. Mukhopadhyay, Dalton Trans. (2008) 6634.
[39] C.K. Mathews, K.E. VanHolde, Biochemistry, 2nd ed., Benjamin Cummings, Publ. Co., Menlo Park, CA, 1956. pp. 482 ff.
[40] A. Das, S. Mukhopadhyay, Transition Met. Chem. 29 (2004) 797.
[41] K.K. Sengupta, T. Sarkar, Tetrahedron 31 (1975) 123.
[42] K.K. Sengupta, H.R. Chatterjee, Inorg. Chem. 17 (1978) 2429.
[43] R. Panda, C. Patnaik, Bull. Korean Chem. Soc. 22 (2001) 909.
[44] B.B. Dhar, R. Mukherjee, S. Mukhopadhyay, R. Banerjee, Eur. J. Inorg. Chem. (2004) 4584.
[45] S. Das, J. Bhattacharyya, S. Mukhopadhyay, Helv. Chim. Acta 89 (2006) 1947.
[46] S. Das, G.S. Chaubey, M.K. Mahanti, Kinet. Catal. 43 (2002) 794.
[47] S. Banerjee, U. Roy Choudhury, R. Banerjee, S. Mukhopadhyay, J. Chem. Soc., Dalton Trans. (2002) 2047.
[48] M.L. Moss, M.G. Mellon, G.F. Smith, Ind. Eng. Chem., Anal. Ed. 14 (1942) 931.
[49] G. Nord, B. Pedersen, E. Bjergbakke, J. Am. Chem. Soc. 105 (1983) 1913.
[50] S. Banerjee, U. Roy Choudhury, B.C. Ray, R. Banerjee, S. Mukhopadhyay, Anal. Lett. 34 (2001) 2797.
[51] H.M. Irving, M.G. Miles, L.D. Pettit, Anal. Chim. Acta 38 (1967) 475.
[52] P.K. Glasoe, F.A. Long, J. Phys. Chem. 64 (1960) 188.
[53] P. Salomaa, L.L. Schaleger, F.A. Long, J. Am. Chem. Soc. 86 (1964) 1.
[54] K. Dutta, S. Bhattacharjee, B. Choudhuri, S. Mukhopadhyay, J. Environ. Monit. 4 (2002) 754.
[55] F. Feigl, Spot Test in Organic Analysis, 5th ed., Elsevier, London, 1956. pp. 340–342.
[56] R.M. Smith, A.E. Martell, Critical Stability Constants, vol. 2, Plenum Press, New York, 1975. p. 251.
[57] D. Ghosh, A.D. Shukla, R. Banerjee, A. Das, J. Chem. Soc., Dalton Trans. (2002) 1220.
[58] K.J. Laidler, Chemical Kinetics, 3rd ed., Harper and Row, New York, NY, 1987. pp. 197–201.
[59] J.N. Butler, Ionic Equilibrium: Solubility and pH Calculations, Wiley-Interscience, New York, NY, 1998 (Chapter 2).
[60] H. Strehlow, Z. Elektrochem. 66 (1962) 392.
[61] Y.I. Tur'yan, Croat. Chem. Acta 71 (1998) 727.
[62] P.E. Sorensen, K. Bruhn, F. Lindelov, Acta Chem. Scand. A28 (1974) 162.
[63] J. Kuta, P. Valenta, Collect. Czech. Chem. Commun. 28 (1963) 1593.
[64] A.R. Rendina, J.D. Hermes, W.W. Cleland, Biochemistry 23 (1984) 5148.
[65] M.-L. Ahrens, Ber. Bunsen. Phys. Chem. 72 (1968) 691.
[66] Y.I. Tur'yan, Croat. Chem. Acta 72 (1999) 13.
[67] M. Xie, A. Feng, Huaxue Tongbao 10 (1986) 40.
[68] H. Patting, H. Strehlow, Ber. Bunsen. Phys. Chem. 73 (1969) 534.
[69] J. Damitio, G. Smith, J.E. Meany, Y. Pocker, J. Am. Chem. Soc. 114 (1992) 3081.
[70] Y. Chiang, A.J. Kresge, P. Pruszynski, J. Am. Chem. Soc. 114 (1992) 3103.
[71] J.A. Kresge, Pure Appl. Chem. 63 (1991) 213.
[72] L. Bracza, K. Michalyi, Z. Phys. Chem. 104 (1977) 213.
[73] L. Bracza, K. Michalyi, Z. Phys. Chem. 104 (1977) 189.
[74] D. Leussing, C.K. Stanfield, J. Am. Chem. Soc. 86 (1964) 2805.
[75] O.H. Muller, J.P. Baumberger, J. Am. Chem. Soc. 61 (1939) 590.
[76] K.D. Asmus, M. Bonifacic, P. Toffel, P. O'Neill, D.S. Frohlinde, S. Steenken, J. Chem. Soc., Faraday Trans. 1 (1978) 1820.
[77] S.K. Ghosh, R.N. Bose, E.S. Gould, Inorg. Chem. 26 (1987) 2688.
[78] E.C. Constable, Metals and Ligand Reactivity, Ellis Horwood, Chichester, UK, 1990.
[79] S. Mukhopadhyay, R. Banerjee, J. Chem. Soc., Dalton Trans. (1994) 1349.
[80] P. Bandyopadhyay, B.B. Dhar, J. Bhattacharyya, S. Mukhopadhyay, Eur. J. Inorg. Chem. (2003) 4308.
[81] L. Maros, I. Molnar-Perl, L. Kover, J. Chem. Soc., Perkin Trans. II (1976) 1327.
[82] P. Manikyamba, React. Kinet. Catal. Lett. 78 (2003) 169.
[83] A. Aziz, S.J. Lyle, J.E. Newbery, J. Inorg. Nucl. Chem. 33 (1971) 1757.
[84] D.E. Tallman, D.L. Leussing, J. Am. Chem. Soc. 91 (1969) 6253.
[85] D.L. Leussing, D.C. Shultz, J. Am. Chem. Soc. 86 (1964) 4846.
[86] P.G. David, P.C. de Mello, Inorg. Chem. 12 (1973) 2188.
[87] P.G. David, J. Inorg. Nucl. Chem. 35 (1973) 1463.
[88] R.B. Jordan, Reaction Mechanisms of Inorganic and Organometallic Systems, 2nd ed., Oxford University Press, New York, 1998 (Chapter 3).
[89] G. McLendon, R.J. Motekaitis, A.E. Martell, Inorg. Chem. 15 (1976) 2306.
[90] P. Chaudhuri, K. Wieghardt, B. Nuber, J. Weiss, Angew. Chem., Int. Ed. Engl. 24 (1985) 778.
[91] F. Arena, C. Floriani, A. Chiesi-Villa, C. Guastini, J. Chem. Soc., Chem. Commun. (1986) 1369.
[92] S. Zhang, R.E. Shepherd, Inorg. Chem. 33 (1994) 5262.
[93] S. Yoon, S.J. Lippard, Inorg. Chem. 42 (2003) 8606.
[94] T.S. Lee, I.M. Kolthoff, D.L. Leussing, J. Am. Chem. Soc. 70 (1948) 3596.
[95] J.C. Thompsen, H.A. Mottola, Anal. Chem. 56 (1984) 755.
[96] A.L. Nivorozhkin, E.A. Anxolabére-Mallart, P. Mialane, R. Davydov, J. Guilhem, M. Cesario, J.-P. Audiére, J.-J. Girerd, S. Styring, L. Schussler, J.-L. Seris, Inorg. Chem. 36 (1997) 846.
[97] U. Bossek, H. Hummel, T. Weyhermüller, E. Bill, K. Wieghardt, Angew. Chem., Int. Ed. Engl. 34 (1995) 2642.
[98] J.D. Armstrong, T. Ramasami, A.G. Sykes, Inorg. Chem. 24 (1985) 3230.
[99] M.J. Baldwin, V.L. Pecoraro, J. Am. Chem. Soc. 118 (1996) 11325.
[100] J.S. Vrettos, J. Limburg, G.W. Brudvig, Biochim. Biophys. Acta 150 (2001) 229.
[101] G. Renger, Biochim. Biophys. Acta 1655 (2004) 195.
[102] S. Mukhopadhyay, S.K. Mandal, S. Bhaduri, W.H. Armstrong, Chem. Rev. 104 (2004) 3981.
[103] M.J. Maroney, R.C. Scarrow, L. Que Jr., A.L. Roe, G.S. Lukat, D.M. Kurtz Jr., Inorg. Chem. 28 (1989) 1342.

[104] L.D. Pearce, D.M. Kurtz Jr., Y-M. Xia, P.G. Debrunner, J. Am. Chem. Soc. 109 (1987) 7286.
[105] S. Ménage, J.M. Vincent, C. Lambeaux, G. Chottard, A. Grand, M. Fontecave, Inorg. Chem. 32 (1993) 4766.
[106] C.C. Page, C.C. Mosar, X. Chen, P.L. Duttan, Nature 402 (1999) 47.
[107] J. Stubbe, D.G. Nocera, C.S. Yee, M.C.Y. Chang, Chem. Rev. 103 (2003) 2167.
[108] J.M. Mayer, I.J. Rhile, Biochim. Biophys. Acta 1665 (2004) 51.
[109] J.M. Mayer, Annu. Rev. Phys. Chem. 55 (2004) 363.
[110] A.R. Crofts, Annu. Rev. Physiol. 66 (2004) 689.
[111] M. Sjödin, S. Styring, H. Wolpher, Y. Xu, L. Sun, L. Hammarström, J. Am. Chem. Soc. 127 (2005) 3855.
[112] W.H. Albery, in: E. Caldin, V. Gold (Eds.), Proton Transfer Reactions, Wiley, New York, 1975 (Chapter 9).
[113] W.J. Albery, M.H. Davis, J. Chem. Soc., Faraday Trans. 1 (68) (1972) 167.
[114] J.D. Armstrong, A.G. Sykes, Inorg. Chem. 25 (1986) 3135.
[115] J. Shorter, C.N. Hinshelwood, J. Chem. Soc. (1950) 3276.
[116] J. Shorter, J. Chem. Soc. (1950) 3425.

Polyhedron 28 (2009) 3169–3170

Contents lists available at ScienceDirect

Polyhedron

journal homepage: www.elsevier.com/locate/poly

Preface



Dr. Aris Terzis

It is a great pleasure for us to see the completion of this special issue of *Polyhedron* entitled "The Impact of Crystallography on Inorganic Chemistry in Greece". The idea for this issue came from the recognition that inorganic chemistry research in our country has undergone a renaissance over the last three decades or so, for the obvious reason, of course, that this period has seen significant changes to the Greek chemistry community. Three new Chemistry Departments were founded or developed during this period (at the Universities of Patras, Ioannina and Crete), and all three created strong research programs in inorganic chemistry. Inorganic chemistry was also developed in a brilliant way at several institutes in the National Center of Scientific Research (NCSR) 'Demokritos' and the Hellenic Research Foundation, both located in Athens. Many appointments by the Universities of Athens and Thessaloniki in the 1950's resulted in the partial or full retirement of a large number of academics 20–30 years ago. As a result, new generations of people with their own new research ideas and directions were appointed, and they are currently helping to shape the future of inorganic chemistry in Greece. Another important reason for the progress of inorganic chemistry in Greece has been the access of researchers to the X-ray crystallographic facilities of the NCSR 'Demokritos'. We do believe that the heart and soul of inorganic chemistry is making new molecules, new substances. There is no doubt that when a solid compound has to be identified, there is nothing to beat a single-crystal, X-ray crystal structure determination.

The scientist who undoubtedly pioneered single-crystal X-ray crystallography of small molecules in Greece, and subsequently made available to outside groups the crystallographic facilities of his laboratory at the Institute of Materials Chemistry, NCSR 'Demokritos', is Dr. Aris Terzis, who holds a Ph.D. from Princeton, USA, and who has just retired. He has worked in many aspects of X-ray crystallography his whole professional career, which has been characterized by outstanding levels of creativity, enthusiasm, innovation and sheer quality. His impact on the scientific community goes far beyond just his tremendous publication list in top quality, peer-reviewed journals and the fact that his work supported more than 100 PhD theses in the five Greek Chemistry Departments. Aris had the ability to inspire most Greek synthetic inorganic chemists to greater efforts and patience, often giving smart ideas and suggesting new projects to us. In addition to being a brilliant scientist, Aris is also a most friendly and generous spirited person (but very strict with us when he found himself solving structures of starting materials) with whom it was a privilege for us to be associated closely for the last 25 exciting years. His extremely broad education and sound political ideas also make him a fantastic speaker on topics outside science.

One issue of a journal is a rather limited forum, but nevertheless we have attempted as far as possible to have this special issue of *Polyhedron* reflect the great development of crystallography-based inorganic chemistry in Greece and the great respect that Aris commands throughout the scientific community in our country and internationally. This issue certainly contains contributions from many of the scientists with whom Aris has been collaborating, but there are also a few others who gladly and indeed eagerly

0277-5387/$ - see front matter © 2009 Elsevier Ltd. All rights reserved.
doi:10.1016/j.poly.2009.09.013

accepted our invitation to participate as a means to show their respect for the man and his scientific impact. There is no unifying scientific theme to the issue, other than that the papers contain crystallography and are all dedicated to Aris Terzis. On behalf of all the authors, and indeed the Greek scientific community as a whole, we wish him a happy retirement (he currently works as before!), and many more years of success in his future scientific endeavors.

Last, but not least, we would like to express our gratitude to the Americas Editor of *Polyhedron*, Professor George Christou, for encouraging us to realize this idea and for his great help during the organization of the special issue.

Guest Editors
Catherine P. Raptopoulou
Institute of Materials Science,
NCSR 'Demokritos',
GR-153 10 Aghia Paraskevi Attikis,
Greece
Tel.: +30 210 6503365; fax: +30 210 6519430
E-mail address: craptop@ims.demokritos.gr

Vassilis Psycharis
Institute of Materials Science,
NCSR 'Demokritos',
GR-153 10 Aghia Paraskevi Attikis,
Greece
E-mail address: vpsychar@ims.demokritos.gr

Spyros P. Perlepes
Department of Chemistry,
University of Patras, GR-265 04 Patras,
Greece
E-mail address: perlepes@patreas.upatras.gr

2. Experimental

2.1. Materials and instrumentation

All laboratory chemicals were reagent grade and were used without further purification. Solvents for high-performance liquid chromatography (HPLC) were HPLC-grade. They were filtered through membrane filters (0.22 μm, Millipore, Milford, MA) and degassed by a helium flux before and during use.

IR spectra were recorded as KBr pellets on a Perkin–Elmer 1600 FT-IR spectrophotometer in the region 4000–500 cm^{-1}. The NMR spectra were recorded in D_2O and DMSO-d_6, at 25 °C on a Bruker 500 MHz Avance DRX spectrometer using DSS and $(CH_3)_4Si$ as internal references, respectively. Elemental analyses for C, H and N were conducted on a Perkin–Elmer 2400 automatic elemental analyzer. HPLC analysis was performed on a Waters 600 chromatography system coupled to both a Waters 2487 Dual λ Absorbance detector and a Gabi gamma detector from Raytest. Separations were achieved on a Nucleosil C18 (10 μm, 250 mm × 4 mm) column eluted with a binary gradient system at a 1 mL min^{-1} flow rate. Mobile phase A was methanol containing 0.1% trifluoroacetic acid, while mobile phase B was water containing 0.1% trifluoroacetic acid. The elution gradient was 0 to 1 min 100% B (0% A), followed by a linear gradient to 75% A (25% B) in 9 min; this composition was held for another 10 min. After a column wash with 95% A for 5 min, the column was re-equilibrated by applying the initial conditions (100% B) for 15 min prior to the next injection.

*Chloroacetiminoethylether hydrochloride (**1**), 2-(chloromethyl)-imidazoline hydrochloride (**2**)* and the precursor $[Et_4N][ReBr_3(CO)_3]$ were synthesized according to literature methods [8–10]. $Na^{99m}TcO_4$ was obtained in physiological saline as a commercial $^{99}Mo/^{99m}Tc$ generator eluate (Mallinckrodt Medical B.V., The Netherlands). The radioactive precursor *fac*-$[^{99m}Tc(OH_2)_3(CO)_3]^+$ was prepared using a commercially available IsoLink kit (Malinckrodt), according to the manufacturers.

2.2. Synthesis of the ligands

2.2.1. Synthesis of N1-ethyl-2-(chloromethyl)imidazoline hydrochloride (**3**)

Chloroacetiminoethylether hydrochloride (15.8 g, 0.1 mol) is added slowly at 0 °C to *N*-ethyl-ethylenediamine (8.8 g, 0.1 mol) in absolute ethanol (80 mL). After 1 h, abs ethanol saturated with HCl (50 mL, 3.6 g HCl) is added and the mixture is slowly warmed to room temperature. The NH_4Cl is removed by filtration and the filtrate is concentrated to dryness at reduced pressure. Recrystallization of the residue from hot abs ethanol affords **3**, as colorless crystals. Yield 13.4 g (73%). M.p.: 100 °C. *Anal.* Calc. for $C_6H_{11}N_2Cl.HCl$: C, 39.36; H, 6.61; N, 15.30. Found: C, 39.03; H, 6.95; N, 15.04%. ^1H NMR (D_2O, δ): 4.50 (s, 2H, CH_2Cl), 3.95–3.85 (m, 4H, im), 3.45 (q, 2H, CH_2CH_3), 1.15 (t, 3H, CH_2CH_3). ^{13}C NMR (D_2O, δ): 167.15, 51.89, 45.42, 43.82, 35.54, 14.34.

2.2.2. Synthesis of the ligand 4-(imidazolin-2-yl)-3-thiabutanoic acid (4)

2-(Chloromethyl)imidazoline hydrochloride (3.1 g, 0.02 mol) and sodium hydroxide (powder, 4.05 g, 0.04 mol) are added to thioglycolic acid (1.84 g, 0.02 mol) in 30 mL abs ethanol. This suspension is refluxed for 3 h. The mixture is cooled and the precipitated NaCl is removed by filtration. The ligand precipitated as colourless crystals after concentration of the filtrate. Crystals suitable for X-ray were isolated by re-crystallization from ethanol. Yield 1.20 g (28.6%). M.p.: 135–140 °C. *Anal.* Calc. for $C_6H_{10}N_2O_2S.H_2O$: C, 37.49; H, 6.29; N, 14.57. Found: C, 37.18; H, 6.43; N, 14.29%. IR (KBr, cm^{-1}): 3482, 3385, 3115, 2979, 2907, 2705, 1625, 1556, 1386, 1283, 1231. ^1H NMR (D_2O, δ): 3.60 (s, 6H, im, im-CH_2S–), 3.20 (s, 2H, SCH_2COO).

2.2.3. Synthesis of the ligand 4-(N-ethylimidazolin-2-yl)-3-thiabutanoic acid (**5**)

The compound is prepared in a similar procedure to the one described above for **4**, using *N*1-ethyl-2-(chloromethyl)imidazoline hydrochloride (2.76 g, 0.015 mol), thioglycolic acid (1.38 g, 0.015 mol) and sodium hydroxide (powder, 1.2 g, 0.03 mol) in 30 mL abs ethanol. The mixture is filtered and the filtrate is concentrated to dryness to give yellow oil (2.7 g). The oil is dissolved in ethanol, diethylether is added and the flask is placed in the freezer (−22 °C). The white solid formed is collected by filtration. Yield 1.30 g (36.4%). M.p.: 133.6–135 °C. *Anal.* Calc. for $C_8H_{14}N_2O_2S$: C, 47.50; H, 6.98; N, 13.85. Found: C, 47.16; H, 7.15; N, 13.64%. IR (KBr, cm^{-1}): 2986, 2914, 1661(sh), 1600(br), 1381, 1296, 1233. ^1H NMR (D_2O, δ): 3.95–3.85 (m, 4H, im), 3.65 (s, 2H, im-CH_2S–) 3.50 (q, 2H, CH_2CH_3), 3.28 (s, 2H, SCH_2COO), 1.22 (t, 3H, CH_2CH_3). ^{13}C NMR (D_2O, δ): 178.97 (COO), 168.99, 51.51, 44.96, 43.65, 27.88, 14.31.

2.3. Synthesis of the rhenium complexes 6 and 7

2.3.1. General method

A mixture of the ligand **4** or **5** (0.1 mmol), $[NEt_4]_2[ReBr_3(CO)_3]$ (0.077 g, 0.1 mmol) in acetonitrile (5 mL) and 1 mL 0.1 N NaOH (0.1 mmol) is refluxed for 2 h. Upon standing at room temperature a pale yellowish crystalline product precipitates and is collected by filtration. The product can be re-crystallized from methanol, ethanol and acetonitrile. Crystals suitable for X-ray were isolated by re-crystallization from ethanol.

*Re-Complex **6***: Yield 0.032 g (72.2%). *Anal.* Calc. for $C_9H_9N_2O_5ReS$: C, 24.38; H, 2.05; N, 6.32. Found: C, 24.18; H, 2.25; N, 6.48%. IR (KBr, cm^{-1}): 3218, 3057, 2991, 2023 (s), 1920 (sh, s) and 1903 (br, s), 1634, 1598. ^1H and ^{13}C NMR in Table 1. t_R: 14.9 min.

*Re-Complex **7**:* Yield 0.031 g (65.7%). *Anal.* Calc. for $C_{11}H_{13}N_2O_5ReS$: C, 28.02; H, 2.78; N, 5.94. Found: C, 27.81; H, 2.95; N, 5.68%. IR (KBr, cm^{-1}): 2988, 2916, 2021(s), 1911(s), 1865 (s), 1641, 1626, 1578. ^1H and ^{13}C NMR in Table 1. t_R: 15.8 min.

2.4. Synthesis of ^{99m}Tc-complexes 8 and 9

[^{99m}Tc]-sodium pertechnetate (370–740 MBq, 1 mL) is added to the Isolink kit formulation (Mallinckrodt Medical B.V.) containing sodium tetraborate (2.85 mg), sodium carbonate (7.15 mg), sodium boranocarbonate decahydrate (2.85 mg) and sodium tartrate dihydrate (8.5 mg) and the mixture was incubated at 95 °C for 20 min. After cooling, the pH was adjusted to 8 by addition of 0.1 N HCl and formation of *fac*-$[^{99m}Tc(OH_2)_3(CO)_3]^+$ was checked by HPLC,

Table 1
^1H and ^{13}C NMR chemical shifts for complexes **6** and **7** in DMSO-d_6 at 25 °C. The numbering of the atoms is shown in Figs. 3 and 4.

	6	**7**		**6**	**7**
H-2	3.56, 3.50	3.53	C-1	177.62	177.39
H-3	4.13, 3.99	4.30, 4.19	C-2	35.81	35.95
H-5	3.84, 3.63	3.78, 3.65	C-3	35.11	34.36
H-6	3.87, 3.64	3.85, 3.68	C-4	175.15	174.08
H-7		3.28	C-5	45.85	49.62
H-8		1.09	C-6	56.24	54.47
NH	8.42		C-7		42.00
			C-8		12.82
			CO	196.12	196.13
				195.43	195.41
				194.65	194.68

t_R = 5.5 min. An amount of the *fac*-[^{99m}Tc(OH$_2$)$_3$(CO)$_3$]$^+$ precursor (450 μL) is added to a vial containing an aqueous solution of **4** or **5** (5 μg, 50 μL). The vial is sealed with a rubber stopper and aluminium crimp cap and the solution is incubated at 70 °C for 20 min. After cooling, a sample is analyzed by HPLC and in each case the formation of a single radioactive complex, in more than 95% yield is observed. The retention time of **8** and **9** is 15.3 and 16.2 min, respectively. The identity of the Tc-99m complexes **8** and **9** is established by comparative HPLC studies using as references the well characterized analogous rhenium complexes **6** and **7**, respectively. In order to evaluate the stability of the ^{99m}Tc complexes samples are periodically analyzed by HPLC for a period up to 6 h.

2.5. Single-crystal X-ray crystallography

Colorless crystals of **4**·H$_2$O (0.30 × 0.40 × 0.50 mm), **6** (0.20 × 0.20 × 0.40 mm) and **7** (0.10 × 0.20 × 0.60 mm) suitable for X-ray analysis were mounted in air and covered with epoxy glue. Diffraction measurements were made on a Crystal Logic Dual Goniometer diffractometer using graphite monochromated Mo Kα radiation. Unit cell dimensions were determined by using the angular settings of 25 automatically centered reflections in the range 11 < 2θ < 23° and they appear in Table 2. Intensity data were recorded using a θ–2θ scan. Three standard reflections monitored every 97 reflections showed less than 3% variation and no decay. Lorentz, polarization and psi-scan absorption corrections were applied using Crystal Logic software. The structure was solved by direct methods using SHELXS-97 [11] and refined by full-matrix least squares techniques on F^2 using SHELXL-97 [12]. Further crystallographic details for **4**·H$_2$O: 2θ_{max} = 50°, scan speed 4.5°/min, scan range 2.3 + $\alpha_1\alpha_2$ separation, reflections collected/unique/used 1590/1522 [R_{int} = 0.0244]/1522, 157 parameters refined, $[\Delta\rho]_{max}/[\Delta\rho]_{min}$ = 0.262/−0.209 e/Å^3, $[\Delta/\sigma]_{max}$ = 0.000, R_1/wR_2 (for all data) = 0.0334/0.0872. Hydrogen atoms were located by difference maps and were refined isotropically. All non-H atoms were refined anisotropically. Further crystallographic details for **6**: 2θ_{max} = 45.5°, scan speed 2.3°/min, scan range 2.3 + $\alpha_1\alpha_2$ separation, reflections collected/unique/used 3051/2993 [R_{int} = 0.0452]/2993, 325 parameters refined, $[\Delta\rho]_{max}/[\Delta\rho]_{min}$ = 2.649/−3.723 e/Å^3, $[\Delta/\sigma]_{max}$ = 0.000, R_1/wR_2 (for all data) = 0.0620/0.1493. Hydrogen atoms were introduced at calculated positions as riding on bonded atoms. All non-H atoms were refined anisotropically. Further crystallographic details for **7**: 2θ_{max} = 50°, scan speed 3.0°/min, scan range 1.7 + $\alpha_1\alpha_2$ separation, reflections collected/unique/used 2806/2581 [R_{int} = 0.0086]/2581, 222 parameters refined, $[\Delta\rho]_{max}/[\Delta\rho]_{min}$ = 1.249/−0.747 e/Å^3, $[\Delta/\sigma]_{max}$ = 0.001, R_1/wR_2 (for all data) = 0.0277/0.0674. Hydrogen atoms were located by difference maps and were refined isotropically or were introduced at calculated positions as riding on bonded atoms. All non-H atoms were refined anisotropically. Plots of the structure were drawn using the Diamond 3 program package [13].

3. Results and discussion

3.1. Synthesis and characterization

The organic compounds **4** and **5** were synthesized by reacting 2-mercaptoacetic acid with the corresponding 2-chloromethylimidazoline **2** or **3** (Scheme 1) and were characterized by elemental analysis, NMR spectroscopy. Ligand **4** was further characterized by X-ray crystallography. These compounds were designed to act as monoanionic tridentate ligands (NSO) with the *fac*-[M(CO)$_3$]$^+$ core (M = Re and Tc).

The synthesis of non-radioactive Re(I)-complexes, **6** and **7**, (Scheme 1) was effected by ligand exchange reaction using the organometallic Re tricarbonyl precursor [NEt$_4$]$_2$[ReBr$_3$(CO)$_3$] and equimolar quantities of **4** and **5**, respectively. HPLC analysis of the reaction mixture showed that in each case only one product is formed with a retention time 14.9 and 15.8 min, respectively. The complexes were isolated as colourless crystals in high yield (70%) and were fully characterized by IR and NMR spectroscopies, elemental analysis and X-ray crystallography. The rhenium complexes are stable in the solid state as well as in solution as shown by HPLC and NMR.

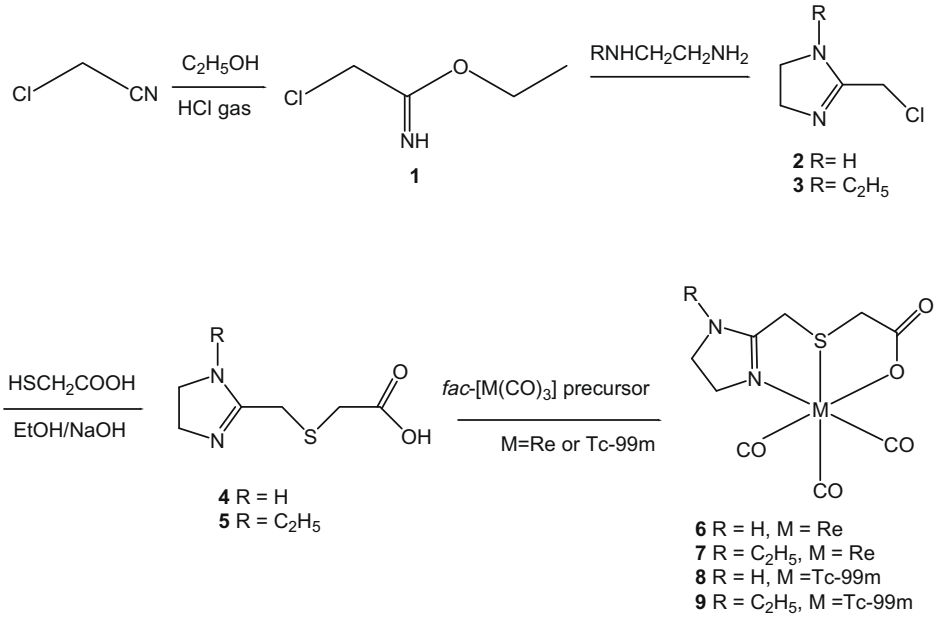
3.2. Description of the structures

The molecular structure of **4** is given in Fig. 1. The compound is present in the crystal in the zwitterionic form with essentially symmetric ionized carboxylate groups and with both nitrogens of the imidazoline bearing protons. In the lattice structure of **4**·H$_2$O there are intermolecular hydrogen bonding interactions which form a 2D network extending parallel to the *bc* plane [N1···O2 (0.5 − *x*, −0.5 − *y*, 1 − *z*) = 2.734 Å, HN1···O2 = 1.899 Å, N1–HN1···O2 = 170.5°; N2···O1 (0.5 − *x*, 0.5 + *y*, 0.5 − *z*) = 2.795 Å, HN2···O1 = 1.956 Å, N2–HN2···O1 = 172.8°; Ow1···O1 (*x*, −*y*, 0.5 + *z*) = 2.854 Å, Hw1A···O1 = 2.131 Å, Ow1–Hw1A···O1 = 151.9°; Ow1···O2 (0.5 − *x*, −0.5 − *y*, 1 − *z*) = 2.841 Å, Hw1B···O2 = 1.992 Å, Ow1-Hw1B···O2 = 162.7°] (Fig. 2).

Table 2
Summary of crystal, intensity collection and refinement data for **4**·H$_2$O, **6** and **7**.

	4·H$_2$O	**6**	**7**
Empirical formula	$C_6H_{12}N_2O_3S$	$C_9H_9N_2O_5ReS$	$C_{11}H_{13}N_2O_5ReS$
Formula weight	192.24	443.44	471.49
Temperature	298	298	298
Wavelength	Mo Kα 0.71073	Mo Kα 0.71073	Mo Kα 0.71073
Space group	*C*2/*c*	*P*2$_1$/*n*	*P*2$_1$/*n*
a (Å)	13.661(7)	12.675(11)	6.901(2)
b (Å)	9.049(4)	7.674(7)	11.659(4)
c (Å)	15.397(8)	25.15(2)	18.572(6)
β (°)	114.18(2)	91.62(3)	97.31(1)
V (Å^3)	1736.3(15)	2445(4)	1482.1(8)
Z	8	8	4
$D_{calc.}$ (Mg m^{-3})	1.471	2.410	2.113
μ (mm^{-1})	0.343	10.125	8.358
F(0 0 0)	816	1664	896
Goodness-of-fit (GOF) on F^2	1.039	1.056	1.080
R indices (R_{int})	R_1 = 0.0304[a]	R_1 = 0.0572[b]	R_1 = 0.0248[c]
	wR_2 = 0.0835[a]	wR_2 = 0.1442[b]	wR_2 = 0.0652[c]

[a] For 1398 reflections with $I > 2\sigma(I)$.
[b] For 2718 reflections with $I > 2\sigma(I)$.
[c] For 2371 reflections with $I > 2\sigma(I)$.



Scheme 1. Synthetic pathway of **4–9**.

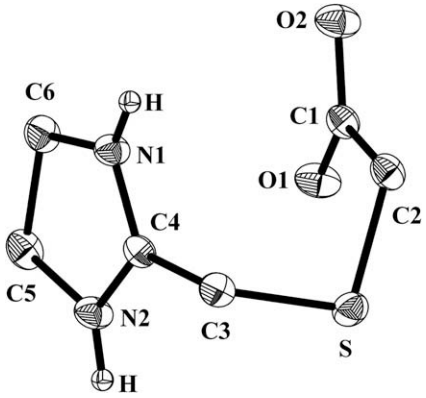


Fig. 1. Labeled plot of **4** with ellipsoids drawn at the 30% probability level. Only the imine hydrogen atoms are shown for clarity purposes.

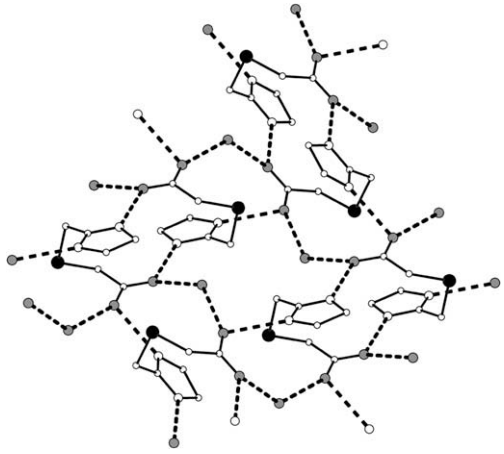


Fig. 2. A part of the 2D structure of **4**·H_2O due to hydrogen bonding interactions.

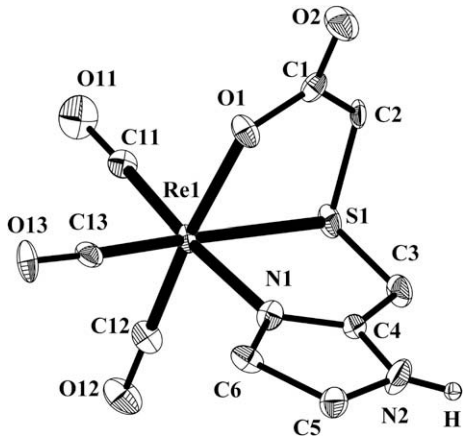


Fig. 3. Labeled plot of **6** with ellipsoids drawn at the 30% probability level. H atoms have been omitted for clarity.

The molecular structures of **6** and **7** are given in Figs. 3 and 4, selected bond distances and angles are listed in Tables 3 and 4, respectively. The asymmetric unit of **6** contains two crystallographically independent molecules, thereafter denoted as A and B. The distorted octahedral environment of the Re atom in the structures of **6** and **7** is defined by the three facially bound CO groups and the NSO donor atom set of the tridentate ligand. The Re-carbonyl bond distances (**6A**: 1.865–1.910 Å, **6B**: 1.890–1.911 Å, **7**: 1.903–1.925 Å) are consistent which those found in other Re-tricarbonyl complexes [14–18]. The Re–S, Re–N and Re–O bond distances fall well in the ranges observed in analogous complexes. In the coordination sphere of **6**, the Re–N–C–C–S five-membered ring is planar (largest deviation ~0.08 and ~0.05 Å for **6A** and **6B**, respectively), while the Re–S–C–C–O five-membered ring adopts the envelope configuration with the sulfur atom being out of the best mean plane defined by the remaining four atoms (0.49 and 0.52 Å for **6A** and **6B**, respectively). In the coordination sphere of **7**, the two five-membered rings defined by Re–N–C–C–S and Re–S–C–C–O adopt the envelope configuration with C3 and C2 being 0.37 and 0.30 Å, respectively, out of the best mean plane of their respective four atoms. In the lattice structure of **6**, there are intermolecular hydrogen bonding interactions which form double chains extending parallel to the *a* axis [N2···O22 (−1 + *x*, −1 + *y*, *z*) = 2.781 Å, HN2···O22 = 1.943 Å,

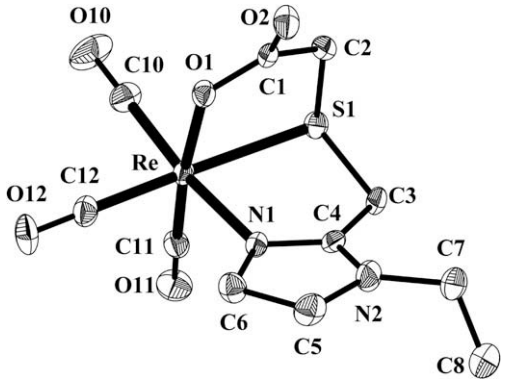


Fig. 4. Labeled plot of **7** with ellipsoids drawn at the 30% probability level. H atoms have been omitted for clarity.

Table 3
Selected bond distances (Å) and angles (°) for **6**.

A		B	
Distances			
Re(1)–C(11)	1.864(15)	Re(2)–C(31)	1.890(16)
Re(1)–C(12)	1.906(16)	Re(2)–C(32)	1.893(17)
Re(1)–C(13)	1.910(16)	Re(2)–C(33)	1.911(17)
Re(1)–N(1)	2.131(11)	Re(2)–N(11)	2.125(11)
Re(1)–O(1)	2.152(9)	Re(2)–O(21)	2.145(9)
Re(1)–S(1)	2.483(4)	Re(2)–S(2)	2.476(4)
Angles			
C(11)–Re(1)–C(12)	89.5(6)	C(31)–Re(2)–C(32)	89.0(6)
C(11)–Re(1)–C(13)	91.9(6)	C(31)–Re(2)–C(33)	90.6(7)
C(12)–Re(1)–C(13)	88.9(6)	C(32)–Re(2)–C(33)	88.1(6)
C(11)–Re(1)–N(1)	174.8(5)	C(31)–Re(2)–N(11)	174.0(6)
C(12)–Re(1)–N(1)	94.5(5)	C(32)–Re(2)–N(11)	95.5(5)
C(13)–Re(1)–N(1)	91.5(5)	C(33)–Re(2)–N(11)	93.6(5)
C(11)–Re(1)–O(1)	93.3(5)	C(31)–Re(2)–O(12)	92.6(5)
C(12)–Re(1)–O(1)	174.5(6)	C(32)–Re(2)–O(21)	176.2(5)
C(13)–Re(1)–O(1)	95.7(5)	C(33)–Re(2)–O(21)	95.3(5)
N(1)–Re(1)–O(1)	82.4(4)	N(11)–Re(2)–O(21)	82.8(4)
C(11)–Re(1)–S(1)	96.3(5)	C(31)–Re(2)–S(2)	95.4(5)
C(12)–Re(1)–S(1)	96.3(5	C(32)–Re(2)–S(2)	97.1(4)
C(13)–Re(1)–S(1)	170.3(4)	C(33)–Re(2)–S(2)	172.1(5)
N(1)–Re(1)–S(1)	80.1(3)	N(11)–Re(2)–S(2)	80.1(3)
O(1)–Re(1)–S(1)	78.6(3)	O(21)–Re(2)–S(2)	79.4(3)

Table 4
Selected bond distances (Å) and angles (°) for **7.**

Distances			
Re(1)–C(11)	1.903(5)	Re(1)–N(1)	2.148(4)
Re(1)–C(12)	1.924(5)	Re(1)–O(1)	2.137(3)
Re(1)–C(10)	1.925(5)	Re(1)–S(1)	2.471(1)
Angles			
C(11)–Re(1)–C(12)	90.5(2)	C(10)–Re(1)–N(1)	172.6(2)
C(11)–Re(1)–C(10)	89.0(2)	N(1)–Re(1)–O(1)	79.7(1)
C(12)–Re(1)–C(10)	88.9(3	C(11)–Re(1)–S(1)	94.4(1)
C(11)–Re(1)–O(1)	174.4(2)	C(12)–Re(1)–S(1)	172.8(1)
C(12)–Re(1)–O(1)	94.2(2)	C(10)–Re(1)–S(1)	96.5(2)
C(10)–Re(1)–O(1)	94.0(2)	N(1)–Re(1)–S(1)	78.9(1)
C(11)–Re(1)–N(1)	97.0(2)	O(1)–Re(1)–S(1)	80.6(1)
C(12)–Re(1)–N(1)	95.2(2)		

N2–HN2···O22 = 164.5°; N12···O2 (x, 1 + y, z) = 2.830 Å, HN12···O2 = 2.007 Å, N12–HN12···O2 = 159.8°] (Fig. 5).

3.3. Synthesis of the ^{99m}Tc complexes

The synthesis of the ^{99m}Tc-complexes **8** and **9** was carried out by ligand substitution reaction employing the tricarbonyl *fac*-$[^{99m}Tc(OH_2)_3(CO)_3]^+$ as precursor. The precursor was prepared by the addition of pertechnetate to a commercially available IsoLink kit that contains sodium boranocarbonate, which acts simultaneously as reductant and "in situ" source of CO [6]. The reaction was monitored by HPLC (Rt of pertechnetate 3.0 min, t_P of precursor 5.5 min under the employed conditions) and was quantitative (>95%).

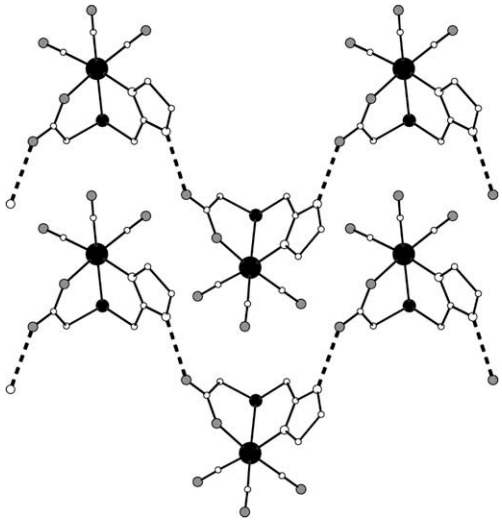


Fig. 5. A part of the 1D structure of **6** due to hydrogen bonding interactions.

Reaction of the ligands **4** and **5** with the precursor *fac*-$[^{99m}Tc(OH_2)_3(CO)_3]^+$ for 20 min at 70 °C resulted in the formation of **8** and **9**, respectively. In each case, the HPLC analysis demonstrated the formation of a single complex with yields greater than 95%, eluting at 15.3 and 16.2 min, respectively. Corroboration of the structure of the Tc-99m complex was effected by comparative HPLC analysis using the analogous non radioactive rhenium complexes **6** and **7,** eluting at 14.9 and 15.8 min, respectively, as references.

Stability studies performed by HPLC, demonstrate that the ^{99m}Tc complexes remained stable for a period of at least 6 h (max time tested). Their stability in the presence of histidine and cysteine at a molar ratio of 1/1000 was also monitored by HPLC and only minor changes were observed in the radiochromatogram indicating the stability of the Tc complexes.

3.4. Spectral properties

The characteristic finding in the infrared spectra of the rhenium complexes **6** and **7** is the presence of three very strong bands in the 2023–1865 cm^{-1} region. These bands are attributed to the symmetric and asymmetric stretching vibration of the C≡O bond and they are characteristic for the *fac*-$[Re(CO)_3]^+$ core [14–18]. In addition, **6** and **7** exhibit two strong broad absorptions at 1634, 1598 cm^{-1} and at 1641, 1578 cm^{-1}, respectively, which correspond to the asymmetrical C═O stretching vibration to the coordinated carboxylate and to the C═N bond.

^{1}H and ^{13}C chemical shift assignments for complexes **6** and **7** were based on the combined analysis of a series of ^{1}H–^{1}H and ^{1}H–^{13}C correlation spectra (Fig. 6) and are reported in Table 1. The numbering of the atoms is according to the crystallographic structures shown in Figs. 3 and 4. As is typically observed with asymmetric complexes, after coordination, the geminal protons on C-2 and C-3, as well as on C-5 and C-6 of the imidazolinyl ring, become diastereotopic, appearing at different chemical shifts in the ^{1}H spectrum (a rare exception is noted in the case of the H-2 protons of complex **7** that coincide and appear as a singlet peak). H-3 protons were distinguished from H-2 based on their NOE

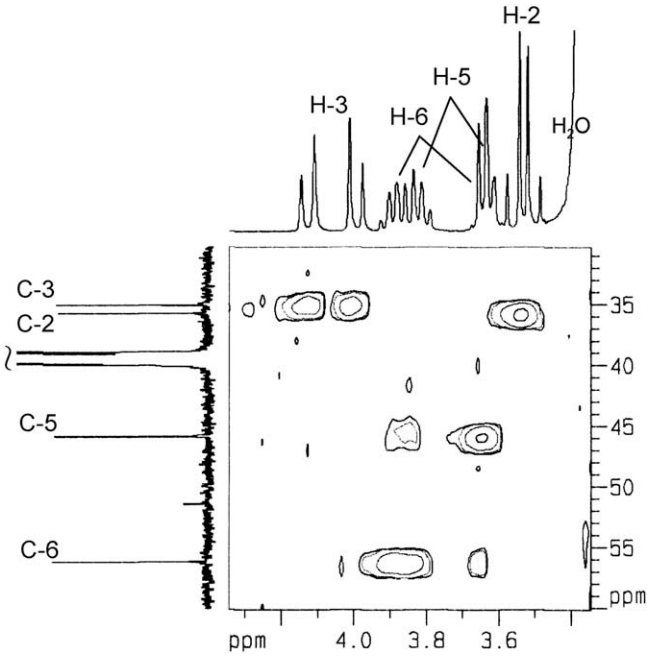


Fig. 6. ^{1}H–^{13}C correlation spectrum for complex **6** in DMSO-d_6 at 25 °C (range δ_H 4.35–3.34, range δ_C 60.1–30.3).

correlation with the imidazolinyl NH proton in **6,** and the *N*-ethyl group protons in **7**. H-5 protons were distinguished from H-6 based on the chemical shift differentiation of their corresponding carbons; specifically, C-6 is shifted downfield compared to C-5 – by appr. 10 ppm in **6** and 5 ppm in **7 –** due to its proximity to the coordinated imidazolinyl nitrogen. In complex **7**, the distinction of H-5 from H-6 is further confirmed by the existence of a long range coupling between C-5 and the H-7 protons of the *N*-ethyl group.

4. Conclusions

In conclusion, two new NSO ligands and their *fac*-$[Re(CO)_3]^+$ complexes have been synthesized and characterized. The ligands, 4-(imidazolin-2-yl)-3-thiabutanoic acid and its *N*-ethyl derivative, bind to the rhenium *fac*-$[M(CO)_3]^+$ core with the imidazolinyl nitrogen, the thioether and the carboxylate oxygen through the resulting in a single stable and neutral complex. The analogous complexes were also prepared at tracer level with the gamma emitting radionuclide ^{99m}Tc. The high affinity of these ligands for the *fac*-$[M(CO)_3]^+$ metal core coupled with their capacity for easy derivatization at the N1-imidazolyl position, indicate that exploitation of this ligand system for development of ^{99m}Tc-radiopharmaceuticals is promising.

Supplementary data

CCDC 721586, 721587 and 721588 contain the supplementary crystallographic data for compound **4** and complexes **6** and **7**, respectively. These data can be obtained free of charge via http://www.ccdc.cam.ac.uk/conts/retrieving.html, or from the Cambridge Crystallographic Data Centre, 12 Union Road, Cambridge CB2 1EZ, UK; fax: (+44) 1223-336-033; or e-mail: deposit@ccdc.cam.ac.uk.

Acknowledgements

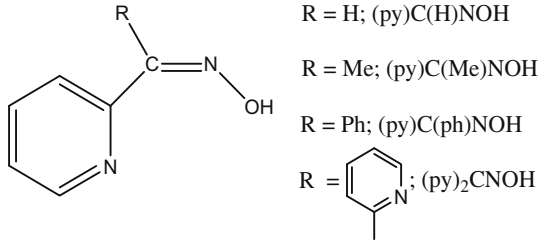
This work was supported by the GSRT, Hellenic Ministry of Development, Measure 3.3., Excellence in Research II, "*Functional and Functionalized Biomolecules in Biodiagnosis and Radiopharmacy*" and Greek-Serbian Bilateral Co-operation Research Project, *No* 709. Mallinckrodt Medical B.V., The Netherlands for the Isolink kits.

References

[1] S. Liu, Adv. Drug Delivery Rev. 60 (2008) 1347.
[2] S.S. Jurisson, J.D. Lydon, Chem. Rev. 99 (1999) 2205.
[3] S.R. Banerjee, K.P. Maresca, L. Francesconi, J. Valliant, J.W. Babich, J. Zubieta, Nucl. Med. Biol. 32 (2005) 1.
[4] W.A. Volkert, T.J. Hoffman, Chem. Rev. 99 (1999) 2269.
[5] R. Alberto, R. Schibli, A. Egli, A.P. Schubiger, J. Am. Chem. Soc. 120 (1998) 7987.
[6] R. Alberto, K. Ortner, N. Wheatley, R. Schibli, A.P. Schubiger, J. Am. Chem. Soc. 123 (2001) 3135.
[7] R. Alberto, Top. Curr. Chem. 252 (2005) 1.
[8] T.G. Hamill, N.J. Brenner, W. Eng, H.D. Burns, J. Labelled Compd. Radiopharm. 41 (1998) 319.
[9] W. Klarer, E. Urech, Helv. Chim. Acta 27 (1944) 1762.
[10] R. Alberto, U. Abram, K. Hegetschweiler, V. Gramlich, A.P. Schubiger, J. Chem. Soc., Dalton Trans. (1994) 2815.
[11] G.M. Sheldrick, SHELXS-97, Structure Solving Program, University of Göttingen, Germany, 1997.
[12] G.M. Sheldrick, SHELXL-97, Crystal Structure Refinement Program, University of Göttingen, Germany, 1997.
[13] DIAMOND – Crystal and Molecular Structure Visualization, Ver. 3.1, Crystal Impact, Rathausgasse 30, 53111, Bonn, Germany.
[14] L. Wei, J. Babich, W.C. Eckelman, J. Zubieta, Inorg. Chem. 44 (2005) 2198. and reference therein.
[15] C. Fernandes, I.C. Santos, I. Santos, H.-J. Pietzsch, J.U. Kunstler, W. Kraus, A. Rey, N. Margaritis, A. Bourkoula, A. Chiotellis, M. Paravatou-Petsotas, I. Pirmettis, J. Chem. Soc., Dalton Trans. (2008) 3215.
[16] R.F. Vitor, S. Alves, J.D.G. Correia, A. Paulo, I. Santos, J. Organomet. Chem. 689 (2004) 4764.
[17] H.-J. Pietzsch, A. Gupta, M. Reisgys, A. Drews, S. Seifert, R. Syhre, H. Spies, R. Alberto, U. Abram, P.A. Schubiger, B. Johannsen, Bioconjugate Chem. 11 (2000) 414.
[18] O. Karagiorgou, G. Patsis, M. Pelecanou, C.P. Raptopoulou, A. Terzis, T. Siatra-Papastaikoudi, R. Alberto, I. Pirmettis, M. Papadopoulos, Inorg. Chem. 44 (2005) 4118.

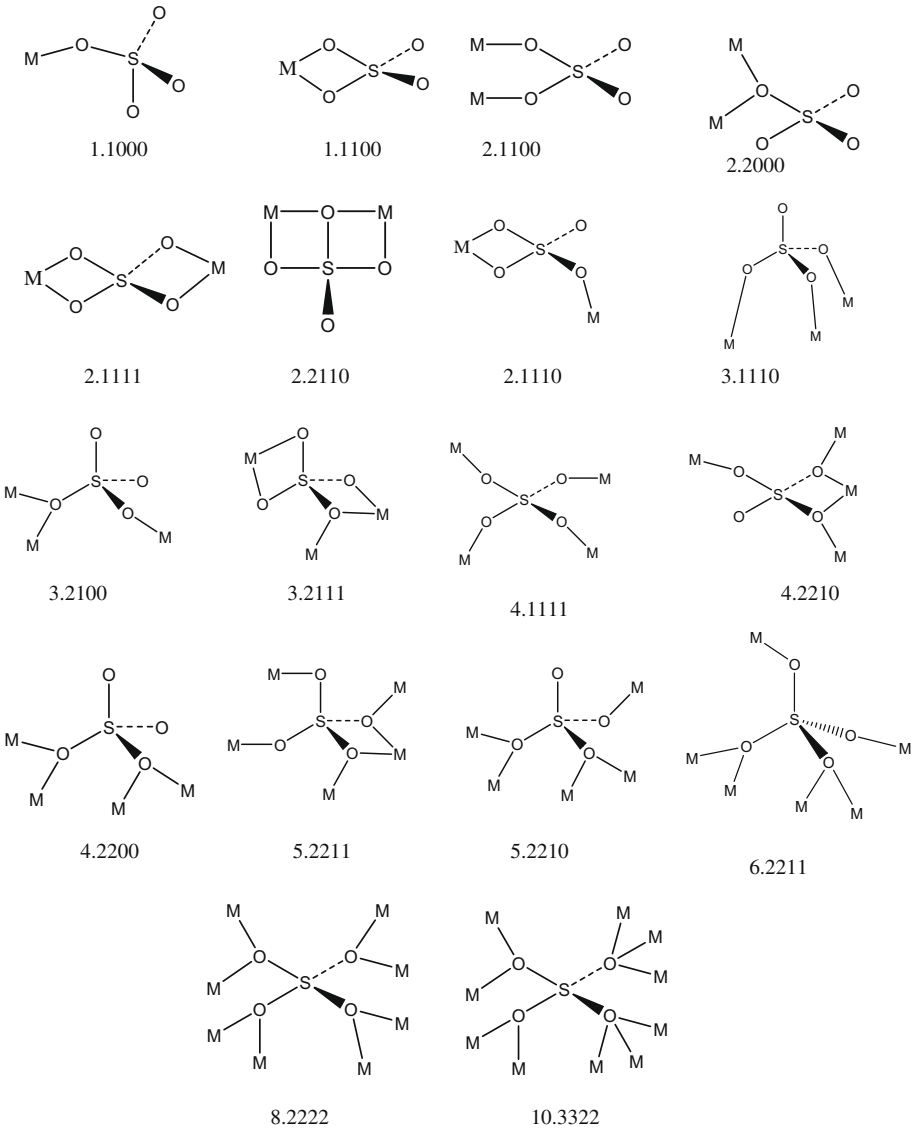
considerable forethought in the ligands, metals and conditions (reaction ratio, 'pH', solvent, etc.) used for any significant progress to be made. As the field develops, the boundary between "designed" and "serendipitous" assembly is becoming blurred [4].

In the context of the several variations of "serendipitous assembly", we have been exploring "ligand blend" reactions involving carboxylates ($R'CO_2^-$) *and* various 2-pyridyloximates [10] (Scheme 1) *with* or *without* additional inorganic monoanions (Cl^-, Br^-, NO_3^-, N_3^-, SCN^-) as a means to high-nuclearity species. The presence of a deprotonated oxime group leads to a great coordinative flexibility due to the well known ability of the oximate group to bridge two or three metal ions. On the other hand, carboxylates are able to deprotonate the oxime group of (py)C(R)NOH under mild conditions (the use of external hydroxides often perplexes the reactions). Besides their deprotonating ability, the $R'CO_2^-$ ions are flexible ligands, a consequence of their ability to adopt a number of different ligation modes, both terminal and bridging as well as both bidentate and tridentate. Thus, the $(py)C(R)NO^-/R'CO_2^-$ (R = H, Me, Ph, py; R′ = H, Me, Et, Ph) "blends", without (*binary* "blends") or with (ternary "blends") additional inorganic anions have led to a variety of Cr, Mn, Fe, Co, Ni and Cu clusters [10–12] with nuclearities ranging from 3 to 12 and with interesting magnetic properties, including SMM behavior [11h,n].



Scheme 1. General structural formula and abbreviations of simple 2-pyridyl oximes, including phenyl(2-pyridyl)ketone oxime [(py)C(ph)NOH].

Three years ago we decided to begin a program which can be considered as a modification of the above mentioned *binary* "ligand blend" approach. We have been exploring the use of the sulfato ligand, SO_4^{2-}, instead of the carboxylato ligand, $R'CO_2^-$, in the 3d-metal cluster chemistry with 2-pyridyloximate ligands. The sulfate ion [13] is currently a ligand of limited interest. However, metal-sulfato complexes have been studied for their roles in the



Scheme 2. The up to now crystallographically established coordination modes of the sulfato ligand and the Harris notation [20] which describes these modes.

field of porous-framework materials [14], in catalysis [15], in the construction of luminescent molecular materials [16], and in medicinal [17], environmental [18] and bioinorganic [19] chemistry. The great coordinative flexibility of the (py)C(R)NO$^-$ family of ligands, as well as the μ_2, μ_3, μ_4, μ_5, μ_6, μ_8 or μ_{10} potential of SO_4^{2-} (Scheme 2), prompted us to combine the two ligand types to aim for new types of clusters. Our belief was that the simultaneous employment of the two ligand types would give tremendous structurally flexibility in these "blends". The possible advantages of using SO_4^{2-} instead of $R'CO_2^-$ include (i) the possibility of triggering aggregation of preformed smaller cationic species into new, higher-nuclearity products, and (ii) the possible diversion of known reaction systems developed using *mono*anionic carboxylates to new species as a result of the higher charge and higher density/bridging capability of sulfates.

In this work, we report the synthesis and the X-ray structural characterization of the hexanuclear sulfato Ni(II) complex $[Ni_6(SO_4)_2\{(py)C(ph)NO\}_8]\cdot 6DMF$ (**1**·6DMF) which contain the anion of phenyl(2-pyridyl)ketone oxime as an organic ligand. Complex **1**·6DMF has also been studied by variable-temperature dc magnetic susceptibility techniques and IR spectroscopy.

2. Experimental

2.1. General and physical measurements

All manipulations were performed under aerobic conditions using materials (reagent grade) and solvents as received. Microanalyses (C, H, N) were performed by the University of Ioannina (Greece) Microanalytical Laboratory using an EA 1108 Carlo Erba analyzer.

IR spectra (4000–400 cm^{-1}) were recorded on a Perkin–Elmer 16 PC FT-spectrometer with samples prepared as KBr pellets. Magnetic susceptibility measurements in the 2–300 K range under a field of 0.3 *T* were performed using a Quantum Design SQUID magnetometer at the Magnetochemistry Service of the University of Barcelona. All measurements were carried out on polycrystalline samples. Data were corrected for diamagnetic contributions calculated from Pascal's constants.

2.2. Compound preparation

2.2.1. $[Ni_6(SO_4)_2\{(py)C(ph)NO\}_8]\cdot 6DMF$ (**1**·6DMF)

DMF (25 mL) was added to a solid mixture containing $NiSO_4\cdot 6H_2O$ (0.158 g, 0.60 mmol), (py)C(ph)NOH (0.119 g, 0.60 mmol) and NaOMe (0.033 g, 0.60 mmol). The mixture was refluxed for 2 h. The resulting red solution was filtered and layered with Et_2O (50 mL). Slow mixing gave X-ray quality, red prismatic crystals of the product. The crystals were collected by filtration, washed with Et_2O (2 × 3 mL) and dried in air; yield 53% (based on the metal). IR (KBr pellet): ν = 3394m, 3060w, 2926w, 1658m, 1594m, 1462s, 1438m, 1384w, 1340w, 1210m, 1124s, 1072m, 1012m, 974w, 786 m, 746m, 704m, 642m, 616m, 474w, 452w. *Anal.* Calc. for $C_{114}H_{114}N_{22}Ni_6O_{22}S_2$ (2560.66): C, 53.47; H, 4.49; N, 12.03. Found: C, 53.61; H, 4.35; N, 11.98%.

2.3. Single-crystal X-ray crystallography

A crystal of **1**·6DMF with approximate dimensions 0.05 × 0.10 × 0.30 mm was mounted in capillary. Diffraction measurements were made on a $P2_1$ Nicolet diffractometer upgraded by CRYSTAL LOGIC using graphite monochromated Cu Kα radiation. Complete crystal data and parameters for data collection and processing are listed in Table 1. Unit cell dimensions were determined and refined by using the angular settings of 25 automatically centered reflections in the range $22 < 2\theta < 54°$. Intensity data were recorded using the θ–2θ scan method. Three standard reflections monitored every 97 reflections showed less than 3% variation and no decay. Lorentz, polarization and Ψ-scan absorption were applied using the CRYSTAL LOGIC software package.

Table 1
Summary of crystal data, data collection and structure refinement for the X-ray diffraction study of complex **1**·6DMF.

Complex	**1**·6DMF
Empirical formula	$C_{114}H_{114}N_{22}Ni_6O_{22}S_2$
Formula weight	2560.66
Colour, habit	red prisms
Crystal system	triclinic
Space group	$P\bar{1}$
a (Å)	17.672(8)
b (Å)	13.305(7)
c (Å)	14.134(7)
α (°)	99.24(2)
β (°)	105.69(2)
γ (°)	111.07(2)
V (Å^3)	2860(2)
Z	1
ρ_{calc} (g cm^{-3})	1.487
Radiation, λ (Å)	Cu Kα, 1.5418
μ (mm^{-1})	2.074
F (0 0 0)	1328
T (K)	298
$2\theta_{max}$ (°)	107.4
Ranges	
h	−17 → 18
k	−13 → 13
l	−14 → 0
Measured reflections	7107
Unique reflections	6635
R_{int}	0.0666
Reflections used ($I > 2\sigma(I)$)	4807
Parameters refined	667
Goodness of Fit (GOF) (on F^2)	1.021
R_1[a] ($I > 2\sigma(I)$)	0.0926
wR_2[b] ($I > 2\sigma(I)$)	0.2406
$(\Delta\rho)_{max}/(\Delta\rho)_{min}$ (e Å^{-3})	0.1203/0.2406

[a] $R_1 = \Sigma(|F_o| - |F_c|)/\Sigma(|F_o|)$.
[b] $wR_2 = \{\sum[w(F_o^2 - F_c^2)^2]/\sum[w(F_o^2)^2]\}^{1/2}$.

The structure was solved by direct methods using SHELXS-86 [21] and refined by full-matrix least-squares techniques on F^2 with SHELXL-97 [22]. The crystals were of poor quality showing large ω-widths with shoulders on one side, a fact that is also reflected in the quality of the crystallographic data (Table 1), while our repeating efforts to improve the quality of the crystals were unsuccessful. The data were collected in increasing 2θ shells and the data collection was terminated when about half of the collected shell data were unobserved. All hydrogen atoms were introduced at calculated positions as riding on bonded atoms; no H-atoms for the solvent molecules (DMF) were included in the refinement. All non-hydrogen atoms were refined anisotropically.

3. Results and discussion

3.1. Brief synthetic comments

Our general synthetic approach for the isolation of heteroleptic Ni(II) clusters was to treat the metal sulfate with (py)C(ph)NOH and a base in a variety of solvents. The addition of base is necessary for the deprotonation of the organic ligand. Note that reactions in the absence of base lead to complexes $[Ni_2(SO_4)_2\{(py)C(ph)NOH\}_4]$ and $[Ni\{(py)C(ph)NOH\}_3](SO_4)$ [23] that contain the neutral ligands.

Treatment of $NiSO_4\cdot 6H_2O$ with 1 equiv. of (py)C(ph)NOH and 1 equiv. of NaOMe in DMF under reflux gave a red solution from

which the new hexanuclear cluster $[Ni_6(SO_4)_2\{(py)C(ph)NO\}_8]\cdot 6DMF$ (**1**·6DMF) has been isolated. Its formation can be summarized in Eq. (1). The methoxide ions act as proton acceptors to facilitate formation of the $(py)C(ph)NO^-$ ligands. As expected, the nature of the base is not crucial for the identity of the product; we were able to isolate **1** by using plethora of bases such as NEt_3, NMe_4OH, NEt_4OH and $LiOH\cdot H_2O$.

$$6NiSO_4\cdot 6H_2O + 8(py)C(ph)NOH + 8NaOMe + 6DMF \xrightarrow[T]{DMF} \underset{\mathbf{1}\cdot 6DMF}{[Ni_6(SO_4)_2\{(py)C(ph)NO\}_8]\cdot 6DMF} + 4Na_2SO_4 + 8MeOH + 36H_2O \quad (1)$$

It should be mentioned at this point that the chemical and structural identity of the products from the $NiSO_4\cdot 6H_2O/(py)C(ph)NOH/OH^-$ general reaction system depends on the solvent used and the oxime to OH^- ratio. For example, the employment of MeOH leads to the *hydroxo* hexanuclear Ni(II) sulfato clusters $Ni_6(SO_4)_4(OH)\{(py)C(ph)NO\}_3\{(py)C(ph)NOH\}_3(MeOH)_3]$ (**2**) and $[Ni_6(SO_4)_4(OH)\{(py)C(ph)NO\}_3\{(py)C(ph)NOH\}_3(H_2O)_3]$ (**3**) [24], whereas employment of an excess of base in MeOH yields the sulfate-free trinuclear complex $[Ni_3\{(py)C(ph)NO\}_6]$ (**4**) [25]. Complexes **2** and **3** have similar structures which contain the $[Ni_6(\mu_3\text{-}OH)(\mu_3\text{-}SO_4)_3(\mu_3\text{-}ONPh)_3]^{2+}$ core. The core consists of six Ni^{II} ions arranged as two parallel equilateral triangular subunits, one small (Ni···Ni = ~3.3 Å) and the other larger (Ni···Ni = ~6.0 Å).

3.2. Description of structure

A partially labelled plot of the hexanuclear molecule present in **1**·6DMF is shown in Fig. 1. Selected interatomic distances and angles are listed in Table 2.

The structure of **1**·6DMF consists of hexanuclear molecules $[Ni_6(SO_4)_2\{(py)C(ph)NO\}_8]$ (Fig. 1) and solvate DMF molecules; the latter will not be further discussed. The hexanuclear molecule lies on a crystallographic inversion center. The metal ions are held together by two 3.211 (using Harris notation, [20]) and six 2.111 $(py)C(ph)NO^-$ ligands, as well as two 5.2210 SO_4^{2-} ions.

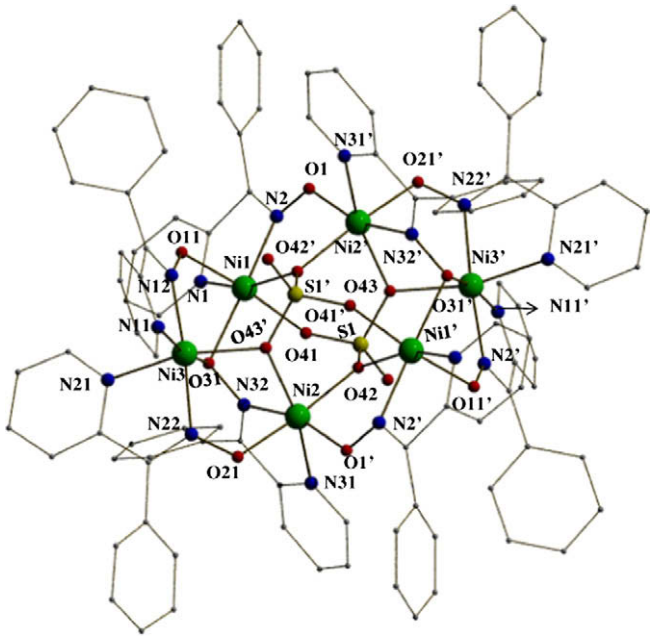


Fig. 1. The structure of **1** in the crystal. Primed and unprimed atoms are related by the crystallographic inversion center.

Table 2
Selected interatomic distances (Å) and angles (°) for **1**·6DMF.

Distances			
Ni(1)···Ni(2)	4.000(3)	Ni(2)–O(1′)	1.858(2)
Ni(1)···Ni(2′)	3.362(2)	Ni(2)–O(43′)	2.120(5)
Ni(1)···Ni(3)	3.303(3)	Ni(2)–N(31)	2.086(10)
Ni(1)–O(11)	2.025(5)	Ni(2)–N(32)	2.031(7)
Ni(1)–O(31)	2.119(5)	Ni(3)–O(31)	2.082(5)
Ni(1)–O(41)	2.038(5)	Ni(3)–O(43′)	2.086(6)
Ni(1)–O(42′)	2.199(5)	Ni(3)–N(11)	2.061(6)
Ni(1)–N(1)	2.057(4)	Ni(3)–N(12)	2.003(6)
Ni(1)–N(2)	2.115(2)	Ni(3)–N(21)	2.070(7)
Ni(2)–O(21)	2.073(7)	Ni(3)–N(22)	2.044(7)
Ni(2)–O(42)	2.143(6)		
Angles			
O(11)–Ni(1)–O(31)	87.6(2)	O(42)–Ni(2)–N(32)	93.8(2)
O(11)–Ni(1)–O(41)	172.3(2)	O(1′)–Ni(2)–O(43′)	109.7(2)
O(11)–Ni(1)–O(42′)	91.1(2)	O(1′)–Ni(2)–N(31)	83.5(3)
O(11)–Ni(1)–N(1)	86.7(2)	O(1′)–Ni(2)–N(32)	160.5(2)
O(11)–Ni(1)–N(2)	94.9(2)	O(43′)–Ni(2)–N(31)	165.7(4)
O(31)–Ni(1)–O(41)	85.5(2)	O(43′)–Ni(2)–N(32)	88.6(2)
O(31)–Ni(1)–O(42′)	103.8(2)	N(31)–Ni(2)–N(32)	77.7(4)
O(31)–Ni(1)–N(1)	92.4(2)	O(31)–Ni(3)–O(43′)	88.2(2)
O(31)–Ni(1)–N(2)	171.3(2)	O(31)–Ni(3)–N(11)	167.9(2)
O(41)–Ni(1)–O(42′)	87.2(2)	O(31)–Ni(3)–N(12)	89.2(2)
O(41)–Ni(1)–N(1)	97.0(2)	O(31)–Ni(3)–N(21)	91.0(2)
O(41)–Ni(1)–N(2)	92.4(2)	O(31)–Ni(3)–N(22)	90.5(2)
O(42′)–Ni(1)–N(1)	163.6(2)	O(43′)–Ni(3)–N(11)	93.9(2)
O(42′)–Ni(1)–N(2)	84.5(2)	O(43′)–Ni(3)–N(12)	97.9(2)
N(1)–Ni(1)–N(2)	79.5(2)	O(43′)–Ni(3)–N(21)	165.4(3)
O(21)–Ni(2)–O(42)	173.3(2)	O(43′)–Ni(3)–N(22)	87.1(3)
O(21)–Ni(2)–O(1′)	86.9(2)	N(11)–Ni(3)–N(12)	78.7(2)
O(21)–Ni(2)–O(43′)	84.0(2)	N(11)–Ni(3)–N(21)	90.0(3)
O(21)–Ni(2)–N(31)	91.4(3)	N(11)–Ni(3)–N(22)	101.6(3)
O(21)–Ni(2)–N(32)	88.3(3)	N(12)–Ni(3)–N(21)	96.6(3)
O(42)–Ni(2)–O(1′)	93.2(2)	N(12)–Ni(3)–N(22)	175.0(3)
O(42)–Ni(2)–O(43′)	89.6(2)	N(21)–Ni(3)–N(22)	78.4(3)
O(42)–Ni(2)–N(31)	95.3(3)		

Symmetry operation used to generate equivalent atoms: $-x, -y, 1-z$.

A distorted octahedral environment is created about each metal center; the chromophores are $Ni(1,2,1',2')(N_{py})(N_{ox})(O_{ox})_2(O_{sulf})_2$ and $Ni(3,3')(N_{py})_2(N_{ox})_2(O_{ox})(O_{sulf})$, where the abbreviations "py", "ox" and "sulf" are for the 2-pyridyl, oximate and sulfato donor atoms, respectively. The average Ni–O_{ox}, Ni–N_{ox} and Ni–N_{py} bond lengths of 2.035(7), 2.048(7) and 2.069(10) Å, respectively, agree well with values expected for high-spin Ni^{II} ions in octahedral environment [11o,p,26,27]. The Ni–O_{sulf} bond lengths are typical [13,24,26,28]. The Ni–O bond distances for the bridging sulfate oxygen atoms are longer than the Ni–O distance exhibited by the terminal oxygen atom from the same sulfato ligand. For example, the Ni(2)–O(43′) and Ni(3)–O(43′) bond distances are 2.119(5) and 2.086(5) Å, respectively, while the Ni(1′)–O(41′) distance is 2.037(6) Å. The bridging Ni–O_{sulf} distances are asymmetric, e.g., the Ni(2)–O(43′) bond length is longer than the Ni(3)–O(43′) distance.

The molecule of **1** contains the $[Ni_6(\mu_5\text{-}SO_4)_2(\mu_2\text{-}ONR)_6(\mu_3\text{-}ONR)_2]$ core, where R^- = –C(py)(ph) (Fig. 2, left). An alternative description of the core (using only the sulfate oxygen atoms) is $[Ni_6(\mu_5\text{-}SO_4)_2]^{8+}$ (Fig. 2, right). The six Ni^{II} atoms have a chair-like conformation (Fig. 2) which is a common topology in organometallic Ni(II) compounds [29], but it is observed only for the second time in non-organometallic Ni(II) clusters [30a]. The most common topologies of the metal ions in Ni_6^{II} complexes are the hexagons, the Chinese-lantern-like objects and the face-shared distorted dicubanes in which one of the corners of each cubane is missing [24,30].

The 5.2210 [20] coordination mode of the SO_4^{2-} (Scheme 2) is very rare in coordination chemistry and novel in Ni(II) chemistry. Hitherto, it has been observed in two polyoxomolybdenate clusters

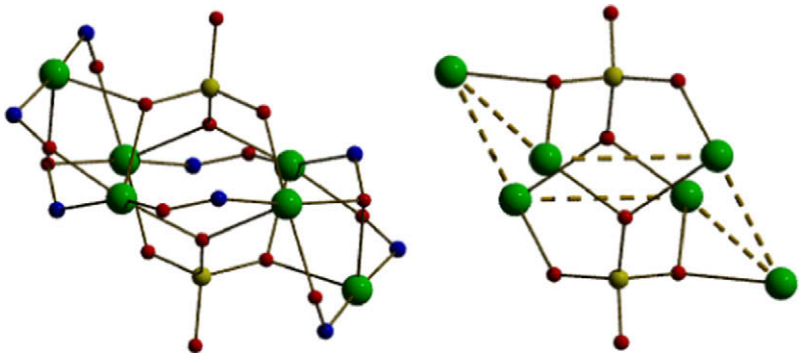


Fig. 2. Left: the $[Ni_6(\mu_5\text{-}SO_4)_2(\mu_2\text{-}ONR)_6(\mu_3\text{-}ONR)_2]$ core of complex **1**, where R^- = −C(py)(ph). Right: the core of **1** using only the sulfate oxygen atoms; the chair-like topology of the Ni^{II} atoms is emphasized with dashed lines.

[31], and in the coordination polymers $[Ag_2(SO_4)(L)]_n$ [32] and $[Zn_2(SO_4)(OH)(L')]_n$ [33], where L = 4,4′-bipyrazine and L' = 1,2,4-triazolato anion. Complex **1** is the third highest-nuclearity nickel(II) sulfato cluster which has been structurally characterized. The other three are the compounds $[Ni_6(SO_4)_4(OH)\{(py)C(Me)NO\}_3\{(py)C(Me)NOH\}_3(MeOH)_2(H_2O)]$, $[Ni_6(SO_4)_4(OH)\{(py)C(ph)NO\}_3\{(py)C(ph)NOH\}_3(MeOH)_3]$ and $[Ni_6(SO_4)_4(OH)\{(py)C(ph)NO\}_3\{(py)C(ph)NOH\}_3(H_2O)_3]$ [24].

Complex **1** joins a small but growing family of structurally characterized metal complexes containing the neutral or anionic forms of phenyl(2-pyridyl)ketone oxime as ligands. Since most of these complexes have been reported only recently, we felt it timely to collect the crystallographically characterized, non-organometallic metal complexes of (py)C(ph)NOH and/or $(py)C(ph)NO^-$ in Table 3, together with the ligands' coordination modes and the cores of the polynuclear complexes for convenient comparison. It should be mentioned at this point that the first structurally characterized complexes of phenyl(2-pyridyl)ketone oxime were the carbonyl compounds $[Os_3(CO)_8\{(py)C(ph)NO\}_2]$, $[Os_3(CO)_8\{(py)C(ph)NO\}\{(py)C(ph)HNH\}]$, $[Os_3H(CO)_9\{(py)C(ph)NO\}]$ and $[Os_3H(CO)_{11}\{(py)C(ph)NO\}]$ which exhibit interesting structural features [34]; these complexes have not been incorporated in Table 3. Inspection of Table 3 clearly shows that: (i) complex **1** is amongst the highest-nuclearity clusters of any metal identified with the $(py)C(ph)NO^-$ ligand; (ii) the 2.111 coordination mode is the most common for the bridging $(py)C(ph)NO^-$ ligands; and (iii) the 3.211 mode of $(py)C(ph)NO^-$ observed in **1** is rare in the complexes containing bridging $(py)C(ph)NO^-$ ligands.

3.3. IR spectra

The medium intensity bands at 1568 and 1094 cm^{-1} in the spectrum of the free ligand (py)C(ph)NOH are assigned to $\nu(C{=}N)_{oxime}$ and $\nu(N{-}O)_{oxime}$, respectively [24,37]. The 1094 cm^{-1} band is shifted to a lower wavenumber (1072 cm^{-1}) in **1**. This shift is attributed to the coordination of the neutral oxime nitrogen [38]. Somewhat to our surprise, the 1568 cm^{-1} band is shifted to a higher wavenumber in the complex (1594 cm^{-1}), overlapping with an aromatic stretch. This shift may be indicative of the oxime nitrogen coordination [38]. Extensive studies on Schiff-base complexes (which also contain a C=N bond) have shown [39] that a change in the s character of the nitrogen lone pair occurs upon coordination such that the s character of nitrogen orbital involved in the C=N bond increases; this change in hybridization produces a greater C=N stretching force constant relative to the free neutral ligand.

The in-plane deformation band of the 2-pyridyl ring of free (py)C(ph)NOH at 622 cm^{-1} shifts upwards (642 cm^{-1}), confirming the involvement of the ring-N atom in coordination [40].

The IR spectrum of the free, *i.e.*, ionic, sulfate (the ion belongs to the T_d point group) consists of two bands at ~1105 and ~615 cm^{-1}, assigned to the $\nu_3(F_2)$ stretching $[\nu_d(SO)]$ and $\nu_4(F_2)$ bending $[\delta_d(O\text{-}SO)]$ modes, respectively [13,41]. The $\nu_1(A_1)$ stretching $[\nu_s(SO)]$ and $\nu_2(E)$ bending $[\delta_d(OSO)]$ fundamentals are not IR-active. The coordination of SO_4^{2-} to metal ions decreases the symmetry of the group and the ν_3 and ν_4 modes are split [13,41]. In the case the SO_4^{2-}-site symmetry is lowered from T_d to C_{3v} (monodentate coor-

Table 3
Formulae, ligands' coordination modes[a] and cores[b] for structurally characterized, non-organometallic metal complexes of (py)C(ph)NOH and/or $(py)C(ph)NO^-$.

Complex[c]	Coordination mode of the oxime/oximate ligand[d]	Core	Ref.
$[Mn(O_2CPh)_2\{(py)C(ph)NOH\}_2]$	1.011		[11c]
$[Mn^{II}_4Mn^{III}_4O_2(OH)_2(O_2CPh)_{10}\{(py)C(ph)NO\}_4]$	2.111	$[Mn_4^{II}Mn_4^{III}(\mu_4-O)_2(\mu_3-OH)_2]^{14+}$	[11c]
$[Mn^{II}_3Mn^{IV}O(N_3)(O_2CPh)_3\{(py)C(ph)NO\}_4]$	2.111	$[Mn_3^{II}Mn^{IV}(\mu_4-O)(\nu^1:\mu-N_3)]^{7+}$	[11i]
$[Mn^{III}_3O(O_2CMe)_3(py)C(ph)NO_3]$	2.111	$[Mn_3^{III}(\mu_3-O)]^{7+}$	[11h]
$[Co_2^{III}Co^{II}\{(py)C(ph)NO\}_6](PF_6)_2$	2.111	$[CO^{II}CO_2^{III}(\mu_2-ONR)_6]^{2+}$	[35]
$[Co\{(py)C(ph)NO\}_3]$	1.011		[35]
$[Cu_3(OMe)(Cl)(ClO_4)\{(py)C(ph)NO\}_3]$	2.111	$[Cu_3(\mu_3\text{-}MeO)(\mu_3\text{-}Cl)(\mu_2\text{-}ONR)_3]^+$	[36]
$[Cu_3(OH)(ClO_4)_2\{(py)C(ph)NO\}_3(MeOH)_2]$	2.111	$[Cu_3(\mu_3\text{-}OH)(\mu_2\text{-}ClO_4)(\mu_2\text{-}ONR)_3]^+$	[36]
$[Ni_4(O_2CMe)_4\{(py)C(ph)NO\}_4(MeOH)_2]$	3.211	$[Ni_4(\mu_3\text{-}ONR)_4]^{4+}$	[11p]
$[Ni_6(SO_4)_4(OH)\{(py)C(ph)NO\}_3\{(py)C(ph)NOH\}_3L_3]$	3.211, 1.011	$[Ni_6(\mu_3\text{-}OH)(\mu_3\text{-}SO_4)_3(\mu_3\text{-}ONR)_3]^{2+}$	[24]
$[Ni_2(SO_4)_2\{(py)C(ph)NOH\}_4]$	1.011	$[Ni_2(\eta^1{:}\eta^1{:}\mu_2\text{-}SO_4)_2]$	[23]
$[Ni\{(py)C(ph)NOH\}_3](SO_4)$	1.011		[23]
$[Ni_6(SO_4)_2\{(py)C(ph)NO\}_8]$	3.211, 2.111	$[Ni_6(\mu_5\text{-}SO_4)_2(\mu_2\text{-}ONR)_6(\mu_3\text{-}ONR)_2]$	this work

[a] Only for (py)C(ph)NOH and/or $(py)C(ph)NO^-$.
[b] Only for the dinuclear and polynuclear complexes.
[c] Solvate molecules have been omitted.
[d] Using Harris notation [20].

dination), both ν_1 and ν_2 appear in the IR spectrum with weak to medium intensity, while ν_3 and ν_4 each splits into two bands. In the case the SO_4^{2-}-site symmetry is lowered from T_d to C_{2v} (bidentate chelating or bridging coordination), again both ν_1 and ν_2 appear in the IR spectrum, while ν_3 and ν_4 each splits into three IR-active vibrations [41]. In the case the SO_4^{2-}-site symmetry is lowered to C_1, ν_3 and ν_4 each splits into three IR-active vibrations, ν_1 appears in the IR spectrum, while ν_2 splits into two IR modes [41]. The symmetry of the sulfato groups in **1** is lower than C_i. The bands at 1210, 1124 and 1072 (overlapping with the $N–O_{oxime}$ stretch) cm^{-1} are attributed to the ν_3 modes [41], while the bands at 616, 642 and 704 cm^{-1} are assigned to the ν_4 modes [13,41] with the intermediate wavenumber band being superimposed by a ligand's vibration. The band at 974 cm^{-1} and the two weak features at 474 and 452 cm^{-1} are assigned [13,41] can be assigned to the ν_1 and ν_2 modes, respectively. These spectral features suggest a low symmetry for the sulfato ligand in the complex.

The ν(C=O) vibrational mode of the lattice DMF molecules appears at 1658 cm^{-1} [42].

3.4. Magnetic properties

Variable-temperature dc magnetic susceptibility studies were performed on a polycrystalline sample of compound **1** in an applied magnetic field of 0.3 *T* (3.0 KG) and in the 2.0–300 K range. The data are plotted as $\chi_M T$ versus *T* in Fig. 3. The $\chi_M T$ value at 300 K is 7.19 $cm^3\,mol^{-1}\,K$, close to the expected value of 7.26 $cm^3\,mol^{-1}\,K$ for six non-interacting $S = 1$ centers assuming $g = 2.20$. As *T* is lowered, the $\chi_M T$ product decreases to reach a final value of 1.02 $cm^3\,K\,mol^{-1}$ at 2 K; the decline is sharper below ~100 K. The data indicate an overall antiferromagnetic behavior. The χ_M versus *T* plot does not exhibit a maximum in the temperature range studied. Magnetization experiments performed at 2.0 K show a continuous increase of *M* as the field increases, reaching a non-saturated value equivalent to two electrons with a non-Brillouin shape, suggesting the population of various spin levels close to the ground state spin.

To fit and interpret the magnetic susceptibility data of **1**, it is first necessary to find all possible magnetic pathways in the complicated structural type. Close inspection of the molecular structure reveals that there are five different superexchange pathways and thus five different kinds of *J* values: J_1 is associated (from now onwards the numbering scheme that will be used is the same with that used in the real structure of **1**, see Fig. 1) with the Ni(1)···Ni(3) and Ni(1′)···Ni(3′) interactions, each through one monoatomic bridge from a 3.211 (py)C(ph)NO^- ligand, a triatomic part of one sulfato ligand and one diatomic oximate group from a 2.111 (py)C(ph)NO^- ligand; J_2 is associated with the Ni(2)···Ni(3) and Ni(2′)···Ni(3′) interactions, each through one monoatomic bridge from a sulfate ion and two diatomic oximate bridges coming from a 2.111 and a 3.211 organic ligands; J_3 is associated with the Ni(1)···Ni(2′) and Ni(1′)···Ni(2) interactions, each through one diatomic oximate group from a 2.111 (py)C(ph)NO^- ligand, one monoatomic bridge from a sulfate ion and one triatomic part of the second (symmetry-related) sulfato ligand; J_4 is associated with the Ni(1)···Ni(2) and Ni(1′)···Ni(2′) interactions, each through two triatomic parts of the two sulfato ligands and one diatomic oximate group from a 3.211 (py)C(ph)NO^- ligand; and finally J_5 is associated with the Ni(1)···Ni(3′) and Ni(2)···Ni(3′) (and their symmetry equivalents) interactions, each through the triatomic part of a sulfato ligand. The spin Hamiltonian for such a system is given by Eq. (2).

$$\begin{aligned} H = &-J_1(S_1\cdot S_3 + S_{1'}\cdot S_{3'}) - J_2(S_2\cdot S_3 + S_{2'}\cdot S_{3'}) \\ &- J_3(S_1\cdot S_{2'} + S_{1'}\cdot S_2) - J_4(S_1\cdot S_2 + S_{1'}\cdot S_{2'}) \\ &- J_5(S_2\cdot S_{3'} + S_{2'}\cdot S_3 + S_{1'}\cdot S_3 + S_1\cdot S_{3'}) \end{aligned} \quad (2)$$

To avoid a vast parameterization, we decided to attempt to fit the susceptibility data using a simpler 3-*J* model. It is known that the superexchange Ni–O–X–O–Ni interactions mediated by tetrahedral anions with electronegative central atoms, e.g. SO_4^-, ClO_4^-, PO_3^{3-}, are negligible [26]. Another simplification can be made according to the kind and the number of the bridges between the Ni^{II} ions; Ni1 and Ni3 (and their symmetry equivalents) are interacting through three pathways involving one monoatomic, one diatomic and one triatomic bridge. The same number and kind of bridges (with similar Ni–N–O–Ni torsion and Ni–O–Ni bond angles) comprise the interaction pathways between Ni1 and Ni2′ (and their symmetry equivalents). Thus, assuming that $J_5 = 0$ and $J_1 = J_3$, the spin Hamiltonian can be expressed in the form of Eq. (3) and the resulting new, simpler interaction scheme is shown in Scheme 3.

$$\begin{aligned} H = &-J_1(S_1\cdot S_3 + S_1\cdot S_{2'} + S_{1'}\cdot S_{3'} + S_{1'}\cdot S_2) - J_2(S_2\cdot S_3 + S_{2'}\cdot S_{3'}) \\ &- J_3(S_1\cdot S_2 + S_{1'}\cdot S_{2'}) \end{aligned} \quad (3)$$

The fit on the interaction pattern of Scheme 3 was performed by means of the computer program CLUMAG [43]. The best fit parameters were $J_1 = -12.7\ cm^{-1}$, $J_2 = -12.9\ cm^{-1}$, $J_3 = -21.0\ cm^{-1}$, $g = 2.32$ and $R = 1.2\cdot10^{-2}$ [$R = \Sigma((\chi_M)^{calc} - (\chi_M)^{obs})^2/\Sigma((\chi_M)^{obs})^2$].

The fitting results are in accordance with the behavior of the system at low temperatures (Fig. 4). A low *T*, simulation of the $\chi_M T$ response of a hexagonal arrangement of six $S = 1$ metal centers results in a well isolated $S = 0$ ground state ($J_1 = J_2$ and $J_3 = 0$). In contrast, increasing the antiferromagnetic interaction J_3 within the hexagonal array of the spin carriers, the ground state remains

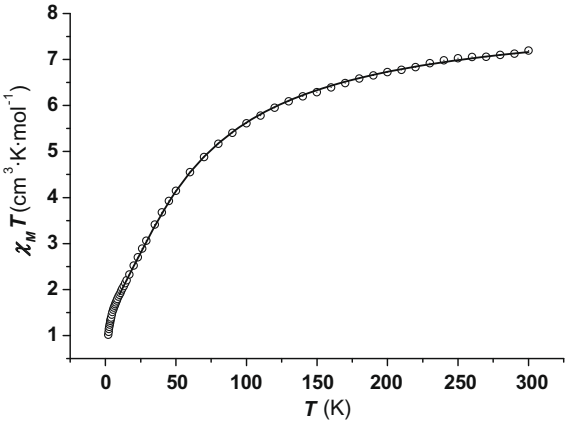
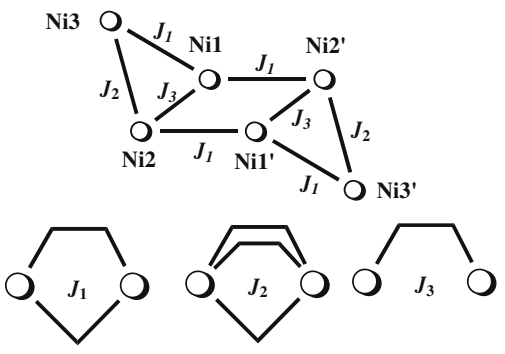


Fig. 3. $\chi_M T$ vs. *T* plot for complex **1**. The solid line represents the best fit to the data as described in the text.



Scheme 3. Top: a 3-*J* exchange-interaction pattern corresponding to the Hamiltonian of Eq. (3) for **1**. Bottom: schematic representation of the bridges involved in each pathway; the monoatomic bridges derive from oximato or sulfato groups.

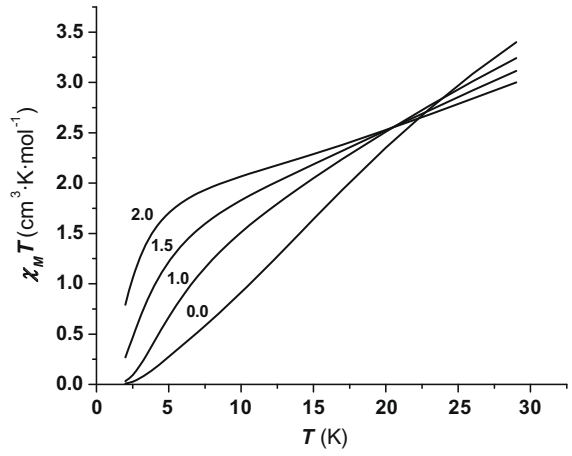


Fig. 4. Low temperature simulation of the response of six $S = 1$ centers arranged in the manner shown in Scheme 3 and assuming $J_1 = J_2$. The four plots correspond to the indicated ratios $J_3/J_{1,2}$.

$S = 0$, but the slope of $\chi_M T$ plot changes and for high $J_3/J_{1,2}$ ratios it tends to values close to 1 $cm^3\,K\,mol^{-1}$ as a result of competitive interactions in the magnetically isosceles triangle Ni1–Ni2–Ni3 (and its equivalent) (Fig. 4), which reduces the gap between the $S = 0$ ground state and the first excited states $S = 1$ and $S = 2$. The vicinity of these S levels leads to the characteristic non-saturated magnetization plot.

The J values are reasonable for $Ni^{II}\cdots Ni^{II}$ magnetic exchange interactions through di-/monoatomic oximato and monoatomic sulfato bridges [24].

4. Conclusions

The present work extends the body of results that emphasize the ability of the sulfate ion to create interesting structural types in 3d-metal chemistry. The study of the coordination chemistry of the *binary* SO_4^{2-}/(py)C(ph)NOH ligand system in the presence of base in DMF has provided access to the novel hexanuclear Ni(II) cluster $[Ni_6(SO_4)_2\{(py)C(ph)NO\}_8]\cdot 6DMF$ (**1**·6DMF). Complex **1** contains the $[Ni_6(\mu_5\text{-}SO_4)_2(\mu_2\text{-}ONR)_6(\mu_3\text{-}ONR)_2]$ core, where $R^- = -C(py)(ph)$, with a chair-like topology of the Ni^{II} ions; it is a valuable addition to the family of hexanuclear Ni^{II} clusters. In compound **1**, the SO_4^{2-} adopts the rare 5.2210 coordination mode. The magnetic properties of **1** have been interpreted using three exchange interactions in a simplified model.

Analogues of **1** with 2-pyridinealdoxime [(py)C(H)NOH], methyl(2-pyridyl)ketone oxime [(py)C(Me)NOH] or di-2-pyridyl ketone oxime [$(py)_2$CNOH] (Scheme 1) are not known, until to date, and it is currently not evident whether the preparation and stability of such hexanuclear complexes are dependent on the particular nature of the R substituent on the oximate carbon.

Acknowledgements

C.P. and S.P.P. thank the European Social Fund (ESF), the Operational Program for Educational and Vocational Training II (EPEAEK II) and particularly the Program PYTHAGORAS (Grant b.365.037), for funding this work. A.E. thanks the Ministerio de Ciencia y Tecnología (Spain), Project CTQ2006-01759 for financial support of this research.

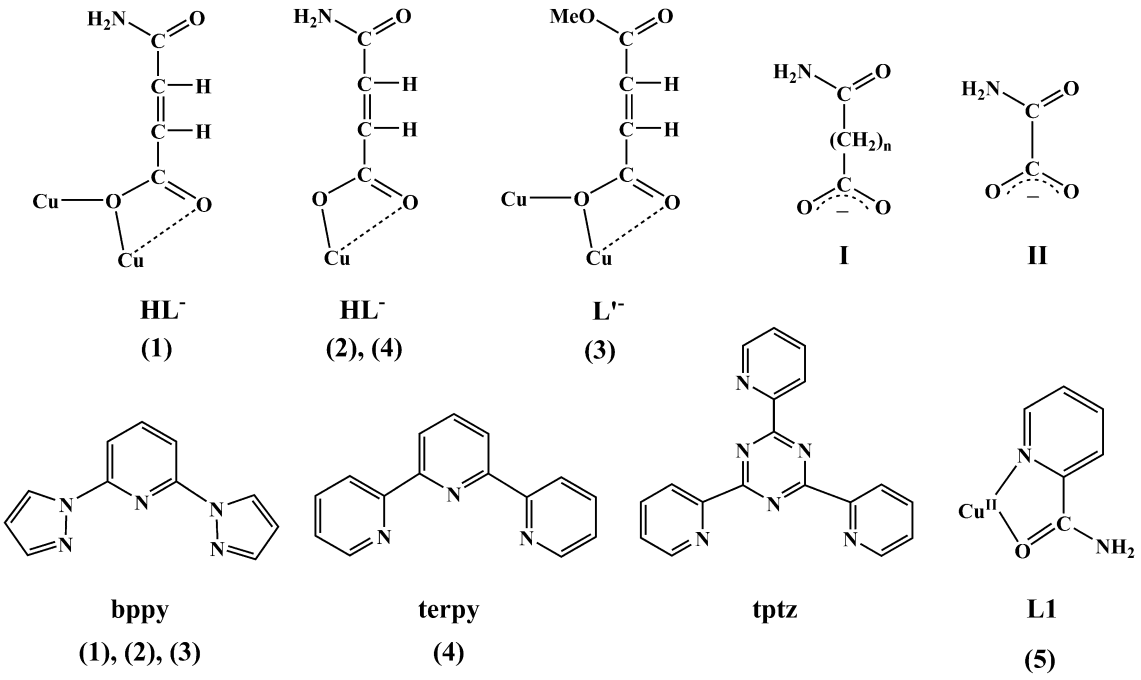
Appendix A. Supplementary data

CCDC 720374 contains the supplementary crystallographic data for **1**·6DMF. These data can be obtained free of charge via http://www.ccdc.cam.ac.uk/conts/retrieving.html, or from the Cambridge Crystallographic Data Centre, 12 Union Road, Cambridge CB2 1EZ, UK; fax: (+44) 1223-336-033; or e-mail: deposit@ccdc.cam.ac.uk.

References

[1] (a) R.A. Grant, D.J. Filman, S.E. Finkel, R. Colter, J.M. Hogle, Nat. Struct. Biol. 5 (1998) 294;
(b) For a minireview see:E.C. Theil, M. Matzapetakis, X. Liu, J. Biol. Inorg. Chem. 11 (2006) 803.
[2] (a) For excellent reviews concerning SMMs, see: G. Christou, D. Gatteschi, D.N. Hendrickson, R. Sessoli, MRS Bull. 25 (2000) 66;
(b) D. Gatteschi, R. Sessoli, Angew. Chem., Int. Ed. 42 (2003) 268;
(c) R. Birchner, G. Chaboussant, C. Dobe, H. Güdel, S.T. Ochsenbein, A. Sieber, O. Waldman, Adv. Funct. Mater. 16 (2006) 209;
(d) G. Aromi, E.K. Brechin, Struct. Bond. 122 (2006) 1.
[3] S. Wang, Coord. Chem. Rev. 215 (2001) 79.
[4] R.E.P. Winpenny, in: J.P. Sauvage (Ed.), Perspectives in Supramolecular Chemistry, vol. 5, Wiley, New York, 1999, p. 193 (Chapter 5).
[5] R.E.P. Winpenny, in: J.A. McCleverty, T.J. Meyer (Eds.), Comprehensive Coordination Chemistry II, vol. 7, Elsevier, Amsterdam, 2004, p. 125 (Chapter 7.3).
[6] E. Breuning, U. Ziener, J.-M. Lehn, E. Wegelius, K. Rissanen, Eur. J. Inorg. Chem. (2001) 1515.
[7] R.W. Saalfrank, U. Reimann, M. Goritz, F. Hampel, A. Scheurer, F.W. Heinemann, M. Buschel, J. Daub, V. Schunemann, A.X. Trautwein, Chem. Eur. J. 8 (2002) 3614.
[8] M. Fujita, K. Umemoto, M. Yoshizawa, N. Fujita, T. Kusukawa, K. Biradha, Chem. Commun. (2001) 509 (feature article).
[9] For a provocative perspective, see: R.E.P. Winpenny, J. Chem. Soc., Dalton Trans. (2001) 1 (Dalton perspective).
[10] For a review, see: C.J. Milios, Th.C. Stamatatos, S.P. Perlepes, Polyhedron 25 (2006) 134 (Polyhedron Report).
[11] (a) C.J. Milios, E. Kefalloniti, C.P. Raptopoulou, A. Terzis, R. Vicente, N. Lalioti, A. Escuer, S.P. Perlepes, Chem. Commun. (2003) 819;
(b) C.J. Milios, C.P. Raptopoulou, A. Terzis, R. Vicente, A. Escuer, S.P. Perlepes, Inorg. Chem. Commun. 6 (2003) 1056;
(c) C.J. Milios, Th.C. Stamatatos, P. Kyritsis, A. Terzis, C.P. Raptopoulou, R. Vicente, A. Escuer, S.P. Perlepes, Eur. J. Inorg. Chem. (2004) 2885;
(d) C.J. Milios, E. Kefalloniti, C.P. Raptopoulou, A. Terzis, A. Escuer, R. Vicente, S.P. Perlepes, Polyhedron 23 (2004) 83;
(e) M. Alexiou, E. Katsoulakou, C. Dendrinou-Samara, C.P. Raptopoulou, V. Psycharis, E. Manessi-Zoupa, S.P. Perlepes, D.P. Kessissoglou, Eur. J. Inorg. Chem. (2005) 1964;
(f) Th.C. Stamatatos, S. Dionyssopoulou, G. Efthymiou, P. Kyritsis, C.P. Raptopoulou, A. Terzis, R. Vicente, A. Escuer, S.P. Perlepes, Inorg. Chem. 44 (2005) 3374;
(g) C.J. Milios, P. Kyritsis, C.P. Raptopoulou, A. Terzis, R. Vicente, A. Escuer, S.P. Perlepes, Dalton Trans. (2005) 501;
(h) Th.C. Stamatatos, D. Foguet-Albiol, C.C. Stoumpos, C.P. Raptopoulou, A. Terzis, W. Wernsdorfer, S.P. Perlepes, G. Christou, J. Am. Chem. Soc. 127 (2005) 15380;
(i) C.J. Milios, S. Piligkos, A.R. Bell, R.H. Laye, S.J. Teat, R. Vicente, E. McInnes, A. Escuer, S.P. Perlepes, R.E.P. Winpenny, Inorg. Chem. Commun. 9 (2006) 642;
(j) Th.C. Stamatatos, A.K. Boudalis, Y. Sanakis, C.P. Raptopoulou, Inorg. Chem. 45 (2006) 7372;
(k) Th.C. Stamatatos, J.C. Vlahopoulou, Y. Sanakis, C.P. Raptopoulou, V. Psycharis, A.K. Boudalis, S.P. Perlepes, Inorg. Chem. Commun. 9 (2006) 814;
(l) C. Papatriantafyllopoulou, C.P. Raptopoulou, A. Escuer, C.J. Milios, Inorg. Chim. Acta 360 (2007) 61;
(m) K.V. Priggouri, C.P. Raptopoulou, A. Escuer, Th.C. Stamatatos, Inorg. Chim. Acta 360 (2007) 69;
(n) Th.C. Stamatatos, D. Foguet-Albiol, C.C. Stoumpos, C.P. Raptopoulou, A. Terzis, W. Wernsdorfer, S.P. Perlepes, G. Christou, Polyhedron 26 (2007) 2165;
(o) Th.C. Stamatatos, E. Diamantopoulou, C.P. Raptopoulou, V. Psycharis, A. Escuer, S.P. Perlepes, Inorg. Chem. 46 (2007) 2350;
(p) Th.C. Stamatatos, C. Papatriantafyllopoulou, E. Katsoulakou, C.P. Raptopoulou, S.P. Perlepes, Polyhedron 26 (2007) 1830.
[12] (a) M. Murugesu, K.A. Abboud, G. Christou, Polyhedron 23 (2004) 2779;
(b) T. Afrati, C. Dendrinou-Samara, C.P. Raptopoulou, A. Terzis, V. Tangoulis, D.P. Kessissoglou, Angew. Chem., Int. Ed. 41 (2002) 2148;
(c) A.J. Stemmler, J.W. Kampf, V.L. Pecoraro, Inorg. Chem. 34 (1995) 2271.
[13] For a review, see: C. Papatriantafyllopoulou, E. Manessi-Zoupa, A. Escuer, S.P. Perlepes, Inorg. Chim. Acta 362 (2009) 634.
[14] (a) M.I. Khan, S. Cevik, R.J. Doedens, Chem. Commun. (2001) 1930;
(b) A.C. Sudik, A.R. Millward, N.W. Ockwig, A.P. Côte, J. Kim, O.M. Yaghi, J. Am. Chem. Soc. 127 (2005) 7110.
[15] J. Moriyama, H. Nishiguchi, T. Ishihara, Y. Takita, Ind. Eng. Chem. Res. 41 (2002) 32. and references cited therein.
[16] (a) S.-Y. Wan, Y.-Z. Li, T.-A. Okamura, J. Fian, W.-Y. Sun, N. Ueyama, Eur. J. Inorg. Chem. (2003) 3783;
(b) Z. He, E.-Q. Gao, Z.-M. Wang, C.-H. Yan, M. Kurmoo, Inorg. Chem. 44 (2005) 862.
[17] J. Reedijk, Inorg. Chim. Acta 198-200 (1992) 873.

[18] D. Peak, R.G. Ford, D.L. Sparks, J. Colloid Interface Sci. 218 (1999) 289.
[19] G. Tamasi, R. Cini, Dalton Trans. (2003) 2928 (and references therein).
[20] R.A. Coxall, S.G. Harris, D.K. Henderson, S. Parsons, P.A. Tasker, R.E.P. Winpenny, J. Chem. Soc., Dalton Trans. (2000) 2349.
[21] G.M. Sheldrick, SHELXS-86: Structure Solving Program, University of Göttingen, Germany, 1986.
[22] G.M. Sheldrick, SHELXL-97: Crystal Structure Refinement Program, University of Göttingen, Germany, 1997.
[23] C. Papatriantafyllopoulou, C.G. Efthymiou, C.P. Raptopoulou, A. Terzis, E. Manessi-Zoupa, S.P. Perlepes, Spectrochim. Acta, Part A 70 (2008) 718.
[24] C. Papatriantafyllopoulou, G. Aromi, A.J. Tasiopoulos, V. Nastopoulos, C.P. Raptopoulou, S.J. Teat, A. Escuer, S.P. Perlepes, Eur. J. Inorg. Chem. (2007) 2761.
[25] C.G. Efthymiou, C.P. Raptopoulou, A. Terzis, S.P. Perlepes, A. Escuer, C. Papatriantafyllopoulou, Polyhedron (2009), submitted for publication.
[26] C. Papatriantafyllopoulou, C.G. Efthymiou, C.P. Raptopoulou, R. Vicente, E. Manessi-Zoupa, V. Psycharis, A. Escuer, S.P. Perlepes, J. Mol. Struct. 829 (2007) 176.
[27] (a) G.S. Papaefstathiou, A. Escuer, F.A. Mautner, C. Raptopoulou, A. Terzis, S.P. Perlepes, R. Vicente, Eur. J. Inorg. Chem. (2005) 879;
(b) C.G. Efthymiou, C.P. Raptopoulou, A. Terzis, R. Boča, M. Korabic, J. Mrozinski, S.P. Perlepes, E.G. Bakalbassis, Eur. J. Inorg. Chem. (2006) 2236.
[28] C. Papatriantafyllopoulou, C.P. Raptopoulou, A. Terzis, J.F. Janssens, S.P. Perlepes, E. Manessi-Zoupa, Z. Naturforsch. 62b (2007) 1123.
[29] (a) M.S. Paquette, L.F. Dahl, J. Am. Chem. Soc. 102 (1980) 6621;
(b) D. Fenske, H. Fleischer, H. Krautscheid, H. Magull, C. Oliver, S. Weisgerber, Z. Naturforsch. 46b (1991) 1384.
[30] (a) Representative references: E. Ilina, V.G. Kessler, Polyhedron 24 (2005) 3052;
(b) A. Cornia, A.C. Fabretti, D. Gatteschi, G. Palyi, E. Rentschler, O.I. Shchegolikhina, A.A. Zhdanov, Inorg. Chem. 34 (1995) 5383;
(c) Y.-B. Jiang, H.-Z. Kou, R.-J. Wang, A.-L. Cui, J. Ribas, Inorg. Chem. 44 (2005) 709;
(d) T.K. Paine, E. Rentschler, T. Weyhermüller, P. Chaudhuri, Eur. J. Inorg. Chem. (2003) 3167;
(e) S. Wörl, H. Pritzkow, I.O. Fritsky, R. Kramer, Dalton Trans. (2005) 27;
(f) M. Mikuriya, K. Tanaka, N. Inoue, D. Yoshioka, J.-W. Lim, Chem. Lett. 32 (2003) 126;
(g) F.A. Cotton, B.H.C. Winquist, Inorg. Chem. 8 (1969) 1304;
(h) M.-L. Tong, M. Monfort, J.M.C. Juan, X.-M. Chen, X.-H. Bu, M. Ohba, S. Kitagawa, Chem. Commun. (2005) 233;
(i) R.E.P. Winpenny, Adv. Inorg. Chem. 52 (2001) 1.
[31] (a) T. Hori, S. Himeno, O. Tamada, J. Chem. Soc., Dalton Trans. (1992) 275;
(b) S.J. Maginn, M.M. Harding, J.W. Campbell, Acta Crystallogr., Sect. B 49 (1993) 520.
[32] K.V. Domasevitch, I.A. Gural'skiy, P.V. Solntsev, E.B. Rusanov, A.N. Chernega, Acta Crystallogr., Sect. C 63 (2007) m259.
[33] W. Ouellette, B.S. Hudson, J. Zubieta, Inorg. Chem. 46 (2007) 4887.
[34] J.S.-Y. Wong, W.T. Wong, New J. Chem. 26 (2002) 94.
[35] Th.C. Stamatatos, A. Bell, P. Cooper, A. Terzis, C.P. Raptopoulou, S.L. Heath, R.E.P. Winpenny, S.P. Perlepes, Inorg. Chem. Commun. 8 (2005) 533.
[36] T. Afrati, C. Dendrinou-Samara, C. Raptopoulou, A. Terzis, V. Tangoulis, D.P. Kessissoglou, Dalton Trans. (2007) 5156.
[37] P. Chaudhuri, M. Winter, U. Flörke, H.-J. Haupt, Inorg. Chim. Acta 232 (1995) 125.
[38] C. Papatriantafyllopoulou, C.P. Raptopoulou, A. Terzis, E. Manessi-Zoupa, S.P. Perlepes, Z. Naturforsch. 61b (2006) 37.
[39] J. Lopez-Carriga, G.T. Badcock, J.F. Harrison, J. Am. Chem. Soc. 108 (1986) 7241.
[40] A.B.P. Lever, A. Mantovani, Inorg. Chem. 10 (1971) 817.
[41] K. Nakamoto, Infrared and Raman Spectra of Inorganic and Coordination Compounds, 4th ed., Wiley, New York, 1986. p. 139, 248.
[42] C. Airoldi, Inorg. Chem. 10 (1981) 998.
[43] D. Gatteschi, L. Pardi, Gazz. Chim. Ital. 123 (1993) 231.



Scheme 1. Some of the ligands discussed in the text and their coordination modes. The ligand used in this work is the maleamate(−1) ion (HL^-).

Safety note. Perchlorate salts are potentially explosive; such compounds should be synthesized and used in small quantities, and treated with utmost care at all times.

2.2. Compound preparation

2.2.1. $[Cu_2(HL)_2(bppy)_2](ClO_4)_2{\cdot}H_2O$ (**1**·H_2O)

A colorless aqueous solution (1.5 ml) of $LiOH{\cdot}H_2O$ (0.018 g, 0.43 mmol) was added to a colorless solution of H_2L (0.049 g, 0.43 mmol) in MeCN (20 ml) to give a white suspension which was stirred for 10 min to afford a colorless solution. Solid bppy (0.061 g, 0.29 mmol) was then added to give a colorless solution. A blue solution of $Cu(ClO_4)_2{\cdot}6H_2O$ (0.107 g, 0.29 mmol) in MeCN (10 ml) was finally added to obtain a dark green solution. Layering of the final solution with a mixture of Et_2O/*n*-hexane (10 ml, 1:1 v/v) afforded X-ray quality, dark blue prismatic crystals of **1**·H_2O, which were collected by filtration under vacuum, washed with cold MeCN (3 ml) and Et_2O (5 ml), and dried in air. Typical yields were in the 45–50% range. FT-IR for **1**·H_2O (KBr pellet, cm^{-1}): 3420mb, 3100m, 3078m, 3040w, 1688s, 1624vs, 1592s, 1530s, 1500m, 1482vs, 1438w, 1404vs, 1350s, 1314w, 1304sh, 1222vw, 1210vw, 1172m, 1130sh, 1112sh, 1094vs, 1074sh, 1048sh, 1036sh, 974s, 910vw, 806s, 774s, 680vw, 656vw, 636sh, 626s, 598m, 484w. *Anal.* Calc. for $C_{30}H_{28}N_{12}O_{15}Cl_2Cu_2$ (994.62): C, 36.23; H, 2.84; N, 16.90. Found: C, 36.28; H, 2.80; N, 16.78%.

2.2.2. $[Cu(HL)(bppy)(ClO_4)]$ (**2**)

Solid $LiOH{\cdot}H_2O$ (0.018 g, 0.43 mmol) was added to a colorless solution of H_2L (0.049 g, 0.43 mmol) in MeOH (20 ml) to give a white suspension which was stirred for 20 min to finally afford a colorless solution. Solid $Cu(ClO_4)_2{\cdot}6H_2O$ (0.107 g, 0.29 mmol) was added to give a light blue solution. A colorless solution of bppy (0.061 g, 0.29 mmol) in MeOH (10 ml) was then added to obtain a final blue solution. Vapor diffusion of Et_2O into the final solution afforded X-ray quality, light blue needle-like crystals of **2** after 15 days. The crystals were collected by filtration under vacuum, washed with cold MeOH (3 ml) and Et_2O (5 ml), and dried in air. Typical yields were in the 60–65% range. FT-IR for **2** (KBr pellet, cm^{-1}): 3408mb, 3194w, 3156w, 3117m, 2923w, 2854vw, 2736vw, 2313vw, 2021vw, 1806w, 1813vw, 1775w, 1685vs, 1644ssh, 1629vs, 1597vs, 1525vs, 1503s, 1485vs, 1435s, 1405vs, 1355vs, 1321s, 1301vs, 1237m, 1216m, 1177m, 1077vsb, 1053vs, 1035sh, 980s, 934w, 911m, 889w, 875w, 865vw, 817sh, 802s, 782vs, 717w, 684m, 662m, 624s, 599m, 591sh, 554mb, 490w, 471w, 459vw. *Anal.* Calc. for $C_{15}H_{13}N_6O_7ClCu$ (488.30): C, 36.90; H, 2.68; N, 17.21. Found: C, 37.02; H, 2.47; N, 16.99%.

2.2.3. $[Cu_2(L')_2(bppy)_2](ClO_4)_2$ (**3**)

Solid bppy (0.061 g, 0.29 mmol) was dissolved in a colorless solution of H_2L (0.049 g, 0.43 mmol) in MeOH (20 ml). A light blue solution of $Cu(ClO_4)_2{\cdot}6H_2O$ (0.107 g, 0.29 mmol) in the same solvent (10 ml) was then added to obtain a green-turquoise solution. X-ray quality, blue prismatic crystals of **3** were formed in a closed vial after 7 days. The crystals were collected by filtration under vacuum, washed with Et_2O (2 × 2 ml) and dried in air. Typical yields were in the 50–55% range. FT-IR for **3** (KBr pellet, cm^{-1}): 3510w, 3424wb, 3150sh, 3116m, 1720vs, 1660s, 1624vs, 1594s, 1532s, 1502m, 1488vs, 1438m, 1404vs, 1354s, 1320m, 1298m, 1222m, 1178m, 1136sh, 1090vs, 1060sh, 1036w, 988w, 974s, 892w, 820w, 792m, 782sh, 772m, 686m, 644sh, 636sh, 624m, 598m, 588w, 488vw, 456vw. *Anal.* Calc. for $C_{32}H_{28}N_{10}O_{16}Cl_2Cu_2$ (1006.32): C, 38.18; H, 2.80; N, 13.91. Found: C, 38.32; H, 2.77; N, 13.76%.

2.2.4. $[Cu(HL)(terpy)(H_2O)](ClO_4)$ (**4**)

A colorless aqueous solution (1.5 ml) of $LiOH{\cdot}H_2O$ (0.018 g, 0.43 mmol) was added to a colorless solution of H_2L (0.049 g, 0.43 mmol) in MeCN (20 ml) to give a white suspension which was stirred for 10 min to afford a colorless solution. Solid terpy (0.068 g, 0.29 mmol) was added to afford a pale yellow, almost colorless, solution. A light blue solution of $Cu(ClO_4)_2{\cdot}6H_2O$ (0.063 g, 0.17 mmol) in MeCN (5 ml) was then added to obtain a dark green solution. Vapor diffusion of Et_2O into the final solution afforded X-ray quality, blue-marine prismatic crystals of **4** after 2 days. The crystals were collected by filtration under vacuum, washed with cold MeCN (3 ml) and Et_2O (5 ml), and dried in air. Typical yields

were in the 60–65% range. FT-IR for **4** (KBr pellet, cm^{-1}): 3538m, 3453m, 3343m, 3204w, 3100vw, 3070vw, 2924vw, 1732vw, 1674s, 1638s, 1598vs, 1573sh, 1499w, 1478m, 1445s, 1406w, 1370m, 1328sh, 1313m, 1300m, 1257w, 1212w, 1183w, 1167w, 1104vs, 1091vs, 1064vs, 1038sh, 1022m, 1009sh, 976m, 932w, 872vw, 834w, 821w, 811w, 779s, 743vw, 733w, 674w, 652m, 621s, 540wb, 509sh, 483w. *Anal.* Calc. for $C_{19}H_{17}N_4O_8ClCu$ (528.37): C, 43.19; H, 3.24; N, 10.60. Found: C, 43.31; H, 3.17; N, 10.29%.

*2.2.5. $[Cu(L1)_2(NO_3)_2]$ (**5**)*

2.2.5.1. Method A. Solid $Cu(NO_3)_2{\cdot}2.5H_2O$ (0.067 g, 0.29 mmol) was dissolved in a colorless solution of H_2L (0.049 g, 0.43 mmol) in MeOH (20 ml) to afford a light blue solution. A pale yellow solution of tptz (0.047 g, 0.15 mmol) in MeOH (8.5 ml) was then added to obtain a final light green solution. X-ray quality light blue plate-needle-like crystals of **5** were formed by layering of the final solution with Et_2O (10 ml). The crystals were collected by filtration under vacuum, washed with MeOH (3 ml) and Et_2O (5 ml), and dried in air. Typical yields were in the 50–55% range. FT-IR for **5** (KBr pellet, cm^{-1}): 3273mb, 3079sb, 2782vw, 2445vw, 2353w, 2033w, 1995vw, 1750vw, 1681s, 1585m, 1566s, 1499m, 1445s, 1408s, 1384vs, 1324vs, 1310sh, 1280m, 1184m, 1172w, 1129m, 1105w, 1055w, 1045vw, 1033m, 908w, 831m, 808m, 793sh, 757m, 707vw, 679w, 660m, 524w, 458sh, 446w. *Anal.* Calc. for $C_{12}H_{12}N_6O_8Cu$ (431.81): C, 33.38; H, 2.80; N, 19.46. Found: C, 33.51; H, 2.69; N, 19.32%.

2.2.5.2. Method B. Solid $Cu(NO_3)_2{\cdot}2.5H_2O$ (0.067 g, 0.29 mmol) was dissolved in a pale yellow solution of tptz (0.091 g, 0.29 mmol) in MeOH (20 ml) to afford a green solution. X-ray quality light blue plate-needle-like crystals of the product were formed by layering of the final solution with Et_2O (10 ml). The crystals were collected by filtration under vacuum, washed with MeOH (3 ml) and Et_2O (5 ml), and dried in air. Typical yields were in the 60–65% range. The identity of the crystals was confirmed by unit cell determination (a = 7.463(9), b = 13.67(2), c = 8.83(1) Å, β = 104.24(3)°, see Table 1).

2.3. Single-crystal X-ray crystallography

Important crystallographic data for the structures of **1**·H_2O and **3** have been previously reported [4b]. Crystals of **2** (0.08 × 0.18 × 0.48 mm), **4** (0.10 × 0.25 × 0.70 mm) and **5** (0.10 × 0.10 × 0.80 mm) were mounted in capillaries. Diffraction measurements were made on a Crystal Logic Dual Goniometer diffractometer using graphite monochromated Mo Kα radiation. Unit cell dimensions were determined by using the angular settings of 25 automatically centered reflections in the range $11 < 2\theta < 23°$. Intensity data were recorded using a θ–2θ scan. Three standard reflections monitored every 97 reflections showed less than 3% variation and no decay. Lorentz, polarization and ψ-scan absorption corrections (for **4**) were applied using CRYSTAL LOGIC software. Important crystallographic and refinement data are listed in Table 1.

The structures were solved by direct methods using SHELXS-97 [7] and refined by full-matrix least-squares techniques on F^2 with SHELXS-97 [8]. Further crystallographic details for **2**: $2\theta_{max}$ = 50°; reflections collected/unique/used, 3528/3256 [R_{int} = 0.0090]/3256; 323 parameters refined; $(\Delta/\sigma)_{max}$ = 0.008; $(\Delta\rho)_{max}/(\Delta\rho)_{min}$ = 1.030/−0.804 e/Å^3; R/R_w (for all data), 0.0624/0.1470. Hydrogen atoms were located by difference maps and refined isotropically. All non-H atoms were refined anisotropically. Further crystallographic details for **4**: $2\theta_{max}$ = 50°; reflections collected/unique/used, 3812/3583 [R_{int} = 0.0072]/3583; 366 parameters refined; $(\Delta/\sigma)_{max}$ = 0.001; $(\Delta\rho)_{max}/(\Delta\rho)_{min}$ = 0.562/−0.324 e/Å^3; R/R_w (for all data), 0.0335/0.0855. Hydrogen atoms were located by difference maps and refined isotropically. All non-H atoms were refined anisotropically. Further crystallographic details for **5**: $2\theta_{max}$ = 50°; reflections collected/unique/used, 1649/1527 [R_{int} = 0.0311]/1527; 148 parameters refined; $(\Delta/\sigma)_{max}$ = 0.000; $(\Delta\rho)_{max}/(\Delta\rho)_{min}$ = 0.777/−0.517 e/Å^3; R/R_w (for all data), 0.0497/0.1323. Hydrogen atoms were located by difference maps and refined isotropically. All non-H atoms were refined anisotropically. Plots of all structures were drawn using the DIAMOND 3 program package [9].

Table 1
Crystallographic data for complexes **2**, **4** and **5**.

	2	**4**	**5**
Formula	$C_{15}H_{13}ClCuN_6O_7$	$C_{19}H_{17}ClCuN_4O_8$	$C_{12}H_{12}CuN_6O_8$
Fw	488.30	528.37	431.82
Space group	$P\bar{1}$	$P\bar{1}$	$P2_1/n$
a (Å)	7.533(5)	9.959(3)	7.460(3)
b (Å)	10.475(9)	10.741(3)	13.653(7)
c (Å)	12.412(6)	11.491(3)	8.818(4)
α (o)	76.96(3)	101.690(10)	90
β (°)	78.74(2)	100.860(10)	104.26(2)
γ (°)	80.15(3)	116.900(10)	90
V (Å^3)	927.5(11)	1016.7(5)	870.5(7)
Z	2	2	2
T (°C)	25	20	20
Radiation	Mo Kα	Mo Kα	Mo Kα
ρ_{calcd} (g cm^{-3})	1.748	1.726	1.648
μ (mm^{-1})	1.377	1.264	1.310
Reflections with $I > 2\sigma(I)$	2742	3332	1369
R_1[a]	0.0519	0.0310	0.0457
wR_2[a]	0.1384	0.0832	0.1273

[a] $w = 1/[\sigma^2(F_o^2) + (\alpha P)^2 + bP]$ and $P = (\max\ F_o^2, 0) + 2F_c^2)/3$, $R_1 = \Sigma(|F_o| - |F_c|)/\Sigma(|F_o|)$ and $wR_2 = \{\Sigma[w(F_o^2F_c^2)^2]/\Sigma[w(F_o^2)^2]\}^{1/2}$.

3. Results and discussion

3.1. Syntheses

Our previous investigation of the tertiary $Cu^{II}/H_2L/N,N'$-chelates reaction system (N,N'-chelates used were 1,10-phenanthroline [4] and 2,2′-bipyridine [5]) led to interesting results concerning the chemical and structural properties of the compounds isolated. From the chemical point of view, interesting Cu^{II}-assisted/promoted transformations of the H_2L ligand to the maleate(−2) and monomethyl maleate(−1) (Scheme 1) ligands were observed, as a result of the hydrolysis and methanolysis of the primary amide group of H_2L to a carboxylate function and an ester group, respectively. From the structural point of view, five different coordination modes of the HL^- ligand were observed, leading to mononuclear, dinuclear and polymeric complexes; the latter formed via the rarely observed coordination of the amide oxygen. Our efforts involved the investigation of various synthetic parameters that might affect the identity of the products, i.e. the reaction solvent, the presence or absence of externally added hydroxides, the inorganic anion in the copper(II) salts, the stoichiometry of the reactants, the crystallization method, and the nature of the aromatic N,N'-chelating ligands.

We have expanded our research to the tertiary $Cu^{II}/H_2L/N,N',N''$-chelate reaction system, in order to examine to what extent the binding of three coordination sites per Cu^{II} center by the tridentate aromatic heterocycle might affect the identity of the products. We have explored the influence of the reaction solvent, the presence or absence of external OH^-s and the inorganic anion in the copper(II) salt, on the products of the above general reaction system.

Our initial efforts involved the reaction of $Cu(ClO_4)_2{\cdot}6H_2O$ with 1.5 equiv. of H_2L and 1 equiv. of bppy in the presence of 1.5 equiv.

of $LiOH\cdot H_2O$ in $MeCN/H_2O$ (10:1 v/v). Layering of the resultant dark green solution with a mixture of Et_2O/*n*-hexane afforded complex **1**·H_2O. The preparation of **1**·H_2O can be summarized in the balanced equation:

$$2Cu(ClO_4)_2\cdot 6H_2O + 2H_2L + 2bppy + 2LiOH\cdot H_2O \xrightarrow{MeCN/H_2O} \underset{\mathbf{1}\cdot H_2O}{[Cu_2(HL)_2(bppy)_2](ClO_4)_2\cdot H_2O} + 2LiClO_4 + 15H_2O \quad (1)$$

In order to examine the influence of the reaction solvent, we have performed the above reaction in MeOH and isolated complex [Cu(HL)(bppy)(ClO_4)] (**2**) by vapor diffusion of Et_2O into the reaction solution. The preparation of **2** can be summarized in the balanced equation:

$$Cu(ClO_4)_2\cdot 6H_2O + H_2L + bppy + LiOH\cdot H_2O \xrightarrow{MeOH} \underset{\mathbf{2}}{[Cu(HL)(bppy)(ClO_4)]} + LiClO_4 + 8H_2O \quad (2)$$

In a next step, we wondered whether the absence of external OH^-s in MeOH, might lead to interesting maleamate(−1) to monomethyl maleate(−1) ligand transformation, as we have previously observed with *N*,*N*′-chelates [4,5]. Thus, we have performed the reaction of $Cu(ClO_4)_2\cdot 6H_2O$ with 1.5 equiv. of H_2L and 1 equiv. of bppy in MeOH. Upon storage of the reaction mixture at room temperature for *ca.* 7 days, complex $[Cu_2L'_2(bppy)_2](ClO_4)_2$ (**3**) was formed; L'^- is the monomethyl maleate(−1) ligand, see Scheme 1. Without any mechanistic implications, we believe that L'^- was formed in situ via the Cu^{II}-assisted/promoted $HL^- \rightarrow L'^-$ transformation, as we have previously observed in the case of bpy- and phen-containing reaction systems [4,5]. The preparation of **3** can be summarized in the balanced equation:

$$2Cu(ClO_4)_2\cdot 6H_2O + 2H_2L + 2bppy + 2MeOH \xrightarrow{MeOH} \underset{\mathbf{3}}{[Cu_2(L')_2(bppy)_2](ClO_4)_2} + 2NH_4ClO_4 + 12H_2O \quad (3)$$

In a subsequent step, we extended our research to the study of the influence of the aromatic *N*,*N*′,*N*″-chelate by introducing 2,2′;6′,2″-terpyridine (terpy) and 2,4,6-tris(2-pyridyl)-1,3,5-triazine (tptz) in the reaction systems.

The reaction of $Cu(ClO_4)_2\cdot 6H_2O$ with 2.5 equiv. of H_2L and 1 equiv. of terpy in the presence of 2.5 equiv. of $LiOH\cdot H_2O$ in $MeCN/H_2O$ afforded complex [Cu(HL)(terpy)(H_2O)](ClO_4) (**4**) by vapor diffusion of Et_2O into the reaction solution. The preparation of **4** can be summarized in the balanced equation:

$$Cu(ClO_4)_2\cdot 6H_2O + H_2L + terpy + LiOH\cdot H_2O \xrightarrow{MeCN/H_2O} \underset{\mathbf{4}}{[Cu(HL)(terpy)H_2O](ClO_4)} + LiClO_4 + 7H_2O \quad (4)$$

The reaction of $Cu(ClO_4)_2\cdot 6H_2O$ with 1.5 equiv. of H_2L and 1 equiv. of tptz in the presence of 1.5 equiv. of $LiOH\cdot H_2O$ in $MeCN/H_2O$ afforded green microcrystalline solids by layering the dark green reaction solution with Et_2O. Repeating efforts to obtain crystals, suitable for X-ray structure analysis, by varying the reaction solvent (MeOH, MeCN/MeOH), the stoichiometry of the reactants, and the crystallization methods, proved unsuccessful.

In order to isolate a complex analogous to **3** from the Cu^{II}/H_2L/tptz reaction system, we performed the 1:1.5:1 CuX_2/H_2L/tptz ($X = ClO_4^-, NO_3^-$) reactions in MeOH and we isolated green microcrystalline solids. The infrared spectra of all products showed peaks at ~1720 cm^{-1}, which are attributed to the carbonyl stretching vibration of the ester group [10] of the monomethyl maleate(−1), L'^-, ligand. The reaction of 2 equiv. of $Cu(NO_3)_2\cdot 2.5H_2O$ with 1.5 equiv. of H_2L and 1 equiv. of tptz in MeOH afforded complex $[Cu(L1)_2(NO_3)_2]$ (**5**) (L1 = pyridine-2-carboxamide); thus the excess of $Cu(NO_3)_2\cdot 2.5H_2O$ in the reaction mixture has dramatically affected the identity of the product. L1 is formed in situ via the Cu^{II}-assisted hydrolysis [11] of 2,4,6-tris(2-pyridyl)-1,3,5-triazine. Lerner and Lippard reported an analogous hydrolytic reaction which occurs with tptz and the chemically similar 2,4,6-tris(2-pyrimidyl)-1,3,5-triazine (tpmtz) in aqueous solutions of copper(II), which promotes the hydrolysis of these triazines yielding the [bis(arylcarbonyl)amido]copper(II) complexes and free pyridine-2-carboxamide [11b,c]. It has also been pointed out that other metal ions promote the hydrolysis of these 2,4,6-trisubstituted triazines [11b]. It is interesting to note that although simple triazines are known to hydrolyze under mild conditions, 2,4,6-triaryltriazines such as tptz and tpmtz are usually stable towards hydrolysis; concentrated mineral acid and temperatures above 150 °C are required to achieve it. Kinetic and thermodynamic data [11d,e] suggest that the hydrolytic reaction of 2,4,6-triaryltriazines that yields the carboximidate ligand may take place via the nucleophilic attack of OH^- or H_2O to the triazine ring; steric considerations have been also suggested to play a significant role [11c]. Julve and coworkers [11a] have proved that the two main products of the hydrolysis of tptz in aqueous solutions of copper(II) are the bis(pyridylcarbonyl)amido anion [$(NC_5H_4CO)_2N$] and pyridine-2-carboxamide ($NC_5H_4CONH_2$); both present in the crystal structure of complex $[Cu\{(NC_5H_4CO)_2N\}(NC_5H_4CONH_2)]ClO_4\cdot H_2O$. In order to examine to what extent the presence of H_2L might be involved to the tptz → L1 transformation mechanism, we have performed the 1:1 reaction between $Cu(NO_3)_2\cdot 2.5H_2O$ and tptz in MeOH and isolated blue-ocean crystals of **5** by layering the reaction solution with Et_2O/*n*-hexane. The identity of the crystals was confirmed by unit cell determination.

3.2. Description of structures

The molecular structures of the dinuclear complexes **1**·H_2O and **3** have been previously communicated [4b] and will not be discussed in detail. The crystallographically established coordination modes of HL^-, L'^- and L1 in complexes **1**–**5** are shown in Scheme 1. Selected interatomic distances and angles for complexes **2**, **4** and **5** are listed in Tables 2 and 3. The molecular structure of the

Table 2
Selected interatomic distances (Å) and angles (o) for complexes **2** and **4**.

2		**4**	
Distances			
Cu(1)–O(1)	1.907(3)	Cu(1)–O(1)	1.912(2
Cu(1)–N(3)	1.947(4)	Cu(1)–N(2)	1.942(2)
Cu(1)–N(1)	2.000(4)	Cu(1)–N(1)	2.018(2)
Cu(1)–N(5)	2.010(4)	Cu(1)–N(3)	2.035(2)
Cu(1)–O(2)	2.740(5)	Cu(1)–Ow(1)	2.379(2)
Cu(1)–O(11)	2.716(5)	Cu(1)–O(2)	2.883(2)
Angles			
O(1)–Cu(1)–N(3)	174.9(1)	O(1)–Cu(1)–N(2)	171.7(1)
O(1)–Cu(1)–N(1)	99.0(1)	O(1)–Cu(1)–N(1)	100.1(1)
N(3)–Cu(1)–N(1)	79.0(2)	N(2)–Cu(1)–N(1)	80.1(1)
O(2)–Cu(1)–O(1)	53.1(1)	O(1)–Cu(1)–N(3)	99.3(1)
O(2)–Cu(1)–N(3)	131.6(2)	N(2)–Cu(1)–N(3)	79.9(1)
O(1)–Cu(1)–N(5)	103.7(2)	N(1)–Cu(1)–N(3)	159.8(1)
N(3)–Cu(1)–N(5)	78.7(2)	O(1)–Cu(1)–Ow(1)	85.1(1)
N(1)–Cu(1)–N(5)	157.1(2)	N(2)–Cu(1)–Ow(1)	103.2(1)
O(2)–Cu(1)–N(1)	97.7(2)	N(1)–Cu(1)–Ow(1)	96.5(1)
O(2)–Cu(1)–N(5)	93.0(2)	N(3)–Cu(1)–Ow(1)	90.8(1)
O(1)–Cu(1)–O(11)	90.0(1)	O(2)–Cu(1)–O(1)	50.5(1)
O(2)–Cu(1)–O(11)	141.3(2)	O(2)–Cu(1)–Ow(1)	135.6(1)
N(1)–Cu(1)–O(11)	99.6(2)	O(2)–Cu(1)–N(1)	90.6(1)
N(3)–Cu(1)–O(11)	85.7(2)	O(2)–Cu(1)–N(2)	121.2(1)
N(5)–Cu(1)–O(11)	84.1(2)	O(2)–Cu(1)–N(3)	97.4(1)

cation **1**·H_2O consists of a [Cu_2] unit bridged by two η^2 carboxylato oxygen atoms of HL^- (Fig. 1). Three nitrogen atoms of the bppy and the second carboxylato oxygen atom of HL^- (Cu(1)···O(12) = 2.861(2) Å, shown as dashed line in Fig. 1) complete distorted octahedral coordination geometry around each metal ion. Intermolecular hydrogen bonding interactions between the cations of **1**, the perchlorate anions and the solvate water molecules form chains. Further π–π stacking interactions between the aromatic rings of the bppy belonging to neighboring chains form a 2D structure parallel to the (1 1 1) plane (Fig. 2, Table 4).

The structure of **2** consists of [Cu(HL)(bppy)(ClO_4)] molecules. The Cu^{II} atom is in a distorted octahedral geometry (Fig. 3). The equatorial coordination sites are occupied by the three nitrogen atoms of the bppy ligand and a carboxylate oxygen atom of the HL^- ion. The second carboxylate oxygen atom and a monodentate perchlorate anion occupy the axial, Jahn–Teller distorted coordination sites (Table 2). The molecules of **2** form dimers through two N(6)···O(3) hydrogen bonding interactions; the dimers are further connected to 1D chains extending parallel to the *a*-axis (Fig. 4, Table 4).

The molecular structure of the cation of **3** (Fig. 5) is quite similar to the structure of the cation of **1**·H_2O, the only difference being that **3** contains the monomethyl maleate(−1) ligand, L'^-, instead of HL^-. The coordination modes of HL^- and L'^- in **1**·H_2O and **3**, respectively, are the same, see Scheme 1. The crystal structure of **3** is stabilized by π–π stacking interactions between the aromatic rings of bppy belonging to neighboring cations, thus 1D chains are formed along the *a*-axis (Fig. 6).

The structure of **4** consists of [Cu(HL)(terpy)(H_2O)]$^+$ cations and perchlorate counterions (Fig. 7). The structure of the cation of **4** is similar to the structure of the molecule that is present in **2**. The coordination geometry of the Cu^{II} atom in the cation of **4** is distorted octahedral. The three nitrogen atoms of terpy and a carboxylate oxygen atom of HL^- define the equatorial plane; the second carboxylate oxygen atom of HL^- and an aquo ligand occupy the axial, Jahn–Teller coordination sites. The cations of **4** are held together through intermolecular hydrogen bonding interactions involving the perchlorate anions and form 1D chains (Fig. 8, Table 4).

The structure of **5** (Fig. 9) consists of centrosymmetric mononuclear [$Cu(L1)_2(NO_3)_2$] molecules. Two oxygen atoms from the two terminal monodentate nitrate ions, two pyridine N atoms and two amide oxygen atoms from the two L1 ligands create the coordination environment around the Cu^{II} atom. The metal coordination geometry is described as octahedral. The Jahn–Teller sites are occupied by the oxygen atoms of the nitrate atoms. The mononuclear molecules are hydrogen bonded through the amide group of L1 and the nitrate anions and form a 3D network (Fig. 10, Table 4).

Table 3
Selected interatomic distances (Å) and angles (°) for complex **5**.

Distances			
Cu(1)–O(1)	1.964(2)	Cu(1)–N(1)	1.979(2)
Cu(1)–O(1′)	1.964(2)	Cu(1)–O(3)	2.422(3)
Cu(1)–N(1′)	1.979(2)	Cu(1)–O(3′)	2.422(3)
Angles			
O(1)–Cu(1)–O(1′)	180.0(1)	N(1′)–Cu(1)–O(3)	95.8(1)
O(1)–Cu(1)–N(1′)	97.1(1)	N(1)–Cu(1)–O(3)	84.2(1)
O(1′)–Cu(1)–N(1′)	82.7(1)	O(1)–Cu(1)–O(3′)	91.9(1)
O(1)–Cu(1)–N(1)	82.7(1)	O(1′)–Cu(1)–O(3′)	88.1(1)
O(1′)–Cu(1)–N(1)	97.3(1)	N(1′)–Cu(1)–O(3′)	84.2(1)
N(1′)–Cu(1)–N(1)	180.0(1)	N(1)–Cu(1)–O(3′)	95.8(1)
O(1)–Cu(1)–O(3)	88.1(1)	O(3)–Cu(1)–O(3′)	180.0
O(1′)–Cu(1)–O(3)	91.9(1)		

Symmetry operation to generate primed atoms: (′) −*x*, 1−*y*, −*z*.

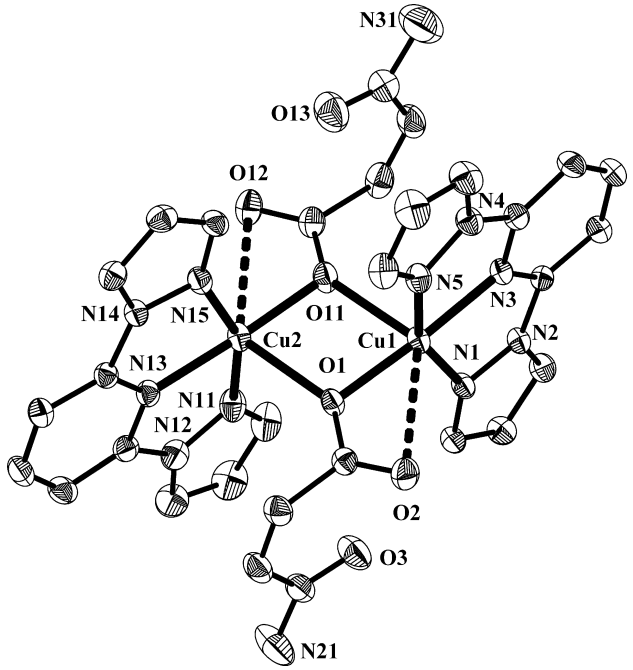


Fig. 1. Partially labelled plot of the cation of **1**·H_2O with ellipsoids drawn at the 30% probability level. H atoms have been omitted for clarity.

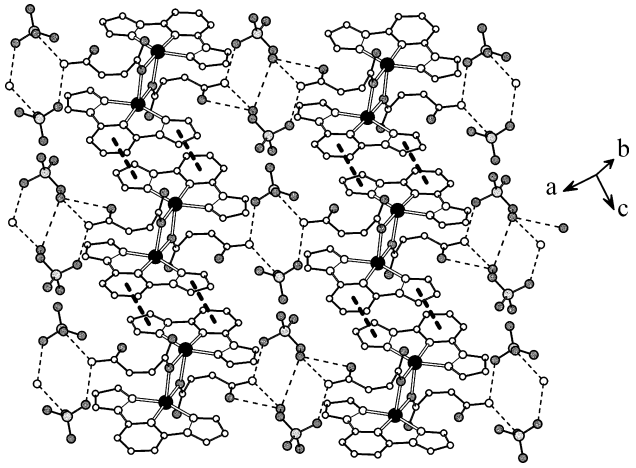


Fig. 2. A part of the 2D structure of **1**·H_2O. Colour code: Cu, black; O, moderate grey; N, large white; C, small white. H bonds are shown as thin dashed lines and π–π interactions are shown as thick dashed lines.

3.3. IR spectra

Dried samples of complexes **1**·H_2O, **2**, **3**, **4** and **5** were characterized by IR spectroscopy. Complexes **1**·H_2O and **4** exhibit a very broad band covering the whole 3450–3150 cm^{-1} range, assignable to ν(OH) vibrations of lattice (**1**·H_2O) or/and coordinated (**4**) H_2O [12]. The broadness and relatively low frequency of this band are both indicative of H-bonding.

In the spectra of **1**·H_2O, **3** and **4** the strong band at 1077–1112 cm^{-1} and the medium-intensity band at ~625 cm^{-1} are attributed to the $\nu_3(F_2)$ [ν_d(ClO)] and $\nu_4(F_2)$ [δ_d(OClO)] modes, respectively, of the uncoordinated T_d ionic perchlorates [13]. The large number of ClO_4^- bands at around 1070 and 640 cm^{-1} in the spectrum of **2** are consistent with the presence of coordinated ClO_4^- groups in this compound [13]. In the spectrum of **5**, the bands at 1445 and 1324 cm^{-1} are assigned [13] to the

Table 4
Hydrogen bonding interactions in complexes **1**·H_2O, **2**, **4** and **5**.

Interaction	D···A (Å)	H···A (Å)	D–H···A (°)	Symmetry operation
***1**·H₂O*				
N(21)–H(21)A···O(22)	3.184(5)	2.012(4)	168.2(3)	−1−*x*, 2−*y*, 1−*z*
N(21)–H(21)B···O(21)	3.392(6)	2.333(5)	174.5(3)	*x*, *y*, *z*
N(31)–H(31)A···Ow(1)	2.965(8)	2.031(5)	153.6(4)	*x*, *y*, −1+*z*
N(31)–H(31)B···O(34)	3.137(7)	1.960(4)	157.6(3)	1+*x*, −1+*y*, *z*
Ow(1)···O(33)	2.970(7)			−*x*, 2−*y*, 1−*z*
Ow(1)···O(13)	3.063(7)			*x*, *y*, 1+*z*
Ow(1)···Ow(1)	3.273(9)			1−*x*, 1−*y*, 2−*z*
2				
N(6)–HN6B···O(3)	3.092(8)	2.114(7)	164.1(6)	2−*x*, −*y*, 1−*z*
N(6)–HN6A···O(2)	3.118(6)	2.367(7)	154.5(7)	1+*x*, *y*, *z*
4				
Ow(1)–Hw1A···O(11)	2.975(4)	2.229(3)	172.9(4)	2−*x*, 1−*y*, 1−*z*
Ow(1)–Hw1B···O(3)	2.825(4)	2.045(5)	171.6(4)	1−*x*, −*y*, 1−*z*
N(4)–HN1A···O(12)	3.043(3)	2.333(3)	169.2(4)	*x*, *y*, *z*
5				
N(2)–HNA···O(5)	2.877(5)	2.019(4)	162.7(4)	0.5−*x*, −0.5+*y*, −0.5−*z*
N(2)–HNB···O(3)	3.021(4)	2.249(5)	160.2(5)	1−*x*, 1−*y*, −*z*

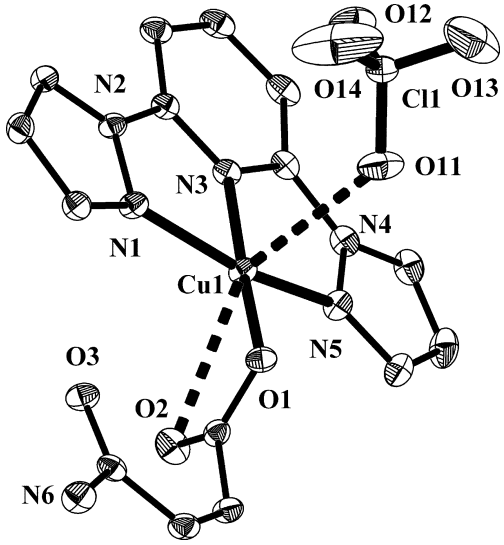


Fig. 3. Partially labelled plot of **2** with ellipsoids drawn at the 30% probability level. H atoms have been omitted for clarity.

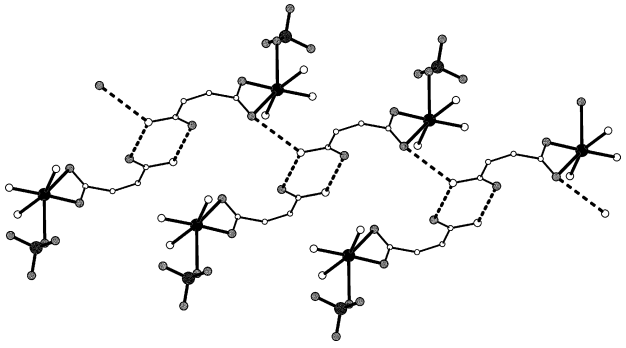


Fig. 4. A part of the 1D structure of **2**. Colour code: Cu, black; O, moderate grey; N, large white; C, small white; Cl, dark grey. H bonds are shown as dashed lines. Only the N atoms of the bppy ligands are shown.

$\nu_5(B_2)[\nu_{as}(NO_2)]$ and $\nu_1(A_1)[\nu_s(NO_2)]$ stretching modes (under C_{2v} symmetry), respectively, of the nitrato ligand; their separation is small ($\sim$120 cm^{-1}) in accordance with the monodentate coordination of the nitrato groups [13].

The very strong band at 1720 cm^{-1} in the spectrum of **3** is assigned to the carbonyl stretching vibration of the ester group [10].

The IR spectra of **1**·H_2O, **2**, **4** and **5** exhibit the typical bands of the primary amide and carboxylate groups [13]. Tentative assignments of few diagnostic bands attributed to these groups are given in Table 5. The assignments have been given in comparison with the data obtained for sodium maleamate, Na(HL), assumed to contain a "free" carboxylate group [14], oxamato(−1) (**II** in Scheme 1) [15], malonamato(−1) (**I** in Scheme 1; $n = 1$) [16] and succinamato(−1) (**I** in Scheme 1; $n = 2$) [17] metal complexes. As a general remark, we must emphasize that some of the vibrational modes shown in Table 5 are strongly coupled and thus the proposed assignments must be regarded as approximate descriptions of

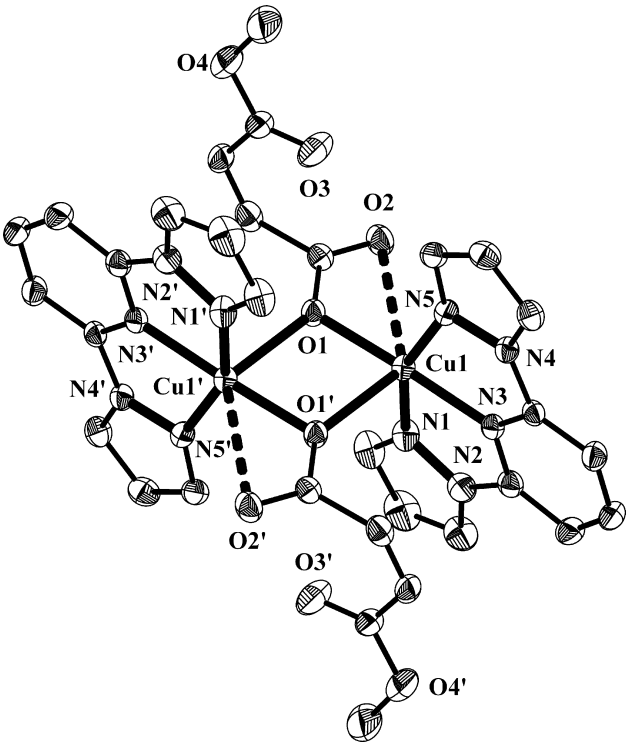


Fig. 5. Partially labelled plot of the cation of **3** with ellipsoids drawn at the 30% probability level. H atoms have been omitted for clarity.

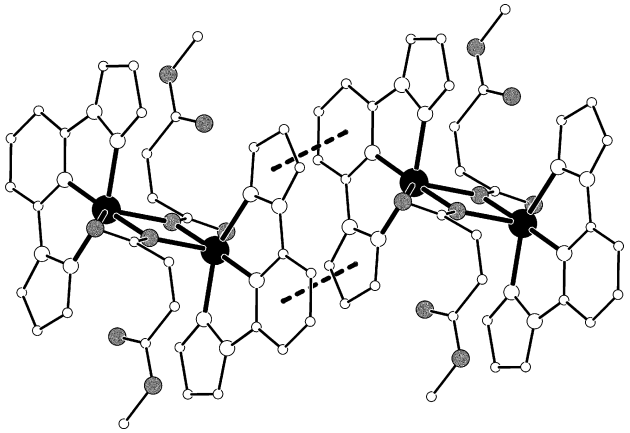


Fig. 6. A part of the 1D structure of **3**. Colour code: Cu, black; O, moderate grey; N, large white; C, small white. The π–π interactions are shown as thick dashed lines.

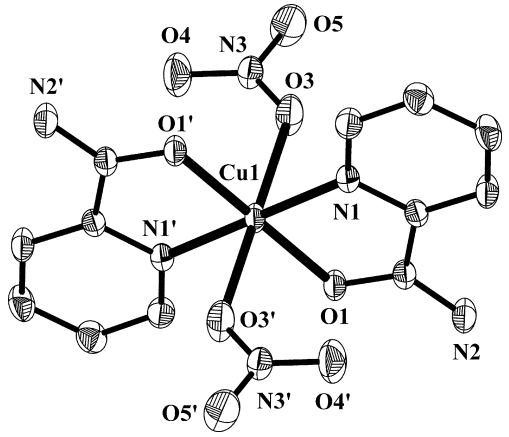


Fig. 9. Partially labelled plot of **5** with ellipsoids drawn at the 30% probability level. H atoms have been omitted for clarity. Primed atoms are generated by symmetry: (′) = −*x*, 1−*y*, −*z*.

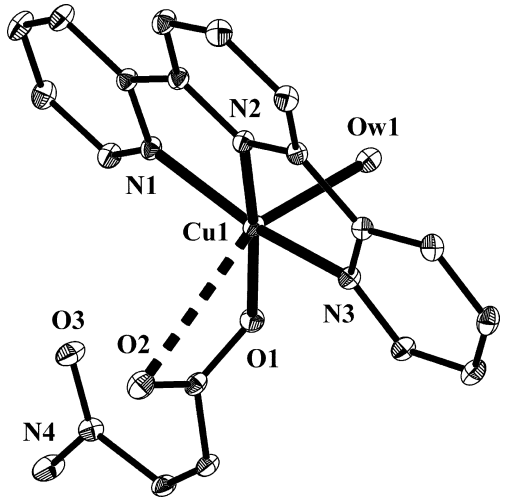


Fig. 7. Partially labelled plot of the cation of **4** with ellipsoids drawn at the 30% probability level. H atoms have been omitted for clarity.

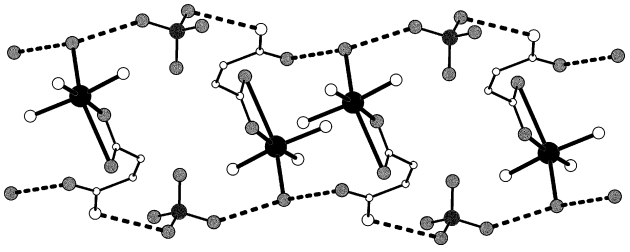


Fig. 8. A part of the 1D structure of **4**. Colour code: Cu, black; O, moderate grey; N, large white; C, small white; Cl, dark grey. H bonds are shown as dashed lines. Only the N atoms of the terpy ligands are shown.

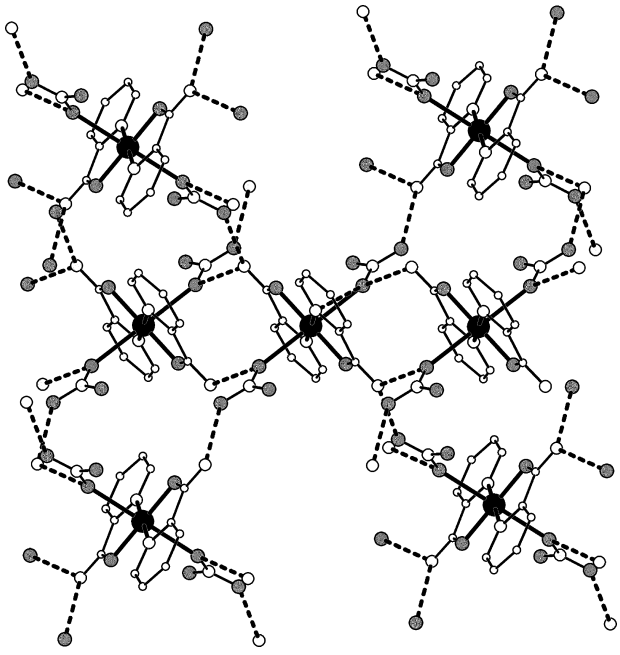


Fig. 10. A part of the 3D structure of **5**. Colour code: Cu, black; O, large white; N, moderate grey; C, small white. H bonds are shown as dashed lines.

the vibrations [10]. The typical bands of the neutral amide group, i.e., $\nu_{as}(NH_2)$, $\nu_s(NH_2)$, ν(C=O) and ν(CN), in the spectra of **1**·H_2O, **2** and **4** are observed at approximately the same wavenumbers as those of Na(HL), confirming the crystallographically established non-participation of the amide group in coordination. The difference Δ, where $\Delta = \nu_{as}(CO_2) - \nu_s(CO_2)$, for **1**·$H_2O$ (242 cm^{-1}) and **3** (276 cm^{-1}) is large, as expected for the crystallographically confirmed, essentially monoatomic bridging mode of the carboxylate ligation [18]. The difference Δ for **2** (192 cm^{-1}) and **4** (192 cm^{-1}) is more than that of the "free" maleamate(−1) ion (169 cm^{-1})

Table 5
Diagnostic amide and carboxylate IR bands (cm^{-1}), and their tentative assignments for sodium maleamate[a] and complexes **1**·H_2O, **2**, **4** and **5**.

Vibration	Na(HL)	**1**·H_2O	**2**	**4**	**5**
$\nu_{as}(NH_2)$	3385sb[b]	3420w[b]	3408m[b]	3538m	3273mb
$\nu_s(NH_2)$	3160mb[b]	3100m[b]	3194m	3343m	3079sb
$\nu(C{=}O)_{amide}$	1677s	1688s	1685vs	1674s	1681s
$\delta(NH_2)$	1636m[d]	1624vs[d]	1644sh	1638s[d]	1585m
ν(C=C)	1636m[d]	1624vs[d]	1629vs	1638s[d]	
$\nu_{as}(CO_2)$[c]	1576s	1592s	1597vs	1598vs	
$\nu(CN)_{amide}$[c]	1449s	1438m	1435s	1445s	1499m
$\nu_s(CO_2)$[c]	1407m	1350s	1405vs	1406w	

Abbreviations: b, broad; m, medium; s, strong; sh, shoulder; v, very.

[a] Prepared from the 1:1 reaction between H_2L and NaOH in EtOH, followed by precipitation with Et_2O.

[b] These bands are components of the ν(OH) manifold.

[c] These vibrations may include an aromatic stretching character.

[d] Overlapping bands.

[19], as expected for the essentially monodentate mode of the carboxylate ligation [14].

4. Concluding comments and perspectives

The use of the HL^-/bppy "ligand blend" in reactions with $Cu(ClO_4)_2{\cdot}6H_2O$ has yielded the new dinuclear and mononuclear complexes **1**·H_2O, **2** and **3**. The chemistry of the $Cu(ClO_4)_2{\cdot}6H_2O$/HL^-/bppy system shows more differences than similarities to that of the corresponding $Cu(ClO_4)_2{\cdot}6H_2O/HL^-$/phen [4a] and $Cu(ClO_4)_2{\cdot}6H_2O/HL^-$/bpy [5a] systems. The binding of an extra Cu^{II} coordination site from bppy, with respect to phen and bpy, did not prove detrimental to the isolation of dinuclear complexes. The Cu^{II}-assisted methanolysis of the primary amide group of HL^- to L'^- has been observed in phen/bpy reaction systems as well as in the bppy-containing systems yielding complex **3**. The main difference is that, in the present case, the isolation of **3** takes place without the formation of an intermediate compound as in the phen/bpy systems. Worth mentioning is also the fact that the Cu^{II}-assisted hydrolysis of the primary amide group of HL^- to a carboxylate, yielding the maleate(−2) ligand, was not observed in the case of the bppy-containing systems. Bppy proved to be a hydrophobic ligand in contrast to bpy. This feature can be justified from the presence of coordinated aquo ligands in the complexes of bpy. On the other hand, terpy which is structurally similar to bppy and not to bpy, afforded complex **4** which contains a coordinated aquo ligand. Complex **4** is similar to complex [19] [Cu(Hsucm)(terpy)(MeOH)](ClO_4) ($Hsucm^-$ is the succinamate ligand, $^-OOC–CH_2CH_2–CONH_2$). The main difference between the two complexes is the terminal monodentate ligand (H_2O versus MeOH) coordinated to the Cu^{II} ion.

The use of HL^-/tptz "ligand blend" in reactions with Cu^{II} salts led to a completely different chemistry. Only one mononuclear complex (**5**) was structurally characterized which does not contain HL^- or L'^-. The impressive feature of this reaction system was the Cu^{II}-assisted hydrolysis [11] of tptz to pyridine-2-carboxamide, L1 (Scheme 1). Our current efforts are oriented on the isolation of X-ray quality crystals from the spectroscopically characterized Cu^{II} complexes of tptz with HL^- or L'^-, as well as the in depth investigation of the synthetic parameters that might affect the products from the terpy and tptz reaction systems.

Appendix A. Supplementary data

CCDC 723352, 723353, and 723354 contain the supplementary crystallographic data for **2**, **4** and **5**. These data can be obtained free of charge via http://www.ccdc.cam.ac.uk/conts/retrieving.html, or from the Cambridge Crystallographic Data Centre, 12 Union Road, Cambridge CB2 1EZ, UK; fax: (+44) 1223-336-033; or e-mail: deposit@ccdc.cam.ac.uk.

References

[1] See for example a recent review on the synthetic approaches and applications of polynuclear metal clusters: A.K. Boudalis, Y. Sanakis, C.P. Raptopoulou, V. Psycharis, in: D. Stamopoulos (Ed.), Magnetism and Superconductivity in Low-Dimensional Systems – Utilization in Future Applications, Nova Science Publishers, New York, 2008, p. 1.

[2] (a) For interesting reviews concerning the chemistry and applications of coordination polymers, see: C. Janiak, Dalton Trans. (2003) 2781 (Dalton Perspective);
(b) S.R. Batten, R. Robson, Angew. Chem., Int. Ed. Engl. 37 (1998) 1460;
(c) M. Munakata, L.P. Wu, T. Kuroda-Sowa, Adv. Inorg. Chem. 46 (1999) 173;
(d) S.R. Batten, Curr. Opin. Solid State Mater. Sci. 5 (2001) 107;
(e) S. Kitagawa, S. Noro, in: J.A. McCleverty, T.J. Meyer (Eds.), Comprehensive Coordination Chemistry II, vol. 7, Elsevier, Amsterdam, 2004, p. 231;
(f) A.Y. Robin, K.M. Fromm, Coord. Chem. Rev. 250 (2006) 2127;
(g) Y. Zhou, M. Hong, X. Wu, Chem. Commun. (2006) 135 (feature article);
(h) C. Coulon, H. Miyasaka, R. Clérac, Struct. Bond. 122 (2006) 163;
(i) D.-K. Bucar, G.S. Papaefstathiou, T.D. Hamilton, Q.L. Chu, I.G. Georgiev, L.R. MacGillivray, Eur. J. Inorg. Chem. (2007) 4559 (microreview);
(j) J.L.C. Rowsell, O.M. Yaghi, Micropor. Mesopor. Mater. 73 (2004) 3.

[3] R.E.P. Winpenny, J. Chem. Soc., Dalton Trans. (2002) 1.

[4] (a) K.N. Lazarou, S.P. Perlepes, V. Psycharis, C.P. Raptopoulou, Polyhedron 27 (2008) 2131;
(b) K.N. Lazarou, I. Chadjistamatis, V. Psycharis, S.P. Perlepes, C.P. Raptopoulou, Inorg. Chem. Commun. 10 (2007) 318.

[5] [a] K.N. Lazarou, V. Psycharis, S.P. Perlepes, C.P. Raptopoulou, Polyhedron 28 (2009) 1085;
[b] K.N. Lazarou, A.K. Boudalis, S.P. Perlepes, C.P. Raptopoulou, in preparation.

[6] D.L. Jameson, K.A. Goldsby, J. Org. Chem. 55 (1990) 4992.

[7] G.M. Sheldrick, SHELXS-97, Structure Solving Program, University of Göttingen, Germany, 1997.

[8] G.M. Sheldrick, SHELXS-97, Crystal Structure Refinement Program, University of Göttingen, Germany, 1997.

[9] DIAMOND – Crystal and Molecular Structure Visualization, Ver. 3.1, Crystal Impact, Rathausgasse 30, 53111, Bonn, Germany.

[10] H.O. Desseyn, in: S. Patai (Ed.), The Chemistry of Acid Derivatives, vol. 2, Wiley, New York, 1992, p. 271.

[11] (a) A. Cantarero, J.M. Amigo, J. Faus, M. Julve, T. Debaerdemaeker, J. Chem. Soc., Dalton Trans. (1988) 2033;
(b) E.I. Lerner, S.J. Lippard, J. Am. Chem. Soc. 98 (1976) 5397;
(c) E.I. Lerner, S.J. Lippard, Inorg. Chem. 16 (1977) 1546;
(d) V.M.S. Gil, R.D. Gillard, P.A. Williams, R.S. Vagg, E.C. Watton, Transition Met. Chem. 4 (1979) 14;
(e) R.D. Gillard, P.A. Williams, Transition Met. Chem. 4 (1979) 18.

[12] C. Papatriantafyllopoulou, C.P. Raptopoulou, A. Terzis, J.F. Janssens, E. Manesssi-Zoupa, S.P. Perlepes, J.C. Plakatouras, Polyhedron 26 (2007) 4053.

[13] K. Nakamoto, Infrared and Raman Spectra of Inorganic and Coordination Compounds, 4th ed., Wiley, New York, 1986.

[14] G.B. Deacon, R.J. Phillips, Coord. Chem. Rev. 33 (1980) 227.

[15] C. Vansant, H.O. Desseyn, S.P. Perlepes, Transition Met. Chem. 20 (1995) 454.

[16] C. Vansant, H.O. Desseyn, V. Tangoulis, C.P. Raptopoulou, A. Terzis, S.P. Perlepes, Polyhedron 14 (1995) 2115.

[17] I. Chadjistamatis, A. Terzis, C.P. Raptopoulou, S.P. Perlepes, Inorg. Chem. Commun. 6 (2003) 1365.

[18] G. Christou, S.P. Perlepes, E. Libby, K. Folting, J.C. Huffman, R.J. Webb, D.N. Hendrickson, Inorg. Chem. 29 (1990) 3657.

[19] I. Chadjistamatis, Ph.D. Thesis, University of Patras, Greece, 2005 (The coordination geometry about the Cu^{II} ion in [Cu(Hsucm)(terpy)(MeOH)](ClO_4) is distorted octahedral comprised of the three nitrogen atoms of the terpy (Cu–N = 1.945(2) – 2.026(3) Å) and the carboxylato oxygen atom of $Hsucm^-$ (Cu–O1 = 1.963(2) Å) in the equatorial positions, whereas the second carboxylato oxygen atom of $Hsucm^-$ and the coordinated MeOH are directed in the Jahn–Teller positions of the distorted octahedron (Cu–Om = 2.274(2), Cu–O2 = 2.581(2) Å)).

$_2NH_2)(HNCH_2\ CH_2NH_2)_3Zn_2Ge_2Se_8$ (**3**). To the best of our knowledge, the 1D chains $[Zn_2Ge_2Se_8]^{4-}$ in **3** are observed for the first time and also **3** is a rare templated semiconductor that contains two different charge balancing organic cations. We report here the synthesis and structural characterization of **3** as well as its optical and thermal properties.

2. Experimental

2.1. Reagents

N-(2-aminoethyl)piperazine (98%) and zinc powder (99.9%) were purchased from Alfa Aesar. Germanium (99.99%) and selenium (99.5%) were purchased from Aldrich. All chemicals were used as received.

2.2. Synthesis of $(H_2NC_4H_8NCH_2CH_2NH_2)(HNCH_2CH_2NH_2)_3Zn_2Ge_2Se_8$ (3)

In a typical synthesis, an amount of Zn (0.052 g, 0.795 mmol), Ge (0.029 g, 0.399 mmol), Se (0.219 g, 2.774 mmol) and 6 ml of *N*-(2-aminoethyl)piperazine were placed in a 45 ml Teflon-lined stainless steel autoclave (Parr Instruments) and heated at 200 °C for 62 h. The product, in the form of transparent, yellow–orange rod like crystals, was isolated by suction filtration and washed with copious amount of CH_3OH. Yield 0.210 g based on Ge.

2.3. Single crystal X-ray crystallography

A STOE IPDS II diffractometer was used to collect intensity data at room temperature, operated at 2000 W power (50 kV, 40 mA) with graphite monochromatized Mo Kα (λ = 0.71073 Å) radiation. An analytical absorption correction was applied using the program X-RED (routine within the X-AREA software package). The structure was solved with SHELXL software (Sheldrick, SHELXL, University of Göttingen, 2002). All non-hydrogen atoms were refined anisotropically expect the carbon atom C9 (–CH_2– group in a piperazinium cation) which was refined using the isor command (six restrains) because the ADPs were found physically not very sensible. The hydrogen atoms were generated with idealized geometries.

2.4. Physical measurements

Powder X-ray diffraction patterns were collected on a Rigaku D/MAX-2000H rotating anode diffractometer (Cu Kα radiation) equipped with a secondary pyrolytic graphite monochromator operated at 40 kV and 178 mA. The scan rate was 0.15°/min with a step size of 0.01°. Simulated PXRD patterns were calculated from the corresponding single crystal data using the program POWDER CELL 2.3. Thermogravimetric analyses (TGA) were performed using a TA SDT Q 600 analysis system. An amount of 20 mg of sample was placed inside an alumina cup and heated up to 600 °C under Argon flow with a heating rate of 5 °C/min. ATR-IR spectra were recorded on a Thermo-Electron Nicolet 6700 FT-IR optical spectrometer with a DTGS KBr. Raman spectrum was recorded at room temperature on a single crystal using a Nicolet Almega XR Raman spectrometer with a 473 nm blue laser (25% of the 15 mW laser power). The beam was focused on the sample through a confocal microscope using a 10× objective lens. Solid state UV–Vis/near IR electronic absorption spectrum was obtained at room temperature on a Perkin Elmer LAMBDA 950 UV/Vis/NIR spectrophotometer in the wavelength range of 200–2500 nm. $BaSO_4$ powder was used as a reference (100% reflectance) and base material on which the powder sample was coated. Reflectance data were converted to absorbance data as described elsewhere [27].

3. Results and discussion

3.1. Synthesis

In templated solvothermal syntheses of metal chalcogenides usually a common solvent such as water, methanol, ethylenediamine, pyridine or acetonitrile is required in addition to the templating molecules. That was the case in the successful synthesis of **1** in which a mixture of CH_3OH and **2** was used under solvothermal reaction conditions. Interestingly, when germanium was used instead of tin, under otherwise the same reaction conditions, we did not observed the isostructural phase of **1** or any other ternary Zn/Ge/Se crystalline phase. In contrast, when only **2** was used as solvent and template we obtained the ternary phase **3** in pure form (see below the powder X-ray data) and high yield (>80%). As we report below, the crystal structure of **3** consists of 1D $[Zn_2Ge_2Se_8]^{4-}$ chains made of edge sharing $[ZnSe_4]$ and $[GeSe_4]$ tetrahedra. Alternatively, the chains can be viewed as made of $[GeSe_4]^{4-}$ anions bridged by Zn^{2+} cations. These results could be explained based on solvent effects as follows: the highly basic nature of the $[GeSe_4]^{4-}$ anions requires a relatively strong basic environment in order to be stabilized and therefore, the fact that the synthesis of **3** requires only the amine **2** as a solvent (basic environment) and not a mixture of **2**/CH_3OH could be explained in terms of the relative basicity of the reaction medium. In fact, the effect of basicity in the stabilization of different germanium chalcogenide species, for example in aqueous solutions, has been document [28]. Accordingly, in highly basic solutions the anions $[GeQ_4]^{4-}$ (Q = S, Se) are stable, while at lower pH, condensation reactions occur leading to the formation of dimeric $[Ge_2Q_6]^{4-}$ and tetrameric, adamantine type $[Ge_4Q_{10}]^{4-}$ species. We note that the pH dependence of metal chalcogenide clusters has also been used as a tool for the controlled formation of ordered mesostructured metal chalcogenides [29].

3.2. X-ray diffraction characterization

The powder X-ray diffraction pattern of **3** is in full agreement with that calculated from the corresponding crystal structure (see Fig. 1) and confirms that the as-made, bulk material is a pure phase.

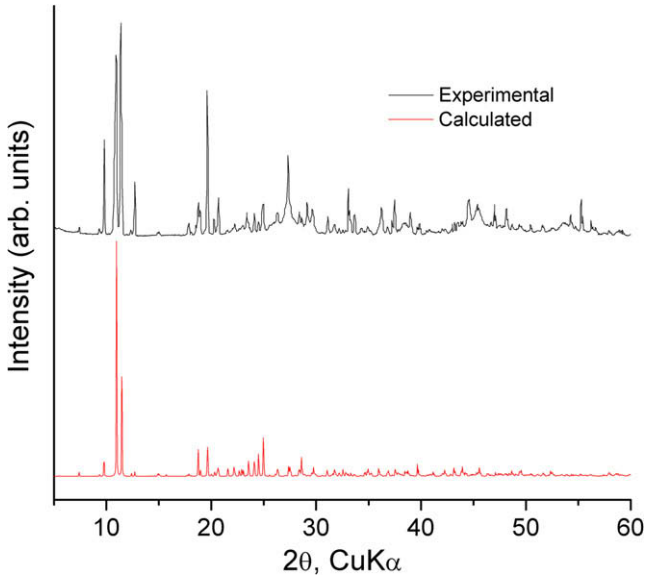


Fig. 1. Experimental (black line) and calculated (red line) powder X-ray diffraction pattern of **3**. (For interpretation of the references to colour in this figure legend, the reader is referred to the web version of this article.)

Compound **3** crystallize in the orthorhombic non-centrosymmetric space group $P2_12_12$ (see Table 1). The unit cell is shown in Fig. 2. The inorganic network consists of 1D $[Zn_2Ge_2Se_8]^{4-}$ chains made of edge sharing $[ZnSe_4]$ and $[GeSe_4]$ tetrahedral, running down the *c*-axis (see Fig. 3). Selected bond distances and bond angles are shown in Tables 2 and 3, respectively. The Zn–Se and Ge–Se bond distances lie between 2.4700(15)–2.5171(16) and 2.3416(15)–2.3580(16) Å, respectively, in the same range to those reported in some crystalline metal chalcogenides, as for example in ZnSe and $GeSe_2$.

Table 1
Crystal data and structure refinement for **3** at 298(2) K.

Empirical formula	$C_{18}H_{49}N_9Zn_2Ge_2Se_8$
Formula weight	1299.19
T (K)	298(2)
Wavelength (Å)	0.71073
Crystal system	orthorhombic
Space group	$P2_12_12$
Unit cell dimensions	
a (Å)	18.928(4)
b (Å)	30.849(6)
c (Å)	6.3954(13)
α (°)	90.00
β (°)	90.00
γ (°)	90.00
Volume (Å^3)	3734.3(13)
Z	4
Density (calculated) g/cm^3	2.295
Absorption coefficient (mm^{-1})	10.
F(0 0 0)	2428
Crystal size (mm^3)	0.3 × 0.1 × 0.1
θ Range for data collection	1.26–29.23°
Index ranges	$-25 \leqslant h \leqslant 25$, $-42 \leqslant k \leqslant 42$, $-8 \leqslant l \leqslant 8$
Reflections collected	56 328
Independent reflections	10 084 [R_{int} = 0.1783]
Completeness to θ = 29.23°	100%
Refinement method	full-matrix least-squares on F^2
Data/restraints/parameters	10 084/6/354
Goodness-of-fit (GOF) on F^2	0.899
Final *R* indices [>2σ(*I*)]	R_{obs} = 0.0589, wR_{obs} = 0.1075
R indices (all data)	R_{all} = 0.1052, wR_{all} = 0.1224
Largest differences in peak and hole (e Å^{-3})	1.017 and −1.762

$R = \sum||F_o|-|F_c||/\sum|F_o|$, $wR = \{\sum[w(|F_o|^2-|F_c|^2)^2]/\sum[w(|F_o|^4)]\}^{1/2}$ and calc. $w = 1/[\sigma^2(F_o^2) + (0.0448P)^2 + 0.0000P]$ where $P = (F_o^2 + 2F_c^2)/3$.

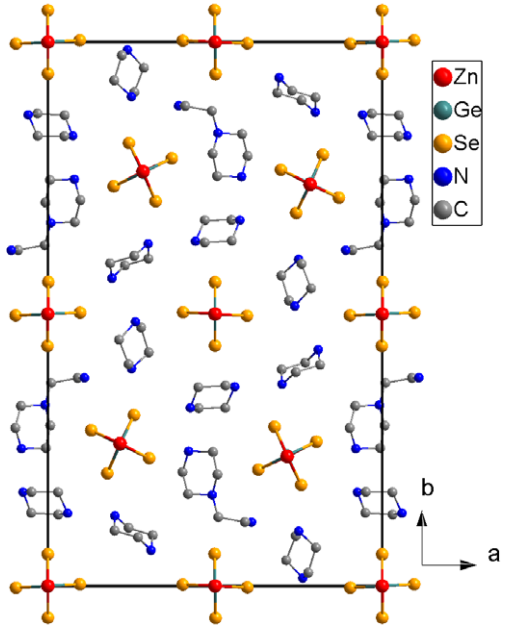


Fig. 2. The unit cell of **3** looking down the *c*-axis. Hydrogen atoms are omitted for clarity.

Notably, although in the system Zn/Sn/Se a number of crystalline ternary and quaternary compounds have been discovered and structurally characterized [30–33], in the system Zn/Ge/Se only the synthesis of Zn_2GeSe_4 and Zn_2GeSe_3 has been reported. The $[ZnSe_4]$ tetrahedra in **3** are highly distorted and the Se–Zn–Se bond angles lie in the range 93.09(7)–119.92(4)° (see Table 3). This large distortion from the ideal T_d symmetry of the zinc cations have been observed in other tetrahedral, transition metal containing metal chalcogenides including the isostructural series $(Me_4N)_2M[Ge_4S_{10}]$ (M = Mn^{2+}, Fe^{2+}, Co^{2+}, Zn^{2+}, Cd^{2+}) [34–37], $(Me_4N)_2M[Ge_4Se_{10}]$ (M = Fe^{2+}, Cd^{2+}) [38], $(Me_4N)_2M[Sn_4Se_{10}]$ (M = Mn^{2+}, Fe^{2+}, Co^{2+}, Zn^{2+}) [39,40] and $(Me_4N)_2Mn[Ge_4Te_{10}]$ [39]. The Se–Ge–Se bond angles lie in the range 100.34(7)–116.21(5)° which is typical for main-group metal chalcogenides [10].

A unique feature in **3** is that the anionic chains $[Zn_2Ge_2Se_8]^{4-}$ are charged balanced by two different organic cations. The asymmetric unit of **3** contains one templating molecule **2** and three piperazine molecules (**4**). Because compound **4** was not included in the starting reaction mixture, their formation indicates that **2** are partially decomposed during the reaction forming **4** and presumably ethylamine. In compound **3**, looking down the *c*-axis, the chain $[Zn_2Ge_2Se_8]^{4-}$ located at the center of the unit cell (Zn^{2+} and Ge^{4+} atoms at +1/2, +1/2, *z*), is surrounded by six molecules **4**, while all the other are surrounded by four molecules **4** and two molecules **2** (see Fig. 2). Taking into account charge balancing considerations, the observed packing indicates that the molecule **2** and the three molecules **4** of the asymmetric unit are monoprotonated forming *N*-(2-aminoethyl)piperazinium and piperazinium cations, respectively that compensate the anionic charge of the chains. Accordingly, the overall charged balanced formula of **3** is $(H_2NC_4H_8NCH_2CH_2NH_2)(HNCH_2CH_2NH_2)_3Zn_2Ge_2Se_8$.

3.3. Infrared and Raman spectroscopy

Infrared spectroscopy confirmed the presence of $-NH_2^+-$, –NH– and $-NH_2$, groups [41] in **3** (see Fig. 4).

Raman spectroscopy was used to further characterize the inorganic part in **3**. The Raman spectrum of **3** in the range 0–500 cm^{-1}, recorded at room temperature on a single crystal, is shown in Fig. 5. At least five vibrational modes were observed and provide information about the local environment of the germanium atoms in the structure. Normally, an ideal $[GeSe_4]^{4-}$ tetrahedron should show only a single Raman peak due to the symmetric (A_g) mode of vibration. The observation of multiple peaks suggests a local symmetry lowering of the tetrahedron, in full agreement with the crystallographic data of **3**. A comparison with the Raman spectra of $ASmGeSe_4$ (A = K^+, Rb^+, Cs^+) [42], $KCeGeSe_4$ [43], $M_{0.5}Pb_{1.75}GeSe_4$ (M = Ag^+, Na^+) [44] and $GeSe_2$ [45] all of which contain linked $[GeSe_4]^{4-}$ distorted tetrahedra, allows for a qualitative assignment of the observed bands. Accordingly, the sharp, intense peak centered at 213 cm^{-1} can be assigned to the primary symmetric Ge–Se stretching modes (A_1 mode, ν_1) of $[GeSe_4]$ tetrahedra. The peaks at 300 and 284 cm^{-1} can be assigned to the asymmetric Ge–Se stretching modes (F) while those at 166 and 101 cm^{-1} to the partially overlapping antisymmetric Se–Ge–Se bends (E).

3.4. Thermal analysis

The thermal stability of **3** was studied by thermogravimetric analysis (TGA). As shown in Fig. 6, the material is stable up to ~105 °C. Between 105 and 450 °C weight loss occur in two steps,

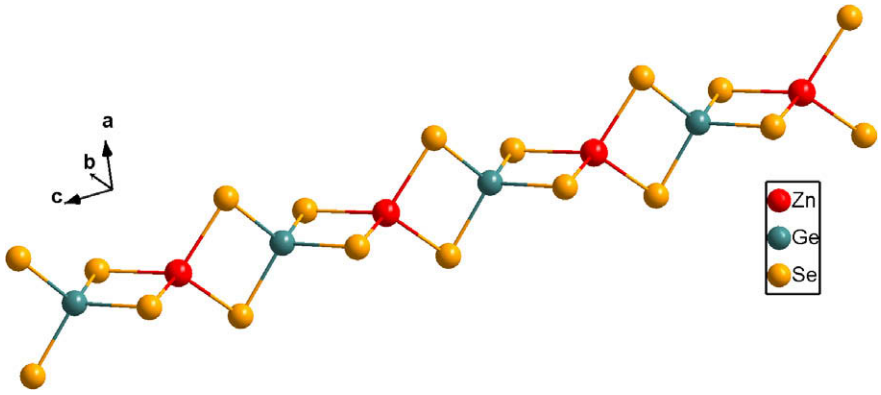


Fig. 3. The 1D $[Zn_2Ge_2Se_8]^{4-}$ chains in **3**.

Table 2
Selected bond lengths [Å] for **3** at 298(2) K with estimated standard deviations in parentheses.

Label	Distances	Label	Distances
Zn(1)–Se(2)$^{\#1}$	2.4924(15)	Ge(1)–Se(3)$^{\#4}$	2.3416(15)
Zn(1)–Se(2)	2.4924(15)	Ge(1)–Se(6)	2.3563(15)
Zn(1)–Se(8)$^{\#1}$	2.5041(15)	Ge(1)–Se(4)	2.3580(16)
Zn(1)–Se(8)	2.5041(15)	Ge(2)–Se(1)$^{\#2}$	2.3436(14)
Zn(2)–Se(6)	2.4759(17)	Ge(2)–Se(1)	2.3436(14)
Zn(2)–Se(5)	2.4845(17)	Ge(2)–Se(7)	2.3556(14)
Zn(2)–Se(3)	2.4871(17)	Ge(2)–Se(7)$^{\#2}$	2.3556(14)
Zn(2)–Se(4)	2.5171(16)	Ge(3)–Se(2)$^{\#4}$	2.3485(13)
Zn(3)–Se(1)	2.4700(15)	Ge(3)–Se(2)$^{\#5}$	2.3485(13)
Zn(3)–Se(1)$^{\#2}$	2.4700(15)	Ge(3)–Se(8)	2.3559(13)
Zn(3)–Se(7)$^{\#3}$	2.4804(15)	Ge(3)–Se(8)$^{\#1}$	2.3559(13)
Zn(3)–Se(7)$^{\#4}$	2.4804(15)	Ge(2)–Se(1)$^{\#2}$	2.3436(14)

Symmetry transformations used to generate equivalent atoms: 1# $-x,-y+1,z$; 2# $-x+1,-y+1,z$; 3# $-x+1,-y+1,z+1$; 4# $x,y,z+1$; 5# $-x,-y+1,z+1$; 6# $x,y,z-1$.

Table 3
Bond angles [°] for **3** at 298(2) K with estimated standard deviations in parentheses.

Label	Angles	Label	Angles
Se(2)$^{\#1}$–Zn(1)–Se(2)	94.18(7)	Se(3)$^{\#4}$–Ge(1)–Se(6)	115.72(6)
Se(2)$^{\#1}$–Zn(1)–Se(8)$^{\#1}$	115.96(4)	Se(3)$^{\#4}$–Ge(1)–Se(4)	113.12(6)
Se(2)–Zn(1)–Se(8)$^{\#1}$	119.92(4)	Se(6)–Ge(1)–Se(4)	101.35(5)
Se(2)$^{\#1}$–Zn(1)–Se(8)	119.92(4)	Se(3)$^{\#4}$–Ge(1)–Se(5)$^{\#4}$	100.89(5)
Se(2)–Zn(1)–Se(8)	115.96(4)	Se(6)–Ge(1)–Se(5)$^{\#4}$	112.92(6)
Se(8)$^{\#1}$–Zn(1)–Se(8)	93.09(7)	Se(4)–Ge(1)–Se(5)$^{\#4}$	113.43(6)
Se(6)–Zn(2)–Se(5)	119.13(6)	Se(1)$^{\#2}$–Ge(2)–Se(1)	100.34(7)
Se(6)–Zn(2)–Se(3)	118.71(7)	Se(1)$^{\#2}$–Ge(2)–Se(7)	116.21(5)
Se(5)–Zn(2)–Se(3)	93.70(5)	Se(1)–Ge(2)–Se(7)	112.21(5)
Se(6)–Zn(2)–Se(4)	93.83(5)	Se(1)$^{\#2}$–Ge(2)–Se(7)$^{\#2}$	112.21(5)
Se(5)–Zn(2)–Se(4)	118.35(6)	Se(1)–Ge(2)–Se(7)$^{\#2}$	116.21(5)
Se(3)–Zn(2)–Se(4)	115.14(6)	Se(7)–Ge(2)–Se(7)$^{\#2}$	100.45(8)
Se(1)–Zn(3)–Se(1)$^{\#2}$	93.55(7)	Se(2)$^{\#4}$–Ge(3)–Se(2)$^{\#5}$	102.02(7)
Se(1)–Zn(3)–Se(7)$^{\#3}$	119.79(5)	Se(2)$^{\#4}$–Ge(3)–Se(8)	111.45(4)
Se(1)$^{\#2}$–Zn(3)–Se(7)$^{\#3}$	116.07(5)	Se(2)$^{\#5}$–Ge(3)–Se(8)	115.76(4)
Se(1)–Zn(3)–Se(7)$^{\#4}$	116.07(5)	Se(2)$^{\#4}$–Ge(3)–Se(8)$^{\#1}$	115.76(4)
Se(1)$^{\#2}$–Zn(3)–Se(7)$^{\#4}$	119.79(5)	Se(2)$^{\#5}$–Ge(3)–Se(8)$^{\#1}$	111.45(4)
Se(7)$^{\#3}$–Zn(3)–Se(7)$^{\#4}$	93.75(7)	Se(8)–Ge(3)–Se(8)$^{\#1}$	101.00(7)

Symmetry transformations used to generate equivalent atoms: 1# $-x,-y+1,z$; 2# $-x+1,-y+1,z$; 3# $-x+1,-y+1,z+1$; 4# $x,y,z+1$; 5# $-x,-y+1,z+1$; 6# $x,y,z-1$.

corresponding to the removal of the organic molecules, with a total weight loss of 22.5%. This value is close to that calculated from the chemical formula of **3** (30 wt%), assuming completely removal of the organic part. The difference between the observed and the calculated weight loss could be explained by remaining carbon in the form of coke, due the calcination of **3** under inert (flow of argon) conditions.

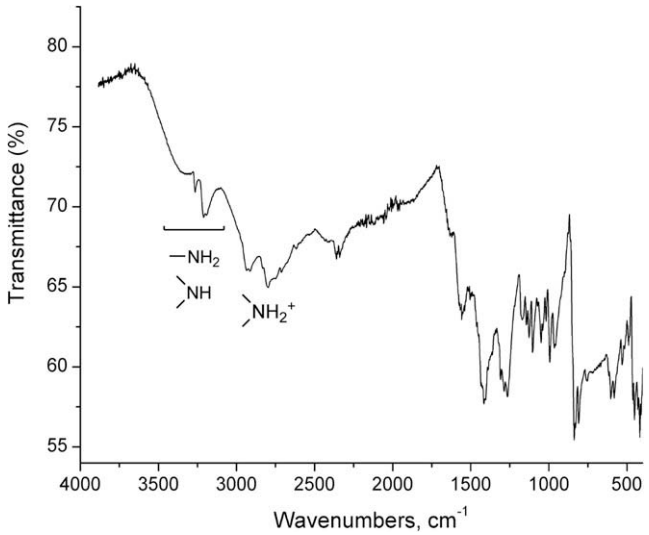


Fig. 4. ATR-IR spectrum of **3**.

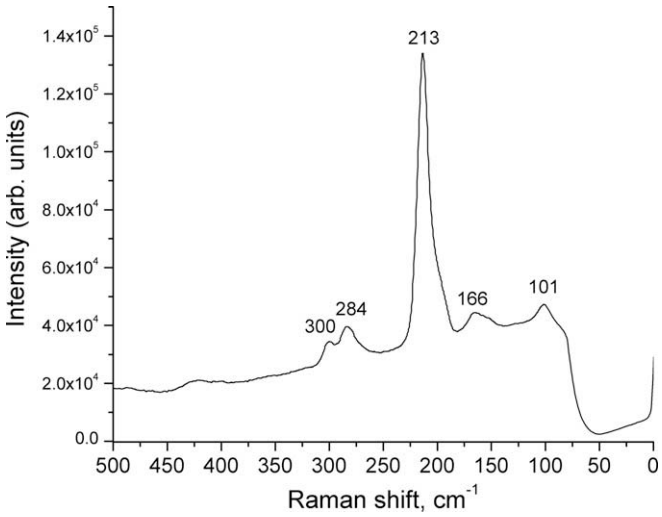


Fig. 5. Raman spectrum for compound **3** recorded at room temperature on a single crystal.

3.5. Solid-state diffuse reflectance spectroscopy

Diffuse reflectance UV–Vis/near IR spectroscopy was used to investigate the optical properties of **3**. As shown in Fig. 7, a well

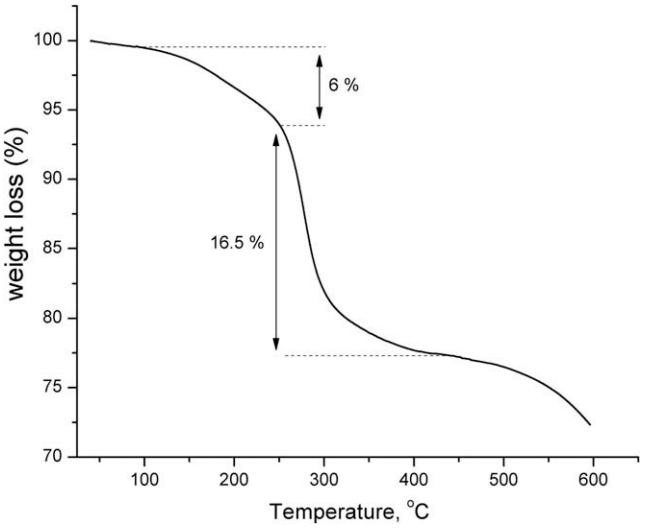


Fig. 6. Thermogravimetric analysis (TGA) curve of **3** recorded under Argon flow.

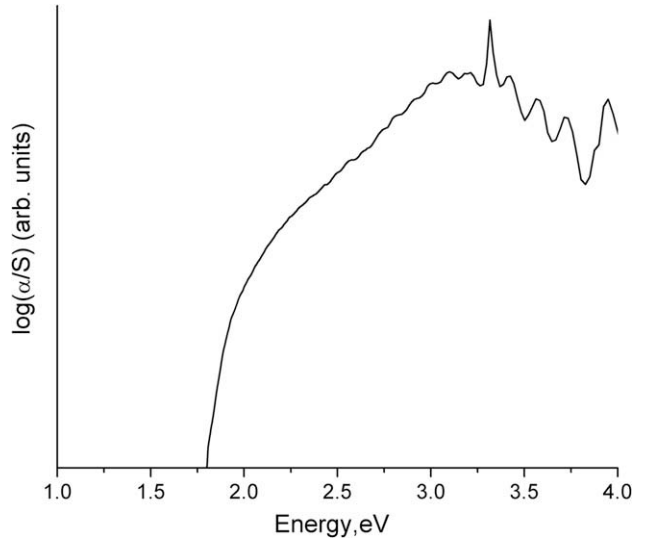


Fig. 7. Solid state UV–Vis/near IR electronic absorption spectrum for compound **3**.

defined optical absorption associated with a band-gap transition at 1.8 eV is observed, indicating that this is a medium gap semiconductor, in the same range of some important chalcogenides such as GaAs (1.43 eV) and CdSe (1.70 eV). Interestingly, the observed band-gap is lower to that found in **1** (2.3 eV). One would expect a higher band-gap in **3** in comparison to **1**, because **1** is a two-dimensional (2D) solid and also contains a heavier main-group metal (Sn instead of Ge). These results indicated that the chemical composition of the inorganic part in **3** is not the decisive factor that controls the optical properties of the material and structural parameters should also be considered. Band structure calculations may seed light into the optical properties of **3** and currently are performed. It is important to note here that similar surprising observations have been reported in other low-dimensional semiconductors such as in the case of the 2D compound $Ga_4Se_7(en)_2(enH)_2$ [46].

4. Conclusions

In conclusion, we have synthesized and characterized the first organically templated semiconductor in the system Zn/Ge/Se. The compound features 1D anionic chains made of alternating edge-shared [$ZnSe_4$] and [$GeSe_4$] tetrahedra that charged balanced by two different organic cations. The material is a medium gap semiconductor with an absorption edge at 1.8 eV. Currently, we are exploring other amine-based organic molecules as templating agents for the development of novel transition metal containing group 14 (Ge and Sn) chalcogenides.

5. Supplementary data

CCDC 721564 contains the supplementary crystallographic data for **3**. These data can be obtained free of charge via http://www.ccdc.cam.ac.uk/conts/retrieving.html, or from the Cambridge Crystallographic Data Centre, 12 Union Road, Cambridge CB2 1EZ, UK; fax: (+44) 1223-336-033; or e-mail: deposit@ccdc.cam.ac.uk.

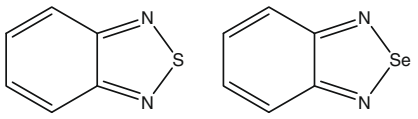
Acknowledgments

Financial support from the European Union (75%) and the Greek Government (25%) through the program PENED-2003 code number 03ED450, from INTERREG IIIA Greece-Cyprus (K2301.004) and from BIOSOLENUTI (REGPOT-2008-1) grant number 229927, is gratefully acknowledged.

References

[1] N.F. Zheng, X.H. Bu, P.Y. Feng, Nature 426 (2003) 428.
[2] K.F. Hsu, S. Loo, F. Guo, W. Chen, J.S. Dyck, C. Uher, T. Hogan, E.K. Polychroniadis, M.G. Kanatzidis, Science 303 (2004) 818.
[3] C.B. Murray, C.R. Kagan, M.G. Bawendi, Science 270 (1995) 1335.
[4] D.B. Mitzi, L.L. Kosbar, C.E. Murray, M. Copel, A. Afzali, Nature 428 (2004) 299.
[5] K. Tanaka, Science 277 (1997) 1786.
[6] W.S. Sheldrick, M. Wachhold, Coord. Chem. Rev. 176 (1998) 211.
[7] M.G. Kanatzidis, A.C. Sutorik, Progress in Inorganic Chemistry, Vol. 43 (1995) 151.
[8] H.L. Li, J. Kim, M. O'Keeffe, O.M. Yaghi, Angew. Chem., Int. Ed. 42 (2003) 1819.
[9] N. Zheng, X.H. Bu, H. Vu, P.Y. Feng, Angew. Chem., Int. Ed. 44 (2005) 5299.
[10] P.Y. Feng, X.H. Bu, N.F. Zheng, Acc. Chem. Res. 38 (2005) 293.
[11] Q.C. Zhang, Y. Liu, X.H. Bu, T. Wu, P.Y. Feng, Angew. Chem., Int. Ed. 47 (2008) 113.
[12] N. Ding, M.G. Kanatzidis, Chem. Mater. 19 (2007) 3867.
[13] P. Vaqueiro, Inorg. Chem. 47 (2008) 20.
[14] T. Jiang, A. Lough, G.A. Ozin, R.L. Bedard, R. Broach, J. Mater. Chem. 8 (1998) 721.
[15] N.F. Zheng, X.G. Bu, B. Wang, P.Y. Feng, Science 298 (2002) 2366.
[16] M.J. Manos, C.D. Malliakas, M.G. Kanatzidis, Chem.-Eur. J. 13 (2007) 51.
[17] J. Zhou, G.Q. Bian, Y. Zhang, Q.Y. Zhu, C.Y. Li, J. Dai, Inorg. Chem. 46 (2007) 6347.
[18] N. Pienack, A. Puls, C. Nather, W. Bensch, Inorg. Chem. 47 (2008) 9606.
[19] J.N. Rebilly, P.W. Gardner, G.R. Darling, J. Bacsa, M.J. Rosseinsky, Inorg. Chem. 47 (2008) 9390.
[20] N.F. Zheng, X.H. Bu, J. Lauda, P.Y. Feng, Chem. Mater. 18 (2006) 4307.
[21] N.F. Zheng, X.H. Bu, H.W. Lu, L. Chen, P.Y. Feng, J. Am. Chem. Soc. 127 (2005) 14990.
[22] J.L. Xie, X.H. Bu, N.F. Zheng, P.Y. Feng, Chem. Commun. (2005) 4916.
[23] X.Y. Huang, J. Li, H.X. Fu, J. Am. Chem. Soc. 122 (2000) 8789.
[24] J. Li, W.H. Bi, W. Ki, X.Y. Huang, S. Reddy, J. Am. Chem. Soc. 129 (2007) 14140.
[25] P. Vaqueiro, M.L. Romero, J. Am. Chem. Soc. 130 (2008) 9630.
[26] P.N. Trikalitis, A. Philippidis, T. Bakas, Chem. Commun. (2009) 2, doi:10.1039/<B821859E>.
[27] T.J. McCarthy, S.P. Ngeyi, J.H. Liao, D.C. Degroot, T. Hogan, C.R. Kannewurf, M.G. Kanatzidis, Chem. Mater. 5 (1993) 331.
[28] B. Krebs, Angew. Chem., Int. Ed. Engl. 22 (1983) 113.
[29] K.K. Rangan, P.N. Trikalitis, C. Canlas, T. Bakas, D.P. Weliky, M.G. Kanatzidis, Nano Lett. 2 (2002) 513.
[30] M.J. Manos, J.I. Jang, J.B. Ketterson, M.G. Kanatzidis, Chem. Commun. (2008) 972.
[31] M. Wu, W.P. Sul, N. Jasutkar, X.Y. Huang, J. Li, Mater. Res. Bull. 40 (2005) 21.
[32] M.K. Brandmayer, R. Clerac, F. Weigend, S. Dehnen, Chem.-Eur. J. 10 (2004) 5147.
[33] E. Ruzin, S. Dehnen, Z. Anorg. Allg. Chem. 632 (2006) 749.
[34] O.M. Yaghi, Z. Sun, D.A. Richardson, T.L. Groy, J. Am. Chem. Soc. 116 (1994) 807.
[35] C.L. Bowes, A.J. Lough, A. Malek, G.A. Ozin, S. Petrov, D. Young, Chem. Berichte 129 (1996) 283.
[36] O. Achak, J.Y. Pivan, M. Maunaye, M. Louer, D. Louer, J. Solid State Chem. 121 (1996) 473.
[37] R.L. Bedard, S.T. Wilson, L.D. Vail, J.M. Bennett, E.M. Flanigen, Zeolites: facts, figures, future, in: P.A. Jacobs, R.A. van Santen (Eds.), Proceedings of the Eighth International Zeolite Conference, Elsevier, Amsterdam, 1989, p. 375.

[38] H. Ahari, A. Garcia, S. Kirkby, G.A. Ozin, D. Young, A.J. Lough, J. Chem. Soc., Dalton Trans. (1998) 2023.
[39] K. Tsamourtzi, J.H. Song, T. Bakas, A.J. Freeman, P.N. Trikalitis, M.G. Kanatzidis, Inorg. Chem. 47 (2008) 11920.
[40] S. Haddadpour, M. Melullis, H. Staesche, C.R. Mariappan, B. Roling, R. Clerac, S. Dehnen, Inorg. Chem. 48 (2009) 1689.
[41] R.M. Silverstein, T.C. Morrill, G. Clayton, Spectrometric Identification of Organic Compounds, John Wiley and Sons Inc, 1974.
[42] B.R. Martin, P.K. Dorhout, Inorg. Chem. 43 (2004) 385.
[43] A. Choudhury, L.A. Polyakova, I. Hartenbach, T. Schleid, P.K. Dorhout, Z. Anorg. Allg. Chem. 632 (2006) 2395.
[44] R.G. Iyer, J.A. Aitken, M.G. Kanatzidis, Solid State Sci. 6 (2004) 451.
[45] J.E. Griffiths, G.P. Espinosa, J.C. Phillips, J.P. Remeika, Phys. Rev. B 28 (1983) 4444.
[46] Y.J. Dong, Q. Peng, R.J. Wang, Y.D. Li, Inorg. Chem. 42 (2003) 1794.



btd bsd

Fig. 1. The structures of 2,1,3-benzothiadiazole (btd) and 2,1,3-benzoselenadiazole (bsd).

temperature. Colorless crystals of **1** were formed over a period of three days. The crystals were isolated by vacuum filtration, washed with Et_2O (2 × 5 mL) and dried in air. Yield ~40%. *Anal.* Calc. for $C_{12}H_8HgCl_2N_4Se_2$: C, 22.60; H, 1.26; N, 8.79. Found: C, 22.51; H, 1.15; N, 8.87%. Selected IR data (cm^{-1}): 3040 (w), 1602 (m), 1530 (s), 1485 (s), 1460 (s), 1350 (m), 1280 (m), 1130 (m), 924 (s), 870 (vs), 848 (s), 709 (vs), 592 (m), 475 (s).

2.2.2. Synthesis of $[HgCl_2(bsd)]_n$ (**2**)

$HgCl_2$ (271 mg, 1.0 mmol) and bsd (183 mg, 1.0 mmol) were dissolved in MeOH (25 mL). The resulting pale yellow solution was allowed to stir for 20 min and left undisturbed to evaporate at room temperature. Pale yellow crystals of **2** were formed over a period of two days. The crystals were isolated by vacuum filtration, washed with Et_2O (2 × 5 mL) and dried in air. Yield ~30%. *Anal.* Calc. for $C_6H_4HgCl_2N_2Se$: C, 15.85; H, 0.89; N, 6.16. Found: C, 15.82; H, 0.76; N, 6.18%. Selected IR data (cm^{-1}): 3038 (w), 1598 (m), 1520 (s), 1479 (s), 1465 (s), 1340 (m), 1276 (m), 1128 (m), 930 (s), 878 (vs), 840 (s), 712 (vs), 588 (m), 468 (s).

2.3. Single-crystal X-ray crystallography

2.3.1. Complex **1**

Slow crystallization from MeOH yielded colorless prismatic crystals. A crystal with approximate dimensions 0.05 × 0.14 × 0.50 mm was mounted in a capillary. Diffraction measurements were made on a Crystal Logic Dual Goniometer diffractometer using graphite monochromated Mo radiation. Unit cell dimensions were determined and refined by using the angular settings of 25 automatically centered reflections in the range 11<2θ<23° and they appear in Table 1. Intensity data were recorded using a θ–2θ scan. Three standard reflections monitored every 97 reflections showed less than 3% variation and no decay. Lorentz, polarization and psi-scan absorption corrections were applied using Crystal Logic software. The structure was solved by direct methods using SHELXS-97 [20] and refined by full-matrix least-squares techniques on F^2 with SHELXL-97 [21]. All hydrogen atoms were introduced at calculated positions as riding on bonded atoms. All non-hydrogen atoms were refined anisotropically.

Table 1
Crystallographic data for complexes **1** and **2**.

Parameter	**1**	**2**
Formula	$C_{12}H_8Cl_2HgN_4Se_2$	$C_6H_4Cl_2HgN_2Se$
Formula weight	637.64	454.56
Crystal colour, habit	colorless, prisms	pale yellow, prisms
Crystal dimensions (mm)	0.05 × 0.14 × 0.50	0.05 × 0.05 × 0.50
Crystal system	triclinic	orthorombic
Space group	$P\bar{1}$	$P212121$
Unit cell dimensions		
a(Å)	9.746(6)	3.9231(19)
b(Å)	11.237(7)	14.756(7)
c(Å)	3.857(3)	16.730(7)
α(°)	84.801(16)	90.00
β(°)	80.174(17)	90.00
γ(°)	79.336(17)	90.00
V(Å^3)	408.2(5)	968.5(8)
Z	1	4
$\rho_{calc.}$(g cm^{-3})	2.594	3.118
Radiation, λ (Å)	Mo Kα, 0.71073	Mo Kα, 0.71073
T (K)	298(2)	298(2)
θ Range (°)	1.85–25	1.84–24.50
μ (mm^{-1})	14.207	20.145
Collected reflections	1659	1897
Independent reflections (R_{int})	1432 (0.0317)	1602 (0.0430)
Observed reflections $I > 2\sigma(I)$	1198	1543
Parameters refined	97	111
$(\Delta\rho)_{max}$, $(\Delta\rho)_{min}$ (e Å^{-3})	2.141, −3.727	0.985, −1.050
Goodness-of-fit (GOF) (on F^2)	1.115	1.080
R_1[a], wR_2[b] (all data)	0.0840, 0.1959	0.0314, 0.0830
R_1[a], wR_2[b] ($I > 2\sigma(I)$)	0.0714, 0.1810[c]	0.0299, 0.0817[d]

[a] $R_1 = \sum(|F_o| - |F_c|)/\sum(|F_o|)$.
[b] $wR_2 = \left\{\sum[w(F_o^2 - F_c^2)^2]/\sum[w(F_o^2)^2]\right\}^{\frac{1}{2}}$.
[c] For 1198 reflections with $I > 2\sigma(I)$.
[d] For 1543 reflections with $I > 2\sigma(I)$.

2.3.2. Complex **2**

Slow crystallization from MeOH yielded yellow prismatic crystals. A crystal with approximate dimensions 0.05 × 0.05 × 0.50 mm was mounted in air and covered with epoxy glue. Diffraction measurements were made on a Crystal Logic Dual Goniometer diffractometer using graphite monochromated Mo radiation. Unit cell dimensions were determined and refined by using the angular settings of 25 automatically centered reflections in the range $11° < 2\theta < 23°$ and they appear in Table 1. Intensity data were recorded using a θ–2θ scan. Three standard reflections monitored every 97 reflections showed less than 3% variation and no decay. Lorentz, polarization and psi-scan absorption corrections were applied using Crystal Logic software. The structure was solved by direct methods using SHELXS-97 [20] and refined by full-matrix least-squares techniques on F^2 with SHELXL-97 [21]. All hydrogen atoms were introduced at calculated positions as riding on bonded atoms. All non-hydrogen atoms were refined anisotropically.

3. Results and discussion

3.1. Brief synthetic comments

Reaction of one mol of $HgCl_2$ with one and two mol of bsd in MeOH results in yellow crystals of $[HgCl_2(bsd)]_n$ (**2**) and colorless crystals of $[HgCl_2(bsd)_2]_n$ (**1**), respectively and therefore, the identity of the products is ratio depended. Higher $HgCl_2$/bsd mole ratios than 1:2 (i.e. 1:3, 1:4) always result in the formation of **1**, while mole ratios of 1:1 or 2:1 result in **2**. The $HgCl_2$/bsd reaction system is not temperature depended since refluxing the reaction mixtures always resulted in the formation of **1** or **2** according to the $HgCl_2$/bsd molar ratio.

3.2. Description of structures

Selected bond distances and angles for compound **1** are listed in Table 2. The structure of **1** consists of 1D $\{Hg(\mu\text{-}Cl)_2\}_n$ linear chains running along the *c*-axis (Fig. 2), with *intra*chain Hg···Hg separations of 3.857(3) (*c*-axis). The shortest *inter*chain Hg···Hg separation is 9.746(6) Å (*a*-axis). The Hg^{II} atom sits on an inversion

Table 2
Selected bond distances (Å) and angles (°) in **1**.

Hg–Cl	2.427(7)	Hg–N1	2.627(1)
Hg–Cl[a]	3.100(1)		
Cl–Hg–N1	91.6(3)	Cl[a]–Hg–N1	81.7(3)
Cl–Hg–Cl[a]	92.4(3)	Cl[c]–Hg–N1	98.3(3)
Cl–Hg–Cl[b]	180.00	Cl[a]–Hg–Cl[c]	180.00
Cl–Hg–Cl[c]	87.6(3)	N1–Hg–N1[b]	180.00
Cl–Hg–N1[b]	88.4(3)		

Symmetry codes: a: −*x*, −*y*, 1−*z*; b: −*x*, −*y*, −*z*; c: *x*, *y*, 1 + *z*.

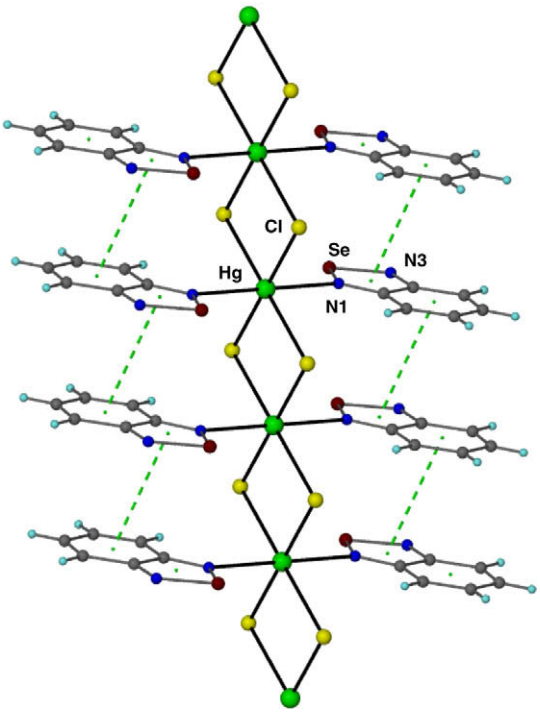


Fig. 2. Ball and stick representation of **1** showing a single chain and the π···π interactions (green dashed lines) between the bsd molecules. Color code: Hg green, Cl yellow, N blue, Se dark-red, C grey, H cyan, centroids small green spheres. (For interpretation of the references to colour in this figure legend, the reader is referred to the web version of this article.)

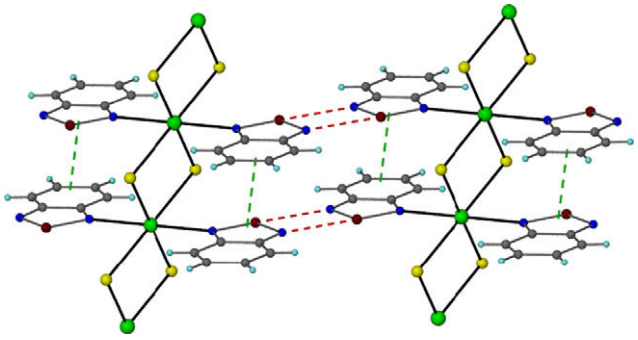


Fig. 3. Ball and stick representation of **1** showing two chains and the N···Se interactions (red dashed lines) between the bsd molecules. Color code: Hg green, Cl yellow, N blue, Se dark-red, C grey, H cyan. (For interpretation of the references to colour in this figure legend, the reader is referred to the web version of this article.)

Table 3
Selected bond distances (Å) and angles (°) in **2**.

Hg–Cl1	2.352(3)	Hg–Cl2^{b}	3.059(3)
Hg–Cl2	2.348(3)	Hg–N1	2.666(9)
Hg–Cl1^{a}	3.050(3)	Hg–N3^{c}	2.718(9)
Cl1–Hg–Cl2	179.11(10)	Cl2–Hg–N3^{c}	85.9(2)
Cl1–Hg–N1	82.8(2)	Cl1^{a}–Hg–N1	81.4(2)
Cl1–Hg–Cl1^{a}	92.24(9)	Cl2^{b}–Hg–N1	99.3(2)
Cl1–Hg–Cl2^{b}	87.70(9)	N1–Hg–N3^{c}	164.4(3)
Cl1–Hg–N3^{c}	93.3(2)	Cl1^{a}–Hg–Cl2^{b}	179.33(8)
Cl2–Hg–N1	98.1(2)	Cl1^{a}–Hg–N3^{c}	83.8(2)
Cl1^{a}–Hg–Cl2	87.99(9)	Cl2^{b}–Hg–N3^{c}	95.6(2)
Cl2–Hg–Cl2^{b}	92.07(10)		

Symmetry codes: a: $-1+x, y, z$; b: $1+x, y, z$; c: $-x, -1/2+y, 3/2-z$.

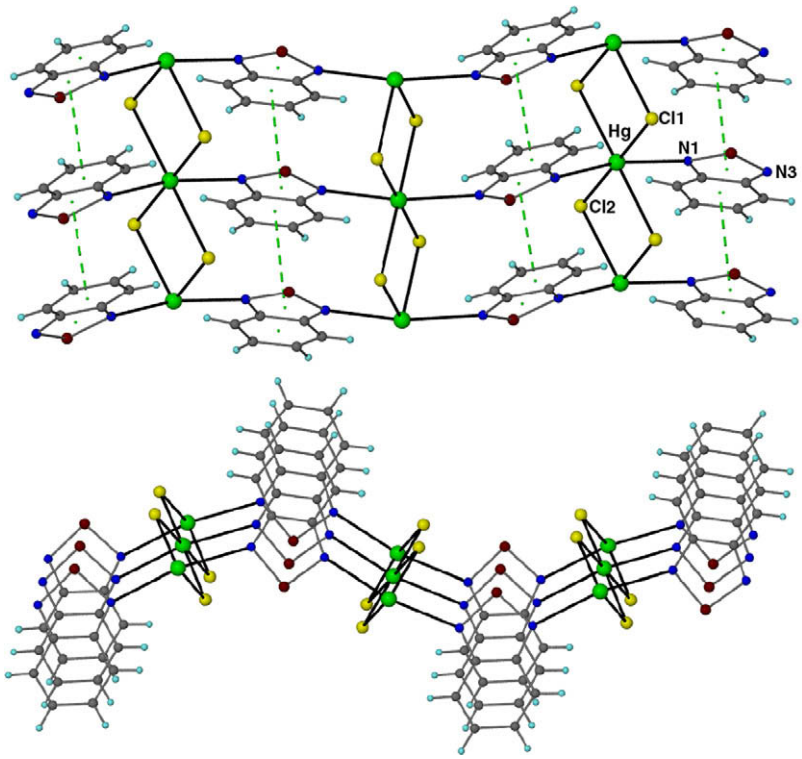


Fig. 4. Ball and stick representation of **2** showing the top and side view of the undulated layer and the π···π interactions (green dashed lines) between the bsd molecules. Color code: Hg green, Cl yellow, N blue, Se dark-red, C grey, H cyan, centroids small green spheres. (For interpretation of the references to colour in this figure legend, the reader is referred to the web version of this article.)

center. Each Hg^{II} atom is octahedrally coordinated to four Cl^- ligands and two terminal bsd molecules. The Hg–Cl distances are 2.427(7) and 3.100(7) Å and the Hg–N bond length is 2.627(1) Å, in good agreement with those of other similar Hg(II) complexes [1].

A characteristic structural feature common to free bsd and **1** is the existence of strong face-to-face stacking interactions between the bsd ligands. The bsd molecules form columns within the crystal lattice, with the *inter*planar distances being 3.576 and 3.474 Å for free bsd [13] and **1**, respectively. In **1** the columns of the bsd molecules are orientated on alternating sides of each $\{Hg(\mu\text{-}Cl)_2\}_n$ chain. The bsd molecules within a column in **1** stack off set such that the five-membered ring (C_2N_2Se) of one molecule forms a π···π stacking interaction with the phenyl ring of a neighboring molecule [centroid···centroid 3.622 Å] (Fig. 2). The centroid···centroid distance between the five-membered ring of one molecule and the phenyl ring of a neighboring molecule in the structure of the free ligand is 3.621 Å. This structural feature has also been observed in the crystal structures of btd [22] and its complexes [10,11].

Neighboring layers of **1** are further bridged in the second dimension via N···Se interactions (Fig. 3). Each bsd molecule forms two complementary N···Se interactions [N···Se 2.876(1) Å] with a bsd molecule belonging to a neighboring chain giving rise to an undulated layer running parallel to the *bc* plane. Similar N···Se conducts are observed in the crystal structure of the free ligand with the N···Se distance being 3.155(6) Å [13].

Selected bond distances and angles for complex **2** are listed in Table 3. Complex **2** consists of 1D $\{Hg(\mu\text{-}Cl)_2\}_n$ linear chains running along the *a*-axis and linked via μ-bsd ligands along the *b*-axis to afford an extended undulated (4,4) 2D layered network (Fig. 4), with *intra*layer Hg···Hg separations of 3.923 Å (via chlorides) and 7.480 Å (via bsd). The shortest *inter*layer Hg···Hg separation is 7.773 Å. The Hg^{II} atom is octahedrally coordinated to four Cl^- ligands and two bsd molecules. There are two kinds of Hg–Cl bonds, short and long. The short Hg–Cl distances are 2.352(3) and 2.348(3) Å, while the long Hg–Cl distances are 3.050(3) and 3.059(3) Å. The Hg–N bond lengths are 2.666(9) and 2.718(9) Å. Complex **2** has a similar structure with $[CuCl_2(btd)]_n$ [10], $[CoCl_2(btd)]_n$ and $[CoBr_2(btd)]_n$ [11].

Complex **2** is dominated by the existence of strong face-to-face *intra*layer stacking interactions between the bsd ligands along the *c*-axis (Fig. 4). Like in **1**, the bsd molecules in **2** form columns within the crystal lattice, with the *inter*planar distances being 3.516 Å. The columns of the bsd molecules in **2** are orientated on alternating sides of each sheet. The bsd molecules within each column in **2** stack off set such that the five-membered ring (C_2N_2Se) of one molecule forms a π···π stacking interaction with the phenyl ring of a neighboring molecule [centroid···centroid 3.624 Å] (Fig. 4).

3.3. Spectroscopic characterization

3.3.1. IR Spectroscopy

The IR spectra of both complexes are similar and exhibit the typical bands of the disubstituted benzene ring and bands assignable to vibrations of the selenadiazole ring. The bands in the 1600–1520 cm^{-1} region are associated with the ν(C=N) and ν(C=C) of the phenyl ring while the bands at *ca.* 1480 and 470 cm^{-1} are associated with the ν(CN) and ν(SeN) vibrational modes of the selenadiazole ring, respectively. Due to coordination these bands are shifted compared to those in free bsd.

4. Conclusions and perspectives

The employment of 2,1,3-benzoselenadiazole in the coordination chemistry of mercury(II) chloride afforded two coordination polymers. Both polymers feature 1D $\{Hg(\mu\text{-}Cl)_2\}_n$ linear chains, while bsd molecules act as terminal ligands in **1** and as bridging ligands in **2** to create a 2D layer in the latter case. The linear chains in **1** are further bridged via N···Se interactions to create a 2D layer. A structural feature observed in the crystal structures of the free ligand and of both complexes is the present of π···π stacking interactions between the bsd molecules. The same feature has been observed in the crystal structures of the similar ligand btd and its complexes [10,11] and seems to be persistent regardless of the different heteroatom in the five-membered ring. Efforts to employ other mercury salts and bsd are continuing.

Supplementary data

CCDC 723314 and 723315 contain the supplementary crystallographic data for **1** and **2**. These data can be obtained free of charge via http://www.ccdc.cam.ac.uk/conts/retrieving.html, or from the Cambridge Crystallographic Data Centre, 12 Union Road, Cambridge CB2 1EZ, UK; fax: (+44) 1223-336-033; or e-mail: deposit@ccdc.cam.ac.uk.

References

[1] S.R. Batten, A.R. Harris, K.S. Murray, J.P. Smith, Cryst. Growth Des. 2 (2002) 87.
[2] S.R. Batten, B.F. Hoskins, R. Robson, Angew. Chem., Int. Ed. Engl. 34 (1995) 820.
[3] M.A. Pitt, D.W. Johnson, Chem. Soc. Rev. 36 (2007) 1441.
[4] E.R.T. Tiekink, CrystEngComm 5 (2003) 101.
[5] R. Ghosh, A.D. Jana, S. Pal, G. Mostafa, H.-K. Func, B.K. Ghosh, CrystEngComm 9 (2007) 353.
[6] C. Hu, I. Kalf, U. Englert, CrystEngComm 9 (2007) 603.
[7] A.K.S. Chauhan, A. Kumar, P. Singh, R.C. Srivastava, R.J. Butcher, J. Beckmann, A. Duthie, J. Organomet. Chem. 691 (2006) 1954.
[8] A. Mosset, M. Bagieu-Beucher, A. Lecchi, R. Masse, J. Zaccaro, Solid State Sci. 4 (2002) 827.
[9] B. Bentria, D. Benbertal, M. Bagieu-Beucher, A. Mosset, J. Zaccaro, Solid State Sci. 5 (2003) 359.
[10] G.S. Papaefstathiou, A. Tsohos, C.P. Raptopoulou, A. Terzis, V. Psycharis, D. Gatteschi, S.P. Perlepes, Cryst. Growth Des. 1 (2001) 191.
[11] G.S. Papaefstathiou, S.P. Perlepes, A. Escuer, R. Vicente, A. Gantis, C.P. Raptopoulou, A. Tsohos, V. Psycharis, A. Terzis, E. Bakalbassis, J. Solid State Chem. 159 (2001) 371.
[12] K. Skorda, G.S. Papaefstathiou, A. Vafiadis, A. Lithoxoidou, C.P. Raptopoulou, A. Terzis, V. Psycharis, E. Bakalbassis, V. Tangoulis, S.P. Perlepes, Inorg. Chim. Acta 326 (2001) 53.
[13] A.C. Gomes, G. Biswas, A. Banerjee, W.L. Duax, Acta Crystallogr. C45 (1989) 73.
[14] A.F. Cozzolino, J.F. Britten, I. Vargas-Baca, Cryst. Growth Des. 6 (2006) 181.
[15] A.F. Cozzolino, N.E. Gruhn, D.L. Lichtenberger, I. Vargas-Baca, Inorg. Chem. 47 (2008) 6220.
[16] A.F. Cozzolino, I. Vargas-Baca, S. Mansour, A.H. Mahmoudkhani, J. Am. Chem. Soc. 127 (2005) 3184.
[17] K.M. Barkigia, M.W. Renner, M.O. Senge, J. Fajer, J. Phys. Chem. B 108 (2004) 2173.
[18] C.-K. Tan, J. Wang, J.-D. Leng, L.-L. Zheng, M.-L. Tong, Eur. J. Inorg. Chem. (2008) 771.
[19] A.-J. Zhou, S.-L. Zheng, Y. Fang, M.-L. Tong, Inorg. Chem. 44 (2005) 4457.
[20] G.M. Sheldrick, SHELXS-97, Structure Solving Program, University of Göttingen, Germany, 1997.
[21] G.M. Sheldrick, SHELXL-97, Program for the Refinement of Crystal Structures from Diffraction Data, University of Göttingen, Germany, 1997.
[22] P.V. Luzzati, Acta Crystallogr. 4 (1951) 193.

which have produced a new family of octanuclear complexes $[Mn_8(N_3)_4(O_2CR)_6(L)_4(py)_6]$ (L = pd^{2-}, R = Et **1**; L = mpd^{2-}, R = Et **2**; L = pd^{2-}, R = Ph **3**) with a near-planar, rod-like topology. The magnetic properties of compounds **1** and **2** were studied by dc and ac magnetic susceptibility measurements, which revealed that both compounds have a diamagnetic spin ground state.

2. Experimental

2.1. General and physical measurements

All manipulations were performed under aerobic conditions using materials (reagent grade) and solvents as received; water was distilled in-house. *Warning: Although no such behavior was observed during the present work, azide salts are potentially explosive; such compounds should be used in small quantities, and treated with utmost care at all times.* $Mn(O_2CEt)_2{\cdot}2H_2O$ [13], $Mn(O_2CPh)_2{\cdot}2H_2O$ [14] were synthesized according to published methods. Elemental analyses (C, H, N) were performed by the in-house facilities of the University of Florida, Chemistry Department.

2.2. Compound preparation

2.2.1. $[Mn_8(N_3)_4(O_2CEt)_6(pd)_4(py)_6]$ (**1**)

To a solution of $[Mn(O_2CEt)_2]{\cdot}2H_2O$ (0.131 g, 0.553 mmol) in a 10:2 ml mixture of MeCN/py was added pdH_2 (0.20 ml, 2.77 mmol) and NaN_3 (0.036 g, 0.55 mmol). The resulting yellowish-brown slurry was then left under magnetic stirring for 10 min. Then, it was filtered off, and the filtrate was left undisturbed at room temperature. After a few days X-ray quality crystals appeared and were collected by filtration, washed with MeCN and dried in vacuum. The yield was 36%. Elemental analysis: *Anal.* calc. for $C_{60}H_{84}O_{20}N_{18}Mn_8$ (**1**): C 39.66, H 4.66, N 13.88. Found: C 39.82, H 4.64, N 13.78%. Selected IR data (KBr): ν~ = 3441s, br, 2980w, 2937w, 2856w, 2073s, 1566s, 1427s, 1300w, 1087s, 1051s, 941w, 817w, 596w, 523w.

2.2.2. $[Mn_8(N_3)_4(O_2CEt)_6(mpd)_4(py)_6]$ (**2**)

To a solution of $[Mn(O_2CEt)_2]{\cdot}2H_2O$ (0.107 g, 0.450 mmol) in a 10:2 ml mixture of MeCN/py was added $mpdH_2$ (0.20 mL, 2.25 mmol) and NaN_3 (0.029 g, 0.45 mmol). The resulting yellowish - brown slurry was left under magnetic stirring for 15 min. Then, it was filtered off, and the filtrate was left undisturbed at room temperature. After a few days, X-ray quality crystals appeared and were collected by filtration, washed with MeCN and dried in vacuum. The yield was 34%. Elemental analysis: *Anal.* calc. for $C_{64}H_{92}O_{20}N_{18}Mn_8$ (**2**): C 41.04, H 4.95, N 13.46. Found: C 41.27, H 5.03, N 13.31%. Selected IR data (KBr): ν~ = 3412s, br, 2979w, 2937w, 2877w, 2862w, 2077s, 1570s, 1429s, 1300w, 1110m, 1042m, 1042m, 951w, 817w, 590m, 537w.

2.2.3. $[Mn_8(N_3)_4(O_2CPh)_6(pd)_4(py)_6]$ (**3**)

To a solution of $[Mn(O_2CPh)_2]{\cdot}2H_2O$ (0.184 g, 0.552 mmol) in a 10:2 ml mixture of Me_2CO/py was added pdH_2 (0.20 mL, 2.77 mmol) and NaN_3 (0.036 g, 0.55 mmol). The resulting yellowish-brown slurry was left under magnetic stirring for 15 min. Then, it was filtered off, and the filtrate was left undisturbed at room temperature. After a few weeks X-ray quality crystals appeared and were collected by filtration, washed with Me_2CO and dried in vacuum. The yield was 23%. Elemental analysis: *Anal.* calc. for $C_{84}H_{84}O_{20}N_{18}Mn_8$ (**3**): C 47.93, H 4.02, N 11.98. Found: C 47.78, H 4.12, N 12.06%. Selected IR data (KBr): ν~ = 3453s, br, 2942w, 2856w, 2070s, 1601s, 1558s, 1445w, 1399s, 1088m, 1052m, 944w, 817w, 723w, 593w.

Table 1
Crystallographic data for complexes **1** and **2**.

Parameter	**1**	**2**
Formula	$C_{60}H_{84}Mn_8N_{18}O_{20}$	$C_{64}H_{92}Mn_8N_{18}O_{20}$
Formula weight	1816.97	1873.08
Crystal system	triclinic	triclinic
Space group	$P\bar{1}$	$P\bar{1}$
Unit cell dimensions		
a (Å)	11.887(2)	11.710(1)
b (Å)	18.562(3)	11.963(1)
c (Å)	19.279(3)	16.307(2)
α (°)	75.43(2)	74.522(6)
β (°)	76.25(2)	88.365(6)
γ (°)	72.05(2)	78.679(5)
V (Å^3)	3857(1)	2158.1(3)
Z	2	1
ρ_{calc} (Mg m^{-3})	1.564	1.441
Radiation, λ (Å)	Mo Kα, 0.71073	Mo Kα, 0.71073
Temperature (K)	100(2)	100(2)
μ (mm^{-1})	1.343	1.203
Data collected/unique (R_{int})	54646/14354(0.0506)	38159/10853(0.0297)
Data with $I > 2\sigma(I)$	7368	6698
R_1 ($I > 2\sigma(I)$)[a]	0.0324	0.0366
wR_2 ($I > 2\sigma(I)$)[b]	0.0592	0.0952

[a] $R_1 = \sum(|F_o| - |F_c|)/\sum(|F_o|)$.
[b] $wR_2 = \{\sum[w(F_o^2 - F_c^2)^2]/\sum[w(F_o^2)^2]\}^{1/2}$.

2.3. Single-crystal X-ray crystallography

Crystals of **1**, **2** and **3** in Paratone-N oil were mounted on glass fibers. Diffraction measurements were made on an Oxford Diffraction CCD instrument using graphite-monochromated Mo radiation. Complete crystal data and parameters for data collection and processing are reported in Table 1. Unit cell dimensions were determined and refined by using 12620 ($3.1 \leqslant \theta \leqslant 30.6°$) and 15442 ($3.1 \leqslant \theta \leqslant 30.4°$) reflections for **1** and **2,** respectively. Empirical absorption corrections (multi-scan based on symmetry-related measurements) were applied using CRYSALIS RED software [15]. Data for **3** were of insufficient quality to allow full structure analysis but were suitable for the atom connectivity, and chemical formula to be confirmed; crystal data of **3** thus are not included in Table 1.

The structures were solved by direct methods using SIR92 [16a] and refined by full-matrix least-squares techniques on F^2 using SHELXL97 [16b]. Programs used: CRYSALIS CCD [15] for data collection, CRYSALIS RED [15] for cell refinement and data reduction, and DIAMOND [17a] and MERCURY [17b] for molecular graphics. All non-hydrogen atoms of the two structures were refined anisotropically. The hydrogen atoms attached to carbon atoms of the ligands of compounds **1** and **2** were positioned geometrically (riding model).

2.4. Other measurements

IR spectra (4000–400 cm^{-1}) were recorded at the University of Cyprus, using a Shimadzu Prestige – 21 spectrometer with samples prepared as KBr pellets. Variable-temperature dc and ac magnetic susceptibility data were collected at the University of Florida using a Quantum Design MPMS-XL SQUID susceptometer equipped with a 7 T magnet. The sample was embedded in solid eicosane to prevent torquing. Diamagnetic corrections to the observed susceptibilities were applied using Pascal's constants.

3. Results and discussion

3.1. Synthesis

Recently, we have been exploring the use of a combination of N_3^- and (m)pdH_2 ligands in Mn carboxylate chemistry. The initial

results of this investigation were the 1-D coordination polymers $[Mn_{17}(\mu_4\text{-}O)_8(N_3)_5(O_2CMe)_4(L)_{10}(py)_6]_\infty$ (L = pd^{2-}, **4** or mpd^{2-}, **5**), consisting of Mn_{17} octahedral units [9,10]. These compounds were isolated from the reaction of $[Mn(O_2CMe)_2]\cdot 4H_2O$, pdH_2 (or $mpdH_2$) and NaN_3 in a 1:5:1 ratio in MeCN/py (py = pyridine). A number of modifications were performed to this reaction system, some of which resulted in a discrete Mn_{17} cluster and also in a 2-D coordination polymer consisting of the same Mn_{17} octahedral unit discussed above [9] and some others resulted in microcrystalline precipitates that we were unable to further characterize. However, the reactions which involved the use of different $[Mn(O_2CR)_2]$ starting materials resulted in the isolation of three new octanuclear compounds with a rod-like topology (**1**–**3**). Thus, the reaction of $[Mn(O_2CEt)_2]\cdot 2H_2O$ with pdH_2 and NaN_3 in a 1:5:1 ratio in MeCN/py (10/2 ml) resulted in the formation of yellowish-brown crystals of **1** in 36% yield. Analogous reactions, using $mpdH_2$ instead of pdH_2, and $[Mn(O_2CPh)_2]\cdot 2H_2O$ as a starting material instead of $[Mn(O_2CEt)_2]\cdot 2H_2O$ were also performed, resulting in the formation of yellowish-brown crystals of complexes **2** and **3** in 34 and 23% yields, respectively. Note that crystals of **3** were isolated only when the reaction took place in an Me_2CO/py solvent system. Although all the reactions took place in organic solvents (MeCN/py, Me_2CO/py) where NaN_3 is nearly insoluble, we should not forget that the solvents, which were used as received, contain small amounts of water and thus NaN_3 is slightly soluble in these solvent systems. The NaN_3 that comes in the solution reacts rapidly, more NaN_3 is then dissolved and the color of the reaction mixture changes to darker yellowish-brown as the reaction proceeds.

Compounds **2** and **3** are similar to **1** since they all possess the same structural core and differ from **1** mainly in the propanediol (mpd^{2-} instead of pd^{2-} in **2**) or the carboxylate (^-O_2CPh instead of ^-O_2CEt in **3**) ligand they contain. In all those reactions, the oxidation state of the starting material is 2+, whereas the average oxidation state of the final products is higher, i.e. 2.25+ although no oxidant was added in the reaction mixture; we believe that the atmospheric O_2 is responsible for this oxidation which is facilitated

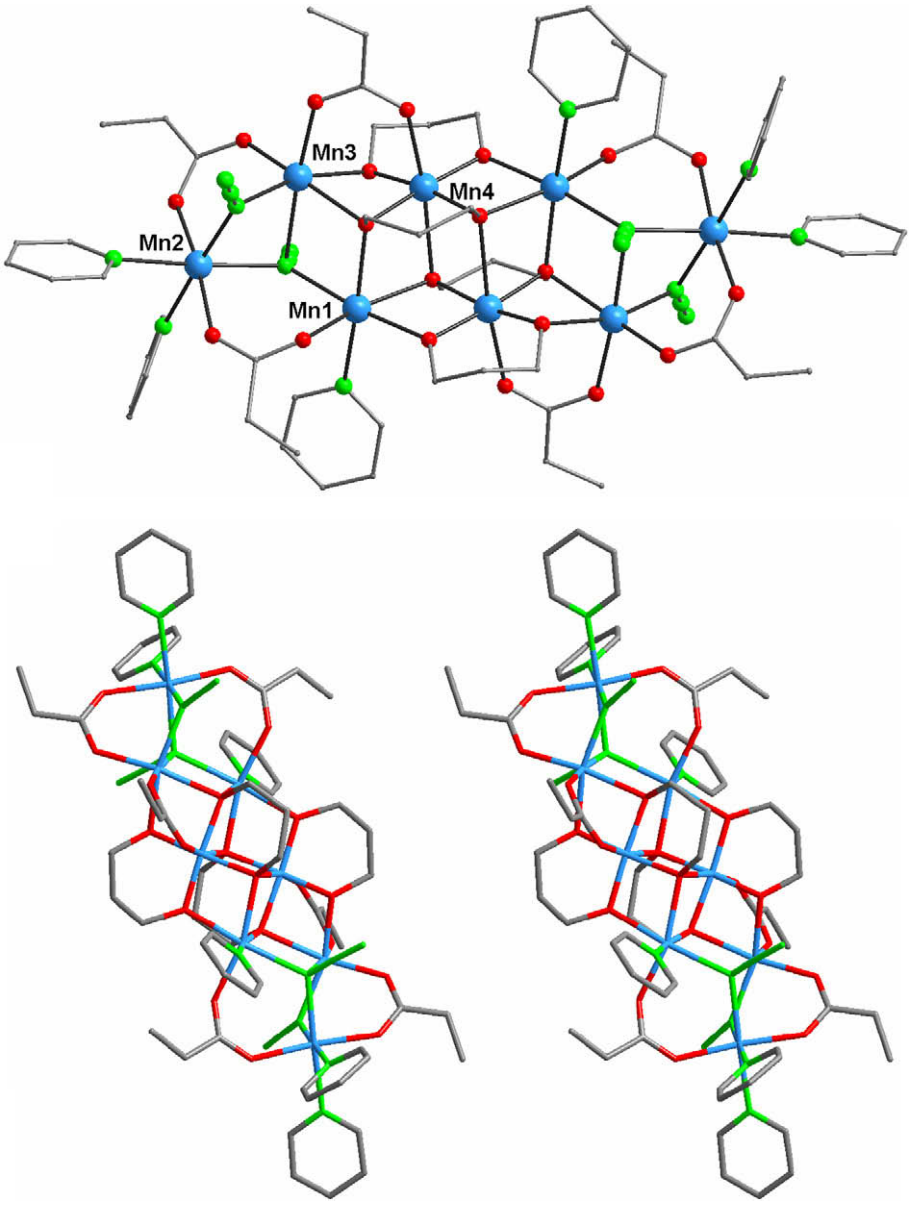


Fig. 1. Molecular structure (top) and stereoview (bottom) of complex **1**. Color code: Mn, blue; O, red; N, green; C, grey. (For interpretation of the references to colour in this figure legend, the reader is referred to the web version of this article.)

by the existence of a large excess of a base (pyridine) as it has also been observed in the past [18]. The formation of compounds **1**–**3** is summarized in Eq. (1).

$$8Mn(O_2CR)_2 \cdot 2H_2O + 4H_2(m)pd + 4NaN_3 + 6py \rightarrow [Mn_8(N_3)_4(O_2CR)_6((m)pd)_4(py)_6] + 6RCO_2H + 4RCOO^-Na^+ + 8xH_2O + 2H^+ + 2e^- (R = C_2H_5, C_6H_5) \quad (1)$$

The isolation of compounds **1**–**3** when $[Mn(O_2CR)_2]\cdot 2H_2O$ (R = Et, or Ph) are used as starting materials does not imply that analogues of **4** and **5** with propionate and benzoate ligands respectively, are not formed as reaction co-products and vise versa. It is possible that the reaction solution in each case consists of a mixture of various species in equilibrium, which could include the analogues of **4** and **5**. However, since the identity of the product that is isolated from such reactions is determined by a number of factors such as relative solubility, lattice energies, crystallization kinetics, etc, it is reasonable that the use of different carboxylate ligands will result in the precipitation of different products.

3.2. Description of the structures

A partially labelled plot and a stereoview of **1** are shown in Fig. 1. A view of the structural core of **1**–**3** emphasizing its two butterfly units is shown in Fig. 2. Selected interatomic distances and BVS calculations data for compound **1** are listed in Tables 2 and 3, respectively. Since, the crystal structures of compounds **1**–**3** are strikingly similar, only the structure of **1** will be described in detail, and the other two structures will be compared to that of **1**. Complex **1** crystallizes in the triclinic space group $P\bar{1}$, with the asymmetric unit consisting of two halves of two octanuclear units of **1**. Bond-valence sum calculations (Table 3), charge considerations, and inspection of metric parameters revealed a mixed-valent complex containing six Mn^{II} and two Mn^{III} ions. The eight Mn ions of **1** are held together by bridging N_3^- and 1,3-propanediol ligands, resulting in a $[Mn^{II}_6Mn^{III}_2(\mu_3\text{-}N_3)_2(\mu\text{-}N_3)_2(\mu_3\text{-}OR)_4(\mu\text{-}OR)_4]^{6+}$ core (Fig. 2) with a near-planar, rod-like topology.

All eight Mn ions are in distorted octahedral geometries with the two Mn^{3+} ions displaying the expected Jahn-Teller elongations. The structure of **1** consists of two symmetry-related butterfly units, which are connected through RO^- groups of pd^{2-} ligands (Fig. 2). The four pd^{2-} ligands are fully deprotonated and two of them sit above and the other two below the plane of the core. Two of the pd^{2-} ligands bridge three Mn ions in a $\eta^2{:}\eta^2{:}\mu_3$ fashion, whereas the other two bridge five Mn ions in a $\eta^3{:}\eta^3{:}\mu_5$ fashion. The Mn^{2+} ions of each butterfly unit are held together by two end-on N_3^- ligands. One of the N_3^- group bridges three Mn^{2+} in a μ_3-1,1,1 fashion, whereas the second N_3^- group bridges two Mn^{2+} ions in a μ_2-1,1 fashion. The peripheral ligation of the compound is completed by six $CH_3CH_2COO^-$ ligands, and six terminal pyridine groups. The six $CH_3CH_2COO^-$ ligands coordinate in their usual *syn*, *syn* μ_2 fashion. A close examination of the packing revealed that there are no intermolecular interactions between neighbouring Mn_8 units which are well separated since the shortest Mn···Mn distance between different Mn_8 units is relatively large (7.958 Å).

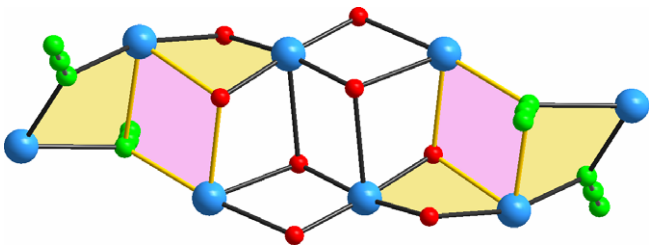


Fig. 2. The metal – oxygen–nitrogen core of **1**; the yellow lines connecting the Mn ions and the yellow and pink planes emphasise the two butterfly units. The color code is as in Fig. 1. (For interpretation of the references to colour in this figure legend, the reader is referred to the web version of this article.)

Table 2
Selected interatomic distances (Å) for complex **1**.

Bond Lengths			
Mn(1)–O(6)	2.110(2)	Mn(5)–O(12)	2.112(2)
Mn(1)–O(9)	2.190(2)	Mn(5)–O(19)	2.166(2)
Mn(1)–O(8)	2.260(2)	Mn(5)–N(13)	2.239(2)
Mn(1)–O(7)	2.269(2)	Mn(5)–O(18)	2.259(2)
Mn(1)–N(1)	2.316(2)	Mn(5)–O(17)	2.274(2)
Mn(1)–N(7)	2.328(2)	Mn(5)–N(10)	2.315(3)
Mn(2)–O(5)	2.150(2)	Mn(6)–O(11)	2.163(2)
Mn(2)–O(2)	2.175(2)	Mn(6)–O(15)	2.187(2)
Mn(2)–N(4)	2.228(2)	Mn(6)–N(16)	2.231(3)
Mn(2)–N(3)	2.291(2)	Mn(6)–N(12)	2.278(2)
Mn(2)–N(2)	2.329(3)	Mn(6)–N(11)	2.294(3)
Mn(2)–N(7)	2.355(2)	Mn(6)–N(13)	2.299(2)
Mn(3)–O(1)	2.118(2)	Mn(7)–O(16)	2.108(2)
Mn(3)–O(3)	2.127(2)	Mn(7)–O(14)	2.148(2)
Mn(3)–O(10)	2.166(2)	Mn(7)–O(20)	2.168(2)
Mn(3)–N(4)	2.215(2)	Mn(7)–N(16)	2.180(3)
Mn(3)–O(8)	2.285(2)	Mn(7)–O(17)	2.269(2)
Mn(3)–N(7)	2.390(2)	Mn(7)–N(13)	2.499(2)
Mn(4)–O(9)	1.890(2)	Mn(8)–O(19)	1.892(2)
Mn(4)–O(10)	1.897(2)	Mn(8)–O(20)	1.899(2)
Mn(4)–O(7)	1.948(2)	Mn(8)–O(18)	1.951(2)
Mn(4)–O(8)	1.970(2)	Mn(8)–O(17)	1.976(2)
Mn(4)–O(4)	2.223(2)	Mn(8)–O(13)	2.179(2)
Mn(4)–O(7)	2.460(2)	Mn(8)–O(18)	2.426(2)

Table 3
Bond-valence sums for the Mn atoms of **1**.[a]

Atom	Complex **1**		
	Mn^{II}	Mn^{III}	Mn^{IV}
Mn1	*1.79*	1.66	1.70
Mn2	*1.88*	1.78	1.76
Mn3	*1.95*	1.81	1.85
Mn4	3.04	*2.78*	2.92
Mn5	*1.88*	1.75	1.78
Mn6	*1.93*	1.83	1.81
Mn7	*1.93*	1.79	1.83
Mn8	3.07	*2.81*	2.95

[a] The italicized value is the one closest to the charge for which it was calculated. The oxidation state of a particular atom can be taken as the nearest whole number to the italicized value.

As it was mentioned above, the structures of compounds **2** and **3** are strikingly similar to this of **1** with the main differences between them being the diolate (mpd^{2-} in **2** instead of pd^{2-}) or carboxylate (benzoate in **3** instead of propionate) ligands included in the compounds.

To our knowledge, the $[Mn^{II}_3Mn^{III}(\mu_3\text{-}N_3)(\mu\text{-}N_3)(\mu_3\text{-}OR)(\mu\text{-}OR)_2]^{4+}$ that is present in **1**–**3** is unknown in discrete form but would be particularly attractive since it is expected to have a large spin ground state because of the presence of the end - on N_3^- ligands. Complexes **1**–**3** are related to compounds $[Mn^{III}_8O_4(O_2CCMe_3)_{10}(thme)_2(py)_2]$ (**6**) [19] (H_3thme = 1,1,1-tris(hydroxymethyl)ethane) and $[Mn^{III}_4Mn^{II}_4(O_2CCMe_3)_2(tmp)_2(Htmp)_4Br_4(H_2O)_2]$ (**7**) (H_3tmp = 1,1,1-tris(hydroxymethyl)propane) reported by Brechin and coworkers [18c] since they are all octanuclear Mn clusters with rod-like topologies. However, there are a number of significant differences between **1**–**3** and **6**, **7** including: (i) the presence in **1**–**3** of end-on N_3^- ligands which lead in very different structural cores, (ii) the existence in **1**–**3** of fully deprotonated diols instead of triols, (iii) different oxidation states of the Mn ions, etc.

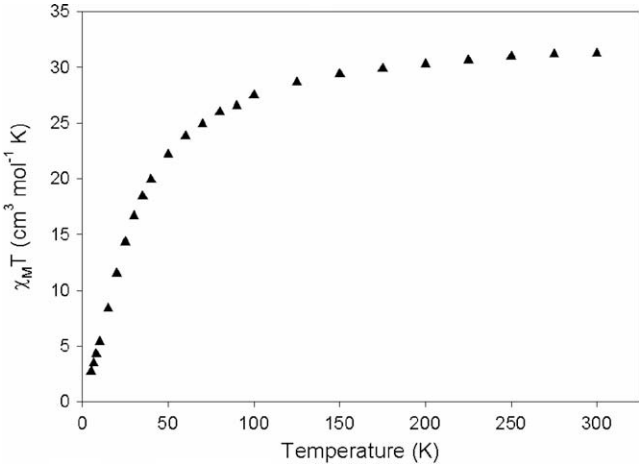


Fig. 3. Magnetic susceptibility data for **1**, shown as $\chi_M T$ vs T curves.

3.3. Magnetism

Variable-temperature, solid-state magnetic susceptibility measurements were performed on powdered polycrystalline samples of **1** and **2** in a 1kG (0.1T) field in the 5.0–300 K range. The obtained data for **1** and **2** are almost identical and thus only those for compound **1** are shown as a $\chi_M T$ vs T plot in Fig. 3. The $\chi_M T$ values at 300 K are 31.26 and 30.96 cm^3 mol^{-1} K for **1** and **2** respectively. These values are slightly smaller than that expected for a cluster comprising six Mn^{II} and two Mn^{III} non-interacting ions (32.25 cm^3 mol^{-1} K with $g = 2$). The $\chi_M T$ values gradually decrease with decreasing temperature to 22.15 cm^3 mol^{-1} K and 22.34 at 50 K before dropping to 2.68 and 2.52 cm^3 mol^{-1} K at 5.0 K. This behavior is indicative of the existence of dominant antiferromagnetic interactions between the metal centers, with the low temperature values suggesting a very small or zero ground spin state. In order to determine the ground state, magnetization data were collected in the temperature and magnetic field ranges 1.8–10.00 K and 0.1–7 T. Attempts were made to fit the resulting data using the program MAGNET [20], which assumes that only the ground state is populated at these temperatures and includes axial zero-field-spliting ($D\hat{S}_z^2$) and Zeeman interactions. However, it was not possible to obtain a satisfactory fit.

Reliable conclusions about the ground state S value, can nevertheless, be reached by using alternating current (ac) magnetic susceptibility measurements [5b,8,11]. The in-phase $\chi_M'T$ vs. T data for compound **1** are shown in Fig. 4. The $\chi_M'T$ signal for both compounds decreases linearly with decreasing temperature in the whole temperature range, and is clearly heading to $\chi_M'T$ values close to 0 at 0 K. This is consistent with the existence of antiferromagnetic interactions within the Mn ions of **1** and **2** and a diamagnetic ground spin state as was suggested on the basis of the dc magnetic susceptibility data. As expected for compounds with diamagnetic ground spin states, there are no out-of-phase ac signals down to 1.8 K.

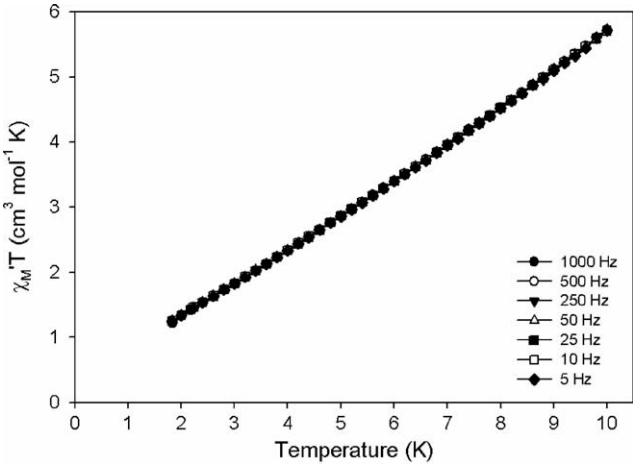


Fig. 4. Plot of the in-phase (χ_M') ac magnetic susceptibility as $\chi_M'T$ vs T for complex **1**, in a 3.5 Oe field oscillating at the indicated frequencies.

An $S = 0$ ground state for compounds such as **1** and **2** with end - on N_3^- ligands, which are expected to mediate ferromagnetic interactions, is somewhat surprising. Since, the $[Mn_3^{II}Mn^{III}(\mu_3\text{-}N_3)(\mu\text{-}N_3)(\mu_3\text{-}OR)(\mu\text{-}OR)_2]^{4+}$ sub-unit does not exist in a discrete form in order to make relatively safe predictions about the sign and the magnitude of the various exchange interactions within **1** and **2**, it is quite difficult to rationalize the diamagnetic spin ground state. However, a rather simple and also reasonable rationalization of the $S = 0$ ground states of **1** and **2** is that whatever the ground state S of each of the two $[Mn_3^{II}Mn^{III}(\mu_3\text{-}N_3)(\mu\text{-}N_3)(\mu_3\text{-}OR)(\mu\text{-}OR)_2]^{4+}$ sub-units of the Mn_8 cluster might be, they are overall interacting antiferromagnetically with each other, and thus yield an $S = 0$ ground state for the complete molecule. Note, that compound **7,** which is the only other Mn_8 cluster with a planar rod-like topology, also has an $S = 0$ ground state [18c].

4. Conclusions

The present work is an extension of our investigations on the use of a combination of pdH_2 or $mpdH_2$ and N_3^- ligands in Mn carboxylate chemistry [9,10]. This study has produced a new family of octanuclear manganese complexes with a near-planar, rod-like topology which appears for first time in Mn–(m)pdH_2 chemistry. In addition, compounds **1**–**3** are the first that combine the rod-like topology with the presence of end – on N_3^- ligands and thus their $[Mn_6^{II}Mn_2^{III}(\mu_3\text{-}N_3)_2(\mu\text{-}N_3)_2(\mu_3\text{-}OR)_4(\mu\text{-}OR)_4]^{6+}$ structural core is unprecedented in Mn cluster chemistry. Magnetic susceptibility studies revealed the existence of antiferromagnetic exchange interactions within the Mn_8 unit that result in a diamagnetic ground state. Finally, it is clear that the Mn-(m)pdH_2 chemistry is proving a rich source of new polynuclear compounds. Further studies are thus in progress, which are expected to result in a number of new Mn clusters with a variety of structural topologies in the near future.

Supplementary data

CCDC 724079 and 724080 contains the supplementary crystallographic data for this paper. These data can be obtained free of charge via http://www.ccdc.cam.ac.uk/conts/retrieving.html, or from the Cambridge Crystallographic Data Centre, 12 Union Road, Cambridge CB2 1EZ, UK; fax: (+44) 1223-336-033; or e-mail: deposit@ccdc.cam.ac.uk.

Acknowledgements

This work was supported by the Cyprus Research Promotion Foundation (Grant: PENEK-ENISX/0505/18), and the USA National Science Foundation (CHE-0414555).

References

[1] (a) J. Barber, Chem. Soc. Rev. 38 (2009) 185;
(b) S. Mukhopadhyay, S.K. Mandal, S. Bhaduri, W.H. Armstrong, Chem. Rev. 104 (2004) 3981.
[2] (a) R. Sessoli, H.-L. Tsai, A.R. Schake, S. Wang, J.B. Vincent, K. Folting, D. Gatteschi, G. Christou, D.N. Hendrickson, J. Am. Chem. Soc. 115 (1993) 1804;

(b) G. Christou, D. Gatteschi, D.N. Hendrickson, R. Sessoli, MRS Bull. 25 (2000) 66;
(c) R. Sessoli, D. Gatteschi, A. Caneschi, M.A. Novak, Nature 365 (1993) 141.
[3] (a) A.M. Ako, I.J. Hewitt, V. Mereacre, R. Clérac, W. Wernsdorfer, C.E. Anson, A.K. Powell, Angew. Chem., Int. Ed. 45 (2006) 4926;
(b) O. Waldmann, A.M. Ako, H.U. Güdel, A.K. Powell, Inorg. Chem. 47 (2008) 3486.
[4] (a) E.K. Brechin, Chem. Commun. (2005) 5141;
(b) A.J. Tasiopoulos, S.P. Perlepes, Dalton Trans. (2008) 5537.
[5] (a) A.J. Tasiopoulos, A. Vinslava, W. Wernsdorfer, K.A. Abboud, G. Christou, Angew. Chem., Int. Ed. 43 (2004) 2117;
(b) A.J. Tasiopoulos, W. Wernsdorfer, K.A. Abboud, G. Christou, Inorg. Chem. 44 (2005) 6324;
(c) C.J. Milios, C.P. Raptopoulou, A. Terzis, F. Lloret, R. Vicente, S.P. Perlepes, A. Escuer, Angew. Chem., Int. Ed. 43 (2004) 210;
(d) C.M. Zaleski, E.C. Depperman, C. Dendrinou-Samara, M. Alexiou, J.W. Kampf, D.P. Kessissoglou, M.L. Kirk, V.L. Pecoraro, J. Am. Chem. Soc. 127 (2005) 12862;
(e) C.M. Zaleski, E.C. Depperman, J.W. Kampf, M.L. Kirk, V.L. Pecoraro, Angew. Chem., Int. Ed. 43 (2004) 3912;
(f) S. Maheswaran, G. Chastanet, S.J. Teat, T. Mallah, R. Sessoli, W. Wernsdorfer, R.E.P. Winpenny, Angew. Chem., Int. Ed. 44 (2005) 5044.
[6] (a) R.T.W. Scott, S. Parsons, M. Murugesu, W. Wernsdorfer, G. Christou, E.K. Brechin, Angew. Chem., Int. Ed. 44 (2005) 6540;
(b) S. Piligkos, G. Rajaraman, M. Soler, N. Kirchner, J. van Slageren, R. Bircher, S. Parsons, H.-U. Güdel, J. Kortus, W. Wernsdorfer, G. Christou, E.K. Brechin, J. Am. Chem. Soc. 127 (2005) 5572;
(c) D. Foguet-Albiol, T.A. O'Brien, W. Wernsdorfer, B. Moulton, M.J. Zaworotko, K.A. Abboud, G. Christou, Angew. Chem., Int. Ed. 44 (2005) 897;
(d) C.J. Milios, M. Manoli, G. Rajaraman, A. Mishra, L.E. Budd, F. White, S. Parsons, W. Wernsdorfer, G. Christou, E.K. Brechin, Inorg. Chem. 45 (2006) 6782.
[7] (a) C.J. Milios, A. Vinslava, W. Wernsdorfer, S. Moggach, S. Parsons, S.P. Perlepes, G. Christou, E.K. Brechin, J. Am. Chem. Soc. 129 (2007) 2754;
(b) J.T. Brockman, T.C. Stamatatos, W. Wernsdorfer, K.A. Abboud, G. Christou, Inorg. Chem. 46 (2007) 9160;
(c) T.C. Stamatatos, V. Nastopoulos, A.J. Tasiopoulos, E.E. Moushi, W. Wernsdorfer, G. Christou, S.P. Perlepes, Inorg. Chem. 47 (2008) 10081;
(d) S.J. Shah, C.M. Ramsey, K.J. Heroux, A.G. DiPasquale, N.S. Dalal, A.L. Rheingold, E. del Barco, D.N. Hendrickson, Inorg. Chem. 47 (2008) 9569;
(e) T.C. Stamatatos, S.J. Teat, W. Wernsdorfer, G. Christou, Angew. Chem., Int. Ed. 48 (2009) 521.
[8] E.E. Moushi, T.C. Stamatatos, W. Wernsdorfer, V. Nastopoulos, G. Christou, A.J. Tasiopoulos, Angew. Chem., Int. Ed. 45 (2006) 7722.
[9] E.E. Moushi, T.C. Stamatatos, W. Wernsdorfer, V. Nastopoulos, G. Christou, A.J. Tasiopoulos, Inorg. Chem. (2009), doi:10.1021/ic801795.
[10] E.E. Moushi, T.C. Stamatatos, V. Nastopoulos, G. Christou, A.J. Tasiopoulos, Polyhedron (2009), doi:10.1016/j.poly.2008.12.023.
[11] E.E. Moushi, C. Lampropoulos, W. Wernsdorfer, V. Nastopoulos, G. Christou, A.J. Tasiopoulos, Inorg. Chem. 46 (2007) 3795.
[12] (a) A. Escuer, G. Aromí, Eur. J. Inorg. Chem. (2006) 4721;
(b) E. Ruiz, J. Cano, S. Alvarez, P. Alemany, J. Am. Chem. Soc. 120 (1998) 11122;
(c) T.C. Stamatatos, G. Christou, Inorg. Chem. 48 (2009) 3308.
[13] T. Lis, Acta Crystallogr. Sect. B 33 (1977) 2964.
[14] M.W. Wemple, H.-L. Tsai, S. Wang, J.P. Claude, W.E. Streib, J.C. Huffman, D.N. Hendrickson, G. Christou, Inorg. Chem. 35 (1996) 6437.
[15] Oxford Diffraction, CRYSALIS CCD and CRYSALIS RED, version p171.29.2, Oxford Diffraction Ltd, Abingdon, Oxford, England, 2006.
[16] (a) A. Altomare, G. Cascarano, C. Giacovazzo, A. Guagliardi, M.C. Burla, G. Polidori, M. Camalli, J. Appl. Cryst. 27 (1994) 435;
[b] G.M. Sheldrick, SHELXL97, University of Göttingen, Germany.
[17] (a) K. Brandenburg, DIAMOND. Version 3.1d. Crystal Impact GbR, Bonn, Germany, 2006.;
(b) I.J. Bruno, J.C. Cole, P.R. Edgington, M. Kessler, C.F. Macrae, P. McCabe, J. Pearson, R. Taylor, Acta Crystallogr. Sect. B 58 (2002) 389.
[18] (a) J. Yoo, A. Yamaguchi, M. Nakano, J. Krzystek, W.E. Streib, L.-C. Brunel, H. Ishimoto, G. Christou, D.N. Hendrickson, Inorg. Chem. 40 (2001) 4604;
(b) R.P. John, K. Lee, B.J. Kim, B.J. Suh, H. Rhee, M.S. Lah, Inorg. Chem. 44 (2005) 7109;
(c) M. Manoli, C.J. Milios, A. Mishra, G. Christou, E.K. Brechin, Polyhedron 26 (2007) 1923.
[19] (a) E. K Brechin, M. Soler, G. Christou, M. Helliwell, S.J. Teat, W. Wernsdorfer, Chem. Commun. (2003) 1276;
(b) G. Rajaraman, M. Murugesu, E.C. Sañudo, M. Soler, W. Wernsdorfer, M. Helliwell, C. Muryn, J. Raftery, S.J. Teat, G. Christou, E.K. Brechin, J. Am. Chem. Soc. 126 (2004) 15445.
[20] E.R. Davidson, MAGNET, Indiana University: Bloomington, IN.

[19,20]. In such systems, Cr(III) is able to react due to its solubility maintained by weaker organic and inorganic ligands.

Undoubtedly, therefore, soluble Cr(III) presents a metal ion linked to a number of abiotic and biological species for which specific knowledge of chemistry and biology are needed. Poised to understand the binary interactions of Cr(III) with low molecular mass substrates in cellular processes, we have launched research efforts targeting the pH-specific reactivity of Cr(III) toward metal-complexing hydroxycarboxylate-containing physiological ligands. In this respect, we herein report the pH-specific synthesis and physicochemical characterization of two new binary pH-structural variants of the Cr(III)–citrate system emerging from the requisite aqueous speciation.

2. Experimental

2.1. Materials and methods

All experiments were carried out in air. Nanopure quality water was used for all reactions. $Cr(NO_3)_3{\cdot}9H_2O$ and citric acid monohydrate, were purchased from Aldrich. Sodium hydroxide was supplied by Fluka and 2,9-dimethylphenanthroline (dmphen) ($C_{14}H_{12}N_2$) by Aldrich.

2.2. Physical measurements

FT-Infrared spectra were recorded on a Thermo, Nicolet IR 200 FT-infrared spectrometer. UV–Vis measurements were carried out on a Hitachi U2001 spectrophotometer in the range from 190 to 1000 nm. A ThermoFinnigan Flash EA 1112 CHNS elemental analyzer was used for the simultaneous determination of carbon, hydrogen, and nitrogen (%). The analyzer is based on the dynamic flash combustion of the sample (at 1800 °C) followed by reduction, trapping, complete GC separation and detection of the products. The instrument is fully automated and controlled by PC via the Eager 300 dedicated software and is capable of handling solid, liquid or gaseous substances.

A TA Instruments thermal analyzer, model Q 600, system was used to run the simultaneous TGA–DTG experiments. The employed heating rate was 5 °C/min. The instrument mass precision is 0.1 μg. About 15.9 mg of sample was placed in an open alumina sample pan for the experiment. High purity air (80/20 in N_2/O_2) was used at a constant flow rate of 100 mL/min. During the experiments, the sample weight loss and rate of weight loss were recorded continuously under dynamic conditions, as a function of time or temperature, in the range 30–1000 °C. Prior to activating the heating routine program, the entire system was purged with the appropriate inert gas for 10 min, at a rate 400 mL/min, to ensure that the desired environment had been established.

The EPR spectra in the solid state and frozen aqueous solutions were recorded on a Bruker ER 200D-SRC X-band spectrometer, equipped with an Oxford ESR 9 cryostat at 9.43 GHz, 10 dB, and in the range 4–150 K. Magnetic susceptibility data were collected on powdered samples of the title complexes with a Quantum Design SQUID susceptometer in the 2–300 K range, under various applied magnetic fields. Magnetization measurements were carried out at three different temperatures in the field range 0–5 T.

Electrochemical measurements were carried out with an Autolab model PGSTAT100 potensiostat–galvanostat. The entire system was under computer control and supported by the appropriate computer Autolab software GPES, running on Windows. The employed electrochemical cell had platinum (disk) working and auxiliary (wire) electrodes. As reference electrode, a saturated Ag/AgCl electrode was used. The water used in the electrochemical measurements was of nano-pure quality. KNO_3 was used as a supporting electrolyte. Normal concentrations used, were 1–6 mM in electroanalyte and 0.1 M in supporting electrolyte. Purified argon was used to purge the solutions prior to the electrochemical measurements. Derived $E_{1/2}$ values are reported versus Ag/AgCl electrode.

2.3. Preparation of complex $Na_3[Cr(C_6H_5O_7)_2]{\cdot}8.5H_2O$ (**1**)

A quantity of $Cr(NO_3)_3{\cdot}9H_2O$ (0.80 g, 2.0 mmol) was placed in a flask and dissolved in 3 mL of H_2O. Subsequently, citric acid (1.3 g, 6.0 mmol) was added slowly and under continuous stirring. Sodium hydroxide was then added slowly to adjust the pH to a final value of ~5.5. The resulting solution was left to stir overnight. Addition of cold ethanol at 4 °C resulted, after a couple of months, in the deposition of a pink-like crystalline material. The crystals were isolated by filtration and dried in vacuo. The yield of the reaction was 0.64 g (~49%). *Anal.* Calc. for **1**, $Na_3[Cr(C_6H_5O_7)_2]{\cdot}8.5H_2O$ (**1**), ($C_{12}H_{27}O_{22.5}Na_3Cr$, M.W. 652.31): C, 22.0; H, 4.1. Found: C, 22.2; H, 4.2%.

2.4. Preparation of complex $(Hdmphen)_6[Cr(C_6H_5O_7)_2]{\cdot}(NO_3)_3{\cdot}14H_2O$ (**2**)

A quantity of $Cr(NO_3)_3{\cdot}9H_2O$ (0.20 g, 0.50 mmol) was placed in a flask and dissolved in 3 mL of H_2O. Subsequently, citric acid (0.42 g, 2.0 mmol) was added slowly and under continuous stirring. 2,9-dimethylphenanthroline ($C_{14}H_{12}N_2$) (0.40 g, 4.0 mmol) was then added slowly to adjust the pH to a final value of ~3.5. The resulting solution was left to stir overnight. Addition of cold ethanol at 4 °C resulted, after a few days, in the deposition of a purple-like crystalline material. The crystals were isolated by filtration and dried in vacuo. The yield of the reaction was 0.30 g (~30%). *Anal.* Calc. for **2**, $(Hdmphen)_6[Cr(C_6H_5O_7)_2]{\cdot}(NO_3)_3{\cdot}14H_2O$ (**2**), ($C_{96}H_{116}CrN_{15}O_{37}$, M.W. 2124.04): C, 54.2; H, 5.5; N, 9.9. Found: C, 54.4; H, 5.5; N, 9.4%.

2.5. X-ray crystal structure determination

2.5.1. $Na_3[Cr(C_6H_5O_7)_2]{\cdot}8.5H_2O$ (**1**)

X-ray quality crystals of compound **1** were grown from mixtures of water–ethanol solutions. A single crystal of **1** with dimensions 0.15 × 0.09 × 0.06 mm was mounted on an Xcalibur Oxford Diffractometer equipped with a Sapphire 3 CCD detector and a 4-cycle Kappa geometry goniometer, using an enhanced Mo X-ray source and a graphite radiation monochromator. Unit cell dimensions for **1** were determined and refined by using the angular settings of all the reflection frames in the range $6.30° < 2\theta < 60.50°$. Relevant crystallographic data appear in Table 1. Intensity data were measured by using a θ–2θ scan. Three standard frames were monitored every 35 reflections, over the course of data collection, to ensure the stability of the sample. Further experimental crystallographic details: for **1**, $2\theta_{max} = 60.64°$; 427 parameters refined; $(\Delta/\sigma)_{max} = 0.001$; $(\Delta\rho)_{max}/(\Delta\rho)_{min} = 0.685/-0.576$ e/Å^3; R/R_w (for all data) = 0.0683/0.1051. CrysAlis CCD and CrysAlis RED software were used for monitoring data collection and carrying out data reduction/cell refinement, respectively [21,22]. The structure was solved by direct methods and refined by full-matrix least-squares techniques on F^2, by using SHELXS-97 [23,24]. Special computer molecular graphics incorporated in the WINGX 3.2 interface were used [25]. All of the non-H atoms were refined anisotropically. The methylene hydrogen atoms of the citrate ligands were introduced at calculated positions as riding on bonded atoms. The remainder of the hydrogen atoms were located by difference Fourier maps and were refined isotropically.

Table 1
Summary of crystal, intensity collection and refinement data for $Na_3[Cr(C_6H_5O_7)_2]\cdot 8.5H_2O$ (**1**) and $(Hdmphen)_6[Cr(C_6H_5O_7)_2]\cdot(NO_3)_3\cdot 14H_2O$ (**2**).

	1	**2**
Formula	$C_{12}H_{27}Na_3O_{22.5}Cr$	$C_{96}H_{116}CrN_{15}O_{37}$
Formula weight	652.31	2124.04
T (K)	100 (2)	298 (1)
Wavelength	Mo Kα 0.71073	Cu Kα 1.54180
Space group	$C2/c$	$P\bar{1}$
a (Å)	37.093(3)	12.823(6)
b (Å)	6.794(1)	13.198(6)
c (Å)	19.949(1)	15.690(7)
α (°)	90.00	77.57(2)
β (°)	112.03(1)	81.30(2)
γ (°)	90.00	89.44(2)
V (Å^3)	4660.3(6)	2563.0(2)
Z	8	1
D_{calcd} (Mg m^{-3})	1.859	1.376
Absolute coefficient (μ), (mm^{-1})	0.655	1.711
Range of h, k, l	−50→41, −9→9, −27→27	−13→0, −13→13, −16→15
Goodness-of-fit (GOF) on F^2	0.931	1.052
R indices[a]	R = 0.0391, R_w = 0.1011[b]	R = 0.0582, R_w = 0.1698[b]

[a] R values are based on F values, R_w values are based on F^2. $R = \frac{\sum||F_o|-|F_c||}{\sum(|F_o|)}$, $R_w = \sqrt{\frac{\sum[w(F_o^2-F_c^2)^2]}{\sum[w(F_o^2)^2]}}$.
[b] For **1**: 3820, for **2**: 5180, refs. $I > 2\sigma(I)$.

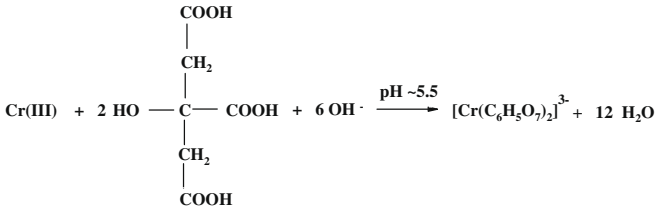
2.5.2. $(Hdmphen)_6[Cr(C_6H_5O_7)_2]\cdot(NO_3)_3\cdot 14H_2O$ (**2**)

X-ray quality crystals of compound **2** were grown from mixtures of water–ethanol solutions. A single crystal, with dimensions 0.15 × 0.25 × 0.40 mm was mounted on a $P2_1$ Nicolet diffractometer upgraded by Crystal Logic, using graphite monochromated Cu Kα radiation. Unit cell dimensions for **2** were determined and refined by using the angular settings of 25 automatically centered reflections in the range 22.00° < 2θ < 54.00°. Crystallographic details are given in Table 1. Intensity data were measured by using θ–2θ scans. Throughout data collection, three standard reflections were monitored every 97 reflections, and showed less than 3% variation and no decay. Lorentz, polarization, and ψ-scan absorption corrections were applied by using Crystal Logic software. Further experimental crystallographic details for **2**: $2\theta_{max}$ = 105.22°; 714 parameters refined; $(\Delta/\sigma)_{max}$ = 0.007; $(\Delta\rho)_{max}/(\Delta\rho)_{min}$ = 0.578/−0.347 e/Å^3; R/R_w (for all data), 0.0629/0.1771. The structure of complex **2** was solved by direct methods using SHELXS-97 [26], and refined by full-matrix least-squares techniques on F^2 with SHELXL-97 [23,24]. All non-H atoms in the structure of **2** were refined anisotropically. Hydrogen atoms were either located by difference maps and were refined isotropically or introduced at calculated positions as riding on bonded atoms; no H atoms for the solvate water molecules were included in the refinement. The third nitrate counterion was found disordered around an inversion center and was refined over two positions.

3. Results

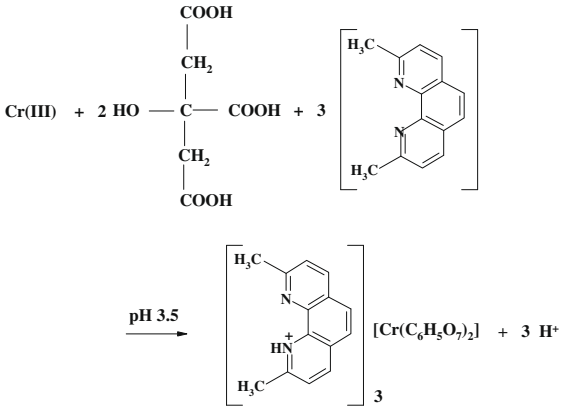
3.1. Synthesis

The synthesis of compound **1** was expediently pursued through a facile reaction between Cr(III) and citric acid (molar ratio 1:3) in aqueous solutions at pH ∼ 5.5. Product **1** was also obtained in the pH-range 5–8.5. The adjustment of pH was achieved by addition of aqueous NaOH solution. NaOH served as a base for the adjustment of the pH of the reaction mixture and the concurrent generation of the counter ion for the assembled anionic complex. This behavior had been previously observed on a number of occasions in metal-citrate chemistry. The stoichiometric reaction leading to the synthesis and isolation of **1** is shown below:



The compound was isolated in pure crystalline form upon addition of ethanol to the reaction mixture at 4 °C. Elemental analysis of the isolated pink crystalline material suggested the molecular formulation $Na_3[Cr(C_6H_5O_7)_2]\cdot 8.5H_2O$ for **1**. Further spectroscopic inspection of **1** by FT-IR revealed the presence of citrate bound to Cr(III), thus affirming the proposed formulation. Remarkably, when the same reaction was run with a molar ratio of Cr(III):citrate 1:2, under identical reaction conditions as above, the same product was obtained at comparable yields, albeit of lower bulk crystallinity.

The synthesis of compound **2** was expediently pursued through a facile reaction between Cr(III) and citric acid (molar ratio 1:4) in aqueous solution at pH 3.5. The adjustment of pH was achieved by addition of 2,9-dimethylphenanthroline (dmphen). 2,9-Dimethylphenanthroline was also used for the concurrent generation of the counter ion for the assembled anionic complex. It is worth noting, that **2** was isolated only at this specific pH and only under the conditions specified. The stoichiometric reaction leading to the formation and isolation of **2** is shown below:



Compound **2** was isolated in pure crystalline form upon addition of ethanol to the reaction mixture at 4 °C. Elemental analysis of the isolated purple crystalline material suggested the molecular formulation $(Hdmphen)_6[Cr(C_6H_5O_7)_2]\cdot(NO_3)_3\cdot 14H_2O$ for **2**. Further spectroscopic inspection of **2** by FT-IR revealed the presence of citrate bound to Cr(III), thus supporting the proposed formulation.

Compounds **1** and **2** are soluble in water. There are insoluble in organic solvents, such as methanol, acetonitrile, chlorinated solvents ($CHCl_3$, CH_2Cl_2), toluene and DMF. The materials are stable in the air at room temperature for a long period of time.

3.1.1. Description of the structure: $Na_3[Cr(C_6H_5O_7)_2]\cdot 8.5H_2O$ (**1**)

The X-ray crystal structure of **1** reveals the presence of discrete cations and anions in the lattice. The compound crystallizes in the monoclinic space group $C2/c$. The structural diagram of **1** is shown

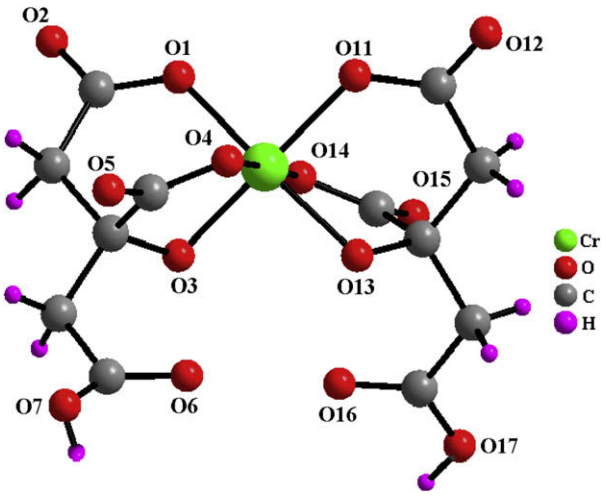


Fig. 1. Labeled plot of the structure of the $[Cr(C_6H_5O_7)_2]^{3-}$ anion in **1**.

in Fig. 1. Selected interatomic distances and bond angles for **1** are listed in Table 2. The structure of **1** consists of a mononuclear core unit composed of a central Cr(III) ion, surrounded by two citrate ligands. The latter ligands bind to Cr(III) through the central carboxylate and alkoxide oxygens, promoting the formation of a stable five-membered ring. An additional carboxylate oxygen from one of the terminal carboxylates of each citrate ligand coordinates to the central metal ion, thus occupying a third coordination site around Cr(III). The second terminal carboxylate group of each citrate does not bind Cr(III). Therefore, the six coordination sites around Cr(III) are taken up by the two citrate ligands bound in the same fashion. The arising geometry from the described citrate coordination is distorted octahedral.

The negative charge of 3- in complex **1** is counterbalanced by three sodium ions. These counter ions likely contribute to the stability of the crystal lattice through interactions with oxygen anchors from the citrate ligands and lattice water molecules. In this respect, Na(1) exhibits a coordination number 6 formulated by oxygen atoms from four different citrate ligands. Na(2) displays a coordination number 5 and binds to oxygen atoms from two different citrate ligands as well as oxygens from three water molecules. Na(3) exhibits a coordination number 6 and is bound to oxygen atoms from one citrate ligand and five water molecules. Overall, sodium ions are diversely coordinated to O-bearing anchors, contributing to the establishment of the crystal lattice (Fig. 2A and B).

Table 2
Bond lengths (Å) and angles (°) in $Na_3[Cr(C_6H_5O_7)_2]\cdot 8.5H_2O$ **(1)** and in $(Hdmphen)_6[Cr(C_6H_5O_7)_2]\cdot(NO_3)_3\cdot 14H_2O$ **(2)**.

1		**2**	
Bond distances			
Cr–O(3)	1.9059(15)	Cr–O(3)	1.956(2)
Cr–O(13)	1.9879(15)	Cr–O(5)	1.972(2)
Cr–O(4)	1.9678(14)	Cr–O(1)	1.965(2)
Cr–O(14)	1.9565(14)		
Cr–O(1)	1.9704(15)		
Cr–O(11)	2.0050(16)		
Angles			
O(3)–Cr–O(13)	91.94(6)	O(3)–Cr–O(3)'	180.0
O(3)–Cr–O(4)	84.39(6)	O(3)–Cr–O(1)	88.7(1)
O(4)–Cr–O(13)	96.66(6)	O(3)'–Cr–O(1)	91.3(1)
O(3)–Cr–O(14)	93.61(6)	O(1)–Cr–O(1)'	180.0
O(14)–Cr–O(13)	82.35(6)	O(3)–Cr–O(5)'	97.6(1)
O(14)–Cr–O(4)	177.75(7)	O(3)–Cr–O(5)	82.4(1)
O(3)–Cr–O(1)	89.97(6)	O(1)–Cr–O(5)'	91.0(1)
O(1)–Cr–O(13)	172.72(6)	O(1)–Cr–O(5)	89.0(1)
O(4)–Cr–O(1)	90.51(6)	O(5)–Cr–O(5)'	180.0
O(14)–Cr–O(1)	90.52(6)		
O(3)–Cr–O(11)	174.19(6)		
O(13)–Cr–O(11)	86.86(6)		
O(4)–Cr–O(11)	90.10(6)		
O(14)–Cr–O(11)	91.86(6)		
O(1)–Cr–O(11)	91.93(7)		

Symmetry operations for **1**: (i) x, y, z; (ii) $-x, y, -z+1/2$; (iii) $x+1/2, y+1/2, z$; (iv) $-x+1/2, y+1/2, -z+1/2$; (v) $-x, -y, -z$; (vi) $x, -y, z-1/2$; (vii) $-x+1/2, -y+1/2, -z$; (viii) $x+1/2, -y+1/2, z-1/2$.
Symmetry operations for **2**: (i) x, y, z (ii) $-x, -y, -z$.

3.1.2. $(Hdmphen)_6[Cr(C_6H_5O_7)_2]\cdot(NO_3)_3\cdot 14H_2O$ (**2**)

Compound **2** crystallizes in the triclinic space group $P\bar{1}$. The structural diagram of **2** is shown in Fig. 3. Selected interatomic distances and bond angles for **2** are listed in Table 2. The structure consists of a mononuclear core unit composed of a central Cr(III) ion, surrounded by two citrate ligands in the same fashion as in compound **1**. The latter ligands each bind to the metal ion through the central carboxylate and alkoxide oxygens, promoting the formation of a stable five-membered ring. An additional carboxylate oxygen from one of the terminal carboxylates of each citrate ligand binds the central metal ion, thus occupying a third coordination site around Cr(III). The second terminal carboxylate group of each citrate does not bind Cr(III). Therefore, the six coordination sites around Cr(III) are taken up by the two citrate ligands bound in the same fashion. The arising geometry from the described citrate coordination is distorted octahedral.

The deprotonation state of the citrate ligand in both complexes **1** and **2** is 3-. A triple (3-) deprotonation state for the citrate ligand had been previously observed in the case of $(NH_4)_3[Ga^{III}(C_6H_5O_7)_2]\cdot 4H_2O$ [27]. The two complexes **1** and **2**, however, are not identical. There is a distinct difference between them. Specifically, the two citrate ligands in **1** are bound to Cr(III) in such a way that (a) the five-membered cyclic rings lie above and below the planes formulated by the six membered rings [O(1),C(1),C(2),C(3),O(3),Cr] and [O(11),C(11), C(12),C(13),O(13),Cr], respectively, and (b) the non-coordinated protonated terminal carboxylates are in the syn-orientation with respect to Cr(III). In **2**, the disposition of the two ligands is dictated by the presence of a center of inversion.

The Cr–O bond distances in $Na_3[Cr(C_6H_5O_7)_2]\cdot 8.5H_2O$ (**1**) (1.906(2)—2.005(2) Å) and $(Hdmphen)_6[Cr(C_6H_5O_7)_2]\cdot(NO_3)_3\cdot 14H_2O$ (**2**) (1.956(2)–1.972(2) Å) are in line with those in other O-containing Cr(III) complexes such as $(NH_4)_4[Cr(C_6H_4O_7)(C_6H_5O_7)]\cdot 3H_2O$ (1.933(2)–1.973(2) Å) [28], $(C_5H_6N)_2[Cr(C_6H_{5.5}O_7)_2]\cdot 4H_2O$ (1.965(2)–1.987(2) Å) [29], $Na_2[Cr(C_5H_7NO_4)_2]$ (1.963(2)–1.948(2) Å) [30], $K_3[Cr(C_2O_4)_3]\cdot 3H_2O$ (1.955(2)–1.985(2) Å) [31], $K_2[Cr_2(C_6H_6NO_6)_2(OH)_2]\cdot 6H_2O$ (1.937(4)–1.983(3) Å) [32], *trans*(O_5)–Na[Cr(ed3ap)]$\cdot 3H_2O$ (ed3ap = ethylenediamine-*N*,*N*,*N*′-triacetate-*N*′-3-propionate) (1.945(6)–1.974(5) Å) [33]. Furthermore, the Cr–O bond distances in **1** and **2** are in line with corresponding bonds in other trivalent metal-citrate complexes such as $(NH_4)_3[Ga^{III}(C_6H_5O_7)_2]\cdot 4H_2O$ [27] (1.890(2)–1.900(2) Å).

It appears that angles similar to those in $Na_3[Cr(C_6H_5O_7)_2]\cdot 8.5H_2O$ (**1**) (82.35(6)—96.66(6)°) and $(Hdmphen)_6[Cr(C_6H_5O_7)_2]\cdot(NO_3)_3\cdot 14H_2O$ (**2**) (82.4(1)–97.6(1)°) are observed in a number of Cr(III)–O_6 core-containing complexes, exhibiting octahedral geometry around the Cr(III) ion. Among such complexes are $K_3[Cr(C_2O_4)_3]\cdot 3H_2O$ (81.5(1)–88.7(1)°) [31], *trans*(O_5)–Na[Cr(ed3ap)]$\cdot 3H_2O$ (ed3ap = ethylenediamine-*N*,*N*,*N*′-triacetate-*N*′-3-propionate) (81.8(1)–98.9(1)°) [33] and $[Cr(C_9H_{12}N_2O_6COOH)(H_2O)]$ (89.43(8)–97.10(10)°) [34].

In the lattice of **2**, there exist intermolecular hydrogen-bonding interactions involving the $[Cr(C_6H_5O_7)_2]^{3-}$ anion, the NO_3^- and $Hdmphen^+$ ions, and the solvate water molecules, which result in the formation of a 2D network extending parallel to the (1 0 1) plane (Fig. 4, Table 3).

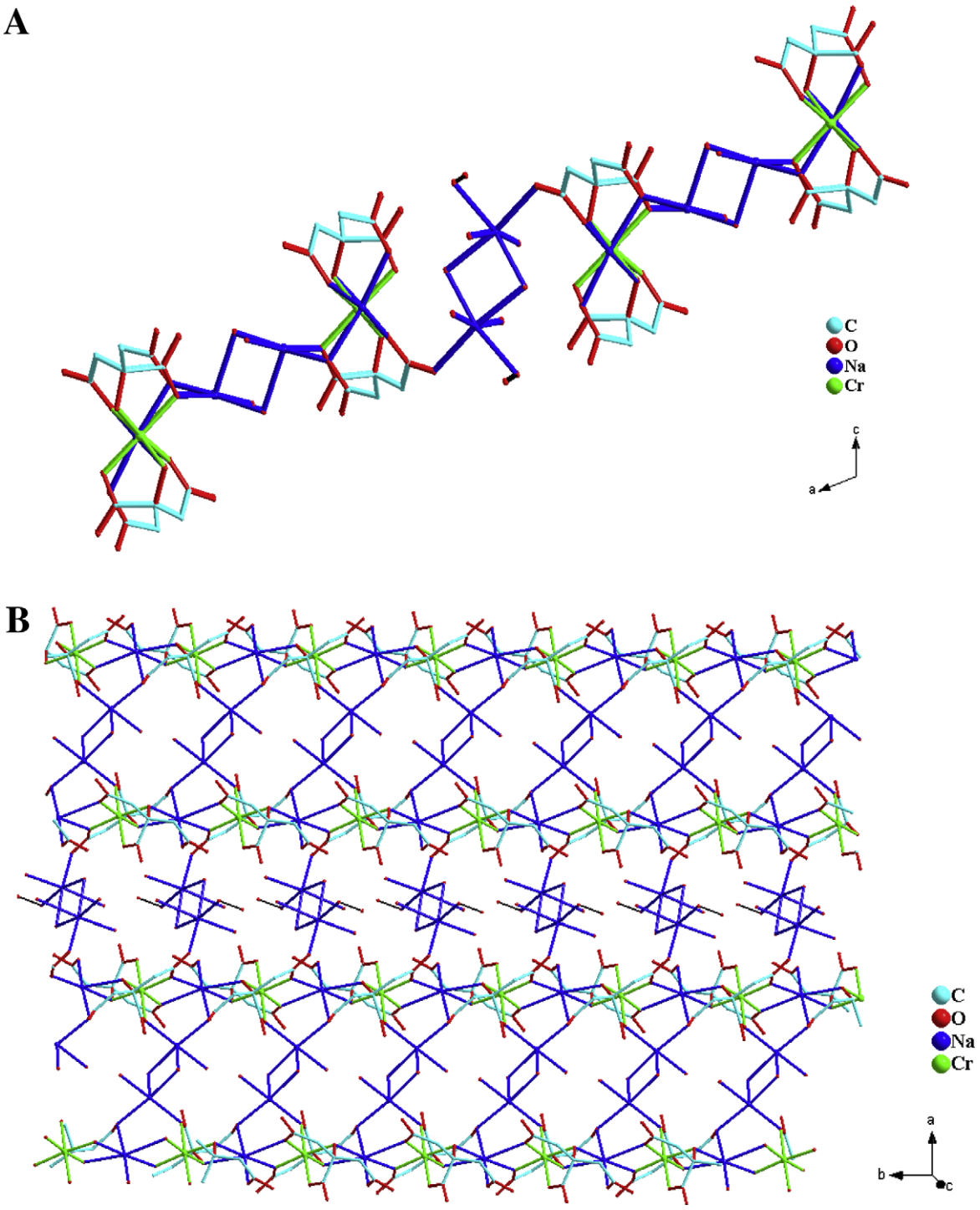


Fig. 2. Packing diagram of **1** along the *ac* (A) and off the *ab* (B) plane.

4. Electronic spectroscopy

The UV–Vis spectra of **1** and **2** were taken in water and are the same. The spectrum of **1** shows a band at $\lambda_{max} = 564$ nm (ε 48 M^{-1} cm^{-1}). At higher energies, a shoulder-like band appears at 443 nm ($\varepsilon \sim 19$ M^{-1} cm^{-1}), ultimately reaching a well-formed major peak at $\lambda_{max} = 395$ nm (ε 51 M^{-1} cm^{-1}). The absorption features are likely due to d–d transitions, which are typical of a Cr(III) d^3 (^4F) octahedral species [35]. The band at 564 nm could be tentatively attributed to the $^4A_{2g} \rightarrow {}^4T_{2g}$ transition. In an analogous fashion, the band at 395 nm could be assigned to the $^4A_{2g} \rightarrow {}^4T_{1g}(F)$ transition. No further definitive assignments could be made in the absence of detailed specific studies.

5. FT-IR spectroscopy

The FT-Infrared spectra of **1** and **2** in KBr revealed the presence of vibrationally active carboxylate groups. Antisymmetric as well as symmetric vibrations for the carboxylate groups of the coordinated citrate ligands were present. Specifically, antisymmetric

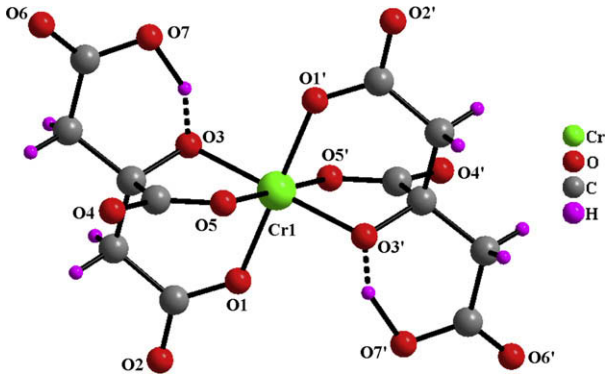


Fig. 3. Partially labeled plot of the structure of the $[Cr(C_6H_5O_7)_2]^{3-}$ anion in **2**. The intramolecular hydrogen bonds are shown as dashed lines. Primed atoms are generated by symmetry: (′) = $-x, -y, 1-z$.

Table 3
Hydrogen bonding interactions in the structure of **2**.

Interaction	D···A (Å)	H···A (Å)	D–H···A (°)	Symmetry operations
O7–HO7···O3	2.430	1.182	152.4	x, y, z
N1–HN1···O23	2.996	2.102	162.0	$1-x, 1-y, 1-z$
N11–HN11···O6	2.799	1.855	163.4	$x, 1+y, z$
N22–HN22···Ow6	2.802	2.052	172.0	x, y, z
Ow1···Ow2	2.802			x, y, z
Ow1···Ow3	2.922			x, y, z
Ow1···O2	2.807			$-x, -y, 1-z$
Ow2···O4	2.762			$x, 1+y, z$
Ow2···Ow2	2.767			$-x, 1-y, 1-z$
Ow4···Ow5	2.766			x, y, z
Ow4···O2	2.840			$-x, -y, 1-z$
Ow5···Ow3	2.805			x, y, z
Ow5···O12	2.857			$1-x, 1-y, 1-z$
Ow6···Ow7	2.752			x, y, z
Ow7···O21	2.698			x, y, z
Ow7···O12	2.809			$x, y, -1+z$
Ow7···Ow3	2.840			x, y, z

stretching vibrations $\nu_{as}(COO^-)$ for the carboxylate carbonyls appeared in the range 1616–1579 cm^{-1} for **1** and in the range 1641–1603 cm^{-1} for **2**, respectively. Symmetric vibrations $\nu_s(COO^-)$ for the same groups were present around 1384 cm^{-1} for both **1** and **2**.

The frequencies of the observed carbonyl vibrations were shifted to lower values in comparison to the corresponding vibrations in free citric acid, indicating changes in the vibrational status of the citrate ligand upon binding to Cr(III) [36]. The difference between the symmetric and antisymmetric stretches, $\Delta(\nu_{as}(COO^-) - \nu_s(COO^-))$, was greater than 200 cm^{-1}, indicating that the carboxylate groups of the citrate ligand were either free or coordinated to Cr(III) in a monodentate fashion [37]. This contention was subsequently confirmed by the X-ray crystal structure of **1** and **2**. All of the above assignments were in agreement with past assignments in mononuclear Cr(III)–O_6 complexes [38], and in line with previous reports on carboxylate-containing substrates bound to variable nature metal ions [39–46].

6. Magnetic susceptibility studies

Magnetic susceptibility studies were carried out on both **1** and **2**. It appears that the two species exhibit the same behavior over the temperature range 2–300 K. Consequently, only the data for **1** are presented here. The temperature dependence $\chi_M T$ (χ_M being the magnetic susceptibility for one Cr(III) ion) for complex **1** is shown in Fig. 5A (solid stars). The $\chi_M T$ value is 1.94 emu mol^{-1} K at 300 K, higher than the value expected for an isolated ion of Cr(III), which is 1.87 emu mol^{-1} K. In the range from 300 to 10 K, there is a smooth linear decrease, while after that temperature and down to 2 K a more pronounced decrease occurs reaching the value of 1.64 emu mol^{-1} K. The shape of this curve is characteristic of the occurrence of large zero field effects along with a temperature independent paramagnetism (TIP) effect. The large zero effects are responsible for the drastic decrease of the susceptibility data in the low temperature range, while the latter effect leads to a

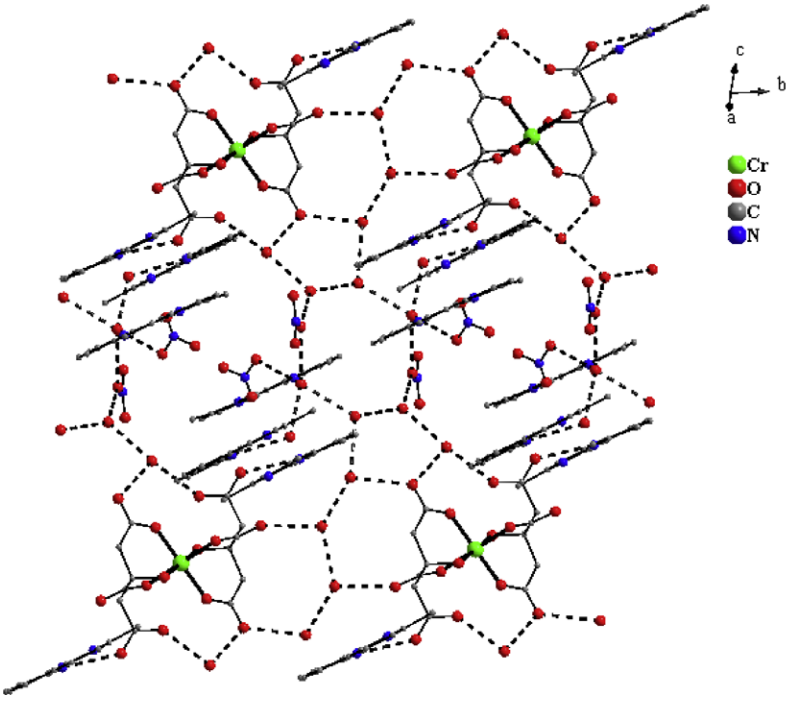


Fig. 4. Part of the 2D network in the lattice structure of **2** due to intermolecular hydrogen-bonding interactions. H bonds are shown as dashed lines.

linear temperature dependence of the susceptibility data in the high temperature range. The susceptibility data were fitted by the following equation:

$$H = D\left[S_z^2 - \frac{1}{3}S(S+1)\right] + E(S_x^2 - S_y^2) + g_z\mu_B H_z S_z + g_x\mu_B H_x S_x + g_y\mu_B H_y S_y \quad (1)$$

where an isotropic g-value was used. The best fit (solid line in Fig. 5A) is given by the parameters $D = 0.78(1)\,cm^{-1}$ and $g = 1.97(1)$, TIP = 800×10^{-6}.

Isothermal magnetization curves at $T = 1.8$–2.5–5 K in an applied field 0–5 T are shown in Fig. 5B. The data were fitted using (Eq. (1)) and the best fit (solid line in Fig. 5B) is given by the parameters of $D = 0.80(1)\,cm^{-1}$, $g = 1.97(1)$ for all temperatures, very close to the values obtained from the susceptibility study, thus verifying the large zero field character of the system.

7. EPR studies

7.1. Solid-state powder spectrum

X-band EPR measurements were carried out on powder samples of **1** and are shown in Fig. 6 (Top). An isotropic magnetic-field domain line width was used for the powder spectrum ($lw = 35$ G), while the broadness of the spectrum reveals the presence of g-strain effects. Gaussian distributions of the g-principal values were used and the results are ($\sigma g_x = \sigma g_y = 0.1$, $\sigma g_z = 0.2$). The principal g-values for the powder spectrum are $g_{xy} = 1.96(1)$, $g_z = 1.98(1)$. The values for the crystal field terms are: $D = 0.45(2)$ cm^{-1} and $\lambda = E/D = 0.30(2)$, revealing the rhombic character of the system. Gaussian distributions of the D and E parameters were also used ($\sigma(D) = 0.3$, $\sigma(E) = 0.03$). The simulation of the powder EPR spectrum of complex **1** verifies the large value of the D parameter, calculated from the simulation of the magnetization curve. The spectrum of **2** was not taken in the solid state.

7.2. Solution spectrum

The EPR spectra of **1** and **2** in aqueous frozen solution are the same. Therefore, only the spectrum of **1** is discussed here (Fig. 6 – Bottom). The effective g-value $g \approx 4$ of the complex is typical of an electronic spin $S = 3/2$, with moderately large zero field splitting (ZFS) and small rhombicity ($D > h\nu \approx 0.3$ cm^{-1} at X-band; $E/D \approx 0$) parameters. In this regime of ZFS, the spin quartet is split into two Kramers doublets, |3/2, ±1/2> and |3/2, ±3/2>, for virtually all fields applied in the EPR spectrometer, with EPR transitions occurring only within these doublets. For $E/D = 0$, only the $m_s = \pm 1/2$ doublet is EPR detectable, whereas the $m_s = \pm 3/2$ doublet is EPR silent. In this limiting case of a large axial ZFS ($D \gg h\nu$, $E/D = 0$), the effective g-values for |3/2, ±1/2> would be expected at (a) $g_{perpendicular} = 2S + 1$ for fields applied in the x/y directions, and (b) $g_{parallel} = 2$ along z, which is in close agreement with the experimental findings. The simulations showed that the experimental line shape can not be reproduced by a single $S = 3/2$ species with a well defined value for E/D, even if one employs angular dependent line

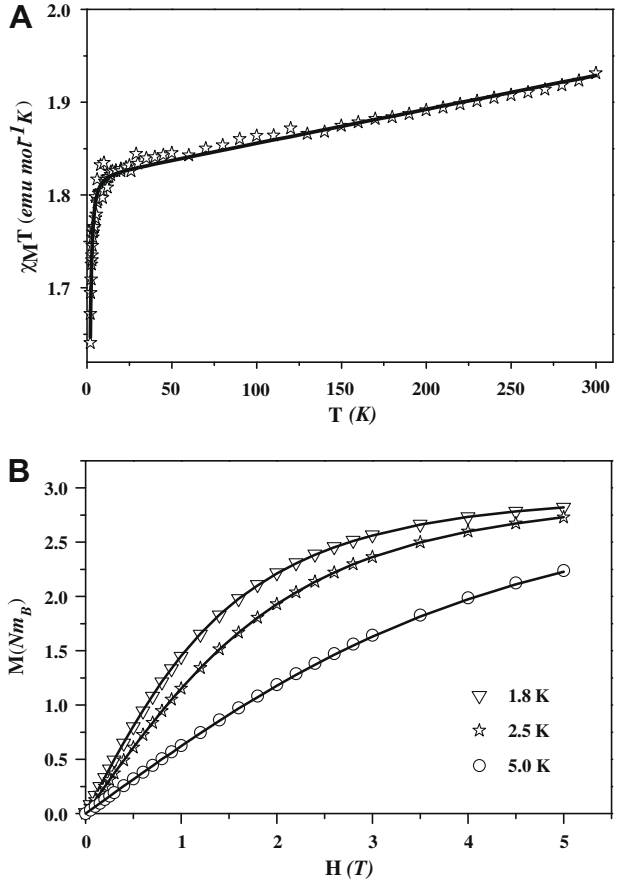


Fig. 5. A. Temperature dependence of the susceptibility data in the form of $\chi_M T$ vs. T (solid stars) and fitting results using the theoretical formula discussed in the text (solid line). B. Magnetization measurements in the field range 0–5 T and at temperatures (1.8, 2.5, 5.0 K), and fitting results using the theoretical formula discussed in the text (solid line).

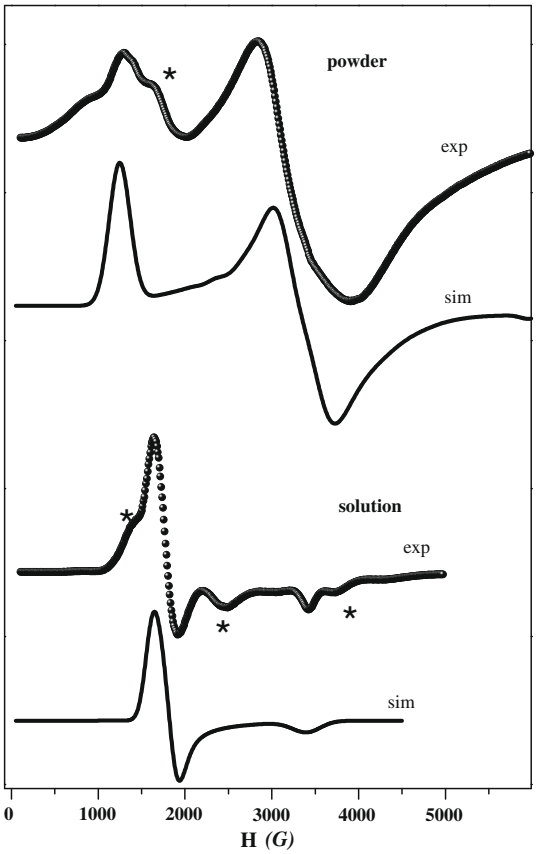


Fig. 6. (Top) Experimental X-Band EPR powder spectra of complex **1** at 4 K along with the simulated spectrum. (Bottom) Experimental X-Band EPR frozen solution spectra of complex **1** at 4 K along with the simulated spectrum. The microwave resonance is 9.43 GHz.

shape distributions of the type $W^2 = \sqrt{\sum W_i^2 l_i^2}$, where l_i denotes the direction cosines of the applied field. An isotropic magnetic-field domain line width was used for the powder spectrum (lw = 25 G), while the broadness of the spectrum reveals the presence of g-strain effects. Gaussian distributions of the isotropic g-value were used ($\sigma g = 0.1$) and the isotropic g-value for the solution spectrum was $g = 1.96(1)$. The values of the crystal filed terms are $D = 1.6(2)\,cm^{-1}$ and $\lambda = E/D = 0.06(2)$ and the Gaussian distributions of the D and E parameters were ($\sigma(D) = 0.3$, $\sigma(E) = 0.03$).

Both simulation procedures were unable to reproduce all the features of the experimental spectra (see asterisks in Fig. 6). Very likely, the population of excited states as well as the inclusion of other terms in the Hamiltonian formalism such as antisymmetric or intermolecular interactions must be taken into consideration. However, such an overparameterization of the final Hamiltonian could lead to parameters with no physical meaning. To this end, no further attempt was made to improve our simulations.

8. Thermal studies

The thermal decomposition of complex **1** was studied by TGA–DTG under an atmosphere of oxygen. Compound **1** is thermally stable up to 65 °C. From that point on, an initial process points to dehydration, with the release of lattice water between 65 and 296 °C, signifying an endothermic process. The observed weight loss amounts to 24.6%, a value close to the calculated value of 24.5% based on the molecular formula of the title complex. Beyond this point, there are multiple steps between 296 and 504 °C involving the decomposition of the organic part of the molecule. No clear plateaus are reached in these stages, suggesting that the derived products are unstable and decompose further. The total weight loss of 55.3% due to the decomposition of the title complex is reached at 504.7 °C with no further loss up to 1000 °C. The DTG profile of the complexes exhibits clear features that depict the aforementioned TGA process.

9. Cyclic voltammetry

Electrochemical measurements for **1** were taken in water, in the presence of KNO_3 as a supporting electrolyte (Fig. 7). A Pt electrode was used as a working electrode and an Ag/AgCl electrode served as a reference electrode. The cyclic voltammogram of **1** reflects a one electron chemically reversible process ($ip_a/ip_c = 1$, $ip_c/\{(v)^{1/2}C\}$ constant) with a value of $E_{1/2} = -615$ mV that corresponds to the Cr(III)/Cr(II) redox couple. Attempts to pursue the isolation of the one electron reduced product of the title complex **1** are currently ongoing.

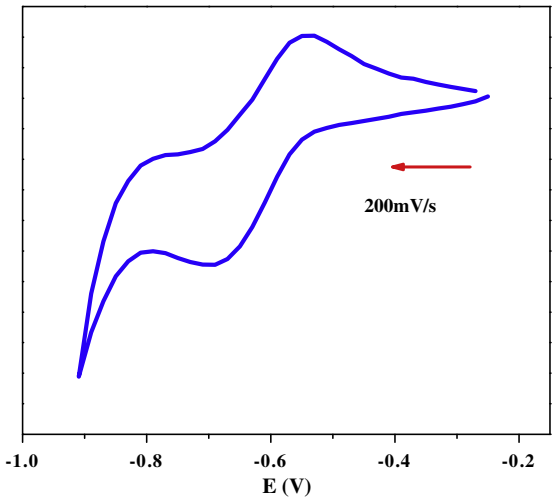


Fig. 7. Cyclic voltammetry of **1** in water (scan rate 200 mV/s).

10. Discussion

The current investigation of the binary Cr(III)–citrate system has led to the emergence of two new mononuclear Cr(III)–citrate species $Na_3[Cr(C_6H_5O_7)_2]\cdot 8.5H_2O$ (**1**) and $(Hdmphen)_6[Cr(C_6H_5O_7)_2]\cdot(NO_3)_3\cdot 14H_2O$ (**2**), with specific properties (analytical, spectroscopic, electrochemical, thermal, magnetic and structural). The following major points are worth pointing out in this work:

(a) The species were synthesized and isolated at specific yet distinct pH values i.e. 5.5 and 3.5, with the use of two different cations arising from the associated bases sodium hydroxide and 2,9-dimethylphenanthroline, respectively. Nevertheless, the isolated complexes contain the same type of anion $[Cr(C_6H_5O_7)_2]^{3-}$, with the two citrate ligands bound to Cr(III) being triply deprotonated, thus leading to the overall charge of 3- for both anionic species.

The structural characterization of **1** and **2** showed that Cr(III), a rather kinetically inert metal ion, follows a similar reactivity with other trivalent metal ions in its aqueous chemistry toward α-hydroxycarboxylic acids, such as citric acid. In fact, the nature of the isolated complexes **1** and **2** is similar to that of the Al(III) and Ga(III) congener species already studied synthetically and structurally. Characteristic examples of relevant anionic M(II,III) complexes include $[Cr(C_6H_4O_7)(C_6H_5O_7)]^{4-}$ [28], $[Al(C_6H_4O_7)_2]^{5-}$ [39], $[Al(C_6H_4O_7)(C_6H_5O_7)]^{4-}$ [47], $[Ga^{III}(C_6H_5O_7)_2]^{3-}$ [27], $[Fe(C_6H_4O_7)_2]^{5-}$ [40], $[Mn(C_6H_4O_7)_2]^{5-}$ [42], $[Mn(C_6H_5O_7)_2]^{4-}$ [42], $[Co_2(C_6H_5O_7)_2(H_2O)_4]^{2-}$ [48], $[Co_2(C_6H_5O_7)_2]^{2-}$ [41] and $[Ni(C_6H_5O_7)(H_2O)_2]_2^{2-}$ [49]. A worth noting remark in the aforementioned series of studied M(III) and M(II)–citrate complexes is that they exhibit variable deprotonation states for the bound citrate ions i.e. 3- and 4-. In the case of **1** and **2**, the deprotonation state of citrate is 3-. A binary species of Cr(III), $(NH_4)_4[Cr(C_6H_4O_7)(C_6H_5O_7)]\cdot 3H_2O$, bearing both triply and fully deprotonated citrate ligands has been synthesized and characterized [28].

The importance of the degree of deprotonation of the Cr(III)-bound citrates is linked to an important observation on the structural identity of **1** and **2**. Specifically, the hydrogen of the non-coordinated terminal carboxylate group of citrate in **2** forms a hydrogen bond with the alkoxide oxygen of the same ligand. This property is specific to the structure of the anion in **2**. No such hydrogen bond exists in the case of the anion in **1**. Therefore, the ability of the triply deprotonated citrate ligand bound to Cr(III) to form an intramolecular hydrogen bond provides an imprint of the conformational identity of compound **2** in comparison to that of compound **1**. That H bond formation in concert with the presence of an appropriately large counter ion (such as $Hdmphen^+$) and nitrate ions may contribute to favorable lattice dynamics necessary to differentiate the solid state structure of **2** relative to that in **1**.

Furthermore, an equally remarkable characteristic of the two compounds **1** and **2** is their distinct structural conformation in the solid state (vide supra). That is reflected into the disposition of the two citrates bound to the Cr(III) ion and suggests that pH-structural variants exist in the requisite binary system. In solution, spectroscopic data (UV–Vis, EPR) support the same identity for both **1** and **2**, with the solid state conformers very likely interconverting rapidly so that it is not easy to discern them as discrete species. Their solid state identity is exemplified through the use of appropriate counter ions giving rise to discrete lattice dynamics and favoring their isolation. It appears, therefore, that under carefully screened and tuned reaction conditions, favorable lattice

dynamics may lead to the capture of conformational structural variants of binary Cr(III)–citrate species that otherwise would not have been able to distinguish easily in solution. That contention may also apply to other binary metal–hydroxycarboxylate systems containing hitherto unknown compounds. To this end, the employment of the Na^+ and $Hdmphen^+$ counter ions (vide infra) facilitates "trapping" of the two conformers in the solid state. Interestingly, the magnetic susceptibility profiles of the two species are the same over the temperature range studied. Ostensibly, the conformational signature of the two species in the solid state does not influence the magnetic susceptibility behavior of Cr(III). It may very well be that the immediate Cr(III)–O_6 coordination sphere in **1** and **2** is rather insensitive to magnetic susceptibility differentiation despite the existing distinctly variable conformational status of the two species.

(b) The importance of cations in the synthetic process leading to the isolation of variable nature binary Cr(III)–citrate complexes from aqueous media is amply exemplified in **1** and **2**. The cations employed in this and previous work [28] on the specific Cr(III)–citric acid binary system derive from the use of inorganic (NaOH, KOH, etc.) and organic bases (dmphen), both acting as essential pH-adjustment agents while concurrently providing the necessary counter ions to balance the arisen charge on the assembled metal ionic complex in solution. Albeit of both inorganic (K^+, Na^+, etc.) and organic ($Hdmphen^+$) nature, these cations affect the solubility of species arising at the specific pH at which the reaction mixture is adjusted, thus influencing (1) the lattice dynamics of the species synthesized and ultimately isolated, and (2) the isolation of variable nature metal ionic complexes at the same or different pH of the aqueous synthesis medium. To this end, the nature of bases from which the cations emerge, the cations themselves, the bulkiness of the cations, the ability of counter ions to (1) interact with solvent molecules and the assembled metal ionic complex, and (2) influence packing forces involved in crystal lattice dynamics, all project the importance of cations in the synthesis of metal ionic complexes, not unlike those in the Cr(III)–citrate system. Undoubtedly, cation significance in delineating the structural speciation of the herein investigated binary system has been high, in view of the fact that (1) pH-structural Cr(III)–citrate variants bearing citrate at different deprotonation states, and (2) pH-structural conformers of the same binary variant Cr(III)–citrate complex (**1** and **2**) could be isolated from the requisite speciation scheme. It is worth pointing out that in other metal–hydroxycarboxylate systems, the employment of cations, originating in the use of bases for the mere adjustment of the pH of the reaction mixture, has not resulted in their participation in the isolated respective lattice, thus influencing again the nature of the isolated metal–ligand assembly (charged or uncharged) [50,51]. Hence, the use of variable nature cations appears to play an important role in the synthetic and structural delineation of binary M(II,III)–ligand aqueous speciation distributions.

(c) The alcoholic moiety of the citrate ligand is deprotonated upon binding to Cr(III). The derived alkoxide group participates in the formation of the five-membered cyclic ring, which further stabilizes the entire mononuclear complex. A similar behavior was observed in the case of other trivalent metal ions such as Al(III), Ga(III), Mn(III) and Fe(III) in aqueous binary systems with citric acid. This is in contrast to the congener complexes of citrate with divalent metal ions, in which the alcoholic moiety in the five member metallacyclic ring remains protonated. The structural features in **1** and **2** seem to be in line with the previously reported $(NH_4)_4[Cr(C_6H_4O_7)(C_6H_5O_7)]\cdot 3H_2O$ [28] and in contrast to the reported complex $(C_5H_6N)_2[Cr(C_6H_{5.5}O_7)_2]\cdot 4H_2O$ [29]. In the latter case, it appears that the alkoxide groups of the two citrate ligands share a proton (half occupancy), thus reflecting partial deprotonation of the alcoholic moiety bound to Cr(III). Undoubtedly, more Cr(III)–citrate pH-structural variants need to be synthesized, isolated and characterized crystallographically in order to settle the issue of deprotonation state of the citrate alcoholic moiety. Such work is currently under way.

(d) In previous work, solution speciation studies were reported on the binary Cr(III)–citric acid system [28]. An important species arising into that speciation scheme was the mononuclear complex $[CrL_2H_{-1}]^{4-}$, reflected into the known $(NH_4)_4[Cr(C_6H_4O_7)(C_6H_5O_7)]\cdot 3H_2O$ [28] complex synthesized and isolated in the solid state. By analogy to the behavior of $(NH_4)_4[Cr(C_6H_4O_7)(C_6H_5O_7)]\cdot 3H_2O$ in the solid state and in solution, the collective spectroscopic and structural data for complexes **1** and **2** suggest that they (a) not retain their crystal structure in solution, and (b) dissociate in solution. In light of the above information, knowledge of (a) the nature of the binary Cr(III)–citrate and by extension other Cr(III)–hydroxycarboxylate species present at pH-specific values in solution, and (b) the physical and chemical properties of the potential speciation participants across the physiological pH-range, will undoubtedly contribute to the understanding of the bioavailability of soluble Cr(III) forms as a prerequisite to (i) its biochemical interactions with low and high molecular mass cellular targets, and (ii) any potential influence of Cr(III) binary and ternary species on toxicity effects or support of cellular physiology.

11. Cr(III) solubility and potential toxicity

Chromium is encountered in forest soils, sediments [52], leather tanning industries and laboratories, and surface and atmospheric waters. Two thermodynamically stable states of chromium exist in that variety of environments, namely Cr(III) and Cr(VI). In biological systems, chromium activities include well-established genotoxic, mutagenic, and carcinogenic actions of Cr(VI) compounds and a more controversial role of Cr(III) as an insulin potentiator in glucose and fat metabolism [53]. A generally accepted mechanism of Cr(VI)-induced genotoxicity [54] involves the following main steps: (i) active transport of Cr(VI) into cells (through anion channels for soluble chromates or through phagocytosis for insoluble compounds such as $PbCrO_4$), (ii) reduction of Cr(VI) within the cells or at the cell surface linked to the formation of potentially DNA damaging Cr(V)/Cr(IV) intermediates (which can be stabilized by intracellular ligands) and organic radicals, (iii) formation of kinetically inert Cr(III) complexes, including highly genotoxic ternary DNA–Cr(III)–protein and DNA–Cr(III)–DNA cross linked species, as a result of such reduction. X-ray absorption spectroscopic (XAS) studies on single cells [54] have confirmed the predominance of the Cr(III) oxidation state in Cr(VI)-treated mammalian cells. In contrast to Cr(VI), most Cr(III) complexes to which cells are exposed, are non-cytotoxic and non-mutagenic even at mM concentrations [55], presumably due to the low cellular permeability related to their octahedral geometry and kinetic inertness [56]. On the other hand, one of the less-studied aspects of Cr(VI)-induced genotoxicity is the possibility of intracellular re-oxidation of Cr(III) complexes accumulated in Cr(VI)-treated cells [54,57–59]. Re-oxidation, involving reactive oxygen species (ROS) arising through the action of cellular redox enzymes, could potentially lead to genotoxic Cr(V)/Cr(IV) complexes and be blamed for the long-term toxicity and carcinogenicity of Cr(VI), when the latter metal ion finds its way into the cellular environment [54,58–60]. Furthermore, a recent thesis [60] has related the reported antidiabetic activities of some Cr(III) complexes [60] to their intra- or extra-cellular oxidation to Cr(VI)/Cr(V) species, which can act as phosphatase inhibitors by mechanisms not unlike those of well-known insulin-mimetic V(V) species [61,62] (its worth pointing out that Cr(VI) is isoelectronic to V(V)). In this regard, it has been shown that Cr(III) dietary supplements could be

oxidized to Cr(VI) by a) biological inorganic oxidants (H_2O_2, OCl^-), or b) enzymatic oxidation, with the emerging Cr(VI) (and Cr(V)) being very efficient inhibitors of phosphatase enzymes in much the same way as V(V) [60]. Enzyme inhibition is one of the postulated mechanisms of the antidiabetic activity of V(IV)/V(V) complexes [62,63].

In view of the above information, it appears that knowledge of well-characterized soluble forms of Cr(III) is important in understanding (a) its aqueous chemistry at the molecular level, and (b) any subsequent toxic repercussions that it potentially gives rise to in the cellular environment. Given that solubility is a prerequisite for bioavailability, with the latter being strongly linked to toxic effects, the presence of well-characterized species of Cr(III) could contribute to (a) comprehending early steps of toxicologically significant chemical processes, and (b) associating initial forms of chromium with cellular damage.

In the present case, the pH-specific chemistry of the binary system Cr(III)–citric acid afforded two species, which can be isolated in a pure crystalline form, studied and characterized. In this effort, the spectroscopic and structural characterization of **1** and **2** in the solid state and in solution projects their distinct fingerprint signature in the progressively growing family of binary Cr(III)–citrate species. Therefore, key physicochemical properties of new Cr(III)–hydroxycarboxylate species have become known and could be used in: (a) the design and development of methodologies for the sensitive and selective detection [63] of that metal ion in a variety of aqueous media (environment, bacteria, plants, humans), and (b) the assessment of the potential of Cr(III) to influence cellular physiology and/or inflict toxic damage to cellular structures.

12. Cr(III) precursors to new materials

Chromium has been known to be a component of multifunctional materials. To this end, chromium is an essential component, among others, of (a) binary Cr/W oxide thin film materials destined for gas sensing [64], (b) Cr-substituted hematites and magnetite materials relevant to the removal of corrosion products-deposits on iron-based alloys in Pressurized Water Reactors [65,66], and (c) mixed oxides of the type $La_{0.9}Sr_{0.1}Ni_{1-x}Cr_xO_3$ exhibiting a perovskite structure [67]. Materials with a perovskite phase are prepared by the citrate method and used as catalysts involving H_2O_2 decomposition. To this end, structurally, spectroscopically and magnetically well-characterized Cr(III) precursor species (vide supra) are needed for the expedient synthesis of new materials leading to the preparation of mixed metal perovskite phases such as the ones mentioned above. Furthermore, synthetic binary and/or ternary Cr(III)–L complexes could facilitate processes leading to the synthesis of new materials destined for an array of technological applications. In this regard, well-characterized Cr(III) complexes with (hydroxy)carboxylate-containing substrates could be competent starting materials for the preparation of variable temperature solid-state phases. Hence, compounds **1** and **2** could serve as promising starting agents in the synthesis of advanced materials.

In line with the aforementioned, a significant area of technology where (a) the nature of the hydroxycarboxylate ligand is important in promoting reactivity toward metal-based (e.g. Cr(III)) starting reagents, and (b) binary Cr(III)–hydroxycarboxylate species could be competent starting agents influencing novel synthetic materials processes, is that of molecule-based magnets. In such materials, the metal ionic binder oxalate (ox) has been demonstrated to be one of the most versatile ligands used in relevant synthetic investigations. As a bidentate chelate linker, it can assist in the tuning of the magnetic properties of materials. To this end, the topology, dimensionality and sign of magnetic exchange can be tuned in emerging systems, thus allowing for the preparation of novel magnetic materials (hybrid magnets [68,69], chiral magnets [70,71], conducting magnets [72] or photoactive magnets) [73,74]. Such versatility is extensively reflected into the employment of dinuclear metal–oxalate complexes. These compounds are obtained by using a $[M^{III}(ox)_3]^{3-}$ octahedral species as a ligand toward paramagnetic divalent ions. Initially, the chemical reactivity affords anionic oligomeric species in solution. Subsequently, employment of bulky cations in the media leads to the self-assembly of these molecular species and formation of insoluble coordination polymers. The first successful example of such an approach was reported by Okawa et al. in the early 1990s. It was then reported that addition of a bulky monovalent cation, such as alkylammonium, affords layered 2D compounds bearing the general formula $[A][M^{II}M^{III}(C_2O_4)_3]$ ($M^{(II)}$ = Mn, Fe, Co, Ni, Cu, Zn; $M^{(III)}$ = Cr, Fe, V, Ru, Mn; A = counter ion). Depending on the identity of the divalent and trivalent metal ions, these compounds behave as ferromagnets, ferrimagnets or weak ferromagnets with critical temperatures between 6 and 45 K [75–83]. Substitution of the bulky monocation by tris(bipyridyl) metal complexes $[M_1^{II}(bpy)_3]^{2+}$ (M_1 = Fe, Co, Ni, Ru; bpy = $C_{10}H_8N_2$) facilitates formation of extended bimetallic oxalate-based 3D networks: $[M_1^{II}(bpy)_3][ClO_4][M^{II}M^{III}(C_2O_4)_3]$ (where M_1(II) and M(III) may or may not be the same). These compounds exhibit ferro- and ferrimagnetic behavior, with lower ordering temperatures than their 2D counterparts. Contrary to the previous cations, the flat $[K(18\text{-crown-}6)]^+$ cation induces reduction of the dimensionality, yielding other less connected 2D anionic layers and even 1D chains [84,85]. These systems, too, reach magnetic ordering at lower temperatures than their 2D counterparts. Other cations, with the help of capping ligands, allow for even further decrease in the dimensionality, thus yielding discrete polynuclear compounds, such as dimers [86–89], trimers [90–92], or tetramers [93–97]. In the framework of such an approach, Cr(III)–citrate complexes could be viable starting materials (synthons) providing soluble metal ionic centers (a) accessible to reactive hetero- or homo-metal ionic complex or cluster species, and (b) eliciting the promotion of interactions toward divalent metal ions, potentially giving rise to novel magnetic materials. This work is currently in progress in our lab.

13. Conclusions

One of the two predominant ionic forms of chromium in nature, Cr(III), was found to (a) react with citric acid, a low molecular mass physiological agent of many structural and chemical attributes, under pH-specific conditions, and (b) afford two new binary Cr(III)–citrate complexes $Na_3[Cr(C_6H_5O_7)_2]\cdot 8.5H_2O$ (**1**) and $(Hdmphen)_6[Cr(C_6H_5O_7)_2]\cdot(NO_3)_3\cdot 14H_2O$ (**2**). The two conformationally discrete pH-structural variants complement the already known Cr(III)–citrate species, justifying the focused effort to delineate the structural speciation of the binary Cr(III)–citrate system. Both **1** and **2** were characterized spectroscopically, structurally and magnetically, thus providing essential information on the relevant binary interactions under pH-variable conditions and molecular stoichiometries dictated by a plethora of factors in abiotic or biological settings. Given that well-characterized forms of Cr(III) in the presence of citrate are likely involved in (bio)chemical processes, underlying physiological and/or toxic manifestations linked with that metal ion's involvement in biological media, further studies targeting (a) the synthesis and characterization of binary and ternary Cr(III)-hydroxycarboxylate-L (L = O-, N-containing substrate) species, and (b) the investigation of the solution chemistry of such species toward variable molecular mass substrates, are needed. Collectively, such studies are expected to provide good understanding of the chemical reactivity of Cr(III) in binary and ternary systems, under variable conditions, leading to species (a)

of specific structural, spectroscopic and magnetic properties, and (b) useful in the development of technologically apt materials. Studies along these lines are currently in progress in our lab.

Acknowledgments

This work was supported by a "PENED" grant co-financed by the E.U.-European Social Fund (75%) and the Greek Ministry of Development-GSRT (25%),

Appendix A. Supplementary data

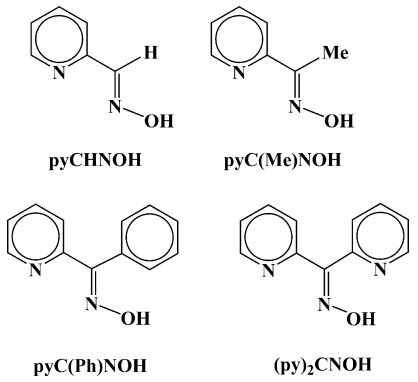
CCDC 722269 and 722270 contain the supplementary crystallographic data for **1** and **2**. These data can be obtained free of charge via http://www.ccdc.cam.ac.uk/conts/retrieving.html, or from the Cambridge Crystallographic Data Centre, 12 Union Road, Cambridge CB2 1EZ, UK; fax: (+44) 1223-336-033; or e-mail: deposit@ccdc.cam.ac.uk.

Supplementary data associated with this article can be found, in the online version, at doi:10.1016/j.poly.2009.05.077.

References

[1] C.J. Smithells, S.V. Williams, Nature 124 (1929) 617.
[2] D.R. Lide (Ed.), CRC Handbook of Chemistry and Physics, 84th ed., CRC Press, Boca Raton, Florida, 2003. Section 4, Properties of the Elements and Inorganic Compounds; Density of Molten Elements and Representative Salts.
[3] E. Oberg et al., Machinery's Handbook, 25th ed., Industrial Press Inc., 1996.
[4] C. Pariya, K.H. Theopold, Curr. Sci. 78 (2000) 1345.
[5] W.B. Jensen, J. Chem. Educ. 84 (2007) 1418.
[6] W.C. Bae, H.K. Lee, Y.C. Choe, D.J. Jahng, S.H. Lee, S.J. Kim, J.H. Lee, B.C. Jeong, J. Microbiol. 43 (2005) 21.
[7] G. Anger, J. Halstenberg, K. Hochgeschwender, C. Scherhag, U. Korallus, H. Knopf, P. Schmidt, M. Ohlinger, "Chromium Compounds" in Ullmann's Encyclopedia of Industrial Chemistry, Wiley-VCH, Weinheim, 2005.
[8] F.L. Pettrilli, W. Miller, Appl. Environ. Microbiol. 33 (1977) 805.
[9] A.G. Levis, V. Bianchi, in: S. Langard (Ed.), Biological and Environmental Aspects of Chromium, Elsevier Science, Amsterdam, 1982, pp. 171–208.
[10] Y.T. Wang, H. Shen, J. Ind. Microbiol. 14 (1995) 159.
[11] J.B. Vincent, Acc. Chem. Res. 33 (2000) 503.
[12] C.M. Davis, J.B. Vincent, Biochemistry 36 (1997) 4382.
[13] G.S. Morris, K.A. Guidry, M. Hegsted, D.L. Hasten, Nutr. Res. 15 (1995) 1045.
[14] D.M. Stearns, J.P. Wise Sr., S.R. Patierno, K.E. Wetterhahn, FASEB J. 9 (1995) 1643.
[15] A.R. Walsh, J. O'Halloran, A.M. Gower, Ecotoxicol. Environ. Saf. 27 (1994) 168.
[16] S. Tsoodol, I.P. Alimarin, Z.A. Gallai, Russ. Chem. Bull. 17 (1968) 1632.
[17] C.B. Black, J.A. Cowan, Eur. J. Biochem. 243 (1997) 684.
[18] L. Fishbein, Int. J. Environ. Anal. Chem. 17 (1984) 113.
[19] W. Mertz, Physiol. Rev. 49 (1969) 163.
[20] V. Harshita, L. Kobla, S. Volpe, Crit. Rev. Food Sci. Nutr. 40 (2000) 291.
[21] CrysAlis CCD, Oxford Diffraction Ltd., Version 1.171.29.9, Release 23-03-2006.
[22] CrysAlis.NET, CrysAlis RED, Oxford Diffraction Ltd., Version 1.171.29.9, Release 23-03-2006.
[23] G. Sheldrick, M. SHELX-97: Program for the Refinement of Crystal Structure, University of Göttingen, Göttingen, Germany (1993–7), Release 97-2.
[24] G. Sheldrick, M. SHELX-97: Program for the Solution of Crystal Structure, University of Göttingen, Göttingen, Germany, 1997.
[25] L.J. Farrugia, J. Appl. Cryst. 32 (1999) 837.
[26] G.M. Sheldrick, SHELXS-97: Structure Solving Program; University of Göttingen, Germany, 1997.
[27] P. O'Brien, H. Salacinski, M. Motevalli, J. Am. Chem. Soc. 119 (1997) 12695.
[28] C. Gabriel, C.P. Raptopoulou, A. Terzis, V. Tangoulis, C. Mateescu, A. Salifoglou, Inorg. Chem. 46 (2007) 2998.
[29] D.M. Quiros, M.L. Goodgame, D.J. Williams, Polyhedron 11 (1992) 1343.
[30] J.S. Suh, S.J. Park, K.W. Lee, I.H. Suh, J.H. Lee, J.H. Song, M.R. Oh, Acta Crystallogr. C53 (1997) 432.
[31] D. Taylor, Aust. J. Chem. 31 (1978) 1455.
[32] J.H. Choi, T. Suzuki, S. Kaizaki, Acta Crystallogr. E59 (2003) m812.
[33] D.J. Radanovic, N. Sakagami, V.M. Ristanovic, S. Kaizaki, Inorg. Chim. Acta 292 (1999) 16.
[34] L.E. Gerdom, N.A. Baenziger, H.M. Goff, Inorg. Chem. 20 (1981) 1606.
[35] R.S. Drago, Physical Methods in Chemistry, W.B. Saunders Company, Philadelphia, 1977. pp. 359.
[36] G.B. Deacon, R. Philips, J. Coord. Chem. Rev. 33 (1980) 227.
[37] C. Djordjevic, M. Lee, E. Sinn, Inorg. Chem. 28 (1989) 719.
[38] K. Nakamoto, Infrared and Raman Spectra of Inorganic and Coordination Compounds, Part B, fifth ed., John Wiley and Sons Inc., New York, 1997.
[39] M. Matzapetakis, C.P. Raptopoulou, A. Terzis, A. Lakatos, T. Kiss, A. Salifoglou, Inorg. Chem. 38 (1999) 618.
[40] M. Matzapetakis, C.P. Raptopoulou, A. Tsohos, B. Papefthymiou, N. Moon, A. Salifoglou, J. Am. Chem. Soc. 120 (1998) 13266.
[41] M. Matzapetakis, M. Dakanali, C.P. Raptopoulou, V. Tangoulis, A. Terzis, N. Moon, J. Giapintzakis, A. Salifoglou, J. Biol. Inorg. Chem. 5 (2000) 469.
[42] M. Matzapetakis, N. Karligiano, A. Bino, M. Dakanali, C.P. Raptopoulou, V. Tangoulis, A. Terzis, J. Giapintzakis, A. Salifoglou, Inorg. Chem. 120 (2000) 4044.
[43] W.P. Griffith, T.D. Wickins, J. Chem. Soc. A (1968) 397.
[44] N. Vuletic, C. Djordjevic, J. Chem. Soc., Dalton Trans. (1973) 1137.
[45] M. Kaliva, T. Giannadaki, C.P. Raptopoulou, V. Tangoulis, A. Terzis, A. Salifoglou, Inorg. Chem. 40 (2001) 3711.
[46] M. Tsaramyrsi, D. Kavousanaki, C.P. Raptopoulou, A. Terzis, A. Salifoglou, Inorg. Chim. Acta 320 (2001) 47.
[47] M. Matzapetakis, M. Kourgiantakis, M. Danakali, C.P. Raptopoulou, A. Terzis, A. Lakatos, T. Kiss, I. Banyai, L. Iordanidis, T. Mavromoustakos, A. Salifoglou, Inorg. Chem. 40 (2001) 1734.
[48] N. Kotsakis, C.P. Raptopoulou, V. Tangoulis, A. Terzis, J. Giapintzakis, T. Jakusch, T. Kiss, A. Salifoglou, Inorg. Chem. 42 (2003) 22.
[49] Z.H. Zhou, Y.J. Lin, H.B. Zhang, G.D. Lin, K.R. Tsai, J. Coord. Chem. 42 (1997) 131.
[50] M. Dakanali, E.T. Kefalas, C.P. Raptopoulou, A. Terzis, T. Mavromoustakos, A. Salifoglou, Inorg. Chem. 42 (2003) 2531.
[51] M. Menelaou, C.P. Raptopoulou, A. Terzis, V. Tangoulis, A. Salifoglou, Eur. J. Inorg. Chem. (2006) 1957.
[52] K. Flogeac, E. Guillon, M. Aplincourt, J. Colloid Interface Sci. 286 (2005) 596.
[53] A. Levina, R. Codd, C.T. Dillon, P.A. Lay, Prog. Inorg. Chem. 51 (2003) 145. and references therein.
[54] C.T. Dillon, P.A. Lay, M. Cholewa, G.J.F. Legge, A.M. Bonin, T.J. Collins, K.L. Kostka, G. Shea-McCarthy, Chem. Res. Toxicol. 10 (1997) 533.
[55] S. De Flora, A. Camoirano, M. Bagnasco, P. Zanacchi, in: G. Berthon (Ed.), Handbook of Metal–Ligand Interactions in Biological Fluids. Bioinorganic Medicine, vol. 2, Marcel Dekker, New York, 1995, pp. 1020–1036.
[56] P.A. Lay, A. Levina, in: J.A. McCleverty, T.J. Meyer (Eds.), Comprehensive Coordination Chemistry II, vol. 4, Elsevier, Oxford, UK, 2004, p. 313.
[57] C.T. Dillon, P.A. Lay, A.M. Bonin, M. Cholewa, G.J.F. Legge, Chem. Res. Toxicol. 13 (2000) 742.
[58] C.T. Dillon, P.A. Lay, A.M. Bonin, N.E. Dixon, Y. Sulfab, Aust. J. Chem. 53 (2000) 411.
[59] I. Mulyani, A. Levina, P.A. Lay, Angew. Chem. Int. Ed. 43 (2004) 4504.
[60] J.B. Vincent, J. Trace Elem. Exp. Med. 16 (2003) 227. and references therein.
[61] P.J. Stankiewicz, A.S. Tracey, D.C. Crans, in: H. Sigel, A. Sigel (Eds.), Metal Ions in Biological Systems, vol. 31, Marcel Dekker, New York, 1995, p. 287.
[62] M. Zhang, M. Zhou, R.L. Van Etten, C.V. Stauffacher, Biochemistry 36 (1997) 15.
[63] A. Massumi, N.M. Najafi, H. Barzegari, Microchem. J. 72 (2002) 93.
[64] C. Cantalini, J. Eur. Ceram. Soc. 24 (2004) 1421.
[65] J. Manjanna, G. Venkateswaran, Hydrometallurgy 61 (2001) 45.
[66] J. Manjanna, G. Venkateswaran, B.S. Sherigara, P.V. Nayak, Hydrometallurgy 60 (2001) 155.
[67] A. Ariafard, H.R. Aghabozorg, F. Salehirad, Catal. Commun. 4 (2003) 561.
[68] A. Alberola, E. Coronado, C. Gimenez-Saiz, C.J. Gomez-Garcia, F.M. Romero, A. Tarazon, Eur. J. Inorg. Chem. 2 (2005) 389.
[69] E. Coronado, J.R. Galan-Mascaros, C.J. Gomez-Garcia, J. Ensling, P. Gutlich, Chem. Eur. J. 6 (3) (2000) 552.
[70] E. Coronado, J.R. Galan-Mascaros, C.J. Gomez-Garcia, J.M. Martinez-Agudo, Inorg. Chem. 40 (1) (2001) 113.
[71] M. Clemente-Leon, E. Coronado, C.J. Gomez-Garcia, A. Soriano-Portillo, Inorg. Chem. 45 (14) (2006) 5653.
[72] E. Coronado, J.R. Galan-Mascaros, C.J. Gomez-Garcia, V. Laukhin, Nature 408 (6811) (2000) 447.
[73] S. Benard, E. Riviere, P. Yu, K. Nakatani, J.F. Delouis, Chem. Mater. 13 (1) (2001) 159.
[74] S. Benard, P. Yu, J.P. Audiere, E. Riviere, R. Clement, J. Guilhem, L. Tchertanov, K. Nakatani, J. Am. Chem. Soc. 122 (39) (2000) 9444.
[75] H. Tamaki, M. Mitsumi, K. Nakamura, N. Matsumoto, S. Kida, H. Okawa, S. Iijima, Chem. Lett. 10 (1992) 1975.
[76] H. Tamaki, Z.J. Zhong, N. Matsumoto, S. Kida, M. Koikawa, N. Achiwa, Y. Hashimoto, H. Okawa, J. Am. Chem. Soc. 114 (18) (1992) 6974.
[77] H. Okawa, N. Matsumoto, H. Tamaki, M. Ohba, Mol. Cryst. Liq. Cryst. 232 (1993) 617.
[78] C. Mathoniere, S.G. Carling, Y.S. Dou, P. Day, J. Chem. Soc., Chem. Commun. 13 (1994) 1551.
[79] S.G. Carling, C. Mathoniere, P. Day, K.M.A. Malik, S.J. Coles, M.B. Hursthouse, J. Chem. Soc., Dalton Trans. 9 (1996) 1839.
[80] C. Mathoniere, C.J. Nuttall, S.G. Carling, P. Day, Inorg. Chem. 35 (5) (1996) 1201.
[81] R. Pellaux, H.W. Schmalle, R. Huber, P. Fischer, T. Hauss, B. Ouladdiaf, S. Decurtins, Inorg. Chem. 36 (11) (1997) 2301.
[82] M.H. Molina, F. Lloret, C. Ruiz-Pérez, M. Julve, Inorg. Chem. 37 (1998) 4131.
[83] K.S. Min, J.S. Miller, Dalton Trans. 20 (2006) 2463.
[84] E. Coronado, J.R. Galan-Mascaros, C. Marti-Gastaldo, Inorg. Chem. 45 (5) (2006) 1882.
[85] E. Coronado, J.R. Galan-Mascaros, C.J. Gomez-Garcia, C. Marti-Gastaldo, Inorg. Chem. 44 (18) (2005) 6197.
[86] O. Kahn, Angew. Chem., Int. Ed. Engl. 24 (10) (1985) 834.
[87] S. Kitagawa, T. Okubo, S. Kawata, M. Kondo, M. Katada, H. Kobayashi, Inorg. Chem. 34 (19) (1995) 4790.

[88] S. Triki, F. Berezovsky, J.S. Pala, E. Coronado, C.J. Gomez-Garcia, J.M. Clemente, A. Riou, P. Molinie, Inorg. Chem. 39 (17) (2000) 3771.
[89] P. Roman, C. Guzman Miralles, A. Luque, J.I. Beitia, J. Cano, F. Lloret, M. Julve, S. Alvarez, Inorg. Chem. 35 (13) (1996) 3741.
[90] N. Stanica, C.V. Stager, M. Cimpoesu, M. Andruh, Polyhedron 17 (10) (1998) 1787.
[91] M. Andruh, R. Melanson, C.V. Stager, F.D. Rochon, Inorg. Chim. Acta 251 (1–2) (1996) 309.
[92] F.D. Rochon, R. Melanson, M. Andruh, Inorg. Chem. 35 (21) (1996) 6086.
[93] E. Coronado, M.C. Gimenez, C.J. Gomez-Garcia, F.M. Romero, Polyhedron 22 (23) (2003) 3115.
[94] M.C. Muñoz, M. Julve, F. Lloret, J. Faus, M. Andruh, Dalton Trans. (1998) 3125.
[95] C.Y. Vivas, F.S. Delgado, C. Ruiz-Pérez, M. Julve, Cryst. Eng. Commun. 6 (2004) 11.
[96] G. Marinescu, M. Andruh, M. Julve, F. Lloret, R. Llusar, S. Uriel, J. Vaissermann, Cryst. Growth Des. 5 (2005) 261.
[97] G. Marinescu, M. Andruh, R. Lescouezec, M.C. Munoz, J. Cano, F. Lloret, M. Julve, New J. Chem. 24 (7) (2000) 527.



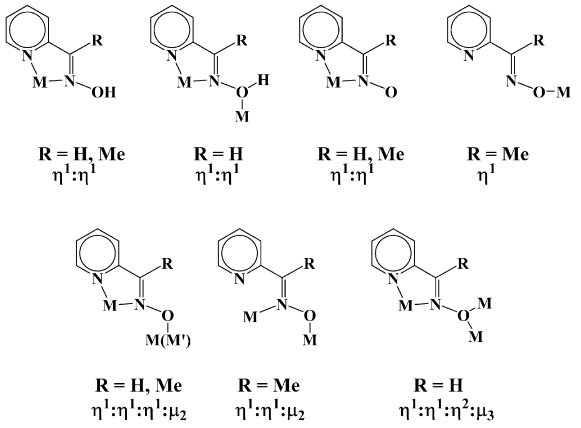
Scheme 1. The 2-pyridyl ketone oxime ligands discussed in the text.

characterized Fe^{III} carboxylato complex of pyC(Me)NOH; its molecular structure contains the $[Fe_4(\mu_3\text{-}O)_2]^{8+}$ 'butterfly' core, and the pyC(Me)NO$^-$ adopts the $\eta^1{:}\eta^1{:}\eta^1{:}\mu_2$ coordination mode (Scheme 2).

2. Experimental

2.1. General and spectroscopic measurements

All manipulations were performed under aerobic conditions using materials as received (Aldrich Co). All chemicals and solvents were reagent grade. The basic iron(III) benzoate $[Fe_3O(O_2CPh)_6(H_2O)_3]Cl$ was synthesised by addition of 2.2 equivalents of NaO_2CPh in an aqueous solution of $FeCl_3{\cdot}6H_2O$. The immediately formed orange precipitate was filtered, washed with Et_2O and dried in vacuo. Methyl 2-pyridyl ketone oxime, pyC(Me)NOH, was synthesised by the reaction of equimolar quantities of 1-pyridin-2-ylethanone (2-acetyl-pyridine). pyC(Me)O, $H_2NOH{\cdot}HCl$ and NaOEt in EtOH [12]. Elemental analyses for carbon, hydrogen, and nitrogen were performed using a Perkin–Elmer 2400/II automatic analyzer. Infrared spectra were recorded as KBr pellets in the range 4000–400 cm^{-1} on a Bruker Equinox 55/S FT-IR spectrometer. Mössbauer spectra for **2** was taken with a constant acceleration spectrometer using a ^{57}Co (Rh matrix) source at RT and a variable temperature Oxford cryostat. Variable-temperature magnetic susceptibility measurements for **2** were carried out on polycrystalline samples in the 2.0–300 K temperature range using a Quantum Design MPMS SQUID susceptometer under a magnetic field of 0.5 T. Data were corrected with standard procedures for the contribution of the sample holder and diamagnetism of the sample. The calculation of the magnetic susceptibility was accomplished by analytical calculation



Scheme 2. The crystallographically established coordination modes of pyC(R)NOH and pyC(R)NO$^-$ (R = H, Me).

of the energy levels associated with the spin Hamiltonian. Minimization was carried out with an adapted version of MINUIT [13]. The error factor R is defined as $R = \sum \frac{x_{exp}-x_{calc}}{Nx^2_{exp}}$, where N is the number of experimental points.

2.2. Compound preparation

2.2.1. $[Fe_4O_2Cl_2(O_2CPh)_2\{pyC(H)NO\}_4]$ (**1**)

2.2.1.1. Method A. A colorless solution of pyC(H)NOH (0.061 g, 0.50 mmol) in dmf (10 mL) was added to a stirred suspension of NaO_2CPh (0.144 g, 1.00 mmol) in dmf (20 mL). The stirring continued for 5 min until an orange solution of $FeCl_3{\cdot}6H_2O$ (0.135 g, 0.50 mmol) in EtOH (10 mL) was added. After 5 min of stirring, the clear brown solution was layered with Et_2O (1:2 v/v) to afford a microcrystalline brown product after ~1 month, which was filtered off and dried *in vacuo*. Yield: 0.055 g, 42%. The resulting powder was analyzed as solvent free. *Anal.* Calc. for $C_{38}H_{30}Fe_4N_8O_{10}Cl_2$: C, 43.35; H, 2.87; N, 10.64; Found: C, 42.48; H, 2.81; N, 10.34%. Main IR data (KBr pellet): ν~ = 3062(w), 1603(s), 1544(s), 1539(s), 1475(m), 1405(vs), 1344(w), 1309(w), 1294(w), 1252(w), 1218(m), 1178(w), 1156(w), 1116(s), 1090(vs), 1015(m), 891(m), 774(m), 720(m), 689(s), 643(m), 604(m), 552(m), 519(m), 470(m), 422(m).

2.2.1.2. Method B. An orange solution of $[Fe_3O(O_2CPh)_6(H_2O)_3]Cl$ (0.170 g, 0.17 mmol) in EtOH (10 mL) was added to a stirred solution of pyC(H)NOH (0.061 g, 0.50 mmol) in dmf (30 mL). The resulting brown solution was stirred for 5 min and layered with Et_2O (1:2 v/v) yielding brown microcrystalline precipitate after 15 days, which was filtered off and dried *in vacuo*. Yield: 0.052 g, 40%. The resulting powder was analyzed as solvent free. *Anal.* Calc. for $C_{38}H_{30}Fe_4N_8O_{10}Cl_2$: C, 43.35; H, 2.87; N, 10.64; Found: C, 42.45; H, 2.79; N, 10.29%. Main IR data (KBr pellet): ν~ = 3064(w), 1604(s), 1544(s), 1529(s), 1475(m), 1406(vs), 1344(w), 1309(w), 1296(w), 1252(w), 1218(m), 1178(w), 1156(w), 1116(s), 1090(vs), 1013(w), 893(w), 774(m), 720(m), 689(s), 642(m), 604(m), 552(m), 518(m), 470(m), 420(m).

2.2.2. $[Fe_4O_2Cl_2(O_2CPh)_2\{pyC(Me)NO\}_4]{\cdot}EtOH{\cdot}Et_2O$ (**2**$\cdot EtOH\cdot Et_2O$)

2.2.2.1. Method A. A colorless solution of pyC(Me)NOH (0.068 g, 0.50 mmol) in dmf (10 mL) was added to a stirred suspension of NaO_2CPh (0.144 g, 1.00 mmol) in dmf (20 mL). The stirring continued for 5 min until an orange solution of $FeCl_3{\cdot}6H_2O$ (0.135 g, 0.50 mmol) in EtOH (10 mL) added. After 5 min of stirring, the clear brown solution was layered with Et_2O (1:2 v/v) yielding microcrystalline brown precipitate after ~1 month, which was filtered off and dried *in vacuo*. Yield: 0.058 g, 42%. The resulting powder was analyzed as solvent free. *Anal.* Calc. for $C_{42}H_{38}Fe_4N_8O_{10}Cl_2$: C, 45.48; H, 3.45; N, 10.10; Found: C, 44.61; H, 3.35; N, 9.88%. Main IR data (KBr pellet): ν~ = 3411(br), 3063(w), 1600(s), 1551(s), 1534(s), 1473(m), 1406(vs), 1374(m), 1293(w), 1256(w), 1151(s), 1100(m), 1074(s), 1051(m), 779(m), 750(w), 727(m), 705(s), 672(m), 642(m), 599(m), 562(w), 504(m), 484(m), 420(m).

2.2.2.2. Method B. To a refluxed orange suspension of $[Fe_3O(O_2CPh)_6(H_2O)_3]Cl$ (0.170 g, 0.17 mmol) in EtOH (10 mL) was added a solution of pyC(Me)NOH (0.068 g, 0.50 mmol) in dmf (30 mL). The color of the solution immediately turned to brown and the reflux stopped. X-ray quality red crystals of **2** were obtained by vapor diffusion or layering of Et_2O (1:2 v/v) to the brown solution after two weeks. Yield: 0.058 g, 42%. The crystals were collected by filtration and were dried *in vacuo*. The resulting powder was analyzed as solvent free. *Anal.* Calc. for $C_{42}H_{38}Fe_4N_8O_{10}Cl_2$: C, 45.48; H, 3.45; N, 10.10; Found: C, 44.57; H, 3.38; N, 9.90%. Main IR data (KBr pellet): ν~ = 3439(br), 3064(vw), 1600(s), 1551(s), 1534(s), 1478(m), 1407(vs), 1375(m), 1294(w), 1258(w), 1151(s), 1100(m), 1075(s),

Table 1
Crystallographic data for complex **2**·EtOH·Et_2O.

	2·EtOH·Et_2O
Formula	$C_{48}H_{54}Cl_2Fe_4N_8O_{12}$
Fw	1229.29
Space group	$P2_1/c$
T (°C)	−93
λ (Å)	Mo Kα (0.71073 Å)
a (Å)	15.150(7)
b (Å)	21.450(8)
c (Å)	17.350(8)
β (°)	103.00(1)
V (Å^3)	5494(4)
Z	4
$\rho_{calculated}$ (g cm^{-3})	1.486
μ, (Mo Kα) (mm^{-1})	1.198
$R1$[a]	0.0642[b]
$wR2$[a]	0.1445[b]

[a] $w = 1/[\sigma^2(F_o^2) + (aP)^2 + bP]$ and $P = (\max)\ (F_o^2,0)+2F_c^2/3$, $a = 0.0394$ and $b = 10.8799$; $R1 = \Sigma\ (|F_o|-|F_c|)/\Sigma(|F_o|)$ and $wR2 = \{\Sigma[w(F_0^2-F_c^2)^2]/\Sigma[w(F_0^2)^2]\}^{1/2}$.
[b] For 8806 reflections with $I > 2\sigma(I)$.

1051(m), 780(m), 727(m), 705(s), 669(m), 642(m), 600(m), 561(w), 504(m), 484(m), 425(m).

2.3. Single-crystal X-ray crystallography

A red prismatic crystal of **2**·EtOH·Et_2O (0.10 × 0.20 × 0.50 mm) was taken directly from the mother liquor and immediately cooled to −93 °C. Diffraction measurements were made on a Rigaku R-AXIS SPIDER Image Plate diffractometer using graphite monochromated Mo Kα radiation. Data collection (ω-scans) and processing (cell refinement, data reduction and Empirical absorption correction) were performed using the CRYSTALCLEAR program package [14]. Important crystal data and parameters for data collection are reported in Table 1. The structure was solved by direct methods using SHELXLS-97 [15] and refined by full matrix least-squares techniques on F^2 with SHELXLS-97 [16]. Further experimental crystallographic details for **2**·EtOH·Et_2O: $2\theta_{max} = 51°$; reflections collected/unique/used, 39051/10042 [$R_{int} = 0.0651$]/10042; 704 parameters refined; $(\Delta/\sigma)_{max} = 0.006$; $(\Delta\rho)_{max}/(\Delta\rho)_{min} = 0.534/-0.481$ e/Å3; $R1/wR2$ (for all data), 0.0745/0.1510. Hydrogen atoms were introduced at calculated positions as riding on bonded atoms. All non-H atoms were refined anisotropically. The ethanol solvate was found disordered and it was refined over two positions with occupation factors summing one. Plots of all structures were drawn using the DIAMOND 3 program package [17].

3. Results and discussion

3.1. Syntheses

Complexes **1** and **2** can be obtained either from the 1:2:1 Fe^{III}/$PhCO^-$/pyC(R)NOH molar ratio reaction in EtOH/dmf, or by the 1:3 $[Fe_3O(O_2CPh)_6(H_2O)_3]Cl$/pyC(R)NOH molar ratio reaction in EtOH/dmf. The large excess of NaO_2CPh used (Fe^{III}/pyC(R)NOH/NaO_2CPh = 1:1:2 or 4:4:8) is beneficial to the preparation of **1** and **2**. The excess of $PhCO_2^-$ helps the deprotonation of the neutral ligand pyC(R)NOH and the so-formed weak acid ($PhCO_2H$) does not decompose the oxide-bridged cluster. The balanced chemical equations describing the synthesis of **1** and **2** may be written in the form of Eqs. (1) and (2):

$$4FeCl_3\cdot 6H_2O + 4pyC(R)NOH + 8NaO_2CPh \xrightarrow{EtOh/dmf} \underset{\mathbf{1,2}}{[Fe_4O_2Cl_2(O_2CPh)_2\{pyC(R)NO\}_4]} + 8NaCl + 2HCl + 6PhCO_2H + 22H_2O \quad (1)$$

In this case, it is assumed that the H_2O from the solvents and/or the starting materials is the source of the O^{2-} ions.

$$6[Fe_3O(O_2CPh)_6(H_2O)_3]Cl + 12pyC(R)NOH + 6NaCl \xrightarrow{EtOH/dmf} 3\,\underset{\mathbf{1,2}}{[Fe_4O_2Cl_2(O_2CPh)_2\{pyC(R)NO\}_4]} + 2''[Fe_3O(O_2CPh)_6(H_2O)_2(OH)]'' + 18PhCO_2H + 10H_2O \quad (2)$$

The 1:1 Fe^{III}/pyC(R)NOH molar ratio reaction is reflected to the stoichiometry of the final product. An excess of the metal ion in the reaction mixture may favor the synthesis of even higher nuclearity metal clusters, a possibility that is currently under investigation in our laboratory.

In an attempt to explore to what extend the presence of counterions might affect the identity of the products isolated, we have performed the 1:3:3 $[Fe_3O(O_2CPh)_6(H_2O)_3]Cl$/pyC(Me)NOH/$NaClO_4$ or Bu_4NBF_4 molar ratio reactions in EtOH and/or EtOH/dmf mixtures. In every case the red precipitate formed was identified as compound **2** by infrared spectroscopy.

The IR spectrum of complexes **1** and **2** exhibit strong absorptions at 1544 and 1406 cm^{-1} (for **1**) and 1551 and 1407 cm^{-1} (for **2**) which are assigned to the $\nu_{as}(CO_2)$ and $\nu_s(CO_2)$ modes of the benzoate ligands, respectively. The difference Δ [$\Delta = \nu_{as}(CO_2)-\nu_s(CO_2)$] is 138 and 144 cm^{-1} for **1** and **2**, respectively, less than that for NaO_2CPh (184 cm^{-1}), as expected for a bidentate bridging mode of the carboxylate ligation [18]. A strong absorption band at ~1600 cm^{-1} and a weak absorption band at ~1294 cm^{-1} are assigned to the (C–N) and (N-Ooximate) stretching vibrations, respectively, of the pyC(R)NO$^-$ ligands [11].

3.2. Description of the structure

The molecular structure of **2** is depicted in Fig. 1 and selected bond distances and angles are listed in Table 2. The tetranuclear complex contains the $[Fe_4(\mu_3\text{-}O)_2]^{8+}$ core comprising four Fe^{III} ions in a "butterfly" disposition and two μ_3-O^{2-} ions, each bridging three Fe^{III} ions forming the 'wings' of the 'butterfly'. Atoms Fe(1) and Fe(2) occupy the 'hinge' or 'body' sites and Fe(3) and Fe(4) occupy the 'wingtip' positions. The topology of the central $[Fe_4(\mu_3\text{-}O)_2]^{8+}$ core can be also described as two edge-sharing $[Fe_3(\mu_3\text{-}O)]^{7+}$ triangular subunits. The dihedral angle between the

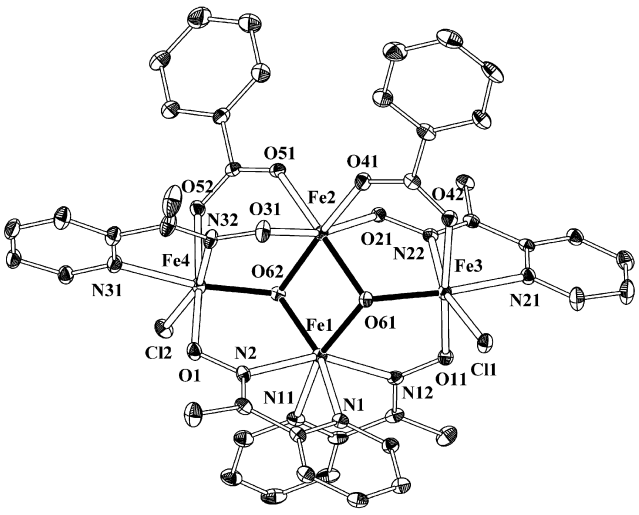


Fig. 1. Partially labeled plot of **2** with ellipsoids drawn at the 30% probability level. Hydrogen atoms have been omitted for clarity. Black bonds describe the $[Fe_4(\mu_3\text{-}O)_2]^{8+}$ core.

Table 2
Selected bond distances (Å) and angles (°) for complex **2**·EtOH·Et_2O.

Distances					
Fe(1)–O(62)	1.911(3)	Fe(2)–O(61)	1.999(3)	Fe(3)–O(61)	1.878(3)
Fe(1)–O(61)	1.922(3)	Fe(2)–O(62)	2.009(3)	Fe(3)–O(11)	2.025(3)
Fe(1)–N(2)	2.133(4)	Fe(2)–O(31)	2.019(4)	Fe(3)–O(42)	2.067(3)
Fe(1)–N(12)	2.132(4)	Fe(2)–O(21)	2.020(3)	Fe(3)–N(22)	2.155(4)
Fe(1)–N(11)	2.192(4)	Fe(2)–O(41)	2.027(3)	Fe(3)–N(21)	2.215(4)
Fe(1)–N(1)	2.208(4)	Fe(2)–O(51)	2.051(3)	Fe(3)–Cl(1)	2.337(1)
Fe(4)–O(62)	1.879(3)	Fe(4)–O(52)	2.049(4)	Fe(4)–N(31)	2.202(4)
Fe(4)–O(1)	2.016(3)	Fe(4)–N(32)	2.175(4)	Fe(4)–Cl(2)	2.326(2)
Fe(1)···Fe(2)	2.910(1)	Fe(1)···Fe(3)	3.390(6)	Fe(1)···Fe(4)	3.359(3)
Fe(2)···Fe(3)	3.279(4)	Fe(2)···Fe(4)	3.266(7)	Fe(3)···Fe(4)	5.969(6)
Angles					
O(62)–Fe(1)–O(61)	86.4(1)	O(61)–Fe(2)–O(62)	81.7(1)	O(61)–Fe(3)–O(11)	89.9(1)
O(62)–Fe(1)–N(2)	84.5(1)	O(61)–Fe(2)–O(31)	98.8(1)	O(61)–Fe(3)–O(42)	95.1(1)
O(61)–Fe(1)–N(2)	114.4(1)	O(62)–Fe(2)–O(31)	90.7(1)	O(11)–Fe(3)–O(42)	170.6(1)
O(62)–Fe(1)–N(12)	116.3(1)	O(61)–Fe(2)–O(21)	91.6(1)	O(61)–Fe(3)–N(22)	88.2(1)
O(61)–Fe(1)–N(12)	84.4(1)	O(62)–Fe(2)–O(21)	99.4(1)	O(11)–Fe(3)–N(22)	88.7(1)
N(2)–Fe(1)–N(12)	153.7(2)	O(31)–Fe(2)–O(21)	166.4(2)	O(42)–Fe(3)–N(22)	83.4(1)
O(62)–Fe(1)–N(11)	97.5(1)	O(61)–Fe(2)–O(41)	90.9(1)	O(61)–Fe(3)–N(21)	159.4(1)
O(61)–Fe(1)–N(11)	157.2(1)	O(62)–Fe(2)–O(41)	168.9(2)	O(11)–Fe(3)–N(21)	81.2(1)
N(2)–Fe(1)–N(11)	88.3(2)	O(31)–Fe(2)–O(41)	82.1(2)	O(42)–Fe(3)–N(21)	91.4(1)
N(12)–Fe(1)–N(11)	73.8(2)	O(21)–Fe(2)–O(41)	89.1(1)	N(22)–Fe(3)–N(21)	73.2(1)
O(62)–Fe(1)–N(1)	155.5(1)	O(61)–Fe(2)–O(51)	170.1(1)	O(61)–Fe(3)–Cl(1)	107.1(1)
O(61)–Fe(1)–N(1)	93.3(1)	O(62)–Fe(2)–O(51)	92.1(1)	O(11)–Fe(3)–Cl(1)	95.4(1)
N(2)–Fe(1)–N(1)	73.4(1)	O(31)–Fe(2)–O(51)	89.1(1)	O(42)–Fe(3)–Cl(1)	90.8(1)
N(12)–Fe(1)–N(1)	87.9(1)	O(21)–Fe(2)–O(51)	81.6(1)	N(22)–Fe(3)–Cl(1)	164.1(1)
N(11)–Fe(1)–N(1)	92.3(1)	O(41)–Fe(2)–O(51)	96.2(1)	N(21)–Fe(3)–Cl(1)	92.3(1)
O(62)–Fe(4)–O(1)	90.8(1)	O(52)–Fe(4)–N(32)	86.1(2)	O(62)–Fe(4)–Cl(2)	105.5(1)
O(62)–Fe(4)–O(52)	94.6(1)	O(62)–Fe(4)–N(31)	161.0(2)	O(1)–Fe(4)–Cl(2)	99.7(1)
O(1)–Fe(4)–O(52)	166.7(2)	O(1)–Fe(4)–N(31)	85.1(1)	O(52)–Fe(4)–Cl(2)	90.6(1)
O(62)–Fe(4)–N(32)	88.3(1)	O(52)–Fe(4)–N(31)	85.9(1)	N(32)–Fe(4)–Cl(2)	166.1(1)
O(1)–Fe(4)–N(32)	81.9(2)	N(32)–Fe(4)–N(31)	72.9(1)	N(31)–Fe(4)–Cl(2)	93.5(1)
Fe(3)–O(61)–Fe(1)	126.3(2)	Fe(1)–O(61)–Fe(2)	95.8(1)	Fe(4)–O(62)–Fe(2)	114.3(2)
Fe(3)–O(61)–Fe(2)	115.5(2)	Fe(4)–O(62)–Fe(1)	124.8(2)	Fe(1)–O(62)–Fe(2)	95.8(1)

planes defined by Fe(1)/Fe(2)/Fe(3) and Fe(1)/Fe(2)/Fe(4) is 176.3(3)°; thus, the four Fe^{III} ions are essentially coplanar. As a result, the two μ_3-O^{2-} ions are forced to leave out of their respective [Fe_3(μ_3-O)] triangle and are displaced above and below the [Fe_4] best mean plane (0.53(1) and 0.55(1) Å for O(61) and O(62)). This is also reflected to the sums of the Fe–O–Fe angles around the μ_3-O^{2-} ions, which severely deviate from 360° (337.7°/334.9° for O(61)/O(62), respectively) and are close to the ideal value of 328.4° expected for pure sp^3 hybridization. A literature survey of tetranuclear complexes presenting the [Fe_4(μ_3-O)$_2$]$^{8+}$ core showed a number of different configurations regarding the position of the 'wing' metal ions and the displacement of the μ_3-O^{2-} ions with respect to their respective [Fe_3] planes. The most common include a) the trans arrangement of the 'wing' metal ions with respect to the central [Fe_2O_2] core and the displacement of the μ_3-O^{2-} ions above and below their respective [Fe_3] planes (type A) [19], (b) the cis arrangement of the 'wing' metal ions with respect to the central [Fe_2O_2] core and the displacement of the μ_3-O^{2-} ions below their respective [Fe_3] planes (type B) [20], and (c) an intermediate configuration between those two (type C) [21]. However, in all cases the sum of the Fe–O–Fe angles around the μ_3-O^{2-} ion falls in the range 350°–359°. Only in the case of K_2[Fe_4(OH)$_2$(PO_4)$_4$(H_2O)$_2$] [22] the sum of the Fe–O–Fe angles around the μ_3-OH group is 339.8°. In the case of **2**, which belong to the first type of configuration described above, the two μ_3-O^{2-} ions show a more pyramidal character than in analogous complexes. Each μ_3-O^{2-} ion presents two short (~1.9 Å) and one longer (~2.0 Å) Fe–O distance, unlike the case of the more symmetrical [Fe_3(μ_3-O)] triangular units found in various 'basic iron(III) carboxylates' [23] where the μ_3-O^{2-} ion is symmetrically coordinated to the iron(III) ions at ~1.9 Å. The two short Fe–O bond distances exert a *trans* influence on the Fe–N bond (Fe–N ~ 2.2 Å).

The two 'body' iron(III) ions [Fe(1) and Fe(2)] are bridged by two μ_3-oxides, while a single μ_3-oxide ion participates in the coordination sphere of the 'wingtip' iron(III) ions. As a result, the central Fe(1)···Fe(2) separation is much shorter (2.910(1) Å) than the body-to-wing separations which fall in the range 3.266(7)–3.390(6) Å. The wing-to-wing separation is the largest one as expected (5.969(6) Å).

The four methyl 2-pyridyl ketone oxime ligands are anionic presenting the η^1:η^1:η^1:μ_2 coordination mode (Scheme 2) around the Fe^{III} ions. Two of the pyC(Me)NO^- ligands are coordinated to the 'body' Fe(1) through their pyridine and oximato nitrogen atoms, and they use their oximato oxygen atom to bridge one of the 'wingtip' ions, Fe(3) and Fe(4). In this way, Fe(1) presents an

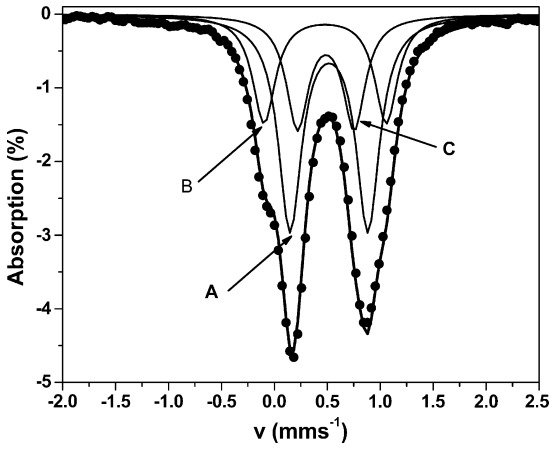


Fig. 2. Zero field Mössbauer spectrum from **2** recorded at 90 K. The solid lines are theoretical spectra assuming three sites as explained in the text.

O_2N_4 distorted octahedral coordination. The remaining two pyC(Me)NO^- ligands are coordinated through their pyridine and oximato nitrogen atoms to the 'wingtip' ions Fe(3) and Fe(4) respectively, and their oximato oxygen atom is bridging the 'body' ion Fe(2). The 'body' Fe(2) ion is also bridged to each of the 'wingtip' ions Fe(3) and Fe(4) through a syn,syn $\eta^1{:}\eta^1{:}\mu_2$ benzoato group. The octahedral coordination around each of the 'wingtip' iron(III) ions is completed by a chloride ion. In this manner, Fe(2) presents an oxygen-rich octahedral coordination environment, while Fe(3) and Fe(4) present an O_3N_2Cl octahedral coordination.

Complex **2** is the forth member of a small family of structurally characterized iron(III) carboxylate complexes with pyC(R)NOH type ligands (R = H, Me, Ph, py); the rest being the analogous tetranuclear compounds $[Fe_4O_2(O_2CMe)_2\{(py)_2CNO\}_4X_2]$ ($X = Cl^-$, N_3^-) featuring 'butterfly' cores [11], and the dodecanuclear compound $[Fe_{12}O_8(OMe)_2(O_2CPh)_{12}(pyCHNO)_6]$ [8b].

3.3. Mössbauer spectroscopy

A Mössbauer spectrum from a powdered sample of **2** recorded in zero field at 90 K is shown in Fig. 2. The spectrum consists of overlapping quadruple doublets. The crystal structure of **2** indicates the presence of at least three different, six coordinated ferric sites, FeO_3N_2Cl, FeO_6, FeO_2N_4 with a ratio 2:1:1. In order to reproduce the spectrum we take into account this information allowing for three different sites **A**, **B**, **C** at a ratio 2:1:1 and assuming close lying values for the isomer shifts. The results are quoted in Table 3.

The values listed in Table 3 are only indicative and by no means unique. The average value of the isomer shift is in the range expected for six-coordinated high-spin ferric ions and consistent with the type of ligands for the iron sites. Moreover, the heterogeneity in the coordination of the iron sites of the complex is depicted in the different values of the quadruple splitting.

3.4. Magnetic susceptibility studies

The $\chi_M T$ value of **2** is 2.50 $cm^3\ mol^{-1}\ K$ at 300 K, significantly below the theoretically expected value for four non-interacting spins (17.51 $cm^3\ mol^{-1}\ K$, $g = 2$), suggesting the interplay of strong antiferromagnetic interactions. This was corroborated by the continuous decrease of the $\chi_M T$ value, down to a plateau of 0.015 $cm^3\ mol^{-1}$ below 20 K (Fig. 3). This plateau is characteristic of a small fraction of high-spin ferric paramagnetic impurity. This impurity is manifested as an abrupt increase of χ_M below 15 K.

For the interpretation of the magnetic susceptibility data, we initially considered two types of interactions, usually considered for butterfly-type complexes, i.e. wingtip-body (J_{wb}) and body–body (J_{bb}) interactions. However, several attempts to fit our data yielded very poor results. After examination of the structural parameters of **2**, we considered that this model should be refined. In particular we note that the Fe(1)/Fe(3) and Fe(1)/Fe(4) pairs are each bridged by one N–O moiety from the pyC (Me)NO^- ligand (excluding the μ_3-O^{2-} bridges) and that the Fe(2)/Fe(3) and Fe(2)/Fe(4) are additionally bridged by one benzoate bridge each. This fact affects the respective Fe–O–Fe angles formed by the μ_3-oxide bridges, which are 126.4(2) and 124.8(2)° for the Fe(1)/Fe(3) and Fe(1)/Fe(4) pairs, respectively, and 115.5(2) and 114.3(2)° for the Fe(2)/Fe(3) and Fe(2)/Fe(4) pairs, respectively. The oxide bridge being considered to provide the main superexchange pathway, we assumed that these differentiations in the Fe–O–Fe angles might affect the exchange couplings. We therefore decided to account for these interactions with two different exchange coupling parameters (Fig. 4). Thus the Hamiltonian used was:

$$\hat{H} = -2[J_1(\hat{\mathbf{S}}_1\hat{\mathbf{S}}_3 + \hat{\mathbf{S}}_1\hat{\mathbf{S}}_4) + J_2(\hat{\mathbf{S}}_2\hat{\mathbf{S}}_3 + \hat{\mathbf{S}}_2\hat{\mathbf{S}}_4) + J_{bb}\hat{\mathbf{S}}_1\hat{\mathbf{S}}_2] \quad (3)$$

It should be noted that the assignment of J_1 and J_2 is arbitrary, since the symmetry of the problem does not allow us to readily distinguish between the two types of interaction, which are topologically equivalent. Adoption of this model yielded significant improvements to the fits. Best-fit parameters were $J_1 = -85\ cm^{-1}$, $J_2 = -27\ cm^{-1}$, $J_{bb} = +25\ cm^{-1}$, $g = 2$ (fixed), $\rho = 0.36\%$, with $R = 4.3 \times 10^{-3}$, where ρ is a small fraction of high-spin ferric paramagnetic impurity. Although the values for J_1 and J_2 are well determined, that of J_{bb} is not. It was found within a wide range of values (e.g. from -25 to $+25\ cm^{-1}$); this parameter did not influence the agreement factor significantly. This is a known issue for this parameter in Fe^{III} butterfly complexes with $S = 0$ ground states, resulting to an indeterminate ground state [11]. Therefore, we present here the best-fit value of this parameter, although it should not be considered as reliable.

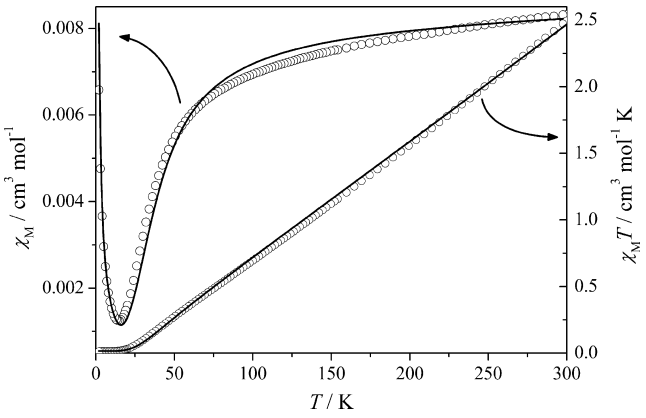


Fig. 3. χ_M vs T and $\chi_M T$ vs T data and best-fit curved according to the model described in the text.

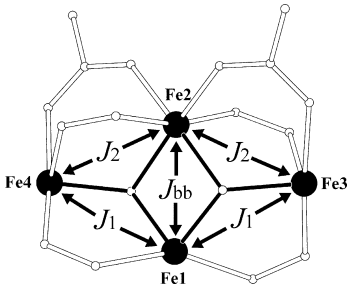


Fig. 4. Spin-coupling scheme used for the interpretation of the magnetic susceptibility data of **2**.

4. Conclusions

The use of 2-pyridyl oximes, pyC(R)NOH (R = H, Me), in Fe^{III}-carboxylate chemistry has yielded tetranuclear clusters that contain the $[Fe_4(\mu_3\text{-}O)_2]^{8+}$ 'butterfly' core, compounds $[Fe_4O_2Cl_2(O_2CPh)_2\{pyC(R)NO\}_4]$ (R = H, **1**; R = Me, **2**). Complex **2** is the first crystallographically characterized Fe^{III} carboxylato complex of

Table 3
Mössbauer parameters of the three different sites A, B, C.

Doublet	δ[a] (mm/s)	ΔE_Q[a] (mm/s)	Area[b] (%)
A	0.52	0.74	50
B	0.48	1.15	25
C	0.49	0.54	25

[a] ±0.01 mm/s.
[b] Fixed.

pyC(Me)NOH. The use of different Fe^{III} sources and the presence of counterions in the reaction mixtures have not affected the isolation of **1** and **2**, thus suggesting that they represent the more thermodynamically stable products of the reactions. From the structural point of view, complex **2** is analogous to the previously reported tetranuclear 'butterfly' complexes of Fe^{III} with di-2-pyridyl ketone oxime, $(py)_2CNOH$, i.e. R = py, $[Fe_4O_2(O_2CMe)_2\{(py)_2CNO\}_4X_2]$ ($X = Cl^-$, N_3^-). From the magnetic point of view, the latter complexes of $(py)_2CNOH$ and **2** present striking differences. Complexes $[Fe_4O_2(O_2CMe)_2\{(py)_2CNO\}_4X_2]$ ($X = Cl^-$, N_3^-) present a $S = 1$ ground state because of the particular value of the J_{bb}/J_{wb} ratio [11], whereas complex **2** presents a diamagnetic ground state as is the case for the majority of the $[Fe_4]$ 'butterfly' complexes. In order to draw safe conclusions regarding the origin of the different magnetic behavior and the possible influence of the R-substituent of the 2-pyridyl oximes we are currently investigating the Fe^{III}-carboxylate chemistry of ligands containing various R groups (Et, Ph, etc).

Supplementary data

CCDC 723976 contains the supplementary crystallographic data for **2**. These data can be obtained free of charge via http://www.ccdc.cam.ac.uk/conts/retrieving.html, or from the Cambridge Crystallographic Data Centre, 12 Union Road, Cambridge CB2 1EZ, UK; fax: (+44) 1223-336-033; or e-mail: deposit@ccdc.cam.ac.uk.

References

[1] (a) For some examples involving manganese and iron complexes see: A.J. Tasiopoulos, A. Vinslava, W. Wernsdorfer, K.A. Abboud, G. Christou, Angew. Chem., Int. Ed. 43 (2004) 2117;
(b) M. Soler, W. Wernsdorfer, K. Folting, M. Pink, G. Christou, J. Am. Chem. Soc. 126 (2004) 2156;
(c) N. Aliaga-Alcalde, R.S. Edwards, S.O. Hill, W. Wernsdorfer, K. Folting, G. Christou, J. Am. Chem. Soc. 126 (2004) 12503;
(d) S. Wang, J.-L. Zuo, H.-C. Zhou, H.J. Choi, Y. Ke, J.R. Long, X.-Z. You, Angew. Chem., Int. Ed. 43 (2004) 5940;
(e) H. Oshio, N. Hoshino, T. Ito, M. Nakano, J. Am. Chem. Soc. 126 (2004) 8805.

[2] (a) Y. Niu, Y. Song, H. Hou, Y. Zhu, Inorg. Chem. 44 (2005) 2553;
(b) K. Susumu, T.V. Duncan, M.J. Therien, J. Am. Chem. Soc. 127 (2005) 5186;
(c) X. Meng, Y. Song, H. Hou, Y. Fan, G. Li, Y. Zhu, Inorg. Chem. 42 (2003) 1306;
(d) L. Tian, W. Zhang, B. Yang, P. Lu, M. Zhang, D. Lu, Y. Ma, J. Shen, J. Phys. Chem. B 109 (2005) 6944;
(e) H. Hou, Y. Wei, Y. Song, L. Mi, M. Tang, L. Li, Y. Fan, Angew. Chem., Int. Ed. 44 (2005) 6067.

[3] (a) G. Yu, S. Yin, Y. Liu, Z. Shuai, D. Zhu, J. Am. Chem. Soc. 125 (2003) 14816;
(b) S. Bordiga, C. Lamberti, G. Ricchiardi, L. Regli, F. Bonino, A. Damin, K.-P. Lillerud, M. Bjorgen, A. Zecchina, Chem. Commun. (2004) 2300;
(c) J.-M. Shi, W. Xu, Q.-V. Liu, F.-I. Liu, Z.-I. Huang, H. Lei, W.-T. Yu, Q. Fang, Chem. Commun. (2002) 756;
(d) E. Coronado, M. Clemente-León, J.R. Galán-Mascarós, C. Giménez-Saiz, C.J. Gómez-García, E. Martínez-Ferrero, J. Chem. Soc., Dalton Trans. (2000) 3955.

[4] (a) Although literature is abundant for various first-row metal complexes, for recent representative examples involving iron complexes see: L. Legros, C. Bolm, Chem. Eur. J. 11 (2005) 1086;
(b) F. Avenier, L. Dubois, P. Dubourdeaux, J.-M. Latour, Chem. Commun. (2005) 480;
(c) L. Bénisvy, J.-C. Chottard, J. Marrot, Y. Li, Eur. J. Inorg. Chem. (2005) 999.

[5] (a) A. Mishra, W. Wernsdorfer, K.A. Abboud, G. Christou, Chem. Commun. (2005) 54;
(b) T.G. Carell, A.M. Tyryshkin, G.C. Dismukes, J. Biol. Inorg. Chem. 7 (2002) 2;
(c) J.P. McEvoy, G.W. Brudvig, Chem. Rev. 106 (2006) 4455.

[6] For a recent review on the coordination chemistry of pyridyl oximes see: C.J. Milios, Th.C. Stamatatos, S.P. Perlepes, Polyhedron 25 (2006) 134.

[7] (a) See for example: C.J. Milios, P. Kyritsis, C.P. Raptopoulou, A. Terzis, R. Vicente, A. Escuer, S.P. Perlepes, Dalton Trans. (2005) 501;
(b) M. Alexiou, C. Dendrinou-Samara, C.P. Raptopoulou, A. Terzis, D.P. Kessissoglou, Inorg. Chem. 41 (2002) 4732;
(c) M. Alexiou, C. Dendrinou-Samara, A. Karagianni, S. Biswas, C.M. Zaleski, J. Kampf, D. Yoder, J.E. Penner-Hahn, V.L. Pecoraro, D.P. Kessissoglou, Inorg. Chem. 42 (2003) 2185;
(d) T. Afrati, C. Dendrinou-Samara, C.P. Raptopoulou, A. Terzis, V. Tangoulis, D.P. Kessissoglou, Angew. Chem., Int. Ed. 41 (2002) 2148;
(e) Th.C. Stamatatos, S. Dionyssopoulou, C. Efthymiou, P. Kyritsis, C.P. Raptopoulou, A. Terzis, R. Vicente, A. Escuer, S.P. Perlepes, Inorg. Chem. 44 (2005) 3374;
(f) M. Alexiou, C. Dendrinou-Samara, C.P. Raptopoulou, A. Terzis, V. Tangoulis, D.P. Kessissoglou, Eur. J. Inorg. Chem. (2004) 3822;
(g) G. Psomas, A.J. Stemmler, C. Dendrinou-Samara, J.J. Bodwin, M. Schneider, M. Alexiou, J.W. Kampf, D.P. Kessissoglou, V.L. Pecoraro, Inorg. Chem. 40 (2001) 1562;
(h) M. Alexiou, E. Katsoulakou, C. Dendrinou-Samara, C.P. Raptopoulou, V. Psycharis, E. Manessi-Zoupa, S.P. Perlepes, D.P. Kessissoglou, Eur. J. Inorg. Chem. (2005) 1964;
(i) J.A. Cabeza, I. del Rio, V. Riera, M. Suárez, C.A. Álvarez-Rúa, S. Garcia-Granda, S.H. Chuang, J.R. Hwu, Eur. J. Inorg. Chem. (2003) 4159;
(j) S.O. Sommerer, B.J. Westcott, A.J. Jircitano, K.A. Abboud, Inorg. Chim. Acta 238 (1995) 149.

[8] (a) For pyCHNOH complexes see for example: P. Chaudhuri, Coord. Chem. Rev. 243 (2003) 143;
(b) M. Murufesu, K.A. Abboud, G. Christou, Polyhedron 23 (2004) 2779;;
(c) Th.C. Stamatatos, A. Bell, P. Cooper, A. Terzis, C.P. Raptopoulou, S.L. Heath, R.E.P. Winpenny, S.P. Perlepes, Inorg. Chem. Commun. 8 (2005) 533;;
(d) H. Miyasaka, S. Furukawa, S. Yanagida, K. Sugiura, M. Yamashita, Inorg. Chim. Acta 357 (2004) 1619;
(e) S. Ross, T. Weyhermüller, E. Bill, K. Wieghardt, P. Chaudhuri, Inorg. Chem. 40 (2001) 6656;
(f) C.J. Milios, E. Kefalloniti, C.P. Raptopoulou, A. Terzis, A. Escuer, R. Vicente, S.P. Perlepes, Polyhedron 23 (2004) 83;
(g) A. Caneschi, D. Gatteschi, N. Lalioti, C. Sangregorio, R. Sessoli, G. Venturi, A. Vindigni, A. Rettori, M.G. Pini, M.A. Novak, Angew. Chem., Int. Ed. 40 (2001) 1760;
(h) A. Caneschi, D. Gatteschi, N. Lalioti, R. Sessoli, L. Sorace, V. Tangoulis, A. Vindigni, Chem. Eur. J. 8 (2002) 286.

[9] (a) For pyC(Me)NOH complexes see for example: K. Riggle, T. Lynde-Kernell, E.O. Schlemper, Coord. Chem. 25 (1992) 117;
(b) A. Pajunen, M. Orama, H. Saarinen, Acta Crystallogr. Sect. C 55 (1999) 2075;
(c) A. Gupta, R.K. Sharma, R. Bohra, V.K. Jain, J.E. Drake, M.B. Hursthouse, M.E. Light, Polyhedron 21 (2002) 2387;
(d) V. Sharma, R.K. Sharma, R. Bohra, R. Ratnani, V.K. Jain, J.E. Drake, M.B. Hursthouse, M.E. Light, J. Organomet. Chem. 651 (2002) 98;
(e) V. Sharma, R.K. Sharma, R. Bohra, V.K. Jain, J.E. Drake, M.E. Light, M.B. Hursthouse, J. Organomet. Chem. 664 (2002) 66;
(f) C. Papatriantafyllopoulou, C.P. Raptopoulou, A. Terzis, E. Manessi-Zoupa, S.P. Perlepes, Z. Naturforsch. 61b (2006) 37;
(g) Th.C. Stamatatos, D. Foguet-Albiol, C.C. Stoumpos, C.P. Raptopoulou, A. Terzis, W. Wernsdorfer, S.P. Perlepes, G. Christou, Polyhedron 26 (2007) 2165;
(h) Th.C. Stamatatos, D. Foguet-Albiol, S.-C. Lee, C.C. Stoumpos, C.P. Raptopoulou, A. Terzis, W. Wernsdorfer, S.O. Hill, S.P. Perlepes, G. Christou, J. Am. Chem. Soc. 129 (2007) 9484;
(i) C. Papatriantafyllopoulou, G. Aromi, A.J. Tasiopoulos, V. Nastopoulos, C.P. Raptopoulou, S.T. Teat, A. Escuer, S.P. Perlepes, Eur. J. Inorg. Chem. (2007) 2761.

[10] (a) For pyC(Ph)NOH complexes see for example: J. Shuk-Yee Wong, W.T. Wong, New J. Chem. 26 (2002) 94;
(b) C.J. Milios, E. Kefalloniti, C.P. Raptopoulou, A. Terzis, R. Vicente, N. Lalioti, A. Escuer, S.P. Perlepes, Chem. Commun. (2003) 819;
(c) C.J. Milios, Th.C. Stamatatos, P. Kyritsis, A. Terzis, C.P. Raptopoulou, R. Vicente, A. Escuer, S.P. Perlepes, Eur. J. Inorg. Chem. (2004) 2885.

[11] Th.C. Stamatatos, A.K. Boudalis, Y. Sanakis, C.P. Raptopoulou, Inorg. Chem. 45 (2006) 7372.

[12] M. Orama, H. Saarinen, J. Korvenranta, J. Coord. Chem. 22 (1990) 183.

[13] F. James, M. Roos, Comput. Phys. Commun. 10 (1975) 345.

[14] Rigaku/MSC (2005). CrystalClear, Rigaku/MSC Inc., The Woodlands, Texas, USA.

[15] G.M. Sheldrick, SHELXS-97: Structure Solving Program, University of Göttingen, Germany, 1997.

[16] G.M. Sheldrick, SHELXL-97: Crystal Structure Refinement, University of Göttingen, Germany, 1997.

[17] DIAMOND – Crystal and Molecular Structure Visualization, Ver. 3.1, Crystal Impact, Rathausgasse 30, 53111, Bonn, Germany.

[18] G.B. Deacon, R.J. Phillips, Coord. Chem. Rev. 33 (1980) 227.

[19] (a) Among many others, see for example: S.M. Gorum, S.J. Lippard, Inorg. Chem. 27 (1988) 149;
(b) V.I. Ponomarev, L.O. Atovmyan, S.A. Bobkova, K.I. Turte, Dokl. Akad. Nauk. SSSR 274 (1984) 368.

[20] (a) Among many others, see for example: W.H. Armstrong, M.E. Roth, S.J. Lippard, J. Am. Chem. Soc. 109 (1987) 6318;
(b) J.K. McCusker, J.B. Vincent, E.A. Schmitt, M.L. Mino, J. Shin, D.A.K. Coggin, P.M. Hagen, J.C. Huffman, G. Christou, D.N. Hendrickson, J. Am. Chem. Soc. 113 (1991) 3012.

[21] (a) M.W. Wemple, D.A.K. Coggin, J.B. Vincent, J.K. McCusker, W.E. Streib, J.C. Huffman, D.N. Hendrickson, G. Christou, J. Chem. Soc., Dalton Trans. (1998) 719;
(b) A.K. Boudalis, V. Tangoulis, C.P. Raptopoulou, A. Terzis, J.-P. Tuchagues, S.P. Perlepes, Inorg. Chim. Acta 357 (2004) 1345.

[22] P.B. Moore, Am. Mineral. 57 (1972) 397.

[23] (a) Among many others, see for example: S.M. Gorun, G.C. Papaefthymiou, R.B. Frankel, S.J. Lippard, J. Am. Chem. Soc. 109 (1987) 3337;
(b) A.M. Bond, R.J.H. Clark, D.G. Humphrey, P. Panayiotopoulos, B.W. Skelton, A.H. White, J. Chem. Soc., Dalton Trans. (1998) 1845;
(c) F. Degang, W. Guoxiong, T. Wenxia, Polyhedron 20 (1993) 2459.

present work is an extension of our research efforts on coordination polymers [12,14–20] and hydrogen-bonded frameworks [21,22].

2. Experimental

2.1. General

All reagents and solvents were of commercially available reagent quality unless otherwise stated. All reactions were performed at room temperature and no special conditions were required.

2.2. Instrumentation

^{13}C and ^{113}Cd NMR spectra were recorded on a Bruker AMX 400 MHz spectrometer. For ^{113}Cd NMR spectra a 0.1 M $Cd(NO_3)_2{\cdot}4H_2O$ solution was used as an external standard. The samples for solution NMR studies were prepared by dissolving $Cd(NO_3)_2{\cdot}4H_2O$ and *trans*-aconitic acid in D_2O; the pH of the D_2O solutions was adjusted with NaOD. Mass spectra were measured on an Agilent 1100 series LC-MSD-TRAP-SL-Spectrometer. The samples for ESI-MS spectra were prepared by dissolving $Cd(NO_3)_2{\cdot}4H_2O$ and *trans*-aconitic acid in a solvent mixture (H_2O/CH_3CN: 90/10) and the pH of the solutions was adjusted using NaOH. The FT-IR spectra were recorded on a Perkin–Elmer Spectrum GX FT-IR spectrophotometer with the samples as KBr pellets. The TG-DTA analysis was carried out under nitrogen, at a scan speed of 5 °C/min, on a Shimadzu DTG 60 apparatus. The weight of the samples was about 5 mg. C, H and N analyses were conducted by Microanalytical Service at the University of Ioannina, Greece.

2.3. Potentiometry

Potentiometric titrations of free ligand (H_3L) and its complexes with Cd(II) ions were carried out at 25 °C, using a total volume of 10.0 mL. The titrations were performed in the presence of 0.1 M KNO_3 over the pH range 2–8 on a Mettler Toledo DL50 automatic titrator and a combined glass-silver chloride electrode calibrated in hydrogen concentrations using HNO_3 [23]. About 0.1 M KOH was used as titrant. The concentrations of *trans*-aconitic acid and the metal ion was 4 mM at a1:1 metal:ligand molar ratio. The experimental data were analyzed using the HYPERQUAD program [24]. Standard deviations computed by HYPERQUAD refer to random errors.

2.4. Preparation of the compounds

2.4.1. Synthesis of $[Cd_3L_2(H_2O)_6]_n$ (**1**)

$Cd(NO_3)_2{\cdot}4H_2O$ (46.4 mg, 0.15 mmol) was dissolved in H_2O (4 mL). To this, an aqueous solution of *trans*-aconitic acid (17.4 mg, 0.1 mmol), was added. The pH of the resulting solution was adjusted to 6.2. This molecular ratio affords the optimum yield for compound **1**. A microcrystalline powder was formed after 1 h, it was collected and washed with ethanol and diethyl ether, and dried in vacuum. Yield 80% (31.4 mg based on L). For the preparation of a suitable sample for crystallographic analysis 1.7 mg of *trans*-aconitic acid were dissolved in 6 mL H_2O. To this solution, 4.64 mg of $Cd(NO_3)_2{\cdot}4\ H_2O$ (dissolved in 4 mL H_2O) was added. The resulting solution was left undisturbed for slow evaporation. The first crop of colourless crystals was isolated after 5 days; a second crop of crystals isolated after 3 weeks. *Anal.* Calc. for $C_{12}H_{18}O_{18}Cd_3$, (**1**): C, 18.30; H, 2.30. Found: C, 17.96; H, 2.22%. IR (KBr, cm^{-1}) = 3448 (s), 2965 (w), 2925 (w), 1638 (m), 1564 (s), 1400 (s), 1307 (w), 1264 (m), 1222 (w), 1106 (w), 964 (w), 941 (m), 887 (m), 791 (m), 700 (m).

2.4.2. Synthesis of $\{[Cd(HL)(1,10\text{-phen})(H_2O)]_n{\cdot}n(H_2O)\}$ (**2**)

$Cd(NO_3)_2{\cdot}3H_2O$ (46.4 mg, 0.15 mmol) was dissolved in H_2O (4 mL). To this, a solution of 1,10-phenanthroline (15 mg, 0.075 mmol) in hot H_2O (1 mL), was added. Separately, *trans*-aconitic acid, (17.4 mg, 0.1 mmol) was dissolved in water (5 mL) and was added to the metal solution. The resulting solution was left undisturbed for slow evaporation. The first crop of colorless crystals was isolated after 5 days; a second crop of colorless crystals was isolated after 1 week. Yield 75% (28.1 mg based on phen). *Anal.* Calc. for $C_{18}H_{16}N_2O_8Cd$, (**2**): C, 43.03; H, 3.21; N, 5.58. Found: C, 42.96; H, 3.18; N, 5.45%. IR (KBr, cm^{-1}) = 3448 (s), 3071 (m), 2992 (w), 2607 (w) (–OH), 1700 (m) (–COOH), 1649 (m), 1567 (s), 1517 (m), 1411 (s), 1332 (m) [phen], 1294 (w), 1273 (w), 1210 (m) [phen], 1103 (m), 924 (w), 848 (m) [phen], 801 (w), 727 (m) [phen].

2.4.3. Synthesis of $\{[Cd(HL)(2,2'\text{-bipy})(H_2O)]_n{\cdot}n(H_2O)\}$ (**3**)

The synthesis of **3** was carried out as for **2** but using 2,2′-bipy instead of 1,10-phenanthroline. The formation of the colorless crystals was slower and the last crop of crystals was collected after almost 8 weeks. Overall yield: 72% (23 mg based on 2,2′-bipy). *Anal.* Calc. for $C_{16}H_{16}N_2O_8Cd$, (**3**): C, 40.17; H, 3.37; N, 5.86. Found: C, 40.06; H, 3.33; N, 5.78%. IR (KBr, cm^{-1}) = 3425 (s), 3296 (m), 3072 (w), 2983 (w), 2951 (w), 2604 (w) (–OH), 1703 (m) (–COOH), 1639 (m), 1576 (s), 1475 (m), 1438 (m), 1377 (s), 1317 (w), 1210 (m), 1171 (m), 1077 (w), 1016 (m), 851 (w), 770 (m).

2.5. X-ray crystallography

The crystals of **1–3** were immersed in cryo-oil, mounted in a Nylon loop, and measured at a temperature of 120 K. The X-ray diffraction data were collected on a Nonius KappaCCD diffractometer using Mo Kα radiation (λ = 0.71073 Å). The EVALCCD [25] program package was used for cell refinements and data reductions. The structures were solved by direct methods using the SIR92 [26] or SIR97 [27] programs with the WINGX [28] graphical user interface. A semi-empirical absorption correction (SADABS) [29] was applied to all data. Structures were refined using the SHELXL-97 program [30]. The H_2O and OH hydrogen atoms were located from the difference Fourier map but constrained to ride on their parent atom, with U_{iso} = 1.5. Other hydrogens were positioned geometrically and constrained to ride on their parent atoms, with C–H = 0.95–0.99 Å and $U_{iso} = 1.2U_{eq}$ (parent atom). The crystallographic details are summarized in Table 1 and selected bond lengths and angles in Tables 2 and 3.

3. Results and discussion

3.1. Description of the structures

The molecular structure of **1** is depicted in Fig. 1 and bond distances and angles are listed in Table 2. The crystal structure of **1** reveals the formation of a neutral 3D metal-organic framework $[Cd_3L_2(H_2O)_6]_n$. [31]. The formation of **1** has been reported under hydrothermal conditions [11]. There are two independent Cd(II) atoms in the asymmetric unit (Table 2). Cd(2) is coordinated to three oxygen atoms belonging to water molecules and three oxygen atoms of three different *trans*-aconitates, forming a distorted octahedral geometry. The three water molecules are placed around the centre in a meridional plane. Cd(1) is coordinated to eight oxygen atoms, which belong to two chelating and two chelating-bridging carboxylates with two elongated Cd(1)–O(6) distances of 2.671(2) Å. In the reported compound, the authors considered that Cd(1) is six coordinate and adopts a distorted octahedral geometry [11]. A detailed analysis of the molecular geometry reveals that

Table 1
Crystallographic data and structure refinement for complexes **1**–**3**.

	1	2	3
Formula	$C_{12}H_{18}Cd_3O_{18}$	$C_{18}H_{16}CdN_2O_8$	$C_{16}H_{16}CdN_2O_8$
FW	787.46	500.73	476.71
Crystal System	monoclinic	triclinic	triclinic
Space group	*C*2/*c*	$P\bar{1}$	$P\bar{1}$
Crystal size (mm^3)	0.17 × 0.14 × 0.11	0.18 × 0.06 × 0.04	0.19 × 0.19 × 0.06
a (Å)	16.9640(19)	8.759(5)	9.0776(3)
b (Å)	9.5416(8)	10.531(3)	9.9059(6)
c (Å)	14.0203(15)	10.698(5)	10.6343(6)
α (°)	90	66.15(2)	115.523(5)
β (°)	115.982(12)	89.46(4)	91.855(4)
γ (°)	90	85.17(4)	94.671(4)
V ($Å^3$)	2040.0(4)	899.0(7)	857.65(9)
Z	4	2	2
D_c (Mg/m^3)	2.564	1.850	1.846
T (K)	120(2)	120(2)	120(2)
μ (mm^{-1})	3.191	1.267	1.323
Independent reflections (R_{int})	2353 (0.0607)	4055 (0.0471)	3932 (0.0365)
Measured reflections	14 933	8545	13 956
Parameters	150	262	244
R_1 (observed)	0.0238	0.0453	0.0263
wR_2 (observed)	0.0537	0.0686	0.0479
R_1 (all)	0.0296	0.0741	0.0394
wR_2 (all)	0.0561	0.0755	0.0506
CCDC number	721 133	721 134	721 135

Table 2
Bond distances (Å), bond angles (°) and hydrogen bonding for **1**.

Cd(1)–O(3)	2.469(2)	Cd(2)–O(1)	2.272(2)
Cd(1)–O(3)#1	2.469(2)	Cd(2)–O(2)	2.284(2)
Cd(1)–O(4)	2.325(2)	Cd(2)–O(6)	2.295(2)
Cd(1)–O(4)#1	2.325(2)	Cd(2)–O(8)	2.262(2)
Cd(1)–O(5)	2.319(2)	Cd(2)–O(7)	2.337(2)
Cd(1)–O(5)#1	2.319(2)	Cd(2)–O(9)	2.3568(19)
Cd(1)–O(6)	2.671(2)		
Cd(1)–O(6)#1	2.671(2)		
O(5)#1–Cd(1)–O(5)#2	83.70(10)	O(4)#3–Cd(1)–O(6)#2	124.11(8)
O(4)–Cd(1)–O(5)#1	98.49(7)	O(5)#1–Cd(1)–O(6)#1	51.53(7)
O(4)–Cd(1)–O(5)#2	148.08(7)	O(5)#1–Cd(1)–O(6)#2	82.07(7)
O(4)#3–Cd(1)–O(5)#1	148.08(7)	O(5)#2–Cd(1)–O(6)#1	82.07(7)
O(4)#3–Cd(1)–O(5)#2	98.49(7)	O(6)#1–Cd(1)–O(6)#2	118.64(8)
O(4)–Cd(1)–O(4)#3	96.04(11)	O(5)#2–Cd(1)–O(6)#2	51.53(7)
O(3)–Cd(1)–O(5)#1	79.07(7)		
O(3)–Cd(1)–O(5)#2	154.49(7)	O(1)–Cd(2)–O(2)#4	163.91(7)
O(3)–Cd(1)–O(4)	54.36(7)	O(1)–Cd(2)–O(6) #4	95.55(7)
O(3)–Cd(1)–O(4)#3	86.71(7)	O(1)–Cd(2)–O(7)	87.23(8)
O(3)#3–Cd(1)–O(5)#1	154.48(7)	O(1)–Cd(2)–O(8)	93.60(8)
O(3)#3–Cd(1)–O(5)#2	79.07(7)	O(1)–Cd(2)–O(9)	92.02(7)
O(3)#3–Cd(1)–O(4)	86.71(7)	O(2)–Cd(2)–O(6)#4	98.86(7)
O(3)#3–Cd(1)–O(4)#3	54.36(7)	O(2)–Cd(2)–O(7)	76.69(7)
O(3)–Cd(1)–O(3)#3	122.84(10)	O(2)#4–Cd(2)–O(8)	87.85(8)
O(3)–Cd(1)–O(6)#1	72.48(7)	O(2)#4–Cd(2)–O(9)	83.47(7)
O(3)–Cd(1)–O(6)#2	142.11(8)	O(6)#4–Cd(2)–O(7)	155.06(7)
O(4)–Cd(1)–O(6)#1	124.11(8)	O(6)#4–Cd(2)–O(8)	111.20(8)
O(4)–Cd(1)–O(6)#2	97.00(7)	O(6)#4–Cd(2)–O(9)	80.14(7)
O(3)#3–Cd(1)–O(6)#1	142.11(8)	O(7)–Cd(2)–O(8)	93.29(8)
O(3)#3–Cd(1)–O(6)#2	72.48(7)	O(7)–Cd(2)–O(9)	74.99(7)
O(4)#3–Cd(1)–O(6)#1	97.00(7)	O(8)–Cd(2)–O(9)	166.74(7)

D–H···A	d(D–H)	d(H···A)	d(D···A)	<(DHA)
O(8)–H(81)...O(9)#5	0.86	2.24	3.088(3)	166.7
O(8)–H(82)...O(4)#6	0.90	1.79	2.672(3)	166.5
O(7)–H(71)...O(3)#7	0.92	2.22	2.819(3)	122.3
O(7)–H(72)...O(5)#7	0.93	1.97	2.868(3)	161.3
O(9)–H(92)...O(1)#8	0.98	1.78	2.750(3)	166.2
O(9)–H(91)...O(5)#9	0.81	2.00	2.787(3)	163.6

Symmetry codes: #1 = −*x*, −*y* + 1, −*z*; #2 = *x*, −*y* + 1, *z* − ½; #3 = −*x*, *y*, −*z* − ½; #4 = −*x* + 1/2, *y* − 1/2, −*z* + ½; #5 = −*x* + 1/2, *y* + 1/2, −*z* + ½; #6 = *x*, −*y*, *z* + ½; #7 = −*x*, −*y*, −*z*; #8 = 1/2 + *x*, *y* − 1/2, *z*; #9 = 1/2 − *x*, −*y* − 1/2, −*z*.

Table 3
Selected bond distances (Å) and bond angles (°) for **2** and **3**.

2		3	
Cd(1)–O(1)	2.260(3)	Cd(1)–O(7)	2.2546(16)
Cd(1)–O(7)	2.271(3)	Cd(1)–O(6)	2.2581(16)
Cd(1)–N(2)	2.303(3)	Cd(1)–O(2)	2.2887(17)
Cd(1)–N(1)	2.344(3)	Cd(1)–O(1)	2.4773(16)
Cd(1)–O(6)#1	2.395(3)	Cd(1)–N(2)	2.3203(19)
Cd(1)–O(5)#1	2.353(3)	Cd(1)–N(1)	2.3271(19)
O(1)–Cd(1)–O(7)	90.21(10)	O(7)–Cd(1)–O(6)	90.11(6)
O(1)–Cd(1)–N(2)	92.69(11)	O(7)–Cd(1)–O(2)	133.35(6)
O(7)–Cd(1)–N(2)	132.02(11)	O(6)–Cd(1)–O(2)	89.52(6)
O(1)–Cd(1)–N(1)	160.04(11)	O(7)–Cd(1)–N(2)	92.90(7)
O(7)–Cd(1)–N(1)	90.45(11)	O(6)–Cd(1)–N(2)	160.51(6)
N(2)–Cd(1)–N(1)	72.26(12)	O(2)–Cd(1)–N(2)	102.21(6)
O(1)–Cd(1)–O(5)#1	93.64(10)	O(7)–Cd(1)–N(1)	136.54(7)
O(7)–Cd(1)–O(5)#1	86.50(11)	O(6)–Cd(1)–N(1)	94.08(6)
N(2)–Cd(1)–O(5)#1	140.91(10)	O(2)–Cd(1)–N(1)	89.98(6)
N(1)–Cd(1)–O(5)#1	106.31(11)	N(2)–Cd(1)–N(1)	70.70(7)
O(1)–Cd(1)–O(6)#1	98.02(10)	O(7)–Cd(1)–O(1)	82.14(6)
O(7)–Cd(1)–O(6)#1	141.09(11)	O(6)–Cd(1)–O(1)	109.73(6)
N(2)–Cd(1)–O(6)#1	85.72(11)	O(2)–Cd(1)–O(1)	54.48(5)
N(1)–Cd(1)–O(6)#1	93.94(11)	N(2)–Cd(1)–O(1)	89.76(6)
O(5)#1–Cd(1)–O(6)#1	55.19(10)	N(1)–Cd(1)–O(1)	135.39(6)

Symmetry codes: #1 = *x* + 1, *y*, *z*.

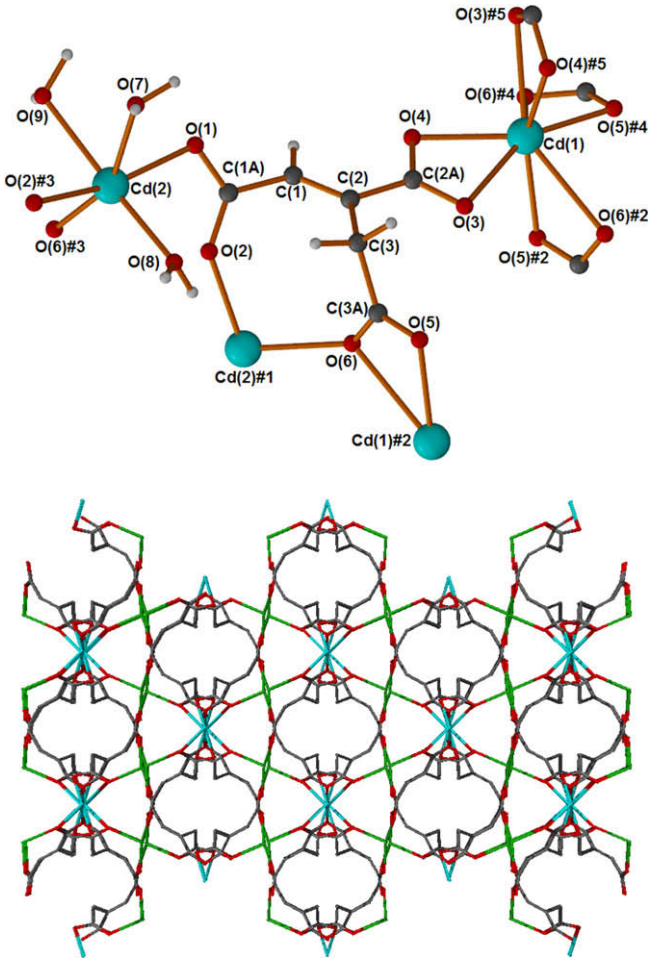


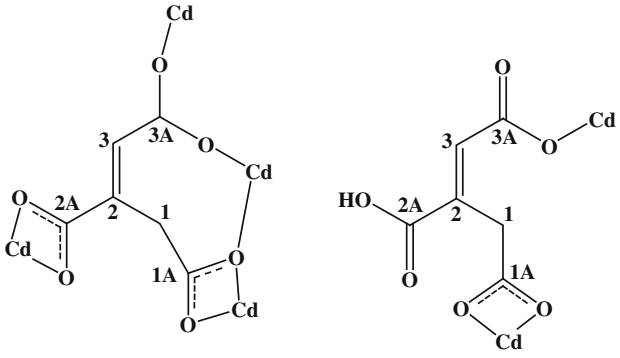
Fig. 1. (top) Asymmetric unit extended to show the coordination of the ligand and coordination sphere of two independent Cd(II) atoms (symmetry operations #1 = 1/2 − *x*, *y* − 1/2, 1/2 − *z*; #2 = −*x*, 1 − *y*, −*z*; #3 = 1/2 − *x*, *y* − 1/2, 1/2 − *z*; #4 = *x*, 1 − *y*, *z* − ½; #5 = −*x*, *y*, −*z* − 1/2) (bottom) A view of the 3D structure down the *c* axis. Cd(1) is represented by sky blue nodes while Cd(2), which acts as a linker between the two ligands, is green. Protons and water molecules have been omitted for clarity. (For interpretation of the references to colour in this figure legend, the reader is referred to the web version of this article.)

Cd(1) has a dodecahedral (*mmmm* Dod) coordination environment [32]. Each *trans*-aconitate bridges four cadmium centers through the six carboxylic oxygen atoms. Three different coordination modes of the ligand carboxylate moieties can be assigned in **1**: a bidentate in a *syn-anti* configuration (η^1:η^2:μ_2) for the C3A carboxylate group, a chelating (η^1:η^1:μ_1) for the carboxylate based on C2A and a chelating - bridging mode (η^1:η^2:μ_2) for the C1A carboxylate (Scheme 1). The water molecules form hydrogen bonds which amplify the construction of the 3D structure (Table 2).

The structure of compound **1** propagates in three directions through the bridging ligand and the metal center Cd(1) (Fig. 1). Topologically, Cd(1) has been replaced by node B and the geometric centroid of the tritopic carboxylate ligand has been substituted by node A. The Cd(2) metal center is not concerned to the *decorated* compound. In this way, a neutral 3D network is formed, formulated as A_2B. Node B is connected through four short pillars to four A nodes possessing a square tetrahedral geometry, whereas node A is bridged to two B and two A nodes through two short and two elongated pillars adopting a tetrahedral configuration. The *decorated* compound that is formed is a four-connected *non-homogeneous binodal* network, possessing a moganite (**mog**) topological structure (Fig. 2). The Schläfli symbol for a **mog** network is $(4.6^4.8)_2(4^2.6^2.8^2)$, while the elongated symbol for each node is $(4.4.6_2.6_2.8_2.8_2)$ and $(4.8_6.6.6.6.6)$ for nodes A and B, respectively.

To our knowledge, few examples of metal-organic frameworks having a **mog** topology have been reported [33–34]. Usually, a typical **mog** network possesses tetrahedral and tetragonal nodes, while there are a few exceptions in which both nodes adopt a tetrahedral configuration. To conclude, the *decorated* compound **1** is a distorted **mog** net with tetrahedral nodes and represent the first example of this topology that originates from this carboxylate ligand.

Both compounds **2** and **3** were characterized crystallographically and they were found to belong to the triclinic $P\bar{1}$ space group. Selected distances (Å) and angles (°) for both compounds are presented in Table 3. The compounds are similar; therefore, only interactions for compound **2** will be further discussed. The crystal structure of **2** consists of linear [Cd(HL)(N–N)] 1D chains (Fig. 3) (for **3**, see Fig. S1), running parallel to the *a*-axis and a lattice water molecule held with H-bonds. The coordination number of each Cd(II) center is six, forming an octahedral coordination polyhedron. Each metal is coordinated by two nitrogen atoms belonging to the chelated Lewis base, three oxygen atoms belonging to two different aconitate anions, and a water molecule [CdN_2O_4]. The equatorial positions are occupied by one nitrogen atom (N(1) for **2** and N(2) for **3**) and three oxygen atoms, two belonging to a chelate carboxylate and one to a terminal water molecule. The second nitrogen atom and one oxygen atom of a monodentate carboxylate



Scheme 1. Coordination mode of L^{3-} and HL^{2-} organic ligand found in **1** (left) and **2**, **3** (right).

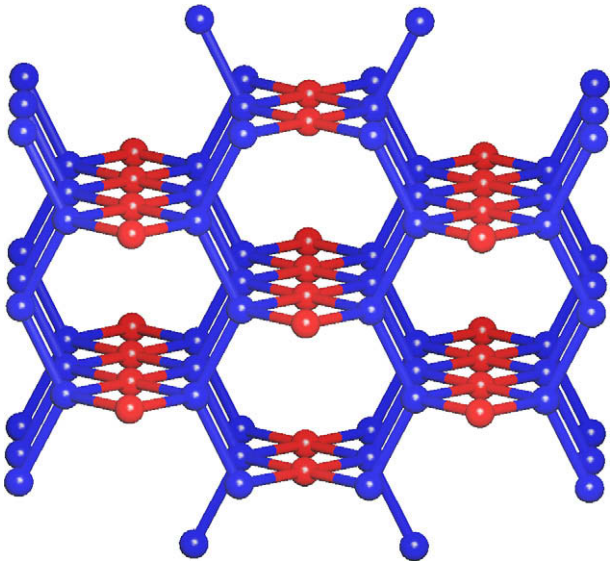


Fig. 2. Topological presentation of the four-connected non-homogeneous binodal network with **mog** topology of compound **1**. (node A; blue, node B; red). (For interpretation of the references to colour in this figure legend, the reader is referred to the web version of this article.)

are placed in the axial positions. The axial angle N–Cd–O displays a significant deviation from linearity (160.04(11)° for **2** and 160.51(6)° for **3**), and the equatorial angles vary from 55.19(10)° to 141.09(11)° for **2** and 54.48(5)° to 136.54(7)° for **3**.

The three carboxylate groups in the doubly deprotonated ligand behave differently (Scheme 1). The carboxylate group of C1A is chelated, carboxylate of C3A is monodentate, while the carboxylate group based on C2A remains protonated. In this way, the ligand bridges two Cd(II) ions leading to the formation of linear chains. To the best of our knowledge, this coordination mode has not been observed previously for this tricarboxylic acid [9–12]. Compared to our recent work, the present coordination mode of the HL^{2-} ligand is completely different from that observed in the one-dimensional 1D [Zn(HL)(N–N), where N–N = Lewis base] linear chains [12]. In both compounds **2** and **3** there are two different kinds of interactions that lead to the formation of 3D metal-supramolecular architectures; hydrogen bonding and stacking interactions. In **2**, the terminal water molecule forms two hydrogen bonds (Table 4) and acts as a bridge between two different 1D chains (Fig. 4). The first hydrogen bond involves hydrogen atom H(71) and a carboxylate oxygen from the chelated carboxylate group O(5) and the second involves the other hydrogen atom of lattice water H(72) and the non-coordinated carboxylate oxygen from the monodentate carboxylate group, O(2), of a different chain. Finally, the lattice water molecule acts as donor and acceptor forming three hydrogen bonds. The former involve hydrogen atoms H(81) and H(82) and oxygen atoms O(4) of the protonated carboxylate group and O(1) of the monodentate carboxylate, respectively, while the latter involves oxygen atom O(8) and forms the third hydrogen bond with the hydrogen atom H(3) of the protonated carboxylate group of a third chain, belonging to a third different chain resulting in the formation of thick layers (Fig. 3, middle–lower). The angle between the planes defined by the Cd(II) atoms in the double chains and the ribbons connected by the lattice water molecules is 80.01° (76.52° for **3**).

The 2D H-bonded undulating layers interact via stacking interactions through symmetry-related phenanthroline moieties that occupy the space between the previously described layers. There is a combination of strong and medium π–π stacking interactions between the aryl moieties resulting in the formation of a 3D

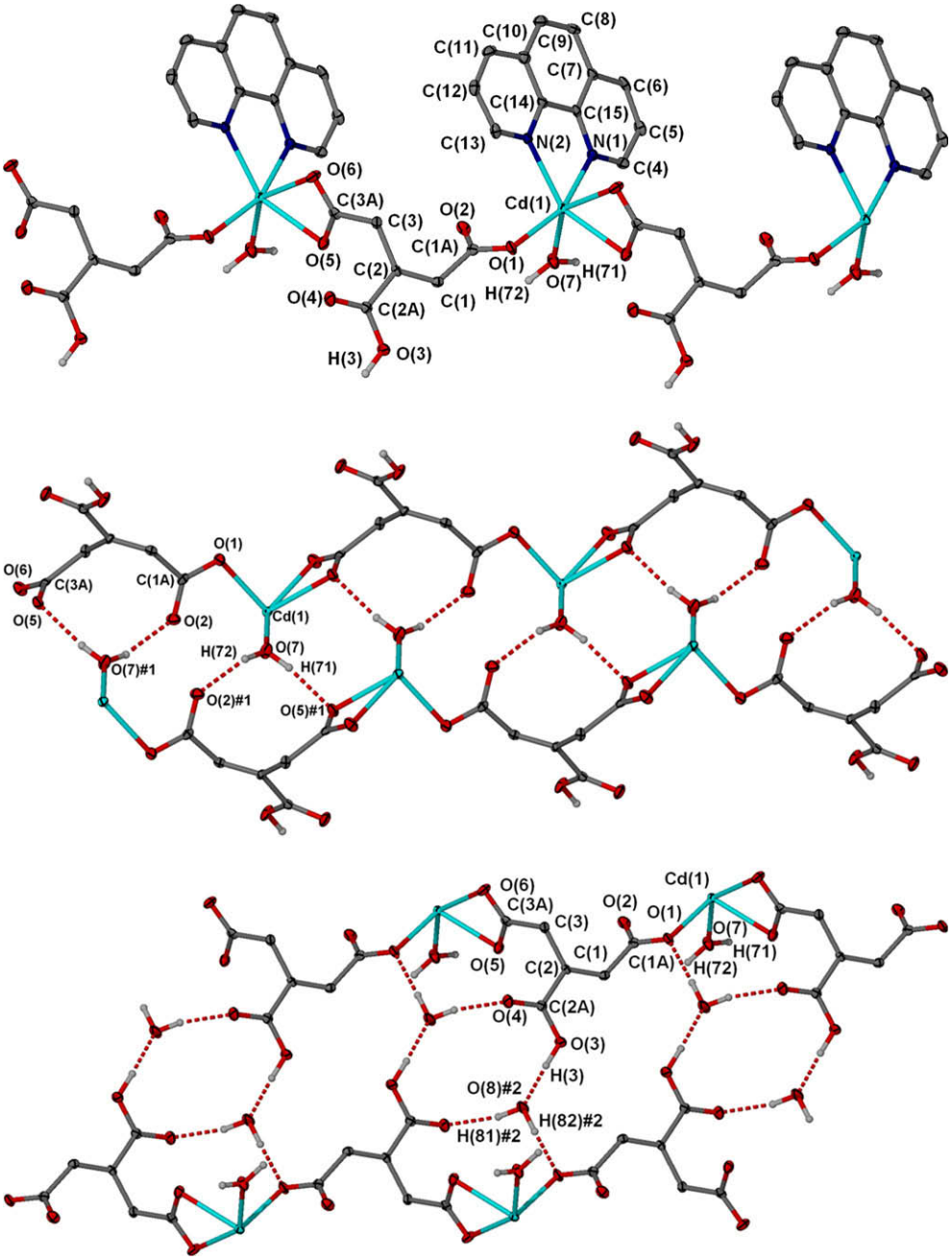


Fig. 3. Part of the 1D polymeric chains of **2** showing the coordination of the ligand (50% probability ellipsoids). Lattice water molecules and organic protons have been omitted for clarity (top). A projection approximately parallel to ac plane showing the interchain H-bonds. Phen molecules and organic protons have been omitted for clarity (middle). An illustration of the interconnection of the 1D chains via lattice water (bottom); symmetry operations #1 = $-x$, $-y$, $1-z$; #2 = x, $y-1$, z.

metal-supramolecular structure (Fig. 4). In **2**, the aromatic ligand utilizes all aromatic rings (a–c, Scheme 2, Table 4) for the stacking interaction. In a similar way, in **3** (Table 5) both aromatic rings participate in the stacking interactions (see Fig. S2) [35,36].

3.2. Solution study

3.2.1. Free ligand protonation constants

Overall protonation and ionization constants (pK_a) derived by the potentiometric measurements on the free ligand are collected in Table 6 while ^{13}C NMR data are presented in Table 7 [5].

Three ionization constants are expected for *trans*-aconitic acid (H_3L) due to the presence of three carboxylate groups (Table 6). The first two pK_α values 2.72 and 3.95 should be assigned to carboxylate groups attached in C=C bond in *trans* position (C2A and C3A), presenting almost the same pK_α difference as the corresponding values of fumaric acid [37], and the last one (5.61) is assigned to C1A. All observed pK_α values are in agreement with similar data already published [38,39].

3.2.2. Cd–ligand interaction

The interaction of Cd(II) and *trans*-aconitic acid was studied in aqueous solutions in 1:1 molar ratios. The titration curves were best fitted assuming the formation of four species over the pH range 2–8, namely CdH_4L_2, $Cd_3L_2H_2$, Cd_3L_2H and Cd_3L_2. The stability constants of the above Cd(II) complexes with the ligand *trans*-

Table 4
Hydrogen bonding and stacking interactions in **2**.

D–H···A	d(D–H)	d(H···A)	d(D···A)	<(DHA)
O(7)–H(71)···O(5)#1	0.83	1.89	2.707(4)	167.1
O(3)–H(3)···O(8)#2	0.94	1.64	2.578(4)	176.8
O(8)–H(81)···O(4)#3	0.90	1.87	2.755(4)	169.2
O(8)–H(82)···O(1)#4	0.94	1.79	2.728(4)	176.7

Centroids	Centroids distance (Å)	Least square planes distance (Å)	Offset (Å)
a···a#5	3.6747	3.307	1.602
a···b#5	3.6651	3.310	1.574
c···b#6	3.4770	3.353	0.920
b···b#6	3.9502	3.373	2.056

Symmetry transformations used to generate equivalent atoms: #1 = $-x, -y, -z+1$; #2 = $x, y-1, z$; #3 = $-x-1, -y, -z+2$; #4 = $-x, -y, -z+2$; #5 = $1-x, 1-y, 1-z$; #6 = $x, 1-y, 1-z$.

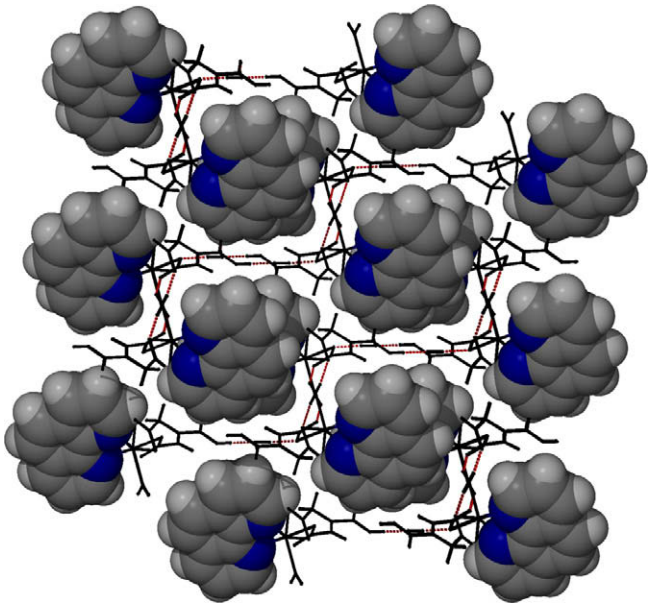
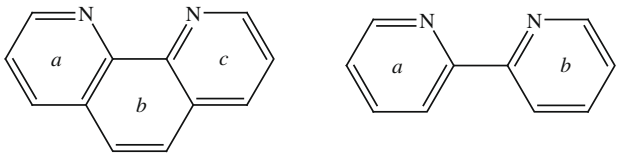


Fig. 4. A packing diagram of **2** viewed along *a*, emphasizing the stacking interactions that stabilize the 3D metalo supramolecular architecture.



Scheme 2. Numbering of aryl moieties in 1,10-phenanthroline for **2** and 2,2'-bipyridine for **3**.

aconitic acid have already been presented in Table 7 and the species distribution diagram of Cd(II) complexes, is presented in Fig. 5.

For the assignment of the species, ESI-MS and ^{113}Cd NMR spectra were also recorded over the pH range 2–5 and in a Cd(II): ligand molar ratio 1:1. It is evident from the speciation diagram that Cd(II)–ligand interaction begins above pH 2 and CdH_4L_2 species are formed. Complexes with stoichiometry 1:2 are not expected in the studied 1:1 system. Nevertheless, the ESI-MS spectra (Fig. 6) recorded in the positive ion mode provides a strong indication for the existence of bis complexes. The spectra recorded at pH 2.5 comprise two peak clusters (marked a and b in Fig. 6) presenting the typical isotopic distribution of Cd(II) ions. The first one can

Table 5
Hydrogen bonding and stacking interactions in **3**.

D–H···A	d(D–H)	d(H···A)	d(D···A)	<(DHA)
O(7)–H(71)...O(1)#1	1.00	1.80	2.765(2)	163.1
O(7)–H(72)...O(5)#2	1.02	1.77	2.673(2)	145.9
O(3)–H(3)...O(8)	0.96	1.60	2.546(2)	170.4
O(8)–H(81)...O(4)#3	1.00	1.80	2.751(2)	157.9
O(8)–H(82)...O(2)#3	1.00	1.76	2.705(2)	156.2

Centroids	Centroids distance (Å)	Least square planes distance (Å)	Offset (Å)
a···a#4	3.6360(16)	3.771	1.557
b···b#5	3.7016(16)	3.310	1.657

Symmetry transformations used to generate equivalent atoms: #1 = $-x+2, -y, -z+1$; #2 = $-x+1, -y, -z+1$; #3 = $-x+1, -y-1, -z$; #4 = $2-x, 1-y, 1-z$; #5 = $1-x, 1-y, 1-z$.

Table 6
Protonation constants (log β), dissociation macroconstants (pKa) of *trans*-aconitic acid and stability constants (log β) of Cd(II) complexes with *trans*-aconitic acid (T = 25 °C, I = 0.1 M KNO_3).

	log βa	pKa
H_3L	12.28(1)	2.72
H_2L	9.56(1)	3.95
HL	5.61(1)	5.61
CdH_4L_2	26.11(1)	
$Cd_3H_2L_2$	25.45(1)	
Cd_3HL_2	20.15(1)	
Cd_3L_2	15.01(1)	

Standard deviations of the last digit are given in parentheses.

Table 7
Chemical shifts ^{13}C (δ, ppm) of *trans*-aconitic acid in D_2O (C = 20 mM) based on literature data [5].

	C1A	C2A	C3A	C2	C3	C1
pH 1.5	174.978	169.589	168.799	139.533	130.789	33.483
pH 3.8	177.085	173.520	173.302	137.894	132.470	35.572
pH 4.5	177.620	174.540	174.540	137.582	132.592	36.342
pH 6.5	179.808	176.615	176.423	139.173	131.405	37.881

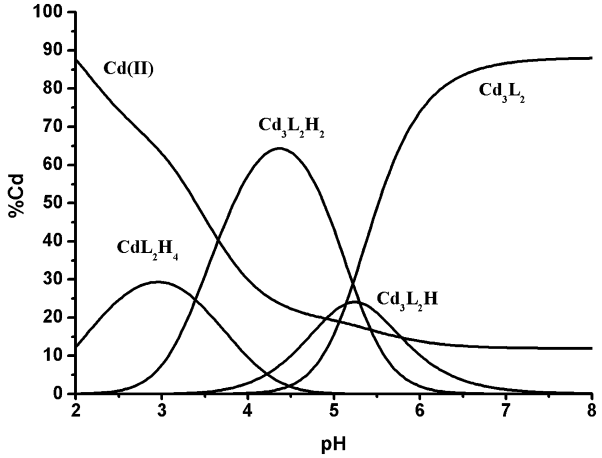


Fig. 5. Speciation curves for the complexes formed in the Cd(II)–*trans*-aconitic acid system at 1:1 metal ion to ligand molar ratio and c_{ligand} = 0.004 M.

be assigned to formula $[CdH_4L_2 + 2Na^+ + 2CH_3CN]$ (m/z = 295) while the second to formula $[CdH_4L_2 + 2Na^+ + 4CH_3CN + H_2O]$ (m/z = 324). The next three species detected were $Cd_3L_2H_2$, Cd_3L_2H and Cd_3L_2 presenting the same stoichiometry as the isolated and

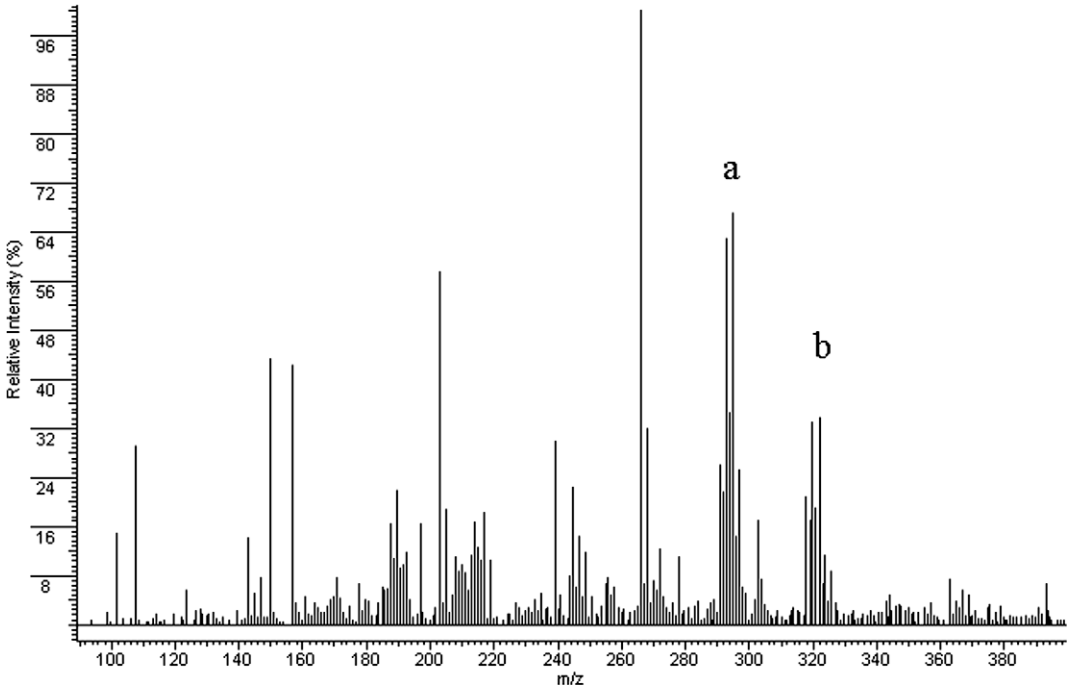


Fig. 6. ESI-MS spectrum recorded in the positive ion mode in the binary Cd(II)–*trans*-aconitic acid system at 1:1 metal ion to ligand molar ratio and c_{ligand} = 0.004 M.

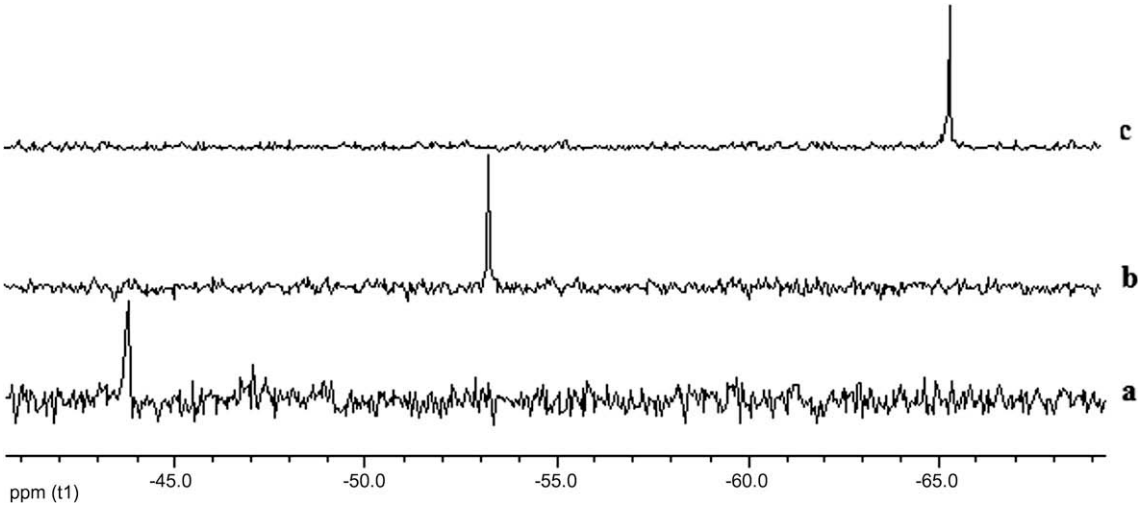


Fig. 7. ^{113}Cd NMR spectra were recorded at pH values 1.8(a), 3.2(b) and 5.8(c).

crystallized compound. Unfortunately, no information regarding the existence of these species can be extracted from ESI-MS spectra recorded at higher pH values in either positive or negative modes, possibly indicating decomposition in the gas phase under ESI-MS conditions. To substantiate the presence of Cd(II)–ligand interaction in solution at higher pH values, ^{113}Cd NMR spectra were recorded at pH values 1.8, 3.2 and 5.8 (Fig. 7a–c, respectively). At 298 K the spectral data clearly suggest metal ion–carboxylate interaction. It is generally known that 6–8 coordinate Cd complexes with oxo ligands give shifts in the range 150 to −100 ppm [40]. In the present case, chemical shifts of −43.77, −53.22 and −65.80 ppm, respectively were observed, corroborating our assumption and suggesting a possible increase of metal coordination number from 6 to 7 or 8 in higher pH values. It should also be mentioned here that a crystalline solid precipitated from the solution at pH 3.2 upon 4 h standing. This solid was identified as compound **1** on the basis of X-ray and Powder XRD measurements, suggesting the existence of species of the above stoichiometry in solution.

3.3. FT-IR spectroscopy

The multiple coordination modes of the ligand L^{3-} in **1** and HL^{2-} in **2** and **3** make it difficult to unambiguously assign the IR spectra; however, some bands can be explained. The IR spectrum of compound **1** displays a broad band centered at 3448 cm^{-1} in agreement with the presence of water molecules, and characteristic asymmetric and symmetric stretching vibrations of carboxylate groups at 1564 and 1400 cm^{-1}. The IR spectra display broad bands centered at 3448 and 3425 cm^{-1} for **2** and **3**, respectively, in agreement with the presence of H-bonded water molecules. The multiple coordination of the ligand HL^{2-} makes the distinct assignment

of the IR bands difficult; however, some bands can be explained. The bands at 1700 cm^{-1} for **2** and 1703 cm^{-1} for **3** can be attributed to the ν(C=O) of the free carboxyl at position 3A (Scheme 1), while the pairs of bands at 1567 and 1411, and 1576 and 1438 cm^{-1} are characteristic for the symmetric and asymmetric COO stretching vibrations for **2** and **3**, respectively [41].

3.4. TG-DTA studies

The TG-DTA spectra of **1** show that there is a loss in the range 116.5–230.0 °C which is possibly due to the loss of six terminal water molecules of two cadmium centers (calc. 13.71%; found 13.23%). The dehydrated product of **1** is stable up to 313 °C, whereupon a simple decomposition process begins which proceeds up to 492 °C, where the white final residue corresponds to CdO (calc. 48.79%; found 48.16%). When the 1D coordination polymer **3** is heated under nitrogen atmosphere, an endothermic dehydration starts at 36 °C which is completed at 187 °C. The observed weight loss of 7.60% corresponds well to the calculated values of 7.56% of two lattice water molecules. The dehydrated product of **3** is stable up to 205 °C and after that temperature a rather complicated decomposition process begins which involves at least three continuous steps as shown by the DTA curve. The decomposition proceeds up to 555 °C, where the white final residue corresponds to CdO (calc. 26.85%; found 25.75%). Similar TG-DTA curves were recorded also for compound **2**.

4. Conclusion

The complexing ability of the binary system *trans*-aconitic acid (H_3L) with regard to Cd(II) is presented. The crystal structures of the species $Cd_3L_2(H_2O)_6$ (**1**) and the ternary system of Cd(II)–(H_3L)–Lewis base [Lewis base = 1,10-phenanthroline (**2**) and 2,2′-bipyridine (**3**)] have been determined. Topological representation of compound **1** reveals a rare binodal four-connected 3D metal-organic framework possessing a **mog** topology, in which both four-connected nodes adopt distorted configurations. Compounds **2** and **3** represent 1D-infinite chains forming 3D metal-supramolecular architectures through H-bond and π–π^* stacking interactions. The coordination mode of HL^{2-} differs from those reported previously. The solution studies support the existence and the formation of compound **1** upon increasing the pH of the solution.

In the binary system, correlation between its behavior in the solid state and in solution with that of species arising from solution speciation studies can be accomplished. We believe that this study can contribute to the elucidation of the mechanism of the action of H_3L and comprise a fundamental research towards the exploration of the substitute action mechanism against other metal ions. The present findings provide new structural data, which could enhance the understanding of the exact mechanism by which Cd(II) toxicity arises. It is worth mentioning that small flexible biological organic ligands are a fruitful source for the construction of coordination polymers.

Acknowledgements

G.E.K. thanks the Stavrou Foundation for a PhD fellowship. Financial support from EU Marie Curie (the Research Training Site *Metals in Biological Systems*), the Swedish Research Council (VR) and EPEAEK "Bioinorganic Chemistry" (financed by EU and Greece) is gratefully acknowledged. Assistant Prof. Dr. Anastasios Troganis (Department of Biological Applications and Technology, University of Ioannina, Ioannina, Greece) is gratefully acknowledged for providing the ^{113}Cd NMR spectra and helpful discussions.

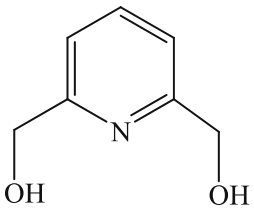
Appendix A. Supplementary data

CCDC 721133, 721134 and 721135 contains the supplementary crystallographic data for **1–3**. These data can be obtained free of charge via http://www.ccdc.cam.ac.uk/conts/retrieving.html, or from the Cambridge Crystallographic Data Centre, 12 Union Road, Cambridge CB2 1EZ, UK; fax: (+44) 1223-336-033; or e-mail: deposit@ccdc.cam.ac.uk.

Supplementary data associated with this article can be found, in the online version, at doi:10.1016/j.poly.2009.05.008.

References

[1] J.E. Fergusson, The Heavy Elements: Chemistry, Environmental Impact and Health Effects, Pergamon Press, Oxford, 1990.
[2] F.T. Bingham, F.J. Peryea, W.M. Jarrell, in: H. Siegel (Ed.), Metal Ions in Biology, vol. 20, Marcel Dekker, New York, 1986, p. 119.
[3] R.B. Martin, in: H. Siegel (Ed.), Metal Ions in Biology, vol. 20, Marcel Dekker, New York, 1986, p. 21.
[4] J.F. Thomson, S.L.M. Nance, K.J. Bush, P.A. Szczepanik, Arch. Biochem. Biophys. 117 (1966) 65.
[5] H. Cai, J. Strouse, D. Dumlao, M.E. Jung, S. Clarke, Biochemistry 40 (2001) 2210.
[6] J.M. Dargay, H.M. Berman, H.L. Carrell, J.P. Glusker, Acta Crystallogr., Sect. B 28 (1972) 1533.
[7] H.L. Carrell, Acta Crystallogr., Sect. B 29 (1973) 2082.
[8] D. Braga, O. Benedi, L. Maini, F. Grepioni, J. Chem. Soc., Dalton Trans. (1999) 2611.
[9] M.-S. Wang, G.-C. Guo, M.-L. Fu, L. Xu, L.-Z. Cai, J.-S. Huang, Dalton Trans. (2005) 2899.
[10] M.-S. Wang, G.-C. Guo, L.-Z. Cai, W.-T. Chen, B. Liu, A.-Q. Wu, J.-S. Huang, Dalton Trans. (2004) 2230.
[11] H.-M. Shen, J. Zhang, P.-X. Yin, Z.-J. Li, Z.-W. Cai, Y.-G. Yao, J. Mol. Struct. 826 (2007) 126.
[12] G.E. Kostakis, E. Nordlander, N. Hadjiliadis, M. Haukka, J.C. Plakatouras, Inorg. Chem. Commun. 9 (2006) 915.
[13] I. Vlahou, N. Kourkoumelis, A. Michaelidis, S. Skoulika, J.C. Plakatouras, Inorg. Chim. Acta 359 (2006) 3540.
[14] G.E. Kostakis, L. Casella, N. Hadjiliadis, E. Monzani, N. Kourkoumelis, J.C. Plakatouras, Chem. Commun. (2005) 3859.
[15] S. Mukherjee, Y. Lan, G.E. Kostakis, R. Clérac, C.E. Anson, A.K. Powell, Cryst. Growth Des. 9 (2009) 577.
[16] S. Mukherjee, Y. Lan, G. Novitchi, G.E. Kostakis, C.E. Anson, A.K. Powell, Polyhedron (2009), doi:10.1016/j.poly.2008.12.003.
[17] R. Abuhmaiera, Y. Lan, A.M. Ako, G.E. Kostakis, A. Mavrandonakis, W. Klopper, R. Clérac, C.E. Anson, A.K. Powell, CrystEngComm 11 (2009). doi:10.139/b820834d.
[18] C. Papatriantafyllopoulou, G.E. Kostakis, C.P. Raptopoulou, A. Terzis, S.P. Perlepes, J.C. Plakatouras, Inorg. Chim. Acta 362 (2009) 2361.
[19] K.C. Mondal, G.E. Kostakis, Y. Lan, C.E. Anson, A.K. Powell, Inorg. Chem., submitted for publication.
[20] G.E. Kostakis, K.C. Mondal, G. Abbas, Y. Lan, G. Novitchi, G. Buth, C.E. Anson, A.K. Powell, CrystEngComm, accepted for publication.
[21] G.E. Kostakis, G. Abbas, C.E. Anson, A.K. Powell, CrystEngComm 10 (2008) 1117.
[22] G.E. Kostakis, G. Abbas, C.E. Anson, A.K. Powell, CrystEngComm 11 (2009) 82.
[23] H. Irving, M.G. Miles, L.D. Pettit, Anal. Chim. Acta 38 (1967) 475.
[24] P. Gans, A. Sabatini, A. Vacca, Talanta 43 (1996) 1739.
[25] A.J.M. Duisenberg, L.M.J. Kroon-Batenburg, A.M.M. Schreurs, J. Appl. Crystallogr. 36 (2003) 220.
[26] A. Altomare, G. Cascarano, C. Giacovazzo, A. Guagliardi, J. Appl. Crystallogr. 26 (1993) 343.
[27] A. Altomare, M.C. Burla, M.C. Camalli, C. Giacovazzo, A. Guagliardi, A.G.G. Moliterni, G. Polidori, R. Spagna, J. Appl. Crystallogr. 32 (1999) 115.
[28] L.J. Farrugia, J. Appl. Crystallogr. 32 (1999) 837.
[29] G.M. Sheldrick, SADABS – Bruker Nonius Scaling and Absorption Correction, v 2.10, Bruker AXS Inc., Madison, Wisconsin, USA, 2003.
[30] G.M. Sheldrick, SHELXL-97, Program for Crystal Structure Refinement, University of Göttingen, Göttingen, Germany, 1997.
[31] This Article Consists Part of G.E.K. Ph.D. Thesis, Ioannina, Greece, June, 2006.
[32] M.G. B Drew, Coord. Chem. Rev. 24 (1977) 179. Parameters for geometry: *dihedral angles* 19.86°, 26.56°, 40.92°, 40.92°, φ angle 14.12°, bide chelate parameters for Cd(1) z_1 = 0.88 and z_2 = 0.92, for ideal dodecahedron z = 0.80.
[33] O. Delgado-Friedrichs, M. O'Keefe, O. M Yaghi, Solid State Sci. 5 (2003) 73.
[34] <http://rcsr.anu.edu.au/nets>.
[35] C. Janiak, J. Chem. Soc., Dalton Trans. (2000) 3885.
[36] V. Russell, M. Scudder, I. Dance, J. Chem. Soc., Dalton Trans. (2001) 789.
[37] J. Cappe, D. Cook, D. Williams, J. Chem. Soc., Dalton Trans. (1974) 1849.
[38] N. Skorik, A. Kochmaneuk, O. Voronkova, Zh. Neorg. Khim. 31 (1986) 1137.
[39] T. Krasovskaya, A. Sorokin, S. Pirkes, Zh. Neorg. Khim. 26 (1981) 910.
[40] M.F. Summers, Coord. Chem. Rev. 86 (1988) 43.
[41] H. Carlsson, M. Haukka, E. Nordlander, Inorg. Chem. 43 (2004) 5681.



pdmH$_2$

Scheme 1. Structural formula and abbreviation of pyridine-2,6-dimethanol.

with suitable chelates (generally denoted as "L") [14]. Thus, we and others have been exploring various such binary (L/RCO_2^- or L/N_3^-) and ternary ($L/RCO_2^-/N_3^-$) reaction schemes as potentially new routes to high-nuclearity molecular species with unprecedented structural motifs.

In particular, some of our current efforts are focused on copper(II) chemistry and, for example, we have recently reported Cu^{II}_6, and 1D $(Cu^{II}_4)_n$ and 2D $(Cu^{II}_2)_n$ cluster and coordination polymers, respectively, by using the di-2-pyridyl ketone $[(py)_2CO]/PhCO_2^-/N_3^-$ 'ligand blend' [15]. Across this line, the initial employment of the pyridyl alkoxide ligand pyridine-2,6-dimethanol ($pdmH_2$, Scheme 1) in $Cu^{II}/MeCO_2^-$ chemistry has provided access to a compound consisting of cocrystallized Cu^{II}_3 and Cu^{II}_4 clusters, the individual Cu^{II}_4 component of the latter "mixed"-species through a designed synthesis, and a unique 1D $(Cu^{II}_5)_n$ coordination polymer [16]. Despite its rather extensive use in *trivalent* 3d-metal cluster chemistry [8a,b,17], there has been only very limited use of $pdmH_2$ in Cu^{II} chemistry (and generally in the *divalent* 3d-metal chemistry), and only one dinuclear [18] and few mononuclear [18] complexes were further reported.

As an extension of the work with $pdmH_2$, we have now asked what kind of products might result from the use of this ligand in Cu^{II} *non*-carboxylate chemistry. Since the RCO_2^- ions are structure-determining components in the $[Cu_3]\cdot[Cu_4]$, Cu_4 and $(Cu^{II}_5)_n$ complexes [16], we anticipated that the absence of RCO_2^- from the reactions would give distinctly different products, and we have therefore explored this possibility. In the present work, we have explored the reactions between $pdmH_2$ and a Cu^{II} non-carboxylate starting material, namely copper(II) nitrate, under basic conditions. This has successfully led to the known [18] mononuclear Cu^{II} compound with a Jahn–Teller distorted octahedral geometry and a new Cu^{II}_4 cluster possessing a distorted tetrahedral metal arrangement; the latter was prepared by using both the "metal complexes as ligands" strategy [19] and "one-pot" procedures. The synthesis, structure and magnetochemical characterization of the tetranuclear compound are described in this paper.

2. Experimental

2.1. General and physical measurements

All manipulations were performed under aerobic conditions using materials (reagent grade) and solvents as received.

Microanalyses (C, H, N) were performed by the University of Ioannina (Greece) Microanalytical Laboratory using an EA 1108 Carlo Erba analyser. IR spectra (4000–450 cm^{-1}) were recorded on Perkin–Elmer 16 PC and Nicolet 520 FTIR spectrometers with samples prepared as KBr pellets, and as Nujol and hexachlorobutadiene mulls between CsI discs. Variable-temperature magnetic studies for complex **2** were performed using a Quantum Design SQUID magnetometer at the Magnetochemistry Service of the University of Barcelona. Diamagnetic corrections were applied to the observed paramagnetic susceptibilities using Pascal's constants.

2.2. Compound preparation

2.2.1. $[Cu(pdmH_2)_2](NO_3)_2$ (**1**)

Solid $pdmH_2$ (0.28 g, 2.00 mmol) was added to a pale blue solution of $Cu(NO_3)_2\cdot 3H_2O$ (0.48 g, 2.00 mmol) in MeCN (30 mL). The solid soon dissolved to give a blue solution. The solution was stirred for 30 min, filtered and the filtrate was layered with Et_2O (60 mL). After 6 days, X-ray quality, blue prismatic crystals of **1** were collected by filtration, washed with MeCN (2×5 mL) and Et_2O (2×5 mL), and dried in air. Yield: 80% (based on the ligand). *Anal.* Calc. for $C_{14}H_{18}CuN_4O_{10}$: C, 36.10; H, 3.89; N, 12.03. Found: C, 36.21; H, 3.94; N, 11.95%. Selected IR data (KBr pellet, cm^{-1}): 3220mb, 2820m, 1612s, 1580m, 1476m, 1380vs, 1292s, 1232m, 1164m, 1102w, 1024vs, 828m, 798s, 660m, 622m.

2.2.2. $[Cu_4(NO_3)_2(pdmH)_4(H_2O)(MeOH)](NO_3)_2\cdot H_2O\cdot MeOH$ (**2**$\cdot H_2O\cdot MeOH$)

Method A. To a pale blue solution of **1** (0.47 g, 1.00 mmol) in MeOH (30 mL) was added solid NaOMe (0.05 g, 1.00 mmol). The solid soon dissolved to give a pale green solution. The solution was stirred for 40 min, during which time no further colour change occurred. The resulting solution was filtered and the filtrate was layered with Et_2O/*n*-hexane (1:1 v/v, 60 mL). After 10 days, pale green prismatic crystals of **2**$\cdot H_2O\cdot$MeOH were collected by filtration, washed with cold MeOH (2×2 mL) and Et_2O (2×5 mL), and dried in air. Yield: 40%. The air-dried sample analyzed as **2**$\cdot H_2O$. *Anal.* Calc. for $C_{29}H_{40}Cu_4N_8O_{23}$: C, 31.02; H, 3.59; N, 9.98. Found: C, 31.13; H, 3.62; N, 9.85%. Selected IR data (KBr pellet, cm^{-1}): 3428mb, 3074sb, 2836m, 2360m, 1610s, 1586m, 1452vs, 1383vsb, 1317s, 1224m, 1162m, 1040vs, 826m, 790m, 696m, 634w, 574m, 432w.

Method B. To a stirred, colourless solution of $pdmH_2$ (0.28 g, 2.00 mmol) and NaOMe (0.11 g, 2.00 mmol) in MeOH (30 mL) was added solid $Cu(NO_3)_2\cdot 3H_2O$ (0.48 g, 2.00 mmol). The resulting pale green solution was stirred for 40 min, filtered and the filtrate was layered with Et_2O/*n*-hexane (1:1 v/v, 60 mL). After 7 days, pale green prismatic crystals of **2**$\cdot H_2O\cdot$MeOH were collected by filtration, washed with cold MeOH (2×2 mL) and Et_2O (2×5 mL), and dried in air. Yield: 70%. The IR spectrum of the product was identical with that of the authentic material prepared by Method A. The purity of the sample prepared from this method was also confirmed by microanalytical data.

2.3. Single-crystal X-ray crystallography

The crystallographic data and structure refinement details for the two complexes are summarized in Table 1. It should be mentioned at this point that the crystal structure of **1** was reported five years ago [18]. Since the X-ray analysis by our group has led to a better quality structure due to the better quality of crystals [e.g., the reported R_1 ($I > 2\sigma(I)$) is 0.0564 [18], while our solution leads to 0.0286], we have included data for this mononuclear compound in Tables 1 and 2, and we briefly discuss its structure in the text of the present paper (vide infra). A selected crystal of **1** ($0.50 \times 0.40 \times 0.35$ mm) was mounted in air, whereas a selected crystal of **2**$\cdot H_2O\cdot$MeOH ($0.30 \times 0.20 \times 0.15$ mm) was mounted in capillary filled with drops of mother liquor. Diffraction measurements for **1** and **2**$\cdot H_2O\cdot$MeOH were made on a Crystal Logic Dual Goniometer diffractometer using graphite-monochromated Mo radiation. Unit cell dimensions were determined and refined by using the angular settings of 25 automatically centered reflections in the range $11° < 2\theta < 23°$. Intensity data were recorded using a θ–2θ scan to a maximum 2θ value of 50°. Three standard reflections monitored every 97 reflections showed less than 3% variation and no decay. Lorentz, polarization corrections were applied using Crystal Logic software. Both structures were solved by direct

Table 1
Crystallographic data for complexes **1** and **2** · H_2O · MeOH.

Parameter	**1**	**2** · H_2O · MeOH
Formula	$C_{14}H_{18}CuN_4O_{10}$	$C_{30}H_{44}Cu_4N_8O_{24}$
Formula weight	465.86	1154.89
Crystal system	monoclinic	monoclinic
Space group	$C2/c$	$P2_1/n$
a (Å)	13.931(5)	10.132(3)
b (Å)	9.044(3)	16.605(5)
c (Å)	15.031(5)	25.813(7)
α (°)	90	90
β (°)	100.72(1)	97.33(1)
γ (°)	90	90
V (Å^3)	1860.7(11)	4307(2)
Z	4	4
ρ_{calc} (g cm^{-3})	1.663	1.781
Radiation, λ (Å), Mo Kα	0.71073	0.71073
T (K)	298	298
μ (mm^{-1})	1.237	2.046
Data collected/unique (R_{int})	1702/1635 (0.0240)	8030/7570 (0.0552)
Data with $I > 2\sigma(I)$	1542	6785
R_1 ($I > 2\sigma(I)$)[a]	0.0286	0.0431
wR_2 ($I > 2\sigma(I)$)[b]	0.0749	0.1145

[a] $R_1 = \Sigma(|F_o| - |F_c|)/\Sigma(|F_o|)$.
[b] $wR_2 = \{\sum[w(F_o^2 - F_c^2)^2]/\sum[w(F_o^2)^2]\}^{1/2}$.

Table 2
Selected bond lengths (Å) and angles (°) for complex **1**.[a]

Parameter		Parameter	
Cu(1)–O(1)	2.163(2)	Cu(1)–N(1)	1.936(2)
Cu(1)–O(2)	2.192(2)		
O(1)–Cu(1)–O(2)	156.8(6)	O(1)–Cu(1)–N(1′)	97.5(7)
N(1)–Cu(1)–N(1′)	174.3(1)	O(2)–Cu(1)–O(2′)	91.9(1)
O(1)–Cu(1)–O(1′)	104.6(1)	O(2)–Cu(1)–N(1)	79.2(7)
O(1)–Cu(1)–O(2′)	86.1(8)	O(2)–Cu(1)–N(1′)	104.9(7)
O(1)–Cu(1)–N(1)	79.0(7)		

[a]Primed atoms are related to the unprimed ones by the symmetry operation $-x$, y, $-z + 1/2$.

methods using SHELXS-97 [20a] and refined on F^2 by full-matrix least-squares techniques with SHELXL-97 [20b]. All H atoms were located by Fourier difference maps and refined isotropically. All non-H atoms were refined anisotropically.

3. Results and discussion

3.1. Brief synthetic comments and IR spectra

Many synthetic procedures [5,10,14a] to polynuclear 3d-metal clusters rely on the reactions of carboxylate starting materials such as $M(O_2CR)_2$ (R = various) with a potentially chelating/bridging ligand. This route was also known from our previous work to yield magnetically and structurally interesting Cu^{II} complexes upon reaction with $pdmH_2$ [16]. In the present study we have investigated the reactions with a simple Cu^{II} source, i.e. $Cu(NO_3)_2{\cdot}3H_2O$, *in the absence of carboxylate groups*.

Various reactions have been systematically explored with differing reagent ratios, reaction solvents, and other conditions. The reaction of $Cu(NO_3)_2{\cdot}3H_2O$ with $pdmH_2$ in a 1:1 molar ratio in MeCN gave a blue solution and the subsequent isolation of well-formed blue crystals of the known complex [18] $[Cu(pdmH_2)_2](NO_3)_2$ (**1**) in excellent yield (~80%). The formation of **1** is summarized in Eq. (1). The "wrong" reaction ratio employed for the preparation of the complex, compared to the stoichiometric ratio (1:2) required by Eq. (1), obviously did not prove detrimental to the formation of the product. The "correct" stoichiometric ratio, i.e. Cu^{II}:$pdmH_2$ = 1:2, was also employed and led to the pure compound in an excellent yield (>80%). Complex **1** was isolated from Weber's group [18] in EtOH/H_2O. Since (i) we have prepared this complex in MeCN and (ii) we have used it as starting material, we give its detailed preparation in Section 2 (Experimental) of this paper.

$$Cu(NO_3)_2 \cdot 3H_2O + 2pdmH_2 \xrightarrow{MeCN} \underset{\mathbf{1}}{Cu(pdmH_2)_2](NO_3)_2} + 3H_2O \quad (1)$$

In an attempt to obtain higher nuclearity Cu^{II} products, several reactions were performed with higher Cu^{II}:$pdmH_2$ ratios, up to 4:1. However, complex **1** was still the only isolable product, in comparable (1.5:1 ratio) or lower (3–4:1 ratio) yields. Complex **1** was also obtained when the reaction was performed in MeOH, EtOH [18] or $MeNO_2$, but in much lower yields (~20–35%), whereas no significant reaction was observed when the solvent was CH_2Cl_2 or $CHCl_3$.

Since we could not easily divert the Cu^{II}/$pdmH_2$ reaction system to higher nuclearity products, we instead decided to investigate reactions of pre-isolated **1**, i.e., we suspected that this mononuclear Cu^{II} compound could act as "ligand" (the so-named "metal complexes as ligands strategy" [19,21]). Its insolubility in many common solvents limited our choices, and we thus employed MeOH in which **1** is very soluble. Given the neutral form of $pdmH_2$ in **1**, we targeted its deprotonation by reaction of **1** with 1–3 equiv. of base, either NEt_3 or NaOMe. Such reactions with NEt_3 gave insoluble amorphous powders that perhaps were polymeric; these products were not further characterized. However, when NaOMe was reacted with one equivalent of **1** in MeOH (Method A of Section 2) a pale green solution was obtained which led to subsequent isolation of well-formed pale green crystals of $[Cu_4(NO_3)_2(pdmH)_4(H_2O)(MeOH)](NO_3)_2 \cdot H_2O \cdot MeOH$ (**2** · H_2O · MeOH) in good yield (~40%) upon layering of the reaction solution with Et_2O. Its formation is summarized in Eq. (2).

$$\begin{aligned} 4\underset{\mathbf{1}}{[Cu(pdmH_2)_2](NO_3)_2} + 4NaOMe + H_2O &\xrightarrow{MeOH} \\ &\times \underset{\mathbf{2}}{[Cu_4(NO_3)_2(pdmH)_4(H_2O)(MeOH)](NO_3)_2} \\ &+ 4NaNO_3 + 4pdmH_2 + 3MeOH \end{aligned} \quad (2)$$

Once the identity of **2** had been established, we also sought and devised a convenient preparation of **2** in MeOH involving the *in situ* deprotonation of $pdmH_2$ (Method B of Section 2). This was the reaction between $Cu(NO_3)_2 \cdot 3H_2O$, $pdmH_2$ and NaOMe in a 1:1:1 ratio in MeOH, which gave **2** in high-yield (~70%) upon layering of the reaction solution with precipitation solvents; the reaction is summarized in Eq. (3).

$$\begin{aligned} 4Cu(NO_3)_2 \cdot 3H_2O + 4pdmH_2 + 4NaOMe &\xrightarrow{MeOH} \\ &\times \underset{\mathbf{2}}{[Cu_4(NO_3)_2(pdmH)_4(H_2O)(MeOH)](NO_3)_2} + 4NaNO_3 \\ &+ 3MeOH + 11H_2O \end{aligned} \quad (3)$$

Note that prolonged solvent evaporation should be avoided because the crystals of the product are contaminated with $NaNO_3$, requiring copious washing with MeOH to obtain an analytically pure sample. An increase in the NaOMe:$pdmH_2$ ratio up to 3:1 gave comparable (or slightly decreased) yields of complex **2** rather than a higher nuclearity product resulting from complete deprotonation of $pdmH_2$ groups. Further increases in the amount of NaOMe led to insoluble amorphous precipitates that may be polymers formed from this further deprotonation.

The IR spectrum of a vacuum-dried sample of complex **1**, arising from a KBr pellet, exhibits a medium intensity band at 3220 cm^{-1}, assignable to $\nu(OH)_{pdmH_2}$ [22]. The broadness and relatively low frequency of this band are both indicative of strong hydrogen-bonding. Several bands appear in the 1610–1383 cm^{-1} range in

the spectra of both **1** and **2**. These are assigned to contributions from the stretching vibrations of the aromatic ring, which overlap with stretches of the nitrate bands; they, thus, do not represent pure vibrations and render exact assignments difficult. The presence of ionic NO_3^- in **1** (established by crystallography) follows from the spectrum of this compound through the appearance of the $\nu_3(E')[\nu_d(NO)]$ mode of the D_{3h} ionic nitrate at $\sim$1380 cm^{-1} [23]. The nitrate vibrations in the mull and KBr spectra of **2** are indicative of the simultaneous presence of coordinated and ionic nitrates (also established by crystallography). The bands at $\sim$1452 and $\sim$1317 cm^{-1} may assigned to the $\nu_5(B_2)$ and $\nu_1(A_1)$ stretching modes (under C_{2v} symmetry), respectively, of the nitrato ligands [23]; their separation is small ($\sim$135 cm^{-1}) in accordance with the monodentate character of two nitrate groups [23]. It should be mentioned at this point that the highest-frequency NO stretching mode belongs to the A_1 species in complexes containing bidentate and to the B_2 species in complexes containing monodentate nitrato ligands [23]. As expected, the strong and broad band at $\sim$1383 cm^{-1} is present in both the KBr and mull spectra of **2**; this band is assigned (as in **1**) to the $\nu_3(E')$ mode of the ionic nitrate [23].

3.2. Description of structures

The molecular structures of the cations of complexes **1** and **2** are depicted in Figs. 1 and 2, respectively. Selected interatomic distances and angles are listed in Tables 2 and 3.

Complex **1** crystallizes in the monoclinic space group *C*2/*c*. Its asymmetric unit contains half of the mononuclear $[Cu(pdmH_2)_2]^{2+}$ cation in a general position (Fig. 1) and one NO_3^- anion. The Cu^{II} center is coordinated by two *N*,*O*,*O*′-tridentate chelating (η^3) $pdmH_2$ ligands. The $pdmH_2$ donor atoms are the nitrogen atom of the pyridyl group and the two oxygen atoms of the neutral alcohol arms. Thus, the Cu^{II} atom is six-coordinate with a compressed, *trans*-octahedral N_2O_4 environment [24]. The pyridyl nitrogen atoms can be viewed as strongly coordinating to the metal [Cu(1)–N(1) = 1.936(2) Å)] in the axial direction (N(1)–Cu(1)–N(1′) = 174.3(1)°), while the four alcohol-type oxygen atoms of the equatorial plane form weaker bonds to Cu^{II} [Cu(1)–O(1) = 2.163(2)/Cu(1)–O(2) = 2.192(2) Å].

The pyridyl rings of the two $pdmH_2$ ligands are planar and almost perpendicular to each other, forming an angle of 71.4° [N(1)C(2)C(3)C(4)C(5)C(6)/N(1′)C(2′)C(3′)C(4′)C(5′)C(6′)]. The two five-membered chelating rings, Cu(1)–N(1)–C(6)–C(7)–O(2) and Cu(1)–N(1)–C(2)–C(1)–O(1), share the common Cu(1)–N(1) edge. The dihedral angle formed between the mean planes Cu(1)–C(6)–C(7)–O(2) and Cu(1)–C(2)–C(1)–O(1) is 7.9°. There are four symmetry-equivalent, interionic OH···O hydrogen bonds involving the protonated $pdmH_2$ O atoms as donors and NO_3^- counterion O atoms as the acceptors. Their dimensions are: O(1)···O(4) 2.639(4) Å, HO(1)···O(4) 1.948(4) Å, O(1)–HO(1)···O(4) 156.3(1)° and O(2)···O(3) 2.739(4) Å, HO(2)···O(3) 2.063(4) Å, O(2)–HO(2)···O(3) 158.5(1)°. These H bonds serve to link neighbouring Cu^{II} monomers into one-dimensional, linear chains along the *b*-axis (Fig. S1) and their existence rationalizes the high thermodynamic stability of **1**.

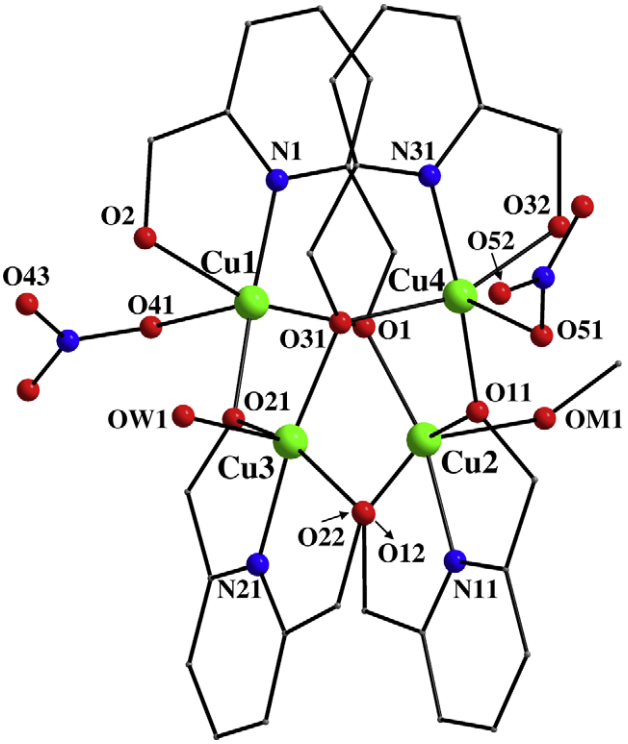


Fig. 2. Partially labelled plot of the cation of complex **2**. H atoms have been omitted for clarity. Colour scheme: Cu^{II}, green; O, red; N, blue; C, gray. (For interpretation of the references to colour in this figure legend, the reader is referred to the web version of this article.)

Complex **2** · H_2O · MeOH crystallizes in the monoclinic space group $P2_1/n$. Its structure consists of $[Cu_4(NO_3)_2(pdmH)_4(H_2O)(MeOH)]^{2+}$ cations (Fig. 2), NO_3^- anions, and solvate H_2O and MeOH molecules; the latter two will not be further discussed.

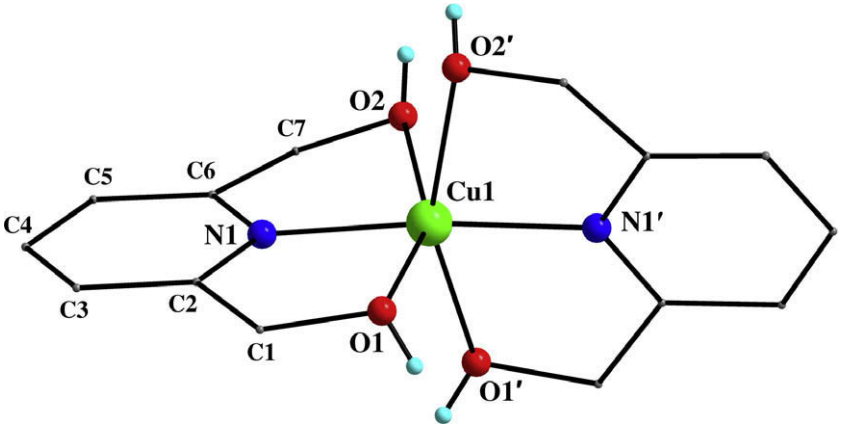


Fig. 1. Partially labelled PovRay representation of the cation of **1**, with some H atoms omitted for clarity. Colour scheme: Cu^{II}, green; O, red; N, blue; C, gray; H, sky blue. (For interpretation of the references to colour in this figure legend, the reader is referred to the web version of this article.)

Table 3
Selected interatomic distances (Å) and angles (°) for complex **2** · H_2O · MeOH.

Parameter		Parameter	
Cu(1)···Cu(2)	3.339(8)	Cu(2)···Cu(3)	3.762(1)
Cu(1)···Cu(3)	3.223(1)	Cu(2)···Cu(4)	3.304(8)
Cu(1)···Cu(4)	3.505(3)	Cu(3)···Cu(4)	3.373(3)
Cu(1)–O(1)	1.950(3)	Cu(3)···O(11)	3.158(6)
Cu(1)–O(2)	2.090(3)	Cu(3)–O(21)	1.937(3)
Cu(1)–O(21)	1.874(3)	Cu(3)–O(22)	2.036(3)
Cu(1)···O(31)	2.812(1)	Cu(3)–O(31)	1.904(3)
Cu(1)–O(41)	2.353(3)	Cu(3)–OW(1)	2.313(4)
Cu(1)–N(1)	1.902(3)	Cu(3)–N(21)	1.923(3)
Cu(2)–O(1)	1.899(3)	Cu(4)···O(1)	3.047(7)
Cu(2)–O(11)	1.942(3)	Cu(4)–O(11)	1.879(3)
Cu(2)–O(12)	2.034(3)	Cu(4)–O(31)	1.965(3)
Cu(2)···O(21)	3.191(4)	Cu(4)–O(32)	2.021(3)
Cu(2)–OM(1)	2.247(4)	Cu(4)–O(51)	2.396(4)
Cu(2)–N(11)	1.923(3)	Cu(4)–N(31)	1.903(3)
Cu(1)–O(1)–Cu(2)	120.3(1)	Cu(2)–O(1)···Cu(4)	80.2(1)
Cu(1)–O(1)···Cu(4)	86.1(1)	Cu(2)–O(11)···Cu(3)	91.9(1)
Cu(1)–O(21)···Cu(2)	77.7(1)	Cu(2)–O(11)–Cu(4)	119.7(1)
Cu(1)–O(21)–Cu(3)	115.5(1)	Cu(2)···O(21)–Cu(3)	91.0(1)
Cu(1)···O(31)–Cu(3)	83.9(1)	Cu(3)···O(11)–Cu(4)	79.7(1)
Cu(1)···O(31)–Cu(4)	92.6(1)	Cu(3)–O(31)–Cu(4)	121.3(1)
O(1)–Cu(1)–O(2)	163.0(1)	O(21)–Cu(3)–O(22)	156.5(1)
O(21)–Cu(1)–N(1)	171.7(1)	O(31)–Cu(3)–N(21)	166.1(1)
O(1)–Cu(2)–N(11)	163.0(1)	O(11)–Cu(4)–N(31)	171.0(1)
O(11)–Cu(2)–O(12)	159.0(1)	O(31)–Cu(4)–O(32)	159.5(1)

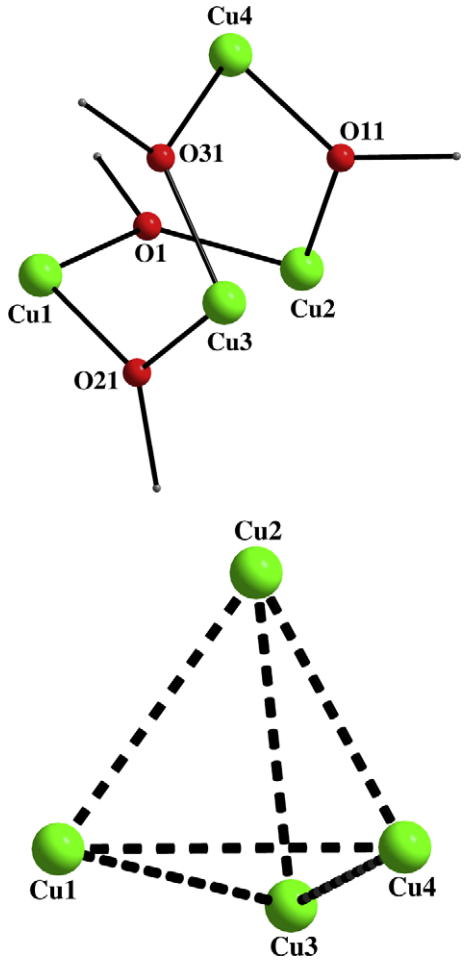


Fig. 3. (top) PovRay representation of the $[Cu_4(\mu_2\text{-}OR)_4]^{4+}$ core of complex **2**. (bottom) The Cu_4 skeleton of **2**, emphasizing its slightly distorted tetrahedral metal topology. Colour scheme: Cu^{II}, green; O, red; C, gray. (For interpretation of the references to colour in this figure legend, the reader is referred to the web version of this article.)

The core of the cation of **2** (Fig. 3, top) consists of four Cu^{II} ions arranged at the vertices of a *slightly* distorted tetrahedron. The Cu_4 topology of **2** is shown in the bottom of Fig. 3. It can be alternatively described as a *very* distorted, non-planar "ring", at the "corners" of which are lying the four Cu^{II} centers (Fig. S2); the deviation of the metal ions from their best least-squares plane ranges from 0.92 to 1.15 Å.

The Cu^{II} ions are held together by four monoatomic RO^- bridges [O(1), O(11), O(21), O(31)] of four pdmH$^-$ groups to give a $[Cu_4(\mu_2\text{-}OR)_4]^{4+}$ core (Fig. 3, top). Each O atom of the μ_2-OR bridges spans an edge of the tetrahedron. The Cu^{II}_4 tetrahedron is only slightly distorted; the bridged Cu···Cu distances are within the 3.223(1)–3.373(3) Å range, while the unbridged Cu···Cu separations are 3.505(3) and 3.762(1) Å for Cu(1)···Cu(4) and Cu(2)···Cu(3), respectively. The Cu···Cu···Cu and Cu–OR–Cu angles are all acute and obtuse, respectively, varying from 53.6(1) to 68.6(1)° and 115.5(1) to 121.3(1)°. The alkoxide bridges involving O(1), O(11), O(21) and O(31) are slightly asymmetrical, with Cu–O distances ranging from 1.874(3) to 1.965(3) Å.

All Cu^{II} ions are five-coordinate with almost ideal [Cu(2) and Cu(3); τ = 0.07 and 0.02, respectively] or slightly distorted [Cu(1)

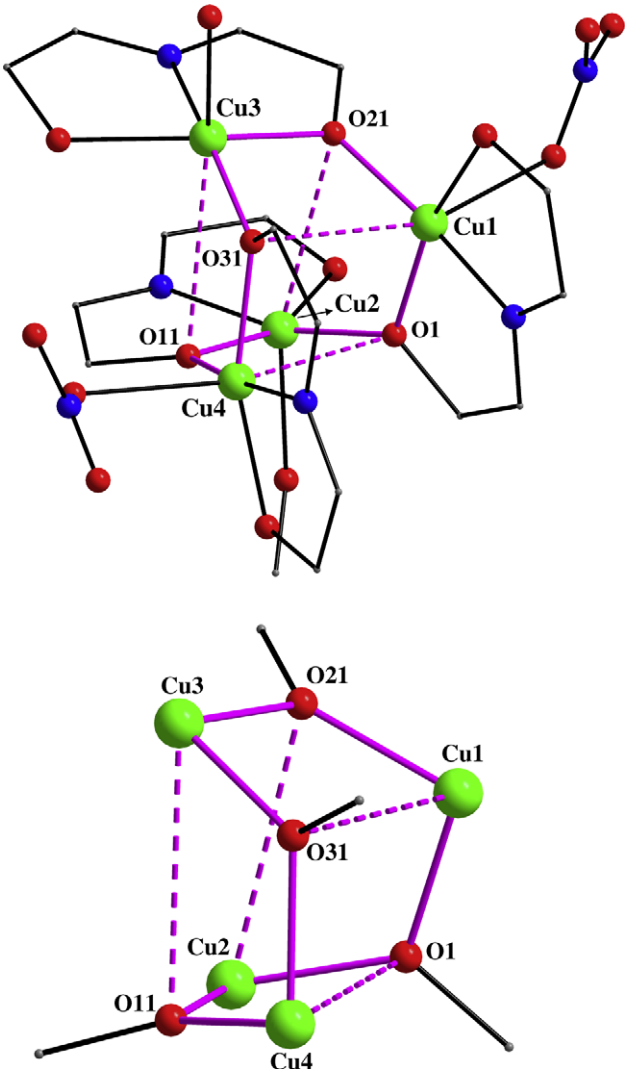


Fig. 4. (top) Molecular structure of the cation of **2**, and (bottom) its $[Cu_4(\mu_3\text{-}OR)_4]^{4+}$ core, emphasizing the very distorted cubane description (purple thick lines). The purple dashed lines represent the four long distances (edges) of the cubane unit. Colour scheme: Cu^{II}, green; O, red; N, blue; C, gray. (For interpretation of the references to colour in this figure legend, the reader is referred to the web version of this article.)

and Cu(4); τ = 0.15 and 0.19, respectively] square pyramidal geometry, where τ is 0 and 1 for perfect square pyramidal and trigonal bipyramidal geometries [25], respectively. The basal planes of the square pyramidal Cu^{II} ions are of the same type, and consist of one N and two O atoms belonging to the 'chelate' part of one $pdmH^-$ ligand and one bridging O atom from an adjacent $pdmH^-$ ligand; these groups are thus $\eta^1{:}\eta^1{:}\eta^2{:}\mu_2$. The two coordinated monodentate NO_3^- ions, as well as the H_2O and MeOH molecules, are each terminally bound to Cu(1)/Cu(4), Cu(3) and Cu(2), respectively, occupying the apical positions of the square pyramids; the Cu^{II} ions lie 0.111 [Cu(1)], 0.230 [Cu(2)], 0.236 [Cu(3)] and 0.177 Å [Cu(4)] Å above the O_3N least-squares basal planes, towards the apical donor atom.

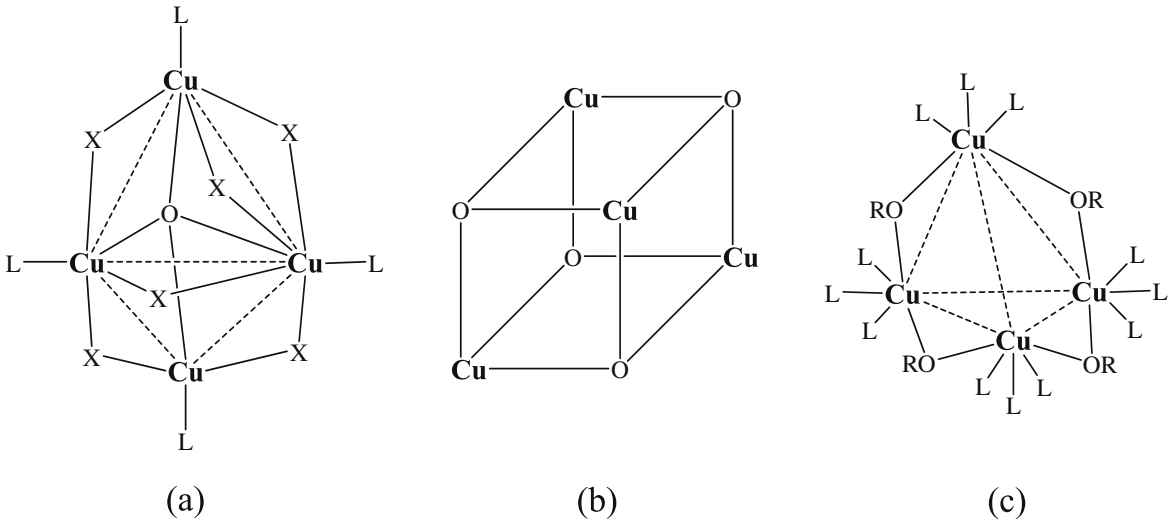
In addition to the tetrahedral or non-planar, ring-like description of **2**, an alternative way of describing it can be presented *if* we consider as bonding the four, abnormally long Cu(1)–O(31) [2.812(1) Å], Cu(2)–O(21) [3.191(4) Å], Cu(3)–O(11) [3.158(6) Å] and Cu(4)–O(1) [3.047(7) Å] distances that involve the RO^- bridges, which thus become μ_3 (Fig. 4, top). Thus, the resulting $[Cu_4(\mu_3\text{-}OR)_4]^{4+}$ core (Fig. 4, bottom) can be described as a very distorted cubane with the four, distorted octahedral Cu^{II} atoms (now six- instead of five-coordinate) and the deprotonated μ_3-O atoms from the four $\eta^1{:}\eta^1{:}\eta^3{:}\mu_3$ (instead of $\eta^1{:}\eta^1{:}\eta^2{:}\mu_2$) $pdmH^-$ ligands occupying alternate vertices.

The structure of complex **2** is stabilized by two strong hydrogen bonds between the protonated, bound OH groups of two $pdmH^-$ ligands and the O atoms of a monodentate or ionic NO_3^- group. The dimensions are: O(2)···O(43) 2.606(4) Å, HO(2)···O(43) 1.768(4) Å, O(2)–HO(2)···O(43) 170.6(1)° and O(32)···O(72) 2.705(3) Å, HO(32)···O(72) 1.918(3) Å, O(32)–HO(32)···O(72) 160.7(1)°. There are also many weak hydrogen bonds involving the remaining protonated OH groups of $pdmH^-$ ligands and the terminal H_2O and MeOH molecules as donors and the monodentate/ionic NO_3^- groups as acceptors, with O···O distances in the 2.9–3.1 Å range, or slightly greater. These serve to link neighbouring Cu_4 cations and NO_3^- anions in the crystal into a 3D H-bonded network. The tetrahedral arrangement of the four Cu^{II} in the 'folded' crystal structure of complex **2** is further stabilized by two intramolecular π–π stacking interactions [26] on the two sides of the molecule that involve the pyridyl groups of two sets of $pdmH^-$ ligands, i.e., those containing N(1)/N(31) and N(11)/N(21). In both sets, the aromatic rings of the $pdmH^-$ ligands are nearly parallel, the angle between their mean planes being 10.3 and 3.9°, respectively. Moreover, the distances between the centroids of rings containing N(1)/N(31) and N(11)/N(21) are 3.805 and 3.755 Å, respectively.

Tetranuclear copper(II) coordination complexes with *N*- and/or *O*-based ligands show a variety of structural types [24,27]. Well known examples are the clusters having the metal ions in a tetrahedral arrangement bridged over the edges by μ_2-halide ions and by a μ_4-O^{2-} in the center of the tetrahedron (Scheme 2a) [28]. More recently tetranuclear compounds of the cubane type have been studied extensively, structurally as well as with respect to their magnetic properties, by Haase, Ruiz and Alvarez, among others (Scheme 2b) [16,29]. The common feature characterizing the tetranuclear compounds studied so far is the fact that monoatomic bridges interconnect the metal ions. Tetranuclear Cu^{II} complexes containing diatomic bridges are also known [30]. Complex **2** joins a handful of structurally characterized Cu_4^{II} complexes with a tetrahedral metal topology that contain *solely* monoatomic bridges (Scheme 2c) [31].

3.3. Magnetochemistry

Variable-temperature dc magnetic susceptibility data in a 0.1 T field and in the 2.0–300 K range were collected on a powdered microcrystalline sample of $\mathbf{2}\cdot H_2O$ restrained in eicosane to prevent torquing. The obtained data are plotted as $\chi_M T$ and χ_M vs. T in Fig. 5. The $\chi_M T$ value at 300 K is 1.23 $cm^3\ mol^{-1}$ K. This value is slightly less than that expected for a cluster comprising four Cu^{II} non-interacting ions (1.50 $cm^3\ mol^{-1}$ K with g = 2). The $\chi_M T$ product continuously decreases with decreasing temperature and gradually tends to 0 $cm^3\ mol^{-1}$ K at the very low temperature range (<20 K). This behaviour is indicative of predominant antiferromagnetic interactions between the metal centers with the low temperature value suggesting a ground state spin of S = 0. The shape of the $\chi_M T$ vs. T plot indicates an overall, moderate antiferromagnetic coupling between the four metal centers. On the other hand, the molar magnetic susceptibility χ_M shows a continuous increase upon cooling, but below ~110 K it exhibits a sudden drop, thus revealing a well-defined maximum. This further supports antiferromagnetic interactions, which are expected to be of moderate strength considering the position of the maximum, and an S = 0 ground state. The Curie tail in the low temperature susceptibility data reveals the existence of a paramagnetic, possibly monomeric, impurity.



Scheme 2. Common structural types in Cu_4^{II} clusters: (a) halide- and oxo-bridged, tetrahedral clusters; (b) cubanes; (c) alkoxide-bridged, tetrahedral clusters (X = halide ion, L = monodentate ligand).

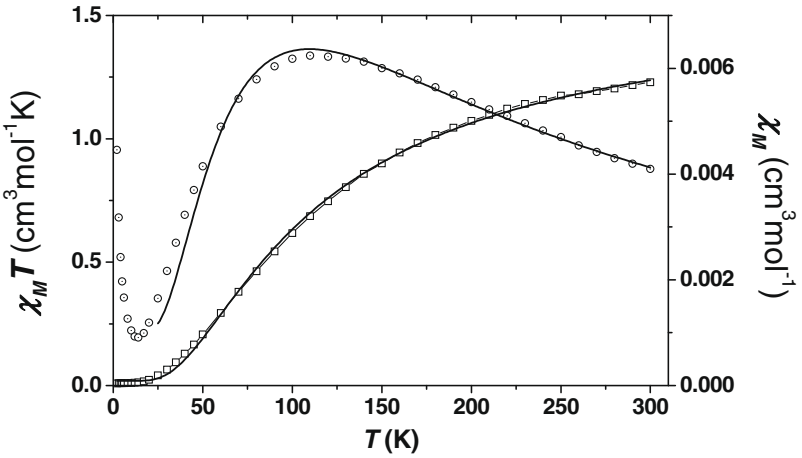


Fig. 5. χ_M vs. T (open cycles) and $\chi_M T$ vs. T (open squares) plots for **2**·H_2O in a 1 kG field. The solid lines are the fit of the data; see the text for the fit parameters.

As we mentioned before, from a structural viewpoint, complex **2** adopts a slightly distorted tetrahedral metal topology; however, magnetically, the system behaves as a ring (vide infra). Considering as bonding the four long Cu(1)–O(31), Cu(2)–O(21), Cu(3)–O(11), and Cu(4)–O(1) distances the system could potentially behave magnetically as a cube; however, given the real rigid shape of the structure, this is clearly not the case and thus there are no superexchange pathways that involve these axial Cu–O–Cu interactions. Nevertheless, from the magnetic point of view, the exact geometric arrangement of the spin carriers in a molecule is of less importance compared with the actual number of interactions through the exchange pathways. In the case of **2**, the system is magnetically defined by four exchange interactions, J_{ij} (Scheme 3).

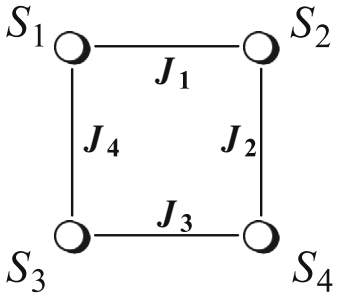
From examination of the structural data of **2**, there are strictly four different Cu–O–Cu bond angles, thus four different superexchange pathways from which derives the spin Hamiltonian (using the atomic numbering in Scheme 3) shown in Eq. (4).

$$H = -J_1(S_1 \cdot S_2) - J_2(S_2 \cdot S_4) - J_3(S_3 \cdot S_4) - J_4(S_1 \cdot S_3) \quad (4)$$

However, the Cu–O–Cu bond angles have similar values (120.3, 119.7, 121.3 and 115.5°); thus, assuming that the four J coupling constants are not identical, an attempt to differentiate J_1, J_2, J_3 and J_4 is not reliable because three of them should be extremely similar to each other, and only the coupling constant related to the smaller angle can be slightly different. Then, the only possibility to simplify the system is to assume a mean value defined by the spin Hamiltonian:

$$H = -J_1(S_1 \cdot S_2 + S_2 \cdot S_4 + S_3 \cdot S_4 + S_1 \cdot S_3) \quad (5)$$

A fit of the experimental data of **2** · H_2O to the expression derived from the simplified spin Hamiltonian shown in Eq. (5), i.e. assuming that all the coupling constants are equal, gives the parameters $J_1 = -99.5$ cm^{-1} and $g = 2.11(4)$, which lead to an overall $S = 0$ ground state. The large, obtuse Cu–O–Cu angles are considered responsible for the moderately strong antiferromagnetic J_1 coupling [15,16,22,29c,32].



Scheme 3. The magnetic coupling scheme of **2** involving four J parameters.

4. Conclusions

The present work extends the body of results that emphasize the ability of $pdmH_2$ to form interesting structural types in copper(II) cluster chemistry. In addition to the $\{[Cu_3(O_2CMe)_2(pdm)_2(MeOH)_2][Cu_4(O_2CMe)_2(pdmH)_4]\}(ClO_4)_2$, $[Cu_4(O_2CMe)_2(pdmH)_4](O_2CMe)_2$ and $[Cu_5(O_2CMe)_6(pdm)_2]_n$ carboxylate-based complexes reported previously [16], the $Cu/NO_3^-/pdmH_2$ reaction system has provided access to the tetranuclear cluster **2** and the known [18] mononuclear compound **1**. Complex **2** is a new addition to the small Cu_4 family of clusters with a tetrahedral metal arrangement bridged solely by monoatomic alkoxide bridges. This compound has been found to possess a $S = 0$ spin ground state and its magnetic behaviour can be interpreted considering a simplified $1-J$ model as a result of its folded ring-like $[Cu_4(\mu_2\text{-}OR)_4]^{4+}$ core. The monomeric complex **1** has been also used as a "ligand" for the construction of the larger, tetranuclear cluster **2** under basic conditions. Thus, from the synthetic inorganic chemistry viewpoint, this work further demonstrates the utility of the "metal complexes as ligands" approach in transition metal cluster chemistry. Preliminary experiments show that the reactions of **1** with sources of other divalent 3d or 4f metals under strong basic conditions lead to a variety of mixed-metal Cu^{II}/M complexes (M = Fe, Mn, Ni, Co, Ln). Finally, an important chemical message from this and our previous [16] work is that the $pdmH_2/X^-$ (X^- = RCO_2^-, NO_3^-) ligand combination looks like a promising candidate system for the generation of interesting new 3d-metal (other than Cu^{II}) clusters and coordination polymers, whose structure may be dependent on the nature of X^-.

Acknowledgements

This work was supported by EPEAEK II (Program PYTHAGORAS I, Grant b.365.037 to S.P.P.) and MEC (Grant CTQ2006-01759 to A.E.).

Appendix A. Supplementary data

CCDC 727367 and 727366 contain the supplementary crystallographic data for **1** and **2** · H_2O · MeOH. These data can be obtained free of charge via http://www.ccdc.cam.ac.uk/conts/retrieving.html, or from the Cambridge Crystallographic Data Centre, 12

Union Road, Cambridge CB2 1EZ, UK; fax: (+44) 1223-336-033; or e-mail: deposit@ccdc.cam.ac.uk. Supplementary data associated with this article can be found, in the online version, at doi:10.1016/j.poly.2009.05.047.

References

[1] (a) R.E.P. Winpenny, in: J.A. McCleverty, T.J. Meyer (Eds.), Comprehensive Coordination Chemistry III, vol. 7, Elsevier, Amsterdam, 2004, p. 125;
(b) Th.C. Stamatatos, G. Christou, Philos. Trans. R. Soc. Lond. A 366 (2008) 113.

[2] (a) A.J. Tasiopoulos, A. Vinslava, W. Wernsdorfer, K.A. Abboud, G. Christou, Angew. Chem., Int. Ed. 43 (2004) 2117;
(b) T. Liu, Y.-J. Zhang, Z.-M. Wang, S. Gao, J. Am. Chem. Soc. 130 (2008) 130;
(c) C.-F. Lee, D.A. Leigh, R.G. Pritchard, D. Schultz, S.J. Teat, G.A. Timco, R.E.P. Winpenny, Nature 458 (2009) 314.

[3] For a review, see: E.C. Theil, M. Matzapetakis, X. Liu, J. Biol. Inorg. Chem. 11 (2006) 803.

[4] (a) For reviews, see: G. Christou, D. Gatteschi, D.N. Hendrickson, R. Sessoli, MRS Bull. 25 (2000) 66;
(b) D. Gatteschi, R. Sessoli, Angew. Chem., Int. Ed. 42 (2003) 268;
(c) R. Birchner, G. Chaboussant, C. Dobe, H.U. Güdel, S.T. Ochsenbein, A. Sieber, O. Waldman, Adv. Funct. Mater. 16 (2006) 209;
(d) G. Aromi, E.K. Brechin, Struct. Bond. 122 (2006) 1.

[5] (a) G. Christou, Polyhedron 24 (2005) 2065;
(b) R.E.P. Winpenny, J. Chem. Soc., Dalton Trans. (2002) 1.

[6] (a) A.J. Tasiopoulos, W. Wernsdorfer, K.A. Abboud, G. Christou, Inorg. Chem. 44 (2005) 6324;
(b) P. King, W. Wernsdorfer, K.A. Abboud, G. Christou, Inorg. Chem. 44 (2005) 8659;
(c) C. Canada-Vilalta, T.A. O'Brien, M. Pink, E.R. Davidson, G. Christou, Inorg. Chem. 42 (2003) 7819;
(d) Th.C. Stamatatos, A.G. Christou, S. Mukherjee, K.M. Poole, C. Lampropoulos, K.A. Abboud, T.A. O'Brien, G. Christou, Inorg. Chem. 47 (2008) 9021.

[7] (a) For reviews, see: P. Chaudhuri, Coord. Chem. Rev. 243 (2003) 143;
(b) C.J. Milios, Th.C. Stamatatos, S.P. Perlepes, Polyhedron 25 (2006) 134 (Polyhedron Report).

[8] (a) For some representative examples, see: Th.C. Stamatatos, K.A. Abboud, W. Wernsdorfer, G. Christou, Angew. Chem., Int. Ed. 46 (2007) 884;
(b) M. Murugesu, M. Habrych, W. Wernsdorfer, K.A. Abboud, G. Christou, J. Am. Chem. Soc. 126 (2004) 4766;
(c) Th.C. Stamatatos, K.A. Abboud, W. Wernsdorfer, G. Christou, Angew. Chem., Int. Ed. 45 (2006) 4134;
(d) Th.C. Stamatatos, K.A. Abboud, W. Wernsdorfer, G. Christou, Angew. Chem., Int. Ed. 47 (2008) 6694.

[9] For a review, see: A.J. Tasiopoulos, S.P. Perlepes, Dalton Trans. (2008) 5537.

[10] For a review, see: E.K. Brechin, Chem. Commun. (2005) 5141.

[11] (a) Selected work from our group: Th.C. Stamatatos, D. Foguet-Albiol, C.C. Stoumpos, C.P. Raptopoulou, A. Terzis, W. Wernsdorfer, S.P. Perlepes, G. Christou, J. Am. Chem. Soc. 127 (2005) 15380;
(b) Th.C. Stamatatos, D. Foguet-Albiol, S.-C. Lee, C.C. Stoumpos, C.P. Raptopoulou, A. Terzis, W. Wernsdorfer, S.O. Hill, S.P. Perlepes, G. Christou, J. Am. Chem. Soc. 129 (2007) 9484;
(c) Th.C. Stamatatos, K.A. Abboud, S.P. Perlepes, G. Christou, Dalton Trans. (2007) 3861;
(d) Th.C. Stamatatos, E. Diamantopoulou, C.P. Raptopoulou, V. Psycharis, A. Escuer, S.P. Perlepes, Inorg. Chem. 46 (2007) 2350.

[12] For a review, see: C.J. Milios, S. Piligkos, E.K. Brechin, Dalton Trans. (2008) 1809.

[13] (a) Th.C. Stamatatos, B.S. Luisi, B. Moulton, G. Christou, Inorg. Chem. 47 (2008) 1134;
(b) S. Khanra, T. Weyhermüller, P. Chaudhuri, Dalton Trans. (2008) 4675;
(c) C. Lampropoulos, Th.C. Stamatatos, K.A. Abboud, G. Christou, Inorg. Chem. 48 (2009) 429.

[14] (a) For recent reviews, see: G.S. Papaefstathiou, S.P. Perlepes, Comment. Inorg. Chem. 23 (2002) 249;
(b) A. Escuer, G. Aromi, Eur. J. Inorg. Chem. (2006) 4721;
(c) Th.C. Stamatatos, G. Christou, Inorg. Chem. 48 (2009) 3308 and references cited therein.

[15] Th.C. Stamatatos, V. Tangoulis, C.P. Raptopoulou, A. Terzis, G.S. Papaefstathiou, S.P. Perlepes, Inorg. Chem. 47 (2008) 7969.

[16] Th.C. Stamatatos, G.C. Vlahopoulou, C.P. Raptopoulou, A. Terzis, A. Escuer, S.P. Perlepes, Inorg. Chem. 48 (2009) 4610.

[17] For example, see: T. Taguchi, Th.C. Stamatatos, K.A. Abboud, C.M. Jones, K.M. Poole, T.A. O'Brien, G. Christou, Inorg. Chem. 47 (2008) 4095.

[18] S. Winter, W. Seichter, E.Z. Weber, Anorg. Allg. Chem. 630 (2004) 434.

[19] G. Denti, S. Serroni, S. Campagna, A. Juris, M. Ciano, V. Balzani, in: A.F. Williams, C. Floriani, A.E. Merbach (Eds.), Perspectives in Coordination Chemistry, VCH, Weinheim, 1992, pp. 153–164.

[20] (a) G.M. Sheldrick, SHELXS-97, Structure Solving Program, University of Göttingén, Germany, 1997;
(b) G.M. Sheldrick, SHELXL-97, Program for the Refinement of Crystal Structures from Diffraction Data, University of Göttingén, Germany, 1997.

[21] (a) Th.C. Stamatatos, A. Bell, P. Cooper, A. Terzis, C.P. Raptopoulou, S.L. Heath, R.E.P. Winpenny, S.P. Perlepes, Inorg. Chem. Commun. 8 (2005) 533;
(b) Th.C. Stamatatos, K.A. Abboud, G. Christou, Dalton Trans. (2009) 41.

[22] For example, see: V. Tangoulis, C.P. Raptopoulou, A. Terzis, S. Paschalidou, S.P. Perlepes, E.G. Bakalbassis, Inorg. Chem. 36 (1997) 3996.

[23] (a) K. Nakamoto, Infrared and Raman Spectra of Inorganic and Coordination Compounds, 4th ed., Wiley, New York, 1986. p. 229, 254;
(b) E. Katsoulakou, V. Bekiari, C.P. Raptopoulou, A. Terzis, P. Lianos, E. Manessi-Zoupa, S.P. Perlepes, Spectrochim. Acta A 61 (2005) 1627.

[24] For example, see: V. Tangoulis, C.P. Raptopoulou, S. Paschalidou, A. Tsohos, E.G. Bakalbassis, A. Terzis, S.P. Perlepes, Inorg. Chem. 36 (1997) 5270.

[25] A.W. Addison, T.N. Rao, J. Reedijk, J.V. Rijin, G.C. Verschoor, J. Chem. Soc., Dalton Trans. (1984) 1349.

[26] For an excellent review, see: C. Janiak, Dalton Trans. (2003) 2781 (Dalton Perspective).

[27] (a) For some representative examples of rarely found Cu^{II}_4 topologies, see: C.A. Bear, J.M. Waters, T.N. Waters, J. Chem. Soc., Dalton Trans. (1974) 1059;
(b) V. Chandrasekhar, L. Nagarajan, R. Clerac, S. Ghosh, S. Verma, Inorg. Chem. 47 (2008) 1067;
(c) K.E. Halvorson, T. Grigereit, R.D. Willett, Inorg. Chem. 26 (1987) 1716.

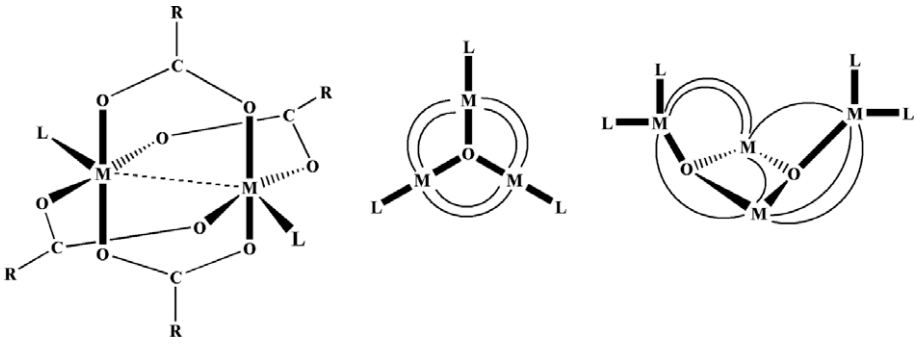
[28] (a) J.A. Bertrand, J.A. Kelley, J. Am. Chem. Soc. 88 (1966) 4746;
(b) H. Bock, H. tom Dieck, H. Pyttlik, M. Schnöller, Z. Anorg. Allg. Chem. 357 (1968) 54;
(c) F.S. Keij, J.G. Haasnoot, A.J. Oosterling, J. Reedijk, C.J. O'Connor, J.H. Zhang, A.L. Spek, Inorg. Chim. Acta 181 (1991) 185;
(d) K. Skorda, E.G. Bakalbassis, J. Mrozinski, S.P. Perlepes, C.P. Raptopoulou, A. Terzis, J. Chem. Soc., Dalton Trans. (1995) 2317;
(e) K. Skorda, Th.C. Stamatatos, A.P. Vafiadis, A.T. Lithoxoidou, A. Terzis, S.P. Perlepes, J. Mrozinski, C.P. Raptopoulou, J.C. Plakatouras, E.G. Bakalbassis, Inorg. Chim. Acta 358 (2005) 565;
(f) R.F. Drake, V.H. Crawford, W.E. Hatfield, J. Chem. Phys. 60 (1974) 4525;
(g) N.S. Gill, M. Sterns, Inorg. Chem. 9 (1970) 1619.

[29] (a) For some representative references, see: L. Schwabe, W. Haase, J. Chem. Soc., Dalton Trans. (1985) 1909;
(b) L. Laurent, J. Bonnet, F. Nepveu, H. Astheimer, L. Walz, W. Haase, J. Chem. Soc., Dalton Trans. (1982) 2433;
(c) J. Tercero, E. Ruiz, S. Alvarez, A. Rodriguez-Fortea, P.J. Alemany, J. Mater. Chem. 16 (2006) 2729;
(d) A. Mukherjee, M. Nethaji, A.R. Chakravarty, Angew. Chem., Int. Ed. 43 (2004) 87.

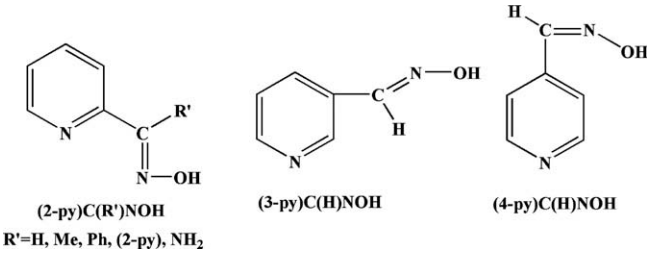
[30] (a) R.W.M. ten Hoedt, F.B. Hulsbergen, G.C. Verschoor, J. Reedijk, Inorg. Chem. 21 (1982) 2369;
(b) R. Prins, R.A.G. de Graaff, J.G. Haasnoot, C. Vader, J. Reedijk, J. Chem. Soc., Chem. Commun. (1986) 1430;
(c) W.-H. Gu, X.-Y. Chen, L.-H. Yin, A. Yu, X.-Q. Fu, P. Cheng, Inorg. Chim. Acta 357 (2004) 4085;
(d) E. Kavlakoglu, A. Elmali, Y. Elerman, I. Svoboda, Polyhedron 21 (2002) 1539;
(e) J. Manzur, A.M. Garcia, M.T. Garland, V. Acuna, O. Gonzalez, O. Pena, A.M. Atria, E. Spodine, Polyhedron 15 (1995) 821.

[31] (a) X.S. Tan, Y. Fujii, R. Nukada, M. Mikuriya, Y. Nakano, Dalton Trans. (1999) 2415;
(b) K.H. Whitmire, J.C. Hutchison, A. Gardberg, C. Edwards, Inorg. Chim. Acta 294 (1999) 153;
(c) U. Ray, K.K. Sarker, G. Mostafa, T.-H. Lu, M.S. El Fallah, C. Sinha, Polyhedron 25 (2006) 2764.

[32] O. Kahn, Molecular Magnetism, VCH Publishers, New York, 1993.



Scheme 1. Paddle wheel (left), trinuclear basis carboxylate (middle) and tetranuclear "butterfly" carboxylate (right) complexes. Curved lines represent bidentate bridging carboxylate groups. The paddle wheel structural type is associated with a variety of metal–metal interactions ranging from no interaction, weak spin-pairing, various orders of metal–metal bonding, to the "super-short" metal–metal bonds. The L groups are often monodentate ligands, but they may represent intercluster association into polymeric structures or (only in the case of the "butterfly" complexes) one donor atom of a bidentate chelate.



Scheme 2. General structural formula and abbreviation of the 2-pyridyl oximes that are used in our laboratories (left); the ligands pyridine-3-carbaldehyde oxime [3-pyridinealdoxime, (3-py)C(H)NOH] and pyridine-4-carbaldehyde oxime [4-pyridinealdoxime, (4-py)C(H)NOH] employed in this work are shown in the middle and right part, respectively, of the scheme.

(the term "simple" means here ligands with only one pyridyl and one oxime group as donors). Our goals are to investigate if clusters and coordination polymers can be prepared from the Zn^{II}/RCO_2^-/(py)C(R′)NOH reaction systems (R′=H, Me, Ph) and to isolate, if possible, photoluminescent complexes. Reactions of $Zn(O_2CR)_2{\cdot}2H_2O$ (R = Me, Ph) with the more complex ligand di-2-pyridyl ketone oxime, (2-py)C(2-py)NOH, have led to compounds $[Zn_4(OH)_2(O_2CR)_2\{(2\text{-py})C(2\text{-py})NO\}_4]$ [11] with the extremely rare inverse 12-metallacrown-4 structural motif. We report here the preparation and characterization of two complexes derived from the reactions of $Zn(O_2CPh)_2{\cdot}2H_2O$ with (3-py)C(H)NOH and (4-py)C(H)NOH (see Scheme 2). Efforts to date with the isomeric pyridine-*x*-carbaldehyde oximes [*x* = 2, (2-py)C(H)NOH, R′ = H in Scheme 2; *x* = 3, (3-py)C(H)NOH; *x* = 4, (4-py)C(H)NOH] have almost completely neglected Zn chemistry; no Zn^{II} complexes of (3-py)C(H)NOH and (4-py)C(H)NOH have been reported, while the only structurally characterized Zn^{II}/(2-py)C(H)NOH or (2-py)C(H)NO^- compound is $[Zn_4(OH)_2Cl_2\{(2\text{-py})C(H)NO\}_4]$ [12].

2. Experimental

2.1. General and spectroscopic measurements

All manipulations were performed under aerobic conditions using materials (reagent grade) and solvents as received. $Zn(O_2CPh)_2{\cdot}2H_2O$ was prepared by the reaction of $Zn(O_2CMe)_2{\cdot}2H_2O$ with and excess of $PhCO_2H$ in $CHCl_3$ under reflux. Microanalyses (C, H, N) were performed by the University of Ioannina (Greece) Microanalytical Laboratory using an EA 1108 Carlo Erba analyzer.

IR spectra (4000–450 cm^{-1}) were recorded on a Perkin–Elmer 16 PC FT-spectrometer with samples prepared as KBr pellets.

2.2. Compound preparation

2.2.1. $[Zn_3(O_2CPh)_6\{(3\text{-py})C(H)NOH\}_2]$ (**1**)

A solution of $Zn(O_2CPh)_2{\cdot}2H_2O$ (0.346 g, 1.00 mmol) in MeCN (10 ml) was added gradually to a stirred solution of (3-py)C(H)NOH (0.122 g, 1.00 mmol) in MeCN (10 ml). Slow evaporation of the resulting solution at room temperature yielded colourless prismatic crystals of **1** after three days. The crystals were collected by filtration under vacuum, washed with MeCN (2 × 5 ml) and Et_2O (5 ml), and dried in air. Typical yields were in the 50–55% range (based on the metal). FT-IR (KBr pellet, cm^{-1}): 3354mb, 3064w, 1622sh, 1612vs, 1602m, 1570s, 1540m, 1490m, 1448w, 1400vs, 1304m, 1192w, 1130w, 1058w, 1026w, 978m, 890w, 874w, 838w, 814w, 720s, 700m, 670m, 654w, 586w, 528w, 446w. *Anal.* Calc. for $C_{54}H_{42}N_4O_{14}Zn_3$ (1167.03): C, 55.57; H, 3.63; N, 4.80. Found: C, 55.29; H, 3.37; N, 4.82%.

2.2.2. $[Zn_2(O_2CPh)_4\{(4\text{-py})C(H)NOH\}_2]$ (**2**)

To a stirred solution of $Zn(O_2CPh)_2{\cdot}2H_2O$ (0.138 g, 0.40 mmol) in MeCN (10 ml) was added a solution of (4-py)C(H)NOH (0.049 g, 0.40 mmol) in the same solvent (10 ml). The reaction solution was stirred for 15 min during which time a white solid precipitated. The precipitate was collected by filtration and the filtrate was allowed to slowly evaporate at room temperature. After

Table 1
Crystallographic data for complexes **1** and **2**.

Parameter	**1**	**2**
Chemical formula	$C_{54}H_{42}N_4O_{14}Zn_3$	$C_{40}H_{32}N_4O_{10}Zn_2$
Formula weight	1167.09	859.48
Crystal system	triclinic	monoclinic
Space group	$P\bar{1}$	$P2_1/n$
a (Å)	10.414(4)	16.485(8)
b (Å)	10.830(4)	13.008(6)
c (Å)	12.690(5)	19.982(9)
α (°)	81.66(1)	90
β (°)	79.73(1)	113.31(2)
γ (°)	66.40(1)	90
V (Å^3)	1286.2(9)	3935(3)
Z	1	4
T (K)	298	298
Radiation, wavelength Mo Kα	0.71073	0.71073
ρ_{calc} (g cm^{-3})	1.507	1.451
μ (mm^{-1})	1.459	1.281
Data collected/unique (R_{int})	4800/4529 (0.014)	6082/5893 (0.031)
Data with $I > 2\sigma(I)$	3719	3735
R_1[a] [$I > 2\sigma > (I)$]	0.0361	0.0516
wR_2[b] [unique data]	0.1159	0.1203

[a] $R_1 = \sum(|F_o| - |F_c|)/\sum(|F_o|)$.
[b] $wR_2 = \{\sum[w(F_o^2 - F_c^2)^2]/\sum[w(F_o^2)^2]\}^{1/2}$.

three days, X-ray quality colourless crystals of **2** were collected by filtration under vacuum, washed with MeCN (2 × 5 ml) and Et_2O (5 ml), and dried in air. Typical yields (including the white solid) were in the 50–55% range. FT-IR (KBr pellet, cm^{-1}): 3221mb, 3066w, 1634vs, 1573s, 1409vs, 1301m, 1225w, 1175vw, 1067vw, 1030w, 990m, 932w, 832m, 714s, 673m, 560w, 536m, 472w, 460w. The IR spectra of the white powder and the colourless crystals (in the form of a powder) are identical. *Anal.* Calc. for $C_{40}H_{32}N_4O_{10}Zn_2$ (859.44): C, 55.90; H, 3.76; N, 6.52. Found: C, 55.62; H, 3.78; N, 6.55%.

2.3. Single-crystal X-ray crystallography

A colourless crystal of **1** (0.10 × 0.20 × 0.60 mm) and a colourless crystal of **2** (0.20 × 0.30 × 0.50 mm) were mounted in air and covered with epoxy glue. Diffraction measurements were made on a Crystal Logic Dual Goniometer diffractometer using graphite monochromated Mo Kα radiation. Details for data collection and processing are listed in Table 1. Unit cell dimensions were determined and refined by using the angular settings of 25 automatically centered reflections in the range $11 < 2\theta < 23°$. Three standard reflections monitored every 97 reflections showed less than 3% variation and no decay. Lorentz, polarization corrections were applied using Crystal Logic software. Ψ-scan data were collected for both structures. The intensity of a certain reflection remains invariant during 360° rotation around the Φ axis, thus absorption correction is not required.

The structures were solved by direct methods using SHELXS-86 [13] and refined by full-matrix least-squares techniques on F^2 with SHELXL-97 [14]. Further experimental crystallographic details for **1**: $2\theta_{max} = 50°$; 424 parameters refined; $(\Delta/\sigma)_{max} = 0.000$; $(\Delta\rho)_{max}/(\Delta\rho)_{min} = 0.557/-0.712$ e/Å^3; R_1 (for all data), 0.0581. All hydrogen atoms were located by difference maps and refined isotropically. All non-hydrogen atoms were refined anisotropically. Further experimental crystallographic details for **2**: $2\theta_{max} = 47.2°$; 633 parameters refined; $(\Delta/\sigma)_{max} = 0.002$; $(\Delta\rho)_{max}/(\Delta\rho)_{min} = 0.292/-0.354$ e/Å^3; R_1 (for all data), 0.1075. All hydrogen atoms were located by difference maps and were refined isotropically. All non-hydrogen atoms were refined anisotropically.

3. Results and discussion

3.1. Brief synthetic comments and IR spectra

The chemical and structural identities of the products from the $Zn(O_2CPh)_2{\cdot}2H_2O$/LH reaction systems in MeCN, where LH is (3-py)C(H)NOH or (4-py)C(H)NOH, depends on the pyridyl oxime ligand. Use of (3-py)C(H)NOH gives the trinuclear cluster **1**, whereas employment of (4-py)C(H)NOH led to the dinuclear compound **2**.

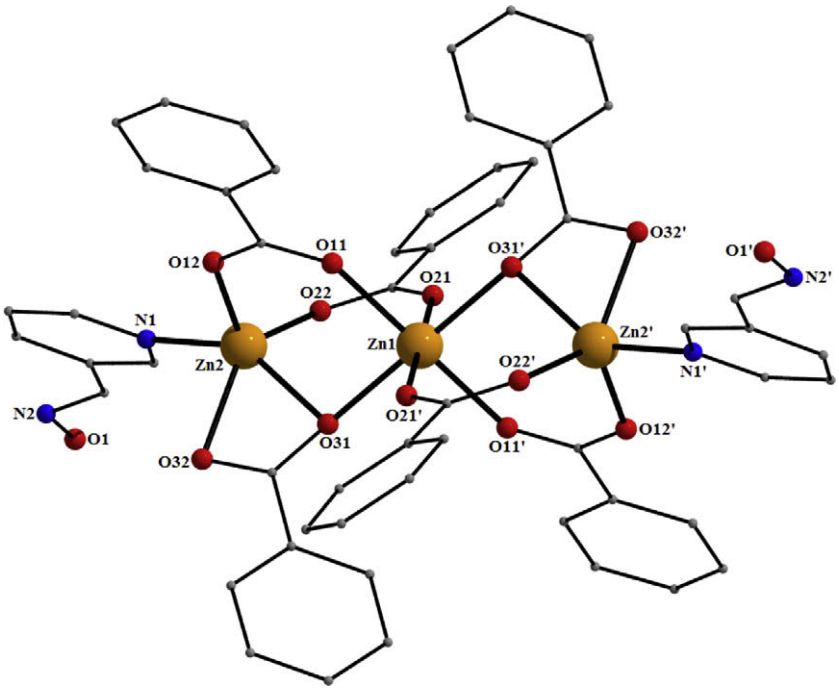


Fig. 1. Partially labeled plot of the molecular structure of **1**. H atoms have been omitted for clarity. Colour code: Zn, orange; O, red; N, blue; C, gray. Primes are used for symmetry related (−*x*, 1 − *y*, −*z*) atoms. (For interpretation of the references to colour in this figure legend, the reader is referred to the web version of this article.)

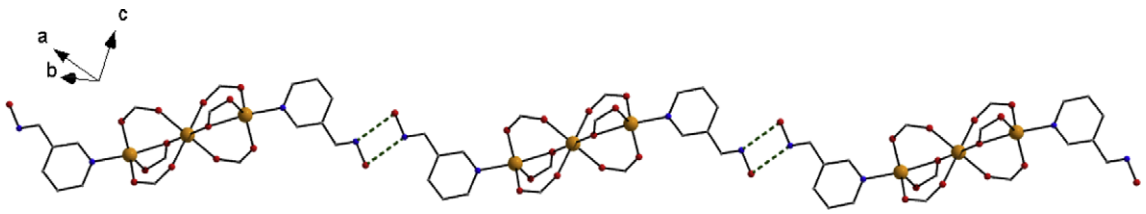


Fig. 2. A part of the 1D structure of **1** due to H-bonding interactions (green dashed lines); colour code as in Fig. 1. H atoms and the phenyl rings of the benzoates have been omitted for clarity. (For interpretation of the references to colour in this figure legend, the reader is referred to the web version of this article.)

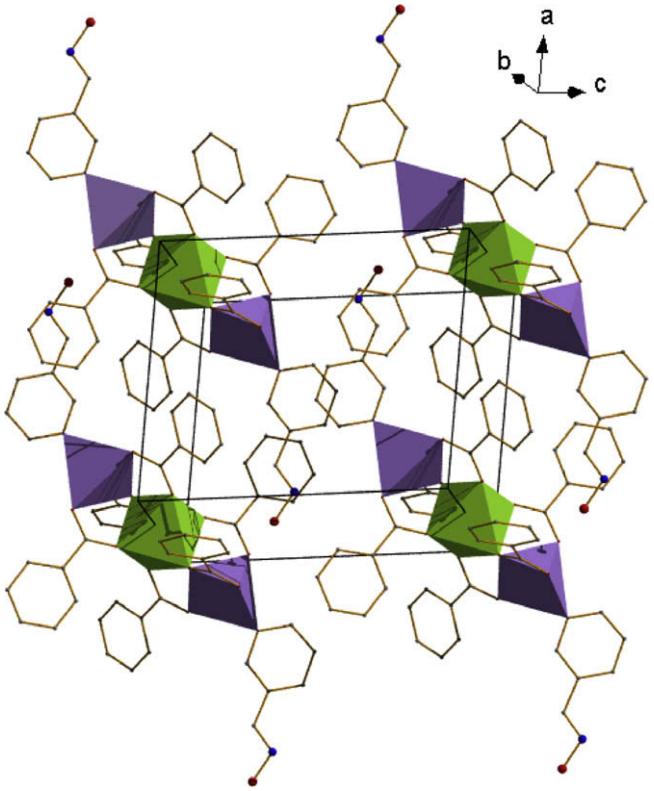


Fig. 3. Crystal packing diagram of complex **1**. The metal coordination spheres are represented as polyhedra [Zn(1), green; Zn(2), purple]. (For interpretation of the references to colour in this figure legend, the reader is referred to the web version of this article.)

The preparation of the two complexes is summarized in the balanced Eqs. (1) and (2):

$$3Zn(O_2CPh)_2 \cdot 2H_2O + 2(3\text{-py})C(H)NOH \xrightarrow{MeCN} [Zn_3(O_2CPh)_6\{(3\text{-py})C(H)NOH\}_2] + 6H_2O \quad (1)$$

$$2Zn(O_2CPh)_2 \cdot 2H_2O + 2(4\text{-py})C(H)NOH \xrightarrow{MeCN} [Zn_2(O_2CPh)_4\{(4\text{-py})C(H)NOH\}_2] + 4H_2O \quad (2)$$

Two features of the reactions represented by the chemical (1) and (2) deserve comments. First, the "wrong" reaction ratio (1:1) employed for the preparation of **1**, compared to the stoichiometric ratio (1.5:1) required by Eq. (1), obviously did not prove detrimental to the formation of the complex. With the identity of **1** crystallographically established (vide infra), the "correct" stoichiometric ratio, i.e. Zn^{II}:(3-py)C(H)NOH = 1.5:1, was employed and led to the pure compound in very good yield (60–65%). Second, complexes **1** and **2** seem to be the only isolable products from the $Zn(O_2CPh)_2{\cdot}2H_2O$/LH reaction systems. The Zn^{II} to ligand reaction ratio (we used 1:2 and 1:3 ratios to "force" the formation of mononuclear complexes, e.g. $[Zn(O_2CPh)_2(LH)_x]$ with $x = 2$ or 3), the presence of counteranions (we added ClO_4^- or PF_6^- in some reaction mixtures to "force" the isolation of cationic complexes), the nature of the solvent (use of alcohols gives the same products) and the precipitation/crystallization method have no influence on the identity of the products.

The IR spectra of **1** and **2** exhibit medium intensity bands at ~3350 and 3320 cm^{-1}, respectively, assignable to the ν(OH) vibration of the coordinated pyridyl oxime ligands [6a,15]. The broadness and low frequency of these bands are both indicative of hydrogen bonding. The medium intensity bands at 1636 and 1124 cm^{-1} in the spectrum of the free ligand (3-py)C(H)NOH are assigned to $\nu(C{=}N)_{oxime}$ and $\nu(N{-}O)_{oxime}$, respectively [6a,16]. The corresponding vibrations in the spectrum of free (4-py)C(H)NOH appear at 1566 and 1096 cm^{-1}. In the spectra of the complexes, these typical bands of the neutral oxime group are situated at approximately the same wavenumbers to those in the spectra of the corresponding free ligands, confirming the crystallographically established (vide infra) non-participation of the oxime group in coordination. For example, the $\nu(C{=}N)_{oxime}$ and $\nu(N{-}O)_{oxime}$ vibrations appear at 1622 and 1130 cm^{-1}, respectively, in the spectrum of **1**. The in-plane deformation band of the pyridyl ring of the free ligands [638 cm^{-1} in (3-py)C(H)NOH, 646 cm^{-1} in (4-py)C(H)NOH] shifts upwards in the complexes (654 cm^{-1} in **1**, 673 cm^{-1} in **2**), confirming the involvement of the ring-N atom in coordination [17]. The strong bands at 1573 and 1409 cm^{-1} in

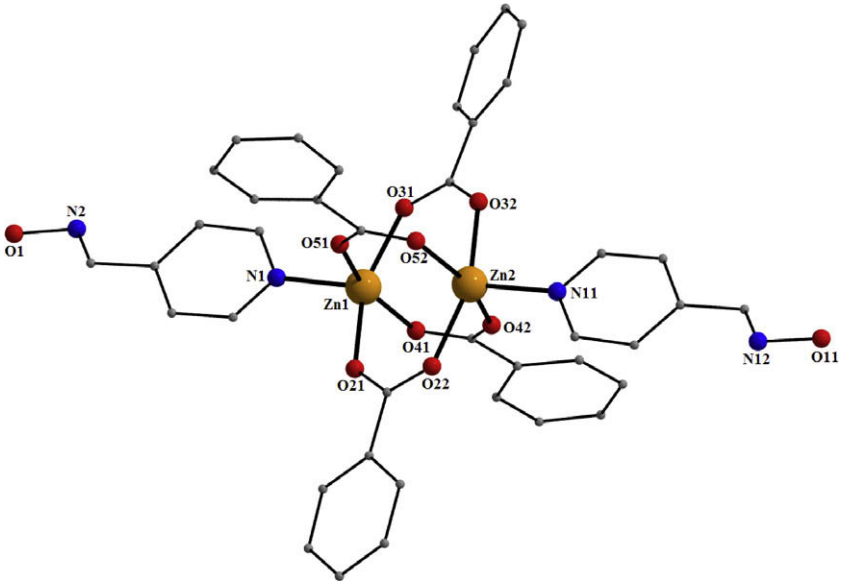


Fig. 4. Partially labeled plot of the molecular structure of **2**. Colour code as in Fig. 1. H atoms have been omitted for clarity. (For interpretation of the references to colour in this figure legend, the reader is referred to the web version of this article.)

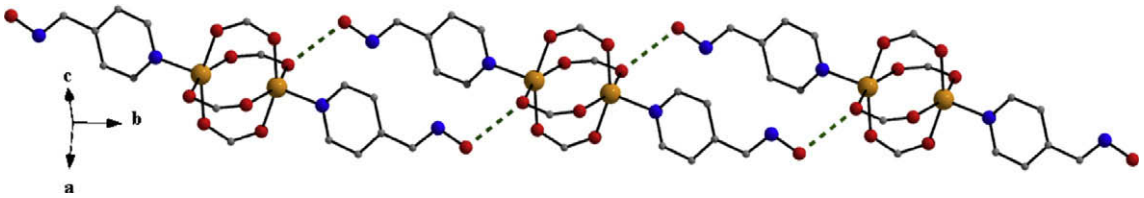


Fig. 5. A small portion of the ladder-like 1D architectures of **2** due to H-bonding interactions (green dashed lines). Colour code as in Fig. 1. The H atoms and the phenyl rings of the benzoates have been omitted for clarity. (For interpretation of the references to colour in this figure legend, the reader is referred to the web version of this article.)

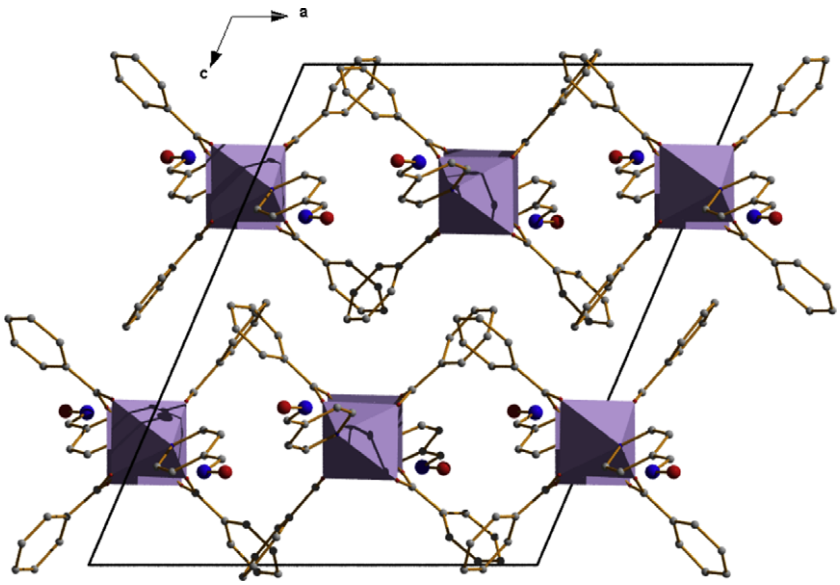


Fig. 6. Crystal packing diagram of complex **2**. The metal coordination spheres are represented as polyhedra (purple colour). (For interpretation of the references to colour in this figure legend, the reader is referred to the web version of this article.)

Table 2
Selected interatomic distances (Å) and angles (°) for complex **1**.

Distances			
Zn(1)–O(11)	2.084(3)	Zn(2)–O(12)	1.955(3)
Zn(1)–O(21)	2.069(3)	Zn(2)–O(22)	1.951(3)
Zn(1)–O(31)	2.144(3)	Zn(2)–O(31)	2.147(3)
Zn(1)–O(11′)	2.084(3)	Zn(2)–O(32)	2.202(3)
Zn(1)–O(21′)	2.069(3)	Zn(2)–N(1)	2.073(4)
Zn(1)–O(31′)	2.144(3)	Zn(1)···Zn(2)	3.392(5)
Angles			
O(11)–Zn(1)–O(21)	93.6(1)	O(11′)–Zn(1)–O(31′)	90.2(1)
O(11)–Zn(1)–O(31)	90.2(1)	O(21′)–Zn(1)–O(31′)	90.3(1)
O(11)–Zn(1)–O(11′)	180.0	O(12)–Zn(2)–O(22)	113.9(1)
O(11)–Zn(1)–O(21′)	86.4(1)	O(12)–Zn(2)–O(31)	107.9(1)
O(11)–Zn(1)–O(31′)	89.8(1)	O(12)–Zn(2)–O(32)	105.7(1)
O(21)–Zn(1)–O(31)	90.3 (1)	O(12)–Zn(2)–N(1)	99.5(1)
O(11′)–Zn(1)–O(21)	86.4(1)	O(22)–Zn(2)–O(31)	94.4(1)
O(21)–Zn(1)–O(21′)	180.0	O(22)–Zn(2)–N(1)	93.2(2)
O(21)–Zn(1)–O(31′)	89.7(1)	O(31)–Zn(2)–N(1)	145.5(1)
O(11′)–Zn(1)–O(31)	89.8(1)	O(22)–Zn(2)–O(32)	138.1(1)
O(21′)–Zn(1)–O(31)	89.7(1)	O(31)–Zn(2)–O(32)	59.9(1)
O(31)–Zn(1)–O(31′)	180.0	O(32)–Zn(2)–N(1)	93.1(1)
O(11′)–Zn(1)–O(21′)	93.6(1)		

Symmetry operations used to generate equivalent atoms: (′) $-x, 1-y, -z$.

the spectrum of **2** are assigned to the $\nu_{as}(CO_2)$ and $\nu_s(CO_2)$ modes of the benzoato ligands, respectively [18]; the former may also involve a pyridyl stretching character. The difference Δ, where $\Delta = \nu_{as}(CO_2) - \nu_s(CO_2)$, is 164 cm^{-1}, less than that for NaO_2CPh (184 cm^{-1}), as expected for bidentate bridging ligation [18]. In the IR spectrum of **1**, the bands at 1570 and 1612 cm^{-1} are assigned to $\nu_{as}(CO_2)$; both may also involve a pyridyl stretching character. The $\nu_s(CO_2)$ modes appear at 1400 and 1448 cm^{-1}. The appearance of two distinct bands for each mode reflects the presence of two different types of $PhCOO^-$ groups in the complex (vide infra) [19]. The 1612, 1400 cm^{-1} pair ($\Delta = 212$ cm^{-1}) are assigned [18–20] to the $\eta^1{:}\eta^2{:}\mu_2$ benzoate, while the 1570, 1448 cm^{-1} pair ($\Delta = 122$ cm^{-1}) to the bidentate bridging ($\eta^1{:}\eta^1{:}\mu_2$) benzoates.

3.2. Description of structures

Aspects of the molecular and crystal structures of complexes **1** and **2** are shown in Figs. 1–6. Selected interatomic distances and angles are listed in Tables 2 and 4, while important hydrogen bonding interactions are presented in Table 5.

Complex **1** crystallizes in the triclinic space group $P\bar{1}$. Its crystal structure consists of trinuclear $[Zn_3(O_2CPh)_6\{(3\text{-py})C(H)NOH\}_2]$ molecules. The central metal center [Zn(1)] is located on a crystallographic inversion center and thus the trinuclear molecule adopts a strictly linear structure. Zn(1) is coordinated by six oxygen atoms belonging to six $PhCO_2^-$ groups. One $\eta^1{:}\eta^2{:}\mu$ and two *syn*, *syn*-$\eta^1{:}\eta^1{:}\mu$ carboxylate groups span each pair of neighbouring Zn^{II} ions. The terminal metal ions [Zn(2), Zn(2′)] are each capped by one monodentate (3-py)C(H)NOH ligand; the donor atom of (3-py)C(H)NOH is the pyridyl nitrogen. The ZnO_6 octahedron is almost perfect with the Zn(1)–O bond lengths and the cis O–Zn(1)–O bond angles being in the ranges 2.069(3)–2.144(3) Å and 86.4(1)–93.6(1)°, respectively. The coordination geometry about the terminal Zn^{II} ions is described as distorted square pyramidal with the carboxylate oxygen atoms O(12) and O(12′) occupying the apical positions for Zn(2) and Zn(2′), respectively. Analysis of the shape-

Table 3
Pentinent structural properties[a] for trinuclear Zn^{II} complexes containing the $[Zn^{II}_3(\eta^1{:}\eta^1{:}\mu\text{-}O_2CPh)_4(\eta^1{:}\eta^2{:}\mu\text{-}O_2CPh)_2]$ unit.

Complex	*B* (Å)	*D* (Å)	*A* (Å)	Zn···Zn (Å)	C–O_b (Å)	C–O_d (Å)	θ (°)	β (°)	α (°)
$[Zn_3(O_2CPh)_6(py)_2]$[b,c]	2.328	2.121	2.141	3.444	1.248	1.241	100.73	86.43	139.45
$[Zn_3(O_2CPh)_6$ (2,3-Me_2pyz)$_2]$[d]	2.103	2.264	2.207	3.370	1.278	1.242	102.85	94.03	139.05
Complex **1**[e]	2.147	2.202	2.144	3.392	1.271	1.247	101.46	91.38	145.52

Abbreviations: 2,3-Me_2pyz = 2,3-dimethylpyrazine; py = pyridine.
[a] See Scheme 3 for the definition of the various structural parameters given in this table.
[b] Ref. [22b].
[c] This discrete cluster cocrystallizes with $[Zn_2(O_2CPh)_4(py)_2]$ in the complex.
[d] Ref. [22b].
[e] This work.

Table 4
Selected interatomic distances (Å) and angles (°) for complex **2**.

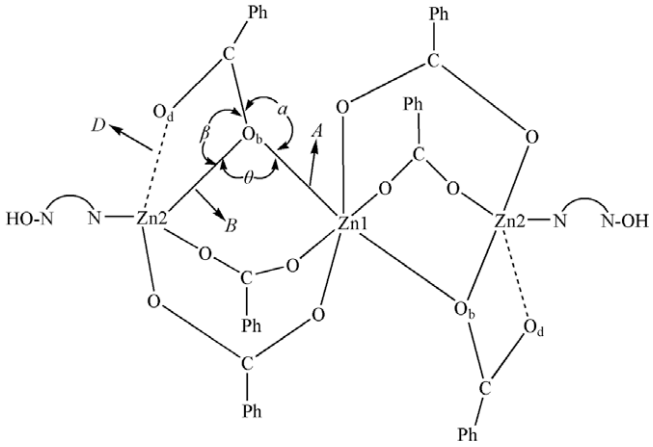
Distances			
Zn(1)–O(31)	2.007(5)	Zn(2)–O(32)	2.019(5)
Zn(1)–O(21)	2.014(5)	Zn(2)–N(11)	2.028(4)
Zn(1)–N(1)	2.028(4)	Zn(2)–O(52)	2.070(4)
Zn(1)–O(41)	2.061(4)	Zn(2)–O(42)	2.105(5)
Zn(1)–O(51)	2.132(5)	Zn(2)–O(22)	2.017(5)
Zn(1)···Zn(2)	2.990(2)		
Angles			
O(31)–Zn(1)–O(21)	157.2(2)	O(22)–Zn(2)–O(32)	158.8(2)
O(21)–Zn(1)–N(1)	100.5(2)	O(32)–Zn(2)–N(11)	98.8(2)
O(21)–Zn(1)–O(41)	89.4(2)	O(32)–Zn(2)–O(52)	89.0(2)
O(31)–Zn(1)–O(51)	89.6(2)	O(22)–Zn(2)–O(42)	88.1(2)
N(1)–Zn(1)–O(51)	93.4(2)	N(11)–Zn(2)–O(42)	94.7(2)
O(31)Zn(1)N(1)	102.2(2)	O(22)–Zn(2)–N(11)	102.0(2)
O(31)Zn(1)O(41)	86.5(2)	O(22)–Zn(2)–O(52)	88.6(2)
N(1)–Zn(1)–O(41)	107.2(2)	N(11)–Zn(2)–O(52)	107.6(2)
O(21)–Zn(1)–O(51)	86.5(2)	O(32)–Zn(2)–O(42)	86.2(2)
O(41)–Zn(1)–O(51)	159.5(2)	O(52)–Zn(2)–O(42)	157.7(2)

determining angles using the approach of Reedijk and co-workers [21] yields a trigonality index, τ, value of 0.12 (τ = 0 and 1 for perfect *sp* and *tbp* geometries, respectively). The coordination of the bridging benzoate oxygen [O(31), O(31′)] is slightly pyramidal [$\sum$O(31) = 341.4(1)°]. The Zn(1)–O(31)–Zn(2) angle is 104.5(1)°.

In the crystal lattice of **1**, the molecules interact through hydrogen bonds building 1D chains parallel to the [2 0 −1] vector.

Complex **1** is the third structurally characterized Zn^{II}_3 complex containing the $[Zn^{II}_3(\eta^1{:}\eta^1{:}\mu_2\text{-}O_2CPh)_4(\eta^1{:}\eta^2{:}\mu_2\text{-}O_2CPh)_2]^0$ unit. The other two complexes are $[Zn_3(O_2CPh)_6(2,3\text{-}Me_2pyz)_2]$ [22a] and the trinuclear part of complex $[Zn_3(O_2CPh)_6(py)_2]\cdot[Zn_2(O_2CPh)_4(py)_2]$ [22b], where 2,3-Me_2pyz and py are 2,3-dimethylpyrazine and pyridine, respectively. Such complexes have been important in the establishment of the "carboxylate shift" concept [23]. Of the various types of metal-carboxylate binding modes, monoatomic bridging between metal ions offers great flexibility. Analysis [23] of the structural characteristics of dinuclear and trinuclear complexes containing monoatomically bridging carboxylate groups reveals that they can be grouped into three classes, depending upon the strength of the interaction of the non-bridging, or dangling (O_d), oxygen atom [O(32) in compound **1**] with one of the bridged metal centers [Zn(2) in **1**]. The application of this analysis to trinuclear Zn^{II} benzoate complexes is demonstrated in Scheme 3 and Table 3. The monoatomic bridging mode is postulated to be an important intermediate between the other, more common carboxylate binding modes, based on observed variation of the geometry for monoatomic bridges in structurally characterized metal complexes. The "movement" from monoatomic bridging to the other binding modes has been termed "carboxylate shift" [23]; such a shift is considered to be kinetically important in carboxylate-containing metalloproteins. Complex **1** is characterized by a moderate *D* value, *D* > *B*, *A*, a rather long Zn···Zn distance, a difference between C–O_d and C–O_b and a distinct tilt (α–β) of the $\eta^1{:}\eta^2{:}\mu$ carboxylate group towards Zn(2); thus, this compound can be placed in class II in Lippard's "carboxylate shift" classification scheme [23].

Compound **1** joins only a handful of structurally characterized metal complexes of (3-py)C(H)NOH [24]; in all the previously reported complexes the 3-pyridinealdoxime ligand is attached to the metal ions through the pyridine nitrogen atom (like in **1**) with



Scheme 3. Schematic structure of complex **1** showing the dangling (O_d) and bridging (O_b) oxygen atoms of the $\eta^1{:}\eta^2{:}\mu_2$ carboxylate groups, and defining the geometry of monoatomic carboxylate-bridged polymetallic centers in relation to the "carboxylate shift" mechanism proposed by Lippard and co-workers [23]; the values of the relevant structural parameters for **1** and the other two, structurally characterized complexes containing the $[Zn^{II}_3(\eta^1{:}\eta^1{:}\mu\text{-}O_2CPh)_4(\eta^1{:}\eta^2{:}\mu\text{-}O_2CPh)_2]^0$ unit are listed in Table 3.

Table 5
Hydrogen bonding interactions in **1** and **2**.

Interaction D–H···A	D···A (Å)	H···A (Å)	D–H···A (°)	Symmetry operation of A
1				
O1–HO1···N2	2.894(6)	1.94(8)	159(7)	2 − *x*, 1 − *y*, −1 − *z*
2				
O1–HO1···O52	2.727(7)	1.92(8)	169(8)	*x*, −1 + *y*, *z*
O11–HO11···O41	2.781(7)	2.05(11)	157(11)	*x*, 1 + *y*, *z*

the free oxime group participating in hydrogen bonding interactions. Complex **1** is the first Zn^{II} complex of (3-py)C(H)NOH.

Complex **2** crystallizes in the monoclinic space group $P2_1/n$. The four *syn*, *syn*-η^1:η^1:μ $PhCO_2^-$ ligands display a paddle wheel arrangement about the Zn···Zn axis. Each Zn^{II} center has a square pyramidal coordination geometry [τ = 0.04 for Zn(1) and 0.02 for Zn(2)], with the apex provided by coordination of the pyridyl nitrogen atom of a monodentate (4-py)C(H)NOH ligand. The metal to apical atom distances are the same, i.e., 2.028(4) Å. The mean Zn–O(carboxylate) bond lengths are 2.054(5) Å for Zn(1) and 2.053(5) Å for Zn(2). These distances are typical and unremarkable [25]. Zn(1) lies 0.386 Å and Zn(2) lies 0.387 Å out of their respective least-squares basal planes towards N(1) and N(11), respectively. The Zn(1)···Zn(2)–N(11) and Zn(2)···Zn(1)–N(1) angles are the same, i.e. 160.8°. Dinuclear $[Zn_2(O_2CR)_4L_2]$ complexes (L = monodentate ligand) have previously been observed to be either collinear [26] or similarly offset [25]. The tetracarboxylate bridging framework can accommodate metal–metal separations of up to ~3.5 Å [25]. The Zn···Zn separation in **1** [2.990(2) Å] is shorter than this maximum, but longer than the Cu···Cu distances in structurally similar Cu_2^{II} complexes [27].

In the crystal lattice of **2**, the dinuclear molecules interact through hydrogen bonds forming double, ladder-like chains along the *b* axis (Table 5, Fig. 5). Both oxime groups act as donors to carboxylate oxygen atoms.

Complex **2** is a new member of a small family of paddle wheel $[Zn_2(O_2CPh)_4L_2]$ complexes [22,28]. It is the sixth structurally characterized metal complex of (4-py)C(H)NOH. The previously reported complexes $[UO_2(acac)_2\{(4\text{-py})C(H)NOH\}]$ [29a], $[Cu(ClO_4)_2(phen)\{(4\text{-py})C(H)NOH\}_2]\cdot(4\text{-py})C(H)NOH$ [29b], $[Ni\{(4\text{-py})C(H)NOH\}_4(H_2O)_2]Br_2\cdot 2(4\text{-py})C(H)NOH$ [29c], $[Ag_4Mn_2(CN)_8\{(4\text{-py})C(H)NOH\}_4(H_2O)_2]_n$ [29d] and $[Cu(dipic)\{(4\text{-py})C(H)NOH\}(H_2O)]$ [29e], where $acac^-$ is the pentane-2,4-dionato (−1) ion and $dipic^{2-}$ is the pyridine-2,6-dicarboxylato (−2) ligand, all involve monodentate (4-py)C(H)NOH ligands with the pyridine nitrogen as the donor atom.

4. Concluding comments and perspectives

The initial use of (3-py)C(H)NOH and (4-py)C(H)NOH in reactions with $Zn(O_2CPh)_2\cdot 2H_2O$ has yielded the first Zn^{II} complexes of these ligands; the complexes have interesting molecular and crystal structures. The nuclearity of the product depends on the isomeric ligand form used. This work demonstrates the synthetic potential of combining 3- or 4-pyridinealdoxime with carboxylate ligands. Complexes **1** and **2** augur well that they are merely the first members of a new family of 3d-metal carboxylate clusters with (*x*-py)C(H)NOH-based ligands (*x* = 2, 3, 4). We currently investigate several M^{II}/RCO_2^-/(3-py)C(H)NOH or (4-py)C(H)NOH reaction systems (M^{II} = Mn^{II}, Co^{II}, Ni^{II}, Cu^{II}, Cd^{II}; R = Me, CMe_3, Ph) as an entry point to clusters with various nuclearities and structural types.

Metal complexes with *N*, *O*- or *N*,*N*′-bidentate bridging behaviours of the two ligands or complexes in which the oxime functionality is deprotonated are not known to date, and it is currently not evident if such species could be capable of existence; such complexes could be high nuclearity clusters or coordination polymers. We are studying these matters. It is also clear that the M^{II}/(3-py)C(H)NOH or (4-py)C(H)NOH chemistry warrants expansion to anionic ligands other than carboxylates, e.g. NO_3^-, SO_4^{2-}, etc.

5. Supplementary data

CCDC 727528 and 727529 contains the supplementary crystallographic data for complexes **1** and **2**. These data can be obtained free of charge via http://www.ccdc.cam.ac.uk/conts/retrieving.html, or from the Cambridge Crystallographic Data Centre, 12 Union Road, Cambridge CB2 1EZ, UK; fax: (+44) 1223-336-033; or e-mail: deposit@ccdc.cam.ac.uk.

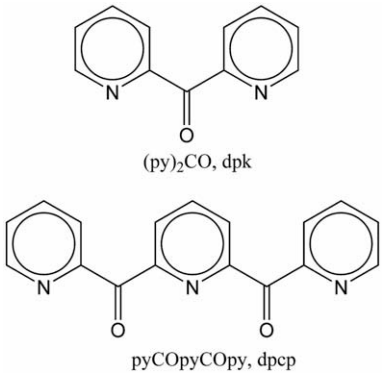
Acknowledgement

E.M.-Z and K.F.K thank the Research Committee of the University of Patras for funding this work (C. Karatheodory Grant 2008, No. C.584).

References

[1] (a) R.C. Mehrotra, R. Bohra, Metal Carboxylates, Academic Press, New York, 1983;
(b) J. Catterick, P. Thornton, Adv. Inorg. Chem. Radiochem. 20 (1977) 291;
(c) C.N.R. Rao, S. Natarajan, R. Vaidhyanathan, Angew. Chem. Int. Ed. 43 (2004) 1466.
[2] (a) W.N. Lipscomb, W. Sträter, Chem. Rev. 96 (1996) 2375;
(b) R.H. Holm, P. Kennepohl, E.I. Solomon, Chem. Rev. 96 (1996) 2239.
[3] M.-L. Tong, S.-L. Zheng, J.-X. Shi, Y.-X. Tong, H.K. Lee, X.-M. Chen, J. Chem. Soc., Dalton Trans. (2002) 1727.
[4] (a) D.J. Darensbourg, J.R. Wildeson, J.C. Yarbrough, Inorg. Chem. 41 (2002) 973;
(b) D.J. Darensbourg, M.S. Zimmer, Macromolecules 32 (1999) 2137.
[5] (a) V.Yu. Kukushkin, A.J.L. Pombeiro, Coord. Chem. Rev. 181 (1999) 147;
(b) A.G. Smith, P.A. Tasker, D.J. White, Coord. Chem. Rev. 241 (2003) 61.
[6] (a) C. Papatriantafyllopoulou, C.G. Efthymiou, C.P. Raptopoulou, A. Terzis, E. Manessi-Zoupa, S.P. Perlepes, Spectrochim. Acta, Part A 70 (2008) 718. and references therein;
(b) C.J. Milios, R. Inglis, A. Vinslava, R. Bagai, W. Wernsdorfer, S. Parsons, S.P. Perlepes, G. Christou, E.K. Brechin, J. Am. Chem. Soc. 129 (2007) 12505.
[7] (a) P. Chaudhuri, Coord. Chem. Rev. 243 (2003) 143;
(b) C.J. Milios, Th.C. Stamatatos, S.P. Perlepes, Polyhedron 25 (2006) 134. Polyhedron Report.
[8] Th.C. Stamatatos, D. Foguet-Albiol, S.-C. Lee, C.C. Stoumpos, C.P. Raptopoulou, A. Terzis, W. Wernsdorfer, S.O. Hill, S.P. Perlepes, G. Christou, J. Am. Chem. Soc. 129 (2007) 9484.
[9] H. Miyasaka, R. Clèrac, K. Mizushima, K. Sugiura, M. Yamasita, W. Wernsdorfer, C. Coulon, Inorg. Chem. 42 (2003) 8203.
[10] (a) H. Kumagai, M. Endo, M. Kondo, S. Kawata, S. Kawata, S. Kitagawa, Coord. Chem. Rev. 237 (2003) 197;
(b) C.J. Milios, P. Kyritsis, C.P. Raptopoulou, A. Terzis, R. Vicente, A. Escuer, S.P. Perlepes, Dalton. Trans. (2005) 501;
(c) C.J. Milios, E. Kefalloniti, C.P. Raptopoulou, A. Terzis, A. Escuer, R. Vicente, S.P. Perlepes, Polyhedron 23 (2004) 83.
[11] (a) M. Alexiou, E. Katsoulakou, C. Dendrinou-Samara, C.P. Raptopoulou, V. Psycharis, E. Manessi-Zoupa, S.P. Perlepes, D.P. Kessissoglou, Eur. J. Inorg. Chem. (2005) 1964;
(b) A.J. Stemmler, J.W. Kampf, V.L. Pecoraro, Inorg. Chem. 34 (1995) 2271.
[12] J.-L. Song, J.-G. Mao, H.-Y. Zeng, R.K. Kremer, Z.-C. Dong, Inorg. Chem. Commun. 6 (2003) 891.
[13] G.M. Sheldrick, SHELXS-86, Structure Solving Problem, University of Göttingen, Germany, 1986.
[14] G.M. Sheldrick, SHELXL-97, Program for the Refinement of Crystal Structures from Diffraction Data, University of Göttingen, Germany, 1997.
[15] K.W. Nordquest, D.W. Phelps, W.F. Little, D.J. Hodgson, J. Am. Chem. Soc. 98 (1976) 1104.
[16] P. Chaudhuri, M. Winter, U. Flörke, H.-J. Haupt, Inorg. Chim. Acta 232 (1995) 125.
[17] A.B.P. Lever, A. Mantovani, Inorg. Chem. 10 (1971) 817.
[18] G.B. Deacon, R.J. Phillips, Coord. Chem. Rev. 33 (1980) 227.
[19] C.C. Stoumpos, N. Lalioti, I.A. Gass, K. Gkotsis, A.A. Kitos, H. Sartzi, C.J. Milios, C.P. Raptopoulou, A. Terzis, E.K. Brechin, S.P. Perlepes, Polyhedron, in press, doi:10.1016/j.poly.2008.12.001.
[20] (a) S.P. Perlepes, E. Libby, W.E. Streib, K. Folting, G. Christou, Polyhedron 11 (1992) 923;
(b) J.-P. Costes, F. Dahan, J.-P. Laurent, Inorg. Chem. 24 (1985) 1018.
[21] A.W. Addison, T.N. Rao, J. Reedijk, J. Rijn, G.C. Verschoor, J. Chem. Soc., Dalton Trans. (1984) 1349.
[22] (a) H. Kwak, S.H. Lee, S.H. Kim, Y.M. Lee, B.K. Park, E.Y. Lee, Y.J. Lee, C. Kim, S.-J. Kim, Y. Kim, Polyhedron 27 (2008) 3484;
(b) A. Karmakar, R.J. Sarma, J.B. Baruah, Inorg. Chem. Commun. 9 (2006) 1169.
[23] R.L. Rardin, W.B. Tolman, S.J. Lippard, New J. Chem. 15 (1991) 417.
[24] (a) C.B. Aakeröy, A.M. Beatty, D.S. Leinen, J. Am. Chem. Soc. 120 (1998) 7383;
(b) C.B. Aakeröy, A.M. Beatty, D.S. Leinen, K.R. Lorimer, Chem. Commun. (2000) 935.
[25] Q. Zhou, T.W. Hambley, B.J. Kennedy, P.A. Lay, P. Turner, B. Warwick, J.R. Biffin, H.L. Regtop, Inorg. Chem. 39 (2000) 3742.
[26] W. Clegg, I.R. Little, B.P. Straugham, J. Chem. Soc., Dalton Trans. (1986) 1283.
[27] R. Sharma, A. Karmakar, J.B. Baruah, Inorg. Chim. Acta 361 (2008) 2081.

[28] (a) H. Necefoglu, W. Clegg, A.J. Scott, Acta Crystallogr. E58 (2002) m121;
(b) V. Zelenak, M. Sabo, W. Massa, J. Cernak, Acta Crystallogr. C60 (2004) m85;
(c) T. Ohmura, W. Mori, T. Takei, T. Ikeda, A. Maeda, Mater. Sci. 23 (2005) 729.
[29] (a) T. Kawasaki, T. Kitazawa, Acta Crystallogr. E64 (2008) m788;
(b) B. Zhang, S. Chu, X. Wang, G. Shen, R.-J. Wang, Acta Crystallogr. E59 (2003) m824;
(c) C.B. Aakeroy, A.M. Beatty, D.S. Leinen, Angew. Chem. Int. Ed. 38 (1999) 1815;
(d) T. Kawasaki, C. Kachi-Terajima, T. Saito, T. Kitazawa, Bull. Chem. Soc. Jpn. 81 (2008) 268;
(e) A.M. Mutambi, Acta Crystallogr. E64 (2008) m979.



Scheme 1. The dpk and dpcp ligands.

2. Experimental

2.1. Materials

All materials were commercially available and used as received expect dpcp, which was synthesized according to a literature procedure [6]. *Caution!* Although no such tendency was observed during the present work, perchlorate salts are potentially explosive and should be handled with care and in small quantities.

2.2. Synthesis

Solid dpcp (15.0 mg, 0.052 mmol) was added to a light orange solution of $Fe(ClO_4)_3$?$9H_2O$ (107.0 mg, 0.208 mmol) in MeOH (45 mL). After cooling, the solution was left for slow evaporation. Yellow crystals of $[Fe_2\{pyCO(OMe)pyCO(OMe)py\}_2(MeO)_2](ClO_4)_2$·MeOH (**1**·MeOH) formed after 3 days, which were filtered off and dried in vacuo. The yield was ~9 mg (~16% with respect to dpcp). The dried complex was analyzed as solvent-free. *Anal.* Calc. for $C_{40}H_{42}Cl_2Fe_2N_6O_{18}$: C, 44.59; H, 3.93; N, 7.80. Found: C, 44.32; H, 3.80; N, 7.72%.

2.3. X-ray crystallography

A crystal with approximate dimensions 0.07 × 0.18 × 0.47 mm was taken from the mother liquor and immediately cooled to −93 °C. Diffraction measurements were made on a Rigaku R-AXIS SPIDER Image Plate diffractometer using graphite monochromated Cu Kα radiation. Data collection (ω-scans) and processing (cell refinement, data reduction and Empirical absorption correction) were performed using the CrystalClear program package [13]. The structure was solved by direct methods using SHELXS-97 [14] and refined by full-matrix least-squares techniques on F^2 with SHELXL-97 [15]. Important crystallographic data are listed in Table 1. Further experimental crystallographic details for **1**·MeOH: $2\theta_{max}$ = 130°; reflections collected/unique/used, 28 753/7696 [R_{int} = 0.0521]/7696; 728 parameters refined; $(\Delta/\sigma)_{max}$ = 0.019; $(\Delta\rho)_{max}/(\Delta\rho)_{min}$ = 0.922/−0.758 e/Å^3; R_1/wR_2 (for all data), 0.0583/0.1417. Hydrogen atoms were either located by difference maps and were refined isotropically or were introduced at calculated positions as riding on bonded atoms. All non-hydrogen atoms were refined anisotropically.

2.4. Physical measurements

Elemental analysis for carbon, hydrogen, and nitrogen was performed on a PerkinElmer 2400/*II* automatic analyzer. Infrared spectra were recorded as KBr pellets in the range 4000–400 cm^{-1} on a Bruker Equinox 55/S FT-IR spectrophotometer. Mössbauer spectra were taken with a constant acceleration spectrometer using a ^{57}Co (Rh) source at RT and a variable temperature Oxford cryostat. Variable-temperature magnetic susceptibility measurements were carried out on a powdered sample of **1** in the 2–300 K temperature range using a Quantum Design MPMS SQUID susceptometer operating under a magnetic field of 1 T for **1**. Magnetization isotherms between 0 and 5.5 T were collected at 2 and 5 K for **1** and at 2 K for **2** and **3**. Diamagnetic corrections for the complexes were estimated from Pascal's constants. The magnetic susceptibility for **1** has been computed by exact calculation of the energy levels associated with the spin Hamiltonian through diagonalization of the full matrix with the enhanced version of a general program for axial symmetry [16]. Least-squares fittings were accomplished with an adapted version of the function-minimization program MINUIT [17]. The error-factor R is defined as $R = \sum \frac{(\chi_{exp}-\chi_{calc})^2}{N\chi^2_{exp}}$, where N is the number of experimental points. X-band EPR spectra at liquid helium temperatures were recorded on a Bruker ER 200D-SRC X-band spectrometer equipped with an Oxford ESR 9 cryostat, an NMR-Gaussmeter, and an Anritsu microwave frequency counter.

Table 1
Crystallographic data for complex **1**·MeOH.

	1·MeOH
Formula	$C_{41}H_{42}Cl_2Fe_2N_6O_{19}$
Fw	1105.41
Space group	$P\bar{1}$
a (Å)	12.6518(2)
b (Å)	13.0239(2)
c (Å)	15.9957(2)
α (°)	98.946(1)
β (°)	94.570(1)
γ (°)	113.199(1)
V (Å^3)	2364.11(6)
Z	2
T (°C)	−93
Radiation	Cu Kα
ρ_{calcd} (g cm^{-3})	1.553
μ (mm^{-1})	6.684
R_1[a]	0.0500[b]
wR_2[a]	0.1302[b]

[a] $w = 1/[\sigma^2(F_o^2) + (\sigma P)^2 + bP]$ and $P = (\max(F_o^2, 0) + 2F_c^2)/3$, $R_1 = \Sigma(|F_o| - |F_c|)/\Sigma(|F_o|)$ and $wR_2 = \{\sum[w(F_o^2 - F_c^2)^2]/\sum[w(F_o^2)^2]\}^{1/2}$.
[b] For 6615 reflections with $I > 2\sigma(I)$.

3. Results and discussion

3.1. Synthesis of $[Fe_2\{pyCO(OMe)pyCO(OMe)py\}_2(MeO)_2](ClO_4)_2$ (**1**)

For the preparation of **1** a simple reaction between iron(III) perchlorate and dpcp in MeOH was employed. The synthesis reaction of **1** can be summarized in the following equation:

$$2(FeClO_4)_3 \cdot 9H_2O + 2pyCOpyCOpy + 4MeOH \xrightarrow{MeOH} [Fe_2\{pyC(O)(OMe)py(H)C(O)(OMe)py\}_2(OMe)_2](ClO_4)_2 + 18H_2O + 4HClO_4 \quad (1)$$

The molecule of dpcp in **1** is present in its monoanionic $\{pyC(O)(OMe)py(H)C(O)(OMe)py\}^-$ form, observed here for the first time. In this form, the two hemiacetal functions are both deprotonated, while the central pyridine is protonated. The reasons for this behavior are currently unclear to us.

The forms of dpcp observed in other iron(III) complexes are $L^{2-} = \{pyC(O)(OMe)pyC(O)(OMe)py\}^{2-}$ in the trinuclear complex $[Fe_3(L)_2Cl_2(OMe)_2][FeCl_4]$ and $L'^- = \{pyCOpyC(O)(OR)py\}^-$ (R = H, Me) in a series of mononuclear complexes of the general formula $[Fe(L')_2Cl_2]$ [12]. Although in the case of the trinuclear complex

hot methanolic solutions were employed, in our work, heating was not required for full methanolysis. This point might be of chemical significance in the understanding of the solvolysis chemistry of dpcp and the synthetic parameters that govern it. However, given the small number of reported ferric complexes, this is not yet an easy task. In the absence of such examples, we believe that useful conclusions are to be drawn from the preparations of ferric complexes of dpk. Three such complexes have been structurally characterized, namely the mononuclear complex $[Fe\{(py)_2C(O)(OH)\}_2](NO_3)$ [18] and the clusters $[Fe_4\{(py)_2C(OMe)O\}_2\{(Hpy)(py)C(OMe)O\}_2(dbcat)_4](ClO_4)_2$ and $(HNEt_3)[Fe_3\{(py)_2C(OH)O\}_2(dbcat)_4]$ ($dbcat^{2-}$ = the dianion of 3,5-di-*tert*-butylcatechol) [19], all of which were prepared at ambient temperatures.

In light of these results, we might say that iron(III) exhibits a higher potential to assist the solvolysis of the C=O bond in dpk and dpcp, even at ambient temperatures. In the case of dpcp, full solvolysis may be expected, provided there is a sufficient quantity of nucleophile (e.g. H_2O and ROH). Thus, in the case of the mononuclear iron(III) complexes of L'^{-}, prepared by Mak and coworkers [12], the use of dry solvents with only small amounts of nucleophile (namely H_2O and MeOH) may be the cause for the partial solvolysis of dpcp.

3.2. Description of the structure

A partially labeled POV-Ray plot of complex **1** is shown in Fig. 1. Important structural parameters are shown in Table 2. Complex **1** crystallizes in the triclinic $P\bar{1}$ space group and consists of two independent dinuclear cationic complexes, each sitting on an inversion centre. The asymmetric unit contains the two half molecules, which generate the two cations through inversion. Due to the similarity of the cations, we will only describe the cation containing Fe(1), shown in Fig. 1. Due to symmetry, we will only describe Fe(1), unless otherwise required.

Fe(1) is hexacoordinate, exhibiting a distorted octahedral coordination sphere with a N_2O_4 chromophore. The Fe–L bond lengths range between 1.94 and 2.16 Å. The longest bonds are formed with the dpcp pyridine donors N(1) and N(3′) (2.158(3) and 2.159(3) Å, respectively), while the shortest ones are formed with the dpcp alkoxo oxygen atoms O(1) and O(3′) (1.946(2) and 1.951(2) Å, respectively).

Bridging within **1** is accomplished through two monatomic $\mu:\eta^2$ methoxo bridges, which form a Fe–O–Fe angle of 105.2(1)°. Additional bridging is provided by the dpcp ligand, present in its *bis*-hemiacetal form. In particular, the ligand is bis-chelating to each Fe atom, adopting a $\mu:\eta^1:\eta^1:\eta^1:\eta^1$ bridging mode, observed for the first time in the structurally characterized complexes of dpcp (Scheme 2). The cause for this coordination mode is the protonation of the central pyridine, which renders it coordinatively inactive.

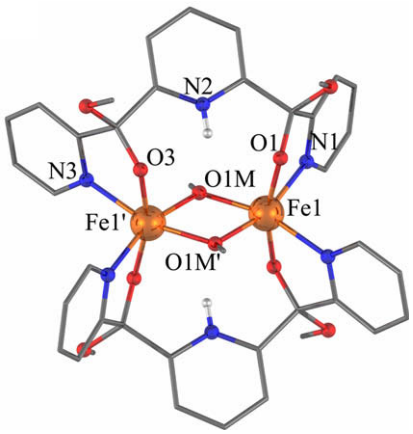
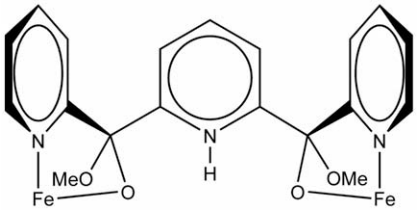


Fig. 1. Partially labeled POV-Ray plot of the cation in **1**.

Table 2
Selected bond distances (Å) and angles (°) for **1**.

Fe(1)–O(1)	1.946(2)	Fe(2)-O(23″)	1.962(2)
Fe(1)–O(3′)	1.951(2)	Fe(2)–O(21)	1.966(2)
Fe(1)–O(1M)	2.012(3)	Fe(2)–O(2M″)	2.008(2)
Fe(1)–O(1M′)	2.015(2)	Fe(2)–O(2M)	2.023(2)
Fe(1)–N(1)	2.158(3)	Fe(2)–N(23″)	2.149(3)
Fe(1)–N(3′)	2.159(3)	Fe(2)–N(21)	2.156(3)
Fe(1)···Fe(1′)	3.200(1)	Fe(2)···Fe(2″)	3.201(1)
O(1)–Fe(1)–O(3′)	162.52(11)	O(23″)–Fe(2)–O(21)	161.40(10)
O(1)–Fe(1)–O(1M)	101.33(10)	O(23″)–Fe(2)–O(2M″)	104.06(10)
O(3′)–Fe(1)–O(1M)	92.23(10)	O(21)–Fe(2)–O(2M″)	90.85(10)
O(1)–Fe(1)–O(1M′)	92.74(10)	O(23″)–Fe(2)–O(2M)	92.34(10)
O(3′)–Fe(1)–O(1M′)	101.49(10)	O(21)–Fe(2)–O(2M)	102.40(10)
O(1M)–Fe(1)–O(1M′)	74.79(10)	O(2M″)–Fe(2)–O(2M)	74.85(10)
O(1)–Fe(1)–N(1)	77.60(11)	O(23″)–Fe(2)–N(23″)	77.36(10)
O(3′)–Fe(1)–N(1)	90.88(11)	O(21)–Fe(2)–N(23″)	91.23(11)
O(1M)–Fe(1)–N(1)	92.87(11)	O(2M″)–Fe(2)–N(23″)	92.16(10)
O(1M′)–Fe(1)–N(1)	162.71(11)	O(2M)–Fe(2)–N(23″)	161.13(12)
O(1)–Fe(1)–N(3′)	91.24(11)	O(23″)–Fe(2)–N(21)	91.82(11)
O(3′)–Fe(1)–N(3′)	77.81(11)	O(21)–Fe(2)–N(21)	77.08(11)
O(1M)–Fe(1)–N(3′)	163.42(11)	O(2M″)–Fe(2)–N(21)	158.24(10)
O(1M′)–Fe(1)–N(3′)	94.03(11)	O(2M)–Fe(2)–N(21)	89.96(10)
N(1)–Fe(1)–N(3′)	100.42(12)	N(23″)–Fe(2)–N(21)	105.95(11)
C(1M)–O(1M)–Fe(1)	122.8(2)	C(2M)–O(2M)–Fe(2″)	122.3(2)
C(1M)–O(1M)–Fe(1′)	123.4(2)	C(2M)–O(2M)–Fe(2)	124.3(2)
Fe(1)–O(1M)–Fe(1′)	105.21(1	Fe(2″)–O(2M)–Fe(2)	105.15(10)

Symmetry operations: ′ = $-x+1, -y+1, -z+2$; ″ = $-x+2, -y+1, -z+1$.



Scheme 2. Bridging mode of dpcp in **1**.

3.3. Ir spectroscopy

A strong band at 3138 and a weaker one at 3110 cm^{-1} are assigned to the υ[C–H(py)] stretching vibrations of the pyridyl moieties of dpcp. A medium-intensity band at 2970 cm^{-1} is assigned to the asymmetric υ_{as}[C–H(CH_3)] stretching vibration of the methyl functions of the dpcp ligands and the bridging methoxides. The symmetric υ_s[C–H(CH_3)] vibration is more sensitive to the adjacent groups [20]. For these two types of methyls, these bands are found at 2931 and 2825 cm^{-1}, respectively.

The bands at 1603, 1491, 1471 and 1444 are attributed to the stretching υ(C···C) and υ(C···N) vibrations of the pyridyl rings of dpcp. A series of bands between 1300 and 1100 cm^{-1} (1320, 1299, 1269, 1245, 1222, 1186, 1133 cm^{-1}) are assigned to the in-plane δ[C–H(py)] deformations of the pyridyl groups of dpcp.

A strong and broad band around 1100 cm^{-1} and the medium band at 624 cm^{-1} are attributed to the $\nu_3(F_2)$ and $\nu_4(F_2)$ modes, respectively, of the uncoordinated T_d perchlorate anions [21].

The band at 1051 cm^{-1} is assigned to the υ[C–O(OCH_3)$_{dpcp}$] stretching vibration of the –OCH_3 function of dpcp, while the 1023 cm^{-1} band is assigned to the υ[C–O(OCH_3)] stretching vibration of the methoxo bridges [22].

The out-of-pane π[C–H(py)] vibrations for the pyridyl rings appear split to two bands at 789 and 767 cm^{-1}, assigned to the two

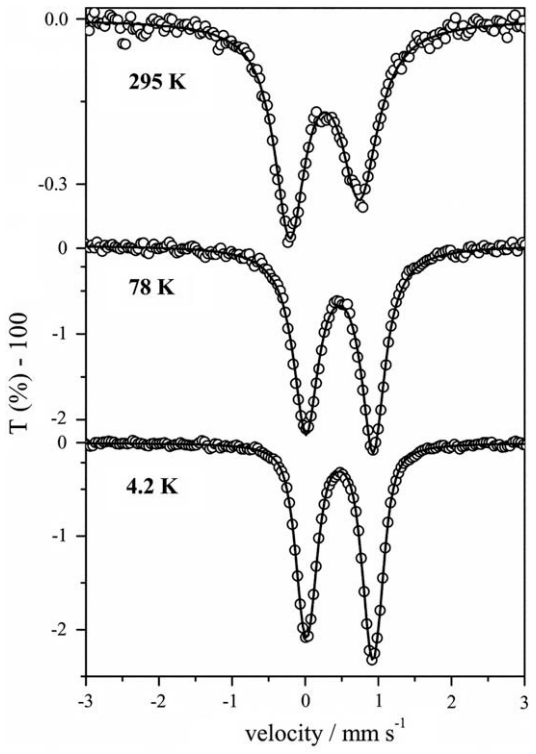


Fig. 2. Mössbauer spectra of 1 at various temperatures.

types of pyridyl functions of dpcp, i.e. external (mono-substituted) and internal (disubstituted).

3.4. Mössbauer spectroscopy

Mössbauer spectra of complex **1** are shown in Fig. 2. Due to the crystallographically imposed symmetry for each cation in **1** and due to the structural resemblance of the two cations, a single quadrupole-split doublet is expected for its Mössbauer spectrum. The 295 K spectrum of **1** consists of an asymmetric quadrupole-split doublet, whose isomer shift is indicative of high-spin ferric ions in octahedral N/O environments.

Initial fitting attempts were carried out using asymmetric Lorentzians. These afforded mediocre fits. High-quality fits were obtained only when Voigt lines were considered; these are the ones presented here. For the fits, the linewidths and areas of the two peaks of each doublet were fitted separately. The results of the fits are shown in Table 3. An increase in the isomer shift upon cooling is attributed to a second-order Doppler effect [23].

From these results it is seen that there are important asymmetries of the quadrupole-split doublets. Such asymmetries have been attributed to several phenomena and can be divided to area asymmetry and linewidth asymmetry.

Area asymmetry ($A_-/A_+ \neq 1$) is attributed to the anisotropy of the recoil-free fraction (Goldanskii–Karyagin effect) [24]. This effect is associated with anisotropic vibrations in the crystal lattice, of sites with lower than cubic symmetry. These anisotropic vibrations produce an anisotropic Debye–Weller factor, which is the source for the anisotropic recoil-free fraction. The result is an asymmetry of the relative intensities of the two Mössbauer lines. Since the area of a line is the measure of its intensity, the Goldanskii–Karyagin effect is perceived as an area asymmetry. Upon heating, the accelerated vibrations cause an increase of the recoil-free fraction anisotropy, and hence of the asymmetry. In our case, however, the area asymmetry being only marginal at high temperatures ($A_-/A_+ = 1.04$), this possibility is discarded.

Another source of area asymmetry are texture effects due to crystallite orientation in the packed sample. However, this should not give rise to a temperature-dependent asymmetry as is the case here, so this possibility is also discarded.

Linewidth asymmetry ($\Gamma_-/\Gamma_+ \neq 1$) has been attributed to the thermal population of the excited $S_T = 1, 2, 3, 4, 5$ states [25], which are expected to exhibit a zero-field splitting (zfs). It has been proposed by Reiff and coworkers, that this zfs of the excited states leads to slow *inter*molecular spin–spin relaxation, due to the poor exchange pathway between neighboring molecules (*intra*molecular spin–spin relaxation is expected to be fast due to the small intermetallic separations). At low temperatures, only the ground $S_T = 0$ state will be populated, which is free of hyperfine splitting or paramagnetic relaxation due to zfs. Therefore, symmetric doublets are expected at those temperatures. Upon heating, thermal population of the anisotropic excited states will cause a decrease of the intermolecular spin–spin relaxation rate and consequently to doublet asymmetries.

Given the fact that our spectra were area symmetric at room temperature and linewidth asymmetric ($\Gamma_-/\Gamma_+ = 0.844$), we conclude that the source of the asymmetry is the thermal population of higher spin multiplicity anisotropic states. The large intermolecular separation (9.47 Å) in **1** is also in agreement with the mechanism of slow *inter*molecular spin–spin relaxation. The same source of asymmetry has been found in other diferric complexes exhibiting weak antiferromagnetic couplings through hydroxo- [25,26] or alkoxo-[27] bridges. In one case [28], a similar behavior was observed for a diferric complex with a postulated benzoquinone bridge and a very weak ($J = -2.0\ \mathrm{cm}^{-1}$) antiferromagnetic coupling.

Table 3
Mössbauer parameters for **1** at various temperatures.

T (K)	δ (mm s^{-1})[a]	ΔE_Q (mm s^{-1})	Γ_+ (mm s^{-1})[b]	Γ_-/Γ_+	A_-/A_+
295	0.374	0.955	0.604	0.844	1.04
78	0.469	0.919	0.389	1.06	0.960
4.2	0.471	0.903	0.258	0.984	1.10

[a] Referenced to iron foil at 300 K.
[b] Half-width at half-maximum.

3.5. Magnetic properties

Magnetic susceptibility data for complex **1** are shown in Fig. 3. The $\chi_M T$ value of **1** at 300 K is 5.34 cm^3 mol^{-1} K, lower than theoretically expected for two non-interacting $S = 5/2$ spins (8.76 cm^3 mol^{-1} K, $g = 2$). This indicates the interplay of antiferro-

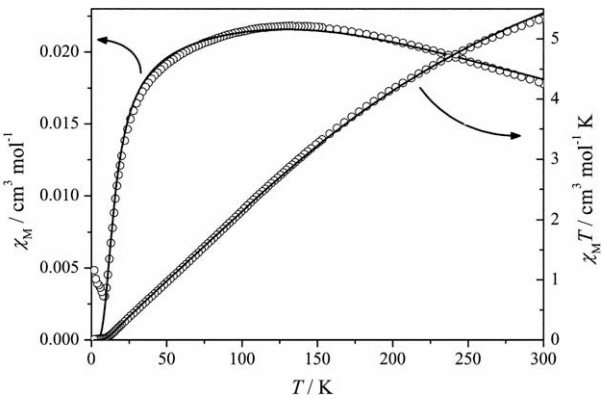


Fig. 3. χ_M and $\chi_M T$ vs T data for complex **1** and calculated curves according to the model described in the text.

magnetic interactions. This is corroborated by the constant drop of the $\chi_M T$ product upon cooling (9.4×10^{-3} cm^3 mol^{-1} K at 2 K), and by a broad maximum of the χ_M versus T curve around 130 K. A small rise of χ_M below 8 K is attributed to a small fraction of high-spin ferric paramagnetic impurity.

For the interpretation of the data, a simple model consisting of two $S = 5/2$ spins was considered. The observation of increased asymmetries in the linewidths of the Mössbauer spectra at high temperatures, prompted us to include a single-ion zfs parameter, common for the two sites. The Hamiltonian used was:

$$\hat{H} = -2J\hat{\mathbf{S}}_1\hat{\mathbf{S}}_2 + D(\hat{S}_{z1}^2 + \hat{S}_{z2}^2) \quad (2)$$

To avoid contributions from the paramagnetic impurity, fits were carried out over the 20–300 K region. Initial fitting attempts were carried out considering $D = 0$. These yielded satisfactory fits with best-fit parameters $J = -15.6$ cm^{-1}, $g = 2.04$ with $R = 9.9 \times 10^{-5}$. This J value is consistent with values derived for other bis-methoxo-bridged diferric complexes, which were found to vary between -5.7 and -28.6 cm^{-1} [29] and implies an $S = 1$ first excited state at 31.2 cm^{-1}.

Additional fitting attempts were made, releasing the D parameter. However, it was found that this parameter did not sufficiently influence the calculated curve for its value to be reliably determined by magnetic susceptibility data.

3.6. Epr spectroscopy

In order to study further the magnetic properties of complex **1** we carried out EPR spectroscopic studies at the X-band. Measurements from powdered samples were carried out over the 4.2–200 K temperature range and indicative spectra are shown in Fig. 4.

At 4.2 K the spectrum consists of relatively weak signals: an absorption peak at g ~ 6.00 and a sharp derivative at $g \sim 4.3$. Both signals are attributed to two different monomeric high-spin ferric species representing a small amount of impurities in agreement with the magnetic susceptibility measurements. As the temperature increases new signals emerge in a wide field range. The temperature dependence of these signals strongly suggests that they arise from excited states ($S > 0$) of the dimer and is consistent with the analysis of the magnetic susceptibility measurements. Similar EPR signals at X-band have been observed from other antiferromagnetically coupled ferric dimers and were attributed to the excited states of the system [30]. Such signals are affected by the combination of single-ion anisotropy and non-Heisenberg exchange interactions. A comparison with the signals observed in other diferric systems [30] suggests that these interactions are also present in the case of **1**.

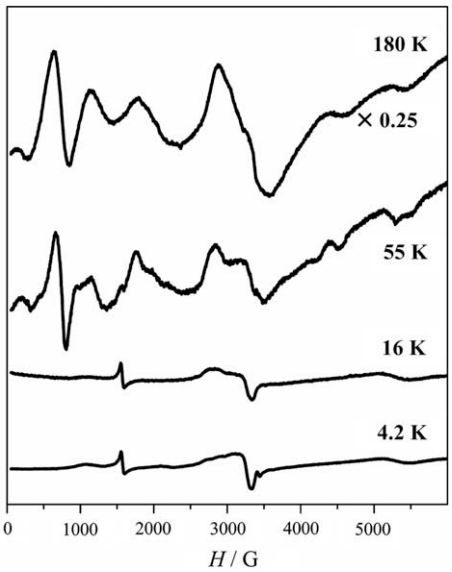


Fig. 4. Temperature dependence of X-band EPR spectra from powdered samples of **1**. The spectra are normalized according to Intensity × Temperature. Other EPR conditions. Modulation amplitude: 25 Gpp, microwave power: 2.2 mW, microwave frequency: 9.43 GHz.

4. Conclusions

Our research on the cluster chemistry of dpcp, continues to reveal new capabilities of this ligand in adopting different forms (of varying degrees of solvolysis or protonation) and coordination modes. Clearly, this chemistry has still a lot of promising results to afford.

In particular, its use in combination with iron(III) gave access to a dinuclear complex bridged by two alkoxo ligands. Complex **1** was found to contain dpcp in a *bis*-hemiacetal, monoanionic form, observed here for the first time. In this form, the two hydroxyl functions were deprotonated, whereas the central pyridine was protonated and coordinatively inactive. This was an interesting finding from a Chemical perspective.

The physical properties for complex **1** were in agreement with its structure. The *bis*-methoxo-bridged core exhibited a weak antiferromagnetic coupling as expected, which gives rise to several phenomena associated with the thermal population of the excited states. On one hand, this thermal population of the anisotropic $S = 1, 2, 3, 4, 5$ states was manifested as a linewidth asymmetry of the Mössbauer spectra at high temperatures. This asymmetry was associated with spin–spin intermolecular relaxation, which is decelerated by the population of these anisotropic states. On the other hand, thermal population of these states gave rise to EPR signals, of increasing intensity upon heating. Thus, from a Physical perspective, complex **1** was found to be interesting, for allowing us to directly monitor the thermal population of its excited magnetic states by different spectroscopic techniques (Mössbauer, EPR), instead of deriving them indirectly from magnetic susceptibility data.

Supplementary data

CCDC 721737. contains the supplementary crystallographic data for this paper. These data can be obtained free of charge via http://www.ccdc.cam.ac.uk/conts/retrieving.html, or from the Cambridge Crystallographic Data Centre, 12 Union Road, Cambridge CB2 1EZ, UK; fax: (+44) 1223-336-033; or e-mail: deposit@ccdc.cam.ac.uk.

Acknowledgments

We are grateful to the Ministerio de Educación y Ciencia (Spain) (Project CTQ2006-15672-C05-03) for its financial support, and FEDER co-financing.

References

[1] See A.K. Boudalis, Y. Sanakis, C.P. Raptopoulou, V. Psycharis, Magnetic phenomena in zero-dimensional transition-metal spin-clusters, in: Magnetism and Superconductivity in Low-dimensional Systems: Utilization in Future Applications, Nova Science Publishers Inc., New York, 2008. and references therein.
[2] M. Soler, W. Wernsdorfer, K. Folting, M. Pink, G. Christou, J. Am. Chem. Soc. 126 (2004) 2156.
[3] A.J. Tasiopoulos, A. Vinslava, W. Wernsdorfer, K.A. Abboud, G. Christou, Angew. Chem., Int. Ed. 43 (2004) 2117.
[4] G.S. Papaefstathiou, S.P. Perlepes, Comments Inorg. Chem. 23 (2002) 249.

[5] A.K. Boudalis, Y. Sanakis, J.M. Clemente-Juan, B. Donnadieu, V. Nastopoulos, A. Mari, Y. Coppel, J.-P. Tuchagues, S.P. Perlepes, Eur. J. 14 (2008) 2514.
[6] B. Abarca, R. Ballesteros, M. Elmasnaouy, Tetrahedron 54 (1998) 15287.
[7] A.K. Boudalis, C.P. Raptopoulou, B. Abarca, R. Ballesteros, M. Chadlaoui, J.-P. Tuchagues, A. Terzis, Angew. Chem., Int. Ed. 45 (2006) 432.
[8] A.K. Boudalis, C.P. Raptopoulou, V. Psycharis, Y. Sanakis, B. Abarca, R. Ballesteros, M. Chadlaoui, Dalton Trans. (2007) 3582.
[9] A.K. Boudalis, C.P. Raptopoulou, V. Psycharis, B. Abarca, R. Ballesteros, Eur. J. Inorg. Chem. (2008) 3796.
[10] A.K. Boudalis, M. Pissas, C.P. Raptopoulou, V. Psycharis, B. Abarca, R. Ballesteros, Inorg. Chem. 47 (2008) 10674.
[11] A. N. Georgopoulou, C.P. Raptopoulou, V. Psycharis, R. Ballesteros, B. Abarca, A.K. Boudalis, Inorg. Chem. 48 (2009) 3167.
[12] X.-D. Chen, M. Du, F. He, X.-M. Chen, T.C.W. Mak, Polyhedron 24 (2005) 1047.
[13] Rigaku/MSC, CrystalClear, Rigaku/MSC Inc., The Woodlands, TX, USA, 2005.
[14] G.M. Sheldrick, SHELXS-97: Structure Solving Program, University of Göttingen, Germany, 1997.
[15] G.M. Sheldrick, SHELXL-97: Crystal Structure Refinement Program, University of Göttingen, Germany, 1997.
[16] J.-M. Clemente-Juan, C. Mackiewicz, M. Verelst, F. Dahan, A. Bousseksou, Y. Sanakis, J.-P. Tuchagues, Inorg. Chem. 41 (2002) 1478.
[17] F. James, M. Roos, Comput. Phys. Commun. 10 (1975) 345.
[18] J. Woltz, B.L. Westcott, G. Grundwell, M. Zeller, A.D. Hunter, S.O. Sommerer, Acta Crystallogr., Sect. E 58 (2002) m609.
[19] A.K. Boudalis, F. Dahan, A. Bousseksou, J.-P. Tuchagues, S.P. Perlepes, Dalton Trans. (2003) 3411.
[20] L.J. Bellamy, The Infra-red Spectra of Complex Molecules, Chapman and Hall, London, 1975. pp. 13–15.
[21] K. Nakamoto, Infrared and Raman Spectra of Inorganic and Coordination Compounds, 4th ed., Wiley, New York, 1986.
[22] H. Houjou, M. Kanesato, K. Hiratani, D. Mandon, Chem. Eur. J. 10 (2004) 4576.
[23] N.N. Greenwood, T.C. Gibbs, Mössbauer Spectroscopy, Chapman and Hall, New York, 1971.
[24] (a) Vi.I. Goldanskii, G.M. Gorodinskii, S.V. Karyagin, L.A. Korytko, L.M. Krizhanskii, E.F. Makarov, V.V. Khrapov, Doklady Akad. Nauk S.S.S.R. 147 (1962) 127;
(b) S.V. Karyagin, Doklady Akad. Nauk S.S.S.R. 148 (1963) 102.
[25] L. Borer, C. Ceccarelli, M. Glick, J.H. Zhang, W.M. Reiff, Inorg. Chem. 22 (1973) 1719.
[26] A.K. Boudalis, J.M. Clemente-Juan, F. Dahan, V. Psycharis, C.P. Raptopoulou, B. Donnadieu, Y. Sanakis, J.-P. Tuchagues, Inorg. Chem. 47 (2008) 11314.
[27] L. Cianchi, F. Del Giallo, M. Lantieri, P. Moretti, G. Spina, A. Caneschi, Phys. Rev. B 69 (2004) 014418.
[28] S.L. Kessel, D.N. Hendrickson, Inorg. Chem. 17 (1978) 2630.
[29] R. Werner, S. Ostrovsky, K. Griesar, W. Haase, Inorg. Chim. Acta 326 (2001) 78.
[30] (a) R.G. Wollmann, D.N. Hendrickson, Inorg. Chem. 17 (1978) 926;
(b) A. Ozarowski, B. McGarvey, J.E. Drake, Inorg. Chem. 34 (1995) 5558;
(c) S.J.W. Holgate, G. Bondarenko, D. Collison, F.E. Mabbs, Inorg. Chem. 38 (1999) 2380.

(**1**) (HAc4Ph denotes the 4-phenyl-2-acetylpyridine thiosemicarbazone molecule) [17]. The anionic $Ac4Ph^-$ acts as a tridentate ligand which coordinates to manganese(II) through the pyridyl nitrogen, N(1), the azomethine nitrogen, N(2), and the thiolato sulfur atom (Scheme 1). The tridentate ligand has a ZEZ configuration based on the C(5)–C(6), N(2)–C(6) and N(3)–C(8) bonds for the donor centres nitrogen, nitrogen and sulfur, respectively. The manganese atom is coordinated in a distorted octahedral configuration in a *trans*-N(2)–*cis*-N(1)–*cis*-S configuration. Complex **1** belongs to a relatively rare class of octahedral Mn(II) complexes exhibiting sulfur coordination.

Among the few octahedral Mn(II) complexes with sulfur coordination two have been studied by EPR spectroscopy [18,19]. In both cases non negligible ZFS was observed. For the complex $[Mn([9]aneN_2S)_2](ClO4)_2$ ([9]aneN$_2$S: 1-thia-4,7-diazacyclononane) [18], simulations of the powder X- and Q-band EPR spectra allowed the determination of the absolute value of the axial Zero Field Splitting term (0.19 cm^{-1}). In the complexes described in Ref. [19] the value of the ZFS terms was not reported. However, the X-band EPR spectrum of frozen solution at 77 K from Mn(Me2L) complex [19] indicates ZFS smaller than 0.3 cm^{-1}.

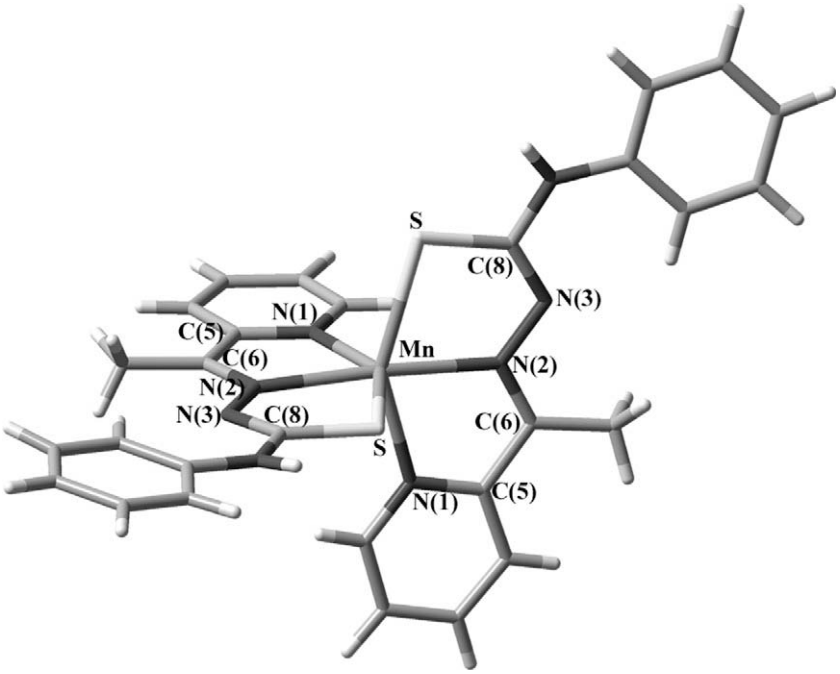
The purpose of the present work is to study the electronic properties of **1** by EPR spectroscopy. In solid state, **1** gives rise to a broad derivative feature at X-band. Such a behavior is indicative of intermolecular interactions. This is consistent with the molecular packing revealed in the crystal structure of **1**, which indicates extended network of hydrogen bonds and π–π stacking interactions. In a frozen DMSO solution, dual mode X-band EPR spectra exhibit signals, that agree with mononuclear Mn(II) species [17]. The spectra, however, are rather complicated spanning several hundred mT at X-band and quantitative information cannot be easily derived without tedious simulation efforts. Therefore we present here a HF EPR investigation for determining the ZFS parameters of **1** in DMF solution. Moreover, the electronic properties of **1** are studied by means of theoretical calculations. A good agreement between theoretical and experimental values is found. In many cases the experimental spectra are characterized by line-broadening. This line-broadening is usually attributed to distributions of the parameters pertinent to the system. For instance, in the present case the line-broadening is correlated with distribution of the D and E parameters. Apparently, distribution on such parameters reflects distribution on the electronic parameters of the system which in turn may originate from geometrical distortions. In the present work, we attempt to correlate the experimentally derived distributions on D and E with distribution on the geometry of the complex. It is found that reasonable structural distortions can account for such distributions.

2. Experimental

2.1. EPR spectroscopy

The synthesis and the crystal structure of **1** have been reported elsewhere [17]. The EPR studies were carried out in frozen solutions of **1** in dimethyl formamide, DMF, or dimethyl sulfoxide, DMSO (∼4 mM). Dual mode X-band EPR measurements were carried out with an upgraded Bruker ER-200D spectrometer equipped with a Bruker Dual Mode cavity, an Anritsu frequency counter, an NMR Gaussmeter and an Oxford ESR-9 cryostat. The spectra were found to be independent on the concentration of the solutions in the 0.4–5.0 mM range. HF-EPR spectra were recorded on a laboratory made spectrometer [20]. Gunn diodes operating at 95 and 115 GHz have been used as the radiation source. The frequency is calibrated via the Gunn diode. The magnetic field was produced by a superconducting magnet (0–12 T). Simulations of the spectra were carried out with SpinCount software kindly provided to us by Prof. M. Hendrich, Department of Chemistry, Carnegie Mellon University, Pittsburgh, PA, USA.

The spectral lineshapes are determined by assuming a distribution on the ZFS parameters D and E/D of Eq. (1). We assume that the variation of these parameters follows a Gaussian distribution specified as one standard deviation, σ_D, $\sigma_{E/D}$. A residual linewidth of σ_B in the magnetic field is also specified to account for other unspecified line-shape determinants, such as unresolved hyperfine from coordinated nitrogen to Mn(II). Gaussian spin-packets with linewidths determined in relation to these linewidth parameters



Scheme 1. The crystal structure of **1**.

(σ_D, $\sigma_{E/D}$ and σ_B) and properly normalized for field-swept experimental spectra are folded into the spectrum at each resonance position.

2.2. Computational

Geometry optimizations were conducted with the GAUSSIAN 03 suite of programs [21] by using DFT methods [22]. The model chemistry used in this particular case was the BP86 [23] functional, along with the TZVP [24] basis set of Ahlrichs, i.e. BP86/TZVP optimizations were performed under C_2 point group symmetry, where the C_2 axis traverses the Mn(II) ion. Harmonic frequencies calculations were also performed at the BP86/TZVP level of theory and produced no imaginary frequencies, which signifies that the optimized structure pertains to an equilibrium point. Tight self consistent field, SCF, and geometry optimization criteria were used throughout the calculations. Due to the $S = 5/2$ ground state, unrestricted, *U*, open shell wavefunctions were used, i.e. different spatial functions were used to describe α and β electrons.

Theoretical calculations of the ZFS parameters were carried out with the ORCA program package [25]. Unrestricted Kohn–Sham formalism was applied for the solution of the SCF equations at the BP86/TZVP level of theory. Tight SCF convergence criteria were applied during the single-point calculations, and for the Mn(II) cation, the integration grid accuracy was increased compared to the atoms remainder. The centre of electric charge is the choice of the gauge origin in our calculations.

In the ZFS tensor calculation, two kinds of contributions have to be considered: (i) the first order terms, i.e. the spin–spin, SS, interactions, and (ii) the second order terms, i.e. the spin–orbit coupling, SOC [26]. SS interactions are a two-electron effect and very difficult to calculate accurately [26]. However, it was included in the $\tilde{D}$ tensor calculation [27a], by using the direct spin density, obtained from the single-point calculation. In the Breit–Pauli approximation, the SOC operator is [27]:

$$\hat{H}_{SOC} = \hat{H}^{(1)}_{SOC} + \hat{H}^{(2)}_{SSOC} + \hat{H}^{(2)}_{SOOC}, \quad (2)$$

which contains one-electron, $\hat{H}^{(1)}_{SOC}$, and two-electron, $\hat{H}^{(2)}_{SSOC}$ and $\hat{H}^{(2)}_{SOOC}$, terms, where SSOC and SOOC stand for spin-same orbit and spin-other orbit coupling, respectively. The SOC operator is also difficult to handle computationally, so the spin–orbit mean-field, SOMF, [28] approximation to the full Breit–Pauli operator, and in particular the variation of the SOMF operator implemented in ORCA, is employed in our study [29]. The second order contribution to $\tilde{D}$ has three components, as was derived elsewhere [30]. If the ground state has a total spin number *S*, then the excited states interacting with the ground state, via SOC, acquire a total spin number of either *S*, $S + 1$ or $S - 1$ [30]. In a more compact form, the ZFS is equal to:

$$D = D_{SS} + D^{S,S}_{SOC} + D^{S,S+1}_{SOC} + D^{S,S-1}_{SOC}. \quad (3)$$

In order to calculate the SOC contribution to ZFS, four types of excitations must be considered [30]:

(i) DOMO → SOMO ($\beta \rightarrow \beta$), which couples excited states with the same multiplicity as the ground state,
(ii) SOMO → VMO ($\alpha \rightarrow \alpha$), which also couples excited states with the same multiplicity as the ground state,
(iii) SOMO → SOMO ($\alpha \rightarrow \beta$), which couples excited states of an $S - 1$ total multiplicity to the ground state, and
(iv) DOMO → VMO ($\beta \rightarrow \alpha$), which couple excited states of an $S + 1$ total multiplicity to the ground state.

DOMO, SOMO and VMO stand for doubly occupied, singly occupied and virtual molecular orbital, respectively. The exact equations used to calculate D_{SS} and D_{SOC} tensor matrix elements can be found in the article by Neese [31]. The SOC contribution to *D* was calculated using the coupled-perturbed method, which uses revised prefactors for the spin-flip terms and solves a set of coupled-perturbed SCF, equations for the SOC perturbation [31].

3. Results and discussion

Preliminary dual mode X-band EPR spectroscopic studies from **1** in DMSO gave rise to complicated spectra spanning several hundred mT, which were consistent with a $|D|$ value of the order of 0.1 cm^{-1} [17]. For this order of magnitude, the EPR spectra recorded at high frequencies (>95 GHz) and high magnetic fields (>2.0 T) are expected to be less complicated and their interpretation almost straightforward. Therefore, we first present the results from HF-EPR studies.

3.1. High frequency/high field EPR studies

In Fig. 1, we show the 5 K EPR spectrum from **1** in a DMF solution recorded at 115 GHz. The part of the spectrum centred at $g = 2.0$ is characterized by a sharp strong feature which has attributed to the transitions occurring between the states $M_s = -1/2$ and $M_s = +1/2$. This part of the spectrum has been removed for clarity purposes from Fig. 1. It is shown in more detail in Fig. 2 and will be discussed separately. Despite the poor S/N the interpretation of the spectrum is quite straightforward [11]. It is consistent with a negative *D* term with moderate rhombicity. Under these conditions, the two peaks at the lower field part of the spectrum arise from the $-\frac{5}{2} \leftrightarrow -\frac{3}{2}$ and $-\frac{3}{2} \leftrightarrow -\frac{1}{2}$ transitions for molecules lying with the *z*-axis of the ZFS tensor parallel to the external magnetic field. First order perturbation treatment [11] of the spin Hamiltonian of Eq. (1) is considered a good approximation for those transitions in high field limit conditions and the separation of these two peaks is given by $\frac{2D}{g\beta}$, independently on the parameter *E*. The separation of the peaks from the spectrum is roughly 20 mT, from which the value of *D* is restricted between −0.1 and −0.09 cm^{-1}. The high magnetic field part of the spectrum arises from molecules lying with their *z*-axis perpendicular to the external magnetic field. The signals from the $-\frac{5}{2} \leftrightarrow -\frac{3}{2}$ and $-\frac{3}{2} \leftrightarrow -\frac{1}{2}$ transitions do not exhibit hyperfine features, whereas the former are broader than the

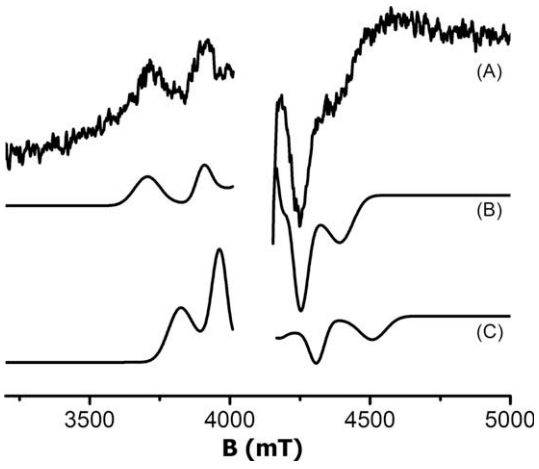


Fig. 1. Experimental (A) and simulated (B and C) 115 GHz EPR spectra from a frozen DMF solution of **1**. Simulated spectra are calculated from Eq. (1) with $D = -0.095$ cm^{-1} (B) or +0.095 cm^{-1} (C), $E/D = 0.15$, $A = 7.8 \times 10^{-4}$ cm^{-1}, $g = 1.999$, $\sigma_D = 0.01$ cm^{-1}, $\sigma_{E/D} = 0.04$, $\sigma_B = 2.0$ mT.

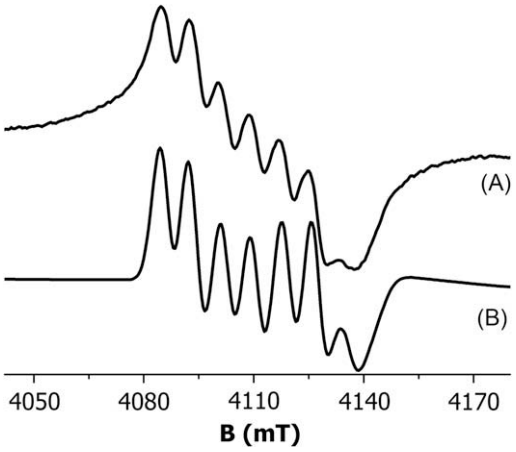


Fig. 2. Experimental (A) and simulated (B) 115 GHz EPR spectra from a frozen DMF solution of **1**. The simulated spectrum is obtained from Eq. (1) with $D = -0.095\ cm^{-1}$, $E/D = 0.15$, $A = 7.8 \times 10^{-3}\ cm^{-1}$, $g = 1.999$ and $\sigma_D = 0.01\ cm^{-1}$, $\sigma_{E/D} = 0.04$, $\sigma_B = 2.0$ mT.

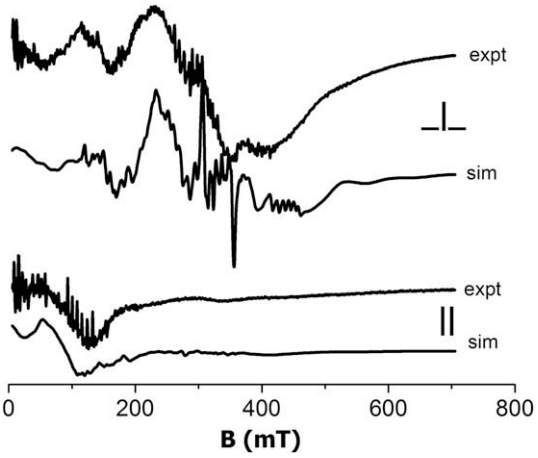


Fig. 3. Dual mode X-band EPR spectra from a frozen solution of **1** in DMF. The simulated spectra are obtained as described in the text. EPR conditions: *T*, 10 K; modulation amplitude, 1.0 mT; microwave power, 2.2 mW; perpendicular mode: 9.59 GHz, parallel mode: 9.31 GHz.

latter. Both observations may be rationalized by the presence of distributions on the ZFS parameters, σ_D and $\sigma_{E/D}$.

In high field limit conditions [16], the signal originating from the transitions $-\frac{1}{2} \leftrightarrow +\frac{1}{2}$ is less sensitive on the parameters *D* and *E*, and therefore, from this transition hyperfine features may be resolved. This is demonstrated in Fig. 2, where we display the magnetic field region corresponding to these transitions. Well resolved hyperfine features are observed and the hyperfine interaction may be determined. The hyperfine lines are superimposed on a broad background which is attributed to the mixing of the in-phase and out-of-phase signals. Finally, no signals are observed from the other transitions $+\frac{1}{2} \leftrightarrow +\frac{3}{2}$ and $+\frac{3}{2} \leftrightarrow +\frac{5}{2}$ along the three magnetic axes. This is due to the fact that at 5 K the corresponding energy levels have considerably lower thermal occupation in comparison with the levels corresponding to the $-\frac{5}{2} \leftrightarrow -\frac{3}{2}$ and $-\frac{3}{2} \leftrightarrow -\frac{1}{2}$ transitions.

More accurate determination of the parameters is obtained by simulating the experimental spectra within the framework of the Hamiltonian of Eq. (1). The obtained parameters are quoted in Table 1. Simulated spectra are included in Figs. 1 and 2. In Fig. 1, we include also a simulated spectrum assuming a positive value for *D*. Clearly a positive value for *D* cannot account for the spectral behavior. The 115 GHz data and analysis presented above are in agreement with similar studies carried out in 95 GHz (not shown).

3.2. Dual mode X-band EPR studies

In Fig. 3 we show the X-band EPR spectra from a DMF frozen solution of **1** recorded either in perpendicular or parallel mode and under non saturating conditions. In perpendicular mode, the spectrum is characterized by signals expanding in a large magnetic field range. The complexity of the X-band EPR spectrum is due to the value of ZFS terms and such spectra have been observed in many mononuclear Mn(II) complexes. Because the ZFS of the energy levels of the $S = 5/2$ manifold is small in comparison with the microwave energy, many transitions are induced at X-band. Hyperfine interactions complicate further the spectrum.

For a Mn(II) system with an approximate $|D|$ value of 0.1 cm^{-1}, transitions are expected when the microwave field oscillates parallel to the external magnetic field. Indeed such signals are observed as it is shown in Fig. 3. Since the transitions which have appreciable transition probability in parallel mode are rather few, the parallel mode spectrum is less complicated than the perpendicular mode one. Still, the interpretation of this spectrum is not straightforward. However, such transitions arise from states which are separated at zero magnetic field. For an $S = 5/2$ system as in the present case such transitions are induced between the $|\pm 1/2\rangle$, $|\pm 3/2\rangle$, and $|\pm 5/2\rangle$ Kramer's doublets. The separation of these doublets depends on *D*. In the axial case, the energy difference between $|\pm 1/2\rangle$ and $|\pm 3/2\rangle$ doublets is $2|D|$ and between $|\pm 1/2\rangle$ and $|\pm 5/2\rangle$ is $6|D|$. Therefore, the position of the signals in the parallel mode spectrum may be used as a rough estimate of *D*.

Superimposed to the experimental spectra are simulated ones obtained using the parameters deduced from the HF-EPR spectra. Even if the simulated spectra do not accurately reproduce the experimental ones, they reproduce the main features with the same set of parameters. At X-band, the EPR spectra are more sensitive for distribution on the ZFS parameters. Because such distributions may not have an ordinary behavior (for instance Gaussian) the exact line-shape of the spectra cannot be accurately reproduced by simulations and probably more sophisticated models for line broadening are required. Although the interpretation of X-band EPR spectra from such species is not straightforward they may be used in order to estimate the magnitude of $|D|$ and this is achieved by simulation. Still, however, the determination of the sign of *D* can be determined only with HF-EPR spectra measurements.

Noteworthy, in the X-band spectra (either in perpendicular or parallel mode) from the DMF frozen solution, characteristic multiline features (with irregular spacing) are present at certain parts of the spectra. These multiline features arise from hyperfine interactions with the ^{55}Mn nucleus. The simulations do not account for these features. In Fig. 4, we compare the X-band dual mode EPR spectra from **1** dissolved in DMSO and DMF. The spectra in both solvents are almost identical suggesting that the ZFS parameters do not depend upon the solvent. The main difference is the lack of hyperfine patterns in the case of DMSO. In order to simulate

Table 1
EPR parameters for **1** determined by simulations of the 115 GHz spectra (Figs. 1 and 2).

$D\ (cm^{-1})$	−0.095
$\sigma_D\ (cm^{-1})$	0.010
E/D	0.15
$\sigma_{E/D}$	0.04
g	1.999
$A\ (cm^{-1})$	7.8×10^{-3}

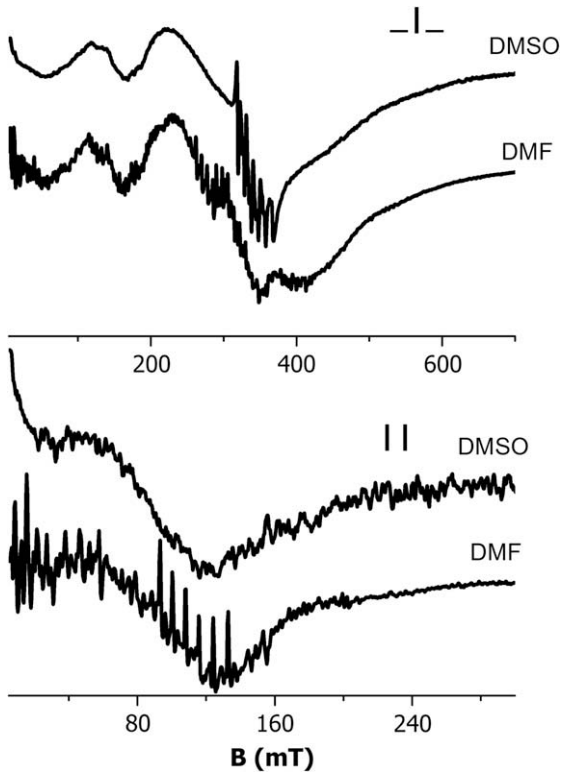


Fig. 4. Dual mode X-band EPR spectra from a frozen solution of **1** in DMSO and DMF. EPR conditions: *T*, 10 K; modulation amplitude. 1 mT, microwave power, 2.2 mW, DMF, perpendicular mode: 9.59 GHz, parallel mode: 9.31 GHz; DMSO, perpendicular mode: 9.60 GHz, parallel mode: 9.32 GHz.

the X-band EPR spectra in the case of DMF, we adopted a simple model assuming Gaussian distributions for the parameters *D* and *E*/*D*. As it was noted earlier it appears that the assumption of a Gaussian distribution is not strictly correct. We suggest that a minority fraction of the molecules are characterized by a rather homogeneous environment, which allows resolved hyperfine features at X-band. However, for the majority of the molecules, a Gaussian distribution of their parameters appears to be a good approximation for the spectral line-shape. It also works better for the X-band EPR spectra in the case of DMSO. Apparently the nature of homogeneity depends upon the solvent. Similar solvent effects were also observed in X- and Q-band EPR studies of some Mn(II) dimers [32] and *trans*-bis(oxalato) Cr(III) complexes [33].

3.3. Theoretical investigations

In the previous sections, we have experimentally determined the ZFS parameters of **1** by means of EPR spectroscopy at high frequency (115 GHz) and X-band. Apart from the determination of these parameters, our studies indicate that in solution distributions are affecting the spectra. In order to rationalize this behavior we have performed DFT calculations.

3.3.1. Geometry optimizations

The optimized structure at the BP86/TZVP level of theory, denoted as **A**, is depicted in Fig. 5 and selected geometric parameters are presented in Table 2. The obtained geometry is a distorted octahedron and well agrees with the experimentally derived crystal structure (Scheme 1). Bond lengths are quite accurately reproduced and certain bond angles deviate by no more than 12° to the crystal structure values. Furthermore, in our calculations, the phenolic ring of the 4-phenyl-2-acetylpyridine thiosemicarbazone is slightly out of plane, compared to the remainder of the anion, i.e. the C(19)–N(21)–C(23)–C(24) and C(51)–N(53)–C(55)–C(56) dihedral angles are equal to −174.6° (due to the C_2 symmetry), whereas in the crystal structure the value is equal to −180.0°. This can be attributed to the internal rotation around the N(21)–C(23) and N(53)–C(55) bond axis, respectively. Finally, the C(19)–N(18)–N(17)–C(12) and C(51)–N(50)–N(49)–C(44) dihedral angles have a value of −172.3° in the optimized structure, **A**, as opposed to the −176.3° value of the crystal structure data, due to the rotation around the N(17)–N(18) and N(50)–N(51) single bonds. All deviations from the crystal structure could be attributed to the fact that π–π interactions and intermolecular hydrogen bonds are present in the crystalline structure but not accounted in the gas phase calculations.

The experimentally obtained EPR spectra were simulated introducing distributions on the parameters *D* and *E*. These distributions may correlate with the electronic properties of the system which in turn may correlate with distributions in specific geometrical elements. Upon closer inspection of **A**, it became evident that the C(19)–N(18)–N(17)–C(12) and C(51)–N(50)–N(49)–C(44) dihedral angles (denoted as δ further on) could vary, as it has been previously mentioned. In the solid state, this motion is restricted by intermolecular hydrogen bonding and π–π stacking. However, in solution such interactions are lost and multiple conformers may be present. While freezing, it is reasonable to assume that a number of conformations in relation with this geometrical element are trapped.

For this reason we have considered four additional conformations by varying the value of the dihedral angle δ around the global minimum of −172.3°. The δ value was held frozen at −174.0°, −176.0°, −170.0° and −168.0° and geometry optimizations were performed, resulting in the structures denoted as **B**, **C**, **D** and **E**, respectively. Selected geometric parameters of all conformers are included in Table 2, along with the corresponding experimental ones. As was the case with the minimum, conformers' structure agrees quite well with the crystal structure, although differences can be located particularly at dihedral angle values, due to the aforementioned lack of effects present in the solid state.

Before proceeding further, it is important to check whether any of these conformations is characterized by significantly larger energy in comparison to the optimized local minimum. The electronic energies of the various conformers with respect to the corresponding one of minimum **A** are given in Table 3. We observe that the energy values of **B**, **C**, **D** and **E** differ only by few cm^{-1} to the corresponding value for **A** suggesting that inter-conversion between different configurations is feasible, since there is no significant rotational energy barrier. Therefore, at room temperature a multitude of configurations in solution are thermally accessible. Such configurations are assumed to be trapped upon freezing rapidly to cryogenic temperatures.

3.3.2. Zero field splitting calculations

The calculation of ZFS parameters was carried out as described previously and the results are given in Table 4. For the local minimum and the four conformers, the mean *D* value is $-0.106\ cm^{-1}$ with standard deviation of $0.014\ cm^{-1}$. The theoretically derived mean value of *D* is very close to the experimentally determined one ($-0.095\ cm^{-1}$). For all conformers the theoretically calculated *E* and |*E*/*D*| values are lower compared to the experimental ones. The good agreement between theoretical and experimental values in the case of *D* is not unprecedented. Similar studies have been carried out for several mononuclear Mn(II) compounds [6,7,14,34] and it was found that the methodology concerning the theoretical calculations followed in the present work leads to reliable results.

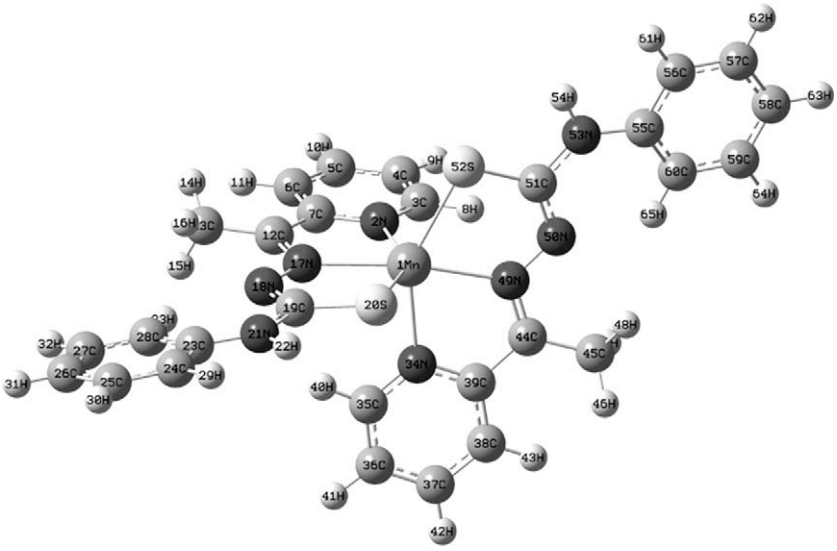


Fig. 5. Optimized structure of **1**, denoted as **A**, at the BP86/TZVP level of theory.

Table 2
Selected optimized structural parameters (bond lengths in Å, and bond angles in °) for the global minimum and the rotational conformers at the BP86/TZVP level of theory, along with the available experimental values.

Geometrical parameter	Theoretical values					Experimental values[a]
	A	**B**	**C**	**D**	**E**	
Mn(1)–N(2)	2.299	2.301	2.304	2.297	2.295	2.261
Mn(1)–N(17)	2.262	2.261	2.258	2.261	2.261	2.252
Mn(1)–S(20)	2.496	2.494	2.492	2.498	2.501	2.510
N(2)–Mn(1)–N(17)	71.3	71.3	71.2	71.4	71.4	71.4
N(2)–Mn(1)–S(20)	148.1	148.2	148.3	147.7	147.3	147.3
N(2)–Mn(1)–N(34)	92.1	91.0	90.0	93.4	94.7	92.7
N(2)–Mn(1)–N(49)	93.6	94.0	94.6	93.2	92.9	101.7
N(2)–Mn(1)–S(52)	93.8	93.6	93.4	94.0	94.1	91.9
N(17)–Mn(1)–S(20)	77.0	77.0	77.1	76.9	76.7	76.0
N(17)–Mn(1)–N(49)	158.6	159.3	160.3	157.9	157.2	170.4
N(17)–Mn(1)–S(52)	118.0	117.3	116.3	118.9	119.7	110.4
S(20)–Mn(1)–S(52)	97.6	98.6	99.9	96.3	95.2	101.3
C(3)–N(2)–Mn(1)–N(17)	−178.1	−178.3	−178.9	−177.7	−177.4	−179.9
C(3)–N(2)–Mn(1)–S(20)	174.5	176.8	179.5	171.6	168.8	−176.2
C(3)–N(2)–Mn(1)–N(34)	−85.0	−84.5	−84.0	−85.5	−86.0	−78.5
C(3)–N(2)–Mn(1)–N(49)	−13.6	−13.2	−12.9	−13.9	−14.4	−6.9
C(3)–N(2)–Mn(1)–S(52)	63.6	64.0	64.4	63.1	62.5	69.2
C(12)–N(17)–Mn(1)–N(2)	−6.3	−5.7	−4.9	−7.1	−7.7	−5.5
C(12)–N(17)–Mn(1)–S(20)	169.6	171.7	174.2	167.0	164.7	176.5
C(12)–N(17)–Mn(1)–N(34)	−97.3	−95.5	−93.3	−99.7	−101.8	−94.4
C(12)–N(17)–Mn(1)–N(49)	−53.3	−52.1	−50.6	−55.0	−56.3	−50.9
C(12)–N(17)–Mn(1)–S(52)	77.9	78.6	79.4	77.0	76.3	79.5
C(19)–S(20)–Mn(1)–N(2)	12.3	8.5	3.7	16.9	21.2	−6.1
C(19)–S(20)–Mn(1)–N(17)	5.0	3.8	2.1	6.4	7.8	−2.5
C(19)–S(20)–Mn(1)–N(34)	−87.8	−89.4	−91.8	−85.9	−84.2	−104.1
C(19)–S(20)–Mn(1)–N(49)	−158.6	−160.2	−162.5	−156.9	−155.2	−175.0
C(19)–S(20)–Mn(1)–S(52)	122.1	120.0	117.1	124.7	127.2	106.0
C(19)–N(21)–C(23)–C(24)	−174.6	−175.2	−177.0	−174.2	−173.9	−180.0
C(19)–N(18)–N(17)–C(12)	−172.3	−174.0	−176.0	−170.0	−168.0	−176.3

[a] Ref. [17].

Table 3
Differences in electronic energy between **A** and its conformers **B**, **C**, **D** and **E**, as were calculated with the GAUSSIAN 03 program [21].

Structure	Energy difference (cm^{-1})
C	25.4
B	3.3
A	0.0
D	10.2
E	37.0

We also calculated the ZFS on the crystal structure of **1**, and the results are included in Table 4. The sign of *D* is correctly reproduced but the absolute magnitude is somehow larger than the configurations **A**–**E** and the experimentally derived values. Theoretical calculations carried out in the geometry dictated by the crystal structure have been successful in reproducing the ZFS parameters derived from powdered samples of Mn(II) complexes [7,14,34,35]. In the present case we observe that the ZFS parameters are better reproduced assuming geometrically optimized structures. This is probably due to the fact that the experimental values are derived

Table 4
Experimental and theoretically calculated ZFS parameters for complex **A**, its conformers **B**, **C**, **D** and **E** and the crystal structure **1**.

ZFS parameters	A	B	C	D	E	1	Experiment
D[a]	−0.103	−0.111	−0.126	−0.096	−0.092	−0.181	−0.095
D_{SOC}[a]	−0.028	−0.041	−0.061	−0.020	−0.016	−0.145	
$\alpha \rightarrow \alpha$	−0.061	−0.046	−0.032	−0.069	−0.075	+0.040	
$\beta \rightarrow \beta$	−0.085	−0.083	−0.078	−0.082	−0.074	−0.030	
$\alpha \rightarrow \beta$	+0.084	+0.060	+0.027	+0.094	+0.095	−0.142	
$\beta \rightarrow \alpha$	+0.034	+0.028	+0.022	+0.037	+0.039	−0.013	
D_{SS}[a]	−0.075	−0.070	−0.065	−0.076	−0.076	−0.037	
1-Centre	−0.075	−0.059	−0.048	−0.081	−0.088	+0.016	
2-Centre-coulomb	+0.001	−0.001	−0.004	+0.002	+0.004	−0.015	
2-Centre-exchange	0.000	0.000	0.000	0.000	0.000	0.000	
2-Centre-hybrid	+0.001	−0.012	−0.020	+0.006	+0.016	−0.059	
3-Centre-coulomb	−0.002	+0.003	+0.007	−0.004	−0.008	+0.022	
3-Centre-exchange	+0.001	+0.001	0.000	+0.001	+0.001	0.000	
4-Centre	0.000	0.000	0.000	0.000	0.000	−0.001	
E[a]	−0.001	−0.001	−0.006	−0.009	−0.013	−0.006	
$\lvert E/D \rvert$	0.008	0.009	0.047	0.092	0.141	0.032	0.150

[a] Values are given in cm^{-1}.

from frozen solutions. In the present work we did not study powder samples of **1** so we have not determined the ZFS in the solid state. Differences in ZFS between the solid state and in frozen solutions have been observed [7].

For the **A–E** structures, SS interactions have the major contribution to the ZFS. The major contribution to the spin-spin coupling comes mostly from one centre terms and in the case of **A**, it is the main contribution. The SOC contribution to the overall D value is quite important, but is not the dominant factor for the **A–E** conformers ($|D_{SOC}| < |D_{SS}|$). An inspection of Table 4 indicates that this is due to the cancelling signs of the terms contributing to D_{SOC}. The relative contributions of SOC and SS are reversed when the calculations are carried out in the geometry of the crystal structure and in this case $|D_{SOC}| > |D_{SS}|$. This is mainly due to the fact that the spin flip term $D_{SOC}^{\alpha \rightarrow \beta}$ has a relatively large negative value whereas $|D_{SS}|$ is almost half the value of those obtained for the optimized structures.

The analysis of the EPR spectra indicates that $|D|$ has a spread of the order of 0.01 cm^{-1} around an average value of the order of 0.1 cm^{-1}. The theoretical calculations indicate that such a spread may be reproduced if we assume different structures of the molecule which do not differ for more than a few tenths of cm^{-1} from the energy of the configuration exhibiting local minimum. Similar correlations were recently made in the case of a high spin, four-coordinate Fe(II) diketiminate complex [36] where the distribution on the hyperfine tensor of the ^{57}Fe, studied by Mössbauer spectroscopy were correlated with narrow distributions ($\sim 0.5^{\circ}$) in a torsion angle φ of the complex.

4. Summary and conclusions

In the present work we determine the ZFS terms of a mononuclear Mn(II) complex in frozen solutions by multifrequency EPR spectroscopy. The absolute value of D lies in the range found for six coordinated Mn(II) ($S = 5/2$) complexes. The experimental values were compared to the theoretical ones on the basis of DFT calculations and a very good agreement was found. The EPR spectra indicate the presence of distributions. The present work shows that theoretical calculations may also be used in order to rationalize these distributions, which can be correlated with structural variations of the complex. Distributions on ZFS parameters have been observed even in the case of paramagnetic ions in single crystals [37]. Other mechanisms, which may lead to broadening of EPR lines, are intermolecular magnetic interactions [32]. More systematic studies are required in order to quantitatively distinguish the contributions of each mechanism in the line-shape of the EPR signals.

Acknowledgements

Dr. Dimitrios A. Pantazis, University of Bonn, is gratefully acknowledged for providing helpful assistance, regarding the EPR parameters calculations. T. D. Tzima has been the recipient of a graduate fellowship from N.C.R.P.S. Demokritos. The electronic structure calculations were supported by the Computer Centre, University of Ioannina.

References

[1] A.F. Miller, Curr. Opin. Chem. Biol. 8 (2004) 162.
[2] T.C. Stamatatos, K.A. Abboud, W. Wernsdorfer, G. Christou, Polyhedron 26 (2007) 2095.
[3] C.G. Torres, B. Lundby, A.T. Sterud, S. McGill, P.B. Gordon, H.S. Bjerknes, Acta Radiol. 38 (1997) 631.
[4] A. Abragam, B. Bleaney, Electron Paramagnetic Resonance of Transition Ions, Dover Publ. Inc., New York, 1986.
[5] L.C. Tabares, N. Cortez, I. Agalidis, S. Un, J. Am. Chem. Soc. 127 (2005) 6039.
[6] C. Duboc, T. Phoeung, S. Zein, J. Pécaut, M.-N. Collomb, F. Neese, Inorg. Chem. 46 (2007) 4905.
[7] C. Duboc, M.-N. Collomb, J. Pécaut, A. Deronzier, F. Neese, Chem. Eur. J. 14 (2008) 6498.
[8] J. Gätjens, M. Sjödin, V.L. Pecoraro, S. Un, J. Am. Chem. Soc. 129 (2007) 13825.
[9] D. Gatteschi, R. Sessoli, J. Villain, Molecular Nanomagnets, Oxford University Press, Oxford, 2006.
[10] D.M.L. Goodgame, H. El Mkami, G.M. Smith, J.P. Zhao, E.J.L. McInnes, Dalton Trans. (2003) 34.
[11] W.B. Lynch, R.S. Boorse, J.H. Freed, J. Am. Chem. Soc. 115 (1993) 10909.
[12] R.M. Wood, D.M. Stucker, L.M. Jones, W.B. Lynch, S.K. Misra, J.H. Freed, Inorg. Chem. 38 (1999) 5384.
[13] C. Mantel, C. Baffert, I. Romero, A. Deronzier, J. Pécaut, M.-N. Collomb, C. Duboc, Inorg. Chem. 43 (2004) 6455.
[14] C. Hureau, S. Groni, R. Guillot, G. Blondin, C. Duboc, E. Anxolabéhère-Mallart, Inorg. Chem. 47 (2008) 9238.
[15] C. Mantel, C. Baffert, I. Romero, A. Deronzier, J. Pécaut, M.-N. Collomb, C. Duboc, Inorg. Chem. 43 (2004) 6455.
[16] C. Duboc, T. Phoeung, D. Jouvenot, A.G. Blackman, L.F. McClintock, J. Pécaut, M.-N. Collomb, A. Deronzier, Polyhedron 26 (2007) 5243.
[17] D. Kovala-Demertzi, U. Gangadharmath, M.A. Demertzis, Y. Sanakis, Inorg. Chem. Commun. 8 (2005) 619.
[18] L.R. Gahan, V.A. Grillo, T.W. Hambley, G.R. Hanson, C.J. Hawkins, E.M. Proudfoot, B. Moubaraki, K.S. Murray, D. Wang, Inorg. Chem. 35 (1996) 1039.
[19] P. Chakraborty, S.K. Chandra, A. Chakravorty, Inorg. Chem. 32 (1993) 5349.
[20] A.-L. Barra, L.C. Brunel, J.B. Robert, Chem. Phys. Lett. 165 (1990) 107.
[21] M.J. Frisch, G.W. Trucks, H.B. Schlegel, G.E. Scuseria, M.A. Robb, J.R. Cheeseman, J.A. Montgomery Jr., T. Vreven, K.N. Kudin, J.C. Burant, J.M. Millam, S.S. Iyengar, J. Tomasi, V. Barone, B. Mennucci, M. Cossi, G. Scalmani, N. Rega, G.A. Petersson, H. Nakatsuji, M. Hada, M. Ehara, K. Toyota, R. Fukuda, J. Hasegawa, M. Ishida, T. Nakajima, Y. Honda, O. Kitao, H. Nakai, M. Klene, X. Li, J.E. Knox, H.P. Hratchian, J.B. Cross, V. Bakken, C. Adamo, J. Jaramillo, R. Gomperts, R.E.

Stratmann, O. Yazyev, A.J. Austin, R. Cammi, C. Pomelli, J.W. Ochterski, P.Y. Ayala, K. Morokuma, G.A. Voth, P. Salvador, J.J. Dannenberg, V.G. Zakrzewski, S. Dapprich, A.D. Daniels, M.C. Strain, O. Farkas, D.K. Malick, A.D. Rabuck, K. Raghavachari, J.B. Foresman, J.V. Ortiz, Q. Cui, A.G. Baboul, S. Clifford, J. Cioslowski, B.B. Stefanov, G. Liu, A. Liashenko, P. Piskorz, I. Komaromi, R.L. Martin, D.J. Fox, T. Keith, M.A. Al-Laham, C.Y. Peng, A. Nanayakkara, M. Challacombe, P.M.W. Gill, B. Johnson, W. Chen, M.W. Wong, C. Gonzalez, J.A. Pople, GAUSSIAN 03, Revision D.01, GAUSSIAN, Inc., Wallingford CT, 2004.

[22] (a) P. Hohenberg, W. Kohn, Phys. Rev. 136 (1964) B864;
(b) W. Kohn, L.J. Sham, Phys. Rev. 140 (1965) A1133.

[23] (a) S.H. Vosko, L. Wilk, M. Nusair, Can. J. Phys. 58 (1980) 1200;
(b) J.P. Perdew, Phys. Rev. B 33 (1986) 8822;
A.D. Becke, Phys. Rev. A 38 (1988) 3098.

[24] A. Schäfer, C. Huber, R. Ahlrichs, J. Chem. Phys. 100 (1994) 5829.

[25] F. Neese, Orca, Version 2.6 – Revision 35, University of Bonn, Bonn, 2008.

[26] F. Neese, E.I. Solomon, in: J.S. Miller, M. Drillon (Eds.), Magnetism: Molecules to Materials, Wiley-VCH, Weinheim, 2002.

[27] (a) F. Neese, J. Am. Chem. Soc. 128 (2006) 10213;
(b) G. Breit, Phys. Rev. 34 (1929) 553;
(c) G. Breit, Phys. Rev. 36 (1930) 383;
(d) G. Breit, Phys. Rev. 39 (1932) 616;
(e) H.A. Bethe, E.E. Salpeter, Quantum Mechanics of One- and Two-Electron Atoms, Springer-Verlag, Berlin, 1977;
(f) J.C. Slater, The Theory of Atomic Structure II, McGraw-Hill, New York, 1960.

[28] (a) B.A. Hess, C.M. Marian, U. Wahlgren, O. Gropen, Chem. Phys. Lett. 251 (1996) 365;
(b) A. Berning, M. Schweizer, H.-J. Werner, P.J. Knowles, P. Palmieri, Mol. Phys. 98 (2000) 1823.

[29] F. Neese, J. Chem. Phys. 122 (2005) 034107.

[30] F. Neese, E.I. Solomon, J. Am. Chem. Soc. 120 (1998) 12829.

[31] F. Neese, J. Chem. Phys. 127 (2007) 164112.

[32] A.P. Golombeck, M.P. Hendrich, J. Magn. Res. 165 (2003) 33.

[33] W.T.M. Andriessen, Inorg. Chem. 14 (1975) 792.

[34] S. Zein, C. Duboc, W. Lubitz, F. Neese, Inorg. Chem. 47 (2008) 134.

[35] S. Zein, F. Neese, J. Phys. Chem. A 112 (2008) 7976.

[36] S.A. Stoian, J.M. Smith, P.L. Holland, E. Münck, E.L. Bominaar, Inorg. Chem. 47 (2008) 8687.

[37] S. Piligkos, I. Laurse, A. Morgenstjerne, H. Weihe, Mol. Phys. 105 (2007) 2025.

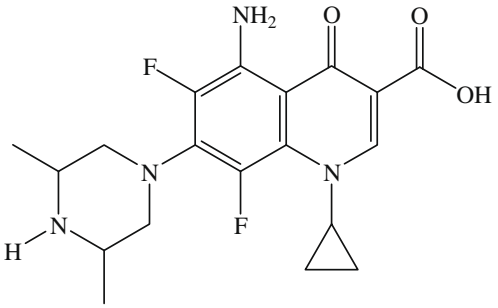


Fig. 1. Sparfloxacin (Hsf = 5-amino-1-cyclopropyl-7-(*cis*-3,5-dimethyl-1-piperazinyl)-6,8-difluoro-1,4-dihydro-4-oxo-3-quinolinecarboxylic acid).

2. Experimental

2.1. Materials

Sparfloxacin, CT DNA and EB were purchased from Sigma, NaCl and all solvents were purchased from Merck, trisodium citrate was purchased from Riedel-de Haen and $NiCl_2 \cdot 6H_2O$, pyridine and KOH were purchased from Aldrich Co. All the chemicals and solvents were reagent grade and were used as purchased.

DNA stock solution was prepared by dilution of CT DNA to buffer (containing 150 mM NaCl and 15 mM trisodium citrate at pH 7.0) followed by exhaustive stirring at 4 °C for 3 days, and kept at 4 °C for no longer than a week. The stock solution of CT DNA gave a ratio of UV absorbance at 260 and 280 nm (A_{260}/A_{280}) of 1.89, indicating that the DNA was sufficiently free of protein contamination [34]. The DNA concentration was determined by the UV absorbance at 260 nm after 1:20 dilution using $\varepsilon = 6600\ M^{-1}\ cm^{-1}$ [35].

2.2. Synthesis of complex $Ni(sf)_2(py)_2 \cdot 6.4H_2O$, **1** $\cdot 6.4H_2O$

Sparfloxacin (0.4 mmol, 157 mg) was dissolved in methanol (15 mL), was deprotonated with KOH (0.4 mmol, 22 mg) and was added to a methanolic solution (10 mL) of $NiCl_2 \cdot 6H_2O$ (0.2 mmol, 48 mg) followed by the addition of 3 mL of pyridine. The solution was left for slow evaporation. Green crystals of $Ni(sf)_2(py)_2 \cdot 6.4H_2O$, **1** $\cdot 6.4H_2O$, suitable for X-ray structure determination, were deposited after a few days. Yield: 280 mg, 70%. *Anal.* Calc. for $Ni(sf)_2(py)_2 \cdot 6.4H_2O$ ($C_{48}H_{64.8}F_4N_{10}O_{12.4}Ni$) (MW = 1115.01): C, 51.71; H, 5.86; N, 12.56. Found: C, 51.40; H, 5.83; N, 12.73%. IR: ν_{max}/cm^{-1}; $\nu(C{=}O)_{ket}$: 1643(vs); $\nu_{as}(CO_2)$: 1600(vs); $\nu_{sym}(CO_2)$: 1380(vs); $\Delta = \nu_{asym}(CO_2) - \nu_{sym}(CO_2)$: 220 cm^{-1} (KBr pellet); UV–Vis: λ_{max}/nm ($\varepsilon/M^{-1}\ cm^{-1}$) as nujol mull: 615, 415(sh), 385, 313, 291; in dmso: 620 (12), 412(sh) (220), 380 (6500), 312 (6800), 286 (13 500). The complex is soluble in dmso and dmf and is non-electrolyte.

2.3. Instrumentation – physical measurements

Infrared (IR) spectra (400–4000 cm^{-1}) were recorded with a Nicolet FT-IR 6700 spectrometer with samples prepared as KBr pellets. UV–Visible (UV–Vis) spectra were recorded as nujol mulls and in solution at concentrations in the range 5×10^{-6}–10^{-3} M with a Hitachi U-2001 dual beam spectrophotometer. C, H and N elemental analysis were performed with a Perkin–Elmer 240B elemental analyzer. Molecular conductivity measurements were carried out with a Crison Basic 30 conductometer. Fluorescence spectra were recorded in solution with a Hitachi F-7000 fluorescence spectrophotometer.

Cyclic voltammetry (CV) studies were performed with an Eco chemie Autolab Electrochemical analyzer. CV experiments were carried out in a 30 mL three-electrode electrolytic cell. The working electrode was platinum disk, a separate Pt single-sheet electrode was used as the counter electrode and a Ag/AgCl electrode saturated with KCl was used as the reference electrode. The cyclic voltammograms of the complexes were recorded in 0.4 mM dmso solutions and in 0.4 mM 1/2 dmso/buffer solutions at ν = 100 mV s^{-1} where teap (=tetraethylammonium perchlorate) and the buffer solution were the supporting electrolytes, respectively. Oxygen was removed by purging the solutions with pure nitrogen which had been previously saturated with solvent vapors. All electrochemical measurements were performed at 25.0 ± 0.2 °C.

2.4. X-ray crystal structure determination

Slow crystallization from methanol yielded green prismatic crystals of **1**. A crystal with approximate dimensions 0.24 × 0.49 × 0.59 mm was taken directly from the mother liquor and immediately cooled to −93 °C. Diffraction measurements were made with Rigaku R-AXIS SPIDER Image Plate using graphite monochromated Cu radiation. Data collection (ω-scans) and processing (cell refinement, data reduction and Empirical absorption correction) were performed using the CrystalClear program package [36].The structure was solved by direct methods using SHELXS-86 and refined by full-matrix least-squares techniques on F^2 with SHELXL-93 using 8326 reflections and refining 921 parameters [37,38]. The final values for R_1, wR_2 and GOF for all data are 0.0481, 0.1242 and 1.045, respectively. The maximum and minimum residual peaks in the final difference map were 1.022 and −0.354 e/Å and the largest shift/esd in the final cycle was 0.001. All non-H atoms were refined anisotropically. There are six water solvate molecules in the structure, which were refined with full occupation factor, and one water solvate molecule which was refined with occupation factor fixed to 0.40. Hydrogen atoms were located by difference maps and were refined isotropically, except those of the partially occupied water solvate molecule which were not included in the refinement. The H-atoms of one of the fully occupied water solvates were not found in the difference maps and were not included in the refinement (Table 1).

2.5. DNA binding studies

The interaction of **1** with CT DNA has been studied with UV spectroscopy and CV in order to investigate the possible binding

Table 1
Crystallographic data for complex **1** $\cdot 6.4H_2O$.

	1 $\cdot 6.4H_2O$
Formula	$C_{48}H_{64.8}F_4N_{10}NiO_{12.4}$
Fw	1115.01
T (K)	180(2)
Crystal system	triclinic
Space group	$P\bar{1}$
a	10.7239(1)
b	14.3709(2)
c	18.1556(3)
α	69.660(1)
β	80.155(1)
γ	77.966(1)
V	2551.03(6)
Z	2
D_{calc} (Mg/m^3)	1.452
Absolute coefficient, μ (mm^{-1})	1.302
F(0 0 0)	1172
θ Range	6.61–65.00
Goodness-of-fit (GOF) on F^2	1.045
R_1	0.0444[a]
wR_2	0.1209[a]

[a] 7441 reflections with $I > 2\sigma(I)$.

mode to CT DNA and to calculate the binding constants to CT DNA (K_b).

In UV titration experiments, the spectra of CT DNA in the presence of **1** have been recorded for a constant CT DNA concentration in diverse [complex]/[CT DNA] mixing ratios (r). The intrinsic binding constants, K_b, of the complex with CT DNA have been determined using the UV spectra of **1** recorded for a constant concentration in the absence or presence of CT DNA for diverse r values.

The interaction of **1** with CT DNA has been also investigated by monitoring the changes observed in the cyclic voltammogram of a 0.40 mM 1/2 dmso/buffer solution of **1** upon addition of CT DNA at diverse r values. The buffer solution was also used as the supporting electrolyte and the cyclic voltammograms were recorded at $v = 100$ mV s^{-1}.

The competitive studies of complex **1** with EB have been investigated with fluorescence spectroscopy in order to examine whether it is able to displace EB from its CT DNA–EB complex. The CT DNA–EB complex was prepared by adding 20 μM EB and 25 μM CT DNA in buffer (150 mM NaCl and 15 mM trisodium citrate at pH 7.0). The intercalating effect of **1** with the DNA–EB complex was studied by adding a certain amount of a solution of **1** step by step into the solution of the DNA–EB complex. The influence of the addition of complex **1** to the DNA–EB complex solution has been obtained by recording the variation of fluorescence emission spectra.

3. Results and discussion

3.1. Synthesis and spectroscopic study of complex *1*

The synthesis of $Ni(sf)_2(py)_2$ **1** was achieved via the reaction of sparfloxacin, deprotonated with KOH, with $NiCl_2 \cdot 6H_2O$ in the presence of pyridine under air, according to the equation:

$$NiCl_2 \cdot 6H_2O + 2C_{18}H_{21}F_2N_4O - COOH + 2KOH + 2C_5H_5N \rightarrow Ni(C_{18}H_{21}F_2N_4O - COO)_2(C_5H_5N)_2 + 2KCl \quad (1)$$

In the IR spectrum of **1**, the observed absorption bands at 3462(br,m) cm^{-1}, 1716(s) cm^{-1} and 1292(s) cm^{-1} attributed to the stretching vibrations ν(H–O), ν(C=O)$_{carboxyl}$, ν(C–O)$_{carboxyl}$, respectively, of the carboxylic group (–COOH) of the sparfloxacin molecule, have been replaced by two very strong characteristic bands at 1600 cm^{-1} and 1380 cm^{-1} assigned as antisymmetric, ν_{asym}(C=O), and symmetric, ν_{sym}(C=O), stretching vibrations, respectively. The difference Δ [=ν_{asym}(C=O) − ν_{sym}(C=O)], a useful characteristic tool for determining the coordination mode of carboxylato ligands, with a value of 220 cm^{-1} is indicative of a monodentate coordination mode [39]. The vibration ν(C=O)$_{ket}$ is slightly shifted from 1640 cm^{-1} to 1643 cm^{-1} upon bonding. The overall changes of the IR spectrum suggest that the sparfloxacinato ligand is coordinated to Ni(II) via the ketone oxygen and a carboxylate oxygen [1,19].

The UV–Vis spectra of the complex have been recorded as nujol mull and in dmso solution and they are similar, with the exception, in some cases, of a few nm shifts suggesting that the complex retains its structure in solution. The UV spectrum of the complex is practically identical with that of sparfloxacin but slightly shifted, indicative of the coordination of sparfloxacin to Ni(II) through the ketone oxygen and a carboxylate oxygen [11]. In the visible region spectra, there is a characteristic band at 620 nm (ε = 12 M^{-1} cm^{-1}) attributed to d–d transitions as expected for distorted octahedral high-spin Ni(II) [21] complexes. Similar behavior has been observed for the distorted octahedral Ni(II) [40] cinoxacin complex as well as for other Ni(II) quinolone complexes [12,41,42]. Additionally, a band assigned to the ligand-to-metal charge transfer transition for the quinolone ligand [41–43] exists at 412 nm (ε = 220 M^{-1} cm^{-1}) as a shoulder.

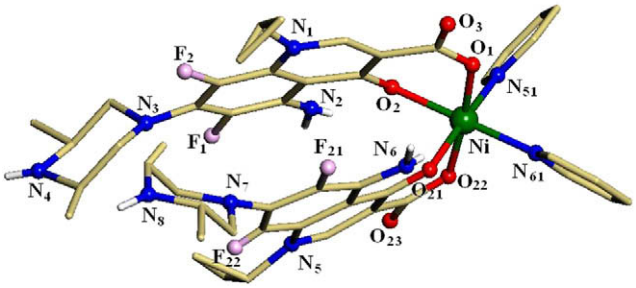


Fig. 2. The molecular structure of **1**.

Table 2
Selected bond distances and angles for complex **1**.

Bond (Å)			
Ni1–O1	2.012(2)	C1–O1	1.265(2)
Ni1–O2	2.072(2)	C1–O3	1.253(3)
Ni1–O22	2.015(2)	C3–O2	1.272(2)
Ni1–O21	2.059(1)	C21–O22	1.266(3)
Ni1–N51	2.073(2)	C21–O23	1.250(3)
Ni1–N61	2.088(2)	C23–O21	1.271(2)
Angles (°)			
O1–Ni1–O2	86.14(6)	O2–Ni1–N61	176.28(7)
O1–Ni1–O21	90.87(6)	O21–Ni1–O22	85.96(6)
O1–Ni1–O22	174.54(6)	O21–Ni1–N51	175.26(7)
O1–Ni1–N51	93.85(7)	O21–Ni1–N61	88.42(7)
O1–Ni1–N61	91.17(7)	O22–Ni1–N51	89.30(7)
O2–Ni1–O21	89.05(6)	O22–Ni1–N61	93.19(7)
O2–Ni1–O22	89.35(6)	N51–Ni1–N61	91.88(7)
O2–Ni1–N51	90.87(7)		

3.2. Description of the structure of $Ni(sf)_2(py)_2 \cdot 6.4H_2O$, ***1*** $\cdot$ $6.4H_2O$

An ORTEP diagram of **1** is shown in Fig. 2, and selected bond distances and angles are listed in Table 2. The complex is monomeric, the sparfloxacinato ligand behaves as a bidentate deprotonated ligand and is coordinated to nickel ion via the ketone oxygen and a carboxylate oxygen.

The nickel atom is six-coordinate and is in an octahedral environment formed by nitrogen atoms from the two pyridine ligands and four oxygen atoms from the two sparfloxacinato ligands.

Two sets of Ni–O distances are observed: the Ni–O$_{carb}$ [Ni(1)–O(1) = 2.012(2) Å, Ni(1)–O(22) = 2.015(2) Å] are shorter than the Ni–O$_{ket}$ [Ni(1)–O(2) = 2.072(2) Å, Ni(1)–O(21) = 2.059(1) Å]. The arrangement of the two sparfloxacinato ligands is such that the two ketone oxygen atoms [O(2)–Ni(1)–O(21) = 89.05(6)°] are in a *cis* arrangement and the two carboxylato oxygen atoms [O(1)–Ni(1)–O(22) = 174.54(6)°] are *trans* to each other.

The Ni–N bond distances [Ni(1)–N(51) = 2.073(2) Å, Ni(1)–N(61) = 2.088(2) Å] are similar to the values reported for other Ni(II) complexes with N-donor heterocyclic ligands [44,45]. The N$_{pyr}$–Ni–N$_{pyr}$ angle [N(51)–Ni(1)–N(61) = 91.88(7)°] shows a *cis* arrangement of the two pyridine ligands.

The lattice structure of **1** is stabilized by an extensive network of hydrogen bonding interactions (Table 3) leading to the overall stability of the structure.

3.3. Cyclic voltammetry for $Ni(sf)_2(py)_2$

The complete scan in the range +1.5 V to −1.0 V of **1** in 0.4 mM dmso solution shows one cathodic wave at −775 mV and one anodic wave at −615 mV (Fig. 3A). This quasi-reversible wave can be assigned to the couple Ni(II)/Ni(I) [8,46,47].

Table 3
Hydrogen bonding interactions in the structure of **1**.

Interaction	D···A (Å)	H···A (Å)	D–H···A (°)	Symmetry operation
N2–H1N2···Ow5	2.936	2.171	147.4	$1+x, y, z$
N4–HN4···Ow7	3.042	2.278	169.3	$-x, 1-y, -1-z$
N6–H2N6···Ow5	2.944	2.123	152.9	x, y, z
Ow1–H1w1···O23	2.891	2.013	172.8	x, y, z
Ow1–H2w1···Ow4	2.789	1.903	174.2	$1+x, y, z$
Ow3–H1w3···Ow7	2.890	2.069	169.7	$x, y, 1+z$
Ow3–H2w3···Ow6	2.867	1.921	173.7	$x, y, 1+z$
Ow4–H1w4···O3	2.862	1.963	178.7	x, y, z
Ow4–H2w4···Ow3	2.938	2.161	155.4	x, y, z
Ow5–H1w5···O23	2.860	2.051	166.4	$-1+x, y, z$
Ow5–H2w5···O3	2.859	2.043	166.9	x, y, z
Ow7–H1w7···N8	2.804	1.935	174.6	x, y, z
Ow7–H2w7···Ow3	2.890	2.446	125.2	$x, y, -1+z$
Ow6···Ow2	2.677			$-1-x, -y, -1-z$
Ow6···Ow2	2.691			x, y, z
Ow6···Ow1	2.741			$-x, -y, -z$
Ow2···Ow3	2.862			$-1-x, -y, -z$

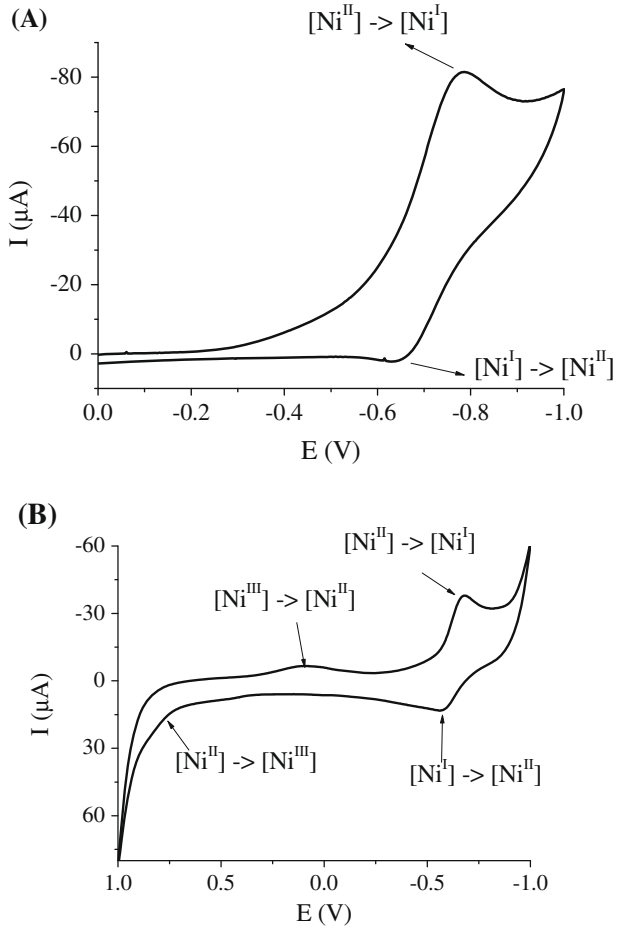


Fig. 3. Cyclic voltammograms of $Ni(sf)_2(py)_2$ **1** in (A) 0.4 mM dmso solution in the range +1.5 V to −1.0 V (supporting electrolyte = teap, 0.1 M); (B) in 0.4 mM 1/2 dmso/buffer (150 mM NaCl and 15 mM trisodium citrate at pH 7.0) solution (supporting electrolyte = buffer solution). Scan rate = 100 mV s^{-1}.

The cyclic voltammogram of complex **1** in 0.4 mM 1/2 dmso/buffer solution shows the existence of one cathodic wave at −686 mV ($[Ni^{II}] \rightarrow [Ni^{I}]$) and two anodic waves at −567 mV and +530 mV ($[Ni^{II}] \rightarrow [Ni^{III}]$), while a second cathodic wave attributed to $[Ni^{III}] \rightarrow [Ni^{II}]$ process appears at +95 mV in the reverse scan [8,47]. The current intensities attributed to the couple Ni(II)/Ni(I) are much higher than the others which are sometimes difficult to distinguish (Fig. 3B).

3.4. Interaction with DNA

Titration with UV absorption spectroscopy is an effective method to examine the binding mode of DNA with metal complexes [48]. The transition metal complexes can bind to DNA via covalent mode (a labile ligand of the complexes is replaced by a nitrogen atom of DNA bases) and/or noncovalent interactions (intercalative, electrostatic and groove binding of metal complexes along outside of DNA helix, along major or minor groove) [49]. It has been reported that the quinolone metal complexes can interact with DNA only via noncovalent interactions comprising groove binding, electrostatic binding to phosphate group or intercalation [50].

The UV spectra of the interaction of CT DNA with **1** have been recorded for a constant CT DNA concentration in different [complex]/[DNA] mixing ratios (r) and are shown in Fig. 4. The changes observed in the absorption spectra of CT DNA in the presence of **1**, i.e. the decrease of the intensity at λ_{max} = 258 nm, which is accompanied by a red-shift of the λ_{max} up to 266 nm, indicate that the interaction of **1** with CT DNA results in the direct formation of a new complex with double-helical CT DNA [51]. The observed

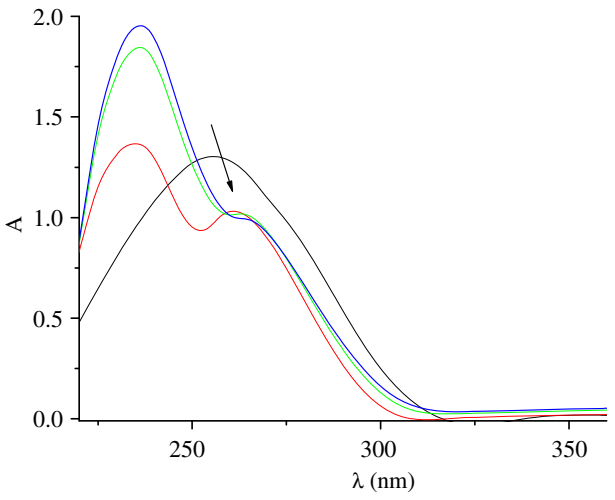


Fig. 4. UV spectra of CT DNA ([DNA] = 2×10^{-4} M) in buffer solution (150 mM NaCl and 15 mM trisodium citrate at pH 7.0) in the presence of $Ni(sf)_2(py)_2$, **1** at diverse r values (r = [**1**]/[DNA]). The arrow shows the changes upon increasing amounts of complex **1** (r = 0–0.08).

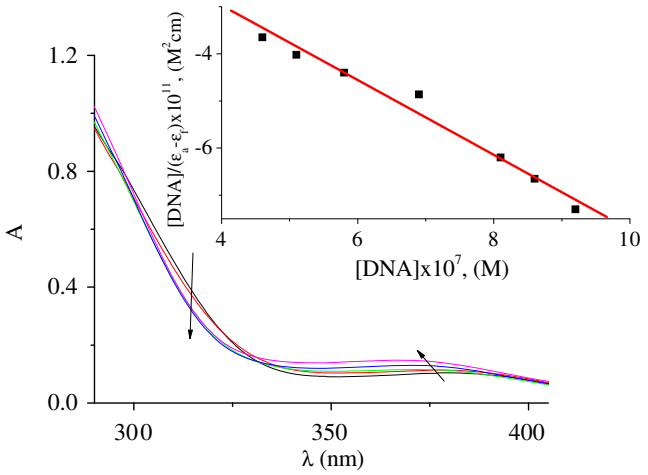


Fig. 5. UV spectra of Ni(sf)$_2$(py)$_2$ ([**1**] = 5 μM) in dmso solution in the absence and presence of CT DNA ([CT DNA] = 0–5 μM) at increasing amounts. The arrows show the changes upon increasing amounts of CT DNA. Inset: plot of $\frac{[DNA]}{(\varepsilon_a-\varepsilon_f)}$ vs. [DNA].

hypochromism is due to stacking interaction between the aromatic chromophore (either from sparfloxacinato and/or pyridine ligands) of **1** and DNA base pairs consistent with the intercalative binding mode [48,52]. Additionally, the observed bathochromism of 8 nm is an evidence of the stabilization of the CT DNA duplex [53].

In Fig. 5, the changes occurred in the spectrum of a 5×10^{-6} M solution of **1** during the titration upon addition of CT DNA in diverse r values can be observed. In the UV region, the intense absorption bands observed in the spectrum are attributed to the intraligand $\pi \rightarrow \pi^*$ transition of the coordinated groups of sparfloxacinato and pyridine ligands. Any interaction between a compound and CT DNA could perturb the intra-ligand centred spectral transitions of the compound [54]. There are not observed any significant changes in the position of the $\pi \rightarrow \pi^*$ transition bands of sparfloxacinato ligand upon addition of CT DNA. On the other hand, the intensity of the band (observed as a shoulder) centred at 315 nm is decreased in the presence of increasing amounts of CT DNA. The observed hypochromic effect suggests tight binding to CT DNA probably due to intercalation induced through the sparfloxacinato ligands [55]. Additionally, the intensity of the band centred at 380 nm is increased in the presence of increasing amounts of CT DNA, while a blue-shift of 10 nm (up to 370 nm) can be observed. The observed hyperchromic effect suggests binding to CT DNA ascribed either to external contact (electrostatic binding) [56] or to the fact that complex could uncoil the helix structure of DNA and make more bases embedding in DNA exposed [57]. One distinct isosbestic point at 320 nm appears upon addition of CT DNA.

The intrinsic binding constant K_b is determined in order to estimate the magnitude of the binding strength of **1** with CT DNA, represents the binding constant per DNA base pair, can be obtained by monitoring the changes in the absorbance at λ_{max} = 315 nm with increasing concentrations of CT DNA and is given by the ratio of the slope to the y intercept in plots $\frac{[DNA]}{(\varepsilon_a-\varepsilon_f)}$ versus [DNA] (inset in Fig. 5), according to the following equation [52]:

$$\frac{[DNA]}{(\varepsilon_a-\varepsilon_f)} = \frac{[DNA]}{(\varepsilon_b-\varepsilon_f)} + \frac{1}{K_b(\varepsilon_b-\varepsilon_f)} \quad (2)$$

where [DNA] is the concentration of DNA in base pairs, $\varepsilon_a = A_{obsd}/[\mathbf{1}]$, ε_f = the extinction coefficient for free complex **1** and ε_b = the extinction coefficient for the compound in the fully DNA-bound form.

The obtained K_b value [=3.87(±0.14) × 10^7 M^{-1}] suggests very strong binding of **1** to CT DNA and it is much higher than that of Hsf (=1.71(±0.02) × 10^5 M^{-1}) [58], indicating that the coordination of sparfloxacinato ligand to Ni(II) ion, in combination with the existence of the N-donor aromatic ligand pyridine, enhances significantly its ability to bind to CT DNA. The K_b for **1** is higher than the binding affinity for CT DNA of EB, a classical intercalator, (K_b = 1.23(±0.07) × 10^5 M^{-1}) [59], suggesting that intercalative interaction may affect EB displacement from the EB–DNA complex [59].

The changes observed in the cyclic voltammogram of a small molecule upon addition CT DNA can provide a useful complement to spectroscopic methods for the molecule–DNA interaction [60] since the electrochemical potential of the molecule will shift positively when the molecule intercalates into DNA double helix, and it will shift into a negative direction, if the molecule is bound to DNA by an electrostatic interaction [61,62].

In Fig. 6, the cyclic voltammograms of **1** in the absence or presence of CT DNA are shown. No new redox peaks appeared after the addition of CT DNA to the complex, but the current intensity of all the peaks decreased significantly, suggesting the existence of an interaction between complex **1** and CT DNA, and can be explained in terms of an equilibrium mixture of free and DNA-bound complex to the electrode surface [63]. It can be observed (Fig. 6) that for increasing amounts of CT DNA, the cathodic potential E_{pc} shows a positive shift up to −672 mV (ΔE_{pc} = +14 mV) and the anodic potential E_{pa} presents a lower positive shift up to −560 mV (ΔE_{pa} = +5 mV). These positive shifts of the potentials may suggest the existence of intercalation between **1** and CT DNA as the most possible interaction mode [8,53,62].

3.5. Competitive studies with ethidium bromide

Complex **1** does not show any fluorescence at room temperature in solution or in the presence of CT DNA, so that the binding to DNA cannot be directly predicted through the emission spectra. Hence, a competitive EB (=3,8-diamino-5-ethyl-6-phenyl-phenanthridinium bromide) binding study will give support for the binding of **1** with DNA. EB, a phenenthridine fluorescence dye and a typical indicator of intercalation [64], does not show any appreciable emission in buffer solution due to fluorescence quenching of the free EB by the solvent molecules [65], while the fluorescence intensity is highly enhanced upon addition of CT DNA, due to its strong intercalation through the planar phenenthridinium ring between the adjacent DNA base pairs [66,67].

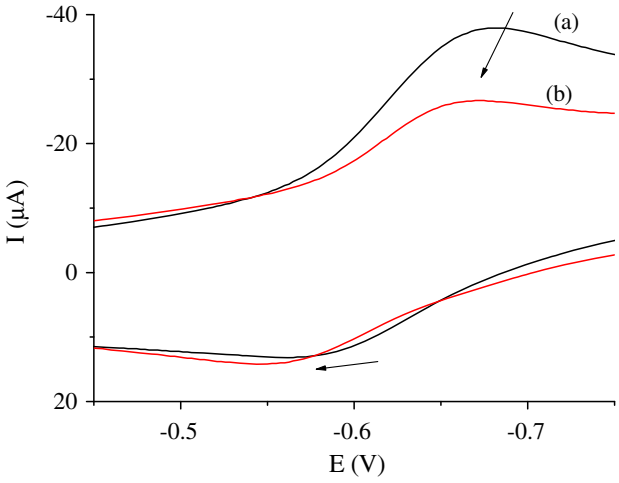


Fig. 6. Cyclic voltammograms of Ni(sf)$_2$(py)$_2$ **1** in 0.4 mM 1/2 dmso/buffer (containing 150 mM NaCl and 15 mM trisodium citrate at pH 7.0) solution (supporting electrolyte = buffer solution) in (a) the absence and (b) presence of CT DNA for r = 2. The arrows show the changes upon addition of CT DNA. Scan rate = 100 mV s^{-1}.

Addition of a second molecule, which can bind to DNA more strongly than EB, would result to a decrease the DNA-induced EB emission [68]. Two mechanisms have been proposed to account for this reduction in the emission intensity: the replacement of EB, and/or electron transfer [69].

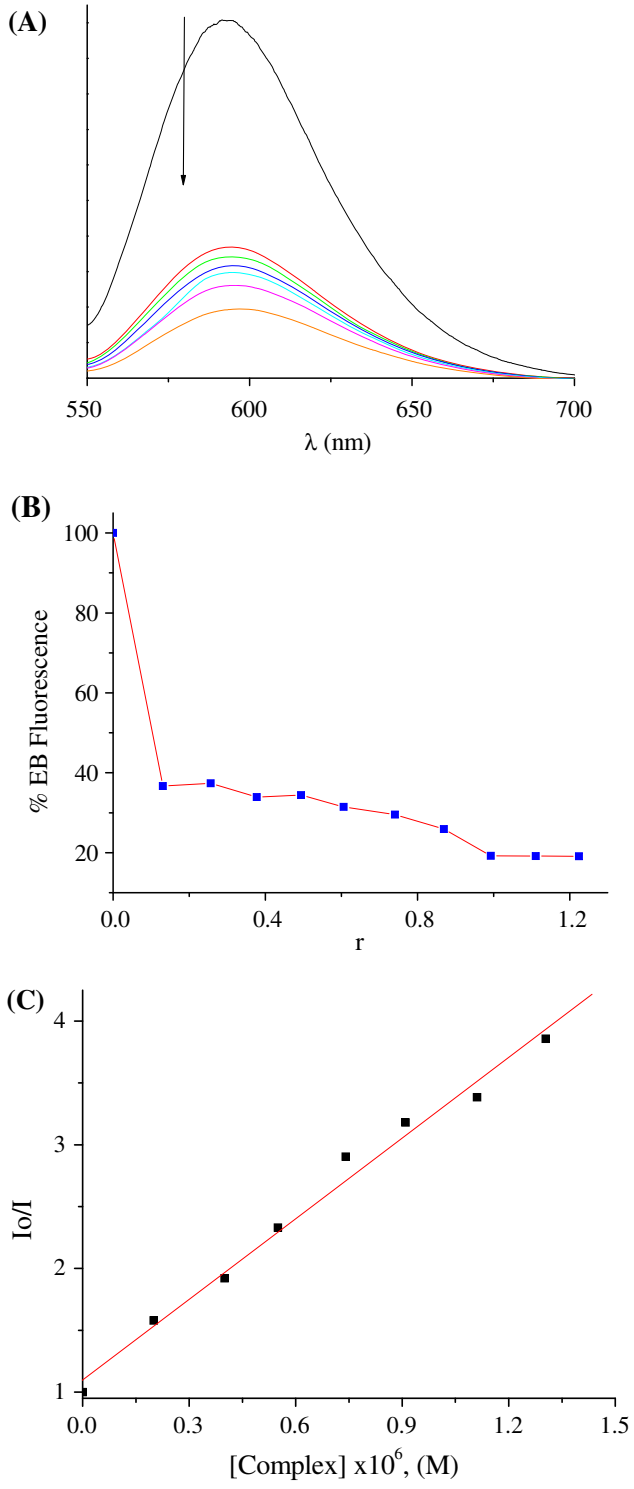


Fig. 7. (A) Emission spectra (λ_{exit} = 540 nm) for EB–DNA in buffer solution (150 mM NaCl and 15 mM trisodium citrate at pH 7.0) in the absence and presence of increasing amounts of complex **1** (r = [**1**] / [DNA] = 0–1.2). The arrow shows the changes of intensity upon increasing amounts of **1**. (B) Plot of EB relative fluorescence intensity (%) vs. r (=[**1**]/[DNA]) for **1** in buffer solution (150 mM NaCl and 15 mM trisodium citrate at pH 7.0). (C) Stern–Volmer quenching plot of EB bound to CT DNA by complex **1**. [EB] = 20 μM, [DNA] = 25 μM, λ_{em} = 592 nm.

The emission spectra of EB bound to CT DNA in the absence and presence of **1** have been recorded for [EB] = 2×10^{-5} M, [DNA] = 2.5×10^{-5} M for increasing amounts of complex **1** (Fig. 7A). The intensity of the emission band at 592 nm of the DNA–EB system decreased in intensity (up to 19% of the initial EB–DNA fluorescence intensity) upon addition of **1** at diverse r values (Fig. 7B) indicating the competition of complex **1** with EB in binding to DNA. The observed quenching of DNA–EB fluorescence for complex **1** suggests that it can displace EB from the DNA–EB complex and it can interact with CT DNA probably by the intercalative mode [8,70].

The Stern–Volmer constant K_{SV} is often used to evaluate the quenching efficiency for a compound, it varies with the experimental conditions and is given by the equation:

$$\frac{I_o}{I} = 1 + K_{SV}[\text{complex}] \quad (3)$$

where I_o and I are the emission intensities in the absence and the presence of the complex, respectively. The Stern–Volmer plot of DNA–EB for **1** (Fig. 7C) illustrates that the quenching of EB bound to DNA by the complex is in good agreement (R = 0.99) with the linear Stern–Volmer equation (Eq. (3)), which proves that the partial replacement of EB bound to DNA by **1** results in a decrease in the fluorescence intensity [71]. The high K_{SV} value of the complex ($K_{SV} = 2.17 \pm 0.16 \times 10^6$ M^{-1}) shows that **1** can be bound tightly to the DNA [55].

4. Conclusions

The synthesis and characterization of the neutral mononuclear nickel(II) complex with the third-generation quinolone antibacterial drug sparfloxacin in the presence of the N-donor heterocyclic ligand pyridine has been realized. The crystal structure of complex $Ni(sf)_2(py)_2$ has been determined with X-ray crystallography revealing a distorted octahedral environment around Ni(II). The interaction of **1** with CT DNA has been studied with UV spectroscopy revealing its ability to bind to DNA. UV spectroscopic titrations have been used in order to calculate the intrinsic binding constant K_b [=3.87(±0.14) × 10^7 M^{-1}], which suggests very strong binding of **1** to CT DNA. Cyclic voltammetric titration has shown that **1** can bind to CT DNA by the intercalative mode. Competitive binding study with EB, performed with fluorescence spectroscopy, has shown that the interaction between DNA–EB complex and **1** releases EB from its DNA complex, indicating that complex **1** can bind to DNA probably via the intercalative mode

Supplementary data

CCDC 716240 contains the supplementary crystallographic data for this paper. These data can be obtained free of charge via http://www.ccdc.cam.ac.uk/conts/retrieving.html, or from the Cambridge Crystallographic Data Centre, 12 Union Road, Cambridge CB2 1EZ, UK; fax: (+44) 1223-336-033; or e-mail: deposit@ccdc.cam.ac.uk

References

[1] I. Turel, Coord. Chem. Rev. 232 (2002) 27. and references cited therein.
[2] K. Sandstrom, S. Warmlander, M. Leijon, A. Graslund, Biochem. Biophys. Res. Commun. 304 (2003) 55.
[3] J.A. Wiles, Q. Wang, E. Lucien, A. Hashimoto, Y. Song, J. Cheng, C.W. Marlor, Y. Ou, S.D. Podos, J.A. Thanassi, C. Thoma, M. Deshpande, M.J. Pucci, B.J. Bradbury, Bioorg. Med. Chem. Lett. 16 (2006) 1272.
[4] E.S. Pfeiffer, H. Hiasa, Antimicrob. Agents Chemother. 48 (2004) 608.
[5] Y. Xia, Z.Y. Yang, P. Xia, K.F. Bastow, Y. Tachibana, S.C. Kuo, E. Hamel, T. Hackl, K.H. Lee, J. Med. Chem. 41 (1998) 1155.
[6] D.K. Saha, U. Sandbhor, K. Shirisha, S. Padhye, D. Deobagkar, C.E. Anson, A.K. Powell, Bioorg. Med. Chem. Lett. 14 (2004) 3027.

[7] I. Turel, A. Golobic, A. Klavzar, B. Pihlar, P. Buglyo, E. Tolis, D. Rehder, K. Sepcic, J. Inorg. Biochem. 95 (2003) 199.
[8] G. Psomas, J. Inorg. Biochem. 102 (2008) 1798.
[9] A. Tarushi, E.K. Efthimiadou, P. Christofis, G. Psomas, Inorg. Chim. Acta 360 (2007) 3978.
[10] N. Jimenez-Garrido, L. Perello, R. Ortiz, G. Alzuet, M. Gonzalez-Alvarez, E. Canton, M. Liu-Gonzalez, S. Garcia-Granda, M. Perez-Priede, J. Inorg. Biochem. 99 (2005) 677.
[11] G. Psomas, A. Tarushi, E.K. Efthimiadou, Polyhedron 27 (2008) 133.
[12] A. Tarushi, P. Christofis, G. Psomas, Polyhedron 26 (2007) 3963.
[13] E.K. Efthimiadou, M.E. Katsarou, A. Karaliota, G. Psomas, J. Inorg. Biochem. 102 (2008) 910.
[14] E.K. Efthimiadou, H. Thomadaki, Y. Sanakis, C.P. Raptopoulou, N. Katsaros, A. Scorilas, A. Karaliota, G. Psomas, J. Inorg. Biochem. 101 (2007) 64.
[15] M.E. Katsarou, E.K. Efthimiadou, G. Psomas, A. Karaliota, D. Vourloumis, J. Med. Chem. 51 (2008) 470.
[16] D.E. King, R. Malone, S.H. Lilley, Am. Fam. Physician 61 (2000) 2741.
[17] Sparfloxacin, in: J.K. Aronson (Ed.), Meyler's Side Effects of Drugs: The International Encyclopedia of Adverse Drug Reactions and Interactions, Elsevier, 2006, pp. 3172–3174.
[18] J.J. Schentag, Clin. Ther. 22 (2000) 372.
[19] E.K. Efthimiadou, Y. Sanakis, C.P. Raptopoulou, A. Karaliota, N. Katsaros, G. Psomas, Bioorg. Med. Chem. Lett. 16 (2006) 3864.
[20] D. Shingnapurkar, R. Butcher, Z. Afrasiabi, E. Sinn, F. Ahmed, F. Sarkar, S. Padhye, Inorg. Chem. Commun. 10 (2007) 459.
[21] F. Meyer, H. Kozlowski, in: J.A. McCleverty, T.J. Meyer (Eds.), Comprehensive Coordination Chemistry II, vol. 6, Elsevier, 2003, pp. 247–554. and references cited therein.
[22] R.K. Andrews, R.L. Blakeley, B. Zerner, in: H. Sigel, A. Sigel (Eds.), Metal Ions in Biological Systems, vol. 23, Marcel Dekker Inc., New York, 1988, pp. 165–284. and references cited therein.
[23] P. Bombicz, E. Forizs, J. Madarasz, A. Deak, A. Kalman, Inorg. Chim. Acta 315 (2001) 229.
[24] G. Morgant, N. Bouhmaida, L. Balde, N.E. Ghermani, J. d'Angelo, Polyhedron 25 (2006) 2229.
[25] O.Z. Yesilel, M.S. Soylu, H. Olmez, O. Buyukgungor, Polyhedron 25 (2006) 2985.
[26] R. Kurtaran, L.T. Yildirim, A.D. Azaz, H. Namli, O. Atakol, J. Inorg. Biochem. 99 (2005) 1937.
[27] M. Alexiou, I. Tsivikas, C. Dendrinou-Samara, A.A. Pantazaki, P. Trikalitis, N. Lalioti, D.A. Kyriakidis, D.P. Kessissoglou, J. Inorg. Biochem. 93 (2003) 256.
[28] Z. Afrasiabi, E. Sinn, W. Lin, Y. Ma, C. Campana, S. Padhye, J. Inorg. Biochem. 99 (2005) 1526.
[29] M.C. Rodriguez-Arguelles, M. Belicchi Ferrari, F. Bisceglie, C. Pelizzi, G. Pelosi, S. Pinelli, M. Sassi, J. Inorg. Biochem. 98 (2004) 313.
[30] J. Garcia-Tojal, J.L. Pizarro, A. Garcia-Orad, A.R. Perez-Sanz, M. Ugalde, A. Alvarez Diaz, J.L. Serra, M.I. Arriortua, T. Rojo, J. Inorg. Biochem. 86 (2001) 627.
[31] M. Belicchi Ferrari, F. Bisceglie, G. Pelosi, P. Tarasconi, R. Albertini, A. Bonati, P. Lunghi, S. Pinelli, J. Inorg. Biochem. 83 (2001) 169.
[32] W. Luo, X. Meng, X. Sun, F. Xiao, J. Shen, Y. Zhou, G. Cheng, Z. Ji, Inorg. Chem. Commun. 10 (2007) 1351.
[33] R. del Campo, J.J. Criado, E. Garcia, M.R. Hermosa, A. Jimenez-Sanchez, J.L. Manzano, E. Monte, E. Rodriguez-Fernandez, F. Sanz, J. Inorg. Biochem. 89 (2002) 74.
[34] J. Marmur, J. Mol. Biol. 3 (1961) 208.
[35] M.F. Reichmann, S.A. Rice, C.A. Thomas, P. Doty, J. Am. Chem. Soc. 76 (1954) 3047.
[36] Rigaku/MSC, CrystalClear, Rigaku/MSC Inc., The Woodlands, TX, USA, 2005.
[37] G.M. Sheldrick, SHELXS-97: Structure Solving Program, University of Göttingen, Germany, 1997.
[38] G.M. Sheldrick, SHELXL-97: Crystal Structure Refinement Program, University of Göttingen, Germany, 1997.
[39] K. Nakamoto, Infrared and Raman Spectra of Inorganic and Coordination Compounds, 4th ed., Wiley, New York, 1986.
[40] M. Ruiz, R. Ortiz, L. Perello, A. Castineiras, M. Quiros, Inorg. Chim. Acta 211 (1993) 133.
[41] E.K. Efthimiadou, Y. Sanakis, N. Katsaros, A. Karaliota, G. Psomas, Polyhedron 26 (2007) 1148.
[42] E.K. Efthimiadou, A. Karaliota, G. Psomas, Polyhedron 27 (2008) 1729.
[43] G. Psomas, A. Tarushi, Y. Sanakis, E.K. Efthimiadou, C.P. Raptopoulou, N. Katsaros, J. Inorg. Biochem. 100 (2006) 1764.
[44] B.A. Frenz, J.A. Ibers, Inorg. Chem. 11 (1972) 1109.
[45] S. Cabaleiro, J. Castro, E. Vazquez-Lopez, J.A. Garcia-Vazquez, J. Romero, A. Sousa, Polyhedron 18 (1999) 1669.
[46] C. Dendrinou-Samara, G. Psomas, C.P. Raptopoulou, D.P. Kessissoglou, J. Inorg. Biochem. 83 (2001) 7.
[47] M. Thirumavalavan, P. Akilan, M. Kandaswamy, Polyhedron 24 (2005) 1781.
[48] T.M. Kelly, A.B. Tossi, D.J. McConnell, T.C. Strekas, Nucleic Acids Res. 13 (1985) 6017.
[49] Q.L. Zhang, J.G. Liu, H. Chao, G.Q. Xue, L.N. Ji, J. Inorg. Biochem. 83 (2001) 49.
[50] B.M. Zeglis, V.C. Pierre, J.K. Barton, Chem. Commun. (2007) 4565.
[51] G.S. Son, J.A. Yeo, M.S. Kim, S.K. Kim, A. Holmen, B. Akerman, B. Norden, J. Am. Chem. Soc. 120 (1998) 6451.
[52] A.M. Pyle, J.P. Rehmann, R. Meshoyrer, C.V. Kumar, N.J. Turro, J.K. Barton, J. Am. Chem. Soc. 111 (1989) 3053.
[53] E.C. Long, J.K. Barton, Acc. Chem. Res. 23 (1990) 271.
[54] V. Uma, M. Kanthimathi, T. Weyhermuller, B.U. Nair, J. Inorg. Biochem. 99 (2005) 2299.
[55] M. Chauhan, K. Banerjee, F. Arjmand, Inorg. Chem. 46 (2007) 3072.
[56] R.F. Pasternack, E.J. Gibbs, J.J. Villafranca, Biochemistry 22 (1983) 2406.
[57] G. Pratviel, J. Bernadou, B. Meunier, Adv. Inorg. Chem. 45 (1998) 251.
[58] E.K. Efthimiadou, A. Karaliota, G. Psomas, Bioorg. Med. Chem. Lett. 18 (2008) 4033.
[59] A. Dimitrakopoulou, C. Dendrinou-Samara, A.A. Pantazaki, M. Alexiou, E. Nordlander, D.P. Kessissoglou, J. Inorg. Biochem. 102 (2008) 618.
[60] M.T. Carter, A.J. Bard, J. Am. Chem. Soc. 109 (1987) 7528.
[61] S.S. Zhang, S.Y. Niu, B. Qu, G.F. Jie, H. Xu, C.F. Ding, J. Inorg. Biochem. 99 (2005) 2340.
[62] M.T. Carter, M. Rodriguez, A.J. Bard, J. Am. Chem. Soc. 111 (1989) 8901.
[63] K. Jiao, Q.X. Wang, W. Sun, F.F. Jian, J. Inorg. Biochem. 99 (2005) 1369.
[64] W.D. Wilson, L. Ratmeyer, M. Zhao, L. Strekowski, D. Boykin, Biochemistry 32 (1993) 4098.
[65] S. Dhar, M. Nethaji, A.R. Chakravarty, J. Inorg. Biochem. 99 (2005) 805.
[66] C.G. Reihardt, T.R. Krugh, Biochemistry 17 (1978) 4845.
[67] J. Olmsted, D.R. Kearns, Biochemistry 16 (1977) 3647.
[68] B.C. Baguley, M. Lebret, Biochemistry 23 (1984) 937.
[69] R.F. Pasternack, M. Cacca, B. Keogh, T.A. Stephenson, A.P. Williams, F.J. Gibbs, J. Am. Chem. Soc. 113 (1991) 6835.
[70] O. Novakova, H. Chen, O. Vrana, A. Rodger, P.J. Sadler, V. Brabec, Biochemistry 42 (2003) 11544.
[71] S. Tabassum, S. Parveen, F. Arjmand, Acta Biomater. 1 (2005) 677.

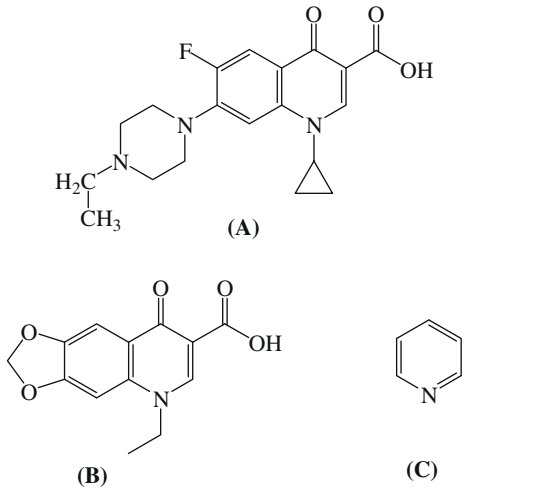


Fig. 1. (A) Enrofloxacin (Herx = 1-cyclopropyl-7-(4-ethyl-piperazin-1-yl)-6-fluoro-4-oxo-1,4-dihydro-quinoline-3-carboxylic acid). (B) oxolinic acid (Hoxo = 5,8-dihydro-5-ethyl-8-oxo-1,3-dioxolo[4,5-g]quinoline-7-carboxylic acid), (C) pyridine (= py).

Cu(oxo)(phen)Cl has been reported in the literature [29]. We have also initiated studies on the co-ordination chemistry of carboxylate-containing herbicides or anti-inflammatory agents with metal ions in an attempt to examine their mode of binding and possible biological relevance. In addition, we have reported studies on the effect of polynuclear metal complexes on the integrity and electrophoretic mobility of nucleic acids [30–39].

The role of zinc in various biological systems is important [40], since zinc is critical for numerous cell processes and is a major regulatory ion in the metabolism of cells [41]. In the literature, diverse zinc complexes with biological activity are reported, but only zinc complexes with drugs used for the treatment of Alzheimer's disease [42] and others showing antibacterial [43], anticonvulsant [44], antidiabetic [45], anti-inflammatory [46], antimicrobial [47] and antiproliferative – antitumor [48–50] activity are structurally characterized.

The synthesis, the characterization and the DNA-binding properties of two novel neutral mononuclear zinc complexes with enrofloxacin, $Zn(erx)_2(py)_2$ **1,** and oxolinic acid, $Zn(oxo)_2(py)_2$ **2**, in the presence the N-donor heterocyclic ligand pyridine (=py) (Fig. 1C) are presented. The ability of these complexes to bind to CT (calf-thymus) DNA has been investigated with UV spectroscopic titration and their intrinsic binding constants, K_b, with CT-DNA have been determined. Competitive binding studies with ethidium bromide (EB), one of the most widely used intercalative agents and fluorescence probes for DNA structure, have been employed in the study of the interaction of the complexes with CT-DNA in order to investigate a potential intercalative binding mode.

2. Experimental

2.1. Materials

Enrofloxacin, oxolinic acid, CT-DNA and EB were purchased from Sigma, NaCl and all solvents were purchased from Merck, trisodium citrate was purchased from Riedel-de Haen and $ZnCl_2$, pyridine and KOH were purchased from Aldrich Co. All the chemicals and solvents were reagent grade and were used as purchased.

DNA stock solution was prepared by dilution of CT-DNA to buffer (containing 150 mM NaCl and 15 mM trisodium citrate at pH 7.0) followed by exhaustive stirring at 4 °C for 3 days, and kept at 4 °C for no longer than a week. The stock solution of CT-DNA gave a ratio of UV absorbance at 260 and 280 nm (A_{260}/A_{280}) of 1.89, indicating that the DNA was sufficiently free of protein contamination [51]. The DNA concentration was determined by the UV absorbance at 260 nm after 1:20 dilution using $\varepsilon = 6600\ M^{-1}\ cm^{-1}$ [52].

2.2. Synthesis of the complexes

2.2.1. Synthesis of $Zn(erx)_2(py)_2 \cdot 6H_2O \cdot MeOH$ ($1 \cdot 6H_2O \cdot MeOH$)

A methanolic solution (15 mL) of enrofloxacin (0.4 mmol, 144 mg), deprotonated with KOH (0.4 mmol, 22 mg), was added to a methanolic solution (10 mL) of $ZnCl_2$ (0.2 mmol, 28 mg) followed by the addition of 3 mL of pyridine. The solution was left for slow evaporation. Colorless crystals of $Zn(erx)_2(py)_2 \cdot 6H_2O \cdot MeOH$, $\mathbf{1} \cdot 6H_2O \cdot MeOH$, suitable for X-ray structure determination, were deposited after ten days. Yield: 260 mg, 70%. *Anal.* Calc. for $Zn(erx)_2(py)_2 \cdot 6H_2O \cdot MeOH$ ($C_{49}H_{58}F_2N_8O_{13}Zn$) (MW = 1080.48): C, 54.47; H, 6.34; N, 10.37. Found: C, 54.92; H, 6.38; N, 10.23%. IR: ν_{max}/cm^{-1}; $\nu(C{=}O)_{ket}$: 1631(vs); $\nu_{as}(CO_2)$: 1611(vs); $\nu_{sym}(CO_2)$: 1384(vs); $\Delta = \nu_{asym}(CO_2) - \nu_{sym}(CO_2)$: 227 cm^{-1} (KBr pellet). The complex is soluble in dmso and dmf and is non-electrolyte.

2.2.2. Synthesis of $Zn(oxo)_2(py)_2 \cdot 6H_2O$, $2 \cdot 6H_2O$

Complex **2** was prepared in a similar way. Oxolinic acid (0.4 mmol, 105 mg) was used instead. Yield: 190 mg, 65%. *Anal.* Calc. for $Zn(oxo)_2(py)_2 \cdot 6H_2O$ ($C_{36}H_{42}N_4O_{16}Zn$) (MW = 852.13): C, 50.74; H, 4.97; N, 6.58. Found: C, 50.40; H, 4.83; N, 6.30%. IR: ν_{max}/cm^{-1}; $\nu(C{=}O)_{ket}$: 1642(vs); $\nu_{as}(CO_2)$: 1596(vs); $\nu_{sym}(CO_2)$: 1388(vs); $\Delta = \nu_{asym}(CO_2) - \nu_{sym}(CO_2)$: 208 cm^{-1} (KBr pellet). The complex is soluble in dmso and dmf and is non-electrolyte.

2.3. Instrumentation – physical measurements

Infrared (IR) spectra (400–4000 cm^{-1}) were recorded on a Nicolet FT-IR 6700 spectrometer with samples prepared as KBr pellets. UV–Visible (UV–Vis) spectra were recorded as nujol mulls and in solution at concentrations in the range 10^{-5}–10^{-3} M on a Hitachi U-2001 dual beam spectrophotometer. C, H and N elemental analysis were performed on a Perkin–Elmer 240B elemental analyzer. Molecular conductivity measurements were carried out with a Crison Basic 30 conductometer. Fluorescence spectra were recorded in solution on a Hitachi F-7000 fluorescence spectrophotometer.

2.4. X-ray crystal structure determination

Slow crystallization from methanol yielded colorless prismatic crystals of $\mathbf{1} \cdot 6H_2O \cdot MeOH$. A crystal with approximate dimensions 0.43 × 0.44 × 0.69 mm was taken directly from the mother liquor and immediately cooled to −93 °C. Diffraction measurements were made on a Rigaku R-AXIS SPIDER Image Plate diffractometer using graphite monochromated Cu radiation. Data collection (ω-scans) and processing (cell refinement, data reduction and Empirical absorption correction) were performed using the CRYSTALCLEAR program package [53]. The structure was solved by direct methods using SHELXS-97 and refined by full-matrix least-squares techniques on F^2 with SHELXL-97 using 4034 reflections and refining 356 parameters for **1** [54,55]. The final values for R_1, wR_2 and GOF for all data for **1** are 0.0463, 0.1264 and 1.075, respectively, and are given in Table 1. The maximum and minimum residual peaks in the final difference map were 0.820 e/Å and −0.440 e/Å and the largest shift/esd in the final cycle was 0.001. Hydrogen atoms were introduced at calculated positions as riding on bonded atoms, except those of the water solvate molecules which were located by difference maps and were refined isotropically. All non-H atoms were refined anisotropically.

Table 1
Crystallographic data for complex **1** · $6H_2O$ · MeOH.

	1 · $6H_2O$ · MeOH
Formula	$C_{49}H_{68}F_2N_8O_{13}Zn$
Fw	1080.48
T (K)	180
Crystal system	triclinic
Space group	$P\bar{1}$
a	9.6854(1)
b	11.5791(2)
c	11.8995(2)
α	78.626(1)
β	81.785(1)
γ	83.825(1)
V	1290.53(3)
Z	1
D_{calc} (Mg/m^3)	1.390
Absolute coefficient, μ (mm^{-1})	1.323
F(0 0 0)	570
θ Range	7.30–63.98
GOF on F^2	1.068
R_1	0.0440[a]
wR_2	0.1247[a]

[a] 3761 reflections with $I > 2\sigma(I)$.

2.5. DNA binding studies

The interaction of the ligands and the complexes with CT-DNA has been studied with UV spectroscopy in order to investigate the possible binding modes to CT-DNA and to calculate the binding constants to CT-DNA (K_b).

In UV titration experiments, the spectra of CT-DNA in the presence of each compound have been recorded for a constant CT-DNA concentration in diverse [compound]/[CT-DNA] mixing ratios (r). The intrinsic binding constants, K_b, of the compounds with CT-DNA have been determined using the UV spectra of the compounds recorded for a constant concentration in the absence or presence of CT-DNA for diverse r values.

The competitive studies of each compound with EB have been investigated with fluorescence spectroscopy in order to examine whether the quinolone or the complex is able to displace EB from its CT-DNA–EB complex. The CT-DNA–EB complex was prepared by adding 20 μM EB and 30 μM CT-DNA in buffer (150 mM NaCl and 15 mM trisodium citrate at pH 7.0). The intercalating effect of the free quinolones and complexes **1**and **2** with the DNA–EB complex was studied by adding a certain amount of a solution of the compound step by step into the solution of the DNA–EB complex. The influence of the addition of each compound to the DNA–EB complex solution has been obtained by recording the variation of the fluorescence emission spectra.

3. Results and discussion

3.1. Synthesis and spectroscopic study of the complexes

The synthesis of the complexes Zn(erx)$_2$(py)$_2$ **1** and Zn(oxo)$_2$-(py)$_2$ **2** was achieved via the reaction of the corresponding quinolone ligand, deprotonated with KOH, in the presence of pyridine with $ZnCl_2$ under air, according to the equations:

$$ZnCl_2 + 2C_{18}H_{21}FN_3O{-}COOH + 2KOH + 2C_5H_5N \rightarrow Zn(C_{18}H_{21}FN_3O{-}COO)_2(C_5H_5N)_2 + 2KCl + 2H_2O$$

$$ZnCl_2 + 2C_{12}H_{10}NO_3{-}COOH + 2KOH + 2C_5H_5N \rightarrow Zn(C_{12}H_{10}NO_3{-}COO)_2(C_5H_5N)_2 + 2KCl + 2H_2O$$

In the IR spectra of the complexes, the observed absorption bands at 3442(br,m) cm^{-1}, 1736(s) cm^{-1} and 1254(s) cm^{-1} and at 3443(br,m) cm^{-1}, 1712(s) cm^{-1} and 1260(s) cm^{-1} attributed to the stretching vibrations ν(H–O), ν(C=O)$_{carboxyl}$, ν(C–O)$_{carboxyl}$, respectively, of the carboxylic group (–COOH) of the Herx and Hoxo molecule, have been replaced by two very strong characteristic bands at 1611 and 1384 cm^{-1} for **1** and at 1596 and 1388 cm^{-1} for **2,** assigned as antisymmetric, ν_{asym}(C=O), and symmetric, ν_{sym}(C=O), stretching vibrations, respectively. The difference Δ [= ν_{asym}(C=O) − ν_{sym}(C=O)] is a useful characteristic tool for determining the coordination mode of the carboxylato ligands and has a value of 227 cm^{-1} for **1** and 208 cm^{-1} for **2** indicating a monodentate coordination mode [56]. The vibration ν(C=O)$_{ketone}$ is slightly shifted from 1627 cm^{-1} in Herx to 1631 cm^{-1} for **1** from 1633 cm^{-1} in Hoxo to 1642 cm^{-1} for **2** upon bonding. The overall changes of the IR spectra suggest that enrofloxacinato and oxolinato ligands are coordinated to the zinc via the ketone oxygen and a carboxylate oxygen [1,22,29].

3.2. Description of the structure of Zn(erx)$_2$(py)$_2$ · $6H_2O$ · MeOH (1 · $6H_2O$ · MeOH)

An ORTEP diagram of **1** is shown in Fig. 2, and selected bond distances and angles are given in Table 2. There are six water and a methanol solvate molecules. The complex is monomeric and the enrofloxacinato ligands behave as bidentate deprotonated ligands and are coordinated to zinc ion via the ketone oxygen and a carboxylate oxygen.

The structure of the complex is centrosymmetric, the Zn(II) ion is sitting on a center of symmetry and it is coordinated to two pyridine and two bidentate enrofloxacinato ligands related by the inversion center. Thus, the zinc ion is six-coordinate and, as a result of the inversion center, it displays a distorted octahedral geometry.

The quinolone ligands in the reported structurally characterized zinc–quinolone complexes may be found in different coordination modes. More specifically, the quinolone is (a) in neutral bidentate mode coordinated through the ketone oxygen and a carboxylate oxygen as in complexes Zn(Hnorf)$_2$(NO$_3$)$_2$ · $2H_2O$ [57], [Zn(Hcf)(1,3-bdc)] (1,3-bdc = 1,3-benzenedicarboxylate) [58] and [Zn$_2$(Hcf)$_4$(1,4-bdc)](1,4-bdc) · $13H_2O$ (1,4-bdc = 1,4-benzenedicarboxylate) [58], (b) in deprotonated bidentate mode coordinated

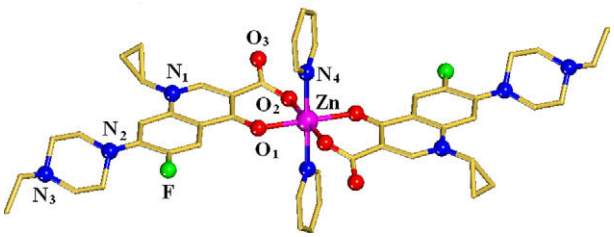


Fig. 2. The molecular structure of **1**.

Table 2
Selected bond distances and angles for complex **1**.

Bond (Å)			
Zn1–N4	2.178(2)	C1–O3	1.234(3)
Zn1–O1	2.082(2)	C1–O2	1.272(3)
Zn1–O2	2.059(2)	C3–O1	1.259(3)
Angles (°)			
N4–Zn–O1	90.62(7)	O1–Zn–O2	88.24(7)
N4–Zn–O2	91.13(7)	N4–Zn–O1′	89.38(7)
O1–Zn–O2′	91.76(6)	N4–Zn–O2′	88.87(7)
N4–Zn–N4′	180.00(12)	O1–Zn–O1′	180.00(8)
O2–Zn–O2′	180.00(13)		

Primed atoms are generated by symmetry operation: (′) = –x, –y, –z.

through the ketone oxygen and a carboxylate oxygen atom as in complexes $[Zn(cx)_2(dmso)_2]\cdot 4H_2O$ [59], $[Zn(cf)_2(H_2O)_2]\cdot 8H_2O$ [60], $[Zn(cf)_2]\cdot 2.5H_2O$ [48,58] and $Zn(gatx)_2(H_2O)_2\cdot 4H_2O$ [33,43], (c) in protonated counter cation mode as in the complex $(H_2norf)(Hnorf)[ZnCl_4]C1\cdot H_2O$ [61], and (d) in deprotonated tridentate mode bound to zinc through the ketone oxygen, a carboxylate oxygen and piperazine nitrogen atom as in the polymeric complex $Zn(norf)_2\cdot 4H_2O$ [57], where Hnorf = norfloxacin, Hcx = cinoxacin, Hcf = ciprofloxacin and Hgatx = gatifloxacin are quinolones.

The Zn–O distances observed, $Zn–O_{carb}$ [Zn–O(2) = 2.059(2) Å] and $Zn–O_{ket}$ [Zn–O(1) = 2.082(2) Å], are quite shorter than the $Zn–N_{pyr}$ [Zn–N(4) = 2.178(2) Å]. The Zn–O distances are longer than those observed in $Zn(Hnorf)_2(NO_3)_2\cdot 2H_2O$ [$Zn–O_{carb}$ = 2.028(3) Å, $Zn–O_{ket}$ = 2.057(3) Å] [57], $[Zn_2(Hcf)_4(1,4–bdc)](1,4–bdc)\cdot 13H_2O$ [$Zn–O_{carb}$ = 2.014(4) Å, $Zn–O_{ket}$ = 2.047(3) Å] [58], $[Zn(cx)_2(dmso)_2]\cdot 4H_2O$ [$Zn–O_{carb}$ = 2.019(2) Å, $Zn–O_{ket}$ = 2.058(2) Å] [59], $[Zn(cf)_2(H_2O)_2]\cdot 8H_2O$ [$Zn–O_{carb}$ = 2.013(17) and 2.030(16) Å, $Zn–O_{ket}$ = 1.983(16) and 2.023(13) Å] [60] and shorter than those in $[Zn(cf)_2]\cdot 2.5H_2O$ [$Zn–O_{carb}$ = 2.0779(19) Å, $Zn–O_{ket}$ = 2.0873(17) Å] [58], $Zn(norf)_2\cdot 4H_2O$ [$Zn–O_{carb}$ = 2.070(3) Å, $Zn–O_{ket}$ = 2.095(3) Å] [47]. In $Zn(gatx)_2(H_2O)_2\cdot 4H_2O$ [43] the $Zn–O_{carb}$ (=1.992(5) Å) is shorter and the $Zn–O_{ket}$ (=2.108(5) Å) is longer than those found in **1**, while in [Zn(Hcf)(1,3-bdc)] [58] the $Zn–O_{carb}$ (=2.085(3) Å) is longer and the $Zn–O_{ket}$ [=2.037(2) Å] is shorter than those found in **1**. In all these complexes, the $Zn–O_{carb}$ is shorter than the $Zn–O_{ket}$ distance as observed in **1**, except those in $[Zn(cf)_2(H_2O)_2]\cdot 8H_2O$ [60] and [Zn(Hcf)(1,3-bdc)] [58] where the $Zn–O_{carb}$ distance is longer than the $Zn–O_{ket}$ one.

The Zn–N distances, [Zn–N(4) = 2.178(2) Å] are longer than those found in $[Zn(S_2CNMe_2)_2(py)]$ (2.079(6) Å) [62], $[Zn(bipy)_2(pybet)](ClO_4)$ (2.081(5)–2.140(6) Å, bipy = 2,2′-bipyridine, $pybet^-$ = pyridinioacetate) [63], $[Zn(bipy)(CC1_3CO_2)_2(H_2O)]$ (2.086(2) and 2.151(2) Å) [64], $[Zn(bipy)_2(ONO)](NO_2)$ (2.122(9)Å) [65] and $[Zn(phen)_2(MeCO_2)](ClO_4)$ (2.100(5)–2.160(5) Å, phen = 1,10-phenanthroline) [63] and shorter than those in $[Zn(pipdtc)_2(bipy)]$ (2.196(3) Å, $pipdtc^-$ = piperidine–carbodithioato anion) [66], $[Zn(cf)_2]\cdot 2.5H_2O$ (2.245(2) Å) [58] and $Zn(norf)_2\cdot 4H_2O$ (2.253(3) Å) [57].

The two pyridine rings are vertical to the mean plane defined by the Zn(II) and the four enrofloxacinato coordinated oxygens. The uncoordinated carboxylato oxygen atoms O(3) [Zn···O(3) = 4.098 Å] lie out the ZnO_4 plane and are displaced at 1.004 Å above and below the mean plane.

3.3. Interaction with DNA

Transition metal complexes can bind to DNA via covalent interactions, where a labile ligand of the complexes is replaced by a nitrogen base of DNA such as guanine N7, and/or noncovalent interactions which include intercalative, electrostatic and groove (surface) binding of metal complexes along outside of DNA helix, along major or minor groove [67]. Quinolone metal complexes can interact with CT-DNA via noncovalent interactions; groove binding, electrostatic binding to phosphate group and intercalation [68].

The UV spectra of CT-DNA in the presence of the quinolones Herx and Hoxo as well as complexes **1** and **2** have been recorded for diverse [compound]/[DNA] mixing ratios (r) and are shown in Fig. 3. The changes observed in the absorption spectra of CT-DNA in the presence of these compounds, i.e. the increase of the intensity at λ_{max} = 258 nm which is accompanied with a red-shift of the λ_{max} up to 267 nm, after mixing with each compound, indicate that the interaction with CT-DNA results in the direct formation of a new complex with double–helical CT-DNA [69]. The absorption intensity at 258 nm is increased due to the fact that the purine and pyrimidine DNA–bases are exposed because of the binding of the compounds to DNA. These characteristics can be attributed to an interaction [70] having caused the changes of the conformation of DNA [71]. Additionally, the observed bathochromism is an evidence of the stabilization of the CT-DNA duplex [72], while the existence of the intercalative binding mode may not be ruled out [15].

In Fig. 4, the changes occurred in the spectrum of a 4×10^{-5} M solution of free quinolones and complexes **1 and 2** during the titra-

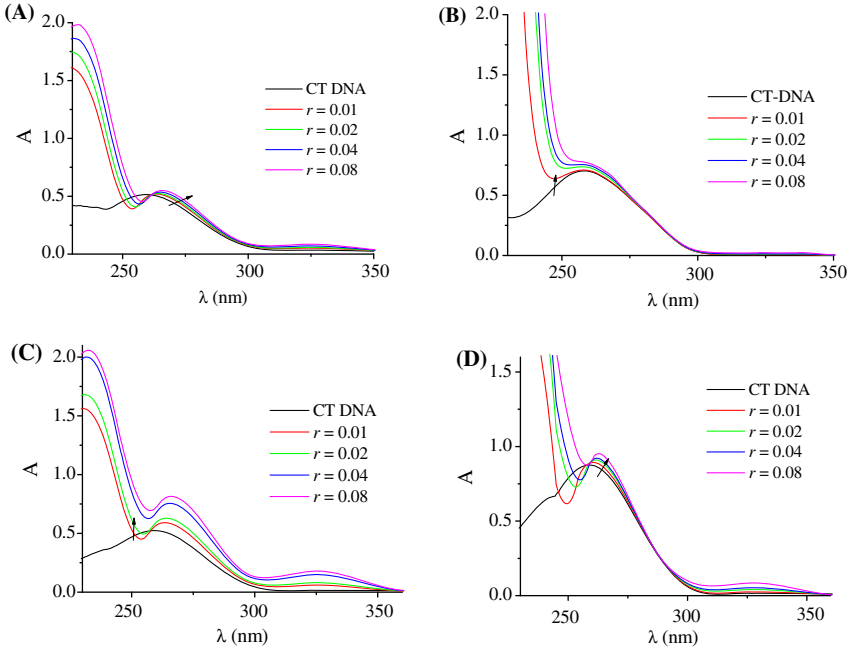


Fig. 3. UV spectra of CT-DNA in buffer solution (150 mM NaCl and 15 mM trisodium citrate at pH 7.0) in the presence of (A) Herx ([DNA] = 0.78×10^{-4} M), (B) Hoxo ([DNA] = 1.10×10^{-4} M), (C) $Zn(erx)_2(py)_2$, **1** ([DNA] = 0.79×10^{-4} M) and (D) $Zn(oxo)_2(py)_2$, **2** ([DNA] = 1.38×10^{-4} M) at diverse r values (r = [complex]/[DNA]) (r = 0–0.08). The arrows show the changes upon increasing amounts of compound.

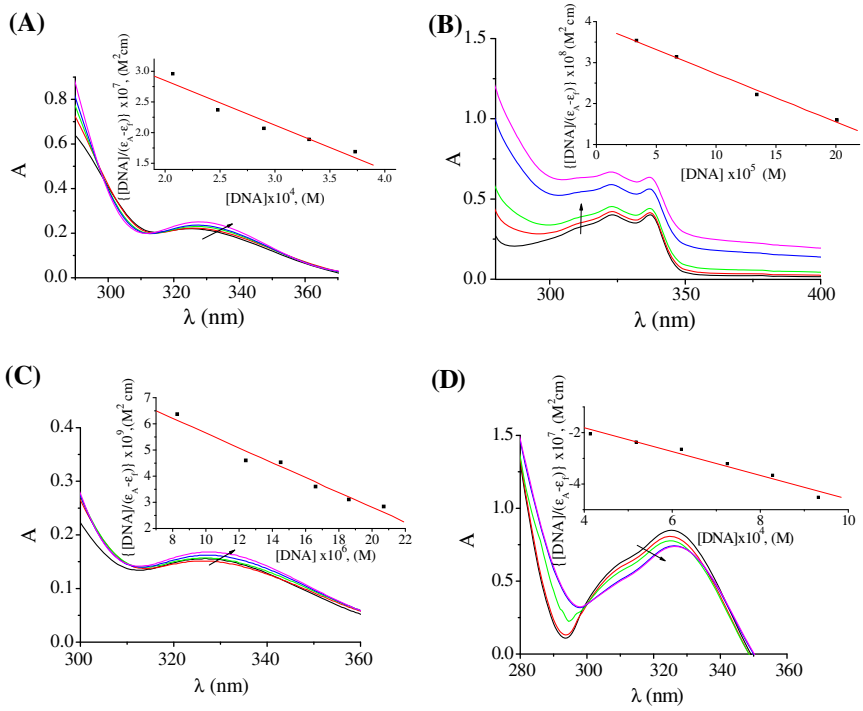


Fig. 4. UV spectra of dmso solution of (A) Herx (2×10^{-5} M), (B) Hoxo (4×10^{-5} M), (C) $Zn(erx)_2(py)_2$, **1** (2.5×10^{-6} M) and (D) $Zn(oxo)_2(py)_2$, **2** (5×10^{-5} M), in the presence of CT-DNA at increasing amounts. The arrows show the changes upon increasing amounts of CT-DNA. Insets: plots of $\frac{[DNA]}{(\varepsilon_a-\varepsilon_f)}$ vs [DNA].

tion upon addition of CT-DNA in diverse *r* values are presented. In the UV region, the intense absorption bands observed in the spectra of the quinolones and the complexes are attributed to the intraligand $\pi \rightarrow \pi^*$ transition of the coordinated groups. Any interaction between each compound and CT-DNA could perturb the intra-ligand centred spectral transition bands of the compound [73].

No significant changes are observed in the position of the $\pi \rightarrow \pi^*$ transition bands of the quinolones upon addition of CT-DNA. For Herx, the band centred at 325 nm shows a hyperchromism in the presence of increasing amounts of CT-DNA (Fig. 4A), which is accompanied with a red–shift of 3 nm (up to 328 nm). For Hoxo, the intensity of the bands centred at 324 nm and 334 nm is increased in the presence of increasing amounts of CT-DNA (Fig. 4B), while a blue-shift of 3 nm (up to 321 nm) and a red-shift of 4 nm (up to 338 nm), respectively, has been observed. The observed hyperchromic effect for Herx and Hoxo suggests binding to CT-DNA ascribed either to external contact (electrostatic binding) [72,74] or to the fact that the quinolones could uncoil the helix structure of DNA and make more bases embedding in DNA exposed [75].

For **1**, the intraligand band of enrofloxacinato ligand at 325 nm presents a red-shift of 3 nm (up to 328 nm), accompanied with a hyperchromism (Fig. 4C), suggesting tight binding to CT-DNA, maybe by electrostatic mode [76], and stabilization. One distinct isosbestic point at 311 nm appears upon addition of CT-DNA.

For **2**, the intensity of the band of oxolinato ligand centred at 325 nm is decreased upon addition of increasing amounts of CT-DNA (Fig. 4D), while a red-shift of 2 nm (up to 327 nm) is observed. The resultant hypochromism suggests tight binding of complex **2** to CT-DNA, probably by the intercalative mode and stabilization [72].

The results derived from the UV titration experiments suggest that all compounds can bind to CT-DNA, resulting in the stabilization of DNA duplex [72]. Nevertheless, the oxolinato ligands provide to **2** a more extended aromatic/planar moiety than the enrofloxacinato ligands in **1,** so that the binding of **2** involving intercalation of such an aromatic/planar ring between the base pairs of CT-DNA cannot be ruled out.

The intrinsic binding constant K_b, a tool to investigate the magnitude of the binding strength of a compound with CT-DNA, which represents the binding constant per DNA base pair, can be obtained by monitoring the changes in the absorbance at the corresponding λ_{max} with increasing concentrations of CT-DNA and is given by the ratio of slope to the *y* intercept in plots $\frac{[DNA]}{(\varepsilon_a-\varepsilon_f)}$ versus [DNA] (Insets in Fig. 4), according to the following equation [70]:

$$\frac{[DNA]}{(\varepsilon_a-\varepsilon_f)} = \frac{[DNA]}{(\varepsilon_b-\varepsilon_f)} + \frac{1}{K_b(\varepsilon_b-\varepsilon_f)} \quad (1)$$

where [DNA] is the concentration of DNA in base pairs, $\varepsilon_a = A_{obsd}/[compound]$, ε_f is the extinction coefficient for the free compound and ε_b is the extinction coefficient for the compound in the fully DNA-bound form. The calculated K_b values for the quinolones and the complexes are given in Table 3.

The K_b values suggest a relatively strong binding of the quinolones and complexes to CT-DNA. Especially, the K_b value obtained for complex **2** ($=1.16(\pm0.14) \times 10^5\ M^{-1}$) is much higher than the other compounds. This can be attributed to the existence of the oxolinato ligands containing a more extended aromatic/planar moiety than the enrofloxacinato ligands.

The K_b for the quinolone ligands and complex **1** are much lower than that of the classical intercalator EB, while the K_b value of **2** is

Table 3
The DNA binding constants (K_b) and the Stern–Volmer constants (K_{SV}) of the quinolones Herx, Hoxo and complexes **1** and **2**.

Complex	K_b (M^{-1})	K_{SV} (M^{-1})
Herx	$1.69(\pm0.04) \times 10^3$	$1.91(\pm0.07) \times 10^5$
Hoxo	$3.02(\pm0.10) \times 10^3$	nd [a]
$Zn(erx)_2(py)_2$, **1**	$3.35(\pm0.05) \times 10^4$	$3.40(\pm0.25) \times 10^5$
$Zn(oxo)_2(py)_2$, **2**	$1.16(\pm0.14) \times 10^5$	$3.68(\pm0.21) \times 10^5$

[a] n.d., not determined.

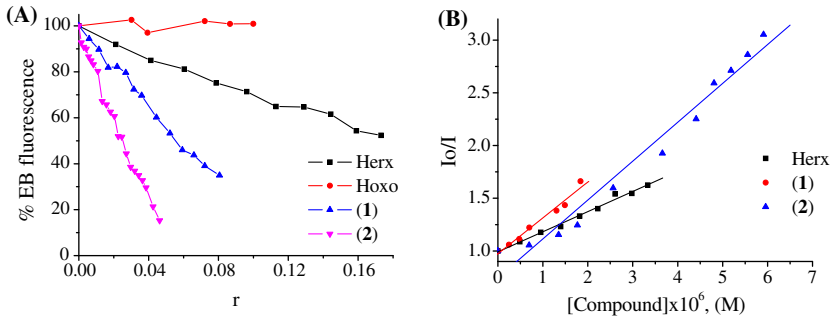


Fig. 5. (A) Plot of EB relative fluorescence intensity (%) vs r (=[complex]/[DNA]) for (■) Herx, (●) Hoxo, (▲) $Zn(erx)_2(py)_2$, **1** and (▼) $Zn(oxo)_2(py)_2$, **2** in buffer solution (150 mM NaCl and 15 mM trisodium citrate at pH 7.0). (B) Stern–Volmer quenching plot of EB bound to CT-DNA by (●) Herx, (▲) $Zn(erx)_2(py)_2$, **1** and (▼) $Zn(oxo)_2(py)_2$, **2**. [EB] = 20 μM, [DNA] = 30 μM, λ_{em} = 592 nm.

comparable to the EB binding affinity for CT-DNA, ($K_b = 1.23(\pm 0.07) \times 10^5\ M^{-1}$) [77], suggesting that electrostatic and/or intercalative interaction could affect EB displacement from the EB–DNA complex [77].

The quinolones and the complexes do not show any fluorescence at room temperature in solution or in the presence of CT-DNA, and their binding to DNA cannot be directly predicted through the emission spectra, so that competitive EB binding studies have been performed to gain support for the binding of each compound with DNA. EB (=3,8-diamino-5-ethyl-6-phenyl-phenanthridinium bromide), a phenenthridine fluorescence dye and a typical indicator of intercalation [78], does not show any appreciable emission in buffer solution due to fluorescence quenching of the free EB by the solvent molecules [79]. It can form soluble complexes with nucleic acids and emitting enhanced fluorescence in the presence of CT-DNA due to the intercalation of the planar phenenthridinium ring between adjacent base pairs on the double DNA-helix [80,81]. Addition of a second molecule, which can bind to DNA more strongly than EB results to a decrease the DNA-induced EB emission [82]. Two mechanisms have been proposed to account for this reduction in the emission intensity: the replacement of EB, and/or electron transfer [83].

The emission spectra of EB bound to CT-DNA in the absence and presence of each compound have been recorded for [EB] = 2×10^{-5} M, [DNA] = 3×10^{-5} M for increasing amounts of each compound. Free oxolinic acid does not provoke any significant changes of the intensity of the emission band at 592 nm of the DNA–EB system indicating that Hoxo cannot displace EB from the DNA–EB complex. On the other hand, the intensity of the emission band at 592 nm of the DNA–EB system decreased in intensity (up to 15% of the initial EB–DNA fluorescence for **2**) upon addition of enrofloxacin and complexes **1** and **2** at diverse r values (Fig. 5A) indicating the competition of the compounds with EB in binding to DNA. The observed quenching of DNA–EB fluorescence for Herx and complexes **1** and **2** may suggest that they can displace EB from the DNA–EB complex interacting with CT-DNA probably by the intercalative mode [15,84].

The Stern–Volmer constant K_{SV} is often used to evaluate the quenching efficiency for a compound and varies with the experimental conditions:

$$\frac{Io}{I} = 1 + K_{SV}\,[\text{compound}] \qquad (2)$$

where Io and I are the emission intensities in the absence and the presence of the compound, respectively. Fig. 5B shows the Stern–Volmer plots for Herx and **1** and **2** and the corresponding K_{SV} values calculated are shown in Table 3. The Stern–Volmer plot of DNA–EB illustrates that the quenching of EB bound to DNA by Herx and complexes **1 and 2** is in good agreement ($R = 0.99$) with the linear Stern–Volmer equation (Eq. 2), which proves that the partial replacement of EB bound to DNA by each compound results in a decrease in the fluorescence intensity [85]. Especially, the high K_{SV} values of the complexes show that they can be bound tightly to the DNA [86]. More specifically, complex **2** presents a higher value for K_{SV} than complex **1**, which is in accordance to the magnitude order observed for the K_b values, indicating its higher affinity to CT-DNA.

4. Conclusions

The synthesis and characterization of two novel neutral mononuclear zinc complexes with the quinolone antibacterial drugs enrofloxacin (second-generation) and oxolinic acid (first-generation) in the presence of the N-donor heterocyclic ligand pyridine has been realized. In these complexes, the quinolone ligands are bound to zinc(II) via the ketone oxygen and a carboxylato oxygen. The crystal structure of the complex $Zn(erx)_2(py)_2$ has been determined with X-ray crystallography revealing a distorted octahedral geometry for Zn(II).

The interaction of the quinolones and the complexes with CT-DNA has been studied with UV spectroscopy revealing their ability to bind to DNA. UV spectroscopic titrations have been used in order to calculate their binding strength with CT-DNA. $Zn(oxo)_2(py)_2$ exhibits the highest K_b value among all the compounds examined, which is comparable to that of EB.

Competitive binding studies with EB have been performed with fluorescence spectroscopy and have shown that the interaction between DNA–EB complex and the complexes release EB from its DNA complex, indicating that the complexes can bind to DNA probably via the intercalative mode.

5. Supplementary data

CCDC 716239 contains the supplementary crystallographic data for this paper. These data can be obtained free of charge via http://www.ccdc.cam.ac.uk/conts/retrieving.html, or from the Cambridge Crystallographic Data Centre, 12 Union Road, Cambridge CB2 1EZ, UK; fax: (+44) 1223-336-033; or e-mail: deposit@ccdc.cam.ac.uk.

References

[1] I. Turel, Coord. Chem. Rev. 232 (2002) 27–47. and references cited therein.
[2] D.E. King, R. Malone, S.H. Lilley, Am. Fam. Phys. 61 (2000) 2741.
[3] K. Sandstrom, S. Warmlander, M. Leijon, A. Graslund, Biochem. Biophys. Res. Commun. 304 (2003) 55.
[4] E. Canton, J. Peman, M.T. Jimenez, M.S. Ramon, M. Gobernado, Antimicrob. Agents Chemother. 36 (1992) 558.
[5] E.S. Pfeiffer, H. Hiasa, Antimicrob. Agents Chemother. 48 (2004) 608.
[6] Y. Xia, Z.Y. Yang, P. Xia, K.F. Bastow, Y. Tachibana, S.C. Kuo, E. Hamel, T. Hackl, K.H. Lee, J. Med. Chem. 41 (1998) 1155.

[7] D.K. Saha, U. Sandbhor, K. Shirisha, S. Padhye, D. Deobagkar, C.E. Anson, A.K. Powell, Bioorg. Med. Chem. Lett. 14 (2004) 3027.
[8] I. Turel, A. Golobic, A. Klavzar, B. Pihlar, P. Buglyo, E. Tolis, D. Rehder, K. Sepcic, J. Inorg. Biochem. 95 (2003) 199.
[9] E.K. Efthimiadou, M.E. Katsarou, A. Karaliota, G. Psomas, J. Inorg. Biochem. 102 (2008) 910.
[10] G. Psomas, A. Tarushi, E.K. Efthimiadou, Polyhedron 27 (2008) 133.
[11] A. Tarushi, E.K. Efthimiadou, P. Christofis, G. Psomas, Inorg. Chim. Acta 360 (2007) 3978.
[12] N. Jimenez–Garrido, L. Perello, R. Ortiz, G. Alzuet, M. Gonzalez–Alvarez, E. Canton, M. Liu–Gonzalez, S. Garcia–Granda, M. Perez–Priede, J. Inorg. Biochem. 99 (2005) 677–689.
[13] P. Drevensek, I. Turel, N. Poklar, Ulrih, J. Inorg. Biochem. 96 (2003) 407.
[14] A. Tarushi, P. Christofis, G. Psomas, Polyhedron 26 (2007) 3963.
[15] G. Psomas, J. Inorg. Biochem. 102 (2008) 1798.
[16] E.K. Efthimiadou, H. Thomadaki, Y. Sanakis, C.P. Raptopoulou, N. Katsaros, A. Scorilas, A. Karaliota, G. Psomas, J. Inorg. Biochem. 101 (2007) 64.
[17] M.E. Katsarou, E.K. Efthimiadou, G. Psomas, A. Karaliota, D. Vourloumis, J. Med. Chem. 51 (2008) 470.
[18] M.J. e Souza, C.F. Bittencourt, L.M. Morsch, J. Pharm. Biomed. Anal. 28 (2002) 1195–1199.
[19] D.M. Boothe, Vet. Med. 89 (1994) 744.
[20] J.-Y. Fan, D. Sun, H. Yu, S.M. Kerwin, L.H. Hurley, J. Med. Chem. 38 (1995) 408.
[21] S. Ameyama, Y. Shinmura, M. Takahata, Antimicr. Agent Chemother. 47 (2003) 2327.
[22] E.K. Efthimiadou, M. Katsarou, Y. Sanakis, C.P. Raptopoulou, A. Karaliota, N. Katsaros, G. Psomas, J. Inorg. Biochem. 100 (2006) 1378.
[23] J. Recillas-Mota, M. Flores-Alamo, R. Moreno-Esparza, J. Gracia-Mora, Acta Crystallogr., Sect. E 63 (2007) m3030–m3031.
[24] E.K. Efthimiadou, N. Katsaros, A. Karaliota, G. Psomas, Bioorg. Med. Chem. Lett. 17 (2007) 1238.
[25] E.K. Efthimiadou, A. Karaliota, G. Psomas, Polyhedron 27 (2008) 349.
[26] E.K. Efthimiadou, A. Karaliota, G. Psomas, Polyhedron 27 (2008) 1729.
[27] R. Piccolomini, G. Ravagnan, Chemioterapia 5 (1986) 249.
[28] D.J. D'Alessio, V.M. Olexy, G.G. Jackson, Antimicr. Agents Chemother. 7 (1967) 490.
[29] G. Psomas, A. Tarushi, E.K. Efthimiadou, Y. Sanakis, C.P. Raptopoulou, N. Katsaros, J. Inorg. Biochem. 100 (2006) 1764.
[30] C. Dendrinou-Samara, L. Alevizopoulou, L. Iordanidis, E. Samaras, D.P. Kessissoglou, J. Inorg. Biochem. 89 (2002) 89.
[31] C. Dendrinou-Samara, G. Psomas, K. Christophorou, V. Tangoulis, V.P. Raptopoulou, A. Terzis, D.P. Kessissoglou, J. Chem. Soc., Dalton Trans. (1996) 3737–3743.
[32] G. Psomas, C. Dendrinou-Samara, P. Philippakopoulos, V. Tangoulis, C.P. Raptopoulou, H. Samaras, D.P. Kessissoglou, Inorg. Chim. Acta 272 (1998) 24.
[33] C. Dendrinou-Samara, G. Tsotsou, C.P. Raptopoulou, A. Kortsaris, D. Kyriakidis, D.P. Kessissoglou, J. Inorg. Biochem. 71 (1998) 171.
[34] G. Psomas, C.P. Raptopoulou, L. Iordanidis, C. Dendrinou-Samara, V. Tangoulis, D.P. Kessissoglou, Inorg. Chem. 39 (2000) 3042.
[35] V. Tangoulis, G. Psomas, C. Dendrinou-Samara, C.P. Raptopoulou, A. Terzis, D.P. Kessissoglou, Inorg. Chem. 35 (1996) 7655.
[36] A. Dimitrakopoulou, C. Dendrinou-Samara, A. Pantazaki, C. Raptopoulou, A. Terzis, E. Samaras, D.P. Kessissoglou, Inorg. Chim. Acta 360 (2007) 546.
[37] I. Tsivikas, M. Alexiou, A.A. Pantazaki, C. Dendrinou-Samara, D.A. Kyriakidis, D.P. Kessissoglou, Bioinorg. Chem. and Appl. 1 (2003) 85.
[38] M. Alexiou, I. Tsivikas, C. Dendrinou-Samara, A. Pantazaki, P. Trikalitis, N. Lalioti, D.A. Kyriakidis, D.P. Kessissoglou, J. Inorg. Biochem. 93 (2003) 256.
[39] C. Dendrinou-Samara, A.N. Papadopoulos, D. Malamatari, A. Tarushi, C. Raptopoulou, A. Terzis, E. Samaras, D.P. Kessissoglou, J. Inorg. Biochem. 99 (2005) 864.
[40] N. Farrell, Coord. Chem. Rev. 232 (2002) 1.
[41] G.K. Walkup, S.C. Burdette, S.J. Lippard, R.Y. Tsien, J. Am. Chem. Soc. 122 (2000) 5644.
[42] M. Di Vaira, C. Bazzicalupi, P. Orioli, L. Messori, B. Bruni, P. Zatta, Inorg. Chem. 43 (2004) 3795.
[43] Z.Q. Li, F.J. Wu, Y. Gong, C.W. Hu, Y.H. Zhang, M.Y. Gan, Chin. J. Chem. 25 (2007) 1809.
[44] J. d'Angelo, G. Morgant, N.E. Ghermani, D. Desmaele, B. Fraisse, F. Bonhomme, E. Dichi, M. Sghaier, Y. Li, Y. Journaux, J.R.J. Sorenson, Polyhedron 27 (2008) 537–546.
[45] H. Sakurai, Y. Kojima, Y. Yoshikawa, K. Kawabe, H. Yasui, Coord. Chem. Rev. 226 (2002) 187.
[46] Q. Zhou, T.W. Hambley, B.J. Kennedy, P.A. Lay, P. Turner, B. Warwick, J.R. Biffin, H.L. Regtop, Inorg. Chem. 39 (2000) 3742.
[47] N.C. Kasuga, K. Sekino, M. Ishikawa, A. Honda, M. Yokoyama, S. Nakano, N. Shimada, C. Koumo, K. Nomiya, J. Inorg. Biochem. 96 (2003) 298.
[48] M. Belicchi Ferrari, F. Bisceglie, G. Pelosi, P. Tarasconi, R. Albertini, S. Pinelli, Inorg. Biochem. 87 (2001) 137.
[49] Z. Travnicek, V. Krystof, M. Sipl, J. Inorg. Biochem. 100 (2006) 214.
[50] J.S. Casas, E.E. Castellano, M.D. Couce, J. Ellena, A. Sanchez, J. Sordo, C. Taboada, J. Inorg. Biochem. 100 (2006) 124.
[51] J. Marmur, J. Mol. Biol. 3 (1961) 208.
[52] M.F. Reichmann, S.A. Rice, C.A. Thomas, P. Doty, J. Am. Chem. Soc. 76 (1954) 3047.
[53] Rigaku/MSC, CRYSTALCLEAR, Rigaku/MSC Inc., The Woodlands, TX, USA, 2005.
[54] G.M. Sheldrick, SHELXS-97: Structure Solving Program, University of Göttingen, Germany, 1997.
[55] G.M. Sheldrick, SHELXL-97: Crystal Structure Refinement Program, University of Göttingen, Germany, 1997.
[56] K. Nakamoto, Infrared and Raman Spectra of Inorganic and Coordination Compounds, 4th ed., Wiley, New York, 1986.
[57] Z.F. Chen, R.G. Xiong, J. Zhang, X.T. Chen, Z.L. Xue, X.-Z. You, Inorg. Chem. 40 (2001) 4075.
[58] D.R. Xiao, E.B. Wang, H.Y. An, Z.M. Su, Y.G. Li, L. Gao, C.Y. Sun, L. Xu, Chem. Eur. J. 11 (2005) 6673.
[59] M. Ruiz, R. Ortiz, L. Perello, A. Castineiras, M. Quiros, Inorg. Chim. Acta 211 (1993) 133.
[60] M.P. Lopez-Gresa, R. Ortiz, L. Perello, J. Latorre, M. Liu-Gonzalez, S. Garcia-Granda, M. Perez–Priede, E. Canton, J. Inorg. Biochem. 92 (2002) 65–74.
[61] I. Turel, K. Gruber, I. Leban, N. Bukovec, J. Inorg. Biochem. 61 (1996) 197.
[62] K.A. Fraser, M.M. Harding, Acta Crystallogr. 22 (1967) 75.
[63] X.M. Chen, Z.T. Xu, X.L. Yu, T.C.W. Mak, Polyhedron 13 (1994) 2079.
[64] S. Sen, S. Mitra, P. Kundu, M.K. Saha, C. Kruger, J. Bruckmann, Polyhedron 16 (1997) 2475.
[65] A. Walsh, B. Walsh, B. Murphy, B.J. Hathway, Acta Crystallogr., Sect. B 37 (1981) 1512.
[66] S. Thirumaran, K. Ramalingama, G. Bocelli, A. Cantoni, Polyhedron 18 (1999) 925.
[67] Q.L. Zhang, J.G. Liu, H. Chao, G.Q. Xue, L.N. Ji, J. Inorg. Biochem. 83 (2001) 49.
[68] B.M. Zeglis, V.C. Pierre, J.K. Barton, Chem. Commun. (2007) 4565–4579.
[69] G.S. Son, J.A. Yeo, M.S. Kim, S.K. Kim, A. Holmen, B. Akerman, B. Norden, J. Am. Chem. Soc. 120 (1998) 6451.
[70] A.M. Pyle, J.P. Rehmann, R. Meshoyrer, C.V. Kumar, N.J. Turro, J.K. Barton, J. Am. Chem. Soc. 111 (1989) 3053.
[71] Y.M. Song, Q. Wu, P.J. Yang, N.N. Luan, L.F. Wang, Y.M. Liu, J. Inorg. Biochem. 100 (2006) 1685.
[72] E.C. Long, J.K. Barton, Acc. Chem. Res. 23 (1990) 271.
[73] V. Uma, M. Kanthimathi, T. Weyhermuller, B.U. Nair, J. Inorg. Biochem. 99 (2005) 2299.
[74] R.F. Pasternack, E.J. Gibbs, J.J. Villafranca, Biochemistry 22 (1983) 2406.
[75] G. Pratviel, J. Bernadou, B. Meunier, Adv. Inorg. Chem. 45 (1998) 251.
[76] A. Janeso, L. Nagy, E. Moldrheim, E. Sletten, J. Chem. Soc., Dalton Trans. (1999) 1587–1594.
[77] A. Dimitrakopoulou, J. Inorg. Biochem. 102 (2008) 618.
[78] W.D. Wilson, L. Ratmeyer, M. Zhao, L. Strekowski, D. Boykin, Biochemistry 32 (1993) 4098.
[79] S. Dhar, M. Nethaji, A.R. Chakravarty, J. Inorg. Biochem. 99 (2005) 805.
[80] C.G. Reihardt, T.R. Krugh, Biochemistry 17 (1978) 4845.
[81] J. Olmsted, D.R. Kearns, Biochemistry 16 (1977) 3647.
[82] B.C. Baguley, M. Lebret, Biochemistry 23 (1984) 937.
[83] R.F. Pasternack, M. Cacca, B. Keogh, T.A. Stephenson, A.P. Williams, F.J. Gibbs, J. Am. Chem. Soc. 113 (1991) 6835.
[84] O. Novakova, H. Chen, O. Vrana, A. Rodger, P.J. Sadler, V. Brabec, Biochemistry 42 (2003) 11544.
[85] S. Tabassum, S. Parveen, F. Arjmand, Acta Biomater. 1 (2005) 677.
[86] M. Chauhan, K. Banerjee, F. Arjmand, Inorg. Chem. 46 (2007) 3072.

2. Experimental

2.1. General and physical measurements

All manipulations were performed under aerobic conditions. Gallium (III) acetylacetonate, [Ga(acac)$_3$], 2-aminophenol and 5-methylsalicylaldehyde (2-hydroxy-5-methyl-benzaldehyde) were obtained from Aldrich. 5-Bromosalicylaldehyde was from Fluka, while salicylaldehyde and the rest of the reagents were from Merck. All chemicals were of the best quality available and were used as received. Microanalyses (C, H and N) were performed by the University of Ioannina (Ioannina, Greece) Microanalytical Laboratory using an EA 1108 Carlo Erba analyser. IR spectra (4000–450 cm^{-1}) were recorded on a Perkin–Elmer 16 PC FT spectrometer with samples prepared as KBr pellets.

2.2. Compound preparation

2.2.1. Synthesis of N-salicylidene-o-aminophenol (saphH$_2$) and derivatives

Synthesis of saphH$_2$ was achieved by the condensation in absolute ethanol of 2-aminophenol with salicylaldehyde in the case of the unsubstituted Schiff base, with 2-hydroxy-5-methyl-benzaldehyde in the case of methyl substituted Schiff base or with 5-bromosalicylaldehyde in the case of bromo-substituted Schiff base, in accordance with literature methods [20]. The chemical structures of the free and substituted Schiff bases are shown in Fig. 1.

2.2.2. [Ga(acac)(saph)(EtOH)] (**1**)

A yellow solution of H$_2$saph (0.021 g, 0.10 mmol) in EtOH (10 mL) was added to a colorless solution of [Ga(acac)$_3$] (0.037 g, 0.10 mmol) in the same solvent (10 mL). The clear yellow solution, obtained was allowed to stand undisturbed for one day at room temperature. Well-formed X-ray quality single crystals of **1** slowly appeared. The yellow crystals were isolated by vacuum filtration, washed with cold EtOH (2 × 3 mL) and dried in air. The yield was 80% based on Ga. *Anal.* Calc. for $C_{20}H_{22}GaNO_5$: C, 56.37; H, 5.21; N, 3.29. Found: C, 55.78; H, 5.12; N, 3.24%. IR (KBr pellets, cm^{-1}): 3440br, 3048w, 2968w, 2790w, 1620s, 1586s, 1546m, 1526s, 1474s, 1446w, 1386s, 1342w, 1308m, 1270m, 1222w, 1176m, 1154m, 1128w, 1090w, 1042m, 928m, 876w, 836m, 774w, 742m, 678w, 626w, 610w, 526w, 538m, 490w.

2.2.3. [Ga(acac)(5Mesaph)(MeOH)] (**2**)

Solid [Ga(acac)$_3$] (0.037 g, 0.10 mmol) was added to a yellow–orange solution of H$_2$5Mesaph (0.023 g, 0.10 mmol) in MeOH/EtOH (1:1 v/v, 20 mL). The yellow solution obtained was filtered and layered with Et$_2$O/hexane (1:1 v/v, 40 mL). Slow mixing yielded well-formed, X-ray quality yellow crystals of **2**. The crystals were isolated by vacuum filtration, washed with Et$_2$O (2 × 3 mL) and dried in air. The yield was 78% based on Ga. *Anal.* Calc. for $C_{20}H_{22}GaNO_5$: C, 56.37; H, 5.21; N, 3.29. Found: C, 57.10; H, 5.75; N, 3.47%. IR (KBr pellets, cm^{-1}): 3450wbr, 3003w, 2760w, 2552w, 1621m, 1588s, 1537s, 1478s, 1433w, 1393m, 1378s, 1315m, 1282m, 1270m, 1252w, 1214w, 1200w, 1161m, 1147w, 1134m, 1028m, 961w, 933w, 891w, 830m, 814w, 785w, 740m, 684w, 652w, 616w, 584w, 564w, 532w, 491w, 478w, 451w.

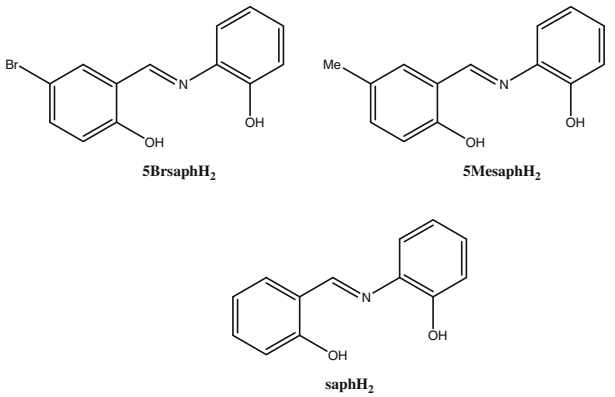


Fig. 1. The chemical structures of the ligands discussed in the text.

2.2.4. [Ga(acac)(5Brsaph)(EtOH)] (**3**)

A colorless solution of [Ga(acac)$_3$] (0.037 g, 0.10 mmol) in EtOH (10 mL) was added to a yellow solution of H$_2$5Brsaph (0.058 g, 0.20 mmol) in the same solvent (10 mL). The yellow solution obtained was filtered and allowed to stand undisturbed in the refrigerator for thirteen days. Well-formed X-ray quality single crystals of **3** slowly appeared. The yellow crystals were isolated by vacuum filtration, washed with Et$_2$O (2 × 3 mL) and dried in air. The yield was 60% based on Ga. *Anal.* Calc. for $C_{20}H_{21}GaNO_5Br$: C, 47.56; H, 4.20; N, 2.77. Found: C, 48.79; H, 5.94; N, 2.84%. IR (KBr pellets, cm^{-1}): 3460br, 2348w, 2284br, 1658w, 1619s, 1589m, 1524s, 1475s, 1458s, 1377s, 1307m, 1261m, 1248m, 1209w, 1169s, 1137w, 1114w, 1087w, 1045w, 875w, 826m, 744s, 678m, 648m, 620w, 580w, 544w, 518w, 493w.

2.3. Single-crystal X-ray crystallography

Crystals of **1** and **2** were mounted in capillary. Diffraction measurements were made on a Nicolet diffractometer upgraded by Crystal Logic using graphite-monochromated Cu radiation. Complete crystal data and parameters for data collection and processing are reported in Table 1. Unit cell dimensions were determined and refined by using the angular settings of 25 automatically centered reflections in the range $22 < 2\theta < 54°$ for **1** and

Table 1
Crystallographic data for complexes **1** and **2**.

Parameter	**1**	**2**
Formula	$C_{40}H_{44}Ga_2N_2O_{10}$	$C_{20}H_{22}GaNO_5$
Formula weight	852.21	426.11
Crystal color, habit	yellow, plates	yellow, plates
Crystal dimensions (mm)	0.10 × 0.20 × 0.30	0.13 × 0.15 × 0.40
Crystal system	monoclinic	triclinic
Space group	$P2_1/n$	$P\bar{1}$
Unit cell dimensions		
a (Å)	12.8150(18)	10.912(5)
b (Å)	16.826(3)	10.065(5)
c (Å)	18.170(3)	11.164(6)
α (°)	90	76.35(2)
β (°)	90.888(6)	61.66(2)
γ (°)	90	63.54(2)
V (Å^3)	3917.3(11)	965.7(8)
Z	8	2
$\rho_{calc.}$ (g cm^{-3})	1.445	1.465
Radiation, λ (Å)	Cu Kα, 1.54180	Cu Kα, 1.54180
T (K)	293	293
$2\theta_{max.}$ (°)	110	118
μ (mm^{-1})	2.184	2.215
Reflections collected/unique (R_{int})	5060/4882 (0.0280)	2928/2772 (0.0205)
Data with $I > 2\sigma(I)$	3557	2674
Parameters refined	543	293
$(\Delta\rho)_{max.}$, $(\Delta\rho)_{min.}$ (e Å^{-3})	0.419, −0.511	1.212, −0.398
Goodness-of-fit (GOF) (on F^2)	1.024	1.060
R_1[a], wR_2[b] (all data)	0.0740, 0.1360	0.0370, 0.1000
R_1[a], wR_2[b] ($I>2\sigma(I)$)	0.0486, 0.1186[c]	0.0361, 0.0991[d]

[a] $R_1 = \sum(|F_o| - |F_c|)/\sum(|F_o|)$.

[b] $wR_2 = \left\{\sum\left[w(F_o^2 - F_c^2)^2\right]/\sum\left[w(F_o^2)^2\right]\right\}^{1/2}$.

[c] For 3579 reflections with $I > 2\sigma(I)$.

[d] For 2674 reflections with $I > 2\sigma(I)$.

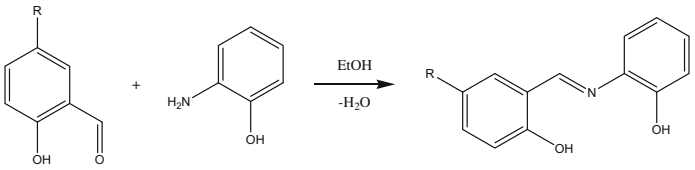
2. Three standard reflections monitored every 97 reflections showed less than 3% variation and no decay. Lorentz, polarization corrections were applied using Crystal Logic software.

The structures were solved by direct methods using SHELXS-86 [21] and refined by full-matrix least-squares techniques on F^2 with SHELXL-97 [22]. For **1**, all hydrogen atoms were introduced at calculated positions as riding on bonded atoms. All non-hydrogen atoms were refined anisotropically. For **2**, the hydrogen atoms were either located by difference maps and were refined isotropically or were introduced at calculated positions as riding on bonded atoms. All non-hydrogen atoms were refined anisotropically.

3. Results and discussion

3.1. Brief synthetic comments

Eq. (1) summarizes the synthesis of the ligands. Complexes **1**–**3** were obtained by ligand substitution reactions between $Ga(acac)_3$ (acacH = 2,4,-pentanedione) and $5XsaphH_2$ (X = H, $saphH_2$; X = Me, $5MesaphH_2$ and X = Br, $5BrsaphH_2$) in alcoholic solutions as yellow crystals. Eq. (1) summarizes the preparation of the representative complex **1**. The ligand substitution reactions can be realized on the basis of the different coordination strength of the acacH and the $5XsaphH_2$ ligands.



R = H : $saphH_2$
R = Br : $5BrsaphH_2$
R = Me : $5MesaphH_2$ (1)

$$Ga(acac)_3 + saphH_2 + EtOH \xrightarrow{EtOH} [Ga(acac)(saph)(EtOH)] + 2acacH \quad (2)$$

3.2. Description of structures

Complexes **1** and **2** were characterized by X-ray crystallography, while preliminary X-ray characterization of complex **3** revealed that it is isostructural to **1** and therefore we did not performed full X-ray characterization.

Table 2
Selected bond distances (Å) and angles (°) in **1**.

Ga(1)–O(1)	1.894(4)	Ga(2)–O(11)	1.910(4)
Ga(1)–O(2)	1.923(4)	Ga(2)–O(12)	1.927(4)
Ga(1)–O(3)	1.925(4)	Ga(2)–O(13)	1.925(4)
Ga(1)–O(4)	1.984(4)	Ga(2)–O(14)	1.977(4)
Ga(1)–O(5)	2.067(4)	Ga(2)–O(15)	2.062(4)
Ga(1)–N(1)	1.966(2)	Ga(2)–N(11)	2.045(2)
O(1)–Ga(1)–O(2)	171.4(2)	O(11)–Ga(2)–O(12)	172.2(2)
O(1)–Ga(1)–O(3)	92.0(2)	O(11)–Ga(2)–O(13)	91.7(2)
O(1)–Ga(1)–O(4)	93.9(2)	O(11)–Ga(2)–O(14)	93.5(2)
O(1)–Ga(1)–O(5)	88.6(2)	O(11)–Ga(2)–O(15)	90.2(2)
O(1)–Ga(1)–N(1)	98.2(6)	O(11)–Ga(2)–N(11)	95.2(6)
O(2)–Ga(1)–O(3)	93.7(2)	O(12)–Ga(2)–O(13)	94.3(2)
O(2)–Ga(1)–O(4)	92.3(2)	O(12)–Ga(2)–O(14)	91.4(2)
O(2)–Ga(1)–O(5)	85.5(2)	O(12)–Ga(2)–O(15)	85.4(2)
O(2)–Ga(1)–N(1)	76.3(6)	O(12)–Ga(2)–N(11)	78.8(6)
O(3)–Ga(1)–O(4)	90.7(2)	O(13)–Ga(2)–O(14)	90.3(2)
O(3)–Ga(1)–O(5)	87.0(2)	O(13)–Ga(2)–O(15)	85.7(2)
O(3)–Ga(1)–N(1)	169.6(6)	O(13)–Ga(2)–N(11)	173.1(6)
O(4)–Ga(1)–O(5)	176.7(2)	O(14)–Ga(2)–O(15)	174.7(2)
O(4)–Ga(1)–N(1)	86.8(4)	O(14)–Ga(2)–N(11)	89.0(5)
O(5)–Ga(1)–N(1)	95.0(4)	O(15)–Ga(2)–N(11)	94.6(5)

Complex **1** crystallizes in the monoclinic space group $P2_1/n$, while there are two crystallographically independent mononuclear complexes in the unit cell. Fig. 2 shows the molecular structure of one monomer of **1**, while selected bond distances and angles are listed in Table 2. The Ga^{III} ion adopts a six-coordinate distorted octahedral geometry. The $saph^{2-}$ ligand chelates the Ga^{III} ion through the imine nitrogen atom and the deprotonated hydroxyl oxygen atoms all on the equatorial plane of the octahedron. The $acac^-$ ligand also chelates the Ga^{III} atom with one O atom completing the equatorial plane of the octahedron and the other on one of the axial positions. The ethanol O atom occupies the second axial position. Although the EtOH hydroxyl hydrogen atom was not located, it appears that each [Ga(acac)(saph)(EtOH)] is hydrogen

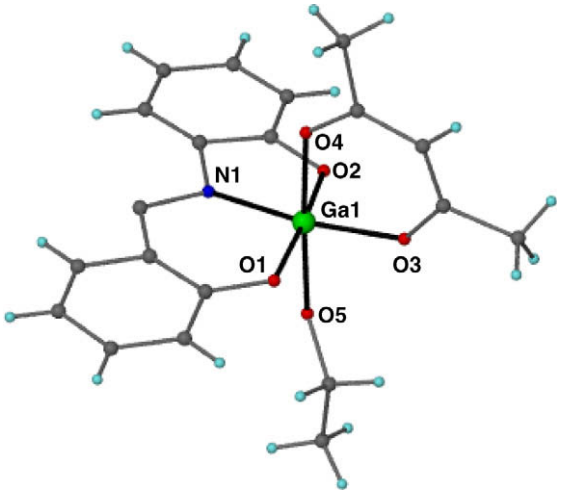


Fig. 2. Ball and stick representation of the molecular structure of **1**.

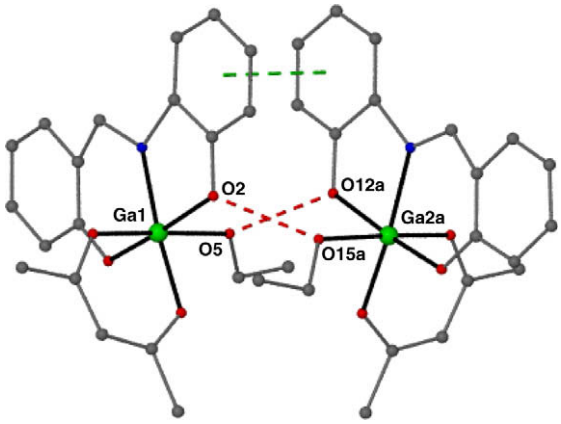


Fig. 3. The hydrogen bonding and the π–π stacking interactions that form the dimer in **1**. All hydrogen atoms have been omitted for clarity. Symmetry code: a, $x-1/2, 3/2-y, 1/2+z$.

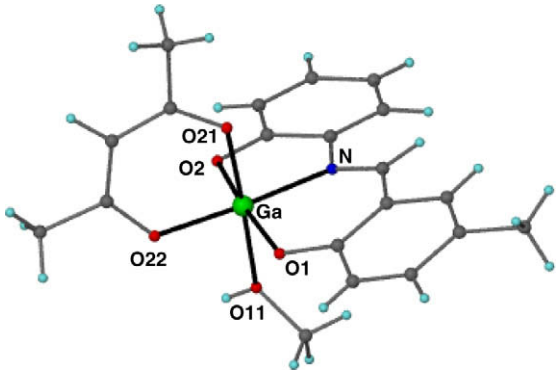


Fig. 4. Ball and stick representation of the molecular structure of **2**.

Table 3
Selected bond distances (Å) and angles (°) in **2**.

Ga–O(1)	1.896(2)	Ga–O(11)	2.060(2)
Ga–O(2)	1.960(2)	Ga–O(21)	1.982(2)
Ga–N	2.032(3)	Ga–O(22)	1.920(2)
O(1)–Ga–O(2)	170.8(1)	O(2)–Ga–O(22)	89.7(1)
O(1)–Ga–N	91.5(1)	N–Ga–O(11)	92.5(1)
O(1)–Ga–O(11)	87.5(1)	N–Ga–O(21)	89.5(1)
O(1)–Ga–O(21)	93.0(1)	N–Ga–O(22)	171.5(1)
O(1)–Ga–O(22)	96.8(1)	O(11)–Ga–O(21)	177.9(1)
O(2)–Ga–N	81.8(1)	O(11)–Ga–O(22)	85.7(1)
O(2)–Ga–O(11)	86.6(1)	O(21)–Ga–O(22)	92.2(1)
O(2)–Ga–O(21)	93.3(1)		

bonded to the other crystallographically indepedented monomer (Fig. 3) through two hydrogen bonds that involve the EtOH oxygen [O5 and O15] and the depropotonated hydroxyl oxygen [O12 and O2] atoms of the saph^{2-} ligand with the O···O distances equal to 2.618 and 2.650 Å for O5···O12a and O2···O15a (a: $x-1/2$, $3/2-y$, $1/2+z$), respectively. A π–π stacking interaction (centroid···centroid distance: 3.638 Å) between the aminophenolate rings of the two monomers assists the hydrogen bonding in forming the dimer (Fig. 3).

Complex **2** crystallizes in the triclinic space group $P\bar{1}$. The molecular structure of **2** is shown in Fig. 4, while selected bond distances and angles are listed in Table 3. The mononuclear complex **2** is very similar to **1**, with the Ga^{III} ion adopting a distorted octahedral environment. A tridentate 5Mesaph^{2-} ligand chelates to the Ga^{III} ion through the imine nitrogen atom and the deprotonated hydroxyl oxygen atoms. A bidentate chelating acac$^-$ ligand and a MeOH molecule complete the octahedron around the metal centre. The NO_2 donor set from the 5Mesaph^{2-} ligand and one oxygen atom from the acac$^-$ ligand are situated on the equatorial plane, while the other acac$^-$ oxygen atom and the methanolic oxygen atom occupy the axial positions of the octahedron. Two

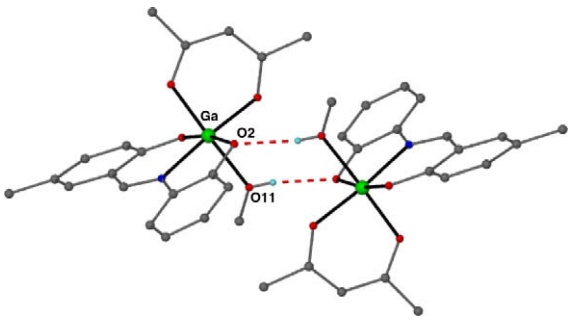


Fig. 5. The hydrogen bonding that form the dimer in **2**. All hydrogen atoms have been omitted for clarity.

[Ga(acac)(5Mesaph)(MeOH)] complexes assemble to form a hydrogen bonded dimer (Fig. 5) through the O11–HO11···O2a [O11···O2a 2.627 Å, a: $1-x,-y,1-z$] hydrogen bond (and its symmetry related) which involves the methanolic oxygen atom O11 and one of the deprotonated hydroxyl oxygen atoms O2 of the 5Mesaph^{2-} ligand.

3.3. Spectroscopic characterization

The IR spectra of all complexes are similar. In the ν(O–H) region, the IR spectra of the complexes exhibit medium-intensity bands at 3440 (**1**), 3450 (**2**) and 3460 (**3**) cm^{-1}, assignable to $\nu(O-H)_{alcohol}$ [23]. The broadness and the relatively low frequency of these bands are both indicative of hydrogen bonding. The ν(C=N) in spectra free ligands appears at 1632, 1628 and 1630 cm^{-1} for saphH$_2$, 5MesaphH$_2$ and 5BrsaphH$_2$, respectively [24]. These bands are shifted to lower wavenumbers in the spectra of **1** (1620 cm^{-1}), **2** (1621 cm^{-1}) and **3** (1619 cm^{-1}) due to complexation. The ν(C=C) and ν(C=O) modes [25] of the acetylacetonate ligand at 1586 and 1532 cm^{-1} in the spectrum of Ga(acac)$_3$ have not shifted significantly in the spectra of **1** (1586 and 1526 cm^{-1}), **2** (1588 and 1537 cm^{-1}) and **3** (1589 and 1524 cm^{-1}), respectively.

4. Conclusions and perspectives

In this manuscript, we presented the chemical aspects of our first results from the exploitation of the Ga(III)/5XsaphH$_2$ reaction system. The Ga(acac)$_3$/saphH$_2$, 5MesaphH$_2$ and 5BrsaphH$_2$ reaction systems provided access to three mononuclear Ga(III) complexes. Two of the complexes were characterized by single-crystal X-ray crystallography, while the identity of the third was confirmed by crystal cell determination and IR data. All three complexes are surrounded by a tridentate-chelate 5Xsaph^{-2} ligand, a chelate acac$^-$ ligand and a terminal alcohol molecule. The optical properties of this series indicated [19] that all three complexes emitted light upon photo- or electro-excitation. Efforts are being devoted to change the acac$^-$ and alcohol molecules with other electron rich molecules.

5. Supplementary data

CCDC 725905 and 725906 contain the supplementary crystallographic data for **1** and **2**. These data can be obtained free of charge via http://www.ccdc.cam.ac.uk/conts/retrieving.html, or from the Cambridge Crystallographic Data Centre, 12 Union Road, Cambridge CB2 1EZ, UK; fax: (+44) 1223-336-033; or e-mail: deposit@ccdc.cam.ac.uk

Acknowledgement

The authors gratefully acknowledge the Research Committee of the University of Patras (Grant "K. Caratheodory, 2004-2007) for support of this work.

References

[1] S. Zanias, C.P. Raptopoulou, A. Terzis, Th.F. Zafiropoulos, Inorg. Chem. Commun. 2 (1999) 48.
[2] G.S. Papaefstathiou, S. Manessi, C.P. Raptopoulou, E.J. Behrman, Th.F. Zafiropoulos, Inorg. Chem. Commun. 7 (2004) 69.
[3] A. Manessi, G.S. Papaefstathiou, C.P. Raptopoulou, A. Terzis, Th.F. Zafiropoulos, Inorg. Biochem. 98 (2004) 2052.
[4] A. Sofetis, G.S. Papaefstathiou, A. Terzis, C.P. Raptopoulou, Th.F. Zafiropoulos, Z. Naturforsch. 59b (2004) 291.
[5] A. Sofetis, C.P. Raptopoulou, A. Terzis, T.F. Zafiropoulos, Inorg. Chim. Acta 359 (2006) 3389.
[6] G.S. Papaefstathiou, A. Manessi, C.P. Raptopoulou, A. Terzis, T.F. Zafiropoulos, Inorg. Chem. 45 (2006) 8823.
[7] G.S. Papaefstathiou, A. Sofetis, C.P. Raptopoulou, A. Terzis, G.A. Spyroulias, T.F. Zafiropoulos, J. Mol. Struct. 837 (2007) 5.

[8] A.R. Barron, A.N. Maclnnes, in: R.B. King (Ed.), Encyclopedia of Inorganic Chemistry, vol. 3, Wiley, New York, 1994, pp. 1249–1269.
[9] F.A. Ponce, D.B. Bour, Nature 386 (1997) 351.
[10] J. Qiao, L.D. Wang, L. Duan, Y. Li, D.Q. Zhang, Y. Qiu, Inorg. Chem. 43 (2004) 5096. and references therein.
[11] C.W. Tang, S.A. Van Slyke, Appl. Phys. Lett. 51 (1987) 913.
[12] C.H. Chen, J.M. Shi, Coord. Chem. Rev. 171 (1998) 161.
[13] P.E. Burrows, L.S. Sapochak, D.M. McCarty, S.R. Forrest, M.E. Thompson, Appl. Phys. Lett. 64 (1994) 2718.
[14] Y. Wang, W. Zhang, Y. Li, L. Ye, G. Yang, Chem. Mater. 11 (1999) 530.
[15] M.A. Jakupec, M. Galanski, V.B. Arion, C.G. Hartinger, B.K. Keppler, Dalton Trans. (2008) 183.
[16] C.G. Hartinger, B.K. Keppler, Electrophoresis 28 (2007) 3436.
[17] M.A. Jakupec, B.K. Keppler, Curr. Top. Med. Chem. 4 (2004) 1575.
[18] L.S. Sapochak, A. Padmaperuma, N. Washton, F. Endrino, G.T. Schmett, J. Marshall, D. Fogarty, P.E. Burrows, S.R. Forrest, J. Am. Chem. Soc. 123 (2001) 6300.
[19] A. Kagkelari, V. Bekiari, E. Stathatos, G.S. Papaefstathiou, C.P. Raptopoulou, T.F. Zafiropoulos, P. Lianos, J. Lumin. 129 (2009) 578.
[20] A.G.J. Ligtenbarg, R. Hage, A. Meetsma, B.L. Feringa, J. Chem. Soc., Perkin Trans. 2 (1999) 807.
[21] G.M. Sheldrick, SHELXS-86, Structure Solving Program, University of Göttingen, Germany, 1986.
[22] G.M. Sheldrick, SHELXL-97, Program for the Refinement of Crystal Structures from Diffraction Data, University of Göttingen, Germany, 1997.
[23] L.S. Gelfand, F.J. Iaconiani, L.L. Pytlewski, A.N. Speca, C.M. Mikulski, N.M. Karayannis, J. Inorg. Nucl. Chem. 42 (1980) 377.
[24] S.M. El-Medani, J. Coord. Chem. 57 (2004) 115.
[25] K. Nakamoto, Infrared and Raman Spectra of Inorganic and Coordination Compounds, fourth ed., Wiley, New York, 1986.

the compositionally ordered $L1_2$ phase before studying the magnetic properties of the products.

2. Experimental

Mn–Pt nanoparticles were synthesized by thermolytic reduction of platinum acetylacetonate ($Pt(acac)_2$, Aldrich) with either 1,2-hexadecanediol (Aldrich) or long-chain amines, in the presence of various manganese precursors, as described below. Several synthesis protocols were employed, based on modifications of literature procedures for the preparation of other nanoparticle systems. Table 1 provides an overview of the prepared samples, classified according to the starting reagents of choice.

Concerning synthesis via the decomposition of manganese(II) acetylacetonate, in a typical procedure (e.g. sample 1 in Table 1), 197 mg $Pt(acac)_2$ (0.5 mmol) and 127 mg (0.5 mmol) of $Mn(acac)_2$ were diluted in 15 mL of oleylamine in a three-neck vessel. The mixture was degassed under stirring at room temperature, with the use of a vacuum pump for 10 min. After heating up to 100 °C, degassing was continued for 1 h. Flow of Ar was applied and the temperature was then raised up to 300 °C with an average rate of 5 °C min^{-1} and kept stable for 1 h. The mixture was allowed to cool at room temperature, the particles were precipitated by ethanol and the solid product was subsequently washed twice with a mixture of *n*-hexane and excess ethanol. Eventually, the particles were dispersed into *n*-hexane.

Regarding decomposition of dimanganese decacarbonyl (e.g. sample 6 of Table 1), 50 mg $Pt(acac)_2$ (0.125 mmol) and 135 mg (0.75 mmol) of 1-adamantanecarboxylic acid (ACA) were introduced in a three-neck vessel containing 3 g hexadecylamine, 10 mL phenyl ether and 162 mg 1,2-hexadecanediol. The mixture was degassed under stirring at room temperature, with the use of a vacuum pump for 10 min. After heating up to 120 °C, degassing was continued for 1 h. Flow of Ar was applied through the reacting solution and 3 mL DMF, containing 147 mg (0.375 mmol) of $Mn_2(CO)_{10}$, were injected. The temperature was then increased up to 196 °C at a rate of 4 °C min^{-1} and maintained constant for 1 h. Natural cooling was followed by precipitation of the formed particles with iso-propanol and the solid product was subsequently washed repeated times with a mixture of hexane and excess iso-propanol. Finally, the particles were stored in *n*-hexane.

In the case of decomposition of manganese acetates (e.g. sample 10 of Table 1), in a three-neck vessel containing 9 mL phenyl ether and 15 mL oleylamine, 5.4 g hexadecylamine, 160 mg $Mn(ac)_3{\cdot}2H_2O$, 100 mg $Pt(acac)_2$, 323 mg 1,2-hexadecanediol and 245 mg 1-adamantanecarboxylic acid were introduced. The mixture was flushed with Ar for 20 min and then heated up to 255 °C at an average rate of 5 °C min^{-1}. The black color at the solution had already appeared at ~205 °C, implying the formation of nanoparticles. After cooling, the particles were isolated by centrifuging with acetone. Repeated washes with hexane and excesses of acetone or ethanol yielded a well purified solid product which was afterwards dispersed into *n*-hexane.

Certain samples were annealed by depositing a few drops of the nanoparticle solutions onto Si wafers, which were inserted in a tube furnace, flashed with argon during 30 min, and then the temperature raised to 600 °C and maintained for 1 h. The crystalline structure of the particles was analyzed using X-ray powder diffraction (XRD) with a Philips PW 1820 diffractometer, using Cu Kα radiation. X-ray photoelectron spectroscopy (VG EscaLab 250-IXL XPS system) provided additional information concerning the elemental composition and chemical state of manganese in the particles. To investigate the size and arrangement of the nanoparticles, samples for transmission electron microscopy (TEM) were prepared by drop-casting from the colloidal dispersions onto carbon-coated copper grids. TEM images were acquired on a Philips CM20 and JEOL JEM 2010F microscopes, both operating at an acceleration voltage of 200 kV and equipped with EDX analyzers. Magnetic properties were measured using a vibrating sample magnetometer (1.2H/CF/HT Oxford Instruments VSM) and a superconducting quantum interference device (SQUID, Quantum Design MPMS-5), between 10 and 300 K.

3. Results and discussion

3.1. Morphology and composition

We have explored the synthesis of Mn–Pt alloy nanoparticles by thermal decomposition of platinum and manganese precursors in high-boiling-point organic solvents in the presence of suitable surfactants. Reaction conditions and particle sizes are summarized in Table 1. Several manganese precursors [$Mn_2(CO)_{10}$, $Mn(acac)_2$, $Mn(ac)_2{\cdot}4H_2O$ and $Mn(ac)_3{\cdot}2H_2O$], possessing different decomposition temperatures and decomposition rates, were employed as Mn sources. Additionally the variety of the applied surfactants, reductants and solvents is also depicted. The analysis of the results is presented by grouping the samples according to the used Mn precursor, as referred in Table 1.

Decomposition of manganese(II) acetylacetonate led to small particle sizes (2.5–4.4 nm), no matter which was the type and ratio of surfactants. The Mn:Pt initial ratio was kept constant at 1:1. The obtained results for the particles size are in agreement with the previously published data for $MnPt_3$ nanoparticles obtained by metal-acetylacetonate decomposition. In particular, $MnPt_3$ particles have been synthesized from decomposition of $Mn(acac)_2$ and $Pt(acac)_2$ and yielded a size of 2 nm [7]. Smaller particle sizes were also

Table 1
Starting reagents and particle sizes for the synthesis procedures applied to prepare Mn–Pt nanoparticles.*

Sample	Mn precursor	Pt precursor	Surfactants	Solvent	Reducing agent	Size (nm)
S1	$Mn(acac)_2$ (0.5 mmol)	$Pt(acac)_2$ (0.5 mmol)		OAm (15 mL)		4.4 ± 0.7
S2	$Mn(acac)_2$ (0.5 mmol)	$Pt(acac)_2$ (0.5 mmol)		TOAm (15 mL)		3.5 ± 0.4
S3	$Mn(acac)_2$ (0.5 mmol)	$Pt(acac)_2$ (0.5 mmol)	TOPO, OA, OAm (0.2, 0.5, 0.5 mmol)	TOAm (15 mL)		3.1 ± 0.3
S4	$Mn(acac)_2$ (0.5 mmol)	$Pt(acac)_2$ (0.5 mmol)	ACA (2.25 mmol)	ODE (15 mL)	HDOL (0.6 mmol)	2.5 ± 0.3
S5	$Mn_2(CO)_{10}$ (0.125 mmol)	$Pt(acac)_2$ (0.125 mmol)	ACA (0.75 mmol)	HDA, DPE (3 g, 5 mL)	HDOL (0.6 mmol)	9.1 ± 1.3
S6	$Mn_2(CO)_{10}$ (0.375 mmol)	$Pt(acac)_2$ (0.125 mmol)	ACA (0.75 mmol)	HDA, DPE (3 g, 10 mL)	HDOL (0.6 mmol)	3.1 ± 0.3
S7	$Mn_2(CO)_{10}$ (0.375 mmol)	$Pt(acac)_2$ (0.125 mmol)	ACA (1.25 mmol)	HDA, DPE (3 g, 10 mL)	HDOL (0.6 mmol)	6.1 ± 0.7
S8	$Mn_2(CO)_{10}$ (0.375 mmol)	$Pt(acac)_2$ (0.125 mmol)	Decanoic acid (0.125 mmol)	ODE (15 mL)	HDOL (0.6 mmol)	2.5 ± 0.3
S9	$Mn(ac)_2{\cdot}4H_2O$ (1.17 mmol)	$Pt(acac)_2$ (0.5 mmol)		OAm (30 mL)		7.1 ± 1.3
S10	$Mn(ac)_3{\cdot}2H_2O$ (0.6 mmol)	$Pt(acac)_2$ (0.25 mmol)	ACA (1.36 mmol)	HDA, OAm, DPE (5.4 g, 15 mL, 9 mL)	HDOL (1.2 mmol)	6.7 ± 0.5

* OAm = oleylamine, OA = oleic acid, TOAm = trioctylamine, TOPO = trioctylphosphine oxide, ACA = 1-adamantanecarboxylic acid, ODE = 1-octadecene, HDOL = 1,2-hexadecanediol, HDA = hexadecylamine, DPE = diphenyl ether. HDA, OAm and TOAm are in some samples listed as solvents, but they act simultaneously as surfactants. In the absence of 1,2-hexadecanediol, the amines are supposed to act also as reducing agents.

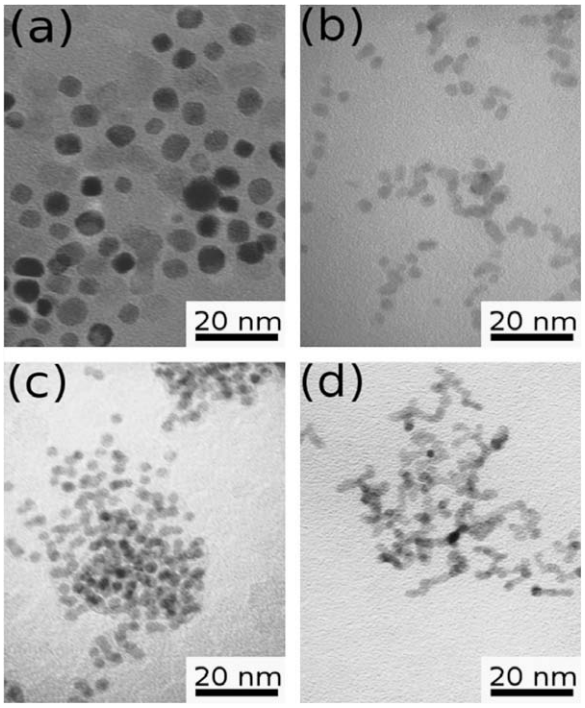


Fig. 1. TEM images of the nanoparticles prepared using manganese acetylacetonate as a precursor (from A–D, images correspond to samples S1–S4 in Table 1).

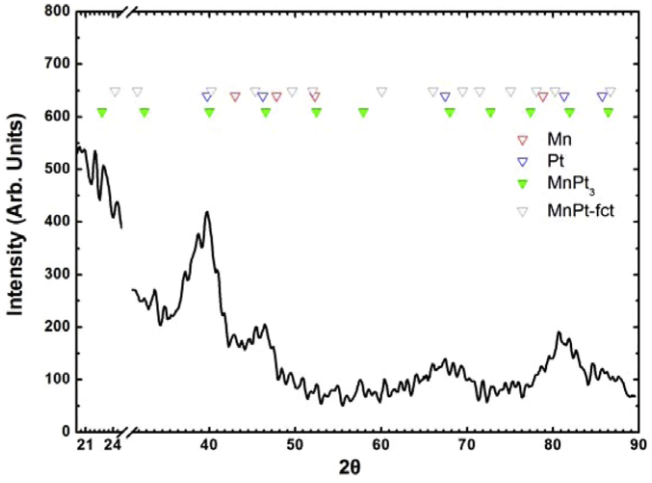


Fig. 2. X-ray diffraction pattern for the sample S2.

reported for FePt nanostructures that were produced from the thermal decomposition of $Fe(acac)_3$ in comparison with other precursors and for a diversity of surfactant/precursor starting ratios [18,19].

Keeping constant the nature and the ratio of the precursors we tried to correlate the role of several surfactants. We started our investigation without the use of any other reagent, except for oleylamine (sample S1) and trioctylamine (sample S2) that are targeted to act in a triple role as high-boiling-point solvents, mild reducing agents and weak-bonding surfactants at the same time. The particles were well separated and the average particle size in sample S1 was 4.4 nm (Fig. 1a), while for S2 an average size of 3.5 nm (Fig. 1b) was measured. Despite the high temperatures used, 303 and 332 °C, respectively, the average particle size did not show any further increase. Aiming to study the effect of other capping ligands on the obtained morphology, the addition of bulky or strongly binding surfactants such as TOPO and oleic acid (S3, Fig. 1c) and ACA (S4, Fig. 1d) was found to lead to a small decrease in particle size, up to 3.1 and 2.5 nm, correspondingly. It is worth mentioning that a slight improvement in monodispersity was obtained in these samples, as compared with S1 and S2. The use of ACA as the only surfactant led to the formation of particles which had some tendency to coalesce (Fig. 1d).

Regarding the composition of these samples, it is interesting to notice the appearance of some faint-colored particles in Fig. 1a, which are most likely Mn-rich particles. Such a difference in contrast has been attributed to the co-existence of separate Mn particles during the preparation of $MnPt_3$ nanocrystals [7]. Moreover, XPS measurements revealed considerable oxidation of manganese for samples S1 and S2. In the XRD pattern of S2 sample (Fig. 2), the main peak at ~39.8° indicates the existence of Pt or Pt-rich particles, supporting the claim for a rather inefficient alloying between the two metals in this sample.

Dimanganese decacarbonyl has been used for the syntheses of the samples S5, S6 and S7. TEM images are displayed in Fig. 3a, b and c, respectively. The first noticeable observation is that the particles from S5 are faceted, with an average particle size of ~9.1 nm, indicating that the use of manganese carbonyl, rather than acetylacetonate, resulted in a significant size increase. Concerning the composition of S5, EDX measurements yielded a Mn/Pt ratio lower than 1/9. This might be related to the high tendency of $Mn_2(CO)_{10}$ to sublime [20], even upon careful handling. In an attempt to obtain nanocrystals with a higher Mn content, we changed the injection temperature of manganese carbonyl from 80 to 120 °C in sample S6, so as to minimize the time interval between injection and decomposition, along with a higher Mn/Pt starting ratio. The increased injection temperature promoted the formation of particles with a significantly smaller average size (~3.1 nm), which is in agreement with literature data for $CoPt_3$ nanocrystals [21].

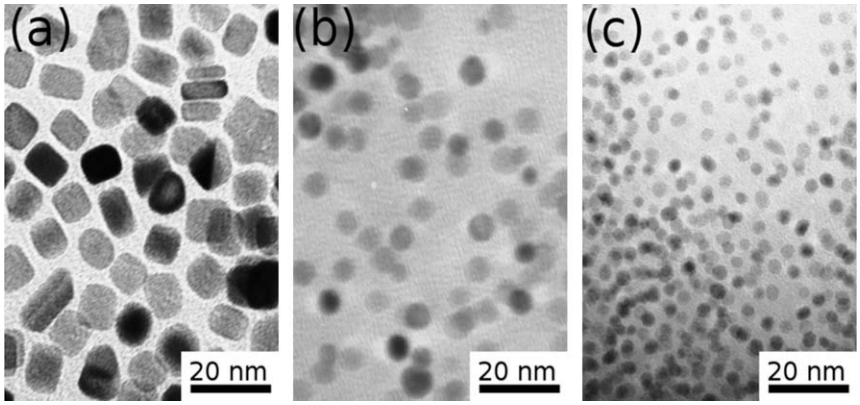


Fig. 3. TEM images of the nanoparticles prepared using manganese carbonyl as a precursor. The injection temperature was 80 °C (S5), 100 °C (S7) and 120 °C (S6) for A, B and C, respectively. (Refer to Table 1 for synthesis details.)

Fig. 4 shows a high resolution image of the particles in sample S6, together with the corresponding EDX microanalysis spectrum. S6 particles show a Mn/Pt ratio of 23/77 when a relatively large area (more than 100 nanoparticles) was sampled, which is close to the theoretical value 1/3 for $MnPt_3$. For the same sample, XRD diffraction data (Fig. 5) revealed the absence of MnPt and manganese oxide phases, as analyzed below. Consequently, we assigned the composition of the material as a $MnPt_3$ alloy.

Chemically synthesized M–Pt (M = Fe, Co or Mn) alloy nanostructures usually possess a disordered face-centered-cubic A1 phase [22], where M and Pt atoms occupy random positions in the crystal lattice and for this reason they do not show so significant magnetic properties. Therefore, annealing was necessary also in our case to transform the disordered phase into the ordered $L1_2$ cubic phase of the $MnPt_3$ alloy, where both elements retain specific positions within the crystal. The X-ray powder diffraction patterns of S6 before and after annealing in Ar atmosphere (Fig. 5) show some characteristic peaks of the $MnPt_3$ alloy, while no Mn-oxide or MnPt peaks were recorded. It is difficult to distinguish the ordered and disordered $MnPt_3$ alloys from the XRD analysis due to the small difference in the position of the main peaks of both alloys. However, magnetic measurements allowed us to perform a more clear assignment of the annealed alloy to the ordered phase (see below). An increment in particle size, explained by sintering phenomena as a result of the annealing treatment, was identified through the sharpness of the XRD peaks. The average crystalline grain size in the sintered material was estimated to be ~18.2 nm from Scherrer's equation.

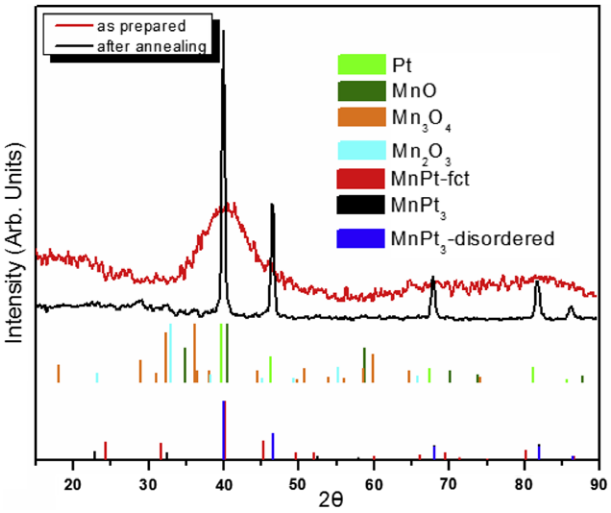


Fig. 5. X-ray powder diffraction pattern from sample S6 before and after annealing.

Increase of the final particle size of the $MnPt_3$ nanoparticles was achieved by injecting the manganese precursor at an intermediate temperature (100 °C) and raising the ACA/Pt ratio from 6/1 up to 10/1. The average particle size in sample S7 was ~6.1 nm, as measured from TEM. The role of ACA toward the size increment of bimetallic nanoparticles has also been observed in the case of $CoPt_3$ particles prepared by Shevchenko et al. [21]. In our case, the larger concentration of ACA in S7 possibly led to the formation of a complex between ACA with either Mn or Pt, which could complicate the nucleation stage, resulting in a bigger size compared to sample S6. From elemental analysis carried out by XPS, a Mn/Pt ratio of 29/71 was derived. The corresponding XRD spectrum indicates the existence of the $MnPt_3$ $L1_2$-phase after annealing (Fig. 6). The average crystalline grain size for the annealed S7 sample, estimated from Scherrer's equation, was only ~12.3 nm, which means that grain growth during annealing was much smaller than that observed for S6, revealing a better surface stabilization of the particles within S7 sample. We believe that the higher concentration of the bulky organic ligand ACA in S7 somehow hindered the coalescing process. Though, it has to be noted that the nanoparticles probably lose their solubility after annealing, due to the

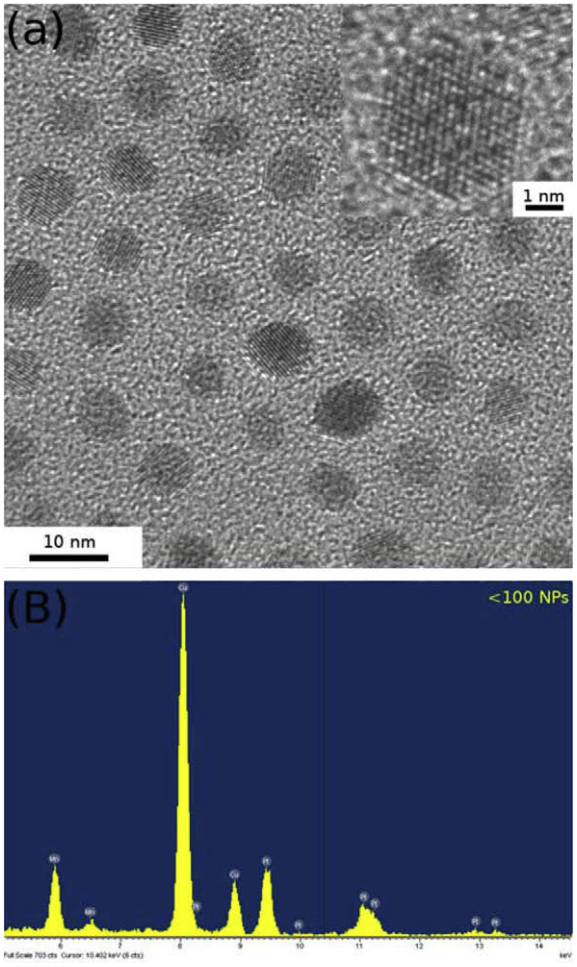


Fig. 4. Representative HRTEM image (a) from sample S6 (the atomic lattice is clearly seen in the inset) and EDX spectrum (b) from an area containing more than 100 nanocrystals.

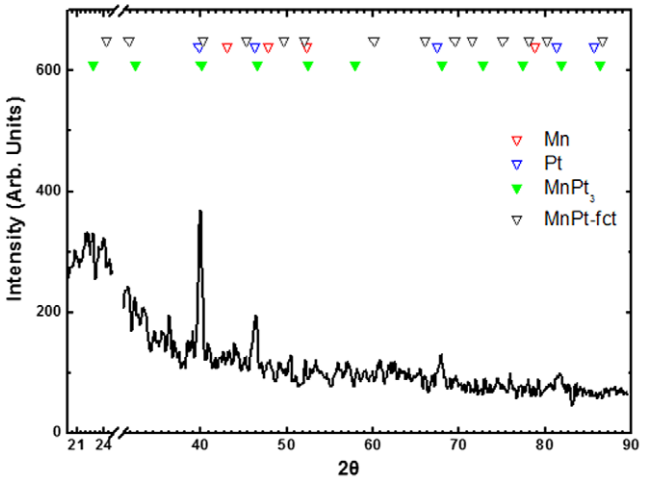


Fig. 6. X-ray diffraction pattern for the annealed S7 sample.

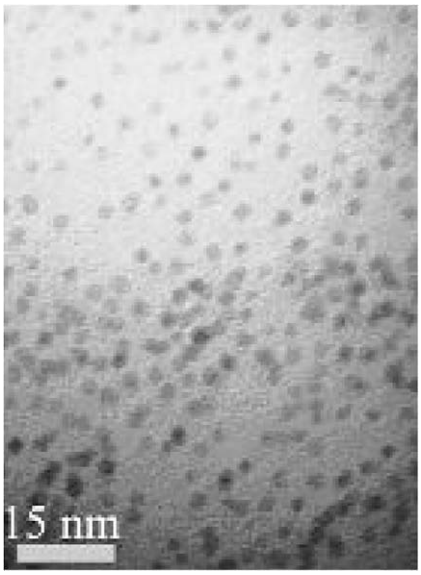


Fig. 7. TEM image of S8 sample.

decomposition of the protective organic layer surrounding the surface of each particle and the unavoidable aggregation and sintering [22].

Synthesis in the presence of a single and relatively short chain surfactant (decanoic acid) leads to rather monodisperse nanoparticles with an average diameter of ~2.5 nm (Fig. 7). In this case (sample S8), only an acid (decanoic) was used as surfactant, and the obtained product was difficult to precipitate and purify, just as in the case of the ACA-capped nanoparticles (S4). It has been observed that occasionally, if the acid surfactants are not combined with surfactants with milder bonding behavior (e.g. amines), the obtained nanoparticle colloids either tend to aggregate or prove difficult to purify and characterize [21,23]. However, after repeated washing cycles with a mixture of hexane/acetone, the S8 particles appeared well separated. The small size obtained in this case can be explained by the molecular structure and low concentration of decanoic acid. For example, in maghemite nanocrystals, decreasing the chain length or reducing the amount of the carboxylic acid ligand has been shown to lead to a decrease in the resulting nanoparticle size [24].

Mn(II) acetate and Mn(III) acetate have been used, respectively for the production of the samples S9 and S10. In the case of S9, the use of Mn(II) acetate in oleylamine yielded ~7.1 nm particles (Fig. 8a) with a polydispersity of 18%. The particles were not well separated as shown by TEM imaging, which might be due to the sole use of oleylamine as solvent, surfactant and reductant simultaneously. Occasionally, amines are weakly binding ligands, and therefore cannot totally prevent the aggregation of the formed particles. In certain areas of the TEM grid, the particles were assembled into big circular structures ($d \sim 400$–450 nm) during the evaporation of the carrier solvent on the grid.

In the case of sample S10, we noticed a remarkable self-assembly, occasionally even forming multilayers, as shown in Fig. 8b. The particles in this sample were highly monodisperse (~6.7 nm), with sufficient interparticle distances. Thus, one can see that by using both Mn(II) and Mn(III) acetates, particle size can be slightly increased as compared to particles obtained from $Mn(acac)_2$, while having similar values to particles made from $Mn_2(CO)_{10}$. It seems that manganese acetylacetonate feeds the solution with atoms in a fast rate, when it starts to decompose, and a rapid nucleation of Mn–Pt clusters takes place followed by a slow growth, leading to a relatively smaller particle size compared to the synthesis using carbonyl or acetate Mn-precursors. An appropriate combination of different types of surfactants (ACA, amines) in sample S10, together with the use of a moderate reaction temperature (255 °C) allow the particles to grow further and then assemble in a controlled way. The Mn/Pt ratio determined for these particles from elemental analysis was 31/69.

3.2. Magnetic characterization

We discuss in what follows the magnetic behavior of two types of samples: (i) a sample with a considerable degree of oxidation

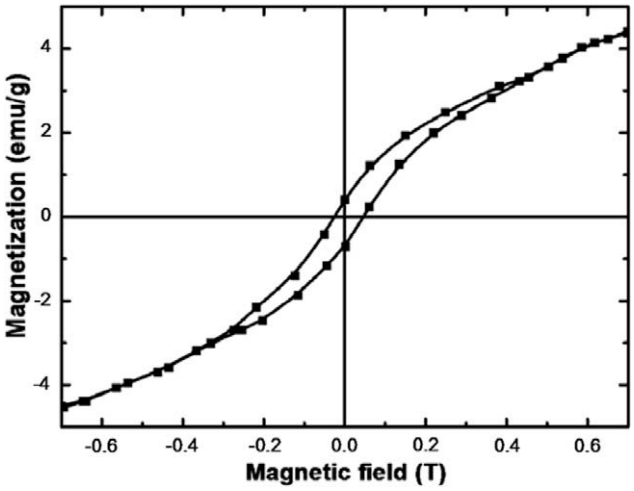


Fig. 9. *M–H* plot for sample S2 obtained by VSM measurement at 77 K.

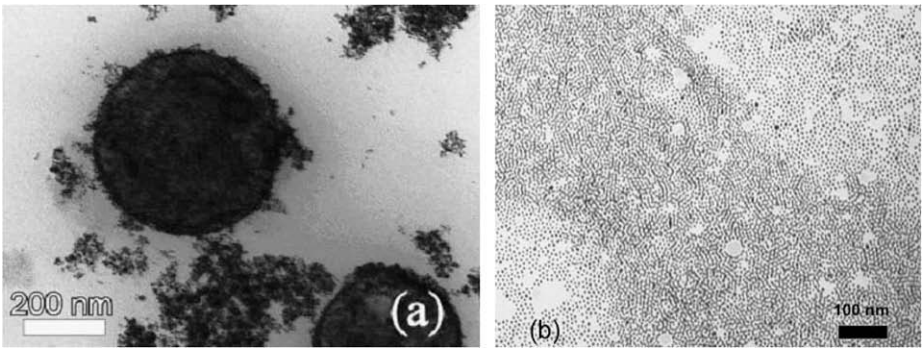


Fig. 8. TEM images of S9 and S10 samples [(a) and (b) images, respectively].

and poor alloying between Mn and Pt (S2) and (ii) two samples which showed an effective formation of the $MnPt_3$ alloy (S6 and S7).

(i) Sample S2: We have plotted in Fig. 9 the hysteresis loop of sample S2, measured at 77 K by vibrating sample magnetometry (VSM). As mentioned above, manganese was oxidized in a significant percentage in this sample. VSM results reveal the presence of a small exchange bias field of ~0.01 T, as derived by

$$H_{ex} = \frac{H_{c(pos)} + H_{c(neg)}}{2}. \quad (1)$$

This result indicates the possible co-existence of antiferromagnetic and ferromagnetic components in this sample. In our case, MnO is the obvious antiferromagnetic component, while Mn_3O_4 is ferrimagnetic. Exchange bias values up to ~0.18 T were recently reported for the case of MnO–Mn_3O_4 core shell nanoparticles [25]. In sample S2, the appearance of H_{ex} above the T_C of Mn_3O_4 is an indication of irreversible switching of antiferromagnetic (MnO) spin lattices by exchanged-coupled uncompensated spins, with the assistance of thermal activation [25]. In Fig. 9, the shift of the hysteresis loop along the horizontal axis of the *M–H* plot is not itself a proof for the co-existence of two magnetically different phases, but it is a strong indication for such consideration. The loop was shifted to the positive-field side of the axis. No magnetic field was applied during the cooling process from room temperature to 77 K. A low value for magnetization remanence is observed (~0.4 emu/g) and no saturation for this system was achieved for fields up to 1 T, as expected from the large amount of antiferromagnetic and paramagnetic materials (MnO and Pt, respectively).

(ii) S6 and S7 alloy samples: The magnetic properties of samples S6 and S7 after annealing have been examined. These specific samples were chosen to be annealed and further investigated because they possessed the optimum composition, close to $MnPt_3$ alloy, as shown above by XRD and elemental analysis measurements among the as-prepared samples. In Fig. 10a, temperature-dependent zero-field-cooled (ZFC) and field-cooled (FC) magnetization scans under an applied field of 0.01 T for the annealed S6 sample are shown. These $L1_2$-phase $MnPt_3$ nanocrystals display a blocking temperature at approximately 50 K. The observed split between the curves happens at much higher temperature than the maximum of the ZFC curve, possibly due to the sintering effect and the consequent breakdown of the size monodispersity caused by the annealing. The decay of the magnetization versus temperature after the maximum of the ZFC deviates from a Curie law behavior, where the magnetization would vary in proportion to the reciprocal of the temperature ($1/T$), probably due to the presence of some interactions among the particles. The presence of dipolar couplings between the nanoparticles is more specifically implied by the shape of the plateau of the FC curve at low temperatures. Regarding the deviation from a Curie law behavior in the superparamagnetic regime, it can also be attributed to the fact that the saturation magnetization varies with temperature. In general, a nanoscale size provides a much lower T_C for a material, compared to the T_c of its corresponding bulk counterpart. Such phenomenon results in the significant variation of M_S with temperature in nanoparticles. The field sweep at 10 K shows hysteresis with a coercivity of ~0.075 T (Fig. 10b).

The magnetic behavior of the annealed sample S7 is shown in Fig. 11. The blocking temperature T_b is similar to that for S6 (~50 K) and the ZFC peak (Fig. 11a) is indicative of superparamagnetic single domain particles. However, also in this case, as in the annealed S6, the shape of the curves implies the existence of some interactions among particles. The coercivity at 10 K reaches 1.1 T (Fig. 11b), which is one of the highest values of coercivity ever reported for Mn–Pt nanocrystals. For instance, Lee et al. have prepared $MnPt_3$ nanoparticles with various sizes, which displayed coercivity values in the range of 0.05–0.22 T at 5 K after annealing [7]. The respective value for the Mn–Pt nanoparticles of Ono et al.

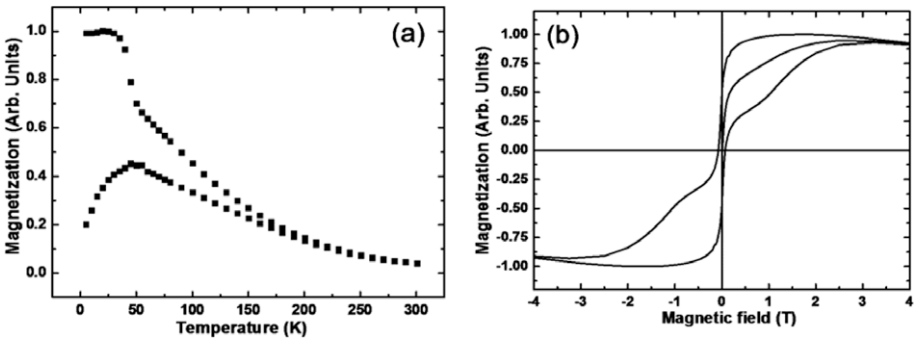


Fig. 10. Magnetic properties for the annealed sample S6: (a) ZFC–FC curves under an applied field of 0.01 T. (b) Field-sweep of the magnetization at 10 K (SQUID).

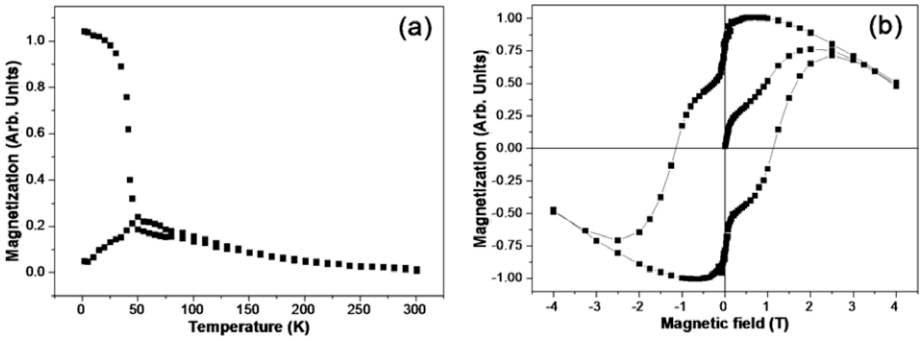


Fig. 11. Magnetic properties for the annealed S7 sample: (a) ZFC–FC curves under an applied field of 0.01 T. (b) Field-sweep of the magnetization at 10 K (SQUID).

was 0.95 T at 5 K [12]. In addition, Ho et al. reported a maximum value for $H_C \sim 0.48$ T at 5 K for their MnPt nanoparticles, having tried several different annealing conditions [13]. Concerning our samples, we notice a big difference in the coercivity values between S6 and S7: 0.075 T for S6 versus 1.1 T for S7, both at 10 K. From the morphological and structural characterization of these samples, some differences were found in particle size and composition. The difference in particle size (18.2 nm of annealed S6 versus 12.3 nm of annealed S7) is not expected to promote such large deviation among the measured coercivity values. Taking into account that the magnetic properties of the $MnPt_3$ alloy are very sensitive to Mn–Pt composition and atomic ordering in the lattice [7], we assume that a small difference in the Mn:Pt ratio recorded by elemental analysis (23/77 for S6 versus 29/71 for S7) and a somewhat better ordering in the $MnPt_3$ lattice of S7 due to the higher reaction temperature (257 °C in S7 versus 196 °C in S6) are responsible for the observed difference in the magnetic properties.

The 'constricted' shape of the hysteresis loops, as depicted in Figs. 10b and 11b, might be attributed to the presence of two magnetically different phases in the product. The peculiar bendings observed at both curves probably imply the co-existence of a 'hard' magnetic phase with a 'soft' one. For instance, it is reasonable to assume that most of the particles of the annealed S7 sample show 'hard' magnetic features (Fig. 11b), thus resulting in the observed large coercivity, but there is also a minority of particles that despite the annealing maintain 'soft' magnetic behavior which however cannot seriously affect the total magnetic behavior of this sample. Since the XRD measurements for S7 (Fig. 6) do not show any sign of oxidation, we speculate that some of the annealed particles transformed into the $L1_2$ (ordered) $MnPt_3$ phase, which is responsible for the 'hard' magnetic contribution, while the rest of the particles maintained the A1 (disordered) $MnPt_3$ phase, with much 'softer' magnetic features.

4. Conclusions

Mn–Pt nanoparticles were synthesized by thermal decomposition/reduction method with variation of metal precursors, organic solvents and capping ligands. Depending on the type and concentration of the starting reagents, monodisperse $MnPt_3$ nanoparticles could be obtained, while in some cases significant oxidation of manganese was observed, together with the formation of Pt-rich or single Pt particles. The size, shape and arrangement of the particles could be tuned by careful choice of proper surfactants. Regarding the magnetic properties, exchange bias phenomena were assumed in the oxidized samples, while $MnPt_3$ particles showed also a two-phase behavior after annealing, displaying high coercivity at 10 K. Further experiments are underway including annealing in reducing atmosphere (93% Ar/7% H_2) instead of simply inert (Ar) so as to facilitate the conversion of the alloy into the compositionally ordered $L1_2$ phase of $MnPt_3$, even via the additional incorporation of oxidized Mn in the alloy.

Acknowledgments

This work has been supported by the European Union Marie Curie Research Training Network – SyntOrbMag – MRTN-CT-2004-0055667, the Spanish Ministerio de Educación y Ciencia through Consolider Ingenio 2010 "Nanobiomed", and the General Secretariat for Research and Technology, Greece – Project No: 03EΔ667. The authors are grateful to Prof. Luis M. Liz-Marzan for his help.

References

[1] R. Skomski, J. Phys.: Condens. Matter 15 (2003) 841.
[2] F. Dumestre, B. Chaudret, C. Amiens, P. Renaud, P. Fejes, Science 303 (2004) 821.
[3] S.I. Cha, C.B. Mo, K.T. Kim, S.H. Hong, J. Mater. Res. 20 (2005) 2148.
[4] M. Han, Q. Liu, J. He, Y. Song, Z. Xu, J. Zhu, Adv. Mater. 19 (2007) 1096.
[5] M. Ghosh, K. Biswas, A. Sundaresan, C.N.R. Rao, J. Mater. Chem. 16 (2006) 106.
[6] W.S. Seo, H.H. Jo, K. Lee, B. Kim, S.J. Oh, J.T. Park, Angew. Chem. Int. Ed. 43 (2004) 1115.
[7] D.C. Lee, A. Ghezelbash, C.A. Stowell, B.A. Korgel, J. Phys. Chem. B 110 (2006) 20906.
[8] M.S. Jagadeesh, M.S. Seehra, Phys. Rev. B 21 (1980) 2897.
[9] S.J. Pickart, R. Nathans, J. Appl. Phys. 33 (1962) 1336.
[10] K.W. Wierman, R.D. Kirby, J. Magn. Magn. Mater. 154 (1996) 12.
[11] K.W. Wierman, J.N. Hilfiker, R.F. Sabiryanov, S.S. Jaswal, R.D. Kirby, J.A. Woollam, Phys. Rev. B 55 (1997) 3093.
[12] K. Ono, R. Okuda, Y. Ishii, S. Kamimura, M. Oshima, J. Phys. Chem. B 107 (2003) 1941.
[13] C.H. Ho, C.H. Lai, IEEE Trans. Magn. 42 (2006) 3069.
[14] C.A. Stowell, R.J. Wiacek, A.E. Saunders, B.A. Korgel, Nano Lett. 3 (2003) 1441.
[15] A. Glaria, M.L. Kahn, A. Falqui, P. Lecante, V. Colliere, M. Respaud, B. Chaudret, ChemPhysChem 9 (2008) 2035.
[16] V.F. Puntes, D. Zanchet, C.K. Erdonmez, A.P. Alivisatos, J. Am. Chem. Soc. 124 (2002) 12874.
[17] X. Peng, L. Manna, W. Yang, J. Wickham, E. Scher, A. Kadavanich, A.P. Alivisatos, Nature 404 (2000) 59.
[18] V. Nandwana, K.E. Elkins, N. Poudyal, G.S. Chaubey, K. Yano, J.P. Liu, J. Phys. Chem. C 111 (2007) 4185.
[19] M. Chen, J.P. Liu, S. Sun, J. Am. Chem. Soc. 126 (2004) 8394.
[20] E. Kang, J. Park, Y. Hwang, M. Kang, J.G. Park, T. Hyeon, J. Phys. Chem. B 108 (2004) 13932.
[21] E.V. Shevchenko, D.V. Talapin, H. Schnablegger, A. Kornowski, O. Festin, P. Svedlindh, M. Haase, H. Weller, J. Am. Chem. Soc. 125 (2003) 9090.
[22] I. Zafiropoulou, E. Devlin, N. Boukos, D. Niarchos, D. Petridis, V. Tzitzios, Chem. Mater. 19 (2008) 1898.
[23] S. Sun, H. Zeng, D.B. Robinson, S. Raoux, P.M. Rice, S.X. Wang, G. Li, J. Am. Chem. Soc. 126 (2004) 273.
[24] M. Yin, A. Willis, F. Redl, N.J. Turro, S.P. O'Brien, J. Mater. Res. 19 (2004) 1208.
[25] A.E. Berkowitz, G.F. Rodriguez, J.I. Hong, K. An, T. Hyeon, N. Agarwal, D.J. Smith, E.E. Fullerton, Phys. Rev. B 77 (2008) 024403.

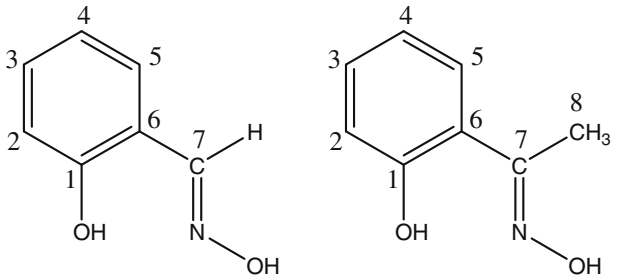


Fig. 1. The structures of the ligands discussed in the text.

^1H and ^{13}C NMR spectra were recorded on a Varian UNITY Plus spectrometer operating at 300 MHz. Samples were run in a 5 mm probe with $CDCl_3$ as internal lock and reference.

2.2. Compound preparation

2.2.1. Synthesis of $Ga(NO_3)_3{\cdot}9H_2O$ and $Ga(acac)_3$

A drop of gallium metal (5.808 g, 83.3 mmol) was weighed in a 100 mL flat bottom flask. Concentrated HNO_3 (65%, 50 mL) was added and the mixture was stirred overnight at room temperature to produce a clear colorless solution. The solution was cooled at 5 °C and seeded with a small crystal of $Ga(NO_3)_3{\cdot}9H_2O$. Almost immediately the whole mass of the solution transformed to a white crystalline solid. The solid was crashed with a glass rod and $Ga(NO_3)_3{\cdot}9H_2O$ isolated by vacuum filtration, washed two times with ice-cold water (2 × 3 mL) and dried over $CaCl_2$. Yield: 25.8 g, 74% based on Ga. The filtrate, including the washing liquids, was transferred to a 250 mL flat bottom flask and diluted with water to a final volume of 100 mL. The pH of the solution was adjusted to ~2–3 with concentrated NH_3 (25%) and then acacH (26.7 mL, 25.9 mmol) was added. The mixture was heated to reflux while concentrated NH_3 was added in drops until no obvious turbidity was observed by adding. $Ga(acac)_3$ was separated as a pale white crystalline solid. The pH of the final solution was ~7–8. The mixture was left to cool at room temperature and then $Ga(acac)_3$ was isolated by vacuum filtration, washed several times with water and dried over $CaCl_2$. Yield: 6.7 g. IR (KBr pellets, cm^{-1}): 2998w, 2966w, 2922w, 1586s, 1532s, 1382sbr, 1278m, 1194w, 1018m, 934m, 795wsh, 776w, 682w, 654w, 582w. The total yield for both $Ga(NO_3)_3{\cdot}9H_2O$ and $Ga(acac)_3$ was 96% based on Ga. Both compounds gave satisfactory analytical data. $Ga(acac)_3$ can be also synthesized by the reaction of an aqua solution of $Ga(NO_3)_3{\cdot}9H_2O$ and 12-fold excess of acacH in the presence of concentrated NH_3 as described above in yields of 80–85%.

2.2.2. Synthesis of $saoH_2$ and Me-$saoH_2$

A water solution (20 mL) containing hydroxylamine hydrochloride (1.40 g, 20.0 mmol) and Na_2CO_3 (1.06 g, 10 mmol) was added to a 100 mL flat bottom flask containing salicylaldehyde (2.46 g, 20 mmol). The resulting mixture was stirred for three days. Salicylaldoxime was separated as a white solid. The solid was isolated by vacuum filtration, washed several times with water and dried over $CaCl_2$. Yield: 1.84 g, 67%. IR (KBr pellets, cm^{-1}): 3371mbr, 1623msh, 1614s, 1573s, 1492s, 1472m, 1408m, 1396msh, 1390m, 1295msh, 1285s, 1258s, 1120m, 1192m, 1152m, 1113w, 1037w, 989s, 957m, 899s, 856w, 786m, 753m, 739msh, 720m, 696m, 648s, 561m, 470m. Me-$saoH_2$ was prepared in a similar manner by replacing salicylaldehyde by 2′-hydroxyacetophenone (2.4 mL, 20 mmol). Yield: 2.65 g, 88%. IR (KBr pellets, cm^{-1}): 3343mbr, 1628s, 1610s, 1584s, 1553w, 1539w, 1505s, 1500s, 1465m, 1403sbr, 1367s, 1310m, 1286s, 1250sbr, 1157m, 1124w, 1070w, 1044s, 1015s, 986w, 942s, 848s, 834s, 781sbr, 748sbr, 652sbr, 561m, 510m.

2.2.3. $[Ga(acac)(saoH)_2]$ (**1**)

$Ga(acac)_3$ (0.13 g, 0.35 mmol) and $saoH_2$ (0.10 g, 0.73 mmol) were dissolved in CH_2Cl_2 (5 mL). The solution was heated gently and hexane (25 mL) was added. The resulting colorless solution was refluxed for 30 min and left undisturbed to cool to room temperature. Colorless crystals of **1** were formed over a period of one day. The crystals were isolated by vacuum filtration, washed with hexane (2 × 5 mL) and dried in air. Yield: 0.12 g, 77%. *Anal.* Calc. for $C_{19}H_{19}GaN_2O_6$: C, 51.74; H, 4.34; N, 6.35. Found: C, 51.78; H, 4.29; N, 6.37%. IR (KBr pellets, cm^{-1}): 3064mbr, 3004w, 1647m, 1595s, 1586ssh, 1552s, 1530s, 1517s, 1465s, 1440s, 1375s, 1350m, 1328m, 1278s, 1195m, 1150m, 1120w, 1013s, 963w, 953w, 930m, 907m, 859w, 806m, 786w, 757s, 740w, 687w, 642m, 599m, 586w, 570w, 548w, 491w, 453m.

2.2.4. $[Ga(acac)_3][Ga(acac)(Me\text{-}saoH)_2]$ (**2**)

$Ga(acac)_3$ (0.12 g, 0.32 mmol) and Me-$saoH_2$ (0.05 g, 0.33 mmol) were dissolved in CH_2Cl_2 (4 mL). The solution was heated gently and hexane (30 mL) was added. The resulting colorless solution was refluxed for 30 min and left undisturbed to cool to room temperature. Light yellow crystals of **1** were formed over a period of two days. The crystals were isolated by vacuum filtration, washed with hexane (2 × 5 mL) and dried in air. Yield: 0.09 g, 65%. *Anal.* Calc. for $C_{36}H_{44}Ga_2N_2O_{12}$: C, 51.71; H, 5.30; N, 3.35. Found: C, 51.76; H, 5.27; N, 3.38%. IR (KBr pellets, cm^{-1}): 3050wbr, 2960w, 1593ssh, 1579s, 1555w, 1528s, 1439m, 1400m, 1337s, 1322w, 1303m, 1275m, 1242m, 1192w, 1160w, 1137w, 1130w, 1076w, 1044w, 1019m, 961w, 953w, 928m, 862m, 770m, 763m, 682w, 644w, 617w, 580w, 565w, 480w.

2.3. Single-crystal X-ray crystallography

The data collection for the single crystals of compounds **1** and **2** was carried out at 22 °C on a SMART CCD 1k diffractometer with graphite monochromated Mo Kα radiation. Complete crystal data and parameters for data collection and processing are reported in Table 1.

The structures were solved by direct methods using SHELXS-86 [36] and refined by full-matrix least-squares techniques on F^2 with SHELXL-97 [37]. The coordinates of the metal atoms were obtained from the initial solutions and for all other non-hydrogen atoms found in subsequent difference Fourier syntheses. All hydrogen atoms were introduced at calculated positions as riding on bonded atoms. All non-hydrogen atoms were refined anisotropically.

3. Results and discussion

3.1. Brief synthetic comments

Complexes **1** and **2**, were obtained by the ligand substitution reactions between $Ga(acac)_3$ (acacH = 2,4,-pentanedione) and R-$saoH_2$ (R = H $saoH_2$, R = Me Me-$saoH_2$) in CH_2Cl_2/hexane solutions as crystalline solids. Eq. (1) summarizes the preparation of the representative complex **1**. Altering the $Ga(acac)_3/saoH_2$ ratio in the same solvent mixture did not affect the identity of the product but the yield of the reaction. The use of more polar solvents such as alcohols, acetone or acetonitrile resulted in oily products that could not turn to solids by adding hexane or diethylether. In the case of Me-$saoH_2$, we were not able to isolate the $[Ga(acac)(Me\text{-}saoH)_2]$ without the presence of $Ga(acac)_3$. The use of polar solvents had the same effect as in the case of **1**.

Table 1
Crystallographic data for complexes **1** and **2**.

Parameter	1	2
Formula	$C_{19}H_{19}GaN_2O_6$	$C_{36}H_{44}Ga_2N_2O_{12}$
Formula weight	441.08	836.17
Crystal color, habit	colorless, plates	colorless, plates
Crystal dimensions (mm)	0.35 × 0.28 × 0.08	0.30 × 0.28 × 0.08
Crystal system	monoclinic	monoclinic
Space group	$P2/c$	$P2_1/n$
Unit cell dimensions		
a (Å)	13.110(3)	19.366(3)
b (Å)	10.720(2)	8.2867(15)
c (Å)	14.975(4)	23.900(4)
α (°)	90	90
β (°)	112.680(7)	98.736(6)
γ (°)	90	90
V (Å^3)	1941.8(8)	3791.0(12)
Z	4	4
$\rho_{calc.}$(g cm^{-3})	1.509	1.465
Radiation, λ (Å)	Mo Kα, 0.71073	Mo Kα, 0.71073
T (K)	298(2)	298(2)
θ Range (°)	1.68–23.49	1.26–23.50
μ (mm^{-1})	1.455	1.485
Collected reflections	7050	13 970
Independent reflections (R_{int})	2840 (0.0373)	5396 (0.0600)
Observed reflections $I > 2\sigma(I)$	2037	3333
Parameters refined	253	469
$(\Delta\rho)_{max.}$, $(\Delta\rho)_{min.}$ (e Å^{-3})	1.955, −0.655	0.817, −0.716
Goodness-of-fit (GOF) (on F^2)	1.066	0.992
R_1[a], wR_2[b] (all data)	0.0946, 0.2081	0.1257, 0.2546
R_1[a], wR_2[b] ($I > 2\sigma(I)$)	0.0687, 0.1966[c]	0.0728, 0.2058[d]

[a] $R_1 = \sum(|F_o| - |F_c|)/\sum(|F_o|)$.
[b] $wR_2 = \left\{\sum\left[w(F_o^2 - F_c^2)^2\right] \Big/ \sum\left[w(F_o^2)^2\right]\right\}^{1/2}$.
[c] For 2037 reflections with $I > 2\sigma(I)$.
[d] For 3333 reflections with $I > 2\sigma(I)$.

Table 2
Selected bond distances (Å) and angles (°) in **1**.

Ga1–O1	1.934(5)	Ga1–O6	1.932(6)
Ga1–O3	1.927(5)	Ga1–N1	2.067(6)
Ga1–O5	1.931(6)	Ga1–N2	2.069(6)
O1–Ga1–O3	166.3(2)	O3–Ga1–N2	86.3(2)
O1–Ga1–O5	95.3(2)	O5–Ga1–O6	92.6(3)
O1–Ga1–O6	91.8(2)	O5–Ga1–N1	178.2(2)
O1–Ga1–N1	85.7(2)	O5–Ga1–N2	86.3(3)
O1–Ga1–N2	84.2(2)	O6–Ga1–N1	89.0(3)
O3–Ga1–O5	94.0(2)	O6–Ga1–N2	175.7(2)
O3–Ga1–O6	97.9(2)	N1–Ga1–N2	92.3(3)
O3–Ga1–N1	84.8(2)		

$$Ga(acac)_3 + 2saoH_2 \xrightarrow[hexane]{CH_2Cl_2} [Ga(acac)(saoH)_2] + 2acacH \quad (1)$$

3.2. Description of structures

Complex **1** crystallizes in the monoclinic space group $P2/c$. The molecular structure of **1** is shown in Fig. 2 while selected bond distances and angles are listed in Table 2. The Ga^{III} ion is in a distorted octahedral geometry. Two saoH$^-$ ligands chelate the Ga^{III} ion through the deprotonated phenoxy oxygen atom and the oximic nitrogen atom with the oxygen atoms in *trans* and the nitrogen atoms in *cis* orientation. A bidentate chelate acac$^-$ ligand completes the octahedron with both oxygen atoms in *trans* orientation with respect to the oximic nitrogen atoms of the saoH$^-$ ligands. The Ga–O_{acac} and Ga–O_{saoH} are very similar ranging from 1.928 to 1.934 Å while the two Ga–N distances are 2.067 and 2.069 Å for Ga1–N1 and Ga1–N2, respectively and compare favorably with those of other octahedral Ga(III) complexes [38]. Each of the two oximic OH groups forms an intramolecular hydrogen bond with the phenoxy oxygen atom of a neighboring saoH$^-$ [O2–H2A···O3, O···O 2.643(9) Å and O4–H4A···O1, O···O 2.621(7) Å].

Complex **2** crystallizes in the monoclinic space group $P2_1/n$, with two mononuclear complexes in the unit cell, namely [Ga(acac)$_3$] and [Ga(acac)(Me-saoH)$_2$]. Fig. 3 shows the asymmetric unit of **2**, while selected bond distances and angles are listed in Table 3. The structure of [Ga(acac)$_3$] within **2** compares well with the structures of [Ga(acac)$_3$] [39] and [Ga(acac)$_3$]·*trans*-CHCl=CHCl [40]. The structure of [Ga(acac)(Me-saoH)$_2$] is very similar to that of **1**. The Ga^{III} ion is in a distorted octahedral geometry with two bidentate chelate Me-saoH$^-$ ligands to coordinate through the deprotonated phenoxy oxygen atom and the oximic nitrogen atom around the Ga^{III} ion with the oxygen atoms in *trans* and the nitrogen atoms in *cis* orientation. The acac$^-$ ligand chelates the central atom with

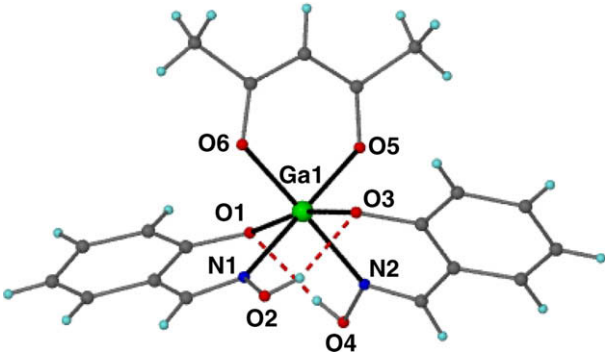


Fig. 2. Ball and stick representation of the molecular structure of **1**.

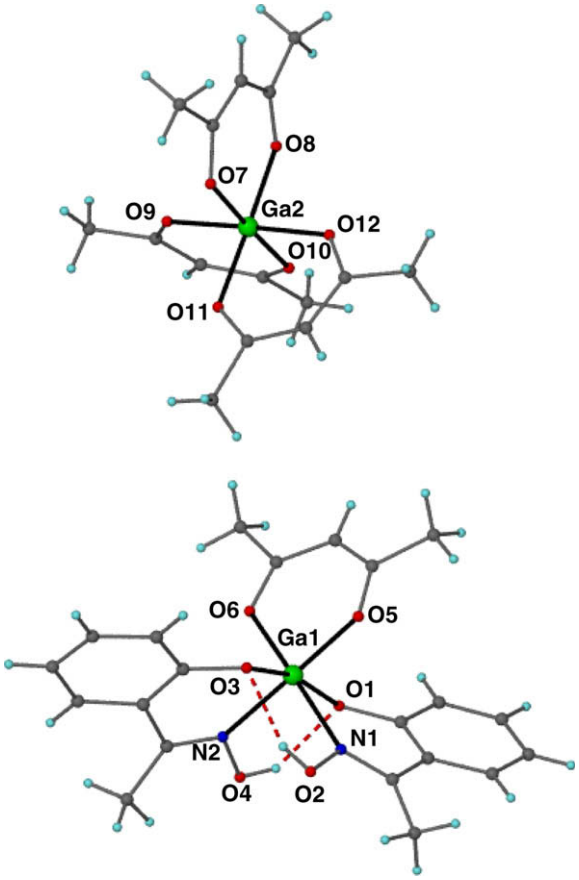


Fig. 3. Ball and stick representation of the asymmetric unit of **2**.

Table 3
Selected bond distances (Å) and angles (°) in **2**.

Ga1–O1	1.920(6)	Ga2–O9	1.925(7)
Ga1–O3	1.901(7)	Ga2–O10	1.947(6)
Ga1–O5	1.935(6)	Ga2–O11	1.938(7)
Ga1–O6	1.932(5)	Ga2–O12	1.935(7)
Ga1–N1	2.112(7)	Ga2–O7	1.938(6)
Ga1–N2	2.069(7)	Ga2–O8	1.953(5)
O1–Ga1–O3	164.6(3)	O8–Ga2–O11	178.9(3)
O1–Ga1–O5	94.4(2)	O8–Ga2–O12	89.3(3)
O1–Ga1–O6	92.8(2)	O9–Ga2–O10	92.5(3)
O1–Ga1–N1	83.2(3)	O9–Ga2–O11	86.4(3)
O1–Ga1–N2	85.3(2)	O9–Ga2–O12	178.1(3)
O3–Ga1–O5	94.2(2)	O10–Ga2–O11	93.2(3)
O3–Ga1–O6	99.5(3)	O10–Ga2–O12	87.3(3)
O3–Ga1–N1	84.1(3)	O11–Ga2–O12	91.7(3)
O3–Ga1–N2	86.4(2)	O8–Ga2–O10	87.3(3)
O5–Ga1–O6	92.6(2)	O7–Ga2–O8	90.9(3)
O5–Ga1–N1	90.1(3)	O7–Ga2–O9	89.4(3)
O5–Ga1–N2	178.6(2)	O7–Ga2–O10	177.5(3)
O6–Ga1–N1	175.4(3)	O7–Ga2–O11	88.6(3)
O6–Ga1–N2	86.1(3)	O7–Ga2–O12	90.9(3)
N1–Ga1–N2	91.3(3)	O8–Ga2–O9	92.6(2)

both oxygen atoms in *trans* orientation with respect to the oximic nitrogen atoms of the Me-saoH$^-$ ligands. The oximic OH groups form two intramolecular hydrogen bonds with the phenoxy oxygen atoms of the neighboring Me-saoH$^-$ ligands [O2–H2A···O3, O···O 2.609(8) Å and O4–H4A···O1, O···O 2.589(8) Å].

3.3. Spectroscopic characterization

3.3.1. IR spectroscopy

In the ν(O–H) region, the IR spectra of the complexes exhibit medium-intensity broad bands at 3064 (**1**) and 3050 (**2**) cm^{-1}, assignable to $\nu(O–H)_{oxime}$. The broadness and the relatively low frequency of these bands are both indicative of hydrogen bonding. The ν(C=N) in spectra free ligands appear at 1623 and 1628 cm^{-1} for saoH$_2$ and Me-saoH$_2$, respectively. These bands are shifted to lower wavenumbers in the spectra of **1** (1595 cm^{-1}) and **2** (1593 cm^{-1}) due to complexation. The ν(C=C) and ν(C=O) modes of the acetylacetonate ligand at 1586 and1532 cm^{-1} in the spectrum of Ga(acac)$_3$ have not shifted significantly in the spectra of **1** (1586 and 1530 cm^{-1}) and **2** (1579 and 1528 cm^{-1}), respectively.

3.3.2. ^{1}H and ^{13}C NMR spectroscopy

^{1}H and ^{13}C NMR spectra of **1**, **2**, Ga(acac)$_3$, saoH$_2$ and Me-saoH$_2$ were recorded in CDCl$_3$ solution at ambient temperature. Figs. 4, 5 and 7, 8 show the ^{1}H and ^{13}C NMR spectra of **1** and **2**, respectively. The signal assignment is based on chemical shifts and comparison between the spectra of the complexes and the spectra of the starting materials. The ^{1}H and ^{13}C NMR spectra of Ga(acac)$_3$, saoH$_2$ and Me-saoH$_2$ are shown in Figs. S1–S6. The methyl (CH$_3$) and methinic (CH) protons of the acac$^-$ ligands in spectrum of Ga(acac)$_3$ appear as two singlets at 2.01 and 5.44 ppm, respectively (Fig. S1). The spectrum of **1** (Fig. 4) is more complex in these two regions exhibiting three distinct signals (singlets) and a shoulder for each of the methyl and methinic protons of the acac$^-$ ligand. The oximic (NOH) and the methinic (C–H) protons in the spectrum of saoH$_2$ appear as two singlets at 10.03 and 8.24 ppm, respectively (Fig. S2). Those signals have shifted downfield in the spectrum of **1** due to the deprotonation and coordination of the saoH$^-$ ligands and split in sets of two peaks at 9.96 and 9.75 for the oximic and 8.22 and 8.20 for the methinic protons. The phenolic proton (OH) appears as a singlet at 7.86 in the spectrum of saoH$_2$ and it is absent in the spectrum of **1**. The aromatic protons in the spectrum of saoH$_2$ appear as two triplets for the C3 and C4 protons and two doublets for C2 and C5 protons (for numbering pattern see Fig. 1). The spectrum of **1** is more complex in the region of the aromatic protons exhibiting not only overlapping signals of triplets and doublets but overlapping of lower integration peaks which indicate the presence of isomers in the CDCl$_3$ solution.

The ^{13}C NMR spectrum of **1** corroborates with the presence of isomers in the CDCl$_3$ solution (Fig. 5). The methyl (CH$_3$), methinic (CH) and carbonyl (CO) carbon atoms of the acac$^-$ ligands appear at 27.36, 100.36 and 192.96 ppm in the spectrum of Ga(acac)$_3$ (Fig. S3). Those signals have not shifted significantly in the spectrum of **1**, but the signals of the methyl and methinic carbon atoms have split in sets of two signals (Fig. 5). The seven carbon atoms of saoH$_2$ appear as seven distinct peaks in the ^{13}C NMR spectrum of

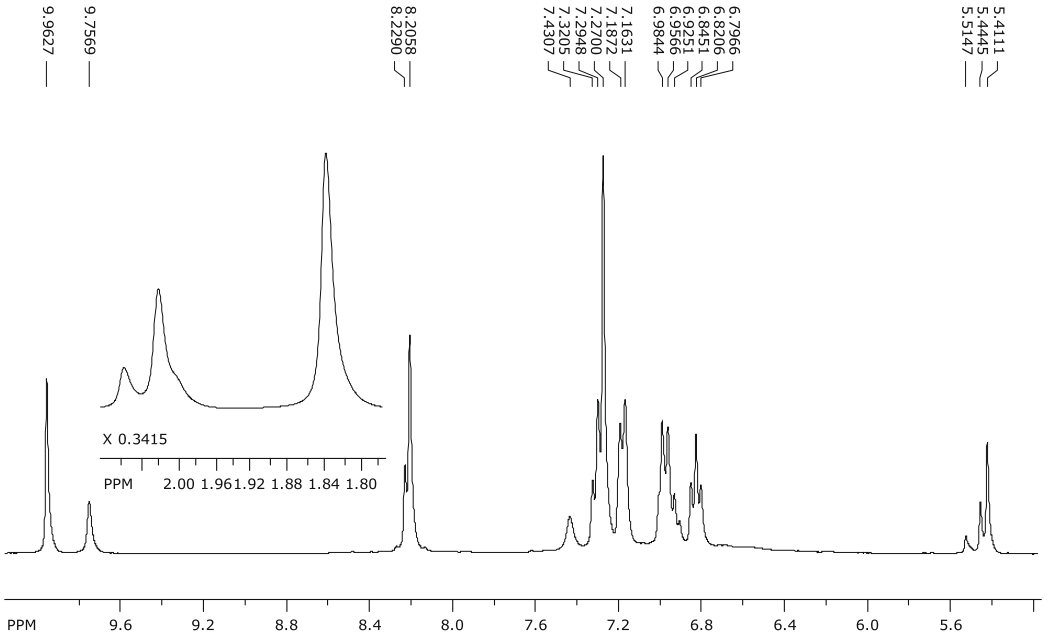


Fig. 4. The ^{1}H NMR spectrum of **1** in CDCl$_3$.

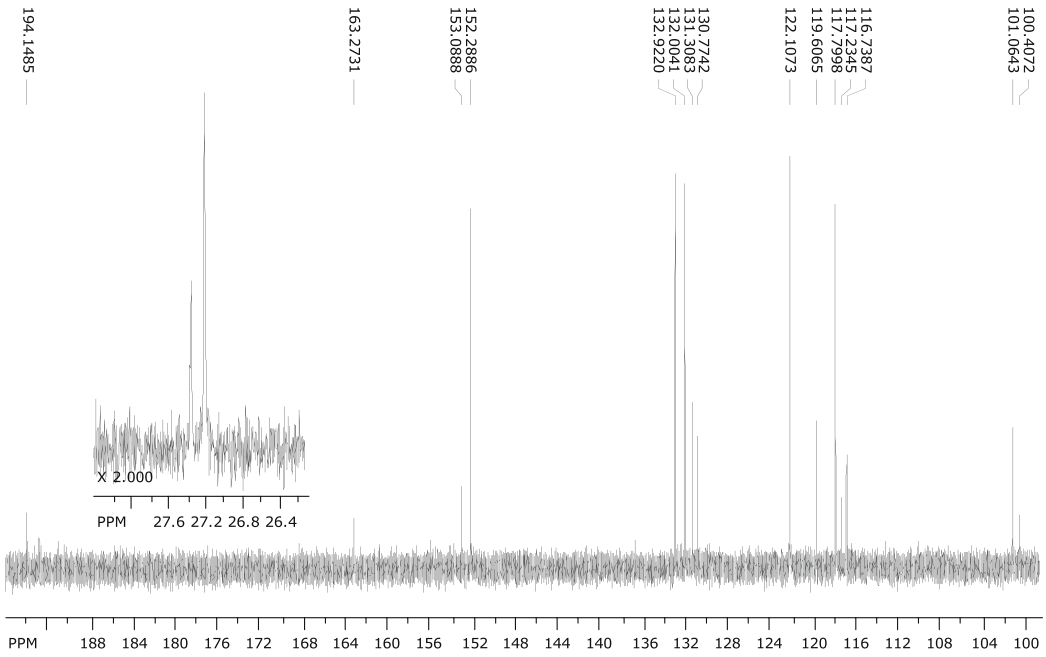


Fig. 5. The ^{13}C NMR spectrum of **1** in $CDCl_3$.

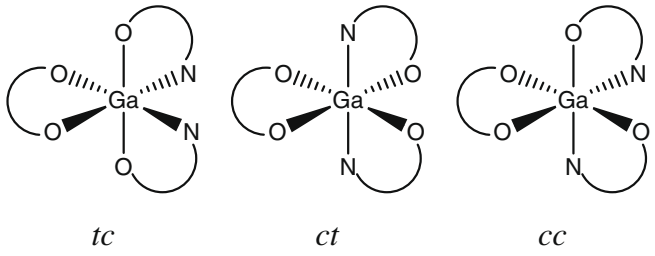


Fig. 6. The structures of the three geometric isomers of the Tris–chelate $[Ga(O,O)(O,N)_2]$ complexes.

the ligand (Fig. S4). Those peaks have shifted and split in sets of two peaks for all carbon atoms of saoH$^-$ except for the C1 and C6 which appear as two single peaks at 194.14 and 117.23 ppm in the ^{13}C NMR spectrum of **1**, respectively (Fig. 5). The fact that those two carbon atoms as well as the carbonyl carbon atoms of the acac$^-$ ligand give very weak signals in the ^{13}C NMR spectra of saoH$_2$ and Ga(acac)$_3$ and given that the minor species of **1** give a small percent signals compared with the signals of the majors species in solution, suggest that the signals of the minor species for those three carbon atoms are within the noise in the spectrum of **1**.

Tris–chelate complexes of the general formula $[Ga(O,O)(O,N)_2]$ such as **1** and the $[Ga(acac)(Me\text{-}saoH)_2]$ in **2** may exist in three iso-

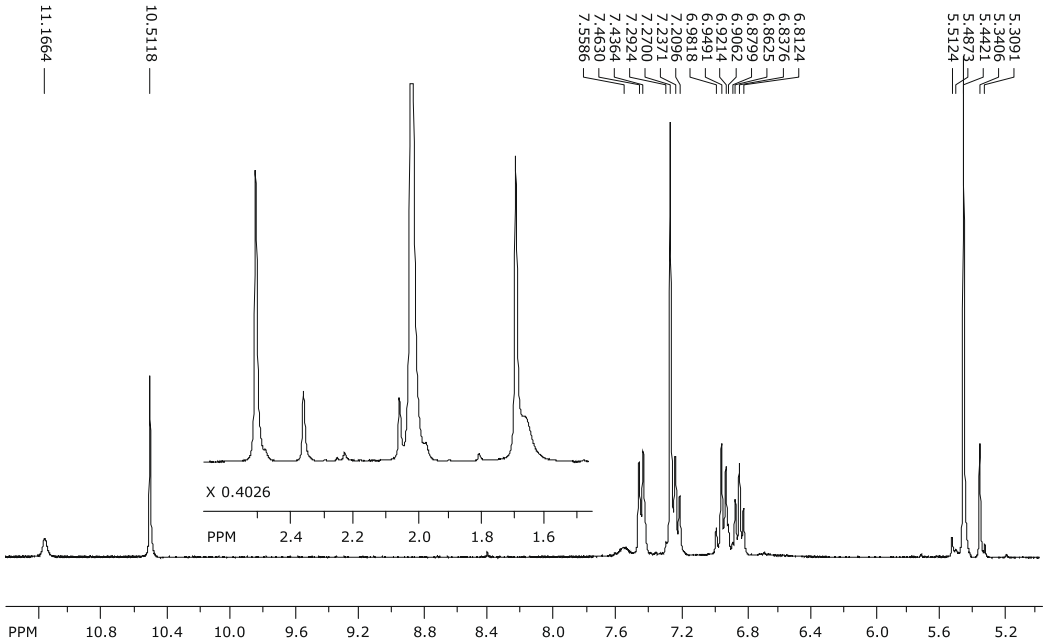


Fig. 7. The ^1H NMR spectrum of **2** in $CDCl_3$.

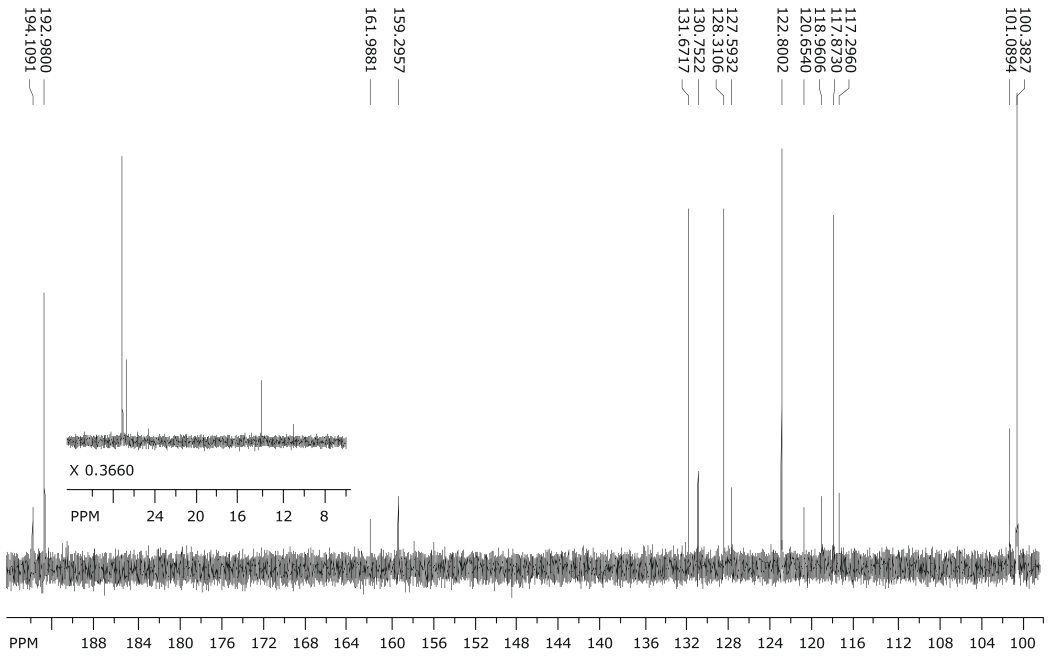


Fig. 8. The ^{13}C NMR spectrum of **2** in $CDCl_3$.

meric forms [41–43]. Those three geometric isomers are shown in Fig. 6 and with respect of the orientation of the N and O atoms of the two (O,N)-ligands are the *cis–cis* (*cc*), the *cis–trans* (*ct*) and the *trans–cis* (*tc*) with the latter being the one isolated in the solid-state in **1** and **2**. The *ct* and *tc* isomers have a C_2-symmetry where as *cc* has a C_1-symmetry. The ^1H and ^{13}C solution NMR spectra support at least the presence of two isomers in different proportion. The overlapping of the signals in the ^1H NMR spectrum of **1** makes the evaluation of the proportion difficult. A rough estimation of the proportion of the two isomers made on the integration of the oximic (NOH) protons, suggests that the two isomers are present in the $CDCl_3$ solution in 72:28% ratio.

The ^1H NMR spectrum of **2** indicates the presence of at least two isomers in $CDCl_3$ solution (Fig. 7). The aliphatic region is more complicated than that in the spectrum of **1** due to the presence of the methyl groups of the $Ga(acac)_3$ and the Me-saoH$^-$. The region where the methinic protons of the acac$^-$ ligands appear exhibits five signals, four of which are attributed to the two isomers and one to the methinic proton of the $Ga(acac)_3$. The aromatic region contains overlapping signals of triplets and doublets as well as lower integration peaks which indicate the presence of the other isomer. A rough estimation of the proportion of the two isomers made again on the oximic protons which appear as two peaks at 10.51 and 11.16 ppm in the spectrum of **2** suggests that the two isomers are present in the $CDCl_3$ solution in 74:26% ratio, which is similar to that observed in **1**. The ^{13}C NMR spectrum of **2** exhibits two peaks for the Me-saoH$^-$ methyl carbon atoms at 10.76 and 13.81 ppm (Fig. 8). The remaining Me-saoH$^-$ carbon atoms except C1, C6 and C7 (for numbering pattern see Fig. 1) appear as two sets of peaks in the ^{13}C spectrum of **2**, while there are eight distinct signals for the carbon atoms in the ^{13}C NMR spectrum of Me-saoH$_2$ (Fig. S6). As in the case of **1**, the C1, C6 and C7 atoms give very weak signals in the ^{13}C NMR spectrum of Me-saoH$_2$ and therefore the signals of the minor species of **2** for those three carbon atoms are not observed. The ^{13}C NMR spectrum of **2** exhibits two peaks for the acac$^-$ methyl carbon atoms around 27 ppm, two peaks for the methinic carbon atom at 100.38 and 101.08 ppm and two peaks for the carbonyl carbon atoms at 194.10 and 192.98 ppm. A closer look at the spectrum of **2** and the spectrum of $Ga(acac)_3$ indicates that the higher intensity signals at 27.36, 101.38 and 192.98 ppm are due to the $Ga(acac)_3$ within **2**. Concentrating our attention at the methinic carbon signals at around 100 ppm in the spectra of **1** and **2**, we can observe that the intense and the weak signals in the spectrum of **1** have been reversed in the spectrum of **2** and that the signals of the minor species in **2** overlap with the signals of the $Ga(acac)_3$ in **2**.

4. Conclusions and perspectives

Our first attempt to employ salicylaldoximes in the coordination chemistry of Ga(III) afforded two mononuclear Ga(III) complexes. Both complexes were characterized by single-crystal X-ray crystallography, IR, ^1H and ^{13}C NMR spectroscopy. Complex **1** is an octahedral Ga(III) complex surrounded by a bidentate-chelate saoH$^-$ ligand and a bidentate chelate acac$^-$ ligand, while complex **2** contains the same core with Me-saoH$^-$ instead of saoH$^-$ and has co-crystallized with one $Ga(acac)_3$ molecule. Both ^1H and ^{13}C NMR spectra of the compounds suggest the presence of at least two geometrical isomers in the $CDCl_3$ solution. Detailed preparations of the starting materials $Ga(acac)_3$, saoH$_2$ and Me-saoH$_2$ as well as $Ga(NO_3)_3{\cdot}9H_2O$ are given along with their IR and ^1H and ^{13}C NMR data. Although we did not manage to isolate higher nuclearity Ga(III) complexes in our first attempt, we continue working toward the synthesis of polynuclear Ga(III) complexes with salicyladoximes.

Appendix A. Supplementary data

CCDC 729176 and 729177 contain the supplementary crystallographic data for (**1**) and (**2**). These data can be obtained free of charge via http://www.ccdc.cam.ac.uk/conts/retrieving.html, or from the Cambridge Crystallographic Data Centre, 12 Union Road, Cambridge CB2 1EZ, UK; fax: (+44) 1223-336-033; or e-mail: deposit@ccdc.cam.ac.uk. Supplementary data associated with this article can be found, in the online version, at doi:10.1016/j.poly.2009.04.039.

References

[1] C.J. Milios, C.P. Raptopoulou, A. Terzis, F. Lloret, R. Vicente, S.P. Perlepes, A. Escuer, Angew. Chem., Int. Ed. 43 (2003) 210.
[2] C.J. Milios, R. Inglis, A. Vinslava, A. Prescimone, S. Parsons, S.P. Perlepes, G. Christou, E.K. Brechin, Chem. Commun. (2007) 2738.
[3] C.J. Milios, A. Prescimone, A. Mishra, S. Parsons, W. Wernsdorfer, G. Christou, S.P. Perlepes, E.K. Brechin, Chem. Commun. (2007) 153.
[4] C.J. Milios, R. Inglis, R. Bagai, W. Wernsdorfer, A. Collins, S. Moggach, S. Parsons, S.P. Perlepes, G. Christou, E.K. Brechin, Chem. Commun. (2007) 3476.
[5] I.A. Gass, C.J. Milios, A. Collins, F.J. White, L. Budd, S. Parsons, M. Murrie, S.P. Perlepes, E.K. Brechin, Dalton Trans. (2008) 2043.
[6] J. Cano, T. Cauchy, E. Ruiz, C.J. Milios, C.C. Stoumpos, T.C. Stamatatos, S.P. Perlepes, G. Christou, E.K. Brechin, Dalton Trans. (2008) 234.
[7] C.J. Milios, I.A. Gass, A. Vinslava, L. Budd, S. Parsons, W. Wernsdorfer, S.P. Perlepes, G. Christou, E.K. Brechin, Inorg. Chem. 46 (2007) 6215.
[8] I.A. Gass, C.J. Milios, A.G. Whittaker, F.P.A. Fabiani, S. Parsons, M. Murrie, S.P. Perlepes, E.K. Brechin, Inorg. Chem. 45 (2006) 5281.
[9] C.J. Milios, A. Vinslava, A.G. Whittaker, S. Parsons, W. Wernsdorfer, G. Christou, S.P. Perlepes, E.K. Brechin, Inorg. Chem. 45 (2006) 5272.
[10] C.J. Milios, P.A. Wood, S. Parsons, D. Foguet-Albiol, C. Lampropoulos, G. Christou, S.P. Perlepes, E.K. Brechin, Inorg. Chim. Acta 360 (2007) 3932.
[11] C.J. Milios, A. Vinslava, P.A. Wood, S. Parsons, W. Wernsdorfer, G. Christou, S.P. Perlepes, E.K. Brechin, J. Am. Chem. Soc. 129 (2007) 8.
[12] C.J. Milios, A. Vinslava, W. Wernsdorfer, S. Moggach, S. Parsons, S.P. Perlepes, G. Christou, E.K. Brechin, J. Am. Chem. Soc. 129 (2007) 2754.
[13] C.J. Milios, A. Vinslava, W. Wernsdorfer, A. Prescimone, P.A. Wood, S. Parsons, S.P. Perlepes, G. Christou, E.K. Brechin, J. Am. Chem. Soc. 129 (2007) 6547.
[14] C.J. Milios, R. Inglis, A. Vinslava, R. Bagai, W. Wernsdorfer, S. Parsons, S.P. Perlepes, G. Christou, E.K. Brechin, J. Am. Chem. Soc. 129 (2007) 12505.
[15] A. Prescimone, C.J. Milios, S. Moggach, J.E. Warren, A.R. Lennie, J. Sanchez-Benitez, K. Kamenev, R. Bircher, M. Murrie, S. Parsons, E.K. Brechin, Angew. Chem., Int. Ed. 47 (2008) 2828.
[16] C.J. Millos, A.G. Whittaker, E.K. Brechin, Polyhedron 26 (2007) 1927.
[17] P. Chaudhuri, M. Hess, E. Rentschler, T. Weyhermüller, U. Flörke, New J. Chem. 22 (1998) 553.
[18] J.M. Thorpe, R.L. Beddoes, D. Collison, C.D. Garner, M. Helliwell, J.M. Holmes, P.A. Tasker, Angew. Chem., Int. Ed. 38 (1999) 1119.
[19] H.-B. Xu, B.-W. Wang, F. Pan, Z.-M. Wang, S. Gao, Angew. Chem., Int. Ed. 46 (2007) 7388.
[20] C.-I. Yang, W. Wernsdorfer, G.-H. Lee, H.-L. Tsai, J. Am. Chem. Soc. 129 (2007) 456.
[21] C.P. Raptopoulou, A.K. Boudalis, Y. Sanakis, V. Psycharis, J.M. Clemente-Juan, M. Fardis, G. Diamantopoulos, G. Papavassiliou, Inorg. Chem. 45 (2006) 2317.
[22] C.P. Raptopoulou, Y. Sanakis, A.K. Boudalis, V. Psycharis, Polyhedron 24 (2005) 711.
[23] C.C. Stoumpos, R. Inglis, G. Karotsis, L.F. Jones, A. Collins, S. Parsons, C.J. Milios, G.S. Papaefstathiou, E.K. Brechin, Cryst. Growth Des. 9 (2009) 24.
[24] G.S. Papaefstathiou, S. Manessi, C.P. Raptopoulou, E.J. Behrman, Th.F. Zafiropoulos, Inorg. Chem. Commun. 7 (2004) 69.
[25] A. Manessi, G.S. Papaefstathiou, C.P. Raptopoulou, A. Terzis, Th.F. Zafiropoulos, J. Inorg. Biochem. 98 (2004) 2052.
[26] A. Sofetis, G.S. Papaefstathiou, A. Terzis, C.P. Raptopoulou, Th.F. Zafiropoulos, Z. Naturforsch. 59b (2004) 291.
[27] G.S. Papaefstathiou, A. Manessi, C.P. Raptopoulou, A. Terzis, Th.F. Zafiropoulos, Inorg. Chem. 45 (2006) 8823.
[28] G.S. Papaefstathiou, A. Sofetis, C.P. Raptopoulou, A. Terzis, G.A. Spyroulias, Th.F. Zafiropoulos, J. Mol. Struct. 837 (2007) 5.
[29] A. Kagkelari, V. Bekiari, E. Stathatos, G.S. Papaefstathiou, C.P. Raptopoulou, Th.F. Zafiropoulos, P. Lianos, J. Lumin. 129 (2009) 578.
[30] A.R. Barron, A.N. MacInnes, in: R.B. King (Ed.), Encyclopedia of Inorganic Chemistry, vol. 3, Wiley, New York, 1994, p. 1249.
[31] F.A. Ponce, D.B. Bour, Nature 386 (1997) 351.
[32] M.A. Jakupec, M. Galanski, V.B. Arion, C.G. Hartinger, B.K. Keppler, Dalton Trans. (2008) 183.
[33] C.G. Hartinger, B.K. Keppler, Electrophoresis 28 (2007) 3436.
[34] M.A. Jakupec, B.K. Keppler, Curr. Top. Med. Chem. 4 (2004) 1575.
[35] S.J. Rettig, A. Storr, J. Trotter, Acta Crystallogr., Sect. C 48 (1992) 1587.
[36] G.M. Sheldrick, SHELXS-86, Structure Solving Program, University of Göttingen, Germany, 1986.
[37] G.M. Sheldrick, SHELXL-97, Program for the Refinement of Crystal Structures from Diffraction Data, University of Göttingen, Germany, 1997.
[38] G. Bandoli, A. Dolmella, F. Tisato, M. Porchia, F. Refosco, Coord. Chem. Rev. 253 (2009) 56.
[39] K. Dymock, G.J. Palenik, Acta Crystallogr., Sect. B 30 (1974) 1364.
[40] L. Pang, M.A. Whitehead, E.A.C. Lucken, Inorg. Chim. Acta 203 (1993) 239.
[41] E.C. Constable, C.E. Housecroft, V. Jullien, M. Neuburger, I. Poleschak, S. Reymann, S. Saxer, S. Schaffner, Polyhedron 26 (2007) 5519.
[42] S.K. Ramalingam, S.A. Samath, Transition Met. Chem. 15 (1990) 374.
[43] P. Byabartta, Spectrochim. Acta, Part A 66 (2007) 521.

to standard procedures. Melting points (m.p.) were determined in open capillaries and are uncorrected. IR and far-IR spectra were recorded on a Perkin–Elmer Spectrum GX Fourier transform spectrophotometer using KBr pellets (4000–400 cm^{-1}) and nujol mulls dispersed between polyethylene disks (400–40 cm^{-1}). NMR spectra were recorded on a Bruker AV-400 spectrometer operating at 400 and 100 MHz for ^1H and ^{13}C acquisition, respectively, or on a Bruker AV-250 spectrometer operating at 250.13 and 62.90 MHz for ^1H and ^{13}C acquisition, respectively. The spectra were acquired at room temperature (298 K). The chemical shifts are reported in ppm for ^1H and ^{13}C NMR). Samples were dissolved in dimethylsulfoxide-d6 and spectra were obtained at room temperature with the signal of free dimethylsulfoxide-d6 (at 2.50 ppm ^1H NMR, 39.5 ppm ^{13}C NMR) as a reference. Elemental analyses were carried out by the microanalytical service of the University of Ioannina, Greece.

*2.1.1. Preparation of pyruvic acid thiosemicarbazone hemihydrate ($H_2pt·1/2H_2O$) (**1**)*

The ligand was synthesized according to a published procedure [6d]. The white powder was recrystallized from diethyl ether and was dried *in vacuo* over silica gel. Yield: 85%. M.p. 188–190 °C. IR (cm^{-1}) [6d]: 3431 m, $\nu(H_2O)$; 3294 m, $\nu(NH_2)$; 1626s, υ(C=N); 1733s, 1702 m, υ(C=O), 1046 m, υ(N—N); 859 m, υ(C=S). ^1H NMR (DMSO): δ 12.10 (s, 1H, OH); 10.74 (s, 1H, NH); 8.67 (d, 2H, NH_2, J_{H-H} = 16.8); 2.11 (s, 3H, Me); ^{13}C NMR: δ 180.3 (C=S); 165.3 (C=O); 139.1 (C—CH_3); 12.6 (Me). *Anal.* Calc. for $C_4H_7N_3O_2S.1/2H_2O$ (Mw: 170.2): C, 28.2; H, 4.7; N, 24.7, S, 18.8. Found: C, 28.0; H, 4.8; N, 24.5; S, 18.9%.

*2.1.2. Preparation of [$Ph_2Sn(pt)$] (**2**)*

Diphenyltin(IV) oxide (0.0867 g, 0.3 mmole) and pyruvic acid thiosemicarbazone hemihydrate (H_2pt) (0.0511 g, 0.3 mmole) in benzene (20 ml) were refluxed overnight under azeotropic removal of water (*Dean-Stark* trap). The resulting clear solution was rotary evaporated under vacuum to a small volume (2 ml), chilled and triturated with diethyl ether to give a white solid. The white powder was recrystallized from diethyl ether and dried *in vacuo* over silica gel. Yield: 15%. M.p. 196–198 °C. IR (cm^{-1}): 3285s, $\nu(NH_2)$; 1610, 1593 m, υ(C=N); 1667s, ν_{as}(COO); 1431s, ν_{sym}(COO); 1070 m, υ(N–N); 766 ms, υ(C=S); 333 m, υ(Sn–C); 310 m, υ(Sn–O); 396 m, ν(Sn–S); 278 m, υ(Sn–N). ^1H NMR (DMSO): δ 8.28 (s, 2H, NH_2); 7.67 (H*o*-Ph); 7.45–7.40 (m, H*m*, *p*-Ph); 2.30 (s, 3H, Me); ^{13}C NMR: δ 175.2 (C=S); 164.6 (C=O); 148.9 (Co-Ph); 146.0 (Cm-Ph); 135.9 (Cp-Ph); 129.5 (C–CH_3); 15.2 (CH_3). *Anal.* Calc. for $C_{16}H_{15}N_3O_2SSn$ (Mw: 432.1): C, 44.5; H, 3.5; N, 9.7; S, 7.4. Found: C, 44.2; H, 3.7; N, 9.4, S, 7.5%.

*2.1.3. Preparation of [$SnMe_2(Hpt)(H_2O)$]Cl (**3**)*

Pyruvic thiosemicarbazone hemihydrate (0.04 g, 0.24 mmole) and equimolar quantity of KOH in methanol (10 ml) were mixed and dimethyltin(IV) dichloride (0.053 g, 0.24 mmole) was added. The reaction mixture was stirred for 2 h. The resulting clear solution evaporated and triturated with distilled diethyl ether to give a pale white solid. The pale white powder was recrystallized from distilled diethyl ether and dried *in vacuo* over silica gel. Yield: 61%. M.p. 157–159 °C. IR (cm^{-1}): 3420 m, $\nu(H_2O)$; 3244s, $\nu(NH_2)$; 1560 m, υ(C=N); 1625s, ν_{as}(COO); 1393s, ν_{sym}(COO); 1062 m, υ(N–N); 768 m, υ(C=S); 517 m, 493 υ(Sn–C); 331sh, 311 m υ(Sn–O); 403 m, ν(Sn–S); 277 m, υ(Sn–N). ^1H NMR (DMSO): δ 12.12 (s, 1H, H_2O); 10.70 (s, 1H, NH); 8.75 (d, 2H, NH_2, $J_{(H)-(H)}$ = 21.5); 2.28 (s, 3H, Me); 1.06/0.81 (s, Sn–Me, $J_{(Sn)-(Me)}$ = 63.6); ^{13}C NMR: δ 185.5; 180.9(C=S); 170.5, 169.4, 156.2 (C=O); 121.3 (C–CH_3); 14.4 (Me); 9. (Me–Sn). *Anal.* Calc. for $C_6H_{14}N_3O_3SSnCl$ (Mw: 362.37): C, 19.9; H, 3.9; N, 11.6, S, 8.8. Found: C, 19.4; H, 3.8; N, 12.0, S, 9.1%.

*2.1.4. Preparation of [$Ph_2Sn(Hpt)(H_2O)$]Cl (**4**)*

Pyruvic thiosemicarbazone hemihydrate (0.04 g, 0.24 mmole) and equimolar quantity of KOH in methanol (10 ml) were mixed and diphenyltin(IV) dichloride (0.0825 g, 0.24 mmole) was added. The reaction mixture was stirred for 2 h. The resulting clear solution evaporated and triturated with distilled diethyl ether to give a pale white solid. The pale white powder was recrystallized from distilled diethyl ether and dried *in vacuo* over silica gel. Yield: 46%. M.p. 124–126 °C. IR (cm^{-1}): 3409 m, $\nu(H_2O$; 3299s, $\nu(NH_2)$; 1597 m, υ(C=N); 1618s, ν_{as}(COO); 1391, ν_{sym}(COO); 1066s, υ(N–N); 766 m, υ(C=S); 340 m, υ(Sn–C); 329 m, 315sh, υ(Sn–O); 397 m, ν(Sn–S); 279 m,, υ(Sn–N). ^1H NMR (DMSO): δ 12.03 (s, 1H, H_2O); 10.65 (s, 1H, NH); 8.68 (d, 2H, NH_2, $J_{(H)-(H)}$ = 20.9); 8.18 (m, H*o*-Ph); 7.87 (m, H*p*-Ph); 7.61 (m, H*m*-Ph); 2.22 (s, 3H, Me); ^{13}C NMR: δ 207.4, 180.7, 175.2 (C=S); 165.7, 164.6 (C=O); 148.9 (Co-Ph); 146.2 (C*m*-Ph); 139.5 (C*p*-Ph); 129.5 (C–CH_3); 15.2 (Me). *Anal.* Calc. for $C_{16}H_{18}N_3O_3SSnCl$ (Mw: 486.5): C, 39.5; H, 3.7; N, 8.6; S, 6.6. Found: C, 39.1; H, 3.5; N, 8.4; S, 6.4%.

2.2. X-ray crystallography

X-ray data for **2** and **3** were collected at low temperature using an Oxford Cryosystem device on a Kuma KM4CCD κ-axis diffractometer with graphite-monochromated Mo Kα radiation (λ = 0.71073 Å). Crystals were positioned at 65 mm from the CCD camera. Six hundred and twelve frames were measured at 0.75° intervals with a counting time of 10–20 s. Accurate cell parameters were determined and refined by least-squares fit of 11 200 and 12 000 the strongest reflections for **1** and **2**, respectively. The data were corrected for Lorentz and polarization effects. Analytical absorption correction was applied for both crystals. Data reduction and analysis were carried out with the Oxford Diffraction (Poland) Sp. z o.o programs [9]. Crystal structures were solved by direct methods (program SHELXS97 [9a]) and refined by the full-matrix least-squares method on all F^2 data using the SHELXL97 [9b] programs. Non-hydrogen atoms were refined with anisotropic displacement parameters; hydrogen atoms were included from geometry of molecules and $\Delta\rho$ maps. During the refinement process they treated as riding atoms [9a–d]. Crystal data are given in Table 1, together with refinement details.

2.3. Antiproliferative assay in vitro

2.3.1. Compounds

Test solutions of the compounds tested (1 mg/ml) were prepared by dissolving the substance in 100 µl of DMSO completed with 900 µl of tissue culture medium. Afterwards, the tested compounds were diluted in culture medium to reach the final concentrations of 100, 50, 10, 1 and 0.1 ng/µl. The solvent (DMSO) in the highest concentration used in test did not reveal any cytotoxic activity.

2.3.2. Cells

The cell lines are maintained in the Cell Culture Collection of the University of Ioannina. Twenty-four hours before addition of the tested agents, the cells were plated in 96-well plates at a density of 10^4 cells per well. The MCF-7 cells were cultured in the D-MEM (Modified Eagle's Medium) medium supplemented with 1% antibiotic and 10% fetal calf serum. L-929 cells were grown in Hepes-buffered RPMI 1640 medium supplemented with 10% fetal calf serum, penicillin (50 U/ml) and streptomycin (50 mg/ml). A-549 cells were grown in F-12 K Ham's medium supplemented with 1% glutamine, 1% antibiotic/antimycotic, 2% $NaHCO_3$ and 10% fetal calf serum. The cell cultures were maintained at 37 °C in a humid atmosphere saturated with 5% CO_2. Cell number was counted by the Trypan blue dye exclusion method. MCF-7, L-929 and A-549

Table 1
Crystal data, data collection and structure refinement for **2** and **3**.

	2	3
Empirical formula	$C_{16}H_{15}N_3O_2SSn$	$C_6H_{14}ClN_3O_3SSn$
Formula weight	432.09	362.40
Temperature (K)	100(2)	100(2)
Wavelength (Å)	Mo Kα 0.71073	0.71073
Crystal system	triclinic	monoclinic
Space group	$P\bar{1}$ (No. 2)	$P21/c$ (No. 14)
a (Å)	8.8155(4)	9.6415(5)
b (Å)	9.2944(6)	8.9202(5) A
c (Å)	11.6818(6)	15.0583(8)
α (°)	89.314(4)	90
β (°)	77.578(4)	101.665(5)
γ (°)	65.230(5)	90
V (Å^3)	845.44(9)	1268.33(12)
Z	2	4
D_{calcd} (Mg m^{-3})	1.697	1.898
μ(Mo Kα) (mm^{-1})	1.646	2.382
F(0 0 0)	428	712
Unit cell dimensions	0.11 × 0.22 × 0.26	0.30 × 0.27 × 0.24
Diffractometer	Kuma KM4CCD	Kuma KM4CCD
θ Range (°)	3.1, 36.6	3.14, 36.58
Ranges of h, k, l	−14 to 14; −13 to 15; −19 to 19	−12 to 16, −14 to 14, −24 to 22
Reflections collected	13 268	20 481
Independent reflections [R_{int}]	7105 [R_{int} = 0.036]	5801 [R_{int} = 0.0318]
Observed data [I > 2.0 sigma(I)]	6180	5009
Data/parameters	7105, 268	5801, 192
Goodness-of-fit (F^2)	1.04	1.097
Final R indices [I > 2 sigma(I)]	0.0283/0.0714	0.0289/0.0684
Minimum and maximum residential density [e/Å^3]	−1.17/1.80	−0.885/2.508

cells were determined by the sulforhodamine B assay [10a], while T-24 cells by the MTT assay [10b]. The in vitro tests were performed as described previously [10c].

3. Results and discussion

3.1. Synthetic aspects

Pyruvic acid thiosemicarbazone hemihydrate (H_2pt·1/2H_2O) was prepared by the condensation of pyruvic acid and thiosemicarbazide hydrochloride [6d]. The reaction of dimethyltin(IV)oxide with pyruvic acid thiosemicarbazone (H_2pt) and subsequent recrystallization from THF leads to the formation two *pseudo*-polymorfs based on triangular $[(CH_3)_2Sn(pt)]_3$ units; one of them $[(CH_3)_2Sn(pt)]_3$·3THF with tubular cavities while the other $[(CH_3)_2Sn(pt)]_3$·1.5THF is a H-bonded 3D network with truncated tetrahedral cavities [6e]. When diphenyltin(IV) oxide was reacted with H_2pt the monomer [*Sn*Ph_2(pt)] (**2**) was formed. Probably, the steric hindrance effect of phenyl groups prevent the formation of a trimer. The stoichiometry of the complex indicates that SnR_2(IV) is coordinated by the doubly charged anion pt^{2-} formed on the loss of the two protons from the carboxylato oxygen and thioamide nitrogen, N. The doubly deprotonated ligand, pt^{2-}, is coordinated as a tridentate ligand *via* the carboxylato oxygen O, the azomethine nitrogen N and the thiolato sulfur S atoms. In the trimer the carboxylato group OCO bridge two tin centers. Reaction of potassium pyruvic thiosemicarbazone with SnR_2Cl_2 (where R = Me or Ph) gives the cationic complexes [$SnMe_2$(Hpt)(H_2O)]Cl (**3**) and [$SnPh_2$(Hpt)(H_2O)]Cl (**4**). The stoichiometries of the cationic complexes indicate that SnR_2(IV) is coordinated by the singly charged anion Hpt^- and one molecule of water. The formula of these diorganotin(IV) complexes were confirmed by elemental analysis, spectroscopic studies and by X-ray analysis, Scheme 1.

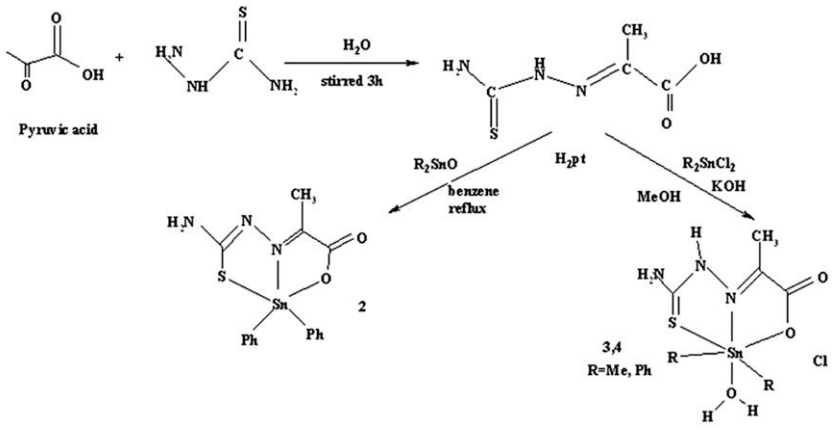
3.2. Structural characterization

Complexes **2** and **3** were recrystallized from C_6H_6/toluene/DMSO/CH_3CN and distilled diethyl ether respectively, to furnish white prisms suitable for single-crystal X-ray analysis. Selected interatomic distances and bond angles are collected in Table 2.

3.2.1. Crystal structure of [$SnPh_2$(pt)] (**2**)

The crystal structure of compound **2** is shown in Fig. 1. The dianionic, tridentate ligand has a ZEZ configuration based on the C(1)–C(2), C(2)–N(1) and N(2)–C(4) bonds. The double deprotonated ligand is coordinated as tridentate ligand *via* the carboxylato oxygen O(1), the azomethine nitrogen N(1) and thiolato sulfur S(1) atoms. The penta-coordination number is completed by two carbon atoms of phenyl groups. The coordinated part of the ligand is made of two chelate rings Sn(1)S(1)N(1)N(2)C(4) and Sn(1)O(1)N(1)C(1)C(2) (I and II). The dihedral angles between the planes of the rings I and II is 4.60(6)°, indicating that the ligand is nearly planar.

Analysis of the shape determining angles using the approach of Reedijk and coworkers [11] yields τ ($(\alpha - \beta)/60$) value of 0.44 for Sn(1) (τ = 0.0 and 1.0 for *SPY* and *TBPY* geometries, respectively). The metal coordination geometry is therefore described as distorted *SPY* with the C(11) occupying the apical position for Sn(1). The donor C(11) is chosen as apex by the simple criterion that neither should be any of the four donor atoms which define the two largest angles, a and b [11]. The angles S(1)–Sn(1)–C(11) and O(1)–Sn(1)–C(11), are 101.16(4)° and 93.46(6)° respectively, and



Scheme 1. The reaction scheme for the synthesis of **1**–**4**.

Table 2
Summary of crystal, intensity collection and refinement data.

2		**3**	
Sn(1)–C(11)	2.1195(17)	Sn(1)–C(6)	2.1065(19)
Sn(1)–C(5)	2.1237(17)	Sn(1)–C(5)	2.1127(18)
Sn(1)–O(1)	2.1536(11)	Sn(1)–O(1W)	2.2975(14)
Sn(1)–N(1)	2.2087(14)	Sn(1)–O(1)	2.3166(12)
Sn(1)–S(1)	2.4986(4)	Sn(1)–N(1)	2.3879(15)
S(1)–C(4)	1.7466(17)	Sn(1)–S(1)	2.6080(5)
O(1)–C(1)	1.289(2)	S(1)–C(4)	1.7003(19)
O(2)–C(1)	1.2304(19)	O(1)–C(1)	1.282(2)
N(1)–C(2)	1.2952(19)	O(2)–C(1)	1.238(2)
N(1)–N(2)	1.3632(19)	N(1)–C(2)	1.291(2)
N(2)–C(4)	1.3252(19)	N(1)–N(2)	1.364(2)
N(3)–C(4)	1.339(2)	N(2)–C(4)	1.356(2)
C(11)–Sn(1)–C(5)	123.25(6)	C(6)–Sn(1)–C(5)	162.50(8)
C(11)–Sn(1)–O(1)	93.46(5)	C(6)–Sn(1)–O(1W)	84.86(7)
C(5)–Sn(1)–O(1)	90.85(6)	C(5)–Sn(1)–O(1W)	89.73(6)
C(11)–Sn(1)–N(1)	110.47(6)	C(6)–Sn(1)–O(1)	87.02(6)
C(5)–Sn(1)–N(1)	124.92(6)	C(5)–Sn(1)–O(1)	87.20(6)
O(1)–Sn(1)–N(1)	73.79(5)	O(1W)–Sn(1)–O(1)	142.48(5)
C(11)–Sn(1)–S(1)	101.16(4)	C(6)–Sn(1)–N(1)	99.36(7)
C(5)–Sn(1)–S(1)	101.46(4)	C(5)–Sn(1)–N(1)	93.76(6)
O(1)–Sn(1)–S(1)	151.06(4)	O(1W)–Sn(1)–N(1)	149.41(5)
N(1)–Sn(1)–S(1)	77.71(3)	O(1)–Sn(1)–N(1)	68.10(5)
C(4)–S(1)–Sn(1)	95.93(5)	C(6)–Sn(1)–S(1)	96.60(5)
C(1)–O(1)–Sn(1)	118.31(10)	C(5)–Sn(1)–S(1)	98.23(5)
C(2)–N(1)–N(2)	119.34(14)	O(1W)–Sn(1)–S(1)	76.02(4)
C(2)–N(1)–Sn(1)	117.09(11)	O(1)–Sn(1)–S(1)	141.39(3)
N(2)–N(1)–Sn(1)	123.55(9)	N(1)–Sn(1)–S(1)	73.40(4)

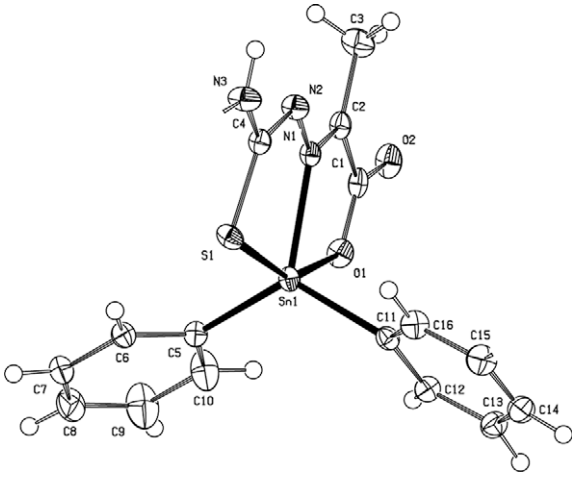


Fig. 1. Molecular structure of the neutral diorganotin complex **2**.

the angles C(5)–Sn(1)–C(11) and N(1)–Sn(1)–C(11) are 123.26(7)° and 110.47(6)° respectively, and deviate by ~20–33° from the 90° expected for a square-base pyramid, so the polyhedron formed is far from being a square pyramid.

The C(3)–N(1) bond length is 1.299(3) Å and is close to a double bond (1.28 Å). The deprotonation of N(2)H produces a negative charge, which is delocalized in the C(3)–N(1)–N(2)–C(4) group. All the metal-donor bond distances, Sn–O and Sn–N were similar to other organotin complexes presented in literature [8c,d]. $\pi \rightarrow \pi$ intermolecular interactions and intra- and intermolecular hydrogen bonds stabilize this structure. The polar hydrogen atom on N(3) participates in intermolecular hydrogen bond. For **2** the monomers of Sn(1) are linked through intermolecular hydrogen bonds of N(3)–H(3A)–O(2) type. A strong π–π interaction is that between the rings Sn(1)–N(1)–N(2)–C(4)–S {Cg(1)–Cg(1); symmetry operation; $1-x, 1-y, 1-z$} at a center to center separation of 4.0360(9) Å, Fig. 2.

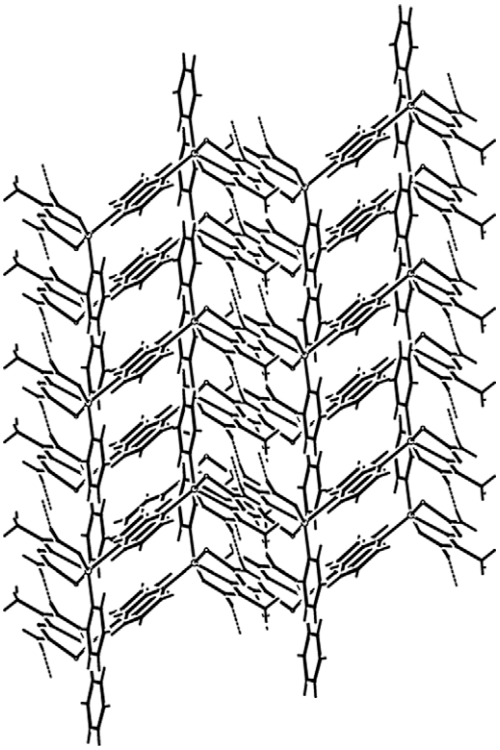


Fig. 2. A view of the extended network of **2** along the *b* axis.

*3.2.2. Crystal structure of [SnMe$_2$(Hpt)(H$_2$O)]Cl (**3**)*

A perspective view of **3** is shown in Fig. 3. The mono deprotonated ligand is coordinated as tridentate ligand *via* the carboxylato oxygen O(1), the azomethine nitrogen N(1) and thiolato sulfur S(1) atoms. The molecule of H_2O is coordinated to the tin through oxygen O(1W) atom. The six coordination number is completed by two carbon atoms of methyl groups. Two axial places are occupied by the two carbon atoms and the basal plane by the three donor atoms of ligand and the O(1W) donor atom. The charge of the organotin fragment is balanced by an ionic chloride anion. The

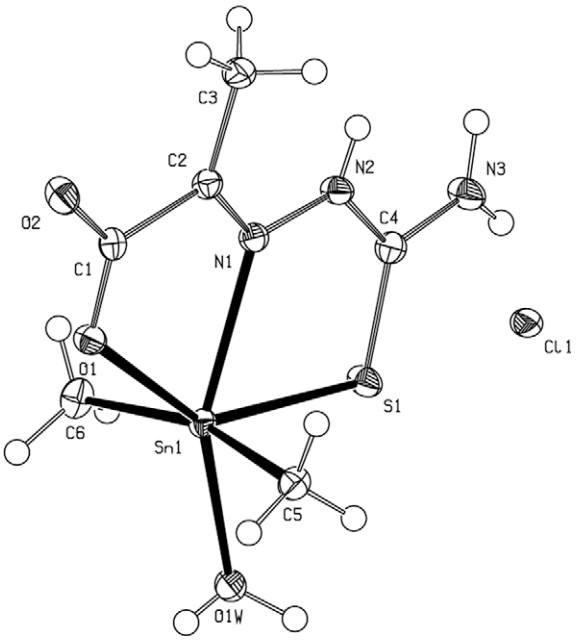


Fig. 3. Molecular structure of the cationic diorganotin complex **3**.

structure is distorted octahedral. The distortion from the ideal octahedral configuration is shown by the C(5)–Sn(1)–C(6) angle of 162.50(7). Also, the angles S(1)–Sn(1)–O(1) and O(1W)–Sn(1)–N(1) in the basal plane are 141.39(3) and 149.41(5) respectively, which deviates from the ideal value of 180°, probably due to the ligand constraint. The organic molecule acts as anionic tridentate with the ONS donors placed in the same side. The tridentate ligand has a ZEZ configuration. The coordinated ligand consists of two chelate rings, SnSNNC and SnONCC, I and II, respectively. The dihedral angle between the planes of the rings I and II is 3.17(6) indicating that the ligand does not deviate appreciably from planarity. The distance between the metal centers is 4.2960(3) Å.

The counter anion participates in five hydrogen bonds. The Cl(1) anion participates in three hydrogen bonds of N(2)–H(2N)···Cl(1), N(3)–H(31N)···Cl(1) and O(1W)–H(2W)···Cl(1) with one monomer of **3**. The polar hydrogen atoms on N(3) partcipate in two intermolecular hydrogen bonds [12]. The monomers of **3** form hydrogen-bonded dimers linked by two N(3)–H(32N)···Cl(1) hydrogen bonds involving the amino N(3)–H(32N) hydrogen atom and the adjacent Cl(1) chloride and *vice versa* of centrocymetrically related pairs of molecules. The observed hydrogen-bonding pattern is of the DA = AD type. Another centrosymmetric pair of hydrogen bonds of the DA = AD type involving the methyl carbon C(3)–H(3) and the same chloride Cl(1) atom connects the dimers and results in the formation of infinite layers, Fig. 4 [12]. Intra and inter molecular hydrogen bonds stabilize this structure and leads to a supramolecular assembly, Table 3.

Table 3
π–π, inter- and intramolecular hydrogen bonds for **2**, inter and intra-molecular hydrogen bonds for **3**[a].

*π–π, intra- and intermolecular hydrogen bonds for **2***					
		Cg–Cg[b]	β[c]	CgI-Perp[d]	CgJ-Perp[e]
Cg(1) → Cg(1)[i]		4.0360(9)	23.08	3.7131(6)	3.7131(6)
D	H	A[b]	D···A	H···A	D–H···A
N(3)	H(3B)	O(2)[ii]	2.844(2)	2.00(3)	169(3)
C(3)	H(3D	O(2)	2.884(2)	2.51(3)	107(3)
*Intra- and intermolecular hydrogen bonds for **3***					
D	H	A[b]	D–H	D···A	D–H···A
O(1W)	H(1W)	O(2)[iii]	1.95(4)	2.659(2)	172(4)
N(2)	H(2N)	Cl(1)[iv]	2.39(4)	3.174(2)	164(4)
O(1W)	H(2W)	Cl(1)[v]	2.15(4)	3.048(2)	176(3)
N(3)	H(31N)	Cl(1)[iv]	2.39(3)	3.226(2)	155(3)
N(3)	H(32N)	Cl(1)	2.41(3)	3.245(2)	174(3)
C(3)	H(3A)	Cl(1)[vi]	2.76(4)	3.505(2)	136(3)
C(3)	H(3B)	O(2)	2.42(4)	2.840(2)	109(3)
C(6)	H(6A)	O(2)[vi]	2.57(4)	3.411(2)	153(3)

[a] Cg(1) refer to the centroid Sn(1)–N(1)–N(2)–C(4)–S for **2**, (i) $1-x, 1-y, 1-z$; (ii) $x, 1+y, z$; (iii) $-x, -y, 2-z$; (iv) $1-x, 1/2+y, 3/2-z$;v,$1-x, -1/2+y, 3/2-z$; (vi) $x, 1/2-y, 1/2+z$.
[b] Cg–Cg is the distance between ring centroids.
[c] Where β is the angle Cg(I) → Cg(J).
[d] CgI-Perp is the perpendicular distance of Cg(I) on ring J.
[e] CgJ-Perp is the perpendicular distance of Cg(J) on ring I.

3.3. Spectroscopy

3.3.1. Infrared spectroscopy

The three medium-strong intensity bands at around 3294, 3210 and 3120 sh cm^{-1} in the spectra of $H_2tpt{\cdot}1/2H_2O$, are assigned to $\upsilon_{as}NH_2$, υ_sNH_2 and υNH, respectively, while the bands at 3430 and 3407 are assigned to υOH mode. These bands are superimposed upon the broader more intense O–H stretching absorption typical of the carboxylic acid functions. The broad band at 3000–2980 cm^{-1} is taken to represent the υ(NH···O) mode, due to intra- or intermolecular hydrogen bonding [8c,d,13,14]. In the NH stretching frequency region the spectral band υ(NH) disappears in the complex **2**, indicating the deprotonation of the NH group. The difference, $\Delta[\upsilon_{as}(COO)-\upsilon_{sym}(COO)]$ between these frequencies for **2**–**4** is close to that found for monodentate carboxylato group (230–240 cm^{-1}). The significant changes in the ligand bands upon complexing are the decrease in υ(C=N) and increase in υ(N–N) and the absence of the large systematic shifts of $\upsilon_{as}(NH_2)$ to lower frequencies. These data indicate coordination through the nitrogen of the azomethine group and no interaction between the terminal amino nitrogen and the metal ion. The υ(CS) bands at 859 cm^{-1} are less intense in the complexes **2**–**4** and are shifted to a lower frequency, suggesting coordination of the metal through sulfur after deprotonation. From the metal–ligand stretching vibrations, which are below 600 cm^{-1}, it is possible to assign the bands characteristic for υ(SnC). Also, υ(SnS) at 403–395 cm^{-1}, υ(SnN) at 270–250 cm^{-1} and υ(SnO) at 330–310 cm^{-1} [8c,d,13,14].

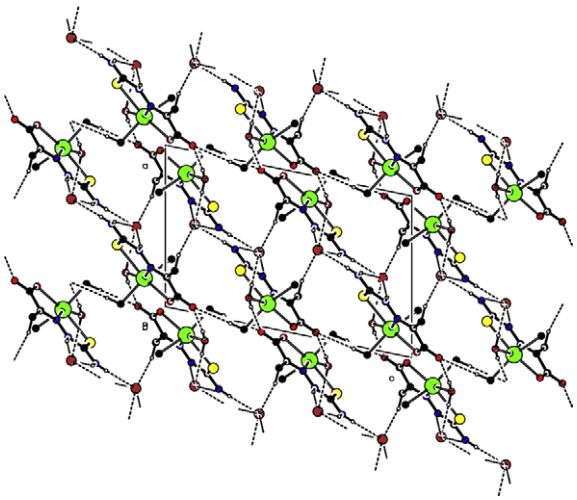


Fig. 4. Arrangement of the intermolecular hydrogen bonds in **3**.

3.3.2. NMR spectra

In the ^{1}H NMR spectra of (H_2pt) (**1**) the appearance of the signal ^{2}NH at δ 10.74 ppm, indicates that this proton is involved in hydrogen bonding [13]. The absence of peak corresponding to the imino proton in the spectrum of **2** indicates that this nitrogen is present in the deprotonated form. The existence of the ^{2}NH resonance in the ^{1}H NMR spectra of the complexes **3** and **4** indicates that the nitrogen atoms remain protonated. The signals corresponding to the hydroxyl groups for **2**–**4** disappear upon interaction with the metal, indicating deprotonation of these atoms and possible coordination to the tin atom. The C=S resonances of the thiosemicarbazone moieties in the free ligand resonated at 180.3 ppm. In the complex **2** an upfield shift was observed, indicating increased electron density at this site on complexation, due probably to π-back bonding for thiolato sulfur [8c,d,14]. ^{13}C NMR spectra for **3** and **4** clearly show the existence of two-three signals for most of the ligand's atoms. For this case, the contemporary presence of two structural isomers or two different complexes could be concluded [14c].

3.4. Pharmacology: Antiproliferative activity in vitro

Platinum(II) complexes of *N*4-ethyl 2-formyl and 2-acetylpyridine thiosemicarbazones showed cytotoxicity and were found to be able to overcome the *cisplatin* resistance of A2780/Cp8 cells [3a]. Pt(II) or Pd(II) complexes with 2-acetyl pyridine N(4)-ethyl-thiosemicarbazone, HAc4Et were tested in a panel of human tumor

Table 4
The antiproliferative activity *in vitro* of **1**–**4** (expressed as as $IC_{50} \pm SD$ (μM)) against MCF-7, T-24, A-549 and L-929 cancer cell lines.

	L-929	A-549	T-24	MCF-7
H_2pt	34.7 ± 1.5	n.a.	18.2 ± 0.5	160.4 ± 5.1
2	0.88 ± 0.04	7.2 ± 0.18	0.43 ± 0.03[a]	0.69 ± 0.03
3	1.02 ± 0.03	0.91 ± 0.05	19.73 ± 0.9	1.24 ± 0.30
4	0.95 ± 0.02	4.83 ± 0.31	4.52 ± 0.14	0.62 ± 0.03
Me_2SnCl_2	20.5 ± 1.0	12.7 ± 0.9	n.a.	8.5 ± 0.05
Ph_2SnCl_2	1.45 ± 0.08	9.89 ± 0.14	n.a.	0.84 ± 0.02
Cisplatin	0.69 ± 0.03	1.53 ± 0.10	41.66 ± 2.2	7.99±0.31

[a] In this case the IC_{50} is $\times 10^{-10}$.

cell lines of different origins (breast, colon, and ovary cancers), and *cisplatin*-refractory/resistant cell lines and were found to exhibit very remarkable growth inhibitory activities with mean IC_{50} values of 0.9–0.5 nM and support the hypothesis that both $[Pt(Ac4Et)_2]$ and $[Pd(Ac4Et)_2]$ complexes can be characterized by cellular pharmacological properties distinctly different from those of *cisplatin* [4d].

The compounds **1**–**4** were tested for their antiproliferative activity *in vitro* against the cells of three human cancer cell lines: MCF-7 (human breast cancer cell line), T-24 (bladder cancer cell line), A-549 (non-small cell lung carcinoma) and a mouse fibroblast L-929 cell line. The results of cytotoxic activity *in vitro* are expressed as IC_{50} – the concentration of compound (in μM) that inhibits a proliferation rate of the tumor cells by 50% as compared to control untreated cells, Table 4.

The ligand **1** is less cytotoxic compared to *cisplatin* against the L929, MCF7, non-toxic against A549 cell lines and more cytotoxic against T-24 cancer cell line. The diorganotin complexes **2**–**4** are in the same μM range compared to *cisplatin* against L929 cancer cell line. The diorganotin complexes **2**–**4** and Ph_2SnCl_2 are more cytotoxic compared to *cisplatin* against MCF-7 and T-24 cancer cell lines.

The IC_{50} values for **2** against MCF-7 and T-24 cell lines are 0.69 μM and 0.43×10^{-10} M, respectively and against A-549 and L-929 cell lines are 7.2 and 0.88 μM, respectively. Complex **2** is 11.6 and 10^6 times more active than *cisplatin* against MCF-7 and T-24 cell lines, respectively. The IC_{50} values for **3** against MCF-7 and T-24 cell lines are 1.24 and 19.73 μM, respectively and against A-549 and L-929 cell lines are 0.91 and 1.02 μM, respectively. Complex **3** is 6.4 times more active than *cisplatin* against MCF-7 cell line and 2.7 times more active than *cisplatin* against T-24 cell line. The IC_{50} values for **4** against MCF-7 and T-24 cell lines are 0.62 and 4.52 μM, respectively and against A-549 and L-929 cell lines are 4.83 and 0.95 μM, respectively. Complex **4** is 12.9 times more active than *cisplatin* against MCF-7 cell line and 9.2 times more active than *cisplatin* against T-24 cell line.

Selectivity was observed for complexes **2**–**4**, which were found especially active against MCF-7 and T-24 cancer cell lines. The most active of all was found the diorganotin complex **2**. The cytotoxic activity shown by these compounds against all these cancer cell lines indicates that coupling of **1** with $R_2Sn(IV)$ metal center result in metallic complexes with important biological properties and remarkable cytotoxic activity, since they display IC_{50} values in a μM range better to that of the antitumor drug *cisplatin*. Compound **2** is considered as agent with potential antitumor activity, and can therefore be candidate for further stages of screening *in vitro* and/or *in vivo*.

4. Conclusions

The reaction of dimethyltin(IV)oxide with pyruvic acid thiosemicarbazone (H_2pt) leads to the formation two *pseudo*-polymorfs based on triangular $[(CH_3)_2Sn(pt)]_3$ units [6e]. When diphenyltin(IV) oxide was reacted with H_2pt the monomer $[SnPh_2(pt)]$ (**2**) was formed. The stoichiometry of the complex indicates that $SnR_2(IV)$ is coordinated by the doubly charged anion pt^{2-} formed on the loss of the two protons from the carboxylato oxygen and thioamide nitrogen, N. Reaction of potassium pyruvic thiosemicarbazone with SnR_2Cl_2 (where R = Me or Ph) gives the cationic complexes $[SnMe_2(Hpt)(H_2O)]Cl$ (**3**) and $[SnPh_2(Hpt)(H_2O)]Cl$ (**4**). The stoichiometries of the cationic complexes indicate that $SnR_2(IV)$ is coordinated by the singly charged anion Hpt^- and one molecule of water. The formula of these diorganotin(IV) complexes were confirmed by elemental analysis, spectroscopic studies and by X-ray analysis.

The *in vitro* cytotoxic activity has been evaluated against the cells of three human cancer cell lines: MCF-7 (human breast cancer cell line), T-24 (bladder cancer cell line), A-549 (non-small cell lung carcinoma) and a mouse L-929 (a fibroblast-like cell line cloned from strain L). Selectivity was observed for complexes **2**–**4**, which were found especially active against MCF-7 and T-24 cancer cell lines. The most active of all was found the diorganotin complex **2**. Compound **2** is considered as agent with potential antitumor activity, and can therefore be candidates for further stages of screening *in vitro* and/or *in vivo*.

Supplementary data

CCDC 721898 and 721899 contain the supplementary crystallographic data for **2** and **3**. These data can be obtained free of charge via http://www.ccdc.cam.ac.uk/conts/retrieving.html, or from the Cambridge Crystallographic Data Centre, 12 Union Road, Cambridge CB2 1EZ, UK; fax: (+44) 1223-336-033; or e-mail: deposit@ccdc.cam.ac.uk.

Acknowledgments

J.W. thanks I.K.Y. for a scholarship for her Ph.D. We also thank the NMR centrum of University of Ioannina.

References

[1] (a) H. Beraldo, D. Gambino, Mini Rev. Med. Chem. 4 (2004) 159;
(b) A. Gomez Quiroga, C. Navarro Ranninger, Coord. Chem. Rev. 248 (2004) 119;
(c) R.A. Finch, M.-C. Liu, S.P. Grill, W.C. Rose, R. Loomis, K.M. Vasquez, Y.-C. Cheng, A.C. Sartorelli, Biochem. Pharmacol. 59 (2000) 983. and references cited therein;
(d) D.R. Richardson, Crit. Rev. Oncol./Hematol. 42 (2002) 267. and references cited therein.
[2] (a) A.E. Liberta, D.X. West, Biometals 5 (1992) 121;
(b) J.G. Cory, A.H. Cory, G. Rappa, A. Lorico, M.C. Liu, T.-S. Lin, A.C. Sartorelli, Biochem. Pharmacol. 48 (1994) 335;
(c) Z. Afrasiabi, E. Sinn, J. Chen, Y. Ma, S. Padhye, Toxicol. Appl. Pharmacol. 197 (2004) 40.
[3] (a) D. Kovala-Demertzi, P. Nath Yadav, M.A. Demertzis, M. Coluccia, J. Inorg. Biochem. 78/4 (2000) 347;
(b) Z. Iakovidou, E. Mioglou, D. Mourelatos, A. Kotsis, M.A. Demertzis, A. Papageorgiou, P.N. Yadav, D. Kovala-Demertzi, Anticancer Drugs 12 (2001) 65;
(c) D. Kovala-Demertzi, M.A. Demertzis, V. Varagi, A. Papageorgiou, D. Mourelatos, E. Mioglou, Z. Iakovidou, A. Kotsis, Chemotherapy 44 (1998) 421;
(d) D. Kovala-Demertzi, A. Domopoulou, M.A. Demertzis, C.P. Raptopoulou, A. Terzis, Polyhedron 13 (12) (1994) 1917.
[4] (a) D. Kovala-Demertzi, M.A. Demertzis, E. Filiou, A.A. Pantazaki, P.N. Yadav, J.R. Miller, Y. Zheng, D.A. Kyriakidis, Biometals 16 (2003) 411;
(b) A. Papageorgiou, Z. Iakovidou, D. Mourelatos, E. Mioglou, L. Boutis, A. Kotsis, D. Kovala-Demertzi, A. Domopoulou, D.X. West, M.A. Demertzis, Anticancer Res. 17 (1997) 247;
(c) D. Kovala-Demertzi, A. Domopoulou, M.A. Demertzis, G. Valle, A. Papageorgiou, J. Inorg. Biochem. 68 (1997) 147;
(d) D. Kovala-Demertzi, A. Boccarelli, M.A. Demertzis, M. Coluccia, Chemotherapy 53 (2007) 148;
(e) D. Kovala-Demertzi, A. Alexandratos, A. Papageorgiou, P.N. Yadav, P. Dalezis, M.A. Demertzis, Polyhedron 27 (2008) 2731.

[5] (a) D. Kovala-Demertzi, M.A. Demertzis, J.R. Miller, C. Papadopoulou, C. Dodorou, G. Filousis, J. Inorg. Biochem. 86 (2001) 555;
(b) D. Kovala-Demertzi, J.R. Miller, N. Kourkoumelis, S.K. Hadjikakou, M.A. Demertzis, Polyhedron 18 (1999) 1005;
(c) D. Kovala-Demertzi, A. Domopoulou, M.A. Demertzis, A. Papageorgiou, D.X. West, Polyhedron 16 (20) (1997) 3625;
(d) D. Kovala-Demertzi, P.N. Yadav, J. Wiecek, S. Skoulika, T. Varadinova, M.A. Demertzis, J. Inorg. Biochem. 100 (2006) 1558;
(e) D. Kovala-Demertzi, A. Papageorgiou, L. Papathanasis, A. Alexandratos, P. Dalezis, J.R. Miller, M.A. Demertzis, Eur. J. Med. Chem. 44 (2009) 1296.

[6] (a) M.B. Ferrari, G.G. Fava, C. Pelizzi, P. Tarasconi, J. Chem. Soc., Dalton Trans. (1992) 2153;
(b) M.B. Ferrari, G.G. Fava, G. Pelosi, P. Tarasconi, Polyhedron 19 (2000) 1895;
(c) M.D. Timken, S.R. Wilson, D.N. Hendrickson, Inorg. Chem. 24 (1985) 3450;
(d) N.I. Dodoff, D. Kovala-Demertzi, M. Kubiak, J. Kuduk-Jaworska, A. Kochel, G.A. Gorneva, Z. Naturforsch. 61b (2006) 1;
(e) D. Kovala-Demertzi, J. Wiecek, J.C. Plakatouras, Z. Ciunik, CrystEngCommun. 10 (2008) 1291.

[7] (a) J.J. Zuckerman (Ed.), Organotin compounds: new chemistry and applications, Advances in Chemistry Series, vol. 157, American Chemical Society, Washington, 1976;
(b) C.J. Evans, S. Karpel, Organotin Compounds in Modern Technology, J. Organomet. Chem. Library 16, Elsevier, 1985.;
(c) S.J. Blunden, P.A. Cusack, R. Hill, Industrial Uses of Tin Chemicals, Royal Society of Chemistry, London, 1985.

[8] (a) M. Gielen, Appl. Organomet. Chem. 16 (2002) 481;
(b) D. Kovala-Demertzi, J. Organomet. Chem. 691 (2006) 1767;
(c) V.N. Dokorou, M.A. Demertzis, J.P. Jasinski, D. Kovala-Demetrzi, J. Organomet. Chem. 689 (2004) 317;
(d) V. Dokorou, D. Kovala-Demettzi, J.P. Jasinsky, A. Galani, M.A. Demertzis, Helv. Chim. Acta 87 (2004) 1940;
(e) D. Kovala-Demertzi, V. Dokorou, Z. Ciunik, N. Kourkoumelis, M.A. Demertzis, Appl. Organomet. Chem. 16 (2002) 360.

[9] (a) M. Sheldrick, Acta Crystallogr. A46 (1990) 467;
(b) G.M. Sheldrick, SHELXL97, program for crystal structure refinement, University of Göttingen, 1997;
(c) A.L. Spek, PLATON, A Multipurpose Crystallographic Tool, A Program for the Automated Generation of a Variety of Geometrical Entities, Utrecht University, Utrecht, The Netherlands, 2001;
(d) L.J. Farrugia, J. Appl. Cryst. 32 (1999) 837.

[10] (a) P. Skehan, R. Storeng, D. Scudiero, A. Monks, J. Mcmahon, D. Vistica, J.T. Warren, H. Bokesch, S. Kenney, M.R. Boyol, J. Natl. Cancer Inst. 82 (1990) 1107;
(b) M. Ohno, T. Abe, J. Immunol. Meth. 145 (1-2) (1991) 199;
(c) D. Kovala-Demertzi, A. Galani, N. Kourkoumelis, J.R. Miller, M.A. Demertzis, Polyhedron 26 (12) (2007) 2871.

[11] A. Addison, R.T. Nageswara, J. Reedijk, J. Van Rijn, G.C. Verschoor, J. Chem. Soc., Dalton Trans. (1984) 1349.

[12] (a) G.A. Jeffrey, H. Maluszynska, J. Mitra, Int. J. Biol. Macromol. 7 (1985) 336;
(b) T. Steiner, B. Lutz, J. van der Maas, A.M.M. Schreurs, J. Kroon, M. Tamm, Chem. Commun. (1998) 171;
(c) M.C. Etter, Acc. Chem. Res. 23 (1990) 120;
(d) G.R. Desiraju, Acc. Chem. Res. 24 (1991) 290.

[13] K. Nakamoto, Infrared and Raman Spectra of Inorganic and Coordination Compounds, fourth ed., Wiley, New York, 1986.

[14] (a) V. Dokorou, Z. Ciunik, U. Russo, D. Kovala-Demertzi, J. Organomet. Chem. 630 (2001) 205;
(b) D. Kovala-Demertzi, N. Kourkoumelis, A. Koutsodimou, A. Moukarika, E. Horn, E.R.T. Tiekink, J. Organomet. Chem. 620 (2001) 194;
(c) A. Pellerito, T. Fiore, C. Pellerito, A. Fontana, R. Di Stefano, L. Pellerito, M.T. Cambria, C. Mansueto, J. Inorg. Biochem. 721 (1998) 115;
(d) A. Galani, M.A. Demertzis, M. Kubicki, D. Kovala-Demertzi, Eur. J. Inorg. Chem. 9 (2003) 1761;
(e) M.A. Demertzis, S.K. Hadjikakou, D. Kovala-Demertzi, A. Koutsodimou, M. Kubicki, Helv. Chim. Acta 83 (2000) 2787.

was characterized by UV–Vis, IR and NMR spectroscopy, as well as by X-ray crystallography. The structure of this complex enables comparisons with the previously characterized [Ni{Ph_2PNPPh_2-*P*,*P*}$_2$] [29] and [Ni{$Ph_2P(Se)NP(Se)Ph_2$-*Se*,*Se*}$_2$] [30] complexes, in which there are four- and six-membered rings, respectively. Furthermore, while investigating the coordination between $Ph_2P(Se)N\{(S)\text{-}CH(CH_3)Ph\}PPh_2$ [31] and Ni(II), single crystals were isolated, the analysis of which revealed the *trans*-[Ni{$Ph_2P(Se)$-$NPPh_2$-*Se*,*P*}{$Ph_2P(Se)N(H)PPh_2$-*Se*,*P*}]$Cl\cdot CH_2Cl_2\cdot H_2O$ (**2**) structure, which contains one Ni–Se–P–N(H)–P and one Ni–Se–P–N–P ring, in the same molecule. This unprecedented structure makes possible to compare the structural characteristics of such rings in the same molecule, as well as in the structure of **1**.

2. Experimental

2.1. UV–Vis, IR and NMR spectroscopy

Electronic spectra were recorded in a Carry 300 Varian spectrophotometer. IR spectra were run in the range 4000–200 cm^{-1} on a Perkin–Elmer 883 IR spectrophotometer, as KBR discs. $^{31}P\text{–}\{^1H\}$ NMR spectra were recorded in a Varian Unity Plus 300 MHz instrument, operating at 121 MHz, using $CDCl_3$ solutions. The ^{31}P chemical shifts are relative to 85% H_3PO_4.

2.2. X-ray crystal structure determination

A dark green crystal of **1** (0.15 × 0.20 × 0.30 mm) was mounted in air, and a yellow–brown crystal of **2** (0.07 × 0.36 × 0.48 mm) was taken directly from the mother liquor and immediately cooled to −93 °C. Diffraction measurements for **1** were made on a Crystal Logic Dual Goniometer diffractometer using graphite monochromated Mo Kα radiation. Unit cell dimensions were determined and refined by using the angular settings of 25 automatically centered reflections in the range $11 < 2\theta < 23°$. Intensity data were recorded using a $\theta\text{–}2\theta$ scan. Three standard reflections monitored every 97 reflections showed less than 3% variation and no decay. Lorentz, polarization corrections were applied using CRYSTAL LOGIC software. Diffraction measurements for **2** were made on a Rigaku R-AXIS SPIDER Image Plate diffractometer using graphite monochromated Mo Kα radiation. Data collection (ω-scans) and processing (cell refinement, data reduction and empirical absorption correction) were performed using the CRYSTALCLEAR program package [32]. Important crystallographic and refinement data are listed in Table 1. The structures were solved by direct methods using SHELXS-97 [33] and refined by full-matrix least-squares techniques on F^2 with SHELXL-97 [34]. Further crystallographic details for **1**: $2\theta_{max} = 50°$; reflections collected/unique/used, 3904/3664 [$R_{int} = 0.0190$]/3664; 340 parameters refined; $(\Delta/\sigma)_{max} = 0.001$; $(\Delta\rho)_{max}/(\Delta\rho)_{min} = 0.664/-0.306$ e/Å^3; R/R_w (for all data), 0.0471/0.0841. Hydrogen atoms were located by difference maps and were refined isotropically. All non-H atoms were refined anisotropically. Further crystallographic details for **2**: $2\theta_{max} = 52°$; reflections collected/unique/used, 93095/9494 [$R_{int} = 0.0426$]/9494; 723 parameters refined; $(\Delta/\sigma)_{max} = 0.002$; $(\Delta\rho)_{max}/(\Delta\rho)_{min} = 0.922/-0.705$ e/Å^3; R/R_w (for all data), 0.0331/0.0841. Hydrogen atoms were located by difference maps and were refined isotropically. All non-H atoms were refined anisotropically.

Table 1
Crystallographic data for **1** and **2**.

	1	**2**
Formula	$C_{48}H_{40}N_2NiP_4Se_2$	$C_{49}H_{45}Cl_3N_2NiOP_4Se_2$
Fw	985.34	1124.73
Space group	$P2_1/n$	$P2_1/n$
a (Å)	9.345(3)	9.7772(2)
b (Å)	21.908(8)	16.9296(3)
c (Å)	10.994(3)	29.4621(5)
β (°)	102.85(1)	96.329(1)
V (Å^3)	2194.4(12)	4846.9(2)
Z	2	4
T (°C)	25	−93
Radiation	Mo Kα	Mo Kα
$\rho_{calc.}$ (g cm^{-3})	1.491	1.541
μ (mm^{-1})	2.283	2.239
R_1[a]	0.0327[b]	0.0331[c]
wR_2[a]	0.0775[b]	0.0797[c]

[a] $w = 1/[\sigma^2(F_o^2) + (\alpha P)^2 + bP]$ and $P = ((\max F_o^2, 0) + 2F_C^2)/3$, $R_1 = \sum(|F_o| - |F_c|)/\sum(|F_o|)$ and $wR_2 = \{\sum[w(F_o^2 - F_C^2)^2]/\sum[w(F_o^2)^2]\}^{1/2}$.
[b] For 3024 reflections with $I > 2\sigma(I)$.
[c] For 7954 reflections with $I > 2\sigma(I)$.

2.3. Synthesis

All manipulations were carried out under a pure Ar atmosphere. All chemical reagents used were purchased from Aldrich. The ligands $Ph_2P(Se)NHPPh_2$ [23] and $Ph_2P(Se)N\{(S)\text{-}CH(CH_3)Ph\}PPh_2$ [31] were prepared according to published procedures.

2.3.1. trans-[Ni{$Ph_2P(Se)NPPh_2$-*Se*,*P*}$_2$] (**1**)

^{t}BuOK (0.0591 g, 0.5 mmol) was added to a solution of $Ph_2P(Se)NHPPh_2$ (0.2322 g, 0.5 mmol) in methanol (20 mL) and the mixture was stirred at room temperature for 30 min. $NiCl_2\cdot 6H_2O$ (0.0594 g, 0.25 mmol) was subsequently added to the mixture, which was stirred for additional 2 h. The resulting dark green precipitate was removed by filtration, washed with methanol (2 × 10 mL) and dried *in vacuo*. Yield: 0.1841 g, 0.1868 mmol, 75%. *Anal.* Calc. for $C_{48}H_{40}N_2NiP_4Se_2$: C, 58.51; H, 4.09; N, 2.84. Found: C, 57.54; H, 4.34; N, 2.79%. IR (cm^{-1}) ν(P–N–P) 1127, ν(P–Se) 541. $^{31}P\text{–}\{^1H\}$ NMR ($CDCl_3$): $\delta = 89.5$ [t, P(Ni), N 167.2 Hz], $\delta = 57.9$ [t, P(Se), N 166.9 Hz].

2.3.2. trans-[Ni{$Ph_2P(Se)NPPh_2$-*Se*,*P*}{$Ph_2P(Se)N(H)PPh_2$-*Se*,*P*}]$Cl\cdot CH_2Cl_2\cdot H_2O$ (**2**)

An appropriate amount of the ligand $Ph_2P(Se)N\{(S)\text{-}CH(CH_3)Ph\}PPh_2$ (0.1000 g, 0176 mmol) was added to a solution of $NiCl_2\cdot 6H_2O$ (0.0418 g, 0.176 mmol) in THF (10 mL). The mixture was stirred for 8 h. During the first hour, the colour of the mixture was dark red and finally changed to brown. The brown precipitate, obtained by addition of 15 mL of Et_2O, was then removed by filtration and dried *in vacuo*. Crystals were obtained from a 1:3 mixture of CH_2Cl_2/*n*-hexane.

3. Results and discussion

3.1. Synthesis and spectroscopic study

The reaction of $Ph_2P(Se)NHPPh_2$ with $NiCl_2\cdot 6H_2O$, in the presence of ^{t}BuOK for the *in situ* deprotonation of the ligand, gave **1** in satisfactory yield, according to the metathesis reaction:

$$2[K\{Ph_2P(Se)NPPh_2\}] + NiCl_2\cdot 6H_2O \rightarrow [Ni\{Ph_2P(Se)NPPh_2\}_2] + 2KCl + 6H_2O$$

Single crystals of **1** were obtained by adding *n*-hexane into a CH_2Cl_2 solution of **1**. It is of interest to note that an attempt, in a different experiment, to synthesize [Ni{$Ph_2P(Se)NHPPh_2$-*Se*,*P*}Cl_2] by mixing equivalent amounts of [Ni$(PPh_3)_2Cl_2$] and $Ph_2P(Se)NHPPh_2$, in the absence of ^{t}BuOK, afforded crystals, the analysis of which revealed the formation of **1**.

On the other hand, crystals of **2** were isolated while studying the reaction between $NiCl_2\cdot 6H_2O$ and the ligand $Ph_2P(Se)N\{(S)\text{-}CH(CH_3)Ph\}PPh_2$ [31]. The IR spectrum of these crystals showed

the presence of N–H bond [3042 cm^{-1}, ν(N–H)], while the ^{31}P NMR showed additional peaks compared to the triplets of **1** (*vide infra*). Therefore, the crystals were studied by X-ray crystallography but no attempt was made to analyse their IR and NMR spectra. The structure of **2** contains one Ni–Se–P–N(H)–P and one Ni–Se–P–N–P five-membered ring (*vide infra*). Therefore, cleavage of the N–C bond and removal of the –C{CH(CH_3)Ph} moiety is responsible for the formation of **2**. A similar observation was previously reported concerning the interaction of M(III) precursors, M = Rh, Ir, with the same ligand $Ph_2P(Se)N\{(S)$-CH(CH_3)Ph$\}PPh_2$, in acetone, which resulted in the formation of the $[(Cp^*)MCl\{Ph_2P(S)NHPPh_2$-*S*,*P*$\}]BF_4$ complexes [19]. The correlation between this type of cleavage reactions and the nature of the solvent in which the reaction takes place will be further investigated.

Fig. S1 shows the electronic spectrum of **1** in CH_2Cl_2. A band at 378 nm is well defined (ε = 5860 M^{-1} cm^{-1}), whereas there are two shoulders at 270 and 307 nm (ε = 27 660 and 19 190 M^{-1} cm^{-1}). Owing to the rather large extinction coefficients determined, most likely these bands correspond to charge transfer transitions [35]. From the spectrum of **1**, it was not possible to clearly identify any bands due to d–d transitions, although a very broad and not well defined feature is observed at about 490 nm, in agreement with the spectra of typical square–planar complexes of Ni(II) [35].

One of the most characteristic IR peaks of chalcogenated imidodiphosphinate systems is due to ν(P–E), which in the case of **1** is observed at 541 cm^{-1} [ν(P–Se)]. Since the free ligand $Ph_2P(Se)NHPPh_2$ exhibits the corresponding IR peak at 551 cm^{-1} [23], it is concluded that the P–Se bond in **1** is slightly weakened compared to the free ligand. This is a typical observation concerning the coordination chemistry of either bis-chalcogenated or monooxidised imidodiphosphinate ligands [2–5].

The assignments in the ^{31}P NMR spectrum of the two different P atoms of **1**, namely the metal bound, P(Ni), and Se-bound, P(Se), are based on the fact that the former is less shielded than the latter. This is borne out by the fact that the P(Se)–N bond is stronger compared to the corresponding P(Ni)–N bond (*vide infra*). The ^{31}P NMR spectrum of **1** (Fig. 1), shows a pair of mutually coupled triplets, consisting of an AA′XX′ type pattern. These triplets are "deceptive" since, based on the structure of **1**, a pair of mutually coupled doublets would have been expected instead. Similar patterns were previously observed in analogous complexes, like *trans*-$[M\{Ph_2P(Se)CH_2PPh_2$-*Se*,*P*$\}_2]^{2+}$, M = Pt [36], Pd [37], *trans*-$[M\{Ph_2P(Se)N(H)PPh_2$-*Se*,*P*$\}_2]^{2+}$, M = Pd [23], Pt [23] and *trans*-$[Ni\{^iPr_2P(Se)NP^iPr_2$-*Se*,*P*$\}_2]$ [38]. In all these cases, the separation of the outermost lines of each triplet, N [= J(A–X) + J(A–X′)], is reported [23]. In the case of **1**, the values of N are 167.2 and 166.9 Hz. The above pattern in the ^{31}P NMR spectrum of **1** shows that the *trans*-Ni(*Se*,*P*)$_2$ arrangement, observed in the solid state, is maintained in solution. Moreover, the ^{31}P chemical shifts in **1** are in the diamagnetic part of the spectrum, which provides evidence that the geometry of the $NiSe_2P_2$ core of the complex remains square–planar in solution. This is in contrast to the analogous square–planar $NiSe_4$-containing complexes, in which the corresponding ^{31}P NMR peaks are in the paramagnetic part of the spectrum, most likely due to the formation of tetrahedral $NiSe_4$ centers, as was shown in the case of $[Ni\{^iPr_2P(Se)NP(Se)^iPr_2$-*Se*,*Se*$\}_2]$ [8]. The above difference shows that in the latter case the coordination sphere, which contains six-membered chelating rings, is more flexible in solution compared to complex **1** with five-membered rings.

3.2. Molecular structures

The structures of **1** and **2** were determined by single crystal X-ray diffraction. The crystal data and refinement characteristics are shown in Table 1. Selected bond lengths and angles are listed in Table 2. In the case of **2**, data are shown separately for its two five-membered rings. The only available crystallographic structures for monooxidised imidodiphosphinate ligands are for $Ph_2P(O)NHPPh_2$ [10] and $^iPr_2P(Se)NHP^iPr_2$ [39]. Therefore, it is not possible to make direct comparisons with the structures of **1** and **2**. However, from the data of Table 2, we can draw the conclusions described in the following paragraphs.

3.2.1. *trans*-[Ni{$Ph_2P(Se)NPPh_2$-*Se*,*P*}$_2$] (**1**)

The ORTEP representation of the crystal structure is shown in Fig. 2. The crystals of **1** contain discrete monomeric molecules, exhibiting square–planar $NiSe_2P_2$ cores, in which Ni(II) ions are coordinated by two (*Se*,*P*) chelates in *trans* arrangement. Overall, the structure contains a center of symmetry, and therefore the two five-membered Ni–Se–P–N–P rings are identical. The equivalent equatorial Ni–Se and N–P bond lengths are 2.296 and 2.239 Å, respectively, and very similar to the corresponding bond

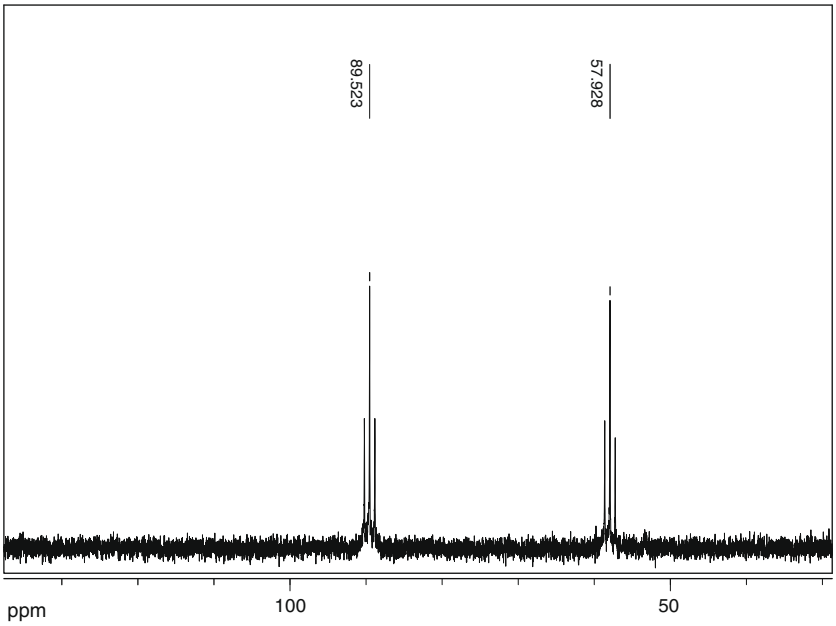


Fig. 1. ^{31}P NMR spectrum of **1** in $CDCl_3$.

Table 2
Selected bond lengths (Å) and angles (°) for **1** and **2**.

Complex	**1**	**2**	
Distances			
		{Ni–Se–P–N–P} ring	{Ni–Se–P–N(H)–P} ring
Ni–Se	2.2961(5)	(Ni–Se2) 2.2995(4)	(Ni–Se1) 2.3057(4)
Ni–P1	2.2391(9)	(Ni–P4) 2.2404(7)	(Ni–P2) 2.2063(7)
Se–P2	2.2098(10)	(Se2–P3) 2.2210(7)	(Se1–P1) 2.1939(7)
P1–N	1.639(3)	(N2–P4) 1.644(2)	(N1–P2) 1.693(2)
P2–N	1.586(3)	(N2–P3) 1.593(2)	(N1–P1) 1.639(2)
Angles			
Se–Ni–Se	180.00(3)	(Se1–Ni–Se2) 178.228(18)	
P1–Ni–P1	180.00(3)	(P2–Ni–P4) 178.34(3)	
P1–Ni–Se	91.16(3)	(P4–Ni–Se2) 90.53(2)	(P2–Ni–Se1) 91.28(2)
Ni–P1–N	114.63(9)	(Ni–P4–N2) 114.93(8)	(Ni–P2–N1) 111.36(8)
P1–N–P2	118.42(15)	(P3–N2–P4) 117.42(13)	(P1–N1–P2) 120.08(13)
N–P2–Se	111.33(10)	(N2–P3–Se2) 111.43(8)	(N1–P1–Se1) 107.50(8)
P2–Se–Ni	98.04(3)	(P3–Se2–Ni) 99.28(2)	(P1–Se1–Ni) 101.38(2)
P1–Ni–Se′	88.84(3)	(P2–Ni–Se2) 87.98(2), (P4–Ni–Se1) 90.18(2)	

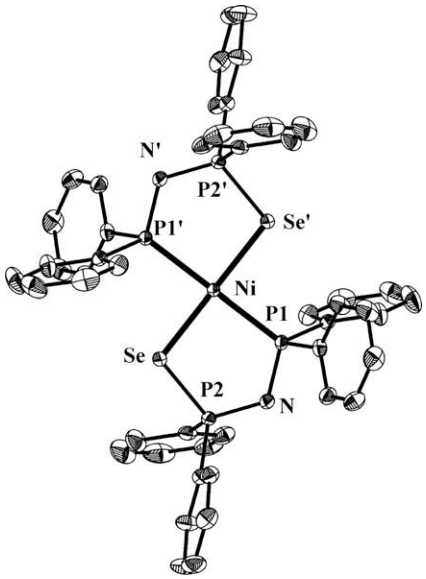


Fig. 2. Partially labelled ORTEP plot of **1** with ellipsoids drawn at the 30% probability level. Primed atoms are generated by symmetry (′ = −*x*, 1−*y*, −*z*).

lengths (2.305 and 2.239 Å, respectively) in the recently characterized *trans*-[Ni{^{i}Pr$_2$P(Se)NP^{i}Pr$_2$-*Se*,*P*}$_2$] complex [38]. The Se–Ni–P and P–N–P angles in **1** (91.16 and 118.42°) and the latter complex (91.33 and 119.03°) are also very similar. Therefore, the difference of the R peripheral groups in the two complexes (Ph or ^{i}Pr) has no effect in their structural characteristics. This observation is in contrast to the marked difference between the corresponding [Ni{Ph$_2$P(Se)NP(Se)Ph$_2$-*Se*,*Se*}$_2$] and [Ni{^{i}Pr$_2$P(Se)NP(Se)^{i}Pr$_2$-*Se*,*Se*}$_2$] complexes, since the former crystallizes in square–planar [30] and the latter in a mixture of tetrahedral and square–planar NiSe$_4$ polymorphs [8]. It is concluded that the six-membered Ni–Se–P–N–P–Se rings in these complexes provide structural flexibility to the NiSe$_4$ core, the geometry of which is affected by the nature of the R groups, not only in solution (*vide supra*) but also in the solid state. This is in contrast to the corresponding five-membered Ni–Se–P–N–P rings of **1** and *trans*-[Ni{^{i}Pr$_2$P(Se)NP^{i}Pr$_2$-*Se*,*P*}$_2$] [38], which maintain a rather rigid square–planar NiSe$_2$P$_2$ coordination sphere, irrespective of the nature of the R groups.

The P–N bond lengths in Ni{Ph$_2$P(Se)NP(Se)Ph$_2$-*Se*,*Se*}$_2$] are almost identical (1.600 and 1.602 Å) [30]. On the other hand, in the case of **1**, these bond lengths are not equal (P2–N, 1.586 and P1–N, 1.639 Å). Therefore, the P–N bond adjacent to the Se atom is strengthened, whereas the other P–N bond is weakened, compared to the P–N bonds in Ni{Ph$_2$P(Se)NP(Se)Ph$_2$-*Se*,*Se*}$_2$]. Related to the above effects, it should be noted that the Ni–Se bond length in **1** (2.296 Å) is smaller by 0.054 Å compared to the Ni–Se bond lengths (average 2.350 Å) in [Ni{Ph$_2$P(Se)NP(Se)Ph$_2$-*Se*,*Se*}$_2$] [30]. For comparison, the Ni–P bond lengths of **1** (2.239 Å) and [Ni{Ph$_2$PNPPh$_2$-*P*,*P*}$_2$] (2.222 Å) [29] differ only by 0.02 Å. These differences might be justified by the higher electronegativity of Se compared to P, which, in complex **1**, would result in electron density flow from N to P2 to Se. A similar trend is also observed in the case of *trans*-[Ni{^{i}Pr$_2$P(Se)NP^{i}Pr$_2$-*Se*,*P*}$_2$] [38], which should be extended in other systems containing five-membered M–E–P–N–P rings by the coordination of monooxidised imidodiphosphinate ligands [10–26].

By comparing the endocyclic angles X–Ni–Y, X, Y = P, P or Se, P or Se, Se, in [Ni{Ph$_2$PNPPh$_2$-*P*,*P*}$_2$] (67.43°) [29], complex **1** (91.16°) and [Ni{Ph$_2$P(Se)NP(Se)Ph$_2$-*Se*,*Se*}$_2$] (99.41°) [30], it is obvious that only **1** exhibits an angle very close to the value of the ideal square–planar geometry, a fact that should be critical in conserving its square–planar NiSe$_2$P$_2$ core geometry in solution (*vide supra*).

3.2.2. *trans*-[Ni{Ph$_2$P(Se)NPPh$_2$-*Se*,*P*}{Ph$_2$P(Se)N(H)PPh$_2$-*Se*,*P*}]Cl·CH$_2$Cl$_2$·H$_2$O (**2**)

The ORTEP representation of the crystal structure is shown in Fig. 3. The crystal was shown to contain the [Ni{Ph$_2$P(Se)NPPh$_2$-*Se*,*P*}{Ph$_2$P(Se)N(H)PPh$_2$-*Se*,*P*}]$^{+}$ ion, along with a Cl^{-} as a counter ion, one solvent molecule (CH$_2$Cl$_2$) and a H$_2$O molecule. As in the case of **1**, the system contains square–planar NiSe$_2$P$_2$ cores, in which Ni(II) ions are coordinated by two (*Se*,*P*) chelates in *trans* arrangement. However, unlike **1**, complex **2** contains two different rings, one protonated at the N atom, Ni–Se–P–N(H)–P, and one unprotonated, Ni–Se–P–N–P, a fact that introduces asymmetry to the system, and affects the bond lengths and angles (Table 2). The Ni–Se bond lengths in **2** are rather similar to those in **1**. On the other hand, a notable difference is the *ca.* 0.03 Å decrease in the Ni–P2 bond length, in the Ni–Se–P–N(H)–P ring, compared to both the Ni–Se–P–N–P ring of **2**, as well as of **1**.

The trend in the P–N bond lengths described above for **1** is conserved in **2** (Table 2). Moreover, the presence of the N–H bond in the Ni–Se–P–N(H)–P ring of **2** weakens the P–N bonds compared to both the Ni–Se–P–N–P ring of **2**, as well as of **1**, since part of the electronic density of N is devoted to the N–H bond formation.

With respect to the angles in **1** and **2**, Table 2 shows that these are rather similar between **1** and the Ni–Se–P–N–P ring of **2**, but

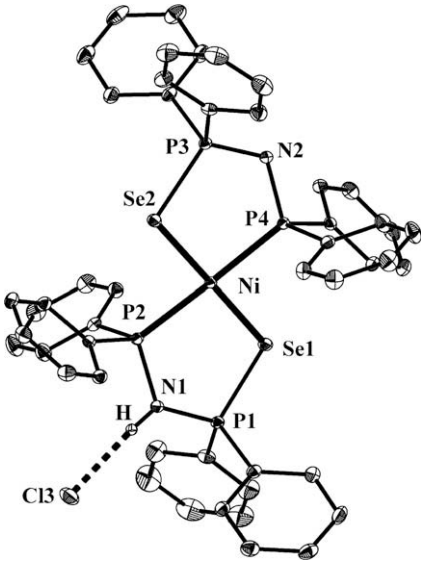


Fig. 3. Partially labelled ORTEP plot of **2** with ellipsoids drawn at the 30% probability level.

there are notable differences in the angles of the Ni–Se–P–N(H)–P ring of **2**. For instance, the P–N–P angle in the latter is increased by 2.7°, whereas the N–P–Se angle is decreased by 3.9°, compared to the Ni–Se–P–N–P ring of **2**. Moreover, the P–N–P angle in the Ni–Se–P–N(H)–P ring of **2** is larger by 1.7° compared to the equivalent P–N–P angles of **1**. Also, the P–Se–Ni angle in the Ni–Se–P–N(H)–P ring of **2** is larger by 3.3°, whereas the N–P–Se is smaller by 3.8° and the N–P–Ni smaller by 3.3° compared to the corresponding angles of **1**. The P–N–P angles in other complexes containing M–Se–P–N(H)–P rings are close to 120° [21,23], indicating an sp^2 hybridization of the N atom [40].

It is of interest that in the case of [Pd{$Ph_2P(S)NP(S)Ph_2$-*S*,*S*}{$Ph_2P(S)N(H)P(S)Ph_2$-*S*,*S*}]Cl [41], which contains one Ni–S–P–N(H)–P–S and one Ni–S–P–N–P–S six-membered ring, the latter contains longer P–S bonds and shorter P–N bonds compared to the former [41]. However, the angles in the two rings are rather similar [41], unlike what has been described above for **1** and **2**.

In [Pd{$Ph_2P(S)NP(S)Ph_2$-*S*,*S*}{$Ph_2P(S)N(H)P(S)Ph_2$-*S*,*S*}]Cl [41], the counter ion Cl^- is hydrogen bonded to the Ni–S–P–N(H)–P–S ring (distances H···Cl 2.20 Å, N···Cl 2.93 Å and angle N–H···Cl 134°) [41]. In the case of the Ni–Se–P–N(H)–P ring of **2**, the analogous distances and angle are H···Cl, 2.19 Å, N···Cl, 3.01 Å and N–H···Cl, 175.2°. The situation is analogous to other systems which contain M–Se–P–N(H)–P five-membered rings, like *trans*-[Pt{$Ph_2P(Se)N(H)PPh_2$-*Se*,*P*}$_2$]Cl_2 [23] and [Ag{$Ph_2P(Se)N(H)PPh_2$-*Se*,*P*}$_2$]Br [21].

The atoms that are coordinated to the Ni(II) ions in **1** and **2** are in the same plane. The five-membered rings exhibit a pseudo-boat conformation. The protonation at the N atom of one ring in **2** does not seem to cause major changes to the ring conformation.

4. Conclusions

The work described here adds more information on the structural and spectroscopic properties of coordination compounds containing monooxidised imidodiphosphinate ligands. The main conclusions drawn from the analysis of spectroscopic and structural data, are the following: (i) The square–planar *trans*-Ni(*Se*,*P*)$_2$ arrangement in **1,** established in the solid state by X-ray crystallography, is maintained in solution and justifies the "deceptive" triplets in the diamagnetic part of its ^{31}P NMR spectrum. (ii) Availability of the structures of **1** and **2** makes possible to establish structural effects due to the higher electronegativity of Se compared to P, as well as to the protonation/deprotonation at the N atom of the five-membered rings. These effects will be further probed by appropriate theoretical calculations, as in the case of the analogous bis-chalcogenated imidodiphosphinate ligands and their complexes [40]. In addition, the NMR properties of **1** will be further investigated by studies in the solid state [42].

Acknowledgements

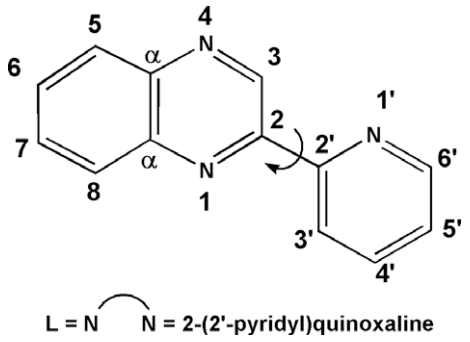
We would like to thank the Special Account of the University of Athens (Grant 70/4/7575), as well as the Empirikion Foundation, for funding. Eleftherios Ferentinos is thanked for technical assistance and helpful discussions. This article is dedicated with gratitude to Dr. Aris Terzis, whose contribution, over the years, to the advancement of our projects, has been invaluable.

Appendix A. Supplementary data

CCDC 721470 and 721471 contains the supplementary crystallographic data for **1** and **2**, respectively. These data can be obtained free of charge via http://www.ccdc.cam.ac.uk/conts/retrieving.html, or from the Cambridge Crystallographic Data Centre, 12 Union Road, Cambridge CB2 1EZ, UK; fax: (+44) 1223-336-033; or e-mail: deposit@ccdc.cam.ac.uk. Supplementary data associated with this article can be found, in the online version, at doi:10.1016/j.poly.2009.05.006.

References

[1] F.T. Wang, J. Najdzionek, K.L. Leneker, H. Wasserman, D.M. Braitsch, Synth. React. Inorg. Met. Org. Chem. 8 (1978) 119.
[2] T.Q. Ly, J.D. Woollins, Coord. Chem. Rev. 176 (1998) 451.
[3] C. Silvestru, J.E. Drake, Coord. Chem. Rev. 223 (2001) 117.
[4] I. Haiduc, J. Organomet. Chem. 623 (2001) 29.
[5] I. Haiduc, Comprehensive Coordination Chemistry II, Elsevier Ltd., Amsterdam, 2003.
[6] G.G. Briand, T. Chivers, M. Parvez, Angew. Chem., Int. Ed. Engl. 41 (2002) 3468.
[7] T. Chivers, J. Konu, J.S. Ritch, M.C. Copsey, D.J. Eisler, H.M. Tuononen, J. Organomet. Chem. 692 (2007) 2658.
[8] N. Levesanos, S.D. Robertson, D. Maganas, C.P. Raptopoulou, A. Terzis, P. Kyritsis, T. Chivers, Inorg. Chem. 47 (2008) 2949.
[9] J.D. Woollins, J. Chem. Soc., Dalton Trans. (1996) 2893.
[10] P. Bhattacharyya, A.M.Z. Slawin, M.B. Smith, J.D. Woollins, Inorg. Chem. 35 (1996) 3675.
[11] R. Haid, R. Gutmann, G. Czermak, C. Langes, W. Oberhauser, H. Kopacka, K.H. Ongania, P. Bruggeller, Inorg. Chem. Commun. 6 (2003) 61.
[12] R. Rossi, L. Marvelli, A. Marchi, L. Magon, V. Bertolasi, V. Ferretti, J. Chem. Soc., Dalton Trans. (1994) 339.
[13] A.M.Z. Slawin, M.B. Smith, J.D. Woollins, J. Chem. Soc., Dalton Trans. (1996) 1283.
[14] K.A. Chatziapostolou, K.A. Vallianatou, A. GrigoropouloS, C.P. Raptopoulou, A. Terzis, I.D. Kostas, P. Kyritsis, G. Pneumatikakis, J. Organomet. Chem. 692 (2007) 4129.
[15] M.R.J. Elsegood, M.B. Smith, S.H. Dale, Acta Crystallogr., Sect. C-Cryst. Struct. Commun. 63 (2007) M7.
[16] M.B. Smith, A.M.Z. Slawin, Inorg. Chim. Acta 299 (2000) 172.
[17] J. Parr, M.B. Smith, M.R.J. Elsegood, J. Organomet. Chem. 664 (2002) 85.
[18] M.B. Smith, A.M.Z. Slawin, J.D. Woollins, Polyhedron 15 (1996) 1579.
[19] E. Simon-Manso, M. Valderrama, P. Gantzel, C.P. Kubiak, J. Organomet. Chem. 651 (2002) 90.
[20] R. Rossi, A. Marchi, L. Marvelli, M. Peruzzini, U. Casellato, R. Graziani, J. Chem. Soc., Dalton Trans. (1992) 435.
[21] J. Wilton-Ely, A. Schier, H. Schmidbaur, J. Chem. Soc., Dalton Trans. (2001) 3647.
[22] W.H. Leung, K.K. Lau, Q.F. Zhang, W.T. Wong, B.Z. Tang, Organometallics 19 (2000) 2084.
[23] P. Bhattacharyya, A.M.Z. Slawin, D.J. Williams, J.D. Woollins, J. Chem. Soc., Dalton Trans. (1995) 3189.
[24] W.M. Cheung, Q.F. Zhang, C.Y. Lai, I.D. William, W.H. Leung, Polyhedron 26 (2007) 4631.
[25] M. Valderrama, R. Contreras, P. Munoz, M.P. Lamata, D. Carmona, F.J. Lahoz, S. Elipe, L.A. Oro, J. Organomet. Chem. 633 (2001) 182.
[26] P. Bhattacharyya, A.M.Z. Slawin, D.J. Williams, J.D. Woollins, J. Chem. Soc., Dalton Trans. (1995) 2489.
[27] M.C. Copsey, T. Chivers, Chem. Commun. (2005) 4938.
[28] J.S. Ritch, T. Chivers, Dalton Trans. (2008) 957.
[29] V.V. Sushev, A.N. Kornev, Y.V. Fedotova, Y.A. Kursky, T.G. Mushtina, G.A. Abakumov, L.N. Zakharov, A.L. Rheingold, J. Organomet. Chem. 676 (2003) 89.
[30] C. Papadimitriou, P. Veltsistas, J. Novosad, R. CeaOlivares, A. Toscano, P.G.Y. Garcia, M. LopezCardosa, A.M.Z. Slawin, J.D. Woollins, Polyhedron 16 (1997) 2727.
[31] J.W. Faller, J. Lloret-Fillol, J. Parr, New J. Chem. 26 (2002) 883.
[32] Rigaku/MSC, Rigaku/MSC Inc., The Woodlands, Texas, USA, 2005.
[33] G.M. Sheldrick, SHELXS-97: Structure Solving Program, University of Göttingen, Germany, 1997.
[34] G.M. Sheldrick, SHELXL-97: Crystal Structure Refinement Program, University of Göttingen, Germany, 1997.
[35] B.N. Figgis, M.A. Hitchman, Ligand Field Theory and its Applications, Wiley-VCH, 2000.
[36] P. Peringer, J. Schwald, J. Chem. Soc., Chem. Commun. (1986) 1625.
[37] D. Cauzzi, C. Graiff, M. Lanfranchi, G. Predieri, A. Tiripicchio, Inorg. Chim. Acta 273 (1998) 320.
[38] S.D. Robertson, T. Chivers, J. Akhtar, M. Afzaal, P. O'Brien, Dalton Trans. (2008) 7004.
[39] S.D. Robertson, T. Chivers, Dalton Trans. (2008) 1765.
[40] D. Maganas, S.S. Staniland, A. Grigoropoulos, F. White, S. Parsons, N. Robertson, P. Kyritsis, G. Pneumatikakis, Dalton Trans. (2006) 2301.
[41] D. Cupertino, R. Keyte, A.M.Z. Slawin, J.D. Woollins, D.J. Williams, Polyhedron 15 (1996) 4441.
[42] B.A. Demko, R.E. Wasylishen, Inorg. Chem. 47 (2008) 2786.



Scheme 1. Structural formula of the 2-(2′-pyridyl)quinoxaline ligand.

source of rhodium(III), along with conducting preliminary biological tests.

In this paper we report on the synthesis and complete characterization of a new rhodium(III) complex, namely *cis*-$[Rh(pqo)_2Cl_2]Cl$ (**1**) together with early results on the inhibitory effect of this compound on PAF-induced rabbit platelet aggregation.

Platelet Activating Factor (PAF), characterized mainly as 1-*O*-alkyl-2-acetyl-sn-glycero-3-phosphochloline [13], is a potent lipid mediator expressed upon inflammation, oxidation or thrombosis [14] (Scheme 2). PAF exhibits its effects at exceptionally low concentrations (10^{-12}–10^{-9} M) through the specific PAF receptor (PAF-R), a transmembrane receptor located in the cell membrane of its target-cells, such as platelets, neutrophils, macrophages, leukocytes and endothelial cells [15].

This mediator participates in both physiological processes (reproduction, haemostasis, neurotransmission, gastrointestinal, vascular homeostasis and kidney function) and in pathological conditions (inflammation, allergy asthma, acute pancreatitis, bowel disease, pulmonary disease, diabetes, cancer, renal damages, pulmonary tissue injury, organ transplantation rejection, and septic shock). Given the spectrum of target cells and tissues, it seems likely that PAF may play an integral role in both pathological and physiological aspects of inflammation throughout the body [16].

Due to the involvement of the Platelet Activating Factor in cancer disease [15] as a next step we are interested to examine the cytotoxicity of this and other rhodium(III) species prepared in our laboratory. Preliminary results towards this goal will be presented in due course.

2. Experimental

2.1. Reagents and materials

All manipulations were performed under aerobic conditions and all chemicals and solvents used in this study were of analytical grade and used as received without further purification. $RhCl_3{\cdot}3H_2O$ was purchased from Johnson Matthey Co. The ligand 2-(2′-pyridyl)quinoxaline (L = pqo) was synthesized according to already published procedures [9].

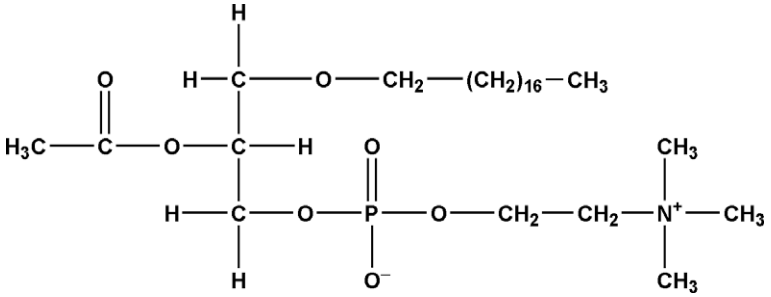
2.2. Physical measurements

Infrared spectra were measured with Perkin–Elmer 883 spectrometer and a Nicolet 550 Magna-IR™ spectrometer as potassium bromide pellets in the spectral range of 4000–400 cm^{-1}. The far-IR measurements were recorded on a Bruker Optics IFS-55 spectrometer as polyethylene plates in the range of 480–100 cm^{-1} with a 4 cm^{-1} spectral resolution. Micro-Raman spectra were measured in backscattering configuration using a Renishaw inVia Reflex microscope with an Ar^+ ion laser (λ = 514.5 nm) and a high power near infrared (NIR) diode laser (λ = 785 nm) as excitation sources. The C, H, N analyses were carried out on a Perkin Elmer 2400 CHN elemental analyzer. Melting or decomposition points were determined using an Electrothermal 9100 (IA9000 series) Digital melting point apparatus and are uncorrected. Absorption spectra were recorded using a CARY 3E UV–Vis spectrometer. ^1H and $^{13}C\{^1H\}$ NMR spectra were measured with a Bruker Avance 500 MHz and a Varian 300 MHz spectrometers in $(CD_3)_2SO$. The ^1H NMR signals of the 2-(2′-pyridyl)quinoxaline ligand in complex **1** were assigned by two dimentional ^1H–^1H, ^1H–^{13}C COSY experiments. Electrospray ionization mass spectra (ESI-MS) were performed using a TSQ 7000 Finnigan Mat spectrometer.

2.3. Synthesis

2.3.1. Synthesis of *cis*-$[RhL_2Cl_2]Cl$ (**1**)

In a two-necked round-bottomed flask 0.105 g (0.385 mmol) of $RhCl_3{\cdot}3H_2O$ was suspended in 5 ml of MeOH. 0.222 g (1.07 mmol) of the ligand pqo dissolved in MeOH (20 ml) was added slowly under stirring to the suspension above. Upon addition, the color of the suspension changed from violet to orange–yellow with the precipitation of an orange solid. The mixture was then heated to a gentle reflux for about 45 min. After 10 min of heating the orange solid was dissolved giving an orange–yellow solution. The slightly cloudy solution was filtered and the clear filtrate was concentrated to the third of the volume and stored in a −20 °C refrigerator overnight. The yellow solid precipitated was washed with small amounts of cold MeOH (4 ml), cold Et_2O (2 × 10 ml) and dried *in vacuo*. The microcrystalline product (0.2 g) was redissolved in hot MeOH (10 ml) filtered off and the clear solution was cooled at ambient temperature. The methanol solution was then placed in the refrigerator for crystallization via slow diffusion of diethyl ether. Some crystals were used for X-ray diffraction measurement and the bulk material was washed with small amounts of Et_2O and dried in vacuo at 50 °C for about 5 h. Yield: 0.12 g (50%). M.p: 190 °C (dec). *Anal.* Calc. for **1** × **1.5**(**H_2O**) $C_{26}H_{21}Cl_3N_6O_{1.5}Rh$ (650.75 g mol^{-1}): C, 47.99; H, 3.25; N, 12.91; Cl, 16.34. Found: C, 48.11; H, 3.05; N, 13.09; Cl, 16.25%. IR (KBr, $\tilde{\nu}$ in cm^{-1}): 3022(w,



Scheme 2. The structure of PAF.

C–H, arom), 1506 (w), 1481 (m, C=C), 1464 (w), 1435 (w), 1367 (w), 1342 (s), 1271 (w), 1209 (m), 1147 (m), 1124 (m), 1080 (w), 1059 (m), 1038 (w), 972 (m), 772 (s), 669 (w), 616 (w), 575 (w), 550 (w), 444 (w). Raman (cm^{-1}): 1603 (s), 1575 (s), 1542 (s), 1485 (s), 1428 (w), 1369 (vs), 1360 (vs), 1348 (s), 1279 (w), 1212(w), 1128 (w), 1042 (s), 1023 (m), 975 (m), 785 (s), 717 (w), 665 (w), 544 (w), 521 (w), 342 (s), 314 (s), 266 (m). UV–Vis (ε/$M^{-1}\,cm^{-1}$): λ_{max} (MeOH) 376 (2384 $M^{-1}\,cm^{-1}$), 363 (2685 $M^{-1}\,cm^{-1}$), 280 nm (sh) (2569 $M^{-1}\,cm^{-1}$), 238 nm (4167 $M^{-1}\,cm^{-1}$) nm. ^1H NMR ($(CD_3)_2SO$, 500 MHz, 298 K): δ = 6.79 (d, ^3J = 8.6 Hz, 2H, $H_{5/8}$), 7.47 (t, ^3J = 7.75 Hz, 2H, $H_{6/7}$), 7.95 (t, ^3J = 7.5 Hz, 2H, $H_{6/7}$), 8.14 (t, ^3J = 6.5 Hz, 2H, $H_{5'}$), 8.30 (d, ^3J = 8.3 Hz, $H_{5/8}$), 8.77 (t, ^3J = 7.5 Hz, 2H, $H_{4'}$), 9.43 (d, ^3J = 7.9 Hz, 2H, $H_{3'}$), 9.55 (d, ^3J = 5.1 Hz, 2H, $H_{6'}$), 10.34 (s, 2H, H_3) ppm. $^{13}C\{^1H\}$ NMR ($(CD_3)_2SO$, 125.8 MHz, 298 K): δ = 124.24 (s, $C_{5/8}$), 128.7 (s, $C_{3'}$), 129.7 (s, $C_{5'}$), 130.5 (s, $C_{5/8}$), 133.1(s, $C_{6/7}$), 133.3 (s, $C_{6/7}$), 140.3 (s, $C_{5\alpha}$), 142.0 (s, $C_{4'}$), 143.6 (s, $C_{8\alpha}$), 145.4 (C_3), 153.4 (s, $C_{6'}$), 154.3 (s, C_2), 156.5 (s, $C_{2'}$) ppm. ESI (*m/z*, QMS, MeOH): 587 (M^+, 100%), 551 (M^+-Cl, 90%), 515 (M^+-2Cl, 25%), 208 ($L+1^+$, 0.5%).

2.3.2. Crystal structure determination

Yellow needles and yellow prismatic single crystals of **1**·2CH_3OH were obtained upon slow diffusion of diethylether into a methanolic solution of the complex at +6 °C. Diffraction measurements were made on a Crystal Logic Dual Goniometer diffractometer using graphite monochromated Mo radiation. Important crystal data and parameters for data collection are reported in Table 1. Unit cell dimensions were determined and refined by using the angular settings of 25 automatically centered reflections in the range $11° < 2\theta < 23°$. Three standard reflections monitored every 97 reflections showed less than 3% variation and no decay. Lorentz, polarization corrections were applied using Crystal Logic software. The structure was solved by direct methods using SHELXS-97 [17] and refined by least-squares techniques on F^2 with SHELXL-97 [18]. Intensity data were recorded using a θ–2θ scan. All hydrogen atoms were introduced at calculated positions as riding on bonded atoms. All non-H atoms were refined anisotropically. The methanol solvate molecules in the prismatic polymorph were found disordered and were refined over two positions with occupation factors fixed to 0.50; no-H atoms for these molecules were included in the refinement.

2.4. Biological assay

2.4.1. PAF-induced aggregation

Washed rabbit platelets were prepared as previously described [13b]. The biological activity of complex **1** against PAF-induced aggregation on washed rabbit platelets was tested. The experiments were performed using two different batches of platelets. The solutions of PAF and of the examined samples, after having being dried under nitrogen stream, were dissolved in 2.5 mg of bovine serum albumin (BSA)/ml of saline. In order to determine the inhibitory effect of each sample, the platelet aggregation induced by PAF (2×10^{-11} M, final concentration in the cuvette) was measured in the absence (0% inhibition) and in the presence of various concentrations of each sample. Consequently, the plot of percent inhibition (ranging from 20% to 80%) versus different sample concentrations is linear. From this curve, the concentration of the sample that inhibited 50% PAF-induced aggregation was calculated, and this value was defined as IC_{50} [13b]. Desensitization experiments were performed using PAF and samples, as previously described [19]. PAF-induced aggregation was measured in a Chrono-Log (Havertown, PA) aggregometer coupled to a Chrono-Log recorder (Havertown, PA). All reagents and chemicals were of analytical grade supplied from Merck (Darmstadt, Germany). PAF standard and BSA were obtained from Sigma (St. Louis, MO).

2.4.2. [^{3}H]-PAF binding to washed rabbit platelets

The experiments involving the specific binding of [^{3}H]-PAF to washed rabbit platelets and its inhibition by complex **1**, were performed as previously described with some modifications [20].

Table 1
Crystallographic data for **1**·2(CH_3OH).

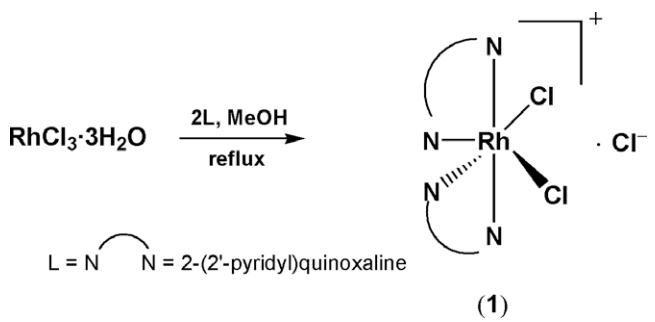
	1·2CH_3OH	**1**·2CH_3OH
Formula	$C_{28}H_{26}Cl_3N_6O_2Rh$	$C_{28}H_{26}Cl_3N_6O_2Rh$
Fw	687.81	687.81
Space group	$P2_12_12_1$	$P\bar{1}$
T [°C]	298 K	298 K
λ (Å)	Mo Kα (0.71073)	Mo Kα (0.71073)
Color, habit	yellow, neeedles	yellow, prisms
Crystal size $(mm)^3$	0.10 × 0.10 × 0.70	0.15 × 0.30 × 0.50
Crystal system	orthorhombic	triclinic
Unit cell dimensions		
a (Å)	13.348(4)	8.647(5)
b (Å)	13.236(5)	13.174(8)
c (Å)	16.476(5)	13.335(8)
α (°)	90	79.58(2)
β (°)	90	71.76(2)
γ (°)	90	89.57(2)
V ($Å^3$)	2910.9(17)	1417.0(15)
Z	4	2
$\rho_{calc.}$ ($g\,cm^{-3}$)	1.569	1.612
μ (Mo Kα) (mm^{-1})	0.899	0.924
$2\theta_{max}$ (°)	50	50
Reflections collected/unique/used	4533/4268 [R_{int} = 0.0588]/4268	5327/4966 [R_{int} = 0.0239]/4966
Reflections with $I > 2(\sigma)I$)	4023	4347
Parameters refined	365	397
$(\Delta/\sigma)_{max}$	0.003	0.011
$(\Delta\rho)_{max}/(\Delta\rho)_{min}$ ($e/Å^3$)	0.674/−0.341	0.625/−0.786
Goodness-of-fit (GOF) on F^2	1.104	1.071
R_1/wR_2 (for all data)	R_1 = 0.0451, wR_2 = 0.1250	R_1 = 0.0473, wR_2 = 0.1075
R_1/wR_2 (for data with $I > 2(\sigma)I$)	R_1 = 0.0420, wR_2 = 0.1225	R_1 = 0.0385, wR_2 = 0.1015

Briefly, [^{3}H]-PAF (1 nM), PAF (1 μM), and *cis*-[RhL_2Cl_2]Cl were diluted in BSA 2.5 mg/ml saline. [^{3}H]-PAF (1 nM) was mixed in the presence or absence of either PAF (1 μM) or *cis*-[RhL_2Cl_2]Cl in various quantities and the volume was adjusted in 100 μl with BSA 2.5 mg/ml saline. The mixture was placed in 360 μl of Tg–Ca^{2+} buffer pH 7.2 (tyrode's buffer pH 7.2 containing $CaCl_2$ 1.72 mM) and the incubation started by adding 40 μl of the washed rabbit platelet suspension (1×10^8 platelets in Tg buffer pH 6.2) at 22 °C for 4 min. Each sample concentration was tested twice and incubation was terminated by adding 0.7 ml ice cold Tg–Ca^{2+} buffer pH 7.2, followed by rapid centrifugation at 11500*g* for 2 min at 4 °C on a Heraeus Labofuge 400R (Hanau, Germany). The specific PAF antagonist, BN 52021, was used as a reference compound [21]. The radioactivity was measured by scintillation counting on a 1209 Rackbeta liquid scintillation counter from Pharmacia (Wallac, Finland). Nonspecific binding was defined as the total binding measured in the presence of excess unlabelled PAF (1 μM) and specific binding was defined as the difference between total binding and nonspecific binding. The percent inhibition was expressed as $\%I = [(\text{total binding} - \text{total binding with tested compound})/\text{specific binding}] \times 100$. The IC_{50} value was defined as the concentration of inhibitor required to obtain 50% inhibition of the PAF specific binding. Scatchard analysis was performed with GRAPHPAD PRISM software (San Diego, Calif, USA). All reagents were purchased by Sigma (St. Louis, MO) unless otherwise stated.

3. Results and discussion

The mononuclear rhodium(III) complex of the formula *cis*-[Rh(pqo)$_2$Cl$_2$]Cl (**1**) was synthesized by a one-pot procedure from the direct reaction of the pqo ligand with $RhCl_3 \cdot 3H_2O$ in a 1:2 molar ratio (Scheme 3). Under the same conditions the reaction of the metal salt with the ligand in the 1:3 (M:L) molar ratio yields complex **1** [22].

After work up of the reaction mixture, the cationic rhodium(III) complex **1** was obtained analytically pure as an orange–yellow solid in 50% yield. This was possible by following a simple crystallization method, i.e. crystallization of the crude product, avoiding therefore the use of time consuming column chromatography. It is an air stable solid that shows remarkable thermal stability and decomposes upon heating at 190 °C. It dissolves well in methanol, ethanol, H_2O, DMF and DMSO, while is less soluble in $CHCl_3$ and insoluble in Et_2O and pentane. The composition of **1** was confirmed by elemental analyses and the spectroscopic properties was examined by FT-IR, FT-Raman, UV–Vis, ^{1}H, ^{13}C NMR spectroscopy and by two-dimensional ^{1}H–^{1}H, ^{1}H–^{13}C COSY experiments. The molecular composition of the rhodium(III) complex was further confirmed by mass spectrometric data (electrospray). All analytical data are in accord with the proposed formulation. The molecular structure of **1**·2CH_3OH was determined by single-crystal X-ray diffraction (vide infra).



Scheme 3. Synthesis of complex **1**.

3.1. IR and Raman spectroscopic data

In the FT-IR spectrum of complex **1** the characteristic in-plane and out-of-plane pyridyl ring deformation bands at 620 and 401 cm^{-1} in free ligand L [9], are shifted to higher frequencies at 669 and 444 cm^{-1}, respectively indicating coordination through the pyridyl nitrogen atom N(1) [23] (see Scheme 1). Also the appearance of a sharp single band at 972 cm^{-1} characterizes the monodentate quinoxaline coordination [24]. The far-IR spectrum of complex **1** in polyethylene exhibits medium intensity bands at 334 and 343 cm^{-1} due to terminal Rh–Cl stretching vibrations [25] in the typical region observed for similar compounds supporting a *cis*-arrangement of the Cl atoms [26]. The Rh–Cl stretching mode of **1** has a slightly lower frequency than those of *cis*-[$Rh(bpy)_2Cl_2$]Cl·2H_2O (350 and 355 cm^{-1}), *cis*-[$Rh(phen)_2Cl_2$]Cl·3H_2O (348 and 353 cm^{-1}) [27] and the related *cis*-[$Rh(pq)_2Cl_2$]Cl complex (pq = 2-(2′-pyridyl)quinoline; 350 and 365 cm^{-1}) [28] reflecting the weaker bonding of Cl to the rhodium center in complex **1**. The low frequency region of the spectrum exhibits weak vibration bands at 269 and 211 cm^{-1}, assignable to ν(Rh–N) vibrations (vide infra).

Fig. 1 compares the solid state Raman spectra of the pqo ligand (L) at 785 nm and the complex **1** at both 514.5 and 785 nm. The luminescence background has been subtracted from the Raman spectra by polynomial fitting and/or cubic spline interpolation routines. However, in the case of the pqo ligand, the strong luminescence precluded detection of the Raman spectrum at 514.5 nm. The NIR Raman spectrum of L (upper trace in Fig. 1) shows distinct vibrational bands at 535, 772, 1369 and 1408 cm^{-1} that lie close to the skeletal bending (536 and 759 cm^{-1}) and ring stretching (1370 and 1416 cm^{-1}) modes of quinoxaline [29]. In addition, several intense bands of the pqo ligand can be identified with those of bipyridine [30] and terpyridine [31] ligands, namely the characteristic ring deformation mode at 997 cm^{-1}, the pyridine ring stretching modes at 1550–1595 cm^{-1} and the strong band at 1321 cm^{-1} arising from the inter-ring C–C vibrations of terpyridine. Significant differences are detected in the corresponding NIR Raman spectrum of complex **1** (middle trace in Fig. 1). Strong Raman bands are observed at 1613, 1603, 1575, 1542, 1485, 1369, 1360, 1348, 1042, 785, 343, 152, 140 and 111 cm^{-1}. The modes at wave numbers above 700 cm^{-1}, comply favorably with previous non-resonant Raman data on coordination compounds containing the 2-(2′-pyridyl)quinoxaline ligand as a bidentate chelate with the pyridine nitrogen and the nearest quinoxaline nitrogen acting as donor atoms to Pd [11h], Cu [32] and Re [33] metal atoms. According to

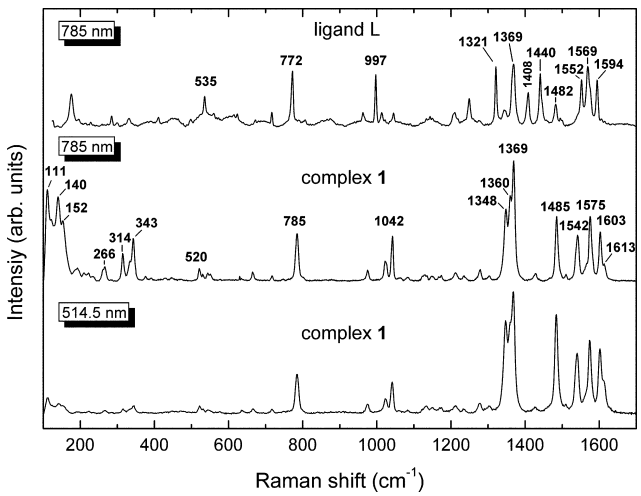


Fig. 1. Micro-Raman spectrum of the ligand (L) and complex **1** in powder form.

density functional theoretical calculations of the normal vibrational modes of these complexes [32,33], the high frequency modes at 1500–1600 cm^{-1} are mostly pyridine based vibrations, while the intense mode at 1485 cm^{-1}, is largely localized on the quinoxaline ligand. A similar but weaker band is also observed in the free 2-(2′-pyridyl)quinoxaline ligand (upper trace in Fig. 1).

At lower frequency, the Raman spectrum of **1** reveals one strong and a medium intensity band for the ν_s(Rh–Cl) stretching mode at 314 and 343 cm^{-1}, respectively. The latter appears as a shoulder with an extra band at 334 cm^{-1}. The band at 266 cm^{-1}, are probably due to the ν(Rh–N) vibrations [25].

Excitation with the green laser line at 514.5 nm results in a significant variation of the relative intensity distribution of most vibrational bands compared to the NIR Raman spectra, as shown in the lower trace of Fig. 1. The intensity of the Raman bands at wave numbers above 700 cm^{-1} becomes considerably enhanced with respect to the lower frequency bands, especially for the higher frequency modes (1300–1650 cm^{-1}), which are mostly localized on the pqo ligand. This is particularly prominent for the quinoxaline based mode at 1485 cm^{-1}. This behavior is consistent with previous resonance Raman studies on 2-(2-pyridyl)quinoxaline metal complexes, where laser excitation with energies around the metal-to-ligand charge transfer (MLCT) transition at 420–450 nm, cause the enhancement of the resonating vibrational modes [32,33]. In the present case, the laser excitation at 514.5 nm approaches the weak MLCT band in the visible range of complex **1**, causing the enhancement of the high frequency modes that involve mostly the vibration of the pyridyl-quinoxaline ligand. This would further indicate that the corresponding MLCT transition is mainly associated with the redistribution of the electron density in the ligand system, in agreement with the resonance Raman study of [Re(pqo)$(CO)_3$Cl] [33].

3.2. Absorption spectra

The absorption spectrum of complex **1** was recorded in methanol and is shown in Fig. 2. The electronic spectrum of the complex cannot be compared with this of the free ligand, due to different conformation in both cases (see NMR discussion as well). The UV–Vis spectrum of the ligand, in methanol, exhibits π–π^* transitions at 275 and 332 nm, respectively.

The electronic spectrum of the cation *cis*-$[RhL_2Cl_2]^+$ displays two ligand centered (LC) bands at 238 and 280 nm and the metal–ligand charge transfer bands (MLCT) as shoulder at 363 and 376 nm, respectively. In this region, MLCT and d–d transitions are present, hindering a complete assignment of the bands. In concentrated solutions, a weak band centered at approximately 540 nm (not seen in the spectrum of Fig. 2) could be responsible for the characteristic yellow color of the complex. These values are in good agreement with the reported data for the *cis*-[Rh$(phen)_2Cl_2$]Cl system [34]. The latter, presents the characteristic π–π^* transitions at 223 and 274 nm and the MLCT bands at 354 and about 380 nm, respectively. Other two bands at 300 nm (sh) and at 337 have also been reported in methanol as a solvent as well.

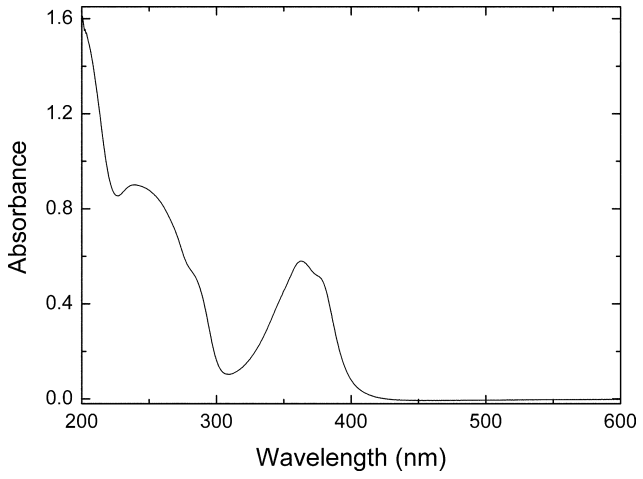


Fig. 2. UV–Vis absorption spectrum of **1** in methanol (2×10^{-4} M) at 298 K.

3.3. NMR spectra

The ^{1}H NMR spectrum of complex **1** was recorded in $(CD_3)_2SO$ at ambient temperature. Signal assignment is based on integration, splitting pattern, chemical shifts, ^{1}H–^{1}H and ^{1}H–^{13}C COSY experiments and literature values concerning similar systems [27].

The aromatic region of the spectrum of **1** displays well resolved narrow resonance signals for all the protons of the ligand as expected for diamagnetic Rh(III) complexes. Each signal corresponds to 2H as is indicated by integration. Upon chelation, the $H_{6'}$ proton is downfield shifted by 0.47 ppm compared to the free ligand [35] due to a decrease in the electron density of the pyridine ligand. Moreover, the chemical shifts of the $H_{6'}$ and $H_{3'}$ protons on going from the 2-(2′-pyridyl)quinoxaline ligand to complex **1** are downfield shifted by 0.73 and 0.88 ppm, respectively. An important feature of the spectrum of **1**, is the presence of a single resonance at δ = 10.34 ppm characteristic of the H_3 proton of the ligand. This pronounced downfield shift ($\Delta\delta$ = 0.46 ppm compared to the free ligand [35]) may be an indication that the N(4) atom of the quinoxaline ligand is coordinated to the meal center [10 m]. This further implies that the structure of **1** in solution is rather different from that in the crystal.

Finally, the ^{13}C{^{1}H} NMR spectrum of **1** reveals twenty six resonance signals in the aromatic region (δ = 120–160 ppm) corresponding to the pyridyl ring carbons. The downfield resonances at 156.5 and 154.3 ppm are assigned to $C_{2'}$, C_2 carbons that are near to the electron withdrawing nitrogen of the coordinated pyridine ring. The remaining carbon atoms were assigned on the basis of the ^{1}H NMR data and by ^{1}H–^{13}C COSY experiments.

3.4. X-ray crystallography

The solid-state structure of complex **1** was determined by single-crystal X-ray diffraction. During crystallization two polymorphs, yellow needles and yellow prismatic crystals, were obtained. The asymmetric unit of the crystal structure of **1** contains two molecules of methanol. The molecular structure of complex **1** crystallizing in the orthorhombic and triclinic crystallographic system is depicted in Figs. 3 and 4, respectively. Selected bond lengths and angles are given in Table 2. All data described below refer to needle like crystals.

In the molecular structure of **1**·$2CH_3OH$ the rhodium environment adopts a distorted octahedral geometry with the chlorine atoms *cis* to each other. This agrees with the results of the NMR studies in solution (vide supra). The 2-(2′-pyridyl)quinoxaline ligand acts in a bidentate manner through N(1), N(2) and N(11), N(12) adopting a *syn* conformation, where the pyridyl and quinoxaline nitrogen atoms are located on the same side of the C(5)–C(6) [C(25)–C(26)] bond. The deviation from the ideal octahedral geometry is shown by the angles N(1)–Rh–N(11) (175.3°(2)), N(1)–Rh–N(2) (80.1°(2)), N(1)–Rh–N(12) (103.2°(2)) and N(2)–Rh–N(12) (94.0°(2)), respectively. The bond lenghts within the coordinated ligand in **1** are in good agreement with the corresponding ones in the free ligand [9] and other pyridyl-quinoxaline complexes with different metal ions [11]. There are two sets of Rh–N

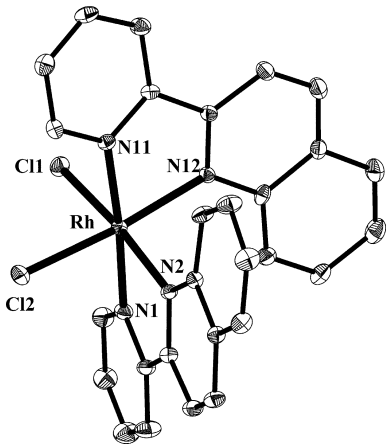


Fig. 3. A perspective view of the cation **1**·2(CH_3OH) in the solid state (needle like polymorph). Thermal ellipsoids are set at the 50% probability. Hydrogen atoms and solvate methanol molecules have been omitted for clarity.

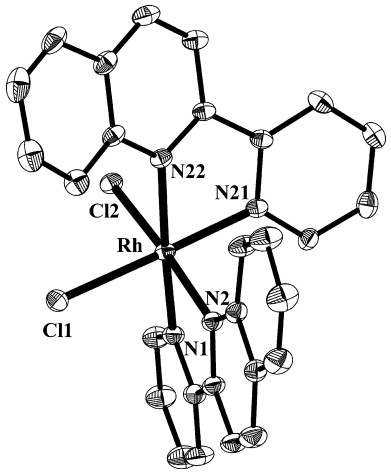


Fig. 4. A perspective view of the cation **1**·2(CH_3OH) in the solid state (prismatic polymorphs). Thermal ellipsoids are set at the 50% probability. Hydrogen atoms and solvate methanol molecules have been omitted for clarity.

distances. An average of 2.031 Å for the pyridyl moiety and 2.096 Å for the quinoxaline moiety, something that implies a stronger bonding of rhodium to the pyridyl nitrogen atoms (N(11) and N(1)). The Rh–Cl bond lengths of 2.318(2) Å (Rh–Cl(1)) and 2.308(2) Å (Rh–Cl(2)) are slightly shorter than those found in *cis*-$[Rh(bpy)_2Cl_2]Cl_2{\cdot}2H_2O$ [36] (Rh–Cl(1) = 2.341(2), Rh–Cl(2) = 2.328(2)) and in *cis*-$[Rh(phen)_2Cl_2]Cl_2{\cdot}H_2O$ [37] (Rh–Cl(1) = 2.329(2), Rh–Cl(2) = 2.320(2)). The atoms N(1), N(2) and C(1)–C(12) defining the (pyridyl)quinoxaline ligand, are planar and the rhodium atom lies 0.43 Å from the mean plane. The second 2-(2′-pyridyl)quinoxaline ligand defined by the N(11), N(12) and C(21)–C(32) atoms is also planar with the Rh atom almost lying on this plane (deviation 0.09 Å).

3.5. Biological activity

The IC_{50} value of **1** was measured as described in the experimental section and calculated to be 210 nM (towards 0.02 nM PAF). IC_{50} value represents the inhibitory potency of this compound against PAF-induced aggregation, thus the smaller the IC_{50} value is, the greater the inhibitory effect. The investigated compound inhibits PAF-induced platelet aggregation in a non-cytotoxic way, even at high concentrations. The respective BN 52021 IC_{50} value, is 24 600 nM (2.5 nM PAF) [21], meaning that the inhibitory effect of **1** is of the same order of magnitude. At 210 nM (IC_{50} value) the *cis*-$[RhL_2Cl_2]Cl$, induced 18% inhibition of PAF binding onto platelet PAF-R, whereas the highest *%I* was observed at 50 nM (34% inhibition). These data indicate that **1** inhibits PAF action on platelets and this effect is attributed only in part to the inhibition of PAF binding onto PAF-R. It seems that at low concentrations, **1** affects PAF-R much more effectively and inhibits PAF action in another pathway.

PAF has been implicated in carcinogenesis and cancer metastasis, whereas BN 52021 has antitumor effects [38]. Perhaps *cis*-$[RhL_2Cl_2]Cl$, that inhibits PAF action, may also be used as a potential anticancer agent.

Table 2
Selected bond lengths (Å) and angles (°) of **1**·2(CH_3OH). Data of both polymorphs are given.

Needles		Prisms	
Rh–N(1)	2.031(5)	Rh–N(1)	2.015(4)
Rh–N(2)	2.083(5)	Rh–N(2)	2.079(3)
Rh–N(11)	2.032(5)	Rh-N(21)	2.026(4)
Rh–N(12)	2.108(5)	Rh–N(22)	2.091(3)
Rh–Cl(1)	2.318(2)	Rh–Cl(1)	2.338(2)
Rh–Cl(2)	2.308(2)	Rh–Cl(2)	2.339(2)
N(1)–C(1)	1.334(9)	N(1)–C(1)	1.335(6)
N(1)–C(5)	1.361(9)	N(1)–C(5)	1.351(6)
N(2)–C(6)	1.329(8)	N(2)–C(6)	1.333(5)
N(2)–C(13)	1.380(8)	N(2)–C(13)	1.374(6)
N(11)–C(21)	1.340(8)	N(21)–C(21)	1.338(5)
N(12)–C(26)	1.328(8)	N(22)–C(26)	1.332(5)
Bond angles (°)			
N(1)–Rh–N(11)	175.3(2)	N(1)–Rh–N(21)	95.8(2)
N(11)–Rh–N(2)	103.3(2)	N(21)–Rh–N(2)	93.4(2)
N(1)–Rh–N(2)	80.1(2)	N(1)–Rh–N(2)	80.1(2)
N(1)–Rh–N(12)	103.2(2)	N(1)–Rh–N(22)	173.5(2)
N(11)–Rh–N(12)	79.9(2)	N(21)–Rh–N(22)	79.3(2)
N(2)–Rh–N(12)	94.0(2)	N(2)–Rh–N(22)	104.3(2)
Cl(2)–Rh–Cl(1)	90.3(7)	Cl(2)–Rh–Cl(1)	89.7(5)
N(1)–Rh–Cl(1)	93.9(2)	N(1)–Rh–Cl(1)	83.6(2)
N(2)–Rh–Cl(2)	86.9(2)	N(2)–Rh–Cl(2)	173.7(1)
C(1)–N(1)–Rh	126.6(5)	C(1)–N(1)–Rh	125.8(3)

4. Conclusions

In summary, a new Rh(III) complex with the 2-(2′-pyridyl)quinoxaline ligand, synthesized in a one pot process, was fully characterized. The new complex crystallizes out from the mother liquor in two polymorphs, with two solvate methanol molecules. The molecular structures in the crystal of both polymorphs have been elucidated by X-ray crystallography. For the first time, an X-ray crystallographic analysis of the Rh(III) complex with the pqo ligand is described. The biological activity of *cis*-$[RhL_2Cl_2]Cl$ on PAF-induced rabbit platelet aggregation showed that this compound is a potent inhibitor with an IC_{50} value of 210 nM. In this study, compound **1** inhibited PAF action partly through PAF-R dependent way.

Our further efforts will be devoted to evaluating the anticancer activity of the new complex **1** and other similar complexes that are under investigation.

Acknowledgments

The authors express their gratitude to Prof. Dr. A.C. Filippou for access to the Central Analytical Group of the Chemistry Department of the University of Bonn. We also thank Dr. N. Weidemann of the same University for his help with the far-IR measurements.

Appendix A. Supplementary data

CCDC 720833 and 720834 contains the supplementary crystallographic data for the two polymorphs of **1**. These data can be obtained free of charge via http://www.ccdc.cam.ac.uk/conts/retrieving.html, or from the Cambridge Crystallographic Data Centre, 12 Union Road, Cambridge CB2 1EZ, UK; fax: (+44) 1223-336-033; or e-mail: deposit@ccdc.cam.ac.uk.

References

[1] (a) M.J. Cleare, Coord. Chem. Rev. 12 (1974) 349;
(b) G. Zassinovich, A. Camus, G. Mestroni, Inorg. Nucl. Chem. Lett. 12 (1976) 865;
(c) B.R. Ramesh, B.S.S. Mallikarjuna, G.K.N. Reddy, Natl. Acad. Sci. Lett. 1 (1978) 24;
(d) G. Mestroni, E. Alessio, A. Sessanti o Santi, S. Geremia, B.A. Bergamo, G. Sava, A. Boccarelli, A. Schettino, M. Coluccia, Inorg. Chim. Acta 273 (1998) 62;
(e) P.K.L. Fu, C. Turrro, Chem. Commun. (2001) 279;
(f) P.K. L Fu, P.M. Bradley, C. Turrro, Inorg. Chem. 42 (2003) 878;
(g) M. Harlos, I. Ott, R. Gust, H. Alborzinia, S. Wölf, A. Kromm, W.S. Sheldrick, J. Med. Chem. 51 (2008) 3924.
[2] U. Koelle, M. Graetzel, Angew. Chem., Int. Ed. Engl. 26 (1987) 567.
[3] (a) S. Swavey, K.J. Brewer, Inorg. Chem. 41 (2002) 6196;
(b) P.M. Bradley, A.M. Angeles-Boza, K.R. Dunbar, C. Turro, Inorg. Chem. 43 (2004) 2450.
[4] C.M. Bolinger, N. Story, B.P. Sullivan, T.J. Meyer, Inorg. Chem. 27 (1988) 4582.
[5] K.E. Erkkila, D.T. Odom, J.K. Barton, Chem. Rev. 99 (1999) 2777.
[6] R.S. Mahnken, M.A. Billddeau, E.P. Nikonowicz, H. Morrison, J. Am. Chem. Soc. 114 (1992) 9253.
[7] (a) J.K. Barton, A.T. Danishefsky, J.M. Goldeberg, J. Am. Chem. Soc. 106 (1984) 2172;
(b) C. Hiort, P. Lincoln, B. Nordén, J. Am. Chem. Soc. 115 (1993) 3448.
[8] L. Menon, R. Perera, M. Navarro, R.J. Kuhn, H. Morrison, Inorg. Chem. 43 (2004) 5373.
[9] S. Kasselouri, A. Garoufis, A. Katehanakis, G. Kalkanis, S.P. Perlepes, N. Hadjiliadis, Inorg. Chim. Acta 207 (1993) 255.
[10] C. Shao, W.-H. Sun, Z. Li, Y. Hu, L. Han, Catal. Commun. 3 (2002) 405.
[11] (a) J.C. Plakatouras, N. Hadjiiadis, S. Perlepes, A. Albinati, G. Kalkanis, Polyhedron 12 (1993) 2069;
(b) E.G. Bakalbassis, J. Mrozinski, S.P. Perlepes, N. Hadjiliadis, F. Lianza, A. Albinati, Polyhedron 13 (1994) 3209;
(c) S. Kasselouri, A. Garoufis, S. Paschalidou, S.P. Perlepes, I.S. Butler, N. Hadjiliadis, Inorg. Chim. Acta 227 (1994) 129;
(d) A. Garoufis, S.P. Perlepes, A. Vreugenhil, I.S. Butler, N. Hadjiliadis, Inorg. Chim. Acta 240 (1995) 673;
(e) S.P. Perlepes, S. Kasselouri, A. Garoufis, F. Lutz, R. Bau, N. Hadjiliadis, Polyhedron 14 (1995) 1461;
(f) A. Garoufis, S.P. Perlepes, N.A. Froystein, J. Sletten, N. Hadjiliadis, Polyhedron 15 (1996) 1035;
(g) A. Garoufis, S.P. Perlepes, A. Schreiber, R. Bau, N. Hadjiliadis, Polyhedron 15 (1996) 177;
(h) S.P. Perlepes, A. Garoufis, J. Sletten, E.G. Bakalbassis, G. Plakatouras, E. Katsarou, N. Hadjliadis, Inorg. Chim. Acta 261 (1997) 93;
(i) A. Garoufis, S. Kasselouri, S. Boyatzis, C.P. Raptopoulou, Polyhedron 18 (1999) 1615;
(j) A. Garoufis, A. Koutsodimou, C.P. Raptopoulou, A. Simopoulos, N. Katsaros, Polyhedron 18 (1999) 3005;
(k) I. Veroni, A. Rontoyianni, C. Mitsopoulou, J. Chem. Soc., Dalton Trans. (2003) 255;
(l) A. Garoufis, G. Malandrinos, N. Hadjiliadis, Eur. J. Inorg. Chem. (2004) 3326;
(m) I. Veroni, C. Makedonas, A. Rontoyianni, C.-A. Mitsopoulou, J. Organomet. Chem. 691 (2006) 267;
(n) C. Makedonas, I. Veroni, C.-A. Mitsopoulou, Eur. J. Inorg. Chem. (2007) 120;
(o) I. Veroni, C.A. Mitsopoulou, F.J. Lahoz, J. Organomet. Chem. 693 (2008) 2451;
(p) A. Garoufis, G. Malandrinos, N. Hadjiliadis, Eur. J. Inorg. Chem. (2004) 3326.
[12] S.I. Mostafa, S.P. Perlepes, N. Hadjiliadis, Z. Naturforsch. 56b (2001) 394.
[13] (a) L.M. McManus, R.N. Pinckard, Crit. Rev. Oral Biol. Med. 11 (2000) 240;
(b) C.A. Demopoulos, R.N. Pinckard, D.J. Hanahan, J. Biol. Chem. 254 (1979) 9355.
[14] C.A. Demopoulos, H.C. Karantonis, S. Antonopoulou, Eur. J. Lipid Sci. Technol. 105 (2003) 705.
[15] S. Ishii, T. Shimizu, Prog. Lipid Res. 39 (2000) 41.
[16] A.B. Tsoupras, C. Iatrou, C. Frangia, C.A. Demopoulos, Infect. Disord. Drug Targets (2009), in press.
[17] G.M. Sheldrick, SHELXS-86: Structure Solving Program, University of Göttingen, Germany, 1986.
[18] G.M. Sheldrick, SHELXL-97: Crystal Structure Refinement Program, University of Göttingen, Germany, 1997.
[19] M. Lazanas, C.A. Demopoulos, S. Tournis, S. Koussissis, K. Labrakis-Lazanas, X. Tsarouhas, Arch. Dermatol. Res. 280 (1988) 124.
[20] S. Antonopoulou, C.A. Demopoulos, C. Iatrou, Int. J. Biochem. Cell Biol. 28 (1996) 43.
[21] T.L. Yue, R. Rabinovici, M. Farhat, G. Feuerstein, J. Lipid Med. 3 (1991) 13.
[22] This was confirmed by a single crystal X-ray analysis on the bulk of the crystals formed upon crystallization of the reaction mixture.
[23] M.G.B. Drew, F.S. Esho, A. Lavery, S.M. Nelson, J. Chem. Soc., Dalton Trans. (1984) 545.
[24] P. Lumme, S. Lindross, E. Lidell, Inorg. Chim. Acta 144 (1998) 75.
[25] K. Nakamoto, Infrared and Raman spectra of Inorganic and Coordination compounds, forth ed., Wiley, New York, 1986.
[26] R.D. Gillard, J.A. Osborn, G. Wilkinson, J. Chem. Soc. (1965) 1951;
I.I. Bhayat, W.R. McWhinnie, Spectrochim. Acta 28 (1972) 743.
[27] L. Pazderski, J. Toušek, J. Sitkowski, L. Kozerski, R. Marek, E. Szłyk, Magn. Reson. Chem. 45 (2007) 24.
[28] (a) M.H. Zaghal, H.A. Qaseer, Inorg. Chim. Acta 163 (1989) 193;
(b) H.A. Qaseer, Croat. Chem. Acta 78 (2005) 79.
[29] R.W. Mitchell, R.W. Glass, J.A. Merritt, J. Mol. Spectrosc. 36 (1970) 310;
H.F. Shurvell, J.W. Russell, J. Raman Spectrosc. 3 (1975) 407.
[30] L. Ould-Moussa, M. Castellà-Ventura, E. Kassab, O. Poizat, D.P. Strommen, J.R. Kincaid, J. Raman Spectrosc. 31 (2000) 377.
[31] S. Schneider, G. Brehm, C.-J. Prenzel, W. Jager, M.I. Silva, H.D. Burrows, S.T. Formosinho, J. Raman Spectrosc. 27 (1996) 163.
[32] M.R. Waterland, S.L. Howell, K.C. Gordon, A.K. Burrell, J. Phys. Chem. A 109 (2005) 8826.
[33] M.R. Waterland, S.L. Howell, K.C. Gordon, J. Phys. Chem. A 111 (2007) 4604.
[34] E.D. McKenzie, R.A. Plowman, J. Inorg. Nucl. Chem. 32 (1970) 199.
[35] A detailed comparison with the NMR data of the free ligand (in the same solvent) cannot be made. Single crystal X-ray crystallography and ^{1}H NMR studies have shown that the free ligand exists in a *trans* conformation. Upon coordination to a metal center the *cis* conformation is adopted.
[36] P. Lahuerta, J. Latorre, R. Martínez-Máñez, S. García-Granda, F. Gómez-Beltrán, Acta Crystallogr. C47 (1991) 519.
[37] Z. Ji, Y. Shan, A.R. Guadalupe, S.D. Huang, Z. Kristallogr. New Cryst. Struct. 214 (1999) 387.
[38] S.H. Xia, D.C. Fang, Chin. Med. J. (Engl.) 120 (2007) 922.

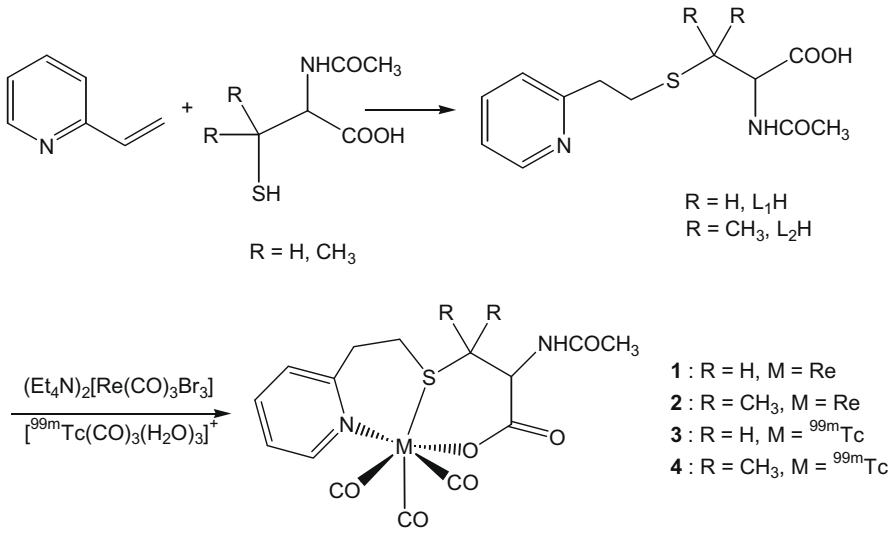


Fig. 1. Synthetic scheme of the ligands and complexes studied.

a novel bifunctional chelating system in the development of target-specific radiopharmaceuticals [12–14].

In this work, we present the synthesis of two *N*-acetylcysteine derivatized ligands, S-(2-(2-pyridyl)ethyl)-*N*-acetyl-L-cysteine, L_1H and S-(2-(2-pyridyl)ethyl)-*N*-acetyl-D-penicillamine, L_2H, as shown in Fig. 1, as well as the synthesis of their corresponding rhenium(I) and technetium(I) complexes. In these ligands the primary amine of the cysteine moiety is acetylated to allow coordination to the $[M(CO)_3]^+$ core through the pyridine nitrogen, the thioether sulfur and the carboxylate oxygen.

2. Experimental

2.1. Materials and methods

All reagents and organic solvents used in this study were purchased from Aldrich and used without further purification. Solvents for high-performance liquid chromatography (HPLC) were HPLC-grade. They were filtered through membrane filters (0.22 μm, Millipore, Milford, MA) and degassed by a helium flux before and during use. Ligand L_1H was prepared by a slightly modified method described elsewhere [15,16]. $[NEt_4]_2[Re(CO)_3Br_3]$ was prepared according to published procedure [17]. For ^{99m}Tc labelling, a kit containing 5.5 mg $NaBH_4$, 4 mg Na_2CO_3 and 10 mg Na–K tartarate, was purged with CO gas prior to addition of $Na^{99m}TcO_4$, as described in literature [6].

IR spectra were recorded as KBr pellets on a Perkin–Elmer 1600 FT-IR spectrophotometer in the region 4000–500 cm^{-1}. NMR spectra were recorded on a Bruker 500-MHz Avance DRX spectrometer using $(CH_3)_4Si$ as the internal reference. Elemental analyses for C, H and N were conducted on a Perkin–Elmer 2400 automatic elemental analyzer. HPLC analysis was performed on a Waters 600 chromatography system coupled to both a Waters 2487 Dual λ Absorbance detector and a Gabi gamma detector from Raytest. Separations were achieved on a Nucleosil C18 (10 μm, 250 × 4 mm) column eluted with a binary gradient system at 1 mL min^{-1} flow rate. Mobile phase A was methanol containing 0.1% trifluoroacetic acid and mobile phase B was water containing 0.1% trifluoroacetic acid. The elution profile was 0–1 min 100% B followed by a linear gradient to 30% B in 10 min; this composition was held for another 10 min. After a column wash with 95% A for 5 min, the column was re-equilibrated by applying the initial conditions (100% B) for 15 min prior to the next injection.

2.2. Synthesis of ligands, S-(2-(2-pyridyl)ethyl)-N-acetyl-L-cysteine, L_1H, and S-(2-(2-pyridyl)ethyl)-N-acetyl-D-penicillamine, L_2H

31 mmol of *N*-acetyl-L-cysteine or *N*-acetyl-D-penicillamine were dissolved in 100 ml methanol and 31 mmol of freshly distilled under vacuum 2-vinylpyridine were added dropwise. The reaction mixture was heated under reflux for 6 h. Methanol was then removed on a rotary evaporator and the remaining thick oil was recrystallized from ethanol.

L_1H: White needles, yield 92%. I.R. (KBr, cm^{-1}): 1720, 1646, 1606, 1534, 1487, 1445. *Anal. Calc.* for $C_{12}H_{16}N_2SO_3$: C, 53.71; H, 6.01; N, 10.44. Found: C, 52.75; H, 6.11; N, 10.65%. NMR (DMSO-d_6, ppm): 8.60, 8.40, 7.90, 7.80, 4.27, 3.26, 2.95, 2.78, 1.93.

L_2H: White needles, yield 90%. I.R. (KBr, cm^{-1}): 1705, 1662, 1603, 1539, 1442, 1371. *Anal. Calc.* for $C_{14}H_{20}N_2SO_3$: C, 56.73; H, 6.80; N, 9.45. Found: C, 56.45; H, 6.91; N, 9.19%. NMR (DMSO-d_6, ppm): 8.40, 8.20, 7.70, 7.50, 3.90, 3.05, 1.93, 1.05, 1.10.

2.3. Synthesis of rhenium complexes, $[Re(CO)_3(L_1)]$, **1** and $[Re(CO)_3(L_2)]$, **2**

Both complexes, **1** and **2**, were prepared according to the following procedure: A solution of L_1H or L_2H (0.2 mmol) in methanol (5 ml) and 0.2 ml NaOH 1 N were added under stirring to a solution of $[NEt_4]_2[Re(CO)_3Br_3]$ (0.154 g, 0.2 mmol) in methanol (10 ml). The mixture was heated under reflux for 2 h. The solution was then cooled at room temperature yielding white crystals which were filtered. The product was washed with CH_2Cl_2 and CH_3CN and characterized by spectroscopic methods and elemental analysis.

$[Re(CO)_3(L_1)]$, **1**: HPLC: t_R = 16.7 min, I.R. (KBr, cm^{-1}): 2021, 1900, 1875, 1686, 1666. *Anal. Calc.* for $C_{15}H_{15}N_2O_6ReS$: C, 33.51; H, 2.81; N, 5.21. Found: C, 33.11; H, 2.75; N, 5.13%.

$[Re(CO)_3(L_2)]$, **2**: HPLC: t_R = 17.6 min, I.R. (KBr, cm^{-1}): 2029, 1928, 1893, 1650. *Anal. Calc.* for $C_{17}H_{19}N_2O_6ReS$: C, 36.10; H, 3.39; N, 4.95. Found: C, 36.38; H, 3.71; N, 4.85. ^1H and ^{13}C NMR in Table 1. Crystals suitable for X-ray crystallography were obtained by slow evaporation from MeOH.

2.4. Single-crystal X-ray crystallography

A colorless crystal of **2** (0.30 × 0.40 × 0.50 mm) suitable for X-ray analysis was mounted in air and covered with epoxy glue. Diffraction measurements were made on a Crystal Logic Dual

Table 1
^{1}H and ^{13}C chemical shifts for complex **2** in DMSO-d_6 at 25 °C.

H-1	8.66	C-1	155.02
H-2	7.58	C-2	125.17
H-3	8.13	C-3	141.21
H-4	7.80	C-4	127.00
H-6	3.66, 3.01	C-5	160.24
H-7	3.54, 2.60	C-6	37.12
H-9	3.44	C-7	24.84
H-12	1.72	C-8	52.45
H-13[a]	1.31	C-9	55.39
H-14[a]	1.20	C-10	170.99
NH	8.01	C-11	169.10
		C-12	22.21
		C-13	25.30
		C-14	23.66
		C=O	195.30, 193.41, 192.80

[a] Assignments of H-13 and H-14 are not position specific and may be interchanged.

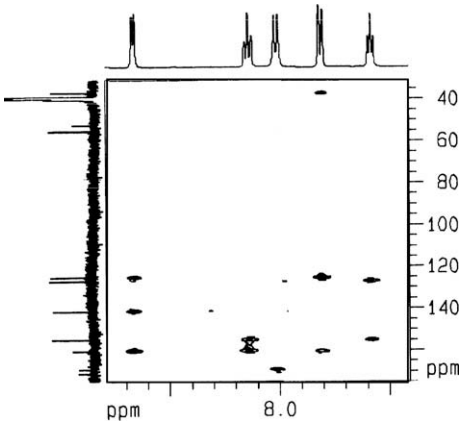


Fig. 2. ^{1}H–^{13}C long range correlation (HMBC) spectrum for complex **2** in DMSO-d_6 at 25 °C (range δH 8.79–7.41, range δC 175.0–30.9).

Goniometer diffractometer using graphite monochromated Mo Kα radiation. Unit cell dimensions were determined by using the angular settings of 25 automatically centered reflections in the range $11 < 2\theta < 23°$ and they are presented in Table 2. Intensity data were recorded using a θ–2θ scan. Three standard reflections monitored every 97 reflections showed less than 3% variation and no decay. Lorentz, polarization and psi-scan absorption corrections were applied using Crystal Logic software. The structure was solved by direct methods using SHELXS-97 [18] and refined by full-matrix least squares techniques on F^2 using SHELXL-97 [19]. Further crystallographic details for **2**: $2\theta_{max} = 50°$, scan speed 5.5°/min, scan range 1.6 + $\alpha_1\alpha_2$ separation, reflections collected/unique/used 3798/3496 [$R_{int} = 0.1400$]/3496, 275 parameters refined, $[\Delta\rho]_{max}/[\Delta\rho]_{min} = 0.538/-1.216$ e/Å^3, $[\Delta/\sigma]_{max} = 0.012$, R_1/wR_2 (for all data) = 0.0523/0.1214. Hydrogen atoms were located by difference maps and were refined isotropically, or introduced at calculated positions as riding on bonded atoms. All non-H atoms were refined anisotropically. Plots of the structure were drawn using the DIAMOND 3 program package [20].

2.5. Synthesis of technetium complexes, [^{99m}Tc(CO)$_3$(L$_1$)], **3** and [^{99m}Tc(CO)$_3$(L$_2$)], **4** and challenge experiments

Synthesis: Technetium-99m complexes, **3** and **4**, were prepared according to the general procedure: 400 μL of a freshly prepared solution of the *fac*-[^{99m}Tc(CO)$_3$(H$_2$O)$_3$]$^+$ precursor (pH 6) were added to a vial containing a 100 μL solution of L$_1$H or L$_2$H (10^{-3} M) in methanol. The vial was sealed, flushed with N_2 and heated for 30 min at 70 °C. The complexes **3, 4** were analyzed by HPLC: **3:** t_R = 17.1 min, **4:** t_R = 18.2 min.

Challenge experiments against L-histidine and L-cysteine: Aliquots of 100 μl of complex **3** or **4** were added to 900 μl of a 10^{-2} M L-histidine and 10^{-2} M L-cysteine solutions in saline. The samples were incubated at room temperature for 24 h. At the 1, 6, and 24 h time points, 100 μl of each sample were removed and analyzed by gradient HPLC under the same solvent system used for the characterization of the complexes.

Table 2
Summary of crystal, intensity collection and refinement data.

	2
Empirical formula	$C_{17}H_{19}N_2O_6ReS$
Formula weight	565.60
Temperature	298
Wavelength	Mo Kα 0.71073
Space group	$P2_12_12_1$
a (Å)	9.532(3)
b (Å)	9.249(3)
c (Å)	22.565(6)
V (Å^3)	1989.4(10)
Z	4
D_{calcd} (Mg m^{-3})	1.888
Absorption coefficient μ (mm^{-1})	6.248
F(0 0 0)	1096
Goodness-of-fit on F^2	1.059
R indices[a]	$R_1 = 0.0494$[b], $wR_2 = 1187$[b]

[a] $w = 1/[\sigma^2(F_o^2) + (\alpha P^2) + bP]$ and $P = (\max(F_o^2, 0) + 2F_c^2)/3, R_1 = \sum(|F_o| - |F_c|)/\sum(|F_o|)$ and $wR_2 = \left\{\sum\left[w\left(F_o^2 - F_c^2\right)^2\right]/\sum\left[w\left(F_o^2\right)^2\right]\right\}^{1/2}$.

[b] For 3305 reflections with $I > 2\sigma(I)$.

3. Results and discussion

3.1. Synthesis and characterization of rhenium complexes

Ligands L$_1$H and L$_2$H react readily with the [NEt$_4$]$_2$[Re(CO)$_3$Br$_3$] precursor in methanol to generate the corresponding neutral Re(CO)$_3$(NSO) complexes **1** and **2** (Fig. 1). HPLC analysis of the reaction mixture showed the formation of a single product. Both compounds were collected as white solids and were characterized by elemental analysis and spectroscopic methods. Complex **1** is insoluble in all common solvents while complex **2** is slightly soluble in methanol and DMSO. Crystals suitable for X-ray crystallography were obtained for **2** by recrystallization from a methanolic solution. Both complexes are stable in the solid state while complex

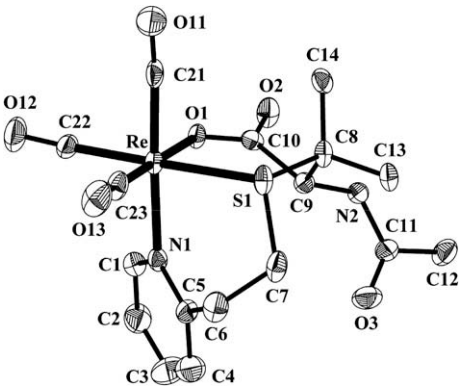


Fig. 3. Labelled plot of **2** with ellipsoids drawn at the 30% probability level. H atoms have been omitted for clarity.

Table 3
Selected bond distances (Å) and angles (°) for **2**.

Distances			
Re–C(23)	1.893(10)	Re–O(1)	2.156(6)
Re–C(22)	1.925(11)	Re–N(1)	2.220(10)
Re–C(21)	1.941(13)	Re–S(1)	2.479(2)
Angles			
C(23)–Re–C(22)	86.9(5)	C(21)–Re–N(1)	173.7(4)
C(23)–Re–C(21)	88.5(5)	O(1)–Re–N(1)	81.7(3)
C(22)–Re–C(21)	86.8(5)	C(23)–Re–S(1)	89.7(4)
C(23)–Re–O(1)	179.1(4)	C(22)–Re–S(1)	176.0(4)
C(22)–Re–O(1)	93.9(4)	C(21)–Re–S(1)	90.9(3)
C(21)–Re–O(1)	92.1(4)	O(1)–Re–S(1)	89.5(2)
C(23)–Re–N(1)	97.8(4)	N(1)–Re–S(1)	89.3(2)
C(22)–Re–N(1)	93.3(4)		

2 is stable in methanol for a period of months as shown by both HPLC and NMR.

The infrared spectra of complexes **1** and **2** demonstrate strong bands in the 2029–1875 cm^{-1} range, attributed to the C≡O stretch of the *fac*-$[Re(CO)_3]^+$ unit [21,22]. In addition, both complexes exhibit strong broad absorptions in the 1686–1650 cm^{-1} region which correspond to the asymmetrical C=O stretching vibration of the coordinated carboxylate and the amide groups.

The NMR assignments for complex **2** in DMSO-d_6 were based on the combined analysis of a series of ^1H–^1H and ^1H–^{13}C correlation spectra and are presented in Table 1. The numbering of the atoms is according to the crystallographic structure and is shown in Fig. 3. Upon complexation of the L_2H ligand, a characteristic chemical shift differentiation of the gemical protons on C-6 (by 0.7 ppm) and C-7 (by 0.9 ppm) takes place. The H-6 protons are distinguished from the H-7 protons based on the presence of a NOESY peak with the neighboring pyridinyl H-4 proton. The assignment is further confirmed through the observation of the long range heteronuclear coupling of H-4 and C-6 (Fig. 2).

3.2. Description of the structure

The molecular structure of **2** is given in Fig. 3 and selected bond distances and angles are listed in Table 3. The distorted octahedral environment of the Re atom in the structure of **1** is defined by the three facially bound CO groups and the NSO donor atom set of the tridentate ligand. The Re-carbonyl bond distances, 1.893(10)–1.941(13) Å, are consistent with those found in other Re-tricarbonyl complexes [23]. The Re–S, Re–N and Re–O bond distances fall well in the ranges observed in the analogous complexes. The Re–N1–C5–C6–C7–S1 six-membered ring in the coordination sphere adopts the boat conformation with C6 and Re displaced by 0.74 and 0.70 Å on the same side of the mean plane defined by the remaining four atoms. The Re–S1–C8–C9–C10–O1 six-membered ring in the coordination sphere adopts a distorted envelope conformation with C9 displaced by 0.81 Å out of the mean plane of the remaining five atoms (the largest deviation for the atoms on the plane is 0.12 Å for C10).

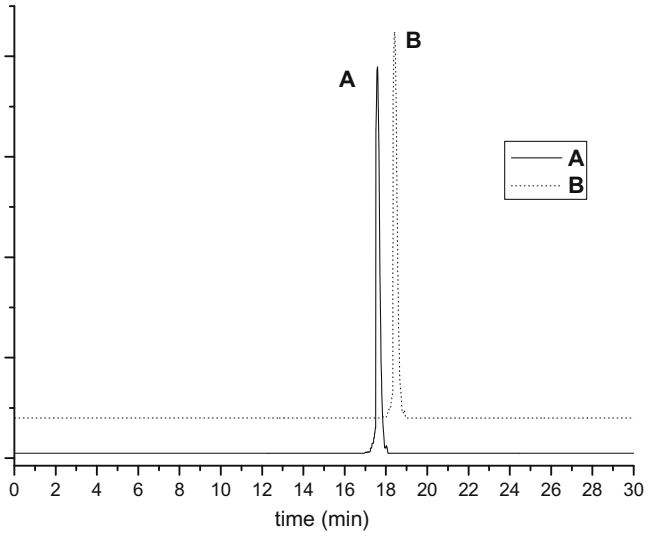


Fig. 4. Comparative reverse-phase HPLC chromatograms: (A) UV recording at 254 nm, complex **2,** retention time: 17.60 min and (B) radiometric detection, complex **4,** retention time: 18.2 min.

3.3. Synthesis of technetium-99m complexes

At technetium-99m level, the complexes *fac*-$^{99m}Tc(CO)_3(NSO)$, **3** and **4**, were obtained almost quantitatively (>90%) by heating the *fac*-$[^{99m}Tc(CO)_3(H_2O)_3]^+$ precursor at 70 °C in water (pH 6) in the presence of a 2×10^{-4} M concentration of the corresponding ligand. The reaction mixture was analyzed by HPLC and the analysis demonstrated that in both cases the reaction produces a single complex. The radioactivity recovery from the HPLC column after the injection of the reaction mixture was monitored and found to be quantitative. The identity of complexes **3** and **4** was established by HPLC comparison of their retention times to those of the analogous well-characterized rhenium complexes, **1** and **2**, respectively, by applying parallel radiometric and photometric detection (Fig. 4).

Both complexes were stable against high concentrations of L-histidine and L-cysteine. The HPLC analysis showed that at 24 h no trans-chelation product is formed and no decomposition of the complexes **3** and **4** occurs.

4. Conclusions

The two *N*-acetylcysteine derivative ligands L_1H and L_2H, synthesized by pyridinethylation (S-alkylation of the *N*-acetyl-L-cysteine and *N*-acetyl-D-penicillamine), react quantitatively with the $[NEt_4]_2[Re(CO)_3Br_3]$ and *fac*-$[^{99m}Tc(CO_3)(H_2O)_3]^+$ precursors and lead to the formation of a single, neutral $[M(CO)_3(NSO)]$ (M = Re, ^{99m}Tc) complex in high yield. The complexes were found to be stable at high concentrations of L-histidine and L-cysteine, a prerequisite for their further exploitation in the development of potential radiopharmaceuticals. The *N*-acetyl group present in cysteine may in principle be replaced by a great variety of pharmacophore groups through the formation of an amide bond. A major advantage of the presented work is that the pharmacophore-coupled cysteine can easily generate – in a single and high yield pyridinethylation step – tridentate SNO ligands suitable for coordination to the $[M(CO)_3]^+$ core.

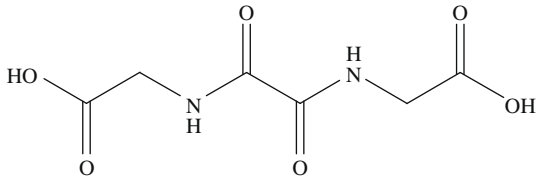
Supplementary data

CCDC 721589 contains the supplementary crystallographic data for complex **2**. These data can be obtained free of charge via <http://www.ccdc.cam.ac.uk/conts/retrieving.html>, or from the Cambridge Crystallographic Data Centre, 12 Union Road, Cambridge CB2 1EZ, UK; fax: (+44) 1223-336-033; or e-mail: deposit@ccdc.cam.ac.uk.

References

[1] S.S. Jurisson, J.D. Lydon, Chem. Rev. 99 (1999) 2205.
[2] S. Liu, D.S. Edwards, Chem. Rev. 99 (1999) 2235.
[3] W.A. Volkert, T.J. Hoffman, Chem. Rev. 99 (1999) 2269.

[4] P.A. Schubiger, R. Alberto, A. Smith, Bioconjugate Chem. 7 (1996) 165.
[5] S.R. Banerjee, K.P. Maresca, L. Francesconi, J. Valliant, J.W. Babich, J. Zubieta, J. Nucl. Med. Biol. 32 (2005) 1.
[6] R. Alberto, R. Schibli, A. Egli, P.A. Schubiger, J. Am. Chem. Soc. 120 (1998) 7987.
[7] R. Alberto, Top. Curr. Chem. 252 (2005) 1.
[8] R. Schibli, R. Bella, R. Alberto, E. Garcia-Garayoa, K. Ortner, U. Abram, P.A. Schubiger, Bioconjugate Chem. 11 (2000) 345.
[9] D. Van Staveren, S. Mundwiler, U. Hoffmanns, J. Pak, B. Spingler, N. Metzler-Nolte, R. Alberto, Org. Biomol. Chem. 2 (2004) 2593.
[10] O. Karagiorgou, G. Patsis, M. Pelecanou, C.P. Raptopoulou, A. Terzis, T. Siatra-Papastaikoudi, R. Alberto, I. Pirmettis, M. Papadopoulos, Inorg. Chem. 44 (2005) 4118.
[11] D. van Staveren, P. Benny, R. Waibel, P. Kurz, J.-L. Pak, R. Alberto, Helv. Chim. Acta 88 (2005) 447.
[12] H. He, J. Morely, E. Silva-Lopez, B. Bottenus, M. Montajano, G. Fugate, B. Twamley, P. Benny, Bioconjugate Chem. 20 (2009) 78.
[13] D. Desbouis, H. Struthers, V. Spiwok, T. Kuster, R. Schibli, J. Med. Chem. 51 (2008) 6689.
[14] C. Xavier, J-K. Pak, I. Santos, R. Alberto, J. Organomet. Chem. 692 (2007) 1332.
[15] R. Alsfasser, R. vanEldik, Inorg. Chem. 35 (1996) 628.
[16] R.H. Fish, J.J. Windle, W. Gaffield, J.R. Scherer, Inorg. Chem. 12 (1973) 855.
[17] R. Alberto, A. Egli, U. Abram, K. Hegetschweiler, V. Gramlich, P.A. Schubiger, J. Chem. Soc., Dalton Trans. (1994) 2815.
[18] G.M. Sheldrick, SHELXS-97, Structure Solving Program, University of Göttingen, Germany, 1997.
[19] G.M. Sheldrick, SHELXL-97, Crystal Structure Refinement Program, University of Göttingen, Germany, 1997.
[20] DIAMOND – Crystal and Molecular Structure Visualization, Ver. 3.1, Crystal Impact, Rathausgasse 30, 53111, Bonn, Germany.
[21] S. Alves, A. Paulo, J.D.G. Correia, A. Domingos, I. Santos, J. Chem. Soc. Dalton Trans. (2002) 4714.
[22] A. Vitor, S. Alves, J.D.G. Correia, A. Paulo, I. Santos, J. Organomet. Chem. 689 (2004) 4764.
[23] L. Wei, J. Babich, W.C. Eckelman, J. Zubieta, Inorg. Chem. 44 (2005) 2198, and references therein.



Scheme 1. The ligand oxamide-*N*,*N*′-diacetic acid (H_4L).

in 3D supramolecular architectures by hydrogen bonding and stacking interactions [22].

Utilization of oxamide-*N*,*N*′-diacetic acid (H_4L) (Scheme 1) represents a sequential step in our systematic study carried out on the assembly of flexible ligands under mild conditions. The flexibility of this ligand is based firstly on different donor atoms that can offer different chelate rings, secondly on the *trans* configuration of amide groups and the antiparallel orientation of the C=O groups of oxalyl moiety. Furthermore, the amide groups of the ligand can be a source of hydrogen bonds leading to the formation of supramolecular architectures. Solution studies which carried out in the absence of metal ions, suggest a total deprotonation of the ligand around pH ~13 [23]. Solid state studies of the ligand regarding Cu(II) suggest that its deprotonation is taking place only at the terminal carboxylic groups, acting as bis-monodentate (H_2L^{2-}), resulting in the configuration of 1D-polymeric chain [23]. According to further solid state studies, the ligand (L^{4-}) is totally deprotonated, acting as bis-tridentate, leading to the formulation of centrosymmetric binuclear molecules either with Ni(II) [23] or Cu(II) [24]. We initiated our synthetic efforts with transition metals (namely Co(II), Ni(II), Zn(II) and Cd(II)) and in all cases we isolated 1D polymers with the diprotonated ligand (H_2L^{-2}) utilizing only the carboxylate groups for coordination. Bearing in mind the spherical charge distribution of Ca^{2+} ions, and believing that it could force a different coordination of the ligand, we decided to include it in our synthetic attempts. This way, we have successfully isolated a novel two-dimensional polymeric structure containing the diprotonated ligand (H_2L^{2-}).

Herein, we report the synthesis and the structural, spectroscopic, and physicochemical characterization of five new oxamide-*N*,*N*′-diacetate complexes with the general formula $\{[M(H_2L)(H_2O)_x]\cdot 2(H_2O)\}_n$ where M = Co(II), $x = 4$ **(1)**; Ni(II), $x = 4$ **(2)**; Zn(II), $x = 3$ **(3)**; Cd(II), $x = 3$ **(4)**; Ca(II), $x = 2$ **(5)**. Compounds **1**–**4** are 1D polymers with the ligand being doubly deprotonated and coordinated through the carboxylic edges. **5** is a 2D polymer with the ligand utilizing all of the available oxygen atoms for coordination. Extended H-bonded networks are present in all of the above coordination polymers leading to interesting supramolecular architectures.

2. Experimental

2.1. General

All reagents and solvents were of commercially available reagent quality unless otherwise stated. All the reactions were performed at room temperature and no special conditions were demanded.

2.2. Instrumentation

IR spectra were recorded on a Perkin–Elmer Spectrum GX FT-IR spectrophotometer with samples as KBr pellets. UV–Vis spectra on solid state (Diffuse Reflectance Spectra) were recorded on a Shimadzu UVPC 2401 spectrophotometer; the samples were prepared as 1:2 solid mixtures in $BaSO_4$, which was also used as reference. TG-DTA analysis was carried out under nitrogen, at a scan speed of 5 °C/min, on a Shimadzu DTG 60 apparatus with the sample size being *ca.* 5 mg. X-ray powder diffraction patterns were recorded on a Siemens (now Bruker) D8 ADVANCE diffractometer. C, H and N analyses were conducted by the University of Ioannina, Greece, Microanalytical Service.

2.3. Preparation of the compounds

The ligand was synthesized by following the procedure reported [23]. All the products are air stable and insoluble in all common organic solvents such as MeOH, EtOH, THF, CH_3CN and DMSO.

H_4L (20.4 mg, 0.1 mmol) was dissolved in H_2O (5 ml) and then a solution of NaOH 0.5 M was added until pH ~5. After that a solution of $Co(NO_3)_2\cdot 6(H_2O)$ in H_2O (5 ml) in a 1:1 molar ratio was added. Suitable crystals for X-ray analysis were obtained by slow evaporation

Table 1
Summary of crystal data and refinement results

	1	**2**	**3**	**4**	**5**
Formula	$C_6H_{18}CoN_2O_{12}$	$C_6H_{18}N_2NiO_{12}$	$C_6H_{16}N_2O_{11}Zn$	$C_6H_{16}CdN_2O_{11}$	$C_6H_{14}CaN_2O_{10}$
FW	369.16	368.94	357.58	404.61	314.27
Crystal system	triclinic	triclinic	monoclinic	monoclinic	orthorhombic
Space group	$P\bar{1}$	$P\bar{1}$	$C2/c$	$C2/c$	$Pbcn$
Crystal size	0.20 × 0.09 × 0.04	0.20 × 0.09 × 0.04	0.25 × 0.18 × 0.09	0.16 × 0.07 × 0.06	0.23 × 0.18 × 0.05
a (Å)	4.9688(5)	4.9548(10)	6.9185(2)	7.0333(3)	12.0318(3)
b (Å)	5.4759(4)	5.5428(11)	7.6934(3)	7.9908(3)	6.8082(4)
c (Å)	12.0615(11)	11.998(2)	23.2758(7)	23.2776(6)	14.5930(8)
α (°)	86.876(7)	86.75(3)	90	90	90
β (°)	78.724(7)	78.98(3)	94.120(2)	92.812(3)	90
γ (°)	86.800(8)	86.93(3)	90	90	90
V (Å^3)	321.02(5)	322.61(11)	1235.69(7)	1306.67(8)	1195.38(10)
Z	1	1	2	2	4
D_{calc} (g cm^{-3})	1.910	1.899	1.922	2.057	1.746
T (K)	120(2)				
μ (mm^{-1})	1.408	1.574	2.051	1.731	0.508
Total reflections (R_{int})	5320 (0.0265)	5285 (0.0426)	7714 (0.0276)	7963 (0.0361)	13980 (0.0619)
Data/restrains/parameters	1472/0/78	1479/0/128	1421/0/116	1495/0/116	1367/0/108
Goodness-of-fit	1.057	1.095	1.082	1.052	1.024
R_1/wR_2 (observed)	0.0231/0.0498	0.0396/0.0877	0.0210/0.0460	0.0199/0.0391	0.0334/0.0810
R_1/wR_2 (all)	0.0292/0.0521	0.0446/0.0898	0.0275/0.0482	0.0257/0.0407	0.0481/0.0871
$\Delta\rho_{max}/\Delta\rho_{min}$ (e Å^3)	0.486/−0.258	1.341/−0.478	0.453/−0.299	0.419/−0.515	0.409/−0.264

after several days. The crystals were collected, washed with cold water and ethanol and dried in air. $[Co(H_2L)(H_2O)_4]\cdot 2(H_2O)$ (**1**), *Anal.* Calc. for (**1**) $C_6H_{18}CoN_2O_{12}$: C, 19.52; H, 4.91; N, 7.59. Found: C, 19.44; H, 4.97; N, 7.33%. IR (cm^{-1}): 3432 (s), 3332 (s), 2942 (w), 1663 (s), 1638(s), 1579 (w), 1518 (m), 1391 (s), 1309 (s), 1217 (m), 1063 (w), 1007 (m), 824 (w), 695 (m). Electronic spectrum (DRS, $BaSO_4$ solution) (nm): 457(sh), 488(sh), 507. 619.

Similar procedures were followed for the preparation of (**2**)–(**5**) compounds. The yields were in the range 65–75%.

$[Ni(H_2L)(H_2O)_4]\cdot 2(H_2O)$ (**2**), *Anal.* Calc. for (**2**) $C_6H_{18}N_2NiO_{12}$: C, 19.53; H, 4.91; N, 7.59. Found: C, 19.42; H, 4.92; N, 7.45%. IR (cm^{-1}): 3434 (s), 3331 (s), 2942 (w), 1657 (s), 1638 (s), 1580 (m), 1520 (s), 1392 (s), 1309 (s), 1217 (m), 1123 (w), 1062 (w), 1007 (w), 827 (w), 697 (w). Electronic spectrum (DRS, $BaSO_4$ solution) (nm): 364, 661.

$[Zn(H_2L)(H_2O)_3]\cdot 2(H_2O)$ (**3**), *Anal.* Calc. for (**3**) $C_6H_{16}N_2O_{11}Zn$: C, 20.15; H, 4.51; N, 7.83. Found: C, 20.02; H, 4.42; N, 7.75%. IR (cm^{-1}): 3384 (s), 3305 (s), 2935 (s), 1663 (s), 1639 (m), 1525 (s),1392 (s), 1292 (s), 1223 (m), 1113 (w), 887 (w), 794 (w), 715 (w), 618 (w).

$[Cd(H_2L)(H_2O)_3]\cdot 2(H_2O)$ (**4**), *Anal.* Calc. for (**4**) $C_6H_{16}CdN_2O_{11}$: C, 17.81; H, 3.99; N, 6.92. Found: C, 17.72; H, 3.92; N, 6.85%. IR (cm^{-1}): 3449 (s), 3352 (s), 2981 (w), 2986 (w), 1655 (s), 1639 (m), 1598 (s), 1540 (m), 1439 (m), 1401 (s), 1324 (w), 1236 (w), 1056 (w), 1001 (w), 933 (w), 720 (m), 644 (m).

$[Ca(H_2L)(H_2O)_2]\cdot 2(H_2O)$ (**5**), *Anal.* Calc. for (**5**) $C_6H_{14}CaN_2O_{10}$: C, 22.93; H, 4.49; N, 8.91. Found: C, 22.44; H, 4.97; N, 8.23%. IR (cm^{-1}): 3453 (s), 3282 (s), 3088 (m), 2950 (m), 1655 (s), 1629 (s), 1533 (m), 1441 (s), 1402 (s), 1326 (m), 1268 (m), 1246 (m), 1064 (m), 999 (m), 928 (m), 882 (m), 786 (m), 719 (m).

2.4. X-ray crystallography

X-ray diffraction intensities were collected at 120 K on a Nonius Kappa CCD diffractometer with φ and ω scans with κ offsets and Mo Kα radiation, $\lambda = 0.71073$ Å. The Denzo-Scalepack [25] or EVALCCD [26] program packages were used for cell refinements and data reductions. A semi-empirical absorption correction (SADABS) [27] was applied to all data. SHELX-97 [28] was used for structure solution (SHELXS) and refinement (SHELXL). The structures were solved by direct methods and all non-hydrogen atoms were refined anisotropically. Some of the methylene H atoms were located from different Fourier maps, but finally all of them were introduced in idealized positions and treated as riding on the parent non-hydrogen atoms. The amide and water protons were located from Fourier maps and refined smoothly isotropically, without any SHELX

Table 2
Selected bond distances (Å) and angles (°) for complexes **1** and **2**.

Complex **1**[a]				
Bond distances				
Co(1)–O(1)	2 × 2.0873(13)	Co(1)–O(1W)		2 × 2.0965(19)
Co(1)–O(2W)	2 × 2.0818(16)			
Bond angles				
O(2W)–Co(1)–O(2W)#1	180.0	O(2W)–Co(1)–O(1)#1		2 × 92.14(7)
O(2W)–Co(1)–O(1)	2 × 87.86(7)	O(1)#1–Co(1)–O(1)		180.0
O(2W)–Co(1)–O(1W)#1	2 × 91.82(7)	O(1)–Co(1)–O(1W)#1		2 × 81.31(6)
O(2W)–Co(1)–O(1W)	2 × 88.18(7)	O(1)–Co(1)–O(1W)		2 × 98.69(6)
O(1W)#1–Co(1)–O(1W)	180.0			
Hydrogen bonds				
Donor–H···acceptor	d(D–H)	d(H···A)	d(D···A)	‹(DHA)
N(1)–H(1)···O(3W)#3	0.82(2)	2.28(2)	2.994(3)	146.0(19)
O(1W)–H(11)···O(2)	0.75(3)	2.24(3)	2.864(2)	141(2)
O(1W)–H(12)···O(2)#4	0.84(3)	2.00(3)	2.815(2)	163(3)
O(2W)–H(21)···O(1)#5	0.80(3)	1.97(3)	2.765(3)	172(2)
O(2W)–H(22)···O(3W)	0.82(3)	1.92(3)	2.736(2)	169(2)
O(3W)–H(31)···O(2)#6	0.83(2)	2.02(2)	2.755(2)	148(2)
Complex **2**[b]				
Bond distances				
Ni(1)–O(1)	2 × 2.050(2)	Ni(1)–O(1W)		2 × 2.061(3)
Ni(1)–O(2W)	2 × 2.069(2)			
Bond angles				
O(1)#1–Ni(1)–O(1)	180.0	O(1)–Ni(1)–O(1W)		2 × 83.30(10)
O(1)–Ni(1)–O(1W)#1	2 × 96.70(10)	O(1W)#1–Ni(1)–O(1W)		180.0
O(1)#1–Ni(1)–O(2W)	2 × 88.72(10)	O(1)–Ni(1)–O(2W)		2 × 91.28(10)
O(1W)#1–Ni(1)–O(2W)	2 × 92.31(11)	O(1W)–Ni(1)–O(2W)		2 × 87.69(11)
O(2W)–Ni(1)–O(2W)#1	180.0			
Hydrogen bonds				
Donor–H···acceptor	d(D–H)	d(H···A)	d(D···A)	‹(DHA)
O(3W)–H(32)···O(3)	0.81(5)	2.03(5)	2.829(4)	171(5)
O(3W)–H(31)···O(2)#3	0.88(4)	2.06(4)	2.776(3)	138(4)
N(1)–H(1)···O(3W)#4	0.85(4)	2.23(4)	3.003(4)	151(4)
O(1W)–H(11)···O(2)#3	0.77(5)	2.11(5)	2.856(4)	162(4)
O(1W)–H(12)···O(2)#1	0.88(6)	2.03(5)	2.777(3)	143(5)
O(2W)–H(21)···O(1)#5	0.82(5)	1.99(5)	2.794(4)	171(4)
O(2W)–H(22)···O(3W)#1	0.81(5)	1.96(5)	2.759(3)	174(4)
O(3W)–H(32)···O(3)	0.80(2)	2.02(2)	2.814(2)	173(2)

[a] Symmetry transformations used to generate equivalent atoms: #1 $-x+1, -y, -z+1$; #2 $-x+1, -y-1, -z+2$; #3 $x+1, y-1, z$; #4 $-x+1, -y-1, -z+1$; #5 $x-1, y, z$; #6 $x, y+1, z$.

[b] Symmetry transformations used to generate equivalent atoms: #1 $-x, -y+1, -z+2$; #2 $-x, -y+2, -z+1$; #3 $x, y-1, z$; #4 $x-1, y+1, z$; #5 $-x-1, -y+1, -z+2$.

restrains. A summary of crystal data and structure refinement for the compounds are provided in Table 1. Figures were drawn with X-Seed [29].

3. Results and discussion

3.1. Synthetic comments

The reaction of $M(NO_3)_2{\cdot}yH_2O$ (M = Co, Ni, Zn, $y = 6$; M = Cd, Ca, $y = 4$) with one equivalent of oxamide-*N*,*N*′-diacetic acid (H_4L) in aqueous media and conventional workup leads to the isolation of the polymeric complexes $\{[M(H_2L)(H_2O)_x]\cdot 2(H_2O)\}_n$ where M = Co(II), $x = 4$ **(1)**; Ni(II), $x = 4$ **(2)**; Zn(II), $x = 3$ **(3)**; Cd(II), $x = 3$ **(4)**; Ca(II), $x = 2$ **(5)** according to the balance Eq. (1):

$$n\mathrm{M(NO_3)_2}\cdot y\mathrm{H_2O} + n\mathrm{H_4L} \xrightarrow{\mathrm{H_2O}} \{[\mathrm{M(H_2L)(H_2O)}_x]\cdot 2(\mathrm{H_2O})\}_n + 2n\mathrm{H^+} + 2n\mathrm{NO_3^-} + (y-x-2)n\mathrm{H_2O} \quad (1)$$

1–5

In all complexes the ligand is in its doubly deprotonated form as it is expected from the low pK_a of the carboxylic group. The solid products are pure and homogeneous as derived from comparisons of the X-ray powder patterns (XRPD's) of the bulk samples with the corresponding patterns simulated from the crystal structures.

Few features of the reaction represented by chemical Eq. (1) deserve comments: First, the appearance of HNO_3 in the products might imply that complexes **1**–**5** (which contain deprotonated organic ligands) decompose under "acidic" conditions, i.e. excess of protons could move the reaction to the left. We did not have such evidence probably due to high dilution. A second point of synthetic interest is the absence of a base from the reaction mixtures that lead to **1**–**5**. The employment of base in the $M(NO_3)_2{\cdot}yH_2O/H_4L$ reaction system in H_2O leads to the precipitation of solids which produce XRPD's with strong background indicating amorphous phases. On the other hand, microanalytical results on the above solids suggest formulations that are not reasonable. When the metal to ligand ratio was changed to 2:1 and in the absence of base the same products were isolated but in smaller yields. Maintaining the metal to ligand ratio to 2:1 and adding small amounts of base (i.e. up to pH = 6.5) insoluble precipitates were isolated which are formulated as $M_2L{\cdot}xH_2O$. Our efforts towards the structural characterization of those products are in progress.

From the use of H_2O viewpoint, the preparation of the five polymeric complexes may be considered as a "green" procedure [30]. The use of environmentally benign solvents (and solventless systems) has been one of the most active areas of green chemistry over the past 10 years [26].

3.2. Description of the crystal structures

Compounds **1** and **2** are isomorphous and only the structure of **2** will be described in detail. Selected inter-atomic bond distances and angles and additionally H-bond's geometrical characteristics, for both compounds are presented in Table 2. The crystal structure of compound **2** consists of linear chains (Fig. 1) running parallel to the $[0\ \bar{1}\ 1]$ crystallographic direction of the unit cell, and two lattice water molecules per metal ion held together with hydrogen bonds.

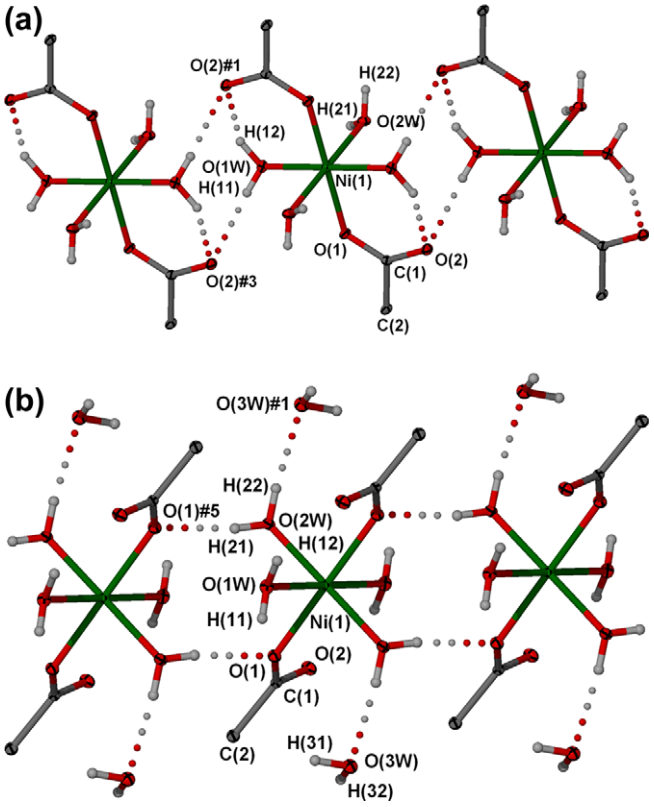


Fig. 2. Parts of the 1D H-bonded chains present in the crystal structure of **2**. (a) H-bonds through water O(1W) parallel to *c*. (b) H-bonds through water O(2W) parallel to *a*. The oxamide part of the ligand has been omitted for clarity. Symmetry transformations to generate equivalent atoms: #1 $-x, -y+1, -z+2$; #3 $x, y-1, z$; #5 $-x-1, -y+1, -z+2$.

Each metal ion is coordinated in a rather regular octahedron to two oxygen atoms belonging to two monodentate carboxylates of two symmetry related H_2L^{2-} ligands and four terminal water molecules (Fig. 1). The oxamide ligand is deprotonated only at the terminal carboxylate groups and acts as a μ_2-bridge.

There is an extended array of H-bonds that stabilize the overall crystal structure and leads to a 3D supramolecular architecture. Practically, each 1D chain is connected to four surrounding chains through H-bonds. The first coordinated water molecule acts as a donor to one intra-chain $\{O(1W)–H(12)\cdots O(2)\#1, (-x, -y+1, -z+2)\}$ H-bond to the uncoordinated oxygen atom of the symmetry related carboxylate in the same metal coordination sphere, and to one inter-chain $\{O(1W)–H(11)\cdots O(2)\#3, (x, y-1, z)\}$ H-bond to the uncoordinated oxygen atom of the symmetry related carboxylate in a different metal coordination sphere. This way, a 1D H-bonded chain is formed that runs parallel to *c* (Fig. 2a). The second water molecule

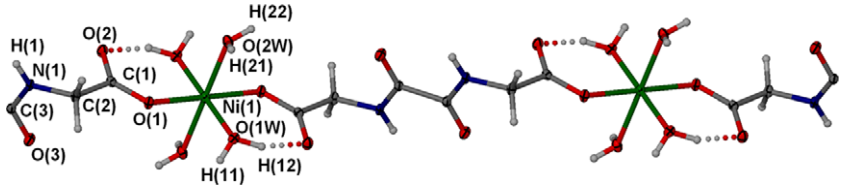


Fig. 1. A part of the linear chains in **2** showing the labeling scheme, the coordination of the ligand, the coordination sphere of the metal ion, and the intra-chain H-bonds with 40% probability thermal ellipsoids. The lattice water molecules have been omitted for clarity. Compound **2** has a very similar structure.

participates in two H-bonds as a donor. The first is to an adjacent coordinated carboxylate oxygen {O(2W)–H(21)···O(1)#5, $(-x-1, -y+1, -z+2)$}, and leads to the formation of H-bonded 1D chains parallel to *a*. The second is to the lattice water molecule {O(2W)–H(22)···O(3W)#1, $(-x, -y+1, -z+2)$} (Fig. 2b).

Apart from the previously described, the lattice water molecule participates in three additional H-bonds, reinforcing this way the overall 3D supramolecular architecture. As an acceptor it interacts with the amide bond {N(1)–H(1)···O(3W)#4, $(x-1, y+1, z)$} of the ligand, and as a donor interacts with a different amide bond {O(3W)–H(32)···O(3)} and an uncoordinated carboxylate oxygen atom {O(3W)–H(31)···O(2)#3, $(x, y-1, z)$}. A packing diagram, including all the previously described interactions is shown in Fig. 3.

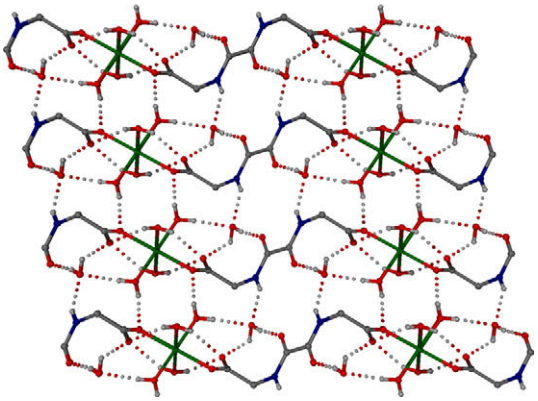


Fig. 3. A packing diagram of **2**, shown down to *b* axis. Methylene hydrogen atoms have been omitted for clarity.

The simplest way to describe the topology of the 3D supramolecular structure [31] is to ignore the lattice water molecule and check the connectivity of the obvious node (either the metal ion or the asymmetric unit). This way, a uninodal 6-connected net is formed with $4^{12}.6^3$-**pcu** topology [32,33]. When the lattice water is taken into account two extra links between the nodes are formed. The new net is a uninodal 8-connected hexagonal primitive net with $3^6.4^{18}.5^3.6$-**hex** topology [32,33].

Compounds **3** and **4** are isomorphous with substantial structural differences due to the larger ionic radius of Cd^{2+}. Again only the structure of **3** will be described in detail and additionally the minor differences between the two structures. Selected interatomic bond distances and angles and H-bond's geometrical characteristics, for both compounds are presented in Table 3.

The crystal structure of compounds **3** and **4** consist of zig-zag chains (Fig. 4) running parallel to the $[\bar{1}\ 0\ 1]$ crystallographic direction of the unit cell, and two lattice water molecules per metal ion held together with hydrogen bonds. In **3**, Zn(II), being bonded to two carboxylate oxygen atoms belonging to two different H_2L^{2-} ligands, and three water molecules, is five coordinated in a trigonal

Table 3
Selected bond distances (Å) and angles (°) for complexes **3** and **4**.

Complex **3**[a]				
Bond distances				
Zn(1)–O(1)	2 × 2.0032(11)	Zn(1)–O(1W)		2 × 2.1601(11)
Zn(1)–O(2W)	1.9911(16)	Zn(1)–O(2)		2 × 2.7815(11)
Bond angles				
O(2W)–Zn(1)–O(1)	2 × 127.74(3)	O(1)–Zn(1)–O(1W)		2 × 89.00(4)
O(1)–Zn(1)–O(1)#1	104.52(6)	O(2W)–Zn(1)–O(1W)		2 × 89.04(3)
O(1)#1–Zn(1)–O(1W)	2 × 92.18(4)	O(1W)–Zn(1)–O(1W)#1		178.08(7)
Hydrogen bonds				
Donor–H···acceptor	d(D–H)	d(H···A)	d(D···A)	‹(DHA)
N(1)–H(1)···O(3W)#3	0.84(2)	2.19(2)	2.9141(19)	144.7(19)
N(1)–H(1)···O(3)#2	0.84(2)	2.32(2)	2.6950(17)	107.6(17)
O(1W)–H(11)···O(3W)	0.78(2)	1.94(2)	2.7205(17)	176(2)
O(1W)–H(12)···O(1)#4	0.86(2)	1.86(2)	2.7242(16)	174(2)
O(2W)–H(21)···O(1W)#5	0.79(2)	1.98(2)	2.7536(16)	166(2)
O(3W)–H(31)···O(2)#6	0.76(2)	2.04(2)	2.7321(18)	152(2)
O(3W)–H(32)···O(3)	0.82(3)	1.96(3)	2.7743(17)	168(2)
Complex **4**[b]				
Bond distances				
Cd(1)–O(1)	2 × 2.2635(14)	Cd(1)–O(1W)		2 × 2.3138(15)
Cd(1)–O(2W)	2.189(2)	Cd(1)–O(2)		2 × 2.6647(15)
Bond angles				
O(2W)–Cd(1)–O(1)#1	2 × 132.87(4)	O(1)#1–Cd(1)–O(1)		94.26(7)
O(2W)–Cd(1)–O(1W)	2 × 91.06(4)	O(1)#1–Cd(1)–O(1W)		2 × 93.96(5)
O(1)–Cd(1)–O(1W)	2 × 84.59(6)	O(1W)–Cd(1)–O(1W)#1		177.89(9)
O(1)–Cd(1)–O(2)	2 × 52.59(5)	O(2W)–Cd(1)–O(2)		2 × 80.55(3)
O(1)–Cd(1)–O(2)#1	2 × 146.20(5)	O(2)–Cd(1)–O(2)#1		161.08(6)
O(1W)–Cd(1)–O(2)	2 × 89.57(5)	O(1W)–Cd(1)–O(2)#1		2 × 90.78(5)
Hydrogen bonds				
Donor–H···acceptor	d(D–H)	d(H···A)	d(D···A)	‹(DHA)
N(1)–H(1)···O(3W)#3	0.81(2)	2.29(2)	2.982(3)	144(2)
O(1W)–H(11)···O(3W)	0.77(3)	1.95(3)	2.719(2)	174(3)
O(1W)–H(12)···O(1)#4	0.76(3)	1.88(3)	2.639(2)	171(3)
O(2W)–H(21)···O(1W)#5	0.81(3)	1.90(3)	2.702(2)	169(3)
O(3W)–H(31)···O(3)	0.78(3)	2.05(3)	2.816(2)	170(3)
O(3W)–H(32)···O(2)#6	0.80(3)	2.09(3)	2.841(2)	157(3)

[a] Symmetry transformations to generate equivalent atoms: #1 $-x+1, y, -z+1/2$; #2 $-x+3/2, -y+1/2, -z$; #3 $x+1, y, z$; #4 $x-1/2, y-1/2, z$; #5 $x+1/2, y-1/2, z$; #6 $x-1/2, y+1/2, z$.

[b] Symmetry transformations to generate equivalent atoms: #1 $-x+1, y, -z+1/2$; #2 $-x+3/2, -y+1/2, -z$; #3 $x+1, y, z$; #4 $x-1/2, y-1/2, z$; #5 $x+1/2, y-1/2, z$; #6 $x-1/2, y+1/2, z$.

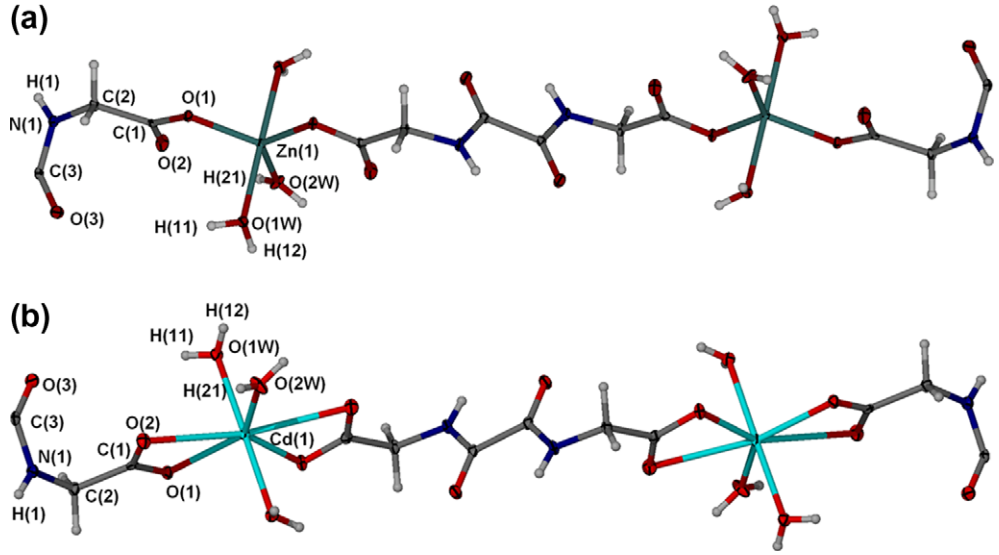


Fig. 4. Parts of the zig-zag chains in **3** (a) and **4** (b) showing the labeling scheme, the coordination of the ligand, the coordination sphere of the metal ion, and the intra-chain H-bonds with 40% probability thermal ellipsoids. The lattice water molecules have been omitted for clarity.

bipyramidal environment. In **4**, Cd(II) can be considered as seven coordinated in a pentagonal bipyramidal environment and it is bonded to asymmetrically chelated carboxylates belonging to two different H_2L^{2-} ligands, and three water molecules. The oxamide ligand is deprotonated only at the terminal carboxylate groups and acts as a bridge between two metal ions in both structures. There are not any more important differences between the crystals structures and we continue describing polymer **3**.

There is an extended array of H-bonds that stabilize both crystal structures and lead to 3D supramolecular architectures. Instead of an inversion center that exists on the metal atoms in **1** and **2**, in **3** and **4** there is a C_2 axis which coincides with the M–O(2W) bond (M = Zn(1) and Cd(1) in **3** and **4**, respectively). Due to this difference, the H-bonded array that formed in the later compounds is different from the array already described for compounds **1** and **2**. As in **1** and **2** each chain is connected via H-bonds to four adjacent chains, but the presence of only three water molecules in the coordination sphere of the metal ions forms a different motif of H-bonds. The water molecule O(2W) acts as a donor to a symmetry related O(1W) {O(2W)–H(21)···O(1W)#5, $(x + 1/2, y - 1/2, z)$} forming, this way, 1D H-bonded chains parallel to *b*. Those chains are connected to each other with another H-bond {O(1W)–H(12)···O(1)#4, $(x - 1/2, y - 1/2, z)$} leading to the formation of 2D layers parallel to *ab* plane (Fig. 5).

The lattice water molecule participates in four H-bonds, as in **1** and **2**, reinforcing this way the overall 3D supramolecular architecture. As an acceptor it interacts with the amide bond {N(1)–H(1)···O(3W)#3, $(x + 1, y, z)$} of the ligand, and one of the coordinated water molecules {O(1W)–H(11)···O(3W)}, and as a donor interacts with a different amide bond {O(3W)–H(32)···O(3)} and

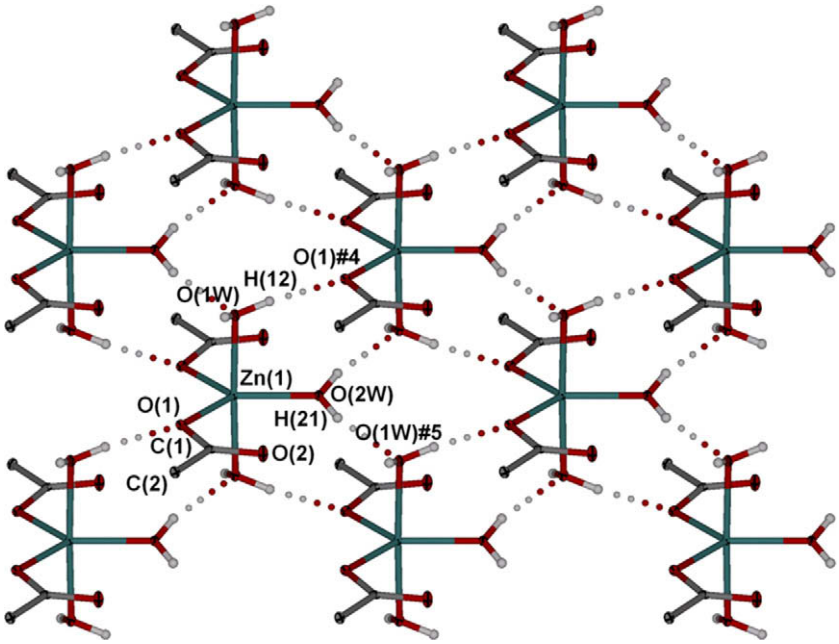


Fig. 5. Part of the 2D H-bonded layers present in the crystal structure of **3** down to *c* axis. The oxamide part of the ligand has been omitted for clarity. Symmetry transformations to generate equivalent atoms: #4 $x - 1/2, y - 1/2, z$; #5 $x + 1/2, y - 1/2, z$.

an uncoordinated carboxylate oxygen atom {O(3W)–H(31)···O(2)#6, $(x-1/2, y+1/2, z)$}. A packing diagram, including all the previously described interactions is shown in Fig. 6.

The same two scenarios used for the description of the topology of the supramolecular structures of **1** and **2**, can be applied here for **3** and **4**, as well; they lead to 6- and 8-connected nets with the same topology.

The crystal structure of **5** consists of 2D layers parallel to the *bc* plane of the cell, and two lattice water molecules per calcium atom held together with H-bonds. Selected inter-atomic bond distances and angles and H-bond's geometrical characteristics, are presented in Table 4.

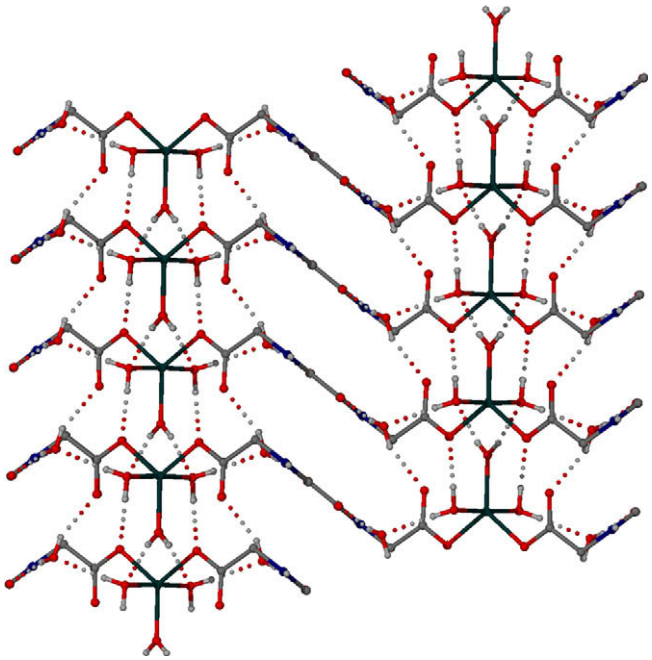


Fig. 6. A packing diagram of **3**, shown down to *a* axis. Methylene hydrogen atoms have been omitted for clarity.

The ligand is doubly deprotonated, but this time utilizes all oxygen atoms for coordination, bridging this way four Ca(II) atoms (Fig. 7a). Each Ca(II) atom is eight coordinated in a distorted square antiprismatic environment [34]. The calcium atom is coordinated to four different ligands via two symmetrically chelated carboxylate groups, and two amide oxygens; its coordination sphere is saturated with two water molecules (Fig. 7b). In this way, a 2D layer is formulated possessing 4^4-**sql** topology [32] (Fig. 8).

Hydrogen bonding interactions are a dominant feature of the crystal structure of **5**, as in the structures of **1**–**4**. Eventually, a 3D supramolecular architecture is formed. There is one intra-layer H-bond generated from the amide N–H, which interacts with a symmetry related coordinated carboxylate oxygen {N(1)–H(1)···O(2)#6, $(-x, -y+1, -z+2)$}. The 2D layers interact directly through H-bonds and indirectly, through the lattice water molecule. The coordinated water molecule O(1W) acts as a donor to a symmetry related coordinated carboxylate oxygen belonging to a different layer {O(1W)–H(11)···O(1)#7, $(-x+1/2, y-1/2, z)$}. The lattice water molecule participates in three hydrogen bonds and acts as a bridge between two different 2D layers. As an acceptor it is connected to the coordinated water molecule {O(1W)–H(12)···O(2W)#2, $(-x, y-1, -z+3/2)$}. As a donor it is connected to a coordinated carboxylate oxygen belonging to the original layer {O(2W)–H(22)···O(2)} and to a coordinated water molecule of an adjacent layer {O(2W)–H(21)···O(1W)#8, $(x-1/2, y+1/2, -z+3/2)$.

An interesting feature of the structure is revealed when we see the crystal down to *b* axis (Fig. 9). An H-bonded water chain is formed by alternating connection of coordinated and lattice water molecules. The water chain can be calcified according to Mascal et al. [35] as C_2. The H-bonds involved in the formation of the chain are: O(1W)–H(12)···O(2W)#2 $(-x, y-1, -z+3/2)$ and O(2W)–H(21)···O(1W)#8 $(x-1/2, y+1/2, -z+3/2)$.

A search in CSD [36] reveals a compound (VUHWEA) with the same chemical formula and lattice geometrical characteristics [37]. The structure of that compound is different from the structure of **5**. The ligand is utilizing all O atoms for coordination to Ca, but it bridges only two metal ions in a much distorted manner.

3.3. Spectroscopy

The IR spectra of all compounds display a broad strong band centered at 3400 cm^{-1}, which reveals the presence of water in all cases.

Table 4
Selected bond distances (Å) and angles (°) for complex **5**.

Bond distances			
Ca(1)–O(1)	2 × 2.4918(13)	Ca(1)–O(2)	2 × 2.5158(14)
Ca(1)–O(3)#2	2 × 2.4342(13)	Ca(1)–O(1W)	2 × 2.3968(14)
Bond angles			
O(1W)#1–Ca(1)–O(1W)	122.66(7)	O(1W)–Ca(1)–O(3)#2	2 × 74.06(5)
O(1W)–Ca(1)–O(3)#3	2 × 79.19(5)	O(1W)#1–Ca(1)–O(1)	2 × 143.69(5)
O(1W)–Ca(1)–O(1)	2 × 76.16(5)	O(3)#2–Ca(1)–O(1)	2 × 137.00(4)
O(3)#3–Ca(1)–O(1)	2 × 80.65(4)	O(1)–Ca(1)–O(1)#1	107.61(6)
O(1W)#1–Ca(1)–O(2)	2 × 95.68(4)	O(1W)–Ca(1)–O(2)	2 × 125.18(5)
O(3)#2–Ca(1)–O(2)	2 × 157.94(4)	O(3)#3–Ca(1)–O(2)	2 × 75.58(4)
O(1)–Ca(1)–O(2)	2 × 52.33(4)	O(1)#1–Ca(1)–O(2)	2 × 77.29(4)
O(2)–Ca(1)–O(2)#1	90.56(6)	O(3)#2–Ca(1)–O(3)#3	122.42(7)

Hydrogen bonds Donor–H···acceptor	d(D–H)	d(H···A)	d(D···A)	∢(DHA)
N(1)–H(1)···O(3)#5	0.90(3)	2.30(2)	2.716(2)	107.8(18)
N(1)–H(1)···O(2)#6	0.90(3)	2.07(3)	2.938(2)	162(2)
O(1W)–H(11)···O(1)#7	0.90(3)	1.89(3)	2.7536(19)	160(3)
O(1W)–H(12)···O(2W)#2	0.93(3)	1.77(3)	2.693(2)	169(3)
O(2W)–H(21)···O(1W)#8	0.88(3)	1.99(3)	2.850(2)	166(3)
O(2W)–H(22)···O(2)	0.89(3)	1.86(3)	2.738(2)	171(3)

Symmetry transformations to generate equivalent atoms: #1 $-x, y, -z+3/2$; #2 $-x, y-1, -z+3/2$; #3 $x, y-1, z$; #4 $x, y+1, z$; #5 $-x, -y+2, -z+2$; #6 $-x, -y+1, -z+2$; #7 $-x+1/2, y-1/2, z$; #8 $x-1/2, y+1/2, -z+3/2$.

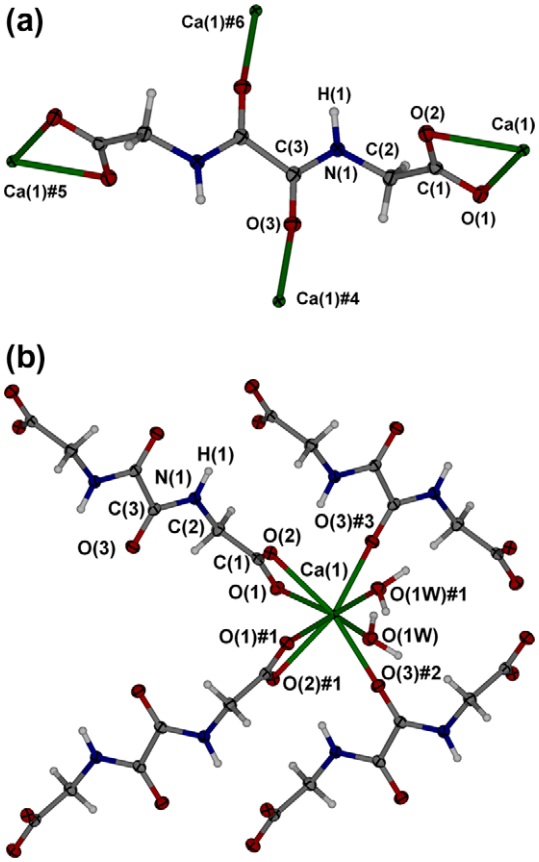


Fig. 7. The coordination of the ligand (a) and the coordination sphere of the metal (b) in **5** with 40% probability ellipsoids and the labeling scheme. Symmetry transformations: #1 $-x, y, -z+3/2$; #2 $-x, y-1, -z+3/2$; #3 $x, y-1, z$; #4 $x, y+1, z$; #5 $-x, -y+2, -z+2$; #6 $-x, -y+1, -z+2$; #7 $-x+1/2, y-1/2, z$; #8 $x-1/2, y+1/2, -z+3/2$.

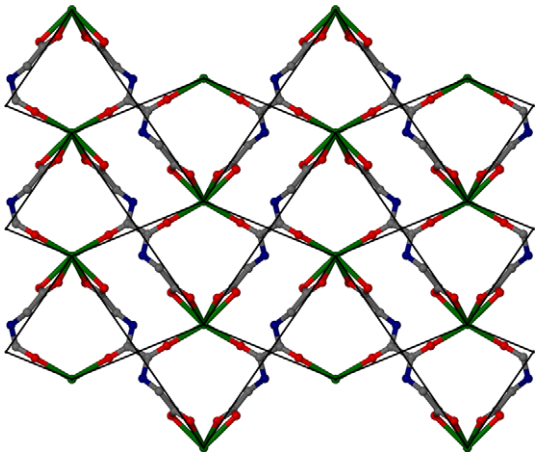


Fig. 8. A part of the 2D layer formed in **5**, shown down to *a*. Hydrogen atoms and coordinated water molecules have been omitted for clarity. The topological net formed is embedded in black.

In addition, a single absorption of medium intensity centered at 3330 cm^{-1} ν(N–H) (stretching band), reveal the existence of N–H amide groups. A strong band centered at 1638 cm^{-1} for compounds **1**–**4** corresponds to the carbonyl group of the amide bond, while for **5** this absorption shifts to lower value (1629 cm^{-1}), indicating also the coordination of the oxalyl moiety. The ν_a(COO) and ν_{as},(COO)

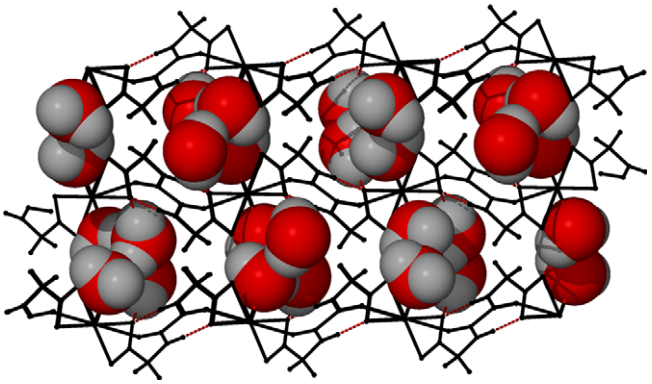


Fig. 9. A packing diagram of **5** shown down to *b*. The water molecules are in space filling mode; the rest of the atoms are drawn black to emphasize the position of the chains between the layers parallel to *bc* plane.

stretching vibrations of carboxylate groups appear as strong absorptions centered at 1663 and 1390 cm^{-1} for **1**–**3**, 1655 and 1402 cm^{-1} for **4** and **5**, respectively. These values are consistent with bis-monodentate carboxylate coordination for **1**–**3** and bis-chelate carboxylate coordination for **4** and **5** [38]. The diffuse reflectance spectra (DRS) of all compounds reveals two absorption bands at 205 and 258 nm which can be assigned to $\pi \rightarrow \pi^*$ transfer transition of the ligand. Furthermore, the DRS of **1** shows subtly distinguishable shoulders around 457 and 488 nm which are attributed to spin–orbit coupling effects or to transitions to doublet states, a shoulder around 619 nm can be attributed to the $^4T_{1g}(F) \rightarrow {}^4A_{2g}$ transition and the major peak at 507 nm can be assigned to the $^4T_{1g}(F) \rightarrow {}^4T_{1g}(P)$ transition. As regard to the diffuse reflectance spectra of compound **2**, this is typical to an octahedral Ni(II) complex, exhibiting two peaks at 364 and 661 nm corresponding to $^3A_{2g} \rightarrow {}^3T_{1g}(P)$ and $^3A_{2g} \rightarrow {}^3T_{1g}(F)$ transitions, respectively [39].

3.4. Thermal analysis

In a typical measurement, TG curve of the cobalt polymer **1** can be divided into two areas corresponding to two different weight losses. When **1** is heated under nitrogen, an endothermic dehydration starts at 79 °C which is completed at 180 °C. The observed weight loss of 28.2% is in agreement with the calculated value of 29.3% of the four coordinated and two lattice water molecules. The anhydrous intermediate is stable up to 248 °C; and at this point the second decomposition process begins (weight loss 46.6%), as shown by the DTA curve. The decomposition proceeds up to 700 °C, where the purple final residue corresponds to Co_2O_3 (found 23.1%, calculated 22.2%). Compounds **2**–**4** show similar TG DTA curves, where the final residues are in good agreement with the calculated values.

The TG curve of the calcium polymer **5** can be divided into three areas corresponding to three different weight losses. When the calcium compound **5** is heated under nitrogen, a two stepped endothermic dehydration occurs; the first step starts at 79 °C and is completed at 123 °C. A curve inflection at 125 °C suggests the initiation of the second step which is completed at 197 °C. The observed weight losses of 11.77% and 11.23%, respectively are in good agreement with the total calculated value of 23.18% of the two lattice and the two coordinated water molecules. The anhydrous intermediate $[Ca(C_6H_6N_2O_6)]$ is stable up to 294 °C; and at this point the second decomposition process begins (weight loss 45.23%), as shown by the DTA curve, and the anhydrous intermediate is converted to $CaCO_3$ (calculated value 45.23%). Further heating up to 700 °C, results in to the final residue which corresponds to CaO (found 14.73%, calculated 14.01%).

4. Concluding remarks

In this work, five new complexes of the oxamidic ligand oxamide-bis-*N*,*N*′-acetate (H_4L) have been synthesized; their structures have been elucidated and their spectroscopic and thermal properties were studied. The selection of mild conditions for the preparation of the complexes allows isolation of pure crystalline products with the ligand being doubly deprotonated.

With transition metals, H_2L^{2-} utilizes only the carboxylates for coordination. In complexes **1** and **2** the carboxylates are monodentate while in **4** and **5** asymmetrically and symmetrically bidentate, respectively. In **3** there is certainly an attractive interaction between zinc and the non-bonded carboxylate oxygen, but their distance could not easily characterize that interaction as a bond (Table 3).

The presence of water in all structures is very important for their stabilization. All water molecules (coordinated and lattice) in all compounds are involved in strong hydrogen bonding, leading to supramolecular architectures. The compounds are reasonably stable, but they can not regain their structures after a dehydration–rehydration procedure, and behave similarly with other hydrated compounds [21].

Attempts to synthesize coordination polymers with oxamide-bis-*N*,*N*′-acetate (H_4L) in the presence of Lewis bases and/or the oxamide in its fully deprotonated form are in progress.

Supplementary data

CCDC 724713–724717 contain the supplementary crystallographic data. These data can be obtained free of charge via http://www.ccdc.cam.ac.uk/conts/retrieving.html, or from the Cambridge Crystallographic Data Centre, 12 Union Road, Cambridge CB2 1EZ, UK; fax: (+44) 1223 336 033; or e-mail: deposit@ccdc.cam.ac.uk.

Acknowledgements

Financial support from the postgraduate course program 'Bioinorganic Chemistry' (financed by EU and Greece) is gratefully acknowledged.

References

[1] S. Kitagawa, R. Kitaura, S. Noro, Angew. Chem., Int. Ed. Engl. 43 (2004) 2334.
[2] S.R. Batten, R. Robson, Angew. Chem., Int. Ed. Engl. 37 (1998) 1460.
[3] M. Eddaoudi, D.B. Moler, H. Li, B. Chen, T.M. Reineke, M. O'Keeffe, O.M. Yaghi, Acc. Chem.Res. 34 (2001) 319.
[4] B. Moulton, M.J. Zaworotko, Chem. Rev. 101 (2001) 1629.
[5] O.R. Evans, W. Lin, Acc. Chem. Res. 35 (2002) 511.
[6] A.J. Blake, N.R. Champness, P. Hubberstey, W.-S. Li, M.A. Withersby, M. Schröder, Coord. Chem. Rev. 183 (1999) 117.
[7] B.F. Abrahams, P.A. Jackson, R. Robson, Angew. Chem., Int. Ed. Engl. 37 (1998) 2656.
[8] M. Eddaoudi, J. Kim, J.B. Wachter, H.K. Chae, M. O'Keeffe, O.M. Yaghi, J. Am. Chem. Soc. 123 (2001) 4368.
[9] O.M. Yaghi, H. Li, J. Am. Chem. Soc. 118 (1996) 295.
[10] O.M. Yaghi, H. Li, T.L. Groy, Inorg. Chem. 36 (1997) 4292.
[11] O.M. Yaghi, H. Li, T.L. Groy, J. Am. Chem. Soc. 118 (1996) 9096.
[12] J. Kim, B. Chen, T.M. Reineke, H.Li, M. Eddaoudi, D.B. Moler, M. O'Keeffe, O.M. Yaghi, J. Am. Chem. Soc. 123 (2001) 8239.
[13] N.L. Rosi, J. Kim, M. Eddaoudi, B. Chen, M. O'Keeffe, O.M. Yaghi, J. Am. Chem. Soc. 127 (2005) 1504.
[14] B.L. Chen, M. Eddaoudi, T.M. Reineke, J.W. Kampf, M. O'Keeffe, O.M. Yaghi, J. Am. Chem. Soc. 122 (2000) 11559.
[15] M. Eddaoudi, J. Kim, N. Rosi, D. Vodak, J. Wachter, M. O'Keeffe, O.M. Yaghi, Science 295 (2002) 469.
[16] S.S.-Y. Chui, S.M.-F. Lo, J.P.H. Charmant, A.G. Orpen, I.D. Williams, Science 283 (1999) 1148.
[17] O.M. Yaghi, M. O'Keeffe, N.W. Ockwig, H.K. Chae, M. Eddaoudi, J. Kim, Nature 423 (2003) 705.
[18] M.-L. Tong, S. Kitagawa, H.-C. Chang, M. Ohba, Chem. Commun. (2004) 418.
[19] P.J. Steel, Acc. Chem. Res. 38 (2005) 243.
[20] G.E. Kostakis, L. Casella, N. Hadjiliadis, E. Monzani, N. Kourkoumelis, J.C. Plakatouras, Chem. Commun. (2005) 3859.
[21] I. Vlahou, N. Kourkoumelis, A. Michaelidis, S. Skoulika, J.C. Plakatouras, Inorg. Chim. Acta 359 (2006) 3540.
[22] G.E. Kostakis, E. Nordlander, N. Hadjiliadis, M. Haukka, J.C. Plakatouras, Inorg. Chem. Commun. 9 (2006) 915.
[23] F. Lloret, J. Sletten, R. Ruiz, M. Julve, J. Faus, M. Verdaguer, Inorg. Chem. 31 (1992) 778.
[24] J.-F. Lou, Y.-T. Li, Z.-Y. Wu, D.-Q. Wang, J.-M. Dou, Acta Crystallogr., Sect. C: Cryst. Struct. Commun. 61 (2005) m400.
[25] Z. Otwinowski, W. Minor, Processing of X-ray Diffraction Data Collected in Oscillation Mode, in: C.W. Carter, J. Sweet (Eds.), Methods in Enzymology, Macromolecular Crystallography Part A, vol. 276, Academic Press, New York, USA, 1997, p. 307.
[26] A.J.M. Duisenberg, L.M.J. Kroon-Batenburg, A.M.M. Schreurs, J. Appl. Crystallogr. 36 (2003) 220.
[27] G.M. Sheldrick, SADABS – Bruker Nonius Scaling and Absorption Correction, v 2.10, Bruker AXS Inc., Madison, Wisconsin, USA, 2003.
[28] G.M. Sheldrick, Acta Crystallogr., Sect. A 64 (2008) 112.
[29] L.J. Barbour, J. Supramol. Chem. 1 (2001) 189.
[30] P.T. Anastas, M.M. Kirchoff, Acc. Chem. Res. 35 (2002) 686.
[31] (a) I.A. Baburin, V.A. Blatov, L. Carlucci, G. Ciani, D.M. Proserpio, Cryst. Eng. Commun. 10 (2008) 1822;
(b) I.A. Baburin, Z. Kristallogr. 223 (2008) 371.
[32] (a) Reticular Chemistry Structure Resource, http://rcsr.anu.edu.au;
(b) M. O'Keeffe, M.A. Peskov, S.J. Ramsden, O.M. Yaghi, Acc. Chem. Res. 41 (2008) 1782.
[33] (a) http://topos.ssu.samara.ru; V.A. Blatov, IUCr Comp. Commun. Newsletter 7 (2006) 4;
(b) V.A. Blatov, L. Carlucci, G. Ciani, D.M. Proserpio, Cryst. Eng. Commun. 6 (2004) 377;
(c) I.A. Baburin, V.A. Blatov, L. Carlucci, G. Ciani, D.M. Proserpio, J. Solid State Chem. 178 (2005) 2452.
[34] M.G.B. Drew, Coord. Chem. Rev. 24 (1977) 179.
[35] M. Mascal, L. Infantes, J. Chisholm, Angew. Chem., Int. Ed. Engl. 45 (2006) 32.
[36] F.H. Allen, Acta Crystallogr., Sect. B 58 (2002) 380.
[37] K.D. Suyarov, L.M. Shkolnikova, A.L. Poznyak, S.S. Sotman, Koord. Khim. (Russ.) (Coord. Chem.) 17 (1991) 635.
[38] G.B. Deacon, R.J. Phillips, Coord. Chem. Rev. 33 (1980) 227.
[39] A.B.P. Lever, Inorganic Electronic Spectroscopy, 2nd ed., Elsevier, Amsterdam, 1984.

organophosphonate substrates and especially bis(phosphonate) substrates that represent a useful class of drugs, have been employed in the treatment of bone diseases (Paget's disease of bone, myeloma) [16,17]. The biological benefit of organophosphonate moieties has emerged primarily because of their influence on calcium metabolism and its availability.

On the basis of the above views, interactions arising between organophosphonate binders and metal ions such as Ni(II), are expected to promote metal ion solubilization and influence metallo(bio)chemical processes. Two representative low molecular mass organophosphonic acids are: (a) imino bis(methylenephosphonic acid) (H_4IDA2P), and (b) *N*-(phosphonomethyl) glycine (glyphosate, H_3IDAP). The first organophosphonate substrate H_4IDA2P acts as a binder with two very important features: (a) it contains two phosphonate moieties, known to promote metal ion binding, and (b) it contains one imino group. Glyphosate, on the other hand, is a well-known herbicide first introduced in 1974 under the trade name "Roundup". It is one of the very few biodegradable commercial herbicides used to kill weeds. It is degraded in the soil to the non-toxic products CO_2, NH_3 and PO_4^{3-} within a few days. As in the case of H_4IDA2P, glyphosate (H_3IDAP) exists in a zwitterionic form. Glyphosate possesses three binding sites capable of coordinating metal ions such as Ni(II): (a) a carboxylate moiety, (b) a phosphonate moiety, and (c) an imino moiety. Complexes arising from interactions of glyphosate with metal ions are expected to exhibit a variety of structural attributes including five-membered rings, bestowing stability to the isolated species. The use of a diphosphonate and a (carboxy)phosphonate ligand respectively, exemplifies structural attributes of various phosphorylated analogs of amino acids and organophosphonate-containing drugs. In both cases, it is important to point out the paucity of structurally characterized complexes of organophosphonates with Ni(II) in aqueous media.

Poised to understand the underlying principles of the aqueous chemical reactivity of Ni(II) toward organophosphonate ligands, variably mimicking phosphorylated and phosphonate species in cellular media, the binary systems of Ni(II) with the aforementioned substrates were investigated. Herein, we report on the pH-specific synthesis, isolation and characterization of two new binary Ni(II)–organophosphonate complexes with distinct properties (a) reflecting the nature of interactions involved in binary species of the corresponding aqueous speciation schemes, (b) exemplifying the solid state and solution features potentially relating to the aqueous speciation of Ni(II) with phospho-substituted ligands of biological relevance, seeking to contribute to physiology and/or toxicity, and (c) projecting physicochemical properties akin to Ni(II)–phosphonate materials.

2. Experimental

2.1. Materials and methods

All experiments were carried out in aqueous media under aerobic conditions. Nanopure quality water was used for all reactions. $Ni(NO_3)_2{\cdot}6H_2O$ was purchased from Carlo Erba, and imino bis(methylphosphonic acid), (H_4IDA2P) from Fluka. Ammonia, KOH and NaOH were also supplied by Fluka. Glyphosate (H_3IDAP) was purchased from Aldrich.

2.2. Physical measurements

FT-IR spectra were recorded on a Perkin Elmer 1760X FT-infrared spectrometer. UV–Vis measurements were carried out on a Hitachi U2001 spectrophotometer in the range from 190 to 1000 nm. A ThermoFinnigan Flash EA 1112 CHNS elemental analyzer was used for the simultaneous determination of carbon, hydrogen and nitrogen (%). The analyzer is based on the dynamic flash combustion of the sample (at 1800 °C) followed by reduction, trapping, complete GC separation and detection of the products. The instrument is (a) fully automated and controlled by PC via the Eager 300 dedicated software, and (b) capable of handling solid, liquid or gaseous substances.

A TA Instruments, model Q 600, system was used to run the simultaneous TGA-DTG experiments. The employed heating rate was 10 °C/min. The instrument mass precision is 0.1 μg. About 20 mg of sample was placed in an open alumina sample pan for each experiment. High purity air (80/20 in N_2/O_2) was used at a constant flow rate of 100 mL/min, depending on the conditions required for running the experiment(s). During the experiments, the sample weight loss and rate of weight loss were recorded continuously under dynamic conditions, as a function of time or temperature, in the range 30–1010 °C. Prior to activating the heating routine program, the entire system was purged with the appropriate inert gas for 10 min, at a rate of 400 mL/min, to ensure that the desired environment had been established.

Magnetic susceptibility data were collected on powdered samples of **1** with a Quantum Design SQUID susceptometer in the 2–300 K temperature range, under various applied magnetic fields. Magnetization measurements were carried out at three different temperatures in the field range 0–5 T.

Electrochemical measurements were carried out with a model PGSTAT30 potensiostat-galvanostat from Autolab Electrochemical Instruments. The entire system was under computer control and supported by the appropriate computer software GPES, running on Windows XP. The employed electrochemical cell had platinum (disk) working and auxiliary (wire) electrodes. An Ag/AgCl electrode was used as reference electrode. Thus, the derived potentials in the cyclic voltammetric measurements are referenced to that electrode. The water used in the electrochemical measurements was of nano-pure quality. KNO_3 was used as a supporting electrolyte. Normal concentrations used were 1–6 mM in electroanalyte and 0.1 M in supporting electrolyte. Purified argon was used to purge the solutions prior to the electrochemical measurements. Derived $E_{1/2}$ values are reported versus Ag/AgCl electrode.

2.3. Synthesis of complex $[Ni(C_2H_8O_6NP_2)_2(H_2O)_2]$ (**1**)

(a) A sample of 0.50 g of $Ni(NO_3)_2{\cdot}6H_2O$, (1.7 mmol) and 0.35 g (1.7 mmol) of imino-bis(methylenephosphonic acid) were dissolved in nano-pure water. The pH of the resulting solution was raised to 3 with 0.1 M aqueous ammonia. The derived reaction mixture was stirred at room temperature overnight. On the following morning, the solution was clear and its color was green. Subsequently, the reaction solution was filtered and allowed to stand at room temperature. After a period of several weeks green needle-like crystals grew out of the solution by slow evaporation. The crystalline material was collected by filtration and dried in vacuo. Yield: 0.56 g (~66%). *Anal.* Calc. for **1**, $[Ni(C_2H_8O_6NP_2)_2(H_2O)_2]$ ($C_4H_{20}O_{14}N_2P_4Ni$, MW = 502.81): C, 9.54; H, 3.98; N, 5.57. Found: C, 9.68; H, 4.03; N, 5.64%.

(b) The same reaction was run in the presence of NaOH or KOH, affording morphologically identical green needle-like crystals. The FT-IR spectrum of the crystals and the X-ray unit cell determination of one of the isolated single crystals identified the material as complex **1**.

(c) The same reaction as in (a) was also run with a metal to ligand stoichiometry of 1:2. In this case, green crystalline material was also isolated. FT-IR spectroscopy in combination with X-ray crystallography identified the isolated material as complex **1**.

2.4. Synthesis of complex [Ni(OOC–CH2–NH–CH2–PO3H)2]·[Ni(H2O)6]·3.3H2O (2)

(a) A sample of 0.23 g of $Ni(NO_3)_2{\cdot}6H_2O$ (0.79 mmol) and 0.26 g (1.5 mmol) of *N*-(phosphonomethyl) glycine (glyphosate) were dissolved in nano-pure water. The pH of the resulting solution was raised to 4 with 0.1 M NaOH. The derived reaction mixture was stirred at room temperature. On the following morning, the solution was clear and its color was blue. Subsequently, ethanol was added and the reaction mixture was placed at 4 °C. A few weeks later, bluish crystals appeared at the bottom of the flask. The crystals were isolated by filtration and dried in vacuo. The yield was 0.75 g (~77%). *Anal.* Calc. for **2**, $[Ni(OOC{-}CH_2{-}NH{-}CH_2{-}PO_3H)_2]{\cdot}[Ni(H_2O)_6]{\cdot}3.3H_2O$ ($C_6H_{30.6}O_{19.3}N_2P_2Ni_2$, MW = 619.08): C, 11.63; H, 4.94; N, 4.52. Found: C, 11.89; H, 5.25; N, 4.34%.

(b) A similar reaction as in (a) was carried out using aqueous ammonia to raise the pH. Blue crystalline material appeared at the bottom of the reaction flask. FT-IR spectroscopy in combination with the X-ray determination of the unit cell of a single crystal identified the isolated crystals as complex **2**.

2.5. X-ray crystal structure determination

X-ray quality crystals of compound **1** were grown from aqueous reaction mixtures upon slow evaporation. A single crystal with dimensions 0.15 × 0.09 × 0.05 mm was mounted on the tip of a glass fiber with epoxy glue. The crystal was mounted on an Xcalibur Oxford Diffractometer equipped with a Sapphire 3 CCD detector and a 4-cycle Kappa geometry goniometer, using an enhanced Mo X-ray source and graphite radiation monochromator. Unit cell dimensions for **1** were determined and refined by using the angular settings of all the reflection frames in the range $6.30 < 2\theta < 60.50°$. Relevant crystallographic data appear in Table 1. An analytical absorption correction was applied using CrysAlis RED software. CrysAlis CCD and CrysAlis RED software were used for monitoring data collection and computing data reduction/cell refinement, respectively [18,19]. The structure was solved by direct methods and refined by full-matrix least-squares techniques on F^2 by using SHELXS-97 [20,21]. Special computing molecular graphics incorporated in the WinGX 3.2 interface were used [22]. Further crystallographic details for **1**: $2\theta_{max} = 62.44°$; reflections collected/unique/used, 11 076/2263 [$R_{int} = 0.0669$]/2263; parameters refined, 136; $[\Delta\rho]_{max}/[\Delta\rho]_{min}$ = 0.895/−0.686 e/Å^3; R/R_w (for all data), 0.0291/0.0720. All of the non-H atoms were refined anisotropically. The methylene hydrogen atoms of the phosphonate ligand were introduced at calculated positions as riding on bonded atoms. The remainder of the hydrogen atoms were located by difference Fourier maps and were refined isotropically. Further details on the crystallographic studies as well as atomic displacement parameters are given as Supporting Information in the form of cif files.

X-ray quality crystals of compound **2** were grown from water–ethanol mixtures. A single crystal, with dimensions 0.06 × 0.20 × 0.28 mm was mounted on a Crystal Logic dual-goniometer diffractometer, using graphite monochromated Mo Kα radiation (λ = 0.71073 Å). Unit cell dimensions for **2** were determined and refined by using the angular settings of 25 automatically centered reflections in the range $11.00 < 2\theta < 23.00°$. Crystallographic details are given in Table 1. Intensity data were measured by using θ–2θ scans. Three standard reflections were monitored every 97 reflections, over the course of data collection at 298 K. They showed less than 3% variation and no decay. Lorentz, polarization and psi-scan absorption corrections were applied by using Crystal Logic software. The structure of complex **2** was solved by direct methods using SHELXS-97 [20]. Refinement was achieved by full-matrix least-squares techniques on F^2 with SHELXL-97 [21]. Further crystallographic details for **2**: $2\theta_{max} = 50.00°$; reflections collected/unique/used, 4042/3915 [$R_{int} = 0.0249$]/3915; parameters refined, 381; $[\Delta\rho]_{max}/[\Delta\rho]_{min}$ = 2.023/−0.861 e/Å^3; R/R_w (for all data), 0.0697/0.1645. All hydrogen atoms were located in difference maps and were refined isotropically; no H-atoms for the partially occupied water solvate molecules were included in the refinement. All non-H atoms were refined anisotropically.

Table 1
Summary of crystal, intensity collection and refinement data for compounds $[Ni(C_2H_8O_6NP_2)_2(H_2O)_2]$ (**1**) and $[Ni(OOC\text{-}CH_2\text{-}NH\text{-}CH_2\text{-}PO_3H)_2]{\cdot}[Ni(H_2O)_6]{\cdot}3.3H_2O$ (**2**).

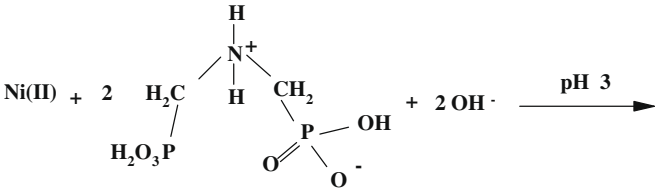
	1	**2**
Chemical formula	$C_4H_{20}N_2O_{14}P_4Ni$	$C_6H_{30.6}O_{19.3}N_2P_2Ni_2$
Formula weight	502.81	619.08
Temperature (K)	100 (2)	298 (1)
Wavelength, λ (Å)	Mo Kα 0.71073	Mo Kα 0.71073
Space group	$P2_1/n$	$P2_1/n$
a (Å)	7.3657(7)	9.138(5)
b (Å)	8.0937(10)	13.352(6)
c (Å)	13.8973(15)	18.382(9)
α (°)	90.00	90.00
β (°)	104.527(9)	94.33(2)
γ (°)	90.00	90.00
V (Å^3)	802.01(15)	2236.5(18)
Z	2	4
ρ_{calcd}/ρ_{obsd} (g/cm^3)	2.082/2.078	1.839/1.831
Absorption coefficient (μ) (mm^{-1})	1.686	1.916
Range of *h*, *k*, *l*	−10 → 10, −10 → 11, −19 → 19	−10 → 10, −15 → 0, −21 → 0
R^a	0.0258[b]	0.0623[b]
$R_w{}^a$	0.0714[b]	0.1559[b]

[a] *R* values are based on *F*'s, R_w values are based on F^2; $R = \frac{\sum ||F_o|-|F_c||}{\sum(|F_o|)}$, $R_w = \sqrt{\sum[w(F_o^2 - F_c^2)^2] / \sum[w(F_o^2)^2]}$.

[b] For 1943 (**1**) and 3456 (**2**) reflections with $I > 2\sigma(I)$.

2.6. Synthesis

The synthesis of compound **1** was pursued through a pH-specific reaction between Ni(II) and imino-bis(methylenephosphonic acid) (H_4IDA2P) in aqueous media. The pH, at which the reaction was developed, was 3. The adjustment of pH was achieved by adding aqueous ammonia (NaOH or KOH). The stoichiometric reaction leading to the isolation of compound **1** is shown below (Reaction 1):

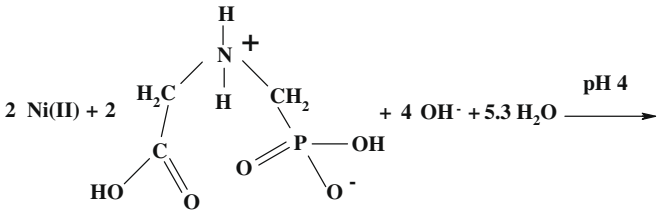


$[Ni(C_2H_8O_6NP_2)_2(H_2O)_2]$

(Reaction1)

Compound **1** was easily isolated in pure crystalline form after several weeks of having the reaction flask stand in the air. Elemental analysis of the isolated green crystalline material suggested the molecular formulation $[Ni(C_2H_8O_6NP_2)_2(H_2O)_2]$ for **1**. It appears that the sole purpose of the employed aqueous base solutions was to adjust the pH of the reaction mixture. No cations arising from the use of such bases were found to be incorporated into the arising lattice of **1**. Further examination of **1** by FT-IR spectroscopy confirmed the presence of the phosphonate moieties bound to Ni(II), thus lending credence to the proposed formulation. Compound **1** is sparingly soluble in water, but it is insoluble in organic solvents, such as acetonitrile, chlorinated solvents ($CHCl_3$, CH_2Cl_2), toluene and DMF.

The pH-specific synthesis of compound **2** was achieved through a similar reaction to that of compound **1**. In the synthesis of **2**, employing the carboxy-phosphonate ligand *N*-(phosphonomethyl) glycine in aqueous media, the pH of the reaction mixture was 4. The adjustment of pH was achieved by adding aqueous NaOH (or ammonia). The stoichiometric reaction leading to the isolation of **2** is shown below (Reaction 2):



(Reaction2)

Elemental analysis of the isolated blue crystalline material suggested the molecular formulation $[Ni(OOC–CH_2–NH–CH_2–PO_3H)_2]·[Ni(H_2O)_6]·3.3H_2O$. It appears that employment of the two separate base solutions used in the synthesis contributed solely to the adjustment of the reaction mixture pH, in view of the fact that Na^+ and NH_4^+ ions were not incorporated in the ultimate lattice of **2**. Further examination of **2** by FT-IR spectroscopy confirmed the presence of phosphonate and carboxylate moieties bound to Ni(II), thus supporting the proposed formulation. Compound **2** is insoluble in water as well as in organic solvents, such as acetonitrile, chlorinated solvents ($CHCl_3$, CH_2Cl_2), toluene and DMF.

2.7. Description of the structures

2.7.1. Compound $[Ni(C_2H_8O_6NP_2)_2(H_2O)_2]$ (1)

The X-ray crystal structure of **1** reveals the presence of discrete species in a molecular type of lattice. The crystal structure diagram of **1** is shown in Fig. 1A, while a packing view of the same complex is provided in Fig. 2A. A list of selected bond distances and angles for **1** is given in Table 2. Complex **1** crystallizes in the monoclinic space group $P2_1/n$ with two molecules per unit cell. The structure shows a mononuclear assembly of Ni(II) bound to two H_3IDA2P^- ligands. In particular, there are two different ligands bound to Ni(II), namely imino bis(methylenephosphonate) ($^-HO_3P–CH_2–NH_2^+–CH_2–PO_3H^-$ = H_3IDA2P^-) and water. The two H_3IDA2P^- ligands in the coordination sphere of Ni(II) are singly deprotonated with the deprotonation site being the hydroxide group of the phosphonate moiety. The second hydroxide group of each phosphonate moiety remains in the protonated form. In this respect, each phosphonate group acts as a monodentate ligand. Finally, two water molecules lie in the equatorial plane of the octahedral metal ion Ni(II).

Analogous cases of bound bis(phosphonate) metal complexes had been previously observed in the case of Co(II) and Mn(II). Specifically, the characterized complexes $[Co(C_2H_8O_6NP_2)_2(H_2O)_2]$ (**3**) [23] and $[Mn(C_2H_8O_6NP_2)_2(H_2O)_2]$ (**4**) [24] exhibit a coordination environment similar to that of Ni(II) generated by two H_3IDA2P^- ligands and two water molecules. A different coordination environment, however, is present in the case of other metal complexes with H_4IDA2P: $Cu[NH(CH_2PO_3H)_2]$ (**5**) [25], $Pb_2[NH(CH_2PO_3)_2]·2H_2O$ (**6**) [26], $Mn[NH_2(CH_2PO_3H)(CH_2PO_3)]·H_2O$ (**7**) [25], $Cu_3[NH_2(CH_2PO_3)_2]_2$ (**8**) [24], $Co_3[NH_2(CH_2PO_3)_2]_2$ (**9**) [24], and $\{Mn[NH(CH_2PO_3H)_2](H_2O)_2\}_2·\{Mn(C_4O_4)(H_2O)_4\}·(C_4H_2O_4)$ (**10**) [27].

The Ni–O bond distances (2.037(1)–2.093(1) Å) in **1** compare favorably with those observed in the crystal structure of complexes $(NH_3CH_2CH_2NH_3)·\{Ni(O_2CCH_2N(CH_2PO_3H)_2](H_2O)_2\}_2$ (2.028(6)–2.097(6) Å) (**11**) [28], $Ni[HO_3PCH_2N(CH_3)CH_2CH_2N(CH_3)CH_2PO_3H](H_2O)_2$ (2.052(4)–2.074(4) Å) (**12**) [29], $[C_{30}H_{50}N_8Ni_2O_2(H_2O)_2]·(ClO_4)_2·CH_3OH·3H_2O$ (2.041(2)–2.141(2) Å) (**13**) [30], and $[Ni(pyr)(H_2O)_4]·[Ni(C_5H_7NO_7P)_2(pyr)(H_2O)_2]·2H_2O$ (2.038(2)–2.110(2) Å) (**14**) [31].

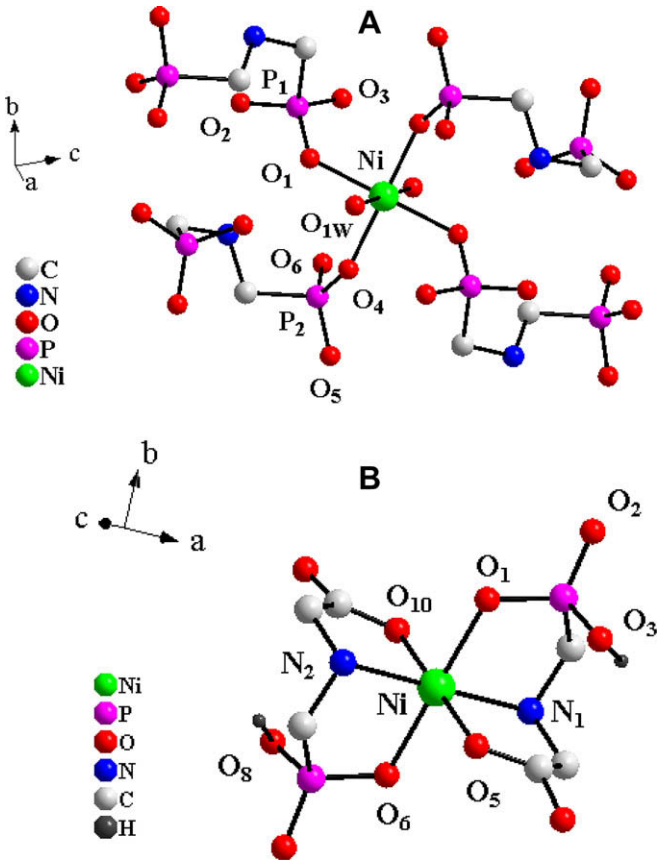


Fig. 1. (A) Crystal structure of $[Ni(C_2H_8O_6NP_2)_2(H_2O)_2]$ (**1**). (B) Partially labeled plot of the anion in **2** with thermal ellipsoids at the 30% probability level.

The angles within the equatorial plane defined by O(4), O(4)′, O(1w) and O(1w)′ are in the range 87.11(5)–92.89(5)°, and hence fairly close to the ideal octahedral angle of 90°. A similar angle variation is observed between the axial donor atoms O(1) and O(1)′ and those in the equatorial plane (range: 86.46(4)–93.54(4)°). The aforementioned angle values are similar to those observed in (**3**)–(**10**) as well as in complexes arisen through interactions of other divalent metals with a diphosphonate ligand similar to H_4IDA2P, i.e. $[Cu(HO_3PC(CH_3)(OH)PO_3H)_2]^{2-}$ (84.7–95.3° and 87.8–92.2°, respectively) [32] and $[Zn(HO_3PC(CH_3)(OH)PO_3H)_2]^{2-}$ (85.0–95.0° and 88.6–91.4°, respectively) [33].

The mode of coordination of the H_3IDA2P^- ligand to Ni(II) in **1** is monodentate. The exact same behavior is observed in the case of the divalent metal ions Co(II) and Mn(II). In the free form, H_4IDA2P consists of two terminal phosphonate groups, both of them capable of binding to Ni(II). However, in the work presented here, the terminal phosphonate group is coordinated to an adjacent Ni(II) ion, which in turn is surrounded by the same type of ligands in an octahedral environment. Finally, the four H_3IDA2P^- binders surrounding the central metal ion Ni(II), are also bound to four other Ni(II) ions due to the presence of the second phosphonate group in each H_4IDA2P molecule. In this sense, saturation of the coordination sites in contiguous octahedral Ni(II) ions extends to infinity, thereby giving rise to the molecular lattice in **1**.

An interesting attribute of the iminodiphosphonate ligand is the presence of a protonated central imino group, reflecting the zwitterionic form of the ligand. Hence, the interaction of the H_3IDA2P^-

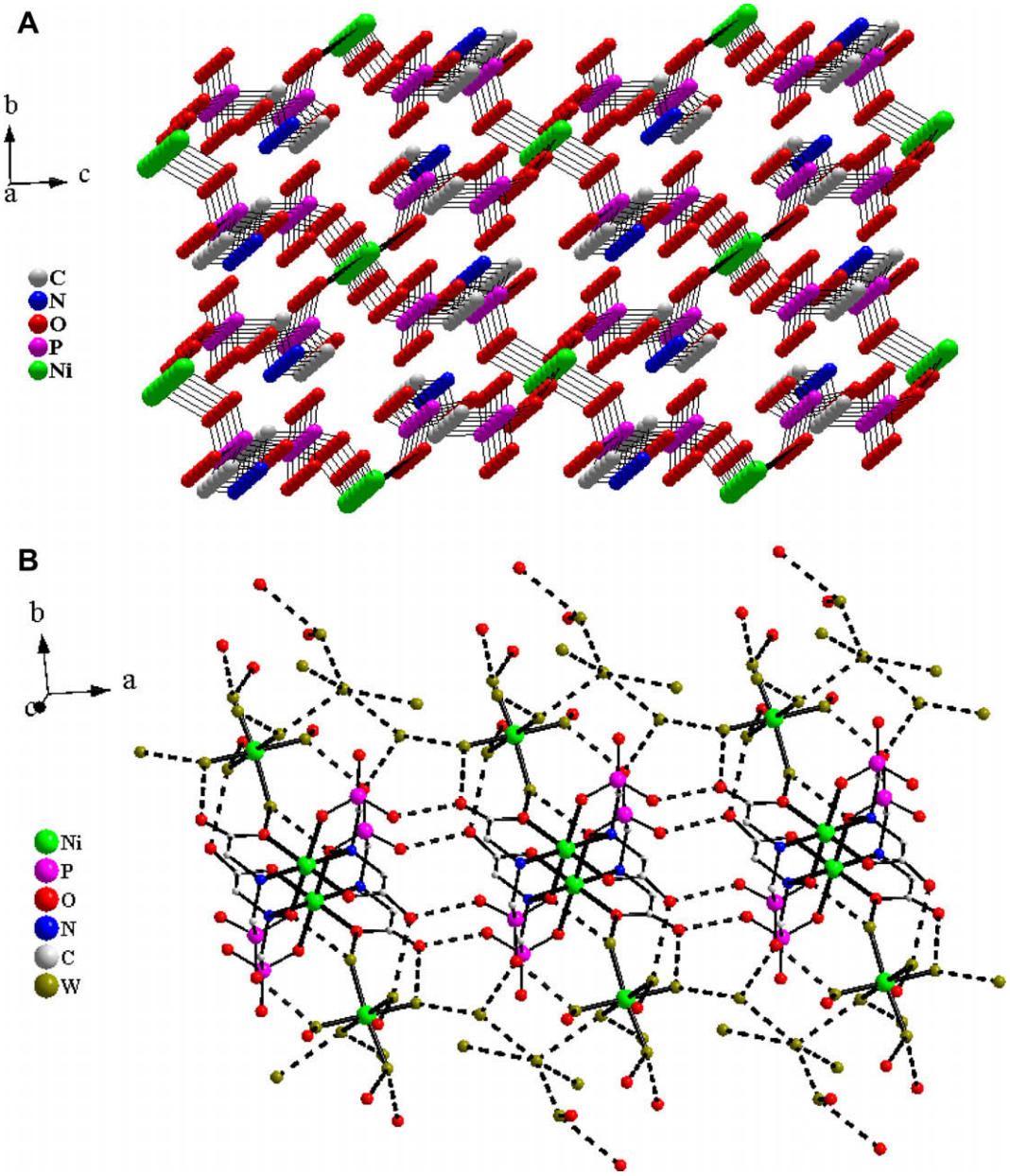


Fig. 2. (A) Packing view of complex **1** in the *bc* plane. (B) Section of the 3D structure of **2** reflecting hydrogen bonding interactions. Water molecules (Ni-bound and free) in the figure are represented as W.

ligand with Ni(II), affording complex **1**, denotes the presence of two singly deprotonated phosphonate groups and a singly protonated imino group. As a result, the overall charge of the iminodiphosphonate ligand coordinated to Ni(II) ion is 1−. Two of these ligands need to balance the overall zero charge of the isolated species. The two additional H_3IDA2P^- ligands coordinated to Ni(II) do not contribute to the overall charge, as they originate in an adjacent mononuclear Ni(II) site and complete the octahedral coordination sphere of Ni(II). The remaining two coordination sites of Ni(II) ion are occupied by two water molecules.

2.7.2. Compound $[Ni(OOC–CH_2–NH–CH_2–PO_3H)_2]·[Ni(H_2O)_6]·3.3H_2O$ (**2**)

Complex **2** crystallizes in the monoclinic space group $P2_1/n$ with four molecules per unit cell. The lattice of **2** consists of discrete mononuclear cations and anions. A list of selected bond distances and angles for **2** is given in Table 2. In the first mononuclear unit, the six coordination sites of Ni(II) (Ni(1)) are occupied by two glyphosate ligands (Fig. 1B). Each glyphosate ligand bound to Ni(II) ion acts as a chelator with a 2− charge ($HIDAP^{2-}$), since the two terminal sites of the glyphosate ligand are deprotonated, i.e. the carboxylate and phosphonate moieties. The second hydroxide moiety of the phosphonate group remains protonated. The imino nitrogen of the bound glyphosate ligand is not protonated as in the case of the H_3IDA2P^- ligand in **1**. As a result, it actively participates in the coordination of the $HIDAP^{2-}$ ligand to the central Ni(II) ion. To this end, in each bound glyphosate two five-membered chelate rings form, defined by Ni–N–C–P–O and Ni–N–C–C–O, respectively, which provide stability to the isolated complex **2**. The two five-membered rings defined by Ni–N–C–P–O adopt the stable envelope configuration with atoms C(4) and C(1) displaced ~0.60 Å out of the best mean plane of the remaining four atoms. In the case of the five-membered rings defined by Ni–N–C–C–O, the out-of-plane atoms are C(2) and C(5), displaced at 0.31 and 0.25 Å, respectively, out of the best mean plane of the remaining four atoms. The negative charge of the first mononuclear unit is counterbalanced

Table 2
Bond lengths [Å] and angles [°] for $[Ni_2(C_2H_8O_6NP_2)_2(H_2O)_2]$ (**1**) and $[Ni(OOC–CH_2–NH–CH_2–PO_3H)_2]\cdot[Ni(H_2O)_6]\cdot 3.3H_2O$ (**2**).

1		2	
Distances			
Ni(1)–O(4)	2.037(1)	Ni(1)–O(1)	2.132(4)
Ni(1)–O(1 W)	2.048(1)	Ni(1)–O(5)	2.059(4)
Ni(1)–O(1)	2.093(1)	Ni(1)–O(6)	2.113(4)
O(2)–P(1)	1.510(1)	Ni(1)–N(1)	2.092(5)
O(5)–P(2)	1.513(1)	Ni(1)–N(2)	2.097(4)
O(4)–P(2)	1.494(1)	Ni(1)–O(10)	2.049(4)
O(3)–P(1)	1.560(1)		
O(1)–P(1)	1.507(1)		
O(6)–P(2)	1.567(1)		
N(1)–C(1)	1.501(2)		
N(1)–C(2)	1.501(2)		
Angles			
O(4)′–Ni(1)–O(4)	180.00(6)	O(10)–Ni(1)–O(5)	179.2(2)
O(4)′–Ni(1)–O(1W)′	87.11(5)	O(10)–Ni(1)–N(1)	97.4(2)
O(4)–Ni(1)–O(1W)′	92.89(5)	O(5)–Ni(1)–N(1)	82.2(2)
O(4)–Ni(1)–O(1W)	87.11(5)	O(10)–Ni(1)–N(2)	82.4(2)
O(1W)′–Ni(1)–O(1W)	180.00(5)	O(5)–Ni(1)–N(2)	98.0(2)
O(4)′–Ni(1)–O(1)′	88.72(4)	N(1)–Ni(1)–N(2)	179.5(2)
O(4)–Ni(1)–O(1)′	91.28(4)	O(10)–Ni(1)–O(6)	90.1(2)
O(1W)′–Ni(1)–O(1)′	86.46(4)	O(5)–Ni(1)–O(6)	89.2(2)
O(1W)–Ni(1)–O(1)′	93.54(4)	N(1)–Ni(1)–O(6)	93.9(2)
O(4)′–Ni(1)–O(1)	91.28(4)	N(2)–Ni(1)–O(6)	86.6(2)
O(4)–Ni(1)–O(1)	88.72(4)	O(10)–Ni(1)–O(1)	90.6(2)
O(1W)′–Ni(1)–O(1)	93.54(4)	O(5)–Ni(1)–O(1)	90.1(2)
O(1W)–Ni(1)–O(1)	86.46(4)	N(1)–Ni(1)–O(1)	86.0(2)
O(1)′–Ni(1)–O(1)	180.00(3)	N(2)–Ni(1)–O(1)	93.5(2)
P(2)–O(4)–Ni(1)	140.06(7)	O(6)–Ni(1)–O(1)	179.2(2)

Symmetry operations for **1** and **2**: (i) x, y, z; (ii) $-x+1/2,\ y+1/2,\ -z+½$; (iii) $-x, -y, -z$ and (iv) $x-1/2, -y-1/2, z-1/2$.

by the positive charge of the second mononuclear unit, which is the well-known hexa-aqua Ni(II) ion $[Ni(H_2O)_6]^{2+}$ (Ni(2)). Ni(2) is coordinated to six water molecules in an octahedral fashion, displaying a 2+ charge.

Finally, it is worth re-emphasizing the presence of the hexa-aqua Ni(II) ion, $[Ni(H_2O)_6]^{2+}$, in the lattice of complex **2**. This mononuclear dicationic unit is not unlikely to appear in a crystal lattice. It was observed in the lattice of other Ni(II)-complexes displaying similar ligand coordination modes, including: $[Ni(H_2O)_6][Ni(H_2O)_2(C_4H_2O_4)]\cdot 4H_2O$ (**20**) [34], $[Ni(H_2O)_6][Ni_2(C_{10}H_4O_4N_2)_3]\cdot 5H_2O$ (**21**) [35], $[Ni(H_2O)_6][Ni(C_4H_4O_4S)_2]\cdot 4H_2O$ (**22**) [36] and $[Ni(H_2O)_6][Ni(C_7H_3O_4N)_2(H_2O)_2]$ (**23**) [37].

The Ni(1)–O distances (2.049(4)–2.132(4) Å) in complex **2** are similar to those observed in other Ni(II)–O, N compounds (**11**–**14**). The glyphosate ligand, on the other hand, is coordinated in a variety of coordination modes exemplified in the following complexes reported in the literature: $[Cd(C_3H_6NO_5P)(H_2O)_2]_n$ (**15**) [38], $NaCu[O_2CCH_2NHCH_2PO_3]\cdot 3.5H_2O$ (**16**) [6], $Pb[O_3PCH_2NH_2CH_2COO]$ (**17**) [39] and the trivalent metal ion complexes $Na_3[Co(C_3H_5PNO_5)_2]\cdot 11H_2O$ (**18**) [40] and $[Eu_2(HO_3PCH_2NH_2CH_2CO_2)_2(H_2O)_7(ClO_4)]\cdot 3ClO_4\cdot H_2O$ (**19**) [41]. The lattice structure of **2** is stabilized by an extensive hydrogen bonding pattern (Fig. 2B, Table 3) in a 3D network.

2.8. UV–Vis spectroscopy

The UV–Vis spectrum of **1** was recorded in water (Fig. 3). The spectrum exhibits a major absorption at $\lambda_{max} = 395$ nm ($\varepsilon \sim 2.5\ M^{-1}\ cm^{-1}$) and a distant band around 208 nm ($\varepsilon \sim 25\ M^{-1}\ cm^{-1}$). The remaining absorption features are most likely due to d–d transitions typical for a Ni(II) d^8 octahedral species [42]. The absorption feature around 395 nm ($\varepsilon \sim 2.5\ M^{-1}\ cm^{-1}$) could be tentatively attributed to the $^3A_{2g} \rightarrow {}^3T_{1g}(P)$ transition. The observed multiple structure containing the 656 and 730 nm features, a region normally corresponding to the $^3A_{2g} \rightarrow {}^3T_{1g}(F)$ transition, is in line with literature reports invoking the presence of an ^1E_g state lying so close to $^3T_{1g}$ that extensive mixing takes place. That mixing leads to the observation of a doublet band, where the spin forbidden transition picks up intensity from the spin-allowed transition, thus accounting for the complexity of the spectrum [43]. In the absence of detailed studies no further assignments could be proposed.

Table 3
Hydrogen bonds in **2**.

Interaction	D···A (Å)	H···A (Å)	D–H···A (°)	Symmetry operation
O3–HO3···O9	2.566	1.416	163.9	$1+x, y, z$
O8–HO8···O4	2.600	1.906	163.7	$-1+x, y, z$
N1–HN1···O6	3.114	2.454	172.4	$-x, -y, -z$
W1–Hw1A···O9	2.763	1.805	165.7	$-x, -y, -z$
W1–Hw1B···W7	2.812	2.243	175.7	$1+x, -1+y, z$
W2–Hw2A···O10	2.714	2.002	164.8	$-x, -y, -z$
W2–Hw2B···O6	2.716	1.888	165.5	x, y, z
W3–Hw3A···O7	2.685	1.989	157.6	x, y, z
W3–Hw3B···O3	2.911	2.071	158.0	$0.5-x, -0.5+y, 0.5-z$
W4–Hw4A···O5	2.723	2.071	163.7	$0.5-x, -0.5+y, 0.5-z$
W4–Hw4B···O2	2.657	1.774	131.7	$x, -1+y, z$
W5–Hw5A···O1	2.716	1.970	162.7	$0.5-x, -0.5+y, 0.5-z$
W5–Hw5B···O4	2.869	2.228	161.5	x, y, z
W6–Hw6A···W8	2.761	1.977	173.1	$x, -1+y, z$
W6–Hw6B···W8	2.817	2.021	166.7	$-x, -y, -z$
W7–Hw7A···O7	2.733	2.185	160.3	$x, 1+y, z$
W7–Hw7B···W1	2.812	1.715	152.2	$-1+x, 1+y, z$
W8–Hw8A···W9	2.680	1.603	159.0	x, y, z
W8–Hw8B···W10	3.230	2.179	166.8	$-x, 1-y, -z$
W9–Hw9A···O1	2.845	1.700	161.2	x, y, z
W9–Hw9B···O4	2.862	1.925	170.7	$0.5-x, 0.5+y, 0.5-z$

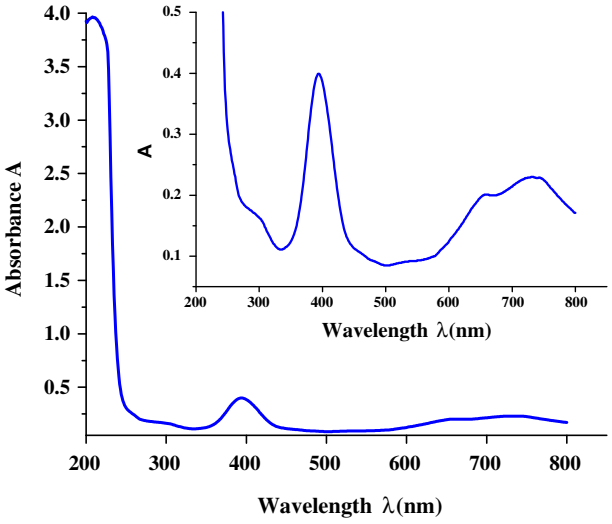


Fig. 3. UV–Vis spectrum of **1** in water.

2.9. FT-IR spectroscopy

The FT-IR spectrum of **1** was recorded in KBr. The spectrum exhibits strong absorptions for the PO_3 groups observed in both the antisymmetric $\nu_{as}(PO_3)$ and symmetric $\nu_s(PO_3)$ vibration regions. Specifically, the antisymmetric stretching vibrations appear in the range between 1090 and 980 cm^{-1}, whereas the symmetric stretching vibrations appear in the range 970–920 cm^{-1}. The frequencies for the aforementioned stretches appear to be shifted to lower values compared to those of free H_4IDA2P acid, indicating changes in the vibrational status of the ligand due to coordination to the Ni(II) ion [23,24].

The FT-IR spectrum for complex **2** in KBr exhibits strong absorptions for the vibrationally active carbonyl moiety of the

carboxylate and PO_3 groups of the glyphosate ligand in both the antisymmetric and symmetric vibration regions. The antisymmetric stretching vibrations $\nu_{as}(COO^-)$ appear in the range from 1600 to 1550 cm^{-1}, whereas the corresponding symmetric stretches $\nu_s(COO^-)$ appear in the range from 1475 to 1385 cm^{-1}. In the same respect, the antisymmetric stretching vibrations $\nu_{as}(PO_3)$ appear in the range from 1209 to 1140 cm^{-1}, whereas the symmetric stretching vibration $\nu_s(PO_3)$ appear in the range from 1074 to 993 cm^{-1}. The frequencies of the various stretches are shifted to lower values compared to those of the free glyphosate binder, due to the coordination of the ligand to the Ni(II) ion [44].

2.10. Thermogravimetric studies

The thermal decomposition of both **1** and **2** was studied by TGA-DTG under an atmosphere of oxygen (see Supplementary data). The TGA diagram shows that an initial process involves the loss of water molecules per formula unit of **1**. The release of Ni(II)-coordinated water molecules until 285 °C, signifies an exothermic process associated with the specific part of the diagram. The observed weight loss amounts to 9.2%, a value very close to the calculated value of 7.2% based on the molecular formula of **1**. Two additional steps are observed in the thermal decomposition of **1**: (a) the release of water molecules due to condensation of the hydrogen phosphonate groups, and (b) the decomposition of the organic moiety. The total weight loss of complex **1** is close to 60.0% and is reached at approximately 1000 °C.

In much the same fashion, the TGA diagram of **2** shows an initial process reflecting the loss of water molecules. The release of all water molecules up until ~300 °C, signifies an exothermic process associated with the specific part of the diagram. The observed weight loss amounts to 28.2%, a value very close to the calculated value of 27.0% based on the molecular formula of the title complex. Two additional steps are observed owing to (a) the carboxylate and phosphonate moieties, and (b) the decomposition of the organic moiety in **2**. The total weight loss due to the decomposition of all the organic composition of **2** is 45.7% and is reached at approximately 935 °C, signifying an endothermic process. The small number of observed TGA peaks reflects simple mechanisms of decomposition for complex **2**.

2.11. Cyclic voltammetry

The cyclic voltammetry of complex **1** was studied in aqueous solutions, in the presence of KNO_3 as a supporting electrolyte (Fig. 4). The cyclic voltammogram projects a well-defined electrochemical behavior, with a pronounced chemically reversible process reflecting: (a) a reduction wave at E_{pc} 0.436 V, and (b) an oxidation wave at E_{pa} 0.616 V, and $E_{1/2}$ 526 mV ($i_{pc}/\{(v)^{1/2}C\}$ constant and $i_{pa}/i_{pc} = 1$). This behavior reflects a process involving the Ni(II)/Ni(III) redox couple. Attempts to pursue the redox chemistry of complex **1** at such high redox potentials are currently ongoing.

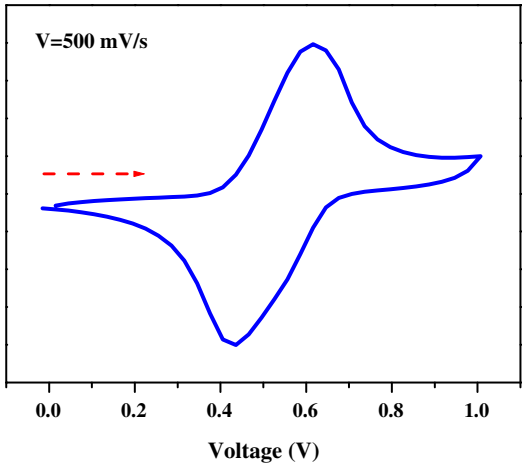


Fig. 4. Cyclic voltammetry of complex **1** in aqueous solutions (scan rate 500 mV/s).

2.12. Magnetic susceptibility studies

Magnetic susceptibility measurements were carried out at different magnetic fields in the temperature range 2–300 K. The temperature dependence of $\chi_M T$ (χ_M being the magnetic susceptibility for one Ni(II) ion) for complex **1** is shown in Fig. 5 (open stars). The $\chi_M T$ value is 1.42 emu mol^{-1} K at 300 K and until 10 K there is a smooth linear decrease. Below that temperature and down to 2 K, a more pronounced decrease occurs reaching the value of 0.8 emu mol^{-1} K. The shape of this curve is characteristic of the occurrence of large zero field effects along with the temperature independent paramagnetism (TIP) effect. The latter effect leads to a linear temperature dependence of the susceptibility data. The susceptibility data were fitted by the following equation:

$$H = D\left[S_z^2 - \frac{1}{3}S(S+1)\right] + E(S_x^2 - S_y^2) + g_z\mu_B H_z S_z + g_x\mu_B H_x S_x + g_y\mu_B H_y S_y \quad (1)$$

where an isotropic g-value was used. The best fit (solid line in Fig. 5) is given by the parameters $D = 4.3(2)$ cm^{-1} and $g = 2.3(1)$, TIP = 9.8×10^{-4}. In the inset of the figure, simulations of the susceptibility function are shown for different values of the D parameter, where the g and TIP values were those obtained from the fitting procedure.

2.13. Magnetization studies

The isothermal magnetization curve at $T = 1.8$ K, in the applied field 0–5 T, is shown in Fig. 6. The curves for the increasing and decreasing fields are identical. The data were fitted using (Eq. (1)) and the best fit (solid line in Fig. 6) is given by the parameters of $D = 3.8(1)$ cm^{-1}, $g = 2.3(1)$. The latter are very close to the values

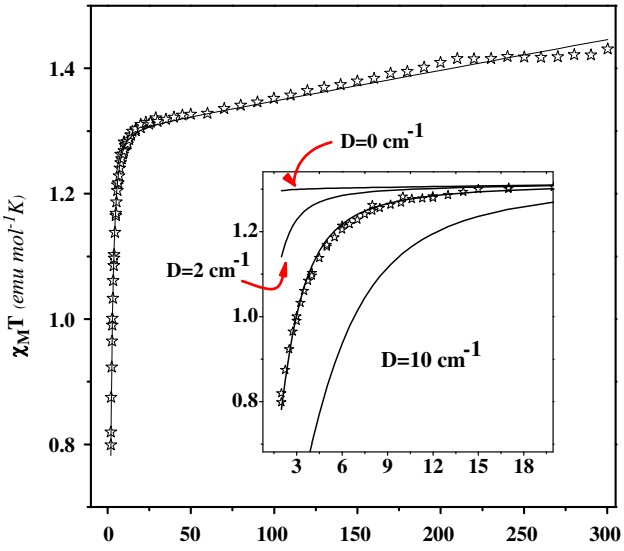


Fig. 5. Temperature dependence of the susceptibility data in the form of $\chi_M T$ vs. T (solid stars) and the fitting results using the theoretical formula discussed in the text (solid line). In the inset simulations of the susceptibility function are shown, in the form of $\chi_M T$ vs. T, for different values of the D parameter.

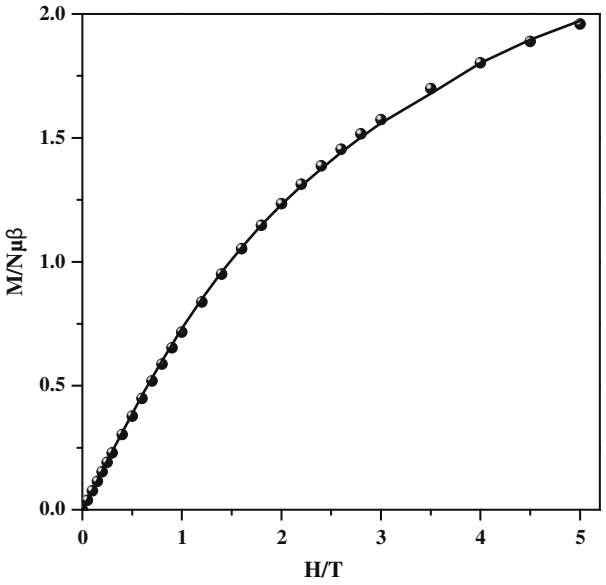


Fig. 6. Magnetization measurements, in the form of $M/N_{\mu\beta}$ vs. H/T, in the field range 0–5 T and at temperature $T = 2$ K, and fitting results using the theoretical formula discussed in the text (solid line).

obtained from the susceptibility study, thus verifying the large zero-field character of the system.

3. Discussion

3.1. The aqueous binary Ni(II)–organophosphonate chemistry

The interaction of two organophosphonate ligands with the divalent metal ion Ni(II), at specific pH values in aqueous media, led to the isolation of two compounds (**1** and **2**). The two ligands employed in these interactions exhibit a zwitterionic form in the free state, i.e. $H_2O_3P–CH_2–NH_2^+–CH_2–PO_3H^-$ and $HOOC–CH_2–NH_2^+–CH_2–PO_3H^-$. This zwitterionic form is essential to the developing synthetic chemistry with Ni(II). In both binary Ni(II)–phosphonate systems, a number of factors appeared to play a role in the isolation of **1** and **2**: (a) the pH of the employed reaction mixture. The acidic reaction conditions in both cases facilitated the formation of the crystalline compounds. Raising the pH of the reaction mixture resulted in the formation of a precipitate of non-crystalline nature in both systems. In the case of the binary Ni(II)–H_4IDA2P system, formation of insoluble precipitate occurred at pH 4, with no dissolution of the precipitate observed at higher pH values. In contrast to that behavior, formation of a precipitate in the second binary system occurred at pH 7. In view of the ostensible pH-dependent behavior of the two binary Ni(II)–organophosphonate systems, it would not be unlikely to consider the existence of the carboxylic moiety in the glyphosate molecule as one of the key factors providing increased solubility to the Ni(II)–glyphosate system compared to the diphosphonate counterpart and (b) the involvement of the alkali solutions in the adjustment of the reaction mixture pH of each binary system investigated. Despite the use of different bases (NaOH, KOH, ammonia) in the binary reaction mixtures, the molecular formulation of the isolated products, as proven by elemental analysis and X-ray crystallography, did not include counter ions originating in those bases. Therefore, the sole use of bases was to adjust the pH and facilitate isolation of the crystalline products **1** and **2**. Moreover, in the case of complex **1**, different molar ratios in the Ni(II)–H_4IDA2P system were employed affording the isolation of **1**. It appears, therefore, that complexes **1** and **2** are stable enough to be isolated under variable reaction conditions. Even though, **1** and **2** are the first isolated products resulting from the interaction of Ni(II) with the two aforementioned phosphonate ligands, the possibility of other Ni(II)-(carboxy)phosphonate species (arising from such specific interactions) being present in solution and currently eluding isolation and characterization, cannot be discounted.

Undoubtedly, the herein described species **1** and **2** project chemical and structural features that emphasize (a) the unique chemistry of phosphonate and mixed carboxy-phosphonate substrates toward Ni(II), and (b) the differentiation of the composition and structure of the derived and ultimately isolated species brought about by the distinct nature of the phosphonate substrates reacting with Ni(II) under the employed conditions. Collectively, therefore, the observed physicochemical behavior of the substrates H_4IDA2P and H_3IDAP influences quite elegantly the nature of binary interactions developing between them and Ni(II). To this end, it would not be unreasonable to envision analogous interactions emerging between that metal ion and corresponding phosphorylated substrates (amino acids, peptides, proteins) and organophosphonate drug substrates in the requisite aqueous speciation of a biological setting. Delving into the exploration of such interactions (a) with low and high molecular mass phospho-derivative biotargets, and (b) at the binary and ternary level, is a challenge of multidisplinary approaches, currently under investigation in the lab.

3.2. Relevance to Ni(II)–organophosphonate materials

Over the last decades, special attention has focused on delineating the reactivity of organophosphonate ligands toward metal ions, such as Ni(II), Co(II), Mn(II), etc. Materials arising from such interactions are employed in a plethora of applications, including catalysis and intercalation chemistry. In this regard, the nature of the organophosphonate binders is crucial in the isolation of metal–ligand frameworks with well-defined properties. Substrates containing one phosphonate group [45,46], such as glyphosate, or various diphosphonic acids [47,48], such as $H_2O_3P–R–PO_3H_2$ (R=alkyl, phenyl, alkylimino, benzylimino, etc.) under diverse reaction conditions are likely to afford new interesting materials with variable physicochemical properties reflected into the size of the employed binder, the shape, the complexity, the nature of the terminal groups, and their chemical reactivity. Under the influence of these factors, various metal frames may emerge, differing in the size of the final metal frame, the inter-layer distance, the lattice, the coordination shape, etc. To date, a limited number of Ni(II)–phosphonate materials have been synthesised either through interactions at room temperature or chemical reactivity at high temperatures (hydrothermal and/or solvothermal conditions) [49].

The organophosphonate ligands presented in this work, are multifunctional binders that bind metalloelements in a variety of ways. The iminodiphosphonate and imino-carboxy-phosphonate ligand bind Ni(II) ions in an octahedral fashion, with each phosphonate group in compounds **1** and **2** being singly deprotonated. The variety of lattices achieved through the interaction of metal ions with such binders is exemplified in both **1** and **2**, given that the iminodiphosphonate ligand is coordinated to Ni(II) ion in a monodentate fashion **1**, whereas the imino-carboxy-phosphonate ligand acts as a chelator in **2**. A reflection of the distinct nature of the arising binary Ni(II)–L interactions due to the nature of the ligand L, is the extended structure of **1**, which is composed of a repeat unit configured by four mononuclear Ni(II) octahedral sites. Therefore, the iminodiphosphonate groups of the H_4IDA2P binders exhibit the role of a linker, bringing four Ni(II) ions in each arising unit. Each such unit is basically a 32-membered ring. Each ring defines the periphery of a large elliptical cavity, with the calculated

dimensions being 8.094 Å (*b* axis) and 13.897 Å (*c* axis). The formulated area of each cavity approaches 88.4 $Å^2$. Furthermore, the height of the void space between contiguous elliptical cavities in the lattice is 7.33 Å (*a* axis), thus leading to a volume of ~648 $Å^3$ for each cavity. Complex **1** is X-ray isomorphous to the already characterized species between Co(II) and H_4IDA2P [23]. In conclusion, the nature of the phosphonate substrate does influence the nature of interactions and the ultimately isolated binary Ni(II)–phosphonate compound.

On the basis of the aforementioned grounds, compounds **1** and **2** exhibit composition (exchangeable water ligands, carboxy-phosphonates, phosphonates) and structural properties that could support chemical reactivity toward other metal ionic species (complexes or clusters) under appropriately configured reaction conditions. To this end, **1** and **2** could serve as viable candidate precursor species that can be used in the synthesis of homometallic or heterometallic Ni(II)-(M)-phosphonate advanced materials of variable nuclearity and physicochemical properties (e.g. magnetic). Research in this direction is currently ongoing in our lab.

4. Conclusions

The pH-specific synthetic chemistry presented in this work led to well-defined binary Ni(II)–organophosphonate species of distinct physical, chemical and structural properties. The collective physicochemical properties of **1** and **2** define the characteristics for which such species could be useful in the synthesis of advanced Ni(II)–(carboxy)phosphonate materials. Moreover, in both complexes, the retention of the octahedral environment around Ni(II), suggests that the particular metal ion could interact aptly, in a unique fashion, with imino-phosphonate ligands, such as imino bis(methylenephosphonic acid) and *N*-(phosphonomethyl) glycine, or similar substrates, such as aminoalkylphosphonate and IDA derivative phosphonate substrates. Given the essentiality of Ni(II) in the biological systems as well as its toxicity potential, the herein presented species reflect the nature of the arising binary interactions in potential participants of variably formulated aqueous Ni(II)–phosphoderivative binary systems. It remains to be seen whether species such as those encountered in **1** and **2** reflect corresponding binary forms of Ni(II) with actual phosphorylated cellular targets (amino acids, peptides, etc.) or organophosphonate drug molecules, further influencing the physiology or toxicity at the cellular level.

Supplementary data

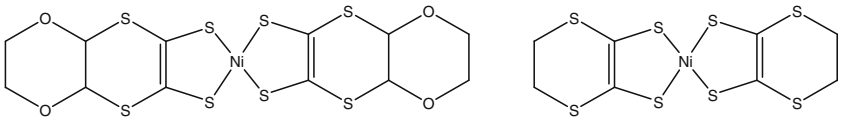
CCDC 722262 and 722263 contain the supplementary crystallographic data for **1** and **2**. These data can be obtained free of charge via http://www.ccdc.cam.ac.uk/conts/retrieving.html, or from the Cambridge Crystallographic Data Centre, 12 Union Road, Cambridge CB2 1EZ, UK; fax: (+44) 1223-336-033; or e-mail: deposit@ccdc.cam.ac.uk.

Acknowledgments

This work was supported by a "PENED" grant co-financed by the EU – European Social Fund (75%) and the Greek Ministry of Development – GSRT (25%).

References

[1] T. Li, W. Zhang, R.Z. Lee, Q. Zhong, Food Chem. 114 (2009) 447.
[2] P. Gikas, J. Hazard. Mater. 159 (2008) 187.
[3] P.A. Olubambi, J.H. Potgieter, L. Cornish, Mater. Design 30 (2009) 1451.
[4] J.M. Ramos, O. Versiane, J. Felcman, C.A.S. Tellez, Spectrochim. Acta A 72 (2009) 182.
[5] Q. Chen, J. Salta, J. Zubieta, Inorg. Chem. 32 (1993) 4485.
[6] E.T. Clarke, P.R. Rudolph, A.E. Martell, A. Clearfield, Inorg. Chim. Acta 164 (1989) 59.
[7] P.R. Rudolph, E.T. Clarke, A.E. Martell, A. Clearfield, J. Coord. Chem. 14 (1985) 139.
[8] B. Bujoli, P. Palvadeau, J. Rouxel, Chem. Mater. 2 (1990) 582.
[9] Y. Zhang, A. Clearfield, Inorg. Chem. 31 (1992) 2821.
[10] G. Huan, A.J. Jacobson, J.W. Johnson, E.W. Corcoran Jr., Chem. Mater. 2 (1990) 91.
[11] D.A. Burwell, K.G. Valentine, J.H. Timmermans, M.E. Thompson, J. Am. Chem. Soc. 114 (1992) 4144.
[12] G.L. Rosenthal, J. Caruso, Inorg. Chem. 31 (1992) 3104.
[13] M.B. Dines, P.C. Griffith, Inorg. Chem. 22 (1983) 567.
[14] M.B. Dines, P.M. DiGiacomo, Inorg. Chem. 20 (1981) 92.
[15] H. Byrd, J.K. Pike, D.R. Talham, J. Am. Chem. Soc. 116 (1994) 7903.
[16] R.G.G. Russell, M.J. Rogers, Bone 25 (1999) 97.
[17] O. Bijvoet, H. Fleisch, R.E. Canfield, R.G.G. Russell, in: Bisphosphonates on Bone, Elsevier, Amsterdam, 1995, p. 1.
[18] CrysAlis CCD, Oxford Diffraction Ltd., Version 1.171.29.9, Release 23.03.06.
[19] CrysAlis.NET, CrysAlis RED, Oxford Diffraction Ltd., Version 1.171.29.9, Release 23.03.06.
[20] G.M. Sheldrick, SHELX-97: Program for the Solution of Crystal Structure, University of Göttingen, Göttingen, Germany, 1997.
[21] G.M. Sheldrick, SHELX-97: Program for the Refinement of Crystal Structure, University of Göttingen, Göttingen, Germany, 1993-7, Release 97-2.
[22] L.J. Farrugia, J. Appl. Cryst. 32 (1999) 837.
[23] H. Jankovics, M. Daskalakis, C.P. Raptopoulou, A. Terzis, V. Tangoulis, J. Giapintzakis, T. Kiss, A. Salifoglou, Inorg. Chem. 41 (2002) 3366.
[24] D. Kong, Y. Li, X. Ouyang, A.V. Prosvirin, H. Zhao, J.H. Ross, K.R. Dunbar, A. Clearfield, Chem. Mater. 16 (2004) 3020.
[25] B.-P. Yang, A.V. Prosvirin, H.-H. Zhao, J.-G. Mao, J. Solid State Chem. 179 (2006) 175.
[26] B.-P. Yang, Z.-M. Sun, J.-G. Mao, Inorg. Chim. Acta 357 (2004) 1583.
[27] B.-P. Yang, J.-G. Mao, Inorg. Chem. 44 (2005) 566.
[28] J.-L. Song, J.-G. Mao, Y.-Q. Sun, H.-Y. Zeng, R.K. Kremer, A. Clearfield, J. Solid State Chem. 177 (2004) 633.
[29] J.G. Mao, Z. Wang, A. Clearfield, J. Chem. Soc., Dalton Trans. 24 (2002) 4541.
[30] D. Kong, J. Reibenspies, J. Mao, A. Clearfield, A.E. Martell, Inorg. Chim. Acta 342 (2003) 158.
[31] F.-N. Shi, F.A.A. Paza, P.I. Girginova, L. Mafra, V.S. Amaral, J. Rocha, A. Makal, K. Wozniak, J. Klinowski, T. Trindade, J. Mol. Struct. 754 (2005) 51.
[32] V.S. Sergienko, G.G. Aleksandrov, E.G. Afonin, Zh. Neorg. Khim. 42 (1997) 1291.
[33] V.S. Sergienko, E.G. Afonin, G.G. Aleksandrov, Zh. Neorg. Khim. 43 (1998) 1002.
[34] Y.Q. Zheng, Z.P. Kong, J. Coord. Chem. 56 (2003) 967.
[35] H. Aghabozorg, R.C. Palenik, G.J. Palenik, Inorg. Chem. 24 (1985) 4216.
[36] T.-T. Pan, J.-R. Su, D.-J. Xu, Acta Cryst. E61 (2005) m1376.
[37] E.E. Sileoa, A.S. Araujob, G. Rigottic, O.E. Piroc, E.E. Castellano, J. Mol. Struct. 644 (2003) 67.
[38] Q.-J. Deng, M.-H. Zeng, H. Liang, K.-L. Huang, Acta Cryst. C62 (2006) m389.
[39] N. Stock, Solid State. Sci. 4 (2002) 1089.
[40] D. Heineke, S.J. Franklin, K.N. Raymond, Inorg. Chem. 33 (1994) 2413.
[41] E. Galdecka, Z. Galdecki, P. Gawryszewska, J. Legendziewicz, New J. Chem. 24 (2000) 387.
[42] R.S. Drago, in: Physical Methods in Chemistry, W.B. Saunders Company, Philadelphia, 1977, pp. 359–410.
[43] A.B.P. Lever, in: Inorganic Electronic Spectroscopy, second ed., Elsevier, Amsterdam, 1984, pp. 507–511.
[44] M. Ramstedt, C. Norgren, J. Sheals, D. Boström, S. Sjöberg, P. Persson, Inorg. Chim. Acta 357 (2004) 1185.
[45] G. Cao, V.M. Lynch, J.S. Swinnea, T.E. Mallouk, Inorg. Chem. 29 (1990) 2112.
[46] G.B. Hix, V.J. Carter, D.S. Wragg, R.E. Morris, P.A. Wright, J. Mater. Chem. 9 (1999) 179.
[47] S. Drumel, P. Janvier, P. Barboux, M. Bujoli-Doeuff, B. Bujoli, Inorg. Chem. 34 (1995) 148.
[48] S. Drumel, P. Janvier, P. Barboux, M. Bujoli-Doeuff, B. Bujoli, New J. Chem. 19 (1995) 239.
[49] B. Menaa, I.J. Shannon, J. Mater. 12 (2002) 350.



Scheme 1. Structural formulas of $Ni(edodddt)_2$ and $Ni(dddt)_2$.

In this paper the synthesis of a new metal 1,2-dithiolene similar to $Ni(dddt)_2$ is described. It contains an ethylene-dioxo group extension, as an additional heteroatom group and the transition metal Ni (Scheme 1). Electrochemical measurements, X-ray measurements and spectral investigations have been made. DFT studies are also included.

2. Experimental

2.1. Materials and methods

All starting materials of analytical grade were obtained commercially and used as received, except the methanol that was dehydrated according to the literature [12].

2.2. Synthesis of 2,3-dichloro-1,4-dioxane (**2**)

The starting material 2,3-dichloro-1,4-dioxane (**2**) was prepared according to the literature by chlorination of 1,4-dioxane. The product was a mixture of *cis* and *trans* isomers [13].

2.3. 4,5-(1,4-Dioxane-2,3-diyldithio)-1,3-dithiole-2-thione (**3**)

2,3-Dichloro-1,4-dioxane (**2**) (1.65 g, 10 mmol) was dissolved in 200 ml acetone and 5 g (5 mmol) of $(Bu_4N)_2Zn(dmit)_2$ were added. The solution was refluxed for 20 h and the color changed from bright red to yellow-brown. The solvent was evaporated and the resulting dark-brown sticky residue was washed with 200 ml of water and extracted with 200 ml of dichloromethane. The organic layer dried with magnesium sulfate and filtered. Purification of the final product was made by column chromatography in silica gel using CH_2Cl_2 as eluent. Yellow-brown crystals were produced.

Yield: 1.7 g, (60%); mp: 187 °C; UV–Vis (CH_3CN, nm): 238, 268, 395, nm; ^1H NMR (300 MHz, $CDCl_3$) δ(ppm): 5.52 (s, 2H), 4.07 (m, 2H), 3.76 (m, 2H); IR data (ν, cm^{-1}): 2967, 2936, 2906, 2860, 1490, 1442, 1366, 1322, 1274, 1241, 1118, 1091, 1037, 1014, 989, 935, 879, 853, 813, 748, 588, 565.

2.4. 4,5-(1,4-Dioxane-2,3-diyldithio)-1,3-dithiol-2-one (**4**)

Oxidation of thione (**3**) with mercuric acetate in acetic acid affords the 4,5-(1,4-dioxane-2,3-diyldithio)-1,3-dithiol-2-one (**4**) as white-yellow crystals [14].

Yield: (77%); mp: 144–146 °C, UV–Vis (CH_3CN, nm): 286, nm; ^1H NMR (300 MHz, $CDCl_3$) δ(ppm): 5.50 (s, 2H), 4.07 (m, 2H), 3.76 (m, 2H); IR data (ν, cm^{-1}): 2980, 2932, 2915, 2865, 1771, 1674, 1644, 1615, 1513, 1445, 1365, 1323, 1273, 1241, 1120, 1095, 1043, 1015, 992, 938, 901, 878, 852, 765, 745, 587, 565, 537.

2.5. Bis[4,5-(1,4-dioxane-2,3-diyldithio)-1,3-dithiole] Nickel tetrabutylammonium [$(Bu_4N)Ni(edodddt)_2$] (**5**)

Ketone (**4**) (100 mg, 0.38 mmol) was added to sodium metal (20 mg, 0.87 mmol) dissolved in 15 ml methanol. The mixture was stirred for an hour, under nitrogen atmosphere. Addition of a solution of Nickel chloride hexahydrate (45 mg, 0.19 mmol) in 5ml methanol was made and has been stirred for 30 min. An addition of a solution of tetrabutyl ammonium bromide (122 mg, 0.38 mmol) in 5 ml methanol followed, resulting to the precipitation of a dark green solid. The solid was removed by filtration in vaccuo and washed repeatedly with methanol to give **5** as a dark powder.

Yield: 108 mg, (76%), of pure product. mp: 156 °C; UV–Vis (CH_2Cl_2, nm): 1089 (ε = 17 385), 581(ε = 2338), 380 (ε = 10 469), 305 (ε = 39 815); IR data (ν, cm^{-1}): 2958, 2926, 2866, 1442, 1388, 1334, 1271, 1232, 1118, 1090, 1066, 1047, 932, 889, 747, 733, 663, 597, 561; Raman Shifts (cm^{-1}): 141, 245, 356, 417, 456, 487, 526, 565, 594, 895, 995, 1138, 1439, 1490, 2863, 2936, 2975; Elemental *Anal. Calc.* for $C_{28}H_{48}NNiO_4S_8$: C, 43.23; H, 6.22. Found: C, 42.95; H, 6.35%.

2.6. Bis[4,5-(1,4-dioxane-2,3-diyldithio)-1,3-dithiole] Nickel [$Ni(edodddt)_2$] (**6**)

The compound **5** (50 mg 0.065 mmol) was dissolved in PhCN (5 ml), heated and filtered. TCNQ (13 mg 0.065 mmol) was dissolved in ACN (5 ml) heated and filtered. The two filtrates ware united and refluxed for 40 min. The solution left to stand at room temperature for 24 h. The dark solid was filtered and washed with ACN.

Yield: 29 mg, (57%); mp: >290 °C; UV–Vis (CH_2Cl_2, nm): 944 (ε = 43 431), 648 (ε = 56992), 374 (ε = 12777); ^1H NMR (300 MHz, $CDCl_3$) δ(ppm): 5.45 (s, 4H), 4.11 (m, 4H), 3.74 (m, 4H); IR data (ν, cm^{-1}): 2975, 2930, 2897, 2845, 1444, 1381, 1368, 1328, 1283, 1263, 1235, 1112, 1085, 1062, 1042, 1022, 981, 935, 894, 880, 851, 756, 610, 564; Raman Shifts (cm^{-1}): 125, 162, 250, 278, 297, 317, 355, 371, 392, 413, 460, 498, 533, 832, 880, 912, 1368, 2668, 2855, 2976; Elemental *Anal. Calc.* for $C_{12}H_{12}NiO_4S_8$: C, 26.92; H, 2.26. Found: C, 26.50; H, 2.35%.

3. Analysis and physical measurements

Elemental analyses were obtained on a Perkin–Elmer 2400 Series II elemental analyser. Melting points were determined in open-end capillaries using a Buchi melting point apparatus (pat. 320–388) at a ramp rate 120 (a.u.) without calibration. Solution 1H NMR spectra were recorded on Varian 300 MHz. Chemical shifts are reported in ppm downfield of TMS. UV–Vis spectra were obtained by the Perkin–Elmer, UV/Vis/Nir Lambda 19 spectrometer FTIR spectra were obtained by a Bruker equinox 55 and. Raman spectra were recorded on a Renishaw inVia Reflex Raman microscope system using the 514 and 785 nm laser lines.

4. Single crystal X-ray crystallography

Data were collected on an Oxford Diffraction Xcalibur-3 diffractometer (equipped with a Sapphire CCD area detector) using a graphite-monochromated Mo Kα radiation (λ = 0.71073 Å). A crystal of compound $[Ni(edodddt)_2]\cdot 1.88H_2O$ (black needle, size 0.1 × 0.04 × 0.03 mm) was attached to a glass fiber using silicone grease and transferred to a goniostat where it was cooled to 100 K for data collection. Data were collected using the ω-scan

Table 1
Crystallographic data for complex $[Ni(edodddt)_2]\cdot 1.88H_2O$.

Formula	$C_{12}H_{15.76}NiO_{5.88}S_8$
Formula weight	569.31
Crystal color, habit	black, needle
Crystal dimensions (mm)	0.1 × 0.04 × 0.03
Crystal system	monoclinic
Space group	$P2_1/n$
a (Å)	10.6122(3)
b (Å)	4.5870(1)
c (Å)	22.2014(8)
β (°)	98.288(3)
V (Å^3)	1069.44(5)
Z	2
$\rho_{Calc.}$ (g cm^{-3})	1.768
Radiation, λ (Å)	Mo Kα, 0.71073
T (K)	100(2)
μ (mm^{-1})	1.714
θ range (°)	3.61–25.00
Ranges of h, k, l	−12/11; −5/5; −26/24
Reflections collected	6545
Independent reflections (R_{int})	1886 (0.0278)
Data/parameters	1886/125
Goodness of fit (Gof) (F^2)	1.209
Final R_1[a]/wR_2[b] indices ($I > 2\sigma_I$)	R_1 = 0.0522/wR_2 = 0.1702
Largest difference in peak/hole (e Å^{-3})	1.497/−0.548

[a] $R_1 = \sum(||F_o| - |F_c||)/\sum(|F_o|)$.
[b] $wR_2 = \sum[w(F_o^2 - F_c^2)^2]/\sum[w(F_o^2)^2]\}^{1/2}$.

method (0.75° frame width). Empirical absorption corrections (multiscan based on symmetry-related measurements) were applied using the CRYSALIS RED software.[15] The structure was solved by direct methods using SHELXS-97, and refined on F^2 using full-matrix least-squares with SHELXL-97 [16]. The non-H atoms were treated anisotropically, whereas the H atoms were placed in calculated, ideal positions and refined as riding on their respective C atoms. The programs used were CRYSALIS CCD [15] for data collection, CRYSALIS RED 15 for cell refinement and data refinement and WINGX [17] for crystallographic calculations. Unit cell parameters and structure solution and refinement data are listed in Table 1.

5. Results and discussion

5.1. Synthesis

The thione **3** was first synthesized by Kotov in 25% yield by [2 + 4] cycloaddition of 1,3-dithiole-2,4,5-trithione oligomer to 1,4-dioxene [18]. We used a new improved method for its preparation with a yield of 60% (Scheme 2). The starting material 1,2-dichlorodioxane **2** was prepared by chlorination of dioxane. The nucleophilic displacement reaction of $(Bu_4N)_2Zn(dmit)_2$ with **1** in one step gave thione **3**. The thione **3** was converted to ketone **4** by treatment with $Hg(CH_3COO)_2$ in CH_2Cl_2/CH_3COOH [14]. Deprotection of ketone **4** with a base (MeONa) in MeOH leads to the formation in situ of the corresponding dithiolene salt **5**. The neutral complex **6** can be obtained by oxidation with TCNQ. The **6** was obtained as a dark powder.

In an attempt to obtain crystals, an acetone–isopropanol (1/1) solution of **5** was left to evaporate. During this open to the air procedure the salt **5** oxidizes to neutral **6** and water condensed in the solution to give crystals of $[Ni(edodddt)_2]\cdot 1.88H_2O$ suitable for crystallographic studies.

5.2. Crystal structure of bis[4,5-(1,4-dioxane-2,3-diyldithio)-1,3-dithiole] Nickel

Compound $[Ni(edodddt)_2]\cdot 1.88H_2O$ crystallizes in the monoclinic space group $P2_1/n$. A labeled ball and stick representation of the compound is given in Fig. 1 and selected bond lengths and angles from the crystal structure determination and calculated values from DFT studies are shown in Tables 2 and 3.

The crystal structure consists of compound $[Ni(edodddt)_2]$ and also 1.88 water molecules of crystallization. The water molecules occupy two sites. Compound $[Ni(edodddt)_2]\cdot 1.88H_2O$ contains one Ni^{2+} ion linked with the two vicinal exocyclic sulfur atoms of the two chelating ligands. The Ni atom is thus tetra-coordinate and has a square planar geometry. The dioxo outer rings adopt a chair conformation preventing the formation of stacks with short intermolecular contacts. The packing motive of the crystal along the α-axis, shown in Fig. 2, reveal a parallel alignment of the $[Ni(edodddt)_2]$ molecules.

A close examination of the packing revealed the existence of intermolecular hydrogen-bonding interactions involving the crystallization H_2O molecules (O···O separations = 2.769 Å) and also the C, O, S atoms of the ligands (C···O, C···S separations = 3.285-3.426 Å). The closest Ni···Ni distance is 4.5870(1) Å which is the length of the b-axis. The Ni–S bond lengths are 2.123(2) [Ni–S1] and 2.132(2) [Ni–S2] Å, whereas the S–C, C = C and C–O bond distances are 1.700(6)–1.751(6) Å, 1.378(8) and 1.415(7)–1.449(7) Å, respectively. These bond distances of the $[Ni(edodddt)_2]\cdot 1.88H_2O$

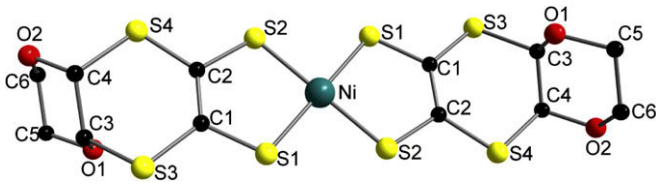
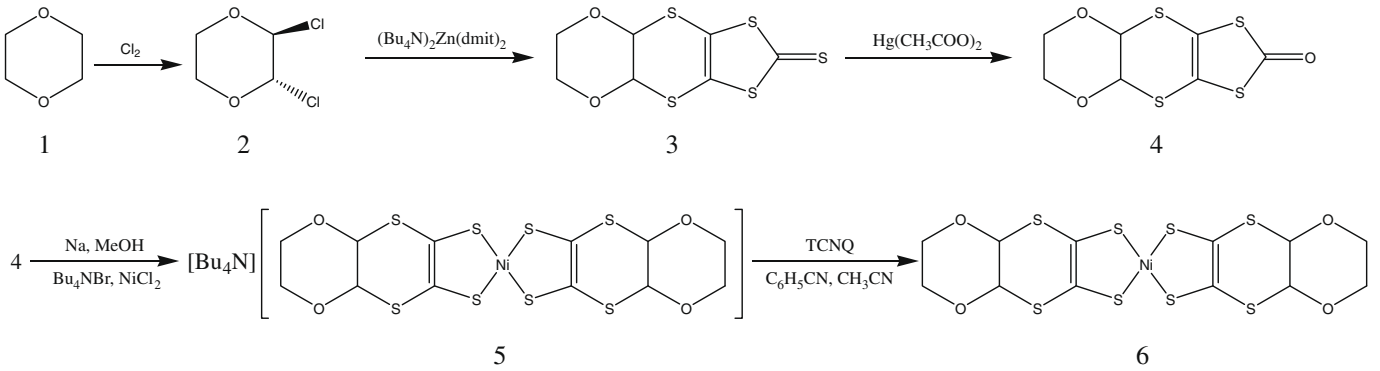


Fig. 1. Ball and stick representation of the structure of compound $[Ni(edodddt)_2]$ with the indication of the atom labels. H atoms were omitted for clarity.



Scheme 2. Synthetic route of the $[Ni(edodddt)_2]$ synthesis.

Table 2
Experimental and theoretically calculated bond distances for Ni(edodddt)$_2$.

Atoms	Experimental distances (Å)	Calculated distances (Å)	Atoms	Experimental distances (Å)	Calculated distances (Å)
Ni–S1	2.123 (1)	2.175	C3–S3	1.792 (6)	1.839
Ni–S2	2.132 (2)	2.169	C3–O1	1.415 (7)	1.415
Ni1–Ni1	4.5870 (1)		C3–C4	1.525 (8)	1.522
C1–S1	1.700 (6)	1.722	C4–S4	1.841 (6)	1.832
C1–S3	1.751 (6)	1.771	C4–O2	1.418 (7)	1.412
C1–C2	1.378 (8)	1.395	C5–O1	1.446 (7)	1.434
C2–S2	1.716 (6)	1.719	C5–C6	1.501 (8)	1.521
C2–S4	1.743 (6)	1.771	C6–O2	1.449 (7)	1.435

Table 3
Experimental and theoretically calculated bond angles for Ni(edodddt)$_2$.

Atoms	Experimental angles (ω°)	Calculated angles (ω°)	Atoms	Experimental angles (ω°)	Calculated angles (ω°)
S1–Ni–S1	180.00	180.00	S1–C1–S3	114.1(3)	112.57
S1–Ni–S2	91.91(5)	91.28	C1–S3–C3	103.4(3)	104.52
S2–Ni–S2	180.00	179.99	S3–C3–O1	110.9(4)	103.95
Ni–S1–C1	104.8(2)	104.47	C3–O1–C5	108.6(4)	110.65
S1–C1–C2	119.9(4)	119.59	O1–C5–C6	110.3(5)	110.11

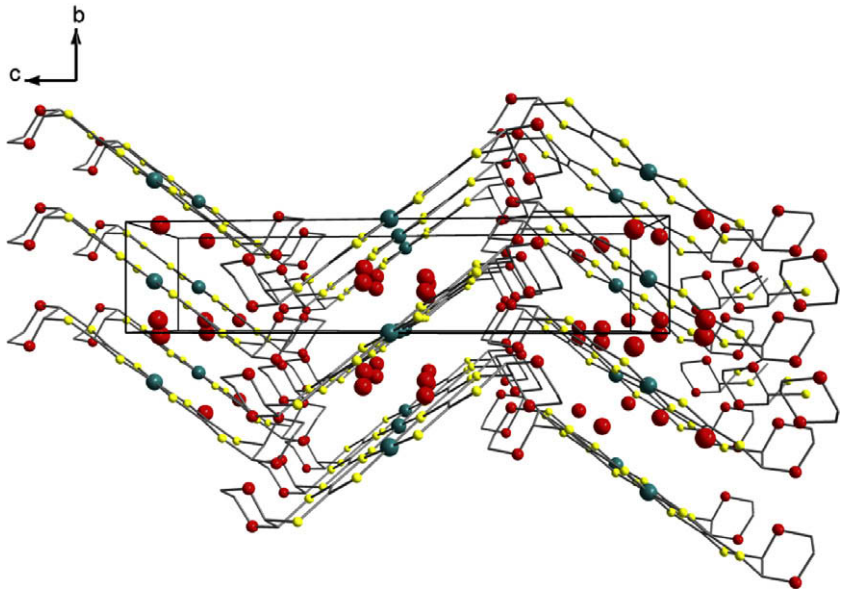
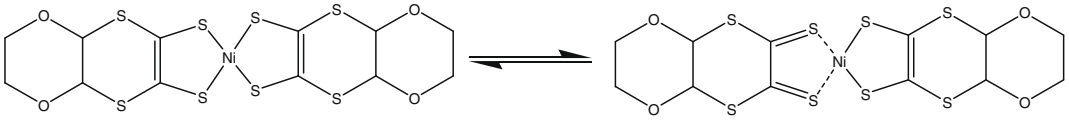


Fig. 2. Packing of [Ni(C_6H_6 O_2 S_4)$_2$] ·1.88H_2O molecules, viewed down the *a*-axis. Color code: Ni, green; O, red; S, yellow; C, gray. H atoms were omitted for clarity. (For interpretation of the references to color in this figure legend, the reader is referred to the web version of this article.)

compound lie within the range observed for other neutral dithiolenes [5,9,19–22]. Finally, it can be seen that the C2–S2 and C1–S1 distances are shorter than the C2–S4 and Cl–S3 distances, respectively. This is not surprising since resonance structures with the ligand in the radical form allow for a partial C1–S1 and C2–S2 double bond (Scheme 3).

5.3. IR, Raman

The Raman spectra of **6** were acquired using the 514 and 785 nm (Fig. 8a) laser lines. It showed in both frequencies the characteristic vibrations of S–Ni–S and Ni–S at 125, 371, 413 and 498 cm^{-1} (125, 417 and 487 cm^{-1} for **5**) and the characteristic vibrations of O–C–C, C–O–C and C–O at 355 cm^{-1}, 392 and 460 cm^{-1} (356 and 456 cm^{-1} for **5**). There are also intensities at 533, 832, 880 and 912 cm^{-1} (526, 565 and 895 cm^{-1} for **5**) which are corresponding to the S–C–S and S–C vibrations. The C=C appears at 1368 cm^{-1} (1439 cm^{-1} for **5**). The intensities at 2668, 2855 and 2976 cm^{-1} correspond to the C–H vibrations and appear only by excitation with the 514 nm and not with the 785 nm laser lines, (in the compound **5** these intensities appear at 2863, 2936 and 2975 cm^{-1} and are enhance due to the existence of the tetrabutyl moiety). This is probably a result of the different Raman crosssection between the two excitation lines.



Scheme 3. Resonance forms of Ni(edodddt)$_2$.

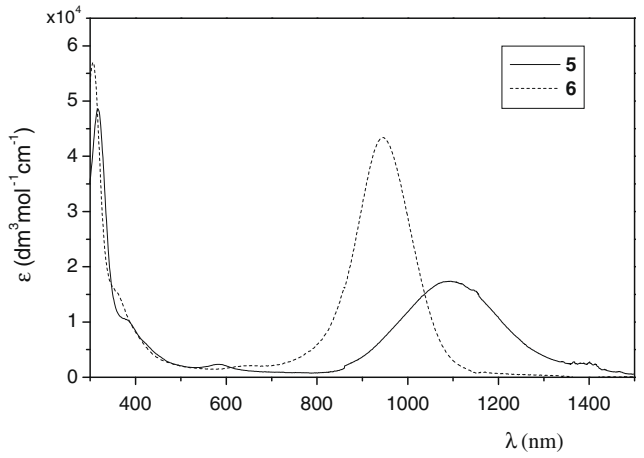


Fig. 3. UV–Vis–NIR spectra of **5** (line) and **6** (dash) in CH_2Cl_2.

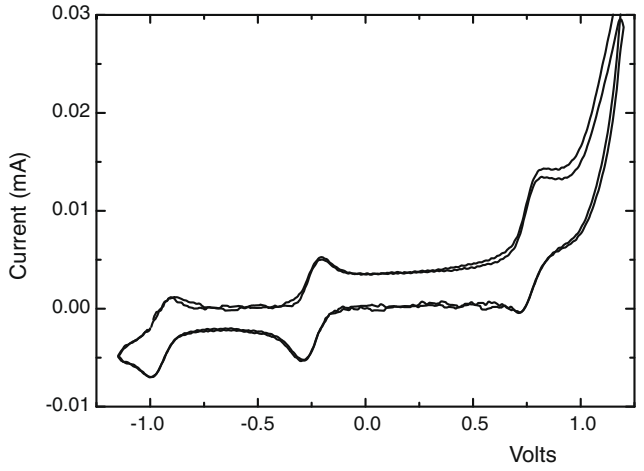


Fig. 4. Cyclic voltammogram of **6** in CH_2Cl_2 with $Ag/AgNO_3$ as reference electrode and 0.4 mol dm^{-3} $BuNPF_6$ as supporting electrolyte with a scan rate of 0.2 V/s.

Table 4
Redox potentials of selected Ni dithiolene complexes.

Compound	$E_1(-2/-1)$ (V)	$E_2(-1/0)$ (V)	$E_3(0/+1)$ (V)	$E_2 - E_1$ (V)
$[Ni(edodddt)_2^{-1}]$[a]	−0.951	−0.250	0.763	0.701
$[Ni(bddt)_2^{-1}]$[b]	−0.625	−0.042	0.907	0.583
$[Ni(cddt)_2^{-1}]$[c]	−0.690	0.080	0.920	0.770
$Ni(dddt)_2$[c]	−0.745	0.058	0.875	0.803
$[Ni(edo)_2]$[a]	−1.550	−0.860	0.110	0.690

[a] vs. $Ag/AgNO_3$ as reference electrode in CH_2Cl_2.
[b] vs. SCE as reference electrode in CH_2Cl_2..
[c] Ag/AgCl as reference electrode in CH_2Cl_2.

$[NBu_4][Ni(edodddt)_2]$ displays a very rich IR spectra with characteristic peaks. The stretching vibrations of O–C bonds are observed at 932, 1047, 1066 and 1090 cm^{-1}. The S–C stretching vibrations are also present in the IR spectra at 747 and 889 cm^{-1}. Furthermore there are also the characteristic bands in the region between 2800 and 3000 cm^{-1} related to the C–H stretching vibrations.

The neutral complex **6** shows the same peaks at 935, 981, 1042, 1085 cm^{-1} for the O–C stretching. The S–C stretching appears at 756, 851, 880 and 894 cm^{-1}. There are also the characteristic bands between 2800 and 3000 cm^{-1} related to the C–H stretching vibrations.

In this paper also the theoretical IR and Raman spectra of the neutral complex **6** were calculated (Figs. 8 and 9). The comparison between them and the experimental ones is discussed later.

5.4. UV–Vis–NIR spectra

The UV–Vis–NIR spectra of complexes **5** and **6** are shown in Fig. 3.

The complex **5** in dichloromethane shows a strong broad absorption at 1089 nm (ε = 17385 dm^3 mol^{-1} cm^{-1}) which is assigned to a $\pi \rightarrow \pi^*$ transition ($2b_{1u} \rightarrow 3b_{2g}$) [19]. The characteristic long wave transition is also found in the **6** complex at 944 nm (ε = 43 431 dm^3 mol^{-1} cm^{-1}).

There are also bands at 581 and 380 nm which are assigned to a $\pi \rightarrow$ Ni and Ni $\rightarrow \pi$ transitions, respectively [19]. These bands are also observed in the neutral complex **6** at 648 and 374 nm.

5.5. Cyclic voltammetry

The electrochemistry of the complex **6** was investigated using cyclic voltammetry in CH_2Cl_2 (versus Ferocene with $Ag/AgNO_3$ as reference electrode and Pt as working electrode, Fig. 4). As

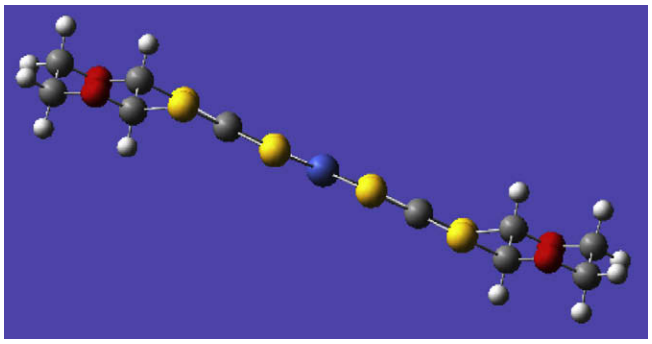


Fig. 6. Calculated geometrical position of the $Ni(edodddt)_2$.

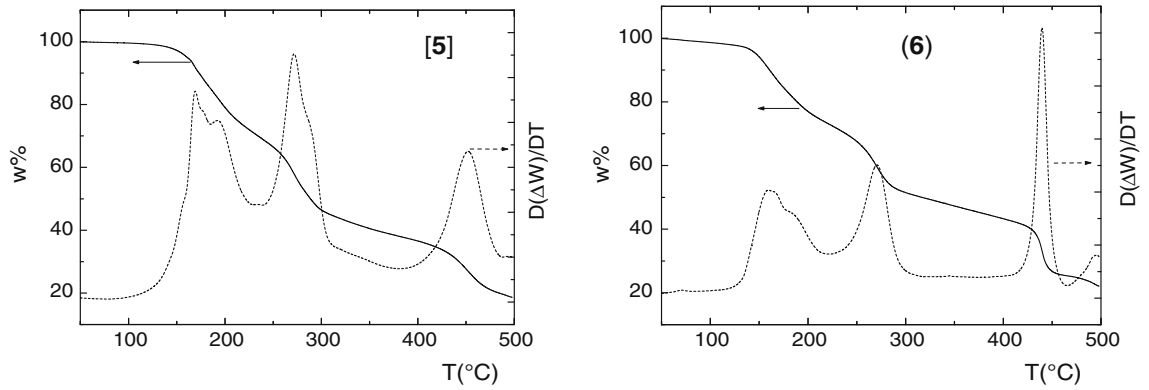


Fig. 5. TGA spectra of **5** and **6**.

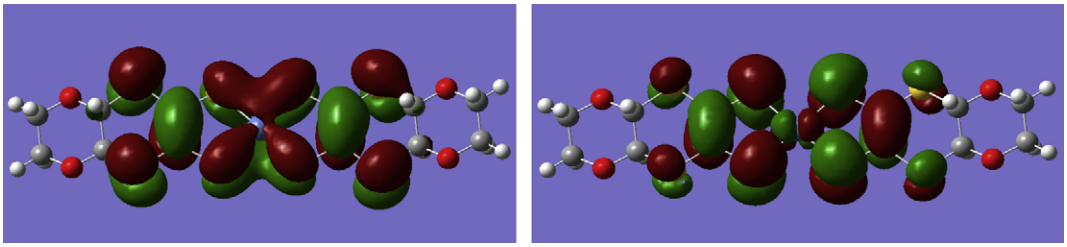


Fig. 7. The HOMO (left) and LUMO (right) molecular orbital of Ni(edodddt)$_2$.

expected, the cyclovoltammogram exhibit three 1e$^-$ reversible redox waves at $E_{1/2}$ = −0.951V versus Ag/AgNO$_3$ (−1.071 V versus Ferocene), −0.250V versus Ag/AgNO$_3$ (−0.370 V versus Ferocene) and 0.763 V versus Ag/AgNO$_3$ (0.640 V versus Ferocene). These oxidations correspond to the equilibrium [Ni(edodddt)$_2$]$^{-2}$ ↔ [Ni(edodddt)$_2$]$^{-1}$ ↔ [Ni(edodddt)$_2$] ↔ [Ni(edodddt)$_2$]$^{+1}$. As it can be seen from Table 4 the potentials of Ni(edodddt)$_2$ are negatively shifted than other molecules with extended outer rings like Ni(bddt)$_2^{-1}$ [20] or Ni(cddt$_2^{-1}$ [21] (the outer ring consist of six or five carbon atoms) indicating that the molecule has stronger donor ability than the other two. On the other hand this expansion did not improve this ability compared with "shorter" molecules like Ni(edo)$_2$ and Ni(dddt)$_2$ [9,23].

5.6. TGA thermal analysis

From the thermal stability spectra (Fig. 5) it seems that this compound either as a salt or as neutral is stable for temperatures till 150 °C. In higher temperatures it decomposes in three stages.

5.7. DFT studies

In the case of Ni(edodddt)$_2$ we additionally performed a theoretical study. For the optimization of molecular geometries as well as the calculation of the vibrational frequencies we used the DFT formalism combined with the B3-LYP [24,25] hybrid functional. The 6-311G(d,p) [26–28] basis set was used for all elements except Nickel for which we used the 6-311++G(d,p) basis set, resulting in 626 basis functions on total. All calculations were done with the GAUSSIAN 03 [29] set of programs.

Selected observed and calculated distances as well as bond angles in the molecule are shown in Tables 2 and 3. In Table 3 the experimental bond angle S3–C3–O1 (110.9°) differs from the calculated one (103.95°). As it has already be mentioned earlier, there is a relatively strong intermolecular (hydrogen-bonding) interaction between O1 and C4 atoms of adjacent molecules (O1···C4 = 3.285 Å). Such intermolecular interactions are not considered in the theoretical calculations and presumably contribute to the observed deviation between the experimental and calculated values for this angle. However there is a good agreement between the experimental and calculated data.

A comparison between the calculated Ni–S and C–S bond length with the Ni(dddt)$_2$ [10] analogous was made. The Ni–S and C–S bonds in the new molecule proved to be shorter than in the case of Ni(dddt)$_2$ [10]. The theoretical calculations show that the most stable position of the molecule is the geometry with the outer rings

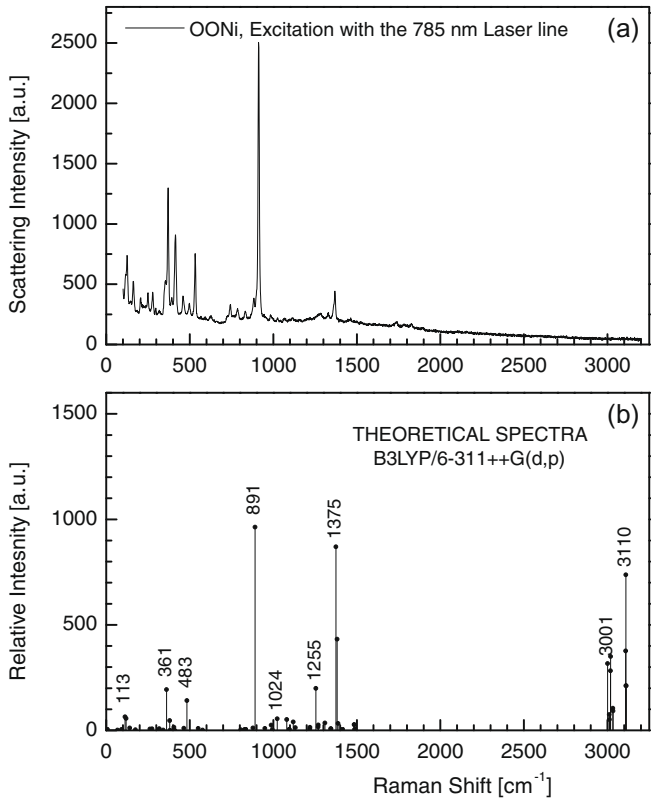


Fig. 8. Experimental (a) and theoretical (b) Raman spectra.

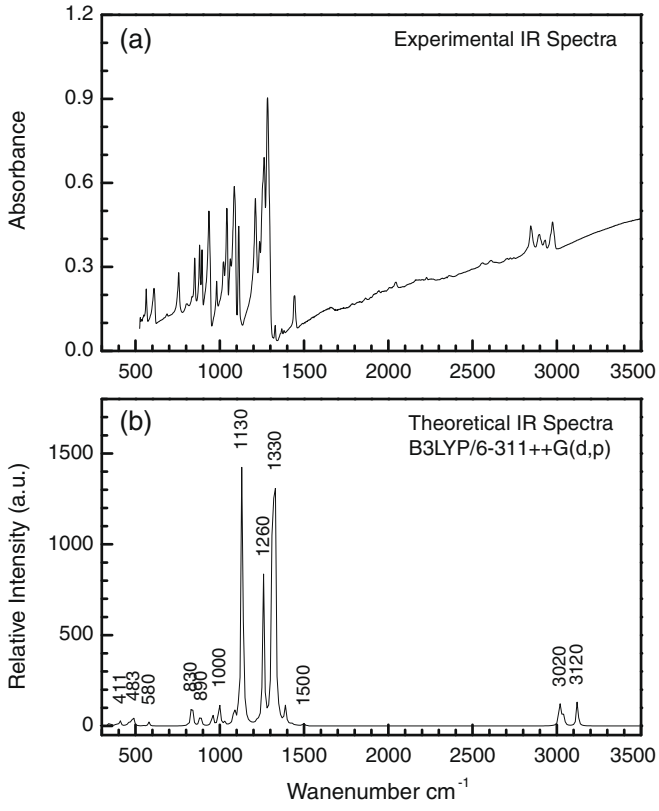


Fig. 9. Experimental (a) and theoretical (b) IR spectra.

Table 5
Normal mode vibrations of the Ni(edodddt)$_2$ molecule with their approximate description of the atomic displacements. Notation: ν – frequency (cm^{-1}), I – IR Intensity (km/mol).

Experiment		Theory				Approximate description
		IR		Raman		
IR (cm^{-1})	Raman (cm^{-1})	ν (cm^{-1})	I (km/mol)	ν (cm^{-1})	I (km/mol)	
		7	1.61	7	4.79	C–S–C b (o.r.) "oop"
		42	1.29			S–Ni–S b "ip"
			68	1.30		C–S–Ni b "oop" + C–S–C b (o.r.) "oop"
			92	4.12		C–S–Ni b "oop"
			113	64.38		S–Ni str
	125		119	56.37		S–Ni str
			141	11.73		S–C–O b "oop"
		122	1.41			C–O–C b "oop" + C–S–C b "oop"
	162	166	4.95	175	2.66	C–O–C b "oop"
		197	3.24			C–O–C b "oop"
		236	1.93			C–S (C of db) str "ip"
	250			262	6.56	O–C–S b "ip"
	278			274	6.95	S–C–S b "oop"
	297	295	2.44			S–Ni–S b "ip" + O–C–S b "ip"
		315	3.42	313	1.58	S–Ni str + S–C–S b "oop"
	317			318	7.50	S–Ni str
	355	341	19.92	341	1.54	O–C–C b "oop"
		356	5.77			S–Ni str + S–C str
	371			361	193.31	S–Ni str + C–O–C b "ip"
				380	46.44	C–O–C b "oop"
	392	382	12.76	382	0.83	C–O–C b "oop"
		403	12.21	403	1.64	S–Ni–S b "ip" + C–O–C b "oop"
				405	15.17	S–Ni–S b "ip" + S–C–O b "oop" + C–C–O b "oop"
	413	411	15.99	411	0.21	S–Ni str + C–O–C b"oop"
		453	4.56			S–Ni–S b "oop"
	460	462	27.15	465	9.84	C–O str
		469	11.26			S–Ni str + S–C–S b h "ip"
	498	483	88.26	483	141.04	S–Ni str + C–S (central) str
564	533	549	1.48	551	9.60	S–C–S b "oop"
610		577	22.08	577	1.71	C–C–O b "oop"
756		808	10.66	805	2.74	S–C str (C of db) + S–C–S b h "ip" + C–O–C b "ip"
		826	105.78	827	3.59	S–C–O b h "ip" + C–C str (of the outer rings) + C–O str
851	832	834	44.46	834	2.61	S–C (left) str "ip" + C–O–C (left) b h "ip"
		835	23.55	835	5.59	S–C(right) str "ip" + C–O–C (right) b h "ip"
880	880	874	58.75	878	11.15	S–C str (C of d.b.) + C–C str (o.r.)
894		882	35.33			
	912			891	963.16	S–C–S b (C of d.b.) "ip"
935		950	76.14	950	9.33	C–O–C b h "ip" + S–C str (o.r.)
981		987	165.49	988	24.73	C–C str (o.r.) + C–O str
		995	28.53	995	3.18	C–C str (o.r.) + C–O str + C–S str (d.p)
1022		1023	22.26	1024	54.74	C = C str + C–S str
1042		1080	196.89	1081	51.69	C–C str + C–O–C b "ip" + C–C str (o.r.)
1062						
1085		1095	13.52	1095	4.53	C–O–C b "ip" (left o.r.)
		1096	10.04	1096	5.03	C–O–C b "ip" (right o.r.)
1112		1114	1706.82	1119	39.87	C–O str + C–C str (o.r.)
		1132	35.96	1132	12.81	C–O str + C–C str (o.r.)
		1219	23.51	1219	6.18	S–C str (o.r.) (right) + C–H w (o.r.) (right)
		1220	11.35	1220	14.30	S–C str (o.r.) (left) + C–H w (o.r.) (left)
1235		1248	1851.33	1255	198.69	C–H(o.r.) w + CH_2 w
1263		1268	7.96	1268	16.01	C–H(o.r. left) w + CH_2 w
		1269	4.61	1269	25.57	C–H(o.r. right) w + CH_2 w
1283		1280	2394.09			C = C str + C–H(o.r.) w + CH_2 w
1328		1310	178.68	1309	35.06	C–H(o.r.) w + CH_2 w
		1344	8.26	1344	7.54	C–H(o.r. right) w + CH_2 w
		1345	8.65	1345	7.46	C–H(o.r. left) w + CH_2 w
	1368		1375	870.02		C = C str + C–H(o.r.) w + CH_2 w
1368		1379	67.41			C–H(o.r.) w + CH_2 w
				1382	432.00	C = C str + C–H(o.r.) w + CH_2 w
1381		1388	4.11	1388	32.57	C–H(o.r.) w + CH_2 w
1444		1415	11.17	1415	5.50	C–H(o.r.) w + CH_2 w
		1484	8.98	1484	26.82	CH_2 (left) sc
		1484	9.12	1485	26.56	CH_2 (right) sc
				1488	3.94	CH_2 (left) sc
				1489	4.82	CH_2 (right) sc
		3000	90.52	3001	316.43	CH_2 str
2845		3011	39.00	3011	74.62	CH_2 (left) str
2897	2668[a]	3012	57.44	3012	51.48	CH_2 (right) str
		3018	2.09	3018	282.55	C–H (o.r. left) str
		3019	1.78	3019	349.94	C–H (o.r. right) str
		3032	26.58	3032	104.89	C–H (o.r. left) str
	2855[a]	3033	28.32	3033	91.94	C–H (o.r. right) str

Table 5 (*continued*)

Experiment		Theory				Approximate description
		IR		Raman		
IR (cm^{-1})	Raman (cm^{-1})	ν (cm^{-1})	I (km/mol)	ν (cm^{-1})	I (km/mol)	
2930		3109	81.86	3109	376.43	CH_2 (left) w
2975	2976[a]	3110	41.47	3110	737.27	CH_2 (right) w
		3111	14.75	3111	211.67	CH_2 (left) w
		3112	15.60	3112	211.22	CH_2 (right) w

b = bending, "oop" = "out of plane", "ip" = "in plane, str = stretching, sc = scissoring, w = wagging, v = vertical, h = horizontal, o.r. = outer ring, d.b. = double bond.
[a] Visible only with the 514 nm excitation line.

adopting a chair conformation (Fig. 6). This is also supported by the X-ray measurements.

The HOMO molecular orbital is of b_{1u} symmetry and as it can be seen from Fig. 7 it is mainly constructed from the p_z atomic orbitals of the sulfur donor atoms and the p_z orbitals of the carbons. The LUMO molecular orbital is of b_{3g} symmetry and shows some contribution from the d_{xz} atomic orbital of Ni. In both MOs we can notice some contribution from atomic orbitals of the sulfurs of the outer rings while there is no contribution from the atomic orbitals of the oxygens partially because they are out of plane. So the main core of the molecule is similar to the core of the $M(dmit)_2$ [30]. The calculated energy in Hartrees of the molecule was $E = -5459.62151$. Addition of the zero point energy gave $E + E_o = -5450.38291$.

The theoretical and experimental Raman spectra of **6** are displayed in Fig. 8. The experimental Raman spectra showed the characteristic vibrations of S–Ni–S and Ni–S at 125, 371, 413 and 498 cm^{-1}. In the theoretical spectra the S–Ni–S vibration peaks appeared at 113, 361, 405 and 483 cm^{-1}. Generally there are several strong lines in the region between 125 and 498 cm^{-1} in the experimental spectra representing not only S–Ni–S bending vibrations but also some C–O–C bending vibrations. The intensity of these peaks seems to be underestimated in our calculations. The C–H stretching vibrations in the experimental spectrum with the 785 nm excitation line did not appear. These vibrations appear at 2668, 2855 and 2976 cm^{-1} in the experimental spectra with the 514 nm excitation line. In the calculated spectrum these peaks were shifted, as expected.

The experimental and the calculated infrared spectra of **6** are displayed in Fig. 9. The Ni–S symmetric and asymmetric stretching appears in the theoretically calculated spectrum at 411 and 483 nm with very low intensities, this area is out of our instrument detection limit. Both infrared spectra of the neutral complex showed absorptions at the region between 890 and 1130 cm^{-1} for the C–O vibrations but with different intensities.

The region from 1130 to 1500 cm^{-1} consists mainly of strechings, S–C, C–C and C–O. The characteristic peaks at 2800–3000 cm^{-1} related to the C–H stretching vibrations in the experimental spectrum are shifted in the theoretical one to higher wavenumbers. Overall it seems that there is a good agreement between the theoretically calculated and the experimentally recorded spectra of the investigated complex. It was very important to propose both Raman and IR band assignments for the investigated donor. These data (Table 5) should be useful for the design of new dithiolene complexes of desired physical properties.

6. Conclusion

The synthesis of the new metal donor $Ni(edodddt)_2$ was made. Its crystal structure was resolved with X-ray crystallography. Structure and spectral investigation was made both experimentally and theoretically. A comparison of the results in both cases showed a very good agreement helping us to understand this new complex.

Supplementary data

CCDC 721320 contains the supplementary crystallographic data for **6**. These data can be obtained free of charge via http://www.ccdc.cam.ac.uk/conts/retrieving.html, or from the Cambridge Crystallographic Data Centre, 12 Union Road, Cambridge CB2 1EZ, UK; fax: (+44) 1223-336-033; or e-mail: deposit@ccdc.cam.ac.uk.

Acknowledgments

This work was financially supported by the Greek General Secretariat for Research and Technology/Ministry of Development through a PENED 2003 Grant.

References

[1] P. Aloukos, S. Couris, J.B. Koutselas, G.C. Anyfantis, G.C. Papavassiliou, Chem. Phys. Lett. 428 (2006) 109.
[2] P. Cassoux, Coord. Chem. Rev. 186 (1999) 213.
[3] Q. Dai, X.F. Chen, H. Chen, X. Gao, X.P. Zhang, Z. Cheng, Supramol. Sci. 5 (1998) 531.
[4] K. Ray, T. Weyhermuller, F. Neese, K. Wieghardt, Inorg. Chem. 44 (2005) 5345.
[5] U.T. Mueller-Westerhoff, B. Vance, D. Ihl Yoon, Tetrahedron 47 (1991) 909.
[6] M. Bousseau, L. Valade, J.P. Legros, P. Cassoux, M. Garbauskas, L.V. Interrante, J. Am. Chem. Soc. 108 (1986) 1908.
[7] A. Kobayashi, H. Kim, Y. Sasaki, R. Kato, H. Kobayashi, S. Moriyama, Y. Nishio, K. Kajita, W. Sasaki, Chem. Lett. (1987) 1819.
[8] N. Robertson, L. Cronin, Coord. Chem. Rev. 227 (2002) 93.
[9] E. Watanabe, M. Fujiwara, J.-I. Yamaura, R. Kato, J. Mater. Chem. 11 (2001) 2131.
[10] G. Liu, Q. Fang, C. Wang, J. Mol. Struct.: THEOCHEM 679 (2004) 115.
[11] C.T. Vance, R.D. Bereman, J. Bordner, W.E. Hatfield, J.H. Helms, Inorg. Chem. 24 (1985) 2905.
[12] B.S. Furniss, A.J. Hannaford, P.W.G. Smith, A.R. Tatchell, Vogel's Textbook of Practical Organic Chemistry, 5th ed., Longman Scientific and Technical, Great Britain, 1989.
[13] R.K. Summerbell, H.E. Lunk, J. Am. Chem. Soc. 79 (1957) 4802.
[14] B. Barszcz, A. Graja, G. Soras, N. Psaroudakis, G.A. Mousdis, J. Phys. Chem. Solids 68 (2007) 1364–1374.
[15] Oxford Diffraction, C.C.a.C.R., version p171.29.2, Oxford Diffraction Ltd., Abingdon, Oxford, England, 2006.
[16] G.M. Sheldrick, SHELXL-97, Program for Crystal Structure Refinement, University of Göttingen, Germany, 1997.
[17] C.L.J. Farrugia, J. Appl. Crystallogr. 32 (1999) 837.
[18] I.A. Kotov, C. Faulmann, P. Cassoux, B.E. Yagubskii, J. Org. Chem. 59 (1994) 2626.
[19] G.N. Schiauzer, V.P. Mayweg, J. Am. Chem. Soc. 87 (1965) 1483.
[20] J.F. Bai, J.L. Zuo, W.L. Tan, W. Ji, Z. Shen, H.K. Fun, K. Chinnakali, I.A. Razak, X.Z. You, C.M. Che, J. Mater. Chem. 9 (1999) 2419.
[21] Y. Ji, J.L. Zuo, L.X. Chen, Y.Q. Tian, Y.L. Song, Y.Z. Li, X.Z. You, J. Phys. Chem. Solids 66 (2005) 207.
[22] J.L. Zuo, T.M. Yao, F. You, X.Z. You, H.K. Fun, B.C. Yip, J. Mater. Chem. 6 (1996) 1633.
[23] G. Anyfantis, Ph.D. Thesis, University of Patras, Patra, 2008.
[24] A.D. Becke, J. Chem. Phys. 98 (1993) 5648.

[25] C. Lee, W. Yang, R.G. Parr, Phys. Rev. B 37 (1988) 785.
[26] A.D. McLean, G.S. Chandler, J. Chem. Phys. 72 (1980) 5639.
[27] A.J.H. Wachters, J. Chem. Phys. 52 (1970) 1033.
[28] M.M. Francl, W.J. Petro, W.J. Hehre, J.S. Binkley, M.S. Gordon, D.J. DeFrees, J.A. Pople, J. Chem. Phys. 77 (1982) 3654.
[29] M.J. Frisch et al., GAUSSIAN 03, Revision C.02 Gaussian, Inc., Wallingford, CT, 2004.
[30] M. Aragoni, M. Area, F. Demartin, F. Devillanova, A. Garau, F. Isaia, F. Lelj, V. Lippolis, G. Verani, J. Am. Chem. Soc. 121 (1999) 7098.

help in the design and synthesis of metal complexes with *desired* supramolecular structures. Hydrogen bonds with carbon donor atoms that may probably develop are very weak and are not expected to affect the tenability of the conclusions. The ligands that will be used in this investigation are various heavily substituted imidazole derivatives of the two types described above. In particular, 1-methyl-4,5-diphenylimidazole (L) (Scheme 1), a monodentate ligand of the first type, has been selected to initiate our studies. So far, there have been only few studies on the coordination chemistry of L [10,11].

An investigation of the $M^{II}/X^-/L$ [M^{II} = Co, Ni, Cu, Zn; X^- = Cl^-, Br^-, I^-, NCS^-, NO_3^-, N_3^-, CH_3COO^-] general reaction system in various solvents is currently under way. We report here on the first Co(II) and Zn(II) complexes based on the neutral monodentate ligand L that have been synthesized, and characterized by spectroscopic methods and single-crystal X-ray diffraction techniques. Their formulae are $[Co(NO_3)_2(L)_2]$ (**1**), $[Zn(NO_3)_2(L)_2]$ (**2**) and $[Co(NCS)_2(L)_2]\cdot EtOH$ (**3**·EtOH). Compounds **1** and **2** are isomorphous. These complexes have proven to be useful starting material for the entry to our supramolecular programme.

2. Experimental

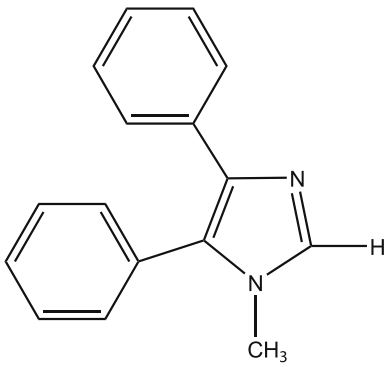
2.1. General remarks

Starting materials were purchased from Merck. All manipulations were performed using materials as received. The ligand 1-methyl-4,5-diphenylimidazole (L) was synthesized according to the literature [12]. Microanalyses (C, H, N) were performed by the University of Ioannina (Greece) Microanalytical Laboratory using an EA 1108 Carlo Erba analyzer.

2.2. Compound preparation

2.2.1. Preparation of $[Co(NO_3)_2(L)_2]$ (**1**)

A pale yellow solution of L (0.30 g, 1.25 mmol) in EtOH (25 ml) and triethylorthoformate, TEOF (3 ml) was treated with solid $Co(NO_3)_2\cdot 6H_2O$ (0.15 g, 0.50 mmol). The resulting pink suspension was refluxed for 1 h and a pink solution was obtained. The solution was left undisturbed at room temperature for 20 min, during which time a pink microcrystalline solid rapidly precipitated. The solution was filtered, and the filtrate left undisturbed at room temperature to slowly concentrate by evaporation. After 2 days, mauve-violet crystals of **1** were collected by filtration, washed with cold EtOH (2 × 2 ml) and Et_2O (2 × 5 ml), and dried in air. Yield 60% (based on the metal). *Anal.* Calc. for $C_{32}H_{28}CoN_6O_6$: C, 58.98; H, 4.34; N, 12.91. Found: C, 58.71; H, 4.32; N, 13.02%. IR data (KBr, cm^{-1}): 3129w, 3118w, 3049w, 2950w, 1762w, 1720w, 1602m, 1573w, 1506s, 1472s, 1443w, 1420w, 1305s, 1274s, 1255sh, 1193m, 1127w, 1073w, 1028m, 1018w, 1001m, 978m, 916m, 858w, 850sh, 810w, 787m, 774m, 744m, 726m, 700s, 654m, 616w, 582m, 518w, 490w. Selected far-IR data (polyethylene, cm^{-1}): 330s, 302s, 284m, 271w, 255m, 235m. Diffuse reflectance spectral data (kK): 18.3, 19.0sh, 8.9, 7.7. Room-temperature effective magnetic moment, μ_{eff} (BM): 4.55.



L

Scheme 1. The ligand 1-methyl-4,5-diphenylimidazole (L) used in this work.

2.2.2. Preparation of $[Zn(NO_3)_2(L)_2]$ (**2**)

A pale yellow solution of L (0.48 g, 2.00 mmol) in EtOH (25 ml) and triethylorthoformate, TEOF (3 ml) was treated with solid $Zn(NO_3)_2\cdot 4H_2O$ (0.27 g, 1.00 mmol). The resulting pale yellow suspension was refluxed for 1 h and soon a homogeneous, yellow solution was obtained. The solution was left undisturbed at room temperature for 20 min, during which time large pale yellow crystals of **2** began precipitating. Once the precipitation of the crystals of **2** was completed, at ~2 days, the solid product was collected by filtration, washed with cold EtOH (2 × 2 ml) and Et_2O (2 × 5 ml), and dried in air. Yield 80% (based on the metal). *Anal.* Calc. for $C_{32}H_{28}ZnN_6O_6$: C, 58.40; H, 4.29; N, 12.77. Found: C, 58.36; H, 4.31; N, 12.73%. IR data (KBr, cm^{-1}): 3120m, 3048m, 1761w, 1719m, 1602m, 1575w, 1522sh, 1500s, 1470s, 1442m, 1420w, 1384m, 1310s, 1286s, 1256sh, 1192m, 1128m, 1074m, 1032m, 1019w, 998m, 978m, 918m, 858w, 812w, 788s, 774s, 744m, 726m, 700s, 654m, 617w, 582m, 516w, 490w. Selected far-IR data (polyethylene, cm^{-1}): 325s, 303s, 279m, 265w, 248m, 219m.

2.2.3. Preparation of $[Co(NCS)_2(L)_2]\cdot EtOH$ (**3**·EtOH)

A pale yellow solution of L (0.15 g, 0.63 mmol) in EtOH (30 ml) and triethylorthoformate, TEOF (2 ml) was treated with solid $Co(NCS)_2$ (0.04 g, 0.25 mmol). The resulting blue suspension was refluxed for 1 h and a homogeneous, blue solution was obtained. The solution was left undisturbed at room temperature for 20 min, during which time a blue microcrystalline solid rapidly precipitated. The solution was filtered, and the filtrate was layered with Et_2O (60 ml). After 2 days, blue crystals of **3**·EtOH were collected by filtration, washed with cold EtOH (2 × 2 ml) and Et_2O (2 × 5 ml), and dried in vacuo over silica gel. The vacuum-dried solid was analyzed as solvent-free (**3**). Yield 65% (based on the metal). *Anal.* Calc. for $C_{34}H_{28}CoN_6S_2$: C, 63.43; H, 4.39; N, 13.06. Found: C, 63.39; H, 4.41; N, 13.10%. IR data (KBr, cm^{-1}): 3130w, 3057w, 3040w, 2962w, 2058vs, 1601m, 1582w, 1522s, 1484m, 1444m, 1422w, 1290w, 1225w, 1192m, 1128m, 1074m, 1048w, 1018m, 1001w, 982m, 910m, 816w, 790s, 774s, 746m, 724m, 700s, 648m, 580m, 505w, 482w. Selected far-IR data (polyethylene, cm^{-1}): 306s, 294s, 250m, 231m. Diffuse reflectance spectral data (kK): 16.0, 8.5, 7.1, 5.9. Room-temperature effective magnetic moment, μ_{eff} (BM): 4.70.

2.3. X-ray crystallographic analysis

Suitable single crystals of **1**, **2** and **3**·EtOH were covered with Paraton N oil and mounted on the tip of a glass capillary. X-ray data for all three compounds were collected (ω-scans) on an Oxford Diffraction Xcalibur diffractometer under a flow of nitrogen gas at 100(2) K using Mo Kα radiation (λ = 0.71073 Å, graphite monochromator). Data collection and reduction was performed with CRYSALIS CCD and RED software [13], respectively. The reflection intensities were corrected for absorption by the multi-scan method. All three structures were solved by direct methods with SIR92 [14] and refined by full-matrix least-squares on F^2 with SHELXL-97 [15]. All non-H atoms were refined anisotropically. Carbon-attached H-atoms were introduced at calculated positions applying the riding model [C(sp^2)–H and C(sp^3)–H 0.93 and 0.96 Å, respectively; $U_{iso}(H) = 1.2U_{eq}(C)$ (1.5 for Csp^3 methyl

Table 1
Crystallographic data and details of structure refinement for complexes **1**, **2** and **3**·EtOH.

	1	**2**	**3**·EtOH
Formula	$C_{32}H_{28}CoN_6O_6$	$C_{32}H_{28}N_6O_6Zn$	$C_{36}H_{34}CoN_6OS_2$
M_r (g mol^{-1})	651.53	657.97	689.74
Crystal system	tetragonal	tetragonal	monoclinic
Space group	$I4_1cd$	$I4_1cd$	$P2_1/c$
a (Å)	28.6967(15)	28.7978(13)	13.2318(3)
b (Å)	28.6967(15)	28.7978(13)	19.7777(8)
c (Å)	14.1071(7)	14.0471(7)	13.0315(4)
α (°)	90	90	90
β (°)	90	90	95.151(2)
γ (°)	90	90	90
V (Å^3)	11617.2(10)	11649.4(9)	3396.50(19)
Z	16	16	4
$D_{calc.}$ (g cm^{-3})	1.490	1.501	1.349
Absorption coefficient (mm^{-1})	0.648	0.901	0.666
F(0 0 0)	5392	5440	1436
Crystal size (mm)	0.27 × 0.14 × 0.11	0.24 × 0.15 × 0.13	0.38 × 0.16 × 0.16
Color	violet	colorless	blue
θ_{min}, θ_{max} for data collection (°)	3.1, 30.0	3.2, 29.0	3.1, 27.5
Index ranges	$-40 \leqslant h \leqslant 39$ $-40 \leqslant k \leqslant 39$ $-19 \leqslant l \leqslant 19$	$-38 \leqslant h \leqslant 38$ $-39 \leqslant k \leqslant 39$ $-19 \leqslant l \leqslant 10$	$-17 \leqslant h \leqslant 17$ $-25 \leqslant k \leqslant 25$ $-16 \leqslant l \leqslant 13$
Reflections collected/unique (R_{int})	104888/8397 (0.0499)	49449/5424 (0.0341)	27187/7713 (0.0227)
Completeness to θ_{max} (%)	99.8	99.2	99.0
Observed reflections [$I > 2\sigma(I)$]	6404	4825	5668
Data/restraints/parameters	8397/2/408	5424/1/408	7713/3/421
Goodness-of-fit on (Gof) F^2	0.941	1.001	0.985
Final R_1[a], wR_2[b] [$I > 2\sigma(I)$]	0.0279, 0.0539	0.0274, 0.0626	0.0289, 0.0719
Final R_1, wR_2 (all data)	0.0403, 0.0550	0.0329, 0.0638	0.0400, 0.0730
Mean/maximum shift/error	0.000/0.002	0.000/0.001	0.000/0.001
$\Delta\rho_{min}/\Delta\rho_{max}$ (e Å^{-3})	−0.238/0.326	−0.259/0.666	−0.380/0.557

[a] $R_1 = \Sigma||F_o| - |F_c||/\Sigma|F_o|$.
[b] $wR_2 = \{\Sigma w(F_o^2 - F_c^2)^2/\Sigma w(F_o^2)^2\}^{1/2}$.

groups) of their parent C atom]. The hydroxyl H-atom of the solvent molecule in **3**·EtOH was found in a difference Fourier map and refined isotropically [U_{iso}(H) = 1.5U_{eq}(O)] applying a soft distance restraint. Geometric calculations were carried out using WINGX [16] and PLATON [17] packages; molecular graphics were prepared with DIAMOND [18] and MERCURY [19]. Crystallographic data and details of the structural analyses are summarized in Table 1.

2.4. Spectroscopic and physical measurements

Room-temperature magnetic susceptibility measurements were carried out by Faraday's method using a Cahn-Ventron RM-2 balance standardized with $HgCo(NCS)_4$; diamagnetic corrections were applied using Pascal's constants. IR spectra were recorded on a Perkin–Elmer PC 16 FT-IR spectrometer with samples prepared as KBr pellets, and as nujol and hexachlorobutadiene mulls between CsI discs. Far-IR spectra were recorded on a Bruker IFS 113v FT spectrometer with samples prepared as polyethylene pellets. Solid-state, diffuse reflectance electronic spectra in the 2000–300 nm range were recorded on a Perkin–Elmer 330 spectrophotometer using spectroscopic grade MgO as reference.

3. Results and discussion

3.1. Brief synthetic comments

Reactions of the metal salts $Co(NO_3)_2{\cdot}6H_2O$, $Zn(NO_3)_2{\cdot}4H_2O$ and $Co(SCN)_2$, and a slight excess of L in EtOH/TEOF under reflux leads to the isolation of the compounds $[Co(NO_3)_2(L)_2]$ (**1**), $[Zn(NO_3)_2(L)_2]$ (**2**) and $[Co(SCN)_2(L)_2]\cdot$EtOH (**3**·EtOH), respectively, according to the balanced Eqs. (1)–(3).

$$Co(NO_3)_2\cdot 6H_2O + 2L \xrightarrow[T]{EtOH/TEOF} \underset{\mathbf{1}}{[Co(NO_3)_2(L)_2]} + 6H_2O \quad (1)$$

$$Zn(NO_3)_2\cdot 4H_2O + 2L \xrightarrow[T]{EtOH/TEOF} \underset{\mathbf{2}}{[Zn(NO_3)_2(L)_2]} + 4H_2O \quad (2)$$

$$Co(SCN)_2 + 2L + EtOH \xrightarrow[T]{EtOH/TEOF} \underset{\mathbf{3}\cdot EtOH}{[Co(SCN)_2(L)_2]\cdot EtOH} \quad (3)$$

Two features of the reactions represented by Eqs. (1)–(3) deserve brief comments. First, the metal to ligand reaction ratio, the nature of the solvents (MeOH and MeCN were also used) and the precipitation/crystallization method have no influence on the identity of the products. Second, it is not possible to isolate completely pure samples of complexes **1**–**3** without use of the dehydrating agent triethylorthoformate (TEOF). Working without TEOF, the isolated products contained 2–3% H_2O, as indicated by analytical data.

3.2. Description of structures of the isomorphous compounds *1* and *2*

To facilitate comparison, all three compounds **1**, **2** and **3** have the same (where applicable) atom, ring and ligand numbering [ligand L_A (rings A1, A2 and A3), ligand L_B (rings B1, B2 and B3)] (see Fig. 1). The X-ray structural analysis reveals that **1** and **2** are not just isostructural but are actually isomorphous since (a) both have the same space group ($I4_1cd$) and quite similar unit cell dimensions and (b) the types and the positions of atoms in both are the same except for a replacement of the Co(II) atom in **1** with a Zn(II) atom in **2**. Therefore, detailed information will be presented mostly for complex **1**. The molecular structure of complex **1** is depicted in Fig. 1. Table 2 contains selected interatomic distances, angles and torsion angles for the three complexes.

Compound **1** consists of discrete neutral mononuclear molecules in which the Co^{II} ion is surrounded by two monodentate 1-

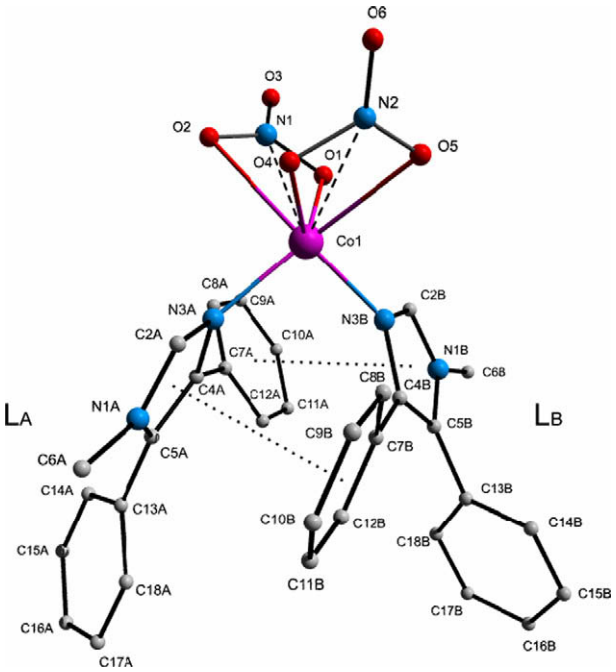


Fig. 1. View of the molecular structure of **1** showing the intramolecular $\pi-\pi$ interactions (dotted lines) between the two ligands L_A and L_B. The dashed lines do not represent bonding interactions (see text). Hydrogen atoms have been omitted for clarity. Ring numeration: A1 (N1A–C2A–N3A–C4A–C5A), A2 (C7A to C12A), A3 (C13A to C18A), B1 (N1B–C2B–N3B–C4B–C5B), B2 (C7B to C12B), B3 (C13B to C18B).

Table 2
Selected bond lengths (Å), angles and torsion angles (°) for **1**, **2** and **3**·EtOH.

Compound	**1**	**2**	**3**·EtOH
M	Co	Zn	Co
M–N3A	2.024(1)	1.996(2)	2.014(1)
M–N3B	2.024(1)	2.014(2)	2.002(1)
M–O1	1.996(1)	2.002(2)	
M–O2	2.709(1)	2.754(1)	
M–O4	2.014(1)	1.988(2)	
M–O5	2.446(1)	2.706(2)	
M–N1	2.749(1)	2.771(2)	1.952(1)
M–N2	2.615(1)	2.714(2)	1.963(1)
N3A–M–N3B	97.6(1)	100.5(1)	107.6(1)
N3A–M–N1	108.9(1)	110.9(1)	116.4 (1)
N3A–M–N2	128.1(1)	128.2(1)	104.1(1)
N3B–M–N1	114.8(1)	114.2(1)	106.4(1)
N3B–M–N2	116.5(1)	111.4(1)	116.0(1)
N1–M–N2	91.6(1)	92.3(1)	106.7(1)
N1–C1–S1			179.3(2)
N2–C2–S2			178.5(2)
A2–A3[a]	64.4(1)	64.8(1)	71.9(1)
B2–B3[a]	75.1(1)	74.7(1)	62.3(1)
C4A–C5A–C13A–C14A	−46.6(2)	−47.4(3)	−62.8(2)
C4B–C5B–C13B–C14B	−64.1(2)	−64.9(3)	−49.6(2)
C5A–C4A–C7A–C12A	−52.4(2)	−52.8(3)	−40.4(2)
C5B–C4B–C7B–C12B	−41.3(2)	−42.0(2)	−34.7(2)

[a] Angle between the mean-planes of the named phenyl rings (see Fig. 1).

methyl-4,5-diphenylimidazole ligands and two chelating nitrates. The ligands L are *cis* to each other. Both nitrate species (with N1 and N2 nitrogen atoms) are planar, the sum of the three O–N–O angles being 360.0° and 361.0°, respectively. According to the criteria suggested by Reedijk and co-workers [20] concerning the nitrate coordination modes (monodentate, anisobidentate and bidentate), the nitrate bearing N1 is at the borderline of anisobidentate/monodentate and the nitrate bearing N2 can be classified as anisobidentate. The Co^{II} ion is therefore in a highly distorted octahedral environment, comprising the two imidazole nitrogen donor atoms and the four nitrate oxygen atoms. The Co–O bonds *trans* to the nitrogen atoms are longer than the other two, as expected for this type of complexes [21]. The severe distortion of the octahedron is due to the acute O–Co–O bite angles [51.7(1)° and 56.5(1)°] of the two chelating nitrato ligands. Alternatively, the six-coordinate Co^{II} center can be regarded as having a distorted quasi-tetrahedral structure with bonds directed towards the centers of the bidentate nitrato groups instead of towards the oxygen atoms (Fig. 1); however, this approach is not without criticism [22]. The situation is similar for complex **2**, with the exception that both nitrates are at the borderline of anisobidentate/monodentate (see Table 2 for comparison).

Table 3
Intramolecular $\pi-\pi$ stacking distances (Å) and angles (°) for **1**, **2** and **3**·EtOH.

Distance/angle	Rings	**1**	**2**	**3**·EtOH
Distance between ring centroids	A1–B2	3.501(1)	3.496(1)	3.724(1)
	B1–A2	3.654(1)	3.649(1)	3.560(1)
Perpendicular distance between ring planes	A1–B2	3.324(1)	3.336(1)	3.660(1)
	B1–A2	3.476(1)	3.472(1)	3.521(1)
Centroid offset	A1–B2	1.102(1)	1.047(1)	0.692(1)
	B1–A2	1.146(1)	1.137(1)	0.525(1)
Dihedral angle between ring mean-planes	A1–B2	6.9(1)	7.0(1)	18.7(1)
	B1–A2	9.0(1)	8.5(1)	13.0(1)

The two 1-methyl-4,5-diphenylimidazole ligands (L_A and L_B) are 'antiparallel' with their methyl groups pointing at opposite directions. The overall conformation of L_A and L_B is similar. The angle between the mean-plane of the phenyl rings A2 and A3 is 64.4(1)° and that between B2 and B3 is 75.1(1)°. The imidazole ring A1 is facing the phenyl ring B2 [angle: 6.9(1)°] and the imidazole ring B1 is equally facing the phenyl ring A2 [angle: 9.0(1)°]; this is most likely attributed to steric effects and the weak $\pi-\pi$ stacking interactions among those pairs of rings. Similar conformations and $\pi-\pi$ interactions among ligands L_A and L_B have also been encountered in a previously characterized Pd^{II} complex with L [11], in a series of analogues complexes of other divalent metals with L [23], as well as in Cu^{II} and Zn^{II} complexes of 2-[2′-(4′,6′-di-*tert*-butylhydroxyphenyl)]-4,5-diphenylimidazole [24,25]. This information brings out a characteristic structural pattern of the complexes and reveals a preferred mode of packing between neighbouring ligands bearing the 4,5-diphenylimidazole moiety.

Table 4
Hydrogen-bond geometries for **1**, **2** and **3**·EtOH (Å, °).

D–H···A	D–H	H···A	D···A	D–H···A
Complex ***1***				
C17A–H17A···O1^{i}	0.93	2.59	3.513(2)	171
C2A–H2A···O3^{ii}	0.93	2.55	3.328(2)	141
C6A–H6A3···O3^{ii}	0.96	2.47	3.267(2)	141
C15A–H15A···O3^{iii}	0.93	2.54	3.423(2)	160
Complex ***2***				
C17A–H17A···O1^{i}	0.93	2.55	3.471(3)	172
C2A–H2A···O3^{ii}	0.93	2.54	3.318(3)	142
C6A–H6A3···O3^{ii}	0.96	2.50	3.292(3)	140
C15A–H15A···O3^{iii}	0.93	2.58	3.472(3)	160
Complex ***3***·*EtOH*				
O1–H1···S1^{iv}	0.84(2)	2.65(2)	3.475(1)	166(2)
C6B–H6B1···O1^{v}	0.96	2.52	3.470(2)	171

Symmetry codes: (i) 1/2 + *y*, 1 − *x*, −1/4 + *z*; (ii) 1 − *x*, *y*, −1/2 + *z*; (iii) 1 − *x*, 1 − *y*, *z*; (iv) −1 + *x*, *y*, *z*; (v) 1 + *x*, ½−*y*, −1/2 + *z*.

Geometrical details of the π–π interactions between L_A and L_B, providing additional stabilization within the complexes, are presented in Table 3. These results confirm the initial considerations with regard to the fitness of ligand L to form such π–π interactions. Dance and Aakeröy have studied aromatic interactions as a crystal engineering tool and have suggested that they can play a role in the assembly and orientation of complexes in inorganic supramolecular chemistry [26,27].

The length of the C–C and C–N bonds of the imidazole groups agree very well for all three structures and are as expected [28]. The Co–N bond lengths are normal for this kind of compound [29–31]. Corresponding information for the isomorphous compound **2** is given in Tables 2 and 3.

The packing of the molecules in the crystal lattice of **1** proceeds through normal van der Waals contacts and weak C–H···O(nitrate) interactions which contribute to the supramolecular aggregation of the mononuclear species (Table 4). In general, it is assumed that C–H···O bonds could play a role in the determination of crystal packing, especially when stronger (classic) hydrogen bonding is absent [32,33]. The geometry of the present C–H···O interactions fulfills the criteria for such bonds as proposed by Jeffrey [34] and other researchers [35].

A least-squares fit of **1** and **2** (Fig. 2) clearly shows that the two compounds are almost superimposable, the most apparent deviation being in the nitrate ligands moiety. As can be seen from Table 4, both **1** and **2** contain the same number and type of C–H···O interactions, a consequence of their isomorphism. The closest Co···Co and Zn···Zn distances in their crystals are 7.289(5) and 7.276(5) Å, respectively.

3.3. Description of structure of compound **3**·EtOH

The structure of **3**·EtOH consists of $[Co(NCS)_2(L)_2]$ and solvate ethanol molecules. It crystallizes in the monoclinic space group $P2_1/c$. The complex molecule has a tetrahedral $Co^{II}N_4$ coordination, involving the pyridine-type nitrogen donor atoms from the L_A and L_B ligands and the two terminal isothiocyanato groups (Fig. 3). The angles around the Co^{II} atom (Table 2) show the tetrahedral environment to be slightly distorted. The two SCN^- ions are almost linear [N1–C1–S1 = 179.3(2)° and N2–C2–S2 = 178.5(2)°] and are coordinated (especially the second one) in a bent fashion, as indicated by the Co–N–CS angles of 173.8(2)° and 160.8(2)°, respectively. The bent coordination at the nitrogen atoms may be caused by intermolecular hydrogen bonding (atom S1 participates in intermolecular hydrogen bonding, see below) and crystal packing [29]. Similar bent geometries have also been observed in a series of six-coordinate Ni(II) and Co(II) complexes [30,36]. An investigation by Noh et al. [37] on the bonding fashion of the SCN^- ion did not reveal any systematic correlation between the C–N bond distance and the Co–N–CS angle, suggesting, in their turn, that the bent angle is determined by steric/packing effects rather than electronic effects of the metal ion.

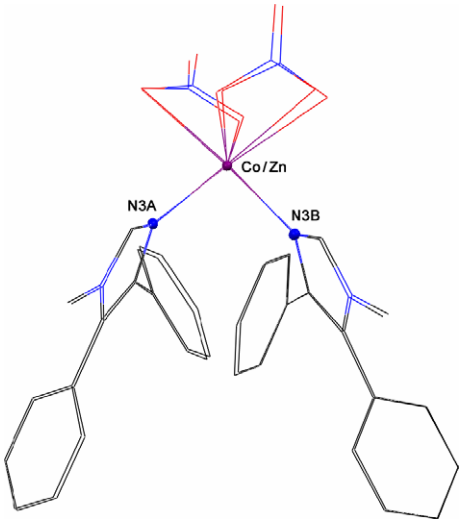


Fig. 2. A least-squares fit of **1** and **2**. The fitting fragment N3A–Co/Zn–N3B of the two complexes has been drawn in ball-and-stick (r.m.s. deviation for fitted atoms: 0.029). Hydrogen atoms have been omitted for clarity.

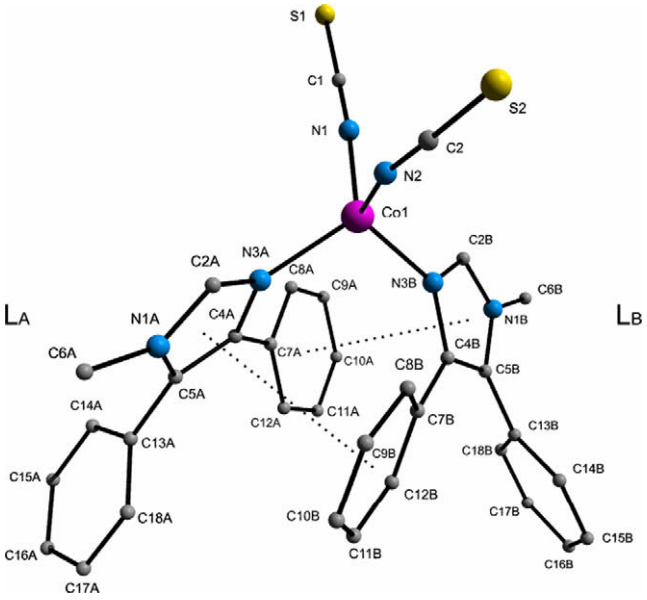


Fig. 3. View of the molecular structure of **3**·EtOH showing the intramolecular π–π interactions (dotted lines) between the two ligands L_A and L_B. The non-coordinated ethanol molecule and hydrogen atoms have been omitted for clarity. The numeration of the rings is identical to that of Fig. 1.

The two ligands L_A and L_B of complex **3** maintain (as in **1** and **2**) the 'antiparallel' orientation of their methyl groups and their conformation is similar. The overall conformation of the complex resembles that of complex **1** (or **2**) preserving the structural pattern of the π–π intramolecular interactions between L_A and L_B (Tables 2 and 3). However, the differences between **3** and **1** (or **2**) are more striking that those between the isomorphous complexes **1** and **2**. The EtOH molecule assists to the stabilization of the crystal structure by forming, through its hydroxyl group, a medium-strength hydrogen bond to the S1 atom of a isothiocyanato ligand, as well as a weak C–H···O interaction (Table 4). The closest Co···Co spacing in the crystal is 5.026(1) Å, significantly different from those of 7.289(5) and 7.276(5) Å for **1** and **2**, respectively.

3.4. IR, magnetochemical and ligand-field studies

The IR bands of L [10] do not shift significantly in the spectra of **1**–**3**. In the spectrum of **3**, the bands at 2058, 816 and 482 cm^{-1} are assigned [38] to the ν(CN), ν(CS) and δ(NCS) modes of the SCN^- ion; the frequencies of these modes are characteristic of terminal isothiocyanato (i.e., *N*-bonded) isothiocyanato groups [38]. The far-IR spectrum of **3** exhibits the two ν(Co–NCS) [306 and 294 cm^{-1}] and the two ν(Co–N_L) bands in the regions expected for pseudotetrahedral C_{2v} stereochemistry [38].

In the spectrum of **1**, the bands at 1472 and 1274 cm^{-1} are assigned to the $\nu_L(A_1)[\nu(N=O)]$ and $\nu_5(B_2)[\nu_{as}(NO_2)]$ modes of the chelating bidentate (C_{2v}) nitrato groups, respectively. The corresponding bands for **2** appear at 1470 and 1286 cm^{-1}. The separation of these two bands is large (198 cm^{-1} for **1**, 184 cm^{-1} for **2**),

in accordance with the bidentate character of the nitrato ligands. The 1700–1800 cm^{-1} region is viewed as the key to differentiate between monodentate and bidentate coordination of nitrato groups [38,39]. The separation of the combination bands $\nu_2 + \nu_3$ and $\nu_2 + \nu_5$ in the spectra of **1** and **2**, appearing around 1760 and 1720 cm^{-1} is about 40 cm^{-1} and this fact is consistent [38,39] with the crystallographically established bidentate character of the nitrato ligands. The great number of the $\nu(M–O_{nitrato})$ [325, 303, 279, 265 cm^{-1} for **2**; 330, 302, 284, 271 cm^{-1} for **1**) and $\nu(M–N_L)$ [248, 219 cm^{-1} for **2**; 255 235 cm^{-1} for **1**) reflects the *cis* stereochemistry of the Co^{II} and Zn^{II} nitrato complexes [38].

The KBr IR spectrum of **2** exhibits a medium intensity band at 1384 cm^{-1}, assigned to the $\nu_3(E')[\nu_d(NO)]$ mode of the D_{3h} ionic nitrate, suggesting [20] that a certain amount of nitrato ligands are replaced by bromides (thus generating ionic nitrates) in the KBr matrix; this spectral phenomenon has been discussed in detail [20,40]. In accordance with this conclusion, the 1384 cm^{-1} band is absent from the mull spectra of **2**.

The room-temperature effective magnetic moment (μ_{eff}) value (4.70 BM) and the electronic spectrum of **3** in the solid state indicate pseudotetrahedral stereochemistry around Co^{II}, the band at 16.0 kK being assigned to the $^4A_2 \rightarrow {}^4T_1(P)$ transition and with the band assigned to the $^4A_2 \rightarrow {}^4T_1(F)$ transition at ~7 kK being split (by virtue of the reduction of symmetry from T_d to C_{2v}) into bands (8.5, 7.1 and 5.9 kK) representing the transitions to the $^4B_1$, $^4A_2$ and $^4B_2$ states [41,42]. These assignments give rise to the parameters 10Dq = 4575 cm^{-1}, B = 672 cm^{-1} and β = 0.69, typical for Co^{II} tetrahedrally surrounded by four nitrogen atoms [30,42].

While the μ_{eff} value of **1** at room-temperature (4.55 BM) is in the region expected for tetrahedral complexes [41], the electronic spectrum of this compound in the solid state differs from spectra of typical tetrahedral Co^{II} complexes. The absorption band at 18.3 kK, although similar in general contour to the visible band of other tetrahedral Co^{II} complexes, is at rather higher energy than would have been expected [42]. Moreover, the color of **1** is abnormally intense for an octahedral complex; octahedral Co^{II} complexes have pink colors. This peculiar magnetochemical and spectral behavior has been found for some other $[Co(NO_3)_2(L')_2]$ complexes, where L′ is a phosphine or arsine oxide [43], a hindered monodentate amine [44] and 1-methylbenzotriazole [30]. The behavior has been explained [43] by postulating that the six-coordinated complex can be regarded as having a rather distorted quasi-tetrahedral structure with bonds directed toward the centers of the bidentate nitrato groups instead of toward the oxygen atoms. In accordance with a quasi-tetrahedral formulation of **1**: (1) The Co–N3(A,B) bond distances (Fig. 1, Table 2) are very similar to those observed in the tetrahedral complex **3**·EtOH (Fig. 3, Table 2); (2) the Co···N(1,2) distances [2.615(1), 2.749(1) Å] may be regarded as *very weakly* bonding; and (3) the N–Co–N angles lie in the 91.6–128.1° range, which is typical for distorted tetrahedral complexes [30]. Lever has suggested that the assumption of a quasi-tetrahedral coordination is perhaps unnecessary [44]. Such molecules have a distorted six-coordinated structure of C_2 symmetry; the degeneracy of the ground state of the Co^{II} ion is lifted [$T_{1g}(O_h) \rightarrow {}^4A$, 2 ^4B in C_2]. The new ground state being an orbital singlet gives rise to a μ_{eff} value closer to the spin-only value than that observed in an octahedral complex (~5 BM). This was observed in **1**. The absence of a center of symmetry could produce a fairly high intensity *d–d* spectrum (since both p and d orbitals span common representations in C_2); this is also observed in **1**.

4. Conclusions and perspectives

This work comprises the initial results of our investigation on a series of divalent, 3d-metal complexes using the 1-methyl-4,5-diphenylimidazole ligand in order to explore the structural consequences of intermolecular forces and the way in which such interactions cooperate, compete and eventually control the supramolecular assembly and architecture of such compounds. Three representative complexes, namely $[Co(NO_3)_2(L)_2]$ (**1**), $[Zn(NO_3)_2(L)_2]$ (**2**) and $[Co(NCS)_2(L)_2]$·EtOH (**3**·EtOH), have been synthesized and subsequent crystallographic analysis showed **1** and **2** to be isostructural and isomorphous. A characteristic structural feature, evidenced in all three compounds, and enhancing the stability and rigidity of the complexes, involves the formation of intramolecular π–π interactions between aromatic rings of adjacent 4,5-diphenylimidazole moieties of the two ligands of the complexes. On the other hand, the observed bent coordination of the isothiocyanate ions in complex **3** seems to be due to intermolecular hydrogen bonding and crystal packing effects.

Further synthetic and structural work (including examples of isomorphism and polymorphism) is in progress; it includes complexes with various imidazole derivatives as ligands (as described in the Introduction) towards a better understanding of their supramolecular organization.

Acknowledgement

This work was supported by the Research Committee of the University of Patras, Greece (K. Caratheodory program, Grant No. C.585 to V.N.).

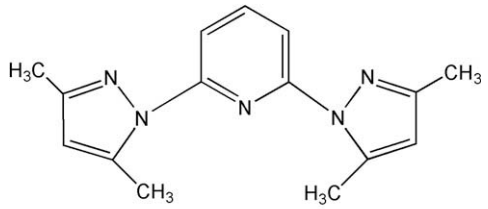
Appendix A. Supplementary data

CCDC 724658, 724659 and 724660 contain the supplementary crystallographic data for **1**, **2** and **3**·EtOH. These data can be obtained free of charge via http://www.ccdc.cam.ac.uk/conts/retrieving.html, or from the Cambridge Crystallographic Data Centre, 12 Union Road, Cambridge CB2 1EZ, UK; fax: (+44) 1223-336-033; or e-mail: deposit@ccdc.cam.ac.uk.

References

[1] J.-M. Lehn, Angew. Chem., Int. Ed. 27 (1988) 89.
[2] J.-M. Lehn, Science 260 (1993) 1762.
[3] J.-M. Lehn, Supramolecular Chemistry. Concepts and Perspectives, Wiley-VCH, Weinheim, 1995.
[4] J.W. Steed, J.L. Atwood, Supramolecular Chemistry, Wiley, New York, 2000.
[5] A.I. Kitaigorodsky, Molecular Crystals and Molecules, Academic Press, New York, 1973.
[6] J.-M. Lehn, Angew. Chem., Int. Ed. 29 (1990) 1304.
[7] D.W. Bruce, D. O'Hare (Eds.), Inorganic Materials, Wiley, Chichester, 1992.
[8] P.S. Corbin, S.C. Zimmerman, P.A. Thiessen, N.A. Hawryluk, T.J. Murray, J. Am. Chem. Soc. 123 (2001) 10475.
[9] C.B. Aakeröy, K.R. Seddon, Chem. Soc. Rev. 22 (1993) 397.
[10] C.P. Raptopoulou, S. Paschalidou, A.A. Pantazaki, A. Terzis, S.P. Perlepes, T. Lialiaris, E.G. Bakalbassis, J. Mrozinski, D.A. Kyriakidis, J. Inorg. Biochem. 71 (1998) 15.
[11] A. Hadzovic, D. Song, Organometallics 27 (2008) 1290.
[12] J. McMaster, R.L. Beddoes, D. Collison, D.R. Eardley, M. Helliwell, C.D. Garner, Chem. Eur. J. 2 (1996) 685.
[13] CRYSALIS CCD and CRYSALIS RED, Programs for Data Collection, Cell Refinement and Data Reduction, Version 1.171.32.15, Oxford Diffraction Ltd., Abingdon, Oxford, England, 2008.
[14] M.C. Burla, M. Camalli, B. Carrozzini, G.L. Cascarano, C. Giacovazzo, G. Polidori, R. Spagna, J. Appl. Crystallogr. 36 (2003) 1103.
[15] G.M. Sheldrick, SHELXL-97, Program for the Refinement of Crystal Structures from Diffraction Data, University of Göttingen, Germany, 1997.
[16] L.J. Farrugia, J. Appl. Crystallogr. 32 (1999) 837.
[17] A.L. Spek, PLATON. A Multipurpose Crystallographic Tool, Utrecht University, The Netherlands, 2003.
[18] K. Brandenburg, DIAMOND, Program for Crystal and Molecular Structure Visualization, Release 3.1f, Crystal Impact GbR, Bonn, Germany, 2008.
[19] C.F. Macrae, P.R. Edgington, P. McCabe, E. Pidcock, G.P. Shields, R. Taylor, M. Towler, J. van de Streek, J. Appl. Crystallogr. 39 (2006) 453.
[20] G.J. Kleywegt, W.G.R. Wiesmeijer, G.J. Van Driel, W.L. Driessen, J. Reedijk, J.H. Noordik, J. Chem. Soc., Dalton Trans. (1985) 2177.
[21] D.L. Kepert, Prog. Inorg. Chem. 23 (1977) 1.

[22] C.C. Addison, N. Logan, S.C. Wallwork, C.D. Garner, Q. Rev. Chem. Soc. 25 (1971) 289.
[23] K.A. Kounavi et al., unpublished results, 2009.
[24] L. Benisvy, A.J. Blake, D. Collison, E.S. Davies, C.D. Garner, E.J.L. McInnes, J. McMaster, G. Whittaker, C. Wilson, Chem. Commun. (2001) 1824.
[25] L. Benisvy, A.J. Blake, D. Collison, E.S. Davies, C.D. Garner, E.J.L. McInnes, J. McMaster, G. Whittaker, C. Wilson, Dalton Trans. (2003) 1975.
[26] I. Dance, Perspectives in Supramolecular Chemistry, The Crystal as a Supramolecular Entity, vol. 2, Wiley, Chichester, 1995.
[27] C.B. Aakeröy, Acta Crystallogr. B53 (1997) 569.
[28] F.H. Allen, O. Kennard, D.G. Watson, L. Brammer, A.G. Orpen, R. Taylor, J. Chem. Soc., Perkin Trans. 2 (1987) S1.
[29] J. van Rijn, E. Bouwman, J.R. Empfield, W.L. Driessen, J. Reedijk, Polyhedron 8 (1989) 1965.
[30] J.C. Plakatouras, S.P. Perlepes, D. Mentzafos, A. Terzis, T. Bakas, V. Papaefthymiou, Polyhedron 11 (1992) 2657.
[31] L. Benisvy, E. Bill, A.J. Blake, D. Collison, E.S. Davies, C.D. Garner, C.I. Guindy, E.J.L. McInnes, G. McArdle, J. McMaster, C. Wilson, J. Wolowska, Dalton Trans. (2004) 3647.
[32] G.R. Desiraju, Acc. Chem. Res. 29 (1996) 441.
[33] G.R. Desiraju, Crystal Engineering. The Design of Organic Solids, Elsevier, Amsterdam, 1989.
[34] G.A. Jeffrey, An Introduction to Hydrogen Bonding, Oxford University Press, Oxford, 1997.
[35] T. Steiner, Angew. Chem., Int. Ed. 41 (2002) 48.
[36] E. Diamantopoulou, T.F. Zafiropoulos, S.P. Perlepes, C.P. Raptopoulou, A. Terzis, Polyhedron 13 (1994) 1593.
[37] T.H. Noh, J.H. Kim, Y.-A. Lee, H. Suh, O.-S. Jung, J. Mol. Struct. 691 (2004) 165.
[38] K. Nakamoto, Infrared and Raman Spectra of Inorganic and Coordination Compounds, 4th ed., Wiley, New York, 1986. pp. 254–257, 282–287, 464.
[39] A.B.P. Lever, E. Mantuvani, B.S. Ramaswamy, Can. J. Chem. 49 (1971) 1957.
[40] E. Katsoulakou, V. Bekiari, C.P. Raptopoulou, A. Terzis, P. Lianos, E. Manessi-Zoupa, S.P. Perlepes, Spectrochim. Acta Part A 61 (2005) 1627.
[41] F.A. Cotton, G. Wilkinson, Advanced Inorganic Chemistry, 5th ed., Wiley, New York, 1988. p. 729.
[42] A.B.P. Lever, Inorganic Electronic Spectroscopy, 2nd ed., Elsevier, Amsterdam, 1984. p. 480.
[43] F.A. Cotton, D.M.L. Goodgame, R.H. Soderberg, Inorg. Chem. 2 (1963) 1162.
[44] A.B.P. Lever, Inorg. Chem. 4 (1965) 1042.



bdmpp

Scheme 1. The ligand 2,6-bis(3,5-dimethylpyrazol-1-yl)pyridine (bdmpp) used in this work.

2. Experimental

2.1. General and spectroscopic measurements

All manipulations were performed under aerobic conditions using materials (reagent grade) and solvents as received. The starting materials $[Ti(Cp)_2Cl_2]$ [11] and bdmpp [12] were synthesized by literature methods, the former under an argon atmosphere using dried THF.

Microanalyses (C, H, N) were performed by the University of Ioannina (Greece) Microanalytical Laboratory using an EA 1108 Carlo Erba analyzer. IR spectra (4000–450 cm^{-1}) were recorded on a Perkin–Elmer 16 PC FT-spectrometer with samples prepared as KBr pellets. The FT-Raman spectrum was recorded on a Bruker IFS 66v spectrometer equipped with an FT-Raman FRA 106 module. The compound was excited by the 1064 nm line of a Nd:YAG laser operating at 200 mW. For the spectrum, 1000 scans were recorded and averaged. The ^1H NMR spectrum of the complex in $CDCl_3$ was recorded with a JEOL FX90Q FT-spectrometer; chemical shifts are reported relative to tetramethylsilane. The solid-state (diffuse reflectance) spectrum in the 300–800 nm range was recorded on a Varian Cary 3 spectrometer equipped with an integration sphere; the sample was diluted with spectroscopic grade MgO.

2.2. Compound preparation

2.2.1. $[TiCl_2(O_2)(bdmpp)]$ (**1**)

A colourless solution of bdmpp (0.08 g, 0.4 mmol) in Me_2CO (10 ml) was added to a red solution of $[Ti(Cp)_2Cl_2]$ (0.09 g, 0.4 mmol) in the same solvent to give an orange–red solution. The reaction solution was stirred overnight. Upon storage of the closed reaction flask at room temperature for few days, orange–red, X-ray quality crystals formed. The crystals were collected by filtration, washed with ice-cooled Me_2CO (1 ml) and Et_2O (2x2 ml), and dried in vacuo over silica gel. Typical yields were in the 55–60% range. *Anal.* Calc. for $C_{15}H_{17}N_5O_2Cl_2Ti$ (418.14): C, 43.08; H, 4.11; N, 16.75. Found: C, 42.88; H, 3.99; N, 16.62%. Selected IR bands (KBr, cm^{-1}) : 2926w, 1600m, 1586m, 1484sh, 1450s, 1378m, 1360m, 1158w, 1060w, 1048w, 990w, 905w, 800m, 720w, 660w, 614w, 551w. ^1H NMR (90 MHz, $CDCl_3$): δ 2.40 (6H, s, pyrazolyl Me), 3.01 (6H, s, pyrazolyl Me), 6.43 (2H, s, pyrazolyl H), 8.22 (3H, m, NC_5H_3). Solid-state (diffuse reflectance) spectrum (MgO, nm): 425.

2.3. Single-crystal X-ray crystallography

A red–orange crystal of **1** with approximate dimensions $0.20 \times 0.30 \times 0.50$ mm was mounted in air and covered with epoxy glue. Diffraction measurements were made on a CRYSTAL LOGIC dual goniometer diffractometer using graphite monochromated Mo Kα radiation. Unit cell dimensions were determined and refined by using the angular settings of 25 automatically centered reflections in the range $11 < 2\theta < 23°$. Intensity data were recorded using a $\theta-2\theta$ scan. Three standard reflections monitored every 97 reflections showed less that 3% intensity fluctuation and no decay. Lorentz, polarization corrections were applied using Crystal Logic software. Important crystal data and parameters for data collection and processing are listed in Table 1.

Table 1
Crystallographic data for complex **1**.

Parameter	**1**
Formula	$C_{15}H_{17}TiN_5O_2Cl_2$
Formula weight	418.14
Crystal system	monoclinic
Space group	$P2_1/c$
a (Å)	9.245(4)
b (Å)	28.070(10)
c (Å)	14.870(6)
β (°)	107.79(2)
V (Å^3)	3674(3)
Z	8
T (°C)	25
Radiation, λ (Å) Mo Kα	0.71073
ρ_{calc} (g cm^{-3})	1.512
μ (mm^{-1})	0.776
F (0 0 0)	1712
Reflections collected	5224
Reflections unique (R_{int})	4731 (0.0210)
Reflections used [$I > 2\sigma(I)$]	3499
R_1[a] [$I > 2\sigma(I)$]	0.0530
wR_2[b] [$I > 2\sigma(I)$]	0.1285

[a] $R_1 = \sum(||F_o|-|F_c||)/\sum(|F_o|)$.
[b] $wR_2 = \left\{\sum\left[w(F_o^2-F_c^2)^2\right]/\sum[w(F_o^2)^2]\right\}^{1/2}$.

The structures were solved by direct methods using SHELXS-86 [13] and refined by full-matrix least squares techniques on F^2 with SHELXL-97 [14]. All H atoms were introduced at calculated positions as riding on bonded atoms. All non-H atoms were refined anisotropically. Further crystallographic details for **1**: $2\theta_{max} = 50.0°$, scan speed = 4.0° min^{-1}, scan range = 1.8° + $\alpha_1\alpha_2$ separation, 473 parameters refined, $(\Delta/\sigma)_{max} = 0.012$, $(\Delta\rho)_{max}/(\Delta\rho)_{min} = 0.474/-0.414$ e/Å^3, R_1/wR_2 (for all data) = 0.0808/0.1617, GOF (on F^2) = 1.077.

3. Results and discussion

The 1:1 reaction between $[Ti(Cp)_2Cl_2]$ and bdmpp in Me_2CO is accompanied by a colour change from red to orange–red; storage of the resulting solution at room temperature gives prismatic, X-ray quality crystals of **1**. We were surprised to see that the product is an η^2-peroxo Ti^{IV} complex also bearing one bdmpp and two chloro ligands (vide infra). This reaction is unusual. Peroxo metal complexes are obtained either by oxidative addition of dioxygen to a low-valent metal complex or by ligand exchange on a high-valent metal complex upon reaction with H_2O_2 [5,15]. These are not the cases here. The Ti^{IV} center in the starting material is d^0 and cannot be oxidized; moreover, there was no peroxide source in the reaction mixture. It should be mentioned at this point that the reaction does not take place in absolute Me_2CO. Although we are far from understanding the reaction mechanism, our first impression is that the reducing equivalents for the dioxygen reduction come from solvent impurities and the whole process is facilitated by $[Ti(Cp)_2Cl_2]$.

With the identity of **1** established by single-crystal, X-ray crystallography (vide infra), the complex could be prepared in excellent yields by the addition of a slight excess of an aqueous H_2O_2 10% solution in the 1:1 $[Ti(Cp)_2Cl_2]$/bdmpp reaction mixture in alcohols or Me_2CO, see Eq. (1).

$$[Ti(Cp)_2Cl_2] + \text{bdmpp} + H_2O_2 \rightarrow \underset{\mathbf{1}}{[TiCl_2(O_2)(\text{bdmpp})]} + 2HCp \qquad (1)$$

Complex **1** crystallizes in the monoclinic space group $P2_1/c$. There are two, crystallographically independent molecules in the asymmetric unit (molecule A and molecule B). Since the two molecules have very similar structures, only the structure of the representative molecule A will be discussed in detail. The structure of A is shown in Fig. 1, while selected bond lengths and angles are listed in Table 2.

The coordination polyhedron of Ti^{IV} is a distorted pentagonal bipyramid. The equatorial positions are occupied by the three nitrogen atoms [N(1), N(3), N(5)] of the chelating bdmpp ligand and the oxygen atoms of the peroxo group. The axial positions are occupied by the two chloro ligands; the Cl(1)–Ti(1)–Cl(2) angle is 163.9(1)°. The distances of O(1), O(2), N(1), N(2) and N(3) from their mean equatorial plane are 0.028, 0.019, −0.058, 0.074 and −0.062 Å, respectively. The distances of the axial ligands Cl(1) and Cl(2) from the mean equatorial plane are −2.363 and 2.366 Å, respectively.

The peroxide group O_2^{2-} binds to Ti^{IV} in a side-on η^2-fashion, occupying two coordination sites in the equatorial plane. The peroxo groups can be (i) part of a three-membered ring, (ii) bridging staggered, (iii) bridging symmetrical, or (iv) bridging through a single oxygen atom [5], see Scheme 2. The two Ti(1)–O(1) and Ti(1)–O(2) bonds are equivalent in **1**. The O–O bond lengths are 1.455(5) and 1.446(5) Å in molecules A and B, respectively. It appears that similar Ti–O, O–O, O–Ti-O and Ti–O–O lengths and angles are observed in **1** and a number of $Ti^{IV}(O_2^{2-})$ complexes exhibiting pentagonal bipyramidal geometry around the Ti^{IV} ion(s) [1,2,16]. Due to the geometric constraints of the η^2-O_2^{2-} group, some coordination angles in the equatorial plane, e.g. O(1)–Ti(1)–O(2) [46.5(2)°], O(1)–Ti(1)–N(5) [85.0(2)°] and O(2)–Ti(1)–N(1) [85.2(2)°] deviate significantly from the ideal value of 72°.

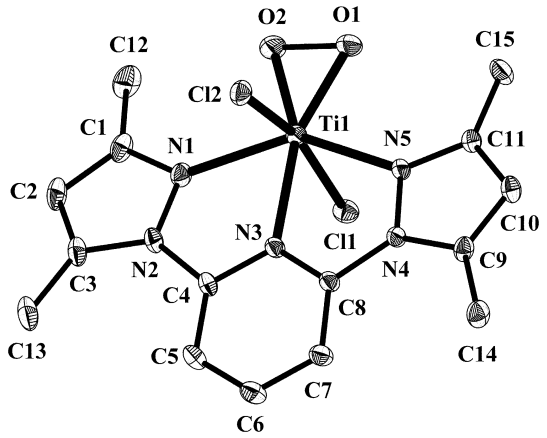


Fig. 1. The structure of one (molecule A) of the two crystallographically independent molecules that is present in the crystal of complex **1**.

Table 2
Selected bond distances (Å) and angles (°) for one (molecule A)[a] of the two crystallographically independent molecules that are present in complex **1**.

Distances			
Ti(1)–O(1)	1.842(3)	C(1)–N(1)	1.342(6)
Ti(1)–O(2)	1.841(4)	N(1)–N(2)	1.393(6)
Ti(1)–N(1)	2.198(4)	N(2)–C(4)	1.413(6)
Ti(1)–N(3)	2.212(4)	C(4)–N(3)	1.342(5)
Ti(1)–N(5)	2.201(4)	N(3)–C(8)	1.324(6)
Ti(1)–Cl(1)	2.371(2)	C(8)–N(4)	1.406(5)
Ti(1)–Cl(2)	2.405(2)	N(4)–N(5)	1.395(5)
O(1)–O(2)	1.455(5)		
O(1)–Ti(1)–O(2)	46.5(2)	N(1)–Ti(1)–N(5)	143.3(2)
O(1)–Ti(1)–N(1)	131.7(2)	N(1)–Ti(1)–Cl(1)	86.9(1)
O(1)–Ti(1)–N(3)	156.0(2)	N(1)–Ti(1)–Cl(2)	88.4(1)
O(1)–Ti(1)–N(5)	85.0(2)	N(3)–Ti(1)–N(5)	71.4(1)
O(1)–Ti(1)–Cl(1)	98.8(2)	N(3)–Ti(1)–Cl(1)	84.0(1)
O(1)–Ti(1)–Cl(2)	95.8(2)	N(3)–Ti(1)–Cl(2)	79.9(1)
O(2)–Ti(1)–N(1)	85.2(2)	N(5)–Ti(1)–Cl(1)	85.7(1)
O(2)–Ti(1)–N(3)	156.9(2)	N(5)–Ti(1)–Cl(2)	88.9(1)
O(2)–Ti(1)–N(5)	131.5(2)	Cl(1)–Ti(1)–Cl(2)	163.9(1)
O(2)–Ti(1)–Cl(1)	99.0(2)	O(1)–O(2)–Ti(1)	66.7(2)
O(2)–Ti(1)–Cl(2)	95.9(2)	O(2)–O(1)–Ti(1)	66.7(2)
N(1)–Ti(1)–N(3)	72.1(2)		

[a] See Fig. 1.

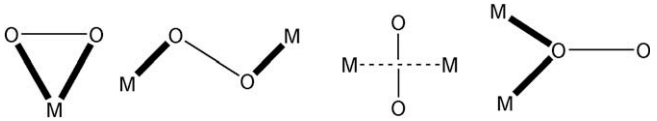
Although the bonding in the three-membered ring (Scheme 2, left) is most easily described by localized bonding, it can also be described by a MO treatment similar to that for the bonding of olefins or acetylenes [5]. Crudely, a σ bond is formed by filled Opπ → Mdσ bonding and back-bonding is due to Mdπ → Opπ* [5]; the latter is not feasible in **1** due to its d^0 nature.

In the crystal structure of the free ligand bdmpp [17], the pyrazolyl rings are oriented away from the pyridine nitrogen atom in order to minimize the electronic repulsion between the nitrogen lone pairs (Scheme 1), in spite of the fact that some steric congestion is thus created by the methyl substituents. A major reorientation of the pyrazolyl rings occurs upon coordination in **1**, thus allowing the molecule to act as a tridentate *N*,*N*′,*N*″-chelate. The interelectronic repulsion of the nitrogen lone pairs is dissipated upon complexation due to the interaction with Ti^{IV} [17]. In addition to this conformational change, the angles N(3)–C(4)–N(2) [113.3(4)°] and N(3)–C(8)–N(4) [113.7(4)°] in the complex are smaller than the corresponding angles in the uncoordinated molecule [average: 117.3(2)°], reasonably due to the formation of the "pocket" for the metal cation [17]. The Ti–N bond lengths are in the range 2.198(4)–2.212(4) Å, very close to the Ti–N(terpy) bond lengths [2.171(4)–2.216(4) Å] in the structurally characterized complex [Ti(Cp^*)($NNC_5H_3Me_2$-2,6)(terpy)](OTf)$_2$ [18], where $^-NNC_5H_3Me_2$-2,6 is the 2,6-dimethyl(1-pyridinio)imido(-1) ligand and OTf^- the triflate ion.

The three bdmpp rings in the molecule A (Fig. 1) of **1** are not coplanar, the dihedral angles between the central pyridine ring and the peripheral pyrazolyl rings being 13.3° [N(3)C(4)C(5)C(6)C(7)C(8)/N(1)N(2)C(3)C(2)C(1)] and 9.12° [N(3)C(4)C(5)C(6)C(7)C(8)/N(4)N(5)C(11)C(10)C(9)]. In molecule B, the three rings are almost coplanar, the corresponding dihedral angles being 0.9 and 7.0°.

Somewhat to our surprise, there are no intermolecular stacking interactions in the crystal lattice. The crystal structure of **1** is stabilized by a series of weak, intermolecular C–H···Cl interactions. In the structure of the complex there are intra- and intermolecular C–H···O (peroxide) H-bonding interactions which stabilize the lattice structure (Fig. 2). Their dimensions are: C(12)···O(2) = 2.913(1) Å, O(2)···H(12A) = 2.261(9) Å, C(12)–H(12A)···O(2) = 124.4(5)°; C(35)···O(22) = 2.829(1) Å, O(22)···H(35A) = 2.256(6) Å, C(35)–H(35A)···O(22) = 117.3(4)°; C(14)···O(22)[x, $-y+1/2$, $z+1/2$] = 3.415(2) Å, H(14A)···O(22)[x, $-y+1/2$, $z+1/2$] = 2.489(1) Å, C(14)–H(14A)···O(22)[x, $-y+1/2$, $z+1/2$] = 162.1(4)°.

Complex **1** is the first, structurally characterized Ti^{IV} complex of bdmpp and it joins a small family of structurally characterized metal complexes of this ligand [9,17,19]. Complex **1** is only the



Scheme 2. The up-to-date crystallographically confirmed coordination modes of the O_2^{2-} ligand.

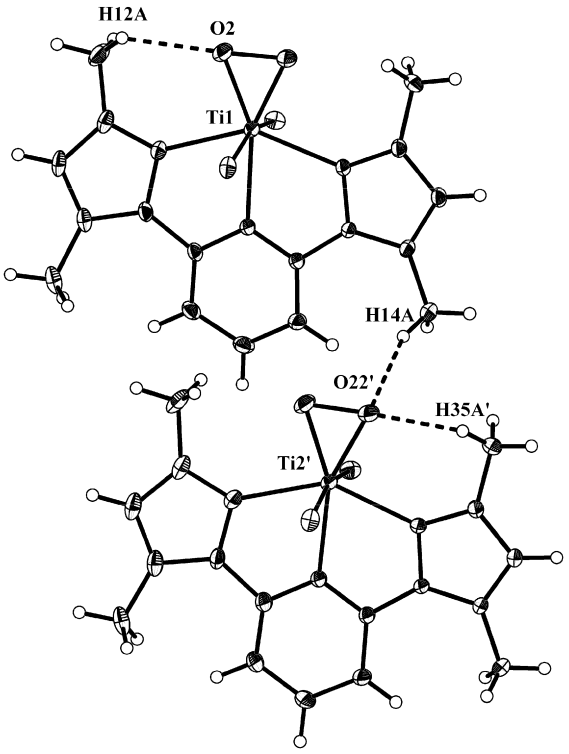


Fig. 2. Partially labeled plot of **1**, with thermal ellipsoids drawn at the 30% probability level, showing the intra- and intermolecular C–H···O (peroxide) H-bonding interactions (dashed lines). Primed atoms are generated by the symmetry operation: (′) = x, $-y + 1/2$, $z + 1/2$.

second, structurally characterized complex of the general type $[Ti^{IV}Cl_2(\eta^2\text{-}O_2)(L\text{–}L\text{–}L)]$, where L–L–L is a neutral, tridentate chelate. The first such complex was $[TiCl_2(O_2)(Me_3tacn)]$ [16b], where Me_3tacn is 1,4,7-trimethyl-1,4,7-triazacyclononane; however, there is strong evidence that there is compositional disorder in the structure and the compound contains an appreciable amount of $[TiCl_2O(Me_3tacn)]$.

The solid-state electronic spectrum of **1** is featureless beyond 500 nm, due to the fact that Ti^{IV} has no d electrons. Attention was focused on the band at ~425 nm. This can be reasonably be attributed to a $\pi_v^* \rightarrow$ d O^{2-} to Ti^{IV} charge-transfer (LMCT) vibration [2,16b].

The IR and Raman spectra of **1** display the expected bands due to the presence of the side-on $\eta^2\text{-}O_2^{2-}$ group [1,2,16b–d]. The ν(O–O), $\nu_s[Ti(O_2)]$ and $\nu_{as}[Ti(O_2)]$ vibrations appear at 905, 614 and 551 cm^{-1}, respectively, in the IR spectrum. The most intense Raman peaks in the 1000–500 cm^{-1} region are located at 908 and 624 cm^{-1}. These spectral features are attributed [1,2,16b] to the O–O and Ti–O_2 symmetric stretching vibrations, respectively, in accordance with the peaks reported in the literature for a peroxide group bound to the Ti^{IV} center in the side-on fashion. The $\nu_{as}[Ti(O_2)]$ mode does not appear in the Raman spectrum, as expected.

The IR bands of **1** at 1600, 1586, 1484 and 1450 cm^{-1} are assigned to carbon–nitrogen ring stretching vibrations of the coordinated bdmpp ligand, while the 800 and 720 cm^{-1} features are typical for out-of-plane C–H bending vibrations [17]. The in-plane deformation band of the pyridine ring of free bdmpp at ~630 cm^{-1} shifts upwards (660 cm^{-1}), confirming the involvement of the pyridine ring N-atom in coordination [20].

The ^{1}H NMR spectrum of **1** in $CDCl_3$ is very similar to that reported for complex *trans*-$[Ru(NO_2)(bdmpp)(PMe_3)_2](ClO_4)$ [9] and is consistent with the tridentate coordination of bdmpp.

4. Concluding comments and perspectives

The main aspect of this work is the discovery that a cyclopentadienyl-free, titanium peroxo complex is synthetically available from the reaction of $[Ti(Cp)_2Cl_2]$ with a *N*,*N*′,*N*″-chelate in acetone under aerobic conditions. The reaction that initially led to complex **1** is neither an oxidative addition of O_2 to low-valent Ti, nor a simple ligand exchange on a Ti^{IV} species by added peroxide sources. It is obvious that the reactivity chemistry of $[Ti(Cp)_2X_2]$ warrants further expansion to other tridentate aromatic *N*-heterocycles (including terpy) to investigate the substitution degree of the Cp^- ligands and the possibility of obtaining other peroxo complexes. Reactions of zircocene and hafnocene derivatives with bdmpp have not been studied to date, and it is currently not evident whether the identity of the products is dependent on the particular nature of the metal ion. Experiments on these projects, as well as on the use of $[Ti(Cp)_2X_2]$ compounds as precursors for the synthesis of heterometallic Ti/3d-metal clusters are currently in progress in our laboratories.

5. Supplementary data

CCDC 727374 contains the supplementary crystallographic data for **1**. These data can be obtained free of charge via http://www.ccdc.cam.ac.uk/conts/retrieving.html, or from the Cambridge Crystallographic Data Centre, 12 Union Road, Cambridge CB2 1EZ, UK; fax: (+44) 1223-336-033; or e-mail: deposit@ccdc.cam.ac.uk.

Acknowledgement

We thank Prof. H.O. Desseyn (Chemistry Department, University of Antwerp, Belgium) for providing us with the Raman and ^{1}H NMR spectra of **1**.

References

[1] M. Kakihana, M. Tada, M. Shiro, V. Petrykin, M. Osada, Y. Nakamura, Inorg. Chem. 40 (2001) 891. and references therein.
[2] M. Dakanali, E.T. Kefalas, C.P. Raptopoulou, A. Terzis, G. Voyiatzis, I. Kyrikou, T. Mavromoustakos, A. Salifoglou, Inorg. Chem. 42 (2003) 4632. and references therein.
[3] K. Schneider, A. Müller, E. Krahn, W.R. Hagen, H. Wassink, K.-H. Knüttel, Eur. J. Biochem. 230 (1995) 666.
[4] For example, see: M. Bochmann, J. Chem. Soc., Dalton Trans. (1996) 255.
[5] F.A. Cotton, G. Wilkinson, C.A. Murillo, M. Bochmann, Advanced Inorganic Chemistry, sixth ed., Wiley, New York, 1999. p. 468.
[6] For example, see: Y. Dang, Coord. Chem. Rev. 135/136 (1994) 93.
[7] (a) R.S. Tobias, G. Doyle, Inorg. Chem. 6 (1967) 1111;
(b) H. Köpf, M. Schmidt, J. Organomet. Chem. 4 (1965) 426;
(c) H. Köpf, T. Klapötke, Chem. Ber. 119 (1986) 1986;
(d) J. Charalambous, M.J. Frazer, W.E. Newton, J. Chem. Soc. A (1971) 2487.
[8] N. Klouras, N. Tzavellas, C.P. Raptopoulou, Monatsh. Chem. 128 (1997) 1201.
[9] C.A. Bessel, R.F. See, D.L. Jameson, M.R. Churchill, K.J. Takeuchi, J. Chem. Soc., Dalton Trans. (1993) 1563.
[10] (a) For example, see: E.C. Constable, Adv. Inorg. Chem. Radiochem. 30 (1986) 69;
(b) P.J. Steel, E.C. Constable, J. Chem. Soc., Dalton Trans. (1990) 1389;
(c) E.C. Constable, M.D. Ward, J. Chem. Soc., Dalton Trans. (1990) 1405;
(d) R. Hage, R. Prins, J.G. Haasnoot, J. Reedijk, J.G. Vos, J. Chem. Soc., Dalton Trans. (1987) 1389.
[11] J. Wilkinson, J.M. Birmingham, J. Am. Chem. Soc. 76 (1954) 4218.
[12] D.J. Jameson, K.A. Goldsby, J. Org. Chem. 55 (1990) 4992.
[13] G.M. Sheldrick, SHELXS-86, Structure Solving Program, University of Göttingen, Germany, 1986.
[14] G.M. Sheldrick, SHELXL-97, Program for the Refinement of Crystal Structures from Diffraction Data, University of Göttingen, Germany, 1997.
[15] R. Guilard, J.-M. Latour, C. Lecomte, J.-C. Marchon, J. Protas, D. Ripoll, Inorg. Chem. 17 (1978) 1228.
[16] (a) Y.-F. Deng, Z.-H. Zhou, H.-L. Wan, K.-R. Tsai, Inorg. Chem. Commun. 7 (2004) 169;
(b) P. Jeske, G. Haselhorst, Th. Weyhermüller, K. Wieghardt, B. Nuber, Inorg. Chem. 33 (1994) 2462;
(c) M. Postel, F. Casabianca, Y. Gauffreteau, J. Fischer, Inorg. Chim. Acta 113 (1986) 173;

(d) H. Mimoun, M. Postel, F. Casabianca, J. Fischer, A. Mitschler, Inorg. Chem. 21 (1982) 1303;
(e) H. Manohar, D. Schwarzenbach, Helv. Chim. Acta 57 (1974) 1086;
(f) D. Schwarzenbach, Helv. Chim. Acta 55 (1972) 2990;
(g) D. Schwarzenbach, Inorg. Chem. 9 (1970) 2391.
[17] F. Calderazzo, U. Englert, C. Hu, F. Marchetti, G. Pampaloni, V. Passarelli, A. Romano, R. Santi, Inorg. Chim. Acta 344 (2003) 197.
[18] M. Retboll, Y. Ishii, M. Hidai, Organometallics 18 (1999) 150.
[19] (a) For example, see: A.J. Blake, S.J. Hill, P. Hubberstey, Chem. Commun. (1998) 1587;
(b) V.J. Catalano, R. Kurtaran, R.A. Heck, A. Öhman, M.G. Hill, Inorg. Chim. Acta 286 (1999) 181;
(c) R. Kurtaran, C. Arici, S. Durmu, D. Ülkü, O. Atakol, Anal. Sci. 19 (2003) 335;
(d) F. Ercan, C. Arici, D. Ülkü, R. Kurtaran, M. Aksu, O. Atakol, Z. Kristallogr. 219 (2004) 295.
[20] A.B.P. Lever, A. Mantovani, Inorg. Chem. 10 (1971) 817.

three phosphonate ligands containing four phosphonate moieties have been studied for their ability to form ionic compounds with non-metal cations, ethylenediammonium (en^{2+}), ammonium (NH_4^+, and the $Zn(H_2O)_6^{2+}$ ion that forms *in situ*. Schematic structures are shown in Fig. 2. These three tetraphosphonate ligands all have the same coordinating moieties (two amino-*bis*(methylenephosphonate) groups), but they are linked by two (EDTMP), four (TDTMP) and six (HDTMP) methylene chains. All three phosphonates are zwitter-ionic (each phosphonate group is monodeprotonated and the N atoms are protonated). The ligand charge is "2−", therefore it requires a "2+" charge balancing cation(s) for electroneutrality.

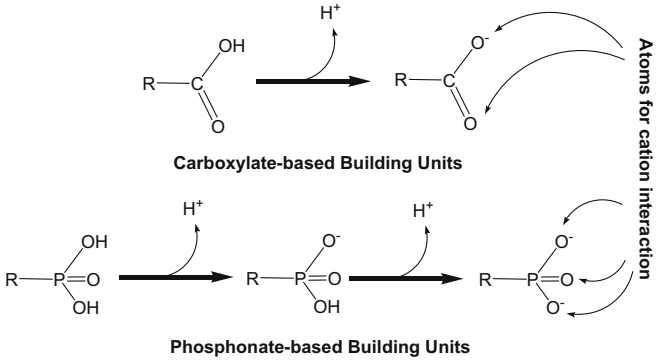


Fig. 1. Structural and functional differences between carboxylic and phosphonic acids.

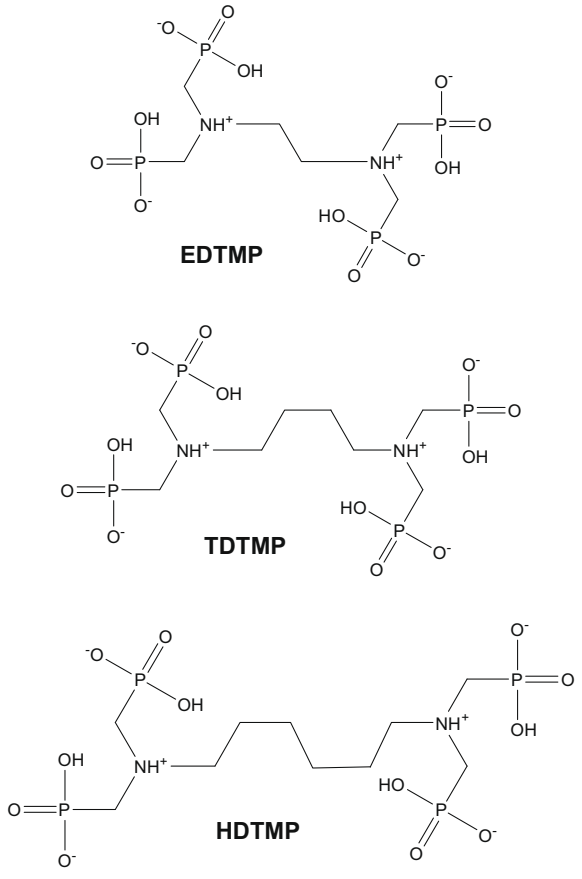


Fig. 2. The three tetraphosphonates (EDTMP, TDTMP and HDTMP) used in this paper in their zwitter-ionic form and an overall ligand charge "2−".

2. Experimental

2.1. Materials

All water-soluble metal salts were commercial samples and were used without further purification. Ethylenediamine was from Fluka. Phosphonic acids (EDTMP, TDTMP and HDTMP) were from Solutia Inc. Stock solutions of HCl and NaOH were used for pH adjustments. In-house, deionized (DI) water was used for all syntheses.

2.2. Syntheses

2.2.1. (en)(HDTMP)·2H$_2$O

The material (en)(HDTMP)·2H_2O was obtained from our attempts to synthesize Zn-HDTMP materials. The Zn^{2+} ion was not incorporated into the final product. (en)(HDTMP)·2H_2O can be synthesized according to the procedure below, without the Zn salt. A quantity of acid HDTMP (1.230 g, 2.5 mmol) is suspended in 40 mL DI water and mixed with 1.2 mL ethylenediamine (neat). The pH is adjusted to 2.0 by addition of HCl stock solution. Then a quantity of $ZnCl_2$·6H_2O is added (0.204 g, 1.5 mmol) under rigorous stirring. Final pH adjustment was done to 2.5. At this point a clear colorless solution forms. This solution is left under quiescent conditions at room temperature. After 2 days colorless crystals appear. They are isolated by filtration, washed with DI water and air-dried. Yield ~40%. Yields can be increased by prolonged crystallization times.

2.2.2. (NH_4)$_2$(EDTMP)

The material (NH_4)$_2$(EDTMP) was obtained from our attempts to synthesize Zn-EDTMP materials. The Zn^{2+} ion was not incorporated into the final product. (NH_4)$_2$(EDTMP) can be synthesized according to the procedure below, without the Zn salt. A quantity of acid EDTMP (0.947 g, 2.00 mmol) is suspended in 40 mL DI water. Sufficient quantity of a stock solution of NH_4OH is added until the solid dissolved. The pH is adjusted to 2.0 by addition of a stock solution of HCl. Then $ZnCl_2$·6H_2O is added (0.270 g, 2.00 mmol) under vigorous stirring and the final pH is adjusted to 1.8. The clear colorless solution is left undisturbed for 3 days, during which a white crystalline precipitate appears. It is filtered, washed with DI water and left to dry at room temperature. Yield ~60%.

2.2.3. Zn(H_2O)$_6$·(TDTMP)

A mixture of TDTMP and $ZnCl_2$ with a molar ratio of 1:1 was prepared in water at room temperature, as follows: 1 mmol (0.450 g) of solid TDTMP was dissolved in water (25 mL) with addition of NaOH until it completely dissolved. The pH was then adjusted to 2.0 by addition of HCl. Then, 1 mmol (0.136 g) of $ZnCl_2$ was gradually added under constant stirring. The pH of the final solution was adjusted to 2.2. After several days single crystals of the final compound appeared. The crystals were collected by filtration and dried in air. Yield ~70%.

2.3. Single crystal determinations

X-ray diffraction data were collected on a SMART 1K CCD diffractometer at 298(2) K with Mo Kα (λ = 0.71073 Å). Data were corrected for absorption using the empirical method employed in Sortav [15]. All structures were subsequently refined by full-matrix least squares refinement on F2 (SHELXL97) [16]. Non-hydrogen atoms were refined anisotropically. Hydrogen atoms were either located in the difference Fourier map or placed geometrically. Subsequent refinement of the thermal parameters was carried out isotropically in all cases. CCDC reference numbers: (en)(HDTMP)·2H_2O CCDC-651135; (NH_4)$_2$-(EDTMP) CCDC-625197; Zn(H_2O)$_6$·(TDTMP) CCDC-287045. Copies of the data may be obtained free of charge from the CCDC, e-mail: deposit@ccdc.cam.ac.uk or www: http://www/ccdc/cam/ac/uk).

Crystallographic details and selected bond distances and angles are given in Tables 1–4.

2.4. Sample characterization

FT-IR spectra were recorded on a FT-IR Perkin–Elmer FT 1760. ATR-IR spectra were collected on a Thermo-Electron NICOLET 6700 FTIR optical spectrometer.

3. Results and discussion

All three crystalline materials described herein share a common structural feature. They are layered compounds. The layered structure is composed of anionic phosphonate layers and charge-balancing cations, see Fig. 3. These layers are held together by complicated networks of hydrogen bonds. Waters of crystallization are found only in the structure of (en)(HDTMP)·$2H_2O$.

Metric features within the tetraphosphonate backbone are trivial and close to values reported in the literature [17]. The P—O bond distances are in the range 1.444–1.591 Å, typical for organophosphonates [18]. However, upon closer examination of the P—O bond lengths it becomes evident that they are separated into two categories, the "short" and the "long" bonds. All "long" bonds are associated with the protonated —P—OH moiety, whereas the "short bonds" are from the non-protonated portion of the —PO_3 moiety. Distinction between the P=O and the P—O— bond lengths is not possible because these are of equivalent length, based on the crystallography results. Therefore, this leads to the conclusion that the negative charge is delocalized over the O=P—O— moiety. Similar observations have been noted for metal-coordinated (and mono-deprotonated) phosphonates [19].

3.1. Crystal structure of (en)(HDTMP)·$2H_2O$

There are discrete $HDTMP^{2-}$ dianions and en^{2+} dications in the structure of (en)(HDTMP)·$2H_2O$, see Fig. 4 (upper). The presence of waters of crystallization, $HDTMP^{2-}$ dianions and en^{2+} dications leads to a complicated network of hydrogen bonds, finally yielding a 2D layered structure, see Fig. 4 (lower). They are described in detail below. The —NH_3^+ portion of the en molecule is hydrogen-bonded with one of the two water molecules of crystallization O(8) (2.974 Å), and with three O—P moieties (all from different phosphonate groups) (2.708, 2.804 and 2.984 Å).

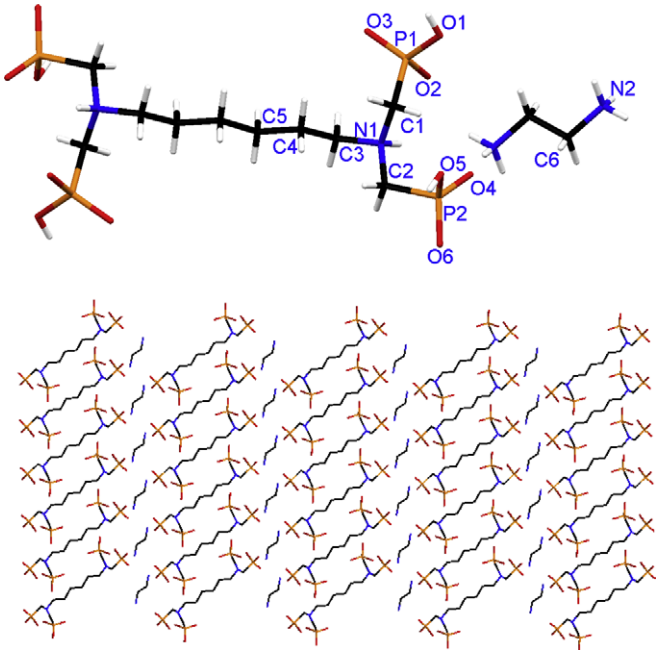


Fig. 4. Structure of $HDTMP^{2-}$ with the en^{2+} dications (upper, the water molecules are ommited for clarity). Layers of $HDTMP^{2-}$ and en^{2+} dications (lower) down the *b*-axis.

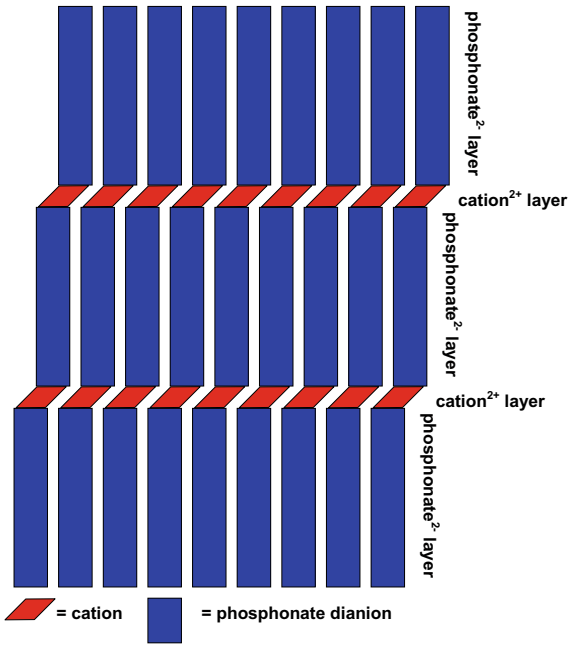


Fig. 3. The common structural feature in the three materials described herein. The cation and anion layers are assembled by hydrogen bonds.

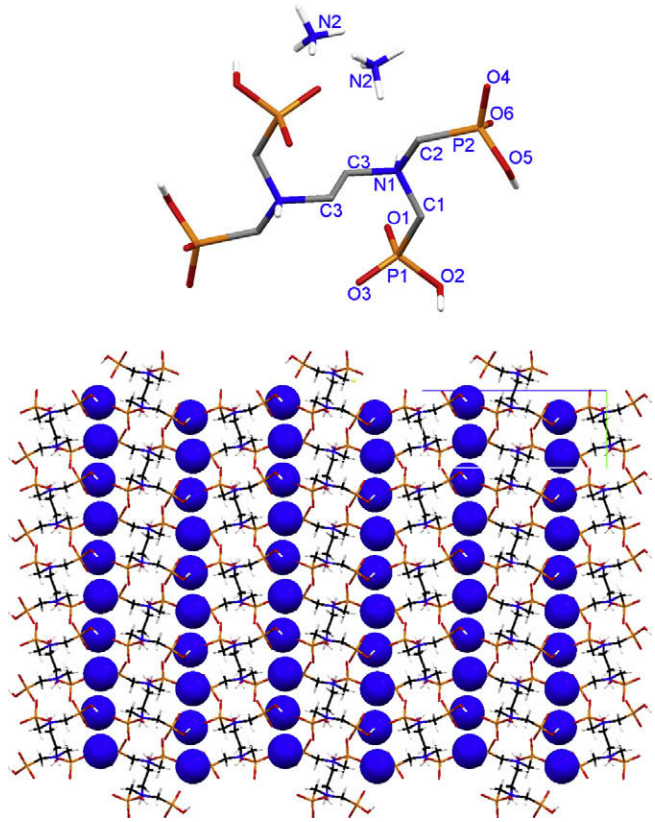


Fig. 5. Structure of $EDTMP^{2-}$ with the two NH_4^+ cations (upper). Layers of $EDTMP^{2-}$ and NH_4^+ cations, shown as blue spheres (lower) down the *a*-axis.

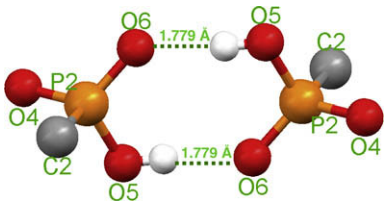


Fig. 6. Structure of the hydrogen-bonded dimer in the structure of $(NH_4)_2$(EDTMP).

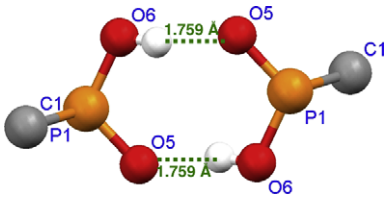


Fig. 9. Structure of the hydrogen-bonded dimer in the structure of $Zn(H_2O)_6$·(TDTMP).

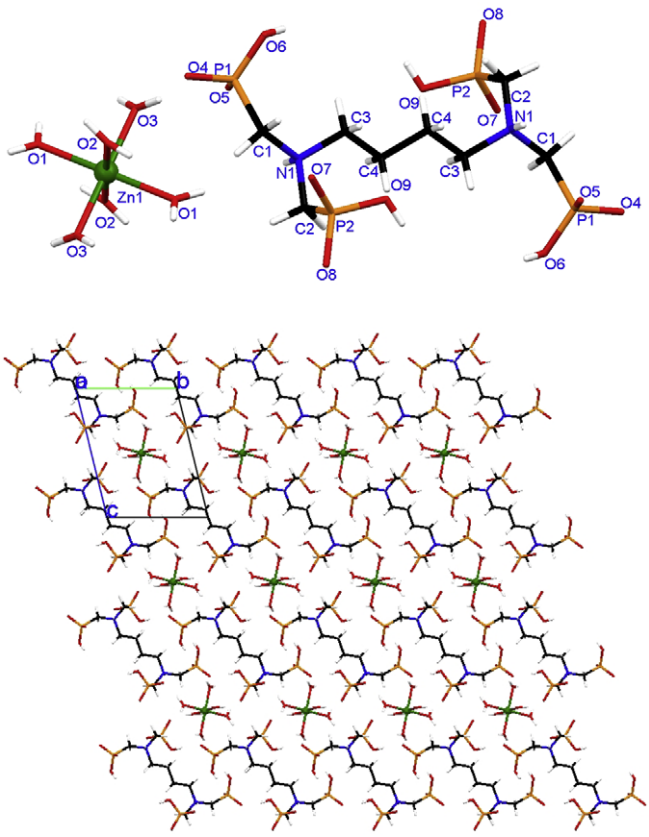


Fig. 7. Structure of $TDTMP^{2-}$ dianion with the $Zn(H_2O)_6^{2+}$ dication (upper). Layers of $TDTMP^{2-}$ and $Zn(H_2O)_6^{2+}$ dications down the *a*-axis (lower).

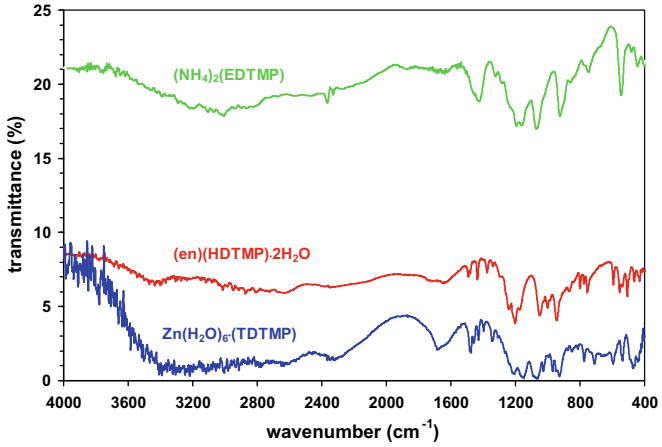


Fig. 10. FT-IR spectra of compounds (en)(HDTMP)·$2H_2O$, $(NH_4)_2$(EDTMP), and $Zn(H_2O)_6$·(TDTMP).

The two waters of crystallization are located in the vicinity of the en^{2+} dication. One water molecule (O(8)) forms hydrogen bonds with the N(1)–H^+ moiety (2.963 Å), with the $^+H_3N(2)$ group of the en^{2+} cation (2.974 Å), and with and the O(4) from a deprotonated phosphonate ligand, ^-O—P (2.999 Å). The second water molecule (O(7)) participates in three hydrogen bonds, one with a —P—O(1)H group (2.553 Å), and two hydrogen bonds with two deprotonated P—$O(3)^-$ moieties (2.729 and 2.743 Å) from neighboring phosphonate ligands.

The $P(1)O_3H^-$ phosphonate participates in four hydrogen bonds. P—O(1) connects to a water molecule O(7) (2.553 Å). P—O(3) forms two hydrogen bonds with two symmetry-related water molecules O(7) (2.743 and 2.729 Å). Finally, P—O(2) is only hydrogen bonded to protonated H—O(5)P(2) (2.533 Å).

The $P(2)O_3H^-$ phosphonate group takes part in five hydrogen bonds. Protonated P—O(5) connects to a P—O(6) group from a neighboring phosphonate (2.533 Å). P—O(4) H-bonds to a water molecule O(8) (2.999 Å) and to a protonated N(2) from en (2.804 Å). Finally, P—O(6) interacts with two protonated N(2) groups from two different en molecules (2.708 and 2.984 Å).

3.2. Crystal structure of $(NH_4)_2$(EDTMP)

There are discrete $EDTMP^{2-}$ dianions and NH_4^+ cations in the structure of $(NH_4)_2$(EDTMP), see Fig. 5 (upper). The presence of $EDTMP^{2-}$ dianions and NH_4^+ cations leads to a complicated network of hydrogen bonds, finally yielding a 2D layered structure, see Fig. 5 (lower). They are described in detail below.

Each of the ammonium cations participates in five hydrogen bonds, all with non-protonated P—O groups from different phosphonate ligands: with O(3)—P(1) (2.895 Å), with O(2)—P(1) (2.929 Å), with O(4)—P(2) (2.949 Å), with O(3)—P(1) (2.799 Å) and with O(6)—P(1) (2.820 Å).

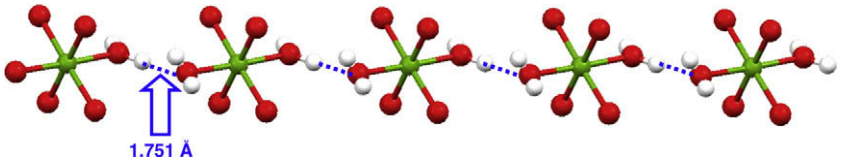


Fig. 8. $Zn(H_2O)_6^{2+}$ dications (part of the "inorganic layer") linked by hydrogen bonds.

The $P(1)O_3H^-$ phosphonate group participates in five hydrogen bonds. Protonated P—O(2)H participates in a hydrogen bond with the ammonium N(2) group of the NH_4^+ cation (2.929 Å) and the non-protonated group O(4)—P(2) from a neighboring phosphonate (2.559 Å). The group P–O(1) forms only one H-bond with the protonated $N(1)H^+$ group belonging to another EDTMP molecule (2.648 Å). Finally, P–O(3) forms two H-bonds with two symmetry-related N(2) groups from two different en molecules (2.799 and 2.895 Å).

The $P(2)O_3H^-$ phosphonate group also participates in five hydrogen bonds. Protonated P–O(5)H participates in a hydrogen bond with the non-protonated P(2)–O(6) group from a neighboring phosphonate. At the same time non-protonated P(2)–O(6) hydrogen bonds with the protonated P(2)–O(5)–H moiety with the same phosphonate group. This creates a hydrogen-bonded dimer, the structure of which is shown in Fig. 6. A similar phosphonate hydrogen-bonded dimmer has been observed in the structure of 2-phosphonobutane-1,2,4-tricarboxylic acid monohydrate ($PBTC{\cdot}H_2O$) [20].

Table 1
Crystallographic data for $(en)(HDTMP){\cdot}2H_2O$, $(NH_4)_2(EDTMP)$ and $Zn(H_2O)_6{\cdot}(TDTMP)$.

Material	$(en)(HDTMP){\cdot}2H_2O$	$(NH_4)_2(EDTMP)$	$Zn(H_2O)_6{\cdot}(TDTMP)$
Empirical formula	$C_6H_{22}N_2O_8\ P_2$	$C_6H_{26}N_4O_{12}P_4$	$C_8H_{34}N_2O_{18}P_4Zn$
Formula weight	312.20	470.19	621.65
Space group	$P\bar{1}$	$P2_1/c$	$P\bar{1}$
a (Å)	6.195(1)	8.012(2)	5.8905(8)
b (Å)	7.489(1)	6.8313(9)	8.990(1)
c (Å)	15.955(3)	16.526(2)	11.817(2)
α (°)	84.472(3)	90	73.506(2)
β (°)	85.319(3)	98.76(1)	76.200(2)
γ (°)	67.881(3)	90	75.428(2)
V (Å)	681.7(2)	893.9(2)	571.2(1)
Z	2	2	1
T (K)	293(2)	293(2)	293(2)
λ (Å)	0.71073	0.71073	0.71073
d_{calc} (g cm^{-3})	1.521	1.747	1.807
μ (mm^{-1})	0.352	0.491	1.442
Meas./Unique/Obs. Refl.	3616/2746/2176	5524/1982/1794	2771/1641/1462
Parameters	161	138	154
R_{int}	0.0185	0.0224	0.0108
R_1 [$R_1(F_0)_{all}$]	0.0547 [0.0683]	0.0341 [0.0385]	0.0292 [0.0338]
wR_2 [$wR_2(F_0^2)_{all}$]	0.1560 [0.1633]	0.0935 [0.0961]	0.0753 [0.0777]
GoF	1.076	1.146	1.061

3.3. Crystal structure of $Zn(H_2O)_6{\cdot}(TDTMP)$

There are discrete $TDTMP^{2-}$ dianions and $Zn(H_2O)_6^{2+}$ dications in the structure of $Zn(H_2O)_6{\cdot}(TDTMP)$, see Fig. 7 (upper). This result is somewhat surprising because reaction of Zn^{2+} with HDTMP in similar conditions yields a Zn-HDTMP inorganic organic hybrid [17a]. At present we have no satisfactory explanation for this. One can link this absence of TDTMP coordination to Zn^{2+} to a reduced basicity of the phosphonate oxygens. The metric features of the $Zn(H_2O)_6^{2+}$ octahedron are expected and comparable to those of $[Zn(H_2O)_6](triflate)_2$ [21] and a Zn6 cluster with the ligand N-(phosphonomethyl)-N-methylglycine containing non-coordinated $Zn(H_2O)_6^{2+}$ dications in the lattice [22]. Also, an Mg ionic material containing non-coordinating aminoethylphosphonate has been reported that contains $Mg(H_2O)_6^{2+}$ dications in the lattice [23]. The presence of $TDTMP^{2-}$ dianions and $Zn(H_2O)_6^{2+}$ dications (there are no waters of crystallization in the structure) leads to an intricate network of hydrogen bonds, finally yielding a 2D layered structure, see Fig. 7 (lower). They are described in detail below.

The $Zn(H_2O)_6^{2+}$ dication participates in a total of fourteen hydrogen bonds. Two of them (O···O 2.733 Å) are with neighboring $Zn(H_2O)_6^{2+}$ dication, thus creating a one-dimensional 'wire', as part

Table 3
Bond lengths [Å] and angles [°] for $(NH_4)_2(EDTMP)$.[a]

Bonds		Angles	
C(1)–N(1)	1.500(2)	N(1)–C(1)–P(1)	114.65(12)
C(1)–P(1)	1.8279(19)	N(1)–C(2)–P(2)	116.25(12)
C(2)–N(1)	1.501(2)	N(1)–C(3)–C(3)#1	112.59(17)
C(2)–P(2)	1.8287(19)	C(1)–N(1)–C(2)	111.81(14)
C(3)–N(1)	1.505(2)	C(1)–N(1)–C(3)	114.52(14)
C(3)–C(3)#1	1.525(3)	C(2)–N(1)–C(3)	112.12(14)
O(1)–P(1)	1.4821(14)	O(1)–P(1)–O(3)	117.90(9)
O(2)–P(1)	1.5639(15)	O(1)–P(1)–O(2)	108.21(9)
O(3)–P(1)	1.5030(14)	O(3)–P(1)–O(2)	111.54(8)
O(4)–P(2)	1.4943(15)	O(1)–P(1)–C(1)	107.25(9)
O(5)–P(2)	1.5745(14)	O(3)–P(1)–C(1)	108.80(9)
O(6)–P(2)	1.5032(15)	O(2)–P(1)–C(1)	101.86(9)
		O(4)–P(2)–O(6)	118.85(9)
		O(4)–P(2)–O(5)	108.31(9)
		O(6)–P(2)–O(5)	109.33(8)
		O(4)–P(2)–C(2)	103.73(9)
		O(6)–P(2)–C(2)	108.63(8)
		O(5)–P(2)–C(2)	107.36(9)

[a] Symmetry transformations used to generate equivalent atoms: #1 $-x+1$, $-y+1$, $-z+2$.

Table 2
Bond lengths [Å] and angles [°] for $(en)(HDTMP){\cdot}2H_2O$.[a]

Bonds		Angles			
C(1)–N(1)	1.488(4)	N(1)–C(1)–P(1)	112.84(19)	O(2)–P(1)–O(1)	109.71(15)
C(1)–P(1)	1.825(3)	N(1)–C(2)–P(2)	114.5(2)	O(3)–P(1)–C(1)	111.02(15)
C(2)–N(1)	1.504(4)	C(4)–C(3)–N(1)	114.9(2)	O(2)–P(1)–C(1)	103.54(14)
C(2)–P(2)	1.830(3)	C(3)–C(4)–C(5)	109.8(2)	O(1)–P(1)–C(1)	101.68(13)
C(3)–C(4)	1.510(4)	C(5)#1–C(5)–C(4)	112.7(3)	O(4)–P(2)–O(6)	120.82(16)
C(3)–N(1)	1.521(4)	N(2)–C(6)–C(6)#2	109.4(3)	O(4)–P(2)–O(5)	106.58(14)
C(4)–C(5)	1.526(4)	C(1)–N(1)–C(2)	113.2(2)	O(6)–P(2)–O(5)	110.12(13)
C(5)–C(5)#1	1.519(6)	C(1)–N(1)–C(3)	113.1(2)	O(4)–P(2)–C(2)	108.03(14)
C(6)–N(2)	1.486(4)	C(2)–N(1)–C(3)	111.5(2)	O(6)–P(2)–C(2)	104.70(14)
C(6)–C(6)#2	1.505(6)	O(3)–P(1)–O(2)	118.24(15)	O(5)–P(2)–C(2)	105.65(15)
N(1)–H(5)	0.91(4)	O(3)–P(1)–O(1)	111.15(14)		
O(1)–P(1)	1.565(2)				
O(2)–P(1)	1.498(2)				
O(3)–P(1)	1.489(3)				
O(4)–P(2)	1.492(3)				
O(5)–P(2)	1.572(2)				
O(6)–P(2)	1.497(2)				

[a] Symmetry transformations used to generate equivalent atoms: #1 $-x+3$, $-y$, $-z$ #2 $-x+1$, $-y+1$, $-z+1$.

Table 4
Selected bond lengths [Å] and angles [°] for $Zn(H_2O)_6$·(TDTMP).

Bonds		Angles			
Zn(1)–O(1)	2.099(2)	O(2)–Zn(1)–O(2)	179.999(2)	O(2)–Zn(1)–O(3)	91.17(10)
Zn(1)–O(2)	2.049(2)	O(2)–Zn(1)–O(1)	91.88(9)	O(1)–Zn(1)–O(3)	91.19(9)
Zn(1)–O(3)	2.106(2)	O(2)–Zn(1)–O(1)	88.12(9)	O(1)–Zn(1)–O(3)	88.81(9)
P(2)–O(7)	1.492(2)	O(1)–Zn(1)–O(1)	180.0(13)	O(3)–Zn(1)–O(3)	180.00(13)
P(2)–O(8)	1.501(2)	O(2)–Zn(1)–O(3)	91.17(10)	O(7)–P(2)–O(8)	117.49(13)
P(2)–O(9)	1.569(2)	O(2)–Zn(1)–O(3)	88.83(10)	O(7)–P(2)–O(9)	107.13(12)
P(1)–O(5)	1.499(2)	O(1)–Zn(1)–O(3)	88.81(9)	O(8)–P(2)–O(9)	112.02(12)
P(1)–O(4)	1.501(2)	O(1)–Zn(1)–O(3)	91.19(9)	O(5)–P(1)–O(4)	116.09(13)
P(1)–O(6)	1.557(2)	O(2)–Zn(1)–O(3)	88.83(10)	O(5)–P(1)–O(6)	111.60(12)
				O(4)–P(1)–O(6)	108.12(14)

of the $[Zn(H_2O)_6^{2+}]_n$ layer, see Fig. 8. The remaining twelve H-bonds are exclusively with phosphonate oxygens from layers below and above. Bond distances are in the range 2.618–2.972 Å.

The $P(1)O_3H^-$ phosphonate group takes part in six hydrogen bonds. Three of them are with Zn-bound water molecules (2.797, 2.972 and 2.809 Å). It is interesting to note that the protonated P(1)–O(6)–H moiety along with a non-protonated group P(1)–O(5) create a hydrogen bonded dimer with the corresponding P–O groups of a neighboring P(1) phosphonate. The structure of this dimer (analogous to that formed in the structure of $(NH_4)_2$(EDTMP) is shown in Fig. 9.

The $P(2)O_3H^-$ phosphonate group takes part in five hydrogen bonds. Three of them are with Zn-bound waters (2.718, 2.737 and 2.621 Å). The protonated P(2)–O(9)–H group hydrogen bonds to a non-protonated P(1)–O(4) moiety (2.569 Å). Finally, there is a hydrogen bond between non-protonated P(2)–O(7) and the —NH^+ amine moiety of a neighboring phosphonate (2.854 Å).

The $P(1)O_3H^-$ phosphonate group takes part in five hydrogen bonds. Two of them participate in the hydrogen-bonded dimer mentioned above. Two of them are with Zn-bound waters (2.752 and 2.949 Å). Finally, there is a hydrogen bond between non-protonated P(1)–O(4) and a protonated P(2)–O(9)–H moiety of a neighboring phosphonate (2.569 Å).

3.4. Vibrational spectroscopy

Vibrational spectroscopy was employed as well to further characterize these compounds. FT-IR spectra are shown in Fig. 10. Mid IR spectra (400–4000 cm^{-1} region) of the tetraphosponate products display a multitude of bands in the region 1100–1270 cm^{-1} assigned to the P=O stretch. A doublet in the region 920–970 cm^{-1} is assigned to the —P—OH antisymmetric and symmetric stretching vibrations. The strong band in the region 1045–1055 cm^{-1} is tentatively assigned to an antisymmetric vibration mode of the —CPO_3 group. Bands in the spectra for all compounds are also observed in the 400–550 cm^{-1} region. These are assigned to the —PO_3 symmetric and —PO_3 antisymmetric bending modes. Broad bands in the region 1640–1670 cm^{-1} in the spectra of (en)(HDTMP)·$2H_2O$ and $Zn(H_2O)_6$·(TDTMP) are due to lattice water and Zn-bound water, respectively. Such bands are absent in the spectrum of $(NH_4)_2$(EDTMP), which is anhydrous.

4. Conclusions

The three ionic materials reported herein share a 2D structural motif. They are layered compounds with anionic tetraphosphonate layers separated with cationic layers. These structures are held together by an intricate network of hydrogen bonds, which act as the driving for the self assembly process. The field of metal phosphonate chemistry is growing rapidly. The area of frameworks composed of organic ionic components is also expected to grow in parallel and act in a supporting fashion. A viable goal is the designed synthesis of supramolecular arrays in a predictable fashion by use of appropriate reactants.

Supplementary data

CCDC 651135, 625197 and 287045 contain the supplementary crystallographic data for compounds (en)(HDTMP)·$2H_2O$, $(NH_4)_2$(EDTMP), and $Zn(H_2O)_6$·(TDTMP). These data can be obtained free of charge via http://www.ccdc.cam.ac.uk/conts/retrieving.html, or from the Cambridge Crystallographic Data Centre, 12 Union Road, Cambridge CB2 1EZ, UK; fax: (+44) 1223-336-033; or e-mail: deposit@ccdc.cam.ac.uk.

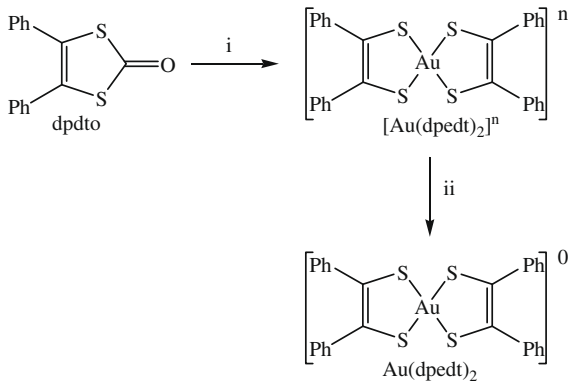
Acknowledgment

K.D.D. thanks the General Secretariat of Science & Technology (Contract # 2006-207c) for partial funding.

References

[1] (a) A.D. Bond, W. Jones, in: W. Jones, C.N.R. Rao (Eds.), Supramolecular Organization and Materials Design, Cambridge University Press, Cambridge, UK, 2002 (and references therein);
(b) C.V.K. Sharma, Cryst. Growth Des. 2 (2002) 465;
(c) D. Braga, L. Brammer, N.R. Champness, Cryst. Eng. Commun. 7 (2005) 1;
(d) M.J. Zaworotko, Cryst. Growth Des. 7 (2007) 4;
(e) L. Brammer, Chem. Soc. Rev. 33 (2004) 476;
(f) I. Goldberg, CrystEngCommun. 10 (2008) 637;
(g) J.S. Miller, CrystEngCommun 7 (2005) 458.
[2] (a) F.A.A. Paz, J. Klinowski, Pure Appl. Chem. 79 (2007) 1097;
(b) B. Moulton, M.J. Zaworotko, Chem. Rev. 101 (2001) 1629;
(c) K. Maeda, Micropor. Mesopor. Mater. 73 (2004) 47;
(d) G. Ferey, C. Mellot-Draznieks, C. Serre, F. Millange, Acc. Chem. Res. 38 (2005) 217.
[3] (a) P.M. Forster, A.K. Cheetham, Topics Catal. 24 (2003) 79;
(b) A. Vioux, J. Le Bideau, P.H. Mutin, D. Leclercq, Top. Curr. Chem. 232 (2004) 232;
(c) M. Hong, Cryst. Growth Des. 7 (2007) 10;
(d) S.L. James, Chem. Soc. Rev. 32 (2003) 276.
[4] D. Kong, J.L. McBee, A. Clearfield, Cryst. Growth Des. 5 (2005) 643.
[5] (a) I.D. Brown, Acta Cryst. A32 (1976) 24;
(b) M.D. Ward, Chem. Commun. (2005) 5838;
(c) E. Matczak-Jon, V. Videnova-Adrabinska, A. Burzynska, P. Kafarski, T. Lis, Chem. Eur. J. 11 (2005) 2357.
[6] A.M. Beaty, B.A. Helfrich, G.A. Hogan, B.A. Reed, Cryst. Growth Des. 6 (2006) 122.
[7] (a) K.D. Demadis, in: R.W. Buckley (Ed.), Solid State Chemistry Research Trends, Nova Science Publishers, New York, 2007, p. 109;
(b) A. Vioux, L. Le Bideau, P. Hubert Mutin, D. Leclercq, Top. Curr. Chem. 232 (2004) 145;
(c) R. Vivani, G. Alberti, F. Costantino, M. Nocchetti, Micropor. Mesopor. Mater. 107 (2008) 58;
(d) T.P. Knepper, Trends Anal. Chem. 22 (2003) 708.
[8] K. Popov, H. Ronkkomaki, L.H.J. Lajunen, Pure Appl. Chem. 73 (2001) 1641.
[9] (a) K.D. Demadis, J.D. Sallis, R.G. Raptis, P. Baran, J. Am. Chem. Soc. 123 (2001) 10129;
(b) J. Jokiniemi, S. Peräniemi, J.J. Vepsäläinen, M. Ahlgrén, CrystEngCommun 10 (2008) 1011;
(c) P.A. Turhanen, K.D. Demadis, S. Peräniemi, J.J. Vepsäläinen, J. Org. Chem. 72 (2007) 1468;

(d) H. Kumpulainen, R. Saari, M. Lehtonen, J. Rautio, T. Järvinen, J. Vepsäläinen, Tetrahedron Lett. 47 (2006) 2003;
(e) R. Murugavel, A. Choudhury, M.G. Walawalkar, R. Pothiraja, C.N.R. Rao, Chem. Rev. 108 (2008) 3549.
[10] S. Bauer, N. Stock, Angew. Chem., Int. Ed. 46 (2007) 6857.
[11] (a) K.M.E. Jones, A.H. Mahmoudkhani, B.D. Chandler, G.K.H. Shimizu, CrystEngCommun 8 (2006) 303;
(b) G. Olive, D.D. Ellis, D. Siri, F. Le Moigne, M. Lutz, A.L. Spek, P. Tordo, J.-P. Reboul, Acta Cryst. C 56 (2002) 720.
[12] (a) D. Kong, J. McBee, L. Holliness, A. Clearfield, Tetrahedron Lett. 49 (2008) 3512;
(b) D. Kong, A. Clearfield, J. Zon, Cryst. Growth Des. 5 (2005) 1767;
(c) C.V.K. Sharma, A. Clearfield, J. Am. Chem. Soc. 122 (2000) 4394;
(d) C.V.K. Sharma, A.J. Hessheimer, A. Clearfield, Polyhedron 20 (2001) 2095.
[13] (a) P. Todorov, E. Naydenova, R. Petrova, B. Shivacheva, K. Troev, Acta Cryst. C62 (2006) o661;
(b) G.B. Hix, V. Caignaert, J.-M. Rueff, L. Le Pluart, J.E. Warren, P.-A. Jaffres, Cryst. Growth Des. 7 (2007) 208;
(c) T. Bailly, R. Burgada, M. Lecouvey, A. Neuman, T. Prangé, ARKIVOC ix (2003) 140;
(d) G. Prochniak, J. Zon, M. Daszkiewicz, A. Pietraszko, V. Videnova-Adrabinska, Acta Cryst. C63 (2007) o434;
(e) A.H. Mahmoudkhani, V. Langer, Phosphorus Sulfur Silicon 177 (2002) 2941;
(f) A.H. Mahmoudkhani, V. Langer, O. Lindqvist, Phosphorus Sulfur Silicon 178 (2003) 2159;
(g) A.H. Mahmoudkhani, V. Langer, Cryst. Growth Des. 2 (2002) 21;
(h) H. Krawczyk, L. Albrecht, J. Wojciechowski, W.M. Wolf, Tetrahedron 64 (2008) 5051.
[14] (a) E. Barouda, K.D. Demadis, S.R. Freeman, F. Jones, M.I. Ogden, Cryst. Growth Des. 7 (2007) 321;
(b) K.D. Demadis, S.D. Katarachia, M. Koutmos, Inorg. Chem. Commun. 8 (2005) 254;
(c) K.D. Demadis, S.D. Katarachia, Phosphorus Sulfur Silicon 179 (2004) 627;
(d) K.D. Demadis, C. Mantzaridis, P. Lykoudis, Ind. Eng. Chem. Res. 45 (2006) 7795;
(e) K.D. Demadis, P. Baran, J. Solid State Chem. 177 (2004) 4768;
(f) K.D. Demadis, S.D. Katarachia, H. Zhao, R.G. Raptis, P. Baran, Cryst. Growth Des. 6 (2006) 836;
(g) K.D. Demadis, M. Papadaki, R.G. Raptis, H. Zhao, J. Solid State Chem. 181 (2008) 679;
(h) K.D. Demadis, M. Papadaki, R.G. Raptis, H. Zhao, Chem. Mater. 20 (2008) 4835;
(i) K.D. Demadis, Z. Anagnostou, H. Zhao, ACS-Appl. Mater. Interf. 1 (2009) 35;
(j) K.D. Demadis, E. Barouda, R.G. Raptis, H. Zhao, Inorg. Chem. 48 (2009) 819;
(k) K.D. Demadis, E. Barouda, N. Stavgianoudaki, H. Zhao, Cryst. Growth Des. 9 (2009) 1250;
(l) S. Lodhia, A. Turner, M. Papadaki, K.D. Demadis, G.B. Hix, Cryst. Growth Des. 9 (2009) 1811;
(m) K.D. Demadis, N. Stavgianoudaki, G. Grossmann, M. Gruner, J.L. Schwartz, Inorg. Chem. 48 (2009) 4154;
(n) R.M.P. Colodrero, A. Cabeza, P. Olivera-Pastor, A. Infantes-Molina, E. Barouda, K.D. Demadis, M.A.G. Aranda, Chem. Eur. J., in press, doi:10.1002/chem.200900558.
[15] (a) R.H. Blessing, Acta Cryst. A51 (1995) 33;
(b) R.H. Blessing, J. Appl. Crystallogr. 30 (1997) 421.
[16] G.M. Sheldrick, Acta Cryst. A46 (1990) 467.
[17] (a) K.D. Demadis, C. Mantzaridis, R.G. Raptis, G. Mezei, Inorg. Chem. 44 (2005) 4469;
(b) G.V. Polyanchuk, L.M. Shkol'nikova, M.V. Rudomino, N.M. Dyatlova, S.S. Makarevich, J. Struct. Chem. 26 (1985) 586;
(c) N. Stock, T. Bein, Angew. Chem., Int. Ed. 43 (2004) 749.
[18] (a) R. Clarke, K. Latham, C. Rix, M. Hobday, J. White, CrystEngCommun 6 (2004) 42;
(b) S. Bauer, T. Bein, N. Stock, J. Solid State Chem. 179 (2006) 145.
[19] K.D. Demadis, P. Lykoudis, R.G. Raptis, G. Mezei, Cryst. Growth Des. 6 (2006) 1064.
[20] K.D. Demadis, R.G. Raptis, P. Baran, Bioinorg. Chem. Appl. 3 (2005) 119.
[21] C. Nguyen-Trung, J.C. Bryan, D.A. Palmer, Struct. Chem. 15 (2004) 89.
[22] C. Lei, J.-G. Mao, Y.-Q. Sun, H.-Y. Zeng, A. Clearfield, Inorg. Chem. 42 (2003) 6157.
[23] A. Schier, S. Gamper, G. Muller, Inorg. Chim. Acta 177 (1990) 179.



i = 1) MeONa in MeOH; 2) $NaAuCl_4$ in MeOH/H_2O;
ii = *n*-Bu_4NBr_3 in MeOH; n = 2- and/or 1-

Scheme 1. Route used for the synthesis of Au(dpedt)$_2$.

on a Bruker IFS-113 V, FT-IR spectrometer, in the range 4000–500 cm^{-1}. Cyclic voltammetry measurements were carried out with a Bipotentiostat AFCBP1 from Pine Instrument Company and controlled with the PINECHEM 2.7.9 software, using a glassy carbon disk working electrode (1.6 mm diameter) and a Ag/Ag$^+$ (0.01 M $AgNO_3$ and 0.5 M *n*-Bu_4NPF_6 in acetonitrile) non-aqueous reference electrode (Bioanalytical Systems, Inc.) with a prolonged bridge (0.5 M *n*-Bu_4NPF_6 in acetonitrile). A Pt foil or gauge (8 cm^2, Sigma–Aldrich) was employed as counter electrode. The working electrode was polished using successively 6, 3, 1 mm diamond paste on a DP-Nap polishing cloth (Struerg, Westlake, OH), washed with water, acetone and air dried. The Pt foil and gauge electrodes were cleaned in a H_2O_2/H_2SO_4 (conc.) solution (1:4 v:v) and oven-dried. The concentration of the sample was 3 mM and that of supporting electrolyte (*n*-Bu_4NPF_6) was 0.5 M. The potential sweep rate varied between 10 and 1000 mV/s. All potentials were reported *versus* the ferrocenium/ferrocene (F_c^+/F_c) couple.

2.2. Synthesis of Au(dpedt)$_2$

In a two-necked 250 mL flask, a solution-suspension of 4,5-diphenyl-1,3-dithiol-2-one (dpdto) (500 mg, 2 mmol) in dry MeOH (40 mL) was prepared with stirring under nitrogen atmosphere. Then, a solution of NaOMe, freshly prepared from Na (115 mg, 5 mmol) and MeOH (20 mL), was added and the mixture stirred at r.t. for 30 min. To the yellow solution obtained, a solution of $NaAuCl_4{\cdot}2H_2O$ (398 mg, 1 mmol in deoxygenated MeOH/H_2O) (5/0.5 mL) was added slowly within 10 min. The resulting brown solution was stirred under nitrogen atmosphere for 1 h at r.t., whereupon the color turned brown–red. Then, a solution of *n*-Bu_4NBr_3 (482 mg, 1 mmol) in MeOH (25 mL) was added, and the mixture stirred for 2 h. Then, it was transferred to a beaker and stirred in air overnight. The precipitate was filtered, washed with water and MeOH and dried in air. The greenish-brown solid was extracted with CS_2 and chromatographed on a short silica-gel column, using CS_2 as eluent. The first greenish-brown fraction contained Au(dpedt)$_2$. Slow evaporation of the solvent gave gray-bronze crystals (190.9 mg, 28%). This compound was obtained in a lower yield as a byproduct of the preparation of Au(dpedt)(dddt) [4b]. M.p.: 234 °C. *Anal.* Calc. for $C_{28}H_{20}S_4Au$ (MW 681.695): C, 49.33; H, 2.96. Found: C, 48.97; H, 2.74%. UV–Vis–NIR (CS_2) $\lambda_{max}1$ = 1485 nm (ε = 50219 M^{-1} cm^{-1}), $\lambda_{max}2$ = 595 nm (ε = 3326 M^{-1} cm^{-1}). IR (cm^{-1}): 562.3 w, 613.4 w, 644.4 w, 694.3 s, 736.8 m, 746.8 s, 761.7 m, 847.7 s, 858.9 s, 869.9 s, 1000.8 w, 1026.9 m, 1075.6 w, 1147.9 s, 1159.1 m, 1175.2 s, 1261.2 w, 1309.8 w, 1401.9 s, 1426.8 m, 1456.9 s, 1496.7 w, 1572.5 w, 1592.2 w, 2851.7 m, 2922.6 m, 2955.3 m, 3018.1 w, 3030.5 w, 3055.3 m, 3074.7 w.

Table 1
Crystal data and structure refinement for Au(dpedt)$_2$.

Empirical formula	$C_{28}H_{20}AuS_4$
Formula weight	681.65
T (°C)	25
Wavelength (Å)	0.71073
Crystal system	triclinic
Space group	$P\bar{1}$
a (Å)	10.045(3)
b (Å)	10.208(3)
c (Å)	12.806(4)
α (°)	81.300(10)
β (°)	87.930(10)
γ (°)	84.010(10)
V (Å^3)	1290.6(7)
Z	2
$D_{calc.}$ (g cm^{-3})	1.754
μ (mm^{-1})	6.038
$2\theta_{max}$ (°)	50
Reflections collected	4800
Reflections unique	4518
Reflections used	4518
R_{int}	0.0383
Parameters refined	378
$(\Delta/\sigma)_{max}$	0.000
$(\Delta e)_{max}$	0.702
$(\Delta e)_{min}$	−1.887
R/Rw (all data)	0.378/0.0856
R_1[a]	0.0322[b]
wR_2[a]	0.0821[b]

[a] $w = 1/[\sigma^2(F_o^2) + (\alpha P)^2 + bP]$ and $P = (\max(F_o^2, 0) + 2F_c^2)/3$; $a = 0.0412$, $b = 0.5309$. $R_1 = \sum||F_o| - |F_c||/\sum|F_o|$ and $wR_2 = \{\sum[w(F_o^2 - F_c^2)^2]/\sum[w(F_o^2)^2]\}^{1/2}$.
[b] For 4056 reflections with $I > 2\sigma(I)$.

2.3. X-ray crystallography

A prismatic single crystal of Au(dpedt)$_2$ (0.18 × 0.36 × 0.70 mm^3) was mounted in capillary. Diffraction measurements were performed on a CRYSTAL LOGIC dual Goniometer diffractometer using graphite-monochromated Mo Kα radiation. Unit cell dimensions were determined and refined by using the angular settings of 25 automatically centered reflections in the range 11° < 2θ < 23°. Three standard reflections monitored every 97 reflections showed less than 3% intensity fluctuation and no decay. Lorentz, polarization corrections were applied using CRYSTAL LOGIC software. Important crystal data and refinement parameters for data collections are given in Table 1. The structure was solved by direct methods using SHELXS-97 [15] and refined by full matrix least-squares techniques on F^2 with SHELXL-97 [16]. Hydrogen atoms were introduced at calculated positions as riding on bonded atoms. All non-H atoms were refined anisotropically. Selected bond lengths and bond angles within the AuC_4S_4 chelate are given in Table 2.

3. Results and discussion

3.1. Formation of Au(dpedt)$_2$

The reaction of dpdto with MeONa, followed by treatment with $NaAuCl_4$ (Scheme 1) afforded the species [Au(dpedt)$_2$]^n (n = 2− and/or 1−). These species cannot be completely oxidized in air, under conditions reported in [4–6]. The oxidation stops when the species [Au(dpedt)$_2$]$^{1-}$ is formed. Further oxidation was performed with *n*-Bu_4NBr_3 to give the required neutral Au(dpedt)$_2$. The preparation of this material under strong oxidation conditions (*n*-Bu_4NBr_3) indicates its stability in air. The complex is soluble in CS_2 (10 mg/mL) and other organic solvents.

Table 2
Selected bond lengths (Å) and bond angles (°) within AuC_4S_4 chelate of $Au(dpedt)_2$.

Au–S(1)	2.288(1)	S(1)–Au–S(3)	90.73(5)
Au–S(3)	2.294(2)	S(4)–Au–S(1)	177.23(5)
Au–S(2)	2.294(1)	S(3)–Au–S(4)	88.77(5)
Au–S(4)	2.295(1)	S(2)–Au–S(1)	88.79(5)
S(1)–C(1)	1.732(5)	S(2)–Au–S(4)	91.71(5)
S(2)–C(11)	1.744(5)	Au–S(4)–C(31)	103.46(17)
S(3)–C(21)	1.723(5)	Au–S(3)–C(21)	103.00(17)
S(4)–C(31)	1.728(5)	Au–S(1)–C(1)	103.77(17)
C(1)–C(11)	1.370(7)	Au–S(2)–C(11)	103.64(17)
C(21)–C(31)	1.367(7)		

3.2. Structural information

Single crystals of the complex $Au(dpedt)_2$ crystallize in the triclinic system, space group $P\bar{1}$ (see Table 1). It is isostructural with β-$Ni(dpedt)_2$ [17a], but not isostructural with α-$Ni(dpedt)_2$ [17b,c], $Pt(dpedt)_2$ [17d] and $Pd(dpedt)_2$·0.5toluene [9a]. Fig. 1 shows the molecular structure of $Au(dpedt)_2$. From this figure and the data, of Table 2, one can see that in the AuC_4S_4 chelate of $Au(dpedt)_2$ molecule the Au–S, C–S and the olefinic C–C bond lengths are 2.288–2.295, 1.723–1.744 and 1.367–1.370 Å, respectively. The theoretically calculated values for $Au(dpedt)_2$ are 2.360, 1.756 and 1.383 Å, respectively [9a]. The experimentally obtained values could be comparable with those reported for $[Au(^2L)_2]\cdot CH_2Cl_2$ [9a], *i.e.*, the Au–S, C–S and olefinic C–C average bond lengths are 2.291(5), 1.749(20) and 1.36(2) Å, respectively. Selected bond lengths for several complexes are listed in Table 3. One can see that the bond length M–S increases with the order Au–S > Pd–S > Pt–S > Ni–S. In $Au(dpedt)_2$ molecule, as in the case of β-$Ni(dpedt)_2$, the conformation of phenyl groups (Fig. 1) is such that the molecule totally lacks reflection and inversion symmetry [17a]. The molecule $Au(dpedt)_2$ is also a dissymmetric molecule and is expected to exhibit optical activity. Fig. 2 shows the packing diagram of $Au(dpedt)_2$ molecules, which are stacked along the *b* crystallographic axis. Both intrastacking and interstacking S···S intermolecular distances are longer than 4.5 Å. These distances are much larger than the sum of the van der Waals radii (3.70 Å). It was found that the long axis of the crystal is almost parallel to the *a*-axis.

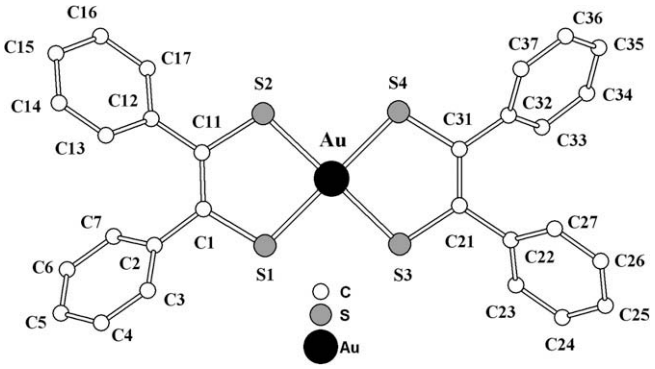


Fig. 1. Molecular structure of $Au(dpedt)_2$ in the crystal.

Table 3
Selected bond lengths (Å) for several complexes.

Complex	M–S	C–S	C=C	Ref.
$Au(dpedt)_2$	2.288–2.295	1.723–1.744	1.367–1.370	this work
$Au(^2L)_2$	2.291(5)	1.749(20)	1.36(2)	[9a]
$Pd(dpedt)_2$	2.251(1)	1.708(4)	1.399(5)	[9a]
$Pt(dpedt)_2$	2.244–2.246	1.699–1.716	1.395	[17d]
β-$Ni(dpedt)_2$	2.120–2.127	1.695–1.701	1.404–1.424	[17a]
α-$Ni(dpedt)_2$	2.101 ± 0.002	1.71 ± 0.01	1.37 ± 0.01	[17b]
α-$Nidpedt)_2$	2.1220(4)–2.1195(6)	1.698(1)–1.712(2)	1.396(2)	[17c]

3.3. EPR spectrum

Fig. 3 shows the EPR spectrum (X-band) of the complex $Au(dpedt)_2$ in frozen CH_2Cl_2 solution (0.1 M n-Bu_4NPF_6). The estimated from this spectrum g_x, g_y and g_z values are 2.064, 2.029 and 1.936, respectively. These values are close to the theoretically calculated ones (2.028, 2.023 and 1.962, respectively) and almost the same as those obtained experimentally from $Au(^2L)_2$ (2.065, 2.030 and 1.944, respective) [9a].

3.4. The electronic optical absorption spectra

Fig. 4 shows the UV–Vis–NIR optical absorption (OA) spectra of $Au(dpedt)_2$ solutions in CH_2Cl_2 and CS_2. One can see that there is an

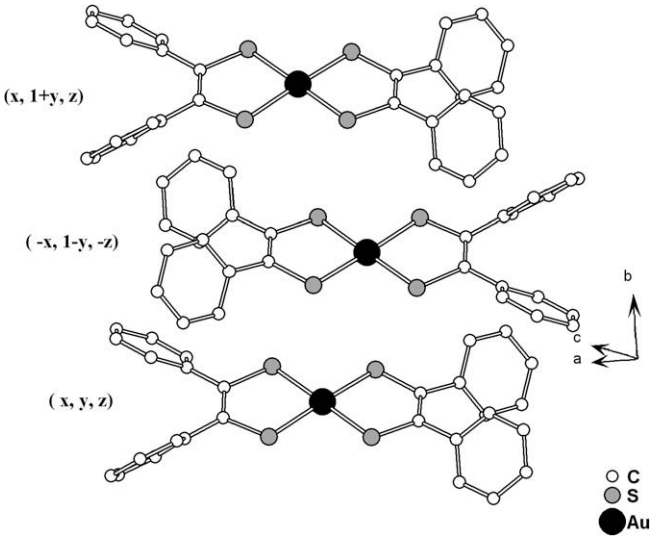


Fig. 2. Packing diagram of $Au(dpedt)_2$.

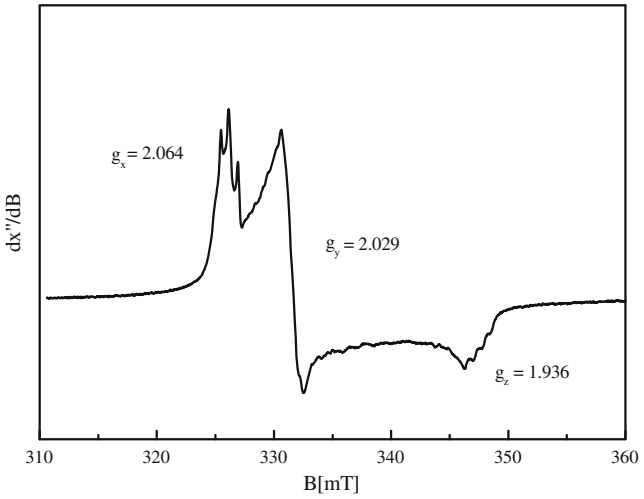


Fig. 3. EPR spectrum of $Au(dpedt)_2$ in frozen CH_2Cl_2 and 90 K. Experimental conditions: microwave frequency 9.41602 GHz, microwave power 3.2 mW, modulation amplitude 0.2 mT, modulation frequency 100 kHz.

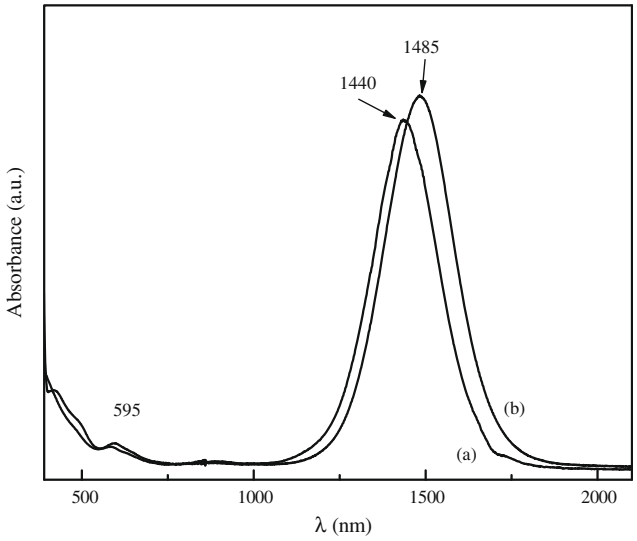


Fig. 4. UV–Vis–NIR optical absorption spectra of Au(dpedt)$_2$ in CH_2Cl_2 (a) and CS_2(b).

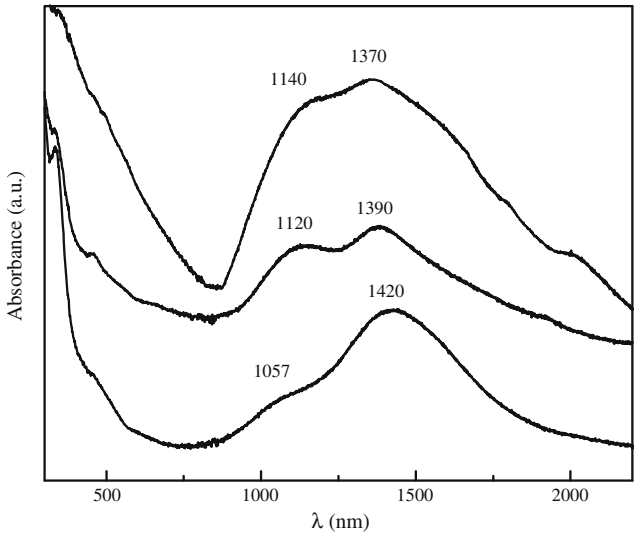


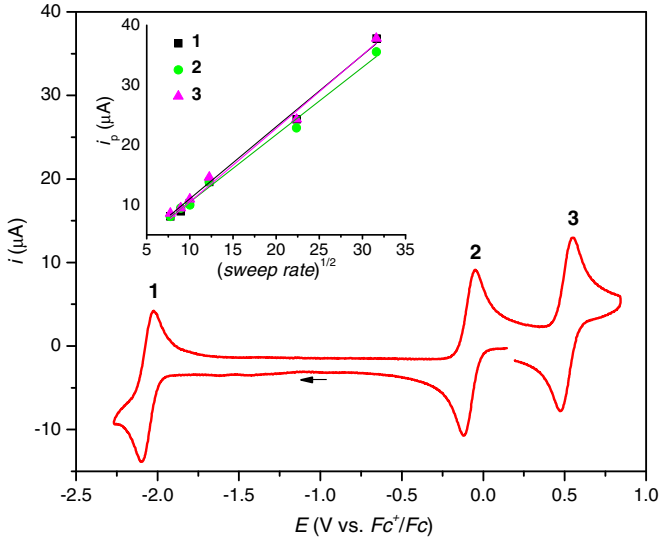
Fig. 5. UV–Vis–NIR optical absorption spectra of Au(dpedt)$_2$ deposited on quartz plates (three samples).

optical absorption onset (E^{opt}_{onset}) at ca. 1750 nm (0.7 eV), and a very strong absorption band at 1440 (CH_2Cl_2) or at 1485 (CS_2) nm. As in the case of Au(^{2}L)$_2$ [9a,10], this band is assigned to the intervalence charge transfer $1b_{1u} \rightarrow 2b_{2g}$ (*x*-polarized $^2B_{1u}$ state) transition. Another weak band at ca. 1180 nm, observed in the spectrum of Au(^{2}L)$_2$ solution in CH_2Cl_2 and assigned to the intervalence charge transfer $1a_u \rightarrow 2b_{2g}$ (*y*-polarized ^2A_u state) transition [9a,10], was not observed in the spectra of Au(dpedt)$_2$ solutions. The low frequency bands are discrete in the solid state spectra of Au(dpedt)$_2$. Fig. 5 shows the spectra of three samples of Au(dpedt)$_2$ deposited on quartz plates from solutions in CH_2Cl_2 or CS_2 by the spin coating technique. One can see that the position, intensity and shape of the low frequency bands vary from sample to sample. This behavior is attributed to the several different kinds of orientation and interaction of crystallites in the deposits. In the spectra of thin deposits the (E^{opt}_{onset}) occurs at ca. 2000 nm (0.61 eV). More discrete bands are expected in the single crystal polarized reflectance spectra, as in the case of Au(bdt)$_2$ (where bdt is benzene-1,2-dithiolate) [11]. The theoretically calculated optical absorption spectrum of Au(dpedt)$_2$ shows the low frequency bands at ca. 1420 and 1370 nm [9a,10].

The low frequency OA band and (E^{opt}_{onset}) of Au(dpedt)$_2$ in solution occur close to those of Au(^{2}L)$_2$ [9a], but at lower frequencies than those of M(dpedt)$_2$ (M = Ni, Pt, Pd) [9,17,18]. The position, intensity and shape of the low frequency the OA band of thin deposits of Au(dpedt)$_2$ remain unchanged for long time. This means that, in the solid state, the complex is stable in air.

3.5. Redox behavior

The key features of the cyclic voltammograms of Au(dpedt)$_2$ in CH_2Cl_2 at r.t. are three chemically and kinetically reversible waves: two reduction waves at $E_{1/2}(1) = -2.061$ V ($\Delta E = 69$ mV, $i_{p,c}/i_{p,a} = 1.07$) and $E_{1/2}(2) = -0.085$ V ($\Delta E = 66$ mV, $i_{p,c}/i_{p,a} = 0.97$) and one oxidation wave at $E_{1/2}(3) = +0.510$ V ($\Delta E = 70$ mV, $i_{p,a}/i_{p,c} = 1.07$). All potential values are given *versus* the ferrocenium/ferrocene (F_c^+/F_c) couple. This behavior was maintained for scan rates ranging from 80 to 1000 mV/s (the ΔE values and the faradaic



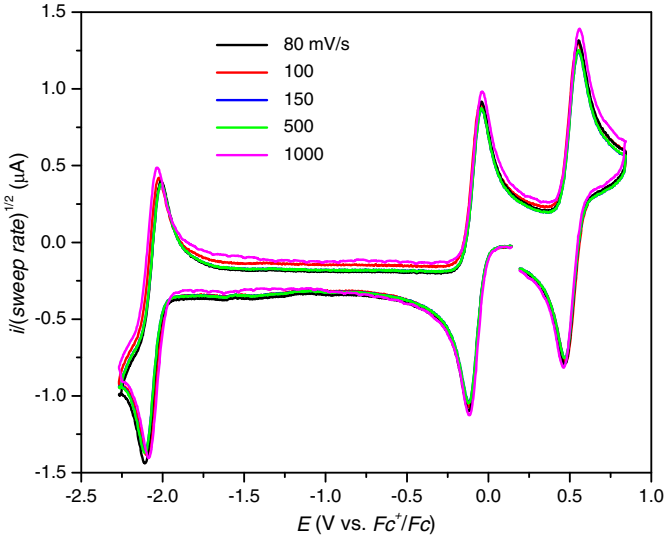


Fig. 6. Left: cyclic voltammetry of Au(dpedt)$_2$ in CH_2Cl_2/0.5 M *n*-Bu_4NPF_6 with a glassy carbon disk electrode (3 mm in diameter); scan rate 100 mV/s. Arrow indicates direction of scan. Inset: Randles–Sevcik plots for the anodic part of the oxidation wave and the cathodic parts of the reduction waves. Right: plots of i/(sweep rate)$^{1/2}$ vs. E for various sweep rates, as indicated.

current ratios given above are taken from the voltammogram recorded at 100 mV/s, Fig. 6, left). At lower scan rates (70–20 mV/s) a small wave appears at ca. −1.36 V, which also affects the reversibility of wave 1. Randles–Sevcik plots yielded straight lines, indicating diffusion controlled processes (Fig. 6, left, inset). Voltammograms normalized by dividing the faradaic current by the square root of the potential sweep rate are superimposable over a wide range of sweep rates, confirming its full chemical and kinetic reversibility (Fig. 6, right).

The electrochemical data exhibit pronounced similarities with data reported previously for analogous compounds [9a]. Thus, the three reversible redox waves can be tentatively assigned to the following transformations:

$$[Au(dpedt)_2]^{2-} \underset{E_{1/2}(1)}{\rightleftharpoons} [Au(dpedt)_2]^{-} \underset{E_{1/2}(2)}{\rightleftharpoons} [Au(dpedt)_2]^{0} \underset{E_{1/2}(3)}{\rightleftharpoons} [Au(dpedt)_2]^{+}$$

At higher potentials (1–2.5 V) further multi-electron oxidation of the complex occurs, as evidenced by the presence of irreversible waves at ca. 1.26, 1.48, 1.79 and 2.18 V. These oxidations have not been further investigated.

The reduction onset (E^{rd}_{onset}) for the neutral complex occurs at ca 0.03 V and the oxidation onset (E^{ox}_{onset}) occurs at ca. 0.42 V. The potential values are very close to those obtained for $Au(^2L)_2$ and similar complexes of Au [9,10], but the $E_{1/2}(2)$ value is larger than the values observed for other $M(dpedt)_2$ compounds (M = Ni, Pt, Pd; [1,4,6,9,10,18] and references therein).

3.6. Calculation of the LUMO and HOMO levels

The LUMO energy level (E_{LUMO}) value was calculated from the reduction onset (E^{rd}_{onset}) value for the 1e process *via* the equation $-E_{LUMO} = 4.8 + (E^{rd}_{onset})$ [19]. This is $E_{LUMO} = -4.83$ eV and is more negative than that obtained from $Ni(dpedt)_2$ [9c,18]. The HOMO energy level (E_{HOMO}) value was calculated from the oxidation onset (E^{ox}_{onset}) value for the 1e process *via* the equation $-E_{HOMO} = 4.8 + (E^{ox}_{onset})$ [19]. This is $E_{HOMO} = -5.22$ eV. The difference $E_{LUMO} - E_{HOMO}$ gives the energy gap of the semiconducting material, $E_g = 0.39$ eV, a value which is little smaller than that obtained from the optical absorption spectra of thin deposits of material on quartz plates (Fig. 4), $(E^{opt}_{onset}) = 0.61\ eV$ [19g]. The $E_{LUMO} = -4.83$ and $E_{HOMO} = -5.22$ eV values of $Au(dpedt)_2$ indicate that the material is stable in air [2]. The complex can be a candidate material for fabrication of n-type or ambipolar FETs in thin film or single crystal form, more stable in air than those based on Ni 1,2-DTs [1–3].

Supplementary data

CCDC 721849 contains the supplementary crystallographic data for $Au(dpedt)_2$. These data can be obtained free of charge via http://www.ccdc.cam.ac.uk/conts/retrieving.html, or from the Cambridge Crystallographic Data Centre, 12 Union Road, Cambridge CB2 1EZ, UK; fax: (+44) 1223-336-033; or e-mail: deposit@ccdc.cam.ac.uk.

Acknowledgement

This work was carried out as part of the «Excellence in Research Institutes» Project No. 64769, supported by GSRT/Ministry of Greece.

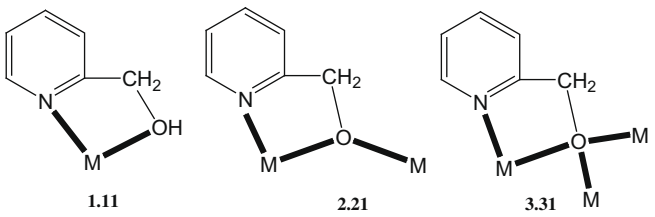
References

[1] (a) J.-Y. Cho, B. Domercq, S.C. Jones, J. Yu, Z. Zhang, Z. An, M. Bishop, S. Barlow, S.R. Marder, B. Kippelen, J. Mater. Chem. 25 (2007) 2642;
(b) T. Taguchi, H. Wada, T. Kabayashi, B. Noda, M. Goto, T. Mori, K. Ishikawa, H. Takezoe, Chem. Phys. Lett. 421 (2006) 395;
(c) H. Wada, T. Taguchi, B. Noda, T. Kambayashi, T. Mori, K. Ishikawa, H. Takezoe, Organ. Electron. 8 (2007) 759.
[2] T.D. Anthopoulos, G.C. Anyfantis, G.C. Papavassiliou, D.M. deLeeuw, Appl. Phys. 90 (2007) 122105.
[3] Y. Takahashi, T. Hasegawa, G.C. Papavassiliou, G.C. Anyfantis, Concerning n-type semiconducting behaviour of Ni(tmedt)(dddt) and ambipolar behaviour of Ni(dpedt)(dddt) single crystals, unpublished work.
[4] (a) G.C. Anyfantis, G.C. Papavassiliou, N. Assimomytis, A. Terzis, V. Psycharis, G.P. Raptopoulou, P. Kyritsis, V. Thoma, I.B. Koutselas, Solid State Sci. 10 (2008) 1729;
(b) G.C. Papavassiliou, G.C. Anyfantis, A. Terzis, V. Psycharis, A. Kyritsis, P. Paraskevopoulou, Z. Naturforsch. 63b (2008) 1377.
[5] G.C. Papavassiliou, G.C. Anyfantis, Z. Naturforsch. 60b (2005) 811.
[6] G.C. Anyfantis, Ph.D. Thesis, University of Patras, 2008.
[7] (a) P. Aloukos, S. Couris, I.B. Koutselas, G.C. Anyfantis, G.C. Papavassiliou, Chem. Phys. Lett. 428 (2006) 109;
(b) W.F. Guo, X.B. Sun, X.Q. Wang, G.H. Zhang, Q. Ren, D. Xu, Chem. Phys. Lett. 435 (2007) 65;
(c) J.-Y. Cho, S. Barlow, S.R. Marder, J. Fu, L.A. Padilha, E.W. van Syland, D.J. Hagan, M. Bishop, Opt. Lett. 32 (2007) 671;
(d) G.C. Anyfantis, G.C. Papavassiliou, P. Aloukos, S. Couris, Y.F. Weng, H. Yoshino, K. Murata, Z. Naturforsch. 62b (2007) 200;
(e) H. Ushijima, T. Kawasaki, T. Kamata, T. Kodzasa, H. Matsuda, T. Fukaya, Y. Fujii, F. Mizukami, Mol. Cryst. Liq. Cryst. 286 (1996) 275.
[8] M. Carla Aragoni, M. Arca, F.A. Devildanova, F. Isaia, V. Lippolis, A. Mancini, L. Pala, G. Verani, T. Agostinelli, M. Caironi, D. Natali, M. Sampietro, Inorg. Chem. Commun. 10 (2007) 191.
[9] (a) S. Kokatam, K. Ray, J. Pap, E. Bill, W.E. Geiger, R.J. LeSuer, P.H. Rieger, T. Weyhermuller, F. Neese, K. Wieghardt, Inorg. Chem. 46 (2007) 1100;
(b) J.M. Tunney, A.J. Blake, E.S. Davies, J. McMaster, C. Wilson, C.D. Garner, Polyhedron 25 (2006) 591;
(c) K. Wang, Prog. Inorg. Chem. 52 (2004) 267;
(d) M. Nomura, C. Takayama, M. Kajitani, Inorg. Chim. Acta 357 (2004) 2294.
[10] (a) K. Ray, T. Weyhermuller, F. Neese, K. Wieghardt, Inorg. Chem. 44 (2005) 5345;
(b) K. Ray, T. Weyhemuller, A. Guossens, M.W.J. Craje, K. Wieghardt, Inorg. Chem. 42 (2003) 4082;
(c) K. Ray, T. Petrenko, K. Wieghardt, F. Neese, Dalton Trans. (2007) 1552.
[11] N.C. Schiodt, T. Bjombolm, K. Bechgaard, J.J. Neumeier, C. Allgeier, C.S. Jacobsen, N. Thorup, Phys. Rev. 53 (1996) 1773.
[12] (a) M.M. Bélombé, J. Nenwa, E. Hey-Hawkings, P. Lonnecke, P. Strauch, K.R. Koch, Polyhedron 27 (2008) 3688;
(b) H. Nishikawa, W. Yasuoka, K. Sakairi, H. Oshio, Polyhedron 28 (2009) 1634.
[13] G.C. Papavassiliou, V.C. Kakoussis, D.J. Lagouvardos, G.A. Mousdis, Mol. Cryst. Liq. Cryst. 181 (1990) 171. and unpublished work.
[14] A.K. Bhattacharya, A.G. Hortmann, J. Org. Chem. 39 (1974) 95.
[15] G.M. Sheldrick, SHELXS-97, Program for the Solution of Crystal Structures, University of Gottingen, Germany, 1997.
[16] G.M. Sheldrick, SHELXL-97, Program for the Refinements of Crystal Structures, University of Gottingen, Germany, 1997.
[17] (a) M. Megnamisi-Bélombé, B. Nuber, Bull. Chem. Soc. Jpn. 62 (1989) 4092;
(b) D. Sartain, M.R. Truter, J. Chem. Soc. A (1967) 1264;
(c) N. Kuramoto, K. Asao, Dyes Pigments 12 (1990) 65;
(d) G. Dessy, V. Fares, C. Bellitto, A. Flamini, Cryst. Struct. Commun. 17 (1982) 1743.
[18] G.A. Bowmaker, P.D.W. Boyd, G.K. Campbell, Inorg. Chem. 22 (1983) 1208. In this paper the redox potentials are given *versus* Ag/AgCl electrode; see also Ref. [7e] cited herein.
[19] (a) X. Gao, W. Wu, Y. Liu, S. Jiao, W. Qiu, G. Yu, L. Wang, D. Zhu, J. Mater. Chem. 17 (2007) 736;
(b) M. Nomura, T. Cauchy, M. Geoffroy, P. Adkine, M. Formique, Inorg. Chem. 45 (2006) 8194;
(c) H. Meng, J. Zheng, A.J. Lovinger, B.C. Wang, P. van Patten, Z. Bao, Chem. Mater. 15 (2003) 1778;
(d) K. Lu, C. Di, H. Xi, Y. Liu, G. Yu, W. Qiu, H. Zhang, X. Gao, Y. Liu, T. Qi, C. Du, D. Zhu, J. Mater. Chem. 18 (2008) 3426;
(e) M.-C. Um, I. Kwark, J.-P. Hong, J. Kang, D.Y. Yoon, S.H. Lee, C. Lee, I.I. Hong, J. Mater. Chem. 18 (2008) 4698;
(f) M. Chikamatsu, A. Itabura, Y. Yoshida, R. Azumi, K. Yase, Chem. Mater. 20 (2008) 7365;
(g) S. Braun, W.R. Salaneck, M. Fahlman, Adv. Mater. 21 (2009) 1450.

of magnetoanisotropy, as measured by the axial, zero-field splitting parameter *D*. An entirely different family of molecular nanomagnets has been recently unearthed with the discovery of single-ion (mononuclear) lanthanide(III) SMM complexes [6]. This innovation represents a crucial step in the miniaturization of nanomagnets [1a].

From the above brief discussion, it is becoming clear that there continues to be a need for new synthetic methods [7] to metal clusters and SMMs. Ligands used in synthesizing 3d-metal clusters are however comparatively restricted and thus discovery of new combinations ("blends") of ligands remains important in the field. With this in mind, we have been exploring "ligand blend" reactions involving carboxylates (RCO_2^-) *and* anioning bridging-chelating ligands (viz., bridging ligands that simultaneously form chelating rings), *with* or *without* additional inorganic annions, e.g., Cl^-, Br^-, NO_3^-, N_3^-, SCN^- and SO_4^{2-}. Besides their deprotonating ability, the RCO_2^- ions are flexible ligands, a consequence of their ability to adopt a number of different ligation modes, both terminal and bridging as well as both monodentate and bidentate. Results with the anionic *gem*-diol derivatives of di-2-pyridyl ketone [5a,b,8], various 2-pyridyloximates [9], a plethora of derivatized salicylaldoximates [5d,10] and the anionic forms of pyridine-2,6-dimethanol [8b,11] have been very encouraging, and a series of Mn, Fe, Co, Ni and Cu carboxylate clusters with nuclearities up to 20 and with interesting properties (including SMM behaviour [5b,c,d,10]) have been prepared.

As part of our continuing search for new ligand combinations in 3d-metal cluster chemistry, we have recently turned our attention to simple 2-pyridyl alcohols that present a kind of structural similarity to 2-pyridyl oximes. Our goals are to investigate to what extent the use of such ligands might affect the identity of the obtained products compared with 2-pyridyl oximes and to what extent this might thus prove to be a route to new cluster types. For example, we have reported [12] that aerobic reactions of $Co(O_2CR)_2$ (R = Me,Ph) with 2-(hydroxymethyl)pyridine (hmpH; for the coordination modes of the neutral ligand and its anion, see Scheme 1), in the presence of ClO_4^- counterions give the hexanuclear, mixed-valence clusters $[Co^{II}_4Co^{III}_2(O_2CR)_4(hmp)_8](ClO_4)_2$ which possess the novel $\{Co^{II}_4Co^{III}_2(\mu_2\text{-}O\acute{R})_4(\mu_3\text{-}O\acute{R})_4\}^{6+}$core [$\acute{R}$ = (2-pyridyl)CH_2–]. In the present work, we report two complexes (one mononuclear, one tetranuclear) resulting from the initial use of hmpH in Ni^{II} acetate chemistry. Ni^{II} with a large single-ion anisotropy and a moderate spin (*S* = 1), may be a good candidate for making SMMs [3b], and there are some reports in the literature of Ni^{II}-based SMMs [13]. The ligand hmpH has been rather extensively used in the synthesis of Mn [14], Fe [15], Co [12] and Cu [16] *carboxylate* clusters, but has been sparingly used with Ni^{II} carboxylates, the only exception being complex $[Ni_4(OH)_2(pypentO)(hmp)(O_2CMe)_2(NCS)_2(H_2O)]$ [17] which contains four (!) bridging ligands [pypentO is the monoanion of 1,5-bis [(2-pyridymethyl)amino] pentane-3-ol]. The deprotonated hmp^- group has been used previously in Ni^{II} *non-carboxlate* chemistry by the groups of Vicente and co-workers [18], Christou/Hendrickson [19] and Hendrickson [20], who reported ferromagnetic cubane clusters (*S* = 4) of the general formula $[Ni_4X_4(hmp)_4(ROH)_4]$ (X = N_3, Cl, Br; R = various), most of which are SMMs. We suspected that there might be a number of Ni^{II}/RCO_2^-/hmp^- cluster species accessible and have therefore been investigating the reactions of hmpH with Ni^{II} carboxylate sources under a variety of conditions; our *initial* investigations on the $Ni(O_2CMe)_2\cdot 4H_2O$/hmpH reaction system are described herein.



Scheme 1. The up-to-now crystallographically confirmed coordination modes of hmpH and hmp^-.

2. Experimental

2.1. General and physical measurements

All manipulations were performed under aerobic conditions using materials (reagent grade) and solvents as received. Microanalyses (C, H, N) were performed by the University of Ioannina (Greece) Microanalytical Laboratory using an EA 1108 Carlo Erba analyzer.

IR spectra (4000–450 cm^{-1}) were recorded on a Perkin–Elmer 16 PC FT-spectrometer with samples prepared as KBr pellets. Magnetic susceptibility measurements in the 1.9–300 K range under a field of 0.5 T were performed with a Quantum Design SQUID-based MPMSXL-5-type magnetometer. The magnetometer was calibrated with a palladium rod sample (Materials Research Corporation, measured purity 99.9985%). The measurements were carried out on polycrystalline samples. Data were corrected for diamagnetic contributions using Pascal's constants; the temperature-independent paramagnetism of the Ni^{II} ion was considered to be $Na = 2.5 \times 10^{-9}$ m^3 mol^{-1} (SI units).

2.2. Compound preparation

2.2.1. $[Ni(O_2CMe)_2(hmpH)_2]$ (**1**)

The ligand hmpH (0.114 ml, 1.20 mmol) was added to an aqueous solution (10 ml) of $Ni(O_2CMe)_2\cdot 4H_2O$ (0.158 g, 0.60 mmol). The resulting blue solution was stirred for about 10 min and was then allowed to slowly concentrate by solvent evaporation at room temperature for a period of 10 d. Well-formed, blue prismatic crystals of the product appeared, which were collected by filtration, washed with Me_2CO (2 × 3 ml) and dried in air; yield 80% (based on the metal). IR (KBr pellet): *v* = 3386 mb, 2838 m, 1600 s, 1568 s, 1480 m, 1416 s, 1358 m, 1286 m, 1236 w, 1154 w, 1082 s, 1048 m, 1024 m, 932 w, 762 m, 730 m, 674 m, 646 m, 492 w cm^{-1}. *Anal.* Calc. for $C_{16}H_{20}NiN_2O_6$: C, 48.65; H, 5.10; N, 7.09. Found: C, 48.69 H, 5.08; N, 7.11%.

2.2.2. $[Ni_4(O_2CMe)_4(hmp)_4(H_2O)_2]\cdot 2.25H_2O\cdot 0.5$(1,4-dioxane) [**2**·2.25H_2O·0.5(1,4-dioxane)]

The ligand hmpH (0.057 ml, 0.60 mmol) was added to an aqueous solution (15 ml) of $Ni(O_2CMe)_2\cdot 4H_2O$ (0.158 g, 0.60 mmol). The resulting deep green solution was stirred for about 15 min, mixed with 1,4-dioxane (10 ml) and left undisturbed in a closed flask at room temperature for about 4 d. Green prismatic crystals of the product formed, which were collected by filtration, washed with Me_2CO (2 × 3 mL) and dried in air; yield 65% (based on the metal). IR (KBr pellet): *v* = 3474 mb, 3356 mb, 2902 m, 2836 m, 1590 s, 1562 s, 1482 m, 1418 s, 1358 m, 1288 m, 1234 w, 1216 w, 1156 w, 1082 s, 1048 m, 1024 m, 818 s, 760 m, 728 m, 672 m, 646 m, 620 w, 498 w, 472 w cm^{-1}. *Anal.* Calc. for $C_{34}H_{48.50}Ni_4N_4O_{17.25}$: C, 39.88; H, 4.77; N, 5.47. Found: C, 39.85; H, 4.78; N, 5.43%.

2.3. Single-crystal X-ray crystallography

A blue prismatic crystal of **1** (0.20 × 0.30 × 0.40 mm) was mounted in air, while a green prismatic crystal of **2**·2.25H_2O·0.5(1,4-dioxane) (0.10 × 0.20 × 0.50 mm) was mounted in capillary. Diffraction measurements for **1** were made on a Nicolet $P2_1$ diffractometer upgraded by Crystal Logic using graphite mono-

chromated Cu radiation. Diffraction measurements for **2**·2.25 H_2O·0.5(1,4-dioxane) were made on a Crystal Logic Dual Goniometer diffractometer using graphite monochromated Mo radiation. Crystal data and details of the data collection and data processing are listed in Table 1. Unit cell dimensions were determined and refined by using the angular settings of 25 automatically centered reflections in the range $22 < 2\theta < 54°$ for **1** and in the range $11 < 2\theta < 23°$ for **2**·2.25H_2O·0.5(1,4-dioxane). Three standard reflections monitored every 97 reflections showed less than 3% variation and no decay for both complexes. Lorentz, polarization and psi-scan absorption corrections were applied using Crystal Logic software.

The structures were solved by direct methods using SHELXS-86 [21] and refined by full-matrix least-squares techniques on F^2 with SHELXL-97 [22]. All hydrogen atoms were located by difference maps and were refined isotropically, except those of the methyl group for structure **2**·2.25H_2O·0.5(1,4-dioxane), which were introduced at calculated positions as riding on their respective bonded atoms. For **1,** all non-hydrogen atoms were refined using anisotropic displacement parameters. All non-hydrogen atoms for **2**·2.25H_2O·0.5(1,4-dioxane) were refined anisotropically, except of the 1,4-dioxane and a water solvate molecule which were refined isotropically with fixed occupation factors. No hydrogen atoms for the solvate molecules were included in the refinement of the structure of **2**·2.25H_2O·0.5(1,4-dioxane).

3. Results and discussion

3.1. Synthetic comments and IR spectra

The chemical and structural identity of the products from the $Ni(O_2CMe)_2$·4H_2O/hmpH reaction system *in H_2O in the absence of counterions*, e.g. ClO_4^-, PF_6^-, Me_4N^+ etc., depends on the Ni^{II}: hmpH reaction ratio. Treatment of $Ni(O_2CMe)_2$·4H_2O with 2 equiv. of hmpH in H_2O leads to the isolation of complex **1**, while the 1:1 reaction gives complex **2**. The preparation of the two compounds is summarized in the balanced Eqs. (1) and (2).

$$Ni(O_2CMe)_2 \cdot 4H_2O + 2hmpH \xrightarrow{H_2O} \underset{\mathbf{1}}{[Ni(O_2CMe)_2(hmpH)_2]} + 4H_2O \quad (1)$$

$$4Ni(O_2CMe)_2 \cdot 4H_2O + 4hmpH \xrightarrow{H_2O} \underset{\mathbf{2}}{[Ni_4(O_2CMe)_4(hmp)_4(H_2O)_2]} + 4MeCO_2H + 14H_2O \quad (2)$$

Few features of the reactions represented by Eqs. (1) and (2) deserve comments. First, the use of different solvents, e.g. MeCN and EtOH, does not affect the identity of the mononuclear product from the 1:2 reaction, but only the quality of the crystals obtained (better crystals were obtained in H_2O); the yields were comparable (70–80%). Second, there is an excess of acetates in the 1:1 reaction (the $MeCO_2^-$: hmpH ratio is 2:1 versus 1:1 in the preparation of **1**). The $MeCO_2^-$ ions play a double role; a quantity of them act as base deprotonating the hmpH ligand, while the remaining acetates behave as ligands. Third, a larger excess of acetates does not lead to another product; the 2:1 $Ni(O_2CMe)_2$·4H_2O/hmpH reaction mixture in H_2O gives again complex **2** (analytical and IR evidences), emphasizing the thermodynamic stability of this neutral tetranuclear cluster. Fourth, compound **2** can be obtained in the form of X-ray quality crystals *only* in the presence of 1,4-dioxane (see Section 2). 1,4-dioxane is a highly non-polar solvent due to its symmetric structure, but it is miscible in all proportions with H_2O [23]. The

Table 1
Summary of crystal data, data collection and structure refinement for the X-ray diffraction study of complexes **1** and **2**·2.25H_2O·0.5(1,4-dioxane).

	1	**2**·2.25H_2O·0.5(1,4-dioxane)
Chemical formula	$C_{16}H_{20}NiN_2O_6$	$C_{34}H_{48.50}Ni_4N_4O_{17.25}$
Formula weight	395.06	1024.11
Colour, habit	blue prisms	green prisms
Crystal size (mm)	0.20 × 0.30 × 0.40	0.10 × 0.20 × 0.50
Crystal system	triclinic	monoclinic
Space group	$P\bar{1}$	$P2_1/n$
a (Å)	7.896(1)	16.671(16)
b (Å)	8.803(1)	13.927(14)
c (Å)	8.504(1)	18.142(18)
α (°)	115.44(1)	90
β (°)	100.13(1)	94.48(3)
γ (°)	115.74(1)	90
V (Å^3)	430.4(1)	4199(7)
Z	1	4
ρ_{calc} (g cm^{-3})	1.524	1.620
T (K)	298	298
Radiation	Cu Kα	Mo Kα
λ (Å)	1.54180	0.71073
μ (mm^{-1})	1.947	1.842
F(0 0 0)	206	2122
Scan mode/speed (° min^{-1})	$\theta - 2\theta/3$	$\theta - 2\theta/2.0$
θ range (°)	7.07–65.00	1.85–25.00
Ranges		
h	−8 → 9	0 → 19
k	−10 → 0	0 → 16
l	−9 → 9	−21 → 21
Measured reflections/unique reflections (R_{int})	1558/1454 (0.0243)	7647/7376 (0.0181)
Reflections used [$I > 2\sigma(I)$]	1427	6005
Parameters refined	155	641
Goodness-of-fit (GOF) (on F^2)	1.078	1.122
R_1[a], wR_2[b] (all data)	0.0299, 0.0791	0.0584, 0.1075
R_1[a], wR_2[b] [$I > 2\sigma(I)$]	0.0294, 0.0787	0.0414, 0.0995
$(\Delta\rho)_{max}/(\Delta\rho)_{min}$ (e Å^{-3})	0.460/−0.241	1.019/−0.696

[a] $R_1 = \Sigma(|F_o| - |F_c|)/\Sigma(|F_o|)$.

[b] $wR_2 = \{\sum[w(F_o^2 - F_c^2)^2]/\sum[w(F_o^2)^2]\}^{1/2}$.

fact that complexes **1** and **2** both contain $MeCO_2^-$ groups and neutral (**1**) or anionic (**2**) 2-(hydroxymethyl)pyridine ligands (the difference being in the number of ligands per Ni^{II} ion) led us suspect that **1** could be transformed into **2** by reacting with an excess of a base; this has indeed turned out to be the case. Treatment of a blue aqueous solution of **1** with 2 equiv. of NaOH led to a green solution and subsequent precipitation of **2** in low yields (<20%) upon slow evaporation of H_2O at room temperature over a period of several days, see Eq. (3); due to the low yield, the preparation of **2** using this method is not given in Section 2. Addition of 1,4-dioxane or Me_2CO in the reaction solution increases the yield, but the product is contaminated with NaO_2CMe and Na(hmp) [IR evidence, presence of colourless microcrystals on the surface of the blue precipitate].

$$4\underset{\mathbf{1}}{[Ni(O_2CMe)_2(hmpH)_2]} + 8NaOH \xrightarrow{H_2O} \underset{\mathbf{4}}{[Ni_4(O_2CMe)_4(hmp)_4(H_2O)_2]} + 4NaO_2CMe + 4Na(hmp) + 6H_2O \quad (3)$$

The IR spectra of **1** and **2**·2.25H_2O·0.5(1,4-dioxane) exhibit medium intesity broad bands in the region 3500–3350 cm^{-1} assignable to the ν(OH) vibration of hmpH [24] and coordinated/lattice H_2O, respectively. The broadness and relatively low frequency of these bonds are both indicative of hydrogen bonding. The in-plane deformation band of the 2-pyridyl ring appears at 674 and 672 cm^{-1} for **1** and **2**, respectively; the high wavenumber for this vibration confirms the involvement of the ring-N atom in coordination [24]. The strong bands at 1600 and 1416 cm^{-1} in the spectrum of **1** are assigned [12,25] to the $\nu_{as}(CO_2)$ and $\nu_s(CO_2)$ vibrations, respectively, of the acetato ligands, both having also a ring stretching character. The difference Δ, where $\Delta = \nu_{as}(CO_2) - \nu_s(CO_2)$, is 184 cm^{-1}, more than that for NaO_2CMe (164 cm^{-1}), as expected for the monodentate mode of the carboxylate ligation [25]. Owing to the presence of two different types of carboxylate ligation (monodentate, bidentate bridging; vide infra) in **2**, two $\nu_{as}(CO_2)$ and two $\nu_s(CO_2)$ bands appear in its spectrum; the modes are strongly coupled with ring stretching vibrations and the proposed assignments should be regarded as approximate descriptions of the vibrations. The 1590, 1418 cm^{-1} pair (Δ = 172 cm^{-1}) are assigned to the monodentate acetates, while the 1562, 1435 cm^{-1} pair (Δ = 127 cm^{-1}) to the bidentate bridging carboxylate groups [25].

3.2. Description of structures

Partially labeled plots of the mononuclear molecule present in complex **1** and the tetranuclear cluster present in complex **2**·2.25H_2O·0.5(1,4-dioxane) are shown in Figs. 1 and 2, respectively. Selected interatomic distances and angles for the two complexes and hydrogen bonding details for **2**·2.25H_2O·0.5(1,4-dioxane) are listed in Tables 2–4.

Complex **1** crystallizes in the triclinic space group $P\bar{1}$. Its structure consists of well-separated $[Ni(O_2CMe)_2(hmpH)_2]$ molecules, with the metal ion lying on an inversion center. The Ni^{II} center is coordinated by two monodentate $MeCO_2^-$ groups (1.10 adopting the Harris notation [26]) and two *N*,*O*-chelating (1.11, Scheme 1) hmpH ligands. The hmpH donor atoms are the oxygen atom of the –OH group and the nitrogen atom of the 2-pyridyl group. The coordination sphere of the Ni^{II} ion exhibits a distorted octahedral geometry; the distortion is a consequence of the relatively small bite angle of the chelating ligand [O(1)–Ni–N(1) = 80.9(1)°]. The Ni–(N,O) bond lengths agree well with values observed for bonds of the some nature in octahedral complexes [24a,27]. There is a very strong intramolecular H-bond between the –OH group and the unbound acetate oxygen [O(3)]. The dimensions are: O(1)–HO(1)···O(3) 2.493 Å, HO(1)···O(3) 1.480 Å, O(1)–HO(1)···O(3) 167.9°. There are neither intermolecular H-bonds nor π–π stacking interactions. Complex **1** joins a very small family of $[NiX_2(hmpH)_2]$ [24a,28] and $[Ni(H_2O)_2(hmpH)_2]^{2+}$ [29] complexes, where X is a

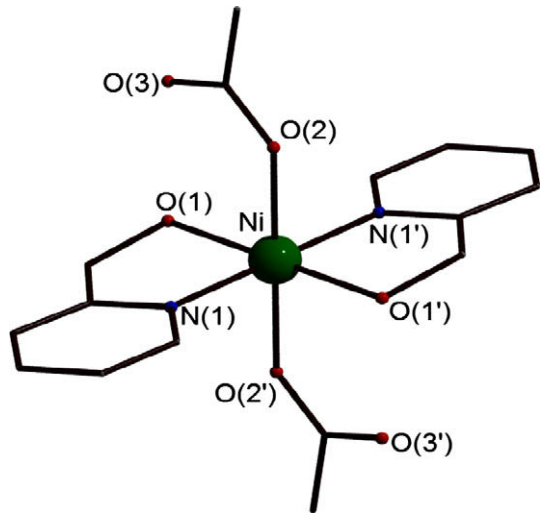


Fig. 1. Partially labeled plot of the molecule present in complex **1**. H atoms have been omitted for clarity. Primes are used for the symmetry-related atoms.

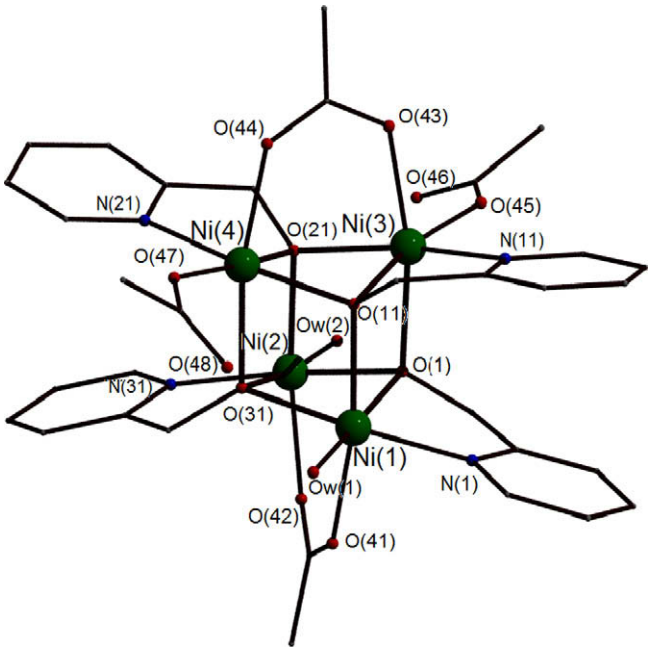


Fig. 2. Partially labeled plot of the tetranuclear cluster molecule present in complex **2**·2.25H_2O·0.5(1,4-dioxane). H atoms have been omitted for clarity.

Table 2
Selected interatomic distances (Å) and angles (°) for complex **1**.[a]

Ni–O(1)	2.074(1)	Ni–N(1)	2.047(2)
Ni–O(2)	2.097(1)		
O(1)–Ni–O(1′)	180.0(1)	O(2)–Ni–O(2′)	180.0(1)
O(1)–Ni–O(2)	91.3(1)	O(2)–Ni–N(1)	92.2(1)
O(1)–Ni–O(2′)	88.7(1)	O(2)–Ni–N(1′)	87.8(1)
O(1)–Ni–N(1)	80.9(1)	N(1)–Ni–N(1′)	180.0(1)
O(1)–Ni–N(1′)	99.2(1)		

[a] Symmetry code: (′) = −*x*, −*y*, −*z*.

Table 3
Selected interatomic distances (Å) and angles (°) for complex **2**·2.25H_2O·0.5(1,4-dioxane).

Ni(1)–O(1)	2.052(3)	Ni(3)–O(43)	2.078(3)
Ni(1)–O(11)	2.076(3)	Ni(3)–O(45)	2.039(3)
Ni(1)–O(31)	2.061(3)	Ni(3)–N(11)	2.070(4)
Ni(1)–O(41)	2.104(3)	Ni(4)–O(11)	2.049(3)
Ni(1)–Ow(1)	2.039(4)	Ni(4)–O(21)	2.087(3)
Ni(1)–N(1)	2.064(4)	Ni(4)–O(31)	2.089(3)
Ni(2)–O(1)	2.057(3)	Ni(4)–O(44)	2.067(4)
Ni(2)–O(21)	2.068(3)	Ni(4)–O(47)	2.034(3)
Ni(2)–O(31)	2.066(3)	Ni(4)–N(21)	2.081(4)
Ni(2)–O(42)	2.093(3)	Ni(1)···Ni(2)	2.889(2)
Ni(2)–Ow(2)	2.012(4)	Ni(1)···Ni(3)	3.220(3)
Ni(2)–N(31)	2.063(4)	Ni(1)···Ni(4)	3.195(3)
Ni(3)–O(1)	2.090(3)	Ni(2)···Ni(3)	3.179(3)
Ni(3)–O(11)	2.119(3)	Ni(2)···Ni(4)	3.183(3)
Ni(3)–O(21)	2.067(3)	Ni(3)···Ni(4)	2.956(3)
O(1)–Ni(1)–O(11)	79.8(1)	O(11)–Ni(3)–O(43)	95.3(1)
O(1)–Ni(1)–O(31)	87.8(1)	O(11)–Ni(3)–O(45)	168.1(1)
O(1)–Ni(1)–O(41)	96.8(1)	O(11)–Ni(3)–N(11)	78.5(1)
O(1)–Ni(1)–Ow(1)	172.5(1)	O(21)–Ni(3)–O(43)	90.9(1)
O(1)–Ni(1)–N(1)	80.3(1)	O(21)–Ni(3)–O(45)	105.4(1)
O(11)–Ni(1)–O(31)	78.9(1)	O(21)–Ni(3)–N(11)	163.8(1)
O(11)–Ni(1)–O(41)	168.0(1)	O(43)–Ni(3)–O(45)	89.8(1)
O(11)–Ni(1)–Ow(1)	94.3(1)	O(43)–Ni(3)–N(11)	90.6(1)
O(11)–Ni(1)–N(1)	101.9(1)	O(45)–Ni(3)–N(11)	90.8(2)
O(31)–Ni(1)–O(41)	89.5(1)	O(11)–Ni(4)–O(21)	86.6(1)
O(31)–Ni(1)–Ow(1)	95.6(1)	O(11)–Ni(4)–O(31)	78.9(1)
O(31)–Ni(1)–N(1)	167.6(1)	O(11)–Ni(4)–O(44)	91.9(1)
O(41)–Ni(1)–Ow(1)	89.9(2)	O(11)–Ni(4)–O(47)	102.9(1)
O(41)–Ni(1)–N(1)	88.7(1)	O(11)–Ni(4)–N(21)	165.7(1)
Ow(1)–Ni(1)–N(1)	96.6(2)	O(21)–Ni(4)–O(31)	79.5(1)
O(1)–Ni(2)–O(21)	80.1(1)	O(21)–Ni(4)–O(44)	93.2(1)
O(1)–Ni(2)–O(31)	87.5(1)	O(21)–Ni(4)–O(47)	170.0(1)
O(1)–Ni(2)–O(42)	90.8(1)	O(21)–Ni(4)–N(21)	79.1(1)
O(1)–Ni(2)–Ow(2)	92.2(2)	O(31)–Ni(4)–O(44)	168.5(1)
O(1)–Ni(2)–N(31)	166.9(1)	O(31)–Ni(4)–O(47)	99.3(1)
O(21)–Ni(2)–O(31)	80.5(1)	O(31)–Ni(4)–N(21)	99.0(1)
O(21)–Ni(2)–O(42)	169.9(1)	O(44)–Ni(4)–O(47)	89.4(1)
O(21)–Ni(2)–Ow(2)	92.2(1)	O(44)–Ni(4)–N(21)	88.3(1)
O(21)–Ni(2)–N(31)	101.1(1)	O(47)–Ni(4)–N(21)	91.4(2)
O(31)–Ni(2)–O(42)	95.0(1)	Ni(1)–O(1)–Ni(2)	89.4(1)
O(31)–Ni(2)–Ow(2)	172.6(1)	Ni(1)–O(1)–Ni(3)	102.0(1)
O(31)–Ni(2)–N(31)	79.8(1)	Ni(1)–O(11)–Ni(3)	100.2(1)
O(42)–Ni(2)–Ow(2)	92.5(1)	Ni(1)–O(11)–Ni(4)	101.5(1)
O(42)–Ni(2)–N(31)	86.8(1)	Ni(1)–O(31)–Ni(2)	88.9(1)
Ow(2)–Ni(2)–N(31)	100.8(2)	Ni(1)–O(31)–Ni(4)	100.7(1)
O(1)–Ni(3)–O(11)	77.9(1)	Ni(2)–O(1)–Ni(3)	100.1(1)
O(1)–Ni(3)–O(21)	79.3(1)	Ni(2)–O(21)–Ni(3)	100.5(1)
O(1)–Ni(3)–O(43)	168.4(1)	Ni(2)–O(21)–Ni(4)	100.0(1)
O(1)–Ni(3)–O(45)	98.6(1)	Ni(2)–O(31)–Ni(4)	100.0(1)
O(1)–Ni(3)–N(11)	97.4(1)	Ni(3)–O(11)–Ni(4)	90.3(1)
O(11)–Ni(3)–O(21)	85.4(1)	Ni(3)–O(21)–Ni(4)	90.7(1)

monodentate anionic ligand; the structure of the 1:3 complex *mer*-[Ni(hmpH)$_3$]Cl_2 has also been recently reported [30].

Complex **2**·2.25H_2O·0.5(1,4-dioxane) crystallizes in monoclinic space group $P2_1/n$. Its structure consists of tetranuclear [$Ni_4(O_2CMe)_4(hmpH)_4(H_2O)_2$] molecules (Fig. 2), and solvate H_2O and 1,4-dioxane molecules; the latter two will not be further discussed. The tetranuclear cluster molecule has a distorted cubane {$Ni_4(\mu_3\text{-}OR')_4$}$^{4+}$ core with Ni^{II} and oxygen atoms occupying alternate vertices of the cube [R′ = (2-pyridyl)CH_2–]. Thus, the molecule consists of two interpenetrating tetrahedra: one of four Ni^{II} ions and one of four μ_3 oxygen atoms originating from the hmp$^-$ ligands. In addition to three μ_3-oxygen atoms, each Ni^{II} center is coordinated to one 2-pyridyl nitrogen atom. For Ni(3) and Ni(4), the remaining two coordination sites per metal ion are occupied by two oxygen atoms coming from one 2.11 and one 1.10 $MeCO_2^-$ groups. The Ni(1) and Ni(2) ions are each coordinated by one aqua ligand and one oxygen atom from the second 2.11 $MeCO_2^-$ ligand. Thus, an octahedral coordination environment is created about each metal center, all chromophores being of the $Ni^{II}O_5N$ type. One octahedral face of each Ni^{II} ion is occupied by the three alkoxide-type oxygen atoms and another contains the remaining donor atoms.

Each hmp$^-$ ion functions as a 3.31 ligand (Scheme 1) forming a five-membered NiNCCO chelating ring with a metal ion and two alkoxide-type bonds to two other Ni^{II} ions. This ligation mode is common for hmp$^-$ [19,20]. Two $MeCO_2^-$ groups are monodentate, while the remaining two behave as 2.11 ligands capping two opposite faces of the cube diagonally. The metal centers that are bridged by the $MeCO_2^-$ ions have the shortest metal–metal distances [Ni(1)···Ni(2) 2.889, Ni(3)···Ni(4) 2.956 Å].

There are two types of Ni–O (alkoxide-type) bonds for each metal ion: one bond is rather short at an average distance of 2.056 Å, whereas the two other bonds are slightly longer (average distance 2.082 Å). The cube deviates from the ideal geometry. The internal cube angles (R′O–Ni–OR′) at the metal vertices average 81.9°, whereas the corresponding angles at the alkoxide corners are much larger averaging 97.0°. The Ni···Ni vectors in the cluster reflect the different Ni–O (alkoxide-type) bond lengths, with the Ni(1)···Ni(3) distance (3.220 Å) being the longest. The shortest Ni(1)···Ni(2) distance (2.889 Å) corresponds to the smaller Ni–O–Ni angles [Ni(1)–O(1)–Ni(2) 89.4, Ni(1)–O(31)–Ni(2) 88.9°], whereas the longest Ni(1)···Ni(3) distance involves the larger Ni–O–Ni angle [Ni(1)–O(1)–Ni(3) 102.0°]. The average Ni–N and Ni–O (alkoxide-type) bond lengths of 2.070 and 2.073 Å, respectively, lie well within the range of reported values for the corresponding bond lengths of other cubane Ni^{II} clusters involving the hmp$^-$ ligand [18–20].

There is an amount of H-bonding in **2**·2.25H_2O·0.5(1,4-dioxane), see Table 4. Each coordinated H_2O molecule is strongly intramolecularly H-bonded to an unbound $MeCO_2^-$ oxygen atom [O(46), O(48)]. One of the aqua ligands [OW(2)] forms an intercubane H-bond with a coordinated $MeCO_2^-$ O atom [O(42)] of a neighbouring tetranuclear molecule. There is also an indication of the presence of H-bonds involving the lattice H_2O molecules; however, due to the fact that their hydrogen atoms were not located, those H-bonds can not be considered in detail. The intermolecular H-bonding interactions form a 2D network which extends parallel to the *ab* crystallographic plane (Fig. S1).

Complex **2** joins a rather large family of Ni_4^{II} cubanes with a {$Ni_4(\mu_3\text{-}OR)_4$}$^{+4}$ core [13c,17–20,27b,31–33]. Williams, Decurtins and co-workers have recently reported [31] a critical survey of the crystal structures containing {$Ni_4(OR)_4$} cubane units. They

Table 4
Hydrogen bonding interactions in complex **2**·2.25H_2O·0.5 (1,4-dioxane).[a]

Interaction	D···A (Å)	H··· A (Å)	D–H···A (°)	Symmetry operator of A
OW(1)–HOW(1B)···O(48)	2.589	1.685	162.5	*x*, *y*, *z*
OW(2)–HOW (2B)···O(46)	2.655	1.807	171.8	*x*, *y*, *z*
OW(2)–HOW(2A)···O(42)	2.749	2.111	176.6	$-x$, $-y$, $1-z$
OW(1)–HOW(1B)···OW(3)[b]	2.930	2.146	166.0	$1-x$, $-y$, $1-z$

[a] A = acceptor, D = donor.
[b] Atom OW(3) (not shown in Fig. 2) belongs to the lattice H_2O molecule.

showed that the average Ni···Ni distances in such complexes is relatively constant. The structures are all distorted from the idealized cube to a T_d symmetry, and most show a further distortion which, however, usually maintains some elements of symmetry. The Ni···Ni distances afford a simple method of analyzing the distortion of the Ni_4 tetrahedron. If the tetrahedron is distorted by extension along a S_4 axis, four Ni···Ni distances will be increased, and two others will remain the same (S_4+ distortion); an S_4+ distortion will increase eight of the Ni–O–Ni angles, and decrease four. Perusal of the Ni···Ni distances and Ni–O–Ni angles for **2** (Table 3) reveals that the distortion mode of the Ni_4 tetrahedron is S_4+.

Complex **2** is a new, welcome addition in the subfamily of the Ni^{II}/hmp$^-$ cubanes. All [18–20], but one [17], contain four 3.31 hmp$^-$ groups. This coordination mode for the four ligands leaves totally eight unoccupied coordination sites, two for each metal center. In the cubanes prepared by the group of Escuer et al. [18], the peripheral ligation is provided by Cl^- or N_3^- groups and MeOH ligands. In the cubanes prepared and studied by the groups of Christou/Hendrickson [19,20], the peripheral ligation is provided by Cl^- or Br^- ligands and a variety of primary alcohols. In the Winter's cubane [34], the coordination number six for each Ni^{II} center is completed by one chelating *O*-ethylxanthate-*S*,*S*′ ligand. In all the just mentioned $4Ni^{II}$/4hmp$^-$ cubanes, the only bridging groups are the μ_3 oxygen atoms of the 3.31 hmp$^-$ ligands. Thus, complex **2** is a unique example amongst these complexes where two opposite faces of the cube are each capped by an additional bridging ligand, i.e., the $MeCO_2^-$ group. *This seems to have an influence on the magnetic properties of cluster* **2**.

3.3. Magnetic study of complex *2*

Solid-state dc magnetic susceptibility measurements were performed on polycrystalline sample of complex **2**, under a constant field of 0.1 T in the temperature range 1.9–300 K.

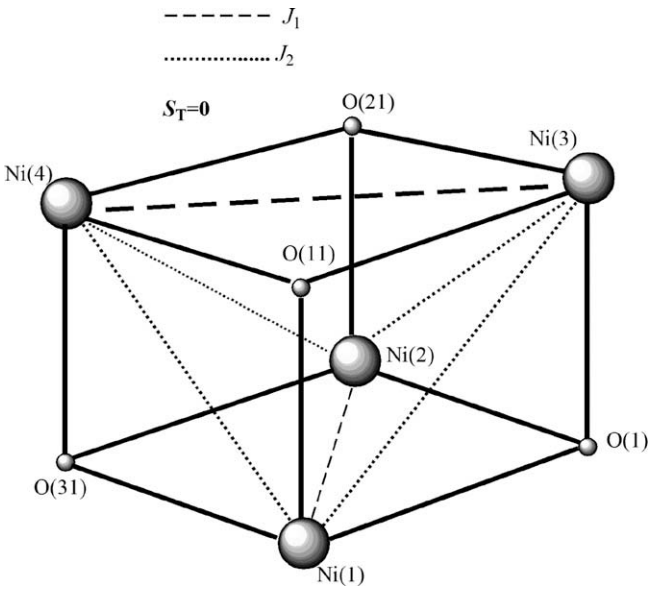
The exchange coupling of four $S = 1$ centers results in $n = 3^4 = 81$ molecular magnetic states which are split into 3 singlets ($S = 0$), 6 triplets ($S = 1$), 6 quintets ($S = 2$), 3 septets ($S = 3$) and 1 nonet ($S = 4$). Depending upon the actual topology, these states can be degenerate (the case of a perfect tetrahedron with a single exchange coupling constant) or the degeneracy can be partially removed.

The structural parameters of **2** suggest a lower symmetry than T_d. The magnetic analysis was carried out using a 2-*J* model and assuming that the tetranuclear structure results from the association of two doubly-bridged dimeric units, see Scheme 2. The intradimer interaction (denoted J_1) is between Ni(1) and Ni(2) on the one hand and between Ni(3) and Ni(4), on the other hand (the numbering scheme used for the magnetic analysis is the same with that employed in the real structure; see Fig. 2), while the interdimer one is denoted J_2. The spin Hamiltonian for such a model, reflecting the S_4 symmetry, is given by Eq. (4).

$$\hat{H}(\mathbf{S}_4) = -J_1(\vec{S}_1\cdot\vec{S}_2+\vec{S}_3\cdot\vec{S}_4) - J_2(\vec{S}_1\cdot\vec{S}_3+\vec{S}_1\cdot\vec{S}_4+\vec{S}_2\cdot\vec{S}_3+\vec{S}_2\cdot\vec{S}_4) + \mu_B Bg(\vec{S}_1+\vec{S}_2+\vec{S}_3+\vec{S}_4) \quad (4)$$

The Hamiltonian matrix in the basis set of coupled kets $|S_1S_2S_{12}S_3S_4S_{34}SM\rangle$ is already diagonal, so that the energy levels are given by a simple formula (Eq. (5)),

$$\begin{aligned}\varepsilon_{B=0}(S) &= \langle S_{12}S_{34}SM|\hat{H}(\mathbf{S}_4)|S_{12}S_{34}SM\rangle \\ &= -(J_2/2)[S(S+1)-S_{12}(S_{12}+1)-S_{34}(S_{34}+1)] \\ &\quad -(J_1/2)[S_{12}(S_{12}+1)+S_{34}(S_{34}+1)] \\ &\quad +(J_1/2)[S_1(S_1+1)+S_2(S_2+1)+S_3(S_3+1)+S_4(S_4+1)]\end{aligned} \quad (5)$$



Scheme 2. Core representation of the tetranuclear molecule of **2** showing the coupling scheme used in the magnetic model. The numbering scheme from Fig. 4 has been used.

where the last, constant term can be omitted. The addition of the Zeeman term results in the formula given by Eq. (6), where a single, isotropic g_{iso}-factor common to all magnetic centers occurs. The identification of the van Vleck coefficients is now an easy task, so that one can apply the van Vleck equation (with a vanishing second-order term) to end up with an analytical formula (Eq. (7)) for the mean magnetic susceptibility, i.e.

$$\varepsilon_B(S,M) = \varepsilon_{B=0}(S) + \mu_B g_{iso} MB \quad (6)$$

$$\tilde{\chi}_{mol} = C_0\frac{g_{iso}^2}{T}\frac{\sum_S\sum_{M=-S}^{+S}M^2\exp[-\varepsilon_{B=0}(S)/kT]}{\sum_S\exp[-\varepsilon_{B=0}(S)/kT]} \quad (7)$$

where the physical constants in the reduced Curie constant $C_0 = N_A\mu_0\mu_B^2/k$ adopt their usual meaning.

There is an evidence for a paramagnetic impurity, in the complex. This admixture has been involved by assuming

$$\chi = (1-x_{PI})\chi^{tetramer} + 4x_{PI}\chi^{monomer} \quad (8)$$

where the Curie law was assumed for the monomer

$$\chi^{monomer} = C_0(g_{PI}^2/T)[S_{PI}(S_{PI}+1)/3] \quad (9)$$

with $S_{PI} = 1$, $g_{PI} = 2.0$.

Fig. 3 shows plots of the experimental data for **2** in the forms of μ_{eff} (effective magnetic moment) per complex, χ_{mol} and χ_{mol}^{-1} versus *T*. The value of μ_{eff} at 300 K is 6.13 μ_B. As the temperature is lowered, μ_{eff} experiences a slight decrease, reaching a value of 5.82 μ_B at 50 K, followed by a much sharper decline at lower temperatures, 1.48 μ_B at 1.9 K. The best fit parameters ($R = 0.057$) are found to be $J_1 = -10.1$ cm^{-1}, $J_2 = -3.14$ cm^{-1} and $g_{iso} = 2.28$.

The zero-field energy levels of **2** are shown in Fig. 4. At temperatures above 100 K, all the levels are almost equally populated, so that the Curie law is obeyed. On cooling, the highest-spin states are consecutively depopulated and thus the magnetic productivity of the populated states gradually decreases to zero at zero temperature (the ground state is a singlet); under the term "magnetic productivity" we mean the contribution of the state $g^2M^2\exp[\varepsilon_{B=0}(S)/kT]$ to the susceptibility function and/or the effective magnetic moment. The low-temperature data for **2** are modulated by the Curie-type susceptibility for the paramagnetic impurity which superimposes the susceptibility curve of the tetranuclear molecule.

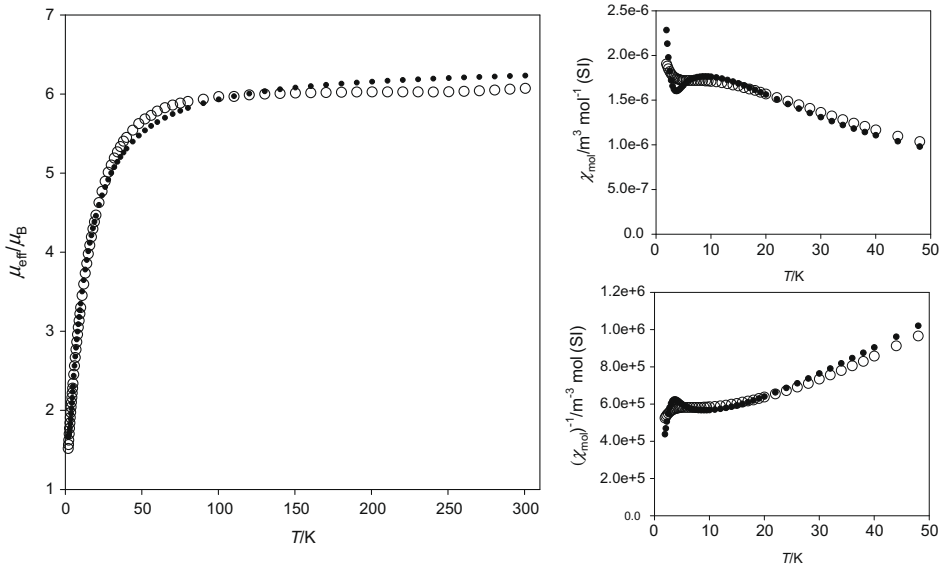


Fig. 3. Plots of experimental (open circles) μ_{eff} (left), χ_{mol} (right up) and χ_{mol}^{-1} (right bottom) vs. T per molecule of **2**. The filled circles are the fits to the experimental data (see text for details).

The magnetic susceptibility of cubane complexes has been studied extensively in recent years. Their high nuclearity and the magnetic exchange pathways offered by the triply bridging oxygen atoms make them particularly interesting, and several complexes have shown potential as SMMs [13c,19,20,35]. The effective magnetic moments of the Ni^{II} cubanes fall into two classes [31]. Type A is generally the most common and shows a rise in μ_{eff} per molecule at low temperatures, until a sharp drop is observed below ~10 K. Type B shows a steady drop in μ_{eff} in the range 100–50 K tending towards zero at very low temperatures. The S_4+ distortion mode of the Ni_4^{II} tetrahedron favours type B behaviour [31]. It is clear from Fig. 3 (left) that compound **2** follows a type B behaviour.

It should be mentioned at this point that the most important parameter in the magnetostructural correlation of tetranuclear clusters possessing the $\{Ni_4(\mu_3\text{-}OR)_4\}^{4+}$ cubane core has been reported [17,27b,31–33,36] to be the average Ni–O–Ni angle of a cubane face. A ferromagnetic exchange interaction is observed for Ni–O–Ni angles lower than 99° and the J value increases as the angle decreases. On the other hand, Ni–O–Ni angles in the vicinity of, and larger than, 99° lead to an antiferromagnetic interaction and the $|J_1|$ value increases as the angle increases. A second, less-significant parameter has been proposed to be the Ni–O–O–Ni torsion angle. The value and the sign ($-3.14\ cm^{-1}$) of the interdimer J_2 parameter (see also Scheme 2) are in line with the previous studies mentioned above. The mean Ni–O–Ni angle for the four Ni_2^{II} pairs (faces of the cube) described by J_2 is 100.6 (1)°; the coupling is thus predicted to be weakly antiferromagnetic, and, indeed, it is. The value of $-3.14\ cm^{-1}$ matches fairly well the linear J versus Ni–O–Ni bridging angle curve established by Christou and co-workers [36] for complexes containing the $\{Ni_4(\mu_3\text{-}OR)_4\}^{4+}$ cubane core. *What was unexpected is the antiferromagnetic value for* J_1 (*$-10.1\ cm^{-1}$*). The opposite faces of the cube including both μ_3-OR'^{-} and $MeCO_2^-$ bridges [Ni(1)O(1)Ni(2)O(31) and Ni(3)O(11)Ni(4)O(21), Fig. 2] have all Ni–O–Ni angles (Table 3) close to orthogonality, the average value being 89.8°. The J_1 coupling parameter that characterizes the Ni(1)···Ni(2) and Ni(3)···Ni(4) exchange interactions was thus expected to be ferromagnetic [17,27b,31–33,36], in agreement with the expectation that the Ni^{II} e_g electrons will couple ferromagnetically through oxygen p orbitals for Ni–O–Ni angles of ~90°. The only *tentative* explanation we can offer for the moment for this discrepancy is the presence of the additional syn, syn bridging $MeCO_2^-$ ligand which caps each of the above mentioned faces. The acetate bridge can provide an additional pathway for antiferromagnetic coupling [17,36], which seems to be strong enough in the case of **2** overcoming the ferromagnetic exchange arising from the triply bridging oxygen atoms of the hmp^- ligands. An analogous effect has been reported previously for complexes $[Ni_4(OH)_2(pypentO)(hmp)(O_2CMe)_2(NCS)_2(H_2O)]$ [17] and $[Ni_4(OMe)_4(O_2CMe)_2(TMB)_4](BPh_4)_2$ [37] which both have two syn, syn bridging (2.11) $MeCO_2^-$ ligands on opposite faces of the cube (TMB is 2,5-dimethyl-2,5-diisocyanohexane); however, in these two complexes the exchange interaction was ferromagnetic, but in both cases the J value was much lower than the predicted on the basis of the correlation established by Christou and co-workers [36]. In complete agreement with this explanation, the cubane complexes $[Ni_4X_4(hmp)_4(ROH)_4]$ [19,20], which do *not* contain additional bridging ligands, are all characterized by ferromagnetic exchange interactions and an $S = 4$ ground state. It should be mentioned at this point that a similar explanation was used by Winpenny to explain the magnetic properties of the $[Ni_4(Piv)_4(Mq)_4]$ cubane [32f], where Piv^- is the pivalate group and Mq^- the anion of 8-hydroxyquinaldine. The mean Ni–O–Ni angle for four Ni_2 pairs is 93.9° in this complex, thus, according to the established magnetostructural

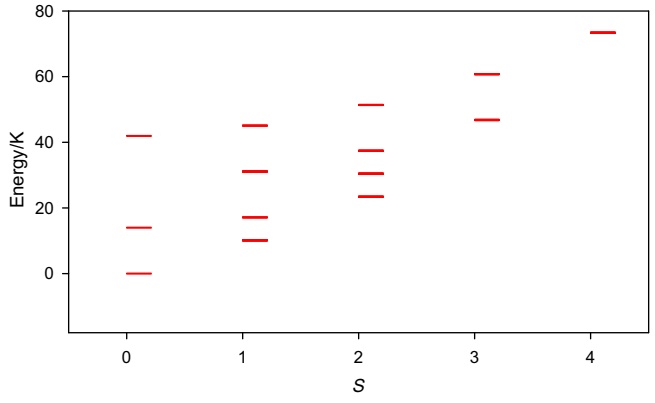


Fig. 4. Calculated spin energy levels for individual total spins in complex **2**.

criteria the coupling is predicted to be ferromagnetic. The fact that the coupling within the four pairs is antiferromagnetic was explained by the presence of an additional carboxylate bridge from the Piv^- ligands in a syn, syn fashion, which favours the antiferromagnetic contribution to the coupling. We refrain from discussing more the unusual J_1 because work is in progress in our laboratories to prepare $[Ni_4(O_2CR)_4(hmp)_4S_2]$, $[Ni_4(O_2CR)_4(hmp)_4]$ and $[Ni_4(O_2CR)_2(hmp)_4S_4]^{2+}$ cubanes (R = various, S = solvent) containing two or four bridging carboxylate groups; their magnetic study will hopefully help us to clarify the presence of ferromagnetic or antiferromagnetic exchange interactions within Ni_2 pairs characterized by low Ni–O–Ni angles and involving carboxylate bridging [38].

4. Concluding comments and perspectives

The present extension of the use of the hmpH ligand in Ni^{II} chemistry is a further demonstration of the ability of this group to yield products with interesting structures and properties. In addition to the Ni^{II}/hmpH and Ni^{II}/hmp^- complexes reported previously and prepared from non-carboxylate Ni^{II} sources, the $Ni^{II}/MeCO_2^-$/hmpH reaction system has provided access to the mononuclear compound **1** and to the antiferromagnetically-coupled, cubane cluster **2**. The latter is a new, welcome addition to the small subfamily of cubane Ni^{II} clusters containing 3.31 hmp^- ligands. Of particular magnetochemical interest is the antiferromagnetic coupling between the Ni^{II} centers that are additionally bridged by $MeCO_2^-$ ligands despite the small (~90°) Ni^{II}–$(\mu_3\text{-}O)_{hmp}^-$–Ni^{II} angles. This matter warrants further investigation and we currently try to prepare a family of structurally similar Ni^{II}/hmp^- cubanes with a variety of carboxylate groups ($Me_3CCO_2^-$, $PhCO_2^-$, $ClCH_2CO_2^-$, etc.).

Both **1** and **2** have been prepared from aqueous media in the absence of counterions. Of particular interest would be the synthetic investigation of the Ni^{II}/RCO_2^-/hmpH and the Ni^{II}/RCO_2^-/hmpH/ClO_4^- or PF_6^- reaction systems in organic solvents. The latter system would hopefully give cubanes with non-bridging RCO_2^- groups, which might introduce ferromagnetic components in the superexchange scheme leading to Ni_4^{II} clusters with an $S = 4$ ground state. The analogue of **2** with 2-(hydroxyethyl)pyridine, hepH, is not known to date, and it is currently not evident whether the preparation and stability of such neutral cubanes are dependent on the nature of the aliphatic chain that connects the 2-pyridyl ring with the hydroxyl oxygen. Work along these lines is currently in progress in our groups.

Acknowledgements

S.P.P. thanks the European Social Fund, the Operational Program for Educational and Vocational Training II (EPEAEK II) and particularly the program PYTHAGORAS (Grant b.365.037) for funding this research. Slovak grant agencies (VEGA 1/2453/05, APVT 20-005204), the Polish Ministry of Science and Computerization, and the 6th Framework Programme EU NoE MAGMANet are also acknowledged.

Appendix A. Supplementary data

CCDC 726561 and 726560 contain the supplementary crystallographic data for **1** and **2**·2.25H_2O·0.5(1,4-dioxane). These data can be obtained free of charge via http://www.ccdc.cam.ac.uk/conts/retrieving.html, or from the Cambridge Crystallographic Data Centre, 12 Union Road, Cambridge CB2 1EZ, UK; fax: (+44) 1223-336-033; or e-mail: deposit@ccdc.cam.ac.uk. Supplementary data associated with this article can be found, in the online version, at doi:10.1016/j.poly.2009.06.049.

References

[1] (a) E. Coronado, K.R. Dundar, Inorg. Chem. 48 (2009) 3293 (preface for the forum of this journal on molecular magnetism);
(b) M. Verdaguer, D. Gatteschi, CR Chimie 11 (2008) 1083 (foreword for the special issue of this journal concerning new trends in molecular magnetism);
(c) D. Gatteschi, L. Bogani, A. Cornia, M. Mannini, L. Sorace, R. Sessoli, Solid State Sci. 10 (2008) 1701.
[2] D. Gatteschi, R. Sessoli, J. Villain, Molecular Nanomagnets, Oxford University Press, Oxford, UK, 2006.
[3] (a) For excellent reviews, see: M. Murrie, D.J. Pric, Annu. Rep. Prog. Chem., Sect. A 103 (2007) 20;
(b) G. Aromi, E.K. Brechin, Struct. Bond. 122 (2006) 1;
(c) R. Bircher, G. Chaboussant, C. Dobe, H. Güdel, S.T. Ochsenbein, A. Sieber, O. Waldman, Adv. Funct. Mater. 16 (2006) 209;
(d) D. Gatteschi, R. Sessoli, Angew. Chem., Int. Ed. 42 (2003) 268;
(e) G. Christou, D. Gatteschi, D.N. Hendrickson, R. Sessoli, MRS Bull. 25 (2000) 66;
(f) J.R. Long, in: P. Yang (Ed.), Chemistry of Nanostructured Materials, World Scientific Publishing, Hong Kong, 2003, pp. 291–315;
(g) R. Bagai, G. Christou, Chem. Soc. Rev. 38 (2009) 1011 (Tutorial Review).
[4] (a) L. Bogani, A. Vindigni, R. Sessoli, D. Gatteschi, J. Mater. Chem. 18 (2008) 4750;
(b) C. Coulon, H. Miyasaka, R. Clérac, Struct. Bond. 122 (2006) 163;
(c) A. Caneschi, D. Gatteschi, N. Lalioti, C. Sangregorio, R. Sessoli, G. Venturi, A. Vindigni, A. Retori, M.G. Pini, M.A. Novak, Angew. Chem., Int. Ed. 40 (2001) 1760.
[5] (a) Recent, representative work with the involvement of our group: Th.C. Stamatatos, V. Nastopoulos, A.J. Tasiopoulos, E.E. Moushi, W. Wernsdorfer, G. Christou, S.P. Perlepes, Inorg. Chem. 47 (2008) 10081;
(b) A.K. Boudalis, Y. Sanakis, J.M. Clemente-Juan, B. Donnadieu, V. Nastopoulos, A. Mari, Y. Coppel, J.-P. Tuchagues, S.P. Perlepes, Chem. Eur. J. 14 (2008) 2514;
(c) Th.C. Stamatatos, D. Foguet-Albiol, S.-C. Lee, C.C. Stoumpos, C.P. Raptopoulou, A. Terzis, W. Wernsdorfer, S.O. Hill, S.P. Perlepes, G. Christou, J. Am. Chem. Soc. 129 (2007) 9489;
(d) C.J. Millios, A. Vinslava, P.A. Wood, S. Parsons, W. Wernsdorfer, G. Christou, S.P. Perlepes, E.K. Brechin, J. Am. Chem. Soc. 129 (2007) 8.
[6] (a) N. Ishikawa, M. Sugita, W. Wernsdorfer, J. Am. Chem. Soc. 127 (2005) 3650;
(b) M.A. Aldamen, J.M. Clemente-Juan, E. Coronado, C. Marti-Gastaldo, A. Gaita-Ariño, J. Am. Chem. Soc. 130 (2008) 8874.
[7] G. Christou, Polyhedron 24 (2005) 2065.
[8] (a) Th.C. Stamatatos, C.G. Efthymiou, C.C. Stoumpos, S.P. Perlepes, Eur. J. Inorg. Chem. (Microreview), doi:10.1002/ejic.200900223.;
(b) A.J. Tasiopoulos, S.P. Perlepes, Dalton Trans. (Dalton Perspective) (2008) 5537;
(c) G.S. Papaefstathiou, S.P. Perlepes, Comment. Inorg. Chem. 23 (2002) 249.
[9] C.J. Millios, Th.C. Stamatatos, S.P. Perlepes, Polyhedron (Polyhedron Report) 25 (2006) 134.
[10] (a) R. Inglis, L.F. Jones, C.J. Millios, S. Datta, A. Collins, S. Parsons, W. Wernsdorfer, S. Hill, S.P. Perlepes, S. Piligkos, E.K. Brechin, Dalton Trans. (2009) 3403;
(b) C.J. Millios, A. Vinslava, W. Wernsdorfer, S. Moggach, S. Parsons, S.P. Perlepes, G. Christou, E.K. Brechin, J. Am. Chem. Soc. 129 (2007) 2754;
(c) C.J. Millios, A. Vinslava, W. Wernsdorfer, A. Prescimone, P.A. Wood, S. Parsons, S.P. Perlepes, G. Christou, E.K. Brechin, J. Am. Chem. Soc. 129 (2007) 6547.
[11 Th.C. Stamatatos, G.C. Vlahopoulou, C.P. Raptopoulou, A. Terzis, A. Escuer, S.P. Perlepes, Inorg. Chem. 48 (2009) 4610.
[12] Th.C. Stamatatos, A.K. Boudalis, K.V. Pringouri, C.P. Raptopoulou, A. Terzis, J. Wolowska, E.J.L. McInnes, S.P. Perlepes, Eur. J. Inorg. Chem. (2007) 5098.
[13] (a) For example, see: H. Andres, R. Basler, A.J. Blake, C. Cadiou, G. Chaboussant, C.M. Grant, H.-U. Güdel, M. Murrie, S. Parsons, C. Paulsen, F. Semadini, V. Villar, W. Wernsdorfer, R.E. Winpenny, Chem. Eur. J. 8 (2002) 4867;
(b) S.T. Ochsenbein, M. Murrie, E. Rusano, H. Stockli-Evans, C. Sekine, H.-U. Güdel, Inorg. Chem. 41 (2002) 5133;
(c) M. Moragues-Cánovas, M. Helliwell, L. Ricard, E. Riviére, W. Wernsdorfer, E. Brechin, T. Mallah, Eur. J. Inorg. Chem. (2004) 2219;
(d) A. Bell, G. Aromi, S.J. Teat, W. Wernsdorfer, R.E.P. Winpenny, Chem. Commun. (2005) 2808;
(e) G. Aromi, S.J. Teat, W. Wernsdorfer, E.K. Brechin, E.J.L. McInnes, Chem. Commun. (2005) 5038.
[14] For example, see: E.K. Brechin, E.C. Sañudo, W. Wernsdorfer, C. Boskovic, J. Yoo, D.N. Hendrickson, A. Yamaguchi, H. Ishimoto, T.E. Concolino, A.L. Rheingold, G. Christou, Inorg. Chem. 44 (2005) 502.
[15] For example, see: E.K. Brechin, M.J. Knapp, J.C. Huffman, D.N. Hendrickson, G. Christou, Inorg. Chim. Acta 297 (2000) 389.
[16] W. Choong, N.C. Stephenson, Cryst. Struct. Commun. 4 (1975) 275.
[17] J.M. Clemente-Juan, B. Chansou, B. Donnadieu, J.-P. Tuchagues, Inorg. Chem. 39 (2000) 5515.
[18] A. Escuer, M. Font-Bardia, S.B. Kumar, X. Solans, R. Vicente, Polyhedron 18 (1999) 909.
[19] (a) E.-C. Yang, W. Wernsdorfer, S. Hill, R.S. Edwards, M. Nakano, S. Maccagnano, L.N. Zakharov, A.L. Rheingold, G. Christou, D.N. Hendrickson, Polyhedron 22 (2003) 1727;

(b) R.S. Edwards, S. Maccagnano, E.-C. Yang, S. Hill, W. Wernsdorfer, D. Hendrickson, G. Christou, J. Appl. Phys. 93 (2003) 7807.
[20] (a) E.-C. Yang, W. Wernsdorfer, L.N. Zakharov, Y. Karaki, A. Yamaguchi, R.M. Isidro, G.-D. Lu, S.A. Wilson, A.L. Rheingold, H. Ishimoto, D.N. Hendrickson, Inorg. Chem. 45 (2006) 529;
(b) J. Lawrence, E.-C. Yang, R. Edwards, M.M. Olmstead, C. Rasmey, N.S. Dalal, P.K. Gantzel, S. Hill, D.N. Hendrickson, Inorg. Chem. 47 (2008) 1965.
[21] G.M. Sheldrick, SHELXL-86, Structure Solving Program, University of Ġottingen, Germany, 1986.
[22] G.M. Sheldrick, SHELXL-97, Crystal Structure Refinement Program, University of Ġottingen, Germany, 1997.
[23] G. Akerlöf, O.A. Short, J. Am. Chem. Soc. 58 (1936) 1241.
[24] (a) V.T. Yilmaz, G. Guney, O. Andac, W.T.A. Harrison, Polyhedron 21 (2002) 2393;
(b) V.T. Vilmaz, S. Hamamci, C. Thöne, Polyhedron 23 (2004) 841.
[25] G.B. Deacon, R.J. Phillips, Coord. Chem. Rev. 33 (1980) 227.
[26] R.A. Coxall, S.G. Harris, D.K. Henderson, S. Parsons, P.A. Tasker, R.E.P. Winpenny, J. Chem. Soc., Dalton Trans. (2000) 2349.
[27] (a) C. Papatriantafyllopoulou, C.G. Efthymiou, C.P. Raptopoulou, A. Terzis, E. Manessi-Zoupa, S.P. Perlepes, Spectrochim. Acta, Part A 70 (2008) 718;
(b) C.G. Efthymiou, C.P. Raptopoulou, A. Terzis, R. Boča, M. Korabic, J. Mrozinsky, S.P. Perlepes, E.G. Bakalbassis, Eur. J. Inorg. Chem. (2006) 2236.
[28] J. Basca, H. Zhao, K.R. Dunbar, Acta Crystallogr., Sect. E 60 (2004) m1040.
[29] S. Hamamci, V.T. Yilmaz, C. Thöne, Acta Crystallogr., Sect. E 60 (2004) m6.
[30] A. Kermagoret, P. Braunstein, Dalton Trans. (2008) 1564.
[31] For a tabulation and a critical structural/ magnetic analysis of Ni_4^{II} cubanes, see: K. Isele, F. Gigon, A.F. Williams, G. Bernardinelly, P. Franz, S. Decurtins, Dalton Trans. (2007) 332.
[32] (a) Representative work from other groups: W. Vreugdenhil, J.G. Haasnoot, J. Reedijk, A.L. Spek, Inorg. Chim Acta 129 (1987) 205;
(b) M.S. El Fallah, E. Rentschler, A. Caneschi, D. Gatteschi, Inorg. Chim. Acta 247 (1996) 231;
(c) M.-L. Tong, S.-L. Zheng, J.-X. Shi, Y.-X. Tong, H.K. Lee, X.-M. Chen, J. Chem. Soc., Dalton Trans. (2002) 1727;
(d) C. Boskovic, E. Rusanov, H. Stoeckli-Evans, H.U. Güdel, Inorg. Chem. Commun. 5 (2002) 881;
(e) T.K. Paine, E. Rentschler, Th. Weyhermüller, P. Chaudhuri, Eur. J. Inorg. Chem. (2003) 3167;
(f) G. Aromi, A.S. Batsanov, P. Christian, M. Helliwell, O. Roubeau, G.A. Timco, R.E.P. Winpenny, Dalton Trans. (2003) 4466;
(g) A. Sieber, C. Boskovic, R. Bircher, O. Waldmann, S.T. Ochsenbein, G. Chaboussant, H.U. Güdel, N. Kirchner, J.v. Slageren, W. Wernsdorfer, A. Neels, H. Stoeckli-Evans, S. Janssen, F. Juranyi, H. Mutka, Inorg. Chem. 44 (2005) 4315;
(h) T. Shiga, H. Oshio, Sci. Techn. Adv. Mater. 6 (2005) 565.
[33] (a) Selected work from our group: G.S. Papaefstathiou, A. Escuer, F.A. Mautner, C. Raptopoulou, A. Terzis, S.P. Perlepes, R. Vicente, Eur. J. Inorg. Chem. (2005) 879;
(b) C. Papatriantafyllopoulou, C.G. Efthymiou, C.P. Raptopoulou, R. Vicente, E. Manessi-Zoupa, V. Psycharis, A. Escuer, S.P. Perlepes, J. Mol. Struct. 829 (2007) 176.
[34] K. Bizilj, S.G. Hardin, B.F. Hoskins, P.J. Oliver, E.R. T Tieking, G. Winter, Aust. J. Chem. 39 (1986) 1035.
[35] K. Bizilj, S.J. Teat, H. Stoeckli-Evans, H.U. Güdel, Angew. Chem., Int. Ed. 42 (2003) 4653.
[36] M.A. Halcrow, J.-S. Sun, J.C. Huffman, G. Christou, Inorg. Chem. 34 (1995) 4167.
[37] W.L. Gladfelter, M.W. Lynch, W.P. Schaefer, D.N. Hendrickson, H.B. Gray, Inorg. Chem. 20 (1981) 2390.
[38] N. Alexopoulou, Ph.D. Thesis, University of Patras.

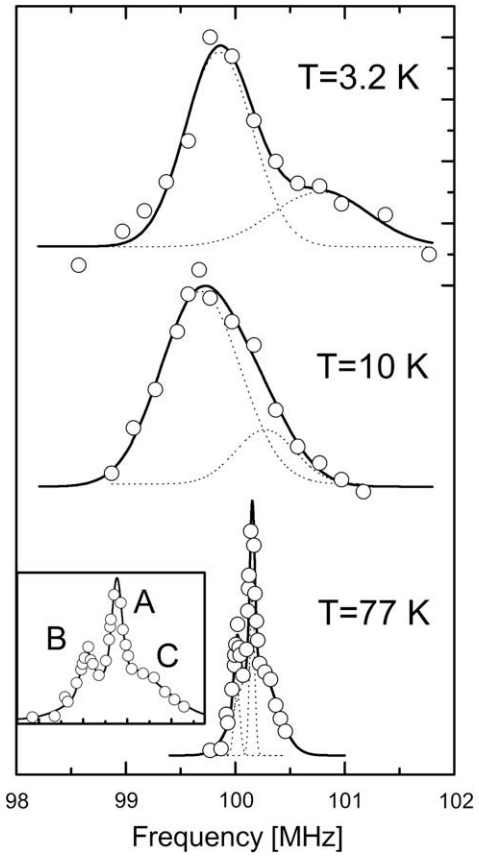


Fig. 1. ^{1}H NMR spectra at $H_0 = 2.35$ T for selected temperatures for $[FeCp_2^*][TCNE]$. The open circles are the experimental data acquired by the point-by-point spin–echo method. The solid lines are fits to the spectra using Gaussian functions. The inset shows the expanded NMR lineshape at 77 K, where three peaks A, B, and C are clearly identified.

magnetic field $H_0 = 2.35$ T. Fig. 1 shows typical ^{1}H NMR spectra for selected low temperatures. Similar results were obtained at $H_0 = 4.7$ T applied magnetic field. The high temperature spectra (not shown) are narrow with a width in the kilohertz range, whereas the low temperature spectra are broadened with a width in the megahertz range.

Fig. 1 clearly shows that the NMR resonance lines exhibit a structure at low temperatures, due to the large number of protons in the system situated at magnetically inequivalent crystallographic sites. At 77 K three peaks (A, B, and C) could be resolved whereas at liquid helium temperatures the line is further broadened and shifted to lower frequencies and could be decomposed into two Gaussian line profiles. The protons are coupled to the electronic spin system through the hyperfine electron–nucleus dipolar interaction. The different hyperfine couplings lead to a distribution of paramagnetic shifts and result in an inhomogeneous broadening of the NMR line. It is also evident from Fig. 1 that the linewidth of the spectra increases substantially below liquid nitrogen temperatures signifying the onset of strong magnetic interactions in the low temperature regime, since the overall width of the inhomogeneous broadened NMR line is proportional to the magnitude of the local magnetic moment.

In order to study the low-energy spin dynamics of $[FeCp_2^*][TCNE]$ we performed ^{1}H T_1 spin–lattice and T_2 spin–spin relaxation time measurements, shown in Fig. 2 as a function of temperature at $H_0 = 2.35$ and 4.7 T.

Both T_1 and T_2 relaxation times at the two applied fields decrease on cooling and exhibit minima at around 15–20 K. Before analyzing the temperature dependence of the relaxation times,

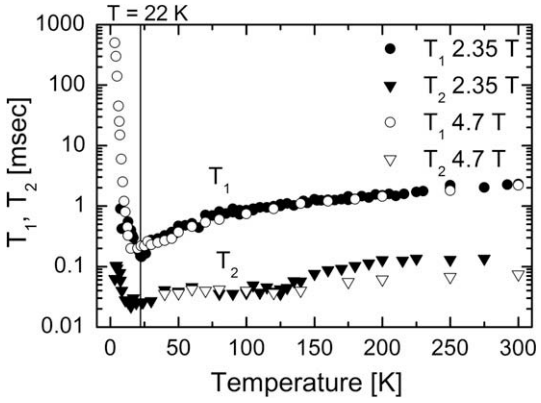


Fig. 2. Temperature dependence of ^{1}H NMR T_1 and T_2 relaxation times for $[FeCp_2^*][TCNE]$ at two applied magnetic fields $H_0 = 2.35$ and 4.7 T.

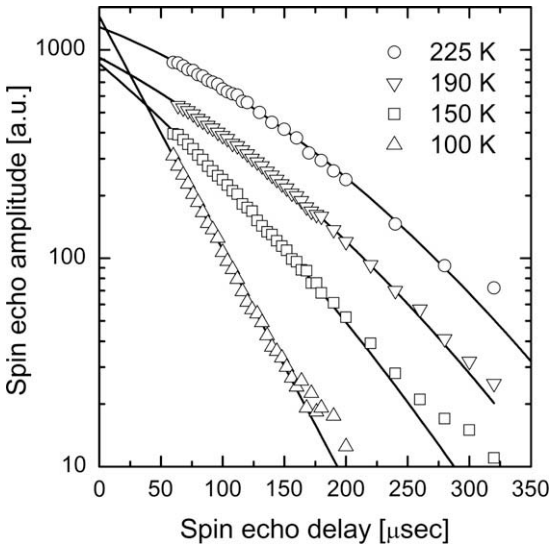


Fig. 3. Spin–echo decays of $[FeCp_2^*][TCNE]$ at $H_0 = 2.35$ T for selected temperatures. The data have been shifted for clarity. The solid lines are fits using a product of a Gaussian and an exponential function (see text). For temperatures between 50 and 100 K, the decays are double exponentials. For the decay at 100 K, only the fast component of the double exponential relaxation (solid line) is shown.

we first consider the analysis of the relaxation decays which determine the values of T_1 and T_2. The longitudinal relaxation decays were single exponentials thus providing a unique value of T_1, whereas the transverse relaxation decays were in general non-exponential functions. The T_2 spin–echo decays for selected temperatures in the high temperature regime at $H_0 = 2.35$ T are shown in Fig. 3.

The spin–echo decays between 100 and 300 K could be analyzed using a function that is a product of a Gaussian and an exponential function shown as solid lines in Fig. 3. Below 100 K we observe a distinct crossover from the Gaussian-exponential to double exponential decay. The Gaussian-exponential function has been frequently encountered in the NMR literature (e.g. high temperature cuprate superconductors), and in general signifies the coupling of the nuclei through the electron spins (Gaussian contribution, T_{2G}) weighted by the T_1 relaxation (Redfield contribution, T_{2R}) [10,11]. The temperature behavior of echo decay can be understood if the measured ^{1}H nuclei are coupled to neighboring spins that experience a fast relaxation time. For very long T_1 the echo decay is Gaussian. As T_1 decreases, the echo decay becomes exponential. However, in our present system, although T_1 decreases

with decreasing temperature and the Gaussian-exponential function seems to adequately describe the relaxation decay data, the fitted parameters are found to be interdependent, and in general, T_{2G} – the Gaussian part was larger than T_{2R} – the exponential part contrary to observation. Therefore, for the present system the exact origin of the observed non-exponential decay at high temperatures is not yet known and further experiments in lower applied magnetic fields are required. For this reason we calculated the $T_2(1/e)$ parameter, which is the time corresponding to the $1/e$ value of the spin–echo decay measured from the origin. The relaxation time $T_2(1/e)$ is plotted in Fig. 2. It can be seen that T_2 decreases on cooling up to 100 K in a manner similar to the T_1 decrease with temperature.

To further investigate the temperature dependence of the relaxation time T_2, we plot T_2 and $\Delta\omega$ (the linewidth of the NMR spectra) as a function of temperature for the data taken at magnetic field $H_0 = 2.35$ T (Fig. 4).

The dotted lines in Fig. 4 indicate the temperature crossovers of the shape of the spin–echo decay. The high temperature crossover at $T = 140$ K marks also the temperature where the linewidth $\Delta\omega$ substantially increases. As a measure of linewidth, the frequency difference $\Delta\omega$ between the A and B peaks (inset in Fig. 1) is plotted in Fig. 4. In the high temperature regime T_2 starts to decrease below 200 K, the shape of the spin–echo decay is non-exponential with a Gaussian short time profile, and the width $\Delta\omega$ of the lineshape is small being approximately independent with temperature. In the same temperature range, T_1 decreases in a continuing fashion (Fig. 2). In this regime, we consider that the spins are in the fast fluctuation limit in a probably magnetically inhomogeneous medium. Between 50 and 140 K, T_2 exhibits a shallow minimum with temperature, while the width $\Delta\omega$ increases by an order of magnitude. It is also observed that at the temperature of the T_2 minimum, the linewidth is comparable to the T_2^{-1} relaxation rate, that is the product $\Delta\omega T_2 \approx 2$.

A minimum at T_2 is not easily explained in NMR experiments when there is no phase transition in the system. Nevertheless, there is a theoretical model, originally proposed by Hu and Hartmann [12], which predicts such a T_2 minimum when $\Delta\omega$ and T_2^{-1} are of comparable order. This model is based on spectral diffusion caused by the fluctuation of the local field at the site of the resonance ions (system of A spins whose resonance is being observed) because of the uncorrelated flipping of a system of B spins at an average flipping rate w. The A and B spins resonate at different Larmor frequencies as for example in our case where the A spins, whose signal are observed, belong to the peak A, (inset of Fig. 1) and the B spins belong to the peak B. The pertinent parameter in the model is the ratio $2w/\Delta\omega_{1/2}$, where w is the B spins flipping rate and $\Delta\omega_{1/2}$ is the half-width at half height of the width of the lineshape in the notation of Hu and Hartmann. The model demonstrates that the product $\Delta\omega_{1/2}T_2$ exhibits a minimum as a function of $2w/\Delta\omega_{1/2}$ (Fig. 5 of Ref. [12]) as observed in our measurements. Further experiments are needed to clarify the applicability of Hu and Hartmann's model in our system.

In the following we consider the low temperature minima ($T \sim 22$ K) in the T_1 and T_2 relaxation times (Fig. 2). In particular, T_1 spin–lattice measurements probe directly the low-frequency spin dynamics of the electronic system through the time dependence of the fluctuating local magnetic fields which in the system examined originates from the fluctuation of the Fe^{3+} electron moment.

Firstly, we consider the high temperature side of the T_1 minimum which is into the paramagnetic regime. To facilitate analysis of the experimental data we plot the relaxation rates T_1^{-1} and T_2^{-1} at both magnetic fields as a function of the inverse temperature T^{-1}, as shown in Fig. 5. No appreciable field dependence was observed for the T_1^{-1} relaxation rates at high temperatures. The T_2^{-1} relaxation data have been multiplied by a factor (4/30) in order to demonstrate the similar temperature dependence of T_1^{-1} and T_2^{-1} in the high temperature side of the relaxation rates maximum.

The relaxation data in the temperature range 20–100 K (Fig. 5) may well be fitted with an Arhenius type relation:

$$T_{1,2}^{-1} = A\exp(E_a/k_BT) \quad (1)$$

indicating that the electron–nucleus interaction is modulated by an thermally activated mechanism. We can safely assume that electronic magnetic fluctuations are expected to dominate in this high temperature regime.

The experimental T_1^{-1} and T_2^{-1} data may well be described by an activation energy $E_a/k_B = 57.8$ K determined from the muon experiments [9] to show the consistency between the different techniques. This activation energy, according to Eq. (1), is shown as solid line in Fig. 5 and fits reasonably well both the T_1^{-1} and T_2^{-1} data in the high temperature side of the maximum. The spin–spin relaxation T_2^{-1} follows the temperature behavior of the spin–lattice relaxation rate T_1^{-1} presumably due to the lifetime broadening factor in the T_2 relaxation. The activation energy $E_a/k_B = 57.8$ K is consistent with a thermal activation process in a ferromagnetic Ising chain, where the basic excitations are the domain walls. In particular, the elementary excitations of such a chain are spin clusters, where an n-fold spin cluster is defined as

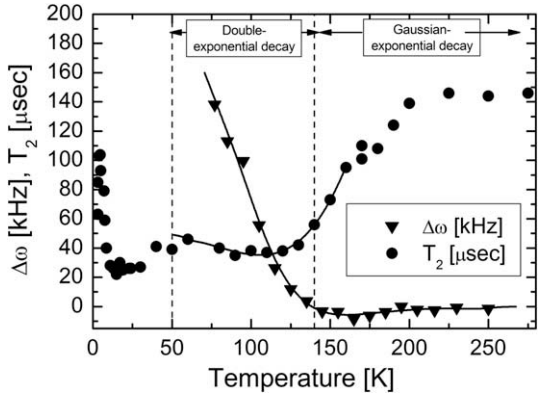


Fig. 4. T_2 relaxation time and $\Delta\omega$ frequency difference between the A and B peaks (inset Fig. 1) as a function of temperature for $[FeCp_2^*][TCNE]$ at magnetic filed $H_0 = 2.35$ T. The solid lines are guides to the eye. The dotted lines mark the crossover temperatures for the shape of the spin–echo decay.

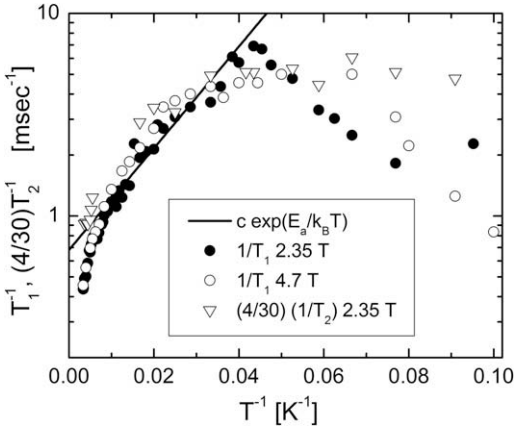


Fig. 5. T_1^{-1} and T_2^{-1} relaxation rates as a function of T^{-1} for $[FeCp_2^*][TCNE]$ at 2.35 and 4.7 T. The solid line is an activated behavior in the high temperature side of the maximum, with an activation energy of $E_a/k_B = 57.8$ K.

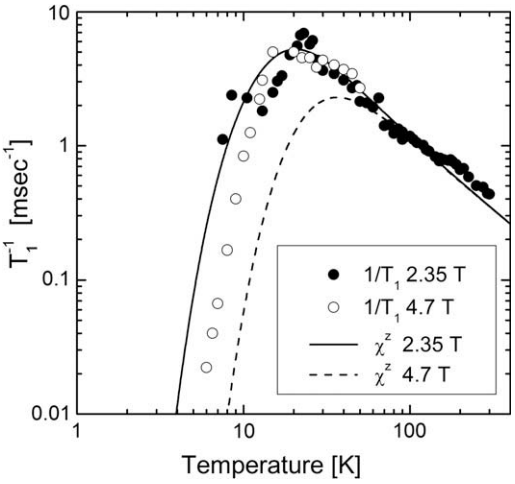


Fig. 6. Temperature dependence of T_1^{-1} for [FeCp$_2^*$][TCNE] at 2.35 and 4.7 T. The curves denote the static longitudinal susceptibility χ^z (normalized to fit the NMR data at 20 K) for 1D ferromagnetic Ising chain (Eq. (3)) at magnetic fields of 2.35 (solid line) and 4.7 T (dashed line).

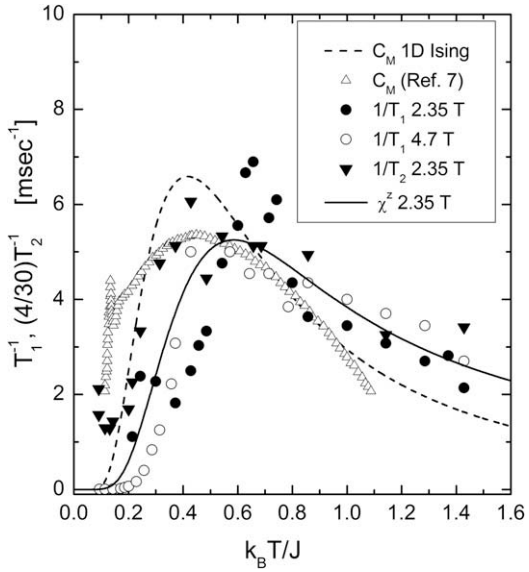


Fig. 7. T_1^{-1} (open and filled circles) and T_2^{-1} (filled inverted triangles) relaxation rates as a function of k_BT/J for [FeCp$_2^*$][TCNE] at 2.35 and 4.7 T. The experimental data are plotted using $J/k_B = 35$ K [7]. The open triangles are experimental specific heat data (C_M) at zero magnetic field, adapted from Ref. [7]. The dashed line is the specific heat for the 1D Ising model. The specific heat data are scaled in order to be compared with the NMR measurements. The solid line is the uniform susceptibility χ^z for 1D ferromagnetic Ising chain at 2.35 T.

n adjacent spins which are reversed with respect to the majority of the spins in the chain [13,14]. In this model, the activation energy is the one required to flip spins within a pair of wall and is equal to 2 J, the intrachain exchange constant, since the energy associated with creating an n-fold spin cluster is localized at the ends of the cluster and is, therefore independent of length [9,13]. Using $E_a = 2$ J, we obtain $J/k_B = 29$ K, consistent with $J_{||} = 27.4$ K as determined from susceptibility measurements [8].

The temperature dependence of the relaxation rates at their maximum values is now considered. This is shown in Fig. 6 where the T_1^{-1} relaxation rates at both magnetic fields show pronounced temperature dependences.

Generally, in the high temperature approximation, the nuclear T_1^{-1} relaxation rate due to fluctuating dipole fields from the electronic spins can be expressed as [15–17]:

$$T_1^{-1} = (g\mu_B\gamma_N)^2/4\pi \int dq A^z(q)(g_z\mu_B)^{-2}\chi^z(q)\cdot 2k_BT/\Gamma_q^z \qquad (2)$$

where $A^\alpha(q)$ are the Fourier transforms of the components of the product of the two dipole-interaction tensors, $\chi^\alpha(q)$ is the static q-dependent susceptibility and Γ_q^α is a damping factor characteristic of the normalized relaxation function. Assuming that Γ_q^α has a weak temperature and field dependence and considering only the $q = 0$ fluctuations because of the ferromagnetic character of the system, one obtains that the part of the relaxation rate T_1^{-1} arising from the longitudinal fluctuation contribution ($\alpha = z$) is simply proportional to the product of the static susceptibility χ^z and the temperature T, that is $T_1^{-1} \sim \chi^z T$ [16,17].

The uniform susceptibility for an Ising linear chain in the presence of a non-zero longitudinal magnetic field is given by [17]:

$$\chi^z = \frac{(g_z\mu_B)^2}{2k_BT}\frac{\mathrm{sech}^2 h\cdot(1+j\tanh^2 h)}{(1+j\mathrm{sech}^2 h)^{1/2}} \qquad (3)$$

where $j = \exp(-2J/k_BT) - 1$ and $h = g_z\mu_B H_z/k_BT$

The temperature dependences of χ^z for $H_0 = 2.35$ and 4.7 T, according to Eq. (3), are shown as solid lines in Fig. 6 (solid and dashed lines respectively), normalized in the y-axis in order to fit the NMR data at the peak temperature. It is observed that the T_1^{-1} relaxation data are represented fairly well by χ^z except from the higher magnetic field at low temperatures. It is to be noted that apart from the normalization constant, no other adjustable parameter has been used to fit the data. In the fitting of the NMR data with χ^z, the value of the exchange constant J/k_B, had little effect on the position of the χ^z maximum, being primarily sensitive to the large values of the external magnetic fields. The result of the analysis of the NMR relaxation data using only the static uniform susceptibility, implies – according to Eq. (2) – that the damping rate Γ_q is more or less proportional to the temperature T, since $T_1^{-1} \sim \chi^z T$. The damping constant of a linear magnetic chain with various degrees of anisotropy has been calculated for low-dimensional spin systems [18]. In the Ising limit, a weak temperature dependence of the damping constant $\Gamma_{q=0}^\alpha$ has been obtained [18], in disagreement with the results of the analysis of the NMR relaxation data. This might be due to the effect of the large applied magnetic field used in the NMR experiments on the temperature dependence of the damping constant.

Another point to be considered is the short range order that is developed in the region above the critical temperature. The NMR relaxation maximum is exactly at the temperature range where short range order is building up. This is shown in Fig. 7, where the T_1^{-1} and T_2^{-1} relaxation rates are plotted as a function of k_BT/J in order to be compared with specific heat measurements.

In Fig. 7, the experimental data of the magnetic specific heat C_M, adapted from Ref. [7] and the theoretical specific heat for the 1D Ising model, are also plotted. For reasons of comparison all the data are plotted using the value of the exchange constant derived from the specific heat measurements of Ref. [7], $J/k_B = 35$ K. These specific heat data show a cusp in C_M at the zero-field magnetic ordering temperature $T_c = 4.82$ K from a 3D ferromagnetic state at low temperatures to a 1D Ising-like behavior at higher temperatures. The broad maximum in C_M at $T \approx 15$ K, is associated with the development of strong short range order characteristic of the 1D structure. This short range order originates from the strong magnetic anisotropy of Ising character present in the compound [7]. It is clearly seen from Fig. 7 that the low temperature NMR data are clearly affected by the development of short range order above the critical temperature.

Therefore, the nuclear relaxation of this ferromagnetic Ising-like magnetic chain is attributed to the temperature dependence of the static uniform susceptibility and it is also affected by the develop-

ment of short range order before the magnetic ordering transition. In the case of 1D magnetic chains this build-up of short range order can lead to maxima or minima of T_1^{-1} as for example in the quasi-1D exchange-coupled paramagnet TMMC [16] and in 1D ferro and antiferro Ising chains [17].

4. Conclusion

The low-frequency electron spin dynamics of $[FeCp_2^*][TCNE]$ has been studied by applying T_1 spin–lattice and T_2 spin–spin ^1H NMR relaxation measurements. In the high temperature paramagnetic phase, the NMR linewidths and T_2 relaxation measurements revealed a magnetically inhomogeneous medium with fast fluctuations of the electronic spins. The T_1 relaxation data were successfully analyzed in the temperature range $13 < T < 110$ K and yielded an Arrhenius activation law for the correlation time of the electron spin fluctuations in very good agreement with previous μSR measurements. The activation energy obtained is consistent with elementary magnetic excitations of 1D ferromagnetic Ising chains. The temperature dependences of T_1^{-1} and T_2^{-1} show significant maxima at temperatures around 22 K, above the paramagnetic–ferromagnetic critical temperature $T_c = 4.8$ K. This behavior has been associated with the temperature dependence of the static uniform susceptibility of 1D ferromagnetic Ising chain and also with the development of significant short range order at temperatures above the magnetic ordering transition. This short range order indicates the presence of strong anisotropic interactions of Ising character in agreement with previous magnetization studies. Further NMR experiments at lower fields are needed to fully investigate the region near the critical temperature.

Acknowledgments

MF acknowledges fruitful discussions with S. Thanos. JSM acknowledges helpful discussions with A. J. Epstein (Ohio State University) and K. I. Pokhodnya, sample preparation by M. L. Taliaferro, and the continued partial support from the U. S. DOE (No. DE FG 03-93ER45504).

References

[1] (a) J.S. Miller, Inorg. Chem. 39 (2000) 4392;
(b) J.S. Miller, A.J. Epstein, Angew. Chem., Int. Ed. Engl. 33 (1994) 385;
(c) S.J. Blundell, F.L. Pratt, J. Phys.: Condens. Matter 16 (2004) R771;
(d) V.I. Ovcharenko, R.Z. Sagdeev, Russ. Chem. Rev. 68 (1999) 345;
(e) M. Kinoshita, Phil. Trans. R. Soc. Lond. (A) 357 (1999) 2855;
(f) J.S. Miller, A.J. Epstein, Chem. Commun. (1998) 1319;
(g) W. Plass, Chem. Zeit 32 (1998) 323;
(h) J.S. Miller, A.J. Epstein, Chem. Eng. News 73#40 (1995) 30;
(i) J.S. Miller, Polyhedron 20 (2001) 1723.
[2] [a] G.T. Yee, J.S. Miller, in: J.S. Miller, M. Drillon (Eds.), Magnetism – Molecules to Materials, vol. 5, Wiley-VCH, Mannheim, 2005, p. 223;
[b] E. Coronado, J.R. Galàn-Mascarós, J.S. Miller, in: R.H. Crabtree, D.M.P. Mingos (Eds.), Comprehensive Organometallic Chemistry III, vol. 12, Oxford, 2006, p. 413.
[3] J.S. Miller, J.C. Calabrese, H. Rommelmann, S.R. Chittipeddi, J.H. Zhang, W.M. Reiff, A.J. Epstein, J. Am. Chem. Soc. 109 (1987) 769.
[4] S. Chittipeddi, K.R. Cromack, J.S. Miller, A.J. Epstein, Phys. Rev. Lett. 58 (1987) 2695.
[5] J.-H. Her, P.W. Stephens, J. Ribas-Ariño, J.J. Novoa, W.W. Shum, J.S. Miller, Inorg. Chem. 48 (2009) 3296.
[6] K.S. Narayan, B.G. Morin, J.S. Miller, A.J. Epstein, Phys. Rev. B 69 (1991) 5953.
[7] A. Chakraborty, A.J. Epstein, W.N. Lawless, J.S. Miller, Phys. Rev. B 40 (1989) 11422.
[8] S. Chittipeddi, M.A. Selover, A.J. Epstein, D.M. O'Hare, J. Manriquez, J.S. Miller, Synth. Met. 27 (1988) B417.
[9] L.P. Le, A. Keren, M.I. Larkin, G.M. Luke, W.D. Wu, Y.J. Uemura, J.S. Miller, A.J. Epstein, Phys. Rev. B 65 (2001) 024432.
[10] N.J. Curro, P.C. Hammel, B.J. Suh, M. Hücker, B. Büchner, U. Ammerahl, A. Revcolevschi, Phys. Rev. Lett. 85 (2000) 642.
[11] A. Goto, W.G. Clark, P. Vonlanthen, K.B. Tanaka, T. Shimizu, K. Hashi, P.V.P.S.S. Sastry, J. Schwartz, Phys. Rev. Lett. 89 (2002) 127002.
[12] P. Hu, S.R. Hartmann, Phys. Rev. B 9 (1974) 1.
[13] J.B. Torrance Jr., M. Tinkham, Phys. Rev. 187 (1969) 595.
[14] M. Date, M. Motokawa, Phys. Rev. Lett. 16 (1966) 1111.
[15] (a) T. Moriya, Prog. Theor. Phys. 16 (1956) 23;
(b) T. Moriya, Prog. Theor. Phys. 28 (1962) 371.
[16] D. Hone, C. Scherer, F. Borsa, Phys. Rev. B 9 (1974) 965.
[17] H. Nishihara, A.M.C. Tinus, K. Kopinga, W.J.M. de Jonge, J. Phys. C: Solid State Phys. 15 (1982) L1103.
[18] K. Kawasaki, Prog. Theor. Phys. 42 (1969) 174.

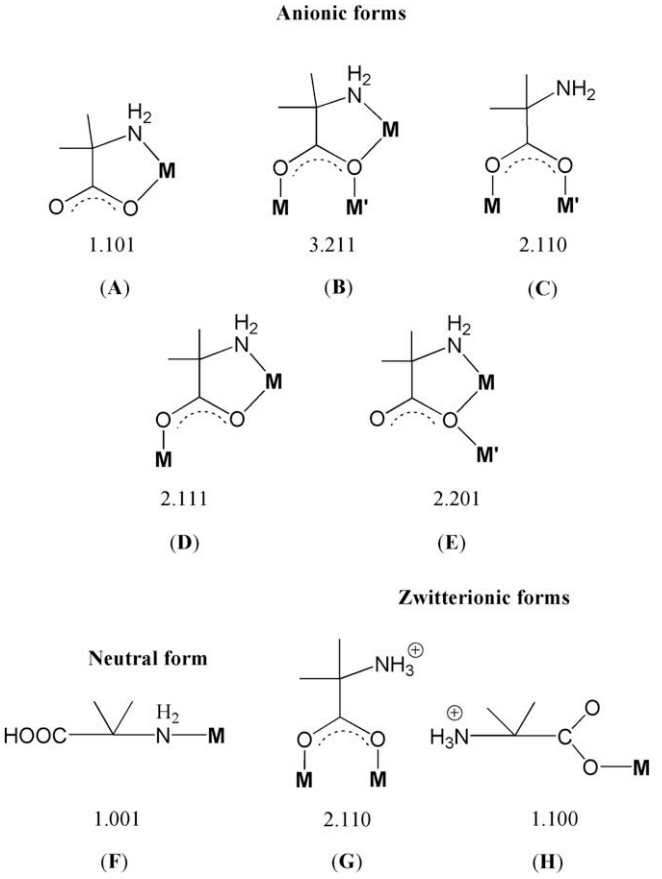
contrast, the structures of metal–oligopeptide complexes are till now scarce, due to the reluctance of the peptide molecules to form crystalline solids. This is specifically valid for the Zn(II)-aminoacid/peptide coordination chemistry. From a careful search in the CCDC base it is evident that crystal structures of Zn(II) complexes with almost all naturally occurring α-aminoacids have been reported. However, there are less than fifteen structure determinations of Zn(II)/dipeptide complexes, including those containing peptide derivatives or –N and –C protected aminoacid constituents. Among them, only three *binary* Zn(II)/*free-peptide* compounds have been structurally characterized: $\{[Zn(H\text{-}Gly\text{-}Gly\text{-}O)_2]\cdot 2H_2O\}_n$ [11a], $\{[Zn(H\text{-}Gly\text{-}L\text{-}Thr\text{-}O)_2]\cdot 2H_2O\}_n$ [11b] and $\{[Zn(H\text{-}Gly\text{-}His\text{-}O)_2]\cdot 7H_2O\}_n$ [11c]; the *ternary* complex $[Zn_2(H\text{-}Gly\text{-}Gly\text{-}O)_2(LH^+)_2](ClO_4)_4\cdot 2H_2O$ (L = 1-methyl-4(6-amino-2-pyridylmethyl) piperazine) is also known [11d]. Furthermore, in the whole Zn(II)/oligopeptide chemistry, only the crystal structure of the coordination polymer $\{[Zn(H\text{-}Gly\text{-}Gly\text{-}Gly\text{-}O)(H_2O)](SO_4)_{0.5}\cdot 2H_2O\}_n$ has been reported so far [11e].

We have initiated a systematic study of the coordination chemistry of α-aminoisobutyric acid (H-Aib-OH), and dipeptides and tripeptides containing the α-aminoisobutyryl residue [–HNC(CH$_3$)$_2$CO–, Aib]. The α-aminoisobutyric acid (also called α-methyl-alanine or α,α-dimethylglycine) is an uncommon natural aminoacid which is commonly found in a family of natural antibiotics produced by microbial sources. As shown by early studies, the replacement of the hydrogen atoms of the C_α carbon of glycine with methyl groups produces severe restrictions on the conformational freedom of the molecule and, consequently, -Aib- is a strong promoter and stabilizer of folded (β-bends) and 3_{10} or α-helical structures [12]. Our interest in this chemistry is mainly to investigate how the inductive and steric properties of the α-carbon methyl groups affect the structures of the complexes in the solid state, to test the possibility of creating helical complexes (helicates) or/and one-dimensional (1D), two-dimensional (2D) and three-dimensional (3D) coordination polymers or polynuclear aggregates (clusters) and to study the supramolecular assemblies of these species through their hydrogen bonding interactions.

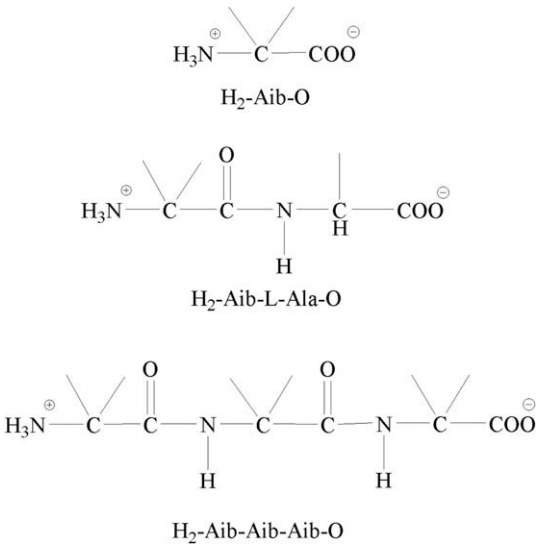
Concerning the coordination chemistry of the free aminoacid (H-Aib-OH), 15 structurally characterized H-Aib-OH/metal ion complexes have been reported. It is impressive that the aminoacid employed in these structures adopts *eight* different coordination modes in its anionic, neutral or zwitterionic forms, as these are illustrated in Scheme 1. The reported metal complexes are listed in Table 1, with the corresponding coordination modes being described using Harris notation [13].

The coordination chemistry of Aib-based *dipeptides* is poorly explored. In our previous work, the crystal structures of Cu(II) complexes with the dianionic forms of dipeptides H-Aib-Aib-OH [27a], H-Aib-Gly-OH, H-Aib-L-Leu-OH H-Aib-L-Phe-OH [27b], and with the monoanionic and dianionic forms of H-Aib-L-Ala-OH [27c] have been reported. Also, the diorganotin complexes [(*n*-Bu)$_2$Sn(H$_{-1}$L) where LH = H-Aib-L-Leu-OH and H-Aib-L-Ala-OH, have been structurally characterized and their antibacterial and antiproliferative acitivities investigated [27d]. Finally, in the coordination chemistry of Aib-based *tripeptides,* the X-ray crystal structure of the remarkable copper(III) complex $[Cu^{III}(H_{-2}Aib_3)].2H_2O.1.5NaClO_4$, containing the trianion of tri-α-amino-isobutyric acid as ligand, has been determined [28a]. Reduction of this complex by 2,4-di-*tert*-butylphenol gave the dinuclear complex $[Cu_2(H_{-1}Aib_3)_2]$ [28b].

We wish to report here the results of our studies concerning the interaction of Zn(II) and the aminoacid H-Aib-OH, the dipeptide H-Aib-L-Ala-OH and the tripeptide H-Aib-Aib-Aib-OH (Scheme 2). Emphasis is given on the characterization of the products in the solid state.



Scheme 1. The crystallographically established coordination modes of H-Aib-OH using Harris notation [13].



Scheme 2. The ligands used in the present work.

2. Experimental

2.1. General procedures and physical measurements

All manipulations were performed under aerobic conditions. All chemicals and solvents were purchased from commercial sources and used without further purification. Microanalyses (C, H, N) were performed by the University of Ioannina (Greece) Microanalytical

Service using an EA 1108 Carlo Erba analyzer. Melting points were taken on a Electrothermal 9200 apparatus and are uncorrected. IR spectra (4000–450 cm^{-1}) were recorded on a Perkin–Elmer 16 PC FT spectrometer with samples prepared as KBr pellets.

2.2. Synthesis of the ligands

2.2.1. H-Aib-L-Ala-OH

The dipeptide was prepared in the liquid phase, as described earlier [27c].

2.2.2. H-Aib-Aib-Aib-OH

The protected aminoacids Z-Aib-OH and p-TsA-Aib-OBzl were prepared according to the literature [29]. Coupling of Z-Aib-OH with *p*-TsA-Aib-Obzl *via* the PyBOP procedure [30], provided Z-Aib-Aib-OBzl [27a]. The dipeptide Z-Aib-Aib-OBzl (0.97 g, 2.5 mmol) was deprotected upon treatment with 2.5 N HBr/CH_3COOH (25 ml) for 1.5 h at room temperature and the HBr salt was precipitated by trituration with dry ether, washed with dry ether repeatedly and dried over P_2O_5/KOH (yield 80%). This salt was dissolved in DMF (4 ml), neutralized with Et_3N and allowed to react with Z-Aib-OH (0.45 g, 2 mmol) dissolved in DMF (4 ml) and preactivated at 0 °C for 30 min with HOBt (0.45 g, 3.0 mmol) and DCC (0.83 g, 4 mmol). The reaction mixture was stirred for 2 h at 0 °C and overnight at room temperature. The precipitated DCU was filtered and the solvent was removed *in vacuo*. The residue was partitioned in AcOEt-H_2O. The organic layer was washed alternatively with 5% $NaHCO_3$ and dried over Na_2SO_4. Evaporation of the solvent and recrystallization of the product from AcOEt/petroleum ether yielded 0.75 g (75%); mp 138-139 °C; TLC: R_f 0.65 (single spot) ($CHCl_3$/MeOH/AcOEt, 85:10:5), R_f 0.87 (single spot) (n-BuOH:MeCOOH-H_2O 3:1:1). The protecting groups were removed by catalytic hydrogenolysis (10% Pd on charcoal) in DMF and the free tripeptide crystallized upon addition of AcOEt-petroleum ether. It was further purified by column chromatography on Sephadex G-10 using AcOH (5%) as the eluent. Yield: 0.33 g (80%); mp 186–187 °C; TLC: 0.40 (single spot) ($CHCl_3$/MeOH/AcOEt, 85:10:5), R_f 0.60 (single spot) (*n*-BuOH:MeCOOH–H_2O 3:1:1).

2.3. Synthesis of zinc(II) complexes

2.3.1. $[Zn_3(H\text{-}Aib\text{-}O)_6]\cdot MeCOOH\cdot H_2O$ (**1**·MeCOOH·H_2O)

H-Aib-OH (0.004 g, 0.04 mmol) was added to a stirred solution of $Zn(O_2CMe)_2\cdot 2H_2O$ (0.011 g, 0.05 mmol) in MeOH (5 ml). After the addition of 4–5 drops of H_2O, the solid soon dissolved. The "pH" of the solution was ~5.5 and adjusted to ~8 with saturated LiOH·H_2O in MeOH. Colourless crystals of the product (suitable for crystallographic studies) were obtained from the solution by vapour diffusion with Et_2O. The crystals were collected by filtration and dried in air. Yield: 57%. The dried solid was analysed as H_2O-free (**1**·MeCOOH). *Anal.* Calc. for $C_{26}H_{52}N_6O_{14}Zn_3$: C, 35.9; H, 6.0; N, 9.7. Found: C, 35.8; H, 6.3; N, 9.6%. Selected IR data (KBr, cm^{-1}): 3430mb [$\nu_{as}(NH_2)$], 3294mb [$\nu_s(NH_2)$], ~3150wb [$\nu(OH)_{acetic\ acid}$], 1655s [$\nu(C{=}O)_{acetic\ acid}$], 1586s [$\nu_{as}(CO_2)$], 1472m [$\delta_d(CH_3)$], 1414mb [$\nu_s(CO_2)$], 1385sh [$\nu_s(CO_2)$], 1216m, 1098m, 902w, 814m, 692m, 624m.

2.3.2. $\{[Zn(H\text{-}Aib\text{-}L\text{-}Ala\text{-}O)_2]\cdot H_2O\}_n$ (**2**·H_2O)

To a stirred solution of $Zn(O_2CMe)_2\cdot 2H_2O$ (0.013 g, 0.06 mmol) in MeOH (6 ml), the dipeptide H-Aib-L-Ala-OH was added (0.016 g, 0.09 mmol). H_2O (1 ml) was added and the solid soon dissolved. The "pH" of the solution was ~6. Colourless X-ray quality crystals of the product were obtained from the solution by vapour diffusion with Et_2O. The crystals were collected by filtration and dried in air. Yield: 60%. The dried solid was analyzed as H_2O-free (**2**). *Anal.* Calc. for $C_{14}H_{26}N_4O_6Zn$: C, 40.8; H, 6.4; N, 13.6. Found: C, 41.1; H, 6.3; N, 13.5%. Selected IR data (KBr, cm^{-1}): 3400mb [$\nu_{as}(NH_2)$], 3265m [$\nu_s(NH)_{peptide}$], 3236m [$\nu_s(NH_2)$], 1646m [$\nu(C{=}O)_{peptide}$ or amide I], 1593sb [$\nu_{as}(CO_2)$], 1559m [$\nu(CN)+\delta(NH)$ or amide II], 1416m [$\nu_s(CO_2)$], 1260m [$\delta(NH+\nu(CN)$ or amide III].

2.3.3. $[Zn(H_2\text{-}Aib\text{-}Aib\text{-}Aib\text{-}O)_4](ClO_4)_2\cdot 5.8H_2O$ (**3**·5.8H_2O)

To a stirred solution of $Zn(ClO_4)_2\cdot 6H_2O$ (0.011 g, 0.03 mmol) in MeOH (6 ml), the tripeptide H-Aib-Aib-Aib-OH was added (0.016 g, 0.06 mmol). The "pH" of the solution was ~4 and no adjustment was made. Colourless crystals of the product (suitable for crystallographic studies) were obtained from the solution by vapour diffusion with Et_2O. The crystals were collected by filtration and dried in air. Yield: 55%. The dried solid was analyzed as H_2O-free (**3**). *Anal.* Calc. for $C_{48}H_{102}N_{12}O_{24}Cl_2Zn$: C, 42.2; H, 7.5; N, 12.3. Found: C, 42.3; H, 7.2; N, 12.4%. Selected IR data (KBr, cm^{-1}): ~3390sb [$\nu(OH)_{water}$], 3254mb [$\nu(NH)_{peptide}$], ~3100m [$\nu(NH_3^+)$], 1654s [$\nu(C{=}O)_{peptide}$ or amide I], 1620s [$\nu_{as}(CO_2)$], 1524s [$\nu(CN)+\delta(NH)$ or amide II], 14 586m [$\delta_d(CH_3)$], 1430m [$\nu_s(CO_2)$], 1284w [$\delta(NH+\nu(CN)$ or amide III], 1094sb [$\nu_d(ClO)$], 624m [$\delta_d(OClO)$].

2.4. X-ray crystallographic studies

Crystals of complexes **1**·MeCOOH·H_2O, **2**·H_2O and **3**·5.8H_2O were mounted in air and covered with epoxy glue. Diffraction measurements were made on a $P2_1$ Nicolet diffractometer upgraded by Crystal Logic using monochromated Cu radiation. Complete crystal data and parameters for data collection and processing are

Table 1
The crystallographically determined Metal/H-Aib-OH complexes.

Compound	Coordination mode[a]	Ref.
$[Cu(H\text{-}Aib\text{-}O)_2]$	1.101 (**A**)	[14]
$[Ni(H\text{-}Aib\text{-}O)_2(H_2O)_2]\cdot xH_2O$ (x = 2, x = 3)	1.101 (**A**)	[15a,b]
$[Cr(H\text{-}Aib\text{-}O)_3]$	1.101 (**A**)	[16]
$[Zn(H\text{-}Aib\text{-}O)_2(H_2O)_2][Zn(H\text{-}Aib\text{-}O)_2(H_2O)]_2$	1.101 (**A**)	[17]
trans-$[Pt(H\text{-}Aib\text{-}O)_2]$	1.101 (**A**)	[18]
$[Pr_2(H_2\text{-}Aib\text{-}O)_4(H_2O)_8]Cl_6\cdot H_2O$	2.110 (**G**)	[19]
$[La_2(H_2\text{-}Aib\text{-}O)_4(H_2O)_8](ClO_4)_6$	2.110 (**G**)	[19]
$[Gd_6Cu_{24}(\mu_3\text{-}OH)_{30}(H\text{-}AibO)_{16}(ClO_4)(H_2O)_{22}]\ (ClO_4)_{17}(OH)_2\cdot 20H_2O$	3.211 (**B**), 2.110 (**C**)	[20]
$Na[Co(H\text{-}Aib\text{-}O)_2(bpy)](ClO_4)_2\cdot 0.5H_2O$ (bpy = 2.2′-bipyridine)	1.101 (**A**)	[21]
$[Co(H\text{-}Aib\text{-}O)(tpa)](ClO_4)_2\cdot H_2O$ (tpa = (2-pyridylmethyl)amine)	1.101 (**A**)	[22]
$[Pt(H\text{-}Aib\text{-}OH)_2Cl_2]$	1.001 (**F**)	[18]
[Cu (H-Aib-O)(pmdt)]$ClO_4\cdot H_2O$ (pmdt = N,N,N′,N″,N″-pentamethyldiethylenetriamine)	1.101 (**A**)	[23]
$[Pt(H\text{-}Aib\text{-}O)Cl(Ph_3P)]\cdot H_2O$	1.101 (**A**)	[24]
$[Cp_2Ti(H_2\text{-}Aib\text{-}O)_2]Cl_2$	1.100 (**H**)	[25]
$[Mn(CO)_3Mo(CO)(\mu_2\text{-}S_2CPCy_3)(H\text{-}Aib\text{-}O)]\cdot CH_2Cl_2$	2.201 (**E**)	[26]
$[Zn_3(H\text{-}Aib\text{-}O)_6]\cdot MeCOOH\cdot H_2O$	1.101 (**A**), 2.111 (**D**)	this work

[a] The coordination modes of the ligands are given using Harris notation [13].

reported in Table 2. Unit cell dimensions were determined and refined by using the angular settings of 25 automatically centered reflections in the range $22° < 2\theta < 54°$. Intensity data were recorded using a $\theta - 2\theta$ scan. Three standard reflections, monitored every 97 reflections, showed less than 3% variation and no decay. Lorenz, polarization and Ψ-scan absorption corrections were applied using Crystal Logic software. The structures were solved by direct methods using SHELXS-86 [31] and refined by full-matrix least-squares techniques on F^2 with SHELXL-97 [32]. Further experimental crystallographic details for **1**·MeCOOH·H_2O: $2\theta_{max} = 118°$; 472 parameters refined; $(\Delta/\sigma)_{max} = 0.052$; $(\Delta\rho)_{max}/(\Delta\rho)_{min} = 2.353/-0.772$ e Å^3; R_1/wR_2 (for all data), 0.0777/0.2052. All hydrogen atoms were introduced at calculated positions as riding on bonded atoms, except those of water solvate which were located by difference maps and were refined isotropically. All non-hydrogen atoms were refined anisotropically. Further experimental crystallographic details for **2**·H_2O: $2\theta_{max} = 125°$; 279 parameters refined; $(\Delta/\sigma)_{max} = 0.003$; $(\Delta\rho)_{max}/(\Delta\rho)_{min} = 0.450/-0.339$ e Å^3; R_1/wR_2 (for all data), 0.0307/0.0832. Hydrogen atoms were either located by difference maps and refined isotropically or were introduced at calculated positions as riding on bonded atoms. All non-hydrogen atoms were refined anisotropically. Further experimental crystallographic details for **3**·5.8H_2O: $2\theta_{max} = 109.4°$; 453 parameters refined; $(\Delta/\sigma)_{max} = 0.010$; $(\Delta\rho)_{max}/(\Delta\rho)_{min} = 0.722/-0.527$ e Å^3; R_1/wR_2 (for all data), 0.1127/0.2549. All hydrogen atoms were introduced at calculated positions as riding on bonded atoms. All non-hydrogen atoms were refined anisotropically, except of water solvate molecules which were refined isotropically.

3. Results and discussion

3.1. Brief synthetic comments

Complexes **1**·MeCOOH·H_2O, **2**·H_2O and **3**·5.8H_2O were prepared according to Eqs. (1)–(3), respectively:

$$3\ Zn(O_2CMe)_2{\cdot}2H_2O + 6\ (H_2\text{-Aib-O}) + 5\ LiOH{\cdot}H_2O \xrightarrow{MeOH} [Zn_3(H\text{-Aib-O})_6]{\cdot}MeCOOH{\cdot}H_2O + 5\ LiO_2CMe + 15\ H_2O$$

1·MeCOOH·H_2O (1)

$$n\ Zn(O_2CMe)_2{\cdot}2H_2O + 2n\ (H_2\text{-Aib-L-Ala-O}) \xrightarrow{MeOH/H_2O} [Zn(H\text{-Aib-L-Ala-O})_2]_n{\cdot}nH_2O + 2n\ MeCOOH + n\ H_2O$$

2·H_2O (2)

$$Zn(ClO_4)_2{\cdot}6H_2O + 4\ (H_2\text{-Aib-Aib-Aib-O}) \xrightarrow{MeOH} [Zn(H_2\text{-Aib-Aib-Aib-O})_4]\ (ClO_4)_2{\cdot}5.8\ H_2O + 0.2\ H_2O$$

3·5.8H_2O (3)

The use of metal-carboxylates is a common practice in our synthetic procedures in metal–peptide chemistry. The reasons are: (i) carboxylate anions can act as strong bases with consequent deprotonation of the ligands, (ii) the by-products (i.e. $MeCO_2H$, $PhCO_2H$) can be easily removed from the reaction mixture without contamination of the product, and (iii) a portion of the anions RCO_2^- can act as ligands with a variety of coordination modes, resulting in the isolation of ternary complexes with interesting and aesthetically pleasant structures.

In fact, the trinuclear complex **1**·MeCOOH·H_2O was isolated from reaction mixture $Zn(O_2CMe)_2{\cdot}2H_2O$/H_2-Aib-O/LiOH·H_2O containing a small excess of Zn(II). The stoichiometric metal/ligand molar ratio of 1:2 was avoided in order to prevent the isolation of the known complex $[Zn(H\text{-Aib-O})_2(H_2O)_2][Zn(H\text{-Aib-O})_2(H_2O)]_2$ [17]. On the other hand, the addition of a strong base (LiOH) seems to be necessary for the deprotonation of the aminoacid (for H_2-Aib-O: $pK_1 = 2.36$, $pK_2 = 10.21$) and its consequent coordination.

The isolation of complex **2**·H_2O was initially succeeded by using the 1:1.5 metal:ligand stoichiometry. With the identity of **2**·H_2O crystallographically established (vide infra), the "correct" stoichiometric ratio, i.e. Zn(II): dipeptide = 1:2, was employed and led to the pure compound in very good yield (60–65%). The same product was also isolated by employing several metal sources (i.e. $Zn(ClO_4)_2.6H_2O$, $ZnCl_2$, $Zn(NO_3)_2{\cdot}4H_2O$) in metal:ligand proportions 1:1or 1:2 and in the presence of LiOH·H_2O. The fact that all the above synthetic procedures had as a result the isolation of the

Table 2
Crystallographic data for complexes **1**·MeCOOH·H_2O, **2**·H_2O and **3**·5.8H_2O.

Parameter	**1**·MeCOOH·H_2O	**2**·H_2O	**3**·5.8H_2O
Chemical formula	$C_{26}H_{54}N_6O_{15}Zn_3$	$C_{14}H_{28}N_4O_7Zn$	$C_{48}H_{113.6}Cl_2N_{12}O_{29.8}Zn$
Formula weight	886.86	429.77	1472.18
Crystal colour, habit	colourless, prismatic	colourless, prismatic	colourless, prismatic
Crystal dimensions (mm)	0.30 × 0.20 × 0.15	0.30 × 0.25 × 0.20	0.25 × 0.20 × 0.15
Crystal system	monoclinic	monoclinic	orthorhombic
Space group	A_1n_1	$P2_1$	$P2_12_12$
a (Å)	18.850(10)	8.2515(8)	13.406(9)
b (Å)	11.752(9)	12.1618(11)	20.140(10)
c (Å)	18.440(10)	10.0928(11)	15.386(7)
α (°)	90.00(3)	90	90
β (°)	93.21	96.161(4)	90
γ (°)	90	90	90
V (Å^3)	4079(4)	1006.99(17)	4154(4)
Z	4	2	2
T (K)	298	298	298
Radiation, Cu Kα (λ, Å)	1.5418	1.5418	1.5418
ρ_{calc} (g cm^{-3})	1.444	1.417	1.177
μ (mm^{-1})	2.632	2.063	1.651
Data collected/unique (R_{int})	5164/5163 (0.0492)	3535/3152 (0.0422)	4891/4531 (0.0810)
Data with $I > 2\sigma(I)$	5040	3152	3425
R_1[a] [$I > 2\sigma(I)$]	0.0766	0.0307	0.0867
wR_2[b] [unique data]	0.2032	0.0832	0.2262

[a] $R_1 = \Sigma(|F_o| - |F_c|)/\Sigma(|F_o|)$.
[b] $wR_2 = \{\sum[w(F_o^2 - F_c^2)^2]/\sum[w(F_o^2)^2]\}^{1/2}$.

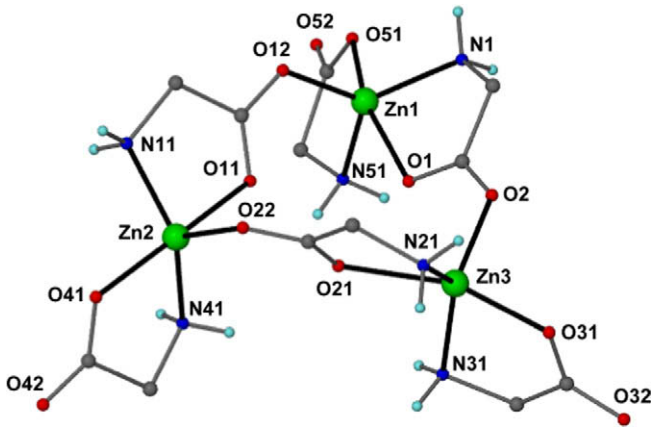


Fig. 1. The molecular structure of **1**·MeCOOH·H_2O. The lattice MeCOOH and H_2O molecules have not been drawn. All methyl groups of the H-Aib-O^- ligands have been omitted for clarity. Color code: Zn = green, O = red, N = blue, C = grey, H = cyan. (For interpretation of the references to colour in this figure legend, the reader is referred to the web version of this article.)

same product demonstrates the high stability of the isolated Zn(II)/dipeptide complex **2**·H_2O.

Our first attempts for the isolation of a Zn(II)/H_2-Aib-Aib-Aib-O complex were made once more by employing $Zn(O_2CMe)_2{\cdot}2H_2O$ as the metal source. Indeed, from the 1:2 (metal:ligand) reaction, a crystalline product was isolated, whose solution of the structure revealed the cationic complex $[Zn(H_2\text{-Aib-Aib-Aib-O})_4]$ $(O_2CMe)_2$. Unfortunately, the full crystallographic analysis of this complex proved impossible. With the aim to stabilize and isolate the above cationic species, where the tripeptide was in its zwitterionic form (a fact scarce in metal/peptide chemistry), the use of $Zn(ClO_4)_2{\cdot}6H_2O$ as starting material was the next step. Complex **3**·5.8H_2O was then isolated employing the "wrong" (1:2) or the "correct"(1:4) metal:ligand ratio.

3.2. Description of structures

The molecular structures of complexes **1**·MeCOOH·H_2O, **2**·H_2O, and **3**·5.8H_2O are shown in Figs. 1, 5 and 9, respectively. Aspects of the crystal structures are shown in Figs. 2–4 (**1**·MeCOOH·H_2O), 6–8 (**2**·H_2O), and 10 and 11 (**3**·5.8H_2O). Selected interatomic distances and angles are listed in Tables 3, 5 and 6 for **1**·MeCOOH·H_2O, **2**·H_2O, and **3**·5.8H_2O, respectively, while important hydrogen bonding interactions are presented in Tables 4 (for **1**·MeCOOH·H_2O), and 7 (for **3**·5.8H_2O).

Complex **1**·MeCOOH·H_2O crystallizes in the monoclinic space group *An*. Its crystal structure consists of trinuclear $[Zn_3(H\text{-Aib-O})_6]$ units and of lattice MeCOOH and H_2O molecules. One H-Aib-O^- ligand chelates to each of the three Zn^{II} atoms through its amino nitrogen atom and one of the carboxylate oxygen atoms, while each of the remaining three anions chelates to each Zn^{II} atom and bridges a neighboring metal ion through the second carboxylate oxygen atom. The carboxylate bridging interaction is of the *syn*, *anti* type (Fig. 1).

Thus, three of the six H-Aib-O^- anions behave as η^1: η^1 ligands or in a 1.101 mode [13], while the other three α-aminoisobutyrate anions behave as $\eta^1{:}\eta^1{:}\eta^1{:}\mu_2$ ligand or in a 2.111 mode (Scheme 1). Each metal center is five-coordinate with an O_3N_2 environment. On the basis of the angular criterion τ, as defined by Addison et al. (τ = 1.00 for an ideal trigonal bipyramid and τ = 0.00 for an ideal square pyramid) [33], the coordination polyhedra around all three Zn atoms lie almost between the two geometrical shapes, with a slight inclination towards the trigonal bipyramidal (τ = 0.55, 0.56 and 0.54 for Zn(1), Zn(2) and Zn(3), respectively). The principal axes and angles for the three trigonal bipyramidal Zn^{II} atoms are O(1)–Zn(1)–O(51) 160.3(3)°, O(11)–Zn(2)–O(41) 164.1(3)° and

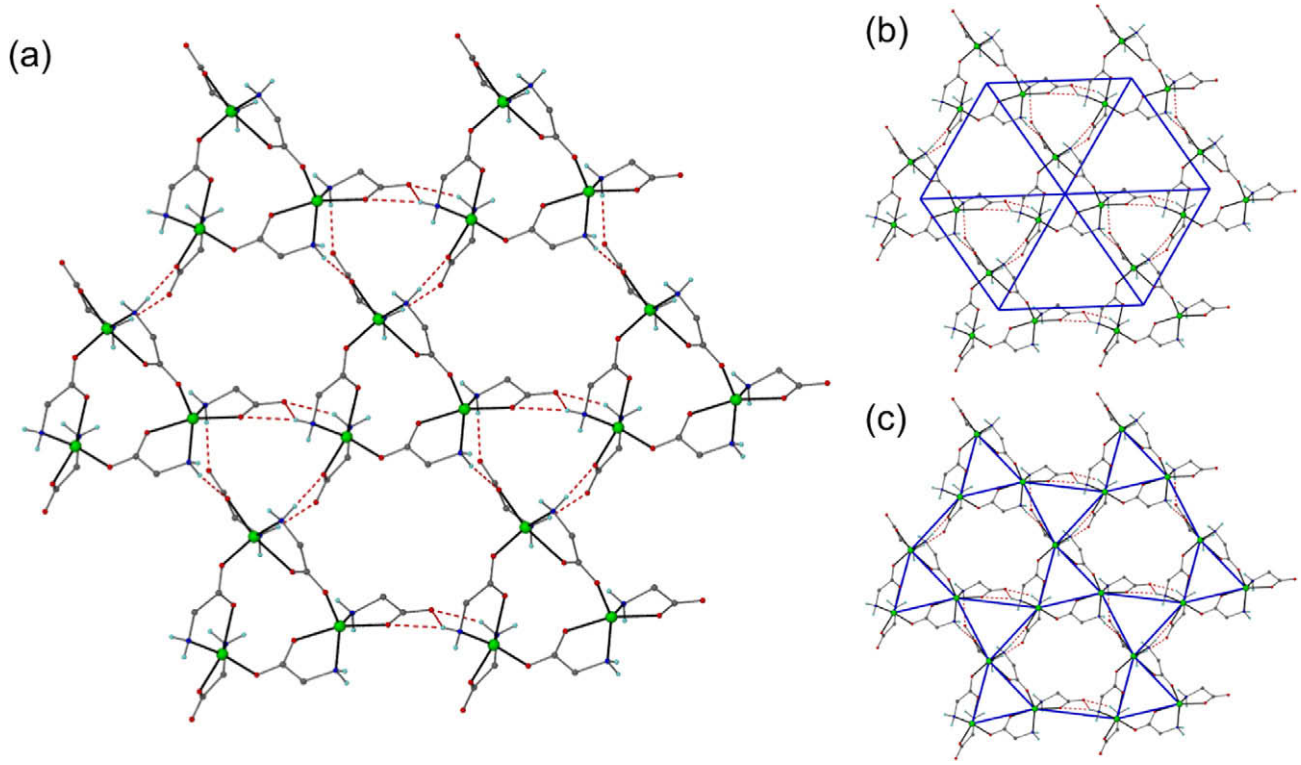


Fig. 2. The 2D hydrogen bonded framework of **1**·MeCOOH·H_2O (a) that conforms to a (3,6)-net (b) or to a (3.6.3.6)-net (c). All methyl groups of the H-Aib-O^- ligands have been omitted for clarity. Color code: Zn = green, O = red, N = blue, C = grey, H = cyan. The blue lines in (b) and (c) are guides for the eye and draw the underline nets. (For interpretation of the references to colour in this figure legend, the reader is referred to the web version of this article.)

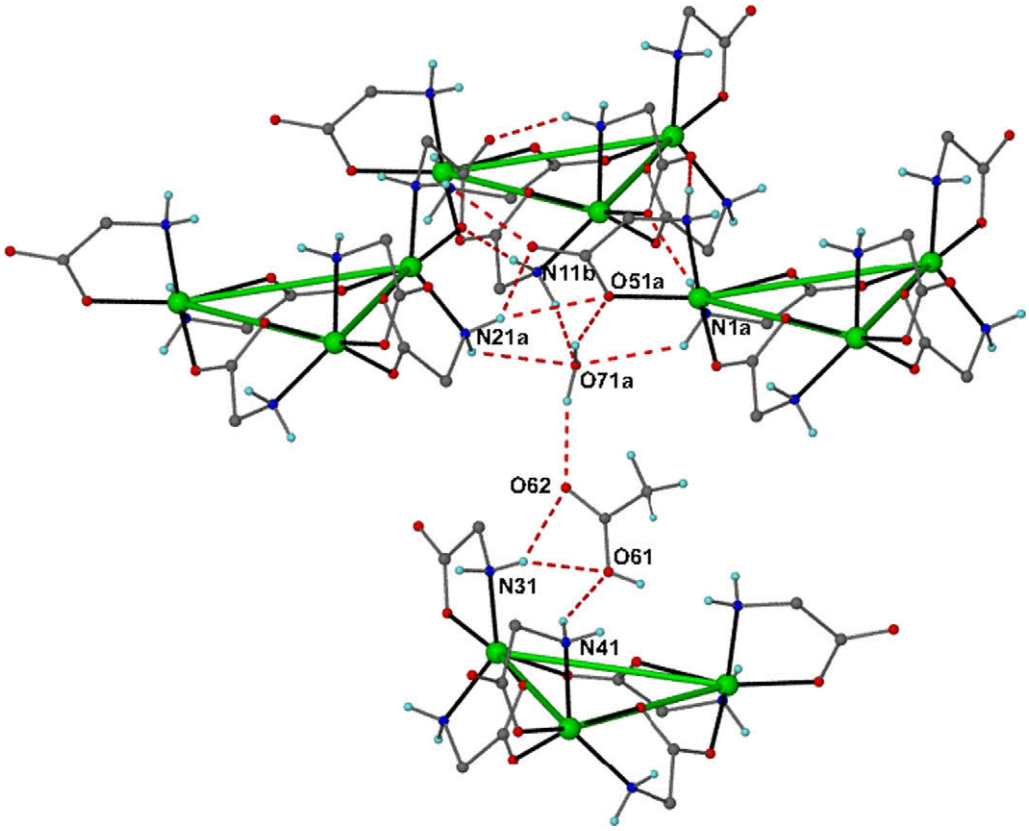


Fig. 3. The hydrogen bonding interactions between the layers in $[Zn_3(\text{-H-Aib-O})_6]\cdot MeCOOH\cdot H_2O$. All methyl groups of the H-Aib-O$^-$ ligands have been omitted for clarity. Color code: Zn = green, O = red, N = blue, C = grey, H = cyan. The green lines are guides for the eye and draw the trinuclear units. Symmetry codes: a 0.5 + *x*, 1.5 − *y*, *z*; b 05 + *x*, 1 − *y*, 0.5 + *z*. (For interpretation of the references to colour in this figure legend, the reader is referred to the web version of this article.)

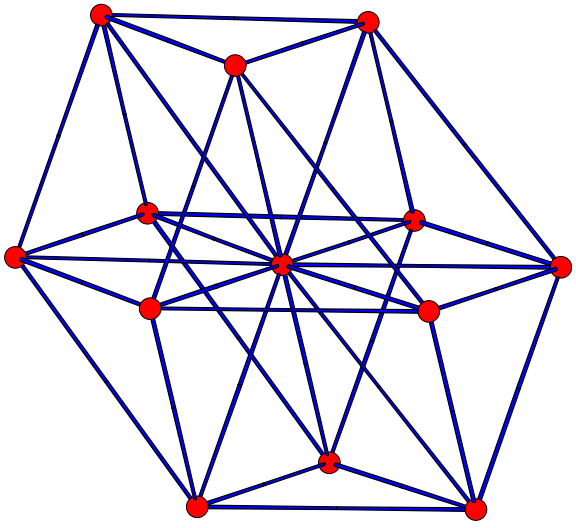


Fig. 4. The 3D 12-connected hydrogen bonded **fcu** net in $\mathbf{1}\cdot MeCOOH\cdot H_2O$. The red circles represent the center of gravity of the trinuclear units.

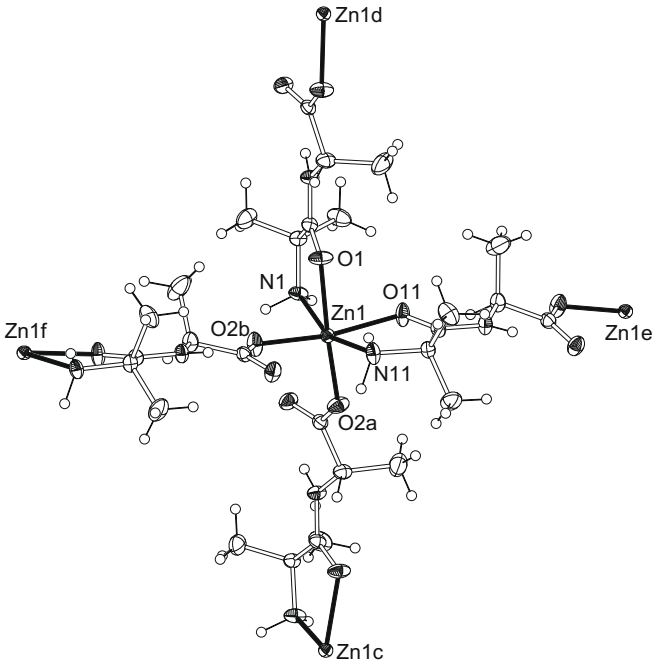


Fig. 5. ORTEP plot (30% probability) of the coordination environment around the central atom in $\mathbf{2}\cdot H_2O$ and the connectivity of the 2D polymer. Symmetry codes: a 2 − *x*, 0.5 + *y*, −*z*; b 1 − *x*, 0.5 + *y*, 1 − *z*; c 2 − *x*, 0.5 + *y*, −*z*; d 1 − *x*, −0.5 + *y*, 1 − *z*; e 2 − *x*, −0.5 + *y*, −*z*; f 1 − *x*, 0.5 + *y*, 1 − *z*.

O(21)–Zn(3)–O(31) 159.2(3)° (Table 3). The Zn(1)···Zn(2) and Zn(1)···Zn(3) and Zn(2)···Zn(3) separations are 5.335, 5.351, and 5.317 Å, respectively.

All twelve values of the C–O carboxylate bonds of the organic ligands lie in the range 1.219–1.292 Å (mean value 1.26 Å), which is referred as the range (1.20–1.33 Å, mean value 1.245 Å) of C–O bond lengths of α-aminoacids in all metal complexes [34].

In complex $\mathbf{1}\cdot\mathbf{MeCOOH}\cdot H_2O$, the aminoacid moiety obviously presents quite different conformation (which is defined by the ϕ = Zn–N–C^a–C' and ψ = N–C^a–C'–O dihedral angles) from the minimum energy conformation, as calculated theoretically, which is

Table 3
Selected bond distances (Å), angles (°) and dihedral angles for complex **1**·MeCOOH·H_2O.

Distances			
Zn(1)–O(1)	2.1888(7)	Zn(2)–N(11)	2.004(10)
Zn(1)–O(12)	1.989(7)	Zn(2)–N(41)	1.987(9)
Zn(1)–O(51)	2.069(7)	Zn(3)–O(2)	1.980(7)
Zn(1)–N(1)	2.029(8)	Zn(3)–O(21)	2.210(6)
Zn(1)–N(51)	2.025(8)	Zn(3)–O(31)	2.033(7)
Zn(2)–O(11)	2.244(6)	Zn(3)–N(21)	1.985(8)
Zn(2)–O(22)	2.001(6)	Zn(3)–N(31)	2.009(8)
Zn(2)–O(41)	2.030(8)		
Angles			
O(1)–Zn(1)–O(12)	97.5(3)	O(41)–Zn(2)–O(22)	101.2(3)
O(1)–Zn(1)–O(51)	160.2(3)	O(41)–Zn(2)–N(11)	102.2(4)
O(1)–Zn(1)–N(1)	77.6(3)	O(41)–Zn(2)–N(41)	80.0(4)
O(1)–Zn(1)–N(51)	90.0(3)	N(11)–Zn(2)–O(22)	109.6(3)
O(51)–Zn(1)–O(12)	102.3(3)	N(11)–Zn(2)–N(41)	130.3(4)
O(51)–Zn(1)–N(1)	93.9(3)	O(2)–Zn(3)–O(21)	100.4(3)
O(51)–Zn(1)–N(51)	81.1(3)	O(2)–Zn(3)–O(31)	100.4(3)
N(1)–Zn(1)–O(12)	116.6(3)	O(2)–Zn(3)–N(21)	111.5(3)
N(1)–Zn(1)–N(51)	127.5(3)	O(2)–Zn(3)–N(31)	121.4(4)
N(51)–Zn(1)–O(12)	115.5(3)	O(21)–Zn(3)–O(31)	159.2(3)
O(11)–Zn(2)–O(22)	94.0(3)	O(21)–Zn(3)–N(21)	76.3(3)
O(11)–Zn(2)–O(41)	164.1(3)	O(210–Zn(3)–N(31)	88.0(3)
O(11)–Zn(2)–N(11)	76.6(3)	O(31)–Zn(3)–N(21)	96.4(4)
O(11)–Zn(2)–N(41)	88.6(3)	O(31)–Zn(3)–N(31)	80.8(3)
O(22)–Zn(2)–N(41)	118.8(4)	N(21)–Zn(3)–N(31)	126.7(3)
Dihedral angles (°) for the aminoacid moieties			
Zn(1)–N(1)–C(2)–C(1)	(ϕ_1) 26.86	Zn(3)–N(31)–C(32)–C(31)	(ϕ_4) 31.17
N(1)–C(2)–C(1)–O(1)	(ψ_1) −14.54	N(31)–C(32)–C(31)–O(31)	(ψ_4) −21.44
Zn(2)–N(11)–C(12)–C(11)	(ϕ_2) 29.26	Zn(2)–N(41)–C(42)–C(41)	(ϕ_5) 28.88
N(11)–C(12)–C(1)–O(11)	(ψ_2) −11.37	N(41)–C(42)–C(41)–O(41)	(ψ_5) −24.31
Zn(3)–N(21)–C(22)–C(21)	(ϕ_3) 26.58	Zn(1)–N(51)–C(52)–C(51)	(ϕ_6) 33.77
N(21)–C(22)–C(21)–O(21)	(ψ_3) −15.82	N(51)–C(52)–C(51)–O(51)	(ψ_6) −27.36

Table 4
Dimensions of the unique hydrogen bonds (distances in Å and angles in °) for **1**·MeCOOH·H_2O.

D[a]–H···A[b]	H···A[b]	D[a]···A[b]	∠D[a]HA[b]
N1–H1A···O41 [x, 1/2 + y, 1/2 + z]	2.00	2.896(12)	172
N11–H11A···O31 [x, 1/2 + y, −1/2+z]	2.04	2.938(12)	178
N21–H21A···O51 [x, −1 + y, z]	2.52	3.397(10)	165
N21–H21A···O52 [x, −1 + y, z]	2.14	2.874(11)	138
N31–H31A···O52 [x, −1 + y, z]	2.43	3.106(12)	132
N41–H41A···O32 [x, 1/2 + y, −1/2+z]	2.01	2.832(16)	150
N51–H51A···O42 [x, 1/2 + y, 1/2 + z]	2.12	2.951(15)	154
N1–H1B···O71	2.51	3.205(13)	134
N11–H11B···O71 [x, −1/2 + y, −1/2+z]	2.34	3.131(12)	146
N21–H21B···O71 [x, −1 + y, z]	2.55	3.127(12)	122
N31–H31B···O61	2.53	3.381(11)	158
N31–H31B···O62	2.35	3.106(12)	142
N41–H41B···O61	2.19	2.992(12)	148
O71–H71B···O62 [−1/2 + x, 3/2 − y, z]	1.97	2.805(13)	165
O71–H71A···O51	2.11	2.922(12)	157

[a] D, donor atom.
[b] A, acceptor atom.

also that commonly observed for α-aminoisobutyric acid residues in peptide crystal structures [12,18]. This conformation, characterized by ϕ and ψ values of about −60°, −30° (or the centrosymmetric 60°, 30°) falls in the helical region of the ϕ–ψ map [35]. In the parent complex, in which the aminoacid anion coordinates in a chelate mode, the observed conformation is folded with values for the ϕ and ψ dihedral angles in the region of 26.58° to 33.77° and −11.37° to −27.36°, respectively.

The trinuclear units assemble through seven hydrogen bonds (and their symmetry related) that involve the $-NH_2$ groups and some of both the coordinated and uncoordinated carboxylate O atoms (Table 4) to form a 2D hydrogen bonded framework (Fig. 2) that conforms to a regular net of a (3,6) topology running parallel to the *bc* plane (Fig. 2a). Due to the size and the shape of the trinuclear complexes which serve as 6-connected nodes within the 2D (3,6) framework, half of the triangular cavities around a trinuclear node are bigger than the others and look like hexagons. The hexagonal cavities could also be envisaged by considering each metal as a 4-connected node. In this perspective, the resulting network is a semi-regular net with (3.6.3.6) topology (kagome net) (Fig. 2c) [36].

The lattice acetic acid and water molecules sit within the layers and connect them to create a 3D hydrogen bonded framework with a $3^{24}.4^{36}.5^6$ topology (**fcu**) [37,38]. The acetic acid molecule sits above the trinuclear unit and is hydrogen bonded to it through three hydrogen bonds [N31–H31B···O61, N31–H31B···O62 and O71–H71B···O62] (Fig. 3). The water molecule sits above a small trigonal cavity and is hydrogen bonded to the three trinuclear units [N1–H1B···O71, N11–H11B···O71, N21–H21B···O71 and O71–H71A···O51] that form the trigonal cavity, while it is also hydrogen bonded to the acetic acid molecule [O71–H71B···O62] (Fig. 3). In this arrangement each trinuclear unit is connected *via* the MeCOOH and the H_2O molecules to six trinuclear units belonging to two neighboring layers above and below the main layer's plane. In this arrangement each trinuclear unit connects to six other trinuclear units that belong to the same (3,6)-layer and to six trinuclear units that belong to neighboring layers, giving rise to a 12-connected 3D network with **fcu** topology (Fig. 4).

Complex **1**·MeCOOH·H_2O is the ninth member of crystallographically established *binary* H-Aib-OH/metal ion complexes (Table 1), and three of its ligands adopt the new coordination mode [2.111], as is seen in Scheme 1.

Concerning the structurally characterized Zn(II)/α-aminoacid *binary* complexes we have to mention the following: (a) The crystal structures of binary complexes of Zn(II) with almost all the natural

Table 5
Selected bond distances (Å) and angles (°) for complex **2**·H_2O[a].

Distances			
Zn(1)–O(1)	2.258(2)	Zn(1d)–O(2)	2.083(2)
Zn(1)–N(1)	2.086(3)	Zn(1e)–O(12)	2.026(2)
Zn(1)–O(11)	2.181(2)	C(4)–O(1)	1.252(3)
Zn(1)–N(11)	2.116(3)	C(4)–N(2)	1.320(4)
Zn(1)–O(2a)	2.026(2)	C(7)–O(2)	1.249(3)
Zn(1)–O(2b)	2.083(2)	C(7)–O(3)	1.244(3)
Angles			
O(2a)–Zn(1)–O(2b)	98.21(11)	O(2a)–Zn(1)–O(1)	176.43(10)
O(2a)–Zn(1)–N(1)	106.74(9)	O(2b)–Zn(1)–O(1)	84.44(9)
O(2b)–Zn(1)–N(1)	87.50(10)	N(1)–Zn(1)–O(1)	75.69(9)
O(2a)–Zn(1)–N(11)	89.20(10)	N(11)–Zn(1)–O(1)	87.81(10)
O(2b)–Zn(1)–N(11)	104.58(9)	O(11)–Zn(1)–O(1)	87.29(10)
N(1)–Zn(1)–N(11)	158.62(12)	N(1)–C(1)–C(4)	108.3(2)
O(2a)–Zn(1)–O(11)	90.12(10)	N(2)–C(5)–C(7)	111.1(2)
O(2b)–Zn(1)–O(11)	171.61(11)	C(1)–C(4)–N(2)	117.9(2
N(1)–Zn(1)–O(11)	89.13(10)	C(1)–C(4)–O(1)	120.7(2)
N(11)–Zn(1)–O(11)	76.41(9)	C(1)–C(4)–N(2)	121.3(2)
Hydrogen bonds			
D[b]–H···A[c]	H···A[c]	D[b]···A[c]	<D[b]HA[c]
Ow1–Hw1A···O3 [2 − *x*, 1/2 + y, 1 − z]	2.19(6)	3.011(4)	135(4)
Ow1–Hw1A···O13 [2−*x*, 1/2 + *y*, −*z*]	2.17(6)	3.004(4)	136(4)
Ow1–Hw1B···O1 [1 + *x*, *y*, *z*]	2.11(6)	2.949(3)	169(6)
N1–Hn1A···Ow1	2.27(6)	3.083(4)	168(4)
N2–Hn2···O13 [*x*, *y*, 1 + *z*]	2.21(3)	3.076(3)	174(3)
N12–Hn12···O3 [*x*, *y*, −1 + *z*]	2.02(3)	2.875(3)	164(3)
N12–Hn12···O13	2.32(3)	2.711(3)	107(3)

[a] Symmetry transformations used to generate equivalent atoms: a = 2 − *x*, 0.5 + *y*, −*z*; b = 1 − *x*, 0.5 + *y*, 1 − *z*; d = 1 − *x*, −0.5 + *y*, 1 − *z*; e = 2 − *x*, 0.5 + *y*, *z*.
[b] D, donor atom.
[c] A, acceptor atom.

α-aminoacids have been reported. (b) The majority of these compounds are monomeric or coordination polymers with only few exceptions, where the Zn(II)/aminoacid coordination results in a cluster formation. These are: $[Zn(Iva)_2]\cdot 2H_2O$ (Iva = isovaline), which is described as a 1D coordination polymer or as a cyclic trimer [39], $[Zn(Iva)_2]\cdot 3.25H_2O$ in which six $[Zn(Iva)_2]$ moieties form the discrete cyclic complex $[Zn_6(Iva)_{12}]$ [39], and the organometallic tetranuclear cluster $[EtZn(\alpha,\alpha\text{-}Ph_2Gly)]_4\cdot CH_3CN$ (α,α-Ph_2Gly = α,α-diphenylglycine) [40]. At this point, a remarkable feature has to be noted: All three aminoacids, i.e. H-Aib-OH, H-Iva-OH and H-Ph_2Gly-OH, are closely related to each other. So, -Iva- is formally derived from -Aib- by replacing a methyl group by an ethyl group, and -Ph_2Gly- by replacing the two methyl groups by two phenyl groups. The dialkylation of the α-carbon, which sterically restricts the conformational freedom of the aminoacid and causes a bent around C[a] atom, seems to favor cluster formation.

Complex **2**·H_2O crystallizes in the monoclinic space group $P2_1$.The Zn^{II} atom and the anionic peptide H-Aib-L-Ala-O^- ligands have assembled to create a two-dimensional (2D) square grid framework laying parallel to the 1 0 1 plane (Figs. 5 and 6). The Zn^{II}

Table 6
Selected bond distances (Å) and angles (°) for complex **3**·5.8H_2O[a].

Distances			
Zn–O(1)	1.968(6)	C(9)–O(4)	1.2369(13)
Zn–O(1a)	1.968(6)	C(9)–N(2)	1.307(15)
Zn–O(11)	1.974(6)	C(5)–O(3)	1.222(13)
Zn–O(11a)	1.974(6)	C(5)–N(1)	1.315(13)
C(1)–O(1)	1.284(12)	C(29)–O(14)	1.195(11)
C(1)–O(2)	1.236(11)	C(29)–N(12)	1.344(13)
C(21)–O(11)	1.262(12)	C(25)–O(13)	1.226(12)
C(21)–O(12)	1.231(12)	C(220–N(11)	1.453(12)
Angles			
O(1)–Zn O(1a)	108.2(4)	N(3)–C(10)–C(9)	105.5(9)
O(1)–Zn–O(11a)	119.7(3)	N(2)–C(6)–C(5)	110.6(9)
O(1)–Zn–O(11)	101.5(3)	N(1)–C(2)–C(1)	106.6(8)
O(1a)–Zn–O(11a)	101.5(3)	N(13)–C(30–C(29)	104.8(7)
O(1a)–Zn–O(11)	119.7(3)	N(12)–C(26)–C(25)	112.3(9)
O(11a)–Zn–O(11)	107.3(4)	N(11)–C(22)–C(21)	107.9(8)
Dihedral angles of the peptide ligand			
N(3)–C(10)–C(9)–N(2)	$(\psi_1) = -172.76$	N(13)–C(30)–C(29)–N(12)	$(\psi_1) = -174.51$
C(9)–N(2)–C(6)–C(5)	$(\phi_2) = -56.89$	C(29)–N(12)–C(26)–C(25)	$(\phi_2) = -62.64$
N(2)–C(6)–C(5)–N(1)	$(\psi_2) = -32.82$	N(12)–C(26)–C(25)–N(11)	$(\psi_2) = -22.67$
C(5)–N(1)–C(2)–C(1)	$(\phi_3) = -172.02$	C(25)–N(11)–C(22)–C(21)	$(\phi_3) = -175.20$
N(1)–C(2)–C(1)–O(1)	$(\psi_3) = 6.83$	N(11)–C(22)–C(21)–O(11)	$(\psi_3) = -3.53$
N(1)–C(2)–C(1)–O(2)	$(\psi'_3) = -179.13$	N(11)–C(22)–C(21)–O(12)	$(\psi'_3) = 174.57$

[a] Symmetry transformations used to generate equivalent atoms: a = −*x*, −*y*, *z*.

atom is in a distorted octahedral N_2O_4 environment. Two dipeptide monoanions bind one Zn^{II} atom *via* their amino nitrogens [N(1), N(11)] and peptide oxygens [O(1), O(11)], with the oxygen atoms in a *cis* orientation and the nitrogen atoms in a *trans* orientation, and two adjacent Zn^{II} atoms each through one of their carboxylate oxygens, adopting the $\eta^1{:}\eta^1{:}\eta^1{:}\mu_2$ or 2.11010 [13] coordination mode. Two monodentate carboxylate oxygen atoms from the C-terminal group of two other H-Aib-L-Ala-O^- ligands in *cis* orientation complete the octahedral environment around the Zn^{II} atom.

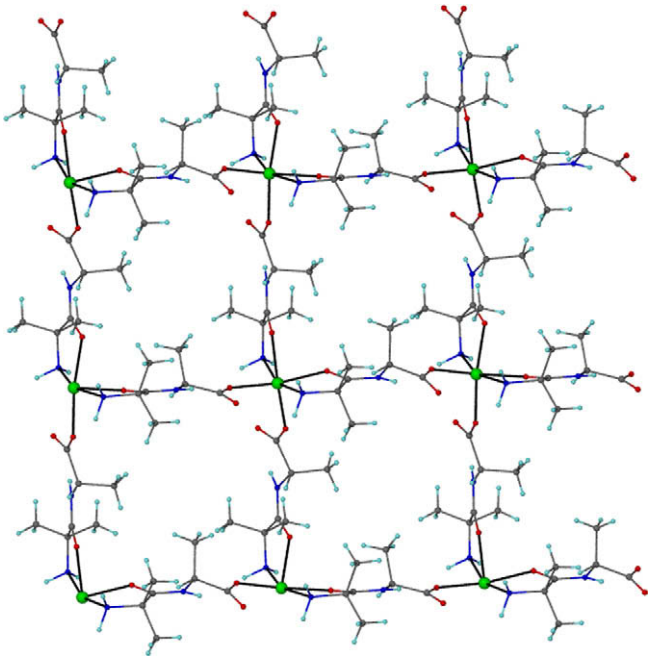


Fig. 6. Perspective view of the 2D layer in **2**·H_2O. Color code: Zn = green, O = red, N = blue, C = grey, H = cyan. (For interpretation of the references to colour in this figure legend, the reader is referred to the web version of this article.)

The 2D layers are parallel and stacked off set in such a way that the Zn^{II} atoms of one layer are placed above the square cavities of the next layer. The layers are connected in the third dimension through two complementary hydrogen bonds (and their symmetry related) that involve the amidic N-H group and the uncoordinated carboxylate O atom [N2–Hn2···O13 and N12–Hn12···O3] (Fig. 7). In this arrangement, each Zn^{II} atom serves as a 4-connected node, by being the vertice of the square grid [(4,4)-net], while each dipeptide ligand might be regarded as a 3-connected node by bridging two Zn^{II} atoms within the same layer and connecting an H-Aib-L-Ala-O^- ligand of a neighbouring net through the two complementary hydrogen bonds. The resulting framework conforms to a **tfa** net (Fig. 8) [38,41]. The solvate H_2O molecules complement this hydrogen bonding pattern by forming a bifurcated hydrogen bond with the two carboxylate O atoms [Ow1–Hw1A···O3 and Ow1–Hw1A···O13] that form the double hydrogen bond bridge between the layers, connecting a neighbouring coordinated carbonyl O atom [Ow1–Hw1B···O1], while accepting a hydrogen bond from a N-H group of the N terminal side [N1–Hn1A···Ow1] (Fig. 7).

Complex **2**·H_2O is the fourth member of a small family of structurally characterized *binary* Zn^{II}/free dipeptide complexes (see Section 1 [11a–c], in all of which the dipeptide anions adopt the same N_{amine}, $O_{peptide}$, $O_{carboxylate}$ coordination mode.

Complex **3**·5.8 H_2O crystallizes in the orthorhombic space group $P2_12_12_1$. Its molecular structure consists of mononuclear complex cations $[Zn(H_2Aib\text{-}Aib\text{-}Aib\text{-}O)_4]^{2+}$, CLO_4^- anions and lattice water molecules. The Zn^{II} atom lies in a distorted tetrahedral environment surrounded by four (two crystallographically independent) tripeptide ligands. Each tripeptide is in its zwitterionic form and coordinated to the metal ion through one of its carboxylate oxygen atoms, while the protonated NH_3^+ group forms an intramolecular hydrogen bond [N3–Hn3A···O12 and N13–Hn13A···O2] with the uncoordinated carboxylate oxygen atom of a neighbouring ligand (Fig. 9).

This "head-to tail" sequence, in which the terminal amine and carboxylate groups are brought in proximity, is also observed in the crystal structure of the free tripeptide (H_2-Aib-Aib-Aib-O)·2H_2O [42]. A comparison of the values of important parameters

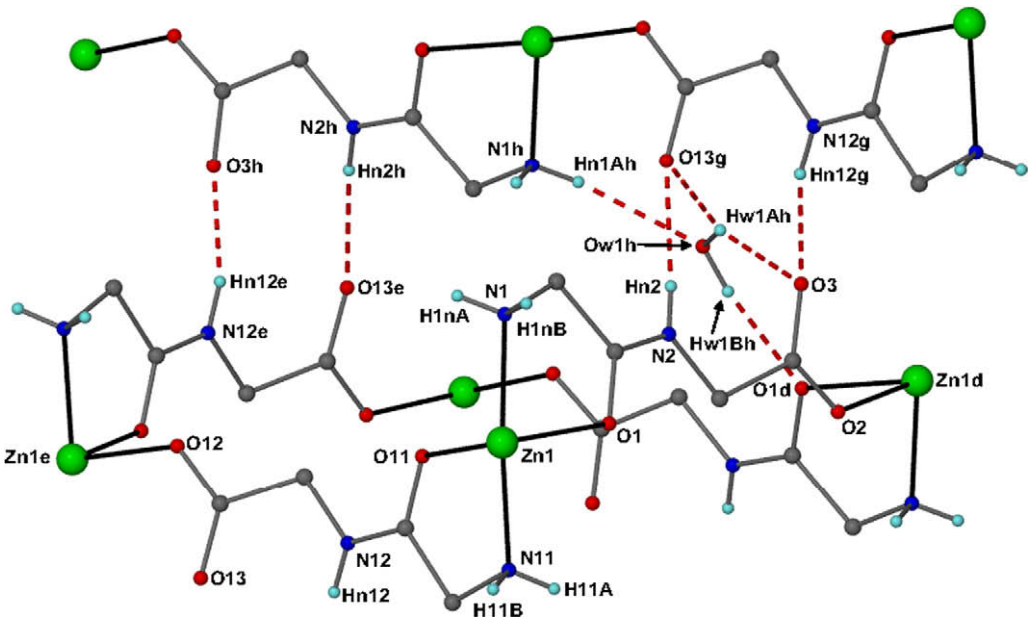


Fig. 7. The hydrogen bonding between the square grid layers and the solvate H_2O molecule in **2**·H_2O. Color code as in Fig. 6. Many H and C atoms have been omitted for clarity. Symmetry codes same as in Fig. 5 and h $2-x, -0.5+y, 1-z$; g $x, y, 1+z$. (For interpretation of the references to colour in this figure legend, the reader is referred to the web version of this article.)

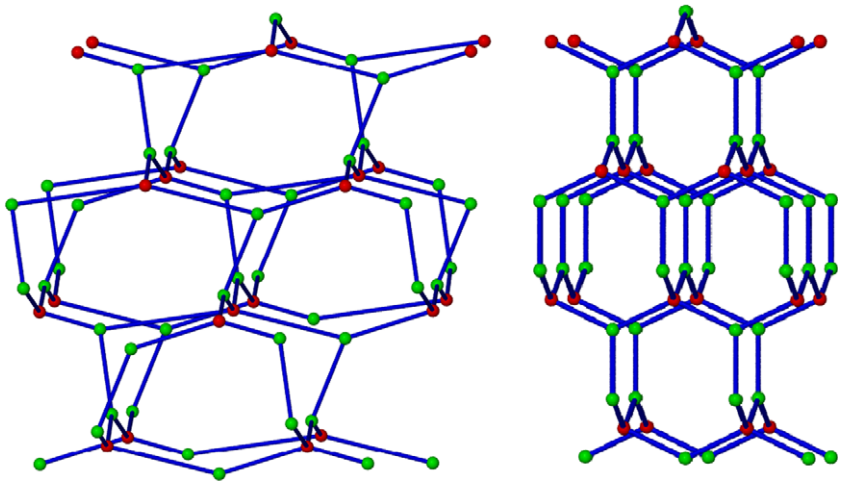


Fig. 8. The real (left) and ideal (right) **tfa** network that **2**·H_2O adopts (see text for details). Color code: Zn = red, H-Aib-Ala-O^- = green. (For interpretation of the references to colour in this figure legend, the reader is referred to the web version of this article.)

of the coordinated and free peptide skeleton can give us a measure of the difference in conformation upon complexation of the ligand. The values of N–C[a]–C' angles are not significantly affected by metal ion coordination, the major difference being the value of the second -Aib- residue [N(2)–C(6)–C(5) = 110.6°/N(12)–C(26)–C(25) = 112.3°], which is larger in the complex than the corresponding value of free peptide (107.1°). Also, small to negligible deviations of the values of C–O and C–N peptide bonds are observed for the free and coordinated tripeptide. The two carboxylate C–O bonds in the free peptide (both of which are involved in hydrogen bonds) (C–O1 = 1.248(3) Å, C–O2 = 1.256(3) Å), are elongated (C(1)–O(1) = 1.284(12) Å, C(21)–O(11) = 1.262(12) Å) and shortened (C(1)–O(2) = 1.236(11) Å, C(21)–O(12) = 1.231(12) Å) after complexation. The planarity of the peptide bonds is retained in the free and complexed tripeptide, as it results from the sum of the angles around the peptide carbon atom (359.5–360.0°). A better description of the peptide backbone conformation is possible by comparing the values of the dihedral angles, (ϕ, ψ) for each residue in the structures of the free and complexed tripeptide. For the first and the third residues these values do not differ essentially for the two forms (ψ_1 = 180°, ϕ_3 = 178.4°, ψ_3 = 4.6° for the free peptide [42], ψ_1 = −172.76° and −174.51, ϕ_3 = −172.02° and −175.20°, ψ_3 = 6.83° and −3.53° for the complex) and these residues are in an extended conformation. A significant difference appears in the values of the second residue (ϕ_2 = 52.9°, ψ_2 = −141.5° for the free ligand, ϕ_2 = −56.89° and −62.64°, ψ_2 = −32.82° and −22.67° for the complexed peptide). The above values indicate a more folded conformation which lies in the limits of the helical region (ϕ = ±60, ψ = ±30) of the ϕ–ψ map [35].

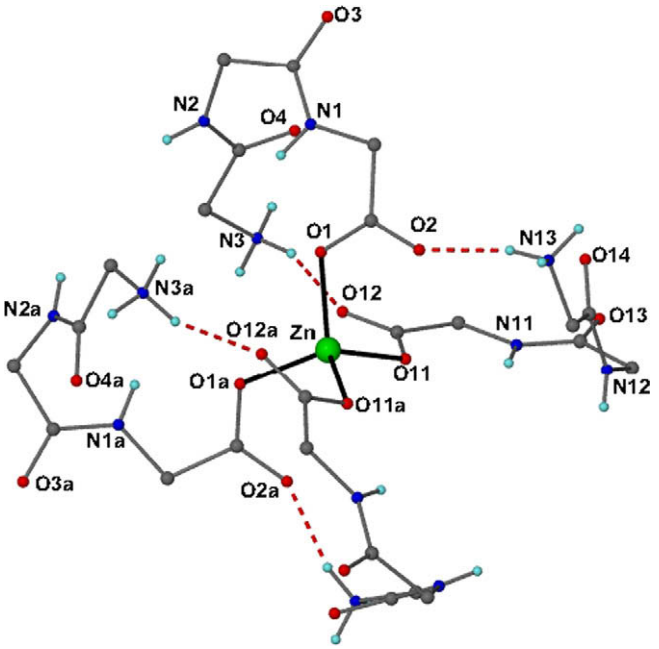


Fig. 9. The coordination environment around the central atom in **3**·5.8H_2O and the intramolecular hydrogen bonding. All methyl groups of the side chains of the tripeptide ligands and the H_2O solvate molecules have been omitted for clarity. Color code: Zn = green, O = red, N = blue, C = grey, H = cyan. Symmetry code: a −*x*, −*y*, *z*. (For interpretation of the references to colour in this figure legend, the reader is referred to the web version of this article.)

Each tripeptide ligand is connected to two other tripeptide ligands belonging to two neighboring $[Zn(H_2\text{-Aib-Aib-Aib-O})_4]^{2+}$ complexes through two hydrogen bonds [N3–Hn3B···O3b and N13–Hn13B···O13c; b −0.5 + *x*, 0.5 − *y*, 1 − *z*; c 05 + *x*, 0.5 − *y*, −*z*] that involve the protonated $-NH_3^+$ group and one of the carbonyl O atoms (Table 7). In this arrangement each $[Zn(H_2\text{-Aib-Aib-Aib-O})_4]^{2+}$ cation is connected to eight neighbouring complexes forming a 3D hydrogen-bonded framework (Fig. 10) that adopts the **bcu** network [38] (Fig. 11) with the Zn^{II} atoms being the nodes of the 8-connected net.

Table 7
Dimensions of the unique hydrogen bonds (distances in Å and angles in °) for **3**·5.8H_2O.

D[a]–H···A[b]	H···A[b]	D[a]···A[b]	∠D[a]HA[b]
N3–Hn3A···O12	1.93	2.784(12)	160
N13–Hn13A···O2	1.90	2.769(11)	164
N3–Hn3B···O3 [−0.5 + *x*, 0.5−*y*, 1 − *z*]	1.94	2.788(13)	158
N13–Hn13B···O13 [05 + *x*, 0.5 − *y*, −*z*]	1.99	2.832(11)	157
N2–Hn2···O21	2.27	3.127(11)	171
N3–Hn3C···Ow1 [−1 + *x*, *y*, *z*]	1.85	2.73(2)	172
N12–Hn12···O24 [*x*, *y*, −1 + *z*]	2.21	2.98(2)	150
N12–Hn12···O22 [−*x*, −*y*, −1 + *z*]	2.19	2.95(2)	146
N13–H13B···O13 [1/2 + *x*, ½ − *y*, −*z*]	1.99	2.832(11)	157
N13–H13C···O31 [1 − *x*, −*y*, *z*]	2.09	2.97(3)	169

[a] D, donor atom.
[b] A, acceptor atom.

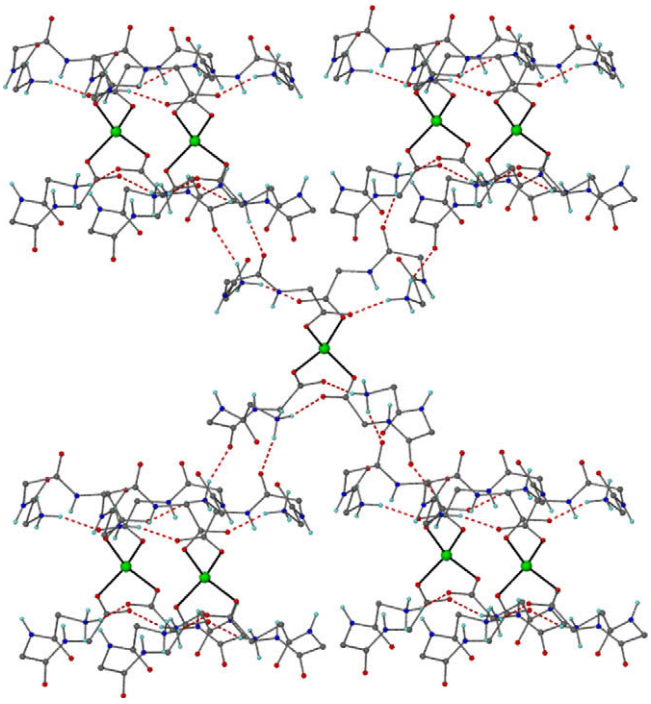


Fig. 10. The hydrogen bonding between the $[Zn(H_2\text{-Aib-Aib-Aib-O})_4]^{2+}$ cations in **3**·5.8H_2O. All methyl groups of the side chains of the tripeptide ligands have been omitted for clarity. Color code: Zn = green, O = red, N = blue, C = grey, H = cyan. (For interpretation of the references to colour in this figure legend, the reader is referred to the web version of this article.)

Alternatively, if we regard each tripeptide ligand as a 3-connected node due to its hydrogen bonding to two other tripeptide ligands and the coordination to the Zn^{II} atom, which can now be regarded as a 4-connected node, the resulting network is a 3,4-connected net with a Schäfli symbol $(8^3)_4{\cdot}8^6$ (topological type: **sqc185**) [43] (Fig. 11).

The above topological analysis is rather oversimplified, giving the connectivity of the $[Zn(H_2\text{-Aib-Aib-Aib-O})_4]^{2+}$ cation in the lattice through the intermolecular hydrogen bonds that form between the coordinated tripeptide ligands, but ignoring the ClO_4^- and the lattice water molecules. The presence of the ClO_4^- (one of which is disordered) ions and the lattice water molecules (also disordered) which participate in the formation of several hydrogen bonds with the tripeptide ligands and with each other, complicate the resulting three-dimensional framework making the topological analysis difficult, if not impossible.

Table 8
The crystallographically established coordination modes of tripeptides in the *binary* M^{n+}/free-tripeptide complexes, in their zwitterionic, mono-, di- and trianionic forms.

Compound	Coordination mode[a]	Ref.
$[Fe_3(\mu_3\text{-O})(H_2\text{-Gly-Gly-Gly-O})_6(H_2O)_3](ClO_4)_7{\cdot}HClO_4{\cdot}H_2O$	2.1100000 **(A)**	[44]
$\{[Mo_4O_{12}(H_2\text{-Gly-Gly-Gly-O})_2]{\cdot}9H_2O\}_n$	2.1100000 **(A)**	[45]
$[Zn(H_2\text{-Aib-Aib-Aib-O})_4](ClO_4)_2{\cdot}5.8H_2O$	1.1000000 **(B)**	This work
$[Cd(H\text{-Gly-Gly-Gly-O})_2{\cdot}H_2O]_n$	3.1100100 **(C)**	[46]
$\{[Zn(H\text{-Gly-Gly-Gly-O})(H_2O)](SO_4)_{0.5}{\cdot}2H_2O\}_n$	2.1010100 **(D)**	[11e]
$[Cd(H\text{-Ala-Ala-Ala-O})_2]_n$	2.1010100 **(D)**	[46]
$\{[Eu(H\text{-Gly-Gly-Gly-O})_3(H_2O)_4](ClO_4)_3{\cdot}H_2O\}_n$	3.1111000 **(E)**	[47]
$[Cu(H\text{-Gly-Leu-Tyr-O})_2]{\cdot}8H_2O{\cdot}Et_2O$	2.1010101 **(F)**	[48]
$[Cu(H\text{-Aib-H}_{-1}\text{Aib-Aib-O})0.5(H_2O)]{\cdot}CH_3CN{\cdot}7H_2O$	2.1100110 **(G)**	[28b]
$Na_2[Cu_2(H\text{-Gly-H}_{-1}\text{GlyH}_{-1}\text{Gly-O})_2]{\cdot}2H_2O$	2.1000111 **(H)**	[49]
$Na[Cu^{III}(H\text{-Aib-H}_{-1}\text{Aib-H}_{-1}\text{Aib-O})](ClO_4){\cdot}2H_2O$	1.1000111 **(I)**	[28a]

[a] The coordination modes of the ligands are given using Harris notation [13].

The monodentate carboxylate coordination of the zwitterionic form of the peptide ligand, as it is observed in complex **3**·5.8H_2O, is very scarce in the metal/peptide coordination chemistry. In fact, there are 16 crystal structures of binary M^{n+}/free tripeptide complexes deposited at CCDC (May 2009). We note a very interesting feature: In the 10 structures (after the exclusion of the tripeptides with coordinated side chains), the tripeptide ligands adopt *eight* different coordination modes (Table 8, Scheme 3); the coordination mode of the tripeptide ligand in **3**·5.8 H_2O is novel. In the remarkable complexes $[Fe_3(\mu_3\text{-O})(H_2\text{-Gly-Gly-Gly-O})_6(H_2O)_3]^{7+}$ [44] and $\{[Mo_4O_{12}(H_2\text{-Gly-Gly-Gly-O})_2]{\cdot}9H_2O\}_n$ [45], the tripeptide is in its zwitterionic form and bridges two metal ions through the bidentate bridging carboxylate group.

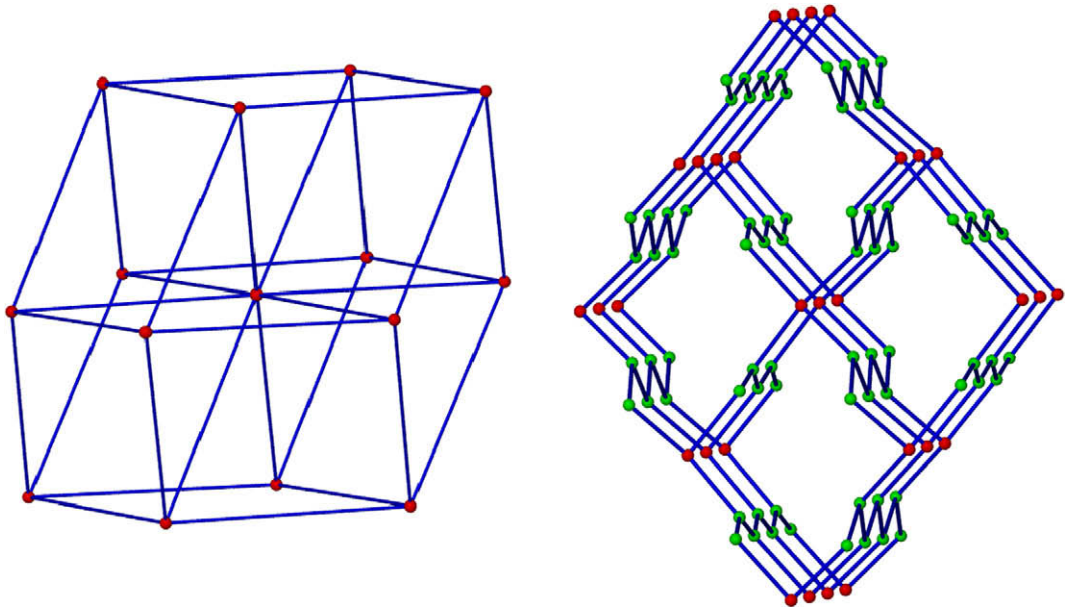
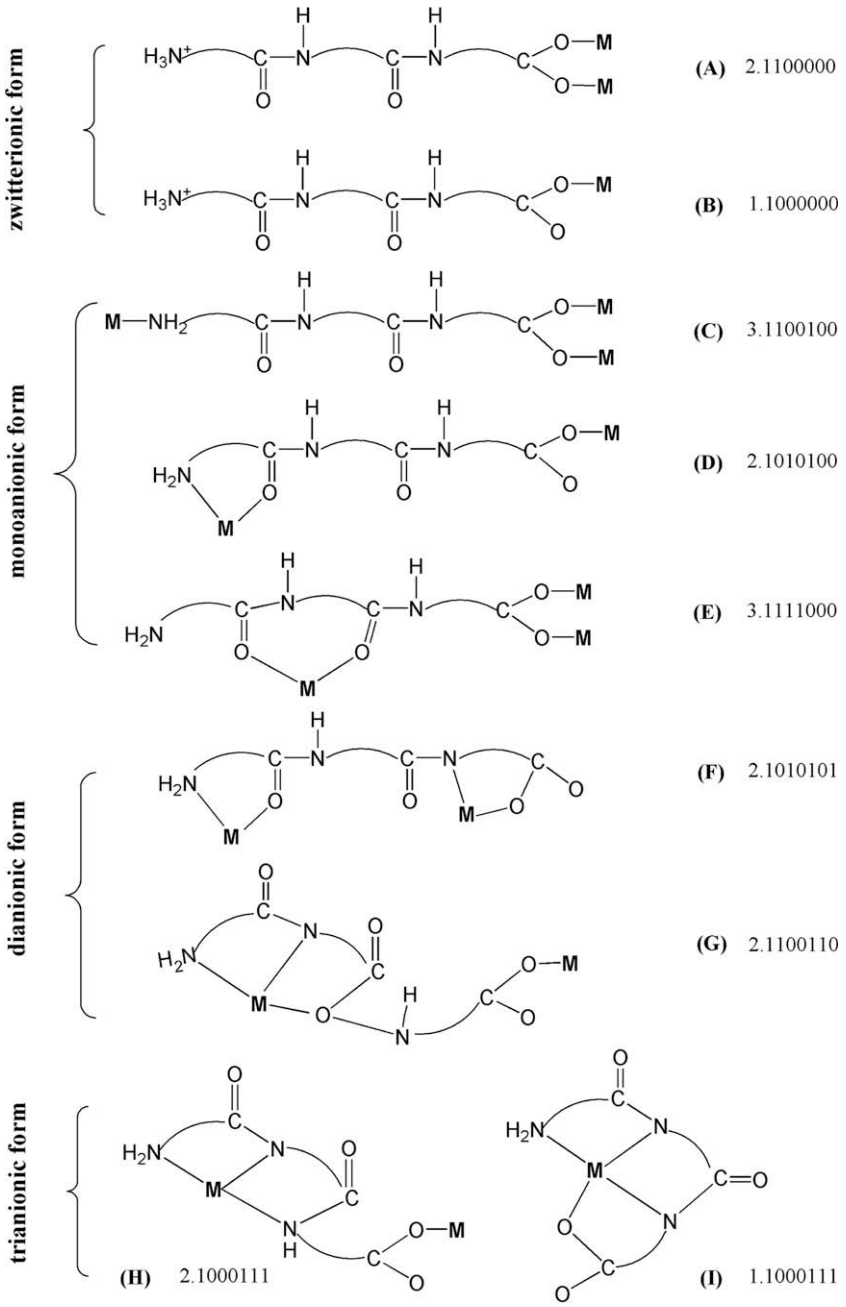


Fig. 11. The 8-connected **bcu** net (left) and the 3,4-connected **sqc185** net (right) in the crystal structure of **3**·5.8H_2O.



Scheme 3. The coordination modes of tripeptides in the *binary* M^{n+}/free-tripeptide complexes (without coordination of their side chains), in their zwitterionic, mono-, di- and trianionic forms. The coordination modes are given using Harris notation [13].

4. Concluding comments and perspectives

The present work extends the body of results that emphasize the ability of α-aminoisobutyric acid and α-aminoisobutyric acid-based peptides to form new structural types in 3d-metal chemistry. The use of H-Aib-OH, H-Aib-L-Ala-OH and H-Aib-Aib-Aib-OH in reactions with Zn^{II} sources has provided access to complexes **1**, **2** and **3**, respectively. Complex **1** is the second, structurally characterized Zn^{II} complex containing any form of H-Aib-OH and proves the ability of the monoanionic ligand to give non-hydroxo/oxo triangular clusters; the 2.111 ligation mode is observed for the first time in the coordination chemistry of this aminoacid. Complex **2** is the first structurally characterized Zn^{II} complex of any form of H-Aib-L-Ala-OH and constitutes a welcome new addition to the family of complexes that adopt the **tfa** network. Compound **3** is a novel example of a complex containing a monodentate tripeptide ligand; of structural interest is also the **bcu** network observed as a result of hydrogen bonding.

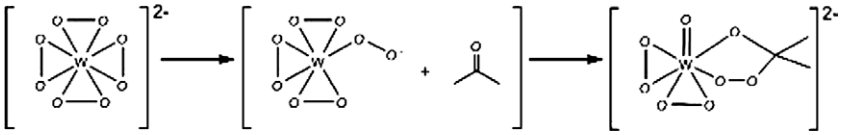
Clearly, Zn^{II}/α-aminoisobutyric acid-based peptide chemistry warrants further expansion to other di- and tripeptides. With complexes **2** and **3** as stimuli, we are also exploring synthetic methods for isolating Zn^{II} complexes involving the dianionic form of H-Aib-L-Ala-OH and the various anionic forms of H-Aib-Aib-Aib-OH as ligands. Finally, analogues of **1**–**3** with the other Group 12 metals, i.e. Cd^{II} and Hg^{II}, are not known to date, and it is currently not evident whether the preparation and stability of such mononuclear, trinuclear and polymeric complexes are dependent on the nature of the metal ion; work along this line is in progress in our group.

Supplementary data

CCDC 738622, 738623 and 738624 contains the supplementary crystallographic data for **1**·MeCOOH·H_2O, **2**·H_2O and **3**·5.8H_2O. These data can be obtained free of charge via http://www.ccdc.cam.ac.uk/conts/retrieving.html, or from the Cambridge Crystallographic Data Centre, 12 Union Road, Cambridge CB2 1EZ, UK; fax: (+44) 1223-336-033; or e-mail: deposit@ccdc.cam.ac.uk.

References

[1] U. Herr, W. Spahl, G. Trojandt, W. Steglich, F. Thaler, R. van Eldik, Bioinorg. Med. Chem. 7 (1999) 699. and references therein.
[2] H. Sigel, R.B. Martin, Chem. Rev. 82 (1982) 385.
[3] I. Sovago, in: K. Burger (Ed.), Biocoordination Chemistry, Ellis Hoorwood, London, 1990. Chapter IV.
[4] L.D. Pettit, J.E. Gregor, H. Kozlowski, in: R.W. Hay, J.R. Dilworth, K.B. Nolan (Eds.), Perspectives on Bioinorganic Chemistry, vol. 1, Jai Press Ltd., London, 1991, pp. 1–41.
[5] H. Kozlowski, W. Bal, M. Dyba, T. Kowalik-Jankowska, Coord. Chem. Rev. 184 (1999) 319.
[6] I. Sovagó, K. Ösz, J. Chem. Soc., Dalton Trans. (2006) 3841.
[7] O. Yamanchi, A. Odani, M. Takani, J. Chem. Soc. Dalton Trans. (2002) 3411.
[8] H.C. Freeman, Adv. Protein Chem. 22 (1967) 257.
[9] H.C. Freemann, in: G.L. Eighhorn (Ed.), Inorganic Biochemistry, vol. 1, Elsevier, Amsterdam, 1973, p. 121.
[10] H. Sigel, in: H. Sigel (Ed.), Metal ions in Biological Systems, Amino Acids and Derivatives as Ambivalent Ligands, vol. 9, Marcel Dekker, New York, 1979.
[11] (a) T. Takayama, S. Ohuchida, Y. Koike, M. Watanabe, D. Hashiznme, Y. Ohashi, Bull. Chem. Soc. Jpn. 69 (1996) 1579;
(b) E. Veda, Y. Yoshikawa, N. Kishimoto, M. Tadokoro, H. Sakurai, N. Kajiwara, Y. Kojima, Bull. Chem. Soc. Jpn. 77 (2004) 981;
(c) M. Förster, H. Vahrenkamp, Chem. Ber. 128 (1995) 541;
(d) J.C.M. Rivas, E. Salvagni, S. Parsons, Chem. Commun. (2004) 460;
(e) D. van der Helm, Acta Crystallogr., Sect. B 26 (1970) 1858.
[12] (a) E. Benedetti, Biopolymers 40 (1996) 3. and references therein;
(b) I.L. Karle, R. Balaram, Biochemistry 29 (1996) 6747;
(c) I.L. Karle, Biopolymers 40 (1996) 57. and references therein.
[13] R.A. Coxall, S.G. Harris, D.K. Henderson, S. Parsons, P.A. Tasker, R.E.P. Winpenny, J. Chem. Soc., Dalton Trans. (2000) 2349.
[14] R. Calvo, M.A. Mesa, G. Oliva, J. Zukerman-Schpector, O.R. Nascimento, J. Chem. Phys. 81 (1984) 4584.
[15] (a) T. Nogushi, Bull. Chem. Soc. Jpn. 35 (1962) 99;
(b) E.E. Castellano, G. Oliva, J. Zukerman-Schpector, R. Calvo, Acta Crystallogr., Sect. C 42 (1986) 16.
[16] H.A. Headlam, C.L. Weeks, P. Turner, T.W. Hambley, P.A. Lay, Inorg. Chem. 40 (2001) 5097.
[17] E.E. Castellano, G. Oliva, J. Zukerman-Schpector, R. Calvo, Acta Crystallogr. Sect. C 42 (1986) 21.
[18] A. Lombardi, O. Maglio, E. Benedetti, B. Di Blasio, M. Saviano, F. Nastri, C. Pedone, C. Pavone, Inorg. Chim. Acta 196 (1992) 241.
[19] K. Aparna, S.S. Krishnamurthy, M. Nethaji, P. Balaram, Polyhedron 13 (1994) 2993.
[20] J.-J. Zhang, S.-M. Hu, S.-C. Xiang, T. Sheng, X.-T. Wu, Y.-M. Li, Inorg. Chem. 45 (2006) 7173.
[21] R.M. Hartshom, S.G. Telfer, J. Chem. Soc., Dalton Trans. (1999) 3217.
[22] C.A. Otter, R.M. Hartshorn, J. Chem. Soc., Dalton Trans. (2004) 150.
[23] T. Murakami, S. Kita, Inorg. Chim. Acta 247 (1998) 247.
[24] A. Lombardi, O. Maglio, V. Pavone, B. di Blasio, M. Saviano, F. Nastri, C. Pedone, E. Benedetti, Inorg. Chim. Acta 204 (1993) 87.
[25] T.M. Klapötke, H. Köpf, I.C. Tornieporth-Oelting, P.S. White, Angew. Chem., Int. Ed. 33 (1994) 1518.
[26] B. Galn, D. Miguel, J. Prez, V. Riera, Organometallics 21 (2002) 2979.
[27] (a) M. Tiliakos, D. Raptis, A. Terzis, C. Raptopoulou, P. Cordopatis, E. Manessi-Zoupa, Polyhedron 21 (2002) 229;
(b) M. Tiliakos, E. Katsoulakou, V. Nastopoulos, A. Terzis, C. Raptopoulou, P. Cordopatis, E. Manessi-Zoupa, J. Inorg. Biochem. 93 (2003) 109;
(c) M. Tiliakos, E. Katsoulakou, A. Terzis, C. Raptopoulou, P. Cordopatis, E. Manessi-Zoupa, Inorg. Chem. Commun. 8 (2005) 1085;
(d) E. Katsoulakou, M. Tiliakos, G. Papaefstathiou, A. Terzis, C. Raptopoulou, E. Geromichalos, K. Papazisis, R. Papi, A. Pantazaki, D. Kyriakidis, P. Cordopatis, E. Manessi-Zoupa, J. Inorg. Biochem. 102 (2008) 1397.
[28] (a) L.L. Diaddario, W.R. Robinson, D.W. Margerum, Inorg. Chem. 22 (1983) 1021;
(b) M.A. Lockwood, T.J. Blubaugh, A.M. Collier, S. Lovell, J.M. Mayer, Angew. Chem., Int. Ed. 38 (1999) 225.
[29] E. Schröder, K.L. Lübke, The Peptides, vol. 1, 1965, vol. 2, 1966, Academic Press, New York.
[30] J. Coste, D. Le Nguyen, B. Castro, Tetrahedron. Lett. 31 (1990) 205.
[31] G.M. Sheldrick, SHELXS-86, Structure Solving Program, University of Göttingen, Germany, 1986.
[32] G.M. Sheldrick, SHELXL-97, Program for the Refinement of Crystal Structures from Diffraction Data, University of Göttingen, Germany, 1997.
[33] A.W. Addison, T.N. Rao, J. Reedijk, J. Rijn, G.C. Verschoor, J. Chem. Soc., Dalton Trans. (1984) 1349.
[34] R.E. Marsh, J. Donohue, Adv. Protein Chem. 22 (1967) 235.
[35] C. Toniolo, E. Benedetti, TIBS 16 (1991) 350.
[36] M. O' Keeffe, B.G. Hyde, Philos. Trans., Royal Soc. London Ser. A: Math. Phys. Sci. 295 (1980) 553.
[37] V.A. Blatov, IUCr CompComm Newsletter 7 (2006) 4. Multipurpose crystallochemical analysis with the program package TOPOS. TOPOS is available at http://www.topos.ssu.samara.ru.
[38] O. Delgado-Friedrichs, M. O' Keeffe, O.M. Yaghi, Acta Crystallogr. Sect. A A59 (2003) 22.
[39] H. Strasoleit, I. Büsching, S. Behrends, W. Saak, W. Barklage, Chem. Eur. J. 7 (2001) 5.
[40] C. Redshaw, M.R.J. Elsegood, Angew. Chem., Int. Ed. 46 (2007) 7453.
[41] M.A.M. Abu-Youssef, V. Langer, L. O hrstrom, Chem. Commun. (2006) 1082.
[42] A.N. Jayashree, C.G. Suresh, M. Vilayan, C. Toniolo, G.M. Bonora, Acta Crystallogr., Sect. C 43 (1987) 1618.
[43] http://epinet.anu.edu.au/sqc185.
[44] E.M. Holt, S.L. Holt, N.W. Alcock, Cryst. Struct. Commun. 11 (1982) 505.
[45] T. Yamase, M. Inone, H. Naruke, K. Fukaya, Chem. Lett. (1999) 563.
[46] H.-Y. Lee, J.W. Kampf, K.S. Park, K.S. Park, E.N.G. Marsh, Cryst. Growth Des. 8 (2008) 296.
[47] K. Apama, P. Balaram, S.S. Krishnamurthy, N. Nethaji, Int. J. Pept. Protein Res. 13 (1994) 19.
[48] W.A. Franks, D. van der Helm, Acta Crystallogr., Sect. B 27 (1971) 1299.
[49] H.C. Freeman, J.C. Schoone, J.G. Sime, Acta Crystallogr. 18 (1965) 381.



Scheme 1. The proposed mechanism for the formation reaction of the acetone peroxide complex.

2. Experimental

2.1. Materials and methods

Sodium tungstate, and guanidinium carbonate obtained from Aldrich were used without further purification. Hydrogen peroxide (30%) obtained from Merck was used as received and de-ionized and distilled water was used throughout this study. Deuterated solvents for use in the NMR, D_2O, and DCl were purchased from Merck. IR spectra were recorded using a KBr pellet on a Perkin Elmer 880 IR spectrophotometer. High-frequency Raman spectra were recorded with a Perkin–Elmer GX Fourier 514.5 nm using an Ar+ laser with a Jobin–Yvon (T64000) triple spectrometer as the excitation source. The UV–Vis absorption spectra in the range 900–200 nm were recorded using a Cary 3E spectrophotometer. NMR spectra were recorded with a Bruker Avance 500 MHz instrument and were processed by X-WIN MR 2.6 (Bruker Analytik GmbH).

2.2. Preparation of $(gu)_2[WO(O_2)_2CO(O)_2(CH_3)_2](CH_3)_2CO$

A solution of sodium tungstate (1.08 g, 3.3 mmol) in 30% H_2O_2 (20 mL) was treated with $(gu)_2CO_3$ (1.35 g, 7.5 mmol) in 20 mL distilled water. The clear yellow solution was stirred for a few minutes and the pH solution was recorded to be 8.7. 120 ml of acetone were slowly added and a white precipitate was formed immediately after the addition of acetone. The solid was filtered off. The filtered solution was cooled at 4 °C and colourless crystals suitable for X-ray diffraction were obtained after 7 days. *Anal.* Calc. for: C. 18.06; H, 4.55; N, 15.79. Found: C, 18.26; H, 4.49; N, 15.85%.

2.3. X-Ray diffraction

Slow crystallization from acetone yielded colourless prismatic crystals. A crystal with approximate dimensions $0.29 \times 0.42 \times 0.56$ mm was taken from the mother liquor and immediately cooled to −10 °C. Diffraction measurements were made on a Rigaku R-AXIS SPIDER Image Plate diffractometer using graphite monochromated Cu Kα radiation. Data collection (ω-scans) and processing (cell refinement, data reduction, Numerical and Empirical absorption correction) were performed using the CRYSTALCLEAR program package [19]. The structure was solved by direct methods using SHELXS-97 [20] and refined by full-matrix least-squares techniques on F^2 with SHELXL-97 [21]. Further experimental crystallographic details for the complex: $2\theta_{max} = 130°$; reflections collected/unique/used, 10 537/2843 [$R_{int} = 0.0539$]/2843; 223 parameters refined; $(\Delta/\sigma)_{max} = 0.007$; $(\Delta\rho)_{max}/(\Delta\rho)_{min} = 0.689/-0.588$ e/Å^3; R_1/wR_2 (for all data), 0.0281/0.0644. All hydrogen atoms were introduced at calculated positions as riding on bonded atoms. All non-hydrogen atoms were refined anisotropically.

3. Results and discussion

3.1. Crystal structure

The crystal data for the complex are given in Table 1 and selected bond lengths and angles in Table 2. The structure of the monomeric oxo diperoxo complex is depicted in Fig. 1.

Table 1
Crystal data and structure refinement for $(gu)_2[WO(O_2)_2CO(O)_2(CH_3)_2](CH_3)_2CO$ complex.

	$(gu)_2[WO(O_2)_2CO(O)_2(CH_3)_2](CH_3)_2CO$
Formula	$C_8H_{24}N_6O_9W$
Formula weight	532.18
Space group	$P2_12_12_1$
T (°C)	−10
λ (Å)	1.54178
a (Å)	10.5039(1)
b (Å)	12.4161(2)
c (Å)	13.5584(2)
α (°)	90
β (°)	90
γ (°)	90
V (Å^3)	1768.25(4)
Z	4
ρ_{calc} (g cm^{-3})	1.999
μ(Cu Kα) (mm^{-1})	12.625
R_1/wR_2[a]	0.0268/0.0633[b]

[a] $w = 1/[\sigma^2(F_o^2) + (aP)^2 + bP]$ and $P = (\max(F_o^2,0) + 2F_c^2)/3$; $R_1 = \sum(|F_o| - |F_c|)/\sum(|F_o|)$ and $wR_2 = \{\sum[w(F_o^2 - F_c^2)^2]/\sum[w(F_o^2)^2]\}^{1/2}$.
[b] For 2729 reflections with $I > 2\sigma(I)$.

Table 2
Selected bond lengths (Å) and angles (°) for the complex.

Bond distances		Bond Angles			
W–O_5	1.733(4)	O_5WO_3	102.5(2)	O_4O_3W	69.3(3)
W–O_3	1.943(5)	O_5WO_1	101.7(2)	O_3O_4W	65.7(2)
W–O_1	1.948(5)	O_3WO_1	84.5(2)	O_XO_6	W110.6(3)
W–O_2	1.985(4)	O_5WO_2	96.0(2)	C_2O_7W	117.1(3)
W–O_4	1.994(4)	O_3WO_2	129.1(2)	$C_2O_XO_6$	105.2(4)
W–O_7	2.005(4)	O_1WO_2	45.1(2)	$O_XC_2O_7$	107.7(5)
W–O_6	2.087(4)	O_5WO_4	96.7(2)	$O_XC_2C_4$	104.3(6)
O_1–O_2	1.509(7)	O_3WO_4	44.9(2)	$O_7C_2C_4$	110.3(6)
O_3–O_4	1.505(7)	O_1WO_4	129.0(2)	$O_XC_2C_3$	110.9(6)
O_6–O_X	1.472(5)	O_2WO_4	166.98(19)	$O_7C_2C_3$	111.1(5)
O_7–C_2	1.431(8)	O_5WO_7	88.77(15)	$C_4C_2C_3$	112.2(7)
O_X–C_2	1.429(7)	O_3WO_7	137.4(2)	$N_3C_8N_1$	118.8(7)
C_2–C_3	1.506(9)	O_1WO_7	133.8(2)	$N_3C_8N_2$	121.6(9)
C_2–C_4	1.505(9)	O_2WO_7	89.38(19)	$N_1C_8N_2$	119.5(7)
C_8–N_3	1.296(9)	O_4WO_7	93.38(19)	$N_5C_9N_4$	122.5(7)
C_8–N_1	1.300(9)	O_5WO_6	165.29(15)	$N_5C_9N_6$	119.0(8)
C_8–N_2	1.309(10)	O_3WO_6	87.8(2)	$N_4C_9N_6$	118.4(8)
C_9–N_5	1.306(10)	O_1WO_6	89.5(2)	$O_{11}C_{11}C_{12}$	120.6(11)
C_9–N_4	1.332(9)	O_2WO_6	85.2(2)	$O_{11}C_{11}$	122.7(11)
C_9–N_6	1.339(9)	O_4WO_6	83.1(2)	$C_{12}C_{11}C_{13}$	116.5(9)
O_{11}–C_{11}	1.180(8)	O_7WO_6	76.57(15)		
C_{11}–C_{12}	1.414(11)	O_2O_1W	68.7(2)		
C_{11}–C_{13}	1.433(14)	O_1O_2W	66.2(2)		

The coordination sphere about the tungsten atom consists of seven oxygen atoms arranged in a pseudotrigonal bipyramid geometry with the oxo ligand O(5) and an oxygen atom of the ligand O(6), in the axial positions. The two peroxo groups and the oxygen O(7) of the ligand lie in the equatorial plane. Similar structural data for peroxo complexes of tungsten W(VI) are reported in a more recent review published in 2008 by Sergienko [18]. The complex compound has a similar structure with the heteroleptic tungsten complex with the quinaldinic ligand reported in our work as it can be seen by the bond angles [9]. The oxo atom, the bond (C–O–W) and the peroxo group of the acetone peroxide ligand are almost copla-

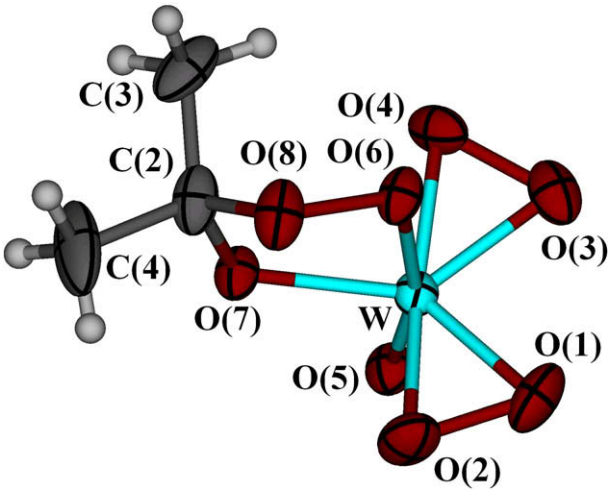


Fig. 1. Structure and atom numbering of $(gu)_2[WO(O_2)_2CO(O)_2(CH_3)_2](CH_3)_2CO$ (where gu^+ = guanidinium ion, $CN_3H_6^+$ ion). Thermal ellipsoids are drawn at the 50% probability level.

nar and perpendicular to the plane of the peroxo oxygen atoms. The acetone peroxide bidentate chelating ligand is coordinated to the metal atom by the oxygen atoms of the oxygen–carbon–tungsten bond (C–O–W) and by two peroxo oxygen atoms and closes the five membered metallocycle $WOCO_2$. The angle between them (O5–W–O7) is 88.7(15) which is close to the angle between the oxo atom the tungsten ion and the oxygen of the quinolinium ring of the quinaldinic tungsten complex [9]. The distance of the W=O double bond is 1.733 (4), whereas the W=O distance is 1.698 Å respectively in the quinaldinic complex. The O–O bond lengths (1.509(7)–1.505(7) Å). The W–O(peroxo) bond lengths are in the range 1.943(4)–1.994(5) Å, which suggests that they are bonded asymmetrically. These data are also in accordance with those reported in our previews work except that the lengths of the O–O (1.509(7)–1.505(7)) bonds are noticeably longer comparing to the quinaldinic complex reported previously [9]. The crystal packing of the complex is dominated by intermolecular O–H···O hydrogen bonds. The co crystallized acetone molecule and the guanidinium N atoms participate in 8 hydrogen bonds of each molecule (Fig. 2) (in) the same way (as) the peroxo tungstate complex with

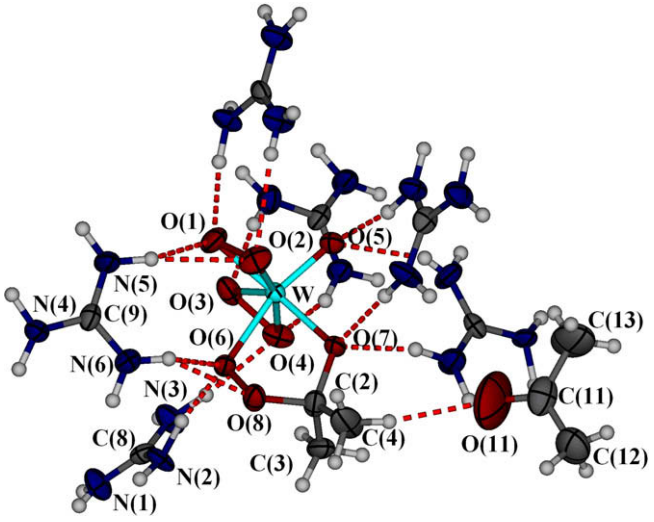


Fig. 2. Crystal packing of $(gu)_2[WO(O_2)_2CO(O)_2(CH_3)_2](CH_3)_2CO$. Hydrogen bonds are represented by dotted lines, and selected donor and acceptor atoms are labelled.

the quinaldinic ligand does [9]. Raczynska et al. reported the richness of intermolecular interactions in guanidinium salts. These are hydrogen bonds, Coulomb and Van der Waals interactions. In particular, the highly symmetric and planar guanidinium ion with six equivalent protons, is a hydrogen bond donor. Since the H-bond donor and acceptor are charged species, the electrostatic interactions in the crystal lattice may additionally modify the hydrogen bond network [15]. The selected hydrogen bond lengths are reported in Table 3.

3.2. Infrared and Raman data

The infrared spectrum of the complex revealed the characteristic spectral pattern main vibrations of which are summarized in Table 4. The spectrum of the complex illustrated in Fig. 3 exhibits a strong sharp band at 929 cm^{-1} consistent with the presence of the W=O bond vibration Two strong and sharp bands packing at 869 and 828 cm^{-1} are ascribed to the O–O vibration [14]. The occurrence of two bands indicates the presence of different peroxo groups side-on bound to the metal. Additional bands in the range of 690–540 cm^{-1} belong to $\nu_{as}(W–O_2)$ and $\nu_s(W–O_2)$ [10]. The bands at 1551 and 1363 are assigned to the methyl group bending motion, and the band at 1227 corresponds to the C–O stretch [16]. The peaks at 3417 and 3182 cm^{-1} are attributed to the asymmetric $\nu_{as}(NH_2)$ and symmetric $\nu_s(NH_2)$vibrations. Drozd et al. in a theoretical vibrational spectra study of guanidine selenate (GUSE) and guanidinium sulphate (GUS), reported that the bands at 3574–3511 cm^{-1} and at 3575–3502 cm^{-1} are assigned in $\nu_{as}(NH_2)$vibrations in (GUS) and (GUSE), respectively, and the symmetric vibrations $\nu_s(NH_2)$ at 3103 and 3315 for (GUS) and (GUSE). In the IR

Table 3
Distances and bending angles for hydrogen bonds in structure of the complex.

D–H···A	D–H	H···A	D–H···A	<D–H···A	
N1–H1N1···O5	0.7200	2.3400	3.000(8)	154.00	4_655
N1–H2N1···O1	0.8100	2.5600	3.226(9)	140.00	2_565
N1–H2N1···O2	0.8100	2.4200	3.221(8)	170.00	2_565
N2–H1N2···O1	0.9500	2.0600	2.911(10)	148.00	2_565
N2–H2N2···O8	1.1000	2.4900	3.404(8)	140.00	1_565
N2–H2N2···O6	1.1000	1.7300	2.822(8)	171.00	1_565
N3–H1N3···O7	1.0300	1.9700	2.971(9)	163.00	4_655
N3–H2N3···O3	1.0000	2.5500	3.353(9)	137.00	1_565
N3–H2N3···O4	1.0000	2.2300	3.224(9)	170.00	1_565
N4–H1N4···O4	0.9600	2.0800	2.992(8)	158.00	2_665
N4–H2N4···O5	1.0100	1.9500	2.950(7)	170.00	4_655
N5–H1N5···O7	0.9700	2.0800	3.052(8)	174.00	4_655
N5–H2N5···O1	1.0000	2.3500	3.101(9)	131.00	1_665
N5–H2N5···O2	1.0000	2.4500	3.428(9)	166.00	1_665
N6–H1N6···O3	0.9500	2.0700	3.006(10)	169.00	2_665
N6–H2N6···O8	0.9200	2.2600	3.065(9)	145.00	1_665
N6–H2N6···O6	0.9200	2.2900	2.895(9)	123.00	1_665
C3–H3C···O4	0.9600	2.5400	3.325(9)	139.00	
C4–H4A···O11	0.9600	2.4100	3.324(11)	159.00	4_555

Table 4
IR and Raman data of the $(gu)_2[WO(O_2)_2CO(O)_2(CH_3)_2](CH_3)_2CO$ complex.

Assign.		
W=O	IR	929
	Raman	896
ν(O–O)	IR	869, 828
	Raman	839, 823
$\nu_s(W–O_2)$	IR	541
	Raman	526
$\nu_{as}(W–O_2)$	IR	687
	Raman	645
ν-CN	IR	1089
	Raman	1011

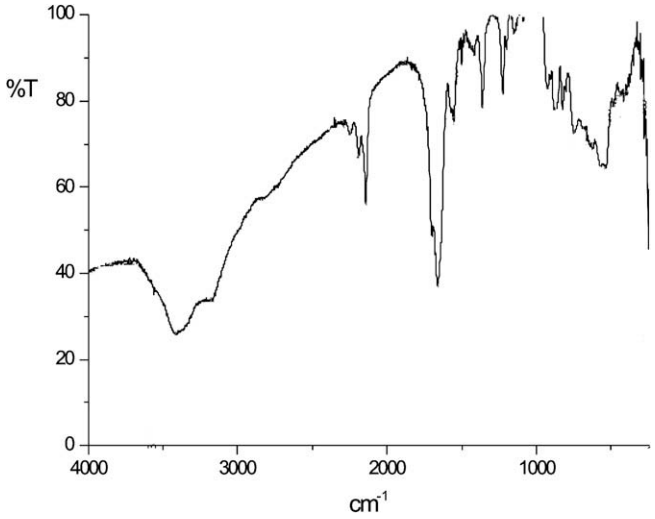


Fig. 3. IR spectra of the acetone peroxide tungsten complex.

spectra reported here the corresponding peaks are shifted due to the hydrogen bonding of the guanidinium cation. Also the band at 3417 cm^{-1} is characterized by higher intensity comparing to the band at 3182 cm^{-1}. This finding is in contrast to Drozd et al. who supported that the ν_s(NH2) is the strongest band in the spectra. The distinct peak at 1661 cm^{-1} has been assigned to the ν_{as}(CN) of the counter ion but also can be attributed to the NH_2 in-plane bending vibrations which are mixed with the ν_{as}(C–N) vibrations. The band at 1089 cm^{-1} with a low-intensity corresponds to the symmetric ν_s(CN) vibration and to the ρNH_2 rocking vibrations. Finally, the bands at 574 and 481 cm^{-1} are also assigned to the in-plane vibrations of CN_3 and are characterized by their low intensities in accordance with Drozd [11].

The wave numbers of the characteristic infrared bands described previously fit those obtained from the Raman spectra (Table 4 and Fig. 4) of the complex. The peaks at 1011, 896, 839, 823, and 645 cm^{-1} correspond to the ν_sC–N, W=O, O–O and ν_{as}(W–O_2) bond vibrations of the complex, respectively. Additionally, the peaks at 526 and 496 cm^{-1} are attributed to the ν_s(W–O_2) and ν_s(W–O–O–C) bond vibrations. The low-intensity, high-frequency peaks at 1668 and 1580 cm^{-1} can be assigned to the bond vibrations of the methyl protons in the acetone peroxide ligand [16].

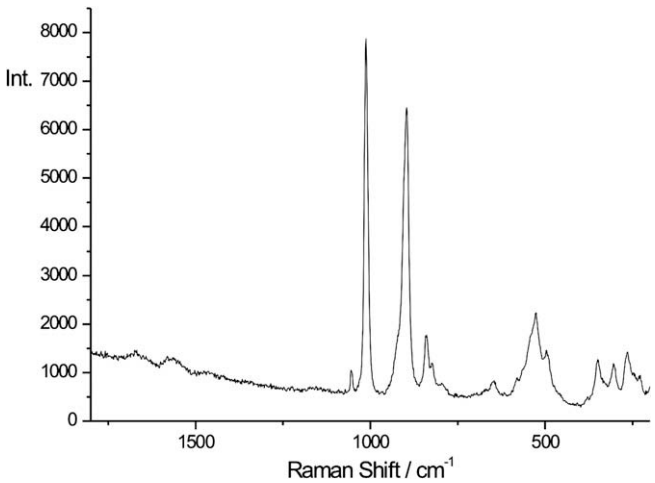


Fig. 4. Raman spectra of the acetone peroxide tungsten complex solution.

3.3. Raman in solution

The Raman spectra of the complex in aqueous solution both in absence and presence of hydrogen peroxide at different pH values, is extremely useful for the identification of the different peroxo species formed and the data are summarized in Table 5. In order to obtain valuable conclusions a strictly specific procedure was followed. Firstly, a spectrum, obtained 20 min after the dissolution of the complex in water, exhibits two main bands at 1013 and 932 cm^{-1} corresponding to the C–N and W=O vibrations, respectively.

After the addition of an appropriate quantity of H_2O_2, capable to prepare a solution with an excess of H_2O_2, a second spectrum obtained which is depicted in Fig. 5. In that spectrum the appearance of four new bands at 876 main, 858 shoulders, 795 broad band, and 573 cm^{-1}, not present before indicates the interaction of H_2O_2 with the complex compound. The band at 876 corresponds to the O–O vibration of the free H_2O_2 and the two bands at 858 and 795 cm^{-1} to the coordinated H_2O_2. The band at 573 cm^{-1} is attributed to the W–O–C vibration [16]. Another interesting difference between the two spectra is the absence of the band at 932 cm^{-1} in the second spectrum. All the peaks mentioned above except for the peak at 573 cm^{-1} appeared in the solid state. The above findings are in accordance with those reported in our work with peroxo tungsten complexes [9]. The disappearance of the band at 932 cm^{-1} indicates the absence of the W=O bond to the compound in the presence of an excess of H_2O_2. Under these conditions a triperoxo form of the complex is dominant. This assertion becomes stronger due to the appearance of the bands at 858 and 795 cm^{-1}. On the contrary, the mono or diperoxo form is present in aqueous solution in the absence of H_2O_2. The Raman spectrum of the complex in aqueous solution also indicated that the complex is rather photosensitive even in the presence of excess hydrogen peroxide.

Table 5
Raman in solution of the $(gu)_2[WO(O_2)_2CO(O)_2(CH_3)_2](CH_3)_2CO$ complex.

Assign.	ν(M=O)	ν(O–O)	ν_s(M–O–C)	ν_s(C–N)
Raman (solution)	932			1013
Raman (solution + H_2O_2)		858, 795	573	1010

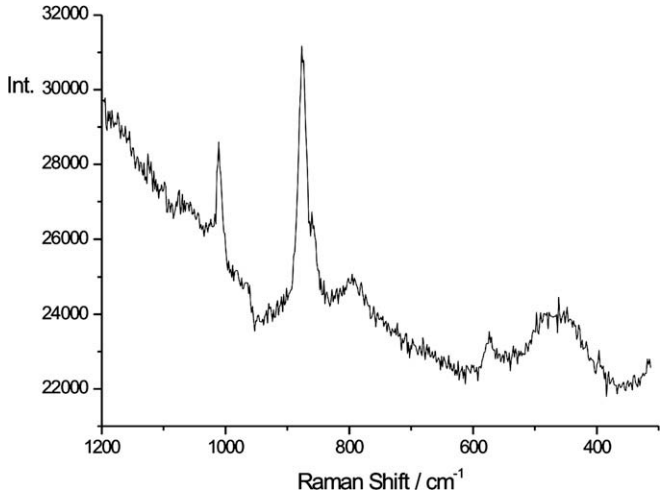


Fig. 5. Raman spectra of the acetone peroxide tungsten complex in aqueous solution in the presence of H_2O_2.

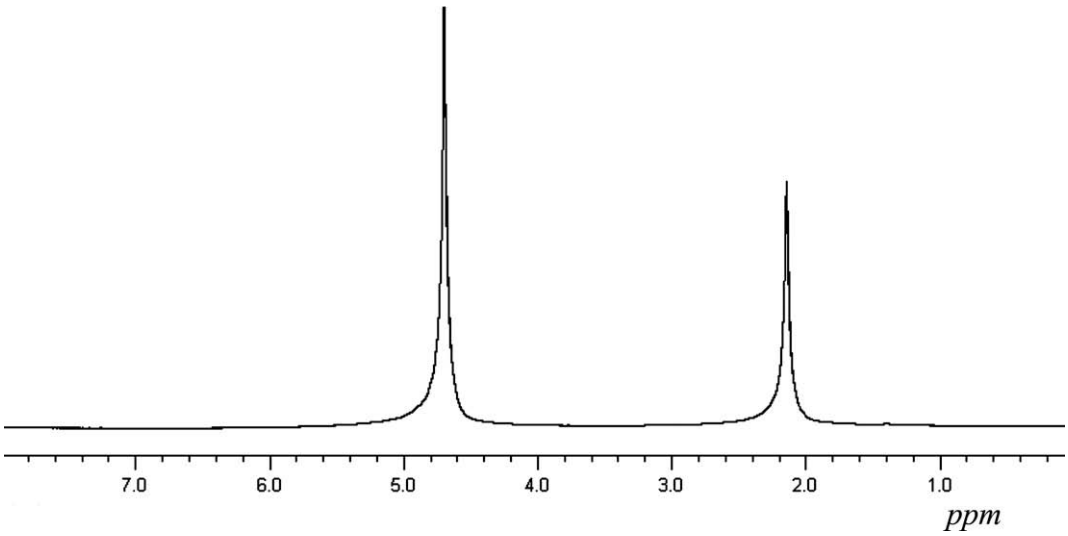


Fig. 6. ^{1}H NMR spectra of the acetone peroxide tungsten complex $(gu)_2[WO(O_2)_2CO(O)_2(CH_3)_2](CH_3)_2CO$ in D_2O solution 10 min after dissolution.

3.4. NMR spectroscopy

The ^{1}H NMR spectrum of the peroxo tungstate complex with the acetonato ligand in D_2O obtained 10 mins after dissolution in D_2O, is illustrated in Fig. 6. The above spectrum exhibits a peak at 2.15 ppm which is the peak of the free non coordinated acetone methyl protons. The source of the free acetone is attributed to the release of the crystal lattice acetone liberated by the dissolution of the complex and also to the acetone from the dissociation of the compound. The rapid dissociation of the complex immediately after the dissolution in water is proved by the fact that the peak which corresponds to the methyl protons of the acetone peroxide ligand at 1.4 ppm [12] is not detected in any spectra. The spectra obtained 7 days later were of no significant difference.

The second sample for NMR spectrum was prepared by the dissolution of the complex in D_2O, and the addition of an appropriate quantity of DCl in order to create acidic environment. In the first spectra obtained 10 mins after the preparation of the sample,

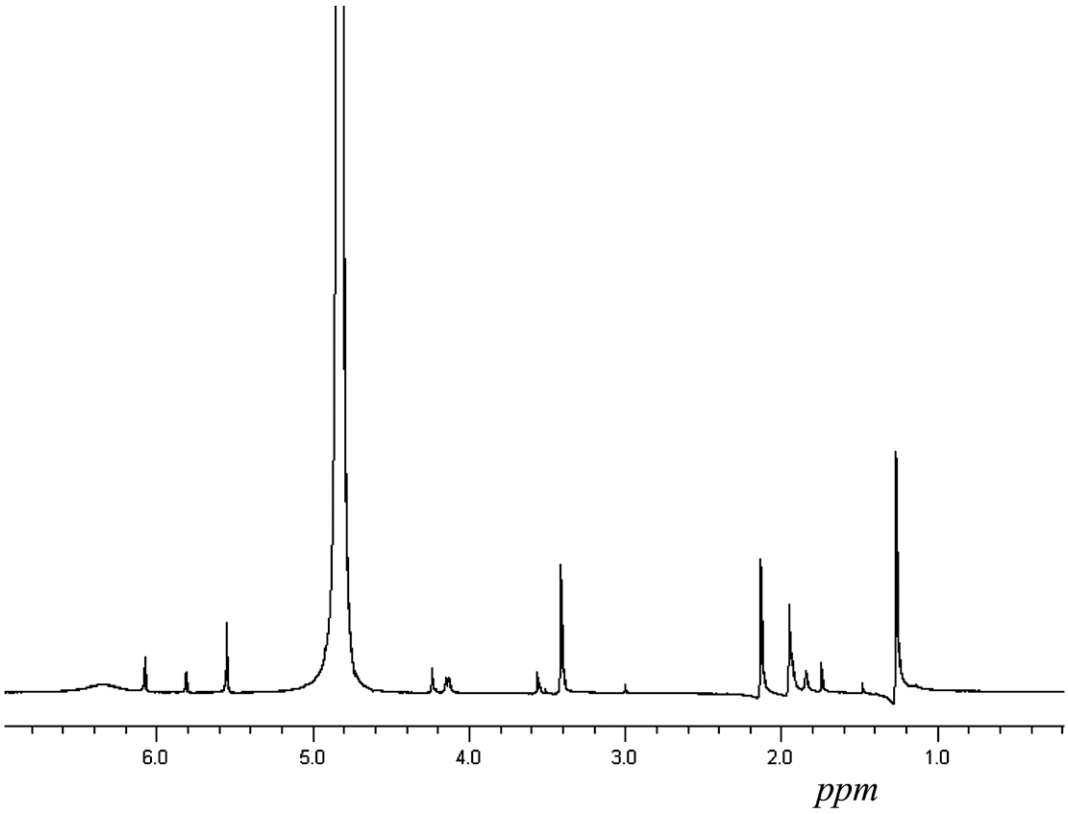
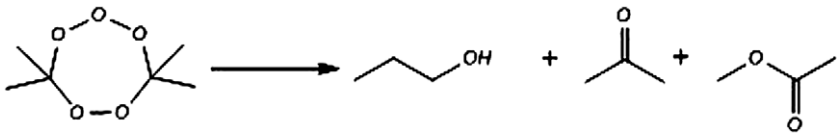
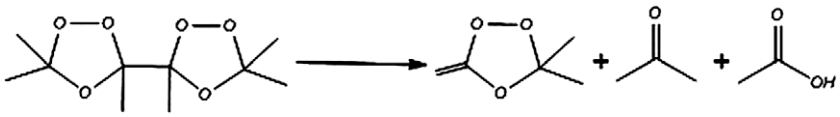


Fig. 7. ^{1}H NMR spectra of the acetone peroxide tungsten complex $(gu)_2[WO(O_2)_2CO(O)_2(CH_3)_2](CH_3)_2CO$ in D_2O solution with DCl 7 days after dissolution.



Scheme 2. Dissociation reaction mechanism of the triacetone triperoxide to acetone and the main intermediate products.



Scheme 3. Decomposition reaction mechanism of a diozonide and the main products.

two new peaks exhibited, at 4.1 ppm (single), and a small peak at 1–1.1 ppm (double), whereas the peak obtained in the previous sample at 2.15 ppm disappeared and a new intense and multiple (triple) peak appeared around 1.8 ppm. The second spectrum obtained 7 days after, exhibited a new range of peaks and is illustrated in Fig. 7.

The peaks at 1.25, 3.4, and 4.15 ppm are attributed to the protons of 2-propanol produced by the reduction of acetone, which is a possible reaction to happen. Dupnicova et al. proposed a mechanism (Scheme 2) of the decomposition reaction of triacetone triperoxide to acetone and ozone and presented the main intermediate products. The above compound has a similar structure with the peroxide complex presented in this paper. The peaks at 3.67 ppm and 2.01 ascribed to CH3–O–C(O)–CH3 are present in this spectrum and the appearance of the peaks at 3.65 and 1.2 indicates the existence of ethanol. The peak at 2.1 is also attributed to the presence of acetone [16]. Griesbaum et al. presented the decomposition reaction (Scheme 3) of a diozonide which gave also an intermediate with analogous structure to the peroxo tungsten complex with the acetone peroxide ligand. This diozonide decomposes to a mixture of an unsaturated form of this compound and acetic acid. The peaks at 5.55, 5.8 and 6.1 ppm indicate the presence of similar unsaturated components, and the peak at 2.15 can be ascribed to acetic acid [17]. Another interesting fact that indicates the decomposition of the compound is the explicit lowering of the peak 1.8 ppm, which was dominant in the spectra obtained immediately after dissolution of the complex.

3.5. Structure and stability towards decomposition

In our previous studies we demonstrated that peroxoniobate and peroxotungstates exhibit low stability toward decomposition in aqueous solution [8,9]. In these studies we also came to the conclusion that the bond length of the O–O bonds influences the chemical reactivity of the complexes. The peroxo O–O bonds of the acetone peroxide complex are noticeably longer than those of the peroxotungsten and peroxoniobate complexes with the quinaldinium ligand [8,9]. The Raman spectra of the complex in aqueous solution indicate that the peroxo groups of the complex are transformed to oxo groups immediately after the dissolution of the complex in water, and that, when H_2O_2 is added, the peroxo groups regenerate; this fact is in accordance with our previous works [8,9]. The NMR spectra in D_2O in both in absence or presence of DCl, indicate that the chelating ligand decomposes immediately after the dissolution of the complex in D_2O releasing acetone, and significantly faster in the presence of DCl; thus a group of products is formed due to various decomposition reactions occurring in acidic environment. The correlation of the above facts indicates that the complex compound is extremely unstable in besides the existence of a chelating ligand which according to the literature induces stability to the complexes in solution. The elucidation of the decomposition reaction mechanism of the complex in aqueous solution and the determination of the intermediate and final products is currently under research.

Supplementary data

CCDC 728377 contains the supplementary crystallographic data for $(gu)_2[WO(O_2)_2CO(O)_2(CH_3)_2](CH_3)_2CO$. These data can be obtained free of charge via http://www.ccdc.cam.ac.uk/conts/retrieving.html, or from the Cambridge Crystallographic Data Centre, 12 Union Road, Cambridge CB2 1EZ, UK; fax: (+44) 1223-336-033; or e-mail: deposit@ccdc.cam.ac.uk.

Acknowledgments

The authors are grateful to Dr. Polycarpos Falaras (Institute of Physical Chemistry NCSR 'Demokritos') for collecting the Raman data and to Dr. Eleni K. Efthimiadou for her assistance. The present work was supported by the Special Research Account of Athens University (E.L.K.E. 70/4/6495) and by the Postgraduate Studies Programme on "Catalysis an Integrated Approach" of Epeaek II Programme of Greek Ministry of Education, and the European Union (75/25).

References

[1] B. Tamami, H. Yeganeh, Eur. Polym. J. 35 (1999) 1445.
[2] D. Bayot, M. Devillers, Coord. Chem. Rev. 250 (2006) 2610.
[3] E.C. Niederhoffer, J.H. Timmons, A.E. Martell, Chem. Rev. 84 (1984) 137.
[4] Thematic issue on "Metal-Dioxygen Complexes", Chem. Rev. 94 (1994) 567–856.
[5] Thematic issue on "Biomimetic Inorganic Chemistry", Chem. Rev. 104 (2004).
[6] M.H. Dickman, M.T. Pope, Chem. Rev. 94 (1994) 569.
[7] V. Nardello, J. Marko, G. Vermeersch, J.M. Aubry, Inorg. Chem. 34 (1995) 4950.
[8] A. Maniatakou, C. Makedonas, C.A. Mitsopoulou, C. Raptopoulou, I. Rizopoulou, A. Terzis, A. Karaliota, Polyhedron 27 (2008) 3398.
[9] A. Maniatakou, S. Karaliota, M. Mavri, C. Raptopoulou, A. Terzis, A. Karaliota, J. Inorg. Biochem. 103 (2009) 859.
[10] L. Barrio, J.M. Campos-Martin, J.L.G. Fierro, J. Phys. Chem. A 111 (2007) 2166.
[11] M. Drozd, J. Mol. Struct.: THEOCHEM 756 (2005) 73.
[12] J. Bordner, G.O. Doak, T. Stephen Everett, J. Am. Chem. Soc. 108 (14) (1986) 4206.
[13] R. Ugo, F. Conti, S. Cenini, R. Mason, G.B. Robertson, Chem. Commun. 1498 (1968) 1.
[14] Shu-Ya Hou, Zhao-Hui Zhou, Tao-Ran Lin, Hui-Lin Wan, Eur. J. Inorg. Chem. (2006) 1670.
[15] E.D. Raczyska, M.K. Cyraski, M. Gutowski, J. Rak, J.F. Gal, P.C. Maria, M. Darowska, K. Duczmal, J. Phys. Org. Chem. 16 (2003) 91.
[16] F. Dubnicova, R. Kosloff, J. Almong, Y. Zeiri, R. Boese, H. Itzhaki, A. Alt, E. Keinan, J. Am. Chem. Soc. 127 (4) (2005) 1146.

[17] K. Griesbaum, W. Volpp, R. Greinert, H.J. Greuning, J. Schmid, H. Henke, J. Org. Chem. 54 (2) (1989) 383.
[18] V.S. Sergienko, Crystallogr. Rep. 53 (2008) 18.
[19] Rigaku/MSC, CRYSTALCLEAR, Rigaku/MSC Inc., The Woodlands, Texas, USA, 2005.
[20] G.M. Sheldrick, SHELXS-97: Structure Solving Program, University of Göttingen, Germany, 1997.
[21] G.M. Sheldrick, SHELXL-97: Crystal Structure Refinement Program, University of Göttingen, Germany, 1997.

using spin-coating techniques [17]. The photoluminescence (PL) of the thin film fabricated by vacuum deposition was measured from cast film of the Al-complex of 8-hydroxyquinoline and a-pyridoin on quartz substrate [18]. Electroluminescence (EL) mechanism of dye-doped vacuum thin film deposition of organic light-emitting diodes (OLEDs) was investigated by using three familiar fluorescent dyes, i.e. (DMQA), (DCJTB) and (Rubrene) [19]. On the other hand, several other techniques are widely used for thin film formation of organic or inorganic deposited materials [20]. These include chemical bath deposition (CBD) [21], electrochemical deposition [22], e-beam evaporation technique [23] Magnetron sputtering technique [24,25] and Langmuir–Blodgett (LB) [26–29].

In our previous report [30], we have presented a simple and direct chemical deposition method for synthesis of nano-sized metal-8-hydroxyquinolate complexes based on layer-by-layer surface deposition of the metal ion followed by 8-hydroxyquinole as the ligating environment for the formation of thin films. In the present work, a comprehensive study is devoted to explore, evaluate and optimize the various affecting and controlling factors in the process of thin film formation of nano-sized Co(II)-8-hydroxyquinalate complex, as a selected example, by surface layer-by-layer chemical deposition technique. In addition, the optical properties of nano-sized Co(II)-8-hydroxyquinolate complex thin film were also aimed to study and explore.

2. Experimental

2.1. Instrumentation

The metal analysis of cobalt contents after acid digestion and suitable dilution of all synthesized Co(II)-8-hydroxyquinolate complexes were determined by flame atomic absorption spectrophotometric measurements by using a Shimadzu model AA-6650 atomic absorption spectrophotometer at the appropriate wavelength. Scanning electron microscope (JSM-6360LA, JEOL Ltd.), (JSM-5300, JEOL Ltd.) and an ion sputtering coating device (JEOL-JFC-1100E) were used to examine the deposited thin film of metal quinolate complexes. SEM specimens were coated with gold to increase the conductivity. The FT-IR spectrum of Co(II)-8-hydroxyquinalate complexes were measured by a Shimadzu Fourier Transform infrared (FT-IR-8400S) spectrophotometer in the range 4000–200 cm^{-1}. Thermal gravimetric analysis (TGA) and thermoanalytical curves of Co(II)-8-hydroxyquinolate complexes were obtained by using a Perkin–Elmer TGA7 Thermobalance at Mubarak City, Egypt. The operating conditions include a temperature heating range is 20–1000 °C with a heating rate 10 °C min^{-1}, a flow rate of 20 ml min^{-1} pure nitrogen atmosphere and the sample mass in the range of 5–12 mg.

Shimadzu gas chromatography-mass spectrometer (GCMS-QP2010 plus) interfaced with a direct insertion probe (DIP), Micro-analytical Laboratory-Cairo University, was used to acquire the electron impact mass spectra (EI-MS) of Co(II)-8-hydroxyquinolate complexes by 70-eV as the ionization energy. Heating temperature programming of the DIP was performed based on 50 °C min^{-1}. The maximum temperature was adjusted to 350 ^{0}C and the run time was completed in 8.0 min.

2.2. Chemical and materials

Cobalt chloride hexahydrate, $CoCl_2{\cdot}6H_2O$, of analytical grade was purchased from Aldrich Chemical Company, USA. 8-Hydroxyquinoline (8-HQ), ethanol and methanol were obtained from BDH limited, Poole, England and used as received. The metal ion solution (0.1 M) was prepared from doubly distilled water by dissolving the appropriate mass of metal salt in a 500 ml flask. Methanolic and ethanolic solutions of 8-HQ (0.1, 0.2 or 0.3 M) were also prepared and used. The micro-slide glass substrates 76.2 mm, 25.4 mm and 1.0 mm were cleaned as previously reported [31].

2.3. Thin film formation of Co(II)-8-hydroxyquinolate complexes via layer-by-layer chemical deposition method

2.3.1. General procedure

The formation of Co(II)-8-hydroxyquinolate complex thin films were carried out according to previously reported procedure [30]. In this method, a clean glass micro-slide of the size 76.2 mm, 25.4 mm and 1 mm was used as the solid substrate. Solutions of $CoCl_2.6H_2O$ and 8-HQ were prepared in the selected solvents. The clean substrate was vertically immersed into the metal ion solution to deposit the Co(II) ion on the substrate surface. The substrate was then immersed in the ligand solution whereas the pre-adsorbed metal ion on the glass substrate was allowed to react with the ligand. A colored and uniform thin film of the Co(II)-8-hydroxyquinolate complex was formed after few dipping cycles. The reaction substrate was rinsed with distilled water after each reaction cycle. This procedure was repeated to increase the film thickness and homogeneity.

2.3.2. Studied and optimized factors

The effect of molar concentration on thin film formation of Co(II)-8-hydroxyquinolate complex was studied by keeping the cobalt ion concentration constant at 0.1 M, while the concentration of 8-HQ was varied to cover three different values of 0.1, 0.2 and 0.3 M. The selected and evaluated number of dipping cycle were kept constant at 2 and 20 cycles while the immersion time values were kept constant at 2 and 20 s.

The effect of number of dipping cycles on Co(II)-8-hydroxyquinolate complex thin films formation was studied at constant immersion time (2-s) and The selected number of dipping cycles is 2, 5, 10, 30, 40 and 50. The (1:1), (1:2) and (1:3) molar stoichiometric ratios of metal to ligand and the immersion time were kept constant.

The effect of immersion time on Co(II)-8-hydroxyquinolate complex thin films formation was also studied. The time of immersion were adjusted to 2, 5, 10, 20, 30, 40 and 50 s. The (1:1), (1:2) and (1:3) are the selected molar stoichiometric ratios of metal to ligand and the number of dipping cycles (five cycles) were kept constant during the course of this evaluation study.

The effect of pH value of metal ion and ligand solution on the Co(II)-8-hydroxyquinolate complex thin film formation was also studied by adjusting the pH value of metal ion solutions to pH 1, 3, 5 and 7. The stoichiometric ratio (1:2) of metal to ligand, the time of immersion (5 s) and the number of dipping cycles (5) were kept constant during the course of this study.

Two different solvents were selected to conduct the study of the effect of solvent and these are ethanol and methanol. The ligand solutions were prepared in ethanol and methanol and the $CoCl_2{\cdot}6H_2O$ solution was prepared in DW. The selected molar stoichiometric ratio was (1:2) of metal to ligand, the time of immersion (5 s) and the number of dipping cycles were (2, 5 and 10 cycles).

2.4. Optical properties

2.4.1. Thin film deposition and optical measurements

Deposited Co(II)-8-hydroxyquinolate complex on solid substrate was re-dissolved in 50 ml absolute methanol at room temperature. Pre-cleaned glass micro slides were used as substrates. Deposited film on glass by dip coating is characterized by high transparency and good quality while its thickness is too small to be measured by optical transmittance. Another technique of thin

film formation was prepared by evaporation of the solvent in air from a Petri dish containing the prepared solution and glass slide. After 24 h the solvent was evaporated and Co(II)-8-hydroxyquinolate thin film with good quality and higher thickness ~0.5 micron was deposited. The optical transmittance was measured by using double beams UV–Vis spectrophotometer type LABOMED of spectral range 190–1100 nm, scan step 2 nm. A reference glass substrate was used.

3. Results and discussion

Layer-by-layer technique for thin film formation is recently used for synthesis of several important classes of nano-compounds and nano-materials. This process is mainly based on deposition of the first target species either ionic or molecular one already dissolved in a solution on the surface of a solid support followed by deposition of the second interacting species from its solution on the same solid support. This initial step is directly leading to the formation of first layer of the aimed compounds. Successive deposition of multilayer thin film is then formed upon repeating the layer-by-layer deposition steps to produce the required thickness and homogeneity of thin film. Several factors are of significant importance on controlling the thin film formation by layer-by-layer technique. These are mainly summarized as (i) the molar concentration of the two interacting species and their effect on the final molar stoichiometric ratio of the produced thin film compound. (ii) The dipping time of the solid substrate in the two interacting solutions and its effect on thickness and homogeneity of the synthesized thin film. (iii) The number of successive dipping cycles and its effect on the thin film thickness. (iv) The effect of pH values of both interacting species on the process of thin film formation, especially if the required deposited compound is a metal complex. (v) The effect of solvent on the possibility and kinetics of the direct thin film formation. Therefore, these factors are extensively studied, evaluated and optimized for thin film formation of Co(II)-8-hydroxyquinolate complex. Table 1 summarizes and compiles all studied factors.

Various spectroscopic methods of detection and analysis were used and applied to follow-up the thin film formation including metal analysis by atomic absorption (AA), scanning electron microscope (SEM), electron impact mass spectrometry (EI-MS), Fourier transform-infrared spectra (FT-IR) and thermal gravimetric analysis (TGA).

3.1. Effect of molar concentration on stoichiometric ratio of Co(II)-8-hydroxyquinolate complexes

The effect of molar concentration of metal ion and ligand solutions was studied based on the selection of a 0.1 M Co(II) solution as a single metal ion concentration, while the molar concentration of 8-HQ was selected and varied as 0.1, 0.2 and 0.3 M. The percentage of the Co(II) in the produced thin film of nano-sized Co(II)-8-hydroxyquinolate complex under these stoichiometric conditions ion was determined by atomic absorption spectrophotometry after dissolution of the deposited thin film in a concentrated nitric acid solution, digestion and dilution in distilled water in order to identify the final stoichiometric ratio of the formed complex in each case. The determined percentage of Co(II) in the three synthesized thin films (1:1, 1:2 and 1:3) were found 17.0 ± 0.3% in all tested nano-sized Co(II)-8-hydroxyquinolate complexes suggesting a unique (1:2) stoichiometric ratio of Co(II) to 8-HQ. This percentage values of Co(II) indicates that the molar concentration values of either Co(II) solution or 8-hydroxyquinoline solution are less important and insignificant in the final stoichiometric ratio of the produced nano-sized metal complexes. In addition, all synthesized thin films of nano-sized Co(II)-8-hydroxyquinolate complex under any examined factors were characterized by the formation of a (1:2) stoichiometric ratio based on the elemental analysis determination of Co(II) constituent.

Table 1
Studied and optimized factors.

Factor	Specifications
Molar stoichiometry	(1:1), (1:2) and (1:3) based on 0.1 M-metal ion solution and 0.1, 0.2 and 0.3-ligand solutions
Dipping cycles	2, 5, 10, 20, 30, 40 and 50 cycles
Dipping time	2, 5, 10, 20, 30, 40 and 50 s
pH-Effect	Buffered metal solution in pH 1, 3, 5 and 7
Solvent effect	Methanol and ethanol for ligand dissolution and DW for metal ion dissolution

The similarities in chemical structure and composition of the three synthesized nano-sized Co(II)-8-hydroxyquinolate complexes by the selected (1:1), (1:2) and (1:3) molar stoichiometric ratios was also confirmed from the study of EI-MS, FT-IR and TGA analysis. The electron impact mass spectra of these three complexes were found to exhibit identical profiles of mass fragmentation patterns confirming similar chemical structures. The molecular ion peaks of the three Co(II)-8-hydroxyquinolate complexes were characterized at *m/z* 347 (Rel. Int. = 100%) assuming that ^{59}Co as the most abundant isotopes of cobalt. These molecular ions were found to exhibit identical losses of 144 amu as the deprotonated 8HQ ligand to form $[Co(II)–8HQ]^+$ fragment ions producing a mass spectral fragment ion peak at *m/z* 203 (Rel. Int. = 28 ± 2%). In addition, characteristic fragment ion peaks that are derived from 8-HQ at *m/z* 145, 117, 89 and 63 are evident in the EI-MS of these three metal complexes. The complete EI-MS data of all ion peaks of the three studied complexes are compiled in Table 2.

The thermal gravimetric analysis of the three nano-sized Co(II)-8-hydroxyquinolate complexes were characterized by producing three identical thermograms revealing another evidence for the similarities of these metal complexes. Two characteristic degradation steps were identified with percentage losses of 9.69–10.21% and 66.01–67.57% at temperature ranges of 371–464 and 646–974 K, respectively. The first degradation steps were suggested to produce from partial decomposition of one of the coordinated 8-HQ ligand and the second degradation steps were identified for the complete decomposition of the two coordinating 8-HQ ligands and producing cobalt oxide as the final fragments in all studied Co(II)-8-hydroxyquinolate complexes. The complete thermal data of the three studied complexes are compiled in Table 2.

The FT-IR spectral analysis was also used to further confirm the similarities outlined for chemical structure and composition of the same three thin film Co(II)-8-hydroxyquinolate. The FT-IR spectra were characterized by the disappearance of the absorption peak υ(OH) due to the deprotonation of H-atom of C_{8-OH} of the ligand moiety, while the υ(C=N) was shifted indicating that coordination of 8-HQ to Co(II) ion in all metal complexes via the C_{8-O} bond as well as nitrogen atom of imin [30]. The FT-IR data and peak assignments of the three studied complexes are compiled in Table 2.

SEM-images of the synthesized thin films of Co(II)-complexes based on the three studied stoichiometric ratios are shown in Fig. 1. The image shown in Fig. 1i represents an identical distribution of deposited thin film of Co(II)-8-hydroxyquinolate complex. The same image was obtained and repeated either the complex was formed by (1:1), (1:2) or (1:3) stoichiometric ratio indicating that the complex is directly formed regardless of the concentration values of the metal ion and the ligand solutions. It is also evident from these image that a uniform and homogeneous film is formed upon layer-by-layer deposition of Co(II) ion followed by the ligand via chemical deposition method. Fig. 1iii represents the SEM-image

Table 2
Thermal analysis, mass spectrometric and FT-IR data of Co(II)-8-hydroxyquinolate complexes.

Compound	Step	Temperature range (K)	ΔTG_{max} (K)	% weight loss	n	Ea (J mol^{-1} K^{-1})	ΔS	R	Ln (A)
Thermal gravimetric data									
Co L_2 based on (1:1)	1	395–448	430.85	9.69	0.67	63.17	−106.47	0.987	17.02
	2	665–813	723.33	66.01	1.0	120.97	−96.22	0.958	18.77
Co L_2 based on (1:2)	1	371–464	423.24	10.21	1.0	48.43	−142.23	0.987	12.7
	2	646–974	723.00	67.57	1.0	81.04	−174.45	0.856	9.59
Co L_2 based on (1:3)	1	393–455	432.86	9.70	0.67	70.90	−91.37	0.976	18.84
	2	652–845	723.00	67.17	1.0	95.61	−137.87	0.948	13.76

Compound	Major m/z peaks (% relative intensity)
EI-MS data	
Co L_2 based on (1:1)	347 (100), 242 (3) 218 (6) 203 (27), 175 (14), 173 (15), 145 (78), 117 (46), 89 (23), 63 (13)
Co L_2 based on (1:2)	347 (100), 242 (3) 218 (7) 203 (28), 175 (16), 173 (16), 145 (76), 117 (45), 89 (22), 63 (12)
Co L_2 based on (1:3)	347 (100), 242 (3) 218 (7) 203 (30), 175 (16), 173 (16), 145 (79), 117 (48), 89 (23), 63 (13)

Compound	% Co (Experimental)	Major FT-IR peaks
FT-IR data		
Co L_2 based on (1:1)	17.07	3097 ν_{CH}, 1581 ν_{CO}, 1366 ν_{ring}, 1284ν_{CN}
Co L_2 based on (1:2)	16.91	3090 ν_{CH}, 1586 ν_{CO}, 1368 ν_{ring}, 1285ν_{CN}
Co L_2 based on (1:3)	17.23	3094 ν_{CH}, 1583 ν_{CO}, 1364 ν_{ring}, 1287ν_{CN}

of Co(II)-8-hydroxyquinolate synthesized based on experimental stoichiometric ratio of (1:1). A quick and uniform film was obtained after only 2 s dipping time and 10 dipping cycles. The quick and homogeneous complex particles distribution are formed as shown by Fig. 1iv and v in which SEM-images of Co(II)-8-hydroxyquinolate were synthesized on the basis of stoichiometric ratios of (1:2) and (1:3), respectively.

The determined particle size of all synthesized Co(II)-8-hydroxyquinolate complexes based on SEM studies were characterized in the range of 50–150 nm as shown in Fig. 2 as a representative image of similar nano-sized Co(II)-8-hydroxyquinolate complexes.

3.2. Effect of number of dipping cycle

The effect of dipping cycles on the thin film formation was extensively studied for the three selected stoichiometric ratios of metal to ligand, 1:1, 1:2 and 1:3. The dipping time was taken as 2-s for all thin film formation and the selected number of cycles are 2, 5, 10, 20, 30, 40 and 50. Fig. 3 clearly shows that a gradual increase in the masses of deposited thin films upon increasing the number of dipping cycles. The mass of deposited thin film was determined by weight difference of glass substrate before and after deposition of the thin film. The maximum masses were identified at 50 dipping cycles as 4.0, 4.8 and 5.2 mg for the three stoichiometric ratios 1:1, 1:2 and 1:3, respectively. In all studies, the highest masses of deposited thin films of Co(II)-complexes were identified in the case of 1:3 stoichiometric ratio while the lowest ones were detected in the case of 1:1. However, the collected data from the mass spectrometric analysis and atomic absorption of cobalt analysis of some selected samples of these synthesized thin film were found to give a 1:2 stoichiometric ratio as described in Section 3.1. In addition, the particle size of Co(II)-complexes synthesized by any selected dipping cycles were found in the range 50–150 nm as determined by the SEM analysis referring to the suitability of the layer-by-layer deposition method for obtaining the desired nano-sized thin films.

3.3. Effect of number of dipping time

The effect of dipping time on layer-by-layer thin film formation of nano-sized Co(II)-8-hydroxyquinolate was also studied as one of the important factors. The time of immersion was varied to cover 2, 5, 10, 20, 30, 40 and 50 s. The selected molar stoichiometric ratios of metal to ligand are (1:1), (1:2) and (1:3) and the number of dipping cycles is five cycles. These factors were kept constant during the course of this evaluation study. The general trend observed from this study can be outlined as the gradual increase in the thin film formation upon increasing the dipping time of substrate in the metal ion and ligand solutions. In the case of (1:2) stoichiometric ratio, the determined masses were found as 0.3, 0.6, 0.9, 1.0, 1.1, 1.1 and 1.1 mg for 2, 5, 10, 20, 30, 40 and 50 dipping time in second, respectively. It evident from these data that very close nano-sized Co(II)-8-hydroxyquinolate complex thin films were formed after 20 s as a dipping time with respect to the deposited masses. Thus, one can easily conclude that the 20 s dipping time is the optimum one for forcing a complete reaction between the deposited metal ion and ligand molecules for the formation of the aimed thin film. This behavior can be interpreted on the basis of mass deposited of initial layer of Co(II) ion on the surface of glass substrate which in this case require at least 20 s to completely react with suitable number of 8-hydroxyquinoline molecules and form the aimed stoichiometric complex species. Moreover, the identified optimum time (20 s) can directly refer to the rapid interaction processes of nano-sized Co(II)-8-hydroxyquinolate complex thin film formation. On the other hand, increasing the contact time to 30, 40 or 50 s was not practically important due to the less pronounced deposition of metal complex than those detected by 20 s dipping time. It is also important to report here that the particle size of Co(II)-complexes synthesized under any selected dipping time as determined by the SEM analysis were found in the range 50–150 nm. This also refers to the suitability of the layer-by-layer deposition method for obtaining good nano-sized thin films.

3.4. Effect of pH and solvent

The effect of pH of metal ion and ligand solutions is also considered of great importance on the process of layer-by-layer deposition of nano-sized thin film formation of Co(II)-8-hydroxyquinolate complex. Four selected buffer solutions of pH 1, 3, 5 and 7 were used to evaluate the process of thin film formation. This study was completed at constant dipping time (5-s) and dipping cycle (5-cycles). The stoichiometric ratio of metal to ligand was taken as 1:2. It was found and identified that a gradual increase in the pH value of deposited metal ion has led to a gradual increase in the mass of deposited thin film. The optimum pH value for thin film formation of Co(II)-8-hydroxyquinolate complex was characterized in pH 5 judging from the 4.8 mg deposited mass of thin

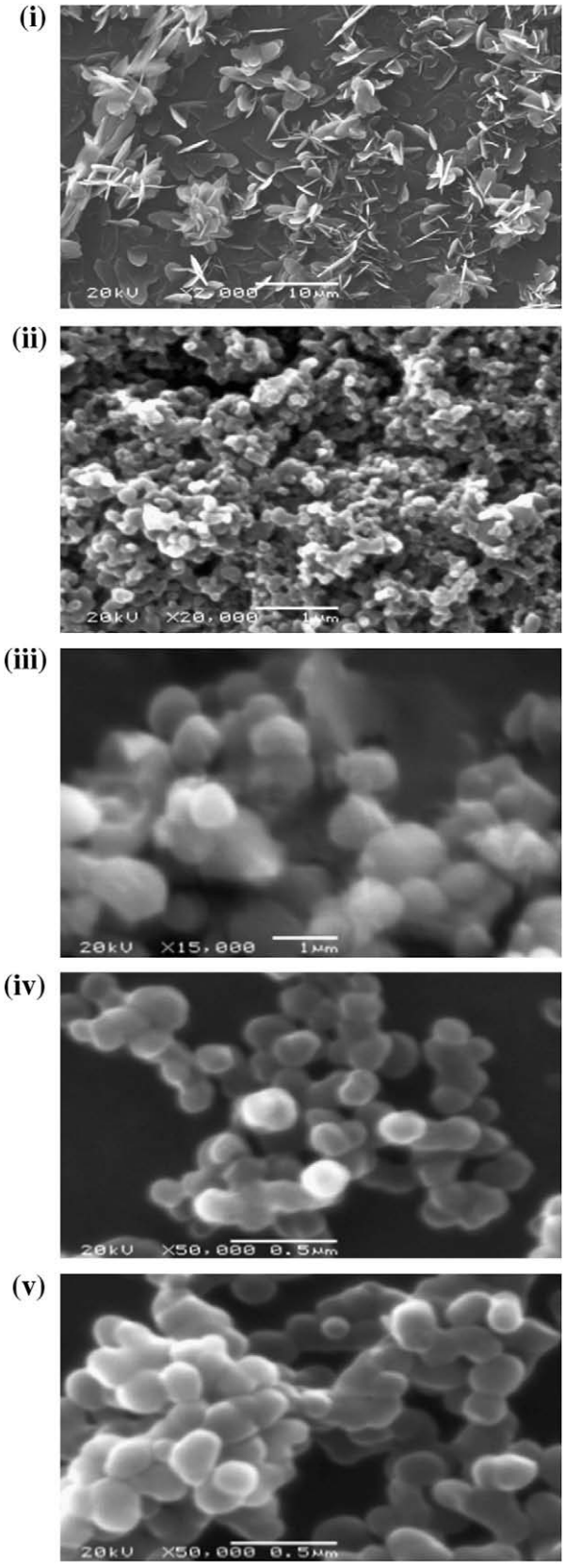


Fig. 1. SEM-images of Co(II)-8-hydroxyquinolate complexes. (i) Thin film image of Co(II)-8-hydroxyquinolate at 2000 magnification times. (ii) General thin film image of Co(II)-8-hydroxyquinolate at 20,000 magnification times. (iii) Co(II)-8-hydroxyquinolate synthesized based on (1:1) ratio at 2 s dipping time and 10 dipping cycles. (iv) Co(II)-8-hydroxyquinolate synthesized based on (1:2) ratio at 2 s dipping time and 10 dipping cycles. (v) Co(II)-8-hydroxyquinolate synthesized based on (1:3) ratio at 2 s dipping time and 10 dipping cycles.

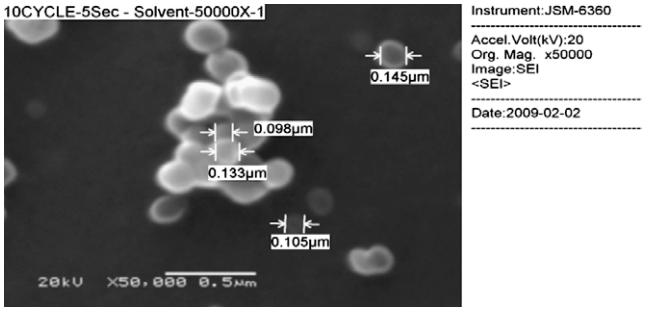


Fig. 2. Representative SEM-image of Co(II)-8-hydroxyquinolate complex for particle size determination.

film. The buffer solution with pH value 7 was also found to produce a thin film of Co(II)-8-hydroxyquinolate complex with a mass equal 3.9 mg. The buffered Co(II) solutions in pH values 1 and 3 were found to produce thin films of Co(II)-8-hydroxyquinolate with low mass values of 0.4 and 0.6 mg, respectively. This indicates that the mass deposited of the initial layer of Co(II) ion was low compared to that at pH 5 and 7 and this behavior may be due to the strong preference of Co(II) ion to exist as dissolved species rather than being deposited on the glass substrate. The results of this study refer to the possibility of thin film formation under any pH values of both contacting metal and ligand solutions. However, the maximum deposited mass and thickness of the required thin film is only obtained when the optimum pH condition is reached. Moreover, the range 50–150 nm as determined by the SEM analysis was also identified as the particle size of Co(II)-8-hydroxyquinolate synthesized under any selected and studied pH value.

Finally, the effect of solvent on nano-sized thin film formation of Co(II)-8-hydroxyquinolate complex was studied and evaluated by using only two solvents, ethanol and methanol, for ligand dissolution and water for Co(II) dissolution. These two solutions were selected on the basis of solubility factor of 8-hydroxyquinoline. The experimental results collected from this study indicated that no pronounced difference in thin film formation between dissolution of 8-hydroxyquinoline in either ethanol or methanol owing to the close polarity of these two solvents. However, other less polar solvents may facilitate the reaction of thin film formation due to rapid deposition of the ligand molecules on the glass substrate. This factor will be comprehensively studied and evaluated in our new thin film works.

3.5. Optical properties of Co(II)-8-hydroxyquinolate complex

The optical transmittance and absorbance of thin films of Co(II)-8-hydroxyquinolate complex is represented in Fig. 4. The average film transmittance in the long wavelength region was >85%. Three absorption bands or edges are evident and referred namely by 1, 2 and 3. The first edge was identified in the UV region with a wavelength range 300–400 nm and the second is located in the wavelength range 400–500 nm. The third is a very weak absorption band and located in the wavelength range 500–700 nm. These absorption edges correspond to optical transitions between occupied and unoccupied energy levels and are commonly referred in organic semiconductors as high occupied molecular orbital "HOMO" and low unoccupied molecular orbital "LUMO" levels. The optical transition between HOMO and LUMO energy levels can be described by the optical absorption coefficient, α, which is given by Eq. (1) [32].

$$\alpha = \left(\frac{A}{h\upsilon}\right)(h\upsilon - E_g)^2 \quad (1)$$

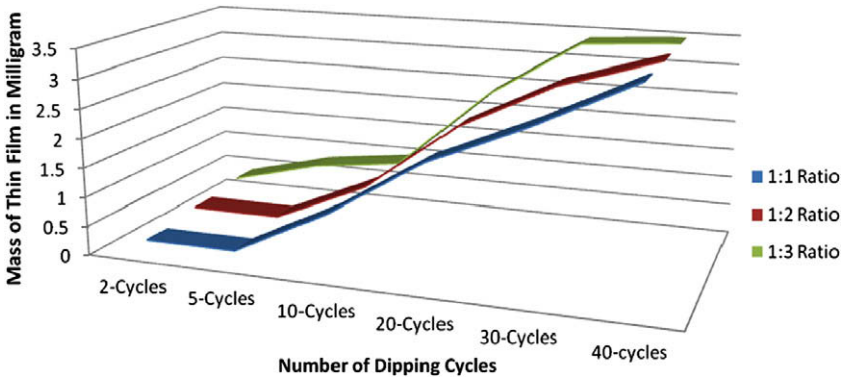


Fig. 3. Effect of dipping cycles on thin film formation at 2-s dipping time.

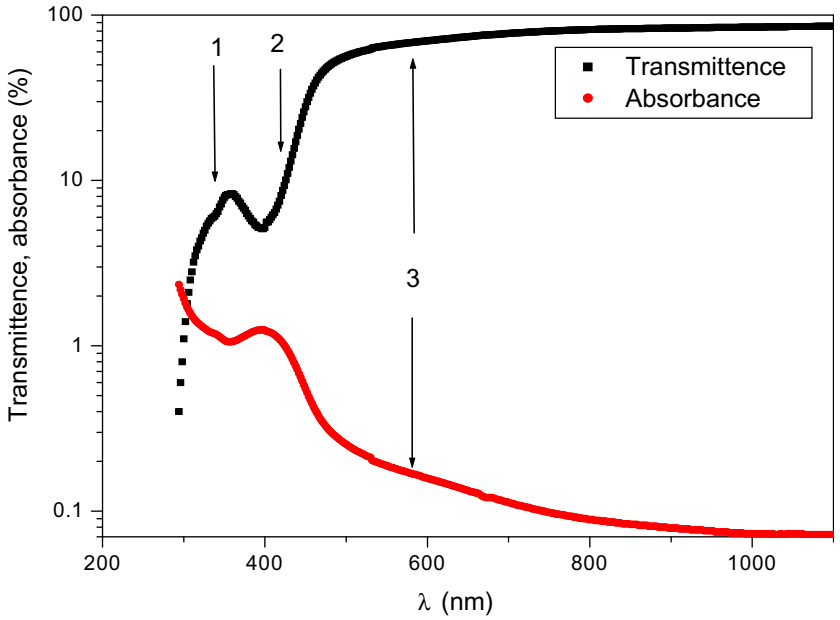


Fig. 4. Optical transmittance of Co(II)-8-hydroxyquinolate complex thin film.

where A is a constant, $h\nu$ is the incident photon energy and E_g is the band gap known as the energy difference between HOMO and LUMO. The exponent m is governed by the type of transition.

In order to obtain information about these transitions, the absorption coefficient α can be calculated according to Eq. (2) [33].

$$\alpha = \frac{1}{d}\ln\left[\frac{\left(1-R^2\right)}{2T}) + \sqrt{\frac{(1-R)^4}{4T^2}+R^2}\right] \tag{2}$$

where T is the transmittance, R is the reflectance and d is the thickness of the film. The value of the reflectance was noticed to be very small compared to the total transmittance and Eq. (2) can be converted to Eq. (3).

$$\alpha = \frac{1}{d}\ln\left(\frac{1}{T}\right) \tag{3}$$

Fig. 5 shows the absorption coefficient dependence upon wavelength in the case of the absorption edge denoted as number 2. It seems that this curve is similar to the absorbance and consists of the pre-mentioned three absorption edges.

The energy band gaps in this case are defined as the difference between the LUMO's and HOMO's levels determined on the basis of spectral absorption edges within the framework of band-to-band transition theory [33]. This theory can be used to analyze the absorption edge data of many organic semiconductors [32–35]. First, the constant m is determined by writing Eq. (1) in natural logarithm form as represented by Eq. (4) and the first derivative with respect to photon energy is given by Eq. (5).

$$\ln(\alpha h\nu) = \ln A + m\ln(h\nu - E_g) \tag{4}$$

$$\frac{d[\ln(\alpha h\nu)]}{d(h\nu)} = \frac{m}{h\nu - E_b} \tag{5}$$

The type of optical transition is based on the determination of m-value. By plotting the data of Eq. (3) by using originlab 6.1 software and differentiating the curve, we can obtain $d\{\ln(\alpha h\nu)\}/d(h\nu)$ versus $h\nu$. This plot shows a peak at 2.5 eV which determines the first estimation of the band gap. Substitution of the obtained value in Eq. (1) to plot the curve $\ln(\alpha h\nu)$ vs $\ln(h\nu - E_g)$ to determine m-value which was then found as 1.89. The nearest optical transition process is found at the $m = 2$ and this represents an indirect allowed transition. Then re-plotting $(\alpha h\nu)^{1/2}$ as a function of photon energy, $h\nu$ gave a straight line as shown in Fig. 6. The optical band gap was determined by extrapolating the linear portion of the plot to $(\alpha h\nu)^{1/2} = 0$. This suggests that the absorption edge is formed by an indirect allowed transition from HOMO to LUMO levels with

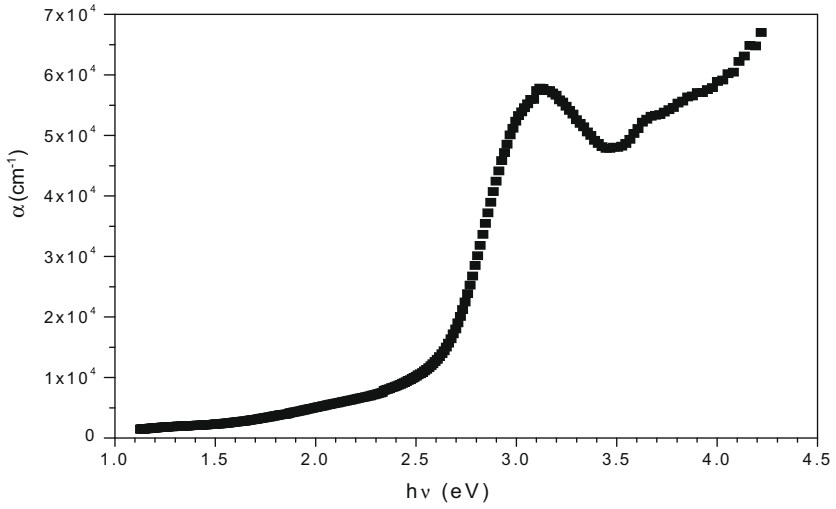


Fig. 5. Absorption coefficient vs. photon energy of Co(II)-8-hydroxyquinolate complex thin film.

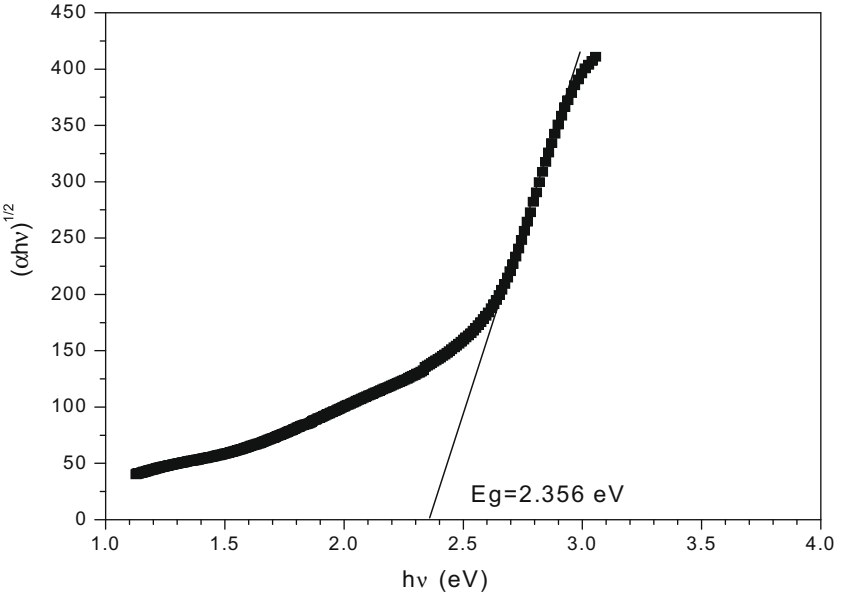


Fig. 6. $(\alpha h\nu)^{1/2}$ vs. hν for indirect transition Co(II)-8-hydroxyquinolate complex thin film.

energy difference of 2.356 eV as shown in Fig. 6. Similar mathematical treatments were also applied for the higher and the lower identified absorption peaks number 1 and 3 (Fig. 4), respectively. It was found that these two edges possess a constant $m = 0.5$ corresponding to the direct allowed transitions. Plotting $(\alpha h\nu)^2$ vs $h\nu$ produces a straight line with an intercept representing the difference between HOMO's and LUMO's in UV and equal 3.13 eV as given in Fig. 7. The lower absorption edge number 3 (Fig. 4) was determined by similar approach to give 1.5 eV. Optical transitions in Co(II)-8-hydroxyquinolate complex can be understood on the basis of two small direct optical transitions from high occupied molecular orbitals (HOMO) to low unoccupied molecular orbitals (LUMO) with transition energy values 1.5 and 3.13 eV. In addition, high indirect optical transition from HOMO to LUMO with transition energy value 2.356 eV is evident. Thus, four main types of electronic transition states are expected and can be outlined in transition metal complexes as discussed by Evans et al. [36].

1. *d–d* States [metal-centered (MC)] transition: When the ligand is coordinated to the metal, the d orbitals are split. Excited d–d states arise from promotion of an electron within d orbital which are essentially confined to the metal center.
2. d–π^* states (metal-to-ligand-charge-transfer (MLCT)): These involve the excitation of a metal centered electron to an anti-bonding orbital located on the ligand system.
3. $\pi-\pi^*$ or $n-\pi^*$ states [intra ligand (IL) transition]: Promotion of an electron from a π-bonding or non-bonding orbital to a higher energy anti-bonding orbital giving rise to these states.
4. π–d states [ligand-to-metal-charge-transfer (LMCT)]: These states arise from the transfer of electronic charge from the ligand π-system to a metal centered orbital.

In Co(II)-8-hydroxyquinolate complex, the highest optical transition is resulting from $\pi-\pi^*$ or n, π^* states with energy gap located in the UV at 3.13 eV. The lowest optical transition results

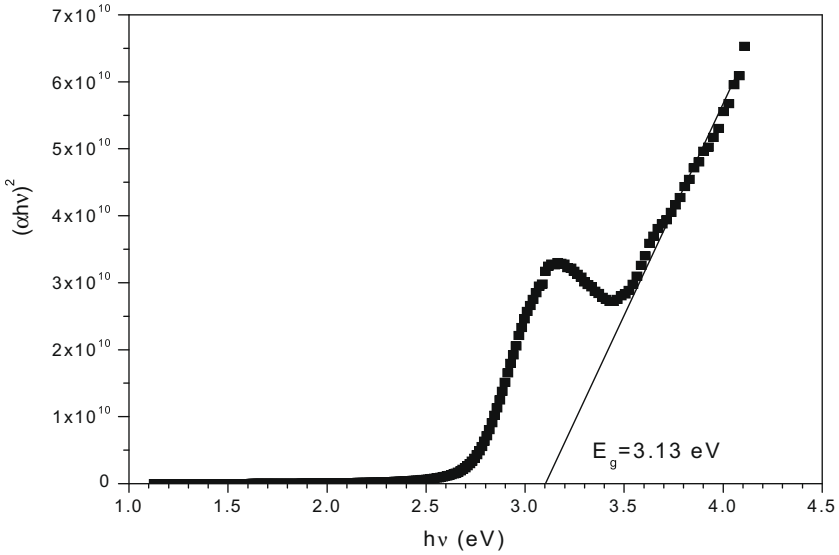


Fig. 7. $(\alpha h\nu)^2$ vs. $h\nu$ for indirect transition Co(II)-8-hydroxyquinolate complex thin film.

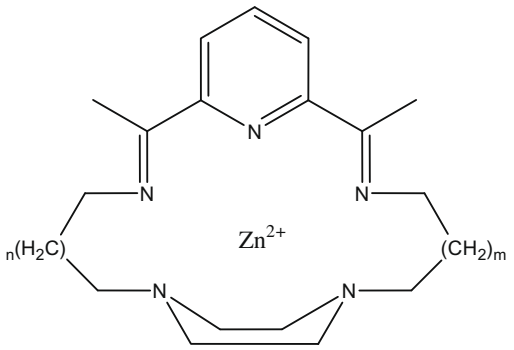
from d–d transition or metal centered transition with energy of 1.5 eV. The optical transition at 2.356 eV corresponds to the contribution of metal–ligand or ligand–metal transition.

4. Conclusion

In the present study, five different controlling factors were studied and explored for layer-by-layer chemical deposition of nano-sized Co(II)-8-hydroxyquinolate complex thin films. First, The molar stoichiometric of metal to ligand was found to be insignificant as the Co(II)-8-hydroxyquinolate complex was identified as 1:2 under any stoichiometric condition. Second, the role of dipping cycles was identified by its strong contribution to thin film formation as the maximum thin film masses were characterized at maximum dipping cycles (50 cycles in this study). Third, evaluation of the optimum dipping time factor was characterized as 20 s with respect to the deposited masses. Fourth, the effect of pH on thin film formation of nano-sized Co(II)-8-hydroxyquinolate complex was found to play a significant role judging from the maximum deposited mass at buffer solution with pH 5 as the identified optimum value. Fifth, the studied solvent effect on thin film formation was proved to exhibit no contribution owing to the similar polarity of the evaluated solvents. Finally, the optical properties of Co(II)-8-hydroxyquinolate complex was studied and confirmed that the highest optical transition from HOMO to LUMO energy levels are located in the visible region at 2.356 eV with indirect transition, while other direct optical transitions at energy values 1.5 and 3.13 eV were observed. Upon these results, Co(II)-8-hydroxyquinolate complex can be accepted as an organic semiconductor with the potential application as a component layer in organic light-emitting diodes (OLEDs).

References

[1] M. Rajeswaran, T.N. Blanton, C.W. Tang, W.C. Lenhart, S.C. Switalski, D.J. Giesen, B.J. Antalek, T.D. Pawlik, D.Y. Kondakov, N. Zumbulyadis, R.H. Young, Polyhedron 28 (2009) 835.
[2] M.M. Amini, M. Sharbatdaran, M. Mirzaeeand, P. Mirzaei, Polyhedron 25 (2006) 3231.
[3] M. Clle, R.E. Dinnebier, W. Brütting, Chem. Commun. (2002) 2908.
[4] M. Albrecht, M. Fiege, O. Osetska, Coord. Chem. Rev. 252 (2008) 812.
[5] C.-F. Leung, C.-Y. Wong, C.-C. Ko, M.-C. Yuen, W.-T. Wong, W.-Y. Wong, T.-C. Lau, Inorg. Chim. Acta 362 (2009) 1149.
[6] H. Filik, M. Hayvali, E. Kilic, Anal. Chim. Acta 535 (2005) 177.
[7] H. Wang, W.-S. Wang, H.-S. Zhang, Talanta 53 (2001) 1015.
[8] M. Buratti, C. Valla, O. Pellegrino, F.M. Rubino, A. Colombi, Anal. Biochem. 353 (2006) 63.
[9] M.E. Mahmoud, Encyclopedia of Chromatography, second ed., 2006, pp. 1–14, 10.1081/E-ECHR-120042798.
[10] M.E. Mahmoud, E.M. Soliman, J. Liq. Chrom. Rel. Technol. 26 (2003) 3045.
[11] A. Goswami, A.K. Singh, B. Venkataramani, Talanta 60 (2003) 1141.
[12] M.L. Firdaus, K. Norisuye, T. Sato, S. Urushihara, Y. Nakagawa, S. Umetani, Y. Sohrin, Anal. Chim. Acta 583 (2007) 296.
[13] C.W. Tang, S.A. VanSlyke, Appl. Phys. Lett. 51 (1987) 913.
[14] C.W. Tang, S.A. VanSlyke, C.H. Chen, J. Appl. Phys. 65 (1989) 3610.
[15] W.S. Jeon, T.J. Park, S.Y. Kim, R. Pode, J. Jang, J.H. Kwona, Org. Electron. 10 (2009) 240.
[16] C. Himcinschia, S. Hartmannb, A. Janssenb, N. Meyerc, M. Friedricha, W. Kowalskyb, D.R.T. Zahna, M. Heukenc, J. Cryst. Growth 275 (2005) e1035.
[17] J.-A. Cheng, C.H. Chen, H.-P.D. Shieh, Mater. Chem. Phys. 113 (2009) 1003.
[18] W.S. Kim, B.-J. Lee, N.M. Tuong, E.M. Son, K.-S. Yang, Y.-S. Kwon, Curr. Appl. Phys. 6 (2006) 596.
[19] W. Li, Y. Jiang, T. Wang, J. Lumin. 128 (2008) 1175.
[20] E. Pál, D. Sebok, V. Hornok, I. Dékány, J. Colloid. Interface Sci. 332 (2009) 173.
[21] M. Ortega-López, A. Avila-García, M.L. Albor-Aguilera, V.M.S. Resendiz, Mater. Res. Bull. 38 (2003) 1241.
[22] Y.F. Gao, M. Nagai, Y. Masuda, F. Sato, K. Koumoto, J. Cryst. Growth 286 (2006) 445.
[23] S. Baskoutas, P. Poulopoulos, V. Karoutsos, M. Angelakeris, N.K. Flevaris, Chem. Phys. Lett. 417 (2006) 461.
[24] S. Singh, R.S. Srinivasa, S.S. Major, Thin Solid Films 515 (2007) 8718.
[25] S. Flickyngerova, K. Shtereva, V. Stenova, D. Hasko, I. Novotny, V. Tvarozek, P. Sutta, E. Vavrinsky, Appl. Surf. Sci. 254 (2008) 3643.
[26] L.Z. Zhang, G.Q. Tang, Opt. Mater. 27 (2004) 217.
[27] M. Safouane, R. Miller, H. Möhwald, J. Colloid Interface Sci. 292 (2005) 86.
[28] S. Singh, R.S. Srinivasa, S.S. Talwar, S.S. Major, Thin Solid Films 515 (2007) 8714.
[29] L. Naszályi, A. Deák, E. Hild, A. Ayral, A.L. Kovács, Z. Hórvölgyi, Thin Solid Films 515 (2006) 2587.
[30] M.E. Mahmoud, S.S. Haggag, T.M. Abdel-Fattah, Polyhedron 28 (2009) 181.
[31] V.R. Shinde, T.P. Gujar, C.D. Lokhande, Sol. Energy Mater. Sol. Cells 91 (2007) 1055.
[32] M.M. El-Nahass, A.A. Atta, H.E.A. El-Sayed, E.F.M. El-Zaidia, Appl. Surf. Sci. 254 (2008) 2458.
[33] G.A. Kumar, J. Thomas, N. George, B.A. Kumar, P. Radhakri, V.P.N. Shnan, C.P.G. Poori, N.V. Vallabhan, Unnikrishnan, Phys. Chem. Glasses 41 (2000) 89.
[34] M.M. El-Nahass, K.F. Abd-El-Rahman, A.A.M. Farag, A.A.A. Darwish, Int. J. Mod. Phys. B 18 (2004) 421.
[35] M.M. El-Nahass, H.S. Soliman, H.S. Metwally, A.M. Farid, A.A.M. Farag, A.A. El-Shazly, J. Opt. 30 (2001) 121.
[36] Rachel C. Evans, Peter Douglas, Christopher J. Winscom, Coord. Chem. Rev. 250 (2006) 2093.



	m	n
L^1	2	3
L^2	3	3

Fig. 1. The template condensation between 2,6-diacetylpyridine and two different amines with piperazine moiety, in the presence of zinc(II) ion.

Safety note: Perchlorate complexes are potentially explosive. While we have not experienced any problems with the compounds described, they should be treated with caution and handled in small quantities.

2.2. Synthesis of metal complexes

2.2.1. Synthesis of $[ZnL^1Br]ClO_4{\cdot}H_2O$ (**1**)

A solution of NaOH (2 mmol) in absolute EtOH (10 cm^3) was added to a suspension of N,N′(2-aminoethyl)(3-aminopropyl)piperazine (0.5 mmol) in absolute EtOH (10 ml). The mixture was stirred at room temperature for a few minutes then filtered, and the precipitate was washed well with absolute EtOH (10 ml). The washings and the filtrate were combined and this solution was added dropwise to a hot solution of $ZnBr_2$ (0.5 mmol) and DAP (0.5 mmol) in absolute EtOH (20 ml) over a period of 2 h. After refluxing the solution for 18 h, then $NaClO_4$ (1 mmol) was added. The solution was filtered and the filtrate was reduced to ca. 10 ml. A crystalline compound was obtained by slow diffusion of Et_2O vapor into this solution. Yield of the complex $[ZnL^1Br]ClO_4{\cdot}H_2O$ **(1)**, 0.27 g, 47%. *Anal.* Calc. for $C_{18}H_{29}BrClN_5O_5Zn$ (MW: 576.2): C, 37.7; H, 5.2; N, 12.1. Found: C, 37.4; H, 5.4; N, 12.0%. IR (KBr, cm^{-1}): 3443, 1644 (νC=N Schiff-base), 1591, 1455 [ν(C=C) and ν(C=N)py], 1092, 623 cm^{-1} ν(ClO_4^-). FAB-MS (*m*/*z*, %): $[ZnL^1Cl]^+$, 412 (85.7%); $[ZnL^1Br]^+$, 458 (100%). Λ_M/Ω^{-1} cm^2 mol^{-1} (in DMF): 120 (2:1).

2.2.2. Synthesis of $[ZnL^2](ClO_4)_2{\cdot}H_2O$ (**2**)

A solution of N,N′-bis(3-aminopropyl)piperazine (0.5 mmol) in absolute methanol (10 ml) was added dropwise to a hot solution of $Zn(ClO_4)_2{\cdot}xH_2O$ (0.5 mmol) and 2,6-diacetylpyridine (0.5 mmol) in absolute methanol (20 ml), over a period of 2 h. After refluxing the solution for 24 h, the resulted solution was reduced to ca. 2–3 ml. The precipitated was filtered off and dried in vacuum. Yield of the complex $[ZnL^2](ClO_4)_2{\cdot}H_2O$ (**2**), 0.24 g, 40%. *Anal.* Calc. for $C_{19}H_{31}Cl_2N_5O_9Zn$ (MW: 607.1): C, 37.4; H, 5.1; N, 11.5. Found: C, 37.0; H, 5.3; N, 11.3%. IR (KBr, cm^{-1}): 3442, 1642, (νC=N Schiff-base), 1591, 1457 1455 [ν(C=C) and ν(C=N)py], 1085, 624 cm^{-1} ν(ClO_4^-). FAB-MS (*m*/*z*, %): $[ZnL^2]ClO_4^+$, 492 (32%). Λ_M/Ω^{-1} cm^2 mol^{-1} (in DMF): 140 (2:1).

2.3. Physical measurements

Elemental analyzes were performed in a Carlo-Erba EA microanalyser. FT-IR spectra in the 4000–400 cm^{-1} region were recorded from KBr pellets on a Bruker VECTOR 22 spectrophotometer. FAB mass spectra were recorded using a Kratos-MS-50T spectrometer connected to a DS90 data system using 3-nitrobenzyl alcohol as the matrix. Conductivity measurements were carried out in 10^{-3} mol dm^{-3} dimethylformamide solutions at 20 °C using a CARISON GLP32 conductivimeter.

2.4. X-ray crystal structure determination

Vapor diffusion of diethyl ether into a solution of $[ZnL^1Br]$ ClO_4 in the mixture of acetonitrile and methanol provided crystals suitable for study by X-ray diffraction. Data were collected on a Bruker SMART CCD area diffractometer operating at room temperature. Data were empirically corrected for absorption and other effects [15]. The structure was solved by direct methods and refined by the full matrix least-squares method on F^2 data using SHELXTL [16]. All non-H atoms were refined anisotropically, except oxygen atoms of the perchlorate ion, which were found to be disordered over two positions with site occupancy factors of 0.40 and 0.60. They were refined isotropically with the restrain bond distances of 1.42 Å. The H atoms were constrained to idealized geometries and refined isotropically. The crystallographic and refinement data are summarized in Table 1.

3. Results and discussion

3.1. Synthesis and characterization

The Schiff-base macrocyclic complexes $[ZnL^n]^{2+}$ (n = 1 and 2) were prepared from [1 + 1] cyclocondensation of 2,6-diacetypyridine and N,N′-bis(3-aminopropyl)piperazine or N,N′(2-amino-

Table 1
Crystal data and structure refinement for $[ZnL^1Br]ClO_4$.

Complex	$[ZnL^1Br]ClO_4$
Empirical formula	$C_{18}H_{27}BrClN_5O_4Zn$
Formula weight	558.18
Temperature	293(2) K
Wavelength (Å)	0.71073 Å
Crystal system, space group	triclinic, P_1
a (Å)	7.7557(11)
b (Å)	11.5602(17)
c (Å)	12.6305(18)
α (°)	100.560(3)
β (°)	90.843(3)
γ (°)	99.148(2)
Volume ($Å^3$)	1098.0(3)
Z, Calculated density	2, 1.688 Mg/m^3
F(0 0 0)	568
Crystal size (mm^3)	0.29 × 0.28 × 0.16 mm
Absorption coefficient (mm^{-1})	3.095
Limiting indices	$-7 \leqslant h \leqslant 10$, $-15 \leqslant k \leqslant 13$, $-16 \leqslant l \leqslant 13$
Maximum and minimum transmission	0.6373 and 0.4672
θ Range for data collection (°)	1.82°–24.71°
Reflections collected/unique	5462/3659 [R_{int} = 0.032]
Completeness to θ	97.5% (24.71°)
Maximum and minimum transmission	0.8592 and 0.7183
Refinement method	Full-matrix least-squares on F^2
Data/restraints/parameters	3659/8/261
Goodness-of-fit on F^2	1.010
Final *R* indices [$I > 2\sigma(I)$]	R_1 = 0.087, wR_2 = 0.243
R indices (all data)	R_1 = 0.135, wR_2 = 0.284
Largest difference in peak and hole (e A^{-3})	1.118 and −1.689

ethyl)(3-aminopropyl)piperazine, respectively. The complexes were characterized by elemental analysis, IR, FAB mass spectrometry and conductivity measurements. The compounds were air stable solids and had elemental analyzes consistent with the formulations given in Section 2. The infrared spectra of the complexes are all very similar and confirm the formation of the macrocyclic compounds by the absence of bands characteristic of carbonyl and amine groups of the starting materials. An important feature is the occurrence of a strong band at approximately 1642–1644 cm^{-1} attributable to C=N stretching modes, indicating the Schiff-base condensation and also bands at ca. 1591 and 1456 cm^{-1} associated with $\nu(C{=}N)_{py}$ and $\nu(C{=}C)$ vibrations from the pyridine and phenyl rings [17]. The absorptions attributable to ionic perchlorate were found at approximately 1090 and 624 cm^{-1} [18]. The lack of splitting these bands suggests that the perchlorate anions are not coordinated. The FAB mass spectra also provide strong evidence for the formation of the macrocyclic ligand systems L^1 and L^2. The FAB mass spectra give the parent peak at *m/z* 458 and 490 corresponding to $[ZnL^1Br]^+$ and $[ZnL^2]ClO_4^+$, respectively. The spectrum in **1** also exhibits a peak due to the $[ZnL^1Cl]^+$ at *m/z* 412. The molar conductance values of the complexes measured in dimethylformamide lie in the range reported for 2:1 electrolytes in this solvent [19]. Due to the dynamic character and low solubility of two complexes (1 and 2), we were unable to obtain suitable NMR spectra of sufficient quality to allow unambiguous assignment of the ^1H and ^{13}C NMR.

3.2. X-ray crystal structure analysis

The structure of the $[ZnL^1Br]^+$ cation, determined by single-crystal X-ray diffraction. Selected bond lengths and angles are given in Table 2. Perchlorate ion was found to be highly disordered resulting in rapid fall-off the intensities and relatively poor statistical parameters for room temperature diffraction data. The $[ZnL^1Br]ClO_4$ complex crystallizes in the triclinic system with space group P-1 (No. 2). Crystal structure of the complex as shown in Fig. 2 represents the Zn(II) ion with a N5Br coordination environment. The geometry around the metal can be better described as in a slightly distorted pentagonal-pyramidal. The pentagonal plane is conformed by the five nitrogen atoms from the ligand (rms 0.4077) with the Zn(II) ion 0.554 Å out of this plane, while the apex of the pyramid is occupied by the bromide ion. The sum of the five

Table 2
Selected bond lengths (Å) and angles (°) for $[ZnL^1Br]ClO_4$.

Bond lengths (Å)	
Zn(1)–N(1)	2.159(9)
Zn(1)–N(2)	2.261(8)
Zn(1)–N(3)	2.248(9)
Zn(1)–N(4)	2.383(9)
Zn(1)–N(5)	2.183(9)
Zn (1)–Br(1)	2.379(9)
Bond angles (°)	
N(1)–Zn(1)–N(2)	71.3(3)
N(1)–Zn(1)–N(3)	135.6(3)
N(1)_Zn(1)–N(4)	118.2(3)
N(1)–Zn(1)–N(5)	73.3(3)
N(2)–Zn(1)–N(3)	72.3(3)
N(2)–Zn(1)–N(4)	122.8(3)
N(2)–Zn(1)–N(5)	144.3(3)
N(3)–Zn(1)–N(4)	64.6(3)
N(3)–Zn(1)–N(5)	139.8(4)
N(4)–Zn(1)–N (5)	77.1(3)
N(1)–Zn(1)–Br(1)	109.7(2)
N(2)–Zn(1)–Br(1)	96.4(2)
N(3)–Zn(1)–Br(1)	98.6(2)
N(4)–Zn(1)–Br(1)	124.9(2)
N(5)–Zn(1)–Br(1)	93.1(3)

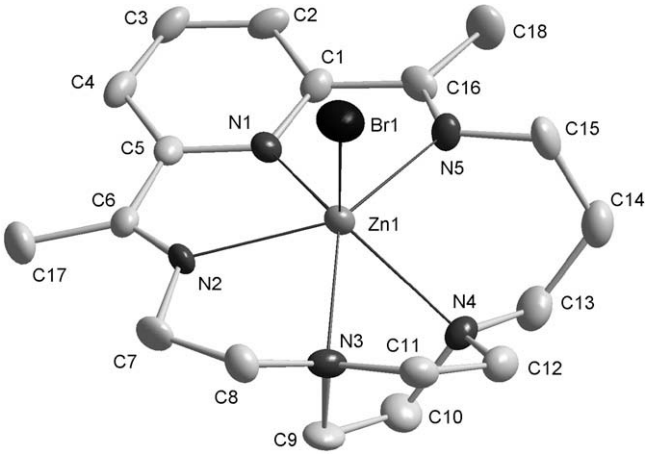


Fig. 2. Crystal structure of the cation $[ZnL1Br]^+$ with atom-numbering scheme. All H atoms are omitted for clarity. Displacement ellipsoids are shown at 30% probability level.

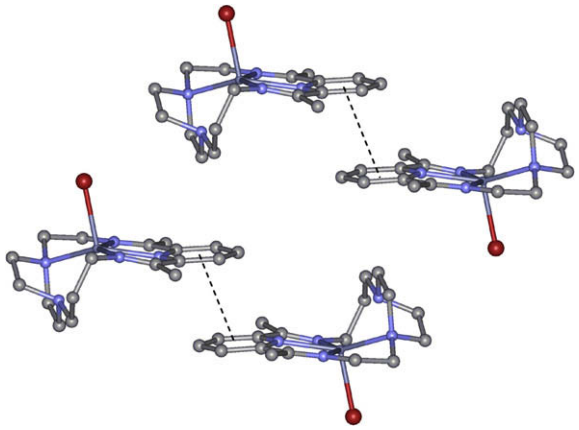


Fig. 3. π,π-Stacking interaction between the pyridine units of adjacent ligand.

N–Zn–N chelate angles (358.6°) is near 360° for an ideal planar structure.

The pyridine group provides the shortest bond to the metal, Zn(1)–N(1) 2.157(8) Å, while the longest belongs to the piperazine nitrogen atoms, Zn(1)–N(3) 2.230(8) and Zn(1)–N(4) 2.379(9) Å. The Zn–N_{imine} bond lengths, Zn(1)–N(2) 2.261(8) and Zn(1)–N(5) 2.183(8) Å show intermediate values. The Zn(1)–Br(1) bond distance of 2.381 Å, is longer than the distance found for this sort of bond in similar complexes [20,21]. The perchlorate ion giving typical bond distances and angles, and the structure shows that it is not coordinated to the Zn(II) ion reflecting the low coordination ability of this anion. Some intermolecular π,π-stacking interactions have been observed between the pyridine rings of adjacent ligands (See Fig. 3). In the net, the pyridine rings lie parallel by pairs, being the distance between the planes containing the rings of 3.33 Å. The distance between centroids (d_{c-c}) is 3.51 Å gives rise to a slipped angle of 18.4°.

4. Conclusion

The template Zn(II) synthesis of the Schiff-base macrocyclic complexes $[ZnL^n]^{2+}$ (n = 1 and 2) prepared from [1 + 1] cyclocondensation of 2,6-diacetylpyridine and N,N′-bis(3-aminopropyl)piperazine or N,N′(2-aminoethyl)(3-aminopropyl)piperazine have been investigated. The crystal structure of $[ZnL^1Br]ClO_4$

shows the metal ion hexacoordinated in a N5Br distorted pentagonal-pyramidal geometry, with the nitrogen atoms from the macrocycle in the pentagonal plane and the bromide ion occupying the axial position.

5. Supplementary data

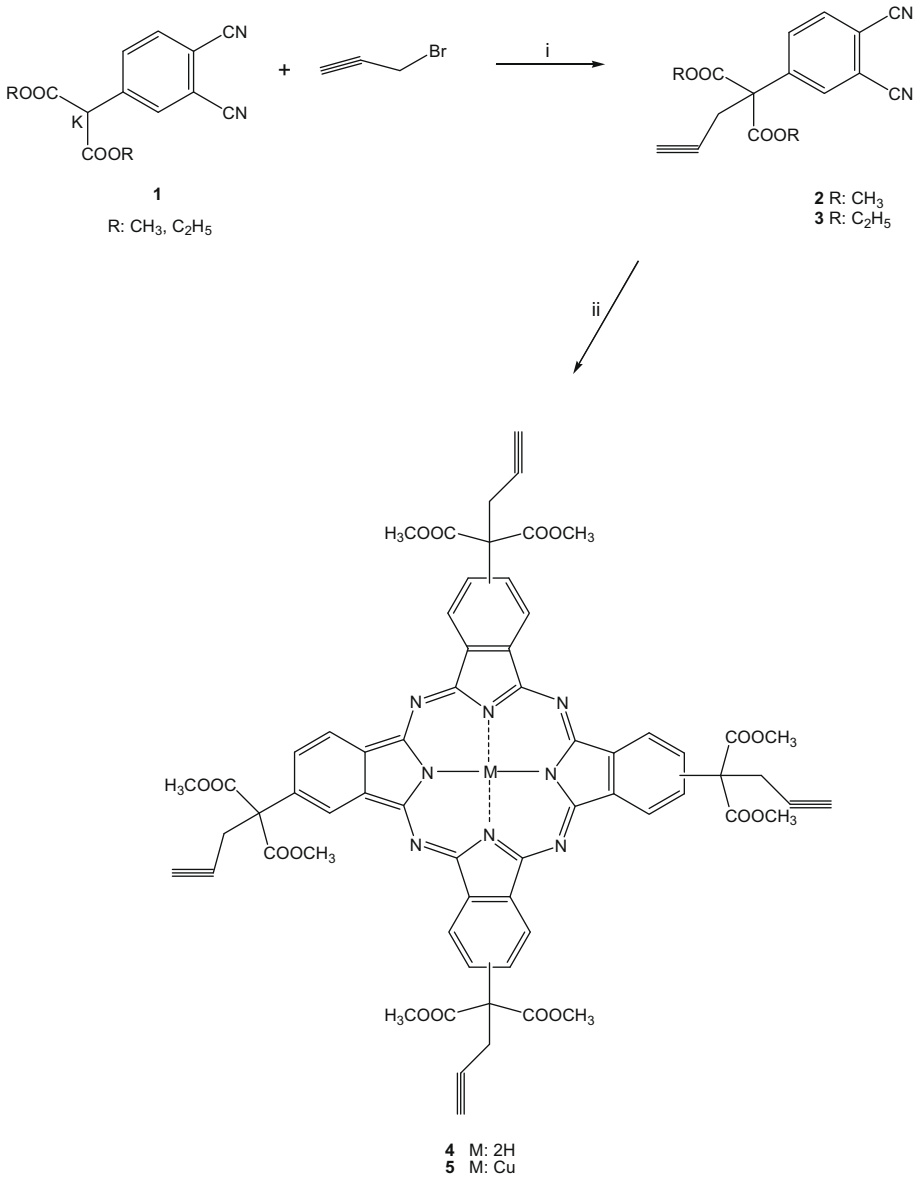
CCDC 699403 contains the supplementary crystallographic data for $[ZnL^1Br]ClO_4$. These data can be obtained free of charge via http://www.ccdc.cam.ac.uk/conts/retrieving.html, or from the Cambridge Crystallographic Data Centre, 12 Union Road, Cambridge CB2 1EZ, UK; fax: (+44) 1223-336-033; or e-mail: deposit@ccdc.cam.ac.uk.

Acknowledgements

We are grateful to the Faculty of Chemistry of Bu-Ali Sina University, Ministry of Science, Research and Technology of Iran for financial support and for a Visiting Fellowship to M. R and Universidade de Vigo (1Z1464102) for financial support.

References

[1] L.F. Lindoy, The Chemistry of Macrocyclic Ligand Complexes, Cambridge University Press, Cambridge, 1989.
[2] W.N. Lipscomb, N. Straeter, Chem. Rev. 96 (1996) 2375.
[3] G. Parkin, J. Chem. Soc., Chem. Commun. (2000) 1971.
[4] C. Kirchner, B. Kerbs, Inorg. Chem. 26 (1987) 3569.
[5] T. Koike, T. Gotoh, S. Aoki, E. Kimura, M. Shiro, Inorg. Chim. Acta 270 (1998) 424.
[6] H. Keypour, H. Khanmohammadi, K.P. Wainwright, M.R. Taylor, Inorg. Chim. Acta 355 (2003) 286.
[7] K. Rissanen, J. Huuskonen, A. Koskinen, J. Chem. Soc., Chem. Commun. (1993) 71.
[8] M.G.B. Drew, S.M. Nelson, Acta Crystallogr., Sect. A 13 (1975) 140.
[9] M.G.B. Drew, S. Hollis, J. Chem. Soc., Dalton Trans. (1978) 511.
[10] J.C. Dabrowiak, L.A. Nafie, S. Bryan Philip, A.T. Torkelson, Inorg. Chem. (1977) 540.
[11] H. Keypour, S. Salehzadeh, R.G. Pritchard, R.V. Parish, Inorg. Chem. 9 (2000) 5787.
[12] H. Keypour, H. Goudarziafshar, A.K. Brisdon, R.G. Pritchard, Inorg. Chim. Acta 360 (2007) 2298.
[13] H. Keypour, H. Goudarziafshar, A.K. Brisdon, R.G. Pritchard, M. Rezaeivala, Inorg. Chim. Acta 361 (2008) 1415.
[14] H. Keypour, M. Rezaeivala, L. Valencia, P. Ṕerez-Lourido, Polyhedron 27 (2008) 3172.
[15] G.M. Sheldrick, Sadabs, Program for Empirical Absorption Correction of Area Detector Data, University of Göttingen, Germany, 1996.
[16] SHELXTL Version, An Integrated System for Solving and Refining Crystal Structures from Diffraction Data (Revision 5.1), Bruker AXS LTD.
[17] N.S. Gill, R.H. Nutall, D.E. Scaife, J. Inorg. Nucl. Chem. 18 (1961) 79.
[18] A.J. Hataway, D.E. Underhill, J. Chem. Soc. (1961) 3091.
[19] W.J. Geary, Coord. Chem. Rev. 7 (1971) 81.
[20] S.J. Brudenell, L. Spiccia, D.C.R. Hockless, E.R.T. Tiekink, J. Chem. Soc., Dalton Trans. (1999) 1475.
[21] A. Bencini, E. Berni, A. Bianchi, P. Fornasari, C. Giorgi, J.C. Lima, C. Lodeiro, M.J. Melo, J. Seixas de Melo, A.J. Parola, F. Pina, J. Pina, B. Valtancoli, J. Chem. Soc., Dalton Trans. (2004) 2180.



Scheme 1. Reagents and conditions: (i) acetone/acetonitrile, reflux; (ii) *n*-pentanol, DBU, reflux, $CuCl_2$ for **5**.

was also synthesized according to the literature procedure, with some minor modifications [31].

2.1. General procedures for the preparation of dialkyl (3,4-dicyanophenyl)propargylmalonates (**2**, **3**)

To the potassium salt of dialkyl-3,4-dicyanophenylmalonate (3.0 mmol, 0.9 g dimethyl-3,4-dicyanophenylmalonate, 0.97 g diethyl-3,4-dicyanophenylmalonate) in 2:1 acetone/acetonitrile (150 mL) was added propargyl bromide (3.6 mmol, 80% in toluene, 0.54 g). The mixture was boiled for 20 h under Ar and then filtered. The solvent was evaporated under reduced pressure to give an oily residue, which was washed with water until the product was free of KBr and finally crystallized from dichloromethane. These compounds were soluble in acetone, chloroform and THF. **2**. Yield: 0.75 g, 84%. Mp: 90–91 °C. FT-IR ν (cm^{-1}): 3288 (H–C≡C–), 3103–3049 (CH, aromatic), 2957 (CH, aliphatic), 2237 (C≡N), 1753, 1731 (C=O). **3**. Yield: 0.79 g, 81%. Mp: 47 °C. FT-IR ν (cm^{-1}): 3278 (H–C≡C–), 3085 (CH, aromatic), 2979–2940 (CH, aliphatic), 2241 (C≡N), 1753, 1724 (C=O); ^{1}H NMR (DMSO-d_6) δ: 8.19–8.16 (aromatic H), 7.96–7.94 (aromatic H), 4.25–4.19 (OCH_2), 3.26 (CH_2), 2.95–2.94 (H–C≡), 1.19–1.16 (CH_3); ^{13}C NMR ($CDCl_3$) δ: 168.1, 142.2, 134.8, 134.4, 134.3, 116.3, 116.2, 115.1, 114.9, 79.4, 75.7, 63.2, 62.2, 25.5, 14.3; GC–MS *m/z*: 324 $[M]^+$, 252 $[M-COOC_2H_5]^+$, 223 $[M-(C_2H_5+COOC_2H_5)]^+$, 205 $[M-(OC_2H_5+COOC_2H_5)]^+$, 179 $[M-2(COOC_2H_5)]^+$, 152 $[M-(2(COOC_2H_5)+HCN)]^+$, 125 $[M-(2(COOC_2H_5)+2(HCN))]^+$.

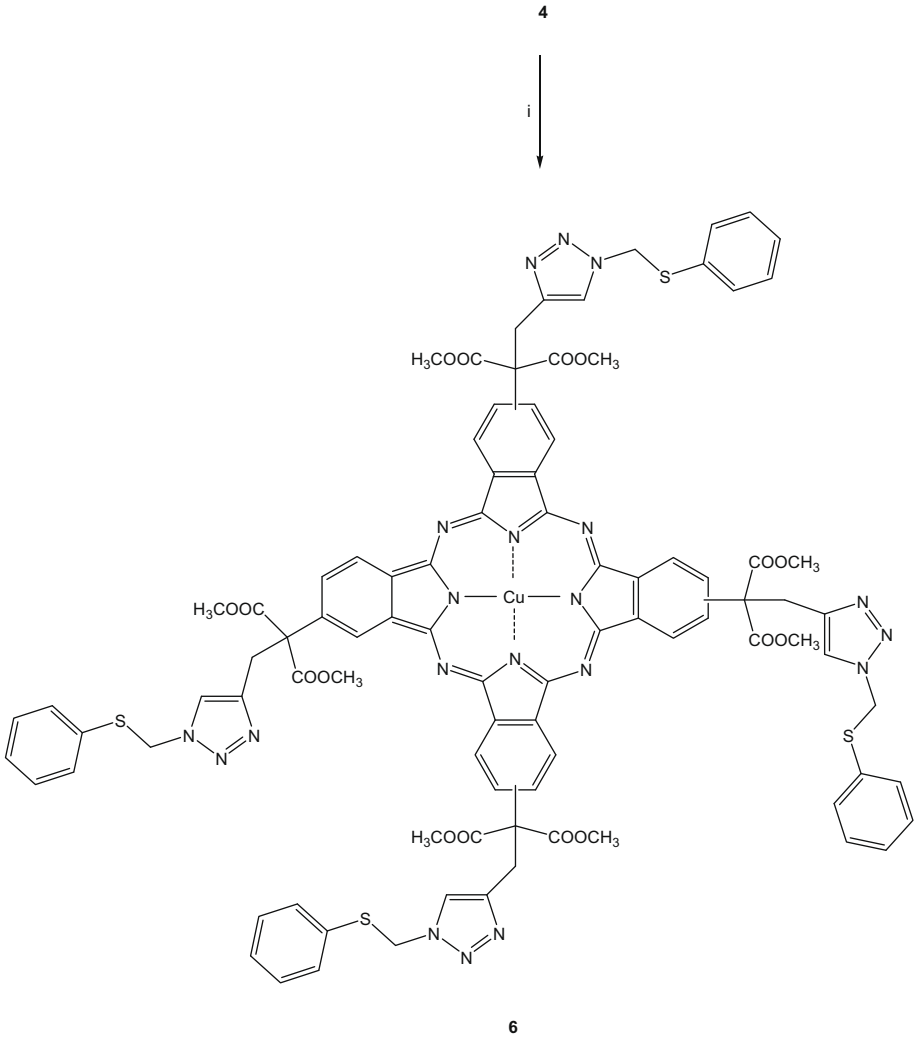
2.2. 2,9,17,23-(1,1-(Dimethoxycarbonyl)-2-(ethynyl)ethyl)phthalocyanine (**4**)

A mixture of dinitrile **2** (0.1 g, 0.33 mmol) and a catalytic amount of DBU in *n*-pentanol (1 mL) was heated at 140 °C with stirring for 20 h. After evaporation of the solvent, the residue was purified by column chromatography (SiO_2, chloroform/methanol 100:1). Yield: 0.075 g, 20%. FT-IR ν (cm^{-1}): 3311 (N–H), 3291 (H–C≡C–), 2956–2856 (CH, aliphatic), 2114 (–C≡C–), 1726 (C=O); UV–Vis λ_{max} (nm) in chloroform: 698, 661, 342; MALDI-TOF MS (2,5-dihydroxybenzoic acid or sinapic acid) *m/z*: 1179.6

$[M-6H]^{6-}$, 2358 $2 \times [M-6H]^{6-}$. *Anal.* Calc. for $C_{64}H_{50}N_8O_{16}$: C, 64.75; H, 4.25; N, 9.44. Found: C, 64.63; H, 4.22; N, 9.41%.

2.3. 2,9,17,23-(1,1-(Dimethoxycarbonyl)-2-(ethynyl)ethyl)phthalocyaninatocopper (**5**)

A mixture of dinitrile **2** (0.1 g, 0.33 mmol), $CuCl_2$ (0.011 g, 0.08 mmol) and a catalytic amount of DBU in *n*-pentanol (1 mL) was heated at 140 °C with stirring for 20 h. The reaction mixture was cooled to room temperature. The precipitate was filtered off and washed with methanol. After extraction of the crude product with chloroform, the purification was carried out by column chromatography on silica gel using chloroform/methanol (100:1) as the eluent to afford **5** as a blue solid. Yield: 0.010 g, 10%. FT-IR ν (cm^{-1}): 3285 (H–C≡C–), 2955–2854 (CH, aliphatic), 2121 (–C≡C–), 1726 (C=O); UV–Vis λ_{max} (nm) in chloroform: 677,



Scheme 2. Reagents and conditions: (i) $CuSO_4 \cdot 5H_2O$, NaAsc., THF/H_2O, rt.

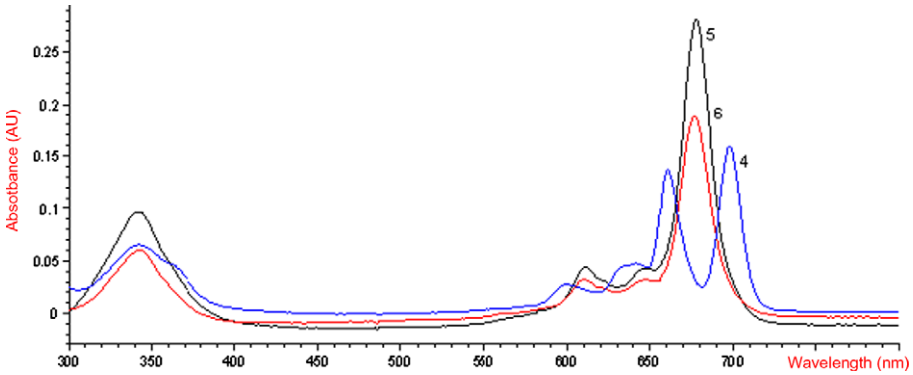


Fig. 1. UV–Vis spectra of **4** (blue line), **5** (black line) and **6** (red line) in chloroform. Concentration: $\sim 10^{-6}$ mol l^{-1}. (For interpretation of the references to colour in this figure legend, the reader is referred to the web version of this article.)

342. *Anal.* Calc. for $C_{64}H_{48}N_8O_{16}Cu$: C, 61.56; H, 3.87; N, 8.97. Found: C, 61.62; H, 3.85; N, 8.93%.

2.4. Preparation of **6** using click chemistry

A mixture of **4** (0.025 g, 0.015 mmol), azidomethyl phenyl sulfide (0.0084 mL, 0.06 mmol), $CuSO_4.5H_2O$ (0.015 g, 0.06 mmol) and sodium ascorbate (0.012 g, 0.06 mmol) were dissolved in 4 mL of THF/H_2O (1:1). The mixture was stirred at room temperature for 24 h under Ar. The solvent was removed under reduced pressure, and the residue was taken up in dichloromethane, washed with water and dried over Na_2SO_4. After the filtration and evaporation of the solvent, the product was washed with methanol to remove unreacted azidomethyl phenyl sulfide. Yield: 0.022 g, 51%. FT-IR ν (cm^{-1}): 3137–3055 (CH, aromatic), 2954–2858 (CH, aliphatic), 1724 (C=O); UV–Vis λ_{max} (nm) in chloroform: 678, 342; MALDI-TOF MS (2,5-dihydroxybenzoic acid) *m/z*: 1901.8 $[M-6H]^{6-}$. *Anal.* Calc. for $C_{92}H_{76}N_{20}O_{16}S_4Cu$: C, 57.87; H, 4.01; N, 14.67. Found: C, 57.93; H, 3.99; N, 14.68%.

3. Results and discussion

The novel phthalocyanines bearing a terminal alkyne moiety were prepared in two steps. First the dialkyl (3,4-dicyano-

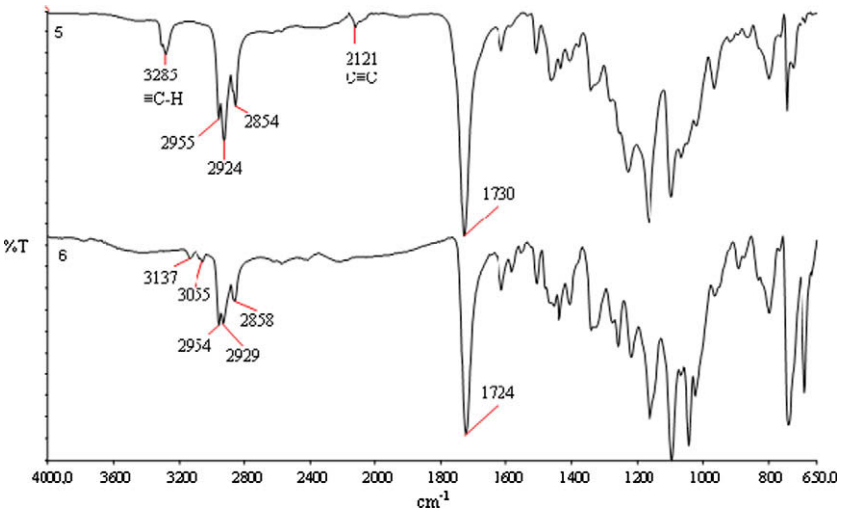


Fig. 2. FT-IR spectra of **5** and **6**.

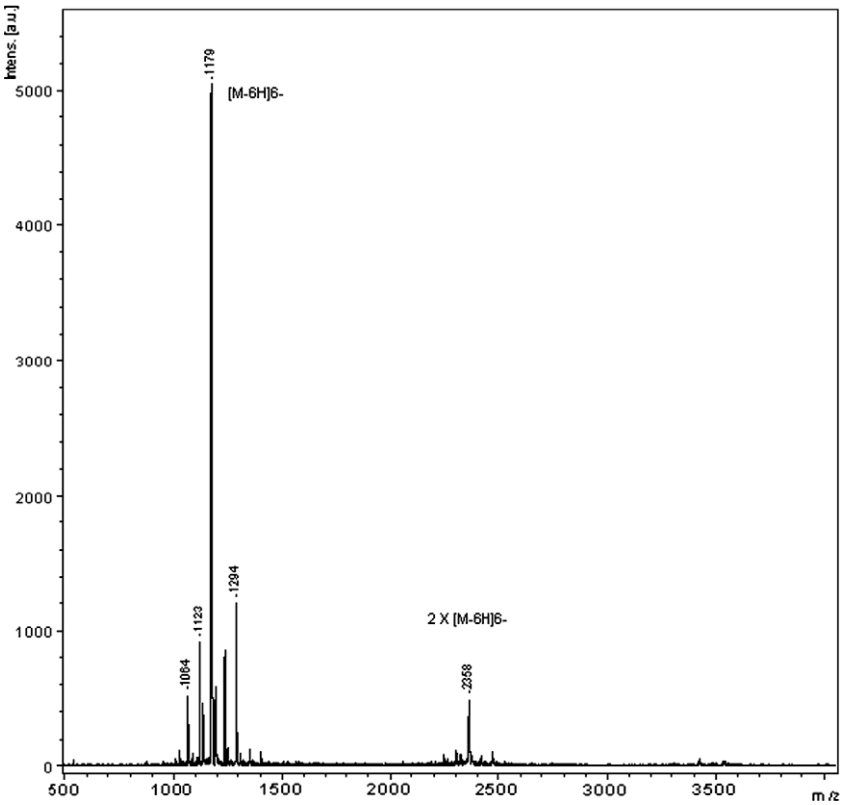


Fig. 3. MALDI-TOF MS spectrum of **4**.

phenyl)propargylmalonates **2**, **3** were synthesized by coupling the potassium salts of dialkyl-3,4-dicyanophenylmalonates **1** with propargyl bromide in acetone/acetonitrile (2:1) at reflux temperature. Then, phthalocyanines **4** and **5** were prepared by the standard method of cyclotetramerization of dialkyl (3,4-dicyanophenyl) propargylmalonates in the presence of DBU in pentanol for 20 h; anhydrous $CuCl_2$ was added when a copper phthalocyanine was desired (Scheme 1). Some difficulties were encountered in trying to obtain copper phthalocyanine (**5**). When the cyclotetramerization reaction was carried out in the presence of anhydrous $CuCl_2$, insoluble polymeric species were obtained with the metallophthalocyanine. The desired product **5** was separated from insoluble polymeric material by extraction with chloroform. The products **4** and **5** were purified by column chromatography using silica gel as the stationary phase and chloroform–methanol (100:1) mixtures as the eluent. The 1,3-dipolar cycloaddition of compound **4** with azidomethyl phenyl sulfide was carried out in THF/H_2O at room temperature using $CuSO_4{\cdot}5H_2O$ as a catalyst and sodium ascorbate as the reducing agent (Scheme 2). Under these reaction conditions, metallation of **4** was also observed (Fig. 1). As a natural consequence of the single substituent on each benzo group, the phthalocyanines (**4**–**6**) are all a mixture of constitutional isomers. Attempts were made to separate each of them by HPLC, but the isomers did not separate [18]. The blue products are easily soluble in a number of solvents, such as chloroform, dichloromethane, THF, acetone, CCl_4. In addition, 1,2,3-triazole-substituted phthalocyanine (**6**) is soluble in DMF as a different solvent.

The structures of the novel compounds were confirmed by elemental analysis together with FT-IR, ^{1}H NMR, ^{13}C NMR, UV–Vis and MS spectroscopic techniques. In the FT-IR spectra of the alkynyl-substituted phthalocyanines, the click functionality propargyl group was evidenced by characteristic bands of H–C≡C– and –C≡C– appearing at 3285 cm^{-1} and 2121 cm^{-1}, respectively. After the click reaction, the characteristic bands of the propargyl group disappeared completely and also the aromatic CH stretchings from the triazole and benzene rings appeared at 3137 and 3055 cm^{-1}, respectively (Fig. 2). The MALDI-TOF MS spectrum of the free-base Pc is especially interesting. The MALDI-TOF mass spectrometry (MS) experiment showed a main peak at *m/z* 1179 which was attributed $[M-6H]^{6-}$. This experiment also showed a peak at *m/z* 2358 which was due to supramolecular association of two molecules of the metal-free phthalocyanine **4** (Fig. 3). In the MALDI-TOF MS spectrum, we observed the $[M-6H]^{6-}$ peak at *m/z* 1901.8 for **6** (Fig. 4). In the ^{1}H NMR spectrum of compound **4**, as a consequence of the presence of four constitutional isomers and supramolecular association, the signals are broad and uninformative. Nevertheless, the integration values of the various assignable signals are consistent with the expected values. The paramagnetic nature of copper(II) phthalocyanines (**5** and **6**) precluded NMR measurements on these compounds [32].

The phthalocyanines display typical electronic spectra with two strong absorption regions, one of them in the UV region at about 300–350 nm (B band) and the other one in the visible region at 600–700 nm (Q band). All the metallophthalocyanines (**4**–**6**) exhi-

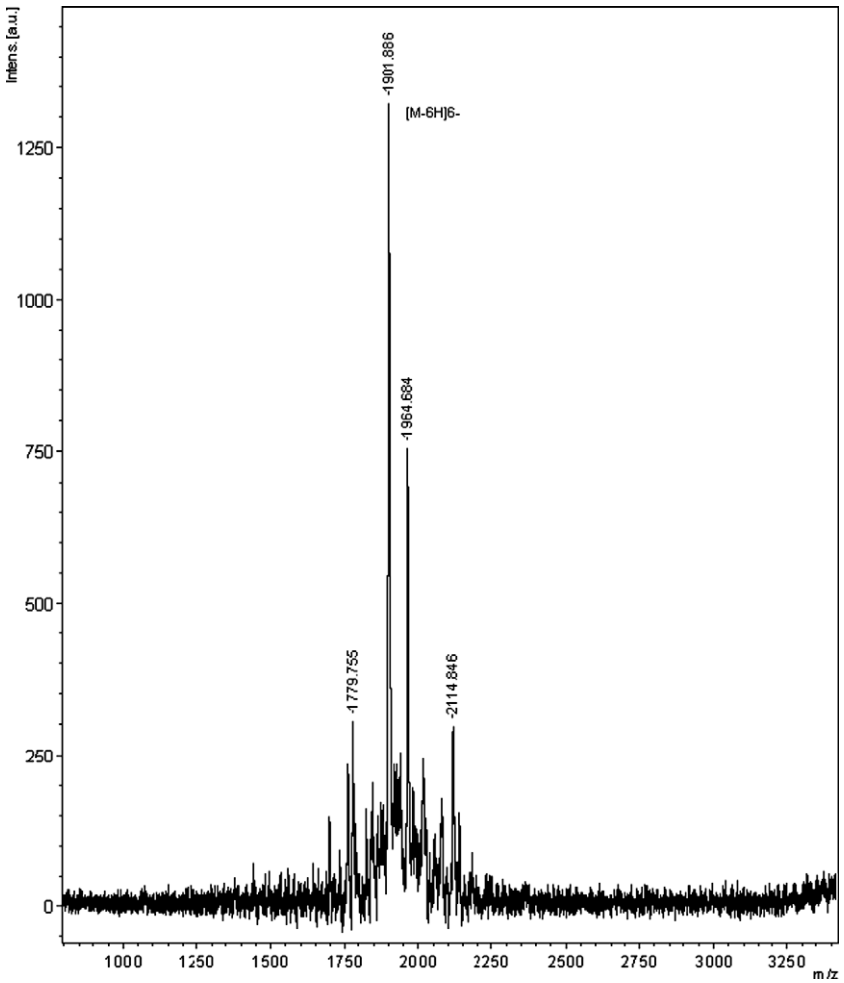


Fig. 4. MALDI-TOF MS spectrum of **6**.

bit intense Q bands around 675–680 nm with a relatively sharp absorption peak and almost no shoulder on the higher energy side, which would correspond to aggregated species [16]. The spectrum of compound **4**, is somewhat different from those of **5** and **6**, with a split Q band (661 and 698 nm) indicating lower symmetry (D_{2h}) of the metal-free derivative (Fig. 1).

In summary, we have synthesized alkynyl-substituted phthalocyanines without protective/deprotective chemistry. In addition, we have applied click chemistry to the synthesis of soluble tetratriazole-functionalized phthalocyanines. Further studies on the click reaction of **4** with functional azides are currently in progress.

Acknowledgement

This work was supported by the Research Fund of the Yıldız Technical University.

References

[1] A.G. Gürek, T. Basova, D. Luneau, C. Lebrun, E. Kol'tsov, A.K. Hassan, V. Ahsen, Inorg. Chem. 45 (2006) 1667.
[2] R. Zhou, F. Josse, W. Göpel, Z.Z. Öztürk, Ö. Bekaroğlu, Appl. Organomet. Chem. 10 (1996) 557.
[3] A. Koca, M.K. Şener, M.B. Koçak, A. Gül, Int. J. Hydrogen Energy 31 (2006) 2211.
[4] V.B. Sharma, S.L. Jain, B. Sain, Tetrahedron Lett. 44 (2003) 383.
[5] E.A. Lukyanets, J. Porphyr. Phthalocyan. 3 (1999) 424.
[6] P.Y. Reddy, L. Giribabu, C. Lyness, H.J. Snaith, C. Vijaykumar, M. Chandrasekharam, J.-H. Yum, K. Kalyanasundaram, M. Gratzel, M.K. Nazeeruddin, Angew. Chem., Int. Ed. 46 (2007) 373.
[7] L. Giribabu, C.V. Kumar, V.G. Reddy, P.Y. Reddy, C.S. Rao, S.-R. Jang, J.-H. Yum, M.K. Nazeeruddin, M. Gratzel, Sol. Energy Mater. Sol. Cells 91 (2007) 1611.
[8] U. Drechsler, M. Pfaff, M. Hanack, Eur. J. Org. Chem. 12 (1999) 3441.
[9] W. Liu, T.J. Jensen, F.R. Fronczek, R.P. Hammer, K.M. Smith, M.G.H. Vicente, J. Med. Chem. 48 (2005) 1033.
[10] C. Choi, P. Tsang, J. Huang, E.Y.M. Chan, W. Ko, W. Fong, D.K.P. Ng, Chem. Commun. 19 (2004) 2236.
[11] H.A. Dinçer, A. Gül, M.B. Koçak, J. Porphyr. Phthalocyan. 8 (2004) 1204.
[12] V.T. Verdree, S. Pakhomov, G. Su, M.W. Allen, A.C. Countryman, R.P. Hammer, S.A. Sopper, J. Fluoresc. 17 (2007) 547.
[13] B. Tylleman, R. Gomez-Aspe, G. Gbabode, Y.H. Geerts, S. Sergeyev, Tetrahedron 64 (2008) 4155.
[14] M.-R. Ke, J.-D. Huang, S.-M. Weng, J. Photochem. Photobiol. A 201 (2009) 23.
[15] S. Sergeyev, O. Debever, E. Pouzet, Y.H. Geerts, J. Mater. Chem. 17 (2007) 3002.
[16] M.K. Şener, A. Gül, M.B. Koçak, J. Porphyr. Phthalocyan. 7 (2003) 617.
[17] M.K. Şener, A. Koca, A. Gül, M.B. Koçak, Polyhedron 26 (2007) 1070.
[18] M.K. Şener, A. Gül, M.B. Koçak, Transition Met. Chem. 33 (2008) 867.
[19] A. Gonzalez-Cabello, P. Vazquez, T. Torres, J. Organomet. Chem. 637–639 (2001) 751.
[20] C.C. Leznoff, B. Suchozak, Can. J. Chem. 79 (2001) 878.
[21] E.M. Garcia-Frutos, S.M. O'Flaherty, E.M. Maya, G. De la Torre, W. Blau, P. Vazquez, T. Torres, J. Mater. Chem. 13 (2003) 749.
[22] A.P. Vogt, B.S. Sumerlin, Macromolecules 39 (2006) 5286.
[23] C. Ornelas, J. Ruiz Aranzaes, E. Cloutet, S. Alves, D. Astruc, Angew. Chem., Int. Ed. 46 (2007) 872.
[24] J.-F. Lutz, H.G. Boerner, Prog. Polym. Sci. 33 (2008) 1.
[25] M.J. Joralemon, R.K. O'Reilly, C.J. Hawker, K.L. Wooley, J. Am. Chem. Soc. 127 (2005) 16892.
[26] M. Juricek, P.H.J. Kouwer, J. Rehak, J. Sly, A.E. Rowan, J. Org. Chem. 74 (2009) 21.
[27] D.D. Diaz, J.J. Cid, P. Vazquez, T. Torres, Chem. Eur. J. 14 (2008) 9261.
[28] S. Campidelli, B. Ballesteros, A. Filoramo, D Diaz-Diaz, G. De la Torre, T. Torres, G.M.A. Rahman, C. Ehli, D. Kiessling, F. Werner, V. Sgobba, D.M. Guldi, C. Cioffi, M. Prato, J.-P. Bourgoin, J. Am. Chem. Soc. 130 (2008) 11503.
[29] H. Yoshiyama, N. Shibata, T. Sato, S. Nakamura, T. Toru, Org. Biomol. Chem. 6 (2008) 4498.
[30] M.P. Roze, E. Berzins, O. Neilands, Zh. Org. Khim. 28 (1992) 827.
[31] S.B. Kahl, J. Li, Inorg. Chem. 35 (1996) 3878.
[32] E. Hamuryudan, Z.A. Bayır, Ö. Bekaroğlu, Dyes and Pigments 43 (1999) 77.

pyrazine, 4,4′-bipyridine, 1,2-bis(4-pyridyl)ethane and 1,2-bis(4-pyridyl)- ethelene. We report the synthesis, structural and spectroscopic studies of the pentanuclear complexes $[Zn_5(bta)_6(acac)_4(dmf)]\cdot dmf$ (**1**·dmf) and $[Zn_5(bta)_6(acac)_4(dmf)]\cdot 3.7dmf$ (**2**·3.7dmf), the enneanuclear complex $[Zn_9(bta)_{12}(acac)_6]\cdot 6dmf$ (**3**·6dmf), and the 1D coordination polymer $[Zn(acac)_2(4,4'\text{-bpy})]_n$ (**4**).

2. Experimental

2.1. General and spectroscopic measurements

All manipulations were performed under aerobic conditions using materials as received (Aldrich Co). All chemicals and solvents were of reagent grade. Elemental analyses for C, H and N were performed on a Perkin Elmer 2400/*II* automatic analyzer. IR spectra were recorded from KBr pellets in the range 4000–400 cm^{-1} on a Bruker Equinox 55/S FT-IR spectrometer.

2.2. Compound preparation

2.2.1. $[Zn_5(bta)_6(acac)_4(dmf)]\cdot dmf$ (**1**·dmf)

A colourless solution of btaH (0.467 g, 4.00 mmol) in dmf (25 mL) was stirred under heating at ~100 °C until solid $Zn(acac)_2$ (0.527 g, 2.00 mmol) was added. The heating immediately turned off and the stirring continued for 10 min. The final colourless solution left for slow evaporation at room temperature and afforded colourless X-ray quality crystals of **1**·dmf after 4 days (Yield: 0.50 g, 80%). The crystals were collected by filtration and dried in air. *Anal.* Calc. for (**1**·dmf) ($C_{62}H_{66}N_{20}O_{10}Zn_5$, fw = 1578.20): C, 47.18; H, 4.22; N, 17.75. Found: C, 47.03; H, 4.24; N, 17.69%. FT-IR (cm^{-1}, KBr pellets): 3432br, 3073m, 3055m, 3025w, 2992w, 2955w, 2922m, 2849m, 1679vs, 1600vs, 1515vs, 1494m, 1451s, 1442s, 1393vs, 1363sh, 1296w, 1275sh, 1260s, 1226m, 1193vs, 1172sh, 1159m, 1147sh, 1129m, 1086m, 1062w, 1013m, 995m, 922s, 846m, 786vs, 752vs, 695m, 640s, 555vs, 430m, 406m.

2.2.2. $[Zn_5(bta)_6(acac)_4(dmf)]\cdot 3.7dmf$ (**2**·3.7dmf)

Solid **1**·dmf (0.158 g, 0.10 mmol) was added to a colourless solution of pyrazin (0.024 g, 0.30 mmol) in dmf (12 mL) and the resultant suspension was refluxed for 30 min. The final colourless solution was filtered and left for slow evaporation at −4 °C. Colourless X-ray quality crystals of **2**·3.7dmf were obtained after 4 days (Yield: 0.10 g, ~60%). The crystals were collected by filtration and dried in air. The resulting powder was analysed as **2**·3dmf. *Anal.* Calc. for (**2**·3dmf) ($C_{68}H_{80}N_{22}O_{12}Zn_5$, fw = 1724.43): C, 47.36; H, 4.68; N, 17.87. Found: C, 47.22; H, 4.70; N, 17.81%. FT-IR (cm^{-1}, KBr pellets): 3438br, 3071m, 3053m, 3020w, 2995w, 2953w, 2920m, 2845m, 1678vs, 1600vs, 1516vs, 1493m, 1449s, 1440s, 1394vs, 1361sh, 1297w, 1277sh, 1259s, 1224m, 1192vs, 1174sh, 1160m, 1148sh, 1130m, 1085m, 1060w, 1012m, 997m, 923s, 845m, 784vs, 752vs, 693m, 641s, 555vs, 432m, 408m.

2.2.3. $[Zn_9(bta)_{12}(acac)_6]\cdot 6dmf$ (**3**·6dmf)

2.2.3.1. Method A. A colourless solution of btaH (0.260 g, 2.18 mmol) and pyrazine (0.052 g, 0.65 mmol) in dmf (25 mL) was stirred under heating at ~100 °C until solid $Zn(acac)_2$ (0.287 g, 1.09 mmol) was added. The heating immediately turned off and the stirring continued for 10 min. The final colourless solution left for slow evaporation at room temperature and afforded colourless X-ray quality crystals of **3**·6dmf after 4 days (Yield: 0.22 g, ~60%). The crystals were collected by filtration and dried in air. *Anal.* Calc. for (**3**·6dmf) ($C_{120}H_{132}N_{42}O_{18}Zn_9$, fw = 3039.06): C, 47.43; H, 4.38; N, 19.36. Found: C, 47.29; H, 4.40; N, 19.30%. FT-IR (cm^{-1}, KBr pellets): 3435br, 3073m, 3055m, 3025w, 2992w, 2958w, 2919m, 2849m, 1679vs, 1600vs, 1515vs, 1494m, 1448s, 1393vs, 1363sh, 1299w, 1260s, 1223m, 1193vs, 1163sh, 1150sh, 1129m, 1089m, 1019s, 995s, 922s, 846m, 786vs, 749vs, 695m, 640s, 555vs, 430m, 409m

2.2.3.2. Method B. Solid **1**·dmf (0.158 g, 0.10 mmol) was dissolved under reflux in dmf (15 mL). The resultant colourless solution was filtered off and left for slow evaporation at room temperature. Colourless X-ray quality crystals of **3**·6dmf were obtained after 10 days. The identity of the crystals was confirmed by unit cell determination (a = 26.40(3), b = 15.89(1), c = 32.41(3) Å, β = 91.22(3) o, see Table 1).

2.2.4. $[Zn(acac)_2(4,4'\text{-bpy})]_n$ (**4**)

A colourless solution of btaH (0.260 g, 2.18 mmol) in dmf (5 mL) was added to a colourless solution of $Zn(acac)_2$ (0.287 g, 1.09 mmol) in dmf (15 mL). A colourless solution of 4,4′-bpy (0.102 g, 0.65 mmol) in dmf (5 mL) was finally added. The final colourless solution was stirred for 10 min and filtered off. X-ray quality crystals of **4** were formed in closed vials at −4 °C after 8 days (Yield: 0.30 g, ~65%). The crystals were collected by filtration and dried in air. *Anal.* Calc. for (**4**) ($C_{20}H_{22}N_2O_4Zn$, fw = 419.77): C, 57.22; H, 5.28; N, 6.67. Found: C, 57.02; H, 5.32; N, 6.63%. FT-IR (cm^{-1}, KBr pellets): 3423br, 3052m, 3003w, 2958w, 2909w, 1597vs, 1536s, 1512vs, 1460s, 1402vs, 1256s, 1220s, 1193m, 1080m, 1044w, 1005s, 919s, 865m, 825s, 761s, 737w, 667w, 652m, 625s, 573m, 552s, 509s, 412s.

Slow evaporation of the final reaction solution at room temperature afforded plate-like crystals of **3**·6dmf and needle-like crystals of **4** after 10 days. The identity of the plate-like crystals was confirmed by unit cell determination (a = 26.43(2), b = 15.93(1), c = 32.52(2) Å, β = 91.36(4)°, see Table 1), and those of the needle-like crystals by infrared spectroscopy.

2.3. Single-crystal X-ray crystallography

Colourless prismatic crystals of **1**·dmf, **2**·3.7dmf, **3**·6dmf and **4** were mounted in capillaries. Diffraction measurements were made on a Rigaku R-AXIS SPIDER Image Plate diffractometer using graphite monochromated Cu Kα (for **1**·dmf and **2**·3.7dmf) and Mo Kα (for **3**·6dmf) radiation. Data collection (ω-scans) and processing (cell refinement, data reduction and Empirical absorption correction) were performed using the CRYSTALCLEAR program package [8]. Diffraction measurements for **4** were made on a Crystal Logic Dual Goniometer diffractometer using graphite monochromated Mo Kα radiation. Unit cell dimensions were determined and refined by using the angular settings of 25 automatically centred reflections in the range $11 < 2\theta < 23°$. Intensity data were recorded using a θ–2θ scan. Three standard reflections monitored every 97 reflections showed less than 3% variation and no decay. Lorentz, polarisation corrections were applied using Crystal Logic software. Important crystal data and parameters for data collection are reported in Table 1. The structures were solved by direct methods using SHELXS-97 [9] and refined by full matrix least-squares techniques on F^2 with SHELXL-97 [10]. Further experimental crystallographic details for **1**·dmf: 2θmax = 130°; reflections collected/unique/used, 48 898/11 716 [R_{int} = 0.0273]/11 716; 1007 parameters refined; $(\Delta/\sigma)_{max}$ = 0.003; $(\Delta\rho)_{max}/(\Delta\rho)_{min}$ = 0.365/−0.366 e/Å^3; R/R_w (for all data), 0.0386/0.0895. Hydrogen atoms of the methyl groups were introduced at calculated positions as riding on bonded atoms, the rest H-atoms were located by difference maps and were refined isotropically. All non-H atoms were refined anisotropically. Further experimental crystallographic details for **2**·3.7dmf: 2θmax = 130°; reflections collected/unique/used, 78 273/14 898 [R_{int} = 0.0333]/14 898; 1027 parameters refined; $(\Delta/\sigma)_{max}$ = 0.004; $(\Delta\rho)_{max}/(\Delta\rho)_{min}$ = 1.214/−0.928 e/Å^3; R/R_w (for

Table 1
Crystallographic data for **1**·dmf, **2**·3.7dmf, **3**·6dmf and **4**.

	1·dmf	2·3.7dmf	3·6dmf	4
Formula	$C_{62}H_{66}N_{20}O_{10}Zn_5$	$C_{70.1}H_{84.9}N_{22.7}O_{12.7}Zn_5$	$C_{120}H_{132}N_{42}O_{18}Zn_9$	$C_{20}H_{22}N_2O_4Zn$
Fw	1578.20	1775.56	3039.06	419.77
Space group	$P\bar{1}$	$P\bar{1}$	$C2/c$	$P2_1$
T (°C)	298	298	298	298
λ (Å)	Cu Kα (1.5418 Å)	Cu Kα (1.5418 Å)	Mo Kα (0.71073 Å)	Mo Kα (0.71073 Å)
a (Å)	15.0975(3)	15.5816(3)	26.4085(6)	7.750(3)
b (Å)	16.3978(3)	16.3545(3)	15.8937(4)	14.857(5)
c (Å)	16.7733(3)	20.1459(4)	32.4121(7)	8.426(3)
α (°)	76.009(1)	110.349(1)	90	90
β (°)	72.339(1)	105.833(1)	91.2109(8)	91.21(1)
γ (°)	65.655(1)	94.580(1)	90	90
V (Å^3)	3572.22(12)	4543.05(15)	13601.3(5)	970.0(6)
Z	2	2	4	2
ρ_{calc} (g cm^{-3})	1.467	1.298	1.484	1.437
μ (mm^{-1})	2.439	2.007	1.635	1.293
R_1[a]	00338[b]	0.0604[c]	0.0483[d]	0.0567[e]
wR_2[a]	0.0862[b]	0.1792[c]	0.1136[d]	0.141[5]

[a] $w = 1/[\sigma 2(F_o^2) + (aP)^2 + bP]$ and $P = (\max(F_o^2,0) + 2F_c^2)/3$; $R_1 = \Sigma(|F_o|-|F_c|)/\Sigma(|F_o|)$ and $wR_2 = \{\Sigma[w(F_o^2-F_c^2)^2]/\Sigma[w(F_o^2)^2]\}^{1/2}$.
[b] For 10 347 reflections with $I > 2\sigma(I)$.
[c] For 11 548 reflections with $I > 2\sigma(I)$.
[d] For 8262 reflections with $I > 2\sigma(I)$.
[e] For 2536 reflections with $I > 2\sigma(I)$.

all data), 0.0745/0.1954. Hydrogen atoms were either introduced at calculated positions as riding on bonded atoms, or were located by difference maps and were refined isotropically. All non-H atoms were refined anisotropically, except of the solvated dmf molecules which were refined isotropically. Further experimental crystallographic details for **3**·6dmf: 2θmax = 50°; reflections collected/unique/used, 91 055/11 948 [R_{int} = 0.0729]/11 948; 819 parameters refined; $(\Delta/\sigma)_{max}$ = 0.005; $(\Delta\rho)_{max}/(\Delta\rho)_{min}$ = 0.716/−0.450 e/Å^3; R/R_w (for all data), 0.0794/0.1302. Hydrogen atoms were introduced at calculated positions as riding on bonded atoms. All non-H atoms were refined anisotropically. Further experimental crystallographic details for **4**: 2θmax = 50°; reflections collected/unique/used, 3489/3218 [R_{int} = 0.0269]/3218; 237 parameters refined; $(\Delta/\sigma)_{max}$ = 0.007; $(\Delta\rho)_{max}/(\Delta\rho)_{min}$ = 0.708/−0.519 e/Å^3; R/R_w (for all data), 0.0803/0.1569. Hydrogen atoms were introduced at calculated positions as riding on bonded atoms. All non-H atoms were refined anisotropically. Plots of all structures were drawn using the Diamond 3.1 application [11].

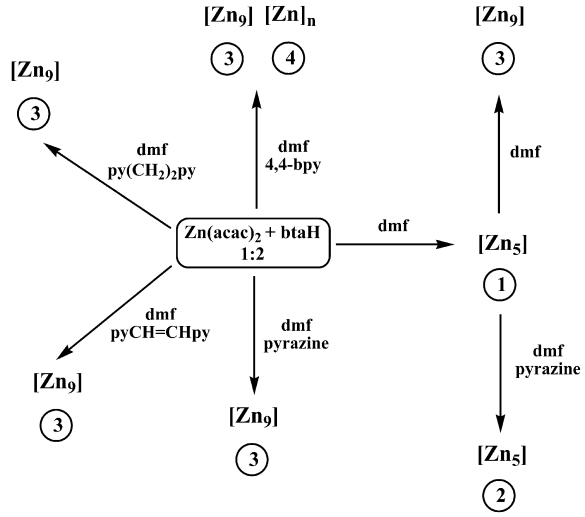
3. Results and discussion

3.1. Syntheses

The reaction of one equivalent of $Zn(acac)_2$ with two equivalents of btaH in dmf afforded a colourless solution which left for slow evaporation. X-ray quality colourless crystals of **1**·dmf were formed after *ca* 4 days (Scheme 1). The chemically balanced equation for the synthesis of **1**·dmf is given below:

$$5Zn(acac)_2 + 6btaH + 2dmf \xrightarrow{dmf} [Zn_5(bta)_6(acac)_4(dmf)] \cdot dmf + 6acacH \quad (1)$$

The molecular structure of **1**·dmf (vide infra), shows that the four peripheral Zn^{II} ions have vacant coordination sites or contain coordinatively labile dmf molecules, which could be completed and/or replaced by neutral ligands. In the particular case of neutral bridging ligands, this approach could be applied for the synthesis of coordination polymers based on $[Zn_5]$ clusters. With this consideration in mind, we have performed the reaction of one equivalent of **1**·dmf with three equivalents of pyrazine in dmf. The colourless solution was refluxed for 30 min, filtered off and left for slow evaporation to yield X-ray quality crystals of **2**·3.7dmf after *ca* 4 days



Scheme 1. The reaction pathways discussed in the text.

(Scheme 1). The molecular structure of **2**·3.7dmf (vide infra) shows that it consists of a $[Zn_5]$ cluster analogous to **1**·dmf; the only difference is the crystallization solvent molecules.

In a subsequent step, we applied a different synthetic approach in order to obtain coordination polymers based on zinc clusters. According to this approach, it was attempted the in situ synthesis of the $[Zn_5]$ clusters in the presence of pyrazine. The reaction of one equivalent of $Zn(acac)_2$ with two equivalents of btaH and 0.6 equivalents of pyrazine in dmf gave a colourless solution. Slow evaporation of the final colourless solution afforded X-ray quality crystals of **3**·6dmf after *ca* 4 days (see Method A in the Experimental Section; Scheme 1). The chemically balanced equation for the synthesis of **3**·6dmf is given below:

$$9Zn(acac)_2 + 12btaH + 6dmf \xrightarrow{dmf} [Zn_9(bta)_{12}(acac)_6] \cdot 6dmf + 12acacH \quad (2)$$

The molecular structure of **3**·6dmf (vide infra) shows that: (i) it does not contain pyrazine and (ii) it consists of $[Zn_9]$ clusters which can be derived from the association of two $[Zn_5]$ clusters followed by abstraction of $Zn(acac)_2$. This alternative was realised by recrys-

tallization of **1**·dmf from dmf. The resultant colourless solution was filtered off and left for slow evaporation. X-ray quality crystals of **3**·6dmf were formed after *ca* 10 days (see Method B in the Experimental Section; Scheme 1). The identity of the crystals was confirmed by unit cell determination. The chemically balanced equation for the synthesis of **3**·6dmf is given below:

$$2[Zn_5(bta)_6(acac)_4(dmf)] \overset{dmf}{\rightarrow} [Zn_9(bta)_{12}(acac)_6] + Zn(acac)_2 + 2dmf \quad (3)$$

In order to explore to what extend the nature of the neutral bridging ligand might affect the preparation of coordination polymers based on $[Zn_5]$ clusters, we performed the reaction of one equivalent of $Zn(acac)_2$ with two equivalents of btaH and 0.6 equivalents of 4,4′-bpy in dmf (Scheme 1). The colourless reaction solution was stirred for 10 min and filtered off. Slow evaporation at room temperature afforded a mixture of plate-like crystals of **3**·6dmf and needle-like crystals of **4**, whereas in closed vials at −4 °C only crystals of **4** were formed. The simultaneous isolation of **3**·6dmf and **4** is indicative of the chemical equilibria in solution and is usually observed in metal ions/ligands reaction mixtures, from which a multitude of products can be isolated due to the labile nature of the coordination bonds and the presence of weak bonding interactions (H-bonds, π–π stacking, etc.). Moreover, the isolation of **3**·6dmf and **4** in mixture, and pure **4**, is indicative of the influence of crystallization methods to the chemical and structural identity of the products from a given reaction system. The chemically balanced equation for the synthesis of **4** is given below:

$$nZn(acac)_2 + n4,4'\text{-bpy} \overset{dmf}{\rightarrow} [Zn(acac)_2(4,4'\text{-bpy})]_n \quad (4)$$

Analogous reactions as the above introducing 1,2-bis(4-pyridyl)ethane and 1,2-bis(4-pyridyl)ethelene also afforded **3**·6dmf from slow evaporation at room temperature (these procedures are not described in the experimental section; Scheme 1).

3.2. Description of structures

The molecular structures of **1**·dmf and **2**·3.7dmf are similar; they differ only in the crystallization dmf molecules, thus only one structure will be described. The structure of **1**·dmf is given in Fig. 1, selected bond distances and angles are listed in Table S1. The complex consists of five Zn^{II} ions, four of which span the corners of a tetrahedron and the fifth lies at its centre. The edges of the tetrahedron fall in the range 5.923–6.064 Å, and the central Zn^{II} lies at 3.616–3.752 Å from the peripheral ones. The central Zn^{II} ion is octahedrally coordinated to six nitrogen atoms from six different bta^- ligands. One of the peripheral Zn^{II} ions possesses distorted octahedral coordination environment comprised by three nitrogen atoms from three different bta^- ligands, and three oxygen atoms, two from a chelating $acac^-$ ligand and one from a coordinated dmf molecule. The rest peripheral Zn^{II} ions adopt a square pyramidal coordination geometry comprised by three nitrogen atoms from three different bta^- ligands and two oxygen atoms from a chelating $acac^-$ ligand. Each μ_3-κ*N*:κN′κN″ bta^- ligand bridges three Zn^{II} ions; two peripheral ones and the central metal ion. The Zn–N and Zn–O bond distances range from 2.018(2)–2.248(2) Å to 1.946(2)–2.243(2) Å, respectively. Compound **1**·dmf is analogous to $[Cu_5(bta)_6(acac)_4]$ [12], $[Cu_5(bta)_6L_4]$ (L = β-diketonates) [13], $[M^{II}Zn_4(L)_6(L')_4]$ (M^{II} = Co, Zn; L = 1,2,3-benzotriazolate derivatives; L′ = Cl^-, $acac^-$) [14] and $[Ni_5(5Mebta)_6(dbm)_4(Me_2CO)_4]$ (5MebtaH = 5-methyl-1,2,3-benzotriazole, dbmH = dibenzoylmethane) [15].

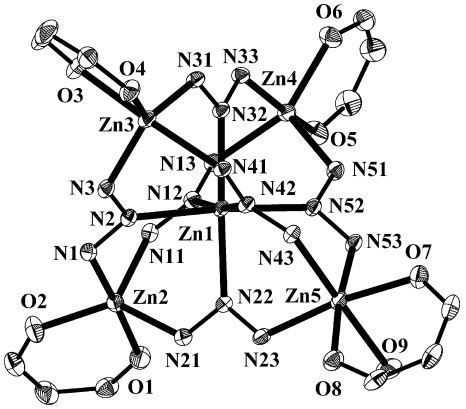


Fig. 1. Partially labelled plot of **1** at 30% thermal probability ellipsoids. The benzene ring of the bta^- ligands, the methyl groups of the $acac^-$ ligands and all hydrogen atoms have been omitted for clarity.

The molecular structure of **3**·6dmf is given in Fig. 2, selected bond distances and angles are listed in Table S2. The complex consists of nine Zn^{II} ions, seven of which reside at the corners of two corner sharing tetrahedra and each of the remaining two lies at the centre of each tetrahedron. The common Zn^{II} ion of the two tetrahedra resides on an inversion centre. The edges of the two tetrahedra fall in the range 5.978–6.066 Å, whereas each of the central Zn^{II} lies at 3.614–3.819 Å from the peripheral ones. The seven peripheral Zn^{II} ions are coordinated to three nitrogen atoms from three different bta^- ligands and two oxygen atoms from a chelating $acac^-$ ligand, thus describing a square pyramidal coordination geometry. The central Zn^{II} ions are coordinated to six nitrogen atoms form six different bta^- ligands thus adopting a distorted octahedral coordination environment. Each μ_3-κ*N*:κN′:κN″ bta^- ligand bridges three Zn^{II} ions; two peripheral ones and the central Zn^{II} of each tetrahedron. The structure of each of the two tetrahedra is similar to the structure of the tetrahedra in **1**·dmf; the structure of **3**·6dmf can be described as derived from the addition of two tetrahedra of **1**·dmf followed by the simultaneous abstraction of two $acac^-$ ligands, two dmf molecules and a Zn^{II} ion. The Zn–N and Zn–O bond distances range from 1.998(4)–2.224(4) Å to 1.943(3)–2.104(4) Å, respectively. Compound **3**·6dmf is analogous to $[Ni_9(5,6Mebta)_{12}(bzac)_6(MeOH)_6]$ (5,6MebtaH = 5,6-dimethyl-1,2,3-benzotriazole, bzacH = benzoylacetone) [15].

A small fragment of the molecular structure of **4** is shown in Fig. 3, selected bond distances and angles are listed in Table S3. The structure consists of $[Zn(acac)_2]$ mononuclear units assembled

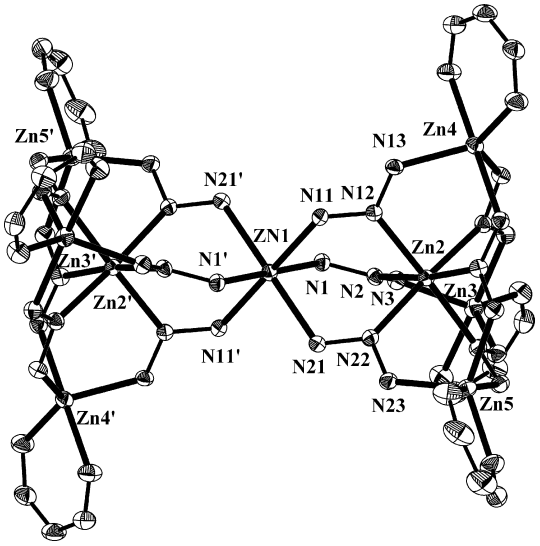


Fig. 2. Partially labelled plot of **3** at 30% thermal probability ellipsoids. The benzene ring of the bta^- ligands, the methyl groups of the $acac^-$ ligands and all hydrogen atoms have been omitted for clarity. Symmetry operations to generate equivalent atoms: (′) = 0.5−*x*, 0.5−*y*, −*z*.

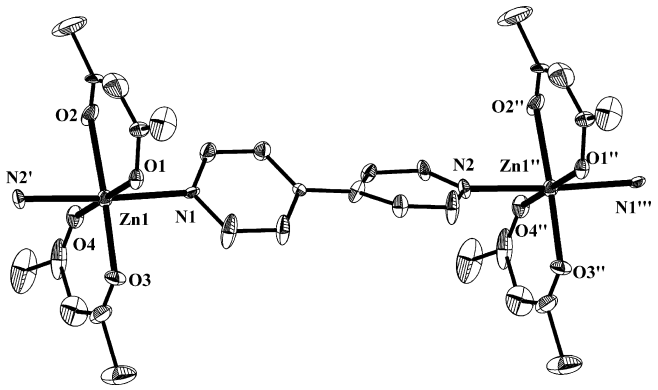


Fig. 3. Partially labelled plot of a small fragment of **4** at 30% thermal probability ellipsoids. Symmetry operations to generate equivalent atoms: (') = $-1 + x, y, 1 + z$; ('') = $1 + x, y, -1 + z$; (''') = $1 + x, y, -1 + z$.

via bridges of 4,4′-bpy in one dimensional polymer. The aromatic rings of the bridging 4,4′-bpy are twisted to each other forming an angle of 32.5° between the respective mean planes. The coordination geometry of the Zn^{II} ions is distorted octahedral with the oxygen atoms of the two $acac^-$ ligands defining the equatorial plane and the nitrogen atoms of two 4,4′-bpy ligands in the apical positions. The Zn–O and Zn–N bond distances range from 1.987(10)–2.122(13) Å to 2.245(11)–2.272(12) Å, respectively. The structure of **4** has been previously described in different space group [16]. The molecular structure of **4** is analogous to the structure of $[Zn(hfac)(4,4'\text{-bpy})]_n$ (hfacH = hexafluoroacetylacetone) [17] and to the various solvate forms of $[Zn(dbm)(4,4'\text{-bpy})]_n$ (dbmH = dibenzoylmethane) [18].

3.3. IR spectra

In the spectra of solid btaH the medium intensity bands in the region 3090–3040 cm^{-1} are attributed to ν(CH) stretching vibrations, and the strong bands in the region 1620–1380 cm^{-1} are attributed to benzene (ν(C=C), ν(N=N), ν(C=N)) and triazole ring stretching vibrations [19]. The bending and breathing vibrations of the benzene and triazole rings are observed as weak and medium intensity bands in the region 1380–1090 cm^{-1} [19]. In the spectra of **1**–**3** the ν(CH) stretching vibrations of the benzotriazolato ligands are observed in the region 3073–3020 cm^{-1}. A series of strong bands in the region 1600–1400 cm^{-1} is found in the spectra of **1**–**3**. Contributions from benzotriazolate ν(C⋯C), ν(N⋯N) and ν(C⋯N) vibrations would be expected in this region [20], but overlap with the $\nu(C\cdots C)_{acac}$ and $\nu(C\cdots O)_{acac}$ bands renders assignments difficult [21]. The presence of coordinated and/or solvate dmf molecules in **1**–**3** is manifested by a strong band at ~1680 cm^{-1} and a medium intensity band at 1494 cm^{-1}, assigned to ν(C=O) and ν(C–N), respectively [22]. In the spectra of **4**, in the region 1600–1400 cm^{-1}, a set of strong bands is attributed to the ν(C⋯C) and ν(C⋯N) bands of the 4,4′-bpy. These bands, also observed in the spectra of free 4,4′-bpy, are sensitive to chelation [23], but overlap with the $\nu(C\cdots C)_{acac}$ and $\nu(C\cdots O)_{acac}$ bands renders assignments difficult. The characteristic bands of the C–H out-of-plane deformations, which appear as a strong band at 757 cm^{-1} and a weak satellite at 735 cm^{-1} in the spectra of free 4,4′-bpy, upon chelation appear as a strong band at 761 cm^{-1} and a weak band at 737 cm^{-1}.

4. Concluding comments and perspectives

Pentanuclear and enneanuclear Zn^{II} clusters, i.e. $[Zn_5(bta)_6(acac)_4(dmf)]\cdot dmf$ (**1**·dmf), $[Zn_5(bta)_6(acac)_4(dmf)]\cdot 3.7dmf$ (**2**·3.7dmf) and $[Zn_9(bta)_{12}(acac)_6]\cdot 6dmf$ (**3**·6dmf), as well as the 1D coordination polymer $[Zn(acac)_2(4,4'\text{-bpy})]_n$ (**4**) were prepared from the $Zn(acac)_2$/btaH reaction system in dmf in the presence or absence of neutral bridging *N*,*N*′-ligands. Recrystallization of **1**·dmf from dmf yielded **3**·6dmf, which can be prepared also from the $Zn(acac)_2$/btaH reaction system in dmf in the presence of pyrazine, 4,4′-bpy, 1,2-bis(4-pyridyl)ethane, and 1,2-bis(4-pyridyl)ethelene. The isolation of **3**·6dmf from various reaction mixtures is indicative of the thermodynamic and/or kinetic stability of the complex. In the case of 4,4′-bpy containing reaction mixtures, the 1D coordination polymer **4** is also formed, either in mixture with **3**·6dmf or in pure form.

Concerning the anticorrosion action of benzotriazole and its derivatives towards certain metals, there are still open matters that need to be elucidated. Coordination chemistry can be used to probe several aspects of corrosion inhibitors such as the bonding of inhibitor molecules on the metal surfaces, the structure of the surface polymeric complexes, the orientation of inhibitors with different functional groups, intramolecular rearrangements, etc. Chemical, physical and structural studies on realistic model complexes, such as **1**·dmf, **2**·3.7dmf and **3**·6dmf, are needed to understand the complex surface chemistry that leads to corrosion inhibition and to create new inhibitors even more efficient than benzotriazole. Studies of the inhibition of zinc corrosion by various triazole derivatives, including benzotriazole, with respect to dependence on pH, potential and other factors, have shown the presence of zinc triazole complex on the zinc surface by XPS spectroscopy [24]. Electrochemical studies of the corrosion inhibition of benzotriazole on brass have shown that the addition of the latter enhances ZnO film formation and insoluble Cu^I/bta film complex on the surface of Cu^I/oxides and Cu^{II}/hydroxides film [25].

From the chemical and structural point of view, compounds **1**·dmf, **2**·3.7dmf and **3**·6dmf represent new members of the family of 3D clusters bearing benzotriazole and its substituted derivatives as ligand. The molecular structures of **1**·dmf, **2**·3.7dmf and **3**·6dmf reveal that the peripheral Zn^{II} ions have vacant coordination sites or contain labile solvate molecules. These sites can be easily modified by the coordination of bridging ligands (spacers); partial or total occupation of these (in)complete sites would increase the nuclearity and/or dimensionality of the complexes. The tetrahedral topology of the Zn^{II} ions in the present complexes, along with coordination completeness is beneficial for the synthesis of porous three dimensional materials (metal–organic frameworks) based on $[Zn_5]$ and $[Zn_9]$ clusters (nodes). On the other hand, the modification of **1**·dmf, **2**·3.7dmf and **3**·6dmf by other β-diketonates and/or benzotriazole derivatives would lead to families of $[Zn_5]$ and $[Zn_9]$ clusters-nodes for the development of polymeric materials with different internal surface environments. These matters are currently under investigation in our lab.

Acknowledgment

C.G and C.P.R. thank NCSR "Demokritos" for financial support through a research Grant (Demoerevna 2005).

Appendix A. Supplementary data

CCDC 731899, 731900, 731901, and 731902 contain the supplementary crystallographic data for **1**·dmf, **2**·3.7dmf, **3**·6dmf and **4**. These data can be obtained free of charge via http://www.ccdc.cam.ac.uk/conts/retrieving.html, or from the Cambridge Crystallographic Data Centre, 12 Union Road, Cambridge CB2 1EZ, UK; fax: (+44) 1223 336 033; or e-mail: deposit@ccdc.cam.ac.uk. Supplementary data associated with this article can be found, in the online version, at doi:10.1016/j.poly.2009.07.020.

References

[1] E. Diamantopoulou, Th.F. Zafiropoulos, S.P. Perlepes, C.P. Raptopoulou, A. Terzis, Polyhedron 13 (1994) 1593 (and references therein).
[2] (a) D. Sockalingum, M. Fleischmann, M.M. Musiani, Spectrochim. Acta 47A (1991) 1475 (and references therein);
(b) B.-S. Fang, C.G. Olson, D.W. Lynch, Surf. Sci. 176 (1986) 476 (and references therein).
[3] (a) D.P. Drolet, D.M. Manuta, A.J. Lees, A.D. Katnani, G.J. Coyle, Inorg. Chim. Acta 146 (1988) 173;
(b) J. Reedijk, G. Roelofsen, A.R. Siedle, A.L. Spek, Inorg. Chem. 18 (1979) 1947.
[4] (a) See for example: R.E.P. Winpenny, J. Chem. Soc., Dalton Trans. (2002) 1;
(b) D. Gatteschi, R. Sessoli, Angew. Chem., Int. Ed. 42 (2003) 268;
(c) E.K. Brechin, C. Boskovic, W. Wernsdorfer, J. Yoo, A. Yamaguchi, E.C. Sanudo, T.R. Concolino, A.L. Rheingold, H. Ishimoto, D.N. Hendrickson, G. Christou, J. Am. Chem. Soc. 124 (2002) 9710;
(d) L.F. Jones, E.K. Brechin, D. Collison, A. Harrison, S.J. Teat, W. Wernsdorfer, Chem. Commun. (2002) 2974;
(e) L.F. Jones, E.K. Brechin, D. Collison, J. Raftery, S.J. Teat, Inorg. Chem. 42 (2003) 6971.
[5] (a) See for example: C.P. Raptopoulou, Y. Sanakis, A.K. Boudalis, V. Psycharis, Polyhedron 24 (2005) 711;
(b) C.P. Raptopoulou, A.K. Boudalis, Y. Sanakis, V. Psycharis, J.M. Clemente-Juan, M. Fardis, G. Diamantopoulos, G. Papavassiliou, Inorg. Chem. 45 (2006) 2317;
(c) C. Gkioni, A.K. Boudalis, Y. Sanakis, C.P. Raptopoulou, Polyhedron 26 (2007) 2536;
(d) C. Gkioni, A.K. Boudalis, Y. Sanakis, L. Leondiadis, V. Psycharis, C.P. Raptopoulou, Polyhedron 27 (2008) 2315;
(e) K.N. Lazarou, S.P. Perlepes, V. Psycharis, C.P. Raptopoulou, Polyhedron 27 (2008) 2131;
(f) C.P. Raptopoulou, A.K. Boudalis, A.N. Lazarou, V. Psycharis, N. Panopoulos, M. Fardis, G. Diamantopoulos, J.-P. Tuchagues, A. Mari, G. Papavassiliou, Polyhedron 27 (2008) 3575;
(g) K.N. Lazarou, V. Psycharis, S.P. Perlepes, C.P. Raptopoulou, Polyhedron 28 (2009) 1085.
[6] (a) For interesting reviews concerning the chemistry and applications of coordination polymers, see: C. Janiak, Dalton Trans. (2003) 2781 (Dalton Perspective);
(b) S.R. Batten, R. Robson, Angew. Chem., Int. Ed. Engl. 37 (1998) 1460;
(c) M. Munakata, L.P. Wu, T. Kuroda-Sowa, Adv. Inorg. Chem. 46 (1999) 173;
(d) S.R. Batten, Curr. Opin. Solid State Mater. Sci. 5 (2001) 107;
(e) S. Kitagawa, S. Noro, in: J.A. McCleverty, T.J. Meyer (Eds.), Comprehensive Coordination Chemistry II, vol. 7, Elsevier, Amsterdam, 2004, pp. 231–261;
(f) A.Y. Robin, K.M. Fromm, Coord. Chem. Rev. 250 (2006) 2127;
(g) Y. Zhou, M. Hong, X. Wu, Chem. Commun. (2006) 135 (feature article);
(h) C. Coulon, H. Miyasaka, R. Clérac, Struct. Bonding 122 (2006) 163;
(i) D.-K. Bucar, G.S. Papaefstathiou, T.D. Hamilton, Q.L. Chu, I.G. Georgiev, L.R. MacGillivray, Eur. J. Inorg. Chem. (2007) 4559 (microreview);
(j) J.L.C. Rowsell, O.M. Yaghi, Micropor. Mesopor. Mater. 73 (2004) 3.
[7] (a) I. Sotofte, K. Nielsen, Acta Chem. Scan. A35 (1981) 739;
(b) R.-F. Hu, J. Zhang, Y. Kang, Y.-G. Yao, Inorg. Chem. Commun. 8 (2008) 828;
(c) V. Tangoulis, C.P. Raptopoulou, V. Psycharis, A. Terzis, K. Skorda, S.P. Perlepes, O. Cador, O. Kahn, E.G. Bakalbassis, Inorg. Chem. 39 (2000) 2522;
(d) C.C. Stoumpos, E. Diamantopoulou, C.P. Raptopoulou, A. Terzis, S.P. Perlepes, N. Lalioti, Inorg. Chim. Acta 361 (2008) 3638;
(e) A.D. Katsenis, N. Lalioti, V. Bekiari, P. Lianos, C.P. Raptopoulou, A. Terzis, S.P. Perlepes, G.S. Papaefstathiou, Inorg. Chem. Commun. 12 (2009) 92.
[8] Rigaku/MSC, 2005. Crystal Clear, Rigaku/MSC Inc., The Woodlands, Texas, USA.
[9] Sheldrick, G.M., SHELXS-97, Structure Solving Program, University of Göttingen, Germany, 1997.
[10] Sheldrick, G.M., SHELXL-97, Crystal Structure Refinement Program, University of Göttingen, Germany, 1997.
[11] DIAMOND, Crystal and Molecular Structure Visualization, Crystal Impact GbR, Bonn, Germany, Version 3.1f, 2008.
[12] J. Handley, D. Collison, C.D. Garner, M. Helliwell, R. Docherty, J.R. Lawson, P.A. Tasker, Angew. Chem., Int. Ed. Engl. 32 (1993) 1036.
[13] M. Murrie, D. Collison, D. Garner, M. Heliwell, P.A. Tasker, S.S. Turner, Polyhedron 17 (1998) 3031.
[14] S. Biswas, M. Tonigold, D. Volkmer, Z. Anorg. Allg. Chem. 634 (2008) 2532.
[15] V. Tangoulis, E. Diamantopoulou, E.G. Bakalbassis, C.P. Raptopoulou, A. Terzis, S.P. Perlepes, Mol. Cryst. Liq. Cryst. 335 (1999) 463.
[16] B.-H. Qian, W.-X. Ma, L.-D. Lu, X.-J. Yang, X. Wang, Acta Cryst. E62 (2006) m2818.
[17] J. Granifo, M.T. Garland, R. Baggio, Acta Cryst. C60 (2004) m97.
[18] (a) D.V. Soldatov, P. Tinnemans, G.D. Enright, C.I. Ratcliffe, P.R. Diamente, J.A. Ripmeester, Chem. Mater. 15 (2003) 3826;
(b) D.V. Soldatov, I.L. Moudrakovski, C.I. Ratcliffe, R. Dutrisac, J.A. Ripmeester, Chem. Mater. 15 (2003) 4810.
[19] I. Popova, J.T. Yates Jr., Langmuir 13 (1997) 6169.
[20] J. Rubim, I.G.R. Gutz, O. Sala, W.J. Orville-Thomas, J. Mol. Struct. 100 (1983) 571.
[21] (a) K. Nakamoto, Infrared and Raman Spectra of Inorganic and Coordination Compounds, fourth ed., Wiley, New York, 1986. pp. 227–231, 259–263;
(b) K. Nakamoto, C. Udovich, J. Takemoto, J. Am. Chem. Soc. 92 (1970) 3973.
[22] E. Manessi-Zoupa, S.P. Perlepes, V. Hondrellis, J.M. Tsangaris, J. Inorg. Biochem. 55 (1994) 217.
[23] A.K. Boudalis, V. Nastopoulos, S.P. Perlepes, C.P. Raptopoulou, A. Terzis, Transition Met. Chem. 26 (2001) 276.
[24] K. Wippermann, J.W. Schultze, R. Kessel, J. Penninger, Corr. Sci. 32 (1991) 205.
[25] S. Mamas, T. Kıyak, M. Kabasakaloğlu, A. Koç, Mater. Chem. Phys. 93 (2005) 41.

For primary aliphatic amines as nucleophiles and hexachlorine-containing clathrochelate iron and ruthenium(II) precursors only partially substituted complexes (mainly tetrasubstituted products) have been isolated [13,16]. The reactions with low-nucleophilic unsubstituted aromatic amines and the amines with electron-withdrawing substituents gave the mixtures of partially substituted clathrochelate products without a stereoselectivity of the substitution. We tried to use silver(I), copper(I,II), mercury(II) and thalium (I,III) derivatives for the activation of the C–Hal bond as well as the deprotonation of the amino- and oxygen-containing nucleophiles with alkaline and alkaline-earth metal amides and alcoholates [13,15,16]. However, in most cases the nucleophilic substitution in such hard conditions leads to the destruction of the clathrochelate framework. On the other hand, we used successfully the imidazol magnesium derivative for synthesis of the bis-imidazolyl iron(II) clathrochelate [26].

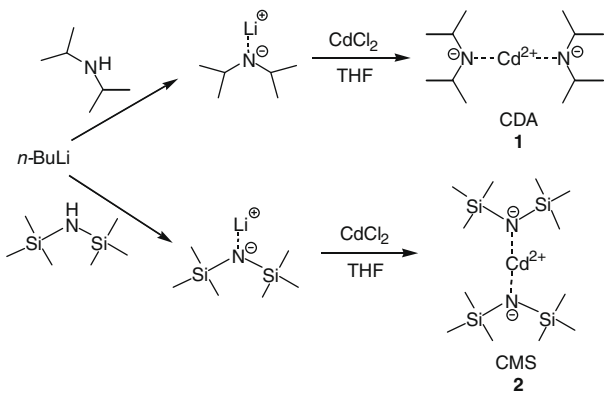
In general, the substitution with soft nucleophilic agents requires an activation of the leaving halogen substituents and an increase of the nucleophilicity of these agents without the use of the strong bases. In this paper, the convenient pathways for ribbed functionalization of the tris-dioximate clathrochelates based on the nucleophilic substitution of the halogen-containing clathrochelate precursors with soft *N*- and *O*-nucleophiles in the presence of cadmium diamides as the promotors are described.

2. Results and discussion

Two cadmium(II) diamides **1** and **2** were used for the activation of the nucleophilic substitution of the ribbed chlorine substituents in the clathrochelate precursors. The THF – hexane solutions of these diamides were obtained *one-pot* by treatment of diisopropylamine and hexamethyldisilazane with *n*-butyl lithium followed by the reactions of the lithium derivatives with $CdCl_2$ (Scheme 1).

The diamide CMS is stable in wide temperature range, whereas the compound CDA is stable only below −20 °C and decomposes at room temperature in few hours with the formation of fine metallic cadmium. The reactivity of these cadmium(II) compounds in the reactions studied is similar. Cadmium(II) derivatives activate the C–Hal bond in the clathrochelate precursors both by the coordination of halogen ribbed substituents to metal ion (Scheme 2) and the formation of anionic forms of a nucleophilic agent due to interaction with cadmium amides, that increases the electron density on a reactive site of this agent. Moreover, the cadmium amides and alcoholates, in the contrast to their lithium-containing analogs, are low-basic reagents.

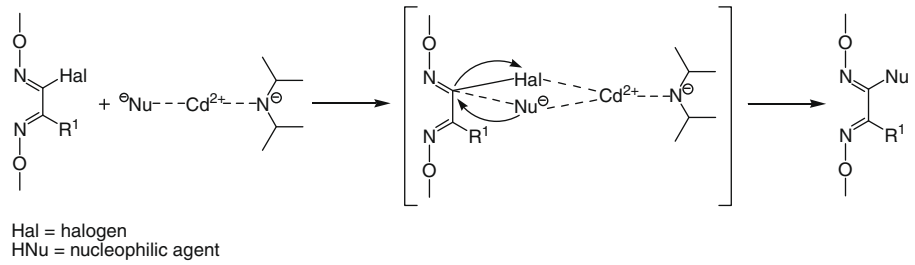
The generation *in situ* low-basic cadmium(II) alcoholates and amides in these nucleophilic substitution reactions allowed us to obtain the derivatives of soft nucleophilic agents [alcohols (including the fluorinated ones) and aromatic amines (including the nucleophiles with electron-withdrawing substituents)] by efficient one-pot procedures in relatively high yields (40%–70%) under mild conditions. The reactions performed for the di- and hexachlorine-containing clathrochelate iron(II) precursors in the presence of cadmium-containing compounds are summarized in Schemes 3–5. The proposed approach allowed to obtain selectively previously unavailable functionalized compounds, in particular, the hexafunctionalized ribbed-substituted clathrochelates with fluorinated alkoxyl groups and monoribbed-functionalized complexes with *n*-butoxyl, crown ether and aromatic amine-, carboxymethyl- and nitro-containing functionalizing fragments.



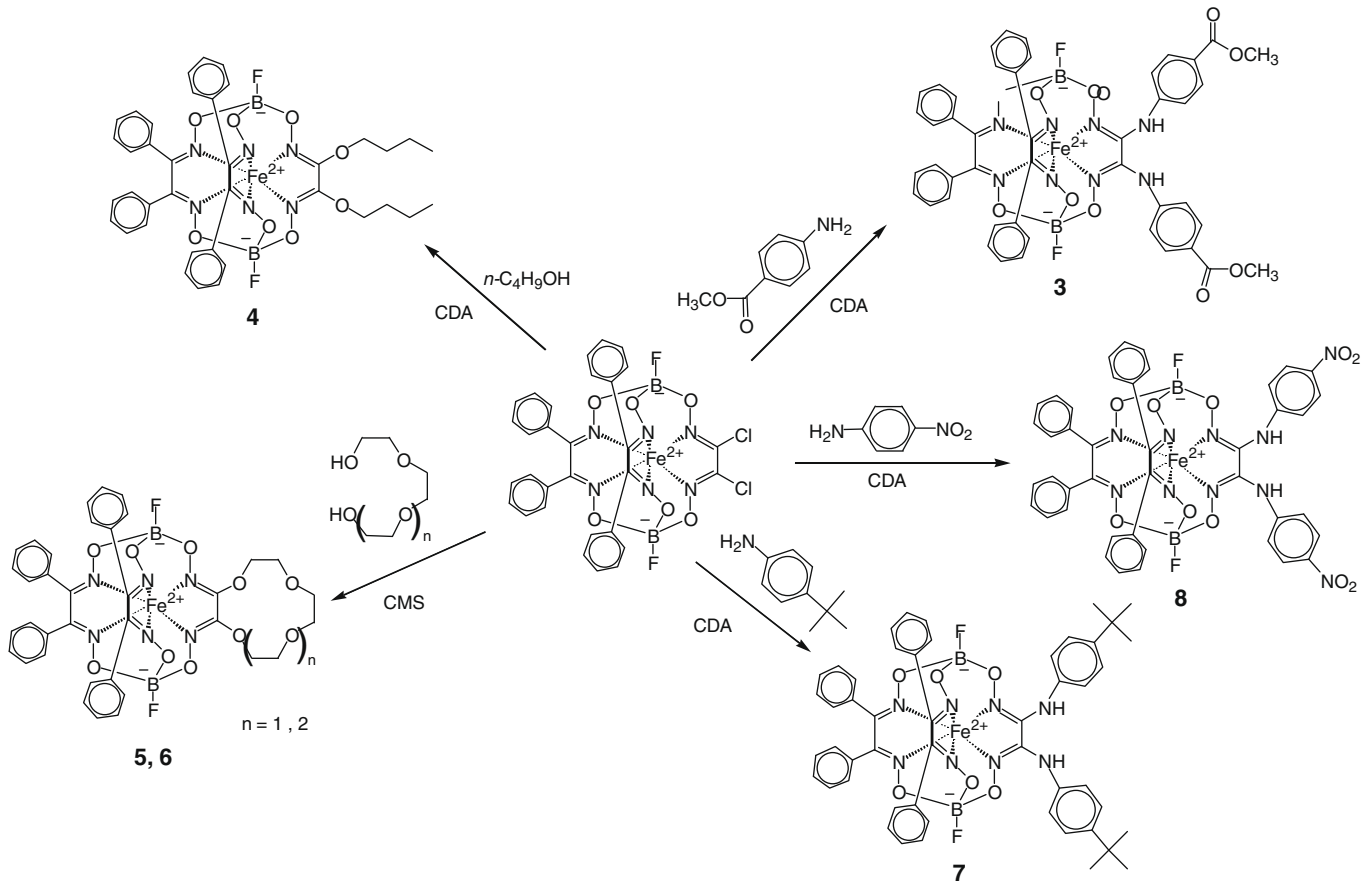
Scheme 1. Synthesis of cadmium(II) amides.

The clathrochelates **3**–**5** were characterized by X-ray crystallography; their molecular structures are shown in Figs. 1–3 and the main geometrical parameters of these molecules are listed in Table 1. The main bond lengths in macrobicyclic frameworks **3**–**5** are almost equal and characteristic of the boron-capped iron(II) clathrochelates [1]. Coordination polyhedra of the encapsulated iron(II) ions are intermediate between a trigonal prism (TP, the distortion angle $\varphi = 0°$) and a trigonal antiprism (TAP, $\varphi = 60°$), which is also characteristic of the hexadentate macrobicyclic ligands [1]. As seen from Table 1, the distortion angle φ values for molecules **3–5** are very close (from 25.3° to 26.9°) as well as the heights *h* of the coordination polyhedra (2.31 Å) and the bite angles α (half the chelate N–Fe–N angles, 39.1°–39.5°). In the earlier-studied mono- and dinitroxide ribbed-functionalized $FeBd_2((TempoNH)GmCl)(BF)_2$ and $FeBd_2((TempoNH)_2Gm)(BF)_2$ clathrochelates (where Bd^{2-} is α-benzyldioxime dianion, Tempo is 2,2,6,6-tetra-methylpyperidinyl-1-oxyl) these values are equal to 2.32 and 2.31 Å, 25.8° and 27.5°, 39.2° and 39.2°, respectively [18]. Thus, the nature of the ribbed substituents in chelate α-dioximate fragments affects the angle φ values only, whereas the height *h* and the α angles remain practically constants.

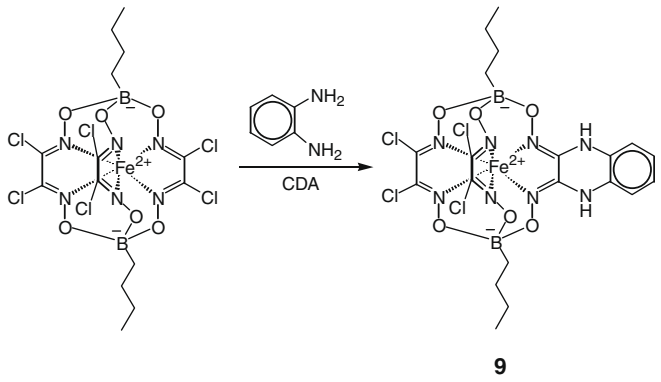
Nevertheless, the nonbonding interactions of the functionalizing ribbed substituents at the C(1) and C(2) atoms affect a molecular geometry of the complexes obtained. The steric hindrances of bulky *n*-butyl and crown ether substituents at α-carbon atoms in the crystals **4** and **5** resulted in *anti*-conformation of these functionalizing groups, whereas in the crystal **3** neighboring *p*-$Ph(COOCH_3)$ aromatic rings are almost parallel (the angle between their planes is equal to 20°) and situated rather close to each other (the minimal distances between the C(31)···C(44) and C(32)···C(39) atoms are equal to 3.34 Å). The functionalized NH-containing dioximate fragment of the molecule **3** has a *syn*-conformation because of the π-staking interactions between its aromatic moieties and is similar to that of the $Fe((n\text{-}C_4H_9NH)_2Gm)_2(Cl_2Gm)(BC_6H_5)_2$ complex [13], whereas in the $FeBd_2((TempoNH)_2Gm)(BF)_2$ [18] and $FeBd_2((tert\text{-}C_4H_9NH)_2Gm)(BF)_2$ [33] molecules these fragments have an *anti*-conformation. These interactions also cause the high distortion of the N–C(1)–N–N–C(2)–N moiety (the dihedral angle is equal to 21.1°), whereas in the molecules **4** and **5** (as well as in the $Fe((n\text{-}C_4H_9NH)_2Gm)_2(Cl_2Gm)(BC_6H_5)_2$, $FeBd_2((TempoNH)_2Gm)(BF)_2$ and $FeBd_2((tert\text{-}C_4H_9NH)_2Gm)(BF)_2$ macrobicycles [13,18,33]) the corresponding dihedral angles are from 8.5° to 18.8°. Nevertheless, the iron(II) coordination polyhedron in the molecule **3** is most regular with all Fe–N distances equal to 1.90(1) Å (Table 1), whereas in the $Fe((n\text{-}C_4H_9NH)_2Gm)_2(Cl_2Gm)(BC_6H_5)_2$, $FeBd_2((TempoNH)_2Gm)(BF)_2$ and $FeBd_2((tert\text{-}C_4H_9NH)_2Gm)(BF)_2$ molecules one of the Fe–N bonds is significantly longer (1.956 1.942 and 1.937 Å, respectively) then the other bonds of this type (the average value is 1.90(1) Å). The elongation of one of the six Fe–N bonds seems to be caused by the steric hindrances between the bulky $n\text{-}C_4H_9$, $tert\text{-}C_4H_9$ and *Tempo* groups [13,18,33]. Other bond lengths and angles in the molecules **3**–**5** are characteristic of the clathrochelate iron(II) tris-dioximates; the dihedral angles between the planes of



Scheme 2. The activation of the C–Hal bond by the coordination to the cadmium(II) ion.



Scheme 3. Synthesis of the monoribbed-functionalized iron(II) clathrochelates.

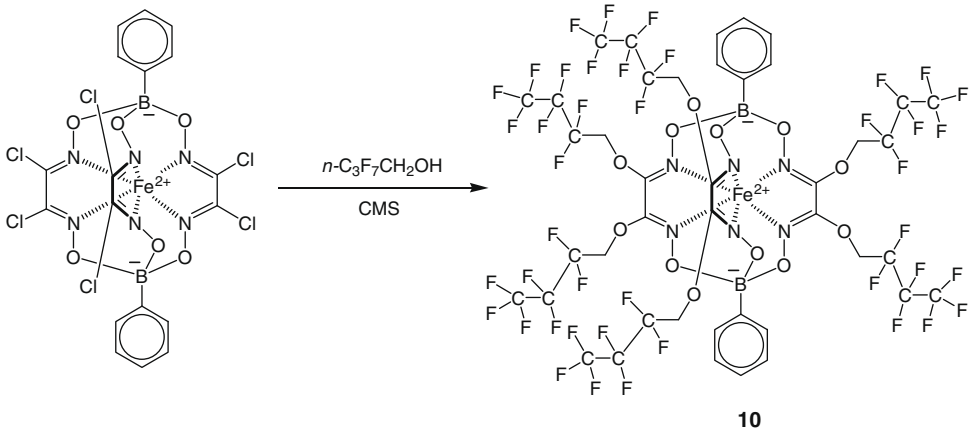


Scheme 4. Reaction of the hexachloride clathrochelate precursor with *o*-phenylenediamine.

neighboring phenyl substituents in the α-benzyldioximate chelate fragments are from 53° to 68°.

Packing diagram for the crystal **3** is shown in Fig. 4. In this crystal the strong intermolecular contacts were found: the dimers are formed by the N(7)–H(7)···O(9) hydrogen bonds with N(7)···O(9) distances equal to 2.924(6) Å and the N–H–O angles *ca* 164°. The crystal packings **4** and **5** (see Supplementary data) are formed by weak intermolecular contacts only.

The isomeric shift (IS) values (0.33–0.44 mm s^{-1}) in the ^{57}Fe Mössbauer spectra of the clathrochelates **3**–**10** allow one to characterize them as the low-spin iron(II) complexes, whereas the quadrupole splitting (QS) values (0.43–1.20 mm s^{-1}) are an evidence of essential trigonal-prismatic distortion of the TP–TAP coordination polyhedra of the encapsulated iron(II) ions. The QS values (Table 1) were deduced for the X-ray crystallography characterized complexes using the partial QS concept from the following equa-



Scheme 5. Reaction of the hexachlorine-containing clathrochelate precursor with fluorinated alcohol.

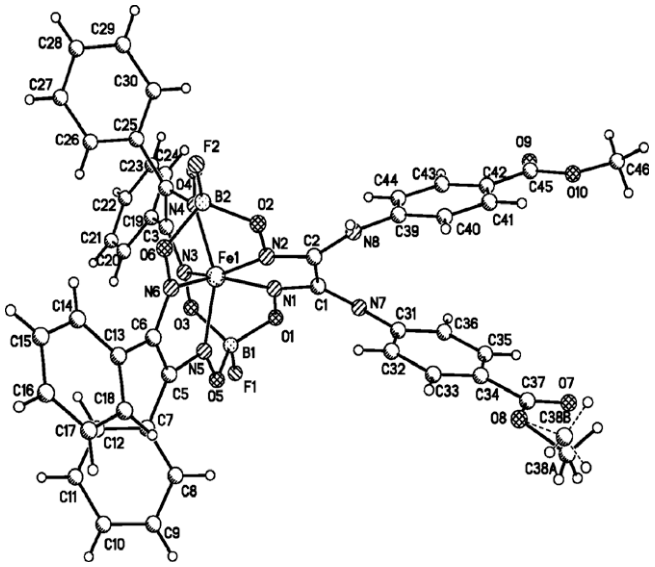


Fig. 1. Molecular structure of **3**. One of the methyl groups is equiprobably disordered (shown with the solid and dashed lines).

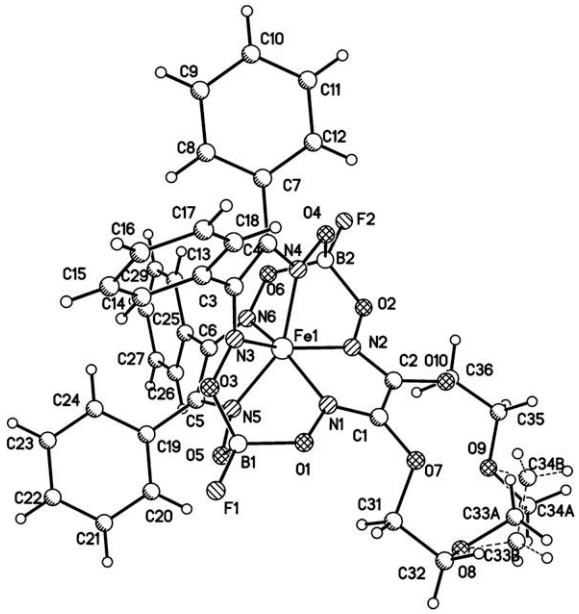


Fig. 3. Molecular structure of **5**. Ethylene moiety is disordered by two positions with occupancies 0.7:0.3 (shown with the solid and dashed lines, respectively).

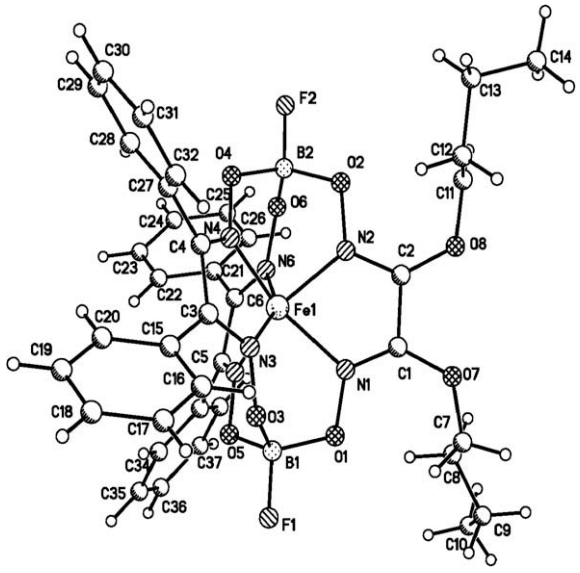


Fig. 2. Molecular structure of **4**.

tion: $QS = 6–9(cos^2\alpha/cos^2(\varphi/2))$ [34]. The essential differences between the experimental and calculated QS values are caused by the absence of symmetry C_3 axis in the molecules studied because of non-equivalence of their ribbed fragments.

In our opinion, the cadmium-promoted reactions have a great potential for synthesis of both the novel heterocyclic systems starting from various halogen-containing heterocyclic precursors and new ribbed-functionalized cage complexes. These previously unavailable compounds with improved properties and functionality might be used for the design of new efficient polyfunctional electro- and photocatalytic systems, biomimetics and pharmaceutical candidates for diagnostics and therapy.

An undoubted interest in cadmium(II) derivatives is caused also by a possible activation of the inert coordination compounds with these reagents. In our opinion, the halogen ligands in the platinum group metal complexes may be activated by the coordination to the Cd^{2+} ion that will allow one to obtain new types of previously unavailable metal complexes starting from precursors with inert metal–halogen bonds.

Table 1
Main geometrical characteristics (Å) of the clathrochelate molecules in the crystals **3–5** and their ^{57}Fe Mössbauer parameters (mm s^{-1}).

Parameter	3	4	5	Parameter	3	4	5
Fe(1)–N(1)	1.912(4)	1.968(6)	1.915(6)	N(5)–O(5)	1.371(5)	1.372(7)	1.383(7)
Fe(1)–N(2)	1.914(4)	1.908(6)	1.920(6)	N(6)–O(6)	1.365(5)	1.399(6)	1.371(8)
Fe(1)–N(3)	1.928(3)	1.890(6)	1.899(6)	B(1)–O(1)	1.465(6)	1.47(1)	1.48(1)
Fe(1)–N(4)	1.871(4)	1.897(5)	1.914(6)	B(1)–O(3)	1.511(6)	1.505(9)	1.470(9)
Fe(1)–N(5)	1.889(4)	1.899(6)	1.892(6)	B(1)–O(5)	1.491(6)	1.47(1)	1.494(9)
Fe(1)–N(6)	1.909(4)	1.884(6)	1.904(6)	B(1)–F(1)	1.343(6)	1.359(9)	1.369(9)
N(1)–C(1)	1.342(6)	1.252(8)	1.24(1)	B(2)–O(2)	1.497(7)	1.46(1)	1.48(1)
N(2)–C(2)	1.323(6)	1.320(9)	1.30(1)	B(2)–O(4)	1.538(6)	1.464(9)	1.49(1)
N(3)–C(3)	1.331(5)	1.335(8)	1.31(1)	B(2)–O(6)	1.464(8)	1.492(9)	1.48(1)
N(4)–C(4)	1.359(5)	1.319(8)	1.305(9)	B(2)–F(2)	1.324(7)	1.374(9)	1.365(9)
N(5)–C(5)	1.325(5)	1.294(8)	1.303(9)	h (Å)	2.32	2.31	2.31
N(6)–C(6)	1.290(6)	1.325(8)	1.314(9)	ϕ (°)	26.1	25.3	26.9
N(1)–O(1)	1.370(5)	1.379(7)	1.381(8)	α (°)	39.5	39.1	39.3
N(2)–O(2)	1.371(5)	1.411(7)	1.370(8)	QS_{exp}	0.78	0.56	0.48
N(3)–O(3)	1.332(4)	1.385(6)	1.374(7)	$QS_{deduced}$(f · PQS)	0.35	0.31	0.30
N(4)–O(4)	1.375(5)	1.379(7)	1.381(7)	QS_{exp}–$QS_{deduced}$	0.43	0.25	0.18

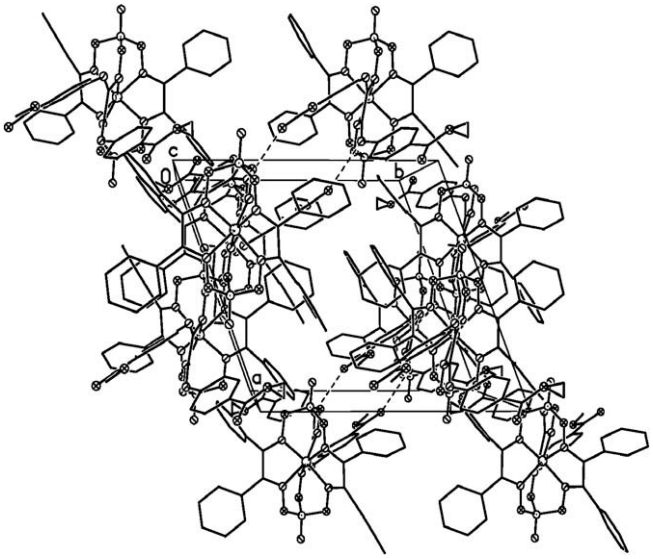


Fig. 4. Packing diagram of **3** along the crystal axis *c*. Solvent molecules and hydrogen atoms are omitted for clarity. The N(7)–H(7)···O(9) hydrogen bonds are shown with a dashed line.

3. Experimental

3.1. General procedures

The reagents used, $CdCl_2{\cdot}2.5H_2O$, n-$C_3F_7CH_2OH$, triethyleneglycol, tetraethyleneglycol, hexamethyldisilazane, n-C_4H_9Li (1.6 M solution in hexane), sorbents, aromatic amines and their derivatives, organic bases and organic solvents were obtained commercially (Fluka). The $Fe(Cl_2Gm)_3(Bn\text{-}C_4H_9)_2$ and $Fe(Cl_2Gm)_3(BC_6H_5)_2$ complexes were prepared as described elsewhere [12,13]. The $FeBd_2(Cl_2Gm)(BF)_2$ complex was prepared as described earlier [15].

Analytical data (C, H, N contents) were obtained with a Carlo Erba model 1106 microanalyzer. Iron content was determined spectrophotometrically.

The MALDI-TOF mass spectra were recorded using a MALDI-TOF-MS Bruker Autoflex mass spectrometer in reflecto-mol mode. The ionization was induced by UV-laser with wavelength 336 nm. The samples were applied to a nickel plate, 2,5-dihydroxybenzoic acid was used as a matrix. The accuracy of measurements was 0.1%.

The IR spectra of solid samples (KBr tablets) in the range of 400–4000 cm^{-1} were recorded with a IR200 Thermo Nicolet FT-spectrophotometer.

The UV–Vis spectra of solutions in dichloromethane were recorded in the range of 230–900 nm with a Lambda 9 Perkin Elmer spectrophotometer. The individual Gaussian components of these spectra were calculated using the SPECTRA program.

The ^{1}H and ^{13}C NMR spectra were recorded from CD_2Cl_2 and $CDCl_3$ solutions with a Bruker AC-200 and AMX-400 FT-spectrometers.

The ^{57}Fe Mössbauer spectra were obtained with a NP-255 (Hungary) spectrometer with a constant acceleration mode. The spectra were collected with a 256-multichannel amplitude analyzer. The isomer shift was measured relative to sodium nitroprusside, and an α-Fe foil was used for the velocity scale calibration. The ^{57}Co in a rhodium matrix was used as the source, which was always kept at room temperature. The minimal absorption line-width in the spectrum of a standard sample of sodium nitroprusside was 0.24 mm s^{-1}.

3.2. Synthesis

3.2.1. Li[N(iso-$C_3H_7)_2$] (LDA)

Diisopropylamine (13.93 g, 138 mmol) was dissolved in THF (62.5 ml) under argon, the solution was cooled to −20 °C and 1.6 M solution of n-BuLi in hexane (87.5 ml, 140 mmol) was added dropwise to the stirring reaction mixture. The resulted 0.92 M solution of LDA in THF–hexane mixture was used for preparation of CDA (**1**).

3.2.2. Cd[N(iso-$C_3H_7)_2]_2$ (CDA, **1**)

0.92 M solution of LDA in THF–hexane mixture (20 ml, 18.4 mmol) was cooled to −20 °C under argon and dry $CdCl_2$ (1.68 g, 9.2 mmol) was added. The reaction mixture was stirred for 2 h at −20 °C. The obtained 0.46 M solution of CDA was used for synthesis of the clathrochelate complexes.

3.2.3. Cd[N(Si($CH_3)_3)_2$] (CMS, **2**)

Hexamethyldisilazane (32.2 g, 200 mmol) was dissolved in THF (183 ml) at −40 °C and 1.6 M solution of n-BuLi in hexane (125 ml, 200 mmol) was added dropwise for 30 min to the stirring reaction mixture under argon. Then $CdCl_2$ (18.3 g, 100 mmol) was added and the reaction mixture was stirred for 1 h. The obtained 0.325 M solution of CMS was used for synthesis of the clathrochelate complexes.

3.2.4. $FeBd_2$((p-$CH_3OOCC_6H_4NH)_2Gm)(BF)_2$. (**3**)

Complex $FeBd_2(Cl_2Gm)(BF)_2$ (0.2 g, 0.27 mmol) and p-carboxymethylaniline (0.163 g, 1.08 mmol) were dissolved/suspended in THF (5 ml) under argon. The reaction mixture was cooled to

−20 °C and 0.46 M solution of CDA (2.32 ml, 1.07 mmol) was added. The reaction mixture was stirred for 1 h at −20 °C and heated to room temperature. Then 0.5% aqueous acetic acid (100 ml) was added and the mixture obtained was extracted with chloroform (30 ml, in 3 portions). The extract was washed with Na_2CO_3 saturated aqueous solution, dried with Na_2SO_4, rotary evaporated to ~5 ml and precipitated with heptane. The precipitate was washed with heptane and dried *in vacuo*. Yield: 0.16 g (62%). *Anal.* Calc. for $C_{46}H_{36}N_8O_{10}B_2F_2Fe$: C, 55.52; H, 3.79; N, 11.78; Fe, 5.78. Found: C, 55.58; H, 3.74; N, 11.65; Fe, 5.73%. MS (MALDI-TOF): *m/z*: −976 $[M]^{-\cdot}$. ^1H NMR (400.13 MHz, CD_2Cl_2): δ = 3.77 (s, 6H, CH_3O), 6.53 (m, 4H, Ar), 7.28–7.60 (m, 26H, Ph+NH) ppm. $^{13}C\{^1H\}$ NMR (100.61 MHz, CD_2Cl_2): δ = 52.2 (s, CH_3O), 120.6 (s, *o*-Ar), 126.3 (s, *m*-Ar), 128.3, 130.3, 130.4, 130.9 (four s, Ar+Ph), 140.7 (NC=N), 143.5 (s, ArNH), 157.6 (s, PhC=N), 166.3 (s, C=O) ppm. IR (KBr): 1714 ν(C=O), 1573m ν(C=N), 1175–1199m ν(B–O)+ν(B–F), 914, 1002, 1057, 1107 ν(N–O), 1623 δ(N–H) cm^{-1}. UV–Vis (CH_2Cl_2): λ_{max} ($\varepsilon \times 10^{-3}$, $mol^{-1}\,l\,cm^{-1}$): 245 (13), 277 (27), 294 (1.8), 306 (9.9), 365 (4.3), 439 (4.5), 490 (14), 500 (4.5) nm. ^{57}Fe Mössbauer (mm s^{-1}): IS = 0.33, QS = 0.78.

3.2.5. $FeBd_2((n\text{-}C_4H_9O)_2Gm)(BF)_2$ (**4**)

Complex $FeBd_2(Cl_2Gm)(BF)_2$ (0.18 g, 0.24 mmol) and *n*-butanol (0.076 ml, 1.07 mmol) was dissolved/suspended in THF (5 ml) under argon. The reaction mixture was cooled to −20 °C and 0.46 M solution of CDA (1.09 ml, 0.5 mmol) was added. The reaction mixture was stirred for 1 h at −20 °C and heated to room temperature. The product was isolated as described above for complex **3**. Yield: 0.11 g (55%). *Anal.* Calc. for $C_{38}H_{38}N_6O_8B_2F_2Fe$: C, 55.54; H, 4.63; N, 10.23; Fe, 6.70. Found: C, 55.41; H, 4.51; N, 10.03; Fe, 6.84%. MS (MALDI-TOF): *m/z*: 822 $[M]^{+\cdot}$, 845 $[M+Na^+]^+$, 861 $[M+K^+]^+$. ^1H NMR (400.13 MHz, CD_2Cl_2): δ = 0.88 (t, 6H, CH_3), 1.38 (m, 4H, CH_2), 1.66 (m, 4H, CH_2), 4.62 (t, 4H, OCH_2), 7.24 (m, 20H, Ph) ppm. $^{13}C\{^1H\}$ NMR (100.61 MHz, CD_2Cl_2): δ = 13.7 (s, CH_3), 19.0 (s, CH_2), 32.3 (s, CH_2), 75.7 (s, OCH_2), 128.3, 129.9, 130.3, 130.9 (four s, Ph), 147.5 (s, OC=N), 157.2 (s, PhC=N) ppm. IR (KBr): 1538, 1579 ν(C=N), 1201m ν(B–O) + ν(B–F), 929, 1033, 1059, 1108 ν(N–O) cm^{-1}. UV–Vis (CH_2Cl_2): λ_{max} ($\varepsilon \times 10^{-3}$, $mol^{-1}\,l\,cm^{-1}$): 244 (30), 265 (1.7), 288 (12), 302 (5.5), 389 (3.9), 466 (7.9), 488 (14), 513 (6.3) nm. ^{57}Fe Mössbauer (mm s^{-1}): IS = 0.38, QS = 0.56.

3.2.6. $FeBd_2(12cw4Gm)(BF)_2$ (**5**)

Complex $FeBd_2(Cl_2Gm)(BF)_2$ (0.4 g, 0.54 mmol) and triethyleneglycol (0.077 ml, 0.55 mmol) were dissolved/suspended in THF (40 ml) at −20 °C under argon and 0.325 M solution of CMS (2.3 ml, 0.75 mmol) was added. The reaction mixture was stirred for 4 h and 0.5% aqueous acetic acid (100 ml) was added. The mixture obtained was extracted with chloroform (30 ml in 3 portions). The extract was washed with Na_2CO_3 saturated aqueous solution, evaporated to dryness and the solid residue was separated by column chromatography on silica gel (0.035–0.070 mm, eluent: chloroform). The major dark-orange elute was evaporated to dryness, washed with hexane and dried in vacuo. Yield: 0.19 g (42%). *Anal.* Calc. for $C_{36}H_{32}N_6O_{10}B_2F_2Fe$: C, 52.49; H, 3.89; N, 10.10; Fe, 6.68. Found: C, 52.60; H, 4.00; N, 10.08; Fe, 6.60%. MS (MALDI-TOF): *m/z*: (positive region) 824 $[M]^{+\cdot}$, 847 $[M+Na^+]^+$, 863 $[M+K^+]^+$, (negative region) – 824 $[M]^{-\cdot}$. ^1H NMR (400.13 MHz, CD_2Cl_2): δ = 3.54 (m, 4H, $CltOCH_2CH_2OCH_2$), 3.68 (m, 4H, $ClTOCH_2CH_2OCH_2CH_2$), 4.74 (m, 4H, $ClTOCH_2CH_2OCH_2$), 7.25 (m, 20H, Ph) ppm. $^{13}C\{^1H\}$ NMR (100.61 MHz, CD_2Cl_2): δ = 71.56 (s, $ClTOCH_2CH_2OCH_2$), 72.3 (s, $ClTOCH_2CH_2OCH_2$), 76.2 (s, $ClTOCH_2CH_2OCH_2CH_2$), 130.0, 131.4, 132.0, 132.5 (four s, Ph), 149.1 (s, OC=N), 158.7 (s, PhC=N) ppm. IR (KBr): 1543, 1581 ν(C=N), 1200m ν(B–O) + ν(B–F), 918, 973, 1041, 1057, 1109 ν(N–O) + ν(C–O–C) cm^{-1}. UV–Vis (CH_2Cl_2): λ_{max} ($\varepsilon \times 10^{-3}$, $mol^{-1}\,l\,cm^{-1}$): 245 (27), 264 (5.9), 276 (8.7), 291 (11), 307 (4.3), 366 (3.0), 441 (5.9), 482 (12), 501 (6.8) nm. ^{57}Fe Mössbauer (mm s^{-1}): IS = 0.33, QS = 0.48.

3.2.7. $FeBd_2(15cw5Gm)(BF)_2$ (**6**)

This complex was obtained like the previous one except that tetraethyleneglycol (0.095 ml, 0.55 mmol) was used instead of triethyleneglycol. Yield: 0.30 g (64%). *Anal.* Calc. for $C_{38}H_{36}N_6O_{11}B_2F_2Fe$: C, 52.60; H, 4.15; N, 9.69; Fe, 6.34. Found: C, 52.76; H, 4.09; N, 9.62; Fe, 6.27%. MS (MALDI-TOF): *m/z*: (positive region) 868 $[M]^{+\cdot}$, 891 $[M+Na^+]^+$, 907 $[M+K^+]^+$; (negative region) – 868 $[M]^{-\cdot}$. ^1H NMR (400.13 MHz, CD_2Cl_2): δ = 3.57 (m, 8H, $ClTOCH_2CH_2OCH_2CH_2$), 3.70 (m, 4H, $ClTOCH_2CH_2OCH_2CH_2$), 4.84 (m, 4H, $ClTOCH_2CH_2OCH_2CH_2$), 7.25 (m, 20H, Ph) ppm. $^{13}C\{^1H\}$ NMR (100.61 MHz, CD_2Cl_2): δ = 71.4 (s, $ClTOCH_2CH_2OCH_2CH_2$), 72.0, (s, $ClTOCH_2CH_2OCH_2CH_2$), 72.7 (s, $ClTOCH_2CH_2OCH_2CH_2$), 76.8 (s, $ClTOCH_2CH_2OCH_2CH_2$), 130.0, 131.5, 132.0, 132.6 (four s, Ph), 148.6 (s, OC=N), 158.9 (s, PhC=N) ppm. IR (KBr): 1543, 1581 ν(C=N), 1200m ν(B–O) + ν(B–F), 922, 981, 1039, 1057, 1109 ν(N–O) + ν(C–O–C) cm^{-1}. UV–Vis (CH_2Cl_2): λ_{max} ($\varepsilon \times 10^{-3}$, $mol^{-1}\,l\,cm^{-1}$): 245 (23), 265 (4.3), 285 (13), 305 (4.8), 367 (2.7), 421 (1.6), 456 (5.7), 484 (4.4), 499 (9.8) nm. ^{57}Fe Mössbauer (mm s^{-1}): IS = 0.35, QS = 0.54.

3.2.8. $FeBd_2((p\text{-}tert\text{-}C_4H_9C_6H_4NH)_2Gm)(BF)_2$ (**7**)

This complex was obtained like the clathrochelate **3** except that *p*-tert-butylaniline (0.16 g, 1.07 mmol) was used instead of *p*-carboxymethylaniline. Yield: 0.18 g (68%). *Anal.* Calc. for $C_{50}H_{48}N_8O_6B_2F_2Fe$: C, 61.79; H, 4.94; N, 11.53; Fe, 5.66. Found: C, 61.88; H, 5.03; N, 11.48; Fe, 5.64%. MS (MALDI-TOF): *m/z*: −972 $[M]^{-\cdot}$. ^1H NMR (400.13 MHz, CD_2Cl_2): δ = 1.17 (s, 18H, *tert*-Bu), 6.32 (d, 4H, *o*-Ar), 6.90 (d, 4H, *m*-Ar), 7.30 (m, 22H, Ph+NH) ppm. $^{13}C\{^1H\}$ NMR (100.61 MHz, CD_2Cl_2): δ = 31.3 (s, CH_3), 34.4 (s, C_q), 122.0 (s, *o*-Ar), 125.6 (s, *m*-Ar), 128.0, 128.4, 129.9, 130.7, 131.0, 133.7 (six s, Ar+Ph), 145.6 (s, *p*-Ar), 148.3 (s, NC=N), 157.3 (s, PhC=N) ppm. IR (KBr): 1563, 1578, 1590 ν(C=N), 1203m ν(B–O) + ν(B–F), 916, 1003, 1018, 1056, 1107 ν(N–O), 1633 δ(N–H) cm^{-1}. UV–Vis (CH_2Cl_2): λ_{max} ($\varepsilon \times 10^{-3}$, $mol^{-1}\,l\,cm^{-1}$): 251 (36), 300 (9.3), 321 (5.7), 382 (5.6), 433 (5.6), 503 (15), 516 (3.8) nm. ^{57}Fe Mössbauer (mm s^{-1}): IS = 0.33, QS = 0.43.

3.2.9. $FeBd_2((p\text{-}NO_2C_6H_4NH)_2Gm)(BF)_2$ (**8**)

This complex was obtained like the clathrochelate **3** except that *p*-nitroaniline (0.15 g, 1.07 mmol) was used instead of *p*-carboxymethylaniline. Yield: 0.16 g (65%). *Anal.* Calc. for $C_{42}H_{30}N_{10}O_{10}B_2F_2Fe$: C, 53.11; H, 3.16; N, 14.75; Fe, 5.80. Found: C, 53.05; H, 3.18; N, 14.66; Fe, 5.74%. MS (MALDI-TOF): *m/z*: −950 $[M]^{-\cdot}$. ^1H NMR (400.13 MHz, CD_2Cl_2): δ = 6.52, 6.65 (two d, 4H, *o*-Ar), 7.25 (m, 20H, Ph), 7.83, 7.91 (two d, 4H, *m*-Ar) ppm. $^{13}C\{^1H\}$ NMR (100.61 MHz, CD_2Cl_2): δ = 120.3 (s, *o*-Ar), 125.0 (s, *m*-Ar), 128.4, 129.7, 130.5, 131.0 (four s, Ph), 142.0, 142.7, 144.2 (three s, *p*-Ar+NC=N), 158.0 (PhC=N) ppm. IR (KBr): 1549, 1577, 1596 ν(C=N), 1185m ν(B–O) + ν(B–F), 914, 1003, 1057, 1109 ν(N–O), 1628 δ(N–H) cm^{-1}. UV–Vis (CH_2Cl_2): λ_{max} ($\varepsilon \times 10^{-3}$, $mol^{-1}\,l\,cm^{-1}$): 237 (32), 291 (3.9), 309 (11), 50 (6.4), 363 (11), 443 (7.8), 484 (17), 521 (11) nm. ^{57}Fe Mössbauer (mm s^{-1}): IS = 0.33, QS = 0.47.

3.2.10. $Fe((HNC_6H_4NH)Gm)(Cl_2Gm)_2(Bn\text{-}C_4H_9)_2$ (**9**)

Complex $Fe(Cl_2Gm)_3(Bn\text{-}C_4H_9)_2$ (0.2 g, 0.3 mmol) and *o*-phenylenediamine (0.043 g, 0.4 mmol) were dissolved/suspended in THF (5 ml) at −20 °C under argon and cooled to −20 °C 0.46 M solution of CDA (0.87 ml, 0.4 mmol) was added. The reaction mixture was stirred for 1 h at −20 °C, heated to room temperature and then the product was isolated as described above for complex **3**. Yield: 0.10g (48%). *Anal.* Calc. for $C_{20}H_{24}N_8O_6B_2Cl4Fe$: C, 34.73; H, 3.47; N, 16.21; Fe, 7.96. Found: C, 34.71; H, 3.45; N, 16.12; Fe, 7.84%. MS (MALDI-TOF): *m/z*: −691 $[M]^{-\cdot}$. ^1H NMR (400.13 MHz, CD_2Cl_2):

δ = 0.47 (s, 4H, BCH_2), 0.80 (s, 6H, CH_3), 1.27 (m, 8H, CH_2CH_2), 6.80 (m, 4H, Ph), 7.94 (br s, 2H, NH) ppm. $^{13}C\{^1H\}$ NMR (100.61 MHz, CD_2Cl_2): δ = 14.2 (s, CH_3), 17.1 (br s, BCH_2), 26.2, 26.6 (two s, CH_2), 115.5, 124.2, 125.3 (three s, Ph), 127.9 (s, ClC=N), 136.8 (s, NC=N) ppm. IR (KBr): 1601m ν(C=N), 1099m ν(B–O) + ν(N–O), 917, 1001, 1046 ν(N–O), 1649 δ(N–H) cm^{-1}. UV–Vis (CH_2Cl_2): λ_{max} ($\varepsilon \times 10^{-3}$, $mol^{-1}\,l\,cm^{-1}$): 250 (23), 287 (4.8), 312 (5.8), 346 (4.7), 384 (7.3), 430 (7.2), 473 (8.7), 570 (1.4) nm. ^{57}Fe Mössbauer spectrum (mm s^{-1}): IS = 0.39, QS = 1.20.

3.2.11. $Fe((n\text{-}C_3F_7CH_2O)_2Gm)_3(BC_6H_5)_2$ (**10**)

Complex $Fe(Cl_2Gm)_3(BC_6H_5)_2$ (0.5 g, 0.72 mmol) and *n*-$C_3F_7CH_2OH$ (1.15 g, 5.76 mmol) were dissolved/suspended in THF (50 ml) at −10 °C under argon and 0.325 M solution of CMS (13.3 ml, 4.32 mmol) was added dropwise to the stirring reaction mixture. The reaction mixture was stirred overnight and 0.5% aqueous acetic acid (100 ml) was added. The mixture obtained was extracted with chloroform (30 ml in 3 portions). The extract was washed with Na_2CO_3 saturated aqueous solution, dried with $CaCl_2$ and filtered through the Silasorb SPH-300 layer (30 mm). The filtrate was evaporated to a small volume and the oily residue was dissolved in hexane. The solution was filtered, evaporated to dryness and the solid product was dried *in vacuo*. Yield: 0.83 g (69%). *Anal.* Calc. for $C_{42}H_{22}N_6O_{12}B_2F_{42}Fe$: C, 30.04; H, 1.31; N, 5.01; Fe, 3.28. Found: C, 30.14; H, 1.35; N, 5.00; Fe, 3.34%. MS (MALDI-TOF): *m/z:* 1678 $[M]^+$, 1701 $[M+Na^+]^+$, 1717 $[M+K^+]^+$). ^1H NMR (200.13 MHz, $CDCl_3$): δ = 5.27 (m, 12H, CH_2), 7.50 (m, 10H, Ph) ppm. $^{13}C\{^1H\}$ NMR (50.32 MHz, $CDCl_3$): δ = 68.8 (t, CH_2), 108.5 (m, CF_3), 114.0, 120.2 (two m, CF_2), 127.8, 128.6, 130.9 (three s, Ph), 144.3 (s, C=N) ppm. ^{19}F NMR (188.31 MHz, $CDCl_3$): δ = −80.6 (m, CF_3), −121.4 (m, β-CF_2), −127.1 (m, α-CF_2) ppm. IR (KBr): 1571 ν(C=N), 1230m ν(B–O), 972, 1018, 1084, 1124 ν(N–O) cm^{-1}. UV–Vis (CH_2Cl_2): λ_{max} ($\varepsilon \times 10^{-3}$, $mol^{-1}\,l\,cm^{-1}$): 238 (8.9), 266 (11), 300 (2.5), 331 (1.6), 426 (2.0), 452 (3.4), 459 (3.6) nm. ^{57}Fe Mössbauer spectrum (mm s^{-1}): IS = 0.44, QS = 0.65.

3.3. X-ray crystallography

Details of the crystal data collection and refinement parameters for the crystals **3–5** are listed in Table 2. Single crystals of these complexes were grown from benzene–isooctane (**4**) and chloroform–heptane (**3** and **5**) mixtures at room temperature.

The single-crystal X-ray diffraction experiments for the complexes **3–5** were carried out with a Bruker SMART APEX II CCD diffractometers at 110 K, using graphite monochromated Mo Kα radiation (λ = 0.71073 Å). Reflection intensities were integrated using SAINT software and corrected for absorption by semi-empirical method (SADABS program) [35,36].

The structures were solved by the direct method and refined by full-matrix least squares method against F^2 of all data, using SHELXTL PLUS software [37]. Non-hydrogen atoms were found on difference Fourier maps and refined with anisotropic displacement parameters except for disordered ones. One methyl group in the crystal **3** is disordered with equal occupancies (C(38A) and C(38B) atoms). One ethylene moiety (atoms C(33A), C(34A) and C(33B), C(34B)) and one solvate chloroform molecule (C(2SA), Cl(4A), Cl(5A), Cl(6A) and C(2SB), Cl(4B), Cl(5B), Cl(6B)) in the crystal **5** are disordered by two positions with occupations 7:3. The positions of hydrogen atoms were calculated and included in refinement in isotropic approximation by the riding model with the U_{iso}(H) = 1.5U_{eq}(C_i) for methyl groups and 1.2 for other groups. All calculations were made with SHELXTL, ver. 5.0 software [36]. The crystal **3** includes unidentified disordered solvate molecules, which have been treated as a diffuse contribution to the overall scattering without specific atom positions by SQUEEZE/PLATON [38]. The best

Table 2
Crystallographic data and experimental details for the crystals **3–5**.

Compound	**3**	**4**	**5**
Empirical formula	$C_{46}H_{36}B_2F_2FeN_8O_{10}\cdot0.5C_6H_{14}$	$C_{38}H_{38}B_2F_2FeN_6O_8\cdot2C_6H_6$	$C_{36}H_{32}B_2F_2FeN_6O_{10}\cdot2CHCl_3$
Formula weight	1019.38	977.42	1062.88
Colour, habit	red, prism	red, needle	red, prism
Crystal dimensions (mm)	0.40 × 0.16 × 0.08	0.34 × 0.25 × 0.20	0.22 × 0.20 × 0.19
Crystal system	triclinic	orthorhombic	orthorhombic
Space group	*P1*	$P2_12_12_1$	*Pbca*
a (Å)	12.628(2)	12.119(4)	17.0468(14)
b (Å)	13.467(2)	14.403(5)	17.2924(14)
c (Å)	18.711(3)	27.095(10)	30.603(3)
α (°)	87.839(3)	90.00	90.00
β (°)	81.445(4)	90.00	90.00
γ (°)	69.369(4)	90.00	90.00
Volume ($Å^3$)	2944.3(8)	4729(3)	9021.3(13)
Z	2	4	8
D_{calc} ($g\,cm^{-3}$)	1.150	1.373	1.565
μ (mm^{-1})	0.32	0.39	0.76
T_{min}	0.939	0.886	0.846
T_{max}	0.976	0.927	0.869
Reflections collected	31592	49310	83435
Independent reflections/R_{int}	13486/0.104	11820/0.324	8817/0.142
Observed reflections	4426	4716	5055
θ_{max} (°)	27.5	28.5	26.0
$R[F^2 > 2\sigma(F^2)]$	0.084	0.085	0.091
$wR(F^2)$	0.169	0.189	0.283
No. of reflections	13486	11820	8817
No. of parameters	539	528	532
Weighting scheme	$w = 1/[\sigma^2(F_o^2) + (0.020P)^2 + 2.2P]$, $P = (F_o^2 + 2F_c^2)/3$	$w = 1/[\sigma^2(F_o^2) + (0.040P)^2 + 3.5P]$, $P = (F_o^2 + 2F_c^2)/3$	$w = 1/[\sigma^2(F_o^2) + (0.110P)^2 + 8.6P]$, $P = (F_o^2 + 2F_c^2)/3$
Largest difference in peak and hole ($e\,Å^{-3}$)	0.92, −0.79	1.08, −0.83	1.37, −1.23
Flack parameter		−0.01 (3)	
F (0 0 0)	1054	2040	4320
Goodness-of-fit	1.004	1.011	0.999

available crystals of **4** and **5** were of poor quality that resulted in relatively high wR and R_{int} values (Table 2).

Acknowledgments

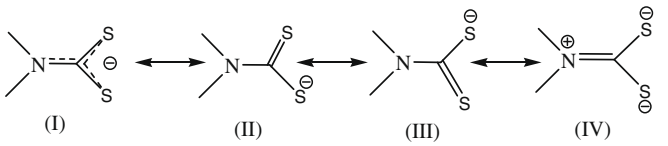
The authors gratefully acknowledge support of the RFBR (grants 09-03-00540, 09-03-90454, 08-03-90441 and 08-03-90107) and RAS (programmes 6, 7, 9 and 18).

Appendix A. Supplementary data

CCDC 716796, 716797 and 716798 contain the supplementary crystallographic data for this paper. These data can be obtained free of charge via http://www.ccdc.cam.ac.uk/conts/retrieving.html, or from the Cambridge Crystallographic Data Centre, 12 Union Road, Cambridge CB2 1EZ, UK; fax: (+44) 1223-336-033; or e-mail: deposit@ccdc.cam.ac.uk. Supplementary data associated with this article can be found, in the online version, at doi:10.1016/j.poly.2009.07.026.

References

[1] Y.Z. Voloshin, N.A. Kostromina, R. Krämer, Clathrochelates: Synthesis, Structure and Properties, Elsevier, Amsterdam, 2002.
[2] A.M. Sargeson, Coord. Chem. Rev. 151 (1996) 89.
[3] D. Burdinski, F. Birkelbach, T. Weyhermüller, U. Flörke, H.-J. Haupt, M. Lengen, A.X. Trautwein, E. Bill, K. Wieghard, P. Chaudhuri, Inorg. Chem. 37 (1998) 1009.
[4] F. Birkelbach, U. Flörke, H.-J. Haupt, C. Butzlaff, A.X. Trautwein, K. Wieghard, P. Chaudhuri, Inorg. Chem. 37 (1998) 2000.
[5] C. Königstein, A.W.-H. Mau, P. Osvath, A.M. Sargeson, Chem. Commun. (1997) 423.
[6] K.A. Anderson, S. Wherland, Inorg. Chem. 30 (1991) 624.
[7] R.Z. Billing, R. Benedix, G. Stich, H. Hennig, Z. Anorg. Allg. Chem. 583 (1990) 157.
[8] D.W. Conrad, H. Zhang, D.E. Stewart, R.A. Scott, J. Am. Chem. Soc. 114 (1992) 9909.
[9] S. Izumoto, K. Miyoshi, H. Yoneda, Bull. Chem. Soc. Jpn. 60 (1987) 3199.
[10] B. Alpha, V. Balzani, J.-M. Lehn, S. Perathoner, N. Sabbatini, Angew. Chem., Int. Ed. 26 (1987) 1266.
[11] L. De Cola, F. Barigelletti, V. Balzani, P. Belser, A. von Zelewsky, F. Vögtle, F. Ebmeyer, S. Grammenudi, J. Am. Chem. Soc. 110 (1988) 7210.
[12] Y.Z. Voloshin, O.A. Varzatskii, A.V. Palchik, A.I. Stash, V.K. Belsky, New J. Chem. 23 (1999) 355.
[13] Y.Z. Voloshin, O.A. Varzatskii, T.E. Kron, V.K. Belsky, V.E. Zavodnik, A.V. Palchik, Inorg. Chem. 39 (2000) 1907.
[14] Y.Z. Voloshin, V.E. Zavodnik, O.A. Varzatskii, V.K. Belsky, I.I. Vorontsov, M.Y. Antipin, Inorg. Chim. Acta 321 (2001) 116.
[15] Y.Z. Voloshin, V.E. Zavodnik, V.K. Belsky, A.V. Palchik, N.G. Strizhakova, I.I. Vorontsov, M.Y. Antipin, Dalton Trans. (2002) 1193.
[16] Y.Z. Voloshin, O.A. Varzatskii, T.E. Kron, V.K. Belsky, V.E. Zavodnik, N.G. Strizhakova, V.A. Nadtochenko, V.A. Smirnov, Dalton Trans. (2002) 1203.
[17] Y.Z. Voloshin, O.A. Varzatskii, A.V. Palchik, N.G. Strizhakova, I.I. Vorontsov, M.Y. Antipin, D.I. Kochubey, B.N. Novgorodov, New J. Chem. 27 (2003) 1148.
[18] A.B. Burdukov, E.G. Boguslavsky, V.A. Reznikov, N.V. Pervukhina, M.A. Vershinin, Y.Z. Voloshin, O.A. Varzatskii, Y.N. Bubnov, Russ. Chem. Bull. Int. Ed. 54 (2005) 1097.
[19] Y.Z. Voloshin, O.A. Varzatskii, A.V. Palchik, I.I. Vorontsov, M.Y. Antipin, E.G. Lebed, Inorg. Chim. Acta 358 (2005) 131.
[20] Y.Z. Voloshin, O.A. Varzatskii, A.V. Palchik, Z.A. Starikova, M.Y. Antipin, E.G. Lebed, Y.N. Bubnov, Inorg. Chim. Acta 359 (2006) 553.
[21] Y.Z. Voloshin, O.A. Varzatskii, I.I. Vorontsov, M.Y. Antipin, Angew. Chem., Int. Ed. 44 (2005) 3400.
[22] Y.Z. Voloshin, O.A. Varzatskii, K.Y. Zhizhin, N.T. Kuznetsov, Y.N. Bubnov, Russ. Chem. Bull. Int. Ed. 55 (2006) 21.
[23] Y.Z. Voloshin, O.A. Varzatskii, A.S. Belov, A.Y. Lebedev, I.S. Makarov, M.E. Gurskii, M.Y. Antipin, Z.A. Starikova, Y.N. Bubnov, Inorg. Chim. Acta 360 (2007) 1543.
[24] Y.Z. Voloshin, O.A. Varzatskii, A.S. Belov, Z.A. Starikova, K.Y. Suponitsky, V.V. Novikov, Y.N. Bubnov, Inorg. Chem. 47 (2008) 2155.
[25] Y.Z. Voloshin, O.A. Varzatskii, D.I. Kochubey, I.I. Vorontsov, Y.N. Bubnov, Inorg. Chim. Acta 362 (2009) 149.
[26] Y.Z. Voloshin, O.A. Varzatskii, Z.A. Starikova, A.S. Belov, A.V. Ignatenko, Y.N. Bubnov, Inorg. Chem. Commun. 11 (2008) 988.
[27] Y.Z. Voloshin, A.S. Belov, O.A. Varzatskii, A.V. Vologzhanina, S. Viswanathan, J. Radecki, Y.N. Bubnov, Inorg. Chim. Acta 362 (2009) 2982.
[28] S. Viswanathan, Y.Z. Voloshin, H. Radecka, J. Radecki, Electrochim. Acta (2009) doi:10.1016/j.electacta.2009.04.034.
[29] A. Mokhir, R. Krämer, Y.Z. Voloshin, O.A. Varzatskii, Bioorg. Med. Chem. Lett. 14 (2004) 2927.
[30] Y.Z. Voloshin, O.A. Varzatskii, Y.N. Bubnov, Russ. Chem. Bull. Int. Ed. 56 (2007) 555 (a review).
[31] Pat. 20050182211 (USA) A1 2005.08.18 Appl. 2004-779939 2004.02.17/S. Nagy, B.M. Tsuie.
[32] O. Pantani, S. Naskar, R. Guillot, P. Millet, E. Anxolabehere-Mallart, A. Aukauloo, Angew. Chem., Int. Ed. 47 (2008) 9948.
[33] A.B. Burdukov, N.V. Pervukhina, M.A. Vershinin, Y.Z. Voloshin, Rus. J. Struct. Chem. 48 (2007) 366.
[34] Y.Z. Voloshin, E.V. Polshin, A.Y. Nazarenko, Hyperfine Interact 141–142 (2002) 309.
[35] BRUKER. APEX2 software package, BRUKER AXS Inc., 5465, East Cheryl Parkway, Madison, WI 5317, 2005.
[36] G.M. Sheldrick, SADABS v.2.01, Bruker/Siemens Area Detector Absorption Correction Program, Bruker AXS, Madison, Wisconsin, USA, 1998.
[37] G.M. Sheldrick, Acta Crystallogr., Sect. A 64 (2008) 112.
[38] A.L. Spek, J. Appl. Cryst. 36 (2003) 7.



Scheme 1. Resonant forms of the $-NCSS^-$ moiety.

using a Bio-Rad Excaliber FT-IR, model FTS 300 MX spectrometer (USA). Raman spectra (±1 cm^{-1}) were measured with an InVia Renishaw spectrometer, using argon-ion (514.5 nm) and near-infrared diode (785 nm) lasers. WIRE 2.0 software was used for the data acquisition and spectra manipulations. The ^1H and ^{13}C NMR spectra were obtained by a Hg-300 MHz spectrometer and the ^{119}Sn NMR spectra were recorded on a Varian Unity 500-MHz instrument using Me_4Sn as external reference.

2.2. Syntheses

2.2.1. Synthesis of 4-benzylpiperidinium 4-benzylpiperidine-1-carbodithioate (L-salt)

Carbon disulfide (in excess) in methanol (50 mL) was added dropwise to 4-benzylpiperidine (5 g, 28.57 mmol) in methanol (50 mL) and the mixture was stirred for 4 h at 273 K. The solvent was evaporated under reduce pressure to yield a white product, which was recrystallized from methanol. (Yield: 4.68 g, 77%). M.p. 132–134 °C. *Anal.* Calc. for $C_{25}H_{34}N_2S_2$ (426.7): C, 70.37; H, 8.03; N, 6.57; S, 15.03. Found: C, 70.22; H, 7.97; N, 6.61; S, 14.91%. Raman (cm^{-1}): 644 ν(C–S), 1075 ν(C=S), 1455 ν(C–N). IR (cm^{-1}): 1017 ν(C–S), 1453 ν(C–N). ^1H NMR (ppm): 3.04–2.96, 2.60–2.58, 2.82–2.67, 2.60–2.58, 1.84–1.64, 1.35–1.27 (m, 18H, piperidine-H), 5.77, 3.79 (d, 4H, CH_2), 7.34–7.14 (m, 10H, Ar–H), 8.3 (s, 2H, NH_2). ^{13}C NMR (ppm): 208.8 (C-1), 51.2, 44.7, 38.2, 36.5, 32.4, 29.7, (piperidine-C), 42.9, 42.8 (CH_2), 140.1, 139.4, 129.1, 129.0, 128.4, 128.3, 126.3, 126.0 (Ar–C).

2.2.2. General procedure for synthesis of complexes

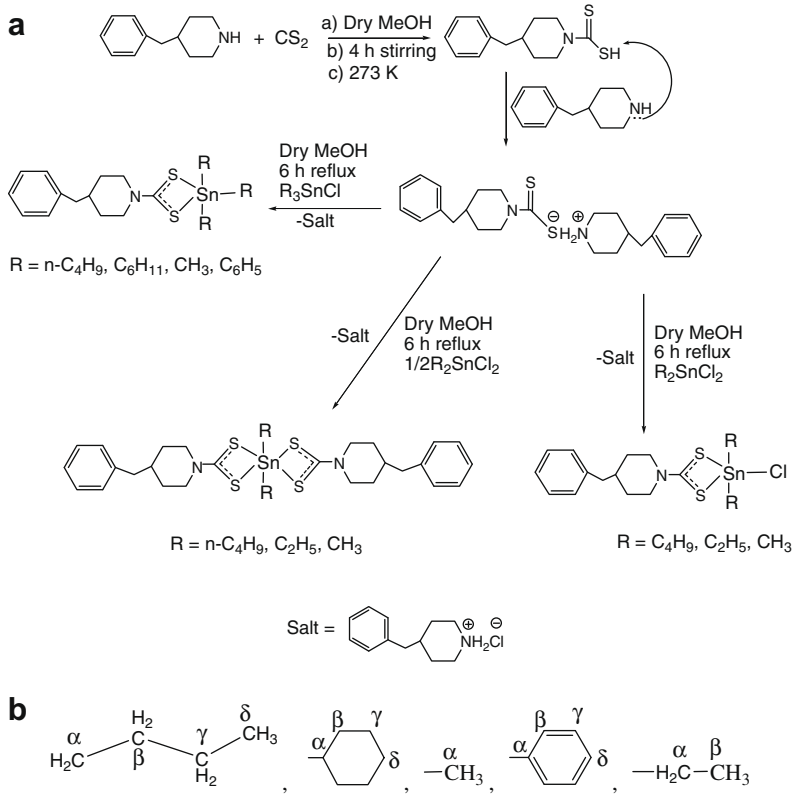
Triorganotin(IV) chloride and diorganotin(IV) dichloride in methanol (30 mL) was added dropwise to the ligand-salt in methanol (50 mL) in the appropriate molar ratio and the mixture was refluxed for 6 h with constant stirring. The salt was allowed to settle and was removed by filtration. The filtrate was rotary evaporated and the product thus obtained was recrystallized from chloroform–ethanol (4:1) mixture (Scheme 2a).

2.2.3. Tributyltin(IV) 4-benzylpiperidine-1-carbodithioate **(1)**

(Yield: 0.46 g, 74%). Sticky material. *Anal.* Calc. for $C_{25}H_{43}NS_2Sn$ (540.5): C, 55.56; H, 8.02; N, 2.59; S, 11.87. Found: C, 55.49; H, 7.93; N, 2.56; S, 11.81%. Raman (cm^{-1}): 587 ν(C–S), 1030 ν(C=S), 1440 ν(C–N), 504 ν(Sn–C), 380 ν(Sn–S). IR (cm^{-1}): 965 ν(C–S), 1467 ν(C–N). ^1H NMR (ppm): 1.38–1.28, 3.08–3.04, 1.85–1.78 (m, 9H, piperidine-H) 5.19 (d, $^3J_{H-H}$ = 12.9 Hz, 2H, CH_2), 7.33–7.12 (m, 5H, Ar–H), 1.65–1.20 (m, 18H, $H_{\alpha,\beta,\gamma}$, SnBu), 0.93 (t, $^3J_{H-H}$ = 7.3 Hz, 9H, H_δ, SnBu). ^{13}C NMR (ppm), [^nJ(^{119}Sn, ^{13}C), Hz]: 197.2 (CS), 36.5, 42.6, 52.4 (piperidine-C), 31.9 (CH_2), 139.8, 129.1, 128.5, 126.3 (Ar–C), 17.5 {(C-α, SnBu), [341]}, 29.1 {(C-β, SnBu), [18]} 27.8 {(C-γ, SnBu), [68]}, 13.7 (C-δ, SnBu). ^{119}Sn NMR: δ −129.6.

2.2.4. Tricyclohexyltin(IV) 4-benzylpiperidine-1-carbodithioate **(2)**

(Yield: 0.51 g, 70%). M.p. 122–124 °C. *Anal.* Calc. for $C_{31}H_{49}NS_2Sn$ (618.6): C, 60.19; H, 7.98; N, 2.26; S, 10.37. Found: C, 60.07; H, 7.90; N, 2.23; S, 10.30%. Raman (cm^{-1}): 547 ν(C–S), 1077 ν(C=S), 1472 ν(C–N), 645 ν(Sn–C), 370 ν(Sn–S). IR (cm^{-1}): 963 ν(C–S), 1460 ν(C–N). ^1H NMR (ppm): 1.34–1.29, 1.82–1.75, 3.07–2.99 (m, 9H, piperidine-H) 5.19 (d, $^3J_{H-H}$ = 13.2 Hz, 2H, CH_2), 7.30–7.11 (m, 5H, Ar–H), 1.96–1.24 (m, 33H, $H_{\alpha,\beta,\gamma,\delta}$, SnC_6H_{11}). ^{13}C NMR (ppm), [^nJ(^{119}Sn, ^{13}C), Hz]: 198.7 (CS), 37.7, 42.8, 52.8 (piperidine-



Scheme 2. (a) Synthesis of ligand-salt and complexes and (b) numbering scheme of organic groups attached to Sn atom.

C), 31.7 (CH_2), 140.1, 129.3, 128.5, 126.3 (Ar–C), 35.0 {(C-α, SnC_6H_{11}), [334]}, 32.2 {(C-β, SnC_6H_{11}), [16]} 29.5 {(C-γ, SnC_6H_{11}), [67]}, 27.2 (C-δ, SnC_6H_{11}). ^{119}Sn NMR: δ 82.3.

2.2.5. Trimethyltin(IV) 4-benzylpiperidine-1-carbodithioate ***(3)***

(Yield: 0.34 g, 71%). M.p. 133–134 °C. *Anal.* Calc. for $C_{16}H_{25}NS_2Sn$ (414.2): C, 46.39; H, 6.08; N, 3.38; S, 15.48. Found: C, 46.33; H, 6.03; N, 3.35; S, 15.39%. Raman (cm^{-1}): 618 ν(C–S), 1030 ν(C=S), 1474 ν(C–N), 521 ν(Sn–C), 361 ν(Sn–S). IR (cm^{-1}): 970 ν(C–S), 1457 ν(C–N). ^{1}H NMR (ppm), [^2J(^{119}Sn, ^{1}H), Hz]: 1.39–1.27, 1.82–1.75, 3.07–3.03 (m, 9H, piperidine-H) 5.07 (d, $^3J_{H-H}$ = 12.6 Hz, 2H, CH_2), 7.34–7.14 (m, 5H, Ar–H), 1.56 {(s, 9H, $H_α$, $SnCH_3$), [57]}.^{13}C NMR (ppm), [^nJ(^{119}Sn, ^{13}C), Hz]: 201.1 (CS), 36.5, 42.5, 51.8 (piperidine-C), 31.8 (CH_2), 126.2, 128.4, 129.1, 139.7 (Ar–C), 15.0 {(C-α, $SnCH_3$), [391]}. ^{119}Sn NMR: δ −49.8.

2.2.6. Triphenyltin(IV) 4-benzylpiperidine-1-carbodithioate ***(4)***

(Yield: 0.55 g, 79%). M.p. 138–139 °C. *Anal.* Calc. for $C_{31}H_{31}NS_2Sn$ (600.4): C, 62.01; H, 5.20; N, 2.33; S, 10.68. Found: C, 61.92; H, 5.17; N, 2.31; S, 10.62%. Raman (cm^{-1}): 617 ν(C–S), 1019 ν(C=S), 1488 ν(C–N), 264 ν(Sn–C), 370 ν(Sn–S). IR (cm^{-1}): 988 ν(C–S), 1470 ν(C–N). ^{1}H NMR (ppm): 1.37–1.33, 1.91–1.79, 3.29–3.21 (m, 9H, piperidine-H) 4.89 (d, $^3J_{H-H}$ = 12.3 Hz, 2H, CH_2), 7.32–7.17 (m, 5H, Ar–H), 7.71–7.41 (m, 15H, $H_{β, γ, δ}$, SnC_6H_5). ^{13}C NMR (ppm): 193.3 (CS), 36.6, 41.8, 53.2 (piperidine-C), 31.6 (CH_2), 125.9, 128.5, 129.0, 140.1 (Ar–C), 142.9 (C-α, SnC_6H_5), 136.4 (C-β, SnC_6H_5), 128.9 (C-γ, SnC_6H_5), 129.1 (C-δ, SnC_6H_5). ^{119}Sn NMR: δ −182.2.

2.2.7. Chlorodibutyltin(IV) 4-benzylpiperidine-1-carbodithioate ***(5)***

(Yield: 0.47 g, 77%). Sticky material. *Anal.* Calc. for $C_{21}H_{34}NS_2SnCl$ (518.8): C, 48.62; H, 6.61; N, 2.70; S, 12.36. Found: C, 48.53; H, 6.54; N, 2.67; S, 12.30%. Raman (cm^{-1}): 619 ν(C–S), 1031 ν(C=S), 1445 ν(C–N), 581 ν(Sn–C), 345 ν(Sn–S), 255 ν(Sn–Cl). IR (cm^{-1}): 968 ν(C–S), 1475 ν(C–N). ^{1}H NMR (ppm): 1.37–1.27, 1.86–1.78, 3.11–3.03 (m, 9H, piperidine-H) 4.72 (d, $^3J_{H-H}$ = 12.9 Hz, 2H, CH_2), 7.31–7.09 (m, 5H, Ar–H), 1.99–1.31 (m, 12H, $H_{α, β, γ}$, SnBu), 0.93 (t, $^3J_{H-H}$ = 6.9 Hz, 6H, $H_δ$, SnBu). ^{13}C NMR (ppm), [^nJ(^{119}Sn, ^{13}C), Hz]: 195.6 (CS), 36.4, 42.5, 52.7 (piperidine-C), 31.9 (CH_2), 139.2, 129.2, 127.5,126.6 (Ar–C), 26.5 {(C-α, SnBu), [590]}, 36.4 {(C-β, SnBu), [18]}, 28.7 {(C-γ, SnBu), [67]}, 13.9 (C-δ, SnBu). ^{119}Sn NMR: δ −175.0.

2.2.8. Dibutyltin(IV) bis[4-benzylpiperidine-1-carbodithioate] ***(6)***

(Yield: 0.33 g, 76%). M.p. 141–142 °C. *Anal.* Calc. for $C_{34}H_{50}N_2S_4Sn$ (733.7): C, 55.65; H, 6.87; N, 3.82; S, 17.48. Found: C, 55.56; H, 6.80; N, 3.78; S, 17.41%. Raman (cm^{-1}): 587 ν(C–S), 1028 ν(C=S), 1473 ν(C–N), 503 ν(Sn–C), 334 ν(Sn–S). IR (cm^{-1}): 969 ν(C–S), 1465 ν(C–N). ^{1}H NMR (ppm): 1.40–1.30, 1.86–1.78, 3.42–3.37 (m, 9H, piperidine-H) 4.89 (d, $^3J_{H-H}$ = 12.3 Hz, 2H, CH_2), 7.28–7.09 (m, 5H, Ar–H), 1.85–1.33 (m, 12H, $H_{α, β, γ}$, SnBu), 0.93 (t, $^3J_{H-H}$ = 7.2 Hz, 6H, $H_δ$, SnBu). ^{13}C NMR (ppm), [^nJ(^{119}Sn, ^{13}C), Hz]: 190.6 (CS), 36.7, 42.5, 52.5 (piperidine-C), 31.9 (CH_2), 139.4, 128.7, 127.5, 126.5 (Ar–C), 26.5 {(C-α, SnBu), [601]}, 36.7 {(C-β, SnBu), [19]}, 29.3 {(C-γ, SnBu), [68]}, 13.9 (C-δ, SnBu). ^{119}Sn NMR: δ −201.1.

2.2.9. Chlorodiethyltin(IV) 4-benzylpiperidine-1-carbodithioate ***(7)***

(Yield: 0.43 g, 79%). M.p. 125–126 °C. *Anal.* Calc. for $C_{17}H_{26}NS_2SnCl$ (462.7): C, 44.13; H, 5.66; N, 3.03; S, 13.86. Found: C, 44.05; H, 5.59; N, 3.00; S, 13.79%. Raman (cm^{-1}): 620 ν(C–S), 1031 ν(C=S), 1446 ν(C–N), 476 ν(Sn–C), 370 ν(Sn–S), 271 ν(Sn–Cl). IR (cm^{-1}): 963 ν(C–S), 1463 ν(C–N). ^{1}H NMR (ppm): 1.32–1.19, 1.82–1.75, 3.11–3.02 (m, 9H, piperidine-H) 4.72 (d, $^3J_{H-H}$ = 13.2 Hz, 2H, CH_2), 7.30–7.08 (m, 5H, Ar–H), 1.81 {(q, $^3J_{H-H}$ = 7.5 Hz, 4H, $H_α$, SnEt), 1.46 {(t, $^3J_{H-H}$ = 7.5 Hz, 6H, $H_β$, SnEt) .^{13}C NMR (ppm), [^nJ(^{119}Sn, ^{13}C), Hz]: 195.5 (CS), 36.4, 42.5, 51.7 (piperidine-C), 31.9 (CH_2), 126.6, 128.7, 129.2, 139.1 (Ar–C), 21.3 {(C-α, SnEt), [534]}, 10.4 (C-β, SnEt). ^{119}Sn NMR: δ −180.2.

2.2.10. Diethyltin(IV) bis[4-benzylpiperidine-1-carbodithioate] ***(8)***

(Yield: 0.29 g, 74%). Sticky material. *Anal.* Calc. for $C_{30}H_{42}N_2S_4Sn$ (677.6): C, 53.17; H, 6.25; N, 4.13; S, 18.93. Found: C, 53.03; H, 6.11; N, 4.10; S, 18.85%. Raman (cm^{-1}): 619 ν(C–S), 1028 ν(C=S), 1455 ν(C–N), 493 ν(Sn–C), 372 ν(Sn–S). IR (cm^{-1}): 961 ν(C–S), 1459 ν(C–N). ^{1}H NMR (ppm): 1.32–1.19, 1.82–1.75, 3.11–3.02 (m, 9H, piperidine-H) 4.74 (d, $^3J_{H-H}$ = 13.2 Hz, 2H, CH_2), 7.28–7.08 (m, 5H, Ar–H), 1.81 {(q, $^3J_{H-H}$ = 7.5 Hz, 4H, $H_α$, SnEt), 1.43 {(t, $^3J_{H-H}$ = 7.5 Hz, 6H, $H_β$, SnEt) .^{13}C NMR (ppm), [^nJ(^{119}Sn, ^{13}C), Hz]: 191.6 (CS), 36.6, 42.6, 52.6 (piperidine-C), 31.9 (CH_2), 126.6, 128.7, 129.2, 139.3 (Ar–C), 29.3 {(C-α, SnEt), [578]}, 10.5 (C-β, SnEt). ^{119}Sn NMR: δ −184.6.

2.2.11. Chlorodimethyltin(IV) 4-benzylpiperidine-1-carbodithioate ***(9)***

(Yield: 0.39 g, 77%). M.p. 161–163 °C. *Anal.* Calc. for $C_{15}H_{22}NS_2SnCl$ (434.6): C, 41.45; H, 5.10; N, 3.22; S, 14.75. Found: C, 41.35; H, 5.04; N, 3.19; S, 14.69%. Raman (cm^{-1}): 621 ν(C–S), 1024 ν(C=S), 1500 ν(C–N), 514 ν(Sn–C), 368 ν(Sn–S), 249 ν(Sn–Cl). IR (cm^{-1}): 961 ν(C–S), 1459 ν(C–N). ^{1}H NMR (ppm), [^2J(^{119}Sn, ^{1}H), Hz]: 1.39–1.36, 1.82–1.78, 3.10–3.02 (m, 9H, piperidine-H) 4.66 (d, $^3J_{H-H}$ = 13.2 Hz, 2H, CH_2), 7.30–7.10 (m, 5H, Ar–H), 1.36 {(s, 6H, SnMe), [82]}. ^{13}C NMR (ppm), [^nJ(^{119}Sn, ^{13}C), Hz]: 194.9 (CS), 36.9, 42.4, 52.7 (piperidine-C), 31.8 (CH_2), 126.6, 128.7, 129.2, 139.5 (Ar–C), 10.2 (C-α, SnMe), [571]}. ^{119}Sn NMR: δ −201.2.

2.2.12. Dimethyltin(IV) bis[4-benzylpiperidine-1-carbodithioate] ***(10)***

(Yield: 0.30 g, 80%). M.p. 180–184 °C. *Anal.* Calc. for $C_{28}H_{38}N_2S_4Sn$ (649.6): C, 51.77; H, 5.90; N, 4.31; S, 19.74. C, 51.67; H, 5.82; N, 4.28; S, 19.66%. Raman (cm^{-1}): 622 ν(C–S), 1030 ν(C=S), 1474 ν(C–N), 511 ν(Sn–C), 364 ν(Sn–S). IR (cm^{-1}): 971 ν (C–S), 1451 ν(C–N). ^{1}H NMR (ppm), [^2J(^{119}Sn, ^{1}H), Hz]: 1.39–1.28, 1.80–1.78, 3.04–2.95 (m, 9H, piperidine-H) 4.66 (d, $^3J_{H-H}$ = 13.2 Hz, 2H, CH_2), 7.30–7.10 (m, 5H, Ar–H), 1.36 {(s, 6H, SnMe), [90]}. ^{13}C NMR (ppm): 195.1 (CS), 36.9, 42.1, 52.7 (piperidine-C), 31.6 (CH_2), 126.6, 128.7, 129.2, 139.3 (Ar–C), 10.5 (C-α, SnMe). ^{119}Sn NMR: δ −337.0.

2.3. X-ray crystallographic studies

A crystal fragment, cut to size to fit in the homogeneous part of the X-ray beam, was mounted on top of a glass fiber and aligned on a Bruker SMART APEX CCD diffractometer (platform with full three-circle goniometer). The crystal was cooled to 100(1) K using the Bruker KRYOFLEX low-temperature device. Intensity measurements were performed using graphite monochromatized Mo Kα radiation from a sealed ceramic diffraction tube (SIEMENS). X-ray diffraction data were collected on a Bruker SMART APEX CCD diffractometer which was equipped with a 4 K CCD detector set 60.0 mm from the crystal. Data integration and global cell refinement was performed with the program SAINT. The program suite SAINTPLUS was used for space group determination (XPREP). The structure was solved by Patterson method; extension of the model was accomplished by direct methods and applied to different structure factors using the program DIRDIF. All refinement calculations and graphics were performed with the program PLUTO and PLATON package.

3. Results and discussion

3.1. Syntheses of ligand-salt and complexes 1–10

The new organotin(IV) 4-benzylpiperidine-1-carbodithioate complexes were prepared by the reaction of the ligand-salt (L-salt)

with the selected triorganotin(IV) chlorides and diorganotin(IV) dichlorides in the appropriate mole ratio in dry methanol (Scheme 2a). The numbering system for the organic groups attached to Sn is given in scheme 2b. The compounds **1**–**10** are quite stable in moist-air and are soluble in common organic solvents.

3.2. Vibrational spectra

The assignment of the Raman bands of the complexes has been made by comparison with the Raman spectra of their related precursors. In the complexes, the appearance of a new peak in the region 334–380 cm^{-1} owing to a Sn–S vibration indicated the formation of complexes. In addition, all the complexes displayed a sharp Sn–C peak in the range 476–645 cm^{-1}, except for the triphenyltin(IV) derivative where a weak vibration appeared at 263 cm^{-1} due to Sn–C stretching. A peak associated with ν(Sn–Cl) was observed in the chlorodiorganotin(IV) derivatives only, which indicates the substitution of one chloride in the diorganotin salt during the reaction.

With respect to the dithiocarboxylate moiety, two main regions of the IR are of particular interest. First, the 1450–1580 cm^{-1} region, which is primarily associated with the 'thioureide' band due to the ν(N–CSS) vibration; second, the 940–1060 cm^{-1} region, which is associated with ν(C–S) stretching. The stretching vibration peak due to ν(N–CSS), in the complexes studied here were located in the range 1457–1475 cm^{-1}. These values lie between the range reported for C–N single bond (1250–1360 cm^{-1}) and C=N double bond (1640–1690 cm^{-1}), and is an indication of partial double bond character in C–N bond [13]. The presence of a band in the above-mentioned range for ν(N–CSS) is due to the four possible resonance structures (Scheme 1). On passing from the ligand-salt to the complexes, the ν(N–CSS) mode is shifted to higher energies, showing an increase of C–N double bond character [14]. Regarding the chlorodiorganotin(IV) derivatives, the ν(N–CSS) band is shifted to higher energy as compared to diorganotin(IV) complexes owing to the presence of electron-withdrawing effect of chloride in the complexes, thus promoting a higher positive charge on nitrogen atom. A single band for C–S in the region of 900–1060 cm^{-1}, in complexes, is in accord with bidentate bonding of 1,1-dithiolate moiety with Sn [15].

3.3. NMR spectra

The ^{1}H NMR spectra were recorded for the compounds **1**–**10** in DMSO-d_6. The characteristic chemical shifts were identified by their intensity and multiplicity patterns. The total number of protons, calculated from the integration curves, is in agreement with the expected molecular composition of the compounds. For the ligand, the piperidine protons demonstrate three triplets (1.78–1.85, 1.27–1.39 and 3.04–3.08 ppm) in the aliphatic region as expected for the structure. The protons of the benzyl part resonate in two regions; a doublet (~5.07 ppm) due to CH_2 protons and a multiplet (7.12–7.33 ppm) because of phenyl moiety. The proton chemical shifts assignment of the organic groups attached to Sn exhibited a singlet at ~1.53 ppm for compounds **3**, **9** and **10** and appeared as multiplets in the aliphatic region in case of compounds **1**, **2**, **5** and **6**. The protons of the ethyltin(IV) derivatives appeared as a quartet and a triplet as expected, while the aromatic protons of the triphenyltin(IV) complex resonate as multiplets in the range 7.42–7.71 ppm. The ^2J [^{119}Sn, ^{1}H] coupling constant value for complex **3** was 57 Hz, in the range normally expected for four-coordinate Sn and consistent with CSnC angle of 110.9° while the angle calculated (Table 1) from ^2J [^{119}Sn, ^{1}H] coupling constant certify the 5- and six-coordinate environment around Sn for compounds **9** and **10**, respectively [16]. However, the coupling constants, ^2J [^{119}Sn, ^{1}H] for *n*-butyl-, cyclohexyl-, ethyl- and triphenyltin(IV) derivatives could not be calculated due to their complex peak pattern. In case of compound **4**, the difference in chemical shift resonances of *ortho* to *meta* and *para* protons (0.3 ppm) is an indication of anisobidentate bonding of 1,1-dithiolate moiety in solution [17].

The ^{13}C NMR chemical shifts due to organic groups, attached to Sn atom, were observed at positions comparable to the other similar compounds [18]. The disappearance of duplicate peak pattern and a small shift in the position of CS carbon confirmed the coordination of ligand to the Sn center via CSS moiety. In organotin compounds, the ^1J(^{119}Sn, ^{13}C) coupling constant can be used to assess the coordination number of the Sn atom. The coupling constants were calculated and found to be in the order of 341 Hz for tributhyltin **1**, 334 Hz for tricyclohexyltin **2** and 391 Hz for trimethyltin **3** compounds which are the typical values for tetrahedral compounds [19] as given in Table 1. A characteristic feature for triphenyltin derivative is the observance of ^{13}C chemical shift of the *ipso*-carbon at about 142.9 ppm which is attributed to a five-coordinated Sn atom [20]. The calculated value of the ^1J(^{119}Sn, ^{13}C) coupling constant for **5**, **6**, **7**, **8** and **9** are 590, 601, 534, 578 and 571 Hz, respectively which described the penta-coordinated environment about the Sn atom in these compounds.

The ^{119}Sn chemical shift values obtained for triorganotin(IV) complexes lie in the range expected for tetrahedral geometry, except for the Ph_3Sn(IV) complex which gave a ^{119}Sn peak corresponding to a five-coordinated Sn atom. The ^{119}Sn NMR data for the chlorodi- and diorganotin(IV) compounds are in conformity with five coordination around the Sn atom. Among the diorganotin(IV) derivatives, only complex **10** furnished a ^{119}Sn peak associated with the octahedral geometry in solution [21].

3.4. X-ray structures

3.4.1. Crystal structures of compound *2*, *4*, *6* and *9*

An ORTEP view of compound **2** together with atomic numbering scheme is depicted in Fig. 1. Pertinent crystallographic parameters, relevant bond lengths and bond angles are given in Tables 2 and 3. The Sn atom is five-coordinate, being chelated by asymmetrically coordinating 4-benzylpiperidine-1-carbodithioate ligand and three cyclohexyl substituents. The Sn–S1 [3.160 Å] bond distance approximately *trans*- to the C26 is longer than the other Sn–S2 [2.4756(9) Å] bond distance. According to Addison et al., the geometry around the Sn atom can be characterized by the value of $\tau = (\beta - \alpha)/60$ [22], where β is the largest of the basal angles around the Sn atom. The angle $\alpha = \beta = 180°$ correspond to a square-pyramidal geometry, and the value of $\alpha = 120°$ corresponds to perfectly trigonal-bipyramidal geometry. Thus, the τ value is equal to zero for a perfect square-pyramidal and unity for a perfect trigonal-bipyramidal. For compound **2**, β is S1–Sn–C26 = 157.39°. The second largest of the basal angles around the Sn atom, α for compound **2** is S2–Sn–C20 = 116.84(8)°. The calculated τ value for the **2** is 0.67, and is an indicative of highly distorted trigonal-bipyramidal

Table 1
(C–Sn–C) angles (°) based on NMR parameters of selected compounds.

Compound Number	^1J(^{119}Sn, ^{13}C) (Hz)	^2J(^{119}Sn, ^{1}H) (Hz)	Angle (°)	
			^1J	^2J
1	341		106.6	
2	334		106.0	
3	391	57	111.0	110.9
5	590		128.5	
6	601		129.5	
7	534		123.6	
8	578		127.4	
9	571	82	126.8	127.5
10		90		135.5

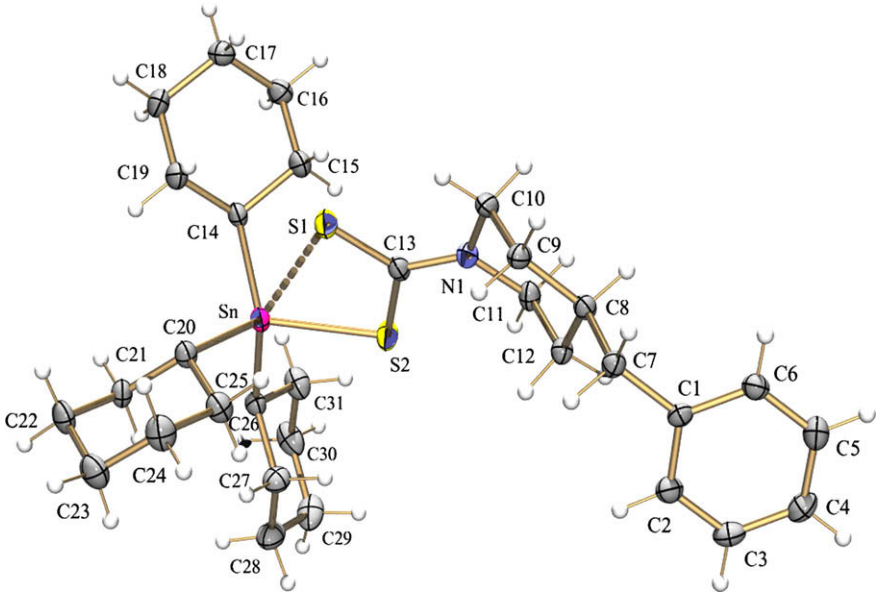


Fig. 1. ORTEP drawing of compound **2** with atomic numbering scheme.

Table 2
Crystal data and structure refinement parameters for compounds **2**, **4**, **6** and **9**.

	2	**4**	**6**	**9**
Empirical formula	$C_{31}H_{46}NS_2Sn$	$C_{31}H_{31}NS_2Sn$	$C_{34}H_{50}N_2S_4Sn$	$C_{15}H_{22}NS_2SnCl$
Formula mass	615.55	600.38	733.75	434.64
Crystal system	triclinic	triclinic	triclinic	monoclinic
Space group	$P\bar{1}$	$P\bar{1}$	$P\bar{1}$	$P2_1$
a (Å)	10.5063(10)	9.2531(8)	9.7767(13)	13.2495(12)
b (Å)	10.6281(10)	10.7273(9)	10.9801(15)	9.7868(9)
c (Å)	15.0438(15)	14.4044(12)	17.105(2)	13.6949(12)
α (°)	109.3918(12)	95.313(10)	89.8273(19)	
β (°)	103.1745(12)	101.880(10)	79.0265(18)	90.7045(11)
γ (°)	92.5424(13)	94.328(10)	80.4534(19)	
V (Å^3)	1529.6(3)	1386.6(2)	1776.9(4)	1775.7(3)
Z	2	2	2	4
Crystal size (mm)	0.44 × 0.37 × 0.17	0.50 × 0.45 × 0.40	0.25 × 0.35 × 0.47	0.55 × 0.50 × 0.42
Total reflections	13801	10780	20874	14351
Independent reflections				
All	7234	4936	10225	8608
For $F_o \geqslant 4.0\sigma(F_o)$	6477		7585	8251
$R(F) = \sum(\|\|F_o\| - \|F_c\|\|)/\sum\|F_o\|$ for $F_o > 4.0\sigma(F_o)$	0.0401	0.0299	0.0528	0.0302
$wR(F^2) = [\sum[w(F_o^2 - F_c^2)^2]/\sum[w(F_o^2)^2]]^{1/2}$	0.1180		0.1302	0.0780
R indices (all data)		$R_1 = 0.0278$, $wR_2 = 0.0750$		
Final R indices [$I > 2\sigma(I)$]		$R_1 = 0.0228$, $wR_2 = 0.0530$		
Goodness-of-fit (GOF)	1.037	1.197	1.034	1.026
θ range for data collections (°)	2.68–28.28	2.41–25.93	2.51–25.68	2.56–28.28
Data/restraints/parameters	7234/0/316	4936/0/316	10225/0/581	8608/0/365

Table 3
Selected bond lengths (Å) and bond angles (°) for compound **2**.

Sn–S2	2.4756(9)	Sn–C14	2.170(3)
Sn–C20	2.181(3)	Sn–C26	2.184(3)
S1–C13	1.691(3)	S2–C13	1.768(3)
Sn–S1	3.160		
S2–Sn–C14	112.09(8)	S1–Sn–C14	86.33
S2–Sn–C20	116.84(8)	S1–Sn–C20	80.78
S2–Sn–C26	95.35(8)	S1–Sn–C26	157.39
C14–Sn–C20	115.11(12)	S1–Sn–S2	62.80
C14–Sn–C26	108.77(11)	Sn–S2–C13	98.97(1)
C20–Sn–C26	106.30(12)	Sn–S1–C13	78.00
Sn–C14–C15	114.36(19)	Sn–C14–C19	109.9(2)
Sn–C20–C21	109.4(2)	Sn–C20–C25	113.4(2)
Sn–C26–C27	112.2(2)	Sn–C26–C31	112.4(2)

geometry. The C26 atom occupies one of the apical positions of the trigonal-bipyramid with the C26–Sn–S2 angle of 95.35(8)°. The quasi-axial S1 atom cannot occupy exactly the position *trans* to C26 and C26–Sn–S1 angle is 157.39°. Thus, ligand chelates the Sn atom via its two sulfur atoms in anisobidentate fashion, forming a four-membered ring with S1–Sn–S2 bond angle of 62.80°. The S–C bond lengths [S1–C13 = 1.691(3) Å and S2–C13 = 1.768(3) Å] also demonstrate the asymmetric nature of the ligand. The packing diagram confirmed trimeric structure for compound **2**, formed as the result of intermolecular H···H interactions (Fig. 2).

The molecular structure of compound **4** is shown in Fig. 3, while crystal data and selected bond lengths and bond angles are given in Tables 2 and 4, respectively. The geometry around Sn is almost a midway between square-pyramidal and trigonal-bipyramidal as evident from the τ value (0.66). The value indicates a highly

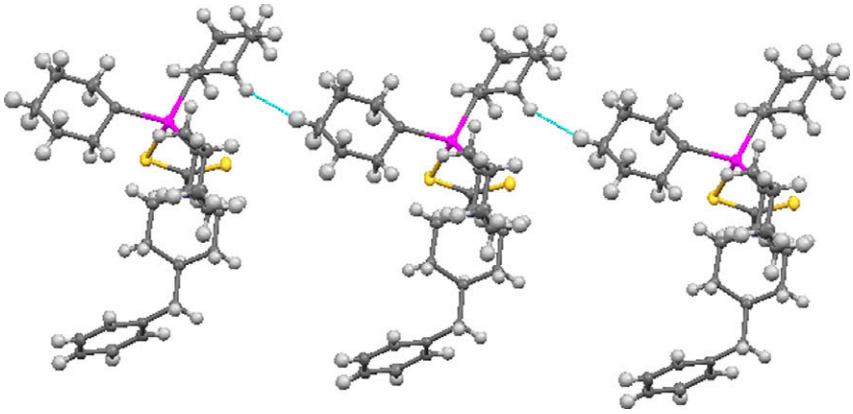


Fig. 2. Loosely associated trimer in compound **2**, connected through weak intermolecular cyclohexyl H···H interactions.

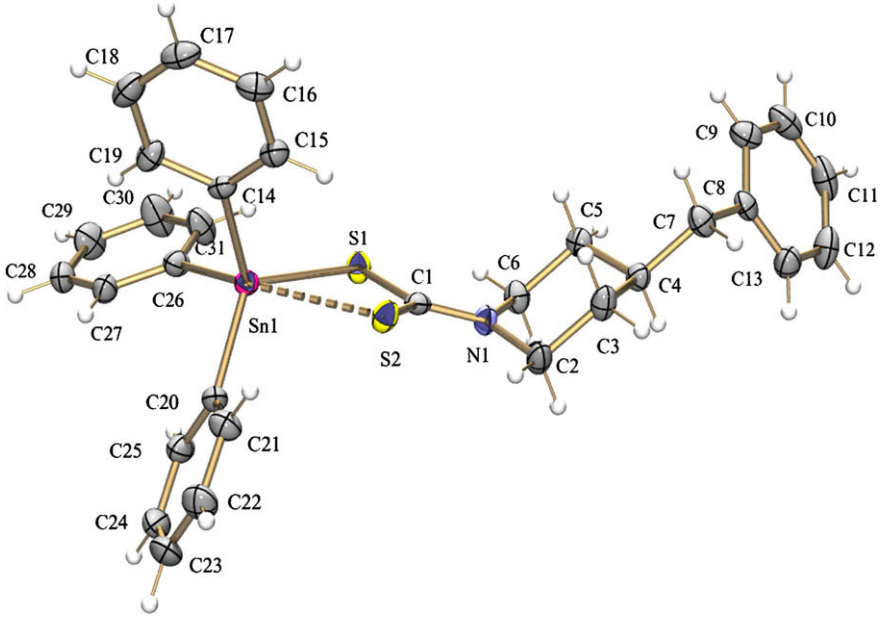


Fig. 3. ORTEP drawing of compound **4** with atomic numbering scheme.

distorted trigonal-bipyramidal arrangement around the Sn1 atom with C26 from a phenyl group and the S2 from the dithiocarboxylate ligand at the axial positions while C14 and C20 from two phenyl groups and S1 in the plane positions. The sum of the equatorial angles is 350° instead of the ideal value of 360°. Being a part of chelate, the angle S2–Sn1–S1 is not 90° but only 65.70°, so the S2 cannot occupy exactly the corresponding *trans* apical position of C26 and the angle between the apical groups is 158.88°. Finally, the C–S bond lengths are characteristic of the 1,1-dithiolate moiety and are intermediate between the values expected for single and double bonds [23]. The packing diagram indicated π···H interactions that gave rise to a dimeric structure (Fig. 4).

Table 4
Selected bond lengths (Å) and bond angles (°) for compound (**4**).

S1–Sn1	2.4892(8)	Sn1–S2	2.935
C14–Sn1	2.144(3)	C20–Sn1	2.156(3)
C26–Sn1	2.173(3)	C1–S2	1.696(3)
C1–S1	1.758(3)		
C14–Sn1–S1			
	115.38(8)	C20–Sn1–S1	119.21(9)
C26–Sn1–S1	93.88(9)	C14–Sn1–S2	89.50
C20–Sn1–S2	83.72	C26–Sn1–S2	158.88
C14–Sn1–C20			
	115.43(11)	C14–Sn1–C26	104.96(11)
C20–Sn1–C26	103.11(11)	C1–S1–Sn1	94.00(10)
C1–S2–Sn1	80.75	S2–C1–S1	118.35(18)
S1–Sn–S2	65.70		

Crystal data and selected interatomic parameters for compound **6** are collected in Tables 2 and 5, respectively. An ORTEP view of the molecule including numbering scheme is shown in Fig. 5. The Sn atom in **6** is coordinated by two butyl groups and two 4-benzylpiperidine-1-carbodithioate ligands, with the latter adopting different asymmetric coordination modes. The first dithiocarboxylate ligand is chelating but forms asymmetric Sn–S bond distances of 2.5315(14) Å and 2.9574(15) Å, respectively, while for the second ligand, Sn–S bond lengths are 2.5470(14) Å and 2.8970 (16) Å. The weaker Sn–S distances are well within the sum of the van der Waals radii for the Sn and S atoms (4.0 Å). The overall geometry at Sn is, however, highly distorted from the *trans* octahedral: the C27–Sn–C31 angle is only 137.3(2)° which is intermediate between *cis* and *trans*, the Sn and the four S atoms of the ligands are nearly coplanar but distorted from square-planar geometry, so that the *cis* S2-Sn–S4 angle is only 83.89(4)° and the *cis* S1-

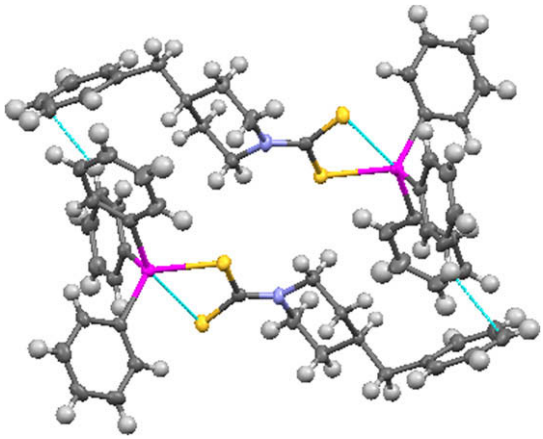


Fig. 4. Loosely associated dimer in compound **4**, connected through weak intermolecular π···H interactions.

Table 5
Selected bond lengths (Å) and bond angles (°) for compound (**6**).

Sn–S1	2.9574(15)	Sn–S2	2.5315(14)
Sn–S3	2.8970(16)	Sn–S4	2.5470(14)
Sn–C27	2.141(7)	Sn–C31	2.135(5)
S1–C13	1.701(5)	S2–C13	1.743(5)
S3–C26	1.695(6)	S4–C26	1.731(5)
S1–Sn–S2	64.95(4)	S1–Sn–S3	145.29(4)
S1–Sn–S4	148.84(4)	S1–Sn–C27	84.57(18)
S1–Sn–C31	84.61(14)	S2–Sn–S3	149.76(5)
S2–Sn–S4	83.89(4)	S2–Sn–C27	107.05(18)
S2–Sn–C31	105.35(15)	S3–Sn–S4	65.87(4)
S3–Sn–C27	82.93(18)	S3–Sn–C31	82.95(14)
S4–Sn–C27	106.03(19)	S4–Sn–C31	104.45(14)
C27–Sn–C31	137.3(2)	Sn–S1–C13	81.33(18)
Sn–S2–C13	94.39(16)	Sn–S3–C26	81.43(18)
Sn–S4–C26	92.06(18)	S1–C13–S2	119.1(3)
S3–C26–S4	120.5(3)		

Sn–S3 angle is 145.29(4)°. In both anisobidentate ligands, each shorter Sn–S bond is associated with a longer C–S bond and vice versa; this is in consonance with the bonding asymmetry of the ligands. The bond angles subtended at the Sn atom by the methylene carbons and S2 and S4 atoms range from 104.45(14)° to 107.05(18)° demonstrating that the Sn–C bonds are bent toward the longer Sn–S bonds. This situation must be a consequence of repulsion between the bonding electron pairs around the central Sn atom. Electronic and steric arguments have also been invoked to account the distortion of the similar structures from the regular octahedral geometry. Thus, the coordination geometry about the Sn atom in compound **6** is best described as being distorted skew trapezoidal-bipyramidal. Secondary π···H and H···H interactions, in compound **6**, result in a supramolecular cyclic structure as shown in Fig. 6.

The asymmetric unit of complex **9** contains two different molecules. An ORTEP diagram for one of the two independent molecules, together with an example of the atom numbering scheme used here is shown in Fig. 7. Crystal data and selected interatomic parameters are collected in Tables 2 and 6, respectively. The configuration about the tin atom is five-coordinate. The sum of the equatorial angles involving the two α-carbons of the methyl groups and a S atom [S11, S22]: 358.7°, show little deviation from the ideal angle of 360°. The coordination geometry, for both molecules, is almost intermediate between square-pyramidal and trigonal-bipyramidal with a slight bias towards the former, based on the τ value (0.40 and 0.44). A concrete explanation is available for the deviation of the coordination geometries towards square-pyramidal. In complex **9**, a secondary Sn···S interaction is responsible for lowering the τ value, which leads to the formation of a supramolecular zig–zag chain structure (Fig 8). For each molecule, the Cl atom occupies one of the apical positions of the highly distorted trigonal-bipyramid with the Cl1–Sn1–S11 and Cl2–Sn2–S22 angles of 86.57(3)° and 86.49(3)°, respectively. The quasi-axial S12 and S21 atoms cannot occupy exactly the position *trans* to Cl and Cl1–Sn1–S12 and Cl2–Sn2–S21 angles are 155.58(3)° and 155.38(3)°. Thus, the dithiocarboxylate group in both molecules is asymmetrically coordinated, and in each molecule Sn–S [Sn1–S12 = 2.6765(11) Å, Sn2–S21 = 2.6961(11) Å] bond length approximately *trans* to the chloride is longer than the other Sn–S [Sn1–S11 = 2.4908(9) Å and Sn2–S22 = 2.4866(9) Å] bond distance. The S–C bond lengths [(Sx1–Cx13 = 1.745(5) Å and 1.706(3) Å) and (Sx2–Cx13 = 1.711(3) Å and 1.763(5) Å)] also illustrate the asymmetric nature of the dithiocarboxylate group in each molecule.

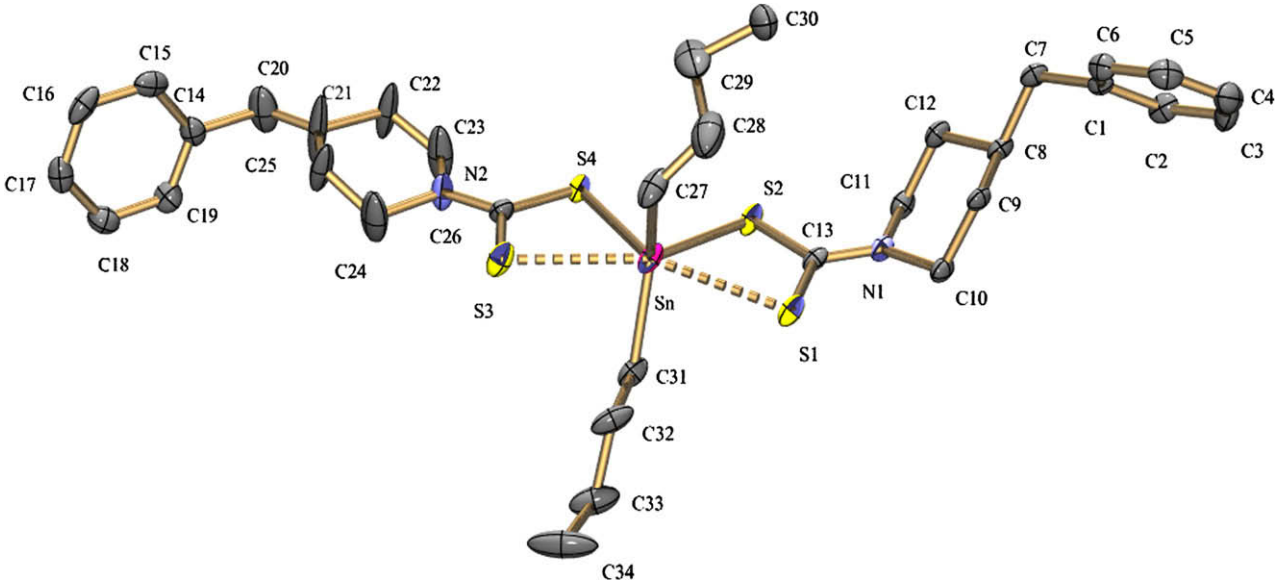


Fig. 5. ORTEP drawing of compound **6** with atomic numbering scheme.

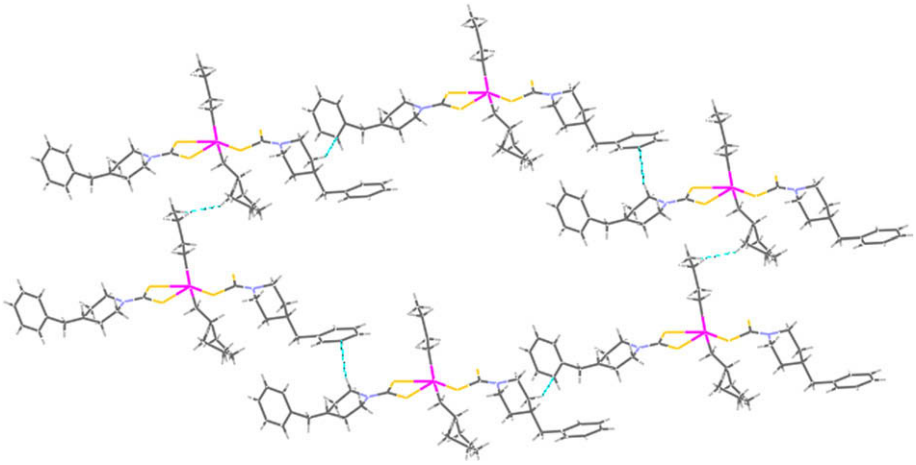


Fig. 6. Supramolecular cyclic structure of compound **9** mediated by secondary π···H and H···H interactions.

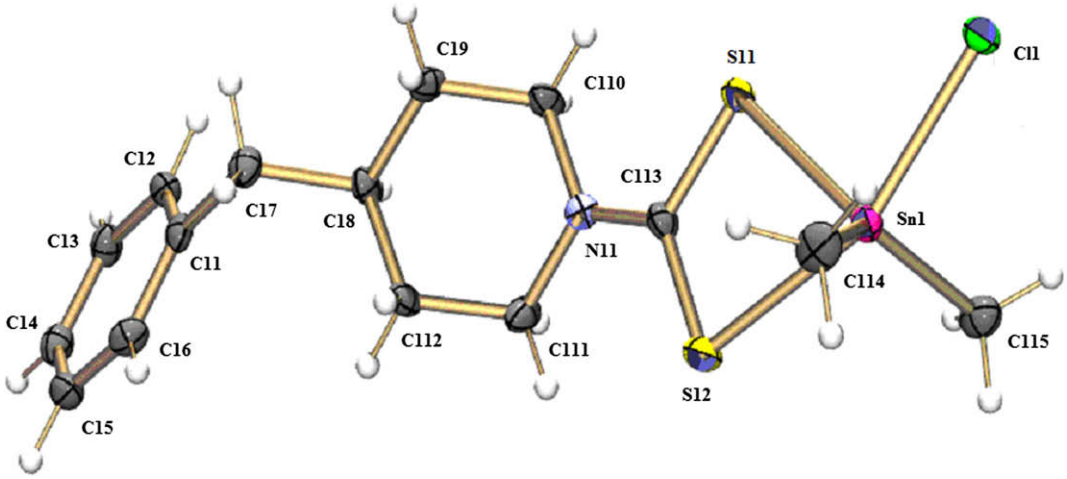


Fig. 7. ORTEP drawing for one of two independent molecules of compound **9** with atomic numbering scheme.

Table 6
Selected bond lengths (Å) and bond angles (°) for compound (**9**).

	x = 1	*x* = 2		*x* = 1	*x* = 2
Snx–Clx	2.5024(10)	2.4976(10)	Snx–Sx1	2.4908(9)	2.6961(11)
Snx–Sx2	2.6765(11)	2.4866(9)	Snx–Cx14	2.122(3)	2.123(3)
Snx–Cx15	2.123(4)	2.131(4)	Sx1–Cx13	1.745(5)	1.706(3)
Sx2–Cx13	1.711(3)	1.763(5)			
Clx–Snx–Sx1	86.57(3)	155.38(3)	Clx–Snx–Sx2	155.58(3)	86.49(3)
Clx–Snx–Cx14	96.86(16)	97.38(13)	Clx–Snx–Cx15	96.32(16)	96.38(13)
Sx1–Snx–Sx2	69.18(4)	69.08(4)	Sx1–Snx–Cx14	112.38(10)	95.20(13)
Sx1–Snx–Cx15	114.86(11)	92.02(13)	Sx2–Snx–Cx14	95.12(16)	113.47(10)
Sx2–Snx–Cx15	91.51(13)	116.36(11)	Cx14–Snx–Cx15	131.48(15)	128.86(15)
Snx–Sx1–Cx13	89.76(11)	84.63(17)	Snx–Sx2–Cx13	84.50(17)	90.16(11)
Sx1–Cx13–Sx2	116.4(3)	116.1(2)			

By comparing the Sn–S bond lengths, the shorter Sn–S bond distance decreases in the following order: **6** > **4** > **2** > **9** and the longer Sn···S bond value decreases in the sequence: **2** > **6** > **4** > **9**. The smallest Sn–S bond distances for compound **9** in the series is presumably due to two reasons: firstly the less steric hindering methyl groups and secondly electron-withdrawing effect of the chloride group that increases electron accepting capability of the Sn atom. For Sn–$S_{shorter}$, the high value for compound **4** might be due to the back-donation capability of the phenyl groups, thus stabilizing Sn atom d-orbitals and reducing their interactions with S-orbitals of the ligand. For complex **6** the highest value can be explained on the basis of electron-donating effect of the butyl groups which increase the electron density on Sn atom as a consequence repulsion between Sn and S atoms increase. In the case of Sn–S_{longer}, the order for complexes **2**, **4** and **6** can be explained on the basis of steric reasons. The high value for complex **2** is due to high steric hindrance of the cyclohexyl groups as compared to the phenyl and butyl groups.

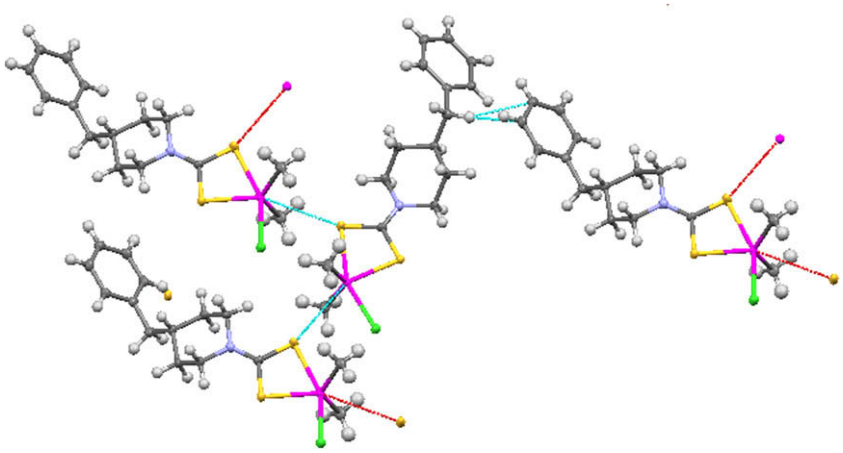


Fig. 8. Supramolecular zig–zag chain in the structure of compound **9** mediated by secondary Sn···S and benzyl-C···H interactions.

Table 7
Antifungal activity[a] of organotin(IV) derivatives **1**–**10**.

Sample	Tested fungi									
	A. nigar		*A. flavus*		*H. solani*		*A. solani*		*Fusarium* sp.	
	Linear growth	% inhibition	Linear growth	% inhibition	Linear growth	% inhibition	Linear growth	% inhibition	Linear growth	% inhibition
Control	85		86		87		90		70	
L[d]	48.0	43.5	63.0	26.7	76.0	12.6	74.0	17.8	56	20
(1)	50.0	41.2	65.0	24.4	80.0	8.0	84.0	6.7	70	0
(2)	78.0	8.2	73.0	15.1	80.0	8.0	76.0	15.6	70	0
(3)	80.0	5.9	78.0	9.3	81.0	6.9	76.0	15.6	70	0
(4)	68.0	20.0	66.0	23.3	70.0	19.5	68.0	24.4	60	14.2
(5)	72.0	15.3	73.0	15.1	61.0	29.9	66.0	26.7	56	20
(6)	66.0	22.4	80.0	7.0	73.0	16.1	70.0	22.2	63	10
(7)	72.0	15.3	74.0	14.0	78.0	10.3	68.0	24.4	63	10
(8)	80.0	5.9	78.0	9.3	68.0	21.8	64.0	28.9	61	12.8
(9)	66.0	22.4	69.0	19.8	73.0	16.1	66.0	26.7	60	14.2
(10)	76.0	10.6	76.0	11.6	80.0	8.0	73.0	18.9	70	0
Clotrimazole	60	29.4	52	39.5	51	41.4	48	46.7	44	37.1

[a] Concentration: 200 μg/mL of DMSO.

A comparison of the τ values for the five-coordinate complexes **2**, **4** and **9** reveals the smallest value for complex **9** because of secondary Sn···S intermolecular interactions. The presence of such kinds of interaction in compound **9** only, is due to the presence of small methyl groups on one end, that allow the molecules to approach one another closely. Secondly the presence of electronegative chloride group makes the Sn atom electron deficient and thus facilitates its interaction with S atom of the adjacent molecule.

3.5. Biocidal activities

3.5.1. Antifungal activity

The agar tube dilution protocol method was employed to test the antifungal activities of the synthesized compounds against the five different strains of fungi *Aspergillus nigar, A. flavus, Helminthosporium solani, Alternia solani, Fusarium* sp. and the results are shown in Table 7. The activity of compounds is highly strain dependent. Triorganotin(IV) derivatives are more active than are the chlorodi- and diorganotin(IV) complexes against the *A. nigar* and *A. flavus*. However, for the other three species, the order is reversed which is an indication of different mode of interaction of these compounds with the strains studied. The different mechanism of these compounds may be due to their ability to form secondary intermolecular interactions (as can be seen in crystal packing diagram) with bioreceptors in the cells of the microorganisms, which in turn block the synthesis of protein by inhibiting the movement of ribosome along with RNA. This situation would inhibit synthesis of DNA in the cell nucleus [10]. The higher activity of complex **1** may be due to highest lipophilic character of tributyltin(IV) derivatives [24]. The ligand and tributyltin(IV) complex are more active than is the standard drug against *A. nigar* and these compounds have potential to be used as fungicides in future.

3.5.2. Antibacterial activity

The compounds **1–10** were tested by agar well diffusion method against five different types of bacteria, namely, *Escherichia coli, Salmonella typhi, Pseudomonas aeroginosa, Staphylococcus auerus* and *Streptococcus, Streptomycin* was used as the reference drug and the results are presented in Table 8. Almost all the compounds were more toxic than was their parent ligand but slightly less so than the standard drug. Among the triorganotin(IV) derivatives, the bactericidal activity of **1** and **4** are fairly good; however, neither of these complexes (**1–4**) demonstrated any activity against *Staphlococcus aureus*. The chlorodiorganotin(IV) complexes were found to be more active than their counterparts without chloride substituents. The most probable reason is the ease of hydrolysis of the former [25]. The enhanced bactericidal activity of the ligand on complexation with organotin moiety may be explained by chelation theory [26], according to which chelation reduces the polarity of the central Sn atom because of the partial sharing of its positive charge with donor groups and possible π-electrons delocalization within the whole chelating ring. As a result, the lipophilic nature

Table 8
Antibacterial activity data[a,b] of organotin(IV) derivatives **1**–**10**.

Bacterium	Clinical implication	Zone of inhibition (mm)											Reference drug
		L	(1)	(2)	(3)	(4)	(5)	(6)	(7)	(8)	(9)	(10)	
E. coli	infection of wounds, urinary tract and dysentery	22	25	12	11	23	14	13	19	17	18	0	34
S. typhi	typhoid fever, localized infection	16	23	12	17	19	19	17	23	20	21	13	31
P. aeroginosa	infection of wounds, eyes, septicemia	17	16	0	13	0	10	0	14	16	14	0	24
Staphylococcus aureus	food poisoning, scaled skin syndrome, endocarditis	12	0	0	0	0	15	19	15	11	11	10	38
Streptococcus	Strep throat	0	18	11	0	21	11	13	17	17	17	11	38

[a] *In vitro*, agar well diffusion method, conc. 1 mg/mL of DMSO.
[b] Reference drug, *Streptomycin*.

of the central Sn atom increases, which favors the permeation of the complexes through the lipid layer of the cell membrane.

4. Conclusions

The presence of intermolecular interactions in packing diagrams can be exploited to conclude that these compounds exert their toxic actions on microorganisms by making similar contacts with the cells constituents. The influence of the metal is clearly visible in the antibacterial activity. This study provides a further step in designing novel antifungal metal-based drugs.

Supplementary data

CCDC 717026, 717715, 717024, and 717025 contain the supplementary crystallographic data for **2, 4**, **6** and **9**. These data can be obtained free of charge via http://www.ccdc.cam.ac.uk/conts/retrieving.html, or from the Cambridge Crystallographic Data Centre, 12 Union Road, Cambridge CB2 1EZ, UK; fax: (+44) 1223-336-033; or e-mail: deposit@ccdc.cam.ac.uk.

Acknowledgements

We thank the Higher Education Commission of Pakistan and the NSERC (Canada) for financial support.

References

[1] F.W. Sunderman, Ann. Clin. Lab. Sci. 9 (1979) 1.
[2] D.L. Bodenner, P.C. Dedon, P.C. Keng, R.F. Borch, Cancer Res. 46 (1986) 2745.
[3] P.J. Nieuwenhuizen, J. Reedijk, M. van Duin, W.J. McGill, Rubber Chem. Technol. 70 (1997) 368.
[4] M. Cicotti, Handbook of Residue Analytical Methods for Agrochemicals, vol. 2, Wiley, Chichester, 2003.
[5] D. Fan, M. Afzaal, M.A. Malik, C.Q. Nguyen, P. O'Brien, P.J. Thomas, Coord. Chem. Rev. 251 (2007) 1878.
[6] P.K. Gogoi, D.P. Phukan, D.K. Das, Asian J. Chem. 11 (1999) 1291.
[7] H.P.S. Chauhan, N.M. Shaik, J. Inorg. Biochem. 99 (2005) 538.
[8] G. Eng, X. Song, Q. Duong, D. Strickman, J. Glass, L. May, Appl. Organomet. Chem. 17 (2003) 218.
[9] H.D. Yin, S.C. Xue, Appl. Organomet. Chem. 20 (2006) 283.
[10] R. Mash, Ann. Appl. Biol. 41 (1954) 652.
[11] Z. Rehman, A. Shah, N. Muhammad, S. Ali, R. Qureshi, I.S. Butler, J. Organomet. Chem. 694 (2009) 1998.
[12] W.F.L. Armarego, C. Chai, Purification of Laboratory Chemicals, 5th ed., Butterworth, Oxford, 2003.
[13] A. Mohammad, C. Varshney, S.A.A. Nami, Spectrochim. Acta, Part A 73 (2009) 20. reference therein.
[14] L. Ronconi, C. Maccato, D. Barreca, R. Saini, M. Zancato, D. Fregona, Polyhedron 24 (2005) 521.
[15] O. Jung, Y.S. Sohn, J.A. Ibers, Inorg. Chem. 25 (1986) 2273.
[16] T.P. Lockhart, W.F. Manders, E.M. Holt, J. Am. Chem. Soc. 108 (1986) 6611.
[17] S. Shahzadi, S. Ali, K. Wurst, M.N. Haq, Heteroat. Chem. 18 (2007) 664. reference therein.
[18] M. Nádvorník, J. Holeček, K. Handlíř, J. Organomet. Chem. 275 (1984) 43.
[19] R. William, I. Verbruggen, M. Gielen, M. Biesemans, B. Mahieu, T.S.B. Baul, E.R.T. Tiekink, Organometallics 17 (1998) 5758.
[20] T.S.B. Baul, S. Dhar, S.M. Pyke, E.R.T. Tiekink, E. Rivarola, R. Butcher, F.E. Smith, J. Organomet. Chem. 633 (2001) 7.
[21] A. Tarassoli, T. Sedaghat, B. Neumüller, M. Ghassemzadeh, Inorg. Chim. Acta 318 (2001) 15.
[22] A.W. Addison, T.N. Rao, J. Reedijk, J. Van Rijn, G.C. Verschoor, J. Chem. Soc., Dalton Trans. (1984) 1349.
[23] G.M. Sheldrick, W.S. Sheldrick, J. Chem. Soc. A (1970) 490.
[24] G.J.M. Van der Kerk, J.G.A. Luijten, J. Appl. Chem. 6 (1956) 56.
[25] E.R.T. Tiekink, Appl. Organomet. Chem. 22 (2008) 533.
[26] R.S. Srivastava, Inorg. Chim. Acta 56 (1981) 65.

coordination chemistry, in the present report we describe the formation of sodium and potassium complexes by the solid-state microwave reaction of alkali salts of ethyl [α-(4-benzeneazoanilino)-*N*-benzyl]phosphonic acid (Na/KA_1) and ethyl [α-(4-benzeneazoanilino)-*N*-4-methoxybenzyl]phosphonic acid (Na/KA_2) with crown ethers containing 18-, 24- and 30-membered macrocyclic rings. As a preliminary screening for their biological activity, the complexes were evaluated for their cytostatic activity *in vitro* against murine leukemia L1210, murine mammary carcinoma FM3A and human T-lymphocyte CEM and MT-4 cell lines, and the results thus obtained were compared with those of the free crown ethers and discussed in terms of their binding behaviour and structure–activity relationships. The antiviral activity of the compounds was evaluated against a number of DNA and RNA viruses.

Similarly to natural cationic ionophores, crown ether compounds were also found to be toxic in prokaryotic and eukaryotic cellular systems. Toxicological research was done in various microorganisms and higher organisms such as mice, rats and dogs, and the results obtained in this field, along with biomedical potentials of crown ethers, have been summarized in our recently published review [17]. In most cases the proposed mechanism for the toxicity of crown ethers is connected with their ability to transport ions, most probably by inserting and integrating into membrane bilayers and conducting cations, as expected for carriers [18,19]. In addition, we reported the antiproliferative activity of several crown ethers and their derivatives *in vitro* against several tumor cell lines and compared their activity to that of valinomycin, an antibiotic known as a selective potassium ionophore [20]. This was the first systematic study of the cytostatic activity of non-functionalized crown compounds. Some crown ethers showed marked tumor cell growth inhibitory activity, presumably as the result of their activity as membrane-active potassium ion transporters, which may promote K^+ efflux. No interaction with double-stranded DNA was detected. There are substantial differences between normal and tumor cells with respect to the membrane potentials of K^+ transport regulation [21,22]. It is worth noting that some functionalized crown ethers, such as acridine, antraquinone, bis(propargilic)sulfone and cisplatin derivatives, were designated to act either as DNA intercalators or DNA metal chelators [17,23–26].

2. Experimental

2.1. Materials and methods

Crown ethers dibenzo-18-crown-6 (DB18C6), bis(4′-di-*tert*-butylbenzo)-18-crown-6 (mtbDB18C6), dibenzo-24-crown-8 (DB24C8) and dibenzo-30-crown-10 (DB30C10), obtained commercially or prepared according to published methods [2], were purified by repeated recrystallizations from the appropriate solvents: acetone (DB18C6), methanol (mtbDB18C6, DB24C8), and *n*-hexane (DB30C10), respectively. Sodium and potassium salts of monoethyl [α-(4-benzeneazoanilino)-*N*-benzyl]phosphonic acid (NaA_1, KA_1) and [α-(4-benzeneazoanilino)-*N*-4-methoxybenzyl]phosphonic acid (NaA_2, KA_2) were prepared and purified following previously described procedures [27,28]. All compounds were dried on P_2O_5 in a vacuum at room temperature and stored in a dry-box before use. The solvents used (AR grade) were purified and dried by standard procedures. Microwave experiments were performed in a microwave oven in an open porcelain vessel at 700 W. Melting points were determined on a hot stage microscope and are uncorrected. FTIR spectra were recorded on an ABB Bomen MB102 spectrometer using KBr pellets. LDI mass spectra were performed on a Finnigan FT/MS 2001 DD instrument (Finnigan, Madison, WI) operating in the linear positive ion mode. The one- and two-dimensional ^1H and ^{13}C NMR spectra (in $CDCl_3$) including ^1H, ^{13}C. APT, ^1H–^1H COSY, ^1H–^{13}C COSY, HMQC and HMBC experiments, were recorded with a Bruker XWIN-600 Fourier-transform spectrometer at ambient temperature. The ^1H and ^{13}C chemical shifts (δ) were referred to $SiMe_4$. All two-dimensional experiments were performed by standard pulse sequences, using Bruker XWIN-NMR software Version 3.5. Elemental analyses (CHN) were performed on a Perkin–Elmer Analyser PE 2400 Series 2. The phosphorus content was determined by the vanadomolybdatophosphoric acid spectrophotometric method, and water by thermogravimetric analysis carried out on a Cahn RG electromicrobalance in an air atmosphere applying a heating rate of 4 °C min^{-1}.

2.2. Preparations of the complexes

The crown ether complexes were prepared by a conventional thermal method in solution and by microwave-promoted solid-state synthesis. Preparation of complexes of DB18C6 (**1**–**4**) and DB24C8 (**7**–**10**) by heating in solution was described earlier [29–31].

2.2.1. Conventional thermal method in solution

The reactions were in general carried out by dissolving an equimolar amount of the crown ether and sodium (NaA_1, NaA_2) and potassium (KA_1, KA_2) salt, respectively, of the corresponding monoethyl ester of benzeneazophosphonic acid in acetonitrile, then refluxing for 2–6 h with vigorous stirring. Only for complex **7** was dry ethanol used as the solvent. The clear hot solution was filtered and allowed to stand at room temperature. Most of the complexes were gradually formed by removal of solvent. The precipitate was filtered off, washed with a small amount of cold reaction solvent, and dried. Complexes of mtbDB18C6 (**5** and **6**) and DB30C10 (**11**) were obtained as a syrup after all the solvent was removed, which solidified slowly on standing, and were washed with cold CH_2Cl_2. All the complexes obtained were hygroscopic compounds, as were the free sodium and potassium phosphonate salts, and were dried under high vacuum at ambient temperature without decomposition, giving stable anhydrous complexes. Only complex **1** was obtained as a monohydrated complex, which was confirmed by thermogravimetric analysis. The purity of the complexes was checked by elemental, thermogravimetric and spectral analyses. Only elemental data for the newly synthesized complexes of mtbDB18C6 and DB30C10 are given.

Na(mtbDB18C6)A_1 (**5**): M.p. 104–106 °C. *Anal.* Calc. for $C_{49}H_{61}N_3O_9PNa$: C, 66.13; H, 6.91; N, 4.72; P, 3.49. Found: C, 66.313; H, 6.78; N, 4.51; P, 3.27%.

K(mtbDB18C6)A_1 (**6**): M.p. 96–98 °C. *Anal.* Calc. for $C_{49}H_{61}N_3O_9PK$: C, 64.95; H, 6.79; N, 4.64; P, 3.42. Found: C, 64.78; H, 6.99; N, 4.54; P, 3.21%.

K(DB30C10)A_1 (**11**): M.p. 93–95 °C. *Anal.* Calc. for $C_{49}H_{61}N_3O_{13}PK$: C, 60.67; H, 6.34; N, 4.33; P, 3.19. Found: C, 60.47; H, 6.59; N, 4.21; P, 3.09%.

2.2.2. Focused solid-state microwave irradiation

Equimolar amounts of the crown ether and the appropriate alkali salt (ca. 0.5 mmol) in a porcelain mortar were ground together until a fine homogenous powder was obtained. This mixture was then irradiated either for 6 min (3 × 2) in the case of complexes **1**–**6** or 4 min (2 × 2) for complexes **7**–**11**, using a 700 W microwave. After the reaction was completed, the liquefied product was allowed to cool down, washed with small amount of cold CH_2Cl_2 and dried *in vacuum* for 24 h giving an orange solid (Yield 92–95%).

2.3. In vitro cytostatic assays

The cytostatic activity of the complexes, uncomplexed crown ethers and alkali benzeneazophosphonate salts NaA_1 and KA_2 was assayed *in vitro* against the murine leukemia L1210 cell line, the murine mammary carcinoma FM3A cells and the human T-lymphocyte CEM and MT-4 cell lines, according to previously described methods [32]. Briefly, the cells were suspended in growth medium and added to 200 μl-microplate wells in the presence of varying concentrations of the test compounds. The cells were then allowed to proliferate in a humidified CO_2-controlled atmosphere for 2 (L1210, FM3A), 3 (CEM) and 5 (MT-4) days, and at the end of the incubation period the number of viable cells was determined by a Coulter counter (L1210, FM3A, CEM) or by the MTT dye exclusion method (MT-4). The activity was expressed as the concentration (in μM) of the compound at which tumor cell growth was inhibited by 50% (IC_{50}).

2.4. In vitro antiviral assays

The assay procedures for measuring the antiviral activity of the compounds against a wide variety of DNA and RNA viruses were based on the inhibition of the virus-induced cytopathic effect in either human lung embryonic HEL, human cervix carcinoma HeLa, African green monkey Vero or human lymphocyte MT-4 cell cultures, as previously described [33,34]. The 50% effective concentration (EC_{50}) was defined as the compound concentration required to confer 50% protection of virus-infected cells against viral destruction. The cytostatic activity of the compounds was assessed in parallel with the antiviral activity, and the cytostatic concentration (CC_{50}) was determined as the concentration of compound to inhibit the number of viable cells in mock-infected cells by 50%.

3. Results and discussion

3.1. Synthesis and properties

Investigations of the reactions of crown ethers containing 18-membered (DB18C6 and mtbDB18C6), 24-membered (DB24C8) and 30-membered (DB30C10) macrocyclic rings with sodium (NaA_1 and NaA_2) and potassium (KA_1 and KA_2) benzeneazophosphonate salts (Fig. 1) in the solid state under microwave irradiation have shown that 1:1 (crown–cation) ion-pair salt complexes are formed, similarly as in conventional thermal reactions in solution. The factors that influence the formation of metal ion complexes with crown ethers are well known [5,35]. The metal–ligand interactions in general depend on the size and charge density of the cation, the size and flexibility of the crown ether, the number and the nature of substituted groups on the macrocyclic ring, the nucleophilicity of the counterion, and the nature of the solvent. In our earlier papers we studied, by electrochemical and UV–Vis spectroscopic methods, the complex formation, solvation and ion-pairing of a number of sodium and potassium salt complexes (picrate, perchlorate, tetraphenylborate, hexafluorophosphate, tetrafluoroborate, anilinobenzylphosphonate) with various crown ethers in organic solutions [29,30,36,37]. Generally, the relative dimensions of the crown ether cavity and the linked cation is the most significant factor for crowns up to 18-membered rings with a planar conformation and limited flexibility. Sodium and potassium ions with cationic diameters of 1.94 and 2.66 Å, respectively, fit well into the 18-membered polyether cavity of 2.6–3.2 Å with anion and solvent molecules having the possibility of interacting with the alkali cation in axial positions. On the other hand, the cavity size effects are not of crucial importance for the larger crown ethers with 24- and 30-membered polyether rings and high conformation mobility which provides a complexation profile of high

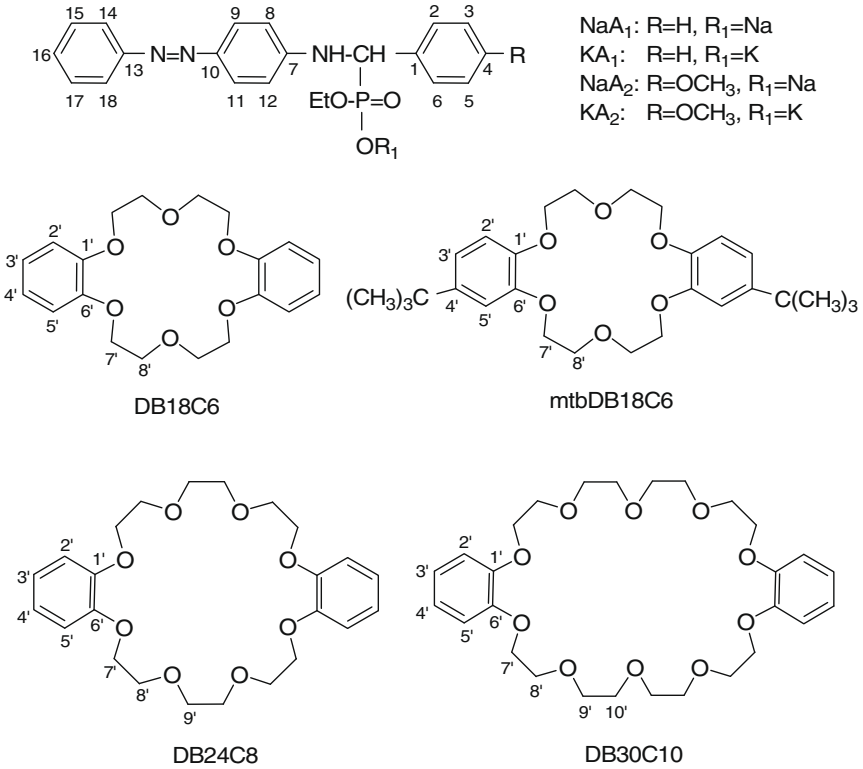


Fig. 1. Sodium and potassium benzeneazophosphonates and crown ethers.

coordination metal geometry, similarly to naturally occurring cyclic ionophores [9,38]. They may form complexes by wrapping around the alkali cation either by expelling the conjugate anion and solvent molecules from the cation coordination sphere or leaving space for bonding with the anion. Thus DB24C8, with a hole diameter of about 4.7 Å, formed sodium and potassium complexes with benzeneazophosphonate salts, while in the case of larger DB30C10 only the potassium complex was obtained. All complexes formed by conventional heating in solution were also obtained by microwave heating in the solid state. A comparative study has shown up to 10% higher yields in the case of DB18C8 (**1**–**4**) and mtbDB18C6 (**5**,**6**) complexes and between 20% and 30% for the DB24C8 (**7**–**10**) and DB30C10 (**11**) complexes. The complexation time is much shorter for the reaction run under microwave irradiation (4–6 min) compared to that with classical heating (2–6 h). In addition, it is twice shorter with respect to the microwave synthesis of the complex of the dioxa-diaza 15-membered macrocycle with NaA_1 (12 min) [11], which confirms the greater affinity towards alkali cations of pure oxa-crown than aza-crown ligands.

It may be presumed that the alkali ion in all the complexes is involved in bonding interactions with all the oxygen atoms of the crown ether and to the phosphonate anion. The low melting points of the complexes (90–140 °C) with respect to the high melting point of the free sodium salts (above 220 °C) [15], indicate that the charge of the alkali ion in the complex is extremely delocalized. Some degree of charge transfer between the metal ion and the anion can take place, increasing the stability of the complex. The X-ray structure determination of complex **1**, obtained in the crystalline form as acetonitrile solvate, shows a strong bonding between the crown ether complexed cation and the phosphonate anion [39]. Sodium is coordinated to all six crown oxygens at distances from 2.601 to 2.769 Å in the base of a hexagonal pyramid and to one of the phosphonate oxygen atoms in the apical position at a distance of 2.183 Å. Therefore, it could be concluded that a stronger interaction exists between the sodium ion and the phosphonate oxygen than with the oxygens in the crown ring, which was supported also by the mass spectra. The low symmetry of the monoalkyl benzeneazophosphonate anions with sites of charge localization may account for the strong cation–anion electrostatic interaction. It is worth noting that the conductometric and UV–Vis spectroscopic studies of sodium and potassium complexes of DB18C6 and DB24C8 reveal also a strong cation–anion interaction in acetonitrile [36,37,40]. A larger ion-pair association was found for DB24C8 complexes, which can be attributed to the lack of solvation of these complex ions compared to those of DB18C6. Furthermore, the potassium complexes are more dissociated than the corresponding sodium analogues, which is in agreement with the assumption that complexes of potassium should be more acceptable to a lipid phase compared to the sodium products. Such effects can be generalized for natural systems and should significantly account for a greater resistance of sodium against complexation with natural carriers and its accumulation outside the cell membrane.

In the present work results of infrared, LDI mass and ^1H and ^{13}C NMR spectroscopic studies as well as the cytostatic and antiviral activity of the benzeneazophosphonate crown ether complexes **1**–**11** are presented.

3.2. Infrared spectra

IR spectra of the crown ether complexes are too complex to allow a complete assignment of the absorption bands. In every case, however, the spectrum of the complex is distinctively different

Table 1
Selected infrared and mass spectroscopic data for the sodium benezeneazophosphonate crown ether complexes.

No.	IR data (cm^{-1})[a]					Mass data, *m/z* (rel. int. %)[b]		
	Complex	ν_{as} (ArCOC) ν(P=O)	ν(aliphCOC) δ(CO–P)	ν(PO–C) ν_s(ArCOC)	$\omega,\tau,\rho(CH_2)$ ν(aliphCC)	$[M+H]^+$	$[L+Na]^+/[L+K]^+$	$[NaA+Na]^+/[KA+K]^+$
1	$Na(DB18C6)A_1$[c]	1254 vs 1219 s	1128 vs	1067 s 1032 s	945 m-s 910 sh	779 (4%)	383 (28%)	440 (53%)
2	$K(DB18C6)A_1$[d]	1252 vs 1219 s	1130 vs	1081 s 1060 s br	948 m-s 910 sh	795 (7%)	399 (31%)	472 (63%)
3	$Na(DB18C6)A_2$[c]	1254 vs 1220 s	1125 vs	1070 sh 1052 s	947 m	809 (4%)	383 (25%)	470 (48%)
4	$K(DB18C6)A_2$[d]	1254 vs 1219 s	1130 vs	1068 sh 1057 s	948 m-s	825 (6%)	399 (32%)	502 (57%)
5	$Na(mtbDB18C6)A_1$	1265 vs 1251 vs 1216 vs	1149 vs 1137 vs	1056 s br	963 m-s 948 m-s	891 (6%)	495 (28%)	440 (51%)
6	$K(mtbDB18C6)A_1$	1266 vs 1254 vs 1218 vs	1146 vs 1136 vs	1058 s br	965 m-s 948 m-s	907 (8%)	511 (35%)	472 (62%)
7	$Na(DB24C8)A_1$	1259 s 1227 s	1138 s 1130 sh 1107 s	1078 s 1050 s	947 m-s br 927 m	867 (4%)	471 (20%)	440 (53%)
8	$K(DB24C8)A_1$	1261 vs 1228 s	1140 vs 1130 sh 1108 s	1080 s 1054 s	952 m 942 m 928 m	883 (7%)	487 (29%)	472 (60%)
9	$Na(DB24C8)A_2$	1257 sh 1249 s 1223 m-s	1140 s 1122 m-s	1075 m-s 1050 s	940 m br 920 sh	898 (4%)	471 (21%)	470 (53%)
10	$K(DB24C8)A_2$	1260 s 1238 sh 1228 s	1136 s br 1107 s	1076 s 1052 s 1038 sh	961 m 942 m 928 m	913 (6%)	487 (31%)	502 (41%)
11	$K(DB30C10)A_1$	1261 s 1240 m 1219 s	1126 vs 1119 s 1101 s	1074 m-s 1050 s 1032 m-s	961 m 943 m 926 m-s 915 w	971 (7%)	576 (35%)	472 (58%)

[a] As KBr pellets. Abbreviations: vs, very strong; s, strong; m, medium; w, weak; br, broad; sh, shoulder.
[b] LDI spectra. *L* = crown ether, $A = A_1, A_2$.
[c] Particular IR data from Ref. [29].
[d] Particular IR data from Ref. [30].

from that of the physical mixture of the constituents, and shows the absence of the uncomplexed constituents [28]. Upon complexation marked changes may be noticed in the 1270–900 cm^{-1} region where bands arising from various modes of vibrations of ether and methylene groups along with the benzeneazoanilinophosphonate ester group are present (Table 1, Fig. 2). Generally, compared with the spectra of the free crown ethers, most of the ligand bands in the complexes are slightly shifted to lower energies, presumably due to less restriction on the coupling of some vibrational modes caused by bonding between the oxygen atoms of the crown ether ring and the sodium and potassium ion, respectively. The greatest changes could be observed in the 1000–900 cm^{-1} region, which contains bands attributed to wagging, twisting and rocking modes of vibration of the methylene groups [29,31,41]. Thus, while free DB18C6 has two strong bands at 997 and 932 cm^{-1} associated with these vibrations, its complexes are characterized by a medium to strong band around 947 cm^{-1} (Fig. 2a–c). In complexes **1** and **2** this band shows a shoulder on the lower frequency side. Complexes of mtbDB18C6 and DB24C8 exhibit either two (**5**, **6**, **7** and **9**) or three bands (**8** and **10**) between 965 and 928 cm^{-1}, while in complex **11** deformation modes of methylene vibrations give a multiple absorption with considerable differences in band intensities compared to those in the free crown ether DB30C10 (Fig. 2d and e).

3.3. Mass spectra

The structures of the complexes were also supported by the LDI mass spectra, and the major structurally informative fragment ions are given in Table 1. All complexes show a weak protonated molecular ion $[M+H]^+$ with a relative abundance of 4–8%. The more abundant ions are those of the sodium $[L+Na]^+$ and potassium $[L+K]^+$ cationic crown ether complexes (20–35%) as well as of the sodium $[NaA+Na]^+$ and potassium $[KA+K]^+$ adduct ions of the corresponding alkali benzeneazophosphonate salts (50–60%). The results obtained are in accordance with the structural data, which indicate strong bonding between the alkali ion and the phosphonate anion.

3.4. NMR spectra

While all the potassium complexes are sufficiently soluble in $CDCl_3$ for NMR spectral analysis, among the sodium complexes only for that of mtbDB18C6 could a satisfactory spectrum be obtained. The complete ^1H and ^{13}C NMR resonance assignments of the complexes and free potassium ethyl benzeneazophosphonate salts KA_1 and KA_2 are summarized in Tables 2 and 3, according to the numbering scheme shown in Fig. 1.

The ^1H NMR spectra of the free non-substituted crown ethers show two separated closely spaced multiplets in the aromatic region characteristic for a four-spin AA′BB′ coupled system, typical of the spectra found for 1,2-disubstituted benzenes. Due to the loss of symmetry in mtbDB18C6, all the aromatic crown ether resonances are separated. In the ether region, are present either two (DB18C6, mtbDB18C6), three (DB24C24) or four (DB30C10) sets of resonant signals for the methylene protons of the chemically non-equivalent ether fragments (Fig. 1). As expected, in mtbDB18C6 these sets of signals are split, as are the corresponding carbon resonances. The assignments were carried out on the basis of the ring current effect of the benzo group for the ether methylenic protons and the inductive effect due to the oxygen for the benzo group protons. Upon complex formation some changes could be observed both in the aromatic and methylene crown ether absorptions. Generally, all the aromatic protons in the complexes show an upfield shift, which varied slightly depending on the crown ether used. The protons 2′,5 in the complexes of non-substituted crown ethers show only a negligible shift of ca. 0.01 ppm,

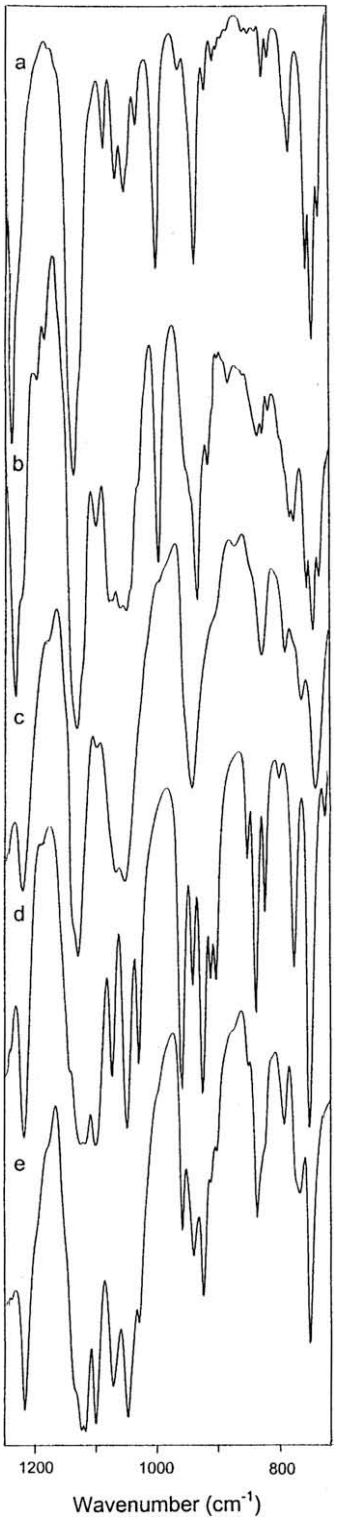


Fig. 2. A part of the infrared spectra of (a) DB18C6; (b) NaA_1; (c) $Na(DB18C6)A_1$; (d) DB30C10; (e) $K(DB30C10)A_1$.

while protons 3′,4′ are shifted by ca. 0.1 ppm in complexes of DB18C6 (**2** and **4**) and DB30C10 (**11**) and ca. 0.02 ppm in complexes of DB24C8 (**8** and **10**). In the complexes of mtbDB18C6 (**5** and **6**) with a weakly electron-releasing *tert*-butyl substituent at the 4′ position, protons 2′ and 5′ show an upfield shift of 0.05–0.1 ppm, while proton 3′ is shifted only by 0.01 ppm. Greater chemical shift differences between complexes could be observed

Table 2
^{1}H NMR (, ppm; *J*, Hz) data of crown ether complexes and potassium benzeneazophosphonate salts[a,b].

Compound	**2**	**4**	**5**	**6**	**8**	**10**	**11**	KA_1	KA_2
H-2,6	7.46 d	7.37 d	7.45 d	7.46 d	7.42 d	7.39 d	7.52 d	7.42 d[c]	7.32 d
	J_{HH} = 7.7	J_{HH} = 7.7	J_{HH} = 7.5	J_{HH} = 7.6	J_{HH} = 7.7	J_{HH} = 7.7	J_{HH} = 7.8	J_{HH} = 7.5	J_{HH} = 7.7
H-3,5	7.03 t	6.59 d	7.14 t	7.05 t	7.17 t	6.74 d	7.17 t	7.24 t	6.79 d
	J_{HH} = 7.6	J_{HH} = 8.6	J_{HH} = 7.5	J_{HH} = 7.6	J_{HH} = 7.7	J_{HH} = 8.5	J_{HH} = 7.7	J_{HH} = 7.5	J_{HH} = 8.4
H-4	6.88[d]		7.07 t	6.91[e]	7.12 t		7.06	7.15 t	
			J_{HH} = 7.7		J_{HH} = 7.7		J_{HH} = 7.7	J_{HH} = 7.5	
OCH_3		3.48 s				3.57 s			3.63 s
H-8,12	6.46 d	6.63 d	6.43 d	6.44 d	6.59 d	6.57 d	6.54 d	6.67 d	6.81d
	J_{HH} = 8.9	J_{HH} = 8.9	J_{HH} = 8.8	J_{HH} = 8.9	J_{HH} = 8.8	J_{HH} = 8.9	J_{HH} = 8.9	J_{HH} = 8.8	J_{HH} = 8.9
H-9,11	7.61 d	7.61 d	7.57 d	7.59 d	7.67 d	7.64 d	7.61 d	7.70 d	7.71 d
	J_{HH} = 8.9	J_{HH} = 8.9	J_{HH} = 8.8	J_{HH} = 8.8	J_{HH} = 8.8	J_{HH} = 8.9	J_{HH} = 8.9	J_{HH} = 8.8	J_{HH} = 8.8
H-14,18	7.75 d	7.75 d	7.75 d	7.78 d	7.77 d	7.75 d	7.71 d	7.76 d	7.75 d
	J_{HH} = 7.4	J_{HH} = 7.4	J_{HH} = 7.9	J_{HH} = 7.8	J_{HH} = 7.5	J_{HH} = 7.5	J_{HH} = 7.4	J_{HH} = 7.6	J_{HH} = 7.4
H-15,17	7.41 t	7.43 t	7.43 t	7.43 t	7.32 t	7.42 t	7.38 t	7.41 t[c]	7.42 t
	J_{HH} = 7.7	J_{HH} = 7.5	J_{HH} = 7.9	J_{HH} = 7.9	J_{HH} = 7.6	J_{HH} = 7.6	J_{HH} = 7.5	J_{HH} = 7.2	J_{HH} = 7.4
H-16	7.32 t	7.31 t	7.36 t	7.36 t	7.29 t	7.33 t	7.28 t	7.34 t	7.32 t
	J_{HH} = 7.3	J_{HH} = 7.2	J_{HH} = 7.2	J_{HH} = 7.3	J_{HH} = 7.5	J_{HH} = 7.3	J_{HH} = 7.4	J_{HH} = 7.3	J_{HH} = 7.3
PCH	4.64 dd	4.59 dd	4.66 dd	4.65 dd	4.59 d	4.58 d	4.64 dd	4.63 d	4.66 dd
	J_{PH} = 21.6	J_{PH} = 21.3	J_{PH} = 21.4	J_{PH} = 21.6	J_{PH} = 22.0	J_{PH} = 21.8	J_{PH} = 21.5	J_{PH} = 22.5	J_{PH} = 21.9
	J_{HH} = 5.8	J_{HH} = 6.1	J_{HH} = 5.9	J_{HH} = 6.0			J_{HH} = 5.8		J_{HH} = 6.0
NH	5.77 dd	5.79 dd	6.02 s br	5.78 dd	5.90 s br	6.10 s br	6.10dd	6.01 t	5.96 dd
	J_{PH} = 10.5	J_{PH} = 10.5		J_{PH} = 10.6			J_{PH} = 10.1	J_{PH} = J_{HH}	J_{PH} = 10.4
	J_{HH} = 5.8	J_{HH} = 6.1		J_{HH} = 5.9			J_{HH} = 5.8	= 8.5	J_{HH} = 6.1
$POCH_2$	3.78 m	3.79 m	3.62 m	3.74 m	3.72 m	3.78 m	3.60[f]	3.69 m	3.71 m
$POCH_2CH_3$	1.08 t	1.10 t	1.01 t	1.08 t	1.05 t	1.04 t	1.00 t	1.09 t	1.07 t
	J_{HH} = 7.0	J_{HH} = 7.0	J_{HH} = 7.1	J_{HH} = 7.1	J_{HH} = 7.0	J_{HH} = 7.1	J_{HH} = 7.0	J_{HH} = 7.0	J_{HH} = 7.0
H-2′	6.875 m	6.876 m	6.752 d	6.712 d	6.878 m	6.883 m	6.877 m		
			J_{HH} = 8.5	J_{HH} = 8.5					
H-3′	6.778 m	6.779 m	6.902 dd	6.901 dd	6.857 m	6.859 m	6.780 m		
			J_{HH} = 8.5; 1.8	J_{HH} = 8.5; 2.0					
H-4′	6.778 m	6.779 m			6.857 m	6.859 m	6.780 m		
H-5′	6.875 m	6.876 m	6.843 d	6.802 d	6.878 m	6.886 m	6.877 m		
			J_{HH} = 1.8	J_{HH} = 2.0					
H-7′	4.022 m	4.029 m	4.059 s br	4.076 s br	4.118 m	4.120 m	4.008 m		
H-8′	4.017 m	4.021 m	4.059 s br	4.076 s br	3.860 m	3.861 m	3.722 m		
H-9′					3.721 s	3.730 s	3.635[g]		
H-10′							3.635[g]		
$C(CH_3)_3$			1.287 s	1.286 s					

[a] Spectra recorded in $CDCl_3$ at room temperature: s, singlet; d, doublet; t, triplet; dd, doublet of doublets; m, multiplet; br, broad signal.
[b] Data for free crown ethers are given for comparative purposes. DB18C6: 6.882 (2′,5′), 6.875 (3′,4′), 4.171 (7′), 4.049 (8′); mtbDB18C6: 6.935 (5′), 6.903 (3′), 6.804 (2′), 4.197, 4.151 (7′), 4.044, 4.016 (8′), 1.280 ($C(CH_3)_3$); DB24C8: 6.885 (2′,5′), 6.876 (3′,4′), 4.149 (7′), 3.918 (8′), 3.837 (9′); DB30C10: 6.888 (2′,5′), 6.886 (3′,4′), 4.146 (7′), 3.877 (8′), 3.772 (9′), 3.687 (10′).
[c] Partly overlapped H-2,6 and H-15,17.
[d] Overlapped with H-2′. Tentative value obtained from a COSY experiment.
[e] Overlapped with H-3′. Tentative value obtained from a COSY experiment.
[f] Overlapped with H-9′ and H-10′. Tentative value obtained from a COSY experiment.
[g] Partly overlapped with $POCH_2$.

in the methylene absorptions, arising from different skeletal structural and conformational changes and charge density variations within the macrocyclic ring during alkali complexation. In complexes of the 18-membered ring crown ethers, the $ArOCH_2$ protons (7′) exhibit an upfield shift of about 0.15 ppm. The $OCH_2CH_2O–CH_2$ protons (8′) are shifted upfield by 0.03 ppm in complexes of DB18C6, while in complexes of mtbDB18C6 this absorption overlaps with that of 7′ giving a broad singlet. The binding of sodium induces the same general spectral pattern observed for potassium complexation. In complexes of DB24C8 protons 7′ show a smaller upfield shift of only 0.03 ppm, while those of 8′ and 9′ are shifted by 0.06 and 0.11 ppm, respectively. Complexation of DB30C10 induces an upfield shift for protons 7′, 8′, 9′ and 10′ of 0.14, 0.16, 0.14 and 0.05 ppm, respectively (Fig. 3). It is worth noting that in spite of the complexation with the alkali cation, which by itself would induce a downfield shift due to the increased electronegativity of the oxygen ether atoms [42,43], in all the complexes the methylene resonances move to a higher field. This may be explained by a change in the position of the ether protons relative to that of the benzo groups, especially in the case of the larger crown ethers DB24C8 and DB30C10, as well as by the proximity of the crown ether molecule to the benzeneazophosphonate aromatic rings. No dissociation of salt complexes could be expected in the examined solvent and no spectral differences were observed as a function of concentration. It should be pointed out that a comparison of the literature spectral data of complexes of various crown ethers as well as those of various alkali metal salts indicates that not only the type of crown ether and cation, but also the anion and solvent could have an important role in the resulting chemical shift of the crown ether ring protons due to different solubilization and charge separation of the complexes in solution [38,44,45].

In the ^{13}C NMR spectra, differences between complexes of crown ethers with different cavity size could also be observed both for the aromatic and methylene carbon absorptions. In the complexes of DB18C6 and mtbDB18C6, all the carbon resonances show a certain upfield shift, which is more pronounced for the aromatic 1′,2′, 5′ and 6′ carbons and both methylene 7′ and 8′ carbons. It varies from 2.0 to 2.4 ppm in complexes **2** and **4**, and between 1.5 and 3.2 ppm in complexes **5** and **6**. While the aromatic protons 1′ and 6′ in the complexes of DB24C8 and DB30C10 show an upfield shift of 1.3–1.5 ppm (complexes **8** and **10**) and 0.6 ppm (complex **11**), the other aromatic carbons 2′–5′ are shifted to towards lower field by

Table 3
^{13}C NMR (δ, ppm; J, Hz) data of crown ether complexes and potassium benzeneazophosphonate salts[a,b].

Compound	**2**	**4**	**5**	**6**	**8**	**10**	**11**	KA_1	KA_2
C-1	140.22 $^2J_{PC}$ = 3.8	132.21 $^2J_{PC}$ = 3.7	139.13 $^2J_{PC}$ = 3.6	141.16 $^2J_{PC}$ = 3.6	140.32 $^2J_{PC}$ = 3.6	132.41 $^2J_{PC}$ = 3.3	140.59 $^2J_{PC}$ = 3.8	139.26 $^2J_{PC}$ = 3.5	131.18 $^2J_{PC}$ = 3.6
C-2,6	127.43 $^3J_{PC}$ = 3.9	128.50 $^3J_{PC}$ = 4.2	127.43 $^3J_{PC}$ = 4.1	127.26 $^3J_{PC}$ = 4.1	127.63 $^3J_{PC}$ = 4.0	128.59 $^3J_{PC}$ = 4.2	127.78 $^3J_{PC}$ = 4.8	127.47 $^3J_{PC}$ = 4.1	128.58 $^3J_{PC}$ = 4.2
C-3,5	127.54 $^4J_{PC}$ = 2.2	113.12	127.70 $^4J_{PC}$ = 2.1	127.45 $^4J_{PC}$ = 2.1	127.68 $^4J_{PC}$ = 2.2	113.45	127.68 $^4J_{PC}$ = 2.1	128.52 $^4J_{PC}$ = 2.3	113.97
C-4	125.67 $^5J_{PC}$ = 2.5	157.76 $^5J_{PC}$ = 2.5	125.87 $^5J_{PC}$ = 2.2	125.51 $^5J_{PC}$ = 2.2	125.65 $^5J_{PC}$ = 2.5	157.93	125.62 $^5J_{PC}$ = 2.4	127.22 $^5J_{PC}$ = 3.4	158.38 $^5J_{PC}$ = 2.5
OCH_3		55.00				55.03			55.18
C-7	151.12 $^3J_{PC}$ = 11.8	151.19 $^3J_{PC}$ = 12.4	151.98 $^3J_{PC}$ = 11.8	151.01 $^3J_{PC}$ = 12.4	151.72 $^3J_{PC}$ = 12.6	151.21 $^3J_{PC}$ = 12.2	151.80 $^3J_{PC}$ = 12.1	150.15 $^3J_{PC}$ = 13.0	150.04 $^3J_{PC}$ = 12.3
C-8,12	112.70	113.12	113.65	112.56	111.36	111.35	112.97	113.40	113.78
C-9,11	124.90	124.95	124.73	124.75	124.83	124.98	124.89	125.06	125.18
C-10	144.08	144.12	143.90	143.88	144.00	144.15	143.76	145.11	145.10
C-13	153.14	153.21	152.97	153.09	153.04	153.23	153.21	152.99	153.40
C-14,18	122.00	122.05	121.88	121.88	122.04	122.08	121.92	122.30	122.31
C-15,17	128.75	128.81	128.62	128.62	128.78	128.83	128.73	128.93	128.98
C-16	129.04	129.08	128.92	128.89	129.01	129.11	128.83	129.69	129.33
PCH	57.18 $^1J_{PC}$ = 130.6	56.38 $^1J_{PC}$ = 133.2	57.45 $^1J_{PC}$ = 135.6	57.28 $^1J_{PC}$ = 130.6	57.58 $^1J_{PC}$ = 130.8	55.81 $^1J_{PC}$ = 130.2	57.79 $^1J_{PC}$ = 130.9	56.70 $^1J_{PC}$ = 140.0	55.84 $^1J_{PC}$ = 133.2
$POCH_2$	60.77 $^2J_{POC}$ = 6.2	60.81 $^2J_{POC}$ = 6.2	61.18 $^2J_{POC}$ = 6.2	60.77 $^2J_{POC}$ = 6.1	60.87 $^2J_{POC}$ = 6.2	61.21 $^2J_{POC}$ = 5.7	60.83 $^2J_{POC}$ = 6.3	62.07 $^2J_{POC}$ = 7.0	62.23 $^2J_{POC}$ = 6.2
$POCH_2\mathbf{C}H_3$	16.79 $^3J_{POOC}$ = 6.2	16.88 $^3J_{POOC}$ = 6.2	16.73 $^3J_{POOC}$ = 6.1	16.70 $^3J_{POOC}$ = 6.2	16.76 $^3J_{POOC}$ = 6.1	16.73 $^3J_{POOC}$ = 6.1	16.68 $^3J_{POOC}$ = 6.2	16.68 $^3J_{POOC}$ = 6.1	16.77 $^3J_{POOC}$ = 6.2
C-1′	146.98	147.06	145.05	144.63	147.88	147.58	148.46		
C-2′	110.90	111.00	110.86	110.00	114.45	114.32	115.93		
C-3′	121.08	121.15	117.40	117.22	121.51	121.54	122.67		
C-4′	121.08	121.15	144.37	144.23	121.51	121.54	122.67		
C-5′	110.90	111.00	109.36	108.35	114.45	114.32	115.93		
C-6′	146.98	147.06	146.77	146.35	147.28	147.58	148.46		
C-7′	66.94	67.04	68.58; 68.55	68.26; 68.29	67.94	68.13	68.65		
C-8′	68.21	68.30	67.18; 67.08	66.84; 66.64	68.91	69.53	68.73		
C-9′					70.02	70.11	68.80		
C-10′							68.97		
$\mathbf{C}(CH_3)_3$			34.30	34.29					
$C(\mathbf{C}H_3)_3$			31.36	31.36					

[a] Spectra recorded in $CDCl_3$ at room temperature.
[b] Data for free crown ethers are given for comparative purposes. DB18C6: 148.92 (1′,6′); 113.28 (2′,5′); 121.13 (3′,4′), 69.05 (7′), 69.71 (8′); mtbDB18C6: 146.71 (1′), 113.64, 113.61 (2′), 117.91, 117.89 (3′), 144.57 (4′), 112.54, 112.50 (5′), 148.28 (6′), 70.08, 70.06, 69.97, 69.96 (7′), 69.48, 69.36, 69.24, 69.11 (8′), 34.20 ($\mathbf{C}(CH_3)_3$), 31.36 ($C(\mathbf{C}H_3)_3$); DB24C8: 148.82 (1′,6′), 113.97 (2′,5′), 121.28 (3′,4′), 69.27 (7′), 69.79 (8′), 71.13 (9′); DB30C10: 149.06 (1′,6′), 114.58 (2′,5′), 121.54 (3′,4′), 69.16 (7′), 69.82 (8′), 70.92 (9′), 70.74 (10′).

0.25–0.4 ppm and about 1.3 ppm, respectively. All the methylene carbons in these complexes are shifted upfield, but to various extents. Thus, in complexes of DB24C8 this shift is about 1.2 ppm for 7′ and 1.0 ppm for 8′ and 9′ carbons, while in the complex of DB30C10 the upfield shift for 7′ is only 0.4 ppm, that for 8′ is 1.2 ppm, while 9′ and 10′ are shifted by about 2 ppm.

The spectral pattern of the benzeneazophosphonate anion in all the complexes examined exhibited similar basic spectral characteristics. In comparison to the free alkali phosphonates some changes could be observed for resonances of the aminophosphonate group and those aromatic protons and carbons in the vicinity of this group. Thus, there is a downfield shift of 0.04–0.09 ppm for the $POCH_2$ protons, and an upfield shift of 0.1–0.2 ppm for the NH resonance and 0.07–0.24 ppm for the aromatic 3,5; 4; 8,12 and 9,11 protons. Small changes could also be observed for the corresponding carbon resonances (0.6–1.8 ppm).

3.5. In vitro cytostatic activity

The cytostatic activity of the crown ether complexes was assayed *in vitro* against the murine leukemia L1210, the murine mammary carcinoma FM3A and the human T-lymphocyte CEM and MT-4 cell lines. The results of the crown ether complexes **1–11**, expressed as the micromolar concentration of the compound required to inhibit tumor cell growth by 50% (IC_{50}), are listed in Table 4, together with those of the free crown ethers as well as the sodium (NaA_1) and potassium (KA_2) salt of the monoethyl benzeneazophosphonic acids. These compounds were assayed in order to evaluate the effect of the constitutional parts of the complex molecules on tumor cell growth and to assess their individual activity.

All the tested compounds showed antiproliferative activity against the examined cell lines. The IC_{50} concentrations of the complexes varied from 2 to 70 μM, while those of the crown ethers and alkali benzeneazophosphonate salts were within 1.4–160 and 300–500 μM, respectively. In general, most of the complexes are slightly more cytostatic to L1210 and FM3A cells than to the CEM and MT-4 cells. Except for DB18C6, this difference is not pronounced in the free crown ethers or in the benzeneazophosphonate salts NaA_1 and KA_2. Very weak, if any, growth-inhibitory effects of the phosphonate salts (IC_{50} > 300 μM) indicate that this part of the complex molecule does not influence the cytostatic ability of the complex. Both the free crown ethers and their complexes have much stronger antiproliferative effects and the results obtained clearly demonstrate that the crown ether part of the complex is responsible for its cytostatic activity. When comparing the activity between

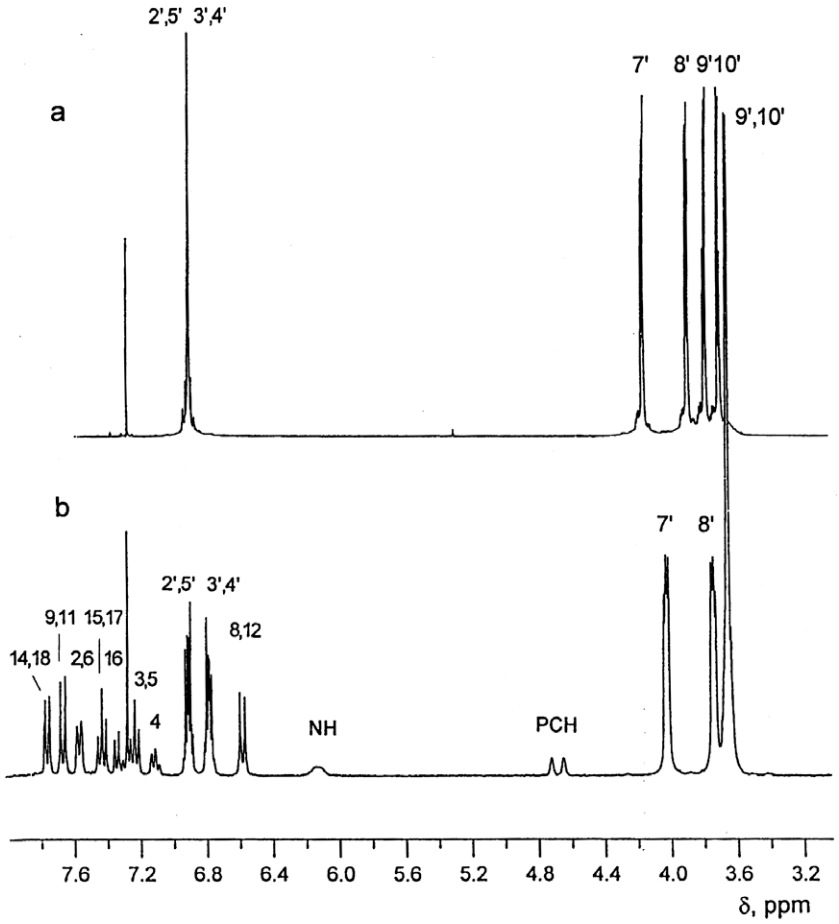


Fig. 3. ^{1}H NMR spectra of (a) DB30C10 and (b) K(DB30C10)A_1.

Table 4
In vitro cytostatic activity of the crown and benzeneazophosphonate compounds.

Compound	IC_{50} (μM)[a]			
	L1210[b]	FM3A[c]	CEM[d]	MT-4[e]
DB18C6	53.1 ± 7.2	44.6 ± 3.9	159 ± 7	>250
1	42.0 ± 0.0	44.4 ± 0.3	71.4 ± 9.4	78 ± 24
2	38.2 ± 1.7	34.0 ± 3.6	46.5 ± 0.8	60 ± 4.3
3	41.4 ± 3.1	40.3 ± 2.7	43.8 ± 2.0	70 ± 8.6
4	16.5 ± 1.4	26.1 ± 2.7	26.8 ± 1.0	13 ± 0.56
mtbDB18C6	1.38 ± 0.02	1.40 ± 0.06	1.61 ± 0.21	1.30 ± 0.25
5	2.09 ± 0.08	1.77 ± 0.19	2.76 ± 0.12	2.30 ± 0.0
6	1.90 ± 0.01	1.74 ± 0.16	2.48 ± 0.01	1.80 ± 0.15
DB24C8	41.2 ± 3.77	66.6 ± 2.66	43.0 ± 14.4	122 ± 15
7	49.3 ± 4.5	52.1 ± 0.1	67.2 ± 9.5	63 ± 66
8	50.3 ± 2.8	53.4 ± 0.3	59.5 ± 15.4	61 ± 7.1
9	42.1 ± 0.1	47.1 ± 1.8	41.6 ± 1.8	51 ± 8.1
10	46.9 ± 0.1	56.7 ± 1.6	45.0 ± 3.5	63 ± 8.3
DB30C10	21.1 ± 0.56	25.1 ± 1.48	25.0 ± 0.74	14 ± 1.5
11	25.0 ± 0.3	9.85 ± 0.91	35.1 ± 3.5	21 ± 13
NaA_1	342 ± 96	301 ± 31	304 ± 20	>300
KA_2	392 ± 101	477 ± 32	462 ± 3	>300
HA_2[f]	198 ± 5		174 ± 1	
EtA_2[g]	25 ± 1		17 ± 3	

[a] 50% Inhibitory concentration.
[b] L1210 – murine leukemia cells.
[c] FM3A – murine mammary carcinoma cells.
[d] CEM – human T-lymphocyte cells.
[e] MT-4 – human T-lymphocyte cells.
[f] Monoethyl ester of [α-(benzeneazoanilino)-*N*-4-methoxybenzyl]phosphonic acid (R = OCH_3, R_1 = H in Fig. 1).
[g] Diethyl ester of [α-(benzeneazoanilino)-*N*-4-methoxybenzyl]phosphonic acid (R = OCH_3, R_1 = Et in Fig. 1).

the crown ethers and their metal complexes, it could be seen that only complexes of DB18C6 are more active than the free parent crown ether, while complexes of the other crown ethers were slightly less active. In general, the tested compounds show a growth-inhibitory effect of the following order:

Crown ethers: mtbDB18C6 >> DB30C10 > DB24C8 ~ DB18C6

Crown ether complexes: mtbDB18C6 (**5**,**6**) >> DB30C10 (**11**) ⩾ DB18C6 (**1**–**4**) > DB24C8 (**7**–**10**).

There is, in general, a good correlation for the IC_{50} values against the different tumor cell lines (Table 4). The greatest activity demonstrated that mtbDB18C6 and its complexes (IC_{50} values of 1.4–2.5 μM) have ca. 10–30 times higher cell growth-inhibitory effects with respect to the other crown ether compounds. These findings may arise from the higher solubility and lipophilicity of these compounds caused by the presence of the bulky *tert*-butyl groups in the crown ether molecule, and this may facilitate their transport through the cellular membranes. The potassium complexes of DB18C6 and mtbDB18C6 are slightly more active than their sodium analogues, while there are no substantial differences in inhibitory activity between the corresponding sodium and potassium complexes of DB24C8. Furthermore, complexes derived from the non-substituted benzeneazophosphonates (Na/KA_1) are slightly less active than those of the methoxy-substituted phosphonates (Na/KA_2), which could be ascribed to lower solubility and lipophilicity of the former complexes. Generally, a fairly good relationship could be seen between the activity and solubility of the complexes and the free crown ethers.

It is interesting to note that comparing the activity of the potassium salt KA_2 with those of the corresponding diester and

monoester phosphonate derivatives EtA_2 and HA_2 (see Table 4), it could be seen that the monoester is ca. twice more active than its alkali salt, while the diester shows about twenty times higher activity. The greater activity of the diester may be ascribed to higher lypophilicity of this compound, which increases with increasing bulkiness from the monoester to the diester derivatives. On the other hand, the presence of the acidic phosphonate group in the monoester may cause the opposite effect. It is important to point out that all phosphonate derivatives, i.e. the ethyl phosphonates, the corresponding sodium salts and their crown ether complexes, were prepared and investigated in the racemic form. These compounds contain an asymmetric PCH carbon atom (diester) or both the carbon and phosphorus atoms (monoester derivatives). The cytotoxicity of the aniline-based ethyl phosphonates (EtA_2 and HA_2) is similar to that of the quinoline-based ethyl phosphonates without a chiral center in their molecules [46] and some palladium(II) and platinum(II) complexes of both types of alkyl phosphonates have shown pronounced antiproliferative effects [47].

3.6. In vitro antiviral activity

The compounds listed in Table 4 were also evaluated for their antiviral activity. The antiviral assays were based on the inhibition of virus-induced cytopathogenicity. Following viruses were investigated: herpes simplex virus type 1 (HSV-1) and type 2 (HSV-2), vaccinia virus (VV) and vesicular stomatitis virus (VSV) in human lung embryonic HEL cell cultures; Coxsackie B4 virus, vesicular stomatitis virus (VSV) and respiratory syncytial virus (RSV) in human cervix carcinoma HeLa cell cultures; parainfluenza-3 virus, reovirus-1, Sindbis virus, Coxsackie B4 virus and Punta Toro virus in African green monkey Vero cell cultures; human immunodeficiency virus type 1 [HIV-1(III_B)] and type 2 HIV-2(ROD) in human lymphocyte MT-4 cell cultures. The results obtained are given as Supplementary material. The antiviral activity of the evaluated compounds, expressed as the concentration of the compound required to reduce virus-induced cytopathogenicity by 50%, as well as their cytotoxicity expressed as the concentration of the compound required to destroy 50% of mock-infected cells, have shown that all compounds exhibited no antiviral activity at subtoxic concentrations to the host cells. For a specific antiviral effect the compound needs to block the virus at a concentration that is $\geqslant$5 fold lower than the cytotoxic concentration.

4. Conclusion

Sodium and potassium benzeneazophosphonate complexes of crown ethers with 18-, 24- and 30-membered macrocyclic rings have been prepared by reactions in the solid state under microwave irradiation, as a first example of microwave-supported synthesis of pure oxa-crown ether complexes. The simple work-up, eco-friendly solvent free reactions resulted in complex formation in a shorter reaction time and with excellent yields, compared to conventional thermal reactions in solution. Investigation of the cytostatic activity *in vitro* of the free crown ethers, their alkali metal complexes and the free benzeneazophosphonate salts in murine leukemia L1210, murine mammary carcinoma FM3A and human T-lymphocyte CEM and MT-4 cell lines have shown that only the crown ethers and their complexes exhibit tumor cell growth-inhibitory effects. The greatest activity with IC_{50} values in the lower micromolar range was observed for *tert*-butyl-substituted dibenzo-18-crown-6 and its complexes, most probably due to a higher lipophilicity and better cellular uptake. Since, in general, there are no substantial differences in activity between the free crown ethers and their complexes, it could be presumed that alkali benzeneazophosphonate complexation does not facilitate or enhance the inherent mode of action of the crown ether. The only exception is a greater activity of complexes of DB18C6 against CEM cells. All investigated compounds had no specific antiviral activity.

Acknowledgements

Financial support granted by the Croatian Ministry of Science, Education and Sports (Grant No. 098-0982915-2950) and the "Geconcerteerde Onderzoeksacties" (No. GOA-05/19) of the K.U.Leuven is gratefully acknowledged. The authors would like to thank Mr. Ž. Marinić for recording the NMR spectra, and Lizette van Berckelaer, Frieda De Meyer, Anita Van Lierde, Kris Uyttersprot and Kristien Erven for excellent technical assistance.

Appendix A. Supplementary data

Supplementary data associated with this article can be found, in the online version, at doi:10.1016/j.poly.2009.07.044.

References

[1] C.J. Pedersen, J. Am. Chem. Soc. 89 (1967) 2495.
[2] C.J. Pedersen, J. Am. Chem. Soc. 89 (1967) 7017.
[3] G. Gokel, Crown Ethers and Cryptands, Royal Society of Chemistry, Cambridge, 1991. pp. 64–98.
[4] J.-M. Lehn, Supramolecular Chemistry, VCH, Weinheim, 1995.
[5] R.M. Izatt, K. Pawlak, J.S. Bradshow, Chem. Rev. 91 (1991) 1721.
[6] J.W. Steed, Coord. Chem. Rev. 215 (2001) 171, and references cited therein.
[7] C.M. Stark, C.L. Liotta, Phase Transfer Catalysis-Principles and Techniques, Academic Press, New York, 1978.
[8] R.M. Izatt, J.J. Christensen, Process in Macrocyclic Chemistry, Wiley Interscience, New York, Vol. 1, 1981; Vol. 2, 1982.
[9] J.D. Lamb, R.M. Izatt, J.J. Christensen, in: R.M. Izatt, J.J. Christensen (Eds.), Progress in Macrocyclic Chemistry, Stability Constants of Cation Macrocycle Complexes, and Their Effect on Facilitaded-Transport Rates, Wiley-Interscience, New York, 1981 (Chapter 2).
[10] B.A. Moyer, in: G.W. Gokel (Ed.), Comprehensive Supramolecular Chemistry, Molecular Recognition: Receptors for Cationic Guests, vol. 1, Elsevier Science Ltd., Oxford, 1996, pp. 377–416.
[11] Lj. Tušek-Božić, E. Marotta, P. Traldi, Polyhedron 26 (2007) 1663–1668.
[12] D.M.P. Mingos, D.R. Baghurst, Chem. Soc. Rev. 20 (1991) 1.
[13] P. Castan, B. Labiad, D. Villemin, F.L. Wimmer, S. Wimmer, J. Organomet. Chem. 479 (1994) 153.
[14] B. Desai, T.N. Danks, G. Wagner, J. Chem Soc., Dalton Trans. (2004) 166.
[15] D.R. Baghurst, S.R. Cooper, D.L. Greene, D.M.P. Mingos, S.M. Reynolds, Polyhedron 9 (1990) 893.
[16] L.S. Hegedus, M.J. Sundermann, P.K. Dorhout, Inorg. Chem. 42 (2003) 4346.
[17] M. Kralj, Lj. Tušek-Božić, L. Frkanec, ChemMedChem 3 (2008) 1478.
[18] M. Naumowicz, A.D. Petelska, Z.A. Figaszewski, Cell. Mol. Biol. Lett. 8 (2003) 383.
[19] W.M. Leevy, M.E. Weber, M.R. Gokel, G.B. Hughes-Strange, D. Daranciang, R. Ferdani, G.W. Gokel, Org. Biomol. Chem. 3 (2005) 1647.
[20] M. Marjanović, M. Kralj, F. Supek, L. Frkanec, I. Piantanida, T. Šmuc, Lj. Tušek-Božić, J. Med. Chem. 50 (2007) 1007.
[21] R. Binggeli, I.L. Cameron, Cancer Res. 40 (1980) 1830.
[22] L.A. Fieber, J. Neurosci. Res. 54 (1998) 495.
[23] R. Fukuda, S. Takenaka, M. Takagi, Chem. Commun. (1990) 1028.
[24] T. Ihara, S. Sueda, A. Inenaga, R. Fukuda, M. Takagi, Supramol. Chem. 8 (1997) 93.
[25] M.M. McPhee, J.T. Kern, B.C. Hoster, S.M. Kerwin, Bioorg. Chem. 8 (2000) 98.
[26] J. Yoo, Y.S. Sohn, Y. Do, J. Inorg. Biochem. 73 (1999) 187.
[27] V. Jagodić, Lj. Tušek, J. Org. Chem. 37 (1972) 1222.
[28] Lj. Tušek, V. Jagodić, Croat. Chem. Acta 49 (1977) 829.
[29] Lj. Tušek-Božić, D. Sevdić, Polyhedron 4 (1985) 1959.
[30] Lj. Tušek-Božić, M. Ćurić, Polyhedron 7 (1988) 2761.
[31] Lj. Tušek-Božić, D. Sevdić, Polyhedron 5 (1986) 877.
[32] J. Balzarini, C. Pannecouque, E. De Clercq, A.Y. Pavlov, S.S. Printsevskaya, O.V. Miroshnikova, M.I. Reznikova, M.N. Preobrazhenskaya, J. Med. Chem. 46 (2003) 2755.
[33] R. Pauwels, E. De Clercq, J. Desmyter, J. Balzarini, P. Goubau, P. Herdewijn, H. Vanderhaeghe, M. Vandeputte, J. Virol. Methods 16 (1987) 175.
[34] J. Balzarini, L. Naesens, J. Slachmuylders, H. Niphuis, I. Rosenberg, A. Holý, H. Schellekens, E. De Clercq, AIDS 5 (1991) 21.
[35] R.M. Izatt, K. Pawlak, J.S. Bradshow, R.L. Bruening, Chem. Rev. 95 (1995) 2529.
[36] Lj. Tušek-Božić, Spectrochim. Acta 45A (1989) 1053.
[37] Lj. Tušek-Božić, Electrochim. Acta 39 (1994) 471. and references cited therein.

[38] I. Matijašić, P. Dapporto, P. Rossi, Lj. Tušek-Božić, Supramol. Chem. 13 (2001) 193.
[39] M. Herceg, Lj. Tušek-Božić, Annual Yugoslav Centre Crystallogr., vol. 24, 1989, S39–S40.
[40] Lj. Tušek-Božić, B. Božić, Electrochim. Acta 35 (1990) 59.
[41] S.V. Trepalin, A.V. Yarkov, A.F. Solotnov, O.A. Raevsky, Spectrochim. Acta A55 (1999) 1715.
[42] D. Live, S. Chan, J. Am. Chem. Soc. 98 (1976) 3769.
[43] S.V. Santhana Mariappan, L. Gomathi, S. Subramanian, Magn. Reson. Chem. 29 (1991) 656.
[44] E. Kleinpeter, S. Stoss, M. Gabler, W. Schroth, Magn. Reson. Chem. 27 (1989) 676.
[45] K.H. Wong, G. Konizer, J. Smid, J. Am. Chem. Soc. 92 (1970) 666.
[46] Unpublished results.
[47] Lj. Tušek-Božić, M. Juribašić, P. Traldi, V. Scarcia, A. Furlani, Polyhedron 27 (2008) 1317, and references cited therein.

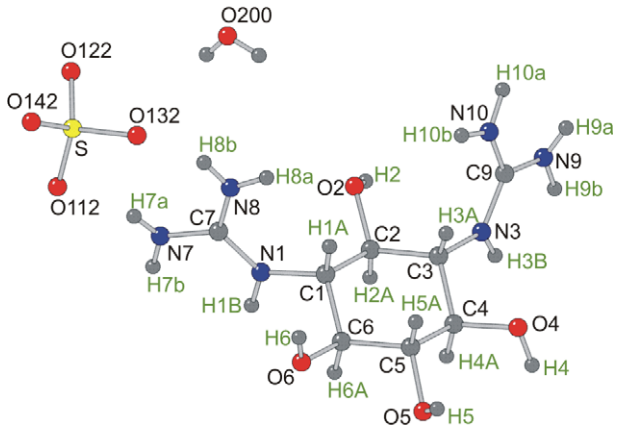


Fig. 1. Atomic numbering and ball and stick representation of the structure $(H_2Std)(SO_4)(H_2O)$, as taken from its crystal structure (*vide infra*). Hydrogen atoms are labeled in green for the sake of clarity. Nitrogen atoms are in dark blue, oxygen in red, sulfur in yellow and carbon and hydrogen in grey colours. (For interpretation of the references to color in this figure legend, the reader is referred to the web version of this article.)

defined parts, both of them with expected bioactivity: (i) as a platinum drug, the anticancer properties of the final complex would be tested; (ii) by utilizing the activity and fluorescence properties of the ligand (H_2Std), *in vitro* studies using digital fluorescence microscopy could be performed and additional antibacterial studies can also be carried.

This paper describes the synthesis and detailed characterization (including Pt L_3- and Cl K-edge XAS) of the first solid platinum–streptidine compound (**1**, $(H_2Std)PtCl_4$). An accurate X-ray diffraction study of the hydrated H_2Std sulfate was performed at room temperature, to assist in the characterization of compound **1**. However, during the preparation for publication of this work, a structural report of H_2Std sulfate at low *T* was published [34], so in this manuscript we will only elude to some of the most relevant features of the former to assist the structural refinement of $(H_2Std)PtCl_4$.

Finally, in this manuscript the results of biological *in vitro* studies of compound **1** (cytotoxicity, UV–Vis titration, fluorescence and antibacterial experiments) will be discussed.

2. Experimental

2.1. Chemistry

K_2PtCl_4 was obtained from Johnson and Matthey and 3-acetylpyridine was used without further purification as purchased from Aldrich. Synthesis was performed in the absence of light, and the final product was kept away from light to avoid any photochemical decomposition.

Infrared spectra were recorded from 4000 to 300 cm^{-1} on Perkin–Elmer Paragon 1000 FTIR spectrometer equipped with a Golden Gate ATR device, using the reflectance technique. ^1H, ^{13}C and ^{195}Pt NMR experiments were performed on a Bruker DPX 300 spectrometer, with measurements carried out at room temperature in dmso-d_6. Elemental analysis of C, H, N were carried out on a Perkin–Elmer 2400 series II analyzer. Pt analysis was carried out by AAS and ICP. Electrospray ionization-mass spectra (ESI-MS) were achieved from dmso (dimethyl sulfoxide) and recorded on a Thermo Finnigan AQA apparatus. XAS and EXAFS experiments were performed at the Stanford Synchrotron Radiation Lightsource (SSRL), as described below.

2.2. X-ray measurements

Diffraction data for the H_2Std sulfate monohydrate were collected at room temperature on a Siemens P4 diffractometer using standard procedures [35] (see Table S1 and the deposited CIF file for details). Handedness of the enantiomorphic space group was arbitrarily chosen and the structure refined in $P3_1$ on the basis of non-corrected data. The relative stereochemistry of chiral centers was assigned after refining a Flack parameter, which corresponds to that expected for a Std derivative. The high resolution of the diffraction data allowed for accurate determination of the H atom positions [36]. The sulfate ion appeared to be disordered over two positions. Sulfate O atoms were found distributed over two sites, and their respective occupancies refined with their sum constrained to 1. Site occupation factors converged to 0.775(7) and 0.225(7). Final least-squares cycles were performed without restraints or constraints for the geometry.

2.3. Cytotoxicity studies

The A2780 and A2780R cells were generously provided by Dr. J.M. Perez (Universidad Autónoma de Madrid, Spain). The cells were grown as monolayers in Dulbecco's modified Eagle's Medium supplemented with 10% fetal calf serum (Gibco, Paisley, Scotland), penicillin (100 units/mL: Dufecha, the Netherlands) and streptomycin (100 μg/mL: Dufecha, the Netherlands). The L1210 and L1210R cell lines were cultured in McCoy's 5a medium supplemented with 10% fetal calf serum (Gibco, Paisley, Scotland), penicillin (100 units/mL: Dufecha, the Netherlands) and streptomycin (100 μg/mL: Dufecha, the Netherlands).

For the cell growth assay, cells were pre-cultured in 96 multiwell plates for 48 h at 37 °C in a 5% CO_2 containing incubator and subsequently treated with 45 μL of compound in triplicate. After 48 h incubation, 50 μL of a 5 mg/mL MTT solution in PBS was added to each well, and allowed to develop at 37 °C for 2 h. After this, the medium was removed carefully and 100 μL of dmso was added to each well. The absorbance of the resulting purple solutions were measured at 590 nm using a Biorad 550 microplate reader. The cytotoxicity is determined by the IC_{50} values of each compound. The IC_{50} values are drug concentrations that inhibit cell growth for 50% with respect to control. The lower the IC_{50} value the better anti-tumor activity can be expected. The numbers were determined graphically using Graphpad Prism analysis software.

2.4. UV–Vis titration

UV–Vis titration experiments were performed in order to clearly discern the behavior of the Pt complex and CT-DNA at different ratios and also to support previous CD analysis. Tris buffer pH 7.2 was used in all the solutions and variations on the amount of platinum compound versus a constant concentration of DNA were accomplished (*R* ratio from 5 to 0.3). Data were collected on Varian Cary 50 UV–Vis Spectrophotometer with new Fiber Optic Dip Probe accessory. The Cary 50 utilizes a very long-life Xenon source lamp with wavelength range between 190 and 1100 nm as well as photometric range of +/−3.3 Å.

2.5. XAS

All data were measured at the Stanford Synchrotron Radiation Lightsource (SSRL) under ring conditions of 3.0 GeV and 60–100 mA.

Pt L_3-edge XAS data were measured on focused 16-pole wiggler beam line 9-3. A Si(2 2 0) monochromator was utilized for energy selection. A harmonic rejection mirror was (set to a 15 keV cutoff) was used to minimize higher harmonic components in the X-ray

beam. Solid samples were prepared in a matrix with boron nitride, pressed into a pellet and sealed between 38 μm Kapton tape windows in a 1 mm aluminum spacer. Solution samples (3.8 mM) were dissolved in dmso. The samples were maintained at 10 K during data collection using an Oxford Instruments CF1208 continuous flow liquid helium cryostat. Data were measured in transmission mode or fluorescence mode, for solid and solution samples, respectively. Internal energy calibrations were performed by simultaneous measurement of a Pt reference foil placed between a second and third ionization chamber. The first inflection point of the Pt L_3-edge was assigned to 11563.0 eV. Data represent three to six scan averages and were processed by fitting a second order polynomial to the pre-edge region and subtracting this background from the entire spectrum. A three-region cubic spline was used to model the smooth background above the edge. The data were normalized by subtracting the spline and normalizing the post-edge 1.0.

All Cl K-edge data were measured using the 54-pole wiggler beam line 6-2 in high magnetic field mode of 10 kG with a Ni-coated harmonic rejection mirror and a fully tuned Si(1 1 1) double crystal monochromator. Data were measured at room temperature by fluorescence, using a Lytle detector. To check for reproducibility, 2–3 scans were measured for each sample. The energy was calibrated from Cl K-edge spectra of Cs_2CuCl_4, run at intervals between sample scans. The maximum of the first pre-edge feature in the spectrum was fixed at 2820.20 eV. Data were averaged, and a smooth background was removed from all spectra by fitting a polynomial to the pre-edge region and subtracting this polynomial from the entire spectrum. Normalization of the data was accomplished by fitting a flattened polynomial or straight line to the post-edge region and normalizing the post-edge to 1.0.

3. Results and discussion

3.1. Synthesis of H_2Std sulfate

Although we have previously reported the preparation of streptidine [21], here we present a more detailed description of the crystalline preparation. Streptomycin (5.38 g, 14.23 mmol) was dissolved in H_2O (420 mL), acetone (350 mL) and concentrated H_2SO_4 (10 mL). After two days refluxing the solution turned orange and a white precipitate gradually appeared, corresponding to the solid streptidine sulfate. The solution was filtered and stored at 4 °C. After few days crystals of $(H_2Std)SO_4(H_2O)$ were formed. The crystals were filtered and washed with acetone and cold water.

3.2. Crystallographic structures of H_2Std sulfate monohydrate

Preliminary crystallographic studies have been reported for this salt, using powdered samples [37] and single crystals [21] very recently Leśniewska et al. [34] reported a low-temperature diffraction study of the streptidine sulfate monohydrate. The Supplementary data of this manuscript shows the high resolution structural analysis that we performed at room temperature, to provide a more precise picture of the free ligand and a better understanding of the final platinum compound.

The refinement of both structures is rather similar, corroborating that the H_2Std sulfate monohydrate conserves at RT the same structural features observed at 100 K. For the following discussion, the projection of the asymmetric unit and a view of the crystal structure are given in Figs. 1 and 2, respectively. Tables with structural parameters, selected bond lengths and angles as well as a more accurate description of the structure are given in the Supplementary data (Tables S1–S3) and in the deposited CIF file.

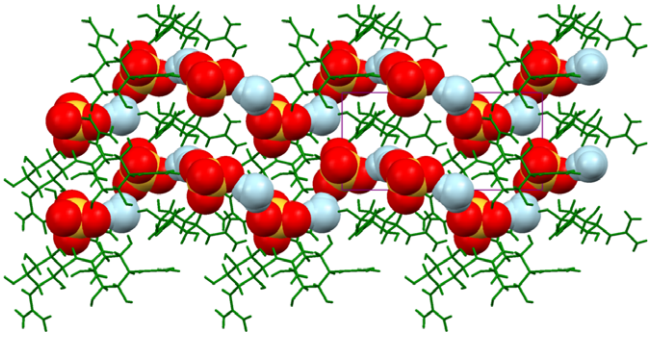


Fig. 2. A part of the crystal structure of $H_2Std^{2+}SO_4^{2-}\cdot H_2O$ viewed along the *b* axis of the trigonal cell. Sulfate (red and yellow) and water molecules (light blue) are displayed using a spacefill style. The 3_1 screw axes are in the plane of projection, generating 1D anionic chains. H_2Std^{2+} cations (green) are represented with capped sticks. For clarity, a single orientation is shown for sulfate, corresponding to the highest site-occupation factor. (For interpretation of the references to color in this figure legend, the reader is referred to the web version of this article.)

A quite original feature of the crystal structure (Fig. 2) is the remarkably complex network of hydrogen bonds, involving all available donor and acceptor groups, i.e. amine and guanidine N–H, hydroxyl O–H, lattice water molecule, and sulfate O atoms (see Supplementary data, Table S3).

In relation to the general goal of our work, the role of the water molecules (light blue, Fig. 2) in the crystal structure deserves a special comment. Lattice solvent does not merely fill the voids in the crystal. It has an essential function as a building block of the anionic matrix, which accommodates cations. On the other hand, because of the limited dimensionality of that matrix, 1D, and the fact that hydrogen bonds are not too strong, we can assume that anionic chains dissociate easily in aqueous media. The salt $H_2Std^{2+}SO_4^{2-}\cdot H_2O$ is therefore a good starting material for our purpose: the H_2Std^{2+} cation, once available in-solution, should work as an efficient shuttle for any anionic Pt-containing moiety, providing that both moieties form a bond, for instance a classic coordination of Std to the metal.

3.3. Synthesis of the platinum–streptidine compound (**1**)

Streptidine (0.025 g, 0.07 mmol), $(H_2Std)(SO_4)(H_2O)$, was dissolved in H_2O (2.5 mL) and added to a 2.5 mL of an aqueous solution of 0.086 mg (0.21 mmol) of K_2PtCl_4. The reaction was protected from the light and stirred at room temperature. After two days, a dark green precipitate ($(H_2Std)PtCl_4$) was isolated by filtration, washed with H_2O and dried with diethyl ether. The observed yield was 20%. IR (KBr), ν (cm^{-1}): 3312, 1634, 1597, 1406, 1392, 1366, 1216, 1084, 1033, 993, 953 and 466; EA: for $Pt(H_2Std)Cl_4\cdot 2H_2O$, *Anal.* Calc. for $C_8H_{24}N_6O_6Cl_4Pt$: C, 15.08; H, 3.80; N, 13.19. Found: C, 14.81; H, 3.16; N, 12.88%. A fit on a second sample also agreed with formula $Pt(H_2Std)(OH)_{0.5}Cl_{3.5}(H_2O)_{2.5}$, *Anal.* Calc. for $C_8H_{25.5}N_6O_7Cl_{3.5}Pt$: C, 15.08; H, 4.04; N, 13.19; Cl, 19.48. Found: C, 14.87; H, 3.42; N, 12.84; Cl, 19.48%.

3.4. Spectroscopic characterization of $(H_2Std)PtCl_4$ (**1**)

After mixing H_2Std sulfate (white solid) with K_2PtCl_4, a dark green precipitate, corresponding to $(H_2Std)PtCl_4$ resulted. The final, colored compound was soluble in dimethyl sulfoxide and dimethyl formamide. However, we were unable to obtain suitable crystals and in the absence of crystallographic information, XAS and EXAFS experiments were thus utilized to characterize the structures (see Section 3.6).

In the solid state, the IR spectrum of the $(H_2Std)PtCl_4$ complex shows shifted and attenuated bands compared with free streptidine, all over the range between 300 and 4000 cm^{-1}; however, one of the most significant changes in the infrared spectrum of **1** is the absence of two intense bands at approximately 1100 and 1068 cm^{-1}, associated to the SO_4^{2-} counterion, suggesting either a neutral species, or an exchange of the counterion from sulfate to Cl^- anions. These observations were reinforced by elemental analysis in which the green precipitate fitted well with a $(H_2Std)PtCl_4(H_2O)_x$ formula ($x = 1–4$ depending on the sample). This formulation involves a streptidine molecule in its protonated form, implying weak interactions between the Pt moiety and the streptidine instead of the formation of a coordination bond. On the other hand, the Pt–ICP results agreed with the theoretical value of 32.67% of Pt, expected for a $(H_2Std)PtCl_4$ molecule.

Several experiments in solution corroborated these results: the molecular ion peaks M^+ (ESI^+-MS in dmso) for $(H_2Std)PtCl_4$ species included Pt and H_2Std in a 1:1 ratio, (see *Fig.* S1). Some of these arrays can only be achieved by varying the charge of H_2Std from +2 to 0, i.e. implying total or partial deprotonation of the streptidine under these conditions. The presence of dmso in the sample as a part of the ionic units shows the replacement of one or more Cl^- ions by dmso molecules. Such a feature is not at all surprising and has been reported before in the literature taking into account the greater affinity that this metal has for S ions [38].

The electronic spectra of $(H_2Std)PtCl_4$ was recorded in dimethyl sulfoxide between 250 and 500 nm. Comparison with the free ligand sulfate was not possible due to the limited solubility of the streptidine in organic solvent. The absorbance of $(H_2Std)PtCl_4$ with time is shown in *Fig.* S2. In dmso, compound **1** resulted in a transparent, yellow solution after continued stirring for several minutes. This change is consistent with the replacement of at least one coordinated Cl^- ion for a dmso molecule. Compound **1** showed a broad and intense band at approximately 290 nm, which can be assigned to a combination of metal–ligand charge transfer and d–d bands [39], and in general, intense bands around 300 nm which may also be indicative of interactions between adjacent platinum atoms, related in this case with the intensity of the color of $(H_2Std)PtCl_4$.

3.5. NMR studies

As mentioned above, detailed comparison of the ^1H NMR of free streptidine and $(H_2Std)PtCl_4$ in dmso was not suitable and did not yield useful information. Nevertheless, the ^1H NMR spectrum of **1** in dmso-d_6 (Fig. 3) presented clean sets of peaks that could be divided in three series depending on their chemical shifts: from 3.11 to 3.30 ppm (broad peaks, partly overlapped with the water from the solvent), from 5.14 to 5.67 ppm (three sets of doublets) and from 7.00 to 7.57 ppm (a broad band and a sharp doublet), respectively. Taking into account the nature of the H_2Std protons, the peaks at ~3.11 ppm were associated to the –CH of the cycle and the rest of signals, to the H atoms from the –OH, –NH and $–NH_2$ groups.

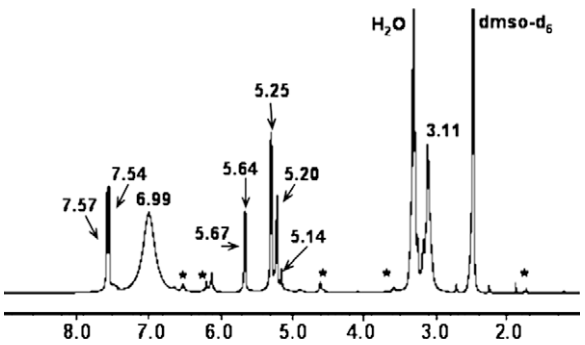


Fig. 3. ^1H NMR of $(H_2Std)PtCl_4$ recorded in dmso-d_6.

The ^{13}C NMR spectrum of the $(H_2Std)PtCl_4$ in dmso-d_6 (Fig. 4) provided even more valuable information: it showed five different chemical shifts at 58.9, 70.9, 71.7, 75.9 and 158.1 ppm. The assignment of the peaks was performed by comparison with the free ligand (in D_2O), their intensity and additional ^{13}C NMR where the quaternary character of the single peak (involving to 2C atoms) at 158.1 ppm and the *tertiary* nature of the rest of the peaks were identified. The spectrum in D_2O of the free-H_2Std showed the same number of peaks with chemical shifts at 59.3, 71.7, 72.4, 75.6 and 159.1, respectively. The intensities for both were 2:1:2:1:2. The number of peaks revealed to basic two aspects: (i) that in solution the final Pt complex exhibited high symmetry, almost identical to the free streptidine and (ii) that the chemical shifts differ slightly from the free ligand (<1 ppm, Table 1) providing some insight on the strength of the interaction between the Pt and the H_2Std.

Altogether, this result was found compatible with our previous work, using additional 3d metals (Ni, Co and Cu) [21], and strongly pointed to the ionic nature of the interactions in complex **1,** where $PtCl_4^{2-}$ would function as a counterion stabilizing the charge of the streptidine ligand. Thus, the putative structure of this compound could be also related to that established for the free streptidine (see Section 3.2), where instead of SO_4^{2-} anions in a pseudo-tetrahedral geometry among the H_2Std^{2+} species, we now would find tetrachloridoplatinate(2−) ions in a square-planar arrangement.

2D NMR correlation experiments with ^{13}C–^1H were performed to assign the H atoms in **1** (Fig. 5). As expected, the peaks observed between 3.11 and 3.30 ppm were clearly related to all *tertiary* C atoms from the ring (–CH type). Following the numbering given in Fig. 1, the chemical shifts of H_{2A}, H_{4A}, H_{5A} and H_{6A}, were found

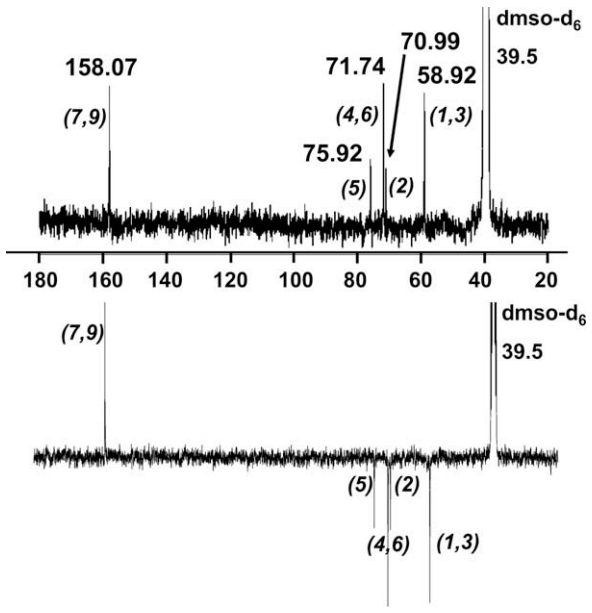


Fig. 4. ^{13}C NMR of $(H_2Std)PtCl_4$ recorded in dmso-d_6. Atom numbering as used in Fig. 1.

Table 1
^{13}C chemical shifts. Comparison between free streptidine and $(H_2Std)PtCl_4$.

Species	C_1/C_3	C_2	C_4/C_6	C_5	C_7/C_9
$(H_2Std)PtCl_4$	58.9	70.9	71.7	75.9	158.1
Free-H_2Std	59.3	71.7	72.4	75.6	159.1

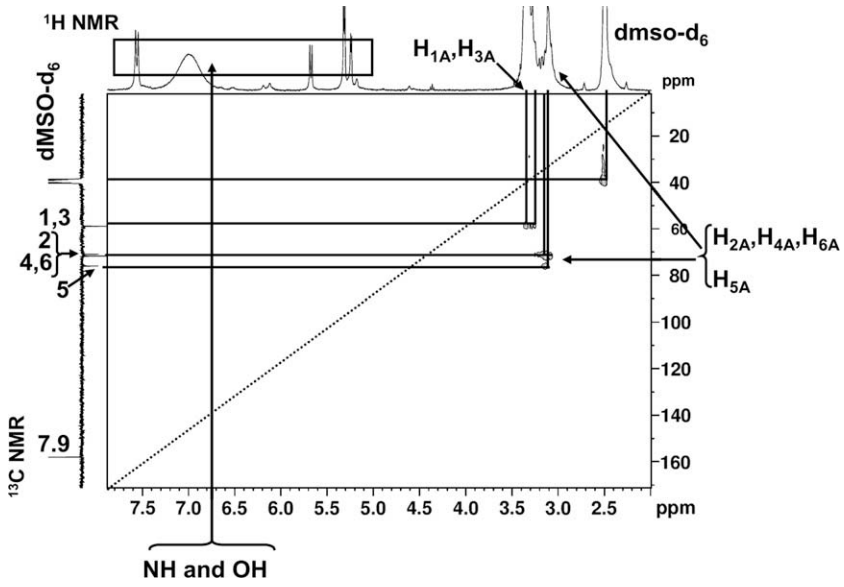


Fig. 5. 2D NMR experiments correlating ^{13}C–^{1}H of $(H_2Std)PtCl_4$ as recorded in dmso-d_6. Atom numbering as in Fig. 1.

at high fields (3.11 ppm) than those for H_{1A} and H_{3A}, shifted downfield and overlapped by an intense peak from the water molecules contained in the solvent (at approximately 3.3 ppm). No further correlation was observed from the other sets of peaks, as was also anticipated by consideration of their possible coordination to O and N atoms (H_2–H_{10}, H_{1B} and H_{3B}).

Furthermore, COSY experiments were performed with the aim of correlating the H atoms previously specified (H_{1A}–H_{6A}) with the adjacent protons from the –OH and –NH groups. Thus it was possible to link the high field chemical shifts corresponding to H_{4A}–H_{6A} and H_{2A} at 3.1 ppm with the three doublets from 5.14 to 5.67 ppm. These peaks were assigned as the protons from hydroxide groups. Similarly, H_{1A} and H_{3A} were related to the singlet at 7.59 ppm corresponding to the H atoms from NH groups. Integrations agreed with the interpretation of the data in all of the peaks. By elimination, the broad band at 7.00 ppm was assigned to the –NH_2 protons from the guanidine (Fig. 6).

At the same time, ^{195}Pt NMR in dmso-d_6 displayed a single peak at −2951 ppm indicative of only one type of Pt species in the sample (Fig. S3). This shift agrees with a platinum center coordinated to one S and three Cl atoms, compatible with other spectroscopic characterization in solution. The substitution of two or more Cl ions by two dmso molecules was discarded, because the resulting peak/s should have appeared at higher fields.

Therefore an additional approach, applying Pt L_3- and Cl K-edge XAS, was employed to compare the results from **1** in the solid and in solution, with the aim of obtaining more insight of the coordination sphere of the Pt ion and the exchange of ligands.

3.6. XAS

Fig. 7 shows a comparison of the Pt L_3-edge spectra of solid and solution $(H_2Std)PtCl_4$ (Fig. 7). The corresponding EXAFS and the fits to the data are shown in (Fig. 8). The Pt L_3-edge data of the solid

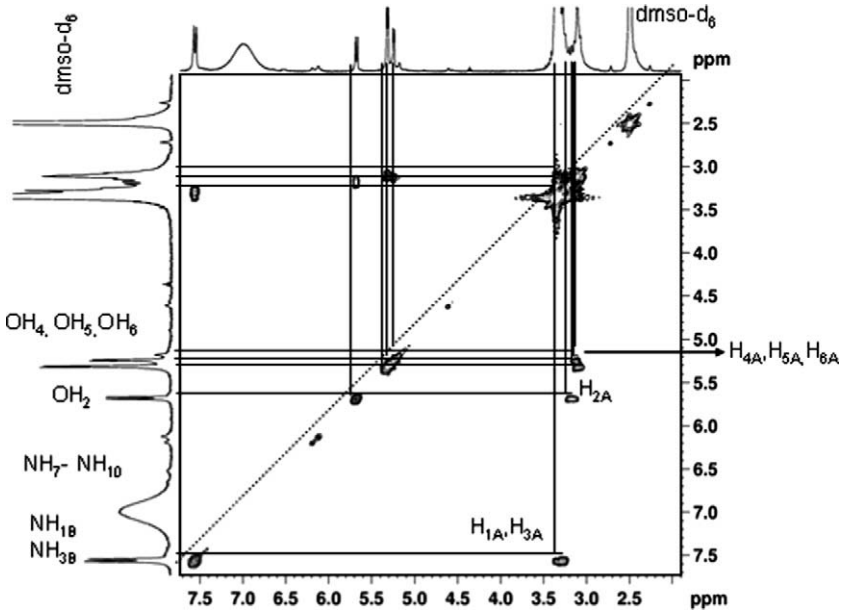


Fig. 6. COSY NMR experiment of $(H_2Std)PtCl_4$ as recorded in dmso-d_6. For the used numbering, see Fig. 1.

complex are shifted to lower energy, indicating a more reduced Pt site or a change in the local coordination environment upon solvation.

The EXAFS data also indicate a change in the local Pt coordination upon solvation of $(H_2Std)PtCl_4$ in dmso. The decrease in amplitude may be attributed to greater disorder in solution and/or a change in local coordination environment (as indicated by the edge data). A good fit to the solid $(H_2Std)PtCl_4$ is obtained by including four Pt–Cl interactions at 2.30 Å (Table 2, fit 1). A slight improvement in the fit is obtained by including an additional Pt–N/O vector at 2.02 Å; however, the improvement in the error value is not statistically significant (Table 2, fit 2). The fit clearly becomes worse if only three Pt–Cl interactions are included (Table 2, fit 3), indicating that the solid $(H_2Std)PtCl_4$ data require four Pt–Cl interactions.

In contrast, the solution $(H_2Std)PtCl_4$ data are best fit by three Pt–Cl at 2.30 Å and one Pt–N/O at 2.04 Å (Table 2, fit 4). The absence of the Pt–N/O vector results in increase in the error to 1.04 (Table 2, fit 5). Thus, these data suggest that oxygen (from dmso) or a N (from Std^{2+}) may be replacing a chloride in solution. However, this is in contradiction with the ^{195}Pt NMR, which should appear at higher fields if the Pt were coordinated to the dmso through the oxygen instead of the sulfur atom. In addition, the strong affinity of Pt for S is well-known.

Table 2
Representative EXAFS fits to solid and solution samples of $(H_2Std)PtCl_4$.

Complex	Fit number	Vector	Length (Å)		σ^2 (Å^2)	ΔE_0	Error[a]
Solid	1	4	Pt–Cl	2.30	0.0024	−4.20	0.594
	2	4	Pt–Cl	2.30	0.0023	−2.19	0.569
		1	Pt–N	2.02	0.0068		
	3	3	Pt–Cl	2.31	0.0013	−4.33	0.671
		1	Pt–N	2.14	0.0005		
Solution	4	3	Pt–Cl	2.30	0.0031	−4.80	0.688
		1	Pt–N	2.04	0.0017		
	5	4	Pt–Cl	2.31	0.0052	−2.10	1.040

[a] Error is given by $\sum[(\chi_{obsd}-\chi_{calcd})^2k^6]/\sum[(\chi_{obsd}{}^2k^6]$.

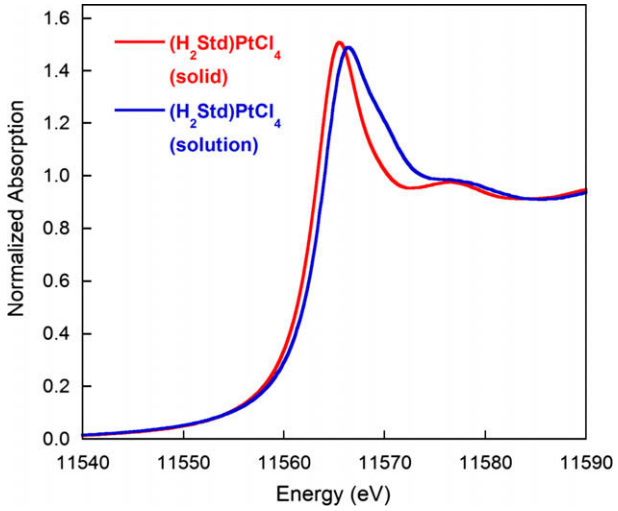


Fig. 7. Comparison of the normalized Pt L_3-edges for $(H_2Std)PtCl_4$ as a solid and as a solution in dmso.

In order to further understand the differences between solid and solution XAS data of $(H_2Std)PtCl_4$, Pt L3-edge data of $(^nBu_4)PtCl_3(NH_3)$, $(^nBu_4)_2[PtCl_4]$ were obtained as both solids and solutions (in CH_2Cl_2). Comparison of the Pt L_3-edge of solid and solution $(^nBu_4)_2[PtCl_4]$ show clear changes in the Pt L_3-edges, while the EXAFS data are identical (Figs. S4–S7). The differences in the edges may be attributed to longer-range order in the solid (perhaps due to the NBu_4 interaction), which are absent in solution. Similarly for $(^nBu_4)PtCl_3(NH_3)$, differences are observed in the edges upon solvation, whereas no changes in the EXAFS data occur. The solution data of all these compounds suggest that caution must be exercised in the interpretation of the Pt L_3-edges. A full XANES analysis of the edge data, however, is beyond the scope of this study.

Cl K-edge XAS data were also obtained for $(^nBu_4)PtCl_3(NH_3)$, $(^nBu_4)_2[PtCl_4]$ and $(H_2Std)PtCl_4$ in the solid state. The presence of a Cl K-pre-edge feature confirms the presence of coordinated Cl in $(H_2Std)PtCl_4$. Interestingly, the Cl K-edge data show a pre-edge energy and intensity for $(H_2Std)PtCl_4$, which is closer to that of $(^nBu_4)PtCl_3(NH_3)$ (Fig. 9). Due to the absorbing nature of dmso at these energies, measurements of $(H_2Std)PtCl_4$ in solution were not possible.

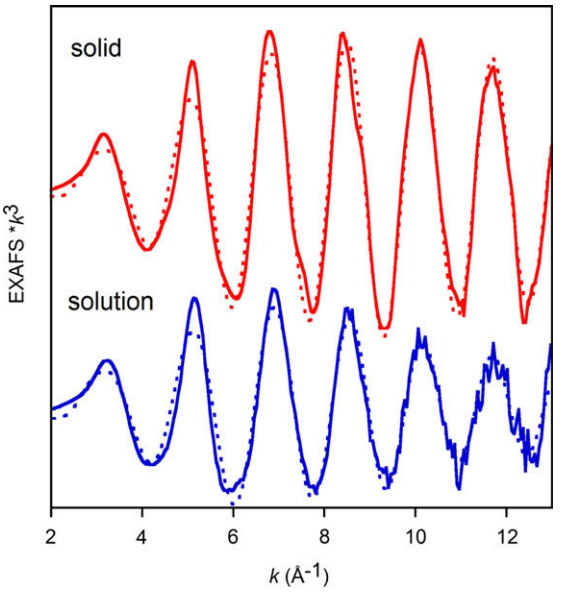


Fig. 8. The k^3-weighted EXAFS data (solid lines) and the fits to the data (dashed lines) $(H_2Std)PtCl_4$ as a solid (top) and as a solution in dmso (bottom).

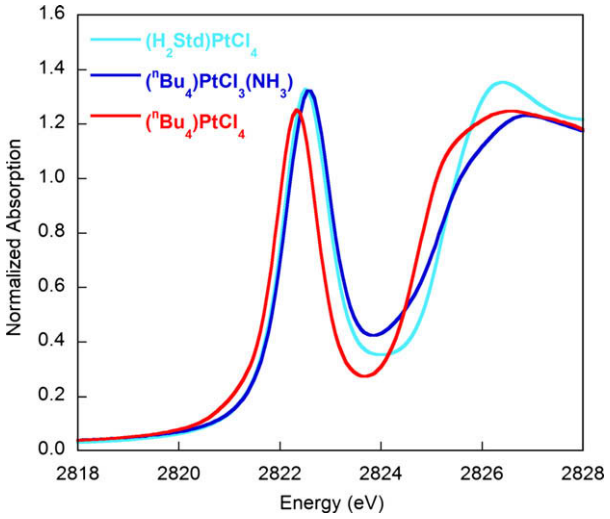


Fig. 9. Comparison of the normalized Cl K-edges of solid $(H_2Std)PtCl_4$, $(^nBu_4)PtCl_3(NH_3)$, and $(^nBu_4)PtCl_4$.

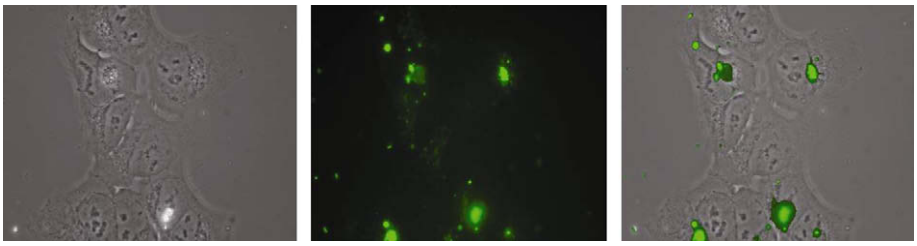


Fig. 10. Pictures with visible and green light (left, center) and overlapped (right) of $(H_2Std)PtCl_4$ in ostereosarcoma cells after 3 h or incubation. (For interpretation of the references to color in this figure legend, the reader is referred to the web version of this article.)

4. Biological assays and biophysical studies

4.1. Growth inhibition assay

Four types of cell lines were used to study the growth inhibition: A2780, L1210 and their respective resistant analogs. The cells were prepared in a complete medium and added to duplicate wells of a 96-well culture plate. They were treated with $(H_2Std)PtCl_4$ that had been previously dissolved in dmso (2% diluted in complete medium) at a 40 μg/mL and incubated for 48 h at 37 °C in a CO_2 incubator. The control set contained tumor cells without test compounds. MTT was added to each well and incubated for 2 h more and later dmso was added to each well. Absorbance values were measured with a microplate reader at 560 nm. The $(H_2Std)PtCl_4$ does not have any apparent activity against the four used cell lines and similar results were found for $(H_2Std)SO_4(H_2O)$, which was found also not toxic in our *in vitro* experiments. Moreover, an additional sample of the platinum complex was checked in the laboratories of Tevapharmachemie, to study a wider range of tumor cancer cells, with analogous results compared with the above cell lines.

4.2. Fluorescence studies

Given the fact that the streptidine sulfate has fluorescent properties [23] it was decided to study the fluorescent activity of $(H_2Std)PtCl_4$ in cells with the aim of having a better understanding on the actions that cancer cells have to shield themselves against the putative anti-tumor actions of this Pt complex. The questions we tried to answer are basically: (i) could the $(H_2Std)PtCl_4$ complex enter into the cells? (ii) once inside: would it be possible to enter the cellular nucleus?

Preliminary studies were performed on free-H_2Std sulfate in H_2O and on the $(H_2Std)PtCl_4$ in dmso, respectively, and their emission spectra at different wavelengths were compared and followed in time. Similarities between the two samples were observed when both solutions were excited at 240 and 410 nm, respectively. The emission spectra at such wavelengths of the final $(H_2Std)PtCl_4$ complex exhibited attenuated bands at 402 and also at 423 and 450 nm, respectively, as well as the free-H_2Std. The rest of the emission bands observed for the free ligand were found to be quenched in **1**.

Fluorescence experiments were performed using ostereosarcoma cells. Fig. 10 shows a picture of the cells after 3 h of being incubated with compound **1**. The overlap of the pictures clearly shows fluorescence inside the cells, although, it appears that this phenomena takes place outside the nuclei, suggesting that to protect themselves, the cells may store the compound in vacuoles and later they disposed them.

The results from these preliminary fluorescence data provide visual explanations on the non-toxicity effects of the $(H_2Std)PtCl_4$. In order to check the activity of the complex with the DNA preliminary binding studies were performed.

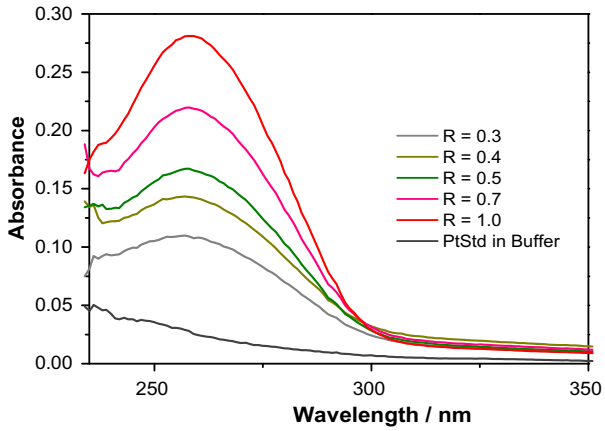


Fig. 11. Titration experiments at different *R* values of DNA and $(H_2Std)PtCl_4$ complex. *R* is defined as the ratio Pt:DNA base pair.

4.3. UV–Vis titration with DNA

Finally, and parallel to the studies of the fluorescence measurements above UV–Vis titrations with DNA were achieved with different ratios Pt/DNA. The *R* values (defined as the ratio Pt:DNA base pair) varied from 0.3 to 1.0 (Fig. 11). The graph of all the *R* values shows the increase of the band of the absorbance of the DNA while increasing the *R* value. At the same time the comparison between *R* = 1, free DNA at this concentration and $(H_2Std)PtCl_4$ shows that the absorbance of the free DNA is lower than the absorbance of the one containing DNA/$(H_2Std)PtCl_4$ at a ratio equal to 1.0. (Fig. S8) This experiment shows that the DNA can indeed be affected upon interaction with **1**, however, the absence of cytotoxic activity in cells could be related to the impossibility of reach the nuclei of the cells.

5. Conclusions

The synthesis of a unique Pt–streptidine compound (**1**) has been achieved and the characterization of this final compound, $(H_2Std)PtCl_4$, was possible based on current spectroscopic techniques. In the absence of crystallographic data, structural characterization was performed using NMR, MS, XAS and EXAFS in the solid state as well as in solution. It was found that compound **1** has anionic nature, where the streptidine acts as cation and the platinum remains present as the $PtCl_4^{2-}$ counterion. In the solution the final arrangement of cations and anions was studied by the XAS edge measurements, suggesting a loss of at least one chloride and perhaps N or O of the Std bonding to the Pt. The substitution of a Cl

ion is in concordance with what was observed by a number of spectroscopic techniques including ^{195}Pt NMR; however, the later suggested coordination with a molecule of solvent (dmso) through a S atoms instead of an O. These results, which initially appear to be contradictory, could be interpreted taking into account that the loss of a Cl will create negative charged, platinum species that may interact electrostatically with Std^{2+} ions and also could be related to the complex network of hydrogen bonds that it was already observed in the crystal structure of H_2Std sulfate.

In addition, biological studies have shown that $(H_2Std)PtCl_4$ does not affect drastically cancer cells or bacteria. Using the fluorescence properties of the compounds it was possible to show that accumulation of **1** occurs in the cells but outside the nuclei of the studied cells. DNA-binding studies have showed the interaction of the complex with the CT-DNA. Although further biological studies would be required with this system, the present results suggest that the lack of anticancer activity may originate from the inability of the compound of passing the nuclear membrane.

Acknowledgments

The authors wish to thank Johnson and Matthey (Reading, UK) for their generous loan of K_2PtCl_4. Continuous support from the Netherlands Research Organisation (NWO) and its Chemical Council (CW) is also gratefully acknowledged for the TOP grant with number 700.53.310. The authors gratefully acknowledge Dr. J.M. Perez (Universidad Autónoma de Madrid, Spain) for providing A2780 and A2780R cell lines.

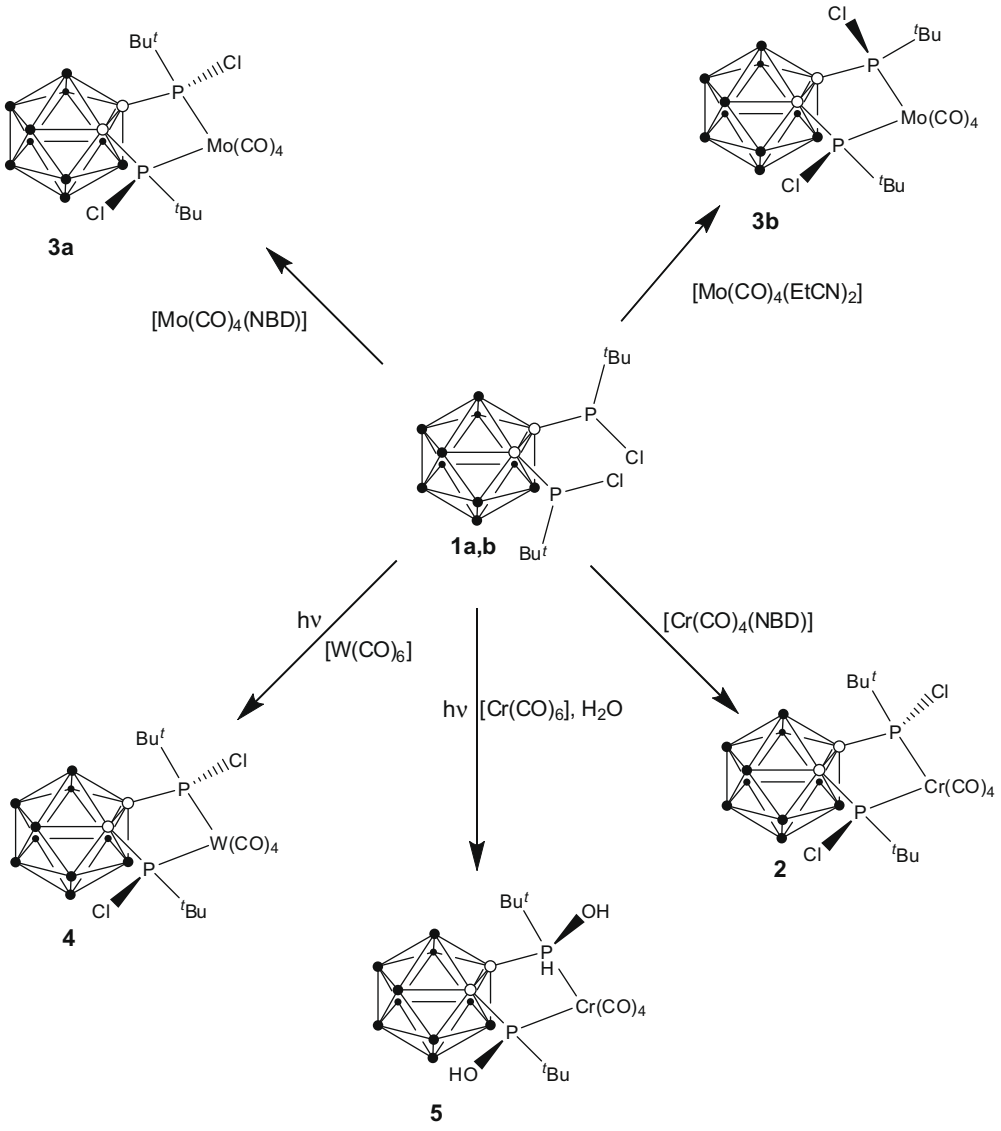
SSRL operations are funded by DOE, BES. The SMB program is supported by NIH, NCRR (grant number 5 P41 RR001209), BMTP and by DOE, BER.

Appendix A. Supplementary data

CCDC 715532 contains the supplementary crystallographic data for H_2Std sulfate monohydrate. These data can be obtained free of charge via http://www.ccdc.cam.ac.uk/conts/retrieving.html, or from the Cambridge Crystallographic Data Centre, 12 Union Road, Cambridge CB2 1EZ, UK; fax: (+44) 1223-336-033; or e-mail: deposit@ccdc.cam.ac.uk. Supplementary data associated with this article can be found, in the online version, at doi:10.1016/j.poly.2009.07.022.

References

[1] P. Bergstrom, K. Grankvist, S. Holm, R. Henriksson, Anticancer Res. 11 (1991) 1039.
[2] J. Fuska, A. Fuskova, P. Nemec, Biologia 34 (1979) 735.
[3] J. Fuska, L. Ivanitsk, K. Horakova, I. Kuhr, J. Antibiot. 27 (1974) 141.
[4] M.A. Hotz, G. Delbino, P. Lassota, F. Traganos, Z. Darzynkiewicz, Cancer Res. 52 (1992) 1530.
[5] D.G. Lee, H.N. Kim, Y.K. Park, H.K. Kim, B.H. Choi, C.H. Choi, K.S. Hahm, BBA-Proteins Proteom. 1598 (2002) 185.
[6] A. Leonardi, V. Papa, I. Fregona, P. Russo, G. De Franchis, G. Milazzo, Cornea 25 (2006) 85.
[7] A.C. Rinaldi, M.L. Mangoni, A. Rufo, C. Luzi, D. Barra, H.X. Zhao, P.K.J. Kinnunen, A. Bozzi, A. Di Giulio, M. Simmaco, Biochem. J. 368 (2002) 91.
[8] K. Satyamoorthy, E.M. Perchellet, J.P. Perchellet, Toxicol. In Vitro 6 (1992) 459.
[9] I.S. Severina, N.V. Pyatakova, A.B. Postnikov, M.N. Preobrazhenskaya, Y.V. Khropov, Eur. J. Pharmacol. 483 (2004) 127.
[10] Y. Xu, L.T. Lai, J.L. Gabrilove, D.A. Scheinberg, Clin. Cancer Res. 4 (1998) 171.
[11] P.J. Bednarski, F.S. Mackay, P.J. Sadler, Anti-Cancer Agents. Med. Chem. 7 (2007) 75.
[12] T.W. Hambley, Coord. Chem. Rev. (1997) 181.
[13] A.G. Quiroga, C.N. Ranninger, Coord. Chem. Rev. 248 (2004) 119.
[14] L. Kelland, Nat. Rev. Cancer 7 (2007) 573.
[15] J. Reedijk, Eur. J. Inorg. Chem. (2009) 1303.
[16] H.C. Hinshaw, W.H. Feldman, K.H. Pfuetze, Am. Rev. Tuberc. Pulm. 54 (1946) 191.
[17] H. Ozbey, G.A. Tireli, T. Salman, Eur. J. Pediatr. Surg. 13 (2003) 116.
[18] H.E. Carter, R.K. Clark, S.R. Dickman, Y.H. Loo, J.S. Meek, P.S. Skell, W.A. Strong, J.T. Alberi, Q.R. Bartz, S.B. Binkley, H.M. Crooks, I.R. Hooper, M.C. Rebstock, Science 103 (1946) 53.
[19] H.E. Carter, R.K. Clark, S.R. Dickman, Y.H. Loo, P.S. Skell, W.A. Strong, Science 103 (1946) 540.
[20] R.L. Peck, C.E. Hoffhine, E.W. Peel, R.P. Graber, F.W. Holly, R. Mozingo, K. Folkers, J. Am. Chem. Soc. 68 (1946) 776.
[21] N. Barba-Behrens, J.L. Bautista, M.E. Ruiz, N.P. Joseph, A. Flores-Parra, R. Contreras, J. Inorg. Biochem. 40 (1990) 201.
[22] O. Granados, G. Meza, Histol. Histopathol. 20 (2005) 357.
[23] G. Meza, N. Barba-Behrens, O. Granados, A. Hernandez-Cruz, A. Toxqui, Histol. Histopathol. 16 (2001) 1143.
[24] G. Gannon, J.A. Larsson, J.C. Greer, D. Thompson, J. Phys. Chem. B 112 (2008) 8906.
[25] B. Rosenberg, L. Vancamp, T. Krigas, Nature 205 (1965) 698.
[26] A. Pasini, F. Zunino, Angew. Chem., Int. Ed. 26 (1987) 615.
[27] J. Reedijk, Chem. Commun. (1996) 801.
[28] J. Reedijk, Proc. Natl. Acad. Sci. USA 100 (2003) 3611.
[29] L. Ronconi, P.J. Sadler, Coord. Chem. Rev. 251 (2007) 1633.
[30] S. van Zutphen, J. Reedijk, Coord. Chem. Rev. 249 (2005) 2845.
[31] H. Robinson, W. Priebe, J.B. Chaires, A.H.J. Wang, Biochemistry 36 (1997) 8663.
[32] W. Priebe, I. Fokt, T. Przewioka, J.M. Woynarowski, G. Pratesi, R. Supino, F. Zunino, Y.H. Ling, R. Perez-Soler, Clin. Cancer Res. 6 (2000) 4538s.
[33] E. Bednarek, J. Sitkowski, R. Kawecki, L. Kozerski, W. Bocian, L. Pazderski, W. Priebe, Dalton Trans. (2008) 4129.
[34] B. Leśniewska, S. Jebors, A.W. Coleman, K. Suwińska, Acta Crystallogr., Sect. C 65 (2009) o290.
[35] Siemens, XSCAnS Users Manual, Siemens Analytical X-ray Instruments Inc., Siemens, Madison, WI, USA, 1996.
[36] G.M. Sheldrick, Acta Crystallogr., Sect. A 64 (2008) 122.
[37] H.A. Rose, Anal. Chem. 26 (1954) 613.
[38] J.A. Beaty, M.M. Jones, Inorg. Chem. 31 (1992) 2547.
[39] W. Caseri, Plat. Met. Rev. 48 (2004) 91.



Scheme 1. Synthesis of complexes **2**–**5**.

metal-coordinated phosphinous acid, $R_2P(OH)$, the free form of which is usually unstable and tautomerizes to give the phosphine oxide $R_2P(O)H$. Complexes containing such type of ligands are rare, and only a limited number of Pt and Ni complexes with phosphinous acid as ligand ($PhP(OH)(CH_2)_2P(OH)Ph$) is described in the literature [30]. Usually, hydrolysis of chlorophosphine complexes is achieved with acids or bases [31,32]. Here, we observed that UV irradiation of **1** with $[Cr(CO)_6]$ in moist THF results in hydrolysis of both P–Cl bonds and formation of $[Cr(CO)_4\{1,2\text{-}(P(OH)^tBu)_2C_2B_{10}H_{10}\}]$ (**5**). The reaction was followed by $^{31}P\{^1H\}$ NMR spectroscopy. After 33 h, only minor amounts of **1** are present. Alternatively, **5** is formed on irradiation of a *rac*/*meso* mixture of **2** in moist THF in 2.5 h according to $^{31}P\{^1H\}$ NMR spectroscopy.

3. Molecular structures of 2, 3a,b, 4 and 5

X-ray structure determinations of **2**–**5** (Figs. 1–3) show that the bis(phosphino)carbaborane coordinates in a chelating fashion. The structural parameters of **1a,b** [21] remain nearly unchanged on coordination to the group 6 metal atom (Table 1).

For the M–CO groups *trans* to the coordinated P atoms, the M–C distances are longer and the C–O bond lengths shorter. Similar trends, that is, lengthening of the Mo–P and C–O bonds and shortening of the Mo–C bonds, are observed for the complexes $[Mo(CO)_4\{1,2\text{-}(PPh_2)_2C_2H_4\}]$ [33] and $[Mo(CO)_4\{1,2\text{-}(PPh_2)_2C_2H_2\}]$ [34]. This suggests increased π-acceptor properties of the P atoms in **1a**,**b** in comparison with other bisphosphines [2,35], due to the presence of the electron-deficient carbaboranyl ligand in **1a** [2].

The compounds *rac*-$[M(CO)_4\{1,2\text{-}(P^tBuCl)_2C_2B_{10}H_{10}\}]$ (M = Cr (**2**), Mo (**3a**), W (**4**)) are isotypic and crystallize in the monoclinic space group $P2_1/n$ with comparable lattice parameters.

4. Spectroscopic properties of 2, 3a,b, 4 and 5

The coordination of the bisphosphine **1a**,**b** leads to a remarkable low-field shift in the $^{31}P\{^1H\}$ NMR spectra (see Table 2) in compounds **2**–**4** (from ca. 160 ppm for **4** to 186 ppm for **3a/b** and to ca. 215 ppm for **2**) in comparison with the starting material (*rac* 116.7 and *meso* 116.4 ppm) [21]. Substitution of the Cl atoms in **2** by OH groups results in a high-field shift (215 ppm in **2**,

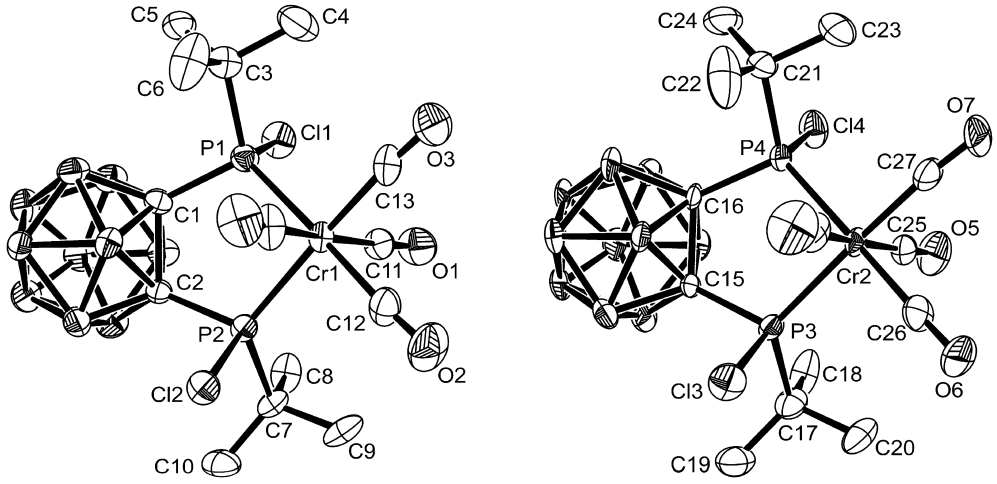


Fig. 1. Molecular structure of *cis-rac*-[Cr(CO)$_4${1,2-(P^{t}BuCl)$_2$C$_2$B$_{10}$H$_{10}$}] (**2**) showing the atom numbering scheme employed (ORTEP) [44]. The two independent molecules in the asymmetric unit are shown. The complexes *cis-rac*-[Mo(CO)$_4${1,2-(P^{t}BuCl)$_2$C$_2$B$_{10}$H$_{10}$}] (**3a**) and *cis-rac*-[W(CO)$_4${1,2-(P^{t}BuCl)$_2$C$_2$B$_{10}$H$_{10}$}] (**4**) are isotypic.

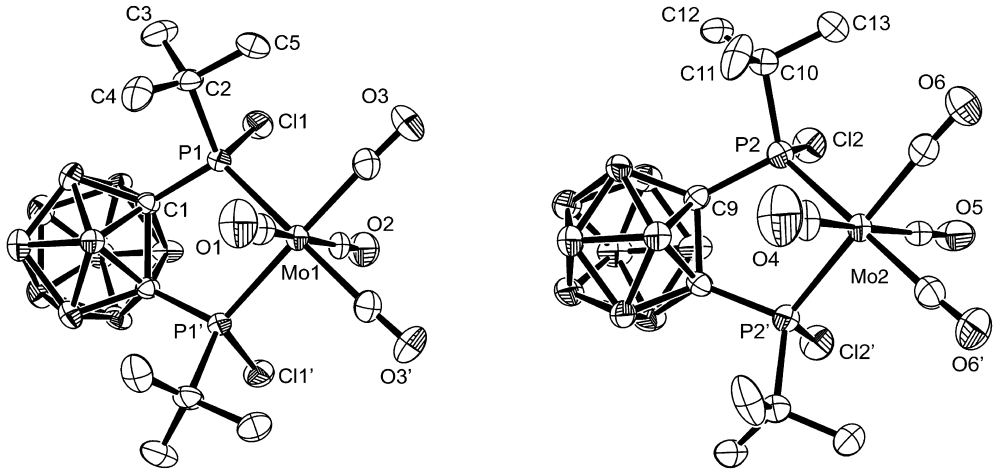


Fig. 2. Molecular structure of *cis-meso*-[Mo(CO)$_4${1,2-(P^{t}BuCl)$_2$C$_2$B$_{10}$H$_{10}$}] (**3b**) showing the atom numbering scheme employed (ORTEP) [44]. The two independent molecules in the asymmetric unit are shown.

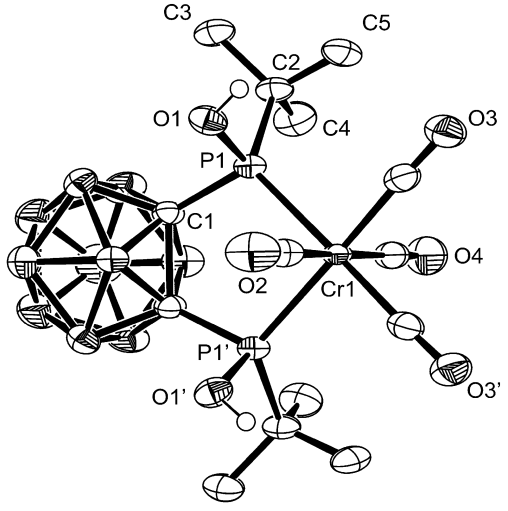


Fig. 3. Molecular structure of *cis-meso*-[Cr(CO)$_4${1,2-(P(OH)^{t}Bu)$_2$C$_2$B$_{10}$H$_{10}$}] (**5**) showing the atom numbering scheme employed (ORTEP) [44].

208 ppm in **5**). Additionally for the tungsten complex **4**, ^{183}W satellites with a $^1J_{PW}$ coupling constant of 289.3 Hz were observed.

The proton NMR spectra show the typical broad multiplets for the cluster protons (2.0–4.0 ppm) and a doublet for the *tert*-butyl protons at ca. 1.15 ppm ($^3J_{HP}$ range from 16.0 to 20.0 Hz).

In the ^{13}C{^{1}H} NMR spectra, all compounds show two signal groups for the four CO ligands. The CO groups *trans* to phosphorus are observed as multiplets due to an ABX spin system for all compounds at 202–223 ppm. For the CO groups *cis* to phosphorus a triplet is observed at 198–216 ppm due to an AA′X spin system in the case of the *rac* isomers **2**, **3a**, and **4** and an A$_2$X spin system for the *meso* isomer in **3b** and **5**. Accordingly, the carbon atoms of the carbaborane cluster also exhibit multiplets due to an ABX spin system. The methyl groups of the *tert*-butyl group show a very broad singlet at ca. 25 ppm, due to hindered rotation at room temperature. A low temperature ^{13}C{^{1}H} NMR spectrum at 213 K revealed a doublet according to C–P coupling. The ^{11}B{^{1}H} NMR spectra of **2**, **3a**, **4** and **5** show four signals in a 2:2:4:2 ratio, whereas compound **3b** shows seven signals in a 2:1:1:2:1:2:1 ratio. The signals can be assigned according to the literature, where boron atoms closest to carbon atoms are observed at the lowest chemical shift and boron atoms furthest from carbon atoms are observed at highest chemical shift [36].

Table 1
Selected bond lengths (in pm) und angles (in °) for **1–5**.

	1a[21]	**1b**[21]	**2**[a]	**3a**[a]	**3b**[a]	**4**[a]	**5**
$C_{cluster}$–$C_{cluster}$	177.0(2)	178.2(3)	172.8(7) [173.0(7)]	176.9(5) [177.0(5)]	176.5(8) [173.5(9)]	175(1) [172(1)]	171.7(8)
$C_{cluster}$–P	189.2(2), 189.7(2)	188.4(2), 189.3(2)	190.1(6), 192.0(6) [188.1(5), 189.7(4)]	191.7(4), 191.2(4) [190.8(4), 192.1(4)]	189.6(4) [190.5(5)]	189(1), 191(1) [190(1), 189(1)]	1.89.7(4)
P–C^{tBu}	188.1(2), 188.7(2)	187.7(2), 187.6(2)	188.7(7), 190.0(6) [187.7(6), 188.7(7)]	189.2(4), 190.1(4) [190.2(4), 190.5(4)]	188.6(5) [188.5(5)]	187(1), 186(1) [187(1), 188(1)]	1.86.8(4)
P–Cl	207.35(9), 207.00(8)	206.95(9), 205.76(9)	207.8(2), 205.4(2) [207.7(2), 210.2(2)]	209.4(2), 207.6(1) [207.9(1), 209.0(2)]	205.5(2), 205.7(2)	208.6(4), 205.9(4) [205.8(4), 209.3(4)]	164.1(3) (P–OH)
P–M			232.5(2), 235.5(2) [232.6(2), 233.5(2)]	248.1(1), 249.1(1) [247.8(1), 248.6(1)]	245.5(1), [249.5(2)]	246.4(3), 245.2(3) [244.7(3), 245.4(3)]	233.7(1)
$C_{cluster}$–$C_{cluster}$–P	112.1(1), 113.2(1)	112.6(1), 113.0(1)	113.8(4), 112.4(4) [113.9(3), 114.0(3)]	115.1(2), 113.9(2) [114.8(2), 115.2(2)]	114.7(1) [113.8(1)]	115.7(6), 113.2(6) [114.7(6), 115.9(6)]	114.3(1)
$C_{cluster}$–P–Cl	99.58(6), 99.66(6)	100.09(7), 99.66(7)	100.0(2), 100.45(2) [100.6(2), 99.8(2)]	100.2(1), 100.2(1) [100.4(1), 99.9(1)]	99.6(2) [100.4(2)]	100.2(4), 99.9(4) [101.1(3), 99.7(4)]	100.4(2) (C–P–O)
$C_{cluster}$–P–M			111.0(2), 112.6(2) [111.7(2), 110.7(2)]	110.8(1), 112.4(1) [112.0(1), 111.0(1)]	112.3(1) [110.7(2)]	110.7(3), 112.5(3) [111.5(3), 110.8(3)]	111.2(1)
P–M–P			87.47(6) [88.96(6)]	85.13(4) [86.20(4)]	86.00(6) [81.99(7)]	85.24(9) [86.26(9)]	89.00(6)

[a] Two independent molecules in the asymmetric unit; values of second molecule in brackets [].

Table 2
NMR data for compounds **2–5** (in C_6D_6).

Compound	$\delta(^{31}P)$ (ppm)	$\delta(^{1}H)$ (ppm)/J_{HP} (Hz)	$\delta(^{13}C)$ (ppm)/J_{CP} (Hz)[a]	$\delta(^{11}B)$ (ppm)/J_{BH} (Hz)
2	215.3	3.5–2.0 (m, vbr, 10H, BH), 1.20 (d, $^3J_{HP}$ = 17.2, 18H, CH_3)	223.1/n.d. (pseudo t, 2x *trans* CO), 216.9/11.2 (t, 2x *cis* CO), 94.9/n.d. (m, $C_2B_{10}H_{10}$), 49.1 (s, C_{quart}, ^{t}Bu), 25.6/n.d. (m, vbr, CH_3, ^{t}Bu)	−0.4/153.7 (2B), −2.5/154.3 (2B), −9.3/116.2 (4B), −11.4/n.d. (2B)
3a	186.7	3.5–2.0 (m, vbr, 10H, BH), 1.15 (d, $^3J_{HP}$ = 20.0, 18H, CH_3)	211.8/n.d. (m, 2x *trans* CO), 206.3/81.5 (t, 2x *cis* CO), 96.7/ n.d. (m, $C_2B_{10}H_{10}$), 47.1 (s, C_{quart}, ^{t}Bu), 24.7/n.d. (m, vbr, CH_3, ^{t}Bu)	−0.4/160.1 (2B), −2.1/161.4 (2B), −9.2/107.5 (4B), −12.1/ n.d. (2B)
3b	185.9	3.5–2.0 (m, vbr, 10H, BH), 1.13 (d, $^3J_{HP}$ = 16.0, 18H, CH_3)	212.0/n.d. (m, 2x *trans* CO), 210.0/6.2 (t, 1x *cis* CO), 202.6/ 11.1 (t, 1x cis CO), 96.2/n.d. (m, $C_2B_{10}H_{10}$), 47.3 (s, C_{quart}, ^{t}Bu), 24.1/n.d. (m, vbr, CH_3, ^{t}Bu)	−0.3/141.0 (2B), −1.3/143.1 (1B), −3.1/158.5 (1B), −7.6/161.6 (2B), −9.1/n.d. (1B), −11.1/ 172.9 (2B), −13.9/165.0 (1B)
4	160.8 ($^1J_{PW}$ = 289.3 Hz)	3.5–2.0 (m, vbr, 10H, BH) 1.15 (d, $^3J_{HP}$ = 19.0, 18H, CH_3)	202.8/n.d. (m, 2x *trans* CO), 198.5/10.0 (t, 2x *cis* CO), 97.7/ n.d. (m, $C_2B_{10}H_{10}$) 48.5 (s, C_{quart}, ^{t}Bu), 24.9/n.d. (m, vbr, CH_3, ^{t}Bu)	−0.5/162.5 (2B), −2.2/160.2 (2B), −9.4/n.d. (4B), −11.4/n.d. (2B)
5	208.3	3.5–2.0 (m, vbr, 10H, BH) 1.14 (d, $^3J_{HP}$ = 16.0, 18H, CH_3)	223.9/n.d. (pseudo t, 2x *trans* CO), 218.4/28.0 (t, 2x *cis* CO), 94.9/n.d.(m, $C_2B_{10}H_{10}$), 44.6 (s, C_{quart}, ^{t}Bu), 26.1/n.d. (m, vbr, CH_3, ^{t}Bu)	−0.5/144.4 (2B), −3.7/149.8 (2B), −10.2/149.3 (4B), −12.5/n.d. (2B)

[a] *cis* = CO *cis* to P; *trans* = CO *trans* to P; in the $^{13}C\{^1H,^{31}P\}$ NMR spectra singlets were observed for the CO and carbaborane carbon atoms (see Supplementary data).

5. Experimental

All experiments were carried out under purified dry nitrogen. For the irradiation experiment, a diving torch with water cooling and polychromatic light was employed. Solvents were dried and freshly distilled under argon. The NMR spectra were recorded with an AVANCE DRX 400 spectrometer (Bruker), ^{1}H NMR: internal standard solvent (benzene), external standard TMS; ^{13}C NMR: external standard TMS, internal standard solvent; ^{31}P NMR: external standard 85% H_3PO_4; ^{11}B NMR: external standard $BF_3(Et_2O)$. The melting points were determined in sealed capillaries under argon and are uncorrected. $[Mo(CO)_4(NBD)]$ [37], $[Mo(CO)_4(EtCN)_2]$ [38], and $[Cr(CO)_4(NBD)]$ [39] were prepared by literature procedures. 1,2-Bis(*tert*-butylchlorophosphino)-1,2-dicarba-*closo*-dodecaborane(12) (**1a,b**) was prepared and the diastereomers separated as described earlier [21]. $[M(CO)_6]$ (M = Cr, Mo, W) are commercially available.

5.1. cis-rac-[1,2-Bis(tert-butylchlorophosphino)-1,2-dicarba-closo-dodecaborane(12)]-tetracarbonylchromium(0) (*2*)

A solution of 0.1 g (0.25 mmol) **1a** and 0.07 g (0.27 mmol) $[Cr(CO)_4(NBD)]$ was stirred at 70 °C in toluene for 35 h. The solution was then cooled to rt, and the solvent evaporated. The residue was washed with *n*-hexane (3 ml) and recrystallized from toluene. At 4 °C pale yellow crystals of **2** were obtained. Yield: 0.06 g (43%), m.p. 230–5 °C (decomp.). *Anal.* Calc. for $C_{14}H_{28}B_{10}Cl_2CrO_4P_2$ (553.30): C, 30.32; H, 5.09. Found: C, 30.10; H, 4.73%. MS (ESI^-, MeOH) *m/z*: 542.1 $(M-B)^-$.

5.2. cis-rac- and cis-meso-[1,2-Bis(tert-butylchlorophosphino)-1,2-dicarba-closo-dodecaborane(12)]-tetracarbonylmolybdenum(0) (*3a,b*)

A mixture of 0.16 g (0.6 mmol) $[Mo(CO)_6]$ and 0.2 g (0.51 mmol) **1** in 5 ml toluene was refluxed for 3 h. Then the solvent was evaporated and the residue kept at rt in vacuum for 30 min to remove $[Mo(CO)_6]$. The residue was suspended in 3 ml *n*-hexane and filtered giving the product as a *rac/meso* mixture of **3a:3b** = 5:1 (0.26 g, 86%). The solid was recrystallized twice from toluene, but the isomers could not be separated. M.p. >210 °C (decomp.). *Anal.* Calc. for $C_{14}H_{28}B_{10}Cl_2MoO_4P_2$ (597.24): C, 28.20; H, 4.70; Cl, 11.89. Found: C, 28.20; H, 4.86; Cl, 11.90%. MS (FAB^+, 3-nitrobenzyl alcohol) *m/z*: 597.0 (28.4%, M^+), 486.1 (68.8%, M^+–4CO), 428.9 (25.2%, M^+–4CO–^{t}Bu).

5.3. cis-rac-[1,2-Bis(tert-butylchlorophosphino)-1,2-dicarba-closo-dodecaborane(12)]-tetracarbonylmolybdenum(0) (*3a*)

A mixture of **1a** (0.1 g, 0.25 mmol) and $[Mo(CO)_4(NBD)]$ (0.08 g, 0.27 mmol) in toluene (5 ml) was stirred at 65–70 °C for 15 h. The mixture was then filtered through 2 cm SiO_2 and washed twice

Table 3
Crystal data and structure refinement for complexes **2**–**5**.

	2	**3a**	**3b**	**4**	**5**
Empirical formula	$C_{14}H_{28}B_{10}Cl_2CrO_4P_2$	$C_{14}H_{28}B_{10}Cl_2MoO_4P_2$	$C_{14}H_{28}B_{10}Cl_2MoO_4P_2$	$C_{14}H_{28}B_{10}Cl_2O_4P_2W$	$C_{14}H_{30}B_{10}CrO_6P_2$
Formula weight	553.30	597.24	597.24	685.15	516.42
Temperature (K)	213(2)	223(2)	216(2)	208(2)	208(2)
Crystals system	monoclinic	monoclinic	orthorhombic	monoclinic	orthorhombic
Space group	$P2_1/n$	$P2_1/n$	$Pmn2_1$	$P2_1/n$	$Pbcm$
Unit cell dimensions					
a (pm)	1381.7(2)	1395.5(3)	1401.5(1)	1381.2(3)	1253.8(2)
b (pm)	1350.4(2)	1374.6(3)	1363.6(1)	1356.9(3)	1425.7(3)
c (pm)	2752.0(3)	2779.6(6)	1353.6(1)	2753.2(6)	1369.6(2)
α (°)	90	90	90	90	90
β (°)	90.107(2)	90.938(4)	90	90.892(4)	90
γ (°)	90	90	90	90	90
Volume (nm^3)	5.135(1)	5.33(1)	2.5869(5)	5.16(1)	2.4481(7)
Z	8	8	4	8	4
Density (calculated) (Mg/m^3)	1.431	1.488	1.534	1.764	1.401
Absorption coefficient (mm^{-1})	0.799	0.833	0.858	4.830	0.628
F(0 0 0)	2256	2400	1200	2656	1064
Crystal size (mm^3)	0.40 × 0.40 × 0.40	0.20 × 0.20 × 0.10	0.20 × 0.15 × 0.15	0.40 × 0.40 × 0.15	0.15 × 0.10 × 0.10
θ Range for data collection (°)	1.65–26.40	1.47–28.57	1.49–28.89	1.64–29.15	1.62–26.37
Index ranges	$-17 \leqslant h \leqslant 17$, $-16 \leqslant k \leqslant 13$, $-34 \leqslant l \leqslant 24$	$-18 \leqslant h \leqslant 12$, $-17 \leqslant k \leqslant 13$, $-35 \leqslant l \leqslant 37$	$-18 \leqslant h \leqslant 13$, $-18 \leqslant k \leqslant 18$, $-15 \leqslant l \leqslant 17$	$-17 \leqslant h \leqslant 18$, $-12 \leqslant k \leqslant 18$, $-36 \leqslant l \leqslant 33$	$-7 \leqslant h \leqslant 15$, $-17 \leqslant k \leqslant 17$, $-16 \leqslant l \leqslant 17$
Reflections collected	28 548	33 057	16 838	31 231	13 058
Independent reflections	10 486 [R_{int} = 0.0429]	12 438 [R_{int} = 0.0875]	6126 [R_{int} = 0.0484]	12 553 [R_{int} = 0.0492]	2618 [R_{int} = 0.0972]
Completeness to θ_{max} (%)	99.5	99.9	94.2	99.9	100.0
Data/restraints/ parameters	10 486/0/608	12 438/0/687	6126/1/332	12 553/0/607	26 18/0/166
Goodness-of-fit on F^2	1.218	0.923	1.029	1.269	1.068
Absolute structure parameter			0.46(5)		
Final R indices [$I > 2\sigma(I)$]	R_1 = 0.0676, wR_2 = 0.1600	R_1 = 0.0438, wR_2 = 0.0906	R_1 = 0.0408, wR_2 = 0.0976	R_1 = 0.0828, wR_2 = 0.1712	R_1 = 0.0594, wR_2 = 0.1491
R indices (all data)	R_1 = 0.0783, wR_2 = 0.1662	R_1 = 0.0948, wR_2 = 0.1063	R_1 = 0.0562, wR_2 = 0.1105	R_1 = 0.1004, wR_2 = 0.1788	R_1 = 0.0998, wR_2 = 0.1740
Largest difference in peak and hole (e Å^{-3})	1.100 and −0.479	1.259 and −0.436	1.588 and −0.415	3.363 and −2.500	0.873 and −0.652

with 5 ml toluene. The solvent was removed in vacuo, and the resulting solid was recrystallized from toluene. At 4 °C pale yellow crystals of **3a** were obtained. Yield: 0.07 g (47%), m.p. >210 °C (decomp.). *Anal.* Calc. for $C_{14}H_{28}B_{10}Cl_2MoO_4P_2$ (597.24): C, 28.20; H, 4.70. Found: C, 28.54; H, 4.80%.

5.4. cis-meso-[1,2-Bis(tert-butylchlorophosphino)-1,2-dicarba-closo-dodecaborane(12)]-tetracarbonylmolybdenum(0) (**3b**)

A solution of 0.07 g (0.18 mmol) **1b** in CH_2Cl_2 (5 ml) was added to a solution of 0.06 g (0.19 mmol) [$Mo(CO)_4(EtCN)_2$] in CH_2Cl_2 (5 ml) and then stirred for 48 h. The solvent was removed in vacuo, and the resulting solid was suspended in *n*-hexane (5 ml) and filtered. The solid was recrystallized from toluene. At 4 °C pale yellow crystals of **3b** were obtained. Yield: 0.05 g (47%), m.p. >210 °C (decomp.). *Anal.* Calc. for $C_{14}H_{28}B_{10}Cl_2MoO_4P_2$ (597.24): C, 28.20; H, 4.70. Found: C, 28.36; H, 4.98%.

5.5. cis-rac-[1,2-Bis(tert-butylchlorophosphino)-1,2-dicarba-closo-dodecaborane(12)]-tetracarbonyltungsten(0) (**4**)

A solution of 0.39 g (1 mmol) **1a** and 0.35 g (1 mmol) [$W(CO)_6$] in THF (15 ml) was irradiated at rt for 42 h. Then the solvent was evaporated and unreacted [$W(CO)_6$] sublimed off. The residue was washed with *n*-hexane (2 × 5 ml) and purified by chromatography (toluene solution, SiO_2 column, eluated with *n*-hexane, then toluene). The product **4** was obtained as pale yellow crystals from toluene at −18 °C. The starting material **1a** was obtained from the *n*-hexane fraction (0.17 g, 49%). Yield: 0.19 g (47% based on reacted **1a**), m.p. 238–42 °C (decomp.). *Anal.* Calc. for $C_{14}H_{28}B_{10}Cl_2O_4P_2W$ (685.15): C, 24.48; H, 4.11. Found: C, 24.80: H, 4.29%. MS (FAB, 3-nitrobenzyl alcohol) *m*/*z*: 685.1 (100%, M^+), 573.1 (69.0%, M^+–4CO), 517.0 (36.8%, M^+–4CO–^{t}Bu).

5.6. cis-meso-[1,2-Bis(tert-butylhydroxophosphino)-1,2-dicarba-closo-dodecaborane(12)]-tetracarbonylchromium(0) (**5**)

A solution of 0.2 g (0.51 mmol) **1** and 0.13 g (0.6 mmol) [$Cr(CO)_6$] in moist THF (10 ml THF and 0.018 g (1 mmol) H_2O) was irradiated at rt for 33 h. The THF was evaporated and the oily residue was washed with *n*-hexane (3 ml) and then passed through SiO_2 (eluated first with *n*-hexane, then with toluene). At room temperature pale yellow crystals of **5** were obtained from toluene. Yield: 0.10 g (38%), m.p. 228–30 °C (decomp.). *Anal.* Calc. for $C_{14}H_{30}B_{10}CrO_6P_2$ (516.42): C, 32.42; H, 5.83. Found: C, 33.10; H, 6.13%. MS (FAB, 3-nitrobenzyl alcohol) *m*/*z*: 516.2 (17.3%, M^+), 432.2 (61.7%, M^+–3CO), 404.2 (100%, M^+–4CO), 387.1 (13.1%, M^+–4CO–OH).

6. Data collection and structural refinement of 2–5

The data were collected on an Siemens CCD diffractometer (SMART [40]) using Mo Kα radiation (λ = 71.073 pm) and ω-scan rotation. Data reduction was performed with SAINT [41] including the program SADABS [42] for empirical absorption correction. All structures were solved by direct methods and the refinement of

all non-hydrogen atoms was performed with SHELX97 [43]. H atoms are calculated on idealized positions with the exception of all boron protons in **3a**. Structure figures were generated with ORTEP [44] Crystal data and structure refinement for complexes **2**–**5** are given in Table 3.

Acknowledgements

We gratefully acknowledge support from the Deutsche For schungsgemeinschaft (GZ: 436 RUS 17/35/06) and the Saxon Ministry of Science and Art (4-7531.50-04-0361-07/2).

Appendix A. Supplementary data

CCDC 715677, 715678 715679, 715680 and 715681 contain the supplementary crystallographic data for compounds **2**, **3a**, **3b**, **4** and **5**, respectively. These data can be obtained free of charge via http://www.ccdc.cam.ac.uk/conts/retrieving.html, or from the Cambridge Crystallographic Data Centre, 12 Union Road, Cambridge CB2 1EZ, UK; fax: (+44) 1223-336-033; or e-mail: deposit@ccdc.cam.ac.uk.

Supplementary data associated with this article can be found, in the online version, at doi:10.1016/j.poly.2009.07.030.

References

[1] S.J. Berners-Price, P.J. Sadler, Phosphines and Metal Phosphine Complexes: Relationship of Chemistry to Anticancer and Other Biological Activity, Bioinorganic Chemistry, Structure and Bonding 70, Springer-Verlag, Berlin–Heidelberg, 1988.
[2] R. Grimes, Carboranes, Academic Press, New York, 1970.
[3] S. Bauer, S. Tschirschwitz, P. Lönnecke, R. Frank, B. Kirchner, M.L. Clarke, E. Hey-Hawkins, Eur. J. Inorg. Chem. 19 (2009) 2776.
[4] S.E. Lyubimov, V.A. Davankov, P.V. Petrovskii, E. Hey-Hawkins, A.A. Tyutyunov, E.G. Rys, V.N. Kalinin, J. Organomet. Chem. 693 (2008) 3689.
[5] S. Tschirschwitz, P. Lönnecke, E. Hey-Hawkins, Organometallics 26 (2007) 4715.
[6] O.M. Ni Dhubhghaill, P.J. Sadler, in: B.K. Keppler (Ed.), Metal Complexes in Cancer Chemotherapy, VCH Verlagsgesellschaft mbH, Weinheim, New York – Basel – Cambridge, 1993.
[7] A. Hollemann, N. Wiberg, Lehrbuch der Anorganischen Chemie, 101 ed., Walter de Gruyter, Berlin – New York, 1995.
[8] V.P. Balema, S. Blaurock, E. Hey-Hawkins, Polyhedron 18 (1998) 545.
[9] (a) M. Fild, R. Schmutzler, in: L. Maier, G.M. Kosolapoff Hrsg. (Eds.), Organic Phosphorus Compounds, vol. 4, John Wiley and Sons, New York, 1972, p. S. 65;
(b) C.S. Kraihanzel, J. Organomet. Chem. 73 (1974) 137;
(c) B. Deschamps, L. Ricard, F. Mathey, Polyhedron 8 (1989) 2671;
(d) G. Salem, G.B. Shaw, A.C. Willis, S.B. Wild, J. Organomet. Chem. 444 (1993) 147;
(e) H. Schumann, L. Eguren, Z. Naturforsch. 46b (1991) 887 (and ref. therein).
[10] F. Bitterer, D.J. Brauer, F. Dörrenbach, F. Gol, P.C. Knüppel, O. Stelzer, C. Krüger, Y.-H. Tsay, Z. Naturforsch. 46b (1991) 1131 (and ref. therein).
[11] (a) S. Stadlbauer, P. Lönnecke, E. Hey-Hawkins, Phosphonate-substituted carbaboranes for potential use in BNCT, in: Y. Nakagawa, T. Kobayashi, H. Fukuda (Eds.), Advances in Neutron Capture Therapy 2006, Proceedings of ICNCT-12, Chemistry and Pharmacy, 2006, p. 215.;
(b) V.A. Ol'shevskaya, A.V. Zaitsev, E.G. Kononova, P.V. Petrovskii, E. Hey-Hawkins, A.A. Shtil', V.N. Kalinin, Doklady Chem. 414 (2007) 120.
[12] M. Scholz, K. Bensdorf, R. Gust, E. Hey-Hawkins, ChemMedChem 4 (2009) 746.
[13] S. Stadlbauer, P. Welzel, E. Hey-Hawkins, Inorg. Chem. 48 (2009) 5005.
[14] R.P. Alexander, H.-J. Schroeder, Inorg. Chem. 2 (1963) 1107.
[15] (a) N.N. Godovikov, V.P. Balema, E.G. Rys, Russ. Chem. Rev. 66 (1997) 1017;
(b) Young-il Park, Se-jin Kim, Jae-jang Ko, Sang Ook Kang, Bull. Korean Chem. Soc. 18 (1997) 1061;
(c) V.P. Balema, F. Somoza Jr., E. Hey-Hawkins, Eur. J. Inorg. Chem. (1998) 651;
(d) S. Paavola, R. Kivekäs, F. Teixidor, C. Vinas, J. Organomet. Chem. 606 (2000) 183;
(e) S. Paavola, F. Teixidor, C. Vinas, R. Kivekäs, J. Organomet. Chem. 645 (2002) 39;
(f) S. Paavola, F. Teixidor, C. Vinas, R. Kivekäs, J. Organomet. Chem. 657 (2002) 187;
(g) S. Paavola, F. Teixidor, C. Vinas, R. Kivekäs, Acta Crystallogr. C58 (2002) m237;
(h) Jianmin Dou, Daopeng Zhang, Dacheng Li, Daqi Wang, Inorg. Chem. Commun. 9 (2006) 1099;
(i) Jianmin Dou, Daopeng Zhang, Yuehua Zhu, Dacheng Li, Daqi Wang, Inorg. Chim. Acta 360 (2007) 3387;
(j) Jianmin Dou, Daopeng Zhang, Dacheng Li, Daqi Wang, Polyhedron 26 (2007) 719;
(k) Jianmin Dou, Daopeng Zhang, Yuehua Zhu, Dacheng Li, Daqi Wang, Polyhedron 26 (2007) 4216;;
(l) Jianmin Dou, Fangfang Su, Yong Nie, Dacheng Li, Daqi Wang, Dalton Trans. (2008) 4152.
[16] (a) G. Allender, H.D. Smith Jr., Inorg. Chim. Acta 26 (1978) L38;
(b) W.E. Hill, W. Levason, C.A. McAuliffe, Inorg. Chem. 13 (1974) 244;
(c) L.I. Zakharkin, G.G. Zhigareva, Zh. Obsh. Khim. 37 (1967) 1791;
(d) H.D. Smith Jr., J. Am. Chem. Soc. 87 (1965) 1817.
[17] (a) J. Dou, D. Zhang, Y. Zhu, D. Li, D. Wang, Polyhedron 26 (2007) 719;
(b) D. Zhang, J. Dou, D. Li, Y. Zhu, D. Wang, Inorg. Chim. Acta 359 (2006) 4243;
(c) J. Guillermo Contreras, L.M. Silva-Trivino, M.E. Solis, Inorg. Chim. Acta 114 (1986) 51.
[18] W.E. Hill, B.G. Rackley, L.M. Silva-Trivino, Inorg. Chim. Acta 75 (1983) 51.
[19] F.A. Hart, D.W. Owen, Inorg. Chim. Acta 103 (1985) L1.
[20] F. Su, Q. Guo, J. Dou, D. Li, D. Wang, Acta Crystallogr. E64 (2008) m134.
[21] A. Sterzik, E.G. Rys, S. Blaurock, E. Hey-Hawkins, Polyhedron 20 (2001) 3007.
[22] (a) O. Crespo, M.C. Gimeno, P.G. Jones, A. Laguna, J.M. Lopez-de-Luzuriaga, M. Monge, J.L. Perez, M.A. Ramon, Inorg. Chem. 42 (2003) 2061;
(b) P.G. Jones, M.D. Villacampa, O. Crespo, M.C. Gimeno, A. Laguna, Acta Crystallogr. C53 (1997) 570;
(c) O. Crespo, M.C. Gimeno, P.G. Jones, A. Laguna, M.D. Villacampa, Angew. Chem., Int. Ed. 36 (1997) 993;
(d) O. Crespo, M.C. Gimeno, P.G. Jones, A. Laguna, Inorg. Chem. 33 (1994) 6128;
(e) O. Crespo, M.C. Gimeno, A. Laguna, P.G. Jones, J. Chem. Soc., Dalton Trans: Inorg. Chem. 10 (1992) 1601;
(f) S. Al-Baker, W.E. Hill, C.A. McAuliffe, J. Chem. Soc., Dalton Trans: Inorg. Chem. 7 (1985) 1387.
[23] (a) O. Crespo, M.C. Gimeno, A. Laguna, P.G. Jones, J. Chem. Soc., Dalton Trans: Inorg. Chem. 24 (1996) 4583;
(b) E. Bembenek, O. Crespo, M.C. Gimeno, P.G. Jones, A. Laguna, Chem. Ber. 127 (1994) 835.
[24] S. Stadlbauer, R. Frank, I. Maulana, P. Lönnecke, B. Kirchner, E. Hey-Hawkins, Inorg. Chem. 48 (2009) 6072.
[25] (a) W.E. Hill, L.M. Silva-Trivino, Inorg. Chem. 17 (1978) 2495;
(b) V.P. Balema, S. Blaurock, V.K. Pechersky, E.G. Rys, E. Hey-Hawkins, Polyhedron 17 (1998) 3771;
(c) V.P. Balema, S. Blaurock, E. Hey-Hawkins, Z. Anorg. Allg. Chem. 625 (1999) 1237;
(d) E. Hey-Hawkins, I. Maulana, A. Sterzik, P. Lönnecke, S. Blaurock, E.G. Rys, Research and Development in Neutron Capture Therapy, Monduzzi Editore S.p.A. Bologna, Italy, 2002, S. 25–29.;
(e) E. Hey-Hawkins, A. Sterzik, I. Maulana, S. Blaurock, P. Lönnecke, E.G. Rys, V.N. Kalinin, Research and Development in Neutron Capture Therapy, Monduzzi Editore S.p.A. Bologna, Italy, 2002, S. 85–88.;
(f) I. Maulana, A. Sterzik, P. Lönnecke, S. Blaurock, E.G. Rys, E. Hey-Hawkins, Boron Chemistry at the Beginning of the 21st Century, in: Yu.N. Bubnov (Ed.), Editorial URSS, Moskau, Russia, 2003, p. S. 183.
[26] P. Machnitzki, O. Stelzer, C. Landgrafe, Z. Naturforsch. 52b (1997) 1103.
[27] (a) P.W. Lednor, W. Beck, G. Thiel, Inorg. Chim. Acta 20 (1976) L11;
(b) P.W. Lednor, W. Beck, H.G. Fick, H. Zippel, Chem. Ber. 111 (1978) 615;
(c) D.E. Berry, K.A. Beveridge, G.W. Bushnell, K.R. Dixon, Can. J. Chem. 63 (1985) 2949.
[28] M. Pabel, A.C. Willis, S.B. Wild, Tetrahedron: Asymmetry 6 (1995) 2369.
[29] H. Trampisch, W. Beck, Z. Naturforsch. 38b (1983) 365.
[30] (a) V.I. Nefedov, Y.V. Salyn, B. Walther, B. Messbauer, R. Schops, Inorg. Chim. Acta 45 (1980) L103;
(b) J. Powell, M.J. Horvath, A. Lough, J. Chem. Soc., Dalton Trans. (1995) 2975;
(c) J. Powell, M.J. Horvath, A. Lough, J. Chem. Soc., Dalton Trans. (1996) 1679.
[31] H. Byrd, J.D. Harden, J.M. Butler, M.J. Jablonsky, G.M. Gray, Organometallics 23 (2004) 3239.
[32] E.H. Wong, F.C. Bradley, Inorg. Chem. 20 (1981) 2333.
[33] I. Bernal, G.M. Reisner, G.R. Dobson, C.B. Dobson, Inorg. Chim. Acta 121 (1986) 199.
[34] Ch.-H. Ueng, L.-C. Leu, Acta Crystallogr. 47C (1991) 725.
[35] F.A. Cotton, G. Wilkinson, Advanced Inorganic Chemistry, fifth ed., John Wiley and Sons, New York, 1988.
[36] S. Hermanek, Inorg. Chim. Acta 289 (1999) 20.
[37] W.P. Fehlhammer, W.A. Herrmann, K. Öfele, in: G. Brauer (Ed.), Handbuch der präparativen anorganischen Chemie, vol. 3, F. Enke, Stuttgart, 1981, p. 1884.
[38] G.F. Kubas, L. Stepan von der Slugs, Inorg. Synth. 28 (1990) 31.
[39] M.A. Bennett, L. Pratt, G. Wilkinson, J. Chem. Soc. (1961) 2037.
[40] SMART, Area-Detector Software Package, Siemens Industrial Automation, Inc.: Madison, WI, 1993.
[41] SAINT, Area-Detector Integration Software. Version 6.01, Siemens Industrial Automation, Inc., Madison, WI, 1999.
[42] SADABS, G.M. Sheldrick, Program for Scaling and Correction of Area-detector Data, Göttingen, 1997.
[43] SHELX97 [Includes SHELXS97, SHELXL97], G.M. Sheldrick, Programs for Crystal Structure Analysis (Release 97-2), University of Göttingen, Germany, 1997.
[44] ORTEP3 for Windows: L.J. Farrugia, J. Appl. Crystallogr. 30 (1997) 565.

phen = 1,10-phenantroline, were prepared according to literature methods [9].

2.2. Apparatus

$^{31}P\{^{1}H\}$ NMR experiments were recorded on a BRUKER equipment 9.4 T (400 MHz for hydrogen frequency) in CH_2Cl_2, using a capillary containing D_2O. The microanalyses were performed in the Microanalytical Laboratory, Department of Chemistry at Universidade Federal de São Carlos, São Carlos (SP), using a FISIONS CHNS, mod. EA 1108 micro analyser.

2.3. X-ray crystallography

Crystals of the isolated complexes were grown by slow evaporation of dichloromethane/diethyl ether solution. These crystals were mounted on an Enraf-Nonius Kappa-CCD diffractometer with graphite monochromated Mo Kα (λ = 0.71073 Å) radiation. The final unit cell parameters were based on all reflections. Data collections were made using the COLLECT program [10]. Integration and scaling of the reflections were performed with the HKL Denzo-Scalepack system of programs [11]. Gaussian absorption corrections were carried out [12]. The structures were solved by direct methods with SHELXS-97 [13]. All hydrogen atoms were stereochemically positioned and refined with the riding model. The ORTEPs shown in Fig. 1 were prepared using ORTEP-3 for windows [14]. Hydrogen atoms of the aromatic rings were set isotropic with a thermal parameter 20% greater than the equivalent isotropic displacement parameter of the atom to which each one is bonded. The data collections and some experimental details are summarized in Table 1.

2.4. Synthesis

cis-[RuCl(L)(P–P)(N–N)](PF_6) type complexes, where N–N = 2,2′-bipyridine (bipy) or 1,10-phenantroline (phen), P–P = 1,4-bis-(diphenylphosphino)butane (dppb) or 1,1′-bis(diphenylphosphino)-ferrocene (dppf), and L = 4-methylpyridine (4-Mepy), benzonitrile (bzCN), and 4-phenylpyridine (4-Phpy), were prepared by reacting the *cis*-[$RuCl_2$(P–P)(N–N)] complex (0.128 mmol) dissolved in CH_2Cl_2 with three times of excess of the L ligands and 0.256 mmol of NH_4PF_6 in methanol (ca. 5 mL) under argon atmosphere for 3 h.

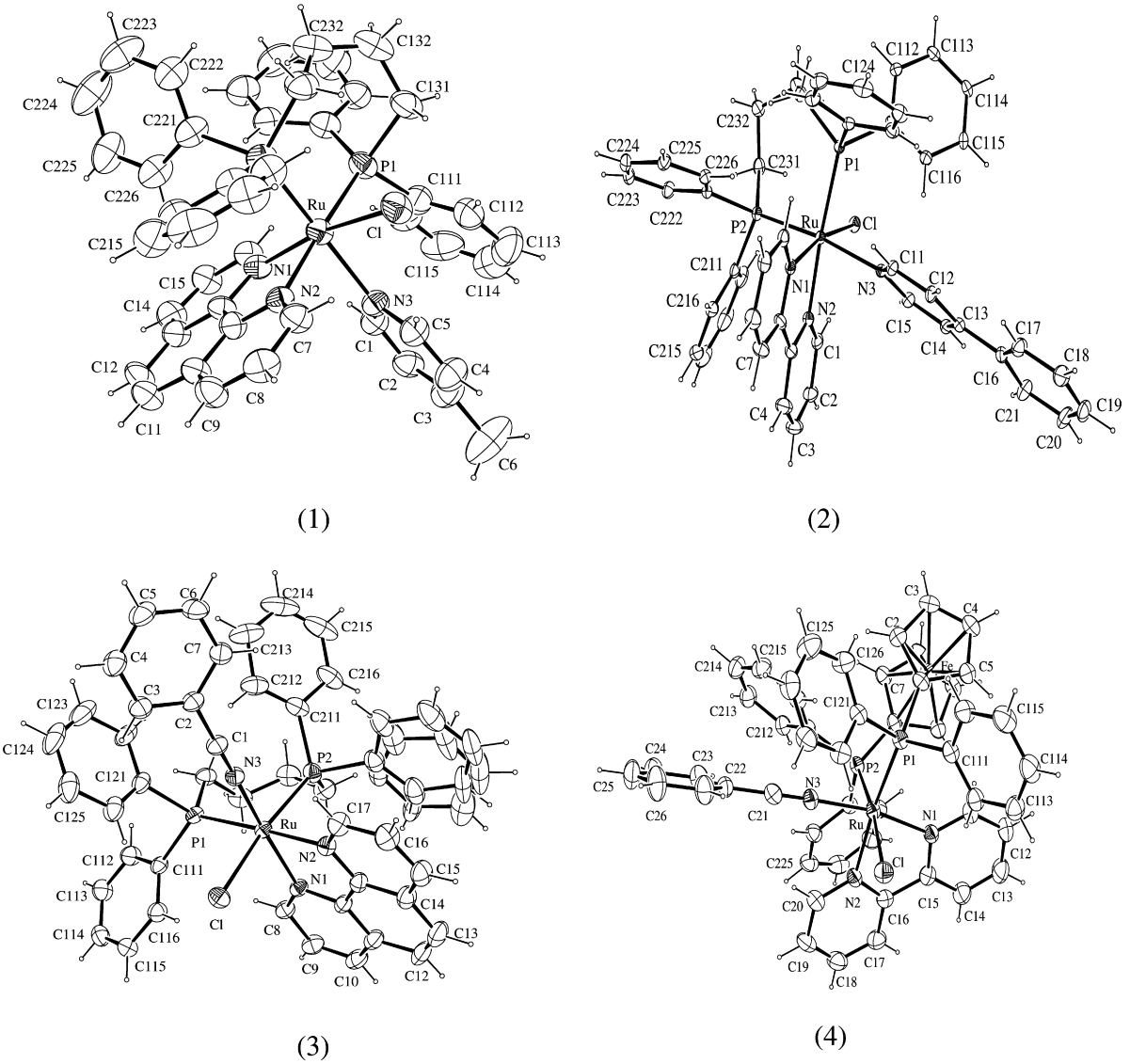


Fig. 1. *ORTEP* [15] view of the [RuCl(4-Mepy)(dppb)(phen)](PF_6)·0.5H_2O **(1)**, [RuCl(4-Phpy)(dppb)(bipy)](PF_6)·CH_2Cl_2 **(2),** [RuCl(bzCN)(dppb)(phen)](PF_6)·0.5H_2O **(3)** and [RuCl(bzCN)(dppf)(bipy)]Cl·H_2O·3/2(C_7H_5N) **(4)** complexes, showing the atoms labeling and the 30% probability ellipsoids.

Table 1
Crystallographic data for the [RuCl(4-Mepy)(dppb)(phen)](PF_6)·0.5H_2O **(1)**, [RuCl(4-Phpy)(dppb)(bipy)](PF_6)·CH_2Cl_2 (**2**), [RuCl(bzCN)(dppb)(phen)](PF_6)·0.5H_2O **(3)** and [RuCl(bzCN)(dppf)(bipy)]Cl·H_2O·3/2(C_7H_5N) **(4)** complexes.

	$C_{46}H_{43}N_3P_3ClF_6Ru·1/2(H_2O)$	$C_{49}H_{45}N_3P_3ClF_6Ru\cdots CH_2Cl_2$	$C_{47}H_{41}N_3P_3ClF_6Ru·1/2(H_2O)$	$C_{51}H_{41}N_3P_2ClFeRu·H_2O·3/2(C_7H_5N)$
Formula weight	990.27	1104.24	1000.27	1158.32
T (K)	293(2)	120(2)	293(2)	293(2)
Crystal system	monoclinic	orthorhombic	triclinic	triclinic
Space group	$P2_1/n$	$Pna2_1$	$P\bar{1}$	$P\bar{1}$
a (Å)	10.6530(8)	11.7052(3)	10.9870(2)	10.5579(3)
b (Å)	30.366(3)	37.922(1)	12.6320(3)	13.9123(5)
c (Å)	16.513(1)	10.6068(3)	17.2550(3)	19.2628(6)
α (°)	90	90.000	74.673(1)	79.203(2)
β (°)	94.032(3)	90.000	73.093(1)	89.644(2)
γ (°)	90.000	90.000	81.746(1)	73.281(2)
V (Å^3)	5328.6(7)	4708.2(2)	2204.00(8)	2658.41(15)
Z	4	4	2	2
ρ_{calcd} (Mg m^{-3})	1.234	1.558	1.507	1.147
Absorption coefficient (mm^{-1})	0.487	0.669	0.590	0.765
F(0 0 0)	2020	2248	1018	1186
Crystal size (mm^3)	0.34 × 0.09 × 0.08	0.23 × 0.18 × 0.16	0.34 × 0.14 × 0.09	0.22 × 0.06 × 0.02
Method/θ range for data collection (°)	2.47–25.00	3.48–27.50	3.00–27.51	3.124–27.52
Index ranges	$-12 \leqslant h \leqslant 12$, $-36 \leqslant k \leqslant 36$, $-19 \leqslant l \leqslant 19$	$-12 \leqslant h \leqslant 15$, $-49 \leqslant k \leqslant 49$, $-13 \leqslant l \leqslant 13$	$-14 \leqslant h \leqslant 14$, $-16 \leqslant k \leqslant 16$, $-22 \leqslant l \leqslant 22$	$-12 \leqslant h \leqslant 13$, $-18 \leqslant k \leqslant 17$, $-25 \leqslant l \leqslant 25$
Reflections collected	25 701	25 549	19 449	58 072
Reflections unique/R_{int}	9078 [R_{int} = 0.1258]	10 320 [R_{int} = 0.0420]	10 026 [R_{int} = 0.0373]	12 113 [R_{int} = 0.0947]
Completeness to θ	25.00° (96.6%)	27.50° (98.7%)	27.51° (98.8%)	27.52° (99.0%)
Data/restraints/parameters	9078/0/545	10 320/1/595	10 026/0/644	12 113/0/667
Absorption correction	gaussian	semi-empirical from equivalents	gaussian	multi-scan
Maximum/minimum transmission	0.981 and 0.887	0.869 and 0.746	0.950 and 0.841	0.998 and 0.824
Final R indices [$I > 2\sigma(I)$][a,b]	R_1 = 0.0897, wR_2 = 0.2412	R_1 = 0.0348, wR_2 = 0.0911	R_1 = 0.0372, wR_2 = 0.0903	R_1 = 0.0526, wR_2 = 0.1107
R indices (all data)	R_1 = 0.1180, wR_2 = 0.2577	R_1 = 0.0443, wR_2 = 0.1124	R_1 = 0.0569, wR_2 = 0.1062	R_1 = 0.1166, wR_2 = 0.1331
Goodness-of-fit (GOF) on F^2, S	1.027	1.151	1.059	1.024
Largest difference in peak and hole (e Å^{-3})	0.885 and −0.724	0.766 and −0.985	0.459 and −0.917	0.736 and −0.655

[a] $R_1 = \sum||F_o|-|F_c||/\sum|F_o|$.
[b] $wR_2 = [\sum w(|F_o|^2-|F_c|^2)^2/\sum w|F_o^2|^2]^{1/2}$.

The solution was then filtered, concentrated to ca. 2 mL and hexane was added to precipitate the products. The solids were filtered off, rinsed with water (3 × 5 mL) and diethyl ether (3 × 5 mL) and dried under vacuum. The complex **(4)** was also synthesized in the same way, but without adding the NH_4PF_6.

*2.4.1. [RuCl(4-Mepy)(dppb)(phen)](PF_6) **(1)**Anal. Calc. for [$C_{46}H_{43}ClF_6N_3P_3Ru$]: C, 55.30; H, 4.42; N, 4.28. Found: C, 55.45; H, 4.30; N, 4.32%. Yield: 90%. $^{31}P\{^1H\}$ NMR: δ 37.9 and δ 37.3 (J_{P-P} = 38.8 Hz).*

*2.4.2. [RuCl(4-Phpy)(dppb)(bipy)](PF_6) **(2)***

Anal. Calc. for [$C_{49}H_{45}ClF_6N_3P_3Ru$]: C, 57.74; H, 4.45; N, 4.12. Found: C, 57.42; H, 4.46; N, 4.28%. Yield: 87%. $^{31}P\{^1H\}$ NMR: δ 38.0. The presence of just one singlet instead of doublets in this type of complex is assigned to solvent and temperature effects as already discussed in our previous works [15,16].

*2.4.3. [RuCl(bzCN)(dppb)(phen)](PF_6) **(3)***

Anal. Calc. for [$C_{47}H_{41}ClF_6N_3P_3Ru$]: C, 56.95; H, 4.17; N, 4.24. Found: C, 56.45; H, 3.97; N, 4.27%. Yield: 91%. $^{31}P\{^1H\}$ NMR: δ 40.9 and δ 32.4 (J_{P-P} = 30.8 Hz).

*2.4.4. [RuCl(bzCN)(dppf)(bipy)]Cl **(4)***

Anal. Calc. for [$C_{51}H_{41}Cl_2N_3P_2FeRu$] **(4)**. C, 63.83; H, 4.27; N, 5.45. Found: C, 53.75; H, 4.33; N, 5.20%. $^{31}P\{^1H\}$ NMR: δ 43.7 and δ 35.6 (J_{P-P} = 27.5 Hz).

*2.4.5. [RuCl(bzCN)(dppf)(bipy)](PF_6) **(5)***

Anal. Calc. for [$C_{51}H_{41}ClF_6N_3P_3FeRu$]: C, 55.93; H, 3.77; N, 3.84. Found: C, 56.12; H, 3.97; N, 4.20%. Yield: 93%. $^{31}P\{^1H\}$ NMR: δ 43.5 and δ 35.3 (J_{P-P} = 27.5 Hz).

3. Results and discussion

The X-ray structures of the complexes **(1–4)** are shown in Fig. 1.

In all cases, the isolated complexes were formed by the displacement of one chloride atom from the respective precursor *cis*-[$RuCl_2$(dppb)(bipy)], *cis*-[$RuCl_2$(dppb)(phen)] or *cis*-[$RuCl_2$-(dppf)(bipy)]. As depicted in Fig. 1, the 4-Mepy and 4-Phpy ligands are coordinated *trans* to phosphorus atoms in complexes **(1)** and **(2)**, respectively, while in complexes **(3)** and **(4)** the benzonitrile ligand occupy the position *trans* to nitrogen atoms of the N–N ligands. Recently the [RuCl(dppb)(bipy)(4-Mepy)]PF_6 complex was synthesized by us showing the same structure of **(1)** and **(2)** [17].

Some selected bond lengths of complexes **(1–4)** are in Table 2.

The bond lengths in Table 2 are in the range found for similar ruthenium phosphine complexes, but the distances Ru–N of the bzCN ligand in complexes **(3)** and **(4)** [Ru–N(3)] are shorter than the other Ru–N bond lengths (involving the nitrogen atoms of the 2,2′-bipyridine or of the 1,10-phenantroline) since the cyano-group is a stronger π acceptor than the nitrogen atoms in the rings of the aromatic amino ligands [9,18–23]. The distances Ru–N(2), which are *trans* to phosphorus atoms in the four complexes, are longer than the distances of Ru–N(1), as a consequence of the strong *trans* influence of the phosphorus atoms of the diphosphine

Table 2
Selected bond lengths (Å) for complexes **(1–4)**, with estimated standard deviations in parentheses.

Complex	Ru–N(1)	Ru–N(2)[a]	Ru–N(3)[b]	Ru–P(1)	Ru–P(2)	Ru–Cl
(**1**) $0.5H_2O$	2.074(5)	2.130(5)	2.190(5)	2.3428(18)	2.3259(19)	2.4352(16)
(**2**) CH_2Cl_2	2.099(3)	2.122(3)	2.170(3)	2.3582(9)	2.3317(9)	2.4168(9)
(**3**) $0.5H_2O$	2.0919(19)	2.111(2)	2.011(2)	2.3434(7)	2.3166(7)	2.4555(7)
(**4**) $H_2O{\cdot}3/2$ (C_7H_5N)	2.089(3)	2.106(3)	2.002(3)	2.3749(10)	2.3163(10)	2.4687(10)

[a] Nitrogen *trans* P(1).
[b] Nitrogen from the entering ligand (L).

ligands. The Ru–P(1) bond lengths of complexes (**1–4)** are longer than the distances Ru–P(2). This observation suggests that the *trans* influence of the bidentate N–N ligands is stronger than the same effect of the monodentates ligands (4-Mepy, 4-Phpy and chloride).

In order to elucidate the mechanism of formation of the $[RuCl(bzCN)(dppb)(phen)]PF_6$ complex with the bzCN ligand coordinated *trans* to the nitrogen atom of the 1,10-phenantroline, the reaction of the benzonitrile ligand with the precursor *cis*-$[RuCl_2(dppb)(phen)]$ was followed by the NMR technique [$^{31}P(^1H)$]. Thus, as can be seen in Fig. 2 initially three complexes are present in the solution: the precursor (δ 42.8 and 31.3); the final product $[RuCl(bzCN)(dppb)(phen)]PF_6$ with the bzCN *trans* to a nitrogen (δ 40.9 and 32.4) and an intermediate complex (δ 40.4 and 37.6). Since in the end of the reaction only the complex $[RuCl(bzCN)(dppb)(phen)]PF_6$ (δ 40.9 and 32.4) with the entering ligand positioned *trans* to the nitrogen atom of the 2,2′-bipyridine molecule is present in solution, according to its X-ray structure (Fig. 1), the intermediate very probably consists of a complex with the same composition as the final product but with the bzCN ligand coordinated *trans* to a phosphorus atom of the diphosphine. The fact that the two doublets for this intermediate are very close from each other reinforce our suggestion that in this case both phosphorus atoms are *trans* to nitrogen atoms (one of the 1,10-phenantroline and the other one of the bzCN ligand).

An interesting point that must be addressed to explain the position of the bzCN ligand in the $[RuCl(bzCN)(dppb)(phen)](PF_6)$ **(3)** and in the [RuCl(bzCN)(dppf)(bipy)]Cl **(4)** complexes is the fact that the phosphorus atom is a strong π acceptor as well as is the cyano-group of the benzonitrile ligand. Thus, when two good π acceptor ligands are mutually *trans*, they compete for electron density residing in the same metal d orbital and the amount of M → C back-bonding is reduced by trying to labilize each other. Consequently, by the competition for the metal center electrons between the diphosphine phosphorus atom and the cyano-group of the bzCN, the bond Ru–NCbz results thermodynamically less stable. Therefore, this ligand is easily dissociated and then located in the position *trans* to one of the nitrogen atoms of the N–N ligands where the competitive effect is less accentuated, since the pyridine rings from the 1,10-phenantroline or from the 2,2′-bipyridine ligand are not strong π electron acceptors. The differential pulse voltammetry experiment supports this suggestion. As shown in Fig. 3, the intermediate complex with the bzCN ligand positioned *trans* to the phosphorus atom (δ 40.4 and 37.6 in the $^{31}P\{^1H\}$ spectra)

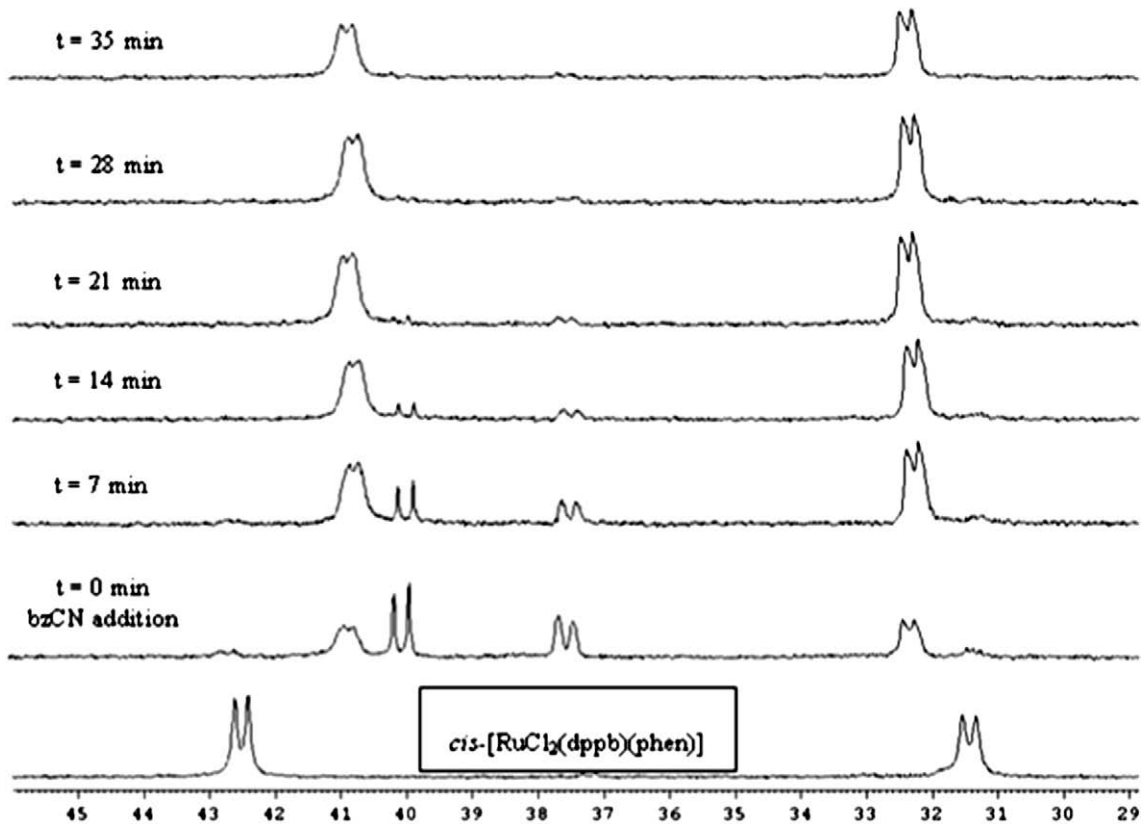


Fig. 2. The $^{31}P\{^1H\}$ NMR spectra, in CH_2Cl_2, following the reaction of the precursor *cis*-$[RuCl_2(dppb)(phen)]$ (bottom) with the bzCN ligand (20 times excess).

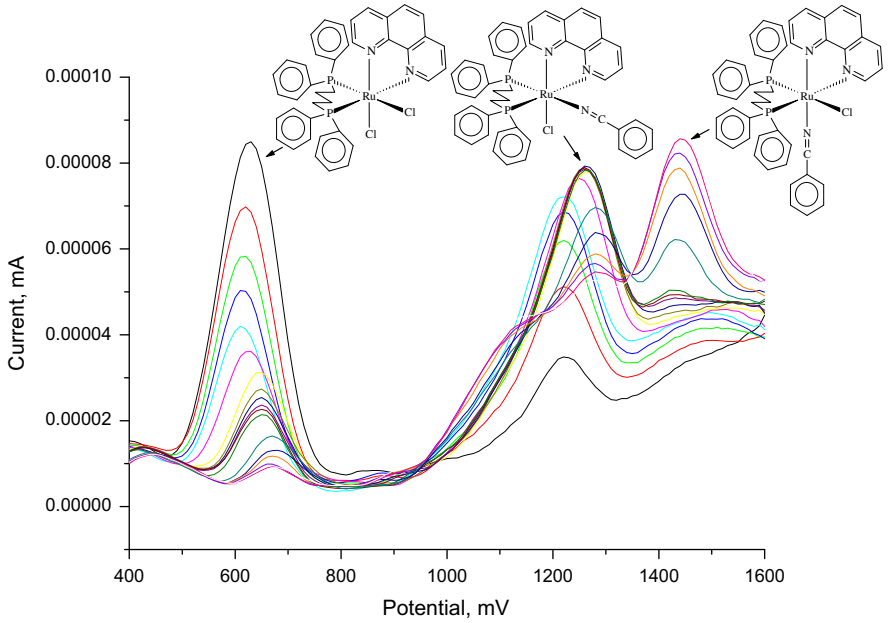


Fig. 3. The differential pulse voltammograms, in CH_2Cl_2, following the reaction of the precursor *cis*-[$RuCl_2$(dppb)(phen)] with the bzCN ligand (20 times excess) (Pt vs. AgCl, 0.1 M PTBA; [Ru] = 1.0×10^{-3} mol L^{-1}; [bzCN] = 20×10^{-3} mol L^{-1}; T = 293 K). Interval of each measurement 7 min.

shows a lower oxidation potential than the other isomer, the final product of the reaction (δ 40.9 and 32.4), with the bzCN ligand sited *trans* to the nitrogen atom. This behavior, provoked by competitive effect, has previously observed by us and by others [24–26].

The same phenomenon observed for the benzonitrile ligand in its reaction with the *cis*-[$RuCl_2$(dppb)(bipy)], *cis*-[$RuCl_2$(dppf)(bipy)] complexes was also observed when acetonitrile (δ 42 e 34 ppm, when acetonitrile is coordinated *trans* to P atom, and δ 43 e 34.5 ppm, when acetonitrile is coordinated *trans* to N atom), a small molecule, was used as entering ligand, suggesting that in these reactions the steric effect does not play a decisive role for the stereochemistry of the final products. Here we would like to point out that in this work "*trans* effect" is used to define the competition for the electron density of the metal that occurs between one strong and one weak π acceptor ligand, while "competitive effect" is used in the case when this competition occurs between two good π acceptor ligands mutually *trans*. These two phenomena are indeed the driving forces in the octahedral complexes studied in this work, leading to thermodynamically stable products, depending of the characteristics of the entering ligand.

The kinetic study of the dissociation of a coordinated chloride, using differential pulse voltammetry for the benzonitrile complex, yielded a rate saturation which is typical of a dissociative mechanism. The limiting first order specific rate of dissociation of the chloride was found to be about $1.0 \pm 0.1 \times 10^{-2}$ s^{-1} and the isomerization rate for the [RuCl(bzCN)(dppb)(phen)]PF_6 (bzCN *trans* to phosphorus to the species *trans* to the nitrogen) was found to be $5.0 \pm 0.1 \times 10^{-4}$ mol L^{-1} s^{-1}. These values are consistent with the data observed in the $^{31}P\{^1H\}$ spectra, in Fig. 2, where the dissociation of the chloride is much faster than the isomerization process. This observed isomerization rate is in the same order as those found for the isomerization of the *trans*-[$RuCl_2$(dppb)(X-bipy)] to the correspondents *cis*-[$RuCl_2$(dppb)(X-bipy)] complexes (X-bipy = 2,2′-bipyridine derivatives) [27].

4. Conclusions

In complexes with general formula *cis*-[$RuCl_2$(P–P)(N–N)] (P–P – diphosphine and N–N = 2,2′-bipyridine or 1,10-phenantroline) the chloride *trans* to the phosphorus atoms is more labile than that one *trans* to the nitrogen atoms, but the final position of an entering good π acceptor ligand is better defined by the competitive effect, which plays a crucial role in the process. The dissociation of the chloride from the *cis*-[$RuCl_2$(dppb)(phen)], *trans* to a phosphorus atoms, follows a dissociative mechanism and its constant rate is $1.0 \pm 0.1 \times 10^{-2}$ s^{-1} while the isomerization rate for the [RuCl(bzCN)(dppb)(phen)]PF_6 (bzCN *trans* to phosphorus to the species *trans* to the nitrogen) is $5.0 \pm 0.1 \times 10^{-4}$ mol L^{-1} s^{-1}.

5. Supplementary data

CCDC 707431, 707432, 707433 and 707434 contain the supplementary crystallographic data for (**1**), (**2**), (**3**) and (**4**), respectively.. These data can be obtained free of charge via http://www.ccdc.cam.ac.uk/conts/retrieving.html, or from the Cambridge Crystallographic Data Centre, 12 Union Road, Cambridge CB2 1EZ, UK; fax: (+44) 1223-336-033; or e-mail: deposit@ccdc.cam.ac.uk.

Acknowledgements

Financial support from CAPES, CNPq, FAPESP.

References

[1] J.E. Huheey, E.A. Keiter, L.K. Richard, Inorganic Chemistry, Principles of Structure and Reactivity, 4th ed., Prentice Hall, 1993.
[2] D.F. Shriver, P.W. Atkins, C.H. Langfor, Inorganic Chemistry, 2nd ed., Oxford, Oxford University Press, 1994.
[3] E.A. Seddon, K.R. Seddon, The Chemistry of Ruthenium, New York, Elsevier Pub., Co., 1984.
[4] M.J. Clarke, Coord. Chem. Rev. 232 (2002) 69.
[5] M. Sykora, J.C. Yang, T.J. Meyer, J. Phys. Chem. B 109 (2005) 1499.
[6] A.M. Joshi, K.S. MacFarlane, B.R. James, J. Organomet. Chem. 488 (1995) 161.
[7] A.A. Batista, A.L. Bogado, R.F. Souza, U. Schuchardt, J. Mol. Catal. A-Chem. 203 (2003) 129.
[8] S.E. Clapham, A. Hadzovic, R.H. Morris, Coord. Chem. Rev. 248 (2004) 2201.
[9] S.L. Queiroz, A.A. Batista, G. Oliva, M.T.P. Gambardella, R.H.A. Santos, K.S. MacFarlane, S.J. Rettig, B.R. James, Inorg. Chim. Acta 267 (1998) 209.
[10] COLLECT, Enraf-Nonius, Nonius BV, Delft, The Netherlands, 1997–2000.
[11] Z. Otwinowski, W. Minor, in: C.W. Carter, R.M. Sweet Jr. (Eds.), Methods in Enzymology, vol. 276, Academic Press, New York, 1997, pp. 307–326.

[12] R.H. Blessing, Acta Crystallogr., Sect. A 51 (1995) 33.
[13] G.M. Sheldrick, Acta Crystallogr., Sect. A 64 (2008) 112.
[14] L.J. Farrugia, J. Appl. Crystallogr. 30 (1997) 565.
[15] E.M.A. Valle, F.B. do Nascimento, A.G. Ferreira, A.A. Batista, M.C.R. Monteiro, S.deP. Machado, J. Ellena, E.E. Castellano, E.R. deAzevedo, Química Nova 31 (2008) 807.
[16] M.P. de Araujo, E.M.A. Valle, E.E. Castellano, E.N. dos Santos, A.A. Batista, Polyhedron 23 (2004) 3163.
[17] L.L. Romualdo, A.L. Bogado, E.M.A. Valle, I.S. Moreira, J. Ellena, E.E. Castellano, M.P. de Araujo, A.A. Batista, Polyhedron 27 (2008) 53.
[18] K.S. MacFarlane, A.M. Joshi, S.J. Rettig, B.R. James, Inorg. Chem. 35 (1996) 7304.
[19] A.L.R. Silva, M.O. Santiago, I.C.N. Diogenes, S.O. Pinheiro, E.E. Castellano, J. Ellena, A.A. Batista, F.B. do Nascimento, I.S. Moreira, Inorg. Chem. Commun. 8 (2005) 1154.
[20] G. Von Poelhsitz, A.L. Bogado, M.P. de Araujo, H.S. Selistre-de-Araújo, J. Ellena, E.E. Castellano, A.A. Batista, Polyhedron 26 (2007) 4707.
[21] G. Von Poelhsitz, A.A. Batista, J. Ellena, E.E. Castellano, E.S. Lang, Inorg. Chem. Commun. 8 (2005) 805.
[22] M.P. Felicíssimo, A.A. Batista, A.G. Ferreira, J. Ellena, E.E. Castellano, Polyhedron 24 (2005) 1063.
[23] A. Batista, K. Wohnrath, A.G. Ferreira, J. Zuckerman-Schpector, E.E. Castellano, Polyhedron 17 (1998) 2013.
[24] A.A. Batista, M.O. Santiago, C.L. Donnici, I.S. Moreira, P.C. Healy, S.J. Berners-Price, S.L. Queiroz, Polyhedron 20 (2001) 2123.
[25] D.W. Krassowski, J.H. Nelson, K.R. Brower, D. Hauenstein, R.A. Jacobson, Inorg. Chem. 27 (1978) 4294.
[26] J. Chatt, B.L. Shaw, A.E. Field, J. Chem. Soc. (1964) 3466.
[27] M.O. Santiago, C.L. Donnici, I.S. Moreira, R.M. Carlos, S.L. Queiroz, A.A. Batista, Polyhedron 22 (2003) 3205.

$[W_3Te_7(dtp)_3]Br$ was prepared according to Ref. [11] by mechanochemical treatment of solid $W_3Te_7Br_4$ and Kdtp. Mechanochemical syntheses were done in a vibration mill, described in Ref. [12] In all cases a cylindrical titanium reactor was used (volume 100 ml, height 50 mm). The reactor was filled with tungsten carbide balls (diameter 10 mm, total mass 320 g), and with a mixture of solid reagents. The reactions were run under the following conditions: frequency of reactor vibrations 25 Hz, amplitude of vertical movement 1 cm, duration – 10 h. IR spectra (4000–400 cm^{-1}) were recorded with an IFS-85 Bruker spectrometer in KBr pellets, Raman spectra were obtained on a Triplimate 21 spectrometer. The elemental analysis was done in the Laboratory of Microanalysis, Institute of Organic Chemistry, Novosibirsk, Russia.

2.2. Electrospray ionization mass spectrometry

A Q-TOF Premier mass spectrometer with an orthogonal Z-spray electrospray source (Waters, Manchester, UK) was used. The temperature of the source block was set to 120 °C and the desolvation temperature to 150 °C. A capillary voltage of 3.5 kV was used in the positive scan mode, and the cone voltage was set to 10 V to control the extent of fragmentation. ESI(+) mass spectra were acquired in the W-scan mode operating at a resolution of ca. 17500 (FWHM). About 2×10^{-5} M CH_3OH:$CHCl_3$ sample solutions were infused via a syringe pump directly connected to the ESI-MS source at a flow rate of 10 μL/min. The observed isotopic pattern of each compound perfectly matched the theoretical isotopic pattern calculated from their elemental composition using the MASSLYNX 4.1 program [13].

2.3. Synthesis of $[Mo_3(_3\text{-}Te)(_2\text{-}Te_2)_3(dtp)_3]I$ (**1**)

About 2.0 g (1.1 mmol) of solid $Mo_3Te_7I_4$ and 0.90 g $(EtO)_2PS_2K$ (4.0 mmol) were treated in a vibration mill. The reaction mixture was extracted with 30 ml of $CHCl_3$, mixed with 60 ml of ethanol and left at 5 °C for two days. A black crystalline solid was filtered off, washed with ethanol and ether and dried in air. Yield 0.37 g (17%). *Anal.* Calc. for $C_{12}H_{30}IMo_3O_6P_3S_6Te_7$: C, 7.73; H, 1.62. Found: C, 7.84; H, 1.37%. IR (cm^{-1}): 3445 w, 2974 w, 2891 w, 1469 w, 1436 w, 1384 w, 1288 w, 1157 m, 1098 w, 1028 s, 1010 s, 959 s, 811 m, 775 s, 635 s, 546 m, 445 w. Raman (cm^{-1}): 278 w, 265 w, 230 w, 213 m, 194 m, 141 w, 123 m, 90 w, 65 s. Electronic spectrum (in $CHCl_3$): λ_{max}/nm (ε_M) = 354 (14500), 391 (9700). ESI(+)-MS: $[Mo_3Te_7((EtO)_2PS_2)_3]^+$ (*m/z* = 1738.2).

2.4. Synthesis of $[W_3Te_{4.25}S_{2.75}((EtO)_2PS_2)_3]Br$ (**2**)

To a solution of $[W_3(\mu_3\text{-}Te)(\mu_2\text{-}Te_2)_3((EtO)_2PS_2)_3]Br$[14] (0.07 g, 0.03 mmol) in 4 ml of $CHCl_3$, bromine (0.02 g, 0.13 mmol) was added. The solution was refluxed for 2 h, a black precipitate was filtered off, and a double volume of ethanol was added to the solution which then was left at −5 °C for 2 days. Red crystals of X-ray quality were separated by decantation, washed with ethanol and ether, and dried in air. Yield 0.010 g (18%). IR (cm^{-1}): 3437 m, 2976 w, 2931 w, 2895 w, 1637 w, 1471 w, 1439 w, 1388 w, 1290 w, 1161 m, 1101 w, 1052 m, 1004 s, 968 s, 816 m, 791 m, 638 m, 531 w. Raman (cm^{-1}): 634 w, 524 w, 399 m, 389 m, 352 w, 281 w, 254 w, 219 w, 203 w, 160 w, 123 w, 100 m, 87 w, 47 s, 29 m. ESI(+)-MS: see Fig. 1.

2.5. Synthesis of $[W_3Te_{4.30}S_{2.70}((EtO)_2PS_2)_3]Br_{0.62}Cl_{0.38}$ (**3**)

To a solution of 0.11 g of $[W_3(\mu_3\text{-}Te)(\mu_2\text{-}Te_2)_3((EtO)_2PS_2)_3]Br$ (0.053 mmol) in 7 ml of $CHCl_3$, a solution of 0.025 g of S_2Cl_2 in 1 ml of $CHCl_3$ (0.19 mmol) was added. The reaction mixture was left stirring for 20 h. A black precipitate was filtered off, and a double volume of ethanol was added to the solution, which then was left at −5 °C for 2 days. Red crystals of X-ray quality were separated by decantation, washed with ethanol and ether, and air-dried. Yield 0.03 g (31%). ESI(+)-MS: see Fig. 1. Recrystallization of the solid, kept for 2 months, from a $CHCl_3$/EtOH mixture at −5 °C gave single crystals of $[W_3Te_{3.91}S_{3.10}((EtO)_2PS_2)_3]Br_{0.64}Cl_{0.36}$ (**4**).

2.6. Synthesis of $[Mo_3Te_{4.74}S_{2.26}((EtO)_2PS_2)_3]I_{0.72}Cl_{0.28}$ (**5**)

To a solution of 0.060 g $[Mo_3(\mu_3\text{-}Te)(\mu_2\text{-}Te_2)_3((EtO)_2PS_2)_3]I$ (0.03 mmol) in 2 ml of $CHCl_3$, a solution of 0.020 g S_2Cl_2 (0.15 mmol) in 2 ml of $CHCl_3$ was added, followed by 7 drops of DMF. The reaction mixture was left stirring for 5 h. A black precipitate of Te was filtered off, and a double volume of CH_3OH was added to the filtrate, and the solution was left at 7 °C overnight. The crystals (suitable for X-ray structural analysis) of $[Mo_3Te_{4.74}S_{2.26}((EtO)_2PS_2)_3]I_{0.72}Cl_{0.28}$ were removed by decantation, washed with methanol and ether, and dried in vacuum. Yield 0.030 g (62%). ESI(+)-MS: see Fig. 2.

2.7. Reaction of **5** with excess of S_2Cl_2

To a solution of 0.022 g of **5** (0.01 mmol) in 2 ml of $CHCl_3$, a solution of S_2Cl_2 (0.020 g, 0.15 mmol) in 2 ml of $CHCl_3$ was added.

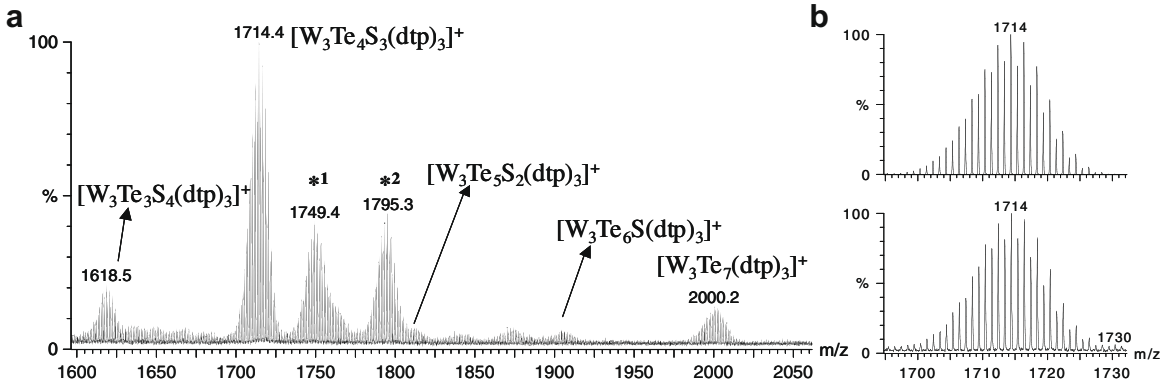


Fig. 1. Electrospray ionization mass spectrum of $[W_3Te_{4.30}S_{2.70}((EtO)_2PS_2)_3]Br_{0.62}Cl_{0.38}$ (**3**) in $CHCl_3$/CH_3OH mixtures (U_c = 10 V) (a) and simulated (top) and experimental (bottom) spectra for $[W_3Te_4S_3((EtO)_2PS_2)_3]^+$ centered at *m/z* = 1714.4 (b). Species marked with ^{*1} and ^{*2} formally correspond to HCl and HBr adducts of the cation $[W_3Te_4S_3(dtp)_3]^+$.

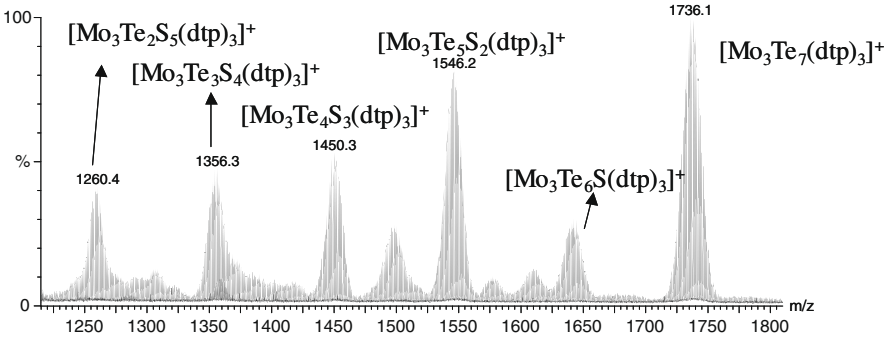


Fig. 2. Electrospray ionization mass spectrum of $[Mo_3Te_{4.74}S_{2.26}((EtO)_2PS_2)_3]I_{0.72}Cl_{0.28}$ (**5**) in $CHCl_3/CH_3OH$ mixtures (U_c = 10 V).

Table 1
Crystal data and structure refinement for **2**–**6**.

Compound	**2**	**3**	**4**	**5**	**6**
Chemical formula	$C_{12}H_{30}BrO_6P_3S_{8.75}Te_{4.25}W_3$	$C_{12}H_{30}Br_{0.62}Cl_{0.38}O_6P_3S_{8.69}Te_{4.30}W_3$	$C_{12}H_{30}Br_{0.63}Cl_{0.36}O_6P_3S_{9.10}Te_{3.91}W_3$	$C_{12}H_{30}C_{10.28}I_{0.72}Mo_3O_6P_3S_{8.26}Te_{4.74}$	$C_{12}H_{30}IMo_3O_6P_3S_9Te_4$
M_r	1817.56	1805.28	1768.37	1621.56	1576.93
Cell setting, space group	monoclinic, $P2_1/n$	monoclinic, $P2_1/n$	monoclinic, $P2_1/n$	monoclinic, $P2_1/n$	monoclinic, $P2_1/n$
Temperature (K)	100.0(2)	100.0(2)	100.0(2)	100.0(2)	100.0(2)
a (Å)	13.2890(3)	13.3101(3)	13.3222(7)	13.3665(9)	13.3619(5)
b (Å)	22.3451(5)	22.4195(5)	22.4156(15)	22.5953(15)	22.4866(8)
c (Å)	13.7593(3)	13.7729(2)	13.7948(9)	13.8358(9)	13.8494(4)
β (°)	111.9090(10)	112.0390(10)	111.927(2)	110.765(3)	110.3620(10)
V (Å^3)	3790.66(15)	3809.59(13)	3821.5(4)	3907.3(4)	3901.2(2)
Z	4	4	4	4	4
D_x (Mg m^{-3})	3.185	3.148	3.074	2.757	2.685
θ range (°)	1.85–25.0	1.81–25.0	1.88–27.5	1.86–37.58	1.81–32.84
μ (mm^{-1})	13.978	13.537	13.270	5.593	5.305
Absorption correction	empirical (using intensity measurements)	empirical (using intensity measurements)	empirical (using intensity measurements)	empirical (using intensity measurements)	empirical (using intensity measurements)
T_{min}	0.577	0.381	0.603	0.495	0.761
T_{max}	0.870	0.762	0.876	0.756	0.899
No. of measured, independent and observed reflections	22148, 6673, 5715	17719, 6354, 5511	23372, 8741, 6920	68412, 19249, 15499	43733, 12220, 7778
Criterion for observed reflections	$I > 2\sigma(I)$	$I > 2\sigma(I)$	$I > 2\sigma(I)$	$I > 2\sigma(I)$	$I > 2\sigma(I)$
R_{int}	0.0406	0.0375	0.032	0.0344	0.039
θ_{max} (°)	25.0	25.0	25.0	25.00	25.00
Refinement on	F^2	F^2	F^2	F^2	F^2
$R[F^2 > 2\sigma(F^2)]$, $wR(F^2)$, S	0.042, 0.100, 1.02	0.0385, 0.0873, 1.076	0.0303, 0.0573, 1.006	0.0417, 0.0857, 1.190	0.0445, 0.0914, 1.026
No. of reflections	6673 reflections	6354 reflections	8741 reflections	19249 reflections	12220 reflections
No. of parameters	346	350	350	369	364
$(\Delta/\sigma)_{max}$	0.000	0.001	0.001	0.001	0.001
$\Delta\rho$ max, $\Delta\rho$ min (e Å^{-3})	4.783, −3.227	1.345, −3.321	2.501, −1.608	3.451, −2.671	1.921, −2.474

Computer programs: APEX2 *v.1.0-8* (Bruker, 2003); SHELXTL *v.6.22* (Bruker, 1990-2003); *local programs*.

Further treatment was as above. Red crystals of $[Mo_3Te_4S_3((EtO)_2PS_2)_3]I$ (**6**) were obtained. Yield 0.007 g (44%). IR (cm^{-1}): 3437 m, 2974 w, 2927 w, 2864 w, 1468 w, 1438 w, 1384 w, 1287 w, 1159 m, 1099 w, 1053 w, 1005 s, 965 s, 814 m, 788 s, 633 m, 528 w, 459 m. ESI(+)-MS: $[Mo_3Te_2S_5((EtO)_2PS_2)_3]^+$ (m/z = 1259), $[Mo_3Te_3S_4((EtO)_2PS_2)_3]^+$ (m/z = 1357), $[Mo_3Te_4S_3((EtO)_2PS_2)_3]^+$ (m/z = 1447), $[Mo_3Te_5S_2((EtO)_2PS_2)_3]^+$ (m/z = 1547).

2.8. X-ray structure determinations

The diffraction data for **2**–**6** were collected on a Bruker *X8APEX* CCD diffractometer with Mo Kα radiation (λ = 0.71073 Å) using φ- and ω-scans of narrow (0.5°) frames. The structure of **3** was solved by direct methods and refined by full-matrix least-squares method against $|F|^2$ in anisotropic approximation using the SHELXTL programs set [14]. The data for the isostructural analogs **2**, **4**, **5** and **6** were refined with the model for **3**. Absorption corrections were applied empirically using the SADABS program [15]. In all cases the statistical occupancies of the sulfur and tellurium atoms in the cluster cores as well as the halogenide counter ions were refined with fixed isotropic atomic displacement parameters, and then with fixed occupancy factors, while the coordinates and anisotropic atomic displacement parameters are equal. The positions of statistically disordered atoms cannot be distinguished except the positions of the chlorine and iodine atoms in the crystal structure of **5**. The Cl and I atoms in **5** were refined anisotropically with equal atomic displacement parameters. Detailed crystallographic data and atomic distances are collected in Tables 1 and 2, respectively. Intermolecular interactions in the crystal and the packing types were analyzed with the program set for multi-purpose crystallochemical analysis TOPOS 4.0 Professional [16].

3. Result and discussion

3.1. Syntheses and electrospray ionization mass spectrometry (ESI-MS)

The starting materials $[M_3Te_7(dtp)_3]X$ (M = Mo, W; X = Br, I; dtp = $(EtO)_2PS_2$) were synthesized from polymeric tellurohalides

Table 2
Selected bond lengths (Å) in **2**–**6**.

Compound	**2**	**3**	**4**	**5**	**6**
M–M	2.78	2.79	2.79	2.83–2.84	2.82–2.83
M-μ_3-Te	2.68–2.69	2.69–2.71	2.69–2.71	2.68	2.68–2.69
M–Q_{eq}	2.51–2.54	2.56–2.62	2.57–2.63		
M–Q_{ax}	2.70–2.74	2.71–2.74	2.72–2.74		
M–S_{cis}[a]	2.51–2.54	2.53–2.55	2.53–2.54	2.54–2.55	2.53–2.55
M–S_{trans}[b]	2.58–2.59	2.58–2.59	2.58–2.59	2.58	2.58–2.59
Q_{ax}–Q_{eq}	2.35–2.39 (Te–S)	2.44–2.46 (mixed occupancy)	2.44–2.46 (mixed occupancy)	2.37 (Te–S) 2.54 (mixed occupancy) 2.66 (Te–Te)	2.48 (mixed occupancy) 2.56 (mixed occupancy) 2.20 (S–S)

[a] M–S_{cis} distance *cis* to the M-μ_3-Te bond.
[b] M–S_{trans} distance *trans* to the M-μ_3-Te bond.

$M_3Te_7X_4$ by mechanochemical treatment in 15–20% yields [11]. The yields are modest, but higher than in the reactions between the solids in the absence of mechanical activation, originally proposed for the synthesis of $[M_3Te_7(dtp)_3]I$ (M = Mo, W) [9].

Initially we turned to the idea of finding a way of converting the M_3Te_7 clusters into Mo_3Te_4 clusters by tellurium abstraction with mild electrophilic reagents, e.g., Ph_3PX_2 (X = Cl, Br). No reaction was found to take place, however, between $[W_3Te_7(dtp)_3]Br$ and either of the phosphine dihalides. A reaction between $[W_3Te_7(dtp)_3]Br$ with free Br_2 did take place, but surprisingly the product was found to be $[W_3Te_{4.25}S_{2.75}(dtp)_3]Br$ (**2**, yield 18%) – the first complex with a new TeS^{2-} ligand. Its formation can be tentatively explained by the following reaction sequence (**1**–**3**):

$$W_3Te_7^{4+} + 3Br_2 \rightarrow W_3Te_4^{4+} + 3\text{“}TeBr_2\text{“} \quad (1)$$

$$2(EtO)_2PS_2^- + Br_2 \rightarrow (EtO)_2P(S)\text{-}S\text{-}S\text{-}P(S)(OEt)_2 + 2Br^- \quad (2)$$

$$W_3Te_4^{4+} + 3(EtO)_2P(S)\text{-}S\text{-}S\text{-}P(S)(OEt)_2 \rightarrow W_3Te_4S_3^{4+} + 3(EtO)_2P(S)\text{-}S\text{-}P(S)(OEt)_2 \quad (3)$$

Uncomplexed $TeBr_2$ is unstable and disproportionates into $TeBr_4$ and Te. It is known that treatment of $M_3Se_4^{4+}$ clusters with alcoholic solutions of P_4S_{10}, which are known to contain both $(RO)_2PS_2H$ and a mixture of polysulfides $(RO)_2P(S)S_xP(S)(OR)_2$ (x = 2, 3, 4), [17] gives $[M_3(\mu_3\text{-}Se)(\mu\text{-}SeS)_3(dtp)_3]^+$ in good yields [18]. It has to be pointed out that this reaction limits the overall reaction yield since the only source of sulfur is provided by the dtp^- ligands, a fact that inherently implies cluster degradation. In order to prevent this undesirable process, we used S_2Cl_2 which can simultaneously chlorinate Te and deliver S to the *in situ* forming $W_3Te_4^{4+}$ core. In this way, $[W_3Te_{4.30}S_{2.70}((EtO)_2PS_2)_3]Br_{0.62}Cl_{0.38}$ (**3**) was obtained in 31% yield, which is higher than in the reaction with Br_2. The formation of $[W_3Te_4S_3((EtO)_2PS_2)_3]^+$ can be explained by the following reactions:

$$[W_3Te_7((EtO)_2PS_2)_3]^+ + 3S_2Cl_2 \rightarrow [W_3Te_4((EtO)_2PS_2)_3] + 3\text{“}TeCl_2\text{”} + 6S$$

$$[W_3Te_4((EtO)_2PS_2)_3]^+ + 3S \rightarrow [W_3Te_4S_3((EtO)_2PS_2)_3]^+$$

As judged by X-ray analysis, there is high degree of regioselectivity in these reactions (irrespective of the use of Br_2 or S_2Cl_2), Te by S replacement being first observed at the equatorial positions (see Table 3), thus leading to μ-TeS ligands. As can be seen in Table 3, Q_{ax} is predominantly Te whereas Q_{eq} is a mixture S/Te. The variable occupation of the Q_{eq} positions disorder is reflected in the bond distances Q_{ax}–Q_{eq} (Table 2). This characteristic regioselectivity is similar to that well-established for M_3Q_7 (Q = S, Se) cluster complexes, where chalcogen abstraction and exchange reactions (by phosphines, KSeCN, polysulfides) take place preferentially at the equatorial positions, probably due to a weaker bonding of the chalcogen atom there [19].

Electrospray ionization mass spectra of $CHCl_3$:CH_3OH solutions of the product formulated as $[W_3Te_{4.30}S_{2.70}((EtO)_2PS_2)_3]Br_{0.62}Cl_{0.38}$ (**3**) and the product obtained by recrystallization of **3** from $CHCl_3$/EtOH after 2 months, $[W_3Te_{4.25}S_{2.75}((EtO)_2PS_2)_3]Br$ (**4**), further confirms the degree of substitution as well as the regioselectivity. Fig. 1 illustrates the ESI mass spectrum of **3** recorded at low cone voltages (typically U_c = 10 V).

Three dominant signals corresponding to the incomplete cuboidal cluster $[W_3Te_4S_3((EtO)_2PS_2)_3]^+$ (m/z = 1713.4) and its HCl and HBr adducts (m/z = 1749.4 and m/z = 1795.4, respectively) are observed, thus indicating a high degree of regioselectivity for the Te by S replacement at the Q_{eq} position. Middle intensity signals attributed to different W/S/Te based species are also detected, namely $[W_3Te_3S_4((EtO)_2PS_2)_3]^+$ (m/z = 1618.4) and the starting material $[W_3Te_7((EtO)_2PS_2)_3]^+$ (m/z = 2000.2), whereas the homologous W/Te/S cations with only one and two incorporated sulfur atoms were observed as minor signals, namely $[W_3Te_5S_2((EtO)_2PS_2)_3]^+$ (m/z = 1810.3) and $[W_3Te_6S((EtO)_2PS_2)_3]^+$ (m/z = 1904.2). The electrospray mass spectrum of **4** revealed a similar speciation to that observed for sample **3**, where the presence of the cluster cation $[W_3Te_4S_3((EtO)_2PS_2)_3]^+$ peak was dominant.

The reactivity described above for W was extended to molybdenum chemistry. The reaction of $[Mo_3Te_7((EtO)_2PS_2)_3]I$ with S_2Cl_2 in a 1:5 molar ratio in a $CHCl_3$/DMF mixture leads to Te by S replacement, yielding a mixture of complexes formulated as $[Mo_3Te_{4.74}S_{2.26}((EtO)_2PS_2)_3]I_{0.72}Cl_{0.28}$ (**5**) on the basis of X-ray analysis. Despite the fact that both W and Mo complexes display roughly an identical degree of Te by S replacement as judged by the overall stoichiometries (for example, $W_3Te_{4.30}S_{2.7}^{4+}$ in **3** and $Mo_3Te_{4.74}S_{2.26}^{4+}$ in **5**), a detailed inspection of the X-ray data reveal some important differences, specifically related to the observed occupation disorder at the Q_{ax} and Q_{eq} sites. While the Q_{ax} and Q_{eq} positions are close to 100% (Te) and 0% (Te), respectively, for the tungsten derivatives **2**–**4** (see Table 3), in the case of Mo these occupancy factors are approximately 90% (Te) and 50% (Te) for Q_{ax} and Q_{eq}, respectively. Such distinctive replacement patterns mean that the degree of regioselectivity at the Q_{eq} sites is higher for the $W_3Te_7^{4+}$ core. This is also very well evident in the ESI(+) mass spectrum of $[Mo_3Te_{4.74}S_{2.26}((EtO)_2PS_2)_3]I_{0.72}Cl_{0.28}$ (**5**) (Fig. 2) where the distribution of species featuring $Mo_3Te_{7-x}S_x^{4+}$ cluster cores ranges from x = 0 to 5.

In order to obtain additional insights on the Te by S replacement, we tried to change the reaction conditions. On one hand, we believe that it is illustrative to investigate the reactivity trends of bridging Te ligands with a large excess of S_2Cl_2, aimed at proving whether further substitution in the axial position or even the inert μ_3-Te ligand takes place. The reaction of **5** with S_2Cl_2 in a 1:15 molar ratio gives a product with the composition $[Mo_3Te_4S_3((EtO)_2$

Table 3
Specific non-bonding contacts (Å) involving the X^- anion in **2**–**6** and their crystallographically ordered isostructural analogs.

Compound	X^-	Q_{ax}	$d(3Q_{ax}\cdots X)$	Q_{eq}	$d(Q_{eq}\cdots X)$	References
$[W_3Te_{4.25}S_{2.75}(dtp)_3]Br$	Br	Te	3.079	0.09Te + 0.91S	3.365	**2**, this work
		Te	3.082	S		
		Te	3.055	S		
$[W_3Te_{4.30}S_{2.69}(dtp)_3]Br_{0.62}Cl_{0.38}$	0.62Br + 0.38Cl	Te	2.963[a]	0.12Te + 0.88S	3.435[a]	**3**, this work
		Te	2.808[a]	S		
		Te	2.954[a]	S		
$[W_3Te_{3.91}S_{3.10}(dtp)_3]Br_{0.64}Cl_{0.36}$	0.64Br + 0.36Cl	0.86Te + 0.14S	3.039	0.13Te + 0.87S	3.337	**4**, this work
		0.85Te + 0.14S	3.077	S		
		0.81Te + 0.19S	3.032	S	3.334	
$[Mo_3Te_{4.74}S_{2.26}(dtp)_3]I_{0.72}Cl_{0.28}$	0.72I + 0.28Cl	0.90Te + 0.10S	3.198	0.47Te + 0.53S	3.233	**5**, this work
		0.90Te + 0.10S	3.284	S		
		0.92Te + 0.08S	3.202	S		
$[Mo_3Te_4S_3(dtp)_3]I$	I	0.75Te + 0.25S	3.196	0.34Te + 0.66S	3.358	**6**, this work
		0.71Te + 0.29S	3.211			
		0.83Te + 0.17S	3.178			
$[W_3Te_7(dtp)_3]Br$	Br	Te	3.123			[11]
		Te	3.243			
		Te	3.140			
$[W_3Se_7(dtp)_3]Br$	Br	Se	3.026	Se	3.241	[21]
		Se	3.077			
		Se	3.030			
$[W_3(\mu_3\text{-}Se)(\mu_2\text{-}SSe)_3(dtp)_3]Cl$	Cl	Se	2.881	S	3.365	[18]
		Se	2.872			
		Se	2.893			
$[Mo_3(\mu_3\text{-}S)(\mu_2\text{-}Se_2)_3(dtp)_3]Cl$	Cl	Se	2.909	S	3.108	[22]
		Se	2.883			
		Se	2.965			
$[Mo_3(\mu_3\text{-}S)(\mu_2\text{-}SSe)_3(dtp)_3]I$	I	Se	3.166	S	3.386	[23]
		Se	3.114			
		Se	3.167			
$[Mo_3Se_7(dtp)_3]Br$	Br	Se	3.039	Se	3.267	[24]
		Se	3.033			
		Se	3.089			

[a] Distances are given to the Cl position.

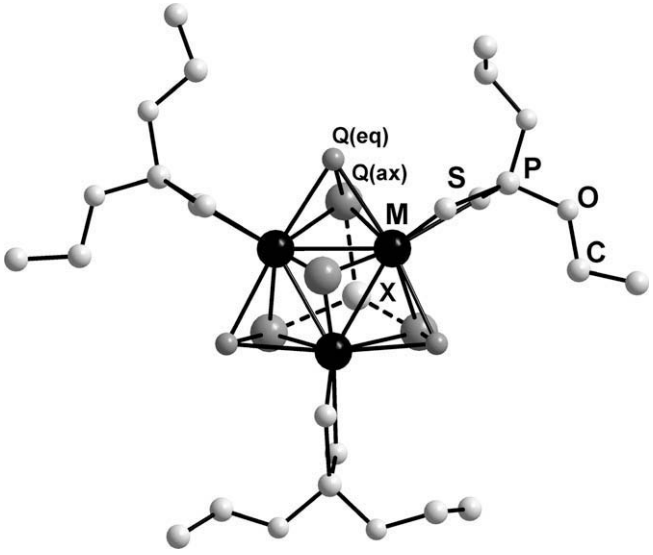


Fig. 3. The ionic pair $[M_3Q_7(dtp)_3]X$ (M = Mo, W; X = Br, I) in **2**–**6**. The Q(ax) and Q(eq) designate axial and equatorial positions statistically occupied by sulfur and tellurium atoms.

$PS_2)_3]I$ (**6**), which really turned out to be a mixture of $[Mo_3Te_2S_5((EtO)_2PS_2)_3]^+$, $[Mo_3Te_3S_4((EtO)_2PS_2)_3]^+$, $[Mo_3Te_4S_3((EtO)_2PS_2)_3]^+$ and $[Mo_3Te_5S_2((EtO)_2PS_2)_3]^+$ with S_2^{2-}, TeS^{2-} and Te_2^{2-} dichalcogenide ligands according to its mass spectrum and occupancy of the Q_{ax} and Q_{eq} positions, in concordance with the following row of decreasing reactivity: $Te_{eq} > Te_{ax} > \mu_3$-Te.

On the other hand, since coordinatively unsaturated species $[W_3Te_4(dtp)_3]^+$ are supposedly involved as a key intermediate during the Te by S replacement process, we attempted to intercept them by doing the reaction of $[W_3Te_7(dtp)_3]^+$ with S_2Cl_2 in the presence of pyridine or DMF, aiming to stabilize the transient coordinatively unsaturated $[M_3Te_4(dtp)_3]^+$ species as the more stable $[M_3Te_4(dtp)_3L_3]^+$ (L = py, DMF) complexes. However, the reaction did not take place at all in the presence of pyridine, while with DMF a product of the composition $[Mo_3Te_{4.74}S_{2.26}((EtO)_2PS_2)_3]I_{0.72}Cl_{0.28}$ (**5**) was obtained, as described above.

3.2. Crystal structures

Crystal structures were determined for all the newly synthesized compounds, **2**–**6**. They are isostructural and crystallize in the monoclinic unit cell ($P2_1/c$ space group). The cluster cation displays an identical geometry to that observed for the closely related $Mo_3Q_7^{4+}$ clusters bearing dithiophosphate ligands (see Fig. 3); the geometrical parameters are summarized in Table 2. The equatorial (Q_{eq}) and axial (Q_{ax}) atoms of the μ_2-Q_2 ligands are mixed-sorted in the most cases, containing both sulfur and tellurium in different ratios. The S/Te composition (see Table 3) determined by X-ray diffraction is in satisfactory agreement with ESI mass spectra and chemical data. From the comparison of interchalcogen bond distances in the coordinated Q_2 ligands, the S–Te bond length was expected to be about 2.35–2.4 Å, as indeed found in **2** and **5** (for comparison: S–S, 2.03–2.04 Å in $[Mo_3S_7(dtp)_3]Cl$ [24], S–Se; 2.20 Å in $[W_3(\mu_3\text{-}Se)(\mu_2\text{-}SSe)_3(dtp)_3]Cl$ [22]; Se–Se, 2.32–2.34 Å in $[W_3Se_7(dtp)_3]Br$ [18]; Se–Te, 2.50–2.52 Å in $K_3\{[W_3Te(SeTe)_3(CN)_6]Br\}$ [8]; Te–Te, 2.68–2.69 Å in $[W_3Te_7(dtp)_3]Br$ [11]).

The crystal packing in **2**–**6** is strongly influenced by specific non-bonding interactions involving the halogen anion (X^-) and

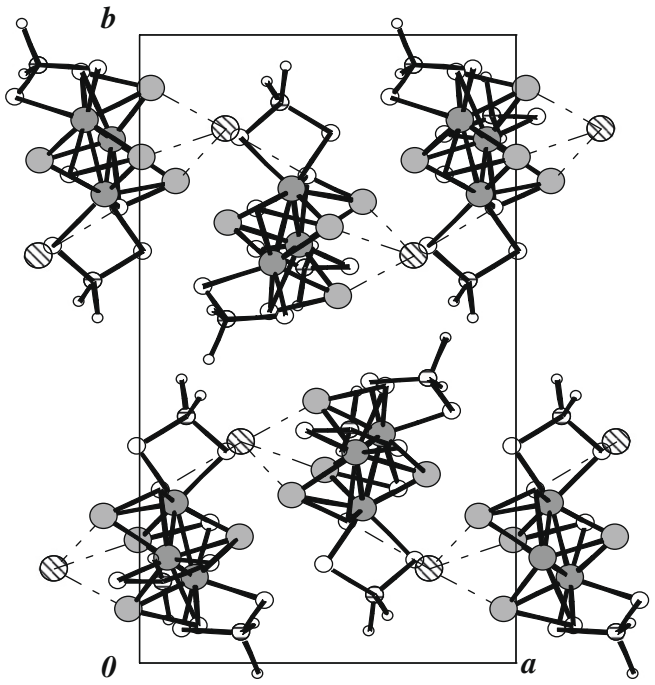


Fig. 4. Crystal packing in **2**–**6**. Shortened halogen···chalcogen contacts are shown by dashed lines. Carbon and oxygen atoms of ethyl groups are omitted for clarity.

both equatorial (Q_{ex}) and axial (Q_{ax}) atoms of the μ_2-Q_2 ligands of the cluster core. These interactions result in two types of shortened halogen···chalcogen contacts, namely, *axial* $3Q_{ax}$···X and *equatorial* Q_{eq}···X [11,20] (Table 3). Cluster anions are joined to halogen anions into ionic pairs *via* axial contacts (Fig. 3). The ionic pairs in turn are joined to each other by means of equatorial contacts into infinite chains running along the crystallographic *a* axis (Fig. 4). According to the crystal packing analysis [16] the cluster cations, as well as cation–anion ionic pairs, form distorted primitive cubic packing. In agreement with this, the cationic–anionic chains form rectangular rod packing.

The compounds **2**–**6** have various isostructural analogs among cluster complexes with the general formula $[M_3Q_7(dtp)_3]X$. In all the structures, similar chains of alternating cluster cations and halogenide anions are found (Table 3). As expected, the Q_{ax}···X and Q_{eq}···X distances demonstrate a tendency to increase along the ranges S–Se–Te and Cl–Br–I.

4. Conclusion

We have found that in the clusters $M_3(\mu_3\text{-Te})(\mu_2\text{-Te}_2)_3^{4+}$ the Te atoms can undergo electrophilic substitution by S (directly or via elimination–addition). The most reactive position was found to be Te_{eq} which makes possible the preparation of complexes with a $Te_{ax}S_{eq}$ bridging ligand.

Supplementary data

CCDC 691116 and 691120 contain the supplementary crystallographic data for **2**–**6**. These data can be obtained free of charge via http://www.ccdc.cam.ac.uk/conts/retrieving.html, or from the Cambridge Crystallographic Data Centre, 12 Union Road, Cambridge CB2 1EZ, UK; fax: (+44) 1223-336-033; or e-mail: deposit@ccdc.cam.ac.uk

Acknowledgements

We would like to thank Professor V.A. Blatov for providing TOPOS 4.0 Professional software. The authors also are grateful to the Serveis Centrals d'Instrumentació Científica (SCIC) of the Universitat Jaume I for providing us with spectrometric facilities.

References

[1] J.W. Kolis, Coord. Chem. Rev. 105 (1990) 195.
[2] L.C. Roof, J.W. Kolis, Chem. Rev. 93 (1993) 1037.
[3] D. Fenske, J.F. Corrigan, in: P. Braunstein, L.A. Oro, P.R. Raithby (Eds.), Metal Clusters in Chemistry, vol. 3, Wiley-VCH, Weiheim, 1999, p. 1303.
[4] I.V. Kalinina, V.P. Fedin, Russ. J. Coord. Chem. 29 (2003) 597.
[5] M.N. Sokolov, V.P. Fedin, A.G. Sykes, Compr. Coord. Chem. II 4 (2003) 761.
[6] M.N. Sokolov, V.P. Fedin, Coord. Chem. Rev. 248 (2004) 925.
[7] D.M. Smith, J.A. Ibers, Coord. Chem. Rev. 200–202 (2000) 187.
[8] M.N. Sokolov, P.A. Abramov, A.L. Gushchin, I.V. Kalinina, D.Yu. Naumov, A.V. Virovets, E.V. Peresypkina, C. Vicent, R. Llusar, V.P. Fedin, Inorg. Chem. 44 (2005) 8116.
[9] (a) X. Lin, H.-Y. Chen, L.-S. Chi, H.-H. Zhuang, Polyhedron 18 (1999) 217; (b) H. Chen, X. Lin, L. Chi, C. Lu, H. Zhuang, J. Huang, Inorg. Chem. Commun. 3 (2000) 331.
[10] V.P. Fedin, H. Imoto, T. Saito, W. McFarlane, A.G. Sykes, Inorg. Chem. 34 (1995) 5097.
[11] A.V. Virovets, A.L. Gushchin, P.A. Abramov, N.I. Alferova, M.N. Sokolov, V.P. Fedin, Russ. J. Struct. Chem. 47 (2006) 326.
[12] V.V. Volkov, K.G. Myakishev, Inorg. Chim. Acta 289 (1999) 51.
[13] MASSLYNX V4.1, Waters Inc., Manchester UK, 2005.
[14] Bruker, SHELXTL Version 6.22 Bruker AXS Inc. Madison, WI, USA, 2003.
[15] G.M. Sheldrick, SADABS Program for Absorption Correction with the SMART System, University of Göttingen, Germany, 1996.
[16] V.A. Blatov, Cryst. Comp. Newsletter N7 (2006) 4; http://topos.ssu.samara.ru.
[17] A.E. Lippman, J. Org. Chem. 31 (1966) 471.
[18] R. Hernandez-Molina, M. Sokolov, P. Nuñez, A. Mederos, J. Chem. Soc., Dalton Trans. (2002) 1072.
[19] M. Mayor-Lopez, M. Weber, K. Hegetschweiler, M.D. Meienberger, F. Jobo, S. Leoni, R. Nesper, G.J. Reiss, W. Frank, B. Kolesov, V. Fedin, V. Fedorov, Inorg. Chem. 37 (1998) 2633.
[20] M.N. Sokolov, A.L. Gushchin, P.A. Abramov, A.V. Virovets, E.V. Peresypkina, V.P. Fedin, Inorg. Chem. 46 (2007) 4677.
[21] V.P. Fedin, M.N. Sokolov, O.A. Geras'ko, A.V. Virovets, N.V. Podberezskaya, V.Y. Fedorov, Polyhedron 11 (1992) 3159.
[22] Jin Hu, Hong-Hui Zhuang, Shi-Xiong Liu, Jin-Ling Huang, Trans. Met. Chem. 23 (1998) 547.
[23] V. Bereau, J.A. Ibers, Acad. Sci. Ser. IIc: Chim. 3 (2000) 123.
[24] H. Jinling, S. Maoyu, H. Jianquan, Z. Honghui, L. Shaofang, L. Jiaxi, Jiegou Huaxue, Chin. J. Struct. Chem. 1 (1982) 1.

polymers containing 4,6,10,12,16,18,22,24-octakis(2-hydroxyethoxy)-2,8,14,20-tetramethylresorcinarene.

2. Experimental

Resorcinarene, 4,5-dichloro-1,2-dicyanobenzene and 4-nitro-1,2-dicyanobenzene were prepared by previously reported procedure [35–37]. FTIR spectra were recorded on a Perkin–Elmer Spectrum 100 Fourier Transform Infrared Spectrometer as KBr pellets. UV–Vis spectra were recorded on a Shimadzu UV–Vis spectrometer. ^{1}H NMR and ^{13}C NMR studies were done on a Varian UNITY INOVA 500 MHz spectrometer. Elemental analyses were performed by the Instrumental Analyses Laboratory of the TÜBİTAK Gebze Research Center. Microwave-assisted syntheses were carried out using a modified BEKO MD domestic microwave oven.

2.1. Microwave-assisted synthesis of 4,6,10,12,16,18,22,24-octakis(2-hydroxyethoxy)-2,8,14,20-tetramethylresorcinarene (**1**)

Resorcinarene (5.44 g, 10 mmol), 2-chloroethanol (5.64 g, 80 mmol) and K_2CO_3 (11.04 g, 80 mmol) were added into *N*,*N*-dimethyl formamide (DMF) (20 mL). This mixture was heated by microwaves for 20 min with a fixed power of 360 W [19,35]. The reaction mixture was poured in an ice bath, added HCl solution to eliminate base trace and the formed solid material was filtered off and washed with water until the filtrate became neutral. The crude product was purified by two successive column chromatographic separations (silica gel, DMF/methanol = 40:1). This compound was soluble in alcohol, DMF and DMSO. Yield: 6.52 g (72%), mp: 213 °C. *Anal.* Calc. for $C_{48}H_{64}O_{16}$: C, 64.20; H, 7.19. Found: C, 63.93; H, 7.19%. FTIR (KBr tablet) ν_{max}/cm^{-1}: 3229 (OH), 2963 (CH), 1620, 1611, 1502, 1431, 1287, 1217, 1100, 895. ^{1}H NMR ($(CD_3)_2SO$), (δ:ppm): 7.40–6.80 (br, 8H, ArCH), 5.20 (br, 4H, CH), 4.23 (s, 8H, OH), 3.42 (t, 16H, CH_2), 3.28 (t, 16H, CH_2), 1.87 (d, 12H, CH_3). ^{13}C NMR ($(CD_3)_2SO$), (δ:ppm): 155.20, 129.89, 105.45, 95.60, 71.26 ($ArOCH_2$), 60.60 (CH_2OH), 31.51, 20.71 (CH_3).

2.2. Microwave-assisted synthesis of tetrakis(4,5-bis(2-hydroxyethoxy))phthalonitrile substituted resorcinarene compound (**2**)

4,6,10,12,16,18,22,24-octakis(2-hydroxyethoxy)-2,8,14,20-tetramethylresorcinarene (**1**) (2.0 g, 2.22 mmol), 4,5-dichloro phthalonitrile (1.75 g, 8.88 mmol) and K_2CO_3 (2.70 g, 19.56 mmol) were added into *N*,*N*-dimethyl formamide (DMF) (20 mL). This mixture was heated by microwaves for 20 min with a fixed power of 360 W [35]. The reaction mixture was poured in an ice bath, added HCl solution to eliminate base trace and the formed solid material was filtered off and washed with water until the filtrate became neutral. The crude product was purified by washing with hot ethanol (5 × 50 mL). This compound was soluble in DMF and DMSO. Yield: 2.72 g (88%), mp > 300 °C. *Anal.* Calc. for $C_{80}H_{64}O_{16}N_8$: C, 68.40; H, 4.63; N, 8.04. Found: C, 67.93; H, 4.25; N, 8.12%. FTIR (KBr tablet) ν_{max}/cm^{-1}: 3076 (=CH), 2969 (CH), 2236 (C≡N), 1583, 1480, 1379, 1273, 1189, 1097, 895. ^{1}H NMR ($(CD_3)_2SO$), (δ:ppm): 8.39 (s, 8H, ArCH), 8.01 (s, 4H, ArCH), 7.10 (s, 4H, ArCH), 4.70–4.20 (m, 4H, CH), 2.82 (t, 16H, CH_2), 2.70 (t, 16H, CH_2), 1.74 (d, 12H, CH_3). ^{13}C NMR ($(CD_3)_2SO$), (δ:ppm): 157.40, 151.20, 136.35, 128.85, 115.10 (CN), 71.26 ($ArOCH_2$), 59.62 (CH_2OAr), 29.51, 20.71.

2.3. Microwave-assisted synthesis of octakis(4-(2-hydroxyethoxy)) phthalonitrile substituted resorcinarene (**3**)

4,6,10,12,16,18,22,24-octakis(2-hydroxyethoxy)-2,8,14,20-tetramethylresorcinarene (**1**) (2.0 g, 2.22 mmol), 4-nitro-1,2-dicyanobenzene (3.08 g, 17.83 mmol) and K_2CO_3 (2.70 g, 19.56 mmol) were added into *N*,*N*-dimethyl formamide (DMF) (20 mL). This mixture was heated by microwaves for 20 min with a fixed power of 360 W [35]. The reaction mixture was poured in an ice bath, added HCl solution to eliminate base trace and the formed solid material was filtered off and washed with water until the filtrate became neutral. The crude product was purified by washing with hot ethanol (5 × 50 mL). This compound was soluble in DMF and DMSO. Yield: 2.64 g (62%), mp > 300 °C. *Anal.* Calc. for $C_{112}H_{80}O_{16}N_{16}$: C, 70.58; H, 4.23; N, 11.76. Found: C, 69.93; H, 4.25; N, 11.69%. FTIR (KBr tablet) ν_{max}/cm^{-1}: 3076 (=CH), 2967 (CH), 2233 (C≡N), 1589, 1568, 1485, 1310, 1279, 1189, 1093, 851. ^{1}H NMR ($(CD_3)_2SO$), (δ:ppm): 7.96 (s, 16H, ArCH), 7.42 (s, 8H, ArCH), 7.21 (s, 4H, ArCH), 7.11 (s, 4H, ArCH) 4.70–4.40 (m, 4H, CH), 2.82 (t, 16H, CH_2), 2.70 (t, 16H, CH_2), 1.12 (d, 12H, CH_3). ^{13}C NMR ($(CD_3)_2SO$), (δ:ppm): 162.40, 156.50, 151.20, 137.45, 124.85, 116.10 (CN), 109.80, 70.26 ($ArOCH_2$), 60.02 (CH_2OR), 31.51, 21.71 (CH_3).

2.4. Microwave-assisted synthesis of octakis(2-hydroxyethoxy)-resorcinarene bridged polymeric phthalocyanines (**2a**–**d**)

The general procedure, employed for synthesis of various metallophthalocyanine (Zn, Cu, Ni, Co) polymers was described as; compound (**2**) (0.5 g, 0.35 mmol), metal salts ($Zn(CH_3COO)_2$, $CuCl_2$, $NiCl_2$, $CoCl_2$) (0.08 mmol), DMAE (*N*,*N*-dimethylaminoethanol) (5 mL) and 2–3 drops DBU (1,8-diazabicyclo [5.4.0]undec-7-ene) were charged together into round bottomed flask. The reaction flask was irradiated by a microwave oven at 360 W for 20 min [19,35]. After cooling to room temperature, the reaction mixture treated with water to precipitate the product which was filtered off. The green product was washed with DMF, hot alcohol and hot chloroform (4 × 50 mL). Yield, melting point, elemental analysis, FTIR and UV–Vis spectra of the products were as following:

Zn-containing polymer (**2a**): Yield: 0.40 g (80%), mp > 300 °C. *Anal.* Calc. for $C_{320}H_{256}O_{64}N_{32}Zn$: C, 68.16; H, 4.58; N, 7.95. Found: C, 67.93; H, 4.90; N, 7.89%. FTIR (KBr tablet) ν_{max}/cm^{-1}: 3060 (=CH), 2931 (CH), 2234 (C≡N), 1774 (C=N), 1724 (C=N), 1587, 1490, 1352, 1276, 1187, 1090, 894. UV–Vis (DMF): λ_{max}/nm: 245, 638, 688.

Cu-containing polymer (**2b**): Yield: 0.43 g (81%), mp > 300 °C. *Anal.* Calc. for $C_{320}H_{256}O_{64}N_{32}Cu$: C, 68.18; H, 4.58; N, 7.95. Found: C, 67.95; H, 4.87; N, 7.90%. FTIR (KBr tablet) ν_{max}/cm^{-1}: 3060 (=CH), 2931 (CH), 2232 (C≡N), 1774 (C=N), 1715 (C=N), 1660, 1489, 1393, 1256, 1160 1093, 896. UV–Vis (DMF): λ_{max}/nm: 289, 298, 748, 762.

Ni-containing polymer (**2c**): Yield: 0.40 g (80%), mp > 300 °C. *Anal.* Calc. for $C_{320}H_{256}O_{64}N_{32}Ni$: C, 68.24; H, 4.58; N, 7.96. Found: C, 67.98; H, 4.87; N, 7.87%. FTIR (KBr tablet) ν_{max}/cm^{-1}: 3060 (=CH), 2931 (CH), 2227 (C≡N), 1770 (C=N), 1719 (C=N), 1692, 1492, 1386, 1253, 1092, 896. UV–Vis (DMF): λ_{max}/nm: 271, 299, 609, 685.

Co-containing polymer (**2d**): Yield: 0.40 g (80%), mp > 300 °C. *Anal.* Calc. for $C_{320}H_{256}O_{64}N_{32}Co$: C, 68.24; H, 4.58; N, 7.96. Found: C, 67.97; H, 4.89; N, 7.87%. FTIR (KBr tablet) ν_{max}/cm^{-1}: 3060 (=CH), 2930 (CH), 2232 (C≡N), 1726 (C=N), 1690 (C=N), 1491, 1385, 1254, 1091, 895. UV–Vis (DMF): λ_{max}/nm: 248, 271, 610, 683.

2.5. Microwave-assisted synthesis of octakis(2-hydroxyethoxy)-resorcinarene bridged polymeric phthalocyanines (**3a**–**d**)

The general procedure, employed for synthesis of various metal phthalocyanine (Zn, Cu, Ni, Co) polymers was described as; compound (**3**) (0.5 g, 0.26 mmol), metal salts ($Zn(CH_3COO)_2$, $CuCl_2$, $NiCl_2$, $CoCl_2$) (0.08 mmol), DMAE (*N*,*N*-dimethylaminoethanol) (5 mL) and 2–3 drops DBU (1,8-diazabicyclo [5.4.0]undec-7-ene)

were charged together into round bottomed flask. The reaction flask was irradiated by a microwave oven at 360 W for 20 min [19,35]. After cooling to room temperature, the reaction mixture treated with water to precipitate the product which was filtered off. The green product was washed with DMF, hot alcohol and hot chloroform (4 × 50 mL). Yield, melting point, elemental analysis, FTIR and UV–Vis spectra of the products were as following:

Zn-containing polymer (**3a**): Yield: 0.40 g (80%), mp > 300 °C. *Anal.* Calc. for $C_{224}H_{160}O_{32}N_{32}Zn$: C, 69.39; H, 4.16; N, 11.56. Found: C, 68.93; H, 4.90; N, 11.52%. FTIR (KBr tablet) ν_{max}/cm^{-1}: 3063 (=CH), 2930 (CH), 2232 (C≡N), 1769 (C=N), 1715 (C=N), 1600, 1474, 1276, 1085, 837. UV–Vis (DMF): λ_{max}/nm: 288, 306, 616, 683.

Cu-containing polymer (**3b**): Yield: 0.27 g (75%), mp > 300 °C. *Anal.* Calc. for $C_{224}H_{160}O_{32}N_{32}Cu$: C, 69.42; H, 4.16; N, 11.57. Found: C, 68.95; H, 4.78; N, 11.50%. FTIR (KBr tablet) ν_{max}/cm^{-1}: 3071 (=CH), 2924 (CH), 2232 (C≡N), 1714 (C=N), 1592, 1434, 1247, 1091, 837. UV–Vis (DMF): λ_{max}/nm: 275, 609, 681.

Ni-containing polymer (**3c**): Yield: 0.40 g (80%), mp > 300 °C. *Anal.* Calc. for $C_{224}H_{160}O_{32}N_{32}Ni$: C, 69.51; H, 4.17; N, 11.58. Found: C, 68.96; H, 4.69; N, 11.52%. FTIR (KBr tablet) ν_{max}/cm^{-1}: 3063 (=CH), 2930 (CH), 2232 (C≡N), 1718 (C=N), 1653, 1595, 1477, 1244, 1085, 836. UV–Vis (DMF): λ_{max}/nm: 270, 289, 674.

Co-containing polymer (**3d**): Yield: 0.41 g (82%), mp > 300 °C. *Anal.* Calc. for $C_{224}H_{160}O_{32}N_{32}Co$: C, 69.51; H, 4.17; N, 11.58. Found: C, 68.91; H, 4.66; N, 11.54%. FTIR (KBr tablet) ν_{max}/cm^{-1}: 3063 (=CH), 2922 (CH), 2225 (C≡N), 1714 (C=N), 1674, 1649, 1465, 1276, 1056, 834. UV–Vis (DMF): λ_{max}/nm: 289, 298, 694.

3. Results and discussion

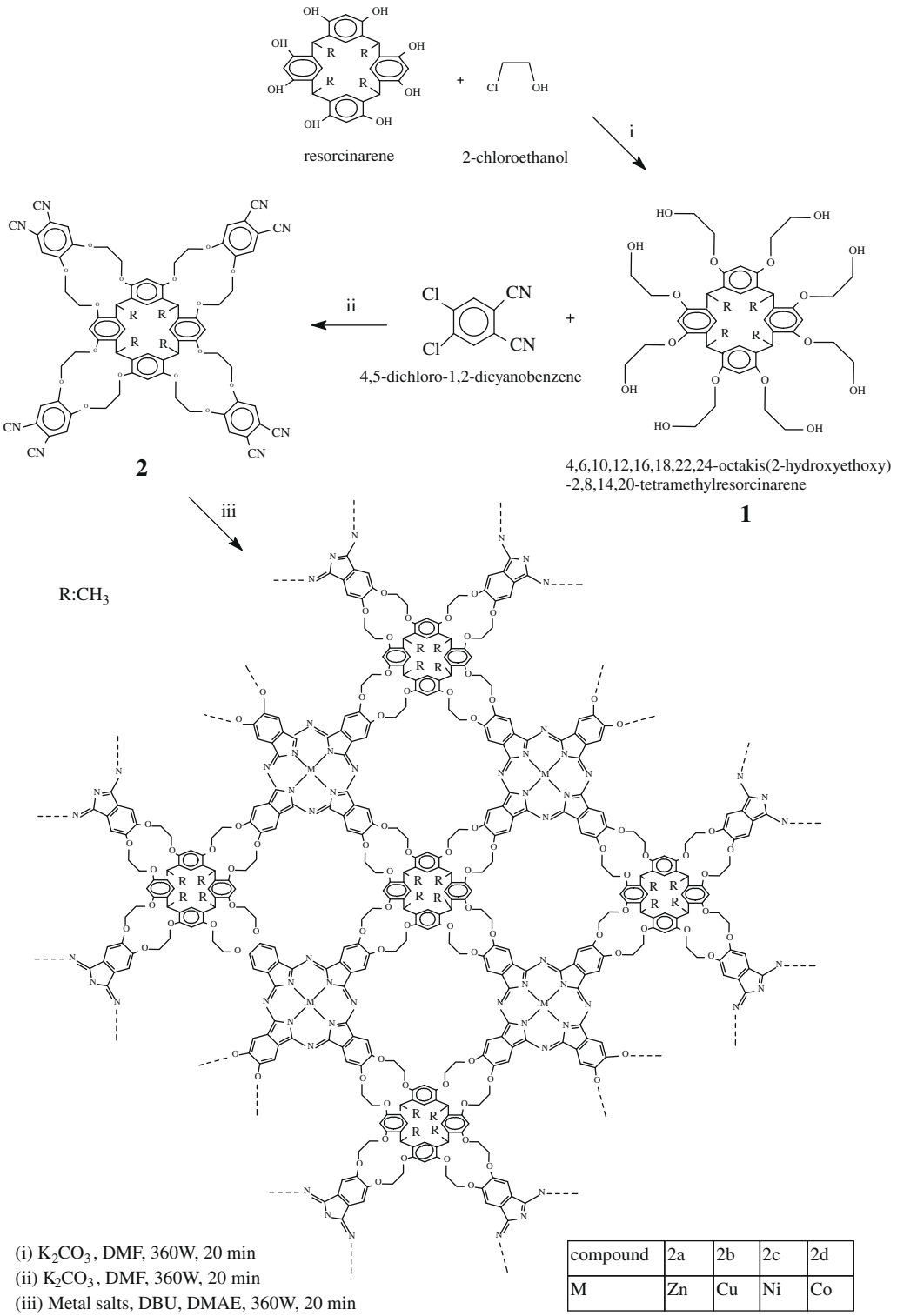
Resorcinarene, 4,5-dichloro-1,2-dicyanobenzene and 4-nitro-1,2-dicyanobenzene were synthesized in according to previously reported literature [35–37]. In order to obtain polymeric phthalocyanines containing octakis(2-hydroxyethoxy)resorcinarene, firstly, 4,6,10,12,16,18,22,24-octakis(2-hydroxyethoxy)-2,8,14,20-tetramethylresorcinarene (**1**) was synthesized by treating resorcinarene with 2-chloroethanol in DMF using K_2CO_3 as the base for nucleophilic substitution, under microwave irradiation 360 W for 20 min [19,35]. All spectroscopic data of 4,6,10,12,16,18,22,24-octakis(2-hydroxyethoxy)-2,8,14,20-tetramethylresorcinarene (**1**) show good agreement with the values reported in literature [38].

The synthesis of phthalonitrile compounds was the most important step in these reaction sequences. For this purpose, tetrakis(4,5-bis(2-hydroxyethoxy))phthalonitrile substituted resorcinarene compound (**2**) and octakis(4-(2-hydroxyethoxy))phthalonitrile substituted resorcinarene compound (**3**) were synthesized by treating compound (**1**) with 4,5-dichloro-1,2-dicyanobenzene and 4-nitro-1,2-dicyanobenzene, respectively, in DMF using K_2CO_3 as the base for nucleophilic substitution under microwave irradiation 360 W for 20 min [35]. The chemical structures of compound (**2**) and (**3**) were determined in according to previously reported paper by Cram et al. [39–41]. At the last step, metallophthalocyanine (Zn, Cu, Ni, Co) polymers were synthesized using microwave irradiation from the corresponding phthalonitrile derivatives and metal salts in DMAE for 20 min [35]. Both microwave irradiation and also conventional methods for the preparation of metal-free phthalocyanine polymer containing octakis(2-hydroxyethoxy)resorcinarene were not successful. Phthalocyanines can be obtained by the metal-template effect [42], however, metal-free phthalocyanine polymers containing octakis(2-hydroxyethoxy)resorcinarene could not be obtained due to absence of metal-template effect. The solubility of metal phthalocyanine polymers containing octakis(2-hydroxyethoxy)resorcinarene was moderate in common organic solvent such as DMF and DMSO. The solubility of the newly synthesized metal phthalocyanine polymers containing octakis(2-hydroxyethoxy)resorcinarene is more than previously synthesized metal phthalocyanine polymers containing resorcinarene by our group [35] in common organic solvents such as DMF and DMSO. The reason for this increase in solubility might be a consequence of the increased intermolecular interactions between solvent and polymeric phthalocyanines containing octakis(2-hydroxyethoxy)resorcinarene groups which have 16 oxygen atoms.

The purification of metallophthalocyanine polymers was carried out by the successive washings with various solvents. Characterization of the products involved a combination of methods including elemental analyses, FTIR, UV–Vis, ^1H NMR and ^{13}C NMR spectroscopy. ^1H NMR and ^{13}C NMR data could not be obtained for metal phthalocyanine polymers due to its insufficient solubility in polar solvents such as $CHCl_3$, DMF and DMSO. Elemental analyses of the phthalonitrile derivatives and the phthalocyanines show good agreement with the calculated values. Phthalonitrile compounds (**2**) and (**3**) are the repeated units in the structures of the newly synthesized metal phthalocyanine (Zn, Cu, Ni, Co) polymers containing octakis(2-hydroxyethoxy)resorcinarene. Microwave-assisted synthesis route of octakis(2-hydroxyethoxy)resorcinarene and new metal phthalocyanine (Zn, Cu, Ni, Co) polymers can be seen in Figs. 1 and 2.

FTIR spectrum of 4,6,10,12,16,18,22,24-octakis(2-hydroxyethoxy)-2,8,14,20-tetramethylresorcinarene (**1**) shows good agreement with the values reported in literature [38]. The formation of compound (**2**) was clearly indicated by the disappearance of the OH band at 3229 cm^{-1} and appearance of the C≡N band at 2236 cm^{-1} in its FTIR spectrum. The FTIR spectra of the polymeric phthalocyanines (**2a–d**) clearly indicate the cyclotetramerization of the phthalonitrile derivatives with the disappearance of the C≡N peak at 2236 cm^{-1}. The formation of compound (**3**) was clearly indicated by the disappearance of the OH band at 3229 cm^{-1} and appearance of the C≡N band at 2233 cm^{-1} in its FTIR spectrum. The FTIR spectra of the polymeric phthalocyanines (**3a–d**) clearly indicate the cyclotetramerization of the phthalonitrile derivatives with the disappearance of the C≡N peak at 2233 cm^{-1}. But, the polymeric phthalocyanines (**2a–d** and **3a–d**) have cyano end groups together with imide functions [11–13], as indicated by the weak absorbtions C≡N at 2234, 2232, 2234, 2232 cm^{-1}, imide at 1774, 1774, 1770 and 1724, 1715, 1719, 1726 cm^{-1}.

^1H NMR and ^{13}C NMR spectra of 4,6,10,12,16,18,22,24-octakis(2-hydroxyethoxy)-2,8,14,20-tetramethylresorcinarene (**1**) show good agreement with the values reported in literature [38]. The formation of compound (**2**) was clearly indicated by the disappearance of the OH peak at 4.23 ppm in its ^1H NMR spectrum. In the ^1H NMR spectrum of compound (**2**) the aromatic protons appear as three singlets at 8.39, 8.01 and 7.10 ppm and aliphatic protons appear as a multiplet at 4.70–4.20 ppm, as two triplet 2.82 and 2.70 and as a doublet at 1.74 ppm. The ^{13}C NMR spectrum of compound (**2**) indicated the presence of nitrile carbon atoms at 115.10 ppm, methyl carbon atoms at 20.71 ppm. The formation of compound (**3**) was clearly indicated by the disappearance of the OH peak at 4.23 ppm in its ^1H NMR spectrum. In the ^1H NMR spectrum of compound (**3**) the aromatic protons appear as four singlets at 7.96, 7.42, 7.21 and 7.11 ppm and aliphatic protons appear as a multiplet at 4.70–4.40 ppm, as two triplet 2.82 and 2.70 and as a doublet at 1.12 ppm. The ^{13}C NMR spectrum of compound (**3**) indicated the presence of nitrile carbon atoms at 116.10 ppm, methyl carbon atoms at 21.71 ppm. ^1H NMR and ^{13}C NMR measurements of the metal phthalocyanine (Cu, Co, Ni) polymers were precluded due to its paramagnetic nature. ^1H NMR and ^{13}C NMR spectra could not be obtained for polymeric phthalocyanines (**2a**) and (**3a**) due to its insufficient solubility in polar solvents such as $CHCl_3$, DMF and DMSO.



compound	2a	2b	2c	2d
M	Zn	Cu	Ni	Co

Fig. 1. Microwave-assisted synthesis of 4,6,10,12,16,18,22,24-octakis(2-hydroxyethoxy)-2,8,14,20-tetramethylresorcinarene (**1**), compound (**2**) and metallophthalocyanine polymers (**2a–d**).

The best indication for the phthalocyanine systems is their UV–Vis spectra in solutions. The newly synthesized metallophthalocyanine polymers (**2a–d** and **3a–d**) showed typical electronic spectra with two strong absorption regions, one of them is in UV region at about 245–289 nm for the compounds (**2a–d**), 270–289 nm for the compounds (**3a–d**) (B band) and the other one is in the visible region at about 683–762 nm for the compounds (**2a–d**), 674–694 nm for the compounds (**3a–d**) (Q band) in DMF. The Q band was attributed to $\pi \rightarrow \pi^*$ transition from the highest occupied molecular orbital (HOMO) to the lowest unoccupied molecular orbital (LUMO) of the Pc ring. The other bands (B) in the UV region are observed due to the transitions from the deeper π levels to the LUMO [3,20]. Q bands shifted to above values due to polymerization of phthalonitrile derivatives [43].

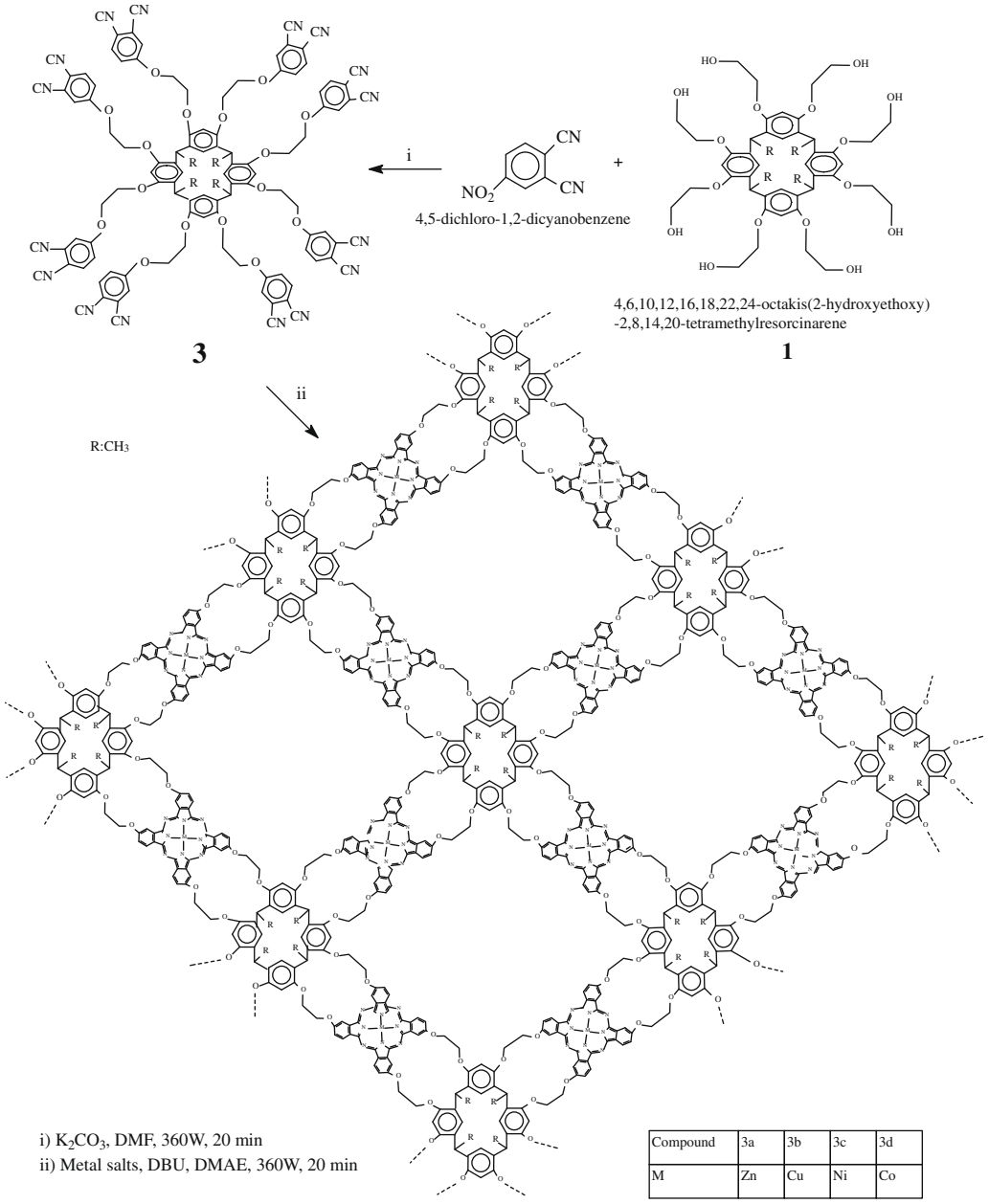


Fig. 2. Microwave-assisted synthesis of compound (**3**) and metallophthalocyanine polymers (**3a–d**).

4. Conclusion

It is the first time, the preparation of metal phthalocyanine (Zn, Cu, Ni, Co) polymers containing octakis(2-hydroxyethoxy)resorcinarene has been achieved by using as starting materials tetrakis(4,5-bis(2-hydroxyethoxy))phthalonitrile substituted resorcinarene and octakis(4-(2-hydroxyethoxy)phthalonitrile substituted resorcinarene under microwave irradiation. The solubility of the newly synthesized metal phthalocyanine polymers is more than previously reported (resorcinarene [35]) metal phthalocyanines polymers in common organic solvents such as DMF and DMSO. Microwave-assisted synthesis technique reduces reaction time and enhances yield in all of carried out reactions.

References

[1] M. Bouvet, The Porphyrin Handbook, vol. 19, Academic Press, New York, 2003.
[2] C.C. Leznoff, A.B.P. Lever, Phthalocyanines: Properties and Applications, vols. 1–4, VCH, Weinheim, 1989–1996.
[3] A. Bilgin, B. Ertem, Y. Gök, Eur. J. Inorg. Chem. 12 (2007) 1703.
[4] B.I. Kharısov, L.M. Blanco, T. Torres, A. Garcia, Ind. Eng. Chem. Res. 38 (1999) 2880.
[5] W. Herbst, K. Hunger, Industrial Organic Pigments, VCH, New York, 1993. pp. 417–421.
[6] H. Moser, L. Thomas, The Phthalocyanines, CRC Press, Boca Raton, Florida, 1983.
[7] C.J. Schramm, R.P. Scaringe, D.R. Stojakovic, B.M. Hofemann, J.A. Ibers, T.J. Marks, J. Am. Chem. Soc. 102 (1980) 6702.
[8] B.N. Dielh, T. Inabe, J.W. Lyding, K.F. Schoch, C.R. Kannewurf, T.J. Marks, J. Am. Chem. Soc. 105 (1983) 1551.
[9] B.N. Archar, G.M. Fohlen, J.A. Parker, J. Appl. Polym. Sci. 29 (1984) 353.
[10] D. Wöhrle, B. Schulte, Die. Macromol. Chimie 186 (1985) 2229.
[11] E. Ağar, S. Şaşmaz, İ. Keskin, B. Karabulut, Dyes Pigments 35 (1997) 269.
[12] E. Ağar, S. Şaşmaz, İ. Keskin, N. Akdemir, Dyes Pigments 36 (1998) 249.
[13] N. Akdemir, E. Ağar, S. Şaşmaz, İ.E. Gümrükçüoğlu, T. Çelebi, Dyes Pigments 69 (2006) 1.
[14] H.M. Kingston, S.J. Haswell, Microwave Enhanced Chemistry, American Chemical Society, Washington, DC, 1997.
[15] N. Safari, P.R. Jamaat, M. Prirouzmand, J. Porph. Phthalocyan 8 (2004) 1209.
[16] W.H. Sutton, Am. Ceram. Soc. Bull. 68 (1989) 376.
[17] F. Bahadoran, S. Dialameh, J. Porph. Phthalocyan 9 (2005) 163.
[18] S.S. Park, E.H. Hwang, B.C. Kim, H.C. Park, Am. Ceram. Soc. Bull. 83 (2000) 1341.

[19] C. Kantar, N. Akdemir, E. Ağar, N. Ocak, S. Şaşmaz, Dyes Pigments 76 (2008) 7.
[20] Z. Bıyıklıoğlu, H. Kantekin, Dyes Pigments 80 (2009) 17.
[21] E. Celenk, H. Kantekin, Dyes Pigments 80 (2009) 93.
[22] B. Kahveci, S. Şaşmaz, M. Özil, C. Kantar, B. Koşar, O. Büyükgüngör, Turk. J. Chem. 30 (2006) 681.
[23] M. Özil, E. Ağar, S. Şaşmaz, B. Kahveci, N. Akdemir, İ.E. Gümrükçüoğlu, Dyes Pigments 75 (2007) 732.
[24] P. Timmerman, W. Verboom, D. Reinhoult, Tetrahedron 52 (1996) 2663.
[25] K.E. Peterson, R.C. Smith, R.S. Mohan, Tetrahedron Lett. 44 (2003) 7723.
[26] W. Sliwa, T. Zujewska, B. Bachowska, Polish J. Chem. 77 (2003) 1079.
[27] B.Q. Ma, P. Coppens, J. Chem. Soc., Chem. Commun. (2003) 412.
[28] K. Yonetake, T. Nakayama, M. Ueda, J. Mater. Chem. 11 (2001) 761.
[29] O. Haba, K. Haga, M. Ueda, O. Morikawa, H. Konishi, Chem. Mater. 11 (1999) 427.
[30] O. Pietraszkiewicz, M. Kozbizl, M. Pietraszkiewicz, Polish J. Chem. 72 (1998) 886.
[31] V.K. Jain, S.G. Pillai, R.A. Pandya, Y.K. Agrawal, P.S. Shrivastav, Anal. Sci. 21 (2005) 129.
[32] V.K. Jain, S.G. Pillai, R.A. Pandya, Y.K. Agrawal, P.S. Shrivastav, Talanta 2 (2005) 466.
[33] M. Hedidi, S.M. Hamdi, T. Mazari, B. Boutemeur, C. Rabia, F. Chemat, M. Hamdi, Tetrahedron 62 (2006) 5652.
[34] Y.K. Agrawal, R.N. Patadia, Syn. Commun. 36 (2006) 1083.
[35] C. Kantar, E. Ağar, S. Şaşmaz, Dyes Pigments 77 (2008) 487.
[36] D. Wöhrle, M. Eskes, K. Shigehara, Synthesis (1993) 194.
[37] J.G. Young, W. Onyebuagu, J. Org. Chem. 55 (1990) 2155.
[38] S. Strandman, H. Tenhu, Polymer 48 (2007) 3938.
[39] D.J. Cram, H.J. Choi, J.A. Bryant, C.B. Knobler, J. Am. Chem. Soc. 114 (1992) 7748.
[40] J.R. Moran, J.L. Ericson, E. Dalcanale, J.A. Bryant, C.B. Knobler, D.J. Cram, J. Am. Chem. Soc. 113 (1991) 5707.
[41] J.R. Moran, S. Karbach, D.J. Cram, J. Am. Chem. Soc. 104 (1982) 5826.
[42] A.L. Thomas, Phthalocyanines. Research and Application, CRC Press, Boca Raton, 1990.
[43] H.H. Jaffe, M.J. Orchin, Theory and Application of Ultraviolet Spectroscopy, John Wiley, London, 1962.

standard methods prior to use. Elemental analyses were performed in a PE240C elemental analyzer. IR spectra were recorded on a BRUKER VECTOR 22 FT-IR spectrometer with KBr pellets. ESI-MS spectra were carried out with a TRACE DSQ instrument.

2.2. Syntheses of complexes **1–5**

2.2.1. [Cu(DMPzA)(2,2′-bipy)]·$(ClO_4)_2$ (**1**)

A solution of $Cu(ClO_4)_2·6H_2O$ (37.1 mg, 0.1 mmol) in acetonitrile (5 ml) was added dropwise to a solution of TMPzA (34.1 mg, 0.1 mmol) in acetonitrile (5 ml) with stirring. To the reaction mixture, a solution of 2,2-bipy (15.6 mg, 0.1 mmol) in acetonitrile (3 ml) was added; the resulting mixture was stirred for 1 h at room temperature. The final mixture was filtered and the filtrate was left to stand for over two weeks. Dark blue single crystals of **1** were obtained. Yield: 52% based on Cu. *Anal.* Calc. for $C_{22}H_{29}Cl_2CuN_7O_9$ (**1**): C, 39.40; H, 4.33; N, 14.63. Found: C, 38.50; H, 5.10; N, 14.20%. IR data (KBr, cm^{-1}): 3553 w, 3308 m, 3140 w, 2924 w, 2022 w, 1613 m, 1616 m, 1555 m, 1500 m, 1476 m, 1447 s, 1426 m, 1391 m, 1314 m, 1251 w, 1237 w, 1097 vs, 883 w, 774 m, 730 w, 663w, 623 s, 557 w.

2.2.2. [(DMPzA)Cu(μ-4,4′-bipy)Cu(DMPzA)]·$(ClO_4)_4$ (**2**)

Complex **2** was prepared by a similar procedure to that of **1** in a CH_3OH/H_2O co-solvent, except using 4,4-bipyridine as the auxiliary ligand instead of 2,2-bipyridine. Yield: 61% based on Cu. *Anal.* Calc. for $C_{34}H_{42}Cl_4Cu_2N_{12}O_{16}$ (**2**): C, 35.67; H, 3.67; N, 14.69. Found: C, 35.38; H, 3.89; N, 14.34%. IR (KBr, cm^{-1}): 3424 br, 3225 w, 3138 w, 3115 m, 3002 w, 1615 s, 1555 s, 1496 m, 1461 s, 1421 s, 1389 s, 1337 w, 1309 w, 1270 m, 1228 m, 1120 vs, 1100 vs, 1071 vs, 1051 vs, 978 m, 928 m, 826 m, 808 m, 728 w, 649 m, 623 vs, 563 w, 511 w.

2.2.3. [(TMPzA)Cu(μ-H_2DPC)Cu(DMPzA)]·$(ClO_4)_2$ (**3**)

A solution of $Cu(ClO_4)_2·6H_2O$ (0.1 mmol, 37.1 mg) in MeOH (10 ml) was added to a solution of TMPzA (0.1 mmol, 34.1 mg) in MeOH (10 ml) with stirring. To the reaction mixture, a solution of H_2DPC (0.05 mmol, 8.4 mg, deprotoned by reacting with NaOH) in water (5 ml) was added, and the resulting mixture was stirred for 1 h at room temperature. The final mixture was filtered, and the filtrate was left to stand for one month. Dark blue single crystals of **3** were isolated (yield: 53% based on Cu). *Anal.* Calc for $C_{37}H_{49}Cl_2Cu_2N_{13}O_{12}$ (**3**): C, 41.66; H, 4.60; N, 17.08. Found: C, 41.34; H, 4.82; N, 17.20%. IR (KBr, cm^{-1}): 3447 br, 3198 w, 2920 w, 2850 w, 2018 w, 1630 s, 1610 vs, 1582 m, 1552 m, 1507 w, 1472 m, 1436 m, 1375 vs, 1281 m, 1243 w, 1120 vs, 1096 vs, 1060 vs, 924 w, 910 w, 823 w, 731 m, 625 m, 597 w, 559 w.

2.2.4. [(DMPzA)Co(μ-H_2DPC)Co(TMPzA)]·$(ClO_4)_2$ (**4**)

Complex **4** was prepared in a way similar to the procedure of **3** except using $Co(ClO_4)_2·6H_2O$ instead of $Cu(ClO_4)_2·6H_2O$. Yield: 60% based on Co. *Anal.* Calc. for $C_{37}H_{51}Cl_2Co_2N_{13}O_{13}$ (**4**): C, 41.32; H, 4.75; N, 16.94. Found: C, 40.88; H, 4.80; N, 17.20%. IR (KBr, cm^{-1}): 3593 w, 3470 br, 2925 m, 2066 m, 1639 s, 1609 s, 1568 s, 1554 s, 1468 s, 1439 m, 1387 m, 1281 m, 1247 m, 1146 s, 1092 vs, 1053 s, 997 w, 738 m, 693w, 625 s, 595 w.

2.2.5. [(TMPzA)Co(μ-HZPC)Co(TMPzA)(H_2O)$_2$]·$(ClO_4)_3$ (**5**)

Complex **5** was prepared in a way similar to the procedure of **4** except using 5-methyl-3-pyrazol-carboxylic acid instead of 2,6-pyridine-dicarboxylic acid as the auxiliary donor. Yield: *ca.* 25% based on Co. *Anal.* Calc. for $C_{41}H_{62}Cl_3Co_2N_{16}O_{16}$ (**5**): C, 39.07; H, 4.92; N, 17.79. Found: C, 38.87; H, 5.10; N, 17.81%. IR (KBr, cm^{-1}): 3852 w, 3746 w, 3647 w, 2926 m, 2018 w, 1733 w, 1649 s, 1576 m, 1555 s, 1468 s, 1425 m, 1386 m, 1277 m, 1247 m, 1093 vs, 1054 s, 984 w, 928 w, 835 m, 794 m, 625 s, 549 w.

Caution! Although we have not met any problems in handling perchlorate salts during this work, these should be treated cautiously because of their potential explosive nature.

2.3. X-ray crystallography

Details of the crystallographic parameters, data collection and refinements are summarized in Table 1. Structure measurements

Table 1
Crystallographic data and structure refinement for **1–5**.

Complex	**1**	**2**	**3**	**4**	**5**
Formula	$C_{22}H_{29}Cl_2CuN_7O_9$	$C_{34}H_{42}Cl_4Cu_2N_{12}O_{16}$	$C_{37}H_{49}Cl_2Cu_2N_{13}O_{12}$	$C_{37}H_{51}Cl_2Co_2N_{13}O_{13}$	$C_{41}H_{62}Cl_3Co_2N_{16}O_{16}$
Formula weight	669.96	1143.68	1065.87	1074.67	1259.28
Crystal system	Triclinic	Orthorhombic	Monoclinic	Triclinic	Triclinic
Space group	$P\bar{1}$	*Pna*2(1)	*P*2(1)/c	$P\bar{1}$	$P\bar{1}$
a (Å)	10.762(5)	16.684(4)	13.506(5)	11.6391(9)	12.4755(14)
b (Å)	11.793(6)	8.326(2)	15.720(6)	12.6261(10)	13.9125(15)
c (Å)	12.213(6)	33.588(9)	22.947(9)	17.3518(14)	18.0850(19)
α (°)	100.021(6)	90	90	95.2530(10)	110.941(2)
β (°)	99.716(7)	90	104.519(6)	90.1870(10)	93.710(2)
γ (°)	93.173(7)	90	90	112.5730(10)	91.757(2)
V (Å^3)	1498.9(13)	4666(2)	4716(3)	2342.7(3)	2920.6(5)
Z	2	4	4	2	2
D_{calc} (g cm^{-3})	1.484	1.628	1.501	1.523	1.432
μ (mm^1)	0.966	1.221	1.087	0.897	0.781
T (K)	293(2)	293(2)	293(2)	293(2)	293(2)
F(0 0 0)	690	2336	2200	1112	1306
Crystal size (mm)	0.37 × 0.26 × 0.16	0.22 × 0.08 × 0.06	0.20 × 0.12 × 0.10	0.22 × 0.16 × 0.14	0.32 × 0.22 × 0.20
θ range (°)	1.72–25.03	2.43–25.03	1.83–25.03	1.76–25.03	1.57–25.01
Limiting indices	$-12 \le h \le 11$, $-14 \le k \le 14$, $-12 \le l \le 14$	$-15 \le h \le 19$, $-9 \le k \le 9$, $-38 \le l \le 39$	$-16 \le h \le 15$, $-18 \le k \le 18$, $-27 \le l \le 25$	$-13 \le h \le 8$, $-15 \le k \le 15$, $-20 \le l \le 20$	$-9 < h < 14$, $-16 < k < 14$, $-17 < l < 21$
Reflections collected/unique	8145/5230 [*R*(int) = 0.0160]	23846/7997 [*R*(int) = 0.0335]	25412/8322 [*R*(int) = 0.0335]	12875/8175 [*R*(int) = 0.0205]	14797/10209 [*R*(int) = 0.0190]
Goodness-of-fit (GOF) on F^2	1.038	1.036	0.970	1.052	1.074
$R_1[I > 2\sigma(I)]$	0.0533	0.0420	0.0665	0.0477	0.0733
ωR_2 (all data)	0.1786	0.1160	0.2132	0.1420	0.2576
Largest difference in peak and hole (e A^{-3})	0.723 and −0.643	0.865 and −0.291	0.595 and −0.317	0.891 and −0.370	0.920 and −0.584
Flack parameter		0.00			

of these complexes were performed on a Bruker SMART 1000 CCD area detector equipped with graphite-monochromated Mo Kα radiation (λ = 0.71073 Å) by the ω-scan mode. The structures were solved by direct methods and refined with the full-matrix least-squares technique using the SHELXS-97 and SHELXL-97 programs [12,13]. The non-hydrogen atoms were refined anisotropically, whereas non-water hydrogen atoms were included in calculated positions and refined with isotropic thermal parameters riding on the parent atoms. The H atoms of water molecules were fixed by difference Fourier E-maps.

3. Results and discussion

3.1. Syntheses

The synthetic methods for complexes **1**–**5** are given in Scheme 1. In the initial stage, the mononuclear complex **1** with TMPzA losing one arm, has been obtained. Then various metal salts have been employed to prepare metal complexes, with pyridyl derivatives as auxiliary ligands also being involved in the system to survey the effect of the metal atom on the structures of the complexes, and complexes **2**, **3** and **4** have been isolated. The same result to that of **1**, namely one pendant arm of the TMPzA ligand is removed in these complexes with various metal atoms, has been observed. In these complexes, the tripodal ligand TMPzA loses a pendant arm and coordinates with the metal center, meanwhile the pyridyl ring also coordinates with the metal center. In order to confirm further the effect of the pyridyl compounds on the cleavage reaction of the tripodal ligand, 5-methyl-3-pyrazolyl-carboxylate as the auxiliary ligand has been employed instead of the pyridyl compounds, and in this case complex **5** has been prepared. It has been found that two TMPzA ligands have coordinated with the metal center and no pendant arm is removed in complex **5**. This result proves further that the metal complexes of TMPzA have the ability to recognize pyridine compounds.

3.2. Descriptions of crystal structures

3.2.1. [Cu(DMPzA)(2,2′-bipy)]·(ClO_4)$_2$ (**1**)

The structure of **1** consists of a mononuclear [Cu(DMPzA)(2,2-bipy)]$^{2+}$ unit and two uncoordinated ClO_4^- anions (Fig. 1). In this complex, TMPzA loses an uncoordinated arm and turns into DMPzA, The Cu(II) atom has a five-coordinated distorted square pyramidal coordination, including two $N_{pyrazole}$ atoms of TMPzA and two $N_{pyridyl}$ of 2,2-bipyridine as well as a N_{amine} atom of TMPzA. The N_{amine} is in an axial site, and the bottom plane is defined by two $N_{pyrazole}$ atoms and two N_{pyrine} atoms. The Cu–$N_{pyrazole}$ and Cu–$N_{pyridine}$ bonds are normal coordinated bonds. The Cu–N_{amine} bond [2.342(4) Å] in the axial site is somewhat longer than a normal bond due to the Jahn–Teller effect from the copper atom and the strain action from the ligand, and the coordination configuration of **1** is best described as a square based pyramid. Selected bond lengths and angles for **1** are listed in Table 2.

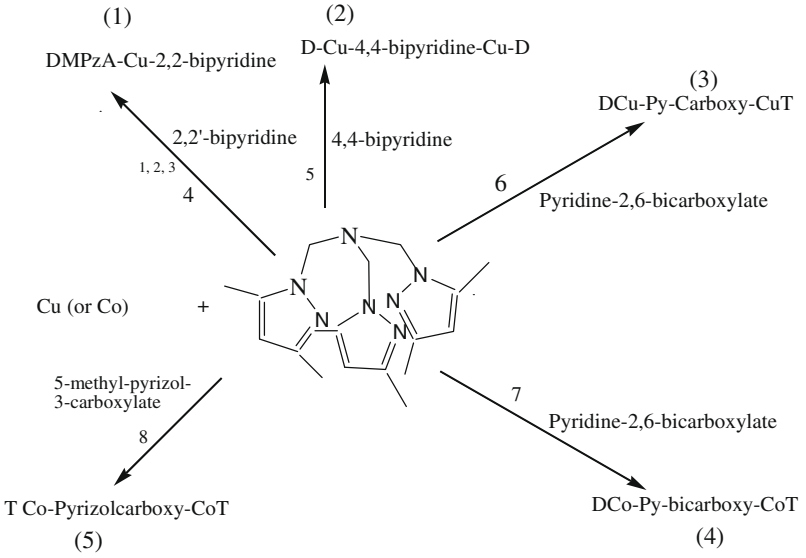
3.2.2. [(DMPzA)Cu(μ-4,4′-bipy)Cu(DMPzA)]·(ClO_4)$_4$ (**2**)

The molecular structure of **2** consists of discrete [Cu_2(DMPzA)$_2$-(4,4-bipy)]$^{2+}$ cations and two perchlorates (Fig. 2a). Both TMPzA molecules lose an arm and become DMPzA. The cation, [Cu_2(DMPzA)$_2$(4,4-bipy)]$^{2+}$, has C_2 symmetry with two-fold axis passing through the center of 4,4-bipyridine. The 4,4-bipyridine molecule bridge links two Cu(II) centers in a bidentate mode, and the two Cu(II) atoms are in square-planar environments involving two $N_{pyrazol}$ atoms, two N_{amine} atoms and two $N_{pyridine}$ atoms. The molecular structure of **2** is quite similar to that of the complex Cu($C_{14}H_9NO_3$)($C_3H_4N_2$) reported by Gao et al. [14]. The Cu–N bond lengths fall in the range 1.9762(12)–2.036(15) Å and they are normal coordination bonds. The Cu–N_{amine} bond is somewhat longer than the Cu–$N_{pyrazol}$ bond, and they can be regarded as normal for this class of complexes [15]. The Cu atoms protrude out from the mean plane by 0.0195 Å. Selected bond lengths and angles for **2** are listed in Table 3.

The symmetry units are developed into a 1D chain through an intermolecular hydrogen bond at the uncoordinated perchlorate groups with O···H–CH_2 = 2.413 Å, shown in Fig. 2b.

3.2.3. Descriptions of the crystal structures of complexes *3* and *4*

The coordinated configurations of complexes **3** and **4** are quite similar, as shown in Figs. 3 and 4, respectively. In these complexes, one carboxyl group of H_2DPC coordinates with the metal center in a monodentate fashion, and the other carboxyl group coordinates with two metal ions in bidentate mode. In **3** and **4**, one metal atom, M(1), coordinated by the four N atoms of TMPzA and one O atom of



Scheme 1. The synthesis methods of the complexes **1**–**5**. (D = bis(3,5-bimethyl-pyrazolmethyl)amine. T = tris(3,5-bimethyl-pyrazolmethyl)amine; bipy = 4,4′-bipyridine; pda = pyridine-2,6-dicarboxylate; pzoa = 5-methyl-3-pyrazole-carboxylate). (1) L:Cu(ClO_4)$_2$ = 1:1; (2) in CH_3OH/H_2O; (3) stirring for 30 min; (4) L:Cu(ClO_4)$_2$:bipy = 1:1:1; (5) L:Cu(ClO_4)$_2$:bipy = 1:1:0.5; (6) L:Cu(ClO_4)$_2$:pda = 1:1:0.5; (7) L:Co(ClO_4)$_2$:pda = 1:1:0.5; (8) L:Co(ClO_4)$_2$:pzoa = 1:1:0.5.

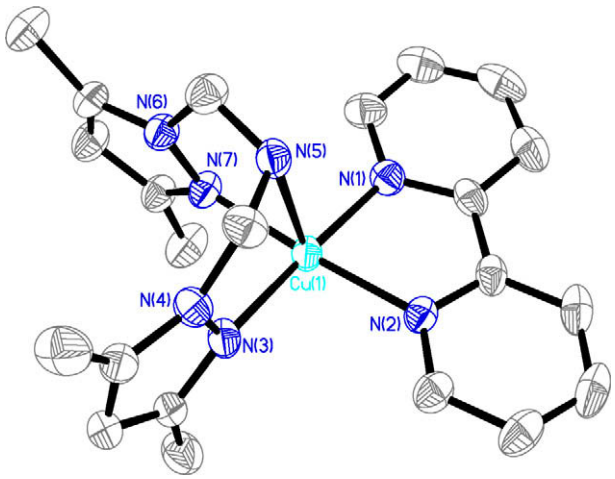


Fig. 1. ORTEP view of complex **1**. Hydrogen atoms are omitted for clarity.

Table 2
Selected bond distances (Å) and angles (°) for **1**.

Bond lengths			
Cu(1)–N(7)	1.971(4)	Cu(1)–N(2)	1.987(4)
Cu(1)–N(1)	2.009(4)	Cu(1)–N(3)	2.020(4)
Cu(1)–N(5)	2.342(4)		
Bond angles			
N(7)–Cu(1)–N(2)	173.8(2)	N(7)–Cu(1)–N(1)	92.83(2)
N(2)–Cu(1)–N(1)	81.36(2)	N(7)–Cu(1)–N(3)	89.82(2)
N(2)–Cu(1)–N(3)	96.00(2)	N(1)–Cu(1)–N(3)	177.3(2)
N(7)–Cu(1)–N(5)	79.50(1)	N(2)–Cu(1)–N(5)	103.8(1)
N(1)–Cu(1)–N(5)	101.2(2)	N(3)–Cu(1)–N(5)	78.87(15)

a carboxyl group, has a distorted trigonal bipyramidal configuration with the axial O–M–N bond angles 176.9(3)° and 177.85(10)°, respectively. The coordination configuration of the other metal atom, M(2), which is different from that of the M(1) atom, is a six-coordinated octahedron with two $O_{carboxyl}$ atoms and one $N_{pyridyl}$ atoms of H_2DPC and two $N_{pyrizale}$ and one N_{amine} of the TMPzA ligand. TMPzA has lost a pendant arm and turns into DMPzA, and coordinates with the metal atoms through the N_{amine} and two $N_{pyrazol}$ atoms. Selected bond lengths and angles for **3** and **4** are listed in Table 4.

3.2.4. Descriptions of crystal structure of complex *5*

Complex **5** also consists of two asymmetric units, and HZPC is employed in the system as an auxiliary ligand (Fig. 5). The configuration of **5** is different from those of the previous four complexes. In complex **5**, two TMPzA molecules are retained and no pendant arm is removed. The carboxyl group of HZPC coordinates with two Co atoms in a bidentate mode, bridging the two metal centers. The Co(1) atom is penta-coordinated trigonal bipyramidal with three $N_{pyrazol}$ atoms, one N_{amine} atom and one $O_{carboxyl}$ atom, which is quite similar to that of the metal(1) atoms in **3** and **4**. Three $N_{pyrazol}$ atoms define the mean plane and the N_{amine} and $O_{carboxyl}$ atoms are in axial sites with the $O_{carboxyl}$–Co–N_{amine} angle being 178.36(4)°. The N(7)–Co(1)–N(3) angle [128.28(5)°] is larger than the angles N(3)–Co(1)–N(5) [106.786(6)°] and N(5)–Co(1)–N(7) [109.70(6)°], which might be due to the strain of the coordinated carboxyl groups.

Table 3
Selected bond distances (Å) and angles (°) for **2**.

Bond lengths			
Cu(1)–N(11)	1.976(1)	Cu(1)–N(1)	1.988(1)
Cu(1)–N(5)	1.992(1)	Cu(1)–N(3)	2.010(1)
Cu(2)–N(10)	1.983(1)	Cu(2)–N(12)	1.988(1)
Cu(2)–N(6)	2.002(1)	Cu(2)–N(8)	2.036(2)
Bond angles			
N(11)–Cu(1)–N(1)	97.44(5)	N(11)–Cu(1)–N(5)	98.62(5)
N(1)–Cu(1)–N(5)	163.65(5)	N(11)–Cu(1)–N(3)	179.05(5)
N(1)–Cu(1)–N(3)	81.65(5)	N(5)–Cu(1)–N(3)	82.31(5)
N(10)–Cu(2)–N(12)	97.81(5)	N(10)–Cu(2)–N(6)	162.62(5)
N(12)–Cu(2)–N(6)	99.21(5)	N(10)–Cu(2)–N(8)	81.37(5)
N(12)–Cu(2)–N(8)	178.32(5)	N(6)–Cu(2)–N(8)	81.71(5)

The Co(2) atom is in an octahedral coordinated environment involving two $N_{pyrazol}$ atoms and one N_{amine} atom of TMPzA, one $N_{pyrazol}$ and one $O_{carboxyl}$ atom of the bridging ligand and one O_{water}. One uncoordinated pendant arm still links with the skeleton of TMPzA. The $O_{carboxyl}$–Co(2)–O_{H2O} defines the in the axial sites, and the mean plane is defined by three $N_{pyrazol}$ atoms and one N_{amine} atom. There are three disordered perchlorate ions and two uncoordinated water molecules, O(16) and O(17), in which one water molecule, O(17), is disordered. Selected bond lengths and angles for **5** are listed in Table 5.

3.3. Study on the cleavage mechanism of the pendant arm on the tripodal ligand

3.3.1. Quantum chemistry calculation

Full geometry optimizations were performed at the DFT/B3LYP levels with the 6-31G(d) basis sets. The vibration analysis was performed on the B3LYP/6-31G(d) geometries to verify the structures of minimum energy and to provide zero-point vibration energies (ZPVEs, scaled by the recommended factor of 0.980619). The C–N bond dissociation enthalpies (BDEs) of model derivatives were corrected for ZPVEs and thermal effects due to transitional, rotational

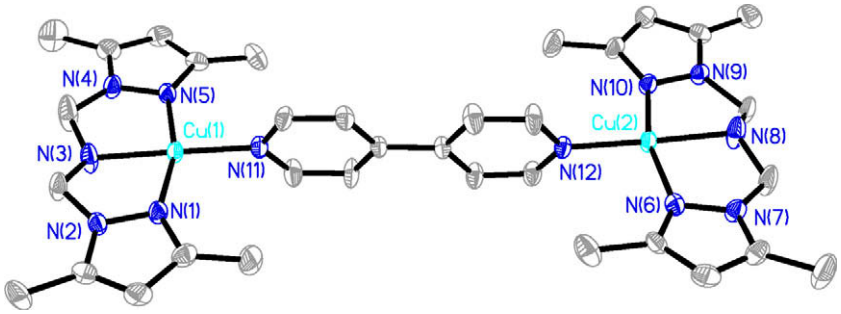


Fig. 2a. ORTEP view of complex **2**. Hydrogen atoms are omitted for clarity.

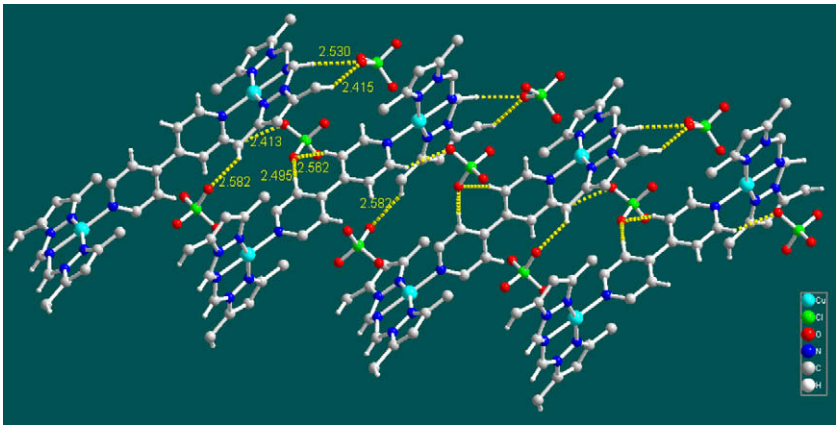


Fig. 2b. The 1D chain formed by the intermolecular hydrogen bond in **2**.

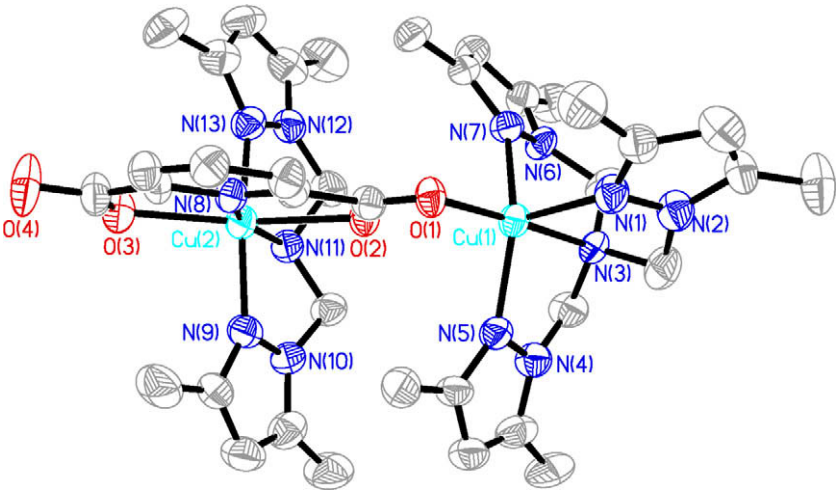


Fig. 3. ORTEP view of complex **3**. Hydrogen atoms are omitted for clarity.

and vibration motions of the related non-linear molecules/radicals. All calculations were carried out with the GAUSSIAN 03 program package [16]. The calculated results by the computation method are collected in Table 6.

From Table 6, it can be seen that the breaking energy of H_2N┼CH_2–pyrazole is lower than that of H_2N–CH_2┼pyrazole, which leads to the methyl–pyrazole group dissociating from N_{amine} of TMPzA, and both bonds are more easily broken than H_2N┼CH_2–pyridine because the energies to break those bonds mentioned above are lower than that of H_2N┼CH_2–pyridine. Thus, the pendant arm of tripodal ligands involving pyrazole arms is more easily broken than that of tripodal ligands involving pyridyl pendant arms, such as TPA, TLA and TEPA, which do not display the cleavage of a pendant arm of the ligand. The cleavage mechanism of the pendant arm on TMPzA might be also illustrated by the special molecular structure of the pyrazole.

3.3.2. The molecular structure of pyrazole

It has been known that the pyrazole molecule has two tautomeric isomers [17–19], as shown in Chart 1.

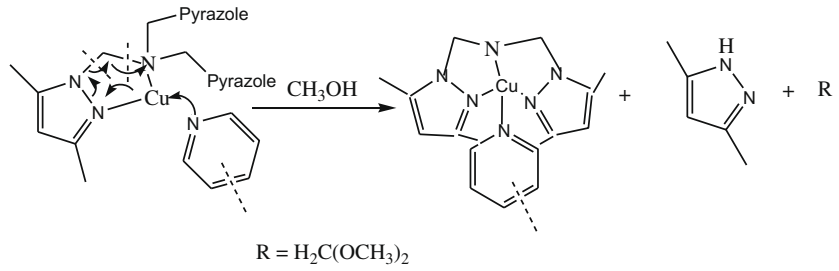
The proton on the nitrogen atom of the pyrazole ring could migrate between both nitrogen atoms, leading to the methyl–pyrazole bond linking with the amine nitrogen of TMPzA being unstable in certain conditions [20]. The mechanism details have been studied and confirmed further by ESI-MS spectra.

3.3.3. ESI-MS spectra and cleavage mechanism studies

After the complex was separated from the reaction system of TMPzA with the metal salt, the mother solution was taken to carry out ESI-MS in order to detect other product molecules. Taking complex **1** as the example, there is a moderate intensity peak of m/z + H at 97.20 (intensity: 4×10^5) assigned to the 3,5-bimethylpyrazole and a peak of m/z – H at 74.2 (intensity: 3.5×10^5) assigned to $CH_2(OCH_3)_2$ in the ESI-MS spectra. A stronger peak of m/z + H at 266.4 (intensity: 12×10^5) assigned to NH(–CH_2–3,5-bimethylpyrazole)$_2$·CH_3OH was also observed.

These results indicate that the complexes with TMPzA have a strong ability of selected recognition of pyridine compounds. The pendant arm on TMPzA can be removed by pyridine derivatives, two C–N bonds of the $N_{pyrazole}$–C–N_{amine} are broken and the pyridyl group coordinates with the metal center on attacking by pyridine compounds. Meanwhile, the complexes with DMPzA give a pyri-

dine-coordinated complex, generated *via* a S_N2-like mechanism. The $-OCH_3$ groups from methanol react with $-CH_2-$ groups to generate $CH_2(OCH_3)_2$ molecules. The reaction can be described as follows:



use the UV–Vis spectral titration method to track the reaction process, but changes of absorptions have not been observed because the rate of the reaction is very slow. A study on the influencing factors for the reaction is under way in our group now.

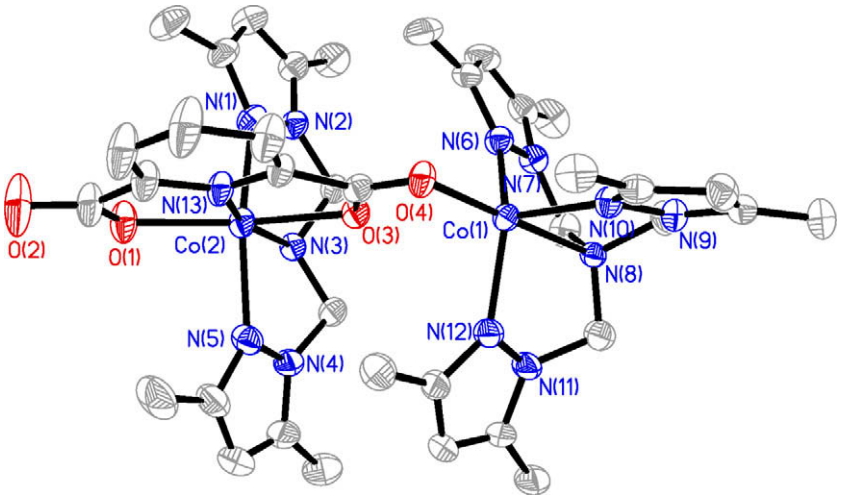


Fig. 4. ORTEP view of complex **4**. Hydrogen atoms are omitted for clarity.

Table 4
Selected bond distances (Å) and angles (°) for **3** and **4**.

3				**4**		
Bond lengths						
Cu(1)–O(1)	1.946(5)	Cu(1)–N(5)	2.029(6)	Co(1)–O(4) 2.011(3)	Co(1)–N(10)	2.032(3)
Cu(1)–N(7)	2.061(6)	Cu(1)–N(3)	2.089(6)	Co(1)–N(6) 2.045(3)	Co(1)–N(12)	2.054(3)
Cu(1)–N(1)	2.089(7)	Cu(2)–N(13)	2.000(7)	Co(1)–N(8) 2.296(3)	Co(2)–N(13)	2.039(3)
Cu(2)–N(9)	2.001(7)	Cu(2)–N(11)	2.038(5)	Co(2)–O(1) 2.112(3)	Co(2)–N(5)	2.119(3)
Cu(2)–N(8)	2.065(6)	Cu(2)–O(3)	2.248(6)	Co(2)–N(3) 2.121(3)	Co(2)–N(1)	2.135(3)
Cu(2)–O(2)	2.373(5)			Co(2)–O(3) 2.223(2)		
Bond angles						
O(1)–Cu(1)–N(3)		176.9(3)		O(4)–Co(1)–N(8)		177.9(1)
N(5)–Cu(1)–N(7)		139.0(3)		N(10)–Co(1)–N(6)		109.4(1)
N(7)–Cu(1)–N(1)		100.9(3)		N(10)–Co(1)–N(12)		105.8(1)
N(5)–Cu(1)–N(1)		112.8(3)		N(6)–Co(1)–N(12)		129.2(1)
N(13)–Cu(2)–N(9)		160.3(3)		N(5)–Co(2)–N(1)		154.1(1)
N(8)–Cu(2)–O(3)		74.4(2)		N(13)–Co(2)–O(1)		76.13(1)
N(11)–Cu(2)–O(3)		126.2(2)		O(1)–Co(2)–N(3)		120.6(1)
N(11)–Cu(2)–O(2)		85.7(2)		N(3)–Co(2)–O(3)		88.6(1)
N(8)–Cu(2)–O(2)		73.6(2)		N(13)–Co(2)–O(3)		74.83(1)

Only pyridine and its derivatives promote the reaction of the pendant arms being broken in the metal complexes, because the pyridine species catalyze the aldol condensation-like reaction in methanol solvent with active hydrogen atoms [21]. Other solvents, such as acetonitrile, chloroform have been employed in these reactions, and the results above have not been obtained. We tried to

4. Conclusion

In summary, it is possible to draw the following conclusions. Firstly, when pyridine and its derivatives coordinate with metal centers, one arm on the metal complexes of TMPzA is removed, which bears no relationship to the various metal atoms used. Thus,

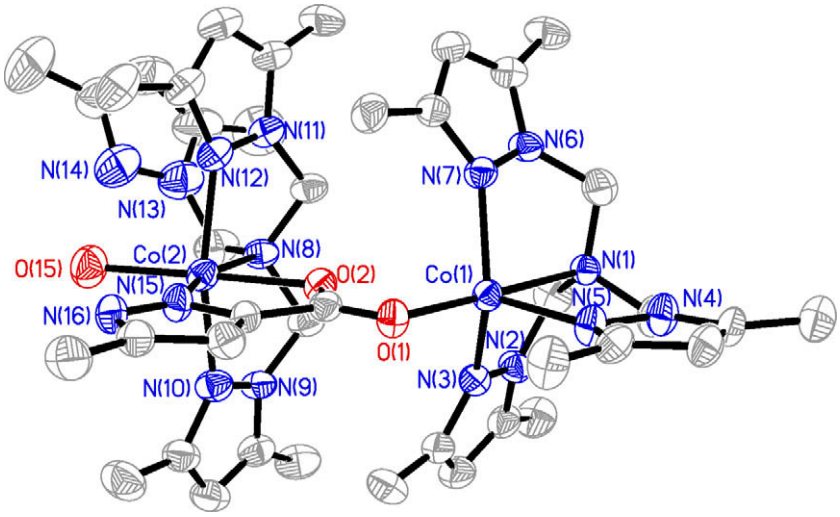


Fig. 5. ORTEP view of complex **5**. Hydrogen atoms and the counter ion are omitted for clarity.

Table 5
Selected bond distances (Å) and angles (°) for **5**.

Bond lengths			
Co(1)–O(1)	2.017(1)	Co(1)–N(5)	2.027(2)
Co(1)–N(3)	2.057(1)	Co(1)–N(7)	2.066(1)
Co(1)–N(1)	2.287(1)	Co(2)–O(15)	2.073(2)
Co(2)–N(12)	2.084(2)	Co(2)–N(10)	2.088(2)
Co(2)–N(15)	2.132(1)	Co(2)–O(2)	2.158(1)
Co(2)–N(8)	2.246(1)		
Bond angles			
N(5)–Co(1)–N(3)	106.8(6)	N(5)–Co(1)–N(7)	109.7(6)
N(3)–Co(1)–N(7)	128.3(5)	O(1)–Co(1)–N(1)	178.4(4)
N(12)–Co(2)–N(15)	103.9(5)	N(10)–Co(2)–N(15)	99.63(5)
N(15)–Co(2)–O(2)	76.94(5)	N(12)–Co(2)–N(8)	76.98(5)
N(10)–Co(2)–N(8)	78.41(5)		

Table 6
Comparison of the energy of the broken bond.

Broken bond	Electron form	Energy/kcal mol^{-1}
H_2N┼CH_2–pyridine	H_2N^-–pyridine$^+$	257.6
H_2N┼CH_2–pyrazole	H_2N^+–pyrazole$^-$	94.4
H_2N–CH_2┼pyrazole	H_2C^+–pyrazole$^-$	173.0

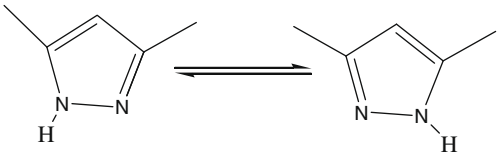
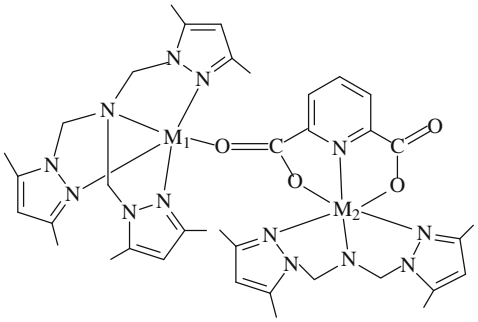


Chart 1. The tautomeric isomers of the pyrazole molecule.



Scheme 2. The coordinated model of the bridging ligand.

we speculate that these complexes have the ability to recognize pyridine compounds, and the complexes might be constructed as a molecular knife in the future. In these complexes, the bond lengths order of M–N (the metal atom with the nitrogen atoms) is: M–$N_{amine(TMPzA)}$ > M–$N_{amine(DMPzA)}$ > M–N_{pyrazo}, which arises from the steric effect of the tripodal ligand; secondly, by comparing the complexes **1**, **2** and **3**, it has been found that when the auxiliary ligands are changed from 2,2-bipy to 4,4-bipy to H_2DPC, the coordinated number changes from 4 to 5 to 6, and their coordination geometries are also changed from square-planar to trigonal bipyramidal (or tetra-pyramidal) to octahedral, which shows that the coordination configurations of the tripodal complexes can be influenced by the molecular structures of the pyridine compounds; finally, the crystal structures of **3** and **4** are quite similar, where one metal center has a six-coordinated octahedral geometry, and the another metal atom is in a five-coordinated trigonal bipyramidal environment. The $N_{pyridine}$ and one $O_{carboxyl}$ of pyridine-2,6-bicarboxylate coordinate with a metal center, and two $O_{carboxyl}$ atoms of the other carboxyl group bridge link two metal centers to form a novel asymmetric binuclear structure, which is different from the symmetric dimers reported in the literature [22,23]. The coordinated model of the bridging ligand is shown in Scheme 2.

5. Supplementary data

CCDC 288920, 288921, 292233, 285074 and 294162 contains the supplementary crystallographic data for **1**, **2**, **3**, **4** and **5**. These data can be obtained free of charge via http://www.ccdc.cam.ac.uk/conts/retrieving.html, or from the Cambridge Crystallographic Data Centre, 12 Union Road, Cambridge CB2 1EZ, UK; fax: (+44) 1223-336-033; or e-mail: deposit@ccdc.cam.ac.uk.

References

[1] (a) D.M. Tagore, K.I. Sprinz, A.D. Hamiton, Supramol. Chem. 19 (1&2) (2007) 129;
(b) Y. Ishimi, A. Kikuchi, J. Biol. Chem. 266 (11) (1991) 7025;
(c) .Y. Mazor, S. Cilead, I. Benhar, E. Gazit, J. Molecul. Biol. 322 (5) (2002) 1013.

[2] (a) M. Berger, F.P. Schmidtchen, Chem. Rev. 97 (1997) 1609;
(b) P.D. Beer, E. Hayes, Coord. Chem. Rev. 240 (2002) 1;
(c) M.S. Han, D.H. Kim, Angew Chem., Int. Ed. 41 (2002) 3809.
[3] (a) L. Fabbrizzi, I. Faravelli, G. Francese, M. Licchelli, A. Perotti, A. Taglietti, Chem. Commun. (1998) 971;
(b) W.R. Cerre, O.W. Michael, Coord. Chem. Rev. 233–234 (2002) 341.
[4] (a) M. Costas, M.P. Mehn, M.P. Jensen, et al., Chem. Rev. 104 (2004) 939;
(b) E.Y. Tshuva, S.J. Lippard, Chem. Rev. 104 (2004) 987;
(c) E. Pidock, H.V. Obias, C.X. Zhang, et al., J. Am. Chem. Soc. 120 (1998) 7841;
(d) Y. Tang, S.-Y. Li, L. Sun, Z.-H. Zhang, Acta Scientiarum Naturalium Univ. Nankaiensis 2 (2006) 75;
(e) G.J. van Driel et al., Inorg. Chem. 24 (19) (1985) 2919.
[5] (a) T. Kojima, T. Sakamoto, Y. Matsuda, Inorg. Chem. 43 (2004) 2243;
(b) T. Kojima, Y. Matsuda, J. Chem. Soc., Dalton Trans. (2001) 958.
[6] Z.-H. Zhang, X. Bu, Z. Zhu, Y. Chen, Polyhedron 15 (16) (1997) 2787.
[7] N.J. Lundin, I.G. Hamilton, A.G. Blackman, Polyhedron 23 (2004) 97.
[8] C.K. Li, W.K. Jang, C.M. Che, K.Y. Wang, R.J. Wang, T.C. Mak, J. Chem. Soc., Dalton Trans (1991) 1909.
[9] J. Bjernemose, A. Hazell, C.J. McKenzie, M.F. Mahon, L.P. Nielsen, P.R. Raithby, O. Simonsen, H. Toftlund, J.A. Wolny, Polyhedron 22 (2003) 875.
[10] J.H. Satcher Jr., M.W. Droege, M.M. Olmstead, A.I. Balch, Inorg. Chem. 40 (2001) 1454.
[11] I. Sanyal, P. Ghosh, K.D. Karlin, Inorg. Chem. 34 (1995) 3050.
[12] G.M. Sheldrick, SHELXL-97 Program for X-ray Crystal Structure Solution, Göttingen University, Germany, 1997.
[13] G.M. Sheldrick, SHELXS-97 Program for X-ray Crystal Structure Refinement, Göttingen University, Germany, 1997.
[14] S. Gao, Z. Shi, J. Hua, S.-H. Feng, R.-R. Xu, S.-X. Liu, L.-H. Huo, P.-G. Chen, Gaodeng Xuexiao Huaxue Xuebao (Chem. J. Chin. Univ.) 21 (2) (2000) 177.
[15] M. Di Vairia, F. Mani, Inorg. Chim. Acta 70 (1983) 99.
[16] GAUSSIAN 03, Revision C.01, M.J. Frisch, G.W. Trucks, H.B. Schlegel, G.E. Scuseria, M.A. Robb, J.R. Cheeseman, J.A. Montgomery Jr., T. Vreven, K.N. Kudin, J.C. Burant, J.M. Millam, S.S. Iyengar, J. Tomasi, V. Barone, B. Mennucci, M. Cossi, G. Scalmani, N. Rega, G.A. Petersson, H. Nakatsuji, M. Hada, M. Ehara, K. Toyota, R. Fukuda, J. Hasegawa, M. Ishida, T. Nakajima, Y. Honda, O. Kitao, H. Nakai, M. Klene, X. Li, J.E. Knox, H.P. Hratchian, J.B. Cross, C. Adamo, J. Jaramillo, R. Gomperts, R.E. Stratmann, O. Yazyev, A.J. Austin, R. Cammi, C. Pomelli, J.W. Ochterski, P.Y. Ayala, K. Morokuma, G.A. Voth, P. Salvador, J.J. Dannenberg, V.G. Zakrzewski, S. Dapprich, A.D. Daniels, M.C. Strain, O. Farkas, D.K. Malick, A.D. Rabuck, K. Raghavachari, J.B. Foresman, J.V. Ortiz, Q. Cui, A.G. Baboul, S. Clifford, J. Cioslowski, B.B. Stefanov, G. Liu, A. Liashenko, P. Piskorz, I. Komaromi, R.L. Martin, D.J. Fox, T. Keith, M.A. Al-Laham, C.Y. Peng, A. Nanayakkara, M. Challacombe, P.M.W. Gill, B. Johnson, W. Chen, M.W. Wong, C. Gonzalez, J.A. Pople, Gaussian, Inc., Wallingford CT, 2004.
[17] C. Foces-Foces, I. Alkorta, J. Elguero, Acta Crystallogr., Sect. B 56 (2000) 1018.
[18] M. Ramos, I. Alkorta, J. Elguero. Tetrahedron 53 (1997) 1403.
[19] L.-R. Wen, G.-L. Zhao, M. Li, W. Qi, X.-L. Zhang, H.-Z. Yang, Chin. Chem. Lett. 16 (9) (2005) 1161.
[20] J. Elguero, Pyrazoles and their Benzo Derivatives, Comprehensive Heterocyclic Chemistry, Pergamon, Oxford, 1996.
[21] J.-T. Wang, Q.-M. Hu, B.-S. Zhang, Y.-M. Wang, Organic Chemistry Textbook, Publishing House of Nankai University, Tianjin, China, 1993. pp. 253–390.
[22] P. Sengupta, S. Ghosh, T.C.W. Mak, Polyhedron 20 (9–10) (2001) 975.
[23] A.E. Martell, R.D. Hancock, R.J. Motekaitis, Coord. Chem. Rev. 133 (1994) 39.

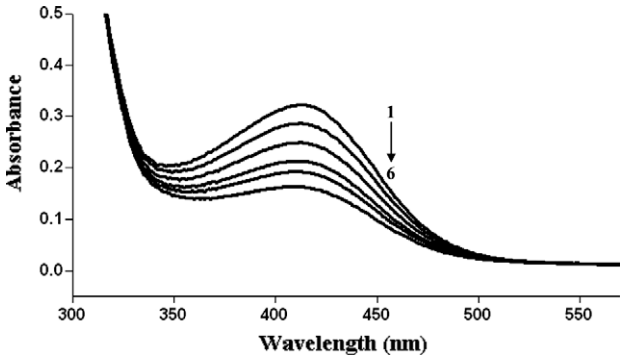


Fig. 1. Spectroscopic changes occurring in the oxidation of ATN by DPC at 27 °C. [DPC] = 5.0×10^{-5}; [ATN] = 5.0×10^{-4}; [OH^-] = 0.04 and I = 0.10 mol dm^{-3} with scanning time interval of 1 min.

2. Experimental

2.1. Materials and reagents

All chemicals used were of reagent grade, and doubly distilled water was used throughout the work. A solution of ATN (M/s. S.S.Antibiotics Pvt. Ltd., Aurangabad, India) was prepared by dissolving an appropriate amount of ATN in doubly distilled water. The required concentration of ATN was prepared from its stock solution. The copper(III) periodate complex was prepared by standard procedure [20,21]. Existence of copper(III) complex was verified by its UV–Vis spectrum, which showed an absorption band with maximum absorption at 415 nm. The aqueous solution of copper(III) was standardized by iodometric titration and gravimetrically by the thiocyanate [22] method. The copper(II) solution was prepared by dissolving the known amount of copper sulfate (BDH) in distilled water. Periodate solution was prepared by weighing the required amount of sample in hot water and used after keeping it for 24 h. Its concentration was ascertained iodometrically [23] at neutral pH by phosphate buffer. KOH and KNO_3 (BDH, AR) were employed to maintain the required alkalinity and ionic strength, respectively, in reaction solutions.

2.2. Kinetic measurements

Since the initial rate was fast, the kinetic measurements were performed on a Hitachi 150-20 UV–Visible spectrophotometer attached to a rapid kinetic accessory (HI-TECH SFA-12). The kinetics was followed under pseudo first order condition, where [ATN] > [DPC] at 27 ± 0.1 °C, unless specified. The reaction was initiated by mixing the DPC with ATN solution, which also contained the required concentration of KNO_3, KOH, and KIO_4, and the progress of the reaction was followed spectrophotometrically at 415 nm by monitoring the decrease in absorbance due to DPC with the molar absorbancy index, ε to be 6230 ± 100 dm^3 mol^{-1} cm^{-1}. It was verified that there is a negligible interference from other species present in the reaction mixture at this wavelength.

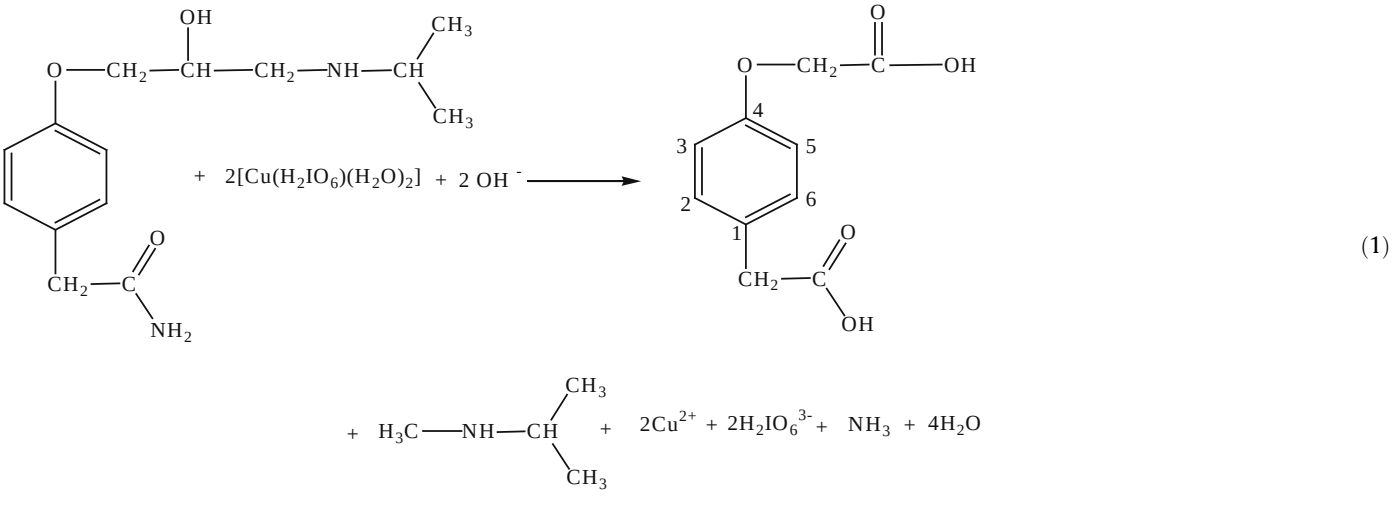
The pseudo first order rate constants, k_{obs}, were determined from the log (absorbance) versus time plots. The plots were linear up to 80% completion of reaction under the range of [OH^-] used. The orders for various species were determined from the slopes of plots of log k_{obs} versus respective concentration of species except for [DPC] in which no variation of k_{obs} was observed as expected to the reaction condition. During the kinetics, a constant concentration viz. 1.0×10^{-4} mol dm^{-3} of KIO_4 was used throughout the study unless otherwise stated. Since periodate is present in the excess in DPC, the possibility of oxidation of ATN by periodate in alkaline medium at 27 °C was tested. The progress of the reaction was followed iodometrically. However, it was found that there was no significant reaction under the experimental conditions employed compared to the DPC oxidation of ATN. The total concentrations of periodate and OH^- was calculated by considering the amount present in the DPC solution and that additionally added. Kinetics runs were also carried out in N_2 atmosphere in order to understand the effect of dissolved oxygen on the rate of reaction. No significant difference in the results was obtained under a N_2 atmosphere and in the presence of air. In view of the ubiquitous contamination of carbonate in the basic medium, the effect of carbonate was also studied. Added carbonate had no effect on the reaction rates. The spectral changes during the reaction are shown in Fig. 1. It is evident from the figure that the concentration of DPC decreases by observing the absorbance at 415 nm.

Regression analysis of experimental data to obtain the regression coefficient r and standard deviation S of points from the regression line was performed using Microsoft 2003 Excel program.

3. Results and discussion

3.1. Stoichiometry and product analysis

Different sets of reaction mixtures containing various ratios of DPC to ATN in the presence of constant amounts of OH^- and KNO_3 were kept for 2 h in a closed vessel under nitrogen atmosphere. The remaining concentration of DPC was estimated by spectrophotometrically. The results indicated 1:2 stoichiometry as given in Eq. (1).



(1)

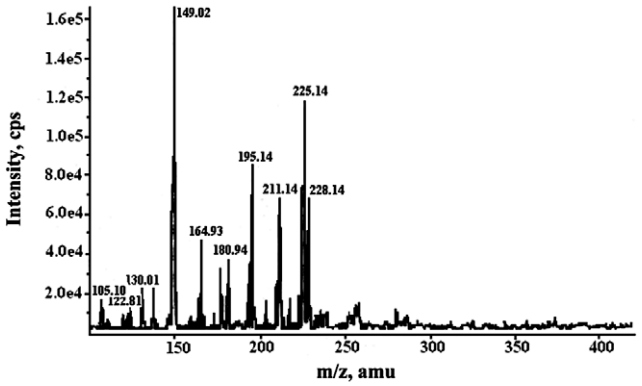


Fig. 2. LC–ESI-MS spectra of ammoniated 4-carboxy methoxy phenyl acetic acid.

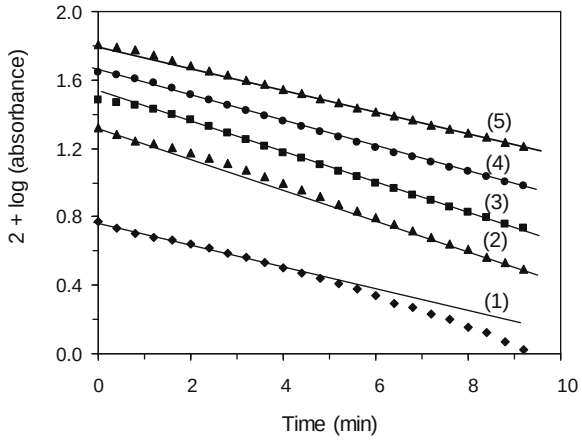


Fig. 3. First order plots on the oxidation of ATN by DPC in aqueous alkaline medium. [DPC]: (1) 1.0, (2) 3.0, (3) 5.0, (4) 7.0 and (5) 10.0×10^{-5} mol dm^{-3}.

The reaction product was extracted with ether and recrystallised form aqueous alcohol and the purity was checked by HPLC. This was identified as 4-carboxy methoxy phenyl acetic acid by its IR spectrum, which showed a band at 1690 cm^{-1} due to >C=O stretching of acid and a broad band at 2845 cm^{-1} due to O–H stretching. 4-Carboxy methoxy phenyl acetic acid was further characterized by ^{1}H NMR spectrum (DMSO), showed a singlet at 9.6 δ due to two carboxylic OH, a doublet at 6.94 δ due to C_3 and C_5-protons, another doublet at at 7.20 δ due to C_2 and C_6-protons, a singlet at 3.53 δ due to methylene protons of ph-CH_2- and another singlet at 4.58 δ due to methylene protons of ph-O-CH_2-, respectively. Further, the product was subjected to LC–Mass spectral analysis with ESI technique (solvents: acetonitrile + water + ammonium acetate). Ammoniated peak at 228 amu (M^+ +17) was obtained, which conforms M^+ at 211 amu, which corresponds to 4-carboxy methoxy phenyl acetic acid (Fig. 2). Ammonia was qualitatively identified using Nessler's reagent. N-isopropylmethylamine, which is highly soluble in water, was identified by spot test [24]. Another product Cu(II), was identified by UV–Vis spectra. The reaction products do not undergo further oxidation under the present kinetic conditions.

3.2. Reaction orders

The reaction orders were determined from the slope of log k_{obs} versus log (concentration) plots by varying the concentrations of ATN, alkali, and periodate in turn, while keeping all other concentrations and conditions constant, except for DPC concentration.

3.3. Effect of [DPC]

The oxidant DPC concentration was varied in the range 1.0×10^{-5}–1.0×10^{-4} mol dm^{-3}, and the fairly constant k_{obs} values indicate that order with respect to [DPC] was unity (Table 1). This was also confirmed by linearity of the plots of log [absorbance] versus time ($r \geqslant 0.986$, $S \leqslant 0.013$) up to 80% completion of the reaction (Fig. 3).

3.4. Effect of [ATN]

The effect of ATN on the rate of reaction was studied at constant concentrations of alkali, DPC, and periodate at a constant ionic strength of 0.10 mol dm^{-3}. The substrate, ATN, was varied in the range 1.0×10^{-4}–1.0×10^{-3} mol dm^{-3}. The k_{obs} values increased with increase in concentration of ATN. The order with respect to [ATN] was found to be less than unity (Table 1) ($r \geqslant 0.991$, $S \leqslant 0.007$) under the experimental concentrations. However, at lower concentrations of ATN, the reaction was first order in [ATN] and at high concentration of ATN, the reaction was independent

Table 1
Effects of [DPC], [ATN], [OH$^-$] and [IO_4^-] for the oxidation of ATN by diperiodatocuprate(III) in alkaline medium at 27 °C, I = 0.10 mol dm^{-3}.

[DPC] $\times 10^5$ (mol dm^{-3})	[ATN] $\times 10^4$ (mol dm^{-3})	[OH$^-$] (mol dm^{-3})	[IO_4^-] $\times 10^4$ (mol dm^{-3})	$k_{obs} \times 10^3$ (s^{-1}) found	calculated
1.0	5.0	0.04	1.0	3.32	3.36
3.0	5.0	0.04	1.0	3.40	3.36
5.0	5.0	0.04	1.0	3.35	3.36
7.0	5.0	0.04	1.0	3.38	3.36
10.0	5.0	0.04	1.0	3.26	3.36
5.0	1.0	0.04	1.0	0.92	0.96
5.0	3.0	0.04	1.0	2.29	2.36
5.0	5.0	0.04	1.0	3.35	3.36
5.0	7.0	0.04	1.0	4.07	4.02
5.0	10.0	0.04	1.0	4.86	4.71
5.0	5.0	0.01	1.0	1.57	1.52
5.0	5.0	0.02	1.0	2.55	2.48
5.0	5.0	0.04	1.0	3.35	3.36
5.0	5.0	0.08	1.0	4.71	4.52
5.0	5.0	0.10	1.0	5.16	4.95
5.0	5.0	0.04	0.5	4.33	4.22
5.0	5.0	0.04	0.7	3.82	3.83
5.0	5.0	0.04	1.0	3.35	3.36
5.0	5.0	0.04	3.0	2.25	2.16
5.0	5.0	0.04	5.0	1.15	1.20

of [ATN]. The order in [ATN] changes from first order to zero order as [ATN] varies.

3.5. Effect of [alkali]

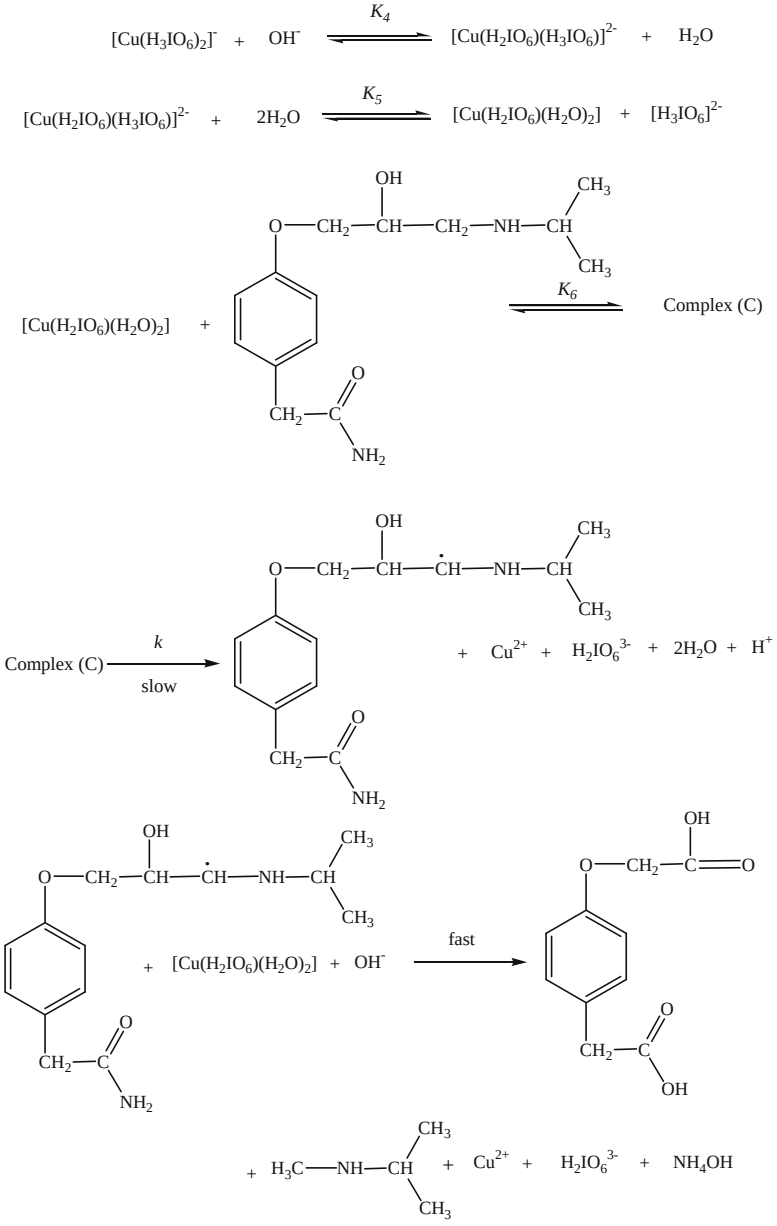
The effect of increase in concentration of alkali on the reaction was studied at constant concentrations of ATN, DPC, and periodate at a constant ionic strength of 0.10 mol dm^{-3} at 27 °C. The rate constants increased with increase in alkali concentration (Table 1), indicating fractional order dependence of rate on alkali concentration ($r \geqslant 0.989$, $S \leqslant 0.006$). Similar to as in the case of ATN, the order in alkali changes from first order to zero order as [OH$^-$] increases.

3.6. Effect of [periodate]

The effect of increasing concentration of periodate was studied by varying the periodate concentration from 5.0×10^{-5} to 5.0×10^{-4} mol dm^{-3} keeping all other reactants concentrations constant. It was found that the added periodate had a retarding effect on the rate of reaction, the order with respect to periodate concentration being negative less than unity (Table 1).

3.7. Effect of ionic strength (I) and dielectric constant of the medium (D)

The addition of KNO_3 at constant [DPC], [ATN], [OH$^-$], and [IO^{-4}] was found that with increasing ionic strength of the medium, rate of the reaction increased. The plot of log k_{obs} versus $I^{1/2}$ was found to be linear with negative slope. Dielectric constant of the medium, D, was varied by varying t-butyl alcohol and water percentage. The D values were calculated from the equation $D = D_wV_w + D_BV_B$, where D_w and D_B are dielectric constants of pure water and t-butyl alcohol, respectively, and V_w and V_B are the volume fractions of components water and t-butyl alcohol, respectively, in the total mixture. With the decrease in dielectric



Scheme 1. Detailed mechanistic scheme for the oxidation of ATN by alkaline diperiodatocuprate(III).

constant of the reaction medium, rate of the reaction increased. The plot of log k_{obs} versus $1/D$ was linear with a negative slope.

3.8. Effect of added products

The externally added product, copper(II) ($CuSO_4$) in the range 1.0×10^{-4}–1.0×10^{-3} mol dm^{-3} did not have any significant effect on the rate of the reaction.

3.9. Polymerization study

The intervention of free radicals in the reaction was examined as follows. The reaction mixture, to which a known quantity of acrylonitrile monomer was initially added, was kept for 2 h in an inert atmosphere. On diluting the reaction mixture with methanol, a white precipitate was formed, indicating the intervention of free radicals in the reaction. The blank experiments of either DPC or ATN alone with acrylonitrile did not induce any polymerization under the same condition as those induced for reaction mixture. Initially, the added acrylonitrile decreased the rate of reaction indicating free radical intervention, which is the case in earlier work [25,26].

3.10. Effect of temperature

The kinetics was studied at four different temperatures under varying concentrations of ATN, alkali, and periodate, keeping other conditions constant. The rate constants were found to increase with increase in temperature. The rate constants (k) of the slow step of Scheme 1 were obtained from the slopes and intercepts of $1/k_{obs}$ versus 1/[ATN], $1/k_{obs}$ versus [$H_3IO_6^{2-}$], and $1/k_{obs}$ versus 1/[OH^-] plots at four different temperatures and were used to calculate the activation parameters. The energy of activation corresponding to these constants was evaluated from the Arrhenius plot of log k versus $1/T$ ($r \geqslant 0.996$, $S \leqslant 0.011$), and other activation parameters obtained are tabulated in Table 2.

Table 2
Thermodynamic activation parameters for the oxidation of ATN by DPC in aqueous alkaline medium with respect to the slow step of Scheme 1.

Temperature (K)			$k \times 10^2$ (s^{-1})
(A) Effect of temperature			
300			0.99
305			1.39
310			1.89
320			3.06
(B) Activation parameters (Scheme 1)			
Parameters			Values
Ea(kJ mol^{-1})			44.7 ± 1.5
$\Delta H^{\#}$ (kJ mol^{-1})			42.2 ± 0.6
$\Delta S^{\#}$ (JK^{-1} mol^{-1})			−142 ± 5
$\Delta G^{\#}$ (kJ mol^{-1})			86 ± 2
Log A			5.8 ± 0.3
Temperature (K)	K_4 (dm^3 mol^{-1})	$K_5 \times 10^3$ (mol dm^{-3})	$K_6 \times 10^{-3}$ (dm^3 mol^{-1})
(C) Effect of temperature on equilibrium constants of Scheme 1 for the oxidation of ATN by diperiodatocuprate(III) in alkaline medium.			
300	1.03 ± 0.02	0.99 ± 0.05	4.1 ± 0.2
305	1.32 ± 0.03	0.71 ± 0.06	5.4 ± 0.2
310	1.54 ± 0.03	0.42 ± 0.03	7.7 ± 0.3
320	2.36 ± 0.04	0.21 ± 0.02	12.0 ± 0.4
Thermodynamic quantities	Values from K_4	Values from K_5	Values from K_6
(D) Thermodynamic quantities using K_4, K_5 and K_6			
ΔH (k J mol^{-1})	32.7 ± 1.4	−62.8 ± 2.0	43.3 ± 1.0
ΔS (J K^{-1} mol^{-1})	110 ± 3	−268 ± 4	215 ± 4
ΔG_{320} (k J mol^{-1})	−2.1 ± 0.1	21.1 ± 1.2	−23.4 ± 1.0

The water-soluble copper(III) periodate complex is reported [27] to be $[Cu(HIO_6)_2]^{5-}$. However, in an aqueous alkaline medium and at a high pH range as employed in the study, periodate is unlikely to exist as HIO_6^{4-} (as present in the complex) as is evident from its involvement in the multiple equilibria [28] ((2)–(4)) depending on the pH of the solution.

$$H_5IO_6 \overset{K_1}{\rightleftharpoons} H_4IO_6^- + H^+ \quad K_1 = 5.1 \times 10^{-4} \tag{2}$$

$$H_4IO_6^- \overset{K_2}{\rightleftharpoons} H_3IO_6^{2-} + H^+ \quad K_2 = 4.9 \times 10^{-9} \tag{3}$$

$$H_3IO_6^{2-} \overset{K_3}{\rightleftharpoons} H_2IO_6^{3-} + H^+ \quad K_3 = 2.5 \times 10^{-12} \tag{4}$$

Periodic acid exists in acid medium as H_5IO_6 and as $H_4IO_6^-$ around pH 7. Thus, under the conditions employed in alkaline medium, the main species are expected to be $H_3IO_6^{2-}$ and $H_2IO_6^{3-}$. At higher concentrations, periodate also tends to dimerize [29]. However, formation of this species is negligible under conditions employed for kinetic study. Hence, at the pH employed in this study, the soluble copper(III) periodate complex exists as diperiodatocuprate(III), $[Cu(H_3IO_6)(H_2IO_6)]^{2-}$, a conclusion also supported by earlier work [30,31].

The reaction between the diperiodatocuprate(III) complex and atenolol in alkaline medium has the stoichiometry 1:2 (ATN:DPC) with a first order dependence on [DPC] and an apparent order of less than unity in [substrate], [alkali] and negative fractional order dependence on the periodate. No effect of added products was observed. Based on the experimental results, a mechanism is proposed for which all the observed orders in each constituent such as [oxidant], [reductant], [OH^-], and [IO^{-4}] may be well accommodated. Lister [32] proposed three forms of copper(III) periodate in alkaline medium as diperiodatocuprate(III)(DPC), monoperiodatocuprate(III) (MPC), and tetrahydroxocuprate(III). The latter is ruled out, as its equilibrium constant is 8.0×10^{-11} at 40 °C. Hence, in the present study, DPC and MPC are to be considered as active forms of copper(III) periodate complex. It may be expected that a lower periodate complex such as MPC is more important in the reaction than the DPC. The results of increase in the rate with increase in alkali concentration and decrease in the rate with increase in periodate concentration suggest that equilibria of different copper(III) periodate complexes are possible as in Eqs. (5) and (6).

$$[Cu(H_3IO_6)_2]^- + OH^- \overset{K_4}{\rightleftharpoons} [Cu(H_2IO_6)(H_3IO_6)]^{2-} + H_2O \tag{5}$$

$$[Cu(H_2IO_6)(H_3IO_6)]^{2-} + 2H_2O \overset{K_5}{\rightleftharpoons} [Cu(H_2IO_6)(H_2O)_2] + [H_3IO_6]^{2-} \tag{6}$$

The less than unit order in [ATN] presumably results from formation of a complex (C) between the oxidant and atenolol prior to the formation of the products. K_6 is the composite equilibrium constant comprising the equilibrium to bind active species of ATN to MPC species to form a complex (C). Then, this complex (C) decomposes in a slow step to form a free radical derived from ATN. This free radical species further reacts with another molecule of MPC species in a fast step to yield the products such as 4-carboxy methoxy phenyl acetic acid, N-isopropylmethylamine, ammonia, Cu(II), and periodate. So, the detailed mechanistic scheme for the oxidation of ATN by diperiodatocuprate(III) is presented in Scheme 1.

Since Scheme 1 is in accordance with the generally well-accepted principle of non-complementary oxidations taking place in sequence of one-electron steps, the reaction between the substrate and oxidant would afford a radical intermediate. A free radical scavenging experiment revealed such a possibility. This type of radical intermediate has also been observed in earlier work [33,34]. Spectroscopic evidence for the complex formation between oxidant and substrate was obtained from UV–Vis spectra

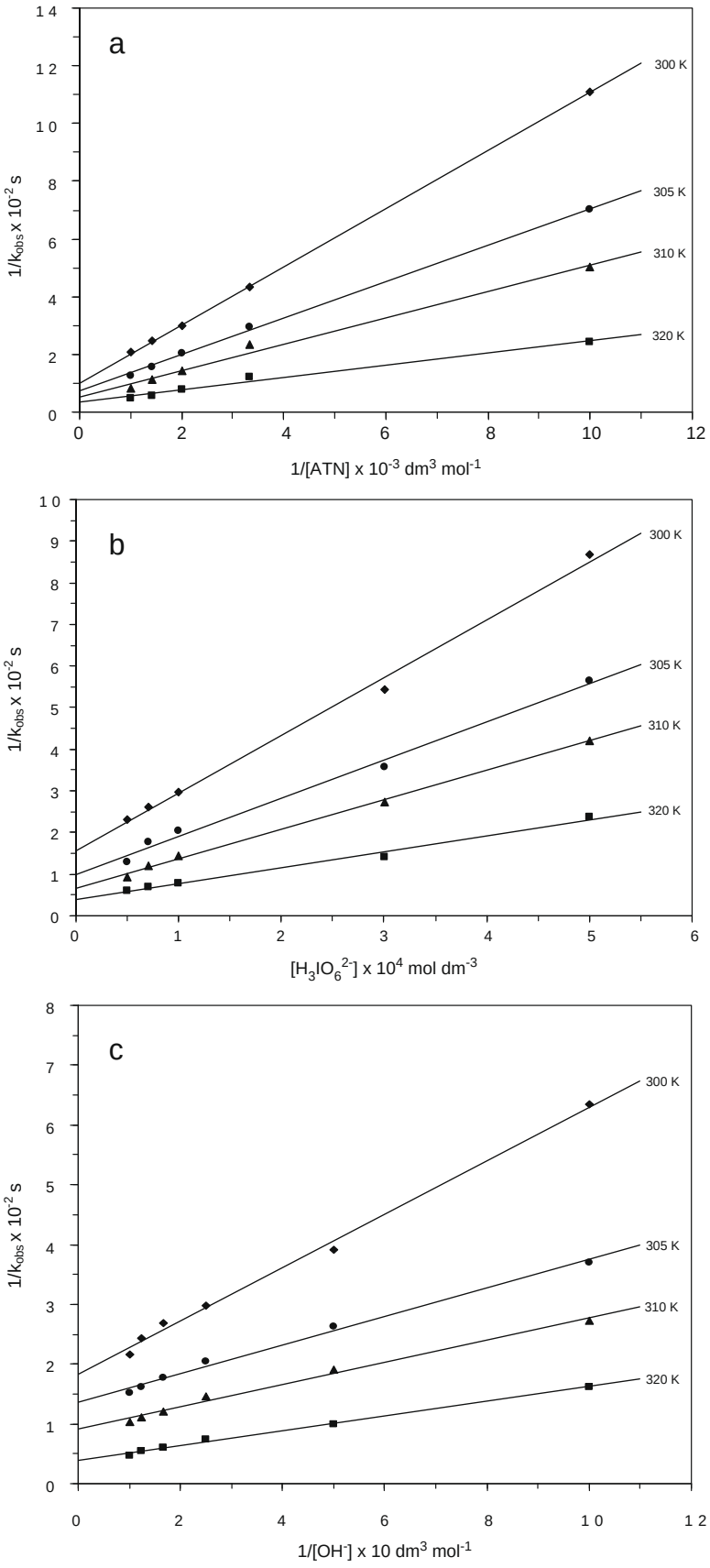


Fig. 4. (a) Plots of $1/k_{obs}$ versus 1/[ATN] at four different temperatures (conditions as in Table 1). (b) Plots of $1/k_{obs}$ versus $[H_3IO_6^{2-}]$ at four different temperatures (conditions as in Table 1). (c) Plots of $1/k_{obs}$ versus $1/[OH^-]$ at four different temperatures (conditions as in Table 1).

of ATN (5.0×10^{-4}), DPC (5.0×10^{-5}), $[OH^-] = 0.04$ mol dm^{-3} and mixture of both. A hypsochromic shift of about 5 nm from 306 to 301 nm in the spectra of ATN was observed. The Michaelis–Menten plot also proved the complex formation between DPC and ATN, which explains the less than unit order dependence on [ATN]. Such a complex between a substrate and an oxidant has been observed in other studies [35,36].

Scheme 1 leads to the rate law as

$$\text{Rate} = \frac{-\text{d}[\text{DPC}]}{\text{dt}} = \frac{kK_4K_5K_6[\text{DPC}][\text{ATN}][\text{OH}^-]}{[\text{H}_3\text{IO}_6^{2-}] + K_4[\text{OH}^-][\text{H}_3\text{IO}_6^{2-}] + K_4K_5[\text{OH}^-] + K_4K_5K_6[\text{ATN}][\text{OH}^-]} \quad (7)$$

which explains all the observed kinetic orders of different species.

$$k_{obs} = \frac{\text{Rate}}{[\text{DPC}]} = \frac{kK_4K_5K_6[\text{ATN}][\text{OH}^-]}{[\text{H}_3\text{IO}_6^{2-}] + K_4[\text{OH}^-][\text{H}_3\text{IO}_6^{2-}] + K_4K_5[\text{OH}^-] + K_4K_5K_6[\text{ATN}][\text{OH}^-]} \quad (8)$$

The rate law (8) can be rearranged into the following form, which is suitable for verification.

$$\frac{1}{k_{obs}} = \frac{[\text{H}_3\text{IO}_6^{2-}]}{kK_4K_5K_6[\text{OH}^-][\text{ATN}]} + \frac{[\text{H}_3\text{IO}_6^{2-}]}{kK_4K_5K_6[\text{ATN}]} + \frac{1}{kK_6[\text{ATN}]} + \frac{1}{k} \quad (9)$$

According to Eq. (9), other conditions being constant, plots of $1/k_{obs}$ versus $1/[OH^-]$ ($r \geqslant 0.995$, $S \leqslant 0.029$), $1/k_{obs}$ versus 1/[ATN] ($r \geqslant 0.997$, $S \leqslant 0.016$), and $1/k_{obs}$ versus $[H_3IO_6^{2-}]$ ($r \geqslant 0.998$, $S \leqslant 0.011$) should be linear and are found to be so (Fig. 4). The slopes and intercepts of such plots lead to the values of K_4, K_5, K_6, and k as (1.03 ± 0.03) dm^3 mol^{-1}, $(9.94 \pm 0.30) \times 10^{-4}$ mol dm^{-3}, $(4.10 \pm 0.10) \times 10^3$ dm^3 mol^{-1}, and $(9.91 \pm 0.40) \times 10^{-3}$ s^{-1}, respectively. The values of K_4 and K_5 are in agreement with earlier data [37]. Using these K_4, K_5, K_6, and k values, the rate constants under different experimental conditions were calculated by Eq. (8) and compared with experimental data. There is a good agreement between them (Table 1), which fortifies the Scheme 1. The equilibrium constant K_4 is far greater than K_5. This may be attributed to the greater tendency of DPC to undergo hydrolysis compared to the dissociation of hydrolyzed species in alkaline medium.

The effect of ionic strength on the rate of reaction is not in accordance with proposed mechanism, which might be due to the presence of high ionic strength used in the reaction. Increase in the content of t-butanol in the reaction medium leads to an increase in the rate of reaction, which seems to be contrary to the expected interaction between neutral species in media of lower relative permittivity. However, an increase in the rate of reaction with decrease in dielectric constant may be due to stabilization of the complex C at low relative permittivity, which is less solvated than MPC at higher dielectric constant because of its larger size.

The thermodynamic quantities for the first, second, and third equilibrium steps of Scheme 1 can be evaluated as follows. The $[H_3IO_6^{2-}]$, [ATN], and $[OH^-]$ (as in Table 1) were varied at four different temperatures. The plots of $1/k_{obs}$ versus $1/[OH^-]$, $1/k_{obs}$ versus 1/[ATN], and $1/k_{obs}$ versus $[H_3IO_6^{2-}]$ should be linear (Fig. 4). From the slopes and intercepts, the values of K_4 were calculated at different temperatures and these values are given in Table 2. A vant Hoff's plot was made for variation of K_4 with temperature (log K_4 vs. $1/T$ ($r \geqslant 0.997$, $S \leqslant 0.006$) and the values of enthalpy of reaction ΔH, entropy of reaction ΔS, and free energy of reaction ΔG were calculated for the first equilibrium step. These values are given in Table 2. A comparison of ΔH value (32.7 ± 1.4) from K_4 with that of $\Delta H^{\#}$ (42.2 ± 0.6) of rate limiting step supports that the first step of Scheme 1 is fairly fast since it involves low activation energy with those obtained for the slow step of the reaction [38,39]. In the same manner, K_5 and K_6 values were calculated at different temperatures and their corresponding values of the thermodynamic quantities are given in the Table 2.

The values of $\Delta H^{\#}$ and $\Delta S^{\#}$ were both favorable for electron transfer processes. The negative value of $\Delta S^{\#}$ indicates that the complex (C) is more ordered than the reactants [40]. The value of $\Delta S^{\#}$ within the range for radical reaction has been ascribed [41] to the nature of electron pairing and unpairing processes and to the loss of degrees of freedom formerly available to the reactants upon the formation of rigid transition state. The observed modest enthalpy of activation and a relatively low value of the entropy of activation as well as a higher rate constant of the slow step indicate that the oxidation presumably occurs via inner-sphere mechanism. This conclusion is supported by earlier observation [42,43].

4. Conclusion

Among the various species of DPC in aqueous alkaline medium, $[Cu(H_2IO_6)(H_2O)_2]$ is considered as active species for the title reaction. The results indicated that in carrying out this reaction, the role of pH in the reaction medium is crucial. Rate constant of slow step and other equilibrium constants involved in the mechanism are evaluated. The activation parameters with respect to slow step of mechanism were computed. The overall mechanistic sequence described here is consistent with product and kinetic studies.

References

[1] M. White, A. Fourney, E. Mikes, F.H.H. Leenen, Am. J. Hypertens. 12 (1999) 151.
[2] D.G. McDevitt, J.K. Nelson, Br. J. Clin. Pharmacol. 6 (1978) 223.
[3] G. Emilien, J.M. Malotcaux, G. Emilion, Eur. J. Clin. Pharmacol. 53 (1998) 389.
[4] C.P. Snook, K. Sigvaldason, J. Kristinsson, J. Toxocol. Clin. Toxicol. 38 (2000) 661.
[5] I.A. Abbasi, S. Sorsby, Clin. Pharmacy 5 (1986) 836.
[6] K.B. Reddy, B. Sethuram, T. Navaneeth Rao, Indian J. Chem. 23A (1984) 593.
[7] A. Kumar, P. Kumar, P. Ramamurthy, Polyhedron 18 (1999) 773.
[8] A. Kumar, Vaishali, P. Ramamurthy, Int. J. Chem. Kinet. 32 (2000) 286.
[9] R.S. Shettar, S.T. Nandibewoor, J. Mol. Cat. A: Chem. 234 (2005) 137.
[10] M.G. RamReddy, B. Sethuram, T. Navaneeth Rao, Indian J. Chem. 16A (1978) 313.
[11] K.D. Karlin, Y. Gultneh, in: S.J. Lippard (Ed.), Progress in Inorganic Chemistry, vol. 35, Wiley, New York, 1997, p. 220.
[12] W.B. Tolman, Acc. Chem. Res. 30 (1997) 227.
[13] E.I. Solomon, P. Chen, M. Metz, S.K. Lee, A.E. Palmer, Angew Chem., Int. Ed. Engl. 40 (2001) 4570.
[14] M.A. Halcrow, Angew Chem., Int. Ed. Engl. 40 (2001) 816.
[15] J. Peisach, P. Alsen, W.E. Bloomberg, The Biochemistry of Copper, Academic Press, New York, 1966. p. 49.
[16] N. Sridevi, J. Padmavathi, K.K.M. Yusuff, Trans. Met. Chem. 26 (2001) 315.
[17] G.C. Hiremath, R.M. Mulla, S.T. Nandibewoor, Catal. Lett. 98 (2004) 49.
[18] Puttaswamy, N. Suresha, Indian J. Chem. 47A (2008) 1649.
[19] T.P. Jose, M.A. Angadi, M.S. Salunke, S.M. Tuwar, Main Group Chem. 7 (2008) 109.
[20] P.K. Jaiswal, K.L. Yadava, Indian J. Chem. 11 (1973) 83.
[21] C.P. Murthy, B. Sethuram, T. Navaneeth Rao, Z. Phys. Chem. 262 (1981) 336.
[22] G.H. Jeffery, J. Bassett, J. Mendham, R.C. Denny, Vogel's Textbook of Quantitative Chemical Analysis, 5th ed., ELBS, Longman, Essex, UK, 1996. p. 455.
[23] G.P. Panigrahi, P.K. Misro, Indian J. Chem. 16A (1978) 201.
[24] F. Feigl, Spot Tests in Organic Analysis, Elsevier, New York, 1975. p. 250.
[25] I.M. Kolthoff, E.J. Meehan, E.M. Carr, J. Am. Chem. Soc. 75 (1953) 1439.
[26] S. Bhattacharya, P. Banerjee, Bull. Chem. Soc. Japan 69 (1996) 3475.
[27] K.B. Reddy, B. Sethuram, T. Navaneeth Rao, Z. Phys. Chem. 268 (1987) 706.
[28] T.S. Kiran, C.V. Hiremath, S.T. Nandibewoor, Appl. Cat. A: Gen. 305 (2006) 79.
[29] B. Sethuram, Some Aspects of Electron Transfer Reactions Involving Organic Molecules, Allied Publishers, New Delhi, 2003. p. 78.
[30] G.C. Hiremath, R.M Mulla, S.T. Nandibewoor, J. Chem. Res. (S) (2005) 197.
[31] C.P. Murthy, B. Sethuram, K.B. Reddy, T. Navaneeth Rao, Indian J. Chem. 23A (1984) 593.
[32] M.W. Lister, Can. J. Chem. 31 (1953) 638.
[33] M. Jaky, M. Szeverenyi, L.I. Simandi, Inorg. Chim. Acta 186 (1991) 33.

[34] R.B. Chougale, G.A. Hiremath, S.T. Nandibewoor, Polish J. Chem. 71 (1997) 1471.
[35] B. Thimmegowda, J. Ishwarabhat, Indian J. Chem. 28A (1989) 43.
[36] D.C. Bilehal, R.M. Kulkarni, S.T. Nandibewoor, Z. Phys. Chem. 217 (2003) 1.
[37] D.C. Hiremath, K.T. Sirsalmath, S.T. Nandibewoor, Catal. Lett. 122 (2008) 144.
[38] K.S. Rangappa, M.P. Raghavendra, D.S. Mahadevappa, D. Channegouda, J. Org. Chem. (1998) 63.
[39] D.C. Bilehal, R.M. Kulkarni, S.T. Nandibewoor, Can. J. Chem. 79 (2001) 1926.
[40] A. Weissberger, E.S. Lewis (Eds.), Investigation of Rates and Mechanism of Reactions in Techniques of Chemistry, Wiley Interscience, New York, 1974. p. 421.
[41] C. Walling, Free Radicals in Solution, Academic Press, New York, 1957. p. 38.
[42] M. Martinez, M.A. Pitarque, R.V. Eldik, J. Chem. Soc., Dalton Trans. (1996) 2665.
[43] S.A. Farokhi, S.T. Nandibewoor, Tetrahedron 59 (2003) 7595.

2.3. Dinuclear Ti(IV) complex **1**

H_4L (0.388 g, 1.0 mmol) was dissolved in 10 mL N,N-dimethylformamide (DMF). To this clear solution *cis*-bis(acetylacetonato)dichloro-titanium(IV), *cis*-[Ti(acac)$_2$Cl$_2$], (0.316 g, 1 mmol) dissolved in 20 mL DMF was slowly added. The color of the solution changed from yellow to orange. The solution was filtered and kept in refrigerator. After 10–15 days the orange colored crystals start separating from the solution. Yield, 57%. M.p: >300 °C (decomp.). *Anal.* Calc. for $C_{70}H_{82}N_8O_{21}Ti_2$: C, 57.30; H, 5.63; N, 7.64. Found: C, 56.80; H, 5.81; N, 7.53%. Selected IR (KBr, cm^{-1}): 3437(s), 3414(s), 1654(s), 1598(s), 1495(w), 1361(s). ^{1}H NMR (DMSO-d$_6$, δ ppm): 8.52 (d, 2H, naph-H), 8.40 (d, 2H, naph-H), 8.14 (d, 2H, naph-H), 7.77 (d, 2H, naph-H), 7.62 (t, 2H, naph-H), 7.52 (d, 2H, naph-H), 7.34 (t, 2H, naph-H), 7.49 (d, 2H, naph-H), 7.01 (t, 2H, naph-H), 6.99 (t, 2H, naph-H), 5.02, 4.79 (s, 4H, Ar–CH$_2$–Ar). ^{13}C NMR (CDCl$_3$, δ ppm): 22.169 (Ar–CH$_2$–Ar), 119.63, 120.55, 121.067, 122.91, 123.28, 124.082, 126.61, 127.40, 128.86, 129.76, 130.78, 131.27, 134.93, 135.52, 159.53, 170.00, 170.93 (Nap-C), 34.47, 35.87, 160.43, 162.77 (DMF-C). Absorption spectral data for **1** in MeOH in terms of λ_{max}/nm (ε/lit mol^{-1} cm^{-1}): 247 (49 690), 263 (44 040), 294 (30 510), 377 (17 800). Single crystals of **1** were obtained from slow evaporation of DMF solution at room temperature.

2.4. Dinuclear Ti(IV) complex **2**

H_4L, 4,4′-methylene-bis(3-hydroxy-2-naphthalene carboxylic acid) (0.388 g, 1.0 mmol) was dissolved in 10 mL DMF. To this clear solution *cis*-bis(acetylacetonato)dichloro-titanium(IV), *cis*-[Ti(acac)$_2$Cl$_2$], (0.316 g, 1 mmol) dissolved in 10 mL DMF was slowly added and the color of the solution changed from yellow to orange. After 1 h of stirring, 4,4′-bipyridine (0.156 g, 1.0 mmol) was added to the reaction mixture and the resulting solution was stirred for 6 h. The solution was then filtered and kept at room temperature. After 10–15 days the orange colored crystals start were obtained from the solution. Yield, 52%. M.p: >300 °C. *Anal.* Calc. for $C_{69}H_{73}N_7O_{20}Ti_2$: C, 58.52; H, 5.20; N, 6.92. Found: C, 58.31; H, 5.19; N, 6.19%. Selected IR (KBr, cm^{-1}): 3435(s), 3043 (s), 1621 (s), 1593(s), 1572(w), 1552(w), 1451(w), 1421(s). ^{1}H NMR (DMSO-d$_6$, δ ppm): 8.79 (d, 4H, 4,4′-BiPy-H), 8.52 (d, 2H, naph-H), 8.40 (d, 2H, naph-H), 8.14 (d, 2H, naph-H), 7.89 (d, 4H, 4,4′-BiPy-H), 7.77 (d, 2H, naph-H), 7.62 (t, 2H, naph-H), 7.52 (d, 2H, naph-H), 7.46 (d, 2H, naph-H) 7.34 (t, 2H, naph-H), 7.01 (t, 2H, naph-H), 6.99 (t, 2H, naph-H), 5.02, 4.79 (s, 4H, Ar–CH$_2$–Ar). ^{13}C NMR (CDCl$_3$, δ ppm): 22.92 (Ar–CH$_2$–Ar), 119.63, 120.55, 121.07, 122.91, 123.28, 124.08, 126.61, 127.40, 128.86, 129.76, 130.78, 131.27, 134.93, 135.52, 158.83, 159.53, 170.00, 170.93 (Nap-C and 4,4′-bipyridine-C), 34.47, 35.87, 160.43, 162.77 (DMF-C). Absorption spectral data for **2** in MeOH in terms of λ_{max}/nm (ε/lit mol^{-1} cm^{-1}): 251(49 540), 264 (46 480), 278 (44 900), 375 (21 690). Single crystals of **2** were obtained by slow evaporation of DMF solution at room temperature.

2.5. Crystallography

Single crystal X-ray diffraction data were collected for H_4L, **1** and **2** on an OXFORD DIFFRACTION XCALIBUR-S CCD system by ω-2θ scan mode and the absorption corrections were applied by using multi-scan method. Preliminary data corresponding to the data collection and refinement are given in Table 1. The structure was solved by direct methods SHELXS97 and refined by full-matrix least squares against F^2 using SHELXL97 software [15]. Non-hydrogen atoms were refined with anisotropic thermal parameters. All hydrogen atoms were geometrically fixed and allowed to refine using a riding model.

3. Results and discussions

3.1. Structure of H_4L

The ligand, H_4L has been synthesized starting from 3-hydroxy-2-naphthoic acid in a single step as reported in the literature [14]

Table 1
Crystal data and structure determination data for H_4L, **1** and **2**.

	H_4L	**1**	**2**
CCDC deposit number	711046	710613	710614
Molecular formula	$C_{23}H_{16}O_6$	$C_{70}H_{82}N_8O_{21}$	$C_{69}H_{73}N_7O_{20}Ti_2$
	H_4L	Ti_2 [(HL)$_2$Ti$_2$(μ-O)	(L)$_2$Ti$_2$(μO)(DMF)$_2$]
		(DMF)$_2$] (DMF)$_6$	(DMF)$_4$(4,4′-bipy-2H)(H$_2$O)
MW	388.36	1467.24	1416.14
Crystal system	monoclinic	triclinic	triclinic
Space group	*C*2/*c*	*P*$\bar{1}$	*P*$\bar{1}$
Z	4	2	2
a (Å)	19.7083(7)	15.4330(16)	15.4892(6)
b (Å)	4.7561(2)	15.820(2)	16.5524(6)
c (Å)	19.0796(7)	17.028(2)	16.8884(7)
α (°)	90	109.524(13)	103.298(3)
β (°)	109.022(4)	107.073(10)	105.685(4)
γ (°)	90	101.910(10)	116.435(4)
V (Å^3)	1690.76(11)	3525.3(8)	3410.6(2)
ρ_{Calc} (g cm^{-3})	1.526	1.382	1.379
Absorption coefficient (mm^{-1})	0.111	0.307	0.314
T (K)	120(2) K	150(2)	150(2) K
λ (Å)	0.71073	0.71073	0.71073
F (0 0 0)	808	1540	1480
Goodness of fit (GOF) (F^2)	1.075	1.096	0.936
Reflections collected/unique	5630/1485	33676/12301	26698/11891
	[R_{int} = 0.0247]	[R_{int} = 0.0396]	[R_{int} = 0.0534]
Data/restraints/parameter	1485/0/140	12301/0/954	11891/0/915
R_1, wR_2 [$I > 2\sigma(I)$]	0.0315, 0.0780	0.0829, 0.2265	0.0532, 0.1217
R_1, wR_2 (all data)	0.0490, 0.0841	0.1054, 0.2381	0.1043, 0.1354
GOF	1.075	1.096	0.936
Largest difference in peak/hole (e Å^{-3})	0.126 and −0.186	2.268 and −0.638	1.344 and −0.372

and the product has been characterized by analytical and spectral methods as given in the experimental. The structure of H_4L has been established by single crystal XRD. It has been crystallized in monoclinic system with *C*2/*c* space group and there is only one half of the molecule in the asymmetric unit. The structure shown in Fig. 1 indicates *anti-like* (*staggered-like*) conformation present in H_4L where in the functional groups are disposed to two different directions, so as the molecule cannot use all its functional groups simultaneously to bind to the same metal ion center. The distances observed between the corresponding atoms of the two pendants, *viz*., O1···O1′ (4.28 Å), C5···C5′ (7.27 Å), O2···O2′ (7.52 Å) and O3···O3′ (9.09 Å) are all indicative of *staggered-like* conformation of the two pendants with respect to the naphthyl moieties (Fig. 1). On the other hand, if the two pendants were to be on the same side, the O1···O1′ distance is expected to be around 3 Å. The inclination angle (C2–C1–C2′) between the two naphthyl moieties was found to be 114.82(0)° and angle between two naphthyl planes was 89.13 (24)°. Crystal structure of H_4L was already known in the literature as DMF adduct [7] where the volume of the unit cell was found to be at least three fold greater when compared to the present one. Though the crystal system was found to be the same in both the cases, the space group was found to be different. Intramolecular dihedral angles (Table 3) between the naphthalene groups were found to be in the same as that observed in the literature [7]. In another report in the literature, the structure of H_4L has been generated from powder X-ray data [12].

In the crystal lattice of H_4L (Fig. 2), each naphthylic-OH is involved in an intramolecular hydrogen bond with the adjacent carboxylic group (O1–H101···O2: 0.968(21), 1.725(19) and 2.623(2) Å, 153.72(6)°) and thus stabilized by two such interactions. Further, such H_4L are connected through intermolecular H-bonds between the neighbor –COOH moieties (O3–H102···O2′: 1.027(23), 1.624(23) and 2.647(2) Å, 175.14(1)°) to result in the formation of supramolecular helical chains as shown in Fig. 2. These hydrogen bonds are reminiscent of the well known benzoic acid dimer in the solid state [16,17]. Thus each H_4L present in the chain is connected through four intermolecular H-bonds, where two were extended from each –COOH moiety. In the lattice, these helices form corrugated sheet structure. These helical chains are further stabilized through weak inter-chain π···π interactions through naphthyl moieties that cuts across the chains where the distance between the two adjacent naphthyl moieties is 4.76 Å.

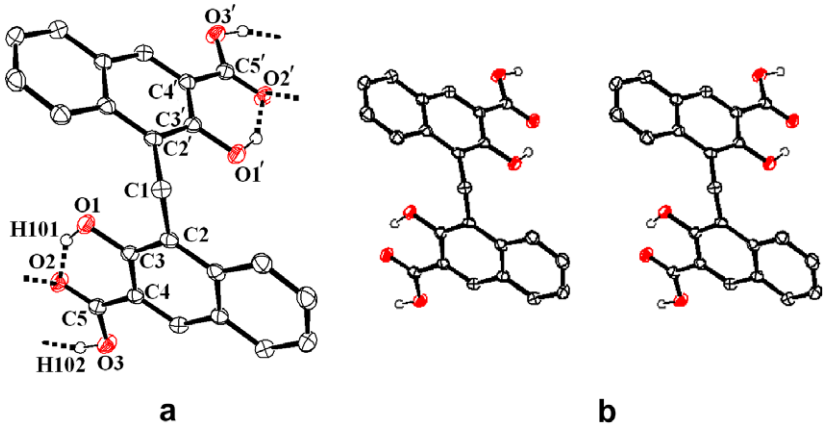


Fig. 1. Crystal structure of H_4L showing 50% ellipsoids: (a) ORTEP picture and (b) stereoview.

Table 2
Selected bond lengths (Å) and angles (°) for the primary co-ordination spheres in **1** and **2**.

	1	**2**		**1**	**2**
Ti–O_{naph}	1.870(4)	1.862(2)	Ti–$O_{\mu\text{-}oxo}$	1.823(4)	1.860(2)
	1.869(3)	1.853(2)		1.801(3)	1.788(2)
	1.872(4)	1.874(2)	Ti–$O_{dmf(o=C)}$	2.067(4)	2.095(2)
	1.883(3)	1.870(2)		2.082(4)	2.080(2)
Ti–$O_{carb(O=C)}$	2.146(4)	2.062(2)	$O_{\mu\text{-}oxo}$–Ti–O_{naph}	95.76(15)	95.55(10)
	2.139(4)	2.158(2)		98.19(16)	98.93(10)
Ti–$O_{carb(O-C)}$	1.982(4)	2.002(2)		97.26(16)	95.90(10)
	1.986(4)	1.988(2)		96.86(15)	98.37(10)
$O_{\mu\text{-}oxo}$–Ti–$O_{carb(O=C)}$	176.21(15)	171.09(10)	O_{naph}–Ti–$O_{carb(O-C)}$	85.64(15)	85.51(10)
	175.50(16)	176.43(10)		164.33(15)	167.49(10)
$O_{\mu\text{-}oxo}$–Ti–$O_{carb(O-C)}$	97.27(16)	96.43(10)		86.01(15)	85.48(10)
	96.33(15)	95.72(10)		166.14(15)	165.19(10)
$O_{\mu\text{-}oxo}$–Ti–O_{dmf}	90.11(16)	88.50(10)	O_{naph}–Ti–O_{dmf}	168.43(15)	167.84(10)
	93.06(16)	95.45(10)		93.70(15)	95.63(10)
O_{naph}–Ti–O_{naph}	95.32(15)	95.36(10)		165.71(16)	164.10(10)
	96.51(15)	94.48(10)		92.02(15)	91.09(10)
O_{naph}–Ti–$O_{carb(O=C)}$	88.03(15)	93.35(10)	O_{dmf}–Ti–$O_{carb(O=C)}$	86.18(15)	82.88(10)
	81.34(14)	82.80(10)		85.06(14)	81.00(9)
	87.09(15)	80.84(9)	O_{dmf}–Ti–$O_{carb(O-C)}$	83.72(15)	82.64(9)
	81.47(14)	85.19(10)		83.04(15)	85.36(10)
$O_{carb(O=C)}$–Ti–$O_{carb(O-C)}$	83.07(14)	84.69(9)			
	85.06(14)	84.40(9)			

naph = naphthyl; carb = carboxylic; dmf = N,N –dimethylformamide.

Table 3
Selected dihedral angles (°) in H_4L, **1** and **2** based on single crystal XRD structures.

Dihedral angle	H_4L	1	2
C2′–C1–C2–C3	−60.49(10)		
C2′–C1–C2–C12	121.53(13)		
C9–C10–C12–C14		67.01	−127.76
C10–C12–C14–C13		49.08	−115.64
C10–C12–C14–C15		−135.31	62.39
C11–C10–C12–C14		−112.58	54.15
C32–C33–C35–C36		66.57	−136.82
C33–C35–C36–C37		59.90	−111.37
C33–C35–C36–C38		−127.05	71.16
C34–C33–C35–C36		−115.84	48.90

Due to the presence of lattice solvent molecules, such supramolecular chain could not be formed in case of structure reported in the literature [7], though the powder diffraction data revealed the formation of such chain structure [12].

3.2. Complexation with Ti(IV)

As reported earlier by us, the reaction of *cis*-$[TiCl_2(acac)_2]$ with a variety of hydroxy-containing ligands in 1:1 mole ratio, resulted only in the formation of mononuclear complexes [18]. On the contrary, in the present case, when one equivalent of H_4L was reacted with one equivalent of *cis*-$[TiCl_2(acac)_2]$ in DMF, it resulted in the formation of oxo-bridged dinuclear titanium(IV) complex wherein the crystals isolated from this reaction exhibited a composition, *viz.*, $[(HL)_2Ti_2(\mu\text{-}O)(DMF)_2]\cdot(DMF)_6$ for **1**. When the same reaction was carried out in the presence of one equivalent of co-ligand, *viz.*, 4,4′-bipyridine, the product **2** obtained from this reaction resulted in crystals having a composition, $[(L)_2Ti_2(\mu\text{-}O)(DMF)_2]\cdot(DMF)_4(4,4'\text{-Bipy-}2H)(H_2O)$. The structural details of **1** and **2**, and their similarities and differences are discussed later in this paper. On the other hand, both **1** and **2** were characterized by spectral and analytical techniques.

3.3. Characterization of *1* and *2*

On going from H_4L to **1** and **2**, the ν_{OH} vibration that appears around 3300 cm^{-1} in H_4L disappears completely, suggesting the binding of naphthylic-OH group to Ti(IV) via deprotonation. A sharp peak arising from $\nu_{C=O}$ at 1659 cm^{-1} shows 10–40 cm^{-1} shift to lower frequency, *viz.*, 1621–1650 cm^{-1}, upon co-ordination to Ti(IV) suggesting the binding of carboxylate moiety. The IR spectrum of **1** and **2** shows asymmetric (1621–1654 cm^{-1}) and symmetric (~1450 and ~1420 cm^{-1}) stretching bands indicating the mono-dentate co-ordination nature of the carboxylate moiety in these complexes. The absorption spectrum of the complexes shows characteristic differences from that of the ligand (H_4L) by exhibiting ligand to metal charge transfer transition bands (Fig. 3, experimental) in solution. The main band observed at 374 nm for H_4L in solution was shifted to 424 nm, while the width of the band was doubled in the solid state. There is no considerable shift observed in this band in solution on going from H_4L to **1** to **2**, however, a substantial shift was observed in this band position in the solid state which moves from 424 to 469 to 495 nm, respectively and the peak widths increase dramatically.

H_4L shows strong fluorescence emission ~500 nm upon exciting the sample at 385 nm whereas the fluorescence intensity was quenched almost completely in **1** and **2** (Fig. 4a and b). In order to find whether this quenching is because of the formation of anion or otherwise, the fluorescence of pamoic acid (H_4L) was measured in NaOH and found enhancement of the fluorescence intensity. Thus the fluorescence quenching in **1** and **2** may be attributed to the binding to Ti(IV) followed by relative orientation of the naphthyl moieties which are inturn responsible for the fluorescence

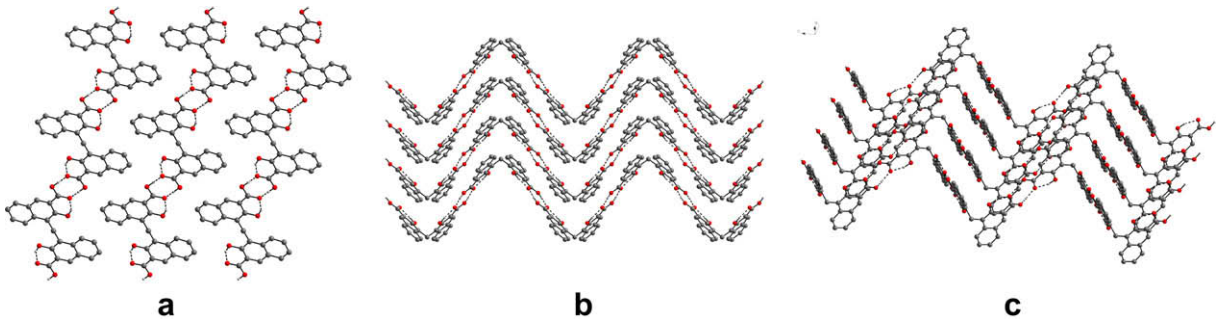


Fig. 2. Lattice structure of H_4L: (a) viewed along *b*-axis, (b) viewed along *a*-axis and (c) viewed along slightly rotated *a*-axis.

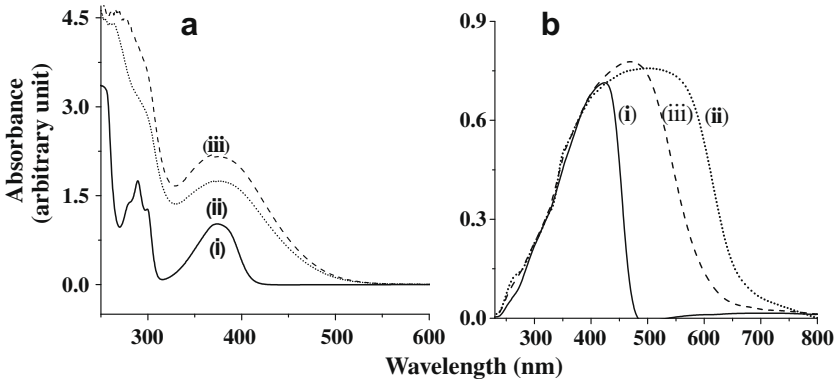


Fig. 3. (a) Absorption spectra measured in DMSO/methanol: (i) H_4L, 0.1 mM; (ii) **1**, 0.1 mM, and (iii) **2**, 0.1 mM. (b) Diffuse reflectance UV–Vis spectra (DRUV): (i) H_4L, (ii) **1** and (iii) **2**.

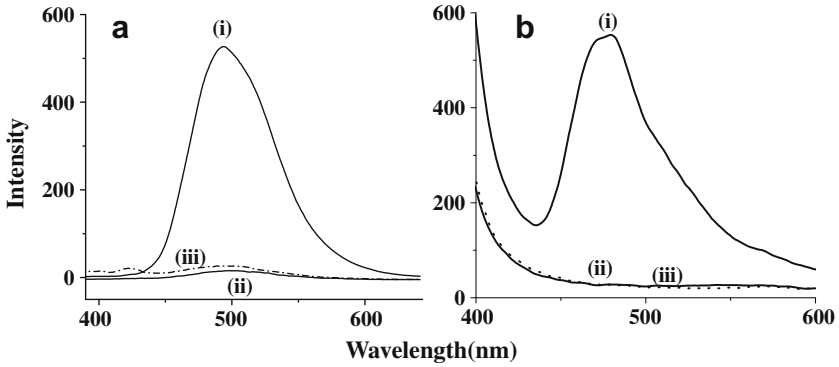


Fig. 4. (a) Fluorescence spectra measured in DMF: (i) H_4L, 1 mM, (ii) **1**, 1 mM and (iii) **2**, 1.mM. (b) Solid state emission spectra upon excitation at 370 nm: (i) H_4L, (ii) **1**, and (iii) **2**.

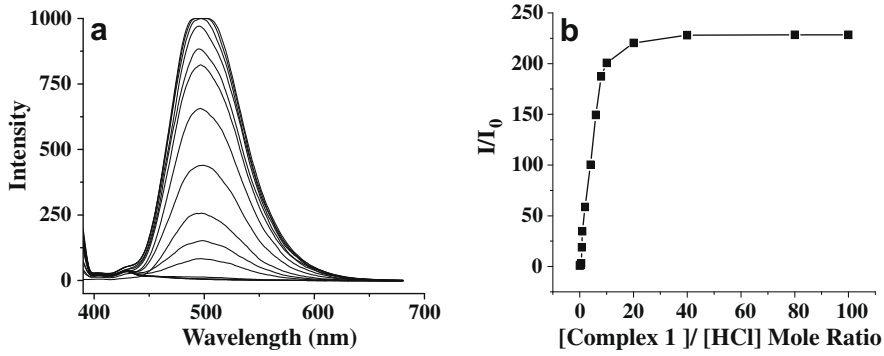


Fig. 5. (a) Fluorescence spectral traces obtained during the titration of **1** with HCl with varying mole ratios of HCl to a maximum of 100 mole equiv., (b) Plot of relative fluorescence intensity (I/I_o) vs. [HCl]/[**1**] mole ratio in the titration of **1** with HCl, at varying concentrations of HCl.

emission. This has been found to be true both in the solution as well as in their solid states.

The complexation in **1** has been further supported by titrating this with HCl and measuring their fluorescence spectra. The titration resulted in an increase of fluorescence as a function of addition of HCl to **1** suggesting the release of the ligand from the complex upon reacting with HCl (Fig. 5). Similar results were observed when **2** was titrated with HCl.

The TGA curves for H_4L, **1** and **2** in the temperature range of 30–1000 °C as measured in N_2 atmosphere are shown in Fig. 6. The weight loss behavior of H_4L can be broken into three parts, one in 255–375 °C (~68%), the second in 375–450 °C (~5%) and the third in 450–1000 °C (~10%) and about 15–17% accounts for residual mass even at 1000 °C, thus indicating the major weight loss being below 400 °C. On the other hand, both **1** and **2** exhibit at least five weight losses under the same conditions. In the entire temperature range, the weight loss observed with **1** is higher than **2**. Within 300 °C the weight loss in case of **1** is ~38% and in **2** it is about ~32%, both accounting the solvent present in their crystals either as bound to metal ion or as loosely present in the lattice. Both **1** and **2** exhibited high residual mass when compared to the ligand as expected owing to the formation of titanium oxides. The residual mass follows a trend, *viz.*, **2** (34%) > **1** (28%) > H_4L (18%) indicating that **2** possessing the protonated 4,4′-bipyridyl needs higher temperature for decomposition.

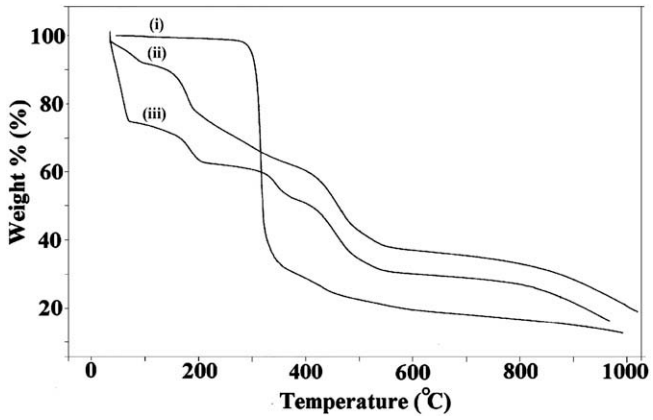


Fig. 6. TGA curves for H_4L and complexes: (i) H_4L, (ii) **2** and (iii) **1**.

3.4. Molecular structures

Both **1** and **2** were crystallized in triclinic crystal system with $P\bar{1}$ space group. The bond lengths and bond angles covering the primary co-ordination sphere are given in Table 2. In **1**, the asymmetric unit contains a dinuclear $[(HL)_2Ti_2(\mu\text{-}O)(DMF)_2]$ moiety besides six unbound DMF molecules whereas in **2**, the asymmetric unit contains a dinuclear $[(L)_2Ti_2(\mu\text{-}O)(DMF)_2]$ moiety besides four unbound DMF molecules, one water molecule and one half of the molecule of protonated 4,4′-bipyridine. In both the cases the metal ion to the ligand ratio is 1:1 with the presence of a 2:2 μ-oxo dinuclear Ti(IV), wherein the molecular structures differ between **1** and **2**.

In **1**, the ligand acts as trinegative through deprotonation of both the naphthylic-OH groups and one of the carboxylic moiety ($H_4L–3H^+ = HL$) but as tetradentate wherein the each half-portions of the pamoic acid binds to one Ti(IV) center as bidentate, thus bridging between the two titanium centers connected by a

μ-oxo moiety to result in a neutral complex species (Fig. 7). In order that each pamoic acid is able to bind to the dinculear Ti(IV) center, the molecule must undergo conformational changes since the functional moieties present on two-halves of the pamoic acids are oriented *trans-like* fashion in the free ligand. The dihedral angles that determines the orientation of the two naphthylic-OH groups of the pamoic acid change from −60.4° and −60.4° in free ligand to 49.11° to 59.90° and −112.58° to −115.85° and brings the naphthylic-OH groups from 4.280 Å to 3.037 Å (Table 3). As a result of these changes, the two-half portions of the pamoic acid orient in such a way that these can simultaneously bind to a dinuclear moiety as seen in case of **1**. However, the structures reported in the literature were polymeric through metal ion complexation and in such cases dihedral changes are not required [5–10].

Another major difference that one finds between **1** and those published in literature is that the involvement of both the naphthylic-OH as well as the carboxylic moieties in the present case, where as it is mainly through carboxylic in case of the reported ones [5–10], owing to their polymeric nature. Among the two carboxylic groups present on the pamoic acid, one of it binds as C–O$^-$ and the other binds through the C=O (Table 4). In **1**, both the titanium centers are co-ordinatively equivalent by exhibiting octahedral geometry wherein each of the pamoic acid moiety extends two of its oxygen centers for binding. The remaining two co-ordinations are filled by a μ-oxo and a DMF. The naphthylic-O$^-$ binds always trans to the carboxylate binding at both the Ti(IV) centers. The charge state of each of these groups, *viz*., naphthylic-OH versus naphthylic-O$^-$ and the –COOH versus –COO$^-$, can also be supported by comparing the metric parameters. In the primary co-ordination sphere (Table 2), while the Ti···O distances vary between 1.801 and 2.146 Å, the trans-angles vary between 164.3° and 176.2°, indicating highly distorted octahedral Ti(IV) centers in **1**. The bond length of Ti···O of the carboxylate moieties is shorter by 0.016 Å when it is bonded through the C–O$^-$ rather than the C=O of the carboxylate moiety and thereby indicate the charge state of this moiety in the complex. Thus the Ti···O distances

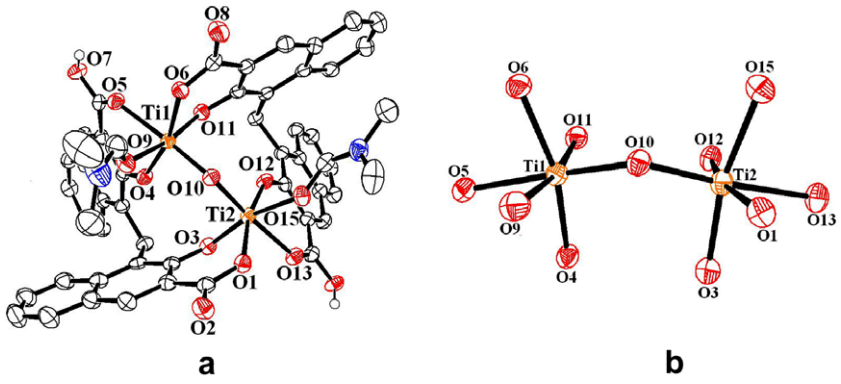


Fig. 7. (a) ORTEP diagram of the dimeric unit present in case of **1** and (b) ORTEP diagram of the metal ion core of **1** showing 50% ellipsoids.

Table 4
The C–O bond lengths (Å) in H_4L, **1** and **2**.

	H_4L	**1**	**2**		H_4L	**1**	**2**
C–O_{naph}	1.364(1)	1.348(6)	1.338(4)	C–O_{carb}	1.316(3)	1.223(6)	1.256(4)
		1.334(6)	1.341(4)			1.236(6)	1.300(4)
		1.334(6)	1.337(4)			1.221(6)	1.312(4)
		1.342(6)	1.341(4)			1.239(6)	1.299(4)
C=O_{carb}	1.242(2)	1.223(6)	1.278(4)	C=O_{dmf}		1.232(7)	1.256(5)
		1.236(6)	1.232(4)			1.243(7)	1.261(4)
		1.221(6)	1.236(4)				
		1.239(6)	1.235(4)				

naph = naphthyl; carb = carboxylic; dmf = N,N –dimethylformamide.

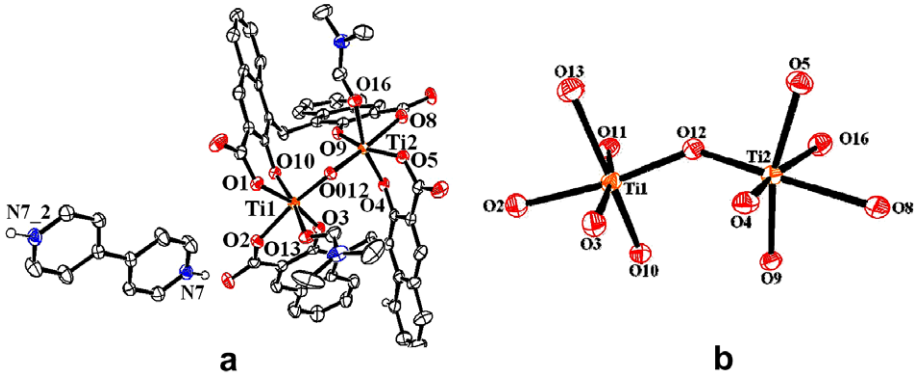


Fig. 8. (a) ORTEP diagram of the dimeric unit present in case of **2** and (b) ORTEP diagram of the metal ion core of **2** showing 50% ellipsoids.

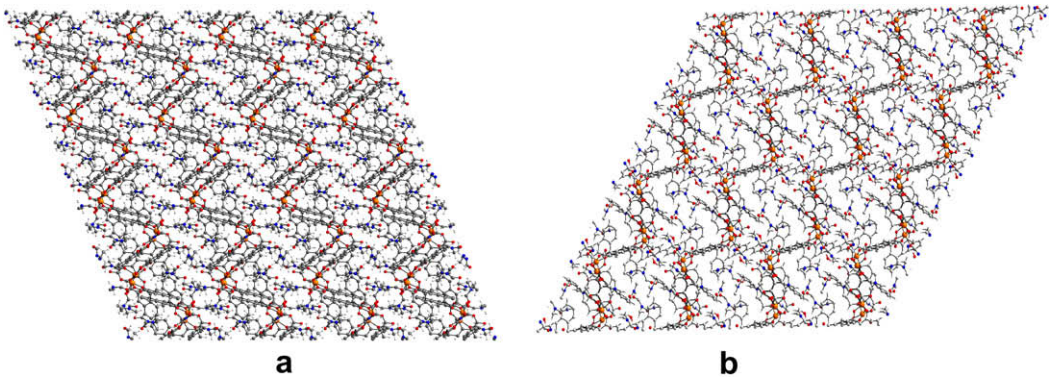


Fig. 9. Lattice structures: (a) **1** and (b) **2**.

follow an order, *viz.*, Ti···O=C > Ti···O–C > Ti···O_{naph}. Even the shorter Ti···O bond observed with DMF (2.07 Å) when compared to the O=C moiety of pamoic acid (2.15 Å) can be attributed to the involvement of nitrogen lone pair present in DMF. Average distance observed for C=O (1.23 Å) is short enough when compared to C–O (1.34 Å) to differentiate the two portions of the carboxylic moiety present in pamoic acid in **1**. The intra-naphthyl inclination angles in any pamoic acid moiety changes between 0° and 10° upon complexation as observed in **1**.

In **2**, the ligand acts as tetranegative through deprotonation of all the naphthylic-OH as well as carboxylic groups ($H_4L–4H^+ = L$), while it is trinegative in **1**, bound across the dinuclear Ti(IV)–O–Ti(IV) unit resulting in an overall di-anionic complex species (Fig. 8). The ionic nature of **2** has been cross checked by measuring the conductance that favors a 1:1 electrolyte. The charge on this anionic species has been neutralized by the di-protonated 4,4′-bipy found in the structure of **2**. Otherwise, the binding features of both the pamoic acid moieties in **2** are same as that noticed in the structure **1**. The orientation of both the naphthyl moieties of the pamoic acid present in **2** has almost same dihedral angles as that observed in case of **1** and hence resulted in $O_{naph}···O_{naph}$ distance of 2.98 Å exhibiting a syn-like orientation. The binding nature of the carboxylate moieties in **2** remains same as that observed in **1**. Binding as well as the metric parameters of the dinuclear Ti(IV) core in **2** is similar to that observed in **1**. In the dinuclear cores, the two titanium centers were separated by 3.408(15) and 3.416(6) Å in **1** and **2**, respectively, indicating no possibility of interaction between the metal centers as no interaction is expected between the two Ti(IV) centers of d^0 nature.

Table 5
Hydrogen bonds (Å, °) **1** and **2**.

D–H···A	D–H (Å)	A···H (Å)	D–A (Å)	D–H···A (°)
*For **1***				
O7–H07···O18	0.937(0.087)	1.661(.102)	2.511(.005)	148.94(9.46)
O14–H104···O17	0.870(.076)	1.673(.077)	2.535(.007)	170.36(7.31)
C63–H63B···O18	0.980(.011)	2.358(.005)	3.295(.013)	159.76(0.70)
C69–H69C···O2	0.980(.010)	2.371(.005)	3.243(.011)	147.86(0.60)
C70–H70B···O2	0.980(.012)	2.528(.004)	3.381(.012)	145.41(0.64)
C57–H57B···O8	0.980(.005)	2.508(.003)	3.413(.006)	153.45(0.39)
C48–H48B···O10	0.980(.007)	2.556(.003)	3.373(.006)	140.75(0.48)
C51–H51B···O19	0.980(.013)	2.508(.011)	3.482(.017)	172.49(0.75)
C57–H57C···O21	0.980(.007)	2.552(.010)	3.372(.012)	141.16(0.42)
C58–H58B···O21	0.980(.008)	2.501(.008)	3.417(.011)	155.43(0.49)
C68–H68B···O21	0.950(.007)	2.435(.008)	3.343(.011)	159.82(0.61)
*For **2***				
N7–H7N···O1	0.949(.059)	1.649(.059)	2.581(.006)	166.48(4.89)
O111–H111···O6	0.886(.040)	1.954(.047)	2.821(.004)	165.55(4.96)
O111–H222···O12	0.823(.052)	1.946(.052)	2.768(.005)	177.42(5.52)
C65–H65···O11	0.950(.005)	2.412(.003)	3.351(.006)	169.92(0.30)
C48–H48C···O012	0.980(.006)	2.541(.003)	3.512(.007)	171.08(0.33)
C18–H18···O14	0.950(.004)	2.704(.005)	3.529(.007)	145.52(0.36)
C49–H49B···O5	0.980(.006)	2.534(.003)	3.467(.007)	159.03(0.35)
C48–H48B···O15	0.980(.006)	2.559(.006)	3.515(.008)	165.09(0.38)
C30–H30···O111	0.950(.004)	2.698(.003)	3.520(.004)	145.20(0.25)
C29–H29···O18	0.950(.004)	2.647(.004)	3.504(.006)	150.17(0.29)
C41–H41···O1	0.950(.005)	2.784(.002)	3.479(.004)	130.79(0.31)
C58–H58A···O15	0.980(.006)	2.384(.006)	3.217(.008)	142.46(0.31)
C53–H53···O12	0.950(.007)	2.689(.004)	3.527(.008)	147.42(0.42)
C52–H52C···O2	0.980(.007)	2.733(.002)	3.533(.006)	139.23(0.44)
C59–H59···O8	0.950(.005)	2.281(.002)	2.999(.005)	131.84(0.25)
C59–H59···O5	0.950(.005)	2.699(.003)	3.548(.006)	149.21(0.29)
C66–H66···O111	0.950(.006)	2.453(.005)	3.388(.007)	168.23(0.33)
C68–H68···O111	0.950(.005)	2.539(.004)	3.473(.006)	167.75(0.27)
C69–H69···O18	0.950(.006)	2.162(.005)	3.084(.008)	163.22(0.34)

3.5. Lattice structures

The lattice structures of **1** and **2** are rather similar in spite of varying solvation in both the cases (Fig. 9). While there are six DMF molecules present per dimer unit in the lattice of **1**, there are four DMF, one water and one di-protonated-4,4′-bipy present per dimer in case of **2**. The dimeric Ti(IV) units stack in the lattice to form columns that exhibit corrugated sheet structures wherein the columns can be described as formed by ABABAB... type repetitivity, where as the immediate adjacent chain runs as BABABA... type. The space between the adjacent columns is being filled by the solvent molecules in **1** and solvent plus the protonated 4,4′-bipy in the lattice of **2**. Thus the neighbor columns interact through weak hydrogen bonds extended by the solvent molecules present between the columns. These hydrogen bonds are extended through the free oxygens of the bound ligand moiety, DMF oxygen and the protonated N–H of 4,4′-bipy as in **2**. This resulted in O–H···O, N–H···O and C–H···O type of hydrogen bonds. List of such hydrogen bond interactions including those of weak type are given in Table 5 for **1** as well as **2**. Within each corrugated chain, the dinuclear Ti(IV) centers are separated by ~13 Å in both the cases. The two nearest dinuclear neighbors present in the adjacent columns are separated by ~9.0 and ~15.0 Å.

4. Conclusions

The ligand, H_4L and complexes **1** and **2** have been synthesized and characterized by analytical and spectral methods and the structures have been established by single crystal XRD. Unlike the reported polymeric structures observed in case of pamoic acid, in the present paper we demonstrate that the anti-conformation of H_4L changes to syn-orientation to avoid poly-metallic complex formation, as noticed in **1** and **2**. Thus, to our knowledge, only **1** and **2** are the first non-polymeric structures to be reported for pamoic acid. The dimeric Ti(IV) units stack in the lattice to form helical col-

umns and the space between the adjacent columns is being filled by the solvent molecules in **1** and solvent plus the protonated 4,4′-bipy in the lattice of **2** and thus the neighbor columns are connected through weak interactions. The presence of protonated 4,4′-bipy in the lattice of **2** was further confirmed by the conductivity experiments. However, the presence of 4, 4′-bipy could not prevent the formation of dinuclear species, but it could bring some changes in the co-ordination characteristics of the pamoic acid moiety, yet maintaining the helical structure.

Supplementary data

CCDC 711046, 710613 and 710614 contains the supplementary crystallographic data for H4L, **1** and **2**. These data can be obtained free of charge via http://www.ccdc.cam.ac.uk/conts/retrieving.html, or from the Cambridge Crystallographic Data Centre, 12 Union Road, Cambridge CB2 1EZ, UK; fax: (+44) 1223-336-033; or e-mail: deposit@ccdc.cam.ac.uk.

Acknowledgements

CPR acknowledges the financial support by DST, CSIR and DAE. GSB acknowledge CSIR, New Delhi for fellowship. We thank Mr. Shaikh M. Mobin for helping with the diffraction data.

References

[1] Z. Fei, A.M.Z. Slawin, J.D. Woollins, Polyhedron 20 (2001) 3355.
[2] D.A. Haynes, J. Van de Streek, J.C. Burley, W. Jones, W.D. Sam Motherwell, Acta Crystallogr., Sect. E E62 (2006) 1170.
[3] T.M. Shang, Q.F. Zhou, J.H. Sun, Acta Crystallogr., Sect. E E63 (2007) 506.
[4] Y.Y. Liu, J.F. Ma, Y.P. Xie, Acta Crystallogr., Sect. E E62 (2006) 3786.
[5] D.A. Haynes, W. Jones, W.D. Samuel Motherwell, Cryst. Eng. Commun. 7 (2005) 538.
[6] J.-J. Wang, M.-L. Yang, H.-M. Hu, G.-L. Xue, D.-S. Li, Q.-Z. Shi, Inorg. Chem. Commun. 10 (2007) 269.
[7] M. Du, C.-P. Li, X.-J. Zhao, Q. Yu, Cryst. Eng. Commun. 9 (2007) 1011.
[8] Q. Zhang, Z. Fei, A.M.Z. Slawin, J.D. Woollins, Main Group Chem. 4 (2005) 145.
[9] Q. Shi, Y. Sun, L. Sheng, K. Ma, M. Hu, X. Hu, S. Huang, Cryst. Growth Des. 8 (2008) 3401.
[10] F. Luo, Y.-T. Yang, Y.-X. Che, J.-M. Zheng, Cryst. Eng. Commun. 10 (2008) 981.
[11] A.C. Blackburn, A.J. Dobson, R.E. Gerkin, Acta Crystallogr., Sect. C: Cryst. Struct. Commun. C52 (1996) 1269.
[12] D.A. Haynes, J. Van de Streek, J.C. Burley, W. Jones, W.D. Sam Motherwell, Acta Crystallogr., Sect. E E62 (2006) 1170.
[13] E. Casassas, A. Izquierdo-Ridorsa, Polyhedron 9 (1990) 1191.
[14] N. Kondekar, S.P. Potnis, Ind. Eng. Chem. Prod. Res. Develop 12 (1973) 135.
[15] G.M. Sheldrick SHELX-97, A Program for Crystal Structure Solution and Refinement, Release 97-2, University of Goettingen, Germany, 1997.
[16] M.R. Johnson, H.P. Trommsdorff, Chem. Phys. Lett. 364 (2002) 34.
[17] X. Holmbäck, Influence of the Drowning-Out Processing Conditions on the Size and Shape of Benzoic Acid Crystals, Royal Institute of Technology, Stockholm, Sweden, 2002. p. 36.
[18] P.V. Rao, C.P. Rao, E.K. Wegelius, E. Kolehmainen, K. Rissanen, J. Chem. Soc., Dalton Trans. (1999) 4469.

$$\text{1-HOCR}_2\text{-2-NMe}_2\text{C}_6\text{H}_4 \xrightarrow{\text{ZnCl}_2} [\text{ZnCl}_2(\text{THF})\{\text{1-HOCR}_2\text{-2-NMe}_2\text{C}_6\text{H}_4\}]$$

$$[\text{R} = \text{Ph}\ (\mathbf{4}),\ \text{R} = \text{C}_6\text{H}_{11}\ (\mathbf{5})]$$

$$\text{1-HOCPh}_2\text{CH}_2\text{-2-NMe}_2\text{C}_6\text{H}_4 \xrightarrow{\text{ZnCl}_2} [\text{ZnCl}_2(\text{THF})\{\text{1-HOCPh}_2\text{CH}_2\text{-2-NMe}_2\text{C}_6\text{H}_4\}]\ (\mathbf{6})$$

Scheme 1. Preparation of **4**–**6**.

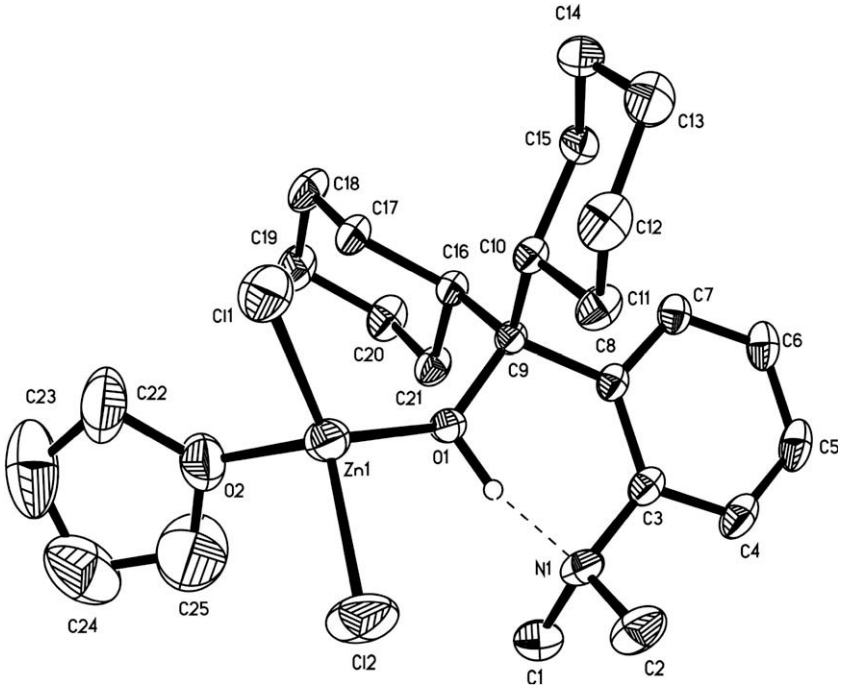


Fig. 1. Molecular structure of **5** showing the atom numbering scheme employed (ORTEP, 50% probability, SHELXTL-PLUS; XP) [18]. Hydrogen atoms (other than O–H) are omitted for clarity.

Table 1
Selected bond lengths (Å) and bond angles (°) for **5**.

Zn(1)–O(1)	1.973(1)	O(1)–Zn(1)–Cl(1)	123.44(4)
Zn(1)–O(THF)$_{av.}$	2.058(2)	O(THF)–Zn(1)–Cl(1)$_{av.}$	102.3(3)
Zn(1)–Cl(1)	2.1949(6)	O(1)–Zn(1)–Cl(2)	98.91(4)
Zn(1)–Cl(2)	2.2092(7)	O(THF)–Zn(1)–Cl(2)$_{av.}$	104.1(4)
Cl(1)–Zn(1)–Cl(2)	122.62(4)	O(1)–Zn(1)–O(THF)$_{av.}$	102.6(6)

$(CH_2OH)C_5H_4N)]$ [2.123(3) Å], and similar to those found in {*N*,*N*′-bis[1-(2-hydroxy-4-methoxyphenyl)ethylidene]ethylenediamine-κ^2O,O'}dichlorozinc(II) [1.975(5) Å] [7]. The Zn–Cl bond lengths (Table 1) are in the same range and comparable to those found in $[ZnCl_2(C_{10}H_{12}NO_2)_2]$ [2.219(2)–2.233(2) Å] [7] and $[ZnCl_2$(8-(diphenylphosphino)quinoline] [2.218(2) and 2.201(2) Å] [17].

The non-involvement of the NMe_2 nitrogen atom in zinc coordination seems to be due to two combined factors: the better donor quality of the THF molecule, and the strong intramolecular O(1)–H(9)···N(1) hydrogen bond [O–H 0.94(3) Å, H···N 1.55(3) Å, O···N 2.464(2) Å, O–H–N 160(3)°]. The intramolecular O(1)–H(9)···N(1) hydrogen bond of **5** is stronger than that in the free ligand **2** [O–H 0.92(2) Å, N···H 1.73(2) Å, N···O 2.591(1) Å, N–H···O 155(2)°] [12]. The bond lengths and angles of the organic fragment of **5** are similar to those observed for the corresponding free ligand **2** [12].

3. Experimental

All experiments were carried out under purified dry nitrogen. Solvents were dried and freshly distilled under nitrogen [19]. The NMR spectra were recorded with an AVANCE DRX 400 spectrometer (Bruker). Chemical shifts for ^1H and ^{13}C NMR spectra are reported in parts per million (ppm) at 400.13 MHz and 100.63 MHz with tetramethylsilane as external standard. Elemental analyses were determined with a VARIO EL (Heraeus). Melting points (Gallenkamp) are uncorrected. Mass spectra were recorded with an MAT-8230 (EI-MS, 70 eV). 1-$HOCPh_2$-2-$NMe_2C_6H_4$ (**1**) [11,12], 1-$HOC(C_6H_{11})_2$-2-$NMe_2C_6H_4$ (**2**) [12], and 1-$HOCPh_2CH_2$-2-$NMe_2C_6H_4$ (**3**) [12,13] were prepared by literature procedures.

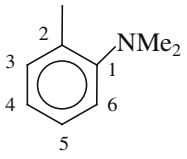
3.1. Preparation of $[ZnCl_2(THF)\{1\text{-}HOCPh_2\text{-}2\text{-}NMe_2C_6H_4\}]$ (**4**)

A 150 ml Schlenk flask was charged with 1-$HOCPh_2$-2-$NMe_2C_6H_4$ (**1**) (0.48 g, 1.6 mmol) and tetrahydrofuran (50 ml). Then $ZnCl_2$ (0.22 g, 1.6 mmol) was added at room temperature. The solution was stirred for about 3 h. The remaining solid was then removed by filtration and the solution was concentrated to give the product in 94% yield. Mp. 177–178 °C. ^1H NMR (DMSO, δ/ppm): 1.76 (m, 4H, CH_2 (THF)), 3.44 (s, 6H, $N(CH_3)_2$), 3.60 (m, 4H, CH_2O (THF)), 6.56–7.54 (m, vbr, 14H, C_6H_4 and C_6H_5), 9.75 (s, 1H, OH). $^{13}C\{^1H\}$ NMR (DMSO, δ/ppm): 21.0 (THF), 45.1 ($N(CH_3)_2$), 67.0 (THF), 82.3 (C–O), 124.3 (s, C6 in C_6H_4), 125.2 (s, C4 in C_6H_4), 126.9 (s, C3 in C_6H_4), 127.8 (s, C5 in C_6H_4), 128.6 (s, *p*-C in C_6H_5), 129.5 (s, *o*-C in C_6H_5), 139.0 (s, *m*-C in C_6H_5), 142.3 (s, C2 in C_6H_4), 147.5 (s, C1 in C_6H_4), 152.0 (s, *ipso*-C in C_6H_5). MS: *m/z* 303.4 (M^+-$ZnCl_2$-THF). Found: C, 58.64; H, 5.69; N, 2.72%. Calcd. for $C_{25}H_{29}Cl_2NO_2Zn$ (511.80): C, 58.67; H, 5.71; N, 2.74%.

Table 2
Crystal data and structure refinement for **5**.

Formula	$C_{25}H_{41}Cl_2NO_2Zn$	Z	2
Formula weight	523.86	D_{calcd} (g cm^{-1})	1.316
Temperature (K)	298(2)	F(0 0 0)	556
Crystal system	Triclinic	Crystal size (mm)	0.60 × 0.50 × 0.40
Space group	$P\bar{1}$	Absorption coefficient (mm^{-1})	1.152
a (Å)	8.9841(7)	Number of reflections collected	12485
b (Å)	9.5300(7)	Number of independent reflections	6197
c (Å)	16.838(1)	R_{int}	0.0231
α (°)	81.206(2)	Number of parameters	459
β (°)	85.350(1)	R_1 ($I > 2\sigma(I)$)	0.0381
γ (°)	68.180(1)	wR_2 (all data)	0.1136
V (Å^3)	1322.1(2)	$(\Delta/\rho)_{min}$ (e Å^{-3})	0.497
Deposition number	194 393	$(\Delta/\rho)_{max}$ (e Å^{-3})	−0.406

Phenylene ring numbering scheme:



3.2. Preparation of [$ZnCl_2$(THF){1-HOCCy$_2$-2-NMe$_2$C$_6$H$_4$}] (**5**)

A similar procedure to that described for **4** was used here, except 1-HOC(C_6H_{11})$_2$-2-NMe$_2$C$_6$H$_4$ (**2**) (0.51, 1.6 mmol) was employed instead of **1** and colorless crystals were obtained from tetrahydrofuran at 20 °C in 80% yield. Mp. 170–172 °C. ^{1}H NMR (DMSO, δ/ppm): 0.69–1.73 (vbr, 22H, C_6H_{11}), 1.77 (m, 4H, CH_2 (THF)), 3.38 (s, 6H, N(CH_3)$_2$), 3.61 (m, 4H, CH_2O (THF)), 10.31 (s, 1H, OH), 7.04–7.39 (m, 4H, C_6H_4). ^{13}C {^{1}H} NMR (DMSO, δ/ppm): 21.0 (THF), 26.4 (s, C4 in C_6H_{11}), 29.2 (s, C3/C5 in C_6H_{11}), 30.4 (s, C2/C6 in C_6H_{11}), 45.8 (s, C1 in C_6H_{11}), 46.4 (N(CH_3)$_2$), 67.0 (THF), 83.2 (C–O), 124.5 (s, C6 in C_6H_4), 125.4 (s, C4 in C_6H_4), 126.1 (s, C3 in C_6H_4), 127.3 (s, C5 in C_6H_4), 137.8 (s, C2 in C_6H_4), 153.3 (s, C1 in C_6H_4). MS: m/z 315.6 (M^+-$ZnCl_2$-THF). Found: C, 57.10; H, 7.87; N, 2.66%. Calcd. for $C_{25}H_{41}Cl_2NO_2Zn$ (523.89): C, 57.32; H, 7.89; N, 2.67%.

3.3. Preparation of [$ZnCl_2$(THF){1-HOCPh$_2$CH$_2$-2-NMe$_2$C$_6$H$_4$}] (**6**)

A similar procedure to that described for **4** was used here, except 1-HOCPh$_2$CH$_2$-2-NMe$_2$C$_6$H$_4$ (**3**) (0.51, 1.6 mmol) was employed instead of **1** and the product was obtained from tetrahydrofuran at 20 °C in 80% yield. Mp. 190–192 °C. ^{1}H NMR (DMSO, δ/ppm): 1.77 (m, 4H, CH_2 (THF)), 2.49 (s, 6H, N(CH_3)$_2$), 3.61 (m, 4H, CH_2O (THF)), 3.73 (s, 2H, CH_2), 7.14 (s, 1H, OH), 7.16–7.45 (m, vbr, 14H, C_6H_4 and C_6H_5). ^{13}C {^{1}H} NMR (DMSO, δ/ppm): 21.0 (THF), 44.7 (CH_2), 45.0 (N(CH_3)$_2$), 67.0 (THF), 77.0 (C–O), 124.5 (s, C6 in C_6H_4), 125.4 (s, C4 in C_6H_4), 126.1 (s, C3 in C_6H_4), 127.6 (s, C5 in C_6H_4), 128.4 (s, p-C in C_6H_5), 130.0 (s, m-C in C_6H_5), 130.9 (s, o-C in C_6H_5), 142.0 (s, C2 in C_6H_4), 148.0 (s, C1 in C_6H_4), 152.3 (s, $ipso$-C in C_6H_5). MS: m/z 317.3 (M^+-$ZnCl_2$-THF). Found: C, 59.37; H, 5.94; N, 2.65%. Calcd. for $C_{26}H_{31}Cl_2NO_2Zn$ (525.83): C, 59.39; H, 5.94; N, 2.66%.

3.4. Data collection and structure refinement of **5**

Crystallographic data are given in Table 2. Data [λ(Mo Kα) = 0.71073 Å] were collected with a Siemens CCD (SMART) diffractometer. All observed reflections were used for determination of the unit cell parameters. Empirical absorption correction was performed with SADABS [20]. The structure was solved by direct methods (SHELXTL-PLUS [15]). H atoms were located by difference maps and refined isotropically, except for the hydrogen atoms of the disordered THF ligand (O2, C22–C25 and O3, C26–C29; these atoms were refined with 63% and 37% occupancy, respectively).

Appendix A. Supplementary data

CCDC 194393 contains the supplementary crystallographic data for **5**. These data can be obtained free of charge via http://www.ccdc.cam.ac.uk/conts/retrieving.html or from the Cambridge Crystallographic Data Centre, 12 Union Road, Cambridge CB2 1EZ, UK; fax: (+44) 1223-336-033; or e-mail: deposit@ccdc.cam.ac.uk.

References

[1] H. Sigel (Ed.), Metal Ions in Biological Systems, vol. 6, Marcel Dekker, New York, 1976.
[2] (a) H.T. Al-Masri, J. Sieler, E. Hey-Hawkins, Appl. Organomet. Chem. 17 (2003) 63;
(b) H.T. Al-Masri, J. Sieler, E. Hey-Hawkins, Appl. Organomet. Chem. 17 (2003) 641;
(c) H.T. Al-Masri, J. Sieler, P. Lönnecke, P.C. Junk, E. Hey-Hawkins, Inorg. Chem. 43 (2004) 7162;
(d) H.T. Al-Masri, J. Sieler, P.C. Junk, K. Domasevitch, E. Hey-Hawkins, J. Organomet. Chem. 690 (2005) 469;
(e) H.T. Al-Masri, J. Sieler, S. Blaurock, P. Lönnecke, P. Junk, E. Hey-Hawkins, Z. Anorg. Allg. Chem. 631 (2005) 518.
[3] W.N. Lipscomb, N. Sträter, Chem. Rev. 96 (1996) 2375.
[4] X. Sun, C. Qi, S. Ma, H. Huang, W. Zhu, Y. Liu, Inorg. Chem. Commun. 9 (2006) 911.
[5] J.K. Nag, P.K. Santra, C. Sinha, F. Liao, T. Lu, Polyhedron 20 (2001) 2253.
[6] R. Walz, K. Weis, M. Ruf, H. Vahrenkamp, Chem. Ber. 130 (1997) 975. and references therein.
[7] (a) X.H. Qiu, X.L. Tong, Acta Cryst. Sect. E 61 (2005) m2302;
(b) Y.-X. Sun, Z.-L. You, Synth. React. Inorg. Metal-Org. Nano-Metal Chem. 36 (2006) 359;
(c) P. Gonzalez-Duarte, R. March, J. Pons, W. Clegg, L. Cucurull-Sanchez, A. Alvarez-Larena, J.F. Piniella, Polyhedron 15 (1996) 2747.
[8] V.B. Arion, V.C. Kravtsov, J.I. Gradinaru, Y.A. Simonov, N.V. Gerbeleu, J. Lipkowski, J.-P. Wignacourt, H. Vezin, O. Mentre, Inorg. Chim. Acta 328 (2002) 123.
[9] D.S. Nesterov, V.G. Makhankova, V.N. Kokzay, B.W. Brian, Inorg. Chim. Acta 358 (2005) 4519.
[10] (a) Z. Zhang, D. Wang, T. Xu, J. Gao, Acta Cryst. Sect. E 62 (2006) m3416;
(b) X. Han, Z.-L. You, Y.-T. Xu, X.-M. Wang, J. Chem. Cryst. 36 (2006) 743.
[11] A.G. Giumanini, A.B. Giumanini, A.R. Lepley, Chim. Ind. (Milan) 51 (1969) 139.
[12] H.T. Al-Masri, J. Sieler, P. Lönnecke, S. Blaurock, K. Domasevitch, E. Hey-Hawkins, Tetrahedron 60 (2004) 333.
[13] R.E. Ludt, G.P. Crowther, C.R. Hauser, J. Org. Chem. 35 (1970) 1288.
[14] I.B. Gorrell, A. Looney, G. Parkin, J. Am. Chem. Soc. 112 (1990) 4068.
[15] K. Folting, J.C. Huffman, R.L. Bansemer, K.G. Caultion, J.L. Martin, P.D. Smith, Inorg. Chem. 23 (1984) 4589.
[16] R.L. Geerts, J.C. Huffman, K.G. Caulton, Inorg. Chem. 25 (1986) 1083.

[17] T. Tsukuda, C. Nishigata, K. Arai, T. Tsubomura, Polyhedron 28 (2009) 7.
[18] SHELXTL PLUS, Siemens Analyt. X-ray Inst. Inc. (1990), XS: Program for Crystal Structure Solution, XL: Program for Crystal Structure Determination, XP: Interactive Molecular Graphics.
[19] D.D. Perrin, W.L.F. Armarego, D.E. Perrin, Purification of Laboratory Chemicals, second ed., Pergamon Press, New York, 1980.
[20] G.M. Sheldrick, SADABS – A Program for Empirical Absorption Correction, Göttingen, 1998.

Table 1
Summarized crystallographic data for $[Co(SEtaaiNEt)_2](ClO_4)_2$ (**2d**) and $[Co(SMeaaiNEt)_2(SCN)_2]$ (**3b**).

	2d	**3b**
Empirical formula	$C_{25.9}H_{32}Cl_2N_8O_8S_2Co$	$C_{26}H_{28}N_{10}S_4Co$
Formula weight	777.30	667.75
T (K)	296(2)	93(2)
Crystal system	orthorhombic	triclinic
Space group	*Pbca*	$P\bar{1}$
Crystal size (mm^3)	$0.20 \times 0.10 \times 0.10$	$0.20 \times 0.20 \times 0.20$
a (Å)	14.4518(13)	10.3386(10)
b (Å)	14.452(7)	10.9941(16)
c (Å)	33.907(3)	15.169(2)
α (°)	90	84.793(13)
β (°)	90	73.717(11)
γ (°)	90	70.876(12)
V ($Å^3$)	7081.7(9)	1563.6(4)
Z	8	2
μ (Mo Kα) (mm^{-1})	0.809	0.851
θ Range (°)	1.20–25.12	2.41–25.35
hkl range	$-10 \leqslant h \leqslant 17$; $-17 \leqslant k \leqslant 17$; $-40 \leqslant l \leqslant 39$	$-10 \leqslant h \leqslant 12$; $-13 \leqslant k \leqslant 12$; $-15 \leqslant l \leqslant 17$
D_{calc} (Mg m^{-3})	1.458	1.418
Refine parameters	466	375
Total reflections	36 756	9304
Unique reflections	6302	5288
R_1[a] [$I > 2\sigma(I)$]	0.0307	0.0379
WR_2[b]	0.1043	0.0915
Goodness-of-fit (GOF)	0.647	1.003

[a] $R = \sum||F_0| - |F_c||/\sum|F_0|$.
[b] $wR_2 = [\sum w(F_0^2 - F_c^2)^2/\sum w(F_0^2)^2]^{1/2}$ | $w = 1/[\sigma^2(F_0)^2+(0.0614P)^2]$ for **2d**: $w = 1/[\sigma^2(F_0)^2 + (0.0460P)^2 + (1.6861P)]$ for 3b where $P = (F_0^2 + 2F_c^2)/3$.

performed with a Siemens SMART CCD diffractometer using fine focus sealed graphite-monochromatized Mo Kα radiation (λ = 0.71073 Å) for $[Co(SEtaaiNEt)_2](ClO_4)_2$ (**2d**) and $[Co(SMeaaiNEt)_2(SCN)_2]$ (**3b**). Reflections were recorded using the ω scan technique. Data were corrected for Lorentz polarization effects and for linear decay. Semi-empirical absorption corrections based on ψ-scans were applied with the help of SADABS (Multi-scan). The structures were solved by direct methods using SHELXS-97 [22] and successive difference Fourier syntheses. Both of the perchlorate anions are disordered. Three oxygen atoms around Cl1 are disordered over two crystallographically independent orientations (O2A/O2B, O3A/O3B, O4A/O4B) with occupancy ratios 0.88/0.12, 0.67/0.37, 0.53/0.47, respectively. In total this affords disordering of the oxygen atoms over 6 positions. One oxygen atom around Cl2 is disordered over two orientations (O6A/O6B) with an occupancy ratio 0.78/0.22. The thermal ellipsoids of the O atoms show that the disordered ClO_4^- ions deviate from the original orientations, which is also supported by the C–H···O(ClO_3) hydrogen bonding interaction. All non-hydrogen atoms were refined anisotropically. The H atoms were not refined but they were treated as riding on their parent atoms. In the final difference Fourier map the residual minima and maxima were [−0.145 and 0.153 (e/$Å^3$) for **2d**; −0.448 and 0.697 (e/$Å^3$) for **3b**], carried out using SHELXL-97 [23]. The structures were drawn using the ORTEP-32 [24], and PLATON-99 [25] programs.

2.4. Synthesis of the complexes

2.4.1. $[Co(SMeaaiNMe)_2](ClO_4)_2$

1-Methyl-2-[*o*-(thiomethyl)phenylazo]imidazole (SMeaaiNMe) (0.4 g, 1.72 mmol) in methanol (15 ml) was added dropwise to $Co(ClO_4)_2{\cdot}6H_2O$ (0.3 g, 0.82 mmol) in the same solvent (10 ml) at 298 K under a N_2 environment. The solution was stirred and refluxed for 3 h. The orange–brown solution was then filtered and N_2 gas was bubbled through to reduce its volume to 10 ml. To this solution a N_2 flushed $NaClO_4$ solution (1 g in 5 ml aqueous solution) was added and the reaction flask was corked. The solution was then kept in a freezer for 12 h. A dark brown mass precipitated at the bottom of the container, which was filtered. The residue was then washed with cold water followed by methanol-water (1:1, v/v) and dried in a vacuum over $CaCl_2$. The yield was 0.37 g (60%).

All the other complexes were prepared by the same procedure. The yields varied from 50–65%.

Microanalytical data: Anal. Calc. for $[Co(SMeaaiNMe)_2](ClO_4)_2$ (**2a**): C, 36.57; H, 3.32; N, 15.51. Found: C, 36.48; H, 3.27; N, 15.48%. *Anal.* Calc. for $[Co(SMeaaiNEt)_2](ClO_4)_2$ (**2b**): C, 38.40; H, 3.73; N, 14.93. Found: C, 38.32; H, 3.70; N, 14.90%. *Anal.* Calc. for $[Co(SEtaaiNMe)_2](ClO_4)_2$ (**2c**): C, 38.40; H, 3.73; N, 14.93. Found: C, 38.32; H, 3.70; N, 14.90%. *Anal.* Calc. for $Co(SEtaaiNEt)_2](ClO_4)_2$ (**2d**): C, 40.11; H, 4.11; N, 14.40. Found: C, 40.02; H, 4.07; N, 14.36%.

2.4.2. $[Co(SMeaaiNMe)_2(SCN)_2]$ (3a)

1-Methyl-2-[*o*-(thiomethyl)phenylazo]imidazole (SMeaaiNMe) (0.4 g, 1.72 mmol)) in methanol 20 ml) was added dropwise to a solution (10 ml) of $Co(OAc)_2{\cdot}4H_2O$ (0.22 g, 0.88 mmol) in the same solvent at 298 K in an inert (N_2) environment. The resulting orange–brown solution was stirred for 30 min. To this solution NH_4SCN (0.15 g, 1.97 mmol) was added in a small volume of water. The resulting brown red solution was then stirred for an additional 1 h, then filtered and left undisturbed for a week. A dark crystalline compound separated out. The crystals were filtered, washed with water, cold methanol and dried over $CaCl_2$ in *vacuo*. The yield was 0.30 g, (54%). All the other complexes were prepared by the same procedure. The yields varied from 50–70%.

Microanalytical data: Anal. Calc. for $[Co(SMeaaiNMe)_2(SCN)_2]$ (**3a**): C, 45.08; H, 3.76; N, 21.91. Found: C, 45.00; H, 3.73; N, 21.85%. *Anal.* Calc. for $[Co(SMeaaiNEt)_2(SCN)_2]$ (**3b**): C, 46.78; H, 4.20; N, 20.99. Found: C, 46.84; H, 4.22; N, 20.92%. *Anal.* Calc. for $[Co(SEtaaiNMe)_2(SCN)_2]$ (**3c**): C, 46.78; H, 4.20; N, 20.99. Found: C, 46.84; H, 4.22; N, 20.92%. *Anal.* Calc. for $[Co(SEtaaiNEt)_2(SCN)_2]$ (**3d**): C, 48.35; H, 4.60; N, 20.15. Found: C, 48.31; H, 4.64; N, 20.28%.

3. Results and discussion

3.1. Synthesis and formulation

1-Alkyl-2-[*o*-(thiomethyl)phenylazo]imidazole ($SRaaiNR^l$) reacts with $Co(ClO_4)_2.6H_2O$ in a 1:2 molar ratio under a N_2

environment in MeOH to isolate shining dark crystals on slow cooling (Scheme 1). The composition of the complexes, $[Co(SRaaiNR^{/})_2](ClO_4)_2$ (**2**) is supported by microanalytical data. Addition of an aqueous solution of NH_4SCN (2 equivalents) to a mixture of $Co(OAc)_2{\cdot}4H_2O$ and $SRaaiNR^{/}$ (1:2 mole ratio) in MeOH in an inert (N_2) atmosphere has isolated crystalline compounds of the formulation $[Co(SRaaiNR^{/})_2(SCN)_2]$ (**3**). The complexes are soluble in methanol, ethanol, chloroform, dichloromethane and acetonitrile, but are insoluble in hexane, benzene and toluene. Complexes **2** show 1:2 molar conductivity (Λ_M = 160–170 Ω^{-1} cm^2 mol^{-1} in MeOH) while complexes **3** are non-conducting in methanol/acetonitrile solution. The effective magnetic moments (μ) of $[Co(SRaaiNR^{/})_2](ClO_4)_2$, **2**, lie in the range 2.0–2.1 BM, and those of **3** show μ values in the range 4.0–4.2 BM. These data undoubtedly suggest low spin $t_{2g}^6eg^1$ for **2** and high spin, $t_{2g}^5eg^2$ for **3**. The magnetic moment data are slightly higher than the spin only value [26].

3.2. Molecular structures

3.2.1. $[Co(SEtaaiNEt)_2](ClO_4)_2$ (2d)

The X-ray structure of $[Co(SEtaaiNEt)_2](ClO_4)_2$ (**2d**) is shown in Fig. 1. Selected bond lengths and angles are given in Table 2. The coordination environment of cobalt includes imidazole-N(N), azo-N($N^{/}$) and thioether-S in a CoN_4S_2 system. The ligands bind in two meridional segments, each of the N, $N^{/}$, S type. Each Co-$NN^{/}S$ fragment is planar (mean deviation <0.03 Å). The donor centres are arranged in a *cis–trans–cis* configuration in the sequence N(imidazole), N(azo) and S donor centres. The bond lengths and angles (Table 2) suggest a distorted octahedral geometry around the Co centre. The Co–N distances vary in the range 1.88–2.05 Å. The distances are comparable with previously reported structures of cobalt(II) complexes of 1-alkyl-2-(arylazo)imidazole [27–29]. The Co–S distances are Co–S(1), 2.3934(12) Å and Co–S(2), 2.3703(13) Å. The N=N distances differ slightly in the two Co(N,$N^{/}$,S) motifs (N(1)–N(2), 1.281(4) Å; N(3)–N(4), 1.293(4) Å) (Table 2), though they are both longer than the free ligand values (1.250(1) Å) [30], 1.261(2) Å [31]). The two chelate planes [Co,S(1),C(1),C(6),N(1), deviation ⩽ 0.1 Å; Co,N(4),C(9),N(1),N(2), mean deviation ⩽ 0.07 Å] are no longer planar and makes a dihedral angle of 4.80(20)°. The chelate angles in Co(N,$N^{/}$) (∠N(1)–Co–N(4), 80.8 (2)°; ∠N(5)–Co–N(8), 79.82(16)°) are smaller than the Co($N^{/}$,S) chelate (∠S(1)–Co–N(1), 86.43(14)° and ∠S(2)–Co–N(8), 85.00(12)°). The two ClO_4^- units are not equivalent. The three oxygen atoms around Cl1 are disordered over two crystallographically independent orientations, with variable occupancy ratios, and one oxygen atom around Cl2 is disordered over two orientations (*vide* Section 2).

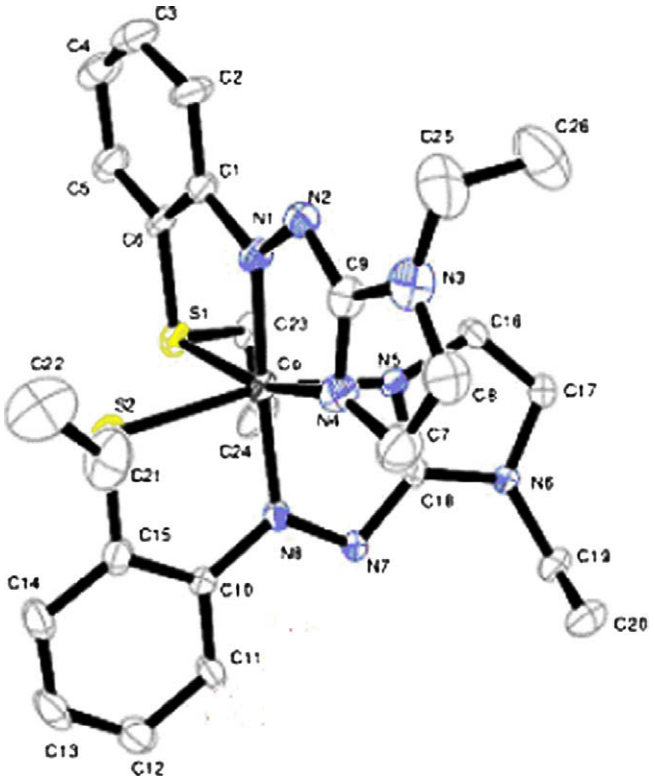
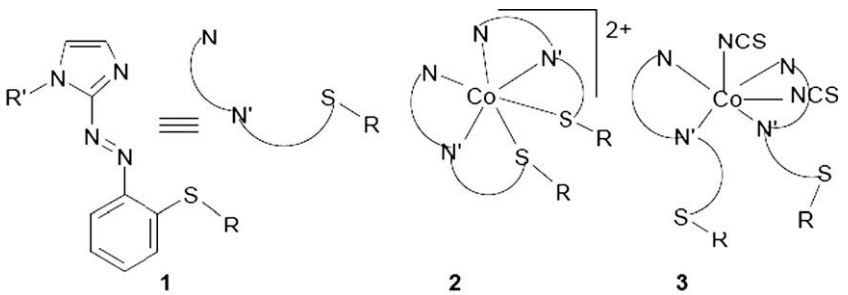


Fig. 1. Molecular structure of $[Co(SEtaaiNEt)_2]^{2+}$ (**2d**).

Table 2a
Bond distances and bond angles of $[Co(SEtaaiNEt)_2(ClO_4)_2]$ (**2d**).

Bond length, Å		Bond angles, °	
Co(1)–N(1)	1.885(4)	N(1)–Co(1)–N(4)	80.8(2)
Co(1)–N(5)	1.891(3)	N(8)–Co(1)–N(5)	79.82(16)
Co(1)–N(4)	2.043(5)	N(1)–Co(1)–S(1)	84.63(14)
Co(1)–N(5)	2.052(4)	N(8)–Co(1)–S(2)	85.00(12)
Co(1)–S(1)	2.3934(12)	N(1)–Co(1)–N(8)	175.93(17)
Co(1)–S(2)	2.3703(13)	N(1)–Co(1)–N(5)	96.61(16)
N(1)–N(2)	1.281(4)	N(4)–Co(1)–N(5)	84.53(14)
N(3)–N(4)	1.293(4)	N(1)–Co(1)–S(2)	98.55(11)
		N(8)–Co(1)–N(4)	96.9(2)
		N(4)–Co(1)–S(2)	97.28(12)
		N(5)–Co(1)–S(2)	164.82(12)
		N(8)–Co(1)–S(1)	97.75(9)
		N(4)–Co(1)–S(1)	165.38(19)
		N(5)–Co(1)–S(1)	97.80(9)
		S(2)–Co(1)–S(1)	84.27(4)



R = $R^{/}$ = Me (**1a**); R = Me,$R^{/}$ = Et (**1b**); R = Et, $R^{/}$ = Me (**1c**); R = $R^{/}$ = Et (**1d**);

$[Co(SRaaiNR^{/})_2]^{2+}$ (**2**); $[Co(SRaaiNR^{/})_2(NCS)_2]$ (**3**)

Scheme 1.

Table 2b
Bond distances and bond angles of $[Co(SMeaaiNEt)_2(NCS)_2]$ (**3b**).

Bond length, Å		Bond Angles, °	
Co(1)–N(1)	2.074(2)	N(21)–Co(1)–N(1)	93.99(8)
Co(1)–N(21)	2.039(2)	N(41)–Co(1)–N(1)	91.58(8)
Co(1)–N(41)	2.031(2)	N(21)–Co(1)–N(27)	71.60(7)
Co(1)–N(42)	2.011(2)	N(42)–Co(1)–N(21)	145.81(8)
Co(1)–N(27)	2.441(2)	N(41)–Co(1)–N(21)	106.48(8)
Co(1)–K(7)	2.488(7)	N(42)–Co(1)– N(1)	103.45(8)
N(6)–N(7)	1.280(3)	N(42)–Co(1)–N(27)	91.73(8)
N(26)–N(27)	1.280(3)	N(41)–Co(1)–N(27)	87.57(7)
		N(1)–Co(1)–N(27)	164.61(8)
		N(42)–Co(1)– N(41)	102.24(9)
		N(1)–Co(1)–N(7)	70.49(4)
		N(41)–Co–N(7)	161.64(5)
		N(42)–Co–N(7)	78.96(2)
		N(21)–Co–N(7)	79.56(4)
		N(27)–Co–N(7)	110.76(8)

Table 2c
Hydrogen bonded metric parameters of **2d**.

	H···A, Å	D···A, Å	∠D–H···A, °
C(7)–H(7)···O(7)	2.39	3.3061	169
C(8)–H(8)···O(6)	2.25	3.1300	158
C(14)···H(14)···O(7)[a]	2.45	3.3268	157
C(16)–H(16)···O(3)	2.40	3.3019	162
C(17)–H(17)···O(4)[b]	2.50	3.1515	127
C(21)–H(21B)···N(4)(Intra)	2.51	3.2787	136

[a] Symmetry: $1/2 - x, -1/2 + y, z$.
[b] Symmetry: $3/2 - x, 1/2 + y, z$.

The hydrogen bonding interaction, C–H···O(ClO_3) forms a 1-D chain. The supramolecular parameters are listed in Table 2c. Intramolecular hydrogen bonding is also observed with the azo-N and imidazole-N(1)–CH_2 group to stabilize the molecular union.

3.2.2. $[Co(SMeaaiNEt)_2(SCN)_2]$ (**3b**)

The X-ray structure of $[Co(SMeaaiNEt)_2(SCN)_2]$ (**3b**) is shown in Fig. 2. Selected bond distances and angles are given in Table 2b. The structure is a distorted octahedron with a CoN_6 configuration. SMeaaiNEt acts as a bidentate N(imidazole), N(azo) chelator, unlike the structure of **2d**, and two –N(CS) groups fulfill the charge and coordination number. The Co–N(azo) distances, Co(1)–N(7), 2.488(7) Å and Co(1)–N(27), 2.441(2) Å, are elongated by 0.4–0.5 Å compared to **2d** (Fig. 1a, Table 2a). The Co–N(azo) distances (Co(1)–N(7/27)) are longer than those of Co–N(imidazole) (Co(1)–N(1/21)) by ~0.4 Å, but the former are sufficiently below the sum of the van der Waals radii of Co(II) (2.00 Å) and azo-N (1.50 Å) [32]. This signifies a covalent interaction between Co(II) and N(azo). The chelate angles are ∠N(1)–Co(1)–N(7), 70.49(4)° and ∠N(21)–Co(1)–N(27), 71.60(7)°. The structural distortion in **3b** may arise from the long Co–N(azo) distance and small Co(N,N′) chelate angles, which may be due to the demand of the larger stereochemical space of azo-N; thus the distortion arises *via* elongation of the Co–N(azo) distance. The N=N bond lengths [N(6)–N(7), 1.280(3) Å; N(26)–N(27), 1.280(3) Å] are longer than the free ligand values (1.250(1) Å) [30], 1.261(2) Å [31]. The elongation of this bond in the complex with reference to the free ligand value (by 0.03 Å) may be due to a dπ(Co)–π*(azo) backbonding charge transfer.

A DFT calculation has been performed for the two different molecules $[Co(SEtaaiNEt)_2](ClO_4)_2$ (**2d**) and $[Co(SMeaaiNEt)_2(SCN)_2]$ (**3b**). The optimized structure of these molecules are developed using the GAUSSIAN 03 analyses package. Structural agreement has been observed from a comparison of bond distances and angles between the calculated and X-ray determined structures. The bond lengths in the theoretically generated molecules are elongated by 0.005–0.01 Å compared to those of the experimental structures.

3.3. Spectral studies

The infrared spectra of the complexes are assigned by comparing with spectra of the free ligands and some cobalt(II) complexes of arylazoimidazoles [20,27–29]. The spectra of the complexes **2** show a strong band at 1085–1093 cm^{-1} with a weak stretch at 624–627 cm^{-1}, which are assigned to $\nu(ClO_4)$. The characteristic strong transmission of **3** at 2060–2075 cm^{-1} is referred to $\nu_{asym}(SCN)$. Moderately intense stretchings at 1583–1600 and 1438–1452 cm^{-1} are due to ν(C=N) and ν(N=N), respectively, for the coordinated SRaaiNR′ ligands.

Solution electronic spectra of the complexes were recorded in acetonitrile solution in the UV–Vis region (250–900 nm). The data are listed in Table 3. The visible region of the spectra show three transitions: for **2** the transitions are 600–635, 450–470 and 410–420 nm, along with two transitions in the UV region; 355–375, 240–255 nm. The complexes **3** exhibit transitions at 530–610, 410–430 and 365–370 nm. The longer wavelength bands are weaker than the bands <430 nm. Based on the low intensity and low energy nature, the bands are considered to be d–d transitions in an octahedral geometry. The high intense transition <430 nm may be assigned to MLCT transitions.

The theoretically generated structures of $[Co(SEtaaiNEt)_2](ClO_4)_2$ (**2d**) and $[Co(SMeaaiNEt)_2(SCN)_2]$ (**3b**) are used to calculate the composition and energy of the functions. These are used to explain the electronic properties of the complexes. The orbital energies along with contributions from the ligands and metal are given in the Supplementary Materials Tables S1 and S2. Fig. 4 depicts the selected occupied and unoccupied frontier orbitals. In the complexes the highest occupied MO is singly occupied and is abbreviated SOMO. The MOs are destabilized on going from $[Co(SEtaaiNEt)_2](ClO_4)_2$ (**2d**) to $[Co(SMeaaiNEt)_2(SCN)_2]$ (**3b**): E_{SOMO} (**2d**), −11.17 eV and E_{SOMO} (**3b**), −4.40 eV; E_{LUMO} (**2d**), −9.14 eV and E_{LUMO} (**3b**), −3.13 eV. This may be attributed to structural distortion, coordination of different donor centres, number of chelate rings etc.

The SOMO of **2d** is constituted of Co (35%) and the chelating ligand, SEtaaiNEt (65%), while the main contribution to HOMO-1, HOMO-2 etc is from SEtaaiNEt (>90%). In $[Co(SMeaaiNEt)_2(SCN)_2]$ (**3b**) the SOMO and other occupied MOs (HOMO-1, HOMO-2 etc) are mainly composed of the –NCS group (>90%) and the unoccupied MOs (except LUMO+2) of SMeaaiNEt (>95%). The LUMO+2 is composed of Co (75%), –NCS (10%) and SMeaaiNEt (15%). The calculated transitions are grouped in the Supplementary Materials Table S2. The intensity of these transitions has been assessed from the oscillator strength (*f*). In **2d**, the visible region (400–570 nm) transitions are assigned to SOMO → LUMO+1, HOMO-1 → LUMO/LUMO+1, HOMO-3 → LUMO/LUMO+1/LUMO+2, HOMO-4 → LUMO/LUMO+1/LUMO+2 etc. The calculated transitions at 470–570 nm are weak (*f*, 0.005–0.007) and are assigned to an admixture of MLCT (metal-to-ligand charge transfer) and ILCT (intraligand charge transfer) transitions. An intense band is calculated at 430 nm (*f*, 0.1095) which is an ILCT band. $[Co(SMeaaiNEt)_2(SCN)_2]$ (**3b**) shows longer wavelength transitions (>600 nm), but they are weaker than those of **2d**. One of these transitions at 833 nm is assigned to XMCT (X = NCS) and is weak (*f*, 0.002). It originates from the SOMO → L+2 transition. The transitions 710–730 and 650–670 nm are also weak (*f*, 0.001–0.002) and have been assigned to an admixture of XMCT, MLCT, ILCT and XLCT. They are characterized as SOMO-1 → LUMO+1/L+2; SOMO-1 → LUMO+1; S−2/S−3 → L+2, etc.

3.4. Redox behavior

Cyclic voltammetry was used to examine the redox nature of the complexes in acetonitrile solution in the potential range −1.6 to 1.2 V versus a SCE electrode. A representative voltammogram

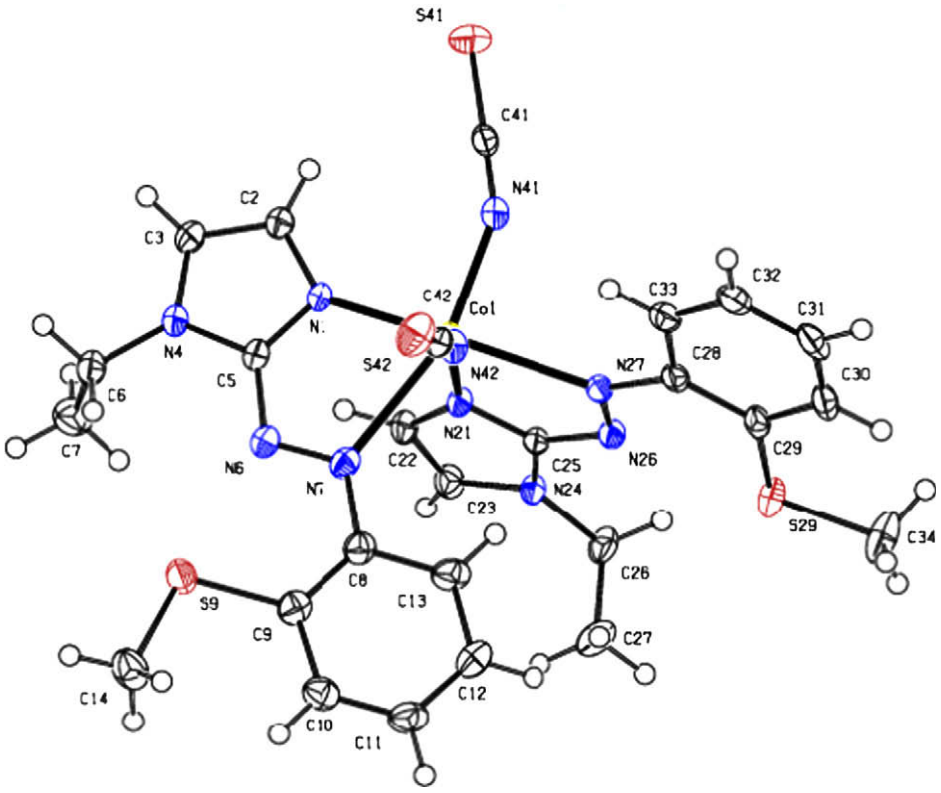


Fig. 2. Molecular structures of $[Co(SMeaaiNEt)_2(NCS)_2]$ (**3b**).

Table 3
UV–Vis spectral and bulk magnetic data.

Compounds	UV–Vis spectra in MeOH Λ_{ms} (nm) (ε in $dm^3\ mol^{-1}\ cm^{-1}$)	Magnetic moment, μ (BM)
$[Co(SMeaaiNMe)_2](ClO_4)_2$ (**2a**)	617 (1450), 412 (11 250), 357 (17 500). 244 (11 250)	2.12
$[Co(SMeaaiNEt)_2](ClO_4)_2$ (**2b**)	605 (1272), 465 (5333), 413(10 000). 357 (15 333). 244(10 667)	2.00
$[Co(SEtaaiNMe)_2](ClO_4)_2$ (**2c**)	602 (1026), 466 (5182), 412 (10 000), 357 (17 273). 256(10 909)	2.18
$[Co(SEtaaiNEt)_2](ClO_4)_2$ (**2d**)	634 (1190), 588 (1690), 471 (5294), 412 (11 176). 360(15 882). 247(11 176)	2.05
$[Co(SMeaaiNMe)_2(NCS)_2]$ (**3a**)	607 (4311), 426 (6431), 368 (7760), 258 (6400)	4.02
$[Co(SMeaaiNEt)_2(NCS)_2]$ (**3b**)	565 (3660), 415 (6692), 368 (7769), 260 (9154)	4.10
$[Co(SEtaaiNMe)_2(NCS)_2]$ (**3c**)	635 (3546). 417 (6155). 369 (6512). 255 (8560)	4.08
$[Co(SEtaaiNEt)_2(NCS)_2]$ (**3d**)	533 (2617), 41S (6498). 366 (7.064). 251 (9.623)	4.12

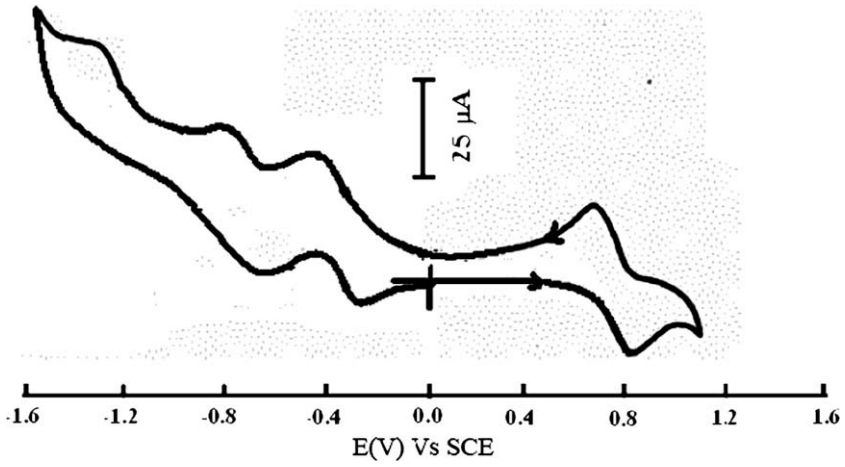


Fig. 3. Cyclic voltammograms $[Co(SMeaaiNEt)_2](ClO_4)_2$ (**2b**) in MeCN solution.

is shown in Fig. 3 and data are given in Table 4. The complexes display a quasireversible (peak-to-peak separation 100–130 mV) one-electron response at 0.6–0.8 V, which may be assigned to a Co(III)/Co(II) redox response. On scanning to the negative direction

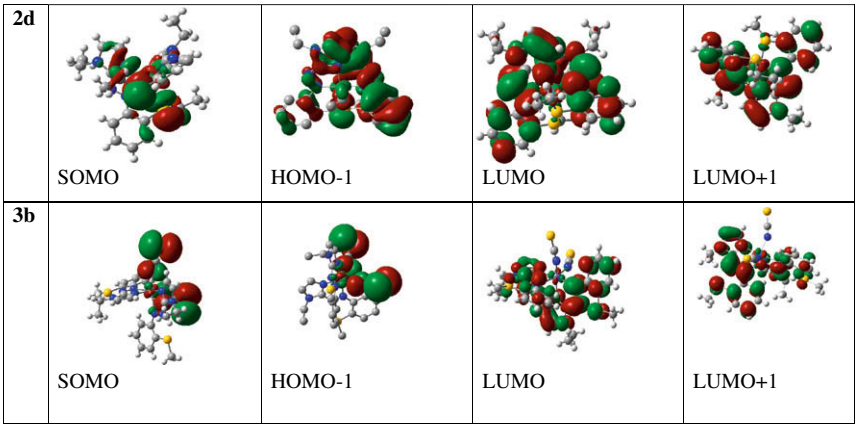


Fig. 4. Some orbital pictures of **2d** and **3b**.

(0.0 to −1.6 V), three redox responses were observed at ∼−0.4, −0.8 and −1.4 V. Two of the reductive couples (∼−0.4, −0.8 V) are quasireversible (ΔEp ⩾ 100 mV), while the third one at −1.4 V is irreversible. The couples negative to SCE are reductive in nature, and the first two reductions are referred to azo/azo^{-} and azo^{-}/azo$^{=}$ respectively [19]. The irreversible reduction at the very high negative potential (−1.4 V) may be considered electron accommodation to a thiocyanato dominated redox level. The coulometric data of $[Co(SRaaiNR^{/})_2]^{2+}$ (**2**) confirms the one-electron stoichiometry, however, we could not run a coulometric oxidation of $[Co(SRaaiNR^{/})(SCN)_2]$ (**3**). The anodic current began to increase progressively above ∼0 .7 V and there were signs of a very ill defined anodic response near 1 V, not associated with a cathodic counterpart on scan reversal. The multicyclic voltammetric response is supportive of this change and it is observed that both the current height and peak-potential position are shifted in a more negative direction. This may support the decomposition of the depolarizer structure under the influence of the electrode field. Ligand reductions appear at more negative values for $[Co(SRaaiNR^{/})_2(SCN)_2]$ compared to $[Co(SRaaiNR^{/})_2](ClO_4)_2$, which may be due to the better stability of the tridentate chelation in latter complex. The higher Co(III)/Co(II) redox potential for $[Co(SRaaiNR^{/})_2]^{2+}$ compared to $[Co(SRaaiNR^{/})_2(SCN)_2]$ suggests a fairly stable Co(II) in **2** compared to that of **3**.

$$[Co(N,N^{/},S)_2]^{3+} + e \rightleftharpoons [Co(N,N^{/},S)_2]^{2+} \quad (1)$$

The cyclic voltammetric behavior of **2** and **3** are readily accountable from the DFT calculation. Because of the significant metal (Co) function in the SOMO of **2d** the complexes show metal oxidation, which is indeed observed. The unoccupied MOs are significantly dominated by the azoimine function, thus reduction may refer to electron accommodation at the azo dominated orbital of the ligand. So the assignments of azo reductions are justified. A DFT calculation on $[Co(SMeaaiNEt)_2(SCN)_2]$ (**3b**) shows a weak Co contribution (<4%) in the SOMO, and HOMO-4 has a significant (46%) Co contribution. The SOMO is dominated by a NCS contribution. The oxidation, which refers to electron extraction from the complex, may be attributed to the NCS group followed by the Co centre. So the terminal oxidation may be assigned to Co(II) → Co(III). The LUMO and other unoccupied MOs are SMeaaiNEt dominated (>95%), so reduction is, as usual, the following:

$$—N{=}N— + e \rightarrow —N^{\cdot\cdot}—N—^{-}. \quad (2)$$

Table 4
UV–Vis spectra[a] cyclic voltametric[b] data.

Compound	CV data E^0 (V) (ΔE_P, mV)			
	E_M[c]	Ligand reductions		
$Co(SMeaaiNMe)_2](ClO_4)_2$ (**2a**)	0.78 (120)	−0.38 (120)	−0.77 (140)	−1.30 (200)
$[Co(SMeaaiNEt)_2](ClO_4)_2$ (**2b**)	0.70 (150)	−0.40 (120)	−0.78 (140)	−1.33 (200)
$[Co(SEtaaiNMe)_2](ClO_4)_2$ (**2c**)	0.72 (130)	−0.42 (110)	−0.80 (140)	−1.34 (180)
$[Co(SEtaaiNEt)_2](ClO_4)_2$ (**2d**)	0.65 (100)	−0.47 (110)	−0.84 (120)	−1.38 (220)
$[Co(SMeaaiNMe)_2(NCS)_2]$ (**3a**)	0.67 (150)	−0.45 (100)	−0.88 (130)	−1.45 (200)
$[Co(SMeaaiNEt)_2(NCS)_2]$ (**3b**)	0.64 (125)	−0.48 (120)	−0.85 (140)	−1.42 (180)
$[Co(SEtaaiNMe)_2(NCS)_2]$ (**3c**)	0.66 (110)	−0.53 (80)	−0.94 (140)	−1.44 (200)
$[Co(SEtaaiNEt)_2(NCS)_2]$ (**3d**)	0.68 (135)	−0.56 (120)	−0.95 (170)	−1.42 (180)

[a] Solvent: MeCN.
[b] Solvent: dry MeCN; Pt-disk working electrode. Pt-wire auxiliary and SCE. TBAP as supporting electrolyte, scan rate 50 mV s^{-1}, potential $E_{1/2} = (Ep_a + Ep_c)/2$, V, $Ep = (Ep_a - Ep_c)$ (mV).

4. Conclusion

Co(II)-1-alkyl-2-[(*o*-thioalkyl)phenylazo]imidazole (SRaaiNR$^{/}$) complexes are described in this work. The complexes have been structurally established. In $[Co(SRaaiNR^{/})_2]^{2+}$ the ligand serves as a tridentate N(imidazole), N(azo), S(thioether) chelator and forms a meridionally bonded octahedral geometry. The complex, $[Co(SRaaiNR^{/})_2(SCN)_2]$ is also distorted octahedral and SRaaiNR$^{/}$ shows a bidentate imidazole-N, azo-N chelation. The X-ray structure parameters confirm a higher degree of distortion in the latter case. The $[Co(SRaaiNR^{/})_2](ClO_4)_2$ complexes are low spin $t_{2g}^6e_g^1$ while the $[Co(SRaaiNR^{/})_2(SCN)_2]$ complexes are high spin $t_{2g}^5e_g^2$. DFT calculations of the optimized geometries of the complexes are used to explain the electronic properties of the complexes.

Acknowledgements

Financial support from the University Grants Commission, CAS-UGC, New Delhi is thankfully acknowledged.

Appendix A. Supplementary data

CCDC 706672 and 706673 contain the supplementary crystallographic data for $[Co(SEtaaiNEt)_2](ClO_4)_2$ (**2d**) and [Co(SMeaai-

$NEt)_2(SCN)_2]$ (**3b**). These data can be obtained free of charge via http://www.ccdc.cam.ac.uk/conts/retrieving.html, or from the Cambridge Crystallographic Data Centre, 12 Union Road, Cambridge CB2 1EZ, UK; fax: (+44) 1223-336-033; or e-mail: deposit@ccdc.cam.ac.uk. Supplementary data associated with this article can be found, in the online version, at doi:10.1016/j.poly.2009.04.043.

References

[1] L. Wang, C. Bailly, A. Kumar, D. Ding, M. Bajic, W.D. Wilson, Proc. Natl. Acad. Sci. USA 97 (2002) 12.
[2] N. Lambercht, K. Munson, O. Vagin, G. Sachs, J. Biol. Chem. 275 (2000) 4041.
[3] W.R. Rypniewski, S. Managani, S. Bruni, P.L. Orioli, M. Casati, K. Wilson, J. Mol. Biol. 251 (1995) 282.
[4] E. Colacio, M. Ghazi, R. Kivekas, M. Klinga, F. Lloret, J.M. Moreno, Inorg. Chem. 39 (2000) 2770.
[5] J.M. Dominguez-Vera, A. Rodriguez, R. Cuesta, R. Kivekas, E. Colacio, J. Chem. Soc., Dalton Trans. (2002) 561.
[6] P. Chattopadhyay, B.K. Dolui, C. Sinha, Indian J. Chem. 36A (1997) 429.
[7] T.K. Misra, D. Das, C. Sinha, P.K. Ghosh, C.K. Pal, Inorg. Chem. 37 (1998) 1672.
[8] J. Dinda, U.S. Ray, G. Mostafa, T.-H. Lu, A. Usman, I. Abdul Razak, S. Chantrapromma, H.-K. Fun, C. Sinha, Polyhedron 22 (2003) 247.
[9] Y.-K. Au, K.-K. Cheung, W.-T. Wong, Inorg. Chim. Acta 238 (1995) 193.
[10] R. Samanta, P. Munshi, B.K. Santra, N.K. Kokanath, M.A. Sridhar, J.S. Prasad, G.K. Lahiri, J. Organomet. Chem. 579 (1999) 311.
[11] K. Pramanik, M. Shivakumar, P. Ghosh, A. Chakravorty, Inorg. Chem. 39 (2000) 195.
[12] B.K. Santra, G.A. Thakur, P. Ghosh, A. Pramanik, G.K. Lahiri, Inorg. Chem. 35 (1996) 3050.
[13] P.K. Santra, R. Roy, C. Sinha, Proc. Indian Acad. Sci. (Chem. Sci.) 112 (2000) 523.
[14] A.K. Ghosh, P. Majumdar, L.R. Falvelo, G. Mostafa, S. Goswami, Organometallics 18 (1999) 5086.
[15] A. Saha, A.K. Ghosh, P. Majumdar, K.N. Mitra, S. Mondal, K. Rajak, L.R. Falvello, S. Goswami, Organometallics 18 (1999) 3772.
[16] J.J. Robertson, A. Kadziola, R.A. Krause, S. Larsen, Inorg. Chem. 28 (1989) 2097.
[17] D. Datta, A. Chakravorty, Inorg. Chem. 22 (1983) 1085.
[18] A.C.G. Hotze, M.E.T. Broekhuisen, A.H. Velders, K. Vander Schilden, J.G. Haasnoot, J. Reedjik, Eur. J. Inorg. Chem. (2002) 369.
[19] D. Graham, R. Brown, W.E. Smith, Chem. Commun. (2001) 1002.
[20] D. Banerjee, U.S. Ray, Sk. Jasimuddin, J.-C. Liou, T.-H. Lu, C. Sinha, Polyhedron 25 (2006) 1299.
[21] A.I. Vogel, A Text Book of Practical Organic Chemistry, second ed., Longman, London, 1959.
[22] G.M. Sheldrick, SHELXS-97, Program for the Solution of Crystal Structure, University of Gottingen, Germany, 1997.
[23] G.M. Sheldrick, SHELXL 97, Program for the Refinement of Crystal Structure, University of Gottingen, Germany, 1997.
[24] L.J. Farrugia, J. Appl. Cryst. 30 (1997) 565.
[25] A.L. Spek, PLATON, Molecular Geometry Program, University of Utrecht, The Netherlands, 1999.
[26] R.L. Dutta, A. Syamal, Elements of Magnetochemistry, second ed., Affiliated East-west Press, New Delhi, 1993. p. 150.
[27] U.S. Ray, B.G. Chand, G. Mostafa, J. Chang, T.-H. Lu, C. Sinha, Polyhedron 22 (2003) 2587.
[28] D. Banerjee, U.S. Ray, S. Chantrapromma, H.-K. Fun, J.-N. Lin, T.-H. Lu, C. Sinha, Polyhedron 24 (2005) 1071.
[29] D. Banerjee, U.S. Ray, J.-S. Wu, T.-H. Lu, C. Sinha, Polyhedron 25 (2006) 3077.
[30] P. Bhunia, B. Baruri, U.S. Ray, C. Sinha, S. Das, J. Cheng, T.-H. Lu, Transition Met. Chem. 31 (2006) 310.
[31] J. Otsuki, K. Suwa, K. Narutaki, C. Sinha, I. Yoshikawa, K. Araki, J. Phys. Chem. A 109 (2005) 8064.
[32] <http://www.ccdc.cam.ac.uk/products/csd/radii/table.php4>.

2. Experimental

2.1. Materials and physical measurements

All chemicals and reagents were of analytical grade, and were used as received from commercial sources (Sigma–Aldrich and Alfa Aesar). Elemental analyses for C, H and N were performed on an Elementar Vario III EL. The FT-IR spectrum was recorded in the 4000–400 cm^{-1} region with a Bruker Optics, Vertex 70 FT-IR spectrometer using ATR techniques. Thermal analysis was performed on a SII Exstar 6000 TG/DTA 6300 model using a platinum crucible with a 10 mg sample. TG/DTA measurement was taken in static air, within the 20–700 °C temperature range. The UV–Vis spectrum was obtained for the solid state, aqueous solution and DMSO solution of the complex (10^{-3} M) and the free ligands, ap and H_2dipic (10^{-3} M), with a SHIMADZU UV-2550 spectrometer in the range 900–200 nm. Magnetic susceptibility measurement at room temperature was performed using a Sherwood Scientific Magway MSB MK1 model magnetic balance by the Gouy method using $Hg[Co(SCN)_4]$ as the calibrant. Molar conductance of the compound was determined in DMSO (10^{-3} M) at room temperature using a WTW Cond 315i/SET Model conductivity meter.

2.2. Synthesis of $[Cu(\mu\text{-ap})(dipic)(H_2O)]_2{\cdot}4H_2O$ (**1**)

A solution of $Cu(CH_3COO)_2{\cdot}H_2O$ (0.199 g, 1 mmol) in water (10 mL) was added dropwise to a mixed-ligand solution of 2,6-pyridinedicarboxylic acid (0.167 g, 1 mmol) and 2-aminopyridine (0.094 g, 1 mmol) in water (20 mL) with stirring at room temperature for 1 h. The reaction mixture was kept at room temperature for 2 weeks to give a green crystalline solid (0.5 g, 66% yield). On recrystallisation, green crystals of **1** suitable for X-ray diffraction were separated and washed with water. *Anal.* Calcd. for $C_{24}H_{30}N_6O_{14}Cu_2$: C, 38.25; H, 4.01; N, 11.15. Found: C, 38.30; H, 4.04; N, 11.21%.

2.3. X-ray data collection and structure refinement

The crystal and instrumental parameters used in the unit-cell determination and data collection are summarized in Table 1 for complex **1**. Diffraction measurements were made at room temperature on a Stoe IPDS II CCD X-ray diffractometer employing plane graphite monochromatized Mo Kα radiation (λ = 0.71073 Å), using the $\omega - 2\theta$ scan mode. Unit-cell dimensions were determined and refined by using the angular settings of 25 automatically centered reflections in the $1.61 \leqslant \theta \leqslant 26.50$ range. The structure was solved by direct methods using SHELXS-97 and refined by full-matrix least-squares techniques on F^2 with SHELXL-97 [32]. Empirical absorption corrections were applied by the integration method via X-RED software [33]. H atoms of NH_2 group and water molecules were located in difference syntheses and refined as riding atoms, with distances of N–H = 0.82(3)–0.84(3) Å and O–H = 0.801(17)–0.818(17) Å and with $U_{iso}(H) = 1.2U_{eq}(N,O)$. The remaining H atoms were placed geometrically at distances of 0.93 Å from their parent atoms for N–H and C–H bonds. ORTEP drawings [34] of complex **1** with 40% probability displacement thermal ellipsoids and the atom-labelling scheme are shown in Figs. 1–3.

Table 1
Crystal data and structure refinement details for complex **1**.

Empirical formula	$C_{24}H_{30}N_6O_{14}Cu_2$
Formula weight	753.62
T (K)	293(2)
λ (Å)	0.71073
Crystal system, space group	monoclinic, $P2_1/c$
Unit cell dimensions	
a (Å)	12.6589(10)
b (Å)	6.4533(4)
c (Å)	18.1088(15)
β (°)	93.026(6)
V (Å^3)	1477.28(19)
Z	2
μ (mm^{-1})	1.520
D_{calc} (Mg m^{-3})	1.694
F(0 0 0)	772
θ Range (°)	1.61–26.50
Crystal size (mm)	0.650 × 0.260 × 0.060
Absorption correction	integration
Limiting indices	$-15 \leqslant h \leqslant 15$, $-7 \leqslant k \leqslant 8$, $-22 \leqslant l \leqslant 19$
Reflections collected	9447
Unique reflections	3057
Observed $I \geqslant 2\sigma(I)$	2516
Number of parameters	240
Refinement method	full-matrix least-squares on F^2
R_{int}	0.0293
$R[F^2 > 2\sigma(F^2)]$	0.0312
$wR(F^2)$	0.0701
Goodness-of-fit on F^2	1.030
Largest difference in peak and hole (Å^{-3})	−0.352 and 0.287

2.4. Bioassays

2.4.1. Antimicrobial assay

2.4.1.1. Microorganisms and inoculum preparation for biological activity. Microorganisms were obtained from various sources (see Table 2) and stored at −85 °C in 50% glycerol until used in the antimicrobial assays. The bacteria and yeasts were first refreshed in Mueller Hinton Broth (Merck) at 35–37 °C, and were then inoculated on Mueller Hinton Agar (Mast Diagnostics) plates for a purity check. After sufficient growth the microbial cultures were transferred to liquid medium and were overnight grown suspensions were calibrated to McFarland No: 0.5 using a densitometer (Biosan).

2.4.1.2. Antimicrobial assay. Micro-dilution broth susceptibility assay was used [35–37]. Stock solutions of the test samples and the standard antibacterial agent Chloramphenicol and the antifungal agent Ketoconazole were prepared in 25% DMSO (Carlo-Erba). Dilution series were prepared from 4 mg/mL to 0.003 mg/mL in 96-well microtiter plates. One hundred microliters of the previously prepared microbial suspensions were then transferred to each well. The last row, containing only the serial dilutions of the antifungal agent without the microorganism, was used as a negative control. After incubation at 37 °C for 24–48 h, the first well without turbidity was determined as the minimal inhibitory concentration (MIC). Ten microliters of tetrazolium salt (TTC) was also added to each well to confirm the MIC values. The assays were repeated twice and the results are given as the average.

2.4.2. Qualitative radical scavenging assay using DPPH·

The test substances were screened for their radical scavenging activity preliminary at 0.5 mg/mL concentration in MeOH qualitatively using a thin layer assay [38,39] to detect possible active substances in comparison with the standard antioxidant substance vitamin C.

3. Results and discussion

3.1. IR spectrum

The significant frequencies in the IR spectrum of **1** are given in Table 3. There is a broad absorption band at 3340 cm^{-1} attributed to the ν(OH) vibrations of water molecules in the crystal. The absorption bands at 3202 and 3280 cm^{-1} are due to the ν(NH)

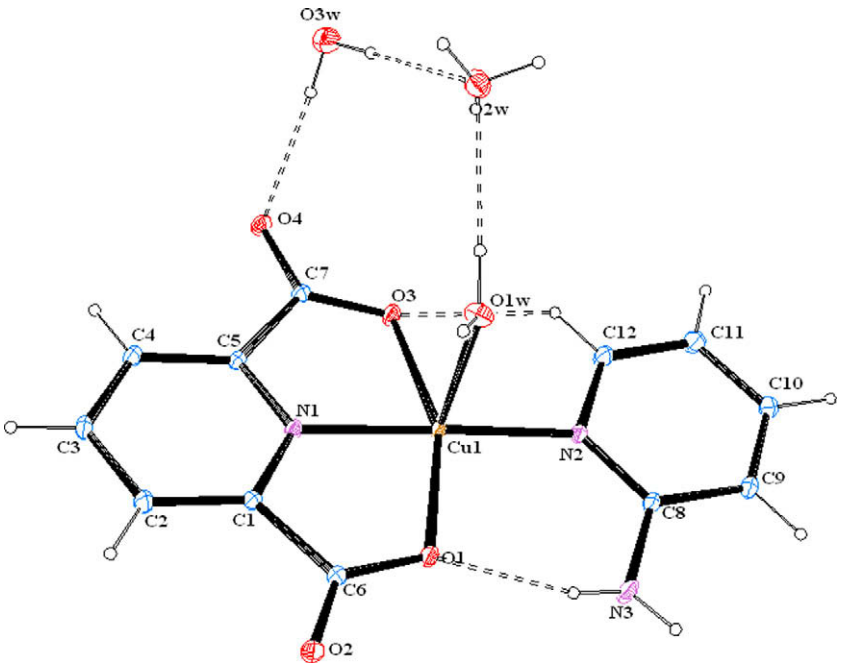


Fig. 1. An ORTEP drawing of **1** with the atom-numbering scheme. Displacement ellipsoids are drawn at the 40% probability level.

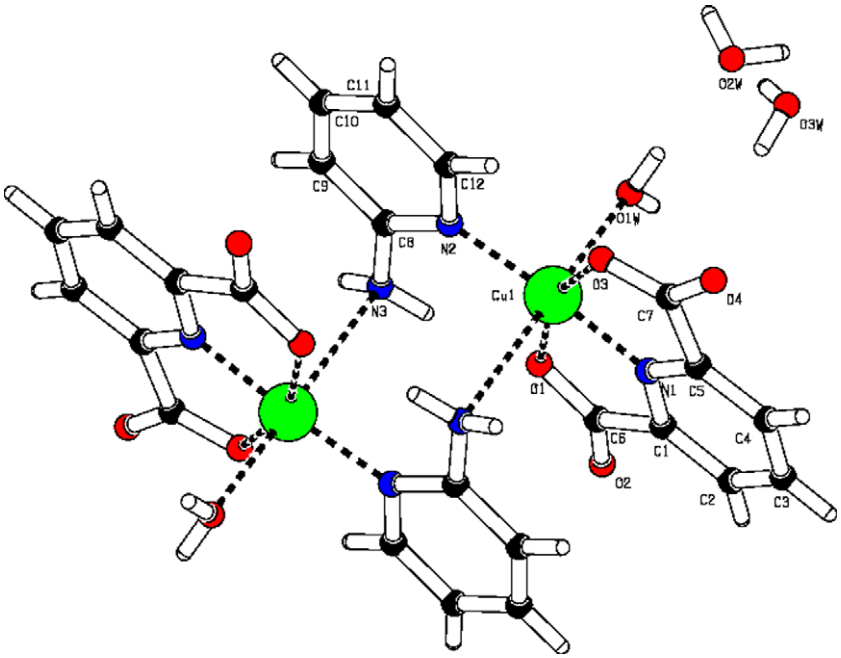


Fig. 2. An ORTEP drawing of **1** with intra- and intermolecular interactions.

vibrations of the coordinated 2-aminopyridine ligand. The relatively weak band at 3098 cm^{-1} is due to ν(CH) vibrations of aromatic rings. The carboxylate groups exhibit strong bands in the region 1690–1570 cm^{-1}. In the Cu(II) complex **1**, these strong bands were shifted and broadened with respect to the corresponding ones in the free dipicolinic acid. The present bands of the carboxylate COO^- group are reflected by IR spectrum of the asymmetric (ν_{as}) and symmetric (ν_s) stretching vibrations at 1660 and 1494 cm^{-1}, respectively. In addition, the differences between the asymmetric and symmetric stretches of the carboxylate groups of **1**, Δ = 166 cm^{-1}, suggest a monodentate binding of the carboxylate group to the metal ion [40]. The strong absorption bands at 1617 and 1566–1592 cm^{-1} are attributed to the ν(C=N) and ν(C=C) vibrations in the ligands, respectively [41]. The ν(C–O) vibrations were observed at 1079, 1275 and 1358 cm^{-1}, as indicated in [42–44]. The ring wagging vibrations of the pyridine groups are also observed at 677 and 760 cm^{-1}. The weak bands at 593 and 432 cm^{-1} are from the Cu–N and Cu–O vibrations, respectively, of complex **1**.

3.2. Crystal structure of $[Cu(\mu\text{-ap})(dipic)(H_2O)]_2{\cdot}4H_2O$ (**1**)

The molecular structure of **1**, with the atom labeling, and the intra- and intermolecular interactions, are shown in Figs. 1 and 2. The crystal packing diagram of **1** is shown in Fig. 3. The details of

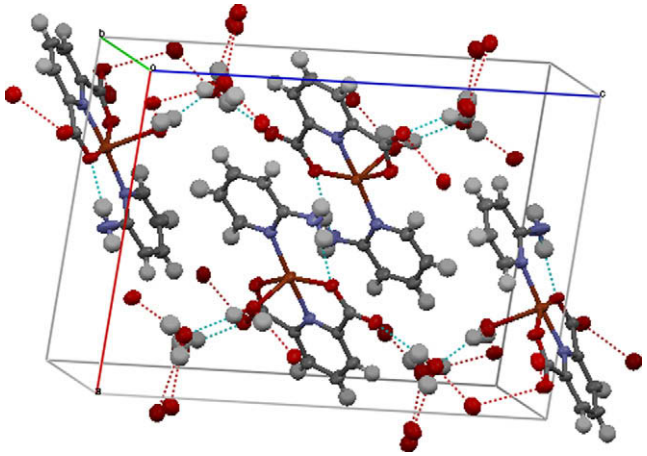


Fig. 3. Crystal packing diagram of **1**.

the crystal structure solution are given in Table 1, whereas the selected bond lengths and angles, and hydrogen bonding geometries are listed in Tables 4 and 5, respectively. The compound crystallizes in the monoclinic $P2_1/c$ space group. The asymmetric unit contains one dipic ion, one ap molecule, one Cu(II) ion, one coordinated water molecule and two uncoordinated water molecules (Fig. 1). The value of the structural index τ is 0.26 and the coordination environment of the Cu(II) atom is best described as a distorted square-pyramid [45]. The penta-coordinated central Cu(II) ion resides on a centre of symmetry comprising two N atoms, one from dipic (N1) and one from the ap ring (N2), two carboxylate O atoms from dipic (O1 and O3) and one O atom from water (O1w). Two N atoms from two different ligands, dipic and ap, fulfill the apical positions with Cu–N distances of 1.9228(17) and 1.9797(17) Å for Cu–N1 and Cu–N2, respectively, and the bond distances are similar to the those found in other related Cu(II) complexes [5,46,47]. The Cu–O bond distances are 2.0533(16) and 2.0543(17) Å, observed from the carboxylate coordination to the center metal ion, and are well consistent with those observed in the literature data [5,44,45,48]. The Cu–O1w bond distance, arising from coordination of the water molecule to the central metal ion, is 2.2776(19) Å, which is much longer than the Cu–O (carboxylate) bond distances.

In the symmetric unit, the distances between the two bilateral pyridine rings are in the range 3.326(3)–3.584(3) Å and these distances are categorized as π–π stacking (Fig. 2). These values are close to the distance between the layers in the structure of graphite. 2-Aminopyridine coordinates the Cu(II) ion through the nitrogen of the ring (N2) (1.9797(17) Å) and the amino group (N3) also participates in coordination with a long distance to combine the asymmetric units (2.918(3) Å). This is categorized as a van der Waals interaction which reduces the molecular volume and thus facilitates the packing in the crystal.

Hydrogen bonds between the carboxylate group and water molecules play important roles in stabilizing the crystal structure. The ranges of the D–H···A angles and those of the H···A and D···A distances indicate the presence of strong and weak hydrogen bonding

Table 3
IR spectral data of **1** (cm^{-1})[a].

Assignment	1
ν(OH)water	3340b
$\nu(NH_2)$	3202m, 3280m
ν(C–H)	3098w
ν(COO)	1660s, 1494s
ν(C=N)	1617s
ν(C=C)	1592s, 1566s
ν(C–O)	1358s, 1275s, 1079s
γ(py)	760vs, 677w
ν(Cu–N)	593w
ν(Cu–O)	432w

[a] *Abbreviations*: w, weak; m, medium; s, strong; vs, very strong; b, broad.

Table 4
Selected bond distances (Å) and angles (°)) for **1**.

Cu1–N1	1.9228(17)	Cu1–O1w	2.2776(19)
Cu1–N2	1.9797(17)	Cu1–N3(a)	2.918(3)
Cu1–O1	2.0533(16)	Cu1(a)–N3^{i}	2.918(3)
Cu1–O3	2.0543(17)		
N1–Cu1–N2	173.89(8)	O1–Cu1–O3	158.57(6)
N1–Cu1–O1	79.02(7)	N1–Cu1–O1w	93.15(7)
N2–Cu1–O1	103.27(7)	N2–Cu1–O1w	92.43(7)
N1–Cu1–O3	79.66(7)	O1–Cu1–O1w	92.07(7)
N2–Cu1–O3	97.74(7)	O3–Cu1–O1w	91.16(8)

Symmetry codes: (i) $1-x, -y, -z$.

Table 5
Hydrogen bonding geometry of **1** (Å, °).

D–H···A	d(D–H)	d(H···A)	d(D···A)	∠D–H···A
N3–H3A···O1	0.86(3)	1.97(4)	2.790(3)	157(3)
N3–H3B···O2^{i}	0.82(3)	2.34(3)	3.129(3)	162(3)
O1w–H5A···O2w	0.810(17)	2.085(17)	2.895(3)	177(3)
O1w–H5B···O4^{ii}	0.801(17)	2.022(18)	2.808(3)	167(3)
O2w–H6A···O3w^{iii}	0.818(17)	1.957(18)	2.773(3)	176(3)
O2w–H6B···O2^{iv}	0.807(17)	2.080(18)	2.886(3)	176(4)
O3w–H7A···O2w	0.808(17)	2.088(18)	2.891(3)	172(4)
O3w–H7B···O4	0.809(17)	2.060(18)	2.862(3)	171(3)

Symmetry codes: (i) $-x+1, -y, -z+1$; (ii) $x, y-1, z$; (iii) $-x+2, y-1/2, -z+1/2$; (iv) $x, -y+1/2, z-1/2$.

Table 2
Inhibition concentrations of the starting materials and crystal complex against microorganisms (MICs are given as mg/mL).

Pathogens	Source	H_2dipic	ap	**1**	Std
Escherichia coli	NRRL B-3008	0.5	>1.0	0.5	0.0078[a]
Pseudomonas aeruginosa	ATCC 27853	0.5	0.5	0.5	0.125[a]
Proteus vulgaris	NRRL B-123	1.0	0.5	0.250	0.0156[a]
Staphylococcus aureus	ATCC 6538	0.25	0.5	0.5	0.032[a]
Candida albicans	Clinical isolate	0.25	0.125	0.125	0.0625[b]
C. albicans	ATCC 90028	0.125	0.0625	0.0625	0.0625[b]
C. albicans	NRRL Y-12983	0.25	0.5	0.125	0.032[b]
C. glabrata	Clinical Isolate	0.125	0.125	0.125	0.032[b]
C. krusei	NRRL Y-7179	0.125	0.25	0.125	0.125[b]
C. parapsilosis	NRRL Y-12696	0.25	0.25	0.125	0.5[b]
C. tropicalis	NRRL Y-12968	0.25	0.25	0.125	0.125[b]

[a] Chloramphenicol for bacteria as antibacterial standard.
[b] Ketoconazole for yeast as antifungal standard.

(Table 5). Two uncoordinated water molecules in the asymmetric unit have no symmetry center; hence they could not be located in the second half of the symmetric unit (Figs. 2 and 3).

3.3. UV–Vis spectrum, magnetic susceptibility and conductivity

The electronic spectra of **1** and the free ligands, ap and H_2dipic, were recorded in the solid state with KBr and in solution at a 1×10^{-3} M concentration at room temperature (Fig. 4). In the solid state absorption spectra of the free ligands there are similar absorption peaks (234 and 298 nm for ap, 230 and 265 nm for H_2dipic) due to the π–π^* transitions. Characteristic π–π^* transitions are in the spectrum of **1** (208, 218, 263 and 272 nm) with the same profiles as the free ligands. These π–π^* transition bands for all compounds are located in two regions, 220 and 270 nm, and are red-shifted in the solution spectra. (Fig. 4a–c and Table 6). The absorption bands profiles of the solution UV–Vis studies are similar to those absorption maxima of the corresponding ligands and complex **1** in the solid state. All the π–π^* transition bands for the ligands and the copper(II) complex in water and DMSO are observed in the range 290–315 nm (Fig. 4b and c and Table 6).

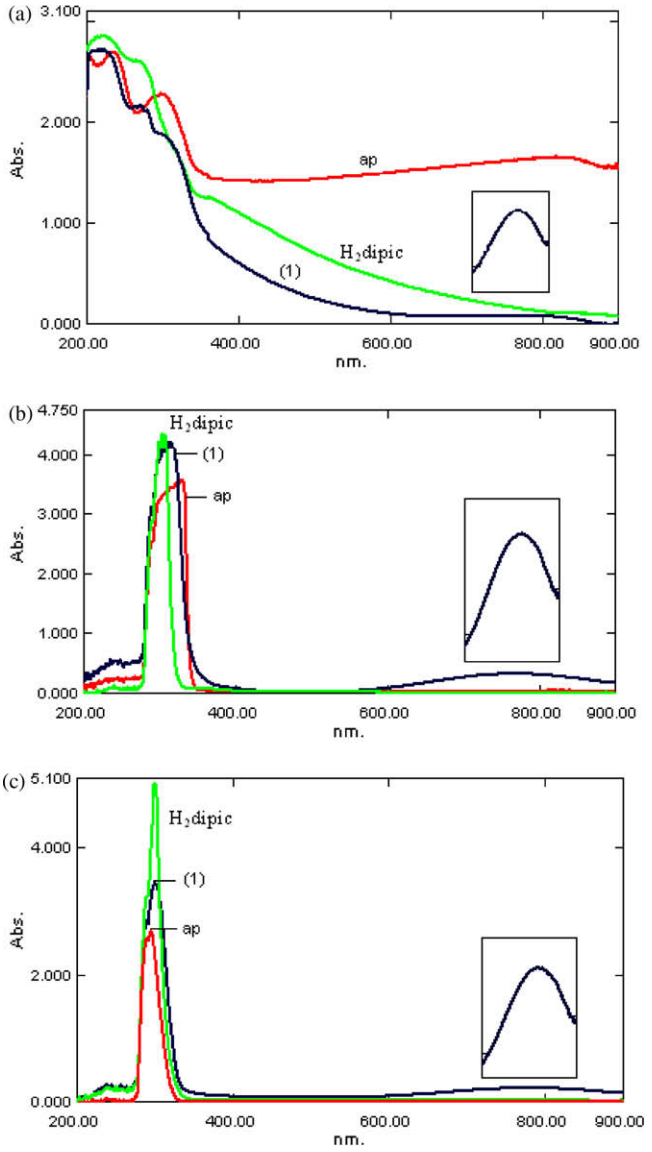


Fig. 4. UV–Vis spectra of complex **1** and the free ligands, ap and H_2dipic, (a) in the solid state phase (KBr), (b) in water, and (c) in DMSO.

Table 6
Optical properties of complex **1** and the free ligands, ap and H_2dipic, in the solid state phase (KBr), water and DMSO.

	λ_{max} (nm) (ε (M^{-1} cm^{-1}))		
	ap	H_2dipic	**1**
Solid		265	777
	298	230	272
	234		263
			218
			208
Water	295 (2678)	299 (10 000)	783 (212)
	290 (2561)		300 (3456)
DMSO	330 (3587)	303 (4340)	768 (325)
	315 (3556)		313 (4229)
			304 (4119)

The bands for the d–d transitions show a similar pattern at the maxima 777 nm in the solid state, 783 nm in water and 768 nm in DMSO for the copper(II) complex and suggest that the Cu(II) ion has the characteristics of a penta-coordinated copper complex with distortion (Fig. 4a–c) [49]. All the data which we obtained from the electronic spectra of the solutions do not show any marked differences from that of the solid, so it may be assumed that the bonding modes of the ligands as well as the geometry of the complex do not change in solution [50].

The room temperature magnetic moment of the Cu(II) complex is 1.63 BM per Cu(II) ion in the crystal structure, indicating the presence of one unpaired electron. The conductivity in DMSO is 1.8 Ω^{-1} cm^2 mol^{-1}, which indicates that complex **1** is non-ionic [51]. This result shows that 2,6-pyridinedicarboxylic acid coordinates to the Cu(II) ion as 2,6-pyridinedicarboxylate to form a neutral coordination compound.

3.4. Thermal analysis of [Cu(μ-ap)(dipic)(H_2O)]$_2$·4H_2O (**1**)

Fig. 5 shows the TG-DTG and DTA curves of complex **1**. The first stage, an endothermic peak (DTG_{max} = 97.4 °C) between 30 and 110 °C, corresponds to the loss of the 6 moles of crystal water molecules (found 14.40, calcd. 14.33%). The second stage, an endothermic peak (DTG_{max} = 269.6 °C) between 110 and 280 °C, corresponds to the loss of the 2 moles of 2-aminopyridine molecules (found 24.90, calcd. 24.95%). Two 2,6-pyridinedicarboxylate ions are decomposed in the third stage between 280 and 369 °C with DTG_{max} at 293.5 and 302.3 °C (found 44.09, calcd. 44.28%). The final decomposition product was CuO, identified by IR spectroscopy (found 20.8%, calcd. 21.1%).

3.5. Biological activity

A panel of selected human microbial pathogens were used to evaluate the effects of the starting materials and the resulting crystal complex. A microdilution assay was used with Ketoconazole and Chloramphenicol as standard antimicrobial agents. The Gram positive and negative bacteria were found to be more resistant when compared with the tested yeasts, where better inhibitory concentrations were observed, as listed in Table 2. The MIC values were determined as 0.0625–0.25 mg/mL, relatively good inhibitions when compared with a standard antifungal agent. The variation in the effectiveness of different compounds against different organisms depend either on the impermeability of the cells of the microbes or the difference in the ribosomes of the microbial cells [52,53].

The preliminary radical scavenging assay resulted in a low activity range, suggesting that these compounds are not of an antioxidative nature in the DPPH assay. However it is also worthwhile to evaluate other antioxidant assays. Compounds such

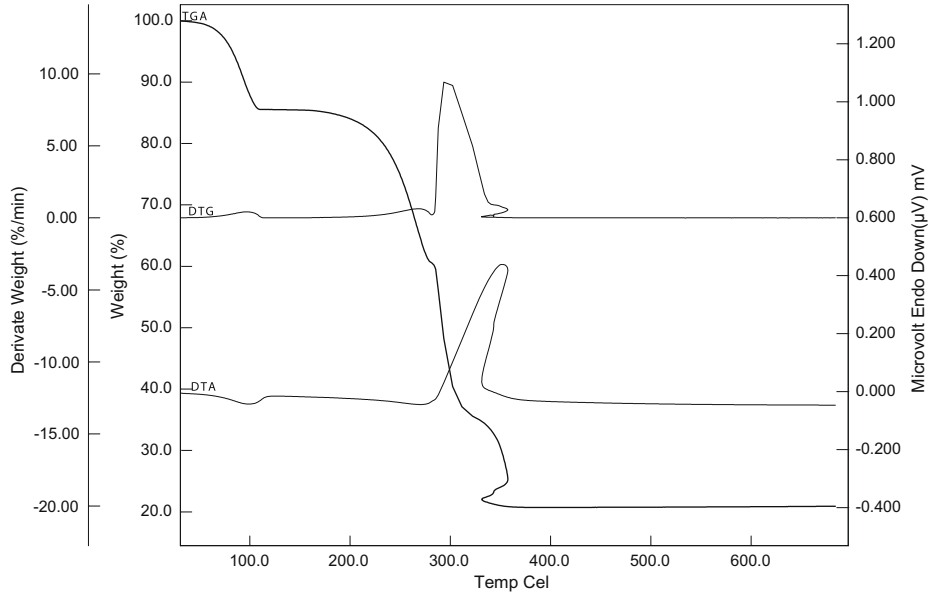


Fig. 5. The TG-DTG and DTA curves of **1**.

as [Cu(L1)(L′)Cl2]·3H2O L1 = 2,6-pyridinedicarboxaldehydebis(*p*-hydroxyphenylimine), L′ = 2-aminopyridine and [Cu(L2)(L′)Cl2]·H2O L1 = 2,6-pyridinedicarboxaldehydebis(*o*-hydroxyphenylimine), L′ = 2-aminopyridine were inactive or less active against some Gram positive and Gram negative bacteria [54]. M(L)Cl2 L = *N*,*N*-diethylpiperazinyl,2,6-pyridinedicarboxylate) and the ligand were also screened against various pathogens in order to study their antibacterial action [55]. The results revealed that the Cu(II) complex has activity comparable with the reference drugs gentamycin and flucanzole. The antibacterial results evidently show that the activity of the ligand becomes more pronounced and significant when coordinated to the metal ion. This enhancement in the activity was suggested to be possibly due to an efficient diffusion of the metal complexes into the bacterial cell or interaction with the bacterial cell walls [55].

4. Conclusions

In this present work, a Cu(II) complex with mixed ligands was prepared for the first time. The Cu(II) ion resides on a centre of symmetry in a distorted square-pyramidal coordination environment comprising two N atoms, one from dipic (N1) and one from the ap ring (N2), two carboxylate O atoms from dipic (O1 and O3) and one O atom from water (O1w). Intermolecular N–H···O and O–H···O hydrogen bonds and π–π stacking interactions seem to be effective in the stabilization of the crystal structure. Elemental analyses and all measurements show good agreement with the structure. The free ligands and the Cu(II) complex possess antifungal activity against *Candida* sp. The preliminary biological evaluation suggests that derivatives of such complexes are worthwhile for further antifungal *in vitro* and *in vivo* tests.

Acknowledgements

The authors acknowledge the support provided (Grant No. 2007/2, Dumlupınar University Research Fund). In addition, the authors would like to thank the Faculty of Arts and Sciences of Ondokuz Mayıs University, Turkey, for the use of the Stoe IPDS-2 diffractometer facilities (Grant F.279). Gökalp İşcan of Anadolu University is also acknowledged for the biological assays.

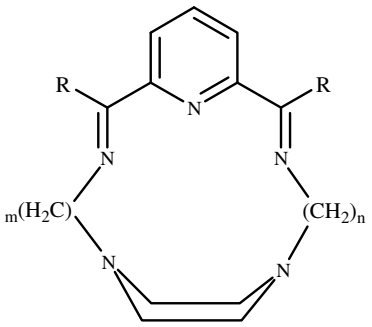
Appendix A. Supplementary data

CCDC 717997 contains the supplementary crystallographic data for **1**. These data can be obtained free of charge via http://www.ccdc.cam.ac.uk/conts/retrieving.html, or from the Cambridge Crystallographic Data Centre, 12 Union Road, Cambridge CB2 1EZ, UK; fax: (+44) 1223-336-033; or e-mail: deposit@ccdc.cam.ac.uk. Supplementary data associated with this article can be found, in the online version, at doi:10.1016/j.poly.2009.05.079.

References

[1] C. Ma, C. Chen, Q. Liu, D. Liao, L. Li, Eur. J. Inorg. Chem. 1 (2003) 1227–1231.
[2] M. Ranjbar, H. Aghabozorg, A. Moghimi, Acta Crystallogr., Sect. E 58 (2002) m304.
[3] M. Devereux, M. McCann, V. Leon, V. McKee, R.J. Ball, Polyhedron 21 (2002) 1063.
[4] C.B. Ma, C. Fan, C.N. Chen, Q.T. Liu, Acta Crystallogr., Sect. C 58 (2002) m553.
[5] M. Koman, M. Melník, M. Moncol, Inorg. Chem. Commun. 3 (2000) 262.
[6] T.D. Barela, A.D. Sherry, Anal. Biochem. 17 (1976) 351–357.
[7] Y. Kanai, Analyst 115 (1990) 809.
[8] P. Laine, A. Gourdon, J.P. Launary, Inorg. Chem. 34 (1995) 5129.
[9] G.F. Bailey, S. Karp, T.E. Sacks, J. Bacteriol. 89 (1965) 984.
[10] B. Setlow, P. Setlow, Microbial 59 (1993) 640.
[11] L.D. Waterbury, C. Serrato, G.R. Martinez, Proc. West. Pharm. Soc. 32 (1989) 9.
[12] J.T. Groves, I.O. Kady, Inorg. Chem. 32 (1993) 3868.
[13] B.R. Cameron, M.C. Darkes, I.R. Baird, R.T. Skerlj, Z.L. Santucci, S.P. Fricker, Inorg. Chem. 42 (2003) 4102.
[14] R. Kempte, S. Brenner, P. Arndt, Organometallics 15 (1996) 1071–1074.
[15] H. Fuhrmann, S. Brenner, P. Arndt, Inorg. Chem. 35 (1996) 6742.
[16] W.R. McWhinnie, J. Chem. Soc. (1964) 2959–2969.
[17] E. Uhlig, M. Madler, Z. Anorg. Allgem. Chem. 338 (1965) 199.
[18] R.K. Poddar, U. Agarwala, J. Inorg. Nucl. Chem. 35 (1973) 3769.
[19] A. Garcia-Raso, J.J. Fiol, A. Lopez-Zafra, A. Cabrero, I. Mata, E. Molins, Polyhedron 18 (1999) 871–878.
[20] P. Lechat, S. Tesleff, W.C. Bownan, Aminopyridines and Similarly Acting Drugs, Pergamon, Oxford, 1982.
[21] M.J.R.P. Queiroz, I.C.F.R. Ferreira, R.C. Calhelha, L.M. Estevinho, Bioorg. Med. Chem. 15 (2007) 1788–1794.
[22] M. Melník, Coord. Chem. Rev. 47 (1982) 239.
[23] M. Kato, Y. Muto, Coord. Chem Rev. 92 (1988) 45.
[24] M.R. Sundberg, R. Uggla, M. Melník, Polyhedron 15 (1996) 1157.
[25] N. Lah, G. Giester, J. Lah, P. Segedin, I. Leban, New J. Chem. 25 (2001) 753.
[26] O. Castillo, A. Luque, F. Lloret, P. Roman, Inorg. Chem. Commun. 4 (2001) 350.
[27] S. Padhye, G.B. Kauffman, Coord. Chem. Rev. 63 (1985) 127.
[28] D.X. West, A.E. Liberta, S.B. Chinate, P.B. Sonawane, A.S. Kumbhar, R.G. Yerande, Coord. Chem. Rev. 123 (1993) 49.
[29] D.X. West, S.B. Padhye, P.B. Sonawane, Struct. Bond. 76 (1991) 1.
[30] N.J.M. Campbell, Coord. Chem. Rev. 15 (1975) 279.

[31] J. Reedijk, W.L. Driessen, J. van Rijn, K.D. Karlin, J. Zubieta (Eds.), Biological and Inorganic Copper Chemistry, Adenine Press, New York, 1986, p. 143.
[32] G.M. Sheldrick, SHELXS97 and SHEXL97. Program for Crystal Structure Solution and Refinement, University of Göttingen, Germany, 1997.
[33] Stoe & Cie, X-AREA (Version 1.18) and X-RED32 (Version 1.04), Stoe & Cie, Darmstadt, Germany, 2002.
[34] L.J. Farrugia, J. Appl. Cryst. 30 (1997) 565.
[35] W.C. Winn, S.D. Allen, W.M. Janda, E.W. Koneman, G.W. Procop, P.C. Schreckenberger, G.L. Woods, Koneman's Color Atlas and Textbook of Diagnostic Microbiology, 6th ed., Lippincott–Williams & Wilkins, Philadelphia, 2006.
[36] NCCLS, Reference Method for Broth Dilution Antifungal Susceptibility Testing of Yeasts; Approved Standard, 2nd ed., NCCLS document M27-A2, 2002.
[37] D. Amsterdam, in: V. Lorian (Ed.), Susceptibility Testing of Antimicrobials in Liquid Media, Antibiotics in Laboratory Medicine, 4th ed., Williams & Wilkins, Maple Press, MD, USA, 1997.
[38] Y. Kumarasamy, M.E. Fergusson, L. Nahar, S.D. Sarker, Pharmaceut. Biol. 40 (2002) 307–310.
[39] S.D. Sarker, Z. Latif, A.I. Gray (Eds.), Natural Product Isolation, Methods in Biotechnology, 2nd ed., vol. 20, Humana Press, Totowa, 2006.
[40] K. Nakamoto, Infrared and Raman Spectra of Inorganic and Coordination Compounds, 5th ed., Wiley-Interscience, NewYork, 1997.
[41] M.V. Kirillova, M.F.C.G. Da Silva, A.M. Kirillov, J.J.R.F. Da Silva, A.J.L. Pombeiro, Chim. Acta 360 (2007) 506.
[42] Z. Vargova, V. Zeleoak, I. Cisaova, K. Györyova, Thermochim. Acta 423 (2004) 149.
[43] L. Mao, Y. Wang, Y. Qi, M. Cao, C. Hu, J. Mol. Struct. 688 (2004) 197.
[44] İ. Uçar, B. Karabulut, A. Bulut, O. Büyükgüngör, J. Mol. Struct. 336 (2007) 834.
[45] A.W. Addison, T.N. Rao, J. Reedijk, J. van Rijn, G.C. Verschoor, J. Chem. Soc., Dalton Trans. (1984) 1349–1356.
[46] J. Shou-Wen, C. Wan-Zhi, Polyhedron 26 (2007) 3074.
[47] C. Julienne, M. Jerome, R. Didier, Acta Crystallogr., Sect. C 60 (2004) m101.
[48] M.C. Subal, Z. Ennio, C.R. Nirmalendu, J. Mol. Struct. 877 (2008) 145.
[49] D. Kroczewska, B. Kurzak, J. Jezierska, Polyhedron 25 (2006) 678.
[50] M. Ghosh, A. Majee, M. Nethaji, T. Chattopadhyay, Inorg. Chim. Acta 362 (2009) 2052.
[51] W.J. Geary, Coord. Chem. Rev. 7 (1971) 81.
[52] N. Sari, S. Arslan, E. Logoglu, I. Sakiyan, G.U. J. Sci. 16 (2003) 283–286.
[53] C. Jayabalakrishnan, K. Natarajan, Transit. Met. Chem. 27 (2002) 75.
[54] G.G. Mohamed, Z.H. Abd El-Wahab, Spectrochim. Acta, Part A 61 (2005) 1059–1068.
[55] S. Khan, S.A.A. Nami, K.S. Siddiqi, E. Husain, I. Naseem, Spectrochim. Acta, Part A 72 (2009) 421.



	m	n	R
L^1	2	3	H
L^2	2	3	CH_3
L^3	3	3	H
L^4	3	3	CH_3

Fig. 1. Ligands under discussion in this paper.

2. Experimental

2.1. Starting materials

2,6-Pyridinedicarbaldehyde was prepared according to the literature method [19]. N,N′(2-aminoethyl)(3-aminopropyl)piperazine was synthesized according to the literature method [18]. 2,6-Diacetylpyridine, N,N′-bis(3-aminopropyl)piperazine, 2-aminoethyl piperazine and the metal salts were commercial products (from Merck, Aldrich and Fluka) and were used without further purification. Solvents were of reagent grade purified by the usual methods.

Caution! Perchlorate salts are potentially explosive. Only small amount of material should be prepared and handled with great care.

2.2. Instrumentation

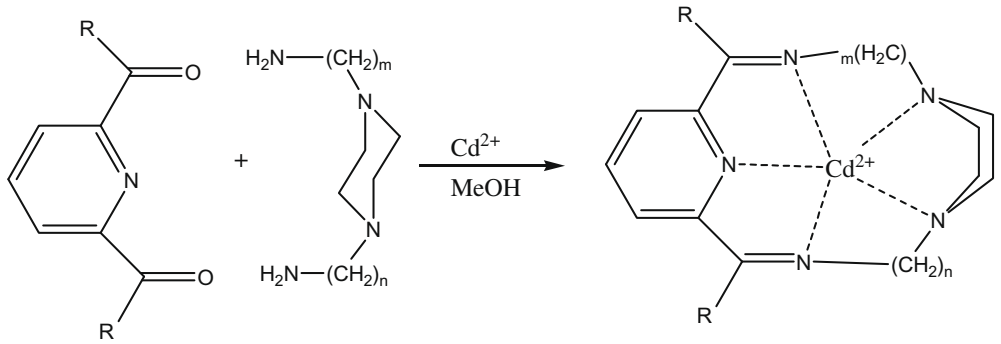
Elemental analyses were performed in a Carlo-Erba EA microanalyser. FT-IR spectra in the 4000–400 cm^{-1} region were recorded from KBr pellets on Bruker VECTOR 22 and Perkin–Elmer GX spectrophotometers. FAB mass spectra were recorded using a Kratos-MS-50T spectrometer connected to a DS90 data system using 3-nitrobenzyl alcohol as the matrix. Conductivimetry measurements were carried out in 10^{-3} mol dm^{-3} dimethylformamide solutions at 20 °C using a CARISON GLP32 conductivimeter. ^1H and ^{13}C NMR spectra were recorded on a Bruker 300 and 400 MHz using DMSO as solvent.

2.3. X-ray crystal structure determination

X-ray data for $[CdL^4|(NO_3)(H_2O)]^+$ was performed on STOE IPDS-II two circle diffractometer, using graphite monochromated Mo Kα X-ray radiation (λ = 0.7107 nm). The data collection was performed at room temperature using the ω-scan technique and using the STOE X-AREA software package [20]. The crystal structures were solved by direct methods [21] and refined by using X-STEP32 crystallographic software package [22]. All of the non-hydrogen atoms were refined anisotropically. All of hydrogen atoms were located in ideal positions. X-ray data for $[CdL^2Cl]^+$ were measured on a Bruker Smart 1000 CCD diffractometer at CACTI (Universidade de Vigo) at 20 °C using graphite monochromated Mo Kα radiation (λ = 0.71073 Å). All data were corrected for Lorentz and polarization effects. Empirical absorption corrections were also applied for all the crystal structures obtained [23]. Complex scattering factors were taken from the program package SHELXTL [24]. The structures were solved by direct methods which revealed the position of all non-hydrogen atoms. All the structures were refined on F^2 by a full-matrix least-squares procedure using anisotropic displacement parameters for all non-hydrogen atoms. Crystal data and structure refinement for both complexes are shown in Table 1.

2.4. Computational method

The geometries of the ligands, L^2 and L^4 and their Cd(II) complexes in the gas phase were fully optimized at DFT (B3LYP) [25] level of theory using the GAUSSIAN 98 set of programs [26]. The ligands were studied using by two different 6-31G* and lanl2dz basis sets [27]. The latter basis set was also used for calculation of the complexes. The standard 6-311+G* basis set was also used for single-point calculations on the structure of ligands derived from above calculations. Vibrational frequency analyses, calculated at the same level of theory, indicate that all optimized structures



	m	n	R
L^1	2	3	H
L^2	2	3	CH_3
L^3	3	3	H
L^4	3	3	CH_3

Scheme 1. The template condensation between 2,6-diacetylpyridine or 2,6-pyridinedicarbaldehyde and two amines with piperazine moiety in the presence of cadmium(II) ion.

Table 1
Crystal data and structure refinement for $[CdL^2Cl](CH_3OH)ClO_4$ and $[CdL^4(NO_3)(H_2O)]ClO_4$.

Complex	$[CdL^2Cl](CH_3OH)ClO_4$	$[CdL^4(NO_3)(H_2O)]ClO_4$
Empirical formula	$C_{19}H_{31}CdCl_2N_5O_6$	$C_{19}H_{31}CdClN_6O_8$
Formula weight	576.26	619.36
Crystal system	monoclinic	orthorhombic
Space group	$P2(1)/c$	$P2_12_12_1$
a (Å)	7.315(14)	11.887(3)
b (Å)	15.457(3)	14.006(3)
c (Å)	21.406(4)	15.097(3)
α (°)	90	
β (°)	98.519(4)	
γ (°)	90	
V (Å^3)	2393.7(8)	2513.6 (9)
Z	4	4
D_{calc} (Mg/m^3)	1.599	1.637
F (0 0 0)	1170	1264
Crystal size (mm^3)	0.45 × 0.34 × 0.32	0.50 × 0.35 × 0.25
T (K)	293(2)	293(2)
Absorption coefficient (mm^{-1})	1.172	1.030
Index ranges	$-8 \leqslant h \leqslant 8$, $-18 \leqslant k \leqslant 12$, $-24 \leqslant l \leqslant 25$	$-15 \leqslant h \leqslant 15$, $-17 \leqslant k \leqslant 17$, $-18 \leqslant l \leqslant 19$
Maximum and minimum transmission	0.7056 and 0.6207	0.760 and 0.650
θ Range for data collection (°)	1.63–25.06	1.98–26.76
λ (Å)	0.71073	0.71073
Number of reflections measured	9750	23613
Number of reflections used in refinement ($F^2 > 0$), NV	3839, 292	5275, 324
R^a, wR_2^b, S	0.0600, 0.1435, 0.943	0.0377, 0.1079, 1.105
$\delta\rho_{max.}$, $\delta\rho_{min.}$ (e Å^{-3})	0.887, −0.492	1.831, −1.428

[a] $R_1 = \Sigma||F_o| - |F_c||/\Sigma|F_o|$.
[b] $wR_2 = \{\Sigma[w(||F_o|^2 - |F_c|^2|)^2]/\Sigma[w(F_o{}^4|)]\}^{1/2}$.

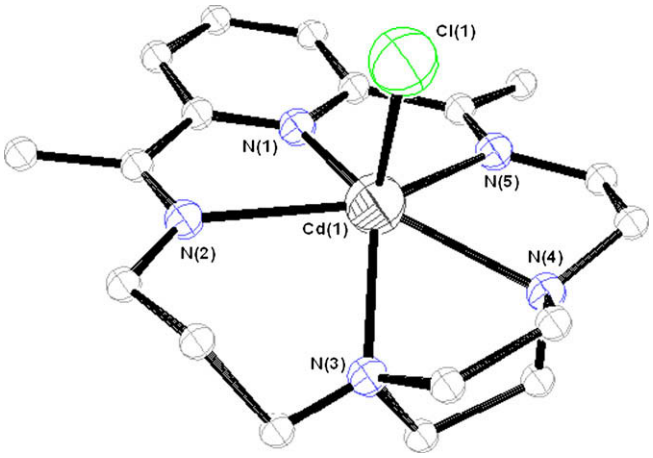


Fig. 2. The molecular structure of the cation $[CdL^2(Cl)]^+$.

are at the stationary points corresponding to local minima without any imaginary frequency. The initial atomic coordinates for DFT calculations were derived from X-ray data.

2.5. Synthesis of complexes

2.5.1. General procedure

2.5.1.1. Method A. A solution of NaOH (2 mmol) in absolute ethanol (10 mL) was added to a suspension of the N,N′(2-aminoethyl)(3-aminopropyl)piperazine tetrahydrochloride (0.5 mmol) in absolute ethanol (10 mL). The mixture was stirred at room temperature for a few minutes then filtered, and the precipitate was washed well with absolute ethanol (10 mL).The washings and the filtrate were

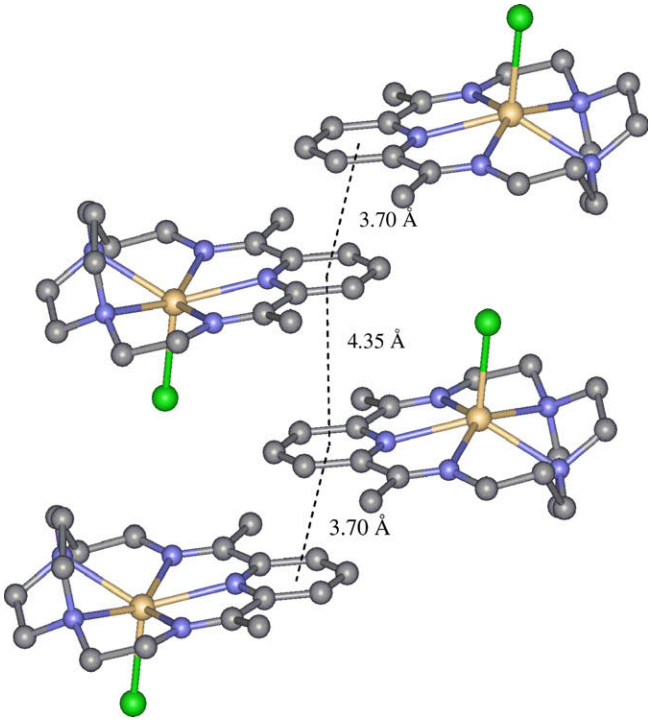


Fig. 3. The π,π-interactions in the cation $[CdL^2Cl]^+$.

combined and this solution was added dropwise to a hot solution of $Cd(ClO_4)_2{\cdot}6H_2O$ (0.5 mmol) and 2,6-diacetylpyridine or 2,6-pyridinedicarbaldehyde (0.5 mmol) in absolute methanol (20 mL), over a period of 2 h. After refluxing the solution for 24 h it was filtered. Crystalline compound was obtained by slow diffusion of diethyl ether vapor into the MeOH/MeCN solution of the above solid.

2.5.2. $[CdL^1Cl]ClO_4{\cdot}H_2O$ (**1**)

Yield: 0.198 g (36%), *Anal.* Calc. for $C_{16}H_{25}CdCl_2N_5O_5$: C, 34.9; H, 4.6; N, 12.7. Found: C, 35.3; H, 4.4; N, 12.9%. IR (KBr, cm^{-1}): 3442, 1659, 1643 $\upsilon_{(C=N)}$, 1589, 1450 [$\upsilon_{(C=C)}$ and $\upsilon_{(C=N)py}$], 1089, 623 cm^{-1} $\upsilon(ClO_4^-)$, FAB-MS, (positive FAB in 3-nitrobenzyl alcohol): m/z (%), $[Cd\ L^1Cl]^+$, 434(100%). Λ_M/Ω^{-1} cm^2 mol^{-1} (in DMF): 120 (2:1).

2.5.3. $[CdL^2Cl](CH_3OH)ClO_4{\cdot}H_2O$ (**2**)

Yield: 0.230g (40%), *Anal.* Calc. for $C_{19}H_{31}CdCl_2N_5O_6$; C: 37.5; H: 5.1; N: 11.5. Found: C, 37.1; H, 4.9; N, 11.7%. IR (KBr, cm^{-1}): 3445, 1652, 1630($_{C=N}$), 1586, 1456 [$\upsilon_{(C=C)}$ and $\upsilon_{(C=N)py}$], 1096, 623 cm^{-1} $\upsilon(ClO_4^-)$, FAB-MS, (positive FAB in 3-nitrobenzyl alcohol): m/z (%): $[Cd\ L^2Cl]^+$, 462(100%). Λ_M/Ω^{-1} cm^2 mol^{-1} (in DMF): 146 (2:1).

2.5.3.1. Method B. A solution of N,N′-bis(3-aminopropyl)piperazine(0.5 mmol) in MeOH(10 mL) was added dropwise to a hot solution of $Cd(NO_3)_2{\cdot}6H_2O$ or $Cd(ClO_4)_2{\cdot}6H_2O$ (0.5 mmol) and 2,6-diacetylpyridine or 2,6-pyridinedicarbaldehyde (0.5 mmol) in absolute methanol (20 mL) over a period of 2 h. After refluxing the solution for 24 h it was filtered whilst hot and $NaClO_4$ (1 mmol) was added to the filtrate. Crystalline compound (**4**) was obtained by slow diffusion of Et_2O vapor into the methanol solution of the above solid.

2.5.4. $[CdL^3](ClO_4)_2$ (**3**)

Yield: 0.230g (38%), *Anal.* Calc. for $C_{17}H_{25}CdCl_2N_5O_8$; C, 33.4; H, 4.1; N, 11.5. Found: C, 33.4; H, 4.4; N, 11.7%. IR (KBr, cm^{-1}): 3441, 1650 $\upsilon_{(C=N)}$, 1590, 1465, [$\upsilon_{(C=C)}$ and $\upsilon_{(C=N)py}$], 1097, 623 cm^{-1}

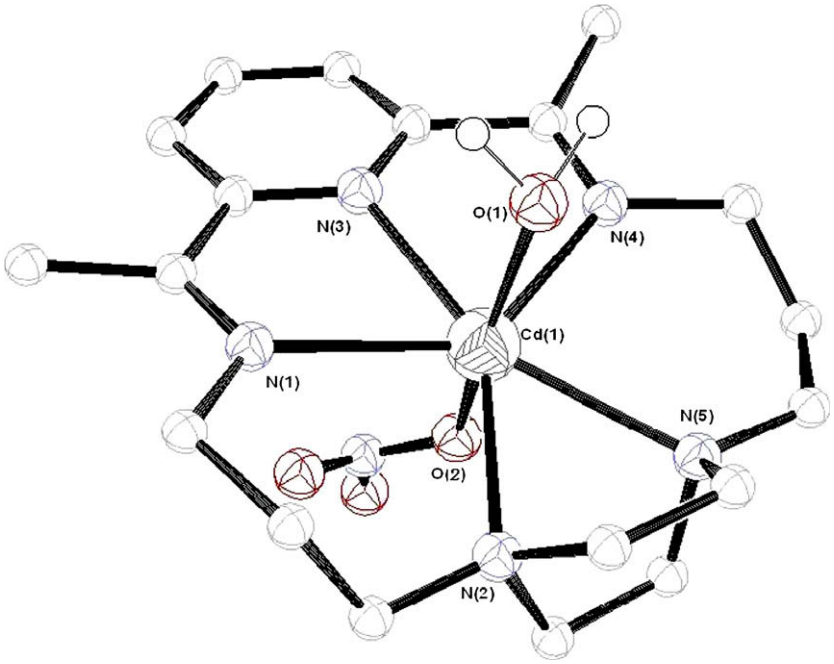


Fig. 4. The molecular structure of the cation $[CdL^4(NO_3)(H_2O)]^+$.

Table 2
Selected bond lengths (Å) and bond angles (°) for $[CdL^2Cl]^+$(**2**) and $[CdL^4(NO_3)(H_2O)]^+$(**4**).

Bond lengths (Å)	**1**	*Bond lengths (Å)*	**2**
Cd(1)–N(1)	2.34(6)	Cd(1)–N(1)	2.41(4)
Cd(1)–N(2)	2.43(6)	Cd(1)–N(2)	2.50(4)
Cd(1)–N(3)	2.34(8)	Cd(1)–N(3)	2.33(4)
Cd(1)–N(4)	2.43(10)	Cd(1)–N(4)	2.48(4)
Cd(1)–N(5)	2.41(6)	Cd(1)–N(5)	2.49(5)
Cd(1)–Cl(1)	2.51(2)	Cd(1)–O(1)	2.39(4)
		Cd(1)–O(2)	2.49(6)
Bond angle (°)		*Bond angle (°)*	
N(1)–Cd(1)–N(2)	68.00(2)	N(1)–Cd(1)–N(2)	82.62(16)
N(1)–Cd(1)–N(3)	134.40(2)	N(1)–Cd(1)–N(3)	148.50(15)
N(1)–Cd(1)–N(4)	67.60(3)	N(1)–Cd(1)–N(4)	142.20(16)
N(1)–Cd(1)–N(5)	67.70(2)	N(1)–Cd(1)–N(5)	61.55(19)
N(2)–Cd(1)–N(3)	134.40(2)	N(2)–Cd(1)–N(3)	67.63(12)
N(2)–Cd(1)–N(4)	147.00	N(2)–Cd(1)–N(4)	135.17(13)
N(2)–Cd(1)–N(5)	134.90(2)	N(2)–Cd(1)–N(5)	143.74(16)
N(3)–Cd(1)–N(4)	65.10(5)	N(3)–Cd(1)–N(4)	68.26(13)
N(3)–Cd(1)–N(5)	125.20(5)	N(3)–Cd(1)–N(5)	148.60(16)
N(4)–Cd(1)–N(5)	67.60(3)	O(1)–Cd(1)–N(1)	95.79(17)
N(1)–Cd(1)–Cl(1)	108.89(14)	O(1)–Cd(1)–N(2)	85.93(15)
N(2)–Cd(1)–Cl(1)	98.90(17)	O(1)–Cd(1)–N(3)	92.15(13)
N(3)–Cd(1)–Cl(1)	109.40(3)	O(1)–Cd(1)–N(4)	88.07(16)
N(4)–Cd(1)–Cl(1)	97.50(3)	O(1)–Cd(1)–N(5)	91.96(19)
N(5)–Cd(1)–Cl(1)	102.61(16)	O(2)–Cd(1)–N(1)	95.00(2)
		O(2)–Cd(1)–N(2)	101.97(18)
		O(2)–Cd(1)–N(3)	81.96(17)
		O(2)–Cd(1)–N(4)	79.40(2)
		O(2)–Cd(1)–N(5)	87.43(19)

$\upsilon(ClO_4^-)$, FAB-MS, (positive FAB in 3-nitrobenzyl alcohol): *m*/*z* $[CdL^3]ClO_4$ 512 (100%), $[CdL^3]^+$(27.33%). Λ_M/Ω^{-1} cm^2 mol^{-1} (in DMF): 160 (2:1).

2.5.5. $[CdL^4(NO_3)(H_2O)]ClO_4$ (**4**)

Yield: 0.200g (32%), *Anal.* Calc. for $C_{19}H_{31}CdClN_6O_8$: C, 35.4; H, 5.3; N, 13.8. Found: C, 35.8; H, 5.2; N, 13.2%. IR (KBr, cm^{-1}): 3465, 1639 $\upsilon_{(C=N)}$, 1587, 1450 [$\upsilon_{(C=C)}$ and $\upsilon_{(C=N)py}$], 1384, 1097, 623 cm^{-1} $\upsilon(ClO_4^-)$, FAB-MS, (positive FAB in 3-nitrobenzyl alco-

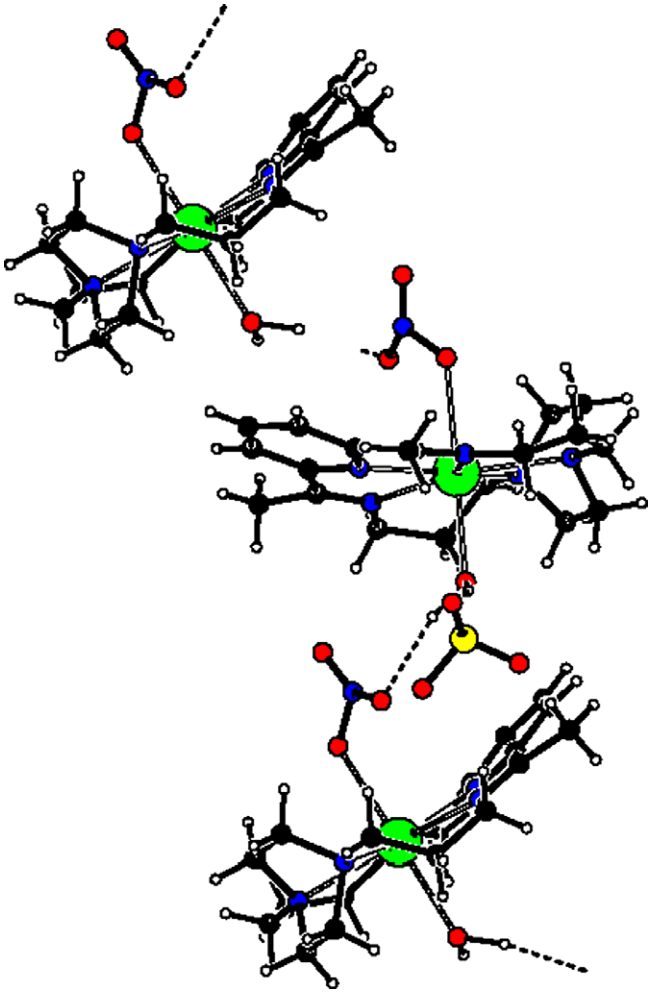


Fig. 5. Hydrogen bonds interactions in $[CdL^4(NO_3)(H_2O)]ClO_4$.

hol): *m*/*z* (%): $[CdL^4NO_3]^+$, 503(100%), $[CdL^4]ClO_4$, 540(71%). Λ_M/Ω^{-1} cm^2 mol^{-1} (in DMF): 169 (2:1).

3. Results and discussion

3.1. Synthesis and characterization

The diimine macrocyclic complexes were synthesized by the metal templated cyclocondensation of 2,6-diacetylpyridine or 2,6-pyridinedicarbaldehyde and the amines N,N′-bis(3-aminopropyl)piperazine and HCl salt of N,N′(2-aminoethyl)(3-aminopropyl) piperazine in refluxing methanol in the presence of appropriate cadmium(II) salts. The complexes were characterized by elemental analysis, IR, NMR (^{1}H, ^{13}C, DEPt, COSY and HMQC) and FAB-MS. The X-ray structure analysis of $[CdL^2Cl](CH_3OH)ClO_4$ and $[CdL^4(NO_3)(H_2O)]ClO_4$ were carried out.

All complexes exhibit a υ(C=N) vibration in the range 1633–1659 cm^{-1} correspond to the imine C=N, and also bands at *ca.* 1600 and 1450 cm^{-1} associated with $\upsilon_{(C=N)py}$ and $\upsilon_{(C=C)}$ vibrations from the pyridine and phenyl rings [28] are present in the spectra, but no bands for the free carbonyls or primary diamines are observed indicating that complete condensation has occurred. Individual spectra are consistent with the presence of water, or other solvent molecules when indicated to be present from the microanalytical data. For the perchlorate complexes, absorptions attributable to ionic perchlorate were found at approximately 1100 and 625 cm^{-1} [29]. The lack of splitting of these bands suggests that the perchlorate anions are not coordinated [30]. The molar conductance values of the complexes measured in dimethylformamide lie in the range reported for 2:1 electrolytes in this solvent [31]. FAB mass spectrometry provided further evidence for cyclocondensation and the formation of the macrocyclic complexes of L^1, L^2, L^3 or L^4. The most intense peak in the spectrum of each complex is observed at *m*/*z* 434, *m*/*z* 462, *m*/*z* 512 and *m*/*z* 540 corresponding to $[CdL^1(Cl)]^+$,$[CdL^2(Cl)]^+$,$[CdL^3](ClO_4)^+$and $[CdL^4](ClO_4)^+$, respectively.

3.2. X-ray crystal structure

The crystal structure of the two Cd(II) complexes with formula $[CdL^2Cl](CH_3OH)ClO_4$ and $[CdL^4(NO_3)((H_2O)]ClO_4$ have been determined by single-crystal X-ray diffraction. The projection view of the molecular structures of the cationic unit present in the complexes with non-hydrogen atoms represented by 50% thermal ellipsoids are shown in Figs. 2 and 4, respectively. Selected bond lengths and bond angles relating the coordination environment of the metals in $[CdL^2Cl](CH_3OH)ClO_4$ and $[CdL^4(NO_3)(H_2O)]ClO_4$ are shown in Table 2.

The $[CdL^2Cl](CH_3OH)ClO_4$ complex crystallizes in the monoclinic $P_{2(1)/c}$ space group and shows that the metal atom is six coordinated in a slightly distorted pentagonal pyramidal geometry, with the metal ion into the macrocyclic cavity, five nitrogen atoms from the ligand lying in a approximately pentagonal plane (rms 0.184) and one Cl ion occupying the axial position. A similar six coordinate geometry has been found for other Cd(II) complexes with N_5 macrocyclic ligands [16].Then, the ligand shows a nearly plane conformation, with the Cd(II) ion 0.553 Å out of the plane formed by the five N atoms. The sum of the five N–Cd–N chelate angles (350.8°) is near 360° for an ideal planar structure. The five Cd–N bond lengths are in the range 2.345–2.434 Å, affording an average Cd–N bond distance of 2.392 Å. The perchlorate ion is non-coordinating reflecting the low coordination ability of this anion.

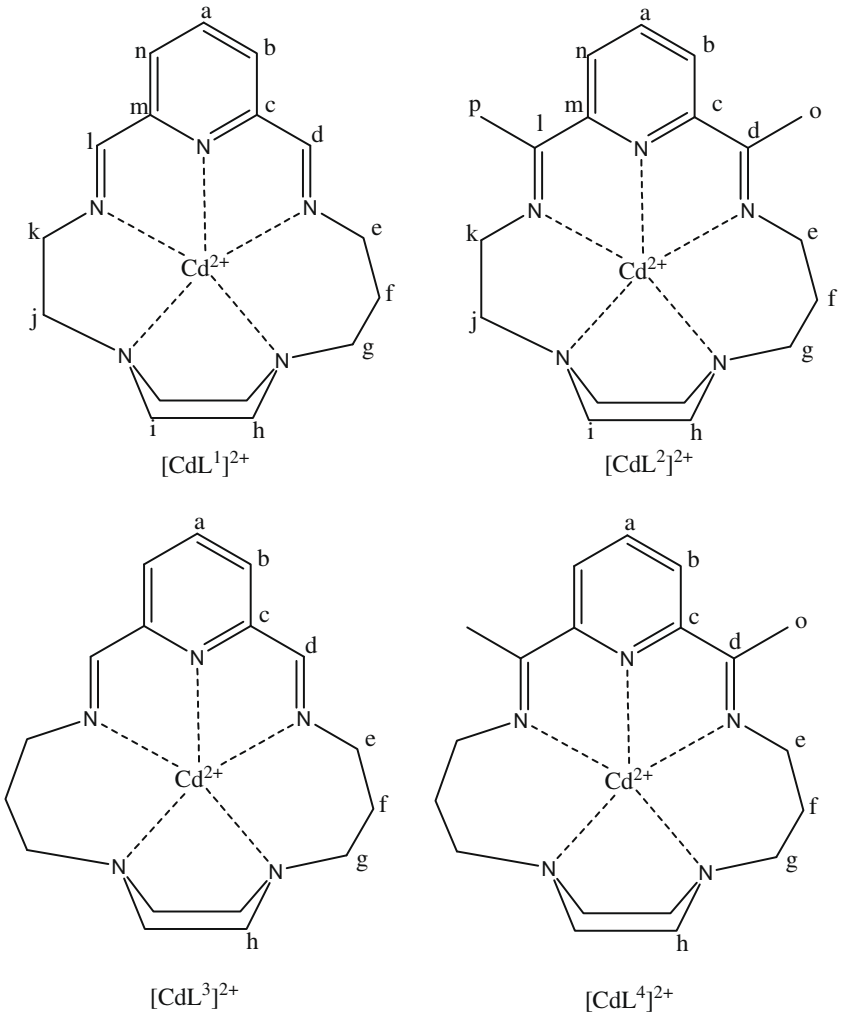
Analysis of short intermolecular interactions reveals the presence of π,π-interactions between the pyridine rings of adjacent ligands (see Fig. 3) giving rise to columnar pyridyl stacks. The pyridine rings involved in the columns are parallel, showing distances between centroids alternatively of 3.70 and 4.32 Å. The planes containing these aromatic groups are 3.44 and 3.45 Å, respectively. No interactions between the chains are observed.

The $[CdL^4(NO_3)(H_2O)]ClO_4$ complex crystallizes in the orthorhombic, $P2_12_12_1$ space group and shows that the metal atom is seven coordinated in a pentagonal bipyramidal geometry, arising from coordination by the five N atoms of the macrocycle with the axial positions being occupied by two oxygen atoms from a water molecule (O(1)) and a monodentate nitrate anion (O(2)). A similar six coordinate geometry has been found for other Cd(II) complexes with N_5 macrocyclic ligands [16].

As in the previous complex, the ligand shows a nearly plane conformation. The rms of the plane formed by the five N atoms is 0.122, showing that these atoms are almost coplanar, with the Cd(II) ion 0.031 Å out of this plane. The sum of the five N–Cd–N

Table 3
^{1}H and ^{13}C{^{1}H} NMR spectral assignments for $[CdL^1]^{2+}$, $[CdL^2]^{2+}$, $[CdL^3]^{2+}$ and $[CdL^4]^{2+}$ recorded at 300 and 400 MHz in DMSO-d_6.

Hydrogen atom	δ_H (ppm)	Carbon atom	δ_C
$[CdL^1]^{2+}$			
H_a	8.48 (t, 1H)	C_a	142.87
H_b	8.15 (d, 1H)	$C_{b,n}$	129.51
H_d	8.91 (s, 1H)	C_l	158.46
H_e	3.94 (b, 2H)		
$H_{f,h,i}$	2.36 (b, 4H)	C_d	160.67
H_g	3.43 (t, 2H)	C_c	146.33
$H_{h,i}$	3.80 (m, 2H) 3.60 (m, 4H)	C_m	147.86
H_j	2.73 (b, 2H)	C_f	23.02
H_k	3.92 (b, 2H)	C_h	50.09
H_l	8.75 (s, 1H)	C_i	50.24
H_n	8.17 (d, 1H)	C_g	52.97
		C_e	54.24
		C_k	56.00
		C_j	56.84
$[CdL^2]^{2+}$			
$H_{a,b,n}$	8.43 (b, 3H)	C_a	142.46
		$C_{b,n}$	125.71, 125.88
		$C_{c,m}$	147.53,147.57
		$C_{d,l}$	163.13,164.16
$H_{e,k}$	3.76, 3.77 (m, 4H)	C_e	44.85
H_f	2.04 (m, 2H)	C_f	24.44
$H_{g,j}$	2.73–2.80 (m, 4H)	C_g	52.04
H_h	2.18 (b, 2H) 3.55 (b, 2H)	C_h	50.83
H_i	2.43 (b, 2H) 3.37 (b, 2H)	C_i	47.67
		C_j	56.92
		C_k	54.41
$H_{o,p}$	2.52, 2.54 (s, 6H)	$C_{o,p}$	15.39, 15.91
$[CdL^3]^{2+}$			
H_a	8.51 (t, 1H)	C_a	143.02
H_b	8.16 (d, 2H)	C_b	129.70
H_d	8.79 (s, 2H)	C_c	146.32
H_e	3.95 (b, 4H)	C_d	160.44
H_f	1.85 (m, 4H)	C_e	60.63
H_g	2.72 (b, 4H)	C_f	24.33
H_h	3.39–3.41 (d,4H) 2.16–2.17 (d, 4H)	C_g	59.50
		C_h	50.73
$[CdL^4]^{2+}$			
$H_{a,b}$ (3H)	8.51 (s, 3H)	C_a	143.21
		C_b	127.15
		C_c	149.11
		C_d	167.46
H_e (4H)	3.75 (m, 4H)	C_e	58.13
H_f (4H)	1.95 (m, 4H)	C_f	24.40
H_g (4H)	2. 59 (b, 4H)	C_g	55.56
H_h (4H)	3.37 (b, 4H) 2.11–2.13 (t, 4H)	C_h	50.90
H_o (6H)	2.57 (s, 6H)	C_o	16.90



Scheme 2. Schematic structures of the $[CdL^n]^{2+}$ cations showing the lettering scheme for NMR assignments.

chelate angles (360.64°) is almost 360° for an ideal planar structure. The five Cd–N bond lengths are in the range 2.33–2.50 Å, affording an average Cd–N bond distance of 2.45 Å. The O(1) and O(2) donor atoms are sited *trans* to the macrocyclic plane, with an angle O(1)–Cd–O(2) of 167.4(2), near to 180°. The pyridine nitrogen atom provides the shortest bond to the Cd atom in both cases. An uncoordinated perchlorate anion balances the ionic charge of the complex cation.

The hydrogen atoms belonging to the bounded water molecule have been encountered and they establish hydrogen bonds interactions with adjacent perchlorate and nitrate anions: [O1–H1C···O4 = 2.180 Å, 166.07°, O1-H1D···O7 = 1.768 Å, 167.96°] (Fig. 5).

No intermolecular π,π-interactions have been observed in the net.

3.3. NMR studies

The ^1H and ^{13}C NMR data for all Cd^{2+} complexes dissolved in DMSO-d_6 are shown in Table 3, which uses the lettering scheme shown in Scheme 2. The ^1H and ^{13}C signals were assigned using one- and two-dimensional ^1H–^1H COSY, ^1H–^{13}C HMQC and DEPT spectra.

The NMR spectra of the complexes confirm the formation of fully condensed macrocyclic Schiff-base complexes. The ^1H NMR spectra of the Cd^{2+} complexes from the asymmetric ligands L^1 and L^2 are more complicated than those from the symmetric L^3 and L^4 ligands.

In $[CdL^1Cl]ClO_4{\cdot}H_2O$ the presence of two signals at *ca.* 8.75 and 8.91 ppm demonstrate the non-equivalence of the two imine protons in the molecule. The ^1H–^{13}C HMQC spectrum shows their correlation with two signals at 158.5 and 160.8 ppm in the ^{13}C NMR spectrum. Also, three signals corresponding to the three aromatic protons of the pyridine rings are observed in the aromatic region of the spectrum. In the aliphatic region of the ^1H NMR spectrum seven signals are observed due to the CH_2 protons belonging to the ethylenic and propylenic protons of the links and also to the piperazine ring. Most of them appear as broad signals reflecting probably intramolecular conformational exchange processes in solution at this temperature. The ^1H NMR spectrum of $[CdL^2Cl](CH_3OH)$-$ClO_4{\cdot}H_2O$ shows that the three pyridine protons collapse in an overlapped broad signal at δ 8.48 ppm as has been previously reported for Nelson and co-workers [32]. The ^1H–^{13}C HMQC spectrum confirm the connectivity between that signal and the three corresponding ones in the ^{13}C NMR spectrum. Two signals due to the imine resonance at δ 163.13, 164.16 ppm in the ^{13}C NMR spectrum, shows again the non-equivalence of the two imine environments. Again, the presence of asymmetric ethylenic and propylenic linkages in L^2 gives rise to a complicated aliphatic region in the spectrum. As in the previous complex, independent signals are

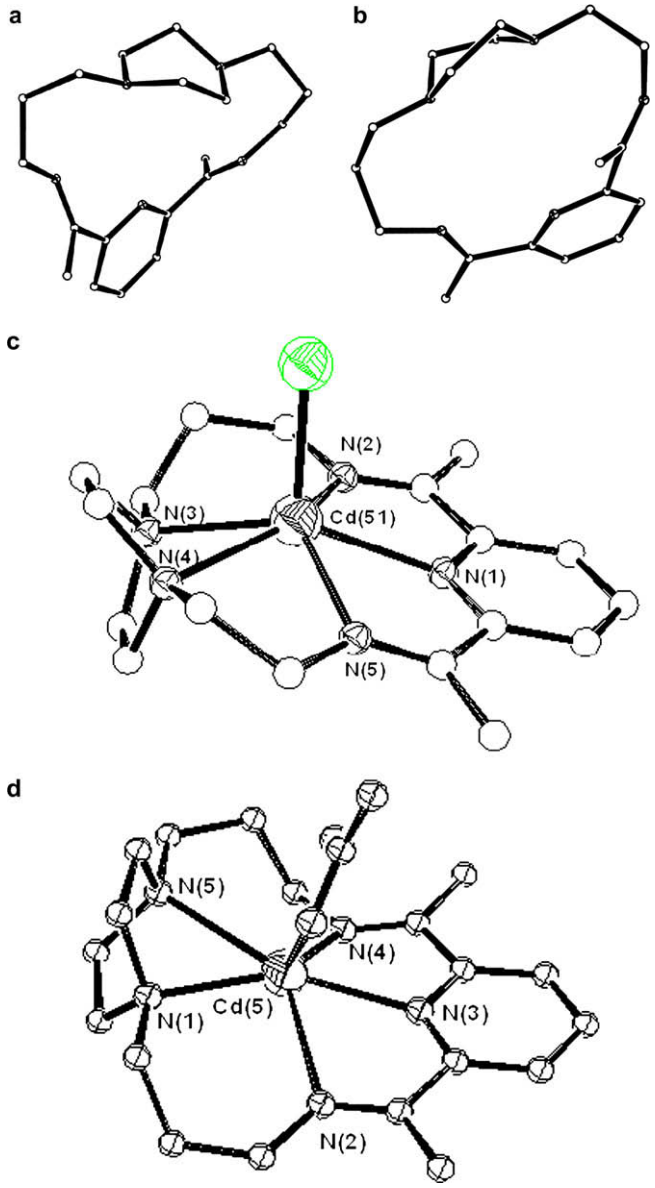


Fig. 6. The DFT optimized structures of the ligands, L^2 and L^4 and their Cd(II) complexes, (a) L^2 at B3lyp/6-31G*; (b) L^4 at B3lyp/6-31G*; (c) $[CdL^2Cl]^+$ at B3lyp/Lanl2dz; (d) $[CdL^4(NO_3)]^+$ at B3lyp/Lanl2dz.

observed for each of the protons of the molecule. The methylene protons of the piperazine ring are all appeared as triplet of doublets. Both the geminal coupling as well as coupling with the adjacent methylene groups (H_h–H_i) was confirmed by the ^1H–^1H COSY spectrum. The ^1H–^{13}C HMQC spectrum clearly shows that the four set of signals observed for latter methylene groups in the ^1H NMR spectrum are connected to two signals at v 47.67 and 50.83 ppm in the ^{13}C NMR spectrum. In this case, the methyl groups belonging to the 2,6-diacetylpyridine precursor appear at δ 2.52 and 2.54 ppm as two singlets, the ^1H–^{13}C HMQC spectrum showing connection with the signals at δ 15.39 and 15.91 ppm.

The ^1H NMR spectrum of $[CdL^3](ClO_4)_2$ shows the imine resonance at δ 8.79 ppm, demonstrating the equivalence of the two imine environments. That signal have two satellite peaks ($^3J \approx 28$ Hz for C_d–H_e) with intensities 1:6:1 due to coupling with neighboring $^{111/113}Cd$ at natural abundance (^{111}Cd, 12.81; ^{113}Cd, 12.22%). This coupling constant is smaller than those reported for other cadmium(II) macrocyclic or macroacyclic Schiff-base complexes [33,34]. The aliphatic region show the presence of the protons from the propylenic chains as broad signals showing again the presence of intermolecular conformational exchange processes, whilst the ethylenic chains protons of the piperazine rings are equivalents and they appear as two doublets due to the geminal coupling. For $[CdL^4(NO_3)(H_2O)]ClO_4$ the ^1H NMR spectrum is very clear. Only one signal appear in the aromatic region at δ 8.51 ppm, as has been observed in $[CdL^2Cl]\,ClO_4{\cdot}H_2O$, which is connected with the two corresponding ones in the ^{13}C NMR spectrum at δ 143.21 and 127.15 ppm. As in the previous complex the protons from the propylenic chains appear as broad signals, whilst two doublets due to the geminal coupling in ethylenic chains protons of the piperazine rings appear at δ 2.12 and 3.37 ppm overlapped with the water signal. The ^{13}C NMR spectrum shows also the imine resonance at δ 167.46 ppm demonstrating the equivalence of the two imine environments, and the signal at δ 16.90 ppm belonging to the methyl groups.

3.4. Ab initio and DFT studies

We have seen that Cd(II) metal ion is an effective template to promote the formation of ligands L^1–L^4 starting from 2,6-diacetylpyridine or 2,6-pyridinedicarbaldehyde with two different amine precursors having piperazine molecules. We were interested to know whether the structures of ligands L^2 and L^4 in the metal complexes are different from their structures in the free state. For that, we have carried out theoretical calculations in order to determine the difference in energy between them. The DFT optimized structures of the ligands, L^2 and L^4 and the related Cd(II) complexes are shown in Fig. 6. Table 4 shows the comparison between some selected calculated bond lengths and angles for the metal complexes with the corresponding X-ray. The results show that in the case of $[CdL^2Cl]^+$ the gas-phase structure is very close to the solid state structure. Although some calculated bond lengths are somewhat different from the solid state values, there is a good agreement between the calculated bond angles and those from the solid state crystal structure. However, the optimized structure for $[CdL^4(H_2O)(NO_3)]^+$ complex was dissimilar with its solid state structure, due to an intramolecular hydrogen bond interaction between the coordinated H_2O molecule and one of the imine nitrogen atoms from the ligand. Thus, we removed the H_2O molecule from its solid state structure and used the resulting structure for present calculations. With it, we found a good agreement between theoretical and experimental data and the results are shown in Table 4.

It has been experimentally/theoretically confirmed that the chair conformation is usually more stable than boat conformation for saturated six-membered rings [35]. On the other hand, obviously, only a boat conformation is suitable for coordination of piperazine nitrogen atoms in ligands L^2 and L^4 to the metal ion (see Figs. 2, 4 and 6). As it can be seen in Fig. 6, due to the ring constraint, a distorted chair conformation is adopted by piperazine rings even in the optimized structures of uncoordinated free ligands. Furthermore, the constraint in macrocyclic rings affect the diacetylpyridine moiety, which shows the methyl groups significantly departed from the plane of pyridine unit in contrast to the structure found in metal complexes, which show the imine-pyridine-imine fragment planar as expected. Thus it seems that the cyclocondensation of the dialdehyde and diamine precursors to give rise the macrocylic ligands L^2 and L^4 in the absence of metal ion is hardly possible and the use of a metal template (Cd(II) in the present study) is necessary to achieve the formation of the ligands. The results of single-point calculations on optimized structure of ligands and on the structure of ligand in their optimized Cd complexes are given in Table 5. The data show that the rearrangement in the structure of ligands L^2 and L^4 from their free state to the corresponding structure in Cd complexes needs energy about 8 and 15.4 kcal/mol, respectively, for Lanl2DZ optimized

Table 4
Selected calculated bond lengths (Å) and bond angles (°) for $[CdL^2Cl]^+$(**2**) and $[CdL^4(NO_3)]^+$(**4**).

	$[CdL^2Cl]^+$		$[CdL^4NO_3]^+$	
	X-ray	(B3lyp/LANL2DZ)	X-ray	(B3lyp/LANL2DZ)
Bond lengths (Å)				
Cd–N(1)	2.345(6)	2.394	2.411(4)	2.414
Cd–N(2)	2.433(6)	2.499	2.501(4)	2.605
Cd–N(3)	2.336(8)	2.473	2.331(4)	2.367
Cd–N(4)	2.434(10)	2.503	2.477(4)	3.483
Cd–N(5)	2.413(6)	2.486	2.494(5)	2.777
Cd–Cl	2.513(2)	2.510		
Bond angles (°)				
N(1)–Cd–N(2)	68.023(2)	67.840	82.622(16)	84.822
N(1)–Cd–N(3)	134.412(2)	135.938	148.501(15)	150.933
N(1)–Cd–N(4)	67.625(3)	68.937	142.202(16)	135.784
N(1)–Cd–N(5)	67.745(2)	67.047	61.553(19)	59.991
N(2)–Cd–N(3)	134.446(2)	135.938	67.631(12)	66.142
N(2)–Cd–N(4)	147.123(3)	145.404	135.174(13)	134.162
N(2)–Cd–N(5)	134.167(2)	133.317	143.744(16)	126.411
N(3)–Cd–N(4)	65.673(5)	61.554	68.265(13)	67.664
N(3)–Cd–N(5)	125.234(5)	121.792	148.606(16)	147.193
N(4)–Cd–N(5)	67.643(3)	68.937	80.783(17)	79.612

Table 5
Single point energies of ligands L^2 and L^4 at B3LYP/6-311+G* level of theory. Optimization were performed at various methods and assigned in column 1.

Level of optimization	L^2		L^4	
	E_{el} (Hartree)[a]	ΔE (kcal/mol)	E_{el} (Hartree)	ΔE (kcal/mol)
B3LYP/6-31G*	−976.06717	0	−1015.39721	0
B3LYP/LanL2DZ	−976.07701	+6.2	−1015.40113	+2.5
B3LYP/LanL2DZ[b]	−976.05433	+14.2	−1015.37253	+17.9

[a] The energy different with most stable structure.
[b] The structure of ligand in its optimized Cd complex is used for single-point calculations.

structures. We also performed the 6-31G* calculations to confirm the result of the Lanl2DZ optimized structure of the ligands in their free state (see Fig. 6). Obviously the optimized structures at LanL2DZ level of theory are less stable than those derived form 6-31G* calculations.

4. Conclusion

The Cd(II) metal templated cyclocondensation of four pentaaza macrocyclic ligands L^1–L^4 starting from 2,6-diacetylpyridine or 2,6-pyridinedicarbaldehyde with two different tetra-amines containing piperazine moiety have been successfully achieved. The crystal structure of $[CdL^2Cl](CH_3OH)ClO_4$ and $[CdL^4(NO_3)(H_2O)]ClO_4$ show the Cd(II) ion endo-macrocyclicly coordinated to the five N atoms from the molecule in slightly distorted pentagonal pyramidal and pentagonal bipyramidal geometries, respectively. It is interesting that in the presence of steric hindrance due to structural restriction of piperazine, which is confirmed by theoretical calculations, cyclocondensation has occurred in the presence of Cd metal ion and pentaaza macrocyclic complexes were produced.

5. Supplementary data

CCDC 672131 and 610457 contain the supplementary crystallographic data for $[CdL^2(Cl)](CH_3OH)ClO_4$ and $[CdL^3(NO_3)(H_2O)]ClO_4$. These data can be obtained free of charge via http://www.ccdc.cam.ac.uk/conts/retrieving.html, or from the Cambridge Crystallographic Data Centre, 12 Union Road, Cambridge CB2 1EZ, UK; fax: (+44) 1223-336-033; or e-mail: deposit@ccdc.cam.ac.uk.

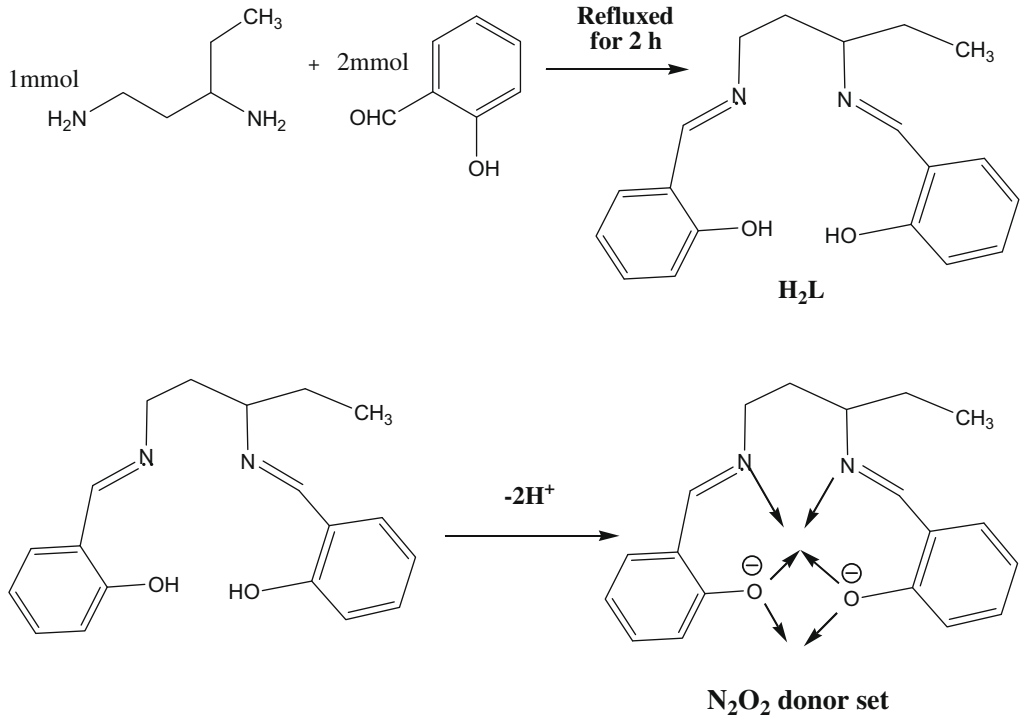
Acknowledgements

We are grateful to the Faculty of Chemistry of Bu-Ali Sina University, Ministry of Science, Research and Technology of Iran for financial support and for a Visiting Fellowship to M.R. and Universidade de Vigo (1Z1464102) for financial support.

References

[1] N.V. Gerbeleu, V.B. Arion, J. Burgess, Template Synthesis of Macrocyclic Compounds, Wiley-VCH, Weinheim, 1999.
[2] K.R. Krishnapriya, M. Kandaswaswamy, Polyhedron 24 (2005) 113.
[3] A. Ramasubbu, K.P. Wainwright, J. Chem. Soc., Chem. Commun. (1982) 1129.
[4] R.D. Hancock, A. Evers, M.P. Ngwenya, P.W. Wade, J. Chem. Soc., Chem. Commun. (1987) 1129.
[5] D.C. Liles, M. Mcpartlin, P.A. Tasker, J. Chem. Soc., Dalton Trans. (1987) 1631.
[6] G. Marcotrigiano, G.C. Pellacani, C. Preti, Z. Anorg. Allg. Chem. 408 (1974) 313.
[7] G. Marcotrigiano, L. Menabue, G.C. Pellacani, Inorg. Chim. Acta 46 (1980) 107.
[8] G. Marcotrigiano, P. Morini, L. Menabue, G.C. Pellacani, Bull. Soc. Chim. Fr. 9 (1977) 815.
[9] O. Schneider, M. Hanack, Chem. Ber. 116 (1983) 2088.
[10] Y. Okishi, Y. Imai, K. Aida, J. Inorg. Nucl. Chem. 35 (1973) 101.
[11] B.S. Manhas, A.K. Trikha, M. Singh, Indian J. Chem., Sect. A 20 (1981) 196.
[12] R. Toenisketter, S. Soloman, Inorg. Chem. 7 (1968) 617.
[13] H. Irvig, D.L. Pettit, J. Chem. Soc. (1963) 3051.
[14] K. Rissanen, J. Huuskonen, A. Koskinen, J. Chem. Soc., Chem. Commun. (1993) 771.
[15] N.W. Alcock, P. Moore, C.J. Reader, S.M. Roe, Chem. Soc., Dalton Trans. (1988) 2959.
[16] S.M. Nelson, S.G. McFall, M.G.B. Drew, A.H. Bin Othman, N.B. Mason, J. Chem. Soc., Chem. Commun. (1977) 167.
[17] D.A. Stotter, J. Inorg. Nucl. Chem. 38 (1976) 1866.
[18] H. Keypour, M. Rezaeivala, L. Valencia, P. Pérez-Lourido, Polyhedron 27 (2008) 3172.
[19] D. Jerchel, J. Heider, H. Wagner, Liebigs Ann. Chem. 613 (1958) 153.
[20] Stoe and Cie, X-AREA, Version 1.30: Program for the Acquisition and Analysis of Data, Stoe and Cie GmbH, Darmatadt, Germany, 2005.
[21] G.M. Sheldrick, SHELX97. Program for Crystal Structure Solution and Refinement, University of Göttingen, Germany, 1997.

[22] Stoe and Cie, X-STEP32, Version 1.07b: Crystallographic Package, Stoe and Cie GmbH, Darmatadt, Germany, 2000.
[23] G.M. Sheldrick, SADABS, Program for Empirical Absorption Correction of Area Detector Data, University of Göttingen, Germany, 1996.
[24] SHELXTL Versio: An Integrated System for Solving and Refining Crystal Structures from Diffraction Data (Revision 5.1), Bruker AXS Ltd.
[25] A.D. Becke, J. Chem. Phys. 98 (1993) 5648.
[26] M.J. Frich, G.W. Trucks, H.B. Schlegel, G.E. Scuseria, M.A. Robb, J.R. Cheeseman, V.G. Zakrazewski, J.A. Montgomery Jr., R.E. Startmann, J.C. Burant, S. Dapprich, J.M. Millam, A.D. Daniels, K.N. Kudin, M.C. Strain, OFarkas, J. Tomasi, V. Barone, M. Cossi, R. Cammi, B. Mennucci, C. Adamo, S. Clifford, J. Ochterski, G.A. Petersson, P.Y. Ayala, Q. Cui, K. Morokuma, D.K. Malik, A.D. Rabuck, K. Raghavachar, J.B. Foresman, J. Cioslowski, J.V. Ortiz, B.B. Stefanov, G. Liu, A. Liashenko, P. Piskorz, I. Komaromi, R. Gomperts, R.L. Martin, D.J. Fox, T. Keith, M.A. Al-Laham, C.Y. Peng, A. Nanyakkara, C. Gonzalez, M. Challacombe, P.M.W. Gill, B. Johnson, W. Chen, M.W. Wong, J.L. Andres, M. Hea-Gordon, E.S. Replogle, J.A. Pople, GAUSSIAN 98 (Revision A.3), Gaussian Inc., Pittsburgh, PA, 1998.
[27] P.J. Hay, W.R. Watt, J. Chem. Phys. 82 (1985) 299.
[28] N.S. Gill, R.H. Nutall, D.E. Scaife, J. Inorg. Nucl. Chem. 18 (1961) 79.
[29] A.J. Hataway, D.E. Underhill, J. Chem. Soc. (1961) 3091.
[30] M.F. Rosenthal, J. Chem. Educ. 50 (1973) 331.
[31] W.J. Geary, Coord. Chem. Rev. 7 (1971) 81.
[32] D.H. Cook, D.E. Fenton, M.G.B. Drew, S.G. McFall, S.M. Nelson, J. Chem. Soc., Dalton (1975) 446.
[33] L. Valencia, H. Adams, R. Bastida, D.E. Fenton, A. Macı'as, Inorg. Chim. Acta 317 (2001) 45.
[34] S. Salehzadeh, S.A. Javarsineh, H. Keypour, J. Mol. Struct. 785 (2006) 54.
[35] M. Boiocchi, M. Bonizzoni, L. Fabbrizzi, F. Foti, M. Licchelli, A. Taglietti, M. Zema, J. Chem. Soc., Dalton Trans. (2004) 653.



Scheme 1. Procedure of synthesis and the coordination mode of the N_2O_2 donor Schiff base ligand [$\mathbf{H_2L}$].

complex were spectroscopically characterised. A single crystal X-ray diffraction study revealed the unusual structural aspects of **1**. Unlike the previously reported antiferromagnetically coupled copper(II) trinuclear complexes, there is a more abrupt decrease in $\chi_m T$ product observed for **1** at very low temperatures and this is attributed to weak antiferromagnetic inter-trimer interactions. Thus the cryomagnetic investigation supported the presence of inter-trimer as well as intra-trimer antiferromagnetic interactions in **1**.

2. Experimental

2.1. Materials

All solvents were of reagent grade and used without further purification. 1,3-diaminopentane and salicylaldehyde were purchased from Aldrich Chemical Company and were used as received. Copper perchlorate hexahydrate was prepared by treatment of copper carbonate (E. Merck, India) with 60% perchloric acid (E. Merck, India) followed by the slow evaporation on the steam bath. It was then filtered through a fine glass-frit and preserved in a $CaCl_2$ desiccator for further use.

2.2. Syntheses

Caution! Perchlorate salts are potentially explosive and should be used in small quantity and with much care.

2.2.1. Synthesis of the Schiff base Ligand [$\mathbf{H_2L}$]

The Schiff base ligand [$\mathbf{H_2L}$] was prepared by the reflux condensation of a methanolic solution of 1,3-diaminopentane (0.59 ml, 5 mmol) with 10 mmol salicylaldehyde (1.04 ml) shown in Scheme 1. The ligand was refluxed for 2 h when yellow coloured solution developed. The colour indicated the formation of the Schiff base. Slow evaporation of the resulting solution yielded shiny yellow crystalline Schiff base [$\mathbf{H_2L}$]. They were dried and stored in vacuo over $CaCl_2$ for subsequent use. *Anal.* Calc. for [$C_{19}H_{22}N_2O_2$]: C, 73.55; H, 7.09; N, 9.03. Found: C, 73.58; H, 7.11; N, 9.04%.

2.2.2. Synthesis of [$Cu_3(\mu$-$\mathbf{L})_2(ClO_4)_2$] [$Cu_3(\mu$-$\mathbf{L})_2(H_2O)(ClO_4)_2$] (**1**)

$Cu(ClO_4)_2{\cdot}6H_2O$ (0.56 g, 1.5 mmol) was dissolved in 20 ml methanol and warmed. About 10 mL of yellow methanolic solution of the Schiff base [$\mathbf{H_2L}$] (0.354 g, 1 mmol), was added to it dropwise. The mixture was allowed to stir for 2 h at 50 °C. The dark green solution was filtered and maintained at 22 °C for crystallisation by slow evaporation. After one week, green block shaped crystals suitable for X-ray crystallography were obtained. Crystals were isolated by filtration and were air-dried. *Anal.* Calc. for [$C_{37}H_{40}Cl_2Cu_3N_4O_{14}$]: C, 43.26; H, 3.90; N, 19.10. Found: C, 43.30; H, 3.92; N, 19.13%.

2.3. Physical measurements

The Fourier transform infrared spectra were recorded in the range 4000–400 cm^{-1} on a Perkin–Elmer RX I FT-IR spectrophotometer with solid KBr disc. The electronic spectra were recorded at 300 K on a Perkin–Elmer Lambda 40 (UV–Vis) spectrometer using HPLC grade acetonitrile as solvent with a 1 cm quartz cuvette in the range 200–800 nm. ^1H NMR spectra were recorded on a BRUKER 300 MHz FT-NMR spectrometer using trimethyl silane as an internal standard in $CDCl_3$. C, H, N microanalysis was carried out with a Perkin–Elmer 2400 II elemental analyser. Electrochemical measurement was performed on a VersaStat-PotentioStat II cyclic voltammeter using HPLC grade acetonitrile as solvent where tetrabutylammonium perchlorate was used as supporting electrolyte at a scan rate 50 mV/s. Platinum and saturated calomel electrode (SCE) were the working and the reference electrodes in the process, respectively. The magnetic susceptibility measurements were carried out in the temperature range 2–300 K with an applied magnetic field of 0.1 T on a polycrystalline sample of **1** (mass = 31.71 mg) with a Quantum Design MPMS-XL-5 SQUID magnetometer. The isothermal magnetization was performed on

the same sample at 2 K with magnetic fields up to 5 T. The susceptibility data were corrected for the sample holders previously measured using the same conditions and for the diamagnetic contributions of the salt as deduced by using Pascal's constant tables ($\chi_{dia} = -534 \times 10^{-6}$ emu mol^{-1}).

2.4. X-ray crystallography

The X-ray diffraction experiment was carried out at 100(2) K on a green block shaped single crystal (0.38 × 0.20 × 0.08 mm) of **1**. The crystal was mounted on a Bruker X8 Apex 2 CCD area diffractometer equipped with Mo Kα radiation (λ = 0.71073 Å). The lattice constants were refined by least-square refinement using 7542 reflections ($2.35° < \theta < 21.31°$), 9171 unique reflection (R_{int} = 0.0863). Structure solution and refinement based on 4644 observed reflections with $I > 2\sigma(I)$ and 579 parameters gave final R = 0.0716, wR = 0.1865 and S = 1.022. Data collection and data reduction were performed with the APEX 2 suite of programs [23]. All non hydrogen atoms were refined anisotropically by full-matrix least-squares based on F^2. The H atoms were generated geometrically (apart from H atoms bound to O2W which were located in the difference map with O–H distances restrained to 0.90(2) Å and all were included in the refinement in the riding model approximation. The components of the disordered ethyl groups (C45 and C45A, C46 and C46A) had relative occupancies refined to 69%:31%, respectively. Restraints were applied to the displacement parameters. 50% Occupancy was assigned as an estimate for ethyl C atoms C22 and C23 because full occupancy resulted in unreasonable displacement ellipsoids. However location of the second disordered ethyl group fragment which would be expected to be bound to C12 was not discernable (highest residual peak 1.156 e Å^{-3}). C–C bond distances in the ethyl groups were restrained to 1.50(2) Å. In the disordered perchlorate ion four of the five O atoms were assigned occupancies of 75%. The fifth retained full occupancy.

Selected crystallographic data, experimental conditions and some important features of the structural refinements of both the complexes are summarized in the Table 1.

Table 1
Crystal structure parameters of **1**.

Parameters	**1**
Empirical formula	$C_{37}H_{40}Cl_2Cu_3N_4O_{14}$
Formula weight	1026.25
Crystal System	monoclinic
Space group	*C*2/*c*
a (Å)	32.7759(16)
b (Å)	8.9878(4)
c (Å)	28.3359(13)
α (°)	90
β (°)	90.532(2)
γ (°)	90
V (Å^3)	8346.9(7)
Z	8
T (K)	100(2)
$\lambda_{Mo\ K\alpha}$ (Å)	0.71073
D_c [Mg m^{-3}]	1.633
[μ(mm^{-1})]	1.714
F(0 0 0)	4184
θ Range for data collection (°)	2.35–21.31
Total data	58 860
Unique data	9171
Observed data [$I > 2\sigma(I)$]	4644
$R_1[I > 2\sigma(I)]$	0.0716
$wR_2[I > 2\sigma(I)]$	0.1865
s	1.022
R_{int}	0.0863
$\Delta\rho_{max}$ (e$^-$ Å^{-3})	1.156
$\Delta\rho_{min}$ (e$^-$ Å^{-3})	−1.163

3. Results and discussion

3.1. Fourier transform IR spectroscopy

The IR spectrum of **1** was analysed and compared with that of its free ligand **H_2L** in the region 4000–400 cm^{-1}. A strong sharp absorption band around 1631 cm^{-1} in the spectrum of the Schiff base ligand can be assigned to the C=N stretching. In the complex, this band is shifted to 1618 cm^{-1} upon complexation with the metal, which can be attributed to the coordination of the imine nitrogen to the metal centre [24–26]. The ligand shows a well-defined band at 3537 cm^{-1} due to O–H stretching which disappears in the complex, indicating the deprotonation of the Schiff base ligand upon complexation. The strong phenolic C–O absorption band at 1214 cm^{-1} observed in the spectrum of **H_2L** shifts to lower frequency at 1192 cm^{-1}, supporting the coordination of the deprotonated phenolic oxygen atoms to the metal centres in the complex [26]. A broad band at 3300–3450 cm^{-1} indicates that water is present in **1**. The characteristic bifurcated absorption band at 1098–1121 cm^{-1} in the spectrum of the complex indicates the presence of perchlorate anions. The ligand coordination to the metal centre is substantiated by a band appearing at 427 cm^{-1} which is mainly attributed to ν_{Cu-N} in the complex.

3.2. UV–Vis spectroscopy

UV–Vis spectra of the free ligand and **1** were recorded at 300 K in HPLC grade acetonitrile solution. The UV–Vis spectrum of the Schiff base ligand [**H_2L**] exhibits two charge transfer (CT) bands at 255 and 308 nm attributed to $\pi \rightarrow \pi^*$ and $n \rightarrow \pi^*$ transitions within the Schiff base ligand. In the spectrum of the complex the CT band at 255 nm remains intact, in agreement with the $\pi \rightarrow \pi^*$ transition of the Schiff base ligand. Another band at 340 nm is detected in the spectrum of **1**. The band at 308 nm observed in the spectrum of the free ligand [**H_2L**] is red shifted to 340 nm (in **1**) in form of ligand to metal charge transfer (LMCT) transition. Unlike the spectrum of the free ligand, much weaker and less well-defined broad bands are found in the spectrum of the complex at 650 and 600 nm which are assigned to the d–d transitions. The two different d–d bands are in good agreement with the presence of two different coordination environments in **1**. The band at 650 nm is associated with a copper(II) centre having square–pyramidal geometry and the d–d transition at 600 nm may be attributed to structurally well characterised square–planar copper(II) complexes [27].

3.3. ^{1}H NMR spectroscopy

^{1}H NMR spectroscopy has been used to extract information regarding the coordination mode of the ligand **H_2L** with the metal ion for **1**. It is generally seen that ^{1}H NMR spectra of the coordination complexes containing paramagnetic metal ions are broadened to some extent but for **1** fairly sharp and well-resolved spectrum was obtained which is probably due to sufficiently short electronic relaxation time [28–30]. Unlike the spectrum of **H_2L**, the chemical shifts of the hyperfine-shifted signals of **1** appeared within a short range 0 to +15 ppm. For **1** the signal due to the protons closer to the respective metal centres experience stronger paramagnetic effects and consequently they are most downfield shifted. The NMR proton numbering scheme of **H_2L** along with the ^{1}H NMR spectra of the ligand and the complex are represented in Fig. 1a and b. The ^{1}H NMR data are summarized in Table 2. In the NMR spectrum of the free ligand **H_2L** no broad peak was observed due to free amine protons in the region 5.0–8.0 ppm indicating that, both $-NH_2$ functions of the 1,3-diamine have undergone condensation with the

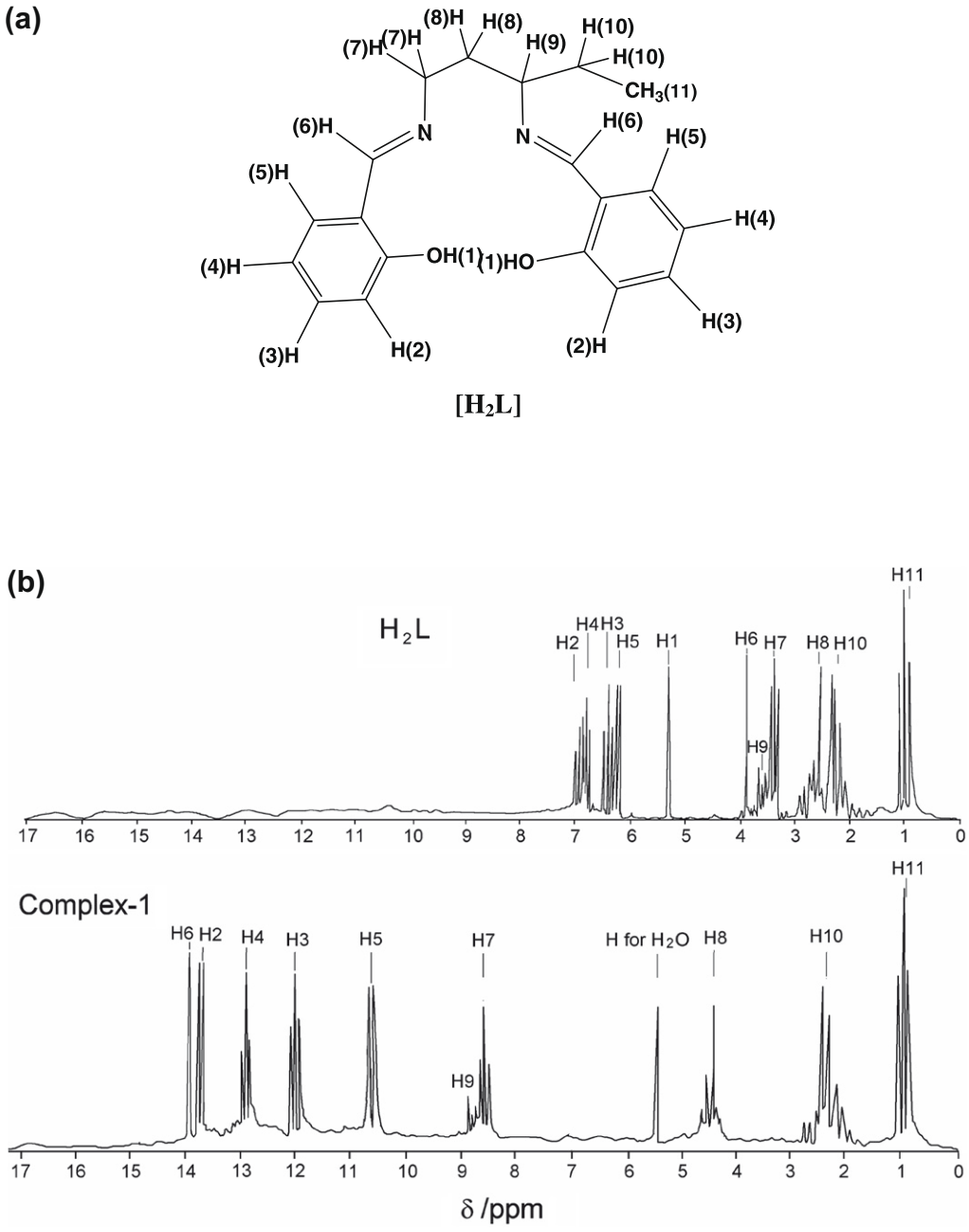


Fig. 1. (a) NMR proton numbering scheme of **H_2L**. (**b**) ^{1}H NMR spectra of **H_2L** and **1**.

Table 2
^{1}H NMR data for the **H_2L** and **1**.

Schiff base/complex	δ (in ppm)
H_2L	0.89 (3H, t, H11); 2.24 (2H, m, H10); 2.5 (2H, m, H8); 3.42 (2H, t, H7); 3.50 (1H, m, H9); 3.8 (2H, s, H6); 5.26 (2H, s, H1); 6.35(2H, d, H5); 6.41 (2H, t, H3); 6.80 (2H, t, H4); 6.85 (2H, d, H2)
1	0.89 (3H, t, H11); 2.24 (2H, m, H10); 4.5 (2H, m, H8); 5.5 (2H, s, H_2O); 8.52 (2H, t, H7); 8.8 (1H, m, H9); 10.55 (2H, d, H5); 11.91 (2H, t,H3); 12.90 (2H, t, H4); 13.75 (2H, d, H2); 13.9 (2H, s, H6)

carbonyl functional group of salicylaldehyde to result the Schiff base ligand **H_2L** [31]. The ^{1}H NMR spectra (Fig. 1) show that the signal due to the phenolic hydrogen (H1) of the free ligand **H_2L** (5.26 ppm) is absent in the spectrum of **1**. The imino proton (H6) is assumed to be significantly downfield shifted (10.1 ppm) due to the coordination of the Schiff base ligand in **1** through imine nitrogen atoms. The largest paramagnetic deshielding effect on H6 indicates that it is in the closest vicinity to the metal centre. The phenyl hydrogens also show significant chemical shifts [4.2 ppm (H5), 5.5 ppm (H3), 6.1 ppm (H4), 6.90 ppm (H2)] indicating the participation of the deprotonated phenolato oxygen in the coordination with the metal centres [31]. The ortho (H2) and para (H4) hydrogens are significantly downfield shifted due to large spin delocalization effect through π-bonding of the aromatic

ring. H2 being ortho to the coordinated phenolato oxygen, is closer to the metal centre and undergoes larger paramagnetic deshielding effect than H4. In **1** the methylene protons (H7) and methine proton (H9) both being very close to imine nitrogens show downfield shifts of 5.1 and 5.3 ppm, respectively from the free ligand values which are attributed to the coordination of the imine nitrogens to the metal centres. Unlike the spectrum of the free ligand the ^{1}H NMR spectrum of **1** contains a singlet at 5.5 ppm which can be assigned to the protons of the coordinated water molecules. The results obtained from the NMR spectra are in agreement with the structure obtained by the X-ray analysis.

3.4. Cyclic voltammetry

The electrochemical behaviour of **1** was studied in HPLC grade acetonitrile medium with tetrabutylammonium perchlorate as supporting electrolyte at a scan rate of 50 mV/s. Complex **1** shows a reductive response at −0.608 V versus SCE, which is assigned to $Cu^{II} \rightarrow Cu^{I}$ reduction and an oxidative response at −0.526 V versus SCE was assigned for $Cu^{I} \rightarrow Cu^{II}$ oxidation (Fig. S1: provided as Supplementary data). This reduction and oxidation are quasi reversible, characterised by a peak to peak separation (ΔE_p) of 82 mV which remain unchanged upon changing the scan rate. The anodic peak current (i_{pa}) is almost equal to the cathodic peak current (i_{pc}) as expected for a quasi reversible electron transfer process. The $E_{1/2}$ value for **1** is −0.57 V. The $E_{1/2}$ value and the quasi reversible nature of the cyclic voltammogram of **1** is in good agreement with that of the earlier reported doubly phenoxo bridged dicopper(II) complex $[Cu_2L^1(ClO_4)_2]\cdot 2CH_3OH\cdot 2H_2O$ (−0.52 V) [32].

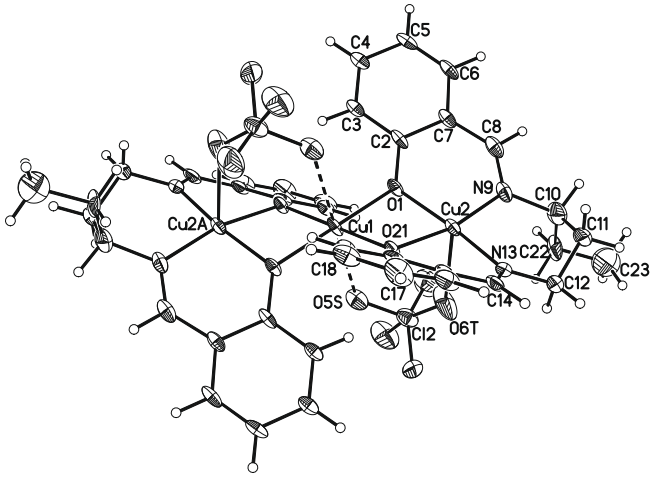


Fig. 2. ORTEP diagram of **I**. The label suffix A denotes the symmetry operation $x + 1/2, -y + 3/2$ used to generate this symmetry equivalent atom.

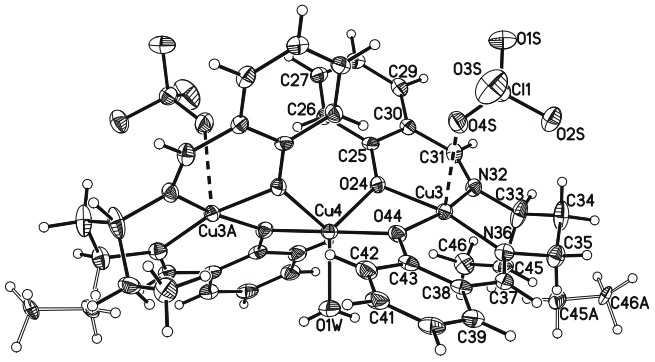


Fig. 3. ORTEP diagram of **II**. The label suffix A denotes the symmetry operation $x + 1, y, -z + 1/2$ used to generate this symmetry equivalent atom.

3.5. Description of the crystal structure of *1*

The asymmetric unit of **1** comprises two structurally independent trinuclear units $[Cu_3(\mu\text{-}\mathbf{L})_2(ClO_4)_2]$ (**I**) and $[Cu_3(\mu\text{-}\mathbf{L})_2(H_2O)(ClO_4)_2]$ (**II**) shown in Figs. 2 and 3, respectively. The main bond lengths and angles are summarised in Tables 3 and 4 and the H-bonding data are listed in Table 5. In the trinuclear units (**I** and **II**) there are two geometrically distinct copper(II) centres [Cu(1) and Cu(2) for **I** and Cu(3) and Cu(4) for **II**]. Cu(1) sits on a centre of inversion, while Cu(4) is positioned on a twofold axis. Thus **I** is constrained by crystallographic symmetry to be linear but **II** can be bent and is found in this case.

The trinuclear unit **I** is very similar to the previously reported trinuclear copper(II) complex $[Cu_3(\mu\text{-}\mathbf{L}')_2(ClO_4)_2]$ (**A**) [**L**′ = $OHC_6H_4CH{=}NCH_2{-}CH_2{-}CH_2N{=}CHC_6H_4OH$] [17], where the three copper(II) centres are held together by two doubly phenoxo bridged oxygen atoms of the deprotonated tetradentate Schiff base ligands $[\mathbf{L}]^{2-}$ and $[\mathbf{L}']^{2-}$, respectively (Fig. 2). In both trinuclear complexes (**I** and **A**) the respective Schiff bases behave as N_2O_2 donor ligands with two perchlorate ions coordinating with the two terminal copper atoms

Table 4
Selected bond angles for **1** [°].

O(21)#1–Cu(1)–O(21)	180.0(3)	O(21)–Cu(1)–O(1)#1	102.51(19)
O(21)–Cu(1)–O(1)	77.49(19)	O(1)#1–Cu(1)–O(1)	179.995(1)
Cu(2)–Cu(1)–Cu(2)#1	180.0	N(9)–Cu(2)–O(1)	93.3(3)
N(9)–Cu(2)–N(13)	96.7(3)	O(1)–Cu(2)–N(13)	168.4(3)
N(9)–Cu(2)–O(21)	168.0(3)	O(1)–Cu(2)–O(21)	77.72(19)
N(13)–Cu(2)–O(21)	91.5(3)	N(9)–Cu(2)–O(6T)	97.8(4)
O(1)–Cu(2)–O(6T)	99.1(4)	N(13)–Cu(2)–O(6T)	85.3(5)
O(21)–Cu(2)–O(6T)	91.5(3)	O(44)–Cu(3)–O(24)	77.1(2)
O(44)–Cu(3)–N(36)	92.5(3)	O(24)–Cu(3)–N(36)	167.3(2)
O(44)–Cu(3)–N(32)	166.6(3)	O(24)–Cu(3)–N(32)	89.9(2)
N(36)–Cu(3)–N(32)	100.0(3)	O(44)–Cu(4)–O(44)#2	179.7(3)
O(44)–Cu(4)–O(1W)	89.83(15)	O(44)–Cu(4)–O(24)	74.7(2)
O(44)#2–Cu(4)–O(24)	105.5(2)	O(1W)–Cu(4)–O(24)	124.68(14)
O(24)–Cu(4)–O(24)#2	110.6(3)	Cu(3)–Cu(4)–Cu(3)#2	161.39(6)
Cu(2)–O(1)–Cu(1)	99.7(2)	Cu(1)–O(21)–Cu(2)	99.6(2)
Cu(3)–O(24)–Cu(4)	98.1(2)	Cu(4)–O(44)–Cu(3)	102.3(3)

Symmetry transformations used to generate equivalent atoms: #1 $-x + 1/2, -y + 3/2, -z$ #2 $-x + 1, y, -z + 1/2$.

Table 3
Selected bond lengths for **1** (Å).

Cu(1)–O(21)#1	1.952(5)	Cu(1)–O(21)	1.952(5)	Cu(1)–O(1)	1.960(4)
Cu(1)–Cu(2)	2.9849(9)	Cu(1)–O(5S)	2.495(7)	Cu(2)–N(9)	1.939(7)
Cu(2)–O(1)	1.946(5)	Cu(2)–N(13)	1.949(8)	Cu(2)–O(21)	1.956(5)
Cu(2)–O(6T)	2.395(9)	O(1W)–Cu(4)	1.956(9)	Cu(3)–O(44)	1.939(5)
Cu(3)–O(24)	1.943(5)	Cu(3)–N(36)	1.954(7)	Cu(3)–N(32)	1.956(6)
Cu(3)–O(4S)	2.529(6)	Cu(3)–Cu(4)	3.0179(9)	Cu(4)–O(44)	1.935(6)
Cu(4)–O(24)	2.051(5)	Cu(4)–Cu(3)#2	3.0180(9)		

Symmetry transformations used to generate equivalent atoms: #1 $-x + 1/2, -y + 3/2, -z$ #2 $-x + 1, y, -z + 1/2$.

Table 5
Hydrogen bonds parameters of **1**.

D—H···A	*d*(D–H) Å	*d*(H···A) Å	*d*(D···A) Å	∠(DHA)°
O(1W)–H(1W)···O(2W)#3	0.84	1.88	2.676(8)	157.6
O(2W)–H(21W)···O(1S)#4	0.901(10)	2.19(13)	2.837(10)	128(9)

Symmetry transformations used to generate equivalent atoms: #3 $x,y+1,z$ #4 $x,-y+1,z-1/2$.

[Cu(2), Cu(2A)] in a monodentate fashion in **A**, but in **I** the perchlorate ions appear bidentate, coordinating to the terminal Cu(2) and central Cu(1) centres. However, this perchlorate is disordered and it is one of the disordered atoms which bonds to Cu(2). The geometry of the terminal copper centres in both these complexes is best described as a distorted (4 + 1) (ONNO + O) square based pyramid with Addison parameters $\tau = 0.057$ for **A** and $\tau = 0.007$ for **I** ($\tau = 0$ corresponds to a perfect square pyramidal geometry and $\tau = 1$ to a perfect trigonal bipyramidal geometry). The four bonds constituting the basal plane of the external Cu(2) ions of **I** show very similar Cu–N and Cu–O bond distances [in the range 1.939(7)–1.956(5) Å]. The axial site is occupied by an oxygen atom of a coordinated perchlorate ion [Cu–O 2.395(9) Å]. The central copper atom in **I** is bound by four phenolato oxygens of the Schiff base ligands [Cu–O 1.952(5) and 1.960(4) Å] and can be described as having square planar coordination if the long Cu(1)–O(5s) [2.495(7) Å] contacts are not included.

The asymmetric unit of **1** contains a second independent bent trinuclear unit $[Cu_3(\mu\text{-}\mathbf{L})_2(H_2O)(ClO_4)_2]$ (**II**) where the three copper centres are also linked by doubly bridging μ-phenolato oxygen atoms of two units of the tetradentate N_2O_2 donor Schiff base ligands (Fig. 3). Unlike **I**, which is constrained to be linear by crystallographic symmetry, **II** is slightly distorted from linearity with a Cu(3)–Cu(4)–Cu(3) angle of 161.39(6)°. Additionally, the coordination environment of the two terminal Cu(3) centres and central Cu(4) centre in **II** are quite different to that in **I**. Although the terminal copper centres are very similar in **I** and **II** being square pyramidal and bound by the N_2O_2 donor atoms of the deprotonated Schiff bases and a terminally coordinating perchlorate anion, the central copper centres have different coordination environments. In **II** perchlorates do not bridge the terminal and central copper atoms, instead one water molecule coordinates to Cu(4) in addition to the four Schiff base oxygen atoms. The central Cu(4) atom has five coordinate trigonal bipyramidal geometry with an Addison parameter, $\tau = 0.917$. The equatorial sites of Cu(4) are occupied by two symmetry equivalent phenolato oxygen atoms [O(24)] and the coordinated water molecule [O(1W)]. The axial sites are occupied by the two remaining deprotonated phenolato oxygen atoms [O(44)] which also have the shortest Cu–O distances in that coordination sphere [Cu(4)–O(44), 1.935(6) Å; O(44)–Cu(4)–O(44)#2, 179.7(3)°, where #2 is the symmetry operation $-x+1, y, -z+1/2$].

A hydrogen bonded chain linking the trinuclear species **II** is formed between the bound water molecule and an uncoordinated solvent water molecule which in turn forms a OH···O hydrogen bond to the perchlorate anion bound to Cu(3) resulting in a double stranded chain running parallel to the *b* axis. Alongside, the trinuclear unit **I** forms parallel stacks and the coordinated perchlorate forms C–H···O hydrogen bonds with the Schiff base (Fig. 4). The benzene rings C(1)–C(6) overlap slightly with their symmetry equivalents in the neighbouring complex in the same stack but their centroids are too far apart for effective π–π-stacking.

3.6. Magnetic properties

The thermal variation of the molar magnetic susceptibility per two copper(II) trimers times the temperature ($\chi_m T$) for compound **1** shows a room temperature value of ca. 1.24 emu K mol^{-1} (Fig. 5), much lower than the spin only expected one for six non interacting copper(II), $S = 1/2$ ions (2.25 emu K mol^{-1}). On lowering the temperature, the $\chi_m T$ product shows a fast decrease that softens at low temperatures to reach a value of ca. 0.80 emu K mol^{-1} at ca. 50 K. At lower temperatures (below ca. 10 K) the $\chi_m T$ product shows a more pronounced decrease to reach a value of ca. 0.70 emu K mol^{-1} at 2 K (inset in Fig. 5). This behaviour clearly indicates that compound **1** presents a strong antiferromagnetic coupling, as deduced form the decrease in the $\chi_m T$ product already observed at room temperatures. The softening observed at low

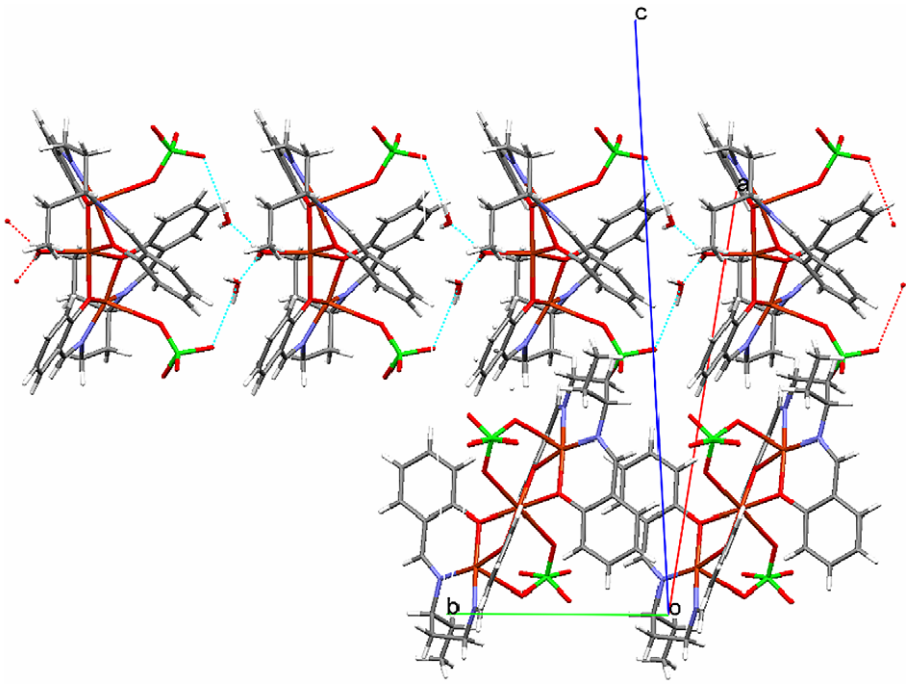


Fig. 4. Hydrogen bonded chains involving **I** alongside stacked molecules of **II** (hydrogen bonds drawn as dotted lines).

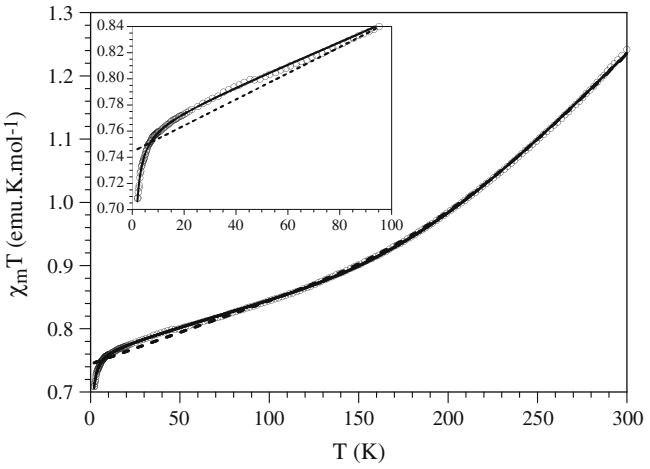


Fig. 5. Thermal variation of the $\chi_m T$ product per two copper(II) trimers for **1**. Inset shows the low temperature region. Solid and dashed lines represent the best fit to the $S = 1/2$ trimer model with and without inter-trimer interactions, respectively (see text).

temperatures suggests that this strong antiferromagnetic exchange does not lead to a diamagnetic spin ground state, in agreement with the expected behaviour for two independent antiferromagnetically coupled copper(II) trimers. Since each copper(II) trimer is expected to present an $S = 1/2$ spin ground state as a result of the intra-trimer antiferromagnetic coupling, the expected $\chi_m T$ value should be ca. 0.40 emu K mol^{-1} per copper(II) trimer (i.e., 0.80 emu K mol^{-1} for the two independent copper(II) trimers), in agreement with the experimental value. The more abrupt decrease observed at very low temperatures should therefore be attributed to weak antiferromagnetic inter-trimer interactions, as confirmed by the fitting results (see below). Since, as already mentioned, the structure of **1** shows the presence of two different copper(II) trimers, we have tried to fit the magnetic properties using a simple model containing the sum of two different $S = 1/2$ copper(II) linear trimers (the Hamiltonian is written as $H = -J_n[S_1S_2 + S_2S_3]$, where J_n is the intra-trimer exchange coupling constant of the trimer n, S_2 is the spin of the central copper(II) ion and S_1 and S_3 correspond to the terminal ones): [33]

$$\chi_{trim} = \frac{Ng^2\beta^2}{4kT}\frac{1 + e^{2x} + 10e^{3x}}{1 + e^{2x} + 2e^{3x}} \quad \text{with } x = J_n/kT \tag{1}$$

This model satisfactorily reproduces the magnetic data of **1** with $g = 1.992(1)$, $J_1 = J_2 = -327(2)$ K $= -227(1)$ cm^{-1} (dashed line in Fig. 5). Note that despite no restriction in the model used, the best values are obtained for $J_1 = J_2$. Although at high temperatures this simple model reproduces satisfactorily the magnetic properties of **1**, the low temperature behaviour is not so well reproduced, especially the sharp decrease observed below ca. 10 K (inset in Fig. 5). In order to better reproduce the magnetic behaviour of **1** at low temperatures, we have included a weak inter-trimer exchange interaction by using the molecular field approximation [34].

$$\chi'_{trim} = \frac{\chi_{trim}}{1 - (2zJ'/Ng^2\beta^2)\chi_{trim}},$$

where χ_{trim} is the susceptibility of the two independent $S = 1/2$ trimers (Eq. (1) with J_1 and J_2 for the two contributing trimers) and J' is the inter-trimer exchange coupling of the z interacting trimers. This more complete model reproduces very satisfactorily the magnetic data of **1** over the whole temperature range with the following parameters: $g = 2.0166(5)$, $J_1 = -291(4)$ K $= -202(3)$ cm^{-1}, $J_2 = -336(5)$ K $= -233(3)$ cm^{-1} and $zJ' = -0.16(1)$ K $= -0.11(1)$ cm^{-1} (solid line in Fig. 5). This model reproduces very satisfactorily the decrease observed at very low temperatures and provides a more realistic g value than the isolated trimers model. However, it could be argued that this improvement may only be due to the increase in the number of adjustable parameters (from two/three to four), so we have run a fit using the second model with J_1 and J_2 fixed to the values obtained in the first one ($J_1 = J_2 = -327$ K). This more restricted model (with only two free parameters) also gives a very good agreement with the experimental data over the whole temperature range, including the decrease at low temperatures with $g = 2.0082(8)$ and $zJ' = -0.13(1)$ K. In all cases the g value is lower than the values usually found for copper(II) complexes, suggesting the presence of a small diamagnetic impurity that reduces the magnetic signal of the sample.

A confirmation of the $S = 1/2$ ground spin state arising from the antiferromagnetically coupled trimers in **1** is provided by the isothermal magnetization data at 2 K (Fig. 6) that shows a saturation value close to 2 μ_B, the expected value for two non interacting $S = 1/2$ ions and that can be very well reproduced with the sum of two identical Brillouin functions for $S = 1/2$ with a reduced g value of 1.967(1) as a consequence of the inter-trimer antiferromagnetic coupling (solid line in Fig. 6).

The strong antiferromagnetic couplings observed in both copper(II) trimers in **1** can be easily rationalized from the similar structural features found in both trimers (Fig. 7). Thus, both trimers present a symmetrical distribution of the copper(II) ions with a perfect linear arrangement in trimer **I** (Fig. 7a) and an almost linear arrangement in trimer **II** (with a Cu3–Cu4–Cu3 angle of 161.4°, Fig. 7b). This arrangement implies that the two possible coupling constants inside each trimer are identical (given the symmetry of both trimers) and that the possible interaction between the terminal copper(II) atoms (Cu2 and Cu3) must be negligible, justifying the symmetrical linear trimer model used to fit the magnetic properties (see above). In both trimers the copper(II) ions are connected through double phenoxo bridges with very similar Cu–O bond distances and Cu–O–Cu bond angles (Fig. 7). Note that the possible perchlorate bridges imply a much longer Cu–O–Cl–O–Cu pathway with Cu–O bond distances ca. 0.5 Å longer than those of the bridging oxygen atoms and, therefore, they are negligible when compared with the much shorter double phenoxo bridges. From the several magneto-structural correlations established for double oxo bridged copper(II) complexes with the oxo bridges laying in the equatorial plane [35–38], the magnetic coupling in both trimers are expected to be strong and antiferromagnetic, in agreement with the observed behaviour. Thus, the correlation

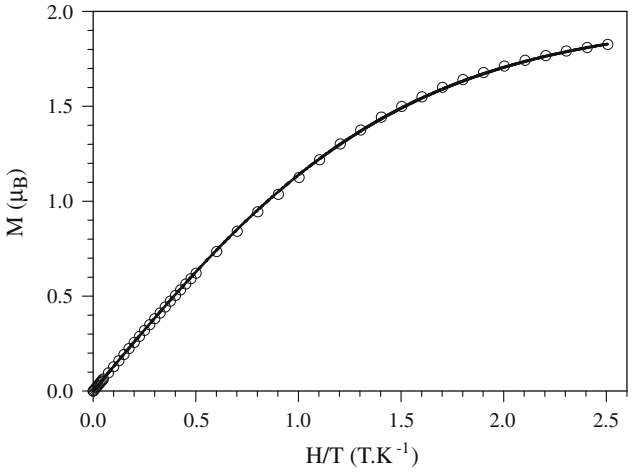


Fig. 6. Isothermal magnetization at 2 K of **1**. Solid line is the best fit to the sum of two identical $S = 1/2$ Brillouin functions (see text).

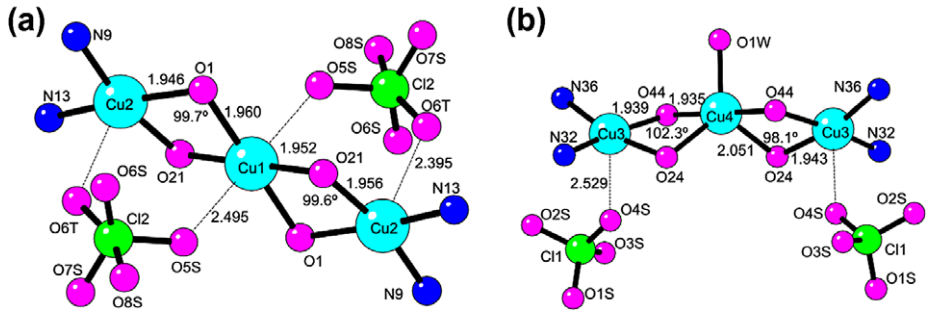


Fig. 7. Coordination environments of the two copper(II) trimers in **1** showing the bridging bond distances (Å) and angles (°) (colour code: Cu = light blue, N = dark blue, O = pink, Cl = green). (For interpretation of the references to colour in this figure legend, the reader is referred to the web version of this article.)

established between the Cu–Cu distance (R) and the J parameter, predicts strong antiferromagnetic couplings of ca. −220 and −290 cm^{-1} for trimers **I** and **II** (where the Cu–Cu distances are 2.985 and 3.018 Å, respectively). Furthermore, the Cu–O–Cu bond angle, which is the other structural parameter also used to estimate the J value, gives an estimation for the J values of ca. −160 cm^{-1} for trimer **I** (where the Cu–O–Cu bond angles are 99.6 and 99.7°, Fig. 7 and Table 4) and ca. −210 cm^{-1} for trimer **II** (where the Cu–O–Cu bond angles are ca. 98.1 and 102.3°, Fig. 7 and Table 4). Note that both magneto-structural correlations give J values in good agreement with the experimental ones even if these estimated values are approximate since these correlations do not include the torsion angle inside the Cu_2O_2 moieties and, even more important, in trimer **II** the central copper(II) ion presents a trigonal bipyramid geometry (τ = 0.92). Nevertheless, these correlations allow us to suggest that in **1** the strongest antiferromagnetic coupling (J_2 = −233(3) cm^{-1}) should be assigned to trimer **II** whereas the weakest coupling (J_1 = −202(3) cm^{-1}) should be attributed to trimer **I**. The weak antiferromagnetic intermolecular coupling can be attributed to the presence of the H-bond network, as also observed in other similar copper(II) trimers [39].

4. Conclusion

In this paper, we have described the structural and magnetic properties of a novel and very original copper(II) complex presenting two structurally different copper(II) trinuclear units. It is really interesting to note that in **1** although the coordination environment of the central copper(II) centres in the two independent linear trinuclear units are quite different from one another, they exist in the same crystallographic asymmetric unit. From the structural point of view, the title compound represents, the first example of two chemically distinct, doubly phenoxo bridged copper(II) trinuclear units. The magnetic properties of the title compound clearly show that both the trinuclear units present similar strong antiferromagnetic coupling between the copper(II) ions through the doubly phenoxo bridges and is in good agreement with the expected value obtained from previous magneto-structural correlations for doubly phenoxo bridged copper(II) complexes.

Acknowledgments

A. Ray is thankful to the Council of Scientific and Industrial Research New Delhi, Govt. of India and Dipali Sadhukhan acknowledge University Grants Commission, New Delhi, Government of India for providing them the financial support to carry out the work. The authors also acknowledge the financial help obtained from All India Council for Technical Education, New Delhi, Government of India, the European Union (MAGMANet network of excellence) and the Spanish Ministerio de Educación y Ciencia (Projects MAT2007-61584 and Consolider-Ingenio 2010 CSD 2007-00010 in Molecular Nanoscience). We also acknowledge use of the EPSRC Chemical Database Service.

Appendix A. Supplementary data

CCDC 719841 contains the supplementary crystallographic data for **1**. These data can be obtained free of charge via http://www.ccdc.cam.ac.uk/conts/retrieving.html, or from the Cambridge Crystallographic Data Centre, 12 Union Road, Cambridge CB2 1EZ, UK; fax: (+44) 1223-336-033; or e-mail: deposit@ccdc.cam.ac.uk. Supplementary data associated with this article can be found, in the online version, at doi:10.1016/j.poly.2009.07.017.

References

[1] D.J. Spira-Solomon, M. Allendorf, E.I. Solomon, J. Am. Chem. Soc. 108 (1986) 5316.
[2] F.H. Allen, Acta Crystallogr., Sect. B 58 (2002) 380.
[3] I.J. Bruno, J.C. Cole, P.R. Edgington, M. Kessler, C.F. Macrae, P. McCabe, J. Pearson, R. Taylor, Acta Crystallogr., Sect. B 58 (2002) 389.
[4] G.A. van Albada, I. Mutikainen, U. Turpeinen, J. Reedijk, Eur. J. Inorg. Chem. (1998) 547.
[5] G.A. van Albada, P.J. Van Koningsbruggen, I. Mutikainen, U. Turpeinen, J. Reedijk, Eur. J. Inorg. Chem. (1999) 2269.
[6] F. Akagi, Y. Nakao, K. Matsumoto, S. Takamizawa, W. Mori, S. Suzuki, Chem. Lett. 2 (1997) 181.
[7] L. Cronin, P.H. Walton, Inorg. Chim. Acta 269 (1998) 241.
[8] M.H.W. Lam, Y.Y. Tang, K.M. Fung, X.Z. You, W.T. Wong, J. Chem. Soc., Chem. Commun. 21 (1997) 957.
[9] T.C. Higgs, K. Spartalian, C.J. O'Connor, B.F. Matzanke, C.J. Carrano, Inorg. Chem. 37 (1998) 2263.
[10] W. Zhang, J.L. Loebach, S.R. Wilson, E.N. Jacobsen, J. Am. Chem. Soc. 112 (1990) 2801.
[11] B. Cornils, W.A. Herrmann, R. Schlogl, Catalysis from A–Z: A Concise Encyclopedia, Wiley, New York, 2000.
[12] J.R. Farraro, J.M. Williams, Introduction to Synthetic Electrical Conductors, Academic Press, New York, 1987.
[13] J.S. Miller, M. Drillon, Magnetism, Molecules to Materials, Wiley-VCH, Weinheim, 2003.
[14] S.R. Marder, J.E. Sohn, G.D. Stucky, Materials for Nonlinear Optics: Chemical Perspectives, ACS Symposium Series, Washington, DC, 1991.
[15] O.R. Evans, W. Lin, Acc. Chem. Res. 35 (2002) 511.
[16] L.C. Nathan, J.E. Koehne, J.M. Gilmore, K.A. Hannibal, W.E. Dewhirst, T.D. Mai, Polyhedron 22 (2003) 887.
[17] A. Datta, C.R. Choudhury, P. Talukder, S. Mitra, L. Dahlenburg, T. Matsushita, J. Chem. Res. (2003) 642.
[18] S.-P. Yang, Y. Hong, H.-M. Chen, F. Zhang, Q.-Q. Chen, X.-B. Yu, Acta Crystallogr., Sect. E 60 (2004) m582.
[19] S. Bandyopadhyay, J.-M. Lo, H.-H. Yao, F.-L. Liao, P. Chattopadhyay, J. Coord. Chem. 59 (2006) 2015.
[20] M. Du, X.-J. Zhao, J.-H. Guo, X.-H. Bu, J. Ribas, Eur. J. Inorg. Chem. (2005) 294.
[21] Y. Song, P. Gamez, O. Roubeau, M. Lutz, A.L. Spek, J. Reedijk, Eur. J. Inorg. Chem. (2003) 2924.
[22] Y.F. Song, G.A. van Albada, M. Quesada, I. Mutikainen, U. Turpeinen, J. Reedijk, Inorg. Chem. Commun. 8 (2005) 975.
[23] APEX2 Version 2.1: Area Detector Control and Integration Software, v. 6.45, Bruker Analytical X-Ray Instruments, Inc., Madison, WI, USA, 2006.
[24] M. Dolaz, M. Tümer, M. Diğrak, Transition Met. Chem. 29 (2004) 528.

[25] K. Nakamoto, Infrared and Raman Spectra of Inorganic and Coordination Compounds: Theory and Applications in Inorganic Chemistry, Part – A, 5th ed., John Willey and Sons Inc., New York, 1997.
[26] Z.-L. You, H.-L.Z. Zhu, Anorg. Allg. Chem. 630 (2004) 2754.
[27] A.B.P. Lever, Inorganic Electronic Spectroscopy, 2nd ed., Elsevier, Amsterdam, 1984. p. 553.
[28] R.C. Holz, B. Bennett, G. Chen, L.-J. Ming, J. Am. Chem. Soc. 120 (1998) 6329.
[29] N.N. Murthy, K.D. Karlin, I. Bertini, C. Luchinat, J. Am. Chem. Soc. 119 (1997) 2156.
[30] J.M. Brink, R.A. Rose, R.C. Holz, Inorg. Chem. 35 (1996) 2878.
[31] W. Kemp, Organic Spectroscopy, 3rd ed., Palgrave Publishers, 1991.
[32] P. Kamatchi, S. Selvaraj, M. Kandaswamy, Polyhedron 24 (2005) 900.
[33] O. Kahn, Molecular Magnetism, VCH Publishers, 1993.
[34] C.J. O'Connor, Prog. Inorg. Chem. 29 (1982) 203.
[35] P.J. Hay, J.C. Thibeault, R. Hoffmann, J. Am. Chem. Soc. 97 (1975) 4884.
[36] W.H. Crawford, H.W. Richardson, J.R. Wasson, D.J. Hodgson, W.E. Hatfield, Inorg. Chem. 15 (1976) 2107.
[37] B. Chiari, J.H. Helms, O. Piovesana, T. Tarantelli, P.F. Zanazzi, Inorg. Chem. 25 (1986) 2408.
[38] F. Setifi, S. Benmansour, S. Triki, C.J. Gómez-García, M. Marchivie, J.-Y. Salaün, M. Mustapha, Inorg. Chim. Acta 360 (2007) 3879.
[39] V. Tudor, V.Ch. Kravtsov, M. Julve, F. Lloret, Y.A. Simonov, B.B. Averkiev, M. Andruh, Inorg. Chim. Acta 358 (2005) 2066.

2. Experimental

2.1. General

All the reactions were carried out under aerobic conditions. $[Fe_3EuO_2(O_2CCCl_3)_8(H_2O)(THF)_3]$ [9a], $[Fe_2CaO(O_2CCCl_3)_6(THF)_4]$ [9b] and $[Fe_3O(O_2CCMe_3)_6(H_2O)_3]NO_3$ [10] were obtained as reported. 1,1′-Ferrocenedicarboxylic acid ($fcdcH_2$) was obtained from commercial sources and was used without further purification. Elemental analyses for C and H were carried out at the Institute for Inorganic Chemistry at the University of Karlsruhe.

2.2. Preparations

2.2.1. $[Fe_4O_2(O_2CCCl_3)_6(fcdc)(THF)_2(H_2O)_2]\cdot 1.5C_7H_8$, (**1**)$\cdot 1.5C_7H_8$

(Method **A**) A mixture of $[Fe_3EuO_2(O_2CCCl_3)_8(H_2O)(THF)_3]$ (0.18 g, 0.10 mmol) and $HOOCC_5H_4FeC_5H_4COOH$ (0.055 g, 0.20 mmol) in toluene (10 ml) was heated to ~50 °C for 30 min, resulting in the immediate formation of a dark red solution. The solution was filtered and the filtrate was allowed to stand undisturbed at room temperature. Dark red crystals of **1** formed over four days. Yield 14%. Elemental *Anal.* Calc. (%) for **1**: $C_{32}H_{28}O_{22}Cl_{18}Fe_5$ (dried): C, 22.85; H, 1.67. Found: C, 22.72; H, 1.78%.

(Method **B**) $[Fe_2CaO(O_2CCCl_3)_6(THF)_4]$ (0.272 g, 0.20 mmol) and $HOOCC_5H_4FeC_5H_4COOH$ (0.055 g, 0.20 mmol) were mixed in toluene (20 ml) and heated to ~50 °C for 30 min, resulting in the formation of a dark red solution. The solution was filtered and the filtrate was allowed to stand undisturbed at room temperature. Dark red crystals of **1** formed over two days, were washed 3 times with water and air dried. Yield ~67%. Elemental *Anal.* Calc. (%) for **1**: $C_{32}H_{28}O_{22}Cl_{18}Fe_5$ (dried): C, 22.85; H, 1.67. Found: C, 22.94; H, 1.81%.

2.2.2. $[Fe_6O_2(OH)_2(O_2CCMe_3)_{10}(fcdc)(H_2O)_2]$ (**2**)

A mixture of $[Fe_3O(O_2CCMe_3)_6(H_2O)_3]NO_3$ (0.19 g, 0.20 mmol) and $HOOCC_5H_4FeC_5H_4COOH$ ($fcdcH_2$) (0.055 g, 0.20 mmol) in toluene (10 ml) was heated under reflux for 3 h, resulting in the immediate formation of a dark green solution. The solution was filtered and the filtrate was allowed to stand undisturbed at room temperature. Dark red crystals of **2** formed over two days and were isolated in an overall yield of 65%. Elemental *Anal.* Calc. (%) for $C_{62}H_{104}O_{30}Fe_7$ (dried): C, 43.28; H, 6.09. Found: C, 43.12; H, 5.94%.

2.3. Physical measurements

2.3.1. Mössbauer measurements

The Mössbauer spectra were acquired using a conventional spectrometer in the constant-acceleration mode equipped with a ^{57}Co source (3.7 GBq) in a rhodium matrix. Isomer shifts are given relative to α-Fe at room temperature. The sample was inserted inside an Oxford Instruments Mössbauer-Spectromag 4000 Cryostat. The sample temperature can be varied between 3.0 and 300 K. The spectra were fitted using the NORMOS Mössbauer Fitting Program.

2.3.2. Magnetic measurements

The magnetic measurements were carried out with the use of a Quantum Design SQUID magnetometer MPMS-XL. This magnetometer works between 1.8 and 400 K for dc applied fields ranging from −7 to 7 T. Measurements were performed on polycrystalline samples. The magnetic data were corrected for the sample holder and the diamagnetic contribution estimated from Pascal constants.

Table 1
Crystallographic data for compounds **1** and **2**.

	1	**2**
Formula	$C_{42.50}H_{40}Cl_{18}Fe_5O_{22}$	$C_{62}H_{104}Fe_7O_{30}$
Mr	1820.09	1720.4
Crystal system	orthorhombic	orthorhombic
Space group	*Pccn*	*Pccn*
a [Å]	19.5009(3)	16.1090(10)
b [Å]	30.8949(5)	16.7640(10)
c [Å]	22.3829(4)	29.880(3)
α [°]	90.00	90.00
β [°]	90.00	90.00
γ [°]	90.00	90.00
V [Å^3]	13485.21(4)	8069.13(10)
Z	8	4
ρ_{calc} [g cm^3]	1.793	1.416
μ (Mo Kα) [mm^{-1}]	1.832	1.298
F(0 0 0)	7256	3592
T [K]	233	233
Collected reflections	50049	17869
Unique reflections	9349	4054
R_{int}	0.1007	0.1194
Reflections with $I > 2\sigma(I)$	9349	4054
Refined parameters	899	486
R_1 [$I > 2\sigma(I)$]	0.0683	0.0727
S (all data)	1.093	1.027
wR_2 (all data)	0.2168	0.1550

2.4. Powder diffraction/crystal structure determination

2.4.1. X-ray crystal and molecular structural analyses

X-ray single-crystal diffraction data for complexes **1** and **2** were collected on a Nonius Kappa CCD diffractometer with graphite-monochromated Mo Kα radiation (λ = 0.71069 Å). Intensities were integrated using DENZO and scaled with SCALEPACK. The structures were solved and refined using the SHELXTL software [11]. The high *R* values of both compounds were caused by a systematic twining and poor diffraction of the small crystals. Further details of the data collection and refinement are given in Table 1.

3. Results and discussion

3.1. Synthesis

Various strategies have been utilized in the synthesis of coordination compounds with ferrocenedicarboxylic acid [4]. All our attempts to synthesize iron(III) complexes using only ferrocenedicarboxylic acid as a ligand failed because of the low solubility of the final products. Therefore, to produce Fe(III) cage complexes featuring ferrocenedicarboxylates we have developed a route in which ferrocenedicarboxylic acid is introduced with a coligand. Small changes to this method in terms of the ratio of starting materials were made and in all cases the reactions gave compounds discussed in this work. Although in the synthetic approach both of the possible starting materials we used, $[Fe_3EuO_2(O_2CCCl_3)_8(H_2O)$- $(THF)_3]$ and $[Fe_2CaO(O_2CCCl_3)_6(THF)_4]$, are heterometallic compounds, the reason why the calcium containing compound leads to a much higher yield of the target compound is unclear.

3.2. Structural analysis

The crystal structure of **1** represents a butterfly structure, but the structure of **2** consists of six Fe^{3+} centres arranged in two triangular subunits bridged at two vertices.

Complex **2** crystallizes in the orthorhombic space group *Pccn* with half a molecule in the asymmetric unit located on a twofold rotation axis (Fig. 2). The core contains the well-known $[Fe_6(\mu_3\text{-}O)_2]^{14+}$ core [12,13], comprising two linked Fe_3O units; a $fcdc^{2-}$ dianion,

Table 2
Selected bond lengths and angles for **1** and **2**.

1	2
Bond lengths (Å)	
Fe1–O1 1.910(4)	Fe1–O1 1.967(6)
Fe1–O1a 1.942(4)	Fe1–O2 1.987(7)
Fe1–O6 2.017(5)	Fe1–O5 2.009(7)
Fe1–O2 2.027(5)	Fe1–O3 2.017(7)
Fe1–O10 2.032(6)	Fe1–O7 2.021(7)
Fe1–O4 2.063(5)	Fe1–O9 2.036(7))
Fe2–O1 1.849(4)	Fe2–O1 1.946(6)
Fe2–O8 1.993(5)	Fe2–O2 1.982(7)
Fe2–O3 2.002(5)	Fe2–O4 1.992(8)
Fe2–O5 2.036(6)	Fe2–O6 1.994(7)
Fe2–O7 2.046(5)	Fe2–O11 2.018(7)
Fe2–O11 2.105(5)	Fe2–O13 2.036(7)
	Fe3–O1 1.864(6)
	Fe3–O8 2.003(7)
	Fe3–O12 2.005(7)
	Fe3–O14 2.026(7)
	Fe3–O10 2.029(7)
	Fe3–O15 2.189(7)
Angles (°)	
Fe2–O1–Fe1 122.1(2)	Fe3–O1–Fe2 119.2(3)
Fe2–O1–Fe1a 131.4(2)	Fe3–O1–Fe1 117.8(3)
Fe1–O1–Fe1a 96.63(18)	Fe2–O1–Fe1 122.5(3)
	Fe2a–O2–Fe1 132.6(4)

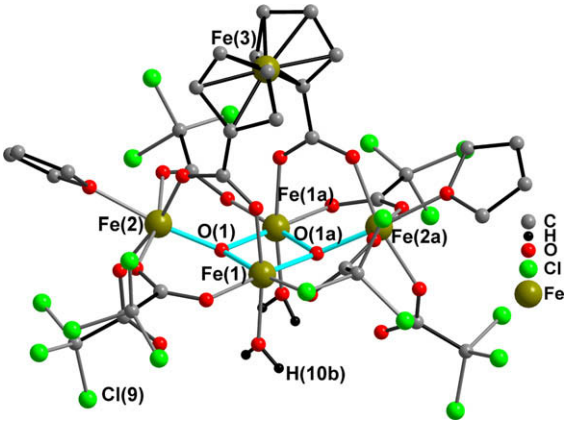


Fig. 1. Molecular structure of **1**. Hydrogen atoms of THF and $fcdc^{2-}$ rings are omitted for clarity.

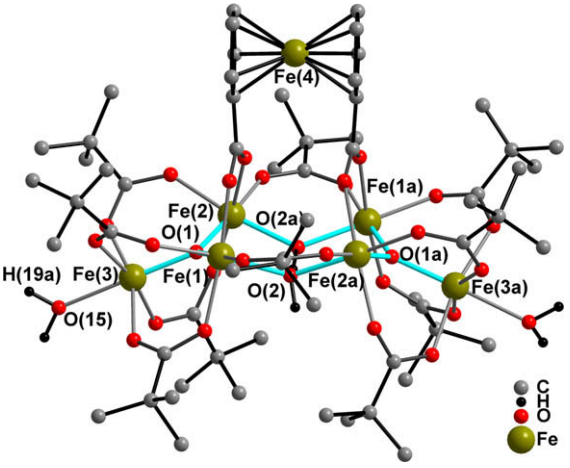


Fig. 2. Molecular structure of **2**. Hydrogen atoms of pivalates and $fcdc^{2-}$ rings are omitted for clarity.

two pivalate and two hydroxide ligands bridge the two Fe_3 halves of the complex, and a trigonal planar oxide and four pivalate ligands bridge within the Fe_3 units at each end. Each Fe^{III} ion is six-coordinate in a distorted octahedral geometry with Fe(3) and Fe(3a) each coordinated to a water molecule.

Complex **1** crystallizes in the orthorhombic space group *Pbcn* with two half molecules again located on twofold rotation axes in the asymmetric unit. One of the essentially identical molecules is shown in Fig. 1. The central $\{Fe_4O_2\}$ core of **1** can be structurally described as two condensed iron Fe_2O units forming a butterfly motif of the iron atoms with a dihedral angle between the planes Fe(1)–Fe(1a)–Fe(2) and Fe(1)–Fe(1a)–Fe(2a) of 29°. In contrast to **2** the terminal iron atom Fe(2) is only bridged by two trichloroacetates and one carboxylate group of fcdc, whereas one THF and one trichloroacetate act as monodentate ligands. The bridging by fcdc leads to a twist of the $\{Fe_3O\}$ unit with a strongly distorted trigonal oxide, which lies 0.336(4) Å out of the iron plane. In comparison with **2**, where the environment of the O(1) atom is trigonal planar with a sum of the angles around O(1) of 359.5°, this twisting in **1** leads to a sum of 350.1° (Table 2).

The $fcdc^{2-}$ ligand acts as a flexible connector between the metal ions because the two cp rings of the $fcdc^{2-}$ can rotate. Different steric configurations are possible, depending on the torsion angle φ of the two carboxylate groups of $fcdc^{2-}$. For **1**, the φ value is about 25°. That is, both carboxylate groups of $fcdc^{2-}$ show a synclinal staggered conformation. For **2**, the φ value is 2°, showing the conformation of carboxylate groups is synperiplanar.

3.3. Mössbauer spectroscopy of *1* and *2*

We used Mössbauer spectroscopy as a means to investigate the electronic structures of both compounds since they are not soluble in any solvents useful for cyclic voltammetry. The Mössbauer spectra of **1** were recorded at 300 and 150 K and are shown in Fig. 3. At both temperatures the spectra consist of an inner- and outer-doublet with a ratio of 4:1. The inner doublet observed at each temperature can be fit by two doublets of equal area originating respectively from the wing- and body-iron atoms of the $Fe_4(\mu_3\text{-}O)_2$ core, whose isomer shifts (δ) and quadrupole splitting (ΔE_Q) values

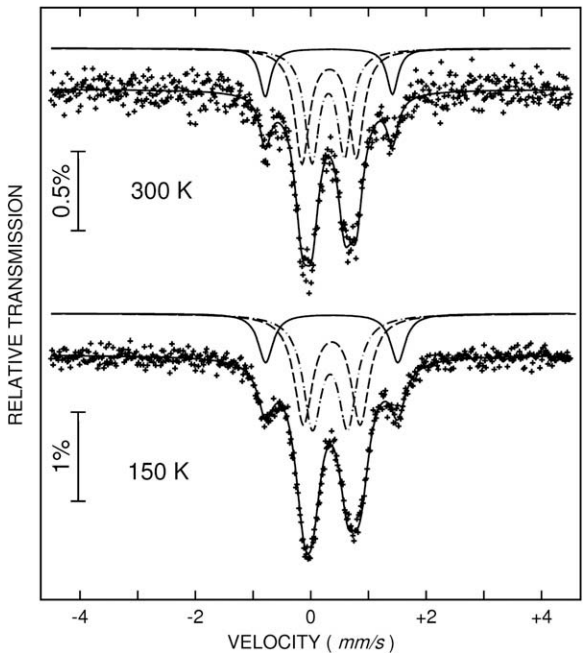


Fig. 3. Zero-field Mössbauer spectra of solid compound **1** at different temperatures.

Table 3
Mössbauer data for compound **1**.

T, K	Type of Fe	δ[a], mm/s	ΔE_Q, mm/s	Γ, mm/s
300	$2 \times Fe_w$	0.42(3)	0.93(1)	0.30(2)
	$2 \times Fe_b$	0.41(2)	0.563(7)	0.29(3)
	$1 \times Fe_{fc}$	0.52(1)	2.204(8)	0.23(2)
150	$2 \times Fe_w$	0.472(7)	0.982(6)	0.383(4)
	$2 \times Fe_b$	0.441(4)	0.610(8)	0.38(2)
	$1 \times Fe_{fc}$	0.54(2)	2.290(3)	0.317(3)

[a] Relative to α-Fe at room temperature. The statistical errors are given in parentheses. The relative area for the spectra for compound **1** has been constrained to 2:2:1 ratios, respectively.

are listed in Table 3. While the δ values for both doublets are very similar, the ΔE_Q values are quite different. The values for δ are within the range expected for iron(III) high-spin complexes and show little temperature dependence. They are comparable to those of other complexes with Fe_4O_2 butterfly cores [14]. The Fe_{body} exhibits an O_6 coordination sphere with distances corresponding to a more symmetric coordination environment than for Fe_{wing} with the bond length distortion values 2.85 and 2.42 for Fe_{wing} and Fe_{body}, respectively. The Mössbauer signal for Fe_{body} is therefore assigned to the smaller ΔE_Q value of 0.563–0.609 mm/s, whereas the doublet showing a ΔE_Q value of 0.937–0.982 mm/s is assigned to the Fe_{wing} ion. The outer-doublet with the δ and ΔE_Q values of ~0.45 mm/s and ~2.25 mm/s, respectively, is characteristic for Fe^{II} low-spin of the ferrocene unit.

The Mössbauer spectra of compound **2** are displayed in Fig. 4. The isomer shifts and quadrupole splitting values at three temperatures in zero applied magnetic field are listed in Table 4. As for **1**, the spectra were fit by three doublets originating respectively from the central and lateral high-spin Fe(III) ions of the $Fe_6(\mu_3\text{-}O)_2(\mu\text{-}OH)_2$ core and Fe^{II} of the $fcdc^{2-}$ anions. The predicted proportions of Fe(II) and Fe(III) from the structural study of compound **2** are 14.3% and 85.7%, respectively. If the fitting of the Mössbauer spectra is done through a free iteration method, then the obtained values for absorption areas for the Fe(II) and Fe(III) centres are close to the predicted percentages; the small discrepancies probably result from different recoilless fractions for the ferrous and ferric subsites in the cluster.

The most important observation from the Mössbauer measurements for both compounds is that the ratio between the areas of the inner- and outer-doublets does not change with temperature. This effect proves that there is no interaction or electron-transfer from the Fe(II) of ferrocene to the Fe(III) ions of the main cores of both compounds. According to the classification scheme proposed by Robin and Day [15], these results support assignment of the complexes **1** and **2** as a class I mixed-valence complexes.

3.4. Magnetic properties of 1–2

The magnetic susceptibility of compounds **1** and **2** was measured at 0.1 T in the range from 1.8 to 300 K. For compound **1**, a plot of $\chi_M T$ per $Fe^{III}{}_4$ (Fe^{II} is diamagnetic) versus temperature is given in Fig. 5 (left). The data clearly indicate that this complex possesses an $S = 0$ ground state, in accord with what has been observed before for molecules of a similar structure [14]. In a qualitative sense, the $S = 0$ state can be thought of in terms of an antiferromagnetic coupling of the four high-spin Fe(III) ions to produce a ground state of zero net spin.

For compound **2**, the room temperature value of $\chi_M T$ per $Fe^{III}{}_6$ (Fe^{II} is diamagnetic) (Fig. 5 (right)) is 5.07 $cm^3\,K\,mol^{-1}$ and it decreases further, reaching a value close to zero already at 8.00 K. The 300 K value is considerably less than the 26.34 $cm^3\,K\,mol^{-1}$ expected for a hexa-nuclear species containing non-interacting Fe^{III} ($S = 5/2$) ions, suggesting the presence of relatively strong

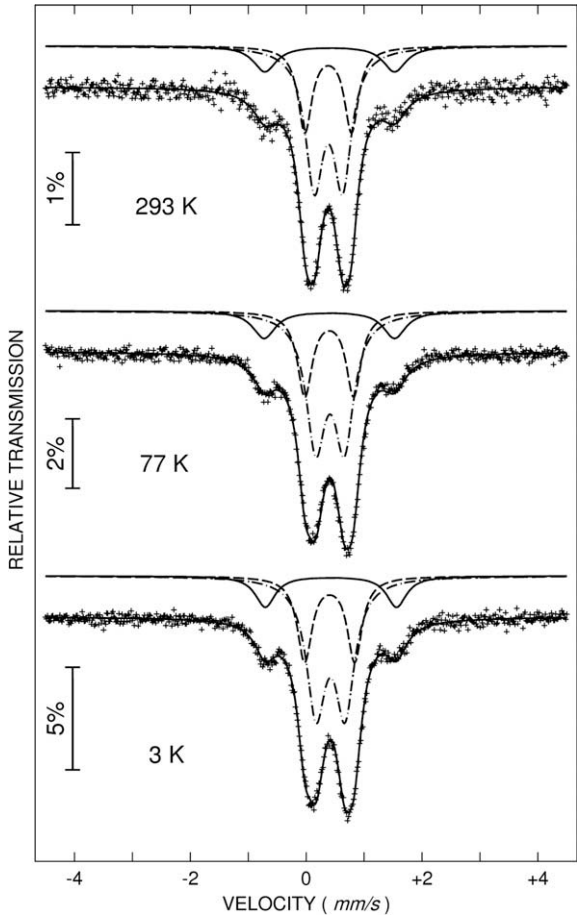


Fig. 4. Zero-field Mössbauer spectra of solid compound **2** at different temperatures.

Table 4
Mössbauer data for compound **2**.

T, K	Type of Fe	δ[a], mm/s	ΔE_Q, mm/s	Γ, mm/s
293	$2 \times Fe_{lat}$	0.486(4)	0.80(2)	0.29(1)
	$4 \times Fe_{centr}$	0.490(2)	0.486(7)	0.37(2)
	$1 \times Fe_{fc}$	0.51(1)	2.23(7)	0.38(1)
77	$2 \times Fe_{lat}$	0.505(7)	0.84(2)	0.31(2)
	$4 \times Fe_{centr}$	0.517(8)	0.492(7)	0.404(2)
	$1 \times Fe_{fc}$	0.527(3)	2.25(1)	0.33(2)
3	$2 \times Fe_{lat}$	0.512(5)	0.862(6)	0.30(1)
	$4 \times Fe_{centr}$	0.526(1)	0.498(3)	0.401(5)
	$1 \times Fe_{fc}$	0.53(1)	2.26(2)	0.41(2)

[a] Relative to α-Fe at room temperature. The statistical errors are given in parentheses. The relative area for the spectra for compound **2** has been constrained to 2:4:1 ratios, respectively.

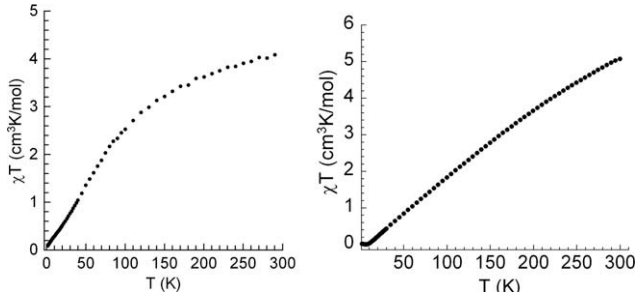


Fig. 5. $\chi_M T$ versus T plot for complexes **1** (left) and **2** (right) in a 1 kG field.

antiferromagnetic exchange interactions in **2**. The continuous decrease at the lowest temperatures is strongly suggestive of an $S = 0$ ground state. The $S = 0$ ground state for such type of compounds with six iron(III) ions, with few exceptions [12], is expected [13b,12c] and the observed overall magnetic behaviour thus indicates that essentially antiferromagnetic coupling interactions are operative between the six Fe^{III} centres and that this topology does not introduce large amounts of spin frustration.

4. Conclusions

In conclusion, the use of ferrocenedicarboxylic acid in reactions with preformed iron clusters has allowed us to obtain two new penta- and hepta-nuclear iron(III) complexes, **1** and **2**. The structures of these compounds are similar to many tetra- and hexa-nuclear iron(III) complexes described in literature [12–14], the main difference here being the presence of one redox centre in the structure. Although the compounds are not soluble in any solvents suitable for cyclic voltammetry, we were able to investigate the electronic structures in the solid-state using Mössbauer spectroscopy. This allowed us to establish that in both cases no electronic communication occurs. Nevertheless, the combination of high-spin Fe(III) with the redox-active ferrocenyl moiety in complexes **1** and **2** could provide a fascinating playground for the study of single electron-transfer. In addition, it should be possible to replace the solvent molecules in **1** (THF) and **2** (H_2O) with other functional (e.g. bridging) ligands. **1** and **2** are therefore possible prototypes for a wide range of crystal engineered one-dimensional redox-active polymers. Studies along these lines are in progress.

Supplementary data

CCDC 661893 and 661896 contains the supplementary crystallographic data for **1** and **2**. These data can be obtained free of charge via http://www.ccdc.cam.ac.uk/conts/retrieving.html, or from the Cambridge Crystallographic Data Centre, 12 Union Road, Cambridge CB2 1EZ, UK; fax: (+44) 1223-336-033; or e-mail: deposit@ccdc.cam.ac.uk.

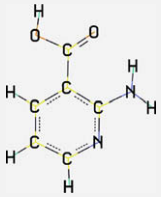
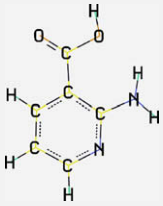
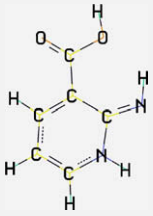
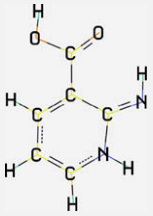
Acknowledgements

This work was supported by the bilateral grant ASM-BMBF (09.820.05.09GF-MDA 08/007) – CSSDT (#08.819.05.01F), D.F.G. (Center for Functional Nanostructures) and INTAS No. 05-1000008-7834.

References

[1] (a) R.D. Cannon, R.P. White, Prog. Inorg. Chem. 36 (1988) 195;
(b) F.A. Cotton, S.A. Duraj, W.J. Roth, Inorg. Chem. 23 (1984) 4042;
(c) T. Sato, F. Ambe, K. Endo, M. Katada, H. Maeda, T. Nakamoto, H. Sano, J. Am. Chem. Soc. 118 (1996) 3450.
[2] (a) O. Jurgens, J. Vidal-Gancedo, C. Rovira, K. Wurst, C. Sporer, P. Bildstein, H. Schottenberger, P. Jaitner, J. Veciana, Inorg. Chem. 37 (1998) 4547;
(b) C. Sporer, H. Heise, K. Wurst, D. Ruiz-Molina, H. Kopacka, P. Jaitner, F. Köhler, J.J. Novoa, J. Veciana, Chem. Eur. J. 10 (2004) 1;
(c) D. Collison, F.E. Mabbs, S.S. Turner, A.K. Powell, E.J.L. McInnes, L.J. Yellowlees, J. Chem. Soc., Dalton Trans. (1997) 1201.
[3] (a) R. Costa, C. Lopez, E. Molins, E. Espinosa, J. Perez, J. Chem. Soc., Dalton Trans. (2001) 2833;
(b) P. Comba, G. Linti, K. Merz, H. Pritzkow, F. Renz, Eur. J. Inorg. Chem. (2005) 383.
[4] (a) D. Braga, G. Cojazzi, A. Abati, L. Maini, M. Polito, L. Scaccianoce, F. Grepioni, J. Chem. Soc., Dalton Trans. (2000) 3969;
(b) G. Dong, M. Hong, D. Chun-Ying, L. Feng, J. Chem. Soc., Dalton Trans. (2002) 2593;
(c) M. Kondo, R. Shinagawa, M. Miyazawa, M.K. Kabir, Y. Irie, T. Horiba, T. Naito, K. Maeda, S. Utsuno, F. Uchida, J. Chem. Soc., Dalton Trans. (2003) 515;
(d) A. Masello, M. Murugesu, K.A. Abboud, G. Christou, Polyhedron 26 (2007) 2276.
[5] G. Dong, L. Yu-ting, D. Chun-ying, M. Hong, M. Quing-jin, Inorg. Chem. 42 (2003) 2519.
[6] M.A.S. Aquino, I.W. Wyman, Trends Inorg. Chem. 8 (2004) 1.
[7] S.D. Christie, S. Subramanian, L.K. Thompson, M.J. Zaworotko, Chem. Commun. (1994) 2563.
[8] V. Mereacre, M. Nakano, J. Gómez-Segura, I. Imaz, C. Sporer, K. Wurst, J. Veciana, C. Turta, D. Ruiz-Molina, P. Jaitner, Inorg. Chem. 45 (2006) 10443.
[9] (a) C. Turta, D. Prodius, V. Mereacre, M. Gdaniec, Yu.A. Simonov, V. Kuncser, G. Filoti, A. Caneschi, L. Sorace, Inorg. Chem. Commun. 7 (2004) 576;
(b) D. Prodius, C.I. Turta, V. Mereacre, S. Shova, M. Gdaniec, Yu.A. Simonov, V. Kuncser, G. Filoti, A. Caneschi, Polyhedron 25 (2006) 2175.
[10] A.B. Blake, L.R. Fraser, J. Chem. Soc., Dalton Trans. (1975) 193.
[11] (a) G.M. Sheldrick, SHELXS-86: Program for Crystal Structure Solutions. University of Göttingen, 1986.;
(b) G.M. Sheldrick, SHELXL-97: Program for Refinement of Crystal Structures. University of Göttingen, 1997.
[12] (a) C. Christmas, H.-L. Tsai, L. Pardi, J. Kesselman, P. Gantzel, R. Chadha, D. Gatteschi, D. Harvey, D. Hendrickson, J. Am. Chem. Soc. 115 (1993) 12483;
(b) L. Jones, P. Jensen, B. Moubaraki, J. Cashion, K. Berry, K. Murray, J. Chem. Soc., Dalton Trans. (2005) 3344;
(c) C. Canada-Vilalta, T.A. O'Brien, E.K. Brechin, M. Pink, E.R. Davidson, G. Christou, Inorg. Chem. 43 (2004) 5505.
[13] (a) J. McCusker, J. Vincent, E. Schmitt, M. Mino, K. Shin, D. Coggin, P. Hagen, J. Huffman, G. Christou, D. Hendrickson, J. Am. Chem. Soc. 113 (1991) 3012;
(b) E.J. Seddon, J. Huffman, G. Christou, J. Chem. Soc., Dalton Trans. (2000) 4446 (and references therein).
[14] (a) S.M. Gorun, S.J. Lippard, Inorg. Chem. 27 (1988) 149;
(b) P. Ammala, J.D. Cashion, C.M. Kepert, B. Moubaraki, K.S. Murray, L. Spiccia, B.O. West, Angew. Chem., Int. Ed. 39 (2000) 1688;
(c) J. Overgaard, D. Hibbs, E. Rentschler, G. Timco, F. Larsen, Inorg. Chem. 42 (2003) 7593.
[15] M.P. Robin, P. Day, Adv. Inorg. Chem. Radiochem. 10 (1967) 247.

Table 1
Calculated (B3LYP/6-311++G**) optimized structures of 2-aminonicotinic acid.

	Structure1	Structure 2	Structure 3	Structure 4
				
Energy (Hartree[a])	−492.3816	−492.3775	−492.3523	−492.3543
Dipole moment (Debye[b])	1.1990	1.4909	3.1303	4.7500

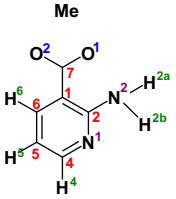
[a] 1 Hartree = 2625.5 kJ/mol.
[b] 1 D = 3.33564 × 10^{-30} C × m.

Table 2
The bond lengths (Å[a]) and bond angles in 2-aminonicotinate (2-AN) molecules in comparison with 2-aminonicotinic acid (2-ANA) and aromaticity indices calculated by the B3LYP/6-311++G** method.

	2-ANA		Li 2-AN	Na 2-AN	K 2-AN
	Experimental [13]	Calculated			
Calculated bond lengths					
C1–C2	1.424	1.430	1.428	1.428	1.428
C2–N1	1.360	1.349	1.350	1.349	1.349
C4–N1	1.348	1.326	1.329	1.330	1.330
C4–C5	1.354	1.398	1.396	1.394	1.393
C5–C6	1.398	1.385	1.388	1.390	1.391
C1–C6	1.374	1.400	1.396	1.394	1.393
C2–N2	1.322	1.351	1.354	1.355	1.356
N2–H2a	0.876	1.006	1.006	1.006	1.005
N2–H2b	0.946	1.010	1.011	1.012	1.013
C1–C7	1.514	1.466	1.481	1.494	1.500
C7–O1	1.234	1.220	1.287	1.282	1.280
C7–O2	1.266	1.358	1.273	1.267	1.265
C4–H4	1.015	1.087	1.088	1.088	1.088
C5–H5	0.911	1.082	1.082	1.083	1.083
C6–H6	0.971	1.082	1.083	1.083	1.083
O1–Me			1.860	2.208	2.529
O2–H/Me		0.968	1.849	2.204	2.512
Calculated bond angles					
C1–C2–N1	118.2	121.6	121.8	122.0	122.0
C2–N1–C4	122.5	118.6	118.5	118.5	118.5
N1–C4–C5	121.2	124.4	124.3	124.2	124.2
C4–C5–C6	118.2	117.4	117.3	117.3	117.3
C5–C6–C1	121.7	120.3	120.5	120.7	120.7
C6–C1–C2	118.2	117.7	117.5	117.3	117.3
C1–C2–N2	124.4	122.5	122.3	122.1	122.1
N1–C2–N2	117.4	115.9	115.9	115.9	115.9
C2–N2–H2a	113.3	120.0	118.9	118.3	118.2
C2–N2–H2b	122.4	117.7	117.9	118.0	118.0
H2a–N2–H2b	124.3	122.3	123.2	123.8	123.8
H4–C4–N1	115.5	115.5	115.5	115.5	115.5
H5–C5–C4	119.1	120.8	120.8	120.9	120.9
H6–C6–C5	119.6	120.9	121.7	121.7	121.7
C2–C1–C7	122.0	120.9	123.3	123.5	123.5
C6–C1–C7	119.8	121.4	119.2	119.2	119.2
O1–C7–O2	125.6	120.7	119.6	122.1	122.0
C1–C7–O1	117.5	125.7	120.4	119.2	119.3
C1–C7–O2	116.9	113.6	120.0	118.7	118.7
C7–O2–H/Me		106.5	84.0	88.9	89.0
O1–Me–O2			73.2	60.7	60.7
Aromaticity indices					
NICS		−5.1615	−4.9987	−5.1369	−5.2662
HOMA[b]	0.8681	0.9088	0.9213	0.9242	0.9249
GEO	0.1283	0.0604	0.0503	0.0492	0.0494
EN	0.0036	0.0307	0.0284	0.0266	0.0257
I_6	69.612	83.509	83.344	83.386	83.287
Δ(CC)[c]	0.076	0.104	0.099	0.098	0.098
Δ(CCC)[d]	4.3	7.0	7.0	6.9	6.9

[a] 1 Å = 10^{-10} m.
[b] HOMA=1−EN−GEO (GEO: geometric contribution to the aromaticity; EN: energetic contribution to the aromaticity).
[c] Differences between the longest and the shortest bond in the ring.
[d] Differences between the largest and the least angle in the ring.

Table 3
The NPA atomic charges [e[a]] for 2-aminonicotinic acid (2-ANA) and 2-aminonicotinates (2-AN) calculated by the B3LYP/6-311++G** method.



Atom	2-ANA	Li 2-AN	Na 2-AN	K 2-AN
C1	−0.262	−0.252	−0.243	−0.240
C2	0.444	0.436	0.430	0.428
N1	−0.519	−0.529	−0.532	−0.535
C4	0.107	0.097	0.089	0.085
C5	−0.304	−0.310	−0.312	−0.314
C6	−0.101	−0.102	−0.110	−0.114
C7	0.793	0.766	0.767	0.771
N2	−0.762	−0.776	−0.784	−0.787
H2a	0.427	0.428	0.429	0.430
H2b	0.398	0.392	0.390	0.388
H/Me	0.487	0.942	0.942	0.960
H4	0.187	0.182	0.179	0.178
H5	0.215	0.211	0.208	0.206
H6	0.227	0.229	0.228	0.227
O1	−0.644	−0.874	−0.858	−0.857
O2	−0.693	−0.841	−0.823	−0.824
Ring	−0.635	−0.660	−0.678	−0.690
COO^-	−0.544	−0.949	−0.914	−0.910
NH_2	0.063	0.044	0.035	0.031

[a] e = 1.6021892 × 10^{-19} C.

molecular and electronic structure and biological activity of new preparations.

Not only is the geometric structure interesting for us, but also the determination of electronic charge distribution and the degree of bond polarity. It is well known that biological activity depends on a compound's reactivity and its stability, which finally depend on the electronic charge distribution. To determine the electronic charge distribution, the following experimental and theoretical methods were used: FT-IR, NMR, FT-Raman, UV/Vis and quantum calculations. Application of the different complementary methods lets us to draw adequate conclusions. To search for the effect of alkali metal series on the electronic structure of ligands, it was necessary to obtain anhydrous complexes, the structures of which are the same. Changes in the number of water molecules or crystallographic structure bring about extra perturbations in the series of the studied salts and complexes.

2. Experimental

Lithium, sodium, potassium, rubidium and cesium 2-aminonicotinates were prepared by dissolving the powder of 2-aminonicotinic acid in a water solution of the appropriate alkali metal hydroxide in a stoichiometric ratio. All reagents were Aldrich analytical chemicals, with the exception of LiOH (Sigma). The mixed solution was slowly condensed at 70 °C. The products precipitated by slow evaporation. Then the salts were dissolved and crystallized from demineralised water. After drying, the IR spectra were recorded. The composition of the obtained salts and degree of dehydration was determined by spectroscopic methods (by analysis of ranges characteristic for H_2O bands in the IR and Raman spectra). Preparing anhydrous salts is important for the comparison of the electronic structures of the studied compounds and to evaluate the alkali metal effect.

The IR spectra were recorded with the EQUINOX 55, BRUKER FT-IR spectrometer within the range 4000–400 cm^{-1}. Samples in the solid state were measured in a KBr matrix and with ATR attachments. Pellets were obtained with a hydraulic press under 739 MPa pressure. Raman spectra of solid samples in capillary tubes were recorded in the range 4000–400 cm^{-1} with a FT-Raman accessory of the Perkin Elmer System 2000. The resolution of the spectrometer was 1 cm^{-1}. The NMR spectra of DMSO saturated solutions were recorded with the NMR AC 200 F, Bruker unit at room temperature. TMS was used as an internal reference.

To calculate the optimized geometrical structures, the DFT hybrid method B3LYP with non-local correlation provided by the Lee–Yang–Parr expression was used. The 6-311++G** basis set was used as the standard basis set available for all atoms in the studied molecules. All theoretical calculations were performed using the GAUSSIAN 98W (version 5.4) package of programs [12] running on a PC computer.

3. Results and discussion

3.1. Calculated geometrical structure

Optimized geometrical structures of 2-aminonicotinic acid were obtained using the B3LYP/6-311++G** quantum chemical method. The obtained data are gathered in Table 1. Structure number 1, whose energy is the least, is the most stable structure. Having calculated the optimal structure for the acid molecule, we performed calculations for alkali metal salts for the same structure. The results of the calculations of 2-aminonicotinates in comparison with the 2-aminonicotinic acid molecule are gathered in Table 2. Our results calculated for the acid molecule were compared with literature experimental data [13]. Quite a good correlation between experimental and calculated values for bond lengths was noted ($R = 0.979$). Magnetic and geometric aromaticity indices [14–17] as well as the values of the largest differences of bond lengths and bond angles in the heterocyclic ring of the lithium, sodium and potassium 2-aminonicotinates in comparison with the acid are also presented (Table 2).

The geometric criterion of aromaticity is based on the π-electron delocalization manifested in planar geometry, symmetry, equalization of the bond lengths and angles. The values of the HOMA geometric aromaticity index (abbreviation from Harmonic Oscillator Model of Aromaticity) significantly increase, which indicates the increase of aromaticity in the series 2-aminonicotinic acid < Li < Na < K 2-aminonicotinate. On the other hand, values of I_6 (Bird's index, which describes the geometric contribution to the aromaticity) decrease, which shows the de-

Table 4
Dipole moments and energies for 2-aminonicotinic acid (2-ANA) and its salts calculated by the B3LYP/6-311++G** method.

	2-ANA	Lithium salt	Sodium salt	Potassium salt
Dipole moment (Debye)	1.199	5.171	8.071	9.812
Energy (Hartree)	−492.382 [0]	−499.381 [−26,26]	−654.143 [61,70]	−1091.788 [47,26]

[In brackets]-the relative energy: E(MeAN)−[E(AN) + E(Me)] in kJ/mol.

Table 5
Wavenumbers (cm^{-1}), intensities and assignments of selected bands in the Raman spectra of 2-aminonicotinates (2-AN) in comparison with 2-aminonicotinic acid (2-ANA).

2-ANA		Li 2-AN		Na 2-AN		K 2-AN		Rb 2-AN		Cs 2-AN		Assignment [18]	
cm^{-1}	int	cm^{-1}	int	cm^{-1}	int	cm^{-1}	int	cm^{-1}	int	cm^{-1}	int		
		3344	w	3339	vw	3393	vw	3357	vw	3345	vw	$\nu_{as}(NH_2)$	
3107	m	3319	w	3304	vw	3272	m	3259	vw	3248	vw	$\nu_{s}(NH_2)$	
		3080	m	3087	w	3089	s	3087	w	3083	w	ν(CH)	2
		3070	sh	3074	w	3077	w	3076	w	3063	w	ν(CH)	20a
3046	w	3017	vw	3031	w	3024	w	3026	vw	3025	vw	ν(CH)	20b
1682	vw											ν(C=O)	
1632	w	1631	w	1625	vw	1630	vw	1630	vw	1628	vw	$\beta_s(NH_2)$, ν(C=C)$_{ar}$	
		1600	w	1614	vw	1607	w	1606	m	1603	m	$\nu_{as}(COO^-)$	
		1581	s	1582	m	1581	s	1579	s	1576	s	ν(C=C)$_{ar}$	8b
1566	m	1552	w	1568	vw	1546	vw	1545	vw	1547	vw	ν(C=C)$_{ar}$	8a
		1504	w	1555	vw	1498	vw	1497	vw	1499	vw,	ν(C=C)$_{ar}$	3
1468	w	1468	w	1459	w	1458	w	1459	w	1447	vw	ν(C–NH_2)	
		1402	s	1404	m	1381	s	1378	m	1375	m	$\nu_{s}(COO^-)$	
		1327	m	1326	m	1323	m	1322	m	1319	m	ν(C–N)	
1370	w											ν(C–C)	14
1318	vs											ν(C–OH)	
1250	m	1253	s	1265	m	1262	s	1262	vs	1263	vs	$\beta_{as}(NH_2)$	
		1207	vw	1205	vw	1214	vw	1218	vw	1216	vw	ν(C–C)	14
1144	w	1157	m	1147	w	1152	m	1151	m	1151	m	β(CH)	18b
1082	vw	1097	m	1076	vw	1083	w	1086	w	1085	vw	$\beta_{as}(NH_2)$	
1058	m											α(CCC)	12
1034	m	1030	w	1028	w	1032	w	1033	m	1032	m	β(CH)	18a
				985	vw	987	vw	990	w	986	w	β(CH)	
		976	vw	966	vw	963	vw	960	vw	963	vw	α(CCC)	12
960	w											γ(OH)	
		898	w	899	w	891	m	891	m	892	m	$\beta_{s}(COO^-)$	
889	m	873	vw	872	vw	875	vw	871	vw	872	vw	γ(CH)	17b
832	vw	838	vw	835	vw	837	w	836	w	837	vw	γ(CH)	10a
808	vs	817	vs	820	vs	811	vs	811	vs	809	vs	α(CCC)	1
		775	w	773	vw	772	vw	774	vw	777	vw	$\gamma_{s}(COO^-)$	
729	vw	753	vw	755	vw	746	vw	747	vw	748	vw	$\gamma_{as}(NH_2)$	
		683	m	679	m	678	s	677	m	675	m	ϕ(C–C)	4
663	s											γ(C=O)	
581	s	591	m	589	m	587	s	585	m	583	m	$\gamma_{s}(NH_2)$	
552	vw	567	w	559	vw	553	vw	556	vw	553	vw	α(CCC)	6a
		541	vw	537	vw			530	vw	532	vw	$\beta_{as}(COO^-)$	
442	vw	448	vw	444	vw			432	w	434	vw	α(CCC)	6b
409	w											β(C–OH)	

ν: Stretching; β: in plane deformations; γ: out of plane deformations; δ: scissoring; ω: wagging; s: strong; vs: very strong; m: medium; sh: shoulder; w: weak.

crease of aromaticity of the salt molecules. The values of the magnetic aromaticity indices NICS (Nucleus-Independent Chemical Shifts) were also calculated. The obtained negative values of NICS (Table 2) denote about the aromaticity of the studied molecules [15,16]. These values show a decrease of aromaticity for lithium 2-aminonicotinate in comparison with the acid molecule, but in the series Li → Na → K-salt an increase of aromaticity was observed.

Atomic charges calculated by NPA (Natural Population Analysis) are gathered in Table 3. The total atomic charges of the carboxylate and amino groups, as well as the heterocyclic ring, are also presented. A significant increase of electron charge density was noted in the case of the carboxylate group for 2-aminonicotinates. A less significant increase of electron charge density for ring atoms and a decrease for the amino group were observed in the series acid → Li → Na → K-salt.

On comparing values of dipole moments (Table 4) for molecules of 2-aminonicotinic acid and alkali metal salts, an increasing tendency along the series: acid → lithium → sodium → potassium 2-aminonicotinate was observed. In the case of nicotinates, the dipole moment increases in the same order (4.394, 4.679, 7.130, 8.713). The values of the energy of aminonicotinates (Table 4) as well as nicotinates (0.00, −31.51, 53.82, 36.76) show a significantly increasing tendency along the series Li < acid < K < Na salts. This indicates that the stability of the studied molecules decreases in this order.

3.2. Vibrational spectra

The vibrational spectra of the synthesized 2-aminonicotinates were recorded and assigned. The observed Raman and IR (KBr, ATR) bands, together with their relative intensities and band assignments, of the studied metal salts are presented in Tables 5 and 6, respectively. The bands are numbered along with the notation used by Varsányi and ourselves [18]. Theoretical calculations by the B3LYP method at the 6-311++G** level were used to obtain values of wavenumbers and intensities of IR and Raman spectra (Table 7). Calculated normal vibrations were characterized by computer animation. A good correlation between experimental and theoretical IR and Raman spectra was noted. The correlation coefficients for the IR spectra are in the range 0.9954–0.9964; for Raman 0.9943–0.9963. Raman and IR (ATR) spectra of 2-aminonicotinic acid and its lithium and cesium salts, as examples, are presented in Figs. 1 and 2.

The changes of intensities and wavenumbers of the bands of the aromatic system and amino group in the case of salts were discussed, in comparison with the free ligand. Characteristic bands occurring in the IR spectra of 2-aminobenzoates (symmetric or asymmetric vibrations of the carboxylic group, for example), which do not exist in the spectra of free acid, as well as the lack of some other bands, which are characteristic for it (the C=O band, 1703 cm^{-1} (KBr) and1696 cm^{-1} (ATR); ν(C–OH) band, 1321 cm^{-1}

Table 6
Wavenumbers (cm^{-1}), intensities and assignments of selected bands in the IR-KBr and IR-ATR spectra of 2-aminonicotinates(2-AN) in comparison with 2-aminonicotinic acid (2-ANA).

2-ANA				Li 2-AN				Na 2-AN				K 2-AN				Rb 2-AN				Cs 2-AN				Assignment [18]	
IR (KBr)		IR (ATR)		IR (KBr)		IR (ATR)		IR (KBr)		IR (ATR)		IR (KBr)		IR (ATR)		IR (KBr)		IR (ATR)		IR (KBr)		IR (ATR)			
cm^{-1}	int	cm^{-1}	int	cm^{-1}	int	cm^{-1}	int	cm^{-1}	int	cm^{-1}	int	cm^{-1}	int	cm^{-1}	int	cm^{-1}	int	cm^{-1}	int	cm^{-1}	int	cm^{-1}	int		
3257	m	3249	vw	3468, 3442	m	3465, 3438	w	3473, 3431	m	3478, 3424	w	3388	m	3381	w	3361	m	3360	w	3386	m	3334	w	$\nu_{as}(NH_2)$	
3099	sh	3095	vw	3344, 3319	m	3342, 3314	w	3342, 3312	m	3339, 3305	w	3271	m	3270	w	3262	m	3250	w	3272	m	3244	w	$\nu_s(NH_2)$	
				3194	w	3200	w	3187	w	3199	vw	3174	sh	3183	vw	3196	w	3200	w			3201	w	ν(CH)	2
				3154	w	3152	vw	3152	w	3166	vw	3153	sh	3139	vw			3141	w			3147	vw	ν(CH)	20a
3045	sh	3043	vw	3078	vw	3083	vw	3080	w	3086	vw	3077	vw	3069	vw	3074	w	3077	w	3077	w	3085	vw	ν(CH)	20b
2950–2658	m	2921–2660	vw																					ν(OH)	
1703	vs	1696	m																					ν(C=O)	
1636	m	1630	w	1630	sh	1627	sh	1632	vs	1623	vs	1627	vs	1620	s	1625	vs			1623	vs			$\beta_s(NH_2)$, $\nu(C{=}C)_{ar}$	
				1611	vs	1608	s	1611	vs	1610	sh	1611	sh			1611	sh	1613	vs	1608	sh	1607	vs	$\nu_{as}(COO^-)$	
1603	m			1578	s	1576	s	1575	s	1575	m	1580	s	1578	m	1578	s	1575	m	1580	s	1572	m	$\nu(C{=}C)_{ar}$	8b
1560	s			1544	s			1552	s			1552	s			1559	w	1540	s	1551	s	1537	s	$\nu(C{=}C)_{ar}$	8a
1544	m	1535	w			1536	s	1535	s	1534	s	1544	s	1542	s	1544	m					1513	sh	$\nu(C{=}C)_{ar}$	3
1463	m	1462	w	1456	m	1450	s	1451	s	1451	m	1448	m	1443	m	1441	m	1441	m	1447	m	1440	s	$\nu(C{-}NH_2)$	
1424	m	1424	w																					β(OH)	
				1398	s	1393	vs	1395	vs	1393	vs	1382	vs	1379	vs	1380	s	1375	vs	1382	s	1372	vs	$\nu_s(COO^-)$	
				1328	m	1326	m	1330	m	1330	m	1324	m	1322	vs	1322	m	1320	m	1324	m	1317	m	ν(C–N)	
1384	m																							ν(C–C)	14
1321	s	1318	m																					ν(C–OH)	
1251	m	1242	m	1255	m	1253	s	1260	m	1258	m	1260	m	1260	m	1260	m	1260	w	1260	s	1261	s	$\beta_{as}(NH_2)$	
				1207	w	1205	w	1206	w	1205	w	1215	w	1223	vw	1214	vw	1225	w	1215	w			ν(C–C)	14
1143	m	1142	w	1154	m	1153	m	1148	m	1147	w	1144	w	1144	w	1143	w	1142	w	1144	m	1141	w	β(CH)	18b
1089	w	1093	w	1079	w			1072	w	1071	w	1079	w	1076	W	1079	w	1077	w	1080	w	1076	m	$\beta_{as}(NH_2)$	
1058	m	1053	m																					α(CCC)	12
1029	m	1028	m	1029	w			1028	w															β(CH)	18a
												986	vw	985	w	989	w	989	m	986	w	984	m	β(CH)	
				973	w	972	w	967	w	956	vw			959	vw	960	vw	957	m	960	w	960	m	α(CCC)	12
948	m	946	w																					γ(OH)	
				894	m	891	m	895	w	894	m	891	w	890	m	891	w	890	m	891	w	889	s	$\beta_s(COO^-)$	
885	m	882	w	859	vw	866	vw	881	w	880	vw			872	vw									γ(CH)	17b
831	w	835	w	839	m	838	m	831	m	830	m	833	w	833	m	835	w	834	m	833	m	834	m	γ(CH)	10a
812	m	807	w	814	m	812	m	817	m	815	m	810	m	808	s	809	m	807	s	810	m	804	s	α(CCC)	1
790	m	785	m																					β(C=O)	
				771	m	768	vs	772	m	772	m	771	m	771	s	771	m	773	s	770	m	777	vs	$\gamma_s(COO^-)$	
				752	w	749	m	755	m	756	s	743	w	745	w	745	w	745	m	744	w	748	m	$\gamma_{as}(NH_2)$	
								739	m	740	m			703	vw									α(CCC)	6a
727	w	733	w	679	m	674	m	672	w	673	m	673	w	672	m	672	w	671	s	675	w	668	vs	ϕ(C–C)	4
664	s	661	s																					γ(C=O)	
617	m																							γ(OH)	
583	m	579	vs	592	m	587	m	587	w	574	m	585	w	583	m	581	w	575	s	586	w	574	s	$\gamma_s(NH_2)$	
557	m																							α(CCC)	6a
				539	m			543	m			551	w			551	w			551	w			$\beta_{as}(COO^-)$	
442	w			446	m			447	m							431	w							α(CCC)	6b
411	m																							β(C–OH)	

ν: Stretching; β: in plane deformations; γ: out of plane deformations; δ: scissoring; ω: wagging; s: strong; vs: very strong; m: medium; sh: shoulder; w: weak.

Table 7
Theoretical IR and Raman spectra of 2-aminonicotinates (2-AN) in comparison with 2-aminonicotinic acid (2-AN).

2-ANA			Li 2-AN			Na 2-AN			K 2-AN				[18]
cm^{-1}	int		cm^{-1}	int		cm^{-1}	int		cm^{-1}	int			
	IR	R		IR	R		IR	R		IR	R		
3769	91.3	125.0										ν(OH)	
3741	118.6	35.6	3712	104.0	63.9	3710	101.5	159.2	3710	104.3	74.7	$\nu_{as}(NH_2)$	
3605	92.8	117.5	3539	112.7	160.8	3524	127.9	159.2	3524	130.8	160.5	$\nu_s(NH_2)$	
3207	7.0	166.4	3203	9.7	153.1	3201	11.3	142.9	3201	11.0	148.1	ν(CH)	2
3193	1.0	54.6	3189	4.3	80.9	3187	6.9	96.7	3186	6.9	94.2	ν(CH)	20a
3145	20.9	135.6	3138	26.2	139.4	3134	29.4	139.8	3135	29.1	142.1	ν(CH)	20b
1775	498.1	104.5										ν(C=O)	
			1537	325.5	18.8	1547	383.0	18.5	1540	328.8	10.1	$\nu_{as}(COO^-)$	
1646	415.0	30.0	1645	485.4	21.9	1644	485.9	21.3	1643	455.4	25.9	$\beta_s(NH_2)$. $\nu(C{=}C)_{ar}$	
1624	155.9	24.0	1610	166.6	34.6	1606	153.1	47.0	1605	163.6	44.8	$\nu(C{=}C)_{ar}$	8b
1590	54.1	23.1	1590	79.0	28.5	1589	67.0	21.0	1587	56.7	19.2	$\nu(C{=}C)_{ar}$	8a
1498	104.6	4.2	1487	197.1	26.4	1485	104.3	8.4	1484	125.4	14.6	$\nu(C{=}C)_{ar}$	3
1478	125.4	7.8	1465	235.2	7.9	1460	191.0	2.4	1460	268.4	6.7	ν(C–NH_2)	
			1410	139.8	41.0	1398	168.5	17.8	1400	193.8	34.6	$\nu_s(COO^-)$	
1348	22.1	16.0										β(OH)	
			1357	28.5	37.4	1350	38.1	28.7	1350	43.8	41.6	ν(C–N)	
			1310	52.1	22.1	1309	58.9	20.1	1308	69.5	30.8	$\beta_{as}(NH_2)$	
1281	108.8	18.5	1285	118.4	24.9	1285	104.6	26.8	1285	112.1	28.1	ν(C–C)	14
1201	98.6	29.4										ν(C–OH)	
1144	54.2	17.1	1134	0.2	7.7	1132	0.8	8.8	1131	0.3	11.9	$\beta_{as}(NH_2)$	
1104	24.7	18.4	1168	39.7	5.8	1165	36.6	6.2	1165	38.2	6.6	β(CH)	18b
			1095	10.5	19.3	1093	11.7	16.4	1093	12.0	16.0	β(CH)	18a
903	4.7	9.1	912	12.1	0.8	909	12.1	1.7	909	20.4	2.9	α(CCC)	12
			849	32.0	45.6	837	24.5	53.0	847	63.4	25.7	$\beta_s(COO^-)$	
825	0.6	0.4										γ(OH)	
783	55.8	0.3										γ(CH)	17b
749	23.4	0.3										γ(C=O)	
740	16.5	26.3	782	56.3	0.6	780	53.1	0.7	781	52.0	0.7	γ(CH)	10a
			759	5.8	0.5	760	5.4	0.6	760	3.9	0.2	$\gamma_s(COO^-)$	
			680	8.1	0.01	695	9.9	0.003	699	10.2	0.03	$\gamma_{as}(NH_2)$	
643	36.5	1.4										β(C=O)	
428	0.002	0.8	441	16.8	0.1	443	14.7	0.1	444	12.7	0.1	ϕ(C–C)	4
			244	16.1	0.6	236	137.4	0.1	244	44.7	1.7	$\gamma_s(NH_2)$	
			545	23.7	1.0	540	7.2	0.5	579	2.4	2.7	$\beta_{as}(COO^-)$	
597	1.8	0.02										γ(OH)	
218	119.3	0.4										$\gamma_s(NH_2)$	
586	4.7	8.7	699	50.9	4.7	691	11.0	4.3	704	26.1	8.2	α(CCC)	6a
393	10.3	3.8	358	3.9	3.0	266	27.2	3.9				α(CCC)	6b
383	5.1	4.6										β(C–OH)	

(KBr) and 1318 cm^{-1} (ATR), for example) were observed. The appearance of bands connected with the carboxylate group $\nu_{as}(COO^-)$, in the range 1612–1608 cm^{-1} IR (KBr), (1613–1607 cm^{-1} – ATR; 1614–1600 cm^{-1} – Raman), $\nu_s(COO^-)$: 1398–1380 cm^{-1} IR (KBr) (1393–1972 cm^{-1} – ATR; 1404–1375 cm^{-1} – Raman), $\beta_{as}(COO^-)$: 551–539 cm^{-1} IR (KBr) (541–530 cm^{-1} – Raman), $\beta_s(COO^-)$: 895–891 cm^{-1} IR (KBr) (894–889 cm^{-1} – ATR; 899–891 cm^{-1} – Raman) and $\gamma_s(COO^-)$: 772–770 cm^{-1} IR (KBr) (777–768 cm^{-1} – ATR; 777–772 cm^{-1} – Raman) was observed.

The wavenumbers of bands connected with symmetric and asymmetric vibrations of amino group in the experimentally obtained IR (KBr and ATR) and Raman spectra increase in the salts in comparison with the acid. In theoretical spectra these values decrease. The bands of $\beta_s(NH_2)$ change to lower values in both experimental and theoretical IR and Raman spectra. Two bands were observed for asymmetrical in plane deformations $\beta_{as}(NH_2)$. In IR (ATR) spectra the wavenumbers of both of them decrease in salts in comparison with the acid. In the IR (KBr) spectra one of the bands changes to a lower wavenumber, but the other changes to a higher value. In IR theoretical obtained spectra, the wavenumbers of these bands increase. The same tendency was observed in Raman spectra (one band changes to lower wavenumbers, but another to higher) except for the sodium salt. Bands of $\gamma_s(NH_2)$ shifted to lower values of wavenumbers in the Raman spectra of salts, but to higher values in the theoretical IR spectra. In the experimentally obtained IR spectra regular changes were not noted.

The influence of the alkali metal in the series Li → Cs on the vibrational structure of 2-aminonicotinic acid was also observed. The wavenumbers of symmetric stretching vibration bands of the carboxylate group in the IR spectra were changed to lower values in the series Li → Na → K → Rb salt, but the asymmetric band does not change. The magnitudes of separation between the wavenumbers due to asymmetrical and symmetrical stretching vibrations of the COO^- group ($\Delta\nu = \nu_{asym} - \nu_{sym}$) increase in the series Li → Na → K → Rb 2-aminonicotinates. These values were used by Nakamoto [19] as a criteria of the way of the carboxylate was bound with metal ions. The structure changes in the order: bidentate (chelating) → bridging → ionic → unidentate with an increase of the $\Delta\nu$(COO) value. The values of $\Delta\nu$(COO) in IR (KBr) spectra of lithium, sodium, potassium, rubidium and cesium 2-aminonicotinates amount to 213, 216, 229, 231and 226 cm^{-1}, respectively. These values are insignificantly higher in comparison with alkali metal nicotinates (193, 211, 192, 209, 210 cm^{-1}, these values are from our previous paper [3]). It suggests that the bonds between the alkali metal cation and the carboxylate anion in 2-aminonicotinate molecules have more ionic nature than those in nicotinates. These values in the Raman spectra are in the range 198–228 cm^{-1} for 2-aminonicotinates and 171–209 cm^{-1} for nicotinates [3]. The values of $\Delta\beta(COO) = \beta_s - \beta_{as}$ amount to 355, 352, 340, 340,

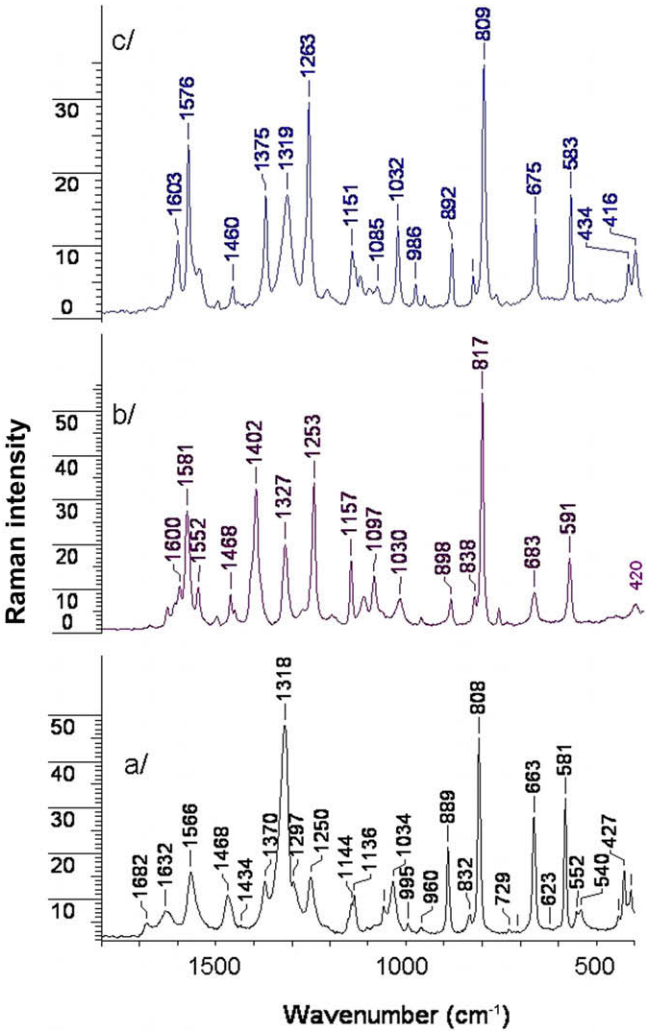


Fig. 1. Raman spectra of 2-aminonicotinic acid (a) and its lithium (b) and cesium (c) salts.

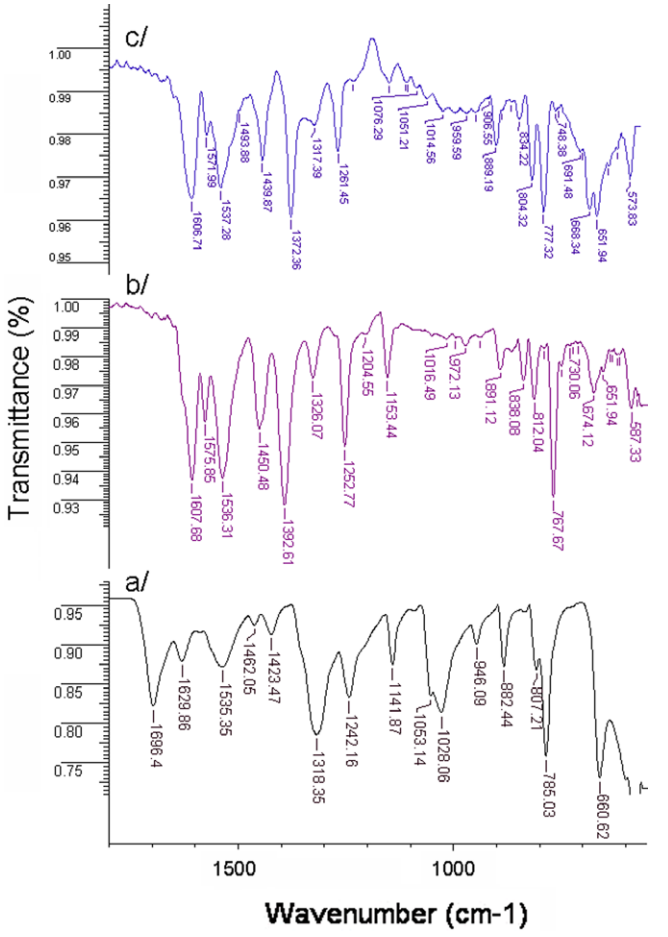


Fig. 2. IR–ATR spectra of 2-aminonicotinic acid (a) and lithium (b) and cesium (c) 2-aminonicotinates.

340 cm^{-1} for 2-AN in the IR(KBr) spectra and for nicotinates they are in the range of 315–323 cm^{-1} [3]. In the theoretical spectra of 2-aminonicotinates, the values of $\Delta\nu$(COO) and $\Delta\beta$(COO) are in the range 127–140 and 268–304 cm^{-1}, respectively.

The wavenumbers of ν(C–NH_2) and $\gamma_s(NH_2)$ in the IR (KBr) spectra decrease in the order Li → Na → K → Rb. A decrease of wavenumbers of ϕ(C–C), β(CH) and $\nu_s(NH_2)$ bands in the IR (ATR) spectra in the series Li → Na → K → Rb → Cs was noted, but an increase of wavenumbers of the $\beta_{as}(NH_2)$ band was noted in the order Li → Na → K = Rb → Cs. In the Raman spectra, the wavenumbers of ϕ(C–C), ν(C–N), $\nu_s(NH_2)$ and $\gamma_s(NH_2)$ bands decrease in following order: Li → Na → K → Rb → Cs.

The decrease of wavenumbers and intensities of the aromatic ring bands indicate an increase in the perturbation of the aromatic system. In the case of the studied molecules, the wavenumbers only of the 8b, 8a and 4 bands change to lesser values in comparison with the acid. The intensity of these bands increases or does not change. Based on this criterion, it is difficult to draw a clear conclusion.

The correlation between selected bands and some metal parameters such as electronegativity, atom and ionic radius, ionization energy and ionic potential (defined as the ratio of the charge of the cation and the ionic radius) was studied. The wavenumbers of those bands correlate in a linear fashion with all the tested factors at a statistically important level. The best correlation coefficients were obtained for electronegativity [$\beta_{as}(COO^-)$: 0.9808] and ionic potential [$\beta_{as}(COO^-)$: 0.9883] in the IR (KBr) spectra; ionic radius [$\nu_s(NH_2)$: 0.9909], atomic radius [$\nu_s(COO^-)$: 0.9998] and ionic potential [β(CH): 0.9888] in IR (ATR) and ionic radius [$\nu_s(NH_2)$: 0.9990] in Raman spectra. According to our previous study on benzoates, salicylates and nicotinates [3,4], the best statistical results were obtained for the ionic potential of the alkali metals.

It was interesting to note the linear correlation between wavenumbers of the $\nu_s(COO^-)$ band in the IR (KBr) spectra and the calculated Me–O bond length. The correlation coefficient amounts to 0.9325.

3.3. NMR spectra

Experimental and theoretical chemical shifts of 2-aminonicotinates in ^1H NMR and ^{13}C NMR spectra were recorded. The geometrical structures of the studied compounds were optimized by the GIAO DFT method [20]. The obtained data, in comparison with 2-aminonicotinic acid, are gathered in Table 8. In order to calculate optimized geometrical structures of the studied compounds, density functional theory at the B3LYP/6-311++G** level was used. Theoretical calculations for optimized structures were performed using the GIAO method in the GAUSSIAN 98W package.

A linear correlation between calculated and experimental data of ^1H and ^{13}C NMR is noted. Correlation coefficients for ^{13}C NMR for 2-aminonicotinic acid, lithium, sodium and potassium salts

Table 8
Experimental and theoretical chemical shifts in ^{1}H and ^{13}C NMR spectra of 2-aminonicotinic acid (2-ANA) and its salts, δ (ppm).

Atom position	2-ANA		Li 2-AN		Na 2-AN		K 2-AN		Rb 2-AN	Cs 2-AN
	Experimental	Theoretical	Experimental	Theoretical	Experimental	Theoretical	Experimental	Theoretical		
H4	8.032	8.417	7.887	8.330	7.860	8.259	7.826	8.281	7.816	7.826
H5	6.596	6.562	6.437	6.442	6.421	6.382	6.396	6.415	6.389	6.395
H6	8.162	8.506	8.028	8.486	7.999	8.529	7.968	8.533	7.941	7.452
C1	105.546	108.733	111.092	113.260	110.957	115.163	110.884	115.974	110.968	111.024
C2	159.742	164.792	160.109	166.701	160.057	166.641	160.123	166.663	160.245	160.241
C4	153.425	162.395	149.172	160.976	148.645	159.438	148.174	159.387	148.245	148.314
C5	111.827	117.478	114.949	116.011	115.495	115.534	116.463	115.466	116.645	116.694
C6	140.056	149.955	139.556	147.699	139.124	148.097	138.887	147.397	138.959	139.017
C7	168.594	171.377	170.535	191.833	170.717	185.927	169.798	187.070	169.608	169.712

amount to 0.9938, 0.9917, 0.9945 and 0.9913, respectively. The corresponding values of correlation coefficients for ^{1}H NMR amount to 0.9994, 0.9999, 0.9993 and 0.9996.

The chemical shifts of protons (^{1}H NMR) and carbons (^{13}C NMR) in the series of alkali metals express the influence of the studied metal on the electronic charge around those atoms. In the ^{1}H NMR spectra of 2-aminonicotinates, all the protons are shifted diamagnetically in comparison to 2-aminonicotinic acid. This suggests that all metals cause a decrease of current intensity, along with the literature data decrease of aromaticity [2]. The differences of chemical shifts of protons along the metal series are small, however they are higher than those of nicotinates [2]. This is an evidence that alkali metals perturb the aromatic system of the 2-aminonicotinic acid molecule to a higher degree than that of nicotinic acid. The chemical shifts of protons numbered 4 and 6 are higher then that of the H5 atom. It means that the electronic charge density around positions 4 and 6 is lower compared to position 5 [21]. The same conclusion was made in the case of nicotinates.

The chemical shifts of the carbon atoms in positions 1, 2, 5 and 7 change to higher values in the salts compared to 2-aminonicotinic acid. The chemical shifts of the carbon atoms in positions 4 and 6 change to smaller values. In the case of nicotinates, all carbon atoms except the C1 and C7 atoms change to lower value chemical shifts. The highest changes of chemical shifts are observed for C1 > C4 > C5 atoms, for the other atoms the chemical shifts change to a lesser degree. The changes of chemical shifts of carbon atoms along metal series are not so clear as in the ^{1}H NMR spectra. Only the chemical shifts of the C5 atom increase regularly in the series Li → Cs. The values of the chemical shifts of the C6, C1 and C4 carbon atoms decrease from lithium to potassium 2-aminobenzoates and from the potassium to the cesium salts they increase. The values of the chemical shifts of the C2 carbon atom decrease from the lithium to the potassium 2-aminobenzoate and increase from the potassium to the rubidium salt, and then decrease again from the rubidium to the cesium salt. For the C7 carbon atom these values change inversely.

The values of chemical shifts for the carbon atoms in positions 1 and 5 are smaller than for the other carbon atoms. The smallest value is observed for carbon 1. It means that the electronic charge density around the C1 atom is bigger than around the other atoms. Comparing the NMR spectra of alkali metal 2-aminonicotinates with those of nicotinates [2], higher values of chemical shifts of all protons and carbons (with the exception of the C1 and C5 atoms) were observed in the case of the nicotinates.

4. Conclusions

Substitution of hydrogen with alkali metals in the carboxylic group brought some characteristic changes in molecular spectra as well as in geometrical structures of the studied molecules.

A decrease of chemical shifts of almost all protons of 2-aminonicotinates in the ^{1}H NMR spectra was observed in comparison with the spectra of the acid, which indicates that the alkali metal ions perturb the electronic system of the molecule and the perturbation significantly increases in the series: H → Li → Na → K → Rb → Cs 2-aminonicotinates. The differences of chemical shifts of protons along this metal series are small, however they are higher than those of nicotinates [2]. This is an evidence that the perturbation effect of alkali metals on the aromatic system of the 2-aminonicotinic acid molecule is higher than that of nicotinic acid. The changes of chemical shifts of carbon atoms along the metal series are not so clear as in the ^{1}H NMR spectra. Comparing the NMR spectra of alkali metal 2-aminonicotinates with those of nicotinates, higher values of chemical shifts of all protons and carbons (with the exception of the C1 and C5 atoms) were observed in the case of nicotinates.

The decrease of wavenumbers and intensities of aromatic ring bands indicates an increase of perturbation of the aromatic system. In the case of the studied molecules, only the wavenumbers of the 8b, 8a and 4 bands change to lesser values in comparison with the acid. The intensities of these bands increase or do not change. Based on this criterion it is difficult to draw a clear conclusion. The values of $\Delta\nu$(COO) suggest that the bonds between the alkali metal cation and carboxylate anion in 2-aminonicotinate molecules have more ionic nature than those in nicotinates. This conclusion is confirmed by the values of dipole moments and the total atomic charge of the carboxylate group.

The conclusions obtained by aromatic indices are not congruent, because the differences between their values are small in the studied series of alkali metal salts. HOMA indices show a slight increase of aromaticity in the series 2-ANA < Li 2-AN < Na 2-AN < K 2-AN. According to the NICS values, an increase of aromaticity is observed in the series Li < Na < K-salts, but for lithium and sodium 2-aminonicotinate a decrease of aromaticity is noted in comparison with 2-aminonicotinic acid molecule.

The conclusions, which are drawn from different applications of work methods are not quite identical. The differences may be explained by the fact that our researches were provided for different states (IR and Raman spectra for solid state, NMR for solution, and calculations for isolated molecules).

Acknowledgment

The presented work was supported by The Scientific Research Committee in Poland (W/WBiIŚ/31/08).

References

[1] P. Koczoń, J. Piekut, M. Borawska, R. Świsłocka, W. Lewandowski, Spectrochim. Acta, Part A 61 (2005) 1917.
[2] P. Koczoń, T. Hrynaszkiewicz, R. Świsłocka, M. Samsonowicz, W. Lewandowski, Vib. Spectrosc. 33 (2003) 215.

[3] W. Lewandowski, B. Dasiewicz, P. Koczoń, J. Skierski, K. Dobrosz-Teperek, R. Świsłocka, L. Fuks, W. Priebe, A.P. Mazurek, J. Mol. Struct. 604 (2002) 189.
[4] W. Lewandowski, M. Kalinowska, H. Lewandowska, J. Inorg. Biochem. 99 (2005) 1407.
[5] S. Bourcier, Y. Hoppiliard, Int. J. Mass Spectrom. 212 (2002) 231.
[6] O. Sala, N.S. Gonçalves, L.K. Noda, J. Mol. Struct. 565–566 (2001) 411.
[7] M.K. Nayak, S.K. Dogra, J. Photochem. Photobiol. A: Chem. 171 (2005) 281.
[8] G. Yang, H.-G. Zhu, B.-H. Liang, X.-M. Chen, J. Chem. Soc., Dalton Trans. (2001) 580.
[9] P.C.R. Soares-Santos, R.A. Śa Ferreira, T. Trindade, L.D. Carlos, H.I.S. Nogueira, J. Alloys Compd. 451 (2008) 575.
[10] M. Toma, A. Sánchez, M.S. Garcia-Tasende, J.S. Casas, J. Sordo, E.E. Castellano, J. Ellena, Appl. Organomet. Chem. 18 (2004) 302.
[11] S.C. Mojumdor, M. Melnik, E. Jóna, Thermochim. Acta 352–353 (2000) 127.
[12] Gaussian 98 (Revision A.1), M.J. Frisch, G.W. Trucks , H.B. Schlegel, G.E. Scuseria, M.A. Robb, J.R. Cheeseman, V.G. Zakrzewski, J.A. Montgomery, R.E. Stratmann, J.C. Burant, S. Dapprich, J.M. Millam, A.D. Daniels, K.N. Kudin, M.C. Strain, O. Farkas, J. Tomasi, V. Barone, M. Cossi, R. Cammi, B. Mennucci, C. Pomelli, C. Adamo, S. Clifford, J. Ochterski, G.A. Petersson, P.Y. Ayala, Q. Cui, K. Morokuma, D.K. Malick, A.D. Rabuck, K. Raghavachari, J.B. Foresman, J. Cioslowski, J.V. Ortiz, B.B. Stefanov, G. Liu, A. Liashenko, P. Piskorz, I. Komaromi, R. Gomperts, R.L. Martin, D.J. Fox, T. Keith, M.A. Al-Laham, C.Y. Peng, A. Nanayakkara, C. Gonzalez, M. Challacombe, P.M.W. Gill, B.G. Johnson, W. Chen, M.W. Wong, J.L. Andres, M. Head-Gordon, E.S. Replogle, J.A. Pople, GAUSSIAN 98 (Revision A.11.2), Gaussian Inc., Pittsburgh PA, 1998.
[13] A.J. Dobson, R.E. Gerkin, Acta Crystallogr., Sect. C 53 (1997) 1427.
[14] T.M. Krygowski, M. Cyrański, Tetrahedron 52 (1996) 1713.
[15] P.R. Schleyer, C. Maerker, A. Dransfeld, H. Jiao, N.J.R.E. Hommes, Org. Lett. 3 (2001) 2465.
[16] P.R. Schleyer, M. Manoharan, Z.X. Wang, J. Am. Chem. Soc. 118 (1996) 6317.
[17] W. Lewandowski, G. Świderski, R. Świsłocka, S. Wojtulewski, P. Koczoń, J. Phys. Org. Chem. 18 (2005) 918.
[18] G. Varsányi, Assignments for Vibrational Spectra of 700 Benzene Derivatives, Akademiai Kiado, Budapest, Hungary, 1973.
[19] K. Nakamoto, Infrared and Raman Spectra of Inorganic and Coordination Compounds, 5th ed., John Wiley and Sons Inc., New York, USA, 1997.
[20] E. Frish, R.D. Denington II, A. Keith, A.B. Nielsen, A.J. Holder, GaussView Reference Manual, Gaussian Inc., Wallingford, 2003.
[21] W. Zieliński, A. Rajca (Eds.), Metody spektroskopowe i ich zastosowanie do identyfikacji związków organicznych, WNT, Warszawa, Poland, 2000.

complexes were obtained (Table 1). IR spectra (4000–450 cm^{-1}) were recorded on a Perkin–Elmer Spectrum One FT-IR spectrometer using KBr pellets. Absorption electron spectra (45 000–9090 cm^{-1}) were carried out on a Perkin–Elmer Lambda 35 UV/VIS spectrophotometer using N,N-dimethylformamide as solvent. Conductivities were measured with an LF 330/SET conductivity meter (WTW GmbH) at 25 °C. Room temperature magnetic susceptibilities were measured by the Faraday method using $Co[Hg(NCS)_4]$ as a calibrant on a laboratory designed instrument with a Sartorius 4434 MP-8 microbalance. Thermal analysis was performed on Exstar 6000 device (Seiko Instruments Inc.).

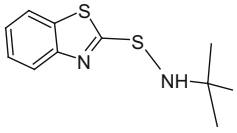
Anticholinesterase activity measurement: Electrochemical strips with platinum working (diameter 1 mm), Ag/AgCl reference and platinum auxiliary electrodes were obtained from BVT (Brno, Czech Republic). Acetylcholinesterase (AChE) from electric eel (obtained from Sigma–Aldrich) was immobilized onto the working electrode as a precipitate with glutaraldehyde and bovine serum albumin (BSA). Two microliter of mixture consisting of total 0.01 nkat of AChE, 1 mg BSA and 0.1% glutaraldehyde was injected onto the working electrode and let to form a layer in a closed chamber.

In order to realize the assay, biosensor was fixed horizontally and connected with an electrochemical device EmStat (Palmsens, Houten, The Netherlands). Twenty microliter of 1 mmol acetylthiocholine chloride (ATChCl) in 50 mmol phosphate buffer pH 7.4 was spread over the electrodes commonly with another 20 μl of tested sample in DMSO. The output current was measured after one minute. The percentage of AChE activity inhibition (***I***) was calculated using the following equation:

$$I = \left(1 - \frac{i_i}{i_t}\right) \times 100$$

where i_i means the current provided by the biosensor inhibited by the sample and i_t by the intact biosensor (20 μl of DMSO solution only) [30].

Vulcanization activity measurement: As standards, the following materials were used: Vuchtalink FMI/G-80 (1.96 dsk, antireversible and adhesion agent); Santocure TBBS GRS 2 MM (0.92 dsk, accelerator of vulcanization: *N*-tert-butyl-2-benzothiazolesulfenamide); Sulphur N (5.03 dsk, vulcanizing agent); Duslin G-80 (0.12 dsk, inhibitor of overvulcanization); Rubber mixture I.° (190.18 dsk).



Vulcanization standard Santocure TBBS GRS 2 MM

The efficiency of the samples as vulcanization accelerators for the side-wall mixtures for car radial tyres was studied. The rubber mixtures were prepared by the double-stirring procedure. In the first step, rubber mixture was recovered directly from the industrial process. In the second step, the accelerator of TBBS type (*N*-tert-butyl-2-benzothiazolesulfenamide) was replaced by the selected samples (other vulcanizing system dopes were unchanged). Preparation of the rubber mixture was performed by Plastograf – Brabender device (Plastograf Duisburg, DE) at 110 °C, during 7 min with a stirring speed 50 min^{-1} according [31]. After the preparation, the rubber mixture was left to stand for 24 h and the appropriate vulcanizing curves were recorded (Table 7). For this purpose, the Monsanto 100 device at 150 °C was used (recording time 60 min) by the normalized procedure mentioned above. The vulcanization of the rubber compound was implemented in a laboratory press BUZULUK (Buzuluk Komárov, CZ) at 150 °C under the pressure of 20 MPa. After vulcanization, the rubber mixtures were left to stand at laboratory temperature for 24 h and the double-sided paddle testing elements for stress–strain measurements were isolated. Stress–strain properties were measured with the shredder machine INSTRON and the hardness of rubber mixture was measured manually by the IRHD device by the normalized procedure [31].

2.2. Syntheses

For syntheses of complexes with the bdt, tdt-ligands, the modified procedure of Darkwa [21] was used: Complexes with the bdt, tdt-ligands were obtained by mixing the appropriate ligand: tdt (0.16 g, 1 mmol) or bdt (0.14 g, 1 mmol) in toluene (10 ml) with triethylamine (0.3 ml). Finally, $NiCl_2{\cdot}6H_2O$ (0.24 g, 1 mmol) in methanol (10 ml) and the appropriate P,P-ligand – dppe (0.40 g), dppp (0.41 g), dppb (0.42 g) or dpppn (0.44 g) in toluene (40 ml). The resulting mixture was stirred under reflux at 50 °C for 1 h. The resulted powder substance was separated by filtration, washed with methanol and diethylether and dried at room temperature (yield 85%).

For syntheses of complexes with mnt, the modified procedure of Bowmaker [28] was performed: $Na_2(CN)_2C_2S_2$ (0.19 g, 1 mmol), $NiCl_2{\cdot}6H_2O$ (0.24 g, 1 mmol) and P,P-ligand – dppe (0.40 g), dppp (0.41 g), dppb (0.42 g) or dpppn (0.44 g) were mixed as solids, and acetone (40 ml) was added. The resulting solution was stirred for 1 h. The complexes were precipitated by the slow addition of water and vigorous stirring. The solid substance was filtered from the solution, washed with water, ethanol and diethylether and dried at room temperature (yield 98%).

Crystals of [Ni(dpppn)(mnt)] for X-ray analysis were obtained in a similar way, using methanol (30 ml). During 24 h, the brown prismatic crystals precipitated and a single crystal suitable for X-ray analysis was selected.

2.3. X-ray crystallography

X-ray data collection for [Ni(dpppn)(mnt)] was performed on an Oxford Diffraction Xcalibur™2 four circle κ-axis diffractometer

Table 1
Analytical data.

Compound	M [g mol^{-1}]	Calc./found				
		Ni (%)	C (%)	H (%)	N (%)	S (%)
I. [Ni(dppe)(mnt)]	597.30	9.83/10.02	60.33/60.09	4.05/4.35	4.69/4.71	10.74/10.97
II. [Ni(dppp)(mnt)]	611.33	9.60/9.75	60.91/60.42	4.29/4.67	4.58/4.37	10.49/10.25
III. [Ni(dppb)(mnt)]	625.36	9.39/9.45	61.46/61.36	4.51/4.90	4.48/4.40	10.26/10.53
IV. [Ni(dpppn)(mnt)]	639.38	9.18/9.25	61.99/61.86	4.73/5.43	4.38/4.00	10.03/9.87
V. [Ni(dppe)(bdt)]	597.30	9.83/10.13	64.34/64.02	4.72/4.61		10.74/10.22
VI. [Ni(dppp)(bdt)]	611.37	9.60/9.79	64.83/64.54	4.95/4.79		10.49/9.22
VII. [Ni(dppb)(bdt)]	625.39	9.39/ 9.30	65.30/65.22	5.16/5.45		10.25/9.34
VIII. [Ni(dpppn)(bdt)]	639.42	9.18/9.21	65.74/65.20	5.36/5.12		10.03/10.65
IX. [Ni(dppe)(tdt)]	612.38	9.58/9.74	64.83/65.32	4.95/4.60		10.49/10.31
X. [Ni(dppp)(tdt)]	627.41	9.35/9.86	65.30/65.28	5.16/5.45		10.25/10.70
XI. [Ni(dppb)(tdt)]	642.45	9.14/9.27	65.74/65.58	5.36/5.29		10.03/9.77
XII. [Ni(dpppn)(tdt)]	657.48	8.93/9.10	65.76/65.11	6.13/6.34		9.75/10.65

equipped with a Sapphire2 CCD detector, a monochromator Enhance and a Cryojet cooler system, using Mo Kα radiation at 105(2) K. CRYSALIS program package (1.171.7, Oxford Diffraction) was used for data reduction. The structure was solved by direct methods using SHELX programs [32,33] and refined anisotropically for all non-hydrogen atoms by full-matrix least-squares procedures. All hydrogen atoms were found from the Fourier map and were refined isotropically. Additional calculations were performed using the PARST program [34]. Basic X-ray data are summarized in Tables 3–5.

3. Results and discussion

3.1. Physical techniques

Selected physical data for all complexes are summarized in Table 2. Results of IR-spectroscopy show that all complexes exhibit vibrations typical for dithiolates υ(C–S) at 866–920 cm^{-1} [35,36]. For P,P-ligands typical υ(P–C_{Ph}) vibrations [37] were found at 1433–1435 cm^{-1} for all complexes (these vibrations for single P,P-ligand are at 1432 cm^{-1}). A small shift can be assigned to the coordination of both P-atoms to the central atom. Moreover, the υ(C≡N) vibrations at 2197–2204 cm^{-1}, typical of complexes **I–IV** with the mnt-ligand are recorded [38,39]. The planar coordination of the nickel is also supported by electron UV/Vis absorbance spectroscopy; the bands of bdt and tdt complexes **V–XII** observed in the 17 180–21 120 cm^{-1} region can be assigned to the $^1A_{1g}$–$^1A_{2g}$ transitions typical of planar nickel(II) complexes [40]. The appropriate bands for complexes **I–III** with mnt-ligand were not observed, probably due to the CT overlap appeared bands in interval 25 700–27 700 cm^{-1}. In good accordance with the assumption of a planar arrangement of the coordination sphere are also the results of conductivity measurements (all complexes are non-electrolytes) [41].

The complexes **I, II, IV, V, VI, VII, VIII, IX**,**X**, and **XI** are diamagnetic, which is also in accord with the supposed square-planar arrangement of NiS_2N_2 chromophore [42]; but for complexes **III** and **XII**, a slight paramagnetism was found (see Table 2) and cannot be eliminated by repeated purification. This fact was recently for similar complexes described [6] and cannot be simply explained; maybe it is due to the exchange intermolecular interactions of the samples [43].

The results of thermal analysis of the selected sample **I** (used also for vulcanization measurements) show that the sample is stable in the range 20–340 °C (Fig. 3). Further thermal decomposition without thermally stable intermediates is accompanied by two sharp *exo*-effects at 339 and 371 °C probably due to the burning of the sample. The final product of thermal decomposition is a mixture of $Ni(PO_3)_2$ and $Ni_2P_2O_7$ (evidence by powder X-ray diffraction). These results are not sufficient for explanation of vulcanization activity, which proceeded under non comparable conditions (high pressure).

Table 3
Crystal data and structure refinement for [Ni(dpppn)(mnt)].

Empirical formula	$C_{33}H_{30}N_2NiP_2S_2$
Formula weight	639.36
Temperature (K)	106(2)
Wavelength (Å)	0.71073
Crystal system, space group	$P2_1/n$
Unit cell dimensions	
a (Å)	14.370(3)
b (Å)	13.746(3)
c (Å)	15.364(3)
α (°)	90
β (°)	95.39(3)
γ (°)	90
Volume (Å^3)	3021.43(11)
Z, Calculated density (Mg/m^3)	4; 1.406
Absorption coefficient (mm^{-1})	0.912
F(0 0 0)	1328
Crystal size (mm)	0.30 × 0.30 × 0.20
θ Range for data collection (°)	3.05–20.0
Index ranges	$-13 \leqslant h \leqslant 12$, $-13 \leqslant k \leqslant 13$, $-14 \leqslant l \leqslant 14$
Reflections collected/unique	11 196/2809 [R_{int} = 0.0356]
Completeness to 2Θ = 32.14° (%)	94.3
Maximum and minimum transmission	0.8386 and 0.7714
Refinement method	Full-matrix least-squares on F^2
Data/restraints/parameters	2809/0/361
Goodness-of-fit on F^2	1.073
Final R indices [$I > 2\sigma(I)$]	R_1 = 0.0295, wR_2 = 0.0740
R indices (all data)	R_1 = 0.0339, wR_2 = 0.0767
Largest difference in peak and hole (e Å^{-3})	0.325 and −0.235

The X-ray structure of [Ni(dpppn)(mnt)] (Fig. 1, Tables 3–5) confirmed a distorted square-planar geometry of NiS_2P_2 chromophore. The deviations of all atoms from an ideal NiS_2P_2 plane are less than 0.2 Å and appropriate bond angles around central atom are in the interval 86.46(3)–93.95(3)°. The dihedral angle between Ni1P1P2S1S2 and Ni1S1S2C1C3 planes is 6.45(6)°. Three possible hydrogen bond interactions between hydrogen atoms of phenyl rings and nitrogen atoms of cyano groups were identified in the structure.

Anticholinesterase activity of the selected compounds [Ni(dppp)(tdt)], [Ni(dppp)(mnt)] and of dppp, mnt as free ligands is shown in Table 6 and Fig. 2. The data were achieved using biosensor technology and it was processed in Origin 6.1. The

Table 2
Results of physico-chemical study.

Compound	λ_M [S cm^2 mol^{-1}]	UV/Vis [cm^{-1}] × 10^3		IR [cm^{-1}]			μ_{ef} [BM]
				υ(C–S)	υ(P–C_{Phenyl})	υ(CN)	
I. [Ni(dppe)(mnt)]	4.45	27.70		880m	1435s	2199s	dia
II. [Ni(dppp)(mnt)]	6.23	26.10		920w	1434s	2204s	dia
III. [Ni(dppb)(mnt)]	4.89	26.10		902w	1434s	2200s	0.40[x]
IV. [Ni(dpppn)(mnt)]	8.46	25.70	20.80	915w	1434s	2197s	dia
V. [Ni(dppe)(bdt)]	6.23	19.15	10.18	880m	1434s		dia
VI. [Ni(dppp)(bdt)]	4.89	19.47	11.42	866w	1435s		dia
VII. [Ni(dppb)(bdt)]	1.34	17.63	11.45	880m	1435s		dia
VIII. [Ni(dpppn)(bdt)]	10.56	20.54	11.78	877m	1435s		dia
IX. [Ni(dppe)(tdt)]	3.56	18.78	11.10	874m	1434s		dia
X. [Ni(dppp)(tdt)]	0.89	18.74	11.15	867m	1434s		dia
XI. [Ni(dppb)(tdt)]	7.12	17.18	11.19	867m	1433s		dia
XII. [Ni(dpppn)(tdt)]	9.81	21.12	11.35	870m	1435s		0.30[x]

[x] A slight paramagnetism cannot be removed by repeated purification.

Table 4
Selected bond lengths (Å) and angles (°) for [Ni(dpppn)(mnt)].

Ni(1)–S(1)	2.1650(11)	S(1)–Ni(1)–S(2)	91.83(4)
Ni(1)–S(2)	2.1707(11)	P(1)–Ni(1)–P(2)	93.98(4)
Ni(1)–P(1)	2.2230(11)	S(1)–Ni(1)–P(1)	86.44(4)
Ni(1)–P(2)	2.2250(11)	S(2)–Ni(1)–P(2)	88.92(4)
S(1)–C(1)	1.737(3)	S(2)–Ni(1)–P(1)	167.96(3)
S(2)–C(3)	1.738(3)	S(1)–Ni(1)–P(2)	174.35(3)
C(1)–C(3)	1.357(4)	C(1)–S(1)–Ni(1)	103.77(12)
C(5)–P(1)	1.835(3)	C(3)–S(2)–Ni(1)	103.60(11)
C(9)–P(2)	1.853(3)	C(20)–P(1)–Ni(1)	108.53(10)
C(5)–C(6)	1.541(4)	C(10)–P(1)–Ni(1)	116.20(10)
C(6)–C(7)	1.531(4)	C(5)–P(1)–Ni(1)	119.81(11)
C(7)–C(8)	1.517(4)	C(9)–P(2)–Ni(1)	118.41(11)
C(8)–C(9)	1.529(4)	C(3)–C(1)–S(1)	120.4(3)
		C(2)–C(1)–S(1)	117.7(2)
		C(1)–C(3)–S(2)	120.4(2)
		C(4)–C(3)–S(2)	119.7(2)
		C(6)–C(5)–P(1)	116.0(2)
		C(8)–C(9)–P(2)	117.7(2)

Table 5
Possible hydrogen bonds for [Ni(dpppn)(mnt)].

Donor–H	Donor···Acceptor	H···Acceptor	Donor–H···Acceptor
C11–H11	C11···N2 (1)	H11···N2 (1)	C11–H11···N2 (1)
0.947(24)	3.374(23)	2.486(12)	156.16(14)
C13–H13	C13···N1 (2)	H13···N1 (2)	C13–H13···N1 (2)
0.858(26)	3.351(70)	2.695(54)	134.25(27)
C32–H32	C32···N2 (3)	H32···N2 (3)	C32–H32···N2 (3)
0.972(36)	3.365(49)	2.600(29)	135.75(18)

Number of possible hydrogen bonds 3.
Equivalent positions: (1) $x+1/2, -y+1/2+1, -z+1/2$ (2) $-x+1, -y+2, -z+1$ (3) $-x+1, -y+2, -z$.

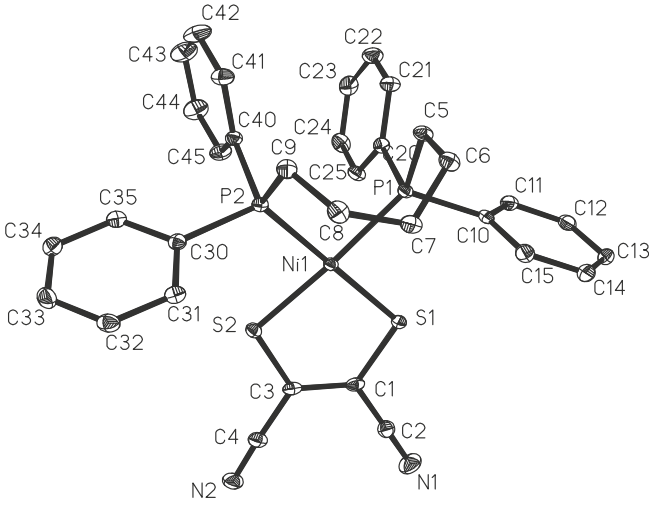


Fig. 1. ORTEP drawing of [Ni(dpppn)(mnt)] with the non-hydrogen atom labeling scheme. Thermal ellipsoids are drawn at the 50% probability level.

experiments confirmed a slow inhibition effect of dppp and mnt-ligands. The ligand dppp was a milder inhibitor. The ligand mnt reached stronger anticholinesterase activity. The dissociable nickel salt ($NiSO_4$) alone was not found to inhibit. However, the complex [Ni(dppp)(tdt)] acts as a strong inhibitor. The strongest inhibition activity was displayed by the [Ni(dppp)(mnt)] complex [44].

As for the influence of selected complexes on the vulcanization process, the basic results are summarized in Tables 7 and 8. All vulcanizing curves are characterized by the slight reversibility. The values of maximal torsion moments (M_L) of samples are lower compared to the standard (the viscosity values of these mixtures

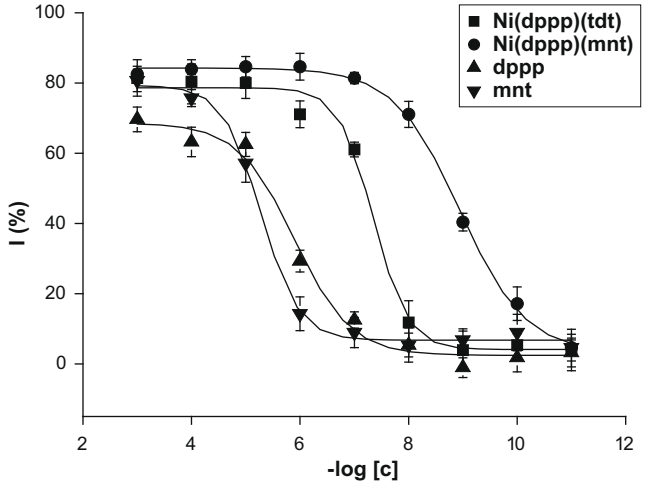


Fig. 2. Expression of ligands and Ni complexes anticholinesterase activity using electrochemical biosensor. Error bars indicate standard deviation ($n = 4$). Data were processed in Origin 6.1 and overlaid with sigmoidal fit.

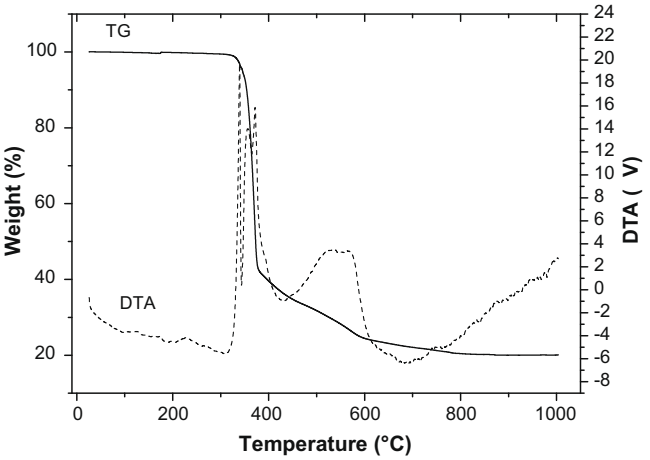


Fig. 3. Thermal analysis of [Ni(dppe)(mnt)].

Table 6
Anticholinesterase activity of selected ligands and complexes.

Compound	IC_{50} [M]
Mnt	5.25×10^{-6}
Dppp	1.30×10^{-6}
II. [Ni(dppp)(mnt)]	1.20×10^{-9}
X. [Ni(dppp)(tdt)]	4.50×10^{-8}

after vulcanization are lower). The minimal torsion moments (M_H) are almost identical with the standard (the viscosity of rubber mixture at the beginning of vulcanization process is almost identical). The start of vulcanization (t_{02} parameter) is also similar. On the other hand, the optimal values of vulcanization (t_{90}) of rubber mixtures with our samples as vulcanizing agents are significantly less than the standard value. The better activity of the vulcanization system with our samples as dopes is confirmed by higher values of vulcanizing speed coefficients (R_V). The obtained values of solidity characteristics are almost identical with the reference sample; the best values were reached by sample **IX** (Table 8), which corresponds to the lowest values of t_{02} and t_{90} (vulcanization process is more effective). The hardness IRHD values are slightly lower than the hardness of reference samples, but the dif-

Table 7
Vulcanizing characteristics of selected compounds.

Compound	M_H [dN/m]	M_L [dN/m]	t_{02} [dN/m]	t_{90} [dN/m]	R_v [min^{-1}]
Santocure TBBS	13.5	104.0	3.0	15.5	8.00
I. [Ni(dppe)(mnt)]	13.0	92.5	2.5	12.5	10.00
V. [Ni(dppe)(bdt)]	14.0	95.0	3.0	12.5	10.53
IX. [Ni(dppe)(tdt)]	15.5	92.0	2.0	12.0	10.00

Table 8
Physical and mechanical properties of selected compounds.

Compound	Tensile strength [MPa]	Elongation [%]	Hardness [IRHD]	Crosslink density [mol/cm^3]
Santocure TBBS	15.93	256	92.6	2.702×10^{-4}
I. [Ni(dppe)(mnt)]	16.52	266	90.8	3.490×10^{-4}
V. [Ni(dppe)(bdt)]	15.91	248	89.9	2.904×10^{-4}
IX. [Ni(dppe)(tdt)]	17.56	281	89.8	2.651×10^{-4}

ferences are not significant. This fact is confirmed by the lower values of viscosity rubber mixture (lower M_L values, Table 7). The grid density is a parameter that gives information about the vulcanization network formation quality. It is connected with the number of cross-bonds in the rubber (tire). Determination of the crosslink density was performed by the [45] methodology; crosslink density values are higher for samples **I** and **V**; in the case of sample **IX** it is only slightly lower than the standard value.

In conclusion, all the measured samples proved to be better sulfur vulcanization accelerators than the commercially used sulfenamide type accelerator TBBS. They increase the vulcanization speed in comparison with the standard by 20%, while the most important physical and mechanical properties and crosslink density values are well-kept. Moreover, the crosslink density of samples **I** and **V**, as well as the vulcanization speed coefficients values, are better than the standard procedure values.

Supplementary data

CCDC 731400 contains the supplementary crystallographic data for JK05. These data can be obtained free of charge via http://www.ccdc.cam.ac.uk/conts/retrieving.html, or from the Cambridge Crystallographic Data Centre, 12 Union Road, Cambridge CB2 1EZ, UK; fax: (+44) 1223-336-033; or e-mail: deposit@ccdc.cam.ac.uk.

Acknowledgements

This work was supported by the project of Ministry of Defense (Czech Republic) – FVZ0000604 (MP, KK). The authors would like to thank Prof. Z. Trávníček for X-ray measurements and data reduction and Assoc. Prof. Z. Šindelář for magnetochemical measurements and Mgr. R. Štarha for thermal analysis.

References

[1] P. Solichová, Diploma Thesis, Palacký University, Olomouc, 2001.
[2] K. Mrkvová, J. Kameníček, Z. Šindelář, Acta Univ. Palacki. Olom. Chem. 43 (2004) 94.
[3] J. Kameníček, P. Solichová, K. Mrkvová, Acta Univ. Palacki. Olom. Chem. 41 (2002) 17.
[4] K. Mrkvová, J. Kameníček, Z. Šindelář, L. Kvítek, Trans. Metal Chem. 29 (2004) 238.
[5] M.M. Belombé, J. Nenwa, E. Hey-Hawkins, P. Lönnecke, P. Strauch, K.R. Koch, Polyhedron 27 (2008) 3688.
[6] J. Kameníček, P. Herich, K. Kuča, D. Jun, M. Olšovský, J. Coord. Chem. 61 (2008) 3525.
[7] T.M. Cocker, R.E. Bachman, Inorg. Chem. 40 (2001) 1550.
[8] Ch. Makedonas, Ch.A. Mitsopoulou, Eur. J. Inorg. Chem. 12 (2006) 2460.
[9] Tie-Xiang Fu, Jun Tao, Dan Li, Wuli Huaxue Xuebao 20 (2004) 843.
[10] R. Pastorek, J. Kameníček, M. Pavlíček, J. Husárek, Z. Šindelář, Z. Žák, Polish J. Chem. 76 (2002) 1545.
[11] R. Pastorek, J. Kameníček, M. Pavlíček, J. Husárek, Z. Šindelář, Z. Žák, J. Coord. Chem. 55 (2002) 1301.
[12] R. Pastorek, J. Kameníček, J. Husárek, B. Cvek, M. Maloň, M. Pavlíček, Z. Šindelář, Polish J. Chem. 78 (2004) 623.
[13] R. Pastorek, J. Kameníček, J. Husárek, M. Pavlíček, Z. Šindelář, Z. Žák, Polish J. Chem. 77 (2003) 805.
[14] R. Pastorek, J. Kameníček, B. Cvek, V. Slovák, M. Pavlíček, J. Coord. Chem. 59 (2006) 911.
[15] A. Manohar, K. Ramalingam, R. Thiruneelakandan, G. Bocelli, L. Righi, Z. Anorg. Allg. Chem. 632 (2006) 461.
[16] M.R.L. Oliveira, J. Amim Jr., I.A. Soares, V.M. de Bellis, C.A. de Simone, C. Novais, S. Guilardi, Polyhedron 27 (2008) 727.
[17] K. Schubert, T. Alpermann, T. Niksch, H. Görls, W. Weigand, Z. Anorg. Allg. Chem. 632 (2006) 1033.
[18] L.G. Katy, D.H. Allen, R.W. Timothy, S.C. Larry, F.L. Francesca, S.A. Jansen-Varnum, Inorg. Chim. Acta 282 (1998) 155.
[19] M. Kajitani, T. Yagisawa, T. Sugiyama, Y. Akama, A. Sugimori, Anal. Sci. 13 (1997) 873.
[20] K. Bei-Sheng, Ch. Zhong-Ning, G. Han-Rong, Z. Zhong-Yuan, W. Bo-Mu, M.C. Thomas, L. Zhong, Huaxue Xuebao 56 (1998) 58.
[21] J. Darkwa, Inorg. Chim. Acta 257 (1997) 137.
[22] W.M. Valentine, H.L. Valentine, K. Amarnath, V. Amarnath, Toxicol. Sci. 50 (1999) 155.
[23] E. Bowman, J. Reedijk, Coord. Chem. Rev. 249 (2005) 1555.
[24] D. Sellmann, D. Häussinger, F. Knoch, M. Moll, J. Am. Chem. Soc. 118 (1996) 5368.
[25] P. Cassoux, L. Valade, H. Kobayashi, R.A. Clark, E. Underhill, Coord. Chem. Rev. 110 (1991) 171.
[26] R. Eisenberg, Prog. Inorg. Chem. 12 (1970) 295.
[27] W.E. Geiger, C.S. Allen, T.E. Mines, F.E. Senftleber, Inorg. Chem. 16 (1977) 2003.
[28] A.G. Bowmaker, W.D.P. Boyd, K.G. Campbell, Inorg. Chem. 21 (1982) 2403.
[29] R. Přibil, Komplexometrické titrace, SNTL Praha, 1955.
[30] M. Pohanka, D. Jun, K. Kuča, Sensors 8 (2008) 5303.
[31] J. Vajdová, M. Štubňa, M. Olšovský, Laboratórium odboru II - Chemické a fyzikálno-mechanické skúšky, FPT TnUAD Púchov, Slovak Republic, 2003.
[32] G.M. Sheldrick, Acta Crystallogr., Sect. A46 (1990) 467.
[33] G.M. Sheldrick, SHELXL-97: Program for Crystal Structure Refinement, University of Göttingen, Germany, 1997.
[34] M. Nardelli, J. Appl. Cryst. 28 (1995) 659.
[35] N.B. Colthup, L.H. Daly, S.E. Wiberley, Introduction to Infrared and Raman Spectroscopy, Academic Press, New York and London, 1964.
[36] M. Horák, D. Papoušek, Infračervená spektra a struktura molekul, Academia Praha, 1976.
[37] A.J. Blacke, G.P. McQuillan, J. Chem. Soc., Dalton Trans. (1984) 1849.
[38] M. Takahashi, N. Robertson, A. Kobayashi, H. Becker, R.H. Friend, A.E. Underhill, J. Mater. Chem. 8 (1998) 319.
[39] D.M. Adams, E.A.V. Ebsworth, Spectroscopic Properties of Inorganic and Organometallic Compounds, vol. 11, Burlington House, London, 1979.
[40] A.B.P. Lever, Inorganic Electronic Spectroscopy, Elsevier, Amsterdam, 1984.
[41] W.J. Geary, Coord. Chem. Rev. 7 (1971) 81.
[42] A.B. Nejding, Magnetochimija komplexnych sojedinenij perechodnych metallov, Mir, Moskva, 1970.
[43] B.A. Kowert, M.J. Fehr, P.J. Sheaff, Inorg. Chem. 47 (2008) 5696.
[44] M. Pohanka, K. Kuča, J. Kassa, Neuro. Endocrinol. Lett. 29 (2008) 755.
[45] M. Olšovský, J. Vajdová, Laboratórne cvičenia z chémie polymérov, TnUAD Trenčín, Slovak Republic, 2007.

$[Zn(L)Cl_2]$ and $[Pd(L)Cl]Cl$, respectively, where L stands for 2-formylpyridine *S*-methylisothiosemicarbazone [35,36].

With 2-acetylpyridine *S*-methylisothiosemicarbazone (HL), a limited number of complexes of Fe(II), Co(II), Ni(II) and Cu(II) have been reported to date, presuming different coordination modes of the ligand [37]. With the aim of checking the coordination mode of the ligand, in this work we performed an X-ray analysis of the ligand itself and its three complexes with copper(II) of the formulae: $[Cu(HL)SO_4(H_2O)]\cdot H_2O$, $[Cu_2(HL)_2(\mu\text{-}SO_4)_2]\cdot 2H_2O$ and [Cu(HL)(NCS)-(SCN)], involving the NNN tridentate coordination mode.

2. Experimental

2.1. Materials and physical measurements

All chemicals for the syntheses were analytical reagent grade. Elemental analysis (C, H, N) was carried out by standard micromethods. Magnetic susceptibility measurements were conducted at room temperature on a MSB-MKI magnetic susceptibility balance, Sherwood Scientific Ltd., Cambridge. Molar conductivities of freshly prepared 1 mM solutions were measured on a Jenway 4010 conductivity meter. IR spectra were recorded at room temperature using KBr pellets, in the range 4000–400 cm^{-1} on a Thermo Nicolet (NEXUS 670 FT-IR) spectrophotometer. Electronic spectra of 0.5–1 mM methanolic solutions of the ligand and complexes were recorded on a T80+ UV/VIS spectrophotometer, PG Instruments Ltd. in the spectral range 190–1100 nm.

TA measurements were carried out using simultaneous TGA-DSC thermal analyzer SDT Q600, TA instruments in open sample holders made of aluminum, with sample masses of about 2 mg. The decomposition was recorded in air and nitrogen atmospheres at a heating rate of 20 °C/min. The carrier gas flow rate was 100 cm^3/min. Before the run, the samples were equilibrated for 5 min at room temperature.

2.2. Preparation of the ligand

Single crystals of 2-acetylpyridine *S*-methylisothiosemicarbazone hydrogen iodide ($H_2L^+I^-$) were obtained by recrystallization from warm EtOH of the product synthesized according to our previous procedure [37]. Conductivity (λ_o, Ω^{-1} cm^2 mol^{-1}) in H_2O and MeOH: 114 and 93, respectively. IR (KBr, cm^{-1}): $\nu(NH_2)$ 3354, 3244, 3143; ν(C=N) 1604; δ(py) 605. UV–Vis [λ_{max}/nm ($\log \varepsilon/M^{-1}cm^{-1}$)]: 219(4.36), 295(4.28), 386(3.23).

2.3. Preparation of the copper(II) complexes

$[Cu(HL)SO_4(H_2O)]\cdot H_2O$ (**1**)/$[Cu_2(HL)_2(\mu\text{-}SO_4)_2]\cdot 2H_2O$ (**2**). To a warm solution of the ligand, $H_2L^+I^-$ (0.34 g, 1 mmol) in 15 cm^3 EtOH/MeOH, respectively, 0.40 g (1.5 mmol) of $CuSO_4\cdot 5H_2O$ dissolved in 5 cm^3 H_2O/MeOH, was added. The mixture was mildly heated to start the formation of CuI, which was filtered off after cooling the solution. After 24 h at room temperature, green single crystals were separated and washed with EtOH and Et_2O. Yield: 0.26 g/0.24 g (65%/32%), respectively.

(**1**) *Anal.* Calc. for $C_9H_{16}CuN_4O_6S_2$: C, 26.76; H, 3.99; N, 13.87. Found: C, 26.55; H, 4.01; N, 13.62%. Magnetic moment (μ, BM): 1.78. Conductivity (λ_o, Ω^{-1} cm^2 mol^{-1}) in MeOH and DMF: 20 and 37, respectively. IR (KBr, cm^{-1}): ν(OH) 3467; ν(NH) 3325; ν(C=N) 1648; $\nu(SO_4)$ 1180, 1115, 619; δ(py) 644. UV–Vis [λ_{max}/nm ($\log \varepsilon/M^{-1}cm^{-1}$)]: 225(4.16), 253sh(4.00), 296(3.93), 317(3.91), 410(3.74), 665(2.03).

(**2**) *Anal.* Calc. for $C_{18}H_{28}Cu_2N_8O_{10}S_4$: C, 28.01; H, 3.66; N, 14.52. Found: C, 27.88; H, 3.59; N, 14.38%. Magnetic moment (μ, BM): 1.57 per Cu atom. Conductivity (λ_o, Ω^{-1} cm^2 mol^{-1}) in MeOH and DMF: 117 and 92, respectively. IR (KBr, cm^{-1}): ν(OH) 3511; ν(NH) 3325, 3367; ν(C=N) 1638; $\nu(SO_4)$ 1180, 1117, 619; δ(py) 650. UV–Vis [λ_{max}/nm ($\log \varepsilon/M^{-1}cm^{-1}$)]: 225(4.43), 259(4.27), 326(4.24), 410(3.49), 681(2.26).

[Cu(HL)(NCS)(SCN)] (**3**). To a warm solution of $H_2L^+I^-$ (0.17 g, 0.5 mmol) in 10 cm^3 MeOH, 0.28 g (0.75 mmol) of $Cu(ClO_4)\cdot 6H_2O$ dissolved in 5 cm^3 MeOH was added and heated mildly. The readily formed CuI was filtered off after 2 h, and 3 cm^3 of triethyl orthoformate was added. After 20 h, 0.09 g (1.2 mmol) of NH_4SCN dissolved in 4 cm^3 MeOH was added and the mixture was heated mildly. After 4 h, green monocrystals were separated and washed with MeOH and Et_2O. Yield: 0.12 g (63%).

Anal. Calc. for $C_{11}H_{12}CuN_6S_3$: C, 34.05; H, 3.12; N, 21.66. Found: C, 34.17; H, 3.18; N, 21.88; Cu. Magnetic moment (μ, BM): 1.80. Conductivity (λ_o, Ω^{-1} cm^2 mol^{-1}) in MeOH and DMF: 69 and 63, respectively. IR (KBr, cm^{-1}): ν(NH) 3330; ν(C=N) 1640; ν(NCS) 2102, 2072; δ(py) 646. UV–Vis [λ_{max}/nm ($\log \varepsilon/M^{-1}cm^{-1}$)]: 223(4.30), 254(4.04), 328(3.97), 404(3.23), 672(2.19).

2.4. X-ray crystal structure determination

Single green crystals of copper(II) complexes **1**–**3** and yellow crystals of $H_2L^+I^-$ were selected and glued onto glass fibers. Diffraction data were collected on an Oxford Diffraction KM4 four-circle goniometer equipped with a Sapphire CCD detector. The crystals to detector distance was 45.0 mm and graphite monochromated Mo Kα (λ = 0.71073 Å) radiation was employed in all measurements. A frame width of 1° in ω, within 1.5–17.4 s was used to acquire each frame for measurements of all crystals in the present work. More than one hemisphere of the three-dimensional data was collected in all measurements. The data were reduced using the Oxford Diffraction program CrysAlis^{Pro}. A semi-empirical absorption-correction based upon the intensities of equivalent reflections was applied, and the data were corrected for Lorentz, polarization, and background effects. Scattering curves for neutral atoms, together with anomalous-dispersion corrections, were taken from the International Tables for X-ray Crystallography [38]. The structures were solved by direct methods [39] and the figures were drawn using Mercury [40]. Refinements were based on F^2 values and done by full-matrix least-squares [41] with all non-H atoms anisotropic. The positions of all non-H atoms were located by direct methods. The positions of hydrogen atoms were found from the inspection of the difference Fourier maps. The final refinement included atomic positional and displacement parameters for all non-H atoms. The non-H atoms were refined anisotropically, while H sites of the water molecules were refined with isotropic displacement parameters. However, at the final stage of the refinement, H atoms belonging to HL were positioned geometrically (N–H = 0.86 and C–H = 0.93 and 0.97 Å for CH and CH_3, respectively) and refined using a riding model with fixed isotropic displacement parameters. Crystal data and refinement parameters are listed in Table 1.

3. Result and discussion

3.1. Synthesis and characterization

The complexes were prepared using the protonated form of the ligand, $H_2L^+I^-$, obtained by the previously described reaction [37]. The ligand is well soluble in H_2O, less soluble in EtOH and MeOH, and insoluble in Et_2O. Molar conductivities in H_2O and MeOH solutions correspond to the electrolyte type 1:1 [42]. The substance is stable in air, not only at room temperature, but also at somewhat elevated temperatures (*vide infra*).

Table 1
Crystal data and refinement parameters for **1**, **2**, **3** and $H_2L^+I^-$.

Crystallographic parameter	Compound			
	1	**2**	**3**	$H_2L^+I^-$
Empirical formula	$C_9H_{16}CuN_4O_6S_2$	$C_{18}H_{28}Cu_2N_8O_{10}S_4$	$C_{11}H_{12}CuN_6S_3$	$C_9H_{13}IN_4S$
Formula weight	403.92	771.81	387.99	336.19
Temperature (K)	293(2)	293(2)	293(2)	293(2)
Wavelength (Å)	0.7107	0.7107	0.7107	0.7107
Crystal size (mm)	0.51 × 0.39 × 0.29	0.48 × 0.35 × 0.25	0.40 × 0.31 × 0.08	0.55 × 0.32 × 0.18
Colour/shape	green/prismatic	green/prismatic	green/platelike	jelow/prismatic
Crystal system	monoclinic	triclinic	monoclinic	triclinic
Space group	$P2_1/n$	$P\bar{1}$	$P2_1/c$	$P\bar{1}$
a (Å)	8.8520(3)	9.0239(4)	11.326(6)	7.752(5)
b (Å)	17.1390(5)	9.0884(7)	18.441(6)	9.642(5)
c (Å)	10.4109(3)	10.2981(7)	7.824(4)	9.782(5)
α (°)	90.0	74.936(6)	90.0	102.540(5)
β (°)	107.728(3)	69.551(5)	109.81(1)	100.058(5)
γ (°)	90.0	64.058(6)	90.0	111.715(5)
Volume (Å^3)	1504.5(2)	705.84(7)	1537.5(2)	636.3(6)
Cell measur. reflect. used	2770	4541	2620	2872
Z	4	2	4	2
D_{calc} (g/cm^3)	1.783	1.818	1.68	1.76
F(0 0 0)	828	394	788	328
θ range (°)	3.14–29.13	3.08–29.23	3.54–26.75	3.60–29.21
Index ranges	$-11 \leqslant h \leqslant 11$, $-21 \leqslant k \leqslant 23$, $-13 \leqslant l \leqslant 13$	$-11 \leqslant h \leqslant 12$, $-12 \leqslant k \leqslant 12$, $-13 \leqslant l \leqslant 12$	$-11 \leqslant h \leqslant 13$, $-23 \leqslant k \leqslant 19$, $-9 \leqslant l \leqslant 9$	$-10 \leqslant h \leqslant 10$, $-12 \leqslant k \leqslant 12$, $-13 \leqslant l \leqslant 12$
Absorption coefficient μ (mm^{-1})	1.763	1.872	1.828	2.657
Absorption correction T_{min}	0.94174	0.65876	0.81425	0.39327
Reflections collected	4944	7245	4779	5357
Unique reflections	2997	3261	2089	2915
Refinement methods	F^2	F^2	F^2	F^2
Data/restraints/parameters	2270/0/220	2590/0/203	1618/0/194	2548/0/141
Goodness-of-fit on F^2	0.885	1.043	1.028	1.019
Final R indices [$F_o > 4\sigma F_o$]	0.0291	0.0321	0.0317	0.0266
R indices (all data)	0.0415	0.0465	0.0470	0.0317
shift/esd$_{max}$	0.075	0.0	0.002	−0.014
Extinction coefficient	–	–	–	0.013(2)
Largest diffraction peak and hole (e/Å^3)	+0.29 −0.36	+0.613 −0.450	+0.36 −0.247	+0.60 −0.58

The sulfato complexes of copper(II), $[Cu(HL)SO_4(H_2O)]\cdot H_2O$ (**1**) and $[Cu_2(HL)_2(\mu\text{-}SO_4)_2]\cdot 2H_2O$ (**2**), were prepared by the reaction of warm EtOH/MeOH solutions of the ligand with a H_2O/MeOH solution of $CuSO_4\cdot 5H_2O$, respectively. The complexes are well soluble in H_2O, MeOH and DMF, and less in EtOH. The molar conductivity of a solution of complex **1** is significantly smaller than λ_o for a complex that is a 1:1 electrolyte, in contrast to λ_o of complex **2**, which corresponds to a 1:1 type of electrolyte, suggesting a lower stability of complex **2** [42]. The μ_{eff} value of complex **1** is characteristic of a mononuclear magnetically isolated Cu(II) complex, in contrast to complex **2** which has a lower μ_{eff} value (1.57 BM), in agreement with its dinuclear structure [43].

Complex [Cu(HL)(NCS)(SCN)] (**3**) was obtained by mixing MeOH solutions of the ligand and $Cu(ClO_4)_2\cdot 6H_2O$, adding triethyl orthoformate and NH_4NCS. The compound is well soluble in MeOH and DMF, less soluble in EtOH and poorly soluble in H_2O. The molar conductivity of its solution corresponds to a 1:1 type of electrolyte, which suggests replacement of one coordinated NCS group with solvent molecules [42]. The effective magnetic moment of complex **3** (μ_{eff} = 1.80 BM), like that of complex **1**, is in agreement with its mononuclear structure [43].

The thermal stability of the compounds was found to be independent of the atmosphere. The onset temperature of the ligand decomposition is 206 °C. The desolvation temperature of **1** is in accordance with its crystal structure. The evaporation of crystal water from **2**, near to the boiling point of water, is probably due to hindered diffusion. The desolvated complexes **1** and **2**, as well as **3**, are thermally stable up to 160 °C. Detailed analysis of the thermal data is given in the Supplementary data.

The IR and electronic spectra of the ligand and complexes are discussed in the Supplementary data.

3.2. Structure of the ligand

The triclinic ($P\bar{1}$) elementary cell of the $H_2L^+I^-$ monocrystal consists of well developed separated structural units of H_2L^+ cations, containing a protonated pyridine nitrogen atom and an I^- anion. Fig. 1 shows the composition of the asymmetric elementary cell unit and enumeration of the ligand atoms, while Table 2 lists the interatomic distances and angles. The magnitude of the angle C(5)–N(4)–C(9) (124.1(2)°) confirms that the nitrogen atom of the pyridine ring is protonated [44]. The H_2L^+ cation has an E-configuration (*cis*-position of N atoms) with respect to the C(1)–N(2) bond. The structure of the ligand is characterized by high polarity, and the deviation from the best mean plane is within the range 0.001–0.145 Å. The iodide anions are located close to the ligand plane. The isothiosemicarbazide fragment is in its amido form, which is characterized by a mild delocalization of the electronic density [30]. The delocalization is also suggested by the N(1)–C(1), C(1)–N(2) and N(2)–N(3) distances of 1.331(4), 1.301(4) and 1.385(2) Å, respectively. The C(3)–N(3) distance (1.285(3) Å) corresponds to a localized double bond.

Apart from the ionic character of the bond, the packing of the structural units is also strongly influenced by hydrogen bonds, as both potential H donors (N atoms from the pyridine and thioamide fragments) participate in the formation of the N–H···I interactions as the only hydrogen bonds. In addition to the hydrogen bonds, the structural units also involve van der Waals contacts, which yield to

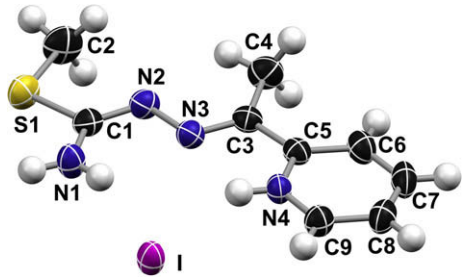


Fig. 1. View of the asymmetric part of the elementary cell and atom labeling in the ligand $H_2L^+I^-$.

Table 2
Selected bond lengths (Å) and angles (°).

	Compound			
	1	**2**	**3**	$H_2L^+I^-$
Cu–N1	1.964(3)	1.949(3)	1.974(3)	–
Cu–N3	1.950(2)	1.967(2)	1.957(3)	–
Cu–N4	2.016(2)	2.016(2)	2.011(3)	–
Cu–N31	–	–	1.908(3)	–
Cu–O1	2.289(2)	1.916(2)	–	–
Cu–O2	–	2.250(2)	–	–
Cu–O5	1.943(2)	–	–	–
Cu–S2	–	–	2.684(2)	–
C2–S1	1.790(3)	1.793(3)	1.772(4)	1.794(4)
S1–C1	1.747(3)	1.738(3)	1.740(3)	1.751(2)
C1–N1	1.285(3)	1.281(4)	1.271(4)	1.331(4)
C1–N2	1.379(3)	1.370(3)	1.367(4)	1.301(4)
N2–N3	1.366(3)	1.354(4)	1.364(4)	1.385(2)
N3–C3	1.283(3)	1.289(3)	1.271(4)	1.285(3)
O1–Cu–O5	93.93(7)	–	–	–
O1–Cu–N3	95.90(7)	94.58(7)	–	–
O1–Cu–N1	99.01(8)	97.19(9)	–	–
O1–Cu–N4	91.77(7)	92.28(7)	–	–
O5–Cu–N3	169.0(1)	–	–	–
O5–Cu–N1	103.6(1)	–	–	–
O5–Cu–N4	94.99(9)	–	–	–
N3–Cu–N1	79.80(9)	78.89(9)	79.0(1)	–
N3–Cu–N4	79.72(7)	78.86(8)	79.0(1)	–
N1–Cu–N4	157.7(1)	156.41(9)	156.5(1)	–
O2–Cu–N4	–	95.25(8)	–	–
O2–Cu–N1	–	103.51(9)	–	–
O2–Cu–N3	–	161.67(8)	–	–
O2–Cu–O1	–	103.04(7)	–	–
N31–Cu–N1	–	–	102.0(1)	–
N31–Cu–N3	–	–	167.3(1)	–
N31–Cu–N4	–	–	97.7(1)	–
S2–Cu–N1	–	–	97.98(9)	–
S2–Cu–N3	–	–	93.81(9)	–
S2–Cu–N4	–	–	91.53(9)	–
S2–Cu–N31	–	–	89.5(1)	–
N1–C1–N2	118.2(2)	117.3(2)	118.3(3)	127.4(3)
C1–N2–N3	112.4(2)	112.9(2)	112.8(3)	111.9(2)
N2–N3–C3	125.1(2)	124.9(2)	125.0(3)	113.8(2)
C5–N4–C9	118.6(2)	119.3(2)	119.3(3)	124.1(2)

the formation of specific supramolecular forms in the shape of double-layer regions along the [1 1 0] direction, about 10.5 Å wide and 3.3 Å thick (see Fig. S1 in the supplementary data). Along their surfaces, the layers are approximately perpendicular to the direction [−1 1 1]. Along each of the double-layer regions, there appear alternate domains populated with I^- and H_2L^+ ions (see Fig. S2 in the supplementary data). The developed network of hydrogen bonds is realized solely within the double-layer areas via the I atom and the N atom of the pyridine ring (N4), and that of the thioamide group (N1). These bonds are characterized by the following parameters: I···H(4)N(4) = 3.513(2) Å, ∠(N(4)–H(4)–I) = 143.2(1)°; I···H(1A)N(1) = 3.729(3) Å, ∠(N(1)–H(1A)···I) = 156.6(2)°, I···H(1B)N(1) = 3.697(3) Å, ∠(I–H(1B)–N(1) = 144.9(2)°. In addition to the hydrogen bonds, the double-layers also involve van der Waals contacts of the type (CH···I): I···C(7) = 4.050(3) Å; I···C(4) = 4.040(5) Å.

3.3. Structure of the complexes

Complexes **1**, **2** and **3** have a slightly distorted square-pyramidal environment around the Cu(II) centers (τ = 0.18, 0.08 and 0.18, respectively). Three coordination sites in the square base are occupied by the neutral 2-acetylpyridine *S*-methylisothiosemicarbazone ligand, which behaves as a tridentate NNN ligand. Namely, HL is coordinated through the pyridine, azomethine and isothioamide nitrogen atoms, forming thus two five-membered metallocycles of high planarity.

The isothioamide and azomethine nitrogens, N(1) and N(3), form bonds with the copper atom, whose lengths are in the range from 1.949 to 1.974 Å, whereas the pyridine nitrogen N(4) forms somewhat longer bonds (2.011–2.017 Å) (Table 2). In contrast to the free ligand, which is in the amido form, the coordinated ligand in all three complexes is in its imido form, resulting from prototropic tautomerization, that is the migration of the hydrogen atom of the NH_2 group of the isothioamide fragment to the adjacent hydrazine N(2) atom. Coordination in the imido form is also characteristic of other isothiosemicarbazones [30]. The existence of the imido form is also unequivocally confirmed by the presence of hydrogen bonds in the crystal structures of all three complexes, in which N(2) appears as an electron donor. In the structure of the coordinated ligand, the bond lengths C(1)–N(2) (1.370–1.379 Å) and N(2)–N(3) (1.354–1.366 Å) are between the values corresponding to the lengths of localized single and double C–N and N–N bonds, which indicates the delocalization of the electronic density in the isothiosemicarbazide fragment [30]. In contrast to these bonds, the bonds C(1)–N(1) (1.271–1.285 Å) and C(3)–N(3) (1.271–1.289 Å) in all three structures correspond to localized double bonds.

The bonds between the atoms of the ligator of the square base and Cu(II) are significantly shorter (1.908–2.016 Å) compared to the bonds of Cu(II) and the apical atoms of the ligator, whose lengths in complexes **1** and **2** are 2.289(2) and 2.250(2) Å, respectively, which has also been observed in a number of copper(II) complexes of a square-pyramidal (4+1) geometry [45]. As expected, the apical Cu–S bond in complex **3** is the longest (2.684(2) Å), and its length is practically identical to the same bond (2.682(1) Å) in the square-pyramidal tridentate triaza complex Cu(NNN)(NCS)(SCN) [46].

3.3.1. Structure of complex *1*

The asymmetric part of the elementary cell (Fig. 2) of **1**, apart from the neutral complex molecule [Cu(HL)SO_4(H_2O)], also contains a molecule of crystal water. The interatomic distances and angles for complex **1** are shown in Table 2.

As is known, in metal-sulfato complexes the SO_4^{2-} ligand can be bonded in many ways, i.e. via two terminal (monodentate, bidentate chelating) and 16 different bridging coordination modes [47]. It has been previously observed that mononuclear square-pyramidal Cu(II) complexes involve a monodentate sulfato group, i.e. the 1.1000 coordinated sulfate mode [47], which can occupy either an equatorial position, with the shortest Cu–O bond length of 1.949(3) Å [48], or an axial position, with the longest Cu–O bond length of 2.414(9) Å [49].

The square base around the Cu(II) in complex **1** is formed of three nitrogen atoms of the chelate ligand and an oxygen atom of the coordinated water (Cu–O(5) = 1.943(2) Å), whereas the apical position is occupied by the O(1) atom of the sulfate group coordinated in the 1.1000 mode (Cu–O(1) = 2.289(2) Å). The Cu(II)

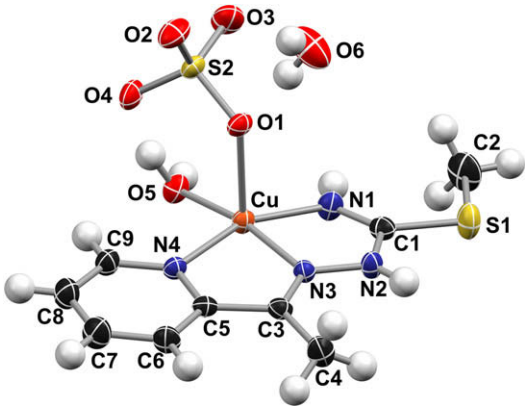


Fig. 2. Contents of the asymmetric part of the elementary cell and atom labeling in the structure of complex **1**.

atom sticks out by 0.177(2) Å from the mean plane of the square base towards the axial position.

The stable bonding of the structural units in the crystal space of complex **1** is realized by the existence of the developed 3-D network of hydrogen bonds, formed thanks to a number of potential donor and acceptor atoms in the structure. Thus, in addition to the O atoms of the coordinated and crystal water, the thioamide nitrogen and the nitrogen of the N(2) hydrazine residue from the chelate ligand play the role of donors. Each oxygen atom of the SO_4 group also plays the role of a single or double hydrogen acceptor. All the existing hydrogen bonds (six in total) are in the range 2.592–3.037 Å and, together with the corresponding angles, are listed in Table 3. The shortest hydrogen bond (O(5)–O(4)) is intramolecular, and it appears between the coordinated water and sulfate group. Packing of the structural units in the crystalline space of complex **1** is presented in Fig. S3 in the supplementary data.

3.3.2. Structure of complex *2*

In the dinuclear complex $[Cu_2(HL)_2(\mu\text{-}SO_4)_2]\cdot 2H_2O$ (**2**), two sulfato *exo*-bidentate ligands are 2.1100 bridged [47] between two metal centers at a distance of 4.744(2) Å, forming a centrosymmetric dinuclear complex with an eight-membered metallo-ring in a chair arrangment, which is a most unusual bridging mode of this ligand. The same coordination mode of two sulfate groups is also found in the structure of the dinuclear Cu(II) complexes $[Cu_2L_2(SO_4)_2]$ (L = dipyridophenazine, diacetyl monoxime-2-pyridyl hydrazone) [50,51], as well as in the tetranuclear $[Cu_4(L)_2(SO_4)_2(H_2O)_{10}](SO_4)_2\cdot 4H_2O$ (L = 3-2(pyridyl)-triazino[5,6-*f*]1,10-phenanthroline) [52].

The square bases of both coordination polyhedra of complex **2** are formed by the nitrogen atoms N(1), N(3) and N(4) from the corresponding HL and the oxygen atoms O(1) from the symmetrically identical (−1) bridging sulfate groups, whereas the apical positions are occupied by the oxygen atoms O(2), also from the bridging sulfate groups (Fig. 3). The Cu(II) atoms deviate by 0.247(2) Å from the mean square base towards the apical position. The Cu–O distance in the apical position is longer (Cu–O(2) = 2.250(2) Å) compared to the equatorial Cu–O(1) distance (1.916(2) Å) (Table 2), which is in good agreement with the corresponding literature data [50,51]. The bridging coordination of the sulfate group distorts its tetrahedral symmetry. The angle O(1)–S(2)–O(2) is the smallest (106.4(1)°), whereas the angle O(4)–S(2)–O(3) is the largest (112.9(1)°). As a consequence of the coordination, the bonds S(2)–O(1) and S(2)–O(2) become longer, amounting to 1.481(2) and 1.494(2) Å, respectively.

Table 3
Hydrogen bonding in complex **1**.

Donor	Acceptor	Distance (Å)	Dist.–vdW (Å)
N2	O1^{i}	2.691	−0.379
N1	O3^{ii}	3.037	−0.033
O5	O2^{ii}	2.691	−0.349
O5	O4^{iii}	2.592	−0.448
O6	O2^{ii}	2.860	−0.180
O6	O3^{iii}	2.858	−0.182
Donor–H–acceptor	Angle (°)	Donor–H–Acceptor	Angle (°)
N1–H1–O3	138.6	O5–H51–O4	159.4
N2–H2–O1	149.2	O6–H61–O3	175.0
O5–H52–O2	174.0	O6–H62–O2	170.0

Symmetry transformations to generate equivalent atoms: (i) (1 − *x*, −*y*, 2 − *z*), (ii) (1/2 + *x*, 1/2 − *y*, 1/2 + *z*), (iii) (*x*, *y*, *z*).

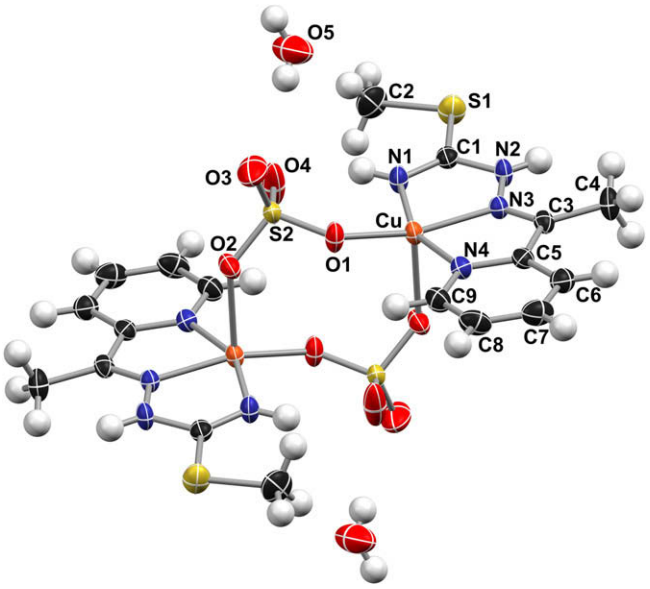


Fig. 3. Contents of the elementary cell and atom labeling in the structure of complex **2**.

The triclinic ($P\bar{1}$) elementary cell of complex **2**, along with the dimeric complex unit, contains also a molecule of crystal water. The bonds between the adjacent units are realized via the branched system of hydrogen bonds. In all, there are four different hydrogen bonds, established between water molecules and N-atoms of the isothioamide group and hydrazine residue of the chelate ligand as hydrogen donors and only O atoms of the sulfate group that do not belong to the basal plane of the coordination polyhedron as hydrogen acceptors. Out of all of them, only N(1)–H(1)···O(4) = 2.799(3) Å, ∠N(1)–H(1)–O(4) = 129.4(2)° is intramolecular, whereas the intermolecular hydrogen bonds in the structure of the complex are: N(2)H···O(1) = 2.668(4) Å, ∠(N(2)–H(2)–O(1)) = 150.0(2)°; O(5)H(51)···O(3) = 2.768(4) Å, ∠(O(5)–H(51)–O(3)) = 164(4)° and O(5)H(52)···O(4) = 2.948(2) Å, ∠(O(5)–H(52)–O(4)) = 156(5)°. The spatial network of hydrogen bonds connects adjacent dimers via water molecules into chains that are parallel in the direction [1 0 1], as is shown in Fig. 4.

3.3.3. Structure of complex *3*

The asymmetric part of the monoclinic ($P2_1/c$) elementary cell contains only one structural unit, and the neutral complex is shown in Fig. 5. The distances and angles in the coordination polyhedron as well as in the chelate ligand are given in Table 2.

The square base around Cu(II) is formed by the tetraaza donor set of atoms, consisting of the tridentate NNN HL ligand and the NCS group, which is coordinated via the nitrogen atom. The apical

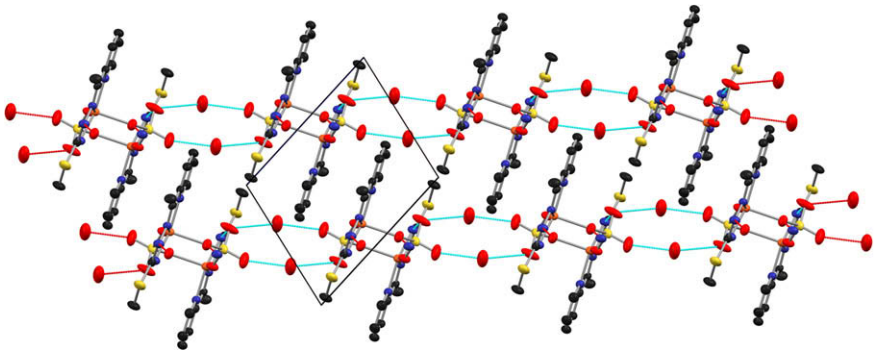


Fig. 4. View along the *b* axis of packing in the structure of complex **2**. H atoms are omitted for better clarity. Crystal water molecules (O5) form hydrogen bonds with free sulfate O atoms, bonding the adjacent dimers along the direction [1 0 1].

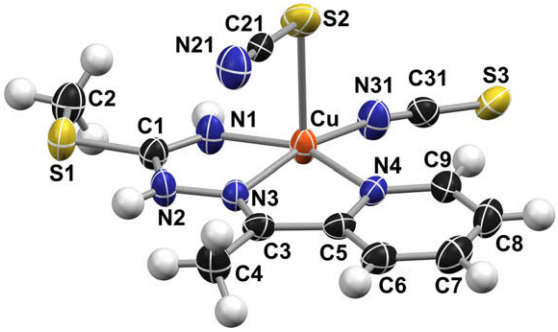


Fig. 5. View of the asymmetric part of the elementary cell and atom labeling in the structure of complex **3**.

position of the square pyramid is occupied by the other NCS group, whose coordination is realized via the sulfur atom. The NCS group of the square base, as well as the apical NCS group, are practically linear, with N–C–S angles of 178.6(4)° and 177.4(4)°, respectively. The NCS group from the square base forms a Cu–N(31)–C(31) angle of 168.8(3)°, whereas the apical NCS group forms almost a right angle (the angle Cu–S(2)–C(21) is 99.8(2)°).

It is known that the ambidenticity of the NCS^- ion allows two modes of its terminal coordination. Copper(II), as a metal of the first transition series, forms most frequently the Cu–N bond with the NCS^- ion, although there are also some examples of S-bonded coordination, which is explained by the formation of NH···N(NCS) hydrogen bonds that stabilize the crystal structure [46,53]. Coordination via the sulfur atom is energetically unfavorable, as it is in contradiction to the Pearson's hard-soft interactions, which assumes that the hardnesses of the base and acid should match each other. The factors influencing bonding properties of this ion are diverse [54], and in the case of the same ligands the condition of the synthesis itself may play a decisive role in the coordination mode of the NCS group [53]. It has been reported [55] that a polynuclear Cu(II) complex, apart from bridging, contains also terminal N- and S-bonded NCS groups. Relatively rare, and difficult to prepare, are metal complexes containing simultaneously one S- and one N-bonded non-bridging thiocyanate to the same metal ion, as was found in the complex [Pd(L)(NCS)(SCN)] (L = 1-phenylphosphino-3-dimethylaminopropane) [56], [Cu(L)(NCS)(SCN) (L = condensation product of 2-(2-aminoethyl)pyridine with 4-methylimidazole-5-carboxaldehyde) [46] and $[Cu^{II}(L)_2][Cu^{I}(L)(NCS)_2(SCN)]$ (L = 2,2′-biimidazole) [57], which the authors [46,57] explain by the formation of the corresponding intermolecular hydrogen bond between the N atom of the thiocyanate and the N–H proton of the ligand L of an adjacent molecule.

In the case of our complex, the S-coordination of the apical NCS group might also be explained by the formation of an intermolecular hydrogen bond between the nitrogen atom of the hydrazine residue N(2) and the rhodanide N(21): N(2)H–N(21) = 2.806(5) Å, ∠(N(2)–H(2)–N(21)) = 167.9(2)°. These hydrogen bridges, formed between adjacent molecules of the complex, give rise to a centrosymmetric pseudo-dimeric structure, which stabilizes an energetically unfavorable mode of coordination of the apical NCS group. Analogous coordination modes of the NCS group, as well as the formation of a pseudo-dimeric structure was also found in the structure of the already mentioned [CuL(NCS)(SCN)] complex [46].

Apart from the above mentioned hydrogen bond, the complex structure also involves a bond between the coordinated sulfur atom of the apical NCS group and the nitrogen atom of the isothioamide group of an adjacent molecule (N(1)H–S(2) = 3.368(3) Å, ∠(N(1)–H(1)···S(2)) = 147.6(2)°), allowing more extensive binding of dimeric units into a 3-D network (see Fig. S4 in the supplementary data). All other intermolecular contacts may be ascribed to van der Waals type bonds, and they exceed 3.50 Å.

4. Conclusion

It has been shown that the coordination mode of the sulfato ligand, and hence the composition and structure of copper(II) complexes with the tridentate NNN 2-acetylpyridine *S*-methylisothiosemicarbazone ligand (HL), is essentially influenced by the conditions of the synthesis. Namely, the reaction of an aqueous solution of $CuSO_4{\cdot}5H_2O$ and an EtOH solution of $H_2L^+I^-$ yielded the mononuclear square-pyramidal complex $[Cu(HL)SO_4(H_2O)]{\cdot}H_2O$, with a monodentate SO_4 group in the apical position. However, the reaction of MeOH solutions of the same reactants resulted in a dinuclear centrosymmetric, also square pyramidal complex $[Cu_2(HL)_2(\mu\text{-}SO_4)_2]{\cdot}2H_2O$, with the *exo*-bidentate coordination of both SO_4 groups, whose oxygen atoms occupy the apical position of both coordination polyhedra, as well as an equatorial position. Beside these two complexes, we also present the complex [Cu(HL)(NCS)(SCN)] which is formed in the reaction of MeOH solutions of $Cu(ClO_4)_2$, $H_2L^+I^-$ and NH_4SCN in the presence of triethyl orthoformate. This, also square pyramidal complex contains differently coordinated NCS groups. For Cu(II), as a moderately hard acid, the usual way of coordination through the sulfur atom of the apical SCN as a soft base, is a consequence of the formation of an intermolecular hydrogen bond.

Acknowledgments

This work was supported by the Ministry of Science and Technological Development of the Republic of Serbia (Grant No.

142028) and the Provincial Secretariat for Science and Technological Development of Vojvodina.

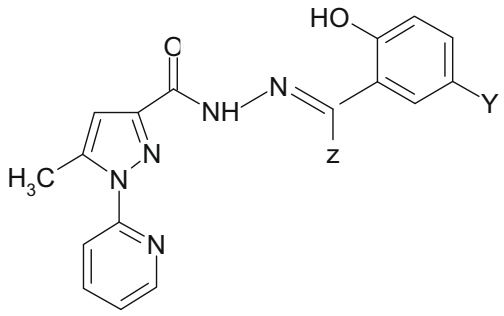
Appendix A. Supplementary data

CCDC 735080, 735081 and 735082 contain the supplementary crystallographic data for **1**, **2** and **3**. These data can be obtained free of charge via http://www.ccdc.cam.ac.uk/conts/retrieving.html, or from the Cambridge Crystallographic Data Centre, 12 Union Road, Cambridge CB2 1EZ, UK; fax: (+44) 1223-336-033; or e-mail: deposit@ccdc.cam.ac.uk.

Supplementary data associated with this article can be found, in the online version, at doi:10.1016/j.poly.2009.07.045.

References

[1] D.X. West, S.B. Padhye, B.P. Sonawane, Structural and Physical Correlations in the Biological Properties of Transition Metal Heterocyclic Thiosemicarbazone and *S*-alkyldithiocarbazate Complexes, Structure and Bonding, vol. 76, Springer-Verlag, Berlin – Heidelberg, 1991.
[2] D.X. West, Transition Met. Chem. 19 (1994) 426.
[3] R.H. Borges, E. Paniago, H. Beraldo, J. Inorg. Biochem. 65 (1997) 267.
[4] M.C. Miller, K.F. Bastow, C.N. Stineman, J.R. Vance, S.C. Song, D.X. West, I.H. Hall, Arch. Pharm. Med. Chem. 331 (1998) 121.
[5] E. Bermejo, R. Carballo, A. Castiniras, R. Domínguez, A.E. Liberta, C. Maichle-Mössmer, M.M. Salberg, D.X. West, Eur. J. Inorg. Chem. (1999) 965.
[6] N.C. Kasuga, K. Sekino, M. Ishikawa, A. Honda, M. Yokoyama, S. Nakano, N. Shimada, C. Koumo, K. Nomiya, J. Inorg. Biochem. 96 (2003) 298.
[7] A.R. Jalilian, P. Rowshanfarzad, M. Sabet, A. Shafiee, Appl. Radiat. Isotopes 64 (2006) 337.
[8] D. Kovala-Demertzi, A. Alexandratos, A. Papageorgiou, P.N. Yadav, P. Dalezis, M.A. Demertzis, Polyhedron 27 (2008) 2731. and references therein.
[9] D.X. West, C.S. Carlson, A.E. Liberta, Transition Met. Chem. 16 (1991) 53.
[10] D.X. West, A.C. Whyte, F.D. Scharif, N. Gebremedhin, A.E. Liberta, Transition Met.Chem. 18 (1993) 238.
[11] D. Kovala-Demertzi, A. Domopoulou, M.A. Demertzis, J. Valdés-Martínez, S. Hernández-Ortega, G. Espinosa-Pérez, D.X. West, M.M. Salberg, G.A. Bain, P.D. Bloom, Polyhedron 15 (1996) 2587.
[12] D.X. West, I.S. Billeh, J.P. Jasinski, J.M. Jasinski, R.J. Butcher, Transition Met. Chem. 23 (1998) 209.
[13] L. Bresolin, R.A. Burlow, M. Hörner, E. Bermejo, A. Castiniras, Polyhedron 16 (1997) 3947.
[14] D.X. West, J.P. Jasinski, J.M. Jasinski, R.J. Butcher, J. Chem. Crystall. 29 (1999) 1089. and references therein.
[15] E. Bermejo, A. Castiniras, L.J. Ackerman, D. Owens, D.X. West, Z. Anorg. Allg. Chem. 627 (2001) 1966.
[16] U. Abram, E. Schulz Lang, E. Bonfada, Z. Anorg. Allg. Chem. 628 (2002) 1873.
[17] D. Kovala-Demertzi, M.A. Demertzis, E. Filiou, A.A. Pantazaki, P.N. Yadav, J.R. Miller, Y. Zheng, D.A. Kyriakidis, Biometals 16 (2003) 411.
[18] A. Sreekanth, S. Sivakumar, M.R. Prathapachandra Kurup, J. Mol. Struct. 655 (2003) 47.
[19] A. Sreekanth, H.K. Fun, Mol. Struct. 737 (2005) 61.
[20] E.N. Nfor, X.Z. You, L. Wei, G. Iniama, Acta Cryst. E 62 (2006) 379.
[21] A.E. Graminha, A.A. Batista, J. Ellena, E.E. Castellano, L.R. Teixeira, I.C. Mendes, H. Beraldo, J. Mol. Struct. 875 (2008) 219.
[22] P.I.S. Maia, F.R. Pavan, C.Q.F. Leite, S.S. Lemos, G.F. Sousa, A.A. Batista, O.R. Nascimento, J. Ellena, E.E. Castellano, E. Niquet, V.M. Deflon, Polyhedron 28 (2009) 398.
[23] G.F. Sousa, R.H.P. Francisco, M.T.P. Gambardella, R.H.A. Santos, A. Abras, J. Braz. Chem. Soc. 12 (2001) 722.
[24] K. Nomiya, K. Sekino, M. Ishikawa, A. Honda, M. Yokoyama, N. Chikaraishi Kasuga, H. Yokoyama, S. Nakano, K. Onodera, J. Inorg. Biochem. 98 (2004) 601.
[25] N. Chikaraishi Kasuga, K. Onodera, S. Nakano, K. Hayashi, K. Nomiya, J. Inorg. Biochem. 100 (2006) 1176.
[26] C.R. Kowol, R. Berger, R. Eichinger, A. Roller, M.A. Jakupec, P.P. Schmidt, V.B. Arion, B.K. Keppler, J. Med. Chem. 50 (2007) 1254.
[27] J.G. da Silva, L.S. Azzolini, S.M.S.V. Wardell, J.L. Wardell, H. Beraldo, Polyhedron 28 (2009) 2301.
[28] T.I. Malinovskii, Yu.A. Simonov, N.V. Gerbeleu, M.A. Yampolskaya, M.D. Revenko, S.G. Shova, in: M.A. Porai-Koshits (Ed.), Problemy Kristalokhimii, Nauka, Moskva, 1985, p. 39.
[29] V.B. Arion, M.D. Revenko, J.D. Gradinaru, Inorg. Chem. 21 (2001) 1.
[30] V.M. Leovac, V.I. Češljević, Coordination Chemistry of Isothiosemicarbazide and Their Derivatives, Department of Chemistry, Faculty of Sciences, Novi Sad, 2002 (In Serbian).
[31] M.A. Malik, D.J. Phillips, Aust. J. Chem. 27 (1974) 1133.
[32] V.M. Leovac, V. Divjaković, V.I. Češljević, M. Rakočević, J. Serb. Chem. Soc. 71 (2006) 593.
[33] S.B. Novaković, G.A. Bogdanović, V.M. Leovac, Polyhedron 25 (2006) 1096.
[34] Z.D. Tomić, A. Kapor, A. Žmirić, V.M. Leovac, D. Zobel, S.D. Zarić, Inorg. Chim. Acta 360 (2007) 2197.
[35] I. Kızılcıklı, B. Ülküseven, Y. Dasdemir, B. Akkurt, Synth. React. Inorg. Metal – Org. Chem. 34 (2004) 653.
[36] I. Kızılcıklı, Y.D. Kurt, B. Akkurt, A.Y. Genel, S. Birteksöz, G. Ötük, B. Ülküseven, Folia Microbiol. 52 (2007) 15. and references therein.
[37] V.I. Češljević, V.M. Leovac, P.N. Radivojša, B. Gordić, G. Argay, J. Serb. Chem. Soc. 63 (1998) 967.
[38] J.A. Ibers, W.C. Hamilton, International Tables for X-ray Crystallography, vol. 4, Kinoch Press, Birmingham, UK, 1974.
[39] M. Sheldrick, Acta Cryst. 46A (1990) 467.
[40] C.F. Macroe, I.J. Bruno, J.A. Chisholm, P.R. Edgington, P. McCabe, E. Pidcock, L. Rodiguey-Monge, R. Taylor, J. Van de Streek, P.A. Wood, J. Appl. Cryst. 41 (2008) 466.
[41] M. Sheldrick, SHELXL-97, University of Göttingen, Germany, 1997.
[42] W.J. Geary, Coord. Chem. Rev. 7 (1971) 81.
[43] F.A. Cotton, G. Wilkinson, C.A. Murillo, M. Bochmann, Advanced Inorganic Chemistry, Wiley-Interscience, New York, 1999.
[44] V.M. Leovac, Lj.S. Jovanović, V. Divjaković, A. Pevec, I. Leban, T. Armbruster, Polyhedron 26 (2007) 49.
[45] B.J. Hathaway, in: G. Wilkinson, R.D. Gillard, J. McCleverty (Eds.), Copper in Comprehensive Coordination Chemistry, vol. 5, Pergamon Press, Oxford, 1887, p. 533 (Chapter 53).
[46] M.G.B. Drew, D. Das, S. De, D. Datta, Inorg. Chim. Acta 362 (2009) 1501.
[47] C. Papatriantafyllopoulou, E. Manessi-Zoupa, A. Escuer, S.P. Perlepes, Inorg. Chim. Acta 362 (2009) 634.
[48] D.C.C. Gomes, H.O. Stumpf, F. Lloret, M. Julve, V. Gonzalez, H. Adams, J.A. Thomas, Inorg. Chim. Acta 358 (2005) 1113.
[49] Yu.M. Chumakov, E. Janneau, N.P. Bejenari, V.I. Tsapkov, A.P. Gulea, Russ. J. Coord. Chem. 34 (2008) 44.
[50] Y.-K. He, Z.-B. Han, Acta Cryst. E 62 (2006) 2676.
[51] C. Basu, S. Biswas, A.P. Chattopadhyay, H. Stoeckli-Evans, S. Mukherjee, Eur. J. Inorg. Chem. (2008) 4927.
[52] X.-H. Zou, J.-W. Cai, X.-L. Feng, X.-P. Hu, Transition Met. Chem. 26 (2001) 704.
[53] S. Youngme, N. Chaichit, C. Pakawatchai, S. Booncoon, Polyhedron 21 (2002) 1279.
[54] M. Kabešová, R. Boča, M. Melnik, D. Valigura, M. Dunaj-Jurčo, Coord. Chem. Rev. 140 (1995) 115.
[55] Z.-Q. Liu, M. Jiang, Y.-T. Li, Z.-Y. Wu, J.-X. Yang, Inorg. Chim. Acta 362 (2009) 1253.
[56] G.R. Clark, G.J. Palenik, D.W. Meek, J. Am. Chem. Soc. 92 (1970) 1077.
[57] J. Carranza, J. Sletten, F. Lloret, M. Julve, Polyhedron 28 (2009) 2249.



Z= H, Y = H, H_2B^1

Z = CH_3, Y = H, H_2B^2

Z = H, Y= Br, H_2B^3

Z = H, Y= NO_2, H_2B^4

Fig. 1. Diagram showing structural formula of the ligands H_2B^1, H_2B^2, H_2B^3 and H_2B^4.

shown that one of these ligands has the potential to demonstrate a metal selective binding mode owing to the presence of multiple binding sites of varying types. Thus our aim is to observe the changes in luminescent behavior of the ligands with different guest (metal ions) inputs. We have also found that fluorescent emissions of the ligands are dependant on the substituents present on the extended conjugated backbone of the ligands. Dioxomolybdenum complexes **1–4** of all the ligands H_2B^1, H_2B^2, H_2B^3 and H_2B^4 have been prepared and characterized. The complexes exhibit quenched emission compared to the respective ligands. One of these complexes, $[MoO_2(B^1)H_2O]$ (**1**), when treated with equimolar amounts of Cu^{2+}, Co^{2+} or Ni^{2+} ions in solution shows further quenching. However with Zn^{2+} ion input to complex **1**, enhancement of fluorescence up to the level of the free ligand was observed. The Cu^{2+} complex (**5**) was isolated and characterized. Again on reduction via oxo abstraction by PPh_3, complex **3** is converted to complex **6**, a monooxo Mo(IV) complex. Fluorescence emission of **6** was found to be less intense than **3**.

2. Experimental

$MoO_2(acac)_2$ was prepared as described in the literature [23]. Reagent grade solvents were used as received. 1-(2-Pyridyl)-5-methyl pyrazole-3-carbohydrazide was prepared from ethyl 1-(2-pyridyl)-5-methyl pyrazole-3-carboxylate [24] by following the literature method. Salicylaldehyde, 5-bromo salicylaldehyde, 5-nitro salicylaldehyde and o-hydroxy acetophenone were purchased from Aldrich Chemical Company, USA and were used as received. Tetraethyl ammonium perchlorate (TEAP) used for electrochemical work was prepared as reported in the literature [25].

2.1. Preparation of the ligands

All the four ligands H_2B^1, H_2B^2, H_2B^3 and H_2B^4 were synthesized in a similar way by refluxing an ethanolic solution (20 ml) of 1-(2-pyridyl)-5-methyl pyrazole-3-carbohydrazide (10 mmol, 2.17 g) with salicylaldehyde (10 mmol, 1.22 g for H_2B^1), *o*-hydroxy acetophenone (10 mmol, 1.36 g for H_2B^2), 5-bromo salicylaldehyde (10 mmol, 2.01 g for H_2B^3) and 5-nitrosalicylaldehyde (10 mmol, 1.67 g for H_2B^4), respectively, also taken in ethanol (20 ml). The reflux was continued for ca. 2 h at water bath temperature, during which a solid compound separated. It was filtered, washed with ethanol and dried over fused $CaCl_2$ .The crude product was recrystallized from an ethanol–water mixture (4:1 V/V). Single crystals of H_2B^2 and H_2B^3 were isolated and their structures were determined.

H_2B^1: M.P.: 193 °C. Yield: 2.57 g (80%). IR (KBr pellet) cm^{-1}: ν(N–H) 3223, ν(O–H) 3066, ν(C=O) 1663, ν(C=C) 1611, ν(C=N) 1546.9. ^1H NMR (D_6-DMSO) δ, ppm: (C_3–H, C_6–H of C_6H_4–) 6.9d(2), (C_4–H, C_5–H of C_6H_4–) 7.45t(2), (–CH=N–) 8.69s(1), (aromatic-OH) 12.08(1), (C_2–H of pyridine) (8.5)d(1), (C_5–H of pyridine) 8.1d(1), (C_3–H and C_4–H of pyridine) 7.25t(2) (pyrazole C–H) 6.79 m(1), (Pyz–CH_3) 2.60s(1).

H_2B^2: M.P.: 138 °C. Yield: 2.68 g. (80%). IR (KBr pellet) cm^{-1}: ν(N–H) 3264, ν(O–H) 3056 ν(C=O) 1698, ν(C=C) 1590, ν(C=N) 1526. ^1H NMR (D_6-DMSO) δ, ppm: (C_3–H, C_6–H of C_6H_4–) 6.85d(2), (C_4–H, C_5–H of C_6H_4–) 7.45t(2), (aromatic-OH) 12.08(1), (C_2–H of pyridine) (8.5)d(1), (C_5–H of pyridine) 8.15d(1), (C_3–H and C_4–H of pyridine) 7.25t(2), (pyrazole C–H) 6.70 m(1), (Pyz–CH_3) 2.60s(1), (–N=C–CH_3) 2.65s(3).

H_2B^3: M.P.: 218 °C. Yield: 3.20 g (80%). IR (KBr pellet) cm^{-1}: ν(N–H) 3308, ν(O–H) 3085, ν(C=O) 1655, ν(C=C) 1591, ν(C=N) 1535. ^1H NMR (D_6-DMSO) δ, ppm: (C_3–H, C_4–H of C_6H_4–) 6.9d(2), (C_6–H of C_6H_4–) 7.9s(1), (–CH=N–) 8.81s(1), (aromatic-OH) 12.20(1), (C_6–H of pyridine) (8.5)d(1), (C_3–H of pyridine) 7.6d(1), (C_4–H of pyridine) 7.4t(1), (C_5–H of pyridine) 8.1t(1), (pyrazole C–H) 6.70 m(1), (Pyz–CH_3) 2.60s(1).

H_2B^4: M.P.: 196 °C. Yield: 2.20 g (60%). IR (KBr pellet) cm^{-1}: ν(N–H) 3304, ν(O–H) 3134 ν(C=O) 1662, ν(C=C) 1620, ν(C=N) 1545. ^1H NMR (D_6-DMSO) δ, ppm: (C_3–H, C_4–H of C_6H_4–) 6.9d(2), (C_6–H of C_6H_4–) 7.9s(1), (–CH=N–) 8.87s(1), (aromatic-OH) 12.08(1), (C_6–H of pyridine) (8.8)d(1), (C_3–H of pyridine) 8.5d(1), (C_4–H of pyridine) 8.0t(1), (C–H of pyridine) 8.3t(1), (pyrazole C–H) 6.70 m(1), (Pyz–CH_3) 2.60s(1).

2.2. Preparation of complexes *1–4*

The complexes $[MoO_2(B^1)H_2O]$ (**1**), $[MoO_2(B^2)EtOH]$ (**2**), $[MoO_2(B^3)EtOH]$ (**3**) and $[MoO_2(B^4)EtOH]$ (**4**) were prepared in a similar way by refluxing an ethanolic solution (10 ml) of $MoO_2(acac)_2$ (0.5 mmol, 0.163 g) with ethanolic solutions of H_2B^1 (0.5 mmol, 0.161 g), H_2B^2 (0.5 mmol, 0.168 g), H_2B^3 (0.5 mmol, 0.200 g) and H_2B^4 (0.5 mmol, 0.183 g), respectively. On mixing the two components, immediately an orange yellow colour was observed. The mixture was then refluxed for 1 h. The respective complexes separated as orange microcrystalline compounds during the reflux or afterwards on slow evaporation of the reaction mixture. These were filtered, washed with ethanol and dried over fused $CaCl_2$.

$[MoO_2(B^1)H_2O]$ (**1**): Yield 0.140 g (60%). Elemental analysis: *Anal.* Calc. for $C_{17}N_5O_5H_{17}Mo$: C, 43.77; H, 3.66; N, 15.02. Found: C, 43.61; H, 3.59; N, 15.23%. IR ($\nu_{(Mo=O)}/cm^{-1}$): 902, 941, UV–Vis (λ_{max}/nm) ($\varepsilon/dm^3\ mol^{-1}\ cm^{-1}$): 392, 327. NMR ($^1H/\delta$ TMS): (–N=CH–) 8.85s, (H_2O) 3.2d. CV (E_{pc}/V): −1.12 [Mo(VI)/Mo(V)], −1.64 [Mo(V)/Mo(IV)].

X-ray quality crystals of (**1**) were obtained from the reaction mixture on slow evaporation.

$[MoO_2(B^2)EtOH]$ (**2**): Yield 0.127 g (50%) Elemental analysis: *Anal.* Calc. for $C_{20}N_5O_5H_{25}Mo$: C, 47.21; H, 4.52; N, 13.77. Found: C, 47.13,; H, 4.50; N, 13.85%. IR ($\nu_{(Mo=O)}/cm^{-1}$): 891, 935. UV–Vis (λ_{max}/nm) ($\varepsilon/dm^3\ mol^{-1}\ cm^{-1}$): 385, 313. NMR ($^1H/\delta$ TMS): (–N=C–CH_3) 2.75s(3), (CH_3CH_2OH) 1.01t, (CH_3CH_2OH) 2.46 m, (CH_3CH_2OH) 3.52s. CV (E_{pc}/V): −1.21 [Mo(VI)/Mo(V)], −1.52 [Mo(V)/Mo(IV)].

$[MoO_2(B^3)EtOH]$ (**3**): Yield 0.143 g (50%) Elemental analysis: *Anal.* Calc. for $C_{19}N_5O_5H_{20}BrMo$: C, 39.72; H, 3.48; N, 12.19. Found: C, 38.80; H, 3.56; N, 11.87%. IR ($\nu_{(Mo=O)}/cm^{-1}$): 917, 936. UV–Vis (λ_{max}/nm) ($\varepsilon/dm^3\ mol^{-1}\ cm^{-1}$): 411, 321, 303. NMR ($^1H/\delta$ TMS):

(–N=CH–) 8.89s, (CH_3CH_2OH) 1.01t, (CH_3CH_2OH) 2.46m, (CH_3CH_2OH) 3.50s. CV (E_{pc}/V): −1.02 [Mo(VI)/Mo(V)], −1.54 [Mo(V)/Mo(IV)].

[$MoO_2(B^4)EtOH$] (**4**): Yield 0.139 g (50%). Elemental analysis: *Anal.* Calc. for $C_{19}N_6O_7H_{20}Mo$: C, 42.30; H, 3.71; N, 15.58. Found: C, 42.25; H, 3.67; N, 15.61%. IR ($\nu_{(Mo=O)}$/cm^{-1}): 917, 945. UV–Vis (λ_{max}/nm) (ε/$dm^3\ mol^{-1}\ cm^{-1}$): 412, 285. NMR ($^1H/\delta$ TMS): (–N=CH) 9.10s, (CH_3CH_2OH) 1.01t, (CH_3CH_2OH) 2.46m, (CH_3CH_2OH) 3.50s. CV (E_{pc}/V): −0.85[Mo(VI)/Mo(V)].

2.3. Preparation of complex **5**

When an ethanolic solution of $Cu(NO_3)_2{\cdot}6H_2O$ (0.295 g, 1 mmol) was added to an ethanolic solution of complex **1** (0.466 g, 1 mmol), immediately a green colloidal precipitate started to appear. To that, acetonitrile was added in a 1:1 proportion (v/v) and the resulting mixture was allowed to reflux for an hour. A clear green solution resulted. It was filtered and kept for slow evaporation. [$Cu(HB^1)NO_3$] (**5**), which may also be treated as the symmetry related binuclear complex [$Cu_2(HB^1)_2(NO_3)_2$], appeared as dark green crystals within a week.

[$Cu(HB^1)NO_3$] (**5**): Yield 0.258 g (50%). Elemental analysis: *Anal.* Calc. for $C_{17}N_6O_5H_{13}Cu$: C, 45.79; H, 3.14; N, 15.71. Found: C, 45.75; H, 3.11; N, 15.64%. UV–Vis (λ_{max}/nm) (ε/$dm^3\ mol^{-1}\ cm^{-1}$): 393, 669. CV (E/V), E_{pa}: 0.480 [Cu(II)/Cu(III)], 0.367 [Cu(III)/Cu(II)], E_{pc}: −0.467[Cu(II)/Cu(I)].

2.4. Preparation of complex **6**

[$MoO(L^3)CH_3CN$] (**6**): Complex **3** (0.25 mmol, 0.143 g) was taken in a suspension of 40 ml degassed acetonitrile, PPh_3 (2.25 mmol, 5.50 g) was added and the mixture was refluxed at water bath temperature under a dinitrogen atmosphere for 1 h. The green compound obtained as a residue was filtered on a sintered gooch crucible and washed with acetonitrile. It was dried in a vacuum desiccator over concentrated H_2SO_4. Yield: 0.055 g (52%). Elemental analysis: *Anal.* Calc. for $C_{19}N_6O_3H_{18}BrMo$: C, 41.30; H, 3.26; N, 15.21. Found: C, 40.8; H, 3.12; N, 15.01%. IR (ν_{max}/cm^{-1}): 926 (Mo=O) UV–Vis (λ_{max}(DMF)/nm) (ε/$dm^3\ mol^{-1}\ cm^{-1}$): 438 (5467), 686 (1765). CV (E/V) E_{pa}: 1.48 [Mo(VI)/Mo(IV)], E_{pc}: −1.21, E_{pa}: −0.71[Mo(IV)/Mo(III)], ΔE_p:0.51, $E_{1/2}$: 0.925.

2.5. Physical measurements

Elemental analyses were performed at IACS, Kolkata on a Perkin–Elmer 2400 CHN analyzer. The ^1H NMR spectra of the complexes and the ligands were recorded on a Bruker AM300L (300 MHz) superconducting FT-NMR spectrometer. IR spectra were recorded in KBr pellets on a Perkin–Elmer FTIR spectrophotometer. UV–Vis spectra and DRS were measured on a Hitachi U-3501 spectrophotometer. Cyclic Voltammetry was carried out using a Sycopel model AEW21820F/L instrument. The measurements were carried out at 293 K in DMF solutions containing 0.2 M TEAP as a supporting electrolyte and 10^{-3} to 10^{-4} M solutions of the complexes deoxygenated by bubbling with nitrogen. The working, counter and reference electrodes used were a Pt wire, platinum coil and an SCE, respectively. The fluorescence spectra were recorded on a Perkin–Elmer LS 50B fluorimeter.

2.6. Crystallographic measurements

The crystals were measured on a Bruker SMART 1K CCD diffractometer using Mo Ka radiation (λ = 0.71073 Å). Positions of the hydrogen atoms were calculated from the geometry of the molecular skeleton and their thermal displacement parameters were refined isotropically on a group-wise basis. Essential crystal parameters for H_2B^2, H_2B^3, complex **1** and complex **5** are provided in Table 1. Selected bond lengths and angles are reported in Table 2. Unit cell and reflection data were obtained by standard methods [26,27]. The structures were solved, refined and prepared for publication using the SHEXTL package [28] (structure solution refinements and molecular graphics). Two of the structures, i.e. ligand H_2B^2 and complex **5**, contained a few disorders. In H_2B^2 the atoms of the pyrimidine ring C14, C15, C16, C17, C18 and N5 are disordered over two positions denoted by A and B suffixes. The occupancies are divided in each case in a ratio A:B of 52.9:47.0. In complex **5** the disorder is limited

Table 1
Crystallographic data table for the ligands H_2B^2 and H_2B^3 and the complexes **1** and **5**.

Crystal parameters	H_2B^2	H_2B^3	**1**	**5**
Empirical formula	$C_{18}H_{17}N_5O_2$	$C_{17}H_{14}BrN_5O_2$	$C_{17}H_{15}MoN_5O_5$	$C_{34}H_{28}Cu_2N_{12}O_{10}$
Formula weight	335.37	400.24	465.28	891.76
T (K)	296(2)	296(2)	200(2)	200(2)
Crystal system	triclinic	monoclinic	triclinic	monoclinic
Space group	$P\bar{1}$	$P121/n1$	$P\bar{1}$	$P121/n1$
Unit cell dimensions				
a (Å)	7.7588(19)	8.1105(2)	9.0853(7)	9.4783(2)
b (Å)	8.417(2)	12.0342(5)	9.5499(6)	10.8104(2)
c (Å)	14.159(4)	17.0769(8)	11.0858(10)	17.5829(4)
α (°)	81.09(2)	90	99.143(6)	90
β (°)	74.42(2)	98.435(4)	109.769(8)	96.5966(19)
γ (°)	70.37(2)	90	94.182(6)	90.00
V (Å^3)	836.8(4)	1648.73(11)	885.31(12)	1789.69(6)
Z	2	4	2	2
F(0 0 0)	352	808	468	908
Crystal size (mm^3)	0.51 × 0.46 × 0.12	0.53 × 0.44 × 0.16	0.3676 × 0.2592 × 0.0853	0.51 × 0.47 × 0.39
θ Range for data collection (°)	4.74–32.45	4.83–32.45	4.32–73.84	4.66–32.52
Reflections collected	12 557	13 948	10 226	20 084
Completeness to θ	99.1% (=25.00°)	98.2% (=25.00°)	99.4% (=67.50°)	99.3% (=25.00°)
Refinement method	full-matrix least-squares on F^2	full-matrix least-squares on F^2	full-matrix least-squares on F^2	full-matrix least-squares on F^2
Data/restraints/parameters	5469/0/224	4998/0/227	3515/3/260	5997/6/267
Goodness-of-fit (GOF) on F^2	0.842	1.116	1.106	1.075
Final R indices [$I > 2\sigma(I)$]	R_1 = 0.0578, wR_2 = 0.1506	R_1 = 0.0557, wR_2 = 0.0798	R_1 = 0.0446, wR_2 = 0.1206	R_1 = 0.0313, wR_2 = 0.0860
R indices (all data)	R_1 = 0.1591, wR_2 = 0.1776	R_1 = 0.1327, wR_2 = 0.1075	R_1 = 0.0472, wR_2 = 0.1222	R_1 = 0.0535, wR_2 = 0.0955
Largest difference in peak and hole (e Å^{-3})	0.449 and −0.504	0.455 and −0.514	1.699 and −0.752	−0.317 and 0.579

Table 2
Selected bond distances and bond angles of the ligands H_2B^2 and H_2B^3 and the complexes **1** and **5**.

Bonds	Bond lengths (Å)	Bond angles	Values (°)
Ligand H_2B^2			
O(1)–C(2)	1.346(2)	O(1)–C(2)–C(1)	124.25(17)
C(1)–C(2)	1.409(3)	N(1)–C(7)–C(8)	122.46(17)
C(1)–C(7)	1.468(2)	C(9)–N(2)–N(1)	120.19(15)
N(1)–C(7)	1.290(2)	O(2)–C(9)–C(10)	123.63(17)
N(1)–N(2)	1.372(2)	N(3)–C(10)–C(9)	119.80(16)
N(2)–C(9)	1.359(2)	N(3)–N(4)–C(14A)	116.4(4)
O(2)–C(9)	1.213(2)		
C(9)–C(10)	1.484(3)		
N(3)–C(10)	1.331(2)		
Ligand H_2B^3			
Br–C(5)	1.908(3)	O(1)–C(2)–C(1)	117.7(3)
C(5)–C(6)	1.377(4)	C(6)–C(1)–C(7)	120.0(3)
C(1)–C(6)	1.388(4)	N(1)–C(7)–C(1)	118.9(3)
C(1)–C(7)	1.470(4)	C(7)–N(1)–N(2)	117.4(3)
N(1)–C(7)	1.267(4)	C(8)–N(2)–N(1)	117.8(2)
N(1)–N(2)	1.371(3)	O(2)–C(8)–C(9)	120.7(3)
N(2)–C(8)	1.348(4)	N(3)–N(4)–C(13)	117.6(2)
O(2)–C(8)	1.207(3)		
C(8)–C(9)	1.484(4)		
N(3)–C(9)	1.322(4)		
*Complex **1***			
Mo–O(3)	1.698(3)	O(5)–Mo–N(1)	156.29(12)
Mo–O(5)	1.722(2)	O(1)–Mo–O(2)	150.88(11)
Mo–O(1)	1.907(2)	O(3)–Mo–O(4)	170.37(12)
Mo–O(2)	2.009(2)	O(5)–Mo–O(1)	101.52(11)
Mo–N(1)	2.240(3)	O(1)–Mo–N(1)	80.77(10)
Mo–O(4)	2.334(3)	O(2)–Mo–N(1)	72.04(10)
C(8)–C(9)	1.471(5)	O(5)–Mo–O(2)	99.36(11)
N(1)–C(7)	1.298(5)		
*Complex **5***			
Cu–O(1)	1.8605(12)	N(1)–Cu–N(3)	168.93(5)
Cu–O(1N)	2.4576(12)	O(1)–Cu–N(2)	169.46(5)
Cu–N(1)	1.9674(14)	O(1N)–Cu–N(1)	98.90(5)
Cu–N(2)	1.8995(12)	O1(N)–Cu–N(2)	90.68(5)
Cu–N(3)	2.0332(13)	O(1N)–Cu–N(3)	81.42(5)
Cu–O(1_a)	2.8408(12)	O(1)–Cu–O(1N)	97.04(5)
N4–C(8)	1.357(2)		
O2–C(8)	1.228(2)		
N1–N(4)	1.4046(18)		

to only one atom of the coordinated nitrate ion, i.e. O2N. Here also the disordered positions are assigned using A and B suffixes (O2NA and O2NB). The occupancies are in a ratio O2NA:O2NB of 17.6(5):82.4(6). The three restrains imposed on the structure of complex **1** are all based on interatomic distances of the coordinated water molecule. They are O4–H41, O4–H42 fixed at 0.82 Å and H41–H42 fixed at 1.29 Å.

2.7. Quantum yield calculation

The fluorescence quantum yields of the ligands H_2B^1, H_2B^2, H_2B^3, their Mo(VI) complexes **1–4** and the solutions resulting by adding equimolar proportions of Cu(II) and Zn(II) salts to solutions of **1** in DMF and methanol solvents are measured relative to recrystallized β-naphthol as the secondary standard, and are calculated on the basis of the following equation [29,30].

$$\Phi_f = \Phi_f^{\circ} \frac{n_{\circ}^2 A^{\circ} \int I_f(\lambda_f) d\lambda_f}{n^2 A \int I_f^{\circ}(\lambda_f) d\lambda_f}$$

where n_0 and n are the refractive indices of the solvents, A^0 and A are absorbances, ϕ°_f and φ_f are quantum yields, and the integrals denote the area of the fluorescence bands for the standard and sample, respectively. The fluorescence quantum yields of the different solutions are given in Table 3.

3. Results and discussion

3.1. Synthesis

The ligand H_2B^1 was prepared by a simple condensation reaction following the same procedure as described in our previous publication [22]. H_2B^2, H_2B^3 and H_2B^4 were also prepared by the same procedure using the same molar ratio. All the Mo(VI) complexes were obtained from a refluxing mixture of the respective ligand and the bis(acetylacetonato) dioxomolybdenum(VI) precursor, taken in a 1:1 molar proportion in purified ethanol. Complex **1** separated with a composition of $[MoO_2(B^1)H_2O]$, while the others separated as $[MoO_2(B^n)EtOH]$ (n = 2–4, complexes **2–4**). These complexes were found to be fairly soluble in most common organic solvents. Magnetic susceptibility and molar conductance data show that the complexes are diamagnetic and electrically non-conducting in nature. Following our observations regarding the change of emission behavior of complex **1** on adding Cu(II) salts, we tried to isolate the resulting species in a solution containing one molar equivalent each of $Cu(NO_3)_2{\cdot}6H_2O$ and complex **1**. The green colloidal precipitate which was obtained first on adding Cu(II) salt to an ethanolic solution of **1** was dissolved in an ethanol–acetonitrile mixture (50:50 v/v), and from that mother liquor, crystals of complex **5** were obtained. The green colloidal precipitate was found to be of same composition as **5**, using common analytical techniques such as UV–Vis spectroscopy, IR and CV studies.

Oxo transfer reactions from dioxomolybdenum(VI) complexes to substrates such as PPh_3 are well known. As complex **3** has the most prominent fluorescence emission among the dioxomolybdenum(VI) complexes, we have chosen it to study the change in emission behavior with oxo abstraction. Thus complex **3** was reacted with PPh_3 under refluxing conditions, and the resulting Mo(IV) complex was also isolated.

3.2. Spectral characterization and electrochemistry

All the dioxomolybdenum(VI) complexes are characterized by the presence of strong IR bands for the symmetric and asymmetric stretching of Mo=O bonds between 891 and 945 cm^{-1} [31]. For the Mo(IV) species, complex **6**, a single peak at 926 cm^{-1} signifies the presence of a single Mo=O bond [32]. The sixth coordination position of complex **1** is occupied by a water molecule. The peaks obtained in the NMR spectra of **1** at δ 3.2 [33] supplements the results obtained from the X-ray crystal analysis. The presence of EtOH as the sixth ligand in complexes **2–4** was indicated by the NMR spectra of these complexes, as shown in the experimental section. In all the complexes, the complexation by the azomethine nitrogen is shown by a more deshielded signal of the azomethine N–H/N–CH_3 compared to those of the ligands [34]. The UV–Vis spectra of complexes **1–4** show CT bands at 385–412 nm, corresponding to ligand to metal charge transfers [35]. The Cu(II) complex **5** also shows a similar CT band at 403 nm [36]. Each of the complexes **1–4** shows two other CT bands at 313–327 nm. The d–d band of complex **5** appears at 669 nm [37]. The DRS spectrum of complex **6** shows a broad CT band, accompanied by a shoulder, at 654 nm which is characteristic of Mo(IV) species [38].

The dioxomolybdenum(VI) complexes **1–4** show two irreversible reductive responses for the Mo(VI)/Mo(V) and Mo(V)/M0(IV) reductions, the latter one taking place at a more negative potential than the former. The electron donating ability of the ligands have a clear effect on the reduction potential values. The Mo(IV) complex **6**, resulting from an oxo-transfer reaction of complex **3**, shows an irreversible oxidation on an anodic scan at 1.48 V. The cathodic scan revealed a redox cycle assigned as a Mo(III)/Mo(IV) response. Complex **5** shows the usual one electron reduction for Cu(II)/Cu(I)

Table 3
Emission behavior of the ligands and their complexes.

Samples	Solvent	$\lambda_{max(abs)}$ (nm)	$\lambda_{max(Emi)}$ (nm)	λ_{Ex} (nm)	ϕ_f
H_2B^1	DMF	325, 390	467, 467	392, 323	2.4×10^{-3}
H_2B^1	MeOH	325, 390	466, 466	310, 380	
H_2B^2	DMF	326, 387	425, 425	352	4.13×10^{-3}
H_2B^3	DMF	332, 397	470, 470	398	3.68×10^{-2}
H_2B^4	DMF	397			
$MoO_2(B^1)H_2O/H_2B^1 + MoO_2(acac)_2$ (1:1)	DMF	327, 390	473, 473	392	7.83×10^{-4}
$MoO_2(B^1)H_2O/H_2B^1 + MoO_2(acac)_2$ (1:1)	MeOH	327, 390	460, 460	310, 380	
$MoO_2(B^2)EtOH/H_2B^2 + MoO_2(acac)_2$ (1:1)	DMF	314, 387	450, 450	368	7.80×10^{-4}
$MoO_2(B^3)EtOH/H_2B^3 + MoO_2(acac)_2$ (1:1)	DMF	321, 411	474, 474	402	3.70×10^{-4}
$MoO_2(B^4)EtOH/H_2B^4 + MoO_2(acac)_2$ (1:1)	DMF	412			
$MoO_2(B^1)H_2O + Cu(NO_3)_2{\cdot}6H_2O$ (1:1)	DMF	317, 390	450, 450 (low intensity)		7.72×10^{-5}
$MoO_2(B^1)H_2O + Co(NO_3)_2{\cdot}6H_2O$ (1:1)	DMF	400	445 (very low intensity)		
$MoO_2(B^1)H_2O + Ni(NO_3)_2{\cdot}6H_2O$ (1:1)	DMF	410	453 (very low intensity)		
$MoO_2(B^1)H_2O + Zn(NO_3)_2{\cdot}6H_2O$ (1:1)	DMF	400, 317	471, 482, 472	395, 393	2.39×10^{-3}
$Cu(HB^1)NO_3$	DMF	317, 390	450, 450	360, 284	7.69×10^{-5}
$MoO_2(B^1)H_2O + MoO_2(acac)_2$ (1:1)	DMF	327, 390	478, 478	388	4.67×10^{-4}

at −0.467 V. The anodic scan of **5** shows a redox cycle with an oxidation peak for Cu(II)/Cu(III) at 0.480 V and the corresponding reduction peak at 0.367 V.

3.3. Description of the crystal structures

The structure of the ligand H_2B^1 has been discussed in an earlier publication [22] on this ligand. Here we present the structures of H_2B^2 and H_2B^3 (Figs. 2 and 3). A notable feature of the structures is that in H_2B^2 the atoms responsible for chelation of the MoO_2^{2+} core, i.e. the phenoxide oxygen, the azomethine nitrogen and the enolate oxygen atoms, are arranged in the same direction as the extended conjugated backbone of the ligands while in H_2B^3 the presence of bulky bromine atoms results in a conformation where the phenoxide and enolate oxygen atoms are trans to each other. The two rings of the fluorophoric 1-(2-pyridyl) 5-methyl pyrazole are essentially planar in H_2B^3 (the same as H_2B^1), but in H_2B^2 the pyridine ring acquires a conformation disordered over two positions. In both of the disordered positions the pyridine ring is not in the same plane as the pyrazole ring (the dihedral angle between the mean planes of the pyrazole and pyridine rings are 12.13° and 17.76°, respectively). However in both ligands the pyrazole ring is fairly planar with the carbohydrazone portion.

The ligand H_2B^1, as expected, acts as a tridentate binegative donor for the MoO_2^{2+} core, donating through the phenolate oxygen (O1), the azomethine nitrogen (N1) and the enolate oxygen (O2). Despite the presence of a highly potential NN donor site at the 1-(2-pyridyl) 5-methyl pyrazole part of the ligand, the highly charged Mo center has chosen the oxygen rich ONO donor center at the other end. The environment of the Mo(VI) center can be described as a distorted octahedral one with a NO_5 chromophore. The ligand donors occupy the three equatorial positions with one oxo group, and the axial positions are shared by the other oxo group and a weakly bonded H_2O molecule. The Mo is found to be raised 0.320 Å above the plane containing the equatorial donors O1, N1, O2 and O5. The ligand maintains a fairly planar conformation as all the atoms, except the phenolate oxygen atom, are at less than 0.2 Å deviation from the ligand mean plane. The phenolate oxygen is raised by 0.38 Å from the mean plane. This ensures sufficient electron delocalization within the ligand and endows stability to the complex. The bond angles in the coordination sphere are unexceptional. Among the Mo-oxo bonds, the axial one is marginally longer. The Mo–enolate O bond is shorter than the Mo–phenolate bond. The Mo–O4 bond is the weakest and has the largest bond distance (2.334 Å). There are two intermolecular H-bonding interactions of considerable strength in the complex between the azomethine nitrogen (N2) and the oxygen (O4) of the H_2O ligand as well as between one oxo atom (O5) and the O4 of H_2O (Fig. 4). This H-bonding pattern mainly governs the packing in this complex. The coordination sphere of complex **5** (Fig. 5) is very similar to another published structure from one of our previous publications [22]. The only difference is in the fifth coordination position. Here it is occupied by a NO_3^- ion instead of ClO_4^- in the earlier structure. The binding mode of the ligand is completely different from that in complex **1** as the ligand adjusts to the change of metal ion to be accommodated. In complex **1**, as we have already

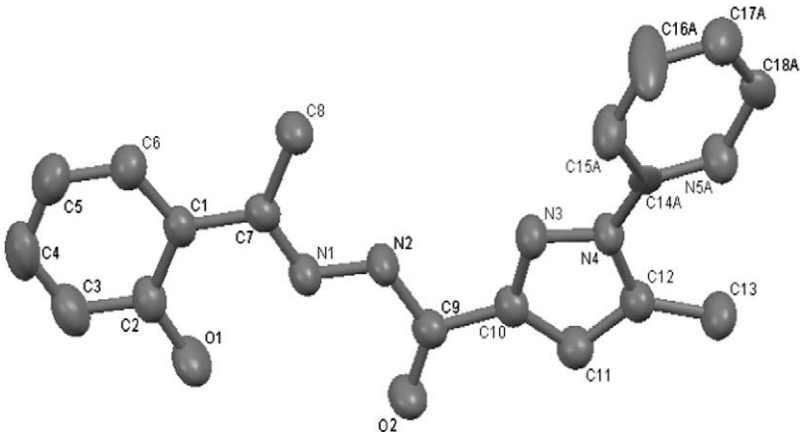


Fig. 2. Representative diagram of the crystal of H_2B^2 (the disorder of the pyridine ring is omitted for clarity).

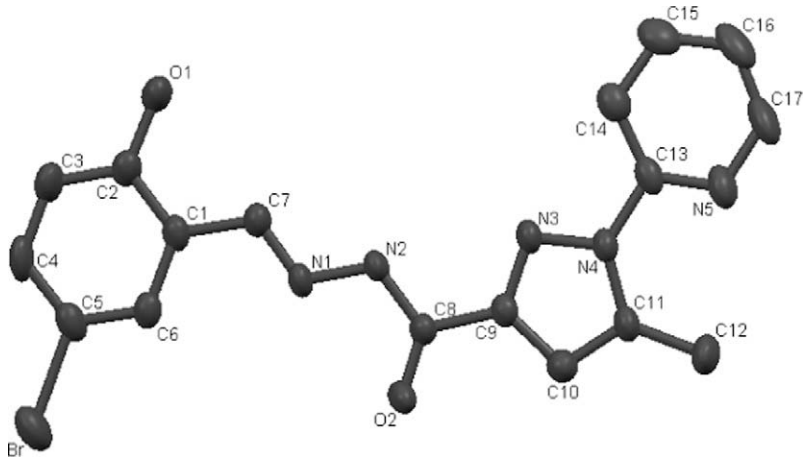


Fig. 3. Representative diagram of the crystal of H_2B^3.

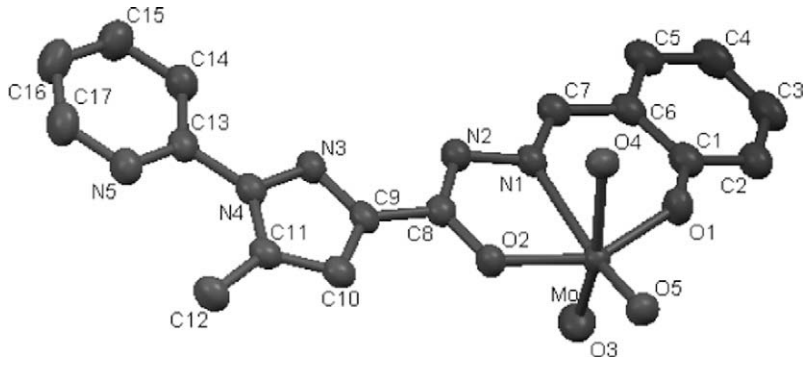


Fig. 4. Representative diagram of the crystal of complex **1**.

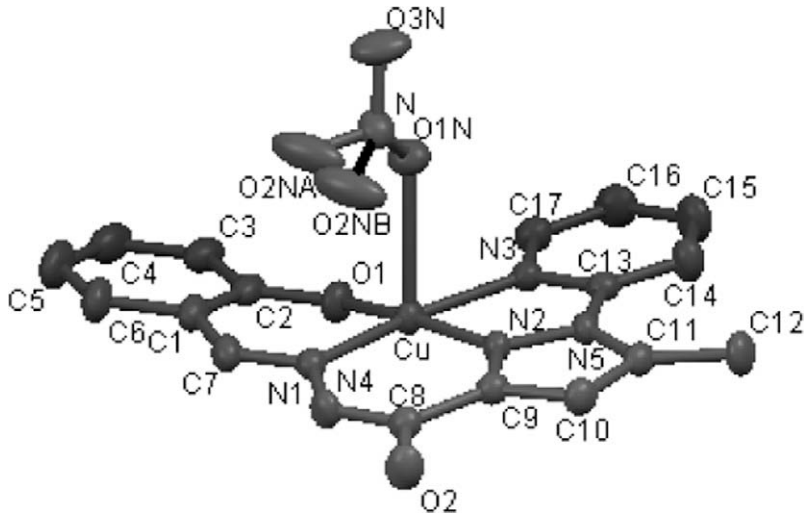


Fig. 5. Representative diagram of the crystal of complex **5** showing the coordination sphere around a single Cu atom.

discussed, the ligand acts as a tridentate binegative one. Here it acts as tetradentate mononegative donor. This change in binding mode probably contributes to the change in emission behavior. The isolation and characterization of **5** is justified as it helps to comprehend the chemistry leading to its formation and also helps to rationalize the change in emission behavior that takes place with its formation in solution.

3.4. Emission behavior

3-(2-Pyridyl) pyrazole and some of its derivatives are known to show considerably high fluorescence [39–41]. Photophysical studies on it and many of its complexes have been explored well. In our ligand system the presence of the 1-(2-pyridyl) 5-methyl pyrazole unit is responsible for the emission behavior. The salicyl

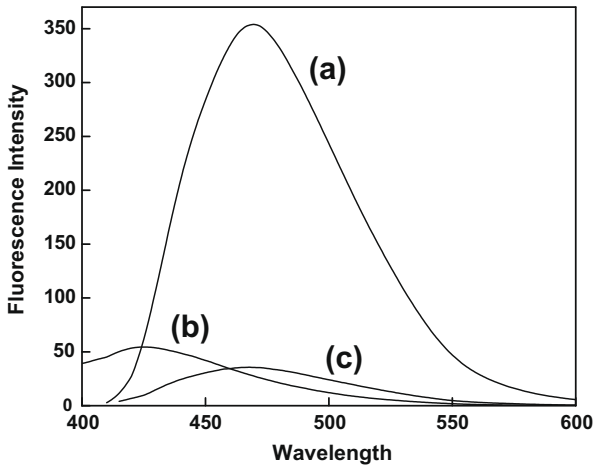


Fig. 6. Fluorescence emissions of the ligands H_2B^3 (a), H_2B^2 (b), H_2B^1 (c). All the spectra were taken in 2×10^{-5} molar solution in DMF. λ_{ex} (H_2B^1) = 390 nm, λ_{ex} (H_2B^2) = 387 nm, λ_{ex} (H_2B^3) = 397 nm.

carbohydrazone substitution at the 3-position of the pyrazole ring, which is in conjugation with the fluorophore, has the capability to regulate its florescence characteristics. Among the ligands H_2B^1, H_2B^2, H_2B^3 and H_2B^4, the former three show emission to a varying degree (Fig. 6). H_2B^4, being the nitro substituted salicyl hydrazone ligand, does not show any fluorescence. In nitro compounds the lowest energy absorption is for a n-π^* transition. Hence no emission could be recorded [42]. Both the ligands H_2B^1 and H_2B^2 shows fluorescence emission which is much diminished in intensity compared to that of H_2B^3. This may be explained by the presence of a fluorescence quenching intra-ligand PET process which takes place from the conjugated salicyl hydrazone portions of the ligands towards the fluorophore [43]. The presence of the electron withdrawing bromo substituent may hinder this process in H_2B^3 to ensure its high quantum yield [44]. Thus H_2B^3 is the ligand which has the highest exploitable fluorescence [45] among these three ligands. As the studies are made in DMF, a polar solvent which facilitates PET, the effects of the presence of an electron withdrawing group is expressed better [46]. The emission from H_2B^2 is blue shifted compared to the other two, in tune with its high energy absorption maxima. It has been observed that the fluorescence excitation spectra exactly follow the absorption spectra in DMF solution, indicating that the fluorescence is taking place from the excited ligand molecules and not from any other species in the solution.

The potential of the ligand molecules to act as a 'FSR' (fluorophore-spacer-receptor) unit has been observed while studying the emission behavior of the metal complexes. The 1:1 dioxomolybdenum(VI) complexes of the ligands exhibit fluorescence quenching compared to the free ligands. However, the position of the fluorescent maxima in each case remains almost unchanged from those of the free ligands. The MoO_2^{2+} unit binds to the salicyl carbohydrazone portion of the ligand leaving the 1-(2-pyridyl) 5-methyl pyrazole free. This should cause a fluorescent enhancement by creating hindrance to the intra-ligand PET process. The observation is, however, quite the opposite. The partial oxidative PET from the fluorophore to the metal center through the conjugated backbone of the ligand combined with the higher probability of radiationless decay (through ISC) in the complexes [47] (heavy metal effect) becomes the overwhelming factors leading to more than a 2/3rds reduction in the fluorescence intensities as compared to free ligands in each case (Fig. 7).

As we have discussed earlier, addition of one molar equivalent of first row transition metal ions, such as Cu(II), to the solution of the dioxomolybdenum(VI) complex **1** lures the ligand to shift its loyalty from the MoO_2^{2+} species to the guest ions with a concomitant change of its binding mode. Thus the formation of complex **5** is achieved with enhanced thermodynamic stability. This action leaves ample evidence with the emission behavior of the newly formed complexes (Fig. 8). The emission intensity is found

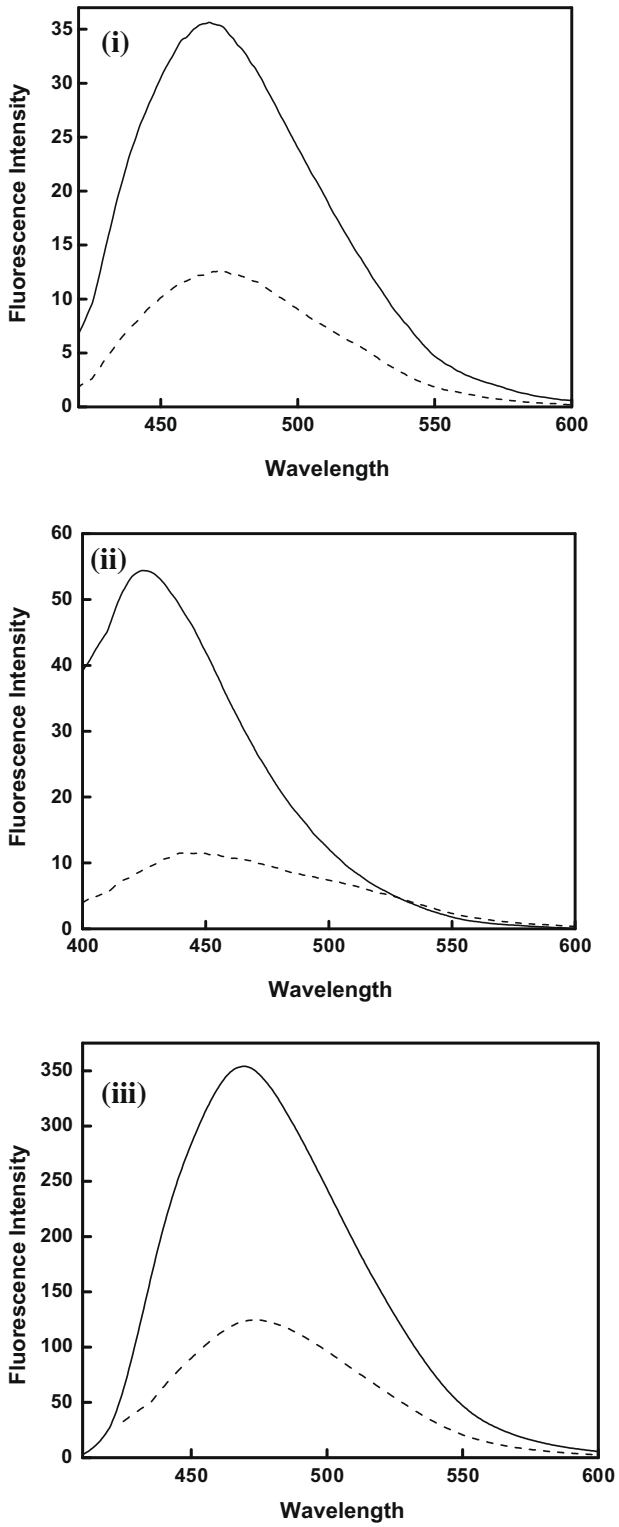


Fig. 7. Comparative emissions of the ligands and their dioxomolybdenum(VI) complexes. All the spectra were taken in 2×10^{-5} molar solution in DMF. (i) H_2B^1 (λ_{ex} = 390 nm, solid line) and complex **1** (λ_{ex} = 390 nm, dotted line). (ii) H_2B^2 (λ_{ex} = 387 nm, solid line) and complex **2** (λ_{ex} = 387 nm, dotted line). (iii) H_2B^3 (λ_{ex} = 397 nm, solid line) and complex **3** (λ_{ex} = 411 nm, dotted line).

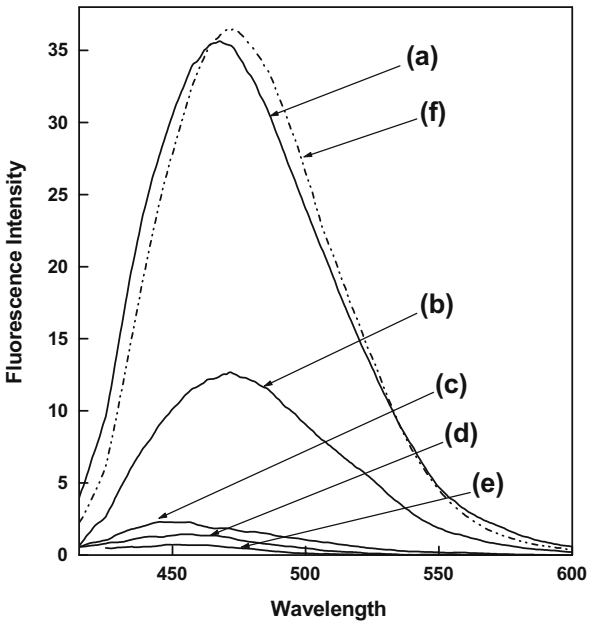


Fig. 8. Fluorescence emissions of (a) a solution of H_2B^1 (λ_{ex} = 390 nm), (b) an equimolar solution of H_2B^1 and $MoO_2(acac)_2$ (λ_{ex} = 390 nm), (c) an equimolar solution containing complex **1** and $Cu(NO_3)_2{\cdot}6H_2O$ (λ_{ex} = 390 nm), (d) an equimolar solution containing complex **1** and $Ni(NO_3)_2{\cdot}6H_2O$ (λ_{ex} = 400 nm), (e) an equimolar solution containing complex **1** and $Co(NO_3)_2{\cdot}6H_2O$ (λ_{ex} = 410 nm) and (f) an equimolar solution containing complex **1** and $Zn(NO_3)_2{\cdot}6H_2O$ (λ_{ex} = 400 nm, 317 nm). All the solutions were 2×10^{-5} molar with respect to each constituent in DMF.

to reduce further from the Mo(VI) complex **1** almost to a 'zero emission' state. We have obtained similar observations with other first row transition metals, such as Co(II) and Ni(II) (Fig. 8). The ligands ability to adjust its binding mode with the change of metal ion seems to be responsible for the secondary quenching. The structure of complex **5** shows that here the ligand actually encompasses the metal ion, occupying all the equatorial positions in its coordination sphere. The nitrogens of the 1-(2-pyridyl) 5-methyl pyrazole unit bind the metal ion with two other N donors from the hydrazone unit. This direct fluorophore–metal interaction enhances the oxidative PET and causes further quenching [48]. A similar change in the metal binding mode can be predicted when Co(II) and Ni(II) are added. However when the zinc(II) ion is added to a solution of complex **1**, a complete restoration of the fluorescence is observed. The closed shell Zn(II) ion is known to be non-quenching in nature as it does not allow a fluorophore–metal oxidative PET [49] (Fig. 8). Although we have not been able to isolate the resulting complex, the complete restoration of fluorescence up to the level of the free ligand indicates that the zinc(II) ion added to complex **1** also causes a stripping of the Mo(VI) species from complex **1**, and a new Zn(II) complex of the ligand H_2B^1 is formed. Most likely, the binding mode of the ligand is different from both **1** and **5**. From the emission properties it may be predicted that the Zn^{2+} ion binds to the heterocyclic chelator end but does not involve the N and O donors of the conjugated backbone as it prefers a tetrahedral arrangement to a square planar one.

When 1 mol equivalent of $MoO_2(acac)_2$ is added to a solution of complex **1** in DMF, fluorescence quenching is observed, but not comparable to the extent that was observed with Cu(II), Co(II) or Ni(II). This indicates that the interaction of complex **1** with the Mo precursor in solution is merely collisional in nature. The free 1-(2-pyridyl) pyrazole portion of complex **1** does not bind the guest Mo(VI) species (Fig. 9).

Emission of the Mo(IV) complex **6** was studied in solid state. Florescence quenching of **6** is much more pronounced than **3**,

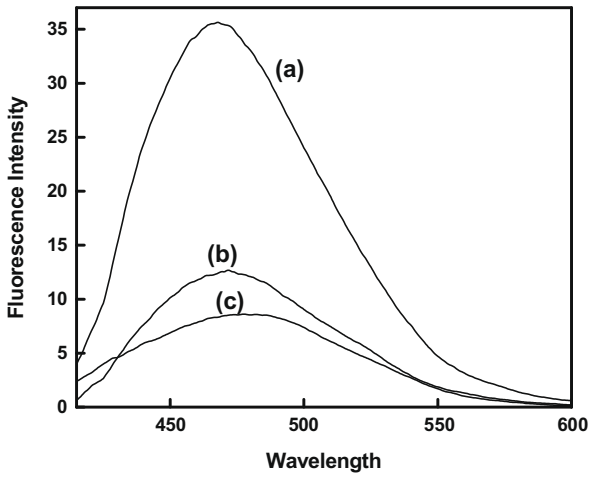


Fig. 9. Fluorescence spectra of the ligand (a) H_2B^1 (λ_{ex} = 390 nm), $H_2B^1 + MoO_2(acac)_2$ (1:1) (λ_{ex} = 390 nm), $H_2B^1 + MoO_2(acac)_2$ (1:2) (λ_{ex} = 390 nm). All the spectra were taken in 2×10^{-5} molar solution in DMF.

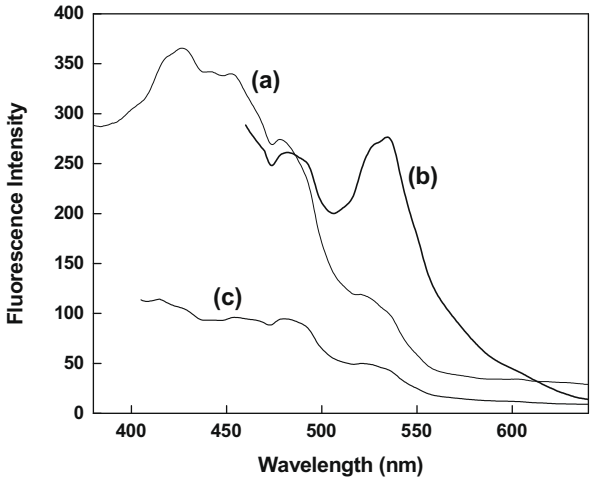


Fig. 10. Solid state fluorescence of (a) H_2B^3 (λ_{ex} = 369 nm), (b) complex **3** (λ_{ex} = 441 nm) and (c) complex **6** (λ_{ex} = 385 nm).

when both are compared to the free ligand H_2B^3. Probably with the reduction of the Mo center to Mo(IV), a metal to ligand reductive PET is initiated which was absent with the d^0 Mo(VI) state (Fig. 10).

Based on these observations, the ligands used here may be used to create a fluorescent 'On–Off' signaling system. The free ligands represent the 'On' state and the Cu(II), Co(II) or Ni(II) complexes represent the 'Off' state. The ligand H_2B^3 is expected to be the most suitable ligand as it exhibits the maximum difference between the 'exploitable fluorescence' in the 'On' state and the 'residual fluorescence' in the 'Off' state. Further using Mo complexes (e.g. complex **1**) inbetween the two states a 'Regulator' effect may be brought in, i.e. by adding 1 equivalent of Mo(VI) salt followed by 1 equivalent of Cu(II) salt to the ligand solution a stepwise quenching of the fluorescence may be achieved. Again an 'On–Off–On' switch may be achieved by the addition of Mo(VI) and Zn(II) salts sequentially in the same molar proportion to the ligand solution. Here the Mo(VI) complex represents the 'Off' state, which is not really a zero emission state but is rather a highly quenched 'On' state. The difference between the 'On' and 'Off' states, i.e. the sensitivity of the system, may be tuned by choosing the most suitable ligand among the three ligands.

4. Conclusion

The stepwise reduction of fluorescence intensity observed here with two different metal ion inputs added to a solution of H_2B^1 is quite unusual, if not unique, in the field of fluorescence signaling. The recovery of fluorescence intensity by altering the second input as Zn^{2+} in place of partially filled shell transition metal ions (Cu^{2+}, Co^{2+} or Ni^{2+}) is also potentially useful in developing a both way switch. The solid state fluorescence of H_2B^3, **3** and **6** shows that reduction of the Mo(IV) center causes further quenching of the fluorescence emission of complex. This observation may be potentially useful in studying enzymatic catalysis reactions of oxo-transferase type molybdoenzymes in living systems with fluorescent tags.

5. Supplementary data

CCDC numbers 716097, 716098, 716099 and 716100 contain the supplementary crystallographic data for the H_2B^2, H_2B^3, complex **5** and complex **1** respectively. These data can be obtained free of charge via http://www.ccdc.cam.ac.ac.uk/conts/retrieving.html, or from the Cambridge Crystallographic Data Center, 12, Union Road, Cambridge CB2 1EZ, UK; fax: +44 1223 336 033; or email: deposit@ccdc.cam.ac.uk.

Acknowledgement

S.K. and S.G. acknowledges Subrata Mohanta and Anuva Samanta for their cooperation in recording the fluorescence spectra. These authors also thank Prof. C.R. Sinha and Papia Dutta of the Department of Chemistry Jadavpur University, Kolkata for their cooperation. T.N.M. thanks the University Grants Commission, New Delhi, India, for a junior research fellowship.

References

[1] (a) A.W. Czarnik (Ed.), Fluorescent Chemosensors of Ion and Molecule Recognition, ACS Symp. Ser. 538, American Chemical Society, Washington, DC, 1993;
(b) L. Fabbrizzi, A. Poggi, Chem. Soc. Rev. 25 (1995) 197;
(c) B. Valeur, in: J.R. Lakowicz (Ed.), Topics in Fluorescence Spectroscopy, vol. IV, Plenum Press, New York, 1994;
(d) A.W. Czarnik, Acc. Chem. Res. 27 (1994) 302.
[2] A.P. de Silva, H.Q.N. Gunaratne, T. Gunnlauggsson, A.J.M. Huxley, C.P. McCoy, J.T. Radmacher, T.E. Rice, Chem. Rev. 97 (1997) 1515.
[3] A.P. de Silva, N.D. McClenaghan, C.P. McCoy, in: V. Balzani (Ed.), Electron Transfer in Chemistry, vol. 5, Wiley-VCH, Weinheim, Germany, 2000.
[4] (a) A.P. de Silva, H.Q.N. Gunaratne, C.P. McCoy, Nature 364 (1993) 42;
(b) A.P. de Silva, H.Q.N. Gunaratne, C.P. McCoy, J. Am. Chem. Soc. 119 (1997) 7891;
(c) A. Credi, V. Balzani, S.J. Langford, J.F. Stoddart, J. Am. Chem. Soc. 119 (1997) 2679;
(d) A.P. de Silva, I.M. Dixon, H.Q.N. Gunaratne, T. Gunnlauggsson, P.R.S. Maxwell, T.E. Rice, J. Am. Chem. Soc. 121 (1999) 1393;
(e) G.J. Brown, A.P. de Silva, S. Pagliari, Chem. Commun. (2002) 2461.
[5] (a) H.-F. Ji, R. Dabestani, G.M. Brown, J. Am. Chem. Soc. 122 (2000) 9306;
(b) K. Ruarck, M. Kollmannsberger, U. Resch-Genger, J. Daub, J. Am. Chem. Soc. 122 (2000) 968;
(c) F. Remacle, S. Speiser, R.D. Levine, J. Phys. Chem. B 105 (2001) 5589;
(d) F.M. Raymo, S. Giordani, J. Am. Chem. Soc. 124 (2002) 2004;
(e) F.M. Raymo, Adv. Mater. 14 (2002) 401.
[6] (a) J. Wolfram, M. Sauer, in: W. Rettig, B. Strehmel, S. Schrader, H. Seifert (Eds.), Applied Fluorescence in Chemistry, Biology and Medicine, Springer-Verlag, Berlin, Germany, 1999;
(b) K. Rurack, Spectrochim. Acta, Part A 57 (2001) 2161.
[7] (a) A.J. Bard, Chem. Eng. News (September 6) (1999) 5;
(b) A.P. Malvino, J.A. Brown (Eds.), Digital Computer Electronics, 3rd ed., Glencoe, Lake Forest, NY, 1993;
(c) A.P. de Silva, N.D. McClenaghan, C.P. McCoy, in: B.L. Feringa (Ed.), Molecular Electronics, Wiley-VCH, Weinheim, Germany, 2001.
[8] (a) I. Oueslati, R.A. Sá Ferreira, L.D. Carlos, C. Baleiza~o, M.N. Berberan-Santos, B. de Castro, J. Vicens, U. Pischel, Inorg. Chem. 45 (2006) 2652;
(b) B. Bag, P.K. Bharadwaj, Chem. Commun. (2005) 513;
(c) K.-C. Chang, I.-H. Su, A. Senthilvelan, W.-S. Chung, Org. Lett. 9 (2007) 3363.
[9] (a) I. Aoki, T. Sakaki, S. Shinkai, Chem. Commun. (1992) 730;
(b) J.-H. Bu, Q.-Y. Zheng, C.-F. Chen, Z.-T. Huang, Org. Lett. 6 (2004) 3301.
[10] (a) I. Leray, J.-P. Lefevre, J.-F. Delouis, J. Delaire, B. Valeur, Chem. Eur. J. 7 (2001) 4590;
(b) S.K. Kim, J.H. Bok, R.A. Bartsch, J.Y. Lee, J.S. Kim, Org. Lett. 7 (2005) 4839;
(c) J.K. Choi, S.H. Kim, J. Yoon, K.-H. Lee, R.A. Bartsch, J.S. Kim, J. Org. Chem. 71 (2006) 8011.
[11] (a) T. Jin, K. Ichikawa, T. Koyana, Chem. Commun. (1992) 499;
(b) S.K. Kim, S.H. Lee, J.Y. Lee, J.Y. Lee, R.A. Bartsch, J.S. Kim, J. Am. Chem. Soc. 126 (2004) 16499;
(c) B. Schazmann, N. Alhashimy, D. Diamond, J. Am. Chem. Soc. 128 (2006) 8607.
[12] (a) T. Jin, Chem. Commun. (1999) 2491;
(b) R.K. Castellano, S.L. Craig, C. Nuckolls, J. Rebek Jr., J. Am. Chem. Soc. 122 (2000) 7876.
[13] W.-S. Yu, C.-C. Cheng, Y.-M. Cheng, P.-C. Wu, Y.-H. Song, Y. Chi, P.-T. Chou, J. Am. Chem. Soc. 125 (2003) 10800.
[14] (a) L. Fabbrizzi, M. Licchelli, P. Pallavicini, A. Perotti, A. Taglietti, D. Sacchi, Chem. Eur. J. 2 (1996) 75;
(b) A.W. Varnes, R.B. Dodson, E.L. Wehry, J. Am. Chem. Soc. 94 (1972) 946;
(c) J.A. Kemlo, T.M. Shepherd, Chem. Phys. Lett. 47 (1977) 158.
[15] (a) B. Turfan, E.U. Akkaya, Org. Lett. 4 (2002) 2857;
(b) P. Pallavicini, L. Pasotti, S. Patroni, J. Chem. Soc., Dalton Trans. (2007) 5670;
(c) P. Ghosh, P.K. Bharadwaj, S. Mandal, S. Ghosh, J. Am. Chem. Soc. 118 (1996) 1553.
[16] (a) T. Lazarides, M.A.H. Alamiry, H. Adams, S.J.A. Pope, S. Faulkner, J.A. Weinstein, M.D. Ward, J. Chem. Soc., Dalton Trans. (2007) 1484;
(b) M.I. Rodríguez-Ćaceres, R.A. Agbaria, I.M. Warner, J. Fluorescence 15 (2005) 185.
[17] M. Camur, M. Bulut, A.R. Ozkaya, M. Kandaz, N. Yayli, Transition Met. Chem. 32 (2007) 642.
[18] R. Sang, L. Xu, Inorg. Chem. 44 (2005) 3731.
[19] S. Kapoor, M. Shastri, J. Chem. Sci. 112 (2000) 459.
[20] Y. Ma, Y. Li, E. Wang, Y. Lu, C. Qin, X. Xu, J. Cluster Sci. 17 (2006) 167.
[21] R.-Q. Zou, C.-S. Liu, Z. Huang, T.-L. Hu, X.H. Bu, Cryst. Growth Des. 6 (2006) 199.
[22] T.N. Mandal, S. Roy, A.K. Barik, S. Gupta, R.J. Butcher, S.K. Kar, Polyhedron 27 (2008) 3267.
[23] G.J.J. Chen, J.W. McDonald, W.E. Newton, Inorg. Chem. 15 (1976) 2612.
[24] N. Adhikari, S. Chowdhury, R.J. Butcher, N. Saha, Polyhedron 18 (1999) 1323.
[25] D.T. Sawyer, J.L. Roberts, Experimental Electrochemistry for Chemists, Wiley, New York, 1974. p. 212.
[26] M. Maus, W. Retigg, D. Bonafoux, R. Lapouyade, J. Phys. Chem. A 103 (1999) 3388.
[27] M. Lukeman, D. Veale, P. Wan, V. Ranjit, N. Munasinghe, J.E.T. Corrie, Can. J. Chem. 82 (2004) 240.
[28] Bruker, SMART (Version 5. 624) and SAINT (Version 6. 04) Programs using the Windows NT System, Bruker AXS Inc., Madison, WI, USA, 2001.
[29] R.J. Butcher, J.C. Bottaro, R. Gilardi, Acta Crystallogr., Sect. E 59 (2003) m591.
[30] G.M. Sheldrick, SHELXTL, Version 5.10, Bruker AXS Inc., Madison, WI, USA, 1997.
[31] M. Kato, K. Nakajima, Y. Yoshikawa, M. Hirotsu, M. Kojima, Inorg. Chim. Acta 311 (2000) 619.
[32] A. Rana, R. Dinda, S.P. Ghosh, A.J. Blake, Polyhedron 22 (2003) 3075.
[33] R.M. Silverstein, F.X. Webster, in: Spectrometric Identification of Organic Compounds, 6th ed. Wiley, New York.
[34] S. Gupta, A.K. Barik, S. Pal, A. Hazra, S. Roy, R.J. Butcher, S.K. Kar, Polyhedron 26 (2007) 133.
[35] R. Hahn, U. Kusthardt, W. Scherer, Inorg. Chim. Acta 210 (1993) 77.
[36] E. Ainscough, A.M. Brodie, N.G. Larsen, Inorg. Chim. Acta 60 (1982) 25.
[37] A.B.P. Lever, Inorganic Electronic Spectroscopy, 2nd ed., Elsevier, Amsterdam, 1984.
[38] R. Dinda, P. Sengupta, S.P. Ghosh, H. Mayer-Figge, W.S. Sheldrick, J. Chem. Soc., Dalton. Trans. (2002) 4434.
[39] R.-Q. Zou, X.-H. Bu, R.-H. Zhang, Inorg. Chem. 43 (2004) 5382.
[40] S.-Z. Zhan, D. Li , X.-P. Zhou, X.-H. Zhou, Inorg. Chem. 45 (2006) 9163.
[41] P.-C. Wu, J.-K. Yu, Y.-H. Song, Y. Chi, P.-T. Chou, S.-M. Peng, G.-H. Lee, Organometallics 22 (2003) 4938.
[42] G.G. Guilbault, in: Practical Fluorescence, CRC Press, 1990, p. 97.
[43] B. Ramachandran, A. Samanta, J. Phys. Chem. A 102 (1998) 10579.
[44] B. Bag, P.K. Bharadwaj, J. Phys. Chem. B 109 (2005) 4377.
[45] P. Pallavicini, L. Pasotti, S. Patroni, J. Chem. Soc., Dalton Trans. (2007) 5670.
[46] T. He, T. Xu, Y. Zhao, C. Chen, J. Chem. Soc., Perkin Trans. 2 (1999) 545.
[47] İ. Kizilcikli, S. Eğlence, A. Gelir, B. Ülküseven, Transition Met. Chem. 33 (2008) 775.
[48] I. Yilmaz, Transition Met. Chem. 33 (2008) 259.
[49] S.M. Brombosz, A.J. Zucchero, R.L. Phillips, D. Vazquez, A. Wilson, U.H.F. Bunz, Org. Lett. 9 (2007) 4519.

2.3. a. Preparation of 1,3-dimethyl-2-(phenylazo)imidazolium iodide

To a solution (20 ml) of 2-(phenylazo)imidazole (HaaiH) (0.2 g, 1.16 mmol) in dry THF, NaH (50% paraffin) was added pinch wise and stirred for 30 min. Methyl iodide (0.39 g, 2.75 mmol) was added drop by drop for 10 min. and the resulting solution was refluxed for another 2 h. It was then cooled, filtered and the filtrate was evaporated in vacuum. The dry orange residue after extracting with $CHCl_3$ was recrystallised from warm water. Yield. 0.3 g (80%).

All other imidazolium iodides were prepared following identical procedure. The microanalitical data of ligands are as follows.

[HaaiMe$_2^+$] I$^-$ (**1a**) (m. p. 215 ± 1 °C): *Anal.* Calc. for $C_{11}H_{13}N_4I$: C, 34.55; H, 3.96; N, 17.07. Found: C, 34.43; H, 3.87; N, 17.02%. [MeaaiMe$_2^+$] I$^-$ (**1b**) (m. p. 218 ± 1 °C): *Anal.* Calc. for $C_{12}H_{15}N_4I$: C, 42.11; H, 4.39; N, 16.37. Found: C, 42.03; H, 4.28; N, 16.26%. [HaaiEt$_2^+$] I$^-$ (**2a**) (m. p. 225 ± 1°C): *Anal.* Calc. For $C_{13}H_{17}N_4I$: C, 43.82; H, 4.78; 15.73. Found: C, 43.77; H,4.71; N, 15.65%. [MeaaiEt$_2^+$] I$^-$ (**2b**) (m. p. 220 ± 2°C): *Anal.* Calc. For $C_{14}H_{19}N_4I$: C, 45.41; H, 5.14; N, 15.14. Found: C, 45.36; H, 5.06; N, 15.07%. [Haai(CH$_2$Ph)$_2^+$] I$^-$ (**3a**) (m. p. > 330 °C): *Anal.* Calc. For $C_{23}H_{21}N_4I$: C, 57.50; H, 4.38; N, 11.67. Found: C, 57.43; H, 4.32; N, 11.58%. [Meaai(CH$_2$Ph)$_2^+$] I$^-$ (**3b**) (m. p. 320 ± 1 °C): *Anal.* Calc. For $C_{24}H_{23}N_4I$: C, 58.29; H, 4.66; N, 11.34. Found: C, 58.21; H, 4.58; N, 11.26%. [HaaiMe(CH$_2$Ph)$^+$] I$^-$ (**4a**) (m. p. 289 ± 1° C): *Anal.* Calc. For $C_{17}H_{17}N_4I$: C, 50.50; H, 4.21; N,13.86. Found: C, 50.42; H, 4.26; N, 13.80%. [MeaaiMe(CH$_2$Ph)$^+$] I$^-$ (**4b**) (m. p. 276 ± 1 °C): *Anal.* Calc. For $C_{18}H_{19}N_4I$: C, 51.69; H, 4.55; N, 13.40%. Found: C, 51.77; H, 4.48; N, 13.46.

2.3. b. Synthesis of [(MeaaiMe(Bz))$^+$]$_2$ [Cu$_2$I$_4$] (**8b**)

To a solution (25 ml) of [MeaaiMe(CH$_2$Ph)]$^+$ I$^-$ (1-methyl-3-benzyl-2-(*p*-tolylazo)imidazolium iodide) (147 mg, 0.35 mmol) in methanol, CuI (70 mg, 0.37 mmol) in acetonitrile, was added, stirred and refluxed for 3 h . The solution was filtered at hot through G4 crucible and was left to evaporate slowly in air. Block shaped black micro crystals, deposited on the wall of beaker, were collected by filtration. X-ray quality black coloured block shaped crystals were obtained by recrystallising from DMF–MeOH (1:2 v/v) solution. The yield was 0.15 g (71%).

All other complexes were prepared by the same procedure. In all cases, crystalline products were obtained. The yield varied from 70% to 80% and microanalytical data of the complexes are as follows. The microanalytical data of the complexes are as follows: [HaaiMe$_2$]$_2$[Cu$_2$I$_4$] (**5a**) *Anal.* Calc. for $C_{11}H_{13}N_4I_2Cu$: C, 25.48; H, 2.53; N, 10.80. Found: C, 25.51; H, 2.54; N, 10.78%. FT-IR (KBr disc, cm^{-1}), ν(N=N), 1420; ν(C=N), 1588 cm^{-1}. UV–VIS spectral data in CH_3CN (λ_{max}(nm)(10^{-3} (dm^3 mol^{-1} cm^{-1}): 245 (46.70), 360 (35.30), 420 (4.35). [MeaaiMe$_2$]$_2$[Cu$_2$I$_4$] (**5b**) *Anal.* Calc. for $C_{12}H_{15}N_4I_2Cu$: C, 27.06; H, 2.84; N, 10.52. Found: C, 27.00; H, 2.82; N, 10.54%. FT-IR (KBr disc, cm^{-1}), ν(N=N), 1428; ν(C=N), 1594 cm^{-1}. UV–VIS spectral data in CH_3CN (λ_{max}(nm)(10^{-3} (dm^3 mol^{-1} cm^{-1}): 244 (39.98), 367 (32.8). [HaaiEt$_2$]$_2$[Cu$_2$I$_4$] (**6a**) *Anal.* Calc. for $C_{13}H_{17}N_4I_2Cu$: C, 28.55; H, 3.11; N, 10.25. Found: C, 28.44; H, 3.04; N, 10.38%. FT-IR (KBr disc, cm^{-1}), ν(N=N), 1416; ν(C=N), 1593 cm^{-1}. UV–VIS spectral data in CH_3CN (λ_{max}(nm)(10^{-3} (dm^3 mol^{-1} cm^{-1}): 248 (44.90), 360 (38.20), 424 (7.80). [MeaaiEt$_2$]$_2$[Cu$_2$I$_4$] (**6b**) *Anal.* Calc for $C_{14}H_{19}N_4I_2Cu$: C, 29.97; H, 3.39; N, 9.99. Found: C, 27.00; H, 2.82; N, 10.54%. FT-IR (KBr disc, cm^{-1}), ν(N=N), 1418; ν(C=N), 1598 cm^{-1}. UV–VIS spectral data in CH_3CN (λ_{max}(nm)(10^{-3} (dm^3 mol^{-1} cm^{-1}): 244 (39.25), 365 (30.73). [HaaiBz$_2$]$_2$[Cu$_2$I$_4$] (**7a**) *Anal.* Calc. for $C_{23}H_{21}N_4I_2Cu$: C, 41.16; H, 3.13; N, 8.35. Found: C, 41.23; H, 3.10; N, 8.42%. FT-IR (KBr disc, cm^{-1}), ν(N=N), 1425; ν(C=N), 1588 cm^{-1}. UV–VIS spectral data in CH_3CN (λ_{max}(nm)(10^{-3} (dm^3 mol^{-1} cm^{-1}): 245 (41.2), 373 (34.5). [MeaaiBz$_2$]$_2$[Cu$_2$I$_4$] (**7b**) *Anal.* Calc. for $C_{24}H_{23}N_4I_2Cu$: C, 42.06; H, 3.36; N, 8.18. Found: C, 42.10; H, 3.35; N, 8.21. FT-IR (KBr disc, cm^{-1}), ν(N=N), 1430; ν(C=N), 1596 cm^{-1}. UV–VIS spectral data in CH_3CN (λ_{max}(nm)(10^{-3} (dm^3 mol^{-1} cm^{-1}): 248 (42.7), 373(35.6). [HaaiMe(Bz)]$_2$[Cu$_2$I$_4$] (**8a**) *Anal.* Calc. for $C_{17}H_{17}N_4I_2Cu$: C, 34.31; H, 2.86; N, 9.42. Found: C, 34.39; H, 2.83; N, 9.39%. FT-IR (KBr disc, cm^{-1}), ν(N=N), 1425; ν(C=N), 1590 cm^{-1}. UV–VIS spectral data in CH_3CN (λ_{max}(nm)(10^{-3} (dm^3 mol^{-1} cm^{-1}): 243(41.5), 376(40.7). [MeaaiMe(Bz)]$_2$[Cu$_2$I$_4$] (**8b**) *Anal.* Calc. for $C_{18}H_{19}N_4I_2Cu$: C, 35.51; H, 3.12; N, 9.20. Found: C, 35.49; H, 3.17; N, 9.18%. FT-IR (KBr disc, cm^{-1}), ν(N=N), 1428; ν(C=N), 1596 cm^{-1}. UV–VIS spectral data in CH_3CN (λ_{max}(nm)(10^{-3} (dm^3 mol^{-1} cm^{-1}): 242.75(38.5), 374.21(32.1).

2.3. c. Synthesis of [MeaaiMe$_2$]2[Ag$_3$I$_5$] (**9b**)

To a solution (25 ml) of [MeaaiMe$_2$]$^+$ I$^-$ (1,3-dimethyl-2-(*p*-tolylazo)imidazolium iodide) (120 mg, 0.35 mmol) in methanol, AgI (75 mg, 0.32 mmol) was added pinch wise, stirred and refluxed for 4 h. The solution was filtered at hot and allowed to evaporate slowly in air. Orange color micro-crystals, deposited at the bottom of the beaker, were collected by filtration. X-ray quality orange cubic crystals were obtained by recrystallising from DMF-MeOH (1:2 v/v) solution. The yield was 0.17 g (71%).

All other complexes were prepared by the same procedure. In all cases, crystalline products were obtained. The yield varied from 70% to 80%. The microanalytical data of the complexes are as follows: [HaaiMe$_2$]$_2$[Ag$_3$I$_5$] (**9a**) *Anal.* Calc. for $C_{22}H_{26}N_8I_5Ag_3$: C, 19.40; H, 1.91; N, 8.23. Found: C, 19.44; H, 1.95; N, 8.21%. FT-IR (KBr disc, cm^{-1}), ν(N=N), 1437; ν(C=N), 1606 cm^{-1}. UV–VIS spectral data in DMF (λ_{max}(nm)(10^{-3} (dm^3 mol^{-1} cm^{-1}): 365(63.4), 462(45.3). [MeaaiMe$_2$]$_2$[Ag$_3$I$_5$] (**9b**) *Anal.* Calc. for $C_{24}H_{30}N_8I_5Ag_3$: C, 20.73; H, 2.16; N, 8.06. Found: C, 20.78; H, 2.15; N, 8.10%. FT-IR (KBr disc, cm^{-1}), ν(N=N), 1437; ν(C=N), 1595 cm^{-1}. UV–VIS spectral data in DMF (λ_{max}(nm)(10^{-3} (dm^3 mol^{-1} cm^{-1}): 373(56.9), 464(41.6). [HaaiEt$_2$]$_2$[Ag$_3$I$_5$] (**10a**) *Anal.* Calc. for $C_{26}H_{34}N_8I_5Ag_3$: C, 22.02; H, 2.40; N, 7.90. Found: C, 22.10; H, 2.38; N, 7.86%. FT-IR (KBr disc, cm^{-1}), ν(N=N), 1432; ν(C=N), 1613 cm^{-1}. UV–VIS spectral data in DMF (λ_{max}(nm)(10^{-3} (dm^3 mol^{-1} cm^{-1}): 370(59.4), 458(48.4). [MeaaiEt$_2$]$_2$[Ag$_3$I$_5$] (**10b**) *Anal.* Calc. for $C_{28}H_{38}N_8I_5Ag_3$: C, 23.25; H, 2.63; N, 7.75. Found: C, 23.18; H, 2.60; N, 7.80%. FT-IR (KBr disc, cm^{-1}), ν(N=N), 1428; ν(C=N), 1602 cm^{-1}. UV–VIS spectral data in DMF (λ_{max}(nm)(10^{-3} (dm^3 mol^{-1} cm^{-1}): 378(58.8), 469(43.5). [HaaiBz$_2$]$_2$[Ag$_3$I$_5$] (**11a**) *Anal.* Calc. for $C_{46}H_{42}N_8I_5Ag_3$: C, 33.15; H, 2.52; N, 6.73. Found: C, 33.11 H, 2.56; N, 6.70%. FT-IR (KBr disc, cm^{-1}), ν(N=N), 1435; ν(C=N), 1602 cm^{-1}. UV–VIS spectral data in DMF (λ_{max}(nm)(10^{-3} (dm^3 mol^{-1} cm^{-1}): 372(58.0), 463(44.8). [MeaaiBz$_2$]$_2$[Ag$_3$I$_5$] (**11b**) *Anal.* Calc. for $C_{48}H_{46}N_8I_5Ag_3$: C, 34.02; H, 2.72; N, 6.62. Found: C, 34.05; H, 2.71; N, 6.60%. FT-IR (KBr disc, cm^{-1}), (N=N), 1434; ν(C=N), 1600 cm^{-1}. UV–VIS spectral data in DMF (λ_{max}(nm)(10^{-3} (dm^3 mol^{-1} cm^{-1}): 378(58.3), 463(41.6). [HeaaiMe(Bz)]$_2$[Ag$_3$I$_5$] (**12a**) *Anal.* Calc. for $C_{34}H_{34}N_8I_5Ag_3$: C, 26.97; H, 2.25; N, 7.40. Found: C, 27.03 H, 2.28; N, 7.42%. FT-IR (KBr disc, cm^{-1}), ν(N=N), 1435; ν(C=N), 1598 cm^{-1}. UV–VIS spectral data in DMF (λ_{max}(nm)(10^{-3} (dm^3 mol^{-1} cm^{-1}): 372(56.2), 464(37.5). [MeaaiMe(Bz)]$_2$[Ag$_3$I$_5$] (**12b**) *Anal.* Calc. for $C_{36}H_{38}N_8I_5Ag_3$: C, 28.03; H, 2.47; N, 7.27. Found: C, 28.05 H, 2.50; N, 7.31%. FT-IR (KBr disc, cm^{-1}), ν(N=N), 1428; ν(C=N), 1592 cm^{-1}. UV–VIS spectral data in CH_3CN (λ_{max}(nm)(10^{-3} (dm^3 mol^{-1} cm^{-1}): 375(61.2), 461(44.1).

2.4. X-ray crystal structure analyses

Crystals suitable for X-ray diffraction study of [(MeaaiMeBz)]$_2$-[Cu$_2$I$_4$] (**8b**) (0.13 × 0.06 × 0.05 mm) and [MeaaiMe$_2$]$_2$[Ag$_3$I$_5$] (**9b**) (0.25 × 0.20 × 0.13 mm) were prepared by slow evaporation of *N*,*N*-dimethylformamide solution by adding methanol (2 vol.) as

Table 1
Summarized crystallographic data for $[MeaaiMe(Bz)^+]_2[Cu_2(\mu\text{-}I)_2I_2]^{2-}$ (**8b**) and $[(MeaaiMe_2)^+]_2[Ag_3I_5]^{2-}$ (**9b**).

	$[MeaaiMe(Bz)^+]_2[Cu_2(\mu\text{-}I)_2I_2]^{2-}$ (**8b**)	$[(MeaaiMe_2)^+]_2[Ag_3I_5]^{2-}$ (**9b**)
Empirical formula	$C_{18}H_{19}I_2N_4Cu$	$C_{24}H_{30}I_5N_8Ag_3$
Formula weight	608.71	1388.67
Temperature (K)	294 (2)	296 (2)
Crystal system	triclinic	monoclinic
Space group	P-1	P 2_1/c
Crystal size $(mm)^3$	$0.13 \times 0.06 \times 0.05$	$0.25 \times 0.20 \times 0.13$
Unit cell dimensions		
a(Å)	9.0523(8)	19.4535(18)
b(Å)	10.5018(9)	13.7069(14)
c(Å)	11.3491(9)	13.3309(12)
α (°)	103.631(2)	90
β (°)	97.527(2)	90.0010(10)
γ (°)	93.272(2)	90
$V(Å)^3$	1035.14(15)	3554.6(6)
Z	2	4
λ(Å)	0.71073	0.71073
μ (Mo Kα) (mm^{-1})	4.045	6.007
D_{calc} $(mg\ m^{-3})$	1.953	2.595
hkl range	$-10 \leqslant h \leqslant 10$, $-12 \leqslant k \leqslant 12$, $-13 \leqslant l \leqslant 13$	$-24 \leqslant h \leqslant 29$, $-19 \leqslant k \leqslant 20$, $-20 \leqslant l \leqslant 20$
θ range (°)	1.87–25.05	1.05–34.05
Refine parameters	226	371
Total reflection	8961	40101
Unique data [$I > 2\sigma(I)$]	3662	12562
R_1[a] [$I > 2\sigma(I)$]	0.0623	0.0452
wR_2[b]	0.1347	0.1155
Goodness of fit	0.905	0.893
Δ_{max} (e $Å^{-3}$)	1.006	1.031
Δ_{min} (e $Å^{-3}$)	−0.648	−2.674

[a] $R = \Sigma|F_0 - F_c|/\Sigma\ F_0$.
[b] $wR = [\Sigma\ w(F_0^2 - F_c^2)/\Sigma\ w\ F_0^4]^{1/2}$ are general but w are different, $w = 1/[\sigma^2(F_0^2) + (0.1000P)^2 + 0.0000P]$ for (8b); $w = 1/[\sigma^2(F^2) + (0.0748P)^2 + (0.0000P)]$ for (**9b**) where $P = (F_0^2 + 2Fc^2)/3$.

precipitant at ambient condition. Diffraction data were collected with the Bruker SMART 1 K CCD area-detector diffractometer using fine focused sealed tube graphite-monochromatized Mo Kα radiation ($\lambda = 0.71073$ Å). Unit cell parameters were determined from least-squares method in the range of $-10 \leqslant h \leqslant 10$, $-12 \leqslant k \leqslant 12$, $-13 \leqslant l \leqslant 13$ and angle varies 3.64 2 50.1° for (**8b**); $-24 \leqslant h \leqslant 29$, $-19 \leqslant k \leqslant 20$, $-20 \leqslant l \leqslant 20$ and angle varies 2.1 2 68.1° for (**9b**). A summary of the crystallographic data and structure refinement parameters are given in Table 1. Data were corrected for Lorentz and polarization effects. Data reduction was carried out by using SAINT programme. The structure was solved by direct method using SHELXS-97 [30] and successive difference Fourier syntheses. All non-hydrogen atoms were refined anisotropically. Full matrix least squares refinements on F_0^2 were carried out using SHELXL-97 [31] with anisotropic displacement parameters for all non-hydrogen atoms. Hydrogen atoms were constrained to ride on the respective carbon or nitrogen atoms with anisotropic displacement parameters equal to 1.2 times the equivalent isotropic displacement of their parent atom in all cases. All calculations were carried out using SHELXS-97 [30], PLATON 99 [32], ORTEP-3 [33] programs.

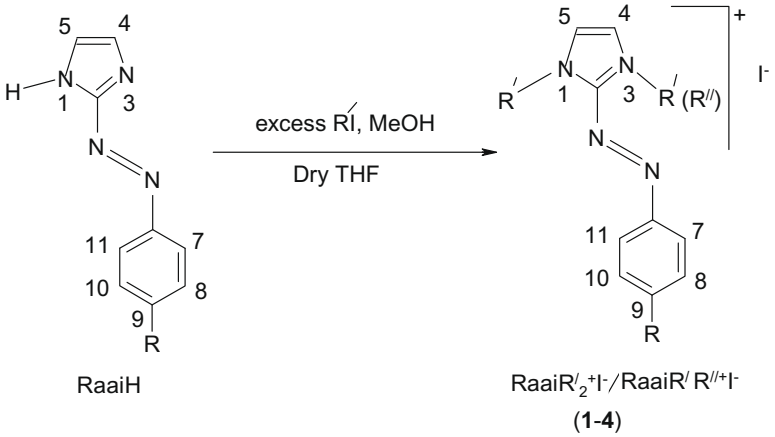
3. Results and discussion

3.1. Azoimidazolium halide

Alkylation of 2-(arylazo)imidazoles (RaaiH) with excess alkyl iodide (MeI, EtI, $PhCH_2I$) in dry THF has afforded 1,3-dialkyl-2-(arylazo)imidazolium iodides ($RaaiR'_2{}^+I^-$, **1**–**3**) and 1-methyl-3-benzyl-2-(arylazo)imidazolium iodides ($RaaiR'R''^+I^-$, **4**). 1-Alkyl-2-(arylazo)imidazoles (RaaiR′) are low melting solids or gummy mass [28] while $[RaaiR'_2{}^+](I^-)$ are orange crystalline compounds. Molar conductance data shows that di-alkyl-imidazolium iodides are 1:1 electrolytes.

The IR spectra of $[[RaaiR'_2{}^+](I^-)]$ (**1**–**3**) and ($RaaiR'R''^+I^-$, **4**) show broad, medium intense band centred at 3420 cm^{-1} which is referred to $\nu(H_2O)$ and a medium intense band at 1620–1640 cm^{-1} corresponding to bending mode of water cluster [34]. Upon heating in the temperature range 90–110 °C the crystallized water is removed and IR spectra do not further show the vibrations corresponding to H_2O even on exposure to air for long time. The –N=N– and –CN– appear at 1400–1420 and 1600–1630 cm^{-1}, respectively. Thermogravimetric analysis (TGA) shows that these compounds do not have any associated solvent molecule, and alkyl iodide is removed from the molecule upon heating.

The absorption spectra of $[RaaiR/] + I- /(RaaiR/R//) + I-)$ in methanol solution show absorption band at 330–400 nm with a molar absorption coefficient in the order of $10^4\ dm^3\ mol^{-1}\ cm^{-1}$ and a tail extending into 500 nm. From the analogy with the



R = H (**a**), Me (**b**); R′, R′ = -$^{12}CH_3$ (**1**); -$^{12}CH_2$-$^{13}CH_3$ (**2**); -$^{12}CH_2$-Ph (13-17) (**3**); R′ = $^{12}CH_3$, R″ = -$^{12}CH_2$-Ph (**4**)

Scheme 1.

absorption spectrum of azobenzene [35], it is likely that the intense absorption band corresponds to $\pi-\pi^*$ transitions, while the tail corresponds to $n-\pi^*$ transition. However, the $\pi-\pi^*$ band exhibits bathochromic shifts by ~30 nm compared with azobenzene, while the $n-\pi^*$ band shows little shift. As a consequence, the energy separation between the $\pi-\pi^*$ and $n-\pi^*$ transitions in arylazoimidazoles is narrower than that of azobenzene.

The ^{1}H NMR spectra of 1,3-dialkyl-2-(arylazo)imidazolium iodide, [RaaiR$'_2^+$](I$^-$) (**1–3**) and 1-methyl-3-benzyl-2-(arylazo)imidazolium iodide [RaaiR$'$R$''^+$](I$^-$) (**4**) are taken in CD_3CN. The atom numbering pattern of the ligands is shown in Scheme 1. The proton signals of [RaaiR$'_2^+$](I$^-$) are assigned on comparing with the spectra of RaaiR$'$ [29,32–35], spin-spin interaction and effect of substitution. 1,3-Dialkyl-2-(arylazo)imidazolium iodide show a single resonance for two R$'$: 1,3-Me$_2$ of (**1**) show a sharp singlet at 4.25 ppm; 1,3-Et$_2$ of [RaaiEt$_2^+$](I$^-$) (**2**) exhibit 1-(CH$_2$)– as quartet at *av.* 4.85 ppm and methyl (-Me) as triplet splitting pattern at *av.* 1.5 ppm; [Raai(CH$_2$Ph)$_2^+$](I$^-$) (**3**) and [Raai(Me)(CH$_2$Ph)$^+$](I$^-$) (**4**) show singlet proton signal at 5.3–5.5 ppm which has been assigned to –CH$_2$– of N(1)–CH$_2$–Ph . Imidazole protons (4-, 5-H) appear as broad single resonance at 7.0–7.2 ppm. The broadening may be due to rapid proton exchange between two positions. The aryl protons (7-H to 11-H) are upfield shifted on going from phenylazo (**a**) to *p*-tolylazo (**b**) which may be due to +I effect of Ar–Me group.

3.2. Iodometallates

1,3-Di-alkyl-2-(arylazo)imidazolium iodides (symmetrical: [RaaiR$'_2^+$]I$^-$, R$'$ = Me, Me (**1**); Et, Et (**2**); CH$_2$Ph, CH$_2$Ph (**3**) and R = H (**a**), Me (**b**); unsymmetrical: [RaaiMe(CH$_2$Ph)$^+$]I$^-$ (**4**)) are used as cation source and I$^-$ are utilized in the formation of iodometallates. The reaction between [RaaiR$'_2^+$]I$^-$ and MI (M = Cu (**5-8**), Ag (**9–12**)) in 1:1 mole ratio in methanol and acetonitrile mixture has afforded polymeric ionic solid (Eqs. (1) and (2)). The molar conductance measurements show that iodocuprates(I) are 1:1 electrolyte while iodoargentates (I) are 2:1 conductor.

$$Cu_2I_2 + 2RaaiR'R'' + I^- \rightarrow \underset{\mathbf{5-8}}{[RaaiR'/R'']_2}[Cu_2I_4] \quad (1)$$

$$3AgI + 2RaaiR'/R'' + I^- \rightarrow \underset{\mathbf{9-12}}{[RaaiR'/R'']_2}[Ag_3I_5] \quad (2)$$

Thermal studies of the complexes show two steps elimination of alkyl iodide within temperature range 200–250 °C and 290–380 °C (Supplementary data). Mass loss perfectly matches with the calculated data.

3.2. Spectral studies

Moderately intense stretching at 1595–1600 and 1435–1445 cm^{-1} are due to ν(C=N) and ν(N=N), respectively, for the complexes. Other bands are shifted to lower frequency in the iodometallates (**5–12**) compared to the free ligand values.

The solution spectra of azoimidazolium iodocuprate (I) (**5–8**) were recorded in acetonitrile. Because of sparing solubility of azoimidazolium iodoargentate(I) (**9–12**) in acetonitrile we have taken solution spectra in DMF in wavelength range 230–600 nm. Intense ($\in \sim 10^4$ mol^{-1} dm^3 cm^{-1}) bands 240–260, 340–360 nm for **5–8** and 240–260, 340–360 and 430–460 nm for **9–12** were observed. On comparing with free ligand spectra [29,32–35], we may conclude that the bands <400 nm are due to intramolecular charge transfer transitions and the bands 430–460 nm may be due to MLCT, d^{10}(Cu(I)/Ag(I)) → π^*(azoimine) transition [26–31].

The ^{1}H NMR spectra of [RaaiR$'$R$''$]$_2$[Cu$_2$I$_4$] (**5–8**) are recorded in $CDCl_3$. The NMR spectra of [RaaiR$'$R$''$]$_2$[Ag$_3$I$_5$] (**9–12**) are recorded in DMSO-d$_6$ due to solubility problem of them in $CDCl_3$. Data (Table 2) reveal that the signals in the spectra of the complexes are shifted to downfield side relative to free ligand values [24,28,29]. This supports some interaction of iodometallates with azoimidazolium unit. Besides, the signals in these compounds are shifted to higher chemical shift data (δ) than that of [azoimidazolium$^+$][Pb(μ-I)$_3^-$] [24]. Imidazole protons suffer downfield shifting by 0.4–0.6 ppm compared to the azoimidazolium ions. Aryl signals shift to the lower field side on Me-substitution to the aryl ring. This is due to electron donating effect of the Me- group.

3.3. Molecular structures

3.3.1. [MeaaiMe(Bz)$^+$]$_2$[Cu$_2$I$_4$]$^{2-}$ (*8b*)

The molecular unit of **8b** is shown in Fig. 1a and bond parameters are listed in Table 3. The iodo-bridged [Cu$_2$(μ-I)$_2$I$_2$]$^{2-}$ (copper(I)-I dimmer) and [MeaaiMe(CH$_2$Ph)]$^+$ are integral parts of the

Table 2
^{1}H NMR data of the complexes.

Complexes	δ, ppm (J, Hz)						
	4-H[a]	5-H[a]	7,11-H[b]	8-10-H	9-Me[d]	1-(3-)- Me	1-(3-)-CH$_2$
[HaaiMe$_2$][CuI$_2$] (**5a**)	7.64	7.64	8.07 (8.0)	7.52[c]		4.32[d]	
[MeaaiMe$_2$][CuI$_2$] (**5b**)	7.74	7.74	7.95 (7.0)	7.42[b] (9.0)	2.52	4.08[d]	
[HaaiEt$_2$][CuI$_2$] (**6a**)	7.62	7.62	8.00 (8.0)	7.50[c]		1.48[e] (7.0)	4.72[g] (9.0)
[MeaaiEt$_2$][CuI$_2$] (**6b**)	7.71	7.71	7.91 (7.0)	7.36[b](9.0)	2.54	1.45[e] (7.00)	4.76[g] (9.0)
[Haai(CH$_2$Ph)$_2$][CuI$_2$] (**7a**)[f]	7.60	7.60	7.97 (8.0)	7.56[c]			5.62[d]
[Meaai(CH$_2$Ph)$_2$][CuI$_2$] (**7b**)[f]	7.54	7.54	7.94 (8.0)	7.42[b](9.0)	2.49		5.85[d]
[HaaiMe(CH$_2$Ph)][CuI$_2$] (**8a**)[f]	7.49	7.58	7.92 (8.0)	7.52[c]		4.18[d]	5.72[d]
[MeaaiMe(CH$_2$Ph)] [CuI$_2$] (**8b**)[f]	7.41	7.41	7.97 (8.0)	7.49[b]	2.52	4.56[d]	6.02[d]
[HaaiMe$_2$]$_2$[Ag$_3$I$_5$] (**9a**)	8.03	8.03	8.11 (7.0)	7.73[c]		4.11	
[MeaaiMe$_2$]$_2$[Ag$_3$I$_5$] (**9b**)	7.97	7.97	8.00 (8.0)	7.51[b](8.0)	2.48	4.09	
[HaaiEt$_2$]$_2$[Ag$_3$I$_5$] (**10a**)	8.00	8.00	8.08 (7.0)	7.70[c]		1.44[e] (8.0)	4.84[g] (9.0)
[MeaaiEt$_2$]$_2$[Ag$_3$I$_5$] (**10b**)	7.95	7.95	8.02 (8.0)	7.50[b] (8.0)	2.44	1.49[e] (8.0)	4.80[g] (9.0)
[Haai(CH$_2$Ph)$_2$]$_2$[Ag$_3$I$_5$] (**11a**)[f]	8.02	8.02	8.07 (8.0)	7.53[c]			5.82[d]
[Meaai(CH$_2$Ph)$_2$]$_2$ [Ag$_3$I$_5$] (**11b**)[f]	7.99	7.99	8.02 (8.0)	7.50[b]	2.49		5.76[d]
[HaaiMe(CH$_2$Ph)]$_2$ [Ag$_3$I$_5$] (**12a**)[f]	8.02	8.02	8.04	7.53[c]		4.04[d]	5.80[d]
[MeaaiMe(CH$_2$Ph)]$_2$ [Ag$_3$I$_5$] (**12b**)[f]	8.06	8.06	8.00 (8.0)	7.53[b]	2.50	4.09[d]	5.74[d]

[a] Broad singlet.
[b] Doublet.
[c] Multiplet.
[d] Singlet.
[e] δ(–N–CH$_2$–)CH$_3$.
[f] –CH$_2$Ph and δ of Ph protons lie 7.35–7.50 ppm.
[g] Quartet.

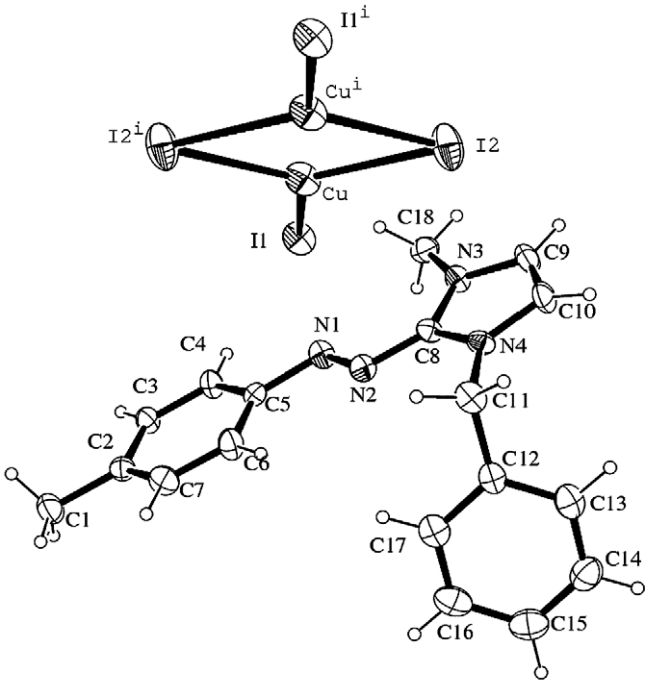


Fig. 1. Molecular unit of $[MeaaiMe(CH_2Ph)^+]_2[Cu_2I_4]^{2-}$ (**8b**).

structure. There are bridge-I and terminal-I bonded to Cu(I) in $[Cu_2(\mu\text{-}I)_2I_2]^{2-}$ motif. The terminal Cu–I bond distances (Cu–I(1), 2.5004(16) Å) are shorter than bridged Cu–I(2) distances (Cu–I(2), 2.5716(19) Å and $Cu^{\#}$–I(2), 2.5888(17) Å). The $[Cu_2(\mu\text{-}I)_2I_2]^{2-}$ is hydrogen bonded to imidazole-H *via* C(9)–H(9)...I1(#1) forming neutral chain (Supplementary material Fig. S1). The hydrogen bonding in C–H–I pattern are scarce [36,37]. In $[MeaaiMe(CH_2Ph)]^+$ the azophenyl and imidazole rings are virtually coplanar as indicated by the torsion angle, C(1)–N(1)–N(2)–C(7), 179.2(9)° and the dihedral angle of two planes, 6.20(12)°. Nonplanarity of benzylic phenyl group (C(11)–C(16)) with imidazole ring is due to $-CH_2-$ group and makes an angle of 112° with imidazole unit. The N(1)–N(2) bond length is 1.234(11) Å which is lower than reported free ligand data (1.252(2) Å for 1-methyl-2-(phenylazo)imidazolium perchlorate) [38–40]. The N(azo)–C(imidazole) distance, N(2)–C(8), 1.359(13) Å, is shorter than N(azo)–C(phenyl), N(1)–C(5), 1.418(13) Å which indicates a stronger intramolecular interaction between azo and imidazole group.

Table 3
Selected bond lengths and bond angles of $[MeaaiMe(CH_2Ph)^+]$ $[CuI_2^-]$ (**8b**) and $[MeaaiMe_2^+]_2$ $[Ag_3I_5^{2-}]$ (**9b**).

Bond lengths (Å)			Bond angles (0)
*[MeaaiMe(CH$_2$Ph)$^+$] [CuI$_2^-$] (**8b**)*			
Cu–I(1)	2.5004(16)	Cu–I(2)–Cu[a]	61.35(6)
Cu–I(2)	2.5716(19)	I(1)–Cu[a]–I(2)	120.92(6)
Cu[a]–I(2)	2.5888(17)	I(1)–Cu–I(2)	120.41(7)
N(1)–N(2)	1.234(11)	I(2)–Cu[a]–I(2)	118.65(6)
N(2)–C(8)	1.359(13)	N(2)–N(1)–C(5)	114.4(9)
N(1)–C(5)	1.418(13)	N(1)–N(2)–C(8)	115.9(9)
Cu–Cu[a]	2.633(2)		
*[MeaaiMe$_2^+$]$_2$ [Ag$_3$I$_5^{2-}$] (**9b**)*			
Ag(1)–I(1)	2.9068(7)	I(4)–Ag(1)–I(3)	109.24(2)
Ag(1)–I(2)	2.9664(8)	I(4)–Ag(1)–I(1)	122.69(3)
Ag(1)–I(4)	2.7806(8)	I(3)–Ag(1)–I(1)	102.08(2)
Ag(1)–I(3)	2.8318(9)	I(4)–Ag(1)–I(2)	116.18(3)
Ag(2)–I(5)	2.7163(9)	I(3)–Ag(1)–I(2)	115.45(3)
Ag(2)–I(1)	2.9781(8)	I(1)–Ag(1)–I(2)	89.78(2)
Ag(2)–I(2)	2.9738(8)	I(5)–Ag(2)–I(3)[b]	110.36(2)
Ag(2)–I(3)[b]	2.8671(8)	I(5)–Ag(2)–I(2)	119.58(3)
Ag(3)–I(1)	2.8972(16)	I(5)–Ag(2)–I(1)	122.63(3)
N(3)–N(4)	1.236(7)	I(3)–Ag(3B)–I(1)	92.96(11)
N(7)–N(8)	1.242(7)	Ag(1)–I(2)–Ag(2)	88.02(2)
		Ag(1)–I(3)–Ag(3B)	53.72(5)

[a] $1-x, -y, 1-z$.
[b] $x, 3/2-y, -1/2+z$.

Azoimidazolium unit contains three different aromatic rings: *p*-tolyl (*p*-Tol), phenyl (Ph) and imidazole (Imz). The face-to-face (Cg(2)–Cg(3)(#1)), 3.7867 Å (symmetry, $-x$, $1-y$, $-z$) ; and Cg(3)–Cg(3)(#3) (3.8424 Å) (symmetry, $1-x$, $1-y$, $-z$) where Cg(20) refers to Imz, N(3)–C(8)–N(4)–C(10)–C(9) and Cg(3), refers to *p*-Tol, C(2)–C(3)–C(4)–C(5)–C(6)–C(7)) π–π stacking interactions are observed between aromatic rings belonging to adjacent chains in the network (Supplementary material Fig. S1b). The π-chains so formed exhibit C–H–π interactions (H or C–Centroid (Cg) of Ph): C(4)-H(4)–Cg(4) (#1), 2.712(7) Å (symmetry, $-x$, $1-y$, $-z$); C(11)–H(11A)–Cg(4) (#2), 3.197(4) Å (symmetry, $-x$, $1-y$, $1-z$); C(18)-H(18C)–Cg(3) (#1), 3.162(8) Å (symmetry, $-x$, $1-y$, $-z$) Cg(2), Cg(3) are defined earlier. Cg(4) is –(N(1)–CH_2–)–Ph (C(12)–C(13)–C(14)–C(15)–C(16)–C(17)) (Fig. 2). Inter-chain face-to-face π–π interaction enable to form a π-sheet (Supplementary material Fig. S2).

3.3.2. Structure of [MeaaiMe$_2^+$]$_2$

The crystal structure unit of $[MeaaiMe_2^+]_2$ $[Ag_3I_5^{2-}]$ (**9b**) is shown in (Fig. 3a) and bond parameters are given in Table 3 (full data are

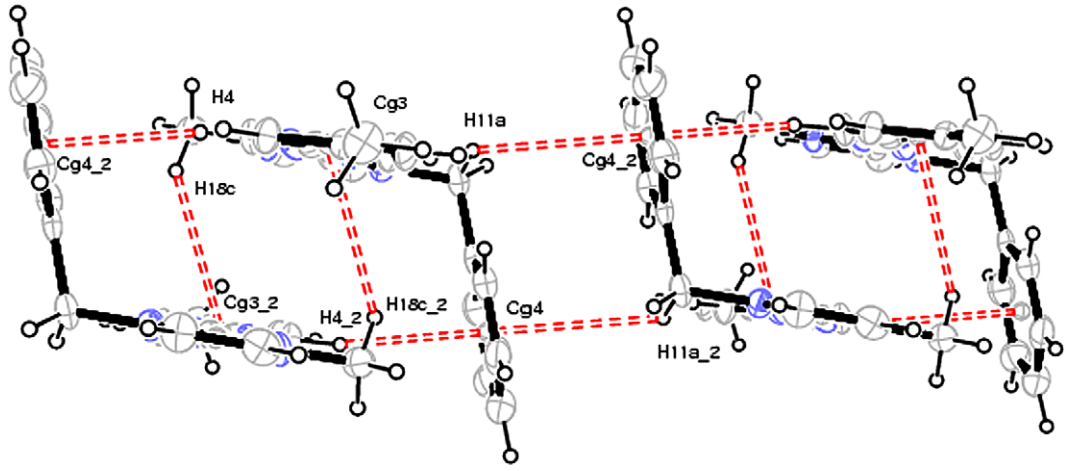


Fig. 2. C–H–π interaction leading to 1-D chain of $[MeaaiMe(CH_2Ph)^+]_2[Cu_2I_4]^{2-}$ (**8b**).

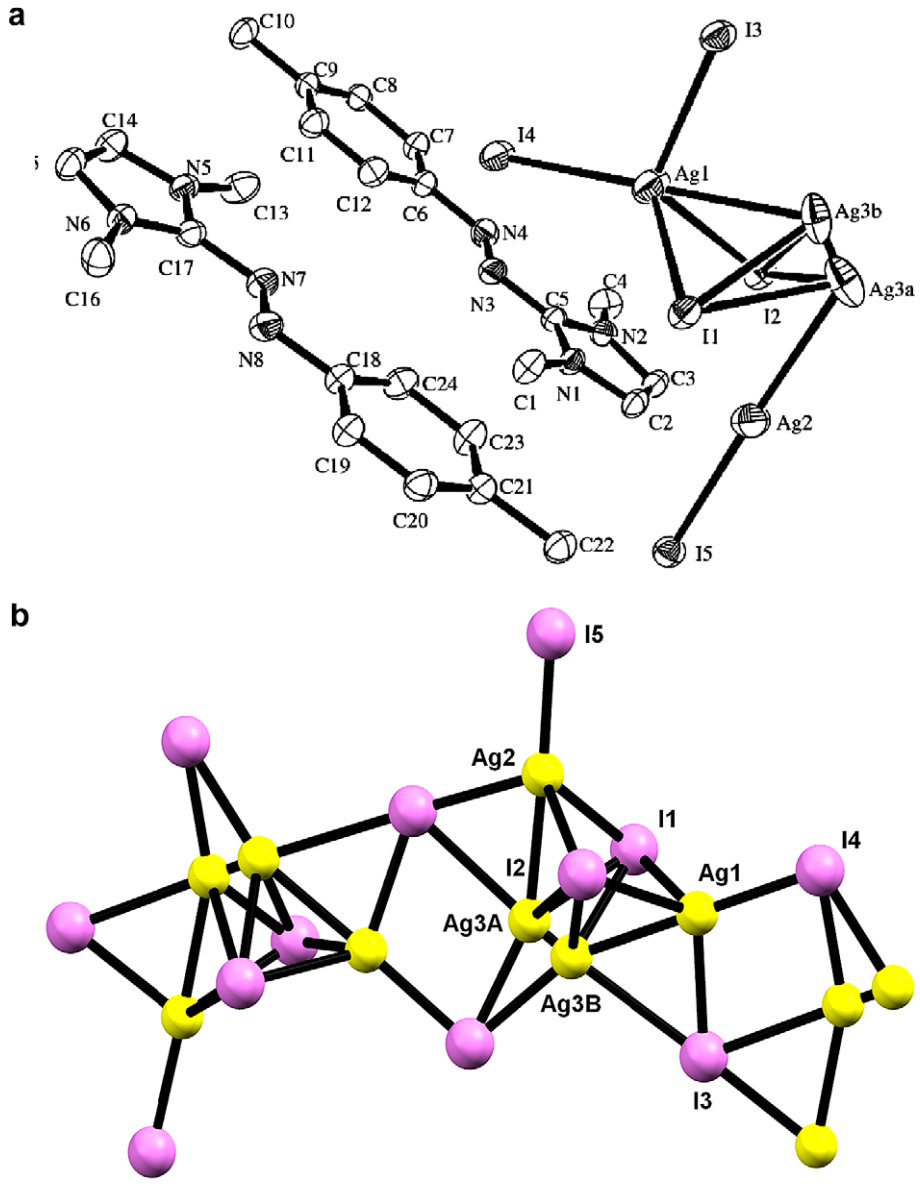


Fig. 3. (a) Structural unit of $[MeaaiMe_2^+]_2\,[Ag_3I_5^{2-}]$ (**9b**) and (b) polymeric chain of $[Ag_3(I_5^{2-}]$.

given in Supplementary Material, Table S1). The structure shows a one-dimensional chain constructed from $[MeaaiMe_2^+]$ and $[Ag_3I_5^{2-}]$. Anion, $[Ag_3I_5^{2-}]$ exists as iodo bridged chain (Fig. 3b). In monomeric unit two Ag atoms (Ag1 and Ag2) are bridged by I(1) and I(2) and Ag(3) is doubly bridged with two μ-I. Ag(3) significantly perturbed and is assigned Ag(3A) and Ag(3B). Three terminal Is (I(3), I(4), I(5)) of $[Ag_3I_5^{2-}]$ are responsible to form chain structure *via* vertices sharing and Ag–I–Ag bridge. Because of the bridging nature of iodine atoms, the coordination environment of the silver atom is distorted from that of a perfect tetrahedron. The AgI_4 tetrahedron is highly distorted, with Ag–I bond distances ranging from 2.7163(9) to 2.9781(8) Å. There are two types of bridging-I: μ_2-I ((I(3), I(4), I(5)) bridge two Ag centers) and μ_3-I (I(1), I(2) bridges three Ag centers Ag(1), Ag(2) and Ag(3A, 3B)). The I–Ag–I bond angles range from 88.28(2) to 122.69(3)° (Table 3), and the Ag–I–Ag bond angles range from 57.42(8) to 172.10(5)°, deviating significantly from 109.5° for an ideal tetrahedron.

The distance between two Ag atoms are Ag(1)–Ag(3B), 2.799(5) and Ag(2)–Ag(3A), 2.8229(17) Å., shorter than sum of van der Waals radii silver (3.44 Å) [41]. The argentophilicity may be the reason for metal–metal interaction between d^{10} and d^{10} closed-shell metals which promotes the aggregation of silver(I) centers. Compounds possessing argentophilicity can be potentially used in silver-containing antibacterial reagents [42]. The *p*-tolylazo and imidazole rings of $MeaaiMe_2^+$, are virtually coplanar and the dihedral angle of two planes is 2.08(19) Å. The N(3)–N(4) and N(7)–N(8) bond lengths are 1.236(7) and 1.242(7) Å which are comparable with $[MeaaiMe(CH_2Ph)^+]_2[Cu_2(\mu\text{-}I)_2I_2]^{2-}$ (**8b**). Pendant phenyl ring and imidazole unit of neighboring cations undergo C–H–π and π–π interaction resulting layers of organic cations. Polyanion chains of $[Ag_3I_5^{2-}]_n$ may act as channels whereas organic cations lie sandwiched between two adjacent chains. Organic groups do not participate in coordination but connect with inorganic moieties by noncovalent interactions: electrostatic force. The organic and inorganic moieties alternate to form a so-called organic-inorganic hybrid structure (Supplementary material, Fig. S3).

4. Conclusion

In summary, we have prepared and structurally characterized hybrid azoimidazolium iodocuprate(I) and iodoargentate(I) compounds. The single crystal X-ray structural characterization shows

di-iodo bridged dimmer $[Cu_2(\mu\text{-}I)_2I_2]^{2-}$ is associated with organic cation $[MeaaiMe(CH_2Ph)^+]$ through electrostatic attraction. In iodoargentate(I) the monomeric unit is $[Ag_3I_5]^{2-}$ that has two μ_3-I and monomer forms 1D chain by Ag–I–Ag bridge. The chains of $[Ag_3I_5^{2-}]_n$ serve as channels wherein organic cations, $[MeaaiMe_2]^+$ is sandwiched. Organic groups do not participate in coordination but connect with inorganic moieties by noncovalent interactions. On the basis of this work, further investigations of new inorganic–organic hybrid metal halides with azoimidazolium derivatives are under way in our laboratory.

5. Supplementary materials

CCDC 614001 and 602165 contain the supplementary crystallographic data for $[MeaaiMe(Bz)^+]_2[Cu_2(\mu\text{-}I)_2I_2]^{2-}$ (**8b**) and for $[MeaaiMe_2^+]_2$ $[Ag_3I_5^{2-}]$ (**9b**). These data can be obtained free of charge via http://www.ccdc.cam.ac.uk/conts/retrieving.html, or from the Cambridge Crystallographic Data Centre, 12 Union Road, Cambridge CB2 1EZ, UK; fax: (+44) 1223-336-033; or e-mail: deposit@ccdc.cam.ac.uk.

Acknowledgements

Financial support from UGC (CAS), New Delhi is thankfully acknowledged. Thanks are also due to Dr. Tapan Kumar Mondal, Department of Chemistry, Jadavpur University for his help in drawing crystallographic drawings.

Appendix A. Supplementary data

Supplementary data associated with this article can be found, in the online version, at doi:10.1016/j.poly.2009.07.034.

References

[1] A.K. Cheetham, Science 264 (1994) 794.
[2] O.M. Yaghi, H. Li, C. Davis, D. Richardson, T.L. Groy, Acc. Chem. Res. 31 (1998) 474.
[3] M.T. Pope, A. Müller, Angew. Chem., Int. Ed. Engl. 30 (1991) 34; C.L. Hill, Chem. Rev. 98 (1998) 1.
[4] C.D. Wu, C.Z. Lu, X. Lin, D.M. Wu, S.F. Lu, H.H. Zhuang, J.S. Huang, Chem. Commun. (2003) 1284.
[5] G. Boche, F. Basold, M. Marsch, K. Harms, Angew. Chem., Int. Ed. 37 (1998) 1684.
[6] J.P. Jasinski, N.P. Rath, E.M. Holt, Inorg. Chim. Acta (1985) 91–97.
[7] K. Singh, J.R. Long, P. Stavropoulos, J. Am. Chem. Soc. 119 (1997) 2942.
[8] M.A. Omary, T.R. Webb, Z. Assefa, G.E. Shankle, H.H. Patterson, Inorg. Chem. 37 (1998) 1380.
[9] H.-H. Li, Z.-R. Chen, J.-Q. Li, C.-C. Huang, Y.-F. Zhang, G.-X. Jia, Cryst. Growth Des. 7 (2006) 1813–1820.
[10] J.L. Zhou, Y.Z. Li, H.G. Zheng, X.Q. Xin, T. Yin, Y.X. Wang, Y.L. Song, Trans. Met. Chem. 29 (2004) 185.
[11] S. Shi, W. Ji, S.H. Tang, J.P. Lang, X.Q. Xin, J. Am. Chem. Soc. 116 (1994) 3615.
[12] M.K.M. Low, H.W. Hou, H.G. Zheng, W.T. Wong, G.X. Jin, X.Q. Xin, W. Ji, Chem. Commun. (1998) 505.
[13] J.B. Howard, D.J. Low, Chem. Rev. 96 (1996) 2965.
[14] R.H. Holm, Adv. Inorg. Chem. 38 (1992) 1.
[15] F.A. Cotton, G. Wilkinson, Advanced Inorganic Chemistry, fifth ed., John Wiley & Sons, New York, 1988.
[16] C. Janiak, L. Uehlin, H.-P. Wu, P. Klufers, H. Piotrowski, T.G. Scharmann, J. Chem. Soc., Dalton Trans. 4 (1999) 3121. and references therein.
[17] H. Hartl, F. Mahdjour-Hassan-Abadi, Angew. Chem., Int. Ed. Engl. 33 (1994) 1841.
[18] J.K. Cheng, Y.-G. Yao, J. Zhang, Z.-J. Li, Z.-W. Cai, X.-Y. Zhang, Z.-N. Chen, Y. Chen, Y.-B. Kang, Y.-Y. Qin, Y.-H. Wen, J. Am. Chem. Soc. 126 (2004) 7796.
[19] D.R. McMillin, K.M. McNett, Chem. Rev. 98 (1998) 1201.
[20] M. Ruthkosky, C.A. Kelly, F.N. Castellano, G.J. Meyer, Coord. Chem. Rev. 171 (1998) 309.
[21] J.R. Nitschke, Am. Chem. Soc. 121 (1999) 4292.
[22] U.S. Ray, G. Mostafa, T.H. Lu, C. Sinha, Cryst. Eng. 5 (2002) 95.
[23] U.S. Ray, B.G. Chand, A.K. Dasmahapatra, G. Mostafa, T.-H. Lu, C. Sinha, Inorg. Chem. Commun. 6 (2003) 634.
[24] K.K. Sarker, A.D. Jana, G. Mostafa, J.-S. Wu, T.-H. Lu, C. Sinha, Inorg. Chim. Acta 359 (2006) 4377.
[25] B.G. Chand, U.S. Ray, G. Mostafa, Polyhedron 23 (2004) (1669).
[26] B.G. Chand, U.S. Ray, G. Mostafa, T.-H. Lu, C. Sinha, J. Coord. Chem. 57 (2004) 627.
[27] B.G. Chand, U.S. Ray, J. Cheng, Chim. Acta 358 (2005) 1927.
[28] T.K. Misra, D. Das, C. Sinha, Polyhedron 16 (1997) 4163.
[29] J. Dinda, U.S. Ray, G. Mostafa, T.-H. Lu, A. Usman, I. Abdul Razak, S. Chantrapromma, H.-K. Fun, C. Sinha, Polyhedron 22 (2003) 247.
[30] G.M. Sheldrick, SHELXS-97, Program for the Solution of Crystal Structure, University of Gottingen, Germany, 1997.
[31] G.M. Sheldrick, SHELXL-97, Program for the Refinement of Crystal Structure, University of Gottingen, Germany, 1997.
[32] A.L. Spek, PLATON, Molecular Geometry Program, University of Utrecht, The Netherlands, 1999.
[33] L.J. Farrugia, J. Appl. Crystallogr. 30 (1997) 565.
[34] J.P. Devlin, J. Sadle, V. Buchi, J. Phys. Chem. A 105 (2001) 974.
[35] N. Nishimura, T. Sueyoshi, H. Yamanaka, E. Imai, S. Yamamoto, S. Hasegawa, Bull. Chem. Soc. Jpn. 49 (1976) 1381.
[36] H. Karutscheid, F. Vielsack, K.N. Frieder, Z. Anorg. Alleg. Chem. 624 (1998) 807.
[37] S.J. Garden, C. Glidewell, J.N. Low, J.M.S. Skakle, J.L. Wardell, Acta Crystallogr. Sect. C, Cryst. Struct. Commun. C61 (2005) 145.
[38] P. Bhunia, B. Baruri, U.S. Ray, C. Sinha, S. Das, J. Cheng, T.-H. Lu, Trans. Met. Chem. 31 (2006) 310.
[39] J. Otsuki, K. Suwa, K. Narutaki, C. Sinha, I. Yoshikawa, K. Araki, J. Phys. Chem. A 109 (2005) 8064.
[40] J. Dinda, K. Bag, C. Sinha, G. Mostafa, T.-H. Lu, Polyhedron 22 (2003) 1367.
[41] A. Bondi, J. Phys. Chem. 68 (1964) 441.
[42] K. Nomiya, S. Takahashi, R. Noguchi, Dalton Trans. (2000) 2091.

(Merck) was distilled over a sodium–potassium alloy under an atmosphere of dry argon. Silica gel (Merck 60, 0.063–0.200 mm) was used for column chromatography. All reactions were performed under a dry argon atmosphere.

2.2. Methods

Thin layer chromatography (TLC) was performed on Merck Silica gel plates (Merck 60, 0.25 mm thickness) with F_{254} indicator. Column chromatography was performed on silica gel (Merck 60, 0.063–0.200 mm; for 3 g crude mixture, 120 g silica gel was used in a column of 3 cm in diameter and 110 cm in length). Mass spectra were recorded on a Bruker MicroTOF LC–MS spectrometer using the electrospray ionisation (ESI) method; ^{35}Cl values were used for calculated masses. Analytical ^{1}H, ^{19}F and ^{31}P NMR spectra were recorded for $CDCl_3$ solutions on a Bruker DRX 500 MHz spectrometer using TMS as an internal reference for ^{1}H, $CFCl_3$ as an internal reference for ^{19}F and 85% H_3PO_4 as an external reference for ^{31}P. In order to assign the signals of some compounds both proton-coupled and proton-decoupled ^{19}F and ^{31}P NMR spectra were recorded.

2.3. Reaction of cyclotriphosphazene (*1*) with 2,2,3,3,4,4,5,5-octafluoro-1,6-hexanediol (*2*)

Cyclophosphazene (3.48 g, 10 mmol) and 2,2,3,3,4,4,5,5-octafluoro-1,6-hexanediol (3,14 g, 12 mmol) were dissolved in 150 mL of dry THF in a 250 mL three-necked round-bottomed flask. The reaction mixture was cooled in an ice-bath and NaH (60% oil suspension, 1 g, 24 mmol) in 20 mL of dry THF was quickly added to the stirred solution under an argon atmosphere. The reaction mixture was stirred for 72 h at room temperature and the reaction was followed on TLC silica gel plates using hexane–DCM (3:1), giving four new products. The reaction mixture was filtered to remove the sodium chloride and any other insoluble material. The solvent was removed at reduced pressure and the resulting colourless oil was subjected to column chromatography, using hexane–DCM (3:1) as the eluant. Unreacted trimer (**1**) (0.81 g, 23%) was eluted first from the column. The first product eluted is the mono-ansa derivative $N_3P_3Cl_4[OCH_2(CF_2)_4CH_2O]$ (**3**), (1.13 g, 21%, mp 124 °C). *Anal.* Calc. for $C_6H_4Cl_4F_8N_3O_2P_3$ (M, 536.8): C, 13.42; H, 0.75; N, 7.83. Found (M^+, 537.9): C, 13.40; H, 0.72; N, 7.80%. ^{1}H NMR, $CDCl_3$, 298 K; complex multiplet, 4.50 ppm, 4H, (OCH_2). The second product is the single-bridged derivative $N_3P_3Cl_5[OCH_2(CF_2)_4CH_2O]N_3P_3Cl_5$ (**4**), (1.20 g, 27%, viscous oil). *Anal.* Calc. for $C_6H_4Cl_{10}F_8N_6O_2P_6$ (M, 884.5): C, 8.15; H, 0.83; N, 9.50. Found (M^+, 876.7): C, 8.12; H, 0.81; N, 8.49%. ^{1}H NMR, $CDCl_3$, 298 K; complex multiplet, 4.49 ppm, 4H, (OCH_2). The third separated product is the double-bridged derivative(s) $N_3P_3Cl_4[OCH_2(CF_2)_4CH_2O]_2N_3P_3Cl_4$ (**5**) shown to exist as a mixture of two isomers by ^{31}P NMR spectroscopy. A compound crystallised from the column fraction solvent was shown by X-ray crystallography to be the double-bridged compound (**5**-*anti* isomer). The ^{31}P NMR spectrum of the solvent residue showed it to be other isomer (**5**-*syn*), as also observed in the ^{31}P NMR spectrum of the reaction mixture. *Anal.* Calc. for isomers $C_{12}H_8Cl_8F_{16}N_6O_4P_6$ (M, 1073.7): C, 13.42; H, 0.75; N, 7.83. (**5**-*anti*) (0.50 g, 9%, mp 141 °C) Found (M^-, 1072.7): C, 13.40; H, 0.74; N, 7.78%. ^{1}H NMR, $CDCl_3$, 298 K; complex multiplet, 4.54 ppm, 8H, (OCH_2). (**5**-*syn*) (0.22 g, 4%, oil) Found (M^+, 1074.8): C, 13.44; H, 0.77; N, 7.75%. ^{1}H NMR, $CDCl_3$, 298 K; complex multiplet, 4.46 ppm, 8H, (OCH_2). The last product eluted is the triple-bridged derivative $N_3P_3Cl_3[OCH_2(CF_2)_4CH_2O]_3N_3P_3Cl_3$ (**6**), (0.12 g, 2%, mp 250.87 °C). *Anal.* Calc. for $C_{18}H_{12}Cl_6F_{24}N_6O_6P_6$ (M, 1262.9): C, 17.12; H, 0.96; N, 6.65. Found (M^+, 1262.7): C, 17.10; H, 0.92; N, 6.63%. ^{1}H NMR, $CDCl_3$, 298 K; complex multiplet, 4.50 ppm, 12H, (OCH_2). Compounds **3**, **5**-*anti* and **6** crystallized from hexane–DCM (3:1) and were obtained as white crystals suitable for X-ray crystallography.

2.4. X-ray crystallography

Intensity data were recorded on a Nonius KappaCCD diffractometer driven by COLLECT [14] and DENZO [15] software. Details of data collection and structure refinement for all compounds are given in Table 2. Structures were determined using the direct methods procedure in SHELXS-97 and refined by full-matrix least squares on F^2 using SHELXL-97 [16].

3. Results and discussion

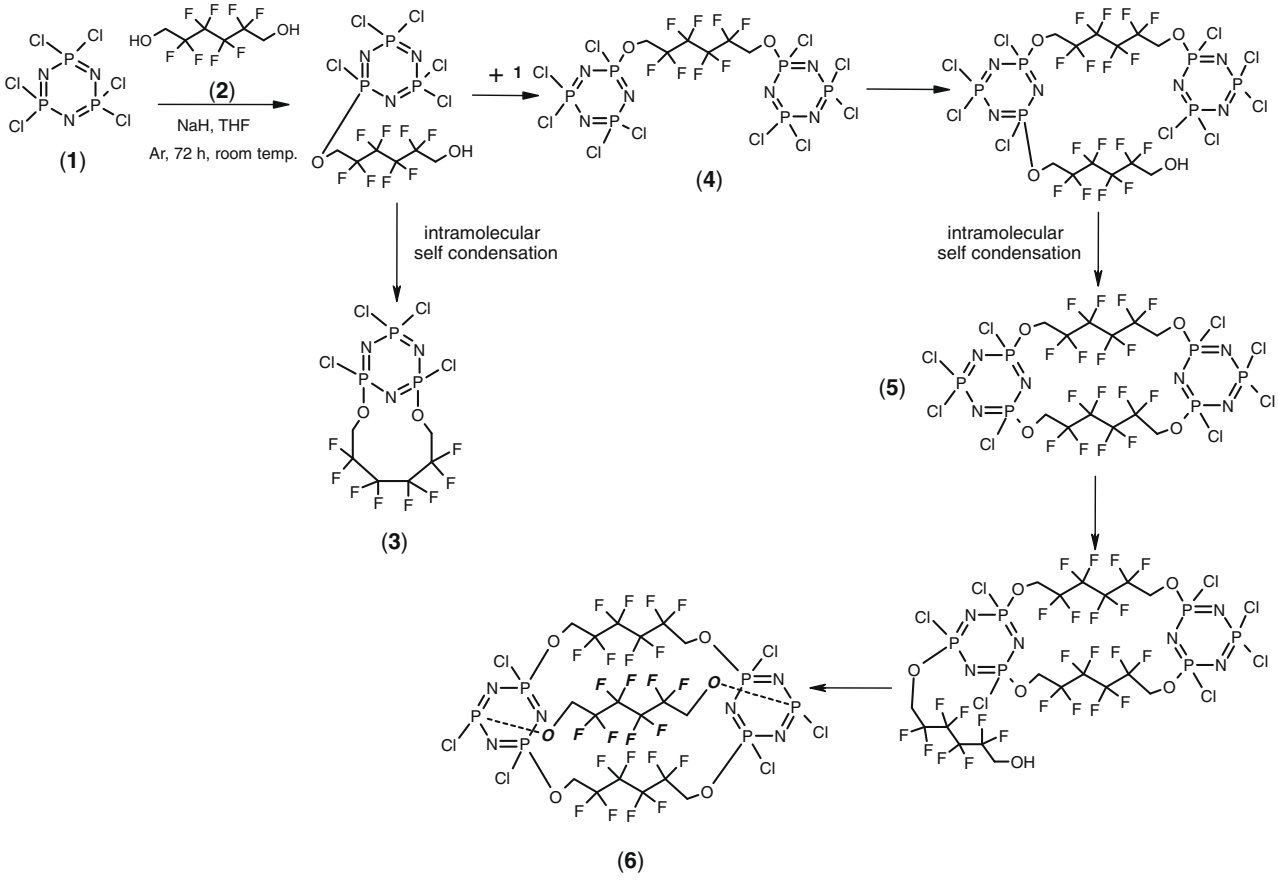
3.1. Characterisation of reaction products by ^{1}H, ^{19}F and ^{31}P NMR spectroscopy

Cyclotriphosphazene (**1**) was reacted with the sodium salt 2,2,3,3,4,4,5,5-octafluorohexane-1,6-diol (**2**) in THF solution under the same solution conditions as those used previously for the reaction of (**1**) with 2,2,3,3-tetrafluorobutane-1,4-diol [10] and 2,2,3,3,4,4-hexafluoropentane-1,5-diol [11]. The ^{31}P NMR spectrum of the reaction mixture indicated five products, which were separated by column chromatography and characterised by ^{1}H, ^{19}F and ^{31}P NMR spectroscopy; the mono-ansa compound $N_3P_3Cl_4(OCH_2(CF_2)_4CH_2O)$ (**3**), the single-bridged compound $N_3P_3Cl_5[OCH_2(CF_2)_4CH_2O]N_3P_3Cl_5$, (**4**), the double-bridged compound $N_3P_3Cl_4(OCH_2(CF_2)_4CH_2O)_2N_3P_3Cl_4$, (**5**) [later characterised as two compounds (**5**-*anti*, **5**-*syn*)], and the triple-bridged compound $N_3P_3Cl_3(OCH_2(CF_2)_4CH_2O)_3N_3P_3Cl_3$ (**6**) (Scheme 1).

Except for the triple-bridged compound (**6**), all the cyclotriphosphazene derivatives contain both PCl(OR) and PCl_2 groups and the ^{31}P NMR spectra are observed as A_2X (or A_2B) spin systems, which can be readily assigned by consideration of signal intensities, chemical shifts and coupling patterns. The triple-bridged cyclophosphazene derivative (**6**) only contains PCl(OR) groups and the ^{31}P NMR spectrum is a single line. The ^{31}P NMR chemical shifts and ^{2}J(PP) values of the compounds are summarised in Table 1. The ^{1}H NMR results for each new compound are provided as part of the analytical data in the synthesis section.

The proton-decoupled ^{19}F NMR spectrum of the bridged forms of the octafluoro-1,6-dioxy moiety shows two single-line signals in a 1:1 ratio (A_2B_2 spin system) for compounds **4**, **5**-*anti*, **5**-*syn* and **6**, whereas the ansa form for compound **3** gives rise to two AB spin systems with ^{2}J(FF) *ca.* 302.6 and 301.7 Hz. Each F atom of the CF_2 groups in the ansa moiety are non-equivalent because they have different spatial relationships with respect to the cyclophosphazene ring and so each peak is split due to geminal coupling ^{2}J(FCF). The ^{19}F chemical shifts and coupling constants of the products are given in Table 1. The magnitudes of ^{2}J(FCF) are in line with previous results on geminal coupling [10,11,17]. It should be noted that the line widths of the ^{19}F NMR signals of the bridged moiety are narrower than those for the ansa moiety, which might reflect the fact that the bridge moiety is more flexible than the ansa moiety.

It is known that there are two configurational isomers for diamino double-bridged cyclotriphosphazene compounds, *i.e.* there are two different meso forms, one has a centre of symmetry and the other has plane of symmetry [9b]. By analogy, the double-bridged diol compound (**5**) has the potential to exist as two configurational isomers (Scheme 2) and so particular attention was taken in analysing by ^{31}P NMR spectroscopy appropriate fractions in the chromatographic separation of the reaction mixture. An example is given (Fig. 1a) for compound (**5**), where the ^{31}P NMR spectrum is observed as two sets of closely spaced signals



Scheme 1. The reaction of cyclotriphosphazene (**1**) with 2,2,3,3,4,4,5,5-octafluorohexane-1,6-diol (**2**) and structures of the products, compounds (**3**)–(**6**).

Table 1
^{31}P and ^{19}F NMR parameters of compounds **3**–**6**.[a,b]

Cpd	Type[c]	^{31}P chemical shift (ppm)		$^{2}J_{PNP}$ (Hz)	^{19}F chemical shift (ppm)		$^{2}J_{FCF}$ (Hz)
		PCl_2	P(OR)Cl		(CF_2)	(CF_2)	
3	ansa	26.70	19.64	69.2	−114.9	−119.5	302.6[d]
					−118.1	−120.7	301.7[e]
4	single-br	23.77	17.57	65.2	−120.3	−123.6	
5-*anti*	double-br	26.01	20.45	67.3	−120.5	−123.7	
5-*syn*	double-br	26.12	20.43	67.7	−120.9	−124.1	
6	triple-br		23.08		−121.0	−123.7	

[a] 202.38 MHz ^{31}P NMR chemical shifts (ppm) in $CDCl_3$ with respect to external 85% H_3PO_4.
[b] 470.36 MHz ^{19}F NMR chemical shifts (ppm) in $CDCl_3$ with respect to internal $CFCl_3$.
[c] br = bridge.
[d] Magnitude of $^{2}J_{FCF}$ corresponds to signals at *ca.* −114 to −119 ppm.
[e] Magnitude of $^{2}J_{FCF}$ corresponds to signals at *ca.* −119 to −121 ppm.

in an approximate 2:1 ratio showing partial separation by column chromatography. The column fraction was then crystallized and the ^{31}P NMR spectrum of the re-dissolved crystal (Fig. 1b) showed one of the diastereoisomers and the ^{31}P NMR spectrum of the solvent residue (Fig. 1c) show the other diastereoisomer. X-ray crystallography is needed to characterise which form of compound (**5**) crystallised.

*3.2. Characterisation of compounds (**3**), (**5**-anti) and (**6**) by X-ray crystallography and, hence, (**5**-syn) by ^{31}P NMR spectroscopy*

The X-ray crystal structures are reported for compounds (**3**), (**5**-*anti*) and (**6**) (Figs. 2–4), with data collection and refinement parameters reported in Table 2.

The cyclophosphazene ring in each structure exhibits no unusual deviations in bond lengths and angles from either that of the parent $N_3P_3Cl_6$ structure (CSD code KAGKUY) [18] or from that observed in similar structures in the Cambridge Structural Database [19]. The cyclotriphosphazene rings are quite planar, with a deviation of individual atoms from the N_3P_3 plane in all structures ranging from 0.024 to 0.137 Å with an average of 0.090 Å, *viz.* **3** (0.024), **5**-*anti* (0.137, 0.137) and **6** (molecule 1, 0.076, 0.122; molecule 2, 0.122, 0.072; molecule 3, 0.080, 0.062; molecule 4 0.058, 0.098 Å).

The molecular structure of **3** (Fig. 2) confirms the *cis*-ansa structure with one diol moiety linked between phosphorus moieties on the same cyclophosphazene ring. The molecular structure of **5** (Fig. 3) show the double-bridged derivative, in which the diol chains are in a *cis*-configuration and the two cyclotriphosphazene rings are in an antiparallel arrangement with respect to the plane of ring formed from the two diol bridges; hence, it has been designated **5**-*anti* to distinguish it from the configurational analogue **5**-

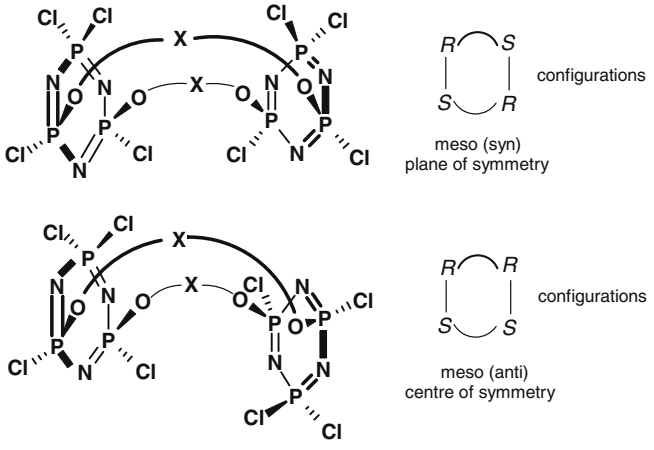
Table 2
X-ray crystallographic data and refinement parameters for compounds **3**, **5**-*anti*, and **6**.

Compound number	**3**	**5**-*anti*	**6**
Empirical formula	$C_6H_4Cl_4F_8N_3O_2P_3$	$C_{12}H_8Cl_8F_{16}N_6O_4P_6$	$C_{18}H_{12}Cl_6F_{24}N_6O_6P_6$
Formula weight	536.83	1073.66	1262.86
Crystal system	monoclinic	monoclinic	triclinic
Space group	$P2_1/c$	$C2/m$	$P\bar{1}$
a (Å)	6.0475(4)	20.9333(3)	16.4477(2)
b (Å)	27.1376(15)	14.5008(2)	16.5533(2)
c (Å)	10.4986(7)	5.9142(2)	33.8473(5)
α (°)	90	90	92.0706(5)
β (°)	96.177(3)	102.975(2)	92.3401(4)
γ (°)	90	90	118.2520(4)
V (Å^3)	1712.97(19)	1758.38(5)	8094.49(18)
Z	4	2	8
Density(calc) (Mg/m^3)	2.082	2.028	2.073
Absorption coefficient (mm^{-1})	1.062	1.035	0.819
F(0 0 0)	1048	1048	4944
Crystal size (mm)	0.10 × 0.06 × 0.02	0.2 × 0.2 × 0.01	0.20 × 0.10 × 0.10
θ_{max} (°)	27.50	27.50	27.50
Reflections collected	17 197	26 252	148 814
Independent reflections ($I > 2\sigma I$)	3849	2105	36 811
R_{int}	0.0523	0.0349	0.0480
Final R indices ($F^2 > 2\sigma F^2$)	R_1 = 0.0633	R_1 = 0.0260	R_1 = 0.055
	wR_2 = 0.1287	wR_2 = 0.0601	wR_2 = 0.1094
$\Delta\rho$ maximum/minimum (e Å^{-3})	0.767/−0.509	0.392/−0.367	2.138/−1.026

syn (Scheme 2). The two phosphorus atoms attached to the diol bridges in a single cyclotriphosphazene moiety of **5**-*anti* exhibit *R* and *S* configurations and an inversion centre in the middle of the molecule generates the opposite handed chirality at the symmetry generated phosphorus centres.

The structure of compound **6** (Fig. 4) shows that it is the triply-bridged derivative, in which the three diol chains connect the two cyclophosphazene rings in a *cis*-configuration and the resulting molecular morphology of the compound is cylindrical, or 'barrel-shaped'. There are four chemically identical, yet crystallographically unique molecules, in the asymmetric unit of **6**, which arise from the number of different torsional degrees of freedom that three bridging 8-membered chains can adopt. The number of degrees of freedom can be demonstrated by the considerable differences in separation between equivalent phosphorus centres connected by a bridge [molecule 1 = 10.03, 9.98, 10.22 Å; molecule 2 = 10.09, 9.91, 10.03 Å; molecule 3 = 10.43, 9.35, 9.99 Å; molecule 4 = 10.14, 9.69, 9.90 Å].

The crystal structure of the double-bridged compound (**5**) shows it to be the *anti*-isomer (Scheme 2) indicating that under these solution conditions, the diastereoisomer with a centre of symmetry crystallises more readily than the *syn*-isomer, which has a plane of symmetry. Characterisation of (**5**-*anti*) by X-ray crystallography enables the ^{31}P NMR spectra of both diastereoisomers of (**5**-*anti*) and (**5**-*syn*) to assign unequivocally (Table 1).



Scheme 2. The (*R*/*S*) configurational isomers of double-bridged cyclotriphosphazene derivatives.

3.3. Effect of size of the ansa ring for fluorinated diol derivatives of cyclophosphazene

The characteristics of the mono-ansa compound (**3**) formed from the octafluorohexane-1,6-diol in this work may be compared with those for analogous compounds (**7**) and (**8**) formed from the hexafluoropentane-1,5-diol [11] and tetrafluorobutane-1,4-diol [10], respectively (Scheme 3). A summary of the structural parameters (Table 3) shows that the size of the ansa ring has little effect on various bond lengths and angles defined in Scheme 3 but that the major difference for the compounds is observed in the maximum deviation from the mean plane of the N_3P_3 ring for ansa compounds (**3**) (0.024), (**7**) (0.099) and (**8**) (0.125 Å), respectively. These values indicate that the greatest strain on the phosphazene ring is caused by the 9-membered ansa ring of compound (**8**), with progressively less strain for the 10-membered ansa ring of (**7**) and the least strain caused by the 11-membered ansa ring (**3**). Previous work has shown that the effect of the strain for cyclotriphosphazenes with smaller ansa rings is also reflected in the minimum value of the P···P distances of the cyclophosphazene ring, which is about 2.6 Å for 8-membered ansa compounds [20,21] but greater than 2.7 Å for unstrained cyclotriphosphazene rings [19]. It is seen in Table 3 that for each of the compounds (**3**), (**7**) and (**8**) the minimum P···P distance is greater than 2.7 Å showing that this parameter is not a sensitive indicator of strain in phosphazene rings caused by derivatives with at least 9-membered ansa rings.

3.4. Influence of chain length of fluorinated diols on the formation of reaction products

There is now available detailed information on the products of the reaction of cyclotriphosphazene (**1**) with three fluorinated diols of different chain length. Reaction of the fluorinated butane- and pentane-diols with (**1**) leads exclusively to the formation of spiro and ansa derivatives [10,11] by intramolecular cyclisation

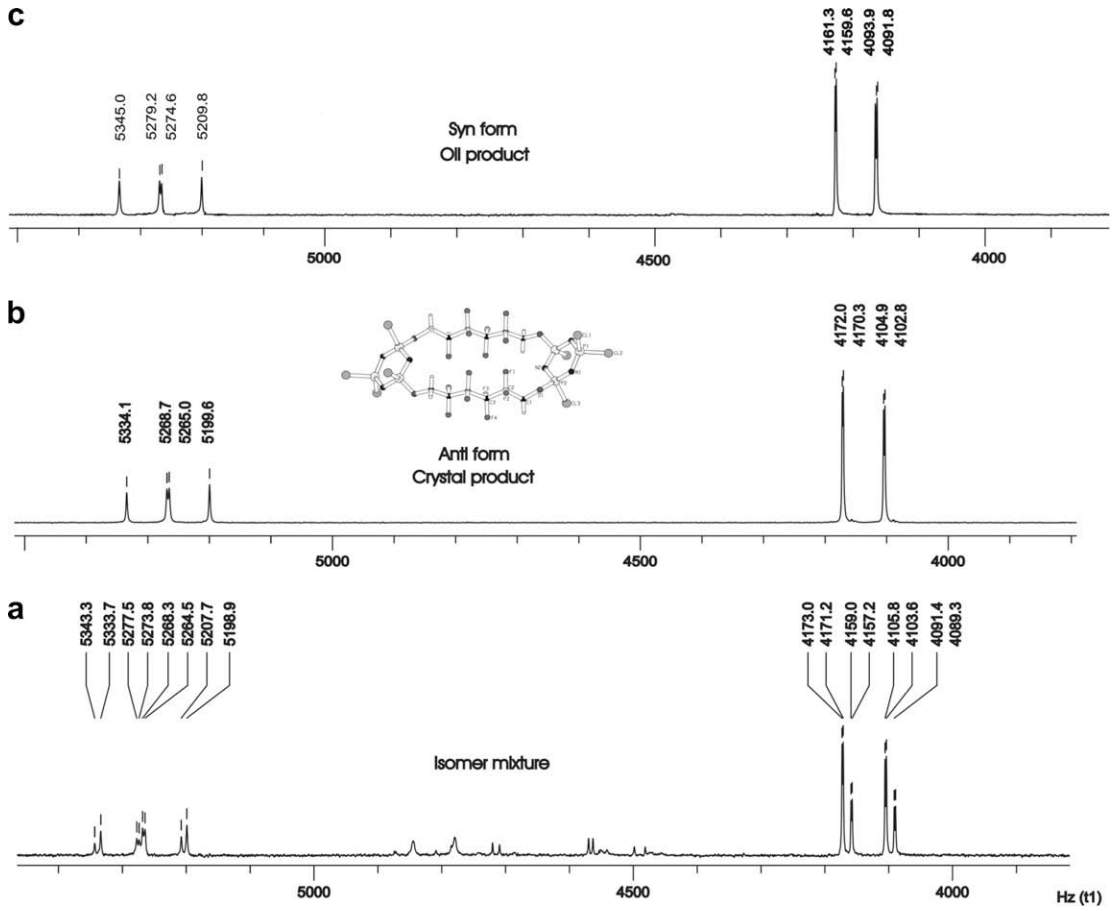


Fig. 1. ^{31}P NMR spectra of (a) mixture of double-bridged diastereoisomers of (**5**), (b) *anti* form of isomer and (c) *syn* form of isomer.

reactions (Scheme 4), whereas for the fluorinated hexanediol intermolecular reactions are predominant to form bridged compounds and the small proportion of intramolecular cyclisation gives the ansa derivative and only a trace of the spiro derivative. Hence, it is important to consider the factors that may be involved in the competition between the intra- and intermolecular mechanisms for reactions of these fluorinated diols with compound (**1**).

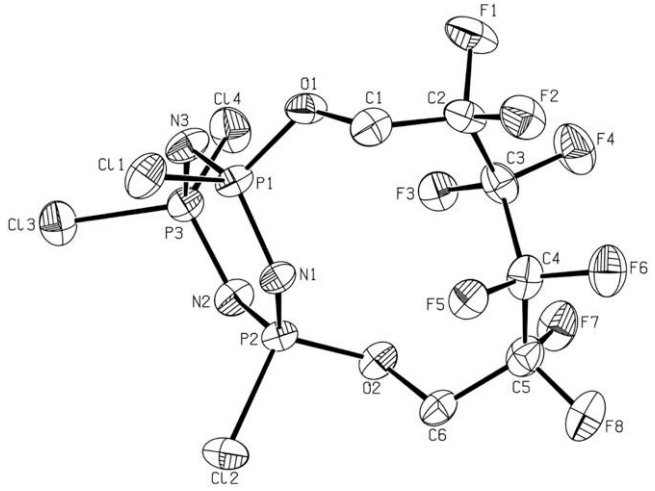


Fig. 2. X-ray crystal structure of (**3**) with ellipsoids plotted at 50% probability.

Using ^{31}P NMR spectra of the reaction mixtures to quantify the formation of products, it is found that the proportion of the monospiro derivative decreases with increasing chain length of the fluorinated diol; 45% of total products for the butane-diol [10], 29% for the pentane-diol [11] and <1% for the hexanediol in this work. Concomitantly, there is an increase in the relative proportion of monoansa derivatives. It is known that reaction of cyclophosphazenes with alkoxides promotes the stereoselective formation of disubstituted derivatives with a *cis*-configuration, which has been rationalised in terms of the co-coordination (cooperative binding) with the attacking oxy-nucleophile of the sodium counterion already present in an oxy-substituent [2,22]. A similar explanation has been given for the stereoselective formation of the *cis*-ansa macrocyclic derivative of cyclotriphosphazene with disodium oxy[tetraethylenoxy] glycolate [23]. Although the cation-assisted mechanism should apply to the formation *cis*-ansa compounds with the fluorinated diols, it is likely that formation of the *cis*-ansa derivatives (**3**, **7** and **8**) will also be influenced by steric effects for these shorter chain diols forming 11-, 10- and 9-membered rings, respectively. Hence, it is not surprising that there is a greater relative proportion of ansa derivatives with increasing chain length, because X-ray crystallographic results have shown (Table 3) that there is less strain in the cyclotriphosphazene ring with increasing size of the ansa ring.

The most interesting finding in the present work on the reaction of cyclotriphosphazene (**1**) with the octafluorohexanediol (**2**) is the formation of single-, double- and triple-bridged derivatives. Although some double-bridged diamino derivatives of (**1**) have been reported previously [9b,12], there is only one mention of a double-bridged diol derivative [13] and its crystal structure was

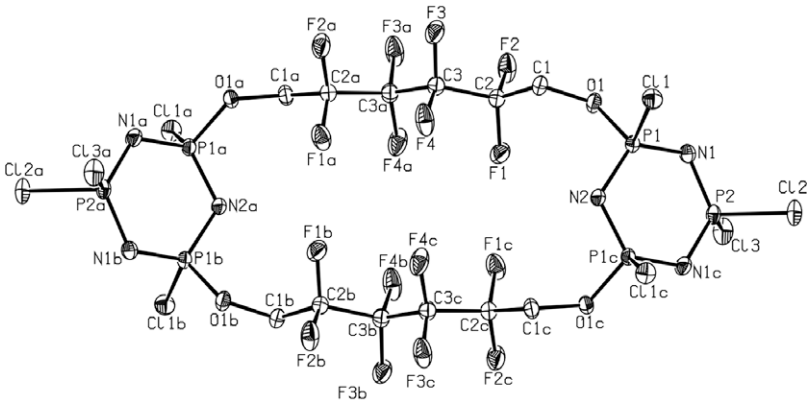


Fig. 3. X-ray crystal structure of (**5**-*anti*) with ellipsoids plotted at 50% probability.

not reported, whereas in this work both a double-bridged (Fig. 3) and a triple-bridged (Fig. 4) have been characterised. It is found that there is a preference for formation of the single-bridged derivative (27% yield) compared to the double-bridged (13% total) and the triple-bridged (2%) derivatives, which is not surprising given the standardised molar ratio of 1:1.2 for reaction of (**1**) with (**2**) for comparison with the other fluorinated diols [10,11]. It is likely that formation of bridged derivatives with the hexanediol results from the flexibility of the longer-chain of the mono-substituted intermediate such that the terminal alkoxy group preferentially reacts with the P–Cl group of a neighbouring cyclotriphosphazene molecule (intermolecular reaction) rather than an intramolecular reaction to form either a spiro or ansa derivative (Scheme 3). It is also of interest to observe that there are two double-bridged diol derivatives that are analogous to the two double-bridged amino derivatives observed previously [9b]. Although the bridging P(OR)Cl group is a centre of chirality, both double-bridged derivatives are meso, one with a centre of symmetry (in which the cyclotriphosphazene are in an *anti* configuration) and the other with a plane of symmetry (*syn*) as summarised in Scheme 2. In principle, one might expect these two stereoisomers to be formed with equal probability but it appears from the ^{31}P NMR of the isomer mixture (Fig. 1) and from the amounts of each compound isolated (**5**-*anti*, 9% yield; **5**-*syn*, 4%) that there is a preference for the stereoisomer having the centre of symmetry. However, ^{31}P NMR of the reaction mixture showed similar proportions for **5**-*anti* and **5**-*syn*, as expected, indicating that the separation procedure favoured the *anti*-

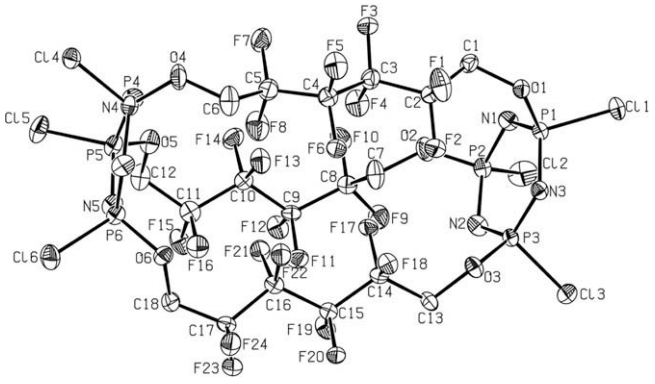
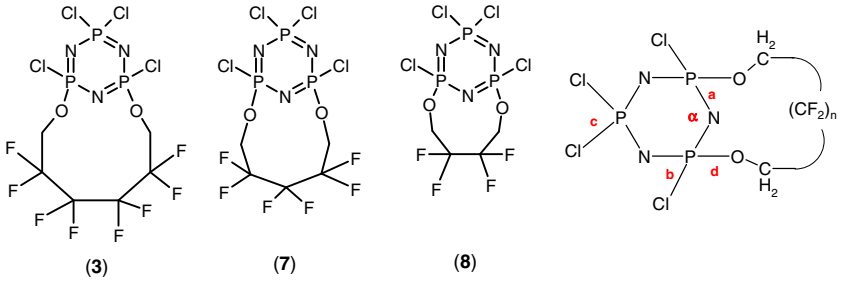


Fig. 4. X-ray crystal structure of one of the four independent molecules of the triple-bridged compound (**6**) with ellipsoids plotted at 50% probability.

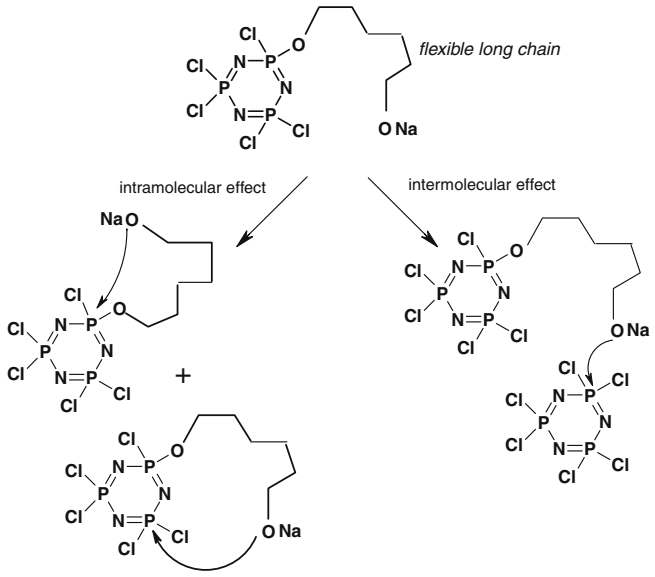
Table 3
Parameters of molecular framework of mono-ansa cyclotriphosphazene compounds.

Structural parameter[a]	Cyclotriphosphazene ansa-compound[b]		
	(**3**)	(**7**)[c]	(**8**)[d]
Number of (CF_2) in ansa ring	4	3	2
Number of atoms in ansa ring	11	10	9
Maximum deviation (Å)[e]	0.024	0.099	0.125
α	121.8(2)	119.9(7)	119.7(3)
a	1.578(3)	1.580(8)	1.582(2)
b	1.989(12)	1.977(3)	1.986(1)
c	1.994(12)	1.997(4)	1.995(1)
d	1.575(3)	1.579(7)	1.573(2)
POC	121.9(2)	121.1(6)	121.9(2)
Minimum P···P (Å)	2.753	2.726	2.735

[a] Structural parameters defined in Scheme 3.
[b] Comparisons are made for ansa derivatives with fluorinated diols; $N_3P_3Cl_4[OCH_2(CF_2)_4CH_2O]$ (**3**), $N_3P_3Cl_4[OCH_2(CF_2)_3CH_2O]$ (**7**) and $N_3P_3Cl_4[OCH_2(CF_2)_2CH_2O]$ (**8**).
[c] Ref. [10].
[d] Ref. [11].
[e] Maximum deviation from the mean plane of the N_3P_3 ring.



Scheme 3. Structures of cyclotriphosphazene ansa compounds (**3**), (**7**) and (**8**) and definitions of bond lengths and bond angles used for their comparison: $n = 2$ (**8**), $n = 3$ (**7**), $n = 4$ (**3**).



Scheme 4. Illustration of the inter- and intramolecular pathways at the first stage of the reaction of (**1**) with (**2**).

compared to the *syn*-configuration of the double-bridged compound.

4. Supplementary data

CCDC 731664, 731667 and 731668 contain the supplementary crystallographic data for compounds (**3**), (**5**-*anti*) and (**6**), respectively. These data can be obtained free of charge via http://www.ccdc.cam.ac.uk/conts/retrieving.html, or from the Cambridge Crystallographic Data Centre, 12 Union Road, Cambridge CB2 1EZ, UK; fax: (+44) 1223-336-033; or e-mail: deposit@ccdc.cam.ac.uk.

References

[1] V. Chandrasekhar, P. Thilagar, B.M. Pandian, Coord. Chem. Rev. 251 (2007) 1045.
[2] C.W. Allen, Chem. Rev. 91 (1991) 119.
[3] M. Gleria, R. De Jaeger (Eds.), Applicative Aspects of Cyclophosphazenes, Nova Science Publishers, New York, 2004.
[4] V. Chandrasekhar, G.T.S. Andavan, R. Azhakar, B.M. Pandian, Tetrahedron Lett. 47 (2006) 8365.
[5] R.P. Singh, A. Vij, R.L. Kirchmeier, J.M. Shreeve, Inorg. Chem. 39 (2000) 375.
[6] K. Muralidharan, P. Venugopalan, A.J. Elias, Inorg. Chem. 42 (2003) 3176.
[7] K. Muralidharan, A.J. Elias, Inorg. Chem. 42 (2003) 7535.
[8] H.R. Allcock, U. Diefenbach, S.R. Pucher, Inorg. Chem. 33 (1994) 3091.
[9] (a) K. Brandt, I. Porwolik-Czomperlik, .M. Siwy, T. Kupka, R.A. Shaw, S. Ture, A. Clayton, D.B. Davies, M.B. Hursthouse, G.D. Sykara, J. Org. Chem. 64 (1999) 7299; (b) D.B. Davies, T.A. Clayton, R.E. Eaton, R.A. Shaw, A. Egan, M.B. Hursthouse, G.D. Sykara, I. Porwolik-Czomperlik, M. Siwy, K. Brandt, J. Am. Chem. Soc. 122 (2000) 12447.
[10] S. Beşli, S.J. Coles, D.B. Davies, R.J. Eaton, M.B. Hursthouse, A. Kılıç, R.A. Shaw, Polyhedron 25 (2006) 963.
[11] S. Beşli, S.J. Coles, D. Davarcı, D.B. Davies, M.B. Hursthouse, A. Kılıç, Polyhedron 26 (2007) 5283.
[12] P. Castera, J.P. Faucher, M. Grainer, J.F. Labarre, Phosphorus Sulfur 32 (1987) 37.
[13] H.A. Al-Madfa, R.A. Shaw, S. Ture, Phosphorus Sulfur Silicon 53 (1990) 333.
[14] R. Hooft, COLLECT: Data Collection Software, Nonius B.V., 1998.
[15] Z. Otwinowski, W. Minor, Methods Enzymol. 276 (1997) 307.
[16] G.M. Sheldrick, Acta Crystallogr. A64 (2008) 112.
[17] J.W. Emsley, L. Phillips, V. Wary, Fluorine Coupling Constants, Pergamon Press, New York, 1977.
[18] G.J. Bullen, J. Chem. Soc. B (1971) 1450.
[19] A.G. Orpen, L. Brammer, F.H. Allen, O. Kennard, D.G. Watson, R. Taylor, International Tables for Crystallography, Volume C, 1992.
[20] (a) S.R. Contractor, M.B. Hursthouse, H.B. Parkes, L.S. Shaw (née Gözen), R.A. Shaw, H. Yılmaz, J. Chem. Soc. Chem. Commun. (1984) 675; (b) S.R. Contractor, M.B. Hursthouse, H.B. Parkes, L.S. Shaw (née Gözen), R.A. Shaw, H. Yılmaz, Phosphorus Sulfur 28 (1986) 267.
[21] (a) K. Muralidharan, N.D. Reddy, A.J. Elias, Inorg. Chem. 39 (2000) 3988; (b) N.D. Reddy, A.J. Elias, A. Vij, Inorg. Chem. Commun. 3 (2000) 29; (c) K. Muralidharan, P. Venugopalan, A.J. Elias, Inorg. Chem. 42 (2003) 3176.
[22] S.B. Lee, S.-Ch. Song, J.-Il. Jin, J. Am. Chem. Soc. 122 (2000) 8315.
[23] K. Brandt, J. Drozd, J. van de Grampel, A. Meetsma, Inorg. Chim. Acta 228 (1995) 187.

hydrophilic tris(hydroxymethyl)phosphine (thp) allowed the preparation of more hydrophilic species stable in aqueous media with improved cytotoxic properties [12]. In particular, mononuclear copper(I) complexes of the type {[L]Cu(thp)$_2$} (L = [HC(CO$_2$)(tz)$_2$]$^-$ or [HC(CO$_2$)[(pz^{Me_2})$_2$]$^-$) were found to possess antiproliferative activity against different human tumor cell lines markedly higher than that shown by cisplatin [12]. Chemosensitivity tests performed on cisplatin sensitive and resistant human cancer cell lines (ovarian cancer 2008 versus C13* and cervix cancer A431 versus A431/Pt) established that (scorpionate)Cu(thp)$_2$ type compounds were able to overcome cisplatin resistance, supporting the hypothesis of a different mechanism of action compared to that exhibited by the reference drug. Marzano et al. hypothesized that the cytotoxic activity of these copper(I) complexes might be correlated to their ability to trigger paraptosis, a non-apoptotic mechanism of cell death [11]. The ^{64}Cu-labeled complexes of two scorpionate ligands, with the thp co-ligands, [HC(CO$_2$)(pz^{Me_2})$_2$Cu(thp)$_2$] and [HC(CO$_2$)(tz)$_2$Cu(thp)$_2$], have been prepared to evaluate their usefulness as PET radiopharmaceuticals [13].

Since the intrinsic difficulty of growing an appropriate crystal of these [(scorpionate)Cu(PR$_3$)$_2$]-type complexes, the local structure of the metal site (Cu) is unknown. However, structural informations are likely to be obtained using the X-ray absorption spectroscopy technique (XAS). In the past decades, XAS has been proved to be a strong structural tool [14–16], for the characterization of amorphous [17] and disordered materials [18], inorganic materials [19–21], biological materials [22,23] solutions [24], has been also applied to in situ techniques [25,26].

This paper describes the identification of the metal sites occupied by copper in the {[H$_2$B(tz$_2^{NO}$)$_2$]Cu(dppe)} [11], {[H$_2$B(tz^{NO_2})$_2$]-Cu[P(p-tolyl)$_3$]$_2$} [11] and {[HC(CO$_2$)(pz^{Me_2})$_2$]Cu(thp)$_2$} [12] complexes.

2. Experimental

2.1. Synthesis

All reagents were purchased from Aldrich and used without further purification. The complexes {[H$_2$B(tz^{NO_2})$_2$]Cu(dppe)} (**1**) [11], {[H$_2$B(tz^{NO_2})$_2$]Cu[P(p-tolyl)$_3$]$_2$} (**2**) [11] and {[HC(CO$_2$)(pz^{Me_2})$_2$]Cu(thp))$_2$} (**3**) [12] were prepared in accordance with the literature methods.

2.2. XAS data collection

Samples for the XAS experiments were mixed with boron nitride and then pressed as pellets (3 tons). X-ray absorption experiments were performed at the synchrotron radiation source (SRS) at Daresbury Laboratory, Warrington, England, using the beam line 7.1. The storage ring operates at 1.6 GeV and a typical current of 240 mA. Internal references for energy calibration were used for copper at each scan. This allows for a continuous monitoring of the energy during consecutive scans. No energy drifts of the monochromator were observed during the experiments. Data were acquired in transmission mode. The ionization chamber was filled with an Ar/He gas mixture. Harmonics were rejected by detuning (80%). X-ray absorption spectroscopy (XAS) spectra were collected from 200 eV before the edge up to k = 13 every 0.03 k with a three second integration time. A Cu foil internal energy calibration was measured simultaneously with each spectrum.

2.3. XAS data analysis

X-ray absorption spectroscopy (XAS) spectra were calibrated using the EXCALIB program. The pre-edge background was removed by subtraction of a linear function extrapolated from the pre-edge region, and the XANES spectra were normalized at the unity (9000 eV) by extrapolation of the atomic background as it comes out from the EXAFS analysis (evaluated using a polynomial function).

The EXAFS analysis has been performed by using the GNXAS package [27,28] that takes into account multiple scattering (MS) theory. The method is based on the decomposition of the EXAFS signals into a sum of several contributions, that are the n-body terms. It allows the direct comparison of the raw experimental data with a model theoretical signal. The procedure avoids any filtering of the data and allows a statistical analysis of the results. The theoretical signal is calculated *ab initio* and contains the relevant two-body $\gamma^{(2)}$ and the three-body $\gamma^{(3)}$ multiple scattering (MS) terms. The contribution from four-body $\gamma^{(4)}$ terms [29] has been checked out, but it was found to be negligible. The two-body terms are associated with pairs of atoms and probe their distances and variances. The three-body terms are associated with triplets of atoms and probe angles, bond–bond and bond–angle correlations. If useful, a single effective MS signal $\eta^{(3)}$ that includes both $\gamma^{(2)}$ and the $\gamma^{(3)}$ contributions can be used for the shells beyond the second one by using the same three-atom coordinates both for the two-atom and the three-atom contributions. The full definition of the parameters associated with the triplet of atoms is found in Ref. [28]. Data analysis is performed by minimizing a χ^2-like function that compares the theoretical model to the experimental signal. The phase shifts for the photoabsorber and backscatterer atoms were calculated *ab initio* starting from the structural model [30]. They were calculated according to the muffin-tin approximation. The Hedin–Lundqvist complex potential [31] was used for the exchange–correlation potential of the excited state. The core hole lifetime, Γ_c, was fixed to the tabulated value [32] and included in the phase shift calculation. The experimental resolution used in the fitting analysis was about 2 eV, in agreement with the stated value for the beamline used. The relevant E_0 values were found to be displaced by several eV with respect to the edge inflection point. They are summarized in Table 1 together with the structural parameters. The values of S_0^2 have been found to be in the 0.81–0.89 range and are also displayed in Table 1. The fitting procedure at the Cu K-edge was also performed including the relevant set of multiple scatter-

Table 1
EXAFS best-fitting results of the investigated samples. The estimated parameter errors are indicated in parentheses.

Bond length (degeneracy) Debye–Waller	(**1**)	(**2**)	(**3**)
Cu–N (Å) (2)	2.03(2)	2.032(12)	1.980(13)
σ^2 (Å^2)	0.028(6)	0.027(6)	0.006(3)
Cu–P (Å) (2)	2.227(12)	2.21(1)	2.279(12)
σ^2 (Å^2)	0.007(3)	0.007(3)	0.014(4)
Cu–O (Å) (1)			2.295(15)
σ^2 (Å^2)			0.004(2)
Cu–N–C(N) (°) (4)	120(2)	124(2)	128(2)
σ_θ^2 (deg^2)	25(20)	60(40)	68(25)
Cu–P–C (°) (6)	110(3)	112(4)	125(4)
σ_θ^2 (deg^2)	30(20)	40(30)	62(25)
P–C (Å) (6)	1.75(4)	1.73(5)	1.85(5)
σ^2 (Å^2)	0.02(1)	0.007(3)	0.009(4)
N–N (C) (Å) (2)	1.37(5)	1.34(4)	1.34(4)
σ^2 (Å^2)	0.009(6)	0.010(2)	0.009(5)
Cu–N(C) (Å)[a]	2.97[a]	2.95[a]	2.98[a]
Cu–C (Å)[a]	3.26[a]	3.27[a]	3.63[a]
E_0	8980(1)	8980.4(8)	8982.9(8)
S_0^2	0.89(5)	0.81(6)	0.83(5)

[a] Data obtained from the three-body configuration (using Cu–P–C angle and P–C distances).

ing paths that may originate from the structure of this class of compounds. Hence, referring to Fig. 1, the theoretical signals included in the fitting procedures are: the two-atom contributions $\gamma_1^{(2)}$ Cu–N with degeneracy of two, the two-atom contributions $\gamma_2^{(2)}$ Cu–P with degeneracy of two, the three-body contribution $\eta^{(3)}$ Cu–N–N with degeneracy of two, the three-body contribution $\eta^{(3)}$ Cu–N–N with degeneracy of two, the three-body contribution $\eta_2^{(3)}$ Cu–P–C with degeneracy of four. Actually the first 2 three-body signals have been grouped considering both the equivalence of the sites where the atoms are placed and the similarity of the C and N atoms in terms of phase shift. Hence, the sum signal is defined in term of $\eta_1^{(3)}$ Cu–N–N(C) with degeneracy of four. This approximation has been checked and produces similar results using less structural parameters. It is noteworthy that the inclusion of the three-body term $\eta^{(3)}$ allows monitoring the shells beyond the first one by using the same three-atom coordinates both for the two-atom and the three-atom contributions. In fact, the three-body signal $\eta_2^{(3)}$ Cu–P–C includes both $\gamma^{(2)}$ Cu–C and $\gamma^{(3)}$ Cu–P–C contributions. Also, the fitting procedure of complex **3** includes the two-atom contributions $\gamma_2^{(2)}$ Cu–O with degeneracy of one. Based on this model, the total number of parameters taken into account in the fitting procedure (including the structural and non-structural terms E_0, S_0^2 and the experimental resolution) is found to be 19 for complexes **1** and **2** and 21 for complex **3**. Besides, it is worth mentioning that in all cases the number of fitting parameters does not exceed the estimated 'number of independent data points' $N_{ind} = (2\delta k \delta R/\pi) + 2$, ensuring that the fit is well determined and does not lead to parameters with very large errors, thus confirming the reliability of the minimization. In order to evaluate the effect of the structural disorder, the simulation was done by considering a non-Gaussian type of pair distribution functions for the $\gamma^{(2)}$ Cu–N and $\gamma^{(2)}$ Cu–P signals. In fact, because of the non-crystalline nature of the compound, a more flexible model replacing the simple Gaussian function might be required. The gamma like (Γ) distribution has been used here [33,34] and proved to be very useful in previous studied systems [35–37]. This function depends on three parameters: the average bond distance, the bond variance, and the asymmetry coefficient (skewness) β, defined as K_3/σ^3 where K_3 is the third cumulant of the distribution. The full definition of the function is described in Refs. [28,34].

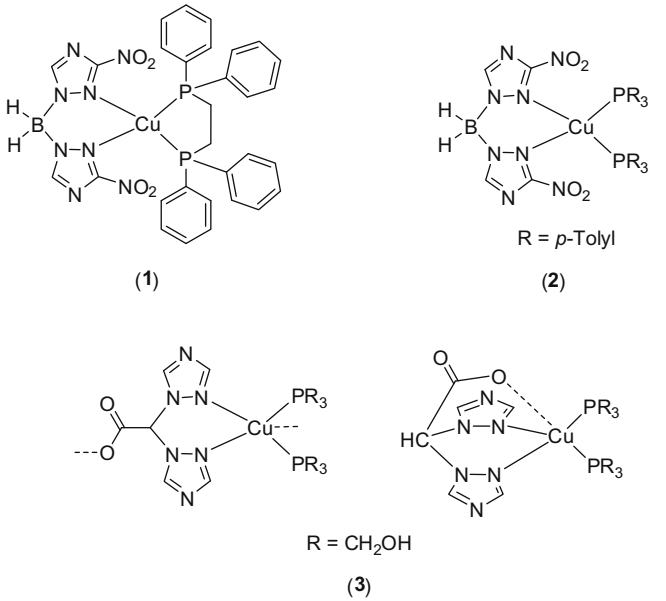


Fig. 1. Structures of the Cu(I) complexes **1**–**3**.

3. Results and discussion

The k^2-extracted EXAFS signals of the investigated samples are shown in Fig. 2 (dot lines). The sinusoidal curves are generated by the atomic environment around the photo-absorber atom, i.e. copper, and are similar for all the investigated compounds. Hence, the structural information provided out by the signals, which is typically extracted by a fitting procedure which compares a model compound with the experimental one, should be not so different. The observed sinusoidal signals for each complex suggest a main contribution of the first shell, which should be the main structural parameter to be studied in the present analysis. As reported in Fig. 1, the first shell of the studied complexes is comparable: the scorpionate ligand coordinates the metal center by two nitrogen atoms, and two additional mono-phosphine co-ligands or a diphosphine complete the 4-fold coordination of Cu(I). In addition, complex **3** is characterized by a carboxylate fragment which makes available an oxygen atom for a possible 5-fold coordination of copper(I). This is not observed insofar and would be a major task of the present analysis, as the EXAFS probe is a unique one for non-crystalline compounds.

As a customary, the EXAFS fitting analysis is conducted by means of a model compound since it permits to compute the various singular EXAFS signals. Because the atomic coordinates of this class of compounds are not available in the literature, we have used those of similar complexes with a different coordinated metal [30]. Of course, the starting theoretical signals have been later recalculated to account for any important structural variation from the model. In fact, when a deviation of more that 10% of a selected structural parameter (e.g. atomic distance or angle) occurred, the corresponding theoretical signal has been recalculated before being used in the fitting procedure. As a consequence, the theoretical model has been adapted to be used in this paper.

The best-fit results concerning the fitting procedures for the investigated complexes (all details specified in Section 2) are illustrated in Figs. 2–4. Fig. 2 shows the comparison of the experimental and theoretical curves of the k^2-extracted EXAFS, and Fig. 3 displays the comparison of the corresponding Fourier Transforms (FTs). We can observe that the theoretical curves match well with the experimental ones, indicating the reliability of the adapted-structural model and the accuracy of the data analysis. The FT curves of Fig. 3 confirm the existence, in all of the three complexes, of a main first shell contribution, and of some multiple scattering (MS) contributions at higher frequencies, i.e. distances. Fig. 4 reports the details of the EXAFS analysis. Each panel reports the various contributions to the theoretical signals and the comparison of

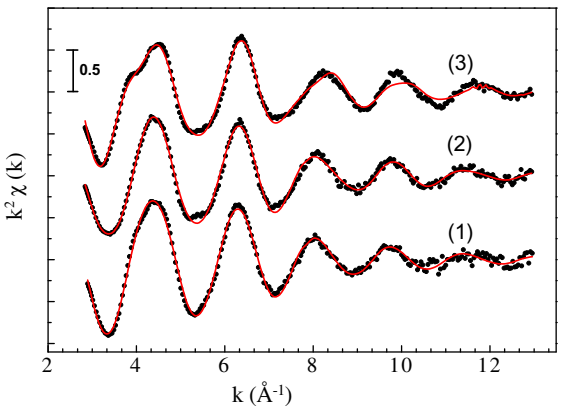


Fig. 2. Best fit of the copper K-edge EXAFS signals of complexes **1**–**3**. The figure shows the comparison of the experimental (···) and theoretical (–) k-extracted EXAFS signals.

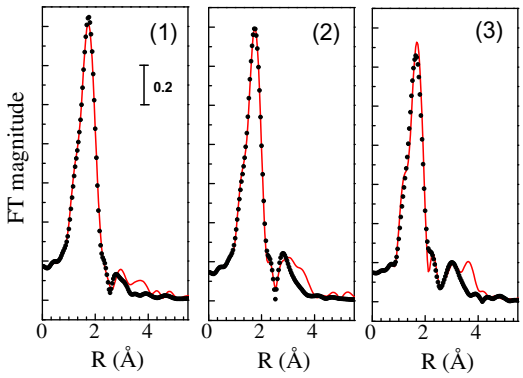


Fig. 3. Best fit of the copper K-edge EXAFS signals of complexes **1**–**3**. The figure shows the comparison of the experimental (···) and theoretical (–) Fourier transform signals, obtained in the 2.5–13 $Å^{-1}$ *k* space, of the EXAFS signals.

the total theoretical signal with the experimental one. Besides the fact that the Cu–P and Cu–N first shell largely contribute in all panels, hence confirming the at-a-glance explanation of Fig. 2 as above, all signals are rather important in the determination of the total theoretical one. It is also interesting to notice the two-body Cu–O signal of the complex **3**, whose intensity is comparable to the three-body ones.

The inter-atomic distances and the corresponding EXAFS Debye–Waller factor (best-fit) of the samples investigated are shown in Table 1. The statistical errors associated with the parameters obtained with the EXAFS analysis are also indicated. They were determined by correlation maps (contour plots) for each pair of parameters. Fig. 5 shows the contour plots for complex **3**, as an example. These plots were selected among the parameters having strong correlation to reflect the highest error. The estimated statistical error [38] is associated with the 95% confidence interval. It is important to emphasize that this evaluation provides only statistical errors on EXAFS refined parameters and it does not accounts for systematic errors in the theory or peculiar to the experimental technique. This values of statistical errors are slightly longer than those normally quoted for non-crystalline and amorphous compounds [36,39].

From Table 1 we can observe that the Cu–N first shell distances, as well as the Cu–P ones for complexes **1** and **2**, are similar and that this holds true also for their bond length variances. Some differences arise in the case of compound **3** where the metallacycle is rather different; the Cu–N distance shortens by about 5 hundredth of an angstrom and the Cu–P interaction becomes longer. Complex **3** also displays a Cu–O interaction at about 2.29 Å, due to the carboxylic tail of the scorpionate ligand. Anyway, these bond lengths reflect the ones normally quoted for copper derivatives of scorpionate ligands [40–43].

A close inspection of Table 1 reveals also other differences of the structural parameters in compounds **1** and **2** in comparison to compound **3**: the Cu–N–N and the Cu–P–C angles are slightly different, and consequently the P–C interaction changes too. This is due to the nature of the metallacycle system, and in particular to the presence, in complex **3**, of a close oxygen for a Cu–O coordination which leads to a slightly different site where the copper is located (the 4-fold coordinated Cu site becomes 5-fold coordinated).

3.1. On the Cu–O interaction in complex *3*

The coordination of copper in compound **3** deserves a special attention. Of course, the structure proposed in Fig. 1 suggests a close interaction between copper and the oxygen fragment. The complex may form the 6-atom cycle Cu–N–N–C–C–O, which seems plausible if a chair configuration of the Cu–N–N–C–N–N cycle takes place (right side of Fig. 1 for complex **3**). The EXAFS probe used in our experiment suggests not only a Cu–O interaction at about 2.29 ± 0.02 Å but also a non-negligible contribution of the Cu–O signal to the total theoretical one. In fact, as underlined by the plot 3 of Fig. 4, the intensity of the $\gamma^{(2)}$ Cu–O is relevant. The importance of this signal has been explored more fully by considering what the fit result would be without the Cu–O interaction (Fig. 6). The upper panel shows the comparison between the total theoretical signal

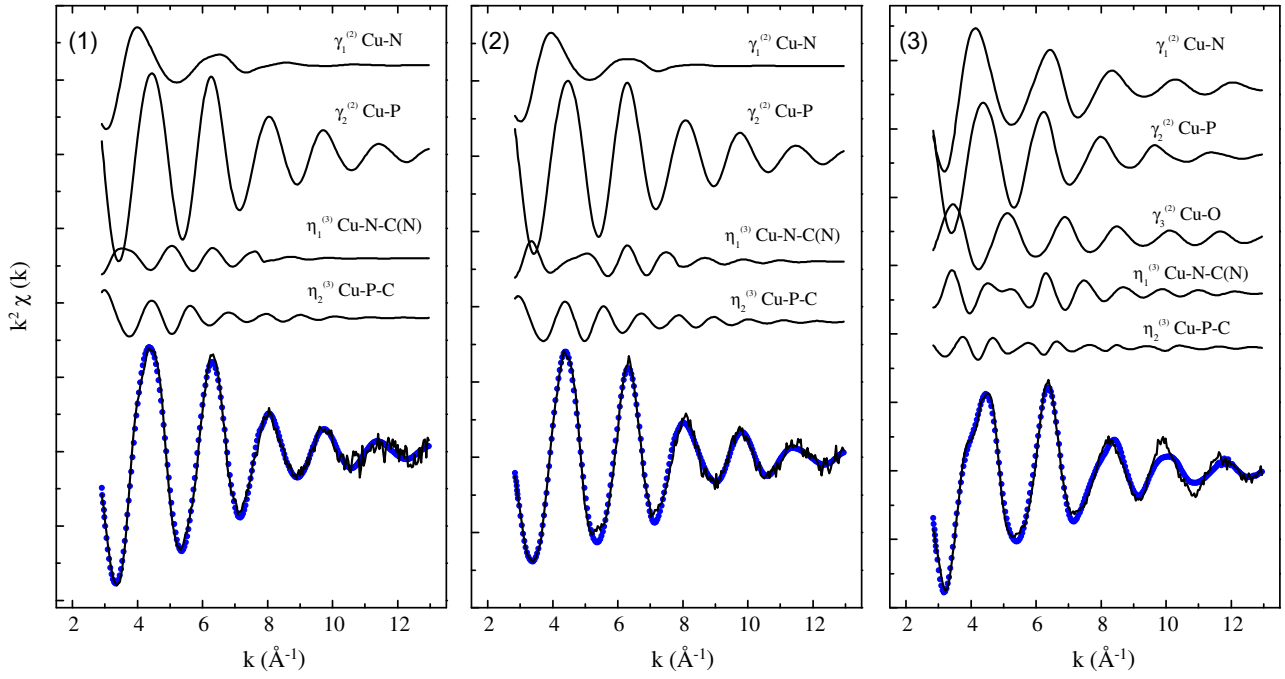


Fig. 4. Details of the EXAFS analysis of the Cu K-edge of complexes **1**–**3**. Each panel of the figure shows the individual EXAFS contributions, in terms of two-body and three-body signals, to the total theoretical signal. The comparison of the total theoretical signal (–) with the experimental one (···) is also reported at the bottom of each panel.

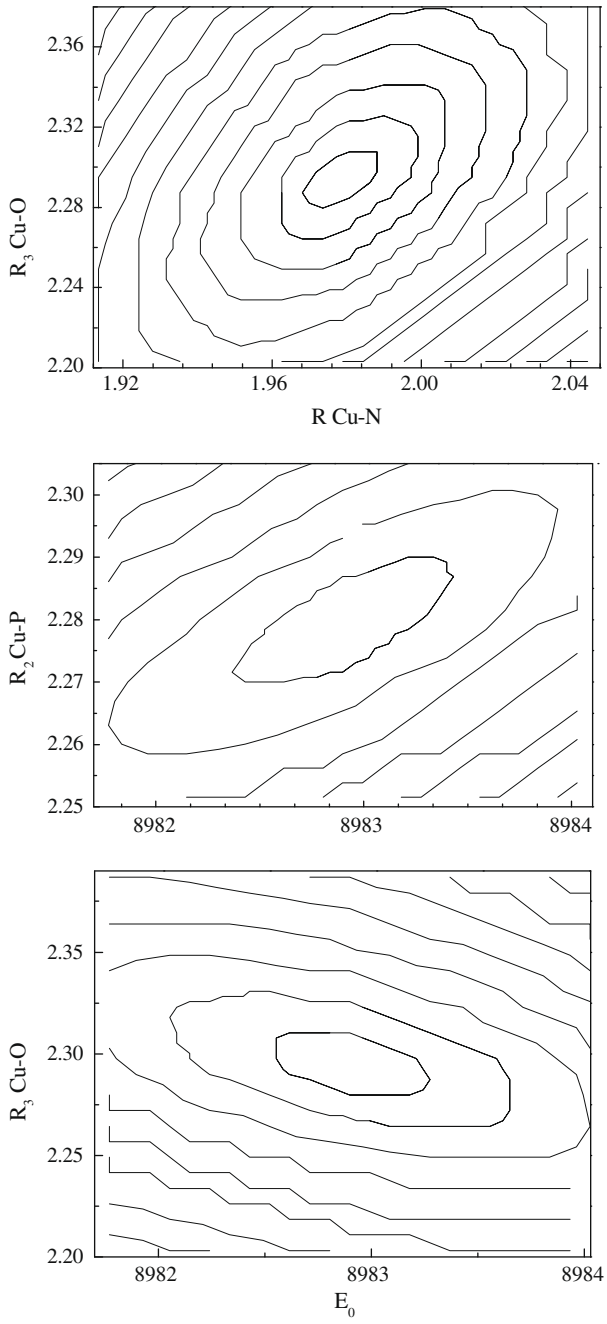


Fig. 5. Examples of the two dimensional section of the parameter space (contour plots) for complex **3**. These plots were selected among the parameters having strong correlation to reflect the highest error. The inner elliptical contour corresponds to the 95% confidence level.

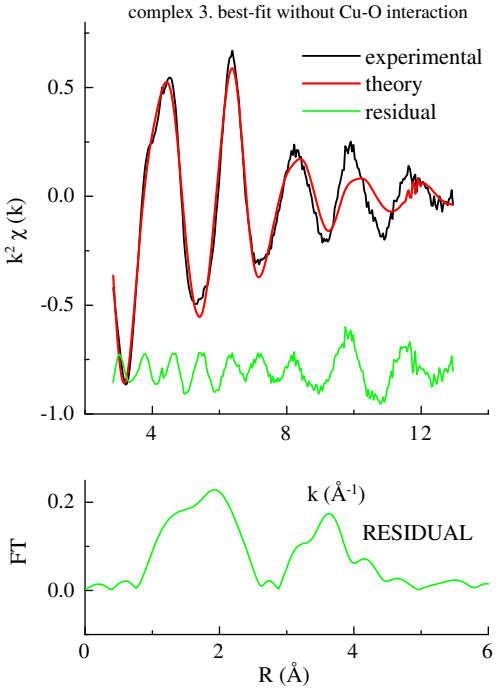


Fig. 6. Former EXAFS analysis of the Cu K-edge of complex **3**. The upper panel displays the comparison of the experimental (···) and theoretical (–) k-extracted EXAFS signals. Fit has been obtained considering a 4-fold coordinated Cu(I) structural model (no Cu–O interaction included). The residual curve is also reported. The lower panel displays the corresponding Fourier transform of the residual curve.

and the experimental one, and the residual curve as well. It is clear that the theoretical curve does not match well with the experimental, especially at high *k*-values. The mismatch appears evident considering the residual curve: a low frequency sinusoidal signal is mainly missed from the calculation, accompanied by a high frequency signal. This is confirmed by the signal at the bottom which displays the corresponding FT curve of the residual curve only. The observed broad peak at about 2 Å confirms a main low-frequency missed and may correspond to the Cu–O contributions, considering the phase shifts issue. The other contributions at higher frequency, from 3 to 4 Å, may origin from the calculation, due to the fact that the missing Cu–O frequency may force other signals, especially those related to the three-body terms, the Multiple Scattering $\eta^{(3)}$s, to compensate the mismatch between the experimental and the theoretical signal, leading to an odd result. Overall, this finding demonstrated the 5-fold coordination geometry of the copper in complex **3**, by means of an additional Cu–O interaction.

In addition, the EXAFS results of complex **3** appear unable to effectively discriminate between the two proposed structures reported in Fig. 1. In any case, the Cu–O bond length quotation at 2.29 Å is short enough to be typical of a strong interaction among Cu and O, and so does the corresponding EXAFS bond variance of 0.004 $Å^2$, which is characteristic of a chemical bond. Hence, both monomeric or polymeric structures depicted for compound **3** in Fig. 1 are probable.

3.2. XANES spectra of Cu(I) complexes

More information about the copper coordination in a complex as well as information about the electronic transitions and the effective charge associated to the absorbing atom, can be obtained from the X-ray absorption near edge structure (XANES) region. XANES spectra of Cu complexes display a pre-edge features which is assigned to the 1s → 4p electronic transition [44,45]. For Cu(I) the pre-edge transition occurs at about 8982–8984 eV, while for Cu(II) it shifts to higher energies, at about 8987 eV. In the case of Cu(I) the transition shows the highest intensity and resolution for linear two-coordinated complexes and becomes less intense and broadened as the coordination number increases and/or the symmetry is lowered [44,45]. This sensitivity of Cu XANES to geometry has proved particularly useful in studies where conversion from two-coordinate to three-coordinate site appeared [46].

Fig. 7 displays the Cu K-edge XANES spectra of complexes **1**–**3**. The general shape of the curves is different, demonstrating the

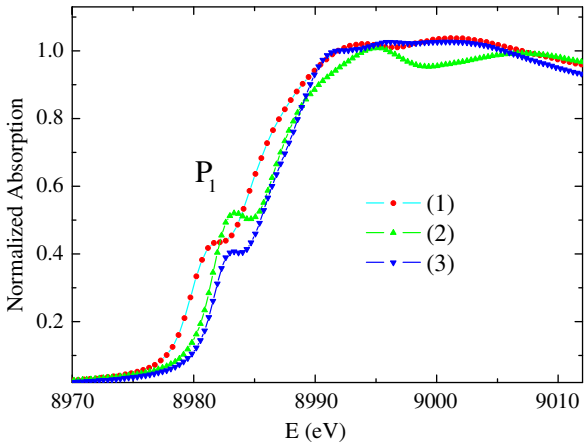


Fig. 7. Normalized XANES spectra at the Cu K-edge of complexes **1**–**3**. The pre-edge features (P_1) is assigned to the 1s → 4p transitions.

sensitivity of the local geometry of the photo-absorber atom (Cu) to the XANES profile. This is not surprisingly by considering the different structures of Fig. 1. As expected for a Cu(I) complex, a pre-edge feature at about 8983 eV appears in each spectrum, and small differences in the normalized intensities are revealed. It can be seen that the intensities of the 8983 eV peak are not indicative of diagonal or trigonal geometry [47,48], but they all resemble those of 4-coordinated Cu(I) complexes [44]. The lower intensity is found for complex **3** whose the present EXAFS analysis indicated to be a *distorted* 5-fold coordinated. This behavior agrees to that observed from Kau et al. about the coordination number increases and symmetry lowering [44]. A close inspection of the figure reveals a 1 eV chemical shift toward lower energy of the 1s → 4p peak for compound **1** respect to **2** and **3**. This may be due to the local coordination geometry as well as to the combined inductive and steric effects of co-ligands in complex **1**, which makes the charge of the coordination metal less positive.

4. Conclusions

The coordination metal core of copper(I) complexes containing the dihydridobis(3-nitro-1,2,4-triazol-1-yl)borate and the bis(1,2,4-triazol-1-yl)acetate ligands have been identified by EXAFS spectroscopy, due to the intrinsic difficulty of growing appropriate crystals of these [(scorpionate)Cu(PR_3)$_2$]-type complexes. The EXAFS analysis has been performed taking into account the Multiple Scattering formalism, allowing the determination of the first shell distances as well as the contribution of the outer shells. Copper is found to be 4-fold coordinated in the dihydridobis(3-nitro-1,2,4-triazol-1-yl)borate complexes, with a CuN_2P_2 core due to the chelation of the scorpionate ligand by two nitrogen atoms and due to two additional mono-phosphine co-ligand or a diphosphine. A $CuON_2P_2$ coordination core is revealed for the copper(I) complex of the bis(1,2,4-triazol-1-yl)acetate due to the carboxylate fragment of the ligand which makes available an oxygen atom for a possible 5-fold coordination of copper(I). The additional interaction of the metal with the oxygen of the acetate sting of the scorpionate ligand is not observed insofar and it is the major task of the present analysis, as the EXAFS probe is a unique one for non-crystalline compounds. The 1s → 4p transition which is a typical feature of the XANES spectrum on Cu(I) samples couples well with the EXAFS results, since the smaller 1s → 4p peak intensity is found for complex **3** and the EXAFS analysis indicates the existence of a 5-fold coordination, with the copper interacting with the acetate of the scorpionate ligand to form a monomeric or polymeric structure.

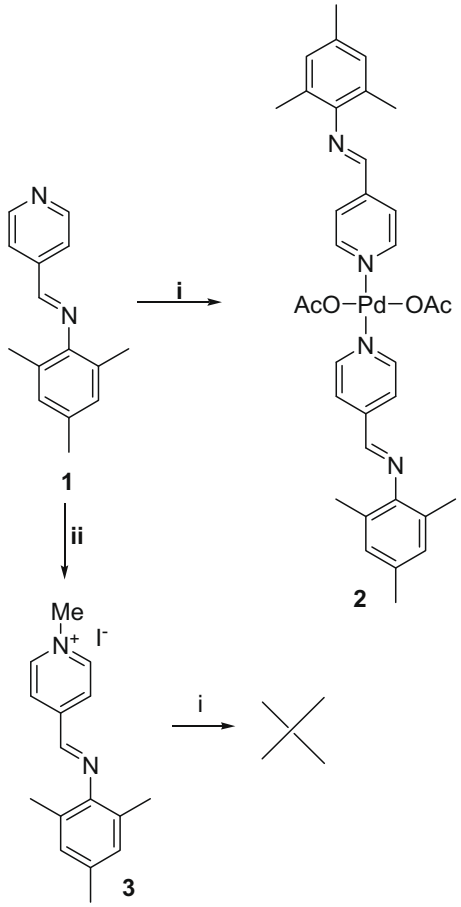
Acknowledgments

Measurements at Daresbury Laboratory were supported by the European Community – Research Infrastructure Action under the FP6 "Structuring the European Research Area" Programme (through the Integrated Infrastructure Initiative "Integrating Activity on Synchrotron and Free Electron Laser Science"). This work was partially supported by Ministero dell'Istruzione, dell'Università e della Ricerca (PRIN 20078EWK9B).

References

[1] C. Marzano, M. Pellei, F. Tisato, C. Santini, Anti-Cancer Agents Med. Chem. 9 (2009) 185.
[2] S.J. Berners-Price, P.J. Sadler, Struct. Bond. 70 (1988) 27.
[3] C.F. Shaw, Chem. Rev. 99 (1999) 2589.
[4] S.J. Berners-Price, C.K. Mirabelli, R.K. Johnson, M.R. Mattern, F.L. McCabe, L.F. Faucette, C.M. Sung, S.M. Mong, P.J. Sadler, S.T. Crooke, Cancer Res. 46 (1986) 5486.
[5] S.J. Berners-Price, M.E. Sant, R.I. Christopherson, P.W. Kuchel, Magn. Reson. Med. 18 (1991) 142.
[6] S.J. Berners-Price, R.K. Johnson, C.K. Mirabelli, L.F. Faucette, F.L. McCabe, P.J. Sadler, Inorg. Chem. 26 (1987) 3383.
[7] C. Marzano, V. Gandin, M. Pellei, D. Colavito, G. Papini, G. Gioia Lobbia, E. Del Giudice, M. Porchia, F. Tisato, C. Santini, J. Med. Chem. 51 (2008) 798.
[8] D. Saravana Bharathi, M.A. Sridhar, J. Shashidhara Prasad, A.G. Samuelson, Inorg. Chem. Commun. 4 (2001) 490.
[9] M.K. Adwankar, C. Wycliff, A. Samuelson, Indian J. Exp. Biol. 35 (1997) 810.
[10] N.J. Sanghamitra, P. Phatak, S. Das, A.G. Samuelson, K. Somasundaram, J. Med. Chem. 48 (2005) 977.
[11] C. Marzano, M. Pellei, S. Alidori, A. Brossa, G. Gioia Lobbia, F. Tisato, C. Santini, J. Inorg. Biochem. 100 (2006) 299.
[12] C. Marzano, M. Pellei, D. Colavito, S. Alidori, G. Gioia Lobbia, V. Gandin, F. Tisato, C. Santini, J. Med. Chem. 49 (2006) 7317.
[13] S. Alidori, G. Gioia Lobbia, G. Papini, M. Pellei, M. Porchia, F. Refosco, F. Tisato, J.S. Lewis, C. Santini, J. Biol. Inorg. Chem. 13 (2008) 307.
[14] D.E. Sayers, E.A. Stern, F. Lytle, Phys. Rev. Lett. 27 (1971) 1204.
[15] P.A. Lee, P.H. Citrin, P. Eisenberger, B.M. Kincaid, Rev. Mod. Phys. 53 (1981) 769.
[16] J.J. Rehr, R.C. Albers, Rev. Mod. Phys. 72 (2000) 621.
[17] M. Giorgetti, S. Passerini, W.H. Smyrl, M. Berrettoni, Inorg. Chem. 39 (2000) 1514.
[18] A. Filipponi, J. Phys.: Condens. Mat. 13 (2001) R23.
[19] E.I. Solomon, B. Hedman, K.O. Hodgson, A. Dey, R.K. Szilagyi, Coord. Chem. Rev. 249 (2005) 97.
[20] P. Cecchi, M. Berrettoni, M. Giorgetti, G. Gioia Lobbia, S. Calogero, L. Stievano, Inorg. Chim. Acta 318 (2001) 67.
[21] M. Tromp, J.A. Van Bokhoven, A.M. Arink, J.H. Bitter, G. Van Koten, D.C. Koningsberger, Chem. Eur. J. 8 (2002) 5667.
[22] M. Giorgetti, I. Ascone, M. Berrettoni, P. Conti, S. Zamponi, R. Marassi, J. Biol. Inorg. Chem. 5 (2000) 156.
[23] A. Levina, R.S. Armstrong, P.A. Lay, Coord. Chem. Rev. 249 (2005) 141.
[24] P. D'Angelo, M. Benfatto, S. Della Longa, N.V. Pavel, Phys. Rev. B: Condens. Mat. Mater. Phys. 66 (2002) 0642091.
[25] M. Giorgetti, S. Mukerjee, S. Passerini, J. McBreen, W.H. Smyrl, J. Electrochem. Soc. 148 (2001) A768.
[26] M. Giorgetti, S. Passerini, W.H. Smyrl, S. Mukerjee, X.Q. Yang, J. McBreen, J. Electrochem. Soc. 146 (1999) 2387.
[27] A. Filipponi, A. Di Cicco, C.R. Natoli, Phys. Rev. B: Condens. Mat. 52 (1995) 15122.
[28] A. Filipponi, A. Di Cicco, Phys. Rev. B: Condens. Mat. 52 (1995) 15135.
[29] M. Giorgetti, M. Berrettoni, A. Filipponi, P.J. Kulesza, R. Marassi, Chem. Phys. Lett. 275 (1997) 108.
[30] M. Pellei, S. Alidori, G. Papini, G. Gioia Lobbia, J.D. Gorden, H.V.R. Dias, C. Santini, Dalton Trans. (2007) 4845.
[31] L. Hedin, B.I. Lundqvist, J. Phys. C: Solid State Phys. 4 (1971) 2064.
[32] M.O. Krause, J.H. Oliver, J. Phys. Chem. Ref. Data 8 (1979) 329.
[33] A. Filipponi, J. Phys.: Condes. Mat. 6 (1994) 8415.
[34] A. Filipponi, A. Di Cicco, Task Quart. 4 (2000) 575.
[35] G. Dalba, P. Fornasini, R. Grisenti, F. Rocca, J. Non-Cryst. Solids 345–346 (2004) 7.
[36] M. Giorgetti, M. Berrettoni, W.H. Smyrl, Chem. Mater. 19 (2007) 5991.
[37] M. Giorgetti, M. Berrettoni, S. Scaccia, S. Passerini, Inorg. Chem. 45 (2006) 2750.
[38] A. Filipponi, J. Phys.: Condens. Mat. 7 (1995) 9343.
[39] M. Giorgetti, M. Berrettoni, Inorg. Chem. 47 (2008) 6001.
[40] C. Pettinari, C. Santini, Compr. Coord. Chem. II 1 (2004) 159.
[41] C. Pettinari, A. Cingolani, G. Gioia Lobbia, F. Marchetti, D. Martini, M. Pellei, R. Pettinari, C. Santini, Polyhedron 23 (2004) 451.
[42] L.M. Mirica, X. Ottenwaelder, T.D.P. Stack, Chem. Rev. 104 (2004) 1013.

[43] W.B. Tolman, J. Biol. Inorg. Chem. 11 (2006) 261.
[44] L.S. Kau, D.J. Spira-Solomon, J.E. Penner-Hahn, K.O. Hodgson, E.I. Solomon, J. Am. Chem. Soc. 109 (1987) 6433.
[45] I.J. Pickering, G.N. George, C.T. Dameron, B. Kurz, D.R. Winge, I.G. Dance, J. Am. Chem. Soc. 115 (1993) 9498.
[46] R.A. Pufahl, C.P. Singer, K.L. Peariso, S.J. Lin, P.J. Schmidt, C.J. Fahrni, V. Cizewski Culotta, J.E. Penner-Hahn, T.V. O'Halloran, Science 278 (1997) 853.
[47] M. Ralle, S. Lutsenko, N.J. Blackburn, J. Biol. Chem. 278 (2003) 23163.
[48] K. Peariso, D.L. Huffman, J.E. Penner-Hahn, T.V. O'Halloran, J. Am. Chem. Soc. 125 (2003) 342.



Scheme 1. (i) $Pd(OAc)_2$, toluene, 60 °C; (ii) MeI, toluene, 90 °C.

analysis. Reaction of the Schiff base ligand **1** with palladium(II) acetate in toluene at 60 °C for 24 h gave the non-cyclometallated complex **2** with two ligands coordinated to the palladium atom through the pyridine nitrogen. The doublet signals assignable to the H2/H6 protons, in the ^{1}H NMR spectrum, was in agreement with absence of Pd–C bond formation in **1**. The values shown by the ν(C=N) stretch, 1610 cm^{-1}, in the IR spectrum and by the the *HC*=N resonance in the ^{1}H NMR spectrum, 8.22 ppm, were similar to those for the free ligand, in accordance with the absence of bonding between the palladium and the non-aromatic iminic nitrogen [22,23]. Two strong bands at 1300 and 1555 cm^{-1} were assigned to the symmetric and asymmetric ν(COO) vibrations, respectively, in agreement with those expected for mono-coordinate acetato ligands [24,25]. The ^{1}H NMR spectrum showed a singlet signal for the acetate CH_3COO^- protons at 2.29 ppm and the ^{13}C{1H} NMR two signals assigned to the CH_3COO and the CH_3COO acetate carbons at 178.36 and 23.23 ppm, respectively. Regardless of the reaction conditions used (dichloromethane, room temperature; acetic acid, reflux) the reaction between ligand **1** and palladium(II) acetate gave in all cases the coordination complex **2** and not the expected cyclometallated compound.

The pyridine nitrogen of ligand **1** could be *N*-methylated with MeI in toluene at 90 °C in order to hinder its coordination through the pyridine nitrogen and, consequently, favour the cyclometallation reaction. However, reaction of the methylated Schiff base **3** with palladium(II) acetate under analogous reaction conditions as used in the synthesis of **2** (toluene, 60 °C) did not yield the desired product; instead of this a large amount of black palladium appeared in the reaction tube and an untreatable reaction mixture was isolated from the solution. Other reaction conditions ($Pd(OAc)_2$, CH_2Cl_2, r.t.; K_2PdCl_4, H_2O, r.t.; Li_2PdCl_4, MeOH, r.t.) failed to produce the expected complexes.

However, treatment of the *N*-oxide of the Schiff base, **4**, with $Pd(OAC)_2$ in toluene at 75 °C for 48 h gave the dimer **5**, metallated at the aromatic C6 carbon atom. The IR spectrum of **5** showed the ν(C=N) stretching band (see Section 3) shifted to lower frequency (compared to the free imine) in agreement with nitrogen coordination to metal center [22]. This was supported by the characteristic upfield shift (0.43 ppm) of the NMR signal for the imine proton, observed in the cyclometallated complexes as a consequence of *N*-coordination [23,26–28]. The IR spectrum showed to strong bands ν_{as}(COO) and ν_s(COO) at 1577 and 1420 cm^{-1}, respectively, in accordance with bridging acetate groups [24,26,28]. The *trans* geometry of the cyclometallated moieties was determined by the presence at 2.44 ppm of a singlet signal in the ^{1}H NMR spectrum, assigned to the two equivalent methyl acetate protons [29]. Complex **5** was also characterized by ^{13}C{1H} NMR spectroscopy, being the most noticeable feature the shift to higher frequency of the C6, C=N, and C1 resonances (as compared to the uncoordinated ligand or the non cyclometallated complex **2**), confirming the formation of the cyclometallated ring [25,30,31]. The FAB-mass spectrum showed at 809 amu the cluster of peaks assigned to $[\{(L\text{-}H)(OAc)Pd\}_2]^+$ (L-H = cyclometallated ligand), thereby confirming the dinuclear nature of the complex [32].

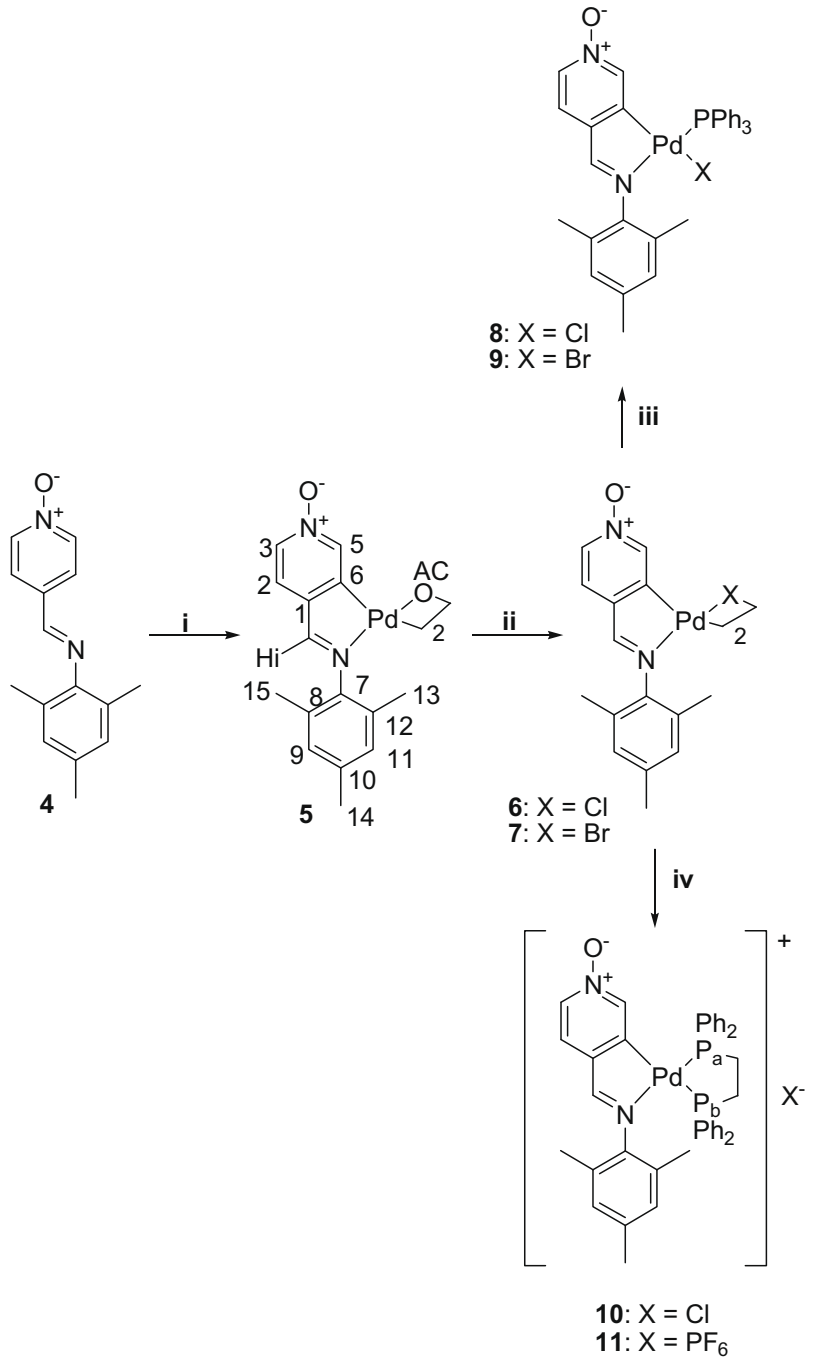
Complex **5** readily experimented metathesis reactions with sodium chloride or lithium bromide in acetone/water or methanol/water, respectively, to give the corresponding complexes with bridging halide ligands **6** and **7**. The mass spectra showed peaks assigned to $[\{(L\text{-}H)XPd\}_2H]^+$ (X = Cl, 763 amu; X = Br, 853 amu), consequent with the dinuclear formulation of the complexes. The IR and ^{1}H NMR spectra were similar to those for complex **5**, being the most noticeable differences the absence of the characteristic acetate bridging ligand signals.

Reaction of the halide-bridged complexes **6** and **7** with triphenylphosphine in chloroform gave the mononuclear complexes **8** and **9**, respectively, which were fully characterized (see Section 3). The IR spectra of these complexes showed the typical low-frequency shift of the ν(C=N) band (*vide supra*). In the ^{1}H NMR spectra the *HC*=N and H5 protons were coupled to the ^{31}P nucleus [δ *ca.* 8.08 ppm (J(PH) = 7.8 Hz) and δ *ca.* 7.0 ppm (J(PH) = 3.9 Hz), respectively], and the ^{31}P{1H} NMR spectra showed singlet resonances at *ca.* 39.5 ppm. In the ^{13}C{1H} spectra the low-field shift observed for the C6, C=N, and C1 resonances was similar to those found in the spectrum of **5** (*vide supra*) and the C5, resonance showed the coupling to the ^{31}P nucleus [J(C5P) *ca.* 11]. The mass spectra of **8** and **9** showed peaks centred at 607 amu corresponding to the loss of the halide ligand and, for complex **8** at 643 amu assigned to the molecular ion.

2.1. Molecular structure of complex **9**

Suitable crystals were grown by slowly evaporating a chloroform solution of **9**. The molecular structure is illustrated in Fig. 1.

The asymmetric unit comprises two solvent molecules of chloroform and a molecule of complex **9**; molecules of **9** are aligned along the *a*-axis and packed in layers parallel to *a* and *c*, between which the chloroform solvent molecules are located. The palladium atom is bonded in a slightly distorted square-planar geometry to the C(1) carbon atom of the pyridine ring, the imine N(1) atom, the Br(1) atom and to the P(1) phosphorus atom of the triphenylphosphine ligand. The angles between adjacent atoms in the coordination sphere of palladium are close to the expected value of 90° with the most noticeable distortions corresponding to the bite angle C(1)–Pd(1)–N(1) of 81.06(9)°. The sum of the angles about palladium is approximately 360°.



Scheme 2. (i) $Pd(OAc)_2$, toluene, 75 °C; (ii) complex **6**: $NaCl_{aq}$, acetone; complex **7**: $LiBr_{aq}$, methanol; (iii) PPh_3, chloroform; (iv) complex **10**: dppe, chloroform; complex **11**: dppe, NH_4PF_6, acetone.

The geometry around palladium is planar [mean deviation from the least square plane Pd(1), C(1), N(1), P(1), Cl(1), (plane 1), of 0.097 Å] and approximately co-planar with the metallated ring [Pd(1), C(1), C(5), C(6), N(1); mean deviation 0.0035 Å (plane 2)] and with the pyridine ring [plane 3, mean deviation of 0.0050 Å] (angles between planes are: plane 1:2, 0.7°; plane 1:3, 0.9°; 2:3, 1.0°). The Pd–N(1), 2.099(2) Å, Pd–C(1), 2.016(2), Pd(1)–P(1), 2.246(1) and Pd(1)–Br(1), 2.459(1), bond distances are within the range found earlier [33–36].

Reaction of complexes **6** and **7** with the diphosphine $Ph_2P(CH_2)_2PPh_2$, (dppe), in a 1:2 molar ratio (followed by treatment with ammonium hexafluorophosphate in the case of **7**) gave the mononuclear complexes, **10** and **11**, respectively, as air-stable solids which were fully characterized (see Section 3). The main difference between them was the counter ion [Cl^- in **10** and PF_6^- in **11**] in spite of which, the NMR spectra showed significant differences indicating that the interaction between the anion and the cation remains in solution. In the ^1H NMR spectrum of **10** the *HC*=N resonance at δ 8.44 ppm was a singlet; however, in the spectrum of **11** it appeared as a doublet at 8.10 ppm, by coupling to the ^{31}P nucleus *trans* to nitrogen (J(HP) = 7.5 Hz); less significant shifts were observed for the signals assigned to the H3 and H9/H11 protons. The $^{31}P\{1H\}$ NMR spectra showed two doublets for the two non-equivalent phosphorus nuclei, but in the spectrum of **10** the

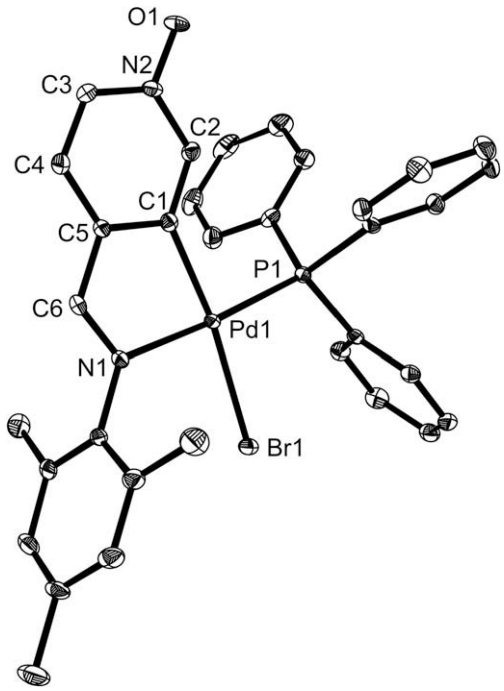


Fig. 1. Molecular structure of Pd{4-(O)$NC_5H_3C(H)$=N[2′,4′,6′-$(CH_3)C_6H_2$]}(Br)(PPh_3)], **9**. Ellipsoids drawn at the 40%. Selected bond distances (Å) and angles (°): Pd(1)–N(1) 2.099(2), Pd(1)–C(1) 2.016(2), Pd(1)–Br(1) 2.459(1), Pd(1)–P(1) 2.246(1), C(1)–C(5) 1.418(3), C(5)–C(6) 1.443(3), N(1)–C(6) 1.284(3), N(2)–O(1) 1.304(3); N(1)–Pd(1)–C(1) 81.06(9), N(1)–Pd(1)–Br(1) 90.85(6), C(1)–Pd(1)–Br(1) 171.87(7), N(1)–Pd(1)–P(1) 175.56(6), C(1)–Pd(1)–P(1) 94.54(7), Br(1)–Pd(1)–P(1) 93.57(2).

signals appeared high-field shifted (δ 55.18, 39.98 ppm; J(PP) = 22.7 Hz, for **10** *vs.* δ 61.12, 46.47 ppm; J(PP) = 24.5 Hz for **11**). The resonance at lower frequency was assigned to the phosphorus nucleus *trans* to the phenyl carbon atom, in accordance with the higher *trans* influence of the latter with respect to the C=N nitrogen atom [37]. The $^{13}C\{1H\}$ spectra showed the HC=N resonance coupled to the *trans*-nitrogen phosphorus nuclei and considerably high-field shifted in the case of **10** [δ 164.66 ppm, J(CP) = 2.0 Hz; 180.11 ppm, J(CP) = 3.1 Hz for **10** and **11**, respectively]. The C5 and C6 resonances also showed coupling to the phosphorus nucleus.

Accordingly, the most significant differing shifts in the ^1H and ^{13}C MNR spectra of complexes **10** and **11** corresponded to the HC=N group. This is indicative that in solution the interaction between the cation and its counteraction takes place through the imine proton. This feature may be used to determine the anions present in the solution and, therefore, complexes **10** and **11** may be used as anion sensors.

In the mass spectra of **10** and **11** the cluster of peaks centred at 743 amu were assigned to the $[\{(L\text{-}H)Pd(dppe)\}]^+$ fragment due to the loss of the counterion. Conductivity measurements were in accordance with a 1:1 electrolyte formulation.

3. Experimental

3.1. General remarks

Solvents were purified by standard methods [38]. Chemicals were reagent grade. Microanalyses were carried out using a Carlo Erba Elemental Analyser, Model 1108. IR spectra were recorded as KBr discs on a Satellite FTIR. NMR spectra were obtained as $CDCl_3$ solutions and referenced to $SiMe_4$ (^1H, $^{13}C\{1H\}$) or 85% H_3PO_4 ($^{31}P\{1H\}$) and were recorded on a Bruker AV-300F spectrometer. All chemical shifts were reported downfield from standards. The FAB mass spectra were recorded using a FISONS Quatro mass spectrometer with a Cs ion gun; 3-nitrobenzyl alcohol was used as the matrix. The ESI mass spectra were recorded using a QSTAR Elite mass spectrometer, using dichloromethane/acetonitrile or dichloromethane/ethanol as solvents.

3.2. Syntheses

3.2.1. Preparation of $NC_5H_4C(H)$=N[2′,4′,6′-$(CH_3)C_6H_2$] (**1**)

4-(COH)NC_5H_4 (0.173 g, 1.61 mmol) and 2,4,6-$Me_3C_6H_2NH_2$ (0.211 g, 1.56 mmol) were added to 50 cm^3 of dry chloroform. The mixture was heated under reflux in a Dean-Stark apparatus for 48 h. After cooling to room temperature, the solvent was evaporated to give a yellow oil. Yield: 93%. *Anal.* Calc. for: $C_{15}H_{16}N_2$: C, 80.2; H, 7.2; N, 12.5. Found. C, 80.0; H, 6.9; N, 12.7%. IR: ν(C=N) = 1605m cm^{-1}. NMR ^1H (300.13 MHz, $CDCl_3$, δ ppm, J Hz): δ = 8.79 [m, 2H, H3/H5]; 8.23 (s, 1H, Hi); 7.78 [m, 2H, H2/H6]; 6.91 (s, 2H, H9/H11); 2.30 (s, 3H, –CH_3); 2.12 (s, 6H, 2CH_3).

3.2.2. Preparation of [Pd{$NC_5H_4C(H)$=N[2′,4′,6′-$(CH_3)C_6H_2$]}$_2$($OCOCH_3$)$_2$] (**2**)

A pressure tube containing Schiff base 1 (0.150 g, 0.666 mmol), palladium(II) acetate (0.150 g, 0.668 mmol) and 20 cm^3 of dry toluene was sealed under argon. The resulting yellow solution was stirred for 24 h at 60 °C. The green solid obtained was filtered off and dried *in vacuo*. Yield: 46%. *Anal.* Calc. for $C_{34}H_{38}N_4O_4Pd$ requires: C, 60.7; H, 5.7; N, 8.3. Found: C, 60.5; H, 5.4; N, 8.6%. IR: ν(C=N) = 1610s; [ν_{as}(COO) = 1558s, ν_s(COO) = 1300s]cm^{-1}. NMR ^1H (300.13 M, $CDCl_3$, δ ppm, J Hz): δ = 8.84 [d, 2H, H3,H5 ^3J(H2H3) = 6.6]; 8.22 (s, 1H, Hi); 7.82 [d, 2H, H2, H6, ^3J(H6H5) = 6.6]; 6.95 (s, 2H, H9/H11); 2.29 (s, 3H, –OAc); 1.89 (s, 3H, –CH_3); 2.10 (s, 6H, 2CH_3). NMR $^{13}C\{1H\}$ (75.47 MHz, $CDCl_3$, δ ppm, J Hz): δ = 178.36 (s, –CO_2CH_3); 158.76 (s, Ci); 122.13 (s, C3/C5); 147.33, 144.83, 134.25, 126.75 (s, C1, C7, C10); 129.01 (s, C2/C6); 128.22 (s, C8/C12); 123.03 (s, C9/C11); 23.23 (s, –CO_2CH_3); 20.76 (s, C13/C15); 18.22 (s, C14).

3.2.3. Preparation of [4-(Me)$NC_5H_4C(H)$=N{2′,4′,6′-$(CH_3)C_6H_2$}][I] (**3**)

A pressure tube containing Schiff base 1 (0.180 g, 0.803 mmol), IMe (0.114 g, 0.803 mmol) and 20 cm^3 of dry toluene was sealed under argon. The resulting yellow solution was stirred for 24 h at 90 °C. The orange solid obtained was filtered off and dried *in vacuo*. Yield: 22%. *Anal.* Calc. $C_{16}H_{19}N_2I$ requires: C, 52.5; H, 5.2; N, 7.6. Found: C, 52.6; H, 5.4; N, 7.6%. IR: ν(C=N) = 1610s cm^{-1}. NMR ^1H (300.13 MHz, $CDCl_3$, δ ppm, J Hz): δ = 8.31 [d, 2H, H3/H5, ^3J(H2H3) = 6.6]; 8.47 (s, 1H, Hi); 8.52 [d, 2H, H2/H6, ^3J(H2H3) = 6.6]; 6.93 (s, 2H, H9/H11); 4.77 (s, 3H, N–CH_3); 2.36 (s, 3H, –CH_3); 2.16 (s, 6H, 2CH_3). Specific molar conductivity Λ_m = 97.5 cm^2 mol^{-1}(in dry acetonitrile).

Compound **4** was obtained as yellow solid, following a similar procedure to that used in the preparation of **1**.

3.2.4. Preparation of 4-(O)$NC_5H_4C(H)$=N[2′,4′,6′-$(CH_3)C_6H_2$] (**4**)

Yield: 93%. *Anal.* Calc. $C_{15}H_{16}N_2O$ requires: C, 75.0.2; H, 6.7; N, 11.7. Found: C, 75.5; H, 6.6; N, 12.0%. IR: ν(C=N) = 1603m cm^{-1}. NMR ^1H (300.13 MHz, $CDCl_3$, δ ppm, J Hz): δ = 8.27 [d, 2H, H3/H5, ^3J(H2H3) = 7.2]; 8.15 (s, 1H, Hi); 7.78 [d, 2H, H2/H6, ^3J(H2H3) = 7.2]; 6.90 (s, 2H, H9/H11); 2.29 (s, 3H, –CH_3); 2.11 (s, 6H, 2CH_3). NMR $^{13}C\{1H\}$ (75.47 MHz, $CDCl_3$, δ ppm, J Hz): δ = 157.76 (s, Ci); 147.57 (s, C7); 139.60 (s, C3/C5); 133.92, 132.91 (s, C1, C10); 128.89 (s, C9/C11); 126.79 (s, C8/C12); 124.70 (s, C2/C6); 20.70 (s, C14); 18.19 (s, C13/C15).

*3.2.5. Preparation of [Pd{4-(O)NC$_5$H$_3$C(H)=N[2′,4′,6′-(CH$_3$)C$_6$H$_2$]}(OCOCH$_3$)]$_2$ (**5**)*

A pressure tube containing Schiff base **4** (0.196 g, 0.816 mmol), palladium(II) acetate (0.186 g, 0.816 mmol) and 20 cm^3 of dry toluene was sealed under argon. The resulting yellow solution was stirred for 48 h at 75 °C, filtered trough celite to remove the black palladium formed and the solvent removed under vacuum. The brown oil obtained was tritured with ether to give a brown solid which was filtered off and dried *in vacuo*. Yield: 93%. *Anal.* Calc. $C_{34}H_{36}N_4O_6Pd_2$ requires: C, 50.4; H, 4.5; N, 6.9. Found: C, 48.9; H, 4.3; N, 6.6%. IR: ν(C=N) = 1576s; [ν_{as}(COO) = 1577s, ν_s(COO) = 1420s]cm^{-1}. NMR ^{1}H (300.13 MHz, $CDCl_3$, δ ppm, *J* Hz): δ = 8.10 [dd, 1H, H3, ^3J(H2H3) = 6.6, ^4J(H3H5) = 1.8]; 7.72 (s, 1H, Hi); 7.48 [d, 1H, H5, ^4J(H3H5) = 1.8]; 7.14 [d, 1H, H2, ^3J(H2H3) = 6.6]; 6.91 (s, 2H, H9/H11); 2.44 (s, 3H, –OAc); 2.34 (s, 3H, –CH$_3$); 1.63 (s, 6H, 2CH$_3$). NMR ^{13}C{1H} (75.47 MHz, $CDCl_3$, δ ppm, *J* Hz): δ = 180.96 (s, –CO_2CH_3); 172.89 (s, Ci); 148.34 (s, C7); 142.61, 141.89 (s, C1, C6); 140.38, 135.76 (s, C3, C5); 137.69 (s, C8/C12); 131.83 (s, C10); 128.84 (s, C9/C11); 121.97 (s, C2); 22.76 (s,--CO_2CH_3); 20.80 (s, C13/C15); 18.26 (s, C14). FAB-mass: [{(L-H)Pd}$_2$H]$^+$ = 691.1; [{(L-H)$_2$(OAc)Pd$_2$}H]$^+$ = 751.1; [{(L-H)(OAc)Pd}$_2$H]$^+$ = 809.1 amu.

*3.2.6. Preparation of [Pd{4-(O)NC$_5$H$_3$C(H)=N[2′,4′,6′-(CH$_3$)C$_6$H$_2$]}(Cl)]$_2$ (**6**)*

A solution of **5** (0.103 g, 0.128 mmol) in 20 cm^3 of acetone was treated with a saturated solution of NaCl in water until complete solution. After stirring for 24 h the yellow precipitate formed was filtered off, washed with water and dried under vacuum. Yield: 82%. *Anal.* Calc. $C_{30}H_{30}N_4O_2Cl_2Pd_2$ requires: C, 47.3; H, 4.0; N, 7.3. Found: C, 47.4; H, 3.8; N, 7.0%. IR: ν(C=N) = 1583m cm^{-1}. NMR ^{1}H (300.13 MHz, DMSO-d$_6$, δ ppm, *J* Hz): δ = 8.28 (s, 1H, H5); 8.26 (s, 1H, Hi); 8.00 [d, 1H, H3, ^3J(H2H3) = 5.7]; 7.41 [d, 1H, H2, ^3J(H2H3) = 5.7]; 6.92 (s, 2H, H9/H11); 2.23 (s, 3H, –CH$_3$); 2.19 (s, 6H, 2–CH$_3$). ESI-mass: [{(L-H)ClPd}$_2$H]$^+$ = 762.98 amu.

*3.2.7. Preparation of [Pd{4-(O)NC$_5$H$_3$C(H)=N[2′,4′,6′-(CH$_3$)C$_6$H$_2$]}(Br)]$_2$ (**7**)*

A brown solution of **5** (0.127 g, 0.157 mmol) in 15 cm^3 of methanol was treated with a saturated solution of LiBr in water (*ca.* 15 cm^3). After stirring for 24 h the yellow–green precipitate formed was filtered off, washed with water and dried under vacuum. Yield: 85%. *Anal.* Calc. $C_{30}H_{30}N_4O_2Br_2Pd_2$ requires: C, 42.3; H, 3.5; N, 6.6. Found: C, 42.5; H, 3.4; N, 6.6%. IR: ν(C=N) = 1600m sh cm^{-1}. NMR ^{1}H (300.13 MHz, DMSO-d$_6$, δ ppm, *J* Hz): δ = 8.38 (br, 1H, H5); 8.29 (s, 1H, Hi); 7.98 [dd, 1H, H3, ^3J(H2H3) = 6.6, ^4J(H3H5) = 1.8]; 7.40 [d, 1H, H2, ^3J(H2H3) = 6.6]; 6.94 (s, 2H, H9/H11); 2.24 (s, 3H, –CH$_3$); 2.20 (s, 6H, 2CH$_3$). FAB-mass: [{(L-H)BrPd}$_2$H]$^+$ = 853.4 amu.

*3.2.8. Preparation of [Pd{4-(O)NC$_5$H$_3$C(H)=N[2′,4′,6′′-(CH$_3$)C$_6$H$_2$]}(Cl)(PPh$_3$)] (**8**)*

PPh$_3$ (0.033 g, 0.124 mmol) was added to a suspension of **6** (0.047 g, 0.062 mmol) in chloroform (15 cm^3). The resulting orange solution was stirred for 24 h and the solvent removed under vacuum to give an orange oil which was recrystallized form chloroform/hexane and the resulting yellow solid filtered off and dried *in vacuo.* Yield: 63%. *Anal.* Calc. $C_{33}H_{30}ClN_2OPdP{\cdot}CHCl_3$ requires: C, 53.5; H, 4.1; N, 3.7. Found: C, 53.0; H, 4.0; N, 4.0%. IR: ν(C=N) = 1581m cm^{-1}. NMR ^{1}H (300.13 MHz, $CDCl_3$, δ ppm, *J* Hz): δ = 8.07 [d, 1H, Hi, ^4J(PHi) = 7.8]; 7.80 [dd, 1H, H3, ^3J(H2H3) = 6.3 , ^4J(H3H5) = 1.8]; 7.19 [d, 1H, H2, ^3J(H2H3) = 6.3]; 7.05 [dd, 1H, H5, ^4J(PH5) = 3.9 , ^4J(H3H5) = 1.8]; 6.86 (s, 2H, H9/H11); 2.31 (s, 6H, –2CH$_3$); 2.25 (s, 3H, –CH$_3$). NMR ^{13}C{1H} (125.76 MHz, $CDCl_3$, δ ppm, *J* Hz): δ = 174.34 (s, Ci); 153.61 [d, C7, ^3J(C7P) = 2.5]; 145.30 [d, C5, ^3J(C5P) = 11.2]; 144.98, 144.47 (s, C1, C6); 136.25 (s, C10); 135.20 [d, C-*orto*, ^2J(C-*orto*,P) = 11.8]; 135.12 (s, C3); 131.34 [d, C-*para*, ^4J(C-*para*,P) = 2.6]; 129.91 (s, C8/C12); 129.66 (s, C-*ipso*, ^1J(C-*ipso*,P) = 43.8]; 128.47 [d, C-*meta*, ^3J(C-*meta*,P) = 11.2]; 128.38 (s, C9/C11); 123.39 (s, C2); 21.0 (s, C14); 19.10 (s, C13/C15). NMR ^{31}P{1H}(121.50 MHz, $CDCl_3$, δ ppm): 39.66 (s). FAB-mass: [{(L-H)Pd(PPh$_3$)}]$^+$ = 607.1; [{(L-H)Pd(PPh$_3$)(Cl)}]$^+$ = 643.1 amu.

Compound **9** was obtained as a yellow solid following a similar procedure.

*3.2.9. Preparation of [Pd{4-(O)NC$_5$H$_3$C(H)=N[2′,4′,6′-(CH$_3$)C$_6$H$_2$]}(Br)(PPh$_3$)] (**9**)*

Yield: 66%. *Anal.* Calc. $C_{33}H_{30}BrN_2OPdP{\cdot}CHCl_3$ requires: C, 50.6; H, 3.9; N, 3.5. Found: C, 51.0; H, 4.3; N, 3.7%. IR: ν(C=N) = 1580m cm^{-1}. NMR ^{1}H (300.13 MHz, $CDCl_3$, δ ppm, *J* Hz): δ = 8.09 [d, 1H, Hi, ^4J(PHi) = 7.8]; 7.82 [dd, 1H, H3, ^3J(H2H3) = 6.3, ^4J(H3H5) = 1.5]; 7.19 [d, 1H, H2, ^3J(H2H3) = 6.3]; 7.00 [dd, 1H, H5, ^4J(PH5) = 3.9 , ^4J(H3H5) = 1.5]; 6.88 (s, 2H, H9/H11); 2.32 (s, 6H, –2CH$_3$); 2.28 (s, 3H, –CH$_3$). NMR ^{13}C{1H} (125.76 MHz, $CDCl_3$, δ ppm, *J* Hz): δ = 174.73 (s, Ci); 154.54 (s, C7); 145.88, 144.42 (s, C1, C6); 144.98 [d, C5, ^3J(C5P) = 11.4]; 136.15 (s, C10); 135.16 (s, C3); 135.07 [d, C-*orto*, ^2J(C-*orto*,P) = 11.7];131.27 [d, C-*para*, ^4J(C-*para*,P) = 2.5]; 130.62 (s, C8/C12); 129.98 (s, C-*ipso*, ^1J(C-*ipso*,P) = 54.9]; 128.38 [d, C-*meta*, ^3J(C-*meta*,P) = 11.2]; 128.23 (s, C9/C11); 123.20 (s, C2); 20.97 (s, C14); 19.18 (s, C13/C15). NMR ^{31}P{1H} (121.50 MHz, $CDCl_3$, δ ppm): 39.39 (s). ESI-mass: [{(L-H)Pd(PPh$_3$)}]$^+$ = 607.12 amu.

*3.2.10. Preparation of [Pd{4-(O)NC$_5$H$_3$C(H)=N[2′,4′,6′-(CH$_3$)C$_6$H$_2$]}(PPh$_2$(CH$_2$)$_2$PPh$_2$)]-[Cl] (**10**)*

Ph$_2$P(CH$_2$)$_2$PPh$_2$ (0.022 g, 0.055 mmol) was added to a suspension of **6** (0.020 g, 0.026 mmol) in chloroform (10 cm^3). The mixture was stirred for 24 h, the solvent removed under vacuum and the residue formed recrystallized form chloroform/hexane to give a yellow solid which was filtered off and dried *in vacuo.* Yield: 49%. *Anal.* Calc. $C_{41}H_{39}ClN_2OP_2Pd$ requires: C, 63.2; H, 5.0; N, 3.6. Found: C, 63.1; H, 4.7; N, 3.5%. IR: ν(C=N) = 1576m cm^{-1}. NMR ^{1}H (300.13 MHz, $CDCl_3$, δ ppm, *J* Hz): δ = 8.44 (s, 1H, Hi); 8.04 [d, 1H, H3, ^3J(H2H3) = 6.0]; 6.78 (s, 2H, H9/H11); 2.30 (s, 3H, –CH$_3$); 1.92 (s, 6H, 2CH$_3$); (H$_5$, occluded). NMR ^{13}C{1H} (125.76 MHz, $CDCl_3$, δ ppm, *J* Hz): δ = 164.66 [d, Ci, ^3J(CiP$_a$) = 2.0]; 161.85 [dd, C6, ^2J(C6P$_b$) = 134.4 , ^2J(C6P$_a$) = 3.5]; 148.59 (s, C7); 142.67 (m, C5); 140.14 (s, C1); 134.87 (s, C3); 133.13 [d, C-*orto*, ^2J(C-*orto*,P$_b$) = 11.4]; 133.02 (s, C10); 132.94 [d, C-*orto*, ^2J(C-*orto*,-P$_a$) = 11.2]; 132.29 [d, C-*para*, ^4J(C-*para*,P$_b$) = 2.3]; 131.43 [d, C-*para*, ^4J(C-*para*,P$_a$) = 2.1]; 129.48 [d, C-*meta*, ^3J(C-*meta*,P$_b$) = 11.2]; 129.19 [d, C-*ipso*, ^1J(C-*ipso*,P$_a$) = 38.7]; 129.16 [d, C-*meta*, ^3J(C-*meta*,-P$_a$) = 10.2]; 128.60 (s, C9/C11); 127.87 [d, C-*ipso*, ^1J(C-*ipso*,P$_b$) = 53.1]; 127.48 (s, C8/C12); 123.66 [d, C2, ^4J(C2,P) = 8.4]; 20.82 (s, C14); 18.62 (s, C13/C15). NMR ^{31}P{1H} (121.50 MHz, $CDCl_3$, δ ppm, *J* Hz): 55.18 [d, P$_a$, ^nJ(P$_a$,P$_b$) = 22.7]; 39.98 [d, P$_b$, ^nJ(P$_a$,P$_b$) = 22.7] ppm. ESI-mass: [{(L-H)Pd(dppe)}]$^+$ = 743.15 amu. Specific molar conductivity: Λ_m = 81.2 cm^2 mol^{-1}(in dry acetonitrile).

*3.2.11. Preparation of [Pd{4-(O)NC$_5$H$_3$C(H)=N[2′,4′,6′-(CH$_3$)C$_6$H$_2$]}(PPh$_2$(CH$_2$)$_2$PPh$_2$)]-[PF$_6$] (**11**)*

Ph$_2$P(CH$_2$)$_2$PPh$_2$ (0.030 g, 0.075 mmol) was added to a suspension of **7** (0.032 g, 0.038 mmol) in acetone (10 cm^3). The mixture was stirred for 45 min after which an excess of ammonium hexafluorophosphate (*ca.* 1:6 molar ratio) was added. The mixture was stirred for a further 1 h, the complex precipitated out by addition of water, stirred for a further 24 h filtered off and dried *in vacuo*, to give the final compound as a pale yellow solid. Yield: 21%. *Anal.* Calc. $C_{41}H_{39}F_6N_2OP_3Pd$ requires: C, 55.4; H, 4.4; N, 3.1. Found: C, 55.0; H, 4.3; N, 3.2%. IR: ν(C=N) = 1575m cm^{-1}. NMR ^{1}H

(300.13 MHz, $CDCl_3$, δ ppm, J Hz): δ = 8.10 [d, 1H, Hi, ^4J(PHi) = 7.5]; 7.88 [d, 1H, H3, ^3J(H2H3) = 6.3]; 6.29 (s, 2H, H9/H11); 2.17 (s, 3H, $-CH_3$); 1.97 (s, 6H, $2CH_3$); (H_5, occluded). NMR $^{13}C\{1H\}$ (125.76 MHz, $CDCl_3$, δ ppm, J Hz): δ = 180.11 [d, Ci, $^3J(CiP_a)$ = 3.1]; 159.48 [d, C6, $^2J(C6P_b)$ = 117.2]; 145.88 (s, C7); 144.94 [dd, C5, $^3J(C5P_b)$ = 11.1, $^3J(C5,P_a)$ = 6.3]; 133.93 (s, C3); 133.88, 133.66 (s, C, C10); 133.68 [d, C-*orto*, ^2J(C-*orto*,P_b) = 11.9]; 133.48 [d, C-*para*, ^4J(C-*para*,P_b) = 2.6]; 133.10 [d, C-*orto*, ^2J(C-*orto*,P_a) = 11.9];132.10 [d, C-*para*, ^4J(C-*para*,P_a) = 2.4]; 130.26 [d, C-*meta*, ^3J(C-*meta*,P_b) = 11.4]; 129.36 [d, C-*meta*, ^3J(C-*meta*,P_a) = 10.4]; 129.00 (s, C9/C11); 127.90 (s, C8/C12); 126.42 [d, C-*ipso*, ^1J(C-*ipso*,P_a) = 41.7]; 125.42 [d, C2, $^4J(C2,P_b)$ = 5.7]; 124.73 [d, C-*ipso*, ^1J(C-*ipso*,P_b) = 52.8]; 20.76 (s, C14); 18.62 (s, C13/C15). NMR $^{31}P\{^1H\}$ (121.50 MHz, $CDCl_3$, δ ppm, J Hz): 61.12 [d, P_a, $^2J(P_a,P_b)$ = 24.5]; 46.47 [d, P_b, $^2J(P_a,P_b)$ = 24.5] ppm. ESI-mass: $[\{(L\text{-}H)Pd(dppe)\}]^+$ = 743.16 amu. Specific molar conductivity Λ_m = 82.1 $cm^2\ mol^{-1}$ (in dry acetonitrile).

3.3. Single-crystal X-ray diffraction analysis

3.3.1. Crystal data

$C_{33}H_{30}BrN_2OPPd{\cdot}2CHCl_3$; M = 926.61. Orthorhombic, a = 13.192(3), b = 19.889(5), c = 29.047(3) Å, U = 7621(4) $Å^3$, Z = 8, D_c = 1.615 g cm^{-3}, Space Group Pbca, μ(Mo Kα) = 2.029 mm^{-1}, T = 100 K. Three-dimensional, room temperature X-ray data were collected on a Bruker X8 Apex diffractometer using graphite-monochromated Mo Kα radiation. Of the 43653 reflections measured, all of which were corrected for Lorentz and polarisation effects and for absorption using a semi-empirical correction based on symmetry-equivalent and repeated reflections (max, min transmissions 0.83, 0.45), 7263 independent reflections exceeded the significance level $|F|/\sigma(|F|) > 4.0$ The structure was solved by direct methods and refined by full matrix least squares on F^2. Hydrogen atoms were included in calculated positions and refined in riding mode. Refinement converged at a final R = 0.0328 (wR_2 = 0.0722 for all 9490 unique data), with allowance for the thermal anisotropy of all non hydrogen atoms. Minimum and maximum final electron density −0.912 and 1.151 $eÅ^{-3}$. The structure solution and refinement were carried out using the program package SHELX-97 [39].

Supplementary data

CCDC 730623 contains the supplementary crystallographic data for compound **8**. These data can be obtained free of charge via http://www.ccdc.cam.ac.uk/conts/retrieving.html, or from the Cambridge Crystallographic Data Centre, 12 Union Road, Cambridge CB2 1EZ, UK; fax: (+44) 1223-336-033; or e-mail: deposit@ccdc.cam.ac.uk.

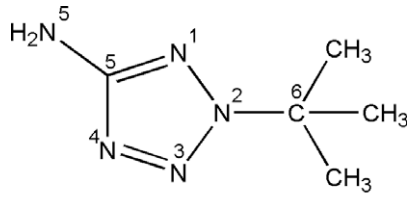
Acknowledgments

We thank the Ministerio de Educación y Ciencia (Projects CTQ2006-15621-C02-01/BQU and CTQ2006-15621-C02-02/BQU), the Xunta de Galicia (Projects INCITE07PXI103083ES and INCITE08ENA209044ES), and the Universidad de la Coruña for financial support.

References

[1] (a) J. Dehand, M. Pfeffer, Coord. Chem. Rev. 18 (1976) 327;
(b) I. Omae, Coord. Chem. Rev. 28 (1979) 97;
(c) I. Omae, Chem. Rev. 79 (1979) 287;
(d) I. Omae, Coord. Chem. Rev. 32 (1980) 235;
(e) I. Omae, Coord. Chem. Rev. 42 (1982) 245;
(f) I. Omae, Coord. Chem. Rev. 248 (2004) 995;
(g) F. Mohr, S.H. Priver, S.K. Bhargava, M.A. Bennett, Coord. Chem. Rev. 250 (2006) 1851.
[2] (a) M.I. Bruce, Angew. Chem., Int. Ed. Engl. 16 (1977) 73;
(b) E.C. Constable, Polyhedron 3 (1984) 1037;
(c) I.P. Rothwell, Polyhedron 4 (1985) 177;
(d) Y. Wu, S. Huo, J. Gong, X. Cui, L. Ding, K. Ding, C. Du, Y. Liu, M. Song, J. Organomet. Chem. 27 (2001) 637;
(e) M. Albrecht, G. van Koten, Angew. Chem., Int. Ed. 40 (2001) 3750.
[3] (a) J. Dupont, M. Pfeffer, J. Spencer, Eur. J. Inorg. Chem. (2001) 1917;
(b) V. Ritleng, C. Sirlin, M. Pfeffer, Chem. Rev. 102 (2002) 1731;
(c) M.E. van der Boom, D. Milstein, Chem. Rev. 103 (2003) 1759;
(d) J. Dupont, C.S. Consorti, J. Spencer, Chem. Rev. 105 (2005) 2527;
(e) H.-Y. Thu, W.-Y. Yu, C.-M. Che, J. Am. Chem. Soc. 128 (2006) 9048;
(f) R. Huang, K.H. Shaugnessy, Organometallics 25 (2006) 4105;
(g) M. Weck, C.W. Jones, Inorg. Chem. 46 (2007) 1865;
(h) R. Johansson, O.L. Wendt, Dalton Trans. (2007) 488;
(i) I. Omae, J. Organomet. Chem. 692 (2007) 2608.
[4] (a) S.B. Wild, Coord. Chem. Rev. 166 (1997) 291;
(b) J. Albert, J.M. Cadena, J.R. Granell, X. Solans, M. Font-Bardia, Tetrahedron: Asymmetry 11 (2000) 1943;
(c) S.P. Flanagan, R. Goddard, P.J. Guiry, Tetrahedron 61 (2005) 9808;
(d) L. Tang, Y. Zhang, L. Ding, Y. Li, K.-F. Mok, W.-C. Yeo, P.-H. Leung, Tetrahedron Lett. 48 (2007) 33;
(e) J. Djukic, A. Hijazi, H.D. Flack, G. Bernardinell, Chem. Soc. Rev. 37 (2008) 406.
[5] (a) W.T.S. Huck, R. Hulst, P. Timmerman, F.C.J.M. van Veggel, D.N. Reinhoudt, Angew. Chem., Int. Ed. Engl. 36 (1997) 1006;
(b) J.R. Hall, S.J. Loeb, G.K.H. Shimizu, G.P.A. Yap, Angew. Chem., Int. Ed. 37 (1998) 121;
(c) W.T.S. Huck, L.J. Prins, R.H. Fokkers, N.M.M. Nibbering, F.C.J.M. van Veggel, D.N. Reinhoudt, J. Am. Chem. Soc. 120 (1998) 6240;
(d) R.F. Carina, A.F. Williams, G. Bernardinelli, Inorg. Chem. 40 (2001) 1827;
(e) M. López-Torres, A. Fernández, J.J. Fernández, A. Suárez, S. Castro-Juiz, J.M. Vila, M.T. Pereira, Organometallics 20 (2001) 1350;
(f) M.Q. Slagt, D.A.P. van Zwieten, A.J.C.M. Moerkerk, R.J.M. Klein Gebbink, G. van Koten, Coord. Chem. Rev. 248 (2004) 2275;
(g) W. Lu, V.A.L. Rpy, C.-M. Che, Chem. Commun. (2006) 3972;
(h) M. Gagliardo, G. Rodríguez, H.H. Dam, M. Lutz, A.L. Spek, R.W.A. Havenith, P. Coppo, L. De Cola, F. Hartl, G.P.M. van Klink, G. van Koten, Inorg. Chem. 45 (2006) 2143.
[6] (a) M. Marcos, in: J.L. Serrano (Ed.), Metallomesogens. Synthesis, Properties and Applications, VCH, Weinheim, 1996;
(b) D. Pucci, G. Barneiro, A. Bellusci, A. Crispini, M. Ghedini, J. Organomet. Chem. 691 (2006) 1138.
[7] (a) S.-W. Lai, T.-C. Cheung, M.C.W. Chan, K.-K. Cheung, S.-M. Peng, C.-M. Che, Inorg. Chem. 39 (2000) 255;
(b) B. Ma, P.I. Djurovich, M.E. Thompson, Coord. Chem. Rev. 249 (2005) 1501;
(c) M. Ghedini, I. Aiello, A. Crispini, A. Golemme, M. La Deda, D. Pucci, Coord. Chem. Rev. 250 (2006) 1373;
(d) M.I.S. Lowry, S. Bernhard, Chem. Eur. J. 12 (2006) 7970;
(e) L.-L. Wu, C.-H. Yang, I-W. Sun, S.-Y. Chu, P.-C. Kao, H.-H. Huang, Organometallics 26 (2007) 2017;
(f) S.C.F. Kui, I.H.T. Sham, C.C.C. Cheung, C.-W. Ma, B. Pan, N. Zhu, C.M. Che, W.-F. Fu, Chem. Eur. J. 13 (2007) 417.
[8] (a) A. Habtemariam, B. Watchman, B.S. Potter, R. Palmer, S. Parsons, A. Parkin, P.J. Sadler, J. Chem. Soc., Dalton Trans. (2001) 1306;
(b) T. Okada, I.M. El-Mehasseb, M. Kodaka, T. Tomohiro, K. Okamoto, H. Okuno, J. Med. Chem. 44 (2001) 4661;
(c) A. Gómez-Quiroga, C. Navarro-Ranninger, Coord. Chem. Rev. 248 (2004) 119;
(d) J. Ruiz, J. Lorenzo, L. Sanglas, N. Cutillas, C. Vicente, M.D. Villa, F.X. Avilés, G. López, V. Moreno, J. Pérez, D. Bautista, Inorg. Chem. 45 (2006) 6347.
[9] M. Chas, D. Abella, V. Blanco, E. Pía, G. Blanco, A. Fernández, C. Platas-Iglesias, C. Peinador, J.M. Quintela, Chem. Eur. J. 13 (2007) 8572.
[10] K. Suzuki, M. Kawano, S. Sato, M. Fujita, J. Am. Chem. Soc. 129 (2007) 10652.
[11] I.S. Chun, J.A. Kwon, H.J. Yoon, M.N. Bae, J. Hong, O. Jung, Angew. Chem., Int. Ed. 46 (2007) 4960.
[12] M. Ferrer, A. Gutiérrez, M. Mounir, O. Rossell, E. Ruiz, A. Rang, M. Engeser, Inorg. Chem. 46 (2007) 3395.
[13] P. Thanasekaran, R.T. Liao, Y.H. Liu, T. Rajendran, S. Rajagopal, K.L. Lu, Coord. Chem. Rev. 249 (2005) 1085.
[14] G.F. Swiegers, T.J. Malefetse, Coord. Chem. Rev. 225 (2002) 91.
[15] M. Fujita, M. Tominaga, A. Hori, B. Therrien, Acc. Chem. Res. 38 (2005) 369.
[16] F. Wurthner, C.C. You, C.R. Saha-Moller, Chem. Soc. Rev. 33 (2004) 133.
[17] M. Broring, C. Kleenberg, Dalton Trans. (2007) 1101.
[18] A. Weisman, M. Gozin, H. Kraatz, D. Milstein, Inorg. Chem. 35 (1996) 1792.
[19] C.H.M. Amijs, A. Berger, F. Soulimani, T. Viasser, G.P.M. van Klink, M. Lutz, A.L. Spek, G. van Koten, Inorg. Chem. 44 (2005) 6567.
[20] H. Meguro, T. Koizumi, T. Yamamoto, T. Kanabara, J. Organomet. Chem. 693 (2008) 1109.
[21] M.C. Lagunas, R.A. Gossage, W.J.J. Smeets, A.L. Spek, G. van Koten, Eur. J. Inorg. Chem. (1998) 163.
[22] (a) H. Onoue, I. Moritani, J. Organomet. Chem. 43 (1972) 431;
(b) H. Onoue, K. Minami, I. Moritani, Bull. Chem. Soc. Jpn. 43 (1970) 431.
[23] Y.A. Ustinyuk, V.A. Chertov, I.V. Barinov, J. Organomet. Chem. 29 (1971) C53.

[24] K. Nakamoto, Infrared and Raman Spectra of Inorganic and Coordination Compounds, 5th ed., Wiley and Sons, New York, 1997.
[25] A. Fernández, D. Vázquez-García, J.J. Fernández, M. López-Torres, A. Suárez, S. Castro-Juiz, J.M. Ortigueira, J.M. Vila, New. J. Chem. 26 (2002) 105.
[26] M.T. Pereira, J.M. Vila, E. Gayoso, M. Gayoso, W. Hiller, J. Strähle, J. Coord. Chem. 18 (1988) 245.
[27] C. Navarro-Ranninger, F. Zamora, I. López-Solera, A. Monge, J.R. Masaguer, J. Organomet. Chem. 506 (1996) 149.
[28] B. Teijido, A. Fernández, M. López-Torres, S. Castro-Juiz, A. Suárez, J.M. Ortigueira, J.M. Vila, J.J. Fernández, J. Organomet. Chem. 598 (2000) 71.
[29] A. Fernández, D. Vázquez-García, J.J. Fernández, M. López-Torres, A. Suárez, S. Castro-Juiz, J.M. Vila, Eur. J. Inorg. Chem. (2002) 2389.
[30] J.M. Vila, M. Gayoso, M.T. Pereira, M. López-Torres, J.J. Fernández, A. Fernández, J.M. Ortigueira, J. Organomet. Chem. 532 (1997) 171.
[31] J. Granell, D. Sáinz, J. Sales, X. Solans, M. Font-Altaba, J. Chem. Soc., Dalton Trans. (1986) 1785.
[32] (a) L. Tusek-Bozic, M. Curic, P. Traldi, Inorg. Chim. Acta 49 (1997) 254;
(b) L. Tusek-Bozic, M. Komac, M. Curic, A. Lycka, M. Dálpaos, V. Scarcia, A. Furlani, Polyhedron 19 (2000) 937.
[33] J.M. Vila, M.T. Pereira, J.M. Ortigueira, M. Lopez-Torres, A. Castineiras, D. Lata, J.J. Fernandez, A. Fernandez, J. Organomet. Chem. 31 (1988) 556.
[34] J. Albert, J. Granell, J. Minguez, G. Muller, D. Sainz, P. Valerga, Organometallics 16 (1997) 3561.
[35] J. Albert, J. Granell, R. Moragas, M. Font-Bardia, X. Solans, J. Organomet. Chem. 59 (1996) 522.
[36] R.B. Bedford, C.S.J. Cazin, M.B. Hursthouse, M.E. Light, K.J. Pike, S. Wimperis, J. Organomet. Chem. 633 (2001) 173.
[37] P.S. Pregosin, R.W. Kuntz, ^{31}P and ^{13}C NMR of transition metal phosphine complexes, in: P. Diehl, E. Fluck, R. Kosfeld (Eds.), NMR, vol. 16, Springer, Berlin, 1979.
[38] D.D. Perrin, W.L.F. Armarego, Purification of Laboratory Chemicals, 4th ed., Butterwort-Heinemann, 1996.
[39] G.M. Sheldrick, Acta Crystallogr., Sect. A 64 (2008) 112.



1

Scheme 1. Classical representation and numbering of 5-amino-2-*tert*-butyltetrazole.

(1.3 g, 77%) as white crystals. Mp 115–116 °C (from water). ^{1}H NMR δ (ppm): 5.90 (s, 2H, NH_2), 1.51 (s, 9H, *t*-Bu); ^{13}C NMR δ (ppm): 167.2 (CN_4), 62.6 (CMe_3), 29.2 (Me). FT-IR (cm^{-1}): 3431 (s), 3324 (s), 3232 (s), 3175 (s), 3080 (m), 2988 (s), 2939 (s), 2912 (m), 2876 (m), 1636 (s), 1565 (s), 1539 (s), 1462 (s), 1403 (m), 1373 (s), 1310 (m), 1219 (s), 1196 (s), 1118 (w), 1081 (w), 1037 (w), 1015 (m), 939 (w), 823 (w), 778 (w), 762 (w), 654 (w br), 578 (w), 429 (vw), 315 (m), 262 (w), 192 (m), 142 (s), 111 (w), 92 (m). *Anal.* Calc. for $C_5H_{11}N_5$: C, 42.5; H, 7.8; N, 49.6. Found: C, 42.7; H, 7.6; N, 49.8%.

2.3. Synthesis of CuL_3Cl_2 (**2**)

Copper(II) chloride dihydrate (1 mmol, 0.17 g) was added to a solution of **1** (2 mmol, 0.282 g) in 20 mL of 1,2-dichloroethane. The resulting mixture was stirred at room temperature for 1 h and filtered. Slow evaporation of obtained solution at ambient conditions gave green crystals of complex **2** with quantitative yield (0.37 g). Calc. for $Cu(C_{15}H_{33}N_{15})Cl_2$: Cu 11.39. Found: Cu 11.20%. FT-IR (cm^{-1}): 3436 (s), 3332 (s), 3188 (s), 3071 (w), 2986 (s), 2938 (s), 2911 (w), 2876 (w), 1624 (vs), 1560 (vs), 1458 (s), 1438 (sh), 1404 (m), 1373 (s), 1331 (s), 1305 (m), 1236 (m), 1190 (vs), 1120 (m), 1083 (vw), 1036 (w), 1015 (s), 937 (w), 828 (m), 785 (m), 752 (m), 699 (w), 655 (w br), 576 (m), 429 (m), 354 (s), 322 (m), 312 (m), 274 (w), 241 (m), 194 (m), 173 (s), 143 (s), 134 (w), 128 (m), 123 (m), 96 (s), 68 (w).

2.4. Synthesis of PtL_2Cl_2 (**3**)

Platinum(II) chloride (1 mmol, 0.266 g) was added to the solution of **1** (2 mmol, 0.282 g) in mixture of toluene–THF (2:1). The resulting mixture was stirred at room temperature for 1 h and filtered. Slow evaporation of obtained solution at ambient conditions gave yellow crystals of **3**. Yield (0.47 g, 86%). Calc. for $Pt(C_{10}H_{22}N_{10})Cl_2$: Pt 35.58. Found: Pt 35.23%. FT-IR (cm^{-1}): 3446 (s), 3350 (s), 3165 (w), 3087 (vw), 2987 (s), 2939 (m), 2874 (w), 1618 (vs), 1550 (s), 1455 (s), 1429 (sh), 1403 (m), 1371 (s), 1331 (s), 1299 (s), 1239 (m), 1189 (vs), 1078 (vw), 1034 (w), 1022 (m), 937 (w), 827 (m), 789 (w), 744 (w), 573 (m), 475 (w), 437 (m), 342 (m), 307 (w), 236 (s), 217 (s), 160 (m), 129 (s), 73 (w).

2.5. Synthesis of PdL_2Cl_2 (**4**)

A solution of **1** (2 mmol, 0.282 g) in 20 ml of ethanol was dropped with stirring to a solution of palladium(II) chloride dihydrate (1 mmol, 0.214 g) in 20 ml of 1% hydrochloric acid. The resulting mixture was stirred at room temperature for 20 min. The resulting yellow solid residue was filtered, washed with water, dried and recrystallized from water/ethanol mixture (1/1) to give yellow crystals of **4**. Yield (0.432 g, 94%). Calc. for $Pd(C_{10}H_{22}N_{10})Cl_2$: Pd 23.15. Found: Pd 22.78%. FT-IR (cm^{-1}): 3440 (s), 3414 (s), 3390 (s), 3347 (s), 3158 (w), 3062 (vw), 2987 (s), 2939 (m), 2874 (w), 1612 (vs), 1551 (s), 1453 (s), 1430 (sh), 1403 (m), 1371 (s), 1327 (s), 1299 (s), 1237 (m), 1192 (vs), 1147 (w), 1078 (vw), 1027 (m), 1022 (m), 937 (w), 827 (m), 786 (w), 745 (w), 572 (m), 439 (w), 353 (m), 332 (w), 319 (w), 307 (w), 253 (w), 226 (s), 160 (m), 132 (s).

2.6. X-ray structure determinations

Suitable single crystals for X-ray analysis were picked directly from the reaction products. In the case of palladium complex **4**, single crystals of two polymorphs, marked as **4a** and **4b**, were found. They are triclinic and monoclinic, respectively. Crystal data, data collection and refinement details for the structures reported are summarized in Table 1. X-Ray data were collected on a Nicolet *R*3*m* diffractometer using graphite monochromated Mo Kα radiation (λ = 0.71073 Å) at room temperature. The structures were solved by direct methods (SIR2004 [18]) and refined by full matrix least square technique (SHELXL 97 [19]). In **1**, **2** and **4b**, rotational disorder of the *tert*-butyl groups over two positions was observed. For the disordered groups, bond lengths C–C(*tert*-butyl) and distances C(methyl)···N (where N is the tetrazole ring atom bonded to the *tert*-butyl group) were restrained to be equal, respectively. The amino group H atoms were localized from difference Fourier maps. For **1**, coordinates of amino H atoms were refined freely, whereas for all complexes, bond lengths N–H were restrained to 0.88 Å. U_{iso}(H) values were set to 1.2U_{eq}(N) for all compounds. Molecular graphics was performed with the program PLATON [20].

2.7. Cytotoxicity

In vitro cytotoxicity tests were performed at N.N. Alexandrov National Cancer Centre of Belarus, Minsk, Belarus.

2.7.1. Cell culture

HeLa cells (human cervical carcinoma) were obtained from the cell culture collection of Research Institute for Epidemiology and Microbiology (RIEM, Minsk, Belarus). The cells were cultured as a monolayer in culture flasks covered with 199 medium (RIEM) supplemented with 10% fetal calf serum (RIEM) and 100 μg/mL kanamycin.

2.7.2. Cytotoxicity assay

All the experiments were carried out on exponentially growing cells. Cell monolayer was detached from the culture flasks with 0.02% versen (DIALEK, Belarus), plated at a concentration of 2×10^5 cells/flask and incubated for 24 h at 37 °C. Stock 10^{-2} M solutions of test compounds were freshly prepared in dimethylsulfoxide (DMSO), then dilutions from 10^{-4} to 10^{-6} M in distilled water were made. On the day of the experiment, 50, 100 or 200 μL of drug dilutions were added into the flasks with cell monolayer at final concentrations of 0–50 μM. The cells were incubated in water bath at 37.0 °C for 48 h. Then treated and control cell monolayers were versenized and viable cells were counted using trypan-blue exclusion on a haemocytometer [21]. The mean ± standard deviation was calculated from three experiments. IC_{50} values (drug concentration at which 50% of the cells are viable relative to the control) were determined for each experiment using regression analysis of the data received.

3. Results and discussion

3.1. Preparation of complexes

Tetrazole **1** was found to react smoothly with transition metal(II) chlorides in solutions without heating giving highly crystalline colored complexes CuL_3Cl_2 (**2**), PtL_2Cl_2 (**3**) and PdL_2Cl_2 (**4**) in

Table 1
Crystal data and refinement details for **1**, **2**, **3**, **4a** and **4b**.

	1	**2**	**3**	**4a**	**4b**
Empirical formula	$C_5H_{11}N_5$	$C_{15}H_{33}N_{15}Cl_2Cu$	$C_{10}H_{22}N_{10}Cl_2Pt$	$C_{10}H_{22}Cl_2N_{10}Pd$	$C_{10}H_{22}Cl_2N_{10}Pd$
Formula weight	141.19	558.00	548.37	459.68	459.68
Crystal system	monoclinic	orthorhombic	triclinic	triclinic	monoclinic
Space group	$P2_1/c$	*Pbca*	$P\bar{1}$	$P\bar{1}$	$C2/c$
Crystal size (mm)	0.48 × 0.32 × 0.30	0.48 × 0.46 × 0.20	0.40 × 0.08 × 0.08	0.48 × 0.38 × 0.22	0.36 × 0.18 × 0.16
a (Å)	5.9538(15)	17.583(4)	9.760(3)	9.7687(14)	17.859(4)
b (Å)	9.978(2)	11.409(3)	9.920(3)	9.983(2)	9.925(2)
c (Å)	13.546(4)	27.551(8)	11.534(3)	11.508(2)	11.811(3)
α (°)	90	90	104.02(2)	104.34(2)	90
β (°)	95.48(2)	90	92.81(2)	93.20(2)	113.97(2)
γ (°)	90	90	115.84(2)	116.02(2)	90
V (Å^3)	801.0(3)	5527(3)	959.7(5)	959.5(3)	1913.0(8)
Z	4	8	2	2	4
ρ_{calc} (g/cm^3)	1.171	1.341	1.898	1.591	1.596
F(0 0 0)	304	2328	528	464	928
μ (Mo Kα) (mm^{-1})	0.081	1.017	7.602	1.259	1.263
θ Range for data collection (°)	2.54–27.54	1.48–27.06	1.85–27.56	1.86–30.07	2.40–30.06
Reflections collected	1920	6318	4693	5940	2895
Independent reflections	1845	6071	4433	5632	2817
Goodness-of-fit on F^2	1.009	1.005	1.046	1.038	1.097
R_1 [$I > 2\sigma(I)$]	0.0550	0.0527	0.0307	0.0281	0.0320
wR_2 [$I > 2\sigma(I)$]	0.1431	0.1225	0.0733	0.0744	0.0705
R_1 [all data]	0.0896	0.1001	0.0402	0.0329	0.0556
wR_2 [all data]	0.1695	0.1481	0.0801	0.0775	0.0804
$\Delta\rho_{min}/\Delta\rho_{max}$ (e Å^{-3})	0.160/−0.152	0.294/−0.654	0.955/−1.626	0.628/−0.612	0.439/−0.580
CCDC	737579	737580	737581	737582	737583

yields >80%. It should be noted that observed composition of copper chloride complex is rather unexpected since till now only complexes with lower content of ligand (CuL_2Cl_2, $CuLCl_2$ or $Cu_3L_4Cl_6$, where L = *N*-alkyltetrazoles) have been synthesized [8].

3.2. Thermal analysis

According to the data of complex thermal analysis (Figs. 1–4), metal complexes show the higher thermal stability in comparison with free ligand. Free ligand undergoes decomposition immediately after melting (117 °C), whereas its complexes decompose at temperature higher ~140 °C. Decomposition of copper, palladium and platinum complexes is characterized with first endothermal peak at 154 °C, 223 °C and 254 °C, correspondingly.

It should be noted that decomposition of tetrazole **1** proceeds endothermally. This behavior is characteristic for N-substituted 5-aminotetrazoles. In spite of high positive enthalpies of formation, they decompose endothermally under flow of nitrogen. Such behavior is explained by the evolution of highly energetic and

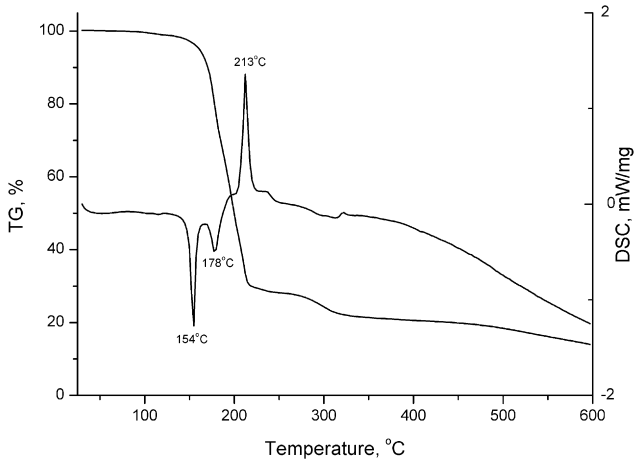


Fig. 2. Curves of thermal analysis of **2**.

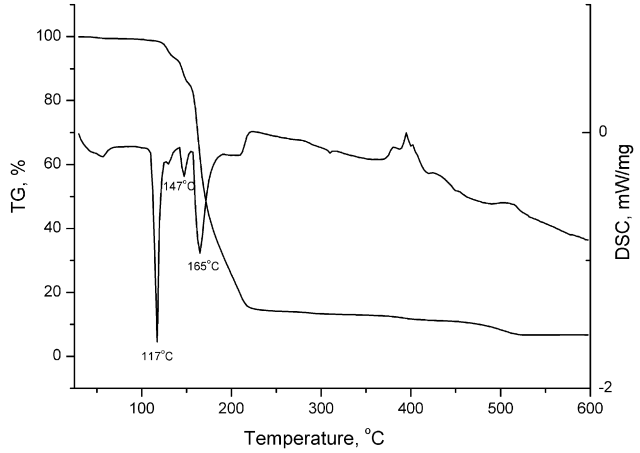


Fig. 1. Curves of thermal analysis of **1**.

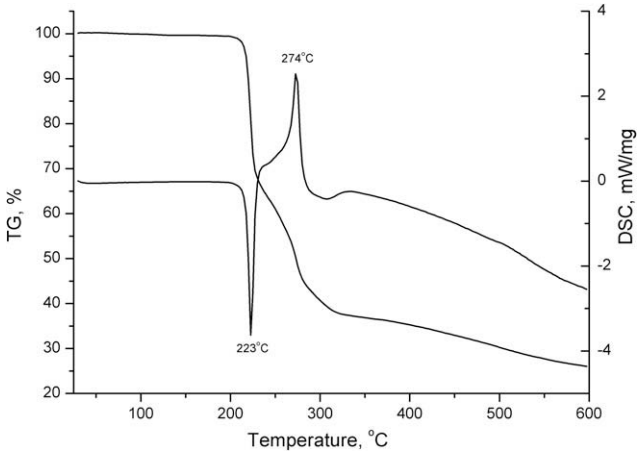


Fig. 3. Curves of thermal analysis of **4**.

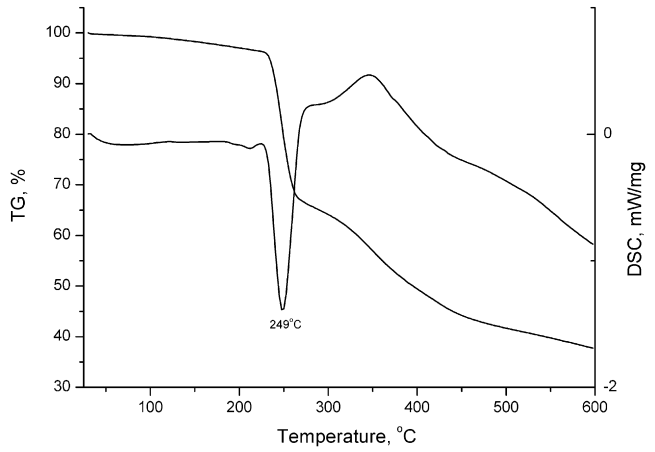


Fig. 4. Curves of thermal analysis of **3**.

readily volatile products which are removed from the reaction zone in the nitrogen steam [2]. Based on data on thermolysis of 2,5-disubstituted tetrazoles we can predict formation of *tert*-butyl azide and cyanamide when tetrazole **1** decomposes [22].

3.3. IR spectra

Free ligand **1** and complexes **2–4** were characterized by vibrational spectroscopy. The assignments were performed based on literature data on IR spectroscopy of related compounds, in particular 1- and 2-methyl-5-aminotetrazoles [12,23], N-alkyltetrazoles and their metal complexes [24]. Coordination with metal ion leads to the significant changes in frequencies of the ν(C=N) (1440–1460 cm^{-1}) and ν(N=N) (1300–1330 cm^{-1}) bands of the tetrazole ring as well as in the region of the stretching ν(N–H) (3450–3330 cm^{-1}) and deformation δ(N–H) (1640–1540 cm^{-1}) bands. The spectrum of the platinum complex has shown the presence of two bands in the stretching ν(N–H) region (3446 and 3350 cm^{-1}), while a number of bands (3347, 3391, 3414, 3342 cm^{-1}) have been observed in the spectrum of the palladium complex, which could be explained by overlapping of the corresponding bands of the two polymorphic modifications of palladium complex **4a** and **4b**, which were revealed during X-ray study.

In general, the spectra of both platinum and palladium complexes in the region 1700–500 cm^{-1} are almost identical. In the spectra of both complexes the bands of combined stretching ν(C–NH_2) and deformation δ(N–H) vibrations were observed at lower frequencies (1550 and 1618 cm^{-1} for **3**; 1551 and 1612 cm^{-1} for **4**) as compared with non-coordinated ligand (1565 and 1635 cm^{-1}), which is in agreement with changes in the spectrum of silver complexes of 5-amino-2-methyltetrazole [12]. No significant change is observed in the $\delta(C–H)_{oop}$ bands (1371–1373 cm^{-1}). The stretching ν(C=N) band of tetrazole ring decreases in frequency by about 10 cm^{-1} from 1462 cm^{-1} in the spectrum of **1** to 1458, 1455, and 1453 cm^{-1} in the spectra of **2**, **3**, and **4**, respectively. The stretching ν(N=N) band (1310 cm^{-1} for **1**) splits in two after the complexation, those are observed at 1299–1305 and 1327–1331 cm^{-1} [24]. The mid-IR spectrum of **2** not significantly differs from both described above. The most noticeable features concern the region of stretching and stretching-deformation vibrations of the tetrazole ring where several bands (1120 and 655 cm^{-1}) almost identical with the spectrum of the ligand are observed.

The far-IR spectra of complexes show ligand vibrations as well as new bands originating from metal–Cl and metal–N stretchings. In particular, the platinum complex gave only one stretching ν(Pt–Cl) band at 342 cm^{-1} which is consistent with a *trans* Cl–Pt–Cl configuration, whereas the palladium complex gave two well separated bands at 332 and at 353 cm^{-1} associated probably with Pd–Cl stretching in the two polymorphic modifications **4a** and **4b**. In the spectrum of copper complex stretching ν(Cu–Cl) band is observed at 354 cm^{-1}. The bands at 241 cm^{-1} for copper, at 253 cm^{-1} for palladium and at 236 cm^{-1} for platinum complexes, respectively, might be described as ν(M–N) stretching bands, although in case of the platinum complex it seems to be rather combinational band with the tetrazole ring vibrations, similarly to assignments in other Pt-heterocyclic amines spectra [25].

3.4. Description of crystal structures

Selected bond lengths for the investigated compounds are given in Table 2. Some structural features are shown in Figs. 5–10.

Compounds **2–4** are molecular complexes in which the ligand molecules are monodentate and coordinate to the metal ion *via* endocyclic N4 atom. In only one structurally characterized complex of 2-substituted 5-aminotetrazoles, namely $AgL(ClO_4)$, where L = 5-amino-2-methyltetrazole, ligand coordinates by N1 and N4 atoms [12].

In the crystal structure of **1**, the tetrazole ring is planar to within 0.0028(17) Å. As seen from Table 2, N2–N3 bond is the shortest in the ring, while the remaining bond lengths are rather similar. This is indicative of essentially aromatic character of this ring. The *tert*-butyl group is disordered over two positions, A and B, with occupancies of 0.564(9) and 0.436(9), respectively (Fig. 5). The amino group is close to planar, with the sum of the angles at amino N atom *ca.* 352°, and lies almost in the tetrazole ring plane. The flattened geometry of the amino group is probably caused by conjugation of the N atom lone pair with the tetrazole ring π-system. Both H atoms of the amino group form hydrogen bonds (HB) with the

Table 2
Selected bond lengths (Å) in the crystal structure of the investigated compounds.[a]

Atoms	1	2			3		4a		4b
N1–N2	1.329(3)	1.328(4)	1.329(5)	1.339(5)	1.335(7)	1.342(6)	1.336(3)	1.337(2)	1.331(4)
N2–N3	1.297(3)	1.299(4)	1.302(4)	1.298(4)	1.288(6)	1.297(6)	1.293(2)	1.299(2)	1.300(3)
N3–N4	1.328(3)	1.320(4)	1.336(4)	1.323(4)	1.330(6)	1.337(6)	1.326(2)	1.334(2)	1.332(3)
N1–C5	1.324(3)	1.329(4)	1.332(5)	1.324(6)	1.332(7)	1.331(6)	1.335(3)	1.330(3)	1.326(4)
N4–C5	1.332(3)	1.350(4)	1.361(5)	1.363(5)	1.343(7)	1.350(7)	1.340(3)	1.357(3)	1.345(4)
N5–C5	1.355(3)	1.358(5)	1.339(6)	1.325(6)	1.347(8)	1.349(7)	1.342(3)	1.348(3)	1.342(4)
N2–C6	1.489(3)	1.501(5)	1.497(5)	1.495(6)	1.498(6)	1.506(6)	1.508(3)	1.508(2)	1.509(3)
M–N4		2.005(3)			2.002(4)		1.9976(17)		2.017(2)
		2.008(3)			2.014(4)		2.0142(16)		2.017(2)
		2.054(3)							
M–Cl		2.2790(12)			2.3045(17)		2.2949(8)		2.2893(9)
		2.5313(12)			2.3052(17)		2.2998(8)		2.2893(9)

[a] For atom-numbering see Scheme 1. M – metal atom.

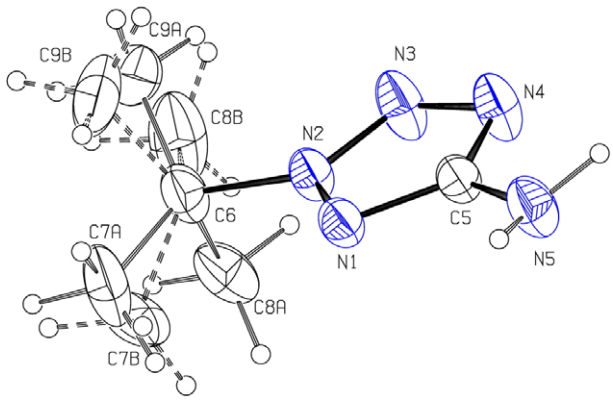


Fig. 5. The molecule of **1** with the atom-numbering scheme (A and B label disorder positions of the *tert*-butyl group). Displacement ellipsoids are drawn at the 30% probability level.

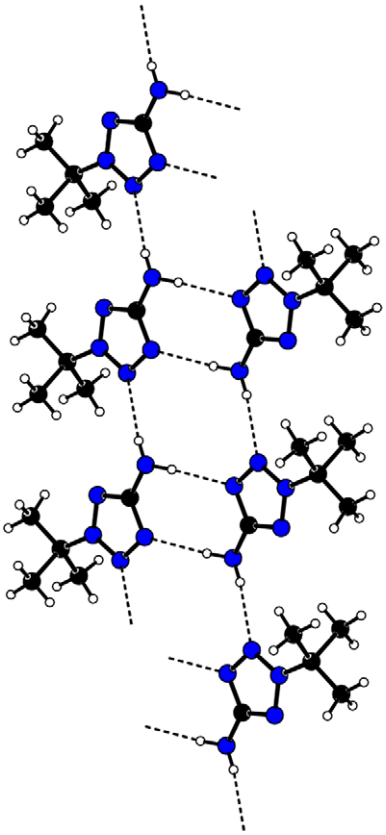


Fig. 6. Hydrogen bonded polymeric chain in the structure of **1**. Dashed lines show hydrogen bonding. Disorder of the *tert*-butyl groups is not shown.

tetrazole ring N atoms, namely N5–H5A···N4^{a} and N5–H5B···N3^{b} (symmetry transformations: *a*: $-x, -y, -z$; *b*: $x-1, y, z$). HB geometry characteristics, distance D···A and angle D–H···A, take of the values 3.090(3) Å, 176(3)° and 3.278(4) Å, 166(3)°, respectively. These HB are responsible for formation of polymeric chains running along the *a* axis, with van der Waals interactions between the chains (Fig. 6).

Asymmetric unit of **2** contains one Cu, two Cl atoms and three ligand molecules. Compound **2** presents molecular complex shown in Fig. 7. Coordination polyhedron of Cu atom is distorted square pyramid with τ descriptor value of 0.28 ($\tau = 0$ for square pyramid and $\tau = 1$ for trigonal bipyramid) [26]. The basal positions are occu-

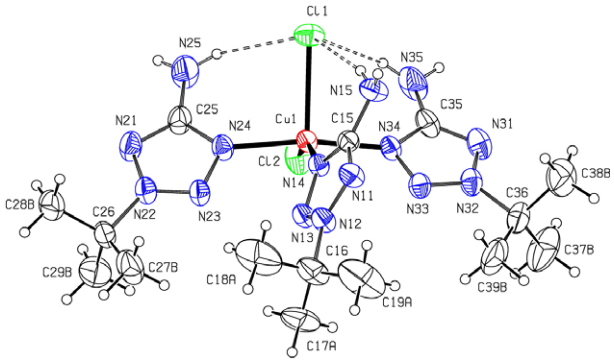


Fig. 7. The complex molecule of **2** with the atom-numbering scheme. Displacement ellipsoids are drawn at the 30% probability level. Disorder of the *tert*-butyl groups is not shown. Dashed lines show intramolecular hydrogen bonds of the amino groups.

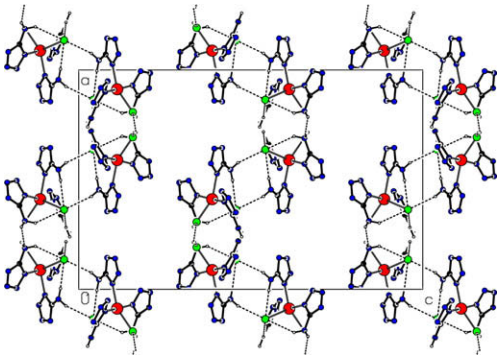


Fig. 8. The crystal packing of **2** viewed along the *b* axis. Dashed lines show hydrogen bonds. *tert*-Butyl groups are omitted for clarity.

pied by one chlorine atom and three N4 atoms of the ligand molecules. Another Cl atom lies in an apical position of the pyramid. In each ligand molecule, the *tert*-butyl group is disordered over two positions with rather different occupancies. Geometries of the tetrazole rings in three ligand molecules are similar being close to that in **1** (Table 2). There are three intramolecular hydrogen bonds N–H···Cl shown in Fig. 7, with distances N···Cl ranged from 3.295(4) to 3.505(6) Å and angles N–H···Cl being in the range of 147(5)–166(4)°, providing additional stabilization of the complex molecule. Three hydrogen atoms, which do not participate in intramolecular hydrogen bonds, form three intermolecular hydrogen bonds N–H···Cl, with distances N···Cl and angles N–H···Cl lying in the ranges 3.234(4)–3.684(5) Å and 146(5)–163(4)°, respectively. These HB link complex molecules into polymeric layers parallel with the *ab* plane (Fig. 8).

Complexes **3** and **4a** are isostructural. They reveal rather distorted square-planar coordination of Pt and Pd atoms, formed by atoms N4 of two ligand molecules and two chlorine atoms. Similar to **2**, these compounds are molecular complexes. As seen from Fig. 9 **3** and **4a** are *trans*-isomers. In both compounds, hydrogen bonds of the amino groups, N–H···Cl and N–H···N, are responsible for formation of polymeric chains along the *c* axis (Fig. 10).

Molecular arrangement in polymorph **4b** is very close to that in **4a**, however some structural differences take place. Pd atom lies on an inversion center and adopts more symmetrical square-planar coordination (*trans*-isomer). In contrast to **4a**, the *tert*-butyl groups are disordered over two positions. In polymorph **4b,** hydrogen bonded polymeric chains (along the *c* axis) are formed due to bonds N–H···Cl and N–H···N of the unique amino group. In **4a**, however, one of two amino group is hydrogen bonded to two Cl

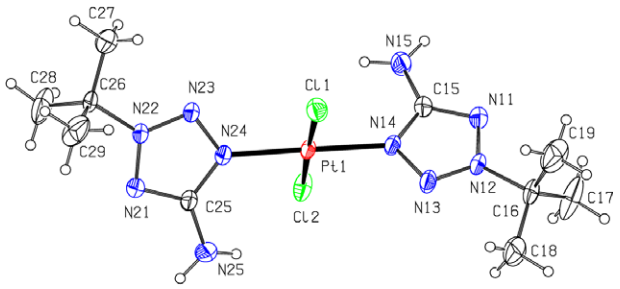


Fig. 9. The molecular structure of **3** with the atom-numbering scheme. Displacement ellipsoids are drawn at the 30% probability level.

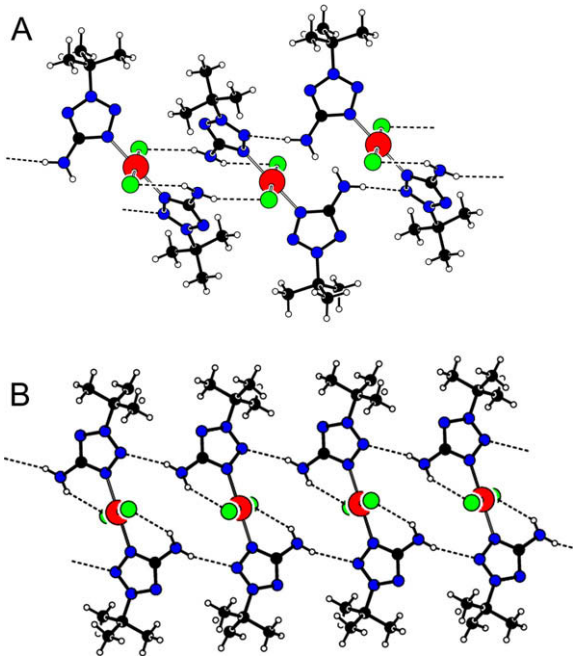


Fig. 10. Infinite chains in the crystal structures of **4a** (A) and **4b** (B). Disorder of the *tert*-butyl groups in **4b** is not shown.

Table 3
IC_{50} values of complexes **2**, **3**, **4**, and control compounds against HeLa cells.

Complex	IC_{50} (μM)
2	82
3	5.6
4	>100
Cisplatin	0.7
Carboplatin	12.5

atoms but another amino group forms only one hydrogen bond N–H···N (Fig. 10).

Comparison of the tetrazole ring geometry of **1** with that in complexes **2**–**4** revealed their similarity. All corresponding bond lengths are the same within 3σ (Table 2). However, they contradict to classical representation of the tetrazole ring (Scheme 1). So, formal single bond N2–N3 is shorter than formal double bonds N3=N4 and N1=C5. These features are observed for some examples of 2-mono- and 2,5-disubstituted tetrazoles [27]. Hence, this question may be a topic of detailed theoretical considerations.

In all compounds **1**–**4,** the amino group atoms lie practically in the tetrazole ring plane, allowing the amino group to be considered as conjugated with the ring π-system similar to other 5-aminotetrazoles [27a,28].

3.5. Cytotoxic activity

The cytotoxic activity of the copper, platinum, and palladium complexes was investigated on human cervical carcinoma cell line (HeLa). Cisplatin and carboplatin were included in the assay as a positive control. The determined IC_{50} values, the concentration of complex needed to inhibit 50% of cell growth, are summarized in Table 3. The palladium complex **4** turned out to be inactive, the copper complex **2** showing only moderate activity. The platinum complex **3** demonstrates promising activity, with IC_{50} value average between those of cisplatin and carboplatin. So its activity is close to those of other *trans*-platinum complexes with N-containing heterocycles [29].

Trans-platinum compounds are of great interest because of their ability to overcome cisplatin resistance. The cytotoxic effect of platinum antitumor drugs is based upon the formation of platinum-DNA adducts and modification of DNA structure. Relatively high activity of *trans*-platinum complexes with planar N-heterocycles is considered to be due to different reactivity of these complexes with DNA and such cellular components as glutathione and ability to form structurally different DNA adducts in different proportions in comparison with *cis*-platinum compounds [30]. Recent studies revealed that cytotoxic properties of platinum complexes strongly depend not only on their geometry, but also on structure of heterocyclic ligands [29b,29c]. Further investigations are required for clarifying influence of the tetrazole containing ligand on mechanistic aspects of compound **3** interactions with DNA and capacity of tetrazole based complexes to overcome tumor resistance to common platinum therapeutics.

4. Conclusion

5-Amino-2-*tert*-butyltetrazole reacts with metal(II) chlorides giving molecular complexes, CuL_3Cl_2, PdL_2Cl_2 and PtL_2Cl_2 in which the ligand molecules are monodentate and coordinate to the metal *via* endocyclic N4 atom. Platinum complex demonstrates promising cytotoxicity against human cervical carcinoma cells, with IC_{50} value being average between those of cisplatin and carboplatin.

4. Supplementary data

CCDC 737579, 737580, 737581, 737582 and 737583 contains the supplementary crystallographic data for **1**, **2**, **3**, **4a** and **4b**. These data can be obtained free of charge via http://www.ccdc.cam.ac.uk/conts/retrieving.html, or from the Cambridge Crystallographic Data Centre, 12 Union Road, Cambridge CB2 1EZ, UK; fax: (+44) 1223-336-033; or e-mail: deposit@ccdc.cam.ac.uk.

Acknowledgements

This work was supported by the Government of Republic of Belarus (The State Program for Oriented Fundamental Researches "Physiologically active substances"). We gratefully acknowledge the support of the Alexander von Humboldt Foundation (Return Research Fellowship of Dr. S. Voitekhovich). We are grateful to Dr. Elena N. Alexandrova (N.N. Alexandrov National Cancer Centre of Belarus, Minsk, Belarus.) for cytotoxicity tests.

References

[1] A.A. Kozyro, V.V. Simirsky, A.P. Krasulin, V.M. Sevruk, G.J. Kabo, M.L. Frenkel, P.N. Gaponik, Y.V. Grigoriev, Zh. Fiz. Khim. 64 (1990) 656 (in Russian).

[2] A.I. Lesnikovich, O.A. Ivashkevich, S.V. Levchik, A.I. Balabanovich, P.N. Gaponik, A.A. Kulak, Thermochim. Acta 388 (2002) 233.
[3] R.N. Butler, in: A.R. Katrizky, C.W. Rees, E.F.V. Scriven (Eds.), Comprehensive Heterocyclic Chemistry, vol. 4, Pergamon, New York, 1996, p. 621.
[4] (a) For recent examples, see: K. Yamazaki, H. Hasegawa, K. Umekawa, Y. Ueki, N. Ohashi, M. Kanaoka, Bioorg. Med. Chem. Lett. 12 (2002) 1275;
(b) T. Schelenz, J. Prakt. Chem. 342 (2000) 205. and references cited therein.
[5] D. Moderhack, B. Holtmann, J. Prakt. Chem. 342 (2000) 591.
[6] (a) T.M. Klapötke, C.M. Sabate, M. Rusan, Z. Anorg. Allg. Chem. 634 (2008) 688;
(b) S.V. Voitekhovich, P.N. Gaponik, A.S. Lyakhov, O.A. Ivashkevich, Tetrahedron 64 (2008) 8721.
[7] T.M. Klapötke, J. Stierstorfer, Helv. Chim. Acta 90 (2007) 2132.
[8] For recent review on metal derivatives of tetrazoles, see: P.N. Gaponik, S.V. Voitekhovich, O.A. Ivashkevich, Russ. Chem. Rev. 75 (2006) 507.
[9] (a) X.-W. Wang, J.-Z. Chen, J.-H. Liu, Cryst. Growth Des. 7 (2007) 1227;
(b) X. He, C.-Z. Lu, D.-Q. Yuan, Inorg. Chem. 45 (2006) 5760;
(c) X. Xue, B.F. Abrahams, R.-G. Xiong, X.-Z. You, Aust. J. Chem. 55 (2002) 495;
(d) J.-G. Zhang, T.-L. Zhang, K.B. Yu, Acta Chim. Sin. 59 (2001) 84.
[10] (a) N. Liu, Q. Yue, Y.-Q. Wang, A.-L. Cheng, E.-Q. Gao, Dalton Trans. (2008) 4621;
(b) T. Jiang, X.-M. Zhang, Cryst. Growth Des. 8 (2008) 3077;
(c) J.-M. Lin, Y.-F. Guan, W. Dong, Acta Crystallogr., Sect. E 64 (2008) m238;
(d) Z.-Q. Liu, W. Donga, S.W. Ng, Acta Crystallogr., Sect. E 63 (2007) m2943;
(e) M. Friedrich, J.C. Galvez-Ruiz, T.M. Klapötke, P. Mayer, B. Weber, J. Weigand, Inorg. Chem. 44 (2005) 8044.
[11] A.J. Zhilin, M.A. Ilyushin, I.V. Tselinsky, A.S. Kozlov, N.E. Kuz'mina, Russ. J. Appl. Chem. 75 (2002) 1849.
[12] K. Karaghiosoff, T.M. Klapötke, C.M. Sabate, Chem. Eur. J. 15 (2009) 1164.
[13] (a) Y. Cui, J. Zhang, T. Zhang, L. Yang, J. Zhang, X. Hu, J. Hazard. Mater. 160 (2008) 45;
(b) Y. Cui, T.-L. Zhang, J.-G. Zhang, L. Yang, X.-C. Hu, J. Zhang, J. Mol. Struct. 889 (2008) 177;
(c) P.N. Gaponik, S.V. Voitekhovich, A.S. Lyakhov, V.E. Matulis, O.A. Ivashkevich, M. Quesada, J. Reedijk, Inorg. Chim. Acta 358 (2005) 2549.
[14] (a) G.-W. Yang, Q.-Y. Li, Y. Zhou, G.-Q. Gu, Y.-S. Ma, R.-X. Yuan, Inorg. Chem. Commun. 11 (2008) 1239;
(b) Q.-Y. Li, G.-W. Yang, R.-X. Yuan, J.-P. Wang, P.-F. Cui, Acta Crystallogr., Sect. C 64 (2008) m26;
(c) Q.-Y. Li, G.-W. Yang, Y.-S. Ma, M.-J. Li, Y. Zhou, Inorg. Chem. Commun. 11 (2008) 795;
(d) G.-W. Yang, Q.-Y. Li, Y. Zhou, G.-Q. Gu, Y.-S. Ma, R.-X. Yuan, Inorg. Chim. Acta 362 (2008) 1234.
[15] G. Steinhauser, T.M. Klapötke, Angew. Chem., Int. Ed. 47 (2008) 3330.
[16] (a) A.V. Smirnov, M.A. Ilyushin, I.V. Tselinskii, Russ. J. Appl. Chem. 77 (2004) 794;
(b) A.Y. Zhilin, M.A. Ilyushin, I.V. Tselinskii, A.S. Kozlov, I.S. Lisker, Russ. J. Appl. Chem. 76 (2003) 572.
[17] B.C. Tappan, M.H. Huynh, M.A. Hiskey, D.E. Chavez, E.P. Luther, J.T. Mang, S.F. Son, J. Am. Chem. Soc. 128 (2006) 6589.
[18] M.C. Burla, R. Caliandro, M. Camalli, B. Carrozzini, G.L. Cascarano, L. De Caro, C. Giacovazzo, G. Polidori, R. Spagna, J. Appl. Cryst. 38 (2005) 381.
[19] G.M. Sheldrick, Acta Crystallogr., Sect. A 64 (2008) 112.
[20] A.L. Spek, J. Appl. Cryst. 36 (2003) 7.
[21] Yu.P. Istomin, E.A. Zhavrid, E.N. Alexandrova, O.P. Sergeyeva, S.V. Petrovich, Exp. Oncol. 30 (2008) 5.
[22] A.I. Lesnikovich, S.V. Levchik, A.I. Balabanovich, O.A. Ivashkevich, P.N. Gaponik, Thermochim. Acta 200 (1992) 427.
[23] A. Bigotto, R. Klingendrath, Spectrochim. Acta, Part A: Mol. Biomol. Spectr. 46A (1990) 1683.
[24] M.M. Degtyarik, P.N. Gaponik, V.N. Naumenko, A.I. Lesnikovich, M.V. Nikanovich, Spectrochim. Acta, Part A: Mol. Biomol. Spectr. 43A (1987) 349.
[25] (a) C. Engelter, A.T. Hutton, D.A. Thornton, J. Mol. Struct. 44 (1978) 23;
(b) J. Kuduk-Jaworska, A. Puszko, M. Kubiak, M. Pełczynska, J. Inorg. Biochem. 98 (2004) 1447;
(c) B.J. Graves, D.J. Hodgson, C.G. van Kralingen, J. Reedijk, Inorg. Chem. 17 (1978) 3007.
[26] A.W. Addison, T.N. Rao, J. Reedijk, J. van Rijn, G.C. Verschoor, J. Chem. Soc., Dalton Trans. (1984) 134.
[27] (a) J.H. Bryden, Acta Cryst. 9 (1956) 874;
(b) K. Yamaguchi, A. Ohsawa, T. Kaihoh, T. Itoh, Acta Crystallogr., Sect. C 46 (1990) 1161;
(c) P.N. Gaponik, S.V. Voitekhovich, A.S. Lyakhov, Chem. Heterocycl. Compd. 36 (2000) 326;
(d) R. Bronisz, Inorg. Chim. Acta 340 (2002) 215.
[28] (a) A.S. Lyakhov, P.N. Gaponik, S.V. Voitekhovich, Acta Crystallogr., Sect. C 57 (2001) 185;
(b) A.S. Lyakhov, A.N. Vorobiov, P.N. Gaponik, L.S. Ivashkevich, V.E. Matulis, O.A. Ivashkevich, Acta Crystallogr., Sect. C 59 (2003) o690.
[29] (a) M.V. Beusichem, N. Farrell, Inorg. Chem. 31 (1992) 634;
(b) G.M. Rakić, S. Grgurić-Šipka, G.N. Kaluđerović, S. Gómez-Ruiz, S.K. Bjelogrlić, S.S. Radulović, Ž.Lj. Teši, Eur. J. Med. Chem. 44 (2009) 1921;
(c) A. Martınez, J. Lorenzo, M.J. Prieto, M. Font-Bardia, X. Solans, F.X. Aviles, V. Moreno, Bioorg. Med. Chem. 15 (2007) 969.
[30] U. Kalinowska-Lis, J. Ochocki, K. Matlawska-Wasowska, Coord. Chem. Rev. 252 (2008) 1328.

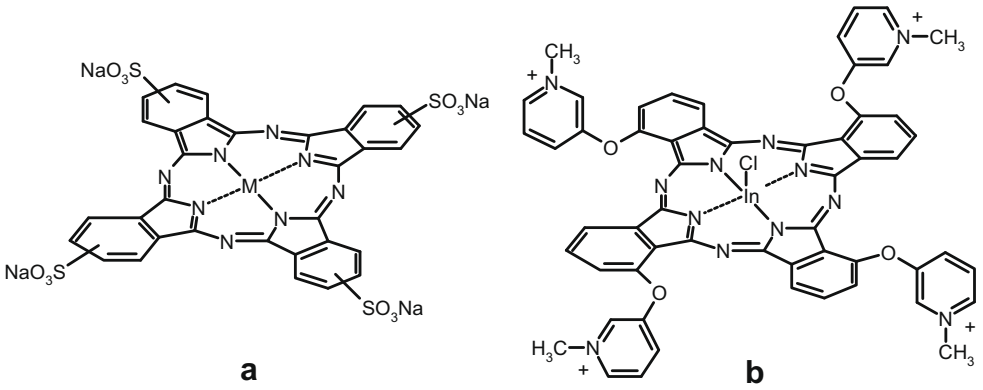


Fig. 1. Molecular structure of (a) tetrasulfo metallophthalocyanine (MTSPc), M = 2H, Mn, Fe, Co, Ni and (b) quaternized 2,(3)-tetra(3-pyridyloxyphthalocyninato) indium (III) (QInPyPc).

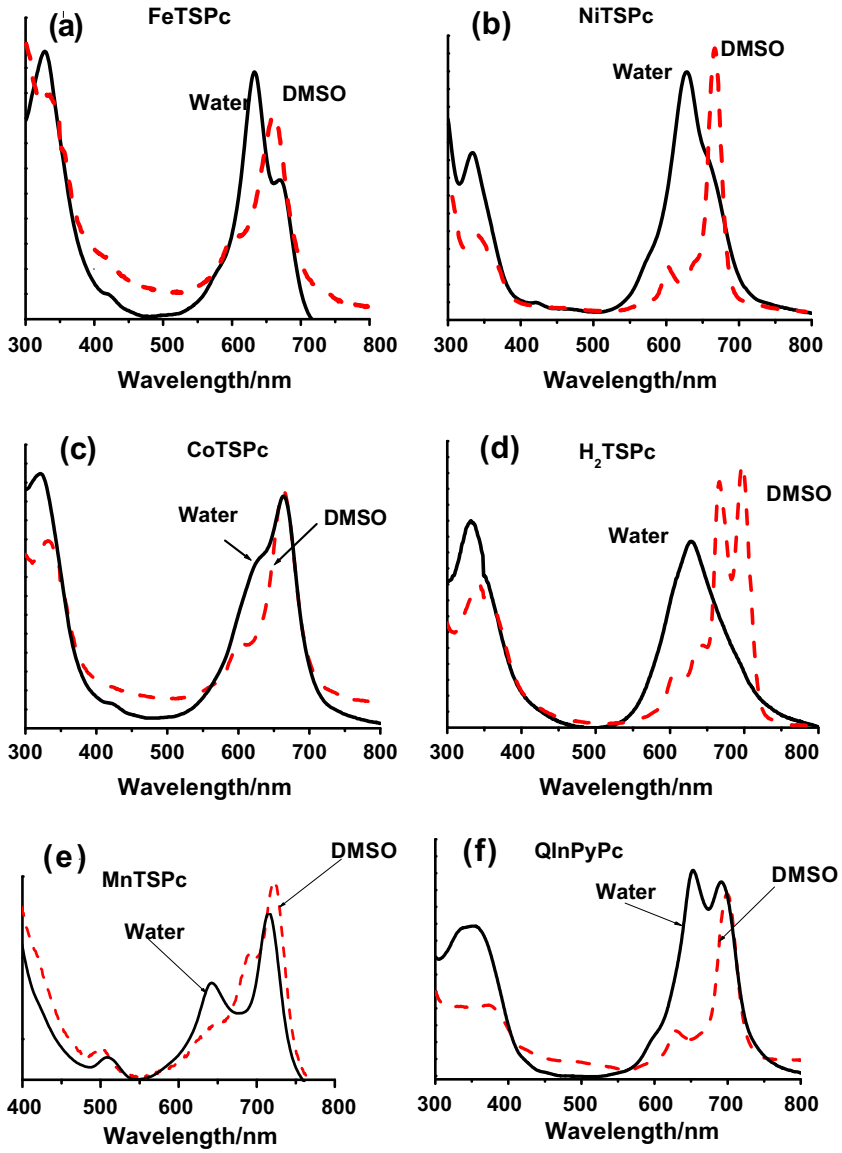


Fig. 2. UV–Vis spectra in water and DMSO for (a) FeTSPc, (b) NiTSPc, (c) CoTSPc, (d) H_2TSPc, (e) MnTSPc and (f) QInPyPc. Concentration $\sim 2 \times 10^{-5}$ M.

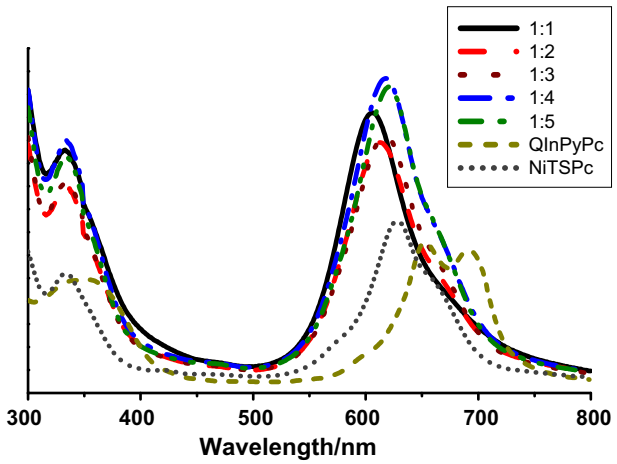


Fig. 3. UV–Vis spectra of various ratios of NiTSPc–QInPyPc in water. Concentration $\sim 3 \times 10^{-5}$ M.

been recently reported [30]. All solutions (315 μM) were prepared in millipore water from a Milli-Q Water system (Millipore Corp., Bedford, MA USA).

2.2. Methods

The fabrication of the nanostructures was performed according to the method of Wang et al. [23] as follows: 3 ml of the freshly prepared negatively charged MTSPc solutions (315 μM) were each mixed with 3 ml of a freshly prepared solution of QInPyPc (315 μM) and kept in the dark for 5 days to aggregate. Afterwards the aggregates were adsorbed on glass surface by putting a few drops of the solution enough to cover the surface and dried in an oven at 70 °C for 30 min. The aggregates in solution or on glass substrate were investigated using UV–Vis spectrophotometer, transmission electron microscopy (TEM) and FT-Raman spectrometer and Ramanscope microscope. The UV–Vis spectra of freshly prepared solutions of the precursors were obtained in water and in DMSO.

2.3. Equipment

UV–Vis spectra were performed using Shimadzu UV-2550 spectrophotometer. Transmission electron microscopy (TEM) images were recorded with a JEOL 1210 (80 KV) and the surface onto which samples were deposited before imaging was carbon coated grids. Raman spectra and images were obtained using Bruker Ram II FT-Raman spectrometer and Ramanscope microscope,

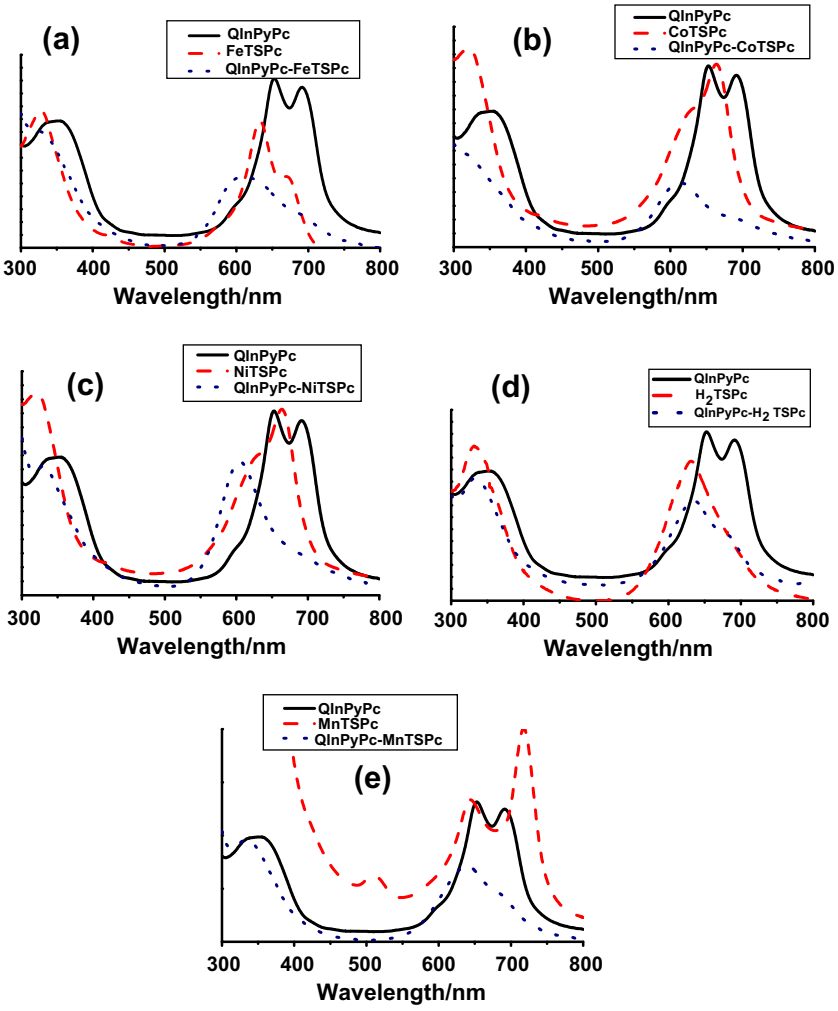


Fig. 4. UV–Vis spectra of precursors and heteroaggregates of the various mixtures (a) FeTSPc–QInPyPc, (b) CoTSPc–QInPyPc, (c) NiTSPc–QInPyPc, (d) H_2TSPc–QInPyPc and (e) MnTSPc–QInPyPc. Concentration of precursors $\sim 2 \times 10^{-5}$ M.

respectively. The excitation source was Nd:YAG of wavelength 1064 nm. Raman spectra were obtained for samples in solution and on glass substrate. The Raman instrument is coupled with a microscope (with a lens of magnification 40×) which was used to study the aggregates on the glass substrate.

3. Results and discussion

3.1. Spectroscopic characterization

Pcs (especially water soluble derivatives) readily form aggregates in solution. Aggregation is usually depicted as a coplanar association of rings progressing from monomer to dimers and higher order aggregates. It is dependent on concentration, nature of the solvent, nature of the substituents, complexed metal ions and temperature. Aggregation generally results in broadening (or splitting) of spectra, with spectra of the aggregate being blue or red shifted, relative to the main absorption peak (the Q band) in MPc complexes. The common aggregation in Pc complexes is characterized by a blue shift in the Q band due to the formation of H aggregates. According to exciton coupling theory [31], the H aggregates are formed when the angle (θ) between the line of the molecular center and the polarization axis is $\geqslant 57.4°$. Its counterpart, the J-aggregate has $\theta \leqslant 57.4°$ resulting in red shifting.

In Fig. 2, the Q bands, observed at the longer wavelengths (~670 nm) are due to the monomeric species and shorter wavelength absorptions (~630 nm) are due to the aggregates (H aggregates) [32]. Thus in water, FeTSPc (Fig. 2a) and NiTSPc (Fig. 2b) are mainly in the aggregated form, while for CoTSPc (Fig. 2c), the monomer peak is more dominant. In DMSO, FeTSPc, NiTSPc and CoTSPc are not aggregated, Fig 2a–c. The H_2TSPc species (Fig. 2d) in DMSO shows splitting of the Q band with maxima at 666 nm and 692 nm. In water H_2TSPc is highly aggregated and does not show the normal splitting of the Q band that is typical of free base phthalocyanines, the lack of split in the Q band in aggregated H_2Pc derivates has been reported before [33]. It has also been documented that in strongly basic solvents, the inner pyrrole hydrogens are acidic enough to dissociate resulting in increased symmetry and an unsplit Q band [34]. However, this is not observed in DMSO (Fig. 2d).

The UV–Vis spectrum of MnTSPc in DMSO has four peaks between 490 nm and 720 nm as seen in Fig. 2e. The peaks have been attributed to the existence of three species [34], Mn^{III}Pc at 721 nm accompanied by a charge transfer band at 500 nm, Mn^{II}Pc at 686 and μ-oxoMnPc at 645 nm. In water the Mn^{II}Pc peak is not observed and three main peaks are observed at 716 nm, 639 nm and 510 nm.

It has been suggested that an equilibrium exists between MnPc species in the presence of oxygen as shown by Eqs. (1)–(5) [35,36].

$$PcMn^{II} + O_2 \rightleftarrows PcMn^{III}(O_2) \quad (1)$$

$$PcMn^{III}(O_2) + PcMn^{II} \rightleftarrows PcMn^{III} - O_2 - Mn^{III}Pc \quad (2)$$

$$PcMn^{III} - O_2 - Mn^{III}Pc \rightleftarrows 2PcMn^{IV}O \quad (3)$$

$$2PcMn^{IV}O + 2PcMn^{II} \rightleftarrows 2PcMn^{III} - O - Mn^{III}Pc \quad (4)$$

$$4PcMn^{II} + O_2 \rightarrow 2PcMn^{III} - O - Mn^{III}Pc \text{ (Net equation)} \quad (5)$$

Eq. (6) is the reversible hydrolysis of μ-oxo-dimer into the oxides species in aqueous media:

$$PcMn^{III} - O - Mn^{III}Pc \overset{H_2O}{\rightleftarrows} 2PcMn^{III} + 2OH^- \quad (6)$$

hence in aqueous media, the $PcMn^{II}$ is not observed.

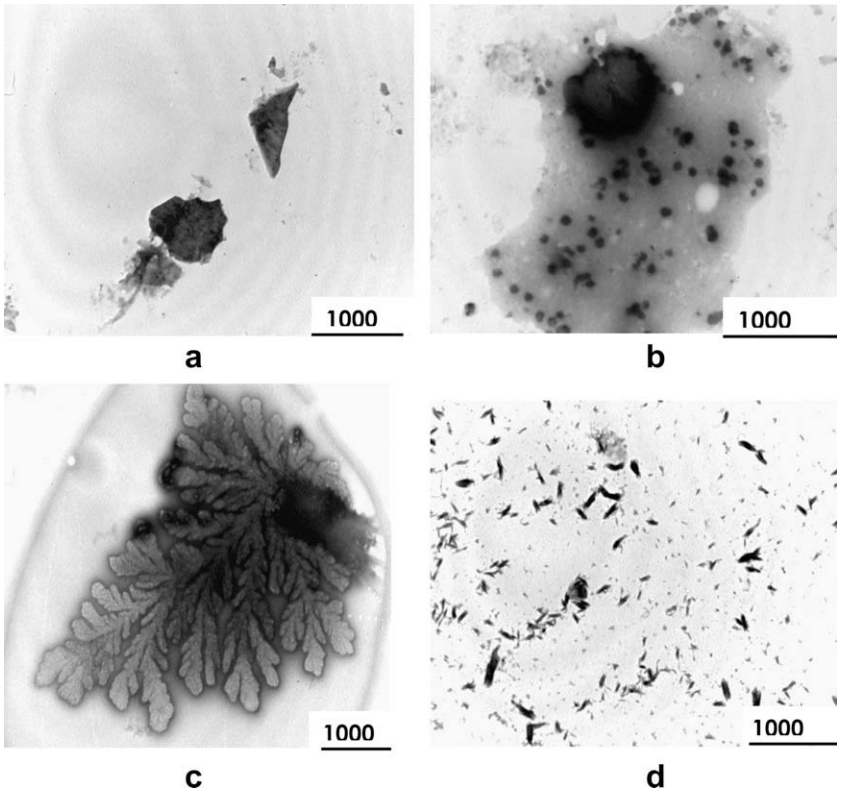


Fig. 5. TEM images of heteroaggregates: (a) H_2TSPc–QInPyPc, (b) MnTSPc–QInPyPc, (c) CoTSPc–QInPyPc and (d) NiTSPc–QInPyPc.

The spectra of QInPyPc showed aggregation in water with two peaks observed at 652 nm (aggregates) and 690 nm (monomer). In DMSO, the aggregate band is completely absent and the band of the monomeric species occurs at 700 nm. The band near 600 nm is vibronic in nature. The broad B-band (350–370 nm) is due to the superimposition of the B_1 and B_2 band [30] (Fig. 2f).

The aggregates in Fig. 2 may be referred to as homoaggregates since they arise from the same Pc molecules. The mixture of oppositely charged Pcs results in aggregated species of a different type, referred to here as heteroaggregates since they are a result of mixing of different Pc molecules. According to Wang et al. [23], the mixtures of oppositely charged porphyrin/phthalocyanine precursors were left to form well-defined heteroaggregates over a period of 3 days but for this work an additional 2 days were required. In this work, a 1:1 mixture of negatively charged MTSPc with positively charged QInPyPc was employed. The ratio of 1:1 of the precursor was chosen based on the data obtained from the UV–Vis spectra (Fig. 3). In Fig. 3 various ratios (1:1–1:5) of QInPyPc:NiTSPc show a shift in the position of the Q band to shorter wavelength as the amount of NiTSPc is decreased and the ratio approaches 1:1. The most blue shifted was the ratio of 1:1 occurring at 605 nm, while ratios 1:2, 1:3, 1:4, 1:5 are at 612 nm, 617 nm, 618 nm and 620 nm, respectively. When the amount of QInPyPc exceeded that of NiTSPC (e.g., QInPyPc:NiTSPc 2:1) no further shifting in spectra (from 605 nm) was observed.

Fig. 4 compares the spectra of the freshly prepared precursors (MTSPc and QInPyPc) in water (which will be aggregated as shown in Fig. 2 forming homoaggregates) with those of the 5-days old aggregate formed by mixing the positively and negatively charged species (heteroaggregates), represented as H_2TSPc–QInPyPc, CoTSPc–QInPyPc, MnTSPc–QInPyPc, NiTSPc–QInPyPc, and FeTSPc–QInPyPc. For FeTSPc (Fig. 4a), CoTSPc (Fig. 4b) and NiTSPc (Fig. 4c), a further blue shift of the Q band is observed for MTSPc–QInPyPc compared to MTSPc or QInPyPc alone. Heteroggregates show extensive broadening in each case. For H_2TSPc (Fig. 4d), the spectrum of the mixture is not shifted, suggesting that the interaction between H_2TSPc and QInPyPc (Fig. 4d) does not result in a heteroaggregation or the heteroaggregates formed do not result in shifted

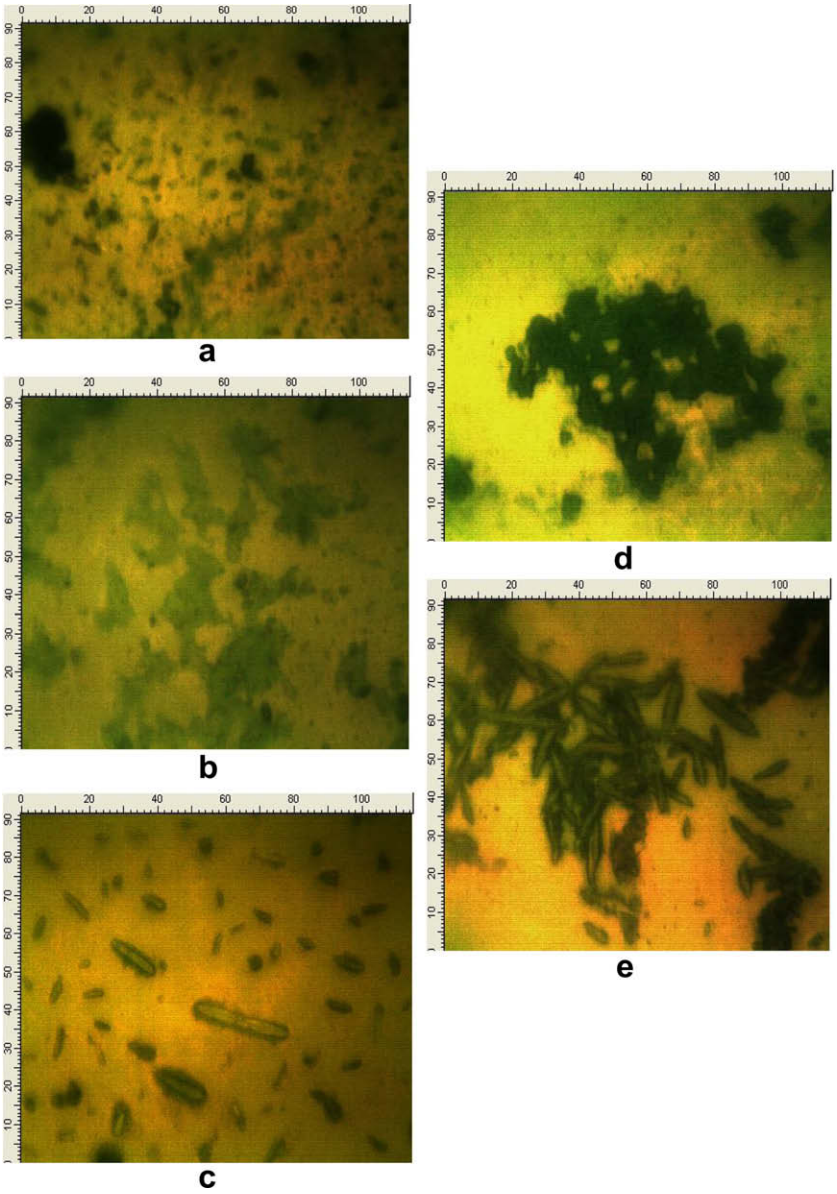


Fig. 6. Ramanscope images of heteroaggregates on glass substrate (a) H_2TSPc–QInPyPc, (b) MnTSPc–QInPyPc, (c) FeTSPc–QInPyPc, (d) CoTSPc–QInPyPc and (e) NiTSPc–QInPyPc.

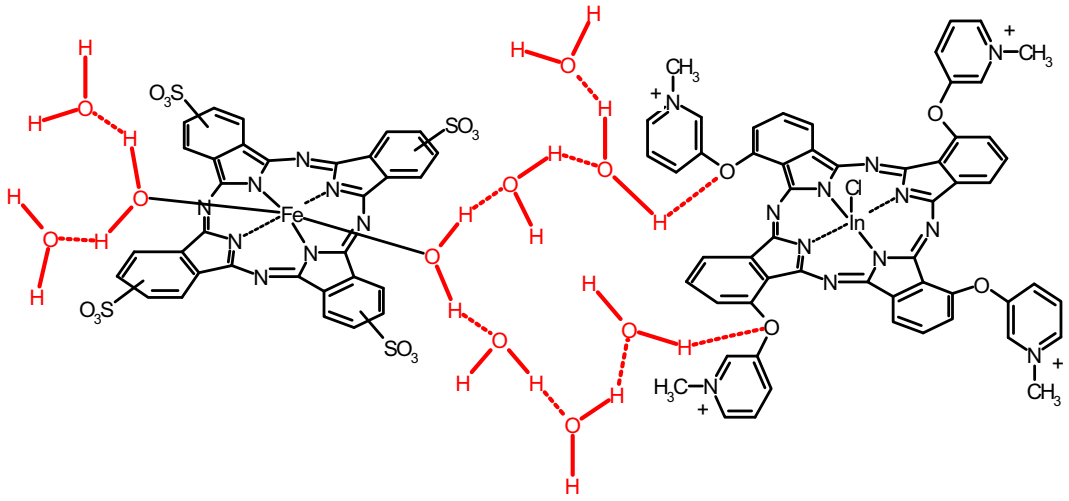


Fig. 7. A representation of the electrostatic and H-bonding interaction responsible for aggregation.

spectra. The mixture between the QInPyPc and MnTSPc (Fig. 4e), gives a peak that has a blue shift of 8 nm from the μ-oxoMnPc at 645 nm and 13 nm from the homoaggregate band peak of QInPyPc, suggesting the formation of the heteroaggregates.

3.2. Imaging studies

Robust nanostructures are structures with well-defined shapes. From the TEM studies, Fig. 5, it was observed that quaternized tetra-(3-pyridyloxyphthalocyaninato)indium phthalocyanines formed robust structures with all the metallated tetrasulfonated Pcs (Fig. 5b–d) and not with the free base tetrasulfonated phthalocyanines (Fig. 5a). The aggregates of MnTSPc–QInPyPc (Fig. 5b) and CoTSPc–QInPyPc (Fig. 5c) appear as leaf-like nanostructures. For MnTSPc, the structure shows a dark ring base and then the aggregates spread out like a leaf. CoTSPc–QInPyPc (Fig. 5c) nanoleaves have veins like a real leaf; those of MnTSPc–QInPyPc (Fig. 5b) have spherical dark specks. FeTSPc–QInPyPc and NiTSPc–QInPyPc (Fig. 5d) formed rod-like nanostructures. H_2TSPc–QInPyPc (Fig. 5a) aggregation did not result in any well-defined structures. The Ramanscope images (Fig. 6) on glass substrate shows the rod-like structures of FeTSPc–QInPyPc (Fig. 6c) and NiTSPc–QInPyPc (Fig. 6e). MnTSPc–QInPyPc (Fig. 6b) and CoTSPc–QInPyPc (Fig. 6d) did not retain the structures seen in the TEM (Fig. 5). H_2TSPc gave less defined structures in the Ramanscope, suggesting the presence of weak heteroaggregates.

It is apparent that to form a robust structure the presence of a metal in the central cavity is required. Previous studies have [28] shown that MTSPc in aqueous solution under aerobic conditions are all spin paired, hence they are less likely to be involved in metal–metal bonding in the aggregates. The central metals in MTSPc complexes are more likely to co-ordinate water and to form H-bond. Fig. 7 is a representation of the proposed arrangement of molecules and interaction with water molecules. The contribution of axial ligation in stacking arrangement in phthalocyanines has been reported in [37].

3.3. FT-Raman spectral studies

Fig. 8 is an example of the Raman spectra obtained for the precursor (QInPyPc and FeTSPc), and the aggregate on glass substrate and in solution. Generally prominent peaks are observed in region between 2700–3300 cm^{-1} and around 1000 cm^{-1} (Tables 1 and 2). Most diagnostic work done on phthalocyanines using this technique has focused on the region 200–2000 cm^{-1} as it highlights the internal vibration of the macrocycle [38–42]. The peaks around 3000 cm^{-1} are assigned to the stretching mode of water (used as a solvent before evaporation and used as a solvent for solution Raman spectra) C–O bonds [41]. These peaks are more intense (×10) than those with wavenumbers less than 2000 cm^{-1}.

Another significant peak is the metal sensitive band which has been calculated to be 1517 cm^{-1} for ZnPc [40]. The shift of this peak has been attributed to the displacement of the C–N–C bridge bond of the internal cavity of the Pc ring depending on the size of the central metal [40]. While this peak is present in the spectra of the precursors (ranging from 1448.9 to 1630.0 cm^{-1} when Pcs are adsorbed on a glass substrate), they appear very weak in solution occurring between 1395 and 1673 cm^{-1} and absent in the spectra of the aggregates deposited on the glass substrate. The Raman spectra also show the peak at 605.3 cm^{-1} for QInPyPc is shifted to higher wave numbers in MnTSPc–QInPyPc (615.1 cm^{-1}) but shift to lower energy in CoTSPc–QInPyPc, NiTSPc–QInPyPc, FeTSPc–QInPyPc (602.9 cm^{-1}) and remained the same for H_2TSPc–QInPyPc (605.3 cm^{-1}). This band according to Bovill et al. [38] might be due to the twisting motion of the pyrrole ring which, being strong in parent molecules become very in weak the spectra of aggregates in solution and is absent in spectra of aggregates on glass substrate

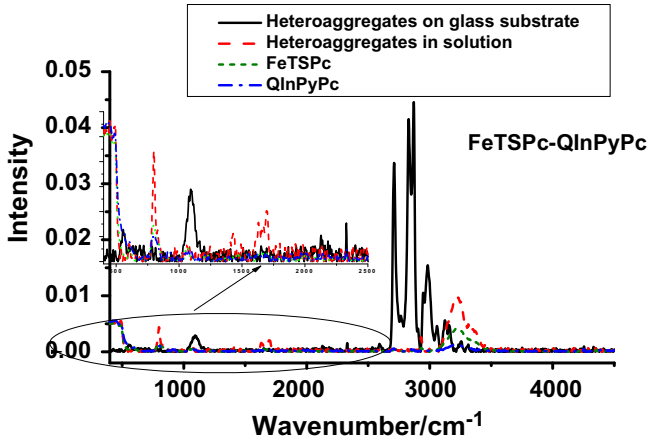


Fig. 8. FT-Raman spectra of aqueous solutions FeTSPc, QInPyPc and FeTSPc–QInPyPc on glass substrate and in solution.

Table 1
Prominent peaks of Raman spectra of parent molecules adsorbed on a glass substrate.[a]

QInPyPc (cm^{-1})	H_2TSPc (cm^{-1})	MnTSPc (cm^{-1})	FeTSPc (cm^{-1})	CoTSPc (cm^{-1})	NiTSPc (cm^{-1})	Assignment
441.9 vs	428.2 vs	448.2 vs	435.3 vs	434.1 vs	435.9 vs	
605.3 s	602.9 vs	601.5 s	603.4 s	606.7 s	604.8 s	Pyrrole ring twisting
803.1 s	801.2 s	804.1 s	799.8 w	791.7 s	800.4 s	
1077.8 w	1089.4 vw	1065.4 vw	1072.2 vw	1046.4 w	1056.3 w	C–H bending
1553.5 vw	1630 w	1448.9 vw	1534.2 vw	1543.6 vw	1557.6 vw	C–N–C
2706.9 w	2703.6 vw	2709.7 w	2711.1w	2710.9 w	2708.1w	C–H stretching
2851.6 w			2865.9 w	2842.3 w	2837.4 w	C–H stretching
3238.3 vs	3224.3 vs	3244.6 vs	3214.8 vs	3240.2 vs	3241.8 vs	H–O–H stretching

[a] w = weak, s = strong, vs = very strong, vw = very weak.

Table 2
Prominent peaks in the Raman spectra of heteroaggregates in solution and on glass substrate.[a]

H_2TSPc–QInPyPc (cm^{-1})		MnTSPc–QInPyPc (cm^{-1})		FeTSPc–QInPyPc (cm^{-1})		CoTSPc–QInPyPc (cm^{-1})		NiTSPc–QInPyPc (cm^{-1})		Assignment
Soln.	Glass substrate	Soln.	Glass substrate	Soln.	Glass substrate	Soln.	Glass substrate	Soln.	Glass substrate	
433.2 s	–	430.2 s	–	442.4 s	–	430.2 s	–	430.2 s	–	–
–	561.2 w	–	561.6 w	–	561.6 w	–	556.7 w	–	549.4 w	–
605.3 w	–	615.1 w	–	602.9 w	–	602.9 w	–	602.9 vw	–	Pyrrole ring twisting
799.9 s	795.0 w	799.0 s	780.4 w	799.9 s	787.9 vw	799.9 s	787.7 vw	797.4 w	797.4 w	–
1057.6 w	1099.0 s	1074.7 w	1099.0 s	1072.2 w	1091.7 s	1072.2 w	1098.9 s	–	1098.9 s	C–H bending
1653.3 s	–	1672.8 s	–	1653.3 w	–	1653.3 vw	–	1395 vw	–	C–N–C
–	2718.5 vs	–	2711.2 vs	–	2725.8 vs	–	2725.8 vs	–	2718.5 vs	C–H bending
–	2849.8 vs	–	2857.1 vs	–	2849.8 vs	–	2849.8 vs	–	2857.1 vs	C–H bending
–	2983.5vs	–	2998.4 vs	–	2983.5 vs	–	2988.4 vs	–	2988.4 vs	C–H bending
–	3134.3 vs	–	3134.3 vs	–	3131.9vs	–	3134.3 vs	–	3134.3 vs	H–O–H stretching
3226.7 vs	3252.5 w	3234.0 vs	3260.8 w	3226.7 vs	3252.5 w	3226.7 vs	3246.2 w	3221.8 vs	3234.0 w	H–O–H stretching

[a] w = weak, s = strong, vs = very strong, vw = very weak.

4. Conclusion

Self-assembly of water soluble phthalocyanine was based on electrostatic interaction between the oppositely charged molecules. The presence of central metal has a major role in the formation of robust nanostructures as it seems to be a contributing force towards the heteroaggregation. Based on the results obtained it is inferred that the arrangement of these molecules in the hetetoaggregates is face-to-face consisting of alternating charged molecules. The formation of rod (for NiTSPc–QInPyPc and FeTSPc–QInPyPc) and leaf-like (for CoTSPc–QInPyPc and MnTSPc–QInPyPc) shapes were revealed by TEM, depending on the nature of the central metal. Further work would be done to investigate the effect on the magnetic properties of the central metal on the shape of the aggregate.

Acknowledgements

This work was supported by the Department of Science and Technology (DST) and National Research Foundation (NRF), South Africa through DST/NRF South African Research Chairs Initiative for Professor of Medicinal Chemistry and Nanotechnology and Rhodes University. RC George thanks the Third World Organization of Women in Science (TWOWS) for the fellowship.

References

[1] R. Bonnet, Chemical Aspects of Photodynamic Therapy, Gordon and Breach Science Publishers, Amsterdam, 2000.
[2] J. Blochwitz, M. Pfeiffer, T. Fritz, K. Leo, Appl. Phys. Lett. 73 (1998) 729.
[3] S.J. Mathew, S.C. Kumar, L. Giribabu, S.V. Rao, Mater. Lett. 61 (2007) 4426.
[4] E. Ben-Hur, W.-S. Chan, in: K.M. Kadish, K.M. Smith, R. Guilard (Eds.), The Porphyrin Handbook, vol. 19, Academic Press, New York, 2004.
[5] N. Nombona, P. Tau, N. Sehotho, T. Nyokong, Electrochim. Acta 53 (2008) 3139.
[6] G. Mbambisa, T. Nyokong, Polyhedron 26 (2007) 5355.
[7] Y. Chen, M. Hanack, Y. Araki, O. Ito, Chem. Soc. Rev. 34 (2005) 517.
[8] A. Ogunsipe, J.-Y. Chen, T. Nyokong, New J. Chem. 28 (2004) 822.
[9] R.D. George, A.W. Snow, J.S. Shirk, W.R. Barger, J. Porphyrins Phthalocyanines 2 (1998) 1.
[10] V. LLiev, V. Alexiev, L. Bilyarska, J. Mol. Catal. A: Chem. 137 (1999) 15.
[11] B. Floris, M.P. Donzello, C. Ercolani, in: K.M. Kadish, K.M. Smith, R. Guilard (Eds.), The Porphyrin Handbook, vol. 18, Academic Press, New York, 2004.
[12] P.-C. Lo, X. Leng, D.K.P. Ng, Coord. Chem. Rev. 251 (2007) 2334.
[13] P. Thordarson, R.J.M. Nolte, A.E. Rowan, in: K.M. Kadish, K.M. Smith, R. Guilard (Eds.), The Porphyrin Handbook, vol. 18, Academic Press, New York, 2004.
[14] H. Engelkamp, S. Middelbeek, R.J.M. Nolte, Science 284 (1999) 785.
[15] T.P. Radhakrishnan, Resonance 3 (1998) 4.
[16] H. Abramczyk, I. Syzmczyk, J. Mol. Liq. 110 (2004) 51.
[17] K. Lang, P. Kubat, J. Mosinger, D.M. Wagnerova, J. Photochem. Photobiol. A: Chem. 119 (1998) 47.
[18] S. FitzGerald, C. Farren, C.F. Stanely, A. Beeby, M.R. Bryce, Photochem. Photobiol. Sci. 1 (2002) 581.
[19] C.F. van Nostrum, R.J.M. Nolte, Chem. Commun. (1996) 2385.
[20] D.K.P. Ng, C.R. Chimie 6 (2003) 903.
[21] M. Hanack, D. Dini, in: K.M. Kadish, K.M. Smith, R. Guilard (Eds.), The Porphyrin Handbook, vol. 18, Academic Press, New York, 2004.
[22] Y. Sun, X. Zhang, C. Sun, Z. Wang, J. Shen, D. Wang, T. Li, Chem. Commun. (1996) 2379.
[23] Z. Wang, C.J. Medforth, J.A. Shelnutt, J. Am. Chem. Soc. 126 (2004) 15954.
[24] Z. Wang, J.H. Kuangchiu, C.J. Medforth, J.A. Shelnutt, Adv. Mater. 18 (2006) 2557.
[25] Z. Wang, Z. Li, C.J. Medforth, J.A. Shelnutt, J. Am. Chem. Soc. (2007) 2440.
[26] G.O. Egharevba, R.C. George, M. Maaza, Synth. React. Inorg. Met.-org. Nano-Met. Chem. 38 (2008) 681.
[27] C.L. Donley, W. Xia, B.A. Minch, R.A.P. Zangmeister, A.S. Drager, K. Nebesny, D.F. O'Brien, N.R. Armstrong, Langmuir 19 (2003) 6512.
[28] J.H. Weber, D.H. Bucsh, Inorg. Chem. 54 (1965) 469.
[29] N.O. Liu, C.-H. Tau, M.-Z. Slain, A.T. Hu, F.-In. Chou, J. Photochem. Photobiol. A: Chem. 165 (2004) 131.
[30] M. Durmuş, T. Nyokong, Photochem. Photobiol. Sci. 6 (2007) 659.
[31] M. Kasha, H.R. Rawls, M.A. EL-Bayomi, Pure Appl. Chem. 11 (1965) 371.
[32] J.E. van-Lier, J.D. Spikes, Photosensitizing Compounds: Their Chemistry, Biology and Clinical Use, John Wiley and sons, Chichester, 1989. p. 17.
[33] S. Arslan, I. Yilmaz, Polyhedron 26 (2007) 2387.
[34] M.J. Stillman, T. Nyokong, in: Phthalocyanines: Properties and Application, VCH publishers, New York, 1989, p. 135.
[35] A.B. Lever, J.P. Wilshire, S.K. Quan, Inorg. Chem. 20 (1981) 761.
[36] W. Pasiuk-Bronikowska, M. Krajewska, I. Flis-Kabulska, Polyhedron 18 (1999) 561.
[37] T. Inabe, J. Porphyrins Phthalocyanines 5 (2001) 3.
[38] A.J. Bovill, A.A. McConnell, J.A. Nimmo, W.E. Smith, J. Phys. Chem. 90 (1986) 569.
[39] D.R. Tackley, G. Dent, W.E. Smith, Phys. Chem. Chem. Phys. 2 (2000) 3949.
[40] D.R. Tackley, G. Dent, W.E. Smith, Phys. Chem. Chem. Phys. 3 (2001) 1419.
[41] B. Brozek-Pluska, I. Szymczyk, H. Abramczyk, J. Mol. Struct. 744 (2005) 481.
[42] Y. Bian, L. Rintoul, D.P. Arnold, R. Wang, J. Jiang, Vib. Spectrosc. 31 (2003) 173.

recent years [12]. Analogous approaches were employed to decompose complex heterometallic compounds with the composition $[Li(H_2O)M(N_2H_3CO_2)_3]\cdot 0.5H_2O$ (M = Co or Ni), which were considered as the only precursors for the preparation of layered $LiMO_2$ materials [13]. In this case, a very low yield of the starting molecular precursors presents a serious problem. Apparently, this precludes the extensive use of these precursors in thermal synthesis.

The aim of the present study was to search for new molecular systems capable of generating lithium cobaltate through mild thermolysis. The requirement for the organic components involved in the heterometallic complexes is that they can be easily eliminated with the retention of the ratio of metals in the final product.

2. Experimental

2.1. Synthesis

The new coordination polymer **1** was synthesised with the use of freshly distilled THF and MeCN. The starting cobalt pivalate $[Co(Piv)_2]_n$ was prepared according to a known procedure [14]. In the synthesis of complex **1**, commercial 2-amino-5-methylpyridine (Fluka) was used.

2.1.1. $[Li_2Co_2(Piv)_6(2\text{-amino-5-methylpyridine})_2]_n$ (**1**)

Tetrahydrofuran (40 ml) was added to a mixture of $[Co(Piv)_2]_n$ (0.5 g, 1.9 mmol), LiPiv (0.207 g, 1.9 mmol) and 2-amino-5-methylpyridine (0.205 g, 0.9 mmol). The reaction mixture was stirred at 60 °C for 20 min. The resulting brown solution was concentrated to 10 ml, MeCN (40 ml) was added, and the mixture was concentrated to 10 ml at 80 °C. The solution was kept at +5 °C for 24 h. Brown crystals suitable for X-ray diffraction were separated from the solution by decantation, washed with cold MeCN, and dried in air. The yield of crystals of **1** is 81% based on $[Co(Piv)_2]_n$. Found (%): C, 52.95; H, 7.35; N, 5.66. $C_{21}H_{35}CoLiN_2O_6$: C, 52.84; H, 7.39; N, 5.87. IR, ν/cm^{-1}: 3384 m, 3130 m, 2960 s, 2928 m, 2868 m, 1612 v.s, 1572 v.s, 1564 v.s, 1520 m, 1504 s, 1484 v.s, 1424 v.s, 1400 v.s, 1376 m, 1364 v.s, 1300 w, 1260 w, 1228 c, 1144 w, 1120 w, 1044 w, 1032 m, 972 m, 952 m, 936 m, 904 s, 848 m, 824 m, 800 s, 792 s, 764 s, 744 w, 664 m, 608 v.s, 568 s, 528 m, 452 v.s, 436 v.s, 416 v.s, 400 v.s.

2.2. Methods

The elemental analysis of complex **1** was carried out on a Carlo Erba analyzer in the Center of Collaborative Research of the N.S. Kurnakov Institute of General and Inorganic Chemistry of the Russian Academy of Sciences. The spectra were measured on a Specord M-80 IR spectrometer in KBr pellets. The magnetochemical measurements were performed on a MPMS-5S SQUID magnetometer (Quantum Design) in the 2–300 K temperature range at a magnetic field strength $H = 5$ kOe. The molar magnetic susceptibility χ was calculated taking into account the atomic diamagnetism according to the Pascal additive scheme. In the paramagnetic region, the effective magnetic moment was calculated by the equation $\mu_{eff} = [(3k/N_A\beta 2)\chi T]^{1/2} \approx (8\chi T)^{1/2}$, where k is the Boltzmann constant, N_A is Avogadro's number and β is the Bohr magneton.

2.3. X-ray data collection

The X-ray diffraction study of complex **1** was carried out on an Enraf Nonius CAD-4 diffractometer (λMo, graphite monochromator, ω-scanning technique, the scan step was 0.3°, the exposure time per frame was 10 s) according to a standard technique [15]. The structure of complex **1** was solved by direct methods and refined by the full-matrix least-squares method with anisotropic displacement parameters for all non-hydrogen atoms. The hydrogen atoms of the carbon-containing ligands were positioned geometrically and refined using a riding model. All calculations were carried out with the use of the SHELX97 program package [16]. The *tert*-butyl substituents at the carboxylate groups are partially disordered. The positions of all methyl carbon atoms in the disordered CMe_3 fragments were located in difference Fourier maps and refined with occupancies of 0.506(12) and 0.494(12) for the *tert*-butyl group at the atom C(1), 0.674(10) and 0.326(10) at the atom C(6), and 0.531(17) and 0.469(17) at the atom C(11). The crystallographic parameters for complex **1** at $T = 293$ K are as follows: $C_{21}H_{35}CoLiN_2O_6$, $fw = 477.38$, blue, prismatic, crystal size $0.45 \times 0.23 \times 0.25$ mm, monoclinic system, space group $P2_1/c$, $a = 12.4255(10)$ Å, $b = 22.1287(10)$ Å, $c = 9.4545(10)$ Å, $\beta = 103.253(10)°$, $V = 2530.4(4)$ Å^3, $\lambda = 0.71073$, $Z = 4$, $\rho_{calc} = 1.253$ g cm^{-3}, $\mu = 7.13$ cm^{-1}, 5775 measured reflections, 3113 reflections with $I > 4.0\sigma(I)$, $R_{int} = 0.0843$, $\theta_{max} = 26.97$, $GOF = 1.047$, R_1 ($I > 2\sigma(I)$) = 0.0502, wR_2 ($I > 2\sigma(I)$) = 0.1365, R_1 (all data) = 0.1173, wR_2 (all data) = 0.1663, $T_{min/max} = 0.9006/0.7397$ [17], full-matrix least-squares on F^2.

The X-ray powder diffraction analysis of the solid decomposition products in air was carried out on a G670 (HUBER) Guinier camera using CuKα1 radiation. The X-ray powder diffraction analysis of the solid decomposition products in an inert atmosphere was performed on a FR-552 monochromator chamber (CuKα1 radiation) using germanium as the internal standard (X-ray diffraction patterns were processed on an IZA-2 comparator with an accuracy of ±0.01 mm).

2.4. Thermal decomposition

The thermal decomposition of compound **1** was studied by differential scanning calorimetry (DSC) and thermogravimetry (TGA). The thermogravimetric measurements were performed in an artificial air flow (20 ml/min) and in an argon flow (20 ml/min) on a *NETZSCH TG 209 F1* instrument in alundum crucibles at a heating rate of 10 °C/min. The composition of the gas phase below 250 °C was studied on a QMS 403C Aëolos mass-spectrometric unit under TGA conditions. The ionizing electron energy was 70 eV; the largest determined mass number (the mass-to-charge ratio) was 300 amu. The weight of the samples for thermogravimetric experiments was 0.5–3 mg. The differential scanning calorimetry study, in a dry artificial air flow (O_2, 20.8%; CH_4, <0.0001%) and in an argon flow (Ar, >99.998%; O_2, 0.0002%; N_2, <0.001%; aqueous vapor, <0.0003%; CH_4, <0.0001%), was carried out on a *NETZSCH DSC 204 F1* calorimeter in aluminum cells at a heating rate of 10 °C/min. The weight of the samples was 4–10 mg. Each experiment was repeated at least three times. The temperature scales and the calorimeter were calibrated based on the phase transition temperatures of standard compounds (C_6H_{12}, Hg, KNO_3, In, Sn, Bi and CsCl; 99.99% purity; ISO/CD 11357-1). For the TGA and DSC experiments, the samples were weighed on a *SARTORIUS RESEARCH R 160P* analytical balance with an accuracy of 1×10^{-2} mg.

2.5. Heat capacity

The heat capacities were measured by DSC on a *NETZSCH 204 F1* instrument in a dry argon flow (10 ml/min) in the 123–373 K temperature range at a heating rate of 10 °C/min in aluminum specimen containers ($V = 56$ mm^3, $d = 6$ mm) equipped with lids with a hole (the ratio of the surface area of the bottom of the container to the surface area of the hole was about 36).

The average weight of the samples for heat capacity measurements was about 10 mg. The heat capacity was calculated in accordance with the *ASTM E 1269* standard by the equation:

$$C_{p,S} = \frac{m_{St}}{m_S}\frac{DSC_S - DSC_{BL}}{DSC_{St} - DSC_{BL}}C_{p,St} \quad (1)$$

where the indices S, St and BL refer to the cell containing the sample, the cell containing the standard compound, and the empty cell, respectively. Sapphire (m = 12.69 mg) was used as the standard. Four series of measurements were carried out. The results were processed statistically. The controlled cooling of the measuring cells was performed manually using a liquid-nitrogen cooling system.

The differential scanning calorimeter was calibrated against the heat flux with the use of sapphire as the standard (ISO/CD 11357-1) according to the equation:

$$E(T) = \frac{DSC_{St}(T) - DSC_{BL}(T)}{m_{St}C_{p,St}(T)\beta} \quad (2)$$

where the indices St and BL refer to the cell containing the standard and the empty cell, respectively, $E(T)$ is the temperature-dependent calibration coefficient, DSC is the experimental DSC signal, m is the mass, C_p is the isobaric heat capacity, and β is the heating rate of the furnace. The calibration against the heat flux was carried out before each measurement throughout the temperature range of interest. The experimental data were processed using the *NETZSCH Proteus Thermal Analysis* program package.

3. Results and discussion

3.1. Synthesis, structure and magnetic properties of the coordination polymer $[Li_2Co_2(Piv)_6(\mu\text{-}L)_2]_n$

We chose the product prepared by the reaction of polymeric cobalt(II) pivalate $[Co(Piv)_2]_n$, lithium pivalate LiPiv and 2-amino-5-methylpyridine (L) in the Co:Li:L ratio of 2:2:1 in THF as the possible molecular precursor for the synthesis of $LiCoO_2$. This reaction afforded a coordination polymer with the composition $[Li_2Co_2(Piv)_6(\mu\text{-}L)_2]_n$ (**1**) in high yield (81%).

According to X-ray diffraction data, compound **1** is a 1D polymer containing the heteronuclear fragment $\{Li_2Co_2(Piv)_6(\mu\text{-}L)_2\}$ as the elementary unit (Fig. 1). This fragment consists of two symmetrically arranged dinuclear units $\{LiCo(Piv)_3\}$, in which the cobalt and lithium atoms are linked by three non-equivalent bridging pivalate anions. The centrosymmetric repeating unit $\{Li_2Co_2(Piv)_6(\mu\text{-}L)_2\}$ contains the square O_2Li_2 fragment (Table 1). The polymer chain is formed by linking adjacent cobalt atoms from different repeating heteronuclear fragments $\{Li_2Co_2(Piv)_6(\mu\text{-}L)_2\}$ by two bridging 2-amino-5-methylpyridine molecules (Fig. 1, Table 1). In the elementary unit, each cobalt atom is coordinated by the pyridine nitrogen atom of one bridging N-donor ligand and the amino nitrogen atom of the bridging ligand from the adjacent fragment. The proton of the coordinated amino group is involved in hydrogen bonding with the oxygen atom of the bridging carboxylate group (Fig. 1, Table 1).

Table 1
Selected bond lengths [Å] and bond angles [°] for compound **1**.

Parameter	Value
Li(1A)–Li(1)–Co(1)	125.7(3)
Li(1)–Co(1)–N(1)	156.76(15)
Li(1)–Co(1)–N(2)	113.79(13)
Li(1)–O(6)–Li(1A)	88.7(3)
O–C–O (range)	119.3(3)–123.7(3)
Co(1)···Li(1)	3.074(5)
Li(1)···Li(1A)	2.709(11)
Co(1)–N(1)	2.131(3)
Co(1)–N(2A)	2.372(3)
Co(1)–O(1)	2.141(3)
Co(1)–O(2)	2.225(3)
Co(1)–O(3)	2.004(2)
Co(1)–O(5)	2.026(2)
Li(1)–O(2)	1.947(6)
Li(1)–O(4)	1.876(6)
Li(1)–O(6)	1.901(6)
Li(1)–O(6A)	1.973(6)
C–O (range)	1.234(4)–1.265(4)
N(2)···O(3)*	2.828(4)

* N(2)–H(2B)–O(3) 155.3°, H(2B)···O(3) 1.98 Å.

It should be noted that the distance between the cobalt atom and the nitrogen atom of the amino group (Co(1)–N(2)) is substantially elongated (2.372(3) Å), which is indicative of weak interactions between these atoms. This situation is typical of amino derivatives of pyridine serving as a bridging ligand in polynuclear cobalt-containing pivalates, and has been observed earlier [18,19].

The magnetic behavior of compound **1** is unusual. At room temperature, the effective magnetic moment of compound **1** is 4.77 μ_B (per cobalt atom) (Fig. 2), which is close to the known experimental values for high-spin Co^{II} atoms (S = 3/2) taking into account spin-orbital interactions (4.4–5.2 μ_B) [20]. The magnetic moment

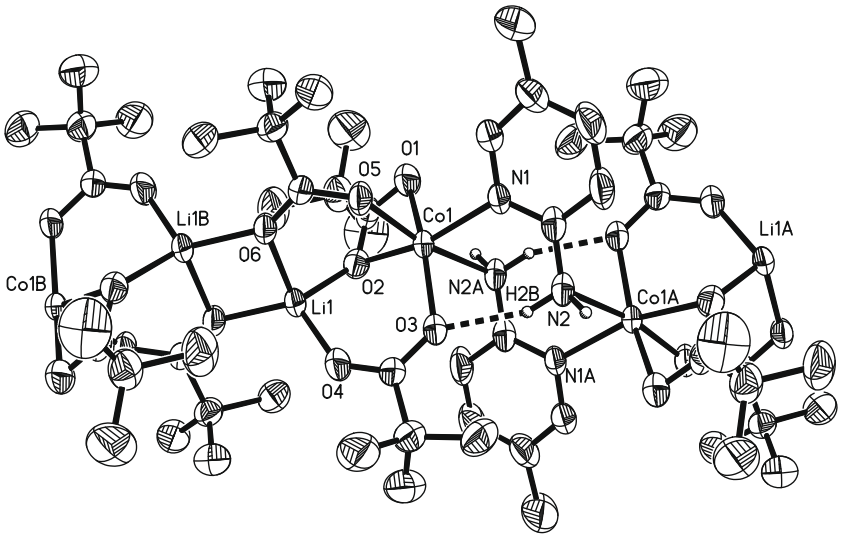


Fig. 1. Fragment of the polymer chain of compound **1** (only one component of each of the distorted *tert*-butyl groups is drawn, hydrogen atoms of the carboxylate and 2-amino-5-methylpyridine ligands (except for amino groups) are omitted for clarity, 50% thermal probability ellipsoids).

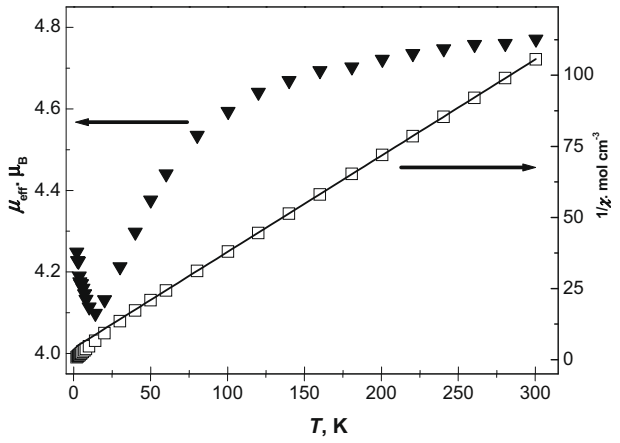


Fig. 2. Magnetic properties of complex **1**: the temperature dependence of the magnetic moment (▼), the curve $1/\chi$ (□); the calculated data are represented by the line.

μ_{eff} decreases with decreasing temperature (to 4.10 μ_B at 14 K). This fact can be attributed to both antiferromagnetic spin-spin exchange interactions between the cobalt atoms and the spin-orbital effect. However, μ_{eff} increases at temperatures below 14 K and reaches 4.25 μ_B at 2 K. Apparently, this effect is indicative of a ferromagnetic contribution to the exchange interactions between the Co^{II} atoms in the polymer chain.

In the 50–300 K temperature range, the temperature dependence of the inverse susceptibility follows the Curie–Weiss law with the parameters $C = 2.96$ mol cm^{-3} and $\theta = -11.96$ K (Fig. 2). The value $C = 2.96$ is larger than the theoretical pure spin value ($C = 1.875$ for $S = 3/2$ and $g = 2$), which is consistent with the orbital contribution to the magnetic susceptibility, typical of Co^{II} ions and g factors larger than 2.

3.2. Thermal decomposition

According to the TGA data, the decomposition of complex **1** in an artificial air flow and in a dry argon flow does not afford stable intermediates (Fig. 3).

The decomposition onset temperature for complex **1** is virtually the same (180 ± 3 °C) both in air and under an inert atmosphere (argon). The mass spectra of the gas phase in the 150–250 °C temperature range correspond to the spectrum of 2-amino-5-methylpyridine [21]. The initial step of decomposition of complex **1** (180–280 °C) is endothermic (the second endothermic peak in the DSC curves; see Fig. 3); the absorbed energy in air is 73.5 ± 5.3 kJ/mol per elementary unit of $Li_2Co_2(Piv)_6(L)_2$. The end of the second endothermic peak (260 ± 3 °C) corresponds to a 22.4 ± 1.5% weight loss. The number of 5-methyl-2-pyridineamine molecules calculated from the empirical formula is 22.67% per $Li_2Co_2(Piv)_6(L)_2$ formula unit. Presumably, heating in air in the above-mentioned temperature range leads to elimination of the N-donor ligand. Under an inert atmosphere, the endothermic effect in this temperature range has a complex character, and it is impossible to separate the thermal effect associated with elimination of the N-donor ligand. The inflection point in the weight loss curve at 280 ± 3 °C corresponds to a 21.7 ± 1.5% weight loss. At higher temperatures, further destructive decomposition of complex **1** is observed. It should be noted that the processes under an inert atmosphere differ from those in air. In an air flow, a highly exothermic oxidative destruction occurs in the 260–410 °C temperature range. The temperature of the end of the exothermic peak in air is virtually equal to the temperature of the end of the weight loss (Fig. 3b).

Under an inert atmosphere, the further weight loss occurs in the 280–470 °C temperature range. This process is accompanied by complex energy changes. According to the X-ray powder diffraction data, a heterogeneous mixture of cobalt oxide CoO and lithium oxide Li_2O is formed as the solid decomposition product of complex **1** under an inert atmosphere at temperatures below 500 °C (Table 2). The weight of the solid residue was 19.5 ± 1.5% of the weight of the starting sample, which agrees within experimental error to the value of 18.91% calculated from the empirical formula on the assumption that the decomposition affords a mixture of the Li_2O and CoO phases.

Unlike the inert conditions, the decomposition of polymer **1** in air (below 500 °C) affords a solid heterogeneous mixture of mixed-valence cobalt oxide Co_3O_4, lithium oxide Li_2O and lithium cobaltate $LiCoO_2$ (X-ray powder diffraction data; Table 2). However, the further storage of the thermolysis product under temperature-controlled conditions at 500 °C for 30–90 min led to the complete disappearance of the simple oxides, which is confirmed by the disappearance of reflections of the simple oxides in the X-ray diffraction patterns (Table 3). The weight of the solid residue upon thermolysis in air is 22.3 ± 1.5% of the weight of the starting sample, which agrees within experimental error to the value of 20.69% calculated from the empirical formula on the assumption that the decomposition affords $LiCoO_2$.

3.3. Heat capacity measurements

Differential scanning calorimetry studies showed that the endothermic effect in the 77–130 °C (350–405 K) temperature range

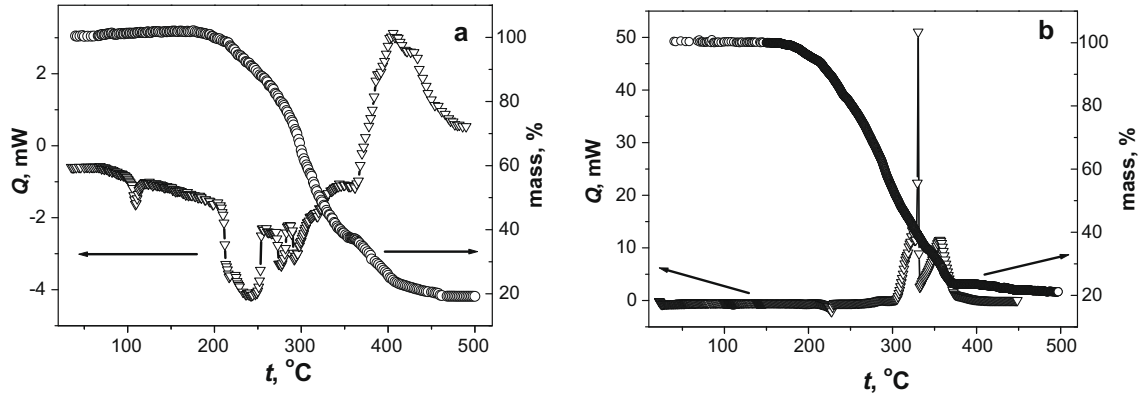


Fig. 3. Dependence of the weight loss (○) and the heat flux (▽) for the sample upon heating (*a*) under an inert atmosphere and (*b*) in an air flow.

Table 2
Phase analysis of the solid decomposition products of compound **1**.

Decomposition product under an inert atmosphere		Decomposition product in air without storage under temperature-controlled conditions		Li_2O [12–0254] *		CoO [48–1719]*		Co_3O_4 [43–1003]*		$LiCoO_2$ [50–653]*	
d (Å)	*I* (%)	*d* (Å)	*I* (%)	*d* (Å)	*I* (%)	*d* (Å)	*I* (%)	*d* (Å)	*I* (%)	*d* (Å)	*I* (%)
		4.695	100					4.667	16	4.6771	87
		2.850	20					2.858	33		
2.670	50			2.664	100						
2.455	50					2.4602	65				
		2.435	80					2.4374	100		
		2.410	40							2.4001	48
2.130	100					2.1307	100				
								2.0210	20		
		2.005	60							2.0019	100
1.650	20			1.6307	40						
		1.550	20					1.5558	32		
1.500	40					1.5066	54				
		1.395	20							1.4074	30

* *Powder Diffraction File*, Swarthmore: Joint Committee on Powder Diffraction Standards.

Table 3
Phase analysis of the solid decomposition product of compound **1** in air after storage under temperature-controlled conditions at 500 °C.

Decomposition product		$LiCoO_2$ [50-653]*	
d (Å)	*I* (%)	*d* (Å)	*I* (%)
4.695	100	4.6771	87
2.409	65	2.400	48
2.000	65	2.002	100
1.162	20	1.152	14

* *Powder Diffraction File*, Swarthmore: Joint Committee on Powder Diffraction Standards.

observed both under an inert atmosphere and in air is not associated with decomposition of the samples (Fig. 3) and is reproduced upon successive cooling and heating of the samples (Fig. 4).

To elucidate the nature of this thermal transformation, we measured the temperature dependence of the heat capacity. In addition, we intended to obtain thermodynamic characteristics for complex **1**, which are necessary for the construction of the thermodynamic model of the thermolysis. This model and the temperature program maintaining the constant level of gas evolution throughout the temperature range of thermolysis, which was calculated from the results of the thermal analysis, allow the optimization of the conditions for the preparation of lithium cobaltate films from the molecular precursor under consideration.

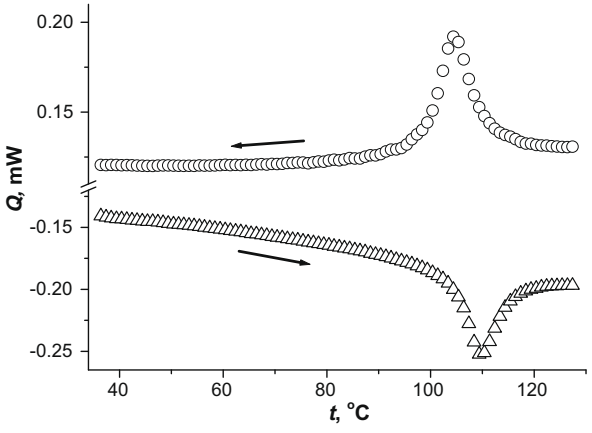


Fig. 4. Changes in the heat flux during heating (△) and cooling (○) of complex **1**.

The results of heat capacity measurements for complex **1** obtained by the statistical processing of experimental data are presented in Fig. 5. The experimental points deviate from the average smoothed curve by no more than 1.4%. The temperature dependence of C_p for complex **1** shows some anomalies. These anomalies are well reproduced, the characteristics of the anomalies being independent of the thermal history of the sample (anomaly 1: T_{onset} = 232.5 ± 0.5 K, Q = 79.1 ± 8.8 J/mol; anomaly 2: T_{onset} = 378.32 ± 0.26 K, Q = 6531 ± 715 J/mol).

According to the X-ray diffraction data, the crystal system and the space group of complex **1** remain unchanged in the 300–190 K temperature range (Table 4), but the unit cell parameters and the unit cell volume change non-monotonically. Hence, the low-temperature anomaly is presumably attributed to the phase transition associated with freezing of vibrations of the *tert*-butyl substituents at the carboxylate groups. Earlier, we have observed an analogous situation for the heteronuclear pivalate complex $Co_2Sm(Piv)_7(2,4\text{-Lut})_2$ [22].

The endothermic effect in the 350–405 K temperature range is apparently attributed to the cleavage of a large number of hydrogen bonds formed between the protons of the coordinated amino group and the oxygen atoms of the bridging and chelate bridging carboxylate groups, accompanied by energy release. The thermal effect of this transformation is comparable with the hydrogen bond energy [23].

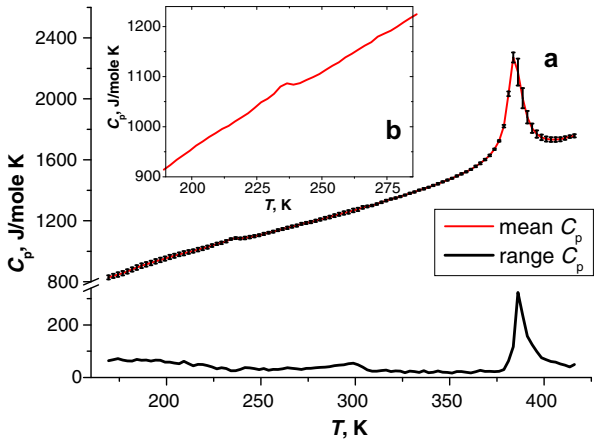


Fig. 5. Average smoothed curve $C_p(T)$, the confidence interval, and the difference between the maximum and minimum experimental values of C_p (*a*), the average smoothed curve $C_p(T)$ in the 190–280 K temperature range (*b*) (DSC, *HR* = 10 °C/min, Ar (10 ml/min), $m \sim 10$ mg).

Table 4
Unit cell parameters for compound **1** depending on the temperature.

T (K)	t (°C)	a (Å)	b (Å)	c (Å)	β (°)	V (Å^3)
403	130	12.596(14)	22.305(16)	9.537(6)	102.83(5)	2614(51)
300	27	12.568(18)	22.32(3)	9.534(13)	103.37(5)	2602(5)
280	7	12.476(12)	22.17(2)	9.461(9)	103.53(3)	2545(2)
260	−13	12.484(11)	22.20(2)	9.458(8)	103.67(5)	2547(5)
210	−63	12.430(7)	22.130(11)	9.366(5)	103.939(17)	2501(4)
190	−83	12.414(5)	22.122(8)	9.332(4)	103.931(17)	2487.4(1.5)

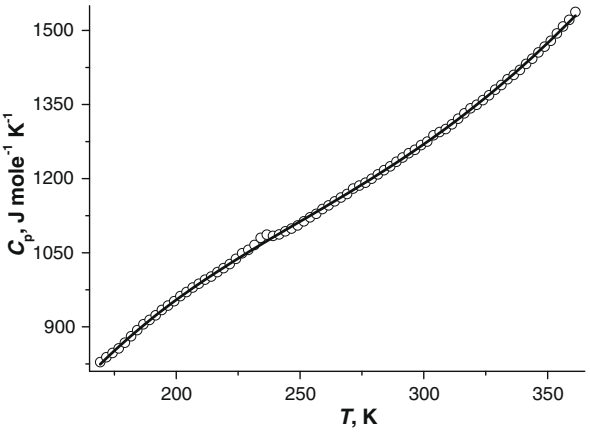


Fig. 6. Dependence of the heat capacity of complex **1**: experimental data (○); the calculated data are represented by the line (a_1 = 1396, θ_1 = 437, a_2 = 7779, θ_2 = 2617).

The absolute entropies of complex **1** were calculated from the limited region of the heat capacity curve (120–350 K) by extrapolating the results of DSC heat capacity measurements from the boiling point of liquid-nitrogen to the absolute zero temperature (0 K). This method gives the physically correct behavior of the temperature dependence of the heat capacity and the mathematically correct standard entropies [22]. To calculate the thermodynamic functions of the complexes, we separated the regular heat capacity contribution and approximated it to 0 by the function:

$$c_p(T) = \sum_i a_i C_{En}\left(\frac{\theta_i}{T}\right) \quad (3)$$

$$\text{where} \quad C_{En}(x) = 3Rx^2\frac{\exp(x)}{[\exp(x)-1]^2}, \quad x = \frac{\theta}{T}$$

The best results were obtained by approximating with function (3), consisting of two summands (Fig. 6).

The standard entropies S^o_{298} of the complexes were estimated by the equation:

$$S(T) = \sum_i a_i S_{En}\left(\frac{\theta_i}{T}\right) \quad (4)$$

$$\text{where} \quad S_{En}(x) = 3R\left[\frac{x}{(\exp(x)-1)} - \ln(1-\exp(-x))\right], \quad x = \frac{\theta}{T}.$$

We took into account the change in the entropy as a result of the transition associated with the anomaly in the curve for C_p according to the equation $\Delta S^{\circ}_{T_{onset}} = \frac{AREA}{T_{onset}}$, where AREA is the measured surface area of the peak in the experimental temperature dependence of the heat capacity. Table 5 gives the experimental (average and smoothed) heat capacities, the temperature contributions to the enthalpy calculated from the heat capacities, and the standard entropies (the latter parameters were determined with the use of the calculated value of S^o_{298}).

Table 5
Thermodynamic functions of compound **1**.

T (K)	C_p (±11.1) (J/mol K)	$H^o_T - H^o_{170}$ (kJ/mol)	S^o_T (J/mol K)
170	828.5	0	403
180	867.8	8.4	451
190	914.2	17.3	500
200	952.0	26.7	547
210	987.2	36.3	595
220	1018.7	46.3	642
250	1105.2	78.3	778
260	1138.5	89.5	822
270	1168.8	101.0	866
280	1199.8	112.8	909
290	1234.0	124.9	952
298	1267.7	137.4	994
310	1300.4	150.2	1036
320	1342.3	163.4	1078
330	1380.1	177.0	1120
340	1420.0	190.9	1162
350	1467.2	205.3	1204

Hence, the study of the heat capacity of coordination polymer **1** in the 123–373 K temperature range revealed two anomalies associated with phase transitions. The parameters of these transitions were determined. The thermodynamic functions ($C^o_p(T)$, $S^0(T)$ and $H^0(T)$–$H^0(170)$) in the 170−350 K temperature range were calculated based on the results of the calorimetric measurements.

4. Conclusions

The above-considered data show that the new heterometallic coordination polymer **1** can apparently be used as an efficient molecular precursor for the synthesis of lithium cobaltate. Under the conditions of the experiments (heating at a rate of 10 °C/min), $LiCoO_2$ can be prepared as the only solid thermolysis product, only after additional storage under temperature-controlled conditions at 500 °C. Preliminary investigations into the preparation of films from saturated solutions of complex **1** on different supports (an alundum support, a stabilized zirconium dioxide support and a sapphire support) showed that homogeneous uniform $LiCoO_2$ films can be formed with the use of a temperature program, which was calculated from the kinetic model of the thermolysis of complex **1**, designed based on the results of thermal analysis and which maintains a constant (3%/min) gas evolution rate during decomposition of coordination polymer **1**.

Supplementary data

CCDC 730046 contains the supplementary crystallographic data for compound **1**. These data can be obtained free of charge via http://www.ccdc.cam.ac.uk/conts/retrieving.html, or from the Cambridge Crystallographic Data Centre, 12 Union Road, Cam-

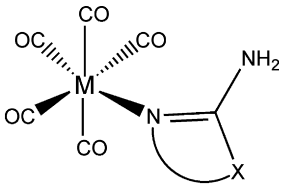
bridge CB2 1EZ, UK; fax: (+44) 1223-336-033; or e-mail: deposit@ccdc.cam.ac.uk.

Acknowledgments

This study was supported by the Russian Foundation for Basic Research (project nos. 07-03-00707, 08-03-00091, 09-03-90441, 09-03-12228, 09-03-12122, and 08-03-00343), the Council on Grants of the President of the Russian Federation (grants NSh-1324.2008.3, NSh-1518.2008.3, MK-156.2009.3), the Federal Agency for Science and Innovations, the Russian Science Support Foundation, the Russian Academy of Science, the Siberian Branch of the Russian Academy of Sciences and the Department of Chemistry and Materials Science.

References

[1] J.N. Reimers, J.R. Dahn, J. Electrochem. Soc. 139 (1992) 2091.
[2] T. Ohzuku, A. Ueda, J. Electrochem. Soc. 141 (1994) 2972.
[3] M. Wang, A. Navrotsky, J. Solid State Chem. 178 (2005) 1230.
[4] B. Garcia, J. Farcy, J.P. Pereira-Ramos, J. Perichon, N. Baffier, J. Power Sources 54 (1995) 373.
[5] Z.S. Peng, C.R. Wan, C.Y. Jaing, J. Power Sources 72 (1998) 215.
[6] S. Myung, N. Kumagai, S. Komaba, J. Appl. Electrochem. 30 (2000) 1081.
[7] C. Julien, S. Gastro-Garsia, J. Power Sources 97–98 (2001) 290.
[8] C.-C. Chang, P.N. Kumta, J. Power Sources 75 (1998) 44.
[9] W. Jang, Y. Lee, K. Baik, M. Lee, Mater. Res. Bull. 38 (2003) 1.
[10] N.V. Kosova, T.V. Larina, E.T. Devyatkina, J. Chem. Sustain. Develop. (2001) 235.
[11] K. Kanamura, A. Goto, R. Young Ho, T. Umegaki, K. Toyoshima, K. Okada, Y. Hakuta, T. Adschiri, K. Aria, Electrochem. Solid-State. Lett. 3 (2000) 256.
[12] M. Hamid, A.A. Tahir, M. Mazhar, M. Zeller, K.C. Molloy, A.D. Hunter, Inorg. Chem. 45 (2006) 10457.
[13] S.L. Tey, M.V. Reddy, G.V.S. Rao, B.V.R. Chowdari, J.J. Ding, J.J. Vittal, Chem. Mater. 18 (2006) 1587.
[14] M.A. Golubnichaya, A.A. Sidorov, I.G. Fomina, M.O. Ponina, S.M. Deomidov, S.E. Nefedov, I.L. Eremenko, I.I. Moiseev, Russ. Chem. Bull. (Engl. Transl.) 48 (1999) 1751.
[15] SMART (Control) and SAINT (Integration) Software, Version 5.0, Bruker AXS Inc., Madison, WI, 1997.
[16] G.M. Sheldrick, SHELX97, Program for the Solution of Crystal Structures, Göttingen University, Götinngen, Germany, 1997.
[17] G.M. Sheldrick, SADABS, Program for Scanning and Correction of Area Detector Data, Göttingen University, Göttinngen, Germany, 1997.
[18] E.V. Pakhmutova, A.E. Malkov, T.B. Mikhailova, A.A. Sidorov, I.G. Fomina, G.G. Aleksandrov, V.M. Novotortsev, V.N. Ikorskii, I.L. Eremenko, Russ. Chem. Bull. Int. Ed. 52 (2003) 2117.
[19] E.V. Pakhmutova, A.E. Malkov, T.B. Mikhailova, I.G. Fomina, A.A. Sidorov, G.G. Aleksandrov, I.F. Golovaneva, V.M. Novotortsev, V.N. Ikorskii, S.E. Nefedov, I.L. Eremenko, Russ. Chem. Bull. Int. Ed. 52 (2003) 139.
[20] Yu.V. Rakitin, V.T. Kalinnikov, Sovremennaya magnetokhimiya (Nauka. St-Petersburg, 1994), Modern magnetochemistry, Science, St. Petersburg, 1994 (in Russian).
[21] http://webbook.nist.gov.
[22] M.A. Bykov, A.L. Emelina, M.A. Kiskin, G.G. Aleksandrov, A.S. Bogomyakov, Zh.V. Dobrokhotova, V.M. Novotortsev, I.L. Eremenko, Russ. J. Inorg. Chem. Int. Ed. 54 (2009) 548.
[23] A. Albinati, V.I. Bakhmutov, N.V. Belkova, C. Bianchini, I. de los Rios, L. Epstein, E.I. Gutsul, L. Marvelli, M. Peruzzini, R. Rossi, E. Shubina, E.V. Vorontsov, F. Zanobini, Eur. J. Inorg. Chem. (2002) 1530.



	M	X	N⌒X
1a	Cr	S	CMeCH
1b	W	S	CMeCH
2a	Cr	S	cyclic(C_6H_4)
2b	W	S	cyclic(C_6H_4)
3a	Cr	S	CH_2CH_2
3b	W	S	CH_2CH_2
4a	Cr	NH	cyclic(C_6H_4)
4b	W	NH	cyclic(C_6H_4)
5a	Cr	NMe	cyclic(C_6H_4)

Scheme 1.

in vacuo, the residue extracted with diethyl ether, the extract filtered through SiO_2 and the filtrate stripped of solvent to obtain the microcrystalline products. The products are soluble in organic solvents but not very stable in solution as the presence of metal hexacarbonyl peaks in the IR spectra indicate (*vide infra*). Crystals suitable for single crystal X-ray diffraction were obtained by slow diffusion of pentane into a solution of the product in diethyl ether (**2a** and **4b**) or acetone (**2b**, **3b**, **4a** and **5a**) at −22 °C.

2.2. Characterisation

The molecular ions of all the new products as well as fragments representing the sequential loss of CO-ligands were observed in their mass spectra, confirming that the 2-aminoazoles were coordinated to the pentacarbonyl group 6 metal fragments. No MS data for **5a** could be collected as the compound is too unstable in solution. This kinetic instability might be the result of greater electron delocalisation in the pseudo-aromatic ring of the 2-amino-azole ligand. The synthesis of the analogous complex with W was not attempted.

$(CO)_5ML$ complexes have C_{4v} local symmetry and thus four vibration bands, ν(CO), are expected in their IR spectra. The characteristic $A_1^{(1)}$ vibration (located at high frequency) was recorded at *ca.* 2065 cm^{-1}(m) for all of the Cr and *ca.* 2070 cm^{-1}(m) for all of the W complexes, followed by the intense E_1 band at *ca.* 1935 cm^{-1} (vs) for the Cr and *ca.* 1930 cm^{-1} (vs) for the W complexes, with one or two weaker bands, which are located to the left (B_1) (~1980 cm^{-1}, obscured by $Cr(CO)_6$ or $W(CO)_6$) and to the right of this band, $A_1^{(2)}$, at *ca.* 1918 cm^{-1}(s) for the complexes recorded in hexane. The normally Raman active but IR inactive band, B_1, if present is obscured by the $M(CO)_6$ peak. These data are very similar to the reported IR data of (4,5-dihydrido-2-methylthiazole)$W(CO)_5$ (2070 w, 1932 vs 1921 m cm^{-1} in pentane) [14]. For complexes **4b** and **5a**, recorded in $CHCl_3$, a vibration representing the E_1 band is observed at *ca.* 1929 cm^{-1} and a shoulder at *ca.* 1890 cm^{-1} can be assigned to the $A_1^{(2)}$ band. The observed decrease in frequency and broadening of the E_1 and $A_1^{(2)}$ bands can be ascribed to the polar solvent, $CHCl_3$ used in the collection of the spectra [15,16]. The E_1 band is less sensitive to the polar solvent than the $A_1^{(2)}$ band as its dipole is perpendicular to the molecular dipole whereas the dipole of the $A_1^{(2)}$ band is parallel to the molecular dipole and thus the $A_1^{(2)}$ band is more affected by interaction with the polar solvent and appears at a lower frequency [17]. An examination of the CO stretching frequency data for the E_1 vibration of 2-aminopyrimidine and 4-aminopyrimidine complexes of $W(CO)_5$ have shown that the infrared technique is not diagnostic of the coordination mode of endocyclic imine versus excocyclic amine donors [12].

The signals in the ^{1}H NMR spectra of the new complexes appear downfield by up to $\Delta\delta$ 0.5 ppm when compared to the corresponding signals for the free ligand, an indication of coordination of the ligand to the metal. The resonances for the NH_2 groups when observed (2-amino-4-methylthiazole, 2-aminothiazoline, and their complexes and 2-aminobenzothiazole) appear between δ 4.71 and 7.81. These signals are known to be solvent and concentration dependent [18]. No NMR data for **5a** could be collected as the compound is too unstable in solution.

In the ^{13}C NMR spectra the resonances for the *cis* and *trans* CO-groups appear with the customary intensities and at the familiar chemical shifts (220 for *trans* and 215 for *cis* CO in Cr complexes and 205 for *trans* and 199 for *cis* CO in W complexes). The $J_{W\text{-}C}$ couplings are not observed as a result of the low signal intensities, a consequence of the long relaxation times of CO carbons. As in the ^{1}H NMR spectra, signals in the ^{13}C NMR spectra generally appear at a lower field strength (>6 ppm) when compared to the corresponding signals in the free ligand. The exceptions are some of the signals for the C atoms located further away from the heterocyclic ring in the benzene rings, in the 2-aminobenzothiazole and 2-aminobenzimidazole derived complexes. The signals for these C atoms can experience a small upfield change (>5 ppm) in chemical shift. This observation is not unusual as the total chemical shift σ ($\sigma = \sigma_p + \sigma_d$) in the ^{13}C NMR does not only reflect shielding and deshielding [19]. The total chemical shift consists of two parts, namely the paramagnetic contribution (σ_p) and diamagnetic contribution (σ_d), in the equation $\sigma = \sigma_p + \sigma_d$. The diamagnetic component can be ignored in ^{1}H NMR spectra where chemical shifts only reflect shielding and deshielding but the diamagnetic contribution plays a more significant role in ^{13}C NMR and cannot be ignored. Thus the ^{13}C NMR chemical shifts do not simply reflect shielding and deshielding as in ^{1}H NMR spectra.

The signal for the NH_2 nitrogen in the ^{15}N NMR spectra of the ligands of complexes **1**–**4** could all be detected by ^{1}H–^{15}N gHMQC or directly (**4**). The resonance for the N=C nitrogens in the thiazole compounds were all located by using ^{1}H–^{15}N gHSQC. In the instance of **4** the signal for NH could not be detected but a signal, possibly, for the N=C nitrogen appears at δ −200, well upfield from the other N=C signals. Delocalisation could render the endocyclic NH and N=C nitrogens in **4** isochronous. Bond distances in the molecular structure determination of 3-methyl-3*H*-imidazo [4,5-f]quinolin-2-ylamine [20], **4a**, **4b** and **5b** also suggest delocalization.

Upon coordination of the ligands, the signal for the N=C nitrogen in the ^{15}N NMR spectra of **1b** and **3b** is detected *upfield* by 70–76 ppm. This is consistent with the results observed for imine coordinated gold(I) complexes of thiazoles [7] and imidazoles [21]. The signal for the NH_2 group appears downfield by 20–24 ppm. Although one would expect a downfield change in chemical shift for the imine N upon metal coordination as a result of the electronic redistribution of charge, this upfield change in chemical shift correlates to results observed for the protonation of imine nitrogens, especially if the isolobal relationship between H^+ and the $W(CO)_5$ unit [22] is taken into consideration. Similar changes in chemical shift were observed during the protonation of prototypical ATP derivatives [23]. An upfield change in chemical shift of about 70 ppm was observed for the imine nitrogen where protonation occurred, in the pyrimidine ring of the adenine unit of these compounds. A downfield change in chemical shift of 9–10 ppm was observed for the exocyclic amine in this instance. These changes were ascribed to the increase in sp^3 character of the imine N and increase in sp^2 character for the excocyclic amine N.

The ^{15}N NMR data suggests endocyclic imine coordination thus providing the only clue from physical measurements as to the site of metal coordination. The endocyclic thioether S is unlikely to be the site of coordination as ^{14}N NMR data suggests that the lone pair of the sulfur is delocalized into the conjugated ring [24].

2.3. Molecular structures of **2a**, **2b**, **3b**, **4a**, **4b** and **5a**

No literature examples of X-ray crystal structure determinations of aminoazole group 6 pentacarbonyl complexes were found. The single crystal X-ray diffraction structure determinations confirmed that the ligands in all complexes are imine coordinated (Figs. 1–6). The unit cells of **2a** and **5a** contain two asymmetric molecules but bond lengths and angles do not differ significantly. The two molecules in the asymmetric unit of **5a** are related by a pseudo-inversion centre. All the complexes essentially display the octahedral coordination geometry adopted by their $M(CO)_6$ synthetic ancestors (C–M–C and C–M–N angles are ~175°). The largest deviation from the ideal 180° angles involving *trans* oriented donor atoms and the central metal, occurs in the *cis* CO-ligands which are slightly bent away from the non-carbonyl ligand in order to accommodate its steric requirements. The ligands are

Table 1
Selected bond lengths (Å) and angles (°) of **2a**, **2b**, **3b**, **4a**, **4b** and **5a** with standard uncertainty in parenthesis.

	2a	2b	3b	4a	4b	5a
Bond lengths						
M1–C1	1.837(4) 1.840(4)	1.960(5)	1.968(5)	1.841(3)	1.967(4)	1.834(6) 1.832(6)
M1–C4	1.922(4) 1.916(4)	2.053(5)	2.047(5)	1.936(3)	2.055(4)	1.899(4)[a] 1.920(4)[a]
M1–C2	1.905(4) 1.897(4)	2.025(5)	2.027(5)	1.891(3)	2.041(4)	1.899(4)[a] 1.920(4)[a]
M1–C3	1.921(4) 1.919(4)	2.041(5)	2.049(6)	1.912(3)	2.053(4)	1.910(4)[b] 1.897(4)[b]
M1–C5	1.911(5) 1.904(4)	2.029(5)	2.042(6)	1.899(3)	2.028(4)	1.910(4)[b] 1.897(4)[b]
M1–N1	2.168(3) 2.174(3)	2.274(4)	2.249(4)	2.136(2)	2.248(3)	2.139(4) 2.136(5)
N1–C10	1.317(5) 1.320(5)	1.325(5)	1.274(7)	1.325(3)	1.334(5)	1.326(6) 1.334(6)
N1–C11	1.416(5) 1.422(5)	1.410(5)	1.489(7)	1.407(3)	1.404(5)	1.395(7) 1.406(7)
N3–C10				1.351(3)	1.352(5)	1.346(7) 1.365(7)
S1–C10	1.749(4) 1.743(4)	1.740(4)	1.762(6)			
N3–C12				1.386(3)	1.391(5)	1.379(7) 1.381(7)
S1–C12	1.747(4) 1.745(4)	1.745(4)	1.707(8)			
C11–C12	1.396(6) 1.402(6)	1.396(6)	1.478(9)	1.402(4)	1.397(5)	1.408(7) 1.414(8)
N2–C10	1.356(5) 1.345(5)	1.333(5)	1.325(8)	1.365(3)	1.346(5)	1.366(7) 1.333(7)
Bond angles						
C1–M1–N1	175.1(2) 177.1(2)	177.2(1)	178.4(2)	177.7(1)	173.0(1)	176.3(2) 176.8(2)
C4–M1–C2	172.4(2) 171.3(2)	176.3(1)	175.0(2)	176.7(1)	175.1(2)	175.5(2)[c] 175.5(2)[c]
C5–M1–C3	176.3(2) 176.8(2)	172.7(2)	173.7(2)	177.3(1)	174.2(2)	175.5(2)[c] 175.5(2)[c]
C10–N1–C11	109.3(3) 109.8(3)	109.8(3)	112.1(5)	104.6 (2)	104.6(3)	104.5(4) 104.9(4)
C10–N3–C12				107.0(2)	107.3(3)	106.6(4) 107.6(4)
C10–S1–C12	88.9(2) 88.9(2)	89.2(2)	90.7(3)			
N3–C10–N1				113.5(2)	113.0(4)	113.9(5) 112.8(4)
N1–C10–S1	116.6(3) 116.6(3)	116.1(3)	116.5(4)			
C12–C11–N1	115.3(3) 114.1(3)	115.0(3)	109.2(5)	109.1(2)	109.6(3)	109.0(4) 109.3(4)
N3–C12–C11				105.7(2)	105.5(3)	105.9(5) 105.5(5)
S1–C12–C11	109.8(3) 110.5(3)	109.9(3)	110.9(5)			
C5–M1–N1–C10	−40.9(3) −52.9(3)	−38.6(4)	−41.4(5)	−42.2(2)	−53.9(4)	45.4(1)[c] 45.1(1)[d]

[a] M1–C4 = M1–C2.
[b] M1–C5 = M1–C3.
[c] C2–M1–C3 = C4–M1–C5.
[d] C5–M1–N1–C10 = C2–M1–N1–C10.

virtually planar and are staggered with respect to the *cis* carbonyl ligands (C5–M1–N1–C10 torsion angles −38 to −55°, Table 1) to avoid steric congestion.

The Cr1–N1 and W1–N1 distances are within the norm set by other M–N bonds in $(CO)_5ML$ complexes with an N(sp^2)-bonded N-heterocyclic ligand (L = 3-ethoxy-1*H*-isoindole [2.134(3) Å] [25], 3,3-diethyl-5-methoxycarbonyl-3*H*-pyrazole [2.138(2) Å] [26], 4-ethoxy-1,2,6,6a-tetrahydro-1-methyl-6-phenylcyclopenta(d)imidazole [2.126(3) Å] [27] and 4-(diethylamino)-2-ethoxy-3-methyl-2,5-diphenyl-2*H*-pyrrole [2.160(2) Å] [28] for M = Cr and L = 4,5-dihydrido-2-methylthiazole [2.287(6) Å] [14], benzoxazole [2.257(6), 2.270(7) Å] [29], 2-methyl-1-(pyridine-2-yl)-1,2,4-triazole [2.273(7) Å] [30] and 5-*t*-butylpyrazol-2-yl [2.236(4) Å] [31] for M = W). The M–CO bonds in each complex *trans* to the M–N bonds are significantly shorter than the other M–CO bonds reflecting the significant *trans* influence of the imine donor. The M–CO bond distances range from 1.832(6) to 1.922(4) Å for M = Cr and from 1.960(5) to 2.055(4) Å for M = W and are in good agreement with the same bond distances in the above mentioned examples.

Bond distances and angles in the ligands (2-aminobenzothiazole [32], 2-aminothiazoline [33], 2-aminobenzimidazole [34] and 2-amino-1-methyl-imidazole compared to 2-amino-3-methylimidazo(4,5-f)quinoline [20]) do not change significantly upon coordination to the metal. The C=N bonds in **2a**, **2b**, **3b**, **4a**, **4b**, and **5a** are somewhat longer than the standard value for a C(sp^2)=N(sp^2) bond (1.30 Å) [35] and the C–N bonds in **4a**, **4b** and **5a** are shorter than the standard value for C(sp^2)–N(sp^3) bonds (1.41 Å) [35]. The two C–S bonds in **2a** and **2b** do not differ significantly from each other whereas they do in **3b**. These facts indicate a degree of delocalization and thus pseudo-aromatic characteristics especially for the 2-aminobenzothiazole and -imidazole ligands.

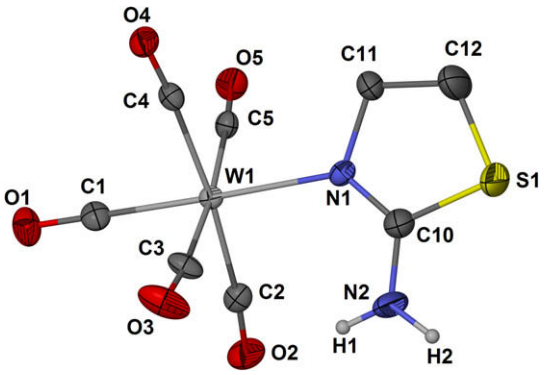


Fig. 3. The molecular structure of **3b**.

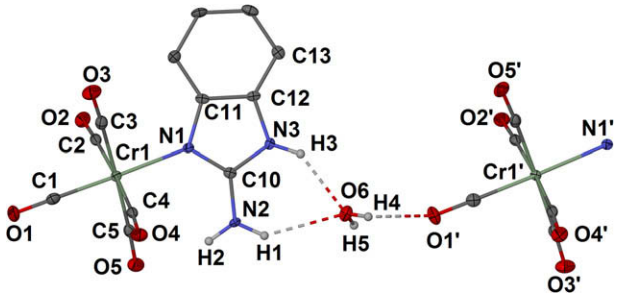


Fig. 4. The molecular structure of **4a**. One symmetry generated ($x-1$, $3/2-y$, $z-1/2$) $Cr(CO)_5$ fragment is shown to indicate the hydrogen bonding motif.

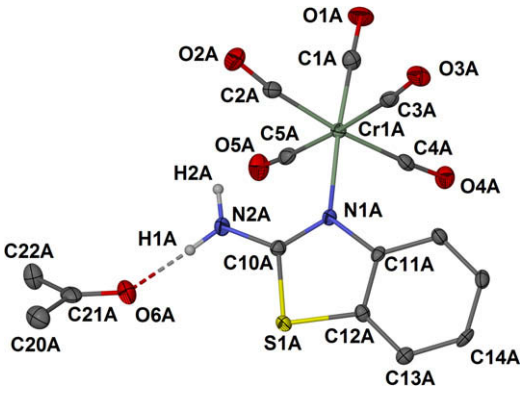


Fig. 1. The molecular structure of **2a**, showing one of the asymmetric molecules per unit cell.

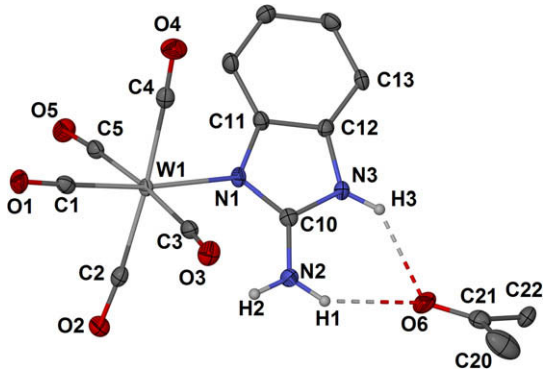


Fig. 5. The molecular structure of **4b**.

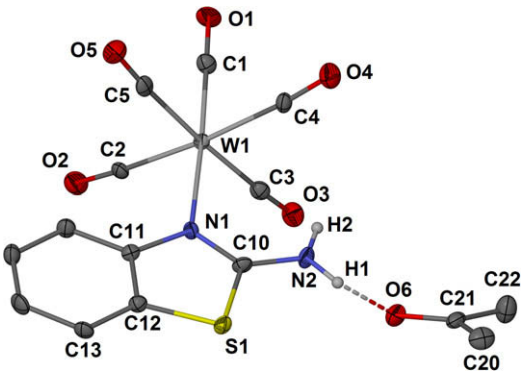


Fig. 2. The molecular structure of **2b**.

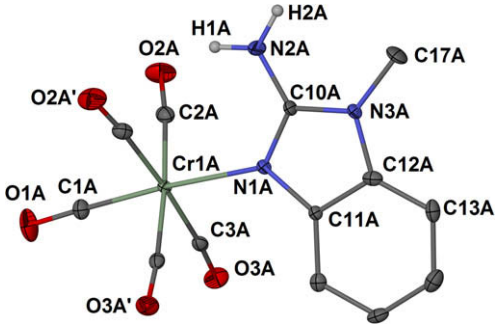


Fig. 6. The molecular structure of **5a**, showing one of the asymmetric molecules per unit cell.

In the crystal structures of **2a**, **2b**, **4a** and **4b** both hydrogen bonding between the amino group on the ligand and included solvent molecules and π-stacking between the 5- and 6-membered rings of neighbouring molecules govern the solid-state arrangement (3.93, 3.78, 3.97 and 3.73 Å in **2a**, 3.99 and 3.76 Å in **2b**, 3.50 Å in **4a**, 3.98 and 3.84 Å in **4b**). The molecular assembly of **5a** is determined by π-stacking between the 5- and 6-membered rings of neighbouring molecules (3.77 and 3.67 Å). No hydrogen bonding is observed in the crystal structure of **3b**.

3. Conclusions

Contrary to expectation when electronic charge redistribution is considered, the signal for the N=C nitrogen in 2-aminothiazoles upon coordination to pentacarbonyl chromium or tungsten, is detected upfield by 70–76 ppm in ^{15}N NMR spectra. This is the only clue presented by IR, NMR and MS analysis of the product complexes as to the preferred coordination site of the metal on the 2-aminoazole ligand. The first molecular structures of pentacarbonyl chromium and tungsten complexes coordinated to 2-aminoazoles were determined and confirmed metal coordination to the softer endocyclic imine rather than the hard excocyclic amine.

4. Experimental

4.1. Synthesis

All reactions were carried out under nitrogen or argon using standard vacuum-line and Schlenk techniques. Tetrahydrofuran (THF), hexane, pentane and diethyl ether were dried and deoxygenated by distillation from sodium benzophenone ketyl, and dichloromethane and *N,N*-dimethylformamide from CaH_2. $Cr(CO)_6$, $W(CO)_6$, 2-amino-4-methylthiazole, 2-aminobenzothiazole, 2-aminothiazoline, 2-aminobenzimidazole and 2-amino-1-methylbenzimidazole were purchased from commercial suppliers and used without further purification. Flash column chromatography was performed with "flash grade" SiO_2 (SDS 230–400 mesh). The starting materials, pentacarbonyl(tetrahydrofuran)chromium(0) and its tungsten analogue [36] and 2-amino-1-methylbenzimidazole [37] were prepared according to literature procedures.

Melting points were determined on a Stuart SMP3 apparatus and are uncorrected. Mass spectra were recorded on a VG 70 SEQ (FAB, 70 eV, *m*-nitrobenzylalcohol matrix) or VG Quattro (ESI, 70 eV, solvent acetonitrile) instrument, the infrared spectra on a Thermo Nicolet Avatar 330 FT-IR instrument equipped with a SMART OMNI ATR (attenuated total reflectance, Zn Se) sampler and NMR spectra on a Varian 300 FT or INOVA 600 MHz spectrometer (^{1}H NMR at 300/600 MHz, ^{13}C{^{1}H} NMR at 75/150 MHz and ^{15}N NMR at 60.8 MHz; δ reported relative to the solvent resonance or external reference, neat CH_3NO_2). Elemental analyses were carried out at the Soil Science Department, University of the Stellenbosch. Prior to elemental analysis, the products were evacuated under high vacuum for 10 h.

4.2. Preparation of (2-amino-4-methylthiazole)pentacarbonylchromium(0), **1a**

The irradiation of hexacarbonylchromium(0) (0.44 g, 2.0 mmol) in 150 ml of THF for 2 h yielded an orange solution. The solution was transferred to a Schlenk tube *via* a cannula whereupon the ligand, 2-amino-4-methylthiazole (0.23 g, 2.0 mmol), was added. The mixture was stirred at room temperature for 2 h. The resulting yellow solution was stripped of solvent *in vacuo*. The yellow residue was then extracted with diethyl ether (60 ml) and filtered through SiO_2 to remove solid impurities. After the removal of solvent from the yellow solution, a yellow microcrystalline product was obtained (0.10 g, 52%). TLC analysis with a 1:1 ratio of hexane/diethyl ether was used to confirm that only one product was present. Mp 86–88 °C (decomp.). IR (hexane, cm^{-1}) ν(CO): 2067 m, 1936 vs 1918 s. ESMS, *m/z* (relative intensity) for $C_9H_6CrN_2O_5S$: 305 (M^+–H, 2), 277 (M−CO–H, 5), 249 (M−2CO−H, 88), 221 (M−3CO−H, 57), 193 (M−4CO−H, 15), 165 (M−5CO−H, 15). ^{1}H NMR (CD_2Cl_2, δ): 6.28 (bs, 1H, SCH), 5.58 (bs, 2H, NH_2), 2.42 (bs, 3H, CH_3). ^{13}C NMR (CD_2Cl_2, δ): 221.7 (s, CO_{trans}), 215.1 (s, CO_{cis}), 170.5 (s, NCS), 150.9 (s, CH_3C), 104.0 (s, SC), 20.2 (s, CH_3). *Anal.* Calc. for $C_9H_6CrN_2O_5S$ (306.22): C, 35.30; H, 1.98; N, 9.15. Found: C, 35.53; H, 1.74; N, 9.09%.

4.3. Preparation of (2-amino-4-methylthiazole)pentacarbonyltungsten, **1b**

The same experimental procedure as described for **1a** was used to prepare **1b** from hexacarbonyltungsten(0) (0.45 g, 1.3 mmol) and 2-amino-4-methylthiazole (0.29 g, 2.0 mmol). Yellow, microcrystalline **1b** was obtained (0.44 g, 50%). Mp 106–108 °C (decomp.). IR (hexane, cm^{-1}) ν(CO): 2071 m, 1931 vs 1919 s. EIMS, *m/z* (relative intensity) for $C_9H_6N_2O_5SW$: 437 (M^+, 27), 407 (M−CO, 35), 381 (M−2CO, 20), 353 (M−3CO, 11), 325 (M−4CO, 4), 114 ($C_4H_6N_2S$, 45), 81 ($C_4H_6N_2S$–NH_2–CH_3, 20). ^{1}H NMR ($(CD_3)_2CO$, δ): 7.17 (bs, 2H, NH_2), 6.56 (s, 1H, CSH), 2.43 (s, 3H, CH_3). ^{13}C NMR ($(CD_3)_2CO$, δ): 203.2 (s, CO_{trans}), 199.9 (s, CO_{cis}), 174.0 (s, NCS), 150.7 (s, CH_3C), 104.5 (s, SC), 22.6 (s, CH_3). ^{15}N NMR ($(CD_3)_2CO$, δ): −198.5 (WN), −293.6 (NH_2). *Anal.* Calc. for $C_9H_6N_2O_5SW$ (438.07): C, 24.68; H, 1.38; N, 6.39. Found: C, 24.41; H, 1.43; N, 6.12%.

4.4. Preparation of (2-aminobenzothiazole)pentacarbonylchromium, **2a**

Complex **2a** was prepared as described above employing hexacarbonylchromium(0) (0.44 g, 2.0 mmol) and 2-aminobenzothiazole (0.19 g, 1.3 mmol), yielding a yellow microcrystalline solid (0.32 g, 47%). Crystals of **2a** were obtained by the slow diffusion of *n*-pentane into a concentrated diethyl ether solution. Mp 149–150 °C (decomp.). IR (hexane, cm^{-1}) ν(CO): 2068 m, 1936 vs 1917 s. ESMS, *m/z* (relative intensity) for $C_{12}H_6CrN_2O_5S$: 341 (M^+−H, 9), 313 (M–CO–H, 15), 285 (M–2CO–H, 2), 229 (M–4CO–H, 19), 201 (M–5CO–H, 17). ^{1}H NMR ($(CD_3)_2CO$, δ): 7.40 (m, 6H, NH_2, CH). ^{13}C NMR ($(CD_3)_2CO$, δ): 222.9 (s, CO_{trans}), 216.3 (s, CO_{cis}), 171.6 (s, NCS), 153.5 (s, NCCHCH), 130.4 (s, SCCHCH), 128.2 (s, SCCHCH), 125.0 (s, NCCHCH), 123.5 (s, SCCHCH), 121.9 (s, NCCHCH). *Anal.* Calc. for $C_{12}H_6CrN_2O_5S$ (342.25): C, 42.11; H, 1.77; N, 8.19. Found: C, 42.25; H, 1.47; N, 8.20%.

4.5. Preparation of (2-aminobenziothiazole)pentacarbonyltungsten, **2b**

Complex **2b** was prepared from hexacarbonyltungsten(0) (0.45 g, 1.28 mmol) and 2-aminobenziothiazole (0.3 g, 2 mmol) as described above. The mixture was stirred for 1 h and after work up a microcrystalline yellow product in a moderate yield (0.476 g, 51%) was isolated. Yellow crystals of complex **2b** were obtained *via* slow diffusion of *n*-pentane into an acetone solution at −22 °C. Mp 146–147 °C (decomp.). IR (hexane, cm^{-1}) ν(CO): 2071 m, 1932 vs 1919 s. EIMS, *m/z* (relative intensity) for $C_{12}H_6N_2O_5SW$: 474 (M^+, 22), 446 (M–CO, 5), 418 (M–2CO, 8), 390 (M–3CO, 12), 362 (M–4CO, 3). ^{1}H NMR ($(CD_3)_2CO$, δ): 7.95 (dm, 1H, ^3J 7.8 Hz, NCCH), 7.81 (bs, 2H, NH_2), 7.75 (dm, 1H, ^3J 7.8 Hz, SCCH), 7.52 (tm, 1H, ^3J 7.8 Hz, NCCHCH), 7.28 (tm, 1H, ^3J 7.8 Hz, SCCHCH). ^{13}C NMR ($(CD_3)_2CO$, δ): 203.4 (s, CO_{trans}), 199.6 (s, CO_{cis}), 172.6 (s, NCS), 153.4 (s, NCCHCH), 129.8 (s, SCCHCH), 128.5 (s, SCCHCH), 125.3 (s, NCCHCH), 123.6 (s, SCCHCH), 123.0 (s,

NCCHCH). *Anal.* Calc. for $C_{12}H_6N_2O_5SW$ (474.11): C, 30.40; H, 1.28; N, 5.91. Found: C, 30.58; H, 1.43; N, 5.85%.

4.6. Preparation of (2-aminothiazoline)pentacarbonylchromium, **3a**

Complex **3a** was prepared using the same method as for the preparation of **2a** employing hexacarbonylchromium(0) (0.46 g, 2.0 mmol) and 2-aminothiazoline (0.21 g, 2.0 mmol), yielding a yellow microcrystalline solid (0.26 g, 45%). TLC analysis in 1:1 hexane/diethyl ether indicated the presence of a single pure product. Mp 81–87 °C (114 °C decomp.). IR (hexane, cm^{-1}) ν(CO): 2066 m, 1934 vs 1917 s. ESMS, *m/z* (relative intensity) for $C_8H_6CrN_2O_5S$: 293 (M^+–H, 1), 237 (M–2CO–H, 88), 209 (M–3CO–H, 10), 181 (M–4CO–H, 29), 153 (M–5CO–H, 19). ^{1}H NMR ($(CD_3)_2CO$, δ): 6.54 (bs, 2H, NH_2), 3.96 (t, 2H, ^3J 7.5 Hz, NCH_2), 3.38 (t, 2H, ^3J 7.5 Hz, SCH_2). ^{13}C NMR ($(CD_3)_2CO$, δ): 222.6 (s, CO_{trans}), 216.5 (s, CO_{cis}), 168.6 (s, NCS), 69.7 (s, NCH_2), 33.9 (s, SCH_2). *Anal.* Calc for $C_8H_6CrN_2O_5S$ (294.21): C, 32.66; H, 2.06; N, 9.52. Found: C, 32.44; H, 2.23; N, 9.27%.

4.7. Preparation of (2-aminothiazoline)pentacarbonyltungsten, **3b**

The same method as above was used to prepare **3b**, utilising hexacarbonyltungsten(0) (1.40 g, 4.0 mmol) and 2-aminothiazoline (0.4 g, 4.0 mmol) producing a yellow microcrystalline product **3b** in low yield (0.60 g, 35%). Yellow needles were obtained by the slow diffusion of *n*-pentane into a concentrated acetone solution of the product. Mp 109–110 °C (153 °C decomp.). IR (hexane, cm^{-1}) ν(CO): 2069 m, 1929 vs 1919 s. EIMS, *m/z* (relative intensity) for $C_8H_6N_2O_5SW$: 424 (M^+, 18), 397 (M–CO, 12), 371 (M–2CO, 10), 342 (M–3CO, 2), 306 ($3 \times C_3H_6N_2S$, 21). ^{1}H NMR ($(CD_3)_2CO$, δ): 6.80 (bs, 2H, NH_2), 4.12 (t, 2H, ^3J 7.5 Hz, NCH_2), 3.42 (t, 2H, ^3J 7.5 Hz, SCH_2). ^{13}C NMR ($(CD_3)_2CO$, δ): 203.7 (s, CO_{trans}), 199.7 (s, CO_{cis}), 170.3 (s, NCS), 71.4 (s, NCH_2), 34.7 (s, SCH_2). ^{15}N NMR ($(CD_3)_2CO$, δ): −233.0 (N≡C), −282.7 (NH_2). *Anal.* Calc. for $C_8H_6N_2O_5SW$ (426.06): C, 22.55; H, 1.42; N, 6.57. Found: C, 22.71; H, 1.67; N, 6.49%.

4.8. Preparation of (2-aminobenzimidazole)pentacarbonylchromium, **4a**

Complex **4a** was prepared implementing the procedures mentioned above using equimolar amounts of hexacarbonylchromium(0) (0.44 g, 2.0 mmol) and 2-aminobenzimidazole (0.27 g, 2.0 mmol). TLC analysis in 1:1 hexane/diethyl ether indicated the presence of a single pure product (0.64 g, 97%). Yellow single crystals were obtained by slow diffusion of *n*-pentane into a concentrated solution of **4a** in acetone maintained at −22 °C. Mp 148–150 °C (decomp.). IR (hexane, cm^{-1}) ν(CO): 2065 m, 1932 vs 1924 sh. ESMS, *m/z* (relative intensity) for $C_{12}H_7CrN_3O_5$: 324 (M^+–H, 7), 296 (M–CO–H, 14), 268 (M–2CO–H, 100). ^{1}H NMR (CD_3OD, δ): 7.53 (dm, 1H, ^3J 7.6 Hz, CrNCC*H*), 7.10 (m, 3H,

Table 2
Crystal data, data collection and refinement for compounds **2a**, **2b**, **3b**, **4a**, **4b** and **5a**.

	2a	**2b**	**3b**	**4a**	**4b**	**5a**
Molecular formula	$C_{12}H_6CrN_2O_5S{\cdot}C_3H_6O$	$C_{12}H_6N_2O_5SW{\cdot}C_3H_6O$	$C_8H_6N_2O_5SW$	$C_{12}H_7CrN_3O_5{\cdot}H_2O$	$C_{12}H_7N_3O_5W{\cdot}C_3H_6O$	$C_{13}H_9CrN_3O_5$
Molecular weight	400.33	532.18	426.06	343.22	515.13	339.23
Crystal system	triclinic	triclinic	monoclinic	monoclinic	triclinic	orthorhombic
Crystal dimensions (mm)	0.19 × 0.16 × 0.11	0.22 × 0.20 × 0.02	0.21 × 0.05 × 0.03	0.30 × 0.10 × 0.05	0.12 × 0.12 × 0.09	0.09 × 0.06 × 0.04
Crystal shape and colour	yellow blocks	yellow prisms	yellow needles	yellow needles	yellow prisms	colourless prisms
Space group	$P\bar{1}$ (No. 2)	$P\bar{1}$ (No. 2)	$P2_1/c$ (No. 14)	$P2_1/c$ (No. 14)	$P\bar{1}$ (No. 2)	*Pnma* (No. 62)
a (Å)	7.6166 (17)	7.666(3)	9.1731(17)	12.3454(15)	7.6522(9)	26.652(8)
b (Å)	11.775(3)	11.253(4)	11.286(2)	10.2483(12)	10.5764(13)	7.268(2)
c (Å)	20.384(4)	11.792(5)	11.945(2)	11.7868(14)	11.5663(14)	14.306(5)
α (°)	81.027(3)	64.333(5)	90	90	108.844(2)	90
β (°)	81.240(3)	74.571(6)	108.203(3)	114.061(2)	103.092(2)	90
γ (°)	74.737(3)	85.210(6)	90	90	94.503(2)	90
Volume (Å^3)	1730.2(7)	883.2(6)	1174.7(4)	1361.7(3)	851.13(18)	2771.2(15)
Z	4	2	4	4	2	8
d_{calc} (g/cm^3)	1.537	2.001	2.409	1.674	2.010	1.626
μ (Mo Kα) (mm^{-1})	0.815	6.690	10.021	0.875	6.823	0.853
F (0 0 0)	816	508	792	696	492	1376
θ Range for data collection (°)	1.81–25.67	1.98–26.42	2.34–26.37	1.81–28.27	1.93 to 28.27	1.53 to 26.42
Index range	$-9 < h < 9$, $-14 < k < 14$, $-24 < l < 24$	$-9 < h < 9$, $-14 < k < 14$, $-14 < l < 14$	$-9 < h < 11$, $-9 < k < 14$, $-14 < l < 14$	$-12 < h < 16$, $-12 < k < 13$, $-15 < l < 13$	$-10 < h < 10$, $-14 < k < 13$, $-14 < l < 15$	$-33 < h < 27$, $-6 < k < 9$, $-17 < l < 17$
Number of reflections collected	17,770	9259	6730	8563	9595	15,691
Number of unique reflections	6518 (R_{int} = 0.0501)	3594 (R_{int} = 0.0465)	2388 (R_{int} = 0.0344)	3230 unique (R_{int} = 0.0400)	3933 (R_{int} = 0.0290)	3054 unique (R_{int} = 0.0552)
Maximum and minimum transmission	0.917 and 0.700	0.878 and 0.471	0.738 and 0.420	0.958 and 0.589	0.544 and 0.431	0.967 and 0.693
Refinement parameters/ restraints	455 parameters, 0 restraints	228 parameters, 0 restraints	154 parameters, 0 restraints	207 parameters, 0 restraints	228 parameters, 0 restraints	243 parameters, 0 restraints
Goodness of fit (GOF) on F^2	1.039	1.090	1.071	1.033	1.048	1.060
Final *R* indices [$I > 2\sigma(I)$]	R_1 = 0.0638	R_1 = 0.0287	R_1 = 0.0282	R_1 = 0.0469	R_1 = 0.0264	R_1 = 0.0711
	wR_2 = 0.1633	wR_2 = 0.0754	wR_2 = 0.0670	wR_2 = 0.1063	wR_2 = 0.0584	wR_2 = 0.1748
R indices (all data)	R_1 = 0.0894	R_1 = 0.0294	R_1 = 0.0312	R_1 = 0.0638	R_1 = 0.0315	R_1 = 0.0903
	wR_2 = 0.1853	wR_2 = 0.0759	wR_2 = 0.0686	wR_2 = 0.1141	wR_2 = 0.0599	wR_2 = 0.1894
Largest difference in peak and hole (e A^{-3})	3.074 and −0.401	1.621 and −0.949	1.619 and −0.969	0.524 and −0.402	1.746 and −1.184	3.370 and −0.387
Weighing scheme [a]	a = 0.1140/b = 0	a = 0.0385/b = 0	a = 0.0311/ b = 2.0279	a = 0.0548/ b = 0.4535	a = 0.0319/b = 0	a = 0.1120/ b = 4.5013

[a] $wR_2 = \{\sum[w(F_o^2 - F_c^2)^2]/\sum[w(F_o^2)^2]\}^{1/2}$; $w = 1/[\sigma^2(F_o^2)+(aP)^2 + bP]$; $P = (F_o^2 + 2F_c^2)/3$.

NCC*H*(*CH*)$_2$). ^{13}C NMR (CD_3OD, δ): 221.5 (s, CO_{trans}), 216.1 (s, CO_{cis}), 157.3 (s, NCN), 144.3 (s, CrN*C*CHCH), 134.0 (s, NC*C*HCH), 121.9 (s, CrNCC*H*CH), 121.5 (s, NCC*H*CH), 116.8 (s, CrCCCH*C*H), 110.2 (s, NCCH*C*H). *Anal.* Calc. for $C_{12}H_7CrN_3O_5$ (325.20): C, 44.32; H, 2.17; N, 12.92. Found: C, 44.56; H, 2.08; N, 12.76%.

4.9. Preparation of (2-aminobenzimidazole)pentacarbonyltungsten, **4b**

Compound **4b** was prepared employing the method described above using hexacarbonyltungsten(0) (0.45 g, 1.3 mmol) and an excess of 2-aminobenzimidazole (0.27 g, 2 mmol) and produced a yellow microcrystalline solid after work up (0.16 g, 27%). Slow diffusion of *n*-pentane into a solution containing **4b** in diethyl ether at −22 °C produced yellow needle-like crystals. Mp 165–167 °C (decomp.). IR ($CHCl_3$, cm^{-1}) ν(CO): 2069 m, 1925 vs 1888 sh. EIMS, *m/z* (relative intensity) for $C_{12}H_7N_3O_5W$: 456 (M^+, 13), 429 (M−CO, 3), 399 (M–2CO, 13), 306 (M–2CO–NH_2–Ph, 22). ^{1}H NMR (CD_3OD, δ): 7.52 (dm, 1H, ^3J 7.6 Hz, CrNCC*H*), 7.10 (m, 3H, NCC*H*(*CH*)$_2$). ^{13}C NMR (CD_3OD, δ): 202.7 (s, CO_{trans}), 199.2 (s, CO_{cis}), 157.7 (s, NCN), 144.6 (s, CrNCCHCH), 133.9 (s, NCCHCH), 122.6 (s, CrNCC*H*CH), 122.4 (s, NCCH*C*H), 118.1 (s, CrCCCH*C*H), 110.8 (s, NCCH*C*H). *Anal.* Calc. for $C_{12}H_7N_3O_5W$ (457.04): C, 31.54; H, 1.54; N, 9.19. Found: C, 31.45; H, 1.73; N, 9.23%.

4.10. Preparation of (2-amino-1-methylbenzimidazole) pentacarbonylchromium, **5a**

Complex **5a** was prepared as described above using hexacarbonylchromium(0) (0.28 g, 1.3 mmol) and 2-amino-1-methylbenzimidazole (0.19 g, 1.3 mmol), yielding a yellow solid (0.18 g, 42%). TLC analysis in 1:1 hexane/diethyl ether indicated the presence of a single pure product. Colourless prisms were obtained by slow diffusion of *n*-pentane into an acetone solution. Mp 148–149 °C (decomp.). IR ($CHCl_3$, cm^{-1}) ν(CO): 2066 m, 1931 vs 1894 sh. *Anal.* Calc. for $C_{12}H_9CrN_3O_5$ (327.22): C, 44.32; H, 2.17; N, 12.92. Found: C, 44.62; H, 2.13; N, 12.83%.

4.11. X-ray data collection

Crystal data collection and refinement details of compounds, **2a**, **2b**, **3b**, **4a**, **4b** and **5a** are summarised in Table 2. Data sets were collected on a Bruker SMART Apex CCD diffractometer with graphite monochromated Mo Kα radiation (λ = 0.71073 Å) [38]. Intensities were measured using the ω-scan mode and were corrected for Lorentz and polarisation effects. Data reduction was carried out with standard methods using the software package Bruker SAINT absorption correction was applied using SADABS [39–41]. All the structures were solved using direct methods, which yielded the position of the metal atoms, and conventional difference Fourier methods. All non-hydrogen atoms were refined anisotropically by full-matrix least-squares calculations on F^2 using SHELX-97 [42] within the X-seed environment [43,44]. The hydrogen atoms were fixed in calculated positions unless otherwise stated. Figures were generated with POV Ray for Windows, with the displacement ellipsoids at 50% probability level.

Supplementary data

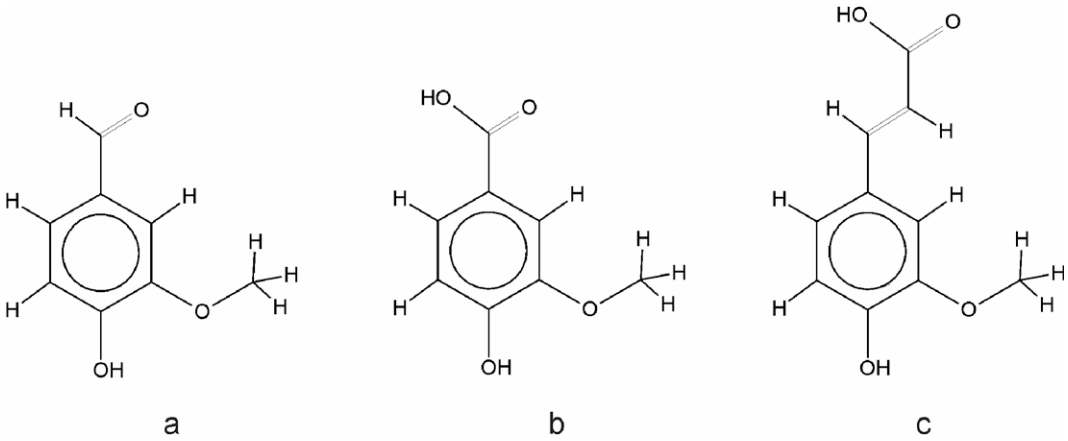
CCDC 729257, 729258, 729259, 729260, 729261 and 729262 contains the supplementary crystallographic data for **2a**, **2b**, **3b**, **4a**, **4b** and **5a**. These data can be obtained free of charge via http://www.ccdc.cam.ac.uk/conts/retrieving.html, or from the Cambridge Crystallographic Data Centre, 12 Union Road, Cambridge CB2 1EZ, UK; fax: (+44) 1223-336-033; or e-mail: deposit@ccdc.cam.ac.uk.

Acknowledgement

We thank the NRF (National Research Foundation, South Africa) for financial support.

References

[1] L. De Luca, Current Med. Chem. 13 (2006) 1.
[2] E. Buncel, I. Onyido, J. Label, Compd. Radiopharm. 45 (2002) 291.
[3] H.-B. Kraatz, N. Metzler-Nolte (Eds.), Concepts and Models in Bioinorganic Chemistry, Wiley, VCH, 2006.
[4] G. Jaouen (Ed.), Bioorganometallics, Wiley, VCH, 2006.
[5] G. Simonneaux (Ed.), Bioorganometallic Chemistry, Springer, 2006.
[6] J.M. Matthews, F.E. Loughlin, J.P. Mackay, Current Opinions in Structural Biology 18 (2008) 484.
[7] S. Cronje, H.G. Raubenheimer, H.S.C. Spies, C. Esterhuysen, H. Schmidbaur, A. Schier, G.J. Kruger, Dalton Trans. (2003) 2859.
[8] F. Téllez, A. Pena-Hueso, N. Barba-Behrens, R. Contreras, A. Flores-Parra, Polyhedron 25 (2006) 2363 (and references therein).
[9] N. Metzler-Nolte, Conjugates of peptides and PNA with organometallic complexes: syntheses and applications, in: G. Jaouen (Ed.), Bioorganometallics, Wiley-VCH, 2006, pp. 160–162.
[10] M. Salmain, Labeling of proteins with organometallic complexes: strategies and applications, in: G. Jaouen (Ed.), Bioorganometallics, Wiley-VCH, 2006, pp. 199–200.
[11] J.E. Huheey, E.A. Keiter, R.L. Keiter, Inorganic Chemistry, Principles of Structure and Reactivity, fourth ed., Harper Collins College Publishers, New York, 1993.
[12] T.W. Stringfield, R.E. Shepherd, Inorg. Chem. Commun. 4 (2001) 760.
[13] T.W. Stringfield, R.E. Shepherd, Inorg. Chim. Acta 343 (2003) 156.
[14] H. Fischer, F. Kirchbauer, A. Früh, M.M. Abd-Elzaher, G. Roth, C.C. Karl, M. Dede, J. Organomet. Chem. 620 (2001) 165.
[15] P.S. Braterman, Metal Carbonyl Spectra, Academic Press, London, 1975. pp. 115–116.
[16] L.M. Haines, M.H.B. Stiddard, Adv. Inorg. Chem. Radiochem. 12 (1969) 100.
[17] M. Bigorgne, J. Organomet. Chem. 94 (1975) 161.
[18] C. Preti, G. Tosi, D. De Filippo, G. Verani, Can. J. Chem. 52 (1974) 2021.
[19] R.F. Fenske, The interpretation of carbon-13 NMR chemical shifts and their correlation with the reaction chemistry of organometallic carbenes, carbynes and related species, in: B.L. Shapiro (Ed.), Organometallic Compounds, Synthesis, Structure and Theory, Texas A & M University Press, Texas, 1983, pp. 305–333.
[20] S. Yokoyama, T. Miyazawa, H. Kasai, S. Nishimura, T. Sugimura, Y. Iitaka, FEBS Lett. 122 (1980) 261.
[21] W.F. Gabrielli, Ph.D. Thesis, University of Stellenbosch, 2006, pp. 91–92.
[22] R. Hoffmann, Angew. Chem., Int. Ed. 21 (1982) 711.
[23] D.T. Major, A. Laxer, B. Fischer, J. Org. Chem. 67 (2002) 790.
[24] M. Witanowski, W. Sicinska, Z. Biedrzycka, Z. Grabowski, G.A. Webb, J. Chem. Soc., Perkin Trans. 2 (1996) 619.
[25] U. Feldhoff, F.-W. Grevels, R.P. Kreher, K. Angermund, C. Kruger, Chem. Ber. 119 (1986) 1919.
[26] M.M. Abd-Elzaher, B. Weibert, H. Fischer, J. Organomet. Chem. 669 (2003) 6.
[27] R. Aumann, H. Heinen, C. Krueger, Chem. Ber. 120 (1987) 1287.
[28] R. Aumann, H. Heinen, C. Krueger, B. Petz, Chem. Ber. 123 (1990) 599.
[29] F.E. Hahn, M. Tamm, J. Organomet. Chem. 456 (1993) C11.
[30] C. O'Flaherty, C. Long, J.G. Vos, R.A. Howie, Inorg. Chim. Acta 180 (1991) 195.
[31] W.L. Jia, L.F. Jang, J.F. Chai, J.T. Wang, Trans. Met. Chem. 26 (2001) 400.
[32] K. Goublitz, E.J. Sonneveld, H. Schenk, Z. Kristallogr. 216 (2001) 176.
[33] D.E. Lynch, Acta Crystallogr. Sect. C60 (2004) o677.
[34] D. Wulff-Molder, M. Meisel, Private Communication, 1999, CCDC 137482.
[35] F.J. Allen, D.G. Watson, L. Brammer, A.G. Orpen, R. Taylor, Typical interatomic distances: organic compounds, in: E. Prince (Ed.), International Tables for X-ray Crystallography **C**, Springer, Heidelberg, 2006, pp. 802–803.
[36] J.A. Costamagna, J. Granifo, Inorg. Synth. 23 (1985) 1.
[37] L.J. Mathias, D. Burkett, Tetrahedron Lett. (1979) 4709.
[38] SMART Data Collection Software (version 5.629), Bruker (2002) AXS Inc., Madison, Wisconsin, USA, 2002.
[39] SAINT, Data Reduction Software (version 6.45), Bruker (2003) AXS Inc., Madison, Wisconsin, USA, 2003.
[40] R.H. Blessing, Acta Crystallogr. Sect. A51 (1995) 33.
[41] SADABS Absorption correction software (Version 2.05), Bruker, AXS Inc., Madison, Wisconsin, USA, 2002.
[42] G.M. Sheldrick, Acta Crystallogr. Sect. A 64 (2008) 112.
[43] L.J. Barbour, J. Supramol. Chem. 1 (2001) 189.
[44] J.L. Atwood, L.J. Barbour, Cryst. Growth Des. 3 (2003) 3.



Scheme 1. The guaiacyl model molecules, vanillin (a), vanillic acid (b) and ferulic acid (c).

off and dried in a desiccator over solid KOH for 24 h, giving final air stable **1a**. Yield: 50% (300 mg, 0.34 mmol); UV–Vis λ_{max}/nm: 250, 340, 450 (sh), 650; IR $\bar{\nu}_{max}$/cm^{-1}: 3350 υ(OH), 2900, 1683, 1635, 1591, 1575 $\upsilon_{as}(O_2C)$, 1511, 1447, 1427, 1401 $\upsilon_s(O_2C)$, 1273; *Anal.* Calc. for $C_{40}H_{36}Cu_2O_{16}$ **1a** (M_r = 899.8): C, 53.4; H, 4.03. Found: C, 53.6; H, 4.22%. Magnetic susceptibility μ_{eff}/B.M.: 1.40; EPR: B_{z1} 15.3 mT, $B_{\perp 2}$ 459 mT, B_{z2} 583 mT, $g_{||}$ 2.35, $g_{\perp}$ 2.08, D 0.329 cm^{-1}, $-J$ 280 cm^{-1}.

*2.1.2. $[Cu_2(C_{10}H_9O_4)_4(C_6H_6N_2O)_2]\cdot 4CH_3CN$ (**2**), $[Cu_2(C_{10}H_9O_4)_4(C_6H_6N_2O)_2]$ (**2a**)*

Eighty milliliter of acetonitrile was added to a solid mixture of 130 mg (0.91 mmol) Cu_2O, 11 mg (0.11 mmol) CuCl and 405 mg (2.1 mmol) of ferulic acid (a diluted version as for **1**, with less CuCl and more Cu_2O to prevent further oxidation). The resulting mixture was allowed to stand in a closed flask at room temperature. The unreacted solid Cu_2O was removed next day by filtration, while the green filtrate was introduced dropwise into the flask with 81 mg (0.66 mmol) of solid nicotinamide ($C_6H_6N_2O$). Small light-green crystals of **2** were noticed and immediately filtered off to prevent side reactions to brown solid. The product **2** was dried in a desiccator over solid KOH for 24 h, resulting in the air stable light-green **2a**. Yield: 41% (309 mg, 0.27 mmol); UV–Vis λ_{max}/nm: 250, 340, 450 (sh), 660; IR $\bar{\nu}_{max}$/cm^{-1}: 3326 υ(OH), 2900, 1679, 1638, 1605, 1579 $\upsilon_{as}(O_2C)$, 1511, 1447, 1426, 1401 $\upsilon_s(O_2C)$, 1273; *Anal.* Calc. for $C_{52}H_{48}Cu_2N_4O_{18}$ **2a** (M_r = 1144.1): C, 54.6; H, 4.23; N, 4.90. Found: C, 54.9; H, 4.19; N, 4.38%. Magnetic susceptibility μ_{eff}/B.M.: 1.48; EPR: B_{z1} 18.3 mT, $B_{\perp 2}$ 461 mT, B_{z2} 582 mT, $g_{||}$ 2.37, $g_{\perp}$ 2.08, D 0.332 cm^{-1}, $-2J$ 245 cm^{-1}.

Some of the crystals obtained by the described procedures for **1** and **2** were suitable also for the XRD single-crystal analysis.

2.2. Measurements

Elemental (C, H, N) analysis was obtained using a Perkin–Elmer Elemental Analyzer 2400 CHN. Infrared spectra of the solid samples were recorded using a Perkin–Elmer Spectrum 100, equipped with a Specac Golden Gate Diamond ATR as a solid sample support. Electronic spectra with nujol suspensions were measured by a Perkin–Elmer UV/VIS/NIR Spectrophotometer Lambda 19. X-ray powder diffraction data were obtained using PANalytical X'Pert PRO MPD with Cu Kα radiation (λ = 1.5406 Å). The magnetic susceptibility data of powdered samples were measured with a Johnson Matthey Alfa Products Sherwood Scientific Magnetic Balance, using Evans's method. Diamagnetic corrections were estimated from Pascal's constants [24]. X-band powder EPR spectra were obtained at various temperatures with a Bruker ELEXSYS E500 spectrometer. The spectra of **1** and **2** were measured by the solid samples on the bottom of the closed tube in the presence of the mother liquid, while the final products **1a** and **2a** as a dry powder.

Single-crystal X-ray diffraction data were collected with a Nonius Kappa CCD diffractometer with the graphite monochromated Mo Kα radiation (λ = 0.71073 Å) at room temperature for **1** and at 150 K for **2**, respectively. A multiscan absorption correction was performed [25]. The structures were solved by direct methods (SHELXS-97 [26] for **1** and SIR-97 [27] for **2**) and refined by a full-matrix least-squares procedure based on F^2 (SHELXL-97) [26]. Hydrogen atoms attached to N2 atoms in **2** were visible in the last stages of refinement and were refined freely. All the remaining H atoms in both structures were placed at calculated positions and treated using appropriate riding models. The atoms of CH_3CN molecules in **2** were refined isotropically and the H atoms of those molecules were not located. The residual density peak in structure of **2** (in the vicinity of CH_3CN molecule) was undefinable and therefore was not included in the model. The crystal data and details of the data collection and refinement are collected in Table 1.

3. Results and discussion

3.1. Crystal structures

X-ray structure determination of $[Cu_2(C_{10}H_9O_4)_4(CH_3CN)_2]$ **1** and $[Cu_2(C_{10}H_9O_4)_4(C_6H_6N_2O)_2]\cdot 4CH_3CN$ **2** reveals tetragonal-pyramidal (4 + 1) arrangement of copper(II) acetate hydrate type, with the inversion center located between copper(II) ions. The coordinated nitrogen atom of the acetonitrile (**1**)/nicotinamide (**2**) group is located on the top of the pyramid and four carboxylato oxygen atoms of four ferulic acid anions in the basal square-plane (Fig. 1). Cu–O (1.964(3)-1.970(3) Å for **1**, 1.965(3)–1.970(3) Å for **2**), Cu–N (2.182(4) Å for **1**, 2.176(3) Å for **2**) and Cu···Cu (2.6277(8) Å for **1**, 2.6371(12) Å for **2**) distances (Table 2) are in agreement with the values reported in the literature [28].

The binuclear moieties are mutually assembled in a canal-like 3D structure, held together by H-bonds (Fig. 2, Table 3). The corners of the canals in **1** are occupied by the dicopper moieties, while these corners are mutually connected by the ferulic acid anions on one side to the carboxylate group on the other. Each of two corners are H-bonded by two such bridges via head to tail orientation (O7–H7···O2 2.828(6) Å, 152°; O8–H8···O3 2.819(7) Å, 150°). The axial acetonitrile molecules in **1** are not H-bonded. A similar canal-like structure is found also in the crystal structure of **2** (Fig. 2), though some differences are noticed due to involvement of the axial nicotinamide ligands in the H-bonding network

Table 1
Experimental data for the X-ray diffraction for compounds **1** and **2**.

	1	**2**
Formula	$C_{44}H_{42}Cu_2N_2O_{16}$	$C_{60}H_{60}Cu_2N_8O_{18}$
Formula weight (g mol^{-1})	981.88	1308.24
crystal size (mm)	0.35 × 0.15 × 0.10	0.30 × 0.15 × 0.10
crystal color	green	green
crystal system	monoclinic	triclinic
Space group	*C*2/*c*	$P\bar{1}$
a (Å)	19.5692 (3)	11.4005(3)
b (Å)	18.5503 (5)	12.1367(3)
c (Å)	16.9057 (4)	12.7181(4)
α (°)	90	65.394(1)
β (°)	124.643 (1)	84.250(1)
γ (°)	90	79.781(1)
V (Å^3)	5049.0 (2)	1573.88(8)
Z	4	1
Calc. density (g cm^{-3})	1.292	1.380
F(0 0 0)	2024	678
θ Range (°)	0.983 – 27.57	0.986 – 27.00
Collected reflections	10 870	11 451
Independent reflections	5753	6782
R_{int}	0.0387	0.0412
Reflections used	4009	5206
Parameters	284	379
$R[I > 2\sigma(I)]$[a]	0.0618	0.0602
wR_2 (all data)[b]	0.2001	0.1559
Goof, *S*[c]	1.057	1.042
Maximum/minimum residual electron density (e Å^{-3})	+0.89/−0.62	+1.12/−0.82

[a] $R = \sum||F_o|-|F_c||/\sum|F_o|$.
[b] $wR_2 = \{\sum[w(F_o^2-F_c^2)^2]/\sum[w(F_o^2)^2]\}^{1/2}$.
[c] $S = \{\sum[(F_o^2-F_c^2)^2]/(n/p)\}^{1/2}$ where *n* is the number of reflections and *p* is the total number of parameters refined.

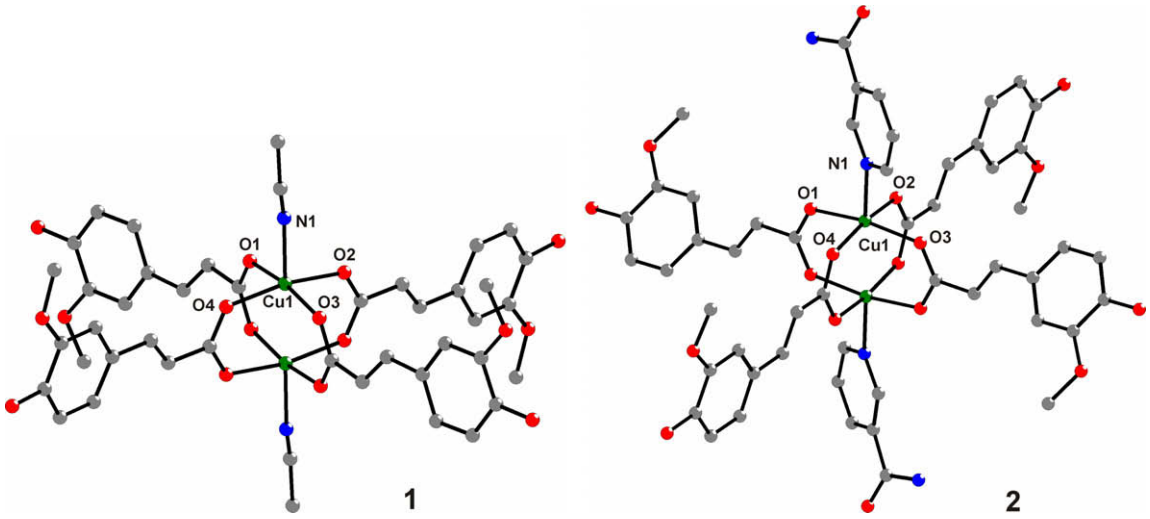


Fig. 1. Molecular structures of coordination compounds **1** and **2**. The hydrogen atoms of both compounds and the lattice CH_3CN molecules of **2** have been omitted for clarity.

(O8–H8···O1 2.738(3) Å, 154°; O7–H7···O8 2.771(3) Å, 151°; N2–H1N···O7 3.011(6) Å, 157(4)°). The solvent acetonitrile molecules in **2** do not participate in any distinguished H-bond, but are found in the voids of the canals. Therefore, the bridging nature of a ferulic acid anion via the carboxylato and phenolato groups is thus seen in both molecular structures of **1** and **2**. This may indeed be possible due to such a H-bonding network as well as coordination bonding. Nevertheless, a stability of **1** and **2** is strongly dependant on the acetonitrile molecules found in both compounds. Namely, the crystal structures of **1** and **2** are not stable outside mother liquid and they both decompose by removal of the acetonitrile molecules (CHN analysis, powder diffraction patterns – see the Supplementary data), giving the final solid products **1a** and **2a**, respectively. It seems that this decomposition is not destruct-

Table 2
Selected bond lengths (Å) and angles (°) for **1** and **2**.

	1	**2**
Cu1–O1	1.966(3)	1.965(3)
Cu1–O2	1.970(3)	1.968(3)
Cu1–O3	1.970(3)	1.970(3)
Cu1–O4	1.964(3)	1.970(3)
Cu1–N1	2.182(4)	2.176(3)
N1–Cu1–O1	97.24(14)	99.64(12)
N1–Cu1–O2	97.04(14)	99.93(11)
N1–Cu1–O3	93.94(14)	91.86(12)
N1–Cu1–O4	94.20(14)	91.31(11)
O1–Cu1–O2	89.87(12)	87.40(10)
O2–Cu1–O3	89.65(12)	90.17(11)
O3–Cu1–O4	88.52(12)	89.62(11)
O4–Cu1–O1	89.77(13)	90.58(11)

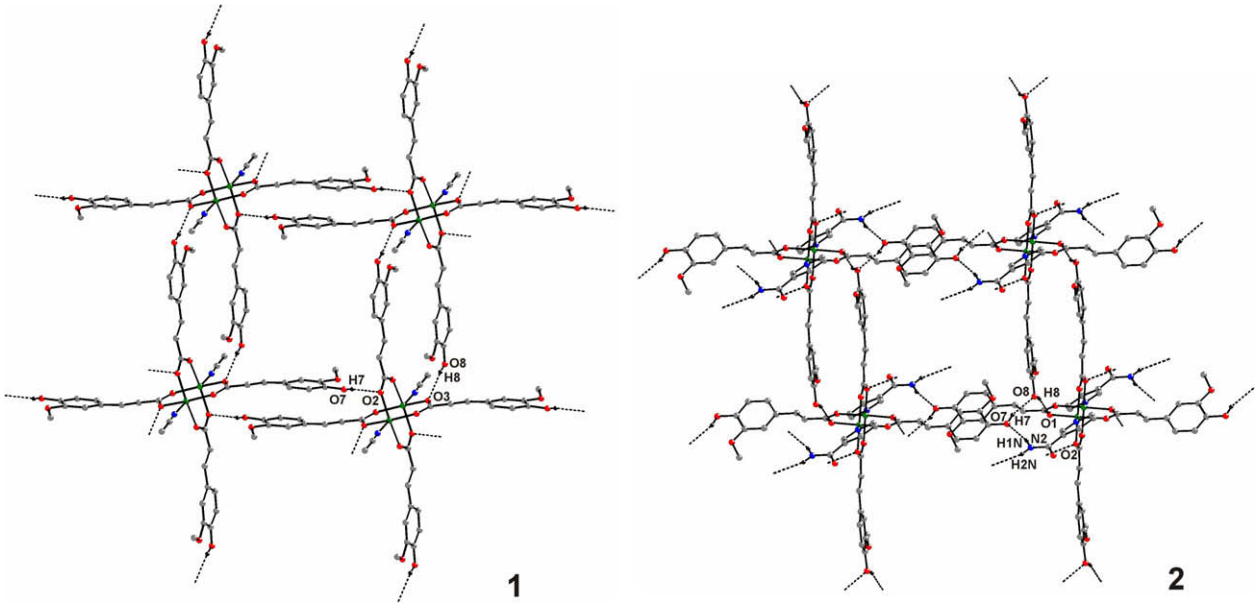


Fig. 2. Parts of the crystal structures of **1** and **2**, showing O–H···O (for **1** and **2**) and O–H···N (for **2**) hydrogen bonds. The lattice CH_3CN molecules of **2** and the hydrogen atoms of both complexes, except those involved in hydrogen bonding, have been omitted for clarity.

Table 3
Hydrogen bonding geometry for **1** and **2**.

D–H···A	*d*(D–H) (Å)	*d*(H···A) (Å)	*d*(D···A) (Å)	<(DHA) (°)	Symmetry transformation for H-bond acceptors
1					
O7–H7···O2	0.82	2.07	2.828(6)	152	$x-1/2, y+1/2, z$
O8–H8···O3	0.82	2.08	2.819(7)	150	$x-1/2, y-1/2, z$
2					
O7–H7···O8	0.84	2.01	2.771(3)	151	$-x+1, -y-1, -z+2$
O8–H8···O1	0.84	1.96	2.738(3)	154	$x, y, z+1$
N2–H1N···O7	0.93(5)	2.13(5)	3.011(6)	157(4)	$-x+1, -y-1, -z+1$
N2–H2N···O2	0.87(6)	2.28(6)	3.112(5)	162(6)	$-x+1, -y, -z+1$

ing a whole structure (see the magnetic susceptibility and EPR analysis) and the dicopper tetracarboxylate moieties may be still present in **1a** and **2a**. Nevertheless, a preservation of the canal-like structure is not certain, though the removed acetonitrile molecules (**1** → **1a**, **2** → **2a**) seem not to support the molecular structures of **1** and **2** significantly. Contrary to **1** and **2**, a similar canal-like binuclear crystal structure with related vanillic acid anions in $[Cu_2(C_8H_7O_4)_4(C_6H_6N_2O)_2]$ [21] retains its 3D structure also outside mother liquid.

3.2. Magnetic susceptibility and EPR

The green color of the air stable **1a** and **2a** is suggesting a presence of copper(II), not differing much to the original solid **1** and **2** from the reaction mixture. Additionally, the room temperature effective magnetic moment μ_{eff}/B.M. 1.40 (**1a**) and 1.48 (**2a**) is as expected for the dicopper(II) tetracarboxylates with a strong antiferromagnetic (AFM) interaction between the dipoles taking place via four carboxylate bridges. A similar conclusion may be drawn from the EPR spectra that show three typical triplet signals ($E \sim 0$) for **1a** and **2a** showing B_{Z1} (15.3, 18.3 mT), $B_{\perp 2}$ (459, 461 mT), B_{Z2} (583, 582 mT) and $-2J = (280, 245\ cm^{-1})$ [29] (Fig. 3). The magnitude of the AFM coupling was determined using the EPR data and equations described by Wasserman (Supplementary) derived from the Hamiltonian (Eq. (1)) [30,31]. The room temperature EPR spectra of **1a** and **2a** additionally show the 300 mT $S = ½$ signals of mononuclear impurities. A weaker intensity of the $S = ½$ signals as compared to those of the triplet $S = 1$ (binuclear) shows that a majority of the copper(II) species remain

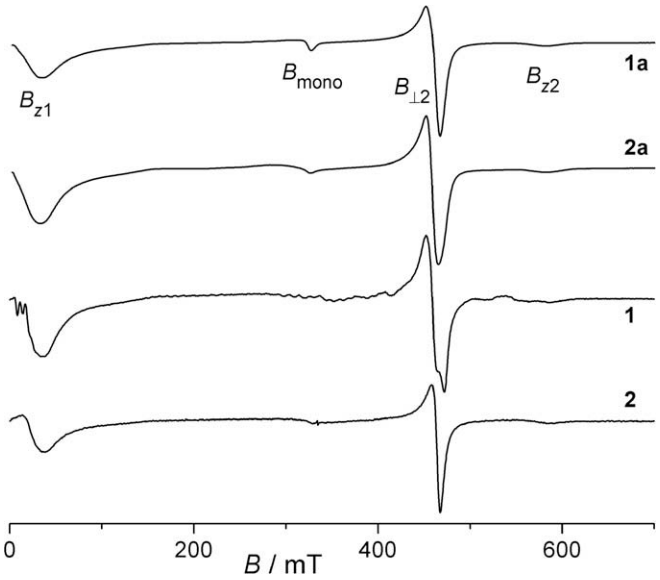


Fig. 3. The room temperature EPR spectra of the solid **1** and **2** (in a presence of the mother liquid) and of the final powdered solid products **1a** and **2a**, all showing the typical triplet signals of $S = 1$ system (**1a**: $g_{||} = 2.35$, $g_{\perp} = 2.08$, $D = 0.329\ cm^{-1}$, $-2J = 280\ cm^{-1}$; **2a**: $g_{||} = 2.37$, $g_{\perp} = 2.08$, $D = 0.332\ cm^{-1}$, $-2J = 245\ cm^{-1}$).

in the binuclear *paddle-wheel* units despite a decomposition (**1** → **1a**, **2** → **2a**). Additionally, the EPR spectra of **2** and **2a** are almost identical, while only some smaller deviations are noticed between the spectra of **1** and **1a** (E is not negligible for **1**). Due to a clear resemblance of the EPR spectra of both pairs, namely **1**/**1a** and **2**/**2a**, respectively, almost complete preservation of the dicopper tetracarboxylato core structure in **1a** and **2a** as found in **1** and **2** is firmly shown. This is proving also a coexistence of the 'oxidative' copper(II) cation and 'antioxidative' ferulic acid anion at a distance of a coordination bond.

$$\hat{H} = \beta B \cdot g \cdot \hat{S} + D\left(\hat{S}_{z^2} - \frac{2}{3}\right) + E(\hat{S}_{x^2} - \hat{S}_{y^2}) \quad (1)$$

4. Conclusions

The first two molecular structures of the coordination compounds with the ferulic acid anion, namely $[Cu_2(C_{10}H_9O_4)_4(CH_3CN)_2]$ **1** and $[Cu_2(C_{10}H_9O_4)_4(C_6H_6N_2O)_2]\cdot 4CH_3CN$ **2** are presented. Due to the reported antioxidative properties of the ferulic acid, and unsuccessful application of copper(II) starting compounds, copper(I) species were used as the starting materials in the acetonitrile solution. Outside the mother liquid, both compounds **1** and **2** decompose by the acetonitrile evaporation, thus giving the final $[Cu_2(C_{10}H_9O_4)_4]$ **1a** and $[Cu_2(C_{10}H_9O_4)_4(C_6H_6N_2O)_2]$ **2a**. The central core structure of the final products most probably remains as in **1** and **2**, as suggested by the magnetic susceptibility data and the EPR spectra. It is thus shown that the 'antioxidative' ferulic acid may be stable in the presence of the 'oxidative' copper(II) ions in the acetonitrile solution and in the solid state. The bridging nature of the ferulic acid is seen herein by the coordination as well as by the H-bonding, both playing the key role in the structure stabilization.

Acknowledgements

We thank Prof. Primož Šegedin for helpful discussions. EPR experiments were conducted at the Jožef Stefan Institute, Ljubljana. Laboratory of Biophysics. The financial support of MVZT, Republic of Slovenia, through grant MVZT PS-511-103 is gratefully acknowledged.

Appendix A. Supplementary data

CCDC 730435 and 730436 contain the supplementary crystallographic data for this paper. These data can be obtained free of charge via http://www.ccdc.cam.ac.uk/conts/retrieving.html, or from the Cambridge Crystallographic Data Centre, 12 Union Road, Cambridge CB2 1EZ, UK; fax: (+44) 1223-336-033; or e-mail: deposit@ccdc.cam.ac.uk.

Supplementary data associated with this article can be found, in the online version, at doi:10.1016/j.poly.2009.07.047.

References

[1] K. Iiyama, T.B.T. Lam, B.A. Stone, Plant Physiol. 104 (1994) 315.
[2] A. Sakakibara, in: D.N.-S. Hon, N. Shiraishi (Eds.), Wood and Cellulosic Chemistry, Marcel Dekker, New York, 1991, pp. 113–175.
[3] F. Natella, M. Nardini, M. Di Felice, C. Scaccini, J. Agric. Food Chem. 47 (1999) 1453.
[4] B. Halliwell, R. Aeschbach, J. Loliger, O.I. Aruoma, Food Chem. Toxicol. 33 (1995) 601.
[5] J.S. Wright, E.R. Johnson, G.A. DiLabio, J. Am. Chem. Soc. 123 (2001) 1173.
[6] A.T. Lithoxoidou, E.G. Bakalbassis, J. Am. Oil Chem. Soc. 81 (2004) 799.
[7] A.M. Khvan, E.L. Kristallovich, K.A. Abduazimov, Chem. Nat. Compd. 37 (2001) 72.
[8] S.Y. Guan, J. Mlynar, S. Sarkanen, Phytochemistry 45 (1997) 911.
[9] B. Kozlevčar, N. Lah, I. Leban, I. Turel, P. Šegedin, M. Petrič, F. Pohleven, A.J.P. White, D.J. Williams, G. Giester, Croat. Chem. Acta 72 (1999) 427.
[10] M. Petrič, R.J. Murphy, I. Morris, Holzforschung 54 (2000) 23.
[11] G.A. Peters, N. Parameswaran, Wood Sci. Technol. 14 (1980) 81.
[12] M. Connel, in: R. Thompson (Ed.), The Chemistry of Wood Preservation, The Royal Society of Chemistry, Cambridge, 1991, pp. 16–33.
[13] A. Kula, L. Mazur, Z. Rzaczynska, J. Coord. Chem. 60 (2007) 843.
[14] R.J. Hobson, M.F.C. Ladd, D.C. Povey, J. Cryst. Mol. Struct. 3 (1973) 377.
[15] T.J. Greenhough, M.F.C. Ladd, Acta Crystallogr. B 34 (1978) 2619.
[16] T.J. Greenhough, M.F.C. Ladd, Acta Crystallogr. B 34 (1978) 2744.
[17] J.N.R. Ruddick, C.S. Xie, F.G. Herring, Holzforschung 55 (2001) 585.
[18] C.S. Xie, J.N.R. Ruddick, S.J. Rettig, F.G. Herring, Holzforschung 49 (1995) 483.
[19] B. Kozlevčar, M. Humar, P. Strauch, I. Leban, Z. Naturforsch. B 60 (2005) 1273.
[20] B. Kozlevčar, B. Mušič, N. Lah, I. Leban, P. Šegedin, Acta Chim. Slov. 52 (2005) 40.
[21] B. Kozlevčar, P. Baškovič, A. Arko, A. Golobič, N. Kitanovski, P. Šegedin, Z. Naturforsch. B 63 (2008) 481.
[22] Z. Longguan, S. Kitagawa, H.C. Chang, H. Miyasaka, Mol. Cryst. Liq. Cryst. 342 (2000) 97.
[23] B. Kozlevčar, D. Odlazek, A. Golobič, A. Pevec, P. Strauch, P. Šegedin, Polyhedron 25 (2006) 1161.
[24] R.L. Dutta, A. Syamal, Elements of Magnetochemistry, Affiliated East-West Press PVT Ltd., New Delhi, 1993, pp. 6–11.
[25] Z. Otwinowski, W. Minor, Methods in enzymology, in: C.W. Carter Jr., R.M. Sweet (Eds.), Macromolecular Crytallography Part A, vol. 276, Academic Press, New York, 1997, pp. 307–326.
[26] G.M. Sheldrick, Acta Crystallogr. A 64 (2008) 112.
[27] A. Altomare, M.C. Burla, M. Camalli, G. Cascarano, C. Giacovazzo, A. Guagliardi, A.G.G. Moliterni, G. Polidori, R. Spagna, SIR97, J. Appl. Crystallogr. 32 (1999) 115.
[28] M.R. Sundberg, R. Uggla, M. Melnik, Polyhedron 15 (1996) 1157.
[29] M. Valko, R.F. Bilton, H. Morris, M. Melnik, J. Coord. Chem. 29 (1993) 257.
[30] E. Wasserman, L.C. Snyder, W.A. Yager, J. Chem. Phys. 41 (1964) 1763.
[31] T.D. Smith, J.R. Pilbrow, Coord. Chem. Rev. 13 (1974) 173.

There are antecedents that the complexation of several drugs with copper ions caused changes in the pharmacological and physiological effects. For instance, copper complex of pindolol has shown higher efficiency than the free ligand regarding its effect on the heart rate of rats [10]. Besides, in the literature reports of several copper complexes with beta-blocker antihypertensive drugs can be found [11,12] but only a few X-ray crystallographic structures have been reported [10,13,14] and none of them with propranolol.

Due to these antecedents and in order to continue our studies on medicinal chemistry [15–17], our aim was to obtain copper beta-blocker complexes in the search of new species with better pharmacological properties and/or that will provide biological information.

In this work, the synthesis and spectroscopic characterization of a new copper complex with propranolol (1-(isopropylamino)-3-(1-naphthyloxy)-2-propanol) are presented.

Fig. 1 shows the structure of propranolol, showing the amino and hydroxyl groups suitable for coordination of metal ions.

First of all we studied the structure in solid state. The X-ray crystal structure of $[Cu(propranolol)_2]\cdot 2H_2O$ was determined and the IR and EPR spectra were analyzed. Besides, this work is the first that reports the chirality of the beta-blocker ligands coordinated to copper. This is an important datum for understanding the pharmacological properties due to the fact that the enantioselectivity influences the pharmacokinetics of these drugs and also it is associated with changes in the pharmacodynamic profile [18].

The structural information in solid state was used as a base for the characterization of the species in DMSO solution that will be administered in the biological assays. Besides, the stability of this solution was studied. Moreover, an analysis of the effect on the contraction force and heart rate, and the block of response to adrenaline were performed.

2. Experimental

2.1. Synthesis of the complex and analytical characterization

Aqueous solutions of *dl*-propranolol hydrochloride (1 mmol, 0.295 g), SIGMA and of $CuSO_4\cdot 5H_2O$ (0.5 mmol, 0.085 g), FLUKA were mixed. After stirring 1 mL of 1 M NaOH was added. Upon mixture a violet precipitate was formed. It was washed with water and recrystallized from methanol. The violet crystals obtained were separated by filtration and dried at room-temperature.

The elemental analysis was performed with a Carlo Erba EA1108 elemental analyzer and copper content was determined by iodimetry.

Anal. Calc. for $[Cu(propranolol)_2]\cdot 2H_2O$ ($C_{32}H_{44}N_2O_6Cu$): C, 62.37; N, 4.55; H, 7.20; Cu, 10.31. Found: C, 62.00; N, 4.44; H, 7.11; Cu, 10.31. Yield 38%.

2.2. Crystal structure determination of $[Cu(propranolol)_2]\cdot 2H_2O$

Room temperature X-ray diffraction data collection for $[Cu(propranolol)_2]\cdot 2H_2O$ was performed on an Enraf-Nonius Kappa-CCD diffractometer, using graphite-monochromated Mo Kα radiation (0.71073 Å). Data were collected up to 50.0° in 2. The final unit cell parameters were based on all reflections. Data collections were made using the COLLECT program [19]. Integration and scaling of the reflections were performed with the HKL Denzo–Scalepack system of programs [20]. Multi-scan absorption corrections were applied [21].

The structure was solved by direct methods with SHELXS-97 [22]. The model was refined by full-matrix least-squares on F^2 with SHELXL-97 [23]. All the hydrogen atoms were stereochemically positioned and refined with the riding model [23]. Data collections and experimental details for the complexes are summarized in Table 1. The programs SHELXL-97, and ORTEP-3 [24] were used within WINGX [25].

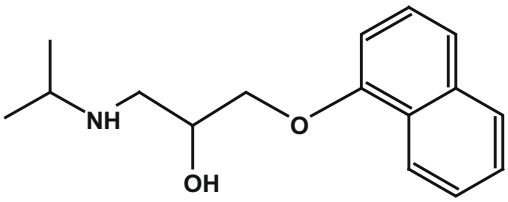


Fig. 1. Scheme of propranolol.

2.3. Spectroscopic measurements

Electronic spectrum of a DMSO solution was registered on a Milton Roy Spectronic 3000 spectrophotometer.

Low-temperature (77 K) EPR experiments were performed using a Varian E109 spectrometer equipped with a rectangular cavity. To perform the experiments on solution-state samples, powder samples of the titled complexes were dissolved in DMSO. The solution-state samples were then centrifuged, and the supernatants were drawn in a quartz sample tube for low-temperature EPR experiments. General experimental conditions were: microwave power, 20 mW; modulation amplitude, 2.0 G; modulation frequency, 100 kHz. The g- and A-values were obtained by means of spectral simulation using the software package EASYSPIN [26].

IR spectra, in the range between 4000 and 200 cm^{-1}, were recorded on a BOMEM M 102 FTIR spectrophotometer using the KBr pellet technique.

Table 1
Crystal data and structure refinement of complex $[Cu(propranolol)_2]\cdot 2H_2O$.

Empirical formula	$C_{32}H_{44}N_2O_6Cu$
Formula weight	616.23
Temperature (K)	293(2)
Wavelength (Å)	0.71073
Crystal system	triclinic
Space group	$P\bar{1}$
Unit cell dimensions	
a = 8.472(1) Å	α = 90.24(1)°
b = 12.057(2) Å	β = 98.94(1)°
c = 15.449(2) Å	γ = 91.548(6)°
V	1558.3(4) Å^3
Z	2
D_{calc} (Mg/m^3)	1.313
Absorption coefficient (mm^{-1})	0.746
F (0 0 0)	654
Crystal size (mm^3)	0.15 × 0.10 × 0.02
Theta range for data collection	2.92–25.00°
Index ranges	$-10 \leqslant h \leqslant 9$, $-14 \leqslant k \leqslant 14$, $-17 \leqslant l \leqslant 18$
Reflections collected	7417
Independent reflections	4963 [R(int) = 0.1269]
Completeness to θ = 22.00°	95.6%
Absorption correction	Semi-empirical from equivalents
Maximum and minimum transmission	0.984 and 0.865
Refinement method	Full-matrix least-squares on F^2
Computing[a]	COLLECT, HKL Denzo and Scalepack SHELXS-97, SHELXL-97
Data/restraints/parameters	4963/0/374
Goodness-of-fit (GOF) on F^2	1.008
Final R indices [$I > 2\sigma(I)$]	R_1 = 0.0784, wR_2 = 0.1480
R indices (all data)	R_1 = 0.2017, wR_2 = 0.2019
Largest differences in peak and hole (e Å^{-3})	0.259 and −0.334

[a] Data collection, data processing, structure solution and structure refinement respectively.

2.4. Thermogravimetric measurements

Thermogravimetric measurements were obtained with a Shimadzu TGA 50 thermobalance, with a platinum cell, working under flowing air (50 mL min^{-1}) and at a heating rate of 6 °C min^{-1}.

2.5. Stability tests

Conductimetric measurements using a Conductivity Meter 4310 Jenway were performed at 37 °C in a DMSO solution (0.5×10^{-3} M). Besides, the DMSO solution was mixed (1:10) with Tyrode solution and the absence of turbidity was observed. Both tests were performed with the aim of studying the stability of the complex in the solution that was administered in the biological studies.

2.6. Biological evaluation by Langendorff technique

The biological evaluation of the complex and the free ligand was performed using an isolated heart technique according to Langendorff [27].

Guinea pigs weighing 400–600 g were heparinized (1000 UI/kg) 10 min before the procedure. Then they were anaesthetized with a sodium pentothal intraperitoneal injection (50 mg/kg).

The hearts were rapidly removed and placed into a dish containing oxygenated Tyrode solution (see composition below) at room-temperature. The aorta was cannulated and the heart was perfused retrogradely via the aortic cannula, at a constant flow rate of 6 mL min^{-1} with Tyrode solution containing: NaCl 137, KCl 2.68, $MgCl_2$ 1.05, $NaHCO_3$ 12, $CaCl_2$ 1.8, NaH_2PO_4 0.38, glucosa 5.5 nM.

By means of Langendorff equipment the perfusate was kept at 36 ± 1 °C. Solution was aerated with a gas mixture of 95% of O_2 and 5% of CO_2 in order to obtain a pH of 7.4. Myocardial contractile force was evaluated measuring the left ventricular pressure. The left atrial appendage was removed to access to the mitral valve orifice, a small hand-made latex balloon was inserted through it, and placed into the left ventricular cavity. The balloon previously filled with saline solution was connected to a pressure transducer (Statham) by means of a catheter. The manometer was connected to a suitable amplifier, and the signals were fed into a digital to analog converter device (Lab Master). Finally signals were displayed and stored into a computer. The basal conditions were controlled and the experiments were started after the parameters reached a steady state.

The protocol followed for the determination of the effect on contraction force and heart rate was the following:

A *bolus* of 0.1 mL of propranolol solution in DMSO (10^{-3} M, $n = 5$) or 0.1 mL of [Cu(propranolol)$_2$]·$2H_2O$ solution in DMSO (0.5×10^{-3} M, $n = 5$) was administered, both equimolar solutions in propranolol. The contraction force and heart rate were measured before and after administration.

The protocol followed for the determination of the inhibition of response to adrenaline was the following:

The heart was stimulated with a *bolus* of 0.1 mL of adrenaline 30 M injected through the side branch of the perfusion cannula. The response in terms of contraction force and heart rate was measured. After this stimulation, the heart was washed and stabilized with the perfusion solution for 15 min. Then a *bolus* of 0.1 mL of propranolol solution

(10^{-3} M, $n = 5$) or 0.1 mL of [Cu(propranolol)$_2$]· $2H_2O$ solution (0.5×10^{-3} M, $n = 4$), was administered and the heart was stabilized during 4 min. Finally, a similar dose of adrenaline was injected and the response was measured and compared with the first stimulation.

Controls with *bolus* of Tyrode, DMSO and with copper salt dissolved in DMSO were performed in both protocols.

3. Results and discussion

3.1. Crystal structure of [Cu(propranolol)$_2$].$2H_2O$

The copper complex crystallized in a triclinic system with a $P\bar{1}$ spatial group as shown Table 1.

The structure consists of two units, each containing a copper center coordinated to two deprotonated propranolol molecules acting as a bidentate ligand, in a distorted square-based environment. Fig. 2 presents an ORTEP view of a unit, showing the atom labels and 50% probability ellipsoids. As Fig. 2 shows each copper ion coordinates through the N atom from the amine group and the O atom from the alkoxide, in a *trans* geometry.

The crystal structure is completed with the presence of two hydration water molecules per complex. Selected bond distances and angles around the copper center are summarized in Table 2.

In comparison with related copper compounds, Cu–$O_{alcohol}$ distances found in this work (1.874 and 1.894 Å) are shorter than those of the Cu(II) complex with nadolol (1.910 Å) [28], with etilefrin (Effortil) (1.905 Å) [29], with propafenone (1900 Å) [30] and clenbuterol (1898 Å) [31] and for one of the Cu–O bonds from the Cu(II) complex with oxprenolol (1.909 Å) [13]. In the case of Cu–N_{amine} distances (2.020 and 2.033 Å) the results are similar to those reported for the compounds mentioned above. The dihedral angle between the planes determined by O11–N1–Cu and O21–N2–Cu is 20.5(3)°, showing the distortion of the arrangement.

The centrosymmetry of the space group found in this work requires that both the R,R and S,S complexes be present. This new complex presents different propranolol isomers coordinated to each copper ion. As it is known propranolol has one chiral carbon

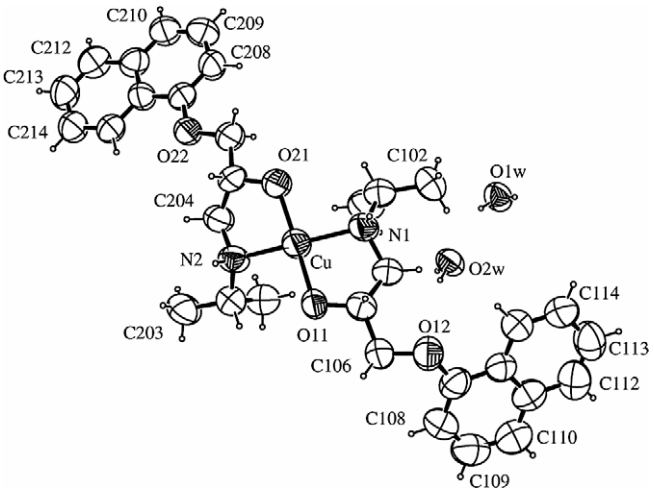


Fig. 2. ORTEP view of one unit of the complex, showing the atom labeling and the 50% probability ellipsoids.

Table 2
Selected bond lengths [Å] and angles [°] of complex [Cu(propranolol)$_2$]·$2H_2O$.

Cu–O(21)	1.874(5)		
Cu–O(11)	1.894(5)		
Cu–N(2)	2.020(6)		
Cu–N(1)	2.033(6)		
O(21)–Cu–O(11)	166.8(3)	C(105)–O(11)–Cu	111.6(4)
O(21)–Cu–N(2)	85.5(3)	C(205)–O(21)–Cu	113.9(5)
O(11)–Cu–N(2)	97.0(2)	C(103)–N(1)–Cu	117.6(5)
O(21)–Cu–N(1)	94.3(2)	C(104)–N(1)–Cu	104.1(4)
O(11)–Cu–N(1)	86.5(2)	C(204)–N(2)–Cu	104.6(4)
N(2)–Cu–N(1)	165.3(3)	C(202)–N(2)–Cu	115.2(5)

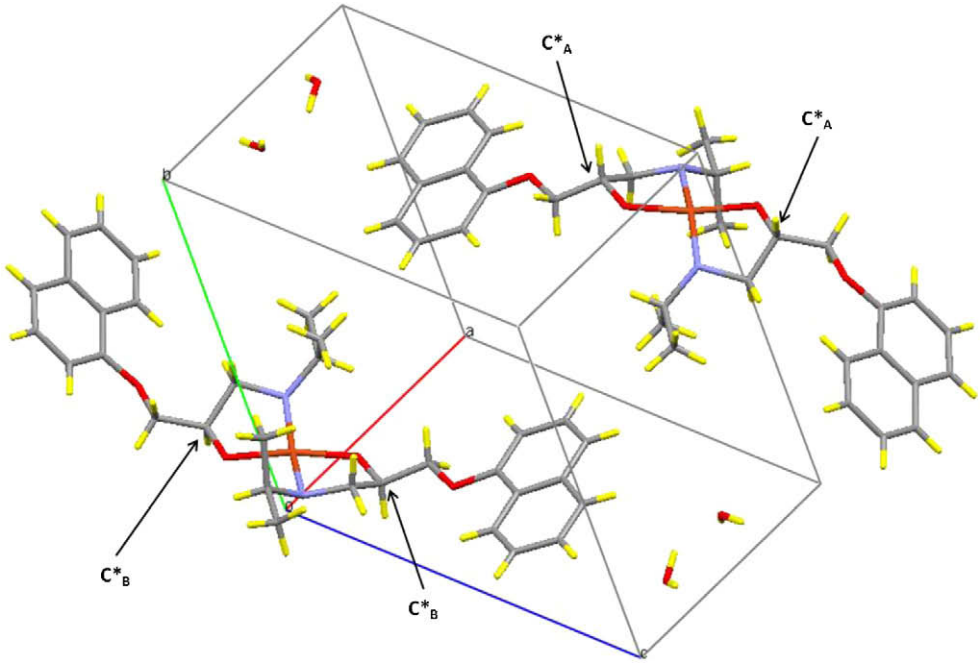


Fig. 3. View of the structure cell showing the S (A) and R (B) propranololate isomers coordinated with copper ions.

atom and it can form two enantiomers. The usual pharmaceutical formulations are prepared with the racemic mixture. In the synthesis of $[Cu(propranolol)_2]\cdot 2H_2O$ a racemic mixture of propranolol was used but as Fig. 3 shows, each copper unit in the obtained structure coordinates with the same isomer, and the compound could be better described as $[Cu(R\text{-propranololate})_2][Cu(S\text{-propranololate})_2]\cdot 4H_2O$.

No report of the coordinated isomers was found in the previously referred articles related to copper complexes with beta-blockers.

The study of the crystal packing shows that the three-dimensional structure is stabilized by six intermolecular hydrogen bonds as shown in Table 3.

All these intermolecular interactions give rise to the formation of double infinite chains and layers of complex molecules alternate with layers of water molecules (see Fig. 4).

This particular crystal packing, with its water channels could be important for pharmacotechnic processes.

3.2. Thermogravimetric measurements

Thermogravimetric results showed that the weight loss at 50–85 °C range was 6%, in accordance with the release of two hydration water molecules. Beyond 230 °C the degradation of the ligand was observed.

Table 3
Intermolecular interaction geometry (Å.°) of $[Cu(propranolol)_2]\cdot H_2O$.

D–H···	D–H	D···A	H···A	D–H···A
O1w–H11w···O2w	0.850	2.789(7)	1.971	161.2(4)
O1w–H12w···O2w^{i}	0.850	2.766(7)	1.944	162.5(4)
N1–H1···O1w^{ii}	0.910	2.975(9)	2.075	169.5(5)
N2–H2 ···O1w^{iii}	0.910	3.036(9)	2.194	153.7(5)
O2w–H21w···O21^{ii}	0.982	2.651(8)	1.738	153.1(4)
O2w–H22w···O11^{iv}	0.979	2.678(7)	1.715	166.9(4)

Symmetry codes: (*i*) $-x+1, y+2, z$; (*ii*) $-x+1,-y+1, -z$; (*iii*) $x-1, y-1, z$; (*iv*) $x+1, y+1, z$.

3.3. Stability tests

The conductivity of a DMSO solution of $[Cu(propranolol)_2]\cdot 2H_2O$ was very similar to that of the pure solvent. This behavior is in agreement with the neutral charge of the complex, according to the stoichiometry. In addition, the conductivity was measured during 24 h and no major changes were observed. This result showed that the complex maintained the neutral charge and therefore the Cu–propranolol bonds remained in the structure in solution. Besides, when the DMSO solution of the complex was mixed with the Tyrode solution no turbidity was observed. Taking into account that the propranolol is insoluble in this solution, this result shows that the propranolol is not free.

3.4. Spectroscopic measurements

The electronic spectrum of $[Cu(propranolol)_2]\cdot 2H_2O$ in DMSO presented one broad band at 685 nm, due to the d–d band transition. This result is in agreement with the reported data for the square planar CuN_2O_2 chromophore [32]. The substitution of the propranolol molecules by DMSO is not observed since the spectrum of copper sulfate in DMSO shows a $\lambda_{max} = 813$ nm.

Low-temperature X-band EPR spectra of the titled compound in the polycrystalline form displayed a single resonance around ~330 mT (Fig. 6A) with no detectable hyperfine interaction between the magnetic moments of the $S = 1/2$ d^9 copper unpaired electron and of the $I = 3/2$ copper nuclear spin. The powder-like spectra is characteristic of monomeric species interacting via weak superexchange interactions, which smear out the hyperfine lines, and are probably mediated by non-covalent bridges as is usually observed in copper complexes in the solid state [33,34]. Simulation of that spectrum yielded g-values: $g_x = g_y = 2.0407$ (perpendicular direction) and $g_z = 2.1312$ (parallel direction), thus indicating an axially symmetric environment experienced by the copper ion, which is in good agreement with the structural data presented above.

Upon dilution in DMSO solvent, EPR spectra of the compound at liquid nitrogen temperature readily showed the four hyperfine

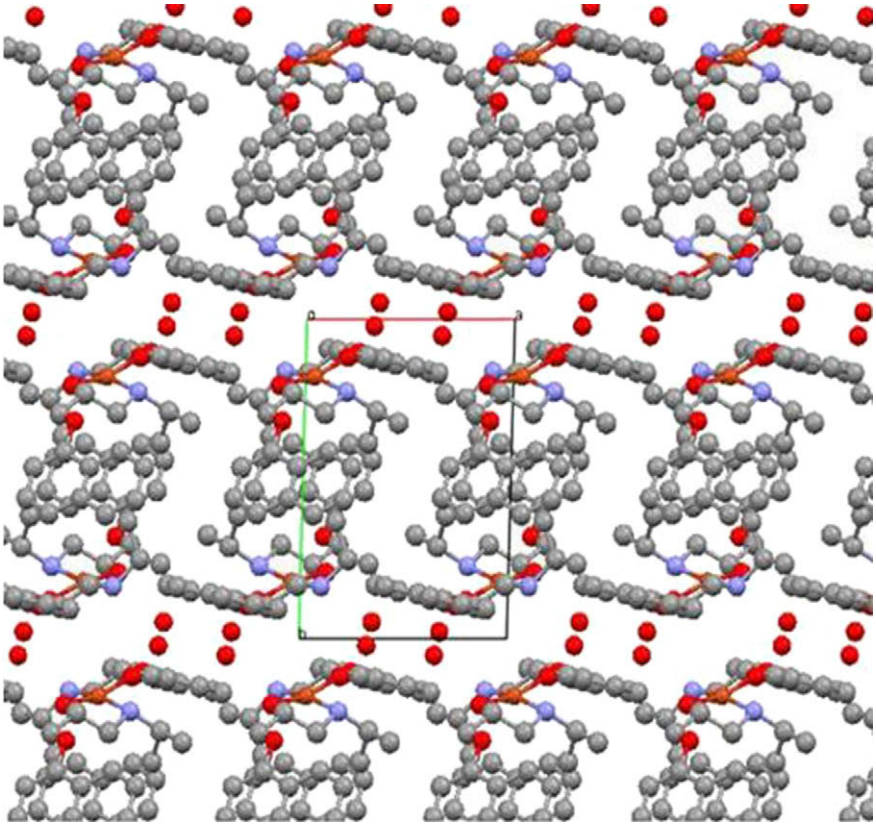


Fig. 4. Crystal packing of $[Cu(propranolol)_2]\cdot 2H_2O$ along *c*-axis.

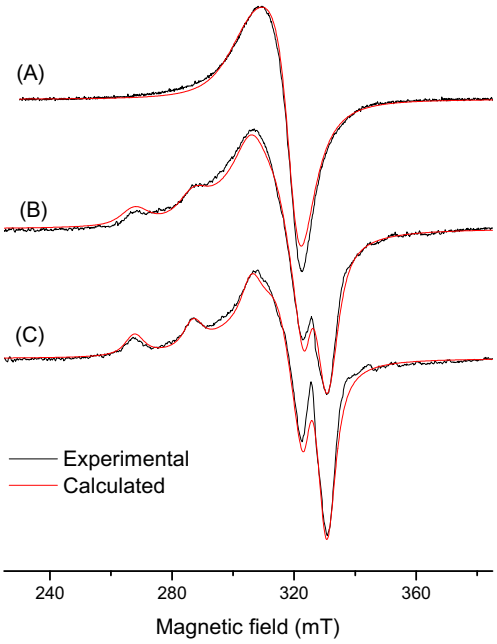


Fig. 5. Low-temperature X-band EPR spectra of $[Cu(propranolol)_2]\cdot 2H_2O$ in: (A) solid state, (B) fresh DMSO solution and (C) DMSO solution after 24 h of the dilution experimental and calculated spectra are shown as black and red lines, respectively. (For interpretation of the references to color in this figure legend, the reader is referred to the web version of this article.)

lines (Fig. 6B) characteristic of a $S = 1/2$ spin system interacting with $I = 3/2$ nuclear spin. The appearance of hyperfine structure suggests that the connections supporting exchange interactions in the solid state are disrupted upon dilution in DMSO, indicating that those connections are not provided by covalent bonds between monomers. To further characterize this spectrum, theoretical simulation was performed using the software EASYSPIN. The simulation involved the use of a spin Hamiltonian constituted by Zeeman and hyperfine interactions along with two linewidth parameters that take care of extra broadening mechanisms. The final calculated spectrum showed a very good agreement with the experimental data and the best-fit magnetic parameters (g and hyperfine) thus determined were: $g_x = 2.059$, $g_y = 2.025$, $g_z = 2.200$, $A_z = 19.2$ mT. The values of the A_x and A_y components could not be determined since the spectrum does not show any splitting due to those components. The g_z and A_z values can be used to determine the atoms coordinated to the copper ion following the method of Peisach that correlate those values with the coordination sphere of copper in several complexes [35]. In our case, the values of g_z and A_z indicate a N_2O_2 equatorial coordination that agrees with the X-ray single-crystal data presented above. Thus, in solution the copper environment is distorted from its solid state axial symmetry, without changes in atoms coordinated (it is maintained with two nitrogen and two oxygen atoms).

To investigate the structural stability of the compound after dilution in DMSO, we also performed a low-temperature EPR experiment on a sample after 24 h of dilution in DMSO. The spectrum is shown in Fig. 5C and shows no major difference when compared with the spectrum measured right after mixture with DMSO (Fig. 5B). The simulation of this last spectrum resulted in the same set of magnetic parameters except for the line widths parameters, which had to be readjusted to achieve optimal fitting of the experimental data. This strongly suggests that the structure of the compound is stable without major difference 24 h after dilution in DMSO.

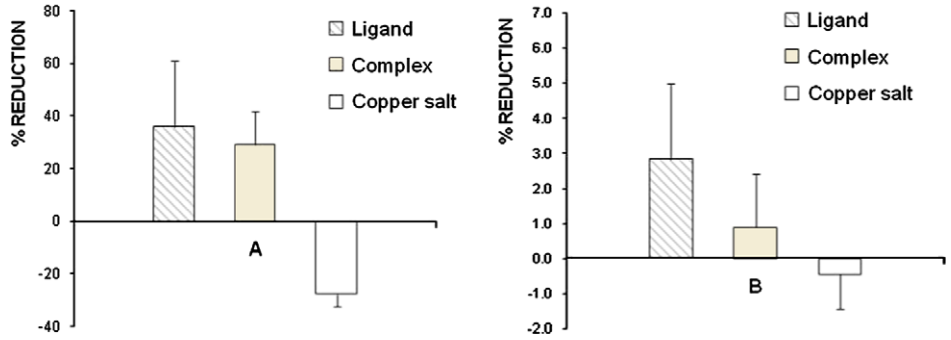


Fig. 6. Effect of *bolus* of $[Cu(propranolol)_2]\cdot 2H_2O$ (0.5×10^{-3} M), propranolol (10^{-3} M) and copper salt (0.5×10^{-3} M) on myocardial contractile force (A) and heart rate (B).

The IR spectrum of the complex was compared with that of the free propranolol and the similar reported complexes [14,36–39].

The free ligand spectrum exhibits three strong bands at 3323, 3281 and 3227 cm^{-1} corresponding to the ν(OH), νa(–NH_2^+–) and νs(–NH_2^+–) engaged in H-bonds. In addition, combination bands, enhanced by Fermi resonance, are found in the range 2710–2395 cm^{-1} [14,36,38]. The $NH2^+$ deformation band is overlapped by the aromatic bands.

After coordination the –NH_2^+– is deprotonated and a band at 3377 cm^{-1} is observed in the complex spectrum in agreement with bibliographic data [36]. Furthermore the disappearance of the bands due to the combination modes, which is characteristic of the protonated amines, is also in agreement with the coordination through this group.

Regarding OH group, in the complex spectrum there is one less band in the range assigned to ν(OH) and ν(–NH_2^+–) engaged in H-bonds, due to the deprotonation of this group upon coordination, and the band at 1324 cm^{-1} in the free ligand, corresponding to σ(HC–OH) shifts to 1312 cm^{-1} upon complexation. This behavior supports the coordination through this group. Further evidence of this is found in the fact that the ν(C–O) band of the ligand at 1107 cm^{-1} shifts to 1098 cm^{-1} [36].

Another observation in the complex spectrum is the appearance of new bands at 604 cm^{-1} and 497 cm^{-1}, assigned to Cu–N and Cu–O bonds respectively, in accordance with bibliographic data [14].

3.5. Biological evaluation

3.5.1. Determination of the effect on contraction force and heart rate

Fig. 6 shows the effect of the administration of propranolol (10^{-3} M), $[Cu(propranolol)_2]\cdot 2H_2O$ (0.5×10^{-3} M) and copper salt (0.5×10^{-3} M) on myocardial contractile force and heart rate.

As can be seen in Fig. 7A the effect of propranolol and $[Cu(propranolol)_2]\cdot 2H_2O$ on myocardial contractile force is to reduce it to a rather similar extent. On the other hand, both complex and free ligand reduced heart rate but the reduction obtained with the complex is lower than that obtained with the free ligand, as shown in Fig. 7B. The reduction on the heart rate performed by the complex is approximately 30% of that produced by the free ligand.

The controls performed with DMSO and Tyrode did not significantly change the signals. On the contrary, the *bolus* of Cu(II) salt produced a slight increase both in myocardial contractile force and heart rate, which differs from the copper complex's effect.

3.5.2. Determination of inhibition of response to adrenaline

Fig. 7 shows that both species block the response to adrenaline to a similar extent when contractility is measured. Adrenaline's effect on heart rate was blocked by either complex or ligand at the dose used.

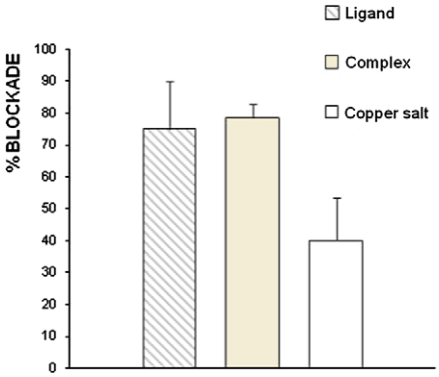


Fig. 7. Percentage of blockade of the complex (0.5×10^{-3} M), free propranolol (10^{-3} M) and copper salt (0.5×10^{-3} M) measuring the response as variation in myocardial contractile force.

The control performed with Cu(II) salt (0.5×10^{-3} M), produced a much lesser blockade when contractility was measured.

4. Conclusions

A new Cu–propranolol complex was synthesized and characterized by spectroscopic measurements including X-ray diffraction. Specially the chirality of this new complex was observed showing that the compound could be better described as $[Cu(R\text{-propranololate})_2][Cu(S\text{-propranololate})_2]\cdot 4H_2O$. Besides, in accordance with the conductivity assay, the electronic spectrum, the propranolol is still coordinates with copper ion in a 10^{-3} M DMSO solution. The magnitude of A_z and g_z obtained from the EPR spectra indicated that Cu is equatorially coordinated through two nitrogen and two oxygen atoms. These structural data in solution agree with the X-ray single-crystal data. In addition, the conductivity measurements and the EPR spectra showed that this solution is stable at least during 24 h.

About the biological assay, the effect of $[Cu(propranolol)_2]\cdot 2H_2O$ on contractility was very similar to that of the free propranolol while the reduction on the heart rate is approximately 30% of that of the free ligand. The block of the response to adrenaline is at least similar for both ligand and complex. Therefore we obtained a new complex that affects specially the contractility and to a minor extent the heart rate.

The results are certainly encouraging due to the fact that the search for new beta-blocker drugs that have lesser effect on heart rate is one of the important topics in cardiac pharmacology.

Supplementary data

CCDC 682936 contains the supplementary crystallographic data for this paper. These data can be obtained free of charge via

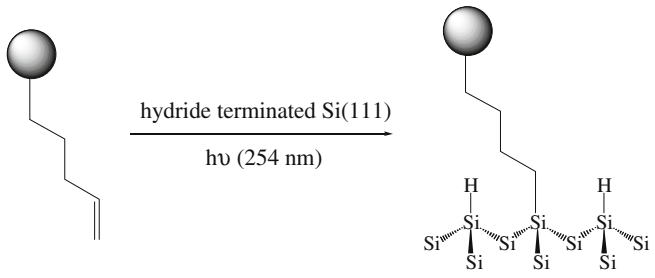
<http://www.ccdc.cam.ac.uk/conts/retrieving.html>, or from the Cambridge Crystallographic Data Centre, 12 Union Road, Cambridge CB2 1EZ, UK; fax: (+44) 1223-336-033; or e-mail: deposit@ccdc.cam.ac.uk.

Acknowledgements

The authors thank Dr. Ricardo Faccio for his help in managing the crystallographic software. We are also grateful to PEDECIBA – Química (Uruguayan organization) and CNPq and FAPESP (Brazilian organizations) for financial support.

References

[1] J.G. Hardman, L.E. Limbird, A.G. Gilman, Goodman and Gilman, Las Bases Farmacológicas De La Terapéutica, McGraw-Hill, 2003.
[2] T.C. Westfall, D.P. Westfall, Adrenergic agonist and antagonist. in: Goodman and Gilmańs. The Pharmacological Basis of Therapeutics, 11th ed., McGraw-Hill, New York, 2007 (Chapter 10).
[3] K. Fox, J.S. Borer, A.J. Camm, N. Danchin, R. Ferrari, J. Am. Coll. Cardiol. 50 (2007) 823.
[4] D.T. Ko, P.R. Hebert, C.S. Coffey, J.P. Curtis, J.M. Foody, A. Sedrakyan, H.M. Krumholz, Arch. Intern. Med. 164 (13) (2004) 1389.
[5] L. Gullestad, J. Wikstrand, J. Am. Coll. Cardiol. 45 (2) (2005) 252.
[6] I. Hamilton, W. Gilmore, J. Strain, Biol. Trace Elem. Res. 78 (2000) 179.
[7] L.M. Klevay, J. Nutr. 130 (2000) 489.
[8] M. Bergomi, S. Rovesti, M. Vinceti, R. Vivoli, E. Caselgrandi, G. Vivoli, J. Trace Elem. Med. Biol. 11 (1997) 166.
[9] C. Russo, O. Olivieri, D. Girelli, G. Faccini, M. Zenari, S. Lombardi, R. Corrocher, J. Hypertens. 16 (1998) 1267.
[10] P. Bontchev, I. Pantcheva, R. Bontchev, D. Ivanov, N. Danchev, Biometals 15 (2002) 79.
[11] P. Bontchev, H. Kadum, B. Evtimova, C. Nachev, E. Zhecheva, D. Mehandjiev, D. Ivanov, J. Inorg. Biochem. 48 (1992) 153.
[12] P.R. Bontchev, G.P. Gochev, Trans. Metal Chem. 25 (2000) 196.
[13] P.R. Bontchev, I.N. Pantcheva, T. Todorov, D.R. Mehandjiev, N.S. Savov, J. Inorg. Biochem. 83 (2001) 25.
[14] P.R. Bontchev, I.N. Pantcheva, Trans. Metal Chem. 27 (2002) 1.
[15] C. Urquiola, D. Gambino, M. Cabrera, M.L. Lavaggi, H. Cerecetto, M. Gonzalez, A.L.d. Cerain, A. Monge, A.J. Costa-Filho, M.H. Torre, J. Inorg. Biochem. 102 (2008) 119.
[16] E. Kremer, G. Facchin, E. Estévez, P. Alborés, E.J. Baran, J. Ellena, M.H. Torre, J. Inorg. Biochem. 100 (2006) 1167.
[17] M. Mondelli, V. Brune, G. Borthagaray, J. Ellena, O.R. Nascimento, C.Q. Leite, A.A. Batista, M.H. Torre, J. Inorg. Biochem. 102 (2008) 285.
[18] R. Mehvar, J. Pharm. Pharm. Sci. 4 (2) (2001) 185.
[19] Enraf-Nonius Collect, Nonius BV, Delf, The Netherlands, 1997–2000.
[20] Z. Otwinowski, W. Minor, in: C.W. Carter, R.M. Sweet (Eds.), Methods in Enzymology, vol. 276, Academic Press, New York, 1997, p. 307.
[21] R.H. Blessing, Acta Cryst. A51 (1995) 33.
[22] G.M. Sheldrick, University of Gottingen, Gottingen, Germany, 1997.
[23] G.M. Sheldrick, University of Göttingen, Göttingen, 1997.
[24] L.J. Farrugia, J. Appl. Cryst. 30 (1997) 565.
[25] L.J. Farrugia, J. Appl. Cryst. 32 (1999) 837.
[26] S. Stoll, A. Schweiger, J. Magn. Reson. 178 (2006) 42.
[27] M. Skrzypiec-Spring, B. Grotthus, A. Szelag, R. Schulz, J. Pharmacol. Toxicol. Methods 55 (2007) 113.
[28] I. Viera, L. Domínguez, J. Ellena, M.H. Torre, Z. Naturforsh. 63b (2008) 543.
[29] P.R. Bontchev, B.B. Ivanova, R.P. Bontchev, D.R. Mehandjiev, D.S. Ivanov, Polyhedron 19 (2000) 1843.
[30] V.T. Getova, R.P. Bontchev, D.R. Mehandjiev, P.R. Bontchev, Polyhedron 25 (2006) 2254.
[31] V.T. Getova, R.P. Bontchev, D.R. Mehandjiev, V. Skumryev, P.R. Bontchev, Polyhedron 24 (2005) 1983.
[32] A.B.P. Lever, Inorganic Electronic Spectroscopy, Elsevier, Amsterdam, 1984.
[33] A.J. Costa-Filho, O.R. Nascimento, R.C.P.C. Bersani, J. Phys. Chem. B 108 (2004) 9549.
[34] E.D. Vieira, N.M.C. Casado, G. Facchin, M.H. Torre, A.J. Costa-Filho, R. Calvo, Inorg. Chem. 45 (2006) 2942.
[35] J. Peisach, W.E. Blumberg, Archives of Biochemistry and Biophysics 165 (1974) 691.
[36] D. Lin-Vien, N.B. Colthup, W.G. Fateley, J.G. Grasselli, The Handbook of Infrared and Raman Characteristic Frequencies of Organic Molecules, Academic Press, Inc., Boston, 1991.
[37] K. Nakamoto, Infrared and Raman Spectra of Inorganic and Coordination Compounds. Part B, John Wiley and Sons, New York, 1997.
[38] K. Florey, Analytical Profiles of Drug Substances and Excipients, vol. 13, Academic Press Inc., London.
[39] M.S. Masoud, S.A.A. El-Enein, I.M. Abed, A.E. Ali, J. Coord. Chem. 55 (2002) 153.



Scheme 1. Functionalization of Si surface with olefin-capped molecule (solid ball represent the head group).

satisfactory combustion analysis results. All four compounds are paramagnetic with the room temperature effective magnetic moments in a narrow range of 3.81–3.93 Bohr magneton, which is consistent with the presence of three unpaired electrons [12,16].

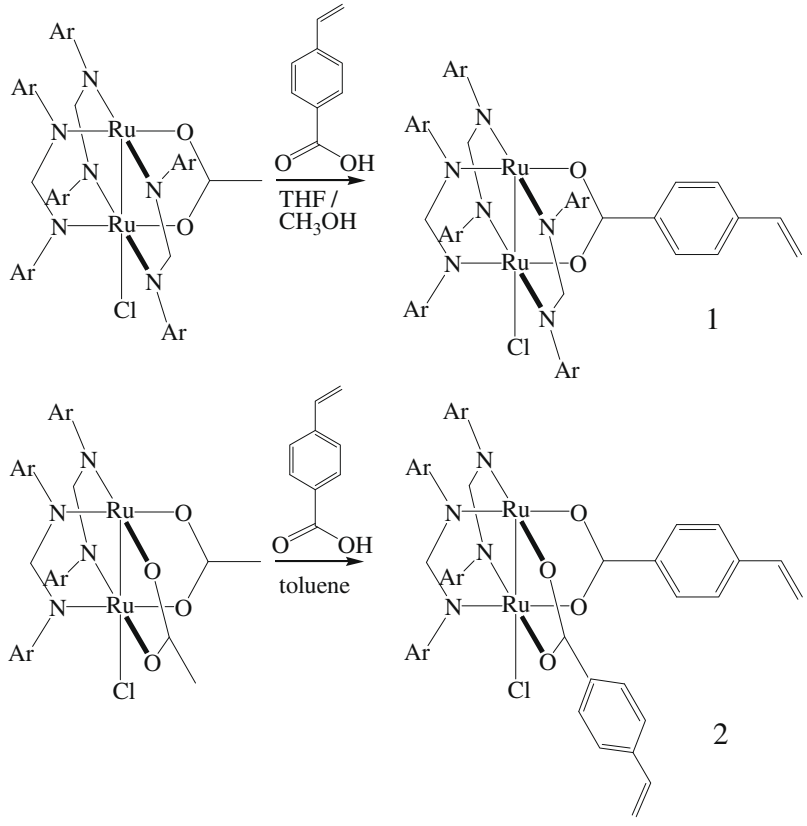
2.2. Molecular structures

Both compounds **1** and **2** crystallize in the space group $P\bar{1}$, and the asymmetric unit contains a complete diruthenium molecule in each case. The structural plot of **1**, Fig. 1, reveals the presence of three D(3,5-Cl_2Ph)F ligands and one 4-vinylbenzoate around the diruthenium core. The coordination sphere of the Ru_2 unit is completed with a chloro and a water ligand in the axial positions, which were disordered over both axial sites and refined with 50% occupancy each for Cl and O (labeled as Cl′ in Fig. 1). Hence, the Ru–Cl′ distance is shorter than the Ru1–Cl1 bond in **2** but longer than the Ru–O(OH_2) distance in Ru_2(D(3,5-Cl_2Ph)F)$_2$(μ-O_2CMe)$_2$Cl(H_2O) (2.362 Å) [9]. It is clear from the structural plot of **2** (Fig. 2) that the coordination sphere of the Ru_2 unit consists of two D(3,5-Cl_2Ph)F and two 4-vinylbenzoate bridging bidentate ligands in a *cis*-arrangement, and a chloro and an ethanol axial ligands.

Listed in Table 1 are the selected bond lengths and angles data for compounds **1** and **2**. The Ru–Ru bond length in **1** (2.3381(4) Å) is slightly longer than that in the precursor Ru_2(D(3,5-Cl_2Ph)F)$_3$(μ-O_2CMe)Cl (2.3220(7) Å), and the shortness of Ru–Ru bond in the latter is attributed to the absence of axial water ligand [9]. The Ru–Ru bond length in **2** (2.319(2) Å) is slightly shorter than that of and Ru_2(D(3,5-Cl_2Ph)F)$_2$(μ-O_2CMe)$_2$Cl(H_2O) (2.327 Å) [9], reflecting the weak ligating ability of ethanol in comparison with water. The equatorial Ru–O and Ru–N bond lengths are all in good agreement with those of related compounds reported earlier [9,11].

2.3. Voltammetry

Similar to other Ru_2(DArF)$_{4-x}$(carboxylate)$_x$ type compounds, compounds **1**–**4** display cyclic voltammograms (CV, Fig. 3) with rich features. Common to all compounds are three Ru_2-centered one-electron events: the quasi-reversible oxidation (**A**), quasi-reversible reduction (**B**), and subsequent irreversible reduction (**D**) as illustrated in Scheme 3. It is clear from Table 2 that the mono-carboxylate species **1**, **3** and **4** have nearly identical electrode potentials. Interestingly, the voltammetric characteristic of the dicarboxylate species **2** is comparable to those of the other three compounds, except that the couple **D** of **2** is anodically shifted. Additional features such as peaks **C** and **E** are related to the dissociation/association of the chloro ligand (Scheme 3), as discussed in our prior study of related species [11]. Peaks **F** and **G** are also prevalent and could be related to the dissociation/association of axially bound solvent molecule, although there is no concrete evidence supporting this speculation.



Scheme 2. Preparation of diruthenium-4-vinylbenzoate compounds.

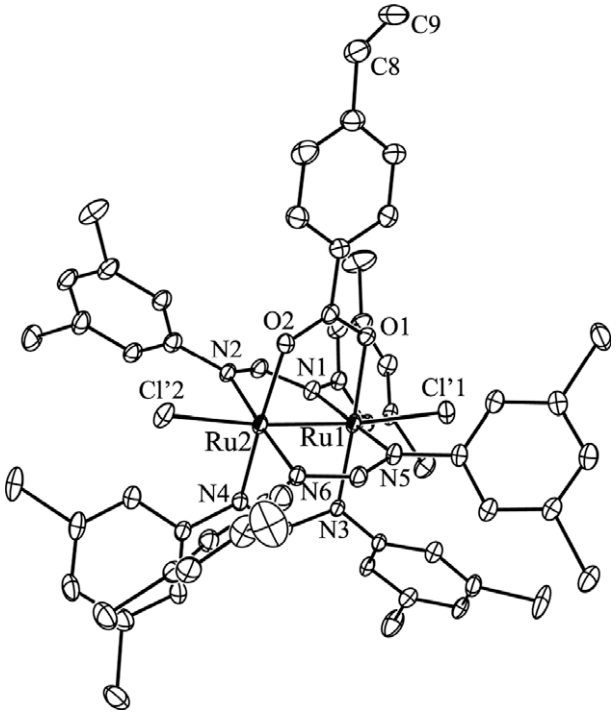


Fig. 1. Structural plot of molecule **1**. Hydrogen atoms were omitted for clarity.

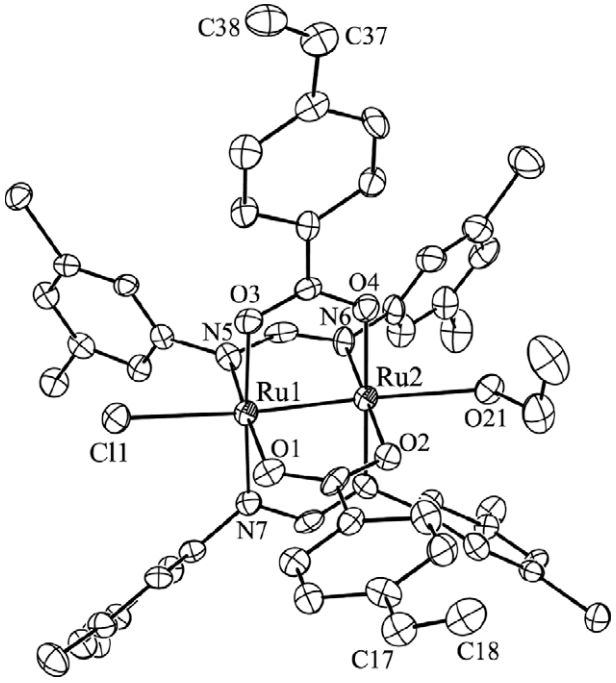


Fig. 2. Structural plot of molecule **2**·(HOEt). Hydrogen atoms were omitted for clarity.

3. Conclusion

We have successfully prepared several diruthenium species with terminal olefin that may be suitable for photolytic immobilization on Si surfaces, and are currently exploring and optimizing conditions for the immobilization of these novel Ru_2 compounds on various Si surfaces.

Table 1
Selected bond lengths (Å) and angles (°) for compounds **1** and **2**.

1		**2**	
Ru1–Ru2	2.3381(4)	Ru1–Ru2	2.319(2)
Ru1–N1	2.085(3)	Ru1–N5	2.03(1)
Ru1–N3	2.069(3)	Ru1–N7	2.03(1)
Ru1–N5	2.073(3)	Ru2–N6	2.03(1)
Ru2–N2	2.059(3)	Ru2–N8	2.04(1)
Ru2–N4	2.058(3)	Ru1–O1	2.075(8)
Ru2–N6	2.087(3)	Ru1–O3	2.064(8)
Ru1–O1	2.067(3)	Ru2–O2	2.063(8)
Ru2–O2	2.080(3)	Ru2–O4	2.048(9)
Ru1–Cl′1	2.437(2)	Ru1–Cl1	2.501(4)
Ru2–Cl′2	2.435(2)	Ru2–O21	2.35(1)
C8–C9	1.307(8)	C17–C18	1.32(2)
		C37–C38	1.28(2)
Ru2–Ru1–Cl1 174.54(4)		Ru2–Ru1–Cl1 171.13(9)	
		Ru1–Ru2–O21 169.7(2)	

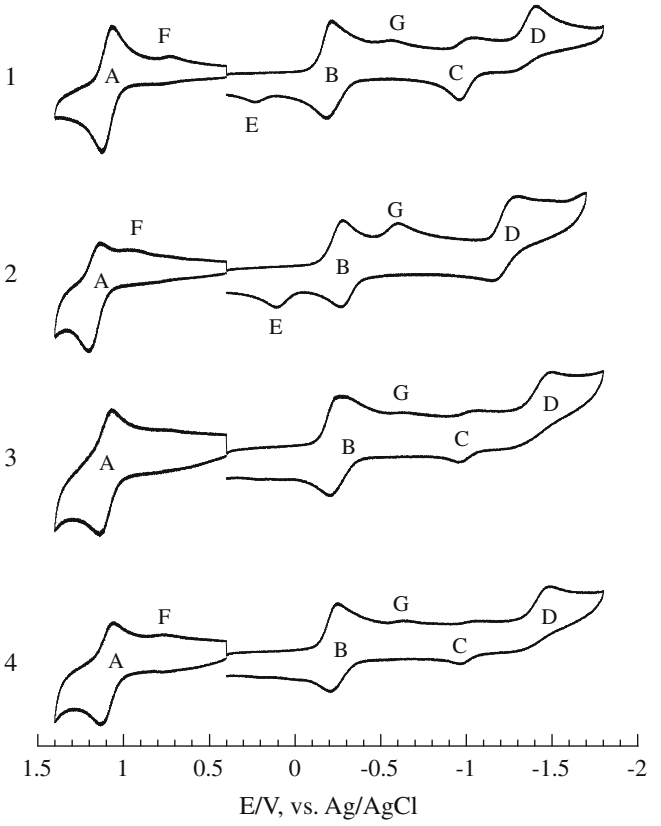
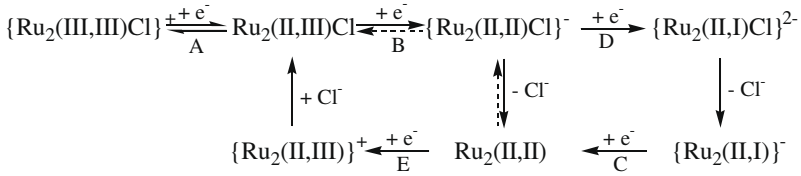


Fig. 3. Cyclic voltammograms of compounds **1–4** recorded in 0.20 M THF solution of Bu_4NPF_6 at a scan rate of 0.10 V/s.

4. Experimental

4.1. General

4-Vinylbenzoic acid, 5-hexenoic acid, and 6-heptenoic acid were purchased from Aldrich. $Ru_2(D(3,5\text{-}Cl_2Ph)F)_3(OAc)Cl$ and *cis*-$Ru_2(D(3,5\text{-}Cl_2Ph)F)_2(OAc)_2Cl$ were prepared using a literature procedure [9]. Vis–NIR spectra in THF were obtained with a JASCO V-670 UV–Vis–NIR spectrophotometer. Magnetic susceptibility was measured at 294 K with a Johnson Matthey Mark-I magnetic susceptibility balance. Cyclic voltammograms were recorded in 0.2 M *n*-Bu_4NPF_6 solution (THF, N_2-degassed) on a CHI620A voltammetric analyzer with a glassy carbon working electrode (diam-



Scheme 3. Assignments of observed Ru_2-based redox couples in compounds **1–4**.

Table 2
Electrode potentials of compounds **1–4**.

Compounds	$E_{1/2}$(**A**) (V)	$E_{1/2}$(**B**) (V)	E_{pc}(**D**) (V)
1	1.09	−0.20	−1.41
2	1.17	−0.27	−1.29
3	1.11	−0.22	−1.50
4	1.10	−0.23	−1.48

eter = 2 mm), a Pt-wire auxiliary electrode, and a Ag/AgCl reference electrode. The concentration of diruthenium species is always 1.0 mM. The ferrocenium/ferrocene couple was observed at 0.606 V (versus Ag/AgCl) under the experimental conditions.

4.2. Preparation of $Ru_2(D(3,5\text{-}Cl_2Ph)F)_3(\mu\text{-}O_2CC_6H_4\text{-}4\text{-}CH{=}CH_2)Cl$ (**1**)

A mixture of $Ru_2(D(3,5\text{-}Cl_2Ph)F)_3(OAc)Cl$ (200 mg, 0.15 mmol), 4-vinylbenzoic acid (222 mg, 1.5 mmol), THF (20 mL), and methanol (20 mL) was refluxed in air overnight. After the solvent removal, the residue was washed with H_2O, ethanol and hexanes to yield a purple solid. Further purification was carried out by recrystallization from a mixed solvent of THF/ethanol (1:5, v:v) to yield a purple solid (172 mg, 83% based on Ru). Vis, λ_{max} (nm, $\varepsilon(M^{-1}\,cm^{-1})$): 520(5000). *Anal. Calc.* for $C_{48}H_{31}N_6O_2Cl_{13}Ru_2{\cdot}H_2O$: C, 41.04; H, 2.37; N, 5.98. Found: C, 40.85; H, 2.36; N, 5.78%. $\mu_{eff} = 3.93\mu_B$.

4.3. Preparation of cis-$Ru_2(D(3,5\text{-}Cl_2Ph)F)_2(\mu\text{-}O_2CC_6H_4\text{-}4\text{-}CH{=}CH_2)_2Cl$ (**2**)

A 100 mL round-bottom flask was charged with *cis*-$Ru_2(D(3,5\text{-}Cl_2Ph)F)_2(OAc)_2Cl$ (200 mg, 0.20 mmol), 4-vinylbenzoic acid (65 mg, 0.44 mmol) and 40 mL toluene. The flask was mounted with a MicroSoxhlet extractor containing a thimble filled with K_2CO_3. The reaction mixture was refluxed in air for 6 h. Solvent was removed, and the residue was washed with H_2O, ethanol and hexanes to yield a dark red solid. Further purification was carried out by recrystallization from a mixed solvent of THF/ethanol (1:5, v:v) to yield a purple solid (182 mg, 76% based on Ru). Vis, λ_{max} (nm, $\varepsilon(M^{-1}\,cm^{-1})$): 535(3550). *Anal. Calc.* for $C_{44}H_{30}N_4O_4Cl_9Ru_2{\cdot}THF$: C, 45.32; H, 3.01; N, 4.40. Found: C, 45.18; H, 3.02; N, 4.38%. $\mu_{eff} = 3.81\mu_B$.

4.4. Preparation of $Ru_2(D(3,5\text{-}Cl_2Ph)F)_3(\mu\text{-}O_2CCH_2CH_2CH_2CH{=}CH_2)Cl$ (**3**)

A mixture of $Ru_2(D(3,5\text{-}Cl_2Ph)F)_3(OAc)Cl$ (200 mg, 0.15 mmol), 5-hexenoic acid (0.18 mL, 1.5 mmol), THF (20 mL), and methanol (20 mL) was refluxed in air overnight. After the solvent removal, the resultant oily residue was dissolved in dichloromethane, and then washed with water, brine and dried with anhydrous Na_2SO_4. After the solvent removal, the residue was mixed with small amount of *n*-pentane, and kept at −20 °C overnight. The precipitate was collected by filtration and washed with a mixed solvent of THF/*n*-pentane (1:10, v:v) to yield a purple solid (145 mg, 71% based on Ru). Vis, (nm, $\varepsilon(M^{-1}\,cm^{-1})$): 520 (5100). *Anal. Calc.* for $C_{45}H_{33}N_6O_2Cl_{13}Ru_2{\cdot}THF$: C, 41.30; H, 2.90; N, 5.90. Found: C, 41.35; H, 2.58; N, 5.87%. $\mu_{eff} = 3.91\mu_B$.

4.5. Preparation of $Ru_2(D(3,5\text{-}Cl_2Ph)F)_3(\mu\text{-}O_2CCH_2CH_2CH_2CH_2CH{=}CH_2)Cl$ (**4**)

This compound was prepared using the same synthetic procedure as that of the above compound except that 6-heptenoic acid (0.20 mL, 1.5 mmol) was used in place of 5-hexenoic acid. Yield: 150 mg (73% based on Ru). Vis, (nm, $\varepsilon(M^{-1}\,cm^{-1})$): 520(5520). *Anal.* Calc. for $C_{46}H_{35}N_6O_2Cl_{13}Ru_2{\cdot}0.5THF$: C, 41.10; H, 2.80; N, 5.99. Found: C, 41.08; H, 2.55; N, 6.01%. $\mu_{eff} = 3.90\mu_B$.

4.6. X-ray diffraction study of compounds **1** and **2**

Single crystals of compound **1** and **2** were obtained by slow diffusion of hexanes into a THF solution and slow cooling of a THF/ethanol (1:5, v:v) solution in refrigerator, respectively. The X-ray intensity data were collected at 150 K on a Nonius Kappa CCD X-ray diffractometer system using Mo Kα (λ = 0.71073 Å). The structures were solved by direct methods using SIR2004 [17] and refined using the SHELX-97 in the space group $P\bar{1}$ for both **1** and **2** [18]. The asymmetric unit of **1** contains one diruthenium molecule and three THF solvent molecules, while that of **2** contains one diruthenium molecule, a coordinating ethanol and four interstitial ethanol molecules. Relevant information on the data collection and the figures of merit of final refinement are listed in Table 3.

Supplementary data

CCDC 735349 and 735350 contain the supplementary crystallographic data for **1** and **2**, respectively. These data can be obtained free of charge via http://www.ccdc.cam.ac.uk/conts/retrieving.html, or from the Cambridge Crystallographic Data Centre, 12

Table 3
Crystal data for compounds **1** and **2**.

	1·3THF	(**2**·HOC_2H_5)·4EtOH
Formula	$C_{60}H_{52}Cl_{13}N_6O_6Ru_2$	$C_{54}H_{58}Cl_9N_4O_9Ru_2$
Formula weight	1616.15	1428.30
Space group	$P\bar{1}$	$P\bar{1}$
a (Å)	12.1831(4)	11.479(4)
b (Å)	12.4481(4)	13.119(3)
c (Å)	25.6312(8)	20.330(5)
α (°)	85.369(2)	78.384(6)
β (°)	85.490(2)	86.27(1)
γ (°)	64.326(2)	83.97(2)
V (Å^3)	3487.8(2)	2979(1)
Z	2	2
T (K)	150	150
λ (Mo Kα) (Å)	0.71073	0.71073
ρ (g cm^{-3})	1.539	1.592
Goodness-of-fit (GOF) on F^2	1.094	1.200
R_1, wR_2	0.049, 0.143	0.101, 0.207

Union Road, Cambridge CB2 1EZ, UK; fax: (+44) 1223-336-033; or e-mail: deposit@ccdc.cam.ac.uk.

Acknowledgments

We thank the support from the National Science Foundation (Grant No. CHE 0715404) and DoD DURIP (Grant No. W911 NF-07-1-0193 for the UV–Vis–NIR spectrophotometer).

References

[1] S. Brase, A. de Meijere, in: A. de Meijere, F. Diederich (Eds.), Metal-Catalyzed Cross-Coupling Reactions, vol. 1, Wiley-VCH, Weinheim, 2004.
[2] R.H. Grubbs (Ed.), Handbook of Metathesis, vols. 1–3, Wiley-VCH, Weinheim, Germany, 2003.
[3] T. Ren, Chem. Rev. 108 (2008) 4185.
[4] (a) E.B. Bauer, J.A. Gladysz, in: R.H. Grubbs (Ed.), Handbook of Metathesis, vol. 2, Wiley-VCH, Weinheim, Germany, 2003;
(b) C.R. Horn, J.A. Gladysz, Eur. J. Inorg. Chem. (2003) 2211;
(c) L. de Quadras, E.B. Bauer, W. Mohr, J.C. Bohling, T.B. Peters, J.M. Martin-Alvarez, F. Hampel, J.A. Gladysz, J. Am. Chem. Soc. 129 (2007) 8296;
(d) L. de Quadras, E.B. Bauer, J. Stahl, F. Zhuravlev, F. Hampel, J.A. Gladysz, New J. Chem. 31 (2007) 1594.
[5] (a) S.F. Bent, Surf. Sci. 500 (2002) 879;
(b) J.M. Buriak, Chem. Rev. 102 (2002) 1271;
(c) Q.L. Li, Mod. Phys. Lett. B 22 (2008) 1183.
[6] N. Gauthier, G. Argouarch, F. Paul, M.G. Humphrey, L. Toupet, S. Ababou-Girard, H. Sabbah, P. Hapiot, B. Fabre, Adv. Mater. 20 (2008) 1952.
[7] (a) M.W. Cooke, G.S. Hanan, F. Loiseau, S. Campagna, M. Watanabe, Y. Tanaka, J. Am. Chem. Soc. 129 (2007) 10479;
(b) M.W. Cooke, M.-P. Santoni, G.S. Hanan, A. Proust, B. Hasenknopf, Dalton Trans. (2009) 3671;
(c) T. Ren, C.R. Chimie 11 (2008) 684;
(d) W.-Z. Chen, T. Ren, Organometallics 23 (2004) 3766;
(e) G.-L. Xu, T. Ren, Organometallics 24 (2005) 2564;
(f) G.-L. Xu, T. Ren, Inorg. Chem. 45 (2006) 10449;
(g) W.-Z. Chen, T. Ren, Inorg. Chem. 45 (2006) 9175;
(h) W.-Z. Chen, P.E. Fanwick, T. Ren, Inorg. Chem. 46 (2007) 3429;
(i) L. Zhang, Z. Huang, W.-Z. Chen, E.-i. Negishi, P.E. Fanwick, J.B. Updegraff, J.D. Protasiewicz, T. Ren, Organometallics 26 (2007) 6529.
[8] W.-Z. Chen, T. Ren, Organometallics 24 (2005) 2660.
[9] W.-Z. Chen, T. Ren, Inorg. Chem. 45 (2006) 8156.
[10] W.-Z. Chen, J.D. Protasiewicz, A.J. Shirar, T. Ren, Eur. J. Inorg. Chem. (2006) 4737.
[11] W.-Z. Chen, J.D. Protasiewicz, S.A. Davis, J.B. Updegraff, L.-Q. Ma, P.E. Fanwick, T. Ren, Inorg. Chem. 46 (2007) 3775.
[12] T. Ren, Organometallics 24 (2005) 4854.
[13] A.K. Mahapatro, J. Ying, T. Ren, D.B. Janes, Nano Lett. 8 (2008) 2131.
[14] (a) T. Ren, V. DeSilva, G. Zou, C. Lin, L.M. Daniels, C.F. Campana, J.C. Alvarez, Inorg. Chem. Commun. 2 (1999) 301;
(b) M.C. Barral, S. Herrero, R. Jiménez-Aparicio, M.R. Torres, F.A. Urbanos, Inorg. Chem. Commun. 7 (2004) 42;
(c) P. Angaridis, J.F. Berry, F.A. Cotton, P. Lei, C. Lin, C.A. Murillo, D. Villagrán, Inorg. Chem. Commun. 7 (2004) 9;
(d) P. Angaridis, J.F. Berry, F.A. Cotton, C.A. Murillo, X. Wang, J. Am. Chem. Soc. 125 (2003) 10327;
(e) M.C. Barral, T. Gallo, S. Herrero, R. Jiménez-Aparicio, M.R. Torres, F.A. Urbanos, Inorg. Chem. 45 (2006) 3639;
(f) W.-Z. Chen, T. Ren, Organometallics 23 (2004) 3766;
(g) H. Miyasaka, C. Kachi-Terajima, T. Ishii, M. Yamashita, Dalton Trans. (2001) 1929;
(h) M.C. Barral, R. Gonzalez-Prieto, S. Herrero, R. Jimenez-Aparicio, J.L. Priego, E.C. Royer, M.R. Torres, F.A. Urbanos, Polyhedron 23 (2004) 2637;
(i) F.A. Cotton, S. Herrero, R. Jimenez-Aparicio, C.A. Murillo, F.A. Urbanos, D. Villagran, X.P. Wang, J. Am. Chem. Soc. 129 (2007) 12666;
(j) M.C. Barral, S. Herrero, R. Jiménez-Aparicio, M.R. Torres, F.A. Urbanos, J. Organomet. Chem. 693 (2008) 1597.
[15] G. Zou, J.C. Alvarez, T. Ren, J. Organomet. Chem. 596 (2000) 152.
[16] (a) F.A. Cotton, A. Yokochi, Inorg. Chem. 36 (1997) 567;
(b) V.M. Miskowski, M.D. Hopkins, J.R. Winkler, H.B. Gray, in: E.I. Solomon, A.B.P. Lever (Eds.), Inorganic Electronic Structure and Spectroscopy, vol. 2, Wiley, New York, 1999, pp. 343–402;
(c) P. Angaridis, in: F.A. Cotton, C.A. Murillo, R.A. Walton (Eds.), Multiple Bonds between Metal Atoms, third ed., Springer Science and Business Media Inc., New York, 2005.
[17] M.C. Burla, R. Caliandro, M. Camalli, B. Carrozzini, G.L. Cascarano, L. De Caro, C. Giacovazzo, G. Polidori, R. Spagna, J. Appl. Cryst. 38 (2005) 381.
[18] G.M. Sheldrick, Acta Crystallogr. A 64 (2008) 112.

POLYHEDRON

The International Journal for Inorganic and Organometallic Chemistry

Executive Editors

The Americas
G. Christou
Department of Chemistry, University of Florida,
Gainesville, FL 32611-7200, USA
E-mail: christou@chem.ufl.edu

Rest of the world
C.E. Housecroft
Department of Chemistry, University of Basel,
Spitalstrasse 51, CH-4056 Basel, Switzerland
E-mail: poly-chemie@unibas.ch

Associate Regional Editor for China
T.C.W. Mak
Department of Chemistry, University Science Centre,
The Chinese University of Hong Kong,
Shatin NT, Hong Kong, People's Republic of China
E-mail: tcwmak@cuhk.edu.hk

Polyhedron Reports
Editor
G. Christou *(Gainesville, FL, USA)*

Symposia-in-print
Editor
G. Parkin *(New York, NY, USA)*

Editorial Board
A.G. Blackman *(Dunedin, New Zealand)*
D.C. Bradley *(London, UK)*
A. Brodie *(Palmerston North, New Zealand)*
A. Castiñeiras *(Santiago de Compostela, Spain)*
X.-M. Chen *(Guangzhou, PR China)*
M.H. Chisholm *(Columbus, OH, USA)*
E.C. Constable *(Basel, Switzerland)*
L. Cronin *(Glasgow, UK)*
G.R. Desiraju *(Hyderabad, India)*
W.J. Evans *(Irvine, CA, USA)*
L.H. Gade *(Heidelberg, Germany)*
G. Girolami *(Urbana, IL, USA)*
J.-F. Halet *(Rennes, France)*
C. Janiak *(Freiburg, Germany)*
C. Kepert *(NSW, Australia)*
P. Kruger *(Canterbury, New Zealand)*
S. Perlepes *(Patras, Greece)*
P.P. Power *(Davis, CA, USA)*
T.B. Rauchfuss *(Urbana, IL, USA)*
J. Reedijk *(Leiden, The Netherlands)*
A.L. Rheingold *(Newark, DE, USA)*
M. Rosales Hoz *(Mexico, D.F., Mexico)*
P. Steel *(Christchurch, New Zealand)*
L.K. Thompson *(St John's, NF, Canada)*
D.A. Tocher *(Oxford, UK)*
M. Yamashita *(Sendai, Japan)*

Aims and Scope

Polyhedron will publish original, fundamental, experimental and theoretical work of the highest quality in all the major areas of inorganic chemistry. These include synthetic chemistry, coordination chemistry, organometallic chemistry, bioinorganic chemistry, and solid-state and materials chemistry. Papers should be complete pieces of work, and the inclusion of results from spectroscopic and/or physical techniques is encouraged. Papers merely reporting the preparation and X-ray structural characterization of only a single compound will not be considered appropriate unless the compound and its structure are particularly interesting.

Similarly, papers concerned solely with stability constants determined by potentiometric titration data unsupported by other e.g. spectroscopic techniques will not be acceptable nor will solvent extraction data unless supported by other data of interest to inorganic chemists. Unnecessary fragmentation of work is not acceptable.

In addition Polyhedron publishes specially commissioned review articles (Polyhedron Reports) and collections of original research papers (Polyhedron Symposia-in-Print) of appropriate timeliness.

Publication Information: Polyhedron (ISSN 0277-5387). For 2009, volume 28 is scheduled for publication. Subscription prices are available upon request from the Publisher or from the Elsevier Customer Service Department nearest you or from this journal's website (http://www.elsevier.com/locate/poly). Further information is available on this journal and other Elsevier products through Elsevier's website (http://www.elsevier.com). Subscriptions are accepted on a prepaid basis only and are entered on a calendar year basis. Issues are sent by standard mail (surface within Europe, air delivery outside Europe). Priority rates are available upon request. Claims for missing issues should be made within six months of the date of dispatch.

Orders, Claims and Journal Enquiries

(no manuscript enquiries)
Please contact the Elsevier Customer Service Department nearest you:

St. Louis
Elsevier Customer Service Department, 3251 Riverport Lane, Maryland Heights, MO 63043, USA; phone: (877) 8397126 [toll free within the USA]; (+1) (314) 4478878 [outside the USA]; fax: (+1) (314) 4478077; e-mail: JournalCustomerService-usa@elsevier.com

Oxford
Elsevier Customer Service Department, The Boulevard, Langford Lane, Kidlington, Oxford OX5 1GB, UK; phone: (+44) (1865) 843434; fax: (+44) (1865) 843970; e-mail: JournalsCustomerServiceEMEA@elsevier.com

Tokyo
Elsevier Customer Service Department, 4F Higashi-Azabu, 1-Chome Bldg, 1-9-15 Higashi-Azabu, Minato-ku, Tokyo 106-0044, Japan; phone: (+81) 3-5561-5037; fax: (+81) 3-5561-5047; e-mail: JournalsCustomerServiceJapan@elsevier.com

Singapore
Elsevier Customer Service Department, 3 Killiney Road, #08-01 Winsland House 1, Singapore 239519, phone: (+65) 6349-0222; fax: (+65) 6733-1510; e-mail: JournalsCustomerServiceAPAC@elsevier.com

USA mailing notice: *Polyhedron* (ISSN 0277-5387) is published triweekly by Elsevier B.V. (Radarweg 29, 1043 NX Amsterdam, the Netherlands). Periodical postage paid at Rahway NJ and additional mailing offices.
USA POSTMASTER: Send change of address to *Polyhedron*, Elsevier Customer Service Department, 3251 Riverport Lane, Maryland Heights, MO 63043, USA.
AIRFREIGHT AND MAILING in USA by Mercury International Limited, 365 Blair Road, Avenel, NJ 07001.

Advertising Information
Advertising orders and enquiries can be sent to: **USA, Canada and South America:** Mr Tino DeCarlo, The Advertising Department, Elsevier Inc., 360 Park Avenue South, New York, NY 10010-1710, USA; tel.: (+1) (212) 633 3815; fax: (+1) (212) 633 3820; e-mail: t.decarlo@elsevier.com. **Europe and ROW:** Miss Katrina Barton, Commercial Sales, Elsevier, 84 Theobald's Road, London, WCIX 8RR, UK; phone: (+44) (0) 20 7611 4117; fax: (+44) (0) 20 7611 4463; e-mail: commercialsales@elsevier.com

Funding body agreements and policies
Elsevier has established agreements and developed policies to allow authors who publish in Elsevier journals to comply with potential manuscript archiving requirements as specified as conditions of their grant awards. To learn more about existing agreements and policies please visit http://www.elsevier.com/fundingbodies

POLYHEDRON

The International Journal for Inorganic and Organometallic Chemistry

Executive Editors

The Americas
G. Christou
Department of Chemistry, University of Florida,
Gainesville, FL 32611-7200, USA
E-mail: christou@chem.ufl.edu

Rest of the world
C.E. Housecroft
Department of Chemistry, University of Basel,
Spitalstrasse 51, CH-4056 Basel, Switzerland
E-mail: poly-chemie@unibas.ch

Associate Regional Editor for China
T.C.W. Mak
Department of Chemistry, University Science Centre,
The Chinese University of Hong Kong,
Shatin NT, Hong Kong, People's Republic of China
E-mail: tcwmak@cuhk.edu.hk

Polyhedron Reports
Editor
G. Christou *(Gainesville, FL, USA)*

Symposia-in-print
Editor
G. Parkin *(New York, NY, USA)*

Editorial Board
A.G. Blackman *(Dunedin, New Zealand)*
D.C. Bradley *(London, UK)*
A. Brodie *(Palmerston North, New Zealand)*
A. Castiñeiras *(Santiago de Compostela, Spain)*
X.-M. Chen *(Guangzhou, PR China)*
M.H. Chisholm *(Columbus, OH, USA)*
E.C. Constable *(Basel, Switzerland)*
L. Cronin *(Glasgow, UK)*
G.R. Desiraju *(Hyderabad, India)*
W.J. Evans *(Irvine, CA, USA)*
L.H. Gade *(Heidelberg, Germany)*
G. Girolami *(Urbana, IL, USA)*
J.-F. Halet *(Rennes, France)*
C. Janiak *(Freiburg, Germany)*
C. Kepert *(NSW, Australia)*
P. Kruger *(Canterbury, New Zealand)*
S. Perlepes *(Patras, Greece)*
P.P. Power *(Davis, CA, USA)*
T.B. Rauchfuss *(Urbana, IL, USA)*
J. Reedijk *(Leiden, The Netherlands)*
A.L. Rheingold *(Newark, DE, USA)*
M. Rosales Hoz *(Mexico, D.F., Mexico)*
P. Steel *(Christchurch, New Zealand)*
L.K. Thompson *(St John's, NF, Canada)*
D.A. Tocher *(Oxford, UK)*
M. Yamashita *(Sendai, Japan)*

Aims and Scope

Polyhedron will publish original, fundamental, experimental and theoretical work of the highest quality in all the major areas of inorganic chemistry. These include synthetic chemistry, coordination chemistry, organometallic chemistry, bioinorganic chemistry, and solid-state and materials chemistry. Papers should be complete pieces of work, and the inclusion of results from spectroscopic and/or physical techniques is encouraged. Papers merely reporting the preparation and X-ray structural characterization of only a single compound will not be considered appropriate unless the compound and its structure are particularly interesting.

Similarly, papers concerned solely with stability constants determined by potentiometric titration data unsupported by other e.g. spectroscopic techniques will not be acceptable nor will solvent extraction data unless supported by other data of interest to inorganic chemists. Unnecessary fragmentation of work is not acceptable.

In addition Polyhedron publishes specially commissioned review articles (Polyhedron Reports) and collections of original research papers (Polyhedron Symposia-in-Print) of appropriate timeliness.

Publication Information: Polyhedron (ISSN 0277-5387). For 2009, volume 28 is scheduled for publication. Subscription prices are available upon request from the Publisher or from the Elsevier Customer Service Department nearest you or from this journal's website (http://www.elsevier.com/locate/poly). Further information is available on this journal and other Elsevier products through Elsevier's website (http://www.elsevier.com). Subscriptions are accepted on a prepaid basis only and are entered on a calendar year basis. Issues are sent by standard mail (surface within Europe, air delivery outside Europe). Priority rates are available upon request. Claims for missing issues should be made within six months of the date of dispatch.

Orders, Claims and Journal Enquiries

(no manuscript enquiries)
Please contact the Elsevier Customer Service Department nearest you:

St. Louis
Elsevier Customer Service Department, 3251 Riverport Lane, Maryland Heights, MO 63043, USA; phone: (877) 8397126 [toll free within the USA]; (+1) (314) 4478878 [outside the USA]; fax: (+1) (314) 4478077; e-mail: JournalCustomerService-usa@elsevier.com

Oxford
Elsevier Customer Service Department, The Boulevard, Langford Lane, Kidlington, Oxford OX5 1GB, UK; phone: (+44) (1865) 843434; fax: (+44) (1865) 843970; e-mail: JournalsCustomerServiceEMEA@elsevier.com

Tokyo
Elsevier Customer Service Department, 4F Higashi-Azabu, 1-Chome Bldg, 1-9-15 Higashi-Azabu, Minato-ku, Tokyo 106-0044, Japan; phone: (+81) 3-5561-5037; fax: (+81) 3-5561-5047; e-mail: JournalsCustomerServiceJapan@elsevier.com

Singapore
Elsevier Customer Service Department, 3 Killiney Road, #08-01 Winsland House 1, Singapore 239519, phone: (+65) 6349-0222; fax: (+65) 6733-1510; e-mail: JournalsCustomerServiceAPAC@elsevier.com

USA mailing notice: *Polyhedron* (ISSN 0277-5387) is published triweekly by Elsevier B.V. (Radarweg 29, 1043 NX Amsterdam, the Netherlands). Periodical postage paid at Rahway NJ and additional mailing offices.
USA POSTMASTER: Send change of address to *Polyhedron*, Elsevier Customer Service Department, 3251 Riverport Lane, Maryland Heights, MO 63043, USA.
AIRFREIGHT AND MAILING in USA by Mercury International Limited, 365 Blair Road, Avenel, NJ 07001.

Advertising Information
Advertising orders and enquiries can be sent to: **USA, Canada and South America:** Mr Tino DeCarlo, The Advertising Department, Elsevier Inc., 360 Park Avenue South, New York, NY 10010-1710, USA; tel.: (+1) (212) 633 3815; fax: (+1) (212) 633 3820; e-mail: t.decarlo@elsevier.com. **Europe and ROW:** Miss Katrina Barton, Commercial Sales, Elsevier, 84 Theobald's Road, London, WCIX 8RR, UK; phone: (+44) (0) 20 7611 4117; fax: (+44) (0) 20 7611 4463; e-mail: commercialsales@elsevier.com

Funding body agreements and policies
Elsevier has established agreements and developed policies to allow authors who publish in Elsevier journals to comply with potential manuscript archiving requirements as specified as conditions of their grant awards. To learn more about existing agreements and policies please visit http://www.elsevier.com/fundingbodies

POLYHEDRON

The International Journal for Inorganic and Organometallic Chemistry

Executive Editors

The Americas
G. Christou
Department of Chemistry, University of Florida,
Gainesville, FL 32611-7200, USA
E-mail: christou@chem.ufl.edu

Rest of the world
C.E. Housecroft
Department of Chemistry, University of Basel,
Spitalstrasse 51, CH-4056 Basel, Switzerland
E-mail: poly-chemie@unibas.ch

Associate Regional Editor for China
T.C.W. Mak
Department of Chemistry, University Science Centre,
The Chinese University of Hong Kong,
Shatin NT, Hong Kong, People's Republic of China
E-mail: tcwmak@cuhk.edu.hk

Polyhedron Reports
Editor
G. Christou *(Gainesville, FL, USA)*

Symposia-in-print
Editor
G. Parkin *(New York, NY, USA)*

Editorial Board
A.G. Blackman *(Dunedin, New Zealand)*
D.C. Bradley *(London, UK)*
A. Brodie *(Palmerston North, New Zealand)*
A. Castiñeiras *(Santiago de Compostela, Spain)*
X.-M. Chen *(Guangzhou, PR China)*
M.H. Chisholm *(Columbus, OH, USA)*
E.C. Constable *(Basel, Switzerland)*
L. Cronin *(Glasgow, UK)*
G.R. Desiraju *(Hyderabad, India)*
W.J. Evans *(Irvine, CA, USA)*
L.H. Gade *(Heidelberg, Germany)*
G. Girolami *(Urbana, IL, USA)*
J.-F. Halet *(Rennes, France)*
L. Hubert-Pfalzgraf *(Villeurbanne, France)*
C. Janiak *(Freiburg, Germany)*
C. Kepert *(NSW, Australia)*
P. Kruger *(Canterbury, New Zealand)*
S. Perlepes *(Patras, Greece)*
P.P. Power *(Davis, CA, USA)*
T.B. Rauchfuss *(Urbana, IL, USA)*
J. Reedijk *(Leiden, The Netherlands)*
A.L. Rheingold *(Newark, DE, USA)*
M. Rosales Hoz *(Mexico, D.F., Mexico)*
P. Steel *(Christchurch, New Zealand)*
L.K. Thompson *(St John's, NF, Canada)*
D.A. Tocher *(Oxford, UK)*
M. Yamashita *(Sendai, Japan)*

Aims and Scope

Polyhedron will publish original, fundamental, experimental and theoretical work of the highest quality in all the major areas of inorganic chemistry. These include synthetic chemistry, coordination chemistry, organometallic chemistry, bioinorganic chemistry, and solid-state and materials chemistry. Papers should be complete pieces of work, and the inclusion of results from spectroscopic and/or physical techniques is encouraged. Papers merely reporting the preparation and X-ray structural characterization of only a single compound will not be considered appropriate unless the compound and its structure are particularly interesting.

Similarly, papers concerned solely with stability constants determined by potentiometric titration data unsupported by other e.g. spectroscopic techniques will not be acceptable nor will solvent extraction data unless supported by other data of interest to inorganic chemists. Unnecessary fragmentation of work is not acceptable.

In addition Polyhedron publishes specially commissioned review articles (Polyhedron Reports) and collections of original research papers (Polyhedron Symposia-in-Print) of appropriate timeliness.

Publication Information: Polyhedron (ISSN 0277-5387). For 2009, volume 28 is scheduled for publication. Subscription prices are available upon request from the Publisher or from the Regional Sales Office nearest you or from this journal's website (http://www.elsevier.com/locate/poly). Further information is available on this journal and other Elsevier products through Elsevier's website (http://www.elsevier.com). Subscriptions are accepted on a prepaid basis only and are entered on a calendar year basis. Issues are sent by standard mail (surface within Europe, air delivery outside Europe). Priority rates are available upon request. Claims for missing issues should be made within six months of the date of dispatch.

Orders, Claims and Journal Enquiries

(no manuscript enquiries)
Please contact the Regional Sales Office nearest you:

St. Louis
Elsevier Customer Service Department, 3251 Riverport Lane, Maryland Heights, MO 63043, USA; phone: (877) 8397126 [toll free within the USA]; (+1) (314) 4478878 [outside the USA]; fax: (+1) (314) 4478077; e-mail: JournalCustomerService-usa@elsevier.com

Oxford
Elsevier Customer Service Department, The Boulevard, Langford Lane, Kidlington, Oxford OX5 1GB, UK; phone: (+44) (1865) 843434; fax: (+44) (1865) 843970; e-mail: JournalsCustomerServiceEMEA@elsevier.com

Tokyo
Elsevier Customer Service Department, 4F Higashi-Azabu, 1-Chome Bldg, 1-9-15 Higashi-Azabu, Minato-ku, Tokyo 106-0044, Japan; Tel.: (+81) 3-5561-5037; Fax: (+81) 3-5561-5047; E-mail: JournalsCustomerService-Japan@elsevier.com

Singapore
Elsevier Customer Service Department, 3 Killiney Road, #08-01 Winsland House 1, Singapore 239519, Tel.: (+65) 6349-0222; Fax: (+65) 6733-1510; E-mail: JournalsCustomerServiceAPAC@elsevier.com

USA mailing notice: *Polyhedron* (ISSN 0277-5387) is published triweekly by Elsevier B.V. (Radarweg 29, 1043 NX Amsterdam, the Netherlands). Periodical postage paid at Rahway NJ and additional mailing offices.
USA POSTMASTER: Send change of address to *Polyhedron*, Elsevier Customer Service Department, 3251 Riverport Lane, Maryland Heights, MO 63043, USA.
AIRFREIGHT AND MAILING in USA by Mercury International Limited, 365 Blair Road, Avenel, NJ 07001.

Advertising Information
Advertising orders and enquiries can be sent to: **USA, Canada and South America:** Mr Tino DeCarlo, The Advertising Department, Elsevier Inc., 360 Park Avenue South, New York, NY 10010-1710, USA; tel.: (+1) (212) 633 3815; fax: (+1) (212) 633 3820; e-mail: t.decarlo@elsevier.com. **Europe and ROW:** Miss Katrina Barton, Commercial Sales, Elsevier, 84 Theobald's Road, London, WCIX 8RR, UK; phone: (+44) (0) 20 7611 4117; fax: (+44) (0) 20 7611 4463; e-mail: commercialsales@elsevier.com

Funding body agreements and policies
Elsevier has established agreements and developed policies to allow authors who publish in Elsevier journals to comply with potential manuscript archiving requirements as specified as conditions of their grant awards. To learn more about existing agreements and policies please visit http://www.elsevier.com/fundingbodies

POLYHEDRON

The International Journal for Inorganic and Organometallic Chemistry

Executive Editors

The Americas
G. Christou
Department of Chemistry, University of Florida,
Gainesville, FL 32611-7200, USA
E-mail: christou@chem.ufl.edu

Rest of the world
C.E. Housecroft
Department of Chemistry, University of Basel,
Spitalstrasse 51, CH-4056 Basel, Switzerland
E-mail: poly-chemie@unibas.ch

Associate Regional Editor for China
T.C.W. Mak
Department of Chemistry, University Science Centre,
The Chinese University of Hong Kong,
Shatin NT, Hong Kong, People's Republic of China
E-mail: tcwmak@cuhk.edu.hk

Polyhedron Reports
Editor
G. Christou *(Gainesville, FL, USA)*

Symposia-in-print
Editor
G. Parkin *(New York, NY, USA)*

Editorial Board
A.G. Blackman *(Dunedin, New Zealand)*
D.C. Bradley *(London, UK)*
A. Brodie *(Palmerston North, New Zealand)*
A. Castiñeiras *(Santiago de Compostela, Spain)*
X.-M. Chen *(Guangzhou, PR China)*
M.H. Chisholm *(Columbus, OH, USA)*
E.C. Constable *(Basel, Switzerland)*
L. Cronin *(Glasgow, UK)*
G.R. Desiraju *(Hyderabad, India)*
W.J. Evans *(Irvine, CA, USA)*
L.H. Gade *(Heidelberg, Germany)*
G. Girolami *(Urbana, IL, USA)*
J.-F. Halet *(Rennes, France)*
L. Hubert-Pfalzgraf *(Villeurbanne, France)*
C. Janiak *(Freiburg, Germany)*
C. Kepert *(NSW, Australia)*
P. Kruger *(Canterbury, New Zealand)*
S. Perlepes *(Patras, Greece)*
P.P. Power *(Davis, CA, USA)*
T.B. Rauchfuss *(Urbana, IL, USA)*
J. Reedijk *(Leiden, The Netherlands)*
A.L. Rheingold *(Newark, DE, USA)*
M. Rosales Hoz *(Mexico, D.F., Mexico)*
P. Steel *(Christchurch, New Zealand)*
L.K. Thompson *(St John's, NF, Canada)*
D.A. Tocher *(Oxford, UK)*
M. Yamashita *(Sendai, Japan)*

Aims and Scope

Polyhedron will publish original, fundamental, experimental and theoretical work of the highest quality in all the major areas of inorganic chemistry. These include synthetic chemistry, coordination chemistry, organometallic chemistry, bioinorganic chemistry, and solid-state and materials chemistry. Papers should be complete pieces of work, and the inclusion of results from spectroscopic and/or physical techniques is encouraged. Papers merely reporting the preparation and X-ray structural characterization of only a single compound will not be considered appropriate unless the compound and its structure are particularly interesting.

Similarly, papers concerned solely with stability constants determined by potentiometric titration data unsupported by other e.g. spectroscopic techniques will not be acceptable nor will solvent extraction data unless supported by other data of interest to inorganic chemists. Unnecessary fragmentation of work is not acceptable.

In addition Polyhedron publishes specially commissioned review articles (Polyhedron Reports) and collections of original research papers (Polyhedron Symposia-in-Print) of appropriate timeliness.

Publication Information: Polyhedron (ISSN 0277-5387). For 2009, volume 28 is scheduled for publication. Subscription prices are available upon request from the Publisher or from the Elsevier Customer Service Department nearest you or from this journal's website (http://www.elsevier.com/locate/poly). Further information is available on this journal and other Elsevier products through Elsevier's website (http://www.elsevier.com). Subscriptions are accepted on a prepaid basis only and are entered on a calendar year basis. Issues are sent by standard mail (surface within Europe, air delivery outside Europe). Priority rates are available upon request. Claims for missing issues should be made within six months of the date of dispatch.

Orders, Claims and Journal Enquiries

(no manuscript enquiries)
Please contact the Elsevier Customer Service Department nearest you:

St. Louis
Elsevier Customer Service Department, 3251 Riverport Lane, Maryland Heights, MO 63043, USA; phone: (877) 8397126 [toll free within the USA]; (+1) (314) 4478878 [outside the USA]; fax: (+1) (314) 4478077; e-mail: JournalCustomerService-usa@elsevier.com

Oxford
Elsevier Customer Service Department, The Boulevard, Langford Lane, Kidlington, Oxford OX5 1GB, UK; phone: (+44) (1865) 843434; fax: (+44) (1865) 843970; e-mail: JournalsCustomerServiceEMEA@elsevier.com

Tokyo
Elsevier Customer Service Department, 4F Higashi-Azabu, 1-Chome Bldg, 1-9-15 Higashi-Azabu, Minato-ku, Tokyo 106-0044, Japan; Tel.: (+81) 3-5561-5037; Fax: (+81) 3-5561-5047; E-mail: JournalsCustomerService-Japan@elsevier.com

Singapore
Elsevier Customer Service Department, 3 Killiney Road, #08-01 Winsland House 1, Singapore 239519, Tel.: (+65) 6349-0222; Fax: (+65) 6733-1510; E-mail: JournalsCustomerServiceAPAC@elsevier.com

USA mailing notice: *Polyhedron* (ISSN 0277-5387) is published triweekly by Elsevier B.V. (Radarweg 29, 1043 NX Amsterdam, the Netherlands). Periodical postage paid at Rahway NJ and additional mailing offices.
USA POSTMASTER: Send change of address to *Polyhedron*, Elsevier Customer Service Department, 3251 Riverport Lane, Maryland Heights, MO 63043, USA.
AIRFREIGHT AND MAILING in the USA by Mercury International Limited, 365 Blair Road, Avenel, NJ 07001.

Advertising Information
Advertising orders and enquiries can be sent to: **USA, Canada and South America:** Mr Tino DeCarlo, The Advertising Department, Elsevier Inc., 360 Park Avenue South, New York, NY 10010-1710, USA; tel.: (+1) (212) 633 3815; fax: (+1) (212) 633 3820; e-mail: t.decarlo@elsevier.com. **Europe and ROW:** Miss Katrina Barton, Commercial Sales, Elsevier, 84 Theobald's Road, London, WCIX 8RR, UK; phone: (+44) (0) 20 7611 4117; fax: (+44) (0) 20 7611 4463; e-mail: commercialsales@elsevier.com

Funding body agreements and policies
Elsevier has established agreements and developed policies to allow authors who publish in Elsevier journals to comply with potential manuscript archiving requirements as specified as conditions of their grant awards. To learn more about existing agreements and policies please visit http://www.elsevier.com/fundingbodies

POLYHEDRON

The International Journal for Inorganic and Organometallic Chemistry

Executive Editors

The Americas
G. Christou
Department of Chemistry, University of Florida,
Gainesville, FL 32611-7200, USA
E-mail: christou@chem.ufl.edu

Rest of the world
C.E. Housecroft
Department of Chemistry, University of Basel,
Spitalstrasse 51, CH-4056 Basel, Switzerland
E-mail: poly-chemie@unibas.ch

Associate Regional Editor for China
T.C.W. Mak
Department of Chemistry, University Science Centre,
The Chinese University of Hong Kong,
Shatin NT, Hong Kong, People's Republic of China
E-mail: tcwmak@cuhk.edu.hk

Polyhedron Reports
Editor
G. Christou *(Gainesville, FL, USA)*

Symposia-in-print
Editor
G. Parkin *(New York, NY, USA)*

Editorial Board
A.G. Blackman *(Dunedin, New Zealand)*
D.C. Bradley *(London, UK)*
A. Brodie *(Palmerston North, New Zealand)*
A. Castiñeiras *(Santiago de Compostela, Spain)*
X.-M. Chen *(Guangzhou, PR China)*
M.H. Chisholm *(Columbus, OH, USA)*
E.C. Constable *(Basel, Switzerland)*
L. Cronin *(Glasgow, UK)*
G.R. Desiraju *(Hyderabad, India)*
W.J. Evans *(Irvine, CA, USA)*
L.H. Gade *(Heidelberg, Germany)*
G. Girolami *(Urbana, IL, USA)*
J.-F. Halet *(Rennes, France)*
L. Hubert-Pfalzgraf *(Villeurbanne, France)*
C. Janiak *(Freiburg, Germany)*
C. Kepert *(NSW, Australia)*
P. Kruger *(Canterbury, New Zealand)*
S. Perlepes *(Patras, Greece)*
P.P. Power *(Davis, CA, USA)*
T.B. Rauchfuss *(Urbana, IL, USA)*
J. Reedijk *(Leiden, The Netherlands)*
A.L. Rheingold *(Newark, DE, USA)*
M. Rosales Hoz *(Mexico, D.F., Mexico)*
P. Steel *(Christchurch, New Zealand)*
L.K. Thompson *(St John's, NF, Canada)*
D.A. Tocher *(Oxford, UK)*
M. Yamashita *(Sendai, Japan)*

Aims and Scope

Polyhedron will publish original, fundamental, experimental and theoretical work of the highest quality in all the major areas of inorganic chemistry. These include synthetic chemistry, coordination chemistry, organometallic chemistry, bioinorganic chemistry, and solid-state and materials chemistry. Papers should be complete pieces of work, and the inclusion of results from spectroscopic and/or physical techniques is encouraged. Papers merely reporting the preparation and X-ray structural characterization of only a single compound will not be considered appropriate unless the compound and its structure are particularly interesting.

Similarly, papers concerned solely with stability constants determined by potentiometric titration data unsupported by other e.g. spectroscopic techniques will not be acceptable nor will solvent extraction data unless supported by other data of interest to inorganic chemists. Unnecessary fragmentation of work is not acceptable.

In addition Polyhedron publishes specially commissioned review articles (Polyhedron Reports) and collections of original research papers (Polyhedron Symposia-in-Print) of appropriate timeliness.

Publication Information: Polyhedron (ISSN 0277-5387). For 2009, volume 28 is scheduled for publication. Subscription prices are available upon request from the Publisher or from the Regional Sales Office nearest you or from this journal's website (http://www.elsevier.com/locate/poly). Further information is available on this journal and other Elsevier products through Elsevier's website (http://www.elsevier.com). Subscriptions are accepted on a prepaid basis only and are entered on a calendar year basis. Issues are sent by standard mail (surface within Europe, air delivery outside Europe). Priority rates are available upon request. Claims for missing issues should be made within six months of the date of dispatch.

Orders, Claims and Journal Enquiries

(no manuscript enquiries)
Please contact the Regional Sales Office nearest you:

St. Louis
Elsevier, Customer Service Department, 11830 Westline Industrial Drive, St. Louis, MO 63146, USA; Tel.: (877) 8397126 [toll free within the USA]; (+1) (314) 4537076 [outside the USA]; Fax: (+1) (314) 5235153; E-mail: JournalCustomerService-usa@elsevier.com

Amsterdam
Elsevier, Customer Service Department, P.O. Box 211, 1000 AE Amsterdam, The Netherlands; Tel.: (+31) 20-485-3757; Fax: (+31) 20-485-3432; E-mail: JournalsCustomerServiceEMEA@elsevier.com

Tokyo
Elsevier K.K., Customer Service Department, 4F Higashi-Azabu, 1-Chome Bldg, 1-9-15 Higashi-Azabu, Minato-ku, Tokyo 106-0044, Japan; Tel.: (+81) 3-5561-5037; Fax: (+81) 3-5561-5047; E-mail: JournalsCustomerServiceJapan@elsevier.com

Singapore
Elsevier, Customer Service Department, 3 Killiney Road, #08-01 Winsland House 1, Singapore 239519, Tel.: (+65) 6349-0222; Fax: (+65) 6733-1510; E-mail: JournalsCustomerServiceAPAC@elsevier.com

USA mailing notice: *Polyhedron* (ISSN 0277-5387) is published triweekly by Elsevier B.V. (Radarweg 29, 1043 NX Amsterdam, the Netherlands). Periodical postage paid at Rahway NJ and additional mailing offices.
USA POSTMASTER: Send change of address to *Polyhedron*, Elsevier, Customer Service Department, 11830 Westline Industrial Drive, St. Louis, MO 63146, USA.
AIRFREIGHT AND MAILING in the USA by Mercury International Limited, 365 Blair Road, Avenel, NJ 07001.

Advertising Information
Advertising orders and enquiries can be sent to: **USA, Canada and South America:** Mr Tino DeCarlo, The Advertising Department, Elsevier Inc., 360 Park Avenue South, New York, NY 10010-1710, USA; tel.: (+1) (212) 633 3815; fax: (+1) (212) 633 3820; e-mail: t.decarlo@elsevier.com. **Europe and ROW:** Miss Katrina Barton, Commercial Sales, Elsevier, 84 Theobald's Road, London, WCIX 8RR, UK; phone: (+44) (0) 20 7611 4117; fax: (+44) (0) 20 7611 4463; e-mail: commercialsales@elsevier.com

Funding body agreements and policies
Elsevier has established agreements and developed policies to allow authors who publish in Elsevier journals to comply with potential manuscript archiving requirements as specified as conditions of their grant awards. To learn more about existing agreements and policies please visit http://www.elsevier.com/fundingbodies

POLYHEDRON

The International Journal for Inorganic and Organometallic Chemistry

Executive Editors

The Americas
G. Christou
Department of Chemistry, University of Florida,
Gainesville, FL 32611-7200, USA
E-mail: christou@chem.ufl.edu

Rest of the world
C.E. Housecroft
Department of Chemistry, University of Basel,
Spitalstrasse 51, CH-4056 Basel, Switzerland
E-mail: poly-chemie@unibas.ch

Associate Regional Editor for China
T.C.W. Mak
Department of Chemistry, University Science Centre,
The Chinese University of Hong Kong,
Shatin NT, Hong Kong, People's Republic of China
E-mail: tcwmak@cuhk.edu.hk

Polyhedron Reports
Editor
G. Christou *(Gainesville, FL, USA)*

Symposia-in-print
Editor
G. Parkin *(New York, NY, USA)*

Editorial Board
A.G. Blackman *(Dunedin, New Zealand)*
D.C. Bradley *(London, UK)*
A. Brodie *(Palmerston North, New Zealand)*
A. Castiñeiras *(Santiago de Compostela, Spain)*
X.-M. Chen *(Guangzhou, PR China)*
M.H. Chisholm *(Columbus, OH, USA)*
E.C. Constable *(Basel, Switzerland)*
L. Cronin *(Glasgow, UK)*
G.R. Desiraju *(Hyderabad, India)*
W.J. Evans *(Irvine, CA, USA)*
L.H. Gade *(Heidelberg, Germany)*
G. Girolami *(Urbana, IL, USA)*
J.-F. Halet *(Rennes, France)*
L. Hubert-Pfalzgraf *(Villeurbanne, France)*
C. Janiak *(Freiburg, Germany)*
C. Kepert *(NSW, Australia)*
P. Kruger *(Canterbury, New Zealand)*
S. Perlepes *(Patras, Greece)*
P.P. Power *(Davis, CA, USA)*
T.B. Rauchfuss *(Urbana, IL, USA)*
J. Reedijk *(Leiden, The Netherlands)*
A.L. Rheingold *(Newark, DE, USA)*
M. Rosales Hoz *(Mexico, D.F., Mexico)*
P. Steel *(Christchurch, New Zealand)*
L.K. Thompson *(St John's, NF, Canada)*
D.A. Tocher *(Oxford, UK)*
M. Yamashita *(Sendai, Japan)*

Aims and Scope

Polyhedron will publish original, fundamental, experimental and theoretical work of the highest quality in all the major areas of inorganic chemistry. These include synthetic chemistry, coordination chemistry, organometallic chemistry, bioinorganic chemistry, and solid-state and materials chemistry. Papers should be complete pieces of work, and the inclusion of results from spectroscopic and/or physical techniques is encouraged. Papers merely reporting the preparation and X-ray structural characterization of only a single compound will not be considered appropriate unless the compound and its structure are particularly interesting.

Similarly, papers concerned solely with stability constants determined by potentiometric titration data unsupported by other e.g. spectroscopic techniques will not be acceptable nor will solvent extraction data unless supported by other data of interest to inorganic chemists. Unnecessary fragmentation of work is not acceptable.

In addition Polyhedron publishes specially commissioned review articles (Polyhedron Reports) and collections of original research papers (Polyhedron Symposia-in-Print) of appropriate timeliness.

Publication Information: Polyhedron (ISSN 0277-5387). For 2009, volume 28 is scheduled for publication. Subscription prices are available upon request from the Publisher or from the Regional Sales Office nearest you or from this journal's website (http://www.elsevier.com/locate/poly). Further information is available on this journal and other Elsevier products through Elsevier's website (http://www.elsevier.com). Subscriptions are accepted on a prepaid basis only and are entered on a calendar year basis. Issues are sent by standard mail (surface within Europe, air delivery outside Europe). Priority rates are available upon request. Claims for missing issues should be made within six months of the date of dispatch.

Orders, Claims and Journal Enquiries

(no manuscript enquiries)
Please contact the Regional Sales Office nearest you:

St. Louis
Elsevier, Customer Service Department, 11830 Westline Industrial Drive, St. Louis, MO 63146, USA; Tel.: (877) 8397126 [toll free within the USA]; (+1) (314) 4537076 [outside the USA]; Fax: (+1) (314) 5235153; E-mail: JournalCustomerService-usa@elsevier.com

Amsterdam
Elsevier, Customer Service Department, P.O. Box 211, 1000 AE Amsterdam, The Netherlands; Tel.: (+31) 20-485-3757; Fax: (+31) 20-485-3432; E-mail: JournalsCustomerServiceEMEA@elsevier.com

Tokyo
Elsevier K.K., Customer Service Department, 4F Higashi-Azabu, 1-Chome Bldg, 1-9-15 Higashi-Azabu, Minato-ku, Tokyo 106-0044, Japan; Tel.: (+81) 3-5561-5037; Fax: (+81) 3-5561-5047; E-mail: JournalsCustomerServiceJapan@elsevier.com

Singapore
Elsevier, Customer Service Department, 3 Killiney Road, #08-01 Winsland House 1, Singapore 239519, Tel.: (+65) 6349-0222; Fax: (+65) 6733-1510; E-mail: JournalsCustomerServiceAPAC@elsevier.com

USA mailing notice: *Polyhedron* (ISSN 0277-5387) is published triweekly by Elsevier B.V. (Radarweg 29, 1043 NX Amsterdam, the Netherlands). Periodical postage paid at Rahway NJ and additional mailing offices.
USA POSTMASTER: Send change of address to *Polyhedron*, Elsevier, Customer Service Department, 11830 Westline Industrial Drive, St. Louis, MO 63146, USA.
AIRFREIGHT AND MAILING in the USA by Mercury International Limited, 365 Blair Road, Avenel, NJ 07001.

Advertising Information
Advertising orders and enquiries can be sent to: **USA, Canada and South America:** Mr Tino DeCarlo, The Advertising Department, Elsevier Inc., 360 Park Avenue South, New York, NY 10010-1710, USA; tel.: (+1) (212) 633 3815; fax: (+1) (212) 633 3820; e-mail: t.decarlo@elsevier.com. **Europe and ROW:** Miss Katrina Barton, Commercial Sales, Elsevier, 84 Theobald's Road, London, WCIX 8RR, UK; phone: (+44) (0) 20 7611 4117; fax: (+44) (0) 20 7611 4463; e-mail: commercialsales@elsevier.com

Funding body agreements and policies
Elsevier has established agreements and developed policies to allow authors who publish in Elsevier journals to comply with potential manuscript archiving requirements as specified as conditions of their grant awards. To learn more about existing agreements and policies please visit http://www.elsevier.com/fundingbodies

POLYHEDRON

The International Journal for Inorganic and Organometallic Chemistry

Executive Editors

The Americas
G. Christou
Department of Chemistry, University of Florida,
Gainesville, FL 32611-7200, USA
E-mail: christou@chem.ufl.edu

Rest of the world
C.E. Housecroft
Department of Chemistry, University of Basel,
Spitalstrasse 51, CH-4056 Basel, Switzerland
E-mail: poly-chemie@unibas.ch

Associate Regional Editor for China
T.C.W. Mak
Department of Chemistry, University Science Centre,
The Chinese University of Hong Kong,
Shatin NT, Hong Kong, People's Republic of China
E-mail: tcwmak@cuhk.edu.hk

Polyhedron Reports
Editor
G. Christou *(Gainesville, FL, USA)*

Symposia-in-print
Editor
G. Parkin *(New York, NY, USA)*

Editorial Board
A.G. Blackman *(Dunedin, New Zealand)*
D.C. Bradley *(London, UK)*
A. Brodie *(Palmerston North, New Zealand)*
A. Castiñeiras *(Santiago de Compostela, Spain)*
X.-M. Chen *(Guangzhou, PR China)*
M.H. Chisholm *(Columbus, OH, USA)*
E.C. Constable *(Basel, Switzerland)*
L. Cronin *(Glasgow, UK)*
G.R. Desiraju *(Hyderabad, India)*
W.J. Evans *(Irvine, CA, USA)*
L.H. Gade *(Heidelberg, Germany)*
G. Girolami *(Urbana, IL, USA)*
J.-F. Halet *(Rennes, France)*
L. Hubert-Pfalzgraf *(Villeurbanne, France)*
C. Janiak *(Freiburg, Germany)*
C. Kepert *(NSW, Australia)*
P. Kruger *(Canterbury, New Zealand)*
S. Perlepes *(Patras, Greece)*
P.P. Power *(Davis, CA, USA)*
T.B. Rauchfuss *(Urbana, IL, USA)*
J. Reedijk *(Leiden, The Netherlands)*
A.L. Rheingold *(Newark, DE, USA)*
M. Rosales Hoz *(Mexico, D.F., Mexico)*
P. Steel *(Christchurch, New Zealand)*
L.K. Thompson *(St John's, NF, Canada)*
D.A. Tocher *(Oxford, UK)*
M. Yamashita *(Sendai, Japan)*

Aims and Scope

Polyhedron will publish original, fundamental, experimental and theoretical work of the highest quality in all the major areas of inorganic chemistry. These include synthetic chemistry, coordination chemistry, organometallic chemistry, bioinorganic chemistry, and solid-state and materials chemistry. Papers should be complete pieces of work, and the inclusion of results from spectroscopic and/or physical techniques is encouraged. Papers merely reporting the preparation and X-ray structural characterization of only a single compound will not be considered appropriate unless the compound and its structure are particularly interesting.

Similarly, papers concerned solely with stability constants determined by potentiometric titration data unsupported by other e.g. spectroscopic techniques will not be acceptable nor will solvent extraction data unless supported by other data of interest to inorganic chemists. Unnecessary fragmentation of work is not acceptable.

In addition Polyhedron publishes specially commissioned review articles (Polyhedron Reports) and collections of original research papers (Polyhedron Symposia-in-Print) of appropriate timeliness.

Publication Information: Polyhedron (ISSN 0277-5387). For 2009, volume 28 is scheduled for publication. Subscription prices are available upon request from the Publisher or from the Regional Sales Office nearest you or from this journal's website (http://www.elsevier.com/locate/poly). Further information is available on this journal and other Elsevier products through Elsevier's website (http://www.elsevier.com). Subscriptions are accepted on a prepaid basis only and are entered on a calendar year basis. Issues are sent by standard mail (surface within Europe, air delivery outside Europe). Priority rates are available upon request. Claims for missing issues should be made within six months of the date of dispatch.

Orders, Claims and Journal Enquiries

(no manuscript enquiries)
Please contact the Regional Sales Office nearest you:

St. Louis
Elsevier, Customer Service Department, 11830 Westline Industrial Drive, St. Louis, MO 63146, USA; Tel.: (877) 8397126 [toll free within the USA]; (+1) (314) 4537076 [outside the USA]; Fax: (+1) (314) 5235153; E-mail: JournalCustomerService-usa@elsevier.com

Amsterdam
Elsevier, Customer Service Department, P.O. Box 211, 1000 AE Amsterdam, The Netherlands; Tel.: (+31) 20-485-3757; Fax: (+31) 20-485-3432; E-mail: JournalsCustomerServiceEMEA@elsevier.com

Tokyo
Elsevier K.K., Customer Service Department, 4F Higashi-Azabu, 1-Chome Bldg, 1-9-15 Higashi-Azabu, Minato-ku, Tokyo 106-0044, Japan; Tel.: (+81) 3-5561-5037; Fax: (+81) 3-5561-5047; E-mail: JournalsCustomerServiceJapan@elsevier.com

Singapore
Elsevier, Customer Service Department, 3 Killiney Road, #08-01 Winsland House 1, Singapore 239519, Tel.: (+65) 6349-0222; Fax: (+65) 6733-1510; E-mail: JournalsCustomerServiceAPAC@elsevier.com

USA mailing notice: *Polyhedron* (ISSN 0277-5387) is published triweekly by Elsevier B.V. (Radarweg 29, 1043 NX Amsterdam, the Netherlands). Periodical postage paid at Rahway NJ and additional mailing offices.
USA POSTMASTER: Send change of address to *Polyhedron*, Elsevier, Customer Service Department, 11830 Westline Industrial Drive, St. Louis, MO 63146, USA.
AIRFREIGHT AND MAILING in the USA by Mercury International Limited, 365 Blair Road, Avenel, NJ 07001.

Advertising Information
Advertising orders and enquiries can be sent to: **USA, Canada and South America:** Mr Tino DeCarlo, The Advertising Department, Elsevier Inc., 360 Park Avenue South, New York, NY 10010-1710, USA; tel.: (+1) (212) 633 3815; fax: (+1) (212) 633 3820; e-mail: t.decarlo@elsevier.com. **Europe and ROW:** Miss Katrina Barton, Commercial Sales, Elsevier, 84 Theobald's Road, London, WCIX 8RR, UK; phone: (+44) (0) 20 7611 4117; fax: (+44) (0) 20 7611 4463; e-mail: commercialsales@elsevier.com

Funding body agreements and policies
Elsevier has established agreements and developed policies to allow authors who publish in Elsevier journals to comply with potential manuscript archiving requirements as specified as conditions of their grant awards. To learn more about existing agreements and policies please visit http://www.elsevier.com/fundingbodies

POLYHEDRON

The International Journal for Inorganic and Organometallic Chemistry

Executive Editors

The Americas
G. Christou
Department of Chemistry, University of Florida,
Gainesville, FL 32611-7200, USA
E-mail: christou@chem.ufl.edu

Rest of the world
C.E. Housecroft
Department of Chemistry, University of Basel,
Spitalstrasse 51, CH-4056 Basel, Switzerland
E-mail: poly-chemie@unibas.ch

Associate Regional Editor for China
T.C.W. Mak
Department of Chemistry, University Science Centre,
The Chinese University of Hong Kong,
Shatin NT, Hong Kong, People's Republic of China
E-mail: tcwmak@cuhk.edu.hk

Polyhedron Reports
Editor
G. Christou *(Gainesville, FL, USA)*

Symposia-in-print
Editor
G. Parkin *(New York, NY, USA)*

Editorial Board
A.G. Blackman *(Dunedin, New Zealand)*
D.C. Bradley *(London, UK)*
A. Brodie *(Palmerston North, New Zealand)*
A. Castiñeiras *(Santiago de Compostela, Spain)*
X.-M. Chen *(Guangzhou, PR China)*
M.H. Chisholm *(Columbus, OH, USA)*
E.C. Constable *(Basel, Switzerland)*
L. Cronin *(Glasgow, UK)*
G.R. Desiraju *(Hyderabad, India)*
W.J. Evans *(Irvine, CA, USA)*
L.H. Gade *(Heidelberg, Germany)*
G. Girolami *(Urbana, IL, USA)*
J.-F. Halet *(Rennes, France)*
L. Hubert-Pfalzgraf *(Villeurbanne, France)*
C. Janiak *(Freiburg, Germany)*
C. Kepert *(NSW, Australia)*
P. Kruger *(Canterbury, New Zealand)*
S. Perlepes *(Patras, Greece)*
P.P. Power *(Davis, CA, USA)*
T.B. Rauchfuss *(Urbana, IL, USA)*
J. Reedijk *(Leiden, The Netherlands)*
A.L. Rheingold *(Newark, DE, USA)*
M. Rosales Hoz *(Mexico, D.F., Mexico)*
P. Steel *(Christchurch, New Zealand)*
L.K. Thompson *(St John's, NF, Canada)*
D.A. Tocher *(Oxford, UK)*
M. Yamashita *(Sendai, Japan)*

Aims and Scope

Polyhedron will publish original, fundamental, experimental and theoretical work of the highest quality in all the major areas of inorganic chemistry. These include synthetic chemistry, coordination chemistry, organometallic chemistry, bioinorganic chemistry, and solid-state and materials chemistry. Papers should be complete pieces of work, and the inclusion of results from spectroscopic and/or physical techniques is encouraged. Papers merely reporting the preparation and X-ray structural characterization of only a single compound will not be considered appropriate unless the compound and its structure are particularly interesting.

Similarly, papers concerned solely with stability constants determined by potentiometric titration data unsupported by other e.g. spectroscopic techniques will not be acceptable nor will solvent extraction data unless supported by other data of interest to inorganic chemists. Unnecessary fragmentation of work is not acceptable.

In addition Polyhedron publishes specially commissioned review articles (Polyhedron Reports) and collections of original research papers (Polyhedron Symposia-in-Print) of appropriate timeliness.

Publication Information: Polyhedron (ISSN 0277-5387). For 2009, volume 28 is scheduled for publication. Subscription prices are available upon request from the Publisher or from the Regional Sales Office nearest you or from this journal's website (http://www.elsevier.com/locate/poly). Further information is available on this journal and other Elsevier products through Elsevier's website (http://www.elsevier.com). Subscriptions are accepted on a prepaid basis only and are entered on a calendar year basis. Issues are sent by standard mail (surface within Europe, air delivery outside Europe). Priority rates are available upon request. Claims for missing issues should be made within six months of the date of dispatch.

Orders, Claims and Journal Enquiries

(no manuscript enquiries)
Please contact the Regional Sales Office nearest you:

St. Louis
Elsevier, Customer Service Department, 11830 Westline Industrial Drive, St. Louis, MO 63146, USA; Tel.: (877) 8397126 [toll free within the USA]; (+1) (314) 4537076 [outside the USA]; Fax: (+1) (314) 5235153; E-mail: JournalCustomerService-usa@elsevier.com

Amsterdam
Elsevier, Customer Service Department, P.O. Box 211, 1000 AE Amsterdam, The Netherlands; Tel.: (+31) 20-485-3757; Fax: (+31) 20-485-3432; E-mail: JournalsCustomerServiceEMEA@elsevier.com

Tokyo
Elsevier K.K., Customer Service Department, 4F Higashi-Azabu, 1-Chome Bldg, 1-9-15 Higashi-Azabu, Minato-ku, Tokyo 106-0044, Japan; Tel.: (+81) 3-5561-5037; Fax: (+81) 3-5561-5047; E-mail: JournalsCustomerServiceJapan@elsevier.com

Singapore
Elsevier, Customer Service Department, 3 Killiney Road, #08-01 Winsland House 1, Singapore 239519, Tel.: (+65) 6349-0222; Fax: (+65) 6733-1510; E-mail: JournalsCustomerServiceAPAC@elsevier.com

USA mailing notice: *Polyhedron* (ISSN 0277-5387) is published triweekly by Elsevier B.V. (Radarweg 29, 1043 NX Amsterdam, the Netherlands). Periodical postage paid at Rahway NJ and additional mailing offices.
USA POSTMASTER: Send change of address to *Polyhedron*, Elsevier, Customer Service Department, 11830 Westline Industrial Drive, St. Louis, MO 63146, USA.
AIRFREIGHT AND MAILING in the USA by Mercury International Limited, 365 Blair Road, Avenel, NJ 07001.

Advertising Information
Advertising orders and enquiries can be sent to: **USA, Canada and South America:** Mr Tino DeCarlo, The Advertising Department, Elsevier Inc., 360 Park Avenue South, New York, NY 10010-1710, USA; tel.: (+1) (212) 633 3815; fax: (+1) (212) 633 3820; e-mail: t.decarlo@elsevier.com. **Europe and ROW:** Miss Katrina Barton, Commercial Sales, Elsevier, 84 Theobald's Road, London, WCIX 8RR, UK; phone: (+44) (0) 20 7611 4117; fax: (+44) (0) 20 7611 4463; e-mail: commercialsales@elsevier.com

Funding body agreements and policies
Elsevier has established agreements and developed policies to allow authors who publish in Elsevier journals to comply with potential manuscript archiving requirements as specified as conditions of their grant awards. To learn more about existing agreements and policies please visit http://www.elsevier.com/fundingbodies

POLYHEDRON

The International Journal for Inorganic and Organometallic Chemistry

Executive Editors

The Americas
G. Christou
Department of Chemistry, University of Florida,
Gainesville, FL 32611-7200, USA
E-mail: christou@chem.ufl.edu

Rest of the world
C.E. Housecroft
Department of Chemistry, University of Basel,
Spitalstrasse 51, CH-4056 Basel, Switzerland
E-mail: poly-chemie@unibas.ch

Associate Regional Editor for China
T.C.W. Mak
Department of Chemistry, University Science Centre,
The Chinese University of Hong Kong,
Shatin NT, Hong Kong, People's Republic of China
E-mail: tcwmak@cuhk.edu.hk

Polyhedron Reports
Editor
G. Christou *(Gainesville, FL, USA)*

Symposia-in-print
Editor
G. Parkin *(New York, NY, USA)*

Editorial Board
A.G. Blackman *(Dunedin, New Zealand)*
D.C. Bradley *(London, UK)*
A. Brodie *(Palmerston North, New Zealand)*
A. Castiñeiras *(Santiago de Compostela, Spain)*
X.-M. Chen *(Guangzhou, PR China)*
M.H. Chisholm *(Columbus, OH, USA)*
E.C. Constable *(Basel, Switzerland)*
L. Cronin *(Glasgow, UK)*
G.R. Desiraju *(Hyderabad, India)*
W.J. Evans *(Irvine, CA, USA)*
L.H. Gade *(Heidelberg, Germany)*
G. Girolami *(Urbana, IL, USA)*
J.-F. Halet *(Rennes, France)*
L. Hubert-Pfalzgraf *(Villeurbanne, France)*
C. Janiak *(Freiburg, Germany)*
C. Kepert *(NSW, Australia)*
P. Kruger *(Canterbury, New Zealand)*
S. Perlepes *(Patras, Greece)*
P.P. Power *(Davis, CA, USA)*
T.B. Rauchfuss *(Urbana, IL, USA)*
J. Reedijk *(Leiden, The Netherlands)*
A.L. Rheingold *(Newark, DE, USA)*
M. Rosales Hoz *(Mexico, D.F., Mexico)*
P. Steel *(Christchurch, New Zealand)*
L.K. Thompson *(St John's, NF, Canada)*
D.A. Tocher *(Oxford, UK)*
M. Yamashita *(Sendai, Japan)*

Aims and Scope

Polyhedron will publish original, fundamental, experimental and theoretical work of the highest quality in all the major areas of inorganic chemistry. These include synthetic chemistry, coordination chemistry, organometallic chemistry, bioinorganic chemistry, and solid-state and materials chemistry. Papers should be complete pieces of work, and the inclusion of results from spectroscopic and/or physical techniques is encouraged. Papers merely reporting the preparation and X-ray structural characterization of only a single compound will not be considered appropriate unless the compound and its structure are particularly interesting.

Similarly, papers concerned solely with stability constants determined by potentiometric titration data unsupported by other e.g. spectroscopic techniques will not be acceptable nor will solvent extraction data unless supported by other data of interest to inorganic chemists. Unnecessary fragmentation of work is not acceptable.

In addition Polyhedron publishes specially commissioned review articles (Polyhedron Reports) and collections of original research papers (Polyhedron Symposia-in-Print) of appropriate timeliness.

Publication Information: Polyhedron (ISSN 0277-5387). For 2009, volume 28 is scheduled for publication. Subscription prices are available upon request from the Publisher or from the Regional Sales Office nearest you or from this journal's website (http://www.elsevier.com/locate/poly). Further information is available on this journal and other Elsevier products through Elsevier's website (http://www.elsevier.com). Subscriptions are accepted on a prepaid basis only and are entered on a calendar year basis. Issues are sent by standard mail (surface within Europe, air delivery outside Europe). Priority rates are available upon request. Claims for missing issues should be made within six months of the date of dispatch.

Orders, Claims and Journal Enquiries

(no manuscript enquiries)
Please contact the Regional Sales Office nearest you:

St. Louis
Elsevier, Customer Service Department, 11830 Westline Industrial Drive, St. Louis, MO 63146, USA; Tel.: (877) 8397126 [toll free within the USA]; (+1) (314) 4537076 [outside the USA]; Fax: (+1) (314) 5235153; E-mail: JournalCustomerService-usa@elsevier.com

Amsterdam
Elsevier, Customer Service Department, P.O. Box 211, 1000 AE Amsterdam, The Netherlands; Tel.: (+31) 20-485-3757; Fax: (+31) 20-485-3432; E-mail: JournalsCustomerServiceEMEA@elsevier.com

Tokyo
Elsevier K.K., Customer Service Department, 4F Higashi-Azabu, 1-Chome Bldg, 1-9-15 Higashi-Azabu, Minato-ku, Tokyo 106-0044, Japan; Tel.: (+81) 3-5561-5037; Fax: (+81) 3-5561-5047; E-mail: JournalsCustomerServiceJapan@elsevier.com

Singapore
Elsevier, Customer Service Department, 3 Killiney Road, #08-01 Winsland House 1, Singapore 239519, Tel.: (+65) 6349-0222; Fax: (+65) 6733-1510; E-mail: JournalsCustomerServiceAPAC@elsevier.com

USA mailing notice: *Polyhedron* (ISSN 0277-5387) is published triweekly by Elsevier B.V. (Radarweg 29, 1043 NX Amsterdam, the Netherlands). Periodical postage paid at Rahway NJ and additional mailing offices.
USA POSTMASTER: Send change of address to *Polyhedron*, Elsevier, Customer Service Department, 11830 Westline Industrial Drive, St. Louis, MO 63146, USA.
AIRFREIGHT AND MAILING in the USA by Mercury International Limited, 365 Blair Road, Avenel, NJ 07001.

Advertising Information
Advertising orders and enquiries can be sent to: **USA, Canada and South America:** Mr Tino DeCarlo, The Advertising Department, Elsevier Inc., 360 Park Avenue South, New York, NY 10010-1710, USA; tel.: (+1) (212) 633 3815; fax: (+1) (212) 633 3820; e-mail: t.decarlo@elsevier.com. **Europe and ROW:** Miss Katrina Barton, Commercial Sales, Elsevier, 84 Theobald's Road, London, WCIX 8RR, UK; phone: (+44) (0) 20 7611 4117; fax: (+44) (0) 20 7611 4463; e-mail: commercialsales@elsevier.com

Funding body agreements and policies
Elsevier has established agreements and developed policies to allow authors who publish in Elsevier journals to comply with potential manuscript archiving requirements as specified as conditions of their grant awards. To learn more about existing agreements and policies please visit http://www.elsevier.com/fundingbodies

POLYHEDRON

The International Journal for Inorganic and Organometallic Chemistry

Executive Editors

The Americas
G. Christou
Department of Chemistry, University of Florida,
Gainesville, FL 32611-7200, USA
E-mail: christou@chem.ufl.edu

Rest of the world
C.E. Housecroft
Department of Chemistry, University of Basel,
Spitalstrasse 51, CH-4056 Basel, Switzerland
E-mail: poly-chemie@unibas.ch

Associate Regional Editor for China
T.C.W. Mak
Department of Chemistry, University Science Centre,
The Chinese University of Hong Kong,
Shatin NT, Hong Kong, People's Republic of China
E-mail: tcwmak@cuhk.edu.hk

Polyhedron Reports
Editor
G. Christou *(Gainesville, FL, USA)*

Symposia-in-print
Editor
G. Parkin *(New York, NY, USA)*

Editorial Board
A.G. Blackman *(Dunedin, New Zealand)*
D.C. Bradley *(London, UK)*
A. Brodie *(Palmerston North, New Zealand)*
A. Castiñeiras *(Santiago de Compostela, Spain)*
X.-M. Chen *(Guangzhou, PR China)*
M.H. Chisholm *(Columbus, OH, USA)*
E.C. Constable *(Basel, Switzerland)*
L. Cronin *(Glasgow, UK)*
G.R. Desiraju *(Hyderabad, India)*
W.J. Evans *(Irvine, CA, USA)*
L.H. Gade *(Heidelberg, Germany)*
G. Girolami *(Urbana, IL, USA)*
J.-F. Halet *(Rennes, France)*
L. Hubert-Pfalzgraf *(Villeurbanne, France)*
C. Janiak *(Freiburg, Germany)*
C. Kepert *(NSW, Australia)*
P. Kruger *(Canterbury, New Zealand)*
S. Perlepes *(Patras, Greece)*
P.P. Power *(Davis, CA, USA)*
T.B. Rauchfuss *(Urbana, IL, USA)*
J. Reedijk *(Leiden, The Netherlands)*
A.L. Rheingold *(Newark, DE, USA)*
M. Rosales Hoz *(Mexico, D.F., Mexico)*
P. Steel *(Christchurch, New Zealand)*
L.K. Thompson *(St John's, NF, Canada)*
D.A. Tocher *(Oxford, UK)*
M. Yamashita *(Sendai, Japan)*

Aims and Scope

Polyhedron will publish original, fundamental, experimental and theoretical work of the highest quality in all the major areas of inorganic chemistry. These include synthetic chemistry, coordination chemistry, organometallic chemistry, bioinorganic chemistry, and solid-state and materials chemistry. Papers should be complete pieces of work, and the inclusion of results from spectroscopic and/or physical techniques is encouraged. Papers merely reporting the preparation and X-ray structural characterization of only a single compound will not be considered appropriate unless the compound and its structure are particularly interesting.

Similarly, papers concerned solely with stability constants determined by potentiometric titration data unsupported by other e.g. spectroscopic techniques will not be acceptable nor will solvent extraction data unless supported by other data of interest to inorganic chemists. Unnecessary fragmentation of work is not acceptable.

In addition Polyhedron publishes specially commissioned review articles (Polyhedron Reports) and collections of original research papers (Polyhedron Symposia-in-Print) of appropriate timeliness.

Publication Information: Polyhedron (ISSN 0277-5387). For 2009, volume 28 is scheduled for publication. Subscription prices are available upon request from the Publisher or from the Regional Sales Office nearest you or from this journal's website (http://www.elsevier.com/locate/poly). Further information is available on this journal and other Elsevier products through Elsevier's website (http://www.elsevier.com). Subscriptions are accepted on a prepaid basis only and are entered on a calendar year basis. Issues are sent by standard mail (surface within Europe, air delivery outside Europe). Priority rates are available upon request. Claims for missing issues should be made within six months of the date of dispatch.

Orders, Claims and Journal Enquiries

(no manuscript enquiries)
Please contact the Regional Sales Office nearest you:

St. Louis
Elsevier, Customer Service Department, 11830 Westline Industrial Drive, St. Louis, MO 63146, USA; Tel.: (877) 8397126 [toll free within the USA]; (+1) (314) 4537076 [outside the USA]; Fax: (+1) (314) 5235153; E-mail: JournalCustomerService-usa@elsevier.com

Amsterdam
Elsevier, Customer Service Department, P.O. Box 211, 1000 AE Amsterdam, The Netherlands; Tel.: (+31) 20-485-3757; Fax: (+31) 20-485-3432; E-mail: JournalsCustomerServiceEMEA@elsevier.com

Tokyo
Elsevier K.K., Customer Service Department, 4F Higashi-Azabu, 1-Chome Bldg, 1-9-15 Higashi-Azabu, Minato-ku, Tokyo 106-0044, Japan; Tel.: (+81) 3-5561-5037; Fax: (+81) 3-5561-5047; E-mail: JournalsCustomerServiceJapan@elsevier.com

Singapore
Elsevier, Customer Service Department, 3 Killiney Road, #08-01 Winsland House 1, Singapore 239519, Tel.: (+65) 6349-0222; Fax: (+65) 6733-1510; E-mail: JournalsCustomerServiceAPAC@elsevier.com

USA mailing notice: *Polyhedron* (ISSN 0277-5387) is published triweekly by Elsevier B.V. (Radarweg 29, 1043 NX Amsterdam, the Netherlands). Periodical postage paid at Rahway NJ and additional mailing offices.
USA POSTMASTER: Send change of address to *Polyhedron*, Elsevier, Customer Service Department, 11830 Westline Industrial Drive, St. Louis, MO 63146, USA.
AIRFREIGHT AND MAILING in the USA by Mercury International Limited, 365 Blair Road, Avenel, NJ 07001.

Advertising Information
Advertising orders and enquiries can be sent to: **USA, Canada and South America:** Mr Tino DeCarlo, The Advertising Department, Elsevier Inc., 360 Park Avenue South, New York, NY 10010-1710, USA; tel.: (+1) (212) 633 3815; fax: (+1) (212) 633 3820; e-mail: t.decarlo@elsevier.com. **Europe and ROW:** Miss Katrina Barton, Commercial Sales, Elsevier, 84 Theobald's Road, London, WCIX 8RR, UK; phone: (+44) (0) 20 7611 4117; fax: (+44) (0) 20 7611 4463; e-mail: commercialsales@elsevier.com

Funding body agreements and policies
Elsevier has established agreements and developed policies to allow authors who publish in Elsevier journals to comply with potential manuscript archiving requirements as specified as conditions of their grant awards. To learn more about existing agreements and policies please visit http://www.elsevier.com/fundingbodies

POLYHEDRON

The International Journal for Inorganic and Organometallic Chemistry

Executive Editors

The Americas
G. Christou
Department of Chemistry, University of Florida,
Gainesville, FL 32611-7200, USA
E-mail: christou@chem.ufl.edu

Rest of the world
C.E. Housecroft
Department of Chemistry, University of Basel,
Spitalstrasse 51, CH-4056 Basel, Switzerland
E-mail: poly-chemie@unibas.ch

Associate Regional Editor for China
T.C.W. Mak
Department of Chemistry, University Science Centre,
The Chinese University of Hong Kong,
Shatin NT, Hong Kong, People's Republic of China
E-mail: tcwmak@cuhk.edu.hk

Polyhedron Reports
Editor
G. Christou *(Gainesville, FL, USA)*

Symposia-in-print
Editor
G. Parkin *(New York, NY, USA)*

Editorial Board
A.G. Blackman *(Dunedin, New Zealand)*
D.C. Bradley *(London, UK)*
A. Brodie *(Palmerston North, New Zealand)*
A. Castiñeiras *(Santiago de Compostela, Spain)*
X.-M. Chen *(Guangzhou, PR China)*
M.H. Chisholm *(Columbus, OH, USA)*
E.C. Constable *(Basel, Switzerland)*
L. Cronin *(Glasgow, UK)*
G.R. Desiraju *(Hyderabad, India)*
W.J. Evans *(Irvine, CA, USA)*
L.H. Gade *(Heidelberg, Germany)*
G. Girolami *(Urbana, IL, USA)*
J.-F. Halet *(Rennes, France)*
L. Hubert-Pfalzgraf *(Villeurbanne, France)*
C. Janiak *(Freiburg, Germany)*
C. Kepert *(NSW, Australia)*
P. Kruger *(Canterbury, New Zealand)*
S. Perlepes *(Patras, Greece)*
P.P. Power *(Davis, CA, USA)*
T.B. Rauchfuss *(Urbana, IL, USA)*
J. Reedijk *(Leiden, The Netherlands)*
A.L. Rheingold *(Newark, DE, USA)*
M. Rosales Hoz *(Mexico, D.F., Mexico)*
P. Steel *(Christchurch, New Zealand)*
L.K. Thompson *(St John's, NF, Canada)*
D.A. Tocher *(Oxford, UK)*
M. Yamashita *(Sendai, Japan)*

Aims and Scope

Polyhedron will publish original, fundamental, experimental and theoretical work of the highest quality in all the major areas of inorganic chemistry. These include synthetic chemistry, coordination chemistry, organometallic chemistry, bioinorganic chemistry, and solid-state and materials chemistry. Papers should be complete pieces of work, and the inclusion of results from spectroscopic and/or physical techniques is encouraged. Papers merely reporting the preparation and X-ray structural characterization of only a single compound will not be considered appropriate unless the compound and its structure are particularly interesting.

Similarly, papers concerned solely with stability constants determined by potentiometric titration data unsupported by other e.g. spectroscopic techniques will not be acceptable nor will solvent extraction data unless supported by other data of interest to inorganic chemists. Unnecessary fragmentation of work is not acceptable.

In addition Polyhedron publishes specially commissioned review articles (Polyhedron Reports) and collections of original research papers (Polyhedron Symposia-in-Print) of appropriate timeliness.

Publication Information: Polyhedron (ISSN 0277-5387). For 2009, volume 28 is scheduled for publication. Subscription prices are available upon request from the Publisher or from the Regional Sales Office nearest you or from this journal's website (http://www.elsevier.com/locate/poly). Further information is available on this journal and other Elsevier products through Elsevier's website (http://www.elsevier.com). Subscriptions are accepted on a prepaid basis only and are entered on a calendar year basis. Issues are sent by standard mail (surface within Europe, air delivery outside Europe). Priority rates are available upon request. Claims for missing issues should be made within six months of the date of dispatch.

Orders, Claims and Journal Enquiries

(no manuscript enquiries)
Please contact the Regional Sales Office nearest you:

St. Louis
Elsevier, Customer Service Department, 11830 Westline Industrial Drive, St. Louis, MO 63146, USA; Tel.: (877) 8397126 [toll free within the USA]; (+1) (314) 4537076 [outside the USA]; Fax: (+1) (314) 5235153; E-mail: JournalCustomerService-usa@elsevier.com

Amsterdam
Elsevier, Customer Service Department, P.O. Box 211, 1000 AE Amsterdam, The Netherlands; Tel.: (+31) 20-485-3757; Fax: (+31) 20-485-3432; E-mail: JournalsCustomerServiceEMEA@elsevier.com

Tokyo
Elsevier K.K., Customer Service Department, 4F Higashi-Azabu, 1-Chome Bldg, 1-9-15 Higashi-Azabu, Minato-ku, Tokyo 106-0044, Japan; Tel.: (+81) 3-5561-5037; Fax: (+81) 3-5561-5047; E-mail: JournalsCustomerServiceJapan@elsevier.com

Singapore
Elsevier, Customer Service Department, 3 Killiney Road, #08-01 Winsland House 1, Singapore 239519, Tel.: (+65) 6349-0222; Fax: (+65) 6733-1510; E-mail: JournalsCustomerServiceAPAC@elsevier.com

USA mailing notice: *Polyhedron* (ISSN 0277-5387) is published triweekly by Elsevier B.V. (Radarweg 29, 1043 NX Amsterdam, the Netherlands). Periodical postage paid at Rahway NJ and additional mailing offices.
USA POSTMASTER: Send change of address to *Polyhedron*, Elsevier, Customer Service Department, 11830 Westline Industrial Drive, St. Louis, MO 63146, USA.
AIRFREIGHT AND MAILING in the USA by Mercury International Limited, 365 Blair Road, Avenel, NJ 07001.

Advertising Information
Advertising orders and enquiries can be sent to: **USA, Canada and South America:** Mr Tino DeCarlo, The Advertising Department, Elsevier Inc., 360 Park Avenue South, New York, NY 10010-1710, USA; tel.: (+1) (212) 633 3815; fax: (+1) (212) 633 3820; e-mail: t.decarlo@elsevier.com. **Europe and ROW:** Miss Katrina Barton, Commercial Sales, Elsevier, 84 Theobald's Road, London, WCIX 8RR, UK; phone: (+44) (0) 20 7611 4117; fax: (+44) (0) 20 7611 4463; e-mail: commercialsales@elsevier.com

Funding body agreements and policies
Elsevier has established agreements and developed policies to allow authors who publish in Elsevier journals to comply with potential manuscript archiving requirements as specified as conditions of their grant awards. To learn more about existing agreements and policies please visit http://www.elsevier.com/fundingbodies

POLYHEDRON

The International Journal for Inorganic and Organometallic Chemistry

Executive Editors

The Americas
G. Christou
Department of Chemistry, University of Florida,
Gainesville, FL 32611-7200, USA
E-mail: christou@chem.ufl.edu

Rest of the world
C.E. Housecroft
Department of Chemistry, University of Basel,
Spitalstrasse 51, CH-4056 Basel, Switzerland
E-mail: poly-chemie@unibas.ch

Associate Regional Editor for China
T.C.W. Mak
Department of Chemistry, University Science Centre,
The Chinese University of Hong Kong,
Shatin NT, Hong Kong, People's Republic of China
E-mail: tcwmak@cuhk.edu.hk

Polyhedron Reports
Editor
G. Christou *(Gainesville, FL, USA)*

Symposia-in-print
Editor
G. Parkin *(New York, NY, USA)*

Editorial Board
A.G. Blackman *(Dunedin, New Zealand)*
D.C. Bradley *(London, UK)*
A. Brodie *(Palmerston North, New Zealand)*
A. Castiñeiras *(Santiago de Compostela, Spain)*
X.-M. Chen *(Guangzhou, PR China)*
M.H. Chisholm *(Columbus, OH, USA)*
E.C. Constable *(Basel, Switzerland)*
L. Cronin *(Glasgow, UK)*
G.R. Desiraju *(Hyderabad, India)*
W.J. Evans *(Irvine, CA, USA)*
L.H. Gade *(Heidelberg, Germany)*
G. Girolami *(Urbana, IL, USA)*
J.-F. Halet *(Rennes, France)*
L. Hubert-Pfalzgraf *(Villeurbanne, France)*
C. Janiak *(Freiburg, Germany)*
C. Kepert *(NSW, Australia)*
P. Kruger *(Canterbury, New Zealand)*
S. Perlepes *(Patras, Greece)*
P.P. Power *(Davis, CA, USA)*
T.B. Rauchfuss *(Urbana, IL, USA)*
J. Reedijk *(Leiden, The Netherlands)*
A.L. Rheingold *(Newark, DE, USA)*
M. Rosales Hoz *(Mexico, D.F., Mexico)*
P. Steel *(Christchurch, New Zealand)*
L.K. Thompson *(St John's, NF, Canada)*
D.A. Tocher *(Oxford, UK)*
M. Yamashita *(Sendai, Japan)*

Aims and Scope

Polyhedron will publish original, fundamental, experimental and theoretical work of the highest quality in all the major areas of inorganic chemistry. These include synthetic chemistry, coordination chemistry, organometallic chemistry, bioinorganic chemistry, and solid-state and materials chemistry. Papers should be complete pieces of work, and the inclusion of results from spectroscopic and/or physical techniques is encouraged. Papers merely reporting the preparation and X-ray structural characterization of only a single compound will not be considered appropriate unless the compound and its structure are particularly interesting.

Similarly, papers concerned solely with stability constants determined by potentiometric titration data unsupported by other e.g. spectroscopic techniques will not be acceptable nor will solvent extraction data unless supported by other data of interest to inorganic chemists. Unnecessary fragmentation of work is not acceptable.

In addition Polyhedron publishes specially commissioned review articles (Polyhedron Reports) and collections of original research papers (Polyhedron Symposia-in-Print) of appropriate timeliness.

Publication Information: Polyhedron (ISSN 0277-5387). For 2009, volume 28 is scheduled for publication. Subscription prices are available upon request from the Publisher or from the Regional Sales Office nearest you or from this journal's website (http://www.elsevier.com/locate/poly). Further information is available on this journal and other Elsevier products through Elsevier's website (http://www.elsevier.com). Subscriptions are accepted on a prepaid basis only and are entered on a calendar year basis. Issues are sent by standard mail (surface within Europe, air delivery outside Europe). Priority rates are available upon request. Claims for missing issues should be made within six months of the date of dispatch.

Orders, Claims and Journal Enquiries

(no manuscript enquiries)
Please contact the Regional Sales Office nearest you:

St. Louis
Elsevier, Customer Service Department, 11830 Westline Industrial Drive, St. Louis, MO 63146, USA; Tel.: (877) 8397126 [toll free within the USA]; (+1) (314) 4537076 [outside the USA]; Fax: (+1) (314) 5235153; E-mail: JournalCustomerService-usa@elsevier.com

Amsterdam
Elsevier, Customer Service Department, P.O. Box 211, 1000 AE Amsterdam, The Netherlands; Tel.: (+31) 20-485-3757; Fax: (+31) 20-485-3432; E-mail: JournalsCustomerServiceEMEA@elsevier.com

Tokyo
Elsevier K.K., Customer Service Department, 4F Higashi-Azabu, 1-Chome Bldg, 1-9-15 Higashi-Azabu, Minato-ku, Tokyo 106-0044, Japan; Tel.: (+81) 3-5561-5037; Fax: (+81) 3-5561-5047; E-mail: JournalsCustomerServiceJapan@elsevier.com

Singapore
Elsevier, Customer Service Department, 3 Killiney Road, #08-01 Winsland House 1, Singapore 239519, Tel.: (+65) 6349-0222; Fax: (+65) 6733-1510; E-mail: JournalsCustomerServiceAPAC@elsevier.com

USA mailing notice: *Polyhedron* (ISSN 0277-5387) is published triweekly by Elsevier B.V. (Radarweg 29, 1043 NX Amsterdam, the Netherlands). Periodical postage paid at Rahway NJ and additional mailing offices.
USA POSTMASTER: Send change of address to *Polyhedron*, Elsevier, Customer Service Department, 11830 Westline Industrial Drive, St. Louis, MO 63146, USA.
AIRFREIGHT AND MAILING in the USA by Mercury International Limited, 365 Blair Road, Avenel, NJ 07001.

Advertising Information
Advertising orders and enquiries can be sent to: **USA, Canada and South America:** Mr Tino DeCarlo, The Advertising Department, Elsevier Inc., 360 Park Avenue South, New York, NY 10010-1710, USA; tel.: (+1) (212) 633 3815; fax: (+1) (212) 633 3820; e-mail: t.decarlo@elsevier.com. **Europe and ROW:** Miss Katrina Barton, Commercial Sales, Elsevier, 84 Theobald's Road, London, WCIX 8RR, UK; phone: (+44) (0) 20 7611 4117; fax: (+44) (0) 20 7611 4463; e-mail: commercialsales@elsevier.com

Funding body agreements and policies
Elsevier has established agreements and developed policies to allow authors who publish in Elsevier journals to comply with potential manuscript archiving requirements as specified as conditions of their grant awards. To learn more about existing agreements and policies please visit http://www.elsevier.com/fundingbodies

POLYHEDRON

The International Journal for Inorganic and Organometallic Chemistry

Executive Editors

The Americas
G. Christou
Department of Chemistry, University of Florida,
Gainesville, FL 32611-7200, USA
E-mail: christou@chem.ufl.edu

Rest of the world
C.E. Housecroft
Department of Chemistry, University of Basel,
Spitalstrasse 51, CH-4056 Basel, Switzerland
E-mail: poly-chemie@unibas.ch

Associate Regional Editor for China
T.C.W. Mak
Department of Chemistry, University Science Centre,
The Chinese University of Hong Kong,
Shatin NT, Hong Kong, People's Republic of China
E-mail: tcwmak@cuhk.edu.hk

Polyhedron Reports
Editor
G. Christou *(Gainesville, FL, USA)*

Symposia-in-print
Editor
G. Parkin *(New York, NY, USA)*

Editorial Board
A.G. Blackman *(Dunedin, New Zealand)*
D.C. Bradley *(London, UK)*
A. Brodie *(Palmerston North, New Zealand)*
A. Castiñeiras *(Santiago de Compostela, Spain)*
X.-M. Chen *(Guangzhou, PR China)*
M.H. Chisholm *(Columbus, OH, USA)*
E.C. Constable *(Basel, Switzerland)*
L. Cronin *(Glasgow, UK)*
G.R. Desiraju *(Hyderabad, India)*
W.J. Evans *(Irvine, CA, USA)*
L.H. Gade *(Heidelberg, Germany)*
G. Girolami *(Urbana, IL, USA)*
J.-F. Halet *(Rennes, France)*
L. Hubert-Pfalzgraf *(Villeurbanne, France)*
C. Janiak *(Freiburg, Germany)*
C. Kepert *(NSW, Australia)*
P. Kruger *(Canterbury, New Zealand)*
S. Perlepes *(Patras, Greece)*
P.P. Power *(Davis, CA, USA)*
T.B. Rauchfuss *(Urbana, IL, USA)*
J. Reedijk *(Leiden, The Netherlands)*
A.L. Rheingold *(Newark, DE, USA)*
M. Rosales Hoz *(Mexico, D.F., Mexico)*
P. Steel *(Christchurch, New Zealand)*
L.K. Thompson *(St John's, NF, Canada)*
D.A. Tocher *(Oxford, UK)*
M. Yamashita *(Sendai, Japan)*

Aims and Scope

Polyhedron will publish original, fundamental, experimental and theoretical work of the highest quality in all the major areas of inorganic chemistry. These include synthetic chemistry, coordination chemistry, organometallic chemistry, bioinorganic chemistry, and solid-state and materials chemistry. Papers should be complete pieces of work, and the inclusion of results from spectroscopic and/or physical techniques is encouraged. Papers merely reporting the preparation and X-ray structural characterization of only a single compound will not be considered appropriate unless the compound and its structure are particularly interesting.

Similarly, papers concerned solely with stability constants determined by potentiometric titration data unsupported by other e.g. spectroscopic techniques will not be acceptable nor will solvent extraction data unless supported by other data of interest to inorganic chemists. Unnecessary fragmentation of work is not acceptable.

In addition Polyhedron publishes specially commissioned review articles (Polyhedron Reports) and collections of original research papers (Polyhedron Symposia-in-Print) of appropriate timeliness.

Publication Information: Polyhedron (ISSN 0277-5387). For 2009, volume 28 is scheduled for publication. Subscription prices are available upon request from the Publisher or from the Regional Sales Office nearest you or from this journal's website (http://www.elsevier.com/locate/poly). Further information is available on this journal and other Elsevier products through Elsevier's website (http://www.elsevier.com). Subscriptions are accepted on a prepaid basis only and are entered on a calendar year basis. Issues are sent by standard mail (surface within Europe, air delivery outside Europe). Priority rates are available upon request. Claims for missing issues should be made within six months of the date of dispatch.

Orders, Claims and Journal Enquiries

(no manuscript enquiries)
Please contact the Regional Sales Office nearest you:

St. Louis
Elsevier, Customer Service Department, 11830 Westline Industrial Drive, St. Louis, MO 63146, USA; Tel.: (877) 8397126 [toll free within the USA]; (+1) (314) 4537076 [outside the USA]; Fax: (+1) (314) 5235153; E-mail: JournalCustomerService-usa@elsevier.com

Amsterdam
Elsevier, Customer Service Department, P.O. Box 211, 1000 AE Amsterdam, The Netherlands; Tel.: (+31) 20-485-3757; Fax: (+31) 20-485-3432; E-mail: JournalsCustomerServiceEMEA@elsevier.com

Tokyo
Elsevier K.K., Customer Service Department, 4F Higashi-Azabu, 1-Chome Bldg, 1-9-15 Higashi-Azabu, Minato-ku, Tokyo 106-0044, Japan; Tel.: (+81) 3-5561-5037; Fax: (+81) 3-5561-5047; E-mail: JournalsCustomerServiceJapan@elsevier.com

Singapore
Elsevier, Customer Service Department, 3 Killiney Road, #08-01 Winsland House 1, Singapore 239519, Tel.: (+65) 6349-0222; Fax: (+65) 6733-1510; E-mail: JournalsCustomerServiceAPAC@elsevier.com

USA mailing notice: *Polyhedron* (ISSN 0277-5387) is published triweekly by Elsevier B.V. (Radarweg 29, 1043 NX Amsterdam, the Netherlands). Periodical postage paid at Rahway NJ and additional mailing offices.
USA POSTMASTER: Send change of address to *Polyhedron*, Elsevier, Customer Service Department, 11830 Westline Industrial Drive, St. Louis, MO 63146, USA.
AIRFREIGHT AND MAILING in the USA by Mercury International Limited, 365 Blair Road, Avenel, NJ 07001.

Advertising Information
Advertising orders and enquiries can be sent to: **USA, Canada and South America:** Mr Tino DeCarlo, The Advertising Department, Elsevier Inc., 360 Park Avenue South, New York, NY 10010-1710, USA; tel.: (+1) (212) 633 3815; fax: (+1) (212) 633 3820; e-mail: t.decarlo@elsevier.com. **Europe and ROW:** Miss Katrina Barton, Commercial Sales, Elsevier, 84 Theobald's Road, London, WCIX 8RR, UK; phone: (+44) (0) 20 7611 4117; fax: (+44) (0) 20 7611 4463; e-mail: commercialsales@elsevier.com

Funding body agreements and policies
Elsevier has established agreements and developed policies to allow authors who publish in Elsevier journals to comply with potential manuscript archiving requirements as specified as conditions of their grant awards. To learn more about existing agreements and policies please visit http://www.elsevier.com/fundingbodies

POLYHEDRON

The International Journal for Inorganic and Organometallic Chemistry

Executive Editors

The Americas
G. Christou
Department of Chemistry, University of Florida,
Gainesville, FL 32611-7200, USA
E-mail: christou@chem.ufl.edu

Rest of the world
C.E. Housecroft
Department of Chemistry, University of Basel,
Spitalstrasse 51, CH-4056 Basel, Switzerland
E-mail: poly-chemie@unibas.ch

Associate Regional Editor for China
T.C.W. Mak
Department of Chemistry, University Science Centre,
The Chinese University of Hong Kong,
Shatin NT, Hong Kong, People's Republic of China
E-mail: tcwmak@cuhk.edu.hk

Polyhedron Reports
Editor
G. Christou *(Gainesville, FL, USA)*

Symposia-in-print
Editor
G. Parkin *(New York, NY, USA)*

Editorial Board
A.G. Blackman *(Dunedin, New Zealand)*
D.C. Bradley *(London, UK)*
A. Brodie *(Palmerston North, New Zealand)*
A. Castiñeiras *(Santiago de Compostela, Spain)*
X.-M. Chen *(Guangzhou, PR China)*
M.H. Chisholm *(Columbus, OH, USA)*
E.C. Constable *(Basel, Switzerland)*
L. Cronin *(Glasgow, UK)*
G.R. Desiraju *(Hyderabad, India)*
W.J. Evans *(Irvine, CA, USA)*
L.H. Gade *(Heidelberg, Germany)*
G. Girolami *(Urbana, IL, USA)*
J.-F. Halet *(Rennes, France)*
L. Hubert-Pfalzgraf *(Villeurbanne, France)*
C. Janiak *(Freiburg, Germany)*
C. Kepert *(NSW, Australia)*
P. Kruger *(Canterbury, New Zealand)*
S. Perlepes *(Patras, Greece)*
P.P. Power *(Davis, CA, USA)*
T.B. Rauchfuss *(Urbana, IL, USA)*
J. Reedijk *(Leiden, The Netherlands)*
A.L. Rheingold *(Newark, DE, USA)*
M. Rosales Hoz *(Mexico, D.F., Mexico)*
P. Steel *(Christchurch, New Zealand)*
L.K. Thompson *(St John's, NF, Canada)*
D.A. Tocher *(Oxford, UK)*
M. Yamashita *(Sendai, Japan)*

Aims and Scope

Polyhedron will publish original, fundamental, experimental and theoretical work of the highest quality in all the major areas of inorganic chemistry. These include synthetic chemistry, coordination chemistry, organometallic chemistry, bioinorganic chemistry, and solid-state and materials chemistry. Papers should be complete pieces of work, and the inclusion of results from spectroscopic and/or physical techniques is encouraged. Papers merely reporting the preparation and X-ray structural characterization of only a single compound will not be considered appropriate unless the compound and its structure are particularly interesting.

Similarly, papers concerned solely with stability constants determined by potentiometric titration data unsupported by other e.g. spectroscopic techniques will not be acceptable nor will solvent extraction data unless supported by other data of interest to inorganic chemists. Unnecessary fragmentation of work is not acceptable.

In addition Polyhedron publishes specially commissioned review articles (Polyhedron Reports) and collections of original research papers (Polyhedron Symposia-in-Print) of appropriate timeliness.

Publication Information: Polyhedron (ISSN 0277-5387). For 2009, volume 28 is scheduled for publication. Subscription prices are available upon request from the Publisher or from the Regional Sales Office nearest you or from this journal's website (http://www.elsevier.com/locate/poly). Further information is available on this journal and other Elsevier products through Elsevier's website (http://www.elsevier.com). Subscriptions are accepted on a prepaid basis only and are entered on a calendar year basis. Issues are sent by standard mail (surface within Europe, air delivery outside Europe). Priority rates are available upon request. Claims for missing issues should be made within six months of the date of dispatch.

Orders, Claims and Journal Enquiries

(no manuscript enquiries)
Please contact the Regional Sales Office nearest you:

St. Louis
Elsevier, Customer Service Department, 11830 Westline Industrial Drive, St. Louis, MO 63146, USA; Tel.: (877) 8397126 [toll free within the USA]; (+1) (314) 4537076 [outside the USA]; Fax: (+1) (314) 5235153; E-mail: JournalCustomerService-usa@elsevier.com

Amsterdam
Elsevier, Customer Service Department, P.O. Box 211, 1000 AE Amsterdam, The Netherlands; Tel.: (+31) 20-485-3757; Fax: (+31) 20-485-3432; E-mail: JournalsCustomerServiceEMEA@elsevier.com

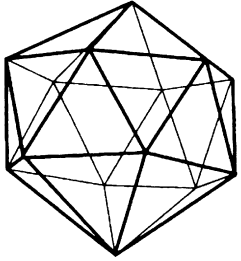
Tokyo
Elsevier K.K., Customer Service Department, 4F Higashi-Azabu, 1-Chome Bldg, 1-9-15 Higashi-Azabu, Minato-ku, Tokyo 106-0044, Japan; Tel.: (+81) 3-5561-5037; Fax: (+81) 3-5561-5047; E-mail: JournalsCustomerServiceJapan@elsevier.com

Singapore
Elsevier, Customer Service Department, 3 Killiney Road, #08-01 Winsland House 1, Singapore 239519, Tel.: (+65) 6349-0222; Fax: (+65) 6733-1510; E-mail: JournalsCustomerServiceAPAC@elsevier.com

USA mailing notice: *Polyhedron* (ISSN 0277-5387) is published triweekly by Elsevier B.V. (Radarweg 29, 1043 NX Amsterdam, the Netherlands). Periodical postage paid at Rahway NJ and additional mailing offices.
USA POSTMASTER: Send change of address to *Polyhedron*, Elsevier, Customer Service Department, 11830 Westline Industrial Drive, St. Louis, MO 63146, USA.
AIRFREIGHT AND MAILING in the USA by Mercury International Limited, 365 Blair Road, Avenel, NJ 07001.

Advertising Information
Advertising orders and enquiries can be sent to: **USA, Canada and South America:** Mr Tino DeCarlo, The Advertising Department, Elsevier Inc., 360 Park Avenue South, New York, NY 10010-1710, USA; tel.: (+1) (212) 633 3815; fax: (+1) (212) 633 3820; e-mail: t.decarlo@elsevier.com. **Europe and ROW:** Miss Katrina Barton, Commercial Sales, Elsevier, 84 Theobald's Road, London, WCIX 8RR, UK; phone: (+44) (0) 20 7611 4117; fax: (+44) (0) 20 7611 4463; e-mail: commercialsales@elsevier.com

Funding body agreements and policies
Elsevier has established agreements and developed policies to allow authors who publish in Elsevier journals to comply with potential manuscript archiving requirements as specified as conditions of their grant awards. To learn more about existing agreements and policies please visit http://www.elsevier.com/fundingbodies



POLYHEDRON

The International Journal for Inorganic and Organometallic Chemistry

Founding Editor: **Sir Geoffrey Wilkinson** ✠

Executive Editors

Regional Editors:

The Americas

G. Christou
Department of Chemistry, University of Florida, Gainesville, FL 32611-7200, USA
E-mail: christou@chem.ufl.edu

Rest of the world

C.E. Housecroft
Department of Chemistry, University of Basel, CH-4056 Basel, Switzerland
E-mail: poly-chemie@unibas.ch

Associate Regional Editor for China

T.C.W. Mak
Department of Chemistry, University Science Centre, The Chinese University of Hong Kong, Shatin NT, Hong Kong, People's Republic of China
E-mail: tcwmak@cuhk.hk

Polyhedron Reports Editor

G. Christou
Department of Chemistry, University of Florida, Gainesville, FL 32611-7200, USA
E-mail: christou@chem.ufl.edu

Symposia-in-print Editor

G. Parkin
Department of Chemistry, Columbia University, New York, NY 10027, USA
E-mail: parkin@chem.columbia.edu

Editorial Board

A.G. Blackman *(Dunedin, New Zealand)*
D.C. Bradley *(London, UK)*
A. Brodie *(Palmerston North, New Zealand)*
A. Castiñeiras *(Santiago de Compostela, Spain)*
X.-M. Chen *(Guangzhou, PR China)*
M.H. Chisholm *(Columbus, OH, USA)*
E.C. Constable *(Basel, Switzerland)*
L. Cronin *(Glasgow, UK)*
G.R. Desiraju *(Hyderabad, India)*
W.J. Evans *(Irvine, CA, USA)*
L.H. Gade *(Heidelberg, Germany)*
G. Girolami *(Urbana, IL, USA)*
J.-F. Halet *(Rennes, France)*
L. Hubert-Pfalzgraf *(Villeurbanne, France)*
C. Janiak *(Freiburg, Germany)*
C. Kepert *(NSW, Australia)*
P. Kruger *(Canterbury, New Zealand)*
S. Perlepes *(Patras, Greece)*
P.P. Power *(Davis, CA, USA)*
T.B. Rauchfuss *(Urbana, IL, USA)*
J. Reedijk *(Leiden, The Netherlands)*
A.L. Rheingold *(Newark, DE, USA)*
M. Rosales Hoz *(Mexico, D.F., Mexico)*
P. Steel *(Christchurch, New Zealand)*
L.K. Thompson *(St John's, NF, Canada)*
D.A. Tocher *(Oxford, UK)*
M. Yamashita *(Sendai, Japan)*



ELSEVIER

Amsterdam — Boston — London — New York — Oxford — Paris — Philadelphia — San Diego — St Louis

Polyhedron 28, issue 6, 23 April 2009

Contents lists available at ScienceDirect

Polyhedron

journal homepage: www.elsevier.com/locate/poly

Contents

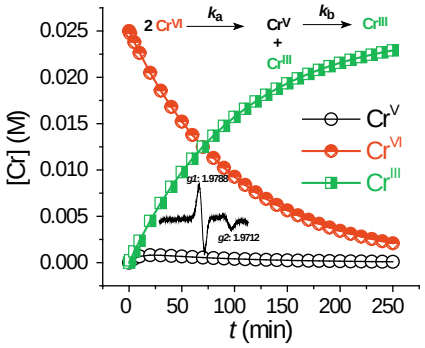
Papers

María Inés Frascaroli, Juan Manuel Salas-Peregrin, Luis F. Sala and Sandra Signorella

Polyhedron 28 (2009) 1049

Kinetics and mechanism of the chromic oxidation of 3-*O*-methyl-D-glucopyranose

The reaction of Cr^{VI} with 3-*O*-methyl-D-glucose yields 2-*O*-methyl-D-arabinose, formic acid and Cr^{III} through a combination of $Cr^{VI} \rightarrow Cr^{IV} \rightarrow Cr^{II}$ and $Cr^{VI} \rightarrow Cr^{IV} \rightarrow Cr^{III}$ pathways.

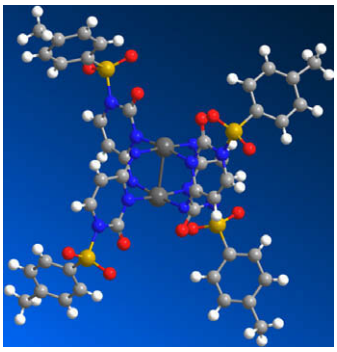


Aleksandar Višnjevac, Marija Luić, Renata Kobetić, Dubravka Gembarovski and Biserka Žinić

Polyhedron 28 (2009) 1057

Stabilization of the *N*-1-substituted cytosinate iminooxo form in dinuclear palladium complexes

The synthesis and characterization of 1-(*p*-toluenesulfonyl)cytosine (**1**), and its dinuclear cytosinato complexes $Pd_2(1\text{-}TosC^{-}\text{–}N3,N4)_4$ (**3**) and $Pd_2(1\text{-}TosC^{-}\text{–}N3,N4)_2DMSO_2Cl_2$ (**4**) are described. Complex **3** has an intriguing paddle-wheel structure with two parallel square-planar coordination spheres, consisting of four N atoms each.

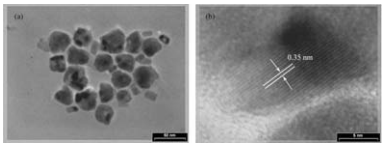


Masoud Salavati-Niasari, Zeinab Fereshteh and Fatemeh Davar

Polyhedron 28 (2009) 1065

Synthesis of cobalt nanoparticles from [bis(2-hydroxyacetophenato)cobalt(II)] by thermal decomposition

[Bis(2-hydroxyacetophenato)cobalt(II)] was used as a new precursor to prepare cobalt (Co) and tricobalt tetraoxide (Co_3O_4) nanoparticles of 15–25 nm in average diameter by thermal decomposition. The products were characterized by X-ray diffraction (XRD), transmission electron microscopy (TEM), high-resolution transmission electron microscopy (HRTEM) and Fourier transform infrared (FT-IR) spectroscopy. The magnetic property was studied with vibrating sample magnetometer (VSM).

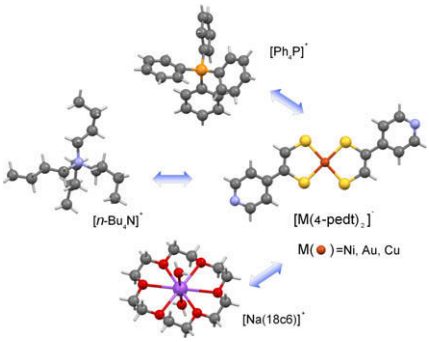


Sandra Rabaça, Ana C. Cerdeira, Ana I.S. Neves, Sandra I.G. Dias, Cécile Mézière, Isabel C. Santos, Laura C.J. Pereira, Marc Fourmigué, Rui T. Henriques and Manuel Almeida

Polyhedron 28 (2009) 1069

Complexes based on asymmetrically substituted pyridine–dithiolene ligands [M(4-pedt)$_2$] (M = Au, Cu, Ni; 4-pedt = 1-(pyridin-4-yl)-ethylene-1,2-dithiolate): Synthesis, structure and physical properties

The synthesis of M(4-pedt)$_2$ complexes of nickel, copper and gold obtained as tetrabutylammonium, tetraphenylphosphonium or sodium 18-crown-6 ether salts are described and these compounds are characterised by single-crystal X-ray diffraction, cyclic voltammetry, EPR and magnetic susceptibility measurements.

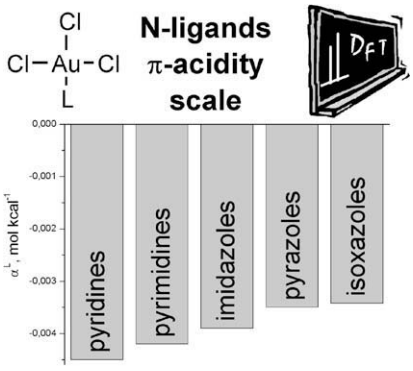


Marco Bortoluzzi, Gino Paolucci, Giuliano Annibale and Bruno Pitteri

Polyhedron 28 (2009) 1079

A new π-acidity scale for several N-donor heterocycles as ligands in neutral gold(III) complexes

A computational DFT approach for the comparison of the π-acceptor character of some N-donor heterocycles L {L = pyridines, pyrimidines, imidazoles, pyrazoles and isoxazoles} in neutral AuCl$_3$L complexes is reported. The π-acceptor ability scale pyridines ≈ pyrimidines < imidazoles < pyrazoles ≈ isoxazoles has been derived. Moreover, the minimum proton affinity value for a meaningful interaction between the ligands and the AuCl$_3$ fragment has been estimated.

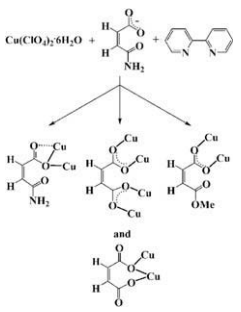


Katerina N. Lazarou, Vassilis Psycharis, Spyros P. Perlepes and Catherine P. Raptopoulou

Polyhedron 28 (2009) 1085

Complexes derived from the copper(II) perchlorate/maleamic acid/2,2′-bipyridine and copper(II) perchlorate/maleic acid/2,2′-bipyridine reaction systems: Synthetic, reactivity, structural and spectroscopic studies

The reactions of Cu(ClO$_4$)$_2$ · 6H$_2$O with the maleamate(−1) ligand, in the presence of 2,2′-bipyridine give dinuclear and polymeric complexes; in some reactions, interesting Cu^{II}-assisted/promoted transformations of the maleamate(−1) ion to the maleate(−2) and monomethyl maleate(−1) ligands are observed.

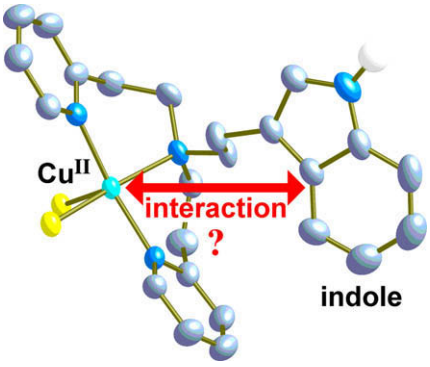


Sang-Tae Lee, Donald C. Craig and Stephen B. Colbran

Polyhedron 28 (2009) 1097

Copper(II) complexes of ligands derived from tryptamine

Copper(II) complexes of novel ligands derived from tryptamine have been prepared in order to assess the mutual perturbation of copper(II) and indole redox centres, which are in close proximity, upon each other.

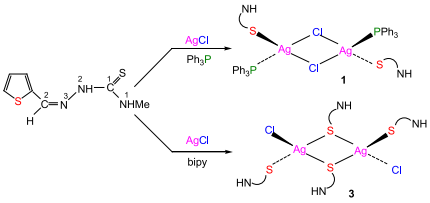


Tarlok S. Lobana, Rekha Sharma and Ray J. Butcher

Polyhedron 28 (2009) 1103

Synthesis, spectroscopy and structures of halogen and sulfur-bridged dinuclear silver(I) complexes with N^1-substituted thiophene-2-carbaldehyde thiosemicarbazone

Reaction of silver(I) chloride with thiophene-2-carbaldehyde N^1-methyl thiosemicarbazone in the presence of coligands has formed dinuclear complexes **1** and **3** with different bridging atoms.

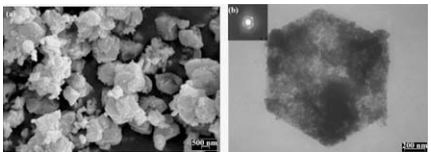


Masoud Salavati-Niasari, Noshin Mir and Fatemeh Davar

Polyhedron 28 (2009) 1111

Synthesis and characterization of NiO nanoclusters via thermal decomposition

Thermal decomposition process has been developed to synthesize nickel oxide (NiO) nanoclusters via the reaction between a new precursor, nickel oxalate $[Ni(O_4C_2)(H_2O)_4]$ and oleylamine ($C_{18}H_{37}N$). The combinations of triphenylphosphine ($C_{18}H_{15}P$) and $C_{18}H_{37}N$ were added as surfactants to control the particle size. The products were characterized different methods. The synthesized NiO nanoclusters have a cubic structure with average size 2–10 nm.

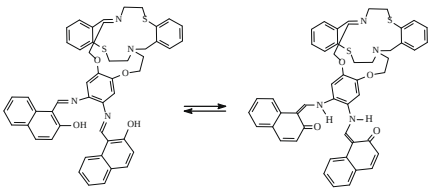


Aysel Başoğlu, Semanur Parlayan, Miraç Ocak, Hakan Alp, Halit Kantekin, Mustafa Özdemir and Ümmühan Ocak

Polyhedron 28 (2009) 1115

Complexation of metal ions with the novel 2-hydroxy-1-naphthaldehyde-derived diamine Schiff base carrying a macrobicyclic moiety with $N_2O_2S_2$ mixed donor in acetonitrile-dichloromethane

A new Schiff base was synthesized by reaction of the corresponding macrobicyclic diamine compound and 2-hydroxy-1-naphthaldehyde. The influence of metal cations such as Zn^{2+}, Mn^{2+}, Fe^{2+}, Fe^{3+}, Co^{2+}, Ni^{2+} and Pb^{2+} on the spectroscopic properties of the Schiff base was investigated by means of absorption and emission spectrometry.

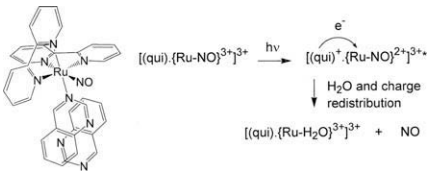


Elisa C. Fornari, Mario S.P. Marchesi, Antônio E.H. Machado and Sofia Nikolaou

Polyhedron 28 (2009) 1121

Exploring weak interactions to assemble a nitrosyl–ruthenium compound able to release NO under visible light irradiation

Compound *cis*-$[Ru(bpy)_2(qui)NO](PF_6)_3 \cdot (qui)$ (qui = quinazoline) was synthesized and characterized. The association with an additional *qui* leads to an absorption band in the visible region which is able to photoinduce the NO release. The transition energy presents reversible dependence on pH and solvent effects, suggesting that the association is driven by π-stacking.

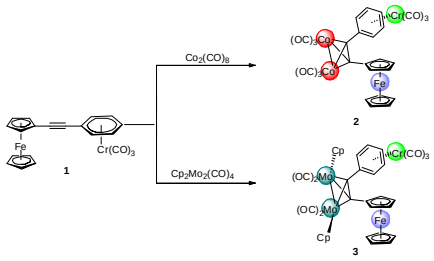


Elton L.S. Gomes and Osvaldo L. Casagrande Jr.

Polyhedron 28 (2009) 1127

Novel heterotetrametallic compounds derived from 1-(ferrocenylethynyl)(η^6-arene)tricarbonylchromium

The compounds $Co_2(CO)_8$ and $Cp_2Mo_2(CO)_4$ readily react with $[Cr(CO)_3(\eta^6\text{-}C_6H_5)C{\equiv}C\text{-}\{(\eta^5\text{-}C_5H_4)Fe(\eta^5\text{-}C_5H_5)\}]$(**1**) to give new heterotetrametallic complexes $[Cr(CO)_3(\eta^6\text{-}C_6H_5)\{Co_2(CO)_6\text{-}\mu^2\text{-}\eta^2\text{-}C{\equiv}C\text{-}\}(\eta^5\text{-}C_5H_4)Fe(\eta^5\text{-}C_5H_5)\}]$(**2**), and $[Cr(CO)_3(\eta^6\text{-}C_6H_5)\{Mo_2Cp_2(CO)_4\text{-}\mu^2\text{-}\eta^2\text{-}C{\equiv}C\text{-}\}(\eta^5\text{-}C_5H_4)Fe(\eta^5\text{-}C_5H_5)]$(**3**).

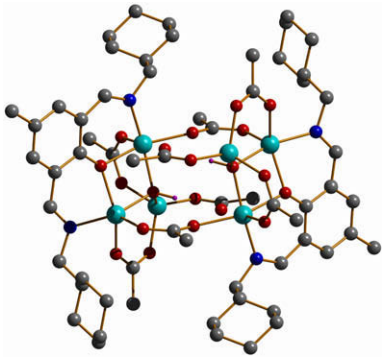


Partha Roy, Mario Manassero, Koushik Dhara and Pradyot Banerjee

Polyhedron 28 (2009) 1133

Synthesis, characterization and fluorescence properties of hexanuclear zinc(II) complexes

Two Schiff-base ligands, 4-methyl-2,6-bis-(cyclohexanemethyliminomethyl)-phenol and 4-methyl-2,6-bis(1-naphthalenemethyliminomethyl)-phenol, have been synthesized and characterized. Two hexanuclear zinc(II) complexes with these N_2O donor ligand have also been synthesized and characterized by X-ray diffraction analysis. Fluorescence property studies of the ligands and their complexes reveal that the quantum yields increase upon complexation.

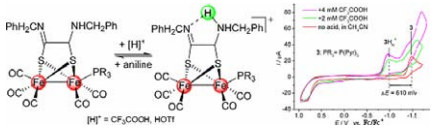


Ting-Ting Zhang, Mei Wang, Ning Wang, Ping Li, Zheng-Yi Liu and Li-Cheng Sun

Polyhedron 28 (2009) 1138

Protophilicity, electrochemical property, and desulfurization of diiron dithiolate complexes containing a functionalized C_2 bridge with two vicinal basic sites

Diiron dithiolate complexes containing a functionalized C_2 bridge with two vicinal basic sites were prepared as models of the FeFe-hydrogenase active site. Protonation of these complexes is instant and reversible, which leads to a large anodic shift (610–650 mV) for the Fe^IFe^I/Fe^IFe^0 reduction potentials. Desulfurization reaction was found for the C_2-bridged diiron complex.

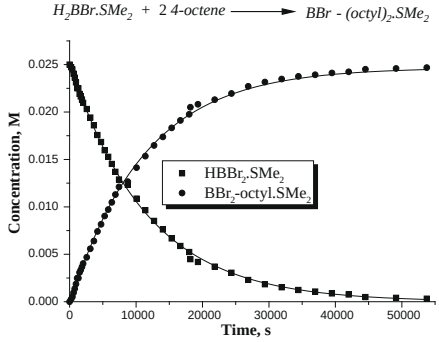


N. Xaba and D. Jaganyi

Polyhedron 28 (2009) 1145

The role of the double bond position in hydroboration using $HBBr_2 \cdot SMe_2$, $HBCl_2 \cdot SMe_2$ and $H_2BBr \cdot SMe_2$: A detailed kinetic and mechanistic study

Exponential decay curve for hydroboration of 4-octene with HBBr2 · SMe2 in CH2Cl2 at 25 °C.

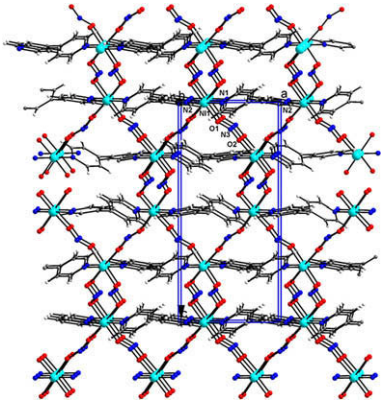


Vien Vo, Youngmee Kim, Nguyen Van Minh, Chang Seop Hong and Sung-Jin Kim

Polyhedron 28 (2009) 1150

Syntheses, crystal structures and magnetic properties of coordination polymers $Ni(NO_2)_2$ and $Ni(4,4'\text{-bipy})(NO_2)_2$

We present the use of solvothermal reaction in formamide to synthesize two new frameworks of $Ni(NO_2)_2$ and $Ni(4,4'\text{-bipy})(NO_2)_2$ containing $\mu_{1,3}$-nitrito bridges. They are the first examples of synthesis of polymeric complexes using solvent as a reducing agent in solvothermal condition. Magnetic measurements show weak ferromagnetism within framework of the two compounds.

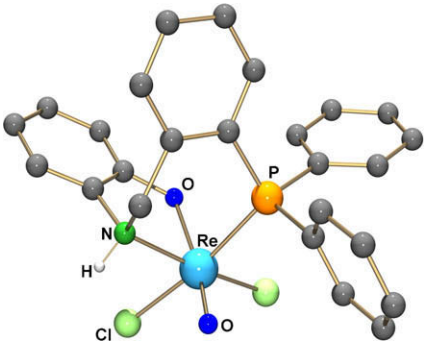


Ali Barandov and Ulrich Abram

Polyhedron 28 (2009) 1155

Heterofunctionalized phosphines derived from (2-formylphenyl)diphenylphosphine and their reactions with oxorhenium(V) complexes

Reactions of $[ReOCl_3(PPh_3)_2]$ or $(NBu_4)[ReOCl_4]$ with Schiff bases derived from (2-formylphenyl)diphenylphosphine and 2-aminophenol result in a rapid decomposition of the imines. Representative rhenium complexes with decomposition products are presented. A stable Re(V) complex was isolated with a tridentate, facially coordinated phosphine amine, which was produced by reduction of a Schiff base with $NaBH_4$.

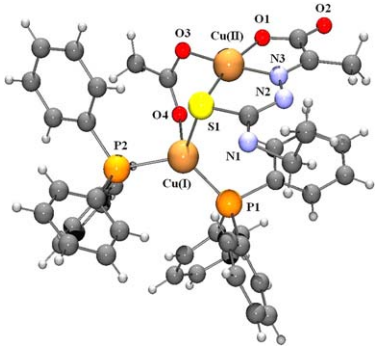


Marisa Belicchi-Ferrari, Franco Bisceglie, Enrico Buluggiu, Giorgio Pelosi and Pieralberto Tarasconi

Polyhedron 28 (2009) 1160

Synthesis, characterization and crystal structure of triphenylphosphine copper(I) methylpyruvate thiosemicarbazones

In the process of synthesis of copper(I) thiosemicarbazone derivatives unexpected mixed valence and cluster copper compounds were isolated and interesting structural features were observed.

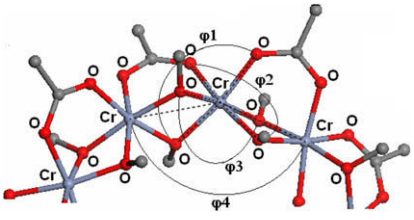


M.Yu. Gorbachev, B.N. Dobrova and A.S. Dimoglo

Polyhedron 28 (2009) 1169

The relative stability of nano-"chromic wheels" $[Cr_n(OCH_3)_{2n}(CH_3COO)_n]$ depending on the number of their coordination units

The relative stability of $[Cr_n(OCH_3)_{2n}(CH_3COO)_n]$ depending on the number n (n = 4, 6, 8, 10, 12 and 14) of its interior groups is studied by means of Hartree–Fock and also Density Functional Theory calculations.

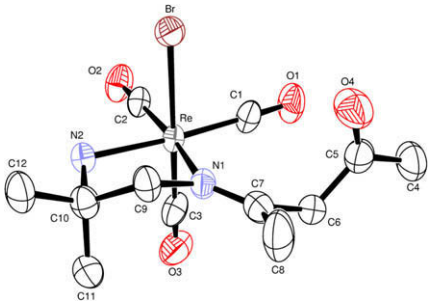


P. Mayer, T.I.A. Gerber, B. Buyambo and A. Abrahams

Polyhedron 28 (2009) 1174

Coordination behaviour of acetylacetone-derived Schiff bases towards rhenium(I) and (V)

Two complexes of Re(I) and (V), containing potentially tridentate Schiff base ligands, based on acetylacetone, were prepared. With Re(I) the ligand coordinates solely via the two nitrogen atoms, but with Re(V) tridentate NNO coordination is observed.

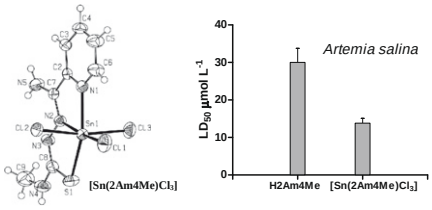


Isolda C. Mendes, Fernanda B. Costa, Geraldo M. de Lima, José D. Ardisson, Isabel Garcia-Santos, Alfonso Castiñeiras and Heloisa Beraldo

Polyhedron 28 (2009) 1179

Tin(IV) complexes with 2-pyridineformamide-derived thiosemicarbazones: Antimicrobial and potential antineoplasic activities

The tin(IV) complexes [Sn(2Am4DH)Cl_3] (**1**), [Sn(2Am4Me)Cl_3] (**2**), [Sn(2Am4Et)Cl_3] (**3**) and [Sn(2Am4Ph)Cl_3] (**4**) with *2-pyridineformamide* thiosemicarbazone (H2Am4DH) and its *N*(4)-methyl (H2Am4Me), *N*(4)-ethyl (H2Am4Et) and *N*(4)-phenyl (H2Am4Ph) derivatives were obtained. The thiosemicarbazones showed moderate antimicrobial activity against *Pseudomonas aeruginosa* and *Candida albicans*. On coordination to tin(IV) the antimicrobial activity increases. The studied compounds were toxic to *Artemia salina*, indicating that they could present antineoplasic activity against solid tumors.

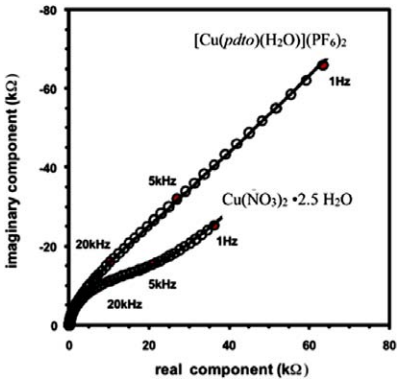


Dayan Rodríguez-Torres, Juan Carlos García-Ramos, Juan Manríquez, Rafael Moreno-Esparza, Mario Altamirano Lozano, Ignacio González, Isabel Gracia-Mora, Lena Ruiz-Azuara, Rene Antaño Lopez and Luis Ortiz-Frade

Polyhedron 28 (2009) 1186

Biological study and electrochemical characterization of Cu(II) and 1,8-bis-(2-pyridyl)-3,6-dithiaoctane (***pdto***) complex

This work presents a biological study and electrochemical characterization of the compound [Cu(***pdto***)H_2O]$^{2+}$ (***pdto*** = 1,8-bis-(2-pyridyl)-3,6-dithiaoctane). In a simple way antitumoral activity of this complex is related to its electrochemical reversibility. In contrast, Cu$(NO_3)_2 \cdot 2.5H_2O$ presented electrochemical irreversibility and no biological activity.

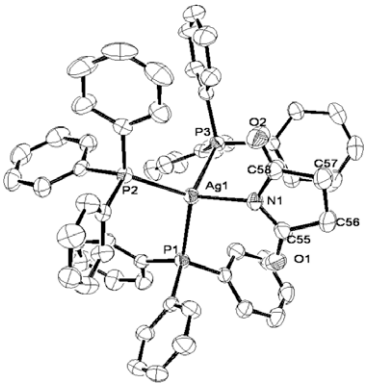


Xian Tao, Yue-Qin Li, Hui-Hua Xu, Ning Wang, Fang-Li Du and Ying-Zhong Shen

Polyhedron 28 (2009) 1191

Synthesis and characterization of organophosphine/phosphite stabilized *N*-silver(I) succinimide: crystal structure of $[(Ph_3P)_3 \cdot AgNC_4H_4O_2]$

Six organophosphine/phosphite stabilized *N*-silver(I) succinimide complexes of the type $L_nAgNC_4H_4O_2$ (L = PPh_3, *n* = 1, **2a**; *n* = 2, **2b**; *n* = 3, **2c**; L = $P(OEt)_3$; *n* = 1, **2d**; *n* = 2, **2e**; *n* = 3, **2f**) have been prepared by reacting $[AgNO_2C_4H_5]$, which could be obtained from $[Ag_2O]$ and $[C_4H_5O_2N]$, with PPh_3 or $P(OEt)_3$ in a 1:1–3 molar ratio. These complexes were obtained in high yields and characterized by elemental analysis, ^1H, $^{13}C\{H\}$ NMR, IR spectroscopy, and thermal analysis (TG and DSC). The molecular structure of **2c** has been determined by X-ray single crystal analysis.



The Publisher encourages the submission of articles in electronic form thus saving time and avoiding rekeying errors. For detailed instructions on the preparation of manuscripts and of electronic artwork, consult the Author Gateway for Elsevier at http://authors.elsevier.com

ScienceDirect

Full text of this journal is available, on-line from **ScienceDirect**. Visit **www.sciencedirect.com** for more information.

Polyhedron 28, issue 5, 1 April 2009

Contents lists available at ScienceDirect

Polyhedron

journal homepage: www.elsevier.com/locate/poly

Contents

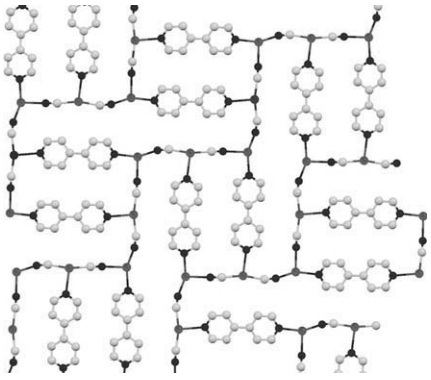
Papers

Safaa El-din H. Etaiw, Dina M. Abd El-Aziz and Ahmed S. Badr El-din

Polyhedron 28 (2009) 873

Self-assembly of supramolecular coordination polymers constructed from AgCN and bipodal spacers

Three novel supramolecular coordination polymers of AgCN, [$(AgCN)_2$.(4,4′-bipyridine)], [$(AgCN)_3$.(*trans*-1,2-bis(4-pyridyl)ethylene)$_2$ · H_2O] and [$(AgCN)_4$.(1,2-bis(4-pyridyl)ethane)], have been synthesized and structurally characterized. Supramolecular interactions play a prominent role in the assembly of these compounds.

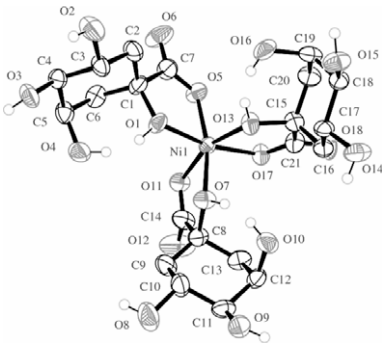


M. Menelaou, C. Mateescu, H. Zhao, N. Lalioti and A. Salifoglou

Polyhedron 28 (2009) 883

The pH-specific synthesis, spectroscopic, structural, and magnetic properties of a new Ni(II) species containing the plant physiological binder D-(−)-quinic acid: Association with the aqueous speciation of the binary Ni(II) quinate system

Reaction of Ni(II) with D-(−)-quinic acid (pH ~5.5) leads to a new species $Na[Ni(C_7H_{11}O_6)_3] \cdot 2.75H_2O$(**1**), characterized analytically, spectroscopically, magnetically, and structurally. The physicochemical profile of **1** is reflected into its partner $[NiL_2]^0$ species in the aqueous speciation of the Ni(II)–quinate binary system, thus aiding in understanding of Ni(II)–hydroxycarboxylate interactions in cellular physiology/toxicity.

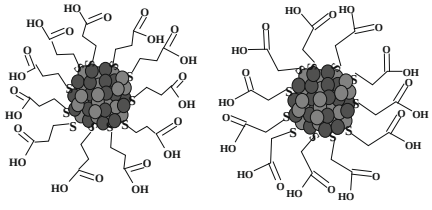


Mopelola Idowu and Tebello Nyokong

Polyhedron 28 (2009) 891

Study of the photophysical behavior of tetrasulfonated metallophthalocyanines in the presence of CdTe quantum dots

Förster resonance energy transfer (FRET) occurs from QDs capped with thioglycolic acid (TGA) or mercaptopropionic acid (MPA) to tetrasulfonated metallophthalocyanines with increase in both the triplet yields and lifetimes of the latter.



QD-MPA **QD-TGA**

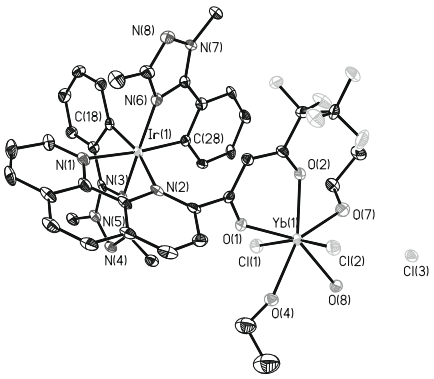
Elsevier Ltd.

Dan Li, Fang-Fang Chen, Zu-Qiang Bian, Zhi-Wei Liu, Yong-Liang Zhao and Chun-Hui Huang

Polyhedron 28 (2009) 897

Sensitized near-infrared emission of Yb^{III} from an Ir^{III} Yb^{III} bimetallic complex

An Ir^{III} complex with a new cyclometalated ligand and the corresponding Ir^{III} Yb^{III} bimetallic complex by the approach of complexes as ligands were synthesized. The near-infrared emission from Yb^{III} was obtained by the efficient energy transfer from the Ir^{III} center.

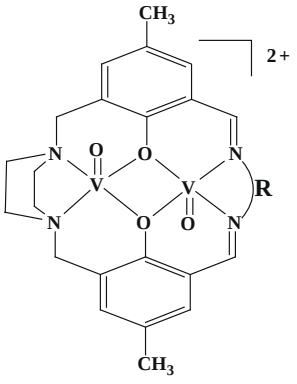


L. Leelavathy, S. Anbu, M. Kandaswamy, N. Karthikeyan and N. Mohan

Polyhedron 28 (2009) 903

Synthesis and characterization of a new series of unsymmetrical macrocyclic binuclear vanadyl(IV) complexes: Electrochemical, antimicrobial, DNA binding and cleavage studies

A series of unsymmetrical macrocyclic binuclear bis-phenoxo bridged oxidovanadium(IV) complexes have been synthesized and characterized by elemental and spectral techniques. A cyclic voltammetric investigation of these complexes evidenced that two successive quasi-reversible one electron transfer reduction waves in the negative and positive potential regions, E^1_{pc} = –0.54 to –0.67 V, E^2_{pc} = –0.80 to –0.85 V and E^1_{pc} = +0.63 to +0.78 V, E^2_{pc} = +0.82 to +0.97 V, respectively, are obtained. The aromatic diimine containing macrocyclic $V^{IV}O$ complexes display better DNA interactions than the aliphatic diimine containing $V^{IV}O$ analogues. These complexes significantly promote the oxidative cleavage of supercoiled plasmid DNA in the presence of H_2O_2. All the complexes display noticeable antifungal and antibacterial activities.

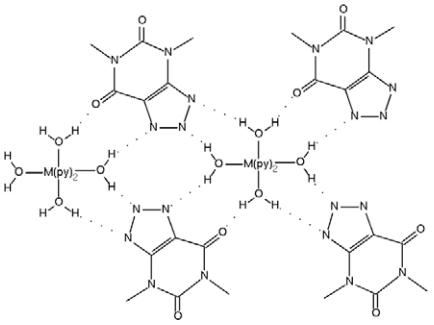


Carmen R. Maldonado, Miguel Quirós and Juan M. Salas

Polyhedron 28 (2009) 911

First and second coordination spheres in divalent metal compounds containing pyridine and 4,6-dimethyl-1,2,3-triazolo[4,5-*d*]pyrimidin-5,7-dione

The crystal structure of compounds containing M(II) (Mn, Co, Ni, Cu, Zn, Cd), pyridine and anionic 4,6-dimethyl-1,2,3-triazolo[4,5-*d*]pyrimidin-5,7-dione (dmax) is described. Mn, Co, Zn and Cd form $[M(py)_2(H_2O)_4](dmax)_2$ salts whereas Ni and Cu form neutral complexes $[M(py)_2(dmax)_2(H_2O)_4] \cdot 2H_2O$. The H-bond superstructures are analyzed.

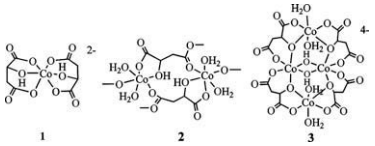


Qiong-Xin Liu, Lu-Bin Ni, Fu-Pei Liang, Zhao-Hui Zhou and Hui-Lin Wan

Polyhedron 28 (2009) 917

pH and molar ratio dependent formation of monomeric, dimeric and tetrameric cobalt malate complexes

The formation of monomeric, dimeric and tetrameric cobalt malate complexes is dependent on the pH value and molar ratio of the reactants, while less relevant to the temperature and counterions. The dimeric species further connects into a two-dimensional coordination polymer, and the tetramer is a mixed-valence cobalt(II/III) complex.

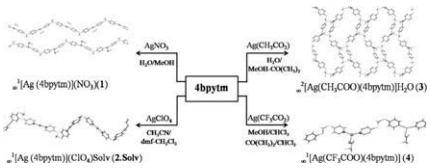


Rosa Carballo, Berta Covelo, Emilia García-Martínez, Ana Belén Lago and Ezequiel M. Vázquez-López

Polyhedron 28 (2009) 923

Role of inorganic and organic anions in the formation of metallosupramolecular assemblies of silver(I) coordination polymers with the twisted ligand bis(4-pyridylthio)methane

The reaction of the twisted ligand 4bpytm with $AgNO_3$ and $AgClO_4$ afforded 1D cationic coordination polymers but with the carboxylate anions, $CH_3CO_2^-$ and $CF_3CO_2^-$ 2D and 1D neutral coordination polymers were obtained. Different anion coordination abilities and different conformation arrangements with different symmetries and axial chirality in the ligand 4bpytm were observed in these compounds. Secondary interactions such as Ag···S, Ag···O or Ag···Ag play a crucial role in the self-organization of supramolecular polymers.

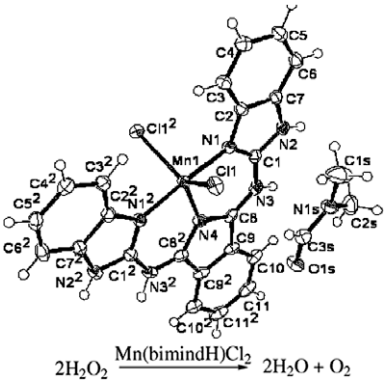


József Kaizer, Balázs Kripli, Gábor Speier and László Párkányi

Polyhedron 28 (2009) 933

Synthesis, structure, and catalase-like activity of a novel manganese(II) complex: Dichloro[1,3-bis(2′-benzimidazolylimino)isoindoline]manganese(II)

The preparations, characterizations, structures, and catalase-like activities of a manganese(II) complex with novel 1,3-bis(2′-benzimidazolylimino)isoindoline (bimindH) ligand are reported. The composition and molecular structure of $Mn(bimindH)Cl_2$ complex was fully determined by IR, UV Vis, ESR, and X-ray crystal analysis.

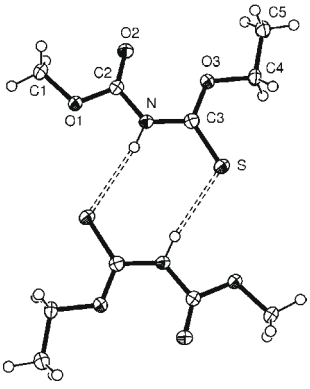


Sonia Torrico Vallejos, Mauricio F. Erben, Oscar E. Piro, Eduardo E. Castellano and Carlos O. Della Védova

Polyhedron 28 (2009) 937

N H···S═C hydrogen bond in O-alkyl N-methoxycarbonyl thiocarbamates, $ROC(S)N(H)C(O)OCH_3$ (R = CH_3 , CH_3CH_2)

The synthesis and full characterization of two O-alkyl N-methoxycarbonyl thiocarbamates, $ROC(S)N(H)C(O)OCH_3$ (R = CH_3 , CH_3CH_2), are reported. The structure and conformation are studied by using a combined experimental (X-ray, IR and Raman spectroscopy) and theoretical approach. The crystal structure of $CH_3CH_2OC(S)N(H)C(O)OCH_3$ shows the presence of centro-symmetric dimeric units held by N–H···S═C hydrogen bonds. The conjugative (resonance) effect in the thiocabamate group OC(S)N(H) is discussed.

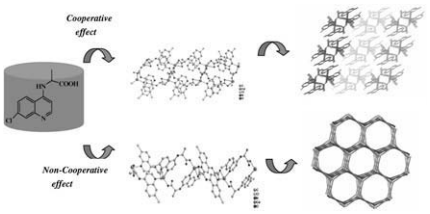


Xiao-Qiang Liang, Chao Chen, Xin-Hui Zhou, Hong-Ping Xiao, Yi-Zhi Li, Jing-Lin Zuo and Xiao-Zeng You

Polyhedron 28 (2009) 947

The architectures of 1D coordination polymers with the versatile 7-chloroquinoline-4-alanine ligand mediated by anions: Syntheses, structures and luminescent properties

Three new coordination polymers based on the 7-chloroquinolin-4-alanine ligand have been synthesized and characterized. The cooperative effect of the anion and the ligand produce a one-dimensional ladder-like polymer and a 3D supramolecular framework formed by π π stacking interactions. The non-cooperative effect of the anion and ligand give a 3D supramolecular framework with 1D channels. The results suggest that the cooperative effect of the anion and the ligand plays a role in mediating the structure in crystal engineering.

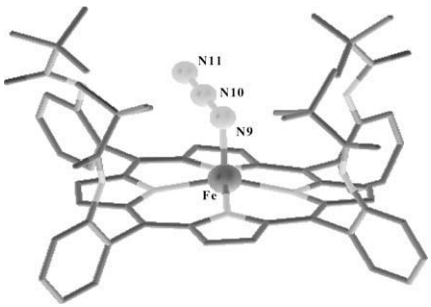


Ibtissem Hachem, Mohamed Salah Belkhiria, Michel Giorgi, Charles E. Schulz and Habib Nasri

Polyhedron 28 (2009) 954

Synthesis and characterization of the azido-bound five-coordinate high-spin iron(II) picket fence porphyrin complex

The present work reports the synthesis, the spectroscopic data and the crystal structure of the Fe(II)-azido five-coordinate picket fence porphyrin complex [Na(2,2,2-crypt)][Fe^{II}-(TpivPP)(N_3)] · $3C_6H_5Cl$ (TpivPP = α,α,α,α-tetrakis(*o*-pivalamidophenyl)porphinato and 2,2,2-crypt is the cryptand-222). The Mössbauer and X-ray data are used to assign the ground state electronic configuration of the iron(II) high-spin (*S* = 2) central ion.

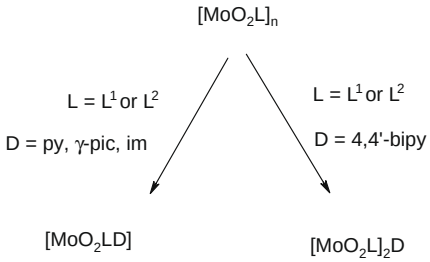


Vi nja Vrdoljak, Ivica Dilović, Marina Cindrić, Dubravka Matković-Calogović, Neven Strukan, Astrid Gojmerac-Iv ić and Predrag Novak

Polyhedron 28 (2009) 959

Synthesis, structure and properties of eight novel molybdenum(VI) complexes of the types: $[MoO_2LD]$ and $[\{MoO_2L\}_2D]$ (L = thiosemicarbazonato ligand, D = N-donor molecule)

Eight molybdenum(VI) complexes have been prepared. All the complexes were characterized by chemical analysis, IR spectroscopy, thermogravimetry and three of them, dioxo[(2-hydroxy-3-methoxybenzaldehyde thiosemicarbazonato)(pyridine)]molybdenum(VI), dioxo[(2-hydroxy-3-methoxybenzaldehyde thiosemicarbazonato)(γ-picoline)]molybdenum(VI) and dioxo[(2-hydroxy-3-methoxybenzaldehyde thiosemicarbazonato)(imidazole)]molybdenum(VI) were characterized by single-crystal X-ray structural analysis.

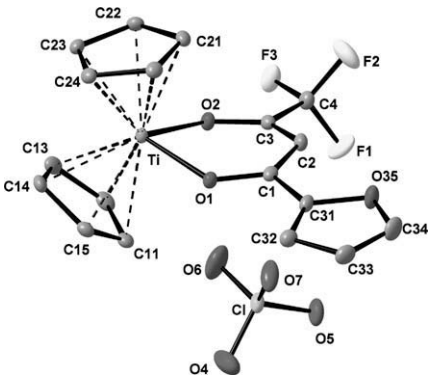


Annemarie Kuhn, Alfred Muller and Jeanet Conradie

Polyhedron 28 (2009) 966

Syntheses, crystal structure and theoretical modelling of tetrahedral mono-β-diketonato titanocenyl complexes

Crystallographic and computational study of new titanocenyl complexes of the type $[Cp_2Ti(CF_3COCHCOR)]^+ClO_4^-$, where R = C_6H_5, C_4H_3S and C_4H_3O.

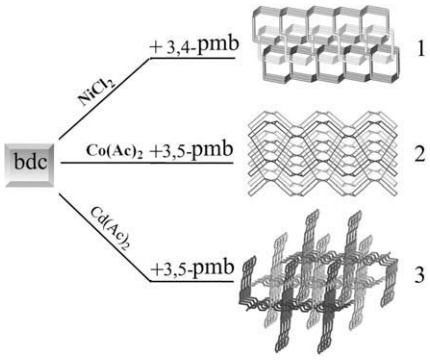


Kother Osman Ashiry, Ya-Hui Zhao, Kui-Zhan Shao, Zhong-Min Su and Guang-Juan Xu

Polyhedron 28 (2009) 975

Syntheses and characterizations of three coordination polymers based on dipyridylbenzoates and 1,4-bezenedicarboxylate

The coordination polymers, [Ni(3,5-pmb)$(bdc)_{0.5}$] (**1**), [Co(3,5-pmb)$(bdc)_{0.5}$] (**2**) and [Cd(3,5-pmb)$(bdc)_{0.5}$] (**3**), have been synthesized by the hydrothermal method. X-ray analysis reveals that complex **1** has a three-dimensional (3D) threefold interpenetrated diamodiod architecture, complex **2** is a 3D fourfold interpenetrated polyrotaxane, while complex **3** is a 2D network with paddle wheel dimeric cadmium tetracarboxylate building units.

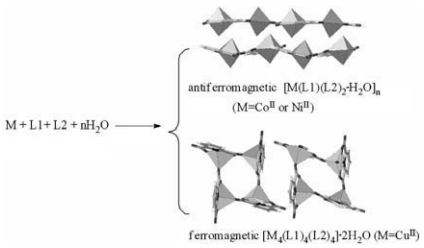


Shu-Xin Cui, Yu-Long Zhao, Jing-Ping Zhang, Qun Liu and Yan Zhang

Polyhedron 28 (2009) 980

Structural and magnetic properties of metal complexes with pyridine-2,6-dicarboxylate and 5-(4-bromophenyl)-2,4′-bipyridine

A series of complexes has been synthesized based on pyridine-2,6-dicarboxylate (L1) and 5-(4-bromophenyl)-2,4′-bipyridine (L2) with different metal ions.

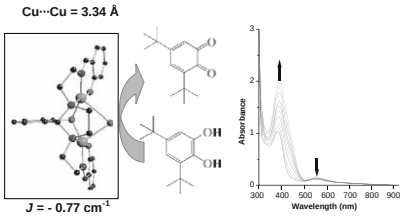


Prasant Kumar Nanda, Valerio Bertolasi, Guillem Aromí and Debashis Ray

Polyhedron 28 (2009) 987

Aqua bridged Cu_2 dimer of a heptadentate N_4O_3 coordinating ligand: Synthesis, structure and magnetic properties

The catechol binding and its oxidation in air have been examined for an aqua and imidazolidinyl phenolate bridged Cu_2 complex with an intermetallic separation of 3.34 Å and exhibiting a very weak antiferromagnetic exchange interaction (J = –0.77 cm^{-1}).

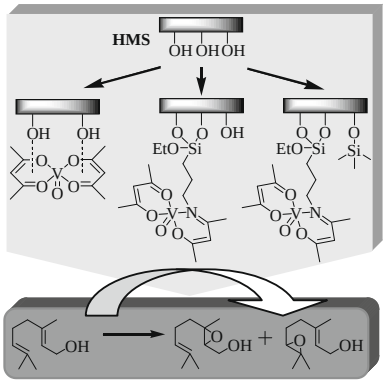


Bruno Jarrais, Clara Pereira, Ana Rosa Silva, Ana P. Carvalho, João Pires and Cristina Freire

Polyhedron 28 (2009) 994

Grafting of vanadyl acetylacetonate onto organo-hexagonal mesoporous silica and catalytic activity in the allylic epoxidation of geraniol

Vanadyl(IV) acetylacetonate was anchored onto a hexagonal mesoporous silica (HMS) using three different methodologies and the catalytic activity of these new materials in the epoxidation of geraniol using *tert*-butyl hydroperoxide (*t*-BuOOH) as oxygen source was assessed.

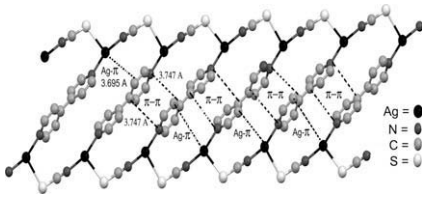


Safaa El-din H. Etaiw, Dina M. Abd El-Aziz, Moustafa Sh. Ibrahim and Ahmed S. Badr El-din

Polyhedron 28 (2009) 1001

Synthesis and crystal structures of three novel coordination polymers constructed from Ag(I) thiocyanate and nitrogen donor ligands

Three novel supramolecular coordination polymers of AgSCN with nitrogen donor ligands; $[AgSCN)_2 \cdot$ (4,4′-bipyridine)], $[AgSCN)_2 \cdot$ (*trans*-1,2-bis(4-pyridyl)ethene)], $[AgSCN)_2 \cdot$ (phenazine)], have been synthesized and structurally characterized by X-ray single-crystal analysis. The length and flexibility of the bipodal ligand affect greatly the structure of the $(AgSCN)_n$ building blocks.

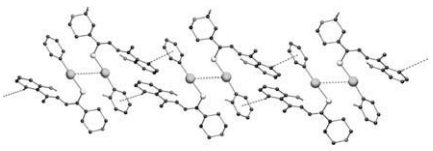


Susobhan Biswas, Golam Mostafa, Ian M. Steele, Saikat Sarkar and Kamalendu Dey

Polyhedron 28 (2009) 1010

Synthesis, crystal structures and luminescent properties of phenylmercury(II) complexes with thiohydrazone ligands having weak Hg π and Hg Hg interactions

The Reaction of phenylmercury(II) acetate with salicylaldehyde morpholine *N*-thiohydrazone (H_2smth) and 2-hydroxyacetophenone morpholine *N*-thiohydrazone (H_2apmth) in dry ethanol under gentle reflux form light yellow complexes [PhHg(Hsmth)] (**1**) and [PhHg(Hapmth)] (**2**) involving formation of Hg S bond from the thiol form of the ligands after deprotonation. Both the complexes form two-dimensional supramolecular assembly by combination of weak intermolecular Hg π, Hg Hg and C H π interactions. All the complexes in this study were found to exhibit rich luminescence properties in both solution and solid state.

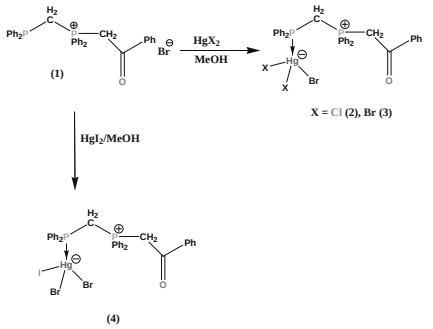


Mothi Mohamed Ebrahim, Krishnaswamy Panchanatheswaran, Antonia Neels and Helen Stoeckli-Evans

Polyhedron 28 (2009) 1017

Synthesis, spectra and crystal structures of zwitterionic mercury(II) complexes formed by the ligand, $[Ph_2PCH_2PPh_2CH_2C(O)Ph]^+$

The unsymmetrical phosphonium salt (**1**) reacts with Hg(II) halides to form different zwitterionic complexes as confirmed by single crystal X-ray analysis.

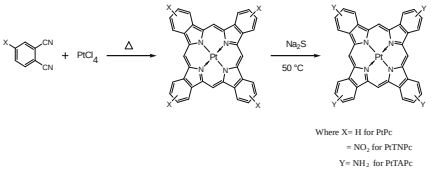


K.S. Lokesh, N. Uma and B.N. Achar

Polyhedron 28 (2009) 1022

The Microwave-assisted syntheses and a conductivity study of a platinum phthalocyanine and its derivatives

Platinum phthalocyanine (PtPc) and its derivatives with tetranitro (PtTNPc) and tetramine (PtTAPc) have been synthesized in the pure state for the first time. These complexes were found to have a monoclinic structure. The electrical conductivities observed at room temperature are in the order PtTAPc > PtTNPc > PtPc. PtTAPc showed an improvement in the intrinsic electrical conductivity by 10^4 times compared to its parent PtPc.

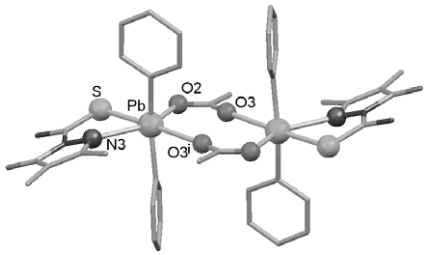


José S. Casas, Eduardo E. Castellano, Javier Ellena, María S. García-Tasende, Agustín Sánchez, José Sordo and Ángeles Touceda

Polyhedron 28 (2009) 1029

Diphenyllead(IV) thiosemicarbazonates and pyrazolonates: Synthesis and characterization

Cyclization of thiosemicarbazones derived from β-keto esters and β-keto amides (HTSC) in the presence of diphenyllead(IV) acetate have been studied. The complexes were isolated and characterized by X-ray crystallography and IR and NMR spectroscopy. Only β-keto ester TSCs underwent cyclization to give the corresponding pyrazolone (HL).

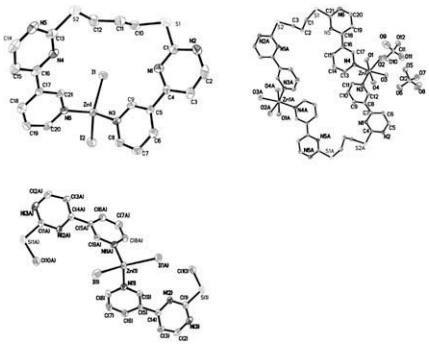


Hua-Ze Dong, Jian Zhao, Shao-Hua Gou and Hai-Bin Zhu

Polyhedron 28 (2009) 1040

Different crystal structures and luminescent properties of zinc and cadmium coordination polymers constructed from two flexible thioether ligands with different alkyl chains

Two series of complexes were prepared from reactions of two dithioether ligands (1,3-bis (4-(pyridin-3-yl) pyrimidin-2-ylthio) propane and 1,2-bis (4-(pyridin-3-yl) pyrimidin-2-ylthio) ethane) with zinc or cadmium salts, respectively. A small difference of the alkyl length between two ligands led to conspicuous changes of the fluorescent properties of both ligands and their complexes with different structural networks.



The Publisher encourages the submission of articles in electronic form thus saving time and avoiding rekeying errors. For detailed instructions on the preparation of manuscripts and of electronic artwork, consult the Author Gateway for Elsevier at http://authors.elsevier.com

ScienceDirect

Full text of this journal is available, on-line from **ScienceDirect**. Visit **www.sciencedirect.com** for more information.

Polyhedron 28, issue 11, 6 July 2009

Contents lists available at ScienceDirect

Polyhedron

journal homepage: www.elsevier.com/locate/poly

Contents

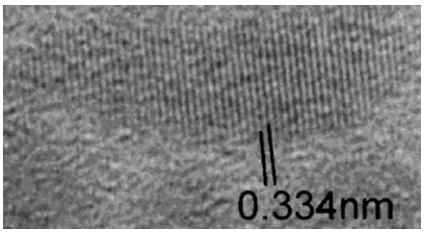
Papers

S.N. Mlondo, N. Revaprasadu, P. Christian, M. Helliwell and P. O'Brien

Polyhedron 28 (2009) 2097

Cadmium thiosemicarbazide complexes as precursors for the synthesis of nanodimensional crystals of CdS

Anisotropic cadmium sulfide nanocrystals have been prepared from two thiosemicarbazide complexes. Thermal decomposition of the precursors in hexadecylamine (HDA) results in the formation of nanorods of different dimensions. The powder X-ray diffraction patterns of the nanodimensional materials reveal differences in the phases of the CdS synthesized from the two complexes. Transmission Electron Microscopy (TEM) was used to study the morphology of the final materials.

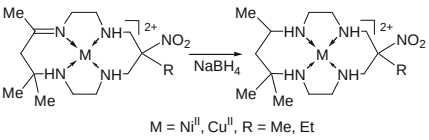


Neil F. Curtis, Kelly Flood, Ward T. Robinson and Joyce M. Waters

Polyhedron 28 (2009) 2103

Synthesis and structures of nickel(II) and copper(II) compounds of 5,5,7,13-tetramethyl-13-nitro-1,4,8,11-tetraazacyclotetradecane and the 13-ethyl-5,5,7-trimethyl-homologue

The imine functions of the nitro-substituted imine–triamine azamacrocycle cations are reduced by $NaBH_4$ to form the nitro-substituted cyclic tetraamine cations. The structures of five compounds with cations with M = Ni^{II}, R = Me and one with M = Cu^{II}, R = Et are reported.



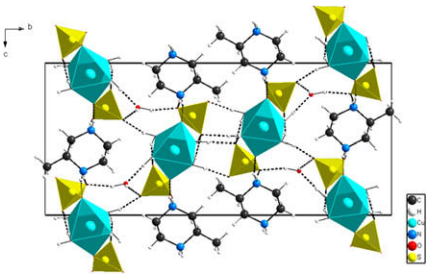
M = Ni^{II}, Cu^{II}, R = Me, Et

Fadhel Hajlaoui, Samia Yahyaoui, Houcine Naïli, Tahar Mhiri and Thierry Bataille

Polyhedron 28 (2009) 2113

Synthesis, structural characterisation and thermal decomposition of a new organic–inorganic hybrid material $(C_5H_{14}N_2)[Cu(SO_4)_2(H_2O)_4] \cdot H_2O$

The centric crystal structure of the title compound was expected from the racemic character of the 2-methypiperazine amine used in the synthesis. The structure consists of $[Cu(SO_4)_2(H_2O)_4]$ units, built from copper (II) octahedron and two sulfate tetrahedra linked by corner sharing, water molecules, and diprotonated 2-methylpiperazine cations connected together by hydrogen bonds only.

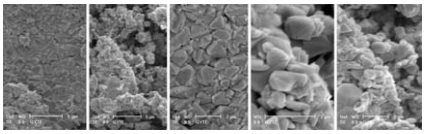


Zehra Durmus, Abdulhadi Baykal, Hüseyin Kavas, Mikail Direkçi and Muhammet S. Toprak

Polyhedron 28 (2009) 2119

Ovalbumin mediated synthesis of Mn_3O_4

By using Mn^{2+} and Mn^{3+} salts, and freshly extracted ovalbumin, Mn_3O_4 nanocrystals have been synthesized successfully. The X-ray diffraction results indicated that the synthesized nanoparticles have only the spinel structure without the presence of any other phase impurities. As the ovalbumin-water mixture was highly basic, the process did not require any use of base to increase the pH where hydrolysis took place. A gel formed where water soluble ovalbumin proteins served as a perfect matrix for entrapment of metal ions (Mn^{2+} and Mn^{3+}). Upon heat treatment, the dried gel precursor decomposed into nanocrystalline Mn_3O_4. The discrepancy between the crystallite size from XRD and particle size SEM analysis reveals polycrystalline nature of the synthesized particles with this route. EPR analysis of Mn_3O_4 show a narrow and symmetric line indicating the absence of hyperfine splitting.

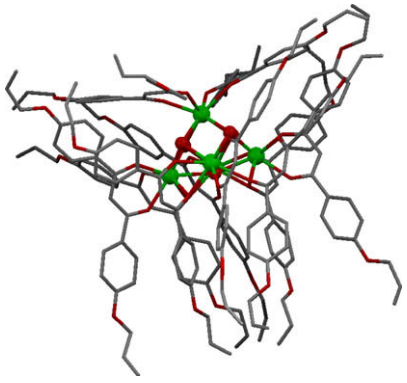


Philip C. Andrews, Tobias Beck, Benjamin H. Fraser, Peter C. Junk, Massimiliano Massi, Boujemaa Moubaraki, Keith S. Murray and Morry Silberstein

Polyhedron 28 (2009) 2123

Functionalised β-diketonate polynuclear lanthanoid hydroxo clusters: Synthesis, characterisation, and magnetic properties

Treatment of methoxy and ethoxy functionalised dibenzoylmethanide ligands with rare earth chlorides yielded mononuclear complexes (Nd), tetranuclear and pentanuclear hydroxo clusters (Ho, Eu), whose structures were determined by X-ray crystallography. An investigation of their magnetic properties is also presented.

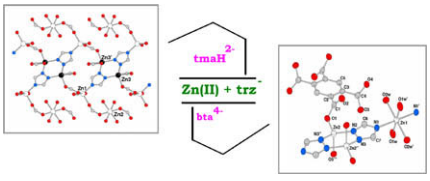


Durga Sankar Chowdhuri, Abhinandan Rana, Madhusudan Bera, Ennio Zangrando and Sudipta Dalai

Polyhedron 28 (2009) 2131

3D zinc(II) coordination polymers built up by triazole and benzene-polycarboxylate anions: Synthesis, crystal structure, thermal and photoluminescence characterization

Two new 3D hydrogen bonded zinc (II) coordination polymers have been synthesized using the benzene-1,3,5-tricarboxylate dianion or the benzene-1,2,4,5-tetracarboxylate tetra anion, with 1,2,4-triazolate. Both compounds were characterized by their X-ray single crystal structures, and by thermal and photoluminescence studies.

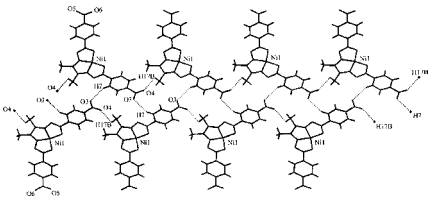


Nahed M.H. Salem, Amal R. Rashad, Laila El Sayed, W. Haase and Magdi F. Iskander

Polyhedron 28 (2009) 2137

Synthesis, characterization, molecular and supramolecular structures of nickel(II) complexes derived from α-diketone and α-ketoaldehyde bisaroylhydrazones

Ni(II) complexes derived from diacetyl bisaroylhydrazones [Ni(L^1-R)] and phenylglyoxal bisaroylhydrazones [Ni(L^2-R)] were prepared and characterized. The molecular and supramolecular structures [Ni(L^1-H)], [Ni(L^1-pCH_3O)] and [Ni(L^1-pNO_2)] were determined by single crystal X-ray analysis. The structure of the mixed ligand Ni(II) complexes [Ni(L^1-H)$(HIm)_2$], [Ni(L^1-pNO_2)$(HIm)_2$] and {Ni(L^2-pCH_3)(HIm)] were also determined.

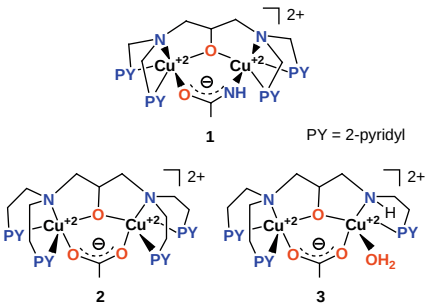


Gnana S. Siluvai and Narasimha N. Murthy

Polyhedron 28 (2009) 2149

X-ray structure and spectroscopic characterization of doubly-bridged binuclear copper(II) complexes in symmetric and asymmetric coordination environments

μ-1,3-Acetamide or acetate bridged, symmetric and asymmetric dicopper(II) complexes *viz* $[Cu_2(P1\text{-}O^-)(NHAc^-)](ClO_4)_2$ (**1**), $[Cu_2(P2\text{-}O^-)(OAc^-)](ClO_4)_2$ (**2**) and $[Cu_2(P2'\text{-}O^-)(OAc^-)(H_2O)](ClO_4)_2$ (**3**) were synthesized by employing classic dinucleating ligands; P1-OH, P2-OH (symmetric), and P2′-OH (asymmetric) and their structures were determined by X-ray crystallography. In solution, they were characterized by various spectroscopic techniques, which include ESI-MS, FT-IR, optical, solution magnetic moment, paramagnetic ^1H NMR and EPR. The solution magnetic moment of these complexes at room temperature suggests a weak magnetic interaction between the two Cu(II) centers.

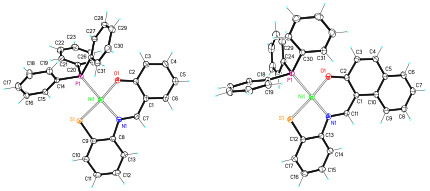


M. Muthu Tamizh, Kurt Mereiter, Karl Kirchner, B. Ramachandra Bhat and R. Karvembu

Polyhedron 28 (2009) 2157

Synthesis, crystal structures and spectral studies of square planar nickel(II) complexes containing an ONS donor Schiff base and triphenylphosphine

Five mononuclear Ni(II) complexes containing an ONS donor Schiff base and triphenylphosphine have been prepared and characterized by analytical and spectral (electronic, IR, ^1H, ^{13}C and ^{31}P NMR) techniques. X-ray crystal structures of two of the complexes have also been discussed. A square planar geometry has been proposed for all the complexes.

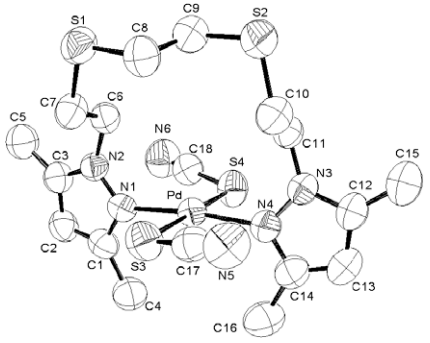


Antonio de León, Josefina Pons, Jordi García-Antón, Xavier Solans, Mercè Font-Bardía and Josep Ros

Polyhedron 28 (2009) 2165

Preparation and characterisation of mononuclear Pd(II) complexes with 1,8-bis(3,5-dimethyl-1-pyrazolyl)-3,6-dithiaoctane (bddo) ligand: Spectroscopy studies and crystal structure of *trans*-$[Pd(SCN)_2(bddo)]$

The reaction of *trans*-$[PdCl_2(bddo)]$ with cyanide, thiocyanate or azide produces the complexes $[PdX_2(bddo)]$. However, the reaction with pyridine yields a mixture of $[Pd(bddo)(py)_2](BF_4)_2$ (78%) and $[Pd(bddo)](BF_4)_2$ (22%) complexes, and the reaction with triphenylphosphine only affords $[Pd(bddo)](BF_4)_2$.

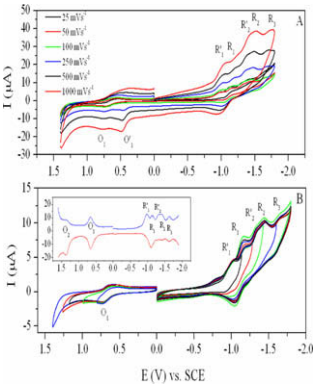


Zekeriya Bıyıklıoğlu, Atıf Koca and Halit Kantekin

Polyhedron 28 (2009) 2171

Synthesis, electrochemical, *in situ* spectroelectrochemical and *in situ* electrocolorimetric characterization of new phthalocyanines peripherally fused to four flexible crown ether moieties

Novel Ni(II), Zn(II), Co(II) and Cu(II) phthalocyanines with four peripheral 4-[methyleneoxy(18-crown-6)] groups have been synthesized via the cyclic tetramerization of 4-[{(18-crown-6)-yl}methyleneoxy]phthalonitrile and the corresponding metal salts ($NiCl_2$, $Zn(CH_3COO)_2$, $CoCl_2$ and $CuCl_2$). The thermal stabilities of the metal-free and metallophthalocyanine compounds were determined by thermogravimetric analysis. The structures of the target compounds were confirmed using elemental analysis, IR, ^1H NMR, ^{13}C NMR, UV–Vis and MS spectral data. Voltammetric and *in situ* spectroelectrochemical measurements show that while the cobalt phthalocyanine complex gives both metal-based and ring-based redox processes, the metal-free, nickel, zinc and copper phthalocyanines show only ring-based reduction and oxidation processes. An *in situ* electrocolorimetric method has been applied to investigate the color of the electro-generated anionic and cationic forms of the complexes.

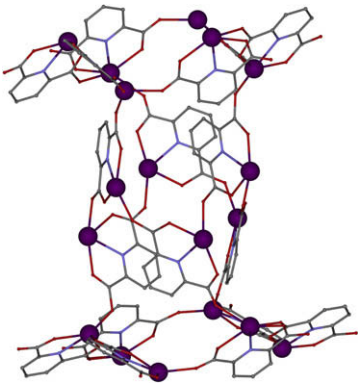


Josef Hamacek, Soumaila Zebret and Gérald Bernardinelli

Polyhedron 28 (2009) 2179

Supramolecular structure of the polymeric Eu-(III) complex with pyridine-2,6-dicarboxylic acid

The europium complex with pyridine-2,6-dicarboxylic acid forms three-dimensional polymers in the solid state, where the europium cation is nine-coordinated by the ligand, two bridging carboxylate oxygens and four water molecules. Interconnecting of mono-(dipicolinate) complexes by carboxylate oxygens results in a compact 3D supramolecular structure with a high density.

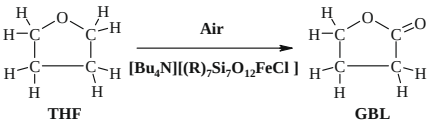


Michael T. Hay, Steven J. Geib and Derek A. Pettner

Polyhedron 28 (2009) 2183

Aerobic oxidation of tetrahydrofuran by a series of iron (III) containing POSS compounds

The aerobic oxidation of tetrahydrofuran was catalysed by a series of iron (III) POSS compounds, $[Bu_4N][(R)_7Si_7O_{12}FeCl]$ (R = isobutyl-, ethyl-, phenyl-, and cyclopentyl-). The major oxidation product was γ-butyrolactone. The corresponding turnover numbers for the aerobic oxidation of THF suggest that smaller substitutents on the POSS ligands improve the stability of the catalytic species.

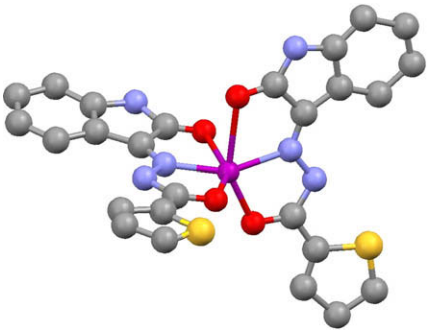


María C. Rodríguez-Argüelles, Roberto Cao, Ana M. García-Deibe, Corrado Pelizzi, Jesús Sanmartín-Matalobos and Franca Zani

Polyhedron 28 (2009) 2187

Antibacterial and antifungal activity of metal(II) complexes of acylhydrazones of 3-isatin and 3-(*N*-methyl)isatin

Three new acylhydrazone ligands and their Co(II), Ni(II), Cu(II) and Zn(II) complexes, were synthesised, characterised and evaluated *in vitro* as antimicrobial agents against a panel of Gram positive and Gram negative bacteria, as well as yeasts and moulds.

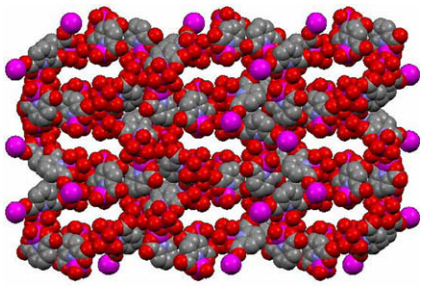


Taoyun Zhu, Koichi Murokawa, Kazuyoshi Uematsu, Tadashi Ishigaki, Kenji Toda, Hirokazu Okawa and Mineo Sato

Polyhedron 28 (2009) 2196

One-dimensional coordination polymers of praseodymium(III)–vanadium(V) complexes with pyridine-2,6-dicarboxylic acid

New isomorphous lanthanide–vanadium complexes with one-dimensional coordination polymers, $[Ln_2(VO_2)_2(dipic)_4(H_2O)_9] \cdot nH_2O$. Three types of chains in the complex provide open channels which can accommodate water molecules. Water molecules were easily removed and absorbed upon heating at 200 °C and exposure of humidity at room temperature, respectively.

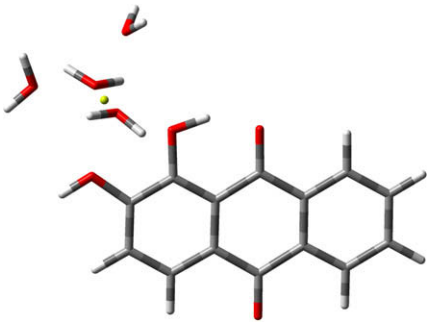


Marek Doskocz, Karolina Kubas, Anna Frąckowiak and Roman Gancarz

Polyhedron 28 (2009) 2201

NMR and *ab initio* studies of Mg^{2+}, Ca^{2+}, Zn^{2+}, Cu^{2+} alizarin complexes

Alizarin acts as a bidendate ligand on forming complexes with the metal ions Mg^{2+}, Ca^{2+}, Zn^{2+} and Cu^{2+}. From the possible structures, the one with the metal attached to two hydroxyl oxygen atoms is of lower energy. A theoretical calculation of the structure of the complex, and NMR parameter analysis lead to the same conclusion.

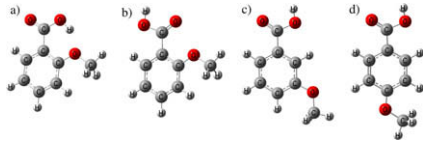


M. Kalinowska, G. Świderski and W. Lewandowski

Polyhedron 28 (2009) 2206

Effect of substituent position and lithium, sodium and potassium on the electronic structure of *o*-, *m*- and *p*-methoxybenzoic acids

FT-IR, FT-Raman, Ar matrix FT-IR, ^1H NMR methods and *ab initio* calculations have been used to study the effect of the substituent position in the ring, and lithium, sodium and potassium ions on the electronic structure of (a, b) *o*-, (c) *m*- and (d) *p*-methoxybenzoic acids. On the basis of the obtained results, we may answer the following: (1) whether the substituents in the benzene ring influence the electronic charge distribution in the carboxylic group of methoxybenzoates, (2) whether metal ions affect the electronic charge distribution in the methoxy group, (3) in what way the alkali metals affect the electronic system of methoxybenzoic acids.

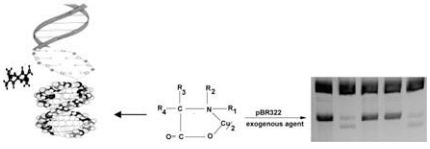


Hoi Ling Seng, Kong Wai Tan, Mohd Jamil Maah, Wee Tee Tan, Hirokazu Hamada, Makoto Chikira and Chew Hee Ng

Polyhedron 28 (2009) 2219

Copper(II) complexes of methylated glycine derivatives: Effect of methyl substituent on their DNA binding and nucleolytic property

DNA interaction and oxidative cleavage by a series of copper(II) methylated glycine derivatives in the presence of hydrogen peroxide alone or ascorbate alone or both reagents are described. Comparison of nucleolytic efficiency and mechanism of cleavage are also discussed.

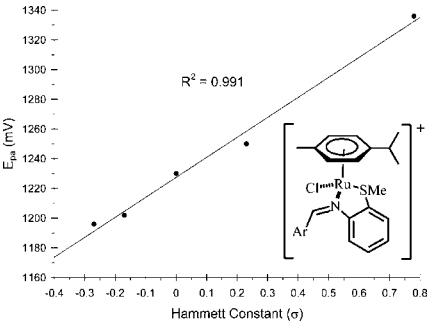


Christopher G. Hamaker and Dominic P. Halbach

Polyhedron 28 (2009) 2228

X-ray structural and electrochemical analysis of η^6-*p*-cymene ruthenium complexes with chelating S∩N ligands derived from 2-(methylthio)aniline and substituted benzaldehydes

A series of cationic, half-sandwich ruthenium complexes with the general formula $[(\eta^6\text{-}p\text{-cymene})RuCl(S\cap N)]^+$, (S∩N = MeS-$C_6H_4$-2-N=CHAr, **1a–f**) have been studied by cyclic voltammetry and X-ray crystallography.

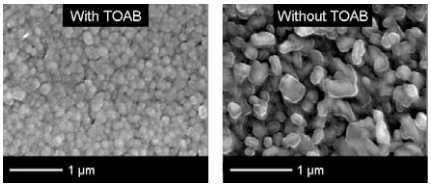


Manfredi Saeli, Russell Binions, Clara Piccirillo, Geoffrey Hyett and Ivan P. Parkin

Polyhedron 28 (2009) 2233

Templated growth of smart nanocomposite thin films: Hybrid aerosol assisted and atmospheric pressure chemical vapour deposition of vanadyl acetylacetonate, auric acid and tetraoctyl ammonium bromide

Hybrid aerosol assisted and atmospheric pressure chemical vapour deposition methodology has been utilised to produce nanocomposite thin films of gold nanoparticles and vanadium dioxide from vanadyl acetylacetonate and auric acid. The addition of tetraoctyl ammonium bromide (TOAB) to the precursor solution gave control of the size and distribution of gold nanoparticles in the vanadium oxide matrix. These reactions led to vanadium dioxide films with reduced crystallite sizes and enhanced thermochromic properties.

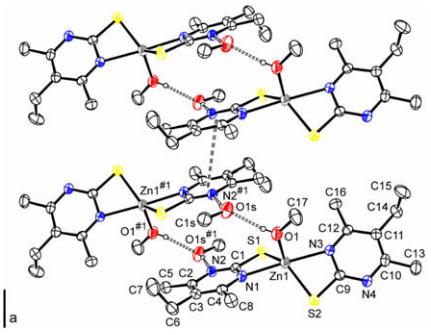


Antonio Rodríguez, Antonio Sousa-Pedrares, José A. García-Vázquez, Jaime Romero and Antonio Sousa

Polyhedron 28 (2009) 2240

Electrochemical synthesis and characterization of zinc(II) complexes with pyrimidine-2-thionato ligands and their adducts with N,N donors

The electrochemical oxidation of a zinc anode in a solution of different pyrimidine-2-thiones in acetonitrile afforded the obtention of the corresponding thionato complexes. When bipy or phen was added to the cell, the heteroleptic complexes are obtained as well. Crystal structures were determined for three of the complexes and the thionato ligands show two different coordination behaviours: –N,S chelating ligand and η^1-S monodentate ligand.

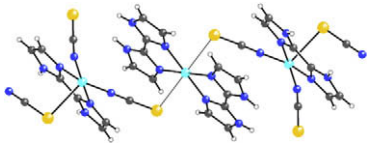


José Carranza, Jorunn Sletten, Francesc Lloret and Miguel Julve

Polyhedron 28 (2009) 2249

Preparation, crystal structures and magnetic properties of three thiocyanato-bridged copper(II) complexes with 2,2′-biimidazole or 2-(2′-pyridyl)imidazole as terminal ligands

Single- (**1** and **2**) and double- (**3**) end-to-end thiocyanato-bridged copper(II) complexes are present in the trinuclear $\{[Cu(H_2bim)_2][Cu(H_2bim)(NCS)_2(SCN)_{0.6667}(NO_3)_{0.3333}]_2\} \cdot 2H_2O$ (**1**) and chain $[Cu(H_2bim)(NCS)_2]_n$ (**2**) and $[Cu(pyim)(NCS)_2]_n$ (**3**) compounds where weak intramolecular (**1**) and intrachain (**2** and **3**) antiferromagnetic interactions occur.

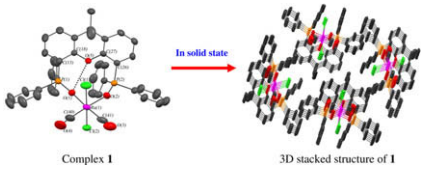


Biswajit Deb and Dipak Kumar Dutta

Polyhedron 28 (2009) 2258

Synthesis, molecular and crystal structure of a new dicarbonylruthenium(II) complex containing a xantphos dioxide chelating ligand

The polymeric precursor $[Ru(CO)_2Cl_2]_n$ reacts with xantphos dioxide (L) in 1:1 molar ratio to generate mononuclear complex $[Ru(CO)_2Cl_2(L)]$(**1**). Each mononuclear unit of **1** is stabilized in their solid state through non-covalent (C–H···O, C–H···Cl and C–H···π) interactions to develop an extended three-dimensional network.

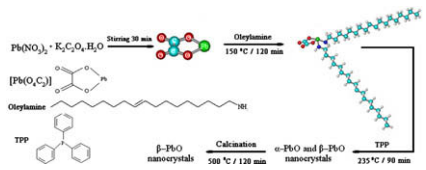


Masoud Salavati-Niasari, Fatemeh Mohandes and Fatemeh Davar

Polyhedron 28 (2009) 2263

Preparation of PbO nanocrystals via decomposition of lead oxalate

The present investigation reports on the synthesis of PbO nanocrystals using thermal decomposition, and its physicochemical characterization. PbO nanocrystals have been prepared using lead oxalate powders as a precursor. The results indicated that the orthorhombic phase β-PbO with a particle size of about 30–45 nm was obtained when the calcination temperature was 500 °C.

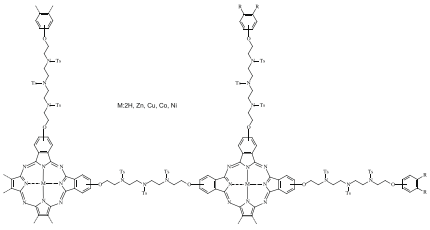


Ahmet Bilgin, Çiğdem Yağcı, Ufuk Yıldız, Ersel Özkazanç and Erdoğan Tarcan

Polyhedron 28 (2009) 2268

Synthesis, characterization, aggregation and thermal properties of a novel polymeric metal-free phthalocyanine and its metal complexes

The novel metal-free (**6**) and its metal complexes (**7**–**10**), containing triazadioxa peripheral units, have been prepared and characterized. The electrical conductivities, thermal and aggregation properties of the novel polymers were also investigated.

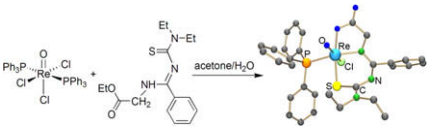


Jennifer Schroer and Ulrich Abram

Polyhedron 28 (2009) 2277

Novel thiourea derivatives of α-amino acids and their oxorhenium(V) complexes

Novel benzamidines prepared from *N*-[(dialkylamino)(thiocarbonyl)]benzimidoyl chlorides and α-amino acid esters react with [ReOCl$_3$(PPh$_3$)$_2$] as monodentate or tridentate ligands depending on the reaction conditions applied. Metal-supported ester hydrolysis and the formation of the tridentate ligands is achieved under mild conditions.

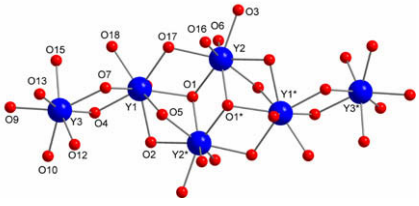


Ananda Kumar Jami, Pilli V.V.N. Kishore and Viswanathan Baskar

Polyhedron 28 (2009) 2284

Functionalised β-diketone assisted self-assembly of a hexanuclear yttrium oxo-hydroxo cluster

A functionalised β-diketone has been used as a ligand for the synthesis of the hexanuclear yttrium oxo-hydroxo cluster [Y$_6$(O-DBM)$_6$(HO-DBM)$_4$(μ$_3$-OH)$_2$(MeOH)$_4$] (**1**). The solid state structure reveals the formation of a novel hexanuclear yttrium cluster with the ligand binding the metal centres in both chelating and chelating- bridging modes.

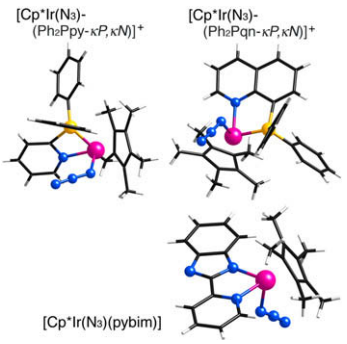


Takayoshi Suzuki, Mai Kotera, Asuka Takayama and Masaaki Kojima

Polyhedron 28 (2009) 2287

Crystal structures of (azido)(pentamethylcyclopentadienyl)iridium(III) complexes containing various types of bidentate ligands

The iridium(III) azido complexes of [Cp*-$Ir^{III}(N_3)_2(Ph_2Ppy$-κP)] (Cp* = η^5-C_5Me_5, Ph_2Ppy = 2-diphenylphosphinopyridine) and [Cp^*Ir^{III}-$(N_3)(L–L')]^{+/0}$ [L–L′ = Ph_2Ppy, bis(dimethylphosphino)methane (dmpm), 8-diphenylphosphinoquinoline (Ph_2Pqn), or 2-(2-pyridyl)-benzimidazolate (pybim)] have been prepared and their crystal structures have been compared together with those of the related complexes.

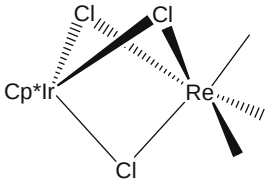


Xiaoping Wang, Casey Hammons and Michael G. Richmond

Polyhedron 28 (2009) 2294

Preparation and reactivity of the heterobimetallic ReIr face-shared bioctahedral compounds $Cp^*Ir(\mu$-$Cl)_3Re(CO)_3$ and $Cp^*Ir(\mu$-SC_6H_4Me-$4)_3Re(CO)_3$: X-ray diffraction structures and redox behavior

Thermolysis of $[Cp^*IrCl_2]_2$ (**1**) with $ClRe(CO)_5$ (**2**) gives the chloride-bridged compound $Cp^*Ir(\mu$-$Cl)_3Re(CO)_3$ (**3**), which when treated with excess HSC_6H_4Me-4 yields the sulfido-bridged product $Cp^*Ir(\mu$-SC_6H_4Me-$4)_3Re(CO)_3$ (**4**). Compounds **3** and **4** have been spectroscopically characterized and their molecular structures established by X-ray crystallography.



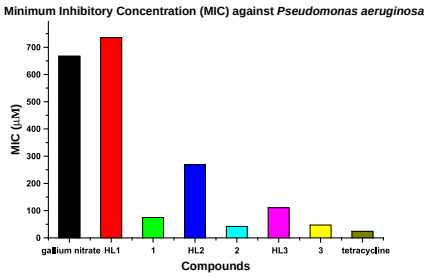
compound **3**

Jeferson G. da Silva, Lucas S. Azzolini, Solange M.S.V. Wardell, James L. Wardell and Heloisa Beraldo

Polyhedron 28 (2009) 2301

Increasing the antibacterial activity of gallium(III) against *Pseudomonas aeruginosa* upon coordination to pyridine-derived thiosemicarbazones

Reaction of *N*(4)-phenyl-2-formylpyridine thiosemicarbazone (H2Fo4Ph, HL1), *N*(4)-phenyl-2-acetylpyridine thiosemicarbazone (H2Ac4Ph, HL2) and *N*(4)-phenyl-2-benzoylpyridine thiosemicarbazone (H2Bz4Ph, HL3) with gallium nitrate gave $[Ga(H2Fo4Ph)_2](NO_3)_3$ (**1**), $[Ga(2Ac4Ph)_2]NO_3$ (**2**) and $[Ga(2Bz4Ph)_2]NO_3$ (**3**). In all complexes coordination of the thiosemicarbazone via the N_{py}–N–S chelating system occurs. Upon coordination the antibacterial activity of both gallium and thiosemicarbazones against *Pseudomonas aeruginosa* significantly increases.



The Publisher encourages the submission of articles in electronic form thus saving time and avoiding rekeying errors. For detailed instructions on the preparation of manuscripts and of electronic artwork, consult the Author Gateway for Elsevier at http://authors.elsevier.com

ScienceDirect

Full text of this journal is available, on-line from **ScienceDirect**. Visit **www.sciencedirect.com** for more information.

Polyhedron 28, issue 8, 10 June 2009

Contents lists available at ScienceDirect

Polyhedron

journal homepage: www.elsevier.com/locate/poly

Contents

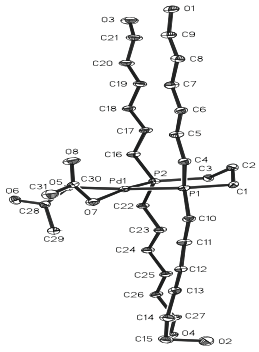
Papers

Mahmoud Sunjuk, Mousa Al-Noaimi, Ghassan Abu Sheikha, Ekkehard Lindner, Bassam El-Eswed and Kamal Sweidan

Polyhedron 28 (2009) 1393

Synthesis and characterization of water-soluble palladium(II)-functionalized diphosphine complexes

Water-soluble functionalized bis(phosphine) ligands **L** (**a**–**h**) of the general formula $CH_2(CH_2PR_2)_2$ where **L** is (**a**: R = $(CH_2)_6OH$; **b**–**g**: R = $(CH_2)_n$ $P(O)(OEt)_2$, n = 2–6 and n = 8; **h**: R = $(CH_2)_3NH_2$ have been prepared photochemically by hydrophosphination of the corresponding 1-alkenes with $H_2P(CH_2)_3PH_2$. Water-soluble palladium complexes *cis*-$[Pd(\mathbf{L})(OAc)_2]$ were obtained by the reaction of $Pd(OAc)_2$ with the ligands **L** in dichloromethane–acetonitrile. A crystallographic study of complex **1** shows that the PdII) ion has a square planar coordination sphere in which the acetate ligands and the diphosphine ligand deviate by less than 0.12 Å from ideal planar.

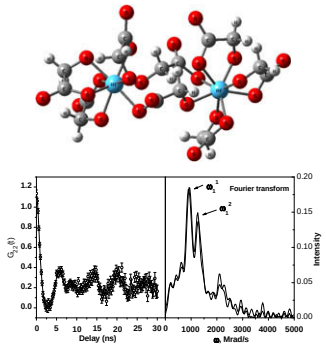


N. Rawat, S. Kumar and B. Tomar

Polyhedron 28 (2009) 1399

The time differential perturbed angular correlation study of binding of hafnium to humic acid and its model compound

Time differential perturbed angular correlation (TDPAC) spectroscopy has been used to study the binding of hafnium to mandelic acid, which is a model compound of humic acid. The Fourier transform of TDPAC spectrum of Hf–mandelate complex showed two ω values, namely, ω_{Q1} = 77 (±0.4) Mrad/s and ω_{Q2} = 111 (±3.1) Mrad/s. The asymmetry parameters for the two sites were found to be 0.7 and 0.3, respectively. The electric field gradient (EFG) around the metal ion was theoretically calculated using the computer code GAMESS. The calculated EFG value was found to be in reasonable agreement with that deduced from experiment. Contrary to Hf–mandelate, the TDPAC spectrum of Hf–humate system did not show characteristic features of discrete binding sites.

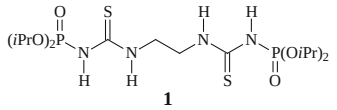


Damir A. Safin, Maria G. Babashkina, Michael Bolte and Axel Klein

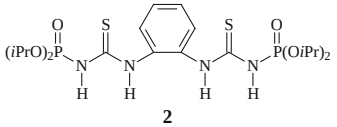
Polyhedron 28 (2009) 1403

The influence of the spacer Z on *N*-phosphorylated bis-thioureas and 2,5-dithiobiurea $Z[C(S)NHP(O)(OiPr)_2]_2$ (Z = —$NHCH_2CH_2NH$—, —NHC_6H_4-2-NH—, —NHNH—) crystal design

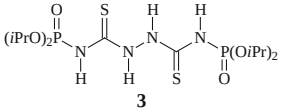
Two new bifunctional *N*-phosphorylated thioureas and a 2,5-dithiobiurea of the common formula $Z[C(S)NHP(O)(OiPr)_2]_2$ [Z = —$NHCH_2$-CH_2NH— (**1**), —NHC_6H_4-2-NH— (**2**), —NHNH— (**3**)] have been synthesized and characterized by NMR spectroscopy and single crystal X-ray diffraction. The structure of the compound **3** has been studied in $CDCl_3$ and DMSO-d_6 solutions.



1



2



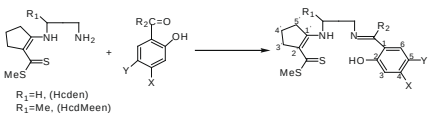
3

Mozaffar Asadi, Khosro Mohammadi, Sheida Esmaielzadeh, Bijan Etemadi and Hoon Kun Fun

Polyhedron 28 (2009) 1409

Some new Schiff base ligands giving a NNOS coordination sphere and their nickel(II) complexes: Synthesis, characterization and complex formation

Some new tetradentate ligands with a N_2OS coordination sphere were prepared and their corresponding nickel(II) and copper(II) complexes were synthesized. The thermodynamic formation constants of the complexes were measured spectrophotometrically at 25 °C in DMF solvent. The structure of {methyl-2-[N-[2-(5-chloro-2-phenolate)methylidynenitrilo]ethyl}-aminato(-1)-1-cyclopentenedithiocarboxyla-te nickel(II), [Ni(cd5Clsalen)], has been determined by X-ray crystallography. The coordination around nickel is essentially square-planar, with a small tetrahedral distortion.

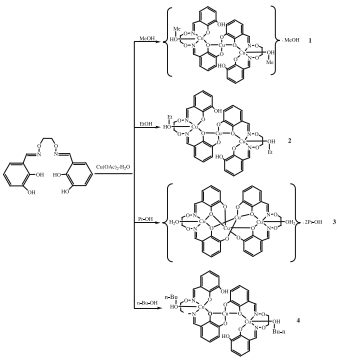


Wen-Kui Dong, Xue-Ni He, Hai-Bo Yan, Zhong-Wu Lv, Xiao Chen, Chun-Yu Zhao and Xiao-Lu Tang

Polyhedron 28 (2009) 1419

Synthesis, structural characterization and solvent effect of copper(II) complexes with a variational multidentate Salen-type ligand with bisoxime groups

Four new solvent-induced Cu(II) complexes have been synthesized and structurally characterized. Because of the introduction of different solvent molecules, these complexes present two kinds of stoichiometric ratio and different structural features with a different performance of the ligand. Complex **3** forms a tetrametal Cu–O–Cu–O–Cu–O–Cu–O eight-membered ring.

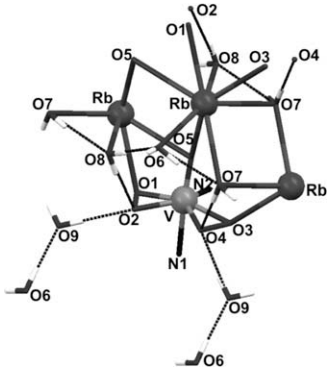


Wojciech Przybylski, Ryszard Gryboś, Dieter Rehder, Martin Ebel, Maciej Grzywa, Wiesław Łasocha, Krzysztof Lewiński and Janusz T. Szklarzewicz

Polyhedron 28 (2009) 1429

Role of the alkali metal ion and hydrogen bonds in $M[VO(O_2)_2bpy] \cdot nH_2O$ (M = Li^+, Na^+, K^+ and Rb^+) and $Cs[VO(O_2)_2bpy] \cdot H_2O_2$ complexes: The X-ray crystal structures and spectroscopic properties

The type of alkali metal ion (M) in the $M[VO(O_2)_2bpy] \cdot nH_2O \cdot mH_2O_2$ complexes influences the degree of hydration, the network of hydrogen bonds involving water molecules and peroxo groups as well the interaction of the M with the oxidovanadium(V) oxygen and/or peroxo ligand.

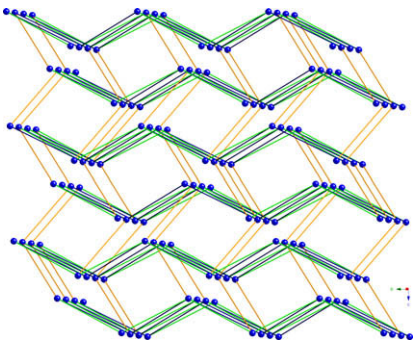


Eric Shyu, Subhashree Mallika Krishnan, Ronald M. Supkowski and Robert L. LaDuca

Polyhedron 28 (2009) 1437

Metal azelate coordination polymers containing a kinked dipyridyl tether: $CdSO_4$ topology and "ligand vacancy" primitive cubic three-dimensional networks

Coordination polymers $[M(aze)(dpa)(H_2O)]_n$ (M = Co, **1**; M = Ni, **2**, aze = azelate, dpa = 4,4′-dipyridylamine) and $\{[Cd(aze)(dpa)] \cdot 2H_2O\}_n$ (**3**) have been prepared. Complexes **1** and **2** possess crystallographically disordered azelate ligands, forming related three-dimensional (3-D) 4-connected "ligand vacancy" primitive cubic coordination polymer networks. Compound **3** manifests a 3-D $6^5 8$ $CdSO_4$ topology coordination polymer network. Luminescent properties for **3** and thermal properties are also discussed.

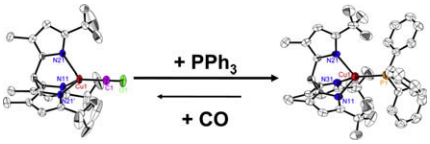


Kiyoshi Fujisawa, Masahiro Yoshida, Yoshitaro Miyashita and Ken-ichi Okamoto

Polyhedron 28 (2009) 1447

Copper(I) complexes with fluorinated hydrotris(pyrazolyl)borate: Influence of electronic effects on their structure, physicochemical properties, and reactivity

Copper(I) coordination complexes of the anionic fluorinated ligand, hydrotris(3-trifluoromethyl-5-methyl-1-pyrazolyl)borate were synthesized and structurally characterized. While X-ray crystallography did not show definitive trends in terms of copper(I) atom geometry, the clear influence of the electronic structure of the pyrazolyl rings is observed by spectroscopic techniques, namely, IR and multinuclear NMR spectroscopy. Finally, the relative stability of the copper(I) complexes is discussed.

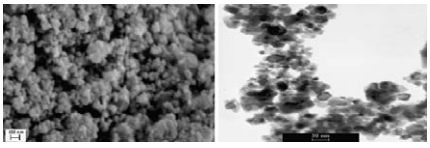


Masoud Salavati-Niasari, Fatemeh Davar and Tahmineh Mahmoudi

Polyhedron 28 (2009) 1455

A simple route to synthesize nanocrystalline nickel ferrite ($NiFe_2O_4$) in the presence of octanoic acid as a surfactant

Nanocrystalline nickel ferrite ($NiFe_2O_4$) powder was prepared by a co-precipitation method from Ni and Fe chlorides. The as-prepared nickel ferrite nanocrystals were characterized by XRD, SEM, TEM, and FTIR. SEM and TEM indicated that the particles were spherical with particle sizes in the range 25 ± 5 nm. The magnetic properties of the sample were measured by using a vibration sample magnetometer, which showed that the sample exhibited typical ferromagnetic behavior at room temperature, while a finite coercivity of 245.5 Oe was present at 300 K.

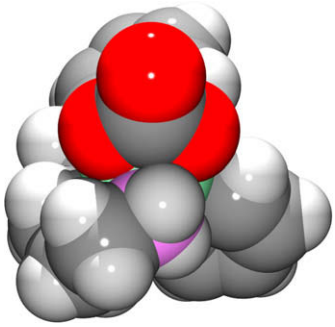


Lisa F. McClintock, Priyanka Bagaria, Henrik G. Kjaergaard and Allan G. Blackman

Polyhedron 28 (2009) 1459

Co(III) complexes of the type $[(L)Co(O_2CO)]^+$ (L = tripodal tetraamine ligand): Synthesis, structure, DFT calculations and ^{59}Co NMR

New $[(L)Co(O_2CO)]ClO_4$ complexes, where L = an "asymmetric" tripodal tetraamine ligand, have been prepared and characterised. The single geometric isomer isolated from these syntheses is generally that predicted by DFT calculations. An excellent correlation between Δ and $\delta(^{59}Co)$ for these, and other similar complexes is detailed.



Daniel L. Reger, J. Derek Elgin, Perry J. Pellechia, Mark D. Smith and Brett K. Simpson

Polyhedron 28 (2009) 1469

Structural organization of a $\{ruthenium[tris(bipyridyl)]\}^{2+}$ complex by strong π–π stacking of a tethered 1,8-naphthalimide synthon: Impact on electrochemical and spectral properties

The $\{Ru(bipyridyl)_2\}^{2+}$ complex of the new ligand *N*-(5-methyl-2,2′-bipyridyl)-1,8-naphthalimide, containing both a bipyridyl and 1,8-naphthalimide group, has been prepared and shown to be organized into dimers in both the solid and solution phase by strong, directionally oriented π–π stacking. UV–VIS, fluorescence spectroscopy and electrochemical studies indicate that the 1,8-naphthalimide groups does not have a significant influence on the properties of the $[Ru(bipy)_3]^{2+}$ core.

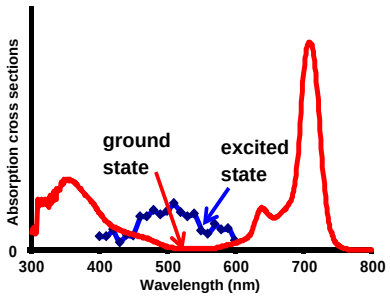


Desmond Kwena Modibane and Tebello Nyokong

Polyhedron 28 (2009) 1475

Synthesis, photophysical and nonlinear optical properties of microwave synthesized 4-tetra and octa-substituted lead phthalocyanines

The ratio of the absorption cross sections of the ground and excited states was larger than unity for lead phthalocyanine complexes containing benzyloxyphenoxy substituents, confirming that the complexes are good optical limiters.

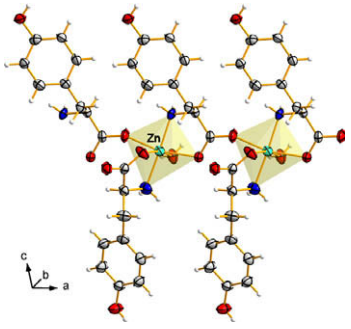


Agnieszka Wojciechowska, Marek Daszkiewicz and Alina Bieńko

Polyhedron 28 (2009) 1481

Polymeric Zn(II) and Cu(II) complexes with exobidentate bridging L-tyrosine: Synthesis, structural and spectroscopic properties

A one-dimensional coordination polymeric structure exists for $\{[Zn(tyr)_2(H_2O)]H_2O\}_n$, due to one tyrosine ligand acting as an exobidentate bridging ligand. The coordination polymer is created as an unstranded chain with a *trans* coordination of the carboxylate groups of L-Tyr(A).

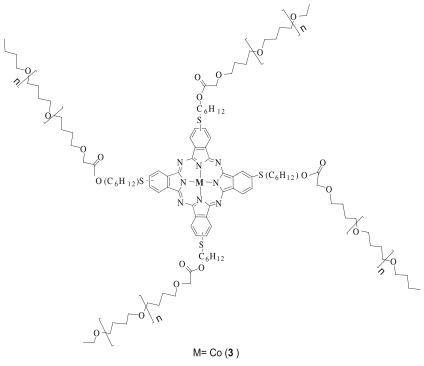


Yeşim H. Gursel, B. Filiz Senkal, Mehmet Kandaz and Fahrettin Yakuphanoglu

Polyhedron 28 (2009) 1490

Synthesis and liquid crystal properties of phthalocyanine bearing a star polytetrahydrofuran moiety

In this study, a new polymeric ligand, 6-(3,4-dicyanophenylthio)-hexyl-2-polytetrahydrofuran-acetate and its liquid crystalline polymeric phthalocyanine, 2,9,16,23-tetrakis-{6-(polytetrahydrofuran-2-carboxylate)-hexylthio-phthalocyaninatocobalt(II) (CoPcLC) have been prepared. CoPcLC promotes a greater interaction between the mesogens resulting in solution aggregations together with a red-shift in the Q-band in the presence of the soft Ag^+ ion. The dielectric anisotropy and phase transition temperature values of CoPcLC doped with 4-cyano-4′-n-pentylbiphenyl (5CB) were found to be 7.17 and 40.5 °C, respectively. The liquid crystal structure changes from the positive to negative type. The current–voltage characteristics of the 5CBCoPcLC liquid crystal show non-linear behaviour.

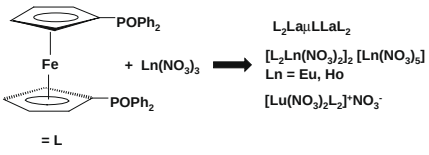


Eileen Buckley-Dhoot, John Fawcett, Roman A. Kresinski and Andrew W.G. Platt

Polyhedron 28 (2009) 1497

Lanthanide nitrate complexes of the redox active ligand $(\eta^5C_5H_4P(O)Ph_2)_2Fe$

The reaction of L with lanthanide nitrates leads to complexes with three distinct structural types. The redox properties have been investigated and show a dependence on the size of the lanthanide ion.

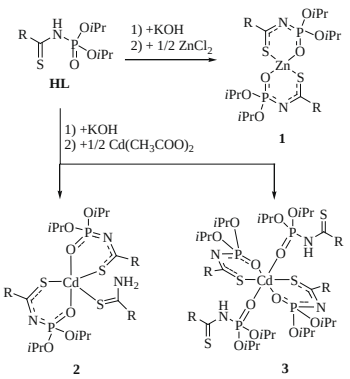


Damir A. Safin, Axel Klein, Maria G. Babashkina, Heinrich Nöth, Dmitriy B. Krivolapov, Igor A. Litvinov and Henryk Kozlowski

Polyhedron 28 (2009) 1504

Versatile coordination of *N*-(diisopropoxyphosphoryl)-*p*-bromothiobenzamide towards Zn(II) and Cd(II)

Reaction of the potassium salt of *N*-(diisopropoxyphosphoryl)-*p*-bromothiobenzamide *p*-$BrC_6H_4C(S)NHP(O)(OiPr)_2$ (**HL**) with Zn(II) and Cd(II) cations in aqueous EtOH leads to the three different complexes: $[Zn(L\text{-}O,S)_2]$ (**1**), $[Cd(p\text{-}BrC_6H_4C(S)NH_2\text{-}S)(L\text{-}O,S)_2]$ (**2**) and $[Cd(HL\text{-}O)_2(L\text{-}O,S)_2]$ (**3**). The structures of these compounds were investigated by single crystal X-ray diffraction analysis, IR, ^1H and ^{31}P NMR spectroscopy, MALDI TOF spectrometry, and microanalysis. The luminescence properties of the novel compounds and previously described complexes of thiobenzamide $C_6H_5C(S)NHP(O)(OiPr)_2$ (**HQ**) with Zn(II) and Cd(II) cations: $[Zn(Q\text{-}O,S)_2]$ (**4**), $[Cd_2(Q\text{-}O,S)_4]$ (**5**), $[Cd(HQ\text{-}O)_2(Q\text{-}O,S)_2]$ (**6**), were also measured.

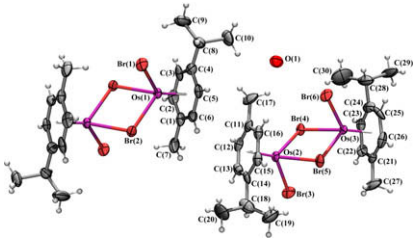


Hadley S. Clayton, Banothile C.E. Makhubela, Hong Su, Gregory S. Smith and John R. Moss

Polyhedron 28 (2009) 1511

Synthesis, characterization, reactivity and molecular structure of arene-osmium complexes: A new synthetic entry into (η^6-arene)osmium(II) chemistry

A novel method for the preparation of areneosium complexes from $K_2[OsO_2(OH)_4]$ is described. The characterization and reactivity of these complexes are reported and single crystal X-ray structures of $[(\eta^6\text{-}p\text{-}MeC_6H_4Pr')OsBr_2]_2$ and $[(\eta^6\text{-p=-}MeC_6H_4Pr')Os(PPh_3)Br_2]$ are resented.

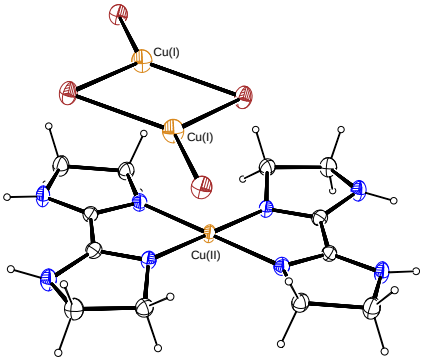


Piotr Drożdżewski and Maria Kubiak

Polyhedron 28 (2009) 1518

The reaction of copper(II) and 2-hydrazino-2-imidazoline leading to the *in situ* formation of bisimidazoline (biz). Crystal structure and vibrational spectroscopy of mixed-valence $[Cu(biz)_2][Cu_2Br_4]$ complex

The "*in situ*" oxidation of 2-hydrazino-2-imidazoline leading to the formation of the Cu(II) complex cation with 2,2′-bi-2-imidazoline is reported. The X-ray analysis monitored the $[Cu_2Br_4]^{2-}$ as the counter ion. The structures and vibrational spectra of both ions have been reproduced in the DFT calculations. The latter theoretical results have been used for the interpretation of the observed IR and Raman spectra.

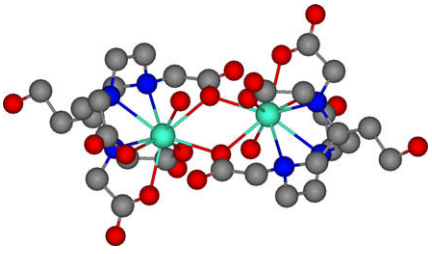


Raghvendra S. Sengar, Archana Nigam, Steven J. Geib and Erik C. Wiener

Polyhedron 28 (2009) 1525

Syntheses and crystal structures of gadolinium and europium complexes of AAZTA analogues

The Gd and Eu complexes of a new AAZTA ligand, with a hydroxyl side chain, show nine-coordinated metal center in dimeric structure with one inner sphere water molecule per metal ion. The hydroxyl side arm does not interfere in the coordination environment of metal and therefore acts as a good anchor for attaching other functional motifs.

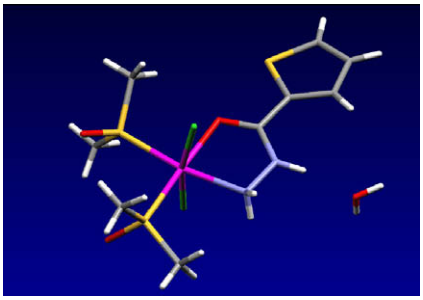


Viswanathan Mahalingam, Nataraj Chitrapriya, Matthias Zeller and Karuppannan Natarajan

Polyhedron 28 (2009) 1532

Ru(II)–DMSO complexes containing aromatic and heterocyclic acid hydrazides: Structure, electrochemistry and biological activity

New Ru(II)–DMSO complexes containing a neutral bidentate ON chelate of carboxylic acid hydrazides have been synthesized and characterized by analytical and spectroscopic methods. The structure of one of the complexes, $[RuCl_2(DMSO)_2(tcah)] \cdot H_2O$ (tcah = thiophene carboxylic acid hydrazide) has been determined by the single crystal XRD technique. The electrochemistry of the complexes has been studied by cyclic voltammetry. The complexes have been shown to bind herring sperm DNA non-intercalatively. The antibacterial activity of the complexes has also been evaluated.

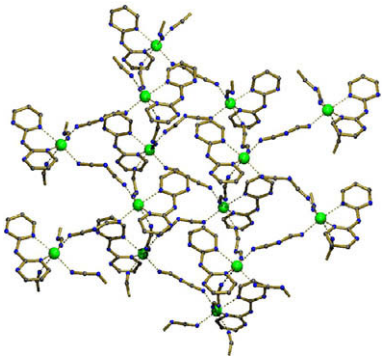


Gerard A. van Albada, Maarten G. van der Horst, Simon J. Teat, Patrick Gamez, Olivier Roubeau, Ilpo Mutikainen, Urho Turpeinen and Jan Reedijk

Polyhedron 28 (2009) 1541

Polynuclear Cu(II), Ni(II) and Cd(II) coordination compounds with bis(pyrimidin-2-yl)amine and dicyanamide

Three novel transition metal polynuclear compounds with formula $[Cu(dipm)(\mu\text{-}dca)_2]_n(H_2O)$ (**1**), $[Ni(dipm)(\mu\text{-}dca)_2]_n(C_2H_6O)_{1/2}$ (**2**) and $[Cd(dipm)(\mu\text{-}dca)_2]_n$ (**3**) (in which dipm = bis-(pyrimidin-2-yl)amine and dca = dicyanamide) are reported. Compounds **1** and **2** contain rare double-bridging end-to-end dca units, connecting two metal ions and a single bridging end-to-end dca unit between subsequent metals. Compound **3** exhibits single bridging end-to-end dca units oriented in three directions, resulting in a 3D framework.

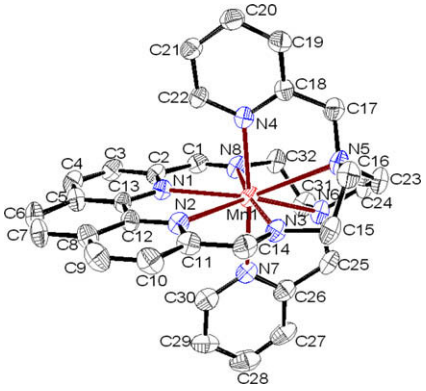


Hassan Keypour, Ahmad Ali Dehghani-Firouzabadi and Hamid Reza Khavasi

Polyhedron 28 (2009) 1546

Synthesis and characterization of three novel manganese(II) octaaza macrocyclic Schiff base complexes containing a phenanthroline and two pyridyl units as pendant arms. X-ray crystal structure determination of one manganese(II) complex

Three novel Schiff base macrocyclic complexes containing a phenanthroline and two 2-pyridylmethyl pendant arms have been prepared by template [1+1] cyclocondensation of 2,9-dicarboxaldehyde-1,10-phenanthroline and three new branched hexadentate amines, in the presence of Mn(II). The one of them crystal structure indicates that in the solid state the complex adopts slightly distorted hexagonal bipyramidal geometry.

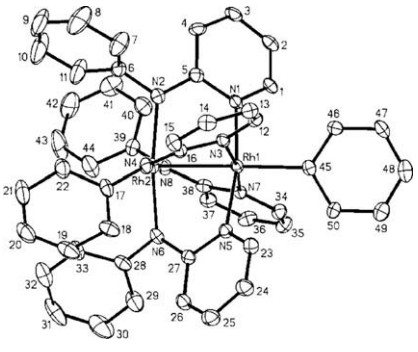


John L. Bear, Baocheng Han, Yulan Li, Siyabonga Ngubane, Eric Van Caemelbecke and Karl M. Kadish

Polyhedron 28 (2009) 1551

Synthesis, spectroscopic properties and electrochemistry of $Rh_2(ap)_4(R)$ where R = CH_3 or C_6H_5 and ap = 2-anilinopyridinate anion

Two sigma-bonded Rh_2^{5+} complexes, $Rh_2(ap)_4(C_6H_5)$ and $Rh_2(ap)_4(CH_3)$, where ap = 2-anilinopyridinate anion were synthesized and examined as to their electrochemical and spectroscopic properties in nonaqueous media.

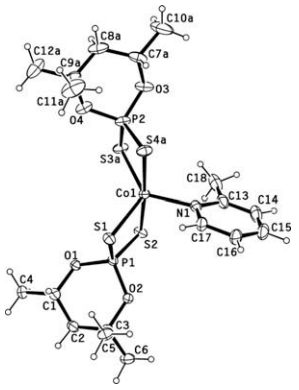


Subhash Bajia, Ray J. Butcher, John E. Drake and Raju Ratnani

Polyhedron 28 (2009) 1556

Synthesis and characterization of adducts of bis(4,4,6-trimethyl-1,3,2-dioxaphosphorinane-2-thione-2-thiolato)cobalt(II) with nitrogen and phosphorus containing Lewis bases: Crystal structures of $[Co(S_2)_2(2\text{-}CH_3\text{-}NC_5H_4)]$ and $[Co(S_2POCMe_2CH_2CHMeO)_2(3\text{-}CH_3\text{-}NC_5H_4)]$

Bis(4,4,6-trimethyl-1,3,2-dioxaphosphorinane-2-thione-2-thiolato)cobalt(II) complexes with nitrogen and phosphorus containing Lewis bases of the type, $[Co(S_2POCMe_2CH_2CHMe_2O)*L_n]$ (where L = pyridine, n = 2; L = 2-picoline, 3-picoline, triphenylphosphine, 2,2′-bipyridine, 1,10-phenanthroline; n = 1) were prepared. These newly synthesized compounds were characterized by elemental analysis, IR and UV–Vis spectroscopy and magnetic measurements. Single crystal X-ray crystal structures of $[Co(S_2POCMe_2CH_2CHMeO)_2(2\text{-}CH_3\text{-}NC_5H_4)]$ and $[Co(S_2POCMe_2CH_2CHMeO)_2(3\text{-}CH_3\text{-}NC_5H_4)]$ were also determined.

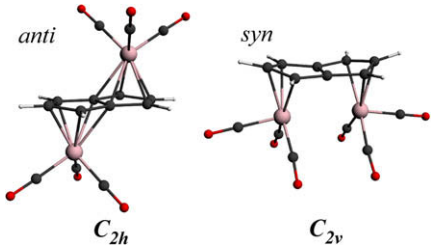


A. Muñoz-Castro, D. Mac-Leod Carey and R. Arratia-Pérez

Polyhedron 28 (2009) 1561

Electronic structure and molecular properties of binuclear group VII pentalene metal carbonyl complexes $[C_8H_6\{M(CO_3)\}_2]$ (M = Mn, Tc, Re, Bh): A relativistic density functional theory study

Homobimetallic systems linked by pentalenediide ligand, of the type *anti*/*syn*-$[C_8H_6\{M(CO_3)\}_2]$ (M = Mn, Tc, Re, Bh): with transitions metals of the group VII, were studied by relativistic DFT methods including spin-orbit coupling, for understand how the electronic and molecular structure change going down in the group. Optical, vibrational and spin-dependent properties (for anionic system) were revisited. These calculations predict that the not yet reported Tc and Bh complexes may be synthesized.

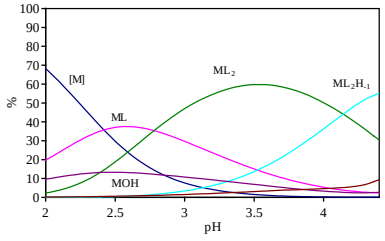


Halina Podsiadły and Zofia Karwecka

Polyhedron 28 (2009) 1568

Complexes of vanadium(III) with aromatic amino acids and L-proline in aqueous solution

The equilibria of the complexation processes of V^{3+} ion with L-phenylalanine, L-tyrosine, L-tryptophan and l-proline in aqueous solution were studied by potentiometric and spectroscopic (UV, Vis, CD) methods. The complexes are relatively weak and hydrolysis of vanadium(III) significantly influenced on complexation process. Only in the vanadium(III)–tyrosine system relatively stable ML_2 species predominantly exists in the pH range 3–4.5.

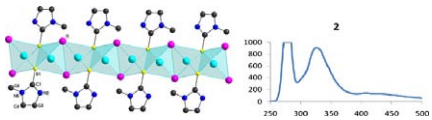


Tarlok S. lobana, Razia Sultana, Geeta Hundal and Alfonso Castineiras

Polyhedron 28 (2009) 1573

Synthesis and crystal structures of polynuclear complexes of Cu^I with 1-methyl-1,3-imidazoline-2-thione

The 1-methyl-1,3-imidazoline-2-thione ($SC_4H_6N_2$) with copper(I) halides have formed uncommon polymers under mild conditions. For example, 1-methyl-1,3-imidazoline-2-thione ($SC_4H_6N_2$) and copper(I) iodide has yielded a 1D polymer, $\{Cu_2(\mu\text{-}I)_2(\mu\text{-}SC_4H_6N_2)_2\}_n$ **2** with twisted ribbon like chain and exhibition of fluorescent emission line at 322 (λ_{ex}, 272 nm).

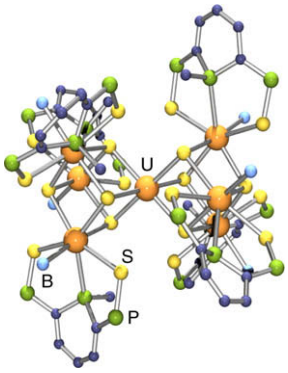


Thérèse Arliguie, Pierre Thuéry, Pascal Le Floch, Nicolas Mézailles and Michel Ephritikhine

Polyhedron 28 (2009) 1578

A homoleptic SPS-based complex and a double-cubane-type sulfur cluster of an actinide element

Treatment of $UI_3(THF)_4$ with $[M(Et_2O)][SPS^{Me}]$ (M = Li, K; $[SPS^{Me}]^-$ = 1-methyl-2,6-bis(diphenylphosphine sulfide)-3,5-diphenylphosphinine anion) gave the tris SPS complex $[U(SPS^{Me})_3]I$ which adopts a tricapped trigonal prismatic configuration. Similar reaction of $U(BH_4)_3(THF)_3$ afforded, in addition to the $[U(SPS)_3]^+$ cation, crystals of the heptanuclear sulfido cluster $[U\{(\mu_3\text{-}S)_4U_3(SPS^{Me})_3(BH_4)_3\}_2]$ which exhibits a corner-shared double-cubane core.

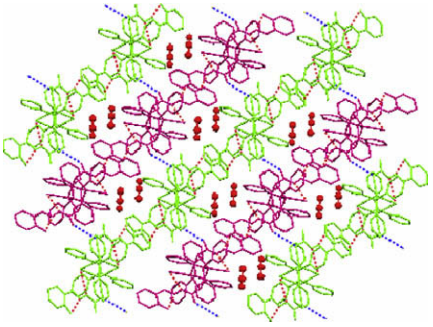


Tarlok Singh Lobana, Sonia Khanna, Geeta Hundal, Pavneet Kaur, Bandana Thakur, Shaweta Attri and Ray Jay Butcher

Polyhedron 28 (2009) 1583

Coinage metal derivatives of salicylaldehyde thiosemicarbazones: Synthesis, structures, bond isomerism and H-bonded networks

Salicylaldehyde thiosemicarbazone (H_2stsc) has formed 1D and 2D polymeric networks in complexes with coinage metals. For example, dimer $[Ag_2Br_2(H_2stsc)_2(PPh_3)_2]$ (**7**) exists as alternate H-bonded linear polymeric chains of halogen bridged $[Ag_2(\mu\text{-}Br)_2(\eta^1\text{-}S\text{–}H_2stsc)_2(PPh_3)_2]$ (**7a**) (green) and sulfur bridged $[Ag_2Br_2(\mu\text{-}S\text{–}H_2stsc)_2(PPh_3)_2]$ (**7b**) (red) bond isomers in the same lattice, forming 2D network.



The Publisher encourages the submission of articles in electronic form thus saving time and avoiding rekeying errors. For detailed instructions on the preparation of manuscripts and of electronic artwork, consult the Author Gateway for Elsevier at http://authors.elsevier.com

ScienceDirect

Full text of this journal is available, on-line from **ScienceDirect**. Visit **www.sciencedirect.com** for more information.

Polyhedron 28, issue 7, 12 May 2009

Contents lists available at ScienceDirect

Polyhedron

journal homepage: www.elsevier.com/locate/poly

Contents

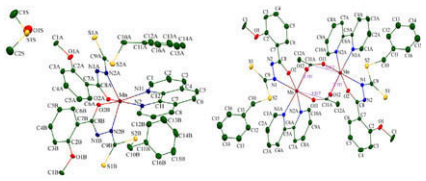
Papers

M. Singh, R.J. Butcher and N.K. Singh

Polyhedron 28 (2009) 1197

First row transition metal complexes of benzyl *N*′-(2-methoxybenzoyl)hydrazinecarbodithioate (H_2mbhcd): X-ray structures of [Mn(Hmbhcd)$_2$-(*o*-phen)] · DMSO and [Mn$_2$(Hmbhcd)$_2$(2,2′-bpy)$_2$(μ-OAc)$_2$]

Complexes of the types [M(Hmbhcd)$_2$]$_n$ {M = Mn(II), Ni(II) and Co(II)} (**2**, **5** and **6**), [Mn-(Hmbhcd)$_2$(*o*-phen)] · DMSO (**3**) and [Mn$_2$-(Hmbhcd)$_2$(2,2′-bpy)$_2$(μ-OAc)$_2$] (**4**) with H_2mbhcd = benzyl *N*′-(2-methoxybenzoyl)-hydrazinecarbodithioate have been synthesized and characterized by spectroscopic methods. The X-ray studies of **3** and **4** indicate that the ligand acts as a uninegative bidentate ligand, forming a five-membered chelate ring.

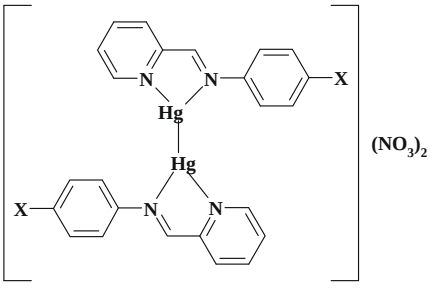


Saeed Dehghanpour, Mehdi Khalaj and Ali Mahmoudi

Polyhedron 28 (2009) 1205

Mercury(I) complexes with bidentate iminopyridine ligands: Synthesis, spectral characterization and structural analysis

The mercury(I) complexes [L^{2}HgHgL^2](NO$_3$)$_2$, where L^2 is a iminopyridine derivative, have been synthesized and characterized by CHN analyses, IR and UV–Vis spectroscopy. The crystal structures of complexes where X=F and Br have been determined.



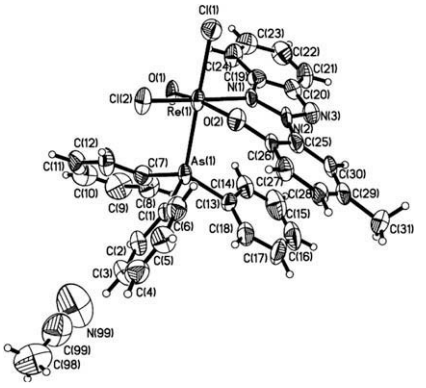
X=F, Cl, Br, I

B. Machura, M. Wolff, R. Kruszynski and J. Kusz

Polyhedron 28 (2009) 1211

Novel oxorhenium complexes with 2-(2′-hydoxy-5′-methylphenyl)benzotriazolato ligand. X-ray studies, spectroscopic characterization and DFT calculations

The [ReOCl$_2$(hmpbta)(AsPh$_3$)]·MeCN, [ReOBr$_2$-(hmpbta)(AsPh$_3$)]·MeCN, [ReOCl$_2$(hmpbta)-(PPh$_3$)]·MeCN, [ReOBr$_2$(hmpbta)(PPh$_3$)]·MeCN, [ReBr$_2$(hmpbta)(PPh$_3$)]·MeCN complexes have been prepared in the reactions of [ReOX$_3$-(EPh$_3$)$_2$] (X=Cl, Br; E=P, As) with 2-(2′-hydoxy-5′-methylphenyl)benzotriazole in molar ratio 1:1. All the compounds were structurally and spectroscopically characterised. The electronic structure of [ReOCl$_2$(hmpbta)(AsPh$_3$)] has been calculated with the density functional theory (DFT) method. The TDDFT/PCM calculations have been employed to produce a hundred of singlet excited-states starting from the ground-state geometry optimized in the gas phase, and the UV-Vis spectrum of [Re-OCl$_2$(hmpbta)(AsPh$_3$)] has been discussed on this basis. The paper reports also X-Ray structure and DFT calculations for the disubstituted [ReOCl(hmpbta)$_2$] chelate.



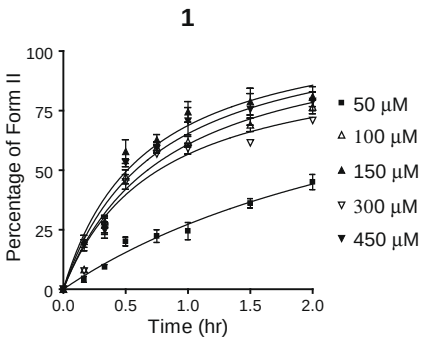
Elsevier Ltd.

Wu Xu, Febee R. Louka, Pierre E. Doulain, Caroline A. Landry, Franz A. Mautner and Salah S. Massoud

Polyhedron 28 (2009) 1221

Hydrolytic cleavage of DNA promoted by cobalt(III)–tetraamine complexes: Synthesis and characterization of carbonatobis[2-(2-pyridylethyl)]-(2-pyridylmethyl)aminecobalt(III) perchlorate

The catalytic cleavage of DNA was studied using a series of *cis*-aquahydroxo–tetraamine–Co(III) complexes (pH 7 and 37 °C). Under pseudo-Michaelis–Menten kinetic conditions, the complexes showed enhancement in rates that is 35 million times greater than the uncatalyzed DNA cleavage.

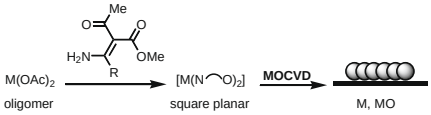


Marino Basato, Elena Faggin, Cristina Tubaro and Augusto Cesare Veronese

Polyhedron 28 (2009) 1229

Volatile square planar β-imino carbonyl enolato complexes of Pd(II) and Ni(II) as potential MOCVD precursors

Reaction of nickel and palladium acetates with a series of β-enaminodiones affords thermally stable, volatile square planar complexes.

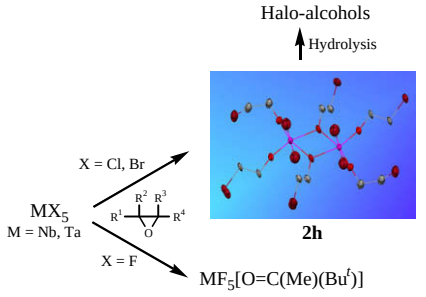


Fabio Marchetti, Guido Pampaloni and Stefano Zacchini

Polyhedron 28 (2009) 1235

Epoxide ring opening and insertion into the M–X bond of niobium and tantalum pentahalides: Synthesis of dihalide-*tris*(2-haloalcoholato) complexes

Multiple epoxide insertion into metal–halide bonds affords the complexes $[MX_2(OR)_2(\mu\text{-}OR)]_2$ (M = Nb, Ta; X = Cl, Br), while the reactions of MF_5 (M = Nb, Ta) with epoxides proceed non-selectively according to various pathways, including formation of C–O and C–F bonds and C–C and C–H bond cleavages: the epoxide to ketone isomerization prevails in some cases.

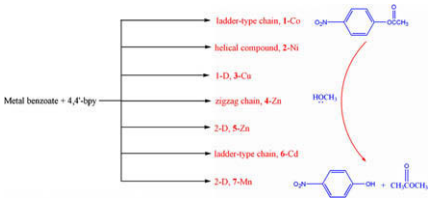


Young Joo Song, Han Kwak, Young Min Lee, Soo Hyun Kim, Sun Hwa Lee, Byeong Kwon Park, Je Yeol Jun, Seung Man Yu, Cheal Kim, Sung-Jin Kim and Youngmee Kim

Polyhedron 28 (2009) 1241

Metal-directed supramolecular assembly of metal(II) benzoates (M = Co, Ni, Cu, Zn, Mn, and Cd) with 4,4′-bipyridine: Effects of metal coordination modes and novel catalytic activities

We have presented a systematic investigation on the coordination polymers assembled from metal benzoates and 4,4′-bpy. Since different structures provide different coordination geometry of each metal ion, it is clear that selection of appropriate metal ions can control the coordination geometry of each metal ion to form different crystal structures. Reactivity study of seven compounds for the transesterification of a variety of esters has shown that **4**-Zn and **5**-Zn are very efficient and the best among them. It can be possible to tune the catalytic activities by changing from Zn to those metals such as Cd, a kinetically inert metal, or Cu, Mn, and Co, the redox-active metals.

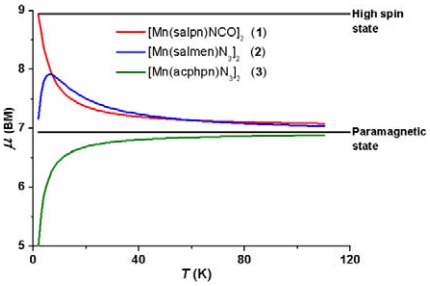


G. Bhargavi, M.V. Rajasekharan, J.-P. Costes and J.-P. Tuchagues

Polyhedron 28 (2009) 1253

Synthesis, crystal structure and magnetic properties of dimeric Mn^{III} Schiff base complexes including pseudohalide ligands: Ferromagnetic interactions through phenoxo bridges and single molecule magnetism

Three phenoxo-bridged dimeric Schiff base complexes of Mn^{III} show very different temperature dependence of magnetic susceptibility due to differences in bridge geometry and intermolecular interactions

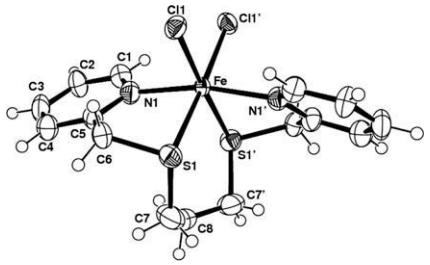


Animesh Patra, Sandipan Sarkar, Michael G.B. Drew, Ennio Zangrando and Pabitra Chattopadhyay

Polyhedron 28 (2009) 1261

Synthesis and crystal structure characterization of iron(II), cobalt(II) and nickel(II) complexes with 1,3-bis(2-pyridylmethylthio)propane

Three complexes, $[Fe^{II}(L)Cl_2]$ (**1**), $[Co^{II}(L)Cl_2]$ (**2**) and $[Ni^{II}(L)Cl_2]$ (**3**) where L = 1,3-bis(2-pyridylmethylthio)propane, were synthesized and characterized by physicochemical and spectroscopic methods. The structural analysis of **1** and **3** shows that the complexes are isomorphous with an octahedral geometry.

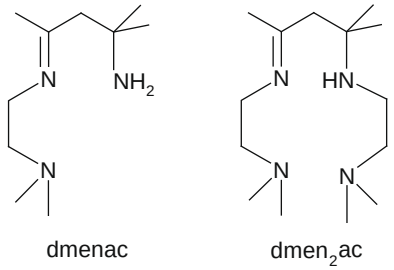


Vitalina M. Nikitina, Oksana V. Nesterova, Vladimir N. Kokozay, Viktoriya V. Dyakonenko, Oleg V. Shishkin and Julia Jezierska

Polyhedron 28 (2009) 1265

N,*N*-Dimethylethylenediamine in direct and direct template syntheses of Cu(II)/Cr(III) complexes

The one-pot synthesis, spectroscopic, magnetic and structural characterization of four new heterometallic Cu(II)/Cr(III) complexes containing novel open-chain Schiff-base ligands, dmenac (*N*′-[(1*Z*)-3-amino-1,3-dimethylbutylidene]-*N*,*N*-dimethylethane-1,2-diamine) and $dmen_2ac$ (*N*′-((1*Z*)-3-{[2-(dimethylamino)ethyl]-amino}-1,3-dimethylbutylidene)-*N*,*N*-dimethylethane-1,2-diamine), are reported.

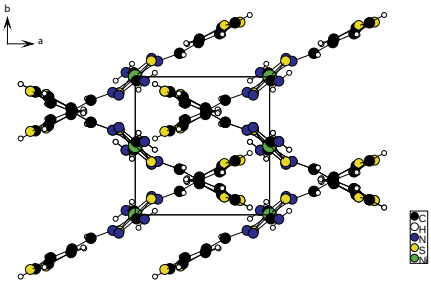


Kusaï Alomar, Mustayeen A. Khan, Magali Allain and Gilles Bouet

Polyhedron 28 (2009) 1273

Synthesis, crystal structure and characterization of 3-thiophene aldehyde thiosemicarbazone and its complexes with cobalt(II), nickel(II) and copper(II)

The reaction of cobalt(II), nickel(II), copper(II) chlorides and bromides with 3-thiophene aldehyde thiosemicarbazone (3TTSCH) leads to the formation of a series of new complexes: $[Co(3TTSC)_2]$, $[Ni(3TTSC)_2]$, $[CuCl(3TTSC)]_2$, $[CuBr(3TTSC)]_2$ and $[CuBr_2(3TTSCH)]$. The crystal structures of the free ligand and the compound $[Ni(3TTSC)_2]$ have been determined by the X-ray diffraction method. For all these complexes, the central ion is coordinated through the sulfur atom and the azomethine nitrogen atom of the thiosemicarbazone.

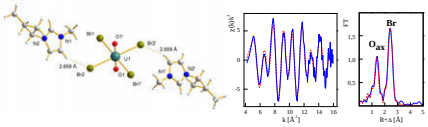


Marie-Olga Sornein, Mickaël Mendes, Céline Cannes, Claire Le Naour, Peter Nockemann, Kristof Van Hecke, Luc Van Meervelt, Jean-Claude Berthet and Christoph Hennig

Polyhedron 28 (2009) 1281

Coordination environment of $[UO_2Br_4]^{2-}$ in ionic liquids and crystal structure of $[Bmim]_2[UO_2Br_4]$

The coordination of uranyl bromide has been investigated in the crystal structure of $[Bmim]_2[UO_2Br_4]$ and in the ionic liquids [Bmim][Tf_2N] and [$MeBu_3N$][Tf_2N].

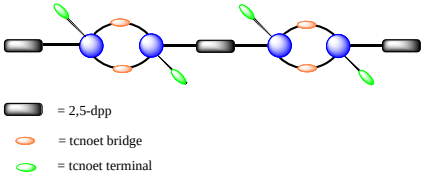


Consuelo Yuste, Abdeslem Bentama, Nadia Marino, Donatella Armentano, Fatima Setifi, Smail Triki, Francesc Lloret and Miguel Julve

Polyhedron 28 (2009) 1287

Copper(II) complexes with 2,5-bis(2-pyridyl)-pyrazine and 1,1,3,3-tetracyano-2-ethoxypropenide anion: Syntheses, crystal structures and magnetic properties

bis-Bidentate 2,5-bis(2-pyridyl)pyrazine occurs in the dicopper(II) complex $[Cu_2(2,5\text{-dpp})(H_2O)_4(CF_3SO_3)_4] \cdot 2H_2O$ (**1**) and in the alternating copper(II) chain $[Cu_2(2,5\text{-dpp})(H_2O)_2(tcneot)_4]_n$ (**2**), with a Curie law behaviour (**1**) and a weak intrachain ferromagnetic interaction (**2**).

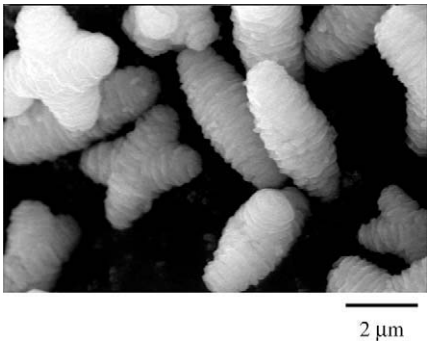


Chie H. Ohnishi, Kimihiro Asano, Hyung-Joon Jeon, Saburo Hosokawa, Shinji Iwamoto and Masashi Inoue

Polyhedron 28 (2009) 1295

Synthesis of alkali-metal cobalt kambaldaite by precipitation method

Alkali-metal cobalt kambaldaite (alkali-metal cobalt carbonate hydroxide hydrate; ideal structure, $M_2Co_8(CO_3)_6(OH)_6 \cdot 6H_2O$; M-CoKBL) was prepared by precipitation of cobalt nitrate with a solution containing a large excess of alkali-metal bicarbonate at 50 °C followed by aging at that temperature for 2–3 h.

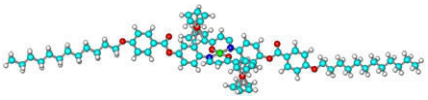


Oleg N. Kadkin, Eun Ho Kim, So Yeon Kim and Moon-Gun Choi

Polyhedron 28 (2009) 1301

Synthesis and liquid crystal properties of copper(II) and palladium(II) chelates with new ferrocene-containing enaminoketones

The syntheses of a series of ferrocene-containing β-aminovinylketone complexes with Cu(II) and Pd(II) ions are described in this article. The synthesized ligands and Cu(II) complexes exhibited disordered soft crystal phases upon cooling from the isotropic liquid state, and the Pd(II) complexes showed monotropic smectic C mesomorphism.

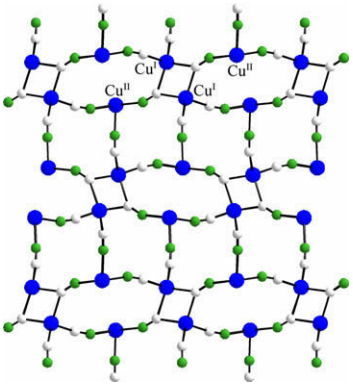


Samia Benmansour, Fatima Setifi, Smaïl Triki, Franck Thétiot, Jean Sala-Pala, Carlos J. Gómez-García and Enrique Colacio

Polyhedron 28 (2009) 1308

High-dimensional mixed-valence copper cyanide complexes: Syntheses, structural characterizations and magnetism

The syntheses, structural characterization and magnetic properties of two mixed-valence copper cyanide compounds $[Cu^{II}(bpy)Cu^{I}(CN)_3]_n$, (**1**) and $\{[Cu^{II}(tn)_2][Cu^{I}_4(CN)_6]\}_n$ (**2**) are presented. The 3-D structure of **1**, is generated by μ_2- and μ_3-cyanide bridges (–Cu^{II}–NC–Cu^{I}– and –Cu^{II}–NC–$(Cu^{I})_2$–), while the 2-D hexagonal networks of **2** are generated by only –Cu^{I}–NC–Cu^{I}– bridges. Compound **1** presents an unexpected weak ferromagnetic coupling through the "a priori diamagnetic" –NC–Cu^{I}–CN– bridges.

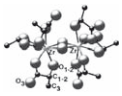


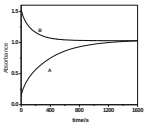
Dilip Kumar Chakravorty, Rozi Ghosh, Rupendranath Banerjee and Diptabhas Sarkar

Polyhedron 28 (2009) 1315

Kinetics of ligand exchange between 2-thenoyltrifluoroacetone and zirconium-lactate solution in weakly acidic lactate buffers

Under the conditions, $T_{HT} \ll T_{Zr} \ll T_L$, "zirconium-lactate" ($Zr_2L_6$) reacts with 2-thenoyltrifluoroacetone (HT) to produce Zr_2L_5E and L; the equilibrium constant $K = 3.2$: $k_{-1} = 4.9 \times 10^{-3}$ s^{-1}, $k_1K_AK_B = 2.62 \times 10^{-6}$ dm^6 mol^{-2} s^{-1} at $T = 25.0$ °C.





$Zr_2L_6 + 2H_2O$ — $Zr_2L_5(OH_2)_2^+ + L^-$ K_A (rapid equilibrium)

$Zr_2L_5(OH_2)_2^+$ — $Zr_2L_5(OH_2)(OH) + H^+$ K_B (rapid equilibrium)

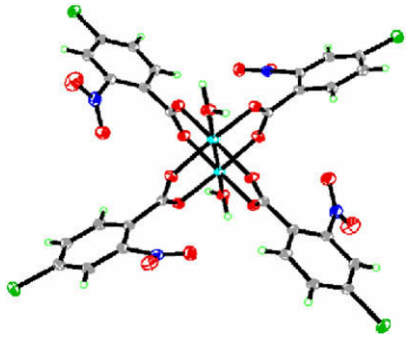
$Zr_2L_5(OH_2)(OH) + HT$ — $Zr_2L_5E + 2H_2O$ k_1 , k_{-1} (slow r.d.s)

Eng-Khoon Lim, Siang-Guan Teoh, Siu-Mun Goh, Cynn-Dee Ch'ng, Chew-Hee Ng, Hoong-Kun Fun, Mohd Mustaqim Rosli, Nazalan Najimudin, Hooi-Kheng Beh, Lay-Jing Seow, Norhayati Ismail, Zhari Ismail, Mohd Zaini Asmawi and Yew-Hoong Cheah

Polyhedron 28 (2009) 1320

Characterization, nucleolytic, cytotoxic and antibacterial property of tetrakis(μ-4-chloro-2-nitrobenzoato-κ^2O,O')bis[aquacopper(II)], tetrakis(μ-2-chloro-6-fluorobenzoato-κ^2O,O')bis[aquacopper(II)] and tetrakis(μ-2-chlorobenzoato-κ^2O,O')bis[aquacopper(II)]

The dimeric Cu(II) complexes are redox active and display two quasi-reversible redox behaviour corresponding to the $Cu^{II}Cu^{II}$ to $Cu^{II}Cu^{I}$ and $Cu^{II}Cu^{I}$ to $Cu^{I}Cu^{I}$ redox process, respectively. Oxidative cleavage of pBr322 DNA occurs in the presence of hydrogen peroxide for which the hydroxyl radical is the reactive oxygen species that is responsible for the cleavage reaction.

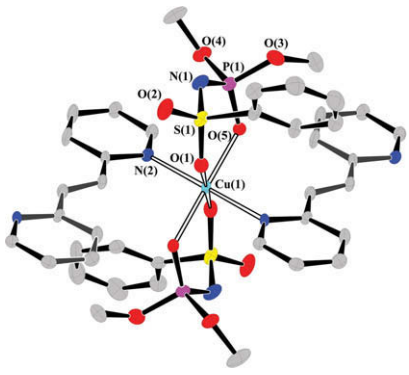


Olesia V. Moroz, Victor A. Trush, Irina S. Konovalova, Oleg V. Shishkin, Yurii S. Moroz, Serhiy Demeshko and Vladimir M. Amirkhanov

Polyhedron 28 (2009) 1331

New copper(II) 1D polymer containing dimethyl(phenylsulfonyl)amidophosphate: Synthesis, crystal structure and magnetic properties

The reaction of sodium dimethyl(phenylsulfonyl)amidophosphate Na**L** (H**L** = $C_6H_5S(O)_2NHP(O)(OCH_3)_2$) with $Cu(NO_3)_2 \cdot 6H_2O$ and **o-bpe** (1,2-bis(pyridine-2-yl)ethane) in appropriate ratio, leads to the formation of 1D coordination polymer $[Cu(\mathbf{L})_2 \cdot \mathbf{o\text{-}bpe}]_n$ in good yield. The structural features, as well as spectroscopic and magnetic properties are reported.

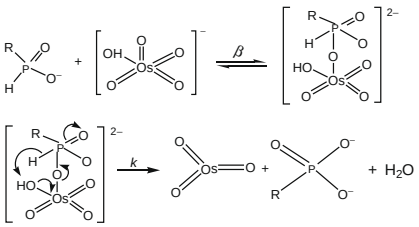


Kamla Sharma and Raj N. Mehrotra

Polyhedron 28 (2009) 1336

Oxidation of hypophosphite and phenylphosphinite ion by perosmate(VIII) ion: Kinetics and mechanism

The oxidation of hypophosphite and phenyl hypophosphinite by OsO_4 is represented by the following steps.

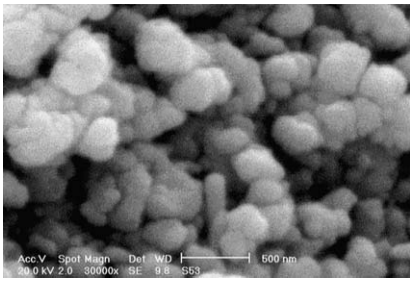


Nilofar Soltanzadeh and Ali Morsali

Polyhedron 28 (2009) 1343

Syntheses and characterization nano-structured bismuth(III) oxide from a new nano-sized bismuth(III) supramolecular compound

Nano-particles of a new Bi(III) supramolecular compound, $\{Bi_2(\mu\text{-}4,4'\text{-bipy})Cl_{10}] \cdot 2(4,4'\text{-Hbipy}) \cdot (4,4'\text{-}H_2bipy) \cdot 2H_2O\}$ (**1**), 4,4′-bipy = 4,4′-bipyridine} were synthesized by a sonochemical method.

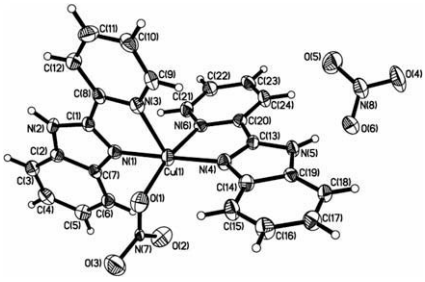


B. Machura, A. Świtlicka, M. Wolff, J. Kusz and R. Kruszynski

Polyhedron 28 (2009) 1348

Synthesis, spectroscopic characterization, X-ray structure and DFT calculations of copper(II) complex with 2-(2-pyridyl)benzimidazole

The $[Cu(pybzim)_2(NO_3)](NO_3)$ complex has been isolated from the reaction of copper(II) nitrate trihydrate and 2-(2-pyridyl)benzimidazole (pybzim) in methanol. The compound has been studied by IR, UV–Vis spectroscopy and X-ray crystallography. The electronic structure of the $[Cu(pybzim)_2(NO_3)]^+$ cation has been calculated with the density functional theory (DFT) method. The spin-allowed doublet–doublet electronic transitions of $[Cu(pybzim)_2(NO_3)]^+$ have been calculated with the time-dependent DFT method, and the UV–Vis spectrum of the title compound has been discussed on this basis.

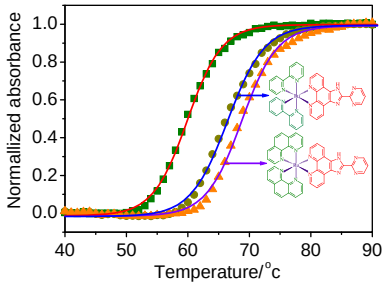


Shuo Shi, Tian Xie, Tian-Ming Yao, Chao-Ran Wang, Xiao-Ting Geng, Dan-Jing Yang, Lin-Jie Han and Liang-Nian Ji

Polyhedron 28 (2009) 1355

Synthesis, characterization, DNA-binding and DNA-photocleavage studies of $[Ru(bpy)_2(pmip)]^{2+}$ and $[Ru(phen)_2(pmip)]^{2+}$ (pmip = 2-(2′-pyrimidyl)imidazo[4,5-f][1,10]phenanthroline

The melting curves of CT-DNA in the absence and presence of the complexes are presented. On addition of **1** or **2**, the T_m of DNA increases to 66.5 and 68.8 °C, respectively, at a concentration ratio [DNA]/[Ru] of 10:1, which indicates that both **1** and **2** can bind to DNA in an intercalative mode and the DNA-binding affinity of **2** is greater than that of **1**.

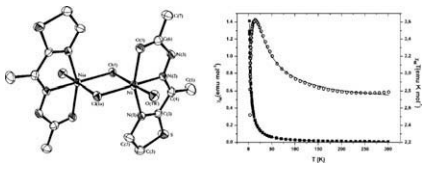


E. Viñuelas-Zahínos, F. Luna-Giles, P. Torres-García and A. Bernalte-García

Polyhedron 28 (2009) 1362

Chloride-bridged Ni(II) complexes with ferromagnetic exchange interaction from thiazoline hydrazone derivative ligands

New ligand 2-acetyl-2-thiazoline acetylhydrazone (ATHAc) and two new chloride-bridged dimeric nickel(II) complexes containing thiazoline hydrazone derivative ligands have been synthesized and structurally characterized. Magnetic susceptibility measurements of complexes revealed that the ferromagnetic coupling occurs among nickel(II) ions.

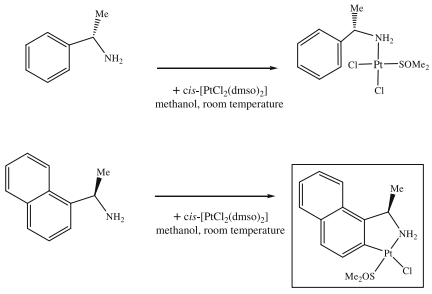


Raquel Martín, Margarita Crespo, Mercè Font-Bardia and Teresa Calvet

Polyhedron 28 (2009) 1369

Steric promotion in the cycloplatination of primary amines

Cycloplatination of primary amines (*S*)-(−)-α-methylbenzylamine and (*R*)-(+)-1-(1-naphthyl)-ethylamine using *cis*-$[PtCl_2(dmso)_2]$ as precursor and standard procedures has been achieved in moderate and quantitative yields, respectively. The ease of formation of the compound derived from the bulky (*R*)-(+)-1-(1-naphthyl)ethylamine is evidenced from the fact that it can also be obtained at room temperature and without requiring the presence of an external base.

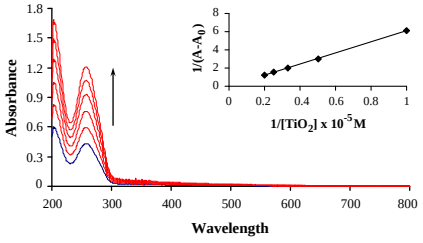


A. Kathiravan and R. Renganathan

Polyhedron 28 (2009) 1374

Photoinduced interactions between colloidal TiO_2 nanoparticles and calf thymus-DNA

Research on the direct interaction occurring between colloidal TiO_2 nanoparticles and DNA is helpful in understanding the interaction between various photosensitizers and DNA. This type of binding study has great importance in the field of using nanoparticles as a carrier for photosensitizers for interaction with DNA in photodynamic therapy (PDT) for cancer treatments.

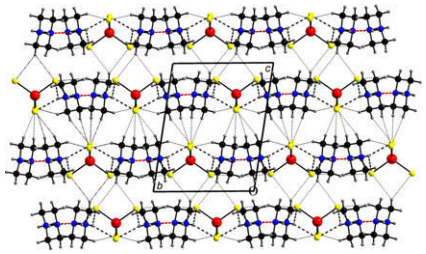


Bikshandarkoil R. Srinivasan, Ashish R. Naik, Martha Poisot, Christian Näther and Wolfgang Bensch

Polyhedron 28 (2009) 1379

Bis(piperazin-1-ium) tetrasulfidometalates: Solid state synthesis, thermal studies and structural characterization

The synthesis, spectroscopic, thermal and structural characterization of two new group VI tetrasulfidometalates $(pipH)_2[MS_4]$ (pipH = piperazin-1-ium; M = W **1**; M = Mo **2**) are described.

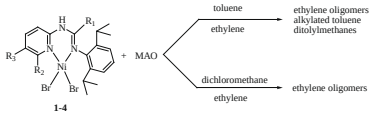


Feng-Shou Liu, Hai-Yang Gao, Ke-Ming Song, Ling Zhang, Fang-Ming Zhu and Qing Wu

Polyhedron 28 (2009) 1386

Nickel complexes bearing [N,N] 2-pyridylbenzamidine ligands: Syntheses, characterizations, and catalytic properties for ethylene oligomerization

Four 2-pyridylbenzamidine nickel complexes were synthesized and characterized. These nickel complexes showed moderate activities for ethylene oligomerization after activated with MAO. The solvent played an important role on catalytic products. In toluene, ethylene oligomers, alkylated toluene and ditolylmethanes were detected, while only ethylene oligomers were found in dichloromethane.



The Publisher encourages the submission of articles in electronic form thus saving time and avoiding rekeying errors. For detailed instructions on the preparation of manuscripts and of electronic artwork, consult the Author Gateway for Elsevier at http://authors.elsevier.com

ScienceDirect

Full text of this journal is available, on-line from **ScienceDirect**. Visit **www.sciencedirect.com** for more information.

Polyhedron 28, issue 15, 13 October 2009

Contents lists available at ScienceDirect

Polyhedron

journal homepage: www.elsevier.com/locate/poly

Contents

Preface **3169**

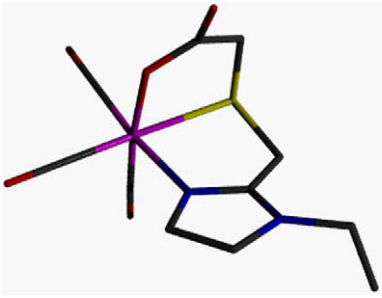
Papers

P. Kyprianidou, C. Tsoukalas, G. Patsis, D. Papagiannopoulou, N. Nikolić, D. Janković, D. Djokić, C.P. Raptopoulou, M. Pelecanou, M. Papadopoulos and I. Pirmettis

Polyhedron 28 (2009) 3171

Rhenium(I) and technetium-99m(I) *fac*-tricarbonyl complexes with 4-(imidazolin-2-yl)-3-thiabutanoic acid derivatives as tridentate ligands: Synthesis and structural characterization

Two rhenium(I) tricarbonyl complexes with the monoanionic tridentate NSO type ligand, 4-(imidazolin-2-yl)-3-thiabutanoic acid and 4-(*N*-ethylimidazolin-2-yl)-3-thiabutanoic acid have been synthesized and fully characterized. The analogous technetium-99m complexes have been also prepared quantitatively and characterized by HPLC.

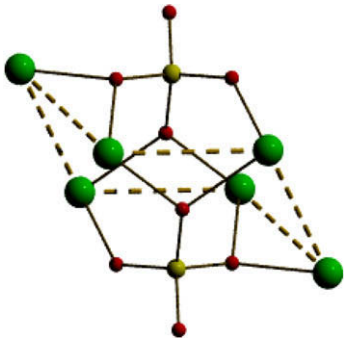


Constantinos G. Efthymiou, Alexandros A. Kitos, Catherine P. Raptopoulou, Spyros P. Perlepes, Albert Escuer and Constantina Papatriantafyllopoulou

Polyhedron 28 (2009) 3177

Employment of the sulfate ligand in 3d-metal cluster chemistry: A novel hexanuclear nickel(II) complex with a chair metal topology

The reaction of $NiSO_4{\cdot}6H_2O$ and phenyl(2-pyridyl)ketone oxime [(py)C(ph)NOH] in DMF in the presence of base has provided access to the novel hexanuclear Ni(II) cluster $[Ni_6(SO_4)_2\{(py)C(ph)NO\}_8]{\cdot}6DMF$ (**1**·6DMF) with the chair-like core $[Ni_6(\mu_5\text{-}SO_4)_2(\mu_2\text{-}ONR)_6(\mu_3\text{-}ONR)_2]$ core; in compound **1** the SO_4^{2-} adopts the rare 5.2210 coordination mode.

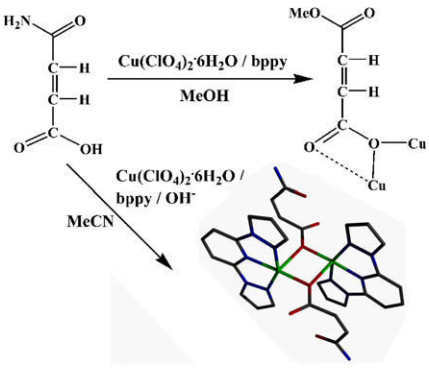


Katerina N. Lazarou, Catherine P. Raptopoulou, Spyros P. Perlepes and Vassilis Psycharis

Polyhedron 28 (2009) 3185

Complexes derived from the general copper(II)/maleamic acid/*N*,*N*′,*N*″-chelate reaction systems: Synthetic, reactivity, structural and spectroscopic studies

The use of maleamic acid (H_2L) in Cu^{II}/*N*,*N*′,*N*″-chelate (bppy, terpy, tptz) reaction systems afforded mononuclear and dinuclear complexes. Interesting Cu^{II}-assisted transformation of the maleamate(−1) ion to the monomethyl maleate(−1) ligand and Cu^{II}-promoted hydrolysis of 2,4,6-tris(2-pyridyl)-1,3,5-triazine to pyridine-2-carboxamide have been observed.



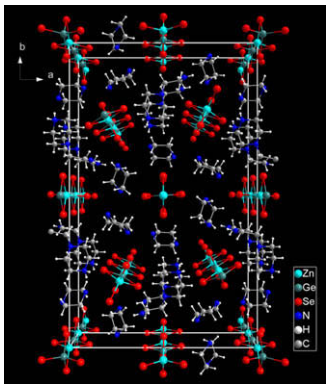
Elsevier Ltd.

Aggelos Philippidis and Pantelis N. Trikalitis

Polyhedron 28 (2009) 3193

$(H_2NC_4H_8NCH_2CH_2NH_2)(HNCH_2CH_2NH_2)_3Zn_2Ge_2Se_8$: A new, templated one-dimensional ternary semiconductor stabilized by mixed organic cations

We present the synthesis and characterization of the first organically templated chalcogenide in the system Zn/Ge/Se. The material is a medium gap semiconductor with an absorption edge at 1.8 eV.

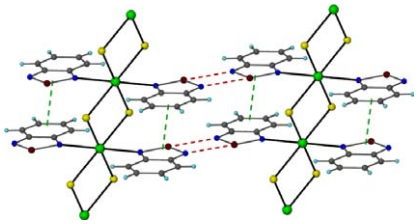


Constantinos J. Milios, Panayiotis V. Ioannou, Catherine P. Raptopoulou and Giannis S. Papaefstathiou

Polyhedron 28 (2009) 3199

Crystal engineering with 2,1,3-benzoselenadiazole and mercury(II) chloride

The employment of 2,1,3-benzoselenadiazole (bsd) in mercury(II) chemistry afforded the polymeric complexes $[HgCl_2(bsd)_2]_n$ (**1**) and $[HgCl_2bsd]_n$ (**2**) Complex **1** is an one-dimensional (1D) coordination polymer, while **2** is a two-dimensional (2D) polymer. Both complexes consist of $(HgCl_2)_n$ chains and are dominated by $\pi\cdots\pi$ interactions between the bsd molecules.

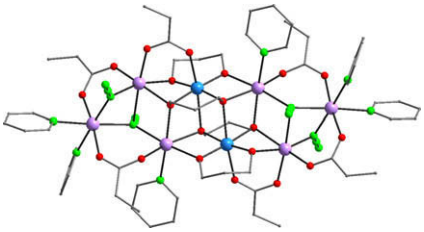


Eleni E. Moushi, Theocharis C. Stamatatos, Vassilios Nastopoulos, George Christou and Anastasios J. Tasiopoulos

Polyhedron 28 (2009) 3203

A new family of octanuclear Mn complexes with a rod-like topology

Three new octanuclear compounds [**1**, **2**, and **3**] (Fig.; color scheme: Mn^{II} purple, Mn^{III} blue, O red, N green, C grey) which were prepared from the use of a combination of pdH_2 or $mpdH_2$ and N_3^- ligands in reactions with $[Mn(O_2CR)_2]\cdot 2H_2O$ (R = Et or Ph) are reported. All three compounds possess a novel $[Mn^{II}_6Mn^{III}_2(\mu_3\text{-}N_3)_2(\mu\text{-}N_3)_2(\mu_3\text{-}OR)_4(\mu\text{-}OR)_4]^{6+}$ structural core with a near-planar, rod-like topology.

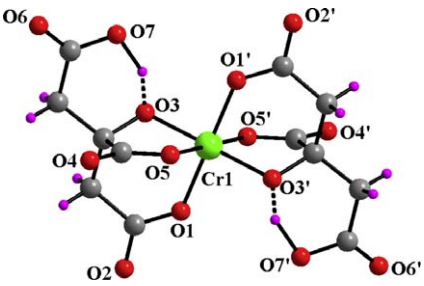


C. Gabriel, C.P. Raptopoulou, C. Drouza, N. Lalioti and A. Salifoglou

Polyhedron 28 (2009) 3209

Synthesis, spectroscopic, structural and magnetic studies of new binary Cr(III)–citrate pH-specific structural variants from aqueous media

Aqueous reactions of Cr(III) with citrate, at pH 5.5 and 3.5, led to the isolation of two new conformationally distinct pH-structural variants $Na_3[Cr(C_6H_5O_7)_2]\cdot 8.5H_2O$ (**1**) and $(Hdmphen)_6[Cr(C_6H_5O_7)_2]\cdot(NO_3)_3\cdot 14H_2O$ (**2**). Both **1** and **2** were characterized by analytical, spectroscopic (UV–Vis, FT-IR, EPR) techniques, magnetic susceptibility, thermal studies, and X-ray crystallography. The collective physicochemical properties of **1** and **2** formulate their profiles and shed light on binary Cr(III)-physiological ligand interactions with relevance to abiotic and biological materials processes.

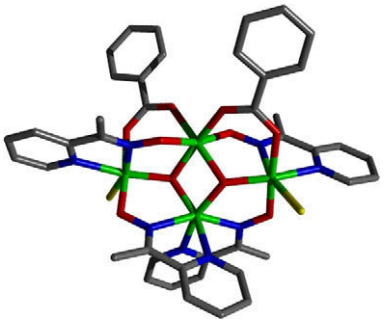


Catherine Gkioni, Athanassios K. Boudalis, Yiannis Sanakis, Vassilis Psycharis and Catherine P. Raptopoulou

Polyhedron 28 (2009) 3221

2-Pyridyl ketone oximes in iron(III) carboxylate chemistry: Synthesis, structural and physical studies of tetranuclear clusters containing the $[Fe_4(\mu_3\text{-}O)_2]^{8+}$ 'butterfly' core

The use of pyC(R)NOH (R = H, Me) in iron(III) benzoate chemistry yielded tetranuclear complexes presenting the $[Fe_4(\mu_3\text{-}O)_2]^{8+}$ 'butterfly' core; the structural, spectroscopic (IR, Mössbauer) and magnetic studies of $[Fe_4O_2Cl_2(O_2CPh)_2\{pyC(Me)NO\}_4]$ are reported.

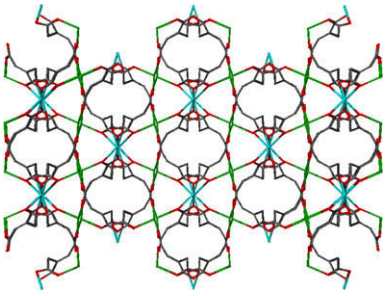


George E. Kostakis, Gerasimos Malandrinos, Ebbe Nordlander, Matti Haukka and John C. Plakatouras

Polyhedron 28 (2009) 3227

Solution and structural studies of the Cd(II) – Aconitate system

The complexing ability of the binary system *trans*-aconitic acid (H_3L) with regard to Cd(II) and the crystal structures of the binary system Cd(II)–(H_3L), $[Cd_3L_2(H_2O)_6]$ (**1**) and ternary systems of Cd(II)–(H_3L)–Lewis base [Lewis base = 1,10-phenanthroline (**2**) and 2,2′-bipyridine (**3**)] have been determined.



Gina C. Vlahopoulou, Dimitris I. Alexandropoulos, Catherine P. Raptopoulou, Spyros P. Perlepes, Albert Escuer and Theocharis C. Stamatatos

Polyhedron 28 (2009) 3235

A tetranuclear complex from the employment of pyridine-2,6-dimethanol in copper(II) nitrate chemistry: Synthetic, structural and magnetic studies

The copper(II) nitrate/pyridine-2,6-dimethanol reaction system has provided access to a mononuclear Cu^{II} complex and an antiferromagnetically-coupled ($S = 0$) tetranuclear cluster containing the $[Cu^{II}_4(\mu_2\text{-}OR)_4]^{4+}$ core.

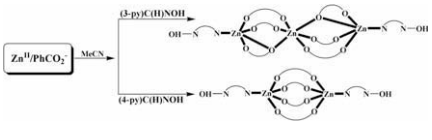


Konstantis F. Konidaris, Michalis Kaplanis, Catherine P. Raptopoulou, Spyros P. Perlepes, Evy Manessi-Zoupa and Eugenia Katsoulakou

Polyhedron 28 (2009) 3243

Dinuclear versus trinuclear complex formation in zinc(II) benzoate/pyridyl oxime chemistry depending on the position of the oxime group

The reaction of $Zn(O_2CPh)_2{\cdot}2H_2O$ and 3-pyridinealdoxime, (3-py)C(H)NOH, in MeCN gives a trinuclear cluster containing the $[Zn_3(\eta^1{:}\eta^1{:}\mu\text{-}O_2CPh)_4(\eta^1{:}\eta^2{:}\mu\text{-}O_2CPh)_2]^0$ core, while an analogous reaction with the isomeric 4-pyridinealdoxime, (4-py)C(H)NOH, yields the dinuclear, paddle-wheel complex $[Zn_2(\eta^1{:}\eta^1{:}\mu\text{-}O_2CPh)_4\{(4\text{-py})C(H)NOH\}_2]$.

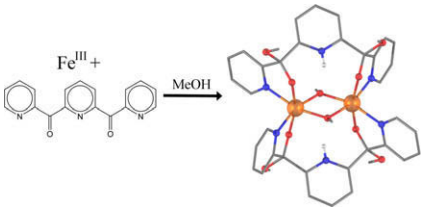


Anastasia N. Georgopoulou, Yiannis Sanakis, Catherine P. Raptopoulou, Vassilis Psycharis and Athanassios K. Boudalis

Polyhedron 28 (2009) 3251

A diferric complex from metal-assisted methanolysis of di-2,6-(2-pyridylcarbonyl)-pyridine: Structural, magnetic and spectroscopic (Mössbauer, EPR) studies

Reaction of iron(III) perchlorate with di-2,6-(2-pyridylcarbonyl)-pyridine (dpcp) leads to a diferric methoxo-bridged complex, exhibiting a weak intramolecular antiferromagnetic interaction as evidenced by magnetic susceptometry.

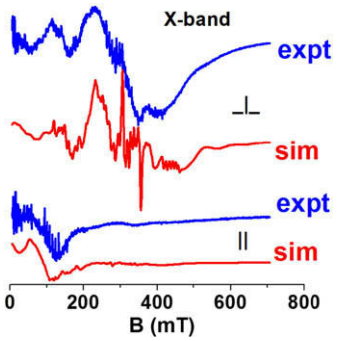


Theodora D. Tzima, George Sioros, Carole Duboc, Demetra Kovala-Demertzi, Vasilios S. Melissas and Yiannis Sanakis

Polyhedron 28 (2009) 3257

Multifrequency electron paramagnetic resonance and theoretical studies of a Mn(II) ($S = 5/2$) complex: The role of geometrical elements on the Zero Field Splitting parameters

The Zero Field Splitting parameters of the mononuclear Mn(II) ($S = 5/2$) compound [Mn(Ac4Ph)$_2$], where HAc4Ph stands for 4-phenyl-2-acetylpyridine thiosemicarbazone, are determined by dual mode X-band and high field/high frequency electron paramagnetic resonance spectroscopy. The results are in agreement with density functional theory calculations.

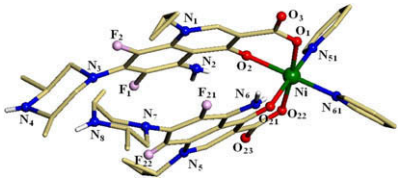


Kalliopi C. Skyrianou, Catherine P. Raptopoulou, Vassilis Psycharis, Dimitris P. Kessissoglou and George Psomas

Polyhedron 28 (2009) 3265

Structure, cyclic voltammetry and DNA-binding properties of the bis(pyridine)bis(sparfloxacinato)nickel(II) complex

The synthesis, the crystal structure, the electrochemical properties and the interaction with calf-thymus DNA of the novel mononuclear complex of the third-generation quinolone antibacterial agent sparfloxacin with Ni(II) in the presence of nitrogen-donor heterocyclic ligand pyridine, bis(sparfloxacinato)bis(pyridine)nickel(II), are presented.

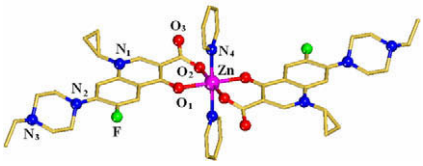


Alketa Tarushi, George Psomas, Catherine P. Raptopoulou, Vassilis Psycharis and Dimitris P. Kessissoglou

Polyhedron 28 (2009) 3272

Structure and DNA-binding properties of bis-(quinolonato)bis(pyridine)zinc(II) complexes

Octahedral mononuclear complexes synthesized by the reaction of $ZnCl_2$ with the quinolone antibacterial drugs enrofloxacin or oxolinic acid in the presence of pyridine interact with CT-DNA revealing their ability to bind to DNA. The binding strengths calculated by UV spectroscopic titrations techniques have shown that Zn(oxo)$_2$(py)$_2$ exhibits the highest K_b value.

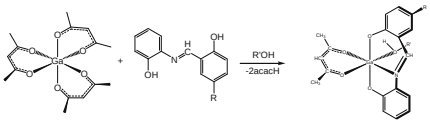


Adamantia Kagkelari, Giannis S. Papaefstathiou, Catherine P. Raptopoulou and Theodoros F. Zafiropoulos

Polyhedron 28 (2009) 3279

Synthesis and structure of *N*-salicylidene-*o*-aminophenolato gallium(III) complexes

Reactions of $Ga(acac)_3$ with *N*-salicylidene-*o*-aminophenol ($saphH_2$) and its 5-methyl and 5-bromo derivatives in alcohols (ROH) resulted in three mononuclear complexes with the general formula [Ga(acac)(5Rsaph)(ROH)]. The structures of the $saph^{2-}$ and $5Mesaph^{2-}$ were determined with single-crystal X-ray crystallography while all complexes were characterized by IR spectroscopy and elemental analysis.

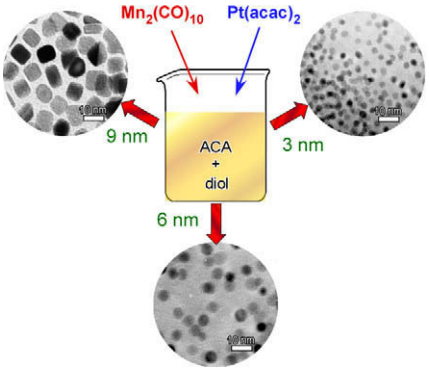


S. Mourdikoudis, A. Shavel, B. Rodríguez-González, C. Serra, K. Simeonidis, M. Angelakeris, C. Dendrinou-Samara and O. Kalogirou

Polyhedron 28 (2009) 3284

Effects of various chemical synthetic routes on structural and magnetic features of Mn–Pt bimetallic nanoparticles

Mn–Pt nanoparticles were synthesized by thermal decomposition/reduction method with variation of metal precursors, organic solvents and capping ligands, as 1-adamantanecarboxylic acid (ACA). Depending on the synthetic conditions, monodisperse $MnPt_3$ nanoparticles could be obtained, while in some cases significant oxidation of manganese was observed, together with Pt-rich particles. Regarding the magnetic properties, exchange bias phenomena were assumed in the oxidized samples.

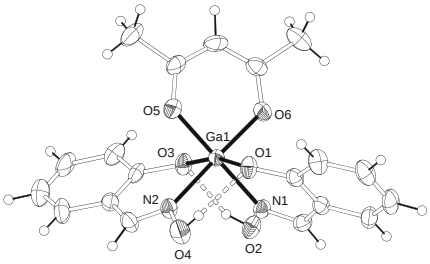


Christiana Birnara, Vadim G. Kessler and Giannis S. Papaefstathiou

Polyhedron 28 (2009) 3291

Mononuclear gallium(III) complexes based on salicylaldoximes: Synthesis, structure and spectroscopic characterization

The reactions of $Ga(acac)_3$ with salicylaldoxime ($saoH_2$) and methylsalicyladoxime ($MesaoH_2$) resulted in two mononuclear complexes with the general formula $[Ga(acac)(RsaoH)_2]$. The structures of both complexes were determined with single-crystal X-ray crystallography. Both complexes were also characterized by IR, ^1H and ^{13}C NMR spectroscopy.

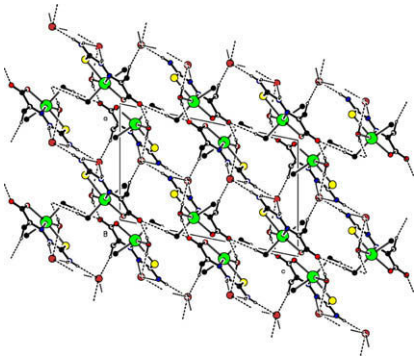


Joanna Wiecek, Vaso Dokorou, Zbigniew Ciunik and Dimitra Kovala-Demertzi

Polyhedron 28 (2009) 3298

Organotin complexes of pyruvic acid thiosemicarbazone: Synthesis, crystal structures and antiproliferative activity of neutral and cationic diorganotin complexes

The synthesis and spectral characterization of novel neutral and cationic organotin complexes with pyruvic acid thiosemicarbazone, H_2pt (**1**), [*Sn*Ph_2(pt)] (**2**), $[SnMe_2(Hpt)(H_2O)]Cl$ (**3**) and $[SnPh_2(Hpt)(H_2O)]Cl$ (**4**) are reported. The crystal structure of the complexes [*Sn*Ph_2(pt)] (**2**) and $[SnMe_2(Hpt)(H_2O)]Cl$ (**3**) have been solved by single-crystal X-ray diffraction. The *in vitro* cytotoxic activity has been evaluated against the cells of three human cancer cell lines: MCF-7 (human breast cancer cell line), T-24 (bladder cancer cell line), A-549 (non-small cell lung carcinoma) and a mouse L-929 (a fibroblast-like cell line cloned from strain L). The most active of all was found the diorganotin complex **2**. Compound **2** is considered as agent with potential antitumor activity, and can therefore be candidate for further stages of screening *in vitro* and/or *in vivo*.

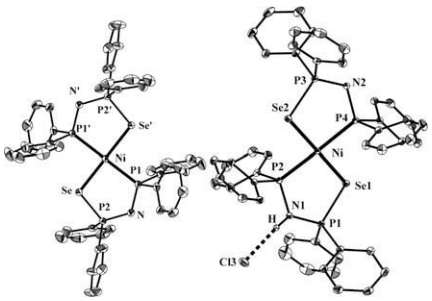


Nikolaos Levesanos, Ioannis Stamatopoulos, Catherine P. Raptopoulou, Vassilis Psycharis and Panayotis Kyritsis

Polyhedron 28 (2009) 3305

Structural effects of the chelating rings in *trans*-[Ni{Ph_2P(Se)$NPPh_2$-*Se*,*P*}$_2$] and *trans*-[Ni{Ph_2P-(Se)$NPPh_2$-*Se*,*P*}{Ph_2P(Se)N(H)PPh_2-*Se*,*P*}]Cl·CH_2-Cl_2·H_2O complexes

The [Ni{Ph_2P(Se)$NPPh_2$}$_2$] complex was structurally and spectroscopically characterized. X-ray crystallography revealed a *trans*-Ni(*Se*,*P*)$_2$ structure, which is conserved in solution, as shown by ^{31}P NMR spectroscopy. The structural features of this complex were compared to those of *trans*-[Ni{Ph_2P(Se)$NPPh_2$-*Se*,*P*}{Ph_2P-(Se)N(H)PPh_2-*Se*,*P*}]Cl, which contains both Ni–Se–P–N(H)–P and Ni–Se–P–N–P five-membered rings.

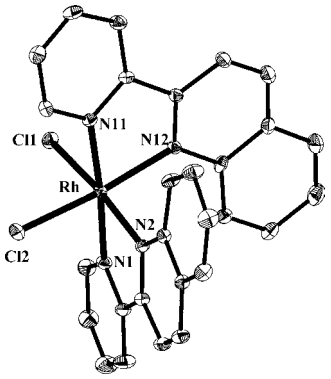


Athanassios I. Philippopoulos, Nektaria Tsantila, Constantinos A. Demopoulos, Catherine P. Raptopoulou, Vlassis Likodimos and Polycarpos Falaras

Polyhedron 28 (2009) 3310

Synthesis, characterization and crystal structure of the *cis*-[RhL_2Cl_2]Cl complex with the bifunctional ligand (L) 2-(2′-pyridyl)quinoxaline. Biological activity towards PAF (Platelet Activating Factor) induced platelet aggregation

The mononuclear Rh(III) complex, *cis*-[RhL_2Cl_2]Cl (**1**) where L = 2-(2′-pyridyl) quinoxaline (pqo) has been prepared and fully characterized. The molecular structure in the crystal of complex **1** is also described, revealing a distorted octahedral geometry. The effect of this compound on PAF-induced rabbit platelet aggregation was investigated.

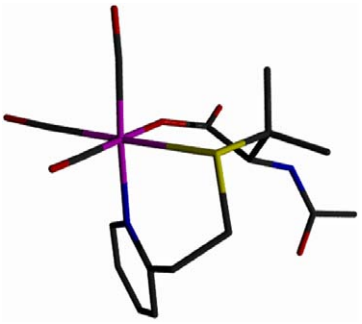


O. Karagiorgou, D. Papagiannopoulou, P. Kyprianidou, G. Patsis, A. Panagiotopoulou, C. Tsoukalas, C.P. Raptopoulou, M. Pelecanou, I. Pirmettis and M. Papadopoulos

Polyhedron 28 (2009) 3317

Synthesis and structural characterization of novel neutral *fac*-M$(CO)_3$(NSO) complexes (M = Re, ^{99m}Tc) with *N*-acetylcysteine derivatives as tridentate NSO ligands

Two *N*-acetylcysteine derivative ligands (NSO) and their stable neutral complexes with the *fac*-[$M(CO)_3(H_2O)_3$]$^+$ (M = Re or ^{99m}Tc) synthons are prepared and fully characterized. These NSO tridentate ligands are promising model compounds for the development of target-specific technetium and rhenium radiopharmaceuticals.

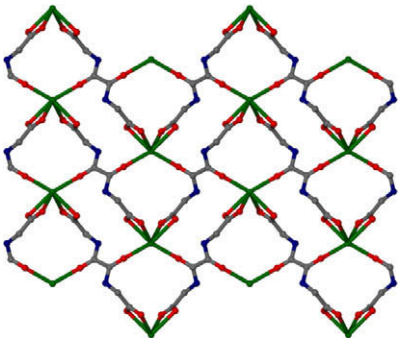


John G. Servetas, George E. Kostakis, Matti Haukka, Thomas Bakas and John C. Plakatouras

Polyhedron 28 (2009) 3322

Synthesis, and characterization of 1- and 2-D coordination polymers derived from the pseudopeptidic ligand oxamide-*N*,*N*′-diacetate: Insights into the supramolecular architectures constructed through H-bonds

Oxamide-*N*,*N*′-diacetic acid forms novel 1- and 2-D coordination polymers upon reaction with metal ions. 3D supramolecular architectures are formulated via H-bonding interactions between the chains or layers and lattice water molecules.

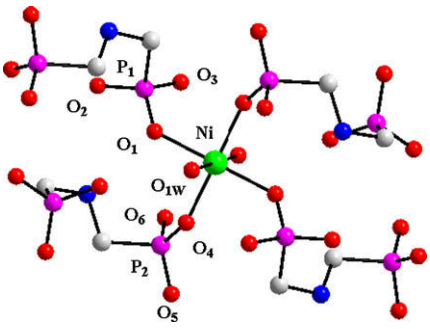


M. Menelaou, M. Dakanali, C.P. Raptopoulou, C. Drouza, N. Lalioti and A. Salifoglou

Polyhedron 28 (2009) 3331

pH-Specific synthetic chemistry, and spectroscopic, structural, electrochemical and magnetic susceptibility studies in binary Ni(II)-(carboxy)phosphonate systems

pH-Specific reactions of Ni(II) with imino-diphosphonic and imino-carboxyphosphonic acids led to the isolation of new complexes $[Ni(C_2H_8O_6NP_2)_2(H_2O)_2]$ (**1**) and $[Ni(OOC–CH_2–NH–CH_2–PO_3H)_2]\cdot[Ni(H_2O)_6]\cdot 3.3H_2O$ (**2**). Compounds **1** and **2** were characterized by analytical, spectroscopic, electrochemical, thermal, magnetic and structural studies. Their collective physicochemical profiles (a) reflect the pH-specific reactivity in aqueous Ni(II)–organophosphonate binary systems, and (b) project the nature of interactions in Ni(II)–organophosphonate species, participating in the requisite aqueous speciation, potentially influencing cellular events and/or materials synthetic processes.

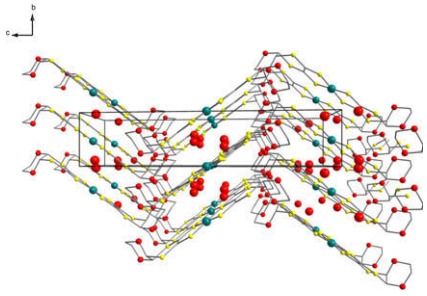


G. Soras, N. Psaroudakis, M.J. Manos, A.J. Tasiopoulos, D.G. Liakos and G.A. Mousdis

Polyhedron 28 (2009) 3340

New type dithiolene complex based on 4,5-(1,4-dioxane-2,3-diyldithio)-1,3-dithiol ligand: Synthesis, experimental and theoretical investigation

A new Nickel complex with an extended multisulfur dithiolene ligand $Ni(edodddt)_2$ (edodddt = 2,3,4α,8α-tetrahydro-dithiine [2,3-b] [1,4] dioxo-6,7-dithiolene) has been synthesized and characterized by electrochemical measurements, IR, UV–Vis and NMR spectroscopy. Its crystal structure was resolved by X-ray diffraction on a single crystal. DFT calculations were made in order to compare the results with the experimental findings and gain an insight of the properties of this new dithiolene complex.

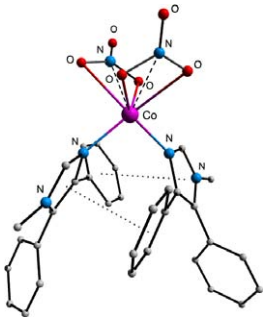


Konstantina A. Kounavi, Constantina Papatriantafyllopoulou, Anastasios J. Tasiopoulos, Spyros P. Perlepes and Vassilios Nastopoulos

Polyhedron 28 (2009) 3349

The supramolecular chemistry of metal complexes with heavily substituted imidazoles as ligands: Cobalt(II) and zinc(II) complexes of 1-methyl-4,5-diphenylimidazole

Two isomorphous, octahedral cobalt(II) and zinc(II) nitrato complexes and one tetrahedral, cobalt(II) isothiocyanato complex, all with two 1-methyl-4,5-diphenylimidazole ligands, possess a characteristic mode of packing between neighbouring ligands of the complexes, expressed through intramolecular π–π interactions between the 4,5-diphenylimidazole moieties.

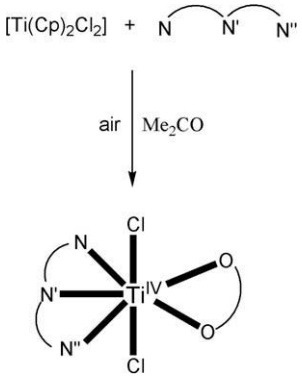


Andreas Sofetis, Fotini Fotopoulou, Catherine P. Raptopoulou, Theodoros F. Zafiropoulos, Spyros P. Perlepes and Nikolaos Klouras

Polyhedron 28 (2009) 3356

Reactions of titanocene dihalides with *N*,*N*′,*N*″-chelates: Preparation, X-ray structure and characterization of bis(chloro){2,6-bis[(3,5-dimethyl)pyrazol-1-yl]pyridine}(η^2-peroxo)titanium(IV)

The reaction of bis(chloro)bis(cyclopentadienyl)titanium(IV) with the *N*,*N*′,*N*″-chelate 2,6-bis(3,5-dimethylpyrazolyl-1-yl)pyridine in acetone gives an interesting, cyclopentadienyl-free 7-coordinate titanium(IV) complex containing a side-on peroxo ligand.

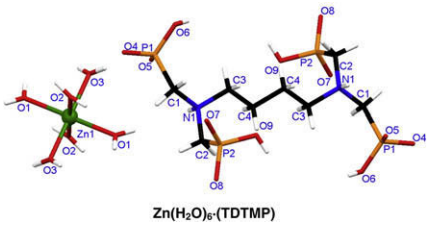


Konstantinos D. Demadis, Eleni Barouda, Hong Zhao and Raphael G. Raptis

Polyhedron 28 (2009) 3361

Structural architectures of charge-assisted, hydrogen-bonded, 2D layered amine···tetraphosphonate and zinc···tetraphosphonate ionic materials

Synthesis and structural characterization of 2D layered, hydrogen bond-assisted ionic salts of three tetraphosphonates (hexamethylenediamine-*tetrakis*(methylenephosphonate), ethylenediamine-*tetrakis*(methylenephospho-nate), and tetramethylenediamine-*tetrakis*(methylenephosphonate)) with ethylenediamonium, ammonium, and $Zn(H_2O)_6^{2+}$ cations are reported.

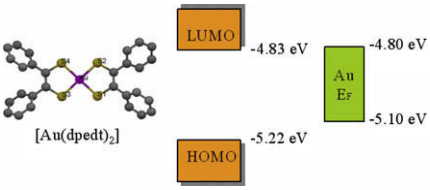


George C. Papavassiliou, George C. Anyfantis, Catherine P. Raptopoulou, Vassilis Psycharis, Nikos Ioannidis, Vassilis Petrouleas and Patrina Paraskevopoulou

Polyhedron 28 (2009) 3368

Bis[1,2-diphenyl-1,2-ethylenedithiolato(2-)-kS_1,kS_2] gold: Preparation, structure and properties

The complex $Au(dpedt)_2$ is isostructural with the β-form of the nickel analogue. Optical and electrochemical data indicate that the complex is stable in air and could be a candidate material for fabrication of electronic devices.

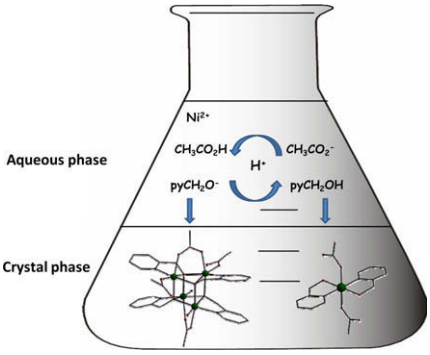


Constantinos G. Efthymiou, Constantina Papatriantafyllopoulou, Nadia I. Alexopoulou, Catherine P. Raptopoulou, Roman Boča, Jerzy Mrozinski, Evangelos G. Bakalbassis and Spyros P. Perlepes

Polyhedron 28 (2009) 3373

A mononuclear complex and a cubane cluster from the initial use of 2-(hydroxymethyl)pyridine in nickel(II) carboxylate chemistry

The acetate/2-(hydroxymethyl)pyridine combination in nickel(II) chemistry has provided access to a mononuclear complex and a tetranuclear cubane cluster containing the neutral and the anionic form of the pyridyl alcohol ligand, respectively; the products have interesting structures and properties.

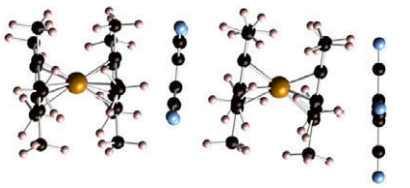


Michael Fardis, George Diamantopoulos, Eleni Karakosta, Ioannis Rabias, George Papavassiliou and Joel S. Miller

Polyhedron 28 (2009) 3382

Spin dynamics in the molecule-based ferromagnet decamethylferrocenium tetracyanoethanide $[FeCp_2^*][TCNE]$, as probed by ^1H NMR relaxation

The electron spin dynamics of the molecule-based ferromagnet decamethylferrocenium tetracyanoethenide, $[FeCp_2^*][TCNE]$, has been investigated at a local level using ^1H NMR experiments. The NMR relaxation measurements verify that $[FeCp_2^*][TCNE]$ is an 1D ferromagnetic Ising-like chain with significant short range order at temperatures above the magnetic ordering transition.

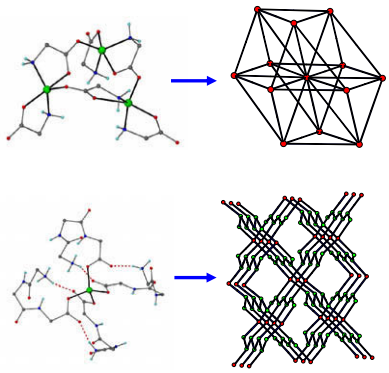


Eugenia Katsoulakou, Giannis S. Papaefstathiou, Konstantis F. Konidaris, George Pairas, Catherine Raptopoulou, Paul Cordopatis and Evy Manessi-Zoupa

Polyhedron 28 (2009) 3387

Synthesis, structural study and topological analysis of Zn/Aib and Aib-based small peptide complexes (H-Aib-OH = α-aminoisobutyric acid)

The synthetic investigation of reaction systems containing Zn^{II} and α-aminoisobutyric acid (H-Aib-OH) or Aib-based peptides gives products with interesting molecular and supramolecular structures.

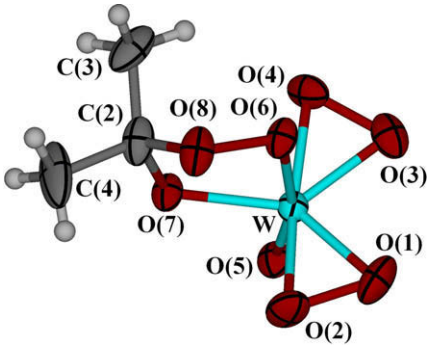


Vasilis Tsitsias, Adamantia Maniatakou, Catherine Raptopoulou and Alexandra Karaliota

Polyhedron 28 (2009) 3400

Synthesis, characterization and crystal structure of a novel mononuclear peroxotungsten(VI) complex with an acetone peroxide ligand

The new mononuclear peroxo complex of tungsten of the formula $(gu)_2[WO(O_2)_2CO(O)_2(CH_3)_2](CH_3)_2CO$ (where gu^+ = guanidinium ion, $CN_3H_6^+$ ion) has been obtained in reaction of sodium tungstate with hydrogen peroxide in the presence of an excess of acetone in aqueous medium. The crystal structure and the spectral characterization of the novel complex have been determined.



The Publisher encourages the submission of articles in electronic form thus saving time and avoiding rekeying errors. For detailed instructions on the preparation of manuscripts and of electronic artwork, consult the Author Gateway for Elsevier at http://authors.elsevier.com

ScienceDirect

Full text of this journal is available, on-line from **ScienceDirect**. Visit **www.sciencedirect.com** for more information.

Polyhedron 28, issue 12, 5 August 2009

Contents lists available at ScienceDirect

Polyhedron

journal homepage: www.elsevier.com/locate/poly

Contents

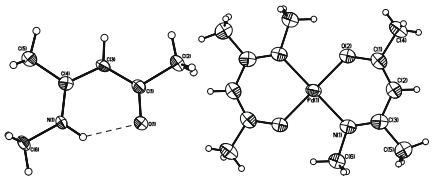
Papers

G.I. Zharkova, P.A. Stabnikov, I.A. Baidina, A.I. Smolentsev and S.V. Tkachev

Polyhedron 28 (2009) 2307

Synthesis, properties and crystal structures of volatile β-ketoiminate Pd complexes, precursors for palladium chemical vapor deposition

Two aminovinylketones and two bis-ketoiminates Pd have been synthesized. All the compounds were identified by elemental analysis, ^{1}H and ^{13} NMR, IR-spectroscopy and were characterized by TGA and a single-crystal X-ray diffraction study. In the chelates, the Pd atom has a square coordination environment, Pd O_2N_2.

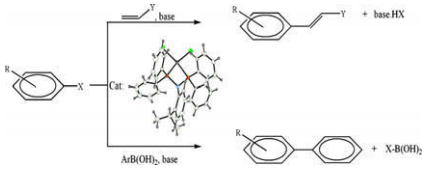


Murat Aydemir, Feyyaz Durap, Akın Baysal, Osman Akba, Bahattin Gümgüm, Saim Özkar and Leyla Tatar Yıldırım

Polyhedron 28 (2009) 2313

Synthesis and characterization of new bis-(diphenylphosphino)aniline ligands and their complexes: X-ray crystal structure of palladium(II) and platinum(II) complexes, and application of palladium(II) complexes as pre-catalysts in Heck and Suzuki cross-coupling reactions

Two new bis(diphenylphosphino)amines and their oxides and selected transition metal complexes (Cu(I), Pd(II), Pt(II)) have been prepared. The Pd complexes exhibit high catalytic activity in the Heck and Suzuki cross-coupling reactions.

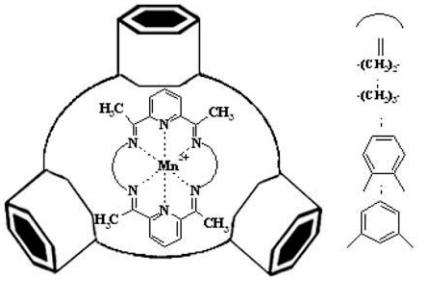


Masoud Salavati-Niasari

Polyhedron 28 (2009) 2321

Synthesis and characterization of 18- and 20-membered hexaaza macrocycles containing pyridine manganese(II) complex nanoparticles dispersed within nanoreactors of zeolite-Y

Manganese(II) complexes of hexaaza macrocyclic complex nanoparticles have been encapsulated in the nanopores of zeolite-Y by the template condensation reaction. The new complex nanoparticles entrapped in the nanoreactor of zeolite-Y have been characterized by FT-IR, DRS, XPS, TGA, UV–Vis spectroscopic techniques, X-ray diffraction (XRD) and elemental analysis as well as by nitrogen adsorption.



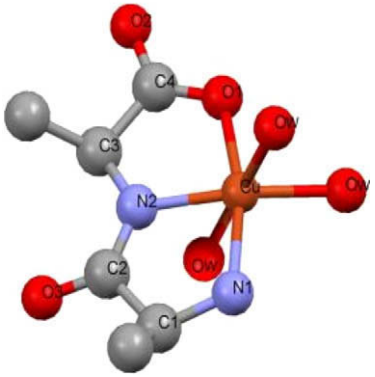
Elsevier Ltd.

Gianella Facchin, Eduardo Kremer, Daniel A. Barrio, Susana B. Etcheverry, Antonio J. Costa-Filho and María H. Torre

Polyhedron 28 (2009) 2329

Interaction of Cu-dipeptide complexes with Calf Thymus DNA and antiproliferative activity of [Cu(ala-phe)] in osteosarcoma-derived cells

The study of the Calf Thymus DNA interaction with several Cu(L-dipeptide) complexes is presented. The binding stoichiometry (amount of copper bound to the DNA) was quantified and in an attempt to clarify the mode of binding, EPR and CD experiments were performed. The effect on cell proliferation determined on rat asteosarcoma-derived cells was stuided.

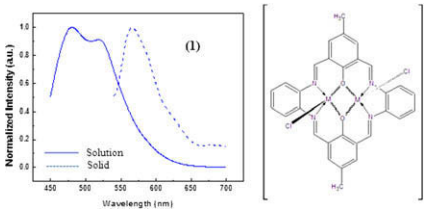


Verónica Paredes-García, D. Venegas-Yazigi, A. Cabrera, P. Valencia-Gálvez, M. Arriagada, D. Ruiz-Leon, N. Pizarro, A. Zanocco and Evgenia Spodine

Polyhedron 28 (2009) 2335

Optical properties of binuclear zinc (II) macrocyclic complexes derived from 4-methyl-2,6-diformylphenol and 1,2-diaminobenzene

DMSO solutions of $[Zn_2LCl_2]\cdot H_2O$ (**1**) and $[Zn_2L](NO_3)_2$ (**2**) show emission bands centred at 480 and 521 nm for (**1**), and at 527 and 480 nm for (**2**). The emission spectra in the solid state show a red shifted band at 565 nm (**1**), and 575 nm (**2**), respectively.

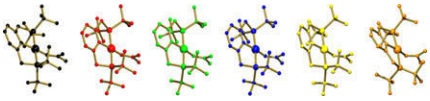


Martin Lutz, Jarl Ivar van der Vlugt, Dieter Vogt and Anthony L. Spek

Polyhedron 28 (2009) 2341

A reversible solid–solid phase transition $Z' = 1$ to $Z' = 6$ in [Ni(OAc)(**PNP^{tBu}**)]OTf

The pincer complex [Ni(OAc)(**PNP^{tBu}**)]OTf has a room temperature structure with $Z' = 1$, which shows signs of disorder. During a phase transition between 230 and 210 K the unit cell volume increases by a factor of six, accompanied by large structural changes, resulting in a well ordered structure with $Z' = 6$.

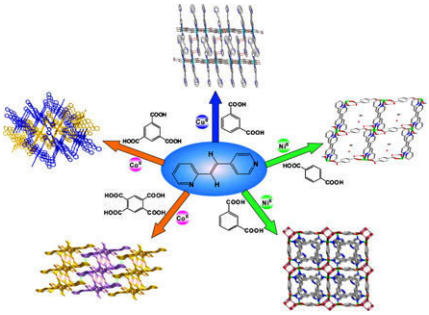


Qian Yu, Cheng-Peng Li, Zhi-Hui Zhang and Miao Du

Polyhedron 28 (2009) 2347

Mixed-ligand complexes with *trans*-1-(2-pyridyl)-2-(4-pyridyl)ethylene terminal and different aromatic polycarboxyl linkers: Synergistic modulation of metallosupramolecular architectures *via* coordinative and secondary interactions

This work presents a series of Co^{II}, Ni^{II}, and Cu^{II} complexes with a bifunctional building block *trans*-1-(2-pyridyl)-2-(4-pyridyl)ethylene and different aromatic polycarboxyl co-ligands, which display diversiform metallosupramolecular networks that are regulated by both coordinative and secondary interactions.

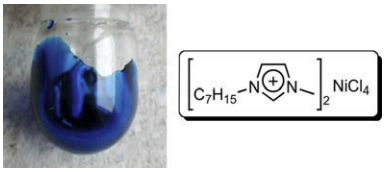


M. Brett Meredith, C. Heather McMillen, Jonathan T. Goodman and Timothy P. Hanusa

Polyhedron 28 (2009) 2355

Ambient temperature imidazolium-based ionic liquids with tetrachloronickelate(II) anions

Tetrachloronickelate(II) salts of 1-alkyl-3-methylimidazolium cations with intermediate chain lengths (C5, C7, C8 or a C4/C6 mixture) are liquid at room temperature (20 °C) and above. Despite the dinegative charge on the anion, their viscosities and thermal stabilities are similar to those of related $[BF_4]^-$ compounds.

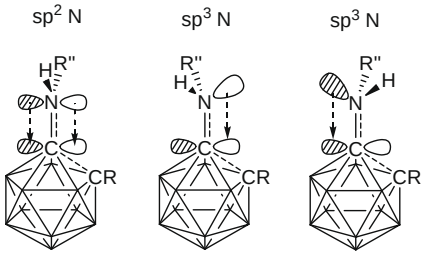


Mark A. Fox, Richard J. Peace, William Clegg, Mark R.J. Elsegood and Kenneth Wade

Polyhedron 28 (2009) 2359

Trends in *ortho*-carboranes 1-X-2-R-1,2-$C_2B_{10}H_{10}$ (R = Ph, Me) bearing an *exo*-CN-bonded substituent group (X = NO, N=NR′ or NHR′′)

The C1–C2 bond distances are remarkably sensitive to the planar (sp^2) or pyramidal (sp^3) nature of the NHR′′ group in 1-NHR′′-2-R-1,2-$C_2B_{10}H_{10}$ systems.

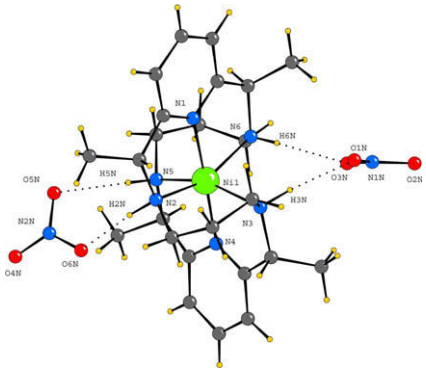


M. del Carmen Fernández-Fernández, Rufina Bastida, Alejandro Macías, Paulo Pérez Lourido and Laura Valencia

Polyhedron 28 (2009) 2371

Ni(II) complexes of stereo-isomeric hexaza-macrocyclic ligands derived from 2,6-diacetylpyridine

A new series of nitrate and perchlorate Ni(II) complexes of the stereo-isomeric hexaazamacrocyclic ligands L^1 and L^2 derived from 2,6-diacetylpyridine were synthesized by reaction of the ligand and the appropriate salt in refluxing acetonitrile. The reactions gave analytically pure products that were characterized by elemental analysis, LSI-MS, conductivity measurements, IR, UV–Vis spectroscopy and magnetic studies.
Crystal structures of $L^1{\cdot}2H_2O$ as well as of the complexes $[NiL^1](ClO_4)_2$ and $[NiL^2](NO_3)_2$ have also been determined. The X-ray studies show the presence of mononuclear endomacrocyclic complexes with the metal ion coordinated to all the nitrogen donor atoms from the macrocyclic framework in a N6 core. The geometry around the metal ions can be described as distorted octahedral. The nitrate and perchlorate anions do not coordinate to the metal ions, but they are involved in intermolecular interactions through hydrogen bonds to the amine groups of the macrocyclic ligands.

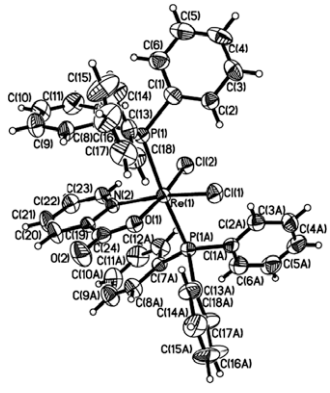


B. Machura, M. Wolff, R. Kruszynski, J. Mroziński and J. Kusz

Polyhedron 28 (2009) 2377

Novel rhenium(III) complexes with the picolinate ligand: Synthesis, spectroscopic investigations, X-ray structures and DFT calculations for $[ReX_2(pic)(PPh_3)_2]$ complexes

The paper presents a combined experimental and computational study of novel rhenium(III) complexes with picolinate ligand – $[ReCl_2(pic)(PPh_3)_2]$ (**1**) and $[ReBr_2(pic)(PPh_3)_2]$ (**2**). The both complexes **1** and **2** have been characterised spectroscopically and structurally (by single-crystal X-ray diffraction). The complex **1** has been additionally studied by magnetic measurement. The magnetic behavior is characteristic of mononuclear complexes with d^4 low-spin octahedral Re(III) complexes ($^3T_{1g}$ ground state) and arise because of the large spin-orbit coupling (ζ = 2500 cm^{-1}), which gives diamagnetic ground state. DFT and time-dependent (TD)DFT calculations have been carried out for complex **1**, and UV–Vis spectra of the $[ReX_2(pic)(PPh_3)_2]$ compounds have been discussed on this basis.

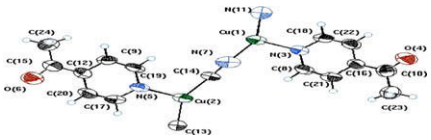


Safaa El-din H. Etaiw, Said A. Amer and Mohamed M. El-bendary

Polyhedron 28 (2009) 2385

3D-supramolecular copper(I) cyanide coordination polymers through hydrogen bonding

The reactions of $K_3[Cu(CN)_4]$, 3-acetylpyridine (3-Acpy) or 4-acetylpyridine (4-Acpy) in the presence of Me_3SnCl in H_2O/acetonitrile media at room temperature afford the 3D-supramolecular coordination polymers (SCPs) $_\infty^3[Cu_2CN(\mu\text{-}CN)\ (3\text{-}Acpy)_2]$ **1** and $_\infty^3[Cu_2CN(\mu\text{-}CN)\ (4\text{-}Acpy)_2]$ **2**.

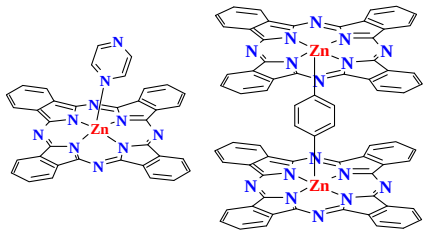


Jan Janczak and Ryszard Kubiak

Polyhedron 28 (2009) 2391

Pyrazine control of the solid-state supramolecular chemistry of zinc phthalocyanine

Monoaxially ligated T-shaped and H-shaped supramolecular zinc(II) phthalocyaninato complexes with pyrazine are obtained. In both types of molecules the central Zn atom of ZnPc complexes with pyrazine exhibits 4 + 1 coordination. The UV–Vis spectrum shows the batochromic shift in the polar solvent like 1-chloronaphthalene in relation to the spectrum in non-polar solvent like benzene.

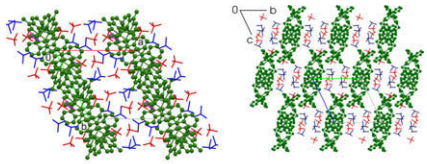


Tamara R. Todorović, Urszula Rychlewska, Beata Warżajtis, Dušanka D. Radanović, Nenad R. Filipović, Ivana A. Pajić, Dušan M. Sladić and Katarina K. Anđelković

Polyhedron 28 (2009) 2397

Synthesis, characterization and antimicrobial activity of Ni(II) and Zn(II) complexes with *N*′,*N*′^{2}-bis[(1*E*)-1-(2-pyridyl)ethylidene]propanedihydrazide. Crystal structures of two highly solvated bimetallic complexes of Ni(II)

The bimetallic Ni(II) complexes with *N*′,*N*′^{2}-bis-[(1*E*)-1-(2-pyridyl)ethylidene]propanedihydrazide (H_2L2), $[Ni_2(H_2L2)_2](ClO_4)_4$ (**1**) and $[Ni_2(HL2)(H_2L2)](ClO_4)_3$ (**2**), were isolated during the fractional crystallization process. The less stable green crystals of (**1**) with a layered structure converted slowly to brown crystals of (**2**) having a channel structure while being kept in the solution.



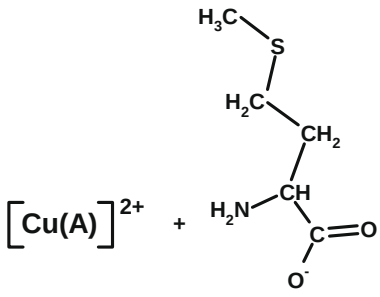
(**1**) (**2**)

Barbara Kurzak, Anna Kamecka, Katarzyna Bogusz, Julia Jezierska and Agnieszka Woźna

Polyhedron 28 (2009) 2403

Stabilities and coordination modes of methionine in copper(II) mixed-ligand complexes with ethylenediamine, diethylenetriamine or N, N, N′, N″, N″-pentamethyldiethylenetriamine in aqueous solution

Solution equilibrium studies on the Cu(II)-polyamine-Methionine ternary systems (polyamine: ethylenediamine, diethylenetriamine, N,N,N′,N″,N″-pentamethyldiethylenetriamine) have been performed by pH-potentiometry, UV–Vis spectrophotometry and EPR methods. Our spectroscopic results indicate the tetragonal geometry for $[Cu(en)(Met)]^+$, the geometry slightly deviated from square pyramidal for the $[Cu(dien)(Met)]^+$ species and strongly deviated from square pyramidal towards trigonal bipyramidal for the $[Cu(Me_5dien)(Met)]^+$ species.

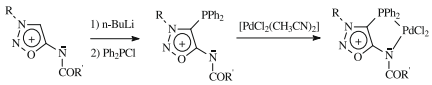


Valeriy N. Kalinin, Sergey N. Lebedev, Il'ia A. Cherepanov, Ivan A. Godovikov, Konstantin A. Lyssenko and Evamarie Hey-Hawkins

Polyhedron 28 (2009) 2411

4-Diphenylphosphinosydnone imines as bidentate ligands

The synthesis and characterization of new 3-substituted-4-diphenylphosphinosydnone imines (1,2,3-oxadiazolium-imines-5) are reported. These compounds react with $[PdCl_2(MeCN)_2]$ in MeCN to afford monomeric *cis*-P,N-coordinated palladium complexes.

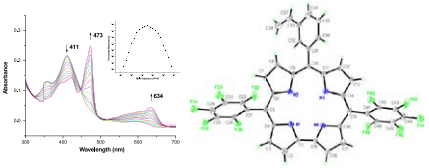


Kibong Kim, Inkoo Kim, Nilkamal Maiti, Seong Jung Kwon, Daniela Bucella, Olga A. Egorova, Yoon Sup Lee, Juhyoun Kwak and David G. Churchill

Polyhedron 28 (2009) 2418

A study of nerve agent model organophosphonate binding with manganese-A_2B-corrole and -A_2B_2-porphyrin systems

Mn A_2B-corrole and *trans*-A_2B_2-porphyrin derivatives have been prepared for a comparison of experimental organophosphonate (OP) binding (e.g., $M^{n+} \leftarrow O{=}PR(OR)_2$). Job plots give a 1:1 metal: ligand stoichiometry which is preferable for the Mn-corrole. Theoretical studies with unsubstituted Mn-corroles/-porphyrins and cyclic voltammetry were also undertaken.

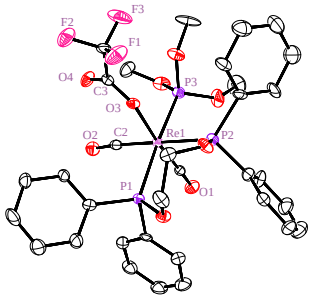


Sandra Bolaño, Jorge Bravo, Jesús Castro, Soledad García-Fontán and María C. Rodríguez

Polyhedron 28 (2009) 2431

Synthesis and characterization of rhenium carbonyltrifluoroacetate complexes with phosphites, phosphonites and phosphinites

The rhenium(I) complexes $[Re(O_2CCF_3)(CO)_3(L)]$ (**1**) and $[Re(O_2CCF_3)(CO)_2LL']$ (L = $Ph_2POCH_2CH_2OPPh_2$; L′ = $PPh_n(OR)_{3-n}$; R = Me, Et; n = 0–2) (**2a–f**) have been synthesised by the reaction of the parent bromo derivatives with AgO_2CCF_3. The metal is in a distorted octahedral environment with the trifluoroacetate ligand acting in a monodentate manner.

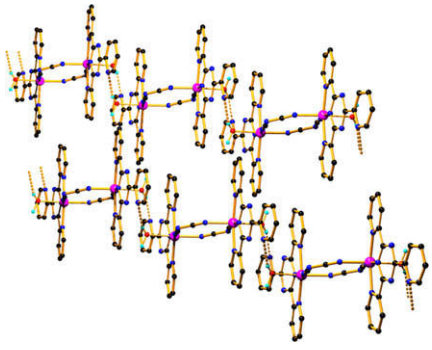


Anamika Das, Christoph Marschner, Joan Cano, Judith Baumgartner, Joan Ribas, M. Salah El Fallah and Samiran Mitra

Polyhedron 28 (2009) 2436

Synthesis, crystal structures and magnetic behaviors of two dicyanamide bridged di- and polynuclear complexes of cobalt(II) derived from 2,4,6-tris(2-pyridyl)1,3,5-triazine and imidazole

Two cobalt(II) coordination compound $[Co(dca)(tptz)(H_2O)]_2{\cdot}2(ClO_4)$ (**1**) and $[Co(dca)_2(imz)_2]_n$ (**2**) [dca, dicyanamide; tptz, 2,4,6-tris(2-pyridyl)1,3,5-triazine; and imz, imidazole] have been synthesized and characterized by elementary analyses, X-ray diffraction study and magnetic measurements.

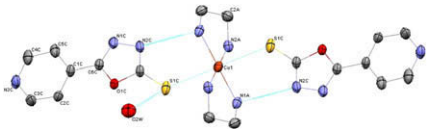


N.K. Singh, M.K. Bharty, R. Dulare and R.J. Butcher

Polyhedron 28 (2009) 2443

Synthesis and X-ray crystallographic studies of Ni (II) and Cu (II) complexes of [5-(4-pyridyl)-1,3,4] oxadiazole-2-thione/thiol formed by transformation of N-(pyridine-4-carbonyl)-hydrazine carbodithioate in the presence of ethylenediamine

The reaction of $[M(H_2L)_2]$ [M = Ni(II) Cu(II)] ($K^+H_2L^-$ = N-(pyridine-4-carbonyl)-hydrazine carbodithioate) with excess of ethylenediamine (en) gave mixed ligand complexes $[Ni(en)_2(4\text{-pytone})_2]$ and $[Cu(en)_2](4\text{-pytol})_2{\cdot}H_2O$. The metal complexes have been characterized with the aid of elemental analyses, IR, magnetic susceptibility and single crystal X-ray studies. The ligand (4-pytone) is bonded through oxadiazole nitrogen in the thione form in **1** and is ionically present in the thioate form in **2**.

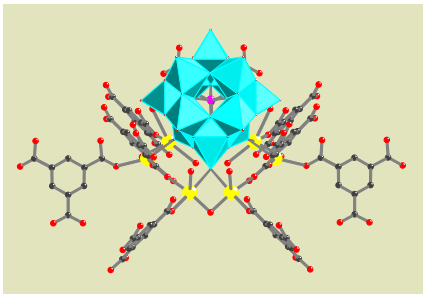


Geeta Hundal, Young Kyu Hwang and Jong-San Chang

Polyhedron 28 (2009) 2450

Formation of nanoporous and non-porous organic–inorganic hybrid materials incorporating α-Keggin phosphotungstate anion: X-ray crystal structure of a 3D polymeric complex $[\{Na_6(C_9H_5O_6)_3(H_2O)_{15}\}\{PW_{12}O_{40}\}]_\infty$ with a 'Ball-in-Bowl' type molecular structure

Two different synthetic approaches to prepare inclusion complexes of Keggin anion $[PW_{12}O_{40}]^{3-}$ and $[Cu_3(BTC)_2(H_2O)_3]_n$ have resulted in the formation of materials **1** and **2**. Compound **1** is a thermally stable, nanoporous material containing the MOF material $[Cu_3(BTC)_2(H_2O)_3]_n$ with half of its pores occupied by the guest Keggin anion. The other product **2** is a crystalline, 3D coordination polymer with a composition of $[Na_6(BTC\text{-}H_2)_3(H_2O)_{15}][PW_{12}O_{40}]$ and is a non-porous, highly water soluble and thermally unstable material.

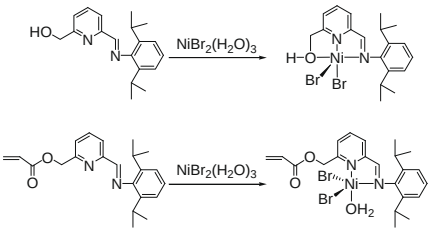


Junpei Kuwabara, Daisuke Takeuchi and Kohtaro Osakada

Polyhedron 28 (2009) 2459

Structures of Co, Pd and Ni complexes with iminopyridine ligands having an hydroxymethyl or acrylate pendant group

The coordination fashion of iminopyridine ligands to Co(II), Pd(II) and Ni(II) centers depends on the central metals, pendant groups of the pyridyl ring and recrystallization conditions. The Ni(II) complex with the hydroxy pendant group has a tridentate *N*,*N*′,*O*-coordination fashion in contrast to a bidentate *N*,*N*′-coordination of the ligand with the acrylate pendant group.

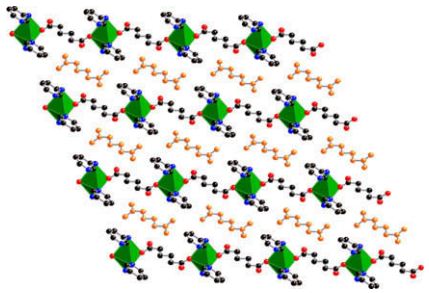


Nina Lah and Rodolphe Clérac

Polyhedron 28 (2009) 2466

Cu(II) coordination polymers incorporating 3-aminopyridine and flexible aliphatic dicarboxylate ligands: Synthesis, structure and magnetic properties

Four new copper coordination polymers with aliphatic dicarboxylates and 3-aminopyridine have been prepared. The association of monomeric building units leads to the formation of chains or layers through the dicarboxylate moiety and unexpectedly also through 3-aminopyridine.

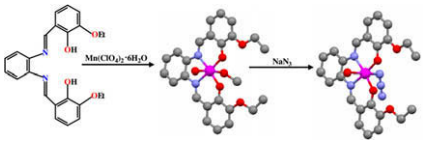


Samit Majumder, Susanta Hazra, Supriya Dutta, Papu Biswas and Sasankasekhar Mohanta

Polyhedron 28 (2009) 2473

Syntheses, structures and electrochemistry of manganese(III) complexes derived from *N*,*N*′-*o*-phenylenebis(3-ethoxysalicylaldimine): Efficient catalyst for styrene epoxidation

Syntheses, characterization, electrochemisty and catalytic properties for styrene epoxidation of three manganese(III) compounds $[Mn^{III}L^1(H_2O)(MeOH)](ClO_4)$ (**1**) $[Mn^{III}L^1(N_3)(H_2O)]\cdot dmf$ (**2**) $[Mn^{III}L^1(Cl)(H_2O)]$ (**3**) derived from the Schiff base compartmental ligand *N*,*N*′-*o*-phenylenebis(3-ethoxysalicylaldimine) (H_2L^1) have been reported. Single crystal X-ray structures of two compounds (**1** and **2**) have been determined.

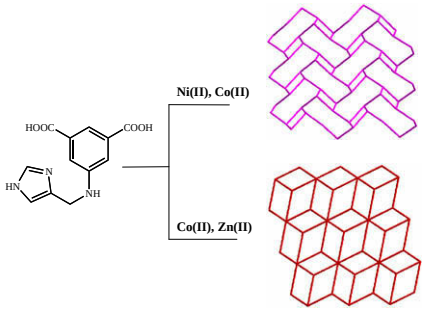


Jing Xu, Zheng-Shuai Bai, Taka-aki Okamura, Man-Sheng Chen, Wei-Yin Sun and Norikazu Ueyama

Polyhedron 28 (2009) 2480

New metal–organic architectures of cobalt(II), nickel(II) and zinc(II) with tripodal ligand 5-(1H-imidazol-4-ylmethyl)aminoisophthalic acid

Four novel coordination polymers with (3, 3)- and (3, 6)-connected 2D network structures have been synthesized by reactions of new imidazol- and carboxylate-containing ligand with Ni(II), Co(II) and Zn(II) salts under hydrothermal conditions. The thermal stability, luminescent, and magnetic properties of the complexes are investigated.

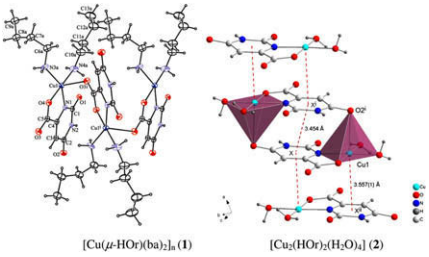


Mustafa Serkan Soylu, Okan Zafer Yeşilel, Bünyamin Karabulut and Orhan Büyükgüngör

Polyhedron 28 (2009) 2487

Syntheses, spectral, thermal and structural characterization of dinuclear and polynuclear copper(II) orotate complexes, $[Cu_2(HOr)_2(H_2O)_4]$ and $[Cu(\mu\text{-}HOr)(ba)_2]_n$

The novel *catena*-*poly*-μ-orotatobis(butylamine)-copper(II), $[Cu(\mu\text{-}HOr)(ba)_2]_n$ (**1**), and diaqua-(orotato)copper(II), $[Cu_2(HOr)_2(H_2O)_4]$ (**2**), complexes have been prepared and characterized by elemental analysis, magnetic measurements, FT-IR spectroscopy, EPR spectroscopy, thermal analysis and X-ray diffraction. In the complexes, the copper(II) ion is chelated by a deprotonated pyrimidine nitrogen atom and a carboxylate oxygen atom of the orotate. While the coordination sphere around Cu(II) is completed by two N atoms from butylamine groups and a carboxylic O atom in the axial position from a neighboring molecule in **1**, the square-planar environment of Cu(II) is completed by two water atoms and one axial position is occupied by the carbonyl oxygen atom from the symmetry related molecule in **2**. Complex **1** shows a polynuclear arrangement, while compound **2** has a dinuclear arrangement.

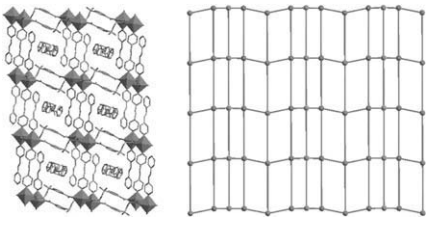


Lu-Fang Ma, Li-Ya Wang, Shu-Hui Chen, Hong-Wei Hou and Stuart R. Batten

Polyhedron 28 (2009) 2494

Various coordination architectures constructed from *N*-[(carboxyphenyl)-sulfonyl]glycine: Structural variation *via* ligand isomerism effects and metal-directed assembly

Using Cu(II), Mn(II) or Co(II) salt and the flexible ligands, *N*-[(4-carboxyphenyl)-sulfonyl]glycine and *N*-[(3-carboxyphenyl)-sulfonyl]glycine, a series of new coordination polymers have been synthesized and structurally characterized. Their structures range from a 0D cation–anion species to a 3D network with different structural motifs. This work indicates that the positional isomer of the anionic *N*-[(carboxyphenyl)-sulfonyl]glycine is significant in the construction of these network structures, which are also well regulated by the metal centers.

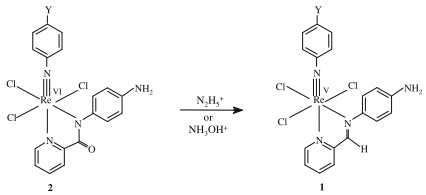


Jaydip Gangopadhyay, Suparna Banerjee, Jiu-Tong Chen and Can-Zhong Lu

Polyhedron 28 (2009) 2503

Intramolecular amide → imine reduction in higher valent rhenium complexes stabilized by arylimido coligand: Rate studies and effect of reductants

Reduction of amide bound imidorhenium(VI) (**2**) into imine coordinated imidorhenium(V) (**1**) occurs in presence of proton cum electron donor nitrogenous reducing agents like $N_2H_5^+$ and NH_3OH^+. The rate is first order on both the substrate (**2**) and the reductant. The reaction is associative and the rate with $N_2H_5^+$ is nearly five times faster than NH_3OH^+.

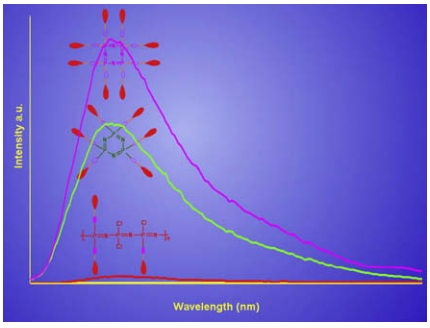


Bünyemin Çoşut, Ferda Hacıelioğlu, Mahmut Durmuş, Adem Kılıç and Serkan Yeşilot

Polyhedron 28 (2009) 2510

The synthesis, thermal and photophysical properties of phenoxycyclotriphosphazenyl-substituted cyclic and polymeric phosphazenes

In this work was shown that synthesis and characterisation of phenoxycyclotriphosphazenyl-substituted cyclic and polymeric phosphazenes. The thermal stability and fluorescence spectral properties of all these novel compounds have been investigated. It is found that the thermal stability and fluorescence spectral properties of cyclic compounds **4** and **5** are superior to those of compound **6**.

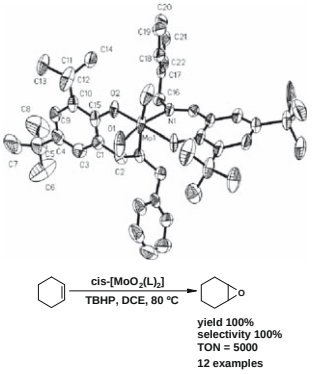


Mojtaba Bagherzadeh, Reza Latifi, Laleh Tahsini, Vahid Amani, Arkady Ellern and L. Keith Woo

Polyhedron 28 (2009) 2517

Synthesis, characterization and crystal structure of a dioxomolybdenum(VI) complex with a N,O type bidentate Schiff base ligand as a catalyst for homogeneous oxidation of olefins

A new complex of molybdenum with 4,6-bis-(*tert*-butyl)-2-{(benzyl)iminomethyl}phenol ligand has been synthesized and characterized using elemental analyses, spectroscopic studies (NMR, IR and electronic) and X-ray structure analysis. The *cis*-$[MoO_2(L)_2]$ complex, in combination with *tert*-butyl hydrogen peroxide (TBHP), shows efficient catalytic activity for the homogeneous epoxidation of various aliphatic olefins at 80 °C, yielding epoxide as the sole product in up to 100% conversion and with a turnover number of up to 5000.

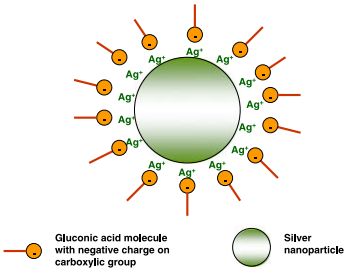


Revathi Janardhanan, Murugan Karuppaiah, Neha Hebalkar and Tata Narsinga Rao

Polyhedron 28 (2009) 2522

Synthesis and surface chemistry of nano silver particles

Silver nano particles of the size 40–80 nm are formed in the process of oxidation of glucose to gluconic acid by amine in the presence of silver nitrate, and the gluconic acid caps the nano silver particle. The presence of gluconic acid on the surface of nano silver particles was confirmed by XPS and FTIR studies. As the nano silver particle is encapsulated by gluconic acid, there was no surface oxidation, as confirmed by XPS studies. The nano silver particles have also been studied for their formation, structure, morphology and size using UV–Visible spectroscopy, XRD and SEM. Further, the antibacterial properties of these nano particles show promising results for *E. coli*. The influence of the alkaline medium towards the particle size and yield was also studied by measuring the pH during the course of the reaction for various bases including DEA, NaOH and Na_2CO_3.



The Publisher encourages the submission of articles in electronic form thus saving time and avoiding rekeying errors. For detailed instructions on the preparation of manuscripts and of electronic artwork, consult the Author Gateway for Elsevier at http://authors.elsevier.com

ScienceDirect

Full text of this journal is available, on-line from **ScienceDirect**. Visit **www.sciencedirect.com** for more information.

Polyhedron 28, issue 4, 12 March 2009

Contents lists available at ScienceDirect

Polyhedron

journal homepage: www.elsevier.com/locate/poly

Contents

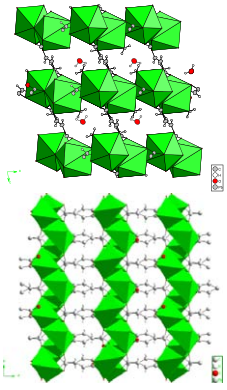
Papers

Kou-Lin Zhang, Wei Liang, Yan Chang, Li-Min Yuan and Seik Weng Ng

Polyhedron 28 (2009) 647

Syntheses, characterization and luminescent properties of two lead(II) fumarate metal-organic frameworks

Two photoluminescent lead(II) MOFs, $\{[Pb_2(fum)_2(H_2O)_4]\cdot 2H_2O\}_n$ (**1**) and $[Pb(fum)]_n$ (**2**), were synthesized by the reaction of the fum dianion with the lead(II) ion in the presence of pyrazole and pyrazine, respectively. The arrangement of the ligands exhibits a coordination gap around the Pb atom, occupied possibly by a stereoactive lone pair of electrons on lead(II), with the coordination around both the eight-coordinated lead atom in **1** and six-coordinated lead atom in **2** exhibiting a hemidirected geometry. The fum ligand shows different ligation behavior toward the lead(II) ions in these complexes.

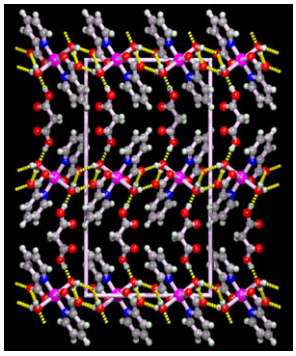


Chaitali Biswas, Atish Dipankar Jana, Michael G.B. Drew, Golam Mostafa and Ashutosh Ghosh

Polyhedron 28 (2009) 653

Segregated self-assembly and pillaring action of aliphatic dicarboxylic acids in the super structure of Cu–picolinate complexes

Co-crystals of [Cu(2-picolinate)$_2$] and malonic or succinic acid reveal that supramolecular association of the monomeric complex units leads to the formation of layers through hydrogen bonding. The co-crystallized dicarboxylic acid connects these 2-D layers, acting as pillars to form the final 3-D supramolecular structure.

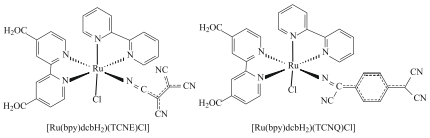


Maria do Socorro de P. Silva, Izaura C.N. Diógenes, Luis Gonzaga de F. Lopes, Ícaro de Sousa Moreira and Idalina M.M. de Carvalho

Polyhedron 28 (2009) 661

Synthesis and physical properties of ruthenium bipyridine complexes with TCNQ and TCNE ligands

The physical properties such as charge uptake, absorption, emission, and oxidation state of the TCNX ligands in the [Ru(bpy)(dcbH$_2$)(TCNQ)Cl] and [Ru(bpy)(dcbH$_2$)(TCNE)Cl] complexes, where bpy = 2,2′-bipyridine and dcbH$_2$ = 4,4′-dicarboxy-2,2′-bipyridine, were investigated. The obtained results suggest not only the anion radical form, $TCNX^{\bullet -}$, for the TCNX ligands upon coordination, but also that the TCNE species presents a higher charge uptake capability than TCNQ ligand.

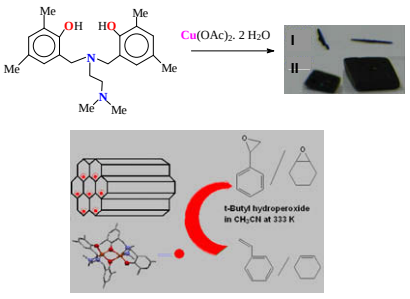


Md. Mijanuddin, Atish Dipankar Jana, Michael G.B. Drew, Chang Seop Hong, Basab Chattopadhyay, Monika Mukherjee, Mahasweta Nandi, Asim Bhaumik, Madeline Helliwell, Golam Mostafa and Mahammad Ali

Polyhedron 28 (2009) 665

Concomitant polymorphism of an antiferromagnetically coupled dicopper(II,II) complex with single strand helical assembly: Synthesis, structure, DSC, magnetic and heterogeneous catalytic studies

Two concomitant polymorphic coordination complexes (**I** and **II**) have been characterized crystallographically. Complex **I** shows the presence of a strong antiferromagnetic interaction and good catalytic efficiency in the liquid phase partial oxidation of olefins when immobilized on 2D-hexagonal mesoporous silica.

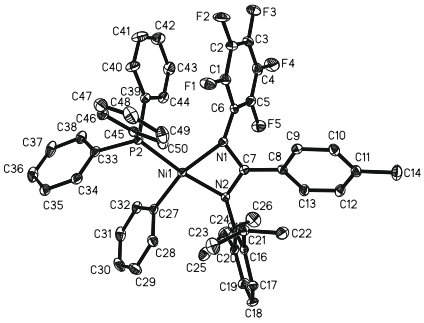


Feng-Shou Liu, Hai-Yang Gao, Ke-Ming Song, Ye Zhao, Jie-Ming Long, Ling Zhang, Fang-Ming Zhu and Qing Wu

Polyhedron 28 (2009) 673

Neutral nickel complexes chelating monoamidinate ligands: Syntheses, characterizations and catalytic properties toward ethylene oligomerization and norbornene polymerization

Three monoamidinate nickel complexes were synthesized, characterized and used as precatalyst for ethylene oligomerization and norbronene polymerization. The nickel complexes oligomerized ethylene producing a mixture of dimers and trimers with a moderate turnover frequency, while exhibited very high activity for the vinyl-addition polymerization of norbornene in the presence of MAO.

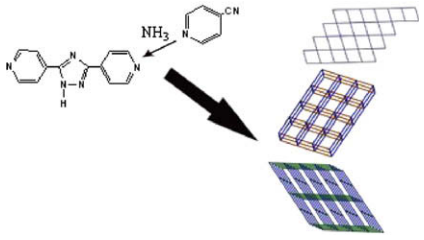


Xiao-Feng Xie, San-Ping Chen, Zheng-Qiang Xia and Sheng-Li Gao

Polyhedron 28 (2009) 679

Construction of metal–organic frameworks with transitional metals based on the 3,5-bis(4-pyridyl)-1*H*-1,2,4-triazole ligand

The versatile ligand 3,5-bis(4-pyridyl)-1*H*-1,2,4-triazole was synthesized using an in situ metal/ligand reaction. Based on which, six coordination complexes have been prepared, in which the bpt ligand manages the metal ions to form 0-D point, (4,4) layers and a variety of 3-D ($4^{12} \cdot 6^3$), ($6^4 \cdot 8^2$) topological networks.

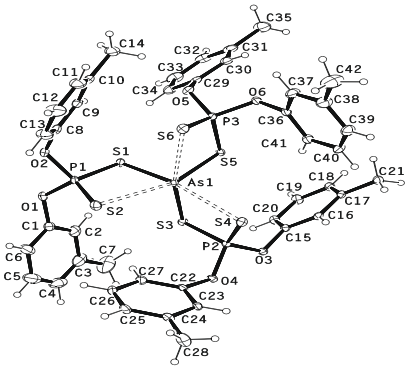


Seema Maheshwari, John E. Drake, Kavita Kori, Mark E. Light and Raju Ratnani

Polyhedron 28 (2009) 689

Synthesis and spectroscopic characterization of tris(*O*,*O*′-ditolyl dithiophosphato) arsenic/antimony/bismuth(III) compounds: Crystal structures of $[As\{S_2P(OC_6H_4Me\text{-}m)_2\}_3] \cdot 0.5C_6H_{14}$, $[Sb\{S_2P(OC_6H_4Me\text{-}m)_2\}_3]$ and $[Bi\{S_2P(OC_6H_4Me\text{-}m)_2\}_3]$

Arsenic(III), antimony(III) and bismuth(III) compounds of the type, $[M\{S_2P(OR)_2\}_3]$ (where M = As, Sb and Bi; R = *o*-, *m*-, *p*-C_6H_4Me) were obtained. These compounds were characterized by elemental analysis, IR, ^1H NMR and ^{31}P NMR spectroscopy. The single crystal X-ray structures of three representative compounds, $[As\{S_2P(OC_6H_4Me\text{-}m)_2\}_3] \cdot 0.5C_6H_{14}$, $[Sb\{S_2P(OC_6H_4Me\text{-}m)_2\}_3]$ and $[Bi\{S_2P(OC_6H_4Me\text{-}m)_2\}_3]$ were determined.

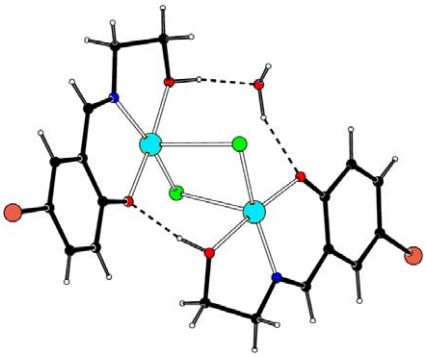


Santarupa Thakurta, Partha Roy, Georgina Rosair, Carlos J. Gómez-García, Eugenio Garribba and Samiran Mitra

Polyhedron 28 (2009) 695

Ferromagnetic exchange coupling in a new bis(μ-chloro)-bridged copper(II) Schiff base complex: Synthesis, structure, magnetic properties and catalytic oxidation of cycloalkanes

A new doubly chloro-bridged complex $[Cu(HL)Cl]_2 \cdot H_2O$ (**1**) has been prepared using a ONO donor Schiff base ligand $\mathbf{H_2L}$, 2-((*E*)-(2-hydroxyethylimino)methyl)-4-bromophenol. Each copper(II) atom in the dimer is square-pyramidal having an axial–equatorial configuration of the bridging chlorine atoms. Temperature dependence of magnetic susceptibility measurements show a high ferromagnetic coupling between two copper(II) ions in **1** with $J = +43.2(5)\ cm^{-1}$. The complex also exhibits efficient catalytic properties leading to the facile oxidation of cyclohexane and cycloheptane in presence of hydrogen peroxide as terminal oxidant.

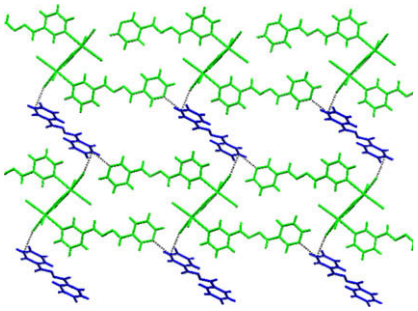


Nilofar Soltanzadeh and Ali Morsali

Polyhedron 28 (2009) 703

Metal–organic supramolecular assemblies generated from bismuth(III) bromide and polyimine ligands

Three new $BiBr_3$ supramolecular complexes, $[Bi_2(3\text{-bpdb})_2Br_8]\cdot(3\text{-}H_2bpdb)$ (**1**), $[Bi_2(3\text{-Hbpdh})_2Br_8]$ (**2**) and $[Bi_2(4\text{-bpdh})Br_9]\cdot 3(4\text{-Hbpdh})$ (**3**) {3-bpdb = 1,4-bis(3-pyridyl)-2,3-diaza-1,3-butadiene, 3-bpdh = 2,5-bis(3-pyridyl)-3,4-diaza-2,4-hexadiene and 4-bpdh = 2,5-bis(4-pyridyl)-3,4-diaza-2,4-hexadiene} have been prepared by the reaction of bismuth(III) bromide with three organic nitrogen donor based ligands under thermal gradient conditions using the branched tube method.

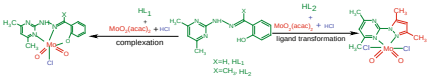


Samik Gupta, Sachindranath Pal, Anil Kumar Barik, Somnath Roy, Arijit Hazra, Tarak Nath Mandal, Ray J. Butcher and Susanta Kumar Kar

Polyhedron 28 (2009) 711

Molybdenum(VI) complexes of a few pyrimidine derived ligands and the study of metal mediated C═N bond cleavage resulting in ligand transformation during complex formation

The syntheses of three mononuclear dioxomolybdenum (VI) complexes and a binuclear oxo μ-oxo molybdenum(VI) complex have been described. Three of these four complexes are the result of an in situ transformation of the used pyrimidine derived Schiff base ligands. The ligand transformation may have been initiated by Mo mediated C═N bond cleavage.

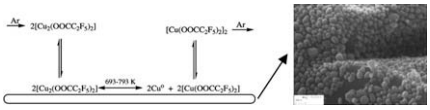


Iwona B. Szymańska, Piotr Piszczek and Edward Szłyk

Polyhedron 28 (2009) 721

Gas phase studies of new copper(I) carboxylates compounds with vinylsilanes and their application in Chemical Vapor Deposition (CVD)

Complexes $[Cu(vinylsilane)(\mu\text{-}O_2CC_2F_5)]_n$ can be the source of the volatile derivative $[Cu_2(O_2CC_2F_5)_2]$, which can be transported in the CVD process and decomposed forming copper materials.

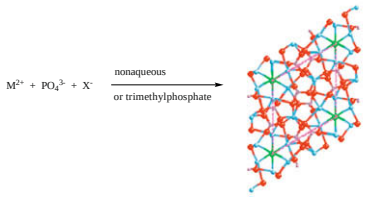


Mitchell P. Sternlieb, Heather M. Brown, Charles D. Schaeffer Jr. and Claude H. Yoder

Polyhedron 28 (2009) 729

The synthesis of apatites with an organophosphate and in nonaqueous media

Ten apatites were synthesized in nonaqueous solvents and three (PbApF, PbApCl, SrApCl) were obtained using trimethylphosphate as the phosphate source. The use of nonaqueous solvents alleviates the formation of hydrogen phosphates which occurs in aqueous solution for some divalent cations.

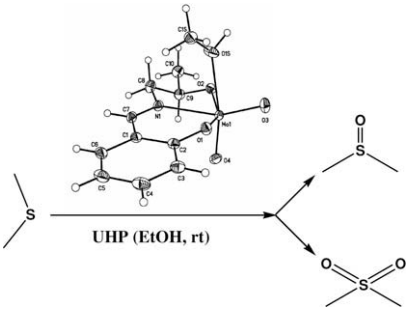


Iran Sheikhshoaie, Abdolreza Rezaeifard, Niaz Monadi and Samira Kaafi

Polyhedron 28 (2009) 733

A novel tridentate Schiff base dioxo-molybdenum(VI) complex: Synthesis, crystal structure and catalytic performance in green oxidation of sulfides by urea hydrogen peroxide

A new dioxo-molybdenum(VI) complex $[MoO_2(L)(CH_3OH)]$ has been synthesized using a tridentate ONO Schiff base ligand (H_2L). The X-ray crystallography showed a monoclinic space group $P2_1/c$ for this complex. The high catalytic activity of this Schiff base complex has been observed in the oxidation of sulfides by urea hydrogen peroxide in ethanol with high/excellent yields and selectivity.

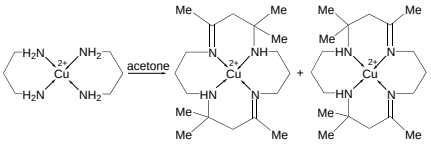


Neil F. Curtis, Kelly Flood, Clifton E. Rickard, Ward T. Robinson and Joyce M. Waters

Polyhedron 28 (2009) 739

The structures of some (hexamethyl-1,5,9,13-tetraazacyclohexadecadiene)copper(II) compounds

Bis(propane-1,3-diamine)copper(II) perchlorate reacts with acetone to form both the *trans*-diimine, (6,8,8,14,16,16-hexamethyl-1,5,9,13-tetraazacyclohexadeca-5,13-diene)copper(II), and *cis*-diimine, (6,8,8,14,14,16-hexamethyl-1,5,9,13-tetraazacyclohexadeca-5,1(16)-diene)-copper(II) macrocyclic cations. The structures of $[Cu(Me_6[16]diene)](ClO_4)_2$, *N-rac*-[Cu(*cis*-$Me_6$[16]diene)][$ZnCl_4$], $[Cu(Me_6[16]diene)(NCS)]ClO_4$ and $[Cu(Me_6[16]diene)(\mu\text{-}NC)Ni(CN)_3] \cdot H_2O$ are reported.

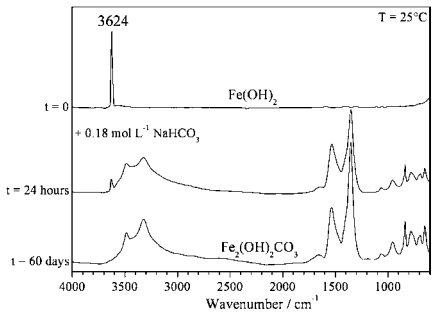


C. Rémazeilles and Ph. Refait

Polyhedron 28 (2009) 749

Fe(II) hydroxycarbonate $Fe_2(OH)_2CO_3$ (chukanovite) as iron corrosion product: Synthesis and study by Fourier Transform Infrared Spectroscopy

$Fe(OH)_2$ was prepared by mixing $FeCl_2 \cdot 4H_2O$ and NaOH solutions. A $NaHCO_3$ solution was then added to the suspension, so that $[NaHCO_3]/[NaOH] = 0.9$. The system was aged at RT. ATR/FT-IR spectra after 24 h and 2 months show that the precipitate transformed progressively into chukanovite.

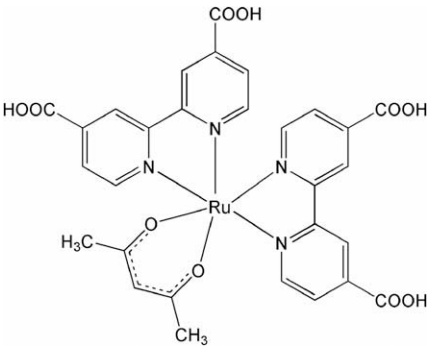


Heléne Gamstedt, Anders Hagfeldt and Lars Kloo

Polyhedron 28 (2009) 757

Photoelectrochemical studies of ionic liquid-containing solar cells sensitized with different polypyridyl–ruthenium complexes

The efficiency of a selection of ionic liquid electrolytes combined with standard, hydrophobic and cationic organometallic sensitizing dyes have been investigated as components in dye-sensitized solar cells. Also effects of co-adsorbent and nanoparticle additives to the electrolytes have been investigated.

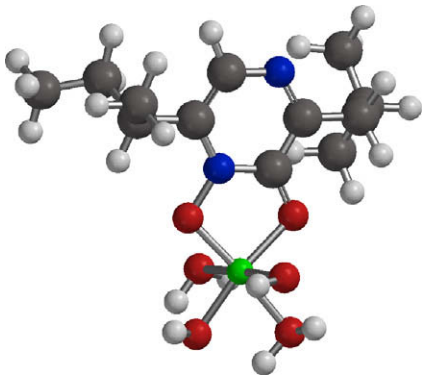


Valeria M. Nurchi, Guido Crisponi, Tiziana Pivetta, Enzo Tramontano, Flaminia Cesare Marincola and Joanna I. Lachowicz

Polyhedron 28 (2009) 763

Interaction between aspergillic acid and iron(III): A potentiometric, UV–Vis, ^{1}H NMR and quantum chemical study

The complex formation equilibria of aspergillic acid with iron(III) were studied potentiometrically and spectrophotometrically. Some structural features of ligand, prepared biosynthetically, are discussed on the basis of NMR results. Iron(III) coordination model is examined on the grounds of quantum chemical calculations and compared with those of two other cyclic hydroxamates.

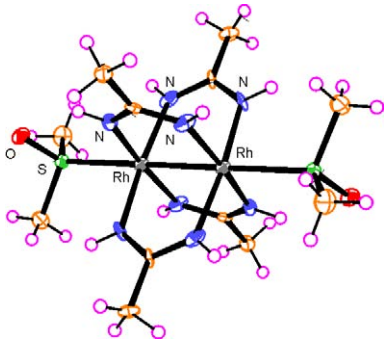


Florian P. Pruchnik, Hanna Pruchnik and Andrzej Kochel

Polyhedron 28 (2009) 769

Structure and properties of tetra-μ-ethanimidamidato-κ*N*:κ*N*′-dirhodium(1+) complexes

Reaction of $Na_4[Rh_2(\mu\text{-}CO_3)_4]$ with ethanimidamide hydrochloride leads to the $[Rh_2\{\mu\text{-}HN(HN{=})CCH_3\}_4L_2]Cl$ complexes. DFT calculations and EPR spectra indicate that δ^*_{RhRh} is SOMO orbital. The rhodium atoms are equivalent in the $[Rh_2\{\mu\text{-}HN(HN{=})CCH_3\}_4L_2]^+$ compounds, and nonequivalent in $[Rh_2\{\mu\text{-}HN(HN{=})CCH_3\}_4LL']^+$ complexes. The intense bands in the electronic spectra in the range 13 000–19 000 cm^{-1} are caused by transitions with prevailing d–d character.

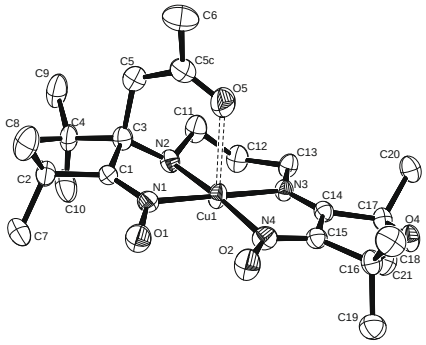


Salma Kiani, Richard J. Staples, S. Ted Treves and Alan B. Packard

Polyhedron 28 (2009) 775

Synthesis and characterization of a tetramethyl furanone functionalized diiminedioxime, a potential ligand for ^{64}Cu radiopharmaceuticals, and its copper(II) and nickel(II) complexes

A novel anionic diiminedioxime ligand containing two tetramethylfuranone moieties was prepared. A Cu(II)-bridged dimer was observed when the complex was prepared in ethanol. However, an acetone adduct of the ligand was observed when the complex was prepared in acetonitrile and acetone (figure). The Ni(II) complex is a square planar monomer.

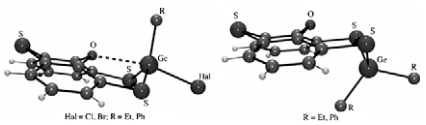


Benito Flores-Chávez, José G. Alvarado-Rodríguez, Noemí Andrade-López, Verónica García-Montalvo and Eliazar Aquino-Torres

Polyhedron 28 (2009) 782

Hypervalence in germanium compounds containing the tetracylic moiety $\{S(C_6H_3S)_2O\}Ge$ via O···Ge transannular interactions: A structural study

The synthesis of $[\{S(C_6H_3S)_2O\}GeR_nHal_{2-n}]$ compounds (R = Et, Ph; Hal = Cl, Br; n = 2–0) is described. The acidity of the $GeRHal^{2+}$ fragment enhances a transannular O···Ge interaction, prompting a trigonal bipyramidal germanium local geometry; the GeR_2^{2+} less acid fragment present has an opposite effect.

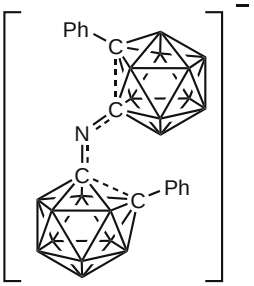


Mark A. Fox, J.A. Hugh MacBride, Richard J. Peace, William Clegg, Mark R.J. Elsegood and Kenneth Wade

Polyhedron 28 (2009) 789

New synthetic and structural studies on nitroso-*ortho*-carboranes $RCB_{10}H_{10}CNO$ and bis-(*ortho*-carboranyl)amines $(RCB_{10}H_{10}C)_2NH$ (R = Ph or Me)

Improved syntheses of nitroso-carboranes and dicarboranylamines are described and crystal structures of $PhCB_{10}H_{10}CNO$ and $[(PhCB_{10}H_{10}C)_2N]^-$ reveal cage C…C distances of 1.68 and 1.99 Å, respectively.

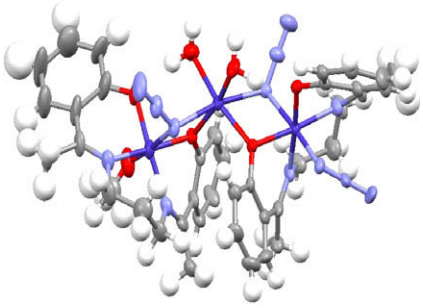


Aurkie Ray, Georgina M. Rosair, Ramakant Kadam and Samiran Mitra

Polyhedron 28 (2009) 796

Three new mono–di–trinuclear cobalt complexes of selectively and non-selectively condensed Schiff bases with N_2O and N_2O_2 donor sets: Syntheses, structural variations, EPR and DNA binding studies

Three new mono–di–trinuclear cobalt complexes of three different Schiff bases have been synthesised. Of the three Schiff bases, $\mathbf{HL^1}$ and $\mathbf{HL^2}$ were obtained by selective condensation of two different 1,3-diamines with 2-hydroxyacetophenone and $\mathbf{H_2L^3}$ resulted from the non-selective condensation of 1,3-diamine with 2-hydroxyacetophenone. The three complexes have been characterised using IR, UV–Vis spectroscopy and cyclic voltammetry. Structural aspects of the cobalt complexes have been described by performing single crystal X-ray analysis. EPR analysis and DNA binding abilities of the complexes have also been studied in detail.

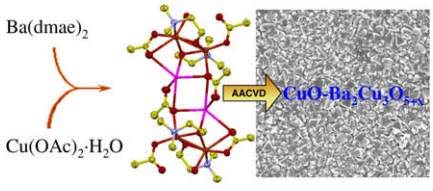


Muhammad Shahid, Muhammad Mazhar, Paul O' Brien, Mohammad A. Malik and James Raftery

Polyhedron 28 (2009) 807

Low temperature and single-source synthesis of a $CuO–Ba_2Cu_3O_{5+x}$ composite: Fabrication of thin films and characterization

The heterobimetallic complex $Ba_2(\mu\text{-}OAc)_4(OAc)_2Cu_4(\mu\text{-}dmae)_4(OH)_2$ (**1**), synthesized by the direct reaction of $Ba(dmae)_2$ and $Cu(OAc)_2 \cdot H_2O$ in toluene, was characterized by melting point, CHNS, FT-IR, TGA, mass spectrometry and single crystal X-ray diffraction. Complex (**1**) was used at 400 °C to deposit thin films of $CuO–Ba_2Cu_3O_{5+x}$ composite which were characterized by XRPD, SEM and EDX.

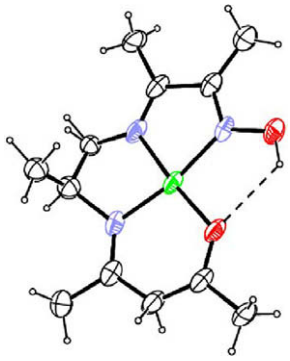


Debdulal Maity, Shouvik Chattopadhyay, Ashutosh Ghosh, Michael G.B. Drew and Gurucharan Mukhopadhyay

Polyhedron 28 (2009) 812

Syntheses, characterization and X-ray crystal structures of Ni(II) complexes of tridentate monocondensed and tetradentate dicondensed Schiff bases

The unsymmetrical tetradentate Schiff base ligands involving 1,2-diaminoethane or 1,2-diaminopropane with 2,4-pentanedione and diacetylmonoxime forms square planar complexes with Ni(II) whereas complexes of symmetrical ligands involving the same diamines and diacetylmonoxime cannot be prepared; instead the bis six-coordinate complex of the monocondensed tridentate Schiff bases were produced.

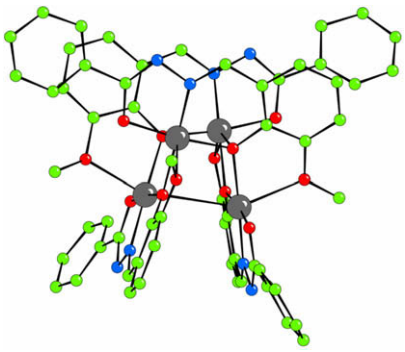


Joy Chakraborty, Santarupa Thakurta, Guillaume Pilet, Dominique Luneau and Samiran Mitra

Polyhedron 28 (2009) 819

A novel tetra(μ_3-phenoxo) bridged copper(II) Schiff base complex containing a Cu_4O_4 cubane core: Synthesis, structural aspects and magneto-structural correlations

A novel tetranuclear copper(II) complex $[Cu_4L_4] \cdot Na \cdot ClO_4$ has been synthesized exploiting the tetradentate donor set of a hydrazone ligand $\mathbf{H_2L}$, *N′*-(2-hydroxy-3-methoxybenzylidene)-benzohydrazide. The Cu_4O_4 core consists of a rare μ_3-phenoxo-bridged copper(II) atoms giving an approximately cubic array of alternating copper and oxygen atoms. Cryomagnetic susceptibility measurements over a wide range of temperature (2–300 K) demonstrate both ferro- [J_{11} = +13.6(4) cm^{-1}] and antiferromagnetic [J_{12} = −34.9(4) cm^{-1}] interactions in a 2*J* model resulting in an overall antiferromagnetic behaviour of the magnetically coupled system.

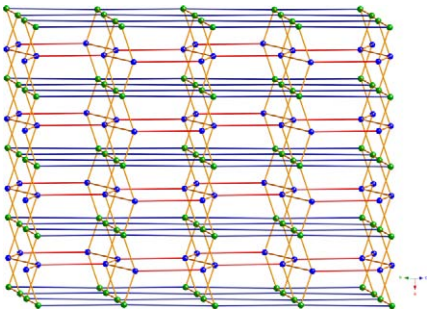


Eric Shyu and Robert L. LaDuca

Polyhedron 28 (2009) 826

Divalent metal succinate/perchlorate coordination polymers incorporating a kinked hydrogen-bonding capable diimine: Chains, layers and a (5,6)-connected binodal network featuring alternating rectangular and hexagonal grids

Hydrothermal synthesis has afforded succinate (suc) or 2,2-dimethylsuccinate (dmsuc) perchlorate coordination polymers incorporating the hydrogen-bonding capable tethering ligand 4,4′-dipyridylamine (dpa). $\{[Co(suc)(Hdpa)_2(H_2O)_2](ClO_4)_2 \cdot 7.5H_2O\}_n$ (**1**) manifests simple cationic 1D polymeric chains, while $\{[Cd_3(suc)_{2.5}(dpa)_2](ClO_4)\}_n$ (**2**) possesses a 3D binodal (5,6)-connected network. The network of **2** can be viewed as alternating (4,4) rectangular and (6,3) hexagonal grids being joined by pillaring ligands. The *gem*-dimethyl substituents within the dmsuc ligands promote a 2D (6,3) herringbone net in $\{[Cd_2(dmsuc)_2(dpa)(Hdpa)](ClO_4) \cdot 6H_2O\}_n$ (**3**).

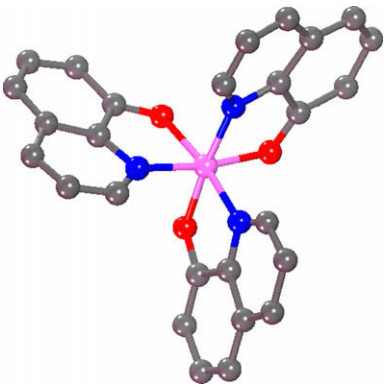


Manju Rajeswaran, Thomas N. Blanton, Ching W. Tang, William C. Lenhart, Steven C. Switalski, David J. Giesen, Brian J. Antalek, Thomas D. Pawlik, Denis Y. Kondakov, Nicholas Zumbulyadis and Ralph H. Young

Polyhedron 28 (2009) 835

Structural, thermal, and spectral characterization of the different crystalline forms of Alq_3, tris(quinolin-8-olato)aluminum(III), an electroluminescent material in OLED technology

The interest in organic materials for use in organic light-emitting diodes (OLEDs) began with the pioneering report of efficient green electroluminescence from Alq_3, by Tang VanSlyke. Alq_3 is used in the electron transport and/or electron-injecting layer in OLED devices. In the present report, a combined structural, thermal, and spectroscopic analysis of different crystalline phases of Alq_3 is presented.

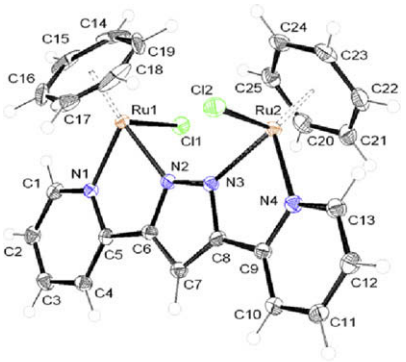


Gajendra Gupta, Glenn P.A. Yap, Bruno Therrien and Kollipara Mohan Rao

Polyhedron 28 (2009) 844

Study of novel η^5-cyclopentadienyl and η^6-arene platinum group metal complexes containing a N_4-type ligand and their structural characterization

Reactions of platinum group metal complexes containing η^5-and η^6-cyclic hydrocarbons with a N_4 donor ligand, *viz.* 3,5-bis(2-pyridyl)pyrazole (bpp-H), yielded mono- and dinuclear complexes. The molecular structures of [**1**]PF_6, [**5**]PF_6 and [**8**]BF_4 have been established by single crystal X-ray diffraction studies



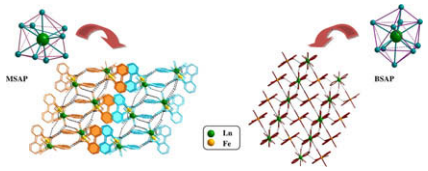
Complex [8]BF_4

Diana Visinescu, Luminita M. Toma, Oscar Fabelo, Catalina Ruiz-Pérez, Francesc Lloret and Miguel Julve

Polyhedron 28 (2009) 851

New 3d–4f supramolecular systems constructed by $[Fe(bipy)(CN)_4]^-$ and partially blocked lanthanide cations

The two different 3D supramolecular arrangements in the 3d–4f isostructural series $[Fe(bipy)(CN)_4][Ln(bpym)(NO_3)_2(H_2O)_3] \cdot H_2O \cdot CH_3CN$ [Ln = Sm (**1**), Gd (**2**), Tb (**3**), Dy (**4**) and Ho (**5**)] (left) and $[Fe(bipy)(CN)_4][Ln(bpym)(NO_3)_2(H_2O)_4]$ [Ln = Pr (**6**), Nd (**7**), Sm (**8**) and Gd (**9**)] (right) are dictated by the lanthanide geometry (mono- or bicapped square antiprism) which is in turn influenced by the nature of the solvent used in the synthesis and the distinct ionic radii of the trivalent rare-earth ions.

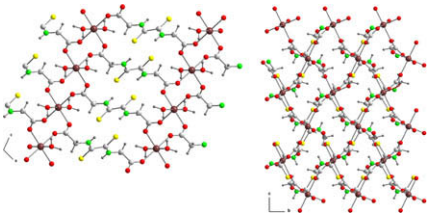


Alfonso Castiñeiras, Isabel García-Santos and José M. Varela

Polyhedron 28 (2009) 860

A manganese(II) coordination polymer with a 3D porous structure: Synthesis, structure, and spectroscopic and magnetic behaviour

A novel Mn^{II} coordination polymer with a porous 3D structure was prepared by the reaction between N,N′-bis(carboxymethyl)dithiooxamide and manganese(II) perchlorate. Variable temperature magnetic measurements reveal the existence of very weak antiferromagnetic interactions through the carboxylate bridge.

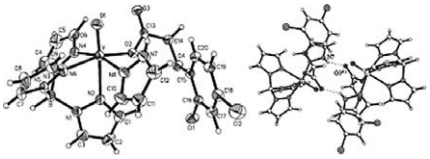


Zhang-Peng Li, Yong-Heng Xing, Yun-Zhu Cao, Xiao-Qing Zeng, Mao-Fa Ge and Shu-Yun Niu

Polyhedron 28 (2009) 865

Synthesis, structure and properties of a series of scorpionate oxovanadium(IV)–carboxylate complexes

The one-step reaction of $VOSO_4 \cdot nH_2O$, pyrazole or 3,5-dimethylpyrazole, potassium poly(pyrazolyl)borate and carboxylic acids in methanol resulted in six new complexes, **1–6**. The synthetic process described here is different from those in literature reports. Structural analyses show that in all of these complexes, the vanadium atoms are six-coordinated with a N_4O_2 donor set in a distorted-octahedral geometry, the carboxylate groups are coordinated as monodentate and the uncoordinated oxygen atom of the carboxylate groups form intra- or inter-molecular hydrogen bonds with the NH group of the corresponding coordinated neutral pyrazole (pzH/pzH*).



The Publisher encourages the submission of articles in electronic form thus saving time and avoiding rekeying errors. For detailed instructions on the preparation of manuscripts and of electronic artwork, consult the Author Gateway for Elsevier at http://authors.elsevier.com

ScienceDirect

Full text of this journal is available, on-line from **ScienceDirect**. Visit **www.sciencedirect.com** for more information.

Polyhedron 28, issue 3, 24 February 2009

Contents lists available at ScienceDirect

Polyhedron

journal homepage: www.elsevier.com/locate/poly

Contents

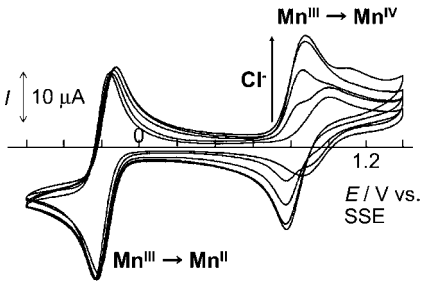
Papers

Megumi Kasuno, Masaki Hayano, Manabu Fujiwara and Takayuki Matsushita

Polyhedron 28 (2009) 425

Effects of chloride ions on electrochemical reactions of manganese(III) complexes

Electrochemical reactions of manganese(III) complexes such as Mn^{III}(R1-salen)Cl were investigated by voltammetry in the absence/presence of Cl^-. By the addition of Cl^-, oxidation processes of Mn^{III}(salen)Cl have been found to be improved from quasi-reversible to reversible, and their oxidation products, $[Mn^{IV}(salen)Cl]^+$ was stabilized by the combination with Cl^- resulting in $[Mn^{IV}(salen)Cl_2]$. The present study may clarify the role of Cl^- being involved in OEC in photosystem II.

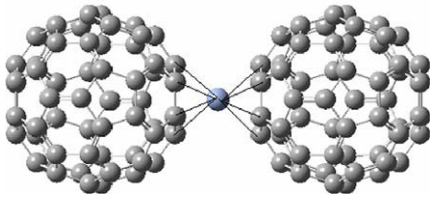


Roberto Salcedo

Polyhedron 28 (2009) 431

Fullerenocene

The nature of the molecule $C_{60}CrC_{60}$ **1** was studied from a theoretical point of view. Calculations on this molecule were carried out at the BPW91 level. The aromaticity of the rings was analyzed by means of HOMA and NICS methods whereas their intrinsic stability was estimated by means of homodesmotic reactions.

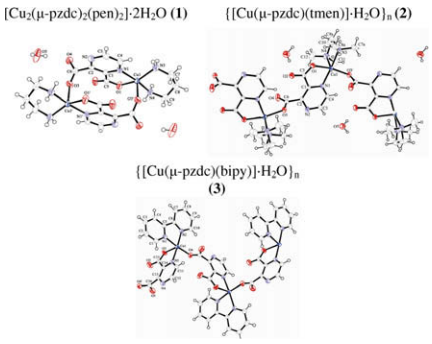


Okan Zafer Yeşilel, Aylin Mutlu and Orhan Büyükgüngör

Polyhedron 28 (2009) 437

Novel dinuclear and polynuclear copper(II)-pyrazine-2,3-dicarboxylate supramolecular complexes with 1,3-propanediamine, *N*,*N*,*N*′,*N*′-tetramethylethylenediamine and 2,2′-bipyridine

We have successfully synthesized and characterized the novel dinuclear and polynuclear Cu(II)-pyrazine-2,3-dicarboxylate complexes. The molecular structures of dinuclear **(1)** and polynuclear **(2, 3)** complexes have also been determined by the single crystal X-ray diffraction technique. The pyrazine-2,3-dicarboxylate ligand acts as a tridentate bridge between the metal ions forming one-dimensional polymeric chains, its coordination sites being the O atom of carboxylate and N atom of ring and one O atom of neighboring carboxylate group.



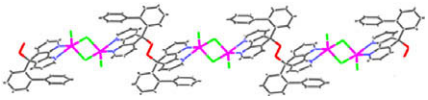
Elsevier Ltd.

Min Hong, Kun Zhang, Yi-Zhi Li and Jin Zhu

Polyhedron 28 (2009) 445

Synthesis and structural characterization of copper(II), cadmium(II) and zinc(II) complexes with 4,5-diazaspirobifluorene and bis-9-biphenyl-4,5-diazafluorenyl peroxide

The synthesis and structural chemistry of four new divalent transition metal complexes (M^{II} = Cu, Cd or Zn) of the fluorene ligands 4,5-diazaspirobifluorene (L1) and bis-9-biphenyl-4,5-diazafluorenyl peroxide (L2) are reported. Single-crystal X-ray diffraction analysis reveal that the four complexes exhibit various frameworks due to diverse coordination modes and different conformations of ligands L1 or L2, as well as nitrate, acetate or chloro counterions. L1 in complexes **1**, **2** and **3** present an asymmetric rigid bidentate ligand with two nitrogen atoms as the donor sites. Novel complex **4** was formed through complexation between conformationally bent shaped peroxide ligands and zinc(II) dichlorides that adopt a linear coordination geometry, which can also give rise to extended polymeric chains with a zigzag secondary structure.

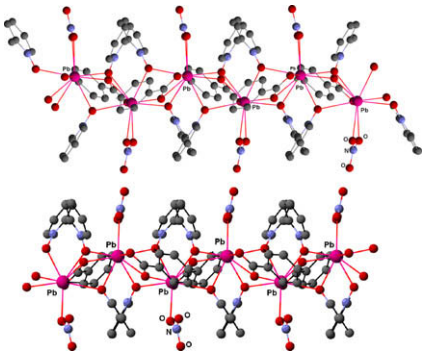


Rupam Sarma and Jubaraj B. Baruah

Polyhedron 28 (2009) 453

A mixed anionic lead(II) N-Oxide coordination polymer containing nitrato and benzoate ligands

The structures of two forms of a mixed anionic one-dimensional coordination polymer of lead(II) nitrate derived from benzoate and 2,2′-bipyridyl N-oxide is reported. Subtle differences in the structures crystals obtained from two independent solvent arises from two binding modes of nitrate.

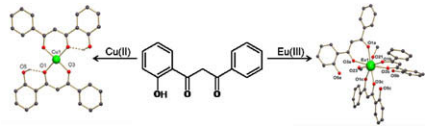


Stefania Tanase, Marta Viciano-Chumillas, Jan M.M. Smits, René de Gelder and Jan Reedijk

Polyhedron 28 (2009) 457

Copper(II) and lanthanoid(III) complexes of a new β-diketonate ligand with an appended non-coordinating phenol group

Mononuclear copper(II) and lanthanoid(III) (Ln = Pr, Nd, Eu, Gd) compounds from a new β-diketone ligand, namely 1-(2-hydroxyphenyl)-3-phenylpropane-1,3-dione have been synthesized and characterized. The structural studies show that in all compounds, the ligand coordinates in a bidentate chelating manner, using the diketone function.

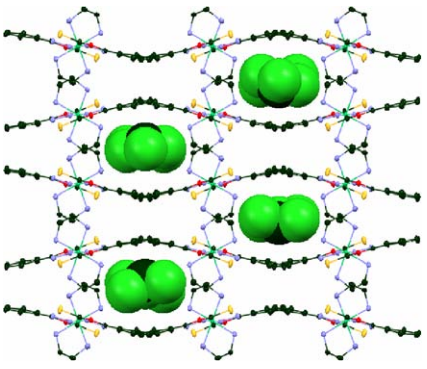


M. Singh, A.K. Pandey, R.J. Butcher and N.K. Singh

Polyhedron 28 (2009) 461

Syntheses and X-ray crystallographic studies of $\{[Ni(en)_2(pot)_2]0.5CHCl_3\}$ and $[Ni(en)_2](3\text{-pytol})_2$

Two new Ni(II) complexes, $\{[Ni(en)_2(pot)_2]0.5CHCl_3\}$(**3**) and $[Ni(en)_2](3\text{-pytol})_2$ (**4**), have been synthesized and characterized by spectroscopic and spectrometric methods, and their X-ray crystallography structures are reported. In complex **3**, the 2D lattices resulting from a parallel stacking of $\{[Ni(en)_2(pot)_2]0.5CHCl_3\}$ form regular open channels in which the $CHCl_3$ solvent molecules are enclosed along the a axis.

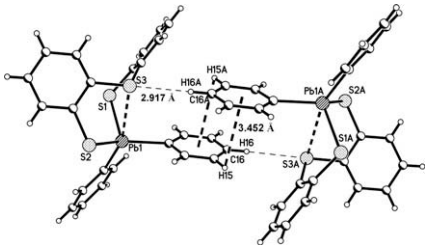


Simplicio González-Montiel, Benito Flores-Chávez, José G. Alvarado-Rodríguez, Noemí Andrade-López and Juan Antonio Cogordan

Polyhedron 28 (2009) 467

Synthesis, characterization and crystal structures of organolead dithiolate compounds displaying transannular interactions D···Pb (D = O, S)

The syntheses of the stable organolead dithiolate compounds $[\{O(C_6H_4S)_2\}PbPh_2]$, $[\{S(C_6H_4S)_2\}PbPh_2]$ and $[\{S(C_6H_3S)_2O\}PbPh_2]$ are described. The lead atom acts as an acceptor atom exhibiting weak intramolecular transannular interactions with the donor D atom. The crystals are stabilized by several intermolecular non-bonded interactions.

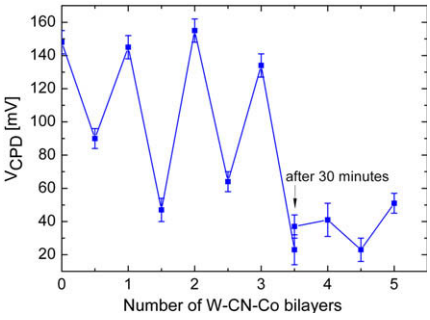


Tomasz Stawski, Janusz Szklarzewicz, Andrzej Kotarba and Paweł Stelmachowski

Polyhedron 28 (2009) 473

The modifications of copper work function by layer-by-layer deposition of $[W(CN)_8]^{4-}$ – Co^{2+} bimetallic nanolayers

The layer-by-layer deposition of a $[W(CN)_8]^{4-}$/Co^{2+}_{aq} on a monocrystalline [3 1 1] and polycrystalline copper resulted in the work function change by 0.4 eV at *ca.* 3 nm layer thickness. The work function change was then independent of layer thickness up to 40 nm. At the low amount of $[W(CN)_8]^{4-}$ ion in solution, deposited layers did not cover totally the copper surface and oscillations in the work function change were observed. The oscillation depended on anion used (Cl^- or NO_3^-) and number of layers deposited. After total surface coverage work function change reached plateau.

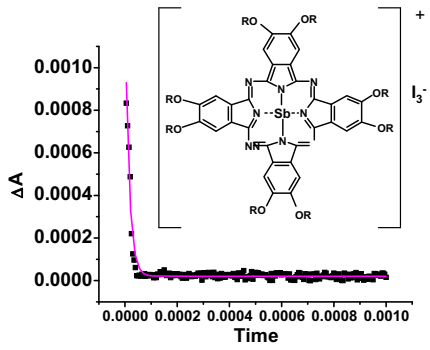


Desmond Kwena Modibane and Tebello Nyokong

Polyhedron 28 (2009) 479

Synthesis, photophysical and photochemical properties of octa-substituted antimony phthalocyanines

Octa-phenoxy ($[Sb^{III}OPPc]^+I_3^-$) and -4-*t*-butylphenoxy ($[Sb^{III}OTBPPc]^+I_3^-$) substituted antimony phthalocyanines and their oxidized $Sb^{V}Pc$ derivatives show very low triplet lifetimes but high triplet yields.

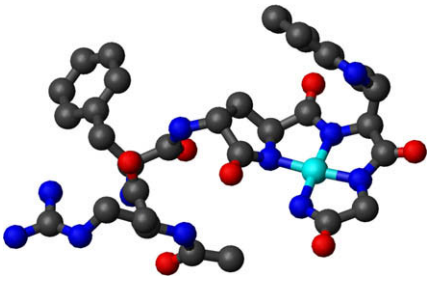


E. Łodyga-Chruścińska, S. Ołdziej, D. Sanna, G. Micera, L. Chruściński, K. Kaczmarek, R.J. Nachman, J. Zabrocki and A. Sykuła

Polyhedron 28 (2009) 485

Coordination ability of insect kinin analogs

Spectroscopic data, including electronic absorption, CD and EPR results, as well as theoretical calculations have shown that the insertion of 4-aminopyroglutamate, a novel *cis*-peptide bond mimic, in the insect kinin peptide leads to an effective ligand towards Cu(II) ions at basic pH ranges.

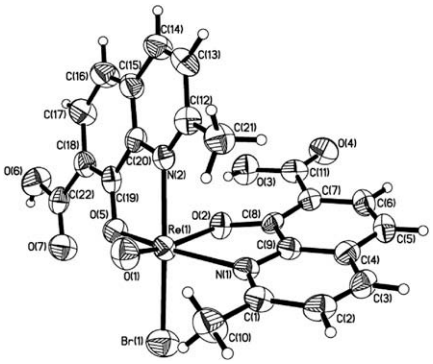


B. Machura, J. Kusz, D. Tabak and R. Kruszynski

Polyhedron 28 (2009) 493

Synthesis, spectroscopic characterization, crystal and molecular structure of [ReOBr(hmquin-7-COOH)$_2$] and [ReOCl(hmquin-7-COOH)$_2$] · MeCN complexes. DFT and TD-DFT calculations for [ReOBr(hmquin-7-COOH)$_2$]

Novel [ReOBr(hmquin-7-COOH)$_2$] (**1**) and [ReOCl(hmquin-7-COOH)$_2$]·MeCN (**2**·MeCN) complexes have been prepared by treatment of [ReOX$_3$(AsPh$_3$)$_2$] with an excess of 8-hydroxy-2-methylquinoline-7-carboxylic acid in acetonitrile. The compounds were characterised structurally and spectroscopically. The electronic structure of **1** has been calculated with the density functional theory (DFT) method, and additional information about binding has been obtained by NBO analysis. The UV-Vis spectrum of **1** has been discussed on the basis of TDDFT calculations.

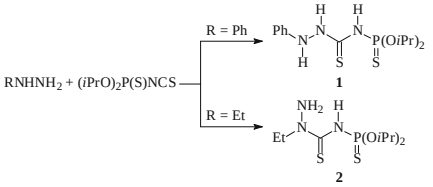


Damir A. Safin, Michael Bolte, Elmira R. Shakirova and Maria G. Babashkina

Polyhedron 28 (2009) 501

The influence of the substituent [PhNHNH– and EtN(NH$_2$)–] on the *N*-thiophosphorylated thiosemicarbazides RC(S)NHP(S)(O*i*Pr)$_2$ crystal design

Two *N*-thiophosphorylated thiosemicarbazides of common formula RC(S)NHP(S)(O*i*pr)$_2$ [R=PhNHNH-(**1**); EtN(NH$_2$)-(**2**)] were synthesized and characterized. Single crystal X-ray diffraction studies showed the thiosemicarbazides to form both intra- and intermolecular hydrogen bonds which in turns lead to the polymeric chains formation. Moreover, according to the X-ray data of the phenylsubstitueted thiosemicarbazide it was established the formation of the intermolecular H$\cdots\eta^6$-phenyl interactions.

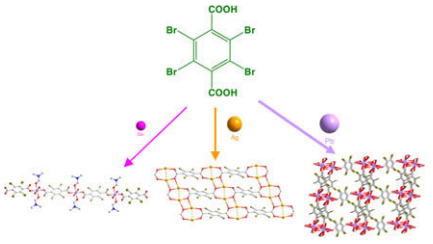


Cheng-Peng Li, Yi-Ling Tian and Ya-Mei Guo

Polyhedron 28 (2009) 505

Cobalt(II), silver(I), and lead(II) tetrabromoterephthalates exhibiting the 1-D linear chain, 2-D CdCl$_2$-type layer, and 3-D penta-nodal mixed-connecting coordination frameworks

This work presents the metal-regulated assembly of three novel coordination polymers of Co^{II}, Ag^{I}, and Pb^{II} with tetrabromoterephthalate, which show distinct coordination frameworks such as the 1-D linear chain, 2-D CdCl$_2$-type layer, and 3-D penta-nodal network.

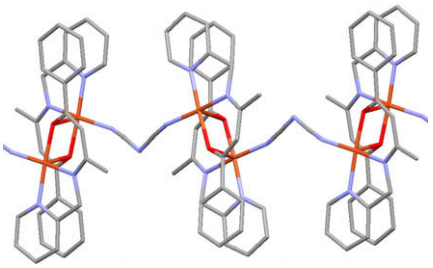


Aurkie Ray, Guillaume Pilet, Carlos J. Gómez-García and Samiran Mitra

Polyhedron 28 (2009) 511

Designing dicyanamide bridged 1D molecular architecture from a mononuclear copper(II) Schiff base precursor: Syntheses, structural variations and magnetic study

A new tridentate N$_2$O donor Schiff base ligand was obtained by 1:1 condensation of benzoylacetone with 2-picolylamine and has been used to synthesise a mononuclear [CuLCl] (**1**) and an *end-to-end* dicyanamide bridged polynuclear {[Cu$_2$(μ-L)$_2$(μ_2-1,5-(CN)$_2$N)]ClO$_4$}$_n$ (**2**) copper(II) complexes. The Schiff base ligand [**LH**] shows a significant variation in its coordination behaviour with copper(II) ion in absence and in presence of dicyanamide ion in **1** and **2** respectively. Variable temperature magnetic susceptibility measurements for **2** in the temperature range 2–300 K reveal the presence of weak antiferromagnetic exchange interactions in the polymeric chain.

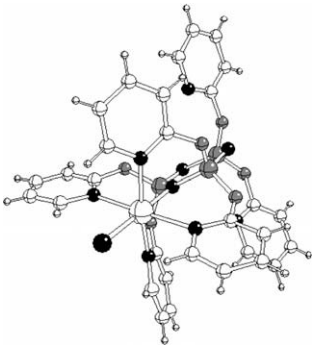


Marián Gall and Martin Breza

Polyhedron 28 (2009) 521

QTAIM study of transition metal complexes with cyclophosphazene-based multisite ligands I: Zinc(II) and nickel(II) complexes

The metal–ligand bonds in $[(ZnCl_2)_2L]$, $[NiLCl]^+$ and two isomers of $[NiLCl_2]$ complexes with multimodal ligand L = hexakis(2-pyridyloxy)-cyclotriphosphazene are investigated at DFT level of theory. Electron density is evaluated in terms of QTAIM topological analysis of electron density.

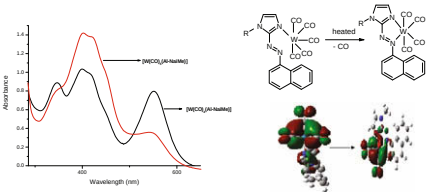


Papia Datta, Ashis Kumar Patra and Chittaranjan Sinha

Polyhedron 28 (2009) 525

Tungsten(0)–carbonyl complexes of naphthylazoimidazoles

$[W(CO)_5(\alpha\text{-NaiR-N})]$ are reported in this work. The complexes have been transformed to $[W(CO)_4(\alpha\text{-NaiR-N,N}')]$ at higher temperatures (where α-NaiR-N is a monodentate imidazole-N donor ligand and α-NaiR-N,N′ denotes a bidentate imidazole-N, azo-N donor ligand). The emission of $[W(CO)_4(\alpha\text{-NaiR-N,N}')]$ shows a higher quantum yield (ϕ = 0.05–0.07) than $[W(CO)_5(\alpha\text{-NaiR-N})]$ (ϕ = 0.01–0.02). Cyclic voltammetry exhibits metal oxidation and ligand reductions. The DFT calculations of $[W(CO)_5(\alpha\text{-NaiMe-N})]$ show contributions from the metal d-orbitals and π-orbitals of the CO ligands to the HOMO while the LUMOs are α-NaiMe dominated. The back bonding interaction thus originates from the $W(CO)_n$ moiety to the LUMO of α-NaiR.

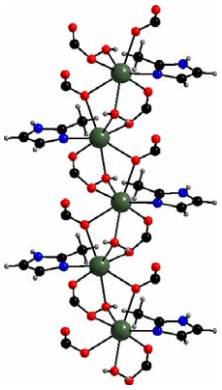


Bikshandarkoil R. Srinivasan, Santosh Y. Shetgaonkar, Christian Näther and Wolfgang Bensch

Polyhedron 28 (2009) 534

Solid state synthesis and characterization of a triple chain calcium(II) coordination polymer showing two different bridging 4-nitrobenzoate coordination modes

In the coordination polymer $[Ca(L^2)(H_2O)(4\text{-nba})_2]_n$ (L^2 = 2-methylimidazole; 4-nba = 4-nitrobenzoate) the aqua and the 4-nba ligands exhibit bridging binding modes leading to the formation of a triple chain coordination polymer.

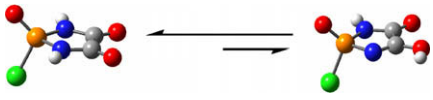


Khodayar Gholivand, Nasrin Oroujzadeh, Mauricio F. Erben and Carlos O. Della Védova

Polyhedron 28 (2009) 541

Synthesis, spectroscopy, computational study and prospective biological activity of two novel 1,3,2-diazaphospholidine-2,4,5-triones

The preparation of two novel diazaphospholidines is reported. D NMR studies complemented by computational methods show that the lactam form dominates the tautomeric equilibrium. The prediction of biological activities using the PASS program invites to test these compounds as HIV-protease inhibitors, antiviral HIV and antineoplastic agents.

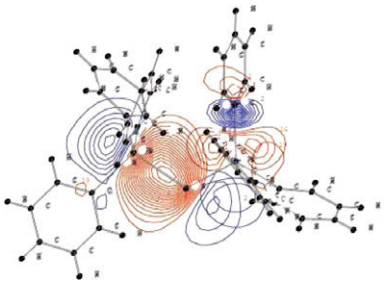


Neetu Singh, Rajendra Prasad and Subrato Bhattacharya

Polyhedron 28 (2009) 548

Structural studies on Ph_3MSMPh_3 (M = Sn, Pb): Quest for a metal–metal bond

Molecular structures of Ph_3MSMPh_3 (M = Sn, Pb) have been studied by X-ray crystallography and DFT to explore the existence of possible M···M interactions.

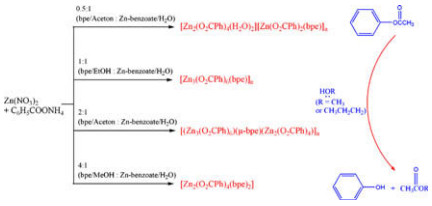


Han Kwak, Sun Hwa Lee, Soo Hyun Kim, Young Min Lee, Byeong Kwon Park, Yu Jin Lee, Je Yeol Jun, Cheal Kim, Sung-Jin Kim and Youngmee Kim

Polyhedron 28 (2009) 553

Controlling self-assembly of zinc(II)-benzoate coordination complexes with 1,4-bis(4-pyridyl)-ethane by varying solvent and ligand-to-metal ratio: Their catalytic activities

Zinc-benzoates can be rationally tuned to form four different structures with a bridging bpe ligand by controlling ligand-to-zinc-benzoate molar ratios and by using different solvent systems, and reveal three coordination polymers having similar one-dimensional characteristics but having different mono-, di-, trinuclear nodes (**1**–**3**), and a dinuclear ring type molecule (**4**). This work reveals that the ligand-to-metal ratio and solvent play very important roles in the formation of different coordination structures. We have also shown that the compounds **1**–**4** catalyzed efficiently the transesterification of a variety of esters.

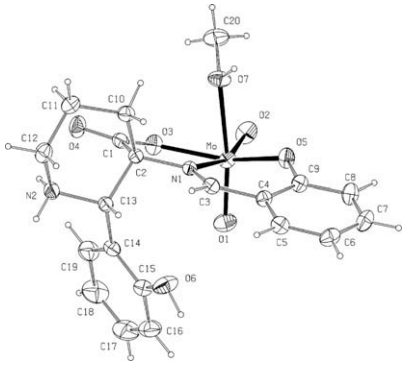


Marina Cindrić, Gordana Galin, Dubravka Matković-Čalogović, Predrag Novak, Tomica Hrenar, Ivan Ljubić and Tanja Kajfež Novak

Polyhedron 28 (2009) 562

Synthesis and characterization of three novel molybdenum(VI) complexes: Mononuclear $[MoO_2(C_6H_4(O)CH{=}NCH(COO)CH_2C{=}(O)NH_2)]$, $[MoO_2(C_{19}H_{19}N_2O_5)(CH_3OH)]Cl \cdot CH_3OH$ and dinuclear $[Mo_2O_4(C_6H_4(O)CH{=}NCH(COO)\text{-}CH_2C{=}(O)NH_2)_2]$

The Schiff base containing a saturated heterocyclic ring is the first example of such a molecule derived from salicylaldehyde and the amino acid, L-ornithine hydrochloride. Our investigation confirmed that the formation of a molybdenum(VI) complex coordinated by the Schiff base containing a saturated heterocyclic ring depends upon the nature of the solvent and upon the presence of molybdenum(VI).

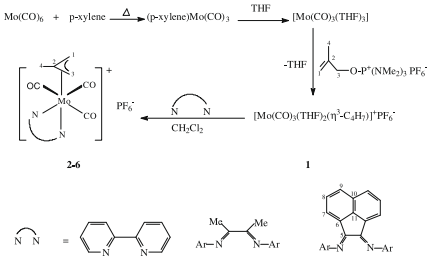


Thouraya Turki, Taha Guerfel and Faouzi Bouachir

Polyhedron 28 (2009) 569

Synthesis and structure of new cationic methallyl molybdenum(II) complexes supported by α-diimine ligands

Cationic methallyl molybdenum(II) complexes with α-diimine ligands have been obtained successfully in high yields by an oxidative addition of methallyloxyphosphonium to the zerovalent $Mo(CO)_3(THF)_3$ in the presence of diimine ligands.

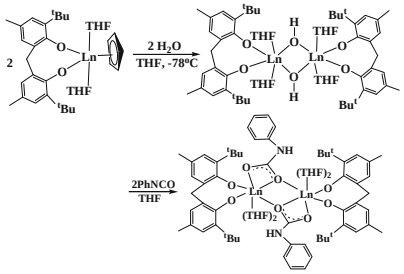


Xiao-Ping Xu, Rui-Peng Qi, Bin Xu, Ying-Ming Yao, Kun Nie, Yong Zhang and Qi Shen

Polyhedron 28 (2009) 574

Synthesis, reactivity and structural characterization of lanthanide hydroxides stabilized by a carbon-bridged bis(phenolate) ligand

Controlled hydrolysis of the carbon-bridged bis(phenolate) lanthanide cyclopentadienyl complexes (MBMP)Ln(C_5H_5)(THF)$_2$ in THF at −78 °C afforded the corresponding lanthanide hydroxides as dimers [{(MBMP)Ln(μ-OH)(THF)$_2$}$_2$] (Ln = Nd (**1**), Yb (**2**)), which reacted with phenyl isocynate in THF to give the desired O–H addition products, [(MBMP)Ln(μ-η^1:η^2-O_2CNHPh)(THF)$_2$]$_2$ (Ln = Nd (**3**), Yb (**4**)) in excellent isolated yields.

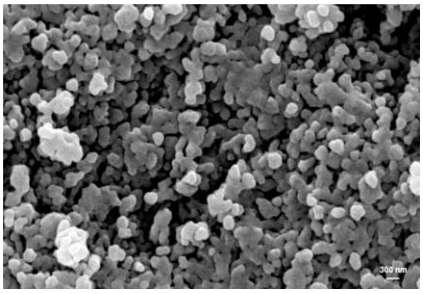


Yogesh Kumar Sharma, Mamta Kharkwal, S. Uma and R. Nagarajan

Polyhedron 28 (2009) 579

Synthesis and characterization of titanates of the formula $MTiO_3$ (M = Mn, Fe, Co, Ni and Cd) by co-precipitation of mixed metal oxalates

The reaction of potassium titanyl oxalate and metal chloride solutions of metals such as Mn, Fe, Co, Ni and Cd did not lead to the formation of a single molecular precursor by a direct salt elimination reaction, but resulted in mixed metal oxalates in the pH range 1.5–3. These oxalates when heated at appropriate temperatures yielded mixed metal oxides.

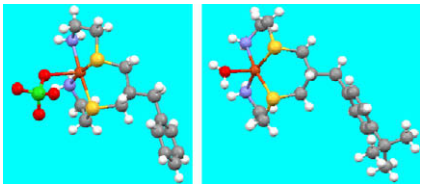


Si-Ping Tang, Lei Hou, Zong-Wan Mao and Liang-Nian Ji

Polyhedron 28 (2009) 586

Synthesis, crystal structures, DNA binding and oxidative cleavage studies of copper(II) complexes of N_2S_2 tetradentate ligands

Mononuclear copper(II) complexes, [Cu(L^1)(ClO$_4$)](ClO$_4$) · 0.5H$_2$O (**1**) and [Cu(L^2)(H$_2$O)](ClO$_4$)$_2$ · H$_2$O (**2**), with aminothioether N_2S_2 ligands L^1 (2-benzyl-1,3-bis(aminoethylthio)propane) and L^2 (2-(4-butylbenzyl)-1,3-bis(aminoethylthio)propane) have been synthesized and characterized. Both complexes exhibit efficient DNA cleavage activity in the presence of ascorbic acid and the activity of **2** is higher than that of **1**.

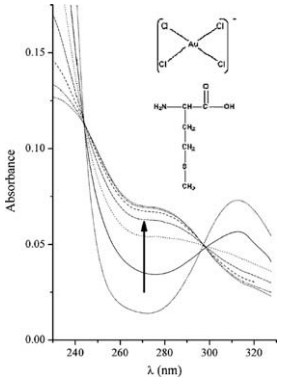


A.V. Vujačić, J.Z. Savić, S.P. Sovilj, K. Mészáros Szécsényi, N. Todorović, M.Ž. Petković and V.M. Vasić

Polyhedron 28 (2009) 593

Mechanism of complex formation between [AuCl$_4$]$^-$ and L-methionine

The kinetics of the reaction between the tetrachloroaurate(III) and L-methionine have been studied spectrophotometrically using a stopped-flow technique at different temperatures. The substitution reaction was ascribed to the formation of the short-lived square-planar Au(III)–(L-Met) that was followed by the replacement of a Cl$^-$ ligand and reduction to Au(I)–(L-Met). The activation parameters for substitution and reduction were determined. IR spectroscopy indicates that L-methionine acts as a bidentate ligand, most likely coordinating *via* the S and N atoms, while ^{1}H and ^{13}C NMR data indicate methionine sulfoxide as the final product. The components of the reaction were treated thermally in order to investigate the solid phase synthesis of the resulting complex.

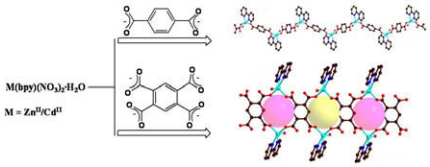


Rishikesh Prajapati, Lallan Mishra, Keisaku Kimura and Pallepogu Raghavaiah

Polyhedron 28 (2009) 600

Metal–organic frameworks (MOFs) constructed from Zn^{II}/Cd^{II}-2,2′-bipyridines and polycarboxylic acids: Synthesis, characterization and microstructural studies

Assembly of $M(bpy)(NO_3)_2 \cdot H_2O$ (M = Zn^{II}/Cd^{II}) separately with 1,4-benzenedicarboxylic acid and 1,2,4,5-benzenetetracarboxylic acid provides a series of photoluminescent porous metal complexes in zig-zag chain and 3D supramolecular architectures. These complexes are characterized by their single crystal X-ray diffraction studies along with their physicochemical properties.

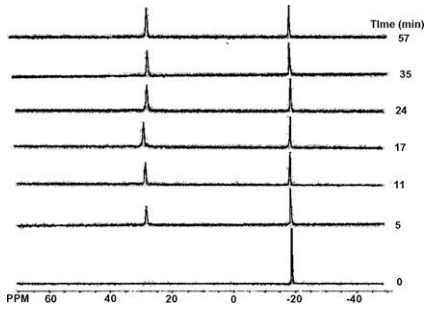


Mahbubeh Pourshahbaz, Mohsen Irandoust, Ezzat Rafiee and Mohammad Joshaghani

Polyhedron 28 (2009) 609

Kinetics of complex formation between palladium(II) acetate and bis(diphenylphosphino)-ferrocene

The kinetics of complex formation between palladium and dppf in $CDCl_3$ and DMSO-d_6 were investigated using ^{31}P-NMR spectroscopy

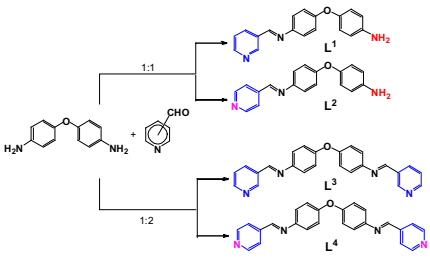


Hye Jung Yun, Sook-Hyun Lim and Soon W. Lee

Polyhedron 28 (2009) 614

Linking patterns of ligands containing pyridyl–amine or two pyridyl terminals and their cadmium compounds: $[CdL^1{}_2(NO_3)_2]$, $[CdL^2{}_2(NO_3)_2]$ and $[Cd_2L^3{}_2(NO_3)_4(H_2O)_4] \cdot (C_4H_8O)_2$ [L^1 = (3-py)–CH=N–C_6H_4–O–C_6H_4–NH_2; L^2 = (4-py)–CH=N–C_6H_4–O–C_6H_4–NH_2; L^3 = (3-py)–CH=N–C_6H_4–O–C_6H_4–N=CH–(3-py)]

We have prepared a 2-D brick-wall coordination polymer $[CdL^1{}_2(NO_3)_2]$, a 1-D double-strand-chain polymer $[CdL^2{}_2(NO_3)_2]$ and a discrete dinuclear macrocycle (molecule) $[Cd_2L^3{}_2(NO_3)_4(H_2O)_4] \cdot (C_4H_8O)_2$: (3-py)–CH=N–$C_6H_4$–O–$C_6H_4$–$NH_2$ (L^1); (4-py)–CH=N–C_6H_4–O–C_6H_4–NH_2 (L^2); [(3-py)–CH=N–C_6H_4–O–C_6H_4–N=CH–(3-py) (L^3).

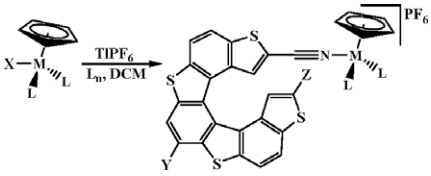


Maria Helena Garcia, Pedro Florindo, Maria de Fátima M. Piedade, Stefano Maiorana and Emanuela Licandro

Polyhedron 28 (2009) 621

New organometallic Ru(II) and Fe(II) complexes with tetrathia-[7]-helicene derivative ligands

Novel organometallic complexes with coordinated new tetrathia-[7]-helicene derivatives.

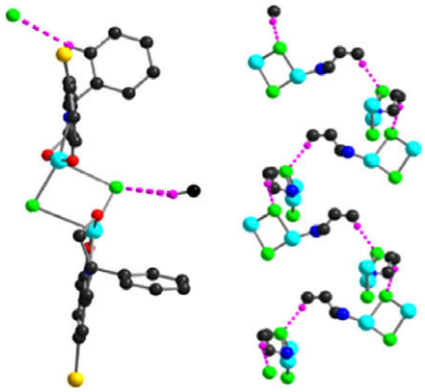


Chullikkattil P. Pradeep and Samar K. Das

Polyhedron 28 (2009) 630

Chiral supramolecular metal-organic architectures from dinuclear copper complexes

Two new chiral dinuclear copper complexes are derived from chiral amino alcohol based ligands and $CuCl_2 \cdot 2H_2O$. Intriguing chiral supramolecular metal-organic architectures are identified in their solid state structures as a result of C–H···Cl–Cu directed H-bonding interactions. Also, the ligand structure found to control the supramolecular structures in these complexes.

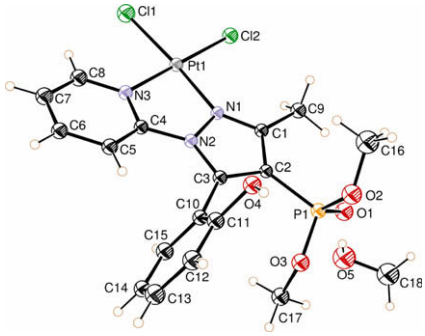


Elzbieta Budzisz, Magdalena Miernicka, Ingo-Peter Lorenz, Peter Mayer, Urszula Krajewska and Marek Rozalski

Polyhedron 28 (2009) 637

Synthesis and X-ray structure of platinum(II), palladium(II) and copper(II) complexes with pyridine–pyrazole ligands: Influence of ligands' structure on cytotoxic activity

The new phosphonic pyrazole ligand has been used to obtain a series of platinum(II), palladium(II) and copper(II) complexes as potential anticancer compounds. The molecular structures of the platinum(II) and copper(II) complexes have been determined by X-ray crystallography. The cytotoxicity of the phosphonic ligand and its carboxylic analog as well as their complexes has been evaluated on leukemia and melanoma cell lines. Copper(II) complexes were found to be the most efficient. Cytotoxic effectiveness of one of copper(II) against melanoma WM-115 cells was two times better than that of cisplatin.



The Publisher encourages the submission of articles in electronic form thus saving time and avoiding rekeying errors. For detailed instructions on the preparation of manuscripts and of electronic artwork, consult the Author Gateway for Elsevier at http://authors.elsevier.com

ScienceDirect

Full text of this journal is available, on-line from **ScienceDirect**. Visit **www.sciencedirect.com** for more information.

Polyhedron 28, issue 2, 3 February 2009

Contents lists available at ScienceDirect

Polyhedron

journal homepage: www.elsevier.com/locate/poly

Contents

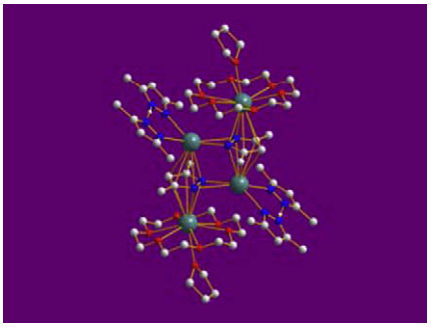
Papers

Miguel-Ángel Velázquez-Carmona, Alejandro-José Metta-Magaña, Sara-Angélica Cortés-Llamas, Virginia Montiel-Palma and Miguel-Ángel Muñoz-Hernández

Polyhedron 28 (2009) 205

Potassium and lithium pyrazolates: The interplay of electronic and steric factors on the hapticity of the pyrazolate ligand and the influence of Lewis bases on nuclearity

The oligomeric potassium complex $[(Me_2pzH)(Me_2pz)_2(18\text{-crown-6})(THF)K_2]_2$ (**1**) and the lithium dimer $[(^tBu_2pz)(THF)Li]_2$ (**2**) were synthesized. Both complexes were fully characterized by spectroscopic methods and single crystal X-ray diffraction. Complex **1** shows π-bound pyrazolate ligands to potassium in a η^5-fashion. Complex **2** was obtained by nucleophilic addition of THF to $[(^tBu_2pz)Li]_4$.

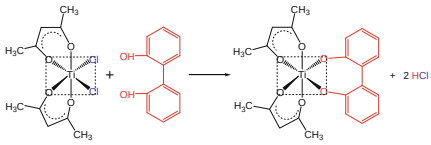


Tsietsi A. Tsotetsi, Annemarie Kuhn, Alfred Muller and Jeanet Conradie

Polyhedron 28 (2009) 209

Substitution kinetics of biphenol at dichlorobis-(acetylacetonato-*O*,*O*′)titanium(IV): Isolation, characterization, crystal structure and enhanced hydrolytic stability of the product bis(acetylacetonato-*O*,*O*′)(biphenyldiolato-*O*,*O*′)titanium(IV)

The substitution of bidentate 2,2′-biphenyldiolato for the two monodentate Cl^- ligands in $Ti(CH_3COCHCOCH_3)_2Cl_2$ affords $Ti(CH_3COCHCOCH_3)_2$biphen with high hydrolytic stability.

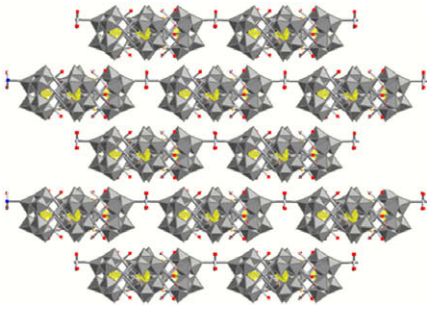


Zhen Luo, Paul Kögerler, Rui Cao and Craig L. Hill

Polyhedron 28 (2009) 215

Synthesis, structure and magnetism of a one-dimensional silicotungstate array: $K_3H_4Cu_{0.5}\{Cu[Cu_{7.5}Si_2W_{16}O_{60}(H_2O)_4(OH)_4]_2\} \cdot 9H_2O$

A multi-copper polyanion linked into a 1D polymer by Cu(II) centers, $K_3H_4Cu_{0.5}\{Cu[Cu_{7.5}Si_2W_{16}O_{60}(H_2O)_4(OH)_4]_2\} \cdot 9(H_2O)$ (**1**) has been characterized by X-ray crystallography and several other methods. Variable temperature magnetic measurements reveal weak ferromagnetic superexchange between Cu(II) centers.



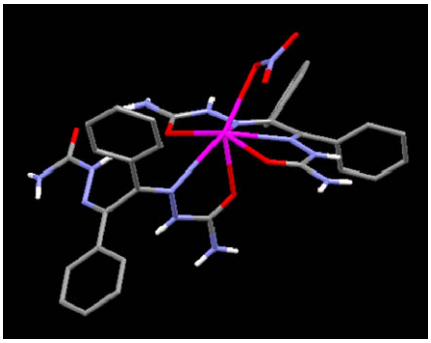
Elsevier Ltd.

Elena López-Torres, M. Antonia Mendiola and César J. Pastor

Polyhedron 28 (2009) 221

Unreported coordination behaviour of a bis(semicarbazone) ligand in a lead(II) complex

A novel lead(II) complex with the Schiff base benzil bis(semicarbazone), $[Pb(LH_2)_2(NO_3)]$-$NO_3 \cdot 1/2H_2O$, has been structurally characterized as well as the free ligand. The most interesting characteristic of this complex is the different behaviour observed in the two bis(semicarbazone) molecules: One of them is a N_2O_2 chelate ligand, whereas the other one is bonded to the lead ion only through one of the semicarbazone branches.

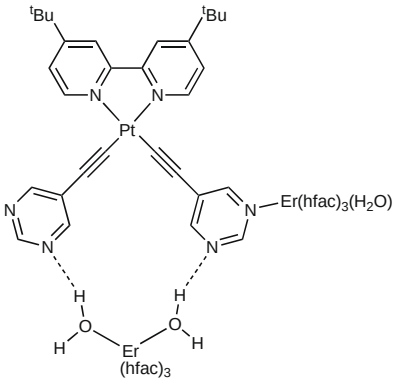


Nawal K. Al-Rasbi, Sofia Derossi, Daniel Sykes, Stephen Faulkner and Michael D. Ward

Polyhedron 28 (2009) 227

Bimetallic Pt(II)-bipyridyl-diacetylide/Ln(III) tris-diketonate adducts based on a combination of coordinate bonding and hydrogen bonding between the metal fragments: Syntheses, structures and photophysical properties

The luminescent Pt(II) complex [Pt(4,4′-^{t}Bu$_2$-bipy){CC-(5-pyrimidinyl)}$_2$] (**1**), which has two pendant pyrimidine rings, forms adducts [**1** · {Ln(hfac)$_3$(H$_2$O)}{Ln(hfac)$_3$(H$_2$O)$_2$}] in which the {Ln(hfac)$_3$} units are associated with pyrimidine rings of **1** *via* a combination of Ln–N coordinate bonds and N···HOH hydrogen bonds. The luminescence of the Pt(II) centre is partially quenched by energy-transfer to the lanthanide when Ln = Er or Nd but not when Ln = Yb.

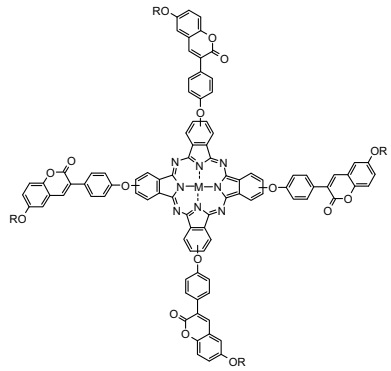


Meryem Çamur, Mustafa Bulut, Mehmet Kandaz and Orhan Güney

Polyhedron 28 (2009) 233

Synthesis, characterization and fluorescence behavior of new fluorescent probe phthalocyanines bearing coumarin substituents

In this study, we report a new ligand, 6-hexyloxy-3-[*p*-(3′,4′-dicyanophenoxy)phenyl]-coumarin, and its fluorescent tetrasubstituted phthalocyanines {M[Pc(OBzCou)$_4$], M = 2H, Zn(II), Co(II); Bz:Benzene}. The effect of the coumarin derivative on the intensity of the fluorescence spectra of the metal-free and zinc phthalocyanine (ZnPc) derivatives was investigated. The change of the emission properties of both the coumarin moieties and phthalocyanine core in the presence of the metal ion and the ring-opening reaction of the coumarin were studied by means of steady-state fluorescence spectroscopy. The novel chromogenic compounds were characterized by elemental analysis, ^{1}H NMR, ^{13}C NMR, Maldi-TOF, IR and UV–Vis spectral data.

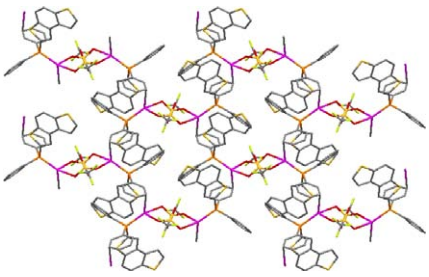


M. Helena Garcia, Pedro Florindo, M. Fátima M. Piedade and M. Teresa Duarte

Polyhedron 28 (2009) 239

Synthesis and structural characterization of silver(I) complexes with moon-shaped benzo[1,2-*b*;4,3-*b*′]dithiophene phosphine derivative ligands

New silver complexes of general formula $[Ag(O_3SCF_3)(PPh_2\{bzt\})_n]$ (n = 1–3, bzt = benzo[1,2-*b*;4,3-*b*′]dithiophene) have been synthesized and characterized. Spectroscopic studies revealed neutral ligand fluxionallity. X-ray crystallographic studies showed a decrease in structure complexity with increasing number of neutral ligands. A very unusual Ag···C short contact was found for compound $[Ag(O_3SCF_3)(PPh_2\{bzt\})]$.

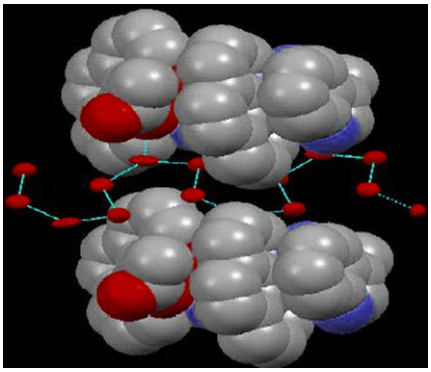


P. Mosae Selvakumar, E. Suresh and P.S. Subramanian

Polyhedron 28 (2009) 245

Single stranded helical supramolecular architecture with a left handed helical water chain in ternary copper(II) tryptophan/diamine complexes

Two single stranded helical coordination polymers with [Cu(DA(AA)] complexes are reported. The left handed helical water chain entrapped in between the Cu^{II}-helical strand is investigated and the change in the supramolecular helical architecture and the change in the chiroptical properties are correlated using various chiral components such as (*P*)/(*M*), (Λ/Δ), and λ/δ in detail, along with CD spectra, single crystal X-ray structures, and thermo-analytical techniques.

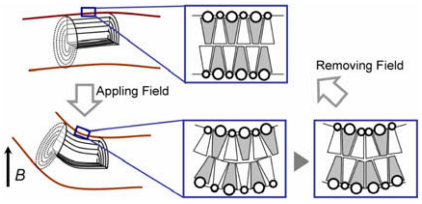


Kentaro Suzuki, Takuya Tomita, Taro Toyota, Masakazu Iwasaka and Tadashi Sugawara

Polyhedron 28 (2009) 253

Hysteretic behavior of diamagnetic molecular assembly: Magnetic field-induced deformation of tubular self-assemblies composed of amphiphilic molecules

Real-time observation of morphologies of a tubular giant vesicle with multi-components was carried out under application of a static magnetic field. The hysteretic behavior in these bending was observed associated with elevating of the fields. To understand the hysteretic behavior, the molecular cooperative effect must be taken into consideration.

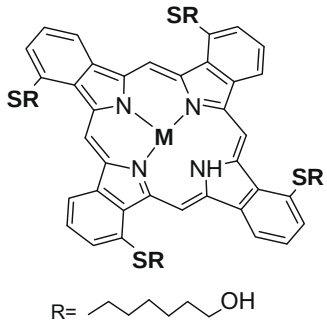


Mehmet Kandaz, Meryem N. Yarasir and Atıf Koca

Polyhedron 28 (2009) 257

Selective metal sensor phthalocyanines bearing non-peripheral functionalities: Synthesis, spectroscopy, electrochemistry and spectroelectrochemistry

The novel alcohol-soluble functional non-peripherally tetrasubstituted phthalocyanines, 1,8,15,22-tetrakis(6-hydroxyhexylthio)-phthalocyanines, M[Pc(α-$SC_6H_{13}OH)_4$] (M=Cu(II), Zn(II), Co(II)) are reported and characterized by elemental analysis, FT-IR, ^{1}H NMR, UV/Vis. MS (MALDI-TOF), electrochemistry, and spectroelectrochemistry. The aggregation and cation binding behaviours of the phthalocyanine compounds in the presence of soft Ag^I and Pd^{II} metal ions was investigated by using UV–vis spectroscopy.



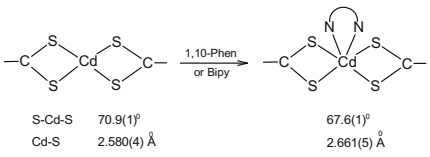
M= Zn(**2**), Cu(**3**), Co(**4**)

S. Thirumaran, K. Ramalingam, G. Bocelli and L. Righi

Polyhedron 28 (2009) 263

XPS, single crystal X-ray diffraction and cyclic voltammetric studies on 1,10-phenanthroline and 2,2′-bipyridine adducts of bis(piperidine-carbodithioato-*S*,*S*′)cadmium(II) with CdS_4N_2 environment – A stereochemical and electronic distribution investigation

The XPS and cyclic voltammetric studies on the complexes show an increase of electron density on the central metal ion in the octahedral complexes compared to the tetrahedral complexes. The S–Cd–S angle in the adducts shows reduction and Cd–S distance in the adducts are longer than those in Cd(dtc)2.

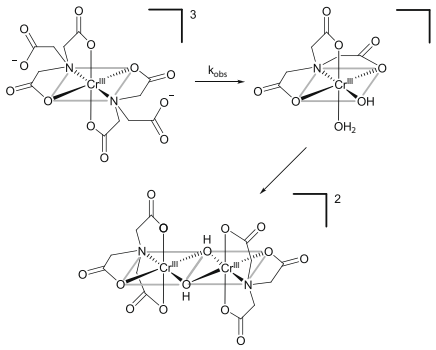


Magdalena E. Mendola, Tias Paul, Timothy J. Strathmann and Richard F. Carbonaro

Polyhedron 28 (2009) 269

Investigation of the kinetics of aquation of the 1:2 complex between Cr^{III} and nitrilotriacetic acid

Kinetics of aquation of the 1:2 complex between Cr^{III} and nitrilotriacetic acid (NTA) was measured using a combination of capillary electrophoresis (CE), UV–Vis spectrophotometry, and ATR-FTIR spectroscopy. The aquation products were identified as the 1:1 Cr^{III} complex with NTA and "free" NTA. Observed first-order rate constants, k_{obs}, exhibited a complicated pH dependence which was successfully modeled by considering five distinct reaction pathways. The 1:1 complex dimerized to form a 2:2 complex in a slower subsequent reaction step.

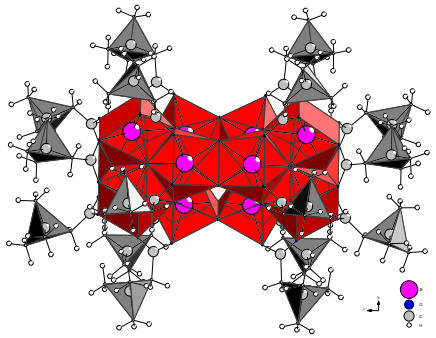


P. Piszczek, A. Radtke, A. Wojtczak, T. Muzioł and J. Chojnacki

Polyhedron 28 (2009) 279

Synthesis, structure characterization and thermal properties of $[Zr_6(\mu_3\text{-}O)_4(\mu_3\text{-}OH)_4(OOCCH_2{}^tBu)_9(\mu_2\text{-}OH)_3]_2$

$[Zr_6(\mu_3\text{-}O_4)(\mu_3\text{-}OH)_4(OOCCH_2{}^tBu)_9(\mu_2\text{-}OH)_3]_2$ has been isolated, when $Zr(O^iPr)_4$ reacted with an 2-fold excess of 3,3-dimethylbutyric acid. Analysis of single crystal X-ray diffraction data showed that this complex crystallizes in hexagonal system ($P6_3/m$ (no. 176)). Results of variable temperature IR spectroscopy and DSC studies revealed phase transitions at 143–183 and 203–293 K. Thermal analysis showed that its decomposition proceeds with complete conversion to ZrO_2 between 603 and 803 K.

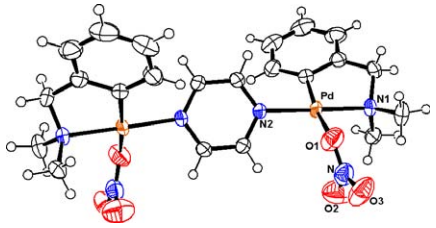


Sandra R. Ananias, Janaina G. Ferreira, Antonio E. Mauro, Adelino V.G. Netto, Stanlei I. Klein and Regina H.A. Santos

Polyhedron 28 (2009) 286

Synthesis and characterization of mono and polymeric cyclopalladated compounds: Crystal and molecular structure of $[\{Pd(dmba)(ONO_2)\}_2(\mu\text{-}pz)] \cdot H_2O$ (pz = pyrazine)

The compound $[Pd(dmba)(NCMe)_2](NO_3)$ (NCMe = acetonitrile) (**1**) reacts with *m*-nitroaniline (*m*-NAN) and pirazine (pz), affording $[Pd(dmba)(ONO_2)(m\text{-}NAN)]$ (**2**), $[\{Pd(dmba)(ONO_2)\}_2(\mu\text{-}pz)] \cdot H_2O$ (**3**), respectively. The IR spectra of (**2**–**3**) display typical bands of monodentade O-bonded nitrate groups. The crystal structure of compound **3** consists of a supramolecular chain formed by hydrogen bonding between the water molecule and the nitrato ligands of two consecutive $[Pd_2(dmba)_2(ONO_2)_2(\mu\text{-}pz)]$ units.

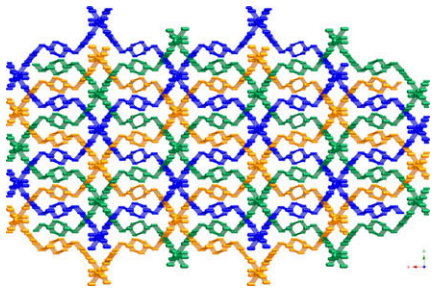


Gregory A. Farnum, Warren R. Knapp and Robert L. LaDuca

Polyhedron 28 (2009) 291

Silver nitrate molecular species and coordination polymers with divergent supramolecular morphology constructed from hydrogen-bonding capable dipyridyl ligands

Solution phase reaction of silver nitrate with various hydrogen-bonding capable dipyridyl ligands has resulted in three 1-D coordination polymers and one discrete cationic species with diverse silver coordination spheres. Long-range Ag···O interactions and/or hydrogen-bonding promote the formation of different supramolecular aggregations such as a 2-D double layer slab and a threefold interpenetrated 3-D diamondoid network. Two of the complexes undergo weak blue–violet luminescence upon irradiation with ultraviolet light.

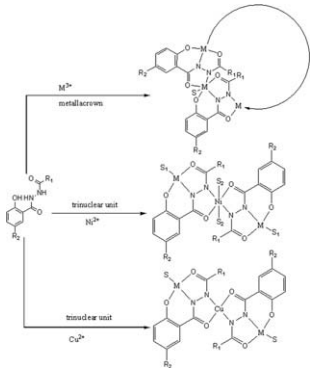


Wei Luo, Xiu-Teng Wang, Xiang-Gao Meng, Gong-Zhen Cheng and Zhen-Ping Ji

Polyhedron 28 (2009) 300

Metal coordination architectures of *N*-acylsalicylhydrazides: The effect of metal ions and steric repulsion of ligands to their structures of polynuclear metal complexes

The chelating modes of ligands around the metal centers are the same, but the different connectivities of them lead to the formation of metallacrowns or trinuclear complexes.

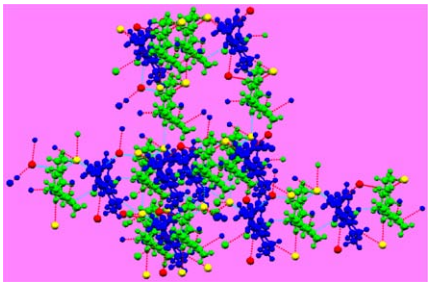


Khodayar Gholivand, Zahra Shariatinia, Seyedeh Mahdieh Mashhadi, Farzaneh Daeepour, Narjes Farshidnasab, Hamid Reza Mahzouni, Nasrin Taheri, Shadi Amiri and Sheida Ansar

Polyhedron 28 (2009) 307

Structural diversity in phosphoramidate's chemistry: Syntheses, spectroscopic and X-ray crystallography studies

A series of various novel phosphorus compounds of bisphosphoramidates, phosphoramidates, and phosphoric triamides were synthesized and characterized. Some interesting and unusual phenomena are noted in this study.

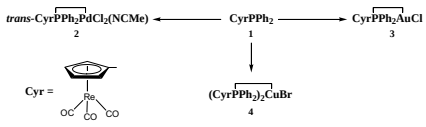


Diego Sierra, Andres Muñoz, Fernando Godoy, A. Hugo Klahn, Andres Ibañez, M. Teresa Garland and Mauricio Fuentealba

Polyhedron 28 (2009) 322

Heterobimetallic Re–Pd, Re–Au and Re–Cu complexes derived from diphenylphosphino cyrhetrene: Synthesis and X-ray structure

The square-planar *trans*-[(η^5-$C_5H_4PPh_2$)Re(CO)$_3$]$PdCl_2$(NCMe) (**2**), linear [(η^5-$C_5H_4PPh_2$)Re(CO)$_3$]AuCl (**3**) and trigonal [(η^5-$C_5H_4PPh_2$)Re(CO)$_3$]$_2$CuBr (**4**) complexes are formed by coordination of diphenylphosphinocyrhetrene ligand (η^5-$C_5H_4PPh_2$)Re(CO)$_3$(**1**) to Pd(II), Au(I) and Cu(I) metal centers. The products were characterized by spectroscopy and X-ray crystallography.

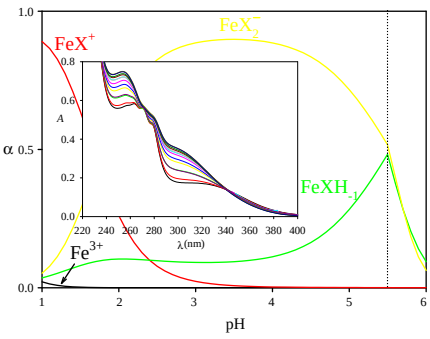


G. Giorgio Bombi, Reheman Aikebaier, Annalisa Dean, Valerio B. Di Marco, Daniele Marton and Andrea Tapparo

Polyhedron 28 (2009) 327

Complexation of 2,6-pyridinedicarboxylic and 2,6-pyridinediacetic acids towards aluminium(III) and iron(III)

The complexes formed by 2,6-pyridinedicarboxylic acid (H_2X) and 2,6-pyridinediacetic acid (H_2A) with Al(III) and Fe(III) were studied by means of potentiometric titrations, UV–Vis, and NMR measurements at 25 °C in (Na)Cl 0.6 m aqueous solution.

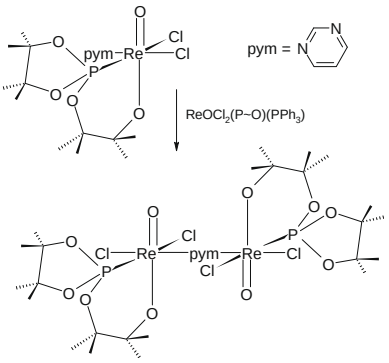


Anna Skarżyńska and Zbigniew Ciunik

Polyhedron 28 (2009) 336

Mono and dinuclear Re(V) complexes with a hydrospirophosphorane HP∼O derived ligand: Synthesis, structural analysis and molecular dynamics

The preparation, crystal structure and molecular dynamics of two oxo-rhenium(V) mono and dinuclear compounds of the formula *cis*-$ReOCl_2$(P∼O)(pym) and *cis*-[$ReOCl_2$(P∼O)] (μ-pym) with the hydrospiro-phosphorane ligand HP∼O (HP∼O = octamethyl-2,2,3,3,7,7,8,8-tetraoxa-5λ^5 1,4,6,9-phosphaspiro-4,4-nonane) are reported.

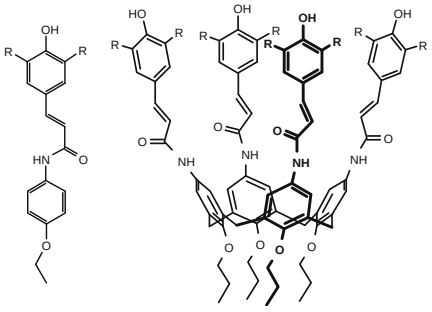


Carmelo Sgarlata, Valeria Zito, Giuseppe Arena, Grazia Maria Letizia Consoli, Eva Galante and Corrada Geraci

Polyhedron 28 (2009) 343

A sinapic acid–calix[4]arene hybrid selectively binds Pb^{2+} over Hg^{2+} and Cd^{2+}

The sinapic acid-calixarene hybrid **2** has a marked selectivity for Pb^{2+} over Hg^{2+} and Cd^{2+}. Its selectivity for Pb^{2+} is much greater than that of the parent "monomer" **1**, owing to the cooperative effect resulting from the simultaneous presence of the sinapyl units arranged on the calix[4]-arene upper rim.

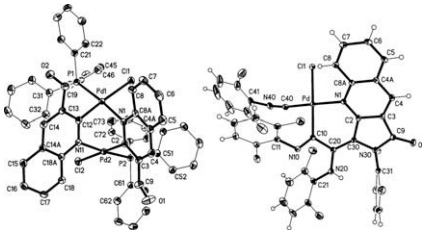


Abdel-Sattar S. Hamad Elgazwy

Polyhedron 28 (2009) 349

Conversion of novel palladacycles into oxopyrrolo[3,4-b]quinolines

Some palladacycles have been synthesized from three simple and readily available building blocks via a one-pot oxidative addition reaction of quinoline chlorides to $Pd(dba)_2$ and isocyanide XyNC or via the direct insertion reaction of XyNC into the prepared novel dinuclear palladium complexes. Depalladation reaction of the palladacycles could convert them into organic molecules. The sequence of reactions led eventually to compounds that could potentially possess pharmacological properties. The solid state structures of selected complexes **2a**, **3a** and **3b** show interesting features.

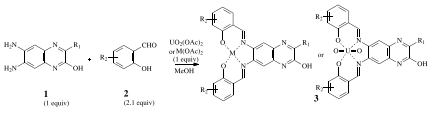


Xianghong Wu, Hannah K. Hubbard, Brandon K. Tate and Anne E.V. Gorden

Polyhedron 28 (2009) 360

One-pot metal templated synthesis for the preparation of 2-quinoxalinol salen metal complexes

Metal complexes of 2-quinoxalinol salen (salqu) ligands can be prepared in a one-pot metal templated synthesis. Using this method, 12 salqu metal complexes have been prepared and characterized from +2 metal ions.

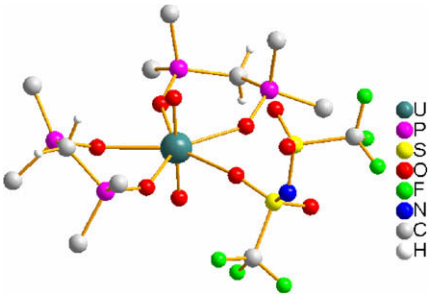


Stéphanie M. Cornet, Iain May, Michael P. Redmond, Andrew J. Selvage, Clint A. Sharrad and Olivier Rosnel

Polyhedron 28 (2009) 363

Coordination of bistriflimide and triflate to the uranyl bis(diphenylphosphino)methane dication, $\{UO_2(DPPMO_2)_2\}^{2+}$

We report the structural characterization of $[UO_2(NTf_2)(DPPMO_2)_2][NTf_2]$ (NTf_2^- = bistriflimide) and $[UO_2(OTf)(DPPMO_2)_2][OTf]$ (OTf^- = triflate). In addition, a spectroscopic and structural investigation of a series of $[UO_2(X)(DPPMO_2)_2]^+$ complexes indicates that the strength of the uranium to X^- ligand bonding interaction decreases along the series $[Cl]^- > [ReO_4]^- > [OTf]^- > [NTf_2^-]$.

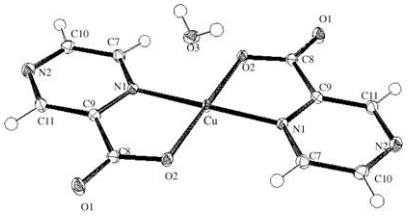


Pratap Chutia, Shigeru Kato, Toshinori Kojima and Shigeo Satokawa

Polyhedron 28 (2009) 370

Synthesis and characterization of Co(II) and Cu(II) supported complexes of 2-pyrazinecarboxylic acid for cyclohexene oxidation

Co(II) and Cu(II) complexes with 2-pyrazinecarboxylic acid were synthesized and characterized. These complexes were immobilized on zeolite–Y, alumina and organically modified silica surfaces. The immobilized complexes were characterized using different experimental techniques. These complexes catalyze the oxidation of cyclohexene in the presence of H_2O_2 giving rise to 2-cyclohexen-1-one as the major product.

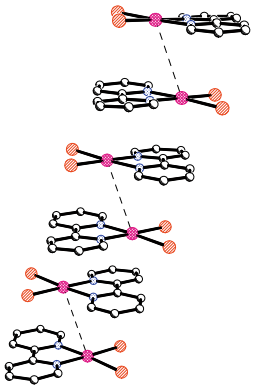


Badri Z. Momeni, Zeinab Moradi, Mehdi Rashidi and Frank Rominger

Polyhedron 28 (2009) 381

Insertion of tin(II) bromide into Pt–X (X = Cl, Br) bond of dimethylplatinum(IV) complexes: A novel polymorphic form of $[PtBr_2(bpy)]$

The platinum(IV) complexes $[PtMe_2X\{(CH_2)_nX\}(bpy)]$ (bpy = 2,2′-bipyridine; n = 1, X = Cl; n = 4, X = Br) were synthesized and characterized by NMR spectroscopy and the insertion of $SnBr_2$ into Pt–X (X = Cl, Br) bond of these platinum(IV) complexes is reported. The crystal structure of the novel polymorphic form of $[PtBr_2(bpy)]$ shows both short and long Pt···Pt separations through the crystal.

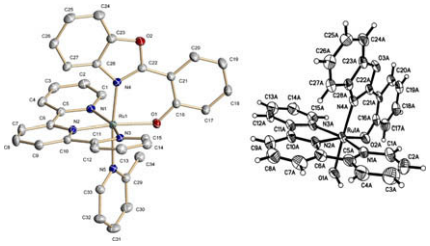


James A. Moore and J. Henry Acquaye

Polyhedron 28 (2009) 386

Crystal structures of $[Ru(terpy)(HPB)(H_2O)](PF_6)_2$ and $[Ru(terpy)(HPB)(2\text{-picoline})](PF_6)$ and the kinetics studies of the aqua ligand substitution by pyridine and substituted pyridines

The kinetics of the substitution of the aqua ligand in $[Ru(terpy)(HPB)(H_2O)](PF_6)_2$ by pyridine, 2-picoline and 4-picoline were studied. The crystal structures of $[Ru(terpy)(HPB)(H_2O)](PF_6)_2$ and $[Ru(terpy)(HPB)(2\text{-picoline})](PF_6)$ have been determined.

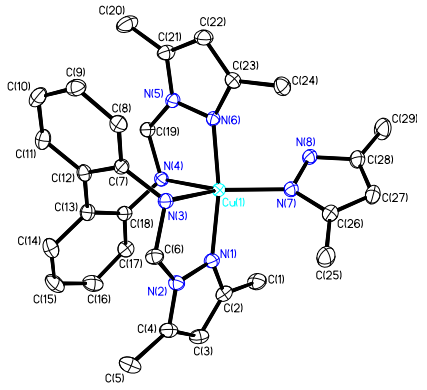


Mitchell R. Malachowski, Ashraf S. Kasto, Mark E. Adams, Arnold L. Rheingold, Lev N. Zakharov, Lawrence D. Margerum and Matthew Greaney

Polyhedron 28 (2009) 393

Copper(II) complexes of a biphenyl-based ligand: Tuning the needs of the metal with those of the ligand

A new biphenyl-based ligand containing pyrazole donors was synthesized and three Cu(II) complexes were prepared from this compound. These complexes were characterized by elemental analysis, FAB-MS and electrochemistry. The X-ray structure of $[Cu(N_4\text{-mpz})(Pz)](ClO_4)_2 \cdot CH_3OH$, **2**, showed the copper coordinated by the ligand donors and a pyrazole that had been extracted from another molecule of the ligand.

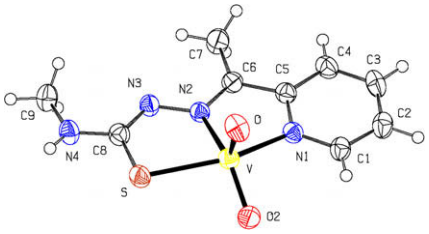


Pedro I. da S. Maia, Fernando R. Pavan, Clarice Q.F. Leite, Sebastião S. Lemos, Gerimário F. de Sousa, Alzir A. Batista, Otaciro R. Nascimento, Javier Ellena, Eduardo E. Castellano, Elke Niquet and Victor M. Deflon

Polyhedron 28 (2009) 398

Vanadium complexes with thiosemicarbazones: Synthesis, characterization, crystal structures and anti-*Mycobacterium tuberculosis* activity

Three oxovanadium(IV) and three *cis*-dioxovanadium(V) complexes with thiosemicarbazone derivatives bearing moieties with different lipophilicity have been prepared and had their inhibitory activity against *Mycobacterium tuberculosis* H37Rv ATCC 27294 evaluated. The analytical methods used included IR, EPR, 1H, 13C and 51V NMR spectroscopies, elemental analysis, cyclic voltammetry, magnetic susceptibility measurement and single crystal X-ray diffractometry.

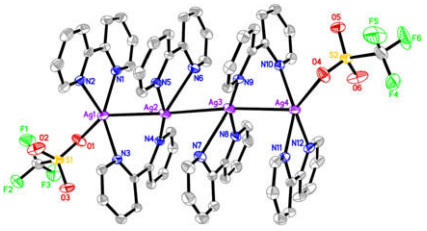


Fernando Hung-Low, Amanda Renz and Kevin K. Klausmeyer

Polyhedron 28 (2009) 407

An X-ray diffraction study of anion and ratio dependence in the formation of discrete molecules versus polymeric arrays involving silver salts and bipyridine ligands

A series of silver(I) complexes, encompassing bimetallic discrete molecules and two-dimension polymeric arrays, were synthesized using different silver salts and the 4,4′-dimethyl-2,2′-bipyridine, 5,5′-dimethyl-2,2′-bipyridine or 2,2′-bipyridine, which are enabled by the highly flexible coordination sphere of the silver(I) cation.

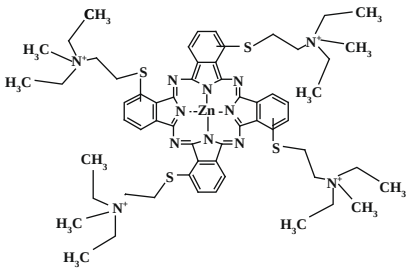


Mopelola Idowu and Tebello Nyokong

Polyhedron 28 (2009) 416

Synthesis, photophysical and photochemical studies of water soluble cationic zinc phthalocyanine derivatives

Quaternized peripherally and non-peripherally substituted 2-diethylaminoethanethiol tetra-substituted zinc phythalocyanine gave low triplet yields and lifetimes in aqueous media which improved on addition of a surfactant, cremophore EL.



The Publisher encourages the submission of articles in electronic form thus saving time and avoiding rekeying errors. For detailed instructions on the preparation of manuscripts and of electronic artwork, consult the Author Gateway for Elsevier at http://authors.elsevier.com

ScienceDirect

Full text of this journal is available, on-line from **ScienceDirect**. Visit **www.sciencedirect.com** for more information.

Polyhedron 28, issue 16, 3 November 2009

Contents lists available at ScienceDirect

Polyhedron

journal homepage: www.elsevier.com/locate/poly

Contents

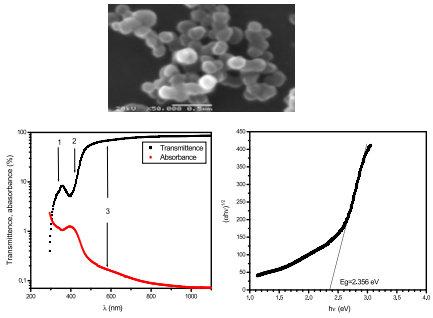
Papers

Mohamed E. Mahmoud, Sawsan S. Haggag, M. Abdel Rafea and Tarek M. Abdel-Fattah

Polyhedron 28 (2009) 3407

Nano-sized Co(II)-8-hydroxyquinolate complex thin film via surface layer-by-layer chemical deposition method: Optimized factors and optical properties

Thin film formation of nano-sized Co(II)-8-hydroxyquinolate complex by surface layer-by-layer chemical deposition method was studied and evaluated on the basis of metal analysis, SEM, EI-MS, FT-IR and TGA. Several controlling factors were optimized for thin film formation including the stoichiometric ratio of metal to ligand, number of dipping cycles and immersion times, pH value of interacting species and the solvent effect. The optical properties of Co(II)-8-hydroxyquinolate thin film were also explored and proved its potential applications as a hybrid organic/inorganic semi-conductor type.

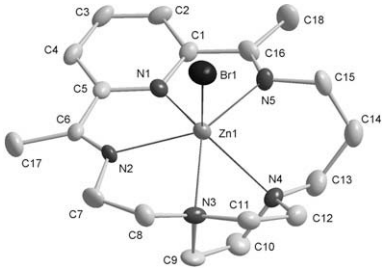


Hassan Keypour, Majid Rezaeivala, Laura Valencia, Paulo Pérez-Lourido and Amir H. Mahmoudkhani

Polyhedron 28 (2009) 3415

Synthesis and characterization of two zinc(II) macrocyclic Schiff-base complexes containing piperazine moiety, crystal structure of one complex

Two new symmetrical and asymmetrical Zn(II) complexes of a pentadentate (N_5) macrocyclic Schiff-base ligands, were prepared via templated [1+1] cyclocondensation of 2,6-diacetylpyridine with two different amines containing piperazine moiety. The complexes have been characterized by variety spectroscopic methods and for asymmetric complex crystal structure was determined by X-ray diffraction.

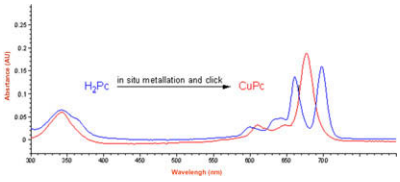


Yusuf Yılmaz, M. Kasım Şener, İbrahim Erden and Ulvi Avcıata

Polyhedron 28 (2009) 3419

Derivatization and in situ metallation of phthalocyanines using click chemistry

Alkynyl phthalocyanines were synthesized without protective/deprotective chemistry. Subsequently, in situ metallation and 'clicking' were employed for the first time as an efficient and quantitative route to tetratriazole-functionalized phthalocyanines.



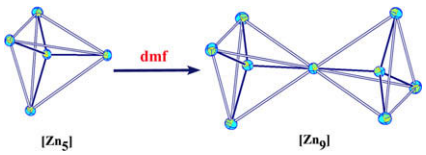
Elsevier Ltd.

Catherine Gkioni, Vassilis Psycharis and Catherine P. Raptopoulou

Polyhedron 28 (2009) 3425

Investigation of the zinc(II) acetylacetonate/benzotriazole reaction system in the presence of bridging *N,N′*-ligands: Pentanuclear, enneanuclear and polymeric complexes

The reaction of $Zn(acac)_2$ with btaH in dmf yields $[Zn_5(bta)_6(acac)_4(dmf)]\cdot dmf$ (**1**·dmf). In the presence of pyrazine, $[Zn_5(bta)_6(acac)_4(dmf)]\cdot 3.7dmf$ (**2**·3.7dmf) and $[Zn_9(bta)_{12}(acac)_6]\cdot 6dmf$ (**3**·6dmf) are obtained, and in the presence of 4,4′-bpy the 1D coordination polymer $[Zn(acac)_2(4,4'\text{-bpy})]_n$ (**4**) is isolated. **3**·6dmf can be alternatively prepared from dissolution of **1**·dmf in dmf.

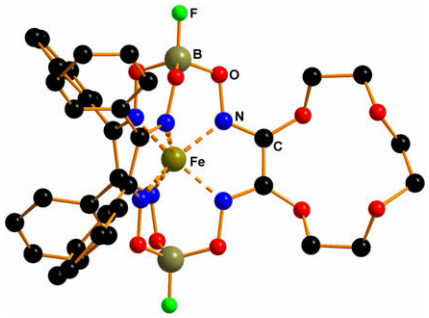


Oleg A. Varzatskii, Yan Z. Voloshin, Sergey V. Korobko, Sergey V. Shulga, Roland Krämer, Alexander S. Belov, Anna V. Vologzhanina and Yurii N. Bubnov

Polyhedron 28 (2009) 3431

On a way to new types of the polyfunctional and polytopic systems based on cage metal complexes: Cadmium-promoted nucleophilic substitution with low-active nucleophilic agents

The one-pot cadmium-promoted nucleophilic substitution of the reactive di- and hexachlorine-containing clathrochelates with soft nucleophilic agents afforded the ribbed-functionalized clathrochelates in high yields under mild conditions. The potential of cadmium-promoted reactions for synthesis of the organic and coordination compounds is discussed.

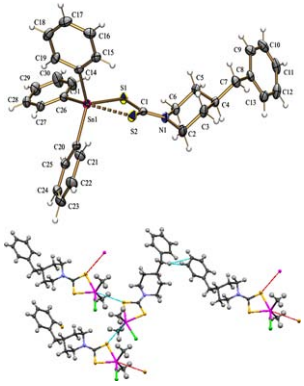


Zia-ur-Rehman, Niaz Muhammad, Shaukat Shuja, Saqib Ali, Ian S. Butler, Auke Meetsma and Momin Khan

Polyhedron 28 (2009) 3439

New dimeric, trimeric and supramolecular organotin(IV) dithiocarboxylates: Synthesis, structural characterization and biocidal activities

Several new organotin(IV) dithiocarboxylates have been synthesised and structurally characterized by spectroscopic techniques. X-ray crystallographic study revealed that these complexes have the ability to form dimeric, trimeric and supramolecular structures via intermolecular non-covalent interactions. Some of the synthesized compounds proved to be good biocides.

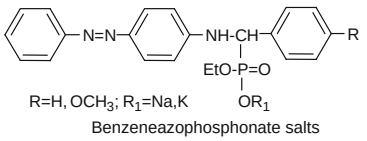


Ljerka Tušek-Božić, Christophe Pannecouque, Erik De Clercq and Jan Balzarini

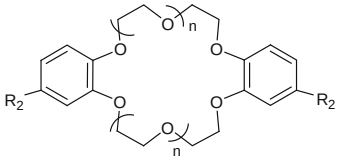
Polyhedron 28 (2009) 3449

Sodium and potassium benzeneazophosphonate complexes with crown ethers: Solid-state microwave synthesis, characterization and biological activity

The eco-friendly synthesis, spectroscopic (IR, MS, ^1H and ^{13}C NMR) study and biological (cytostatic, antiviral) activity of sodium and potassium benzeneazophosphonate complexes, obtained by the solid-state microwave-assisted reaction of alkali monoethyl [α-(4-benzeneazoanilino)-*N*-benzyl]phosphonates and alkali monoethyl [α-(4-benzeneazoanilino)-*N*-4-methoxybenzyl]phosphonates with crown ethers containing 18-, 24- and 30-membered macrocyclic rings, have been described.



Benzeneazophosphonate salts



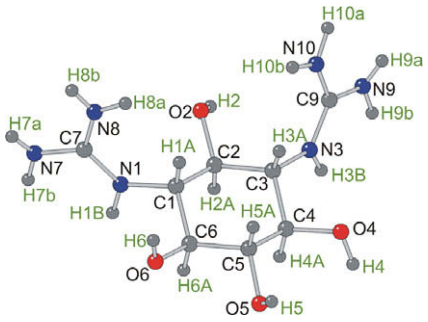
Crown ethers: n=1-3, R_2=H; n=1, R_2=t-Bu

Núria Aliaga-Alcalde, Serena DeBeer George, Israel Alfaro-Fuentes, Geoffrey J.T. Cooper, Norah Barba-Behrens, Sylvain Bernès and Jan Reedijk

Polyhedron 28 (2009) 3459

Physical characterization and biological studies of a (streptidine)($Pt^{II}Cl_4$) compound

The physical characterization with spectroscopy and EXAFS, and biological activity studies of a cationic streptidine complex with platinum are reported.

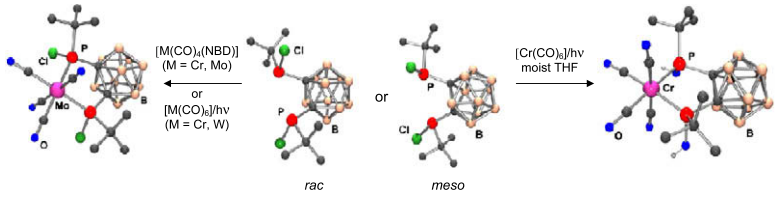


Evgeny G. Rys, Peter Lönnecke, Sven Stadlbauer, Valery N. Kalinin and Evamarie Hey-Hawkins

Polyhedron 28 (2009) 3467

Chiral functionalized bisphosphine ligands: Transition metal complexes of 1,2-bis(*tert*-Butylchlorophosphino)-1,2-dicarba-*closo*-dodecaborane(12)

rac- or *meso*-[$M(CO)_4${1,2-($P^tBuCl)_2C_2B_{10}H_{10}$}] (M = Cr, Mo, W) are readily obtained from *rac*- or *meso*-1,2-($P^tBuCl)_2C_2B_{10}H_{10}$. UV irradiation of 1,2-($P^tBuCl)_2C_2B_{10}H_{10}$ with [$Cr(CO)_6$] in moist THF proceeds with hydrolysis and formation of [$Cr(CO)_4${1,2-($P(OH)^tBu)_2C_2B_{10}H_{10}$}].

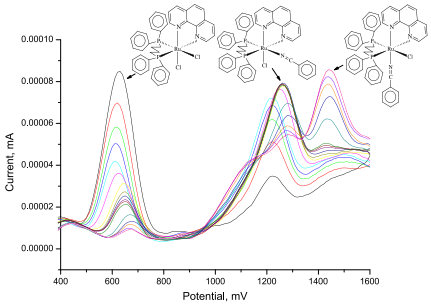


Eliana M.A. Valle, Benedicto A.V. Lima, Antonio G. Ferreira, Fábio B. do Nascimento, Victor M. Deflon, Izaura C.N. Diógenes, Ulrich Abram, Javier Ellena, Eduardo E. Castellano and Alzir A. Batista

Polyhedron 28 (2009) 3473

Driving forces in substitution reactions of octahedral complexes: The influence of the competitive effect

The preparation and crystal structure of four Ru(II) complexes of formula [RuCl(L)(dppb)(N-N)]PF_6 (L = 4-methylpyridine, 4-phenylpyridine, benzonitrile; dppb = 1,4-bis(diphenylphosphino)-butane or 1,1′-bis(diphenylphosphino)ferrocene; N-N = 2,2′-bipyridine or 1,10-phenantroline are reported here. In these complexes the chloride *trans* to the phosphorus atoms is more labile than that one *trans* to the nitrogen atoms, but the final position of the entering good π acceptor ligand is better defined by the competitive effect.

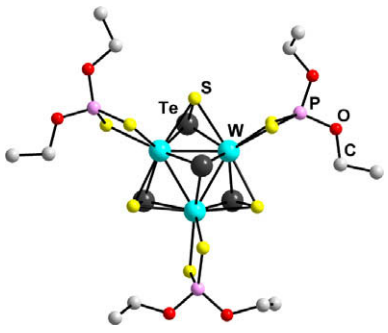


Artem L. Gushchin, Maxim N. Sokolov, Cristian Vicent, Alexander V. Virovets, Eugenia V. Peresypkina and Vladimir P. Fedin

Polyhedron 28 (2009) 3479

Reactions of $M_3Te_7^{4+}$ (M = Mo, W) clusters with electrophilic reagents: Chalcogen exchange in the Te_2 ligand and the first complexes of $(TeS)^{2-}$

Reactions of triangular telluride-bridged clusters [$M_3(\mu_3$-Te)(μ_2-$Te_2)_3((EtO)_2PS_2)_3]^+$ (M = Mo, W) with S_2Cl_2 or Br_2 lead to Te/S exchange in the Te_2 ligands with the formation of complexes with a novel TeS^{2-} ligand. Electrospray ionization mass spectrometry complements the information gathered from X-ray analysis regarding the degree of Te by S substitution.

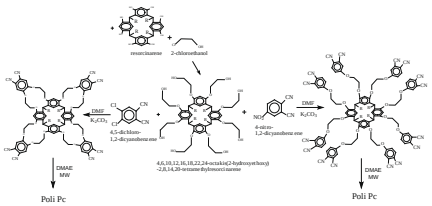


Cihan Kantar, Erbil Ağar and Selami Şaşmaz

Polyhedron 28 (2009) 3485

The microwave-assisted synthesis and characterization of novel, octakis(2-hydroxyethoxy)-resorcinarene bridged polymeric metallophthalocyanines

The new metallophthalocyanine (Zn, Cu, Ni, Co) polymers containing 4,6,10,12,16,18,22,24-octakis(2-hydroxyethoxy)-2,8,14,20-tetramethylresorcinarene are described. Firstly, 4,6,10,12,16,18,22,24-octakis(2-hydroxyethoxy)-2,8,14,20-tetramethylresorcinarene compound (**1**) was synthesized by treating resorcinarene with 2-chloroethanol under microwave irradiation. Then, tetrakis(4,5-bis(2-hydroxyethoxy))phthalonitrile substituted resorcinarene compound (**2**) and octakis(4-(2-hydroxyethoxy))phthalonitrile substituted resorcinarene compound (**3**) were synthesized by treating compound (**1**) with 4,5-dichloro-1,2-dicyanobenzene and 4-nitro-1,2-dicyanobenzene, respectively, under microwave irradiation. The chlorides Cu (II), Ni (II), Co (II), were employed in order to synthesize the corresponding metallophthalocyanine polymers (**2b–d** and **3b–d**) and $Zn(CH_3COO)_2$ was used for the preparation of zinc phthalocyanine polymers (**2a** and **3a**). All products were synthesized by microwave-assisted synthesis method. The structures were characterized by elemental analyses, ^1H NMR, ^{13}C NMR, UV–Vis and FTIR spectroscopy.

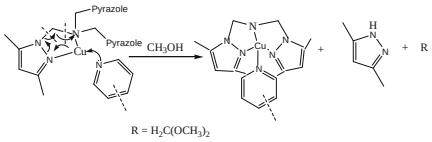


Hong Yang, Yu Tang, Zhen-Feng Shang, Xin-Li Han and Zhi-Hui Zhang

Polyhedron 28 (2009) 3491

Synthetic and structural studies of metal complexes derived from tris(3,5-bimethyl-pyrazolylmethyl)amine and pyridine derivatives

A series of metal complexes with the tripodal ligand (TMPzA) have been synthesized and characterized, and their single crystal structures have been analyzed by X-ray techniques. It was found that when pyridyl derivatives as auxiliary ligands are added to the reaction system, the complexes have the ability to recognize pyridine compounds.

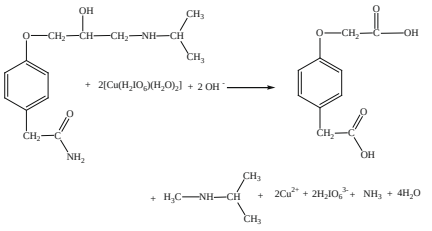


Rajesh N. Hegde, Nagaraj P. Shetti and Sharanappa T. Nandibewoor

Polyhedron 28 (2009) 3499

Oxidative degradation and deamination of atenolol by diperiodatocuprate(III) in aqueous alkaline medium: A mechanistic study

The kinetics of oxidation of atenolol (ATN) by diperiodatocuprate(III) (DPC) in alkaline medium at a constant ionic strength of 0.10 mol dm^{-3} was studied spectrophotometrically. The main oxidative products were identified by spot test, IR, NMR and LC–ESI-MS studies. The reaction constants involved in the different steps of the mechanism were calculated.

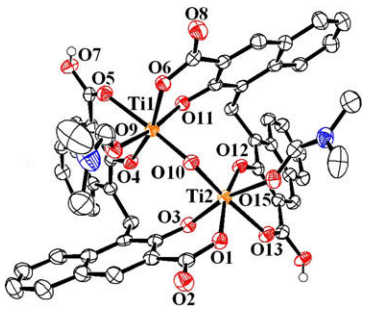


Garima Singh Baghel and Chebrolu P. Rao

Polyhedron 28 (2009) 3507

Pamoic acid in forming metallo-organic framework: Synthesis, characterization and first crystal structure of a dimeric Ti(IV) complex

The ligand, 4,4′-methylene-bis (3-hydroxy-2-naphthalene carboxylic acid) (H_4L) and its dimeric Ti(IV) complexes, having compositions, $[(HL)_2Ti_2(\mu\text{-}O)(DMF)_2]\cdot(DMF)_6$ (**1**) and $[(L)_2Ti_2(\mu\text{-}O)(DMF)_2]\cdot(DMF)_4$(4,4′ Bipy-2H)($H_2O$), (**2**) have been synthesized and characterized by analytical and spectral methods and the structure has been established by single crystal XRD. Both the complexes exhibit dinuclear Ti(IV) centers, though the co-ordination characteristics vary from **1** to **2**. Both the structures exhibited helical chains in their lattices.

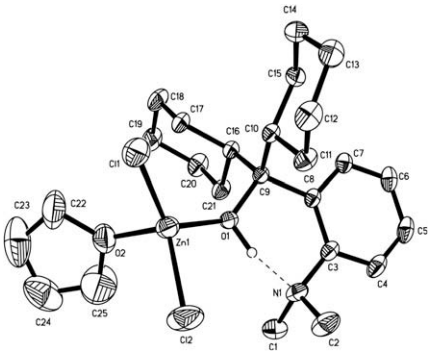


Harbi Tomah Al-Masri, Jens Baldamus and Evamarie Hey-Hawkins

Polyhedron 28 (2009) 3515

Alcohol adducts of zinc dichloride: Molecular structure of $[ZnCl_2(THF)\{1\text{-}HOC(C_6H_{11})_2\text{-}2\text{-}NMe_2C_6H_4\}]$

The aminoalcohols $1\text{-}HOCR_2(CH_2)_n\text{-}2\text{-}NMe_2\text{-}C_6H_4$ react with $ZnCl_2$ in tetrahydrofuran to give the alcohol adducts $[ZnCl_2(THF)\{1\text{-}HOCR_2(CH_2)_n\text{-}2\text{-}NMe_2C_6H_4\}]$ (R = Ph, n = 0, 1; R = Cy, n = 0).

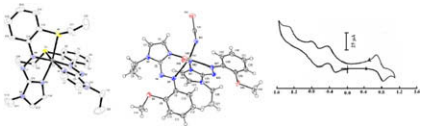


S. Nandi, D. Bannerjee, P. Datta, T.-H. Lu, A.M.Z. Slawin and C. Sinha

Polyhedron 28 (2009) 3519

Cobalt-thioalkylazoimidazole complexes: Structures, spectra and redox properties

$[Co(SRaaiNR^{/})_2](ClO_4)_2$ compounds have been isolated from the reaction between $Co(ClO_4)_2.6H_2O$ and $SRaaiNR^{/}$. A mixture of $Co(OAc)_2{\cdot}4H_2O$, NH_4SCN and $SRaaiNR^{/}$ has isolated $[Co(SRaaiNR^{/})_2(SCN)_2]$. In the previous compound, the ligand acts as a $SRaaiNR^{/}$ tridentate N(imidazole), N(azo), S(thioether) chelator, whilst in the latter compound it serves as a bidentate N(imidazole), N(azo) chelator. Structures are established by X-ray crystallography. Redox chemistry shows Co(III)/Co(II) and azo reductions, azo/azo^{-} and azo^{-}/azo$^{=}$.

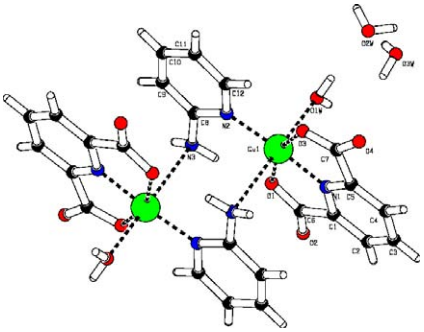


Cengiz Yenikaya, Mehmet Poyraz, Musa Sarı, Fatih Demirci, Halil İlkimen and Orhan Büyükgüngör

Polyhedron 28 (2009) 3526

Synthesis, characterization and biological evaluation of a novel Cu(II) complex with the mixed ligands 2,6-pyridinedicarboxylic acid and 2-aminopyridine

The central Cu(II) ion in novel bridged binuclear Cu(II) complex resides on a centre of symmetry in a distorted square-pyramidal geometry. Free ligands and their complex possess antifungal activity against *Candida* sp.

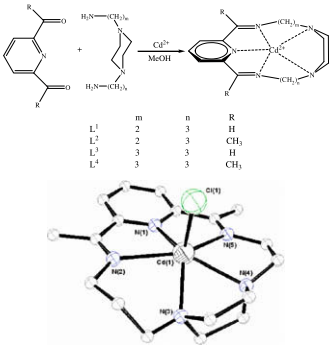


Hassan Keypour, Majid Rezaeivala, Laura Valencia, Sadegh Salehzadeh, Paulo Pérez-Lourido and Hamid Reza Khavasi

Polyhedron 28 (2009) 3533

Synthesis and crystal structure of some new cadmium (II) macrocyclic Schiff-base complexes containing piperazine moiety

The Cd(II) metal templated cyclocondensation of four new pentaaza macrocyclic ligands starting from 2,6-diacetylpyridine or 2,6-pyridinedicarbaldehyde with two different tetraamines containing piperazine moiety have been successfully achieved. The complexes have been characterized by a variety of methods including IR, ^{1}H, ^{13}C NMR, DEPT, COSY(H,H), HMQC(H,C), FAB spectrometry and conductivimetry measurements. The crystal structures of $[CdL^{2}Cl(CH_3OH)]ClO_4$ and $[CdL^{4}(NO_3)(H_2O)]ClO_4$ have been also determined.

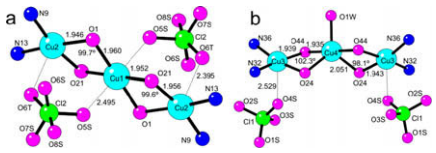


Aurkie Ray, Dipali Sadhukhan, Georgina M. Rosair, Carlos J. Gómez-García and Samiran Mitra

Polyhedron 28 (2009) 3542

An unprecedented Cu^{II}–Schiff base complex existing as two different trinuclear units with strong antiferromagnetic couplings

A new tetradentate N_2O_2 donor Schiff base ligand was obtained by 1:2 condensation of 1,3-diaminopentane with salicylaldehyde and has been used to synthesise an unusual copper(II) complex (**1**) whose asymmetric unit presents two structurally different almost linear trinuclear units. The ligand and the complex were characterised by elemental analysis, FT-IR, ^{1}H NMR, UV–Vis, electrochemical and single crystal X-ray diffraction studies. The magnetic properties of **1** reveal the presence of strong intra-trimer and as well as very weak inter-trimer antiferromagnetic interactions.

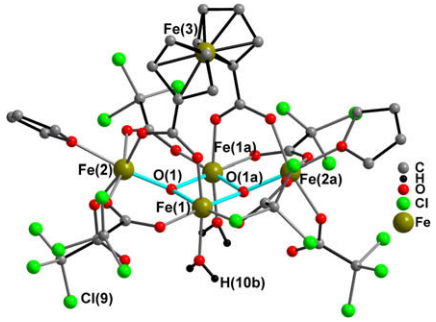


Valeriu Mereacre, Denis Prodius, Ayuk M. Ako, Sergiu Shova, Constantin Turta, Klaus Wurst, Peter Jaitner and Annie K. Powell

Polyhedron 28 (2009) 3551

New penta-nuclear and hepta-nuclear iron(II, III) complexes with ferrocenedicarboxylic acid

Reaction of preformed iron clusters with 1,1′-ferrocenedicarboxylic acid ($fcdcH_2$) yielded penta- and hepta-nuclear $[Fe_4O_2(O_2CCCl_3)_6(fcdc)(THF)_2(H_2O)_2]$ and $[Fe_6O_2(OH)_2(O_2CCMe_3)_{10}(fcdc)(H_2O)_2]$, respectively, which are the first clusters comprising Fe^{III} and the ferrocenedicarboxylic organometallic ligand.

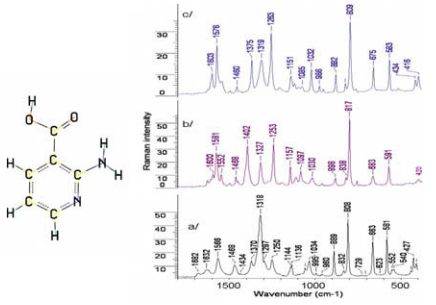


R. Świsłocka, E. Regulska, M. Samsonowicz and W. Lewandowski

Polyhedron 28 (2009) 3556

Experimental (FT-IR, FT-Raman, ^{1}H, ^{13}C NMR) and theoretical study of alkali metal 2-aminonicotinates

The influence of lithium, sodium, potassium, rubidium and cesium on the electronic system of the 2-aminonicotinic acid was studied by the molecular spectroscopy methods. Optimized geometrical structures of studied compounds were calculated by B3LYP method using 6-311++G** basis set. The theoretical NMR, IR and Raman spectra were determined.

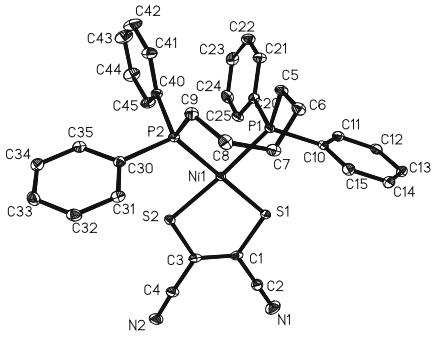


Peter Herich, Jiří Kameníček, Kamil Kuča, Miroslav Pohanka and Milan Olšovský

Polyhedron 28 (2009) 3565

Planar Ni(II) 1,2-dithiolenes involving bidentate *P*-donor ligands

Molecular electronic properties of Ni(II) dithiolene complexes with P,P-ligands and their practical applications (anticholinesterase activity, vulcanization accelerators) were studied. The figure in the graphical abstract shows a molecular structure of [Ni(dppn))(mnt)] complex, dppn = l,5-bis(diphenylphodphino)-pentane, mnt = maleonitriledithiol. The geometry of NiS_2P_2 chromophore is approximately planar.

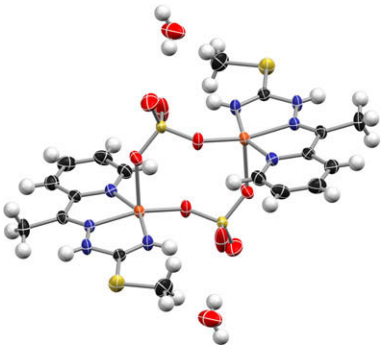


Vukadin M. Leovac, Valerija I. Češljević, Ljiljana S. Vojinović-Ješić, Vladimir Divjaković, Ljiljana S. Jovanović, Katalin Mészáros Szécsényi and Marko V. Rodić

Polyhedron 28 (2009) 3570

Transition metal complexes with thiosemicarbazide-based ligands. Part 56. Square-pyramidal complexes of copper(II) with 2-acetylpyridine *S*-methylisothiosemicarbazone

The subject of this work is the synthesis and single-crystal X-ray analysis of two sulfato and one thiocyanato copper(II) complex with 2-acetylpyridine *S*-methylisothiosemicarbazone (HL) of the formulae: $[Cu(HL)SO_4(H_2O)]\cdot H_2O$ (**1**), $[Cu_2(HL)_2(\mu\text{-}SO_4)_2]\cdot 2H_2O$ (**2**) and $[Cu(HL)(NCS)(SCN)]$ (**3**), as well as the structure of the protonated ligand $H_2L^+I^-$. In contrast to complex **2**, which is an authentic dimer, formed on account of the *exo*-bidentate coordination of both sulfato ligands, the structure of complex **3**, thanks to hydrogen bonding, may be thought of as being a pseudo-dimer. All three complexes have slightly deformed square-pyramidal structures with the tridentate NNN neutral ligand in the basal plane. For complex **3**, different modes of bonding of the ambidentate NCS group were discussed.

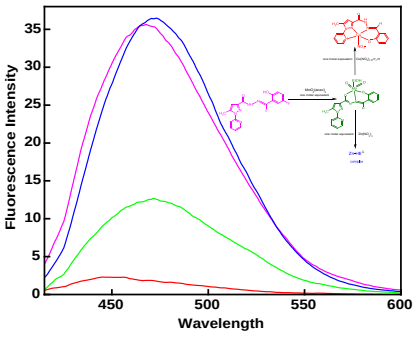


Samik Gupta, Bijan Kumar Paul, Anil Kumar Barik, Tarak Nath Mandal, Somnath Roy, Nikhil Guchhait, Ray J. Butcher and Susanta Kumar Kar

Polyhedron 28 (2009) 3577

Modulation of fluorescence emission of 1-(2-pyridyl) pyrazole derived Schiff base ligands by exploiting their metal ion sensitive binding modes

A two way fluorescence signaling system may be generated by administering two successive metal ion inputs to 1-(2-pyridyl) pyrazole derived ligands which exhibits metal ion sensitive binding modes.

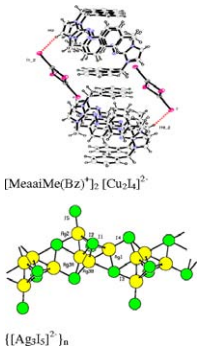


G. Saha, K.K. Sarker, C.-J. Chen, J. Cheng, T.-H. Lu, G. Mostafa and C. Sinha

Polyhedron 28 (2009) 3586

Azoimidazolium iodocuprate(I) and iodoargentate(I)

1,3-Di-alkyl-2-(arylazo)imidazolium iodocuprate(I) and iodoargentate(I) are described in this work. Iodocuprate forms iodo bridged dimmer ($Cu_2I_4^{2-}$) that is electrostatically attracted and has hydrogen bonded to imidazole-H of imidazolium ion. Iodoargentate forms trimeric unit $[Ag_3I_5]^{2-}$ who constitutes iodo bridged 1D chain and anion is placed in the network formed by imidazolium motif.

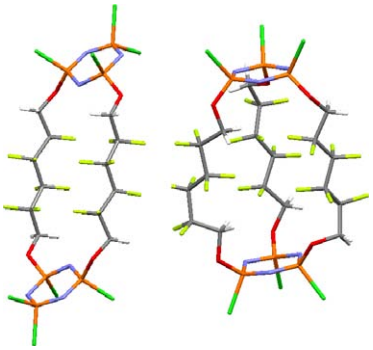


Serap Beşli, Simon J. Coles, David B. Davies, Ayşen O. Erkovan, Michael B. Hursthouse and Adem Kılıç

Polyhedron 28 (2009) 3593

Single-, double- and triple-bridged derivatives of cyclotriphosphazenes with an octafluorohexane-1,6-diol

Novel bridged compounds predominate in the reaction of cyclotriphosphazene with a longer-chain diol.

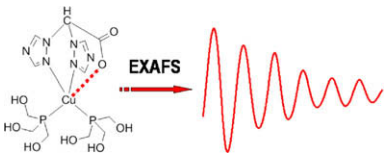


Marco Giorgetti, Lorella Guadagnini, Steven G. Fiddy, Carlo Santini and Maura Pellei

Polyhedron 28 (2009) 3600

Cu K-edge EXAFS on copper(I) complexes containing dihydridobis(3-nitro-1,2,4-triazol-1-yl)-borate and bis(1,2,4-triazol-1-yl)acetate ligand: Evidence for the Cu–O interaction

The EXAFS probe has permitted to check the 5-fold geometry of the Cu(I) with the bis(1,2,4-triazol-1-yl)acetate ligands. An additional bond interaction, due to the oxygen of the acetate sting of the scorpionate ligand, is revealed while comparing other copper(I) complexes, containing the dihydridobis(3-nitro-1,2,4-tryazol-1-yl)borate.

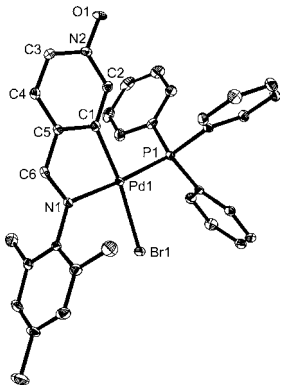


Nina Gómez-Blanco, Jesús J. Fernández, Alberto Fernández, Digna Vázquez-García, Margarita López-Torres, Antonio Rodríguez and José M. Vila

Polyhedron 28 (2009) 3607

Synthesis and characterization of new heterocyclic Schiff base palladacycles: Ring activation through *N*-oxide formation

Schiff base ligands with heterocyclic nitrogen rings may be activated towards metallation to give the corresponding palladacycles through *N*-oxide formation.

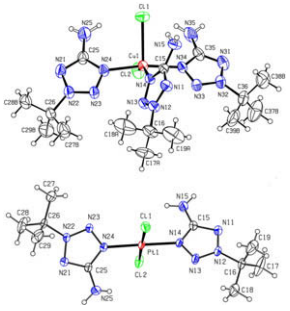


Sergei V. Voitekhovich, Tatiyana V. Serebryanskaya, Alexander S. Lyakhov, Pavel N. Gaponik and Oleg A. Ivashkevich

Polyhedron 28 (2009) 3614

Copper(II), palladium(II) and platinum(II) chloride complexes with 5-amino-2-*tert*-butyltetrazole: Synthesis, characterization and cytotoxicity

Complexes CuL_3Cl_2, PdL_2Cl_2 and PtL_2Cl_2, where L is 5-amino-2-*tert*-butyltetrazole, have been synthesized by the reaction of metal(II) chlorides with L and characterized by IR spectroscopy, thermal and X-ray analyses. In complexes L acts as a monodentate ligand coordinated to the metal *via* endocyclic N4 atom.

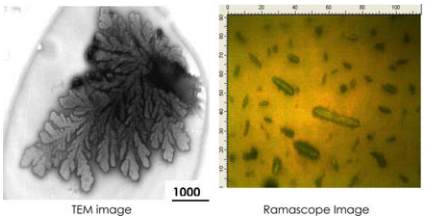


Reama C. George, Mahmut Durmuş, Gabriel O. Egharevba and Tebello Nyokong

Polyhedron 28 (2009) 3621

Electrostatic self-assembly of quaternized 2,(3)-tetra(oxo-pyridine) phthalocyaninato chloroindium(III) with a series of tetrasulfonated phthalocyanines

The interaction of positively charged quaternized 2,(3)-tetra(oxo-pyridine) phthalocyaninato chloroindium (III) (QInPyPc) and a series of negatively charged tetrasulfonate phthalocyanine (MTSPc), M = Mn, Fe, Co and Ni result in the formation of heteroaggregates, whose TEM or Ramanscope images show norod and nanoleaf shapes.

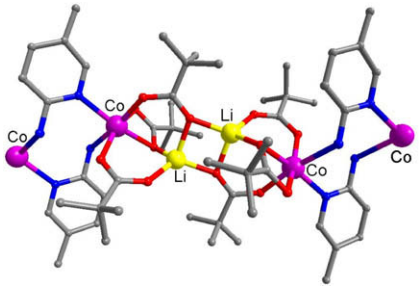


Mikhail Bykov, Anna Emelina, Mikhail Kiskin, Aleksei Sidorov, Grigory Aleksandrov, Artem Bogomyakov, Zhanna Dobrokhotova, Vladimir Novotortsev and Igor Eremenko

Polyhedron 28 (2009) 3628

Coordination polymer $[Li_2Co_2(Piv)_6(\mu\text{-}L)_2]_n$ (L = 2-amino-5-methylpyridine) as a new molecular precursor for $LiCoO_2$ cathode material

The solid-state thermolysis (420–450 °C) of the new heterometallic coordination polymer $[Li_2Co_2(Piv)_6(\mu\text{-}L)_2]_n$ followed by annealing of the decomposition products at 500 °C was shown to afford $LiCoO_2$ in quantitative yield.

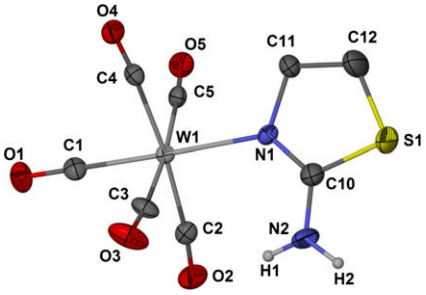


Leigh-Anne de Jongh, Christoph E. Strasser, Helgard G. Raubenheimer and Stephanie Cronje

Polyhedron 28 (2009) 3635

Imine coordinated 2-aminoazole complexes of $(CO)_5Cr(0)$ and $(CO)_5W(0)$, verification by structural characterisation

The structural characterisation of $(CO)_5M$(2-aminoazole), where M = Cr or W, showed preferred endocyclic imine coordination when provided with endocyclic soft thioether or endocyclic hard amine, endocyclic borderline imine and exocyclic hard amine coordination sites. An upfield shift of 70–76 ppm is observed for the ^{15}N NMR signal of the imine nitrogen upon coordination.

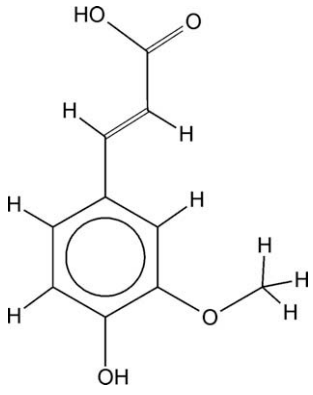


Nives Kitanovski, Andrej Pevec and Bojan Kozlevčar

Polyhedron 28 (2009) 3642

Copper(II) coordination compounds with ferulic acid

The first two molecular structures of the ferulic acid coordination compounds in $[Cu_2(C_{10}H_9O_4)_4(CH_3CN)_2]$ **1** and $[Cu_2(C_{10}H_9O_4)_4(C_6H_6N_2O)_2]\cdot 4CH_3CN$ ($C_6H_6N_2O$ = nicotinamide) **2** are presented. Both compounds were synthesised from the starting copper(I) upon copper oxidation in the acetonitrile solution. They are unstable outside mother liquid giving final $[Cu_2(C_{10}H_9O_4)_4]$ **1a** and $[Cu_2(C_{10}H_9O_4)_4(C_6H_6N_2O)_2]$ **2a**. The triplet $S = 1$ EPR spectra and $\mu_{eff} \sim 1.45$ B.M. confirm the antiferromagnetic interaction in the final products, and consequently a preservation and stability of the *paddle–wheel* structures in **1a** and **2a** by 'oxidative' copper(II) cations and 'antioxidative' ferulic acid anions.

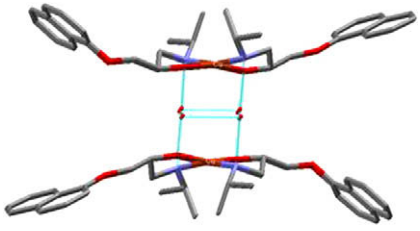


I. Viera, M.A. Gómez, J. Ellena, A.J. Costa-Filho, E.R. Migliaro, L. Domínguez and M.H. Torre

Polyhedron 28 (2009) 3647

Synthesis, structural characterization and *ex vivo* biological properties of a new complex $[Cu(propranolol)_2]\cdot 2H_2O$, a potential beta-blocker

Cu(II) complex with a betablocker propranolol was synthesized and characterized (UV–Vis, IR, EPR, X-ray diffraction) in solid state and in solution, showing the coordination of each copper ion with two S and R propranolol isomers. Analysis of the effect on heart contraction force and on heart rate is reported.

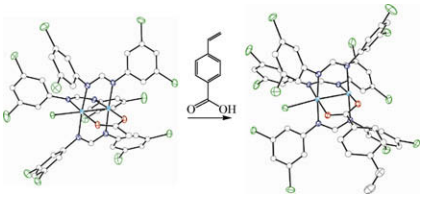


Yang Fan, Phillip E. Fanwick and Tong Ren

Polyhedron 28 (2009) 3654

Preparation and characterization of diruthenium-(II,III) compounds containing terminal olefin groups

Diruthenium compounds containing terminal olefin have been synthesized and characterized.



The Publisher encourages the submission of articles in electronic form thus saving time and avoiding rekeying errors. For detailed instructions on the preparation of manuscripts and of electronic artwork, consult the Author Gateway for Elsevier at http://authors.elsevier.com

ScienceDirect

Full text of this journal is available, on-line from **ScienceDirect**. Visit **www.sciencedirect.com** for more information.

Polyhedron 28, issue 13, 2 September 2009

Contents lists available at ScienceDirect

Polyhedron

journal homepage: www.elsevier.com/locate/poly

Contents

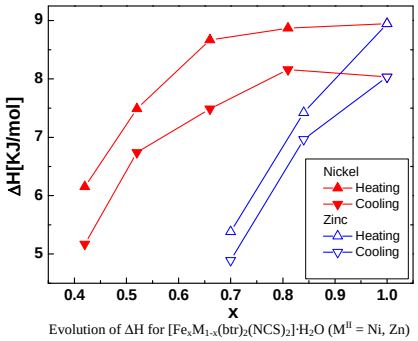
Papers

Aurelian Rotaru, Marinela M. Dîrtu, Cristian Enachescu, Radu Tanasa, Jorge Linares, Alexandru Stancu and Yann Garcia

Polyhedron 28 (2009) 2531

Calorimetric measurements of diluted spin crossover complexes $[Fe_xM_{1-x}(btr)_2(NCS)_2]\cdot H_2O$ with M^{II} = Zn and Ni

We have measured by Differential Scanning Calorimetry (DSC) the heat capacity in the heating and cooling modes and then calculated the enthalpy and the entropy variations at the phase transition of $[Fe_xM_{1-x}(btr)_2(NCS)_2]\cdot H_2O$ with M^{II} = Zn and Ni spin crossover complexes.



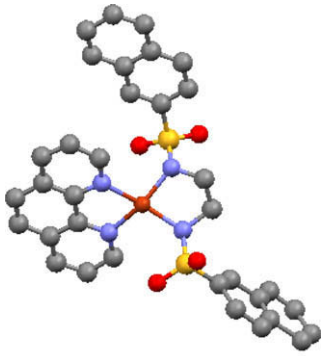
Evolution of ΔH for $[Fe_xM_{1-x}(btr)_2(NCS)_2]\cdot H_2O$ (M^{II} = Ni, Zn)

Andreea Bodoki, Adriana Hangan, Luminita Oprean, Gloria Alzuet, Alfonso Castiñeiras and Joaquín Borrás

Polyhedron 28 (2009) 2537

Oxidative DNA cleavage by copper ternary complexes of 1,10-phenanthroline and ethylenediamine-sulfonamide derivatives

Three ternary copper(II) complexes of 1,10-phenanthroline and ethylenediamine-R-sulfonamide derivatives have been synthesized and structurally characterized. The interaction of the complexes with CT-DNA stabilizes the native DNA conformation. All three complexes were found to be very efficient agents of plasmid DNA cleavage in the presence of ascorbate as reducing agent.



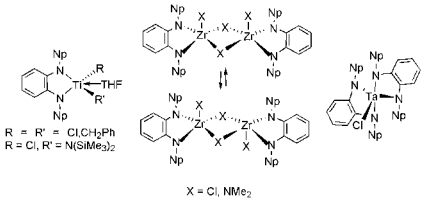
[Cu(L3)(phen)]

Vanessa Tabernero, Tomás Cuenca, Marta E.G. Mosquera and Carmen Ramírez de Arellano

Polyhedron 28 (2009) 2545

Early transition metal derivatives stabilised by the phenylenediamido 1,2-$C_6H_4(NCH_2tBu)_2$ ligand: Synthesis, characterisation and reactivity studies: Crystal structures of [Ta{1,2-C_6H_4-$(NCH_2tBu)_2$}$_2$Cl] and [Zr{(1,2-$C_6H_4(NCH_2tBu)_2$}-$(NMe_2)(\mu$-$NMe_2)]_2$

A series of phenylenediamido titanium, zirconium and tantalum derivatives have been prepared by different synthetic pathways and have been fully characterised. Reactions with alkylating reagents, the tendency to coordinate donor ligands and their reactivity with Lewis acid reagents are described.

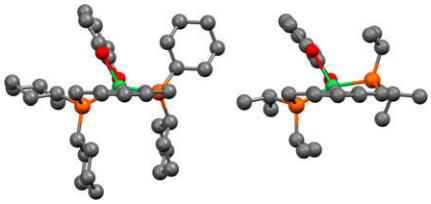


Konstantin A. Kozhanov, Michael P. Bubnov, Nina N. Vavilina, Larisa Yu. Efremova, Georgy K. Fukin, Vladimir K. Cherkasov and Gleb A. Abakumov

Polyhedron 28 (2009) 2555

Novel structurally characterized *o*-semiquinonato PCP-pincer nickel complexes

Structural study of dialkyl (PCP)-pincer *o*-semiquinonato nickel complexes indicated sloped relative positions of bi- and tri-dentate ligands. It became bright confirmation of propositions made on the base of their EPR spectra followed by molecular modelling.

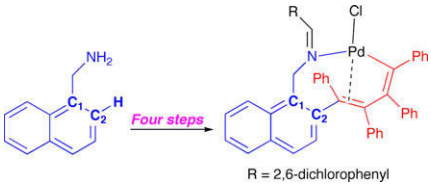


Joan Albert, Lucía D'Andrea, Graciela García, Jaume Granell, Abdelouahab Rahmouni, Mercè Font-Bardia and Teresa Calvet

Polyhedron 28 (2009) 2559

Cyclopalladation of (*E*)-N-(2,6-dichlorobenzylidene)(naphthalen-1-yl)methanamine: Synthesis and X-ray molecular structure of [κ^2-***N,C1***-η^2-***C3,C4***-**Pd{(PhC═CPh)**$_2$–$C_{10}H_6$–CH_2–N═CH–(2,6-$Cl_2C_6H_3$)}Cl]·CH_2Cl_2

A selective palladation at the 2 position of a naphthyl group and a diinsertion of diphenylacetylene into the Pd–C σ bond formed is reported.

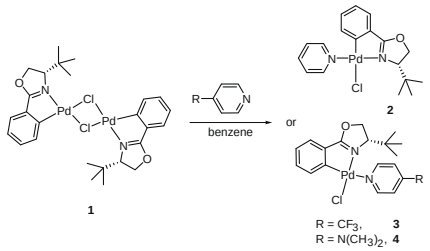


Zhong-Lin Lu, Xiao-Sheng Yang, Rui-Yao Wang, Hoong-Kun Fun and Suchada Chantrapromma

Polyhedron 28 (2009) 2565

Substituted pyridine coordinated *N,N-trans* and *N,N-cis* cyclopalladated complexes of (*S*)-4-*tert*-butyl-2-phenyl-2-oxazoline: Crystal structures, spectral study and catalysis of the decomposition of P═S pesticides

Three cyclopalladated complexes with a chiral oxazoline backbone and substituted pyridine co-ligand show different coordination configurations in the solid state and different catalytic activities on the decomposition of P═S pesticides.

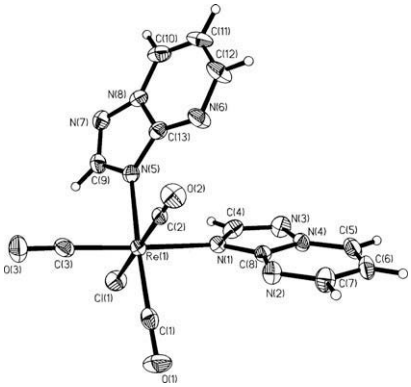


B. Machura, M. Jaworska, P. Lodowski, J. Kusz, R. Kruszynski and Z. Mazurak

Polyhedron 28 (2009) 2571

Synthesis, spectroscopic characterization, X-ray structure and DFT calculations of [$Re(CO)_3L_2Cl$] (L = 1,2,4-triazolo-[1,5-a]pyrimidine)

The paper presents a combined experimental and computational study of novel tricarbonyl complex – *fac*-[$Re(CO)_3(tp)_2Cl$] (tp = 1,2,4-triazolo-[1,5-a]pyrimidine). The compound has been characterised spectroscopically and structurally (by single-crystal X-ray diffraction). The absorption and emission spectra of the complex have been discussed on the basis of DFT and time-dependent (TD)DFT calculations.

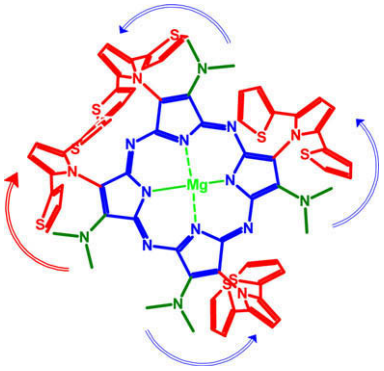


Tomasz Goslinski and Andrew J.P. White

Polyhedron 28 (2009) 2579

Synthesis, characterization and spectroscopic properties of novel periphery – functionalized unsymmetrical porphyrazines containing mixed dithienylpyrrolyl and dimethylamino groups

The novel porphyrazines bearing mixed dithienylpyrrolyl and dimethylamino groups in the periphery have been prepared *via* macrocyclization reaction. The asymmetry imposed by the non-alternate order of the two peripheral substituents, breaking C_4 symmetry, was confirmed by X-ray and NMR studies. The newly synthesized, unsymmetrical magnesium porphyrazine revealed interesting solvatochromic properties.

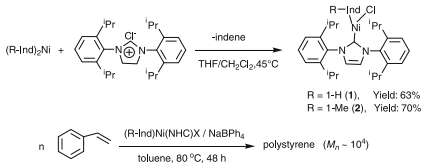


Ling-Zhi Xie, Hong-Mei Sun, Dong-Mei Hu, Zhi-Hong Liu, Qi Shen and Yong Zhang

Polyhedron 28 (2009) 2585

Synthesis and structure of indenylnickel(II) chlorides bearing free *N*-heterocyclic carbene ligands and their catalysis for styrene polymerization

Neutral indenylnickel(II) halides bearing a free *N*-heterocyclic carbene (NHC) ligand (**1** and **2**) have been synthesized and characterized by X-ray structural analysis. A close relationship between the structure and catalytic activity of NHC indenylnickel(II) halides is observed for the first time.

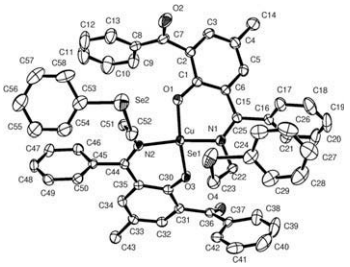


Vinay K. Verma, Ashish K. Asatkar, Tripti A. Jain, Santosh K. Tripathi, Rajendra Singh, Peter B. Hitchcock, Siddhi Nigam and Sushil K. Gupta

Polyhedron 28 (2009) 2591

Synthesis, structure and DNA binding studies of mononuclear copper(II) complexes with mixed donor macroacyclic ligands, 2,6-bis({*N*-[2&3-(phenylselenato)alkyl]}benzimidoyl)-4-methylphenol

Two new phenol based macroacyclic Schiff base ligands, 2,6-bis({*N*-[2-(phenylselenato)ethyl]}benzimidoyl)-4-methylphenol (bpebmpH, **1**) and 2,6-bis({*N*-[3-(phenylselenato)propyl]}benzimidoyl)-4-methylphenol (bppbmpH, **2**) of the Se_2N_2O type have been prepared by the condensation of 4-methyl-2,6-dibenzoylphenol (mdbpH) with the appropriate (for specific reactions) phenylselenato(alkyl)amine. These ligands with Cu(II) acetate monohydrate in a 2:1 molar ratio in methanol form complexes of the composition $[(C_6H_2(O)(CH_3)\{(C_6H_5)C{=}N(CH_2)_n\text{-}Se(C_6H_5)\}\{(C_6H_5)C{=}O\}_2Cu]$ (**3** (n = 2), **4** (n = 3)) with the loss of phenylselenato(alkyl)amine and acetic acid. In both these complexes, one arm of the ligand molecule undergoes hydrolysis, and links with Cu(II) in a bidentate (NO) fashion, as confirmed by single crystal X-ray crystallography of complex **3**. The selenium atoms do not form part of the copper(II) distorted square planar coordination sphere which has a *trans*-CuN_2O_2 core. The average Cu–N and Cu–O distances are, respectively, 1.973(3) and 1.898(2) Å. The N–Cu–N and O–Cu–O angles are, respectively, 167.4(11)° and 164.5(12)°. The compounds **1**–**4** have been characterized by elemental analysis, conductivity measurements, mass spectrometry, IR, electronic, ^1H and $^{77}Se\{^1H\}$ NMR spectroscopy and cyclic voltammetry. The interaction of complex **3** with calf thymus DNA has been investigated by a spectrophotometric method and cyclic voltammetry.

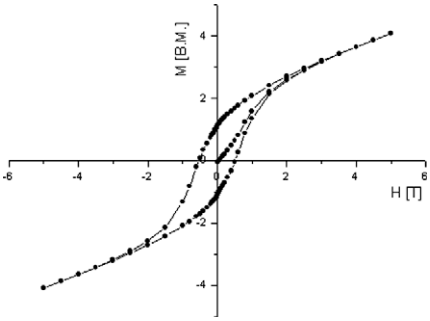


Angad Kumar Singh, Sanyucta Kumari, K. Ravi Kumar, B. Sridhar, Miroslaw Wrzecion, Jerzy Mroziński and T.R. Rao

Polyhedron 28 (2009) 2599

Complexes of 3*d* metal ions of the Schiff-base, 4-hydroxy-*N*′-(4′-octadecyloxybenzylidene)benzohydrazide: Synthesis, spectral studies, crystal structure and magnetic interactions

A *nematic* hydrazide-based Schiff-base, 4-Hydroxy-*N*′-(4′-octadecyloxybenzylidene)benzohydrazide, (HL^3), yields non-mesogenic complexes, $[M(HL^3)_2](OAc)_2$, (M = Mn, Co, Cu and Zn) and a mesogenic Ni^{II} complex. The Mn^{II} and Co^{II} complexes show anti-ferromagnetic interaction and a weak ferromagnetic coupling at lower temperatures; further, the former complex shows magnetic hysteresis loops.

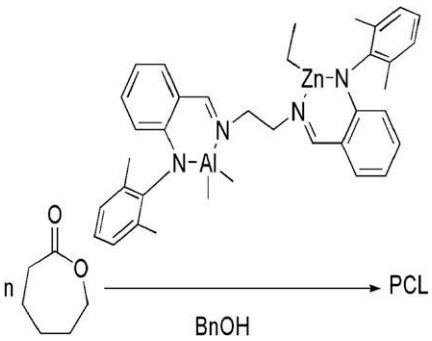


Ai-Hong Gao, Wei Yao, Ying Mu, Wei Gao, Ming-Tai Sun and Qing Su

Polyhedron 28 (2009) 2605

Heterobimetallic aluminium and zinc complex with *N*-arylanilido-imine ligand: Synthesis, structure and catalytic property for ring-opening polymerization of -caprolactone

A heterobimetallic Al/Zn complex and a monometallic Al complex were synthesized. Both complexes are efficient catalysts for the ring-opening polymerization of ε-caprolactone in the presence of benzyl alcohol.

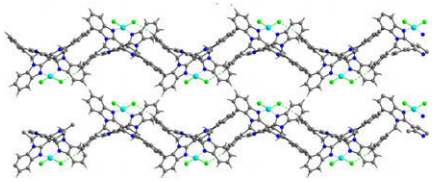


Bao-Ming Ji, Shao-Bin Miao, Dong-Sheng Deng and Chen-Xia Du

Polyhedron 28 (2009) 2611

The C–H···Cl_2Cu(II) synthon in the structural direction and assembly of supramolecular complexes with the 3,3′-bis(2-benzimidazolyl)-2,2′-dipyridine ligand and its N-substituted derivatives

Three new Cu(II) supramolecular complexes were constructed from the 3,3′-bis(2-benzimidazolyl)-2,2′-dipyridine ligand and its N-substituted derivatives. In the three crystal structures, the C–H···Cl_2Cu supramolecular synthons, play a significant role in the formation and stabilization of the structures, and additional non-covalent interactions, such as C–H···π, can extend the discrete (0-D) or low-dimensional (1-D) motifs into high-dimensional architectures.

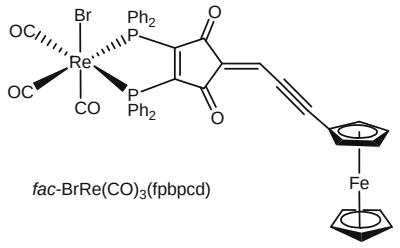


Bhaskar Poola, Xiaoping Wang and Michael G. Richmond

Polyhedron 28 (2009) 2619

New rhenium(I) compounds containing the donor–acceptor diphosphine ligands 2-(ferrocenylidene)-4,5-bis(diphenylphosphino)4-cyclopenten-1,3-dione (fbpcd) and 2-(3-ferrocenylprop-2-ynylidene)-4,5-bis(diphenylphosphino)4-cyclopenten- 1,3-dione (fpbpcd): Electrochemical behavior, MO properties, and X-ray diffraction structure of *fac*-Br$Re(CO)_3$(fpbpcd)

The diphosphine ligands fbpcd and fpbpcd react with $BrRe(CO)_3(THF)_2$ to furnish the diphosphine-substituted compounds *fac*-$BrRe(CO)_3$(fbpcd) (**2**) and *fac*-$BrRe(CO)_3$(fpbpcd) (**3**), respectively. The more highly conjugated fpbpcd ligand was prepared from 3-ferrocenylpropynal and 4,5-bis(diphenylphosphino)-4-cyclopenten-1,3-dione (bpcd) via a Knoevenagel condensation. **2** and **3** have been isolated and fully characterized by a combination of IR and NMR spectroscopies, mass spectrometry, and X-ray diffraction analysis in the case of **3**. Cyclic voltammetric studies reveal well-defined 0/1^+ and 0/1^- redox couples for both new rhenium compounds, and the nature of the HOMO and LUMO levels is discussed relative to MO calculations at the extended Hückel level.

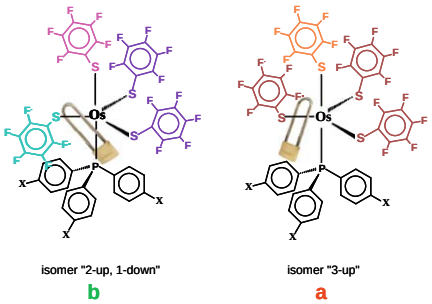


Maribel Arroyo, Consuelo Mendoza, Sylvain Bernès, Hugo Torrens and Hugo Morales-Rojas

Polyhedron 28 (2009) 2625

Five-coordinate pentafluorobenzothiolate osmium(IV) complexes $[Os(SC_6F_5)_4(P(C_6H_4X\text{-}4)_3)]$ (X = OCH_3, CH_3, F, Cl or CF_3): Solid and solution structural characterization

X-ray diffraction studies of $[Os(SC_6F_5)_4(P(C_6H_4X\text{-}4)_3)]$ exhibit a tbp coordination with the three *eq*-C_6F_5-rings towards the *ax*-thiolate (isomers "3-up"). NMR studies at r.t. reveal in addition the "2-up, 1-down" isomer with two *eq*-C_6F_5-rings towards the *ax*-thiolate and the third *eq*-C_6F_5-ring towards the phosphane. At low temperatures are observed restricted rotations about specific bonds in these molecules.

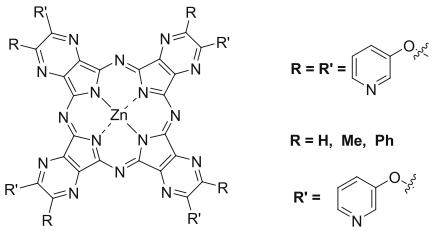


Eva H. Mørkved, Trygve Andreassen and Per Bruheim

Polyhedron 28 (2009) 2635

Zinc azaphthalocyanines with pyridin-3-yloxy peripheral substituents

Four new zinc azaphthalocyanines, octa-substituted with pyridin-3-yloxy groups, or substituted with pyridin-3-yloxy in combination with H, Me and Ph groups, have been synthesized and characterized. Two new complexes between the pyridin-3-yloxy substitutents of the monomer pyrazine-2,3-dicarbonitriles and zinc(II) have been isolated as well.

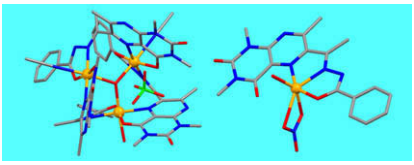


Sonia B. Jiménez-Pulido, Fátima M. Linares-Ordóñez and Miguel N. Moreno-Carretero

Polyhedron 28 (2009) 2641

Novel coordination behavior of a pteridine-benzoylhydrazone ligand (BZLMH): Theoretical calculations, XRD structures and luminescence studies

The reactivity of the benzoylhydrazone of 6-acetyl-1,3,7-trimethyl-(1*H*,3*H*)-pteridine-2,4-dione) towards Ni(II), Zn(II) and Hg(II) has been investigated and the XRD structure of a nickel trimer and a monomeric Zn(II) complexes reported. A wide variety of coordinating patterns for the ligand are reported, which may influence the fluorescence spectroscopic properties of the complexes.

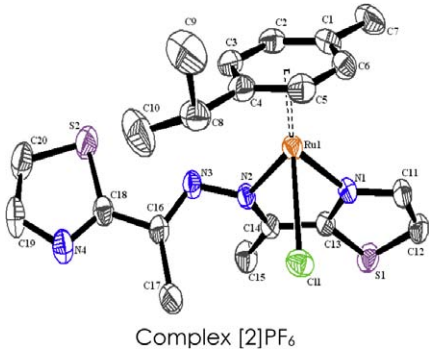


Kota Thirumala Prasad, Gajendra Gupta, Anna Venkateswara Rao, Babulal Das and Kollipara Mohan Rao

Polyhedron 28 (2009) 2649

New series of platinum group metal complexes bearing η^5- and η^6-cyclichydrocarbons and Schiff base derived from 2-acetylthiazole: Syntheses and structural studies

Series of platinum group metal complexes bearing η^5- and η^6-cyclichydrocarbons and 2-acetylthiazole azine ligand have been synthesized.

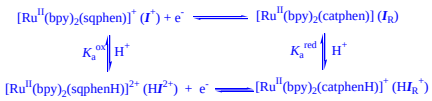


Amit Mondal, Piyali De, Subrata Mukhopadhyay, Rupendranath Banerjee, Prasenjit Kar, Amilan D. Jose and Amitava Das

Polyhedron 28 (2009) 2655

Kinetics of oxidation of quinol and ascorbic acid with the phen substituted semiquinone ligand, (5,6-dioxolene-1,10-phenanthroline-O,O), bound to the $Ru^{II}(bipy)_2$ moiety

The phen substituted semiquinone ligand, 5,6-dioxolene-1,10-phenanthroline-O,O (sqphen), while bound to the RuII(bpy)2 moeity, oxidizes ascorbic acid and quinol at a slower rate than does the semiquinone (sq) bound to the same moiety; the basicity of sqphen decreases considerably on coordination to $Ru^{II}(bpy)_2$, moreover, bound sqphen is less basic than bound sq, but the basicity of bound sqphen enhances on reduction to its catechol form, catphen.

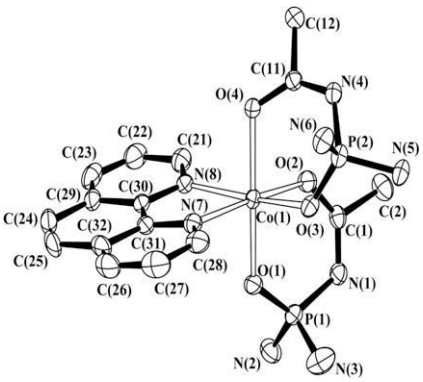


Kateryna E. Gubina, Oleg A. Maslov, Elizaveta A. Trush, Victor A. Trush, Vladimir A. Ovchynnikov, Svetlana V. Shishkina and Vladimir M. Amirkhanov

Polyhedron 28 (2009) 2661

Novel heteroligand complexes of Co(II), Cu(II), Ni(II) and Mn(II) formed by 2,2′-dipyridyl or 1,10-phenanthroline and phosphortriamide ligands: Synthesis and structure

Examples of mixed-ligand Co(II), Cu(II), Ni(II) and Mn(II) complexes having a distorted octahedral coordination geometry with 2,2′-dipyridyl or 1,10-phenanthroline and phosphortriamide ligands have been prepared and characterised by means of X-ray diffraction, IR, UV–Vis spectroscopy. The phosphortriamide ligands are coordinated *via* the oxygen atoms of the phosphoryl and carbonyl groups, and are involved in six-membered metal cycles. The additional ligands 2,2′-dipyridyl or 1,10-phenanthroline are coordinated to the central atom, forming five-membered cycles.

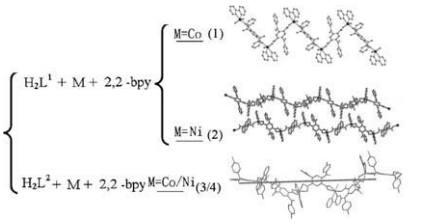


Yanhong Zhou, Li Guan and Hong Zhang

Polyhedron 28 (2009) 2667

Synthesis, crystal structure and properties of cobalt(II) and nickel(II) coordination polymers supported by functionalized dicarboxylate ligands

Four new coordination polymers with carboxylate ligands, namely, $[CoL^1(2,2'\text{-bpy})(H_2O)]$ (**1**), $[NiL^1(2,2'\text{-bpy})(H_2O)]\cdot H_2O$ (**2**), $[Co_2(L^2)_2(2,2'\text{-bpy})_2(H_2O)]$ (**3**) and $[Ni_2(L^2)_2(2,2'\text{-bpy})_2(H_2O)]$ (**4**), where H_2L^1 = 2,5-dibenzoylterephthalic acid, H_2L^2 = 4,6-bis(4-methylbenzoyl)isophthalic acid and 2,2′-bpy = 2,2′-bipyridine, have been synthesized and characterized. They are chain structures which further extend into 2D structures via superamolecular forces; in addition, **3** and **4** are isomorphous.

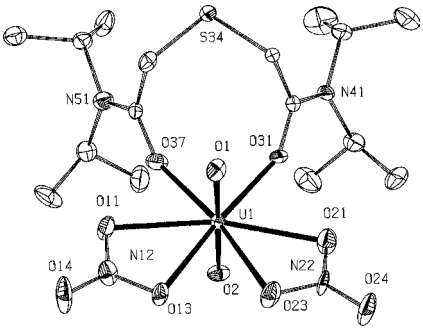


S.B. Deb, J.S. Gamare, S. Kannan and M.G.B. Drew

Polyhedron 28 (2009) 2673

Uranyl(VI) and lanthanum(III) thio-diglycolamides complexes: Synthesis and structural studies involving nitrate complexation

New tri-functional ligands of the type $R_2NCOCH_2SCH_2CONR_2$ (R = iso-propyl, *n*-butyl or iso-butyl) were prepared and their coordination chemistry with the uranyl and lanthanum(III) nitrates has been established. The structures of the uranyl and lanthanum(III) nitrates show the chelating mode of bonding for these ligands in the solid state. Solvent extraction studies show that the ligand can extract the uranyl ion from nitric acid medium but does not show any ability to extract the americium(III) ion.

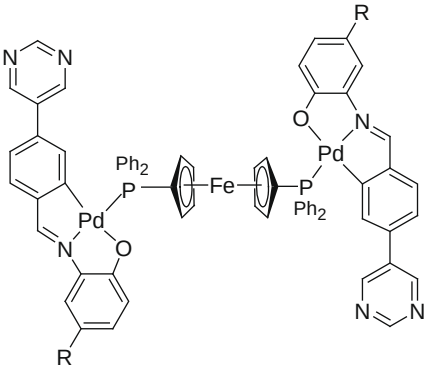


Jesús J. Fernández, Nina Gómez-Blanco, Alberto Fernández, Digna Vázquez-García, Margarita López-Torres and José M. Vila

Polyhedron 28 (2009) 2679

Seeking new metalloligands: Synthesis and reactivity of palladacycles with pyridine and pyrimidine rings

Terdentate [C,N,O] Schiff bases with pyridine or pyrimidine rings yield new mono- and polynuclear palladacycles bearing non-coordinated heterocyclic nitrogen donors.

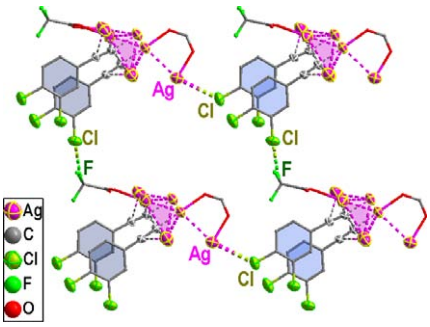


Siegfried M.J. Wang and Thomas C.W. Mak

Polyhedron 28 (2009) 2684

Coordination networks constructed with supramolecular synthon R_X–C≡C⊃Ag_n (n = 4, 5; R_X = halophenyl)

Silver–halophenylethynide Supramolecular Synthon. In eight new silver(I)–ethynide complexes constructed with the R_X–C≡C⊃Ag_n (n = 4, 5; R_X = halophenyl) supramolecular synthon, various types of silver···halogen and halogen···halogen interactions are found to contribute to stabilization of their network structures.

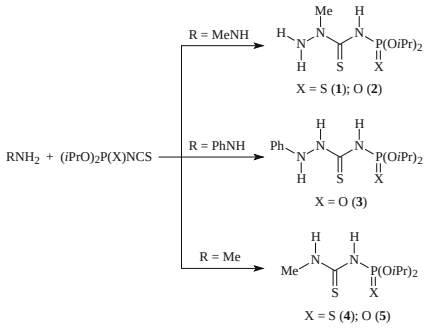


Maria G. Babashkina, Damir A. Safin, Michael Bolte and Axel Klein

Polyhedron 28 (2009) 2693

Synthesis of *N*-(thio)phosphorylated thiosemicarbazides RC(S)NHP(X)(O*i*Pr)$_2$ (X = S, R = NH_2N(Me)–; X = O, R = NH_2N(Me)–, PhNHNH–): Reaction of NH_2N(Me)C(S)NHP(S)(O*i*Pr)$_2$ with acetone

Three new *N*-(thio)phosphorylated thiosemicarbazides of the common formula R–C(S)–NH–P(X)(O*i*Pr)$_2$ [X = S, R = NH_2N(Me)– (**1**); X = O, R = NH_2N(Me)– (**2**), PhNHNH– (**3**)] have been synthesized and characterized by NMR spectroscopy. The structures of the thiosemicarbazides **1–3** in $CDCl_3$ and acetone-d_6 solutions have been discussed in comparison with the *N*-(thio)phosphorylated thioureas Me–NH–C(S)–NH–P(X)(O*i*Pr)$_2$ [X = S (**4**), O (**5**)]. Reaction of **1** with acetone leads to the five-membered substituted 1,3,4-thiadiazolidine S—C(Me)$_2$—NH—N(Me)—C=N—P(S)(O*i*Pr)$_2$ (**6**).

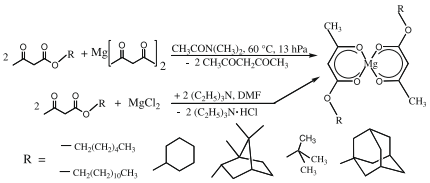


L.I. Koval, V.I. Dzyuba, V.V. Bon, O.L. Ilnitska and V.I. Pekhnyo

Polyhedron 28 (2009) 2698

Synthesis and structure of anhydrous complexes of magnesium(II) with β-ketoesters of higher alcohols

Methods for the synthesis of anhydrous complexes of magnesium(II) with β-ketoesters of higher alcohols have been developed. A number of novel magnesium complexes of the general formula MgL_2 have been synthesized. It has been found by X-ray crystallography that bis(1-adamantyl acetoacetato)magnesium(II) has a trimeric structure. The structure of the complexes in solutions is discussed.

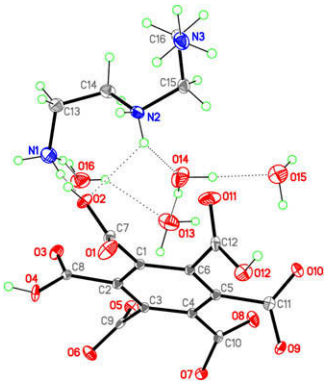


Giuseppe Bruno, Alessandro De Robertis, Ottavia Giuffrè, Archimede Rotondo and Silvio Sammartano

Polyhedron 28 (2009) 2703

Binding of benzene-1,2,3,4,5,6-hexacarboxylate by polyammonium cations

The interaction between mellitate (benzene-1,2,3,4,5,6-hexacarboxylate) and diethylenetriamine and spermidine was studied by potentiometric and calorimetric techniques in aqueous solution at t = 25 °C, moreover by diffractometric technique in the solid state. It was also evaluated the dependence of sequestering ability on ionic strength, temperature and pH.

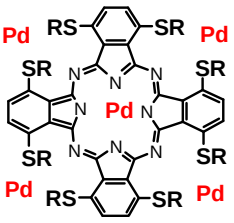


Taofeek B. Ogunbayo and Tebello Nyokong

Polyhedron 28 (2009) 2710

Synthesis and Pd(II) binding studies of octasubstituted alkyl thio derivatised phthalocyanines

Unmetalated octapentylthiophthalocyanine show Pd coordination at the central metal and at the ring, however the nature of the complexes form depends on the point of substitution, peripheral versus non peripheral.

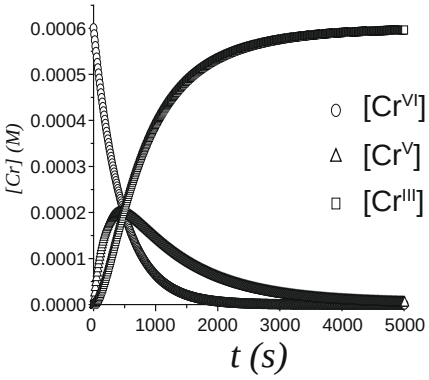


Juan C. González, Silvia I. García, Sebastián Bellú, Ana María Atria, Juan Manuel Salas Pelegrín, Antal Rockenbauer, Lazlo Korecz, Sandra Signorella and Luis F. Sala

Polyhedron 28 (2009) 2719

Oligo and polyuronic acids interactions with hypervalent chromium

Kinetic studies show that the redox reaction proceeds through a mechanism combining $Cr^{VI} \rightarrow Cr^{IV} \rightarrow Cr^{II}$ and $Cr^{VI} \rightarrow Cr^{IV} \rightarrow Cr^{III}$ pathways. The mechanism is supported by the observation of free radicals, CrO_2^{2+} and Cr^{V} as reaction intermediates.

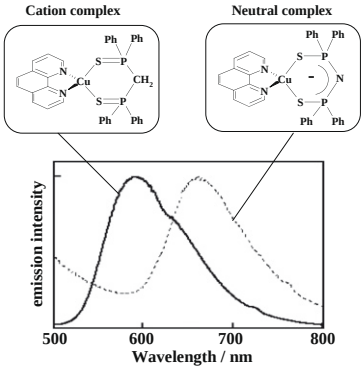


Ayumi Dairiki, Toshiaki Tsukuda, Kenji Matsumoto and Taro Tsubomura

Polyhedron 28 (2009) 2730

Structure and emission properties of mixed-ligand Cu(I) complexes containing phosphinesulfide ligands

Mixed-ligand Cu(I) complexes containing phosphinesulfide ligands were synthesized, and the structure and emission properties were studied for the Cu(I) complexes. The complexes coordinated by a chelating phosphinesulfide and a diimine have been identified by X-ray crystallographic study in solid state and NMR spectra in solution. Photoluminescence of the complexes in the solid state is also discussed.

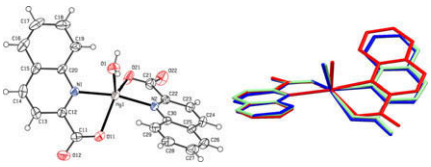


Željka Soldin, Dubravka Matković-Čalogović, Gordana Pavlović, Jasminka Popović, Marijana Vinković, Dražen Vikić-Topić and Zora Popović

Polyhedron 28 (2009) 2735

Various coordination modes in mercury(II) complexes with quinoline-2-carboxylic acid: Preparation and structural characterization

In this work we report the synthesis, IR, ^{1}H and ^{13}C NMR spectroscopy, and crystal and molecular structures determined by X-ray single crystal diffraction of several mercury(II) complexes with quinaldic acid: $[Hg(quin)_2(OH_2)]$, aquabis(quinoline-2-carboxylato-κ^2N,O)mercury(II), $[(quinH_2)(HgCl_3)]\cdot 2quinH\cdot H_2O$, quinolinium-2-carboxylic acid trichloromercurate(II) bis(quinolinium-2-carboxylate) monohydrate, $[Hg(quin)_2(EtOH)]\cdot H_2O$, bis(ethanol-$\kappa O$)bis(quinoline-2-carboxylato-κ^2N,O)mercury-(II) monohydrate, [HgCl(quin)(quinH)], chloro(quinoline-2-carboxylato-κ^2N,O)(quinoline-2-carboxylic acid-κ^2N,O)mercury(II).

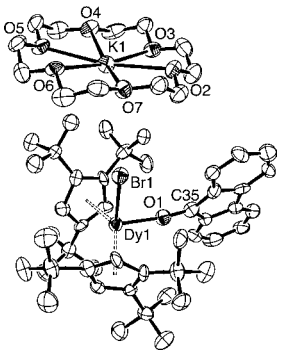


Florian Jaroschik, François Nief and Xavier-Frédéric Le Goff

Polyhedron 28 (2009) 2744

Sterically hindered cyclopentadienyl and phospholyl ligands in dysprosium chemistry

A general method for the synthesis of unsolvated organometallic complexes of dysprosium(III) with very sterically hindered π-ligands is presented. It consists in the reaction of potassium cyclopentadienides or phospholides with a dysprosium(III) iodide in refluxing toluene. A dysprosium(II) ate-complex, obtained by reduction of a bis(cyclopentadienyl)dysprosium(III) bromide, was re-oxidised with fluorenone into a charge-separated dysprosium(III) ionic complex featuring a fluorenone radical-anion liganded to dysprosium through the oxygen atom.

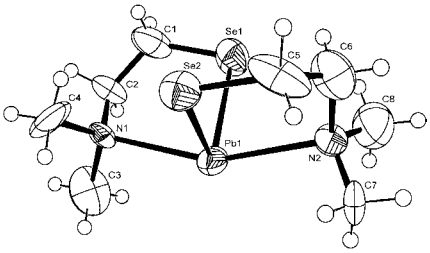


Gotluru Kedarnath, Liladhar B. Kumbhare, Sandip Dey, Amey P. Wadawale, Vimal K. Jain and Goutam K. Dey

Polyhedron 28 (2009) 2749

β-Functionalized ethylchalcogenolate complexes of lead(II): Synthesis, structures and their conversion into lead chalcogenide nanoparticles

Complexes of the general formula $[Pb(ER)_2]$ (ER = $SCH_2CH_2NMe_2$, $SeCH_2CH_2NMe_2$, $SeCH_2CH_2COOMe$) have been isolated and characterized by elemental analyses, UV–Vis and ^1H NMR data. Structures of $[Pb(ECH_2CH_2NMe_2)_2]$ (E = S or Se) have been established by single crystal X-ray analyses. Pyrolysis of these complexes in a furnace or in HDA (hexadecylamine) afforded PbE nanoparticles which were characterized by various techniques.

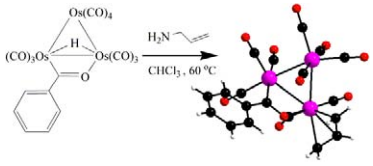


M.Ju. Afonin, V.A. Maksakov, V.P. Kirin, L.A. Scheludyakova, A.V. Golovin and V.G. Vasil'ev

Polyhedron 28 (2009) 2754

Transformations of allylamine and N-allylacetamide on triosmium cluster complexes with hemilabile ligands

The cluster complexes $(\mu\text{-}H)Os_3(\mu\text{-}O{=}CR)(CO)_{10}$ (R = Me (**1**); R = Ph (**2**)) catalyze allylic rearrangement of N-allylacetamide at room temperature. This reaction is accelerated thousands times at microwave irradiation of **2** and allylacetamide solution. The interaction of **2** with allylamine both at room temperature and when heated results in the C–N bond cleavage and formation of $Os_3(CO)_9(\mu,\eta^2\text{-}O{=}C\text{-}Ph)(\eta^3\text{-}Allyl)$ (**3**) cluster.

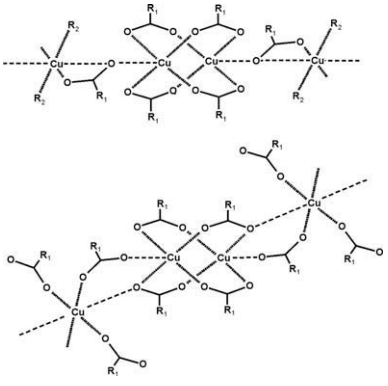


Bojan Kozlevčar, Elizabeta Mate, Zvonko Jagličić, Lea Glažar, Amalija Golobič, Peter Strauch, Jan Moncol, Nives Kitanovski and Primož Šegedin

Polyhedron 28 (2009) 2759

A small methanoato ligand in the structural differentiation of copper(II) complexes

Monomeric $[Cu(O_2CH)_2(2\text{-mpy})_2]$, dimeric $[Cu_2(\mu\text{-}O_2CH)_4(2\text{-mpy})_2]$ and two polymeric complexes of alternate monomeric and dimeric building blocks, $\{[Cu(\mu\text{-}O_2CH)_2(2\text{-mpy})_2][Cu_2(\mu\text{-}O_2CH)_4]\}_n$ (2-mpy = 2-methylpyridine) and $\{Na_2[Cu(\mu\text{-}O_2CH)_2(O_2CH)_2][Cu_2(\mu\text{-}O_2CH)_4]\}_n$, have been characterized. A very strong antiferromagnetic (AFM) interaction is found for all the complexes with *paddle-wheel* building blocks $[Cu_2(\mu\text{-}O_2CH)_4]$ ($2J$ = 444–482 cm^{-1}), attributed to the methanoate intra-binuclear bridges. This strong AFM coupling also plays an important role in the EPR signals of the two polymeric complexes, and differs structurally, especially with the monomer-dimer intra-chain bridges.

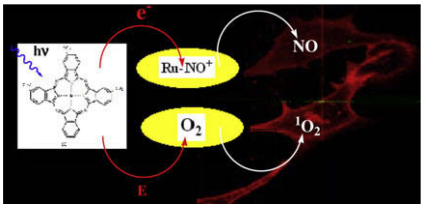


Simone Aparecida Cicillini, Ana Carolina Lemos Prazias, Antonio Claudio Tedesco, Osvaldo Antonio Serra and Roberto Santana da Silva

Polyhedron 28 (2009) 2766

Nitric oxide and singlet oxygen photo-generation by light irradiation in the phototherapeutic window of a nitrosyl ruthenium conjugated with a phthalocyanine rare earth complex

The photoinduced electron transfer studies of an aqueous solution containing nitrosyl ruthenium complex and rare earth complex are discussed in this paper.

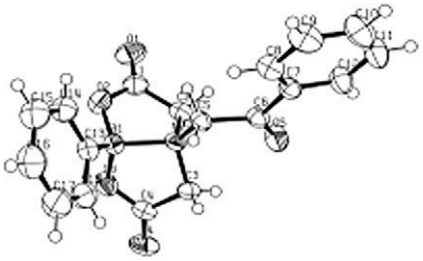


Teresa Mancilla Percino, Roxana Magaly Flores Ancona and Marisol López Martínez

Polyhedron 28 (2009) 2771

New strategy to the synthesis of (N → B) phenyl[N-alkyliminodiacetate-O,O′,N]boranes: The crystal structure of (N → B) phenyl[N-benzyliminodiacetate-O,O′,N]borane, (N → B) phenyl[N-(4-methyl)benzyliminodiacetate-O,O′,N] borane and (N → B) phenyl[N-phenacylimino-diacetate-O,O′,N]borane

A new, mild and friendly method for the synthesis of (N → B) phenyl[N-alkyliminodiacetate-O,O′,N]boranes **2**–**7** is reported. All compounds were identified by NMR and their high resolution mass spectra (HRMS) are reported. The structures of the compounds **2**, **4** and **5** were established by single crystal X-ray. These molecular structures established the bicyclic structure showing a N → B bond length of 1.666 (**2**) Å for **2A**, 1.675 (**2**) Å for **2B**, 1.675 (**3**) Å for **4A**, 1.663 (**3**) Å for **4B** and 1.679 (**2**) Å for **5**.

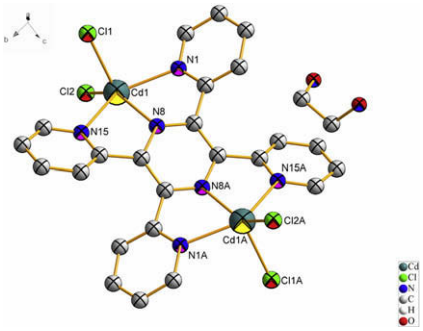


Hassan Hadadzadeh, Seyedeh Raziyeh Hosseinian and S. Jamil A. Fatemi

Polyhedron 28 (2009) 2776

Rhodium(III) and cadmium(II) complexes based on the polypyridyl ligand 2,3,5,6-tetrakis-(2-pyridyl)pyrazine (tppz)

Tppz (2,3,5,6-tetrakis(2-pyridyl)pyrazine) complexes [Rh(tppz)(bpy)Cl][PF_6]$_2$.acetylacetone (bpy = 2,2′-bipyridine) and [{$CdCl_2$}$_2$(μ-tppz)]. ethylene glycol have been synthesized and characterized. Solid state structures of both complexes have been determined by single-crystal X-ray crystallography. The structural determination shows that the dinuclear Cd(II) complex, [{$CdCl_2$}$_2$(μ-tppz)], is a 1D coordination polymer. An ORTEP drawing of [Rh(tppz)-(bpy)Cl][PF_6]$_2$.acetylacetone shows that the coordination geometry around the Rh(III) is a distorted octahedron.

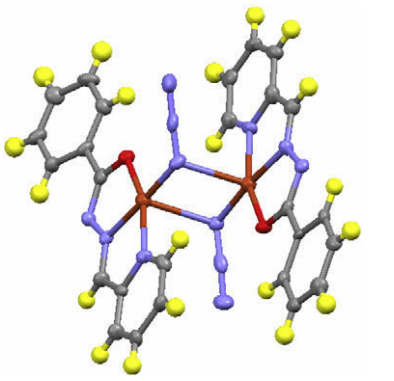


Sambuddha Banerjee, Susmita Mondal, Writachit Chakraborty, Soma Sen, Ratan Gachhui, Ray J. Butcher, Alexandra M. Z. Slawin, Chitra Mandal and Samiran Mitra

Polyhedron 28 (2009) 2785

Syntheses, X-ray crystal structures, DNA binding, oxidative cleavage activities and antimicrobial studies of two Cu(II) hydrazone complexes

This paper describes the synthesis, crystal structures and various spectroscopic studies of a dinuclear Cu(II) hydrazone complex, [{Cu(PBH)-($\mu_{1,1}$-NNN)}$_2$] (**2**), obtained from its mononuclear precursor, [Cu(PBH)$_2$] (**1**), having bridging azido groups in a $\mu_{1,1}$ fashion. The paper also describes the ability of both the complexes to bind with calf thymus DNA using various spectroscopic, viscometric and electrochemical methods. Both **1** and **2** show chemical nuclease activity via an oxidative mechanism. Both the complexes and the free ligand were tested for their ability to act as antimicrobial agents against various bacterial cell lines.

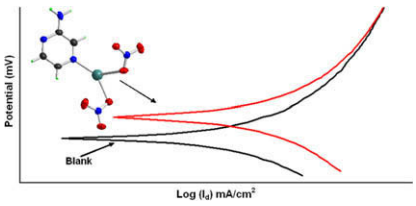


Alshima'a A. Massoud, Ahmed Hefnawy, Vratislav Langer, Mohamed A. Khatab, Lars Öhrstrom and Morsy A.M. Abu-Youssef

Polyhedron 28 (2009) 2794

Synthesis, X-ray structure and anti-corrosion activity of two silver(I) pyrazino complexes

Synthesis, X-ray single crystal structure analysis, elemental analysis as well as IR spectra for $[Ag_2(ampyz)(NO_3)_2]_n$, complex **1** and $\{[Ag(pyzdic)](NO_3)\}_n$, complex **2** are presented. The complexes show anti-corrosion behavior for mild steel in 0.1 M HNO_3 medium. The anti-corrosion test is carried via potentiodynamic polarization technique. Both complexes are mixed type corrosion inhibitors with dominant anodic effect. Only complex **2** fits the Langmuir adsorption isotherm, K = 898. Both complexes fit to the kinetic-thermodynamic model, K1 = 3263 and K2 = 1147.

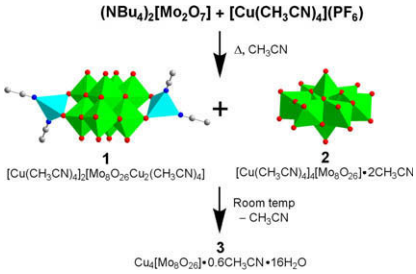


John Fielden, De-Liang Long, Leroy Cronin and Paul Kögerler

Polyhedron 28 (2009) 2803

Synthesis of Cu(I) octamolybdates using *tetra-kis*-acetonitrilecopper(I) hexafluorophosphate

Reaction of $(NBu_4)_2[Mo_2O_7]$ with $[Cu(CH_3CN)_4](PF_6)$ in acetonitrile results in isolation of the orange β-octamolybdate $[Cu(CH_3CN)_4]_2[Mo_8O_{26}Cu_2(CH_3CN)_4]$ (**1**) along with the colourless α-octamolybdate $[Cu(CH_3CN)_4]_4[Mo_8O_{26}]\cdot 2CH_3CN$ (**2**). Both products decompose rapidly upon removal from their mother liquors, forming an insoluble phase with the composition $Cu_4[Mo_8O_{26}]\cdot 0.6CH_3CN\cdot 16H_2O$ (**3**). The copper(I) acetonitrile derivatised isopolyanion in **2** thus represents an intermediate structure between underivatised octamolybdate **1** and the fully condensed, polymeric phase **3**.

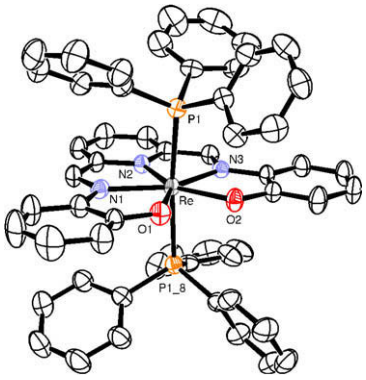


K. Potgieter, P. Mayer, T.I.A. Gerber and I.N. Booysen

Polyhedron 28 (2009) 2808

Coordination behaviour of the multidentate Schiff base 2,6-bis(2-hydroxyphenyliminomethyl)pyridine towards the *fac*-$[Re(CO)_3]^+$ and $[ReO]^{3+}$ cores

The reaction of *cis*-$[ReO_2I(PPh_3)_2]$ with the potentially pentadentate N_3O_2-donor ligand 2,6-bis(2-hydroxyphenyliminomethyl)pyridine (H_2dhp) led to the disproportionation of Re(V) and the isolation of the seven-coordinate Re(III) complex salt $[Re(dhp)(PPh_3)_2]X$ (X = I, ReO_4).



The Publisher encourages the submission of articles in electronic form thus saving time and avoiding rekeying errors. For detailed instructions on the preparation of manuscripts and of electronic artwork, consult the Author Gateway for Elsevier at http://authors.elsevier.com

ScienceDirect

Full text of this journal is available, on-line from **ScienceDirect**. Visit **www.sciencedirect.com** for more information.

Polyhedron 28, issue 14, 23 September 2009

Contents lists available at ScienceDirect

Polyhedron

journal homepage: www.elsevier.com/locate/poly

Contents

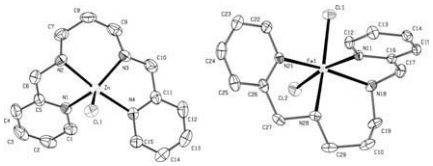
Papers

Aminou Mohamadou, Gerard A. van Albada, Ilpo Mutikainen, Urho Turpeinen, Jérôme Marrot and Jan Reedijk

Polyhedron 28 (2009) 2813

Synthesis, crystal structure, hydrogen bonding and spectroscopy of transition-metal complexes with the ligand (N,N′-bis(2-pyridylmethyl)-1,3-propanediamine)

The tetradentate ligand N,N′-bis(2-pyridylmethyl)-1,3-propanediamine can fold around transition-metal ions in 2 ways, generating either 2 cis octahedral positions for anion ligands, or 1 or 2 axial positions in square pyramidal or octahedral geometries.

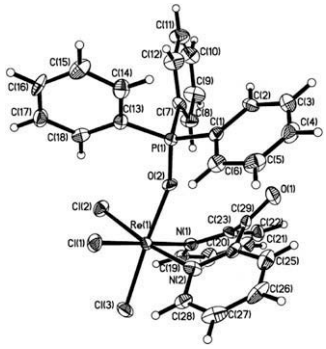


B. Machura, J. Mroziński, R. Kruszynski and J. Kusz

Polyhedron 28 (2009) 2821

Coordination chemistry of di-2-pyridylketone. Synthesis, spectroscopic investigations, X-ray studies and DFT calculations of Re(III) and Re(V) complexes

The paper presents a combined experimental and computational study of Re(III) and Re(V) complexes containing di-2-pyridylketone and its gem-diol form – $[ReCl_3(dpk\text{-}N,O)(PPh_3)]$ (**1**), $[ReCl_3(dpk\text{-}N,N')(OPPh_3)]$ (**2**) and $[ReOBr_3(dpk\text{-}OH)]\cdot 2(dpkH^+Br^-)$ (**3**). All the complexes have been characterized spectroscopically and structurally (by single-crystal X-ray diffraction). The complex **2** has been additionally studied by magnetic measurement. The magnetic behavior is characteristic of mononuclear octahedral Re(III) complex with d^4 low-spin ($^3T_{1g}$ ground state) and arise because of the large spin–orbit coupling (ζ = 2500 cm^{-1}), which gives diamagnetic ground state. DFT and time-dependent (TD)DFT calculations have been carried out for $[ReCl_3(dpk\text{-}N,N')(OPPh_3)]$ and $[ReOBr_3(dpk\text{-}OH)$, and their UV–vis spectra have been discussed on this basis.

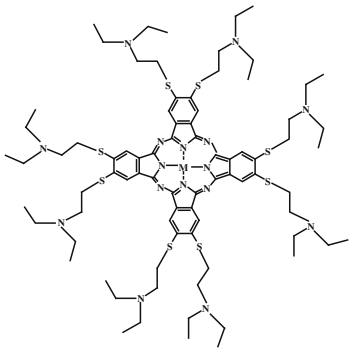


Akinbulu Isaac Adebayo and Tebello Nyokong

Polyhedron 28 (2009) 2831

Synthesis, spectroscopic and electrochemical properties of manganese, nickel and iron octakis-(2-diethylaminoethanethiol)-phthalocyanine

Manganese (**3**), nickel (**4**) and iron (**5**) phthalocyanine complexes, octa-substituted at the peripheral positions with diethlyaminoethanethiol substituents show that the central metal plans a significant role in the aggregation behavior, with Mn phthalocyanine derivatives showing the presence of μ oxo dimers.



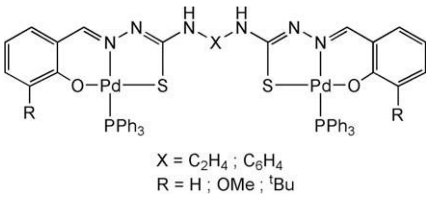
Elsevier Ltd.

Tameryn Stringer, Prinessa Chellan, Bruno Therrien, Nelusha Shunmoogam-Gounden, Denver T. Hendricks and Gregory S. Smith

Polyhedron 28 (2009) 2839

Synthesis and structural characterization of binuclear palladium(II) complexes of salicylaldimine dithiosemicarbazones

Binuclear palladium(II) salicylaldiminato dithiosemicarbazone complexes have been synthesized and characterized by NMR and IR spectroscopies, ESI-mass spectrometry, elemental analyses. Two representative complexes were determined by X-ray diffraction.

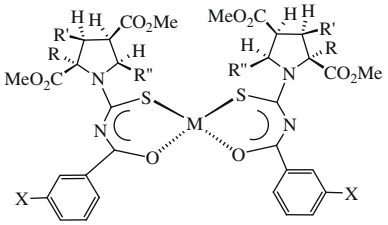


Yahya Nural, Rafet Kilincarslan, H. Ali Dondas, Bekir Cetinkaya, Mehmet Sami Serin, Ronald Grigg, Tuncay Ince and Colin Kilner

Polyhedron 28 (2009) 2847

Synthesis of Ni(II), Pd(II) and Cu(II) metal complexes of novel highly functionalized aroylaminocarbo-*N*-thioyl pyrrolidines and their activity against fungi and yeast

A series of Ni(II), Pd(II) and Cu(II) metal complexes of highly functionalized aroylaminocarbo-*N*-thioyl pyrrolidines were prepared and characterized by microanalysis, spectroscopic methods, magnetic susceptibility measurements and single crystal X-ray diffraction studies. The antifungal activity of the metal complexes against the yeast *Saccharomyces cerevisae* and against the fungus *Penicillium digitatum* was studied.

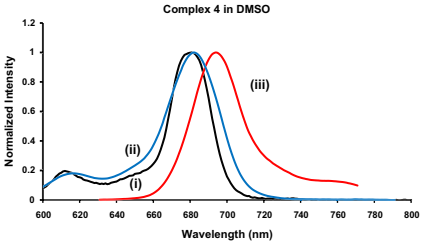


Ali Erdoğmuş and Tebello Nyokong

Polyhedron 28 (2009) 2855

New soluble methylendioxy-phenoxy-substituted zinc phthalocyanine derivatives: Synthesis, photophysical and photochemical studies

Photophysical and photochemical studies of the peripherally tetrakis- (**4**) and octakis- (**6**) and non-peripherally (**5**) tetrakis-3,4-(methylendioxy)-phenoxy-substituted zinc phthalocyanines show complex **4** to have higher singlet oxygen quantum yields, fluorescence quantum yields, triplet quantum yields and triplet life times than complexes **5** and **6**.

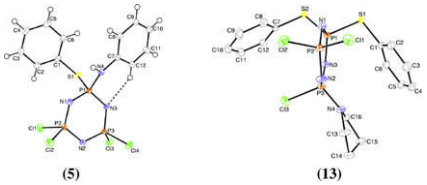


Hanife İbişoğlu, Hakan Dal, Tuncer Hökelek, Adem Kılıç, İlker Ün and Sinan Varı

Polyhedron 28 (2009) 2863

The reaction of thiophenoxide with amino-substituted chloro-cyclotriphosphazenes

Six products were synthesised from the reaction of primary or secondary amino-substituted cyclotriphosphazenes with thiophenol. The structures of these compounds were characterised by elemental analysis and MS, ^{1}H and ^{31}P NMR spectroscopies. Molecular and crystal structures of $N_3P_3Cl_4(NHPh)(SPh)$ **(5)** and $N_3P_3Cl_4(NC_4H_8)(SPh)$ **(13)** were investigated by X-ray crystallography.

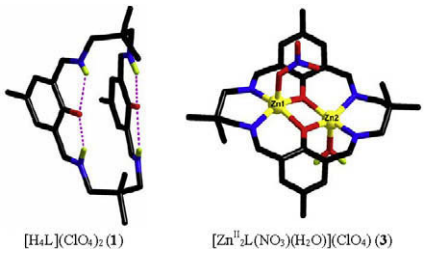


Susanta Hazra, Samit Majumder, Michel Fleck, Rajesh Koner and Sasankasekhar Mohanta

Polyhedron 28 (2009) 2871

Syntheses, structures, absorption and emission properties of a tetraiminodiphenol macrocyclic ligand and its dinuclear Zn(II) and Pb(II) complexes

Synthesis of a Robson type macrocyclic ligand $[H_4L](ClO_4)_2$ (**1**) obtained on condensation of 2,6-diformyl-4-methylphenol and 2,2′-dimethyl-1,3-diaminopropane, template synthesis of a dinuclear lead(II) complex $[Pb^{II}_2L(NO_3)_2]$ (**2**), synthesis of a dinuclear zinc(II) complex $[Zn^{II}_2L(NO_3)(H_2O)](ClO_4)$ (**3**) through metal substitution reaction and synthesis of another dinuclear zinc(II) complex $[Zn^{II}_2L(H_2O)_2](ClO_4)_2.(H_2O)_2$ (**4**) obtained directly from **1** are described in the present study. Crystal structures of **1** and **3** have been determined. Spectrophotometric and spectrofluorometric titrations of **1** with triethylamine as well as with zinc(II) acetate were studied also.

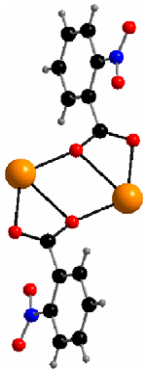


Bikshandarkoil R. Srinivasan, Santosh Y. Shetgaonkar and Pallepogu Raghavaiah

Polyhedron 28 (2009) 2879

A calcium(II) coordination polymer based on a tricyclic dicalcium-bis(2-nitrobenzoate) building block

A pair of μ_2–η^2:η^1 carboxylate ligands bridge two symmetry related Ca(II) ions leading to the formation of a tricyclic dicalcium-bis(2-nitrobenzoate) unit which constitutes the building block of the coordination polymer.

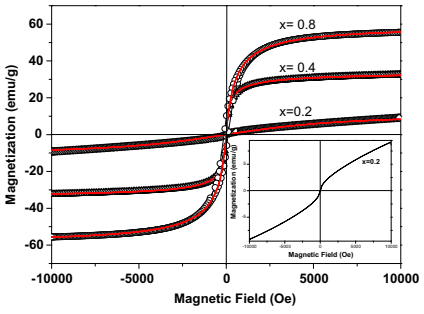


Y. Köseoğlu, A. Baykal, F. Gözüak and H. Kavas

Polyhedron 28 (2009) 2887

Structural and magnetic properties of $Co_xZn_{1-x}Fe_2O_4$ nanocrystals synthesized by microwave method

Microwave assisted combustion method was used to produce nanocrystalline cobalt doped zinc ferrite, $Co_xZn_{1-x}Fe_2O_4$, from stoichiometric mixture of $(Co(NO_3)_2{\cdot}6H_2O)$, $(Fe(NO_3)_3{\cdot}9H_2O)$, $(Zn(NO_3)_2{\cdot}6H_2O)$, and urea $(CO(NH_2)_2)$ as a fuel. The structural, morphological and magnetic properties of the products were determined by X-ray powder diffractometry (XRD), Fourier transmission infrared spectroscopy (FTIR), scanning electron microscopy (SEM), vibrating sample magnetometer (VSM) respectively. The average crystallite sizes obtained from XRD were between 35 and 39 nm. Magnetization measurements indicate that samples with less Co content have superparamagnetic behavior at room temperature. When the Co substitution increases the saturation magnetization and coercivity also increase due to anisotropic nature of cobalt. The $Co_xZn_{1-x}Fe_2O_4$ nanoparticles exhibit typical features of an assembly of magnetic particles with a distribution of blocking temperatures and indicate the spin-glass behavior.

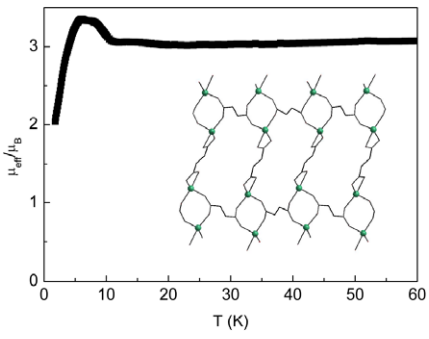


Juraj Černák, Anna Pavlová, Alžbeta Orendáčová, Marcela Kajňaková and Juraj Kuchár

Polyhedron 28 (2009) 2893

A novel two-dimensional Ni(II) fumarato complex: Solvothermal synthesis, crystal structure and magnetic properties

[Ni(*fum*)(*phen*)], prepared by the solvothermal method, exhibits a 2D crystal structure with bridging fumarato ligands. The presence of $\{Ni\}_2$ pairs in the structure, forming antiferromagnetic $S = 1$ dimers with magnetic anisotropy $D/k_B = -6$ K comparable to intra-dimer exchange coupling J, is reflected by magnetic measurements down to 2 K.

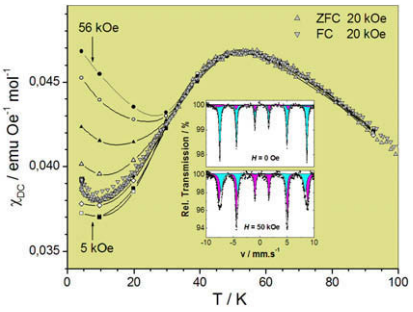


A. Bhattacharjee, M. Bałanda, Y. Miyazaki, M. Sorai and P. Gütlich

Polyhedron 28 (2009) 2899

Uncompensated magnetization in the layered molecular antiferromagnet $\{N(n\text{-}C_5H_{11})_4[Mn^{II}\text{-}Fe^{III}(ox)_3]\}_\infty$

The honeycomb layered $\{N(n\text{-}C_5H_{11})_4[Mn^{II}\text{-}Fe^{III}(ox)_3]\}_\infty$ antiferromagnet, where both Mn^{II} and Fe^{III} ions have spin $S = 5/2$, shows anisotropy and an uncompensated moment below T_N of 27 K. The Mössbauer spectrum in the applied magnetic field reveals the presence of two $Fe^{III}{}_A$ and $Fe^{III}{}_B$ spin sites with different responses towards the external magnetic field that is most probably responsible for the uncompensated magnetization. Breaking the local symmetry of the Fe^{III} sites by the bulky $N(n\text{-}C_5H_{11})_4$ cations together with a small difference in g-factors for Mn^{II} and Fe^{III} ions and a relatively large zero-field splitting for Mn^{II} may be a reason for the two non-equivalent sites within the iron sublattice.

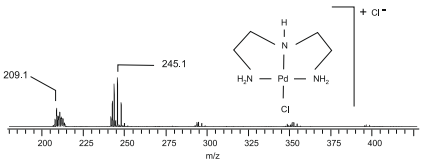


Ana Vujačić, Živadin D. Bugarčić, Jürgen Schiller, Vesna Vasić and Marijana Petković

Polyhedron 28 (2009) 2905

Matrix-assisted laser desorption and ionisation time-of-flight mass spectrometry of Pt(II) and Pd(II) complexes

In this manuscript, we present the characteristic pattern of the matrix-assisted laser desorption and ionisation time-of-flight (MALDI-TOF) mass spectra of Pt(II) and Pd(II) complexes. Experimental conditions (matrix, addition of trifluoro acetic acid and addition of inorganic salt) were varied in order to find the best suitable conditions for reliable analysis of MALDI-TOF mass spectra of selected Pt(II) and Pd(II) complexes.

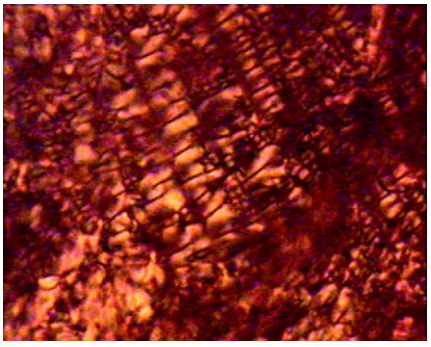


Zolfaghar Rezvani, Mohammad Ali Ghanea, Kamellia Nejati and Sara Abodollahzadeh Baghaei

Polyhedron 28 (2009) 2913

Syntheses and mesomorphic properties of new oxygen-bridged dicopper complex homologous derived from azo-containing salicylaldimine Schiff base ligands

Copper (II) complexes derived from 5-((4-^{n}alkoxyphenyl)azo)-N-(3-hydroxypropyl) salicylaldimine homologous are reported. The mesogenic properties of these complexes were studied by differential scanning calorimetry (DSC) and polarizing microscope. None of the free ligands exhibit liquid crystalline behavior but all of the copper complexes show a smectic A mesophase.

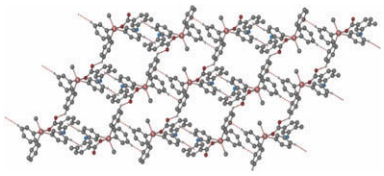


Han-Dong Yin, Li-Yuan Wen, Ji-Chun Cui and Wen-Kuan Li

Polyhedron 28 (2009) 2919

Synthesis, characterizations and crystal structures of new organoantimony(V) complexes with various isomers of fluoromethylbenzoate ligands

Six new organoantimony(V) complexes containing various isomers of fluoromethylbenzoate ligands $[RC_6H_3COO]_2SbPh_3$ and $[RC_6H_3COO]\text{-}SbPh_4$ [R = 3-F-4-(CH_3) (**1**, **4**), 4-F-2-(CH_3) (**2**, **5**), 5-F-2-(CH_3) (**3**, **6**)] have been synthesized by the reactions of triphenylantimony(V) dichloride or tetraphenylantimony(V) bromide with various isomers of fluoromethylbenzoate ligands in 1:2 or 1:1 stoichiometries. All the complexes have been characterized by elemental analysis, IR and NMR [^{1}H, ^{13}C and ^{19}F] studies. The crystal structures of complexes **1**, **3**, **4**, **5** and **6** have been determined by X-ray single crystal diffraction. The structure of complexes show that the five-coordinated antimony(V) atom adopts a distorted trigonal bipyramidal geometry. Furthermore, weak but significant intermolecular C–H···O, C–H···F hydrogen bonds, C–H···Pi stacking lead to aggregation and assembly of these complexes into 1D and 2D supramolecular frameworks.

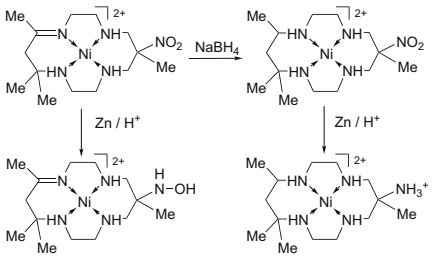


Neil F. Curtis, Horst Puschmann and Ward T. Robinson

Polyhedron 28 (2009) 2927

Synthesis and structures of (13-hydroxylamino-5,7,7,13-tetramethyl-1,4,8,11-tetraazacyclotetradec-4-ene-κ^4)nickel(II) tetrachlorozincate(II) and (13-azonium-5,5,7,13-tetramethyl-1,4,8,11-tetraazacyclotetradecane-κ^4)nickel(II) tetrachlorozincate(II) chloride 2.25 water

Reduction by zinc/acid of the nitro function of (5,5,7,13-tetramethyl-13-nitro-1,4,8,11-tetraazacyclotetradec-4-ene)nickel(II) yields (13-hydroxylamino-5,7,7,13-tetramethyl-1,4,8,11-tetraazacyclotetradec-4-ene)nickel(II), isolated as the tetrachlorozincate salt, for which the structure was determined. Reduction by zinc/acid of the nitro function of (5,5,7,13-tetramethyl-13-nitro-1,4,8,11-tetraazacyclotetradecane)nickel(II) yields (13-amino-5,5,7,13-tetramethyl-1,4,8,11-tetraazacyclotetradecane)nickel(II), isolated as the tetrachlorozincate chloride salt of the protonated cation for which the structure was determined.

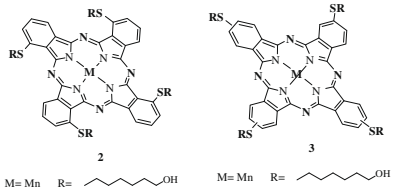


Mehmet Kandaz and Atıf Koca

Polyhedron 28 (2009) 2933

Synthesis, *in situ* spectroelectrochemical, *in situ* electrocolorimetric and electrocatalytic investigation of brown-manganese phthalocyanines

α- and β-substituted tetrakis{6-hydroxyhexylthiol)phthalocyaninato manganese (III) chloride complexes have been prepared via cyclotetramerization and characterized by elemental analysis, FTIR, MS and UV–Vis spectral data. The voltammetric and *in situ* spectroelectrochemical studies of the complexes reveal that both complexes exhibit an oxidation and three reduction processes having reversible, one-electron, and diffusion controlled mass transfer characters, which are assigned to $Mn^{III}Pc^{2-}/Mn^{II}Pc^{2-}$, $Mn^{II}Pc^{2-}/Mn^{I}Pc^{2-}$, $Mn^{I}Pc^{2-}/Mn^{I}Pc^{3-}$ and $Mn^{III}Pc^{2-}/Mn^{IV}Pc^{2-}$ couples respectively. Existence of oxygen in solution significantly affects the *in situ* spectroelectrochemical behaviors of the complexes due to the formation of μ-oxo MnPc species. An *in situ* electrocolorimetric method has been applied to investigate the colors of the electro-generated anionic and cationic forms of the complexes for the first time in this study. The complexes coated on a glassy carbon electrode potentiostatically show considerably high electrocatalytic activity to the hydrogen evolution reaction in aqueous solution.

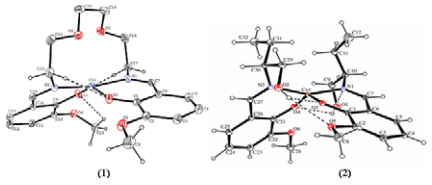


Figen Arslan, Mustafa Odabaşoğlu, Halis Ölmez and Orhan Büyükgüngör

Polyhedron 28 (2009) 2943

Synthesis, crystal structure, spectral and thermal characterization of bis(*o*-vanillinato)-triethylenglycoldiiminecopper(II) and bis[(R)-(−)-hydroxymethylpropylimine *o*-vanillinato]-copper(II)

The novel complexes, bis(*o*-vanillinato)-triethyleneglycoldiiminecopper(II) (**1**) and bis[(R)-(−)-hydroxymethylpropylimine *o*-vanillinato]-copper(II) (**2**) were synthesized and characterized by elemental analysis, magnetic susceptibility, spectral methods (UV–Vis and FT-IR), simultaneous TG, DTA techniques and X-ray diffraction. The crystal structures of (**1**) and (**2**) determined as: Cu atom is coordinated by two imine N atoms and two phenol O atoms from the Schiff base ligand in a slightly distorted square-planar coordination.

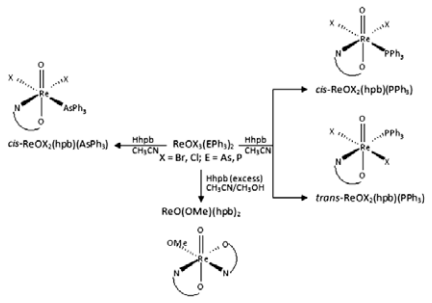


B. Machura, M. Wolff, J. Kusz and R. Kruszynski

Polyhedron 28 (2009) 2949

Reactivity of $[ReOX_3(PPh_3)_2]$ and $[ReOX_3(AsPh_3)_2]$ towards 2-(2-hydroxyphenyl)-1H-benzimidazole: Synthesis, X-ray studies, spectroscopic characterization and DFT calculations for $[ReOX_2(hpb)(EPh_3)]$ and $[ReO(OMe)(hpb)_2]\cdot$MeCN

The paper presents a combined experimental and computational study of mono- and disubstituted Re(V) oxocomplexes obtained in the reactions of $[ReOX_3(EPh_3)_2]$ (X=Cl, Br; E=P, As) with 2-(2-hydroxyphenyl)-1H-benzimidazole (Hhpb). From the reactions of $[ReOX_3(PPh_3)_2]$ with Hhpb in molar ratio 1:1 *cis* and *trans* stereoisomers of $[ReOX_2(hpb)(PPh_3)]$ were isolated, whereas the $[ReOX_3(AsPh_3)_2]$ oxocompounds react with Hhpb to give only *cis*-halide isomers. The $[ReOX_2(hpb)(EPh_3)]$ and $[ReO(OMe)(hpb)_2]$ MeCN complexes have been characterised spectroscopically and structurally (by single-crystal X-ray diffraction). The DFT and TDDFT calculations have been carried out for the *trans*-$[ReOBr_2(hpb)(PPh_3)]$, *cis*-$[ReOBr_2(hpb)(AsPh_3)]$ and $[ReO(OMe)(hpb)_2]$, and their UV-Vis spectra have been discussed on this basis.

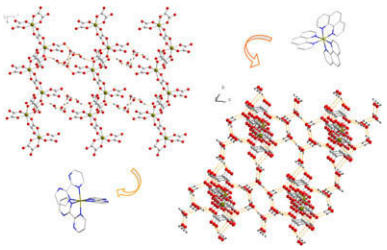


Teresa F. Mastropietro, Donatella Armentano and Giovanni De Munno

Polyhedron 28 (2009) 2965

Self-assembly of water cluster in iron(III) oxalate-bridged complexes

The synthesis and crystal structural characterization of the compound of formula $\{[Fe^{II}(phen)_3]_2[Fe_2^{III}ox_5]\}\cdot 11H_2O$ (**1**) has been reported. The most interesting feature of the solid state structure of **1** is the formation of decanuclear water clusters self-assembled by means of hydrogen bonding interactions between water molecules. The $(H_2O)_{10}$ clusters display extensive multiple interactions with the dimeric units, leading to the formation of an extended 3D supramolecular assembly, wherein hexameric water clusters interconnected with dodecameric hybrid water–$O_{oxalate}$ clusters can be recognized. The comparison of this supramolecular architecture with that found in the already known compound of formula $[Fe(bpm)_3]_2[Fe_2(ox)_5]\cdot 8H_2O$ (**2**) allows some preliminary observations on the design and control of hydrate formation depending on the size and shape of templating cations.

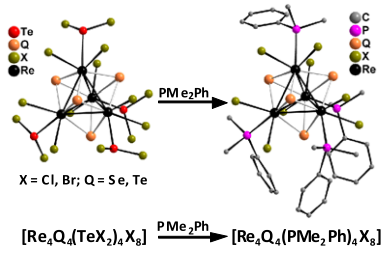


Olga A. Efremova, Yuri V. Mironov, Konstantin A. Brylev, Vladimir E. Fedorov, Hans-Jürgen Pietzsch and Holger Stephan

Polyhedron 28 (2009) 2973

Isomerism in tetrahedral rhenium cluster complexes $[Re_4Q_4(PMe_2Ph)_4X_8]\cdot nCH_2Cl_2$ (Q = Se, X = Br; Q = Te, X = Cl, Br)

Three new tetrahedral rhenium cluster compounds $[Re_4Q_4(PMe_2Ph)_4X_8]\cdot nCH_2Cl_2$ (X = Br, Q = Se (**1**), Te (**2**); X = Cl, Q = Te (**3**)) have been synthesized by reaction $[Re_4Q_4(TeX_2)_4X_8]$ (X = Br, Q = Se (for **1**), Te (for **2**); X = Cl, Q = Te (for **3**)) with dimethylphenylphosphine in dichloromethane. All compounds have been characterized by single-crystal X-ray diffraction analysis. Different isomers were found to be crystallized out by layering of diethylether on CH_2Cl_2 solution.

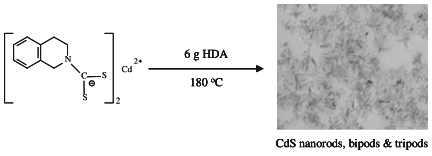


Thandeka Mthethwa, V.S.R. Rajasekhar Pullabhotla, Phumlani S. Mdluli, James Wesley-Smith and Neerish Revaprasadu

Polyhedron 28 (2009) 2977

Synthesis of hexadecylamine capped CdS nanoparticles using heterocyclic cadmium dithiocarbamates as single source precursors

Heterocyclic cadmium dithiocarbamates, $[Cd(S_2CNC_5H_{10})_2]$ and $[Cd(S_2CNC_9H_{10})_2]$ were synthesized. The complexes were thermolysed in hexadecylamine (HDA) to give HDA capped CdS nanoparticles. A combination of close to spherical, rod, bipods and tripods was obtained by varying the reaction parameters such as precursor concentration and temperature. The optical properties and X-ray diffraction studies of the particles are also reported.

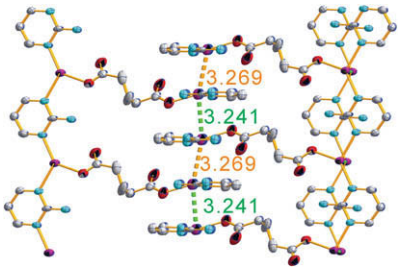


Di Sun, Geng-Geng Luo, Na Zhang, Jian-Hua Chen, Rong-Bin Huang, Li-Rong Lin and Lan-Sun Zheng

Polyhedron 28 (2009) 2983

Influence of dicarboxylic acids on self-assembly process: Syntheses and structural characterization of new Ag(I) complexes derived from mixed ligands

Three new luminescent silver coordination polymers have been successfully synthesized by solution phase reaction of silver nitrate with different dicarboxylates and a cooperative heterocyclic 2-aminopyrimidine ligand under the ammoniacal condition. The structures of the three complexes which span from 2-D to 3-D networks, indicating that dicarboxylates play important roles in the formation of such coordination architectures.

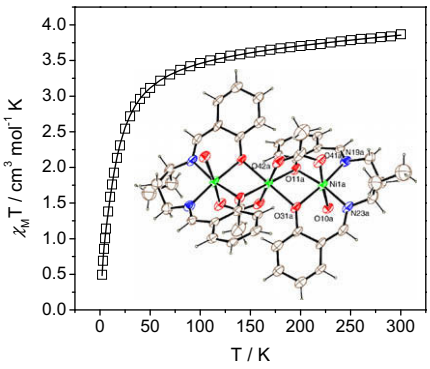


Pampa Mukherjee, Michael G.B. Drew, Vassilis Tangoulis, Marta Estrader, Carmen Diaz and Ashutosh Ghosh

Polyhedron 28 (2009) 2989

Facile strategies for the synthesis and crystallization of linear trinuclear nickel(II)-Schiff base complexes with carboxylate bridges: Tuning of coordination geometry and magnetic properties

Structural analysis and magnetic susceptibility measurements of a series of Ni(II)-Schiff base complexes reveal that the coordination geometry around Ni(II) and the magnetic interactions can be tuned by changing the bridging carboxylate group.

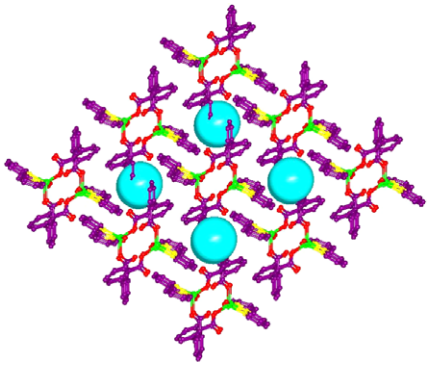


Xin-Xin Xu, Xiao-Xia Liu, Xia Zhang and Ting Sun

Polyhedron 28 (2009) 2997

Mixed-ligand coordination polymers constructed from flexible 2,2′-biphenyldicarboxylate and rigid isomeric bipyridines

In this article, we describe the synthesis of six new coordination polymers, among these complexes, complex **6** exhibits an interesting supramolecular network.

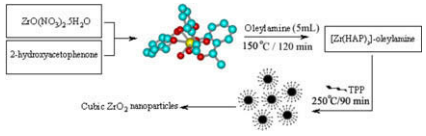


Masoud Salavati-Niasari, Mahnaz Dadkhah and Fatemeh Davar

Polyhedron 28 (2009) 3005

Pure cubic ZrO_2 nanoparticles by thermolysis of a new precursor

The present investigation reports on the synthesis and characterization of zirconium oxide (ZrO_2) nanoparticles using thermolysis. Pure zirconium oxide (ZrO_2) nanoparticles with diameters of 30–40 nm are fabricated from [bis(2-hydroxyacetophenato)oxozirconium(IV)], $[Zr(HAP)_3(H_2O)_2](NO_3)$, as a precursor in the presence of oleylamine and triphenylphosphine as the solvent and capping agent.

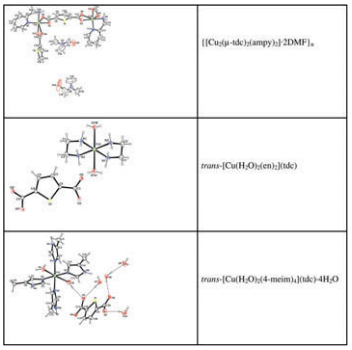


Okan Zafer Yeşilel, İnci İlker and Orhan Büyükgüngör

Polyhedron 28 (2009) 3010

Three copper(II) complexes of thiophene-2,5-dicarboxylic acid with dissimilar ligands: Synthesis, IR and UV–Vis spectra, thermal properties and structural characterizations

We have synthesized and structurally characterized three 3D Cu(II) complexes which are derived from 2,5-thiophenedicarboxylate with dissimilar ligands. One of the complexes has a 1-D zigzag polymeric structure and tdc behaves as a bidentate ligand. In the other complexes, the tdc dianion acts as a counter ion. In all these complexes the Cu(II) atom has a distorted octahedral coordination geometry. Three-dimensional frameworks are constructed though hydrogen bonding and/or C–H···π interactions in all the synthesized complexes.

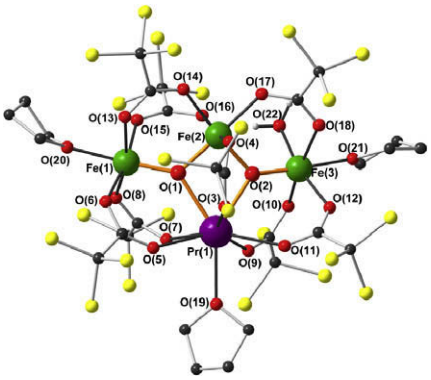


Valeriu Mereacre, Denis Prodius, Constantin Turta, Sergiu Shova, George Filoti, Juan Bartolomé, Rodolphe Clérac, Christopher E. Anson and Annie K. Powell

Polyhedron 28 (2009) 3017

The synthesis, structural characterization, magnetochemistry and Mössbauer spectroscopy of $[Fe_3LnO_2(CCl_3COO)_8H_2O(THF)_3]$ (Ln = Ce, Pr, Nd, Sm, Eu, Gd, Tb, Dy, Ho, Lu and Y)

The new tetranuclear complexes $[Fe_3Ln(_3\text{-}O)_2(CCl_3COO)_8(H_2O)(THF)_3]$ (Ln = Ce^{III} - Lu^{III}) have been prepared. Magnetic susceptibility measurements show dominant intramolecular antiferromagnetic exchange interactions for all the complexes. At the time scale of the Mössbauer spectroscopy, evidence of magnetization blocking, i.e. slow relaxation of the magnetization, is observed below 3 K for Tb^{III} derivative, which was confirmed by ac susceptibility measurements

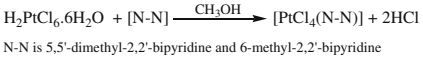


Vahid Amani, Nasser Safari, Hamid Reza Khavasi and Mehmet Akkurt

Polyhedron 28 (2009) 3026

Synthesis, characterization and crystal structure determination of platinum(IV) complexes containing, bipyridine derivatives and chloride, $[Pt(5,5'\text{-dmbipy})Cl_4]$ and $[Pt(6\text{-mbipy})Cl_4]$

$[Pt(5,5'\text{-dmbipy})Cl_4]$ and $[Pt(6\text{-mbipy})Cl_4]$ complexes, (5,5′-dmbipy is 5,5′-dimethyl-2,2′-bipyridine and 6-mbipy is 6-methyl-2,2′-bipyridine) were prepared and characterized by elemental analysis, IR, UV–Vis, ^1H NMR, ^{13}C NMR and ^{195}Pt NMR spectroscopies and X-ray diffraction.

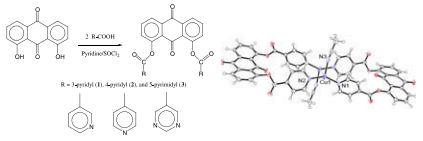


Stephanie S. Peterson, Tishal Kirby, Mariappan Kadarkaraisamy, Richard M. Hartshorn and Andrew G. Sykes

Polyhedron 28 (2009) 3031

Chelating, bridging, and chain structures within Ag(I) and Cu(I) complexes of *bis*(nicotinyloxy), *bis*(isonicotinyloxy), and *bis*(pyrimidine-5-carboxyloxy)-1,8-disubstituted anthraquinone ligands

Bis-substituted anthraquinone ligands containing nitrogen heterocycles form both chelating and bridging complexes with Ag(I) and Cu(I), as well as two new coordination polymers.

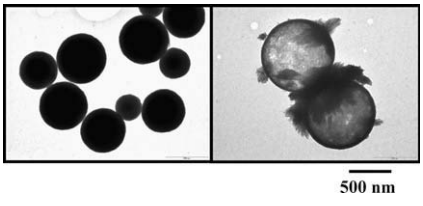


Kazuhiko Kandori, Kazuma Takeguchi, Masao Fukusumi and Yoshiaki Morisada

Polyhedron 28 (2009) 3036

Preparation and characterization of calcium hydroxyapatite and balloon-like calcium phosphate particles from forced hydrolysis of $Ca(OH)_2$–triphosphate solution

Tem pictures of spherical solid and ballon-type particles.

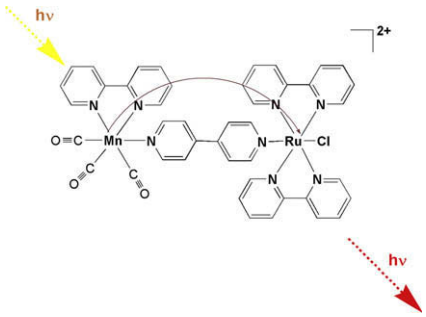


Murugesan Velayudham and Seenivasan Rajagopal

Polyhedron 28 (2009) 3043

Synthesis, characterization and photophysics of bimetallic manganese(I) and ruthenium(II) complexes

A series of new manganese(I) monometallic and bimetallic complexes and manganese(I)–ruthenium(II) heterobimetallic complexes are synthesized and characterized. A weak interaction between two metal centers in Mn–Ru heterobimetallic complexes is observed. The Mn–Ru heterobimetallic complexes, show interesting photophysical properties.

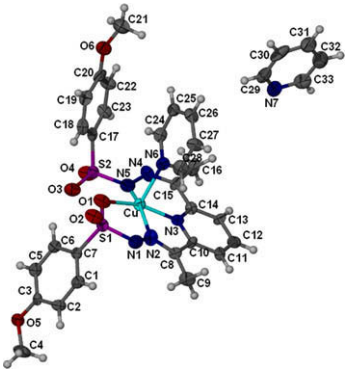


Juahir Yusnita, Subramaniam Puvaneswary, Hapipah Mohd. Ali, Ward T. Robinson and Thong Kwai-Lin

Polyhedron 28 (2009) 3050

Synthesis, structural characterization and antibacterial activity of 2,6-diacetylpyridine bis(benzenesulfonohydrazide) Schiff bases and their copper(II) complexes

X-ray crystallographic analysis on $[CuL^{3}\cdot(py)]\cdot py$ shows that the complex has a near square pyramidal, penta-coordinate geometry. The bi-negatively charged tetradentate Schiff base is asymmetrically coordinated to the Cu(II) ion via the pyridine N, the azomethine N, the sulfonyl O and the hydrazine N. A pyridine molecule is apically coordinated to the Cu(II) ion.

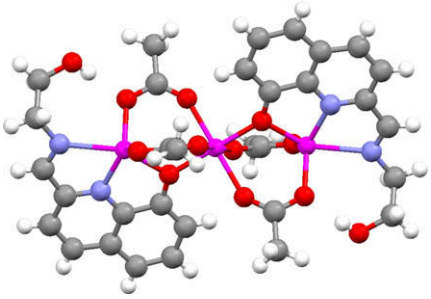


Isabel García-Santos, Jesús Sanmartín, Ana M. García-Deibe, Matilde Fondo and Esther Gómez

Polyhedron 28 (2009) 3055

Structural and photophysical studies on a linear trinuclear zinc complex of 2-[(2-hydroxyethylimino)methyl]quinolin-8-ol

Single crystal X-ray diffraction studies on $Zn_3(HL)_2(OAc)_4$ evidence that HL^- is acting as an *O,N*-donor. A study of the luminescence properties in methanol solution showed that the quantum yield of $Zn_3(HL)_2(OAc)_4$ is slightly higher than that of 8-hydroxyquinoline-2-carboxaldehyde.

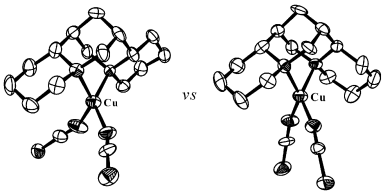


Yong-Min Lee, Bun-Joo Kim, Hee-Jin Kim, Sang-Yub Kim, Sung Kwon Kang and Sung-Nak Choi

Polyhedron 28 (2009) 3060

Crystal structures and spectroscopic properties of copper(II) pseudohalide complexes with two sparteine epimers, having a CuN_4 chromophore

Tetrahedrally distorted copper(II) sparteine pseudohalide complexes having the CuN_4 chromophore were prepared and characterized by various spectroscopic techniques and X-ray crystallography. The results of X-ray crystallography and ESR spectroscopy are in a good agreement with the assumption that the degree of distortion from planar to tetrahedral will reduce the $A_{||}$ value of four-coordinate copper(II) sparteine pseudohalide complexes.

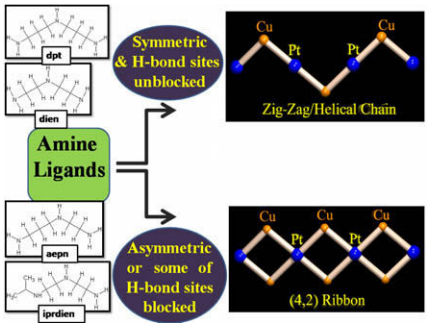


A.D. Jana, R. Saha, A.K. Ghosh, S. Manna, J. Ribas, N. Ray Chaudhuri and G. Mostafa

Polyhedron 28 (2009) 3065

Role of weak interactions in controlling the topology of coordination polymeric chains in $[Pt(CN)_4]^{2-}$ bridged Cu(II) complexes: Syntheses, crystal structure and magnetic studies

Four coordination polymers of $[Pt(CN)_4]^{2-}$ bridged Cu(II) complexes reveal that zig-zag/helical chains or (4,2) ribbons are the result of competition between hydrogen bonding and coordinative forces.

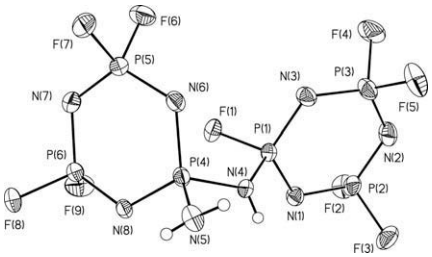


V. Richterová, M. Alberti, J. Příhoda, P. Kubáček, J. Taraba and Z. Žák

Polyhedron 28 (2009) 3078

New results in the ammonolysis of hexafluoro-*cyclo*-triphosphazene: Crystal structure of $P_3N_3F_5$–NH–$P_3N_3F_4NH_2$

The reaction of hexafluoro-*cyclo*-triphosphazene $P_3N_3F_6$ with ammonia in acetonitrile has been studied and new compounds, (2-imino-2,4,4,6,6-pentafluoro-2λ^5,4λ^5,6λ^5-*cyclo*-triphosphaza-1,3,5-trienyl)-2-amino-4,4,6,6-tetrafluoro-2λ^5,4λ^5,6λ^5-*cyclo*-triphosphaza-1,3,5-triene, $P_3N_3F_5$–NH–$P_3N_3F_4NH_2$ (**2**), *cis* and *trans* isomers of *non-gem*-2,4-diamino-2,4,6,6-tetrafluoro-2λ^5,4λ^5,6λ^5-*cyclo*-triphosphaza-1,3,5-triene, $P_3N_3F_4(NH_2)_2$ (**4**, **5**), were identified in the reaction mixture. Two conformers of the compound **2,** denoted as **2A** and **2B,** were isolated (conformational polymorphism).

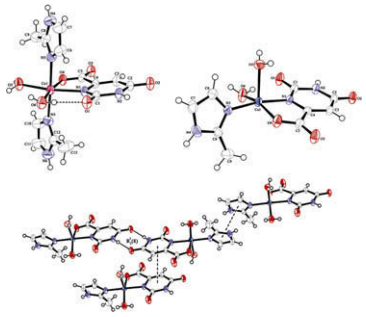


Hakan Erer, Okan Zafer Yeşilel, Cihan Darcan and Orhan Büyükgüngör

Polyhedron 28 (2009) 3087

Synthesis, spectroscopic, thermal Studies, antimicrobial activities and crystal structures of Co(II), Ni(II), Cu(II) and Zn(II)-orotate complexes with 2-methylimidazole

Four M(II)-orotate complexes with 2-methylimidazole, *mer*-$[Co(HOr)(H_2O)_2(2\text{-meim})_2]$ (**1**), *mer*-$[Ni(HOr)(H_2O)_2(2\text{-meim})_2]$ (**2**), $[Cu(HOr)(H_2O)_2(2\text{-meim})]$ (**3**) and $[Zn(HOr)(H_2O)_2(2\text{-meim})]$ (**4**), (H_3Or = orotic acid, 2-meim = 2-methylimidazole) have been synthesized and characterized. The complexes **1** and **2** have distorted octahedral geometries with two monodentate 2-methylimidazole ligands, chelated to the deprotonated nitrogen atom of pyrimidine ring and to the carboxylate oxygen atom of the orotate dianion and two aqua ligands. Complex **3** has distorted square pyramidal and **4** has distorted trigonal bipyramidal geometries with one 2-methylimidazole, bidentate orotate and an aqua ligands. The antimicrobial activities of **1** and **4** were found to be more active gram (+) than gram (−) and **4** could be use for treatment *Sthapylococcus aureus.*

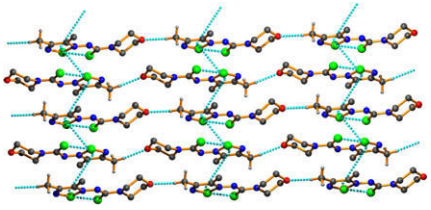


Susobhan Biswas, Glenn P.A. Yap and Kamalendu Dey

Polyhedron 28 (2009) 3094

Reaction of diacetylmonoxime with morpholine N-thiohydrazide in the absence and in presence of a metal ion: Facile synthesis of a thiadiazole derivative with non-bonded S···S interaction

The reaction of diacetylmonoxime with morpholine N-thiohydrazide under refluxing (16 h) conditions in ethanol afforded the zwitterionic nitrogen–sulfur heterocyclic compound N-(3,4-dimethyl-1,2,5-thiadiazole-2-ium-2-yl)morpholine-4-carbothioate (dtmc), with a non-bonded S···S interaction. This heterocyclic compound forms a 2D supramolecular sheet *via* C–H···O and π···π interactions. However, reaction of these two components in the presence of $Zn(OAc)_2{\cdot}2H_2O$ in ethanol yielded the zinc complex $[Zn(Hdammthiol)(H_2O)(OAc)]{\cdot}H_2O$. A 1D supramolecular chain, diagonal to the *ab* plane, has been formed in this molecule, through O–H···O hydrogen bonding. The zinc complex shows a blue emission in chloroform at room temperature.

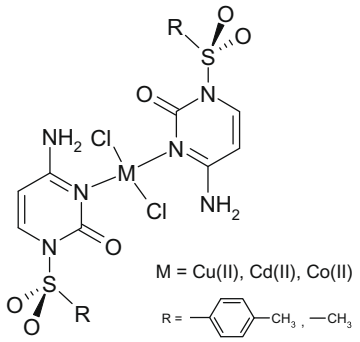


Aleksandar Višnjevac, Nikola Biliškov and Biserka Žinić

Polyhedron 28 (2009) 3101

Transition metal complexes of *N*-1-tosylcytosine and *N*-1-mesylcytosine

The syntheses as well as chemical and X-ray structural characterization of dichlorobis[1-(*p*-toluenesulfonyl)cytosine]copper(II) (**2**), its solvated pseudopolymorph containing two methanol molecules (**3**), dichlorobis[1-(*p*-toluenesulfonyl)cytosine]cadmium(II) (**4**), 1-methanesulfonylcytosine (**6**) and its copper complex dichlorobis(1-methanesulfonylcytosine)copper(II) (**7**) are described. In addition, spectroscopic studies of dichlorobis[1-(*p*-toluenesulfonyl)cytosine]cobalt(II) (**5**), as well as of dichlorobis(1-mesylcytosine)cadmium(II) (**8**) are presented. The X-ray structure of complex **3** revealed charge delocalization inside the cytosine ring, prompted by copper coordination, as the first step towards tautomerization which has not been observed previously in the copper complexes of *N*-1 substituted cytosine.

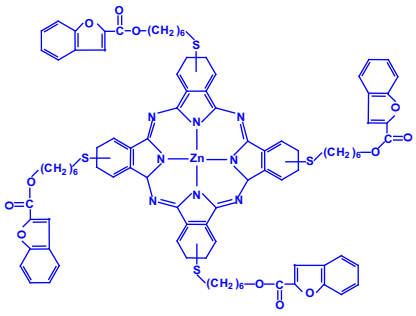


Mehmet Kandaz, Orhan Güney and Filiz B. Senkal

Polyhedron 28 (2009) 3110

Fluorescent chemosensor for Ag(I) based on amplified fluorescence quenching of a new phthalocyanine bearing derivative of benzofuran

A new fluorescent chemosensor for Ag(I) as a family of peripherally functionalized zinc-phthalocyanine, 2(3),9(10),16(17),23(24)-tetrakis-{6-(-benzofuran-2-carboxylate)-hexylthio} phthalocyaninatozinc(II) has been synthesized. Both absorbance and fluorescence spectra of compound exhibit distinct changes in visible region in response to treatment with Ag(I) ion.

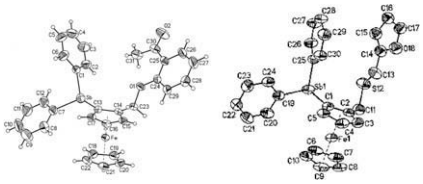


D. Pérez, P. Sharma, A. Cabrera, N. Rosas, I. Arellano, A. Toscano and S. Hernández

Polyhedron 28 (2009) 3115

Preparation of new 1,2-disubstituted ferrocenyl stibine derivatives containing ether/thioether pendant arm from a quaternary ferrocenyl ammonium salt

New 1,2-disubstituted ferrocenyl stibines viz. containing $-CH_2OR$ or $-CH_2SR$ pendant arm at the *ortho*-position have been synthesized and characterized by various physicochemical methods. These new ferrocenylstibines were prepared by the nucleophilic substitution reaction of diphenyl[(*N,N,N*-trimethylaminomethyl ferrocenyl)iodide]stibine by different phenols and thiol viz. *o*-salicyldehyde, *m*-hydroxyacetaphenone, *o*-hydroxyaceto-phenone and furan-2-ylmethylthiol. Molecular structure of stibines (**2**), (**3**), (**4**) and (**5**) have been determined by X-ray crystallography. Molecular structure show that none of these hetero-bimetallic compound possess hypervalent interaction in the solid state. This type of interaction was found in similar compounds with CH_2NR_2 pendant arm.

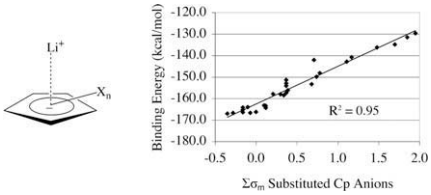


Kevin W. Cormier and Michael Lewis

Polyhedron 28 (2009) 3120

Lithium and sodium cation binding of cyclopentadienyl anions: Electronic effects of cyclopentadienyl substitution

Cp–Li and Cp–Na complexes involving substituted Cp rings were investigated using high-level ab initio molecular orbital theory. The Cp-metal distances and binding energies correlate very well with the Cp $\sum\sigma_m$ values. Furthermore, the metal charge correlates very well with the Cp $\sum|\sigma_m|$ values.

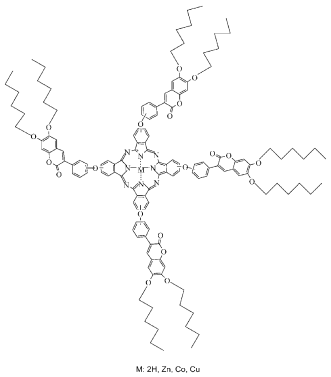


Aliye Aslı Esenpınar and Mustafa Bulut

Polyhedron 28 (2009) 3129

Synthesis and characterization of novel α- or β-tetra[6,7-dihexyloxy-3-(4-oxyphenyl)coumarin]-substituted metal-free and metallo phthalocyanines

The synthesis of novel phthalonitriles substituted at 3- or 4-position with 6,7-dihexyloxy-3-(4-oxyphenyl)coumarin were performed. The metal-free and metallo phthalocyanines (MPcs) (M = Zn, Co, Cu) were prepared by cyclotetramerization of 6,7-dihexyloxy-3-[*p*-(2′,3′-dicyanophenoxy)phenyl]coumarin or 6,7-dihexyloxy-3-[*p*-(3′,4′-dicyanophenoxy)phenyl]-coumarin. The newly prepared compounds, phthalonitriles and Pcs, have been characterized by elemental analysis, ^{1}H NMR, ^{13}C NMR, MALDI-TOF, IR, UV–Vis and fluorescence spectral data. The electronic spectra exhibit bands of coumarin identity along with characteristic Q and B bands of the Pc core. The IR-spectra of all Pcs showed three characteristic intense bands at 1709–1700 cm^{-1} for lactone carbonyl, two bands at 1489–1604 cm^{-1} for conjugated olefinic system.

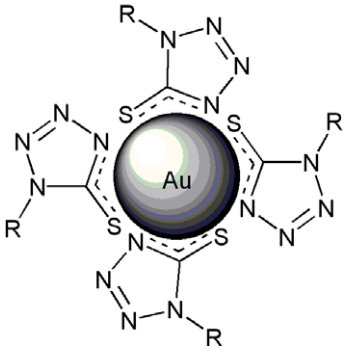


Maria N. Nichick, Sergei V. Voitekhovich, Alexey Shavel, Anatoly I. Lesnikovich and Oleg A. Ivashkevich

Polyhedron 28 (2009) 3138

1-Substituted 5-thiotetrazoles as novel capping agents for stabilization of gold nanoparticles

Stable and nearly monodispersed Au nanoparticles were synthesized by reduction of tetrachloroaurate salts in a toluene-water system in the presence of 1-R-5-thiotetrazoles (R = Et, t-Bu, 1-adamatyl).

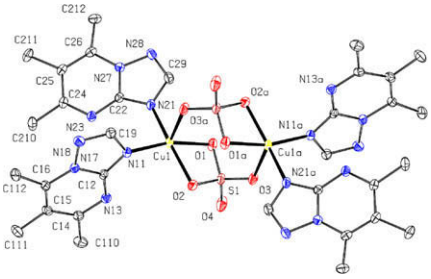


J. Huub Adriaanse, Sven H.C. Askes, Yorrick van Bree, Stefan van Oudheusden, Eelke D. van den Bos, Esref Günay, Ilpo Mutikainen, Urho Turpeinen, Gerard A. van Albada, Jaap G. Haasnoot and Jan Reedijk

Polyhedron 28 (2009) 3143

Coordination chemistry of 5,6,7-trimethyl-[1,2,4]triazolo[1,5-*a*]pyrimidine with first-row transition-metal salts: Synthesis, spectroscopy and single-crystal structures, with counter-anion dependence of the structures

The coordination of the ligand 5,6,7-trimethyl-[1,2,4]triazolo[1,5-*a*]pyrimidine towards transition-metal ions is strongly dependent on the counter ion.

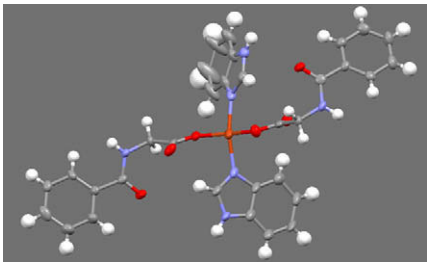


Danuta Dobrzyńska, Tadeusz Lis, Joanna Woźniak, Julia Jezierska, Marek Duczmal, Agnieszka Wojciechowska and Rafał Wysokiński

Polyhedron 28 (2009) 3150

Crystal structure, spectroscopic, magnetic and theoretical studies of [bis(hippurato)bis(benzimidazole)copper(II)] propanol 1/4hydrate

$[Cu(hipp)_2(bim)_2]\cdot PrOH\cdot 0.25H_2O$ (**1**) has been prepared in a one pot synthesis. The crystal structure of **1** consists of layers formed by molecules of the complex and solvent connected via hydrogen bonds. The unsymmetrical CuN_2O_2 core has been investigated by a spectroscopic (EPR and UV–Vis) magnetic study. DFT calculations have been performed.

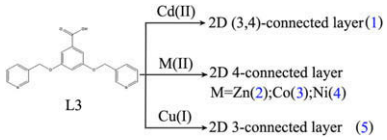


Guang-Juan Xu, Ya-Hui Zhao, Kui-Zhan Shao, Guang-Sheng Yang, Ya-Qian Lan, Zhong-Min Su and Li-Kai Yan

Polyhedron 28 (2009) 3155

Syntheses and characterizations of five coordination polymers constructed by 3,5-bis(pyridin-3-ylmethoxy)benzoic acid ligand

Five coordination polymers, $[Cd(L3)_2]\cdot H_2O$ (**1**), $[Zn(L3)_2]$ (**2**), $[Co(L3)_2]$ (**3**), $[Ni(L3)_2]$ (**4**) and $[Cu_2(L3)_2]\cdot 3H_2O$ (**5**), where L3 = 3,5-bis(pyridin-3-ylmethoxy)benzoic acid, have been synthesized under hydrothermal conditions. **1** is a (3,4)-connected net with $(6^3)(6^6)$ topology. **2**–**4** are isostructural and described by the $(4^4\cdot 6^2)$ topology. The structure of **5** is a 2D binodal (6,3) net.

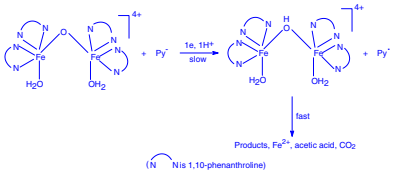


Pulak Chandra Mandal, Jhimli Bhattacharyya, Suranjana Das, Subrata Mukhopadhyay and Louis J. Kirschenbaum

Polyhedron 28 (2009) 3162

Mechanistic studies on the oxidation of pyruvic acid by an oxo-bridged diiron(III,III) complex in aqueous acidic media

$[Fe_2(\mu\text{-}O)(phen)_4(H_2O)_2]^{4+}$ (**1**) equilibrates with $[Fe_2(\mu\text{-}O)(phen)_4(H_2O)(OH)]^{3+}$ (**2**) and $[Fe_2(\mu\text{-}O)(phen)_4(OH)_2]^{2+}$ (**3**) in aqueous solution (phen = 1,10-phenanthroline). In presence of excess phen, an aqueous solution of **1** oxidizes pyruvic acid to acetic acid and carbon dioxide; itself being reduced to two moles of $[Fe(phen)_3]^{2+}$. The reactive species are **1**, **2** and the pyruvate anion (Py^-). The reaction proceeds through a rate limiting 1e, $1H^+$ electroprotic mechanism.



The Publisher encourages the submission of articles in electronic form thus saving time and avoiding rekeying errors. For detailed instructions on the preparation of manuscripts and of electronic artwork, consult the Author Gateway for Elsevier at http://authors.elsevier.com

ScienceDirect

Full text of this journal is available, on-line from **ScienceDirect**. Visit **www.sciencedirect.com** for more information.

Polyhedron 28, issues 9–10, 22 June 2009

Contents lists available at ScienceDirect

Polyhedron

journal homepage: www.elsevier.com/locate/poly

Contents

Papers

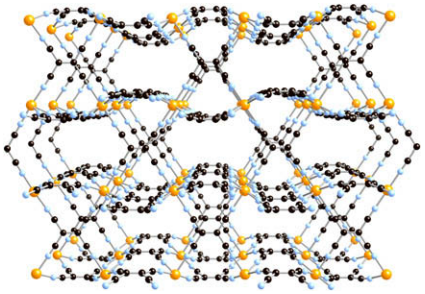
Preface 1595

Joel S. Miller

Polyhedron 28 (2009) 1596

Oliver Kahn Lecture: Composition and structure of the $V[TCNE]_x$ (TCNE = tetracyanoethylene) room-temperature, organic-based magnet – A personal perspective

The formulation and structure of the $V[TCNE]_x$ (TCNE = tetracyanoethylene) room temperature, inhomogeneous, nonstoichiometric, organic-based magnet is reviewed. It is best described as $V^{II}[TCNE]^{\cdot-}_{z}[TCNE]^{2-}_{1-z/2}$ ($1 < z < 2$).

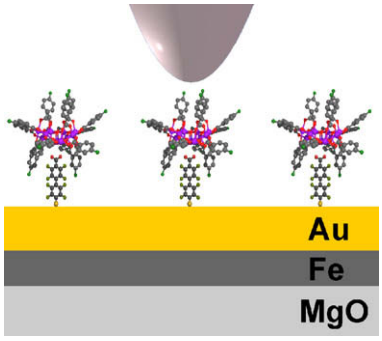


S. Voss, M. Fonin, F. Zinser, M. Burgert, U. Groth and U. Rüdiger

Polyhedron 28 (2009) 1606

A possible approach towards spin-polarized transport through single molecule magnets: Mn_{12} on Au(1 0 0)/Fe(1 0 0)/MgO(1 0 0)

Mn_{12} single molecule magnets have been deposited on a Au/Fe/MgO layer system. The results represent the first deposition of Mn_{12} molecules on Au(1 0 0) and provide evidence that the iron layer is not oxidized during the wet chemical preparation.

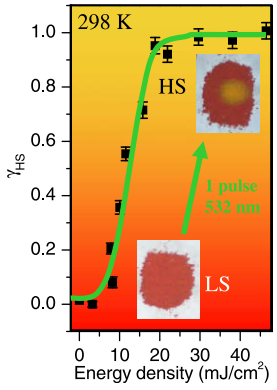


Sébastien Bonhommeau, Gábor Molnár, Saioa Cobo, Denis Ostrovskii and Azzedine Bousseksou

Polyhedron 28 (2009) 1610

One laser shot induced complete phase transition in the spin crossover complex Fe(pyrazine)$[Pt(CN)_4]$

A complete photo-induced phase transition from the low-spin to the high-spin state is triggered by exciting the spin crossover complex Fe(pyrazine)$[Pt(CN)_4]$ with a single laser shot at 532 nm. A non-linear behaviour of the photo-conversion efficiency characterised by the occurrence of an energy density threshold is notably observed.



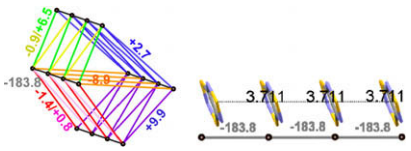
Elsevier Ltd.

C.S. Clarke, J. Jornet, M. Deumal and J.J. Novoa

Polyhedron 28 (2009) 1614

The origin of the bistability in the thiazyl radical 1,3,5-trithia-2,4,6-triazapentalenyl (TTTA): A first principles bottom-up investigation of the magnetic properties of its high temperature polymorph

View of the 3D network created by the non-negligible magnetic interactions in the high temperature phase of the TTTA crystal (left figure). The dominant magnetic interactions, found along the columns in the left view, are shown in the right view in detail.

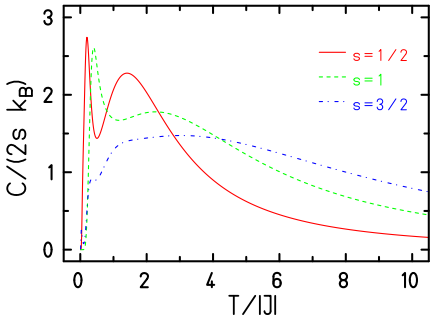


Jürgen Schnack and Roman Schnalle

Polyhedron 28 (2009) 1620

Frustration effects in antiferromagnetic molecules: The cuboctahedron

Frustration of magnetic systems which is caused by competing interactions is the driving force of several unusual phenomena such as plateaus and jumps of the magnetization curve as well as of unusual energy spectra with for instance many singlet levels below the first triplet state. The antiferromagnetic cuboctahedron can serve as a paradigmatic example of certain frustrated antiferromagnets. The graphics displays the heat capacity for the regular cuboctahedron with $s = 1/2$, $s = 1$, and $s = 3/2$. The low-lying singlets lead to a prominent sharp peak at low temperatures especially in the case of $s = 1/2$.

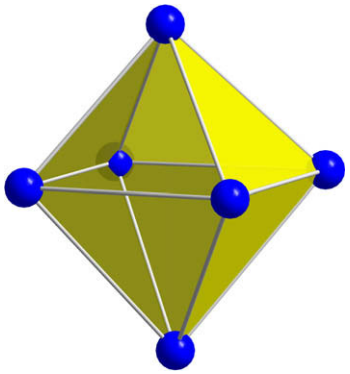


Theocharis C. Stamatatos, Konstantina V. Pringouri, Khalil A. Abboud and George Christou

Polyhedron 28 (2009) 1624

High-spin molecules: A mixed-valence Mn_6 octahedron with an $S = 11$ ground state

A new $Mn^{II/III/IV}_6$ cluster with an octahedral topology has been obtained from the use of 1,1,1-tris(hydroxymethyl)ethane ($thmeH_3$) in higher oxidation state Mn cluster chemistry. The complex is entirely ferromagnetically coupled, possessing the maximum possible $S = 11$ ground state.

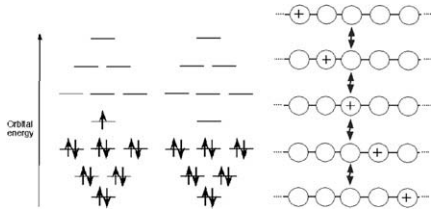


S. Nishihara, S. Yamanaka, K. Nakata, Y. Kitagawa, Y. Yonezawa, M. Okumura, H. Nakamura, T. Takada and K. Yamaguchi

Polyhedron 28 (2009) 1628

A resonating broken-symmetry CI study of cationic states of phenalenyl dimeric compounds

We investigated phenalenyl cation dimers by several ab initio methods. As in the case of simple diatomic cation dimers, the resonating configuration interaction (Res-CI) method correctly yields both the potential surface and the charge distribution of the through-space phenalenyl cation dimer, while the B3LYP and UHF methods fail to describe the potential surface and the charge distribution, respectively. On the other hands, the UHF solution reduces to the ROHF solution for the acethylene-bridged phenalynyl dimer, implying that this bridge plays a role to enhance the conductivity between phenalenyl units. In contrast, the ethylene-bridge leads to a slightly complicated Res-CI solutions based on spin-density wave types of UHF solutions.

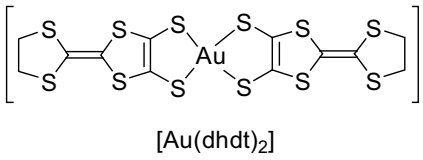


Hiroyuki Nishikawa, Wataru Yasuoka, Kumiko Sakairi and Hiroki Oshio

Polyhedron 28 (2009) 1634

Synthesis and physical properties of a new single-component molecular conductor [Au(dhdt)$_2$]

New Au(III) complexes coordinated by π-reduced TTF-type ligands were prepared and crystal structure of the tetraphenylphosphonium salt was clarified. A neutral complex [Au(dhdt)$_2$] was obtained by the electrochemical oxidation of (n-Bu$_4$N)[Au(dhdt)$_2$]. Conducting behavior of [Au(dhdt)$_2$] was semiconductive with conductivity at room temperature of 8.3 Scm^{-1}, indicating the neutral complex [Au(dhdt)$_2$] is a single-component conductor. Magnetic susceptibility of [Au(dhdt)$_2$] was well explained by the sum of the Curie and temperature independent components.

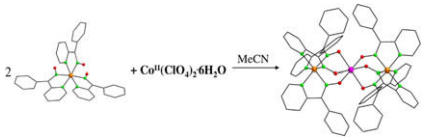


Theocharis C. Stamatatos, Eugenia Katsoulakou, Aris Terzis, Catherine P. Raptopoulou, Richard E.P. Winpenny and Spyros P. Perlepes

Polyhedron 28 (2009) 1638

A family of mononuclear Co^{III}/2-pyridyloximate complexes and their conversion to trinuclear, mixed-valence linear Co$^{II/III}_3$ clusters

A family of new linear, trinuclear mixed-valence Co^{III}Co^{II}Co^{III} clusters have been synthesized using 2-pyridyloximato ligands; the mononuclear "ligand" Co^{III} units of the trinuclear clusters have been also prepared and characterized.

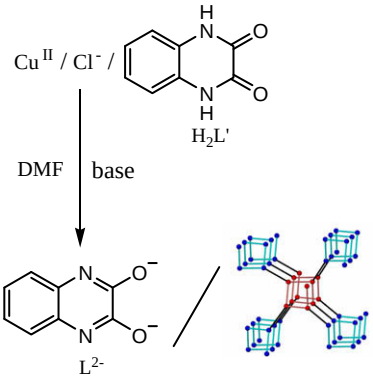


Konstantis F. Konidaris, Giannis S. Papaefstathiou, Guillem Aromi, Simon J. Teat, Evy Manessi-Zoupa, Albert Escuer and Spyros P. Perlepes

Polyhedron 28 (2009) 1646

A three-dimensional copper(II) coordination polymer featuring the 2,3-dioxyquinoxalinate(-2) ligand: Preparation, structural characterization and magnetic study

The initial use of 1,4-dihydro-2,3-quinoxalinedione (H$_2$L′) in Cu^{II} chemistry has led to a 3D coordination polymer featuring the 2,3-dioxyquinoxalinate (L^{2-}) ligand; the complex has the extremely rare (8^2.10)-a, **lig** (LiGe) architecture and is characterized by the propagation of weak antiferromagnetic exchange interactions through the "quinoxaline" part of L^{2-}.

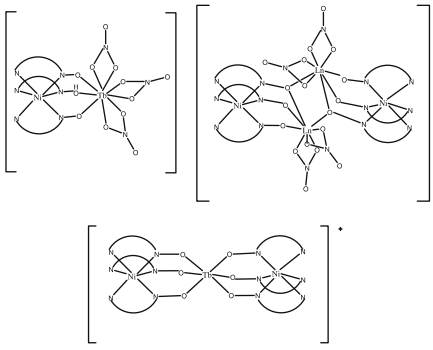


Constantina Papatriantafyllopoulou, Marta Estrader, Constantinos G. Efthymiou, Despina Dermitzaki, Konstantinos Gkotsis, Aris Terzis, Carmen Diaz and Spyros P. Perlepes

Polyhedron 28 (2009) 1652

In search for mixed transition metal/lanthanide single-molecule magnets: Synthetic routes to Ni^{II}/Tb^{III} and Ni^{II}/Dy^{III} clusters featuring a 2-pyridyl oximate ligand

Employing methyl 2-pyridyl ketone oxime, the 'metal complexes as ligand' strategy and various 'one-pot' approaches, NiTb, Ni$_2$Tb$_2$, Ni$_2$Ln$_2$, and Ni$_2$Tb complexes with interesting structural and magnetic features were prepared.

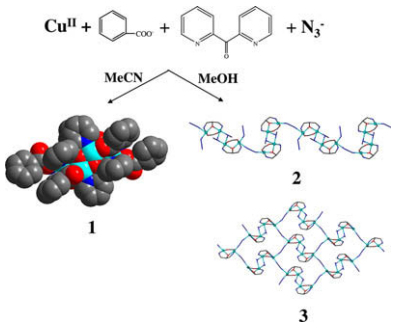


Theocharis C. Stamatatos, Jina C. Vlahopoulou, Vassilis Tangoulis, Catherine P. Raptopoulou, Aris Terzis, Giannis S. Papaefstathiou and Spyros P. Perlepes

Polyhedron 28 (2009) 1656

New copper(II) clusters and coordination polymers from the amalgamation of azide/benzoate/di-2-pyridyl ketone ligands

The employment of the $PhCO_2^-/N_3^-/(py)_2CO$ ternary 'blend' of ligands in copper(II) chemistry has provided access to a Cu^{II}_6 cluster with a novel core and to two $(Cu^{II}_8)_n$ and $(Cu^{II}_2)_n$ coordination polymers (the former 1D, the latter 2D) depending on the reaction solvent; the products have unique structural characteristics.

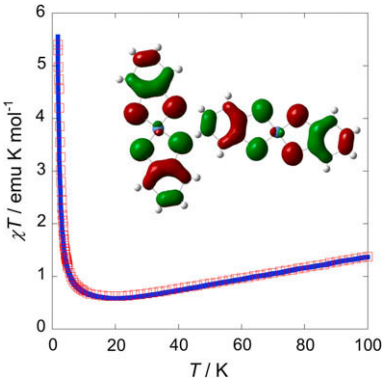


Junichi Nishijo, Shigenori Numao, Ken Judai and Nobuyuki Nishi

Polyhedron 28 (2009) 1664

Ferromagnetic interaction between $[Ni(bdt)_2]^-$ anions in $[Mn_2(Saloph)_2(\mu\text{-}OH)][Ni(bdt)_2](CH_3CN)_2$

A new molecule-based magnetic material $[Mn_2(Saloph)_2(\mu\text{-}OH)][Ni(bdt)_2](CH_3CN)_2$ shows ferromagnetic interaction $2J = +4.5$ K between $[Ni(bdt)_2]^-$ anions. The origin of the ferromagnetic interaction is attributed to the orthogonality of the SOMOs and the large overlap between the NOHOMO and the SOMO of adjacent $[Ni(bdt)_2]^-$ anions.

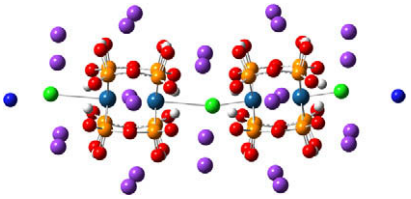


Y. Kitagawa, M. Ito, Y. Nakanishi, T. Saito, S. Yamada, T. Kawakami, M. Okumura and K. Yamaguchi

Polyhedron 28 (2009) 1668

Theoretical studies on electronic structures and magnetic interactions of $K_4[Pt_2(pop)_4X] \cdot 2H_2O$ (X = Cl, Br) complexes

Electronic structures, CDW/CP stability and magnetic properties of $K_4[Pt_2(pop)_4X] \cdot 2H_2O$ (X = Cl, Br) complexes are examined by UB3LYP method.

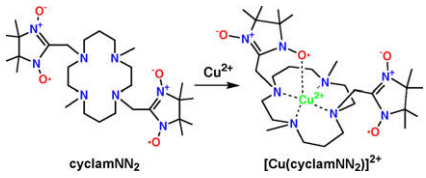


Kazuki Igarashi, Takashi Nogami and Takayuki Ishida

Polyhedron 28 (2009) 1672

Ferromagnetic coupling of copper(II) and nickel(II) complexes with a cyclam-based paramagnetic host

We prepared host–guest complexes $[M(cyclamNN_2)](ClO_4)_2$ (M = Cu (**1**), Ni (**2**)) and investigated their metal–radial exchange couplings. Compound **1** showed ferromagnetic coupling ($2J/k_B = +44(3)$ K), which is ascribable to the axial NN–Cu coupling. Ferromagnetic coupling was also observed in **2**, but the molecular structure was unknown at present.

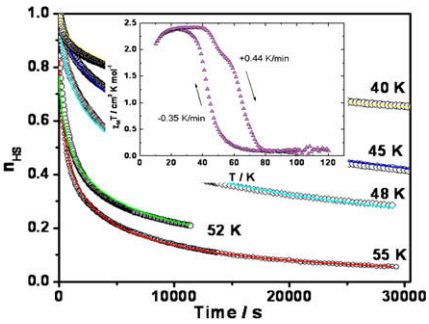


Haritosh Mishra, Vibha Mishra, François Varret, Rabindranath Mukherjee, Chérif Baldé, Cédric Desplanches and Jean-François Létard

Polyhedron 28 (2009) 1678

Opposite effects of interactions and disorder on the switching properties of the spin transition compound $[Fe^{II}(L)_2][ClO_4]_2 \cdot C_7H_8$

The apparent discrepancy between the stretched character of the relaxation curves and the cooperative origin of the LITH loop is investigated in the frame of a model which combines long-range interaction and short- and long-range distributions of molecular parameters.

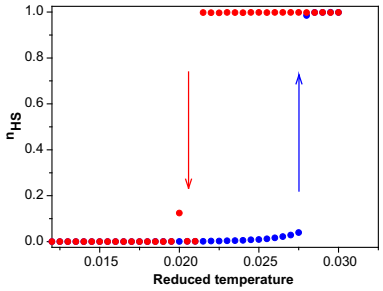


Aurelian Rotaru, Adrian Carmona, Flavien Combaud, Jorge Linares, Alexandru Stancu and Jamil Nasser

Polyhedron 28 (2009) 1684

Monte Carlo simulations for 1- and 2D spin crossover compounds using the atom–phonon coupling model

Thermal behaviour of an one and two dimensional lattice spin crossover systems has been simulated using MonteCarlo-Metropolis technique in the framework of the atom-phonon coupling model.The high spin fraction evolution in function of the reduced temperature, obtained for 2D system using:

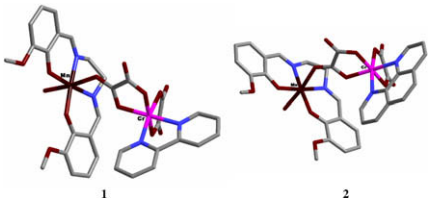


Silviu Nastase, Catalin Maxim, Floriana Tuna, Carine Duhayon, Jean-Pascal Sutter and Marius Andruh

Polyhedron 28 (2009) 1688

First binuclear Cr(III)–Mn(III) oxalato-bridged complexes: Synthesis, crystal structures and magnetic properties

Two Cr(III)–Mn(III) binuclear complexes, with the general formula $[\{Mn(H_2O)(valen)\}\{Cr(AA)(C_2O_4)_2\}] \cdot 3H_2O$, have been obtained by assembling $[Mn((H_2O)(CH_3CN)(valen)]^+$ and $[Cr(AA)(C_2O_4)_2]^-$ ions.

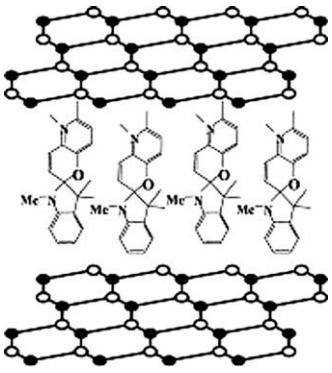


Noriyuki Kida, Masanori Hikita, Izuru Kashima, Masaya Enomoto, Miho Itoi and Norimichi Kojima

Polyhedron 28 (2009) 1694

Mössbauer spectroscopic study of photo-sensitive organic–inorganic hybrid system, (SP)[Fe(II)Fe(III)(dto)$_3$](dto = $C_2O_2S_2$, SP = spiropyran)

^{57}Fe Mössbauer measurement are presented for the photo-sensitive organic–inorganic hybrid system $(SP)[Fe^{II}Fe^{III}(dto)_3]$ (SP = spiropyran, dto = $C_2O_2S_2$) in order to investigated the photo-induced effect on them. The sample without UV-irradiation shows the charge transfer phase transition between 200 and 70 K and the higher and lower temperature phases coexist below 70 K, whereas the UV-irradiated sample does not undergo the charge transfer phase transition and the higher temperature phase is stable between 200 and 6 K.

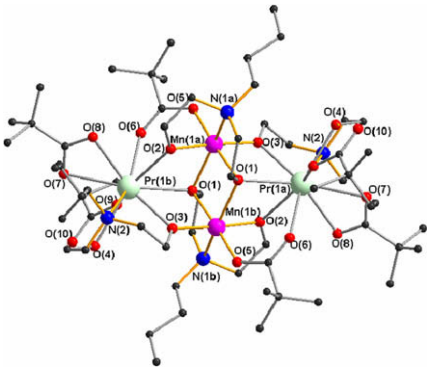


Muhammad Nadeem Akhtar, Yanhua Lan, Valeriu Mereacre, Rodolphe Clérac, Christopher E. Anson and Annie K. Powell

Polyhedron 28 (2009) 1698

Synthesis, structures and magnetic properties of heterometallic $Mn^{III}_2Ln^{III}_2$ tetranuclear complexes

Four isostructural heterometallic Mn–Ln tetranuclear complexes of formula $[Mn^{III}_2Ln_2(bdea)_2(bdeaH)_2(piv)_6]\cdot 2MeCN$ (Ln = La (**1**), Ce (**2**), Pr (**3**) and Nd (**4**)), where $bdeaH_2$ is *N*-butyldiethanolamine and $(piv)^-$ is pivalate, are reported. X-ray crystallographic structure analysis shows that complexes **1**–**4** are centrosymmetric with a "butterfly" core. The magnetic susceptibilities (dc and ac) for all these complexes have been measured. Slow relaxation of the magnetization is observed in compounds **2** and **4**.

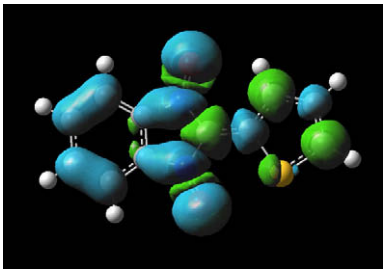


Steven E. Bowles, Brynn M. Dooley, Jason B. Benedict, Werner Kaminsky and Natia L. Frank

Polyhedron 28 (2009) 1704

The competing roles of topology and spin density in the magnetic behavior of spin-delocalized radicals: Donor–acceptor annelated nitronyl nitroxides

Toward the development of multifunctional materials, the electronic, structural and magnetic properties of acceptor–donor benzonitronyl nitroxides was investigated. The radicals exhibit low energy (~950 nm) charge transfer bands consistent with Robin-Day ClassII/III mixed valency in solution, and p-stacked chains with weak antiferromagnetic interactions due to planar disorder.

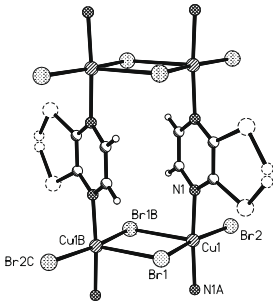


Robert T. Butcher, Louise N. Dawe, Christopher P. Landee and Mark M. Turnbull

Polyhedron 28 (2009) 1710

Copper diazine spin ladders: Synthesis, structure and magnetic analyses of Cu(2-methylthiopyrazine)Br_2

Reaction of $CuBr_2$ with 2-methylthiopyrazine yields the coordination polymer $[Cu(meSpz)Br_2]_n$. Analysis of the temperature dependant magnetic data indicates that the complex is a strong-rung magnetic ladder.

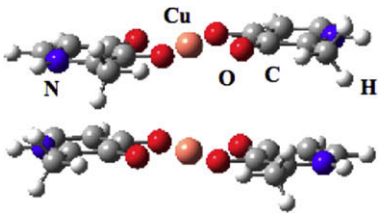


Y. Nakanishi, Y. Kitagawa, Y. Shigeta, T. Saito, T. Matsui, H. Miyachi, T. Kawakami, M. Okumura and K. Yamaguchi

Polyhedron 28 (2009) 1714

Theoretical studies on magnetic interactions between Cu(II) ions in hydroxypyridone nucleobases

The origin of ferromagnetic interaction between Cu^{2+} ions in Cu^{2+}–DNA system is examined by using DFT calculations. In order to consider effects of an entanglement and a dis-entanglement of the double helix chain, three types of structural disorders.

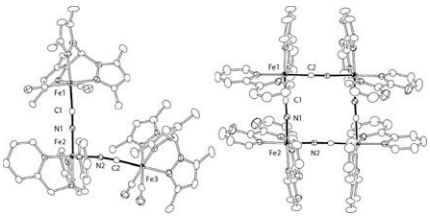


Masayuki Nihei, Mayumi Ui and Hiroki Oshio

Polyhedron 28 (2009) 1718

Cyanide-bridged tri- and tetra-nuclear spin crossover complexes

Cyanide-bridged tri- and tetra-nuclear complexes of $[Fe^{III}_2Fe^{II}(CN)_6(tp^*)_2(tpa)] \cdot 4MeCN \cdot t$-BuMeO (**1**) and $[Fe^{II}_4(CN)_4(bpy)_4(bpym)_4](PF_6)_4 \cdot 6MeOH \cdot 4H_2O$ (**2**) (tp^* = hydrotris(dimethylpyrazolyl)borate, tpa = tris(2-pyridylmethyl)amine, bpy = 2,2′-bipyridine, bpym = 2,2′-bipyrimidine) were prepared. Compound **1** has a right angled trinuclear core, while the tetranuclear core in **2** is almost square. Magnetic susceptibility measurements revealed that both complexes showed thermally induced spin crossover.



Shinya Hayami, Soushi Miyazaki, Jun Kawamata and Katsuya Inoue

Polyhedron 28 (2009) 1722

Second-order non-linear optical response in LB films for the metal complexes

The complexes with long alkyl chains were synthesized. Langmuir–Blodgett (LB) films of the compounds were also prepared. The second harmonic generation (SHG) were estimated for the LB films formed by the metal complexes with long alkyl chains in LB film. The order of the intensity for the SHG related with the number of unpaired d electrons or the d electron configurations. The goal of this study is switching of NLO response by using of SCO and LIESST effect.

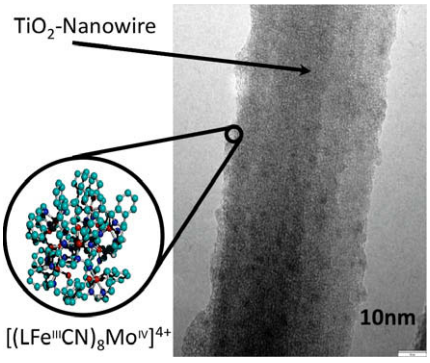


Muhammad Nawaz Tahir, Markus Messerschmidt, Michael Klein, Victor Martinez, Patrick Theato, Nadine Metz, Sonngard Hartmann, Ute Kolb, Vadim Ksenofontov, Franz Renz and Wolfgang Tremel

Polyhedron 28 (2009) 1728

Synthesis and immobilization of molecular switches onto titaniumdioxide nanowires

Application of molecular switches as functional units requires the addressing individual molecules, which is imaging, probling, and eventually manipulating individual molecules. In this contribution we describe the immobilization of switchable $[(LFe^{III}NC)_8Mo^{IV}]^{4+}$ units onto the surface of TiO_2 nanowires using electrostatic interactions.

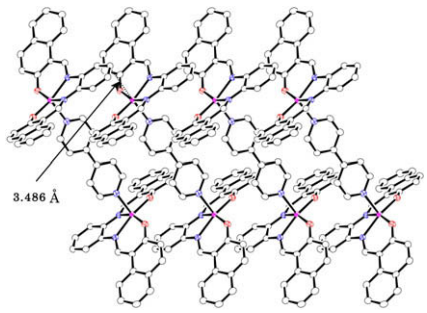


Atsuhiro Nabei, Takayoshi Kuroda-Sowa, Toshiyuki Shimizu, Takashi Okubo, Masahiko Maekawa and Megumu Munakata

Polyhedron 28 (2009) 1734

Ferromagnetic interaction in iron(II)–bis-Schiff base complexes

Three Fe(II)–bis-Schiff base complexes, a bpy-bridged dimer, a monomer with one-dimensional chain and a dimer through $\pi\cdots\pi$ interaction, show ferromagnetic interaction at low temperature, probably due to the Fe$\cdots\pi$ interaction as indicated for the first compound.

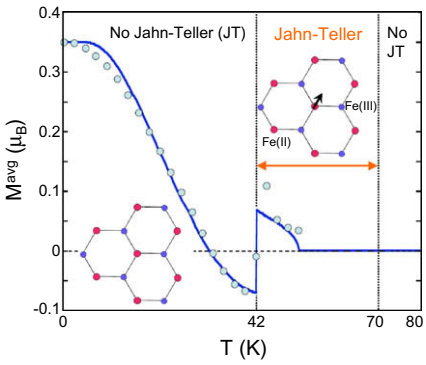


Randy S. Fishman, Satoshi Okamoto and Fernando A. Reboredo

Polyhedron 28 (2009) 1740

Spin–orbit coupling and Jahn–Teller distortion in bimetallic oxalates

A Jahn–Teller distortion of the Fe(II) ions in Fe(II)Fe(III) bimetallic oxalates gains electronic energy but costs elastic energy. In compounds that exhibit magnetic compensation, the distortion only appears above the compensation temperature due to the competition with the spin–orbit coupling.

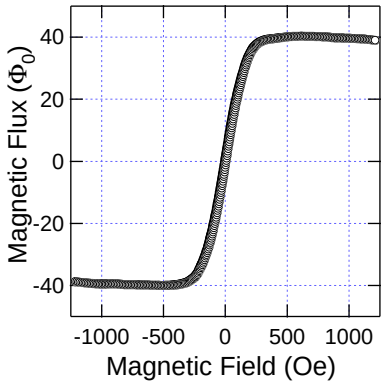


Keiji Takeda, Hiroko Tokoro, Fumiyoshi Hakoe, Akira Yamaguchi, Hatsumi Mori, Hidehiko Ishimoto, Takayoshi Nakamura, Shinya Kuriki and Shin-ichi Ohkoshi

Polyhedron 28 (2009) 1746

High temperature superconductor micro SQUID magnetometer for molecular-based magnets

The magnetic hysteresis curve of the ferrimagnetic microcrystal of $[Mn_2(H_2O)_2(CH_3COO)][W(CN)_8]\cdot 2H_2O$ ($15 \times 15 \times 13$ μm) was obtained by the high temperature superconductor (HTS) micro SQUID magnetometer. The dipole approximation, considering the relative arrangement of the sample and the SQUID loop, reasonably explained the flux of 40 Φ_0 from the saturation magnetic moment.

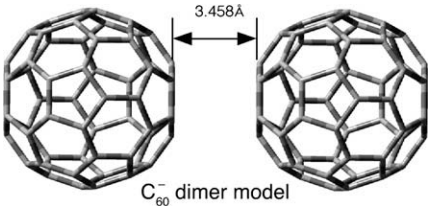


Y. Kitagawa, Y. Nakanishi, T. Saito, K. Koizumi, M. Shoji, S. Yamada, T. Kawakami, M. Okumura and K. Yamaguchi

Polyhedron 28 (2009) 1750

Theoretical study of magnetic interaction between C_{60} anion radicals

The magnetic interactions between two C_{60} anions are investigated by using unrestricted B3LYP (UB3LYP) calculations. One type of SOMO–SOMO interactions shows a week ferromagnetic interaction.

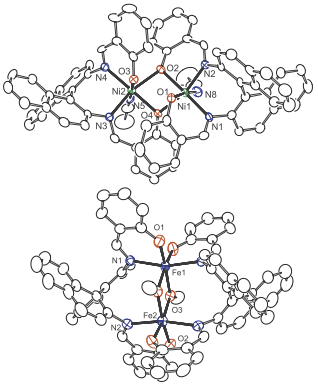


Norihisa Hoshino, Takuya Shiga, Masayuki Nihei and Hiroki Oshio

Polyhedron 28 (2009) 1754

Chiral dinuclear complexes with tetradentate ligands derived from (*R*)-(+)-1,1′-binaphthyl-2,2′-diamine

Novel chiral dinuclear complexes of Δ,Δ-$[Ni^{II}_2((R)\text{-Hsalbn})((R)\text{-salbn})(MeCN)_2](ClO_4)\cdot 2\text{-MeCN}$ (**1**) and Λ,Λ-$[Fe^{III}_2((R)\text{-salbn})_2(OMe)_2]\cdot Et_2O\cdot H_2O$ (**2**) ((*R*)-H_2salbn = ((*R*)-(+)-*N*,*N*′-bissalicylidene-1,1′-binaphthyl-2,2′-diamine) were prepared. Dc magnetic susceptibility measurements suggested antiferromagnetic interactions operative in **1** and **2**.

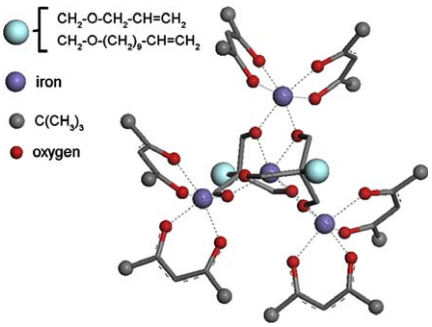


G. Pellegrino, A. Motta, A. Cornia, I. Spitaleri, I.L. Fragalà and G.G. Condorelli

Polyhedron 28 (2009) 1758

One pot grafting of tetrairon(III) single molecule magnets on silicon

Two Fe_4 derivatives have been specifically designed to be directly anchored on the H-terminated silicon surface via the hydrosilylation reaction. The complexes were grafted by a *one pot* route based on the photoinduced hydrosilylation followed by a ligand exchange step in the same reaction solution.

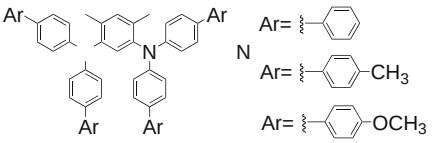


Masafumi Yano, Yorichika Okino, Yuji Ichihara, Masakazu Tatsumi, Munetaka Oyama, Kazunobu Sato and Takeji Takui

Polyhedron 28 (2009) 1764

Organic high-spin systems: Synthesis, electrochemical and spectroscopic studies of π-extended tetraaryl *m*-phenylenediamines

A series of highly π-extended tetraaryl-*m*-phenylenediamines were designed and synthesized as a precursor of positively charged high-spin systems. The electrochemical and spectroscopic properties were examined.

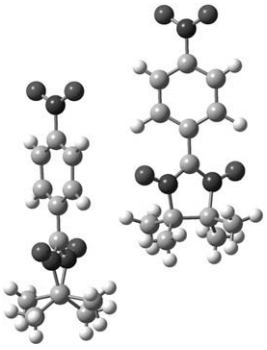


Mitsutaka Okumura, Yohei Nishimura, Yasutaka Kitagawa, Takashi Kawakami and Kizashi Yamaguchi

Polyhedron 28 (2009) 1768

Theoretical calculations of magnetic properties of the α-, β-, γ- and δ-phases of *p*-NPNN

Hybrid density functional theory (HDFT) calculations have been carried out for clusters of *p*-NPNN extracted from the experimental crystal structures of the α-, β-, γ- and δ-phases in order to investigate the weak magnetic interactions between the organic radicals theoretically.

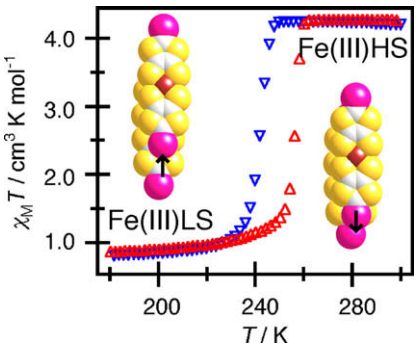


Kazuyuki Takahashi, Hatsumi Mori, Hayao Kobayashi and Osamu Sato

Polyhedron 28 (2009) 1776

Mechanism of reversible spin transition with a thermal hysteresis loop in $[Fe^{III}(qsal)_2][Ni(dmise)_2] \cdot 2CH_3CN$: Selenium analogue of the precursor of an Fe(III) spin-crossover molecular conducting system

The cooperative spin transition of a novel Fe(III) complex with an $Ni(dmise)_2$ anion accompanies a reversible molecular slipping of π-dimer of $Ni(dmise)_2$ along the molecular long axis, which is due to intermolecular π–π interactions between the Fe(III) spin-crossover cation and $Ni(dmise)_2$ anion.

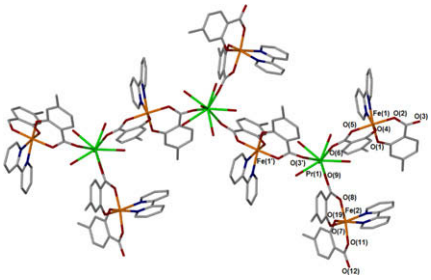


Sudarshana Mukherjee, Yanhua Lan, Ghenadie Novitchi, George E. Kostakis, Christopher E. Anson and Annie K. Powell

Polyhedron 28 (2009) 1782

Syntheses, structures and magnetic studies of three heterometallic Fe_2Ln 1D coordination polymers

Three new heterometallic 1D coordination polymers $[Fe^{III}_2Pr(4\text{-Me-sal})_4(2,2'\text{-bipy})_2(H_2O)_6](NO_3)\cdot 2MeOH\cdot 1.5H_2O$ (**1**), $[Fe^{III}_2Gd(4\text{-Me-sal})_4(2,2'\text{-bipy})_2(H_2O)_5]Cl_{1/2}(NO_3)_{1/2}\cdot 5H_2O$ (**2**) and $[Fe^{III}_2Dy(4\text{-Me-sal})_4(2,2'\text{-bipy})_2(H_2O)_5]Cl_{1/2}(NO_3)_{1/2}\cdot 5H_2O$ (**3**) have been synthesized and structurally characterized. Magnetic studies show that the three compounds show a similar temperature dependence of their magnetic susceptibilities over the range 1.8–300 K.

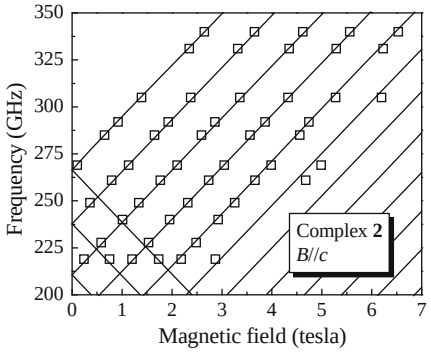


Saiti Datta, Erica Bolin, Ross Inglis, Constantinos J. Milios, Euan K. Brechin and Stephen Hill

Polyhedron 28 (2009) 1788

A comparative EPR study of high- and low-spin Mn_6 single-molecule magnets

The results of high-frequency (50–350 GHz) electron paramagnetic resonance (EPR) studies of two complexes from a family of recently discovered Mn^{III}_6 single-molecule magnets (SMMs), are presented. The experimental findings were compared with numerical calculations, where the total anisotropy for a complex is determined in terms of single-ion anisotropies using both projection operator techniques and exact matrix diagonalization methods. It is shown clearly that the product of the molecular anisotropy, D, and spin, S, does not change significantly upon switching from $S = 4$ to 12, i.e. D goes down as S goes up but the barrier height to the magnetization reversal, U, does increase, and it goes roughly as S^1 rather that S^2 or S^0.

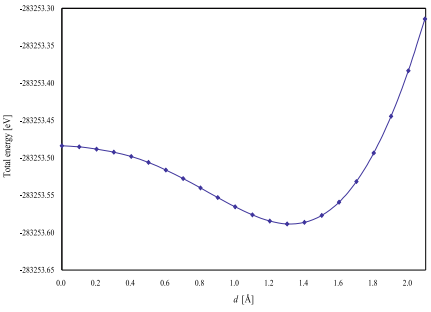


Taku Onishi

Polyhedron 28 (2009) 1792

The theoretical study for the perovskite-type manganese fluorides of $KMnF_3$, $RbMnF_3$ and $K_{1-x}Li_xMnF_3$

The potential energy curve for $LiMn_8O_{12}$ model, changing the displacement distance (d) from the cubic center toward <100> direction (UBHHLYP method).

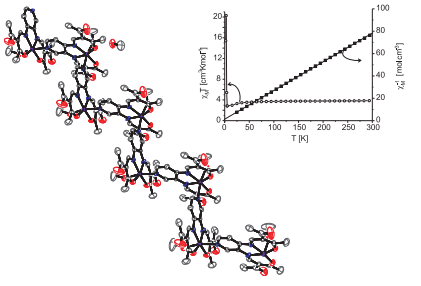


Sebastian Thallmair, Wolfgang Bauer and Birgit Weber

Polyhedron 28 (2009) 1796

Strategies towards the purposeful design of long-range ferromagnetic ordering due to spin canting

A new modification of N_2O_2 coordinating Schiff-base like ligands allows the synthesis of a 1D zigzag chain with a strong spontaneous magnetization due to spin canting.

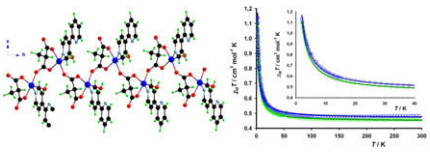


Jorge Pasán, Joaquín Sanchiz, Laura Cañadillas-Delgado, Oscar Fabelo, Mariadel Déniz, Francesc Lloret, Miguel Julve and Catalina Ruiz-Pérez

Polyhedron 28 (2009) 1802

Copper(II)-methylmalonate complexes with unidentate N-donor ligands: Syntheses, structural characterization and magnetic properties

The methylmalonate ligand has been used to synthesize two novel and very similar carboxylate-bridged copper(II) chains. The N-donor coligands 3-Iodopyridine and 2,4′-bipyridine determine the structural differences, mainly the pore size which in the case of the 2,4′-bipyridine is capable to accommodate chains of fused pentagonal motives of water molecules. Both complexes exhibit intrachain ferromagnetic couplings through the equatorial–equatorial *anti-syn* carboxylate bridges.

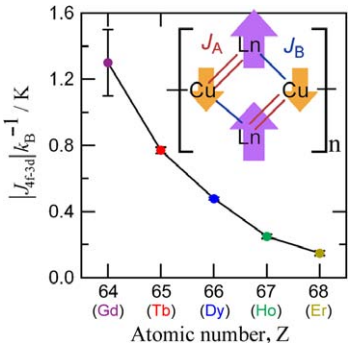


Atsushi Okazawa, Ryo Watanabe, Hiroyuki Nojiri, Takashi Nogami and Takayuki Ishida

Polyhedron 28 (2009) 1808

Magnetic properties and exchange couplings of one-dimensionally arrayed 4f–3d heterometallic $[Ln_2Cu_2]_n$ compounds

The exchange couplings J_{4f-3d} in $[Ln_2Cu_2]_n$ (Ln = Tb, Ho, and Er), which are analogs of the known ferrimagnetic $[Gd_2Cu_2]_n$ and $[Dy_2Cu_2]_n$, were precisely evaluated by high-frequency EPR and pulsed-field magnetization studies. The $|J_{4f-3d}|$ value monotonically decreases in the order of Gd, Tb, Dy, Ho, and Er.

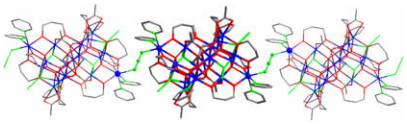


Eleni E. Moushi, Theocharis C. Stamatatos, Vassilios Nastopoulos, George Christou and Anastasios J. Tasiopoulos

Polyhedron 28 (2009) 1814

1-D coordination polymers consisting of a high-spin Mn_{17} octahedral unit

The use of the combination of pdH_2 or $mpdH_2$ and N_3^- ligands in reactions with Mn^{II} carboxylate salts resulted in two one-dimensional coordination polymers $[(\mathbf{1})_\infty$ and $(\mathbf{2})_\infty]$ (figure; color scheme: Mn, blue; O, red; N, green; C, grey) consisting of a $[Mn^{III}{}_{11}Mn^{II}{}_6(\mu_4\text{-}O)_8(\mu_3\text{-}N_3)_4]^{25+}$ octahedral unit. The Mn_{17} unit seems to have a giant spin ground state (S); however, both polymers display $S \approx 0$ spin ground states due to intermolecular antiferromagnetic interactions between the neighboring Mn_{17} units.

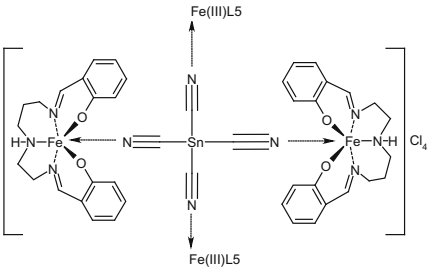


F. Renz, St. Jung, M. Klein, M. Menzel and A.F. Thünemann

Polyhedron 28 (2009) 1818

Molecular switching complexes with iron and tin as central atom

We present a molecular switching complex with a main group metal element, i.e. tin, as central atom. For this compound we can show valence tautomerism between Sn(II) and Sn(IV) and electron switching for Fe(III) between high-spin and low-spin state.

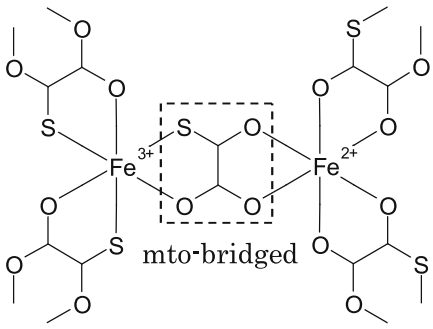


Koichi Kagesawa, Yuki Ono, Masaya Enomoto and Norimichi Kojima

Polyhedron 28 (2009) 1822

Study on the valence fluctuation and the magnetism of an iron mixed-valence complex, $(n\text{-}C_4H_9)_4N[Fe^{II}Fe^{III}(mto)_3]$(mto = C_2O_3S)

Iron mixed-valence complex, $(n\text{-}C_4H_9)_4$ $N[Fe^{II}Fe^{III}(mto)_3]$ (mto = monothiooxalato), behaves as a ferrimagnet with its magnetic transition temperature of T_N = 38 K and Weiss temperature of θ = –93 K. From the analysis of ^{57}Fe Mössbauer spectra of $(n\text{-}C_4H_9)_4$ $N[Fe^{II}Fe^{III}(mto)_3]$ in which Fe^{II} or Fe^{III} was substituted with ^{57}Fe and the dielectric constant, the valence fluctuation between Fe^{II} and Fe^{III} exists in the paramagnetic phase.

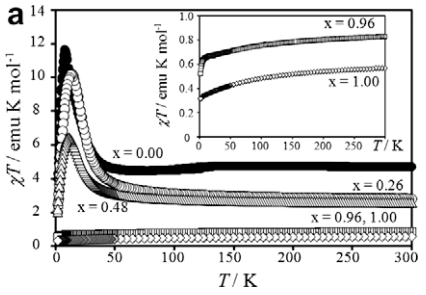


Masaya Enomoto and Norimichi Kojima

Polyhedron 28 (2009) 1826

Magnetic dilution effect on the charge transfer phase transition and the ferromagnetic transition for an iron mixed-valence complex, $(n\text{-}C_3H_7)_4N[Fe^{II}{}_{1-x}Zn^{II}{}_xFe^{III}(dto)_3]$ (dto = $C_2O_2S_2$)

An magnetic diluted complex, $(n\text{-}C_3H_7)_4N[Fe^{II}{}_{1-x}Zn^{II}{}_xFe^{III}(dto)_3]$ (dto = $C_2O_2S_2$) was synthesized and measured its magnetic properties in order to investigate the magnetic structure of $(n\text{-}C_3H_7)_4N[Fe^{II}Fe^{III}(dto)_3]$, whose magnetic transition is coupled with charge transfer between adjacent iron sites. In this system, the charge transfer phase transition disappears above x = 0.26, while the ferromagnetic interaction changes to the antiferromagnetic one between x = 0.48 and 0.96.

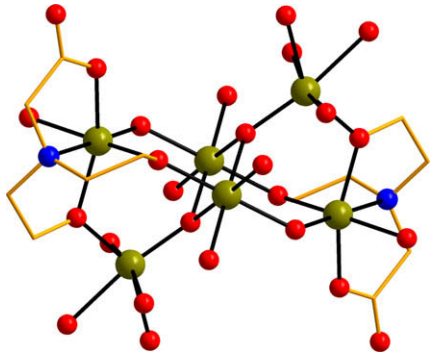


Kristoffer Graham, Amiera Darwish, Alan Ferguson, Simon Parsons and Mark Murrie

Polyhedron 28 (2009) 1830

Synthesis and characterisation of Fe_6 and Fe_{12} clusters using bicine

We report two new Fe(III) complexes using a bicine/pivalate ligand blend. Magnetic characterisation reveals S = 5 and S = 0 ground states for the hexa- and dodeca-nuclear complexes, respectively.

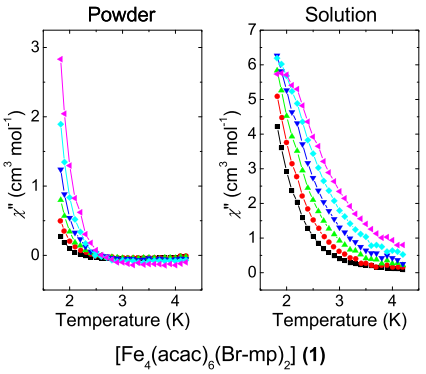


C. Schlegel, J. van Slageren, M. Manoli, E.K. Brechin and M. Dressel

Polyhedron 28 (2009) 1834

Synthesis, structures and magnetic properties of two novel tetranuclear iron(III) single-molecule magnets: Enhanced energy barriers in solution

Two new tetranuclear iron(III) single-molecule magnets were synthesized and fully characterized. AC susceptibility measurements show that the energy barrier increases going from powder to frozen solution samples.

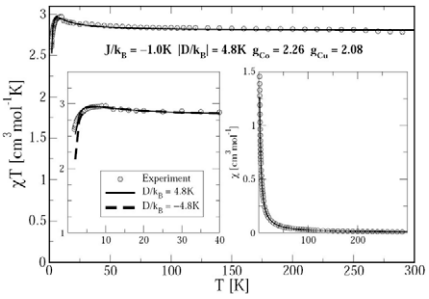


Paweł Sobczak, Artur Barasiński, Andrzej Drzewiński, Grzegorz Kamieniarz, Julia Kłak, Alina Bieńko and Jerzy Mroziński

Polyhedron 28 (2009) 1838

Magnetic properties and DMRG modeling of the 1D bimetallic thiocyanate bridged compound $\{(CuL_1)[Co(NCS)_4]\}$ (L_1 = *N*-rac-5,12-Me_2-[14]-4,11-dieneN_4)

The magnetic properties of the bimetallic compound $\{(CuL_1)[Co(NCS)_4]\}$, where L_1 = *N*-rac-5,12-dimethyl-1,4,8,11-tetraazacyclotetradeca-4,11-diene have been numerically analysed on the basis of the anisotropic Heisenberg spin-chain model. In the model the single-ion anisotropy of the Co(II) ions is taken into account and the interchain interactions are neglected. The thermodynamic properties are calculated using the DMRG technique adapted to the molecular-based chains for the first time which is reliable in the entire temperature region. The high accuracy results of our simulations have been successfully fitted to the corresponding experimental susceptibility and magnetization data measured for the powder sample and the model parameters (the exchange coupling *J*, the absolute value of the anisotropy constant *D*, the anisotropic *g* factors) have been estimated. The quantum model parameters are consistent with the previous findings, although the ferromagnetic interactions between Cu(II) and Co(II) ions through the thiocyanate bridge are somewhat weaker (J/k_B = 1.0 ± 0.1) than found before.

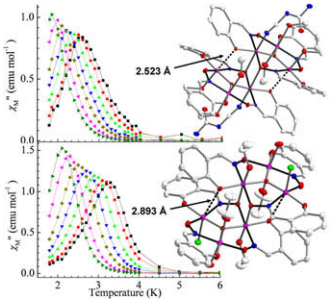


Chen-I Yang, Kai-Hung Cheng, Motohiro Nakano, Gene-Hsiang Lee and Hui-Lien Tsai

Polyhedron 28 (2009) 1842

Synthesis, structures and magnetic properties of two hexanuclear complexes

Two Mn^{III}_6 single-molecule magnets with a ground state S = 4 have been synthesized and structurally characterized. The structural distortions of complexes make the variation of magnetic properties.

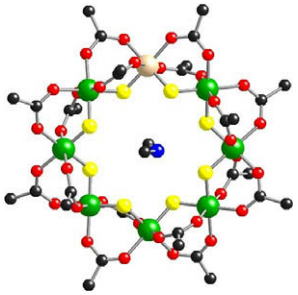


P. Kozłowski, G. Kamieniarz, M. Antkowiak, F. Tuna, G.A. Timco and R.E.P. Winpenny

Polyhedron 28 (2009) 1852

Phenomenological modeling of the anisotropic molecular-based ringCr_7Cd

The properties of the $[(CH_3)_2NH_2][Cr_7CdF_8\{OOCC(CH_3)_3\}_{16}]$ complex are investigated by means of magnetic measurements modeled by two exact techniques: quantum transfer matrix and exact diagonalization. The existence and role of two different types (exchange and single ion) of anisotropy are discussed.

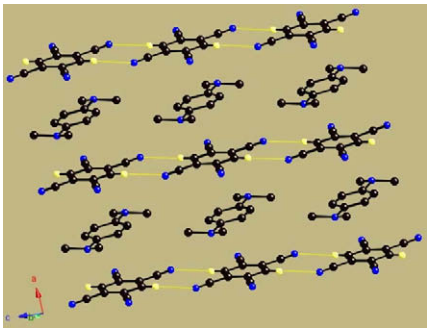


Prasanna S. Ghalsasi

Polyhedron 28 (2009) 1856

Crystal structure and magnetic properties of hydrogen bonded charge-transfer compound – TMPD:TCNB

TMPD:TCNB complex showed presence of two distinct non-covalent interactions: (i) charge-transfer interaction and (ii) ribbon-like CN···HAr hydrogen bonding motif amongst electron acceptor molecules. Magnetic measurements on the powdered compound using SQUID magnetometer (5–20 K) showed that the complex is weakly antiferromagnetic (θ = –0.85 K).

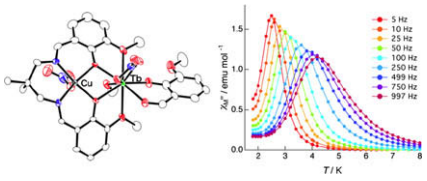


Takashi Kajiwara, Kohei Takahashi, Tomonari Hiraizumi, Shinya Takaishi and Masahiro Yamashita

Polyhedron 28 (2009) 1860

Coordination enhancement of single-molecule magnet behavior of Tb(III)–Cu(II) dinuclear systems

Single-molecule magnet (SMM) behaviors of two Tb(III)-Cu(II) complexes, [TbCu(**L3**)$(No_3)_3$-(H_2O) and [TbCu(**L3**)(NO_3)(*o*-vanilate)-(MeOH)]NO_3 (**L3**$^{2-}$ denotes a Schiff-base ligand formed with *o*-vanilate and 2,2-dimethyl-1,3-propanediamine), were investigated to reveal the relationship between coordination geometry around Tb(III) ion and the magnetic anisotropy.

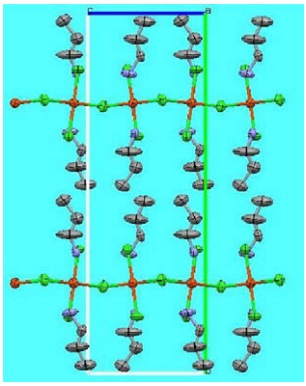


Prasanna S. Ghalsasi and Katsuya Inoue

Polyhedron 28 (2009) 1864

Distorted perovskite structured organic–inorganic hybrid compounds for possible multiferroic behavior: [*n*-alkyl]$_2FeCl_4$

We have synthesized simple double salts, distorted perovskite structured compounds, with formula Cn_2FeCl_4, (Cn = *n*-propyl or *n*-butyl ammonium ions). $(C_3)_2FeCl_4$, crystallize in orthorhombic space group, $Cmc2_1$, at room temperature. The overall structure consists of two-dimensional Fe(II)–chloride network, parallel to the *ac*-plane, interlayered by the ammonium ions. Magnetic measurements using SQUID magnetometer show that these compounds are antiferromagnets with $T_N \sim 90$ K. Preliminary studies using DSC and AC-conductivity have shown promising transitions above room temperature.

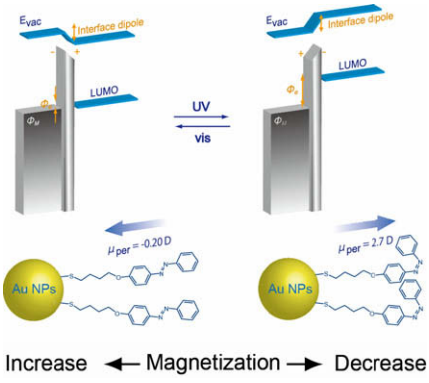


Masayuki Suda, Naoto Kameyama, Aya Ikegami, Motohiro Suzuki, Naomi Kawamura and Yasuaki Einaga

Polyhedron 28 (2009) 1868

Size-reduction induced ferromagnetism and photo-magnetic effects in azobenzene-thiol-passivated gold nanoparticles

We have observed size-reduction induced ferromagnetism and significant photo-magnetic effects in azobenzene-thiol-modified gold nanoparticles. This photo-magnetic effect could be attributed to photo-induced changes in the values of d-charge losses due to the photo-isomerization of azo-ligands, which were accompanied by the inversion of surface dipole values to the opposite sign.

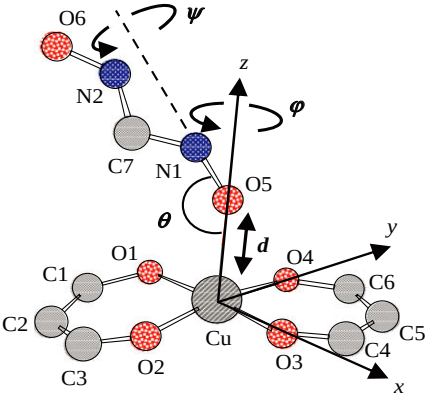


Naoki Matsuoka and Naoki Yoshioka

Polyhedron 28 (2009) 1875

Electronic structures and magnetic properties of copper(II) complexes with axially coordinated nitronyl nitroxide radicals

Electronic structures and magnetic properties of Cu(II) complexes with axially coordinated nitronyl nitroxide radicals are discussed on the basis of computational study using density functional theory (DFT) calculation.

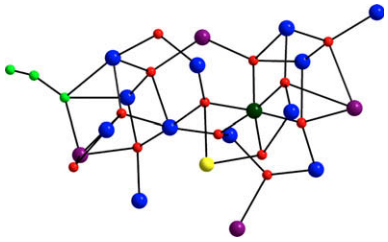


Theocharis C. Stamatatos, Khalil A. Abboud and George Christou

Polyhedron 28 (2009) 1880

Old ligands with new coordination chemistry: A $Mn_{17}Na$ cluster bearing triethanolamine and azide groups and exhibiting slow magnetization relaxation

A new $Mn_{17}Na$ cage-like cluster has been observed from the amalgamation of azide, carboxylate and triethanolamine ligands in Mn cluster chemistry. The complex exhibits frequency-dependent out-of-phase tails of signals, characteristics of the superparamagnetic-like slow relaxation of an SMM.

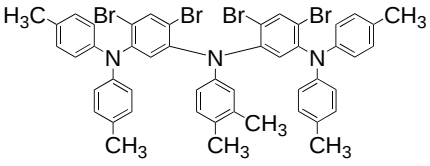


Masafumi Yano, Shohei Tsuda, Masakazu Tatsumi, Munetaka Oyama, Kazunobu Sato and Takeji Takui

Polyhedron 28 (2009) 1883

Amine-based organic high-spin systems; a room-temperature-stable one-dimensional oligoaryl triamine-based trication

A polyalkylated oligoaryl triamine was designed and synthesized as a precursor of positively charged high-spin systems. The highly oxidized tricationic state is very stable at ambient temperature for 15 min. The electrochemical and spectroscopic properties were examined.

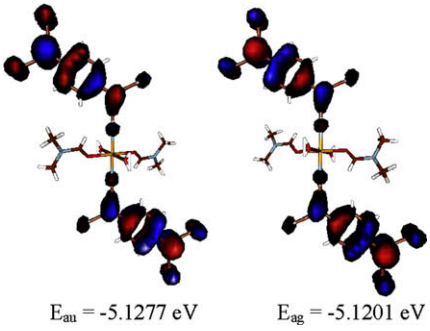


You-Cun Chen, Hong-Bo Zhou, Guang-Xiang Liu, Xiao-Ming Ren and You Song

Polyhedron 28 (2009) 1888

Crystal structure, magnetic property and DFT analysis for a bis(tetracyanoquinodimethane)-zinc(II) complex

A bis(tetracyanoquinodimethane)zinc(II) complex shows biradical characteristic and two SOMOs possess small energy gap.

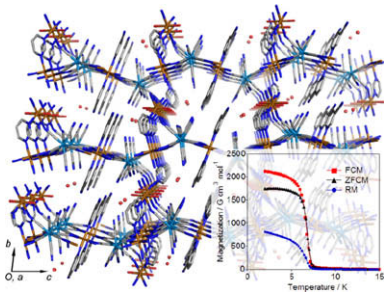


Souhei Kaneko, Yoshihide Tsunobuchi, Koji Nakabayashi and Shin-ichi Ohkoshi

Polyhedron 28 (2009) 1893

Synthesis, crystal structure, and magnetic properties of a copper(II) octacyanotungstate(V)-based magnet containing two types of organic ligands

$[Cu_3[W(CN)_8]_2(pyrimidine)_2(3\text{-cyanopyridine})_2 \cdot 4H_2O]_n$, a three-dimensional cyanide-bridged copper(II) octacyanotungstate(V) containing two different organic ligands (pyrimidine and 3-cyanopyridine), is prepared, and shows ferrimagnetism with a Currie temperature of 7 K, a saturation magnetization of 2.9 μ_B, and a coercive field of 7 Oe at 2 K.

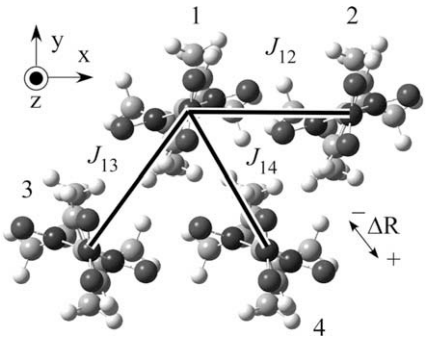


Mitsutaka Okumura, Yasutaka Kitagawa, Takashi Kawakami and Kizashi Yamaguchi

Polyhedron 28 (2009) 1898

Theoretical calculations of the pressure effect for the β-phase of *p*-NPNN

Hybrid DFT (HDFT) calculations were carried out for model clusters of paranitrophenyl nitronyl nitroxide (*p*-NPNN) whose geometrical structures were based on its β-phase crystal structure. The effective exchange integrals between the neighboring *p*-NPNN molecules were calculated for the qualitative understanding of the pressure-induced transition form ferro- to antiferro-magnetic state.

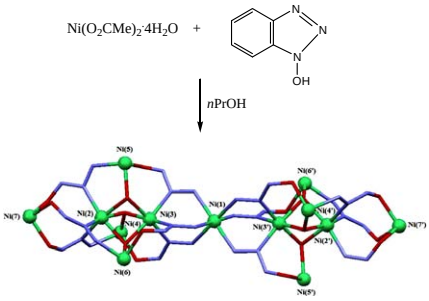


Constantina Papatriantafyllopoulou, Eleanna Diamantopoulou, Aris Terzis, Vassilis Tangoulis, Nikolia Lalioti and Spyros P. Perlepes

Polyhedron 28 (2009) 1903

High-nuclearity nickel(II) clusters: Ni_{13} complexes from the use of 1-hydroxybenzotriazole

The 1:1 $Ni(O_2CMe)_2 \cdot 4H_2O$/1-hydroxybenzotriazole reaction system in propanol gives a tridecanuclear cluster which has the shown $\{Ni_{13}(\mu_3\text{-}OH)_6(\mu_3\text{-}ONNNR)_{12}\}^{8+}$ core; the compound is the biggest metal 1-hydroxybenzotriazole cluster discovered to date and the first Ni_{13} complex. The μ_3-OH^- groups can be replaced by end-on, triply bridging N_3- ligands.

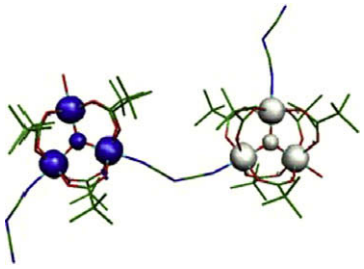


Pablo Alborés and Eva Rentschler

Polyhedron 28 (2009) 1912

DFT broken-symmetry exchange couplings calculation in a 1D chain of bridged iron basic carboxylates

DFT broken-symmetry calculations of the exchange coupling constants in a 1D chain of iron basic carboxylates bridged by dicyanamide, and two related Fe_3O moieties were performed. The chain complex was modeled as two Fe_3O units preserving all features of the real system. The calculated *J* constants are in good agreement with experiment.

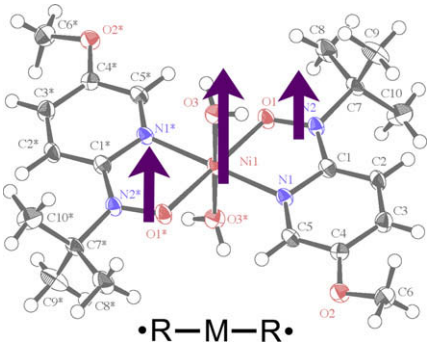


Atsushi Okazawa, Takashi Nogami and Takayuki Ishida

Polyhedron 28 (2009) 1917

Strong intramolecular ferromagnetic couplings in nickel(II) and copper(II) complexes chelated with *tert*-butyl 5-methoxy-2-pyridyl nitroxide

New chelated compounds $[M^{II}(meopyNO)_2(H_2O)_2] \cdot (ClO_4)_2$ (M = Ni and Cu) were characterized, where meopyNO stands for *tert*-butyl 5-methoxy-2-pyridyl nitroxide. The magnetic studies showed that they were ground high-spin molecules with $2J/k_B$ = +288(5) and +178(3) K, respectively.

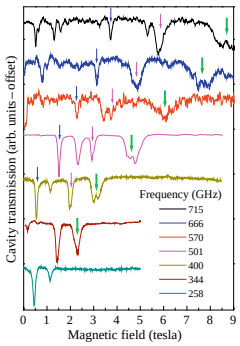


Junjie Liu, Saiti Datta, Erica Bolin, Jon Lawrence, Christopher C. Beedle, En-Che Yang, Philippe Goy, David N. Hendrickson and Stephen Hill

Polyhedron 28 (2009) 1922

Anisotropic exchange in a tetranuclear Co^{II} complex

The results of very high-frequency (50–715 GHz) electron paramagnetic resonance (EPR) studies of the tetranuclear Co^{II} complex $[Co(hmp)(dmb)Cl]_4$ (**1**), are presented. We consider the effect of anisotropic exchange interactions between the effective spin $S' = 1/2$ Kramers ions within the tetranuclear complex to understand the origin of the ZFS within the ground state spin multiplet of **1**, as well as the slow magnetization relaxation observed from low-temperature hysteresis measurements.

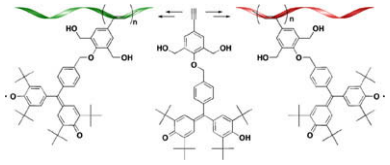


Takashi Kaneko, Hiroo Katagiri, Yasuhiro Umeda, Takeshi Namikoshi, Edy Marwanta, Masahiro Teraguchi and Toshiki Aoki

Polyhedron 28 (2009) 1927

Optically active helical structure and magnetic interaction of poly(phenylacetylene)-based polyradicals

An optically active polyradical possessing an enantiomeric helical backbone was synthesized by helix-sense-selective polymerization (HSSP) of the corresponding achiral monomer. The stronger antiferromagnetic interaction was observed for the polyradical synthesized by HSSP in comparison with the polyradical via polymerization under the racemic condition.

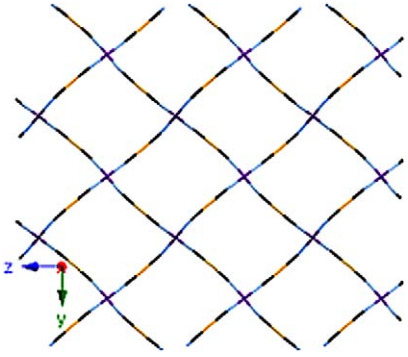


Takashi Kosone, Chikahide Kanadani, Toshiaki Saito and Takafumi Kitazawa

Polyhedron 28 (2009) 1930

Synthesis, crystal structures, magnetic properties and fluorescent emissions of two-dimensional bimetallic coordination frameworks $Fe^{II}(3\text{-fluoropyridine})_2[Au^{I}(CN)_2]_2$ and $Mn^{II}(3\text{-fluoropyridine})_2[Au^{I}(CN)_2]_2$

New interesting two-dimensional bi-metallic coordination polymers $\{Fe^{II}(3\text{-fluoropyridine})_2[Au^{I}(CN)_2]_2\}_n$ (**1**), $\{Mn^{II}(3\text{-fluoropyridine})_2[Au^{I}(CN)_2]_2\}_n$ (**2**) were synthesized and characterized by using single-crystal X-ray analysis and IR and elemental analyses and magnetic measurements. We have found that both compounds show strong fluorescent emissions in the solid state at room temperature.

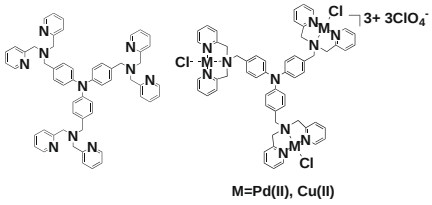


Masafumi Yano, Mitsuru Manabe, Masakazu Tatsumi, Munetaka Oyama, Kazunobu Sato and Takeji Takui

Polyhedron 28 (2009) 1935

Synthesis and properties of a redox active starburst ligand with three bispicorylamino groups and its trinuclear complexes

A novel starburst shaped ligand with a redox active triarylamine unit and its trinuclear palladium and copper complexes were designed and synthesized. Electrochemical and spectroscopic properties of the complexes were examined.

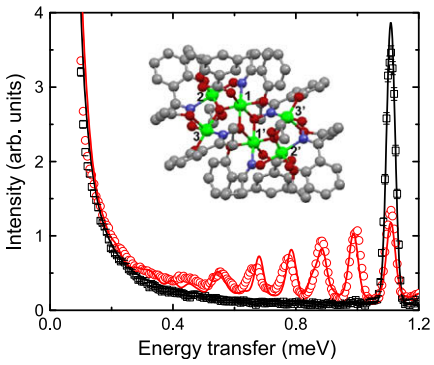


S. Carretta, T. Guidi, P. Santini, G. Amoretti, O. Pieper, B. Lake, J. van Slageren, F. El Hallak, W. Wernsdorfer, H. Mutka, M. Russina, C.J. Milios and E.K. Brechin

Polyhedron 28 (2009) 1940

Neutron spectroscopy and magnetic relaxation of the Mn_6 nanomagnets

Inelastic neutron scattering has been used to determine the microscopic Hamiltonian describing two high-spin variants of the high-anisotropy Mn_6 nanomagnet. Several excited total-spin multiplets partially overlap the $S = 12$ ground multiplet. We show that both the height of the energy barrier and resonant tunnelling processes are greatly influenced by these low-lying excited total-spin multiplets.

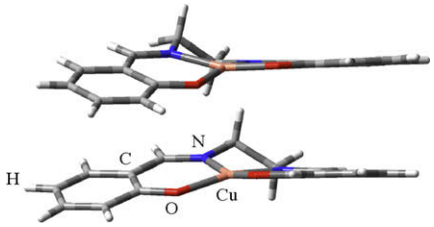


Y. Nakanishi, Y. Kitagawa, Y. Shigeta, T. Saito, T. Matsui, H. Miyachi, T. Kawakami, M. Okumura and K. Yamaguchi

Polyhedron 28 (2009) 1945

Theoretical studies on magnetic interactions between Cu(II) ions in salen nucleobases

The magnetic and other physical properties between Cu^{2+} ions coordinated by salen–base pairs (Cu^{2+}–DNA) are examined by using DFT calculations. In order to consider effects of entanglement and dis-entanglement of the double helix chain, three types of structural disorders.

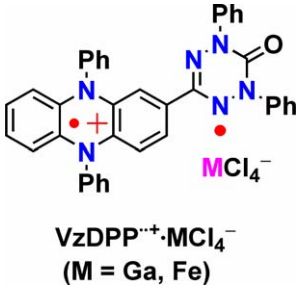


Yuki Masuda, Masato Kuratsu, Shuichi Suzuki, Masatoshi Kozaki, Daisuke Shiomi, Kazunobu Sato, Takeji Takui and Keiji Okada

Polyhedron 28 (2009) 1950

Preparation and magnetic properties of verdazyl-substituted dihydrophenazine radical cation tetrachloroferrate salts

New oxoverdazyl-substituted dihydrophenazine radical cation MCl_4^- (M = Ga, Fe) salts, $\mathbf{VzDPP}^+ \cdot MCl_4^-$, were prepared. The molecular and packing structures, the intramolecular exchange interactions, and the magnetic properties were investigated.

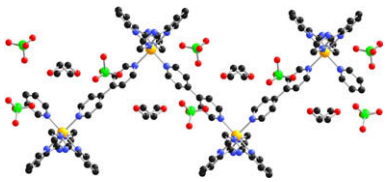


Yurii Chumakov, Galina S. Matouzenko, Serguei A. Borshch and Andrei Postnikov

Polyhedron 28 (2009) 1955

Quantum chemical studies of spin crossover polymers: Periodic DFT approach

The zigzag chain spin crossover polymer has been studied by DFT methods with periodic boundary conditions. The calculations allow to describe the energetic and structural features of the compound.

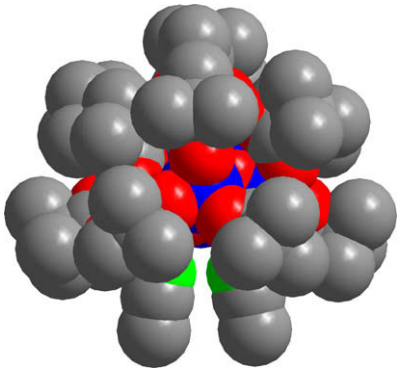


Christos Lampropoulos, Theocharis C. Stamatatos, Khalil A. Abboud and George Christou

Polyhedron 28 (2009) 1958

A convenient Mn^{III} starting material for the synthesis of homo- and heterometallic manganese carboxylate clusters: Mn_9 and $Mn_{10-x}Fe_x$ complexes

The $[Mn(OR)(O_2CR')_2]_n$ family of 1-D polymers has proven a convenient MnIII starting material, and it has been used in the present work for the synthesis of homometallic Mn_9 cage and heterometallic $Mn_{10-x}Fe_x$ wheel products.

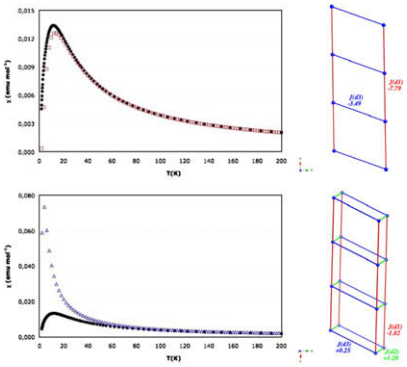


Joaquim Jornet-Somoza, Mercè Deumal, Mark M. Turnbull and Juan J. Novoa

Polyhedron 28 (2009) 1965

On the existence of temperature induced changes in the magnetic topology of crystals that show no first-order crystallographic phase transitions

A First-Principles *Bottom-Up* study of the 88 K and 273 K X-ray diffraction structures of bis-2,3-dimethylpyridinium tetrabromocuprate shows that the magnetic topology and magnetic susceptibility curves of the 88 K and 273 K structures differ (only the 88 K curve reproduces well the experimental properties). The crystal does not show any first-order phase transition, and anisotropic thermal effects are the cause of this transition.

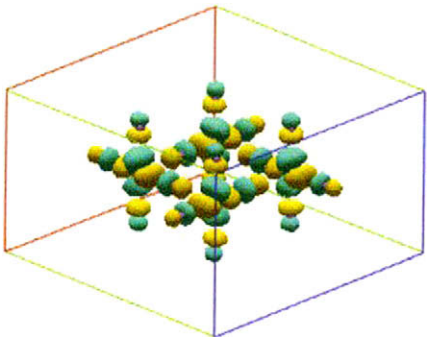


Taku Onishi and Kizashi Yamaguchi

Polyhedron 28 (2009) 1972

Theoretical calculations of effective exchange integrals by spin projected and unprojected broken-symmetry methods II: Cluster models of Jahn–Teller distorted K_2CuF_4 solid

For the cluster model of K_2CuF_4, the singly occupied natural orbital was obtained by hybrid-DFT method. The alternate orbital ordering was reproduced.

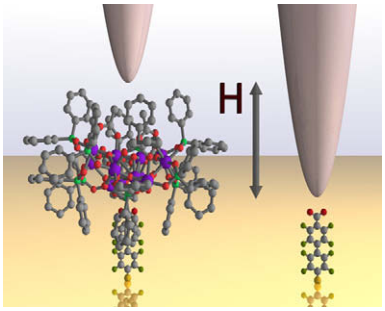


M. Fonin, S. Voss, S. Herr, G. de Loubens, A.D. Kent, M. Burgert, U. Groth and U. Rüdiger

Polyhedron 28 (2009) 1977

Influence of the ligand shell on the surface orientation of Mn_{12} single molecule magnets

Scanning tunneling microscopy experiments show that the substitution of the ligand shell may have a major impact on the surface orientation of the Mn_{12} clusters deposited on Au, i.e. on the orientation of the easy magnetization axis.

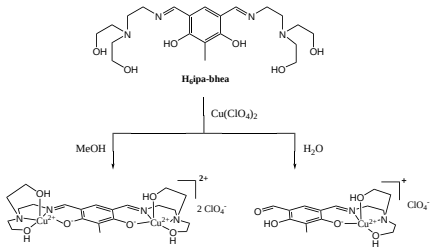


Daniel Plaul, Daniel Geibig, Helmar Görls and Winfried Plass

Polyhedron 28 (2009) 1982

Mono- and dinuclear copper(II) complexes with *meta*-phenylene-bridging ligands: Synthesis, structure and magnetic properties

Starting from the resorcinol based symmetric double-Schiff-base ligand H_6ipa-bhea the selective synthesis of either a dinuclear or a mononuclear copper(II) complex is reported. X-ray crystal structures of all complexes as well as temperature-dependent magnetic measurements and DFT calculations for the dinuclear complex are reported.

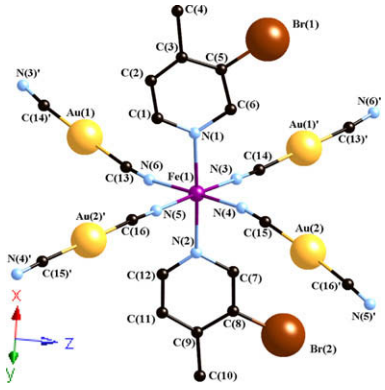


Takashi Kosone, Chikahide Kanadani, Toshiaki Saito and Takafumi Kitazawa

Polyhedron 28 (2009) 1991

Spin crossover behavior in two-dimensional bimetallic coordination polymer Fe^{II}(3-bromo-4-picoline)$_2$[$Au^{I}(CN)_2]_2$: Synthesis, crystal structures, and magnetic properties

A novel hetero-metal $Fe^{II}Au^{I}$ spin-crossover coordination compounds based on 3-bromo-4-picoline and cyano substituents ligands, {Fe^{II}(3-bromo-4-picoline)$_2$[$Au^{I}(CN)_2]_2$}$_n$, were synthesized and characterized by elemental analyses and IR, using single-crystal X-ray analysis at 293 K (high-spin (HS) state) and at 90 K (low-spin (LS) state) and magnetic measurements.

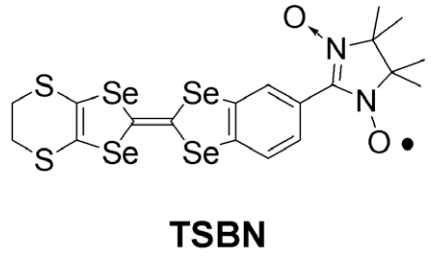


Hideji Komatsu, Ryoji Mogi, Michio M. Matsushita, Tadashi Miyagi, Yuzo Kawada and Tadashi Sugawara

Polyhedron 28 (2009) 1996

Synthesis and properties of TSF-based spin-polarized donor

A novel organic donor radical, **TSBN**, which is a benzotetraselenafulvalene derivative carrying a nitronyl nitroxide group in a cross-conjugated manner was prepared. The neutral microcrystals of **TSBN** which were mounted on interdigitated electrodes showed distinct nonlinear *I-V* characteristics at 2 K and exhibited negative magnetoresistance (-5% at 2 K under 5 T).

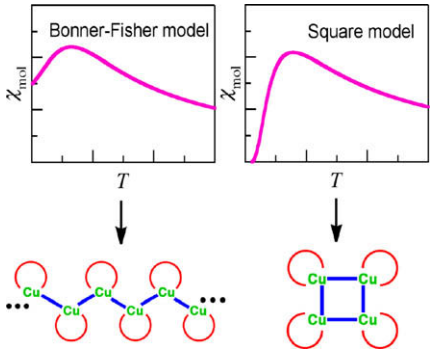


Nobumasa Koyama, Ryo Watanabe, Takayuki Ishida, Takashi Nogami and Tamizo Kogane

Polyhedron 28 (2009) 2001

Structures and magnetic properties of imidazolate-bridged tetranuclear and polymeric copper(II) complexes

Eight kinds of imidazolate-bridged copper(II) complexes were found to be classified into two categories from the magnetic and structural studies. The polymeric and tetrameric structures could be clearly distinguished from each other by fitting the magnetic data to appropriate models, the Bonner-Fisher and square models.

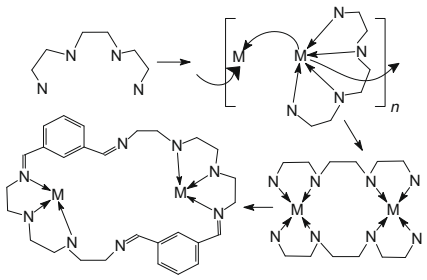


Konstantin Tokarev, Mikhail Kiskin, Aleksei Sidorov, Grygory Aleksandrov, Artem Bogomyakov, Vladimir Novotortsev and Igor Eremenko

Polyhedron 28 (2009) 2010

Chemical assembly of an antiferromagnetic macrocyclic molecule containing two inner Co^{II} centers from polymeric cobalt pivalate

New high spin binuclear of Co^{II} and Fe^{II} with chelate-bridging triethylenetetramine were synthesized. The formation of macrocyclic molecule at the cobalt centers as the mediators chemical assembling was found.

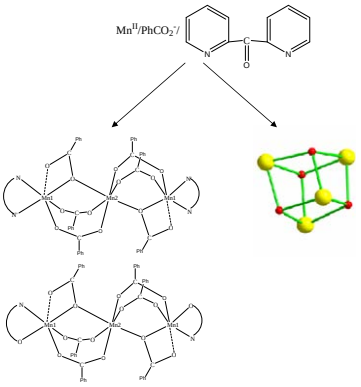


Constantinos C. Stoumpos, Nikolia Lalioti, Ian A. Gass, Konstantinos Gkotsis, Alexandros A. Kitos, Harikleia Sartzi, Constantinos J. Milios, Catherine P. Raptopoulou, Aris Terzis, Euan K. Brechin and Spyros P. Perlepes

Polyhedron 28 (2009) 2017

Linear Mn^{II}_3 and cubane Mn^{II}_4 carboxylate clusters derived from di-2-pyridyl ketone: Synthesis, characterization and magnetic properties

The full synthetic investigation of the $Mn(O_2C\text{-}Ph)_2{\cdot}2H_2O$/di-2-pyridyl ketone reaction system has led to two interesting Mn^{II}_3 linkage isomers containing the ketone form of the ligand and to one Mn^{II}_4 cubane containing the singly deprotonated *gem*-diol form of the ligand; the complexes have interesting properties.

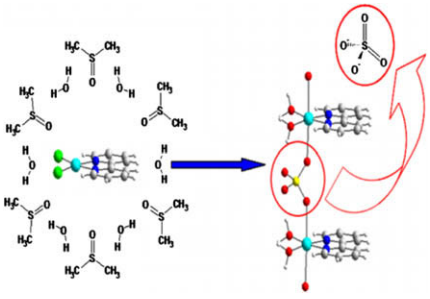


Rafael A. Allão, Jackeline S. Martins, Antonio S. Florencio, Guilherme P. Guedes, José Walkimar de M. Carneiro, Mauricio Lanznaster, Sauli Santos Jr and Maria G.F. Vaz

Polyhedron 28 (2009) 2026

Dimethyl sulfoxide oxidation mediated by a copper(II) diamine complex: A possible source of problem in the synthesis of molecular magnetic compounds

Dimethyl sulfoxide, initially used as solvent, undergoes oxidation to form sulfate, which then participates to the formation of the linear one-dimensional copper chain $[Cu(bipy)(H_2O)_2(SO_4)]_n$. Magnetic measurements was performed and DFT calculations demonstrate that the pathway for the weak antiferromagnetic interaction is through the sulfate bridge.

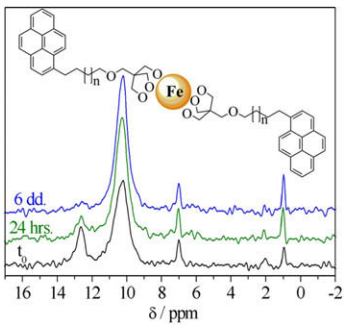


Chiara Danieli, Andrea Cornia, Claudia Cecchelli, Roberta Sessoli, Anne-Laure Barra, Glauco Ponterini and Barbara Zanfrognini

Polyhedron 28 (2009) 2029

A novel class of tetrairon(III) single-molecule magnets with graphene-binding groups

Tetrairon(III) single-molecule magnets with a propeller-like structure have been functionalized with pyrenyl groups suitable for non-covalent binding to graphene surfaces. The new clusters have a $S = 5$ ground spin state and exhibit complete quenching of pyrene fluorescence in solution.

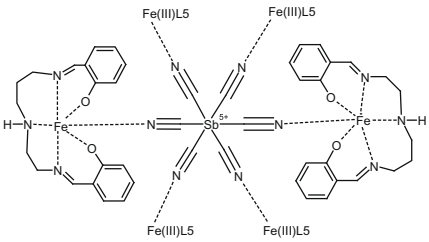


F. Renz, C. Zaba, L. Roberg, St. Jung, M. Klein, G. Klingelhöfer, A. Wünsche, S. Reinhardt and M. Menzel

Polyhedron 28 (2009) 2036

Spin transition in heptanuclear star-shaped iron(III)–antimony(V) NCS- and CN-bridged compounds

We describe multinuclear complexes with the main group metal element antimony as central atom. For such compounds we show that the switchability for Fe(III) from high-spin to low-spin state turns on if we choose CN as Fe–Sb-bridging unit and turns off while bridged with NCS.

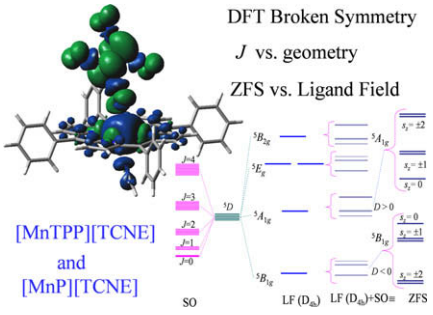


Fanica Cimpoesu, Marilena Ferbinteanu, Bogdan Frecuş and Mihai A. Gîrţu

Polyhedron 28 (2009) 2039

The DFT rationalization of exchange and anisotropy in one-dimensional *d-p* magnets: The [Mn^{III}(porphyrin)][TCNE] case study

We report numerical experiments and modeling of [Mn(porphyrin)]$^+$[TCNE]$^-$ quasi-one-dimensional magnets. Broken Symmetry DFT calculations reveal the geometry dependence of the effective exchange coupling. The intrinsic anisotropy of these systems is studied in an original manner, extracting Ligand Field and Spin Orbit parameters by combined fits to non-relativistic and relativistic DFT calculations.

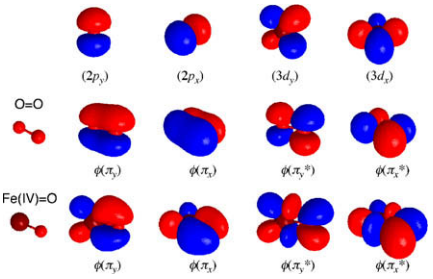


Kizashi Yamaguchi, Mitsuo Shoji, Hiroshi Isobe, Syusuke Yamanaka, Jiro Shimada, Yasutaka Kitagawa and Mitsutaka Okumura

Polyhedron 28 (2009) 2044

Theory of chemical bonds in metalloenzymes XII: Electronic and spin structures of metallo–oxo and isoelectronic species and spin crossover phenomena in oxygenation reactions

The broken-symmetry (BS) and multi-determinant approaches to atomic oxygen (O), molecular oxygen (O_2) and iron–oxo (Fe(IV)═O) core in P450 have elucidated electronic structures of the ground triplet and excited singlet states, which indicate isoelectronic characteristics of the species. This isolobal analogy has indeed enabled us to propose possible reaction mechanisms of oxygenation reactions by the Fe(IV)═O species on the basis of available theoretical and experimental results for O and O_2.

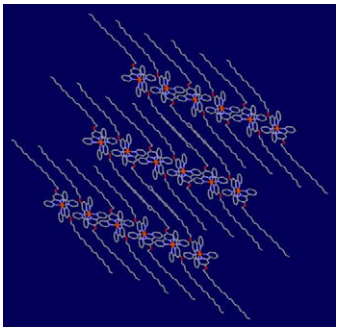


Shinya Hayami, Yoshihiro Kojima, Daisuke Urakami, Kazuchika Ohta and Katsuya Inoue

Polyhedron 28 (2009) 2053

Mesophase and magnetic behavior in cobalt(II) and iron(II) compounds

The metal complexes with long alkyl chains [Co(C16-terpy)$_3$](BF$_4$)$_2$ (**1**) and [Fe(C16-terpy)$_2$](BF$_4$)$_2$ (**2**) were synthesized and the physical properties of the complex were characterized. The complex **1** exhibited unique spin transition ($T_{1/2}\downarrow$ = 217 K and $T_{1/2}\uparrow$ = 260 K) induced by structural phase transition, and the complex **2** was in the low-spin state in the temperature region of 5–400 K before the first mesophase transition. The compound **1** exhibited mesophase transitions, K to SmE at 371 K, SmE to SmC at 430 K, SmC to SmA at 511 K, and the compound **2** also exhibited mesophase transitions, K_3 to D_{L2} at 466 K. After mesophase transition, the complex **1** exhibited only slight spin transition ($T_{1/2}\downarrow$ = 266 K and $T_{1/2}\uparrow$ = 279 K), and the complex **2** was in the low-spin state. The compounds with multifunction, i.e., magnetic property and liquid-crystal properties, are important in the development of molecular materials.

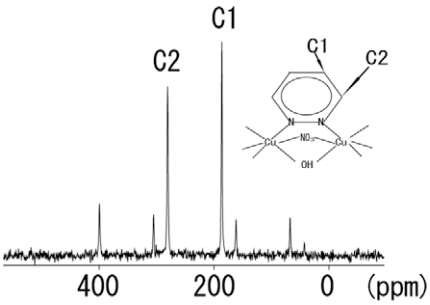


Tetsuya Yamada, Goro Maruta and Sadamu Takeda

Polyhedron 28 (2009) 2058

Determination of spin susceptibility and intrachain exchange interaction of $S = 1/2$ one-dimensional antiferromagnetic Heisenberg chain $[Cu(OH)(NO_3)(pydz)]H_2O$ by solid-state high-resolution NMR

Spin susceptibility of $S = 1/2$ one-dimensional antiferromagnetic Heisenberg chain $[Cu(OH)(NO_3)(pydz)]H_2O$ (pydz = pyridazine), was studied with solid-state ^{13}C MAS NMR measurement. We determined that one-dimensional intrachain exchange interaction is very large, J/k_B is 590–695 K, and a measure of one-dimensionality kBTNJ is less than 3.4×10^{-3}. This result indicates that this compound has very high one-dimensionality.

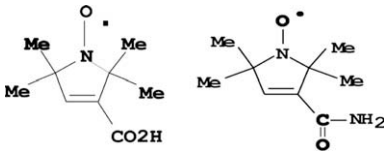


Yasuhiro Kawahashi, Goro Maruta and Sadamu Takeda

Polyhedron 28 (2009) 2063

Electron spin density distribution of a series of nitroxide radicals with five-member ring as studied by solid-state ^1H, ^2H and ^{13}C NMR

Hyperfine coupling constants (hfcc) of ^1H, ^2H and ^{13}C of a series of nitroxide radicals with five-member ring were determined by solid-state magic angle spinning ^1H, ^2H and ^{13}C NMR. Experimental values of hfcc were compared with those deduced from calculations based on density functional theory. Magnetic susceptibility and UV–Vis absorption spectra were also measured and discussed.

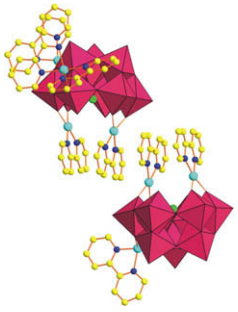


Firasat Hussain, Chris Ritchie, Robert W. Gable, Boujemaa Moubaraki, Keith S. Murray and Colette Boskovic

Polyhedron 28 (2009) 2070

Tungstoarsenate(III) polyoxoanions as inorganic ligands for polynuclear copper complexes

$[\{Cu(2,2'\text{-bpy})\}_3(\alpha\text{-}AsW_9O_{33})]^{3-}$ and $[\{Cu(2,2'\text{-bpy})_2\}\{Cu(2,2'\text{-bpy})\}_3(\alpha\text{-}AsW_9O_{33})]^-$ are the first two complexes of 3d metal centers to feature inorganic tungstoarsenate ligands and organic 2,2′-bpy ligands. They co-crystallize following the hydrothermal reaction between $[\alpha\text{-}AsW_9O_{33}]^{9-}$, Cu(II) and 2,2′-bipyridine in acetate buffer. Very weak antiferromagnetic exchange interactions are evident between the copper centers in the two complexes.

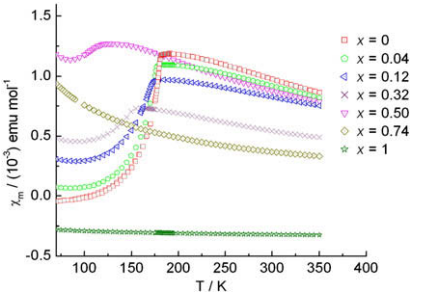


Xiao-Ming Ren, Guang-Xiang Liu, Heng Xu, Tomoyuki Akutagawa and Takayoshi Nakamura

Polyhedron 28 (2009) 2075

Doping effect of nonmagnetic impurity on the spin-Peierls-like transition in the quasi-one-dimensional (quasi-1D) spin system of 1-(4′-nitrobenzyl)pyridinium bis(maleonitriledithiolato)nickelate

Nonmagnetic and isostructural compound $[NO_2BzPy][Cu(mnt)_2]$ was doped into the lattice of the quasi-1D spin-Peierls-like transition compound $[NO_2BzPy][Ni(mnt)_2]$ to give five molecular alloys with formula $[NO_2BzPy][Cu_xNi_{1-x}(mnt)_2]$ (x = 0.04–0.74), and the doping strongly effect the transition behavior.

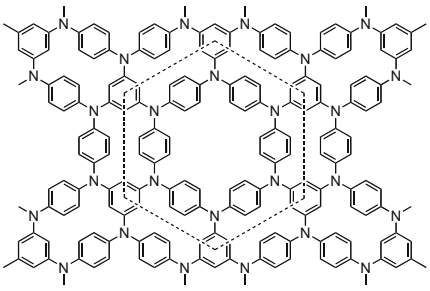


Akihiro Ito, Haruhiro Ino and Kazuyoshi Tanaka

Polyhedron 28 (2009) 2080

Electronic structures of newly designed two-dimensional high-spin organic polymers

Spin electronic structures of newly designed two-dimensional organic polymers are investigated on the basis of the ab initio two-dimensional self-consistent-field crystal orbital method.

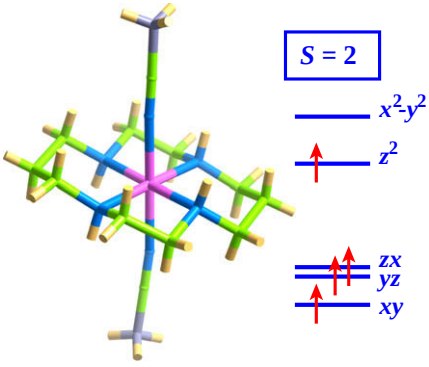


Haruyuki Baba and Motohiro Nakano

Polyhedron 28 (2009) 2087

Magnetostructural examination of Mn(III) complexes $[Mn(cyclam)X_2]^+$ with strong axial ligands

Three novel Mn(III) complexes, *trans*-$[Mn(cyclam)X_2](CF_3SO_3)$ ($X^- = NCBH_3^-$, $NCBPh_3^-$, $NCSe^-$), were synthesized. Magnetic measurements showed they are in high-spin states with $S = 2$. Their large uniaxial zero-field splittings suggested that the axial ligand field strength in these complexes is not far from the spin-crossover boundary according to the AOM calculations.

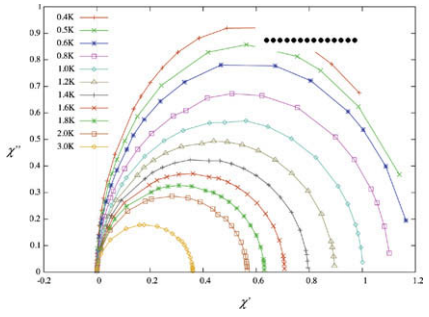


T. Kawakami, H. Nitta, M. Takahata, M. Shoji, Y. Kitagawa, M. Nakano, M. Okumura and K. Yamaguchi

Polyhedron 28 (2009) 2092

Quantum dynamic simulations for single molecular magnets using anisotropic spin models

We performed quantum spin dynamics in anisotropic electron-spin systems to clarify the mechanism in single molecular magnets (SMM) theoretically. In order to examine the effects of such anisotropic magnetic terms (D and E), model systems with large spin multiplicity of the ground state were treated. In DC-external magnetic field, magnetic quantum tunneling (MQT) behavior was found. Moreover, in AC-external magnetic field, frequency dependence of real (χ') and imaginary (χ'') parts of χ can be shown and Cole-Cole plot can be drawn.



The Publisher encourages the submission of articles in electronic form thus saving time and avoiding rekeying errors. For detailed instructions on the preparation of manuscripts and of electronic artwork, consult the Author Gateway for Elsevier at http://authors.elsevier.com

ScienceDirect

Full text of this journal is available, on-line from **ScienceDirect**. Visit **www.sciencedirect.com** for more information.

Polyhedron 28, issue 1, 14 January 2009

Contents lists available at ScienceDirect

Polyhedron

journal homepage: www.elsevier.com/locate/poly

Contents

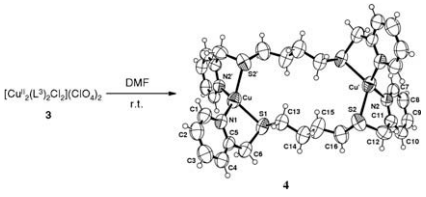
Papers

S. Sarkar, A. Patra, M.G.B. Drew, E. Zangrando and P. Chattopadhyay

Polyhedron 28 (2009) 1

Copper(II) complexes of tetradentate N2S2 donor sets: Synthesis, crystal structure characterization and reactivity

Three copper(II) complexes of NSSN type ligands, two mononuclear $[Cu^{II}(L^1)Cl]ClO_4$ (**1**), $[Cu^{II}(L_2)Cl]ClO_4$(**2**) and one binuclear $[Cu^{II}_2(L^3)_2Cl_2](ClO_4)_2$ (**3**) were isolated in pure form. The dinuclear copper(II) complex **3** changed to a colorless dinuclear copper(I) species of formula $[Cu^{I}_2(L^3)_2](ClO_4)_2$ (**4**) in dimethylformamide even in the presence of air at ambient temperature, while complexes **1** and **2** showed no change under similar conditions.

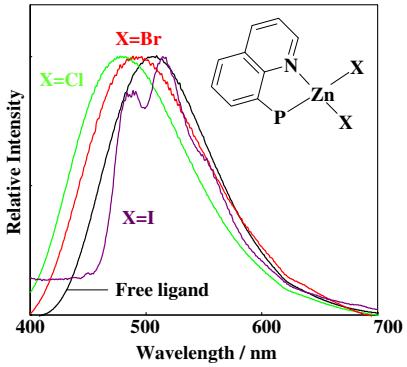


Toshiaki Tsukuda, Chikamine Nishigata, Kodai Arai and Taro Tsubomura

Polyhedron 28 (2009) 7

Photophysical properties of copper(I) and zinc(II) complexes containing phosphinoquinoline ligands

Copper(I) and zinc(II) complexes of 8-phosphinoquinoline derivatives containing both imine and phosphine moieties have successfully been synthesized and characterized. Emissive properties of these complexes both in solution and in the solids state are described.

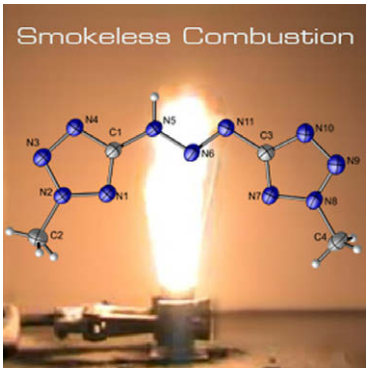


Thomas M. Klapötke, Norma K. Minar and Jörg Stierstorfer

Polyhedron 28 (2009) 13

Investigations of bis(methyltetrazolyl)triazenes as nitrogen-rich ingredients in solid rocket propellants – Synthesis, characterization and properties

The synthesis and characterization of several bis(methyltetrazolyl)-triazenes and triazenates is reported. The compounds are, due to their high thermal stability and positive heat of formation, promising candidates as additives in new solid propellants. Therefore a comprehensive description of the crystal structures and energetic properties (thermal behavior, sensitivities, calculation of detonation and propulsion parameter) is given.



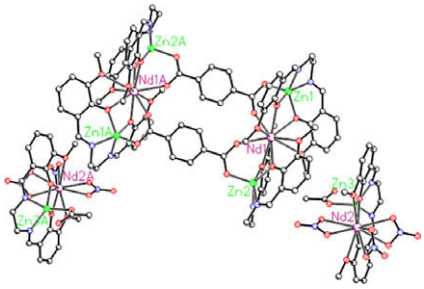
Elsevier Ltd.

Xingqiang Lü, Weiyu Bi, Wenli Chai, Jirong Song, Jianxin Meng, Wai-Yeung Wong, Wai-Kwok Wong, Xiaoping Yang and Richard A. Jones

Polyhedron 28 (2009) 27

Multinuclear NIR luminescent 1,4-BDC bridged Schiff-base complexes of Nd(III)

Solvent and reaction stoichiometry dictate the products from reactions $[ZnNdL(H_2O)(NO_3)_3]$ (H_2L = *N*,*N*′-bis(3-methoxy-salicylidene)ethylene-1,2-diamine) with 1,4-benzenedicarboxylate (1,4-BDC). A 2:1 molar ratio of ZnNd:1,4-BDC in CH_3CN–EtOH gave $[Zn_2Nd_2L_2(1,4\text{-}BDC)(NO_3)_4(EtOH)_2] \cdot 2MeCN$ (**1**) while hexanuclear $[Zn_4Nd_2L_4(1,4\text{-}BDC)_2] \cdot (NO_3)_2 \cdot 2Et_2O \cdot 4H_2O$ (**2**) is formed in a DMF–EtOH mixture. A 4:1 mole ratio in DMF–EtOH gave $[Zn_4Nd_2L_4(1,4\text{-}BDC)_2] \cdot [ZnNdL(NO_3)_3(OAc)]_2$ (**3**).

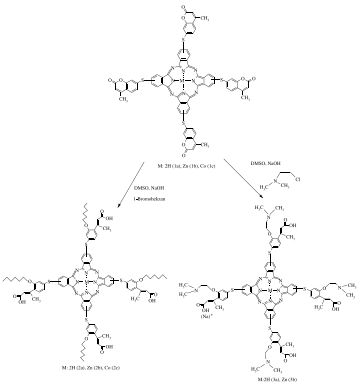


Aliye Aslı Esenpınar, Ali Rıza Özkaya and Mustafa Bulut

Polyhedron 28 (2009) 33

Synthesis and electrochemistry of tetrakis(7-coumarinthio-4-methyl)-phthalocyanines, and preparation of their cinnamic acid and sodium cinnamate derivatives

Novel water soluble free-base, Zn(II) and Co(II) metallo phthalocyanines with four cinnamic acid moieties were prepared from the corresponding tetrakis(7-coumarinthio-4-methyl)-phthalocyanine by the lactone ring opening reaction. The new compounds were purified and characterized by elemental analysis, ^1H NMR, Maldi-TOF, FT-IR and UV–Vis spectral data. Cyclic and differential pulse voltammetry and *in situ* spectroelectrochemistry of the 2,9,16,23-tetrakis(7-coumarinthio-4-methyl) substituted free-base **1a**, Zn(II) **1b** and Co(II) **1c** phthalocyanines, employed as the starting compounds have been studied. This allowed us not only to identify metal- and phthalocyanine ring-based redox processes of the complexes, but also the effect of aggregation on these processes.

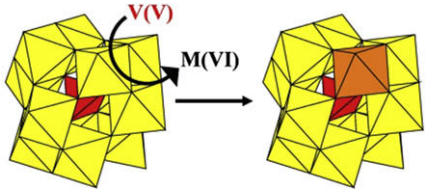


Tadaharu Ueda, Jun-ichi Nambu, Hirofumi Yokota and Masashi Hojo

Polyhedron 28 (2009) 43

The effect of water-miscible organic solvents on the substitution reaction of Keggin-type heteropolysilicates and -germanates with vanadium(V) ion

The substitution reaction of Keggin-type polyoxometalates, $[XM_{12}O_{40}]^{n-}$ (X = Si, Ge, P, or As; M = Mo or W), with vanadium(V) ion was investigated with cyclic voltammetry, Raman spectroscopy, and ^{31}P NMR. The effect of organic solvents, such as acetonitrile, tetrahydrofuran, formamide, N-methylformamide, and N-methylacetoamide, on their substitution reactions was examined.

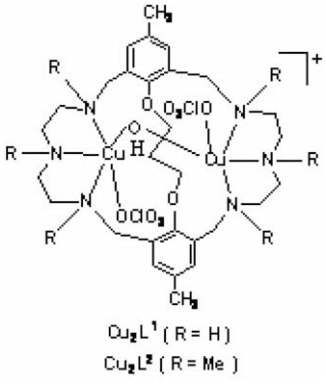


S. Anbu, M. Kandaswamy, Pon. Sathya Moorthy, M. Balasubramanian and M.N. Ponnuswamy

Polyhedron 28 (2009) 49

New polyaza macrobicyclic binucleating ligands and their binuclear copper(II) complexes: Electrochemical, catalytic and DNA cleavage studies

A new symmetrical polyaza macrocyclic binucleating ligand $\mathbf{L}^1$ and its permethylated derivative ligand $\mathbf{L}^2$ have been synthesized by using the precursor compound 2-[2-(2,6-diformyl-4-methylphenoxy)propoxy]-5-methylisophthalaldehyde and bis(aminoethyl) amine. The molecular structure of the precursor compound and the ligand $\mathbf{L}^2$ were determined by the single crystal XRD method. The ligands $\mathbf{L}^1$ and $\mathbf{L}^2$ were treated with two equivalents of $Cu(ClO_4)_2 \cdot 6H_2O$ to afford the new binuclear complexes $[Cu_2L^1(\mu\text{-}OH)(ClO_4)_2](ClO_4)$ (**1**) and $[Cu_2L^2(\mu\text{-}OH)(ClO_4)_2](ClO_4)$ (**2**), respectively. Both the complexes were characterized by elemental and spectral methods. A cyclic voltammetric investigation of these Cu(II) complexes show a quasireversible followed by an irreversible one electron reduction process around E^1_{pc} = −0.59 V and −0.55 V, and E^2_{pc} = −1.07 V and −1.02 V. ESR spectra of the copper(II) complexes **1** and **2** show a broad signal at g = 2.08 and 2.10, and μ_{eff} values of 1.43 and 1.46 BM, respectively, which convey a spin–spin interaction between the two copper(II) ions. The initial rate (V_{in}) for the oxidation of 3,5-di-*tert*-butylcatechol to *o*-quinone by the binuclear Cu(II) complexes **1** and **2** are 1.15×10^{-4} and 1.66×10^{-4} Ms^{-1}, respectively. Both the complexes remarkably promote the hydrolytic cleavage of supercoiled plasmid DNA under physiological conditions in the presence of H_2O_2 at pH 7.2 and 37 °C. The reaction profile for the complex **1** mediated reaction displayed approximately pseudo-first-order kinetic behavior, with $k_{obs} \sim 0.07$ min^{-1} and R^2 = 0.984.

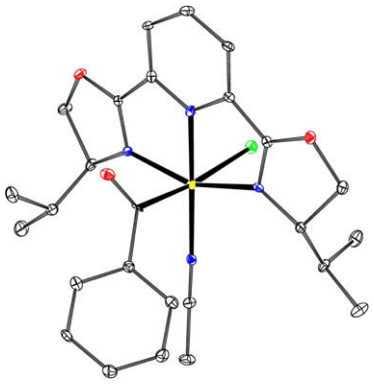


Paloma Paredes, Josefina Díez and M. Pilar Gamasa

Polyhedron 28 (2009) 57

Novel η^1-allyl– and acyliridium(III)/pybox complexes

The synthesis of enantiopure η^1-allyliridium(III) complexes [IrCl(η^1-$CH_2CH{=}CHR$)(L)(κ^3-*N*,*N*,*N*-^{i}Pr-pybox)][PF_6] (R = H, L = $MeO_2CC{\equiv}CCO_2Me$, MeCN; R = Ph, L = C_2H_4, MeCN), [IrCl(η^1-$CH_2CH{=}CHPh$)(η^2-C_2H_4)(κ^3-*N*,*N*,*N*-Ph-pybox)][PF_6] is reported. The results suggest that a η^1-coordination of allyl group is favoured in the case of DMAD and MeCN ligands. The complexes [IrCl(COR)(MeCN)(κ^3-*N*,*N*,*N*-^{i}Pr-pybox)][PF_6] (R = Me, Ph) are obtained by the stereoselective oxidative addition of acyl chloride to the iridium(I) precursors. The structure of the complex **7** · CH_2Cl_2 has been determined by an X-ray monocrystal study.

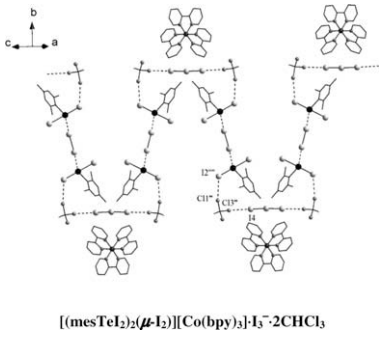


Eliandro Faoro, Gelson Manzoni de Oliveira and Ernesto Schulz Lang

Polyhedron 28 (2009) 63

Attainment of new Te^{II} and Te^{IV} iodides by unexpected removal of the mesityl group of [mesTeI_2]$^-$: Synthesis and structural features of [TeI_4][Co(*en*)$_3$] · I, [TeI_6][Co(*en*)$_3$] · I, [{TeI_6}-{Te_2I_{10}}][Co(NH_3)$_6$]$_2$ · 2I · 6H_2O and [(mesTeI_2)$_2$(μ-I_2)][Co(bpy)$_3$] · I_3 · 2$CHCl_3$ (mes = 2,4,6-trimetylphenyl; *en* = ethylenediamine; bpy = bipyridine)

(MesTe)$_2$ reacts with I_2 and [CoL_n]I_3 {L = (NH_3)$_6$, (*en*)$_3$} in a chloroform/water mixture to give [TeI_4][Co(*en*)$_3$] · I^-, [TeI_6][Co(*en*)$_3$] · I^- and [{TeI_6}-{Te_2I_{10}}] [Co(NH_3)$_6$]$_2$ · 2I^- · 6H_2O in the interface of the two phases. If the crystallization occurs with [Co(bpy)$_3$]I_3 under addition of THF, the final product is [(mesTeI_2)$_2$(μ-I_2)][Co(bpy)$_3$] · I_3^- · 2$CHCl_3$, obtained in the organic phase. The known species {mesTeI···I(mes)Te–Te(mes)$_2$} appears as subproduct in the three first syntheses.

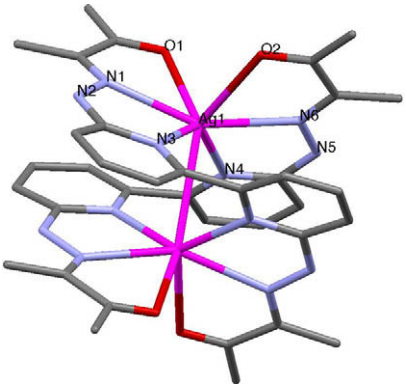


Abdurrahman Şengül, Wen-Jwu Wang and Simon J Coles

Polyhedron 28 (2009) 69

A novel dinuclear double-stranded helical complexes of bis(terdentate) N_4O_2 donor ligand with silver(I) and zinc(II) d^{10} metal ions

A novel hexadentate N_4O_2 ligand 6,6′-bis(3-hydrazonobutan-2-one)-2,2′-bipyridine was shown to self-assembly into double-stranded helical complexes with d^{10} silver and zinc cations in solution; the corresponding $[Ag_2L_2]^{2+}$ helicate (**1a**) shows a pseudo octahedral geometry about each silver(I) centre sharing a short Ag···Ag interaction to accomplish a seven-coordinate mono-capped trigonal prismatic arrangement.

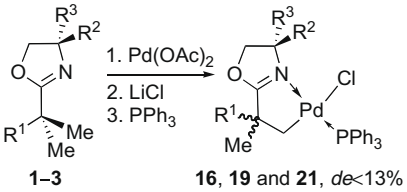


Relindis Y. Mawo and Irina P. Smoliakova

Polyhedron 28 (2009) 77

Cyclopalladation of enantiopure oxazolines having the prochiral CMe_2 moiety at position 2 of the heterocycle

Reactions of Pd(OAc)$_2$ with enantiopure oxazolines **1–3** with the prochiral CMe_2 moiety at position 2 of the heterocycle followed by treatment with LiCl and PPh_3 resulted in the formation of the corresponding diastereomeric cyclopalladated complexes **16**, **19**, and **21** with de < 13%.

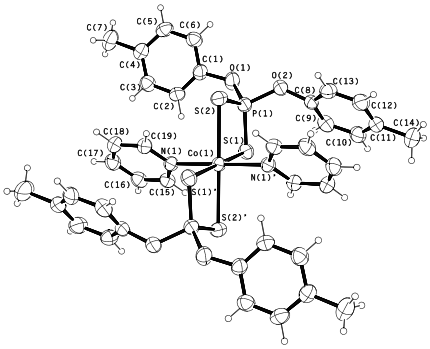


Subhash C. Bajia, John E. Drake, Mark E. Light, Manisha Nirwan, Sushil K. Pandey and Raju Ratnani

Polyhedron 28 (2009) 85

Synthesis and characterization of adducts of bis(*O,O′*-ditolyl/dibenzyl dithiophosphato)cobalt(II) with pyridine: Crystal structures of $[Co\{S_2P(OC_6H_4Me\text{-}p)_2\}_2(C_5H_5N)_2]$ and $[Co\{S_2P(OC_6H_4Me\text{-}p)_2\}_2(NH_3)]$

Bis(*O,O′*-ditolyl/dibenzyl dithiophosphato)-cobalt(II) complexes with pyridine ligands of the type $[Co\{S_2P(OR)_2\}_2(C_5H_5N)_2]$ (R = *o*-, *m*-, *p*-C_6H_4Me, CH_2Ph) have been synthesized by the reaction of $CoCl_2(C_5H_5N)_2$ and the corresponding ammonium salt of *O,O′*-ditolyl/dibenzyl dithiophosphate in methanol. These newly synthesized adducts were characterized by elemental analysis, IR, UV–Vis spectroscopy, magnetic susceptibility measurements and single crystal X-ray diffraction. These structures confirm that in the pyridine complex the geometry around the cobalt metal centre is distorted octahedral, and in the amine complex it is distorted trigonal bipyramidal.

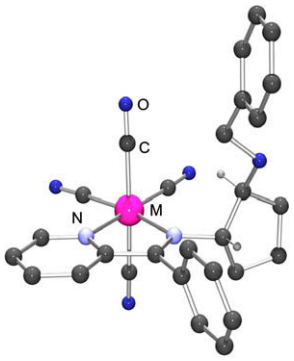


Mehmet Karakus, Gulnihal Davulga, Santiago Gómez-Ruiz, Steffen Tschirschwitz and Evamarie Hey-Hawkins

Polyhedron 28 (2009) 91

Chiral molybdenum(0) and tungsten(0) carbonyl diimine complexes

The chiral diimine ligand C_5H_4N-2-$C(C_6H_5)$═N{(1*S*,2*S*)-C_5H_8-2-$OCH_2C_6H_5$)} (**1**) (=L) reacts with $M(CO)_6$ in toluene to give the respective chiral metal(0) complexes $[M(CO)_4(L\text{-}\kappa N,N')]$ (M = Mo (**2**) and W(**3**)).

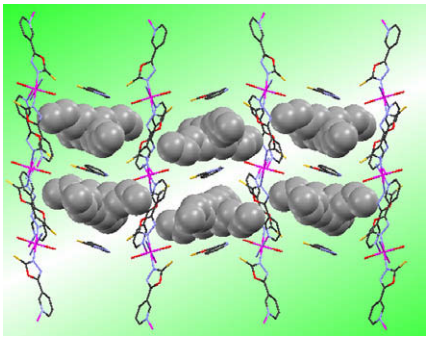


M. Singh, R.J. Butcher and N.K. Singh

Polyhedron 28 (2009) 95

Spectroscopic and structural studies of the 2D Mn(II) coordination polymer from a bridging N_{oxa}, N_{py} bidentate ligand; tetra-*n*-butylammonium[5-(3-pyridyl)-1,3,4-oxadiazole-2-thiolate]

The newly synthesized ligand tetra-*n*-butylammonium{5-(3-pyridyl)-1,3,4-oxadiazole-2-thiolate $\{[N(n\text{-}Bu)_4]^+[3\text{-}pyt]^-\}$ bonds to Mn(II) via N_{py}, $N_{oxa.}$ in a bidentate bridging mode and generates a coordination polymer $\{[Mn(3\text{-}pyt)_2(H_2O)_2][N(n\text{-}Bu)_4]^+[3\text{-}pyt]^-\}_n$. The specific arrangement of molecules along *b* axis, afforded two dimensional metal–organic framework which stacked the molecules in parallel layered manner resulting in a supramolecular architecture.

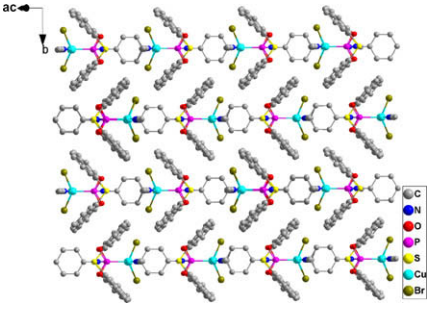


Benudhar Punji, Joel T. Mague, Shaikh M. Mobin and Maravanji S. Balakrishna

Polyhedron 28 (2009) 101

Copper(I) complexes of a thioether-functionalized short-bite aminobis(phosphonite), $[PhN\{P(\text{–}OC_{10}H_6(\mu\text{-}S)C_{10}H_6O\text{–})\}_2]$

The copper(I) complexes of a thioether-functionalized, short-bite aminobis(phosphonite), $PhN\{P(\text{–}OC_{10}H_6(\mu\text{-}S)C_{10}H_6O\text{–})\}_2$ (**1**) are reported. The copper complexes show strong π–π stacking interactions as well as ligand-supported Cu···Cu metallophilic interactions.

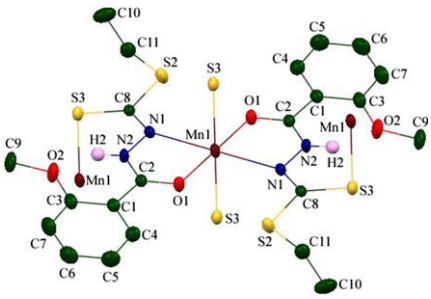


Mamata Singh, Vaibhave Aggarwal, Udai P. Singh and Nand K. Singh

Polyhedron 28 (2009) 107

Synthesis, characterization and spectroscopic studies of a new ligand [N′-(2-methoxybenzoyl)hydrazinecarbodithioate] ethyl ester and its Mn(II) and Cd(II) complexes: X-ray structural study of Mn(II) complex

Complexes of the types $[M(Hmbhce)_2]_n$ {M = Mn(II), Cd(II)} with a new ligand, H_2mbhce = [N′-(2-methoxy-benzoylhydrazine]-scarbodithioic acid ethyl ester have been synthesized and characterized. X-ray study of $[Mn(Hmbhce)_2]_n$ indicates, the ligand acts as an uninegative, tridentate forming five membered chelate ring. The intermediate bond distances in the chelate ring suggest delocalization of charge and support the development of aromaticity in the chelate ring.

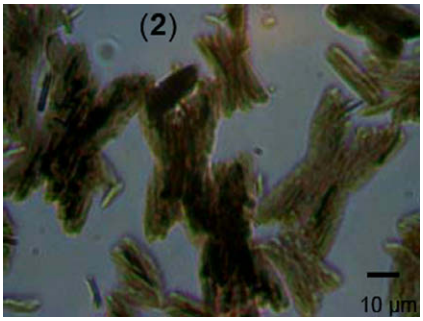


Walid M. Hikal and H. James Harmon

Polyhedron 28 (2009) 113

Photocatalytic self-assembled solid porphyrin microcrystals from water-soluble porphyrins: Synthesis, characterization and application

The formation of highly stable multi-porphyrin micro-crystals using water-soluble porphyrins at room temperature is described. The structure is characterized by means of powder X-ray diffraction, UV-vis spectroscopy, fluorescence spectroscopy, and optical microscopy. The micro-crystals are shown to be a photocatalytic agent for the degradation of 2,4,6-trinitrotoluene.

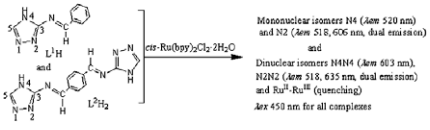


Vinod K. Yadav, Sanjib Kar and L. Mishra

Polyhedron 28 (2009) 121

Reactivity of triazolyl Schiff bases with Ru(II)-2,2′-bipyridyl: Synthesis, spectroscopic characterization of isomers and their photo-physical properties

Trizolyl Schiff bases complexed with *cis*-$[Ru(bpy)_2Cl_2] \cdot 2H_2O$ provide mononuclear (N2, N4) and dinuclear (N4N4, N2N2 and Ru^{II}–Ru^{III}) isomers which are characterized spectroscopically. Out of all the isomers, the N2 and N2N2 isomers show dual emission at room temperature, whereas emission quenching is observed from the Ru^{II}–Ru^{III} complex.

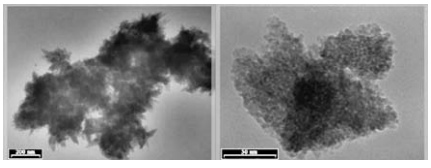


Masoud Salavati-Niasari, Zeinab Fereshteh and Fatemeh Davar

Polyhedron 28 (2009) 126

Synthesis of oleylamine capped copper nanocrystals via thermal reduction of a new precursor

The present investigation reports the novel synthesis of copper nanocrystals using thermal reduction, and their physicochemical characterization. The Cu nanocrystal powders have been prepared using [bis(2-hydroxyacetophenato)copper(II)] as a precursor. Transmission electron microscopy (TEM) analysis has demonstrated that the copper nanocrystals have an average diameter of about 3 nm.

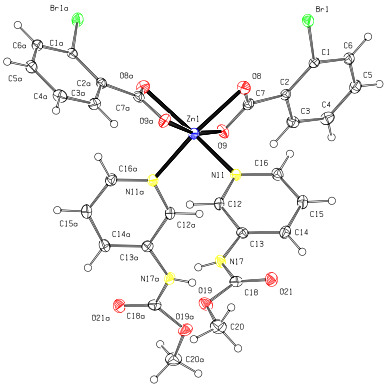


Annamária Erdélyiová, Katarína Győryová, Róbert Gyepes, Ladislav Halás and Jana Kovářová

Polyhedron 28 (2009) 131

Synthesis, spectral, thermal and structural study of bis(2-bromobenzoato-*O,O′*)-bis-(methyl-3-pyridylcarbamate-*N*)-zinc(II)

A new complex, $[Zn(2\text{-}BrC_6H_4COO)_2mpc_2]$ (mpc – methyl-3-pyridylcarbamate), has been synthesised and characterized by elemental analysis, IR spectroscopy, thermal analysis, mass spectrometry, single-crystal X-ray diffraction and DFT studies. It was found that the zinc is coordinated in a pseudo-octahedral geometry (ZnO_4N_2 – chromophore).

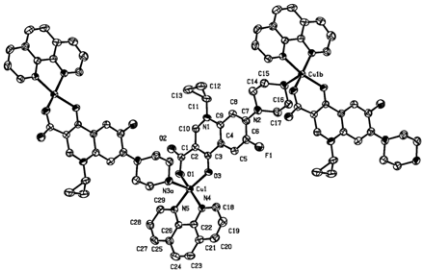


J. Hernández-Gil, L. Perelló, R. Ortiz, G. Alzuet, M. González-Álvarez and M. Liu-González

Polyhedron 28 (2009) 138

Synthesis, structure and biological properties of several binary and ternary complexes of copper(II) with ciprofloxacin and 1,10 phenanthroline

A new binary complex $[Cu(HCip)_2](NO_3) \cdot 6H_2O$ (**1**) has been synthesized and characterized by X-ray structure analyses. In addition, the synthesis and characterization of two new ternary complexes of ciprofloxacin–copper(II)–1,10-phenanthroline, $[Cu(phen)(Cip)](NO_3) \cdot 4H_2O$ (**2**) and $Cu(phen)(HCip)(NO_3)_2 \cdot H_2O$ (**3**), have been accomplished. The chemical nuclease activity of compounds **2** and **3** has also been studied, revealing that both compounds behave as efficient chemical nucleases.

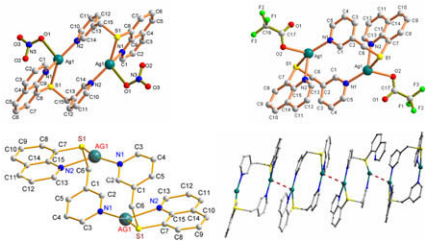


Jing-An Zhang, Mei Pan, Jian-Yong Zhang, Hai-Ke Zhang, Zhi-Jin Fan, Bei-Sheng Kang and Cheng-Yong Su

Polyhedron 28 (2009) 145

Syntheses, structures and bioactivities of silver(I) complexes with a tridentate heterocyclic N- and S-ligand

The reaction of the semi-rigid tridentate ligand TQMP3 with different silver salts afford discrete or connected dimetallic ring subunits. Assembly of these subunits gives rise to a 1D chain and two 2D nets, sustained by intermolecular interactions. A preliminary bioactivity study indicates that these complexes show distinct antibacterial and pesticide activities.

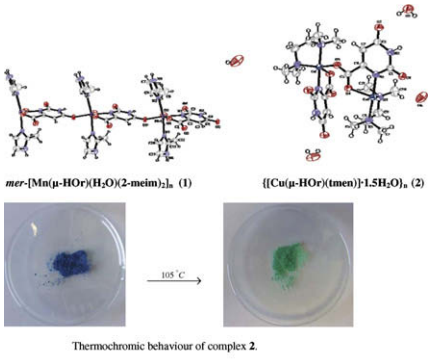


Okan Zafer Yeşilel, Hakan Erer, Aylin Mutlu and Orhan Büyükgüngör

Polyhedron 28 (2009) 150

Coordination polymers of Mn(II) and Cu(II) orotate with 2-methylimidazole and *N,N,N′,N′*-tetramethylethylenediamine ligands: Syntheses, spectroscopic and thermal analyses and crystal structures of *mer*-$[Mn(\mu\text{-}HOr)(H_2O)(2\text{-}meim)_2]_n$ and thermochromic $\{[Cu(\mu\text{-}HOr)(tmen)] \cdot 1.5H_2O\}_n$ complexes

Two novel coordination polymers of Mn(II) and Cu(II) orotate with 2-methylimidazole and *N,N,N′,N′*-tetramethylethylenediamine ligands have been synthesized and described. The orotate ligand acts as a bridging ligand with two different coordination modes, forming a one-dimensional (1D) chain. These polymer chains are linked by hydrogen-bond interactions, forming a three-dimensional network. The complex $\{[Cu(\mu\text{-}HOr)(tmen)] \cdot 1.5H_2O\}_n$ (**2**) exhibits irreversible thermochromism and on dehydration the color of the complex changes from blue to green.



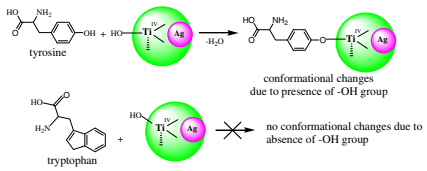
Thermochromic behaviour of complex **2**.

A. Kathiravan, R. Renganathan and S. Anandan

Polyhedron 28 (2009) 157

Interaction of colloidal $AgTiO_2$ nanoparticles with bovine serum albumin

The interaction between colloidal $AgTiO_2$ nanoparticles and bovine serum albumin (BSA) has been studied by absorption, steady state, time resolved and synchronous fluorescence spectroscopic techniques. The quenching rate constant, binding constant and number of binding sites were calculated according to the relevant fluorescence quenching data. From the synchronous fluorescence spectra, it can be shown that the conformational change of BSA is induced by the interaction of colloidal $AgTiO_2$ nanoparticles with the tyrosine micro-region of BSA molecules. This study is expected to provide important insight in the interactions of physiologically important protein BSA with metal nanoparticles.

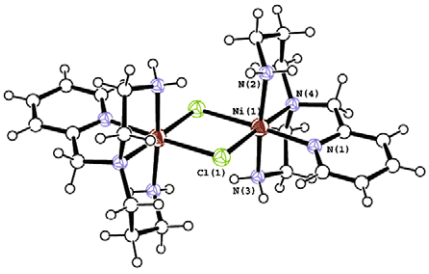


Sadegh Salehzadeh, Reza Golbedaghi, Ian. S. Tidmarsh, Lorenzo Sorace, Harry Adams and Michael D. Ward

Polyhedron 28 (2009) 162

Syntheses, crystal structures and magnetic properties of three new binuclear Ni(II) complexes derived from tripodal tetradentate (N_4) ligands

Three binuclear Ni(II) complexes have been prepared by the reaction of three previously known tetraamine ligands, bearing pyridyl group, with nickel(II) perchlorate in equimolar ratios. The resulting compounds were characterized by elemental analysis, IR and single crystal X-ray diffraction. The magnetic properties in two cases were investigated.

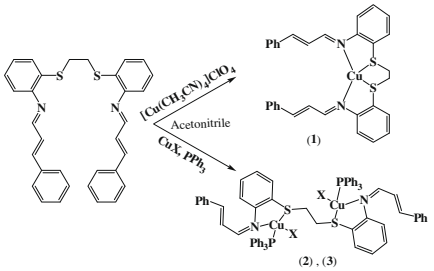


Mahbod Morshedi, Mehdi Amirnasr, Alexandra M.Z. Slawin, J Derek Woollins and Aliakbar Dehno Khalaji

Polyhedron 28 (2009) 167

Synthesis and coordination chemistry of new tetradentate N_2S_2 donor Schiff-base ligand ca_2-dapte: Mononuclear and dinuclear copper(I) complexes $[Cu(ca_2dapte)]ClO_4$ and $[\{Cu(PPh_3)(X)\}_2(ca_2dapte)]$ (X = I and Br)

A mononuclear copper(I) complex, $[Cu(ca_2dapte)]ClO_4$ (**1**), and two dinuclear copper(I) complexes, $[\{Cu(PPh_3)(X)\}_2(ca_2dapte)]$ (X = I (**2**) and Br (**3**)), with the new tetradentate N_2S_2 donor Schiff-base ligand, ca_2dapte, has been prepared. The ca_2dapte, with versatile coordination capability, acts as a simple tetradentate ligand in **1** and as a bis-bidentate bridging ligand in **2** and **3**.

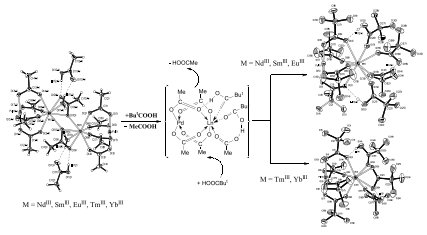


Sergei E. Nefedov, Natalia Yu. Kozitsyna, Michael N. Vargaftik and Ilya I. Moiseev

Polyhedron 28 (2009) 172

Palladium(II)–rare-earth metal(III) paddlewheel carboxylate complexes: Easy total acetate to pivalate metathesis

Bis-paddlewheel heterobimetallic Pd^{II}-Ln^{III} complexes $[Pd(\mu\text{-}OOCMe)_4Ln(OH_2)(\mu,\eta^2\text{-}OOCMe)]_2 \times 2HOOCMe$ (Ln = Nd, Sm, Eu, Yb and Tm were synthesised by the reaction of $Pd_3(\mu\text{-}OOCMe)_6$ with the Ln^{III} acetates. The tetra-acetate-bridged complexes are readily transformed into the mono-paddlewheel tetrapivalate-bridged analogues maintaining the $[Pd(\mu\text{-}OOCR)_4Ln]$ paddlewheel structure with the intra- and intermolecular H-bonding.

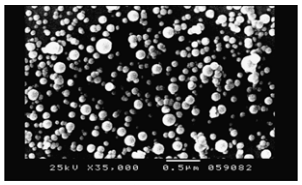


Mohamed E. Mahmoud, Sawsan S. Haggag and Tarek M. Abdel-Fattah

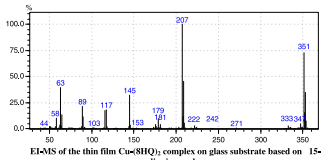
Polyhedron 28 (2009) 181

Surface layer-by-layer chemical deposition reaction for thin film formation of nano-sized metal 8-hydroxyquinolate complexes

A novel, simple and rapid layer-by-layer chemical deposition method for the preparation of nano-Fe(III), Co(II), Ni(II), Cu(II) and Zn(II) 8-hydroxyquinolate complexes is explored and reported. The structures of these complexes were confirmed by SEM, EI-MS, FT-IR, UV–Vis spectroscopic methods as well as TGA.



SEM image of the thin film Ni(8HQ)$_2$ complex on glass substrate based on 30-dipping cycles



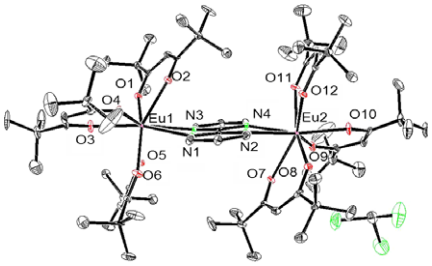
EI-MS of the thin film Cu-(8HQ)$_2$ complex on glass substrate based on 15-dipping cycles

Madelyn H. Baker, Jason D. Dorweiler, Amanda N. Ley, Robert D. Pike and Steven M. Berry

Polyhedron 28 (2009) 188

Structure and emission spectra of dinuclear lanthanide(III) β-diketonate complexes with a bridging 2,2′-bipyrimidine ligand

Formation of 2,2′-bipyrimidine (bpm) adducts of the β-diketonate complexes of Eu(III), Sm(III), or Yb(III) with 2,2′,6,6′-tetramethyl-2,4-heptanedione (tmhd) result in dinuclear species. The synthesis and X-ray structure of these three new dinuclear lanthanide complexes are reported along with emission spectra and electrochemical characterization.

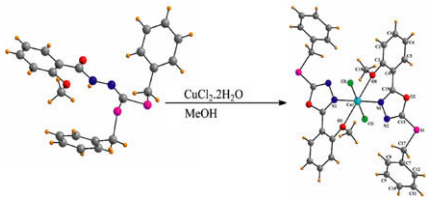


M. Singh, V. Aggarwal, U.P. Singh and N.K. Singh

Polyhedron 28 (2009) 195

Synthesis, spectroscopic and crystal structure investigation of [Cu(bzsmp)$_2$Cl$_2$]; {bzsmp = 2-benzylsulfanyl-5-(2-methoxyphenyl)-1,3,4-oxadiazole}: cyclization of N^2-[bis(benzylsulfanyl)-methylene]-2-methoxybenzohydrazide to 2-benzylsulfanyl-5-(2-methoxyphenyl)-1,3,4-oxadiazole during complexation

The ligand [N^2-Hbmbh] (1) {N^2-[bis(benzylsulfanyl)methylene]-2-methoxybenzo-hydrazide in MeOH solvent on reaction with $CuCl_2 \cdot 2H_2O$, underwent cyclization to afford the complex [Cu(bzsmp)$_2$Cl$_2$] (**2**) {bzsmp = 2-benzylsulfanyl-5-(2-methoxy-phenyl)-1,3,4-oxadiazole}.

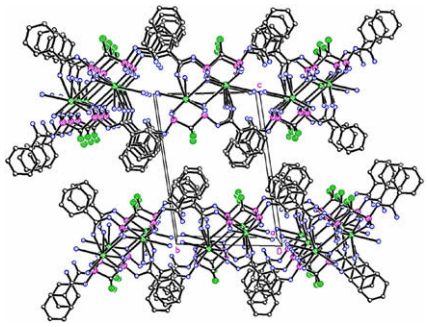


Susan Kunnas-Hiltunen, Mervi Matilainen, Jouko J. Vepsäläinen and Markku Ahlgrén

Polyhedron 28 (2009) 200

X-ray diffraction study of bisphosphonate metal complexes: Mg, Sr and Ba complexes of (dichloromethylene)bisphosphonic acid *P,P′*-dibenzoyl anhydride

Mg, Sr and Ba complexes of (dichloromethylene)bisphosphonic acid *P,P′*-dibenzoyl anhydride have been prepared and characterised by X-ray crystallography, elemental analysis and infrared spectroscopy. The monomeric units of $[Mg\{[Cl_2C(PO_2O(C(O)C_6H_5))_2](H_2O)_5\} \cdot H_2O]$ (**1**) and the polymeric chains of $[Sr_2\{[Cl_2C(PO_2O-(C(O)C_6H_5))_2]_2(H_2O)_9\} \cdot H_2O]_n$ (**2**) and $[Ba\{Cl_2C(PO_2O(C(O)C_6H_5))_2\} \cdot (H_2O)_2]_n$ (**3**) form 2D layer-like structures through intermolecular hydrogen bonds.



The Publisher encourages the submission of articles in electronic form thus saving time and avoiding rekeying errors. For detailed instructions on the preparation of manuscripts and of electronic artwork, consult the Author Gateway for Elsevier at http://authors.elsevier.com

ScienceDirect

Full text of this journal is available, on-line from **ScienceDirect**. Visit **www.sciencedirect.com** for more information.